Organic Electronics 12 (2011) 1–7

Contents lists available at ScienceDirect

Organic Electronics

journal homepage: www.elsevier.com/locate/orgel

Efficient extraction of singlet–triplet excitons for high-efficient white organic light-emitting diode with a multilayer emission region

Yoga Divayana, Shuwei Liu, Aung Ko Ko Kyaw, Xiao Wei Sun *

School of Electrical and Electronic Engineering, Nanyang Technological University, Nanyang Avenue, Singapore 639798, Singapore

ARTICLE INFO

Article history:
Received 5 August 2010
Received in revised form 11 October 2010
Accepted 11 October 2010
Available online 23 October 2010

Keywords:
White organic light-emitting diode
Fluorescence
Phosphorescence
Singlet-triplet
Multilayer emission region

ABSTRACT

We reported a highly efficient white organic light-emitting diode (WOLED) with a multilayer emission region made of sequentially evaporated host and guest layers. The singlet and triplet excitons were harvested in two separate channels. An external quantum efficiency of 16.3% photons/electron (~41 cd/A) was achieved with a good color rendering index (CRI) of 76, and a Commission Internationale de l'éclairage (CIE) coordinate of ($x = 0.38$, $y = 0.46$). At brightness of 100 and 500 cd/m^2, the external quantum efficiencies reached 11% and 10%, respectively. The performance of the WOLED is better than that fabricated by co-evaporation method due to an improved exciton capture and emission efficiencies. This work presents an alternative way of fabricating WOLED.

© 2010 Elsevier B.V. All rights reserved.

The tremendous developments of monochrome red, green and blue organic light-emitting diodes (OLEDs) since their first inception in 1987 [1] have paved the way for the recent advancement of the white organic light-emitting diode (WOLED). Various architectures have been applied to achieve efficient and color-balanced devices. The multiple emission layers architecture reported in the literature has been able to achieve the much desired saturated-white emission [2–5]. For multiple emission layers, the carrier recombination, carrier trapping, and exciton diffusion, the emission of red, green, and blue portion can be tuned appropriately to obtain desired color purity. This technique however suffers from a color-shift with an increase in current [3]. To eliminate color-shift, devices with a single emission layer doped with two or three dopants have been developed [6–9]. To balance red, green and blue emissions, the concentration of each dopant is carefully controlled. The highest efficiency is obtained for device that uses phosphorescent dopants [6]. Phosphorescence enables extraction of the forbidden triplet exciton to potentially increase the efficiency to unity. The architecture has been used to produce a WOLED with a high efficacy of 42 lm/W [6].

The blue-emitting phosphorescent molecule is unstable and has a relatively low operational lifetime. This resulted in color degradation with time, i.e. the blue portion reduces significantly. The device with three-phosphorescent dopants also suffers a large efficiency roll-off. Sun et al. showed that by harvesting the singlet and triplets into two different channels, the efficiency roll-off can be improved [10]. Previous study has shown that the diffusion length of the triplet is much longer than that of the singlet [11]. Sun et al. harvested the singlet (using fluorescent dye) near the exciton formation region and making use of the long diffusion length of triplet, harvested the triplet excitons at a distance from the formation region (using phosphorescent dyes). This structure also eliminates the need for high efficient blue phosphorescent materials, which are still relatively unstable and suffer a short lifespan when incorporated in WOLED. Similar method has been used to achieve WOLED with a power efficiency of 45 lm/W [12,13]. Recently WOLED with efficacy exceeding fluorescent tube has been reported [14].

The device reported by Sun et al. represents a clever technique to fully harvest the singlet and triplet excitons for white light creation. However despite of the high

* Corresponding author.
E-mail address: exwsun@ntu.edu.sg (X.W. Sun).

1566-1199/$ - see front matter © 2010 Elsevier B.V. All rights reserved.
doi:10.1016/j.orgel.2010.10.005

efficiency achieved, the performance somehow diminishes at low current injection, similar to fluorescent OLED. Fluorescent OLED normally uses a very small guest (dopant) concentration (with guest molecule spacing larger than the typical Förster radius) to reduce the aggregation and quenching effects [15,16]. At a low current (exciton) density, the spacing between the excitons is large, resulting in an incomplete energy transfer from the host to the guest. The device reported in Ref. [10] consists of doped and undoped regions where the excitons are harvested in the doped region. However due to the small doping concentration and thin doped region, the excitons was not fully extracted at low current density, resulting in a loss. As the current increases, the spacing between the excitons reduces. This increases the chance of exciton being captured by the guest molecules and improves the efficiency. Although the WOLED is normally operated at high current injection, for some application such as the tandem structure, the performance at low current density is still very important.

Another issue with the device reported in Ref. [10], or doped-OLED devices in general, is the uniformity of the device for large-area fabrication. Fabrication of high-efficiency WOLED (or in general OLED) involves co-evaporation of the guest and host materials with specified concentration [17,18]. Recently it has been shown that the thickness of the organic semiconductor can be controlled well with a variation of less than 3% for a large-area manufacturing [19]. However the current-efficiency of the device varies significantly throughout the regions. The large variation was attributed to the small variation of the doping concentration of the guest/host materials in the emission layer which can significantly influence the performance of the device. To control the doping concentration, thickness sensors are placed near the guest and host materials to monitor the deposition. However since the organic sources are placed at some distance from the substrate, where the layers are being deposited, the doping concentration of the organic materials may vary from region to region on the substrate. To have a better control of the organic deposition, one may place the thickness sensors near the substrate which render better control of the thickness uniformity of the film. However these sensors could not determine the doping concentration of the guest/host material. Therefore the control of the doping concentration for the large area device remains a problem.

Reineke et al. recently applied a rather different device architecture for OLED [20]. The emission region consists of a multilayer architecture, where the doped area is separated by a pure host repeatedly. This method has been used to improve the efficiency roll-off with the critical current density (current density when the efficiency drops to 50%) increased from 140 to 270 mA/cm^2 by confining the exciton within the guest molecule. In spite of the better roll-off performance, the device reported by Reineke et al. show a lower external quantum efficiency (EQE). We recently show that one can even further eliminate the requirement for doping [21], an OLED with a similar architecture was fabricated with the doped regions being replaced with pure guest layers. By carefully controlling the thickness of the guest and host layers, device with efficiency comparable to that fabricated by co-evaporation method was reported.

In this work, we utilized the multilayer structure to produce a highly efficient WOLED. The method to extract both the singlet and triplet follows that reported previously [10]. We showed that device with a multilayer design performs better compared to the device fabricated by the co-evaporation method. The maximum EQE of 16.3% photons/electron was achieved at a current density of 0.05 mA/cm^2. At high current injection, the EQE is comparable to that reported in Ref. [10]. At brightness of 100 and 500 cd/m^2, the EQE reach 11% and 10%, respectively. The multilayer approach is promising for tandem WOLED.

The OLED (or WOLED) was fabricated on ITO glass (50 Ω/square) which was earlier subjected to the standard cleaning procedure that involves ultra-sonication in acetone, ethanol, rinsing in de-ionized water and oxygen plasma treatment at 15 Pa for 3 min. Evaporation of organic materials and metals was carried out in a high vacuum condition of about 2×10^{-4} Pa with deposition rates of 0.5–4 Å/s. The quartz crystal microbalance thickness sensor was positioned near the ITO glass for better accuracy. For each run, up to four samples were fabricated simultaneously without breaking the vacuum, to ensure similar deposition condition. Electroluminescence (EL) spectra of the fabricated devices were measured with a calibrated PR650 Spectra Scan spectrometer. Current density–voltage characteristics were recorded by Yokogawa source measurement unit. We assumed the emission pattern was Lambertian, and calculated the EQE from the luminance, current density and EL spectrum [22]. All measurements were carried out at room temperature under ambient atmosphere without any encapsulation.

The efficiency of the guest–host OLED device is determined by two factors, the rate of energy transfer from the host to the guest molecules (exciton capture) and the efficiency of the guest molecules (exciton emission). Let's compare the rate of energy transfer of the following devices with the same emission region thickness. Device A with emission region consists of x nm (sub-monolayer) of guest and y nm of host, device B consists of two repeated $x/2$ nm of guest and $y/2$ nm of host layers and device C consists of k repeated x/k nm of guest and y/k nm of host layers, as shown in Fig. 1(a). If the intermolecular spacing in the planar guest layer of device A is r nm, guest spacing in devices B and C will be $\sqrt{2}r$ and $\sqrt{k}r$ nm, respectively. As the excitons diffuse toward the guest layer, some of them will be captured while some will escape. The rate of energy transfer (capture) of the exciton follows the Förster process [23] with a rate $\propto (r_F/r)^6$ for device A, while for devices B and C, the rates are $\propto 2(r_F/\sqrt{2}r)^6 = \frac{1}{4}(r_F/r)^6$ and $\propto k(r_F/\sqrt{k}r)^6 = \frac{1}{k^2}(r_F/r)^6$, respectively, where r_F is the Förster radius. This shows that exciton capture rate is higher for device with thicker guest layer (device A) than that with dispersed guest molecules (devices B and C). This is only so because the energy transfer follows Förster process. If the excitons were captured by impact (trapping), the rate would be proportional to the cross section of the guest molecules (r^{-2}), correspondingly, the capture rate

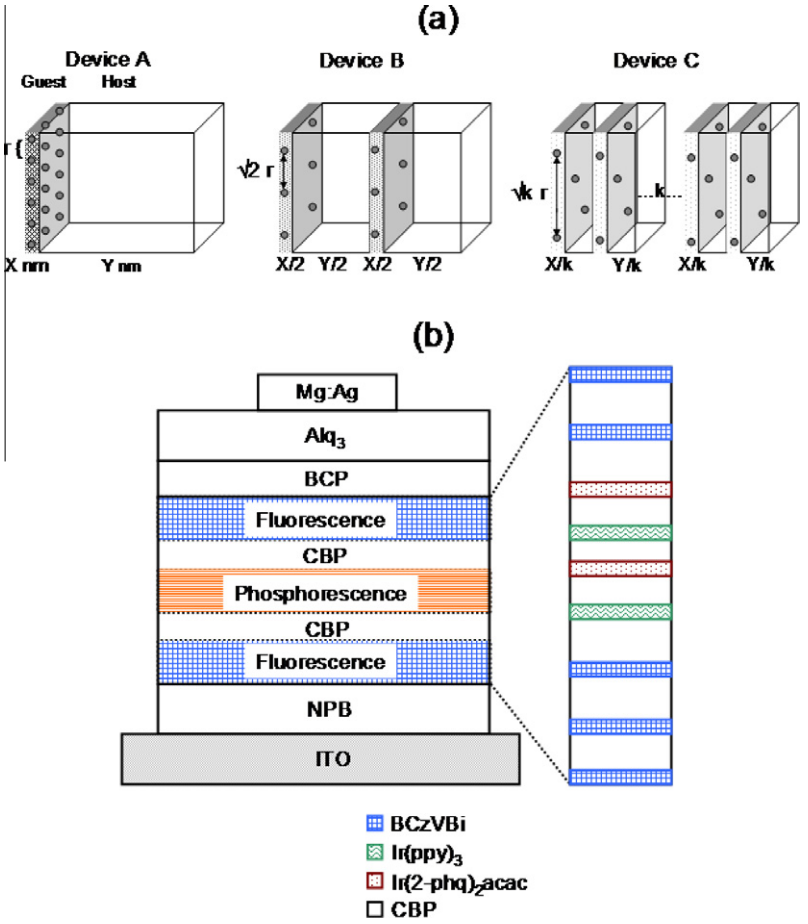

Fig. 1. (a) Illustration for devices with different doping (host/guest) architectures. (b) Schematic diagram of the WOLED with multilayered emission region.

would be the same for all devices. The second factor is the efficiency of the guest molecules. It has been recently shown that the efficiency of the guest molecules decreases significantly when the intermolecular spacing is less than certain quenching radius (~1–1.3 nm) [15]. However by using a very thin layer of guest layer (<1 nm), the intermolecular spacing in the planar guest layer is larger than this typical quenching radius. Assuming monolayer corresponds to 1 nm thickness with intermolecular spacing of 1 nm [24], device with 0.5 nm thick guest layer has an intermolecular spacing of approximately $\sqrt{2}$ nm which is larger than the typical quenching radius. Thus devices with multilayer architecture should out-perform those made of dispersed (co-evaporated) system.

Fig. 1(b) shows the schematic of the WOLED with multilayered architecture. NPB is *N*,*N*′-di(naphth-2-yl)-*N*,*N*′-diphenyl-benzidine used as the hole-transporting layer, CBP is 4,4′-bis(*N*-carbazolyl)biphenyl as the host, BCzVBi is 4,4′-bis(9-ethyl-3-carbazovinylene)-1–1′-bisphenyl as the blue-emitting fluorescent guest, $Ir(ppy)_3$ is tris(2-phenylpyridine) iridium(III) as the green-emitting phosphorescent guest, $Ir(2\text{-phq})_2(acac)$ is bis(2-phenylquinoline) (acetylacetonate) iridium(III) as the red-emitting phosphorescent guest, BCP is 2,9-dimethyl-4,7-diphenylphenanthroline as the hole blocking layer, and Alq_3 is tris-(8-hydroxyquinoline) aluminum as the electron transporting layer. The emission region consists of two separate parts for singlet and triplets harvesting. The singlet regions are placed near the interfaces of the heterojunctions, where most of the excitons are formed, while the triplet region is positioned in the middle of the emission layer. Instead of co-evaporating the guest and host molecules together, the singlet and triplet regions are formed by evaporating the guest and host molecules sequentially. The thickness ratio of the guest and host layers corresponds to the doping concentration of the co-evaporated system. Since the deposition thickness can be controlled very well throughout large-area [19], the uniformity of the device manufacturing should be improved.

Before constructing the WOLED, we studied the exciton (singlet and triplets) distribution in the device. To do this, we placed a thin layer of fluorescent and phosphorescent dye in various positions in the device. We used the BCzVBi and $Ir(2\text{-phq})_2(acac)$ to detect the distribution of the singlet and triplets exciton, respectively. The dye was deposited in two different positions inside CBP and NPB layers (Fig. 1). The structures are NPB (50 nm)/CBP (*x* nm)/dye (0.5 nm BCzVBi or 0.1 nm $Ir(2\text{-phq})_2acac$)/CBP (30-*x* nm)/BCP(20 nm)/Alq_3 (30 nm) for device with dye in CBP, and

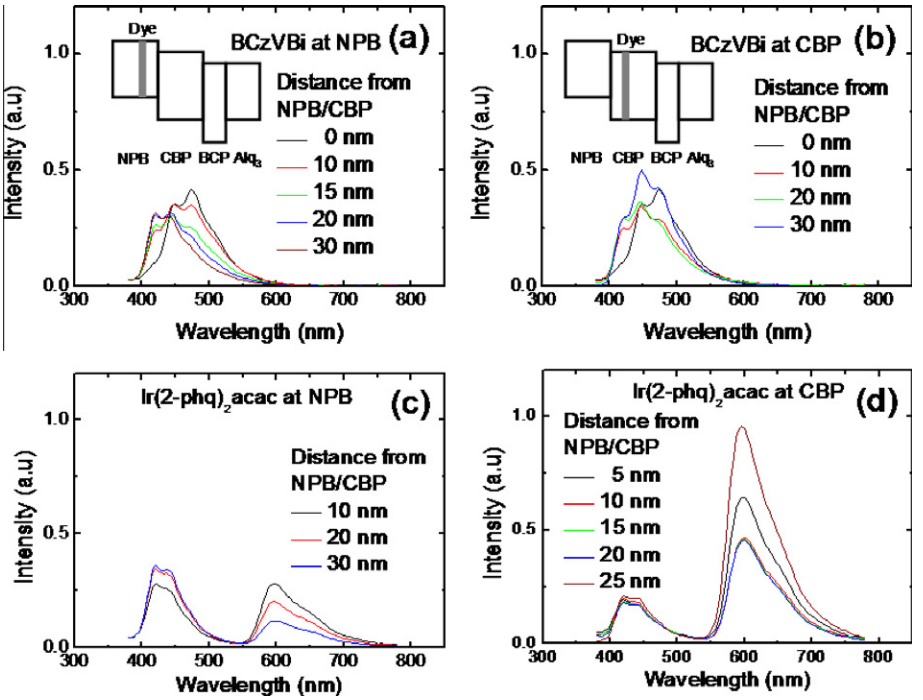

Fig. 2. Emission spectra for devices with a thin BCzVBi layer deposited in NPB (a) and CBP (b). Emission spectra for devices with a thin Ir(2-phq)$_2$acac layer deposited in NPB (c) and CBP (d).

NPB (50-y nm)/dye (0.5 nm BCzVBi or 0.1 nm Ir(2-phq)$_2$-acac)/NPB (y nm)/CBP (30 nm)/BCP (20 nm)/Alq$_3$ (30 nm) for device with dye in NPB, where x and y are the distances from NPB/CBP interface to dyes in NPB and CBP layers, respectively. Fig. 2(a)–(d) show the emission spectra for devices with a thin layer of BCzVBi and Ir(2-phq)$_2$acac deposited at various locations. Significant variation of the emission from the host and the dye can be seen. The host emission consists of that the NPB (peaking at 420 nm) [22] and CBP (peaking at 370 nm) [25]. Although the CBP emission peak is beyond our measurement range, the emission tail can still be seen at the wavelength of 380 nm. For devices with the dye deposited at the NPB (or CBP) side, only the NPB (or CBP) host varies significantly. The guest emission, on the other hand, reduces as the distance of the dye increases from the NPB/CBP or CBP/BCP interfaces. This signifies that the exciton formation is the largest at these interfaces.

Fig. 3 shows the intensities of the BCzVBi and Ir(2-phq)$_2$acac as a function of position in the device. It can be seen that the singlet and triplet excitons distributions are largest at the NPB/CBP or CBP/BCP interfaces. This can be understood since the interfaces have the largest accumulation of both electron and hole. The excitons are formed almost at the same rate at both the NBP/CBP and CBP/BCP interfaces.

The singlet exciton distribution at the NPB layer can be fitted with an exponential decay of $\exp(-y/L_{D(NPB)})$ with a diffusion length ($L_{D(NPB)}$) of 16 nm, where y is the distance from the NPB/CBP interface toward the NPB layer. The exciton distribution at the CBP layer can be fitted with the solution of the diffusion in a confined-space of $\lfloor n_1 \sinh(x/L_{D(CBP)}) + n_2 \sinh((L-x)/L_{D(CBP)}) \rfloor / \sinh(L/L_{D(CBP)})$ with diffusion length ($L_{D(CBP)}$) of 10 nm, where n_1 and n_2 are the exciton densities at CBP/BCP and NPB/CBP interfaces, respectively, L is the thickness of the CBP layer which is 30 nm and x is the distance from the NPB/CBP interface toward the CBP layer. Instead of being confined within the emission layer (CBP), it can be seen that the singlet leaks to the NPB layers.

From Fig. 2(c) and (d), it can be seen that the intensity of the phosphorescent dye in NPB side is much lower than in

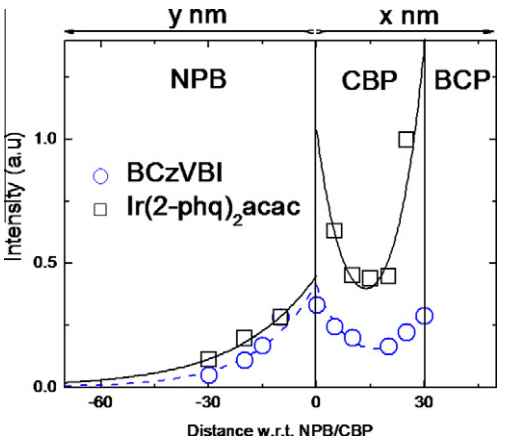

Fig. 3. The intensity of the fluorescent and phosphorescent dyes at various positions in the device.

CBP. Thus the phosphorescence emission in NPB layer is originated from the singlet exciton that leaks to the layer and transfers to the dye. Moreover the intensity profile of triplet exciton is similar to that of the singlet exciton in NPB as shown in Fig. 3. Therefore, it can be concluded that the triplets are well confined within the CBP emission layer. Similar with the case of the singlet exciton, the triplet exciton in CBP layer can be fitted with the same formula with a diffusion length $L^{T}_{D(CBP)}$ of 9 nm. Previously it has been reported that the triplet excitons have a larger diffusion length (~100 nm) [11] compared to the singlet excitons due to their long radiative lifetime. However here it seems the triplet distribution profile is similar to that of the singlet in CBP. This is probably because of the thin CBP layer (30 nm) used in the experiment, where Dexter [26] or Förster [23] processes still dominate the energy transfer besides diffusion.

We then deposited multilayer of BCzVBi near the NPB/CBP interfaces to harvest the singlet exciton. Since much of the singlet excitons are distributed in the NPB side, depositing the fluorescent dye at the hole-transporting layer seems a logical way to extract the singlet excitons. So we deposited the BCzVBi in the NPB layer. Two structures were fabricated, NPB (50 nm)/BCzVBi (0.5 nm)/CBP (30 nm)/BCP (20 nm)/Alq_3 (30 nm) with single guest layer at the interface, and NPB (30 nm)/[NPB (5 nm)/BCzVBi (0.5 nm)]$_4$/CBP (30 nm)/BCP (20 nm)/Alq_3 (30 nm) with four repeating host/guest layers. Fig. 4 shows the emission spectra of the two devices biased at the same current density. The inset of Fig. 4 shows the EQE of the devices. It can be seen that adding the BCzVBi layer at the NPB does not increase the EQE. The deposition of single BCzVBi layer at the interface prevents the excitons diffusion toward the NPB side, confining them in the CBP layer.

So we deposited the fluorescent BCzVBi dye in the CBP layer. The structure is NPB (50 nm)/[BCzVBi (0.5 nm)/CBP (7 nm)]$_p$ /CBP (40–7(p + q) nm)/[CBP (7 nm)/BCzVBi (0.5 nm)]$_q$ /BCP (20 nm)/Alq_3 (30 nm), where p and q are the numbers of repeating host/guest layers and varied from 1 to 3. Fig. 5(a) shows the emission spectra. The inset of Fig. 5(a) shows the external quantum efficiency (EQE) as a function of current density for devices with different

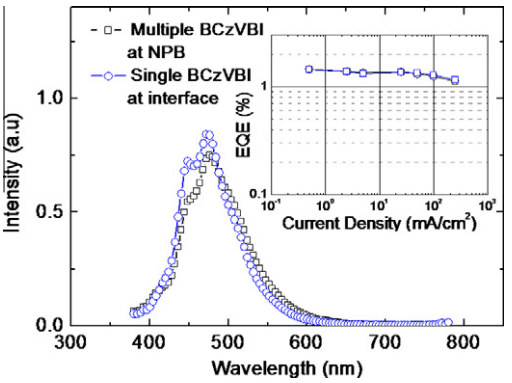

Fig. 4. Emission spectra for devices with singlet excitons extracted with single and multiple BCzVBi layers. Inset shows EQE as a function of current density of the corresponding devices.

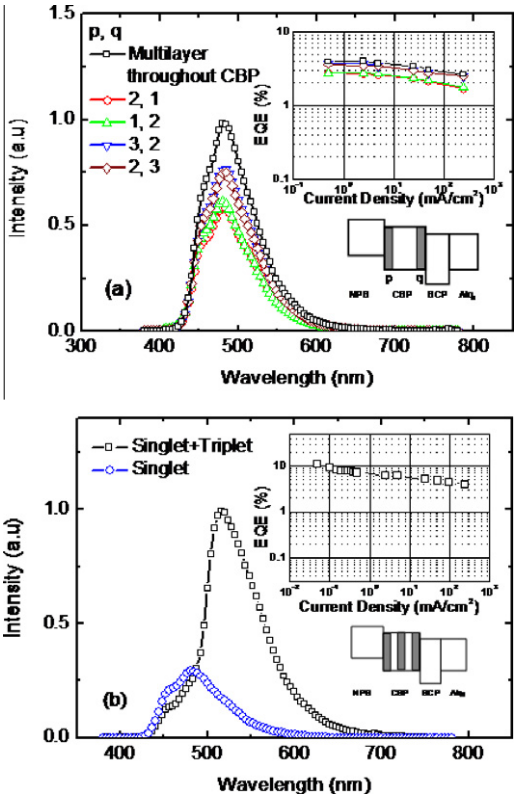

Fig. 5. Emission spectra for devices with p and q multiple BCzVBi layers deposited near the NPB/CBP and CBP/BCP interfaces, respectively, to harvest the singlet exciton (a). Emission spectrum for device in (a) with addition of multiple Ir(ppy)$_3$ layers deposited at the middle of the emission region to harvest the triplet excitons (b). Insets in (a) and (b) shows the EQE as a function of current density of the corresponding devices.

numbers of BCzVBi layers, also shown in the figure is the EQE for device where the whole emission region was replaced by multilayer of BCzVBi and CBP. It can be seen that the EQE steadily increases as the numbers of BCzVBi layers increases. The maximum EQE for device with (p,q) = (3,2) is still 3.5%, which is slightly lower compared to the device with the whole emission region replaced by a multilayer of BCzVBi and CBP (3.9%). This shows that a small amount of singlet excitons still diffuse toward the middle region (escaping the BCzVBi layers), contributing to the loss. It can also be seen that there is no drop in EQE at low current density, unlike the conventional fluorescent OLED fabricated using the co-evaporation method [10]. This shows that the multilayered structure harvests the exciton better at low current density, due to a better capture and confinement of exciton by the thin layer of guest molecules.

The middle emission region was then added with green phosphorescent Ir(ppy)$_3$ layer. The structure of the device is NPB (50 nm)/[BCzVBi (0.5 nm)/CBP (7 nm)]$_3$/[Ir(ppy)$_3$ (0.5 nm)/CBP (6 nm)]$_2$/Ir(ppy)$_3$ (0.5 nm)/[CBP (7 nm)/BCzVBi (0.5 nm)]$_2$/BCP (20 nm)/Alq_3 (30 nm). Fig. 5(b) shows the emission spectrum of the corresponding devices. Also plotted in the figure is the emission spectrum for device without Ir(ppy)$_3$ [device in Fig. 5(a)]. It can be seen that

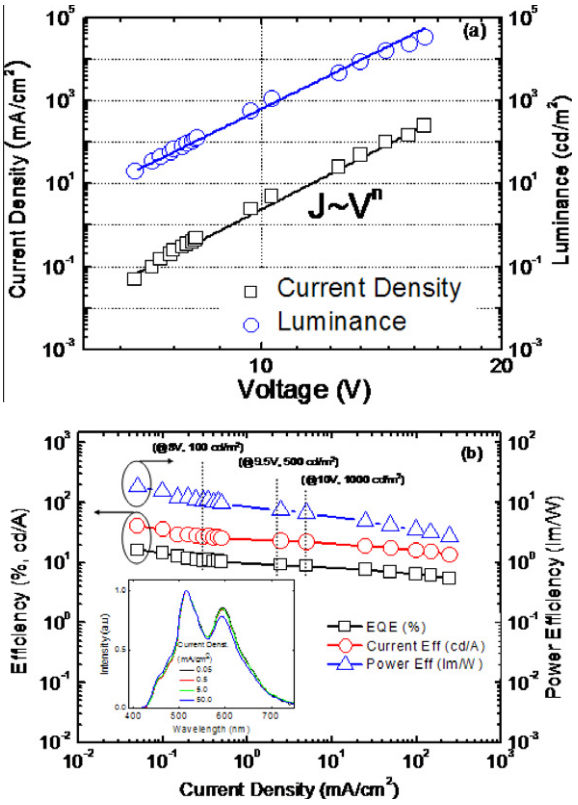

Fig. 6. Current density and luminance versus voltage for the WOLED device (a). The EQE, current and power efficiency as a function of current density for the WOLED [dotted lines @8V, 100 cd/m^2; @9.5V, 500 cd/m^2; and @10V, 1000 cd/m^2] (b). Inset in (b) shows emission spectrum of the WOLED at different current density.

the addition of Ir(ppy)$_3$ layer in the middle section of the emission layer reduces the BCzVBi emission by 40%, which indicates a significant energy transfer (enabled by the Förster process) from the singlet BCzVBi to the Ir(ppy)$_3$ molecule. In previous report, a CBP spacing region as thin as 4 nm was shown adequate to isolate the singlet exciton [10]. Here despite the large 7 nm CBP spacing region, we can still observed a significant energy transfer. This is understandable since the contribution of the molecules within the plane adds to the overall energy transfer, increasing the Förster transfer rate. From the intensity of the emission spectrum, it can be concluded that most of Ir(ppy)$_3$ emission is produced by the triplet exciton in the CBP layer. Direct energy transfer from the triplet of the BCzVBi to Ir(ppy)$_3$ is unlikely. Such a transfer can only occur via Dexter process which has limited range (~10 Å). The large CBP spacing (~7 nm) minimizes the direct energy transfer. The inset of Fig. 5(b) shows the EQE versus current density for the corresponding device. The EQE reaches a maximum of 11% at current density of 0.05 mA/cm^2. The EQE drops monotonously as the current increases, similar to the BCzVBi guest only device [Fig. 5(a)].

Finally we constructed a WOLED with a structure of NPB (50 nm)/[BCzVBi (0.5 nm)/CBP (7 nm)]$_3$/[Ir(ppy)$_3$ (0.5 nm)/CBP (6 nm)/Ir(2-phq)$_2$acac (0.1 nm)/CBP (6 nm)/Ir(ppy)$_3$ (0.5 nm) CBP (6 nm)/Ir(2-phq)$_2$acac (0.1 nm)/[CBP (7 nm)/BCzVBi (0.5 nm)]$_2$/BCP (20 nm)/Alq$_3$ (30 nm) (Fig. 1). Fig. 6(a) shows the current density and luminance versus the voltage for the device. It can be seen from the logarithmic plot that the current density versus voltage shows a power law relationship. The current density (J) can be written as $J \sim V^n$, where V is the voltage and n is equal to 9. This power law behavior is commonly observed in organic devices [27]. It can be seen that the operating voltage is larger than that reported previously which is due to the thick layer of organic semiconductor used in the device. The maximum luminance of >34,000 cd/m^2 was obtained.

Fig. 6(b) shows the EQE and power efficiency as a function of current density. The EQE, current and power efficiencies reach 16.3%, 41 cd/A and 18.5 lm/W at current density of 0.05 mA/cm^2, respectively. The EQE at low current density is much higher than that reported in Ref. [10]. At brightness of 100 and 500 cd/m^2, the EQE reaches 11% and 10%, respectively, comparable with that fabricated by co-evaporation method [10]. This shows that the multilayered emission layer architecture enables an efficient extraction of excitons.

The inset in Fig. 6(b) shows the emission spectra for the white OLED at different current densities. It can be seen that a good coverage of the visible spectrum is achieved. The color rendering index (CRI) reaches a reasonable value of 76 with Commission Internationale de l'éclairage (CIE) coordinate of (x = 0.38, y = 0.46). It can also be seen that variation of the emission at different current density is small.

The device structure has the potential for further optimization, such as the usage of LiF [28] or CsF [29] cathodes, electron-blocking layer [30], doped carrier-transporting layers [30], or corrugated substrate [31] in order to further reduce the operating voltage and increase the efficiency of the device.

In conclusion, we have shown that singlet and triplet excitons can be efficiently extracted from WOLED with a multilayered emission region. The performance of the WOLED is better at low current density and comparable to those fabricated by co-evaporation method at high current density. We also found that there is significant singlet exciton diffusion toward the hole-transporting layer. However the addition of a thin layer of BCzVBi at the NPB/CBP interface was able to confine the singlet exciton within the emission region (CBP). Triplet excitons were well confined within the emission region, enabling an efficient extraction. The method reported here is of significance to tandem WOLED operating at relatively lower current density.

References

[1] C.W. Tang, S.A. VanSlyke, Appl. Phys. Lett. 11 (1987) 913.
[2] C.H. Kim, J. Shinar, Appl. Phys. Lett. 80 (12) (2002) 2201.
[3] C.H. Chen, H.F. Meng, Appl. Phys. Lett. 86 (2005) 201102.
[4] Y.S. Huang, J.H. Jou, W.K. Weng, J.M. Liu, Appl. Phys. Lett. 80 (15) (2002) 2782.
[5] Y. Divayana, X.W. Sun, B.J. Chen, G.Q. Lo, C.Y. Jiang, D.L. Kwong, K.R. Sarma, Jpn. J. Appl. Phys. Part 1 – Regul. Pap. Brief Commun. Rev. Pap. 46 (8A) (2007) 5164.
[6] B.W. D'Andrade, R.J. Holmes, S.R. Forrest, Adv. Mater. (Weinheim, Ger.) 16 (2004) 624.

[7] T.Y. Chu, J.F. Chen, S.Y. Chen, C.H. Chen, Appl. Phys. Lett. 89 (2006) 113502.
[8] J.H. Jou, Y.S. Chiu, C.P. Wang, R.Y. Wang, H.C. Hu, Appl. Phys. Lett. 88 (2006) 193501.
[9] B.W. D'Andrade, J. Brooks, V. Adamovich, M.E. Thompson, S.R. Forrest, Adv. Mater. (Weinheim, Ger.) 14 (2002) 1032.
[10] Y. Sun, N.C. Giebink, H. Kanno, B. Ma, M.E. Thompson, S.R. Forrest, Nature 440 (2006) 908.
[11] M.A. Baldo, D.F. O'Brien, M.E. Thompson, S.R. Forrest, Phys. Rev. B 60 (1999) 14422.
[12] G. Schwartz, M. Pfeiffer, S. Reineke, K. Walzer, K. Leo, Adv. Mater. (Weinheim, Ger.) 19 (21) (2007) 3672.
[13] G. Schwartz, S. Reineke, T.C. Rosenow, K. Walzer, K. Leo, Adv. Funct. Mater. 19 (9) (2009) 1319.
[14] S. Reineke, F. Lindner, G. Schwartz, N. Seidler, K. Walzer, B. Lussem, K. Leo, Nature 459 (7244) (2009) 234.
[15] Y. Kawamura, J. Brooks, J.J. Brown, H. Sasabe, C. Adachi, Phys. Rev. Lett. 96 (2006) 017404.
[16] Y. Divayana, X.W. Sun, Appl. Phys. Lett. 90 (2007) 203509.
[17] C.W. Tang, S.A. VanSlyke, C.H. Chen, J. Appl. Phys. 65 (1989) 3610.
[18] M.A. Baldo, D.F. O'Brien, Y. You, A. Shoustikov, S. Sibley, M.E. Thompson, S.R. Forrest, Nature 395 (1998) 151.
[19] M. Eritt, C. May, K. Leo, M. Toerker, C. Radehaus, Thin Solid Films 518 (2010) 3042.
[20] S. Reineke, G. Schwartz, K. Walzer, K. Leo, Appl. Phys. Lett. 91 (2007) 123508.
[21] Y. Divayana, X.W. Sun, Phys. Rev. Lett. 99 (2007) 143003.
[22] Y. Divayana, X.W. Sun, B.J. Chen, G.Q. Lo, C.Y. Jiang, K.R. Sarma, Appl. Phys. Lett. 89 (2006) 173511.
[23] T. Förster, Discuss. Faraday Soc. 27 (1959) 7.
[24] S. Lamansky, P. Djurovich, D. Murphy, F. Abdel-Razzaq, R. Kwong, I. Tsyba, M. Bortz, B. Mui, R. Bau, M.E. Thompson, Inorg. Chem. 40 (2001) 1704.
[25] T. Tsuboi, H. Murayama, S.-J. Yeh, C.-T. Chen, Opt. Mater. 29 (11) (2007) 1299.
[26] D.L. Dexter, J. Chem. Phys. 21 (1953) 836.
[27] M.A. Baldo, S.R. Forrest, Phys. Rev. B 64 (2001) 085201.
[28] L.S. Hung, C.W. Tang, M.G. Mason, Appl. Phys. Lett. 70 (1997) 152.
[29] M.Y. Chan, S.L. Lai, M.K. Fung, C.S. Lee, S.T. Lee, Chem. Phys. Lett. 374 (2003) 215.
[30] M. Pfeiffer, S.R. Forrest, K. Leo, M.E. Thompson, Adv. Mater. (Weinheim, Ger.) 14 (2002) 1633.
[31] Y.J. Lee, S.H. Kim, J. Huh, G.H. Kim, Y.H. Lee, S.H. Cho, Y.C. Kim, Y.R. Do, Appl. Phys. Lett. 82 (2003) 3779.

Organic Electronics 12 (2011) 8–14

Contents lists available at ScienceDirect

Organic Electronics

journal homepage: www.elsevier.com/locate/orgel

Light-emitting field-effect transistors made of single crystals of an ambipolar thiophene/phenylene co-oligomer

Toshifumi Katagiri [a,b], Yasuhiro Shimizu [a,1], Kohei Terasaki [a], Takeshi Yamao [a], Shu Hotta [a,*]

[a] Department of Macromolecular Science and Engineering, Graduate School of Science and Technology, Kyoto Institute of Technology, Matsugasaki, Sakyo-ku, Kyoto 606-8585, Japan
[b] Technical Office, Sumitomo Seika Chemicals Co., Ltd., 346-1 Miyanishi, Harima, Hyogo 675-0145, Japan

ARTICLE INFO

Article history:
Received 6 August 2010
Received in revised form 30 September 2010
Accepted 4 October 2010
Available online 20 October 2010

Keywords:
Ambipolar charge transport
Organic light-emitting field-effect transistor
External quantum efficiency
Thiophene/phenylene co-oligomer

ABSTRACT

We have developed an ambipolar thiophene/phenylene co-oligomer (TPCO) by introducing the trifluoromethyl group and the methoxy group to molecular terminals of the parent (unsubstituted) TPCO molecule. The crystals of the compound exhibit the ambipolar carrier transport on the field-effect transistors with homogeneous Au electrodes and heterogeneous MgAg and Au electrodes. The latter device definitively emits the light by applying sinusoidal-wave and square-wave alternating-current (AC) voltages to the gate electrode. Time-dependent emission measurements indicate that major emissions take place twice during each period of the AC gate bias.

© 2010 Elsevier B.V. All rights reserved.

1. Introduction

Organic light-emitting field-effect transistors (OLEFETs) are currently attracting increasing attention as reliable devices that can combine signal transformation and its amplification, since a prototype device was proposed and developed [1]. Their device performance is based upon simultaneous injection of electrons and holes into the organic layer and their subsequent recombination. Several attempts were made to facilitate these processes. A typical example is a combination of n-type and p-type organic semiconductor materials. Muccini et al. investigated bi-layered structures [2] and blended films [3] composed of both the types of semiconductors. Recently, they demonstrated high external quantum efficiency (EQE) of 5% using trilayer heterostructure device composed of a light-emitting layer sandwiched between p-type and n-type layers [4]. To achieve the effective charge injection and transport, researchers developed a novel class of ambipolar organic semiconductors. Using poly(9,9-dioctylfluorene-*alt*-benzothiadiazole) (F8BT) [5,6], Sirringhaus et al. were successful in making an ambipolar OLEFET with a single-component semiconductor layer [7,8]. The morphology of amorphous films of F8BT, however, had to be optimized in order to achieve a good balance between charge transport and emission characteristics [8]. More specifically, the annealing temperatures of the processed F8BT were carefully set to prevent the films from forming polycrystalline morphology. Moreover, gold (source and drain) electrodes were modified with a self-assembled monolayer (SAM) to improve the ambipolar device operation [8]. Meanwhile, the ambipolar transport was attained in the OLEFETs using heterogeneous source and drain metal electrodes [9,10]. This is principally because electrons are hard to inject; very unstable metals such as calcium have to be used to improve their injection [9,10].

Thus organic semiconductors that ensure the steady ambipolar device operation are highly desired. With these circumstances as a background we have designed and developed a novel class of ambipolar organic semiconductors based on thiophene/phenylene co-oligomers (TPCOs)

* Corresponding author. Tel.: +81 75 724 7793; fax: +81 75 724 7780.
E-mail address: hotta@kit.ac.jp (S. Hotta).
[1] Present address: Materials Engineering Division, Daihatsu Motor Co., Ltd., 1-17-18 Koda, Ikeda, Osaka 563-0043, Japan.

1566-1199/$ - see front matter © 2010 Elsevier B.V. All rights reserved.
doi:10.1016/j.orgel.2010.10.003

[11]. The TPCOs consist of inline thiophene and phenylene rings with those rings suitably arranged at molecular level. The ambipolar TPCO materials pertinent to the present studies have *both* an electron donating group and an electron withdrawing group on molecular terminals. We have conceived this molecular design strategy on the basis of the fact that the modification of the molecular terminals with the electron donating (withdrawing) groups produces p-type (n-type) semiconductors [12]. Typical examples of them include a methoxy-substituted TPCO, 2,5-bis(4'-methoxybiphenyl-4-yl)thiophene (BP1T-OMe) [12], as the p-type material and a trifluoromethyl-substituted TPCO, 1,4-bis{5-[4-(trifluoromethyl)phenyl]thiophen-2-yl}benzene (AC5-CF_3) [12,13], as the n-type material. Notice that unmodified (i.e. unsubstituted) compounds are of p-type. An example is 2,5-bis(4-biphenylyl)thiophene (BP1T) [11], a parent molecule of BP1T-OMe. The compound we have particularly designed is 2-{4-[5-(4-methoxyphenyl)-2-thienyl]phenyl}-5-[4-(trifluoromethyl)phenyl]thiophene (henceforth abbreviated as AC5-1CF_3-12OMe); see Fig. 1 for the structural formula. We introduced the methoxy group and trifluoromethyl group to the molecular terminals of a parent molecule, 1,4-bis(5-phenylthiophen-2-yl) benzene, AC5 [11].

The devices based on a crystal of AC5-1CF_3-12OMe not only show the ambipolar carrier transport, but produce the characteristic light emission. The emission feature of the devices is probed by the recently-proposed novel operating method that is characterized by applying alternating-current (AC) biases to the gate electrodes [14,15]. For this purpose we have used both a sinusoidal-wave and a square-wave for the gate bias. In both the cases we successfully correlate the time-dependent light emission with the injection of carriers of both the types (i.e. holes and electrons).

2. Results

Fig. 2 depicts a schematic device structure. We used several combinations of metals for source and drain electrodes for the device to have homogeneous electrodes or heterogeneous electrodes (see Section 5.2.). Care should be taken with the electrodes designation according to whether the device is operated for the purpose of measuring the carrier mobility or performing the light-emitting experiments. When we determined the electron mobility on a device with heterogeneous electrodes of MgAg and Au, we solely designated the MgAg electrode as the electron-injection contact. This was because we obtained the higher electron mobility for this electrode designation than the reversed designation. For this measuring configuration we assigned the MgAg (Au) electrode to the source (drain) contact according to the convention [16]. With the hole-enhancement measurement, the electrode designation

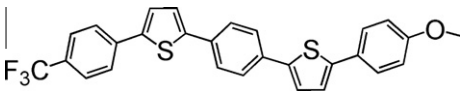

Fig. 1. Structural formula of AC5-1CF_3-12OMe.

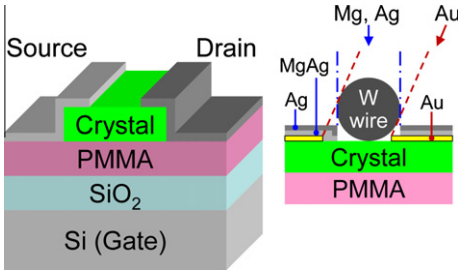

Fig. 2. Schematic structure of a single crystal field-effect transistor. Three combinations of metals of (MgAg, MgAg), (Au, Au), and (MgAg, Au) were used for source and drain electrodes. The former two cases are for the homogeneous electrodes and the last case is relevant to the heterogeneous electrodes. The inset shows an enlarged cross-sectional view of and near the channel of a device with the heterogeneous MgAg and Au electrodes. Care should be taken with the electrode designation according to whether the device is operated for the purpose of measuring the carrier mobility or performing the light-emitting experiments (see text).

was reversed. Regarding the light-emitting experiments we defined the source (drain) electrode as the electron (hole) injection contact. For this purpose the MgAg electrode was chosen as the electron-injection contact as well. A negative (positive) DC voltage with the same absolute value was routinely applied to the source (drain) contact.

The device with homogeneous MgAg electrodes showed typical n-type conduction. The field-effect electron mobility was estimated to be 1.9×10^{-4} $cm^2\,V^{-1}\,s^{-1}$ at the linear region. This device, however, did not show the hole transport (p-type) characteristic. For the device with homogeneous Au electrodes, on the other hand, we observed ambipolar transport feature. The electron and hole mobilities were estimated at the linear regions to be 3.4×10^{-5} and 5.1×10^{-5} $cm^2\,V^{-1}\,s^{-1}$, respectively. In this specific device, the hole mobility was slightly greater than the electron one. For a device with heterogeneous electrodes of MgAg and Au, the ambipolar transport is again evident. The output characteristics of the device were depicted in Fig. 3a for the electron-enhancement mode and Fig. 3b for the hole-enhancement mode. Notice once again that in Fig. 3a we designated the MgAg electrode as the source contact and that in Fig. 3b we assigned that same electrode to the drain contact. In the electron-enhancement mode (Fig. 3a) the drain currents started increasing in the region $V_{DS} \leqslant 10$ V. In the hole-enhancement mode (Fig. 3b) the drain currents rose up around $V_{DS} \approx -30$ V. In both modes, the drain currents were modulated with the gate voltages of $|V_G| \geqslant 60$ V. The electron and hole mobilities at the linear regions were 1.1×10^{-4} and 6.0×10^{-6} $cm^2\,V^{-1}\,s^{-1}$, respectively. The electron mobility is larger than the hole mobility, contrary to the device with homogeneous Au electrodes in the present studies and other unsubstituted TPCO-based ambipolar devices with heterogeneous electrodes [10,17].

Of the devices indicating the ambipolar characteristics, the current-injected light emission is clearly noted by eye under AC gate biases [14] for the device with the heterogeneous MgAg and Au electrodes. This is due to improved electron injection from the MgAg source electrode. Fig. 4a illustrates a micrograph of an unlit device and Fig. 4b represents that lighted in the dark under the AC gate bias

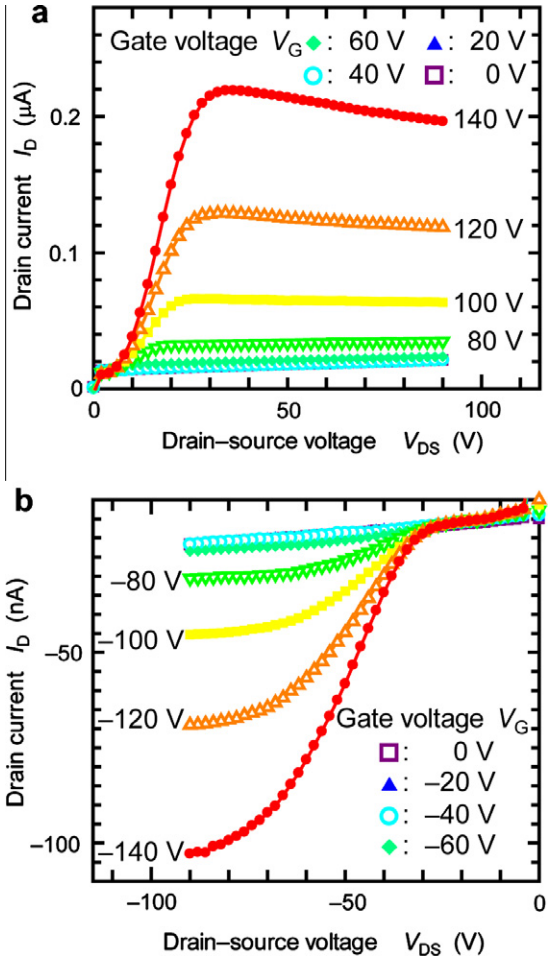

Fig. 3. Output characteristics of the device with heterogeneous MgAg and Au electrodes (a) in the electron-enhancement mode and (b) in the hole-enhancement mode.

application. For the latter, the green emission dominantly takes place from the channel region. Emissions near the source and drain contacts were noticed as well. In Fig. 4b direct current (DC) voltages of −100 and 100 V were applied to MgAg and Au electrodes, respectively (see Section 5.3.). We simultaneously applied a sinusoidal-wave AC gate voltage with an amplitude 120 V and frequency 500 Hz. Fig. 4c shows the emission spectrum taken under the AC gate bias application using another device. To record the emission spectrum, the device was operated by applying a square-wave AC gate voltage with its amplitude 120 V and frequency 20 kHz. A DC voltage of −100 (100) V was applied to the MgAg (Au) electrode. In Fig. 4c we compare the electrically-excited spectrum with an optically-excited one. Both the spectral profiles are closely related with the same peak position of the dominant line occurring at 538.40 nm. The full width at half maximum (FWHM) was 39.67 nm for the electrically-excited spectrum and 39.07 nm for the optically-excited spectrum.

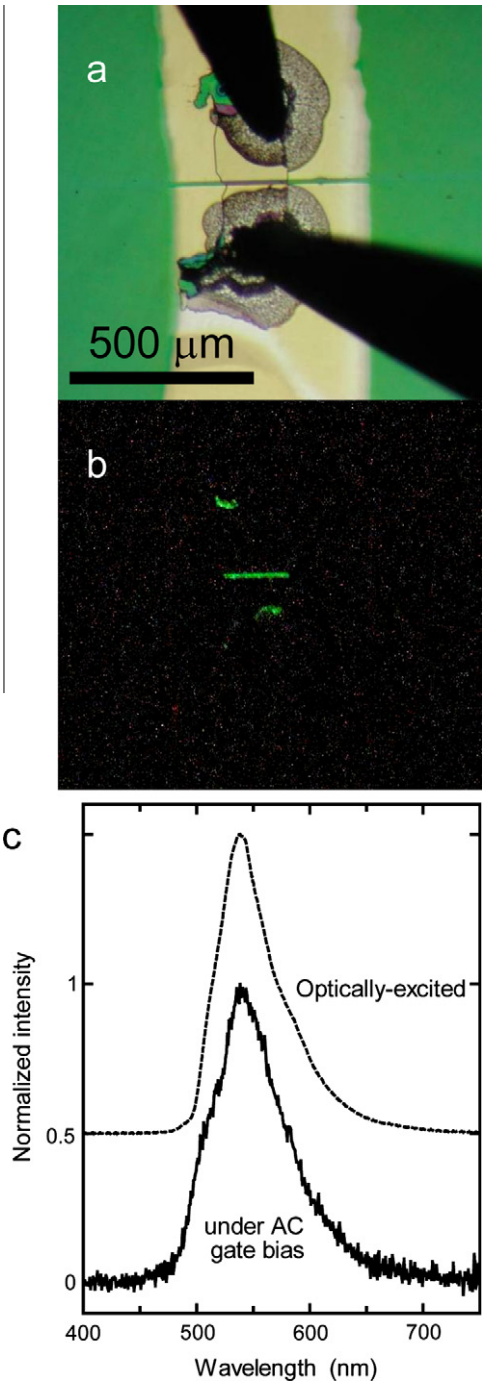

Fig. 4. (a) Micrograph of an AC5-1CF_3-12OMe single-crystal OLEFET. The two dark parts on the top and the right of the micrograph are tungsten needle microprobes. (b) Micrograph of the device lit in the dark under the application of a sinusoidal-wave AC gate bias. Green emissions were noted as a horizontal bar at the channel and as semicircles near the source and drain contacts. (c) Emission spectrum from the device operated under a square-wave AC gate bias. The spectrum is compared with an optically-excited emission spectrum from an AC5-1CF_3-12OMe crystal. (For interpretation of the references to colour in this figure legend, the reader is referred to the web version of this article.)

Fig. 5a and b compare the time-dependent emission intensity characteristics of the devices operated under the sinusoidal-wave AC gate bias and the square-wave gate bias. The temporal waveforms of the gate biases are indicated as a guide. In the sinusoidal-wave case we set the DC voltages and the amplitude and frequency of AC gate bias at values the same as the above. We observed emissions when both the maximum and minimum gate biases were reached (Fig. 5a). For the square-wave bias, in turn, we set DC voltages of the MgAg and Au electrodes at −70 and 70 V, respectively, and applied to the gate electrode an AC bias with an amplitude 90 V and frequency 5 kHz. Strong emissions clearly take place when the gate bias switches its polarity traversing 0 V. We stress that the maximum instantaneous intensity reaches several tens of times that recorded for the sinusoidal-wave case. Correspondingly the EQE for the square-wave device (Fig. 5b) was estimated at 0.16%. This number was higher by five times than 0.032% obtained for the sinusoidal-wave device (Fig. 5a). For both the sinusoidal-wave and square-wave cases, we have observed major emissions *twice* with each period (a 2π-phase change). This observation means that the moment the gate polarity is switched, electrons and holes are alternately injected through the source and drain electrode to produce the light emission. This provides a striking contrast to the results of our previous studies where BP1T was used for a device [14]. In that case we noticed a major emission only once with each period.

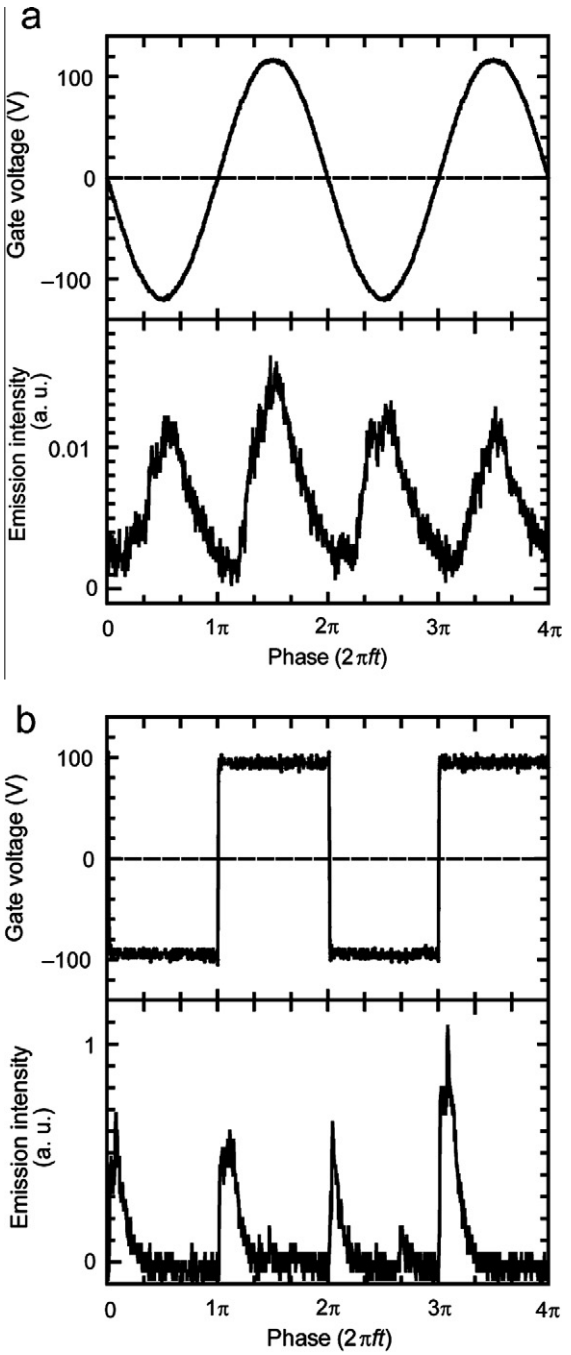

Fig. 5. Emission intensities of the devices as a function of phase. The devices were operated under (a) the sinusoidal-wave and (b) the square-wave AC gate biases. The temporal waveforms of the gate biases are indicated as a guide.

3. Discussion

Occurrence of the two major emissions is interpreted as follows: The electrons (holes) are injected from the source (drain) electrode when the gate bias is positive (negative). The injected carriers flow in the channel and are transported toward the opposite electrode. They recombine with carriers of the opposite polarity which are injected from that electrode when the polarity of the gate voltage is switched. This process evenly takes place twice during the individual period. The rapid polarity switching of the gate bias is responsible for the increase in the emission intensities, as previously observed in the devices with a p-type semiconductor such as BP1T [14,15]. The increased emission intensity is because principally of suppression of the depletion of carriers without the radiative recombination [15]. EQEs of the present studies are larger than those obtained for the BP1T thin film devices [14]. This results from the balanced injection and transportation of both the electrons and holes in the AC5-1CF_3-12OMe crystals.

Fig. 6a depicts an energy diagram where energy levels of the lowest unoccupied molecular orbital (LUMO) and highest occupied molecular orbital (HOMO) for AC5-1CF_3-12OMe are indicated relative to Fermi levels of Au (−5.1 eV [18]) and Mg (−3.66 eV [18]). The LUMO and HOMO levels were −1.86 and −5.16 eV, respectively. The HOMO level is close to the Fermi level of Au. This is consistent with the observation that the homogeneous Au device indicates a good p-type characteristic. Meanwhile, the Au Fermi level is separated from the LUMO level by 3.24 eV. The n-type feature of the homogeneous Au device means that electrons can be injected from the Au electrode into the AC5-1CF_3-12OMe layer beyond the energy barrier of 3.24 eV. This number is exceptionally large and should be compared with a corresponding value of ∼1.8 eV for an ambipolar OLEFET device based on the F8BT thin film equipped with homogeneous Au electrodes [8].

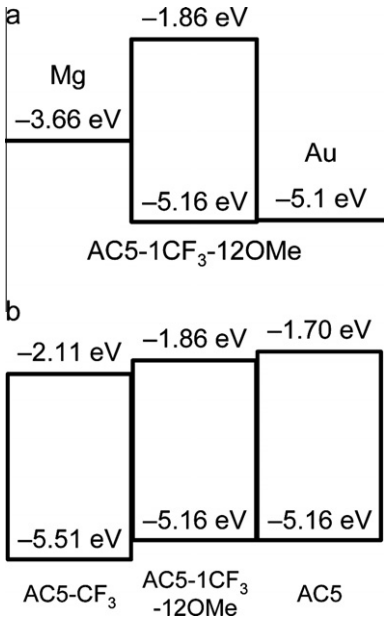

Fig. 6. (a) Energy diagram of the LUMO and HOMO levels of AC5-1CF_3-12OMe relative to Fermi levels of Mg and Au. The levels are indicated with respect to the vacuum level. (b) HOMO and LUMO levels of several TPCOs sharing the parent AC5 structure.

The Mg Fermi level, in turn, is located halfway between the LUMO and HOMO levels (Fig. 6a). Experimental results in the present studies again imply that electrons are easily injected from Mg beyond a barrier 1.80 eV into the AC5-1CF_3-12OMe layer. This is similarly the case with the AC5-CF_3 devices with homogeneous MgAg electrodes [13] to which the corresponding value is 1.55 eV; see Fig. 6b where we compare the HOMO and LUMO levels of several TPCOs sharing the parent AC5 structure. Of these, AC5-1CF_3-12OMe combines the superior abilities of the electron and hole injection. The energy diagram of Fig. 6 means that the hole injection barrier from Mg is 1.50 eV (1.85 eV) for AC5-1CF_3-12OMe (AC5-CF_3). These numbers are smaller than the above-mentioned electron injection barrier from Au into AC5-1CF_3-12OMe. This is indicative of the comparative difficulty in the hole injection from Mg [13]. The origin would therefore need seeking appropriately.

4. Conclusion

We have developed an ambipolar TPCO, AC5-1CF_3-12OMe, by introducing the trifluoromethyl group and the methoxy group to molecular terminals of the parent molecule AC5. The compound AC5-1CF_3-12OMe exhibits the ambipolar carrier transport on the FETs with the devices of homogeneous Au electrodes and heterogeneous MgAg and Au electrodes. Under the AC bias application to the gate electrode the device of the heterogeneous electrodes definitively shows the current-injected light emission. An EQE under square-wave gate bias was 0.16%. The time-dependent emission measurements obviously demonstrate that the major emissions take place twice during each period. This indicates that the moment the gate polarity is switched, electrons and holes are alternately injected through the source and drain electrodes to produce the light emission.

In combination with the AC gate bias operation method, the molecular design strategy in the present studies not only supports a platform display technology but also gives a powerful clue to exploring the charge injection and transport mechanisms associated with light emission.

5. Experimental details

5.1. Synthesis and characterization of AC5-1CF_3-12OMe

We show the synthetic route of AC5-1CF_3-12OMe in Scheme 1. The synthesis of AC5-1CF_3-12OMe is based on the Suzuki coupling reactions [19]. 2-Bromo-5-(4-trifluoromethylphenyl)thiophene [20] (**1**) and 4-(2-thienyl)phenylboronic acid [21] (**2**) were synthesized following the literature methods. Compounds **1** (6.1 g, 20 mmol), **2** (4.9 g, 24 mmol), and tetrakis(triphenylphosphine)palladium(0) [abbreviated as $Pd(PPh_3)_4$ in Scheme 1] (1.2 g, 1.0 mmol) were dispersed and dissolved in chlorobenzene (400 mL) and aqueous sodium carbonate (2.5 g, 24 mmol in 400 mL of water) at room temperature under a nitrogen environment. The mixture was warmed to 90 °C and stirred for 5 h. The reaction mixture was cooled to yield precipitates. The filtered precipitates were washed with cyclopentyl methyl ether and dried under reduced pressure to give

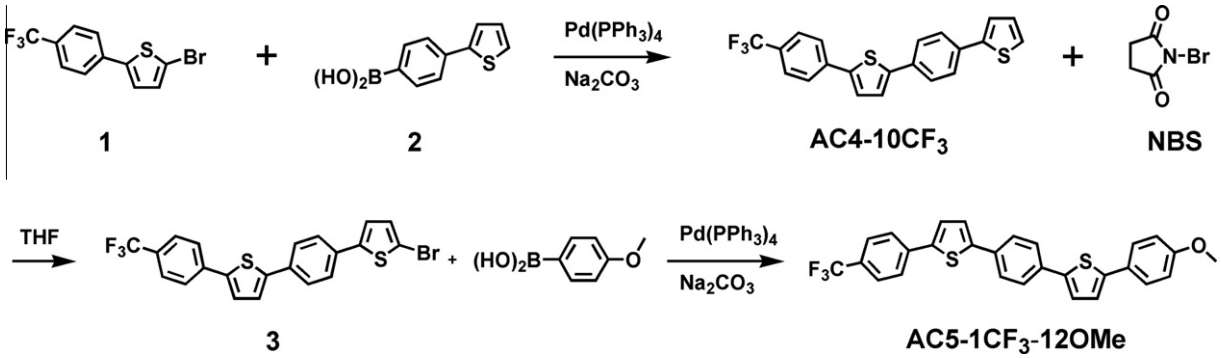

Scheme 1. Synthetic route of AC5-1CF_3-12OMe.

yellow crystals of 5.4 g (70%, 14 mmol) of 2-[4-(2-thienyl) phenyl]-5-(4-trifluoromethylphenyl)thiophene (AC4-10CF_3).

AC4-10CF_3 (3.9 g, 10 mmol) was dissolved in tetrahydrofuran (THF, 1000 mL). To this solution was added dropwise *N*-bromosuccinimide (abbreviated as NBS; 2.5 g, 14 mmol) at room temperature under a dry nitrogen environment and the mixture was stirred for 2 h. The resulting reaction solution was cooled to yield precipitates. The filtered precipitates were washed with THF and dried under reduced pressure to produce yellow crystals of 3.4 g (73%, 7.3 mmol) of 2-[4-(5-bromo-2-thienyl)phenyl]-5-(4-trifluoromethylphenyl)thiophene (**3**).

Compound **3** (2.8 g, 6.0 mmol) was dissolved in chlorobenzene (120 mL) and water (120 mL). To this solution, 4-methoxyphenylboronic acid (1.1 g, 7.2 mmol), sodium carbonate (0.8 g, 7.5 mmol), and $Pd(PPh_3)_4$ (0.3 g, 0.3 mmol) were added successively. The resulting solution was then warmed to 90 °C and stirred for 5 h. The reaction solution was cooled to produce precipitates. The precipitates were washed with cyclopentyl methyl ether and dried under reduced pressure to give 2.7 g (92%, 5.5 mmol) of AC5-1CF_3-12OMe as yellow crystals. m.p. 338 °C. ^{1}H NMR (400 MHz, THF-d_8, δ, ppm): 3.81 (s, 3H, methoxy protons), 6.95 (d, J = 8.8 Hz, 2H, phenylene protons), 7.27 (d, J = 3.8 Hz, 1H, thienylene proton), 7.42 (d, J = 3.8 Hz, 1H, thienylene proton), 7.49 (d, J = 3.8 Hz, 1H, thienylene proton), 7.57–7.60 (m, 3H), 7.67–7.71 (m, 6H), 7.87 (d, J = 8.1 Hz, 2H, phenylene protons). IR (KBr cm^{-1}): 3075 (w), 2941 (w), 1497 (m), 1453 (m), 1414 (w), 1331 (s), 1261 (m), 1129 (m), 1032 (m), 835 (m), 797 (vs). UV–vis (THF): λ_{max} = 384 nm. EIMS (m/z): 492 (M^+). Anal. Calc. for $C_{28}H_{19}F_3OS_2$ (%): C, 68.27; H, 3.89; F, 11.57. Found: C, 68.36; H, 4.00; F, 11.54.

To characterize AC5-1CF_3-12OMe, ^{1}H NMR spectra were measured on a Varian Mercury-400BB spectrometer (400 MHz) in a solution of deuteriotetrahydrofuran and chemical shifts were recorded in ppm (δ) relative to tetramethylsilane as an internal standard. IR spectra were taken on a JEOL JIR-6500 FT-IR spectrophotometer with finely pulverized samples dispersed and embedded in a potassium bromide matrix. Electron impact mass spectra were collected on a SHIMADZU GCMS-QP5000 mass spectrometer. Elementary analyses were performed with a J-Science Micro Corder JM10 and an Orion model 920A after two time purifications of the material by train sublimation technique [22]. UV–vis spectra were recorded on a HITACHI U-4100. Melting points were determined on a Seiko Instruments EXSTAR DSC 6220 thermal analysis system.

5.2. Device fabrication

Crystals of AC5-1CF_3-12OMe (of 240–1040 μm in size and 225–1920 nm in thickness) were grown according to the literature method [23] under nitrogen gas flow (35–50 mL/min). The AC5-1CF_3-12OMe crystals were laminated on a poly(methyl methacrylate) (PMMA) layer (143–330 nm in thickness) that was spin-coated with its 5 wt.% toluene solution on an Si substrate (as the gate contact) covered with a 300-nm thick SiO_2 layer (see Fig. 2). The devices were completed as the top-contact and bottom-gate configuration by depositing metal electrodes in vacuum (~10^{-3} Pa). These metal electrodes were deposited on top of the AC5-1CF_3-12OMe crystal over a tungsten wire in close contact with the crystal. For the electrodes we chose three different combinations of metals either homogeneous or heterogeneous: (i) MgAg (100-nm thick), (ii) Au (50 nm), and (iii) MgAg (30–40 nm) and Au (30 nm). The homogeneous MgAg electrodes were formed first by co-depositing Mg and Ag (15 nm) and depositing Ag (85 nm) subsequently. For the fabrication of heterogeneous MgAg and Au electrodes, the Au (30 nm) was first evaporated obliquely relative to the channel (see the inset of Fig. 2). The Mg and Ag were successively evaporated from directly above the channel; the MgAg layers were formed by co-depositing Mg and Ag (20 nm) and subsequently depositing Ag (10–20 nm) such that the total thickness of the resulting heterogeneous electrodes was 60–70 nm. Note that the innermost parts of the electrodes (i.e. either Au or MgAg) determine the carrier injection (see the inset of Fig. 2). The channel length and width of the devices ranged from 8.3–11.2 μm and 0.16–1.53 mm, respectively.

5.3. Device operation and spectroscopic measurements

For the purpose of estimating the carrier mobility, we routinely operated the device in vacuum (~10^{-3} Pa) in either the electron-enhancement or hole-enhancement mode [13]. For the emission measurements, AC biases were applied to the gate contact. We used either a sinusoidal-wave or a square-wave form with various AC voltage amplitudes and frequencies according to the purposes of experiments.

The experimental setups for the light-emitting experiments and spectroscopic measurements were similar to those employed in our previous studies [14,15]. The device was mounted on a sample stage in a vacuum chamber (~10^{-3} Pa). The emissions occurring from the device were collected with an OLYMPUS SZ61 stereo microscope through a glass window of the vacuum chamber. The emission spectra were recorded in a manner similar as before [14,15]. The optically-excited emission spectrum was measured using the setup and method identical to those used in the previous study [24] except a sharp cut filter was not used in the present studies.

5.4. Quantum chemical calculations

We carried out molecular orbital (MO) calculations of AC5-1CF_3-12OMe. The density functional theory (DFT) calculations were performed to optimize the geometry and estimate the HOMO and LUMO energies at the B3LYP/6-31G(d) level using Gaussian 03 program [25]. We also calculated the energy levels for the parent material AC5 [26] and a homogeneously substituted material AC5-CF_3.

Acknowledgements

We thank Dr. Reiko Azumi and Mr. Satoshi Ota for their helpful discussions and suggestions on the single crystals growth. This work was supported by a Grant-in-Aid for Science Research on Priority Areas "Super-Hierarchical Structures" (No. 17067009) and a Grant-in-Aid for Challenging

Exploratory Research (No. 20655041) from the Ministry of Education, Culture, Sports, Science and Technology, Japan.

References

[1] A. Hepp, H. Heil, W. Weise, M. Ahles, R. Schmechel, H. von Seggern, Physical Review Letters 91 (2003) 157406.
[2] F. Dinelli, R. Capelli, M.A. Loi, M. Murgia, M. Muccini, A. Facchetti, T.J. Marks, Advanced Materials 18 (2006) 1416–1420.
[3] C. Rost, S. Karg, W. Riess, M.A. Loi, M. Murgia, M. Muccini, Applied Physics Letters 85 (2004) 1613–1615.
[4] R. Capelli, S. Toffanin, G. Generali, H. Usta, A. Facchetti, M. Muccini, Nature Materials 9 (2010) 496–503.
[5] Y. He, S. Gong, R. Hattori, J. Kanicki, Applied Physics Letters 74 (1999) 2265–2267.
[6] L.-L. Chua, J. Zaumseil, J.-F. Chang, E.C.-W. Ou, P.K.-H. Ho, H. Sirringhaus, R.H. Friend, Nature 434 (2005) 194–199.
[7] J. Zaumseil, C.L. Donley, J.-S. Kim, R.H. Friend, H. Sirringhaus, Advanced Materials 18 (2006) 2708–2712.
[8] M.C. Gwinner, S. Khodabakhsh, H. Giessen, H. Sirringhaus, Chemistry of Materials 21 (2009) 4425–4433.
[9] J.S. Swensen, C. Soci, A.J. Heeger, Applied Physics Letters 87 (2005) 253511.
[10] S.Z. Bisri, T. Takenobu, Y. Yomogida, H. Shimotani, T. Yamao, S. Hotta, Y. Iwasa, Advanced Functional Materials 19 (2009) 1728–1735.
[11] S. Hotta, H. Kimura, S.A. Lee, T. Tamaki, Journal of Heterocyclic Chemistry 37 (2000) 281–286.
[12] T. Katagiri, S. Ota, T. Ohira, T. Yamao, S. Hotta, Journal of Heterocyclic Chemistry 44 (2007) 853–862.
[13] T. Yamao, Y. Shimizu, H. Kuriki, T. Katagiri, S. Hotta, Japanese Journal of Applied Physics 49 (2010) 01AB01.
[14] T. Yamao, Y. Shimizu, K. Terasaki, S. Hotta, Advanced Materials 20 (2008) 4109–4112.
[15] T. Yamao, K. Terasaki, Y. Shimizu, S. Hotta, Journal of Nanoscience and Nanotechnology 10 (2010) 1017–1020.
[16] S.M. Sze, Physics of Semiconductor Devices, second ed., John Wiley & Sons, New York, 1981 (chapter 8).
[17] Y. Wang, R. Kumashiro, Z. Li, R. Nouchi, K. Tanigaki, Applied Physics Letters 95 (2009) 103306.
[18] H.B. Michaelson, Journal of Applied Physics 48 (1977) 4729–4733.
[19] N. Miyaura, A. Suzuki, Chemical Reviews 95 (1995) 2457–2483.
[20] K. Kobayashi, A. Sugie, M. Takahashi, K. Masui, A. Mori, Organic Letters 7 (2005) 5083–5085.
[21] S. Hotta, Journal of Heterocyclic Chemistry 38 (2001) 923–927.
[22] H.J. Wagner, R.O. Loutfy, C.-K. Hsiao, Journal of Materials Science 17 (1982) 2781–2791.
[23] T. Yamao, S. Ota, T. Miki, S. Hotta, R. Azumi, Thin Solid Films 516 (2008) 2527–2531.
[24] S. Hotta, Y. Sakurai, Y. Okuda, T. Miki, K. Matsunaga, F. Hirato, T. Yamao, H. Jinnai, Journal of Nanoscience and Nanotechnology 10 (2010) 440–447.
[25] M.J. Frisch, G.W. Trucks, H.B. Schlegel, G.E. Scuseria, M.A. Robb, J.R. Cheeseman, J.A. Montgomery Jr., T. Vreven, K.N. Kudin, J.C. Burant, J.M. Millam, S.S. Iyengar, J. Tomasi, V. Barone, B. Mennucci, M. Cossi, G. Scalmani, N. Rega, G.A. Petersson, H. Nakatsuji, M. Hada, M. Ehara, K. Toyota, R. Fukuda, J. Hasegawa, M. Ishida, T. Nakajima, Y. Honda, O. Kitao, H. Nakai, M. Klene, X. Li, J.E. Knox, H.P. Hratchian, J.B. Cross, V. Bakken, C. Adamo, J. Jaramillo, R. Gomperts, R.E. Stratmann, O. Yazyev, A.J. Austin, R. Cammi, C. Pomelli, J.W. Ochterski, P.Y. Ayala, K. Morokuma, G.A. Voth, P. Salvador, J.J. Dannenberg, V.G. Zakrzewski, S. Dapprich, A.D. Daniels, M.C. Strain, O. Farkas, D.K. Malick, A.D. Rabuck, K. Raghavachari, J.B. Foresman, J.V. Ortiz, Q. Cui, A.G. Baboul, S. Clifford, J. Cioslowski, B.B. Stefanov, G. Liu, A. Liashenko, P. Piskorz, I. Komaromi, R.L. Martin, D.J. Fox, T. Keith, M.A. Al-Laham, C.Y. Peng, A. Nanayakkara, M. Challacombe, P.M.W. Gill, B. Johnson, W. Chen, M.W. Wong, C. Gonzalez, J.A. Pople, Gaussian 03, Revision D.01, Gaussian, Inc., Wallingford CT, 2004.
[26] X.M. Hong, H.E. Katz, A.J. Lovinger, B.-C. Wang, K. Raghavachari, Chemistry of Materials 13 (2001) 4686–4691.

Organic Electronics 12 (2011) 15–21

Contents lists available at ScienceDirect

Organic Electronics

journal homepage: www.elsevier.com/locate/orgel

Polarized phosphorescent organic light-emitting devices adopting mesogenic host–guest systems

Su-Hao Liu [a], Ming-Shiang Lin [a], Li-Yin Chen [a], Yun-Hua Hong [a], Chih-Hung Tsai [a], Chung-Chih Wu [a,*], Anurach Poloek [b], Yun Chi [b,*], Chien-An Chen [c], Shaw H. Chen [c,*], Hsiu-Fu Hsu [d]

[a] Department of Electrical Engineering, Graduate Institute of Electronics Engineering, and Graduate Institute of Photonics and Optoelectronics, National Taiwan University, Taipei 10617, Taiwan, ROC
[b] Chemistry Department, National Tsing-Hua University, Hsin-Chu 30013, Taiwan, ROC
[c] Chemical Engineering Department, Rochester University, Rochester, New York, 14623-1212, USA
[d] Chemistry Department, Tamkang University, Taipei 25137, Taiwan, ROC

ARTICLE INFO

Article history:
Received 30 August 2010
Received in revised form 7 September 2010
Accepted 12 September 2010
Available online 23 October 2010

Keywords:
OLEDs
Phosphorescence
Polarized emission
Liquid crystal

ABSTRACT

We report successful realization of workable polarized phosphorescent organic light-emitting devices (OLEDs) by combining a recently developed mesogenic phosphorescent Pt(II) complex and a mesogenic oligofluorene host to form the corresponding mesogenic host–guest emitting system. In the host–guest film, the mesogenic Pt(II) complex tends to aggregate and self-assemble into the columnar stacking arrangement, exhibiting metal–metal-to-ligand charge transfer (MMLCT) emission of the Pt(II) complex. Both the host molecules and guest aggregates in the host–guest films were successfully aligned by using the rubbed conducting polymer as the alignment layer. With such aligned host–guest films, polarized red-emitting OLEDs were successfully implemented, showing an EL polarization ratio of ~2, a maximal brightness exceeding 2000 cd/m^2, and a cd/A efficiency up to 2.4 cd/A. Due to the particular alignment mechanism of guest aggregates and the unique MMLCT emission mechanism, the polarized OLED exhibiting stronger electroluminescence perpendicular to the rubbing direction than along the rubbing direction.

© 2010 Elsevier B.V. All rights reserved.

1. Introduction

The polarization control of light is of particular importance for optical information processing devices, such as displays, optical storage, and stereoscopic imaging systems etc. [1,2]. For instance, linearly polarized electroluminescence (EL) devices would be useful for backlights of liquid–crystal displays (LCDs) [3,4]. With polarized backlights, the displays can be made "greener" (i.e. more power-efficient) and simplified by removing polarizers needed for conventional non-polarized backlights and the optical losses it induced. As such, there had been substantial efforts in developing polarized organic light-emitting devices (OLEDs) [5–19]. Among them, linearly polarized OLEDs adopting mesogenic polyfluorenes/oligofluorenes together with appropriate molecular alignment techniques are some distinctive examples [5–11]. S.H. Chen et al. also reported the use of liquid–crystalline oligofluorenes as hosts to guide molecular orientation of guest emitters, forming the polarized host–guest emitting systems [7–10]. The previous efforts in polarized OLEDs were mainly on fluorescent OLEDs. Yet, the development of OLEDs in recent years has largely shifted toward phosphorescent OLEDs [20,21], since phosphorescent OLEDs could effectively utilize both singlet and triplet excitons and realize ideally 100% internal quantum efficiencies [22,23]. As such,

* Corresponding authors. Tel.: +886 2 33663636; fax: +886 2 3366 9404.
E-mail addresses: chungwu@cc.ee.ntu.edu.tw (C.-C. Wu), ychi@mx.nthu.edu.tw (Y. Chi), shch@lle.rochester.edu (S.H. Chen).

1566-1199/$ - see front matter © 2010 Elsevier B.V. All rights reserved.
doi:10.1016/j.orgel.2010.09.020

it is of both scientific and technical importance to explore the possibility of achieving polarized phosphorescent OLEDs.

In this paper, we report an initial attempt to realize workable and functional polarized phosphorescent OLEDs by using a recently developed mesogenic phosphorescent metal (Pt(II)) complex, which is combined with a mesogenic oligofluorene host to form the corresponding mesogenic host–guest emitting system.

2. Experiments

2.1. Materials

Fig. 1 shows the mesogenic materials, a Pt(II) complex N200, $Pt(N^{\wedge}N)_2$ [*N* = 2-(3-(3,4,5-trihexyloxyphenyl)-1H-pyrazol-5-yl)pyridine], and a fluorene oligomer F(MB)5, penta[9,9-bis(2-methylbutyl)fluorene], used in this work. The Pt(II) complex N200 adopts the distinctive pyridyl azolate as ligands, which are known to form strong chelate bonding with Pt ions and render the molecule a square-plannar geometry, affording distinctive emission (phosphorescent) properties [24–26]. Indeed, the Pt(II) complex N200 exhibits rather efficient green phosphorescence at room temperature in dilute solutions [26]. Further attaching alkyloxyphenyl groups onto the ligands gives certain flexibility to the molecular core and mesomorphic characteristics, thereby yielding luminescent metallomesogens [26–30]. As studied by polarizing optical microscopy and differential scanning calorimetry, the Pt(II) complex N200 shows liquid–crystalline properties within a rather wide temperature range. Upon heating of the bulk crystalline samples, a transition from the solid to the hexagonal columnar mesophase (as verified by X-ray diffraction [26]) and a transition from the mesophase to the isotropic liquid occurs around 98 °C and 340 °C, respectively. The details of syntheses and basic material properties of the Pt(II) complex N200 had been reported elsewhere recently [26].

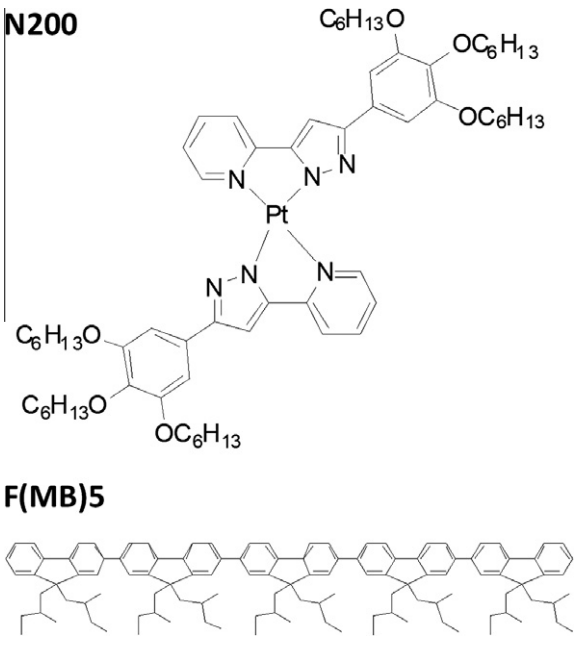

Fig. 1. Molecular structures of N200 and F(MB)5.

On the other hand, the fluorene oligomer F(MB)5 consists of five fluorene units on the backbone and two 2-methylbutyl substituents on C9 atoms [8,9]. F(MB)5 belongs to the class of glass-forming nematic oligofluorenes, that is, materials that exhibit the nematic mesophase at elevated temperatures and yet also the stable glass phase at room temperature [7–10]. As studied by polarizing optical microscopy and differential scanning calorimetry, F(MB)5 exhibits a glass transition (Tg) at ~89 °C and a nematic-to-isotropic transition at 167 °C. It had been demonstrated that liquid–crystal glass of F(MB)5 could be formed by freezing its mesophase down to room temperature without crystallization, and that the aligned glassy nematic film of F(MB)5 could be formed by utilizing mesophase-mediated alignment (e.g. assisted by the rubbed polyimide alignment layer) at elevated temperatures [8,9]. F(MB)5 is also an efficient fluorescent blue emitter with a thin-film quantum yield of >50% [8,9]. Detailed Syntheses and characterizations of F(MB)5 could be found in previous publications [8].

2.2. Molecular alignment

To conduct and study molecular alignment of the Pt(II) complex N200 for polarized emission, different sample structures and alignment approaches were tested: (1) In the first scheme, the active thin films under investigation were spin-coated onto the quartz substrates and then were uniaxially rubbed with a dustless cloth for surface alignment. (2) In the second scheme, a conducting polymer Poly(3,4-ethylenedioxythiophene):poly(styrenesulfonate) (PEDOT:PSS) was used as the alignment layer. PEDOT:PSS was spin-coated onto quartz substrates, dried at 130 °C in air, and uniaxially rubbed with the dust-free cloth. The active thin films under investigation were then spin-coated onto the rubbed PEDOT:PSS for surface alignment. In (1) and (2), the active layer to be aligned could be a neat film of the Pt (II) complex N200 or a F(MB)5:N200 host–guest film. To induce mesophase mediated molecular alignment, after sample preparation, the neat N200 films and the F(MB)5:N200 mixture films were further annealed at 150 °C and 120 °C, respectively, for 1 h.

2.3. Photophysical characterization

The UV–visible absorption spectra were measured on a spectrophotometer. Photoluminescence (PL) spectra were measured on a luminescence spectrometer with a liquid-nitrogen cooled charge coupled device (CCD) coupled to a monochromator, using the 325-nm line of He-Cd laser as the excitation [31,32].

The polarized PL spectra of the aligned samples were measured with a polarizer inserted between the sample and the spectrograph. The polarizer and the rubbing/alignment orientation was set at 45° relative to the entrance-slit/grating orientation of the spectrograph, so that the

polarization dependence of the detection system (e.g. effects of slit orientation, diffraction gratings etc.) can be avoided and the intensities of PL parallel and perpendicular to the rubbing direction could be directly compared. The polarized UV–visible absorption spectra of the aligned samples were measured with a polarizer inserted between the lamp source and the sample.

2.4. Device fabrication and characterization

The OLED device on the glass substrates was composed of multiple organic layers sandwiched between the transparent bottom indium-tin-oxide (ITO) anode and the top aluminum (Al) cathode. In general, the layer structure of the polarized OLED in sequence consisted of: ITO/rubbed PEDOT:PSS (30 nm)/F(MB)5:25 wt.% N200 (55 nm)/TPBi (45 nm)/LiF (0. 5 nm)/Al (150 nm). The ITO-coated glass substrate was cleaned by sequential ultrasonication in detergents and in organic solvents, followed by UV ozone treatments. The uniaxially rubbed PEDOT:PSS (30 nm) was used as the hole injection layer (HIL) and also as the alignment layer [7–10]. F(MB)5:25 wt.% N200 was spin-coated on top of the rubbed PEDOT:PSS layer as the emitting layer (EML). Before deposition of subsequent functional layers, the film of F(MB)5:25 wt.% N200 was annealed at 120 °C for 1 h. Then, 1,3,5-tri(phenyl-2-benzimidazoly)-benzene (TPBi) [33–35], thin lithium fluoride (LiF) (0.5 nm) [36], and Al were deposited as the electron transport layer (ETL), the electron injection layer (EIL), and the cathode, respectively. TPBi, LiF, and Al were deposited by thermal evaporation in a vacuum chamber with a base pressure of $<10^{-6}$ torr. The evaporation system permitted the fabrication of the complete device structure in a single pump-down without breaking vacuum.

The current–voltage-brightness (I–V-L) characterization of the light-emitting devices was performed with a source-measurement unit and a Si photodiode calibrated with the Photo Research PR650 spectroradiometer. The electroluminescence (EL) spectra of devices were collected by a CCD spectrograph. For polarized EL spectra, the measurement was conducted in a way same as the polarized PL measurements.

3. Results and discussions

3.1. Photophysical properties

Fig. 2 shows the absorption and PL spectra of N200 in the dilute CH_2Cl_2 solution (5×10^{-6} M) at 298 K, the absorption and PL spectra of the spin-coated N200 neat film at 298 K, and the PL spectra of the N200 neat film at 77 K.

Based on photophysical properties of previously reported Pt(II) complexes possessing cyclometalating chelates and previous quantum chemical calculations [37–43], the absorption spectrum of N200 in solution can be ascribed to several domains in terms of the absorption wavelength and intensity. The intense absorption bands in the higher-energy region (<300 nm) mainly originate from the ligand-centered transitions, as supported by the similar

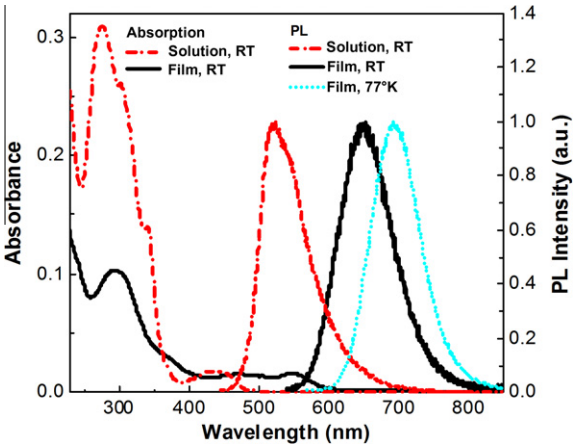

Fig. 2. Absorption and emission spectra of N200 in CH_2Cl_2 solution and in thin films.

transition documented for the free anionic ligands [44,45]. The much weaker lower-energy absorption bands around 380–480 nm can be assigned to the metal-to-ligand charge transfer band (MLCT) [46,47]. In the CH_2Cl_2 solution at 298 K, the Pt(II) complex N200 shows intense green luminescence with a peak wavelength of about 520 nm. The 520-nm phosphorescence band appears to be a mirror image of the lowest absorption band, suggesting it be monomeric MLCT emission from the molecules in the dilute solution.

In sharp contrast with absorption and PL spectra of N200 in the dilute solution, the absorption of the N200 neat film extends to a much longer wavelength of ~600 nm (and shows a lowest-energy peak around 550 nm), together with a significant red shift of the room-temperature PL to red emission peaking around 650 nm. Spectral properties of the spin-cast films suggest N200 molecules exhibit strong ground-state intermolecular interactions (instead of simply excited-state interaction, like excimers) and they tend to self-assemble to form aggregates in films. Previous luminescence characterization of bulk samples of these Pt(II) complexes revealed that they exhibited red emission only in the columnar mesophase, while monomer-like green emission was observed in the isotropic liquid state or in the crystalline state (in which N200 molecules are packed in an antiparallel format) [26]. Thus the appearance of red emission in N200 samples appears to be a good indication of columnar-mesophase-like molecular packing. Due to the columnar mesomorphic nature of N200 and the resemblance of photophysical properties in spin-cast films to those of bulk samples in the liquid crystal phase [26], presumably the square-planar N200 molecules also pack into a one-dimensional columnar stacking arrangement in spin-cast films. The extension of the absorption to longer wavelengths (lower energies) and red emission in neat films can then be reasonably assigned to metal–metal-to-ligand charge transfer (MMLCT) transitions that are associated with the intermolecular interaction between the Pt(II) metal cores [46,47]. As such, the further red shift in PL of N200 films at the lowered temperature (77 K, Fig. 2) can

be attributed to metal–metal bond shortening and thus enhanced intermolecular interaction at lowered temperatures [48–50]. Such temperature dependence of luminescent properties is very different from (i.e. opposite to) that originating from excited-state interaction (e.g. excimers), but is a typical behavior for the metal–metal-stacked compounds and further supports such supramolecular packing and interaction mechanisms [48–50].

Fig. 3 shows the PL spectra of the spin-cast F(MB)5:N200 mixture films with different N200 weight ratios, compared to that of a neat N200 film. It is seen that for the N200 concentrations shown, the emission is more or less comprised of a deep blue emission and a red emission, with the relative intensities depending on the N200 ratios. The deep blue emission can be unambiguously assigned to contribution from F(MB)5 [8,9], while the red emission resembles N200 MMLCT emission in the neat N200 film. It suggests in the spin-cast F(MB)5:N200 mixture films, N200 molecules also aggregate and self-assemble into the column-like stacking arrangement during the casting process, thereby exhibiting MMLCT emission of the Pt(II) complex. The PL spectra also indicate excited-state energy transfer from F(MB)5 to aggregates of N200. The energy transfer increases with the N200 ratios and the aggregate MMLCT emission becomes dominant when the N200 ratio is >20 wt.%.

3.2. Molecular alignment and polarized transitions

With an aim to construct polarized phosphorescent OLED using the mesomorphic N200 complex, we first tried the use of the rubbed PEDOT:PSS film to align the neat N200 film spin-cast onto it, since PEDOT:PSS was to be used as the conductive alignment layer in the polarized OLED. Fig. 4 shows the PL spectra of the annealed N200 film on the rubbed PEDOT:PSS, measured with the polarization parallel with the rubbing direction ($PL_{//}$) and with the polarization perpendicular to the rubbing direction ($PL_{\perp}$). Both show the characteristic MMLCT red emission of N200. $PL_{//}$ and $PL_{\perp}$ spectra are basically of the same

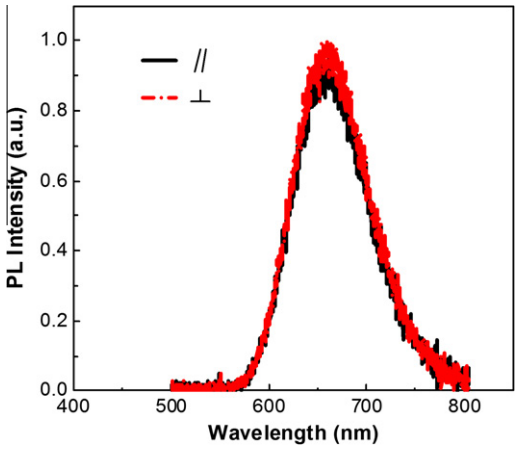

Fig. 4. PL spectra of the annealed N200 film on the uniaxially rubbed PEDOT:PSS layer, measured with the polarization parallel with (//) and perpendicular to (⊥) the rubbing direction.

intensity, indicating that N200 cannot be effectively aligned using the rubbed PEDOT:PSS layer beneath.

We then further studied alignment of the N200 neat films via directly rubbing the surface of the cast N200 film, followed by annealing. Fig. 5 shows the PL and absorption spectra of the uniaxially rubbed N200 film, measured with the polarization parallel with (//) and perpendicular to (⊥) the rubbing direction. With this alignment scheme, now both PL and absorption show distinctive polarization dependence (i.e. polarized transitions), indicating alignment of N200 molecules. In PL, $PL_{\perp}$ shows a larger intensity than $PL_{//}$ and the PL dichroic ratio $PL_{\perp}/PL_{//}$ is about 3. The dichroic phenomena in absorption are more complicated and depend on the wavelength ranges. For the higher-energy ligand-centered transition region (e.g. ~300 nm), the absorption along the rubbing direction is stronger than that perpendicular to the rubbing direction. For the low-energy MMLCT transition region (e.g. 520–600 nm), however, the situation is reversed; the absorption along the rubbing direction is

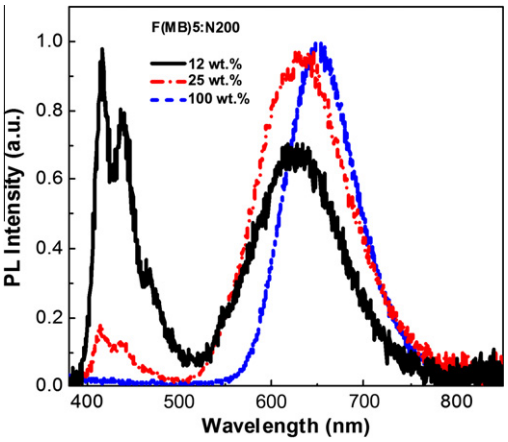

Fig. 3. PL spectra of the F(MB)5:N200 mixture films with different N200 weight ratios.

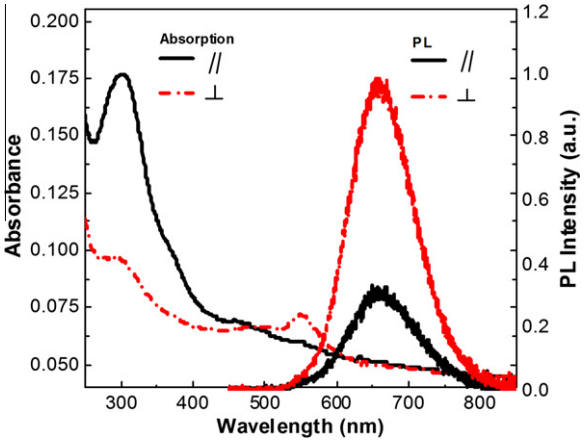

Fig. 5. PL and absorption spectra of the uniaxially rubbed N200 neat film, measured with the polarization parallel with (//) and perpendicular to (⊥) the rubbing direction.

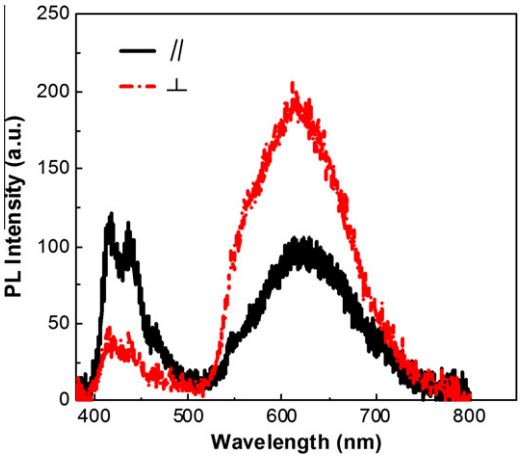

Fig. 6. PL spectra of the annealed F(MB)5:N200 (25 wt.%) mixture film coated onto the rubbed PEDOT:PSS layer, measured with the polarization parallel with (//) and perpendicular to (⊥) the rubbing direction.

weaker than that perpendicular to the rubbing direction. From the polarized absorption in the higher-energy ligand-centered transition region in Fig. 5, one concludes that the pyridyl azolate ligands with alkyloxyphenyl groups are roughly aligned with the rubbing direction. From the consistency of polarized absorption in the low-energy MMLCT transition region and polarized PL (Fig. 5), one can conclude that the axis of the columnar stack of N200 molecules in aggregates is more or less perpendicular to the rubbing direction, since the MMLCT transition is typically along the chain of the metal cores [51–53].

Although polarized emission of N200 was successfully achieved by directly rubbing the N200 neat film, yet the attempt to construct polarized OLEDs using the directly rubbed N200 neat film failed, due to the roughness and damages caused by the mechanic rubbing mechanism. Thus, we next investigated the alignment of the F(MB)5:N200 mixture films. It had been reported that mesomorphic oligofluorenes similar to F(MB)5 can be effectively aligned with a rubbed PEDOT:PSS at elevated temperatures [8–9]. Thus it was hoped that F(MB)5 in F(MB)5:N200 mixture films can also be aligned by the rubbed PEDOT:PSS layer coated beneath and at the same time guide (align) the orientation of N200 molecules in the F(MB)5 host. Fig. 6 shows the PL spectra of the annealed F(MB)5:N200 (25 wt.%) mixture film coated onto the rubbed PEDOT:PSS layer, measured with the polarization parallel with (//) and perpendicular to (⊥) the rubbing direction. Both deep blue emission of F(MB)5 and MMLCT red emission of N200 show polarization dependence (i.e. polarized emission), indicating both F(MB)5 and N200 could be aligned by this configuration. For the F(MB)5 emission, the emission along the rubbing direction is stronger than that perpendicular to the rubbing direction. For N200 MMLCT emission, however, the situation is reversed; the emission along the rubbing direction is weaker than that perpendicular to the rubbing direction, with a PL dichroic ratio $PL_{\perp}/PL_{//}$ of about 2.

For the F(MB)5:N200 mixture film, from the polarized F(MB)5 emission and the polarized N200 MMLCT emission in Fig. 6, it is induced that the oligofluorene backbone are roughly aligned with the rubbing direction and that the axis of the columnar stack of N200 molecules in aggregates is more or less perpendicular to the rubbing direction, similar to the case in Fig. 5. With overall considerations of the mesomorphic characteristics, photophysical characteristics, and polarized transitions of these materials in various states and compositions, a proposed schematic representation of the morphologies and molecular alignments in the aligned F(MB)5:N200 mixture (host–guest) film is shown Fig. 7. Although more advanced characterizations may be needed to further elucidate details of the morphologies (e.g. dimensions and packing parameters of the N200 aggregates in the mixture etc.), it is worthy of mentioning that this

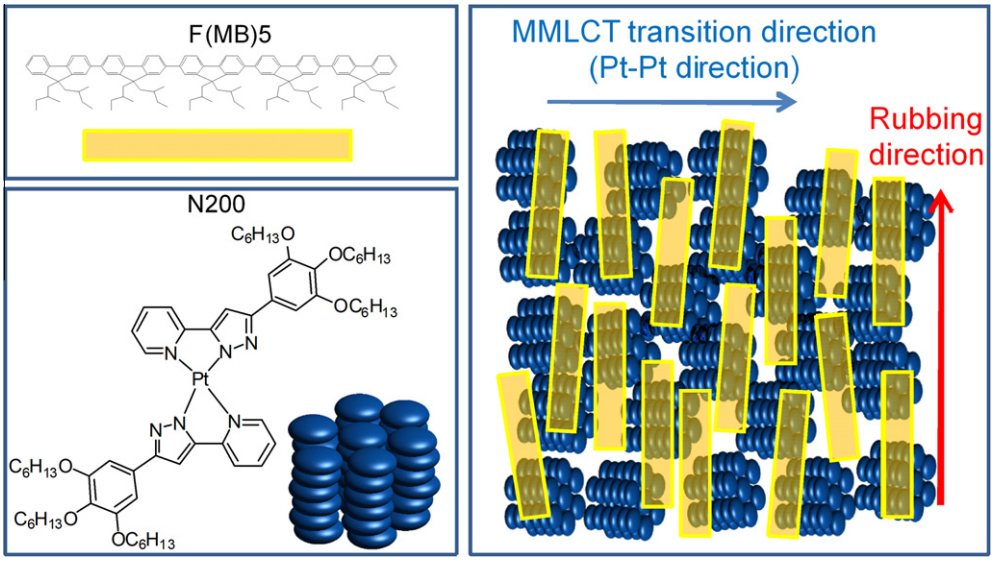

Fig. 7. The schematic representation of the morphologies and molecular alignments in the aligned F(MB)5:N200 mixture (host–guest) film.

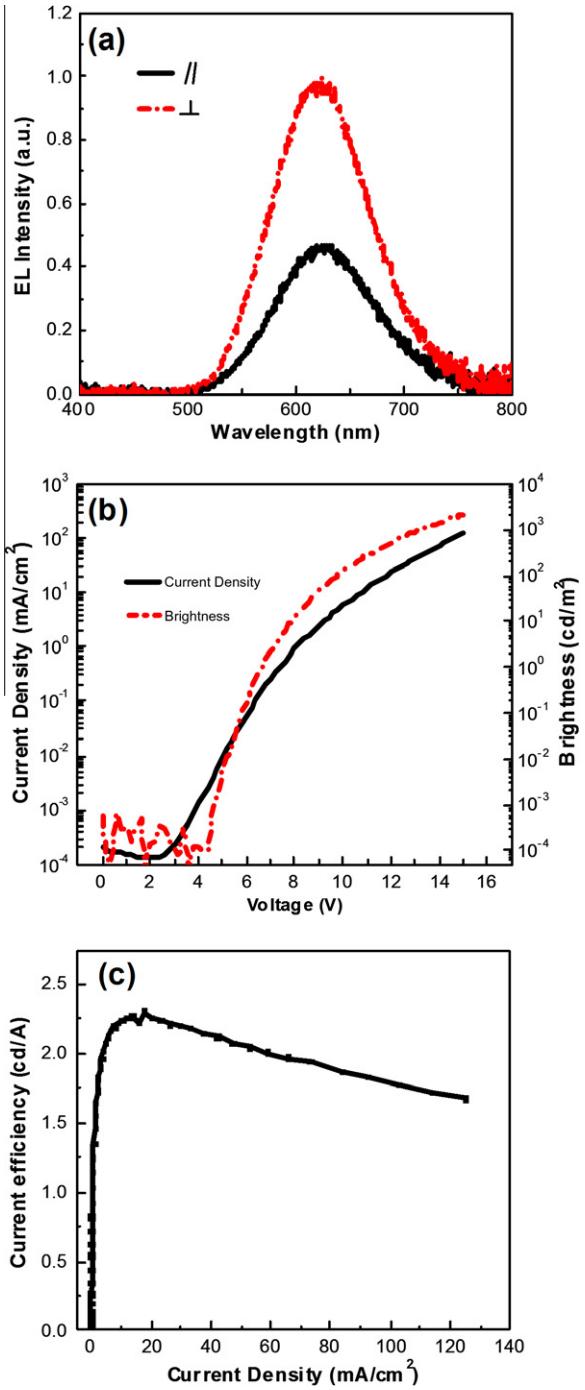

Fig. 8. EL characteristics of the polarized OLEDs: (a) EL spectra measured with the polarization parallel with (//) and perpendicular to (⊥) the rubbing direction; (b) I–V-L characteristics; (c) cd/A efficiency.

proposed picture is rather consistent with all the physical and photophysical characterizations conducted.

3.3. Characteristics of polarized OLEDs

Fig. 8(a) shows the EL spectra of the polarized OLED: ITO/rubbed PEDOT:PSS (30 nm)/F(MB)5:25 wt.% N200 (55 nm)/TPBi (45 nm)/LiF (0. 5 nm)/Al (150 nm), measured with the polarization parallel with ($EL_{//}$) and perpendicular to ($EL_{\perp}$) the rubbing direction. Different from the PL of the F(MB)5: N200 mixture film in Fig. 3 and Fig. 6 [that show emission from both F(MB)5 and N200], EL of the device shows purely N200 MMLCT emission, indicating carrier trapping and direct recombination of holes and electrons on N200 guest molecules (in addition to energy transfer) play important roles in EL [54]. Similar to N200 MMLCT emission in PL of the aligned mixture film (Fig. 6), EL perpendicular to the rubbing direction ($EL_{\perp}$) is stronger than that along the rubbing direction ($EL_{//}$), with an EL dichroic ratio $EL_{\perp}/EL_{//}$ of about 2. For comparison, a control OLED with the same layer structure but no rubbing on PEDOT:PSS (thus no alignment) shows no polarization dependence in EL. It is interesting to note the EL polarization of the present polarized OLED (roughly perpendicular to the rubbing direction) is very different from that of many previously reported polarized (fluorescent) OLEDs (i.e., parallel with the rubbing direction) [5–11], mainly due to the unique emission mechanisms in the present polarized OLED.

Fig. 8b and c show the I–V-L and the efficiency characteristics of the polarized OLED. The red-emitting polarized OLED exhibits a turn-on voltage of 3–4 V, a maximum brightness exceeding 2000 cd/m^2, and a maximum cd/A efficiency of 2.4 cd/A. The EL efficiency achieved for the polarized OLED may not be impressive compared to the state-of-art phosphorescent OLEDs nowadays, but it is worthy of mentioning that this work represents an initial attempt to realize workable polarized phosphorescent OLEDs.

4. Conclusions

In summary, we have successfully realized workable polarized phosphorescent OLEDs by combining a recently developed mesogenic phosphorescent metal (Pt(II)) complex and a mesogenic oligofluorene host to form the corresponding mesogenic host–guest emitting system. In the host–guest film, the mesogenic Pt(II) complex tends to aggregate and self-assemble into the columnar stacking arrangement, exhibiting MMLCT emission of the Pt(II) complex. Both the host molecules and guest aggregates in the host–guest films were successfully aligned by using the rubbed conducting polymer PEDOT:PSS as the alignment layer. With such aligned host–guest films, polarized red-emitting OLEDs were successfully implemented, showing an EL polarization ratio of ~2, a maximal brightness exceeding 2000 cd/m^2, and a cd/A efficiency up to 2.4 cd/A. Due to the particular alignment mechanism of guest aggregates and the unique MMLCT emission mechanism, the polarized OLED exhibiting stronger EL perpendicular to the rubbing direction than along the rubbing direction.

Acknowledgements

The authors gratefully acknowledge the financial support from National Science Council of Taiwan under the grant NSC 98-2120-M-002-005.

References

[1] J.Y. Son, B. Javidi, IEEE J. Dispaly Technol. 1 (2005) 125.
[2] S. Jung, J.H. Park, H. Choi, B. Lee, Appl. Opt. 42 (2003) 2513.
[3] R.H. Friend, R.W. Gymer, A.B. Holmes, J.H. Burroughes, R.N. Marks, C. Taliani, C. Taliani, D.D.C. Bradley, D.A. Dos Santos, D.A. Dos Santos, J.L. Brédas, M. Lögdlun, W.R. Salaneck, Nature 397 (1999) 121.
[4] M. Grell, D.D.C. Bradley, M. Inbasekaran, E.P. Woo, Adv. Mater. 9 (1997) 798.
[5] M.C. Quiles, P.G. Etchegoin, D.D.C. Bradley, Phys. Rev. B. 72 (2005) 045209.
[6] M. Grell, D.D.C. Bradley, Adv. Mater. 11 (1999) 895.
[7] Y. Geng, A.C.A. Chen, J.J. Ou, S.H. Chen, K. Klubek, K.M. Vaeth, C.W. Tang, Chem. Mater. 15 (2003) 4352.
[8] Y. Geng, S.W. Culligan, A. Trajkovska, J.U. Wallace, S.H. Chen, Chem. Mater. 15 (2003) 542.
[9] S.W. Culligan, Y. Geng, S.H. Chen, K. Klubek, K.M. Vaeth, C.W. Tang, Adv. Mater. 15 (2003) 1176.
[10] A.C.A. Chen, S.W. Culligan, Y. Geng, S.H. Chen, K.P. Klubek, K.M. Vaeth, C.W. Tang, Adv. Mater. 16 (2004) 783.
[11] M. Jandke, D. Hanft, P. Strohriegl, K. whitehead, M. Grell, D.D.C Bradley, Proc. SPIE 4105 (2001) 338.
[12] A. Bolognesi, F. Bertini, G. Bajo, A. Provasoli, D. Villa, O. Ahumada, Thin Solid Films 289 (1996) 129.
[13] V. Cimrova, M. Remmers, D. Neher, G. Wegner, Adv. Mater. 8 (1996) 146.
[14] A. Bolognesi, G. Bajo, J. Paloheimo, T. Östergård, H. Stubb, Adv. Mater. 9 (1997) 121.
[15] M. Hamaguchi, K. Yoshino, Polym. Adv. Technol. 8 (1997) 399.
[16] M. Jandke, P. Strohriegl, J. Gmeriner, W. Brütting, M. Schwoerer, Adv. Mater. 11 (1999) 1518.
[17] P. Dyreklev, M. Berggren, O. Inganäs, M.R. Andersson, O. Wennerström, T. Hjertberg, Adv. Mater. 7 (1995) 43.
[18] M. Grell, W. Knoll, D. Lupo, A. Meisel, T. Miteva, D. Neher, H.G. Nothofer, U. Scherf, A. Yasuda, Adv. Mater. 11 (1999) 671.
[19] T. Yasuda, H. Ooi, J. Morita, Y. Akama, K. Minoura, M. Funahashi, T. Shimomura, T. Kato, Adv. Funct. Mater. 19 (2009) 411.
[20] M.A. Baldo, D.F. O'Brien, Y. You, A. Shoustikov, S. Sibley, M.E. Thompson, S.R. Forrest, Nature 395 (1998) 151.
[21] S. Reineke, F. Lindner, G. Schwartz, N. Seidler, K. Walzer, B. Lüssem, K. Leo, Nature 459 (2009) 234.
[22] C. Adachi, M.A. Baldo, M.E. Thompson, S.R. Forrest, J. Appl. Phys. 90 (2001) 5048.
[23] Y. Kawamura, K. Goushi, J. Brooks, J.J. Brown, H. Sasabe, C. Adachi, Appl. Phys. Lett. 86 (2005) 071104.
[24] J. Kavitha, S.Y. Chang, Y. Chi, J.K. Yu, Y.H. Hu, P.T. Chou, S.M. Peng, G.H. Lee, Y.T. Tao, C.H. Chien, A.J. Carty, Adv. Funct. Mater. 15 (2005) 223.
[25] S.Y. Chang, J. Kavitha, S.W. Li, C.S. Hsu, Y. Chi, Y.S. Yeh, P.T. Chou, G.H. Lee, A.J. Carty, Y.T. Tao, C.H. Chien, Inorg. Chem. 45 (2006) 137.
[26] C.T. Liao, H.H. Chen, H.F. Hsu, A. Poloek, H.H. Yeh, Y. Chi, K.W. Wang, C.H. Lai, G.H. Lee, C.W. Shih, P.T. Chou, Chem. Eur. J. (2010). DOI: 10.1002/chem.201000994.
[27] M.H. Qi, G.F. Liu, J. Phys. Chem. B 107 (2003) 7640.
[28] E. Terazzi, S. Suarez, S. Torelli, H. Nozary, D. Imbert, O. Mamula, J.P. Rivera, E. Guillet, J.M. Benech, G. Bernardinelli, R. Scopelliti, B. Donnio, D. Guillon, J.C.G. Bunzli, C. Piguet, Adv. Funct. Mater. 16 (2006) 157.
[29] K. Binnemans, J. Mater. Chem. 19 (2009) 448.
[30] V.N. Kozhevnikov, B. Donnio, D.W. Bruce, Angew. Chem., Int. Ed. 47 (2008) 6286.
[31] J.C. de Mello, H.F. Wittmann, R.H. Friend, Adv. Mater. 9 (1997) 230.
[32] C.C. Wu, W.Y. Hung, T.L. Liu, L.Z. Zhang, T.Y. Luh, J. Appl. Phys. 93 (2003) 6465.
[33] P. Kundu, K.R.J. Thomas, J.T. Lin, Y.T. Tao, C.H. Chien, Adv. Funct. Mater. 13 (2003) 445.
[34] C.C. Wu, Y.T. Lin, K.T. Wong, R.T. Chen, Y.Y. Chien, Adv. Mater. 16 (2004) 61.
[35] G. Schwartz, M. Pfeiffer, S. Reineke, K. Walzer, K. Leo, Adv. Mater. 19 (2007) 3672.
[36] L.S. Hung, C.W. Tang, M.G. Mason, Appl. Phys. Lett. 70 (1997) 152.
[37] A.S. Ionkin, W.J. Marshall, Y. Wang, Organometallics 24 (2005) 619.
[38] B. Yin, F. Niemeyer, J.A.G. Williams, J. Jiang, A. Boucekkine, L. Toupet, H. LeBozec, V. Guerchais, Inorg. Chem. 45 (2006) 8584.
[39] J.A.G. Williams, S. Develay, D.L. Rochester, L. Murphy, Coord. Chem. Rev. 252 (2008) 2596.
[40] S. Develay, J.A.G. Williams, Dalton Trans. (2008) 4562.
[41] S.Y. Chang, Y.M. Cheng, Y. Chi, Y.C. Lin, C.M. Jiang, G.H. Lee, P.T. Chou, Dalton Trans. (2008) 6901.
[42] B. Ma, P.I. Djurovich, M. Yousufuddin, R. Bau, M.E. Thompson, J. Phys. Chem. C 112 (2008) 8022.
[43] J. Liu, C.J. Yang, Q.Y. Cao, M. Xu, J. Wang, H.N. Peng, W.-F. Tan, X.X. Lue, X.C. Gao, Inorg. Chim. Acta. 362 (2009) 575.
[44] P.C. Wu, J.K. Yu, Y.H. Song, Y. Chi, P.T. Chou, S.M. Peng, G.H. Lee, Organometallics 22 (2003) 4938.
[45] P.T. Chou, Y. Chi, Chem. Eur. J. 13 (2007) 380.
[46] S.W. Lai, M.C.W. Chan, T.C. Cheung, S.H. Peng, C.M. Che, Inorg. Chem. 38 (1999) 4046.
[47] S.W. Lai, C.M. Che, Top. Curr. Chem. 241 (2004) 41.
[48] G. Gliemann, H. Yersin, Struct. Bonding 62 (1985) 87.
[49] H. Isci, W.R. Mason, Inorg. Chem. 14 (1975) 905.
[50] H.Q. Liu, T.C. Cheung, C.M. Che, Chem. Commun. 9 (1996) 1039.
[51] Y. Sun, K. Ye, H. Zhang, J. Zhang, L. Zhao, B. Li, G. Yang, B. Yang, Y. Wang, S.W. Lai, C.M. Che, Angew. Chem. 118 (2006) 5738.
[52] B.H. Xia, C.M. Che, D.L. Phillips, K.H. Leung, K.K. Cheung, Inorg. Chem. 41 (2002) 3866.
[53] M.Y. Yuen, V.A.L. Roy, W. Lu, S.C.F. Kui, G.S.M. Tong, M.H. So, S.S.Y. Chui, M. Muccini, J.Q. Ning, S.J. Xu, C.M. Che, Angew. Chem., Int. Ed. 47 (2008) 9895.
[54] M. Uchida, C. Adachi, T. Koyama, Y. Taniguchi, J. Appl. Phys. 86 (1999) 1680.

Organic Electronics 12 (2011) 22–28

Contents lists available at ScienceDirect

Organic Electronics

journal homepage: www.elsevier.com/locate/orgel

Nanocomposites of single-walled carbon nanotubes and poly(3,4-ethylenedioxythiophene) for transparent and conductive film

Tran Thanh Tung, Tae Young Kim *, Kwang S. Suh *

Department of Materials Science and Engineering, Korea University, 5-1, Anam-dong, Seongbuk-gu, Seoul 136-713, Republic of Korea

ARTICLE INFO

Article history:
Received 4 September 2010
Received in revised form 14 October 2010
Accepted 17 October 2010
Available online 30 October 2010

Keywords:
Carbon nanotubes
Poly(3,4-ethylenedioxythiophene)
Poly(ionic liquid)
Hybrids
Transparent conductive film

ABSTRACT

We report a conductive hybrid material composed of single-walled carbon nanotubes (SWCNTs) and poly(3,4-ethylenedioxythiophene) (PEDOT). The hybridization of SWCNT and PEDOT was achieved by the use of poly(ionic liquid) (PIL), specifically poly(1-vinyl-3-ethylimidazolium) salt as the bridging molecules between the two conductive components. The use of PIL not only allows the formation of effective 3D network of SWCNT bundles in the PEDOT matrix, but also enables the resulting SWCNT-PIL:PEDOT hybrid material to be suspended selectively in water or organic solvents. Thin films of SWCNT-PIL:PEDOT were more conductive as compared to the PEDOT-based films, demonstrating the surface resistivity of 6.2×10^4 Ω/sq and optical transparency of 85.5% at a 0.2 wt.% SWCNT loading. The composites were also found to be thermally stable, showing less change in surface resistivity as compared to PEDOT-based films.

Crown Copyright © 2010 Published by Elsevier B.V. All rights reserved.

1. Introduction

Electrically conducting nanocomposites with interconnected 3D network of carbon nanotubes (CNTs) in polymer matrix have attracted widespread scientific and technological interests as robust and highly conductive material [1–4]. The macroscopic electrical conductivity of a CNT-based composite material is strongly dependent on the CNT loading in the polymer matrix, which is described by the percolation threshold [5–8]. Sufficient high loadings of CNTs are generally required to form electrical pathways within composites and thus enable percolation. In order to use CNTs efficiently as conductive fillers and achieve lowest percolation threshold, there are several considerations to be addressed. For example, CNTs are held together in bundles by strong van der Waals interactions and thus difficult to disperse individually in polymer matrix unless dispersing agents (i.e. electrically insulating surfactant molecules) are incorporated [9–11]. The tendency of CNTs to agglomerate in the composites results in diminished electrical properties as compared to theoretical predictions yielded of individual CNTs. In addition, the presence of electrically insulating tube-to-tube junctions compromise overall conductivity of the composites, and this often generates limitations in most proposed applications [12,13]. Therefore, in the specific case of CNT-based composites, the major challenge is to achieve high conductivity at low percolation by dispersing individual CNTs into polymer matrix with reduced junction resistance across the tubes.

For this purpose, the use of intrinsically conducting polymers as the polymer matrix for CNTs has been explored in the hopes of improving the electrical properties. For example, the enhancement of electrical properties has been shown to be more pronounced for CNT-based composites when conducting polymer was utilized as matrix polymer [14–17]. However, a simple mixture of CNTs and conducting polymers may be segregated into individual components due to limited miscibility, which prevents the fine dispersion of CNTs in conducting polymer matrix. Considerable efforts have been made to efficiently disperse individual CNTs in a conducting polymer matrix. One can modify

* Corresponding authors. Tel.: +82 29274546; fax: +82 29294408.
E-mail address: thomas75@korea.ac.kr (T.Y. Kim).

1566-1199/$ - see front matter Crown Copyright © 2010 Published by Elsevier B.V. All rights reserved.
doi:10.1016/j.orgel.2010.10.009

either the conducting polymer to enhance interaction with the π-system of CNT walls or modify the CNT surface via functionalization [18–22]. It is also possible to use a third component to assist the effective coupling of CNTs and conducting polymers, and thus achieve effective 3D network of individual CNTs within the conducting polymers by improving miscibility between the two. For example, poly(3,4-ethylenedioxythiophene):poly(styrenesulfonate) (PEDOT:PSS) has been combined with CNTs to produce composites with conductivities of up to $\sim 7.0 \times 10^4$ S/m. However, it is basically processed from aqueous phase since this method is based on the use of water soluble PSS [23,24].

Here, we have employed poly(ionic liquid) (PIL), a polymer from ionic liquid (IL) monomer, to combine single-walled carbon nanotubes (SWCNTs) with PEDOT. In addition to an effective association of SWCNTs and PEDOT, the use of PIL allows the resulting SWCNT–PEDOT composites to be processed in both aqueous and organic solvents. Recently, PIL, specifically of poly(1-vinyl-3-ethylimidazolium) salt has been proposed as a functional molecule to hybridize SWCNT with PEDOT. The hybrid material (here referred to as SWCNT-PIL:PEDOT) could be an attractive alternative for practical applications using CNT-based composites, since their selective suspension in water or organic solvent is expected to be achievable by a simple chemistry such as anion exchange of PIL [25]. In an extension of our previous work, we report here our progress toward tuning the electrical properties of SWCNT-PIL:PEDOT composites. By modifying the synthetic procedure of the SWCNT-PIL:-PEDOT hybrid composites, we show that these composite films could be more conductive than the ones that are not hybridized. Finally we show that these materials are thermally stable, displaying much lower change in surface resistivity at high temperature, as compared to PIL-modified PEDOT film.

2. Experimental

2.1. Materials

SWCNTs were purchased from Carbon Solutions Inc. under the trade name P3-SWCNT. (1-vinyl-3-ethylimidazolium bromide) (ViEtIm$^+$Br$^-$) was synthesized according to literature method [26]. EDOT monomer was provided from H.C. Starck. All other reagents and solvents were purchased from Aldrich and used as received.

2.2. Synthesis of SWCNT-PIL:PEDOT hybrid materials

Modification of SWCNTs with PIL was carried out according to previous literature [27]. Briefly, the P3-SWCNTs were further oxidized in HNO_3–H_2SO_4 (3:1, v:v) mixture for 3 h at 80 °C. After cooling to room temperature, it was washed with DI water and dried under vacuum at room temperature for 24 h. Acid-treated SWCNTs (30 mg) were suspended in water (80 ml), with polymerizable IL monomer, i.e. (1-vinyl-3-ethylimidazolium) bromide (ViEtIm$^+$Br$^-$) (3.0 g) in ethanol (30 ml). Polymerization of IL was carried out by adding a solution of azobis(2-methylpropionitrile) (AIBN) (30 mg of AIBN in 10 mL ethanol) dropwise to the suspension and stirring at 70 °C for 10 h under N_2 atmosphere. To terminate the reaction, an excess amount of acetone was poured into the suspension, which causes the gel formation of PIL-modified SWCNT (SWCNT-PIL) at the bottom of the flask. The SWCNT-PIL in a gelatinous form was then obtained by filtration through a polycarbonate (PC) membrane and re-suspended in water.

In a typical experiment, the hybrid materials of SWCNT and PEDOT were prepared by adding EDOT monomer (0.2 g) into the aqueous suspension of SWCNT-PIL (0.25 g in 80 ml H_2O) with a dropping of an aqueous solution of APS (0.3 g in 20 ml H_2O). The mixture was then vigorously stirred for 48 h at room temperature, which resulted in an aqueous suspension of SWCNT-PIL:PEDOT hybrid material (hydrophilic SWCNT-PIL:PEDOT). An aqueous suspension of the hydrophilic SWCNT-PIL:PEDOT was then subjected to a phase transfer process in which an aqueous solution of lithium bis(trifloromethanesulfonyl)amide ($Li^+NTf_2^-$) was added into the suspension (1.2 equiv. of NTf_2^- with respect to the repeating units of PIL cations). The addition of $Li^+NTf_2^-$ leads to an immediate replacement of hydrophilic and water soluble anions in the PILs with hydrophobic and water-immiscible NTf_2^- anion, which resulted in the precipitation of the product in water. Due to the increased hydrophobicity, as-produced SWCNT-PIL:PEDOT hybrid became readily dispersible in a range of organic solvents such as acetone, propylene carbonate (PC), dimethylformamide (DMF), acetonitrile, *N*-methyl-pyrollidone (NMP), nitromethane (NM), methyl ethyl ketone (MEK). For comparison, the PIL-modified PEDOT (without any SWCNTs) (PEDOT:PIL) sample was also prepared separately under same condition.

2.3. Characterization and instrumentation

The IR spectrum was measured using a FT-IR spectrometer (Avatar 320, Nicolet) with KBr pellets. X-ray photoelectron spectroscopy (XPS) measurements were performed with ESCA2000 (VG Microtech) system using a monochromatized aluminum Kα anode. The zeta potential was measured in aqueous solution by electrophotoretic light scattering spectrophotometry (ELS-8000, Otsuka). Thermal gravimetric analysis (TGA) was carried out on a NETZSCH STA 409 PC/PG instrument with a heating rate of 10 °C min^{-1} under nitrogen. XRD data were collected on a Rigaku D/Max Ultima II Powder X-ray diffractometer. Scanning electron microscopy (SEM) images were recorded using a JEOL JSM-6700F instrument. AFM image was obtained on a AFM XE-100 (Park system) equipped. High resolution transmission electron microscope (HR-TEM) was conducted on a TECNAI 20 microscope operated at 200 kV. The surface resistivity was obtained using a CMT series JANDEL four-point probe at room temperature.

3. Results and discussion

A suspension of SWCNT-PIL:PEDOT composites in organic solvent was obtained through a three-step procedure (Scheme 1). The first step involved the PIL modification of the acid-treated SWCNT surfaces. In this step, solution of

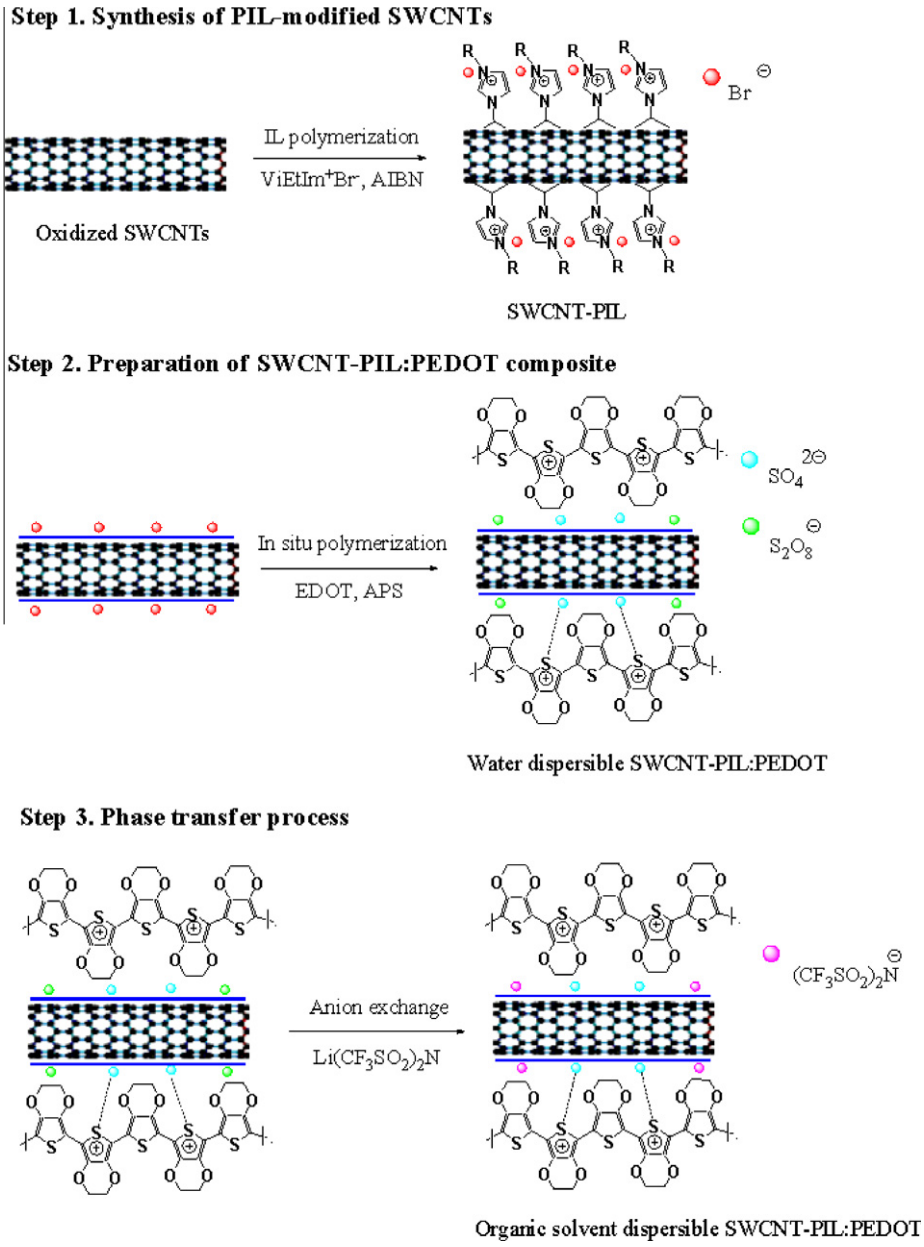

Scheme 1. Schematic illustration of synthetic process for the SWCNT-PIL:PEDOT composites.

(1-vinyl-3-ethylimidazolium) (IL) monomer in ethanol was introduced into an aqueous suspension of the acid-treated SWCNTs, followed by the in situ polymerization of IL with AIBN to form PIL-modified SWCNTs. The SWCNT-PIL in water phase was then collected as gelatinous form by pouring an excess amount of acetone into the suspension, as shown in the photo (Fig. 1(a)). In Fig. 1(b), scanning electron microscope (SEM) image showed the PIL is coated on SWCNT surfaces with an increase in the diameter of individual SWCNT, and the resulting SWCNT-PIL are interlocked with one another in the gelatinous matrix. Transmission electron microscopy (TEM) images of the SWCNT-PIL shows untangled and individualized SWCNTs embedded in PIL matrix (Fig. 1(c)) and also confirm the presence of thin PIL layer on the SWCNT surface (Fig. 1(d)). The decoration of PIL on the SWCNT surface was also evidenced by the zeta potential measurement. The value of the zeta potential from the SWCNT suspension in water was −4.04 mV due to the negatively charged carboxylic acid on the SWCNTs. In contrast, the introduction of PIL into the SWCNT suspension resulted in the reversal of zeta potential with the value of 8.77 mV. These results indicate that the negatively charged carboxylic groups on SWCNTs were covered with the positively charged polycations in PIL, which suggests a noncovalent functionalization of PILs o the graphitic structure of SWCNTs through

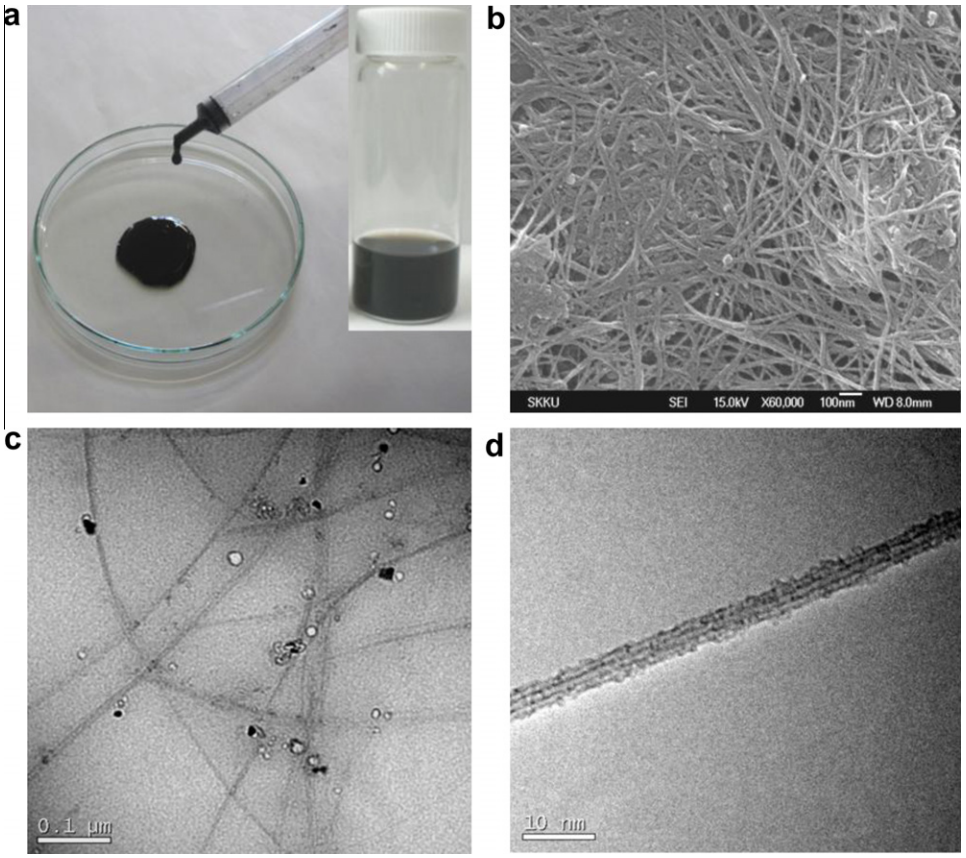

Fig. 1. (a) Photograph of PIL-modified SWCNTs (SWCNT-PIL) in a gelatinous form and its aqueous solution (inset photo). (b) The SEM image and (c and d) TEM images of SWCNT-PIL.

possible interactions may include the $\pi-\pi$ interactions or an electrostatic interaction between SWCNT and PILs [22,28]. The conductivity value of this SWCNT-PIL sample was measured as 0.68 S/cm.

In the second step, gelatinous SWCNT-PIL was re-dispersed in water via mild sonication, and EDOT monomer was added with ammonium persulfate (APS), an oxidizing agent. It is noteworthy that the addition of APS into the SWCNT-PIL suspension immediately led to an exchange of anions (Br^-) in PIL with persulfate anion, which effectively initiates the polymerization of EDOT along the PIL chains on the SWCNT. Therefore, the growth of PEDOT mainly takes place in the vicinity of SWCNT by PIL-mediated polymerization, and the PIL functions to provide a linkage between PEDOT and SWCNT to form a SWCNT-PIL:PEDOT hybrid materials, as shown in Scheme 1. We also note some portion of PILs are intact by PEDOT chains and contains hydrophilic anions such as bromide and persulfate, which preserves the good dispersion of the resulting SWCNT-PIL:PEDOT in water. In the next step, a phase transfer of the SWCNT-PIL:PEDOT from water to organic solvent was carried out by substituting the hydrophilic anions ($S_2O_8^-$ and Br^-) in PIL with hydrophobic anions with details described in the experimental section. As-produced SWCNT-PIL:PEDOT hybrid materials are readily dispersed in organic solvents such as dimethylformamide (DMF), propylene carbonate (PC), and acetonitrile (AN) by mild sonication. These suspensions remained stable for more than 3 months.

A successful hybridization of PEDOT and SWCNTs with the aid of PIL was confirmed by a FT-IR, X-ray photoelectron spectroscopy (XPS) and electron microscopy. Fig. 2 shows the IR spectra of SWCNT-PIL (red curve[1]) and SWCNT-PIL:PEDOT (blue curve). For SWCNT-PIL, the IR peak at 1720 cm^{-1} corresponds to carboxylic acid group in SWCNT, while the multiple peaks at 3130, 3080, 2990, 2880, and 1550 cm^{-1} arise from cation in the PIL and the peak centered at 3430 cm^{-1} was assigned to bromide anion in the PIL [29]. In the case of SWCNT-PIL:PEDOT hybrid, the IR spectrum shows additional characteristic peaks assigned to PEDOT (C–C stretching in the thiophene ring, 1355 cm^{-1}; vibration modes of the ethylenedioxy group, 1200, 1138, 1095 and 1050 cm^{-1}; S–O stretches, 980 and 932 cm^{-1}). The chemical composition of the SWCNT-PIL:PEDOT composites was also investigated by XPS analysis. For SWCNT-PIL (Fig. 2(b)), the C 1s XPS spectrum can be deconvoluted into three main components corresponding to carbon atoms in different functional groups: the non-oxygenated ring C (285.08 eV), the C in C–N bonds (286.55 eV) and the carbonyl C (C=O, 288.20 eV). The

[1] For interpretation of color in Fig. 2, the reader is referred to the web version of this article.

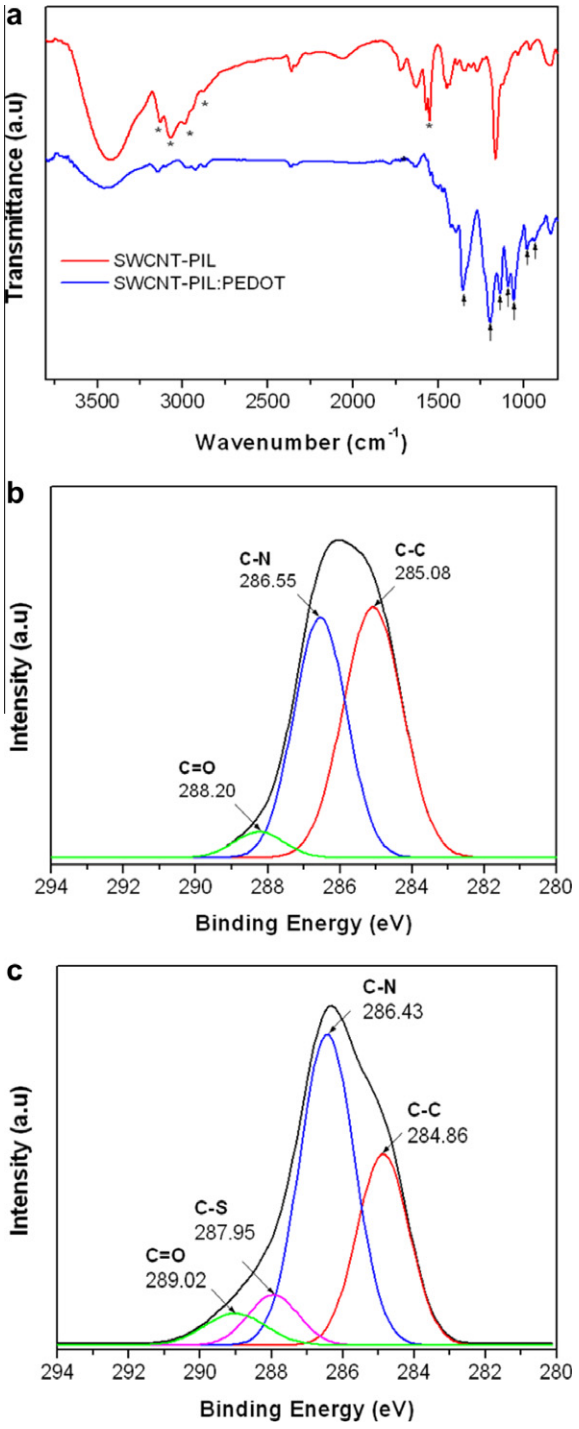

Fig. 2. (a) FT-IR spectra of SWCNT-PIL and SWCNT-PIL:PEDOT composites. (b) C 1s XPS spectra of SWCNT-PIL, and (c) C 1s XPS spectra of SWCNT-PIL:PEDOT composites (with NTf_2^- anions in PIL).

C 1s XPS spectrum of SWCNT-PIL:PEDOT composite (with NTf_2^- being anions of PIL) also exhibited the same functionalities that have been assigned for SWCNT-PIL. However, there is an additional peak at 287.95 eV assigned to the C–S bonds of PEDOT, indicating a creation of SWCNT-PIL:PEDOT hybrid material. The S 2p, O 1s, N 1s XPS spectra (Fig. S1) and XRD data (Fig. S2) in the Supporting information (SI) also support a successful hybridization of SWCNT and PEDOT with the use of PIL as interlinking functional molecules.

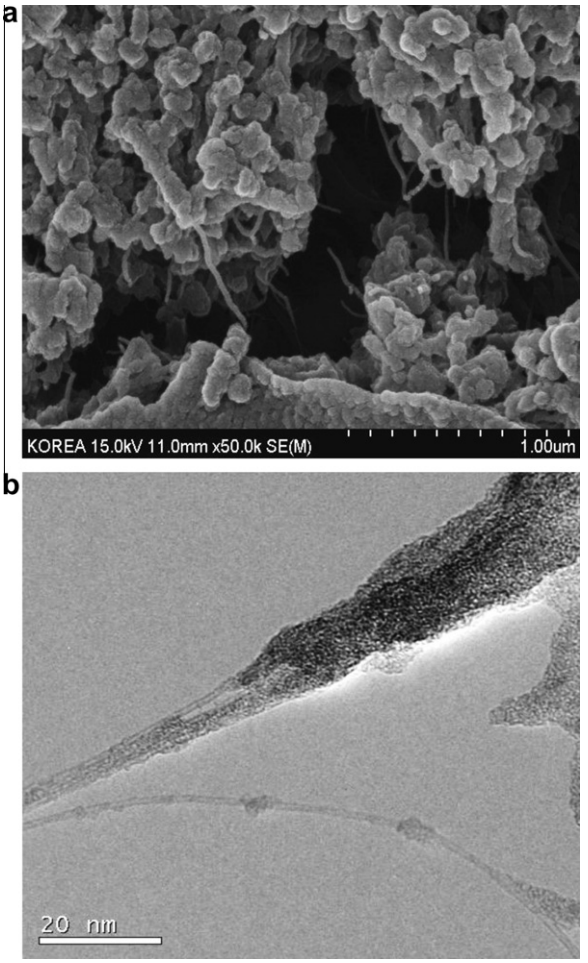

Fig. 3. (a) SEM image on the crack-section of SWCNT-PIL:PEDOT composite film. (b) TEM images of SWCNT-PIL:PEDOT composites.

Based on scanning electron microscopy (SEM) observations (Fig. 3(a)), a good homogeneity of SWCNTs was achieved in the crack-section of composites film; we could also see the SWCNTs bundles bridging the crack faces in the wake. An AFM image showed the SWCNTs randomly distributed on the small particulates of PEDOT matrix (Fig. S3). In addition, the TEM image (Fig. 3(b)) of selected parts confirms the presence of a PEDOT layer adsorbed onto the SWCNT surface, suggesting that PIL is effective to interlink SWCNTs and PEDOT for their hybridization.

The electro-conductive properties of organic solvent dispersible SWCNT-PIL:PEDOT composites were evaluated by measuring electrical conductivity of the composite film (Fig. 4). While the control PIL-modified PEDOT sample (exclusive of SWCNTs) showed a conductivity of 0.083 S/cm, SWCNT-PIL:PEDOT hybrid composite showed increasing conductivity values of up to 1.68 S/cm with increasing

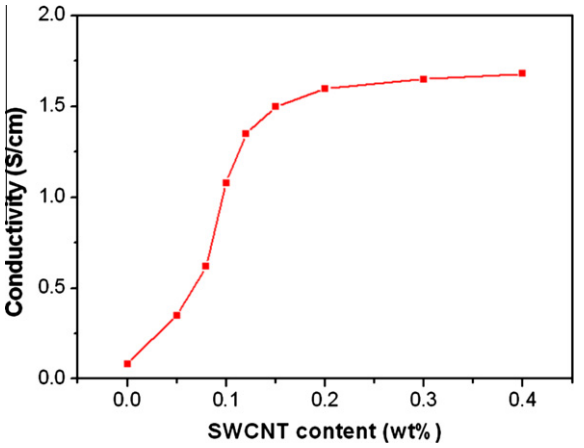

Fig. 4. The electrical conductivity of SWCNT-PIL:PEDOT composite films as a function of SWCNTs content in the composite.

SWCNT contents in the composites in the ranges up to 0.4 wt.%. As in the figure, the conductivity of the composite film increases sharply with increasing SWCNT loading level up to 0.2 wt.% (showed a conductivity of 1.62 S/cm) and then saturated with higher SWCNT concentration, which gives an estimation that a percolation threshold is in the proximity of 0.11 wt.%. This percolation threshold value is comparable to or even lower than the values previously reported in SWCNT nano-composites with PEDOT:PSS matrices [30,31]. This could be explained by means of enhanced inter-tubular charge carrier transfer due to the improved contact between the SWCNTs. The tube-to-tube junction resistance could be reduced by a conductive PEDOT on the SWCNTs, which enhances a charge carrier hopping rate. It should be noted that the conductivity of water dispersible sample with 0.2 wt.% of SWCNTs content was 1.05 S/cm, which was little lower than those of organic solvent dispersible sample. We thought that a difference in conductivity values of the two film samples may come from several factors including solvent-induced morphological changes.

In order to evaluate the possible application of SWCNT-PIL:PEDOT composites as a transparent, flexible, and conductive film, we have fabricated thin films of SWCNT-PIL:PEDOT on polyethylene terephthalate (PET) and investigated their optical and electrical properties. A suspension of SWCNT-PIL:PEDOT (in a mixture of propylene carbonate/ethanol, inset of Fig. 5(a)) was applied on PET films using draw-down bar method and dried at 80 °C to form a homogeneous conductive composite film with a thickness of ~1 μm (Fig. 5(a)). We note that a suspension of SWCNT-PIL:PEDOT in solvent mixture of PC:EtOH (8:2 v:v) resulted

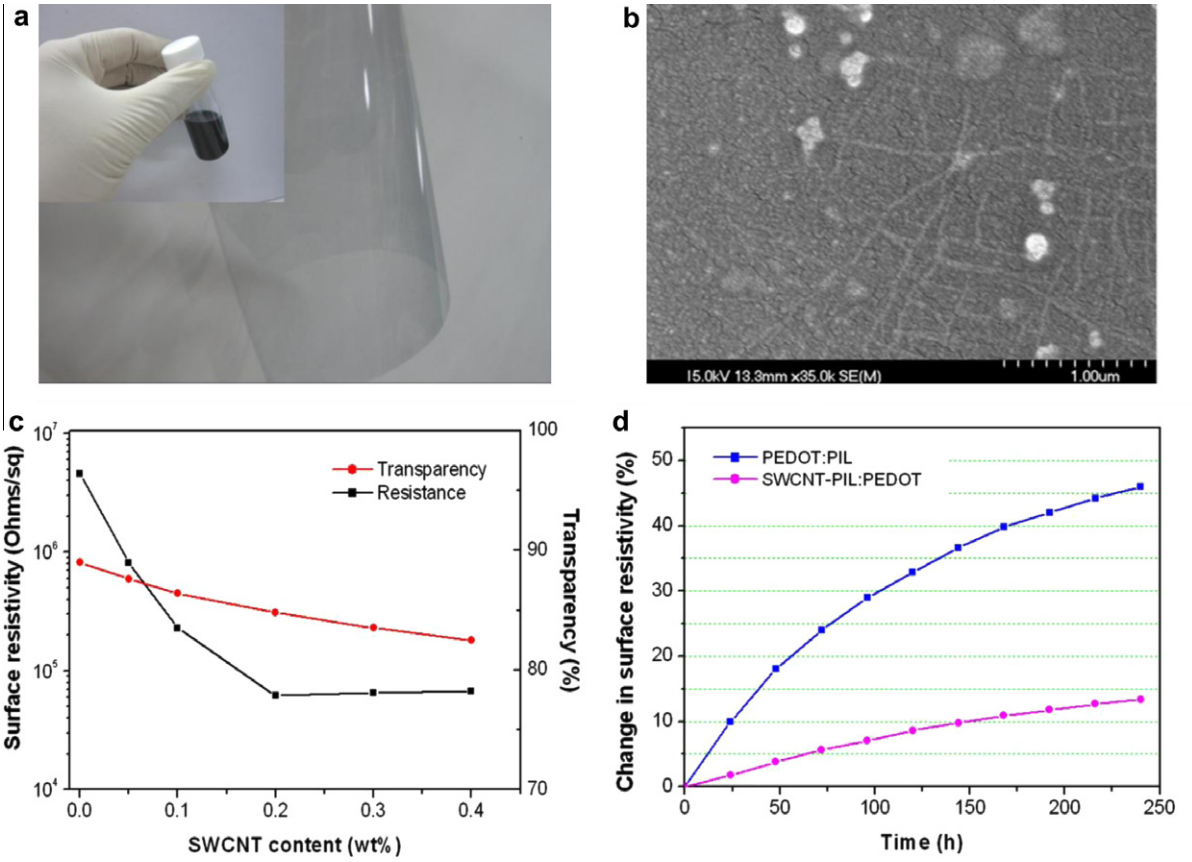

Fig. 5. (a) A hybrid composite film of SWCNT-PIL:PEDOT on the PET substrate. Inset photograph shows a suspension of SWCNT-PIL:PEDOT in organic solvent. (b) SEM image of the hybrid composite film. (c) Surface resistivity and optical transparency vs. SWCNTs concentration in the composite film. (d) Plot of a change in surface resistivity over aging time.

in the most uniform coating on PET film, while other organic solvents such as PC, DMF, THF, NMP, and MEK can be used in the suspension. Fig. 5(b) shows a SEM image of uniform coating of SWCNT-PIL:PEDOT on a PET substrate. It can be seen that the conductive nanotubes channels are formed in PEDOT matrix, which is valuable for achieving reduced overall surface resistivity and thus effective charge transport in the films. Fig. 5(c) shows the surface resistivity and optical transmission of the films as a function of SWCNT concentration in the composite films. For comparison, the control PIL-modified PEDOT film was also tested and it shows a surface resistivity of $4.6 \times 10^6\ \Omega$/sq with an optical transmittance of 87.8% (at 550 nm wavelength). On the other hand, the SWCNT-PIL:PEDOT composite film shows a decrease in the surface resistivity by an order of 2, as the SWCNT concentration in the composite increases up to 0.2 wt.%. This result indicates that the hybridization of SWCNT with PEDOT can effectively reduce the surface resistivity of the film. However, the SWCNT-PIL:PEDOT composite films also show a decrease in the transmittance from 87.8% to 82.5%, which is proportional to the weight percentage of the SWCNT in the composite. The lowest surface resistivity of $6.2 \times 10^4\ \Omega$/sq at optical transmittance of 85.5% was achieved with 0.2 wt.% SWCNT loading, and then increases slightly at loading levels in exceed of 0.2 wt.% due to increase tube-to-tube junction resistance of SWCNTs. The transparent and conductive properties of the present film are consistent with other reports involving CNT/polyethylene composites film [32], PMMA/CNT composites [33], PEDOT–PSS/SWNT composites [34], and lower than that of the SWCNTs films only [35,36]. However, the homogeneous conductive composites relatively low percolation threshold of expensive SWCNTs showed their good adhesion to the plastic substrate with large scale. This feature makes the composites practically easier in industrial approach.

These composite films were subjected to a further testing for thermal stability. Fig. 5(d) shows a change in surface resistivity of the composite films over aging time, while the films were kept at a constant temperature of 80 °C. As it can be seen, the surface resistivity of the control PEDOT film increases over time, while the SWCNT-PIL:PEDOT composite film displays much lower change in surface resistivity. This is indicative of an improved thermal stability of SWCNT-PIL:PEDOT, which is supported by thermal gravimetric analysis (TGA) data (Fig. S4). These results also suggest that the coupling of SWCNT and PEDOT could delay the thermal degradation of PEDOT chains due to a specific interaction between SWCNT and PEDOT, which needs to be in need of further investigation.

4. Conclusions

In this work, a hybrid material of SWCNT and PEDOT was prepared by poly(ionic liquid)-mediated coupling method. Poly(ionic liquid) (PIL) functions to tightly bind exfoliated SWNTs together with PEDOT with enhanced miscibility, and thus generates a uniformly interconnected 3D network of SWCNTs in a PEDOT matrix. This organic solvent dispersible SWCNT-PIL:PEDOT hybrid composites show excellent transparency, electrical conductivity, and thermal stability holds great potential for application in variety of optoelectronic devices where these properties together with room temperature fabrication technologies are required.

Acknowledgements

This work was supported by a Korea University Grant and InsCon Tech. Co. Ltd., Korea.

Appendix A. Supplementary data

Supplementary data associated with this article can be found, in the online version, at doi:10.1016/j.orgel.2010.10.009.

References

[1] R.H. Baughman, A.A. Zakhidov, W.A. de Heer, Science 297 (2002) 787.
[2] G. Cellot, E. Cillia, S. Cipollone, et al., Nat. Nanotechnol. 4 (2009) 126.
[3] M. Endo, M.S. Strano, P.M. Ajayan, Top. Appl. Phys. 111 (2008) 13.
[4] T. Sekitani, Y. Noguchi, K. Hata, et al., Science 321 (2008) 1468.
[5] E. Kymakis, G.A.J. Amaratunga, J. Appl. Phys. 99 (2006) 084302.
[6] C. Li, E.T. Thostenson, T.W. Chou, Comp. Sci. Technol. 68 (2008) 1445.
[7] J. Sandler, M.S.P. Shaffer, T. Prasse, et al., Polymer 40 (1999) 5967.
[8] A. Nogales, G. Broza, Z. Roslaniec, et al., Macromolecules 37 (2004) 7669.
[9] C. Park, Z. Ounaies, K.A. Watson, et al., Chem. Phys. Lett. 364 (2002) 303.
[10] Y.H. Hyun, S.T. Lim, H.J. Choi, et al., Macromolecules 34 (2001) 8084.
[11] A. Thess, R. Lee, P. Nikolaev, et al., Science 273 (1996) 483.
[12] N. Grossiord, J. Loos, O. Regev, et al., Chem. Mater. 18 (2006) 1089.
[13] M.T. Byrne, Y.K. Gun'ko, Adv. Mater. 22 (2010) 1672.
[14] G.B. Blanchet, C.R. Fincher, F. Gao, Appl. Phys. Lett. 82 (2003) 1290.
[15] D.W. Steuerman, A. Star, R. Narizzano, et al., J. Phys. Chem. B 106 (2002) 3124.
[16] Y. Xiao, C.M. Li, Electroanalysis 20 (2008) 648.
[17] H. Ago, K. Petritsch, M.S.P. Shaffer, et al., Adv. Mater. 11 (1999) 1281.
[18] R.J. Chen, Y. Zhang, D. Wang, H.J. Dai, J. Am. Chem. Soc. 123 (2001) 3838.
[19] A. Star, J.F. Stoddart, D. Steuerman, et al., Angew. Chem. Int. Ed. 40 (2001) 1721.
[20] V.C. Moore, M.S. Strano, E.H. Haroz, et al., Nano Lett. 3 (2003) 1379.
[21] F. Liang, A.K. Sadana, A. Peera, et al., Nano Lett. 4 (2004) 1257.
[22] J. Wang, H. Chu, Y. Li, ACS Nano 2 (2008) 2540.
[23] C. Fu, L. Meng, Q. Lu, et al., Adv. Funct. Mater. 18 (2008) 857.
[24] G.F. Wang, X.M. Tao, R.X. Wang, Nanotechnology 19 (2008) 145201.
[25] S. De, P.E. Lyons, S. Sorel, et al., ACS Nano 3 (2009) 714.
[26] T.Y. Kim, T.T. Tung, T.H. Lee, et al., Chem. Asian J. 5 (2010) 256.
[27] R. Marcilla, J.A. Blazquez, J. Rodríguez, et al., J. Polym. Sci. Part A: Polym. Chem. 42 (2004) 208.
[28] S.H. Hong, T.T. Tung, T.Y. Kim, et al., Colloid Polym. Sci. 288 (2010) 1013.
[29] R. Marcilla, J.A. Blazquez, R. Fernandez, et al., Chem. Phys. 206 (2005) 299.
[30] M.C. Hermant, B. Klumperman, A.V. Kyrylyuk, et al., Soft Matter 5 (2009) 878.
[31] M.C. Hermant, P. van der Schoot, B. Klumperman, et al., ACS Nano 4 (2010) 2242.
[32] I. O'Connor, S. De, J.N. Coleman, et al., Carbon 47 (2009) 1983.
[33] R.H. Schmidt, I.A. Kinloch, A.N. Burgess, et al., Langmuir 23 (2007) 5707.
[34] T. Mustonen, K. Kordas, S. Saukko, et al., Phys. Status Solidi B 244 (2007) 4336.
[35] Z. Wu, Z. Chen, X. Du, et al., Science 305 (2004) 1273.
[36] C.M. Aguirre, S. Auvray, S. Pigeon, Appl. Phys. Lett. 88 (2006) 183104.

Organic Electronics 12 (2011) 29–33

Contents lists available at ScienceDirect

Organic Electronics

journal homepage: www.elsevier.com/locate/orgel

High-efficiency and high-quality white organic light-emitting diode employing fluorescent emitters

Yu Yang, Tai Peng, Kaiqi Ye, Ying Wu, Yu Liu *, Yue Wang *

State Key Laboratory of Supramolecular Structure and Materials, Jilin University, Changchun 130012, PR China

ARTICLE INFO

Article history:
Received 13 July 2010
Received in revised form 8 October 2010
Accepted 9 October 2010
Available online 23 October 2010

Keywords:
White organic light-emitting diode
Fluorescent
Beryllium complex
Energy transfer
Color rendering index

ABSTRACT

This paper reports a highly efficient organic light-emitting diode (OLED) with high-quality white emission that employs a deep blue-emitting beryllium complex bis(2-(2-hydroxyphenyl)-pyridine)beryllium ($Bepp_2$) doped with a wide-bandwidth orange-emitting fluorescent dye 4-(dicyanomethylene)-2-methyl-6-(4-dimethylaminostyryl)-4-*H*-pyran (DCM) through incomplete energy transfer from the blue host to the orange dopant. The two-component WOLED exhibits ideal and stable CIE coordinates (0.334 ± 0.002, 0.337 ± 0.007) with a high color rendering index equal to 79–81 upon variation in brightness from 10 to 10,000 cd m^{-2}. As an all-fluorophore-doped white OLED, it yields very high EL efficiencies with the peak luminescence efficiency. The peak value of luminescence efficiency (LE), power efficiency (PE), and external quantum efficiency (EQE) is 14.0 ± 0.35 cd A^{-1}, 9.2 ± 0.25 lm W^{-1}, and 5.6 ± 0.15%, respectively.

© 2010 Elsevier B.V. All rights reserved.

1. Introduction

White organic light-emitting diodes (WOLEDs) have attracted considerable attention in recent years due to their potential applications in next-generation, full-color, flat-panel displays, and solid-state lighting sources [1]. Due to the limited spectral bandwidth of organic molecules, however, single-molecular species cannot provide white-light emission. Therefore, high-quality white light is generally achieved by mixing several materials that give rise to the three primary colors (blue, green, and red) or two complementary colors (cyan and orange) by stacking multiple emitting layers [2] or by co-doping (blending for polymers) several compounds (one host and two emitters at least) [3] in a single emitting layer. However, each of these approaches suffers from some drawbacks such as complicated device fabrication, high driving voltages, and driving voltage-dependent Commission Internationale de L'Eclairage (CIE) coordinates. Another problem with multiple-component systems is that the CIE coordinates of white-light emission change over time for either all-phosphor or fluorophore/phosphor systems due to the limited stability of blue triplet emitters and the different operational lifetimes between singlet and triplet emitters. Therefore, the strategy of using less emitting layers and dopants based on conventional and relatively inexpensive fluorescent materials in multiple-color band architecture should be reconsidered and adopted. The goal is to generate highly efficient white EL emission and to retain ideal and stable CIE coordinates with a high CRI (Color Rendering Index).

Recently, many fluorescent WOLEDs with simple emitting layers containing one blue host and one yellow (or orange) dopant [4] or only one blue emitter that forms an excimer (or exciplex) at longer wavelengths [5] have been developed. However, their performance remains unsatisfactory due to issues such as high turn-on voltage, moderate efficiency, and undesired white CIE coordinates. This paper employs the deep-blue-emitting material bis(2-(2-hydroxyphenyl)-pyridine)beryllium ($Bepp_2$) [6] as the host, which is lightly doped with the wide-bandwidth orange-emitting 4-(dicyanomethylene)-2-methyl-6-(4-dimethylaminostyryl)-4-*H*-pyran (DCM) as the two-component

* Corresponding authors.
E-mail addresses: yuliu@jlu.edu.cn (Y. Liu), yuewang@jlu.edu.cn (Y. Wang).

1566-1199/$ - see front matter © 2010 Elsevier B.V. All rights reserved.
doi:10.1016/j.orgel.2010.10.006

emitting layer, in order to obtain a highly efficient WOLED. This WOLED results from an incomplete energy transfer from $Bepp_2$ to DCM which currently shows the highest EL performance as an all-fluorophore WOLED together with high-quality white emission. The peak value of luminescence efficiency (LE), power efficiency (PE), and external quantum efficiency (EQE) is 14.0 ± 0.35 cd A^{-1}, 9.2 ± 0.25 lm W^{-1}, and $5.6 \pm 0.15\%$, respectively. White light has CIE coordinates (0.334 ± 0.002, 0.337 ± 0.007) which are close to those of the ideal equal-energy white (0.33, 0.33) and remains almost constantly bright (from 10 to 10,000 cd m^{-2}). This chromaticity-stable WOLED also yields a high CRI of 79–81 and a Correlated Color Temperature (CCT) of about 5500, which is appropriate for white-light illumination [1a].

2. Experimental section

2.1. Instrumentation

Photoluminescence spectra were recorded on a Perkin–Elmer LS 55 spectrophotometer, whereas UV–visible spectra were recorded on a Shimadzu UV-2550 PC spectrometer. Electrochemical measurements were performed in anhydrous CH_2Cl_2 with a BAS 100 W bioanalytical electrochemical work station, using Pt as the working electrode, platinum wire as the auxiliary electrode, and a porous glass wick Ag/Ag^+ as the reference electrode. It was standardized against a ferrocene/ferrocenium couple with a scan rate of 100 mV s^{-1}. Elemental analyses were performed on a Flash EA 1112 spectrometer. The EL spectra, brightness, CIE coordinates, and current–luminance–voltage characteristics of the devices were measured with a rapid scan system using a Photo Research PR650 spectrophotometer combined with a computer-controlled, programmable direct-current (DC) source (Keithley 2400).

2.2. Materials and OLED fabrication

The chemical structures and proposed energy diagram of the emitting materials ($Bepp_2$ and DCM) are shown in Fig. 1. Prior to deposition, all organic materials were purified by sublimation. The devices were grown on a glass substrate pre-coated with an indium tin oxide (ITO) anode having a sheet resistance of 20 Ω per square. The ITO substrate was routinely cleaned via ultrasonic treatment in detergent solutions, followed by rinsing with acetone, boiling in isopropanol, rinsing in methanol, and finally rinsing in de-ionized water. The substrate was dried in a vacuum oven between each cleaning step. The devices were fabricated by successive vacuum deposition of organic materials onto the substrate. A very thin layer of LiF can enhance electron injection from the aluminum cathode. A shadow mask with 2×3 mm^2 openings was used to define the cathodes.

3. Results and discussion

3.1. Absorption and photoluminescent (PL) properties

The UV absorption of DCM and the PL spectrum of $Bepp_2$ are shown in Fig. 2. Due to a perfect overlap between the absorption spectrum of DCM and the emission spectrum of $Bepp_2$, the energy transfer from $Bepp_2$ to DCM is possible and efficient. The PL spectra of the $Bepp_2$:DCM co-deposited films with different concentrations prove this point. As shown in Fig. 2, the reduction of $Bepp_2$ emission intensity (with a peak of about 450 nm) in the doped films is notable along with an increase in the concentration of DCM. When the DCM concentration reaches or exceeds 1 wt.%, complete quenching of $Bepp_2$ is achieved. For the DCM doped film with 0.5 wt.% concentrations, the simultaneous emission from $Bepp_2$ to DCM (with a peak of about 560 nm) with comparable emission intensity is achieved, indicating a broad band covering the range of 400–650 nm. These phenomena suggest that the $Bepp_2$:DCM system is well suited as a white EL emitter potentially through the incomplete energy transfer from $Bepp_2$ to DCM.

3.2. EL properties

To examine the EL properties, three organic EL devices (I, II, and III) were fabricated. The compound 4,4-bis(*N*-(1-naphthyl)-*N*-phenylamino)biphenyl (NPB) was employed

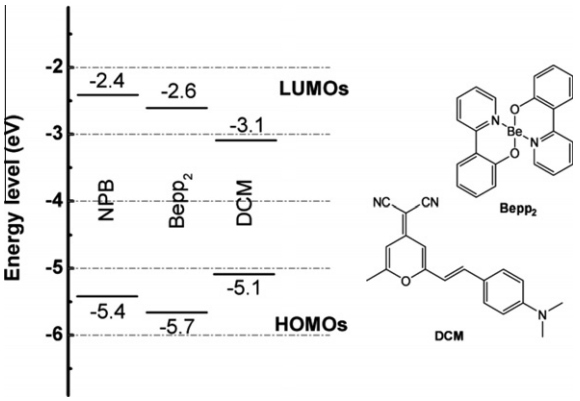

Fig. 1. Proposed energy diagram of the materials used in OLED (left) and the chemical structures of the emitting materials (right).

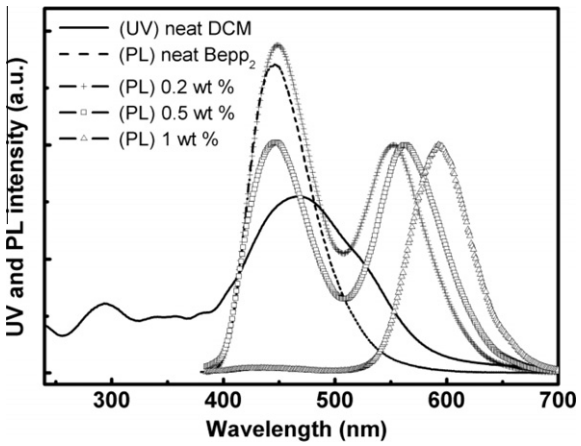

Fig. 2. UV absorption of the DCM film and PL spectra of $Bepp_2$ and $Bepp_2$:DCM co-deposited films with different concentrations.

as a hole-transporting layer (HTL), and DCM-doped $Bepp_2$ with different concentrations was used as the emitting layer (EML) and electron-transporting layer (ETL). The device structures are shown below:

Device I: ITO/NPB (400 nm)/$Bepp_2$:DCM (1 wt.%, 45 nm)/LiF (1 nm)/Al.
Device II: ITO/NPB (400 nm)/$Bepp_2$:DCM (0.5 wt.%, 45 nm)/LiF (1 nm)/Al.
Device III: ITO/NPB (400 nm)/$Bepp_2$:DCM (0.2 wt.%, 3 nm)/ $Bepp_2$:DCM (0.5 wt.%, 42 nm)/LiF (1 nm)/Al.

Fig. 3 top displays the EL spectra of devices I (inset) and device II (normalized). When the concentration of DCM in the emitting layer was 1 wt.% (device I), a dominant emission with a peak at λ_{max} = 580 nm together with a slight emission at the wavelength of about 450 nm was observed at the brightness of 10,000 cd m^{-2}. This was due to an almost complete energy transfer from $Bepp_2$ to DCM. This is also consistent with the PL spectral characteristics shown in Fig. 2. When the doping concentration of DCM decreased to 0.5 wt.% (device II), a broad white emission band with two major emissions at 450 nm (from $Bepp_2$) and 570 nm (from DCM) was obtained. However, with an increase in blue-emission intensity, brightness-dependent

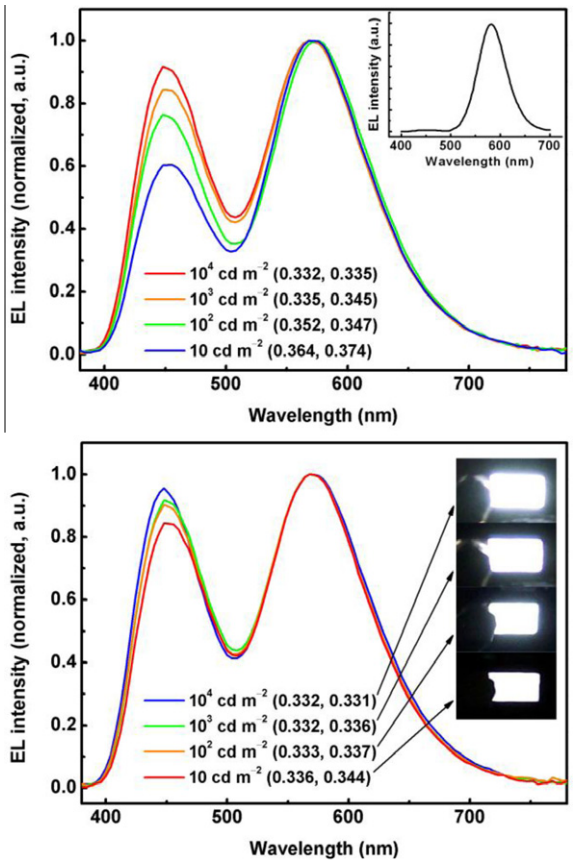

Fig. 3. EL spectra and CIE coordinates of devices II (top) and III (bottom) at brightness of 10, 100, 1000, and 10,000 cd m^{-2}. Inset (top): EL spectrum of device I at brightness 10,000 cd m^{-2}. Inset (bottom): images of device III at brightness of 10, 100, 1000, and 10,000 cd m^{-2}.

(corresponding to voltage dependence) EL spectra became more obvious than the orange dopant as the brightness increased. The CIE coordinates of this cell at brightness 10, 100, 1000, and 10,000 cd m^{-2} were all in the white light region. The EL of device II originated from the uniformly doped layer, so the relative change in EL intensity for blue and orange emissions was partly attributed to the requirement of higher energy excitation for blue light. Moreover, the competition between efficient energy transfer from the blue host to the orange dopant and exciton formation on the orange dopant (DCM) by charge trapping [7] due to a higher HOMO and a lower LUMO of DCM than those of $Bepp_2$ (Fig. 1) would also have a considerable effect on the relative emission intensity.

Due to the similar device structures and comparable EL properties between $Bepp_2$ and Alq_3 [6a,b], the dominant mobile carriers in the diamine (NPB) layer are holes and the emission zone in the doped emitting layer is adjacent to the HTL/EML interface within 5 nm for devices I and II, which is similar to a previously reported doping of NPB/Alq_3 (tris-(8-hydroxyquinoline)aluminum):DCM [8]. To further improve the color stability of the WOLED used, device III was fabricated and designed by decreasing the doping concentration from 0.5 to 0.2 wt.% within 3 nm of EML adjacent to the HTL/EML interface and by maintaining the total thickness of the doped EML at 45 nm.

Fig. 3 bottom summarizes the normalized EL spectra of device III at brightness 10, 100, 1000, and 10,000 cd m^{-2}. The WOLED with the ideal CIE coordinates (0.334 ± 0.002, 0.337 ± 0.007) exhibited better color stability than that of device II within the whole range of diving voltages. This result strongly supports another hypothesis that the recombination zone should be located mainly within the region where the doping concentration is 0.2 wt.% at low driving voltages. The very low concentration effectively decreased orange emission by suppressing the charge trapped on the orange dopant and increased the ratio of blue emission in the mixed EL spectra due to incomplete energy transfer. This led to more pure white CIE coordinates [(0.336, 0.344) and (0.333, 0.337)] in device III than the coordinates [(0.364, 0.374) and (0.352, 0.347)] of device II at brightness 10 and 100 cd m^{-2}, respectively. The similarity between the EL spectra of devices II and III at high diving voltages (corresponding to a high brightness of more than 1000 cd m^{-2}) suggests that the recombination zone in device III extends to the region with a doping concentration of 0.5 wt.% similar to that of device II. Both incomplete energy transfer and charge trapping contribute to the EL emission of device III. The balanced emission of blue and orange with ideal and stable white CIE coordinates in both devices II and III at high brightness (exceeding 1000 cd m^{-2}) also suggests that the saturation of orange-emission sites occurs in the gradually broadened recombination zone as the current increases. The images of device III at brightness 10, 100, 1000, and 10,000 cd m^{-2} shown in the inset of Fig. 3 bottom presents the color stability of the white emission intuitively. This wide EL emission from device III effectively covered the visible spectral region and largely enriched the color rendering capability with a CRI as high as 79–81 and a CCT between 5400 and 5600 which are required for high-quality white-light illumination.

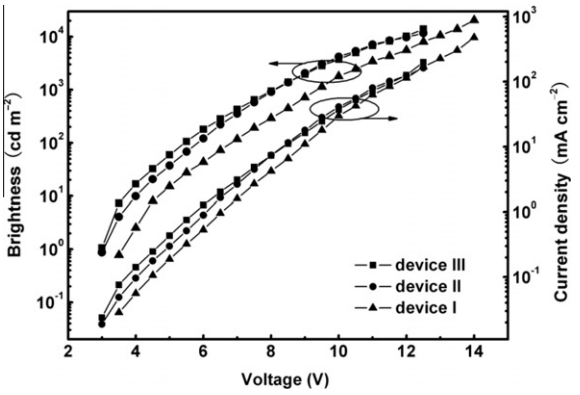

Fig. 4. Brightness–voltage and current density–voltage curves of devices I, II, and III.

The brightness–current density–voltage characteristics of devices I, II, and III are plotted in Fig. 4. Device III exhibited the lowest turn-on voltage of 3.0 V (recorded at 1 cd m^{-2}), and the maximum brightness of 14,010 cd m^{-2} was reached at 12.5 V. Brightness increased linearly with current density, indicating a highly efficient WOLED. The trend of reduction in driving voltage with the doping levels decreased from device I to device III due to DCM in the $Bepp_2$ layer which acted as trapping sites for holes and electrons in terms of the proposed energy diagram (Fig. 1). The almost superposed characteristics of the brightness–voltage and current density–voltage curves in the region of high driving voltage also suggests that a similar EL process should be existent in both devices at high voltages for devices II and III.

Fig. 5 shows the LE, PE, and EQE of the devices as functions of current density. device III exhibited a slightly higher efficiency than device II, and a decrease in efficiency as the concentration increased from 0.5 wt.% (device II) to 1 wt.% (device I) indicated that significant concentration quenching occurred in device I. The highest EL performance was realized in device III. Here, the maximum LE of 14.0 ± 0.35 cd A^{-1} and the maximum EQE of 5.6 ± 0.15% were obtained at brightness 180 cd m^{-2} (6 V), whereas the maximum PE of 9.2 ± 0.25 lm W^{-1} was obtained at brightness 20 cd m^{-2} (4 V). The EL efficiencies of device III remained as high as 12 cd A^{-1} (for LE) and 5.0% (for EQE) upon a variation in brightness from 20 to 2000 cd m^{-2}, indicating the good operational stability of device III. Notably, the EL efficiencies (LE, PE, and EQE) at the practical brightness of 100 cd m^{-2} remained at 14.0 cd A^{-1}, 8.2 lm W^{-1}, and 5.6%, respectively. For lighting applications, the light emitted from all sections of the substrate can, in principle, be redirected to the forward direction via certain lighting fixtures applied to the forward viewing efficiencies by a factor of 1.7–2.3 [1a,9]. Therefore, the total values of LE, PE, and EQE of device III at 100 cd m^{-2} can reach 23.8–32.2 cd A^{-1}, 13.9–18.9 lm W^{-1}, and 9.7–13.1%, respectively. These are comparable to that of an incandescent light bulb (12–17 lm W^{-1}) [1a]. Overall, the values demonstrate high EL efficiencies for a WOLED based on fluorescent materials and illustrate the high potential of an all-fluorophore host/guest doped system for the development of WOLEDs.

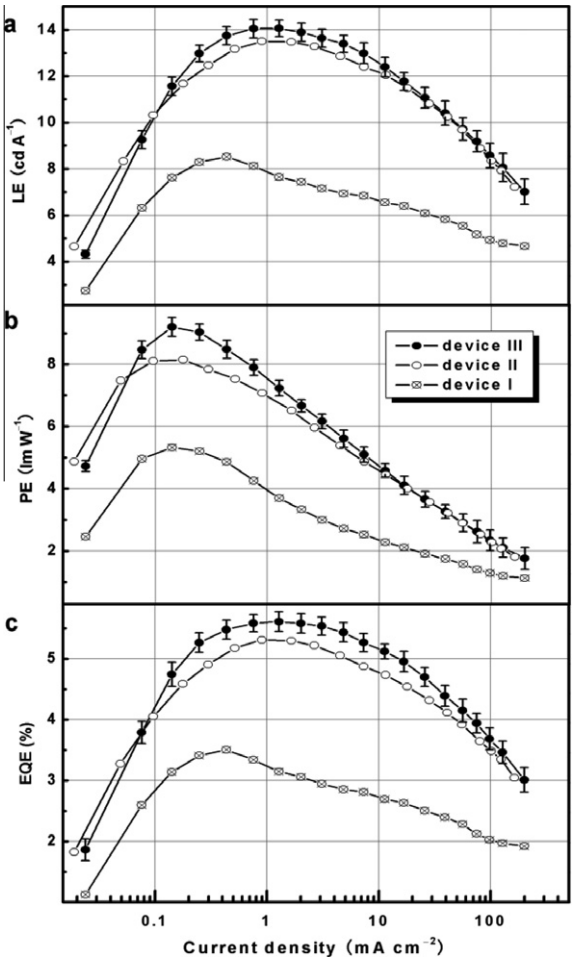

Fig. 5. Luminescence efficiency-current density (a), power efficiency–current density (b), and external quantum efficiency–current density (c) curves of devices I (forks and circles), II (open circles), and III (filled circles). Data are Mean ± SD (standard deviation) values of three experiments in the measurement of device III; the SD falls within the size of the symbol.

4. Conclusion

Using two commercial fluorescent emitting materials, deep-blue beryllium complex $Bepp_2$ (host) and orange organic dye DCM (dopant), a two-component all-fluorophore-doped WOLED was successfully demonstrated. This WOLED yielded a high CRI of 79–81 and stable CIE coordinates close to those of the ideal equal-energy white (0.33, 0.33) at brightness from 10 to 10,000 cd m^{-2}. As a WOLED based on typical fluorescent materials, this device also presented high EL performance not only with a peak efficiency of 14.0 ± 0.35 cd A^{-1} for LE, 9.2 ± 0.25 lm W^{-1} for PE, and 5.6 ± 0.15% for EQE but also high LE and EQE values such as 12 cd A^{-1} and 5.0%, respectively, upon a variation in practical brightness from 20 to 2000 cd m^{-2}. Considering the potential of improved out-coupling, the total PE value

can reach the general efficiency of an incandescent light bulb. The high-efficiency and high-quality white emission of the WOLED, together with inexpensive fluorescent emitters, makes this device a promising candidate for low-cost flat-panel displays and solid-state lighting sources. However, further measurements of the lifetime of encapsulated devices are needed.

Acknowledgements

This work was partly supported by National Basic Research Program of China (973 Program, 2009CB623600), Natural Science Foundation of China (50733002 and 50903036), Jilin Provincial Science and Technology Bureau of Jilin Province (20070107), Special Project from MOST of China (10409A111463).

References

[1] (a) B.W. D'Andrade, S.R. Forrest, Adv. Mater. 16 (2004) 1585;
(b) Y. Sun, N.C. Giebink, H. Kanno, B. Ma, M.E. Thompson, S.R. Forrest, Nature 440 (2006) 908.

[2] (a) G. Schwartz, K. Fehse, M. Pfeiffer, K. Walzer, K. Leo, Appl. Phys. Lett. 89 (2006) 083509;
(b) C.-L. Ho, W.-Y. Wong, Q. Wang, D.G. Ma, L.X. Wang, Z.Y. Lin, Adv. Funct. Mater. 18 (2008) 928;
(c) S.J. Su, E. Gonmori, H. Sasabe, J. Kido, Adv. Mater. 20 (2008) 4189;
(d) H.B. Wu, J.H. Zou, F. Liu, L. Wang, A. Mikhailovsky, G.C. Bazan, W. Yang, Y. Cao, Adv. Mater. 20 (2008) 696;
(e) Y.-S. Park, J.-W. Kang, D.M. Kang, J.-W. Park, Y.-H. Kim, S.-K. Kwon, S.C. Shin, J.-Joo. Kim, Adv. Mater. 20 (2008) 1957;
(f) C.-H. Chang, Y.-H. Lin, C.-C. Chen, C.-K. Chang, C.-C. Wu, L.-S. Chen, W.-W. Wu, Y. Chi, Org. Electronics 10 (2009) 1235.

[3] (a) S.O. Jeon, K.S. Yook, C.W. Joo, J.Y. Lee, Opt. Lett. 34 (2009) 407;
(b) Q. Wang, J.Q. Ding, D.G. Ma, Y.X. Cheng, L.X. Wang, Appl. Phys. Lett. 94 (2009) 103503;
(c) F. Huang, P. Shih, C.-F. Shu, Y. Chi, A.K.-Y. Jen, Adv. Mater. 21 (2009) 361;
(d) H.B. Wu, G.J. Zhou, J.H. Zou, C.-L. Ho, W.-Y. Wong, W. Yang, J.B. Peng, Y. Cao, Adv. Mater. 21 (2009) 4181.

[4] (a) C.H. Chuen, Y.T. Tao, Appl. Phys. Lett. 81 (2002) 4499;
(b) Z.L. Zhang, X.Y. Jiang, W.Q. Zhu, X.Y. Zheng, Y.Z. Wu, S.H. Xu, Synth. Met. 137 (2003) 1142;
(c) B. Geffroy, N. Lemaitre, J. Lavigne, C. Denis, P. Maisse, P. Raimond, Nonlinear Opt. Quantum Opt. 37 (2007) 9;
(d) O. Fadhel, M. Gras, N. Lemaitre, V. Deborde, M. Hissler, B. Geffroy, R. Réau, Adv. Mater. 21 (2009) 1261.

[5] (a) J. Feng, F. Li, W. Gao, S. Liu, Y. Wang, Appl. Phys. Lett. 78 (2001) 3947;
(b) Y. Liu, J.H. Guo, H.D. Zhang, Y. Wang, Angew. Chem. Int. Ed. 41 (2002) 182;
(c) M. Mazzeo, V. Vitale, F.D. Sala, M. Anni, G. Barbarella, L. Favaretto, G. Sotgiu, R. Cingolani, G. Gigli, Adv. Mater. 17 (2005) 34;
(d) Y. Liu, M. Nishiura, Y. Wang, Z. Hou, J. Am. Chem. Soc. 128 (2006) 5592.

[6] (a) Y.Q. Li, Y. Liu, W.M. Bu, Da. Lu, Y. Wu, Y. Wang, Chem. Mater. 12 (2000) 2672;
(b) Y. Liu, J.H. Guo, J. Feng, H.D. Zhang, Y.Q. Li, Y. Wang, Appl. Phys. Lett. 78 (2001) 2300;
(c) J. Chen, D. Ma, Y. Liu, Y. Wang, J. Phys. D: Appl. Phys. 38 (2005) 3366.

[7] (a) Y. Hamada, H. Kanno, T. Tsujioka, H. Takahashi, T. Usuki, Appl. Phys. Lett. 75 (1999) 1682;
(b) X.H. Zhang, B.J. Chen, X.Q. Lin, O.Y. Wong, C.S. Lee, H.L. Hwong, S.T. Lee, S.K. Wu, Chem. Mater. 13 (2001) 1565;
(c) B. Liang, Y.H. Xu, Z. Chen, J.B. Peng, Y. Cao, Synth. Met. 159 (2009) 1876.

[8] C.W. Tang, S.A. VanSlyke, C.H. Chen, J. Appl. Phys. 65 (1989) 3610.

[9] S. Reineke, F. Lindner, G. Schwartz, N. Seidler, K. Walzer, B. Lüssem, K. Leo, Nature 459 (2009) 234.

Organic Electronics 12 (2011) 34–38

Contents lists available at ScienceDirect

Organic Electronics

journal homepage: www.elsevier.com/locate/orgel

High speed responsive near infrared photodetector focusing on 808 nm radiation using hexadecafluoro–copper–phthalocyanine as the acceptor

J.B. Wang [a], W.L. Li [a,*], B. Chu [a,*], C.S. Lee [b], Z.S. Su [a], G. Zhang [a], S.H. Wu [a], F. Yan [a]

[a] Key Laboratory of Excited State Processes, Changchun Institute of Optics, Fine Mechanics and Physics, Chinese Academy of Sciences, 3888-Dong NanHu Road, Changchun, Jilin 130033, PR China
[b] Center of Super-Diamond and Advanced Films COSDAF, City University of Hong Kong, Hong Kong SAR, PR China

ARTICLE INFO

Article history:
Received 31 May 2010
Received in revised form 25 August 2010
Accepted 28 September 2010
Available online 11 November 2010

Keywords:
Organic photodetector
Near infrared
High speed response

ABSTRACT

We have demonstrated an organic photodetector (PD) which can detect 808 nm radiation in near infrared (NIR) region. The photodiode has a hybrid planar-mixed heterojunction structure: ITO/CuPc (10 nm)/CuPc:F16CuPc (1:2, 30 nm)/F16CuPc (20 nm)/LiF (1 nm)/Al. Here, CuPc and F16CuPc denote copper–phthalocyanine and hexadecafluoro–copper–phthalo-cyanine complexes, respectively. The photodiode behaves a response time of 80 ns and a bandwidth of 14 MHz, which are higher than those of recent reports. At the same time, the response waveband of the photodiode covers longer wavelength in NIR comparing to the PD reported. It is conjectured that the high detection performance is due to high electron-mobility of F16CuPc, the large band edge offset between D/A molecules as well reasonable design of the diode structure. The detail working mechanism is also augured.

© 2010 Elsevier B.V. All rights reserved.

1. Introduction

Organic photodetectors (PDs) have been the subject of extensive research in the past decade due to several inherent advantages such as large-area detection, wide selection of materials and low-cost fabrication on flexible substrates [1–4]. Except for ultraviolet and visible PDs, organic near-infrared (NIR) PDs also have tremendous potential in industrial and scientific applications, especially commercial and military field including night vision, tomography and so on. Communication applications also need to extend organic PD sensitivity to the NIR waveband [5–8]. It is considered that the more the NIR absorption of an organic compound is, the stronger the PD response is in NIR spectral region. However, the photo-response spectrum of the reported NIR PDs were almost apart from NIR waveband [5–7], even a photo-response spectrum covered some red light radiation [6,7]. Campbell et al. have reported a photoconductive type NIR PD, but its response bandwidth was too low (only 3 kHz) [8]. Image generation demands periodic read-out of a detector signal, hence the frame rate for image generation is dependent on the response speed of a PD [9]. It has been recognized that upon optical excitation of an organic material, localized Frenkel or charge-transfer excitons are generated, then energy level offsets at heterojunctions are essential to separate excitons because of the fundamental nature of the photogeneration process in organic materials [10].

We note that a CuPc derivative, hexadecafluoro–copper–phthalocyanine (F16CuPc) complex, presents two absorption peaks, 725 and 808 nm in the NIR spectral region, and is used as an electron acceptor in solar PV cells [11]. In addition, the complex behaves the highest occupied molecular orbital (HOMO) of −6.3 eV and lowest unoccupied molecular orbital (LUMO) of −4.9 eV [12]. In light of above spectral and electrical behaviors of F16CuPc and well-known hole transporting property of CuPc, in this letter CuPc and 16FCuPc will be used as the electron donor and acceptor of the PD, respectively. The photocurrent response peak of

* Corresponding authors.
E-mail addresses: wllioel@yahoo.com.cn (W.L. Li), beichu@163.com (B. Chu).

1566-1199/$ - see front matter © 2010 Elsevier B.V. All rights reserved.
doi:10.1016/j.orgel.2010.09.015

the fabricated photodiode lies at 808 nm in the NIR waveband and it behaves fast response speed which could satisfy some special applications, such as medical back-check [13], etching technique [14].

2. Experimental

The NIR PD has the three-layer structure, ITO/CuPc (10 nm)/CuPc:16FCuPc (1:2, 30 nm)/F16CuPc (20 nm)/LiF (1 nm)/Al (200 nm), which is called as an organic hybrid planar-mixed heterojunction (H-PMHJ), that is, the blend of CuPc and 16FCuPc is sandwiched in between two layers. The advantage of this PD structure is that two diodes with planar heterojunction and mixed heterojunction, respectively, can be combined into a single device by stacking their high-efficiency regions in the H-PMHJ diode.

F16CuPc is purchased from Suzhou-Nakai Sunatech Inc., and other materials were commercial materials which were not further purified before use. The photodiodes were fabricated on cleaned indium tin oxide (ITO) coated glass substrates with a sheet resistance of 25 Ω/sq in vacuum chamber and the device active area is $2 \times 2\ mm^2$. The organic layers were deposited at a rate of 2 Å/s, and the evaporating rate of LiF and Al cathode were controlled to be 0.5 and 10 Å/s with the thickness of 1 and 200 nm, respectively. All the vacuum chambers were also controlled at a pressure of 5×10^{-4} Pa and deposition rates and thickness of the layers were monitored using oscillating quartz monitors. Absorptions of films and photocurrent spectral responses of the PDs were measured with a Shimadzu UV-3101 PC spectrophotometer and a Hitachi F-4500, respectively. Current–voltage (I–V) characteristics of the PD devices were recorded in dark and under illumination of 808 nm NIR light with different intensities and through the ITO side. NIR light source was provided by an LD-009 infrared laser diode with 808 nm radiation which was powered by a Keithley 2400 SMU. Transient response was measured and the output signal was displayed on a 500 MHz digital oscilloscope (TDS 3052, Tektronix). The LUMO and HOMO levels of CuPc were cited from Ref. [15]. All the measurements were carried out at room temperature under an ambient condition.

3. Results and discussion

Fig. 1a depicts schematic energy level diagram at the interface of CuPc/F16CuPc and the LUMO level difference between CuPc and F16CuPc is 1.4 eV. This indicates that

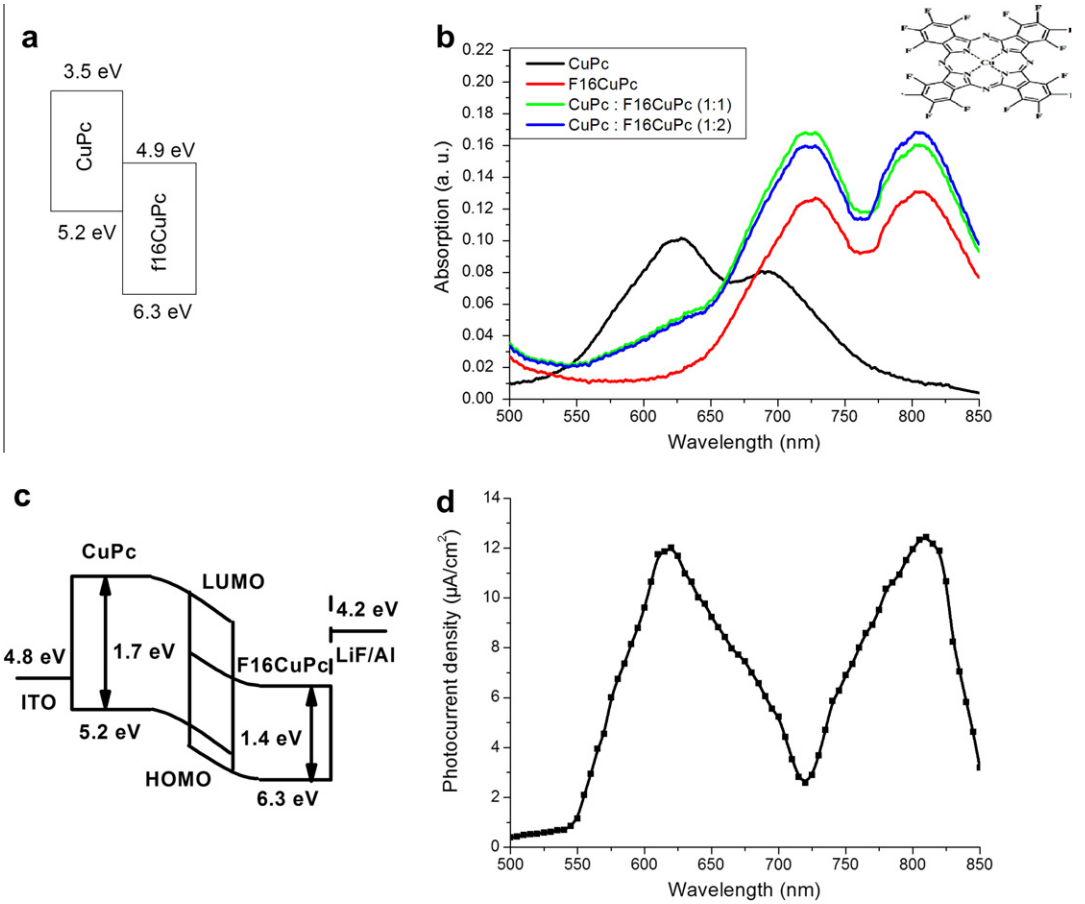

Fig. 1. (a) Schematic energy level diagram at the interface of CuPc/F16CuPc. (b) The solid state absorption spectra of neat films of CuPc and F16CuPc as well blend films of CuPc:F16CuPc with 1:1 and 1:2 ratios by weight, respectively, inset: chemical structure F16CuPc. (c) The schematic level diagram corresponding to the H-PMHJ structure PD. (d) The photocurrent response as a spectrum at zero bias.

at such a DA interface the charge separation of the photo-generated excitons easily occurs because 1.4 eV is markedly larger than the coulombic force of the binding electron and hole pair (exciton) [16]. Fig. 1b illuminates the solid state absorption spectra of the neat films of CuPc and F16CuPc as well the blend films of CuPc:F16CuPc with 1:1 and 1:2 by weight ratio, respectively. From Fig. 1b it can be seen that the neat F16CuPc film shows the two absorption bands which locate at 725 and 808 nm, respectively, in NIR range and the longer waveband can be extended out to 1000 nm. We also note that both the two blend films have higher absorption intensity over the neat F16CuPc film at the NIR spectral region and the 808 nm absorption intensity of the 1:2 blend film is considerably higher than that of the 725 nm peak.

In terms of above the absorption properties of the blend films and energy level alignment between CuPc and F16CuPc, the 1:2 blend film was used to construct a PD which has H-PMHJ structure with ITO/CuPc (10 nm)/CuPc:F16CuPc (1:2, 30 nm)/F16CuPc (20 nm)/LiF (1 nm)/Al. The schematic level diagram of the photodiode is described in Fig. 1c can offer a maximum photocurrent response of about 12.5 μA/cm^2 at 808 nm peak, while 725 nm absorption peak (see Fig. 1b) does not almost contribute to the response, as showed in Fig. 1d. It is surprised that there is a wave-trough at 720 nm which response is around 5.7 times lower than response for 808 nm. Thus, an organic PD with pure 808 nm NIR photo-response could be realized by using a cut-off filter (see the latter of the text).

In order to understand the photo-response feature, we used the 808 nm NIR laser diode with continuous work mode and the monochromatic light source to determine the photo-response. Fig. 2a illuminates the current–voltage (I–V) characteristics of the photodiode. From Fig. 2a we can speculate a rectification ratio of 10^4 at ±10 V biases. Power conversion efficiency (PCE) of 0.2% was obtained under 808 nm laser illumination. The device showed an external quantum efficiency (EQE) of 9.22% at −9 V under illumination with 808 nm radiation. The photodiode figure of merit is the noise equivalent power (NEP), i.e., the minimum impinging optical power that a detector can distinguish from the noise can be shown by the formula (1)

$$\mathrm{NEP} = (A\Delta f)^{1/2}/D^* \tag{1}$$

where A is the effective area of the photodiode in cm^2, Δf is the electrical bandwidth in Hz, and D^* is the detectivity measured in units of Jones. The detectivity can be

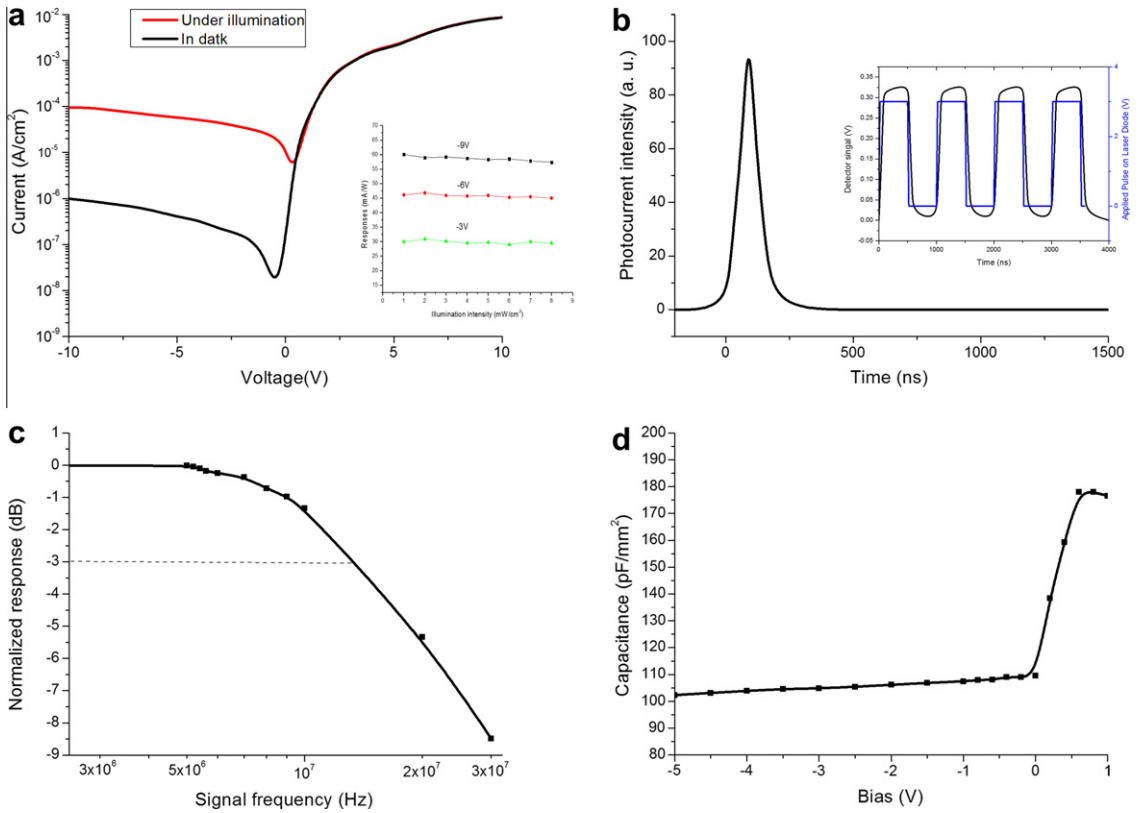

Fig. 2. (a) I–V characteristics of the photodiode in the dark and under 808 nm laser radiation with an intensity of 3 mW/cm^2. Inset: the photocurrent response of the NIR PD at different biases. (b) Photocurrent response of the photodiode based on the structure of ITO/CuPc/CuPc:F16CuPc/F16CuPc/LiF/Al under 808 nm stimulation with 100 ns pulse-width, inset: time response of the same detector to a train of light pulses at a wavelength of 808 nm and with a 1 MHz repetition frequency. (c) Frequency response of the photodiodes with a device area of 2 × 2 mm^2. (d) Capacitance–voltage measurements at frequency of 10 kHz.

expressed as reported by Refs. [17,18], D^* is shown by the formula (2)

$$D^* = R/(2qJ_d)^{1/2} \quad (2)$$

where R is the response (as shown in Fig. 2a inset), q is the absolute value of electron charge (1.6×10^{-19} C) and J_d is the dark current. At zero bias the calculated detectivity using Eq. (2) is, respectively, $D^* = 4.6 \times 10^{10}$ Jones at −9 V and 5.2×10^{10} Jones at −6 V for our NIR photodiode under illumination of 808 nm NIR laser with an intensity of 3 mW/cm^2. Fig. 2b displays the photocurrent response of the photodiode under 808 nm NIR stimulation with 100 ns pulse-width, and inset is the time response of the same detector to a train of light pulses at a wavelength of 808 nm and with a 1 MHz repetition frequency. From Fig. 2b both the rise and fall times of 80 ns were obtained. Fig. 2c indicates the frequency response of the photodiode with an area of 2×2 mm^2, it has been attained that at this area a bandwidth is about 14 MHz at −9 V bias. According to Fig. 2a and c using Eq. (1), a NEP of 1.7×10^{-12} W was calculated. Capacitance of the PD was almost independent of reverse bias by capacitance–voltage measurements in Fig. 2d, which was in contrast to the p-i-n or Schottky-barrier PDs made of inorganic semiconductors. Thus, fast response could be achieved even at zero or low biasing voltage.

In light of the data shown in Fig. 2, we concluded that our 808 nm NIR PD behaved more fast response speed and wider response bandwidth than those of reported NIR PDs [5–9]. At the same time, the spectral peak of our NIR detector focuses on 808 nm which was also much longer than those of reported NIR PDs [5–8], though the EQE at 808 nm needs to be improved further.

The achievement of so good NIR detection performance can be understood as bellow. One of main reasons is the higher hole mobility of 7×10^{-4} cm^2/V s for CuPc [15] and electron mobility of 4.2×10^{-4} cm^2/V s for 16FCuPc which were measured in our lab; another is that the larger band edge offsets between DA molecules [11] is beneficial to exciton dissociation. The response time of planar heterojunction device was 80 ns, which also thanked to adoption of H-PMHJ structure which favoured the efficient exciton dissociation and charge-carrier generation throughout the blend layer as well at the interfaces between the mixed and two adjacent homogeneous layers in the NIR PD. So, excitons had higher probability to reach at DA interfaces prior to recombination. By adding the charge transport layers at two sides of the blend layer, a higher efficiency for extraction of photogenerated charges from and through the blend layer was obtained because the intermolecular distances in D:A blend extent were significantly shorter than that of corresponding charge collection length at either built in field or in addition of the reverse bias. The higher hole and electron mobilities would be in favor of balancing the charge carrier transports in order to collect charge carriers generated.

In addition, we noted that the photocurrent response spectrum of our NIR photodiode also covered visible region from 400 to 700 nm. If the PD is required to detect the NIR waveband, we could use a filter – IPG-700T2 filter to block visible light so that only the NIR radiation can enter into the PD. The photocurrent response of the diodes with the filter is shown in Fig. 3. It is seen that the NIR waveband response is unchanged.

4. Conclusion

In conclusion, CuPc and 16FCuPc with high carrier mobilities act as the D and A species were used in the NIR photodiode and its photocurrent response spectral peak focused on 808 nm. The photodiode having H-PMHJ structure offered a response time of 80 ns and a response bandwidth of 14 MHz, respectively, which were higher than the recent reported results, though the EQE needed to be further improved. The high performance of a PD would be ascribed to larger energy edge offsets of CuPc and F16CuPc, balance of free carrier transport forwards to the two electrodes and stronger absorption at the NIR waveband of the F16CuPc,

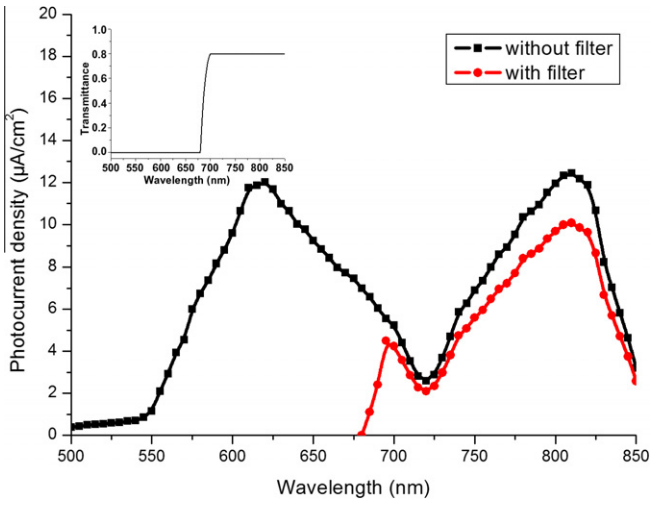

Fig. 3. The photo-response spectra of the H-PMHJ structure photodiode with the NIR through filter. Inset: transparency of IPG-700T2 type filter.

as well skillfully diode design. If the PD is asked to only detect NIR waveband, the photo-response at the visible spectral region must be reduced by selecting such DA materials having no visible absorption.

Acknowledgements

This work was supported by the National Natural Science Foundation of China under Grant Nos. 60877027, 61076047 and Knowledge Innovation Project of Chinese Academy of Sciences under Contract No. KJCX2-YW-M11.

References

[1] D. Ray, K.L. Narasimhan, Appl. Phys. Lett. 91 (2007) 093516.
[2] Z.S. Su, W.L. Li, B. Chu, T.L. Li, J.Z. Zhu, G. Zhang, F. Yan, X. Li, Y.R. Chen, C.S. Lee, Appl. Phys. Lett. 93 (2008) 103309.
[3] G. Yu, J. Wang, J. McElvain, A.J. Heeger, Adv. Mater. 10 (1998) 1431.
[4] G. Yu, G. Srdanov, H. Wang, Y. Cao, A.J. Heeger, Proc. SPIE-Int. Soc. Opt. Eng. 48 (2001) 4108.
[5] L. Wang, J. Wang, J. Pei, Yong Cao, Adv. Mater. 20 (2008) 3745.
[6] Y. Yao, Y. Liang, V. Shrotriya, S. Xiao, L. Yu, Y. Yang, Adv. Mater. 19 (2007) 3979.
[7] M. Binda, Tiziano Agostinelli, Mario Caironi, Dario Natali, Marco SampietroLuca Beverina, Riccardo Ruffo, Fabio Silvestr, Org. Electron. 10 (2009) 1314.
[8] T. Agostinell, M. Caironi, D. Natali, M. Sampietro, G. Dassa, E.V. Canesi, C. Bertarelli, G. Zerbi, J.C. Gonzalez, S.D. Silvestri, G. Lanzani, J. Appl. Phys. 104 (2008) 114508.
[9] I.H. Campbell, B.K. Crone, Appl. Phys. Lett. 95 (2009) 263302.
[10] P. Schilinsky, C. Waldauf, J. Hauch, C.J. Brabec, Thin Solid Films 451 (2004) 105.
[11] P. Peumans, A. Yakimov, S.R. Forrest, J. Appl. Phys. 93 (2003) 3693.
[12] X. Jiang, J. Dai, H. Wang, Y. Geng, D. Yan, Chem. Phys. Lett. 446 (2007) 329.
[13] H. Wei, D. Xing, G. Wu, H. Gu, Y. Jin, Chin. J. Laser 3 (2004) 305.
[14] Z.Y. Wang, Micro. Tech. 6 (2007) 320 (in Chinese).
[15] B.P. Rand, J. Xue, F. Yang, S.R. Forrest, Appl. Phys. Lett. 87 (2005) 233508.
[16] J.-L. Brédas, D. Beljonne, V. Coropceanu, J. Cornil, Chem. Rev. 104 (2004) 4917.
[17] A.R. Jha, Infrared Technology, Wiley, New York, 2000. pp. 245–359.
[18] P. Bhattacharya, Semiconductor Optoelectronics Device, Prentice-Hall, Upper Saddle River, NJ, 1997. pp. 345–367.

Organic Electronics 12 (2011) 39–44

Contents lists available at ScienceDirect

Organic Electronics

journal homepage: www.elsevier.com/locate/orgel

Surface dipole of F4TCNQ films: Collective charge transfer and dipole–dipole repulsion in submonolayers

Zoltán G. Soos, Benjamin J. Topham *

Department of Chemistry, Princeton University, Princeton NJ 08544, United States

ARTICLE INFO

Article history:
Received 15 July 2010
Received in revised form 3 September 2010
Accepted 12 September 2010
Available online 26 October 2010

Keywords:
Surface dipole
Charge transfer
Submonolayer

ABSTRACT

A charge transfer (CT) model is introduced for strong acceptors like A = F4TCNQ that are ionized on surfaces at low coverage θ. Each A forms a CT dimer with a surface state S. Dipole–dipole repulsion grows as $\theta^{3/2}$ up to $\theta = 1$ in a full monolayer. Electron transfer $\rho(\theta)$ within dimers is found self-consistently and decreases with increasing coverage. The surface dipole and work function shift $\Delta\Phi$ are proportional to $\theta\rho(\theta)$. The CT model has implications for photoemission and accounts for $\Delta\Phi(d)$ profiles of F4TCNQ films of thickness d on Cu(1, 1, 1) or on hydrogenated diamond (1, 0, 0). The CT model also describes $\Delta\Phi(\theta)$ of organic donors on metals and is contrasted to previous treatments of dipoles on a surface.

© 2010 Elsevier B.V. All rights reserved.

1. Introduction

F4TCNQ (tetrafluorotetracyanoquinodimethane) is a powerful π-electron acceptor (A), even stronger than TCNQ. TCNQ forms mixed stacks with π-donors (D) and an extensive series of salts with segregated stacks of A^- or $(A_2)^-$anion radicals and closed-shell cations between stacks [1,2]. As reviewed by Chen et al., [3] recent interest in F4TCNQ films has been in the context of organic electronics [4–6] and promoting hole injection [7] by modulating the work function via surface dipoles. Initial adsorption of F4TCNQ on semiconductors or metals is as A^- anion radicals as shown by two diagnostic electronic states, E_1 and E_2, separated by ~ 1.2 eV in photoemission [8,9]. Adsorption beyond a monolayer (ML) involves neutral molecules A with photoemission at higher binding energy E_3 and suppression of E_1 and E_2. Indeed, surface dipole [3] and other data [10] indicate that A^- coverage saturates below a ML. There is broad agreement about the principal features of F4TCNQ films. There are different estimates of the saturation coverage of A^-, however, or how adsorption evolves from A^- to A. Moreover, agreement about A^- on surfaces does not extend to cations D^+ when the adsorbed molecule is a donor. Photoemission evidence is much less accessible because D^+ has higher binding energy than D. Nevertheless, initial adsorption of D = TTF (tetrathiafulvalene) on Au(1 1 1) is also as D^+ leading to ordered sub ML structures that were attributed to dipole–dipole repulsion [11].

Metal-organic (m-O) interfaces have been extensively studied in connection with organic electronics applications, as reviewed by Ishii et al. [12] and Hwang et al. [13]. A major advance has been to identify surface dipoles $\Delta(d)$ that are formed or almost formed at film thickness $d = d_{ML}$. By contrast, interfaces between metals and wide band inorganic semiconductors show band bending over a length scale that is an order of magnitude longer. There is a fundamental difference between metal-semiconductor and m-O interfaces. Possible physical origins of Δ have been discussed [12,13]. Density functional theory (DFT) and quantum chemical calculations have mainly addressed the magnitude of $\Delta \sim \Delta(d_{ML})$. The evolution of $\Delta(d)$ with $d \leqslant d_{ML}$ has not been modeled in general, to the best of our knowledge. In this paper, we model $\Delta(d)$ profiles of sub ML F4TCNQ films by a method that is applicable to any m-O interface with weak nonspecific bonding. Profiles yield information about the charge of adsorbed species and discriminate among possible contributions to surface dipoles.

* Corresponding author.
E-mail address: btopham@princeton.edu (B.J. Topham).

1566-1199/$ - see front matter © 2010 Elsevier B.V. All rights reserved.
doi:10.1016/j.orgel.2010.09.022

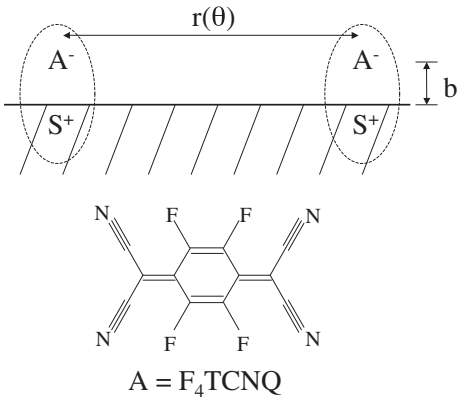

Fig. 1. Schematic representation of adsorbed F4TCNQ molecules on a surface separated by r(θ) at coverage $\theta \leqslant 1$. Each A forms a charge transfer (CT) dimer with a surface state S.

The phenomenological model of $\Delta(d)$ profiles is presented in Section 2. Here we introduce the principal ideas. As sketched in Fig. 1, we suppose that each adsorbed molecule A forms a charge transfer (CT) dimer with a surface state S of the metal. Following Mulliken's treatment of DA dimers, the wave function is a linear combination of a neutral state $|AS\rangle$ and an ionic state $|A^-S^+\rangle$ with dipole $\mu_0 < 0$ normal to the surface. The coefficient $\rho(\theta)^{1/2}$ of the ionic state gives the fraction $\rho(\theta)$ of transferred charge. The separation $r(\theta)$ between adsorbed molecules decreases with increasing $\theta = d/d_{ML} \leqslant 1$, and dipole–dipole repulsion reduces $\rho(\theta)$. Collective CT refers to the self-consistent treatment of dimers on an infinite surface. We follow previous CT studies of organic crystals [14,15] or molecular aggregates [16,17]. The energies of the two states are $E(AS)$ and $E(A^-S^+)$ when the CT integral is $t = 0$. Although t is small by hypothesis, strong mixing is possible when $E(AS) \sim E(A^-S^+)$ are nearly degenerate, as required for neutral-ionic transitions or crossovers [15,17].

In addition to surface dipoles, m-O interfaces typically have an induced density of interfacial states (IDIS) as shown by deviations from the Schottky–Mott limit [12,13]. Induced states are consistent with CT. Weak nonspecific bonding is thought [13] to describe m-O interfaces in contrast to covalent bonds in MLs of alkanethiols on Au or at chemically modified surfaces. Chemisorption also involves strong interactions with $t > 1$ eV in the Newns model [18]. While there is no sharp boundary between weak and strong interactions, CT models assume small t and emphasize electron correlation. DFT or direct calculations are more detailed but less correlated descriptions. Quite generally, dipoles have been associated with atoms or molecules adsorbed on metals, semiconductors or insulators, and qualitative aspects of interfaces are well known. Dipole models have also been criticized and are best for weak interactions.

The Topping model also describes nonspecific bonding that can be applied to $\Delta(d)$ profiles [19,20]. The model assumes a fixed dipole p_0 and polarizability α for every adatom. The dipole field $F(\theta)$ at coverage θ is found self-consistently for induced dipoles $\alpha F(\theta)$ that reduce the net dipole to $p(\theta)$. An example of a quantitative fit [19] is the $\Delta(d)$ profile of Cs on Si(1, 1, 1). Fixed p_0 and depolarization is quite different from variable dipoles and dipole–dipole repulsion in the CT model. But the sharp mathematical difference is less sharp physically since both polarization and CT involve charge redistribution. The models describe work function shifts that cannot uniquely be partitioned into CT and polarization. Since different profiles are predicted, however, observed shifts may point to either model. CT is the natural starting point for F4TCNQ films in view of evidence for ions at $\theta \sim 0$ and molecules at $\theta \sim 1$. We are applying [21] the CT model to published $\Delta(d)$ profiles with CT from molecule to metal and find equally good agreement for D^+ ions at $\theta \sim 0$.

The CT model of interacting dimers is presented in Section 2. Its parameters are $\rho(0)$ and $\rho(1)$, the initial and final degree of CT. Alternatively, the parameters are $E(A^-S^+)$–$E(AS)$ and dipole–dipole repulsion V, both in units of $t = 1$. Two scale factors enter the work function shift $\Delta\Phi(d)$, the ML thickness d_{ML} and the shift Φ_0 of an ionic ($\rho = 1$) ML. Section 3 has applications to F4TCNQ films. Calculated $\Delta\Phi(d)$ profiles are compared to work function shifts of F4TCNQ films on hydrogenated diamond (1, 0, 0) and Cu(1, 1, 1) surfaces. The Discussion contrasts the Topping and CT models and comments briefly on direct approaches to m-O interfaces. We mention extensions of the CT model and emphasize its phenomenological nature.

2. Collective CT model of submonolayers

An isolated A on the surface is modeled as a CT dimer with a localized surface state S whose precise nature is left open. The neutral state $|AS\rangle$ has energy $E(AS)$ and dipole μ_N that we neglect for simplicity. The ionic singlet state $|A^-S^+\rangle$ has energy $E(A^-S^+)$ and large dipole $\mu_0 = -eb$ normal to the surface with $b \sim 3.5$ Å for a planar conjugated molecule in the prone position. The energy difference is $2\Gamma(0) = E(A^-S^+)$–$E(AS)$ in the limit $t = 0$. The two states are coupled by a small CT integral $t = \langle A^-S^+|H|AS\rangle/\sqrt{2}$ that does not perturb the electronic structure of A and A^- significantly. The ground state (gs) of this 2×2 configuration interaction (CI) problem is [14].

$$|\psi(0)\rangle = \sqrt{1-\rho(0)}\,|AS\rangle + \sqrt{\rho(0)}\,|A^-S^+\rangle \tag{1}$$

The ratio $t\sqrt{2}/\Gamma(0) = \tan 2\gamma$ and $\rho(0) = \sin^2\gamma$ determines the relative neutral and ionic contributions. Without loss of generality we set $t = 1$ as the unit of energy and obtain

$$\varepsilon(0) = -2\sqrt{2\rho(0)(1-\rho(0))} + 2\rho(0)\Gamma(0) \tag{2}$$

for an isolated dimer. The parameter $\Gamma(0)$ fixes $\rho(0)$, with $\Gamma(0) < 0$ for $\rho(0) > 1/2$.

F4TCNQ covers $A_0 \sim 100$ Å^2 in Fig. 1, so that a ML has $\sim 10^{14}$ acceptors/cm^2. We consider decreasing electron transfer $\rho(\theta) < 1$ with increasing θ due to dipole–dipole repulsion. The nearest-neighbor separation scales as $r(\theta) = r_0\theta^{-1/2}$ for an invariant surface structure. The model Hamiltonian for $0 < \theta \leqslant 1$ is

$$H(\theta) = \sum_p h_p + \frac{1}{2}\sum_{pp}{}' V_{pp'}\rho_p(\theta)\rho_{p'}(\theta) \tag{3}$$

where h_p describes an isolated dimer and $V_{pp'} = \mu_0^2/r_{pp'}^3$ is the dipole–dipole interaction. We introduce a BCS-type trial function for $N_d = N\theta$ dimers at coverage θ

$$|\psi(\theta)\rangle = \prod_{p=1}^{N_d}(\sqrt{1-\rho(\theta)} + \sqrt{\rho(\theta)}\, b_p^+)|N\rangle. \quad (4)$$

$|N\rangle$ is a product of $N\theta$ neutral dimers whose interactions with the surface or with each other are neglected. The operator b_p^+ acts on the pth dimer to generate the singlet $|A_p^- S_p^+\rangle$. The trial function contains all possible distributions of $|AS\rangle$ and $|A^-S^+\rangle$ states on the surface, and it is strongly peaked at $\rho(\theta)$. CI mixing $\rho(\theta)$ is the same for all dimers by construction. As in BCS, there is perfect correlation of two states ($k\alpha$, $-k\beta$ there, electron–hole excitation of dimers here) and a mean-field approximation otherwise.

The gs expectation value of $|\psi(\theta)\rangle$ is

$$E(\theta) = N_d\varepsilon(\theta) + \rho(\theta)^2 {\sum_{pp'}}' V_{pp'}/2. \quad (5)$$

The first term is Eq. (2) with $\rho(\theta)$ instead of $\rho(0)$. The second term contains sums over $1/r_{pp'}{}^3$ that scale as $\theta^{3/2}$

$$\sum_{p,p'} V_{pp'} = 2kN_d\mu_0^2\theta^{3/2}/r_0^3 \equiv 2V_0\theta^{3/2}N_d. \quad (6)$$

Topping [20] evaluated the sum accurately and obtained $2k \sim 9$ per unit area of either a hexagonal or square planar lattice. $2V_0$ is the repulsion per dimer in a ML with $\rho(1) = 1$. Minimization of $E(\theta)$ with respect to $\rho(\theta)$ gives the self-consistency condition

$$\frac{1-2\rho(\theta)}{\sqrt{2\rho(\theta)(1-\rho(\theta))}} = \Gamma(0) + V\theta^{3/2}\rho(\theta) \equiv \Gamma(\theta) \quad (7)$$

with $V = V_0/t$. A dimer with $\rho(0) > 1/2$ and $\Gamma(0) < 0$ at $\theta = 0$ becomes less ionic with increasing θ. The states are degenerate at θ_1, where $\rho(\theta_1) = 1/2$, $\Gamma(\theta_1) = 0$ and

$$V\theta_1^{3/2} = -2\Gamma(0) \quad (8)$$

The relation between V and $\Gamma(0)$ is independent of t. Alternatively, the model's two parameters may be taken as $\rho(0)$ and $\rho(1)$, the initial and final CT in Eq. (7).

The surface dipole is $\mu_0\theta\rho(0)$, linear in coverage for $V = 0$. Repulsion $V > 0$ gives nonlinear profiles and superlinear $\theta^{3/2}$ may even produce a $\theta\rho(\theta)$ maximum. The derivative

$$\mu'(\theta) = \mu_0\rho(\theta)\left(\frac{(2+\Gamma(\theta)^2)^{3/2} - V\theta^{3/2}/2}{(2+\Gamma(\theta)^2)^{3/2} + V\theta^{3/2}}\right) \quad (9)$$

vanishes at the $\theta\rho(\theta)$ maximum. Since $\Gamma(\theta_1) = 0$, we have $\Gamma(0) = -2\sqrt{2}$ and $\rho(0) = 0.9476$ when $\mu'(\theta_1) = 0$. The maximum shifts to $\theta < \theta_1$ for $\Gamma(0) < -2\sqrt{2}$ and to $\theta > \theta_1$ for $\Gamma(0) > -2\sqrt{2}$. There is no maximum when the numerator of Eq. (9) is positive at $\theta = 1$.

The surface dipole is $b\sigma_-(\theta)$, with charge density $\sigma_-(\theta) = -e\theta\rho(\theta)/A_0$. The change of electrostatic potential across the acceptor layer is $-4\pi eb\sigma_-(\theta)$. The work function shift is

$$\Delta\Phi(\theta) = -4\pi eb\sigma_- \equiv \Phi_0\theta\rho(\theta). \quad (10)$$

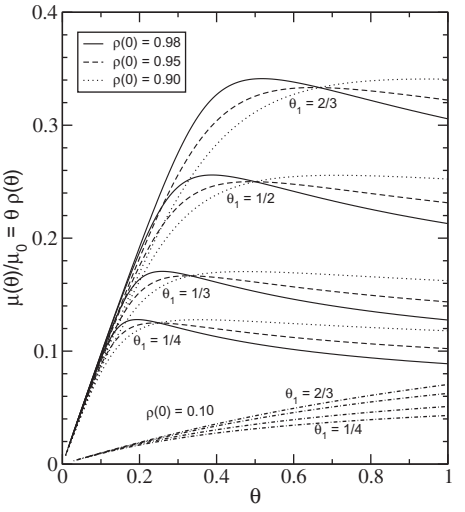

Fig. 2. Surface dipole $\mu(\theta)/\mu_0 = \theta\rho(\theta)$, Eq. (10), at coverage $\theta \leqslant 1$. The dipole $\mu_0\rho(0)$ of isolated dimer decreases to $\mu_0/2$ at θ_1 due to repulsion V in Eq. (7); increasing V decreases θ_1 in Eq. (8). Maxima of $\theta\rho(\theta)$ are given by Eq. (9). Small $\rho(0) = 0.10$ surface dipoles with the same θ_1 are nearly linear in θ.

The prefactor $\Phi_0 = -4\pi e\mu_0/A_0$ is the shift a full ML of A^- ions with $\mu_0 = -eb$. Comparison with experiment requires Φ_0 and d_{ML}. First we consider the CT model itself. Fig. 2 shows $\theta\rho(\theta) = \mu(\theta)/\mu_0$ for the indicated θ_1 and $\rho(0) \sim 1$. Curves with $\rho(0) > 1/2$ cross at θ_1. Increasing θ_1 amounts to decreasing dipole–dipole repulsion V in Eq. (8). The surface dipole is $\sim\mu_0\theta_1/2$ over a broad range with a maximum at $\theta = \theta_1$ for $\rho(0) = 0.95$ as expected from Eq. (9) and at $\theta < \theta_1$ for $\rho(0) = 0.98$. Saturation at $\sim\theta_1/2$ is sudden because the repulsion $\theta^{3/2}$ in Eq. (6) is superlinear. The change becomes more collective with increasing $\rho(0)$.

Fig. 2 also shows $\theta\rho(\theta)$ for largely neutral dimers with $\Gamma(0) \to -\Gamma(0)$, and hence $\rho(0) \to 1-\rho(0) = 10\%$, and unchanged repulsion V based on θ_1. The surface dipole is small and nearly linear, with little indication of cooperative behavior at $\rho(0) = 10\%$ and even less for $\rho(0) < 10\%$. We have neglected the dipole μ_N of $|AS\rangle$ compared to μ_0. The model is readily generalized to include μ_N as another parameter. It is then convenient to redefined $\mu_0 \to \mu_0 - \mu_N$ and the self-consistent analysis holds with minor changes. Our reasons for setting $\mu_N = 0$ are that there are other contributions to $\Delta(d)$ and that CT addresses CI while μ_N reflects local bonding.

3. F4TCNQ on metals or semiconductors

F4TCNQ films have been discussed in terms of ions A^- on the surface and molecules A in thick films. The growth mode is not known, but a full ML or a thick film surely has more adsorbed molecules than the ~20% coverage of A^- inferred from $\Delta\Phi$ shifts. [3,7,10,22,23] CT dimers are linear combinations of A^- and A according to $|\psi(\theta)\rangle$ in Eq. (4), with $\rho(\theta)$ found self-consistently via Eq. (7) to yield the profile $\Delta\Phi(\theta)$ in Eq. (10). There are several ways to compare with experiment: (1) the magnitude of $\Delta\Phi(d)$

for films of thickness d; (2) $\Delta\Phi(d)$ profiles as a function of d with $d_{ML} \sim 4$ Å for F4TCNQ; (3) photoemission spectra or other probes that identify surface species; (4) the surface roughness of sub ML films, which is open at present. The generality of the CT model invites comparison with sub ML films of any m-O interface.

Fig. 3 shows published $\Delta\theta(d)$ profiles to $d = 10$ Å for F4TCNQ on Cu(1, 1, 1) from Fig. 2 of [22] and for the surface dipole contribution on hydrogenated diamond (1, 0, 0) from Fig. 3.5b of [3]. To calculate profiles, we took $\Phi_0 = -4\pi e\mu_0/A_0 = 6.3$ eV in Eq. (10) with $A_0 = 100$ Å^2 and $\mu_0 = -eb$ with b = 3.5 Å. Such inputs pertain to the interface rather than the model. The calculated profiles have $\rho(0) = 0.50$ and $\rho(1) = 0.09$ in Eq. (7), a five fold decrease in the ML, or alternatively $\Gamma(0) = 0.0$ and $V = 22.5$. The shift $\Delta\Phi(d_{ML}) = \Phi_0\rho(1)$ gives an estimated $\rho(1)$. The initial slope of $\Phi_0\rho(0)/d_{ML}$ is an estimate of $\rho(0)$. Shifts beyond $d = d_{ML}$ are small (~0.10 eV), comparable to experimental uncertainties, and not modeled. The fit demonstrates the viability of the model. Moreover, F4TCNQ/Ag(1, 1, 1) has [23] $\Delta\Phi \sim 0.65$ eV and the larger $\Delta\Phi = 1.3$ eV on a passivated Si surface, [9] comparable to diamond (1, 0, 0), was not resolved into surface dipole and band bending. Similar $\Delta \sim \Delta(1)$ for F4TCNQ on different surfaces points to nonspecific bonding.

Photoemission indicates $TCNQ^-$ or $F4TCNQ^-$ on surfaces. Grobman et al. [8] assigned $TCNQ^-$ photoemission at energy E_1 to ionization of the anion's singly occupied HOMO, the neutral molecule's LUMO. The next emission at E_2 was assigned to a "relaxed HOMO" level, perturbed by the partially filled LUMO. This assignment is regrettably still current, [3,22] long after Masuda et al. [10] pointed out the proper interpretation of E_2. Photoemission of an anion generates the electronic spectrum of the neutral molecule. The final state for E_2 emission is the lowest triplet of TCNQ or F4TCNQ. The same MOs give a singlet excited state at higher binding energy. With resolution limited to ± 0.1 eV at best, the reported values of $E_2 - E_1$ for F4TCNQ are 1.3 eV on graphite, [10] 1.4 eV on passivated [9] Si, 1.0 eV on polycrystalline [7] Au, 1.2 eV on [2] Ag(1, 1, 1), 1.0 eV on hydrogenated diamond [3] (1, 0, 0), and 0.9 eV on Na-doped [24] Al_2O_3. Density functional theory (B3LYP) with the reasonably large 6–311++G** basis in the GAUSSIAN 03 program [25] returns 1.09 eV for the vertical triplet state of F4TCNQ.

Photoemissions E_1 and E_2 indicate $F4TCNQ^-$ at sub ML coverage, while E_3 indicates neutral molecules. The three features sometimes coexist, [9,24] with E_3 gaining and E_1, E_2 losing intensity with increasing film thickness. The CT model assumes weakly perturbed A or A^- in the trial function $|\psi(\theta)\rangle$ at least for the π-MOs that are mixed by CI. The electronic spectrum of the model at any θ is a superposition of an ionic fraction $\rho(\theta)$ and a neutral fraction $1-\rho(\theta)$. The CT model implies the coexistence of A^- and A at sub ML coverage, a point whose confirmation is a matter of resolution.

4. Discussion

The CT fit in Fig. 3 of vacuum level shifts is preliminary for several reasons. First, more accurate $\Delta\Phi$(d) data are assured if profiles become the focus rather than the existence and magnitude of Δ. Second, there may be better interface inputs such as d_{ML} or A_0. Third, the CT model can be generalized if warranted by good fits. The principal conclusion is that initial adsorption has considerable ionic character with $\rho(0) \sim 0.5$ that decreases to $\rho(1) \sim 0.1$ in a full ML. The precise value of $\rho(\theta)$ may change on considering other contributions. Since $\Delta\Phi$(d) is linear in coverage for noninteracting dipoles, deviations from linearity indicate $V > 0$ in the CT model or a depolarization field in the Topping model. Profiles with large deviation from linearity bring out differences.

Most m-O interfaces have $\Delta < 0$ and electron transfer from molecule to metal. The vacuum level shifts [26] of α-NPD on Au are shown in Fig. 4 up to $d = 20$ Å. D = α-NPD (N,N′diphenyl-N,N′bis(1-naphthyl)-1,1′biphenyl-4,4′diamine) is not planar and its orientation on the surface is not known. Its molecular volume is almost twice that of F4TCNQ, but the estimated $d_{ML} = 11$ Å gives a similar A_0 and larger $\Phi_0 = -12.0$ eV. A flat $-\Delta\Phi(d)$ profile following

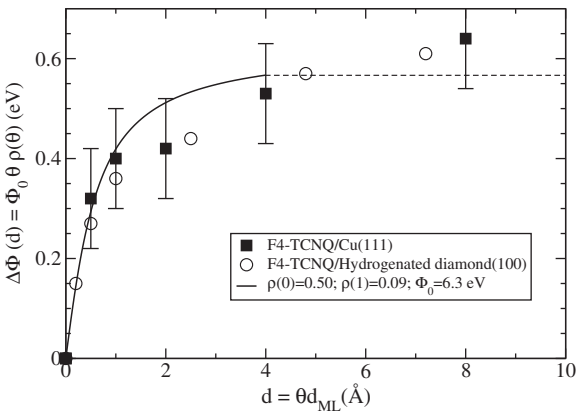

Fig. 3. Work function shift $\Delta\Phi(d)$ of F4TCNQ films. The Cu and diamond data are from Fig. 2 of [22] and Fig. 3.5b of [3], respectively. The curve is Eq. (10) with the $d_{ML} = 4$ Å, $\Phi_0 = 6.3$ eV and the indicated $\rho(0)$ and $\rho(1)$.

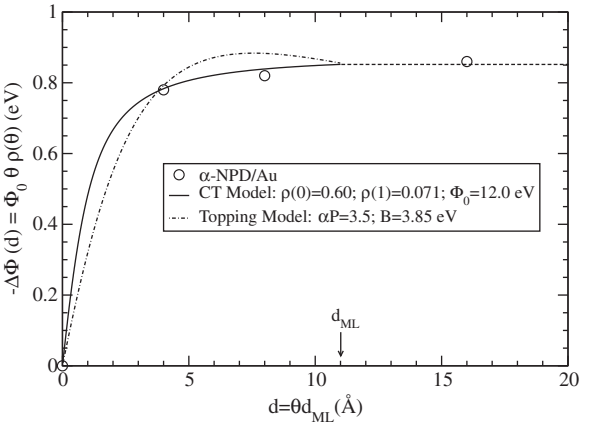

Fig. 4. Work function shift $-\Delta\Phi(d)$ of α-NPD films from [26]. The CT fit is Eq. (10) with the indicated $\rho(0)$, $\rho(1)$ and Φ_0. The Topping fit is Eq. (11) with $\alpha P = 3.5$ and $B = 3.85$ eV.

a steep initial increase is typical of other m-O interfaces [12,13,27] and points to strong repulsion. The CT model fits the profile with $\rho(0) = 0.60$ and $\rho(1) = 0.071$ for μ_0 = eb and b = $d_{ML}/2 + 1.5$ Å for the atomic radius of Au. Larger b and smaller A_0 increases dipole–dipole repulsion in Fig. 1. CT in the ML is about nine times less than at $\theta \sim 0$.

The Topping model works well for adatoms on semiconductors. [19] Its parameters are the dipole p_0 and polarizability α of an adatom on the surface. Topping [20] first scaled the surface structure in Fig. 1 as $r(\theta) = r_0\theta^{-1/2}$. The depolarization field $F(\theta)$ is found self-consistently for induced dipoles $\alpha F(\theta)$. The net dipole $p(\theta)$ and hence $\Delta\Phi_T(\theta)$ is [19]

$$\Delta\Phi_T(\theta) = -B\theta/(1 + \alpha P\theta^{3/2}) \tag{11}$$

where P contains the sum over r^{-3} in Eq. (6) and $B = -4\pi ep_0/A_0$. The dashed line in Fig. 4 has $\alpha P = 3.5$ and $B = 3.85$ eV in Eq. (11). It does not produce an extended flat region. The shift clearly goes as $\theta^{-1/2}$ when αP is large, and $\alpha P < 2$ is required to avoid a maximum at $\theta < 1$. Although $\Delta\Phi_T(\theta)$ with $\alpha P < 2$ differs from the CT profile, small differences from linearity call for accurate profiles. The CT model's $\Gamma(\theta)$ in Eq. (7) has a similar $V\theta^{3/2}$ factor, but its increase is limited by decreasing $\rho(\theta)$. Rearrangement of Eq. (7) with $\Gamma(0) = 0$ immediately shows that $\theta\rho(\theta)$ is constant for large V up to small corrections in $\rho(\theta) << 1$. Hence $\Delta\Phi(d)$ profiles can in principle discriminate among models.

As noted in the Introduction, $\Delta\Phi(\theta)$ profiles indicate charge redistribution but not the origin of surface dipoles. The present model invokes CT, the Topping model invokes polarizability, the pillow effect [28,13] invokes the compression of the metal's electron density on adsorption. Since the pillow contribution is always $\Delta < 0$, the surface dipole of F4TCNQ films contains a larger $\Delta > 0$ contribution. Also, local compression implies a linear profile while the observed profiles in Fig. 3 or Fig. 4 require interactions between adsorbed molecules. The $\Delta(d)$ profiles of all published m-O interfaces [12,13,27] are nonlinear to some extent. The pillow effect for p_0 plus a depolarization field amounts to a Topping model with p_0 due to compression.

In principle, the polarizability tensor α of an adsorbed molecule can be added to variable dipoles $\mu_0\rho(\theta)$ in the CT model. The CT dimer has polarizability α_d normal to the surface. An electric field F along μ_0 changes $E(A^-S^+)$ by $-ebF$ and leads to $\rho(F)$. Charge redistribution within a dimer gives [29]

$$\alpha_d = eb\left(\frac{\partial\rho}{\partial F}\right)_0 = \frac{e^2b^2}{2(\Gamma^2+2)^{3/2}} \tag{12}$$

with $\Gamma(\theta)$ defined in Eq. (7). The α_d contribution depends on θ and is largest at $\Gamma(\theta_1) = 0$ where CT is most sensitive to F. The remainder $\alpha' = \alpha - \alpha_d$ is due to charge redistribution that is beyond a CT dimer. The same logic applies to organic molecular crystals with anisotropic α tensors. Fractional atomic charges [30] yield α_C, which is part of $\alpha = \alpha_C + \tilde{\alpha}$, and the remainder $\tilde{\alpha}$ is associated with atomic polarizability; α_C is typically large and may even exceed [31] α, in which case $\tilde{\alpha} < 0$. In contrast to independent molecular computation of α, however, the polarizability of an adsorbed molecule is a model parameter. We may or may not choose CT to represent charge redistribution. Once the choice is made, however, the depolarization factor in Eq. (11) becomes $\alpha' = \alpha - \alpha_d$ instead of α and the shift $\Delta\Phi(\theta)$ in Eq. (10) is multiplied by $1/(1 + \alpha' P\theta^{3/2})$.

The CT model is phenomenological. It gives a two-parameter expression for the surface dipole $\mu(\theta) = \mu_0\theta\rho(\theta)$ that is nonlinear in the coverage $\theta \leqslant 1$. The parameters $\Gamma(0)$ and V in Eq. (7) lead to $\rho(0)$ and $\rho(1)$ for the initial and final CT. Direct evaluation $\Gamma(0)$ or t requires explicit consideration of both molecules and surfaces. Related models of ion-radical or CT salts [1,14,15] or of molecular aggregates [16,17] are based on small t. The present model is designed for D or A that are ionized on surfaces at low coverage. Large dipoles μ_0 are generated in systems with quite different bonding. Some approximations, less important ones, are readily relaxed. Small μ_N and depolarization can be included at the cost of extra parameters. Charges at finite b can be used instead of point dipoles. Films thicker than one ML can be considered. The $\theta^{3/2}$ dependence of dipole–dipole repulsion is required, but not the magnitude of V or $\Gamma(0)$ or t.

Detailed analysis of m-O interfaces is possible using DFT or quantum chemistry. Theoretical interest in surface dipoles has focused on the magnitude [13] of Δ, the pillow effect, [28] induced density of interface states [32] and cluster calculations [33]. Some studies have considered both [23,34] $\theta = 1/2$ and $\theta = 1$ or variable [35] θ in sub MLs with constrained structures. Direct modeling is limited to one interface at a time and starts with an optimized ML structure that is either retained for $\theta < 1$ or optimized again at $\theta = 1/2$. Direct modeling is more appropriate, indeed mandatory, for strong adsorption with the formation of covalent bonds. The results sometimes [34–36] map into $\Delta\Phi_T(\theta)$ in Eq. (11) with *derived* rather than model parameters. CT dimers and related solid-state models focus on small t and on collective properties as discussed above. Some shared challenges are noted below.

Rangger et al. [23] studied F4TCNQ bonding on Au(1, 1, 1) and Ag(1, 1, 1) at $\theta = 1$ and $\sim 1/2$ and on Cu(1, 1, 1) at $\theta \sim 1/2$ using DFT and supercells. They report backbonding at CN groups that accounts for significant deviations from planar F4TCNQ and hence generates a dipole μ_N (their "molecular contribution", ΔE_{vac}) normal to the surface. The μ_N contribution is opposite to their CT contribution and reduces it by almost a factor of two. Such DFT analysis of σ-bonds is complementary to the CT model with $\mu_N = 0$ and weakly coupled π-electronic states. But correlated models with small t are used precisely where DFT or MO methods have difficulties. The DFT transfer [23] of 1.8 π-electrons leads to $F4TCNQ^{1.8-}$ that in our opinion is not consistent with either E_1, E_2 evidence for $F4TCNQ^-$ anions or for extensive solid-state spectra that point to radical ions rather than dianions, even in stacks with σ-bonded $TCNQ^-$ that are not planar. [37] DFT with on-site repulsion U should limit transfer to one π-electron without major changes in σ-bonding.

In a computational study, Natan et al. [34] analyzed reconstructed Si surfaces at coverage $\theta = 1/2$ and 1 by p-substituted phenyls with the formation of Si–C σ-bonds. They find a linear dependence of the surface dipole on

the gas-phase dipole p_0. They emphasize the collective nature of dipole formation and find good agreement with Eq. (11) with $\alpha P \sim 0.9$ for the calculated α. They conclude that CT or other contributions to surface dipoles are small in these systems. Without disagreeing with the conclusion, we note such small deviations from linear $\Delta(d)$ profiles can be fit with the CT model, and that CT may be appropriate in some contexts.

Romaner et al. [35] studied depolarization and dielectric constants in self-assembled monolayers of 4′substituted 4-mercaptobiphenyl derivatives using DFT and related their results to Eq. (11). The ML structure is accurately known: polar molecules of length b are standing on the surface with a small tilt angle and are tightly packed with separation $r_0 < b$. The point dipole approximation of Eq. (11) requires modification, [35] as expected, for $b > r_0$ and the issue comes up whenever r_0 and d_{ML} are comparable. They assumed that sub ML structures retain erect molecules while scaling $r(\theta)$ as $r_0\theta^{-1/2}$. Scaling is a convenient fiction when covalent bonds are formed on adsorption, especially for standing molecules. Nevertheless, the dependence of polarization or other properties on b/r_0 or on θ can be extracted from such conceptual studies. Surface structure is a general concern in sub ML films.

In summary, we have modeled sub ML films of F4TCNQ in terms of CT dimers with surface states of the metal, as shown in Fig. 1. Small t mixes the neutral and ionic states and leads to variable electron transfer $\rho(\theta)$ due to dipole–dipole repulsion that is treated self-consistently. Collective CT accounts for having both A^- and A on the surface of F4TCNQ films and provides a general approach to profiles of work function shifts or surface dipoles. The model is phenomenological, well suited for modeling $\Delta\Phi(d)$ profiles of m-O interfaces. It is closely related to quantum cell models of donors and acceptors in π-radical solids.

Acknowledgements

ZGS thanks Antoine Kahn for stimulating discussions about interfaces and work function shifts. We gratefully acknowledge support for work by The National Science Foundation under the MRSEC program (DMR-0819860).

References

[1] Z.G. Soos, Ann. Rev. Phys. Chem. 25 (1974) 121;
Z.G. Soos and D.J. Klein, in Treatise on Solid State Chemistry, Vol. III (N.B. Hannay, Ed., Plenum, New York, 1976) p. 689.
[2] J.S. Miller (Ed.), Extended Linear Chain Compounds, vol. 3, Plenum, New York, 1983.
[3] W. Chen, D. Qi, X. Gao, A.T.S. Wee, Prog. Surf. Sci. 84 (2009) 279.
[4] W. Gao, A. Kahn, Org. Electron. 3 (2002) 53.
[5] J. Blochwitz, M. Pfeiffer, T. Fritz, K. Leo, Appl. Phys. Lett. 73 (1998) 729;
X. Zhou, M. Pfeiffer, J. Blochwitz, A. Werner, A. Nollau, T. Fritz, K. Leo, Appl. Phys. Lett. 78 (2001) 410.
[6] T. Takenobu, T. Kanbara, N. Akima, T. Takahashi, M. Shiraishi, K. Tsukagoshi, H. Kataura, Y. Aoyagi, Y. Iwasa, Adv. Mater. 17 (2005) 2430.
[7] N. Koch, S. Duhm, J.R. Rabe, A. Vollmer, R.L. Johnson, Phys. Rev. Lett. 95 (2005) 237601.
[8] W.D. Grobman, R.A. Pollak, D.E. Eastman, E.T. Maas Jr., B.A. Scott, Phys. Rev. Lett. 32 (1974) 534.
[9] K. Mukai, J. Yoshinobu, J. of Electr. Spectr. Rel. Phen. 174 (2009) 55.
[10] S. Masuda, H. Hayashi, Y. Harada, S. Kato, Chem. Phys. Lett. 180 (1981) 279.
[11] I. Fernandez-Torrente, S. Monteret, K.J. Franke, J. Fraxedas, N. Lorente, J.I. Pascual, Phys. Rev. Lett. 99 (2007) 176103.
[12] H. Ishii, K. Sugiyama, E. Ito, K. Seki, Adv. Mater. 11 (1999) 605.
[13] J. Hwang, A. Wan, A. Kahn, Mater. Sci. Eng. R 64 (2009) 1.
[14] Z.G. Soos, H.J. Keller, W. Moroni, D. Nöthe, N.Y. Acad. Sci. 313 (1978) 442.
[15] Z.G. Soos, A. Painelli, Phys. Rev. B 75 (2007) 155119.
[16] A. Painelli, F. Terenziani, J. Amer. Chem. Soc. 125 (2003) 5624;
F. Terenziani, A. Painelli, Phys. Rev. B 68 (2003) 165405.
[17] A. Painelli, F. Terenziani, Z.G. Soos, Theor. Chem. Acc. 117 (2007) 915.
[18] D.M. Newns, Phys. Rev. 178 (1969) 1123.
[19] W. Mönch, Semiconductor Surfaces and Interfaces, Springer Series in Surface Sciences 26, Springer-Verlag, Berlin, 1993. p. 236.
[20] J. Topping, Proc. Roy. Soc. A 114 (1927) 67.
[21] B.J. Topham, M. Kumar and Z.G. Soos, Adv. Func. Mater., submitted for publication.
[22] L. Romaner, G. Heimel, J.L. Brédas, A. Gerlach, F. Schreiber, R.L. Johnson, J. Zegenhagen, S. Duhm, N. Koch, E. Zojer, Phys. Rev. Lett. 99 (2007) 256801.
[23] G.M. Rangger, O.T. Hofmann, L. Romaner, G. Heimel, B. Bröker, R.P. Blum, R.L. Johnson, N. Koch, E. Zojer, Phys. Rev. B 79 (2009) 165306.
[24] S. Braun, W.R. Salaneck, Chem. Phys. Lett. 438 (2007) 259.
[25] M.J. Frisch et al., Gaussian 03, Revision C.02, (Gaussian, Inc), Wallingford, CT, 2003.
[26] W. Gao, A. Kahn, J. Appl. Phys. 94 (2003) 359.
[27] H. Ishii, N. Hayashi, E. Ito, Y. Washizu, K. Sugi, Y. Kimura, M. Niwano, Y. Ouchi, K. Seki, Phys. Stat. Sol. 201 (2004) 1075;
B. Broker, R.-P. Blum, L. Beverina, O.T. Hofmann, M. Sassi, R. Ruffo, G.A. Pagani, G. Heimel, A. Vollmer, J. Frisch, J.P. Rabe, E. Zojer, N. Koch, Chem. Phys. Chem. 10 (2009) 2947.
[28] H. Vasquez, Y.J. Dappe, J. Ortega, F. Flores, J. Chem. Phys. 126 (2007) 144703.
[29] A. Painelli, Z.G. Soos, Chem. Phys. 325 (2006) 48.
[30] E.V. Tsiper, Z.G. Soos, Phys. Rev. B 64 (2001) 195124.
[31] E.V. Tsiper, Z.G. Soos, Phys Rev. B 68 (2003) 085301.
[32] E. Abad, J. Ortega, F. Flores, J. Vac. Sci. Technol. B 27 (2009) 2008.
[33] I. Avilov, V. Geskin, J. Cornil, Adv. Funct. Mater. 19 (2009) 624.
[34] A. Natan, Y. Zidon, Y. Shapira, L. Kronik, Phys. Rev. B 73 (2006) 193310.
[35] L. Romaner, G. Heimel, C. Ambrosch-Draxl, E. Zojer, Adv. Funct. Mater. 18 (2008) 3999.
[36] M. Piacenza, S. D'Agostino, E. Fabiano, F. Della Sala, Phys. Rev. B 80 (2009) 153101.
[37] R.H. Harms, H.J. Keller, D. Nöthe, M. Werner, D. Gundl, H. Sixl, Z.G. Soos, R.M. Metzger, Mol. Cryst. Liq. Cryst. 65 (1981) 179.

Organic Electronics 12 (2011) 45–50

Contents lists available at ScienceDirect

Organic Electronics

journal homepage: www.elsevier.com/locate/orgel

Vertically stacked hybrid organic–inorganic complementary inverters with low operating voltage on flexible substrates

J.B. Kim, C. Fuentes-Hernandez, D.K. Hwang, W.J. Potscavage Jr., H. Cheun, B. Kippelen *

Center for Organic Photonics and Electronics (COPE), School of Electrical and Computer Engineering, Georgia Institute of Technology, Atlanta, GA 30332, USA

ARTICLE INFO

Article history:
Received 20 August 2010
Received in revised form 11 October 2010
Accepted 19 October 2010
Available online 31 October 2010

Keywords:
Thin-film transistors
Vertically stacked complementary inverter
Pentacene
Indium gallium zinc oxide
Noise margin

ABSTRACT

Hybrid organic–inorganic complementary inverters were demonstrated on a flexible polyethersulfone (PES) substrate with vertically stacked *p*-channel pentacene and *n*-channel amorphous indium gallium zinc oxide thin-film transistors (TFT). Al_2O_3 layers grown by atomic layer deposition were used as top- and bottom-gate dielectric layers. Common-gate top-contact *p*- and bottom-contact *n*-channel TFTs showed saturation mobility values of 0.3 ± 0.02 and 5.3 ± 0.2 cm^2/Vs and low threshold voltage values. Complementary inverters yielded high gain values of 61 V/V with high and balanced noise margins at a low supply voltage of 5 V. The independent control of the thickness of the gate dielectric layer used for each transistor in this proposed vertically stacked geometry, allows for the realization of high-density low-power complementary circuits with high gain and balanced noise margins.

Published by Elsevier B.V.

1. Introduction

Thin-film transistors recently have attracted considerable attention as an emerging technology for unique consumer markets that will allow the development of microelectronic circuits on flexible substrates, over very large-areas and potentially at a very low cost. Organic and oxide-based TFTs are two technologies that offer advantages over *n*-channel amorphous silicon TFTs technologies in that these materials are capable of larger mobilities, can be processed at lower temperatures [1–4] and if combined, they could lead to complementary electronic circuits. To date, most complementary inverters used two-dimensional (2D) geometries. Recently a vertically stacked organic TFT-based inverter was demonstrated using two *p*-channel transistors on a glass substrate [5]. This vertical inverter with two pentacene TFTs stacked on top of one another yielded a maximum gain of 13.4 V/V and a switching threshold voltage of −11 V with noise margin low and high values of 9.4 and 6.6 V, respectively, at a supply voltage of 20 V. However, practical electronic devices are expected to use *p*- and *n*-channel TFT-based complementary inverters to operate with low power consumption, high gain, high noise margins, and on flexible substrates.

Organic materials provide a natural framework for the development of complementary technologies, since *n*-channel or *p*-channel TFTs can readily be fabricated. However, they tend to be more susceptible to degradation in air and have lower mobilities than metal oxide semiconductors. On the other hand, transistors based on oxide semiconductors that can be processed at low temperatures with high mobility values operate mainly as *n*-channel transistors [3,6,7]. Hence, hybrid complementary structures comprising *p*-channel organic and *n*-channel metal oxide TFTs are particularly attractive to realize complementary circuit designs because they benefit from the intrinsic advantages of these two material systems.

Most hybrid TFT-based complementary inverters use horizontally distributed *n*- and *p*-channel semiconductor layers with a bottom-gate geometry [8–10] with a shared gate dielectric layer. Recently, we demonstrated organic–inorganic hybrid complementary inverters with high gain

* Corresponding author. Tel.: +1 404 385 5163; fax: +1 404 385 5170.
E-mail address: Kippelen@ece.gatech.edu (B. Kippelen).

1566-1199/$ - see front matter Published by Elsevier B.V.
doi:10.1016/j.orgel.2010.10.012

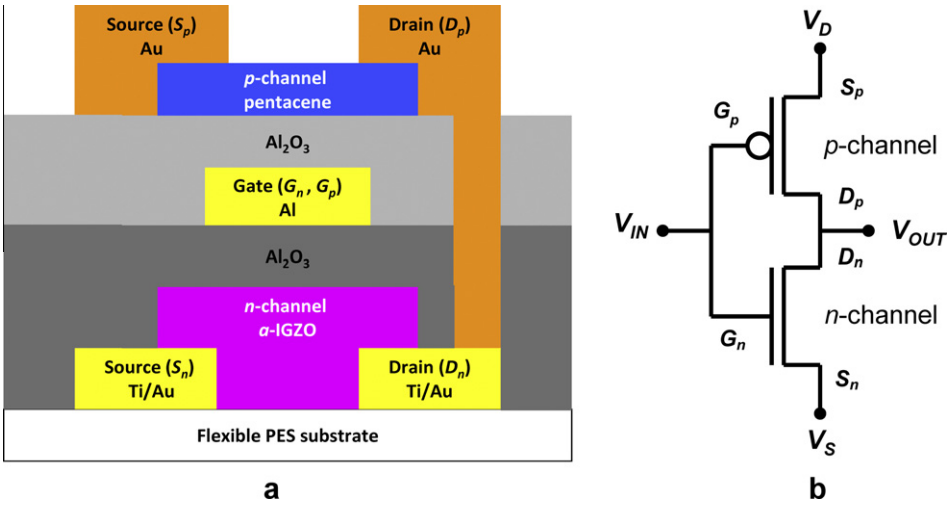

Fig. 1. (a) Schematics of the complementary inverter with vertically stacked pentacene and amorphous *a*-IGZO thin-film transistors on a flexible polyethersulfone substrate. (b) Complementary inverter circuit diagram.

values of 130 V/V and high and balanced noise margins employing *n*-channel *a*-IGZO and *p*-channel pentacene TFTs horizontally distributed on flexible substrates [10]. Here, we report on a novel flexible hybrid organic–inorganic vertically stacked complementary inverter geometry in which a *p*-channel pentacene TFT is stacked on top of an *a*-IGZO *n*-channel TFT. This geometry shown in Fig. 1 has the following advantages. The potential damage to the organic semiconductor layer associated with the deposition of gate dielectric materials and further fabrication steps of the *n*-channel TFT is avoided by employing a *p*-channel organic TFT on the top of a burried *n*-channel oxide TFT. Furthermore, the thickness of each of the gate dielectric layer used for the *n*- and *p*-channel TFTs can be controlled independently which is an important design parameter to achieve complementary circuits with high gain and balanced noise margins. In this study, a 100 nm-thick Al_2O_3 was used as top-gate dielectric for the *n*-channel oxide TFT and a 75 nm-thick Al_2O_3 was used as bottom-gate dielectric for the *p*-channel organic TFT. In both cases, atomic layer deposition was used to grow the Al_2O_3 layers. Balanced "*on*-currents" at the same operating voltages were obtained by independently controlling the size and width of the *n*- and *p*-channels, and by adjusting the thickness of the Al_2O_3 layers.

2. Device fabrication and electrical characterization

Hybrid organic–inorganic complementary inverters with vertically stacked TFTs were fabricated on a flexible polyethersulfone (PES) substrate. A bottom-gate top-contact *p*-channel TFT was fabricated on the top of a top-gate bottom-contact *n*-channel TFT by sharing the gate electrode, as shown in Fig 1(a). First, Ti/Au (6 nm/50 nm) electrodes were deposited using electron-beam (e-beam) at room temperature on a glass substrate through a shadow mask to define the source and drain electrodes for the top-gate *n*-channel TFT. A 30 nm-thick *a*-IGZO (Ga_2O_3:In_2O_3:ZnO = 1:1:1 mol%) layer was then deposited by radio frequency (rf) sputtering without intentional substrate heating using a power of 125 W, a working pressure of 3 mTorr, and an O_2/Ar (2/98) atmosphere through a shadow mask. Then, a 100 nm-thick Al_2O_3 gate dielectric layer was deposited by atomic layer deposition (ALD) system (Savannah100, Cambridge Nanotech Inc.) on top of the *a*-IGZO to form a TFT with a top-gate geometry. The Al_2O_3 films were deposited at 110 °C using alternating exposures of tri-methyl-aluminum ($Al(CH_3)_3$) and H_2O vapor at a deposition rate of approximately 0.1 nm per cycle. Each deposition cycle (one monolayer) lasted 25 s, yielding a total deposition time of 7 h and 20 min for 1000 cycles [11]. Al_2O_3 layers deposited by ALD had a dielectric constant of nine, which yielded highly conformal and defect-free gate dielectrics with high capacitance densities [12,13]. A 50 nm-thick Al electrode was fabricated by thermal evaporation through a shadow mask to serve as a common gate electrode. Then, another 75 nm-thick Al_2O_3 was deposited by ALD on the top of the *n*-channel *a*-IGZO TFT to serve as the gate dielectric for the pentacene TFT. A 50 nm-thick layer of pentacene was deposited through a shadow mask using thermal evaporation at a substrate temperature of 25 °C and an initial pressure of 2×10^{-8} Torr. Prior to its thermal evaporation, pentacene was purified using gradient zone sublimation. Finally, Au (100 nm) source/drain electrodes were deposited through a shadow mask over the pentacene channel. Here, a small offset, of around 400 μm, was introduced along the channel width direction to allow independent access to the source and drain electrodes of the top and bottom TFTs. This offset is not necessary but was use to facilitate the individual characterization of both TFTs. The samples were then transferred into a nitrogen-filled glove box (O_2, H_2O <0.1 ppm) for electrical testing. Gold was used as source and drain electrodes because it provides a similar charge-injection energy barrier of 0.6 eV for the injection of holes into pentacene and electrons into *a*-IGZO [14,15]. In these complementary inverters with a vertical stacked

geometry, further optimization of the injection characteristics can easily be achieved by separately selecting suitable metals for the source and drain electrodes of each channel. Complementary inverter circuits with the structure shown in Fig. 1(b) were fabricated using *p*-channel pentacene and *n*-channel *a*-IGZO TFTs with a channel length of $L_p = L_n = 180$ μm. A channel width of $W_p = 4000$ μm was used for the *p*-channel TFT and $W_n = 400$ μm for the *n*-channel TFT. The *n*- to *p*-channel ratio $W_p/W_n = 10$ and the different thicknesses of the top- and bottom-gate dielectric layers were optimized to compensate for: (1) differences in hole (μ_h) and electron mobility (μ_e) in the pentacene and
a-IGZO transistors; and (2) differences in the threshold voltages of the two transistors. The selected choice of the relative channel widths and gate dielectric thicknesses allowed the *n*- and *p*-channel TFTs to achieve balanced on-currents at comparable operating voltages. To test the inverter characteristics of these vertically stacked TFTs, the drain electrodes of the top and bottom TFTs were connected by using a single probe at the region of overlap. The common gate electrode for both *n*- and *p*-channel TFTs served as the input voltage (V_{IN}) of the inverter circuit.

The dielectric properties of parallel plate capacitors with a geometry PES/Ti/Au/Al_2O_3 (100 nm)/Al/Al_2O_3 (75 nm)/Au fabricated on the same flexible substrate were measured in capacitors of various areas ranging from 1 to 5 mm^2. Measurements of the leakage current and capacitance were performed by first, grounding the Ti/Au bottom electrode (floating top Au electrode) and applying a voltage ranging from −25 to 25 V to the Al electrode, biasing the 100 nm-thick Al_2O_3 layer. Then, the experiment was repeated by grounding the top Au electrode (floating bottom Ti/Au electrode) and applying a voltage ranging from −20 to 20 V to Al electrode, biasing the 75 nm-thick Al_2O_3 layer. Very low leakage current densities, below 10^{-7} A/cm^2 at 2.0 MV/cm were measured. High capacitance density of 81 ± 1 and 108 ± 2 nF/cm^2, with a dielectric constant value of $\varepsilon_r = 9$, were measured for the 100 nm-thick and the 75 nm-thick Al_2O_3 layers, respectively. Variations of the capacitance density smaller than 2% were observed for frequencies ranging from 1 to 100 kHz and electric fields between −2.5 and 2.5 MV/cm. The properties of these Al_2O_3 layers deposited by ALD are consistent with our previous reports [11,12]. The combined dielectric properties of these layers are indicative of a low defect concentration [16].

The current–voltage characteristics of the vertically stacked, bottom-gate *p*-channel and top-gate *n*-channel TFTs with channel widths ($L_p = L_n = 180$ μm) and lengths ($W_p = 4000$ μm and $W_n = 400$ μm) are shown in Fig 2(a and d). The output characteristics (drain current I_{DS} vs. drain–source voltage V_{DS} at multiple constant gate–source voltages V_{GS}) and transfer characteristics (I_{DS} vs. V_{GS} at fixed V_{DS}) of the TFTs were measured using an Agilent E5272A medium-power source/monitor unit connected to a probe station. Hysteresis-free transfer curves and leakage cur-

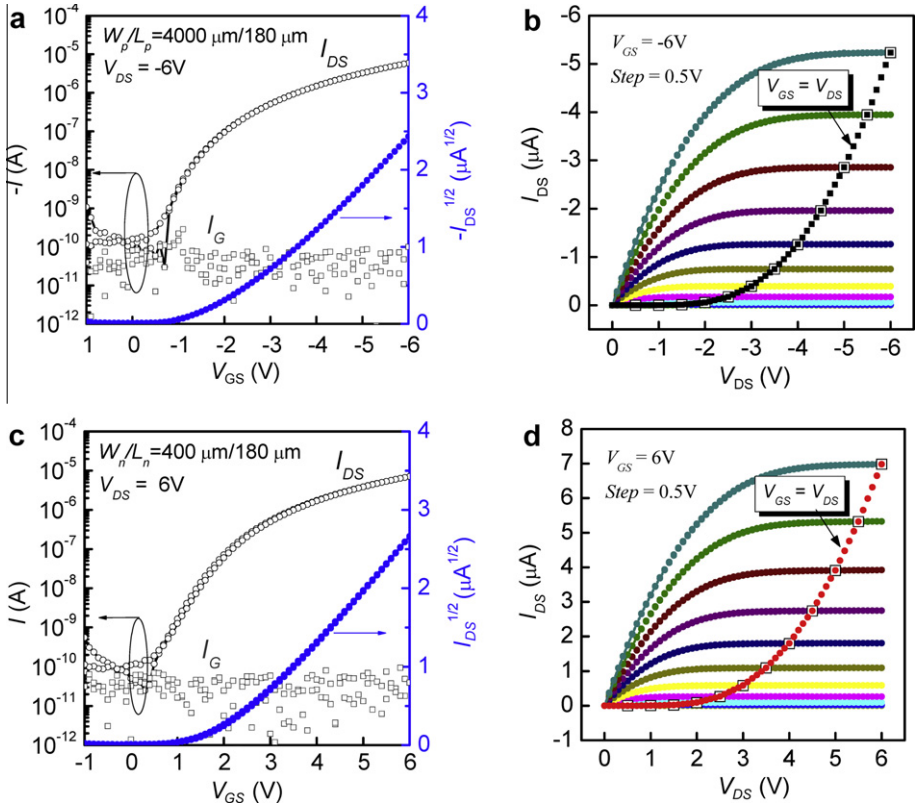

Fig. 2. Representative (a) hysteresis transfer and (b) hysteresis output characteristics of pentacene TFTs with $L = 180$ μm and $W_p = 4000$ μm. Representative (c) hysteresis transfer and (d) hysteresis output characteristics of *a*-IGZO TFTs with $L = 180$ μm and $W_n = 400$ μm.

rents measured for both forward and reverse gate biases are shown in Fig. 2(a) (*p*-channel) and Fig. 2(c) (*n*-channel). Saturation mobility values of 0.3 ± 0.02 and 5.3 ± 0.2 cm^2/Vs and threshold voltage values of −2.0 ± 0.2 and 2.1 ± 0.2 V were obtained for the *p*-channel pentacene and *n*-channel *a*-IGZO TFTs, respectively. Higher mobility values have been obtained from bottom-gate geometry *a*-IGZO TFTs because differences in processing conditions are expected to yield *a*-IGZO films with a slightly different stoichiometry than previously obtained [12,17]. Higher mobility values are expected upon further optimization of the deposition process. The hysteresis output curves shown in Fig. 2(b) (*p*-channel) and Fig. 2(d) (*n*-channel) exhibit good linearity at low drain-to-source voltage (V_{DS}) despite the relatively large energy barrier for charge injection and show no hysteresis.

3. Vertically stacked organic–inorganic hybrid complementary inverters

The static performance of an inverter is evaluated by its static gain and noise margin values, both extracted from the measured voltage transfer characteristics (VTCs). Achieving high and balanced noise margin values is necessary for reliable circuit operation in complex logic circuits such as ring oscillators. Noise margin values are defined by low noise margin ($NM_L = V_{IL} - V_{OL}$) and noise margin high ($NM_H = V_{OH} - V_{IH}$), where V_{IH}, V_{IL}, V_{OH}, and V_{OL} are input (V_{IN}) and output (V_{OUT}) voltages at high and low levels of a given inverter VTCs. The noise margin is limited by the steepness ($\Delta V_{IN} = V_{IH} - V_{IL}$) of the transition, where ΔV_{IN} is the difference of input voltages at high and low levels, and by the position of the switching threshold voltage ($V_M = V_{IN} = V_{OUT}$). High and balanced noise margins are found when the ideal condition $V_M = 0.5V_D$ is met, hence when $V_M = V_{IN} = 0.5V_D = V_{OUT}$. However, the value of V_{IN} at which this transition occurs is generally not $0.5V_D$. A complementary inverter can be modeled as two series-connected voltage-dependent variable resistors. In general, for a given supply voltage, V_D, V_M corresponds to the input voltage where the resistance of the *n*-channel TFT ($R_n = V_{DS}/I_{DS}$) is equal to that of the *p*-channel TFT ($R_p = -V_{DS}/-I_{DS}$). The conventional analytical equation used to find V_M, derived from the MOSFET square law model, assumes that the mobility and threshold voltage remain constant during operation [18,19]. However, in organic or oxide TFTs, this analytical approach may not always hold true. Therefore, an accurate calculation of V_M would require a fitting procedure to get the functional dependence of the mobility and threshold voltage as a function of V_{GS} and V_{DS}. Recently, we have proposed a method that does not require any fitting parameters, such as the carrier mobility or the threshold voltage, and in principle requires just a pair of measurements of R_n and R_p, which can be extracted from the output characteristics of independent TFTs, as a function of $V_{GS} = V_{DS}$ (as shown in Fig. 2(b) and (d)) [10]. Note, that testing at different V_D values is not really necessary once the output characteristics are measured for a large enough range of $V_{GS} = V_{DS}$. This is because the values of I_{DS} and consequently R_n and R_p can be interpolated from the measured output characteristics of the *n*-channel and *p*-channel TFTs. The absolute values of the difference of R_n and R_p, $R_d = |R_n - R_p|$, can be estimated for arbitrary values of V_D. Here, the value of V_M is given as the $V_{GS} = V_{DS}$ value where R_d reaches a minimum value.

Fig. 3(a) shows absolute values of R_d. Fig. 3(b) shows the corresponding hysteresis VTCs and static gain (dV_{OUT}/dV_{IN})

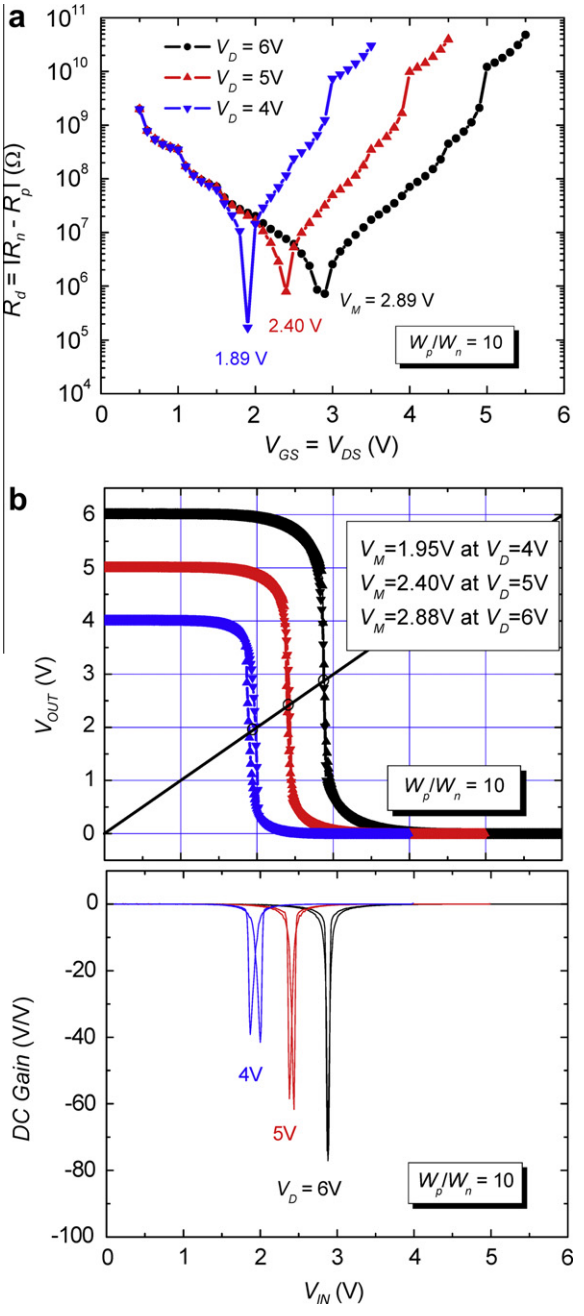

Fig. 3. (a) Absolute values of the differences of total resistances of pentacene *p*-channel and *a*-IGZO *n*-channel TFTs at $V_{GS} = V_{DS}$ by sweeping V_{GS} from 0 to ±4 V, ±5 V, ±6 V (positive for *n*-channel TFT, negative for *p*-channel TFT); (b) their corresponding voltage transfer characteristics and static gains of the hybrid complementary inverters for $W_p/W_n = 10$ at different supply voltages of 4, 5, and 6 V.

Table 1
Performance of an inverter using vertically stacked *p*-channel (pentacene) TFT on the top of an *n*-channel (*a*-IGZO) TFT.

W_p/W_n (μm/μm)	V_D (V)	*Maximum* dV_{OUT}/dV_{IN}	NM_L (V)	NM_H (V)	ΔV_{IN} (V)	V_M (measured) (V)	V_M (calculated) (V)	$R_p = R_n$ (MΩ)
4000/400	4	−42	1.57	1.72	0.39	1.95	1.89	24
	5	−61	1.87	2.07	0.47	2.41	2.40	11
	6	−78	2.17	2.46	0.62	2.88	2.89	5.8

values of the inverters for V_D = 4, 5, and 6 V. As expected from the comparison of the V_M extracted as the minimum value of R_d, at the optimum value of V_D, a reasonably centered V_M with high and balanced noise margins was achieved. Note that hysteresis-free VTCs of the inverter are desirable for stable circuit operations. Negligible hysteresis of the inverters for forward and reverse input biases can be attributed to the hysteresis-free current voltage characteristics, a necessary but not sufficient condition to assure the long-term operational stability of inverters. While this inverters show good short-term stability, under continuous prolonged operation we would expect variations of the threshold voltage, due to deep trapping events at the semiconductor/gate dielectric interfaces, to affect the long-term stability of these inverters. However, this geometry offers a clear path for the optimization of the long-term operational stability because it allows independent passivation of the interfaces of each individual TFT. The performance of this complementary inverter is summarized in Table 1. The maximum static gain value at V_D = 5 V was −61 V/V at V_M = 2.41 V. The corresponding value of NM_L and NM_H are 1.87 and 2.07 V with the steepness of ΔV_{IN} = 0.47 V (9.4% of max V_{IN}). At the switching threshold voltage values, $R_p = R_n$ was found to be 11 MΩ. Further reduction of the operating voltage and size of the TFTs could be achieved without significant degradation of performance because the high quality of the dielectric layers produced by ALD will allow increasing the capacitance density of the gate dielectrics by reducing the thicknesses of the top- and bottom-gate Al_2O_3 layers. Furthermore, the low temperature process of the ALD method makes the proposed geometry and fabrication method also compatible with the use of all-organic semiconductors.

4. Conclusion

In summary, we demonstrated a novel hybrid flexible organic–inorganic complementary inverter geometry with vertically stacked *p*-channel and *n*-channel TFTs. To implement this geometry a pentacene *p*-channel TFTs was stacked on top of an *a*-IGZO *n*-channel TFT. The complementary inverters used *n*- and *p*-channel TFTs with channels having different aspect ratios and dielectric layers with a different thickness to achieve high and balanced noise margins with high static gains. Al_2O_3 layers grown by atomic layer deposition were used as bottom- (100 nm) and top-gate (75 nm) dielectric layers for the *n*-channel *a*-IGZO and *p*-channel pentacene TFTs, respectively. These layers had a high capacitance density of 81 ± 1 and 108 ± 2 nF/cm^2, respectively. With a shared common gate electrode positioned in between two gate dielectric layers, bottom source/drain contact *n*- and top source/drain contact *p*-channel TFTs showed saturation mobility values of 0.3 ± 0.02 and 5.3 ± 0.2 cm^2/Vs and threshold voltages of −2.0 ± 0.2 and 2.1 ± 0.2 V, respectively. Complementary inverters showed voltage transfer curves with negligible hysteresis due to hysteresis-free transfer and output characteristics of the individual TFTs. Hybrid complementary inverters yielded a high gain of 61 V/V and high and balanced noise margins with low and high noise margin values of 1.87 and 2.07 V, respectively. These values correspond to 75% and 83% of their theoretical maximum, with high steepness of 0.47 V at a low voltage of 5 V. Balanced "*on*-currents" during inverter operations could be obtained because this geometry allows for independent control of the channel widths, the *n*- to *p*-channel ratios, as well as separate control of the thickness of the gate dielectric layers. The use of vertically stacked *p*- and *n*-channel TFTs in complementary circuits is a promising way to realize higher packing density and higher interconnectivity with low power by the reduction of the interconnection lengths and parasitic resistances.

Acknowledgements

This material is based upon work supported in part by the STC Program of the National Science Foundation under Agreement No. DMR-0120967 and by the Office of Naval Research (Grant No. N00014-04-1-0120). This work was performed in part at the Microelectronics Research Center at Georgia Institute of Technology, a member of the National Nanotechnology Infrastructure Network, which is supported by NSF (Grant No. ECS-03-35765).

References

[1] S. Lee, B. Koo, J. Shin, E. Lee, H. Park, H. Kim, Appl. Phys. Lett. 88 (2006) 162109.
[2] H. Klauk, U. Zschieschang, J. Pflaum, M. Halik, Nature 445 (2007) 745.
[3] K. Nomura, H. Ohta, A. Takagi, T. Kamiya, M. Hirano, H. Hosono, Nature 432 (2004) 488.
[4] E.M.C. Fortunato, P.M.C. Barquinha, A. Pimentel, A.M.F. Goncalves, A.J.S. Marques, L.M.N. Pereira, R.F.P. Martins, Adv. Mater. 17 (2005) 590.
[5] C. Baek, S.M. Seo, Appl. Phys. Lett. 94 (2009) 153305.
[6] W.T. Lim, J.H. Jang, S.H. Kim, D.P. Norton, V. Craciun, S.J. Pearton, F. Ren, H. Shen, Appl. Phys. Lett. 93 (2008) 082102.
[7] Y. Ogo, H. Hiramatsu, K. Nomura, H. Yanagi, T. Kamiya, M. Hirano, H. Hosono, Appl. Phys. Lett. 93 (2008) 032113.
[8] M.S. Oh, W. Choi, K. Lee, D.K. Hwang, S. Im, Appl. Phys. Lett. 93 (2008) 033510.
[9] J.H. Na, M. Kitamura, Y. Arakawa, Appl. Phys. Lett. 93 (2008) 213505.
[10] J.B. Kim, C. Fuentes-Hernandez, S.J. Kim, S. Choi, B. Kippelen, Org. Electron. 11 (2010) 1074.
[11] J.B. Kim, C. Fuentes-Hernandez, S.J. Kim, W.J. Potscavage, S. Choi, B. Kippelen, Org. Electron. 11 (2010) 1351.
[12] J.B. Kim, C. Fuentes-Hernandez, W.J. Potscavage, X.H. Zhang, B. Kippelen, Appl. Phys. Lett. 94 (2009) 142107.
[13] X.H. Zhang, B. Domercq, X.D. Wang, S. Yoo, T. Kondo, Z.L. Wang, B. Kippelen, Org. Electron. 8 (2007) 718.
[14] C. Baldacchini, C. Mariani, M.G. Betti, L. Gavioli, M. Fanetti, M. Sancrotti, Appl. Phys. Lett. 89 (2006) 152119.

[15] Y. Shimura, K. Nomura, H. Yanagi, T. Kamiya, M. Hirano, H. Hosono, Thin Solid Films 516 (2008) 5899.
[16] X.H. Zhu, D.N. Zheng, W. Peng, J.G. Zhu, X.W. Yuan, J. Li, M.J. Zhang, Y.F. Chen, H.Y. Tian, X.P. Xu, Mater. Lett. 58 (2004) 3591.
[17] J.B. Kim, C. Fuentes-Hernandez, B. Kippelen, Appl. Phys. Lett. 93 (2008) 242111.
[18] S.-M. Kang, Y. Leblebici, CMOS Digital Integrated Circuits Analysis & Design, third ed., McGraw-Hill, New York, 2003.
[19] J.M. Rabaey, Digital Integrated Circuits: A Design Perspective, first ed., Prentice Hall, New Jersey, 1995.

Organic Electronics 12 (2011) 51–61

Contents lists available at ScienceDirect

Organic Electronics

journal homepage: www.elsevier.com/locate/orgel

Theoretical investigation on electronic structure and luminescent properties of 6-phenyl-4-(*p*-R-phenyl)-2,2′-bipyridyl (R = Me, COOMe, $P(O)(OEt)_2$) (C^N^N) platinum(II)R′(R′ = Cl or C≡CPh) complexes

Xiao-Na Li [a,b], Zhi-Jian Wu [a], Liang Zhou [a,b], Xiao-Juan Liu [a], Hong-Jie Zhang [a,*]

[a] State Key Laboratory of Rare Earth Resource Utilization, Changchun Institute of Applied Chemistry, Chinese Academy of Sciences, Changchun 130022, People's Republic of China
[b] Graduate School of the Chinese Academy of Sciences, Beijing, People's Republic of China

ARTICLE INFO

Article history:
Received 29 August 2010
Received in revised form 4 October 2010
Accepted 16 October 2010
Available online 31 October 2010

Keywords:
Density functional theory
Pt(II) complexes
Phosphorescence
Electroluminescence

ABSTRACT

Quantum chemical method was used to investigate the geometrical structures, electronic properties, absorption and phosphorescent mechanism of four Pt(II) complexes 6-phenyl-4-(*p*-R-phenyl)-2′,2-bipyridyl (C^N^N)Pt(II)Cl, (R = Me, (**1a**); COOMe (**1b**), $P(O)(OEt)_2$ (**1c**), and 6-phenyl-4-(*p*-Me-phenyl)-2′,2-bipyridyl (C^N^N)Pt(II) C≡CPh (**2a**). The geometrical structures and electronic properties of **1a**–**1c** are insensitive to the variation of substituents, because of their longer distance to Pt(II) center. However, changes are significant for **2a** with respect to **1a** due to the direct connection of C≡CPh group with phosphorescent Pt(II) center. The oscillator strengths of the lowest energy absorptions for **1a**–**1c** are small, and this intensity for **2a** gets a remarkable enhancement due to the increase of electronic delocalization on the acetylide and Pt(II). More importantly, different phosphorescent quantum yields of these complexes are compared, especially between **1a** and **2a**. It is believed that the higher e_g^*-like Pt d-orbital, the larger ^{3}MC–^{3}MLCT energy gap as well as the deeper potential energy surface (PES) of **2a** than **1a** are the main reasons accounting for its higher efficiency of **2a**. In addition, the potential as light-emitting layer materials of these complexes are investigated.

© 2010 Elsevier B.V. All rights reserved.

1. Introduction

Phosphorescent d^6 and d^8 transition-metal complexes have been attracting an increased interest for the design and synthesis of new functional molecular materials. Due to the strong spin–orbit coupling effect, these complexes produce bright emission from excited states with an increased contribution from the metal-to-ligand charge transfer (MLCT) character, which effectively breaks down the spin-selection rule, facilitating a change in multiplicity and the subsequent radiative transition from the triplet state to the ground state [1]. The potential applications of these complexes include the chromophores for promoting photoinduced charge separation in artificial photosynthesis [2]. High-efficiency Ir(III) and Os(II) complexes represent the examples of phosphorescent transition-metal complexes with d^6 electronic configuration [3]. Because they generally possess an octahedral geometry, which can efficiently prevent the triplet–triplet annihilation arising from strong bimolecular interactions of phosphor, such that the respective emission can be produced in a rather effective manner: high phosphorescent quantum yield and short lifetime. Pt(II) complexes are typical phosphorescent materials with d^8 electronic configuration. The dsp^2 hybridization determines the square-planar structure of these complexes which can facilitate electron delocalization and thus lead to various charge transfer states, such as MLCT, ligand-to-ligand charge transfer (LLCT), or intraligand charge transfer (ILCT). Furthermore, similar to octahedral geometry,

* Corresponding author. Tel.: +86 431 85262127; fax: +86 43185698041.
E-mail address: hongjie@ciac.jl.cn (H.-J. Zhang).

1566-1199/$ - see front matter © 2010 Elsevier B.V. All rights reserved.
doi:10.1016/j.orgel.2010.10.011

square-planar structure is also in favor of electron–hole creation and separation, therefore, these complexes are ideal candidates in OLEDs fabrication and related super-molecular devices.For Pt(II) complexes, the presence of low-lying metal-centered (MC) dd excited states are often used to account for the nonemissive behavior, as the potential-energy minima of its dd excited states is markedly displaced from that of the ground-state structure, and thus efficient nonemissive decay pathways are provided. A general strategy for promoting emission over nonemissive behavior has emerged, namely to ensure that dd excited states involving the population of the strong antibonding $d_{x^2-y^2}$ orbital are not thermally accessible to either the MLCT or ligand-centered (LC) excited state for emission quenching. The key to increase the energy of the dd nonemissive decay is to introduce strong-field ligands. Yip et al. [4] have shown that the introduction of electron-releasing substituents at the 4′-position of the terpyridine ligand in [Pt(tpy)Cl$^-$] leads to emission in fluid solution at room temperature with lifetimes of microseconds. However, only coordination of transition metal ion with strong-field ligand is not enough. Simple modification of the electronic properties of ligands and changes of substituents were expected to perturb the relative energies of MLCT, LLCT or dd excited states, and consequently the phosphorescent quantum yields and lifetimes. For instance, Pt(II) complexes containing tridentate ligands, 6-phenyl-4-(*p*-R-phenyl)-2′,2-bipyridyl (C^N^N)Pt(II)Cl, (R = Me, (**1a**); COOMe (**1b**), and P(O)(OEt)$_2$ (**1c**)) [5], the phosphorescent efficiency changes from 0.066 to 0.035, and lifetime changes from 580 to 385 ns, respectively. If Cl group in **1a** is replaced by acetylide (**2a**) [6], the phosphorescent quantum yield can be improved to 0.073 in CH_2Cl_2 solution. In this case, it is expected that the dd excited states splitting would be increased and the resultant dd excited states raise to higher energies with respect to MLCT states. Therefore, an in-depth understanding of the effect of substituents and coordinating ligand on the photophysical behavior is desirable for rational syntheses of highly emissive phosphorescent materials. In this paper, DFT and time-dependent DFT (TDDFT) calculations have been performed to rationalize the reasons resulting in the different phosphorescent properties and provide a further insight into the spectroscopic origins of this class of complexes.

2. Computational details

The ground-state and the lowest-lying triplet excited-state geometries were optimized by DFT [7] with Becke's LYP (B3LYP) exchange-correlation functional [8] and the unrestricted B3LYP (UB3LYP) [9] approach, respectively. There were no symmetry constraints on these complexes. At the respective optimized geometries of ground and excited states, TDDFT/B3LYP [10] calculations associating with the conductor polarized continuum model (CPCM) [11] in dichloromethane (CH_2Cl_2) media were carried out in order to obtain the vertical excitation energies of singlet (S_n) and triplet (T_n) states. Recent calculations with TDDFT method for transition-metal complexes have supported its credibility and gave good agreement with experimental spectra [12]. Spin–orbital coupling (SOC) causes mixture of singlet and triplet states, and the latter is allowed to participate in both absorption and emission; however, no SOC factor is included in current TDDFT calculation under G03 software. Su and co-workers explored the SOC effect on the excited energy of Re complexes [13]. The results revealed that SOC has a tiny effect on transition and it provides available spectral features for transition-metal Re complexes.

In the calculation, the quasi-relativistic pseudo-potentials of **Pt** atoms proposed by Hay and Wadt [14] with 16 valence electrons were employed, and a "double-ξ" quality basis set LANL2DZ was adopted. 6-31G(d) was used for nonmetal atoms. All calculations were performed with Gaussian 03 software package [15].

3. Results and discussion

3.1. Geometries in the ground and the lowest-lying triplet excited states

The sketch map for the four complexes is presented in Chart 1 and the optimized ground-state structure of **1a** is shown in Fig. 1. The main structural parameters are summarized in Table 1 together with the X-ray crystal structures data of **1a** [5]. For **1a**–**1c**, the main bond lengths and bond angles are insensitive to the variation of substituents, i.e., nearly the same for the three complexes, as shown in Table 1. The Mulliken atom charges on the related atoms of **1a**–**2a** are presented in Fig. S1 (Supporting Information). Fig. S1 indicates that charge is influenced locally, mostly from the atoms to which the substituents are attached. Therefore, the Mulliken charges on Pt(II) and its surrounding atoms are insensitive to the variation of substituents, which leads to the similar bond lengths among **1a**–**1c**. Our conclusions are in good agreement with the results reached by Tong and Che recently [16], who reported a series of platinum complexes similar to systems in this paper. Table 1 indicates that the optimized bond lengths of **1a** are in general agreement with the experimental values [5]. The largest discrepancies are Pt–N2 bond and C2–C3–C4–C5 dihedral angle, which deviate from the measured data of about 0.08 Å and 37.3°, respectively. This is due to the fact that the optimized **1a** is a free molecule in the gas phase, while the measured condition is in the tight crystal lattice. As shown in Fig. 1, the repulsion between H1 and H2 distorts the complex in the gas phase. Moreover, there is π-stacking (∼3.33 Å) of bipyridyl parts of C^N^N ligands between adjacent molecules. This is because the π-accepting ability of pyridine ring is stronger than the cyclometalated phenyl ring, and the co-planar structure of the pendant phenyl ring with the cyclometalated portion of two C^N^N ligands results from the crowded intermolecular stacking. For **1a**–**1c**, Pt–N1 bond (1.978 Å) is ca. 0.21 Å longer than Pt–N2 (2.188 Å). This can be attributed to the fact that side pyridine is localized *trans* to the phenyl ring, which has strong *trans* effect and weakens the metal–nitrogen interaction.

Compared with **1a**, the replacement of Cl group with acetylide in **2a** causes the elongation of Pt–C and Pt–N distances, especially for Pt–N1 bonds. In **2a**, Pt–C6 bond is ca. 0.03 Å shorter than Pt–C1 bond. This is due to the fact that

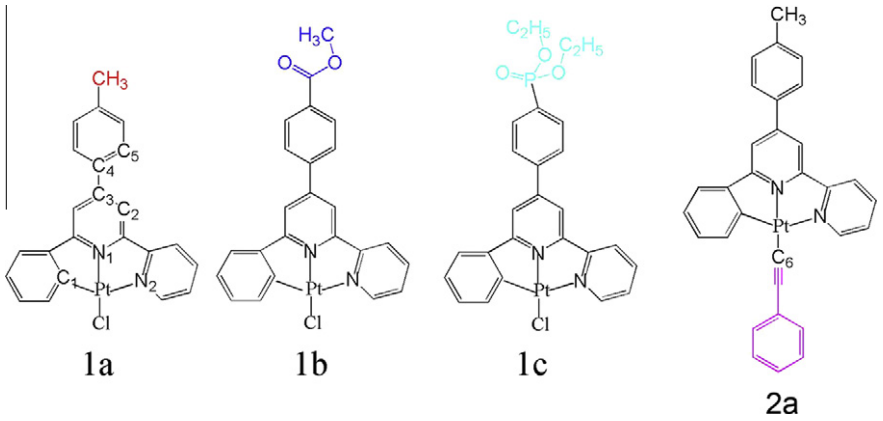

Chart 1. Schematic structures of the investigated complexes.

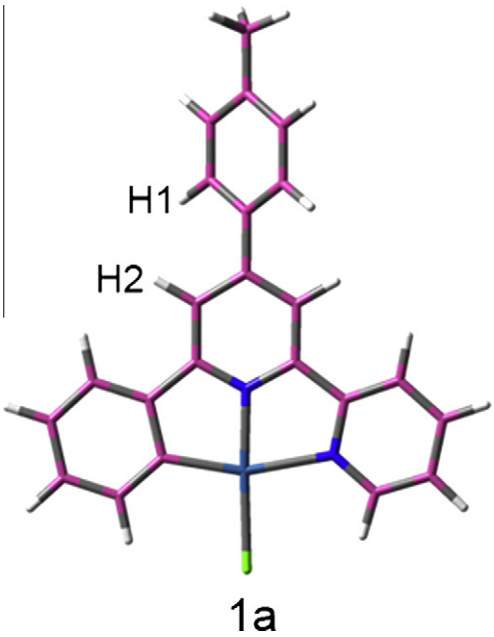

Fig. 1. Optimized structure of 1a in the ground states at DFT/B3LYP level.

phenyl ring in acetylide exhibits a stronger conjugating effect on the C≡C bond, thus leads to higher negative electron density on C6(−0.365 |e⁻|) than C1(−0.241 |e⁻|) and results in shorter Pt–C6 bond than Pt–C1 bond. This substituent effect of phenyl ring on ligand has been observed previously [17]. Moreover, we noted that Pt–N1 bond is elongated significantly with respect to that in **1a**. This indicates that the strong σ donation of Pt–C_{ethyne} bond resulting in the elongation of Pt–N1 bond at its *trans* position.

The calculated geometrical parameters of the lowest-lying triplet excited states for **1a**–**2a** are also listed in Table 1. For all the four complexes, Pt–C1 bond elongates in T_1 states compared with those in S_0 states, while all the other metal–ligand interaction becomes strengthened in T_1 states. This indicates that under higher energy excitation, Pt–C1 bond will be broken first due to its anbibonding combination with Pt d-orbital. In T_1 states, there is negligible change of C1–pt–N1 angle, while N1–pt–N2 bond angles increase about 1° for all the four complexes, which results from the contraction of Pt–N1 and Pt–N2 bonds. In addition, the distortion between phenyl ring and C^N^N moiety significantly reduced for **1a**–**1c** because of the decrease of C2–C3–C4–C5 dihedral angles. However, this change for **2a** is much smaller. Furthermore, bite

Table 1
The calculated geometrical parameters of the investigated complexes together with the measured values.

	1a		**1b**		**1c**		**2a**		Exptl. [5]
	S_0	T_1	S_0	T_1	S_0	T_1	S_0	T_1	
Bond length (Å)									
Pt–C1	1.995	2.008	1.995	2.001	1.994	2.001	1.997	2.024	1.993
Pt–N1	1.978	1.927	1.978	1.931	1.978	1.931	2.024	1.986	1.954
Pt–N2	2.188	2.178	2.188	2.180	2.188	2.176	2.197	2.180	2.109
Pt–Cl	2.363	2.345	2.361	2.348	2.361	2.349			2.3657
Pt–C6							1.965	1.920	
C3–C4	1.482	1.464	1.483	1.461	1.483	1.465	1.483	1.474	
Bond angle (°)									
C1–Pt–N1	82.2	82.4	82.2	82.5	82.2	82.5	81.8	81.6	82.08
N1–Pt–N2	78.3	79.4	78.3	79.2	78.2	79.2	77.0	78.2	79.31
C1–Pt–N2	160.5	161.9	160.5	161.7	160.5	161.8	158.8	159.7	
Dihedral angel (°)									
C2–C3–C4–C5	37.3	26.1	38.3	24.7	38.7	26.8	37.6	30.5	

angles (C1–pt–N2) of the chelating ligands play an important role in determining the photophysical properties of Platium(II) complexes [18]. Decrease in bite angle usually indicates faster non-radiative decay via MC states. The optimal bite angle for maximum orbital overlap would be 180° to offer sufficient ligand field strength. However, the calculated bite angles for **1a**–**1c** are around 160°, these small bite angles result from the binding to large transition metal ion. We noticed that the bite angles slightly increase in T_1 states for all the complexes, which is favorable to improve the phosphorescent quantum yield.

3.2. Frontier molecular orbital properties

It is well understood that the photophysical properties are strongly dependent on the character of frontier orbitals and the resulting HOMO–LUMO energy gap, which in turn are governed by their basic skeletal arrangement and the electronic properties of substituents anchored to these chelating chromophores. Frontier molecular orbital (FMO) compositions for **1a**–**2a** are given in Tables S1–S4 (supporting information). The HOMO and LUMO distribution, energy levels and energy gaps are plotted in Fig. 2.

For **1a**, the HOMO is composed of the mixture of Pt d-orbital (42%), Cl p-orbital (21%) and phenyl ring moiety of C^N^N ligand (37%), and Pt is antibonding combination with both moieties. We noticed negligible participation of phenyl ring connected to the central pyridine of C^N^N ligand in HOMO. Therefore, one can anticipate that attaching different substituents on this phenyl ring will not cause a significant difference in orbital distribution and energy levels for **1b** and **1c**, as shown in Tables S1–S3 and Fig. 2. HOMO−1 of **1a** has similar composition with HOMO and is calculated only 0.04 eV lower than HOMO. Thus, HOMO and HOMO−1 is a couple of nearly degenerate orbitals. HOMO−2, localized at about 0.19 eV lower than HOMO−1, has large composition from Cl group (47.6%) and with the remaining mainly distributed over Pt d-orbital ($31.3d_{xy}$) and C^N^N ligand. HOMO−3 lying at −6.06 eV is dominantly composed of 91% Pt d-orbital ($71.6d_{z^2}$ + $1.5d_{xy}$) and HOMO−4 is mainly localized on C^N^N ligand.

Comparing **2a** with **1a**, the replacement of Cl with acetylide causes significant differences in composition and energy levels, in which HOMO is controlled by acetylide ligand mixed with some contribution from Pt d-orbital as shown in Table S4. HOMO−1 has increased participation from C^N^N moiety, which is different from that of HOMO, and this can be used to account for the large energy gap between HOMO and HOMO−1.

Due to the stronger electron accepting ability of pyridine than phenyl ring, LUMO for the four complexes is predominantly arising from the bipyridines moiety of C^N^N ligand. Since the substituents and ancillary ligands are not connected directly to C^N^N moiety, thus LUMO distribution and energy levels are not pertured much. In **1b**, the slightly lower LUMO energy and the increased participation from phenyl ring result from the electron-withdrawing effect of –COOH group. There is a large energy gap between LUMO+1 and LUMO for **1a**–**2a**, because the orbital composition extends greatly to phenyl ring moiety in the LUMO+1. Other unoccupied orbitals with higher energy tend to localized on both the phenyl ring and C^N^N ligand across, with the exception of LUMO+2 in **1a** and **2a**.

The dd state is usually regarded as the intrinsic reason for the nonemission of square-planar Pt(II) complexes in solution. Therefore, destabilizing and deactivating the dd excited state is of great significance in experiments. In the calculation, the calculated e_g^*-like orbitals are localized at 0.03, −0.08, −0.06, and 0.54 eV, which are higher than HOMO about 5.58, 5.58, 5.59, and 5.30 eV for **1a**–**2a**, respectively, and are much larger than MLCT, LLCT and ILCT energies.

Fig. 2 shows that the replacement of Cl with acetylide increases the HOMO energy level more markedly than that of the LUMO and results in the narrow HOMO–LUMO gap (ΔE_{H-L}) than **1a**–**1c**. Moreover, for **2a**, the energy gaps between HOMO and HOMO−1, LUMO and LUMO+1 are large. These large energy gaps may demonstrate the difficulty of electron transition from HOMO−1 or lower occupied MOs to LUMO+1 or higher unoccupied MOs. This implies that HOMO–LUMO transition may be dominant for the lowest singlet excited states.

3.3. Absorption spectra

Starting from the ground-state geometries, singlet and triplet excited states of **1a**–**2a** were calculated by TDDFT/B3LYP method with CPCM in CH_2Cl_2 media, thus allowing the simulation of absorption spectra up to 280 nm. The calculated transition states, oscillator strength, and assignment for singlet and triplet excited states are listed in Table 2 and Table S5 (Supporting Information), respectively.

As shown in Table 2, for **1a**–**1c**, the calculated lowest energy absorption follows the order **1b** > **1c** > **1a**, which is consistent with the variation rule of energy gaps because HOMO–LUMO transition configurations are predominantly $S_0 \rightarrow S_1$ transition. As a result of the negligible intensity in the range 0.0012–0.0022, the $S_0 \rightarrow S_1$ transition is probably forbidden and would be practically absent in the absorption spectra. However, for **2a**, the transition intensity of S_1 state (0.2716) is significantly improved compared with **1a**–**1c**. The calculated transition dipole moments for **1a**–**2a** are 0.1844, 0.1377, 0.1520 and 2.1241 a.u., respectively. The increased intensity in **2a** originates from the increased transition dipole moments, which is defined as the transition density weighted by the distance of the atom from the center of the gravity [19]. The co-planar molecular structure of C≡CPh and C^N^N moieties is most favorable to achieve an enlargement of the absorption intensity and transition dipole moment. From the above discussion on FMO, the calculated 470, 478 and 475 nm transitions for **1a**–**1c** can all be described as {[d(Pt) + π(Cl + trph) → π*(trph)]} transition with characters of MLCT, LLCT, ILCT. For **2a**, the charge transfer (CT) transition of MLCT and LLCT {[d(Pt) + π(C≡Cph) → π*(trph)]} contributes to S_1 excitation as shown in Table 2.

For **1a**–**2a**, the lower lying distinguishable absorption bands in experiment do not appear in the singlet excited states calculation, which indicates that they are singlet-to-triplet in nature as shown in Table S5. The measured 436, 440 and 439 nm triplet absorptions for **1a**–**1c** all

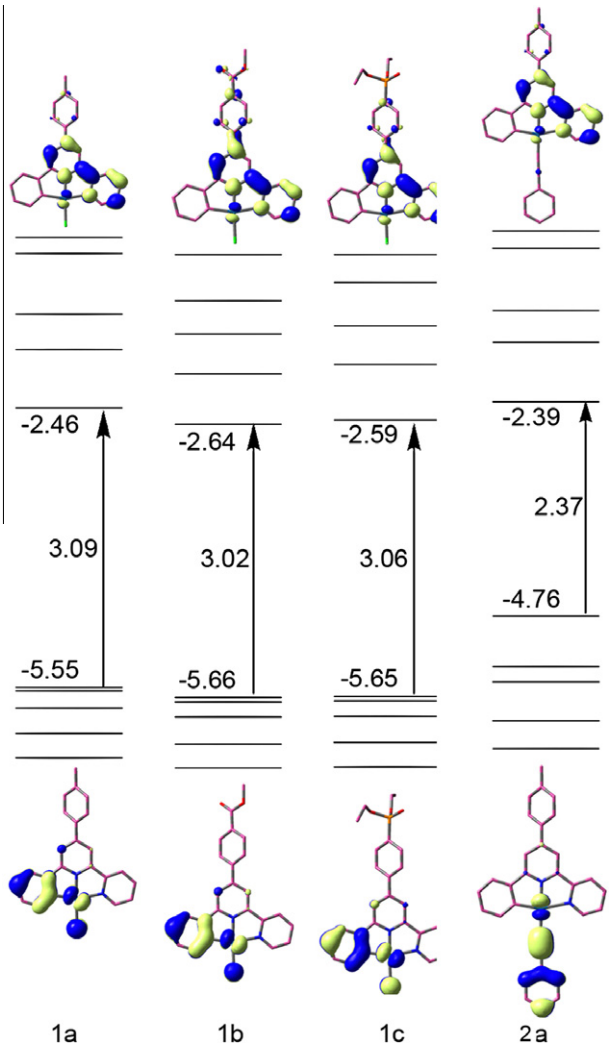

Fig. 2. Energy levels, energy gaps (in eV) and orbital composition distribution of HOMO and LUMO for the four complexes.

correspond to MLCT, LLCT and ILCT characters. For **2a**, the calculated 463 and 444 nm triplet absorptions correspond to the 461 and 448 nm measured values in experiment, respectively, which also have MLCT, LLCT and ILCT characters.

The first distinguishable lower energy absorption bands appear at around 370 nm for the four complexes, and transition with the largest oscillator strengths localized at 352, 352, 350 and 362 nm for **1a**–**2a**, respectively. For **1a**, the Pt d-orbital to trph π^*-orbital transition (MLCT) is the main character, and for **1b** and **1c**, ligand-based transition dominants the 352 and 350 nm absorption. In **2a**, mixed transition characters of MLCT, LLCT and ILCT from Pt d-, C≡Cph and trph π-orbital to trph-based π^*-orbital is predominantly for the 362 nm absorption. The observed strongest absorptions in experiment localized at higher energy region are 291, 288, 285 and 283 nm for **1a**–**2a**, respectively. With the exception of **1a**, the other three complexes appear to be composed of a series of transitions, and each is dominated by two more intense excitations as shown in Table 2. The 291 nm absorption for **1a** is mainly contributed by transition configuration of HOMO−3 → LUMO+1(92%) with MLCT excitation to ph and trph π^*-orbital. The 288 and 283 nm shoulders for **1b** and **2a** appear to be composed of mixed π–π^* and MLCT transitions also with ph-and-trph-based π^*-orbital as arrival orbital. For **1c**, the calculated 298 and 293 nm absorptions compose the 285 nm shoulder, which are both π–π^* transitions in characters.

The calculated results agree with the experimental observations that MLCT component is more remarkable in lower energy region and triplet excitation is appearance in the absorption spectra, which indicates that spin-selection rules are not strictly obeyed for heavy third-row transition-metal complexes. Though the participation of MLCT is weak, it is an efficient process to collect light and therefore enhances the luminescence quantum yields. The selection of substituents with electron-donating properties or ancillary ligand with large π-conjugation planar can also improve the light absorption efficiency.

Table 2
Calculated singlet absorption for **1a–2a** in CH_2Cl_2 media at TD-B3LYP level, together with experimental values.

Complex	States	λ (nm)/E (eV)	Oscillator	Main configuration	Assign	Exptl. [5,6]
1a	S_1	470/2.64	0.0022	H → L(100%)	d(Pt) + π(Cl + trph) → π*(trph)/MLCT/LLCT/ILCT	
	S_6	352/3.52	0.2082	H-3 → L(70%)	d(Pt) → π*(trph)/MLCT	369
	S_7	343/3.61	0.1177	H-1 → L + 1(75%)	d(Pt) + π(Cl + trph) → π*(ph + trph)/MLCT/LLCT/ILCT	
	S_9	327/3.80	0.1661	H-5 → L(93%)	π(Cl + ph) → π*(trph)/LLCT	336
	S_{14}	297/4.18	0.3150	H-3 → L + 1(92%)	d(Pt) → π*(ph + trph)/MLCT	291
1b	S_1	478/2.59	0.0012	H → L(100%)	d(Pt) + π(Cl + trph) → π*(ph + trph)/MLCT/LLCT/ILCT	
	S_6	352/3.53	0.2540	H-4 → L(75%)	π(trph) → π*(ph + trph)/LLCT/ILCT	369
	S_7	342/3.62	0.1329	H-1 → L + 1(76%)	d(Pt) + π(trph) → π*(ph + trph)/MLCT/LLCT/ILCT	336
	S_{11}	303/4.10	0.3380	H-1 → L + 2(58%)	d(Pt) + π(trph) → π*(ph + trph)/MLCT/LLCT/ILCT	
				H-5 → L(34%)	π(Cl + ph) → π*(ph + trph)/LLCT/ILCT	
	S_{13}	297/4.18	0.2454	H-4 → L + 1(52%)	π(trph) → π*(ph + trph)/LLCT/ILCT	288
				H → L + 3(27%)	d(Pt) + π(Cl + trph) → π*(ph + trph)/MLCT/LLCT/ILCT	
	S_{15}	295/4.20	0.1893	H-4 → L + 1(41%)	π(trph) → π*(ph + trph)/LLCT/ILCT	
				H → L + 3(40%)	d(Pt) + π(Cl + trph) → π*(ph + trph)/MLCT/LLCT/ILCT	
1c	S_1	475/2.61	0.0015	H → L(100%)	d(Pt) + π(Cl + trph) → π*(trph)/MLCT/LLCT/ILCT	
	S_6	350/3.54	0.2301	H-4 → L(76%)	π(trph) → π*(trph)/ILCT	376
	S_8	339/3.65	0.1456	H-1 → L(82%)	d(Pt) + π(Cl + trph) → π*(trph)/MLCT/LLCT/ILCT	336
	S_{11}	298/4.16	0.2698	H-5 → L(74%)	π(Cl + ph) → π*(trph)/LLCT	
	S_{14}	293/4.23	0.3889	H-4 → L + 1(75%)	π(trph) → π*(ph + trph)/LLCT/ILCT	285
2a	S_1	505/2.46	0.2716	H → L(100%)	d(Pt) + π(C≡Cph) → π*(trph)/MLCT/LLCT	
	S_6	362/3.42	0.1524	H-1 → L + 1(96%)	d(Pt)) + π(C≡Cph + trph) → π*(ph + trph)/MLCT/LLCT/ILCT	370
	S_{10}	335/3.70	0.2215	H-4 → L(84%)	π(C≡Cph)→π*(trph)/LLCT	337
	S_{20}	287/4.32	0.1590	H-5 → L + 1(72%)	π(trph) → π*(ph + trph)/LLCT/ILCT	
	S_{22}	284/4.35	0.5597	H → L + 4(89%)	d(Pt) + π(C≡Cph) → π*(ph+trph)/MLCT/LLCT	283

3.4. Phosphorescence

On the basis of the optimized lowest triplet excited-state structures, TDDFT method was used to calculate emission energies. The calculated results are listed in Table 3 and the molecular orbital compositions related to emission are listed in Table 4. The transition responsible for the emission is simulated in Fig. 3.

Table 3 shows that the calculated lowest energy emissions of the four complexes are localized at 619, 629, 621, and 761 nm, respectively. The calculated Stokes shifts between the ^{3}MLCT absorption and the lowest energy emissions are in the range of 0.32–0.41 eV for **1a–2a**, and they are comparable with our investigation of Ir complexes [20]. These larger Stokes shifts indicate that the lowest-lying emissions for **1a–2a** will be in a larger mixture of ^{3}MLCT and ligand-based $^3(\pi \rightarrow \pi^*)$ transitions [21]. Our calculated results agree with the experimental observations that the measured emission spectra give structured emission with several shoulders [5]. Because emission bands from ^{3}MLCT states are generally broad and featureless, while $^3(\pi \rightarrow \pi^*)$ states typically give highly structured emissions [21].

For **1a–1c**, the predicted emissions deviate from measured values by 42, 55 and 48 nm, respectively, which is comparable with the results reported recently [22]. However, the calculated absolute emission of 761 nm for **2a** deviates largely from the measured result of 595 nm [6]. One reason is that the excited-state geometry we used here was optimized in the gas phase, and another reason is the limited dimensions of the basis set. Table 3 and Fig. 3 show that the 619, 629 and 621 nm emissions for **1a–1c** are all nearly evenly contributed by HOMO → LUMO and HOMO-1 → LUMO transition configurations, and the three complexes have similar orbital compositions. In Table 4, the HOMO−1 of **1a–1c** is localized on Pt d-orbital, Cl p-orbital, phenyl ring and center pyridine moieties of C^N^N ligand, which covers the whole molecule across. The HOMO is mainly the anbibonding combination of Pt d-orbital with C^N^N moiety. Therefore, the 619, 629 and 621 nm emissions can be described as {[d(Pt) + π(Cl + ph + trph)]→[π*(ph + trph/trph)]} transition with MLCT, LLCT and ILCT characters, and {[d(Pt) + π(trph)]→[π*(ph + trph/trph)]} transition with MLCT and ILCT characters. As expected, the 761 nm emission of T_1 state for **2a** arises mainly from HOMO → LUMO transition and has the

Table 3
Phosphorescent emissions of **1a–2a** in CH_2Cl_2 solution under the TDDFT calculations, together with the experimental values.

Complex	States	λ (nm)/E (eV)	Main configuration	Assign	Exptl. [5,6]
1a	T_1	619/2.00	H-1→L(54%)	d(Pt) + π(Cl + ph + trph) → π*(trph)/MLCT/LLCT/ILCT	577(max), 640(sh)
			H → L(37%)	d(Pt) + π(trph) → π*(trph)/MLCT/ILCT	
1b	T_1	629/1.97	H-1 → L(54%)	d(Pt) + π(Cl + ph + trph) → π*(ph + trph)/MLCT/LLCT/ILCT	574(max), 610(sh)
			H → L(49%)	d(Pt) + π(trph) → π*(ph + trph)/MLCT/LLCT/ILCT	
1c	T_1	621/2.00	H-1 → L(47%)	d(Pt) + π(Cl + ph+trph) → π*(ph + trph)/MLCT/LLCT/ILCT	573(max), 600(sh)
			H → L(39%)	d(Pt) + π(trph) → π*(ph + trph)/MLCT/LLCT/ILCT	
2a	T_1	761/1.62	H → L(100%)	d(Pt) + π(trph) → π*(trph)/MLCT/ILCT	595(max), 645(sh)

Table 4
Frontier molecular orbital compositions (%) in the excited states for complexes **1a–2a** at the UB3LYP/LANL2DZ level (where R′ = Cl (**1a–1c**) and C≡CPh (**2a**), R = CH_3 (**1a** and **2a**), $COOCH_3$ (**1b**), and $PO(OC_2H_5)_2$ (**1c**)).

Complex	Orbital	Energy (eV)	Pt	MO composition (%)				Main bond type
				R′	ph	trph	R	
1a	L	−3.68	5.4	1.0	8.7	84.3	0.6	π*(trph)
	H	−6.11	23.8/23.5 d_{xz}	0.7	1.2	74.3		d(Pt) + π(trph)
	H−1	−6.51	20.9/20.8 d_{yz}	13.5	38.1	24.1	3.4	d(Pt) + π(Cl + ph + trph)
1b	L	−3.87	5.7	1.1	11.0	80.5	1.8	π*(ph + trph)
	H	−6.34	25.0/23.5 d_{xz}	1.0	1.2	72.8		d(Pt) + π(trph)
	H−1	−6.72	27.4/26.6 d_{yz}	22.9	19.2	28.2	2.4	d(Pt) + π(Cl + ph + trph)
1c	L	−3.83	5.7	1.1	10.0	82.3		π*(ph + trph)
	H	−6.32	24.8/23.8 d_{xz}	1.0	1.1	73.1		d(Pt) + π(trph)
	H−1	−6.71	27.9/27.0 d_{yz}	24.1	15.4	30.4	2.3	d(Pt) + π(Cl + ph + trph)
2a	L	−3.14	4.2	4.0	6.4	85.0		π*(trph)
	H	−5.58	23.1/22.8 d_{xz}			76.0		d(Pt) + π(trph)

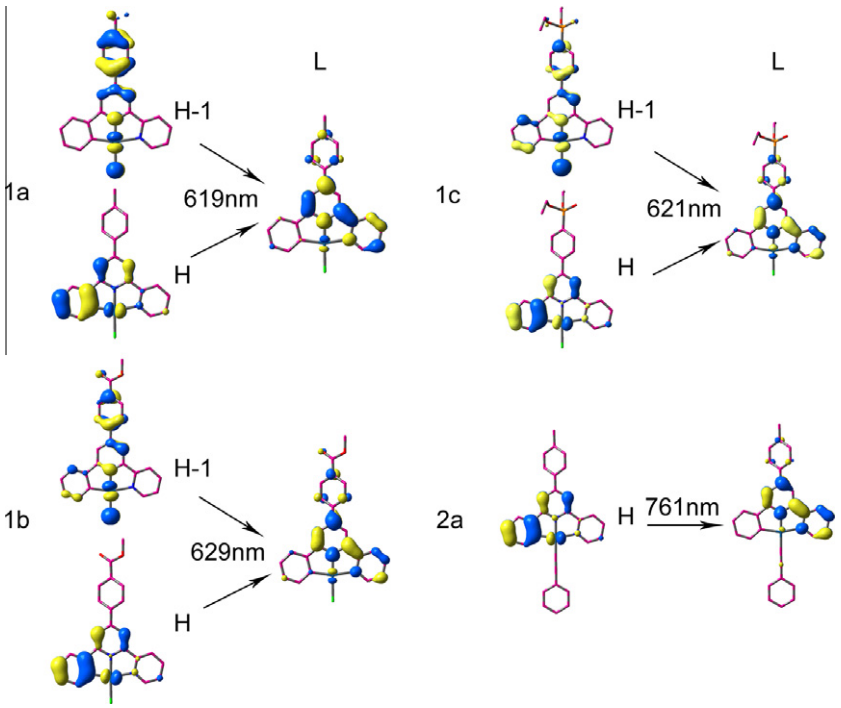

Fig. 3. Singlet electron emission for **1a–2a**, calculated at TDDFT/B3LYP level in CH_2Cl_2 solution.

characters of MLCT, LLCT and ILCT {[d(Pt) + π(trph)]→[π*(trph)]} as shown in Fig. 3.

In experiment, the measured phosphorescent quantum yields for **1b** and **1c** are lower than **1a**, however, the replacement of Cl with acetylide group in **1a** increases the quantum yield in **2a**. From the experimental quantum yields (Φ) and lifetime (τ) data, we obtained the k_r (radiative decay rate) and k_{nr} (non-radiative decay rate) values and the results are listed in Table 5, in which $k_r = \Phi/\tau$ and $k_{nr} = (1 - \Phi)/\tau$. Obviously, Φ can be affected by the competition between k_r and k_{nr}, namely, $\Phi = k_r/(k_r + k_{nr})$. Therefore, to increase the quantum yield, k_r should be increased and k_{nr} should be decreased simultaneously or respectively [23]. As shown in Table 5, the k_r values for **1a–2a** are found to be 3.6–7.9 times larger than k_{nr} values, probably, represent the main factor for regulating the luminescence behavior of these complexes. For **1a–1c**, the calculated k_r values decrease in the order **1a** → **1b** → **1c** and the k_{nr} values increase also in the order **1a** → **1b** → **1c**. According to the above expression, the resulting Φ values decrease in the order **1a** → **1b**→**1c**. The increased k_{nr} values for **1b** and **1c** than **1a** may result from the

Table 5
The calculated radiative decay rate (k_r) and nonradiative decay rate (k_{nr}), together with the measured lifetime (τ) and quantum yields (Φ).

	k_r ($\times 10^6$ s^{-1})	k_{nr}($\times 10^6$ s^{-1})	Φ [5,6]	τ (ns) [5,6]
1a	1.130	0.161	0.066	580
1b	0.974	0.247	0.038	390
1c	0.909	0.251	0.035	385
2a	1.510	0.190	0.073	485

electron-withdrawing effect of COOH and $PO(OC_2H_5)_2$ groups relative to CH_3, which can slightly decrease the metal–ligand interaction as reported previously for Ir complexes with COOH groups, though there no obviously bond lengths difference was observed [24]. The weakened metal–ligand interaction will facilitate the nonemissive transition decay. For **2a**, the larger k_{nr} value than **1a** results from the slightly weakened metal–ligand interaction as shown in Table 1. In addition, according to energy gap law, non-radiative rates increase for longer wavelength emission [25]. The larger Φ of **2a** than **1a**–**1c** can be ascribed to the increased k_r value, which is resulting from the increased light absorption section due to the presence of phenyl ring. It can increase the transition dipole moment of **2a** than **1a**–**1c**, which reflects the transition probability from the ground state to the excited states. The higher transition probability to the excited states means the larger emission probability and higher phosphorescent quantum yields [26].

The excited-state decay in these complexes can be attributed to a balance between activated decay via ^{3}MC state and non-radiative decay. Therefore, in this section, to gain insight into the nature of different phosphorescent quantum yields, the orbital diagram of triplet excited states, energy difference between ^{3}MC and ^{3}MLCT states, ground- and excited-states potential energy surface (PES) for **1a** and **2a** are represented in Fig. 4 by elongating and selectively freezing Pt–C bonds. The choice of Pt–C bond is due to the fact that Pt–C distance shows elongation on going from S_0 to T_1 minima. As shown in Fig. 4(a) and (b), along with the Pt–C bond stretching, the e_g^* -like Pt d-orbital is stabilized and rapidly become more accessible for the occupied orbitals, and the energy separation between ^{3}MC and ^{3}MLCT is significantly reduced for both complexes (Fig. 4(c)). The LUMO+2 for **1a** and LUMO+4 for **2a** are the lowest virtual orbitals receiving electron density in ^{3}MC states as Pt–C distance longer than 2.40 Å, and the ^{3}MC–^{3}MLCT energy separation for **1a** is smaller than that in **2a** as shown in Fig. 4(c). It is generally believed that far separation between metal-center ^{3}MC and the responding emissive state of ^{3}MLCT/$^3(\pi \rightarrow \pi^*)$ plays a key role to reduce non-radiative transition. In this case, the smaller ^{3}MC–^{3}MLCT energy separation in **1a** will facilitate non-radiative from ^{3}MC state. The T_1-PES was calculated by using the constrained geometry optimization method at UB3LYP level when the variations in Pt–C bond lengths changed in the range 1.80–2.40 Å. Then SCF energies of T_1 and S_0 states were calculated based on the T_1 optimized geometries. For S_0 and T_1 PES, the vertical axis indicates the SCF energy relative to the optimized ground-state geometry. As shown in Fig. 4(d) and (e), both S_0 and T_1 states become less stable in energy when Pt–C distance becomes shorter and longer. In addition, the T_1-PES for **2a** is slightly deeper than **1a**, which indicates larger energy barrier to its surrounding state. Furthermore, we noted that in **2a**, the T_1–S_0 energy separation increased when Pt–C distance is longer than 2.40 Å, which means that less surface crossing and radiationless transition from ^{3}MC take place in **2a** than in **1a**. These calculated results may also account for the measured slightly higher phosphorescent quantum yields of **2a** than **1a**.

3.5. Electroluminescent (EL) properties

Due to the bright phosphorescent emission of these complexes in CH_2Cl_2 solution and in the solid state, we are very interested in the EL properties of the complexes as light-emitting layer materials in OLED. In this section, ionization potentials (IPs), electron affinities (EAs), reorganization energy (λ), hole and electron extraction potential (HEP and EEP) are calculated, and the results are listed in Table 6. The details for these definitions can be obtained from our previous work [20,24]. For photoluminescent materials, a smaller IP value means easier hole injection ability and a larger EA value will facilitate electron injection.

The IP value for **2a** (6.08 eV) is much smaller than **1a**–**1c** (6.99–7.11 eV), which is consistent with the measured oxidation potentials of 0.94 V for **2a** and 1.10–1.14 V for **1a**–**1c** [5,6]. This also implies that the difficulties of hole injection from hole-transporting layer (HTL) to these complexes gradually decrease in the order **1c** → **1b** → **1a** → **2a**. By analysis of EA values, **1b** and **1c** can more easily accept an electron than **1a** and **2a** due to the slightly increased electron-withdrawing effect of COOH and $PO(OC_2H_5)_2$ substituents.

According to Marcus/Hush model [27], the charge (hole or electron) transfer rate k can be expressed by the following formula:

$$\kappa = \left(\frac{\pi}{\lambda \kappa_b T}\right)^{1/2} \frac{V^2}{\eta} \exp\left(-\frac{\lambda}{4\kappa_b T}\right) = A \exp\left(-\frac{\lambda}{4\kappa_b T}\right) \quad (1)$$

where T is the temperature, κ_b is the Boltzmann constant, λ is the reorganization energy, and V is the coupling matrix element between the ions and molecules which is dictated by the overlap of orbitals. As shown in Eq. (1), two factors, λ and V determine the k. Due to the limited intermolecular charge transfer range in solid-state, the mobility of charges has been demonstrated dominantly related to the internal reorganization energy λ for OLEDs materials [28], and the expression of λ can be obtained from previous reports [20,24]. Emitting layer materials need to achieve hole and electron injection and transport balance, and the lower reorganization energy is necessary for an efficient charge transport process. As shown in Table 6, the reorganization energy for hole (λ_{hole}) of the four complexes are all smaller than that of electron ($\lambda_{electron}$), which indicates the better hole than electron transfer abilities. After careful analysis, we noted that both the hole and electron reorganization energy values, together with the energy difference between $\lambda_{electron}$ and λ_{hole} for **2a** are smaller than **1a**–**1c**. This can be rationalized by the replacement of Cl atom with C≡Cph group, which is co-planer with the molecular framework. The extended planer structure is in favor of electron–hole creation and separation than **1a**–**1c**. In addition, the confinement of recombination zone within the light-emitting layer has been claimed to play a major role in the long-term stability of the phosphorescent device [29]. In a doped system, unequal carrier trappings were expected if the corresponding trap depths are different [30]. The traps characterizing the electron transport in the material are as the states in which the injected electron

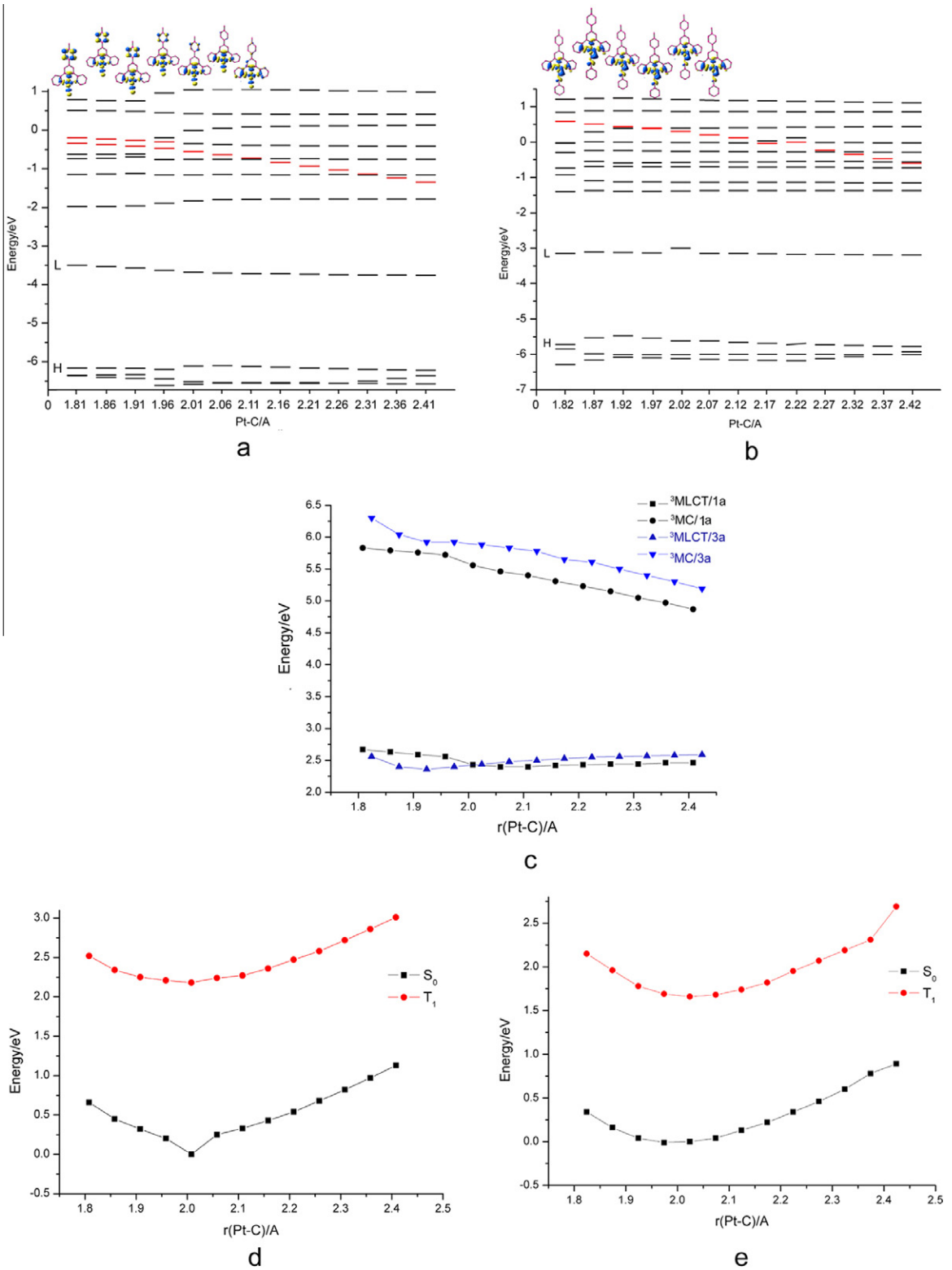

Fig. 4. The partial e_g^*-like orbitals (red lines in a (**1a**) and b (**2a**)), ^{3}MC–^{3}MLCT energy gaps (eV) and potential energy surface (PES) for **1a** (d) and **2a** (e). (For interpretation of the references to colour in this figure legend, the reader is referred to the web version of this article.)

Table 6
Ionization potentials (IP), electron affinities (EA), extraction potentials (HEP and EEP), stabilization energy (SPE) and internal reorganization energies for the investigated complexes (eV).

	IP(v)	IP(a)	HEP	SPE(h)	λ_{hole}
1a	6.99	6.88	6.80	0.11	0.19
1b	7.09	6.98	6.90	0.11	0.19
1c	7.11	6.96	6.87	0.15	0.24
2a	6.08	6.01	5.90	0.07	0.18
	EA(v)	EA(a)	EEP	SPE(e)	$\lambda_{electron}$
1a	1.14	1.29	1.43	0.15	0.29
1b	1.39	1.57	1.72	0.18	0.33
1c	1.33	1.51	1.67	0.18	0.34
2a	1.19	1.29	1.43	0.10	0.24

is self-trapped in an individual molecular accompanied by structure relaxation. However, such a procedure provides an estimate of exciton trap energy rather than that of the injected electrons [31]. In Table 6, **2a** has smaller SPEs for both the hole and electron than **1a**–**1c**. Moreover, the much higher HOMO energy level of **2a** than other three complexes can provide a more stable potential well for hole trapping. The λ and SPE values for **2a** are comparable with recently reported highly efficient phosphorescent and electroluminescent Iridium complexes based on C^N═N ligands [32–34]. Therefore, among the four complexes, **2a** may be ideal candidate as light-emitting material in OLED devices.

4. Conclusions

We investigated the electronic structures, absorption, phosphorescent and electroluminescent mechanism of four Pt(II) complexes 6-phenyl-4-(*p*-R-phenyl)-2′,2-bipyridyl (C^N^N)Pt(II)Cl, (R = Me, (**1a**); COOMe (**1b**), $P(O)(OEt)_2$ (**1c**), and 6-phenyl-4-(*p*-Me-phenyl)-2′,2-bipyridyl (C^N^N)Pt(II) C≡CPh (**2a**). The similar geometrical structures and electronic properties of **1a**–**1c** result from the longer distance between different substituents and central Pt(II) ion, making them insensitive to the variation of substituents. However, for **2a**, the C≡CPh group connects directly to the Pt(II) center and causes significant difference in electronic properties from **1a** to **1c**. The oscillator strength of lowest lying absorptions for **1a**–**1c** are much smaller than **2a**, due to the presence of the extended π-delocalization between C≡CPh and Pt(II) center in **2a**. Highly important, different phosphorescent quantum yields between **1a** and **2a** are investigated. The calculated results reveal that the higher e_g^*-like Pt d-orbital, the larger ^{3}MC–^{3}MLCT energy gap as well as the deeper potential energy surface (PES) for **2a** than that in **1a** are the main reasons resulting in the higher efficiency of **2a**. In addition, the electroluminescent properties of these complexes were reported, and the results indicate that **2a** is more suitable as light-emitting materials in OLED device than **1a**–**1c**.

Acknowledgments

The authors are grateful to the financial aid from the National Natural Science Foundation of China (Grant Nos. 20490210, 20631040, 20602035, and 20771099) and the MOST of China (Grant Nos. 2006CB601103 and 2006DFA42610).

Appendix A. Supplementary data

Supplementary data associated with this article can be found, in the online version, at doi:10.1016/j.orgel.2010.10.011.

References

[1] (a) T. Matsushita, T. Asada, S. Koseki, J. Phys. Chem. A 110 (2006) 13295–13302;
(b) L.S. Forster, Coord. Chem. Rev. 250 (2006) 2023–2033;
(c) T. Matsushita, T. Asada, S. Koseki, J. Phys. Chem. C 111 (2007) 6897–6903.
[2] (a) S.Y. Chang, J.L. Chen, Y. Chi, Y.M. Cheng, G.H. Lee, C.M. Jiang, P.T. Chou, Inorg. Chem. 46 (2007) 11202–11212;
(b) X.F. Ren, D.J. Giesen, M. Rajeswaran, M. Madaras, Organometallics 28 (2009) 6079–6089.
[3] (a) I. Avilov, P. Minoofar, J. Cornil, L. De Cola, J. Am. Chem. Soc. 129 (2007) 8247–8258;
(b) H.C. Su, H.F. Chen, F.C. Fang, C.C. Liu, C.C. Wu, K.T. Wong, Y.H. Liu, S.M. Peng, J. Am. Chem. Soc. 130 (2008) 3413–3419;
(c) F.C. Hsu, Y.L. Tung, Y. Chi, C.C. Hsu, Y.M. Cheng, M.L. Ho, P.T. Chou, S.M. Peng, A.J. Carty, Inorg. Chem. 45 (2006) 10188–10196.
[4] H.K. Yip, L.K. Cheng, K.K. Cheung, C.M. Che, Dalton Trans. (1993) 2933–2938.
[5] J. Schneider, P. Du, X. Wang, W.W. Brennessel, R. Eisenberg, Inorg. Chem. 48 (2009) 1498–1506.
[6] J. Schneider, P. Du, P. Jarosz, T. Lazarides, X. Wang, W.W. Brennessel, R. Eisenberg, Inorg. Chem. 48 (2009) 4306–4316.
[7] (a) J.P. Perdew, Y. Wang, Phys. Rev. B 45 (1992) 13244–13249;
(b) J.P. Perdew, J.A. Chevary, S.H. Vosko, K.A. Jackson, M.R. Pederson, D.J. Singh, C. Fiolhais, Phys. Rev. B 46 (1992) 6671–6687.
[8] S.L. Mayo, B.D. Olafson, W.A. Goddard III., J. Phys. Chem. 94 (1990) 8897–8909.
[9] A. Igor, M. Payam, C. Jérôme, C.D. Luisa, J. Am. Chem. Soc. 129 (2007) 8247–8258.
[10] (a) R.E. Stratmann, G.E. Scuseria, M.J. Frisch, J. Chem. Phys. 109 (1998) 8218–8224;
(b) M.E. Casida, C. Jamorski, K.C. Casida, D.R. Salahub, J. Chem. Phys. 108 (1998) 4439–4449;
(c) R. Bauernschmitt, R. Ahlrichs, Chem. Phys. Lett. 256 (1996) 454–464.
[11] B. Mennucci, J. Tomasi, J. Chem. Phys. 106 (1997) 5151–5158.
[12] (a) X.N. Li, Z.J. Wu, X.J. Liu, H.J. Zhang, Synth. Met. 159 (2009) 1090–1098;
(b) X.N. Li, Z.J. Wu, H.J. Zhang, J. Phys. Org. Chem. 23 (2010) 181–189.
[13] L.L. Shi, Y. Liao, L. Zhao, Z.M. Su, Y.H. Kan, G.C. Yang, S.Y. Yang, J. Organomet. Chem. 692 (2007) 5368–5374.
[14] (a) P. Hay, W.R. Wadt, J. Chem. Phys. 82 (1985) 270–283;
(b) P.J. Hay, W.R. Wadt, J. Chem. Phys. 82 (1985) 299–310.
[15] M.J. Frisch, G.W. Trucks, H.B. Schlegel, G.E. Scuseria, M.A. Robb, J.R. Cheeseman, J.A. Montgomery Jr., T. Vreven, K.N. Kudin, J.C. Burant, J.M. Millam, S.S. Iyengar, J. Tomasi, V. Barone, B. Mennucci, M. Cossi, G. Scalmani, N. Rega, G.A. Petersson, H. Nakatsuji, M. Hada, M. Ehara, K. Toyota, R. Fukuda, J. Hasegawa, M. Ishida, T. Nakajima, Y. Honda, O. Kitao, H. Nakai, M. Klene, X. Li, J.E. Knox, H.P. Hratchian, J.B. Cross, V. Bakken, C. Adamo, J. Jaramillo, R. Gomperts, R.E. Stratmann, O. Yazyev, A.J. Austin, R. Cammi, C. Pomelli, J.W. Ochterski, P.Y. Ayala, K. Morokuma, G.A. Voth, P. Salvador, J.J. Dannenberg, V.G. Zakrzewski, S. Dapprich, A.D. Daniels, M.C. Strain, O. Farkas, D.K. Malick, A.D. Rabuck, K. Raghavachari, J.B. Foresman, J.V. Ortiz, Q. Cui, A.G. Baboul, S. Clifford, J. Cioslowski, B.B. Stefanov, G. Liu, A. Liashenko, P. Piskorz, I. Komaromi, R.L. Martin, D.J. Fox, T. Keith, M.A. Al-Laham, C.Y. Peng, A. Nanayakkara, M. Challacombe, P.M.W. Gill, B. Johnson, W. Chen, M.W. Wong, C. Gonzalez, J.A. Pople, Gaussian 03, Revision D.01, Gaussian, Inc., Wallingford, CT, 2004.
[16] G.S.M. Tong, C.M. Che, Chem. Eur. J. 15 (2009) 7225–7237.
[17] C. Dragonetti, L. Falciola, P. Mussini, S. Righetto, D. Roberto, R. Ugo, A. Valore, F. De Angelis, S. Fantacci, A. Sgamellotti, M. Ramon, M. Muccini, Inorg. Chem. 46 (2007) 8533–8547.

[18] (a) K.L. Garner, L.F. Parkes, J.D. Piper, J.A.G. Williams, Inorg. Chem. 49 (2010) 476–487;
(b) Y.Z. Hu, M.H. Wilson, R. Zong, C. Bonnefous, D.R. MeMillin, R.P. Thummel, Dalton Trans. (2005) 354–358.
[19] F. Niedermair, O. Kwon, K. Zojer, S. Kappaun, G. Trimmel, K. Mereiter, C. Slugovc, Dalton Trans. (2008) 4006–4014.
[20] X.N. Li, Z.J. Wu, Z.J. Si, H.J. Zhang, L. Zhou, X.J. Liu, Inorg. Chem. 48 (2009) 7740–7749.
[21] S. Lamansky, P. Djurovich, D. Murphy, F.A. Razzaq, H.E. Lee, C. Adachi, P.E. Burrows, S.R. Forrest, M.E. Thompson, J. Am. Chem. Soc. 123 (2001) 4304–4312.
[22] X. Gu, T. Fei, H. Zhang, H. Xu, B. Yang, Y. Ma, X. Liu, J. Phys. Chem. A 112 (2008) 8387–8393.
[23] (a) S. Fantacci, F. De Angelis, A. Sgamellotti, A. Marrone, N. Re, J. Am. Chem. Soc. 127 (2005) 14144–14145;
(b) A.B. Tamayo, S. Garon, T. Sajoto, P.I. Djurovich, I.M. Tsyba, R. Bau, M.E. Thompson, Inorg. Chem. 44 (2005) 8723–8732.
[24] X.N. Li, Z.J. Wu, H.J. Zhang, X.J. Liu, L. Zhou, Z.F. Li, Z.J. Si, Phys. Chem. Chem. Phys. 11 (2009) 6051–6059.
[25] S.D. Cummings, R. Eisenberg, J. Am. Chem. Soc. 118 (1996) 1949–1960.
[26] (a) T.Y. Chu, M.H. Ho, J.F. Chen, C.H. Chen, Chem. Phys. Lett. 415 (2005) 137–140;
(b) K.L. Tong, S.K. So, H.F. Ng, L.M. Leung, M.Y. Yeung, C.F. Lo, Synth. Met. 147 (2004) 199–203;
(c) R.H. Young, J.J. Fitzgerald, J. Chem. Phys. 102 (1995) 2209–2221.
[27] (a) N.S. Hush, J. Chem. Phys. 28 (1958) 962–972;
(b) R.A. Marcus, Rev. Mod. Phys. 62 (1993) 599–610;
(c) R.A. Marcus, J. Chem. Phys. 24 (1956) 966–978.
[28] (a) M. Malagoli, J.L. Brédas, Chem. Phys. Lett. 327 (2000) 13–17;
(b) B.C. Lin, C.P. Cheng, Z. Ping, M.J. Lao, J. Phys. Chem. A 107 (2003) 5241–5251;
(c) K. Sakanoue, M. Motoda, M. Sugimoto, S.J. Sakaki, J. Phys. Chem. A 103 (1999) 5551–5556;
(d) Y.Z. Lee, X.W. Chen, S.A. Chen, P.K. Wei, W.S. Fann, J. Am. Chem. Soc. 123 (2001) 2296–2307.
[29] T. Peng, H. Bi, Y. Liu, Y. Fan, H. Gao, Y. Wang, Z.J. Hou, J. Mater. Chem. 19 (2009) 8072–8074.
[30] B.D. Chin, C. Lee, Adv. Mater. 19 (2007) 2061–2066.
[31] Y. Wu, W. Zhu, X.Y. Zheng, R. Sun, X. Jiang, Z. Zhang, S.J. Xu, J. Lumin. 122–123 (2007) 532–629.
[32] B.X. Mi, P.F. Wang, Z.Q. Gao, C.S. Lee, S.T. Lee, H.L. Hong, X.M. Chen, M.S. Wong, P.F. Xia, K.W. Cheah, C.H. Chen, W. Huang, Adv. Mater. 20 (2008) 1–5.
[33] Z.Q. Gao, B.X. Mi, H.L. Tam, K.W. Cheah, C.H. Chen, M.S. Wong, S.T. Lee, C.S. Lee, Adv. Mater. 20 (2008) 774–778.
[34] B. Tong, Q. Mei, S. Wang, Y. Fang, Y. Meng, B. Wang, J. Mater. Chem. 18 (2008) 1636–1639.

Organic Electronics 12 (2011) 62–69

Contents lists available at ScienceDirect

Organic Electronics

journal homepage: www.elsevier.com/locate/orgel

Laser action in a surface-structured free-standing membrane based on a π-conjugated polymer-composite

Yujie Chen [a], Johannes Herrnsdorf [a], Benoit Guilhabert [a], Alexander L. Kanibolotsky [b], Allan R. Mackintosh [b], Yue Wang [c], Richard A. Pethrick [b], Erdan Gu [a], Graham A. Turnbull [c], Peter J. Skabara [b], Ifor D.W. Samuel [c], Nicolas Laurand [a], Martin D. Dawson [a,*]

[a] Institute of Photonics, SUPA, University of Strathclyde, Glasgow G4 0NW, UK
[b] WestCHEM, Department of Pure and Applied Chemistry, University of Strathclyde, Glasgow G1 1XL, UK
[c] Organic Semiconductor Centre, SUPA, School of Physics and Astronomy, University of St. Andrews, St. Andrews, Fife KY16 9SS, UK

ARTICLE INFO

Article history:
Received 30 August 2010
Received in revised form 8 September 2010
Accepted 12 September 2010
Available online 23 October 2010

Keywords:
Distributed feedback organic laser
π-Conjugated polymer-composite
Free-standing membrane

ABSTRACT

A free-standing organic composite membrane distributed feedback (DFB) laser template-patterned by a commercially-available blank digital versatile disk (DVD) is demonstrated. This laser operates at room-temperature and ambient atmosphere and is based on a specifically designed composite incorporating a recently introduced organic semiconductor polymer system, green light-emitting π-conjugated poly[2,5-bis(2′,5′-bis(2″-ethylhexyloxy)phenyl)-*p*-phenylene vinylene] (BBEHP-PPV), as the gain element. This flexible organic membrane laser oscillates around 521 nm above a 1.1 mJ/cm^2 threshold. Optical gain characteristics of the composite material are also reported. The approach represents a step towards viable low-cost, even 'disposable' organic solid-state lasers.

© 2010 Elsevier B.V. All rights reserved.

1. Introduction

Since the realization of organic light-emitting diodes (OLEDs) [1,2], great effort has been put into the investigation of light amplification in organic materials for laser applications [3–8]. Attractive features of organic compounds for the fabrication of lasers and other active photonic devices include the potential for low-cost, high-throughput processing and the possibility to obtain 'plastic-like', mechanically flexible structures that have desired amplifying characteristics [9–11]. Such structures could be employed in conformal photonic devices and integrated circuits for a range of potential applications [9–17] in fields as varied as flexible displays, lighting, sensors and bio-sensing/monitoring. If their fabrication can be made cost-effective enough and their lifetime under typical operating conditions extended, they could also form the backbone for a range of 'disposable' visible laser sources [18]. In this study, we report a simple and potentially cost-effective way to produce all-organic flexible composite membrane lasers that operate under photo-pumping in air and at room-temperature. They are made of a specifically designed surface-patterned composite incorporating a recently introduced semiconducting polymer as the gain element.

Conjugated semiconducting polymers have been identified as a promising class of materials for laser applications owing to their high-emission efficiency, large cross sections for stimulated emission and wide spectral coverage [8]. Among these π-conjugated polymers, poly(*p*-phenylene vinylene) (PPV) and its derivatives, including BuEH-PPV, BCHA-PPV, MEH-PPV, M3O-PPV, TOP-PPV and DOO-PPV, have demonstrated high-gain and low laser oscillation threshold [8,19–22]. Recently, the synthesis of poly[2,5-bis(2′,5′-bis(2″-ethylhexyloxy)phenyl)-*p*-phenylene vinylene] (BBEHP-PPV) has been reported for laser chemo-sensing applications [23]. This green-emitting material has potential for a range of applications due in part to its low

* Corresponding author. Tel.: +44 1415484663; fax: +44 1415521575.
E-mail address: m.dawson@strath.ac.uk (M.D. Dawson).

1566-1199/$ - see front matter © 2010 Elsevier B.V. All rights reserved.
doi:10.1016/j.orgel.2010.09.021

stimulated emission threshold and improved photo-stability compared to other organic materials. A further, complementary, way to improve the stability of organic-based amplifying devices, and in turn make them relevant for real-world applications, is to incorporate the active elements into a transparent host matrix [24–28]. In such a configuration, the polymer matrix effectively protects the gain medium from degradation by isolating it from the ambient environment [26–29]. The resulting material benefits from the combination of its constituents and can be tailored to obtain desired optical and mechanical characteristics. Doing so, it is possible to obtain a photo-polymerized sheet that can emit and amplify light. Other functionalities – such as thermal and/or photo-initiated crosslinking – can also be added to the composite to further extend its processability.

In this paper we use this approach to demonstrate laser action in a surface-structured free-standing composite membrane based on BBEHP-PPV. A light-emitting free-standing membrane is obtained by depositing a layer of composite solution on a substrate, photo-curing and subsequent peeling-off of the solidified composite. Because the refractive index of the composite is higher than air, emitted light is effectively confined within the membrane, which acts as a waveguide. By exciting the active element of the composite – BBEHP-PPV – the generated light can then, in principle, be amplified. In order to trigger laser oscillation a feedback mechanism to re-circulate the amplified light needs to be added. For this membrane geometry, a distributed feedback (DFB) grating is ideally suited. In our case, the DFB is inherently integrated to the membrane at the fabrication stage. To this end, an exposed standard commercial blank digital versatile disk (DVD) is used as the substrate/template, in effect transferring its sub-micron scale grating structure onto one of the membrane surfaces. Blank DVDs consist of repeating tracks – in fact a very long spiral on the disc – with a pitch, Λ, of 740 nm. As we will see in Section 3, this pitch can correspond to a higher Bragg reflection order for green wavelengths and therefore enables resonant feedback in our composite. Compared with custom-made DFB grating structures, the use of mass-produced blank DVDs has the advantage of simplicity and low-cost [8,30]. By casting the film on a mass-produced substrate we show the potential for simple low-cost fabrication.

In Section 2, the optical characterization of neat BBEHP-PPV and of the composite, including optical gain, is reported. The fabrication and demonstration of the free-standing membrane laser based on this specifically-tailored material are then detailed in Section 3.

2. Gain measurements

2.1. Optical gain in pure BBEHP-PPV neat film

In this work, BBEHP-PPV was first synthesized following the method described in [23]. Results of the optical characterization of a 250-nm thin film of pure BBEHP-PPV, including absorption, photoluminescence (PL) and amplified spontaneous emission (ASE) are summarized here. For more details the reader is referred to the Section 5. Two obvious vibrational modes can be identified [23] in the PL spectrum (Fig. 1) at around 496 nm (0–0 transition) and 528 nm (0–1 transition), respectively. The solid-state PL quantum yield (PLQY) of the neat film is 86%. For ASE measurements, the film was excited by a 4-ns-pulsed pump beam shaped as a stripe and the full-width at half-maximum (FWHM) of the emission spectrum and the relative output power as a function of the pump intensity were both monitored from the edge of the sample (Fig. 2). It is seen that the FWHM of the edge-emitted PL narrows from 20 nm to 6 nm when pumping above a pump energy density of 1.1 $\mu J/cm^2$. Optical loss measurements suggest a very low loss coefficient of 0.83 cm^{-1} in the neat film (Fig. 3 and Table 1). The net gain coefficient at 535 nm was found to be $g = 19\ cm^{-1}$ for a pump energy density of 12 $\mu J/cm^2$ (Fig. 4 and Table 2). At higher pump energy densities the gain coefficient no longer increases because of gain saturation in the polymer film.

2.2. Optical gain in BBEHP-PPV/CHDV composite

For the composite, as-synthesized BBEHP-PPV material was incorporated into a UV transparent polymerisable host

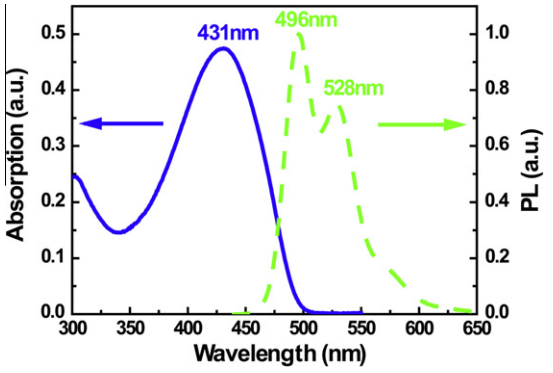

Fig. 1. Absorption (solid line) and photoluminescence (PL) (dashed line) spectra of a neat BBEHP-PPV film.

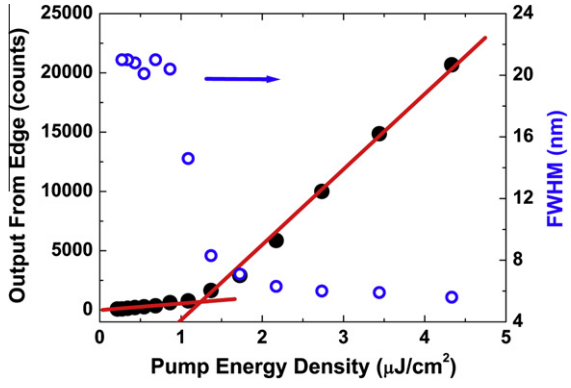

Fig. 2. Output intensity and full width at half maximum (FWHM) versus the pump energy density for a neat BBEHP-PPV film, indicating a threshold of 1.1 $\mu J/cm^2$.

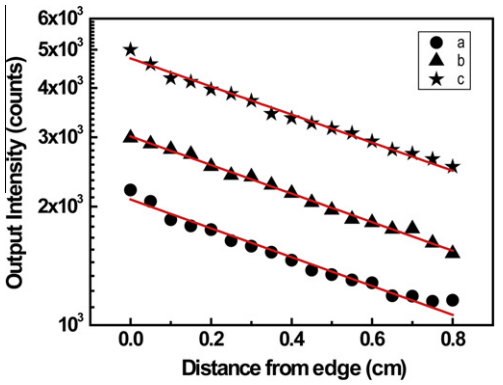

Fig. 3. Optical loss measurements on a neat BBEHP-PPV film via shifting the laser pumping stripe position relative to the sample edge. The data details are given in Table 1.

Table 1
Parameters obtained from fits of Eq. (2) to the data in Fig. 3. Average loss = 0.83 cm^{-1}.

	Pump energy density ($\mu J/cm^2$)	I_{pump} (a.u.)	α (cm^{-1})
a	7.20	2075	0.83
b	9.96	3014	0.83
c	15.6	4755	0.82

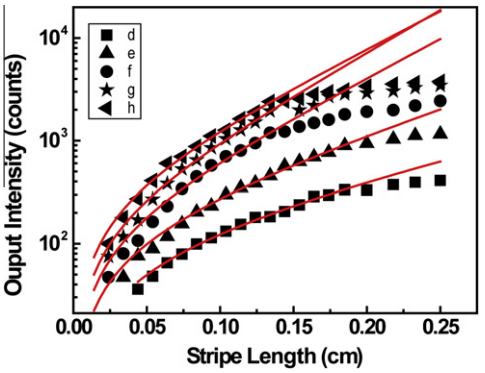

Fig. 4. Gain measurement on a neat BBEHP-PPV film via the variable-stripe-length technique. The data details are given in Table 2.

Table 2
Parameters obtained from fits of Eq. (3) to the data in Fig. 4.

	Pump energy density ($\mu J/cm^2$)	AI_{pump} (a.u.)	$g(\lambda)$ (cm^{-1})
d	2.33	809	7.8
e	4.56	1474	11.2
f	7.84	2235	17.4
g	12.0	3114	19.0
h	13.5	3999	18.3

matrix, 1,4-cyclohexanedimethanol divinyl ether (CHDV) (Sigma–Aldrich, Inc.). A UV initiator (the 'photo-acid generator' or PAG) for cationic polymerization, *para*-octyloxy-functionalized diphenyliodonium hexafluoroantimonate (Gelest, Inc.), was added to trigger the photo-crosslinkable behavior via the vinyl ether moieties [31]. This crosslinking process is achieved when the vinyl ether moieties polymerize, and a carbon-based backbone with associated vinyl ether groups is produced [29,31]. In the experiment, BBEHP-PPV was incorporated at a 10 mg/ml concentration into CHDV monomer solution, with 0.2 wt.% of PAG to trigger the polymerization process. The uncured composite solution was drop-cast onto a smooth planar substrate and cured under UV light forming a 25-μm solid film for gain measurements.

Optical characterization, including absorption, PL and ASE measurements (threshold, gain and loss), was conducted on such a plane composite film. Both absorption and PL features (Fig. 5) are slightly blue-shifted (6 nm for absorption and 8 nm for PL on average) compared to the results from the pure BBEHP-PPV neat film (Fig. 1). This small shift is similar to other cases of doping organic light-emitting materials into a CHDV matrix [26,27,29,31]. The PLQY of the composite material is measured to be 61%, which is lower than in the case of neat BBEHP-PPV. This indicates that some quenching of the radiative transition occurs when BBEHP-PPV is incorporated into CHDV and that some of this effect comes from added non-radiative recombination. Nevertheless, ASE measurements on such a film demonstrate that stimulated emission can be achieved, with a 4 mJ/cm^2 threshold and ~9-cm^{-1} propagation loss coefficient (Figs. 6 and 7 and Table 3). Because the thick membrane supports many transverse optical modes, it is difficult to directly compare results with those of the thin film characterization. However, net gain at saturation is found to be ~19 cm^{-1} at 33 mJ/cm^2 excitation density (Fig. 8 and Table 4) similar to a neat film of BBEHP-PPV (Fig. 4 and Table 2). Measurements were also done on membranes with higher BBEHP-PPV concentrations (20 and 40 mg/ml). Gains at saturation were found to be lower at 13 cm^{-1} (20 mg/ml) and 11 cm^{-1} (40 mg/ml), respectively. For photostability characterization, we photo-pumped a 50-μm thick BBEHP-PPV/CHDV (10 mg/ml) film sample in ambient atmosphere for about an hour while monitoring the PL peak intensity from the sample edge. The result shows no obvious degradation for about an hour (~3.5×10^4 pump pulses) at the pump fluence of about 1.0 mJ/cm^2.

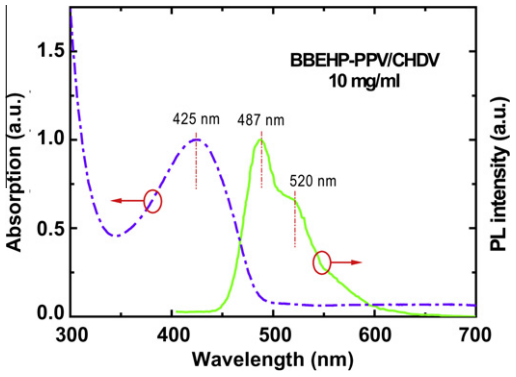

Fig. 5. Absorption and PL spectrum of BBEHP-PPV/CHDV film on a plane glass substrate. The absorption measurement was conducted by Cary 50 UV–Vis spectrophotometer. The PL measurement was conducted under the photo-pumping with a GaN-based cw laser (374 nm).

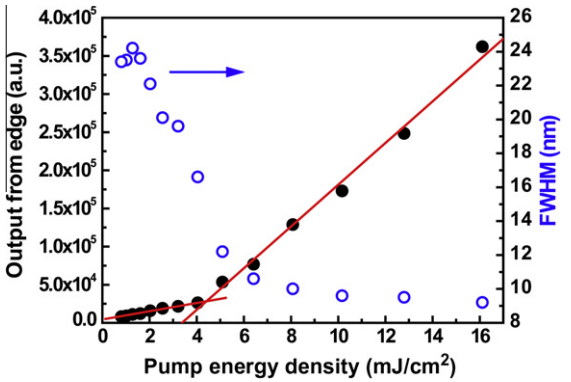

Fig. 6. Output intensity and full width at half maximum (FWHM) versus the pump energy density for a (10 mg/ml) BBEHP-PPV/CHDV membrane. The ASE threshold of BBEHP-PPV/CHDV membrane is found to be 4.6 mJ/cm^2 in this sample.

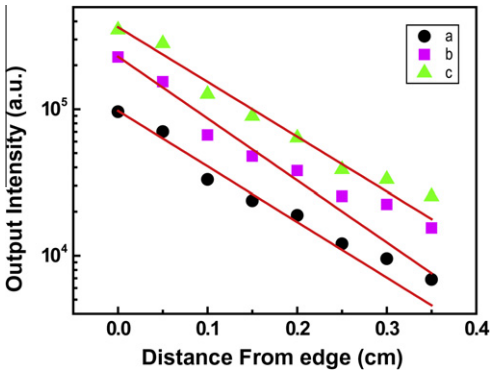

Fig. 7. Optical loss measurements via shifting the laser pumping stripe position relative to the sample edge (10 mg/ml BBEHP-PPV/CHDV membrane). The data details are given in Table 3.

Table 3
Parameters obtained from fits of Eq. (2) to the data in Fig. 7. Average loss = 9.0 cm^{-1}.

	Pump energy density (mJ/cm^2)	I_{pump} (a.u.)	α (cm^{-1})
a	7.7	97536	8.7
b	15	229017	9.7
c	26	364541	8.6

3. Laser action in BBEHP-PPV/CHDV composite

The uncured composite solution was drop-cast onto a blank DVD with exposed track under UV light. The solidified composite was then gently peeled-off from the DVD substrate resulting in a free-standing membrane with the DVD nanopatterns replicated onto one of its surfaces. The sample preparation process and morphology can be seen in Fig. 9, of which details can be found in the Section 5.

A crude but straightforward way to check the uniformity of the replicated grating structure on a surface-patterned membrane is to look at the as-prepared sample from different angles to see whether there exists any effect of diffraction caused by the grating. Here, we simply used a

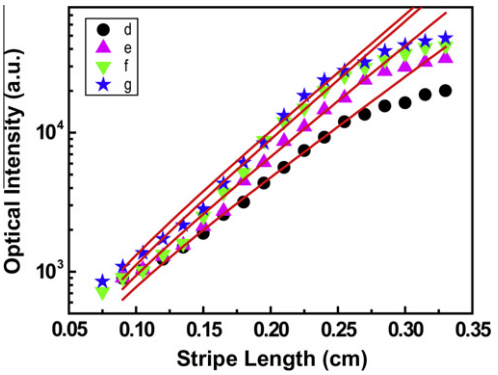

Fig. 8. Gain measurements on a (10 mg/ml) BBEHP-PPV/CHDV membrane via the variable-stripe-length technique. The data details are given in Table 4.

Table 4
Parameters obtained from fits of Eq. (3) to the data in Fig. 8.

	Pump energy density (mJ/cm^2)	AI_{pump} (a.u.)	g (λ) (cm^{-1})
d	28	3067	16.4
e	30	3312	18.2
f	33	3628	19.4
g	40	4358	19.2

camera to take photographs of the DVD-patterned membrane under white-light illumination. Photographs taken at several different angles are shown in Fig. 9c. Changes in the recorded colours indicate that regular structure is indeed present on the membrane surface. In order to examine details at the micron-scale, we used scanning electronic microscopy (SEM) to study a piece of the membrane and also scanned a sample of blank DVD for comparison. The SEM images in Fig. 9d clearly show that the two patterns are complementary, confirming the accurate replication of the grating structure from the blank DVD substrate (Fig. 9d1) to the as-prepared membrane laser (Fig. 9d2). Atomic force microscopy (AFM) was also applied to analyze the membrane surface profile (Fig. 9e), suggesting that the modulation depth of the DFB-textured surface is about 130 nm (Fig. 9e2 and e3), which is suitable to provide sufficient feedback for laser action in a DFB laser structure [32,33]. The thickness of the polymer membrane was estimated from the optical image of the membrane's cross-section profile to be about 50 μm.

In our experimental demonstration, we photo-pumped the membrane laser on its textured side with a stripe at 355 nm (pulse width: 5 ns, repetition rate of 10 Hz and averaged spot size on the membrane: ~0.1 × 2.9 mm^2) incident at about 45° and measured the edge and vertical emission simultaneously (Fig. 10). The results show that, when pumping above a certain energy, a laser peak emerges at 521.3 nm in the edge direction while only normal PL is recorded in the vertical direction (Fig. 10b) at the same time. The edge laser emission was projected onto a paper screen placed about 5 cm away, showing a bright green spot (~5 mm in size) in Fig. 10c. Above the threshold, the laser peak linewidth reaches the resolution limit

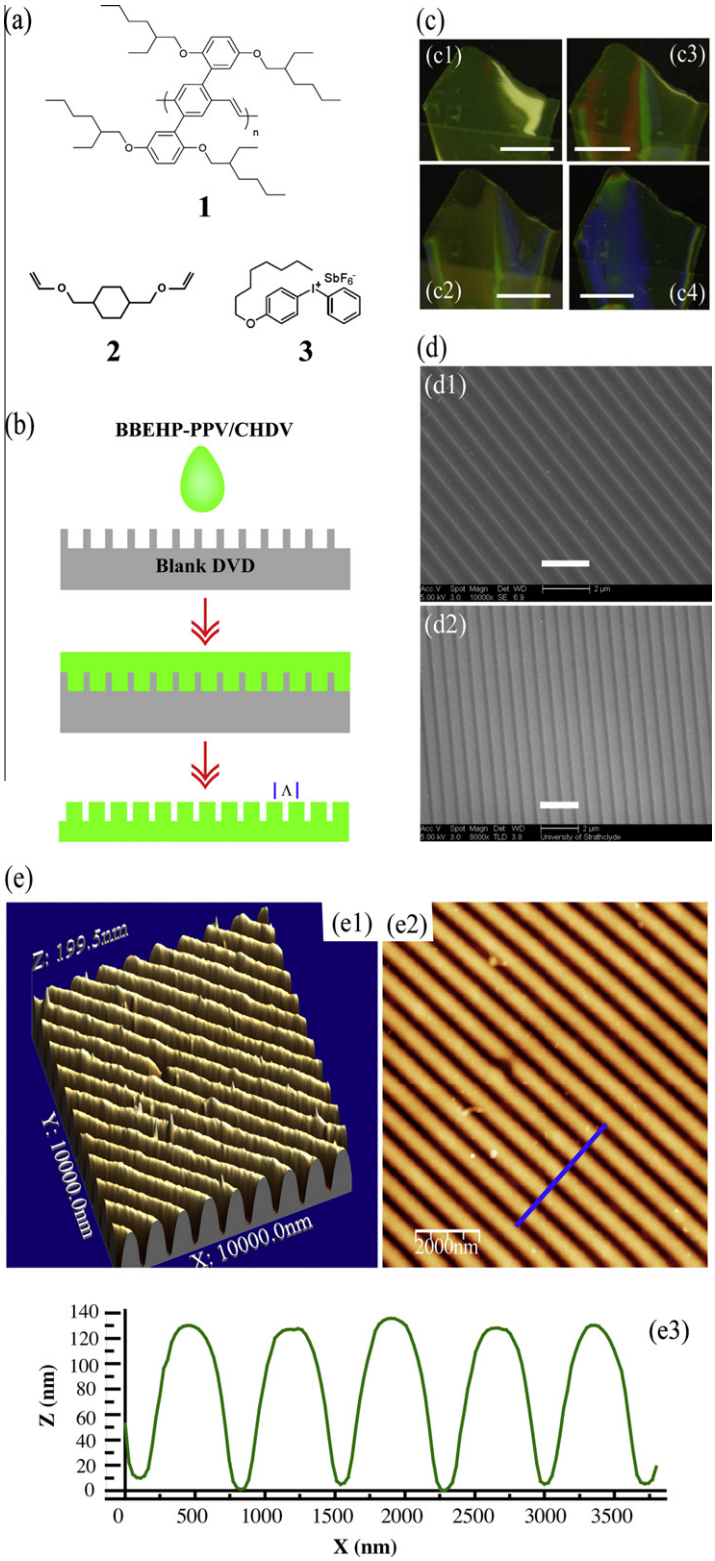

Fig. 9. (a) Chemical structures of the materials used in this work: (**1**) BBEHP-PPV, (**2**) CHDV, (**3**) 'PAG'. (b) Diagram of the fabrication process of the free-standing composite membrane with replication of the grating structure on a blank DVD surface. (c) Optical images of the as-prepared composite membrane sample taken at different angles (c1–c4) demonstrating the light diffraction effect. The scale bar (white line) represents a 1-cm length. (d) SEM images of (d1) a blank DVD surface; and (d2) the as-prepared membrane surface. The scale bar (white line) represents a 2-μm length. (e) AFM images (e1: 3-dimensional; e2: 2-dimensional) of the membrane surface structure, with grating profile (e3) marked by the blue line in (e2) (For interpretation of the references to colour in this figure legend, the reader is referred to the web version of this article.).

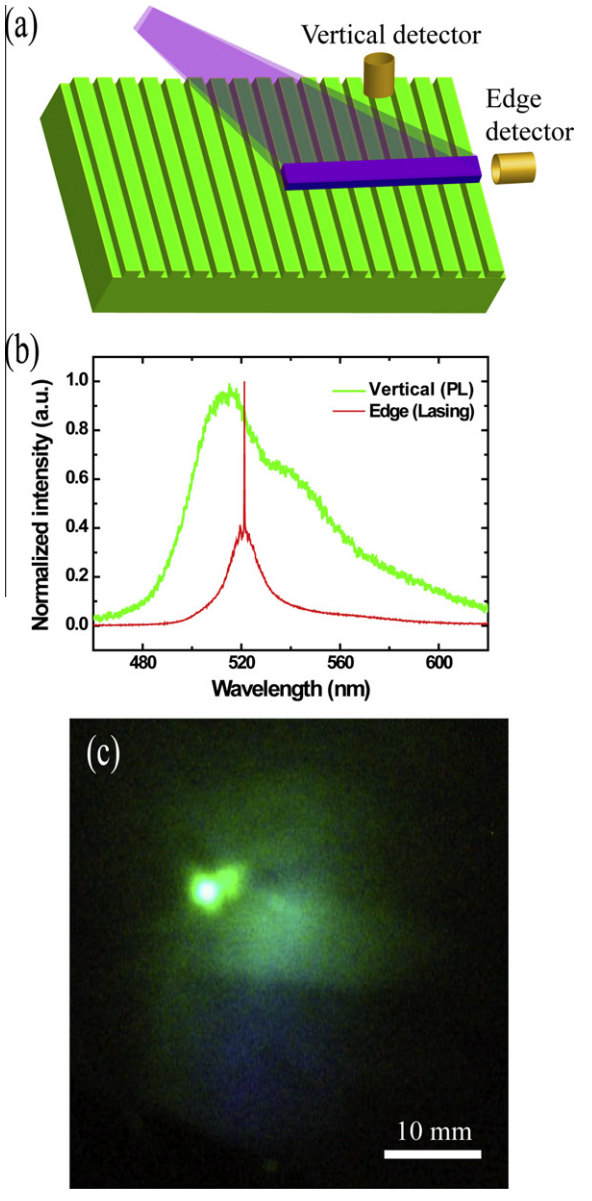

Fig. 10. (a) Diagram of the photo-pumping setup. (b) Above-threshold, edge emission (lasing) spectrum and vertical-emission (PL) spectrum. (c) Photo image of edge emission lasing spot (green) projected onto a paper screen (~5 cm away the sample edge). (For interpretation of references to color in this figure legend, the reader is referred to see the web version of this article.)

of our spectrometer (~0.2 nm). One can also see corrugation in the spectrum with a ~1.9-nm separation (close to the dominant peak) formed by non-lasing transverse modes. The size and shape of the pump stripe on the membrane limits to a certain extent the number of lateral modes but there are still several transverse modes that can potentially oscillate. Given the thickness (~50 μm) of the membrane, one would expect the spectral separation between consecutive transverse modes to be around 1.9 nm, which correspond to the observations. The evolution of the laser emission behavior under different pumping energy was investigated (Fig. 11a). Results show a laser threshold at around 1.1 mJ/cm^2. It can also be seen in the inset of Fig. 11a that there is a 1.5-nm blue-shift of the spectral peak (i.e. the gain maximum) between low pumping levels and threshold.

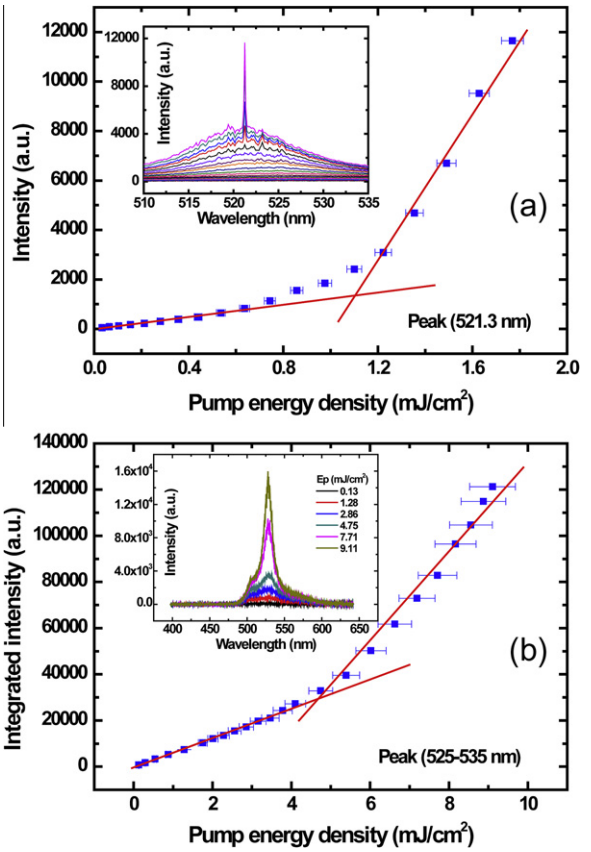

Fig. 11. (a) Laser threshold curve derived from (inset) the evolution of the sample (membrane with grating pattern) edge emission spectra under various pump energy densities. (b) ASE threshold curve and (inset) typical spectra evolution of the plane membrane (no grating pattern) at various pump energy densities.

A similar membrane but prepared on a flat substrate, i.e. with no embedded grating on its surface, was pumped under the same conditions. In that case, no laser oscillation signature was observed but only ASE (Fig. 11b) with a 4.6 mJ/cm^2 threshold. These measurements indicate that the emergence of the laser mode is enabled, or at least facilitated, by the surface grating. In a DFB grating, the in-line resonant feedback is realized when propagating waves fulfill the Bragg condition [8]:

$$m\lambda_{Bragg} = 2n_{eff}\Lambda \quad (1)$$

where n_{eff} is the effective refractive index of the mode in the gain medium, Λ is the period of the grating structure as seen by the propagating mode, and m is the diffraction order. For our composite membrane, at this wavelength, the refractive indices of BBEHP-PPV and CHDV are approximately $n_{\text{BBEHP-PPV}} \approx 1.7$ [23] and $n_{\text{CHDV}} = 1.472$ (Sigma–Aldrich, Inc.), respectively. Given the low concentration of BBEHP-PPV (10 mg/ml in CHDV) in the composite

and the rather thick membrane, the effective refractive index can be taken to be close to the matrix index for lower order transverse modes. Because the period of the grating is 740 nm, it is probably the 4th order diffraction that provides the resonant feedback. For $m = 4$ and a wavelength of 521.3 nm, corresponding to the observed laser emission, one obtains $n_{eff} \sim 1.41$. This is slightly below the composite index and indicates that higher order transverse modes are probably favoured due to a higher modal overlap with the grating.

4. Conclusion

In summary, we have demonstrated a green-emitting free-standing membrane DFB laser that uses a novel guest–host organic composite with π-conjugated BBEHP-PPV as the chromophore. The composite approach protects the light-emitting elements to a certain extent and benefits from improved processability. The composite membrane itself acts as an amplifying waveguide for the light it generates under optical excitation and the feedback is obtained by a grating embedded onto its surface. This surface-grating is directly formed at the fabrication stage and in this case was obtained by template-patterning the membrane with a commercially-available blank DVD. The resulting membrane laser operates at room-temperature and ambient atmosphere. Such a technique is easy to implement, and promising for the fabrication of low-cost and even 'disposable', green-emitting organic lasers.

5. Experimental methods

5.1. ASE measurements

BBEHP-PPV was synthesized according to the literature [23]. For the pure material (BBEHP-PPV), neat films of 250-nm thickness were made by spin-coating from 25 mg/ml Chlorobenzene solutions at 2800 rpm for 60 s on quartz substrates for absorption, photoluminescence and ASE characterization. For the BBEHP-PPV/CHDV composite, membrane samples on plane glass substrates were prepared with concentration of 10, 20 and 40 mg/ml for optical gain and loss measurements. In the ASE measurements, the film or membrane samples were located in a vacuum chamber with a pressure of approximately 10^{-5} mbar. The excitation light was generated by a Nd:YAG laser pumped optical parametric oscillator (OPO) with 4-ns output pulses at a repetition rate of 20 Hz. The pump wavelength was selected to be 425 nm which is close to the absorption maximum (431 nm, see Fig. 1) of BBEHP-PPV. Calibrated neutral density filters were inserted in the beam path to adjust the pump intensity incident on the samples. A cylindrical lens was used to shape the excitation beam into a narrow stripe with a width of approximately 0.046 cm and a length of 0.35 cm. The edge emission from the film was collected and recorded with a fibre-coupled grating spectrograph and a charge coupled device (CCD) detector.

To measure the waveguide loss coefficient, α, the pumped stripe on the film was moved away up to 0.8 cm from the edge of the sample without changing its length. The pump stripe was fixed in the loss measurements to be 0.47 cm $\times$ 0.046 cm. The emission from the edge should then be given by [8]:

$$I = I_{pump} e^{(-\alpha x)} \tag{2}$$

where x is the distance between the end of the pump stripe and the sample edge.

For gain measurements, the output intensities were recorded as a function of excitation length for a range of pump intensities. The pump stripe was able to vary in the range of 0.01 cm to 0.25 cm controlled by an adjustable aperture. In theory, when ASE occurs the output intensity from one end of the pump stripe is given by [8]:

$$I(\lambda) = \frac{A I_{pump}}{g(\lambda)} (e^{g(\lambda) l} - 1) \tag{3}$$

where l is the length of the pump stripe.

5.2. Membrane laser preparation

BBEHP-PPV was incorporated into the CHDV monomer to form a composite solution (BBEHP-PPV concentration of 10 mg/ml). A 0.2 wt.% of PAG, to act as a UV initiator for later polymerization, was also added to the solution [26,27,29]. To ensure the BBEHP-PPV is properly dissolved, the overall mix was stirred in an ultrasonic bath for 30 min. A layer of this BBEHP-PPV composite was then drop-coated onto a piece of standard blank DVD substrate ($\sim$3 cm $\times$ 3 cm). Prior to this over-coating, the DVD substrate was left in an ultrasonic bath of methanol for 30 s in order to remove the protective coating and expose the grating tracks. The composite spread to form a uniform layer due to its low viscosity. The next step was to use a UV lamp ($\sim$370 nm and power density: $\sim$200 mW/cm^2) to cure (30 s) the BBEHP-PPV/CHDV composite layer [27]. Finally, the cured composite layer (thickness: $\sim$50 μm) was peeled off from the DVD substrate. The resulting free-standing membrane was mechanically flexible and one of its surfaces was embossed with the negative of the DVD surface tracks. As a control experiment, a set of BBEHP-PPV/CHDV membrane samples on plane glass substrates were prepared with concentration of 10, 20 and 40 mg/ml. The optical characterizations of ASE threshold, gain and loss measurements on these samples were conducted in the ASE setup described above. PLQY measurements were made on a 10 mg/ml membrane (25 ± 5 μm thick) using an integrating sphere, following the method of Greenham et al. [34], with excitation at 442 nm from a He-Cd laser for excitation. The thicknesses of the membranes were measured using a DekTak 150 Surface Profiler.

5.3. Laser demonstration

The static PL measurement on the BBEHP-PPV/CHDV film was conducted under photo-pumping by a GaN-based cw laser (peak: λ_m = 374 nm, power: 15 mW and spot size: $\sim$3 mm in radius). For laser action, photo-pumping of the composite membrane was done in air with a frequency-tripled Q-switched Nd:YAG laser system yielding 5-ns pump

pulses at a repetition rate of 10 Hz and an excitation wavelength of 355 nm. The membrane was pumped at an angle of about 45°. A cylindrical lens was used to shape the pump beam as a stripe resulting in a 0.1×2.9 mm^2 pump area on the membrane surface. Both edge and vertical emission of the sample were collected by a lens-optical fibre combination, which was fed into a spectrometer (Avantes) for analysis.

Acknowledgements

This work was supported by EPSRC under the project of 'HYPIX'. Y. Chen acknowledges support from SUPA. We thank Yanfeng Zhang and Prof. Robert Martin from University of Strathclyde for the support of SEM measurement.

Reference

[1] C.W. Tang, S.A. VanSlyke, Appl. Phys. Lett. 51 (1987) 913.
[2] J.H. Burroughes, D.D.C. Bradley, A.R. Brown, R.N. Marks, K. Mackay, R.H. Friend, P.L. Burns, A.B. Holmes, Nature 347 (1990) 539.
[3] N. Tessler, Adv. Mater. 11 (1999) 363.
[4] V.G. Kozlov, S.R. Forrest, Curr. Opin. Solid State Mater. Sci. 4 (1999) 203.
[5] G. Kranzelbinder, G. Leising, Rep. Prog. Phys. 63 (2000) 729.
[6] M.D. McGehee, A.J. Heeger, Adv. Mater. 12 (2000) 1655.
[7] U. Scherf, S. Riechel, U. Lemmer, R.F. Mahrt, Curr. Opin. Solid State Mater. Sci. 5 (2001) 143.
[8] I.D.W. Samuel, G.A. Turnbull, Chem. Rev. 107 (2007) 1272.
[9] K. Geetha, M. Rajesh, V.P.N. Nampoori1, C.P.G. Vallabhan, P. Radhakrishnan, J. Opt. A: Pure Appl. Opt. 8 (2006) 189.
[10] C. Kallinger, M. Hilmer, A. Haugeneder, M. Perner, W. Spirk, U. Lemmer, J. Feldmann, U. Scherf, K. Müllen, A. Gombert, V. Wittwer, Adv. Mater. 10 (1998) 920.
[11] F. Scotognella, A. Monguzzi, F. Meinardi, R. Tubino, Phys. Chem. Chem. Phys. 12 (2010) 337.
[12] G.H. Gelinck, H. Edzer, A. Huitema, E. van Veenendaal, E. Cantatore, L. Schrijnemakers, J.B.P.H. van der Putten, T.C.T. Geuns, M. Beenhakkers, J.B. Giesbers, B.-H. Huisman, E.J. Meijer, E.M. Benito, F.J. Touwslager, A.W. Marsman, B.J.E. van Rens, D.M. de Leeuw, Nat. Mate. 3 (2004) 106.
[13] T. Someya, Y. Kato, T. Sekitani, S. Iba, Y. Noguchi, Y. Murase, H. Kawaguchi, T. Sakurai, Proc. Natl. Acad. Sci. USA 102 (2005) 12321.
[14] Y. Noguchi, T. Sekitani, T. Someya, Appl. Phys. Lett. 89 (2006) 253507.
[15] C. Bartic, G. Borghs, Anal. Bioanal. Chem. 384 (2006) 354.
[16] M. Lu, S.S. Choi, U. Irfan, B.T. Cunningham, Appl. Phys. Lett. 93 (2008) 111113.
[17] T. Sekitani, T. Yokota, U. Zschieschang, H. Klauk, S. Bauer, K. Takeuchi, M. Takamiya, T. Sakurai, T. Someya, Science 326 (2009) 1516.
[18] B.H. Wallikewitz, M. de la Rosa, J.H.-W.M. Kremer, D. Hertel, K. Meerholz, Adv. Mater. 22 (2010) 531.
[19] N. Tessler, G.J. Denton, R.H. Friend, Nature 382 (1996) 695.
[20] F. Hide, M.A. Díaz-García, B.J. Schwartz, M.R. Andersson, Q. Pei, A.J. Heeger, Science 273 (1996) 1833.
[21] H.J. Brouwer, V.V. Krasnikov, A. Hilberer, J. Wildeman, G. Hadziioannou, Appl. Phys. Lett. 66 (1995) 3404.
[22] S.V. Frolov, M. Ozaki, W. Gellermann, Z.V. Vardeny, K. Yoshino, Jpn. J. Appl. Phys. 35 (1996) L1371.
[23] A. Rose, Z. Zhu, C.F. Madigan, T.M. Swager, V. Bulović, Nature 434 (2005) 876.
[24] K.-C. Yee, T.-Y. Tou, S.-W. Ng, Appl. Opt. 37 (1998) 6381.
[25] J. Clark, L. Bazzana, D.D.C. Bradley, J. Cabanillas-Gonzalez, G. Lanzani, D.G. Lidzey, J. Morgado, A. Nocivelli, W.C. Tsoi, T. Virgili, R. Xia, J. Nanophoton. 2 (2008) 023504.
[26] M. Wu, Z. Gong, A.J.C. Kuehne, A.L. Kanibolotsky, Y. Chen, I.F. Perepichka, A.R. Mackintosh, E. Gu, P.J. Skabara, R.A. Pethrick, M.D. Dawson, Opt. Express 17 (2009) 16436.
[27] B. Guilhabert, N. Laurand, J. Herrnsdorf, Y. Chen, A.R. Mackintosh, A.L. Kanibolotsky, E. Gu, P.J. Skabara, M.D. Dawson, J. Opt. 12 (2010) 035503.
[28] A. Costela, I. García-Moreno, C. Gómez, F. Amat-Guerri, M. Liras, R. Sastre, Appl. Phys. B 76 (2003) 365.
[29] A.J.C. Kühne, Ph.D. Thesis, University of Strathclyde, 2008.
[30] B. Kaplan, H. Guner, O. Senlik, K. Gurel, M. Bayindir, A. Dana, Plasmonics 4 (2009) 237.
[31] A.J.C. Kuehne, D. Elfström, A.R. Mackintosh, A.L. Kanibolotsky, B. Guilhabert, E. Gu, I.F. Perepichka, P.J. Skabara, M.D. Dawson, R.A. Pethrick, Adv. Mater. 21 (2009) 781.
[32] J.R. Lawrence, G.A. Turnbull, I.D.W. Samuel, Appl. Phys. Lett. 82 (2003) 4023.
[33] R. Xia, G. Heliotis, P.N. Stavrinou, D.D.C. Bradley, Appl. Phys. Lett. 87 (2005) 031104.
[34] N.C. Greenham, I.D.W. Samuel, G.R. Hayes, R.T. Phillips, Y.A.R.R. Kessener, S.C. Moratti, A.B. Holmes, R.H. Friend, Chem. Phys. Lett. 241 (1995) 89.

Organic Electronics 12 (2011) 70–77

Contents lists available at ScienceDirect

Organic Electronics

journal homepage: www.elsevier.com/locate/orgel

Spectral response tuning and realization of quasi-solar-blind detection in organic ultraviolet photodetectors

Hai-guo Li, Gang Wu *, Hong-Zheng Chen, Mang Wang

MOE Key Laboratory of Macromolecule Synthesis and Functionalization, Department of Polymer Science and Engineering, Zhejiang University, State Key Lab of Silicon Materials, Hangzhou 310027, People's Republic of China

ARTICLE INFO

Article history:
Received 4 August 2010
Received in revised form 21 September 2010
Accepted 8 October 2010
Available online 21 October 2010

Keywords:
Triazine derivative
Tunable response region
UV photoresponse
Solar-blind

ABSTRACT

A silane-containing triazine derivative (NSN) with ultrawide bandgap and excellent thermal stability was used as electron acceptor for organic ultraviolet photodetectors. Poly (9,9-dihexylfluorene-2,7-diyl) (PFH), 4,4′,4″-tris(3-methylphenylphenylamino)-triphenylamine (*m*-MTDATA), 2,7-bis(3′,5′-diphenylphenyl)-9,9-diphenylfluorene (PFP) and poly(*N*-vinylcarbazole) (PVK) were applied as electron donors and respectively combined with NSN to construct planar heterojunction devices: indium tin oxide (ITO)/poly(3,4-ethylenedioxythiophene)-poly(styrenesulfonate) (PEDOT:PSS)/donor/NSN/LiF/Al. Under illumination through the ITO electrode, though all the devices exhibit near-ultraviolet (NUV) response, the cutoff wavelength can be well tuned by selecting donors with different bandgaps. If a semitransparent Al cathode is applied for the incidence of light, the response region can be further extended to deep-ultraviolet (DUV) region. Particularly for PFP/NSN and PVK/NSN based devices, quasi-solar-blind response can be realized by combining home-made NUV-blocking organic filters. As a result, the devices are capable of NUV and DUV-selective response for radiation, respectively from ITO and Al sides. The study shown here may provide a useful guideline to achieve low-cost organic detectors with spectral selective response.

© 2010 Elsevier B.V. All rights reserved.

1. Introduction

During the past two decades, organic semiconductors have attracted much attention and found lots of applications in optoelectronic devices such as solar cells, light-emitting diodes, transistors and so on [1–5]. They are also proved to be candidates for ultraviolet (UV) photodetection [6–20]. For example, Li et al. reported efficient organic UV photodetectors using 4,4′,4″-tris(3-methylphenylphenylamino)-triphenylamine (*m*-MTDATA, as donor) and 1,3,5-tris(*N*-phenylbenzimidazol-2-yl)-benzene (as acceptor) and Lin et al. succeeded in applying wide-bandgap triaryldiamine and oxadiazole-containing oligoaryls for UV detection [10,19]. Conjugated polymers like poly(3,6-(*N*-(2-ethylhexyl))carbazole) were also employed as the active materials by Cao et al. [21].

For UV detection, materials with wide-bandgap are generally preferable to ensure the device visible-blind [22]. Since deep-ultraviolet (DUV, with wavelength shorter than 300 nm) can be hardly found in the solar radiation that comes into the aerosphere, device with DUV-selective response is especially attractive. With those devices, detection of weak UV emitters in full sunlight can be realized, which has lots of applications [23]. Nevertheless, almost all the organic UV detectors reported show the response cutoff wavelength round or beyond 400 nm. Though Li et al. succeeded in shifting the response peak to 280 nm by filtering part of near-ultraviolet (NUV) in the incident light, the cutoff wavelength round 400 nm is unchanged [16]. So much work is still needed to tune the spectral response of organic UV detectors.

* Corresponding author. Tel.: +86 571 87952557; fax: +86 571 87953733 (G. Wu).
E-mail address: wmang@zju.edu.cn (G. Wu).

1566-1199/$ - see front matter © 2010 Elsevier B.V. All rights reserved.
doi:10.1016/j.orgel.2010.10.004

In this article, we synthesized a silane-containing triazine derivative (NSN) with strong DUV absorption and employed it as electron accepter for organic ultraviolet photodetectors. Poly (9,9-dihexylfluorene-2,2-diyl) (PFH), *m*-MTDATA, 2,7-bis(3′,5′-diphenylphenyl)-9,9-diphenylfluorene (PFP) and poly(*N*-vinylcarbazole) (PVK) were applied as electron donors to combine with NSN to construct planar heterojunction devices: indium tin oxide (ITO)/poly(3,4-ethylenedioxythiophene)-poly(styrenesulfonate) (PEDOT:PSS)/donor/NSN/LiF/Al. Due to the different bandgaps of the donors, NUV response with varied cutoff wavelengths was achieved for ITO side illumination and the response region was further extended to DUV region by employing the semitransparent counter electrode for the light incidence. Moreover, in PFP/NSN and PVK/NSN based devices, by combining home-made organic filters, quasi-solar-blind response was also realized.

2. Experimental

2.1. Materials

2-Chloro-4,6-diphenyl-1,3,5-triazine (**1**) [24], diphenyl-[4,4′-bis(4,4,5,5-tetramethyl-1,3,2-dioxaborolane-2-yl)diphenyl]silane (**2**) [25], (3,5-diphenylphenyl)boronic acid (**3**) [26], 2,7-dibromo-9,9-diphenylfluorene (**4**) [27], 2,7-dimethyl-3,6-diazacyclohepta-1,6-diene perchlorate (FM1) and chlorinated derivative of FM1 (FM2) [23,28] were synthesized according to the literatures. All other chemicals were purchased from commercial suppliers and used as received. The synthesis routes to bis(4-(4,6-diphenyl-1,3,5-triazine-2-yl)phenyl)diphenylsilane (NSN) and 2,7-bis(3,5-diphenylphenyl)-9,9-diphenylfluorene (PFP) are shown in Scheme 1. The organic UV filters for DUV detection were prepared as follows: first FM1, FM2 or their blend was dissolved in water solution of polyvinyl alcohol (PVA), then the solution was poured into a mould and evaporated slowly at room temperature [23]. After drying, a transparent film with thickness of round 0.1 mm was obtained, which can be placed in front of the devices to filter the NUV in the incident light.

2.2. Synthesis of NSN

A mixture of **1** (0.59 g, 2.2 mmol), **2** (0.59 g, 1 mmol), 15 mg $Pd(PPh_3)_4$, 25 mL tetrahydrofuran (THF) and 5 mL 2 M K_2CO_3 aqueous solution was stirred at 65 °C for 24 h under nitrogen atmosphere. The resulting mixture was cooled to room temperature and then poured into water. The organic layer was extracted with ethyl acetate and dried over $MgSO_4$. The crude product was purified by chromatography using petroleum ether and dichloromethane (4:1, v/v) as eluent. Yield: 0.54 g (68%). FT-IR (in KBr) υ cm^{-1}: 3066, 3028 (CH_{ar}), 1587, 1562, 1520, 1446, 1428 ($C{=}C_{ar}$). ^1H NMR (300 MHz, $CDCl_3$, δ ppm): 8.79 (m, 12H), 7.86 (d, 4H), 7.68 (d, 4H), 7.55–7.64 (m, 12H), 7.41–7.52 (m, 6H). Anal. Calcd. for $C_{54}H_{38}N_6Si$: C, 81.17; H, 4.79; N 10.52. Found: C, 81.43; H, 4.91; N 10.02.

2.3. Synthesis of PFP

A mixture of **3** (0.48 g, 1.76 mmol), **4** (0.38 g, 0.8 mmol), 30 mg $Pd(PPh_3)_4$, 30 mL THF and 5 mL 2 M K_2CO_3 aqueous solution was stirred at 65 °C for 24 h under nitrogen atmosphere. The resulting mixture was cooled to room temperature and then poured into water. The organic layer was extracted with ethyl acetate and dried over $MgSO_4$. The crude product was purified by chromatography using petroleum ether and dichloromethane (5:1, v/v) as eluent. Yield: 0.4 g (65%). FT-IR (in KBr) υ cm^{-1}: 3056, 3030 (CH_{ar}), 1593, 1575, 1476, 1454 ($C{=}C_{ar}$). ^1H NMR (300 MHz, $CDCl_3$, δ ppm): 7.92 (d, 2H), 7.71–7.79 (m, 10H), 7. 69 (d, 8H), 7. 49 (t, 8H), 7.30–7.44 (m, 8H), 7.18–7.30 (m, 6H). Anal. Calcd. for $C_{61}H_{42}$: C, 94.54; H, 5.46. Found: C, 93.64; H, 5.43.

2.4. Characterization

^1H NMR spectra were recorded on a 300 MHz Varian spectrometer in $CDCl_3$. FT-IR spectra were recorded using a Brucker VII FT-IR spectrometer. Element analysis results were obtained on ThermoFinnigan Flash EA1112. UV–vis absorption spectra were taken on a Cary Bio 100 spectro-

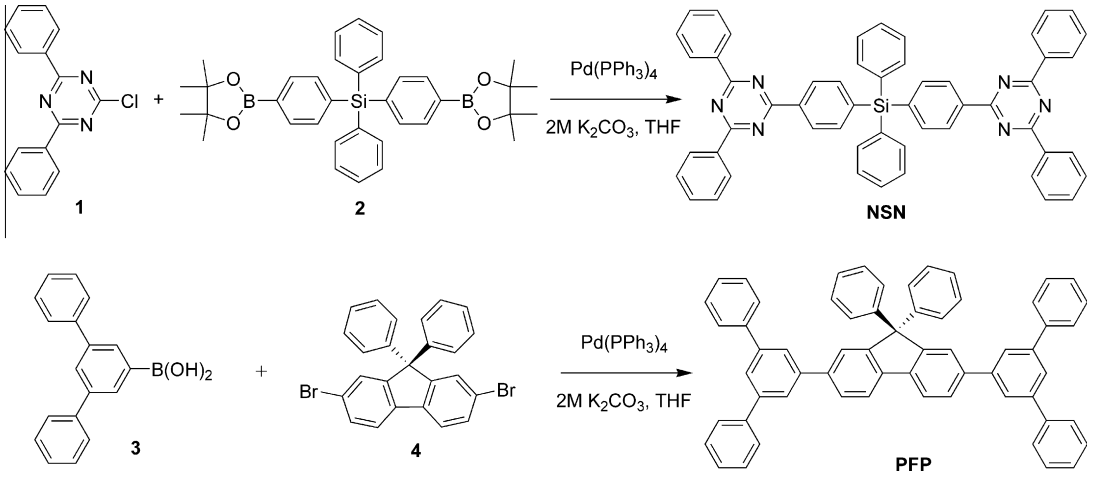

Scheme 1. Synthetic routes for NSN and PFP.

photometer. The thermogravimetric analysis (TGA) was performed under a nitrogen atmosphere on a PE Pyris 1 TGA at heating rates of 20 °C min^{-1}. Cyclic voltammetry (CV) measurements were conducted in a 0.1 M tetrabutylammonium hexafluorophosphate (Bu_4NPF_6) acetonitrile solution at room temperature using a CHI 660C electrochemical workstation at a scan rate of 50 mV s^{-1}. A saturated calomel electrode (SCE), a platinum wire and a platinum disk were used as the reference electrode, counter electrode and working electrode, respectively.

2.5. Device fabrication and performance characterization

For the device fabrication, glass plates covered with patterned ITO were used as substrates. They were first ultrasonically cleaned in detergent and a series of organic solvents (isopropanol, ethanol and acetone) and then precoated with a buffer layer (40 nm) of PEDOT:PSS. Then, organic layers were deposited. For small molecules (*m*-MTDATA, PFP, NSN), thermal evaporation in vacuum chamber at 5×10^{-4} Pa was used, while for polymers (PFH, PVK), spin-coating was applied. The thickness of every organic layer is 30 nm. Finally, LiF (0.5 nm) and aluminum (12 nm) film was evaporated through a mask onto the active layers under high vacuum (about 10^{-4} Pa) as the top electrode.

The photoresponse studies were made with a Keithley 236 Source-Measure Unit under the excitation of a high pressure mercury lamp (CHG-200) filtered by 365 or 340 nm bandpass filters. For spectral response measurement, a 500 W Xenon lamp and a grating monochromator were used. The beam was chopped at 23 Hz and the photocurrent was measured using Stanford Research Systems (USA) SR830 DSP lock-in amplifier. The radiant power was calibrated with a standard silicon photodetector for the calculation of responsivity. Both the spin-coating of the films and photoresponse measurement of the devices were conducted at room temperature in ambient conditions.

3. Results and discussion

3.1. Synthesis and characterization of electron acceptor

NSN was synthesized by palladium-catalyzed Suzuki coupling of **1** and **2**. The structure was confirmed by ^1H NMR spectroscopy and elemental analysis. Though there are two triphenyltriazine (TTA) units in the molecule, they are not conjugated due to the interruption of silicon atom. Thus, the effective conjugation scale for NSN is close to that of TTA, while the thermal stability of NSN shall be much improved due to its larger molecular size and the silane moiety included [29]. According to TGA analysis, the 5% weight loss temperature is as high as 490 °C. Fig. 1 shows the absorption spectra of NSN. In THF, NSN exhibits strong absorption in the region below 300 nm with a peak at 276 nm, indicating that this material may be good for DUV detection. For NSN film, the peak of absorption redshifts to 282 nm and the onset is round 323 nm, from which a bandgap of 3.84 eV can be obtained. Such wide bandgap may facilitate the response cutoff wavelength control in device fabrication. Due to the presence of electron-withdrawing triazine moieties, NSN is expected to work as an electron acceptor and its lowest unoccupied molecular orbital (LUMO) level is round 3.0 eV according to the CV measurement.

3.2. Structure and absorption of electron donors

In order to construct heterojunction, four materials were selected as electron donors to combine with NSN. The chemical structures of the donors are shown in Scheme 2a. Among them, PFP is newly synthesized by Suzuki coupling of **3** and **4** (Scheme 1), while the other three materials are commercial hole-transporting materials. Fig. 2 shows the absorption spectra of corresponding films of the donors. Due to the difference in conjugation scale, the absorption onset for PFH, *m*-MTDATA, PFP and PVK decreases in sequence with a value of 420, 400, 370 and 360 nm, respectively. On the above films, NSN was then further deposited and the absorption spectra of the obtained bilayer films were also measured. As shown in Fig. 3, the absorption is simply the summation of that of the two single layers without additional absorption peaks. Besides, the absorption onsets of all bilayer films keep the same as that of the corresponding donor due to the much wider bandgap of NSN than the donors. Thus, by applying those molecules as donors to construct heterojunction with NSN, we may realize UV photoresponse with different cutoff wavelengths.

3.3. J–V curves and spectral response

By employing the above-mentioned bilayer films as active layers, UV photodetectors with planar heterojunction structure were fabricated. The device structure and the energy level diagram of the materials are shown in Scheme 2. Energy levels for PFH, *m*-MTDATA and PFH are quoted from the literatures [19,30,31], while those for PFP and NSN are obtained by CV measurement. Charge transfer between the

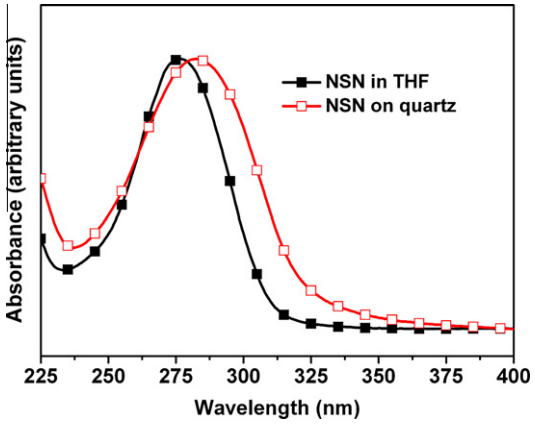

Fig. 1. Absorption spectra of NSN in THF (10^{-5} mol L^{-1}) and in solid state. The symbols on the lines are for distinguishing between different plots (hereinafter the same).

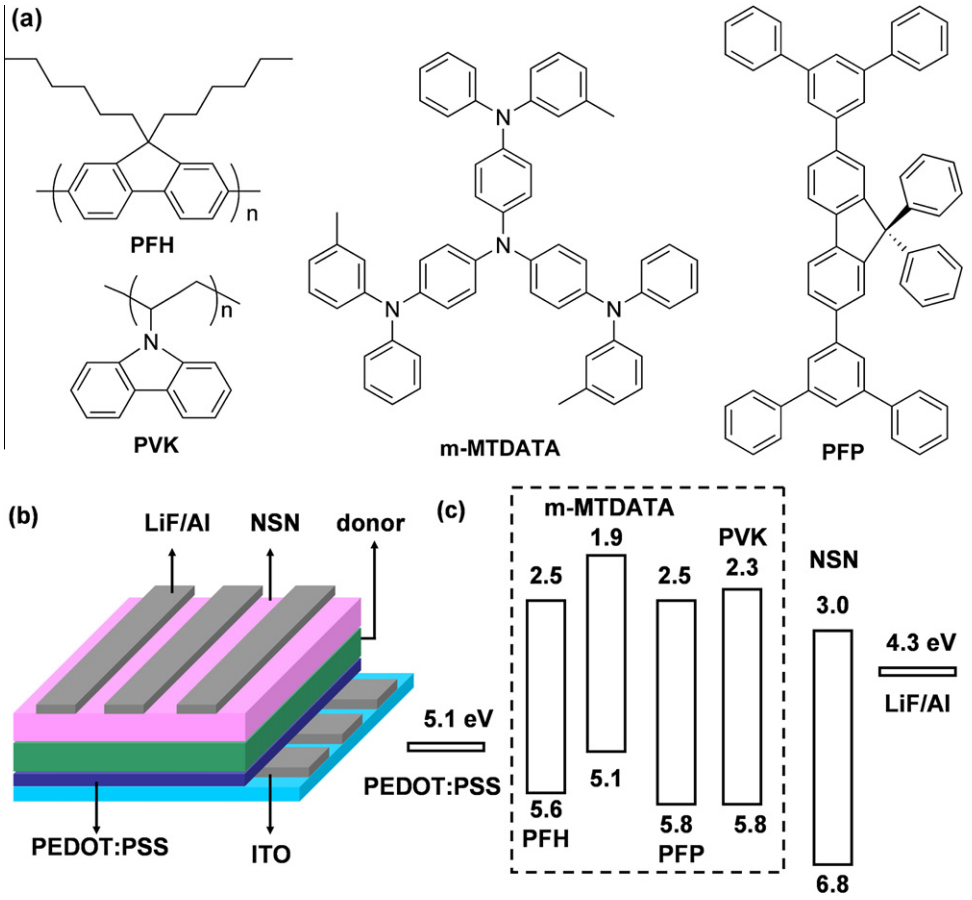

Scheme 2. (a) Chemical structures of the materials used as electron donors. (b) Schematic diagram of the devices. (c) Energy level diagram of the devices.

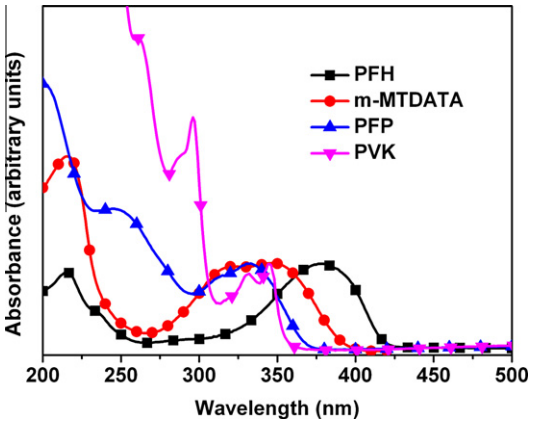

Fig. 2. Absorption spectra of the films of PFH, *m*-MTDATA, PFP and PVK.

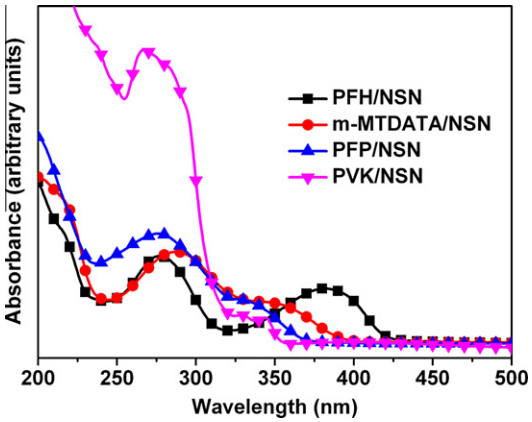

Fig. 3. Absorption spectra of the bilayer films of PFH/NSN, *m*-MTDATA/NSN, PFP/NSN and PVK/NSN.

donors and NSN can be expected from the relative energy level alignment. Fig. 4 shows the *J*–*V* curves for ITO/PEDOT:PSS/PFH/NSN/LiF/Al. Under illumination of 1 mW/cm^2 UV light at 365 nm through ITO-coated substrate, the device presents a high open-circuit voltage of round 2 V, which shall be attributed to the large gap between the highest occupied molecular orbital (HOMO) level of PFH (5.6 eV) and LUMO level of NSN (3.0 eV). However, the short-circuit current is relative small. This is reasonable if we consider the charge transporting ability of NSN. Since the conjugation scale of NSN is small, and the film is amorphous due to the nonplanar molecule structure, the electron mobility of NSN shall be low. As a result, under

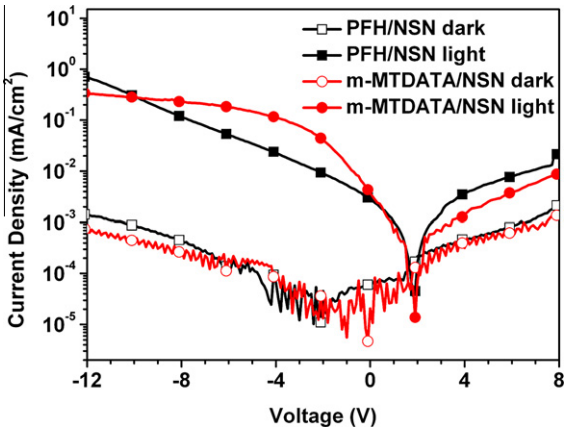

Fig. 4. Semi-log plot of *J–V* curves in the dark and under illumination of 1 mW/cm^2 UV light at 365 nm through ITO electrode for ITO/PEDOT:PSS/PFH/NSN/LiF/Al and ITO/PEDOT:PSS/*m*-MTDATA/NSN/LiF/Al.

build-in electric field, the separated charge carriers from the interface may be unable to be efficiently transported out before recombination. This problem can be solved by applying a reverse bias to facilitate the charge transportation. As shown in Fig. 4, the current density increases quickly with the increase of reverse bias. At −12 V, the photocurrent reaches 0.697 mA/cm^2, while the dark current is 1.4 μA/cm^2. Accordingly, the responsivity and the photo-to-dark current ratio under this bias are 0.696 A/W and 498, respectively. It is found that the quantum yield is over unity, the origin of which is still debatable [15,32–36]. Fig. 4 also shows the results for *m*-MTDATA/NSN based device. *m*-MTDATA is a well-known hole-transporting material widely used in organic light-emitting diode (OLED) and also in ultraviolet photodetectors [19]. Though its conjugation scale is a little lower than that of PFH, the photovoltaic performance is comparable and the responsivity at low reverse bias is even better (Fig. 4). At high reverse bias, the photocurrent tends to saturate and reaches 0.334 mA/cm^2 at −12 V.

The *J–V* curves for devices with PFP/NSN and PVK/NSN heterojunctions were also investigated. Due to the larger energy gaps, the absorption of PFP and PVK at 365 nm is small, so UV light at 340 nm was employed for the photoresponse study. As shown in Fig. 5a, under illumination of 0.5 mW/cm^2 UV light at 340 nm, the photocurrent at −12 V for the PFP/NSN heterojunction is 0.124 mA/cm^2 and the photo-to-current ratio is round two orders of magnitude. After correcting the photocurrent with the dark current, a responsivity of 0.245 A/W can be obtained. As for the PVK/NSN heterojunction, though the photocurrent is a little higher, the dark current is also large, especially at high reverse bias, leading to a poor photo-to-current ratio. For this device, operating at lower bias may be more preferable, though the responsivity will be lower.

According to the above results, the four devices exhibit different *J–V* characters, which may be related to different charge transporting properties of the donors. Nevertheless, the response is all quick. Take PFP/NSN based device for example, as shown in Fig. 5b, the current increases quickly

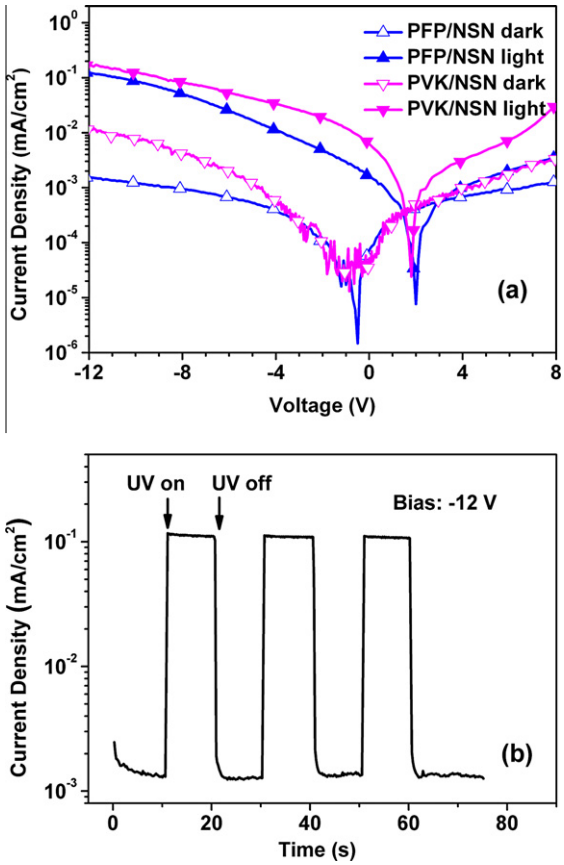

Fig. 5. (a) Semi-log plot of *J–V* curves in the dark and under illumination of 0.5 mW/cm^2 UV light at 340 nm through ITO electrode for ITO/PEDOT:PSS/PFP/NSN/LiF/Al and ITO/PEDOT:PSS/PVK/NSN/LiF/Al. (b) The transient response curve for ITO/PEDOT:PSS/PFP/NSN/LiF/Al at −12 V.

as the light is illuminated and recovers to its original level once the light is removed. The response is stable and reproducible, which is beneficial for UV detection.

The photocurrent response spectra of the four devices under ITO side illumination are integrated in Fig. 6 for comparison. Due to the absorption of ITO substrates, DUV in the incident light can hardly reach the active layers. As a result, only NUV detection can be realized. The response peak for PFH, *m*-MTDATA, PFP and PVK based devices is at 375, 345, 340 and 330 nm, respectively. Moreover, the response cutoff at longer wavelength is also different. In consistent with the optical absorption, the response cutoff blue-shifts sequentially from PFH, *m*-MTDATA, PFP to PVK with a value of 425, 410, 375 and 370 nm, respectively. So, by selecting donors with different bandgaps to combine with NSN, the response cutoff wavelength can be well tuned. In particular, the PFP/NSN and PVK/NSN based devices can be applied as visible-blind UV photodetectors.

3.4. Realization of DUV detection

Since the ITO substrate can block the UV light with wavelength below 300 nm, a semitransparent Al electrode

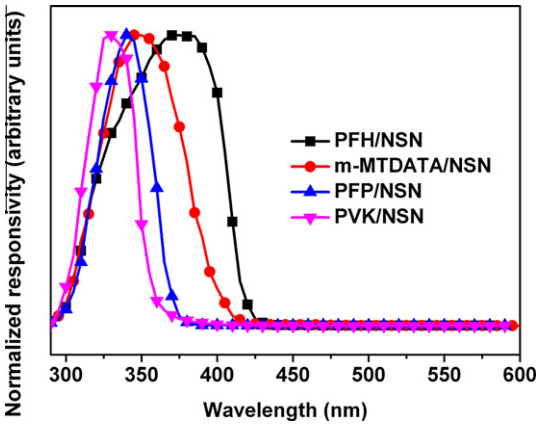

Fig. 6. Normalized photocurrent response spectra of ITO/PEDOT:PSS/donor (PFH, *m*-MTDATA, PFP and PVK)/NSN/LiF/Al for illumination through ITO side.

with thickness of 12 nm was thus employed for the purpose of DUV detection. Fig. 7a shows the response spectrum for illumination through Al side in the PFP/NSN based device. Due to the permission of DUV transmission by Al electrode, the response spectral covers 200–375 nm, which can be further restricted within the DUV region only by filtering the NUV part of the incident light. The UV filter can be simply prepared by doping dyes in PVA film [23]. The structure and absorption of the dyes applied are shown in Fig. 8a. Both FM1 and FM2 exhibit a strong absorption peak in the NUV region but retain a transmission window in the DUV region. The transmittance spectra shown in Fig. 8b indicate that filters based on FM1 and FM2 can respectively block the light in the region of 290–350 and 310–375 nm. Considering the response cutoff wavelength of PFP/NSN based device mentioned above, FM2-based filter seems especially appropriate to block the NUV that can excite this device. In order to further widen the block region of the filter, the doping concentration and final thickness can be increased. However, the transmittance in the DUV region will be also reduced. Alternatively, adding a small amount of FM1 in the FM2-based filter can also extend the blocking region to the lower wavelength. As shown in Fig. 8b, for a filter based on blend of FM1:FM2 (1:8, by weight), UV light in the region of 300–375 nm can be totally blocked. Meanwhile, a transmittance of 45% can still be obtained at 270 nm. With this filter put in front of the semitransparent

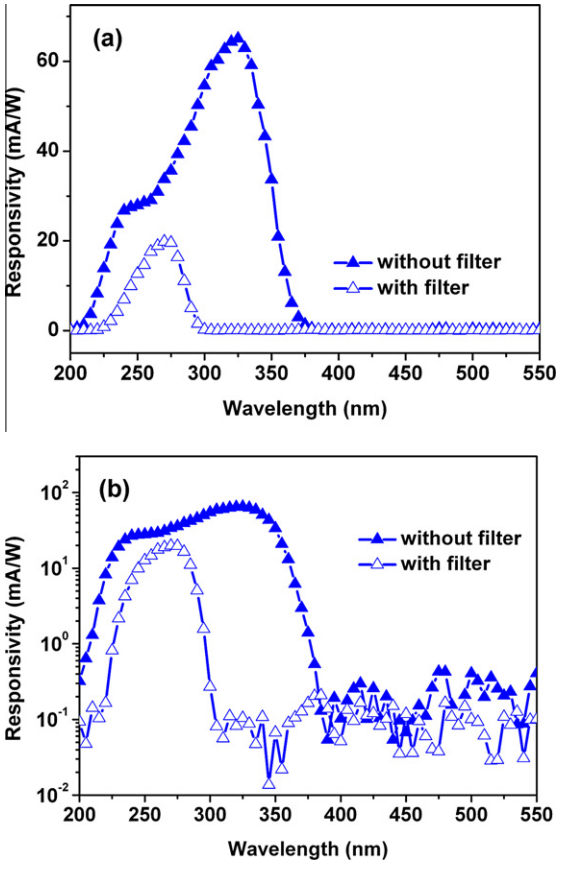

Fig. 7. Photocurrent response spectra of ITO/PEDOT:PSS/PFP/NSN/LiF/Al (a) in linear scale and (b) in semi-log scale for illumination through Al side. The applied bias is −9 V. Both curves with and without UV filter applied are given.

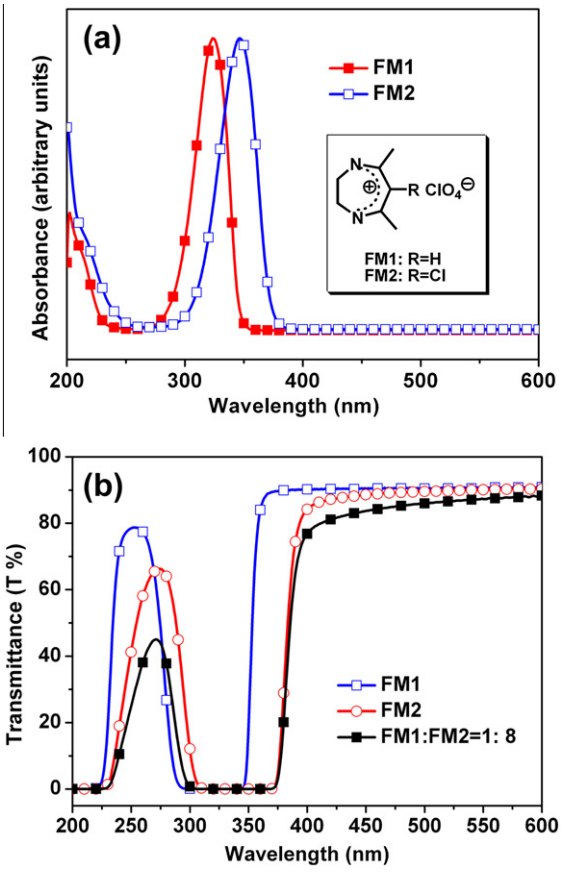

Fig. 8. (a) Absorption spectra of FM1 and FM2 in methanol. The structures for FM1 and FM2 are also shown in the inset. (b) Transmittance spectra of the home-made UV filters.

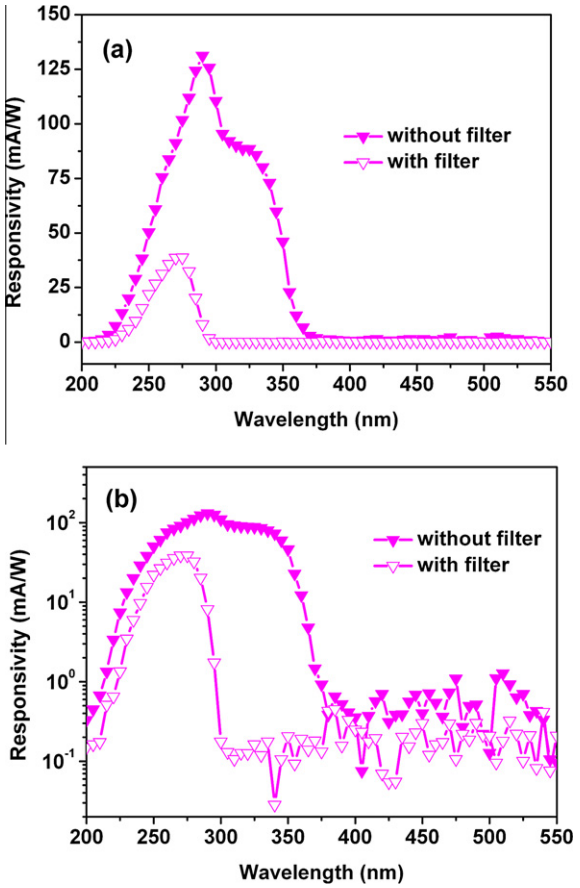

Fig. 9. Photocurrent response spectra of ITO/PEDOT:PSS/PVK/NSN/LiF/Al (a) in linear scale and (b) in semi-log scale for illumination through Al side. The applied bias is −9 V. Both curves with and without UV filter applied are given.

Al electrode, the response cutoff shifts to 300 nm just as expected and a peak responsivity of 19.87 mA/W can be obtained round 270 nm under reverse bias of −9 V (Fig. 7a). From the semi-log plot shown in Fig. 7b, it is observed that the cutoff at 300 nm is very sharp. As a result, quasi-solar-blind response is realized. Since the intrinsic cutoff wavelength for the PVK/NSN based device is even lower, similar effect can be achieved. As shown in Fig. 9, by combining the above-mentioned filter, the device only responses to the UV light in the region of 200–300 nm and the peak responsivity round 275 nm is 38.76 mA/W. To achieve more efficient devices, there are at least two routes. One is developing organic filters with higher transmittance in DUV region and also excellent blocking ability in NUV or even visible region to broaden the selection space of the active materials. The other is applying wide bandgap semiconductors with higher carrier mobility for the devices.

Though the good blindness to NUV of the present devices is not intrinsic, the applied filters can be easily fabricated and will not increase the cost too much. Moreover, the filters are flexible and can be easily integrated with the device during encapsulation. Contrarily, as to the reported solar-blind detectors based on wide-bandgap inorganic semiconductor such as MgZnO and AlGaN, the fabrication is rather complicated and the cost is high [37,38]. Thus, the study shown here may provide a useful guideline to achieve low-cost organic detectors for DUV-selective detection. Besides, by combining the organic NUV filter, the devices based on PFP/NSN and PVK/NSN heterojunctions are also capable of dual-band UV detection. In practical application, the devices can respectively response to NUV and DUV radiating through ITO side and Al side, which facilitates distinguishing complicated UV signals.

4. Conclusion

Organic ultraviolet photodetectors based on a wide bandgap acceptor of triazine derivative (NSN) and four different donors (PFH, *m*-MTDATA, PFP and PVK) were fabricated with device structure of ITO/PEDOT:PSS/donor/NSN/LiF/Al. The devices present NUV response to the radiation from ITO side with varied response cutoff wavelengths due to the different energy gaps of the donors. By employing semitransparent Al electrode for the light incidence, the response region was further extended to DUV region. Specifically, in PFP/NSN and PVK/NSN based devices, by combining home-made organic NUV filters, quasi-solar-blind response was also realized. Since those devices can not only detect NUV radiation from the ITO side, but also give sensitive response to the DUV radiation from the Al side, they may be applied as low-cost NUV/DUV dual-band photodetectors.

Acknowledgments

The work is financially supported by the National Natural Science Foundation of China (Grant Nos. 50773067, 50520150165, 51011130028 and 50990063) and of the Research Fund for the Doctoral Program of Higher Education in China (No. 20060335078). The authors also like to thank the developing program of Changjiang Scholar and Innovation Team from the Ministry of Education of China (Grant No. IRT0651).

References

[1] Y. Shirota, H. Kageyama, Chem. Rev. 107 (2007) 953.
[2] S. Gunes, H. Neugebauer, N.S. Sariciftci, Chem. Rev. 107 (2007) 1324.
[3] H. Spanggaard, F.C. Krebs, Sol. Energy Mater. Sol. Cells 83 (2004) 125.
[4] G. Yu, J. Gao, J.C. Hummelen, F. Wudl, A.J. Heeger, Science 270 (1995) 1789.
[5] C.D. Dimitrakopoulos, P.R.L. Malenfant, Adv. Mater. 14 (2002) 99.
[6] Y.C. Cui, L.H. Liu, C.B. Liu, Q.W. Wang, W.L. Li, G.B. Che, C.H. Xu, M. Liu, Synth. Met. 160 (2010) 373.
[7] Z.G. Kong, W.L. Li, G.B. Che, B. Chu, D.F. Bi, L.L. Han, L.L. Chen, Z.Z. Hu, Z.Q. Zhang, Appl. Phys. Lett. 89 (2006) 161112.
[8] H.G. Li, G. Wu, M.M. Shi, L.G. Yang, H.Z. Chen, M. Wang, Appl. Phys. Lett. 93 (2008) 153309.
[9] J.Y. Li, C.S. Lee, S.T. Lee, J. Mater. Chem. 15 (2005) 3268.
[10] H.W. Lin, S.Y. Ku, H.C. Su, C.W. Huang, Y.T. Lin, K.T. Wong, C.C. Wu, Adv. Mater. 17 (2005) 2489.
[11] Y.Y. Lin, C.W. Chen, W.C. Yen, W.F. Su, C.H. Ku, J.J. Wu, Appl. Phys. Lett. 92 (2008) 233301.
[12] D. Ray, K.L. Narasimhan, Appl. Phys. Lett. 91 (2007) 093516.
[13] Z.J. Si, B. Li, L.H. Wang, S.M. Yue, W.L. Li, Sol. Energy Mater. Sol. Cells 91 (2007) 1168.
[14] Z.S. Su, B. Chu, W.L. Li, Solid State Electron. 54 (2010) 605.
[15] Z.S. Su, W.L. Li, B. Chu, T.L. Li, J.Z. Zhu, G. Zhang, F. Yan, X. Li, Y.R. Chen, C.S. Lee, Appl. Phys. Lett. 93 (2008) 103309.

[16] S.H. Wu, W.L. Li, B. Chu, C.S. Lee, Z.S. Su, J.B. Wang, F. Yan, G. Zhang, Z.Z. Hu, Z.Q. Zhang, Appl. Phys. Lett. 96 (2010) 093302.
[17] F. Yan, H.H. Liu, W.L. Li, B. Chu, Z.S. Su, G. Zhang, Y.R. Chen, J.Z. Zhu, D.F. Yang, J.B. Wang, Appl. Phys. Lett. 95 (2009) 253308.
[18] G. Yu, Y. Cao, G. Srdanov, SPIE Proc. 3629 (1999) 349.
[19] G. Zhang, W.L. Li, B. Chu, Z.S. Su, D.F. Yang, F. Yan, Y.R. Chen, D.Y. Zhang, L.L. Han, J.B. Wang, H.H. Liu, G.B. Che, Z.Q. Zhang, Z.Z. Hu, Org. Electron. 10 (2009) 352.
[20] G. Zhang, W.L. Li, B. Chu, F. Yan, J.Z. Zhu, Y.R. Chen, Appl. Phys. Lett. 96 (2010) 073301.
[21] Y. Cao, J. Peng, M. Xu, CN101345291-A, 2009.
[22] E. Monroy, F. Omnes, F. Calle, Semicond. Sci. Technol. 18 (2003) R33.
[23] Z.H. Xu, X.X. Zhuang, G.B. Su, Opt. Mater. 31 (2009) 1741.
[24] H. Henneberger, M. Wagner, US 5438138, 1995.
[25] R. Koguchi, N. Kobayashi, M. Kijima, Macromolecules 42 (2009) 5946.
[26] S.K. Kim, B. Yang, Y. Ma, J.H. Lee, J.W. Park, J. Mater. Chem. 18 (2008) 3376.
[27] K.T. Wong, Z.J. Wang, Y.Y. Chien, C.L. Wang, Org. Lett. 3 (2001) 2285.
[28] R.G.S. Pong, S.R. Flom, J.S. Shirk, US 6994885, B2, 2006.
[29] J.W. Kang, D.S. Lee, H.D. Park, Y.S. Park, J.W. Kim, W.I. Jeong, K.M. Yoo, K. Go, S.H. Kim, J.J. Kim, J. Mater. Chem. 17 (2007) 3714.
[30] S.H. Chen, Y. Chen, C.S. Shiau, C.J. Tsai, J. Polym. Sci. Polym. Chem. 45 (2007) 136.
[31] H. Etori, X.L. Jin, T. Yasuda, S. Mataka, T. Tsutsui, Synth. Met. 156 (2006) 1090.
[32] J. Reynaert, V.I. Arkhipov, P. Heremans, J. Poortmans, Adv. Funct. Mater. 16 (2006) 784.
[33] J. Gao, F.A. Hegmann, Appl. Phys. Lett. 93 (2008) 223306.
[34] I.H. Campbell, B.K. Crone, J. Appl. Phys. 101 (2007) 024502.
[35] J.S. Huang, Y. Yang, Appl. Phys. Lett. 91 (2007) 203505.
[36] G. Yu, K. Pakbaz, A.J. Heeger, Appl. Phys. Lett. 64 (1994) 3422.
[37] Y.G. Yuan, Y. Zhang, K.H. Chu, X.Y. Li, D.G. Zhao, H. Yang, Sci. China Ser. E: Technol. Sci. 51 (2008) 820.
[38] L.K. Wang, Z.G. Ju, J.Y. Zhang, J. Zheng, D.Z. Shen, B. Yao, D.X. Zhao, Z.Z. Zhang, B.H. Li, C.X. Shan, Appl. Phys. Lett. 95 (2009) 131113.

Organic Electronics 12 (2011) 78–82

Contents lists available at ScienceDirect

Organic Electronics

journal homepage: www.elsevier.com/locate/orgel

High-mobility polymer space–charge-limited transistor with grid-induced crystallinity

Yu-Chiang Chao [a], Mu-Chun Niu [a], Hsiao-Wen Zan [b,*], Hsin-Fei Meng [a,*], Ming-Che Ku [b]

[a] Institute of Physics, National Chiao Tung University, 1001 Ta Hsueh Rd., 300 HsinChu, Taiwan
[b] Department of Photonics and Institute of Electro-Optics, National Chiao Tung University, 1001 Ta Hsueh Rd., 300 HsinChu, Taiwan

ARTICLE INFO

Article history:
Received 28 June 2010
Received in revised form 8 September 2010
Accepted 12 September 2010
Available online 26 October 2010

Keywords:
Vertical transistor
Space–charge-limited current

ABSTRACT

The vertical mobility of a polymer film prepared on a textured substrate is enhanced from 10^{-5} cm^2/Vs to 10^{-3} cm^2/Vs by a slow drying process which is unattainable in planar substrate. Highly ordered structure is observed for polymer film treated with high-boiling-point solvent and slow solvent annealing. The enhanced vertical mobility enables the polymer space–charge-limited transistor (SCLT) capable of outputting current density as high as 100 mA/cm^2 while maintaining good current gain and on–off ratio. Such vertical transistor is able to drive high-power devices or mechanical actuator in large-area and flexible array.

© 2010 Elsevier B.V. All rights reserved.

1. Introduction

Flexible electronics based on solution-processed semiconductors is an exciting emerging technology with the potential applications with very large areas. It enables displays and sensor arrays to cover the surfaces of clothes, buildings, robots, and cars [1,2]. In such large-area array, the pixel size may be over one centimeter and transistors need to drive high-power devices in the pixel as an organic light-emitting diode with high luminance or a motor and other mechanical actuator in robotic applications. For current output over 100 mA it is difficult to achieve using polymer field-effect transistors. Indeed for a channel length of 50 micron typically made by shadow mask the drain current is only 4 mA for channel width as long as 100 cm, given the carrier mobility of 0.1 cm^2/Vs, drain bias of 20 V, and capacitance of 10 nF/cm^2. In principle, the 100 cm channel width can be made by 50 pairs of 1 cm long inter-digited source and drain fingers, resulting in a 1 cm by 1 cm active area. Nevertheless in addition to the insufficient current output, the fabrication of this structure is fragile because any defect would break the entire finger. Furthermore, the operation voltage of organic field-effect transistor is usually over 20 V, so the Joule heating and power consumption will be a major problem for high-current applications. Polymer field-effect transistor is therefore not suitable for the driving of high-current load in the large-area flexible arrays.

Organic vertical transistors offer another approach to this requirement [3–10]. It has intrinsically low operation voltage and the current is directly proportional to its surface area for easy scaling up. One of the most successful vertical transistors is the space–charge-limited transistor (SCLT) which is a solid-state version of vacuum tube triode, with a metal grid embedded in an organic diode to control its vertical current [7–10]. SCLT shows low-operation voltage, below 1 V, and has a robust fabrication using self-assembled sub-micron plastic spheres as the shadow mask [9]. However, so far its current density (J_C) is only 1 mA/cm^2 due to the poor vertical mobility of the polymer. While the field-effect mobility of P3HT and some other polymers is over 0.1 cm^2/Vs, the vertical bulk mobility is only 10^{-5} cm^2/Vs. The surface treatment for the gate dielectric enhances the chain alignment near the interface but not in the bulk. Besides, the high carrier density at the interface also increases the mobility by filling the traps.

* Corresponding authors. Tel.: +886 35731955.
E-mail addresses: hsiaowen@mail.nctu.edu.tw (H.-W. Zan), meng@mail.nctu.edu.tw (H.-F. Meng).

1566-1199/$ - see front matter © 2010 Elsevier B.V. All rights reserved.
doi:10.1016/j.orgel.2010.09.023

In this work we demonstrate that the polymer vertical mobility can be greatly enhanced by a slow drying process using high-boiling-point solvent, i.e. solvent annealing, in a textured surface with 200 nm scale defined by the grid. The vertical columns promote the chain alignment of P3HT during the slow solvent annealing and result in an ordered structure unattainable in planar substrate. The vertical mobility is raised from 4×10^{-5} cm^2/Vs to 2×10^{-3} cm^2/Vs and the SCLT can deliver output current density as high as 100 mA/cm^2 while maintaining good current gain and on–off ratio. With such high current density, 100 mA current out-put can be delivered by a 1 cm^2 active area which is very easy to fabricate with high reliability. With this grid-induced crystallinity SCLT solves the problem of power transistor for large-area flexible electronics.

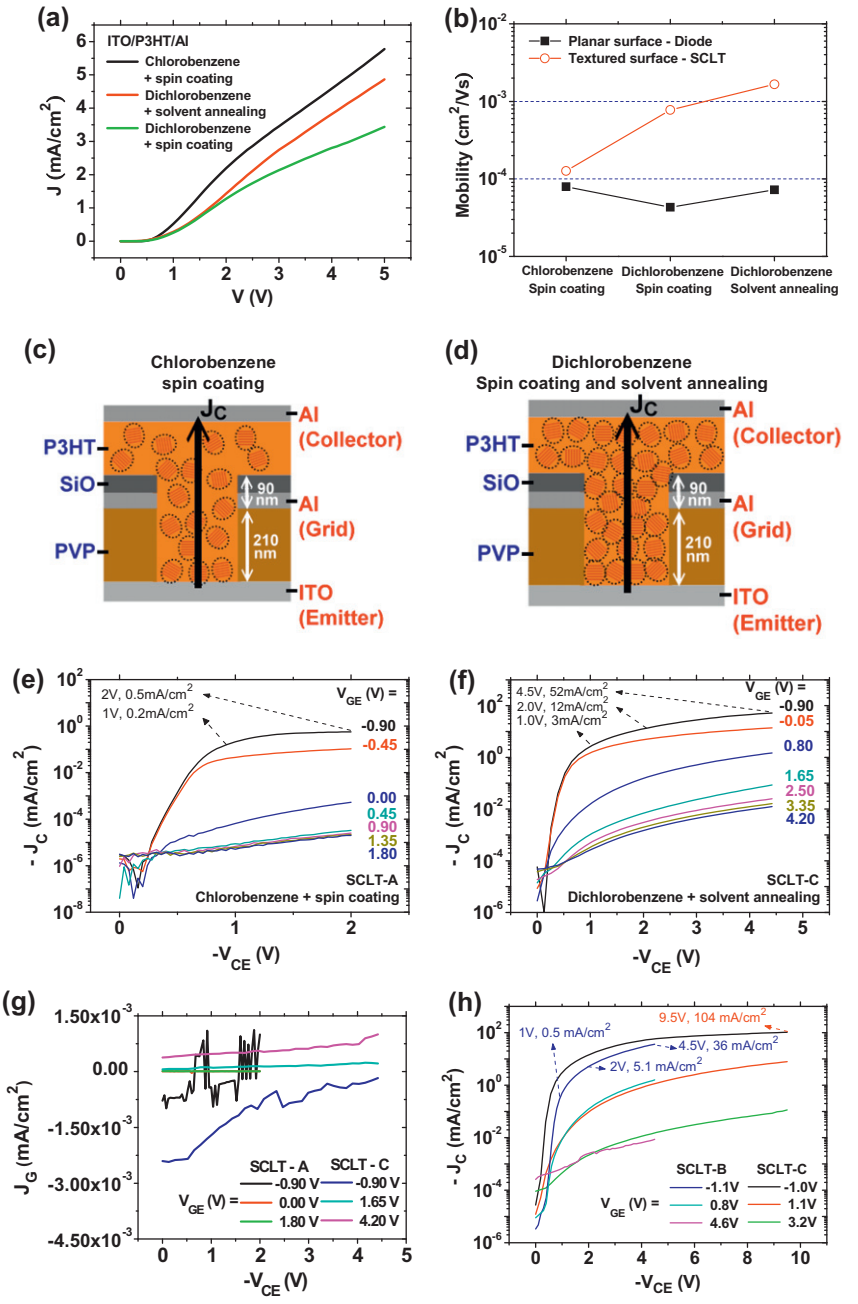

Fig. 1. Device characteristics fabricated by various solutions and processes. (a) Diode characteristics. (b) Mobilities of diodes and SCLTs. (c) and (d) Device structure of SCLT. (e) Transistor characteristics of SCLT-A fabricated by chlorobenzene spin coating. (f) Transistor characteristics of SCLT-C fabricated by dichlorobenzene solvent annealing. (g) Grid current density of SCLT-A and SCLT-C. (h) Transistor characteristics of SCLT-B fabricated by dichlorobenzene spin coating and Transistor characteristics of SCLT-C under high collector bias.

2. Experimental

The SCLT is fabricated on an ITO glass substrate. Cross-linkable poly(4-vinyl phenol) (PVP) of 210 nm is spin coated and cross-linked on the ITO substrate. Poly (melamine-co-formaldehyde) methylated is utilized as a cross-linking agent for PVP. After treating the PVP surface with 50 W O_2 plasma, the substrate is then submerged into 200 nm positively charged polystyrene spheres (Merck, K6-020) dilute ethanol solution with 0.8 wt.% for 3 min. The substrate is transferred into a beaker with boiling isopropanol solution for 10 s, and then blown dry immediately. Forty nanometer Al and 50 nm SiO are sequentially evaporated as metal base electrode and upper insulating layer. After removing the polystyrene spheres by an adhesive tape (Scotch, 3 M), the PVP at sites without base electrode coverage is removed by 13 min 150 W O_2 plasma treatment. Three hundred and fifty nanometer P3HT is then deposited with or without solvent annealing. For the device prepared by spin coating, P3HT in chlorobenzene or dichlorobenzene is spin coated on the substrate until the film dried. As for the device prepared by dichlorobenzene solvent annealing, P3HT in dichlorobenzene (2.5 wt.%) is spin-coated at 450 rpm for 30 s and then 1200 rpm for 1.2 s to form a P3HT wet film. The wet film is then holding still in the glove box until the film dried. The P3HT film is annealed at 140 °C for 10 min. Finally, the Al collector is deposited to complete the SCLT with active area as 1 mm^2. Transistor characteristics are recorded using an Agilent E5270B modular parameter analyzer. SEM image is obtained with a field-emission SEM (JEOL JSM-7401). XRD pattern is obtained with high resolution X-ray diffractometer, D1, Bede.

3. Results and discussions

Diodes and SCLTs with P3HT thickness of 350 nm are prepared from chlorobenzene (b.p. ~130 °C) and dichlorobenzene (b.p. ~180 °C) to understand the influence of solvent and drying process on the characteristics of devices. Because of the high boiling point of dichlorobenzene, the drying time is 7 s for spin coating P3HT chlorobenzene solution while it is 4 min for spin coating P3HT dichlorobenzene solution. Longer drying time about 20 min is achieved by a solvent annealing procedure which is the first spin coat P3HT dichlorobenzene solution for a short time then letting P3HT dichlorebenzene wet film dry slowly in the glove box. The drying time is visually judged by the change in film color. Diode structure and characteristics are shown in Fig. 1a. The output current density (J) of the P3HT diode prepared by spin coating chlorobenzene is higher than the one prepared by spin coating dichlorobenzene. With dichlorobenzene solvent annealing, J is enhanced but still inferior to the one achieved by chlorobenzene spin coating. The mobility, deduced from J follows space–charge-limited current (SCLC), of the diode prepared by spin coating P3HT chlorobenzene solution is therefore the highest one among various diodes as shown in Fig. 1b. The influence of the solvent and drying process on the SCLT is, however, not in the same trend as in diode as shown in Fig. 1e–h. The structure of SCLT is shown in Fig. 1c and d. The active layer of SCLT is fabricated by spin coating P3HT chlorobenzene solution (SCLT-A), spin coating P3HT dichlorobenzene solution (SCLT-B), and spin coating P3HT dichlorobenzene solution for a while then letting wet film dry slowly (SCLT-C). The ITO emitter is commonly grounded and the Al collector is negatively biased at collector-to-emitter voltage (V_{CE}). J_C is obtained by dividing output current by device active area of 1 mm^2. The grid-to-emitter voltage (V_{GE}) is varied to modulate J_C. As the transistor is turned on with $V_{GE} = -0.9$ V, J_C of SCLT-C (shown in Fig. 1f) is higher than the one of the SCLT-A (shown in Fig. 1e) for over one order of magnitude. Besides, as shown in Fig. 1h, J_C is 36 mA/cm^2 for SCLT-B ($V_{GE} = -1.1$ V and $V_{CE} = -4.5$ V) while 52 mA/cm^2 for SCLT-C ($V_{GE} = -1$ V and $V_{CE} = -4.5$ V). J_C of the SCLT fabricated by dichlorobenzene is higher than the one fabricated by chlorobenzene. The SCLT fabricated with dichlorobenzene solvent annealing can output higher current than the one fabricated with spin coating. As a whole, high-boiling-point solvent and long drying time enhance the output current. Furthermore, for SCLT-C, J_C of 104 mA/cm^2 is achieved when V_{CE} is −9.5 V as shown in Fig. 1h. With operation voltage below 10 V, this transistor is able to delivered 100 mA output current by a 1 cm^2 area which could drive

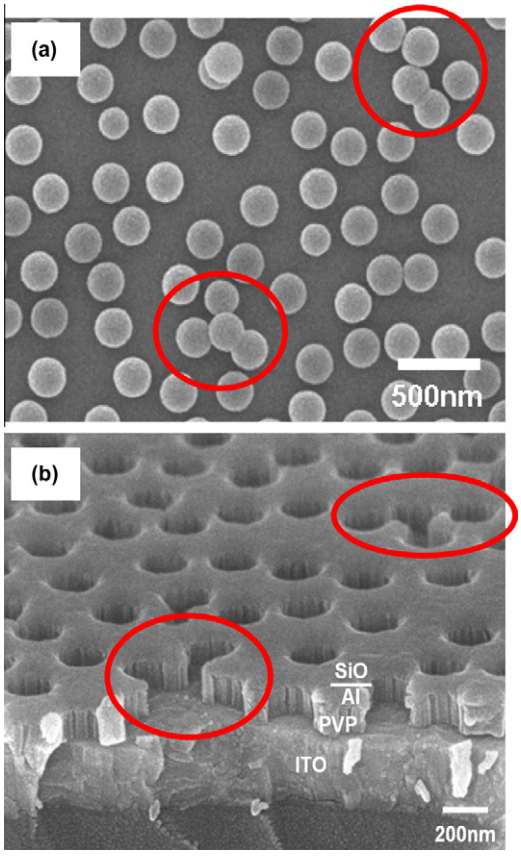

Fig. 2. Scanning electron microscopic images. (a) Top view of polystyrene spheres on poly(4-vinyl phenol). (b) The openings form at sites without Al grid.

high-current load in the large-area flexible arrays. As the SCLT is turned off, the off current of SCLT-C is still higher than SCLT-B and SCLT-A. The output current of SCLT is enhanced no matter in on state or off state. However, on/off ratios of these SCLTs are in the same order of 10^4. As shown in Fig. 1g the gird current density (J_G) is in the order of 10^{-4} to 10^{-3} mA/cm^2 and hence the current gain $|J_C/J_G|$ is as large as 10^4 to 10^5.

The reason why on and off current of SCLT-C are higher than other devices can be understood from scanning electron microscopy (SEM) images at difference phase of device fabrication. Top view of polystyrene spheres on poly(4-vinyl phenol) (PVP) is shown in Fig. 2a. The openings form at sites without Al grid is shown in Fig. 2b. Although most polystyrene spheres are separate to each other, aggregates contain more than two spheres can still be observed. Large openings will occur at sites with these randomly occurred aggregates. The grid control of the current is strong near the edge of the grid. The vertical carrier channel in the region far away from the grid can not be effectively modulated by grid. As large openings occur, the grid control on the current far away from the grid is small. Despite the on current is benefit from the slow drying process enhanced carrier mobility, the off current can not be suppressed by V_{GE} since the grid control on the current in the region away from the grid is less. The off current of SCLT is higher than J_G.

The mobilities of SCLTs are shown in Fig. 1b. Since the current channel is formed only at the openings, the device active area is recalculated according to the amount of openings for estimating the current density and the mobility. Mobilities deduced form SCLTs are higher than those from diodes except the one of SCLT-A. The highest mobility attainable in SCLT-C is 2×10^{-3} cm^2/Vs. With high-boiling-point solvent and solvent annealing process, P3HT can be self-organized into semicrystalline lamellar and yield high carrier mobility [11]. The carrier mobility is different in diode and SCLT which can be explained as vertical channel columns induced chain alignment of P3HT during the slow solvent annealing. To understand the reason why mobility increases in SCLT, atomic force microscopy (AFM) images of P3HT surface on textured surface are shown in Fig. 3a–c. The root mean square roughness of 13.6 nm is achieved for spin-coated film from chlorobenzene solution. The roughness increases to 15.3 nm when high boiling point dichlorobenzene is used. As dichlorobenzene solvent annealing process is used, the roughness is further increased to 22.2 nm. It has been demonstrated that polymer

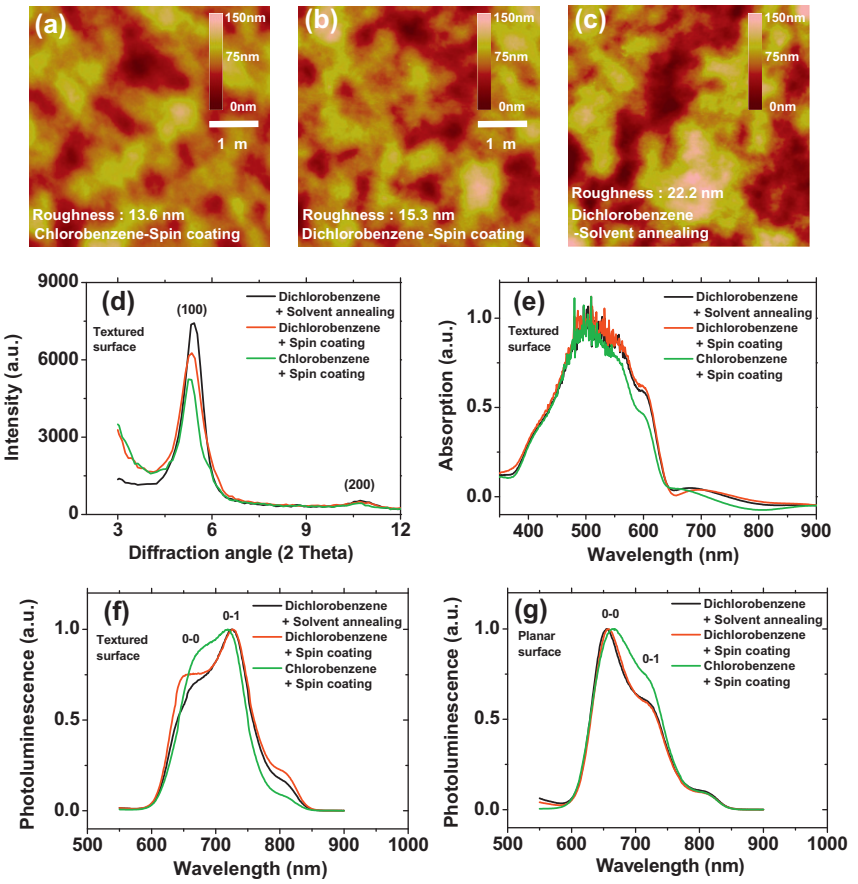

Fig. 3. (a–c) Atomic force microscopy images of P3HT surfaces on textured surface. P3HT layers are prepared from three processes those are chlorobenzene spin coating, dichlorobenzene spin coating, and dichlorobenzene solvent annealing. (d) Grazing incidence X-ray diffraction pattern, (e) UV–Vis absorption spectroscopy, and (f) photoluminescence spectroscopy of P3HT film prepared from three processes on textured surface. (g) Photoluminescence spectroscopy of P3HT film prepared from three processes on planar surface.

film with high surface roughness indicates polymer organization [12]. The increased mobility in SCLT may come from the enhanced degree of the polymer chain alignment. To confirm this, grazing incidence X-ray diffraction (GIXRD), UV–visible absorption spectroscopy, and photoluminescence spectroscopy are utilized to get more in-depth information inside the film since AFM images represent only film surface condition. From out-of plane GIXRD spectra shown in Fig. 3d, stronger reflection of the (100) layer can be observed at $2\theta = 5.4^\circ$ for film prepared with dichlorobenzene solvent annealing [13]. All P3HT films show well-organized intra plane structure which means P3HT self-organizes into two-dimensional π-stacked lamellar structures. The intensity increases when using dichlorobenzene and solvent annealing process. Crystallinity of P3HT is indeed improved by using high boiling point dichlorobenzene and solvent annealing process as illustrated in Fig. 1c and d. Besides, from UV–visible absorption spectra shown in Fig. 3e, prominent vibronic features can be observed at 600 nm for film prepared from dichlorobenzene. Previous work demonstrated that the enhanced vibronic absorption peak indicates strong interchain interactions and enhanced P3HT ordering [14]. This represents the utilization of high boiling point dichlorobenzene helps to induce ordered film with strong inter chain interactions. The influences of π-stacked polymer chains on photoluminescence spectra are shown in Fig. 3f. The 0–0 to 0–1 peak intensity ratio, S_R, is usually used as an effective probe for disorder [15,16]. The 0–0 peak is forbidden by symmetry in disorder-free aggregates. As disorder occurred the symmetry is broken and the 0–0 emission is allowed. The S_R is high as P3HT is spin-coated from chlorobenzene; however, as dichlorobenzene is used as the solvent, the S_R is decreased and reached the lowest value when solvent annealing process is used. This indicates that, on the textured surface, the P3HT film prepared from dichlorobenzene solvent annealing has less disorder while the one prepared from chlorobenzene spin coating has lots of disorder. The mobility is therefore high in P3HT film prepared from dichlorobenzene solvent annealing. Longer drying time may attribute to well-ordered lamellar structure. However, on the planar surface, the film prepared from dichlorobenzene solvent annealing is most disorder while the film prepared from chlorobenzene spin coating is less disorder as shown in Fig. 3g. The difference in photoluminescence spectra of P3HT on textured surface and planar surface reveal the level of disorder and may be used to explain the difference in device performance as shown in Fig. 1. With this grid-induced crystallinity, SCLT treated with dichlorobenzene solvent annealing can output high current which is suitable for large-area flexible electronics. The improved P3HT ordering in grid structure can be explained by improved π-π stacking due to nanoconfinement-induced chain alignment. The nanostructure-induced crystallinity in P3HT was also reported by several other groups [17–19]. Coakley et al. reported that P3HT nanopillars with diameters ranged from 20 to 75 nm have larger hole mobility than P3HT neat film. For pore diameter above 75 nm, the hole mobility falls off and approaches the mobility value for a neat film [17]. In our experiment, with pore diameter as 200 nm, hole mobilities in P3HT nanopillars are still higher than those in neat film. The discrepancy may come from the influences of solvent, drying method, and the pore sidewall properties. The nanostructure-induced crystallinity, however, is a clear phenomenon in all these works.

4. Conclusion

In conclusion, the SCLT capable of outputting current density as high as 100 mA/cm^2 is realized while maintaining good current gain and on–off ratio. The slow drying process using high-boiling-point solvent is utilized to enhance the polymer vertical mobility. The vertical columns promote the chain alignment of P3HT during the slow solvent annealing and result in an ordered structure unattainable in planar substrate. Such vertical transistor can be used to drive high-power devices or other mechanical actuator in large-area and flexible array.

Acknowledgement

This work is supported by the National Science Council of Taiwan under Contract No. NSC98-2628-M-009-001.

References

[1] T. Someya, T. Sekitani, S. Iba, Y. Kato, H. Kawaguchi, T. Sakurai, Porc. Natl. Acad. Sci. USA 101 (2004) 9966.
[2] T. Sekitani, H. Nakajima, H. Maeda, T. Fukushima, T. Aida, K. Hata, T. Someya, Nat. Mater. 8 (2009) 494.
[3] K. Kudo, D.X. Wang, M. Iizuka, S. Kuniyoshi, K. Tanaka, Thin Solid Films 331 (1998) 51.
[4] L.P. Ma, Y. Yang, Appl. Phys. Lett. 85 (2004) 5084.
[5] K. Fujimoto, T. Hiroi, K. Kudo, M. Nakamura, Adv. Mater. 19 (2007) 525.
[6] A.J. Ben-Sasson, E. Avnon, E. Ploshnik, O. Globeman, R. Shenhar, G.L. Frey, N. Tessler, Appl. Phys. Lett. 95 (2009) 213301.
[7] Y.C. Chao, H.F. Meng, S.F. Horng, Appl. Phys. Lett. 88 (2006) 223510.
[8] Y.C. Chao, H.F. Meng, S.F. Horng, C.S. Hsu, Org. Electron. 9 (2008) 310.
[9] Y.C. Chao, Y.C. Lin, M.Z. Dai, H.W. Zan, H.F. Meng, Appl. Phys. Lett. 95 (2009) 203305.
[10] Y.C. Chao, C.Y. Chen, H.W. Zan, H.F. Meng, J. Phys. D: Appl. Phys. 43 (2010) 205101.
[11] G. Li, Y. Yao, H. Yang, V. Shrotriya, G. Yang, Y. Yang, Adv. Funct. Mater. 17 (2007) 1636.
[12] G. Li, V. Shrotriya, J. Huang, Y. Yao, T. Moriarty, K. Emery, Y. Yang, Nat. Mater. 4 (2005) 864.
[13] J.S. Kim, Y. Park, D.Y. Lee, J.H. Lee, J.H. Park, J.K. Kim, K. Cho, Adv. Funct. Mater. 20 (2010) 540.
[14] P.J. Brown, D.S. Thomas, A. Kohler, J.S. Wilson, J.S. Kim, C.M. Ramsdale, H. Sirringhaus, R.H. Friend, Phys. Rev. B 67 (2003) 064203.
[15] J. Clark, C. Silva, R.H. Friend, F.C. Spano, Phys. Rev. Lett. 98 (2007) 206406.
[16] F.C. Spano, J. Clark, C. Silva, R.H. Friend, J. Chem. Phys. 130 (2009) 074904.
[17] K.M. Coakley, B.S. Srinivasan, J.M. Ziebarth, C. Goh, Y. Liu, M.D. McGehee, Adv. Funct. Mater. 15 (2005) 1927.
[18] M. Aryal, K. Trivedi, W. Hu, ACS Nano 3 (2009) 3085.
[19] J.S. Kim, Y. Park, D.Y. Lee, J.H. Lee, J.H. Park, J.K. Kim, K. Cho, Adv. Funct. Mater. 20 (2010) 540.

Organic Electronics 12 (2011) 83–91

Contents lists available at ScienceDirect

Organic Electronics

journal homepage: www.elsevier.com/locate/orgel

Accessing OLED emitter properties by radiation pattern analyses

Michael Flämmich *, Dirk Michaelis, Norbert Danz

Fraunhofer Institute for Applied Optics and Precision Engineering IOF, Albert-Einstein-Str. 7, 07745 Jena, Germany

ARTICLE INFO

Article history:
Received 23 August 2010
Received in revised form 28 September 2010
Accepted 30 September 2010
Available online 14 October 2010

Keywords:
Organic light-emitting diode
Optical simulation
In situ characterization
Internal spectrum
Emission zone
Dipole emitter orientation

ABSTRACT

The optical features of the internal dipole radiation have major impact on the emission pattern and overall device efficiency of organic light-emitting diodes (OLEDs). We provide some general directives on how the OLED layered stack should be designed in order to enable precise measurements of the *active* optical properties of the emissive material (namely internal electroluminescence spectrum, profile of the emission zone and dipole moment orientation) by radiation pattern analyses. We discuss a model layered system and deduce universal emitter positions most suitable for the determination of the particular OLED internal features of interest. Furthermore, we evaluate the real benefit of conducting radiation pattern analyses utilizing a substrate index-matched glass-hemisphere.

© 2010 Elsevier B.V. All rights reserved.

1. Introduction

In the past two decades considerable progress has been achieved in improving the lifetime and efficiency of organic light-emitting diodes (OLEDs) as well as in studying the basic physics of such devices. However, one factor still limiting the overall device performance is the rather low light extraction efficiency. This is due to the fact that the energy of an excited emitter can be radiated into different optical channels and only a small fraction of the light energy is finally extracted from the device. In order to perform comprehensive optical analysis and optimization of the OLED layered system, which promise improved device efficiency, the optical features of both the internal dipole radiation and the layered stack need to be known.

The radiation pattern of an OLED is generated by the interplay of the *active* optical properties of the emissive material (which are the internal electroluminescence (EL) spectrum, the profile of the emission zone, the orientation of the transition dipole moments and the internal luminescence quantum efficiency) and the *passive* optical properties of the layered system (which are the material refractive indices and the layer thicknesses). While the *passive* optical properties, material dispersions and thin film thicknesses, can be measured utilizing standard spectroscopic methods [1–3], the *active* optical properties of the emissive system are difficult to access. Frequently, photoluminescence (PL) experiments are performed to determine the spectrum of the emissive material [4] as well as the molecular dipole orientation [3–6]. However, PL experiments generally suffer from the fact that the initially photo-generated excited states are not necessarily identical to the excited states in EL operation [7]. Consequently, *in situ* investigations of OLEDs are desirable, and a promising approach is based on measurements of the optical far-field of OLEDs in electrical operation and subsequent optical reverse simulations. A variety of methods utilizing the full angular, spectral and polarization resolved radiation pattern or some essential aspects of these have been proposed, allowing conclusions to be drawn to the profile of the emission zone [8–12] as well as the orientation of the emissive dipoles [13]. However, in order to observe the internal features of the dipole radiation in the OLED far-field accurately, devices with well-adapted layered systems are needed to optically enhance the feature of interest. Although this is a crucial point, the potential of adapted devices to OLED characterization has not been investigated yet.

* Corresponding author. Tel.: +49 3641807420; fax: +49 3641807603.
E-mail address: michael.flaemmich@iof.fraunhofer.de (M. Flämmich).

1566-1199/$ - see front matter © 2010 Elsevier B.V. All rights reserved.
doi:10.1016/j.orgel.2010.09.019

In this paper we provide some general principles concerning the design of the OLED layered stack in order to enable for precise measurements of the *active* optical properties of the emissive material, namely the internal EL spectrum, the profile of the emission zone and the dipole moment orientation. Starting from basic considerations of the dipole radiation characteristics, we discuss a model layered system with sufficient detail to be meaningful for discussions of most real OLED configurations. We utilize the fact that the emitter–cathode distance is the most crucial factor in enhancing or suppressing certain dipole contributions to the optical far-field. Additionally, for the reverse simulation we take advantage of the fact that perpendicular dipoles only contribute to transverse-magnetic polarized light emission. Moreover, we evaluate the real benefit of conducting radiation pattern analyses utilizing an index-matched glass-hemisphere to access the substrate internal pattern. Finally, broadly suitable emitter positions are deduced, which allow the internal features of particular interest to be determined with greatest accuracy and in a manner almost independent of the other *active* properties of the emissive material.

2. Method

2.1. Optical modeling

In OLEDs, the electroluminescent emissive process can be considered as a dipole transition from an excited molecular state into the ground state. The emissive dipole transition moment at position z in the emissive material has a defined orientation φ, where φ denotes the internal angle between dipole moment and layered system normal. The angular (θ, angle to the layered system normal) and spectral (λ, wavelength) radiant intensity $I^{class}(\theta,\lambda,z,\varphi)$ of an emitter inside the OLED stack is simulated assuming a classical, continuously oscillating dipole source, yielding the emitted power $P^{class}(\theta,\lambda,z,\varphi)$ per solid angle $\mathrm{d}\Omega$ and wavelength $\mathrm{d}\lambda$ interval:

$$I^{class}(\theta,\lambda,z,\varphi)=\frac{\mathrm{d}^2P^{class}(\theta,\lambda,z,\varphi)}{\mathrm{d}\Omega\mathrm{d}\lambda}. \tag{1}$$

In the following discussion, all power values of classical dipoles are normalized with respect to the total irradiated power of a corresponding dipole in the homogeneous infinite emitter medium. The electromagnetic dipole fields in the system are evaluated using a transfer-matrix formulation of the well-known Green's function model [14]. For further details on the generation of the dipole fields see Ref. [15] and references therein.

The classical emission pattern of an arbitrarily oriented dipole can be decomposed into contributions of three orthogonal dipoles ($\|$TE, $\|$TM, $\perp$ TM) [16]:

$$\begin{aligned}I^{class}(\theta,\lambda,z,\varphi)=\sin^2(\varphi)\cdot[I^{class}_{\|\mathrm{TE}}(\theta,\lambda,z)+I^{class}_{\|\mathrm{TM}}(\theta,\lambda,z)]\\+\cos^2(\varphi)\cdot[I^{class}_{\perp\mathrm{TM}}(\theta,\lambda,z)].\end{aligned} \tag{2}$$

These orthogonal dipoles are specified according to their orientation with respect to the interfaces of the layered system (parallel "$\|$", perpendicular "$\perp$") and the corresponding polarization of the emitted radiation (transverse-electric "TE", transverse-magnetic "TM").

In order to ensure normalization of power emitted from the dipole in the layered system, we utilize the equivalence between the probability for spontaneous emission of a photon via a dipole transition and the radiated power of a classical dipole source in the corresponding layered system [17]:

$$I(\theta,\lambda,z,\varphi)\propto\frac{1}{\Gamma_{rel}(q,z,\varphi)}I^{class}(\theta,\lambda,z,\varphi), \tag{3}$$

where $\Gamma_{rel}(q,z,\varphi)$ denotes the emission rate of the dipole at position z with orientation φ in the cavity normalized to the emission rate in the infinite emitter medium. By this means, the influence of the OLED stack on the rate of emission, the so-called microcavity effect, is taken into account. For all rate calculations performed in this study, a representative internal luminescence quantum efficiency of $q = 0.7$ was assumed. Although the q-value has a major impact on the overall efficiency of OLEDs, it has very minor quantitative impact on the considerations we address here. For a more detailed discussion of the q-value see for example Refs. [17–20].

At this point it is worth noting that although the applied optical model is similar to the simulation tools established by other groups and discussed elsewhere [18,21–24], all calculations are performed with a self-developed, in-house software tool [25]. Each layer within the OLED stack is assumed to have smooth, parallel interfaces and a certain thickness. The interaction between materials and radiation is considered by the wavelength dependent complex refractive index ($n + i\kappa$, with refractive index n and extinction coefficient κ), and the light propagation through the multilayer system is simulated utilizing a transfer-matrix method [26].

In real OLED devices the emissive material can be treated as an ensemble of incoherent radiators. Distributions in (i) emitter location z, (ii) dipole orientation φ, and (iii) wavelength dependent spectral intensity account for (i) the profile of the emission zone $N(z)$, (ii) the distribution of emitter orientation $g(\varphi)$, and (iii) the internal EL spectrum $S(\lambda)=(hc/\lambda)\cdot\hat{s}(\lambda)$, respectively. The internal EL spectrum takes the photon energy hc/λ into account, where h denotes the Planck constant and c the speed of light in vacuum. The integrals of all distributions are normalized to one: $\int N(z)\mathrm{d}z=1$, $\int g(\varphi)\sin\varphi\mathrm{d}\varphi=1$, and $\int\hat{s}(\lambda)\mathrm{d}\lambda=1$. By this means, the integrated distribution weight yields a single emissive event in total and $\int S(\lambda)\mathrm{d}\lambda$ yields the mean photon energy with respect to the spectral distribution $\hat{s}(\lambda)$. The emission pattern from the OLED layered system $I^{LS}(\theta,\lambda)$ can be obtained by an incoherent superposition of all contributions [27]:

$$\begin{aligned}I^{LS}(\theta,\lambda)&=S(\lambda)\int_z\int_\varphi N(z)g(\varphi)\frac{I^{class}(\theta,\lambda,z,\varphi)}{\Gamma_{rel}(q,z,\varphi)}\sin\varphi\mathrm{d}\varphi\mathrm{d}z\\&=S(\lambda)\left\langle\frac{I^{class}(\theta,\lambda,z,\varphi)}{\Gamma_{rel}(q,z,\varphi)}\right\rangle_{\varphi,z}.\end{aligned} \tag{4}$$

Hence, $I^{LS}(\theta,\lambda)$ includes only optical effects due to the layered system. Electrical phenomena, like charge carrier

injection and recombination, are excluded from this investigation. Consequently, it is this quantity which should be considered for optical analyses. It is related to the experimentally accessible spectral radiant intensity of a device $I(\theta,\lambda)$ by the formula:

$$I(\theta,\lambda) = (I_{inj}/e)\cdot\gamma\cdot\eta_{S/T}\cdot q\cdot I^{LS}(\theta,\lambda). \quad (5)$$

Eq. (5) also includes the number of injected charge carriers I_{inj}/e, where I_{inj} denotes the current applied to the device and e denotes the elementary charge. Furthermore, the radiant intensity is limited by (i) the probability of charge carrier recombination and subsequent exciton formation γ, and (ii) by the generation of excited singlet as well as triplet states according to spin statistics, where allowed and forbidden transitions are regarded by the singlet/triplet-factor $\eta_{S/T}$. Additionally the internal luminescence quantum efficiency q of the emissive system limits the radiant intensity.

The fraction of photons emitted from a device $\eta_{out}^{LS} = 2\pi\cdot\int_\lambda\int_\theta I^{LS}(\theta,\lambda)/(hc/\lambda)\mathrm{d}\theta\mathrm{d}\lambda$, with respect to the infinite emissive material, yields a measure of how the number of emitted photons is influenced by the presence of the layered system. It defines the overall device efficiency, represented by the well-known external quantum efficiency:

$$EQE = \gamma\cdot\eta_{S/T}\cdot\langle q_{eff}\cdot\eta_{out}^{class}\rangle_{\varphi,z} = \gamma\cdot\eta_{S/T}\cdot q\cdot\eta_{out}^{LS}, \quad (6)$$

giving the number of emitted photons per injected charge. The middle term of Eq. (6) is well established: in any microcavity the quantum efficiency of excited state luminescence is system dependent due to near field effects, represented by the effective quantum efficiency q_{eff}, and only a fraction of the internally generated light can leave the structure, taken into account by the classical outcoupling-factor η_{out}^{class}. In this notation, however, q_{eff} accounts for the variation of the emissive rate due to the surrounding layered system, and the outcoupling-factor η_{out}^{class} is calculated by classical theory. Thus, both quantities, q_{eff} and η_{out}^{class}, depend on the emitter position z within the system as well as on the emitter orientation φ, a fact which is often disregarded. In order to transform q_{eff} to an emissive system specific constant, the internal luminescence quantum efficiency q is introduced into Eq. (6) on the right hand side, with the advantage that the material dependent quantities $(\gamma,\eta_{S/T},q)$ are separated from the layered system specific effects (η_{out}^{LS}).

2.2. Optical reverse simulation or the inverse outcoupling problem

Eqs. (4) and (6) illustrate the fundamental reason why optical reverse simulation from external device measures is not straight forward: externally measured device outputs are necessarily an average of all single emitter contributions. Starting from *EQE* measurements it is almost impossible to estimate features of the internal dipole radiation, since it is also an integral over all angular and spectral components. Furthermore, the other factors in Eq. (6) have to be known precisely in order to deduce meaningful results from the measured *EQE*. By contrast, angular, spectral and polarization resolved measurements of the radiation pattern are more likely to allow for conclusions about the *active* optical properties of the emissive sites. However, in order to separate the contributions from emitters with distinct locations or orientations [see Eq. (4)], two ideas are fundamental: (i) According to Eq. (2), parallel dipoles emit TE and TM polarized radiation, whereas perpendicular dipoles contribute to TM polarized radiation only. Consequently, investigations of the internal EL spectrum and the emission zone can be performed independently of the dipole orientation distribution in the emissive material by analyzing TE polarized radiation only. Although straight-forward, this consideration has not been utilized in recent studies [9,11,12]. However, by subsequently analyzing TM polarized radiation, the emitter orientation remains the only unknown parameter, which can be adjusted to match TM experiment and simulation. (ii) The emitter–cathode distance mainly determines the interference conditions at the position of the emissive sites and is most crucial to enhance or suppress certain dipole contributions to the OLED far-field. Thus, the device architecture should be well adapted in order to optically enhance the feature of interest.

Solving the inverse outcoupling problem is based on performing a least-squares fit to the measured angle, wavelength and polarization dependent radiant intensity of a device. In order to circumvent the complexity of absolute measurements and the consideration of absolute factors [like in Eq. (5)], a non-absolute reverse simulation based on Eq. (4) is usually performed. Commonly, a number of discrete emitter positions within the emissive layer are assumed, each with identical internal spectrum $S(\lambda)$ and orientation distribution $g(\varphi)$. Some investigations are conducted considering a single dipole at a single position within the emissive layer [18,19]. Other studies take an extended emission zone into account, assuming a parametric distribution $N(z)$ deduced from electrical considerations [9–11,13] with numerically reasonable emitter position discretizations of e.g. ~10 nm [10] and ~20 nm [11]. However, applying a parametric distribution $N(z)$ is intrinsically limited, since the resulting emission zone is always within the frame of the electrical model. Consequently, the results derived are as open to debate as is the underlying electrical model. This is especially relevant for investigations considering the emission from positions very close to interfaces [10,11]. Unfortunately, optical reverse simulations based on a large number of discrete emitter positions without assuming a distribution $N(z)$ fail, because the radiation patterns of the emissive sites are not sufficiently distinct and not linearly independent. Regarding the orientation of the emissive sites, it is impossible to measure the detailed orientation distribution $g(\varphi)$, but rather the fraction of parallel and perpendicular dipole contributions generating the radiation pattern. This has been shown by experiments using both optical [6] and electrical [13] excitation. However, knowledge of the detailed emitter orientation distribution is not necessary for optical evaluations and information on the ratio of parallel to perpendicular dipole contributions is sufficient [see Eq. (2)].

A glass-hemisphere or -prism is frequently attached to the OLED substrate [11,12,18,28] in order to cancel the

total internal reflection at the substrate–air interface. Thus the radiant intensity in the OLED substrate $I^{sub}(\theta^s, \lambda)$, where θ^s denotes the propagation angle in the substrate with respect to the system normal, is accessed and an extended fraction of the internally generated angular radiation pattern is investigated. However, attaching a glass-hemisphere to the OLED substrate using an index-matched oil considerably increases the difficulty of experiments. In the following, we conduct our analyses for both cases, i.e. the emission pattern in air, $I^{LS}(\theta, \lambda)$ and in the substrate, $I^{LS,sub}(\theta^s, \lambda)$, in order to evaluate the real benefit of hemisphere measurements for accessing OLED emitter properties by radiation pattern analyses.

2.3. Model layered system

The basic considerations in this study are illustrated by monochromatic analyses (λ = 550 nm) of an artificial OLED system (see Fig. 1). Conventional OLED substrates are about 1 mm thick and exhibit refractive indices around n = 1.5 with negligible absorption. An indium–tin–oxide (ITO) layer of about 100 nm thickness is typically utilized as transparent anode, covered by a hole transport layer (HTL) of either several 10 nm or around 200 nm thickness. However, the anode-side part of the OLED stack has a minor impact on the basic effects we address. In this study, we have adjusted the HTL thickness to 60 nm, corresponding approximately to an optimized radiation into air. An electron transport layer (ETL) performs as the optical spacer between the emissive sites and the opaque metallic cathode of, in our case, silver. The organic materials and ITO utilized in conventional OLED systems have refractive indices around n = 1.8 at λ = 550 nm accompanied by, for our considerations, negligible absorption [1,13,17]. The optical properties of silver were taken from Ref. [29].

We believe that the proposed configuration (Fig. 1) adequately represents most real OLED systems. It is apparently very similar to bottom emitting structures based on small-molecule materials, where charge carrier injection and blocking layers have refractive indices around n = 1.8 as well. Top emitting OLEDs could be reproduced by inverting the whole structure without the substrate and exchanging the ITO layer by a thin (~20 nm) metal layer. However, in such a system the distance between the emissive sites and the semi-transparent metal has to be carefully adjusted as well, in order to observe the effects we address later in this paper. Typical polymeric OLEDs have a combined emissive and electron transport layer and a rather broad emission zone [30]. Nevertheless, for the purpose of optical analyses it is meaningful to divide the origin of this emission into single, discrete sheets. Furthermore, polymeric OLEDs can exhibit a confined emission zone at the anode-sided interface of the emissive layer (EML) if the charge transport inside the emissive material is electron dominated [10]. Consequently, this case is included by an association of the real polymeric EML with a combination of ETL and emissive sites in the model system. In summary, we believe that the proposed model system matches most real OLED systems well enough to describe the experimental aspects addressed in this contribution.

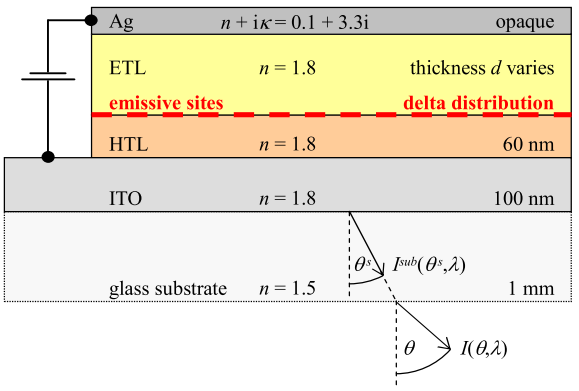

Fig. 1. Model OLED stack as used in the present considerations. Attaching an index-matched, macroscopic glass-hemisphere to the substrate additionally, allows investigation of the substrate radiation pattern $I^{sub}(\theta^s, \lambda)$.

3. Results and discussion

3.1. TE polarization: determination of internal EL spectrum and emission zone

As mentioned above, only TE polarized radiation has to be considered, if an investigation of the internal EL spectrum and/or emission zone is intended. To illustrate the following reasoning, Fig. 2(a) depicts the dependence of the normalized radiant flux ($\Phi_{TE} = 2\pi \cdot \int I^{LS}_{TE}(\theta, 550\,\text{nm}) \sin\theta \mathrm{d}\theta$) of TE polarized radiation from the model device into air on the emitter cathode distance d. In this context the radiant flux from a device can be interpreted as a measure of the optical efficiency of an OLED. An optically optimized device architecture ensures the emissive sites are placed at a distance of about d = 65 nm to the cathode (roughly corresponding to a quarter wavelength distance $\lambda/4n$, n = 1.8, shifted additionally by the non-ideal phase change upon reflection at the non-ideal cathode mirror). The emission into air is enhanced at this distance due to constructive interference of light emitted directly into the substrate direction with that reflected at the metal cathode. For an ETL thickness of about 140 nm (corresponding to about a half wavelength distance $\lambda/2n$) radiation from the emissive sites experiences destructive interference and emission into air is suppressed. Note that the behavior of the TE radiant flux represents the characteristics of the overall radiant flux from a device as well.

The shape of the angular radiation pattern is related to the interference conditions at the position of the emissive site. Fig. 2(b)–(k) shows the TE angular radiation pattern in air [$I^{LS}_{TE}(\theta, 550\,\text{nm})$ according to Eq. (4)] for some representative ETL thicknesses. The characteristics shown in Fig. 2(b)–(d) and (h)–(k) correspond to emissive sites located at values of emitter–cathode distance in the first and second maximum of the normalized TE polarized radiant flux into air, respectively. The angular pattern is nearly Lambertian like for these cases and all characteristics are very similar to each other due to the constructive interference conditions for moderate emission angles around

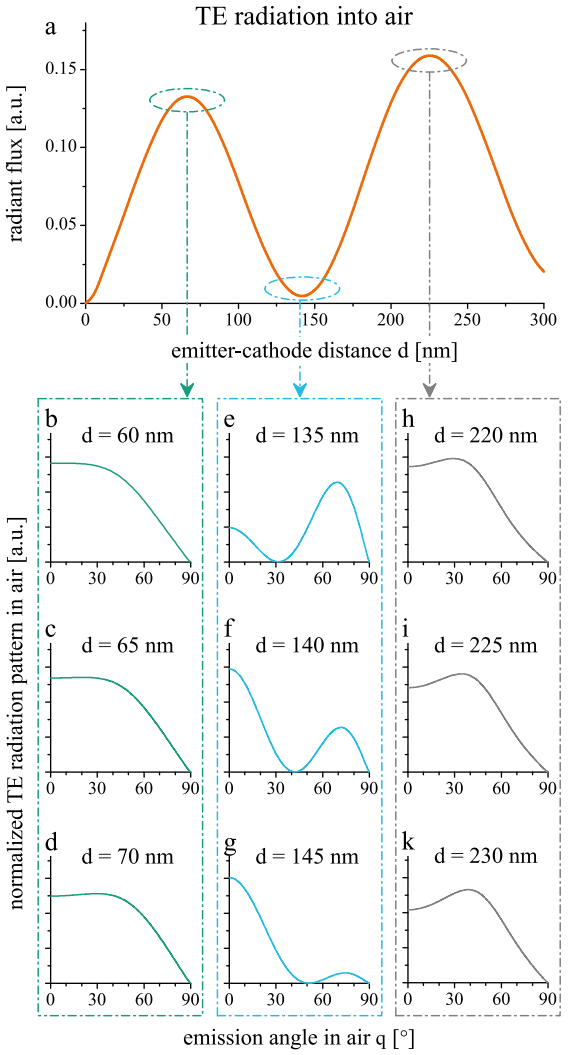

Fig. 2. As a measure for the optical efficiency of the model OLED stack, the normalized TE polarized radiant flux into air for $\lambda = 550$ nm is shown (a). The normalized TE polarized angular radiation patterns for discrete emitter positions around the first maximum (b)–(d), the minimum (e)–(g), and the second maximum (h)–(k) are plotted as well.

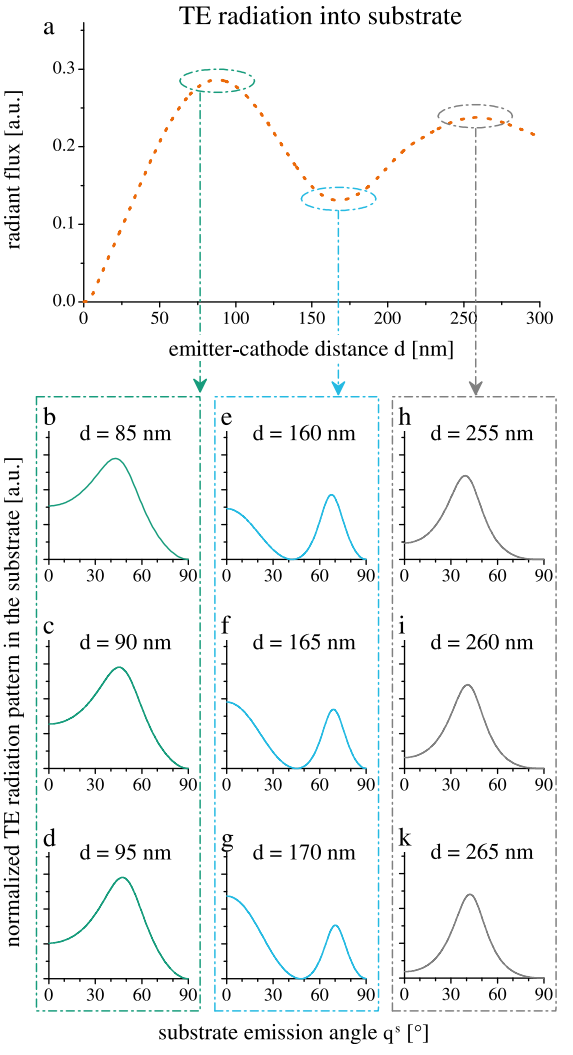

Fig. 3. The normalized TE polarized radiant flux into the substrate for $\lambda = 550$ nm is shown (a). The normalized TE polarized angular radiation patterns for discrete emitter positions around the first maximum (b)–(d), the minimum (e)–(g), and the second maximum (h)–(k) are plotted as well.

these positions. By contrast, the angular characteristics of emissive sites around the minimum of the normalized TE polarized radiant flux into air [Fig. 2(e)–(g)] are significantly modulated, deviating strongly from a Lambertian emission pattern. Furthermore, the absolute emission intensity is considerably reduced due to destructive interference. Surprisingly, it can be seen that the angular characteristics vary considerably for emitters displaced by just a few nanometers. For emissive sites at a distance $d \approx 140$ nm to the cathode, there is destructive interference for emission into oblique angles of $\theta \approx 40°$. This condition shifts significantly towards lower or higher emission angles upon moving the emissive sites closer to or further from the cathode, causing a variation of the balance between radiation into normal or oblique angles.

Fig. 3 illustrates the same characteristics as Fig. 2, but for radiation into the OLED substrate. The normalized TE polarized substrate radiant flux [Fig. 3(a)] consists of an extended fraction of the internally generated angular radiation pattern and is less modulated than the radiant flux into air. All angular patterns from emitter–cathode distances corresponding to maxima of the normalized TE polarized radiant flux into the substrate Fig. 3(b)–(d) and (h)–(k) exhibit enhanced radiation into larger substrate angles, yielding a higher flux due to solid angle considerations. Their characteristics deviate from a Lambertian emission significantly and are very similar to each other. The angular characteristics of emissive sites around the minimum of normalized TE polarized radiant flux into the substrate [Fig. 3(e)–(g)] are again significantly modulated and the absolute emission intensity is considerably reduced. However, compared to the data minimum of the normalized TE polarized radiant flux into air in

Fig. 2(e)–(g), there is much less effect of the emitter–cathode distance on the radiation pattern shape.

In order to quantify the variation of angular radiation pattern due to the emitter–cathode distance, we introduce the parameter

$$V_\theta(d) = \int_{\theta=0^\circ}^{90^\circ} \left| \frac{I^{LS}_{\mathrm{TE},d_{(-)}}(\theta, 550\ \mathrm{nm})}{\Phi_{\mathrm{TE},d_{(-)}}} - \frac{I^{LS}_{\mathrm{TE},d}(\theta, 550\ \mathrm{nm})}{\Phi_{\mathrm{TE},d}} \right| \cdot \frac{\sin\theta \mathrm{d}\theta}{\Delta d}, \tag{7}$$

where $I^{LS}_{\mathrm{TE},d}(\theta, 550\ \mathrm{nm})$ denotes TE polarized radiation emitted into the angle θ in air from an emissive site at a distance d to the cathode. $d_{(-)}$ denotes the next distance closer to the cathode, depending on the discretization $\Delta d = |d - d_{(-)}|$ of the emitter–cathode distances chosen for the calculation of $V_\theta(d)$. In Eq. (7), normalization with respect to the radiant flux at the particular distance to the cathode is important to distinguish the desired relative variation of the shape of the angular pattern from a variation of the absolute emitted power. In other words, all radiation patterns are normalized to the same area in terms of solid angle and only the relative variation of the characteristics is considered. By this means, $V_\theta(d)$ provides a measure of how distinguishable are the radiation pattern shapes of two neighboring positions, $d_{(-)}$ and d, in the device. Replacing $I^{LS}_{\mathrm{TE}}(\theta, 550\ \mathrm{nm})$ by the TE radiation pattern in the substrate as a function of the substrate angle θ^s and normalizing to the radiant flux in the substrate in Eq. (7) yields the corresponding variation of angular radiation pattern in the substrate as a function of emitter–cathode distance.

The angular radiation pattern variation $V_\theta(d)$ versus emitter–cathode distance is shown in Fig. 4 for both radiation in air and in the substrate. It can be seen that $V_\theta(d)$ is low for almost all emitter–cathode distances, including the case of optically optimized devices, apart from emission from around the radiant flux minimum. The latter feature can be explained by the destructive interference conditions for emission into certain oblique angles, which considerably modulates the angular radiation pattern, as discussed above. Surprisingly, analyzing the substrate radiation pattern yields only little more information, to the emission in air. The radiation in air exhibits even better contrast to the exact emission origin, if the emissive sites are placed around the radiant flux minimum. This might be surprising at first, because one might expect the substrate radiation, containing an extended fraction of the OLED-internal radiation pattern, to yield much more information than the radiation into air. However, the suggested approach is based on observing radiation pattern changes, and the substrate pattern variations are largest at small emission angles. This sensitive interval is expanded in air, because the transition from the substrate into air restricts the observed fraction of the OLED-internal radiation pattern. Hence, the qualitative impression from the shape of the angular emission patterns [Figs. 2(b)–(k) and 3(b)–(k)] is confirmed by the quantitative measure $V_\theta(d)$.

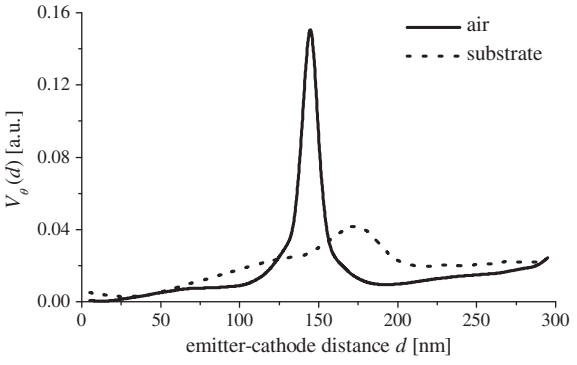

Fig. 4. The variation of the TE polarized angular radiation pattern for $\lambda = 550$ nm in air and in the substrate, respectively, is plotted according to Eq. (7). Maxima of $V_\theta(d)$ correspond to minima of optical outcoupling [see Figs. 2(a) and 3(a)]. Thus, placing the emissive sites around $d \approx 140$ nm and $d \approx 165$ nm, for emission into air and in the substrate, respectively, enables for an accurate determination of the exact emission origin.

Of course, when designing an experiment to measure the internal EL spectrum of a material, relatively weak changes of the interference conditions are desired in order to minimize the influence of the actual position of the emissive sites on the result. Consequently, the emissive sites should be placed around a maximum for optical outcoupling which additionally ensures a high outcoupling intensity.

By contrast, the radiation pattern is most sensitive to the position of the emissive sites at the minimum of optical output where destructive interference conditions apply. We take as an example the following experiment: the EML of a small-molecular device has a width of 10 nm and the exact emission origin is of particular interest. In this case, the ETL thickness should be adjusted in order to match the efficiency minimum in air (corresponding to 140 nm for the present model system). Even analyzing the angular radiation pattern in air in a purely qualitative manner provides information about how the emission zone is balanced. If the angular emission pattern is larger at larger angles, the origin of the emission is at the cathode side of the EML, whereas a larger emission in the perpendicular direction provides evidence for anode-side emission [see Fig. 2(e)–(g)]. Of course, quantitative reverse simulations using an extended spectral range promise even more accurate results.

These monochromatic considerations can be extended in a straightforward manner to the case of real emissive materials for OLEDs with a spectral width of typically about 100 nm, where the layered stack should be designed to match the desired criterion for maximum or minimum outcoupling at the mean wavelength of the spectrum under investigation. As can be seen from Fig. 4, the interference conditions do not change significantly with emitter–cathode distance around the quarter wavelength distance, which implies that the interference conditions do not change significantly with wavelength as well. Consequently, for emitters around the optical maximum the determination of the internal EL spectrum is almost independent of the actual position of the emissive sites, as discussed above. For the profile of the emission zone one would expect to gather more information if the investigated spectral range is extended. However, the condition showing good contrast on the emitter position, corre-

sponding to the $V_\theta(d)$ maximum, is wavelength dependent. This is potentially a positive feature when analyzing extended emission zones but yields no benefit when investigating rather confined emission zones.

The problematic case of measuring the emission profile of broad emission zones, which are typical for polymeric systems, is now discussed. It is essentially critical for such experiments that, in general, positions with good extraction efficiency and thus high far-field contribution possess low sensitivity to the emission origin, as indicated by a low $V_\theta(d)$. By contrast, positions featuring a high sensitivity to the emission origin have only weak contributions to the far-field. In other words, radiation from positions around the efficiency minimum might not be visible in the far-field of the OLED, because it is much weaker than the brighter signal from positions around the efficiency optimum. Although there have been extensive studies on measurements of the profile of the emission zone in polymeric OLEDs recently, this general and problematic issue has not been considered yet [10–12].

3.2. TM polarization: determination of dipole emitter orientation

As discussed above, parallel dipole moments contribute to both TE and TM polarized radiation, whereas perpendicular moments contribute to the TM polarized radiation only [see Eq. (2)]. One basic idea for a dipole orientation measurement is to analyze the TE polarized radiation first and determine the contribution from parallel dipoles to the radiation pattern. Subsequently analyzing TM polarized radiation, the emitter orientation can be adjusted to match TM experiment and simulation.

In order to detect perpendicular dipoles in the TM polarized optical far-field of an OLED, their contributions to the radiation pattern must be sufficiently large compared to the TM polarized contributions arising from parallel dipoles. As a measure of the far-field contribution, the normalized radiant flux ($\Phi_{\mathrm{TM}} = 2\pi \cdot \int I^{LS}_{\mathrm{TM}}(\theta, 550\,\mathrm{nm}) \sin\theta \mathrm{d}\theta$) at $\lambda = 550$ nm of the two TM dipoles embedded in the model OLED stack was calculated as a function of the emitter–cathode distance (see Fig. 5) for radiation into air and in the substrate. Evidently, the emission from parallel and perpendicular emissive sites is governed by opposite interference conditions, discussed in detail in Ref. [13]. A comparison with Figs. 2(a) and 3(a) reveals that emission from ∥TM dipoles shows the same characteristics as emission from ∥TE dipoles.

To quantify the visibility of perpendicular emitters in the TM polarized OLED radiation pattern, we introduce the parameter

$$V_\perp(d) = \frac{\Phi_{\perp\mathrm{TM},d}}{\Phi_{\parallel\mathrm{TM},d} + \Phi_{\perp\mathrm{TM},d}}, \tag{8}$$

giving the relative fraction from ⊥ TM dipole contributions to the overall TM polarized emission in air and in the substrate, respectively, for a given emitter–cathode distance d. The dependence of the $V_\perp(d)$-parameter on the emitter–cathode distance is plotted in Fig. 6. Positions close to the cathode are not suitable for any optical experiment, because they suffer from strong coupling to the surface plasmon mode and the overall outcoupling efficiency is very weak. However, the interference conditions around the optical maximum enhance radiation from parallel dipoles and suppress light from perpendicular emitters. Consequently, the distribution of the dipole moment orientation is almost impossible to obtain using standard, efficient OLED geometries which are optimized for maximum emission, because almost all light generated by perpendicularly oriented emitters is trapped inside the OLED stack. This holds for both the emission in air and in the substrate. By contrast, changing the emitter–cathode distance to the minimum of optical outcoupling yields a large far-field contribution from perpendicular dipole moments accompanied by weaker outcoupling of the radiation from parallel dipoles, which is the desired case for an emitter orientation analysis. Again, this is valid for both, air and substrate emission. Measurements using a glass-hemisphere will yield more information for very large emitter–cathode distances ($d > 150$ nm) only, but offer no benefits compared to an emitter orientation investigation

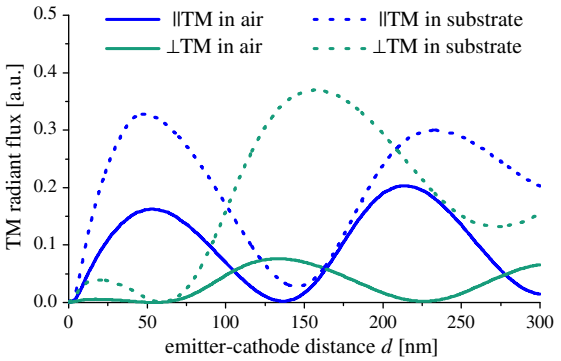

Fig. 5. The normalized TM polarized radiant flux of the two TM dipoles is shown for radiation in air and in the substrate, respectively, as a measure of their far-field contributions. Radiation from parallel and perpendicular dipoles experiences opposite interference conditions, enabling a measurement of the dipole emitter orientation.

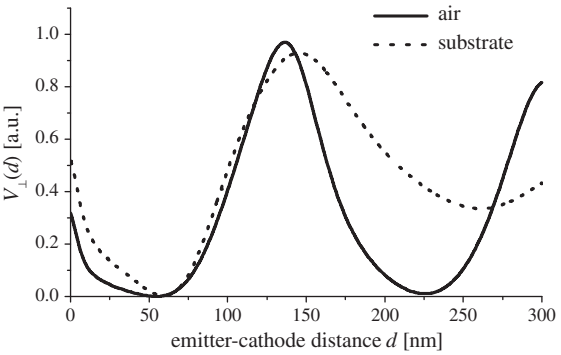

Fig. 6. The contribution of radiation from perpendicular dipoles ($\Phi_{\perp\mathrm{TM},d}$) to the overall TM polarized far-field ($\Phi_{\parallel\mathrm{TM},d} + \Phi_{\perp\mathrm{TM},d}$) in air and in the substrate, respectively, according to Eq. (8) for $\lambda = 550$ nm is shown versus the emitter–cathode distance d. Maxima of $V_\perp(d)$ correspond to minima of optical outcoupling [see Figs. 2(a) and 3(a)]. Thus, positions around $d \approx 140$ nm are favorable for a measurement of the dipole orientation.

based on the radiation pattern in air utilizing a well-adapted OLED stack.

4. Conclusions

In summary, we have proposed general strategies for accessing OLED emitter properties by radiation pattern analyses. Taking advantage of the fact that perpendicular dipoles contribute to TM polarized light emission only, one should analyze TE polarized radiation only if an investigation of internal EL spectrum or emission zone is intended. Provided the OLED layered stack is designed carefully, subsequently analyzing TM polarized radiation yields information about the orientation of the emissive sites.

We have shown that the OLED layered stack design is important for the successful characterization of the emissive sites from radiation pattern measurements. Consequently, well-adapted devices have to be utilized to enable an accurate determination of the *active* optical properties of emissive materials used in OLEDs. In this context, the distance from the emissive sites to the metallic cathode plays a decisive role, as it alters the interference conditions in the device. To illustrate our reasoning, we consider the emitter–cathode distance in terms of device efficiency. Then, placing the emissive sites at a position:

(i) around the emission maximum and analyzing TE polarized radiation allows a determination of the internal EL spectrum,
(ii) around the emission minimum and analyzing TE polarized radiation allows an accurate determination of the emission zone, and
(iii) around the emission minimum and analyzing TM polarized radiation allows a determination of the orientation of the emissive dipoles,

almost independent of the other *active* optical properties, respectively. These rules apply very well to systems where the emissive sites are relatively well confined and the emitter–cathode distance is easily adjustable. Consequently, small-molecular emissive materials can be analyzed in the proposed way. However, the strategies developed are also valid for polymeric materials, where extended emission zones can reduce the contribution of the desired feature to the OLED far-field and thus potentially reduce the quality of the measurement. Considering white OLEDs, the red, green, and blue emissive sites should be analyzed separately, using device architectures adapted to the particular color. However, without loss of generality different molecular moieties can be modeled as a superposition of an appropriate number of emissive species with different emission spectra, emission zones and orientation distributions. Provided the emission spectra are sufficiently distinct, the presented approaches can be extended to analyze all emitters individually. For this purpose additional OLED stacks, featuring ETL thicknesses adapted to the particular color, might be required.

Additionally, we have demonstrated that investigations utilizing a substrate index-matched glass-hemisphere to access the substrate radiation pattern are not necessarily superior to analyses of the emission pattern in air. Glass-hemisphere measurements yield slightly more information only when analyzing extended emission zones, which are problematic in general.

Finally, it is worth underlining again that the proposed concepts are based on adapted OLED stack designs which might differ significantly from common, electrically and optically optimized devices. Hence, one needs to ensure that the emitter properties are unchanged when varying the layered system in order to obtain results which are also meaningful for optimized devices. It has been shown that such an assumption is valid for examples of both polymeric and small-molecular emissive sites [17,19,20].

Acknowledgements

The authors thank Alexander Brown and Enda McGlynn for valuable comments, and acknowledge financial support from the German Federal Ministry of Education and Research (BMBF) through the HOBBIT-project (FKZ 13N8951) and TOPAS2012-project (FKZ 13N10474).

References

[1] C.M. Ramsdale, N.C. Greenham, The optical constants of emitter and electrode materials in polymer light-emitting diodes, J. Phys. D: Appl. Phys. 36 (4) (2003) L29–L34.
[2] M. Flämmich, N. Danz, D. Michaelis, A. Bräuer, M.C. Gather, J.H.-W.M. Kremer, K. Meerholz, Dispersion-model-free determination of optical constants: application to materials for organic thin film devices, Appl. Opt. 48 (8) (2009) 1507–1513.
[3] D. Yokoyama, A. Sakaguchi, M. Suzuki, C. Adachi, Horizontal orientation of linear-shaped organic molecules having bulky substituents in neat and doped vacuum-deposited amorphous films, Org. Electron. 10 (1) (2009) 127–137.
[4] J.A.E. Wasey, A. Safonov, I.D.W. Samuel, W.L. Barnes, Efficiency of radiative emission from thin films of a light-emitting conjugated polymer, Phys. Rev. B 64 (20) (2001) 205201-1–205201-9.
[5] D. Yokoyama, M. Moriwake, C. Adachi, Spectrally narrow emissions at cutoff wavelength from edges of optically and electrically pumped anisotropic organic films, J. Appl. Phys. 103 (12) (2008) 123104-1–123104-13.
[6] J. Frischeisen, D. Yokoyama, C. Adachi, W. Brütting, Determination of molecular dipole orientation in doped fluorescent organic thin films by photoluminescence measurements, Appl. Phys. Lett. 96 (7) (2010) 073302-1–073302-3.
[7] H. Becker, S.E. Burns, R.H. Friend, Effect of metal films on the photoluminescence and electroluminescence of conjugated polymers, Phys. Rev. B 56 (4) (1997) 1893–1905.
[8] W.M.V. Wan, N.C. Greenham, R.H. Friend, Interference effects in anisotropic optoelectronic devices, J. Appl. Phys. 87 (5) (2000) 2542–2547.
[9] T. Granlund, L.A.A. Pettersson, O. Inganäs, Determination of the emission zone in a single-layer polymer light-emitting diode through optical measurements, J. Appl. Phys. 89 (11) (2001) 5897–5902.
[10] M.C. Gather, M. Flämmich, N. Danz, D. Michaelis, K. Meerholz, Measuring the profile of the emission zone in polymeric organic light-emitting diodes, Appl. Phys. Lett. 94 (26) (2009) 263301-1–263301-3.
[11] S.L.M. van Mensfoort, M. Carvelli, M. Megens, D. Wehenkel, M. Bartyzel, H. Greiner, R.A.J. Janssen, R. Coehoorn, Measuring the light emission profile in organic light-emitting diodes with nanometre spatial resolution, Nat. Photonics 4 (2010) 329–335.
[12] B. Perucco, N.A. Reinke, D. Rezzonico, M. Moos, B. Ruhstaller, Analysis of the emission profile in organic light-emitting devices, Opt. Exp. 18 (13) (2010) A246–A260.
[13] M. Flämmich, M.C. Gather, N. Danz, D. Michaelis, A.H. Bräuer, K. Meerholz, A. Tünnermann, Orientation of emissive dipoles in OLEDs: quantitative in situ analysis, Org. Electron. 11 (6) (2010) 1039–1046.

[14] R.R. Chance, A. Prock, R. Silbey, Molecular fluorescence and energy transfer near interfaces, Adv. Chem. Phys. 37 (1978) 1–67.
[15] N. Danz, R. Waldhäusl, A. Bräuer, R. Kowarschik, Dipole lifetime in stratified media, J. Opt. Soc. Am. B 19 (3) (2002) 412–419.
[16] N. Danz, J. Heber, A. Bräuer, R. Kowarschik, Fluorescence lifetimes of molecular dye ensembles near interfaces, Phys. Rev. A 66 (6) (2002) 063809-1–063809-7.
[17] M. Flämmich, M.C. Gather, N. Danz, D. Michaelis, K. Meerholz, In situ measurement of the internal luminescence quantum efficiency in organic light-emitting diodes, Appl. Phys. Lett. 95 (26) (2009) 263306-1–263306-3.
[18] S. Nowy, B.C. Krummacher, J. Frischeisen, N.A. Reinke, W. Brütting, Light extraction and optical loss mechanisms in organic light-emitting diodes: influence of the emitter quantum efficiency, J. Appl. Phys. 104 (12) (2008) 123109-1–123109-9.
[19] B.C. Krummacher, S. Nowy, J. Frischeisen, M. Klein, W. Brütting, Efficiency analysis of organic light-emitting diodes based on optical simulation, Org. Electron. 10 (3) (2009) 478–485.
[20] M. Flämmich, N. Danz, D. Michaelis, C.A. Wächter, A.H. Bräuer, M.C. Gather, K. Meerholz, Measuring the internal luminescence quantum efficiency of OLED emitter materials in electrical operation, Proc. SPIE 7617 (2010) 761715-1–761715-9.
[21] D.M. Whittaker, I.S. Culshaw, Scattering matrix treatment of patterned multi-layer photonic structures, Phys Rev. B 60 (4) (1999) 2610–2618.
[22] B. Ruhstaller, T.A. Beierlein, H. Riel, S. Karg, J.C. Scott, W. Riess, Simulating electronic and optical processes in multilayer organic light-emitting devices, IEEE J. 9 (3) (2003) 723–731.
[23] H. Greiner, O.J.F. Martin, Numerical modeling of light emission and propagation in organic LEDs using the Green's tensor, Proc. SPIE 5214 (2004) 248–259.
[24] K. Celebi, T.D. Heidel, M.A. Baldo, Simplified calculation of dipole energy transport in a multilayer stack using dyadic Green's functions, Opt. Exp. 15 (4) (2007) 1762–1772.
[25] "Radiating Slabs", contact norbert.danz@iof.fraunhofer.de for further information.
[26] C.C. Katsidis, D.I. Siapkas, General transfer-matrix method for optical multilayer systems with coherent, partially coherent, and incoherent interference, Appl. Opt. 41 (19) (2002) 3978–3987.
[27] At this point it is worth noting that Eq. (4) supports different types of ensemble-averaging methods regarding the orientation of the dipole transition moment φ, where the particular character of the emissive species is accounted in the detailed calculation of $\Gamma_{rel}(q,z,\varphi)$ [16]. In this contribution, we assume the orientation of the dipole transition moment φ to be fixed during the process of emission. However, applying different ensemble-averaging methods typically results in small quantitative differences only, which have no qualitative impact on the considerations we present.
[28] M. Roberts, Optical modelling and efficiency optimization of P-OLED devices, in: OEC'06, Organic Electronics Conference, Frankfurt, 2006.
[29] E.D. Palik, Handbook of Optical Constants of Solids, Academic Press, 1991.
[30] C.A. Wächter, N. Danz, D. Michaelis, M. Flämmich, S. Kudaev, A.H. Bräuer, M.C. Gather, K. Meerholz, Intrinsic OLED emitter properties and their effect on device performance, Proc. SPIE 6910 (2008) 691006-1–691006-11.

Organic Electronics 12 (2011) 92–97

Contents lists available at ScienceDirect

Organic Electronics

journal homepage: www.elsevier.com/locate/orgel

The improvement of near-ultraviolet electroluminescence of ZnO nanorods/MEH-PPV heterostructure by using a ZnS buffer layer

Da-Wei Wang, Su-Ling Zhao *, Zheng Xu, Chao Kong, Wei Gong

Institute of Optoelectronic Technology, Beijing Jiaotong University, Beijing 100044, China
Key Laboratory of Luminescence and Optical Information, Beijing Jiaotong University, Ministry of Education, Beijing 100044, China

ARTICLE INFO

Article history:
Received 4 June 2010
Received in revised form 1 September 2010
Accepted 28 September 2010
Available online 17 November 2010

Keywords:
ZnO nanorods
Electroluminescence
Heterostructure
Modification buffer layer
ZnS thin film

ABSTRACT

A near-ultraviolet light emitting diode (LED) consisting of ZnO nanorods/MEH-PPV heterostructure and a layer of ZnS as the modification buffer layer is reported. Specially, the ZnO nanorods are grown on the ZnS hole-injecting buffer layer by hydrothermal method. Then the devices of ITO/ZnS/ZnO/ZnOnanorods/MEH-PPV/Al are prepared. Under forward bias, not only strong near-ultraviolet (N-UV) electroluminescence (EL) at 380 nm of ZnO band edge emission and weak defect-related emissions of ZnO nanorods at 410, 510 and 760 nm are observed, but also the exciton emission of MEH-PPV at 580 nm is detected. Along with increasing the thickness of ZnS film, the emission at 580 nm strengthens. Compared with the device ITO/ZnO/ZnOnanorods/MEH-PPV/Al we have reported in the past, the experimental results show that the suitable insertion of a ZnS thin layer can enhance the N-UV EL. Under the same voltage, the light intensity can be increased up to 10 times more than that of the device without a ZnS layer. Moreover, the turn-on voltage is reduced remarkably. The effect of ZnS as the hole-injecting buffer layer with different thickness on the EL of ZnO nanorods/MEH-PPV heterostructure is investigated.

© 2010 Elsevier B.V. All rights reserved.

1. Introduction

Zinc oxide is a promising semiconductor that has a wide direct band gap of 3.37 eV and a very large exciton binding energy of 60 meV at room temperature. Thus, ZnO materials have been regarded as very attractive candidates for the next generation of UV light emission [1]. However, as we known, the *p*-type doping ZnO is always a bottleneck since wide band gap materials usually show a poor doping efficiency. It is an important problem for the application of ZnO based UV LEDs [2,3]. Thus, the *p*-n heterostructures consisting of *n*-type ZnO as the active layer and other *p*-type materials have been introduced, but still lack high efficiency [4–6].

Recently, great focus has been placed on the research of ZnO nanostructures to realise UV light emission. A few studies have been reported on LEDs by using ZnO thin film [7–10], ZnO nanowires [4,11,12], ZnO nanorods [5,6,13,14], or ZnO nanoparticles [15]. Among these studies, low-dimensional nanostructural ZnO has attracted great interest because of its unique physical and chemical properties [16]. For example, ZnO or other semiconductor nanowires or nanorods can offer additional advantages for optoelectronic device applications due to the increased junction area, enhanced polarization dependence, and improved carrier confinement in one dimension [17]. Hsu et al. reported that the *p*-type undoped ZnO nanorods could be obtained by hydrothermal method through adjusting the properties of the seed layer [18]. Light emitting diodes have been created by using this simple and useful fabrication method. However, the electroluminescence of these diodes is weak, particularly the lower UV intensity than that of the visible emission. In order to realise UV electroluminescence, we have reported a device based on ZnO nanorods/MEH-PPV heterostructure in which the polymer MEH-PPV was used as the electron

* Corresponding author. Tel.: +86 10 51688675; fax: +86 10 51683933.
E-mail address: slzhao@bjtu.edu.cn (S.-L. Zhao).

1566-1199/$ - see front matter © 2010 Elsevier B.V. All rights reserved.
doi:10.1016/j.orgel.2010.09.018

injection layer. Under DC bias, the N-UV electroluminescence of ZnO at 380 nm was detected [14]. But the intensity of N-UV is weak. In order to enhance N-UV electroluminescence, a layer of ZnS as the modification layer was introduced to the ZnO nanorods/MEH-PPV heterostructure. ZnO nanorods were grown on the ZnS buffer layer by hydrothermal method. The as-grown ZnO nanorods were then used to fabricate the devices of ITO/ZnS/ZnO/ZnOnanorods/MEH-PPV/Al. Under forward bias, these devices emitted a relatively strong N-UV light at 380 nm and weaker visible light. This is a developmental approach in the synthesis of ZnO nanorods on the substrates, and this method shows an innovative feature in the ZnO nanostructure LED field [19,20].

2. Experimental setup

The process of the device preparation is as follows. The indium tin oxide (ITO) glass substrates were cleaned in an ultrasonic cleaner with acetone, ethanol, deionised water sequentially, and then were dried with nitrogen for later use. ZnS thin films with varying thicknesses from 2 to 8 nm were deposited on the ITO substrates (3×3 cm) by thermal evaporation in a high vacuum condition of 2.5×10^{-3} Pa. The ZnO nanorods were grown using a two-step hydrothermal method at low temperature. Firstly, to facilitate the nucleation of ZnO nanorod growth, a seeding layer, prepared with Zinc acetate dehydrate solution, was spin-coated on the substrates. Then, they were annealed at 360 °C for 20 min in ambient atmosphere. The hydrothermal reaction solution for ZnO nanorod fabrication was prepared by mixing 25 mM zinc nitrate hexahydrate ($Zn(NO_3)_2{\cdot}6H_2O$) and 25 mM hexamethylenetriamine ($C_6H_{12}N_4$) in 200 ml of deionised water in a glass beaker. During the growth of ZnO nanorods, the glass beaker was placed in an electrically heated thermostatic water bath and maintained at 92 °C for 15 min. Subsequently, the samples were removed from the solution and washed with ethanol and deionised water repeatedly and annealed for 30 min in ambient atmosphere. A *p*-type polymer poly [2-methoxy-5-(2-ethylhexyloxy)-1, 4-phenylene vinylene] (MEH-PPV) was dissolved in chloroform with a concentration of 5 mg/ml, then spin-coated on as-grown ZnO nanorod layers with a rotation rate of 1200 rpm (rotations per minute). This specific rotation rate was used in order to cover the top of the ZnO nanorods with a thin MEH-PPV layer, and provide a smooth surface for subsequent thin film deposition. About 150 nm thick Al film was deposited by thermal evaporation in a high vacuum condition of 2×10^{-4} Pa. Finally, four devices with different ZnS thicknesses of 2 nm (device 1), 4 nm (device 2), 6 nm (device 3) and 8 nm (device 4) were prepared for comparison. In this experiment, the forward bias on the device indicated that the ITO is anode and Al is cathode. The schematic diagram and energy band structure of the device under forward bias is given in Fig. 1. The morphology of the ZnO nanorods was observed by using field emission scanning electron microscopy (FE-SEM, S-4800). The device testing consisted of measuring the EL spectrum of the devices under different forward bias, and the current–voltage (I–V)

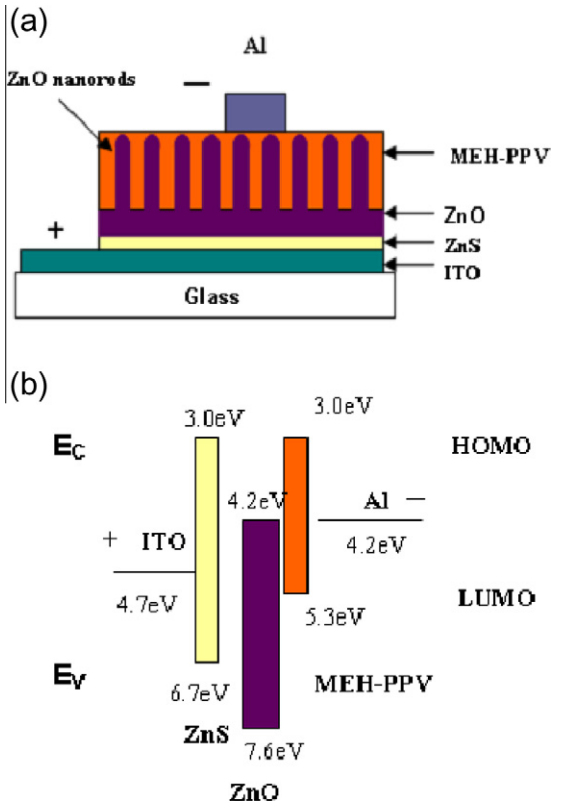

Fig. 1. (a) Schematic diagram of the device (b) Energy band diagram of the device.

and EL characteristics were measured by a system of an ACTON 150 CCD spectrometer, a Keithley 2410, and a Newport 1830-C Optical Power Meter Mainframe controlled by a computer. The photoluminescence (PL) of ZnO nanorods was measured by a fluorolog-3 spectrophotometer. The crystallinity of ZnO nanorods was carried out by X-ray diffraction (XRD) system. All of these tests were carried out at room temperature and in ambient atmosphere.

Device 1: ITO/ZnS(2 nm)/ZnO/ZnOnanorods/MEH-PPV/Al
Device 2: ITO/ZnS(4 nm)/ZnO/ZnOnanorods/MEH-PPV/Al
Device 3: ITO/ZnS(6 nm)/ZnO/ZnOnanorods/MEH-PPV/Al
Device 4: ITO/ZnS(8 nm)/ZnO/ZnOnanorods/MEH-PPV/Al

3. Results and discussion

Fig. 2(a) and (b) present the top-view and cross-sectional SEM of ZnO nanorods grown on the substrate with a 2 nm ZnS layer. It can be observed that ZnO nanorods were compact, and primarily aligned along the perpendicular direction of the substrate. The average diameter and height of the nanorods was about 30 and 100 nm, respectively. The seed layer was about 50 nm thick. Fig. 2(c) and (d) show the top-view and cross-sectional SEM images

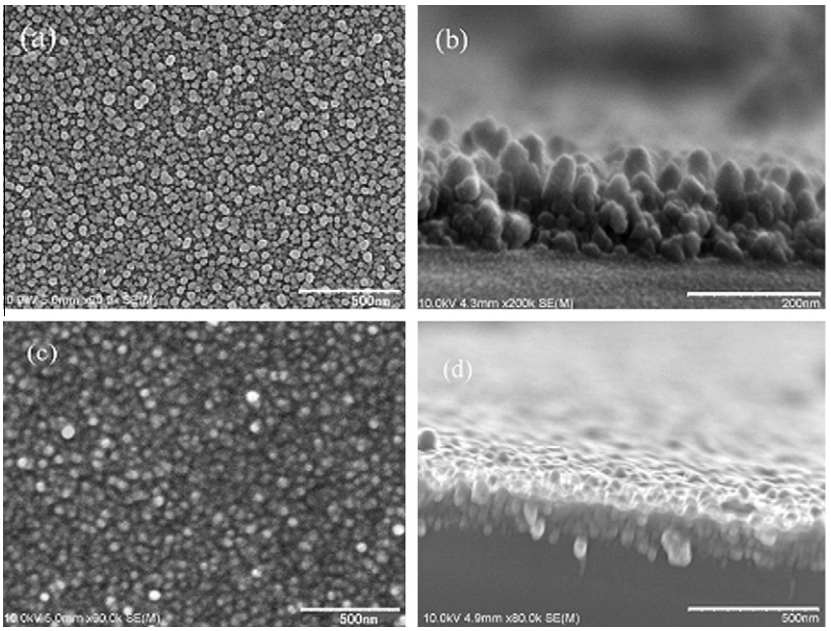

Fig. 2. Top-view (a) and cross-sectional (b) SEM of ZnO nanorods grew on the substrate with 2 nm ZnS layer; Top-view (c) and cross-sectional (d) SEM of ZnO nanorods grew on the substrate with 2 nm ZnS layer after covered by MEH-PPV thin film.

of as-grown ZnO nanorods after being coated with an approximately 30 nm MEH-PPV layer at a rotation rate of 1200 rpm. Moreover, the MEH-PPV layer on the top of every nanorod must be thin (less than 5 nm), which is optimal to allow the electrons to tunnel to the ZnO nanorods and recombine with the holes. However, MEH-PPV should cover ZnO nanorods completely to avoid carrier leakage from ZnO nanorods to the Al electrode directly and form the ZnO nanorods/MEH-PPV *p*-n junction. Unlike the more common process, in these experiments no insulator material was used to fill the interspaces of nanorods.

Fig. 3(a), (b), (c) and (d) show the EL spectra of devices 1, 2, 3, and 4 under different forward biases. From Fig. 3(a) and (b), strong N-UV EL at 380 nm of ZnO band edge emission was observed. The full width at half maximum of this emission was only 25 nm. The turn-on voltage for N-UV electroluminescence was about 14 V for device 1. This value was lower than that reported in reference [14]. In addition, a wide emission with a peak at 510 nm and a weak emission at 760 nm were detected under higher voltage, and regarded as defect-related emissions of ZnO nanorods. In order to make these emission peaks distinguishable, the Gaussian fitting EL of device 1 under 22 V is shown in Fig. 3(e). Another defect-related emission at 410 nm of ZnO and an exciton emission of MEH-PPV at 580 nm were observed. However, there was no MEH-PPV emission detected under low forward bias. Thus, this device was suitable for pure N-UV emission under low bias. Along with the increased voltage, the N-UV light intensity increased faster than other emissions.

Compared with the device with no ZnS as the modification layer [14], the following conclusions can be made: (1) the turn-on voltage of N-UV electroluminescence was reduced from 22 to 14 V. Fig. 1(b) shows the energy band structure of the device under forward bias. From this diagram, it can be seen that the ZnS thin film can lower the hole-injecting barrier by laddering it, and thus the turn on voltage can be reduced. In addition, the thinner MEH-PPV film at the top of ZnO nanorods allowed the electrons to tunnel into the ZnO nanorods more easily, which might also have contributed to the reduction of the turn-on voltage. (2) The MEH-PPV exciton emission at 580 nm couldn't be observed when the voltage was low. The MEH-PPV film was considered sufficiently thin. Most of the electrons could quickly tunnel to the ZnO nanorods even under low bias and recombine with holes. Thus, there was no obvious emission at 580 nm. (3) There were two more defect-related emissions at 410 and 510 nm, which was not reported in reference.

Fig. 4 shows the XRD pattern of the ZnO nanorods grown on the substrate, both with and without 2 nm ZnS thin film (the process of growing ZnO nanorods is same as described above). Only a high intensity of (0 0 2) diffraction peak was detected and implied that ZnO nanorods have a typical wurtzite structure and grow along a c-axis direction perpendicular to the substrate well. However, the diffraction peak of the ZnO nanorods directly grown on the substrate was higher than that grown on the substrate on which a 2 nm ZnS layer had been deposited. This suggests that a ZnS layer affects the vertical alignment and the crystallinity of the ZnO nanorods, and may cause defects in ZnO nanorods [21].

Fig. 5 shows the normalized PL spectrum of as-grown ZnO nanorods. The emissions at 410 and 510 nm were enhanced by the ZnO nanorods grown on the ZnS layer. Thus, it can be confirmed that the insertion of a ZnS thin layer caused the defect-related emissions at 410 and 510 nm of ZnO nanorods.

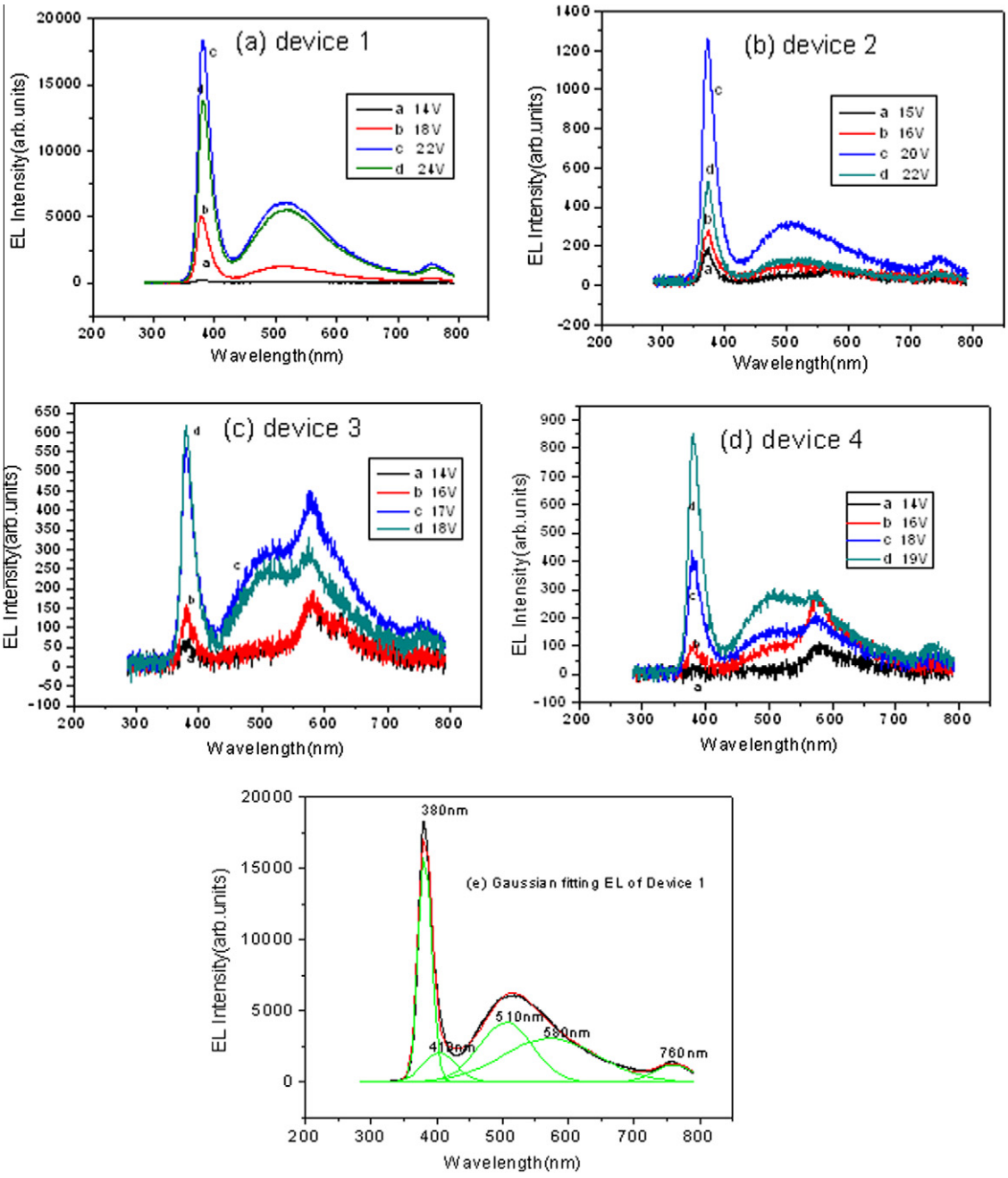

Fig. 3. EL spectra of (a) device 1, (b) device 2, (c) device 3 and (d) device 4 under different forward biases; (e) Gaussian fitting EL of device 1.

From Fig. 3(c), (d) and (e), it can be seen that the exciton emission of MEH-PPV at 580 nm strengthened as the thickness of ZnS film increased. This can be explained as followed: As the thickness of ZnS film increased, a larger portion of applied voltage was dropped on the ZnS/ZnO nanorods. Correspondingly, the portion of applied voltage dropped on the MEH-PPV layer reduced. Thus, the tunnelling probability of electrons decreased. Fewer electrons tunnelled into the conduction band of the ZnO nanorods, and more electron hole recombination occurred in the MEH-PPV layer. In addition, the hole mobility of ZnO was larger than the electron mobility of MEH-PPV. Thus, holes reached the organic layer more quickly compared with devices 1 and 2. As a result, the emission at 580 nm strengthened as the ZnS thickness increased.

Fig. 6(a) and (b) show the I–V characteristics and EL power of devices 1, 2, 3 and 4, respectively. Fig. 6(a) shows that the devices exhibited stable rectifying diode behaviour. The series resistance of device 1 was relatively small, as concluded from its I–V characteristic. When ZnS film

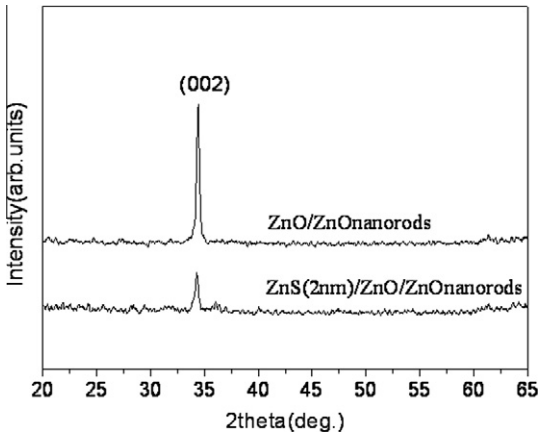

Fig. 4. The XRD pattern of the ZnO nanorods grew on the substrate with and without 2 nm ZnS.

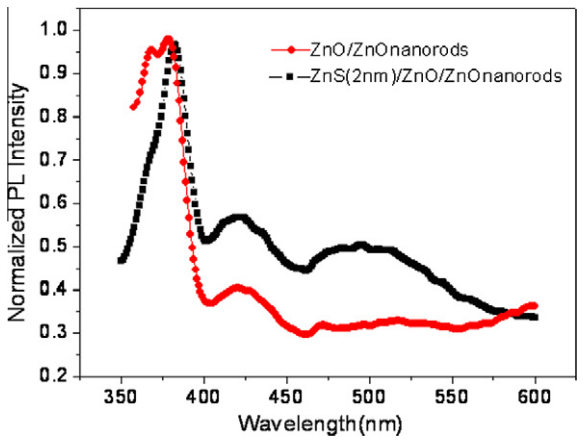

Fig. 5. The normalized photoluminescence spectrum of the ZnO nanorods grew on the substrate with and without 2 nm ZnS (Excitation wavelength is 320 nm).

became thicker, the series resistance of the devices increases. It means that with the increased thickness of ZnS layer, the devices have a decreased current injection. That may be due to the fact that thicker ZnS films resulted in defects in ZnO nanorods and high series resistance in the devices. Under the same forward bias, device 1 had the maximum brightness and the EL intensity could be increased up to 10 times more than that of a device without a ZnS layer. Moreover, the turn-on voltage was reduced remarkably [14]. It was demonstrated that the ZnS buffer layer laddered the hole-injecting barrier, increased the hole injection, and balanced the carrier concentration in the emission layer, all of which contributed to more exciton emission in the ZnO nanorods region. Meanwhile, the intensity of the device weakened as the ZnS thickness increased. From this, it can be acknowledged that excessively thick ZnS film is disadvantageous to the EL of the devices. In addition, the turn-on voltages of devices 2, 3, and 4 were a little higher than that of device 1, which would also be attributed to the excessively thick ZnS film.

4. Conclusions

In summary, it was shown that the suitable insertion of a ZnS modification buffer layer can significantly enhance the N-UV EL of ZnO nanorods/MEH-PPV heterostructure and reduce the turn-on voltage, which can be attributed to a decrease of the hole-injecting barrier and more electron hole recombination in the ZnO nanorods region. When ZnS film is 2 nm thick, the devices ITO/ZnS/ZnO/ZnOnanorods/MEH-PPV/Al show a strong N-UV EL at 380 nm of ZnO band edge emission under DC bias. In addition, not only defect-related emissions at 410 nm, 510 nm and a weak emission at 760 nm of ZnS nanorods were detected under higher voltage, but also an exciton emission of MEH-PPV at 580 nm was observed. However, there was no MEH-PPV emission detected under low forward bias. Also, the exciton emission of MEH-PPV at 580 nm was strengthened when the thickness of ZnS film was increased. The experiment results show that the vertical alignment and crystallinity of the ZnO nanorods grown on ZnS modification layer becomes poor. This affected the EL and I–V characteristics of ITO/ZnS/ZnO/ZnOnanorods/MEH-PPV/Al. The method in this study is a first attempt to improve

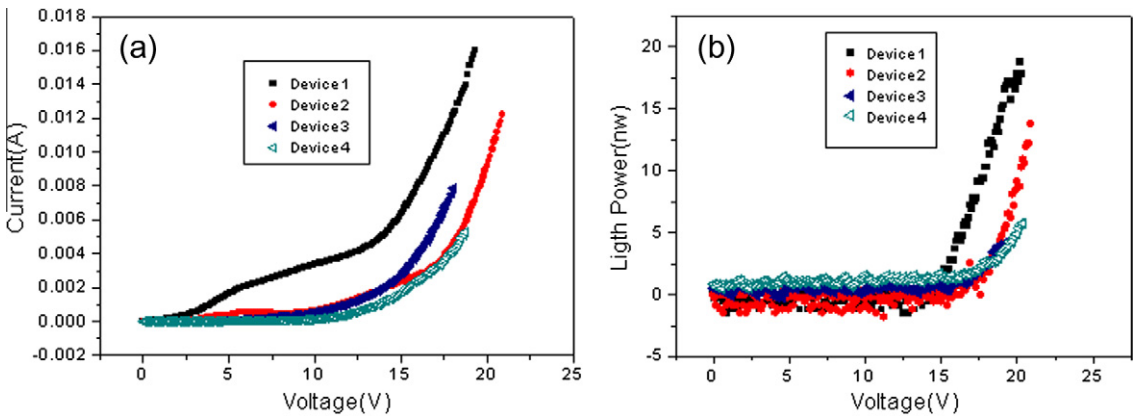

Fig. 6. The I–V characteristics (a) and EL power (b) of devices 1, 2, 3 and 4.

the N-UV EL of ZnO nanorods/MEH-PPV heterostructure and is valuable in the development of growth of ZnO nanorods on the buffer layer, as well as in the improvement of ZnO nanostructure based LED.

Acknowledgements

The authors would like to express their thanks to the NSFC (109740139, 10774013 and 60825407), RFDP (20090009110027, 20070004024 and 20070004031), the Beijing NOVA program (2007A024), BMNSF (1102028), and 973 Program (2010CB327705).

References

[1] Ü. Özgür, Ya.I. Alivov, C. Liu, A. Teke, M.A. Reshchikov, S. Doğan, V. Avrutin, S.-J. Cho, H. Morkoç, A comprehensive review of ZnO materials and devices, J. Appl. Phys. 98 (2005) 041103–041301.
[2] Sachindra Nath Das, Ji-Hyuk Choi, Jyoti Prakash Kar, Tae Il Lee, Jae-Min Myoung, Fabrication of *p*-type ZnO nanowires based heterojunction diode, Mater. Chem. Phys. 121 (2010) 472–476.
[3] S.B. Zhang, S.H. Wei, A. Zunger, Intrinsic *n*-type versus *p*-type doping asymmetry and the defect physics of ZnO, Phys. Rev. B. 63 (2001) 075205–075211.
[4] Xinyu Wang, Cole Jesse, M. Dabiran Amir, O. Jacobs Heiko, ZnO nanowire/p-GaN heterojunction LEDs, Mater. Res. Soc. Symp. Proc. 1018 (2007) 157–162.
[5] X.W. Sun, J.Z. Huang, J.X. Wang, Z. Xu, A ZnO nanorod inorganic/organic heterostructure light-emitting diode emitting at 342 nm, Nano Lett. 8 (2008) 1219–1223.
[6] Hui Sun, Qi-Feng Zhang, Jin-Lei Wu, Electroluminescence from ZnO nanorods with an *n*-ZnO/*p*-Si heterojunction structure, Nanotechnology 17 (2006) 2271–2274.
[7] I.E. Titkov, L.A. Delimova, A.S. Zubrilov, N.V. Seredova, I.A. Liniichuk, I.V. Grekhov, ZnO/GaN heterostructure for LED applications, J. Mod. Opt. 56 (2009) 653–660.
[8] In-Sung Yoo, On-Jin So, Choon-Bae Park, Fabrication of high mobility *p*-type ZnO thin film by ampoule-tube method, 2006 IEEE Nanotechnology Materials and Devices Conference, NMDC. 1 (2006) 538–539.
[9] Q.-X. Yu, B. Xu, Q.-H. Wu, Y. Liao, G.-Z. Wang, R.-C. Fang, H.-Y. Lee, C.-T. Lee, Optical properties of ZnO/GaN heterostructure and its near-ultraviolet light-emitting diode, Appl. Phys. Lett. 83 (2003) 4713–4715.
[10] Deok Kyu Kim, Kyeong Min Kim, Choon Bae Park, Characteristics of *p*-type ZnO: as thin films prepared by the ampoule-tube method and ZnO *p*-n homojunction, Appl. Phys. A: Mater. Sci. Process. 98 (2010) 913–917.
[11] R. Könenkamp, A. Nadarajah, R.C. Word, J. Meiss, R. Engelhardt, ZnO nanowires for LED and field-emission displays, J. Soc. Inf. Disp. 16 (2008) 609–613.
[12] Ying He, Jun-An Wang, Xiao-Ban Chen, Wen-Fei Zhang, Xu-Yu Zeng, Qiu-Wen Gu, Blue electroluminescence nanodevice prototype based on vertical ZnO nanowire/polymer film on silicon substrate, J. Nanopart. Res. 12 (2010) 169–176.
[13] Xuan Fang, Jinhua Li, Dongxu Zhao, Dezhen Shen, Binghui Li, Xiaohua Wang, Phosphorus-doped *p*-type ZnO nanorods and ZnO nanorod *p*-n homojunction LED fabricated by hydrothermal method, J. Phys. Chem. C 113 (2009) 21208–21212.
[14] Su-Ling Zhao, Peng-Zhi Kan, Zheng Xu, Chao Kong, Da-Wei Wang, Yue Yan, Yong-Sheng Wang, Electroluminescence of ZnO nanorods/MEH-PPV heterostructure devices, Org. Electron.: Phys. Mater. Appl. 11 (2010) 789–793.
[15] Chun-Yu Lee, Yuen-Yung Hui, Wei-Fang Su, Ching-Fuh Lin, Electroluminescence from monolayer ZnO nanoparticles using dry coating technique, Appl. Phys. Lett. 92 (2008) 2611071–2611073.
[16] A. Javey, S.W. Nam, R.S. Friedman, H. Yan, C.M. Lieber, Layer-by-layer assembly of nanowires for three-dimensional, multifunctional electronics, Nano Lett. 7 (2007) 773–777.
[17] Yun-Yue Lin, Chun-Wei Chen, Wei-Che Yen, Wei-Fang Su, Chen-Hao Ku, Jih-Jen Wu, Near-ultraviolet photodetector based on hybrid polymer/zinc oxide nanorods by low-temperature solution processes, Appl. Phys. Lett. 92 (2008) 2333011–2333013.
[18] Yuk Fan Hsu, Yan Yan Xi, Kai Hang Tam, Aleksandra B. Djurišić, Jiaming Luo, Chi Chung Ling, Chor Keung Cheung, Alan Man Ching Ng, Wai Kin Chan, Xin Deng, Christopher D. Beling, Stevenson Fung, Kok Wai Cheah, Patrick Wai Keung Fong, Charles C. Surya, Undoped *p*-type ZnO nanorods synthesized by a hydrothermal method, Adv. Funct. Mater. 18 (2008) 1020–1030.
[19] Jing-lei Zhang, Fei Zhong, Peng-yi Liu, Efficient organic light-emitting diodes with ZnS thin films as hole buffer layer, Chin. J. Electron Devices 31 (2008) 40–43.
[20] Fei Zhong, Qin Ye, Peng-yi Liu, Lin Zhai, Jing Wu, Jing-lei Zhang, Organic light-emitting diodes with nano-ZnS thin films as hole buffer layer by RF magnetron sputtering, Chin. J. Lumin. 27 (2006) 881–887.
[21] Baoyi Wang, Rengang Zhang, Dongyun Wan, Yutian Wang, Long Wei, Electroluminescent ZnS-based thin films and their preparation, Mater. Rev. 17 (2003) 33–35.

Organic Electronics 12 (2011) 98–107

Contents lists available at ScienceDirect

Organic Electronics

journal homepage: www.elsevier.com/locate/orgel

One-step micropatterning of highly-ordered semi-crystalline poly(vinylidene fluoride-*co*-trifluoroethylene) films by a selective shear and detachment process

Jiyoun Chang [a], Hee Joon Jung [a], Huisu Jeong [b], Youn Jung Park [a], Jinwoo Sung [a], Seok Ju Kang [a], Gun Young Jung [b], Myung M. Sung [c], Cheolmin Park [a,*]

[a] Department of Materials Science and Engineering, Yonsei University, Seoul 120-749, Republic of Korea
[b] Department of Materials Science and Engineering, Gwangju Institute of Science and Technology (GIST), 261 Cheomdan-gwagiro (Oryong-dong) Buk-gu, Gwangju 500-712, Republic of Korea
[c] Department of Chemistry, Hanyang University, Seoul 133-791, Republic of Korea

ARTICLE INFO

Article history:
Received 1 July 2010
Received in revised form 14 September 2010
Accepted 10 October 2010
Available online 23 October 2010

Keywords:
Ferroelectric polymer
Static shear
Detachment
Micropattern
Crystal orientation
Non-volatile memory

ABSTRACT

We present a one-step route for micropatterning a thin ferroelectric poly(vinylidene fluoride-*co*-trifluoroethylene) (PVDF-TrFE) film with both molecular and microstructural crystal control over a large area. The method is based on the static mechanical shearing and subsequent detachment of a film spin coated on pre-patterned Al which has been lithographically prepared on a SiO_2 substrate under appropriate thermal conditions. Selective detachment of the film in contact with the SiO_2 substrate gave rise to micropatterns of PVDF-TrFE film positioned only on the Al regions. Further, the PVDF-TrFE film showed 25-nm-thick crystalline lamellae aligned perpendicular to the shear direction, wherein the *c* axis of the crystals was globally ordered parallel to the shear direction. The sheared and patterned PVDF-TrFE thin films are readily incorporated into non-volatile memory units of metal/ferroelectric/metal capacitors and bottom gate-top contact field effect transistors, leading to arrays of memory devices with enhanced performance.

© 2010 Elsevier B.V. All rights reserved.

1. Introduction

Non-volatile memories fabricated from ferroelectric polymers such as poly(vinylidene fluoride) (PVDF) and its copolymers with trifluoroethylene (TrFE) are of great interest among various organic non-volatile memory technologies such as flash [1,2] and resistive type ones [1,3] for potential use in organic information storage, one of the most essential technologies for realization of full organic electronic devices [4–6]. Solution-processed thin ferroelectric polymer films are easily incorporated into both destructive and non-destructive memory elements of metal/ferroelectric/metal (MFM) capacitors and ferroelectric field-effect transistors (FeFETs), respectively [4–12]. The macroscopic polarization of a ferroelectric film is attributed to the cooperative dipole moments pointing from fluorine to hydrogen in the ferroelectric polymer molecules, which are in turn hierarchically self-assembled into the characteristic crystalline structures. Non-volatile switching of the polarization is accomplished by rotating the polymer backbone around the chain axis upon exposure to a large polarization-opposing electric field [5].

There are, in our opinion, two main issues for realizing organic memories based on thin PVDF-TrFE films. First of all, in order to optimize ferroelectric properties such as remanent polarization, operating voltage, retention, fatigue and so on, the degree of crystallinity needs to be maximized. In addition, the effective crystal orientation in the *b* axis should be favorably aligned parallel to the electric field of the PVDF-TrFE [13–15]. Secondly, micropatterning of thin ferroelectric films should be possible

* Corresponding author. Tel.: +82 2 2123 2833; fax: +82 2 312 5375.
E-mail address: cmpark@yonsei.ac.kr (C. Park).

1566-1199/$ - see front matter © 2010 Elsevier B.V. All rights reserved.
doi:10.1016/j.orgel.2010.10.007

such that microarrays of the memory elements are readily fabricated without harming the intrinsic properties of the PVDF-TrFE.

A globally oriented PVDF-TrFE thin film with effective crystal orientation has been achieved via various techniques which rely on the ability to couple an externally applied field to some molecular and/or supermolecular feature in the polymer. These techniques include crystallographic matching on a surface known as epitaxy [16,17], using a localized thermal gradient [18], directional solvent evaporation [19] and the employment of mechanical fields [20–22]. We have recently demonstrated two approaches for producing highly-ordered crystalline structures of ferroelectric polymer thin films spin coated onto substrates suitable for memory device architecture: high throughput epitaxy of a thin PVDF-TrFE film on a friction transferred poly(tetrafluoroethylene) (PTFE) surface [23] and global orientation of the film by static shear [24]. In particular, the static shear turned out to be very effective for centimeter scale orientation of the ferroelectric polymer without requiring an additional interlayer, which significantly increases the operating voltage.

Although photolithography with subsequent dry and wet etching processes, available in the current semiconductor industry, is the most common and is powerful for micropattern fabrication, it is, in general, not applicable to PVDF-TrFE patterning because the polymer is significantly damaged or suffers alteration of its intrinsic properties under the harsh patterning conditions. Great care should be taken when fabricating patterned structures of PVDF-TrFE using the conventional etching process [25]. Thus, there is a need for a new non-invasive method based on printing technologies. Several techniques have been demonstrated for micropatterning ferroelectric polymers, including microimprinting [26,27], capillary molding [28] and microcontact printing [19]. Ferroelectric blend layers have also been micropatterned by solid state transfer methods in which a thin blend film floated on a water/air interface was deposited onto metal-coated poly(dimethylsiloxane) pre-patterned mold, and, subsequently, both the ferroelectric and metal layers were directly transferred to another metal electrode surface, resulting in arrays of MFM capacitors [29]. A recent work by Sekitani et al. successfully demonstrated printed non-volatile ferroelectric memory for communication system based on solution processes including ink-jet printing [30].

Most of the previous works, including our approaches, are, however, limited to the fabrication of patterned ferroelectric polymers without successful control of crystal orientation in the patterned films. In other words, the micropatterns have semi-crystalline ferroelectric domains that are randomly oriented. It would be ideal to develop a non-invasive printing technique which is able to simultaneously control both the molecular structure and the microstructure of the ferroelectric crystals. Furthermore, the method would ideally have industrial potential when combined with the spin coating process, one of the most desirable methods for large area uniform polymer film formation.

In this study, we demonstrate a new one-step micropatterning technique which allows us not only to fabricate micropatterns of thin PVDF-TrFE films but also to control both the molecular and microstructural orientations of the ferroelectric crystals in the patterned regions. Our method is based on the static-shearing of a PVDF-TrFE film spin-coated onto a lithographically defined Al pre-pattern, followed by selective detachment of the film. Our shear and detachment process allows for the fabrication of a globally ordered crystalline structure of a PVDF-TrFE film on the pre-patterned Al regions in which the crystalline lamellae are globally oriented perpendicular to the shear direction. Furthermore, facile formation of thin patterned ferroelectric films on metallic surfaces with ordered crystalline structure enables us to fabricate arrays of both MFM capacitors and bottom-gate FeFET devices with enhanced memory performance.

2. Experimental section

2.1. Al patterned substrate preparation

Conventional photolithography was used to prepare various Al pre-patterns on SiO_2 substrates. First, a positive photoresist was spin-coated onto a 200-nm-thick SiO_2 grown wafer that had been chemically cleaned. After soft-baking to eliminate residual solvents, the photoresist was exposed to ultraviolet light through a photomask for development. Subsequently, an ~80-nm-thick layer of Al was deposited onto the patterned photoresist by thermal evaporation under a pressure of 10^{-6} mB at room temperature with a deposition rate of ~0.1 nm/s. The photoresist was then completely removed by lift-off. Finally, Al micropatterns with a variety of shapes and sizes were produced on the SiO_2 substrate, including 1.5-μm- and 5-μm-wide lines with periodicities of 5 and 10 μm, respectively, and 2 and 5 μm squares arrayed into a 4 mm symmetry. Hexagons with 2 μm sides were also prepared and arrayed into a 6 mm symmetry. For non-volatile memory devices, alternating Al lines 300 and 700 μm in width with a periodicity of 1500 μm were prepared on SiO_2 substrate through a shadow mask by thermal evaporation under the same conditions as described above.

2.2. Thin film preparation

The PVDF-TrFE with 27.5 wt% TrFE employed in our study was kindly supplied by MSI Sensor, PA. The melting (T_m) and Curie (T_c) temperatures of the polymer were 150 and 80 °C, respectively. PVDF-TrFE solutions in methylethylketone (MEK) with concentrations ranging from 1 to 5 wt% were spin-coated at a spin rate of 2000 rpm for 1 min to form thin polymer films on the micropatterned Al substrates.

2.3. Static shearing process

The same shearing process was applied for the current experiments as were used in our previous experiment [24]. A poly(methylsiloxane) (PDMS) pad 100 μm in thickness and $1.0 \times 1.0\ cm^2$ in size was placed onto the PVDF-TrFE film on a pre-patterned Al substrate. Then, the

samples were fixed onto the bottom heating plate of our lab-made apparatus, were heated above the melting temperature for 30 min, and were then cooled to 140 °C. The sample was subsequently pressurized to approximately 10^5 Pa using a pressure controller, and a lateral force of about 1 N was applied. The resulting shear stress ($\sim 10^4$ Pa) caused the immediate elastic distortion of the PDMS pad and subsequently gave rise to a slow linear displacement from the viscous shear flow of the PVDF-TrFE. The static shear field was also combined with thermal treatments of PVDF-TrFE thin films spin coated and covered with PDMS pad on Al substrate as described in our previous work [21]. A PVDF-TrFE film was heated over its melting temperature during 30 min and subsequently cooled down to 135 °C at which shear force begins to be exerted on the sample with the pressure applied. All shearing experiments were performed within 2 h, and the maximum displacement in our experimental setup was approximately 2 mm with a velocity of 1.0 mm/h. The translation velocity after shear stress was measured to be approximately 300 nm s^{-1}, and the shear rate became 2 s^{-1} with a 150-nm-thick film. The shear field direction was varied with respect to the pattern geometry.

2.4. Ferroelectric property characterization

MFM capacitors were prepared by depositing Al top electrodes 200 μm in diameter onto the sheared PVDF-TrFE thin films previously prepared with alternating 300 and 700 μm Al lines by thermal evaporation under a 10^{-6} mB pressure with a deposition rate of ~0.1 nm/s. Ferroelectric polarization–voltage measurements were performed using a virtual ground circuit (Radiant Technologies Precision LC units).

For the FeFET memory elements, a pentacene active channel and source/drain Au electrodes were sequentially deposited through a shadow mask onto the sheared, patterned PVDF-TrFE thin film on the alternating Al lines for MFM elements at room temperature by thermal evaporation in a vacuum chamber at a base pressure of 9.0×10^{-7} torr. The deposition rates were fixed at 0.2–0.3 Å/s for the pentacene and at 1 Å/s for the Au electrodes. The pentacene and Au films were 60 and 100 nm in thickness, respectively. The pentacene channel length and width were 100 and 200 μm, respectively. The electrical properties of the devices were recorded using semiconductor systems (E5270B, HP4284A, Agilent Technologies). All measurements were performed in a metallic shielded box at room temperature in air.

2.5. Microstructure characterization

The microstructures of the sheared PVDF-TrFE thin films were characterized by field emission scanning electron microscopy (FESEM) (Jeol 2000) and tapping mode atomic force microscopy (TM-AFM) (Nanoscope IV, Digital Instrument). The molecular ordering of the PVDF-TrFE crystals was investigated by two-dimensional (2D) grazing-incidence X-ray diffraction (GIXD). The GIXD was performed on the 4C2 beam line at the Pohang Accelerator Laboratory in Korea (incidence angle: 0.09–0.15°). The samples were mounted onto X and Y axes goniometers. Monochromatized X-rays ($\lambda = 0.1608$ nm) under vacuum were used, and the full range of available incidence angles were employed. The scattered beam intensity was recorded with an SCX: 4300–165/2 CCD detector (Princeton Instruments). Two-dimensional GIXD patterns were obtained in the range of $0 < q_z < 2.33$ Å^{-1}, $0 < q_{xy} < 2.33$ Å^{-1} ($q = 4\pi \sin\theta/\lambda$, with Z perpendicular to and XY parallel to the substrate).

3. Results and discussion

Fig. 1 illustrates the procedure of our patterning technique in which the crucial steps for the successful patterning with the controlled crystalline structure lie in the static shear of a PVDF-TrFE film covered by a PDMS layer and in the selective detachment of the PVDF-TrFE film after shearing. In our previous work [24], good adhesion between PVDF-TrFE and PDMS gave rise to an excellent crystal ordering over a large area under the proper conditions, i.e., a Weissenberg number, the dimensionless product of a characteristic relaxation time and the shear rate, $W_e = \dot{\gamma}\tau > 1$. Additionally, a firm interface should be formed in order to avoid the possible slipping of PVDF-TrFE at the interface with a solid substrate, frequently resulting in mechanical deformation and tearing of the film without proper crystal orientation [24]. The work of adhesion given by $W_{12} = 4\{(\gamma_1^d\gamma_2^d/(\gamma_1^d + \gamma_2^d)) + (\gamma_1^p\gamma_2^p/(\gamma_1^p + \gamma_2^p))\}$ can be a gauge for evaluating the interfacial strengths between 1 and 2 materials, where γ^p and γ^d correspond to the polar and dispersion contributions to the surface energy. The surface tension of a PVDF-TrFE film was obtained from the equation based on the geometric-mean method, described by $(1 + \cos\ \theta_t\ )\ \gamma_t = 2\{(\gamma_t^d\gamma_s^d)^{1/2} + (\gamma_t^p\gamma_s^p)^{1/2}\}$ [31], where θ is the contact angle of a testing liquid on the PVDF-TrFE surface, and γ_t and γ_s are the surface energies of the testing liquid and the solid surface, respectively. Water and ethylene glycol were chosen as the test liquids to measure the contact angle on the surface. The resulting $\gamma^d_{\text{PVDF-TrFE}}$ and $\gamma^p_{\text{PVDF-TrFE}}$ of the PVDF-TrFE film calculated from the contact angle measurement were 35.5 and 1.5 mJ/m^2, respectively, slightly lower values compared to the 38.6 and 2.6 mJ/m^2 of the PVDF [32].

We employed various substrates (metals, oxides and polymers) to investigate adhesion with PVDF-TrFE, as shown in Table 1. The surface energies of those substrates were obtained either from the literature or from experiments, similar to that performed for PVDF-TrFE. Both the surface energies and the calculated adhesion values for the PVDF-TrFE surface are summarized in Table 1. As shown, most metallic substrates have adhesion values close to that of a homogeneous interface between two PVDF-TrFE layers (~75 mJ/m^2). Recalling that excellent orientation of the crystalline PVDF-TrFE lamellae was achieved on an Al surface in our previous work [24], good adhesion of PVDF-TrFE with a solid substrate is essential for the shear-induced ordering of the ferroelectric crystals. In order to confirm this, we also sheared several hundred-nanometer-thick PVDF-TrFE films on both Ag and Au substrates and again observed excellent crystal orientation

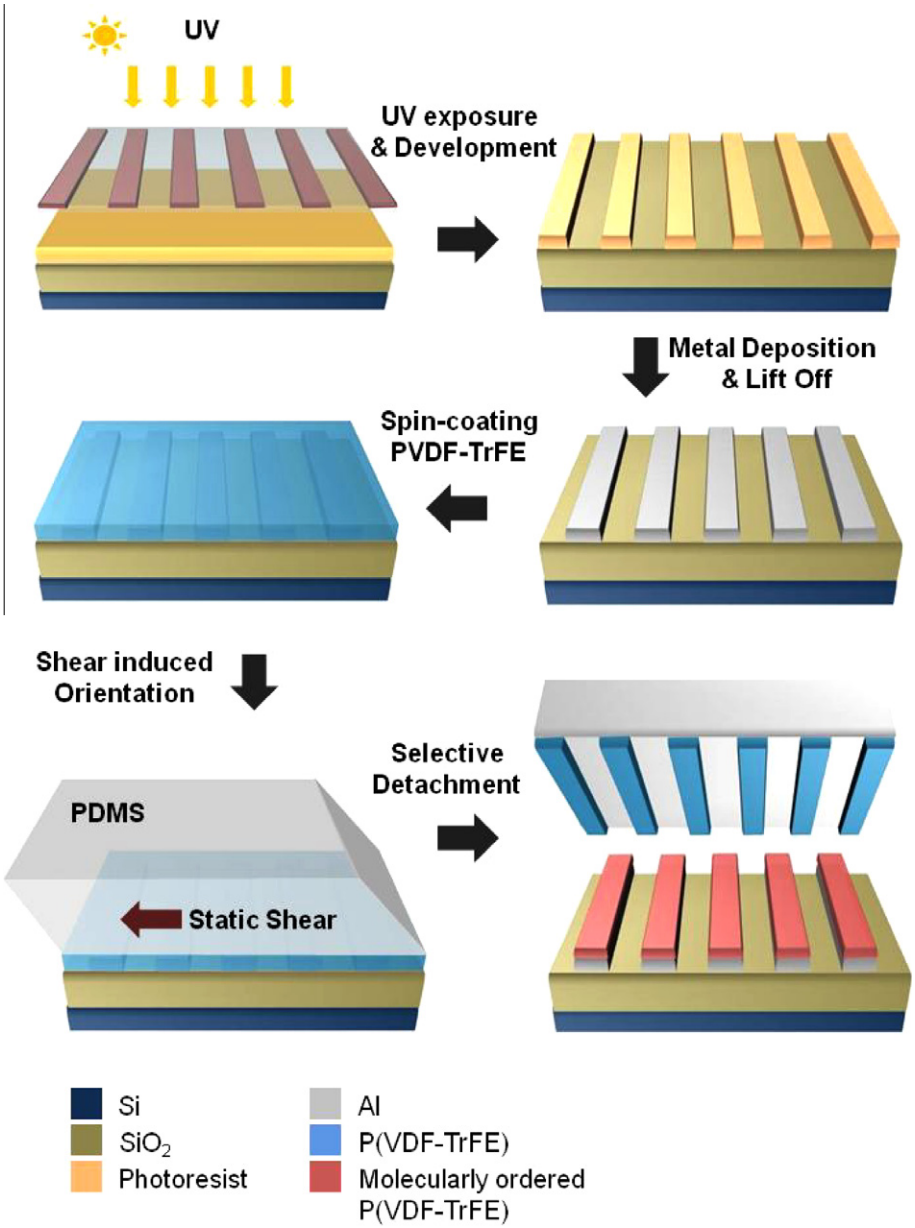

Fig. 1. (a) A schematic diagram of a one-step micropatterning process of a thin PVDF-TrFE film by selective shear and detachment. A thin PVDF-TrFE film is spin-coated onto an Al micropattern defined on SiO_2 substrate by conventional photolithography and lift-off. The static shear of the film with a PDMS pad and subsequent removal of the pad result in a micropatterned PVDF-TrFE selectively on the pre-patterned Al regions in which crystalline PVDF-TrFE lamellae are highly aligned perpendicular to the shear direction, with the *c*-axis of the crystals parallel to the shear field.

over a large area, confirmed by both electron micrographs and GIXD results (see Supporting Information). The edge-on crystalline lamellae of the PVDF-TrFE were well aligned perpendicular to the direction of the shear field on both the Au and Ag substrates. On the other hand, other substrates including SiO_2, Al_2O_3, ITO and PVP have relatively lower adhesion values with thin PVDF-TrFE films. In particular, SiO_2, which has the lowest adhesion value, gave rise to a significantly deformed and torn film with randomly ordered crystals after static shear, implying that the shear field generated from the PDMS layer was not effectively transferred to the PVDF-TrFE film due to slippage of the film on the substrate.

The different shearing behaviors of the PVDF-TrFE film, which depended on the surface properties of the substrates, prompted us to introduce a patterned substrate composed of two different materials having extremely different adhesions with PVDF-TrFE. For instance, alternating periodic lines of Al were prepared on a SiO_2 substrate by conventional lithography. A PVDF-TrFE thin film was spin-coated over the entire pre-pattern, and a shear field was subsequently applied using the PDMS

Table 1
Surface tension values of various solid substrates and the adhesions between the substrates and the PVDF-TrFE thin film.

Substrate	γ ($\gamma^d + \gamma^p$)/ (mJ m^{-2})	γ^d (mJ m^{-2})	γ^p (mJ m^{-2})	$W_{PVDF\text{-}TrFE}$ (mJ m^{-2})
PVDF-TrFE[a]	37.0	35.5	1.5	75
Al[b]	72.4	34.6	37.8	75.8
Ag[b]	45.1	41.8	3.3	80.9
Au[b]	46.8	34.9	11.9	75.7
Si[b]	65.1	29.9	35.2	70.0
SiO_2	71.9	21.9	50	59.9
Al_2O_3[a]	28.9	27.7	1.2	65.0
ITO[b]	47.1	24.3	22.8	63.3
PVP[a]	36.6	26.1	10.5	65.4

[a] Calculated from the geometric mean equation shown in the text, based on the contact angle measurement of water and ethylene glycol.
[b] Obtained from the literatures [31,33–35].

pad. Thereby, we envisioned that the shear field would effectively be exerted onto the pre-patterned Al regions, while the films on the SiO_2 regions would selectively detach from the surface after shearing. Our process thus allows for the one-step fabrication of a micropatterned PVDF-TrFE in which both the molecular structure and the microstructure were precisely controlled by shear direction, as shown in the schematic of Fig. 1.

Micropatterned PVDF-TrFE films were successfully obtained on a 5 μm Al line patterned substrate by our one-step shear and detachment process, as shown in an optical microscopy image in Fig. 2a. A cross-polarized image in the inset exhibits highly birefringent periodic lines of PVDF-TrFE, arising from its crystalline domains. The TM-AFM topography image in Fig. 2b clearly displays highly oriented crystalline lamellae of approximately 25 nm in width aligned perpendicular to the shear direction. We also confirmed the crystal orientation by GIXD, as shown in the inset, in which there are two distinguishable diffraction peaks at 13.5 nm^{-1} (i.e., ≈4.6 Å), on the meridian of the diffraction pattern, and 60° from the meridian. As described in our previous work, these two reflections resulted from the PVDF-TrFE crystal phase having an orthorhombic lattice where (2 0 0) and (1 1 0) have nearly equal spacings. This also indicates that the *c*-axis of the PVDF-TrFE crystals is predominantly parallel to the shear direction. Combined with our previous results on a flat Al substrates [24], the schematic in Fig. 2c depicts the molecular and microstructural orientations of PVDF-TrFE lamellae on an Al pattern after the one-step shear and detachment process.

A SEM image of the patterned PVDF-TrFE film in Fig. 2d again shows the global orientation of the PVDF-TrFE crystalline lamellae perpendicular to the shear direction, which occurs only at the Al lines. There is almost no residual PVDF-TrFE over the large area SiO_2 region, as shown the inset of Fig. 2d. Our patterning technique works well even when the width of an Al line was reduced to 1.5 μm, as shown in Fig. 2e. AFM images both in height (Fig. 2e) and phase contrast (the inset of Fig. 2e) clearly exhibit well aligned crystalline PVDF-TrFE lamellae on Al line patterns with a periodicity of 5 μm. In this case, however, the line edge became slightly irregular, possibly due to the non-uniform detachment of the film along such a narrow line. The confined crystalline lamellae look very straight and perpendicular to the line (Fig. 2e) compared to those in the larger line pattern in Fig. 2d which appear a little wavy. We also employed a two-dimensionally patterned Al substrate consisting of hexagons, with a 2 μm inside length, arrayed into a 6 mm symmetry, as shown in Fig. 2f. Micropatterned PVDF-TrFE thin films were also developed on Al patterned regions by a one-step shear and detachment process. A magnified image of an individual hexagon in the inset of Fig. 2f shows highly ordered crystalline lamellae aligned perpendicular to the shear direction and confined in the hexagon. In this case, the edges of the hexagon are not perfectly defined due to inhomogeneous detachment of the film in the SiO_2 regions.

Our micropatterning technique illustrated very effective control of the orientation of the PVDF-TrFE crystals with respect to the geometry of the pre-pattern, since the static shear, which always results in the crystalline lamellae being oriented perpendicular to the shear direction, can be easily applied in any direction regardless of the pattern geometry. For instance, the static shear direction was readily changed to be either parallel to or perpendicular to the line axis of the periodic line pre-pattern, as shown in Fig. 3a and b. It is apparent that the ordered crystalline lamellae were formed perpendicular to the line edge when shear was applied along the patterned line axis in Fig. 3a, while the ordered lamellae were all aligned parallel to the line edge upon shearing perpendicular to the line axis in Fig. 3b. The control of the lamellae orientation in the patterned domains was successfully achieved with 2D square-shaped pre-patterns in Fig. 3c and d. When the shear was applied parallel to the side of the square patterns 5 μm in the length, as indicated with an arrow in Fig. 3c, the crystalline lamellae were well oriented parallel to the two sides of the square patterns and, at the same time, perpendicular to the other two sides, as shown in the inset of Fig. 3c. Interestingly, the shear field applied diagonal to the direction of the square pattern, i.e., tilted 45° to each side of the square pattern, gave rise to the lamellae of PVDF-TrFE aligned with the 45° tilted direction against all sides of the square pattern, as shown in the inset of Fig. 3d. Highly birefringent individual patterned domains of Fig. 3d indicate the existence of ordered PVDF-TrFE thin films on the Al patterned regions after our process. It should be noted, however, that there are some crystalline lamellae grown from the edges of 2D hexagons or squares, as evidenced in Fig. 2f and d, respectively, possibly due to the nature of the highly defective pattern edge between Al and SiO_2 at which PVDF-TrFE may trans-crystallize with the directionally grown crystals.

Although the oriented PVDF-TrFE and PVDF crystals were achieved via confinement of the crystals in either micron or nanometer scale templates, the facile control of the crystal orientation of PVDF-TrFE with respect to the geometry of a micropattern by the direction of the static shear field has only rarely been demonstrated. The orientation of the polymer crystals confined into micron or nanoscale templates mainly depends upon the interfacial interaction

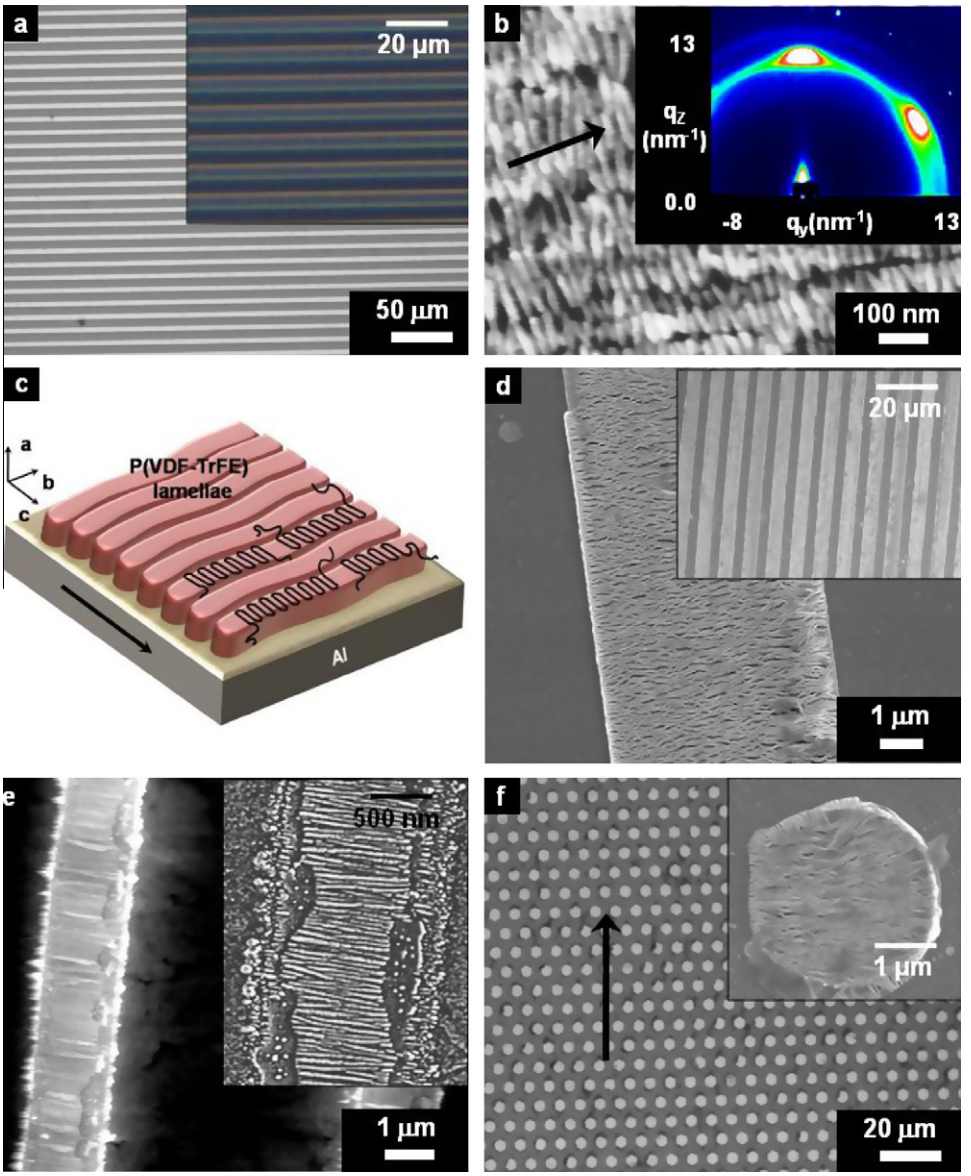

Fig. 2. (a) An optical microscopy image of a PVDF-TrFE film sheared at 140 °C on 5-μm-wide Al lines patterned on a SiO_2 substrate. The inset shows a cross-polarized image of the sample. (b) A TM-AFM image in height contrast of the sheared and micropatterned PVDF-TrFE on a pre-patterned Al substrate where the semi-crystalline PVDF-TrFE lamellae 25 nm in width are highly ordered. A 2D GIXD pattern from a sheared PVDF-TrFE thin film is shown with the incident angle parallel to the shear direction in the inset of (b). (c) A schematic illustration of a PVDF-TrFE film ordered by static shear on an Al surface. The crystalline lamellae and the *c* axis of the crystals are oriented perpendicular and parallel to the shear direction, respectively. (d) A FESEM image of the sample in (a). The inset of (d) exhibits the patterned PVDF-TrFE over a large area. (e) A TM-AFM topography image shows highly ordered PVDF-TrFE produced by the shear field on Al line patterns 1.5 μm in width. An AFM image in phase contrast of the sample is also shown in the inset. (f) A bright field optical microscopy image of a PVDF-TrFE sheared and micropatterned on hexagonal Al pre-pattern. An individual hexagon with the highly ordered crystalline lamellae of PVDF-TrFE is shown in the inset of (f).

between the template surface and the polymer crystal. In general, the polymer crystals tend to grow from a specific unit cell surface preferential to the template surface. For example, the PVDF crystalline lamellae were always aligned parallel to the pore direction of the anodic aluminum oxide (AAO) when they were confined and re-crystallized from the melt state [36]. In our previous work, we also achieved crystalline PVDF lamellae aligned perpendicular to the line pattern when the crystals were molded by capillary printing [37]. As noted, it would be difficult to change the crystal orientation with respect to the pattern geometry without further chemical modification of either the polymer crystals or the template surface. Our shear and detachment process can be one effective way to overcome this issue.

The highly ordered crystalline domains of PVDF-TrFE preferentially formed on a patterned metallic Al surface were readily incorporated into non-volatile ferroelectric

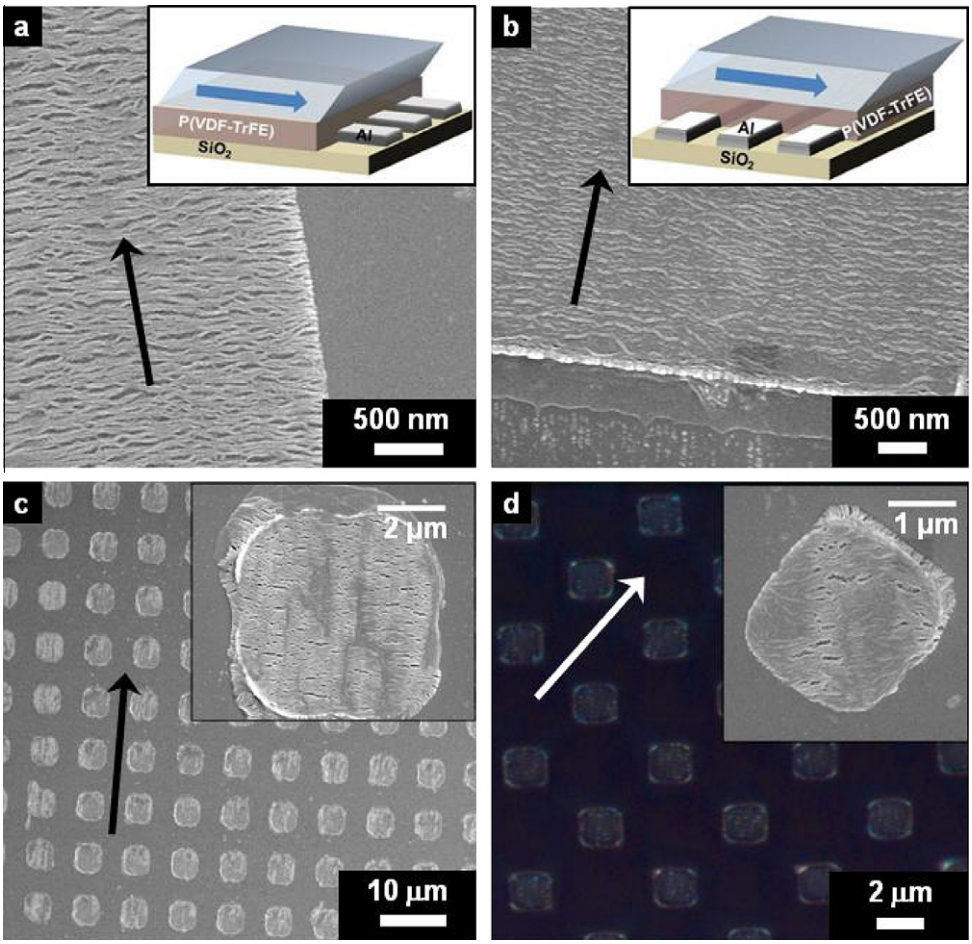

Fig. 3. FESEM images of thin PVDF-TrFE film sheared with the direction (a) parallel and (b) perpendicular to pre-patterned Al lines. The inset of (a) and (b) exhibit the schematics of shear direction with respect to the orientation of the Al lines. (c) An FESEM image of a micropatterned PVDF-TrFE film sheared in the direction indicated with an arrow on 5 μm Al squares. An individual domain highlighted with the ordered crystalline lamellae is shown in the inset. (d) A cross-polarized OM image of a micropatterned PVDF-TrFE film on 2 μm square pattern when the shear field was applied diagonal to the square, as indicated with an arrow. An individual domain with ordered crystalline lamellae is shown in the inset. The crystalline PVDF-TrFE lamellae are always aligned perpendicular to the shear direction regardless of the geometry of the pre-pattern.

memory unit devices such as metal/ferroelectric polymer/metal (MFM) capacitors and bottom gate ferroelectric field effect transistors (FeFETs). Our method allowed for the fabrication of arrays of both devices containing controlled crystalline PVDF-TrFE domains, as shown in Fig. 4a and c. First of all, arrays of Al/ordered PVDF-TrFE/Al capacitors were formed on alternating Al line patterns of 300 and 700 μm on SiO_2 substrate by our one-step shear and detachment method, as shown in Fig. 4a. The static shear on a spin-coated PVDF-TrFE film was applied in the line direction, and Al top electrodes 200 μm in diameter were subsequently deposited by thermal evaporation. Since there was no PVDF-TrFE on the SiO_2 substrate remaining after the shear process, the ferroelectric capacitors were formed in only the regions of the Al bottom electrodes on which the crystalline PVDF-TrFE lamellae were well aligned perpendicular to the shear direction.

Fig. 4b exhibits two different ferroelectric hysteresis loops as determined by polarization-voltage measurements obtained from two different sets of capacitors fabricated on Al bottom electrode at the same time: one with 150 nm thick sheared PVDF-TrFE and the other with non-sheared PVDF-TrFE. MFM capacitors with non-sheared PVDF-TrFE were prepared from the area of a spin-coated film not in contact with the PDMS pad during shearing at appropriate thermal conditions. At sufficient voltage sweep between ±20 V, the remanent polarization (P_r) of 6.49 μC/cm^2 and the coercive voltage (V_c) of 7.91 V, which corresponds to coercive field of approximately 50 MV/m, were obtained from the capacitor measurement with the sheared film. On the other hand, the capacitor with the non-sheared film showed a lower P_r of 2.94 μC/cm^2 with a similar V_c of 7.9 V. The higher P_r value of the sheared PVDF-TrFE arose from the orientation of the crystalline lamellae, as reported in our previous work [13]. Since the PVDF-TrFE thin films in all of our samples were pre-melted before shearing at 140 °C, the thin PVDF-TrFE film without the shear field generally consisted of face-on lamellae whose *c* and *b* axes were aligned normal and parallel to the substrate, respectively [22]. The ineffective orientation

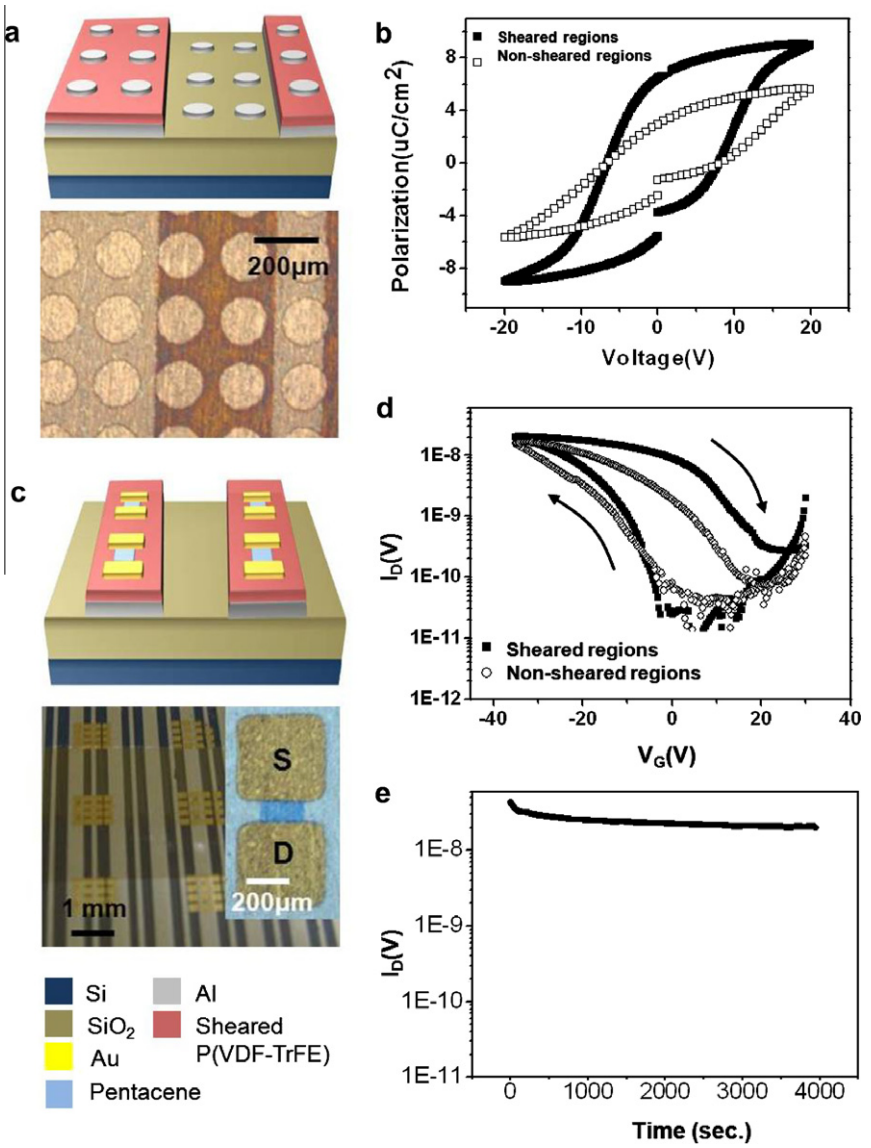

Fig. 4. A bright field optical microscopy image and a schematic of the arrays of (a) MFM capacitors and (c) FeFETs with sheared and patterned PVDF-TrFE films. (b) Polarization P vs. applied voltage V hysteresis loops of Al/PVDF-TrFE/Al capacitors from the sheared region and the outside (not-sheared) region, with a thickness of approximately 160 nm. (d) I_{SD}–V_G transfer curves of the FeFET with highly ordered PVDF-TrFE (square) and the outside (circle) region on an Al gate substrate. The drain voltage V_D, channel length L, and width W are −5 V, 100 and 200 μm, respectively. (e) Data retention of a FeFET memory with pentacene measured with the ON state drain current taken per second. The currents were detected at zero gate voltage with the continuous drain voltage of −5 V after single voltage pulse of −35 V for ON current.

of the b axis with respect to the electric field resulted in a low P_r in the non-sheared sample. In contrast, the sheared PVDF-TrFE film with the oriented edge-on lamellae effectively rotated its permanent dipoles upon exposure to an electric field, leading to the high P_r.

For the fabrication of the arrays of FeFETs with patterned and sheared PVDF-TrFE films, a 300-nm-thick ferroelectric film was spin-coated onto a 700-μm-wide Al line pattern in order to prevent gate leakage between the gate and drain electrodes. Each Al line pattern, on which ferroelectric PVDF-TrFE crystalline lamellae were oriented, served as a bottom gate, as shown in Fig. 4c. The subsequent thermal deposition of semi-conducting pentacene as an active channel and Au as the source and drain electrodes was performed using shadow masks on micropatterned PVDF-TrFE films on the Al line pattern. The photograph and optical microscopy images of Fig. 4c and the inset in Fig. 4c represent the arrays of FeFETs and the top view of an individual device, respectively. The fabricated FeFET exhibits a characteristic hysteresis arising from the bistability of the ferroelectric PVDF-TrFE film in the current between the source and drain when the gate voltage was applied, as shown in Fig. 4d. As the gate voltage was increased, holes accumulated at the interface between the pentacene and the oriented PVDF-TrFE, after which, the On state was achieved when I_{DS} increased to

1×10^{-8} A as indicated by an arrow in Fig. 4d. Although the gate voltage was zero, I_{DS} still remained in the On state due to the remanent ferroelectric polarization of the PVDF-TrFE. When sufficient positive voltage was applied to rotate the dipole of the PVDF-TrFE, the device turns to the Off state. The On/Off bistability of the FeFET increases with programming gate voltage sweep and was maximized of approximately $10^{2.6}$ under ambient conditions with a gate voltage sweep of ±35 V. Further increase of program voltage sweep did not significantly change the value. In order to examine retention properties of On state of a FeFET device, we measured I_{DS} of written On state under zero gate bias with a constant V_{DS} of −5 V after programming at 35 V. On current taken per second is not significantly altered even after period longer than 4000 s as shown in Fig. 4e. It should be noted that our retention measurement last approximately an hour due to air-sensitive pentacene active channel in our FeFETs without additional passivation. Extrapolation of the current with time allows us to expect long time data retention capability of our device as long as the chemical and physical properties of pentacene are preserved without environmental degradation.

Our FeFET with the sheared PVDF-TrFE film operated at gate voltage sweep of ±35 V even without an additional interlayer, which helped to reduce the gate leakage [38]. We also compared the device performance of FeFET containing the sheared film with that of a non-sheared film. The *I*–*V* characteristics of FeFET with non-sheared PVDF-TrFE exhibited notably worse device performance in which the On/Off bistability ratio was approximately $10^{1.4}$, or ten times less than that of the device with the sheared film, as shown in Fig. 4d. Due to many structural defects and large surface roughness arising from semi-crystalline grain–grain mismatch, pinholes and residual solvent trapped in the film, a thick ferroelectric gate insulator is often required to minimize the electric leakage, resulting in high operating gate voltage. Most of previous studies suggest insertion of various interlayers between gate electrode and ferroelectric layer including SiO_2 [39], poly(vinyl phenol) [29,40], and poly(styrene-random-methylmethacrylate) copolymer [38]. For low voltage operation of a device, one should design an interlayer as thin as possible with high capacitance. Our shear and detachment method seems beneficial for reducing surface roughness of a film because a PVDF-TrFE film was flattened out under a PDMS mold during shearing process. In fact, surface of a sheared film is lower in roughness than that of non-sheared one. Highly aligned crystalline domains by shear method may be also efficient for reducing leakage current possibly due to fewer structural defects. The performances of memory devices with sheared and non-sheared films are summarized in Table 2.

Table 2
Device performances of MFM capacitors and FeFETs with PVDF-TrFE films, based on shearing and non-shearing process.

Region	P_r (μC/cm^2)	V_c (V)	ON/OFF	Memory window
Sheared	6.4	7.9	400	26
Non-sheared	2.9	7.9	25	17

All device performances were based on the mean value from three different sets of samples.
Each set of samples was made from the same batch.

4. Conclusions

We developed a facile one-step micropatterning technique for ferroelectric PVDF-TrFE film in which each patterned domain has highly oriented crystalline lamellae of PVDF-TrFE due to selective static shear and detachment. The proper choice of pre-patterned surfaces based on the adhesion with PVDF-TrFE allowed us to orient the crystalline lamellae perpendicular to the shear direction, with the *c* axis of the crystals preferentially oriented parallel to the shear direction on good adhesive regions. At the same time, the film selectively detached from poorly adhesive regions, leading to a micropatterned PVDF-TrFE with controlled molecular structures and microstructures. Our method is also beneficial because the orientation of crystalline lamellae is able to be readily controlled regardless of the micropattern geometry simply by changing the shear direction with respect to the geometry of the prepattern. Arrays of non-volatile MFM and FeFET memory units with patterned and sheared PVDF-TrFE thin films exhibited excellent device performances with both high P_r and On/Off bistability ratio in MFM and FeFET, respectively, compared to those with non-sheared PVDF-TrFE. Our patterning capability in a few micron level can potentially make it possible to realize higher density memory than other state-of-art printing techniques of ink-jet and screening printing.

Acknowledgements

This project was supported by The National Research Program for Memory Development sponsored by the Ministry of Knowledge and Economy, Republic of Korea. This work was partly supported by the IT R&D Program of MKE/KEIT [10030559, Development of next generation high performance organic/nano materials and printing process technology] and the Seoul R&BD Program (10816). The X-ray experiments at PAL (4C2 beamline), Korea, were supported by MEST and POSCO, Korea. This work was supported by the Second Stage of the Brain Korea 21 Project in 2006, the Converging Research Center Program funded by the Ministry of Education, Science and Technology (2010K001149), and the National Research Foundation of Korea (NRF) grant funded by the Korea government (MEST) (No.2010-0000425).

Appendix A. Supplementary data

Supplementary data associated with this article can be found, in the online version, at doi:10.1016/j.orgel.2010.10.007.

References

[1] Q. Linga, D. Liawb, C. Zhuc, D.S. Chanc, E. Kanga, K. Neoha, Prog. Polym. Sci. 33 (2008) 917.
[2] T. Sekitani, T. Yokota, U. Zshieschang, H. Klauk, S. Bauer, K. Takeuchi, M. Takmiya, T. Sakurai, T. Someya, Science 326 (2009) 1516.

[3] T. Kim, H. Choi, S. Oh, G. Wang, D. Kim, H. Hwang, T. Lee, Adv. Mater. 21 (2009) 2497.
[4] S. Ducharme, T.J. Reece, C.M. Othon, R.K. Rannow, IEEE Trans. Device Mater. Reliab. 5 (2005) 720.
[5] R.C.G. Naber, C. Tanase, P.W.M. Blom, G.H. Gelinck, A.W. Marsman, F.J. Touwslager, S. Setayesh, D.M. de Leeuw, Nat. Mater. 4 (2004) 243.
[6] R.C.G. Naber, K. Asadi, P.W.M. Blom, D.M. de Leeuw, B. de Boer, Adv. Mater. 22 (2010) 933.
[7] V. Bune, V.M. Fridkin, S. Ducharme, L.M. Blinov, S.P. Palto, A.V. Sorokin, S.G. Yudin, A. Zlatkin, Nature 391 (1998) 874.
[8] A.J. Lovinger, Science 220 (1983) 1115.
[9] R.C.G. Naber, B. de Boer, P.W.M. Blom, D.M. de Leeuw, Appl. Phys. Lett. 87 (2005) 203509.
[10] C.A. Nguyen, S.G. Mhaisalkar, J. Ma, P.S. Lee, Org. Electron. 9 (2008) 1087.
[11] R.C.G. Naber, P.W.M. Blom, A.W. Marsman, D.M. de Leeuw, Appl. Phys. Lett. 85 (2004) 2032.
[12] F. Xia, Q.M. Zhang, Appl. Phys. Lett. 85 (2004) 1719.
[13] Y.J. Park, S.J. Kang, K.J. Kim, H.S. Lee, M.S. Lee, U.-I. Chung, I.J. Park, C. Park, Appl. Phys. Lett. 88 (2006) 242908.
[14] Y.J. Park, S.J. Kang, C. Park, B. Lotz, A. Thierry, K.J. Kim, J. Huh, Macromolecules 41 (2008) 109.
[15] T. Furukawa, S. Kanai, A. Okada, Y. Takahashi, R.J. Yamamoto, Appl. Phys. Lett. 105 (2009) 061636.
[16] K. Noda, K. Ishida, T. Horiuchi, K. Matsushige, A.J. Kubono, J. Appl. Phys. 86 (1999) 3688.
[17] J.K. Krüger, B. Heydt, C. Fischer, J. Baller, R. Jiménez, K.-P. Bohn, B. Servet, P. Galtier, M. Pavel, B. Ploss, M. Beghi, C. Bottani, Phys. Rev. B 55 (1997) 3497.
[18] K. Kimura, K. Kobayashi, H. Yamada, K. Matsushige, Langmuir 23 (2007) 4740.
[19] S.J. Kang, Y.J. Park, J. Sung, P.S. Jo, C. Park, K.J. Kim, B.O. Cho, Appl. Phys. Lett. 92 (2008) 012921.
[20] D.C. Yang, E.L. Thomas, J. Mater. Sci. Lett. 3 (1984) 929.
[21] D.C. Yang, E.L. Thomas, J. Mater. Sci. Lett. 6 (1987) 593.
[22] W. Kaufmann, J. Petermann, N. Reynolds, E.L. Thomas, S.L. Hsu, Polymer 30 (1989) 2147.
[23] Y.J. Park, S.J. Kang, B. Lotz, M. Brinkmann, A. Thierry, K.J. Kim, C. Park, Macromolecules 41 (2008) 8648.
[24] H.J. Jung, J. Chang, Y.J. Park, S.J. Kang, B. Lotz, J. Huh, C. Park, Macromolecules 42 (2009) 4148.
[25] J.-W. Yoon, S.-I. Ohmi, B.-E. Park, H. Ishiwara, Appl. Phys. Lett. 93 (2008) 162904.
[26] S.J. Kang, Y.J. Park, J. Hwang, H.J. Jeong, J.S. Lee, K.J. Kim, H.-C. Kim, J. Huh, C. Park, Adv. Mater. 19 (2007) 581.
[27] L. Zhang, S. Ducharme, J. Li, Appl. Phys. Lett. 91 (2007) 172906.
[28] M. Steinhart, S. Senz, R.B. Wehrspohn, U. Gosele, J.H. Wendorff, Macromolecules 36 (2003) 3646.
[29] S.J. Kang, Y.J. Park, I. Bae, K.J. Kim, H.-C. Kim, S. Bauer, E.L. Thomas, C. Park, Adv. Funct. Mater. 19 (2009) 2812.
[30] T. Sekitani, K. Zaitsu, Y. Noguchi, K. Ishibe, T. Takamiya, T. Sakurai, T. Someya, IEEE Trans. Elec. Dev. 56 (2009) 1027.
[31] H. Kim, B. Yoon, J. Sung, D.-G. Choi, C. Park, J. Mater. Chem. 18 (2008) 3489.
[32] W. Ma, J. Zhang, S. Chen, X. Wang, Colloid Polym. Sci. 286 (2008) 1193.
[33] R.H. Hurt, G. Krammer, G. Crawford, K. Jian, C. Rulison, Fuel Chem. Div. Prepr. 47 (2002) 423.
[34] I.S. Bayera, A. Biswas, A. Tripathi, D.K. Avasthi, J.P. Singh, C.M. Megaridis, Polym. Adv. Technol. 20 (2009) 775.
[35] J.S. Kim, R.H. Friend, F. Cacialli, Synth. Met. 111–112 (2000) 369.
[36] M. Steinhart, P. Goring, H. Dernaika, M. Prabhukaran, U. Gosele, Phys. Rev. Lett. 97 (2006) 027801.
[37] Y.J. Park, Y.S. Kang, C. Park, Eur. Polymer J. 41 (2005) 1002.
[38] J. Chang, C.H. Shin, Y.J. Park, S.J. Kang, H.J. Jeong, K.J. Kim, C.J. Hawker, T.P. Russell, D.Y. Ryu, C. Park, Org. Electron. 10 (2009) 849.
[39] A. Gerber, M. Fitsilis, R. Waser, T.J. Reece, E. Rije, S. Ducharme, H. Kohlstedt, J. Appl. Phys. 107 (2010) 124119.
[40] S.J. Kang, I. Bae, Y.J. Park, T.H. Park, J. Sung, S.C. Yoon, K.H. Kim, D.H. Choi, C. Park, Adv. Funct. Mater. 19 (2009) 1609.

Organic Electronics 12 (2011) 108–112

Contents lists available at ScienceDirect

Organic Electronics

journal homepage: www.elsevier.com/locate/orgel

Letter

Air-processed organic photovoltaic devices fabricated with hot press lamination

Brian A. Bailey [a], Matthew O. Reese [b], Dana C. Olson [b], Sean E. Shaheen [a], Nikos Kopidakis [b,*]

[a] Department of Physics and Astronomy, University of Denver, Denver, Colorado 80208, United States
[b] National Renewable Energy Laboratory, 1617 Cole Blvd, Golden, Colorado 80401, United States

ARTICLE INFO

Article history:
Received 24 August 2010
Received in revised form 8 October 2010
Accepted 10 October 2010
Available online 2 November 2010

Keywords:
Lamination
Organic photovoltaics
Inverted OPV
PEDOT:PSS
P3HT
Sorbitol

ABSTRACT

A detailed method for air-processed, inverted Organic Photovoltaic (OPV) devices using lamination of the metal electrode with a doped conducting polymer adhesive is presented. A poly(3-hexylthiophene) (P3HT) - [6,6] phenyl C_{61} butyric methyl ester (PCBM) bulk heterojunction is used, with a solution-processed ZnO electron collection layer. The top contact consists of modified polyethylene dioxythiophene:polystyrene sulfonate (PEDOT:PSS) that is spin-coated onto a Ag electrode, and the entire structure is laminated onto the active layer. Lamination produces devices with 3.19% power conversion efficiency at 1 sun illumination, which is higher than the value for control devices produced with the standard sequential process with an evaporated top metal electrode. The laminated interface yields an ohmic contact, as shown by the high fill factor and low series resistance of the laminated devices compared to devices with a thermally evaporated top metal electrode. We examine the lamination parameters and their effect on device performance, and we identify the treatment of the adhesion layer to be one of the more important parameters to control for efficient devices. The optimized protocol described here allows one to fabricate efficient inverted OPV devices in air, without the need for an expensive, high quality evaporation chamber for top contact deposition.

© 2010 Elsevier B.V. All rights reserved.

1. Introduction

Recent progress on materials optimization for organic photovoltaics (OPV) has resulted in efficiencies exceeding 8% [1]. While these advances bring the technology closer to commercialization, there is also strong motivation to improve the processing techniques for the fabrication of these devices. Of particular concern is compatibility with large-area manufacturing on flexible substrates and encapsulation for mechanical robustness and stability against degradation [2]. Due to the nature of the polymeric materials involved in OPV, unconventional methods of fabrication that encompass these traits become possible. One of these methods is the simple lamination (“gluing”) of two parts of the device to finish the final OPV structure, as was shown over a decade ago for polymer–polymer bilayers [3] and was recently demonstrated for polymer-fullerene bulk heterojunctions [4,5]. In contrast to lamination of inorganic PV that is performed to encapsulate a finished device, the OPV lamination process brings two active elements of the device into contact with the goal of forming a functioning charge-collecting interface, as shown in Fig. 1.

In this paper we report on OPV devices fabricated in-air with a hot press lamination process. Lamination as a method to fabricate OPV has several potential advantages over conventional bottom-up fabrication. First, the processing step of thermal evaporation of a metal onto the active layer is eliminated, as the metal electrode is now deposited onto a bare substrate. Thermal damage of the active layer has been proposed to occur during conventional metal evaporation, and high parasitic resistances have been measured

* Corresponding author. Tel.: +1 303 384 6222.
E-mail address: nikos.kopidakis@nrel.gov (N. Kopidakis).

1566-1199/$ - see front matter © 2010 Elsevier B.V. All rights reserved.
doi:10.1016/j.orgel.2010.10.008

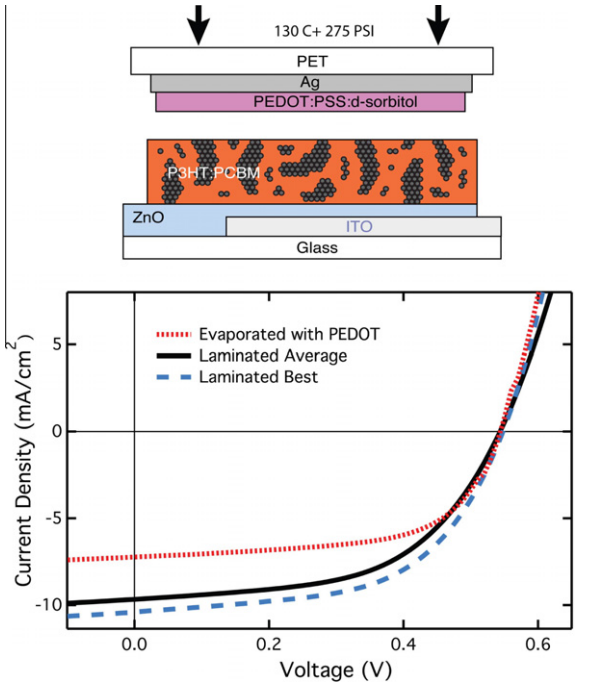

Fig. 1. The laminated device structure and typical *J–V* curves of inverted OPV devices made by hot press lamination (solid black) compared to ones with thermally evaporated top contact (dotted red). The best performing laminated device is also shown (dashed blue). (For interpretation of the references to color in this figure legend, the reader is referred to the web version of this paper.)

in evaporated metal-organic interfaces, compared to laminated ones [6]. It has been shown that the rate of metal evaporation onto a polymer:fullerene active layer is an important determining factor for the efficiency of the device [7]. Therefore, unless one has access to a high quality (and potentially expensive) thermal evaporation system that allows precise control of the evaporation rate, the fabrication of consistently performing inverted OPV devices may be problematic. As we will show, lamination enables the in-air fabrication of devices with power conversion efficiencies equivalent to evaporated contact devices fabricated in parallel. Second, lamination produces a self-encapsulated device that is mechanically protected on both sides. Utilization of flexible substrates with good oxygen and moisture barrier properties should also result in enhanced lifetimes of laminated devices. Third, the methodology presented here allows one to prepare, optimize and characterize two parts of the device independently before bringing them to contact. The method is compatible with roll-to-roll processing on flexible substrates and with solution-processed metal electrodes [8]. Finally, lamination provides a method to bring organic materials to device-grade electrical contact that can be applied to various Organic Electronic devices beyond OPV.

To demonstrate hot press lamination we use the prototypical poly(3-hexylthiophene) (P3HT) – [6,6] phenyl C_{61} butyric methyl ester (PCBM) bulk heterojunction in an inverted geometry, [7,9–11] using a solution-cast Zinc Oxide (ZnO) underlayer as the electron collecting contact and a laminated polyethylene dioxythiophene:polystyrene sulfonate (PEDOT:PSS)/Ag layer as the hole collecting top electrode. The device structure is shown in Fig. 1. The devices reach 3.19% power conversion efficiency at 1 sun, and their high fill factors (typically over 0.55) relative to evaporated devices indicate good electrical contact between the laminated layers. We present studies of the effect of various parameters of lamination on device performance as well as demonstrate the processing steps that are important and must be carefully controlled in order to consistently obtain efficient devices.

The two parts of the device, one on glass and the second on a flexible polyethylene terephthalate (PET) substrate, are fabricated in air as follows. A glass slide with patterned ITO is sonicated in acetone and isopropyl alcohol, then treated with an oxygen plasma for 5 min. Zinc oxide (ZnO) is deposited from zinc acetate solution followed by thermal conversion at 300 °C in air [7]. The active layer is 320 nm thick and it is spun from a 1:1 weight ratio of P3HT:PCBM dissolved in chlorobenzene with 2% dibromooctane added to promote phase separation without the need for solvent or thermal annealing [12,13]. On the PET film, 100 nm of silver is thermally deposited, followed by a 40 nm spin-coated film of PEDOT:PSS. For the best devices the PEDOT:PSS was doped with 10% by weight d-sorbitol [14], unless otherwise stated. The PET substrate is then annealed at 115 °C for varying annealing times as discussed below. The two parts of the device are then placed in contact as shown in Fig. 1, and placed in a hydraulic hot press for lamination. Both top and bottom plates of the press are preheated to 130 °C (verified within 2%) and the sample is pressed with 1.9 MPa (275 psi) of pressure for 5 min. Control devices were fabricated in parallel with evaporated top Ag contacts by spin coating PEDOT:PSS on top of the P3HT:PCBM active layer and annealing at 130 °C, followed by thermal evaporation of 100 nm Ag. To facilitate adhesion of the PEDOT:PSS layer in this case, the active layer was exposed to a mild oxygen plasma treatment.

Current–voltage (*J–V*) curves are measured on an AM 1.5G solar simulator with a Xenon lamp calibrated to 1 sun intensity. The device area of 0.11 cm^2 defined by the electrode geometry is inaccurate because of the high conductivity of the doped PEDOT:PSS layer, so an aperture was used to define a device area of 0.0517 cm^2 [15,16]. It was verified that the external quantum efficiency (EQE) of devices integrated with the AM 1.5G spectrum reproduces the short circuit current density with a 10% accuracy. Although an aperture is unnecessary for evaporated contact devices, the evaporated contact control devices were apertured to .0401 cm^2 for a more accurate comparison to the laminated contact devices. Aperturing evaporated contact devices to 0.0401 cm^2 from 0.11 cm^2 decreases their open circuit voltages (V_{OC}) and increases fill factors (*FF*) while keeping the short circuit current (J_{SC}) constant. The efficiency is consistent within error of the measurements.

Typical *J–V* curves of laminated devices and comparison to devices with a thermally evaporated top contact with a PEDOT:PSS hole transport layer are shown in Fig. 1. The device performance parameters are summarized in Table 1, where the average and standard deviation of performance

Table 1
Performance characteristics of laminated contact devices compared to evaporated contact ones. The control and laminated devices were made during this study, while the best evaporated device data was taken from previous work [7].

	V_{OC} (mV)	J_{SC} (mA/cm^2)	*FF* (%)	R_S (Ω)	η(%)
Avg evap control w/ PEDOT	545 ± 2.5	7.23 ± .47	60.8 ± .23	41 ± 1.5	2.40 ± 0.17
Avg laminated	545 ± 4.8	9.78 ± .73	54.5 ± 1.8	77 ± 20	2.92 ± .27
Best evap [7]	556	11.22	47.5		2.97
Best laminated	549	10.39	56	37	3.19

parameters taken from six laminated devices is also shown. As we will discuss below, optimizing the annealing step of the PEDOT:PSS layer impacts both the efficiency and the reproducibility of the devices. The best laminated device has an efficiency of 3.19% and was achieved when the zinc acetate precursor solution was prepared fresh, stirred overnight at room temperature, then spun just before device fabrication. As documented in previous work, inverted devices benefit from aging in air, with efficiencies gradually improving due to change of the work function of the top Ag electrode [17]. This phenomenon is also observed in the laminated inverted devices presented here, but to a lesser extent. The best efficiencies are reached 5–7 days after the fabrication of the device, but the overall improvement is around 20% over the performance immediately after fabrication. During that period the devices were stored in the dark in ambient conditions. We note that the time evolution during storage in air of inverted OPV devices using ZnO has been shown to result in more dramatic changes (up to 67%) in efficiency over 9 days [17]. It has been suggested that evolution of the ZnO layer also plays a role in the aging of inverted OPV devices. During traditional fabrication the devices are exposed to various environments, including high vacuum for top contact deposition that may cause metastability of the ZnO layer. In this work the part of the device that contains the ZnO remains in ambient conditions throughout fabrication and characterization, therefore we do not expect ZnO evolution to play a major role in device performance.

Compared to the best ZnO-based inverted device presented by White et al. [7] laminated devices have similar V_{OC} of 549 mV and much higher *FF* of 56%. The J_{SC} of the laminated device is lower at 10.3 mA/cm^2, but efficiency is still improved compared to evaporated contact devices. As can be seen from Table 1, the presence of PEDOT:PSS between the active layer and the Ag top contact improves the fill factor of the devices, resulting in values consistently over 54%.

The performance of OPV devices fabricated with hot press lamination is critically affected by the composition and thermal treatment of the PEDOT:PSS layer. Fig. 2 demonstrates the significance of the PEDOT:PSS layer and the d-sorbitol additive on the performance of laminated devices. These samples were fabricated at the same time under conditions that allowed us to compare different compositions of the laminated contact. The best laminated device of the series contained d-sorbitol additive (10% by liquid weight) and had an efficiency of 2.67%. This differs from the 3.19% laminated device since the other parameters mentioned in the study had not yet been optimized.

With no PEDOT:PSS interlayer, the devices have poor efficiency with very low V_{OC} of 173 mV, and J_{SC} of

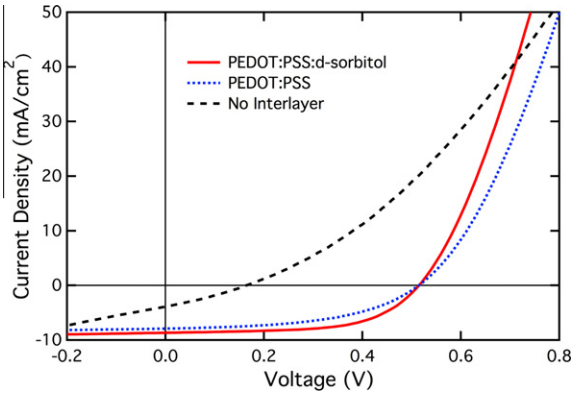

Fig. 2. *J–V* curves under 1 sun illumination of devices using various layers at the lamination interface. The black dashed line shows performance from a device laminated without an interlayer between the bulk heterojunction and the Ag on PET. The blue dashed line has a PEDOT:PSS interlayer, and the solid red line has a PEDOT:PSS:d-sorbitol interlayer. (For interpretation of the references to color in this figure legend, the reader is referred to the web version of this paper.)

3.9 mA/cm^2. This indicates the presence of a barrier for charge collection at the laminated (hole collecting) side of the device in the absence of PEDOT:PSS. The low *FF* of 29%, and high series resistance of ca. 200 Ω, measured from the inverse slope of the curve at 1 V indeed suggests poor electrical contact at the laminated interface, also evidenced by structural failure of the devices under mild mechanical stress. The presence of a PEDOT:PSS interlayer drastically improves the device performance: V_{OC} is 506 mV, J_{SC} is 8.1 mA/cm^2, series resistance drops to 50 Ω, and *FF* increases to 52%. These observations verify that the PEDOT:PSS is providing an ohmic contact for hole extraction [4,14]. The addition of d-sorbitol to the PEDOT:PSS interlayer further increases the J_{SC} to 8.7 mA/cm^2 and the *FF* to 58%. In some cells, the fill factor is over 60%, and the series resistance is reduced to 35 Ω. The decreased series resistance and increased *FF* are consistent with increased conductivity of the PEDOT:PSS:d-sorbitol. The d-sorbitol doped films exhibit much enhanced adhesion, and devices from these films are made more physically robust during the lamination process. About 25% of the undoped PEDOT:PSS devices delaminated when the plates of the press were pulled apart, while none of the doped PEDOT:PSS devices failed in this manner.

Sublimation of d-sorbitol occurs at 120 °C at atmospheric pressure and is responsible for the increase in the conductivity of the PEDOT:PSS film [18]. The enhanced mechanical robustness of laminated devices that incorporated

d-sorbitol (as discussed above) indicates that at least some d-sorbitol remains in the film after lamination at 130 °C. The d-sorbitol treatment also alters the work function from 5.1 to 4.8 eV in PEDOT:PSS films deposited on glass [18]. However, in the devices shown in this work, the V_{OC} is relatively unchanged between PEDOT:PSS with and without d-sorbitol. This is in contrast to what is seen in non-inverted devices, in which formulating the PEDOT:PSS with sorbitol results in a decrease in V_{OC} [19]. We also note that the V_{OC} of inverted devices using a thermally evaporated Ag top contact has been seen to correlate with the work function of the Ag [17]. That the behavior of this laminated electrode is different suggests that either the chemical potential at the laminated interface is decoupled from the work-function of the electrode, presumably due to a lack of Fermi level pinning, or that it is the Ag in the PEDOT:PSS:d-sorbitol/Ag that is dominating the chemical potential. Further studies into this issue are underway.

During annealing of the PEDOT:PSS:d-sorbitol layer a balance needs to be achieved between removing water from the film, while maintaining levels of d-sorbitol at the lamination interface until an electrical connection is made. Careful control of the annealing conditions of the PEDOT:PSS:d-sorbitol layer is one of the most important parameters for efficient and reproducible laminated devices. Fig. 3 shows the effect of different pre-lamination treatments of the PEDOT:PSS:d-sorbitol interlayer on device performance. The error bars correspond to the standard deviation between six devices on the same substrate. The following types of treatment were used: (i) drying in ambient conditions, (ii) a 10 min vacuum step without heat and (iii) an annealing step on a hot plate in-air set to 115 °C. In treatment (iii) the time on the hot plate was varied between 2 and 10 min. Annealing above 115 °C leads to delamination during fabrication and poor reproducibility. Fig. 3 shows that both the J_{SC} and the *FF* of devices increase and become more consistent when the samples are heated, while the V_{OC} is relatively unchanged. We conclude that annealing the PEDOT:PSS:d-sorbitol layer at 115 °C for 10 min increases both the performance and reproducibility of laminated devices. Note that the efficiency of the optimized devices in Fig. 3 is ca. 2.4%, lower than the 3+% reported above. The results shown in Fig. 3 are taken from devices measured shortly after the lamination process without allowing them to age, which improves their efficiency.

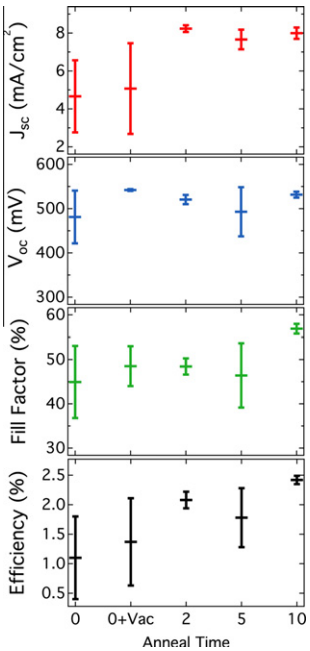

Fig. 3. Device performance parameters for different pre-lamination treatments of the PEDOT:PSS:d-sorbitol interlayer. "0" represents drying the layer in ambient conditions, and "0 + Vac" represents drying the layer in vacuum of 10^{-1} torr at room temperature for 10 min. The other points correspond to annealing the layer at 115 °C in-air for 2, 5, and 10 min.

Additional parameters were explored and were found to have less effect on device performance. Lamination pressure was varied from 0.7 to 2.4 MPa (100–350 psi) with a broad performance peak between 1.31 and 2.07 MPa but with small variations outside that range. Lamination time was varied from 0.5 to 30 min with devices laminated 2 min or less showing poor reproducibility, and devices annealed longer than 5 min showing no significant improvement. Thickness of the active layer was varied from 230 to 560 nm, with thicker layers showing higher J_{SC} and lower *FF* values. The optimum thickness was near 320 nm, the same as reported in evaporated devices [7].

In summary, we demonstrate that lamination of the Ag contact can produce inverted OPV devices with efficiencies higher than devices made in parallel with thermal evaporation of the top contact. This approach greatly reduces the cost of the equipment required for fabrication as devices are processed in air without the need for a high quality evaporation chamber for metal contact deposition. This will allow research groups to investigate other, more novel OPV materials without the need for extensive financial investment into vacuum deposition equipment. It also opens pathways for low cost deposition of electrode materials, such as solution cast electrodes. The processing parameters that are important in the fabrication process are the presence of a PEDOT:PSS:d-sorbitol interlayer at the lamination interface, the pre-lamination treatment of that layer. If these parameters are adequately controlled, devices with a P3HT:PCBM active layer routinely achieve efficiencies over 3%.

Acknowledgements

Funding of this work by the Department of Energy's EERE Solar Technology Program through the National Center for Photovoltaics Seed Fund Program is gratefully acknowledged. We would also like to thank the group of Dr. Arthur Frank for use of the hydraulic hot press.

References

[1] www.solarmer.com.
[2] M. Jorgensen, K. Norrman, F.C. Krebs, Sol. Energy Mater. Sol. Cells 92 (2008) 686–714.
[3] M. Granstrom, K. Petritsch, A. Arias, A. Lux, M. Andersson, R. Friend, Nature 395 (1998) 257–260.
[4] J. Huang, G. Li, Y. Yang, Adv. Mater. 20 (2008) 415–419.

[5] M. Nakamura, C. Yang, K. Tajima, K. Hashimoto, Sol. Energy Mater. Sol. Cells 93 (2009) 1681–1684.
[6] J. Zaumseil, K. Baldwin, J. Rogers, J. Appl. Phys. 93 (2003) 6117–6124.
[7] M. White, D. Olson, S. Shaheen, Appl. Phys Lett (2006).
[8] C. Girotto, B.P. Rand, S. Steudel, J. Genoe, P. Heremans, Org. Electron. 10 (2009) 735–740.
[9] C. Waldauf, M. Morana, P. Denk, P. Schilinsky, K. Coakley, S.A. Choulis, C.J. Brabec, Appl. Phys. Lett. 89 (2006) 233517.
[10] H.-H. Liao, L.-M. Chen, Z. Xu, G. Li, Y. Yang, Appl. Phys. Lett. 92 (2008) 173303.
[11] S.K. Hau, H.-L. Yip, N.S. Baek, J. Zou, K. O'malley, A.K.-Y. Jen, Appl. Phys. Lett. 92 (2008) 253301.
[12] Y. Yao, J. Hou, Z. Xu, G. Li, Y. Yang, Adv. Funct. Mater. 18 (2008) 1783–1789.
[13] J.K. Lee, W.L. Ma, C.J. Brabec, J. Yuen, J.S. Moon, J.Y. Kim, K. Lee, G.C. Bazan, A.J. Heeger, J. Am. Chem. Soc. 130 (2008) 3619–3623.
[14] J. Ouyang, Y. Yang, Adv. Mater. 18 (2006) 2141–2144.
[15] A. Cravino, P. Schilinsky, C.J. Brabec, Adv. Funct. Mater. 17 (2007) 3906–3910.
[16] M.-S. Kim, M.-G. Kang, L.J. Guo, J. Kim, Appl. Phys. Lett. 92 (2008) 133301.
[17] M.T. Lloyd, D.C. Olson, P. Lu, E. Fang, D.L. Moore, M.S. White, M.O. Reese, D.S. Ginley, J.W.P. Hsu, J. Mater. Chem. 19 (2009) 7638.
[18] A. Nardes, M. Kemerink, M. Dekok, E. Vinken, K. Maturova, R. Janssen, Org. Electron. 9 (2008) 727–734.
[19] F. Zhang, A. Gadisa, O. Inganas, M. Svensson, M. Andersson, Appl. Phys. Lett. 84 (2004) 3906–3908.

Organic Electronics 12 (2011) 113–118

Contents lists available at ScienceDirect

Organic Electronics

journal homepage: www.elsevier.com/locate/orgel

Flexible inverted polymer solar cells containing an amorphous titanium oxide electron collection electrode

Ikumi Sasajima, Shogo Uesaka, Takayuki Kuwabara *, Takahiro Yamaguchi, Kohshin Takahashi *

Graduate School of Natural Science and Technology, Kanazawa University, Kakuma-machi, Kanazawa, Ishikawa 920-1192, Japan

ARTICLE INFO

Article history:
Received 7 September 2010
Received in revised form 4 October 2010
Accepted 16 October 2010
Available online 11 November 2010

Keywords:
Air-stable
Amorphous titanium oxide
Flexible solar cell
Polymer solar cell

ABSTRACT

An inverted polymer solar cell was fabricated on a polyethylene terephthalate (PET) substrate. The cell structure was ITO/amorphous titanium oxide (TiO_x)/[6,6]-phenyl C_{61} butyric acid methyl ester (PCBM): regioregular poly(3-hexylthiophene) (P3HT)/poly(3,4-ethylenedioxylenethiophene):poly(4-styrene sulfonic acid) (PEDOT:PSS)/Au (TiO_x cell). It was achieved using low boiling point diethyl amine (DEA) as a Ti^{4+} complexing agent, and high boiling point 1,2,3,4-tetrahydronaphthalene (Tetralin) containing 2 vol.% 1,8-octanedithiol (ODT) as the solvent for PCBM:P3HT film preparation. With heat treatment at 100 °C, the use of DEA and Tetralin:ODT made it possible to prepare a TiO_x electron collection layer and PCBM:P3HT photoactive layer, respectively. Fabricating the TiO_x cell on the thin PET film was possible, as PET did not warp at 100 °C. The power conversion efficiency (PCE) of the TiO_x cell fabricated on PET was 2.43%, under AM1.5G conditions. When fabricated on glass, the PCE was 2.76%. When [6,6] diphenyl C_{62} bis(butyric acid methyl ester) (bis-PCBM) was instead used as the electron acceptor in the photoactive blend layer, the flexible air-stable cell provided a PCE of 2.81%.

© 2010 Elsevier B.V. All rights reserved.

1. Introduction

Much attention has recently been given to polymer solar cells, as candidates for the next generation of solar cells. They are expected to provide a low-cost, environmentally friendly, flexible, easily scaled up and lightweight alternative to the silicon solar cells currently in widespread use [1–3]. The organic active layer of polymer solar cells typically consists of a *p*-conjugated polymer donor and fullerene derivative acceptor, and is prepared by wet-processes such as spin-coating or roller-printing. The power conversion efficiency (PCE) of polymer solar cells has recently achieved 6–7%, which has arisen from the development of new *p*-conjugated polymers [4–7] and fullerene derivatives [8,9]. The *p*-conjugated polymers such as copolymers of benzodithiophene and thienothiophene absorb at long wavelengths and may also possess a low energy HOMO level. Studies investigating their commercial viability (e.g. durability improvement, cost effective production of large-scale flexible cells) are also of great interest and importance, in addition to those investigating their efficiency enhancement. We have been developing air-stable inverted polymer solar cells. Such inverted cells are comprised of a multilayered structure and have a reverse geometry compared with that of a normal cell. Both cell geometries are depicted schematically in Fig. 1. In a normal solar cell, the back Al electrode effectively collects electrons because of its low work function. However, its performance is quickly degraded when Al surface deposition is not carried out under ultrahigh vacuum [10]. High durability can be obtained for the inverted solar cell geometry because the transparent metal oxide (e.g. amorphous titanium oxide (TiO_x) or zinc oxide (ZnO)) provides a non-corrosive electron collection electrode. We previously reported that the performance of an unsealed inverted polymer solar cell with the structure ITO/TiO_x/PCBM:P3HT/PEDOT:PSS/Au (denoted as TiO_x cell) was maintained

* Corresponding authors. Tel.: +81 76 234 4770; fax: +81 76 234 4800.
E-mail address: tkuwa@t.kanazawa-u.ac.jp (T. Kuwabara).

1566-1199/$ - see front matter © 2010 Elsevier B.V. All rights reserved.
doi:10.1016/j.orgel.2010.10.010

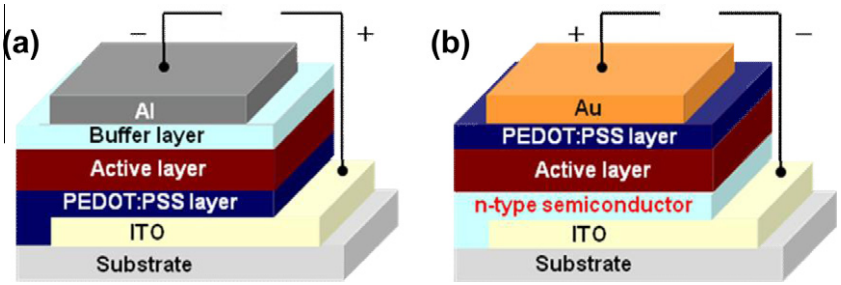

Fig. 1. Schematic illustrations showing the structures of normal (a) and inverted (b) polymer solar cells.

under continuous light irradiation for 100 h in an ambient atmosphere [11]. This structure is a promising candidate for further studying polymer solar cell durability improvement [12–14].

Preparing robust, light weight, flexible polymer solar cells is important for encouraging their widespread use. Several papers have reported the fabrication of polymer solar cells on flexible substrates [15–21]. Krebs et al. fabricated modules from PET-ITO/ZnO nanoparticles/PCBM:P3HT/PEDOT:PSS/Ag cells using a roll-to-roll process [22], and showed that the PCE reached 2.33% from a working area of 4.8 cm^2. Flexible inverted polymer solar cells containing ZnO nanoparticles as an electron collection layer [22,23], or Cs_2CO_3 as a buffer layer [24], have been reported by other research groups. However, such solar cells containing TiO_x films have not been reported, because the PET substrate easily warps during heat treatment. In the current study, we report a flexible TiO_x cell fabricated on a PET substrate, with a photoactive area of 1 cm^2. This cell exhibited a maximum PCE of 2.8% under AM1.5G conditions.

2. Experimental section

2.1. Materials

Titanium (IV) isopropoxide ($Ti(OCH(CH_3)_2)_4$), acetylacetone (AA) ($CH_3C(O)CH_2C(O)CH_3$), diethylamine (DEA) ($CH_3CH_2NHCH_2CH_3$), regioregular P3HT (Mw 87,000), PEDOT:PSS 1.3 wt.% dispersion in water, polyoxyethylene tridecyl ether (PTE), chlorobenzene (CB), o-dichlorobenzene (DCB), 1,2,3,4-tetrahydronaphthalene (Tetralin) and 1,8-octanedithiol (ODT) were purchased from Sigma–Aldrich Chemical Co., Inc. PCBM was purchased from Frontier Carbon Corporation. Bis-PCBM was purchased from ATR Company. All chemicals were used as received. Glass-ITO substrates (sheet resistance = 10 Ω/sq.) and Au wires were purchased from the Furuuchi Chemical Corporation. PET-ITO substrates (sheet resistance = 30 Ω/sq., thickness of PET sheet = 125 μm) were obtained from Nakai Industrial Co., Ltd.

2.2. Preparation of TiO_x layers

TiO_x precursor solutions were prepared under a N_2 atmosphere as described in our previous paper [12]. Precursor solutions were stored under a N_2 atmosphere following filtration, and were then diluted with 2-propanol, to prepare TiO_x layers by spin-coating onto the ITO electrode at 2000 rpm. The films were then hydrolyzed for 30 min in a controlled atmosphere with a relative humidity about 45%. The films were heated at various temperatures for 1 h on a hot plate, to remove the solvent and complexing agent. Two kinds of TiO_x films prepared from the precursor solutions containing complexing agents AA and DEA were denoted as AA-TiO_x and DEA-TiO_x, respectively. Fig. S1 shows the plots of the thickness of TiO_x film versus the concentration of the DEA-TiO_x precursor solution. The thickness was estimated by cross-sectional AFM imaging. The TiO_x films of 30 and 100 nm in thickness were used for the TiO_x cells containing Glass-ITO and PET-ITO substrates, respectively.

2.3. Fabrication of organic solar cells

ITO-Glass electrodes were cleaned by sonication in 2-propanol, washed in boiling 2-propanol, and then dried in air. PET-ITO electrodes were cleaned only by sonication in 2-propanol to prevent substrate warping. For spin-coating, PET-ITO electrodes were fixed on glass plates using adhesive tape. Cell fabrication was carried out in a N_2 filled glove box with less than 1 ppm moisture and 1 ppm oxygen as follows. The AA-TiO_x or DEA-TiO_x films were prepared by the method described above. A mixed solution of P3HT and PCBM (weight ratio = 5:4) was spin-coated onto the ITO/TiO_x substrate. A PEDOT:PSS dispersion in water containing 0.01 wt.% PTE was heated to 85 °C, and then spin-coated onto the PCBM:P3HT layer. The Au back electrode was vacuum-deposited at 2×10^{-5} torr onto the PEDOT:PSS layer. Finally, the device was heated at various temperatures for 5 min to crystallize the P3HT, and then at 70 °C for 30 min. The effective area of the solar cell was restricted to 1 cm^2, by depositing the Au electrode with a shadow mask.

2.4. Measurements

I–V curves of solar cells were measured by linear sweep voltammetry at a scan rate of 5 V min^{-1}, under AM 1.5G simulated sunlight conditions of 100 mW cm^{-2} intensity. The light source was a SAN-EI Electric XES-502S solar simulator calibrated by an EKO MS-601 pyranometer. All electric measurements were performed using a Hokuto Denko HZ-5000 electrochemical analyzer. UV–vis absorption

spectra were measured using a Hitachi U-3310 spectrophotometer. Atomic force microscopy (AFM) was carried out using a SII SPI3800N AFM apparatus. All measurements were carried out under an ambient atmosphere (15–30 °C, 40–60% relative humidity).

3. Results and discussion

3.1. TiO_x layer prepared by drying at 100 °C

The boiling points of DEA (55 °C) and AA (140 °C) are sufficiently low to allow their use as complexing agents for TiO_x precursor solutions, and to fabricate TiO_x cells at low-temperature. TiO_x films on ITO-glass substrates prepared from the AA-TiO_x and DEA-TiO_x precursor solutions were dried at 100 or 150 °C. Fig. 2 shows *I–V* curves of the polymer solar cells containing TiO_x films, and cell performance is summarized in Table 1. When the TiO_x layer was dried at 150 °C, and TiO_x cells containing PCBM:P3HT were annealed at 150 °C, both AA-TiO_x and DEA-TiO_x cells exhibited PCE values of ~2.2%. These two cells are denoted as AA-150/CB-150/glass and DEA-150/CB-150/glass, respectively. Throughout this manuscript, the first label represents the complexing agent and TiO_x film heating temperature. The second label represents the solvent and PCBM:P3HT film heating temperature. The third label represents the substrate, as glass or PET. For a controlled experiment, a TiO_x cell was fabricated using a TiO_x layer prepared from a precursor solution containing no complexing agent (denoted as Non-150/CB-150/glass). TiO_x layers prepared from precursor solutions containing complexing agents acted as electron collection layers, and were superior to that prepared from a precursor solution without complexing agent. When TiO_x layers were dried at 100 °C, PCE values of the AA-TiO_x and DEA-TiO_x cells decreased to 0.66% and 1.10%, respectively. TiO_x cells containing PCBM:P3HT blend film prepared from the CB solution, were heated at 80 °C for 5 min (denoted as AA-100/CB-80/glass and DEA-100/CB-80/glass). Their PCE values were small compared with those of the cells prepared by treatment at 150 °C, and the performance of DEA-100/CB-80/glass was better than that of AA-100/CB-80/glass. DEA could more easily be removed from the TiO_x film by heat treatment at 100 °C than AA, as the DEA boiling point was lower than the drying-temperature. This may have resulted in a small electrical resistance of the DEA-TiO_x film, and a higher PCE was obtained for DEA-100/CB-80/glass prepared at lower temperatures.

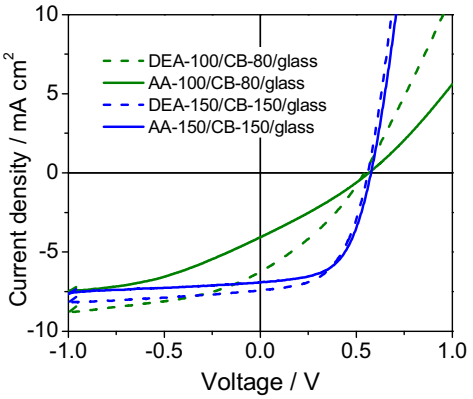

Fig. 2. *I–V* curves of polymer solar cells containing TiO_x on glass substrates, prepared from AA-TiO_x and DEA-TiO_x precursor solutions.

3.2. PCBM:P3HT films prepared by heating at 100 °C

When the DEA-TiO_x layer was dried at 150 °C, DEA-150/CB-80/glass exhibited a low PCE of ~1.1% (Table 1). This was probably because P3HT in the blend film had not crystallized at 80 °C, and suggested that PCBM:P3HT did not act as a sufficient photoactive layer. Solvent annealing is one of the major methods used so far to improve the performance of P3HT:PCBM bulk-heterojunction solar cells [25–27]. The blend film was slowly prepared by using high boiling point solvents such as o-DCB (180.5 °C), and the crystallization of P3HT was achieved without thermal annealing. Thus, DCB was used instead of CB to obtain a more effective photoactive layer. Fig. 3 shows *I–V* curves of cells containing CB and DCB, and their performance is summarized in Table 2. For DEA-100/DCB-80/glass, a PCE of ~2.4% was obtained, because P3HT crystallization had proceeded considerably. This was confirmed from absorption spectra of the PCBM:P3HT film, where crystalline P3HT showed an enhanced shoulder at around 600 nm (Fig. S2).

3.3. Fabrication of flexible TiO_x cells

DEA-TiO_x cells containing PCBM:P3HT prepared using DCB, were fabricated on ITO-glass and PET-ITO substrates at a relatively low temperature of 100 °C. DEA-100/DCB-100/glass showed the short-circuit photocurrent (J_{sc}) of

Table 1
Performance of TiO_x cells on ITO-glass containing Non-TiO_x, AA-TiO_x and DEA-TiO_x layers. The PCBM:P3HT film was prepared from the CB solution.

Name	$T_{(TiOx)}$[a]/°C	$T_{(PCBM:P3HT)}$[b]/°C	J_{sc}/mA cm^{-2}	V_{oc}/V	FF	PCE/%
Non-150/CB-150/glass	150	150	7.25	0.57	0.46	1.93
AA-150/CB-150/glass	150	150	6.92	0.58	0.57	2.26
DEA-150/CB-150/glass	150	150	7.40	0.56	0.54	2.22
AA-100/CB-80/glass	100	80	4.08	0.57	0.28	0.66
DEA-100/CB-80/glass	100	80	5.70	0.57	0.34	1.11
DEA-150/CB-80/glass	150	80	6.26	0.54	0.32	1.10

[a] Drying-temperature of TiO_x.
[b] Heating-temperature of PCBM:P3HT.

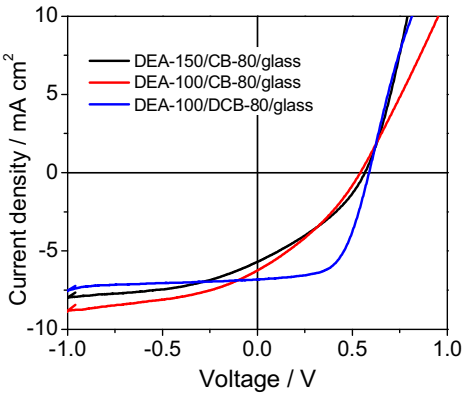

Fig. 3. *I–V* curves of polymer solar cells on glass substrates containing DEA-TiO_x layers dried at 100 and 150 °C.

6.91 mA cm^{-2}, an open-circuit voltage (V_{oc}) of 0.59 V, a fill factor (FF) of 0.60, and a resulting PCE of 2.45% (Table 3). DEA-100/DCB-100/PET exhibited J_{sc} = 6.54 mA cm^{-2}, V_{oc} = 0.58 V, FF = 0.60, and a PCE of 2.27%. The PCE was ~10% lower than that for DEA-100/DCB-100/glass. This originated from a lower transmittance at wavelengths below 600 nm, especially in the UV region (see transmission spectra of glass-ITO and PET-ITO, Fig. S3). None the less, a fabrication method for TiO_x-containing inverted polymer solar cells on thin PET films was successful.

To improve the performance of the flexible cell, we tested Tetralin as a high boiling point solvent, [28] and Tetralin containing a small amount of ODT (denoted as Tetralin:ODT). Tetralin was chosen in attempt to more efficiently generate and separate photo-charge. Fig. S2 shows absorption spectra of PCBM:P3HT films prepared using these solvents. When the blend film was prepared using Tetralin and heated at 100 °C, an enhanced shoulder was observed at ~600 nm, indicating a greater degree of P3HT crystallinity. The addition of ODT into the PCBM:P3HT solution enhanced the PCE because of improvements in nanoscale phase separation [29,30]. Thus, a 2% ODT vol. ratio was added to DCB and Tetralin (denoted as DCB:ODT and Tetralin:ODT, respectively). The performance of DEA-100 solar cells prepared using DCB, Tetralin, DCB:ODT and Tetralin:ODT is summarized in Table 3. For DEA-100/DCB:ODT-100/glass, the PCE was 2.4%. This was the same as for DEA-100/DCB-100/glass, regardless of addition of ODT. DEA-100/Tetralin-100/glass showed a relatively small PCE of 1.48%, although greater crystallinity was observed for P3HT in the blend film (Fig. S2). For PCBM:P3HT prepared using Tetralin:ODT, the absorbance at ~600 nm was lower than that of the blend film prepared without ODT (Fig. S2). The performance of DEA-100/Tetralin:ODT-100/glass exhibited J_{sc} = 7.09 mA cm^{-2}, V_{oc} = 0.59 V, FF = 0.66, and a PCE of 2.76%. The PCE was much larger than that for DEA-100/Tetralin-100/glass. Fig. 4 shows surface AFM images of PCBM:P3HT films prepared using Tetralin containing varying ODT vol.%. Lee et al. reported AFM images of exposed *p*-conjugated polymer PCPDTBT networks after selective removal of C_{71}-PCBM from PCPDTBT:C71-PCBM blend film using alkanedithiol [30]. They distinguished interconnected regions consisting of polymer and porous domains consisting of PCBM by such a method. On the analogy from such an investigation, we

Table 2
Performance of TiO_x cells on ITO-glass containing a DEA-TiO_x layer dried at 100 °C, and a PCBM:P3HT film prepared from CB or DCB solution.

Name	Solvent	$T_{(PCBM:P3HT)}$[a]/°C	J_{sc}/mA cm^{-2}	V_{oc}/V	FF	PCE /%
DEA-100/CB-80/glass	CB	80	6.26	0.54	0.32	1.10
DEA-100/CB-100/glass	CB	100	6.87	0.54	0.36	1.33
DEA-100/DCB-RT/glass	DCB	Room temp.	5.18	0.59	0.56	1.72
DEA-100/DCB-80/glass	DCB	80	6.83	0.59	0.59	2.38
DEA-100/DCB-100/glass	DCB	100	6.91	0.59	0.60	2.45

[a] Heating-temperature of PCBM:P3HT.

Table 3
Performance of TiO_x cells on ITO-glass and PET-ITO, containing DEA-TiO_x layers dried at 100 °C and PCBM:P3HT layers prepared from various solvents and heating at 100 °C.

Sample		J_{sc}/mA cm^{-2}	V_{oc}/V	FF	PCE/%
Substrate	Solvent (volume ratio)				
DEA-100/DCB-100/glass		6.91	0.59	0.60	2.45
Glass-ITO	DCB				
DEA-100/DCB:ODT-100/glass		6.32	0.59	0.64	2.38
Glass-ITO	DCB:ODT (98:2)				
DEA-100/Tetralin-100/glass		4.60	0.59	0.54	1.48
Glass-ITO	Tetralin				
DEA-100/Tetralin:ODT-100/glass		7.09	0.59	0.66	2.76
Glass-ITO	Tetralin:ODT (98:2)				
DEA-100/DCB-100/PET		6.54	0.58	0.60	2.27
PET-ITO	DCB				
DEA-100/Tetralin:ODT-100/PET		6.89	0.57	0.61	2.43
PET-ITO	Tetralin:ODT (98:2)				

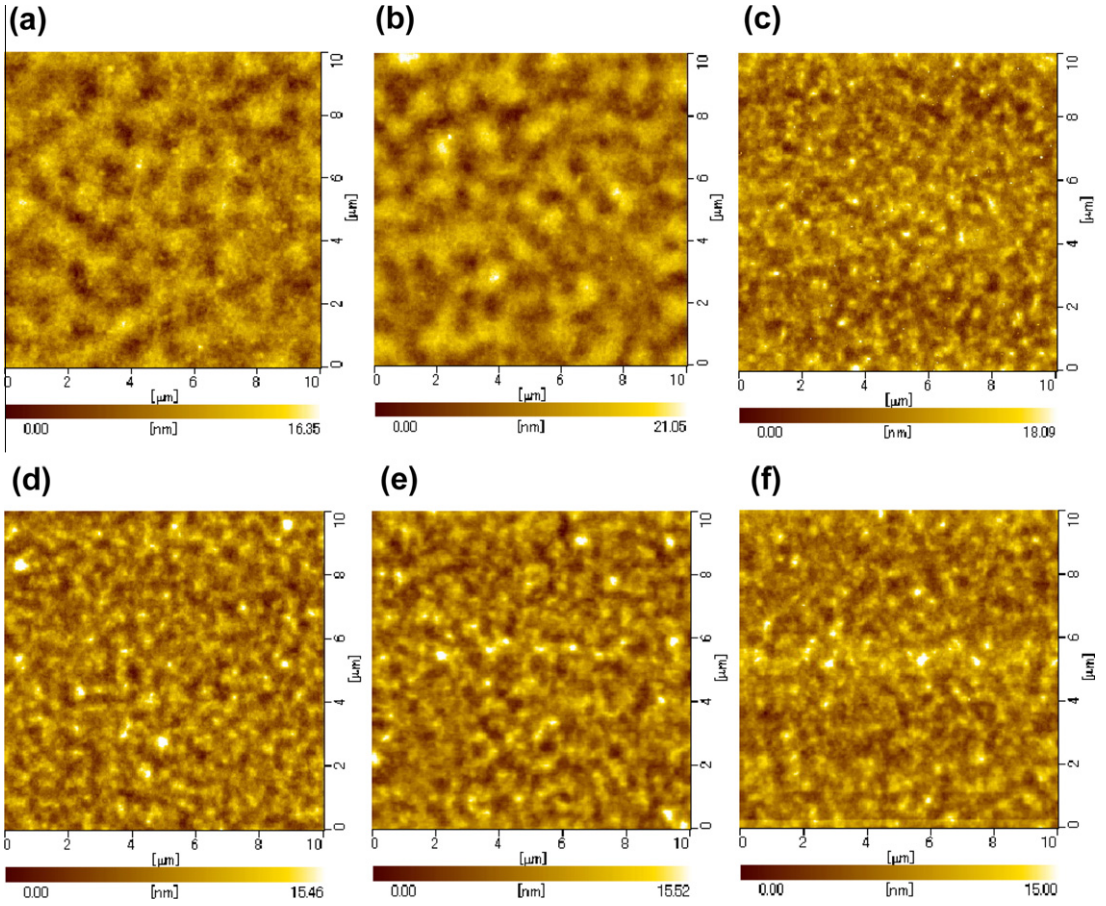

Fig. 4. Surface AFM images of PCBM:P3HT blend films prepared using Tetralin containing varying ODT vol.%. (a) 0, (b) 1, (c) 2, (d) 2.5, (e) 3 and (f) 6 vol.%.

presumed that interconnected regions of lower height were P3HT-rich domains and dotted regions of higher height were PCBM-rich domains from the surface AFM images of PCBM:P3HT films in Fig. 4. For PCBM:P3HT prepared by adding ODT of 2 vol.% or greater, the phase particle size of P3HT-rich and PCBM-rich domains greatly diminished, compared with those in films prepared using Tetralin containing 0 or 1 vol.% ODT. Fig. S4 shows plots of PCE and J_{sc} against vol.% of ODT for DEA-100/Tetralin:ODT-100/glass. When the blend film was prepared using Tetralin containing 2 vol.% ODT, a better performance with J_{sc} = 7.09 mA cm^{-2} and a PCE of 2.76% was observed. When the blend film was prepared using Tetralin containing ODT of 6 vol.%, J_{sc} and PCE values decreased. This was despite AFM images showing little particle size change (compare Fig. 4(c) and (f)). This may have been caused by residual ODT in the PCBM:P3HT film. These results suggest that controlling the morphology of the blend film, in addition to enhancing P3HT crystallinity, is important for overall cell performance. Fig. 5 shows *I–V* curves of DEA-100/Tetralin:ODT-100/glass and DEA-100/Tetralin:ODT-100/PET, where PCBM:P3HT films were prepared using Tetralin containing 2 vol.% ODT, and heated at 100 °C. The flexible DEA-100/Tetralin:ODT-100/PET exhibited better performance, with J_{sc} = 6.89 mA cm^{-2}, V_{oc} = 0.57 V, FF = 0.61,

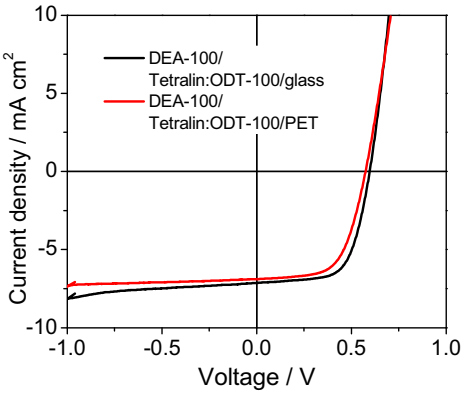

Fig. 5. *I–V* curves of DEA-TiO$_x$ cells prepared on glass and PET substrates, by treatment at 100 °C. PCBM:P3HT films were prepared using Tetralin containing 2 vol.% ODT.

and a PCE of = 2.43%. Its PCE was smaller than that of DEA-100/Tetralin:ODT-100/glass at 2.76%.

It is known that blending bis-PCBM as an acceptor into P3HT as a donor enhances the V_{oc} of polymer solar cells compared to blending PCBM as the acceptor, because bis-PCBM has ca. 100 meV higher LUMO than PCBM [11,31]. Hence, we tried to use the bis-PCBM as the acceptor. A

Tetralin:ODT solution containing 21.8 mg mL^{-1} P3HT and 17.4 mg mL^{-1} bis-PCBM (weight ratio = 5:4) was spin-coated as the organic active layer. The film thickness was ca. 250 nm. As we would expect, the flexible DEA-100/Tetralin:ODT-100/PET containing bis-PCBM acceptor showed higher performance of J_{sc} = 6.22 mA cm^{-2}, V_{oc} = 0.72 V, FF = 0.62, and a PCE of 2.81%.

4. Conclusions

When DEA was used as the complexing agent in the TiO_x precursor solution, the resulting DEA-TiO_x film functioned sufficiently well as an electron collection layer, even when drying at 100 °C was carried out. When using a solvent of high boiling point such as Tetralin containing 2 vol.% ODT, the morphology of the resulting PCBM:P3HT blend film gave higher cell performance. Combining these two techniques, we have fabricated a PET-ITO/TiO_x/PCBM:P3HT/PEDOT:PSS/Au cell without warping of the thin PET film. The resulting PCE was 2.43%, for the unsealed device with a 1 cm^2 working area in air. A PCE value of 2.81% was obtained for the PET-ITO/TiO_x/bis-PCBM:P3HT/PEDOT:PSS/Au cell, when bis-PCBM was instead used as the electron acceptor. We employed a spin-coating method for preparing the TiO_x electron collection and PCBM:P3HT photoactive layers. However, this device could have easily been fabricated by other coating methods such as doctor blading and roller printing.

Acknowledgments

This work was supported by a Grant-in-Aid for Young Scientists (A) from the Ministry of Education, Culture, Sports, Science and Technology (21686011), and the Environment Research and Technology Development Fund (B-0807) of the Ministry of the Environment, Japan.

Appendix A. Supplementary data

Supplementary data associated with this article can be found, in the online version, at doi:10.1016/j.orgel.2010.10.010.

References

[1] B. Kippelen, J.-L. Bredas, Energy Environ. Sci. 2 (2009) 251–261.
[2] J. Peet, A.J. Heeger, G.C. Bazan, Acc. Chem. Res. 42 (2009) 1700–1708.
[3] M. Helgesen, R. Sondergaard, F.C. Krebs, J. Mater. Chem. 20 (2010) 36–60.
[4] H.-Y. Chen, J. Hou, S. Zhang, Y. Liang, G. Yang, Y. Yang, L. Yu, Y. Wu, G. Li, Nat. Photon. 3 (2009) 649–653.
[5] S.H. Park, A. Roy, S. Beaupre, S. Cho, N. Coates, J.S. Moon, D. Moses, M. Leclerc, K. Lee, A.J. Heeger, Nat. Photon. 3 (2009) 297–302.
[6] C.-H. Hsieh, Y.-J. Cheng, P.-J. Li, C.-H. Chen, M. Dubosc, R.-M. Liang, C.-S. Hsu, J. Am. Chem. Soc. 132 (2010) 4887–4893.
[7] Y. Liang, Z. Xu, J. Xia, S.T. Tsai, Y. Wu, G. Li, C. Ray, L. Yu, Adv. Mater. 22 (2010) E135–E138.
[8] G. Zhao, Y. He, Y. Li, Adv. Mater. 22 (2010) 4355–4358.
[9] Y. He, G. Zhao, B. Peng, Y. Li, Adv. Funct. Mat. 20 (2010) 3383–3389.
[10] K. Murata, S. Ito, K. Takahashi, B.M. Hoffman, Appl. Phys. Lett. 71 (1997) 674–676.
[11] T. Kuwabara, H. Sugiyama, M. Kuzuba, T. Yamaguchi, K. Takahashi, Org. Electron. 11 (2010) 1136–1140.
[12] T. Kuwabara, T. Nakayama, K. Uozumi, T. Yamaguchi, K. Takahashi, Sol. Energy Mater. Sol. Cells 92 (2008) 1476–1482.
[13] T. Kuwabara, H. Sugiyama, T. Yamaguchi, K. Takahashi, Thin Solid Films 517 (2009) 3766–3769.
[14] L.M. Chen, Z. Hong, G. Li, Y. Yang, Adv. Mater. 21 (2009) 1434–1449.
[15] F.C. Krebs, S.A. Gevorgyan, B. Gholamkhass, S. Holdcroft, C. Schlenker, M.E. Thompson, B.C. Thompson, D. Olson, D.S. Ginley, S.E. Shaheen, H.N. Alshareef, J.W. Murphy, W.J. Youngblood, N.C. Heston, J.R. Reynolds, S. Jia, D. Laird, S.M. Tuladhar, J.G.A. Dane, P. Atienzar, J. Nelson, J.M. Kroon, M.M. Wienk, R.A.J. Janssen, K. Tvingstedt, F. Zhang, M. Andersson, O. Inganäs, M. Lira-Cantu, R. de Bettignies, S. Guillerez, T. Aernouts, D. Cheyns, L. Lutsen, B. Zimmermann, U. Würfel, M. Niggemann, H.-F. Schleiermacher, P. Liska, M. Grätzel, P. Lianos, E.A. Katz, W. Lohwasser, B. Jannon, Sol. Energy Mater. Sol. Cells 93 (2009) 1968–1977.
[16] M. Al-Ibrahim, H.K. Roth, M. Schroedner, A. Konkin, U. Zhokhavets, G. Gobsch, P. Scharff, S. Sensfuss, Org. Electron. 6 (2005) 65–77.
[17] M. Al-Ibrahim, H.K. Roth, U. Zhokhavets, G. Gobsch, S. Sensfuss, Sol. Energy Mater. Sol. Cells 85 (2005) 13–20.
[18] L. Blankenburg, K. Schultheis, H. Schache, S. Sensfuss, M. Schrödner, Sol. Energy Mater. Sol. Cells 93 (2009) 476–483.
[19] F. C. Krebs, J. Fyenbo, M. Jorgensen, J. Mater. Chem. (2010) <http://dx.doi.org/10.1039/c1030jm01178a>.
[20] R. Steim, P. Schilinsky, S.A. Choulis, C.J. Brabec, Sol. Energy Mater. Sol. Cells 93 (2009) 1963–1967.
[21] F.C. Krebs, T.D. Nielsen, J. Fyenbo, M. Wadstrom, M.S. Pedersen, Energy Environ. Sci. 3 (2010) 512–525.
[22] F.C. Krebs, S.A. Gevorgyan, J. Alstrup, J. Mater. Chem. 19 (2009) 5442–5451.
[23] F.C. Krebs, Org. Electron. 10 (2009) 761–768.
[24] W. Gaynor, J.-Y. Lee, P. Peumans, ACS Nano 4 (2009) 30–34.
[25] G. Li, V. Shrotriya, J. Huang, Y. Yao, T. Moriarty, K. Emery, Y. Yang, Nat. Mater. 4 (2005) 864–868.
[26] G. Li, Y. Yao, H. Yang, V. Shrotriya, G. Yang, Y. Yang, Adv. Funct. Mat. 17 (2007) 1636–1644.
[27] H.-Y. Chen, H. Yang, G. Yang, S. Sista, R. Zadoyan, G. Li, Y. Yang, J. Phys, Chem. C 113 (2009) 7946–7953.
[28] B. Zimmermann, U. Würfel, M. Niggemann, Sol. Energy Mater. Sol. Cells 93 (2009) 491–496.
[29] J. Peet, J.Y. Kim, N.E. Coates, W.L. Ma, D. Moses, A.J. Heeger, G.C. Bazan, Nat. Mater. 6 (2007) 497–500.
[30] J.K. Lee, W.L. Ma, C.J. Brabec, J. Yuen, J.S. Moon, J.Y. Kim, K. Lee, G.C. Bazan, A.J. Heeger, J. Am. Chem. Soc. 130 (2008) 3619–3623.
[31] M. Lenes, G.-J.A.H. Wetzelaer, F.B. Kooistra, S.C. Veenstra, J.C. Hummelen, P.W.M. Blom, Adv. Mater. 20 (2008) 2116–2119.

Organic Electronics 12 (2011) 119–124

Contents lists available at ScienceDirect

Organic Electronics

journal homepage: www.elsevier.com/locate/orgel

Pentacene thin film transistors with (polytetrafluoroethylene) PTFE-like encapsulation layer

M. Rapisarda *, D. Simeone, G. Fortunato, A. Valletta, L. Mariucci

CNR-IMM, Via del Fosso del Cavaliere 100, Roma 00133, Italy

ARTICLE INFO

Article history:
Received 16 July 2010
Received in revised form 22 October 2010
Accepted 28 October 2010
Available online 12 November 2010

Keywords:
Pentacene TFT
PTFE
Encapsulation layer
OTFT reliability

ABSTRACT

(Polytetrafluoroethylene) PTFE-like films, deposited by using CHF_3/Ar gas mixtures in a plasma reactor, have been used as encapsulation layers in pentacene thin film transistors. The PTFE-like encapsulation layers allow to carry out photolithographic processes without damaging pentacene film. However, the PTFE-like encapsulation layers are not effective in reducing hysteresis of electrical characteristics when measured in air. On the contrary, the degradation of the device electrical characteristics, induced by oxygen diffusion into pentacene film after storing the devices in air, is almost completely suppressed by the encapsulation with the PTFE-like films.

© 2010 Elsevier B.V. All rights reserved.

1. Introduction

Organic thin film transistors (OTFTs) based on pentacene show, at present, the best OTFT performance [1–3]. Pentacene OTFTs are promising candidates for the large area, printable and flexible electronic applications like sensor arrays, radio frequency identification tags (RFID) and paper-like displays. In this context patterning and stability of organic semiconductors are key factors for OTFTs applications.

Unfortunately, the interaction with the common solvents, during the fabrication processes, can lead to a degradation of the exposed pentacene layer [4]. In addition, it has been shown that organic devices are very sensitive to exposure to air. Pentacene OTFTs exhibit a hysteresis of the transfer characteristics when measured in air and this phenomenon has been related to the diffusion of water molecules into the device active layer [5,6]. Furthermore, permanent variation of transfer characteristics has been observed when the devices are exposed to air for a long time [7,8], with the degradation of the main electrical parameters (field effect mobility, threshold voltage and subthreshold swing). So, it is mandatory to find out a suitable barrier layer that reduces gas diffusion into the OTFT active layer, preventing pentacene damage during lithographic processes and acting as encapsulating layer for further integration. Several encapsulation layers have been proposed based on solution processed materials, as PVA with single [9] or multilayer structures [10,11], or vapour deposited materials, as parylene [12–14], polyimide [15] and evaporated PTFE [16]. While all these materials show good properties as barriers for lithographic processes, they are not equally effective as a barrier for water and oxygen diffusion. In addition, the deposition of the encapsulation layer often induces a degradation of the electrical characteristics of the pentacene OTFTs. In this work, we have investigated the performance, as encapsulation layers, of polytetrafluoroethylene-like (PTFE-like) films deposited by using different CHF_3/Ar gas mixtures in a plasma reactor.

2. Experimental

Bottom contact devices have been fabricated on heavily doped silicon wafers (acting as gate electrode), with thermal silicon dioxide, 90 nm thick, as gate dielectric. Source

* Corresponding author.
E-mail address: matteo.rapisarda@artov.imm.cnr.it (M. Rapisarda).

1566-1199/$ - see front matter © 2010 Elsevier B.V. All rights reserved.
doi:10.1016/j.orgel.2010.10.018

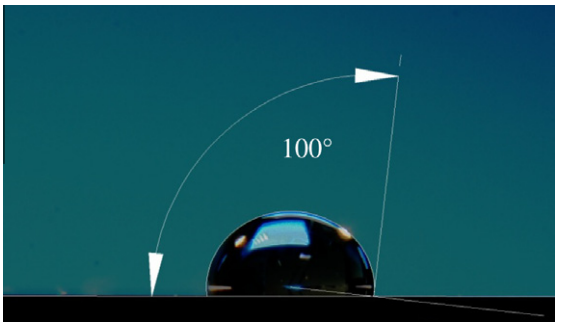

Fig. 1. Measurement of PTFE contact angle for water.

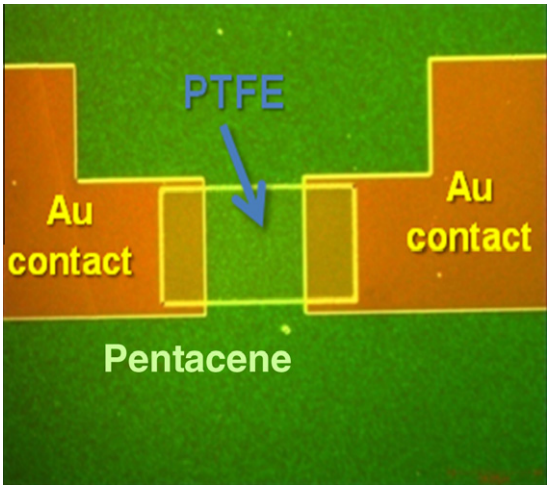

Fig. 2. FTIR measurements of the PTFE layers deposited with different Ar dilutions.

and drain gold contacts, 20 nm thick, are defined using optical lithography and wet-etching ($W = 200$ μm, $L =$ 20–100 μm). A thin film of polycrystalline pentacene, 30 nm thick, has been thermally evaporated, at growth rate of 0.01 nm/s, on a PMMA buffer layer used to improve the structural properties of pentacene [17]. Indeed, the atomic force microscopy showed that the pentacene layers have a highly ordered polycrystalline structure with large grain size (>1 μm). PTFE-like films, about 200 nm thick, have been deposited by using different CHF_3/Ar gas mixtures (20%, 50%, 60% and 70% of Ar) in a plasma reactor. All the deposited PTFE-like films result hydrophobic with a contact angle of about 100° for water (Fig. 1). After the PTFE deposition the device active regions have been defined by conventional photolithography and oxygen plasma etching, without damaging the pentacene active layer (Fig. 2).

The device electrical characteristics were measured in a MMR cryostat using a Keythley 236 source/measure unit and a Keythley 2635 source/meter. In order to measure the hysteresis of the transfer characteristics, the measurements have been performed sweeping the gate voltage, sequentially, from off-to-on and from on-to-off (between 20 V and −30 V).

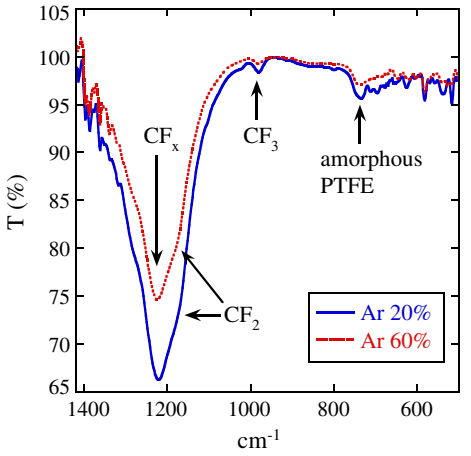

Fig. 3. Optical image of a pentacene-OTFT with PTFE-like encapsulation layer.

3. Results and discussion

3.1. FTIR measurements

The Ar influence on the deposited PTFE-like films has been studied by FTIR analysis. Independently on the CHF_3/Ar ratio, the FTIR spectra (see Fig. 3) of PFTE-like films show a broad peak, located at 1220 cm^{-1} induced by CF_x [18]. The asymmetry of this absorption peak indicates the existence of strong CF_2 symmetric and asymmetric stretch vibration modes. In particular, it is evident a shoulder located approximately at 1180 cm^{-1}, induced by CF_2 symmetric stretching mode [18], that highlights the "Teflon-like" character of the film. Minor peaks can be observed at 980 cm^{-1}, induced by CF_3 stretch, and at 739 cm^{-1}, which is identified as amorphous PTFE [19]. No absorptions induced by C–C and C–O bonds have been observed in the range 1800–1700 cm^{-1}.

3.2. OTFTs electrical characteristics and numerical simulations

Fig. 4 shows the transfer characteristics of the device measured before and after the PTFE deposition with

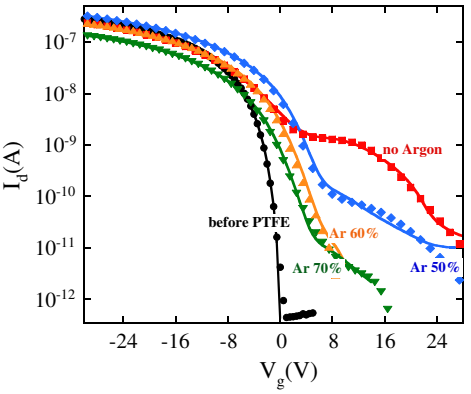

Fig. 4. Experimental (symbols) and simulated (solid lines) transfer characteristics of a pentacene OTFT before and after the PTFE encapsulation. The PTFE-like layers were deposited with different Ar dilutions, as indicated.

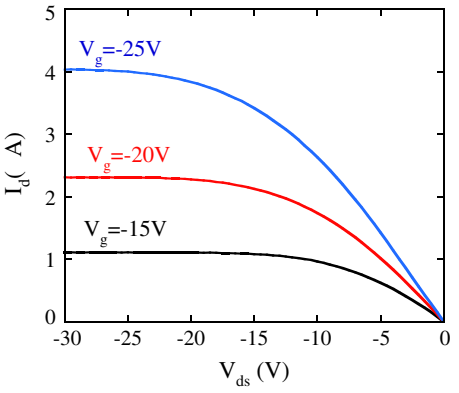

Fig. 5. Output characteristics of a pentacene OTFT before the PTFE encapsulation.

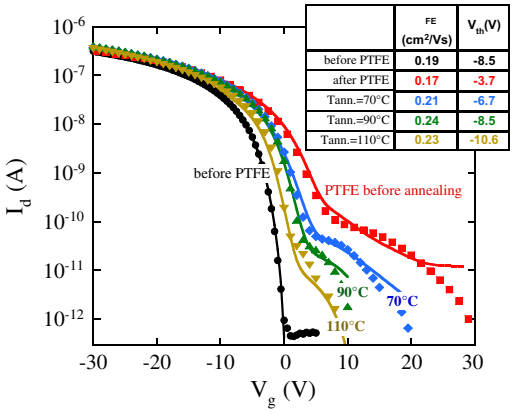

Fig. 6. Experimental (symbols) and simulated (solid lines) transfer characteristics of a pentacene OTFT without and with the PTFE encapsulation layer (deposited with 50% of Ar) after annealing at different temperatures. The field effect mobility and the threshold voltage of each characteristic are shown in the table.

different CHF_3/Ar ratio. Before the PTFE deposition the pentacene OTFTs show a field-effect mobility of about 0.2–0.3 cm^2/V s and no hysteresis of the transfer characteristics is observed, when measured in vacuum. Furthermore, the output characteristics (Fig. 5) show a good linear behaviour at low V_d, suggesting a low contact resistance of the pentacene/PMMA/Au contacts. After the PTFE deposition, the transfer characteristics show a hump in the subthreshold region that decreases with increasing Ar partial pressure in the gas mixture (Fig. 4). The hump disappears for Ar concentration equal or higher than 60%, whereas a degradation of subthreshold slope can be still observed. The encapsulated devices have been thermally annealed (1 h in vacuum) at increasing temperatures, from 70 °C up to 130 °C. The device transfer characteristics improve up to 110°–130 °C (see Fig. 6) and the electrical characteristics in sample annealed at 110 °C, with encapsulation layer deposited at 60% (or higher) Ar dilution, almost completely recover the electrical characteristics before the encapsulation.

In order to gain a physical insight on the effect of the PTFE-like encapsulation layer on the electrical characteristics of pentacene OTFTs, the experimental data have been fitted by using one-dimensional numerical simulations. It has been shown [20,21] that it is possible to perfectly reproduce the pentacene-based OTFT characteristics assuming drift-diffusion transport model and a spatially uniform distribution of localized states, that includes the contributions of the in-grain and grain boundary defects as well as of the dielectric/pentacene interface defects. The density of interface states can be approximated by the sum of two exponential terms (one for the acceptor-like states and one for the donor-like states): $N(E) = N_a e^{-(E_c-E)/E_a} + N_d e^{(E-E_v)/E_d}$, where E is the energy, E_c is the energy of the bottom of the conduction band, E_v is the energy of the top of the valence band, E_a and E_d are the characteristics energies for the acceptor-like and donor-like states distributions, respectively, and N_a and N_d are the acceptor-like and donor-like densities for $E = E_c$ and $E = E_v$, respectively. In the following analysis we are considering a symmetric distribution of interface states, with $N_a = N_d$ and $E_a = E_d$. The transfer characteristics have been computed by evaluating the channel conductance using a one-dimensional approach, by solving numerically the Poisson equation in the direction perpendicular to the channel surface. In order to speed up the computation, the charge trapped in the localized states is evaluated assuming an approximation for the Fermi function: for E ranging in an interval of 3 kT around the Fermi level, a third order polynomial approximation is used, while, for E lying outside this interval, an exponential approximation is employed [22]. Once discretized, the non-linear Poisson's equation is iteratively solved using the Newton's method (or relaxation method) and the resulting carrier distribution, along the depth of the channel, is computed. The density of states (DOS) parameters have been determined by using a least squares approach: the optimization method used is the Levenberg–Marquardt method [23].

The experimental characteristics have been perfectly reproduced by the numerical simulations (see Figs. 4 and 6) considering fixed negative charge and interface traps at the pentacene/PTFE-like interface. Both types of defects can be generated during the early stage of the deposition of PTFE-like films and could be ascribed to the poor quality of the interface between PTFE-like film and pentacene as well as to the plasma damage. The negative fixed charge appearing at the PTFE-like film/pentacene interface produces the formation of a back-channel (see Fig. 7a). Since the pentacene active layer is very thin, the back channel can be modulated by the gate for high positive gate voltages, originating a normally-on back-channel transistor. Due to the different threshold voltage of front and back transistors, the contribution of the back channel to the total current is dominant when the front channel is in either off or subthreshold regime (as schematized in Fig. 7b), producing the hump observed in the experimental characteristics. The fixed charge and interface states densities are related to the deposition conditions and thermal annealing process and by the numerical simulations we have been able to evaluate these quantities as a function of the Ar concentration (Fig. 8) and annealing temperatures (Fig. 9). In the analysis we have considered as parameter the integral of the interface states, $N(E)$, over the lower half of the

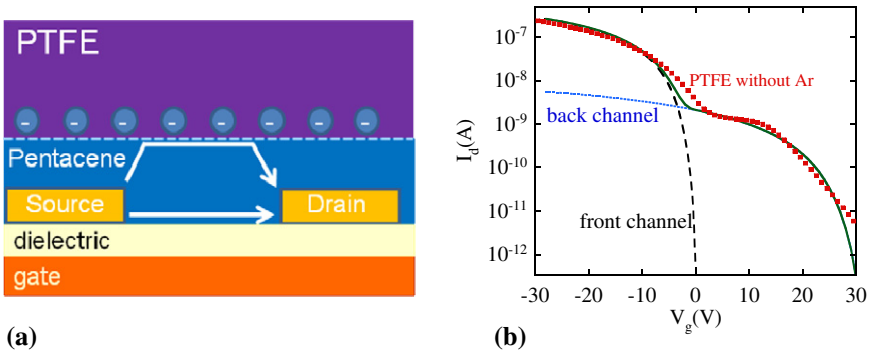

Fig. 7. (a) Schematic of current paths in presence of back-channel conduction. (b) Simulated front (dashed line) and back (dotted line) channel contribution to the device transfer characteristics (solid line) compared to the experimental data (symbols) after PTFE deposition with no argon dilution.

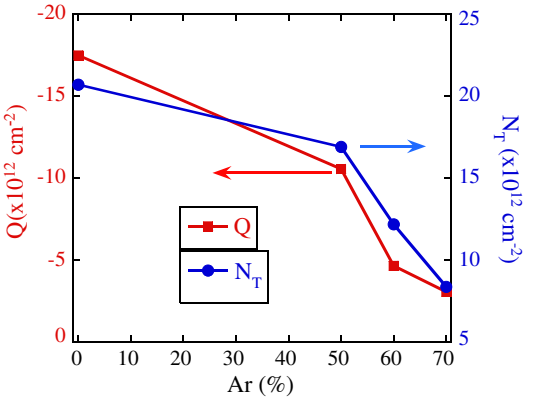

Fig. 8. Negative fixed charge density, Q, and integrated interface state density, N_T, deduced from the analysis of device characteristics after PTFE encapsulation, vs. Ar-dilution used during PTFE-like film deposition.

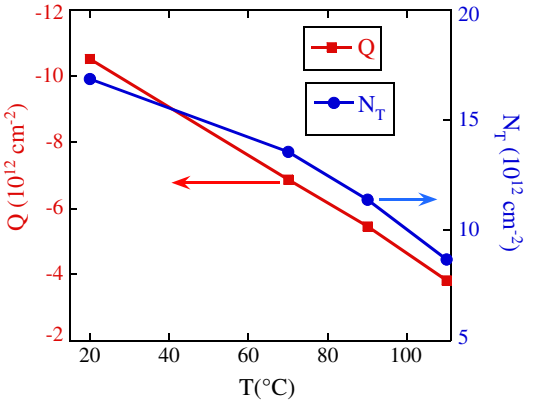

Fig. 9. Negative fixed charge density, Q, and integrated interface state density, N_T, deduced from the analysis of the device characteristics after PTFE encapsulation, vs. annealing temperatures. The PTFE-like film was deposited with 50% Ar-dilution.

bandgap, N_T. As can be seen in Fig. 8, the improvement of the characteristics with increasing Ar partial pressure in the gas mixture is related to a decreasing of both fixed charge, Q, and interface state density, N_T. The fixed charge reduction decreases the threshold voltage of the back transistor, reducing its contribution to the total current in the subthreshold region of front transistor. Furthermore, the reduction of the interface states allows a more efficient modulation of the gate on the back transistor with a sharper reduction of the back-channel current for increasing gate voltage, resulting in an improvement of the transistor subthreshold slope. Similarly, the annealing process decreases both the fixed charge and the interface states (Fig. 9), allowing to restore almost completely the electrical characteristics measured prior to the encapsulation.

3.3. Reliability evaluation

We have investigated the stability of the pentacene OTFTs with the PTFE-like encapsulation layer measuring the devices in air and after several days of storing in air. The above analysis showed that the devices with encapsulation layer deposited at higher Ar dilutions have, after annealing, electrical characteristics comparable with those of the OTFTs before the encapsulation. Therefore, in order to compare the performance of the non-encapsulated and encapsulated devices, reliability tests were carried out on devices with the encapsulation layer deposited at 60% Ar dilution. Fig. 10 compares the transfer characteristics, measured in air, of a non-encapsulated pentacene OTFT and a OTFT with PTFE-like encapsulation layer, before and after the thermal annealing at 110 °C. The measurements have been performed sweeping the gate voltage, sequentially, from off-to-on and on-to-off between 20 V and −30 V, in order to point out the hysteresis of the transfer characteristics. As can be seen, the hysteresis observed in the non-encapsulated device is still present in the encapsulated OTFT, whereas it is slightly reduced after the annealing process. The reduction of the hysteresis after annealing is probably a consequence of the improved structural properties of pentacene that reduces water diffusion in the active layer. This result shows that the PTFE-like layer is not an efficient barrier against water diffusion.

In order to evaluate the aging effects, a PTFE-encapsulated and a non-encapsulated OTFTs have been stored in air for several days, and they have been repeatedly measured,

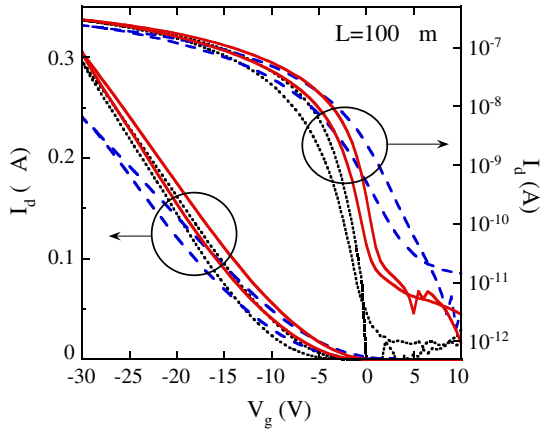

Fig. 10. Transfer characteristics of pentacene OTFTs measured in air without (dotted line) and with encapsulation layer, before (dashed line) and after annealing at 110 °C (solid line). The PTFE-like film was deposited with 60% Ar-dilution.

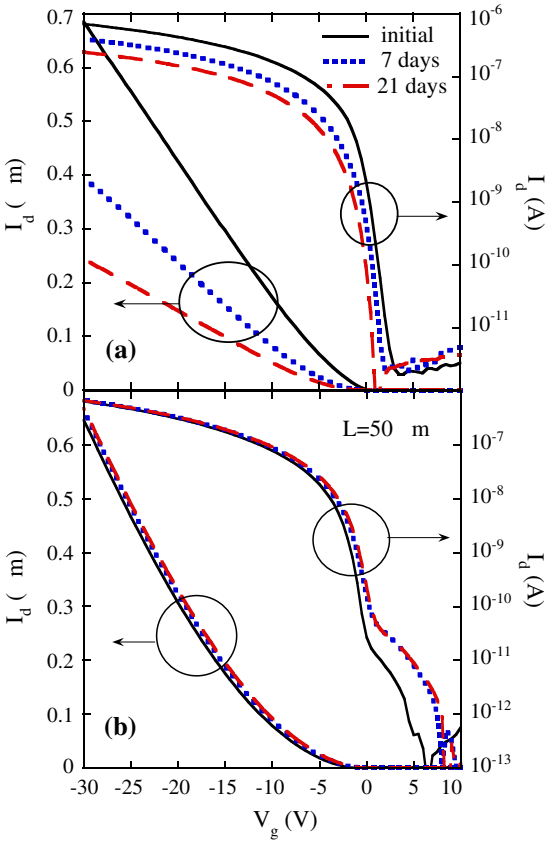

Fig. 11. Transfer characteristics of non-encapsulated (a) and PTFE-encapsulated (b) pentacene OTFTs measured before (solid line) and after storing the device in air for 7 (dotted line) and 21 (dashed line) days. The PTFE-like film was deposited with 60% Ar-dilution.

in vacuum, as a function of the aging time. As can be seen in Fig. 11, after a few days by the starting of aging, the non-encapsulated device (Fig. 11a) shows a large decrease of field effect mobility ($\Delta\mu/\mu_0 = 0.35$) and a small variation of the V_{onset}, $\Delta V_{onset} = -0.9$ V (V_{onset}, can be defined as the gate voltage for which current starts to increase). At the same time, the PTFE-encapsulated device shows an increase of the hump in the subthreshold regime (Fig. 11b), while the field effect mobility remains unchanged. After 3 weeks the degradation of electrical characteristics of the non-encapsulated OTFT continued, with $\Delta\mu/\mu_0 = 0.63$ and a $\Delta V_{onset} = -0.8$ V. On the contrary, no further variation of the electrical characteristics is observed in the PTFE-encapsulated device. In particular, from the linear regime of the transfer characteristics, it is evident that the field effect mobility remains unchanged, relative to the curve before aging, and only a small rigid shift of the curve is observed. From these results we can conclude that the encapsulation with the PTFE-like layer efficiently prevents the diffusion of oxygen into the active layer, which induces degradation of the electrical characteristics in non-passivated pentacene OTFTs.

4. Conclusions

PTFE-like films, deposited by using different CHF_3/Ar gas mixtures in a plasma reactor, have been used for the first time as encapsulating layer for pentacene-OTFTs. They show good structural properties, as demonstrated by FTIR spectra, and allow pentacene channel photolithographic definition and annealing of the passivated OTFTs. After the PTFE-like film deposition, the pentacene OTFT transfer characteristics show, depending on the presence of Argon during the deposition, degraded transfer characteristics in the subthreshold regime, whereas smaller changes are observed in the linear regime. We showed, by numerical simulations, that the subthreshold degradation is related to the formation of a back-channel, at the PTFE-pentacene interface, induced by fixed negative charge and interface traps. These defects, related to the poor quality of the interface between PTFE-like film and pentacene as well as to plasma damage, can be removed by thermal process. Indeed, after the annealing at 110 °C, prior to encapsulation characteristics have restored almost completely.

The reliability of the encapsulated devices has been tested by measuring the electrical characteristics in air and after storing the devices in air for several days. The results show that the PTFE-like encapsulation layer is not effective in reducing the water diffusion, indeed the electrical characteristics show hysteresis when measured in air, with a small reduction of the effect obtained through the annealing process. On the contrary, the degradation of device characteristics after air exposure, due to oxygen interaction with pentacene film, is almost completely suppressed (apart from a minor increase of drain current in subthreshold regime), suggesting that the PTFE-like films act as effective barriers for oxygen.

Acknowledgments

This work has been supported by the Plast_IC project funded by Italian Ministry of Research.

References

[1] S.H. Lee, D.J. Choo, S.H. Han, J.H. Kim, Y.R. Son, J. Jang, Appl. Phys. Lett. 90 (2007) 033502.
[2] C. Rolin, S. Steudel, K. Myny, D. Cheyns, S. Verlaak, J. Genoe, P. Heremans, Appl. Phys. Lett. 89 (2006) 203502.
[3] T. Toccoli, A. Pallaoro, N. Coppedè, S. Iannotta, F. De Angelis, L. Mariucci, G. Fortunato, Appl. Phys. Lett. 88 (2006) 132106.
[4] D.J. Gundlach, T.N. Jackson, D.G. Schlom, S.F. Nelson, Appl. Phys. Lett. 74 (1999) 3302.
[5] L. Mariucci, S. Cipolloni, D. Simeone, M. Cuscunà, L. Maiolo, A. Minotti, A. Pecora, A. Valletta, G. Fortunato, J. Korean Phys. Soc. 54 (2009) 505.
[6] G. Gu, M.G. Kane, Appl. Phys. Lett. 92 (2008) 053305.
[7] F. De Angelis, S. Cipolloni, L. Mariucci, G. Fortunato, Appl. Phys. Lett. 88 (2006) 193508.
[8] W.L. Kalb, K. Mattenberger, B. Batlogg, Phys. Rev. B78 (2008) 035334.
[9] H. Klauk, G. Schmid, W. Radlik, W. Weber, L. Zhou, C. Sheraw, J.A. Nichols, T.N. Jackson, Solid-State Electron. 47 (2003) 297.
[10] M. Kawasaki, S. Imazeki, M. Ando, Y. Sekiguchi, S. Hirota, S. Uemura, T. Kamata, IEEE Trans. Electron. Dev. 53 (2006) 435.
[11] S.H. Han, J.H. Kim, J. Jang, S.M. Cho, M.H. Oh, S.H. Lee, D.J. Choo, Appl. Phys. Lett. 88 (2006) 073519.
[12] I. Kymissis, C.D. Dimitrakopoulos, S. Purushothaman, J. Vac. Sci. Technol. B 20 (2002) 956.
[13] T. Sekitani, S. Iba, Y. Kato, Y. Noguchi, T. Sakurai, T. Someya, J. Non-Cryst. Solids 352 (2006) 1769.
[14] D. Simeone, S. Cipolloni, L. Mariucci, M. Rapisarda, A. Minotti, A. Pecora, M. Cuscunà, L. Maiolo, G. Fortunato, Thin Solid Films 517 (2009) 6379.
[15] G.W. Hyung, J. Park, J.H. Kim, J.R. Koo, Y.K. Kim, Solid State Electron. 54 (2010) 439.
[16] M. Scharnberg, V. Zaporojtchenko, R. Adelung, F. Faupel, C. Pannemann, T. Diekmann, U. Hilleringmann, Appl. Phys. Lett. 90 (2007) 013501.
[17] F. De Angelis, S. Cipolloni, L. Mariucci, G. Fortunato, Appl. Phys. Lett. 88 (2005) 151902.
[18] F. Favia, G. Cicala, A. Milella, F. Palumbo, P. Rossini, R. d'Agostino, Surf. Coat. Technol. 169–170 (2003) 609.
[19] R. d'Agostino, F. Cramarossa, F. Fracassis, F. Illuzzi, in: R. d'Agostino (Ed.), Plasma Deposition and etching of Polymers, Academic, San Diego, 1990, pp. 95–162.
[20] A.R. Volkel, R.A. Street, D. Knipp, Phys. Rev. B 66 (2002) 195336.
[21] F. De Angelis, L. Mariucci, S. Cipolloni, G. Fortunato, J. Non-Cryst. Solids 352 (2006) 1765.
[22] Y.-T. Tsai, K.-D. Hong, Y.-L. Yuan, IEEE Trans. Comput.-Aided Des. Integr. Circ. Syst. 13 (1994) 725.
[23] S.A.W.H. Teukolsky, W.T. Vetterling, B.P. Flannery, Numerical Recipes in C, second ed., Cambridge University Press, 1988.

Organic Electronics 12 (2011) 125–135

Contents lists available at ScienceDirect

Organic Electronics

journal homepage: www.elsevier.com/locate/orgel

Efficient triphenylamine-based dyes featuring dual-role carbazole, fluorene and spirobifluorene moieties

Ping Shen [a,b,*], Yuhua Tang [a], Shenghui Jiang [a], Huajie Chen [a], Xiaoyan Zheng [a], Xueye Wang [a], Bin Zhao [a,b], Songting Tan [a,b,*]

[a] College of Chemistry and Key Laboratory of Environmentally Friendly Chemistry and Applications of Ministry of Education, Xiangtan University, Xiangtan 411105, PR China

[b] Key Laboratory of Advanced Functional Polymeric Materials, College of Hunan Province, Xiangtan University, Xiangtan 411105, PR China

ARTICLE INFO

Article history:
Received 1 July 2010
Received in revised form 19 October 2010
Accepted 25 October 2010
Available online 10 November 2010

Keywords:
Dye-sensitized solar cells
Dual-role moieties
Triphenylamine
Photovoltaic performance

ABSTRACT

Three triphenylamine-based organic dyes **SD6**, **SD7**, and **SD8** containing the bulky dual-role moieties (fluorene, carbazole, and spirobifluorene) in the molecular frameworks were synthesized, characterized and applied in dye-sensitized solar cells (DSSCs). The effects of dual-role moieties of organic dyes on their photophysical, electrochemical, and photovoltaic properties have been investigated in detail. These dyes exhibit strong charge transfer absorption bands in the visible region. Their redox potential levels were estimated by cyclic voltammetry and found to suit well to the charge flow in DSSCs. Inserting the dual-role moieties as the secondary donor between the triphenylamine and thiophene units increased the electron density of the donor groups, therefore reduced the HOMO–LUMO band gaps. The combination of ultraviolet–visible (UV–vis) region broad absorption bands with fairly high extinction coefficients and appropriate redox properties observed in these triphenylamine-based dyes make them promising dyes for DSSCs. For a typical solar cell device based on dye **SD6**, the maximal monochromatic incident photon-to-current conversion efficiency (IPCE) can reach to ~73%, with a short-circuit photocurrent density (J_{sc}) of 14.25 mA/cm^2, an open-circuit photovoltage (V_{oc}) of 0.70 V, and a fill factor (FF) of 0.705, which corresponds to a power conversion efficiency (PCE) of 7.03%.

© 2010 Elsevier B.V. All rights reserved.

1. Introduction

The growing worldwide demand for environment friendly energy sources has led to a great focus on solar energy conversion devices. Dye-sensitized solar cells (DSSCs) have attracted significant attention [1,2] since their report by Regan and Grätzel et al. in 1991 [3]. The relatively high performance and low production costs render DSSCs as competitive alternatives to conventional silicon-based photovoltaic devices [4]. Photosensitizers play a crucial role for highly efficient DSSCs. Ruthenium-based sensitizers (e.g., N719 dye [5]) have achieved power conversion efficiencies (PCEs) over 11% in standard air mass 1.5 sunlight. In the meantime, there are also increasing interests in metal-free organic dyes [6] due to their many advantageous features, such as high molar extinction coefficients, easily modified molecular structure and relatively low cost materials. Power conversion efficiencies up to ~9% have been achieved for DSSCs based on metal-free dyes [7–9]. Moreover, highly impressive PCEs (~10%) and excellent stability were also reported in very recent publications of Wang et al. [10,11].

A common strategy in the design of highly efficient metal-free dyes for DSSCs is the linking of electron donor/acceptor (D–A) systems through π-conjugated bridges (called as D–π–A molecular structure), with TiO_2 surface

* Corresponding author at: College of Chemistry and Key Laboratory of Environmentally Friendly Chemistry and Applications of Ministry of Education, Xiangtan University, Xiangtan 411105, PR China.

E-mail addresses: shenping802002@163.com (P. Shen), tanst2008@163.com (S. Tan).

1566-1199/$ - see front matter © 2010 Elsevier B.V. All rights reserved.
doi:10.1016/j.orgel.2010.10.016

anchoring groups (e.g., carboxylate) integrated onto the acceptor moiety. Among the metal-free organic dyes, it has been demonstrated that triphenylamine (TPA) [12,13], thiophene based aromatics [14–17] and cyanoacetic acid [18,19] are the effective electron donating moiety, π-conjugated bridge and electron acceptor (anchoring group), respectively. At the same time, metal-free organic dyes with D–D–π–A structure were also reported by several groups [20–23]. Their results indicated that organic dyes with D–D–π–A structure can achieved better photovoltaic performances than those of dyes with the simple D–π–A molecular configuration due to the increased electron-density of donor and enhanced molar extinction coefficient by introducing a secondary electron donor into the dye molecules [24–26]. On the other hand, some studies [24,27,28] suggested that the extended π-conjugated bridge benefits the improvement of the photovoltaic performances of DSSCs due to the broadened absorption range. Moreover, our group developed some series of triarylamine-based metal-free dyes for DSSCs [29–32]. The results indicated that the hexyl-substituted thiophene moiety was found to be capable of efficient π-conjugated bridge to enhance the performances due to effectively inhibiting dye aggregation and suppressing the charge recombination.

Organic dyes possessing carbazole [28,33–36] and fluorene [13,16,37–39] moieties have achieved good photovoltaic performances in the application of DSSCs. Nevertheless, there are few reports on DSSCs with spirobifluorene [40,41] unit in the framework of dyes. Expanding on the foregoing points and as part of our efforts to investigate the structural modifications of triphenylamine-based dyes, we herein reported three new D–D–π–A structural metal-free dyes (**SD6**, **SD7**, and **SD8**, see Fig. 1) featuring the dual-role carbazole, fluorene and spirobifluorene moieties, apart from the blocks of a triphenylamine electron-donor (D) and a cyanoacrylic acid electron-acceptor (A). Here, carbazole, fluorene and spirobifluorene moieties inserted between D and 3-hexylthiophene not only acted as the secondary donor but also as the extended π-conjugated bridge together with 3-hexylthiophene. On the one hand, TPA unit incorporated with the electron-rich carbazole, fluorene and spirobifluorene moieties would enhance electron-donating ability of donors which facilitates intramolecular charge transfer (ICT) between the donor and the acceptor and leads to a red shift of the absorption; on the other hand, the bulky structural dual-role moieties combined with thiophene spacer could be beneficial to obtaining high molar extinction coefficients of the absorption as well as suppressing dye aggregation due to incorporation of the hydrophobic alkyl chain. In this study, we mainly investigated the photophysical, electrochemical, and photovoltaic properties of the three as-synthesized dyes with dual-role moieties. DSSCs with excellent performance characteristics were successfully fabricated using these organic dyes. In particular, **SD6** exhibited the highest PCE of 7.03% under AM 1.5 irradiation with 100 mW/cm^2 simulated sunlight, indicating its potential application as metal-free organic dyes in DSSCs.

2. Experimental details

2.1. Materials and reagents

All starting materials were purchased from commercial suppliers (Pacific ChemSource and Alfa Aesar) in analytical grade. THF and toluene were dried and distilled over sodium and benzophenone. DMF, $CHCl_3$, and CH_3CN were dried over by accustomed methods and distilled before using. All other solvents and chemicals used in this work were analytical grade and used without further purification. All chromatographic separations were carried out on silica gel (200–300 mesh).

2.2. Analytical instruments

^{1}H NMR and ^{13}C NMR spectra were recorded on a Bruker Avance 400 instrument. UV–vis spectra of the dyes were measured on a Perkin–Elmer Lamada 25 spectrometer. The PL spectra were obtained using Perkin–Elmer LS-50 luminescence spectrometer. FT-IR spectra were obtained on Perkin–Elmer Spectra One spectrophotometer. The elemental analysis of all compounds was performed

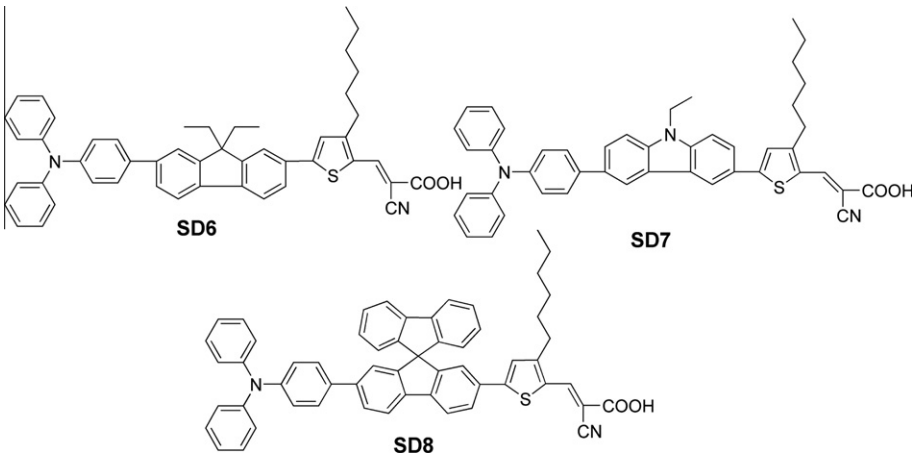

Fig. 1. Molecular structures of the dyes **SD6**–**SD8**.

with an Elementar Vario EL III element analyzer for C, H, N and S determination. Mass spectra were recorded on a Bruker AutoFlex III MALDI-TOF (Germany). Electrochemical redox potentials were obtained by cyclic voltammetry (CV) using a three-electrode cell and an electrochemistry workstation (CHI830B, Chenhua Shanghai). The working electrode was a Pt ring electrode; the auxiliary electrode was a Pt wire, and saturated calomel electrode (SCE) was used as reference electrode. Tetrabutylammonium perchlorate (TBAP) 0.1 M was used as supporting electrolyte in dry acetonitrile. Ferrocene was added to each sample solution at the end of the experiments, and the ferrocenium/ferrocene (Fc^+/Fc) redox couple was used as an internal potential reference. The potentials of dyes vs. NHE were calibrated by addition of 0.63 V to the potentials vs. Fc^+/Fc [14]. The solutions were purged with argon and stirred for 15 min before the measurements.

2.3. General procedure for fabrication and characterization of DSSCs

Fluorine-doped SnO_2 conducting glass (FTO) were cleaned and immersed in aqueous 40 mM $TiCl_4$ solution at 70 °C for 30 min, then washed with water and ethanol, sintered at 450 °C for 30 min. The TiO_2 colloid was prepared from 12 g P25 (Degussa AG, Germany) following a literature procedure [5]. First the 20–30 nm particles sized TiO_2 colloid was coated onto the above FTO glass by sliding glass rod method to obtain a TiO_2 film of 10–15 μm thickness after drying. Subsequently, the 200 nm particles sized TiO_2 colloid was coated on the electrode by same method, resulting in a TiO_2 light-scattering layer of 4–6 μm thickness. The double-layer TiO_2-coated FTO glass were sintered at 450 °C for 30 min, then treated with $TiCl_4$ solution and calcined at 450 °C for 30 min again. After cooling to 100 °C, the TiO_2 electrodes were soaked in a solution with 0.5 mM dyes and kept at room temperature under dark for 24 h.

The dye-adsorbed TiO_2 electrode washed with ethanol and dried. A drop of electrolyte solution was deposited onto the surface of the electrode and a Pt foil counter electrode was clipped onto the top of the TiO_2 electrode to assemble a dye-sensitized solar cells for photovoltaic performance measurements. The electrolyte consisted of 0.5 M LiI, 0.05 M I_2, and 0.5 M 4-*tert*-butylpyridine (TBP) in 3-methoxypropionitrile and the efficient irradiated area of cell was 0.196 cm^2. The photocurrent–voltage (*J–V*) characteristics of solar cells were measured using a Keithley 2602 Source meter under the 100 Mw/cm^2 irradiation of a 500 W Xe lamp with a global AM 1.5 filter for solar spectrum simulation. Meanwhile, the photoelectric conversion efficiency was calculated. The measurement of monochromatic incident photon-to-current conversion efficiencies (IPCE) was performed by a Zolix DCS300PA Data acquisition system and other optical system.

2.4. The detailed experimental procedures and characterization data

2-(4-(*N*,*N*-Diphenylaminephenyl)-4,4,5,5-tetramethyl-1,3,2-dioxaborolane (**1**), [42] 3-hexylthiophene-2-carbaldehyde (**2**) [43], 2-(3-hexylthiophen-2-yl)-1,3-dioxolane (**3**) [31], (5-(1,3-dioxolan-2-yl)-4-hexylthiophen-2-yl)tributylstannane (**4**) [31] 2,7-dibromo-9,9-diethylfluorene (**5**) [44], and 3,6-dibromocarbazole (**6**) [45] were synthesized according to the methods reported in the literatures with some modification. The synthetic routes to the three dyes were shown in Scheme 1. The detailed synthetic procedures were as follows.

2.4.1. 3,6-Dibromo-9-ethylcarbazole (**7**)

Under nitrogen atmosphere, a mixture of **6** (3.25 g, 10 mmol), bromoethane (1.31 g, 12 mmol), KOH (1.68 g, 30 mmol) and DMSO (30 mL) was stirred at 50 °C for 24 h. After cooling, the reaction mixture was quenched by the addition of water and extracted with dichloromethane. The combined organic layer was washed with dilute HCl and brine several times, dried over anhydrous $MgSO_4$, filtered and evaporated under vacuum. The crude product was purified by recrystallization from anhydrous ethyl alcohol to obtain **7** as a light yellow solid. Yield: 82% (2.88 g). ^1H NMR (400 MHz, $CDCl_3$): δ (ppm) 8.15 (s, 1H), 7.56 (d, 2H, J = 8.5 Hz), 7.27 (d, 2H, J = 8.7 Hz), 4.45 (q, 2H, J = 7.1 Hz), 1.53 (t, 3H, J = 7.2 Hz). ^{13}C NMR (100 MHz, $CDCl_3$): δ (ppm) 131.5, 121.4, 121.2, 120.1, 117.2, 113.3, 38.3, 13.8. Elem. Anal. Calcd. for $C_{14}H_{11}Br_2N$: C, 47.63; H, 3.14; N, 3.97. Found: C, 47.30; H, 3.17; N, 4.02.

2.4.2. 2-Bromo-7-(4-(diphenylaminephenyl)-9,9-diethylfluorene (**8**)

Under nitrogen atmosphere, a mixture of compound **5** (0.95 g, 2.5 mmol), **1** (0.74 g, 2 mmol), aqueous K_2CO_3 (2 M, 5 mL) and toluene (20 mL) was added in a 50 mL three-necked flask. When the mixture was heated up to 60 °C, $Pd(PPh_3)_4$ (115 mg, 0.1 mmol) was added into the mixture solution quickly, and then the mixture was stirred at 90 °C for 48 h. After cooling to room temperature, the mixture was extracted with dichloromethane. The combined organic layer was washed with dilute HCl and brine several times, dried over anhydrous $MgSO_4$, filtered and evaporated under vacuum. The crude product was purified by silica gel column chromatograph eluted with petroleum ether to obtain **8** as a white solid. Yield: 67% (0.73 g). ^1H NMR (400 MHz, $CDCl_3$): δ (ppm) 7.71–7.69 (m, 2H), 7.55–7.51 (m, 8H), 7.46–7.29 (m, 2H), 7.15–7.13 (m, 6H), 7.05–7.02 (m, 2H), 2.04 (q, 4H, J = 7.0 Hz), 0.36 (t, 6H, J = 7.1 Hz). ^{13}C NMR (100 MHz, $CDCl_3$): δ (ppm) 151.2, 148.4, 147.2, 144.2, 140.6, 139.6, 135.9, 133.4, 130.8, 130.6, 130.4, 129.7, 129.5, 128.9, 128.8, 125.8, 123.2, 123.1, 122.7, 122.5, 50.1, 35.8, 8.8. Elem. Anal. Calcd. for $C_{35}H_{30}BrN$: C, 77.20; H, 5.55; N, 2.57. Found: C, 77.02; H, 5.64; N, 2.60.

2.4.3. 3-Bromo-6-(4-(diphenylaminephenyl)-9-ethylcarbazole (**9**)

Compound **9** was synthesized according the same procedure as that of **8**, except that compound **7** (0.88 g, 2.5 mmol) was used instead of **5**. Yield: 72% (0.75 g). ^1H NMR (400 MHz, $CDCl_3$): δ (ppm) 8.25–8.24 (m, 2H), 7.74–7.72 (d, 1H, J = 8.4 Hz), 7.60–7.56 (m, 3H), 7.46 (d, 1H, J = 8.5 Hz), 7.32–7.7.26 (m, 4H), 7.21–7.16 (m, 7H), 7.06–7.03 (m, 2H), 4.38 (q, 2H, J = 7.1 Hz), 1.46 (t, 3H, J = 7.2 Hz). ^{13}C NMR (100 MHz, $CDCl_3$): δ (ppm) 147.6,

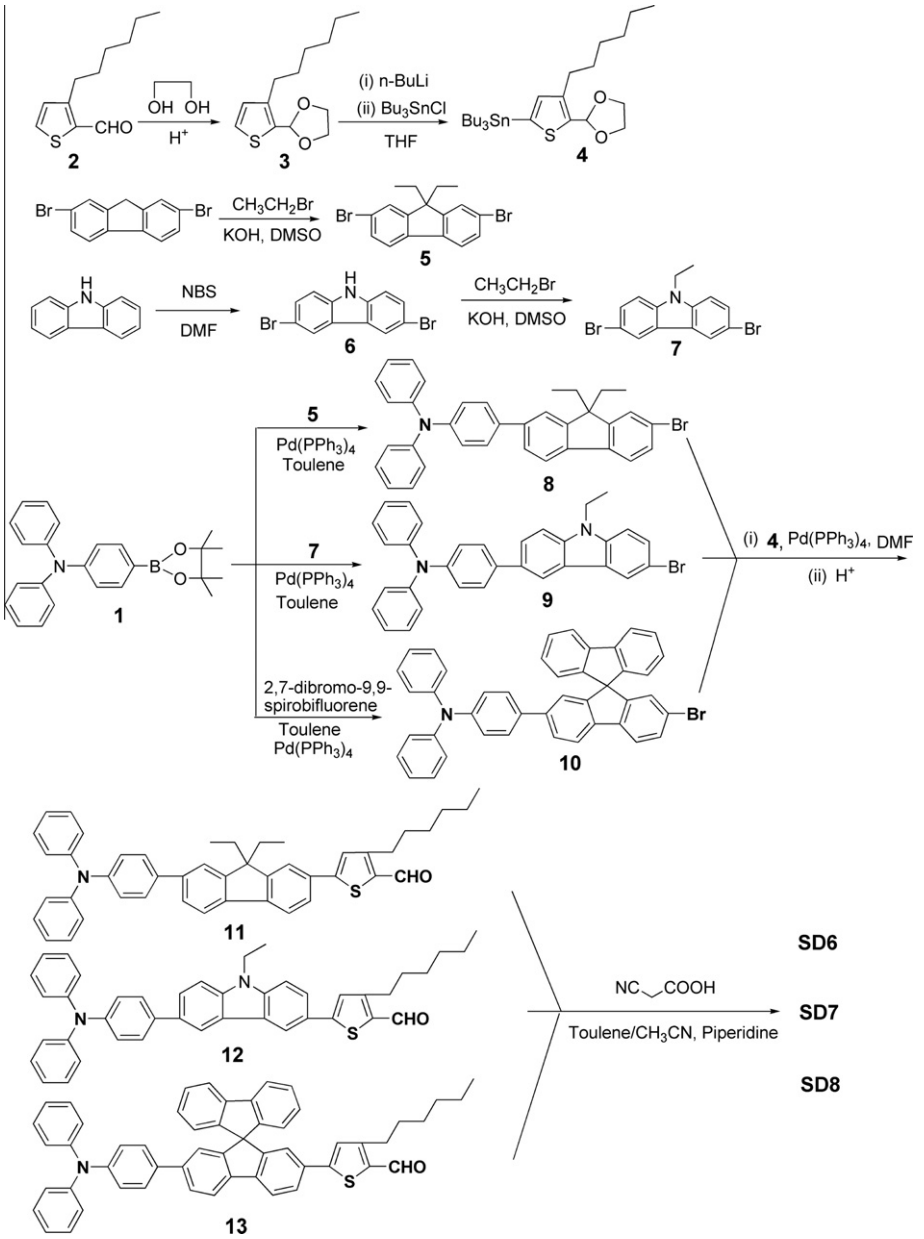

Scheme 1. Synthetic routes to the three new dyes.

146.4, 144.3, 143.7, 135.7, 134.2, 129.5, 128.8, 125.6, 123.9, 123.2, 122.7, 121.2, 121.1, 119.6, 117.5, 117.1, 113.4, 111.2, 106.3, 37.3, 13.7. Elem. Anal. Calcd. for $C_{32}H_{25}BrN_2$: C, 74.28; H, 4.87; N, 5.41. Found: C, 74.12; H, 4.89; N, 5.46.

*2.4.4. 2-Bromo-7-(4-(diphenylaminephenyl)-9,9-spirobifluorene (**10**)*

Compound **10** was *synthesized* according the same procedure as that of **8**, except that 2,7-dibromo-9,9-spirobifluorene (1.19 g, 2.5 mmol) was used instead of **5**. The crude product was purified by silica gel column chromatograph eluted with petroleum ether/dichloromethane (10/1, v/v) to obtain **10** as a white solid. Yield: 69% (0.88 g). ^{1}H NMR (400 MHz, $CDCl_3$): δ (ppm) 7.86 (d, 2H, J = 7.7 Hz), 7.79–7.77 (m, 1H), 7.60–7.58 (m, 1H), 7.51–7.35 (m, 3H), 7.25–7.21 (m, 8H), 7.16–7.14 (m, 3H), 7.07–7.00 (m, 6H), 6.89 (s, 1H), 6.85 (s, 1H), 6.79–6.77 (d, 2H, J = 7.4 Hz). ^{13}C NMR (100 MHz, $CDCl_3$): δ (ppm) 150.1, 148.5, 147.9, 147.7, 147.3, 144.3, 141.2, 140.3, 139.4, 135.8, 133.2, 130.8, 130.5, 130.2, 129.7, 129.6, 128.9, 128.8, 128.7, 128.3, 128.1, 126.9, 125.9, 123.4, 122.7, 122.6, 46.8. Elem. Anal. Calcd. for $C_{43}H_{28}BrN$: C, 80.87; H, 4.42; N, 2.17. Found: C, 80.65; H, 4.48; N, 2.21.

*2.4.5. 5-(2-(4-(Diphenylaminephenyl)-9,9-diethylfluorene-7-yl)-3-hexylthiophene-2-carbaldehyde (**11**)*

Under nitrogen atmosphere, a mixture of compound **8** (0.71 g, 1.3 mmol), **4** (0.86 g, 1.6 mmol), and DMF (30 mL)

was added in a 50 mL three-necked flask. When the mixture was heated up to 60 °C, $Pd(PPh_3)_4$ (115 mg, 0.1 mmol) was added into the mixture solution quickly, and then the mixture was stirred at 100 °C for 48 h. After cooling to 70 °C, the mixture was treated with dilute aqueous HCl (10 mL) solution and stirred for 30 min. Then the resulting mixture was changed into a yellow-green color and extracted with dichloromethane at room temperature. The combined organic layer was washed with brine several times, dried over anhydrous $MgSO_4$, filtered and evaporated under vacuum. The crude product was purified by silica gel column chromatograph eluted with petroleum ether/dichloromethane (5/1, v/v) to obtain **11** as a yellow sticky oil. Yield: 43% (0.37 g). FT-IR (KBr, cm^{-1}): 1667 ($\nu_{C=O}$). ^1H NMR (400 MHz, $CDCl_3$): δ (ppm) 10.04 (s, 1H), 7.76–7.71 (m, 2H), 7.70–7.68 (m, 2H), 7.62–7.56 (m, 6H), 7.31–7.28 (m, 3H), 7.19–7.17 (m, 6H), 7.10–7.05(m, 2H), 2.99 (t, 2H, J = 7.8 Hz), 2.12–2.10 (m, 4H), 1.80–1.76 (m, 2H), 1.56–1.36 (m, 6H), 0.88 (t, 3H, J = 6.5 Hz), 0.40 (t, 6H, J = 7.3 Hz). ^{13}C NMR (100 MHz, $CDCl_3$): δ (ppm) 182.6, 156.4, 148.6, 148.3, 147.6, 147.3, 144.2, 141.1, 140.8, 139.9, 135.9, 133.3, 130.9, 130.6, 130.1, 129.8, 128.9, 128.7, 127.3, 125.9, 125.5, 123.2, 122.6, 50.1, 35.8, 32.0, 31.9, 29.1, 24.7, 22.8, 14.2, 8.9. Elem. Anal. Calcd. for $C_{46}H_{45}NOS$: C, 83.72; H, 6.87; N, 2.12; S, 4.86. Found: C, 83.86; H, 6.53; N, 2.01; S, 5.02.

2.4.6. 5-(3-(4-(Diphenylaminephenyl)-9-ethylcarbazole-6-yl)-3-hexylthiophene-2-carbaldehyde (**12**)

Compound **12** was synthesized according the same procedure as that of **11**, except that compound **9** (0.67 g, 1.3 mmol) was used instead of **8**. Yield: 42% (0.34 g). FT-IR (KBr, cm^{-1}): 1665 ($\nu_{C=O}$). ^1H NMR (400 MHz, $CDCl_3$): δ (ppm) 10.02 (s, 1H), 8.43 (s, 1H), 8.33 (s, 1H), 7.85 (d, 1H, J = 8.4 Hz), 7.78 (d, 1H, J = 8.4 Hz), 7.60 (d, 2H, J = 8.5 Hz), 7.47 (d, 1H, J = 8.4 Hz), 7.43 (d, 1H, J = 8.5 Hz), 7.31–7.26 (m, 4H), 7.21–7.16 (m, 7H), 7.05–7.04 (m, 2H), 4.41 (q, 2H, J = 7.2 Hz), 2.99 (t, 2H, J = 8.2 Hz), 1.78–1.72 (m, 2H), 1.48 (t, 3H, J = 7.0 Hz), 1.43–1.26 (m, 6H), 0.86 (t, 3H, J = 6.8 Hz). ^{13}C NMR (100 MHz, $CDCl_3$): δ (ppm) 182.5, 157.0, 148.9, 147.6, 147.5, 144.3, 143.8, 140.8, 136.6, 132.3, 130.9, 129.8, 129.7, 128.7, 127.2, 125.3, 123.2, 122.8, 119.4, 119.2, 116.7, 111.6, 106.3, 48.5, 32.1, 31.9, 29.1, 24.8, 22.8, 15.8, 14.2. Elem. Anal. Calcd. for $C_{43}H_{40}N_2OS$: C, 81.61; H, 6.37; N, 4.43; S, 5.07. Found: C, 81.76; H, 6.53; N, 4.64; S, 5.61.

2.4.7. 5-(2-(4-(Diphenylaminephenyl)-9,9-spirobifluoren-7-yl)-3-hexylthiophene-2-carbaldehyde (**13**)

Compound **13** was synthesized according the same procedure as that of **11**, except that compound **10** (0.71 g, 1.1 mmol) was used instead of **8**. The crude product was purified by silica gel column chromatograph eluted with petroleum ether/dichloromethane (8/1, v/v) to obtain **12** as a yellow solid. Yield: 33% (0.27 g). FT-IR (KBr, cm^{-1}): 1665 ($\nu_{C=O}$). ^1H NMR (400 MHz, $CDCl_3$): δ (ppm) 10.03 (s, 1H), 7.89–7.88 (m, 4H), 7.72 (d, 1H, J = 7.4 Hz), 7.63 (d, 1H, J = 7.4 Hz), 7.48–7.45 (m, 2H), 7.40–7.20 (m, 10H), 7.14–7.12 (m, 2H), 7.06–6.99 (m, 6H), 6.98 (s, 1H), 6.80 (d, 1H, J = 7.6 Hz), 2.95 (t, 2H, J = 7.7 Hz), 1.67–1.63 (m, 2H), 1.54–1.26 (m, 6H), 0.88 (t, 3H, J = 7.8 Hz). Elem. Anal. Calcd. for $C_{55}H_{47}NOS$: C, 85.79; H, 6.15; N, 1.82; S, 4.16. Found: C, 85.66; H, 6.43; N, 1.80; S, 4.61.

2.4.8. 3-(5-(2-(4-(Diphenylaminephenyl)-9,9-diethylfluorene-7-yl)-3-hexylthiophene-2-yl)-2-cyanoacrylic acid (**SD6**)

Under nitrogen atmosphere, a mixture of compound **11** (0.40 g, 0.61 mmol), cyanoacetic acid (0.1 g, 1.22 mmol), piperidine (0.5 mL), toluene (15 mL) and CH_3CN (5 mL) was refluxed at 80 °C for 12 h. After cooling, the solution was extracted with dichloromethane and 0.1 M aqueous solution of HCl. The organic layer was dried over anhydrous $MgSO_4$, filtered and evaporated under vacuum. The crude product was purified by silica gel column chromatograph eluted with chloroform/methanol (15/1, v/v) to obtain **SD6** as a red solid. Yield: 68% (0.30 g). FT-IR (KBr, cm^{-1}): 2216 ($\nu_{\equiv}$), 1682 ($\nu_{C=O}$). ^1H NMR (400 MHz, $CDCl_3$): δ (ppm) 8.50 (s, 1H), 7.79–7.76 (m, 3H), 7.65(s, 1H), 7.62–7.57 (m, 4H), 7.38 (s, 1H), 7.32–7.28 (m, 4H), 7.20–7.06 (m, 6H), 7.08–7.04 (m, 2H), 2.86 (t, 2H, J = 8.1 Hz), 2.15–2.14 (m, 4H), 1.72 (br, 2H), 1.43–1.28 (m, 6H), 0.93 (br, 3H), 0.39 (t, 6H, J = 7.2 Hz). MALDI-TOF: m/z 726.169.

2.4.9. 3-(5-(3-(4-(Diphenylaminephenyl)-9-ethylcarbazole-6-yl)-3-hexylthiophene-2-yl)-2-cyanoacrylic acid (**SD7**)

SD7 was synthesized according the same procedure as that of **SD6**, except that compound **12** (0.2 g, 0.32 mmol) was used instead of **11**. The crude product was purified by silica gel column chromatograph eluted with chloroform/methanol (10/1, v/v) to obtain **SD7** as a red solid. Yield: 59% (0.13 g). FT-IR (KBr, cm^{-1}): 2210 ($\nu_{\equiv}$), 1679 ($\nu_{C=O}$). ^1H NMR (400 MHz, $CDCl_3$): δ (ppm) 8.49 (s, 1H), 8.47 (s, 1H), 8.40 (s, 1H), 7.85 (d, 1H, J = 7.7 Hz), 7.74 (d, 1H, J = 7.9 Hz), 7.64 (d, 2H, J = 8.1 Hz), 7.49–7.45 (m, 3H), 7.38 (s, 1H), 7.17–7.13 (m, 9H), 7.05–7.04 (m, 2H), 4.42 (br, 2H), 2.86 (t, 2H, J = 7.6 Hz), 1.72–1.65 (m, 2H), 1.50 (t, 3H, J = 7.3 Hz), 1.41–1.26 (m, 6H), 0.89 (t, 3H, J = 6.4 Hz). MALDI-TOF: m/z 699.093.

2.4.10. 3-(5-(2-(4-(Diphenylaminephenyl)-9,9-spirobifluoren-7-yl)-3-hexylthiophene-2-yl)-2-cyanoacrylic acid (**SD8**)

SD8 was synthesized according the same procedure as that of **SD6**, except that compound **13** (0.16 g, 0.21 mmol) was used instead of **11**. The crude product was purified by silica gel column chromatograph eluted with chloroform/methanol (20/1, v/v) to obtain **SD8** as a red solid. Yield: 75% (0.13 g). FT-IR (KBr, cm^{-1}): 2214 ($\nu_{\equiv}$), 1689 ($\nu_{C=O}$). ^1H NMR (400 MHz, $CDCl_3$): δ (ppm) 8.40 (s, 1H), 7.92–7.90 (m, 4H), 7.78 (d, 1H, J = 7.4 Hz), 7.65 (d, 1H, J = 7.4 Hz), 7.45–7.40 (m, 2H), 7.28–7.21 (m, 6H), 7.17–7.14 (m, 2H), 7.09–7.00 (m, 9H), 6.88 (s, 1H), 6.81 (d, 2H, J = 7.6 Hz), 2.73 (t, 2H, J = 7.6 Hz), 1.69–1.55 (m, 2H), 1.34–1.27 (m, 6H), 0.87 (t, 3H, J = 7.9 Hz). MALDI-TOF: m/z 820.267.

3. Results and discussion

3.1. Synthesis and characterization

The molecular structures and synthetic routes of the three organic dyes **SD6**, **SD7**, and **SD8** are shown in Fig. 1 and Scheme 1, respectively. All of the dyes have been synthesized by the stepwise synthetic protocol. Firstly, the dual-role fluorene, carbazole and spirobifluorene moieties were introduced through the Suzuki coupling reaction between triphenylamine-based boric ester (**1**) and dibrominated aryl compounds (**5**, **7**, and 2,7-dibromo-9,9-spirobifluorene). Then, the extension of π-conjugated aryl chain in **8**, **9**, and **10** was accomplished by Stille coupling reactions for adding a 3-hexylthiophenyl-2-carbaldehyde moiety (compound **2**), respectively. Finally, the Knoevenagel condensation reactions of aldehyde derivatives **10**–**13** with cyanoacetic acid afforded the target dyes **SD6**–**SD8** in the presence of piperidine. It is necessary to note that tributylstannyl compound **4** was obtained according to our previous report [31] started from compound **2** which was synthesized from 2-bromo-3-hexylthiophene in the presence of Mg and DMF using the method as described by Demandrille et al. [43] The yields of compounds **8**–**10** via Suzuki coupling reactions were quite satisfactory, i.e., in a range of 67–72%. Whereas, for compounds **11**–**13** by Stille coupling reactions exhibited relatively low yields (33–43%). The structures of all dye molecules were characterized unambiguously with FT-IR, ^{1}H NMR spectroscopy as well as MALDI-TOF. All final products can be crystallized into deep color solids.

3.2. Optical properties

The ultraviolet–visible (UV–vis) absorption spectra of the three dyes in diluted $CHCl_3$ solution (10^{-5} M) are displayed in Fig. 2, and the corresponding data are collated in Table 1. All the dyes exhibit two distinct absorption bands: one absorption band is in the UV region (300–370 nm) corresponding to the π–π^* electron transitions of the conjugated molecules; and the other is in the visible region (400–550 nm) that can be assigned to an intramolecular charge transfer (ICT) between the triphenylamine containing double donating unit and the cyanoacrylic acid anchoring moiety [46]. It can be seen that the maximum absorption (λ_{max}) of the visible region red-shifts from 450 nm to 457 and 469 nm for **SD8**, **SD6**, and **SD7**, respectively. This red-shifted phenomenon may be ascribed to the following two aspects. The first reason is the various ability of electron-denoting of spirobifluorene, fluorene and carbazole moieties. Among the three dual-role moieties, the ability of electron-denoting of carbazole moiety is the strongest, which results in an obviously red shift of **SD7** compared to **SD6** and **SD8**. The other reason may be ascribed to the more planar geometry in **SD7** and **SD6**, because the inserting carbazole and fluorene moieties between phenyl rings and thiophenyl group show longer conjugation relative to spirobifluorene moiety for it's non-coplanar geometry.

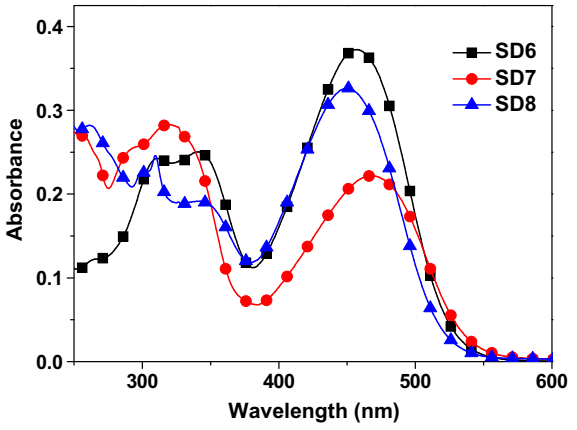

Fig. 2. Absorption spectra of the three dyes in $CHCl_3$ solutions (10^{-5} M) at 25 °C.

As depicted in Table 1, the molar extinction coefficient (ε) of the ICT bands of the three dyes ($2.2–3.7 \times 10^4$ M^{-1} cm^{-1}) are higher than that of SD2 (1.9×10^4 M^{-1} cm^{-1}) [29], indicating a better ability of light harvesting of the D–D–π–A structure than that of the corresponding D–π–A counterpart. Moreover, the ε of the ICT bands increases in the order of **SD8** < **SD7** < **SD6**, which suggests that **SD6** may have the best ability of light harvesting. The higher ε of the organic dyes allows a correspondingly thinner nanocrystalline film so as to avoid the decrease of the film mechanical strength. This also benefits the electrolyte diffusion in the film and reduces the recombination possibility of the light-induced charges during transportation [47,48].

We also measured the emission spectra of dyes **SD6**–**SD8** when they are excited with their λ_{max} of the visible region in $CHCl_3$ solution (10^{-5} M). The corresponding data are also summarized in Table 1. As shown in Fig. 3, the maximum emission (λ_{em}) of **SD7** (556 nm) is very obviously blue-shifted in comparison with **SD6** (667 nm) and **SD8** (666 nm) which indicates that the excited states of **SD7** need more energy for the excited from the ground state. It is unfavorable for light harvesting of the solar spectrum.

The absorption spectra of dyes **SD6**–**SD8** absorbed onto the surface of TiO_2 displayed broader and a slight red shift of 11 nm (**SD7**) and 6 nm (**SD8**) or blue shift of 7 nm (**SD6**) with respect to those in solutions, respectively (Fig. 4). It is presumed that the red and blue shifts of the absorption spectra may be contributed to the formation of aggregates [14,28] on the TiO_2 surface. Such a slight shifts indicates that the aggregates of dyes are not obvious which may be explained that the introduction of the bulk dual-role moieties incorporated with the long alkyl of thiophenyl unit inhibits the aggregates to some extent. Another noteworthy feature in the spectra of dyes adsorbed on TiO_2 surfaces is an apparent tailing toward longer wavelength region (Fig. 4). In solutions the low energy edge of absorption bands does not exceed 600 nm (Fig. 2), yet on TiO_2 the absorption threshold extends to 750 nm. The long wavelength absorption should be result from the formation of a certain degree of aggregates on the surface of TiO_2. The

Table 1
Maximum absorption and emission data of the three dyes.

Dye	λ_{max}[a]/nm (ε/M^{-1} cm^{-1})			λ_{max}[b]/nm	λ_{em}[c]/(nm)
SD6	457(37,000)	342(25,000)	309(24,000)	450	667
SD7	469(22,000)	319(28,000)	–	480	556
SD8	450(33,000)	342(19,000)	309(24,000)	456	666

[a] Maximum absorption in $CHCl_3$ solution (10–5 M).
[b] Maximum absorption on TiO_2 film.
[c] Maximum emission of the dyes in $CHCl_3$ solution (10^{-5} M). ε is the extinction coefficient at λ_{abs} of maximum absorption.

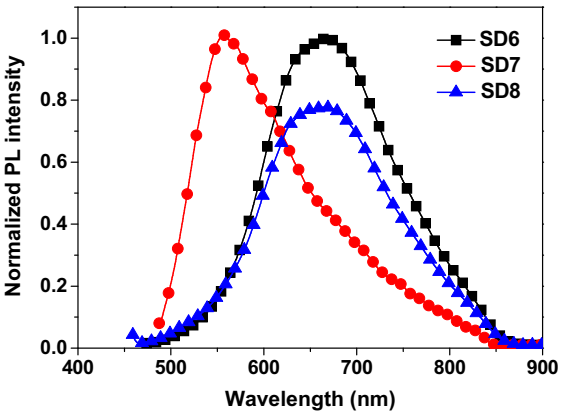

Fig. 3. Emission spectra of the three dyes in $CHCl_3$ solutions (10^{-5} M) at 25 °C.

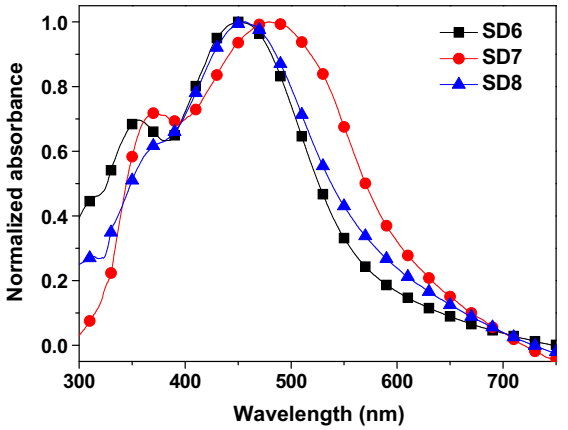

Fig. 4. Absorption spectra of the three dyes adsorbed on TiO_2 surface.

absorption of aggregates is responsible for the induction of photocurrent in the regions of ⩾600 nm (Fig. 6) [49].

3.3. Electrochemical properties

To evaluate the possibility of electron transfer from the excited dye molecule to the conductive band of TiO_2, cyclic voltammetry (CV) was performed in CH_3CN with 0.1 M tetrabutylammonium perchlorate (TBAP) as a supporting electrolyte (Fig. 5). The first oxidation potential vs. NHE (E_{ox}), which corresponds to the highest occupied molecular orbital (HOMO vs. NHE), was calibrated by addition of

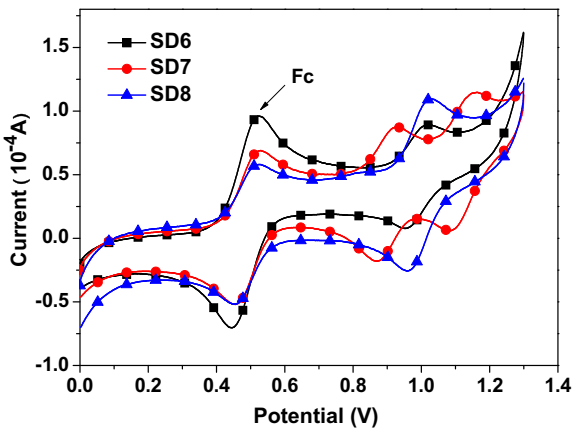

Fig. 5. Cyclic voltammograms of the three dyes: working electrode, Pt ring; auxiliary electrode, Pt wire; reference electrode, Hg/Hg_2Cl_2; scanning rate is 100 mV/s.

Table 2
Electrochemical data of the three dyes.[a]

Dye	λ_{int}/nm	E_{0-0}/eV	E_{ox}/V vs. NHE	E_{red}/V vs. NHE	E_{gap}/V
SD6	531	2.34	1.13	−1.21	0.71
SD7	514	2.41	1.03	−1.38	0.88
SD8	521	2.38	1.13	−1.25	0.55

[a] E_{0-0} values were calculated from intersection of the normalized absorption and the emission spectra (λ_{int}): $E_{0-0} = 1240/\lambda_{int}$. The first oxidation potential (vs. NHE), E_{ox} was measured in acetonitrile and calibrated by addition of 0.63 V to the potential vs. Fc/Fc^+. The reduction potential, E_{red}, was calculated from E_{ox}–E_{0-0}. E_{gap} is the energy gap between the E_{red} of dye and the CB level of TiO_2 (−0.5 V vs. NHE).

0.63 V to the potential (vs. SCE) vs. Fc/Fc^+ by CV. The first oxidation potentials of **SD6** and **SD8** were measured as same as 1.13 V, which shifted in positive direction compared with **SD7** (1.03 V) (Table 2). Moreover, the three dyes show higher E_{ox} than that of SD2 dye (0.93 V) [29], which predicts that a higher open-circuit voltage (V_{oc}) may be obtained for **SD6**–**SD8** due to the comparatively lower-lying HOMO levels [24]. It is can be seen that all the HOMO levels of three dyes are more positive than the iodide/triiodide redox couple (~0.42 V vs. NHE), ensuring that there is enough driving force for efficient regeneration of the dye through the recapture of the injected electrons by the dye cation radical.

By neglecting any entropy change during light absorption, the reduction potential vs. NHE (E_{red}), which corresponds to the lowest unoccupied molecular orbital

(LUMO vs. NHE), can be obtained from the first oxidation potential (E_{ox}) and the E_{0-0} value determined from the intersection of absorption and emission spectra, namely, E_{ox}–E_{0-0}. The calculated LUMO levels of **SD6**, **SD7**, and **SD8** were −1.21, −1.38, and −1.25 V vs. NHE (Table 2), respectively, which all are sufficiently higher than that of the conduction band (CB) level of TiO_2 (−0.5 V vs. NHE). A visible positive shift of the reduction potential (E_{red}) in **SD6** relative to that of **SD7** and **SD8** may be due to more delocalization of the π-conjugation system. The E_{gap} between the CB of TiO_2 and the E_{red} (vs. NHE) ranges from 0.55 (**SD8**) to 0.88 eV (**SD7**) (Table 2). Provided that energy gap of 0.2 eV is necessary for efficient electron injection [7,18], these driving forces are sufficiently large for effective electron injection. Therefore, the three dyes used as sensitizers will have sufficient driving force for electron transfer from the excited dye molecules to the conduction band of TiO_2 electrode. Table 2 summarizes all the electrochemical properties of the three dyes.

3.4. Electronic structure quantum chemical calculations

In order to gain an insight into the molecular structure and electron distribution, density functional theory (DFT) calculations were performed on the dyes **SD6**–**SD8** using the Gaussian 03 program package. In particular we used B3LYP as exchange–correlation functional and 3-21G* as basis set. The electron distribution of the HOMO and LUMO of the dyes is shown in Table 3. It is obvious that the electron density of HOMO is localized mainly on the triphenylamine moiety and is extended along the π-conjugated bridge to the central region of the molecule. On the other hand, the LUMO is localized over the cyanoacrylic unit through thiophene. We notice that the HOMO–LUMO excitation induced by light irradiation could move the electron distribution from the TPA-unit to the cyanoacrylic acid moiety via dual-role moiety-containing π-conjugated bridges and the photo-induced electron transfer from the dyes to the TiO_2 electrode can occur efficiently by the HOMO–LUMO transition.

To gain insight into the excited states giving rise to the optically active absorption bands in the UV–vis region, we performed time dependent DFT (TDDFT) excited states calculations at the B3LYP/6-31G* level in vacuo with the B3LYP/6-21G* optimized ground-state geometries, given the negligible effect of solvation on the electronic structure. The lowest transition of three dyes is calculated at 2.13–2.20 eV (Table 4) and corresponds to the intramolecular charge transfer (ICT) excitation from the triphenylamine-dual moiety-based the HOMO to the LUMO, localized on thiophene–cyanoacrylate moieties. Another transition calculated at 2.75–2.83 eV is a $\pi-\pi^*$ excitation from the HOMO−1 to the LUMO, therefore taking place within the thiophene–cyanoacrylate moiety.

Table 3
Frontier molecular orbitals of the HOMO and LUMO calculated with DFT on a B3LYP/3-21G* level of the dyes **SD6**, **SD7**, and **SD8**.

Dye	HOMO	LUMO
SD6	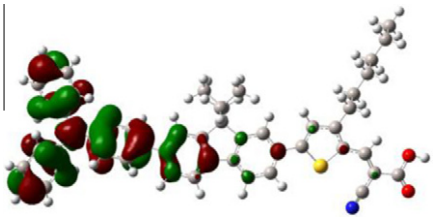	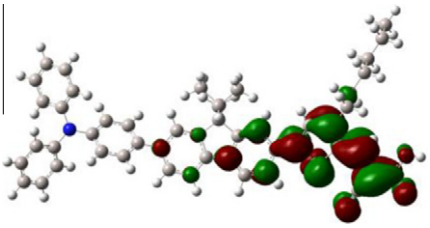
SD7	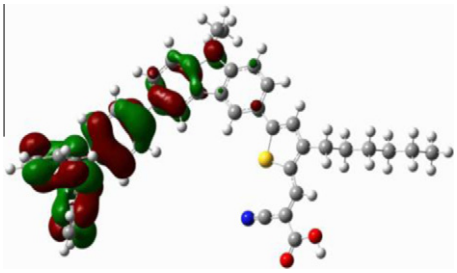	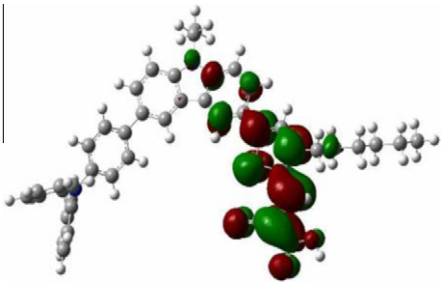
SD8	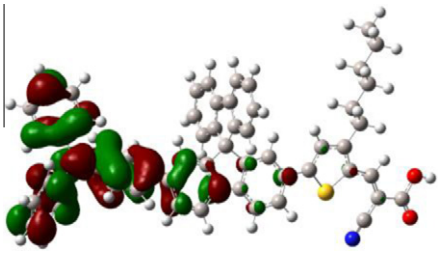	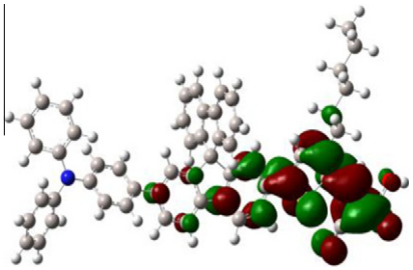

Table 4
Calculated TDDFT excitation energies for the lowest transition (eV, nm), oscillator strengths (*f*), composition in terms of molecular orbital contributions, and experimental absorption maxima.

Dye	State	Composition	*E* (eV, nm)	*f*	Exp. (eV, nm)
SD6	S1	70%, HOMO → LUMO	2.19(566)	0.32	457
	S2	64%, HOMO−1 → LUMO	2.81(441)	1.11	342
SD7	S1	70%, HOMO → LUMO	2.13(583)	0.04	469
	S2	65%, HOMO−1 → LUMO	2.75(451)	0.52	319
SD8	S1	70%, HOMO → LUMO	2.20(563)	0.31	450
	S2	64%, HOMO−1 → LUMO	2.83(438)	0.90	342

The calculated absorption wavelength increases in the order of **SD8** < **SD6** < **SD7** (Table 4), which is in qualitative agreement with experimental absorption spectra. However, the calculated wavelengths are considerably red-shifted compared to the experimental absorption maximum. This is expected since traditional exchange–correlation functionals, such as B3LYP, underestimate the energies for ICT transitions and the error increases with the distance between the negative and positive charges of the charge-transfer state [50].

3.5. Photovoltaic performance of DSSCs

DSSCs were fabricated using these dyes as the sensitizers, with an effective area of 0.196 cm^2, TiO_2 particles on FTO, and the electrolyte composed of 0.5 M LiI, 0.05 M I_2, and 0.5 M 4-*tert*-butyl-pyridine (TBP) in 3-methoxy-propionitrile. Fig. 6 shows incident photon-to-electron conversion efficiency (IPCE) as a function of the wavelength for the sandwiched DSSCs based on the three dyes as sensitizers. As shown in Fig. 6, the IPCE action spectrum for DSSC based on **SD7** is broader than those of **SD6** and **SD8**, which is consistent with the tendency of UV–vis absorption spectra on TiO_2 surface (Fig. 4). The IPCE spectrum of **SD8** is blue shifted compared to those of **SD6** and **SD7** as a result from distortion of dual-role unit, which is in agreement with bulk steric hindrance of spirobifluorene moiety in **SD8** framework. In comparison with **SD8**, **SD6** and **SD7** give the higher IPCE values with the maximum of ~73% at 427 nm and 68% at 443 nm, respectively, which implies the two sensitizers would show a relatively large photocurrent in DSSCs. The higher IPCE values might attribute to an effective intramolecular cascade energy transfer from the double donor to cyanoacetic acid acceptor via π-bridge.

Fig. 7 shows current density–voltage (*J*–*V*) characteristics of devices based on the three dyes. The detailed photovoltaic performances are listed in Table 5. Compared to **SD7** and **SD8**, the **SD6**-sensitized cell exhibited better photovoltaic performances with a short-circuit photocurrent density (J_{sc}) of 14.25 mA/cm^2, an open-circuit voltage (V_{oc}) of 0.70 V, and a filled factor (FF) of 0.705, corresponding to a power conversion efficiency (PCE) of 7.03% (Table 5). According to Fig. 7, it is clear that the photovoltaic performances of the DSSCs can be evidently affected by the dual-role moieties in the dye molecules. In comparison with **SD8**, the J_{sc} and V_{oc} values of **SD6** and **SD7** are significantly improved by introducing better electron-donating ability of fluorene and carbazole moieties to act as the secondary donor. The remarkably increased J_{sc} values can be reflected in their broad and high maximum IPCEs values of **SD6** and **SD7**. The improved V_{oc} values of **SD6** and **SD7** compared to **SD8** could be attributed to the effective retardation of charge recombination between the electrons at the TiO_2 and the oxidized dyes, which may be resulted from the extra hydrophobic alkyl chains of fluorene and carbazole groups in the dyes **SD6** and **SD7** [28–31]. In addition, the broader absorption band and higher IPCEs in range of 500–650 nm of **SD7** likely results in a higher J_{sc} (14.79 mA/cm^2) value compared with

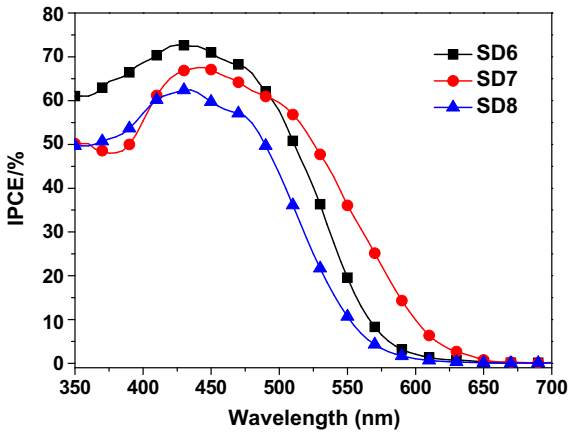

Fig. 6. IPCE plots for the DSSCs based on the three dyes.

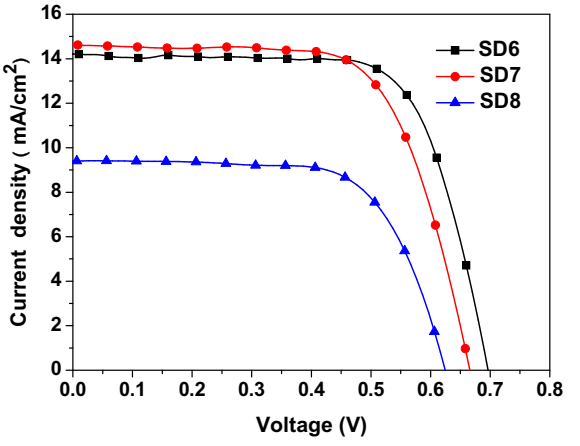

Fig. 7. Current density–voltage characteristics for DSSCs based on the three dyes.

Table 5
Photovoltaic performance of DSSCs based on the three dyes.

Dye	J_{sc} (mA/cm^2)	V_{oc} (V)	FF	PCE (%)
SD6	14.25	0.70	0.705	7.03
SD7	14.79	0.66	0.667	6.51
SD8	9.12	0.63	0.717	4.12

that of **SD6** (14.25 mA/cm^2), but the lower V_{oc} (0.66 V) and FF (0. 667) for the device of **SD7** lead to the lower efficiency (6.51%) finally. The higher V_{oc} of **SD6** than that of **SD7** might be due to the comparatively lower-lying HOMO of the former (estimated from the CV), which offers enough larger driving force for the reduction of the oxidized dye. This, in turn, will lead to a slower back electron transfer from TiO_2 to the dye and result in a lager V_{oc} value [24].

3.6. Electrochemical impedance spectroscopy studies

Electrochemical impedance spectroscopy (EIS) is a powerful technique of characterizing the important interfacial charge transfer processes in a DSSC. The EIS was measured in the dark to elucidate correlation of V_{oc} with those dyes. The Nyquist plots of DSSCs with three dyes are shown in Fig. 8. Three semicircles were observed in the Nyquist plots. The small and large semicircles, respectively located in the high- and middle frequency regions, are assigned to the charge transfer at Pt/electrolyte and TiO_2/dye/electrolyte interface, respectively [24,28,51,52]. Another small semicircle, which should have appeared at the low-frequency region, is overlapped by the middle frequency large semicircle. The charge recombination resistance (R_{rec}) on the TiO_2 surface, which is related to the charge recombination rate between injected electron and electron acceptor (I_3^-) in the electrolyte, is estimated by the large semicircle width. A large R_{rec} means the small charge recombination rate and vice versa. The R_{rec} values for **SD6**, **SD7**, and **SD8** were estimated to be 52, 40 and 29 Ω, respectively. The significantly increased R_{rec} values in the cells of **SD6** and **SD7** imply the retardation of the charge recombination between injected electron and electron acceptor (I_3^-) in the electrolyte, with a consequent increase of V_{oc}. The result appears to be consistent with the above-mentioned changing tendencies of V_{oc} values in the cells of three dyes.

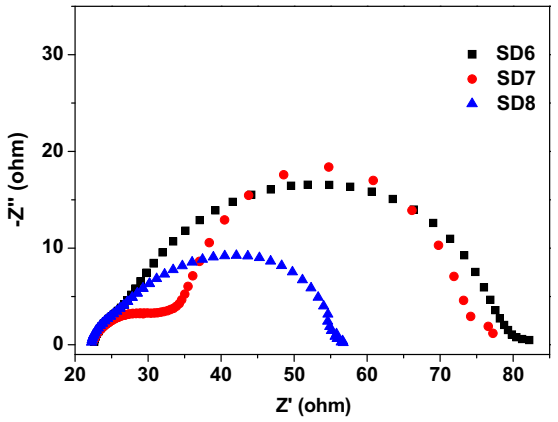

Fig. 8. EIS Nyquist plots for DSSCs based on the three dyes measured in the dark.

4. Conclusions

In summary, we have synthesized and characterized three triphenylamine-based D–D–π–A sensitizers **(SD6–SD8)**, featuring dual-role carbazole, fluorene and spirobifluorene moieties, for the application in DSSCs. There are several advantages preformed by these D–D–π–A structural dyes: (1) enhanced light-harvesting ability as reflected from the improvement of extinction coefficients in the visible region and as a result of high short-circuit photocurrent density (J_{sc}); (2) lower-lying HOMO levels of the dyes, which are favorable for achieving high open-circuit voltage (V_{oc}); (3) reduced dyes aggregates and effective retardation of charge recombination due to the extra hydrophobic alkyl chains of dual-role moieties incorporated with the long alkyl of thiophenyl unit. The DSSCs fabricated by using these dyes display remarkable PCEs, typically in a range of 4–7%. The optimal IPCE value reaches beyond 70%. The best photovoltaic performance among the three dyes exhibits a J_{sc} value of 14.25 mA/cm^2, V_{oc} value of 0.70 V, and FF value of 0.705, all summed up to a PCE of 7.03%. Our results continue to show that the molecular design and modification of organic dyes are a very effective strategy to achieve highly efficient DSSCs.

Acknowledgements

This work was supported by the General Program of the Education Department of Hunan Province (No. 09C946), National Nature Science Foundation of China (No. 50973092), and the Open Project Program of Key Laboratory of Advanced Functional Polymeric Materials (Xiangtan University), College of Hunan Province (No. AFPM200903).

References

[1] S. Gunes, N.S. Sariciftci, Inorg. Chim. Acta 361 (2008) 581.
[2] M. Grätzel, Acc. Chem. Res. 42 (2009) 1788.
[3] B.O. Regan, M. Grätzel, Nature 353 (1991) 737.
[4] L. Moreira Goncalves, V. de Zea Bermudez, H. Aguilar Ribeiro, A. Magalhães Mendes, Energy Environ. Sci. 1 (2008) 655.
[5] M.K. Nazeeruddin, A. Kay, L. Rodicio, R. Humphry-Baker, E. Müller, P. Liska, N. Vlachopoulos, M. Grätzel, J. Am. Chem. Soc. 115 (1993) 6382.
[6] A. Mishra, M.K.R. Fischer, P. Büerle, Angew. Chem. Int. Ed. 48 (2009) 2474.
[7] S. Ito, M. Zakeeruddin, R. Hummphrey-Baker, P. Liska, R. Charvet, P. Comte, M.K. Nazeeruddin, P. Péchy, M. Takata, H. Miura, S. Uchida, M. Grätzel, Adv. Mater. 18 (2006) 1202.
[8] S. Ito, H. Miura, S. Uchida, M. Takata, K. Sumioka, P. Liska, P. Comte, P. Pechy, M. Grätzel, Chem. Commun. (2008) 5194.
[9] H. Choi, C. Baik, S.O. Kang, J. Ko, M.-S. Kang, M.K. Nazeeruddin, M. Grätzel, Angew. Chem. Int. Ed. 47 (2008) 327.
[10] G. Zhang, H. Bala, Y. Cheng, D. Shi, X. Lv, Q. Yu, P. Wang, Chem. Commun. (2009) 2198.
[11] W. Zeng, Y. Cao, Y. Bai, Y. Wang, Y. Shi, M. Zhang, F. Wang, C. Pan, P. Wang, Chem. Mater. 22 (2010) 1915.
[12] A. Baheti, P. Tyagi, K.R.J. Thomas, Y.-C. Hsu, J.T. Lin, J. Phys. Chem. C 113 (2009) 8541.
[13] T. Marinado, K. Nonomura, J. Nissfolk, M.K. Karlsson, D.P. Hagberg, L. Sun, S. Mori, A. Hagfeldt, Langmuir 26 (2010) 2592.

[14] D.P. Hagberg, T. Edrinsson, T. Marinado, G. Boschloo, A. Hagfeldt, L. Sun, Chem. Commun. (2006) 2245.
[15] S. Kim, H. Choi, C. Baik, K. Song, S.O. Kang, J. Ko, Tetrahedron 63 (2007) 11436.
[16] H. Qin, S. Wenger, M. Xu, F. Gao, X. Jing, P. Wang, S.M. Zakeeruddin, M. Grätzel, J. Am. Chem. Soc. 130 (2008) 9202.
[17] M. Xu, S. Wenger, H. Bala, D. Shi, R. Li, Y. Zhou, S.M. Zakeeruddin, M. Grätzel, P. Wang, J. Phys. Chem. C 113 (2009) 2966.
[18] K. Hara, T. Sato, R. Katoh, A. Furube, Y. Ohga, A. Shinpo, S. Suga, K. Sayama, H. Sugihara, H. Arakawa, J. Phys. Chem. B 107 (2003) 597.
[19] W. Xu, J. Pei, J. Shi, S. Peng, J. Chen, J. Power Sources 183 (2008) 792.
[20] L. Zhang, Y. Liu, Z. Wang, M. Liang, Z. Sun, S. Xue, Tetrahedron 66 (2010) 3318.
[21] G. Li, Y.F. Zhou, X.B. Cao, P. Bao, K.J. Jiang, Y. Lin, M.L. Yang, Chem. Commun. (2009) 2201.
[22] Z. Ning, Q. Zhang, W. Wu, H. Pei, B. Liu, H. Tian, J. Org. Chem. 73 (2008) 3791.
[23] H. Tian, X. Yang, J. Pan, R. Chen, M. Liu, Q. Zhang, A. Hagfeldt, L. Sun, Adv. Funct. Mater. 18 (2008) 3461.
[24] K.R.J. Thomas, Y.-C. Hsu, J.T. Lin, K.-M. Lee, K.-C. Ho, C.-H. Lai, Y.-M. Cheng, P.-T. Chou, Chem. Mater. 20 (2008) 1830.
[25] D.P. Hagberg, J.-H. Yum, H.J. Lee, F.D. Angelis, T. Marinado, K.M. Karlsson, R. Humphry-Baker, L. Sun, A. Hagfeldt, M. Grätzel, M.K. Nazeeruddin, J. Am. Chem. Soc. 130 (2008) 6259.
[26] T. Dentani, Y. Kubota, K. Funabiki, J. Jin, T. Yoshida, H. Minoura, H. Miura, M. Matsui, New J. Chem. 33 (2009) 93.
[27] D.P. Hagberg, T. Marinado, K.M. Karlsson, K. Nonomura, P. Qin, G. Boschloo, T. Brinck, A. Hagfeldt, L. Sun, J. Org. Chem. 72 (2007) 9550.
[28] Z. Wang, N. Koumura, Y. Cui, M. Takahashi, H. Sekiguchi, A. Mori, T. Kubo, A. Furube, K. Hara, Chem. Mater. 20 (2008) 3993.
[29] P. Shen, Y. Liu, X. Huang, B. Zhao, N. Xiang, J. Fei, L. Liu, X. Wang, S. Tan, Dyes Pigm. 83 (2009) 187.
[30] Y. Liu, N. Xiang, X. Feng, P. Shen, W. Zhou, C. Weng, B. Zhao, S. Tan, Chem. Commun. (2009) 2499.
[31] H. Chen, H. Huang, X. Huang, John N. Clifford, A. Forneli, E. Palomares, X. Zheng, L. Zheng, X. Wang, P. Shen, B. Zhao, S. Tan, J. Phys. Chem. C 114 (2010) 3280.
[32] B. Zhao, Z. Tian, P. Shen, H. Huang, S. Tan, Dyes Pigm. 87 (2010) 181.
[33] D. Kim, J.K. Lee, S.O. Kang, J. Ko, Tetrahedron 63 (2007) 1913.
[34] Q. Li, L. Lu, C. Zhong, J. Shi, Q. Huang, X. Jin, T. Peng, J. Qin, Z. Li, J. Phys. Chem. B 113 (2009) 14588.
[35] C. Teng, X. Yang, C. Yuan, C. Li, R. Chen, H. Tian, S. Li, A. Hagfeldt, L. Sun, Org. Lett. 11 (2009) 5542.
[36] C. Zafer, B. Gultekin, C. Ozsoy, C. Tozlu, B. Aydin, S. Icli, Sol. Energy Mater. Sol. Cells 94 (2010) 655.
[37] S. Kim, J.K. Lee, S.O. K.J. Kang, J.-H. Yum, S. Fantacci, F. De Angelis, D. Di Censo, M.K. Nazeeruddin, M. Grätzel, J. Am. Chem. Soc. 128 (2006) 16701.
[38] G. Zhou, N. Pschirer, J.C. Schöneboom, F. Eickemeyer, M. Baumgarten, K. Müllen, Chem. Mater. 20 (2008) 1808.
[39] J.T. Lin, P.-C. Chen, Y.-S. Yen, Y.-C. Hsu, H.-H. Chou, M.-C. Yeh, Org. Lett. 11 (2009) 97.
[40] N. Cho, H. Choi, D. Kim, K. Song, M. Kang, S.-O. Kang, J. Ko, Tetrahedron 65 (2009) 6236.
[41] D. Heredia, J. Natera, M. Gervaldo, L. Otero, F. Fungo, C.-Y. Lin, K.-T. Wo, Org. Lett. 12 (2010) 12.
[42] Y.J. Pu, K. Takashi, S. Minoru, J.J. Kido, N. Iroyuki, Synth. Met. 143 (2004) 207.
[43] R. Demandrille, M. Firon, J. Leroy, P. Rannou, A. Pron, Adv. Funct. Mater. 16 (2006) 1694.
[44] A. Xia, Z. Yuan, S. Tan, Y. Zou, Z. Tan, Y. Yang, Y. Li, Eur. Polym. J. 43 (2007) 1394.
[45] K.-T. Wong, Y.-M. Chen, Y.-T. Lin, H.-C. Su, C.-C. Wu, Org. Lett. 7 (2005) 5361.
[46] S. Roquet, A. Cravino, P. Leriche, O. Alévêque, P. Frère, J. Roncali, J. Am. Chem. Soc. 128 (2006) 3459.
[47] A.C. Khazraji, S. Hotchandani, S. Das, P.V. Kamat, J. Phys. Chem. B 103 (1999) 4693.
[48] K. Sayama, K. Hara, N. Mori, M. Satsuki, S. Suga, S. Tsukagoshi, Y. Abe, H. Sugihara, H. Arakawa, Chem. Commun. (2000) 1173.
[49] Y.J. Chang, T.J. Chow, Tetrahedron 65 (2009) 9626–9632.
[50] A. Dreuw, M.J. Head-Gordon, Am. Chem. Soc. 126 (2004) 4007.
[51] C. Longo, A.F. Nogueira, M.-A. De Paoli, H. Cachet, J. Phys. Chem. B 106 (2002) 5925.
[52] R. Kern, R. Sastrawan, J. Ferber, R. Stangl, J. Luther, Electrochim. Acta 47 (2002) 4213.

Organic Electronics 12 (2011) 136–142

Contents lists available at ScienceDirect

Organic Electronics

journal homepage: www.elsevier.com/locate/orgel

White organic light-emitting diodes based on a novel Zn complex with high CRI combining emission from excitons and interface-formed electroplex

Yuying Hao [a,b,*], Weixin Meng [a], Huixia Xu [b], Hua Wang [b], Xuguang Liu [c], Bingshe Xu [b,*]

[a] Department of Physics and Optoelectronics, Taiyuan University of Technology, Taiyuan 030024, China
[b] Key Laboratory of Interface Science and Engineering in Advanced Materials of Taiyuan University of Technology, Taiyuan 030024, China
[c] College of Chemistry and Chemical Engineering, Taiyuan University of Technology, Taiyuan 030024, China

ARTICLE INFO

Article history:
Received 1 February 2010
Received in revised form 5 October 2010
Accepted 31 October 2010
Available online 12 November 2010

Keywords:
White organic light-emitting diodes
bis(2-(4-trifluoromethyl-2-hydroxyphenyl)benzothiazolate)zinc [Zn(4-TfmBTZ)$_2$]
Electroplex

ABSTRACT

An efficient white-light emitting diode ITO/NPB/Zn(4-TfmBTZ)$_2$/Alq$_3$/LiF/Al was obtained when a new material bis(2-(4-trifluoromethyl-2-hydroxyphenyl)benzothiazolate)zinc [Zn(4-TfmBTZ)$_2$] was used as an electron-acceptor emitting layer, NPB as an electron-donor emitting and hole-transporting layer, and Alq$_3$ as an emitting and electron-transporting layer. In this device, the exciton emissions of NPB, Zn(4-TfmBTZ)$_2$ and Alq$_3$ in addition to the electroplex emissions of Zn(4-TfmBTZ)$_2$/NPB interface render white light output. Inserting an Alq$_3$ layer with appropriate thickness can increase EL efficiency and improve chromaticity. The most pure white light emission with CIE coordinates of (0.30, 0.34) and CRI of 90.2 can be attained by adjusting Alq$_3$ layer thickness to 20 nm. Moreover, CIE coordinates are very insensitive to the applied voltage. The CIE coordinate region is (0.29–0.30, 0.33–0.34) at various forward bias (8–13 V). This device showed the maximum luminance of 2445 cd/m^2 at 14 V and the maximum current efficiency of 1.39 cd/A, which will be improved further by optimizing the preparation technique of device.

© 2010 Elsevier B.V. All rights reserved.

1. Introduction

In recent years, white organic light-emitting diodes (WOLEDs) have attracted a great deal of interest due to their potential applications in full color displays, back lighting of flat-panel display, and lighting purposes [1–3]. Several routes have been typically employed to obtain white light: (i) multilayer structure, (ii) multi-doped system in a single layer, (iii) bimolecular excited species (exciplex/excimer/electroplex/electromer), and so on. Among them the method based on bimolecular species is considered to be a simple, cheap and general technique [4–7]. The bimolecular excited states are a kind of transient complexes formed under energy and/or charge exchange between neighbor molecules and usually lead to an additional redshifted broad band emission, and consequently can be utilized to tune emission color and design white OLED by a simple device structure [8–18]. Unless the dissociation process of the excited states into the separated ion pair is facile, photoexcitation rarely generates free charge carriers. Therefore, the electroplexes are visible mostly in electroluminescence (EL) spectrum but not normally in photoluminescence (PL) spectrum. However, exciplexes are readily observed in EL and PL processes [19].

It is well known that bis(2-(2-hydroxyphenyl)benzothiazolate)zinc (Zn(BTZ)$_2$) can be used as an effective white light emissive and electron transport material in EL device [20,11,21,22]. Hamada et al. [20] reported a greenish white OLED combining the emissions of Zn(BTZ)$_2$ exciton and Zn(BTZ)$_2$/TPD interface exciplex. Recently, Singh et al. [11] demonstrated an improvement white OLED with a broadened EL spectrum and the CIE coordinate of (0.38, 0.40) due to formation of exciplexes and electroplexes at Zn(BTZ)$_2$/TPD interface. But the latest report [21] had

* Corresponding authors at: Department of Physics and Optoelectronics, Taiyuan University of Technology, Taiyuan 030024, China (Y. Hao). Tel.: +86 351 6066938.
E-mail addresses: haoyuyinghyy@sina.com (Y. Hao), xubs@tyut.edu.cn (B. Xu).

1566-1199/$ - see front matter © 2010 Elsevier B.V. All rights reserved.
doi:10.1016/j.orgel.2010.10.019

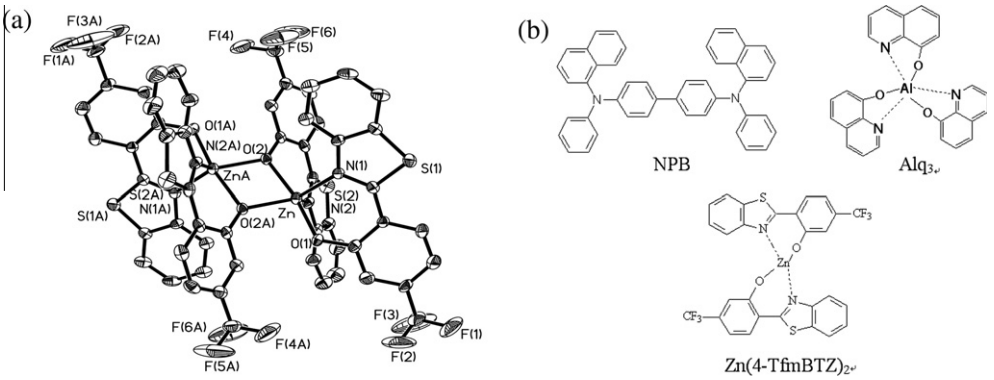

Fig. 1. Crystal structure of $Zn(4\text{-}TfmBTZ)_2$ (a) and chemical structures of materials used in this study (b).

showed that the unusually broad white-light emitting of the device based on $Zn(BTZ)_2$/TPD is due to optical interference effect and light emission originating from fluorescence and phosphorescence.

To date, zinc complexes based on functionalized 2-(2-hydroxyphenyl)benzothiazole derivatives for WOLEDs have not been reported to the best of our knowledge. In this paper, we will demonstrate an excellent WOLED with bis(2-(4-trifluoromethyl-2-hydroxyphenyl)benzothiazolate)-zinc ($Zn(4\text{-}TfmBTZ)_2$) as an electron-acceptor emitting layer, N,N′-diphenyl-N,N'-bis(1-naphthyl)-(1,1′-biphenyl)-4,4′-diamine (NPB) as an electron-donor emitting and hole-transporting layer, and Alq_3 as an emitting and electron-transporting layer. $Zn(4\text{-}TfmBTZ)_2$, which was synthesized in our laboratory [23], is a derivative of $Zn(BTZ)_2$, one additional electron-withdrawing group trifluoromethyl incorporating in 4-position of BTZ. The single crystal structure of $Zn(4\text{-}TfmBTZ)_2$ was determined by single crystal X-ray diffraction (see Fig. 1) [23]. $Zn(4\text{-}TfmBTZ)_2$ forms a monoclinic crystal; $a = 16.866$, $b = 9.8055$, $c = 16.912$ Å; $\alpha = \gamma = 90$, $\beta = 115.771°$, space group P21/n. It can be seen from Fig. 1 that $Zn(4\text{-}TfmBTZ)_2$ exists as an anhydrous dimer structure, where the zinc ions are five-coordinate to 2-(4-trifluoromethyl-2-hydroxyphenyl)benzothiazolate) ligands. $Zn(4\text{-}TfmBTZ)_2$-based WOLED is a typical electroplex light-emitting-device. The best performances for exciplex-type WOLEDs at present had been reported by Kalinowski et al. [6,24]. They combined PtL^2Cl phosphorescence with excimer and exciplex emissions to yield white light with high color rendering index (CRI = 90) and efficiency (EQE = 6.5%, PE = 9.0 lm/W) [6]. Recently, they utilized molecular exciton and excimer phosphorescence from new organic phosphor $PtL^{26}Cl$ to realize white light with high color purity (CIE coordinates $x = 0.34$, $y = 0.35$) and efficiency (EQE = 11.5%, PE = 6.8 lm/W) [24]. Compared with these advanced WOLEDs, $Zn(4\text{-}TfmBTZ)_2$-based WOLED has high CRI (=84.0–90.2), color stability and purity (CIE coordinate region $x = 0.29$–0.30, $y = 0.33$–0.34 at 8–13 V), but its luminous efficiency is required to improve further.

2. Experimental

The chemical structures of organic materials used here are shown in Fig. 1. The devices have structure A: ITO/NPB (35 nm)/$Zn(4\text{-}TfmBTZ)_2$ (30 nm)/Alq_3 (x nm)/LiF (1.8 nm)/Al (150 nm), where x, Alq_3 thickness, was changed from 0 to 40 nm by step of 10 nm. Herein, relatively thin, 30 nm-thick $Zn(4\text{-}TfmBTZ)_2$ layer was chosen with the aim of removing the aforementioned optical interference effect.

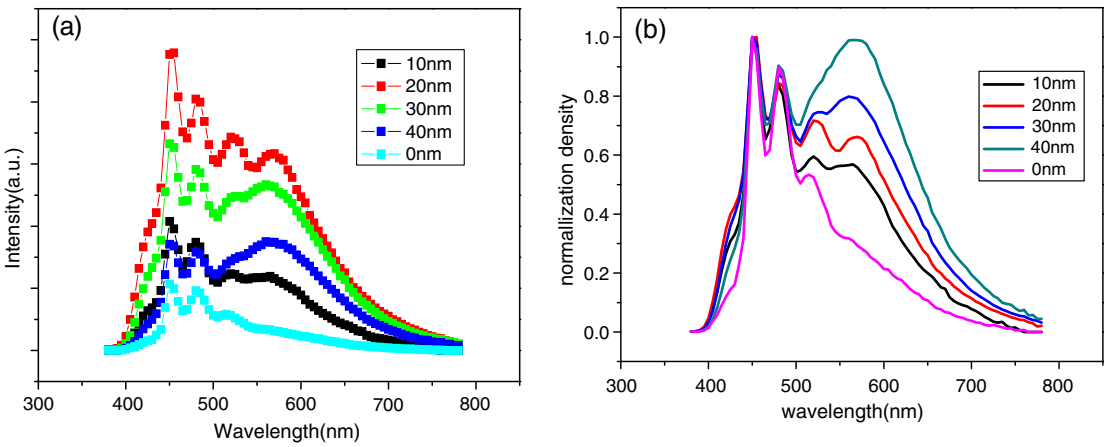

Fig. 2. EL spectra (a) and normalized EL spectra (b) of device A at applied voltage of 12 V.

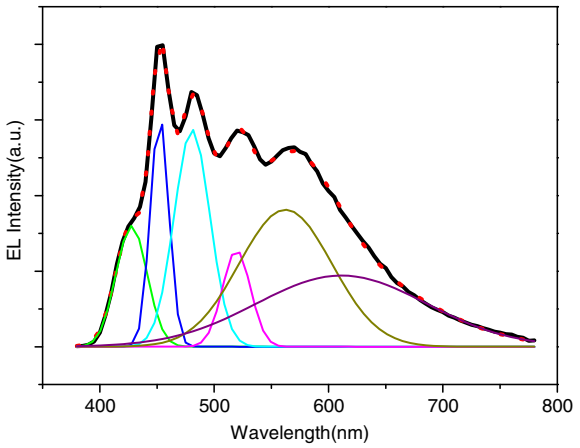

Fig. 3. EL spectra of device A with Alq_3 layer thickness of 20 nm at applied voltage of 12 V: the experiment (black solid) and Gaussian fitting (red dot). (For interpretation of the references in colour in this figure legend, the reader is referred to the web version of this article.)

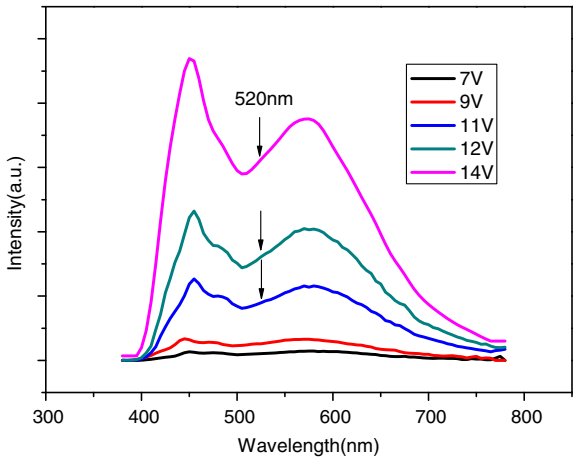

Fig. 4. EL spectra of device B at different driving-voltage.

As comparison, the devices with structure B: ITO/NPB (35 nm)/Zn(4-TfmBTZ)$_2$ (30 nm)/BCP (20 nm)/Alq_3 (20 nm)/LiF (1.8 nm)/Al (150 nm) and C: ITO/NPB (35 nm)/Zn(4-TfmBTZ)$_2$ (x nm)/LiF/Al (x = 20, 30, 40 nm) were designed. The device B was inserted a hole-blocking layer BCP (2,9-dimethy-4,7-diphenyl-1,10-phenanthroline). The device C contain no Alq_3 layer and the thickness of Zn(4-TfmBTZ)$_2$ was changed from 20 to 40 nm by step of 10 nm. All devices were fabricated by successive vacuum deposition of the organic materials onto ITO-coated glass substrates at a deposition rate of 0.1–0.2 nm/s in vacuum of 4.0×10^{-4} Pa and sequential deposition of LiF and aluminum layer without breaking vacuum. The luminance–current–voltage characteristics were measured by a keithley 2400 source meter and ST-900 M photometer. The EL spectra, Commission International De I'Eclairage (CIE) and color rendering index (CRI) were obtained with the SPR-920D spectrofluorometer. The NPB (200 nm) film, Zn(4-TfmBTZ)$_2$ (200 nm) film and layered NPB (100 nm)/Zn(4-TfmBTZ)$_2$ (100 nm) film were prepared on quartz substrates. The PL spectra were measured by Cary Eclipse fluorescence spectrophotometer. The absorption spectra were measured by Cary 300. All measurements were carried out at room temperature under ambient.

3. Results and discussion

As shown in Fig. 2, the EL spectra of device A are composed of multi-emission bands and cover the range from 400 to 700 nm uniformly, approaching an ideal white light. In order to confirm the origins of every emission band, we fit EL spectrum of the device with 20 nm-thick Alq_3 layer at 12 V, as shown in Fig. 3. The EL spectrum is decomposed into six curves by Gaussian fitting. The six emission peaks are located at 425, 454, 481, 519, 561, and 613 nm, respectively. Undoubtedly, the second emission peak is associated with NPB exciton, the third with Zn(4-TfmBTZ)$_2$ exciton. The first peak might be due to optical interference effect because this peak appears only when NPB thickness is 35 nm, but disappears when NPB layer is thicker or

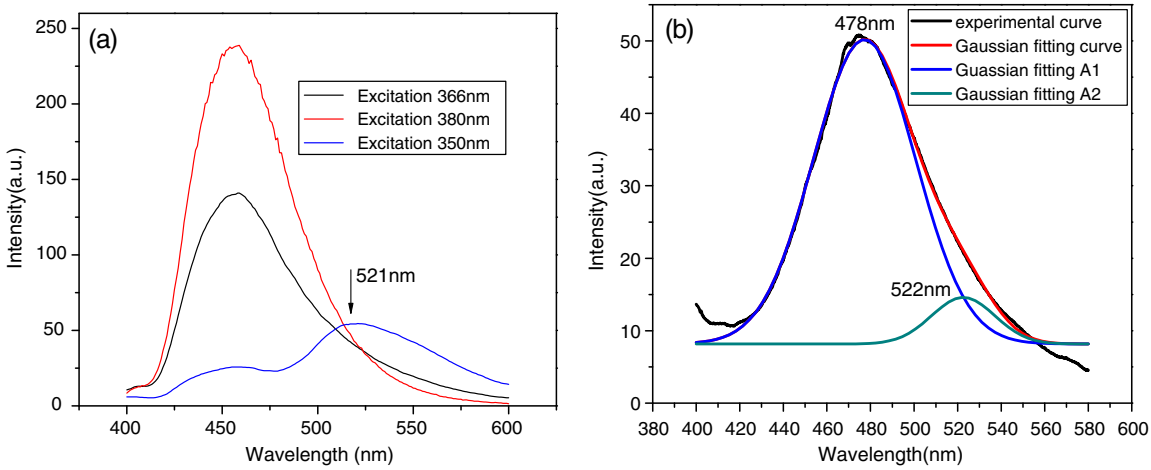

Fig. 5. PL spectra of Zn(4-TfmBTZ)$_2$ in THF solution (a) and film state (b) under excitation of 350 nm including fitting and deconvoluted components.

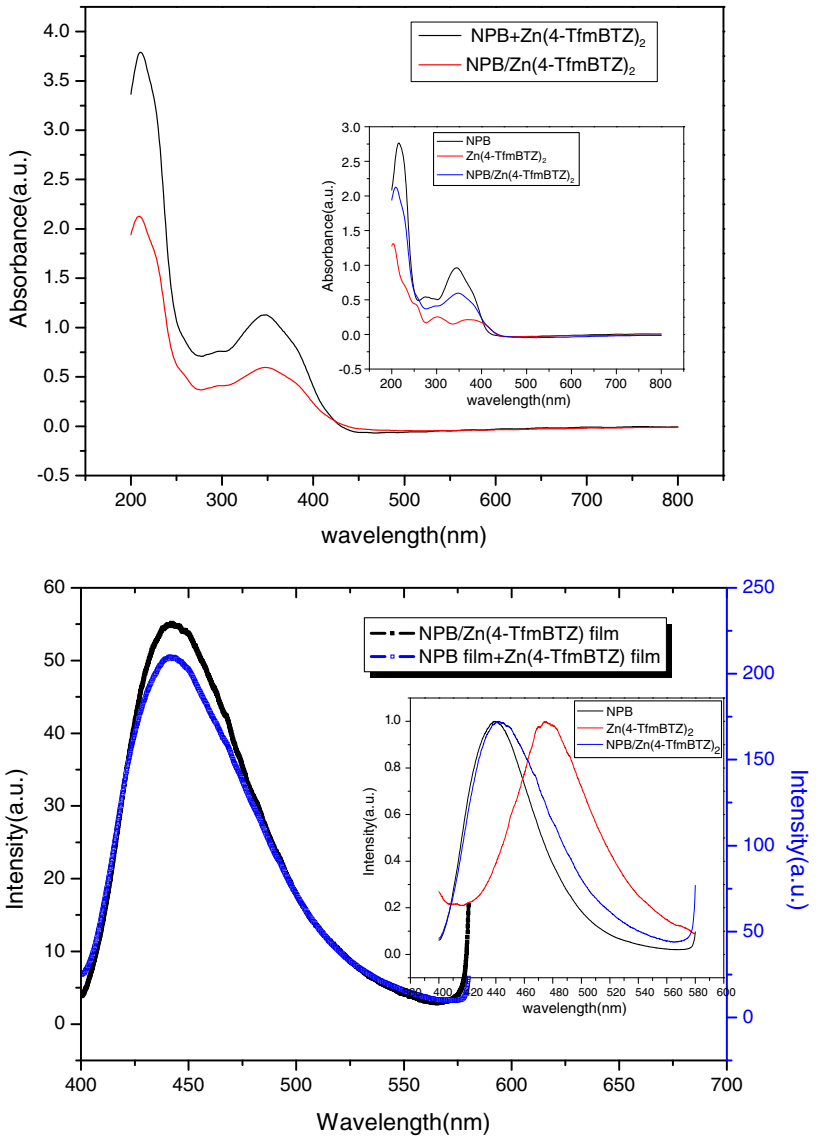

Fig. 6. Absorption (upper) and PL (lower) spectra of NPB film, $Zn(4\text{-TfmBTZ})_2$ film, and layered NPB/$Zn(4\text{-TfmBTZ})_2$ film.

thinner. It seems that the emission band peaked at 519 nm comes from Alq_3 exciton. In order to confirm this point of view, the device B with a hole-blocking layer BCP was designed. Its EL spectra at different voltage were displayed in Fig. 4, where the peak of 519 nm almost disappears. The most likely reason is the eliminating of Alq_3 emission because the holes are blocked not to inject Alq_3 layer resulting from low HOMO level of BCP (−6.4 eV [10]). But this peak also appears in the EL spectra of device C containing no Alq_3 layer (see Fig. 8). This means that $Zn(4\text{-TfmBTZ})_2$ also has contribution on the emission peaked at 519 nm. Though the single crystal structure of $Zn(4\text{-TfmBTZ})_2$ shows a dimer, it is not representative of the entire sample. In order to confirm this point of view, the PL spectra of $Zn(4\text{-TfmBTZ})_2$ in THF solution with the concentration of 10^{-5}M was measured, as shown in Fig. 5, where two emission bands peaked at 456 and 521 nm appear under photoexcitation of 350 nm. These two emission bands are not attributed to ligand 4-TfmBTZ, whose PL peaks at 508 nm in THF solution. Similarly, the PL spectra for $Zn(4\text{-TfmBTZ})_2$ film is decomposed into two curves peaked at 478 and 522 nm by Gaussian fitting, respectively. Thereby, we suggest that $Zn(4\text{-TfmBTZ})_2$ may exist in different oligomeric forms, and tentatively assign the emission of 456 nm to the dimer $[Zn(4\text{-TfmBTZ})_2]_2$ and that of 521 nm to other oligomeric species of $Zn(4\text{-TfmBTZ})_2$. In $Zn(4\text{-TfmBTZ})_2$ film, the dimer is dominant, while other oligomeric species is present in a small amount. Thus, the emission of dimer red-shifts 22 nm in film state compared with that in solution state because of intermolecular interaction while the emission of other oligomeric species is basically unchanged in film and solution state because of similar

molecule space-separation. The emission from dimer is more efficient under photoexcitation so that the emission from other oligomeric species is enshrouded. While the EL emission of other oligomeric species as electron traps becomes obvious by direct charge trap. In a word, the bulk emissions of Zn(4-TfmBTZ)$_2$ and Alq$_3$ are responsible to the emission band peaked at 519 nm. What do the latter two emission peaks stem from? In order to explain this question, we measured the absorption and PL spectra of NPB film, Zn(4-TfmBTZ)$_2$ film, and layered NPB/Zn(4-TfmBTZ)$_2$ film, as shown in Fig. 6. The superposition of absorption spectra of NPB, Zn(4-TfmBTZ)$_2$ film is in accord with that of NPB/Zn(4-TfmBTZ)$_2$ film, where no new absorption is observed. This means that no new components occur in layered NPB/Zn(4-TfmBTZ)$_2$ film. Similarly, the superposition of PL spectra of NPB, Zn(4-TfmBTZ)$_2$ film is in accord with that of NPB/Zn(4-TfmBTZ)$_2$ film. This result confirms that no exciplex appears in NPB/Zn(4-TfmBTZ)$_2$ interface under photoexcitation, that is, the emission of 561, and 613 nm do not belong to exciplex. Thus, we can conclude that these two new emitting components are assigned to the electroplex at NPB/Zn(4-TfmBTZ)$_2$ interface. The abovementioned phenomena can be explained by the energy band diagram of the device A (see Fig. 7), where the HOMO and LUMO of Zn(4-TfmBTZ)$_2$ were measured by Cyclic voltammetry in our experiment. Fig. 7 displays distinctly the exciton distribution and electroplex formation within multilayer device. The electrons can easily inject into Alq$_3$ layer, then partially into Zn(4-TfmBTZ)$_2$ layer and to NPB/Zn(4-TfmBTZ)$_2$ interface region. Further, a fraction of electrons at interface tunnel into NPB layer, the others are limited at NPB/Zn(4-TfmBTZ)$_2$ interface. Similarly, the holes injecting NPB layer partially drift to NPB/Zn(4-TfmBTZ)$_2$ interface region, and then a fraction of holes at interface can leak through Zn(4-TfmBTZ)$_2$ and Alq$_3$ layer, the others are accumulated at NPB/Zn(4-TfmBTZ)$_2$ interface. As a result, not only NPB, Zn(4-TfmBTZ)$_2$ and Alq$_3$ excitons form but also effective cross transition recombination between electrons blocked on LUMOs of Zn(4-TfmBTZ)$_2$ and holes blocked on HOMOs of NPB occurs, that is, electroplex forms. Additionally, other oligomeric species of Zn(4-TfmBTZ)$_2$ as charge traps can capture directly charge to form excitons contributing to EL of 519 nm. The emission band maximum position of electroplex approximated by [10,18].

$$hV_{EX}^{\max} = I_D - A_A - E_c \quad (1)$$

Herein I_D and A_A is the ionization potential of the donor and electron affinity of the acceptor of the electroplex components, respectively. E_c is the coulombic attraction energy between donor and acceptor ion represented by

$$E_c = \frac{e^2}{4\pi\epsilon_0\epsilon r} \quad (2)$$

where r is the donor–acceptor intermolecular distance and $\varepsilon_0\varepsilon$ is the dielectric constant. For most organic semiconductors, ε = 3.5–5.5 [25]. Here ε = 3.8 for Zn(4-TfmBTZ)$_2$ referring to that of Alq$_3$ [26], ε = 2.6 for NPB referring to that of TPD [27], thus, an average dielectric constant ε = 3.2 is obtained to calculate r. The ionization potential of NPB is 5.46 eV and electron affinity of Zn(4-TfmBTZ)$_2$ is 2.99 eV. Thereby, corresponding to 561, and 613 nm emissions give r_{EC1} = 1.67 nm and r_{EC2} = 0.99 nm according to Eqs. (1) and (2), respectively. These values are larger than those reported by Kalinowski et al. [28], where all r fall below 1 nm. Such largely separated ion pairs should originate from the dimeric configuration of Zn(4-TfmBTZ)$_2$. Subsequently, we investigated whether optical interference effect is responsible for the white-light emitting of the device A. For this purpose, we designed a series of devices with structure C. Its EL spectrum profiles are independent on the thickness of Zn(4-TfmBTZ)$_2$, as shown in Fig. 8, therefore the optical interference effect is excluded. Thus, we can conclude that the white light emission of device A results from the overlap of the emissions of NPB, Zn(4-TfmBTZ)$_2$, Alq$_3$ exciton in addition to NPB/Zn(4-TfmBTZ)$_2$ interface electroplex. Because of the amorphous nature of

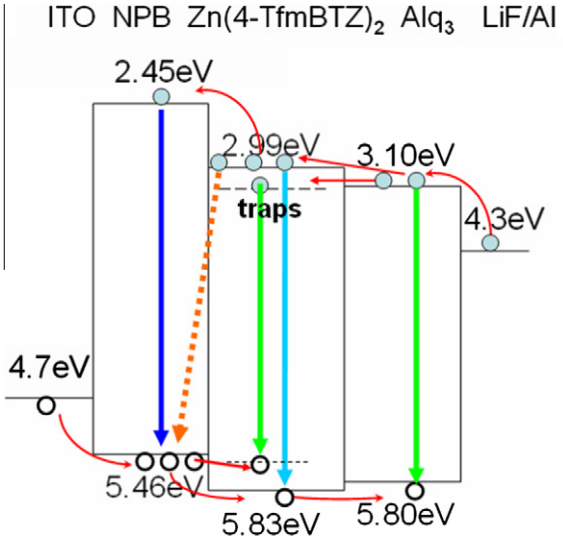

Fig. 7. Energy band diagram of device ITO/NPB/Zn(4-TfmBTZ)$_2$/Alq$_3$/LiF/Al.

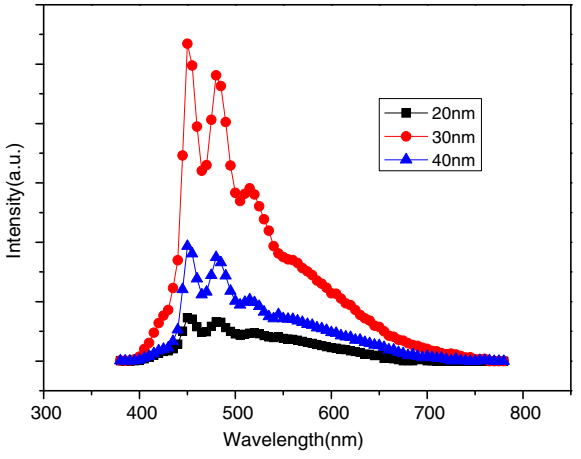

Fig. 8. EL spectra of the devices ITO/NPB (35 nm)/Zn(4-TfmBTZ)$_2$ (x nm)/LiF (1.8 nm)/Al (150 nm) at applied voltage of 8 V, x = 20, 30, 40 nm.

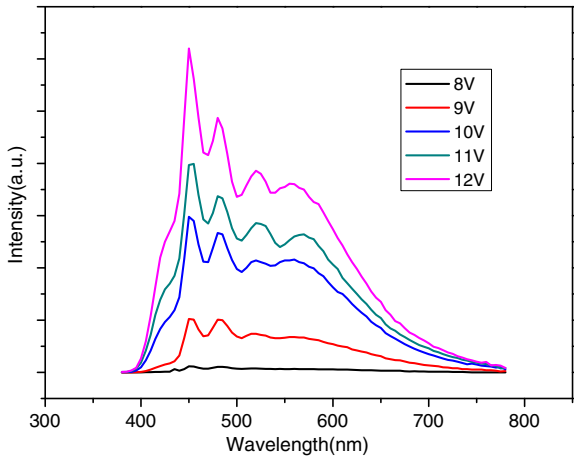

Fig. 9. EL spectra of device A with 20 nm Alq_3 layer at different applied voltage.

organic material film, a wide range of intermolecular distance and relative orientations exist at organic/organic interface, none of donor and accept molecular pairs are necessarily optimum for electroplex formation. This results in a wide range electroplex emission frequencies and efficiencies.

As can be seen from Fig. 2, EL spectra of device A at a certain voltage are dramatically controlled by thickness of Alq_3 layer. A similar phenomenon had been reported [29]. The intensity of all emission bands can be increased with increasing thickness of Alq_3 layer from 0 to 20 nm, and then decreased from 20 to 40 nm. The Alq_3/LiF/Al forms an Ohmic contact [30] so that inserting Alq_3 layer increases injecting of electrons, moreover, Alq_3 as an excellent electron transporting material also improves electron transporting rate. Thus, the charge injection and transport are balanced to lead to high recombination of electron–hole pair in every layer and NPB/Zn(4-TfmBTZ)$_2$ interface. Here, the optimization thickness of Alq_3 is 20 nm, which is just the diffusion length of Alq_3 exciton [31]. An evaporated Alq_3 film appears to be microcrystalline with grain size [31]. So Alq_3 layer is too thin to play well electron transporting role, moreover, Alq_3 excitons diffuse easily to cathode to be quenched in this case. But if Alq_3 becomes thicker than 20 nm, electric-field distributed in every layer at a certain voltage becomes weaker so that charge mobility was deduced, thus, the electron–hole pair ratios are decreased in every bulk and NPB/

Table 1
CIE coordinates and CRI of WOLEDs with Alq_3 layer thickness of 20 nm and 30 nm, respectively.

Driving bias (V)	Alq_3 with 20 nm			Alq_3 with 30 nm		
	CIE coordinates		CRI	CIE coordinates		CRI
	x	*y*		*x*	*y*	
8	0.30	0.34	90.2	0.32	0.36	88.5
9	0.30	0.35	85.8	0.32	0.36	88.2
10	0.30	0.35	85.9	0.32	0.36	85.8
11	0.29	0.32	88.1	0.31	0.36	84.0
12	0.29	0.33	87.9	0.31	0.35	86.2
13	0.30	0.33	89.9	0.31	0.35	86.4

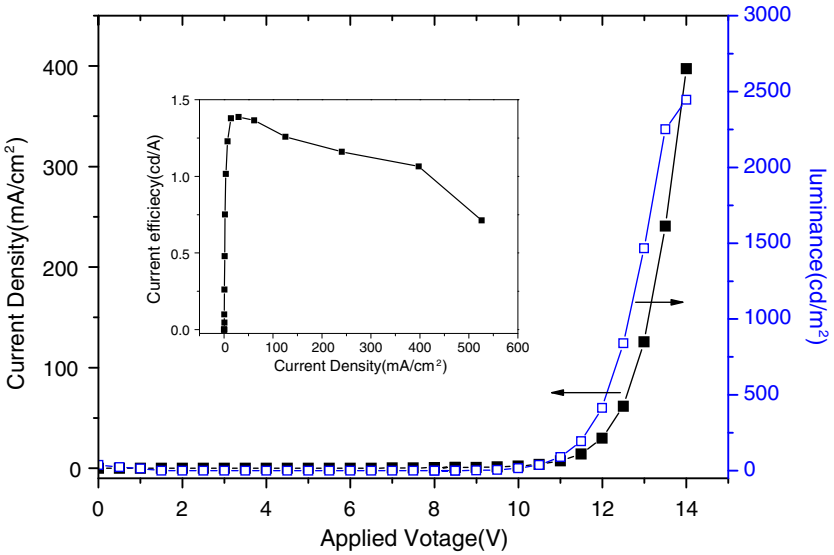

Fig. 10. Current density–luminance–voltage curves of device A with 20 nm Alq_3 layer, the inset shows its current efficiency vs current density curve.

$Zn(4\text{-}TfmBTZ)_2$ interface. When Alq_3 is 20 nm, electron transporting and Alq_3 exciton emission reach optimization simultaneously. It can be seen from the normalized EL spectra that the emission of electroplex increases in relative intensity with increasing thickness of Alq_3 layer. This is the reason that the charge tunneling through NPB/$Zn(4\text{-}TfmBTZ)_2$ interface becomes relatively more difficult because of weaker electric-field for the device with thicker Alq_3. In this case, the electroplex formation is relatively favorable in comparison with excions. Of course, Alq_3 exciton radiations also increase in relative intensity with increasing thickness of Alq_3 layer. The EL spectra of the device A with 20 nm Alq_3 at different applied voltage were shown in Fig. 9. Rising operating voltage will lead to an increased exciton emission at a larger rate than that of electroplex. This further indicates that the electroplex emission at low electric-field is relatively favorable while the exciton emissions are relatively facilitated at high electric-field.

Above mentioned results indicate that pure white light emission can be attained by adjusting Alq_3 layer thickness for device A. The CIE coordinates of device A at 12 V change from (0.29, 0.32) to (0.34, 0.38) when Alq_3 thickness changes from 10 nm to 40 nm. The most pure white-light emitting with CIE coordinate (0.30, 0.34) is obtained when Alq_3 layer thickness is 20 nm. Moreover, CIE coordinate of the devices are very insensitive to the applied voltage. For example, CIE coordinate region of the device A with Alq_3 thickness of 20 nm is (0.29–0.30, 0.33–0.34) at various forward bias (8–13 V). Its maximum CRI is 90.2 at 8 V (see Table 1), and maximum luminance reaches 2445 cd/m^2 at 14 V and maximum current efficiency 1.39 cd/A, as shown in Fig. 10. The brightness and luminous efficiency of the devices here are worse than the advanced WOLEDs at present, but it is believed that these characterizations will be improved further by optimizing the prepared technique of device.

4. Conclusion

In this paper, a new material $Zn(4\text{-}TfmBTZ)_2$ was used for white-light emitting. For the device ITO/NPB/$Zn(4\text{-}TfmBTZ)_2$/Alq_3/LiF/Al, the radiative processes from two different excited states: (i) molecular excited states (NPB, $Zn(4\text{-}TfmBTZ)_2$ and Alq_3 exciton), and (ii) bimolecular excited species (electroplexes at NPB/$Zn(4\text{-}TfmBTZ)_2$ interface) render white light output. Inserting an Alq_3 layer with appropriate thickness can increase intensity of every emission species. The most pure white light emission with CIE coordinates of (0.30, 0.34) can be attained by adjusting the Alq_3 layer thickness to 20 nm. Moreover, CIE coordinate of the devices are very insensitive to the applied voltage. The CIE coordinate region of the device with Alq_3 layer thickness of 20 nm is (0.29–0.30, 0.33–0.34) at various forward bias (8–13 V). For this device, the maximum CRI is 90.2 at 8 V, the maximum luminance reaches 2445 cd/m^2 at 14 V and the maximum current efficiency 1.39 cd/A.

Acknowledgements

This research work was financially supported by National Natural Scientific Foundation of China (21071108, 60976018), Program for Changjiang Scholar and Innovative Research Team in University (IRT0972), Key Program of Science and Technology of Ministry of Education (207015), Scientific and Technological Research Program of Taiyuan City (07020401) and Shanxi Natural Scientific Foundation (2008011008, 2010021023-2).

References

[1] B.W. D'Andrade, S.R. Forrest, Adv. Mater. 16 (2004) 1585.
[2] S. Reineke, F. Lindner, G. Schwartz, N. Seidler, K. Walzer, B. Lüssem, K. Leo, Nature 459 (2009) 234.
[3] D. Gupta, M. Katiyar, M. Deepak, Opt. Mater. 28 (2006) 295.
[4] J. Thompson, R.I.R. Blyth, M. Mazzeo, M. Anni, G. Gigli, R. Cingolani, Appl. Phys. Lett. 79 (2001) 560.
[5] D. Wang, W.L. Li, Z.S. Su, T.L. Li, B. Chu, D.F. Bi, L.L. Chen, W.M. Su, H. He, Appl. Phys. Lett. 89 (2006) 233511.
[6] J. Kalinowski, M. Cocchi, D. Virgili, V. Fattori, J.A.G. Williams, Adv. Mater. 19 (2007) 4000.
[7] C.E. Finlayson, J.S. Kim, M.J. Liddell, R.H. Friend, S.H. Jung, A.C. Grimsdale, K. Müllen, J. Chem. Phys. 128 (2008) 044703.
[8] Y.Y. Hao, J.F. Lei, X.H. Fang, W.H. Fan, B.S. Xu, Curr. Appl. Phys. 10 (2010) 744.
[9] J. Kalinowski, J. Non-Crystalline Solids 354 (2008) 4170.
[10] M. Cocchi, D. Virgili, C. Sabatini, J. Kalinowski, Chem. Phys. Lett. 421 (2006) 351–355.
[11] S.P. Singh, Y.N. Mohapatra, M. Qureshi, S.S. Manoharan, Appl. Phys. Lett. 86 (2005) 113505.
[12] M.T. Li, W.L. Li, L.L. Chen, Z.G. Kong, B. Chu, B. Li, Appl. Phys. Lett. 88 (2006) 091108.
[13] M. Cocchi, J. Kalinowski, D. Virgili, V. Fattori, S. Develay, J.A.G. Williams, Appl. Phys. Lett. 90 (2007) 163508.
[14] B.W. D'Andrade, J. Brooks, V. Adamovich, M.E. Thompson, S.R. Forrest, Adv. Mater. 14 (2002) 1032.
[15] S.A. Jenekhe, Adv. Mater. 7 (1995) 309.
[16] E.L. Williams, K. Haavisto, J. Li, G.E. Jabbour, Adv. Mater. (Weinheim, Ger.) 19 (2007) 197.
[17] B.W. D'Andrade, M.E. Thompson, S.R. Forrest, Adv. Mater. 14 (2002) 147.
[18] S.Y. Yang, M.X. Jiang, Chem. Phys. Lett. 484 (2009) 54.
[19] C.C. Yang, C.J. Hsu, P.T. Chou, H.C. Cheng, Y.O. Su, M.K. Leung, J. Phys. Chem. B 114 (2010) 756.
[20] Y. Hamada, T. Sano, H. Fujii, Y. Nishio, H. Takahashi, K. Shibata, Jpn. J. Appl. Phys. Part 1 35 (1996) 1339.
[21] X. Xu, Y. Liao, G. Yu, H. You, C. Di, Z. Su, D. Ma, Q. Wang, S. Li, S. Wang, J. Ye, Y. Liu, Chem. Mater. 19 (2007) 1740.
[22] G. Yu, S. Yin, Z. Shuai, D. Zhu, J. Am. Chem. Soc. 123 (2003) 14816.
[23] B.S. Xu, H.X. Xu, X.H. Fang, L.Q. Chen, H. Wang, Y.Y. Hao, China Patent, 200910073701.7, 2009.
[24] M. Cocchi, J. Kalinowski, L. Murphy, J.A. Gareth Williams, V. Fattori, Organic Electronics 11 (2010) 388.
[25] A.W. Hains, Z. Liang, M.A. Woodhouse, B.A. Gregg, Chem. Rev. Article ASAP. doi:10.1021/cr9002984..
[26] J. Kalinowski, N. Camaioni, P. Di Marco, V. Fattori, A. Martelli, Appl. Phys. Lett. 72 (1998) 513.
[27] J. Kalinowski, M. Cocchi, G. Giro, V. Fattori, P. Di Marco, J. Phys. D: Appl. Phys. 34 (2001) 2274.
[28] J. Kalinowski, M. Cocchi, P. Di Marco, W. Stampor, G. Giro, V. Fattori, J. Phys. D: Appl. Phys. 33 (2000) 2379.
[29] J. Feng, F. Li, W.B. Gao, S.Y. Liu, Y. Liu, Y. Wang, Appl. Phys. Lett. 78 (2001) 3947.
[30] M. Stößel, J. Staudigela, F. Steubera, J. Blässinga, J. Simmerera, A. Winnackerb, H. Neunerc, D. Metzdorfc, H.-H. Johannesc, W. Kowalskyc, Syn. Metals 111–112 (2000) 19–24.
[31] C.W. Tang, S.A. VanSlyke, C.H. Chen, J. Appl. Phys. 65 (1989) 3610.

Organic Electronics 12 (2011) 143–147

Contents lists available at ScienceDirect

Organic Electronics

journal homepage: www.elsevier.com/locate/orgel

Percolation behaviour in high mobility p-channel polymer/small-molecule blend organic field-effect transistors

Jeremy Smith [a], Martin Heeney [b], Iain McCulloch [b], Jennifer Nekuda Malik [c], Natalie Stingelin [c], Donal D.C. Bradley [a], Thomas D. Anthopoulos [a,*]

[a] Department of Physics and Centre for Plastic Electronics, Blackett Laboratory, Imperial College London, London SW7 2BW, UK
[b] Centre for Plastic Electronics and Department of Chemistry, Imperial College London, London SW7 2AZ, UK
[c] Centre for Plastic Electronics and Department of Materials, Exhibition Road, Imperial College London, London SW7 2AZ, UK

ARTICLE INFO

Article history:
Received 5 September 2010
Received in revised form 22 October 2010
Accepted 25 October 2010
Available online 10 November 2010

Keywords:
Organic field-effect transistors
Electronic percolation
Blend organic semiconductors

ABSTRACT

Organic transistors based on blends of 2,8-difluoro-5,11-bis(triethylsilylethynyl) anthradithiophene (diF-TES ADT) and poly(triarylamine) [PTAA] are strong candidates for application in future large-volume organic electronics because of their record breaking carrier mobility and environmental stability. Here we report on the dependence of hole transport on the composition of diF-TES ADT:PTAA blends. Maximum mobility is obtained only for blends containing $\geqslant$39 wt.% diF-TES ADT. At compositions below this threshold the hole mobility is drastically reduced and is found to be equal to that of the neat polymer matrix, i.e. PTAA ($\sim 10^{-3}$ cm^2/V s). Scanning atomic force and polarised light microscopy, combined with differential scanning calorimetry, show that this threshold corresponds to the appearance of crystalline, acene-rich regions in such blend films, and the formation of high mobility conduction pathways between the source and drain electrodes. The dependence of hole mobility on diF-TES ADT concentration can be modelled using a simple percolation model. The present results provide important insights into the microstructure evolution in this high performance semiconducting blend and could prove valuable for the development of the next generation organic transistors.

© 2010 Elsevier B.V. All rights reserved.

1. Introduction

Blends comprising small-molecular and polymeric organic semiconductors have recently shown great promise for organic electronics due to their high charge carrier mobilities, ease of solution processing and device performance uniformity [1–9]. One such system based on 2,8-difluoro-5,11-bis(triethylsilylethynyl) anthradithiophene (diF-TES ADT) blended with amorphous poly(triarylamine)s [PTAA], has demonstrated a hole mobility up to 2.4 cm^2/V s when integrated in organic field-effect transistor architectures (OFETs) [1]. The microstructure of the diF-TES ADT:PTAA blend film is the key factor in achieving this high mobility value. Spin casting of the blend solution onto a suitably treated substrate produces a highly desirable vertical phase separation of the two components, which leads to the formation of large acene crystals at the top surface. A carefully designed top-gate bottom-contact (TG-BC) transistor architecture can then be used to exploit the excellent charge carrier properties at this blend film/air interface. It is important to note, however, that the solid-state microstructure of such blend films is most likely more complex; lateral phase separation may occur and grain boundaries between the high mobility acene-dominated crystalline domains can form [3].

One specific problem associated with the polymer matrix used in the diF-TES ADT:PTAA blend is its low hole mobility, which is typically several orders of magnitude lower ($\sim 10^{-3}$ cm^2/V s) than that of diF-TES ADT (>1 cm^2/V s) [10]. In order to overcome this limitation, efficient

* Corresponding author. Tel.: +44 (0) 207 594 6669; fax: +44 (0) 207 594 2077.
E-mail address: thomas.anthopoulos@imperial.ac.uk (T.D. Anthopoulos).

1566-1199/$ - see front matter © 2010 Elsevier B.V. All rights reserved.
doi:10.1016/j.orgel.2010.10.017

percolation of charge carriers through the diF-TES ADT phase is required to realise good device performance [5,11,12]. A high polymer content yields lower mobility values due to the fact that insufficient amount of the acene phase is formed at the semiconductor–dielectric interface. This has already been previously shown for blends based on triisopropylsilylethynyl (TIPS) pentacene – another promising small-molecular semiconductor – and an amorphous polymer. A minimum TIPS-pentacene concentration in the range 40–50 wt.% was required to achieve efficient vertical phase separation in such binaries, with the acene being expelled towards the dielectric, resulting in a good transistor performance [7]. However, in the case of diF-TES ADT blends, if the semiconductor content is too high, the film starts to become non-uniform, and increased dewetting occurs during solution processing. Therefore, judicious formulation of the blend composition is necessary in order to allow sufficient percolation while maintaining good film forming properties and at the same time minimising the quantity of diF-TES ADT required.

Here we study the microstructural evolution of diF-TES ADT:PTAA blend films as a function of diF-TES ADT concentration and its effect on field-effect hole mobility. The diF-TES ADT:PTAA blend was selected because it is known to exhibit the highest hole mobility ever measured in solution processed blend based OFETs. A connection between the solid-state microstructure, degree of crystallinity and the electronic properties of OFETs using such blends is established based on the percolation model outlined below. The latter could provide valuable information for the development of next generation of high-performance organic semiconducting blends.

2. Percolation theory

Percolation thresholds have been observed previously in other polymer/small-molecule blend OFETs and have been successfully modelled using a percolation analysis based upon high and low mobility materials [4]. In this analysis the overall measured mobility (μ) in the OFET can be fitted by a sigmoidal function of the form,

$$\mu = \mu_{\text{polymer}} + \frac{\mu_{\text{blend-max}}}{1 + \exp(\frac{c_0 - c}{d})} \quad (1)$$

where c is the concentration of high mobility material, c_0 is the percolation threshold and d a fitting parameter. The two carrier mobilities are the mobility of the low mobility material, i.e. the matrix polymer (μ_{polymer}) in this case, and the maximum mobility ($\mu_{\text{blend-max}}$) obtainable in the blend. If we now consider the morphology at the conduction interface (i.e. the top film/dielectric interface in the case of a TG-BC transistor) both small-molecule rich and polymer rich phases will be present, with the former dominating charge transport. It is therefore reasonable to assume that conduction pathways from source to drain (S–D) electrodes will contain certain fractions of each of these two phases. A particular percolation pathway in the film will have a mobility of μ_{path} given by,

$$\mu_{\text{path}}(f) = \frac{\mu_H}{1 + f(\frac{\mu_H}{\mu_L} - 1)} \quad (2)$$

where f is the volume fraction of low mobility material and the subscripts H and L correspond to high and low mobility, respectively. When μ_H becomes considerably larger than μ_L then μ_{path} becomes essentially independent of μ_H. In diF-TES ADT:PTAA blend systems, the low mobility regions will be approximately equal to the mobility of the pure polymer ($\mu_L \approx \mu_{\text{polymer}}$). It is to be noted that the high mobility region must have a mobility value equal to or greater than the maximum possible value in the blend. The latter should, in principle, be equal to the intrinsic mobility of the neat small-molecule material (i.e. the high mobility component) but in practice is not measureable in a thin film OFET due to problems related to processing a small-molecular material from solution without dewetting, the presence of grain boundaries, and/or limited charge carrier injection from the S-D contacts, all of which can negatively affect transport. Hence we can assume that $\mu_H \geqslant \mu_{\text{blend-max}}$. Finally, combining the fit of Eq. (1) to data and Eq. (2), the fraction of high mobility phase ($1-f$) at the conduction interface (i.e. the transistor channel) can be determined as a function of small-molecule concentration, c, from the measured device mobility, μ, of these blend structures.

3. Experimental

Thin films were deposited onto glass substrates that had been cleaned by sonication in detergent solution (DECON 90) from 4 wt.% (total solid content) 1,2,3,4-tetrahydronaphthalene (tetralin) solutions by spin coating at 500 rpm for 10 s followed by 2000 rpm for 20 s. Neat diF-TES ADT was spin coated at 3000 rpm for 30 s from a 1 wt.% solution in chloroform. The PTAA had a weight average molecular weight of 96 kDa. All films were then annealed at 100 °C for 5 min in nitrogen. Light microscopy images were taken in transmission between crossed polarisers using a Nikon LV100. Atomic force microscopy was carried out using a Pacific Nanotechnology Nano-R2 machine in close-contact mode.

Differential scanning calorimetry (DSC) was conducted on drop-cast films (prepared from solutions as described above), which had been dried at 100 °C for > 1 h to ensure that no solvent peaks were measured. Drop-cast films were employed because spin-casting could not provide enough material to perform the DSC measurements. Thermograms were recorded under nitrogen at a scan rate of 10 °Cmin^{-1} with a Mettler Toledo DSC822 instrument. The sample weights were ~5 mg.

Top-gate, bottom-contact transistors were fabricated on glass using the same spin conditions and solutions detailed above. Gold source and drain electrodes (30 nm) were first deposited by thermal evaporation and then treated with a pentafluorobenzene thiol monolayer (see reference [1]). Channel lengths and widths were in the range of 20–100 μm, and 0.5–2 mm, respectively. After semiconductor deposition, a fluoropolymer dielectric (CYTOP) was spin coated at 2000 rpm for 60 s to form a 900 nm layer. The CYTOP was cured at 100 °C for 20 min. Finally, aluminium top-gate electrodes were thermally evaporated. Electrical characterisation of the OFETs was carried out in nitrogen using a Keithley 4200 semiconductor parameter analyser. The field effect mobility in saturation was calculated from,

$$\mu_{sat} = \frac{L}{WC_i}\frac{\partial^2 I_{D,sat}}{\partial V_G^2} \quad (3)$$

where L is the device channel length, W the channel width, C_i the geometric capacitance of the dielectric (2.1 nFcm^{-2} for our films), V_G the gate voltage and $I_{D,sat}$ the drain current in the saturation regime.

4. Results and discussion

Blend films prepared on glass as described above were first characterised using polarised optical microscopy (PLM) and atomic force microscopy (AFM) (Fig. 1). In the PLM images, crystallisation of a diF-TES ADT rich phase is evident for compositions of > 37.5 wt.% diF-TES ADT, with grain sizes of the crystals formed being of the order of 50 μm. Above 75 wt.% the thin-films started to become non-uniform with some regions of the substrates found to be not fully covered. At 95 wt.% diF-TES ADT, the films severely dewetted from the substrates, resulting in only small semiconducting islands. In order to create a thin film of neat diF-TES ADT, it was necessary to spin cast from chloroform rather than tetralin. The lower boiling point of this solvent allowed rapid solvent removal, and thus prevented dewetting from occurring. However, chloroform is not an ideal solvent for the blends since it does not allow time for significant phase separation or the formation of large ordered grains. Indeed, the grain size of diF-TES ADT crystals in such neat films were found to be considerably smaller (~5 μm) compared to the crystalline blend structures.

Crystallisation of the organic semiconductor on the top surface of the blend architecture, especially for higher diF-TES ADT content, is also evident using AFM (Fig. 1, bottom panels). In addition, peak-to-peak surface roughness, R, can be deduced from the AFM data. For blend compositions below 25 wt.% diF-TES ADT the roughness was found to be (2.1 ± 0.7) nm, whereas at 50 wt.% R increased to (10.7 ± 1.3) nm. At an intermediate small-molecule content (37.5 wt.%), partial crystallisation is observed with diF-TES ADT domains on the micron scale forming. At high diF-TES ADT content, extremely non-uniform thin-film structures are again observed. The surface roughness of the neat diF-TES ADT film cast from chloroform was significantly more pronounced (~100 nm) compared to blend films, rendering such structures less suitable for use in top-gate OFETs.

In addition to domain/grain size, the degree of crystallinity of the semiconductor in the diF-TES ADT:PTAA blend was quantified using differential scanning calorimetry (DSC). Melting endotherms were observed for blends of a diF-TES ADT content of ⩾25 wt.% (Fig. 2a). The melting temperature, T_m, was affected by addition of PTAA only at a polymer concentration of >40 wt.% (Fig. 2b), indicating that for blends comprising more than ~70 wt.% small-molecule, the latter can crystallise essentially unhindered. From the melting endotherms we also can deduce the enthalpy of fusion, ΔH_f, which is directly correlated to the degree of crystallinity of the diF-TES ADT structures in such blends. For diF-TES ADT rich blends (75–100 wt.%), ΔH_f first linearly decreases with PTAA content (Fig. 2c), however, then stabilises for blends comprising 32.5–62.5 wt.% at around a value of 30 J/g. Only when decreasing the diF-TES ADT content further, is ΔH_f drastically reduced. This suggests that for the interim blend compositions (37.5–62.5 wt.% diF-TES ADT) the degree of crystallinity of the small-molecule component, while lower than for neat structures, is essentially unaffected by the further addition of PTAA, but below this there is a rapid reduction in crystallinity.

Top-gate, bottom-contact thin film transistors were then fabricated from blends of a range of compositions. Fig. 3 shows the transfer characteristics for devices based on blends with low (Fig. 3a) and high (Fig. 3b) concentrations of diF-TES ADT. It is evident that there is a significant enhancement of the channel current in devices based on blends with high diF-TES ADT concentrations with virtually no change to the threshold voltage, current on/off ratio or hysteresis during transistor operation. All devices exhibit threshold voltages between +5 and −5 V, on/off ratios of $10^{3.5}$–$10^{4.2}$ and generally display well behaved characteristics. The minor degradation of the subthreshold

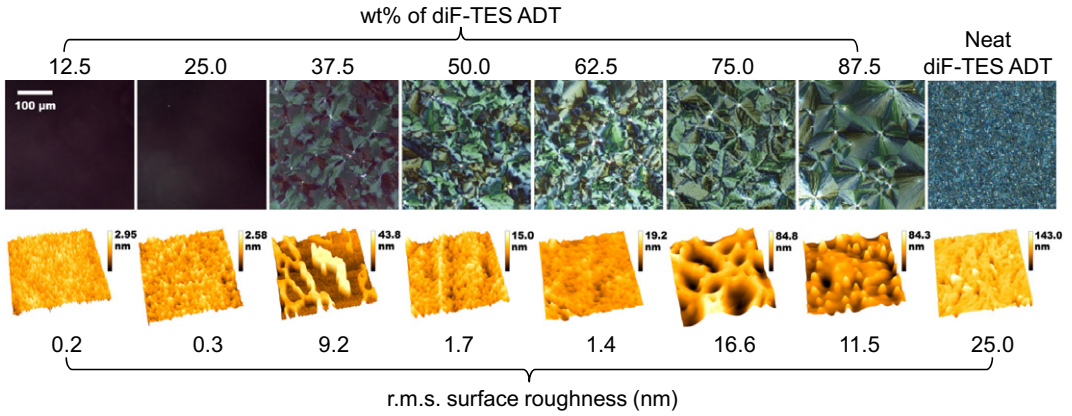

Fig. 1. Polarised optical microscopy and atomic force microscopy images for blend films of diF-TES ADT and PTAA. Numbers indicate the wt.% of diF-TES ADT in the blend. All films were spin cast from tetralin except the neat diF-TES ADT which was spin cast from chloroform. AFM images are of a 5 × 5 μm area and r.m.s. surface roughnesses, as well as peak-to-peak heights, are indicated.

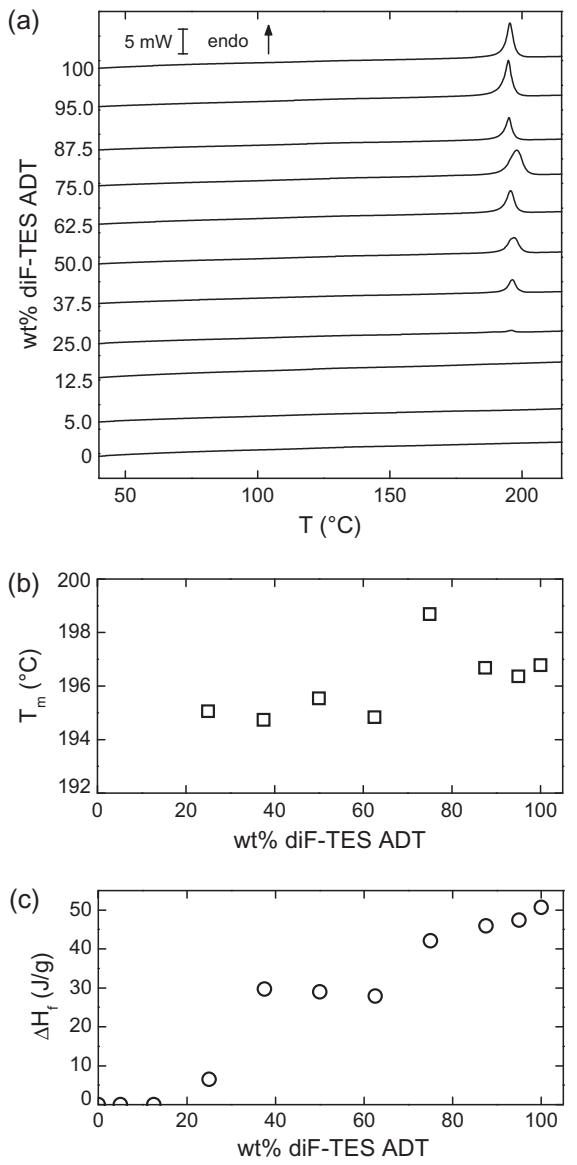

Fig. 2. (a) Differential scanning calorimetry first-heating thermograms obtained for diF-TES ADT:PTAA blends of a range of compositions (heating rate at 10 °C min^{-1}). (b) Melting temperatures of the diF-TES ADT rich phase as function of blend composition. (c) Enthalpies of fusion as deduced from the thermograms presented in (a), which can be directly correlated to the degree of crystallinity of the diF-TES ADT fraction. Crystallisation is evident above ~20 wt.% diF-TES ADT.

slope in OFETs with high diF-TES ADT concentrations may be attributed to the formation of traps at the grain boundaries of the polycrystalline acene phase [13]. There is also a very slight decrease in on/off ratio on the addition of more diF-TES ADT, most likely as a result of the increased bulk conductivity of the small molecule leading to higher off currents. The hole mobility, measured in saturation, is plotted in Fig. 4 as a function of diF-TES ADT content, with averages taken over at least three transistors, and demonstrates a clear threshold concentration. When fitting the OFET data using Eq. (1) for compositions of less than 62.5

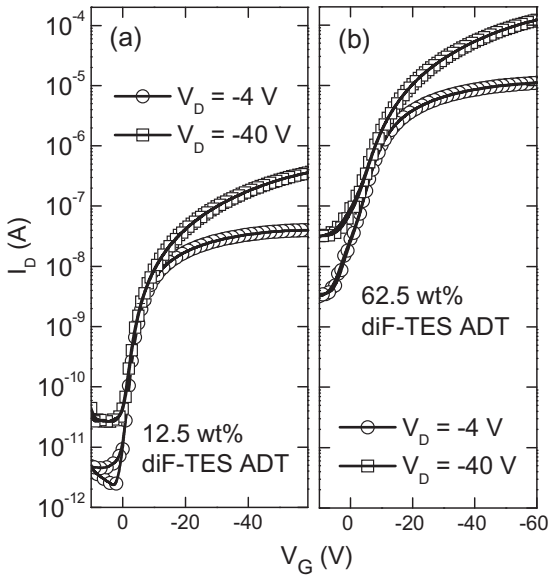

Fig. 3. Transfer characteristics for diF-TES ADT:PTAA OFETs with (a) 12.5 wt.% diF-TES ADT and (b) 62.5 wt.% diF-TES ADT. Devices had a top-gate bottom-contact architecture and were measured at $V_D = -4$ V (linear) and -40 V (saturation). Devices had channel lengths and widths of 50 μm and 1 mm, respectively.

wt.% diF-TES ADT, the following parameters were extracted: $\mu_{polymer} = 0.0048$ $cm^2/V\,s$, $\mu_{blend-max} = 1.79$ $cm^2/V\,s$, $c_0 = 38.9$ wt.% and $d = 2.06$ wt.%. From Eq. (2), f was calculated as a function of diF-TES ADT concentration and the fraction of high mobility phase, $(1-f)$, is also plotted in Fig. 4. The reduction in mobility and increase in mobility variation above 62.5 wt.% can be attributed to the decreased unifor-

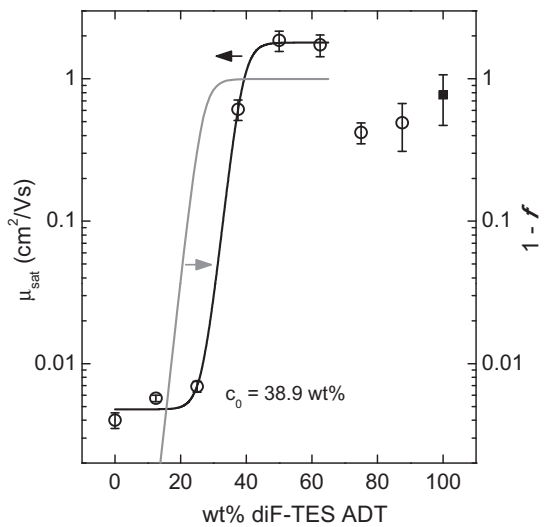

Fig. 4. Hole mobility calculated for OFETs with varying blend composition. The data is fitted with Eq. (1) to extract a percolation threshold, c_0. Right axis shows the fraction of diF-TES ADT $(1-f)$ in the conducting pathways based on the percolation model. (The 100 wt.% diF-TES ADT film was processed from chloroform while all other compositions were processed from tetralin).

mity and increased surface roughness of the blend film as the semiconductor appeared to be able to crystallise essentially unhindered, which is evidenced by the fact that the melting point was not significantly affected by addition of the polymer. Increased grain boundary density may also play a role in the relatively poor device performance found in the case of neat diF-TES ADT. This observation further highlights the benefit of blending small-molecules with polymers since a $\mu_{blend-max}$ can be obtained that is greater than the OFET mobility obtained by simple solution deposition of neat diF-TES ADT.

The percolation threshold for hole mobility corresponds well with the observation of birefringence in the PLM images, and evidence of crystallinity from DSC, which suggests that the diF-TES ADT rich phase forms molecularly ordered regions suitable for high device performance. At very low diF-TES ADT content, the blend films appear to exhibit a single amorphous phase and hence the mobility is low. For diF-TES ADT concentrations between ~20–39 wt.% the fraction of the crystalline phase in the conduction pathways, $(1-f)$, increases sharply but it is only when it becomes significant (i.e.>0.5) that a rapid enhancement of the measured mobility is seen. Above the percolation threshold $(1-f)$ is very close to 1. This highlights the importance of electronic percolation between high mobility regions in the thin film and demonstrates that for the best device performance there must be a very high fraction of diF-TES ADT rich phase at the charge transporting interface. In our case, for the highest mobility blends, only ~0.3 wt.% polymer phase is present in the conduction pathways. This is consistent with the previously observed vertical phase separation effect measured using dynamic secondary ion mass spectrometry and dual-gate transistor architectures [1] whereby the small-molecule moves to the top surface. Such effects are one of the major factors contributing to the high hole mobilities achieved, however, the dependence of crystalline grain microstructure on blend composition also plays a role.

5. Summary and conclusions

In summary, we have demonstrated that for the diF-TES ADT:PTAA blend system there is a critical concentration of small-molecular material required to obtain high performance OFETs. The saturation mobility in these devices can be fitted using a percolation model with the threshold relating to the formation of a crystalline, high mobility, diF-TES ADT rich phase. For diF-TES ADT concentrations greater than ~20 wt.%, the acene-rich phase starts to form but percolation only occurs when a significant fraction of this phase accumulates into conduction pathways. The measured mobility threshold is observed to be ~39 wt.% diF-TES ADT. Above this value uniform, polycrystalline films can be fabricated yielding OFETs with hole mobilities approaching 2 cm^2/V s. However, high concentrations of diF-TES ADT lead to the formation of non-uniform films and a significantly reduced hole mobility. Further improvements to the device performance could therefore be made by increasing the polymer mobility whilst ensuring that phase separation still leads to a high fraction of diF-TES ADT rich phase in the conducting pathways of the OFET. To this end, the understanding of relevant interrelationships between microstructure and charge transport, and in particular knowledge of how to induce efficient percolating pathways in such binaries, is vital to produce blend semiconductor systems that combine excellent mobilities with good film forming characteristics and uniformity. The present work provides an important contribution to OFET design for future high performance applications.

Acknowledgments

We are grateful to the Engineering and Physical Sciences Research Council (EPSRC) grant numbers EP/E02730X/1, EP/C539516/1, Research Councils UK (RCUK), European Community's Seventh Framework Programme (FP7/2007-2013) under grant agreement n 212311 of the ONE-P project and the Lee-Lucas endowment for financial support. T.D.A. is an RCUK Fellow/Lecturer.

References

[1] R. Hamilton, J. Smith, S. Ogier, M. Heeney, J.E. Anthony, I. McCulloch, D.D.C. Bradley, J. Veres, T.D. Anthopoulos, Adv. Mater. 21 (2009) 1166.
[2] J. Smith, R. Hamilton, M. Heeney, D.M. de Leeuw, E. Cantatore, J.E. Anthony, I. McCulloch, D.D.C. Bradley, T.D. Anthopoulos, Appl. Phys. Lett. 93 (2008) 253301.
[3] J. Smith, R. Hamilton, I. McCulloch, N. Stingelin-Stutzmann, M. Heeney, D.D.C. Bradley, T.D. Anthopoulos, J. Mater. Chem. 20 (2010) 2562.
[4] D.M. Russell, C.J. Newsome, S.P. Li, T. Kugler, M. Ishida, T. Shimoda, Appl. Phys. Lett. 87 (2005) 222109.
[5] S. Goffri, C. Muller, N. Stingelin-Stutzmann, D.W. Breiby, C.P. Radano, J.W. Andreasen, R. Thompson, R.A.J. Janssen, M.M. Nielsen, P. Smith, H. Sirringhaus, Nature Mater. 5 (2006) 950.
[6] N. Stingelin-Stutzmann, E. Smits, H. Wondergem, C. Tanase, P. Blom, P. Smith, D. de Leeuw, Nature Mater. 4 (2005) 601.
[7] M.-B. Madec, D. Crouch, G.R. Llorente, T.J. Whittle, M. Geogheganc, S.G. Yeates, J. Mater. Chem. 18 (2008) 3230.
[8] L. Qiu, J.A. Lim, X. Wang, W.H. Lee, M. Hwang, K. Cho, Adv. Mater. 20 (2008) 1141.
[9] J. Kang, N. Shin, D.Y. Jang, V.M. Prabhu, D.Y. Yoon, J. Am. Chem. Soc. 130 (2008) 12273.
[10] O.D. Jurchescu, S. Subramanian, R.J. Kline, S.D. Hudson, J.E. Anthony, T.N. Jackson, D.J. Gundlach, Chem. Mater. 20 (2008) 6733.
[11] R.A. Street, J.E. Northrup, A. Salleo, Phys. Rev. B 71 (2005) 165202.
[12] P. Wolfer, C. Müller, P. Smith, M.A. Baklar, N. Stingelin-Stutzmann, Synth. Met. 157 (2007) 827.
[13] J. Smith, R. Hamilton, Y. Qi, A. Kahn, D.D.C. Bradley, M. Heeney, I. McCulloch, T.D. Anthopoulos, Adv. Funct. Mater. 20 (2010) 2330.

Organic Electronics 12 (2011) 148–153

Contents lists available at ScienceDirect

Organic Electronics

journal homepage: www.elsevier.com/locate/orgel

Concomitant tuning of metal work function and wetting property with mixed self-assembled monolayers

Chun-Yu Chen [a], Kun-Yang Wu [b,c], Yu-Chiang Chao [a], Hsiao-Wen Zan [d,*], Hsin-Fei Meng [a,*], Yu-Tai Tao [b,*]

[a] Institute of Physics, National Chiao Tung University, Hsinchu 300, Taiwan
[b] Institute of Chemistry, Academia Sinica, Taipei 115, Taiwan
[c] Department of Materials Science and Engineering, National Tsing-Hua University, Hsinchu 300, Taiwan
[d] Department of Photonics, National Chiao Tung University, Hsinchu 300, Taiwan

ARTICLE INFO

Article history:
Received 6 July 2010
Received in revised form 13 October 2010
Accepted 19 October 2010
Available online 2 November 2010

Keywords:
Self-assembled monolayer
Wetting property
Polymer light-emitting diode

ABSTRACT

The effect of the surface composition of a mixed self-assembled monolayer on the work function and wetting property of silver substrate are investigated with the mixtures of a fluorinated alkanethiol and a carboxyl-terminated alkanethiol of various chain lengths. The work function of silver can be tuned from 4.3 to 5.3 eV by changing the mixing ratio while the wetting property can be modulated by adjust the relative chain length of the fluorinated thiol and the carboxyl-terminated thiol. Thus solution-processed poly(para phenylene vinylene)-based polymer light-emitting diode was made possible with high efficiency of 6.7 cd/A and brightness of 40,000 cd/m^2.

© 2010 Elsevier B.V. All rights reserved.

1. Introduction

The operation of most organic semiconductor devices depends on a proper energy alignment of the metal electrodes and the organic layers. For example, low energy barriers for both hole and electron injection are required for the organic light-emitting diode, whereas the organic transistor requires Ohmic contact between the source-drain and the semiconductor [1–3]. For relatively stable and common metals, there are however practically very few choices of work functions: 4.3 eV for silver and aluminum, and 5.0 eV for gold [4–6]. The device design will become much more flexible if the work functions of the metals can be continuously tuned in a wide range. Modification/treatment of a metal surface by the adsorption of a specific species changes the tendency for charge departure from or attraction to the surface due to the local dipole moment introduced by the adsorbates [7–9]. In particular, self-assembled monolayers (SAMs) have been used to systematically modulate the work function of a metal through the various functional groups of the adsorbed molecules. Among these, SAMs of fluorinated hydrocarbon chains have been frequently used to increase the work function of various electrodes due to the strongly electron-withdrawing fluorine atoms [10–12]. It is demonstrated that carrier injection in hole-only devices can be enhanced by such modification. Whereas, SAMs of hydrocarbon were found to decrease the work function and suppress hole charge injection [13]. It is further demonstrated that continuous tuning of the work function can be achieved by the use of mixed SAMs of a fluorocarbon and a hydrocarbon [13,14], so that the amount of hole carriers can be systematically modulated by controlling the composition of the two compounds [13]. However, for devices prepared by solution process such as spin coating, there is a dilemma that the highly electronegative fluorine atoms provide not only the desired dipole moment for work function tuning but also the undesired poor wettability due to the low surface energy of the substrate it creates. In a mixed SAM where fluorinated hydrocarbon is mixed with a non-polar

* Corresponding authors. Tel.: +886 35731955 (H.F. Meng).
E-mail addresses: hsiaowen@mail.nctu.edu.tw (H.-W. Zan), meng@mail.nctu.edu.tw (H.-F. Meng), ytt@chem.sinica.edu.tw (Y.-T. Tao).

1566-1199/$ - see front matter © 2010 Elsevier B.V. All rights reserved.
doi:10.1016/j.orgel.2010.10.013

hydrocarbon component, wettability did not improve because the non-polar nature of hydrocarbon component, but the work function is reduced simultaneously. The poor wettability may cause problem in process such as spin-coating as the semiconducting materials may not adhere to the substrate. It is therefore of interest to control the work function and the wetting property of the metal independently.

Mixed monolayers containing one hydrophobic component and one hydrophilic component offer the opportunity to modulate the wetting property of the surface over a wide range [15]. It has also been demonstrated that the contact angle is highly surface-sensitive since the wetting liquid senses the structural change at the very top 2–3 Å region of the surface [15]. Thus by controlling the relative chain length of the two components, it is possible to "shield" the non-wetting character of one component by the wetting character of the other, or vice versa. In this work, mixtures of a fluorinated alkanethiol and a carboxyl-terminated alkanethiol with different chain lengths are used to form mixed SAMs on silver substrate in order to decouple their effect on the work function and surface wetting. The fluorinated alkanethiol serves to increase the work function, whereas the carboxyl-terminated alkanethiol is used to impart the needed wettability. The effect of the carboxyl group can be further enhanced by adjusting the relative chain length of the two in the mixture. As shown in Fig. 1(b), the carboxyl-terminated thiol is chosen to be longer than the fluorinated thiol such that solution containing the semiconductor is in contact mostly with the hydrophilic carboxyl groups. In the case where the two components are of the same chain length (Fig. 1(a)), the solution is in contact with both the hydrophilic carboxyl groups and the hydrophobic CF_3 groups. By forming mixed SAMs with different lengths, the work function of silver can be increased from 4.3 eV for the bare silver metal to 5.3 eV for modified silver without compromising the wetting/spreading of emissive conjugated polymer for PLED.

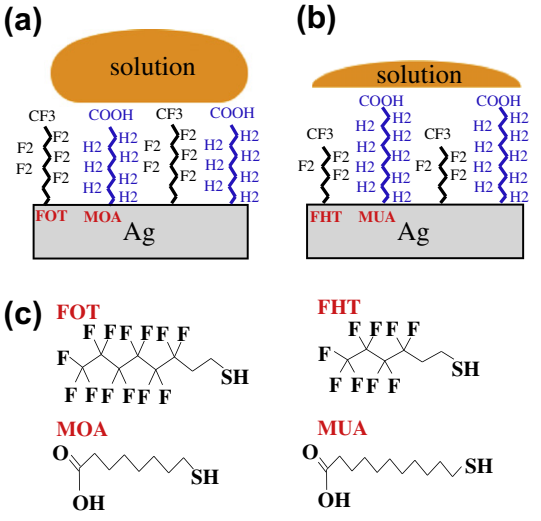

Fig. 1. The schematic plots showing the shapes of the solution drops on the mixed-SAMs with (a) equal molecular lengths and (b) non-equal molecular lengths. (c) Molecular structures of the molecules used for mixed self-assemble monolayer formation.

With proper SAM-modified silver as anode, polymeric light-emitting diodes with high efficiency and brightness close to that with ITO/PEDOT:PSS as anode were achieved for both top and bottom emission devices. This offers the opportunity to replace the commonly used but more resistive and expensive indium-tin-oxide (ITO)/poly(3,4-ethylenedioxythiophene):poly(styrenesulfonate) (PEDOT:PSS) anode with the low resistive and low cost silver metal anode for large area PLED and polymer solar cell application.

2. Experimental

Silver substrates were prepared on chromium-primed glass slides by thermal evaporation. The mixed SAM was prepared by submersing Ag substrate into a 1 mM ethanolic solution containing a fluorinated alkanethiol and a carboxyl-terminated alkanethiol in different ratios. The fluorinated alkanethiol used was either 3,3,4,4,5,5,6,6,6-nonafluoro-1-hexanethiol (FHT) or 3,3,4,4,5,5,6,6,7,7,8,8,8-tridecafluoro-1-octanethiol (FOT), and the carboxyl-terminated alkanethiol used was either 8-mercaptooctanoic acid (MOA) or 11-mercaptoundecanoic acid (MUA), all obtained from Aldrich and used without purification. The molecular structures of these SAM-forming components are shown in Fig. 1(c). Reflection–absorption IR spectra were taken with a Biorad FTS-60 Infrared spectrometer equipped with a MCT detector. A custom-designed optics unit with 86° incidence angle and p-polarized light were employed. Plasma-cleaned gold wafer was used as reference for all spectra. Contact angle was taken with a GBX DIGIDROP Goniometer, and Teflon-coated needles were used to dispense water and Toluene as the contacting liquid onto the surface of the monolayers. The data reported are the average of 4–5 drops measured on both sides. The structure of the PLED is Cr/Ag/mixed-SAMs/emission layer/cathode. The Cr is used as the adhesive layer for Ag. The thickness of Cr is 100 Å for top-emitting device and 30 Å for bottom-emitting device. The thickness of Ag is 800 Å for top-emitting device and 150 Å for bottom-emitting device. The substrate was immersed for 1 h before rinsing with absolute ethanol, acetone and blown dry with a pure nitrogen flow. Poly(para-phenylene vinylene, 800 Å) (Super Yellow from Merck) was spin-coated from a toluene solution (0.8 wt.%) as emission layer. The sample was annealed at 80 °C for 20 min in a glove box to remove the residual solvent. The cathode was Ca (100 Å)/Ag (150 Å) for top-emitting devices and Ca (350 Å)/Al (1000 Å) for bottom-emitting devices. ITO/PEDOT:PSS is used as anode for standard device. A 40 nm PEDOT:PSS (CLEVIOS™ P VP AI 4083) layer is spin coated on a cleaned and patterned ITO substrate and annealed at 200 °C in nitrogen for 10 min. The active area of the PLED was 1 mm^2. Electrode deposition was done by thermal evaporation under 10^{-6} torr. The work functions of the SAM-modified Ag surfaces were measured with a photoelectron spectrometer (AC-2, Riken Keiki) in ambient air with a UV source. The work function was calculated by plotting the square root of the total electron counts versus photoelectron energy and extrapolating the linear fit of the counts to zero as described in

literature [16]. The current density–voltage (J–V) and luminance–voltage (L–V) characteristics of the devices were measured by Keithly 2400 source meter and spectrophotometer PR650.

3. Results and discussion

Ellipsometry measurement of the mixed monolayer was carried out to confirm the monolayer nature of the co-adsorbed films. For example, in the MUA/FHT system, the measured film thickness varies between 6.5 Å (for single component FHT) and 12.0 Å (for single component MUA), depending on the composition.

Reflection absorption IR spectra were taken for the mixed monolayers as a function of the solution composition. With 8-mercaptooctanoic acid (MOA) mixed with the same chain length fluorinated thiol FOT, the intensity of characteristic absorption for carboxyl group at 1712 cm^{-1} decreases with increasing amount of FOT in the adsorbing solution, whereas that for the characteristic absorptions for C–F stretches between 1350 and 1250 cm^{-1} increase with more FOT in the adsorbing solution (Fig. 2). The surface composition correlates with the solution composition. Similar trends for the IR spectra of mixed monolayers composed of MOA and FHT or MUA and FHT, where the carboxyl-terminated thiol is longer than the fluorinated thiol. Based on the integration of the respective peaks, the surface composition was estimated and plotted versus solution composition, as shown in Fig. 3. The surface composition may deviate from the solution composition. Particularly when the chain lengths are much different. Thus for MUA/FHT system, the longer chain MUA will be more favored on the surface than the shorter chain. For the same chain length mixed system of MOA/FOT, the fluorinated component is more favored, presumably because its lower solubility in the ethanol solvent used [15].

One concern is the possible phase separation of the fluorinated component and the carboxyl-terminated alkyl component. In earlier work for mixed monolayer of fluorinated chain and alkyl chain [13], phase separation is possible but of small scale (tens of nanometers) that it is insignificant in affecting the macroscopic properties such as wetting and work function. In the current case where carboxyl groups are introduced, the potential H-bonding interaction between carboxyl group and fluorinated hydrocarbon [17,18] is expected to alleviate, not aggrevate the problem of phase separation.

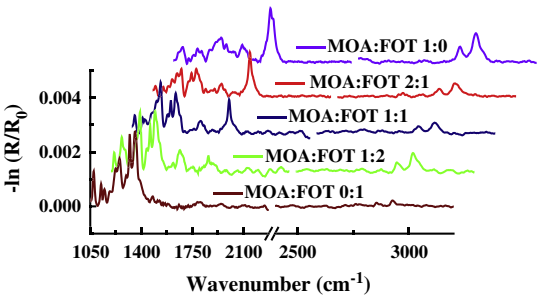

Fig. 2. Reflection–absorption IR spectra of mixed monolayers of MOA (carboxyl-terminated thiol) and FOT (fluorinated thiol) on Ag.

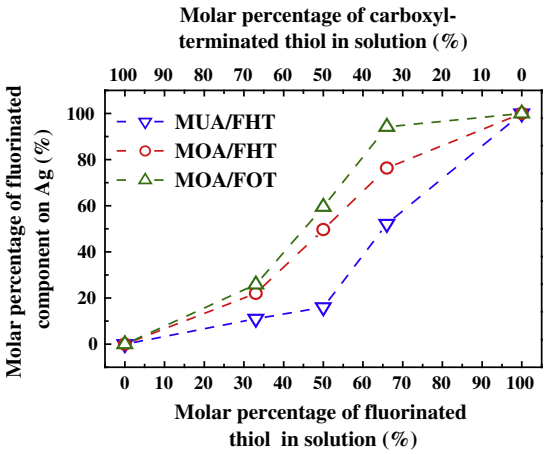

Fig. 3. Plots of surface composition as a function of solution composition, based on the integrated areas under the ν_s (CF-) band (~1350 cm^{-1}) and ν_s (C=O in COOH) band (~1712 cm^{-1}), for the mixed SAMs.

The influences of the molar percentage and chain length of fluorinated and carboxyl-terminated thiols on the wetting property of Ag are shown in Fig. 3(a). On Ag surface covered by a single component MOA or MUA monolayer, the water contact angle is lower than 20°, due to the hydrophilic nature of carboxyl group at the outmost surface. The contact angle increases with increasing amount of fluorinated alkanethiol in the solution. For mixed-SAMs with equal chain length (MOA/FOT), the water contact angle reaches a plateau over 90° as the molar percentage of FOT is higher than 50%.

For Ag surface modified by mixed-SAMs of MOA/FHT, where the carboxyl-terminated thiol is two carbon atoms longer than the fluorinated thiol, the water contact angle increases with increasing ratio of FHT in solution and reaches a plateau as the percentage of FHT is higher than 80%. The wetting property is improved (contact angle decreased) comparing the contact angles at the same mixing ratios. For mixed monolayers prepared from MUA/FHT, where the carboxyl-terminated thiol is six carbon atoms longer than the fluorinated thiol, the contact angle of FHT/MUA-modified Ag surface increases linearly without a plateau and reaches the highest water contact angle around 110° for pure FHT monolayer. This implies the wettability of the MUA/FHT-modified Ag surface is further improved if comparing the contact angles at the same mixing ratios in solution. Longer carboxyl-terminated thiol seems to shield the hydrophobic component down under and rendering the surface relatively more "hydrophilic".

Wettability relates to the sticking property of a polymer by spin-coating. In this work, it was found that formation of polymer film by spin-coating is impossible or very difficult when the substrate surface is highly hydrophobic (for example, the water contact angle is higher than 90°). The polymer solution tends to slip away from the substrate while the substrate spins. It is noted that toluene is used as the solvent for the polymer solution. Similar wetting behavior for toluene on the modified surface was observed (Fig. 4). For the equal length MOA/FOT mixed

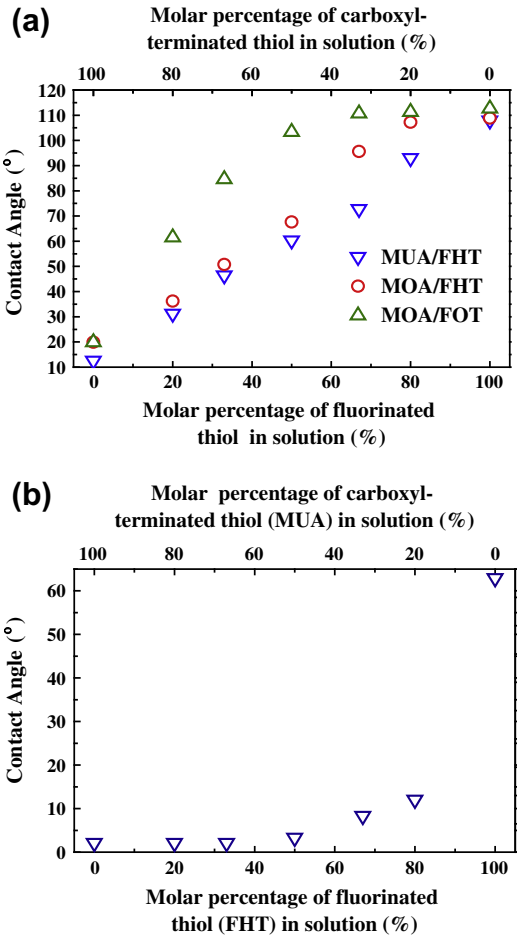

Fig. 4. (a) The water contact angle on mixed SAMs-modified Ag. FHT and FOT are fluorinated alkanethiol with six and eight carbon atoms, respectively. MOA and MUA are carboxyl-terminated alkanethiol with eight and eleven carbon atoms, respectively. (b) The toluene contact angle on mixed SAMs containing MUA and FHT on Ag.

monolayer-modified Ag, the polymer cannot be spun on as the amount of FOT is higher than 50%. For the Ag surface modified by MUA/FHT monolayer, the wetting property of the surface is improved as stated above. Higher percentage of FHT is allowed before the surface becomes too hydrophobic to retain the polymer upon spin coating. The higher amount of FHT serves to increase the work function and reduce the hole injection barrier.

SAM-induced work function change was measured by AC2 in ambient, as shown in Fig. 5. The work function of bare Ag is 4.3 eV (compare to a value of 4.4 eV reported in literature [10]). For Ag modified with carboxyl-terminated SAM (MOA or MUA), the work function increases to about 4.9–5.0 eV which is still not sufficient for hole injection into most luminescent polymers. By increasing the amount of fluorinated component in a mixed monolayer, the work function of the modified Ag now can be tuned. It is noted that for MOA/FHT or MUA/FHT systems, where the carboxyl-terminated chain is longer than the fluorinated chain, the work functions initially remained similar or even decreased until the

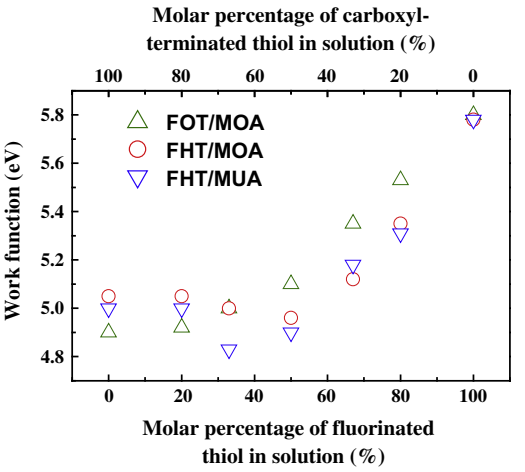

Fig. 5. The work function of mixed SAMs-modified Ag. FHT and FOT are fluorinated alkanethiol with six and eight carbon atoms, respectively. MOA and MUA are carboxyl-terminated alkanethiol with eight and eleven carbon atoms, respectively.

solution percentage for fluorinated component is more than 50%, when the work function increased steadily, up to around 5.8 eV as the amount of fluorinated component is 100%. This value is somewhat higher than the 5.5 eV reported for perfluorinated C10 alkanethiol monolayer on Ag [10]. With equal length MOA/FOT monolayer as modifier, no such dip in work function was observed. The initial decrease of the work function may be due to the re-orientation of the carboxyl groups at the interface. Nevertheless, the amount of FOT is limited to well below 50% to give acceptable wettability for spin-coating to work. This will limit the work function to be below 5.0 eV. With fluorinated component shorter than the carboxyl-terminated component, higher amount of fluorinated component is allowed to give acceptable wettability and the work function can be increased up to 5.3 eV, which is favorable for reducing charge injection barrier.

To further demonstrate the continuous work function change of mixed-SAM-modified Ag surfaces indeed influence the hole injection property of Ag electrode, the current density (J)–voltage (V) relationship of hole-only diodes are compared. J–V curves of the device in the structure Cr/Ag/mixed SAMs (FHT/MUA)/super yellow (SY) or poly(3-hexyl thiophene) (P3HT)/Al are demonstrated in Fig. 6. SY and P3HT layers are fabricated by blade and spin coating technique [19,20]. The blade and spin coating technique can be utilized to deposit a film on all mixed-SAM-modified Ag electrodes no matter the wetting property of the metal. The highest occupied molecular orbital (HOMO) of P3HT and SY are 5.1 and 5.4 eV, respectively. For the P3HT diode, J increases as the FHT ratio increases from 0% to 66%. However, J of devices with 66% and 80% FHT are similar. This is attributed to the work function of FHT modified Ag electrodes with FHT ratio larger than 66% are higher than the HOMO level of P3HT and hence forming an Ohmic contact between electrode and P3HT. As for the diode made by SY with higher HOMO level, J increases as the FHT ratio increases from 0% to 80%. This

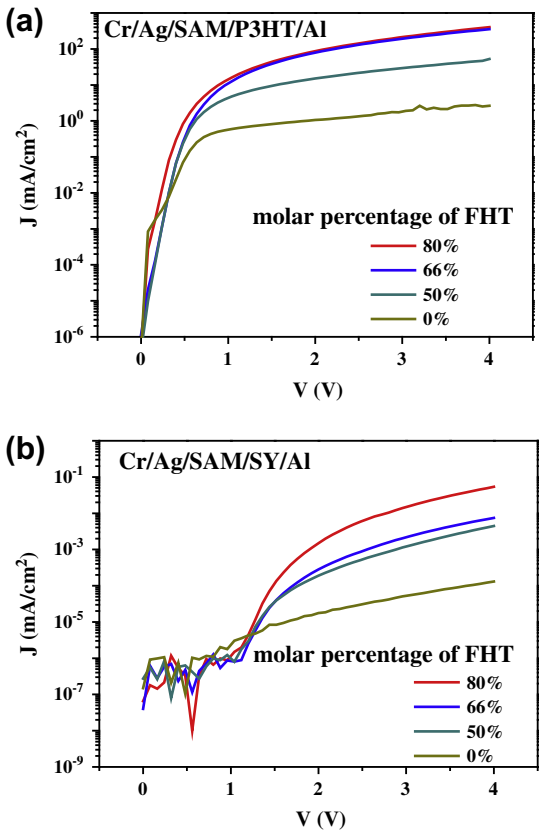

Fig. 6. The current density as a function of voltage of the hole-only devices made by (a) P3HT and (b) super yellow.

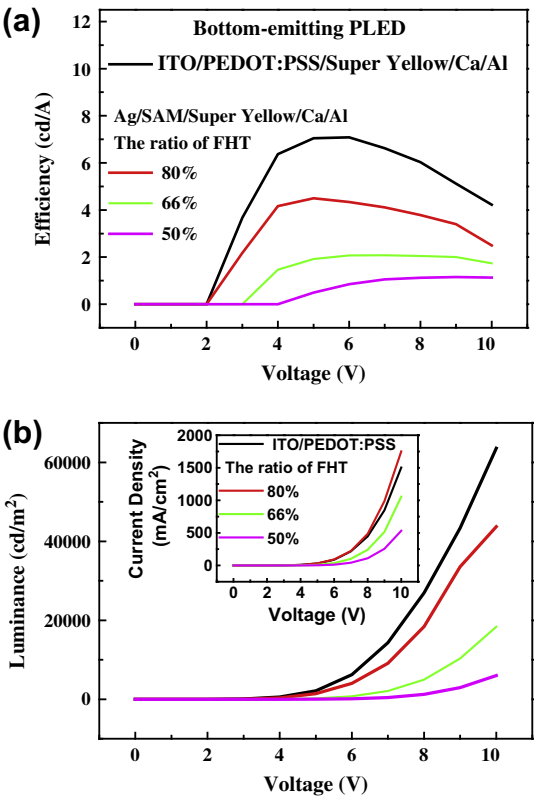

Fig. 7. Characteristics of bottom-emission polymer light-emitting diodes with the structure of anode/super yellow/Ca/Al. FHT/MUA mixed-SAMs-modified Ag and ITO/PEDOT:PSS are utilized as anode. (a) The current efficiency as a function of voltage. (b) The luminance as a function of voltage. The inset shows the current density as a function of voltage.

demonstrates that the mixed-SAM indeed modifies the work function continuously which is suitable serving as an anode.

The effect of mixed SAM-modification on charge injection is demonstrated by a bottom-emitting PLED, as shown in Fig. 7. The current density at same bias increases with increasing amount of FHT in the monolayer, presumably due to the increase in work function of FHT/MUA-modified Ag. The maximum current efficiency of the devices with 80%, 66%, 50% FHT is 4.5 cd/A (at 5 V), 2.1 cd/A (at 7 V), and 1.2 cd/A (at 9 V), respectively. The maximum luminance of the device with 80% FHT is higher than 40,000 cd/m^2 at 10 V. This demonstrates the mixed SAMs-modified Ag can be used as anode to replace ITO. Standard device with ITO/PEDOT:PSS anode is also fabricated for comparison. The standard device achieves a maximum current efficiency of 7.1 cd/A at 6 V. The lower efficiency in the device with 80% FHT results from the reduced transparency of the anode (30 Å Cr/150 Å Ag) as shown in Fig. 8. The top-emitting PLED with FHT/MUA-modified Ag as anode is also fabricated and its characteristics are shown in Fig. 9 (a) and (b). The current density at same bias also increases with increasing amount of FHT. The maximum current efficiency of the devices with 80%, 66%, 50% FHT is 6.7 cd/A (at 6 V), 3.7 cd/A (at 7 V), and 0.8 cd/A (at 8 V), respectively. The maximum luminance of the device with 80% FHT is also

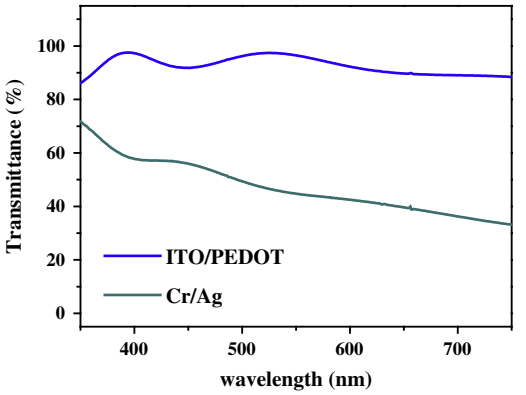

Fig. 8. The optical transmittance of ITO/PEDOT and Cr/Ag electrode.

higher than 40, 000 cd/m^2 at 10 V. Finally, a top-emitting green phosphorescence PLED is also fabricated with FHT/MUA-modified Ag as anode. The emission layer is a blend of tris[2-(p-tolyl)pyridine]iridium(III) (Ir(mppy)$_3$), *N*,*N*′-bis(3-methylphenyl)-*N*,*N*′-bis(phenyl)-benzidine (TPD), 2-(4-biphenylyl)-5-(4-tert-butylphenyl)-1,3,4-oxadiazole (PBD) into poly(vinylcarbazole) (PVK, Mw = 1100,000) in the weight ratio of 6:9:24:61. Some spike can be observed in the current density–voltage curve shown in Fig. 9(c)

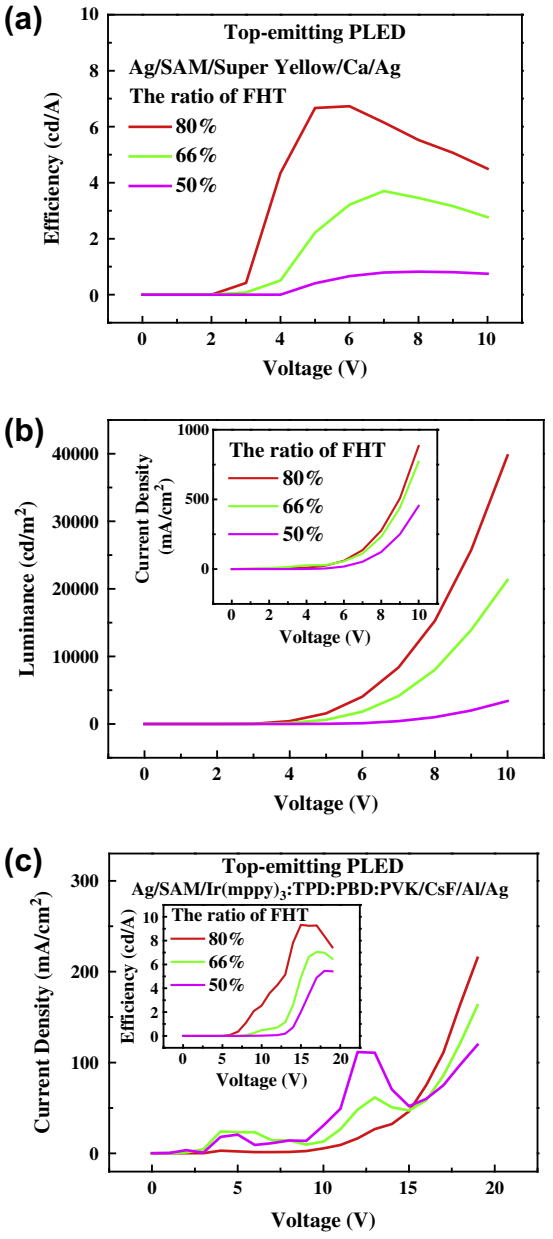

Fig. 9. Characteristics of top-emission polymer light-emitting diode with the structure of Cr/Ag/SAM/super yellow/Ca/Ag. FHT/MUA mixed-SAMs-modified Ag electrodes are utilized as anode. (a) The current efficiency as a function of voltage. (b) The luminance as a function of voltage. The inset shows the current density as a function of voltage. (c) Current density–voltage plot of top-emission polymer light-emitting diode with the structure of Cr/Ag/SAM/Ir(mppy)$_3$:TPD:PBD:PVK/CsF/Al/Ag. The inset shows the current efficiency as a function of voltage.

which may result from current leakage path. The current efficiency is 9.3 cd/A at 15 V. The leakage path may results from the pinhole or aggregation of the component which formed during spin coating. Interaction between SAM-modified Ag surface and polymer solution plays an important role during spin coating process.

4. Conclusion

In conclusion, mixed monolayers of a fluorinated alkanethiol and a carboxyl-terminated alkanethiol of different chain lengths can be used to decouple the effect on the work function and surface wetting for silver. Using a longer carboxyl-terminated component, which may shield or and bury the shorter fluorinated component in the SAM allows higher amount of fluorinated component to be used for increasing the work function of silver, without compromising the wetting property of the substrate needed for spin-coating of emissive conjugated polymer for PLED. PLED with high efficiency and brightness close to the case of ITO/PEDOT:PSS anode are achieved for both top and bottom emission PLED. The tunability in both work function and wettability of silver electrode offers more flexibility in device design.

Acknowledgments

This work is supported by the National Science Council of Taiwan under Contract No. NSC98-2628-M-009-001. The authors thank Merck Inc. for providing the Super Yellow polymer.

References

[1] H. Ishii, K. Sugiyama, E. Ito, K. Seki, Adv. Mater. 11 (1999) 605–625.
[2] P. Marmont, N. Battaglini, P. Lang, G. Horowitz, J. Hwang, A. Kahn, C. Amato, P. Calas, Org. Electron. 9 (2008) 419–424.
[3] Y.L. Wu, Y.N. Li, B.S. Ong, J. Am. Chem. Soc. 128 (2006) 4202–4203.
[4] C.W. Chen, P.Y. Hsieh, H.H. Chiang, C.L. Lin, H.M. Wu, C.C. Wu, Appl. Phys. Lett. 83 (2003) 5127–5129.
[5] C.P. Cho, Y.T. Tao, Langmuir 23 (2007) 7090–7095.
[6] W. Chen, C. Huang, X.Y. Gao, L. Wang, C.G. Zhen, D.C. Qi, S. Chen, H.L. Zhang, K.P. Loh, Z.K. Chen, A.T.S. Wee, J. Phys. Chem. B 110 (2006) 26075–26080.
[7] I.H. Campbell, J.D. Kress, R.L. Martin, D.L. Smith, N.N. Barashkov, J.P. Ferraris, Appl. Phys. Lett. 71 (1997) 3528–3530.
[8] J.Y. Lee, Appl. Phys. Lett. 88 (2006) 073512.
[9] X. Crispin, V. Geskin, A. Crispin, J. Cornil, R. Lazzaroni, W.R. Salaneck, J.L. Bredas, J. Am. Chem. Soc. 124 (2002) 8131–8141.
[10] B. de Boer, A. Hadipour, M.M. Mandoc, T. van Woudenbergh, P.W.M. Blom, Adv. Mater. 17 (2005) 621–625.
[11] D.M. Alloway, M. Hofmann, D.L. Smith, N.E. Gruhn, A.L. Graham, R. Colorado, V.H. Wysocki, T.R. Lee, P.A. Lee, N.R. Armstrong, J. Phys. Chem. B 107 (2003) 11690–11699.
[12] L.W. Chong, Y.L. Lee, T.C. Wen, T.F. Guo, Appl. Phys. Lett. 89 (2006) 233513.
[13] K.Y. Wu, S.Y. Yu, Y.T. Tao, Langmuir 25 (2009) 6232–6238.
[14] N.V. Venkataraman, S. Zurcher, A. Rossi, S. Lee, N. Naujoks, N.D. Spencer, J. Phys. Chem. C 113 (2009) 5620–5628.
[15] (a) P.E. Laibinis, R.G. Nuzzo, G.M. Whitesides, J. Phys. Chem. 96 (1992) 5097–5105;
(b) G.M. Whitesides, P.E. Laibinis, Langmuir 6 (1990) 87–96;
(c) J.P. Folkers, P.E. Laibinis, G.M. Whitesides, Langmuir 8 (1992) 1330–1341.
[16] Y.M. Chang, L. Wang, W.F. Su, Org. Electron. 9 (2008) 968–973.
[17] Y.F. Miura, M. Takenaga, T. Koini, M. Graupe, N. Garg, R.L. Graham, T.R. Lee, Langmuir 14 (1998) 5821–5825.
[18] M. Graupe, M. Takenaga, T. Koini, R. Colorado, T.R. Lee, J. Am. Chem. Soc. 121 (1999) 3222–3223.
[19] S.R. Tseng, H.F. Meng, K.C. Lee, S.F. Horng, Appl. Phys. Lett. 93 (2008) 153308.
[20] J.D. You, S.R. Tseng, H.F. Meng, F.W. Yen, I.F. Lin, S.F. Horng, Org. Electron. 10 (2009) 1610–1614.

Organic Electronics 12 (2011) 154–160

Contents lists available at ScienceDirect

Organic Electronics

journal homepage: www.elsevier.com/locate/orgel

Efficient multilayer electrophosphorescence white polymer light-emitting diodes with aluminum cathodes

Tengling Ye [a], Minrong Zhu [b], Jiangshan Chen [a], Dongge Ma [a,*], Chuluo Yang [b,*], Wenfa Xie [c], Shiyong Liu [c]

[a] State Key Laboratory of Polymer Physics and Chemistry, Changchun Institute of Applied Chemistry, Graduate School of Chinese Academy of Sciences, Chinese Academy of Sciences, Changchun 130022, People's Republic of China
[b] Department of Chemistry, Hubei Key Lab on Organic and Polymeric Optoelectronic Materials, Wuhan University, Wuhan 430072, People's Republic of China
[c] State Key Laboratory on Integrated Optoelectronics, College of Electronic Science and Engineering, Jilin University, 2699 Qianjin Street, Changchun 130012, People's Republic of China

ARTICLE INFO

Article history:
Received 23 September 2010
Received in revised form 27 October 2010
Accepted 31 October 2010
Available online 16 November 2010

Keywords:
Polymer light emitting diodes
Multilayer
Alcohol soluble conjugated polymer
Li_2CO_3
Solution-processed

ABSTRACT

By simply doping Li_2CO_3 in an alcohol soluble neutral conjugated polymer poly[9,9-bis(6′-diethoxylphosphorylhexyl)fluorene] (PF-EP), we demonstrate highly efficient multilayer electrophosphorescence white polymer light-emitting diodes with air-stable Al cathode. From the mechanism studies, we find that the phosphate groups can make Li ions movable in the PF-EP film, resulting in great improvement in the electron injection and transport ability of PF-EP. The hole-blocking ability is also strengthened.

© 2010 Elsevier B.V. All rights reserved.

1. Introduction

White polymer light emitting diodes (WPLEDs) have gained much research interest nowadays due to their potential applications in solid-state lighting sources and full-color displays. The low-cost manufacturing technology, the easy fabrication of large-area device and the compatibility with flexible substrate are the major charming merits for WPLEDs [1]. In order to generate the desired white-light emission, the blending of two complementary colors or three primary colors is typically required. Various approaches have been reported to realize this goal, including the synthesis of polymers incorporating different color moieties, blending several color complementary polymers, doping several dyes into a single emitting layer (EML) and usage of excimer or exciplex system [2–7]. However, the performance of WPLEDs is often poor due to imbalanced hole and electron transport and mismatched injection energy barriers, especially for electron injection. The imbalanced charge transport can be adjusted by introducing charge transport materials or dopants, and lots of highly successful works have been reported in this aspect. On the other hand, considerable efforts have also been devoted to the researches on cathode interfacial engineering. The low work function metals (Ca and Ba) [3,4] and inorganic salts (LiF, CsF, Cs_2CO_3 and Li_2CO_3) [2,8–10] were used as an electron injection layer in an attempt to enhance the electron injection in PLEDs. However, the low work function metals Ca and Ba are highly reactive and still not low enough to match the lowest unoccupied molecular orbital (LUMO) levels of most conjugated polymers. Comparatively, the alkaline metal salt can release Li or Cs by the Ca or Al covered on top of it, behaving more effectively

* Corresponding authors. Tel.: +86 431 85262357; fax: +86 431 85262873.
E-mail addresses: ytl@ciac.jl.cn (T. Ye), mdg1014@ciac.jl.cn (D. Ma), clyang@whu.edu.cn (C. Yang).

1566-1199/$ - see front matter © 2010 Elsevier B.V. All rights reserved.
doi:10.1016/j.orgel.2010.10.025

[9,11]. Recently, several water/alcohol soluble conjugated polymers were reported to significantly improve electron injection with high work-function Al cathode [12–22]. It is believed that the metal ions contained in the interlayer or the polar groups on their side chains can form interfacial dipoles between the electron injection layer (EIL) and metal cathode to enhance electron injection [16,20]. More recently, Huang et al. [10] reported a highly efficient WPLEDs with a power efficiency of 23.4 lm W^{-1} by doping a water/alcohol soluble conjugated polymer poly[9,9-bis(2-(2-(2-diethanolaminoethoxy)ethoxy)ethyl)fluorene] (PF-OH) with Li_2CO_3 as electron injection layer. This supplies an effective method to improve electron injection property by introducing effective electron transport layer, thus balancing electrons and holes to fabricate high efficiency multilayer PLEDs.

In this article, we achieved high efficiency WPLEDs by simply doping Li_2CO_3 in an alcohol soluble neutral conjugated polymer poly[9,9-bis(6′-diethoxylphosphorylhexyl)fluorene] (PF-EP) with air-stable Al cathode. It can be seen that the electron injection and transport ability of PF-EP can be dramatically enhanced due to the doping of Li_2CO_3. The WPLEDs show a peak luminous efficiency (LE) of 25.7 cd A^{-1} and a peak power efficiency (PE) of 13.1 lm W^{-1}, which are equivalent to those of incandescent light bulbs. As we see, the WPLED will show significant advantages in practical applications due to the utilization of simple solution-processed active layer and air-stable Al cathode.

2. Experimental

2.1. Materials

The polymer PF-EP was synthesized as follows: 2,7-dibromo-9,9-bis(6′-diethoxylphosphorylhexyl)-fluorene **1** was prepared according to the procedure reported previously, which in turn underwent cross-coupling with the pinacol ester of diboron to give the aryboronic ester **2**. The Suzuki-polycondensation of monomers **1** and **2** with the $Pd(PPh_3)_4$ as catalyst and Na_2CO_3 as base gives the polymer PF-EP. The ^1H NMR is consistent with the PF-EP prepared through Yamomoto polycondensation reaction [15]. $(fbi)_2Ir(acac)$ was synthesized using a method previously described [23]. Poly(styrenesulfonate) (PEDOT:PSS, Baytron P VP CH 8000) was obtained from H.C. Stark. PVK was purchased from Aldrich. Firpic and OXD-7 were purchased from Nichem Fine Technology Co. Ltd. All materials were used as received.

2.2. Device fabrication

First, an 80 nm thick layer of PEDOT/PSS mixture was spin-coated on top of oxygen plasma treated indium tin oxide (ITO). This coated PEDOT on substrate was baked at 80 °C overnight and then at 120 °C for 30 min in a vacuum oven. Afterwards, the PEDOT:PSS-coated substrate was moved into a glovebox under a nitrogen-protected environment to perform the subsequent multilayer process. A 60 nm thick emitting layer was spun-cast from chlorobenzene (PVK:OXD-7(70 w/30 w):10 wt% Firpic:0.2 wt% $(fbi)_2Ir(acac)$). The samples were annealed on a hot plate at 120 °C for 30 min to remove residual solvent. Following that, about 30 nm thick PF-EP films (doped with 0 wt%, 0.75 wt%, 1.25 wt%, 2.5 wt% and 5 wt% Li_2CO_3) as EILs were casted from MeOH:H_2O (3:1). Finally, after annealing on a hot plate at 95 °C for 30 min, a 100 nm thick Al was thermally deposited as a cathode. All the solutions will be filtered using 0.22 μm filter membranes before spin-coating. The vacuum was $<10^{-4}$ Pa. The device area was 16 mm^2.

2.3. Measurements

The EL spectra of WPLEDs were measured with Keithley 2400 source meter and a coupled PR650 spectroscan photometer. *J–V–L* characteristics were measured by a Keithley source measurement unit (Keithley 2400 and Keithley 2000) with a calibrated silicon photodiode. For photovoltaic measurement, the photocurrent–voltage characteristics were recorded using a computer-controlled Keithley 236 source meter under a white light illumination with intensity of 100 mW cm^{-2}. XPS experiments were performed in Thermo ESCALAB250 using monochromatic Al Kα (1486.6 eV). The thickness of the evaporated films were monitored by frequency counter and calibrated by Dektak 6M Profiler (Veeco). The thicknesses of spin-coated films were controlled by Dektak 6M Profiler (Veeco) directly. AFM studies were carried out directly on the devices after EL performance measurement. All the device testing was carried out in ambient atmosphere. Except that the measures in Fig. 5 were carried out in glovebox, all other measurements were performed in ambient atmosphere.

3. Results and discussion

3.1. Device performance

Device structure and energy diagrams used in this study are shown in Fig. 1(a) [24]. The device structure is ITO/PEDOT:PSS(80 nm)/[(PVK:OXD-7)(7:3)]:FIrpic(10 wt%):$(fbi)_2Ir(acac)$(0.2 wt%)(60 nm)/EIL(30 nm)/Al(100 nm), where PEDOT:PSS is used as both the hole injection and transport layer (HITL), a blend containing poly(N-vinylcarbazole) (PVK), 1,3-bis[2-(4-tert-butylphenyl)-1,3,4-oxadiazo-5-yl] benzene (OXD-7), [bis(4,6-difluorophenyl)-pyridinato-N,C^2] picolinate iridium (III) (FIrpic), and bis(2-(9,9-diethyl-9H-fluoren-2-yl)-1-phenyl-1H-benzoimidazol-N,C^3) iridium-(acetylacetonate) ($(fbi)_2Ir(acac)$) [24] as the EML. Alcohol soluble PF-EP doped with 0 wt%, 0.75 wt%, 1.25 wt%, 2.5 wt% and 5 wt% Li_2CO_3 is used as the EIL. The chemical structures of the relevant materials are shown in Fig. 1(b).

Fig. 2(a) and (b) compares the efficiency of the fabricated WPLEDs for different Li_2CO_3 doping concentrations in PF-EP. It can be seen that the Li_2CO_3-doping in PF-EP EIL leads the devices to higher efficiency than that of the Li_2CO_3-undoped device. The performances of the white devices are summarized in Table 1. The maximum current efficiency and power efficiency of the device with pure PF-EP as EIL reach 21.5 cd A^{-1} and 9.0 lm W^{-1}, respectively.

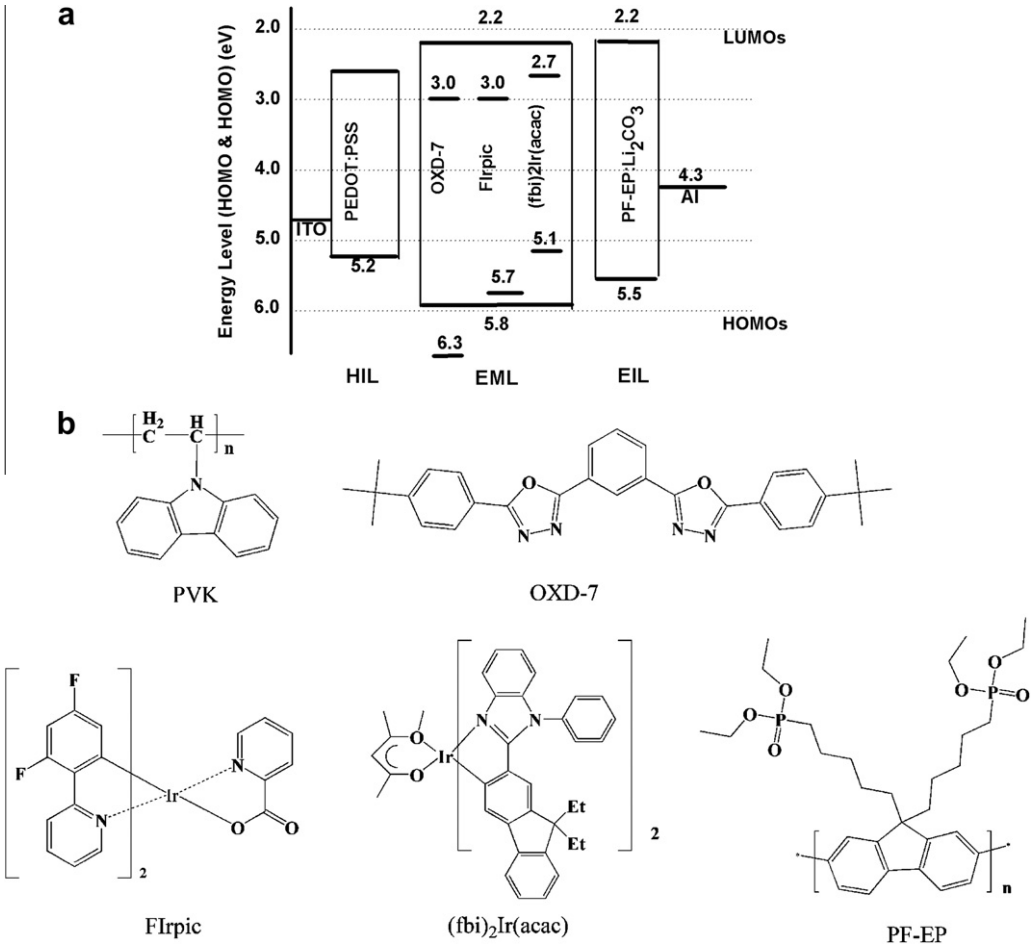

Fig. 1. (a) Device structure and energy diagrams used in this study. (b) Molecular structures of the relevant materials.

Correspondingly, when Li_2CO_3 (0.75 wt%, 1.25 wt%, 2.5 wt% and 5 wt%) is introduced into PF-EP as EILs, the maximum luminance efficiency is 25.6, 25.7, 23.8 and 15.4 cd A^{-1} and the power efficiency is 11.9, 13.1, 11.5, and 6.6 lm W^{-1}, respectively. All devices can realize white-light emission, and the Commission Internationale de l'éclairage (CIE) coordinates of the WPLED device with 1.25 wt% Li_2CO_3 doped EIL are shown in Fig. 2(c), the CIE coordinates variation is negligible and only shifts from (0.41, 0.46) at 8 V to (0.39, 0.45) at 12 V. Fig. 2(d) gives the brightness–voltage (*B*–*V*) curves. It can be found that the devices with Li_2CO_3-doped EILs showed much lower operating voltage than that of the Li_2CO_3-undoped device. The turn-on voltage is decreased from 5.3 V to 4.1 V (Table 1). The inset in Fig. 2(d) gives the current density–voltage (*J*–*V*) curves. Three regions can be identified. For an applied voltage less than 4 V where light output is not observed, called region 1, the current density *J* is sensitive to various factors, such as preparation procedure and diffusion of the cathode [25]. As the applied voltage is increased to 4 V where the devices turn on, the curves go to region 2. The current density is increased with the increase of Li_2CO_3 concentration. After going up to 10 V where the brightness tends to be maximum and the efficiency has fallen (region 3), the high Li_2CO_3 concentration will accelerate the degradation of the devices. The significantly different performances mean that the transport or injection processes of the devices are greatly influenced by Li_2CO_3 doping in EIL.

3.2. Mechanism

In order to get insight into the improvement mechanism of the doped Li_2CO_3 in PF-EP EIL in device performance, we first study electron injection properties by photovoltaic (PV) measurements of the open-circuit voltage (V_{oc}) across the light-emitting devices under steady state forward bias with the scan rate of 0.3 V/s [5,18]. As the anode of each device is identical, the V_{oc} is only dependent on the effective work function of the cathode. As shown in Fig. 3, the V_{oc} increases with the increase of Li_2CO_3 concentration. This indicates that the electron-injection ability of PF-EP EIL is improved upon Li_2CO_3 doping. It is well known that alkali metal salts are a kind of excellent electron injection material and have been successfully used as n-dopants in OLEDs [2,9,10]. Therefore, it is reasonable to infer that the lower barrier is caused

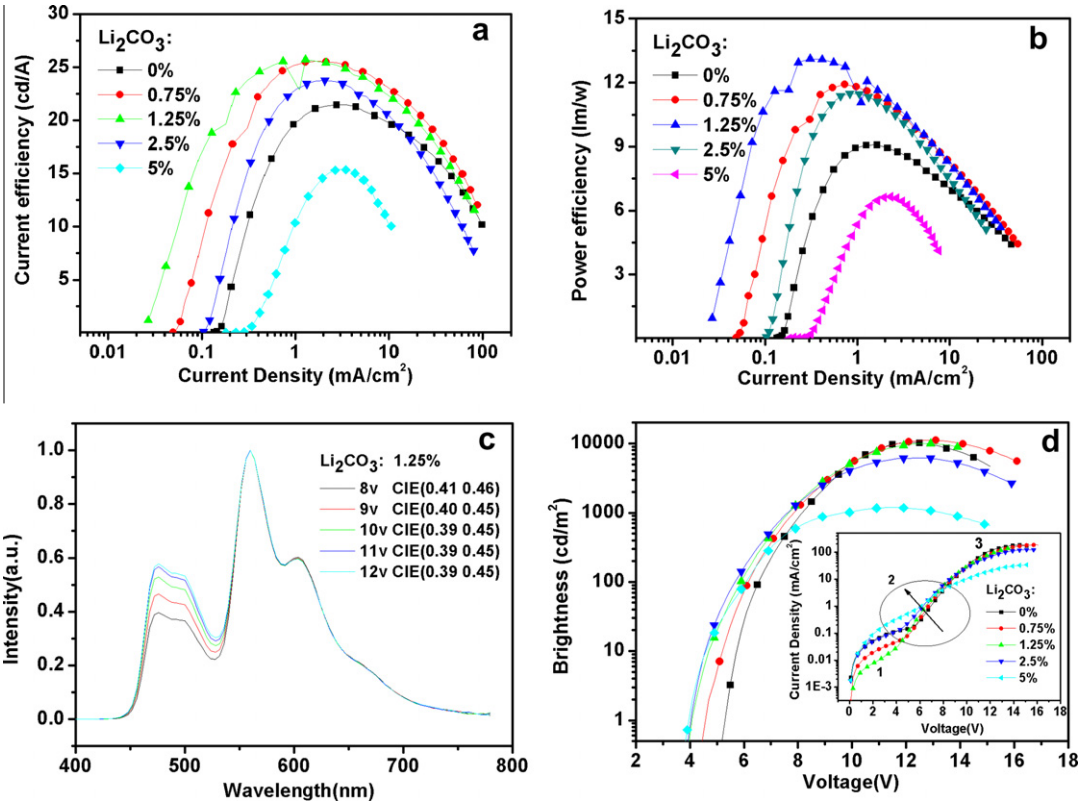

Fig. 2. (a, b) CE and PE vs *J* characteristics of the devices with different Li_2CO_3-doped EILs. (c) The EL spectra of the WPLED with 1.25 wt% Li_2CO_3 doped EIL. (d) *J–B–V* characteristics of the devices with different Li_2CO_3-doped EILs.

Table 1
Device performance of WPLEDs with different Li_2CO_3-doped EILs.

Li_2CO_3-doped PF-EP concentration:	0 wt%	0.75 wt%	1.25 wt%	2.5 wt%	5 wt%
Maximum LE (cd A^{-1})	21.5	25.6	25.7	23.8	15.4
Maximum PE (lm W^{-1})	9.0	11.9	13.1	11.5	6.6
Maximum PE at 1000 cd m^{-2} (lm W^{-1})	7.9	9.8	9.9	9.2	3.6
Max brightness (cd m^{-2})	10,288	11,190	9995	6201	1190
Turn-on voltage at 1 cd m^{-2} (V)	5.3	4.7	4.1	4.1	4.1

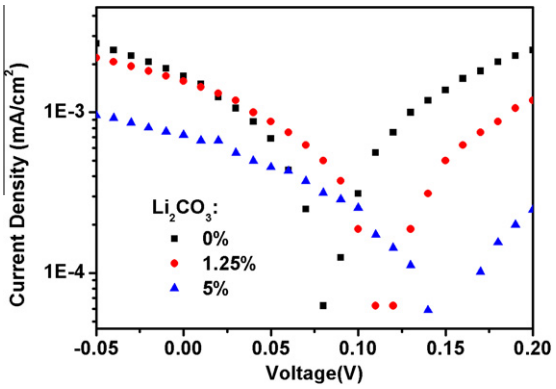

Fig. 3. Photovoltaic characteristics of the WPLEDs with different Li_2CO_3-doped EILs.

by the enhanced interfacial dipole or the space charge electrical field [18].

To further understand the mechanism of the enhanced electron injection, the pure PF-EP film and 2.5 wt% Li_2CO_3 doped PF-EP film are studied by XPS. Fig. 4(a) shows the spectra corresponding to the P 2p core levels. For the sample of pure PF-EP film, the P 2p peak at 133.15 eV is assigned to P═O/P—O (Fig. 4(a)) [26]. However, for the sample of 2.5 wt% Li_2CO_3 doped PF-EP film, the P 2p spectra are broadened. The higher-energy part is not present in the control sample (Fig. 4(a)). We attribute this extra part to an interaction between P and Li. The O 1s signals from the Li_2CO_3-doped and -undoped PF-EP films are shown in Fig. 4(b). For the sample of pure PF-EP film, the peaks at 531.45 eV and 532.75 eV are assigned to P═O and P—O groups (Fig. 4(b)) [27,28], respectively. After doping with

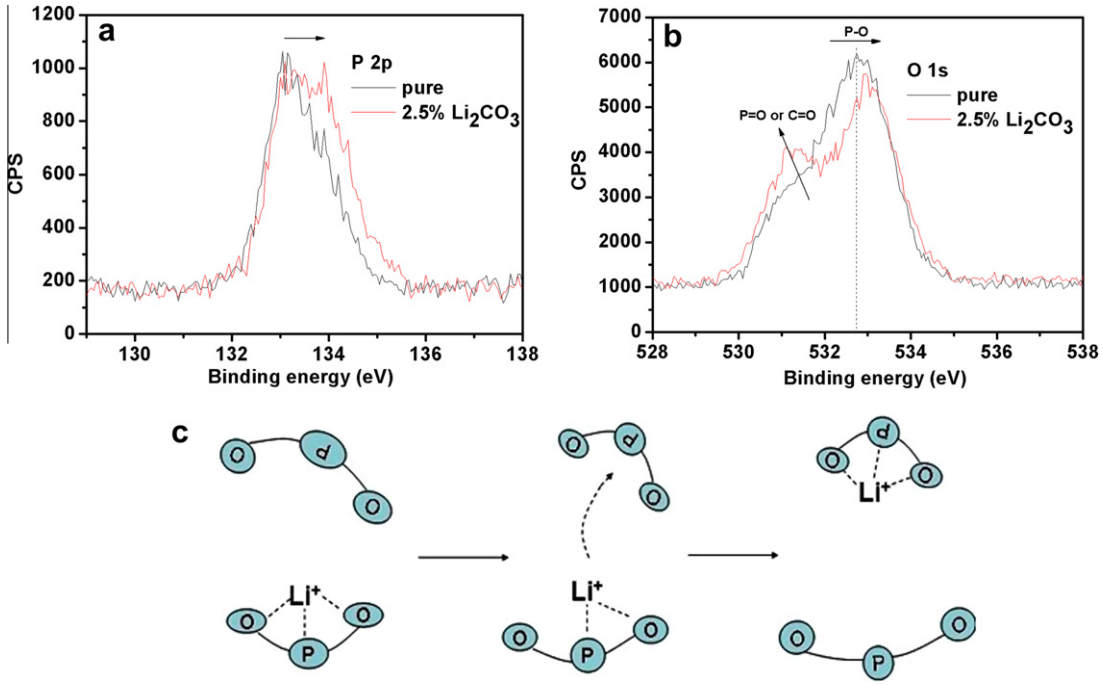

Fig. 4. XPS spectra of the pure PF-EP film and 2.5 wt% Li_2CO_3 doped PF-EP film: (a) XPS of the P 2p and (b) XPS of the O1s. (c) Schematic diagram of the Li ions transport process in the Li_2CO_3-doped PF-EP film.

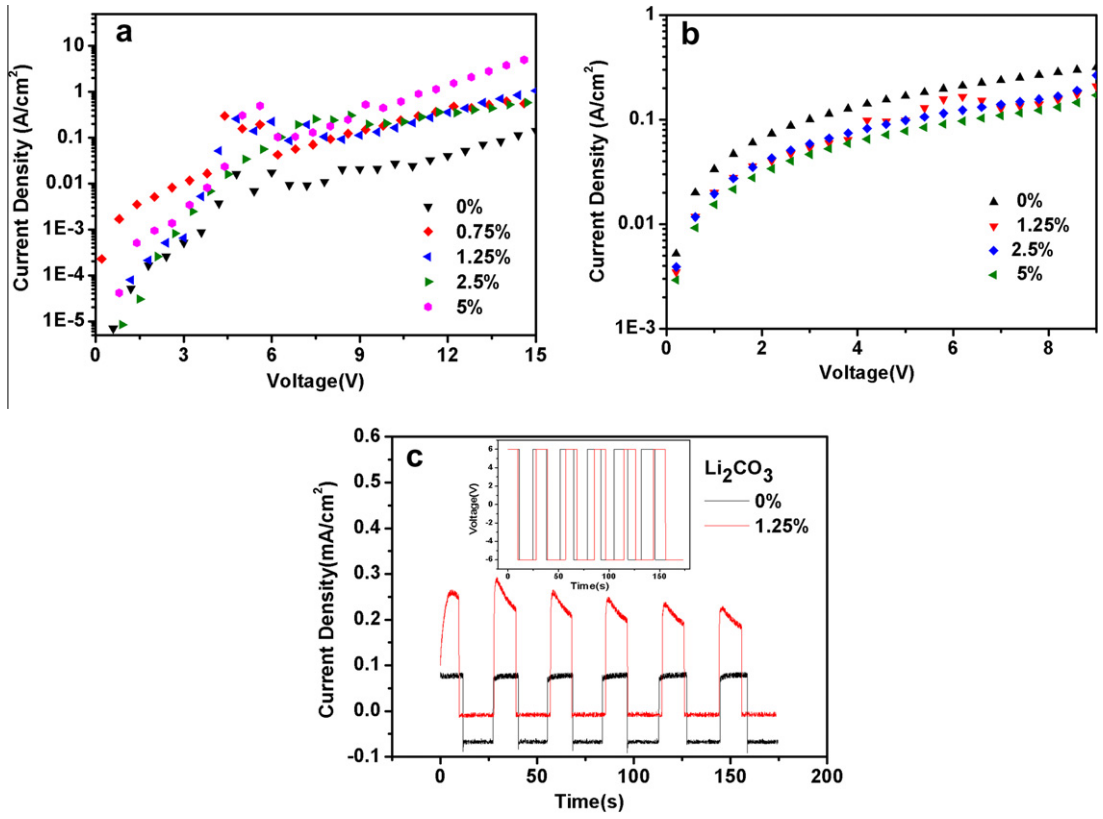

Fig. 5. *J–V* characteristics of the single-carrier devices: (a) electron-dominated device and (b) hole-dominated device. (c) Current density as a function of time for ITO/PEDOT:PSS/EML/PF-EP + Li_2CO_3 (0% or 1.25%)/Al device.

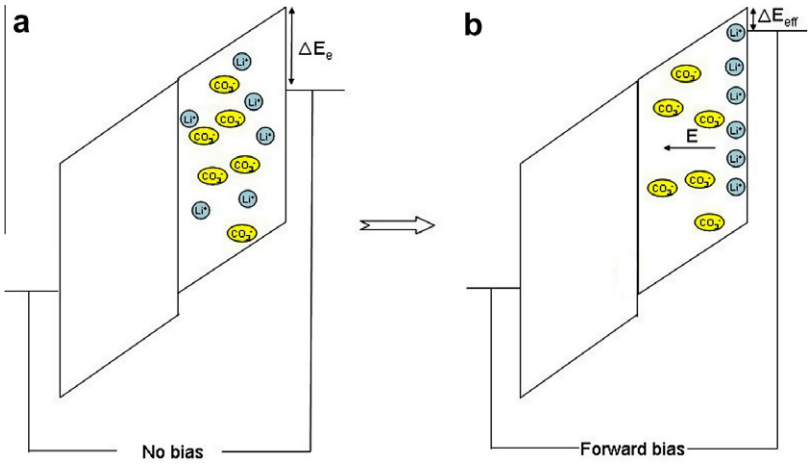

Fig. 6. Schematic of the interface mutative processes: (a) no bias and (b) forward bias across the light emitting device.

Li_2CO_3, the O 1s peak at 531.45 eV becomes strong which is caused by the C═O groups. The O 1s peak at 532.75 eV shows 0.2 eV positive shifts to higher binding energy (532.95 eV). This indicates that the introduction of Li ions also has an effect on O atoms [29,30]. The interaction between P, O and Li makes it possible to transport the Li ions in the EIL, which is similar with the typical polymer electrolytes like PEO and alkali metal salts system [31]. Fig. 4(c) gives the schematic diagram of this transport process [32]. One mechanism of the enhanced electron injection in devices due to Li_2CO_3 doping in EIL can be attributed to the mobile Li ions. Li ions can easily transport into the EIL due to the interaction with the phosphate groups.

Furthermore, two kinds of single-carrier devices are fabricated as follows:

(A) The electron-dominated device: ITO/Ca(20 nm)/[(PVK:OXD-7)(7:3)](60 nm)/EIL(30 nm)/Al(100 nm).
(B) The hole-dominated device: ITO/PEDOT:PSS(80 nm)/[(PVK:OXD-7)(7:3)](70 nm)/EIL(30 nm)/Au(20 nm)/Al(30 nm).

As shown in Fig. 5(a) and (b), the doping of Li_2CO_3 in EIL greatly enhances electron current, but reduces hole current. This indicates that the doping of Li_2CO_3 improves the electron injection and transport of EIL and also plays the role of blocking the hole at the interface of EML/EIL at the same time. Fig. 5(c) shows the *J–V* characteristics of the devices as a function of time with pure PF-EP film and 1.25 wt% Li_2CO_3 doped PF-EP film as EILs. The inset of Fig. 5(c) gives the periodic square wave signal (the amplitude is 6 V and the cycle is about 20 s). It can be found that the rectification ratio of the PLED with 1.25 wt% Li_2CO_3 doped PF-EP EIL is obviously larger than that of the PLED with the pure PF-EP film as EIL. This further verifies that the doped PF-EP film can more effectively enhance the electron injection and transport, and prevent the hole injection into the EILs than the pure PF-EP film does. Furthermore, as we see, the current in device with Li_2CO_3 doped PF-EP EIL shows a long time response. This should indicate that the Li ions are movable in EIL. In this case, the Li ions will gradually move to the interface at the cathode with time at electrical field. As a result, the electron current will gradually increase due to the enhancement of electron injection by formation of interface dipole, leading to the time delay. As reverse bias, the partial ions will leave the interface again, therefore, as again positive bias, the response time becomes short.

On the basis of the above analyses, we draw a scheme to clarify the mechanism on how the movable ions enhance electron injection. As shown in Fig. 6, the ions are freely dispersive in the EIL initially. When the forward bias is applied, the ions redistribute. The Li^+ cations move towards the EIL/cathode interface by interacting with the phosphate groups at electrical field and accumulate at the EIL/cathode interface. These accumulated Li^+ cations can form stronger interfacial dipoles between the EIL and metal cathode than that of pure PF-EP. Thus, the electron injection barrier can be more effectively reduced. For the CO_3^{2-} anions, we infer that the mobility is limited by the big diameter (CO_3^{2-}: 0.402 nm, Li^+: 0.152 nm) [33,34] and shows indistinct interaction with the PF-EP. The CO_3^{2-} anions cannot move to the interface like the Li^+ cations. One of the roles is that the holes are effectively blocked within EML. Therefore, the improved efficiency of PLEDs can be attributed to balance the carriers via enhancing electron injection and blocking hole injection into EIL. As we see, the efficiency is dependent on the doping concentration of Li_2CO_3; higher Li_2CO_3 doping will quench the excitons, leading to the gradual decrease of efficiency. Obviously, it is necessary to optimize the doping concentration of Li_2CO_3 in EIL when fabricating devices.

4. Conclusion

We demonstrate efficient multilayer WPLEDs with air-stable Al cathode by introducing Li_2CO_3-doped PF-EP EIL. The results from the mechanism research reveal that the electron injection and transport ability of PF-EP EIL can be

dramatically improved upon Li_2CO_3 doping. Facilitated migration of Li ions by ion transporting phosphate groups greatly improves the electron injection and transport. What is more, the hole-blocking ability is greatly strengthened. Consequently, the devices with Li_2CO_3-doped EIL exhibit much better performances than the ones without Li_2CO_3 doping. The best efficiencies of 25.7 cd A^{-1} and 13.1 lm W^{-1} are obtained in WPLEDs with air-stable Al cathode.

Acknowledgements

The authors thank the Science Fund for Creative Research Groups of NSFC (20921061), the National Natural Science Foundation of China (50973104, 60906020, 60937001, 90922020), the Ministry of Science and Technology of China (973 Program Nos. 2009CB623604, 2009CB930603), and the Foundation of Jilin Research Council (20080337, 20090127) for the support of this research.

References

[1] H.B. Wu, L. Ying, W. Yang, Y. Cao, Chem. Soc. Rev. 38 (2009) 3391–3400.
[2] J. Huang, G. Li, E. Wu, Q. Xu, Y. Yang, Adv. Mater. 18 (2006) 114–117.
[3] H.B. Wu, J.H. Zou, F. Liu, L. Wang, A. Mikhailovsky, G.C. Bazan, W. Yang, Y. Cao, Adv. Mater. 20 (2008) 696–702.
[4] H.B. Wu, G.J. Zhou, J.H. Zou, C.L. Ho, W.Y. Wong, W. Yang, J.B. Peng, Y. Cao, Adv. Mater. 21 (2009) 4181–4184.
[5] J. Liu, X. Guo, L.J. Bu, Z.Y. Xie, Y.X. Cheng, Y.H. Geng, L.X. Wang, X.B. Jing, F.S. Wang, Adv. Funct. Mater. 17 (2007) 1917–1925.
[6] J. Liu, Z.Y. Xie, Y.X. Cheng, Y.H. Geng, L.X. Wang, X.B. Jing, F.S. Wang, Adv. Mater. 19 (2007) 531–535.
[7] X. Guo, C.J. Qin, Y.X. Cheng, Z.Y. Xie, Y.H. Geng, X.B. Jing, F.S. Wang, L.X. Wang, Adv. Mater. 21 (2009) 3682–3688.
[8] L.S. Hung, C.W. Tang, M.G. Mason, Appl. Phys. Lett. 70 (1997) 152.
[9] P. Piromerium, H. Oh, Y. Shen, G.G. Malliaras, J.C. Scott, P.J. Brock, Appl. Phys. Lett. 77 (2000) 2403–2405.
[10] F. Huang, P.I. Shih, C.F. Shu, Y. Chi, A.K.Y. Jen, Adv. Mater. 21 (2009) 361–365.
[11] K.M. Vaeth, J. DiCillo, Synth. Met. 143 (2004) 75–79.
[12] H. Wu, F. Huang, Y. Mo, W. Yang, D. Wang, J. Peng, Y. Cao, Adv. Mater. 16 (2004) 1826–1830.
[13] H. Yan, Q.L. Huang, B.J. Scott, T.J. Mark, Appl. Phys. Lett. 84 (2004) 3873.
[14] H. Yan, P. Lee, N.R. Armstrong, A. Graham, G.A. Evmenenko, P. Dutta, T.J. Mark, J. Am. Chem. Soc. 127 (2005) 3172–3183.
[15] G. Zhou, G. Qian, L. Ma, Y.X. Cheng, Z.Y. Xie, L.X. Wang, X.B. Jing, F.S. Wang, Macromolecules 38 (2005) 5416–5424.
[16] F. Huang, Y.H. Niu, Y. Zhang, J.W. Ka, M.S. Liu, A.K.Y. Jen, Adv. Mater. 19 (2007) 2010–2014.
[17] X. Niu, C.J. Qin, B.H. Zhang, J.W. Yang, Z.Y. Xie, Y.X. Cheng, L.X. Wang, Appl. Phys. Lett. 90 (2007) 203513.
[18] S.H. Oh, D. Vak, S.I. Na, T.W. Lee, D.Y. Kim, Adv. Mater. 20 (2008) 1624–1629.
[19] C.V. Hoven, A. Arcia, G.C. Bazan, T.Q. Nguyen, Adv. Mater. 20 (2008) 3793–3810.
[20] C.V. Hoven, R. Yang, A. Garcia, V. Crockett, A.J. Heeger, G.C. Bazan, T.Q. Nguyen, Proc. Natl. Acad. Sci. USA 105 (2008) 12730–12735.
[21] Y.H. Xu, R.Q. Yang, J.B. Peng, A.A. Mikhailovsky, Y. Cao, T.Q. Nguyen, G.C. Bazan, Adv. Mater. 21 (2009) 584–588.
[22] B.H. Zhang, C.J. Qin, J.Q. Ding, L. Chen, Z.Y. Xie, Y.X. Cheng, L.X. Wang, Adv. Funct. Mater. 20 (2010) 2951–2957.
[23] W.S. Huang, J.T. Lin, C.H. Chien, Y.T. Tao, S.S. Sun, Y.S. Wen, Chem. Mater. 16 (2004) 2480–2488.
[24] Q. Wang, J.Q. Ding, D.G. Ma, Y.X. Cheng, L.X. Wang, X.B. Jing, F.S. Wang, Adv. Funct. Mater. 19 (2009) 84–95.
[25] H.A.A. Attar, A.P. Monkman, Adv. Funct. Mater. 16 (2006) 2231.
[26] D.Q. Chen, Y.Z. Wang, X.P. Hu, D.Y. Wang, M.H. Qu, B. Yang, Polym. Degrad. Stab. 88 (2005) 349–356.
[27] D.Y. Wang, H. Li, S.Q. Shi, X.J. Huang, L.Q. Chen, Electrochim. Acta 50 (2005) 2955–2958.
[28] A.M. Puziy, O.I. Poddubnaya, A.M. Ziatdinov, Appl. Surf. Sci. 252 (2006) 8036–8038.
[29] A.M. Andersson, D.P. Abraham, R. Haasch, S. MacLaren, J. Liu, K. Amine, J. Electrochem. Soc. 149 (2002) A1358–A1369.
[30] B.V.R. Chowdari, K.L. Tan, W.T. Chia, R. Gopalakrishnan, J. Non-Cryst. Solids 119 (1990) 95–102.
[31] C.A. Angell, C. Liu, E. Sanchez, Nature 362 (1993) 137–139.
[32] M.B. Armand, J.B. Chabagno, M.J. Duclot, in: P. Vashishta, J.N. Mondy, G.K. Shenoy (Eds.), Fast Ion Transport in Solid, Elsevier, Amsterdam, 1979, pp. 131–136.
[33] A.V. Gogolev, V.P. Shilov, A.M. Fedoseev, A.K. Pikaev, Russ. Chem. Bull. 39 (1990) 21–25.
[34] J.Y. Xi, S.J. Miao, X.Z. Tang, Macromolecules 37 (2004) 8592–8598.

Organic Electronics 12 (2011) 161–168

Contents lists available at ScienceDirect

Organic Electronics

journal homepage: www.elsevier.com/locate/orgel

Meyer–Neldel rule for charge carrier transport in fullerene devices: A comparative study

A. Pivrikas [a,*], Mujeeb Ullah [b], Th.B. Singh [a], C. Simbrunner [b], G. Matt [a], H. Sitter [b], N.S. Sariciftci [a]

[a] Linz Institute for Organic Solar Cells (LIOS), Physical Chemistry, Johannes Kepler University, Altenberger Str. 69, A-4040 Linz, Austria
[b] Institute of Semiconductor and Solid State Physics, Johannes Kepler University, Altenberger Str. 69, A-4040 Linz, Austria

ARTICLE INFO

Article history:
Received 21 May 2010
Received in revised form 21 October 2010
Accepted 21 October 2010
Available online 12 November 2010

Keywords:
Meyer–Neldel rule
Arrhenius
CELIV
OFET
Carrier mobility
Charge transport

ABSTRACT

Charge transport is comparatively studied in the bulk and at the interface of disordered fullerene films fabricated using physical vapour deposition. Charge carrier concentration and temperature dependent electron mobilities are comparatively studied using charge extraction by linearly increasing voltage (CELIV) technique and organic field-effect transistors (OFET) measurements. Electron mobility is at least two orders of magnitude higher than hole mobility in the fullerene films. Lower mobility values and stronger concentration dependence in diodes is observed. Carrier concentration dependent activation energy is experimentally measured in both types of devices. Larger activation energy for electron transport is required at lower carrier concentrations. Meyer–Neldel rule (MNR) for electron mobility is observed in both the bulk of the fullerene films and in the transistor channel at the interface. Meyer–Neldel energy (E_{MN} = 35 meV), which is interpreted as disorder parameter, is the same in both device geometries, which suggest that the level of disorder and energetical landscape for charge transport is similar in the bulk of fullerene films and at the interface with the insulator. Disorder formalism is used to qualitatively explain that either carrier concentration or the nature of non-equilibrium charge carrier transport in CELIV compared to steady-state OFET measurements is responsible for observed transport properties.

© 2010 Elsevier B.V. All rights reserved.

1. Introduction

The charge carrier transport mechanisms are fundamentally important for understanding the electronic phenomena in organic semiconductor devices. In general, charge carrier transport is dependent on the material structure and nanoscale order in the film [1]. One of the advantages of organic electronic devices is their solution processability, which results in disordered film structures. The absence of translational symmetry with a three-dimensional periodic lattice in disordered films results in a random distribution of potential wells yielding a distribution of localized density of states (DOS). Hopping type of charge transport leads to a lower carrier mobility compared to crystalline inorganic semiconductors. Charge carrier transport studies in disordered organic semiconductors are challenging due to low charge carrier mobility (<1 $cm^2 V^{-1} s^{-1}$) (limits the applicability of Hall effect), a significant amount of thermally generated carriers (limits the applicability of time-of-flight – TOF), pronounced trapping, dispersive transport, non-Ohmic contacts (limits the applicability of space charge limited current – SCLC) makes the standard measurement methods difficult to apply [2–7].

Various physical processes, including charge carrier transport in disordered media, are thermally activated and follow the Arrhenius exponential law of the form [8]:

$$\mu = \mu_0 \exp\left(-\frac{E_A}{kT}\right), \quad (1)$$

where k is the Boltzmann constant, T is the temperature, μ_0 is the prefactor and E_A is the activation energy. Meyer and

* Corresponding author.
E-mail address: almantas.pivrikas@jku.at (A. Pivrikas).

1566-1199/$ - see front matter © 2010 Elsevier B.V. All rights reserved.
doi:10.1016/j.orgel.2010.10.014

Neldel first observed the exponential dependence of the prefactor μ_0 on the activation energy E_A:

$$\mu_0 = \mu_{MN} \exp\left(\frac{E_A}{kT_{MN}}\right), \quad (2)$$

where μ_{MN} is the Meyer–Neldel mobility and $kT_{MN} = E_{MN}$ is the Meyer–Neldel energy. Substituting Eq. (2) into Eq. (1) leads to the consequence that there exist an isokinetic temperature $T = T_{MN}$, where the charge carrier mobility becomes independent on activation energy E_A. In a plot of $\ln(\mu)$ versus the inverse temperature (Arrhenius plot), the lines of different Arrhenius dependencies should show one common intersection at T_{MN}. Charge carrier concentration is a parameter which changes the activation energy in MNR. During the transport, the charge carriers become detrapped by being excited from localized states to extended states (or to the states with higher energies where density of states is higher if delocalized states do not exist) by acquiring thermal energy (Arrhenius type behaviour) [9]. Carrier concentrations determines the occupation of DOS as well as the activation energy required for carriers to acquire in order to be promoted to states with higher mobility. Therefore, higher carrier mobility is expected at high concentrations.

The Meyer–Neldel rule (MNR) was observed in charge carrier mobility of fullerenes [10], porous and amorphous silicon [11], microcrystalline silicon films [12], ionic conductivity [13] glassy materials [14] organic materials [15] in various devices such as charge-coupled devices [16], liquid semiconductors [17] and thin-film transistors [18]. Meyer–Neldel temperature was even attributed as a figure-of-merit for the quality of materials used in field-effect transistors [19]. Even though a number of theoretical models were proposed to explain the origin of MNR, none of them is universally accepted. One common explanation is based on the Fermi level shift with temperature [20]. Others suggest that MNR arises for processes for which the total energy is provided by multiple excitations [21,22]. It was also shown that multiple processes coexisting at the same time also lead to the MNR [23]. Theoretical studies by Fishchuk et al., proposed this Meyer–Neldel energy kT_{MN} to be directly proportional to the width of the DOS in the disordered energy band [24].

Usually electric current, conductivity, diffusion and other physical parameters are used to determine the presence of MNR. In order to clearly understand the mechanisms of MNR it is important to demonstrate the MNR in fundamental quantities such as charge carrier mobility. Other quantities might depend on non-transport parameters, for instance material conductivity or total current are dependent on both charge carrier mobility and density which hinders the interpretation of experimental results.

In order to understand and be able to develop device independent unifying models of charge transport it is important to study transport in various device configurations. A number of studies have comparatively studied the charge transport using TOF and OFETs is the past [25–28]. The charge carrier mobility as a function of carrier concentration and temperature is comparatively studied in the bulk of fullerene (C_{60}) diodes and at the interface with gate insulators in OFETs. Usually a large discrepancy between the bulk and the interface mobility values is observed, which is attributed to the difference in charge carrier concentrations and to the difference of the DOS at the interface and in the volume of the film [29,30].

Due to the possibility to experimentally vary carrier concentration and temperature, charge extraction with linearly increasing voltage (CELIV) technique and organic field effect transistor (OFET) measurements are advantageous for studying the charge carrier transport, whereas carrier concentration cannot be varied in classical time-of-flight technique. However, non-equilibrium transport of photogenerated charge carriers is studied using CELIV, whereas steady-state transport is measured in OFETs. Photogenerated carriers lose their excess energy during thermalization processes (downward jumps in energy scale) and their mobility decreases with time after photogeneration resulting in a time-dependent dispersive transport [31]. Therefore, when comparing photogenerated with steady-state transport this has to be taken into account.

In this work the charge carrier mobility as a function of carrier concentration and temperature is studied in fullerene (C_{60}) diodes and OFETs. Comparative studies of charge transport in the bulk of the film and at the interface of fullerene and dielectric are reported using CELIV as well as OFET techniques. MNR parameters have been used to determine the quality of the films and the degree of disorder [19]. Activation energy of electron transport is experimentally measured as a function of carrier concentration.

2. Experimental

The schematic structures of the devices studied here are shown in Fig. 1. Diodes are made of sandwich type geometry, where the semiconducting film is placed between aluminum and PEDOT covered ITO electrodes. OFETs are planar contacted structures where charge carrier transport proceeds between the source and drain electrodes within the channel at the interface of the semiconductor and insulator.

2.1. Charge carrier mobility measurements by charge extraction by linearly increasing voltage (CELIV)

CELIV allows the charge carrier mobility and concentration to be measured from current transients directly and independently. Moreover, time, density, electric field and temperature dependent charge carrier mobility can be studied in the films with rather dispersive charge transport, where other methods (e.g. time-of-flight) are inapplicable due to required experimental conditions [2]. It was shown in the past that the charge carrier mobility measured from CELIV is in good agreement with values measured by TOF [32]. Schematic time dependence of the applied triangle rising voltage pulse and current transient response is shown in Fig. 2.

A linearly increasing voltage pulse with the slope $A = U_{max}/t_{pulse}$, here U_{max} is the maximum voltage of triangle pulse and t_{pulse} is the pulse duration) is applied to the sample to extract the equilibrium charge carriers. The

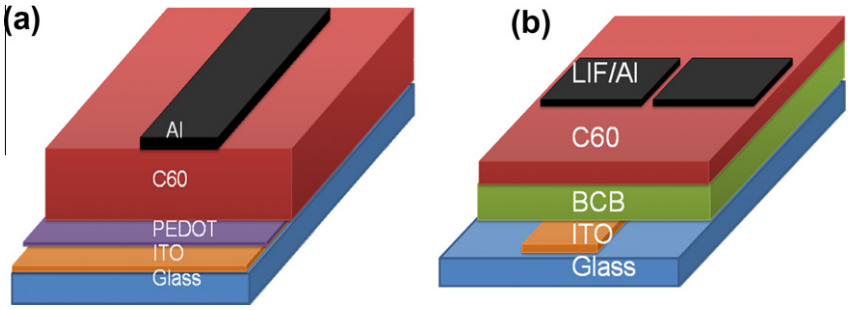

Fig. 1. Schematic illustration of diodes (a) for CELIV and organic field effect transistor (b) for OFET structures used to comparatively study the charge carrier transport in the bulk of the C_{60} film (between Al and ITO/PEDOT contacts) and at the interface of fullerene with the gate insulator (between LiF/Al contacts but at the C_{60}/insulator (BCB) interface).

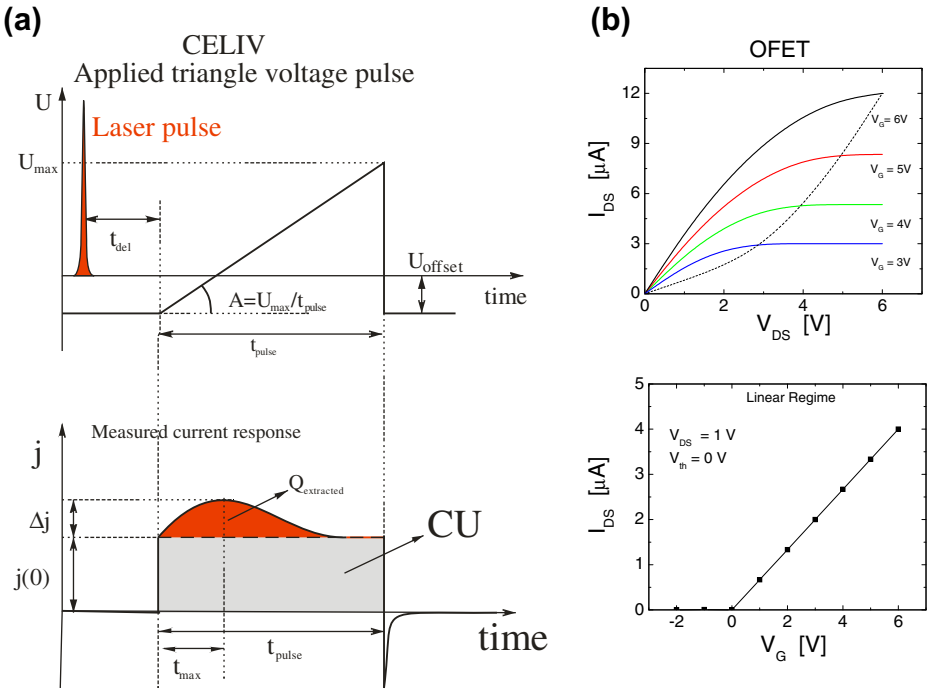

Fig. 2. Schematic charge extraction by linearly increasing voltage (CELIV) current transients (a) and organic field effect transistor (FET) output and transfer curves (b) used to experimentally measure the charge carrier mobility. The charge carrier mobility was studied as a function of the following parameters: temperature, time t_{del} from CELIV, electric field (by changing the rising slope of triangle voltage pulse in CELIV and drain-source voltage V_{DS} in OFET), charge carrier concentration (by changing t_{del} and measuring extracted charge $Q_{extracted}$ in CELIV and changing V_G in OFET).

charge carriers inside the film can also be photogenerated by a light pulse (sometimes called photo-CELIV technique, herein referred also as CELIV). Then, the photogenerated charge carriers are extracted by the linearly increasing voltage pulse after some delay time t_{del}. At the beginning of the CELIV current transient a capacitive current step $j(0)$ is seen (Fig. 2a). The following current increase Δj is related to the extraction current caused by the charge carriers transported in the film. The current continues to increase as the voltage increases until the charge carriers are extracted from the film and the current drops down to the capacitive step level. In practice, if the duration of the applied triangle voltage pulse t_{pulse} is not long enough, then there might be some carriers left in the film and the extraction current will end at a higher level than the capacitive step. The charge carrier mobility is estimated from the extraction maximum [33]:

$$\mu = K\frac{d^2}{At_{max}^2}, \tag{3}$$

where d is the film thickness, $K = 2/3$ for volume ($\alpha d \ll 1$, where α is light absorption coefficient from Beer–Lambert's law) and $K = 2$ for surface photogeneration ($\alpha d \gg 1$).

The charge carrier concentration ($n = Q_{extracted}/e/V$, where $Q_{extracted}$ is the extracted charge, e the elementary charge and V is the volume) is estimated from the integrated extraction photocurrent transient with respect to time. By changing the delay time (t_{del}) between the laser pulse and applied voltage pulse, or by changing the laser

intensity, the charge carrier mobility was measured as a function of time and concentration [34]. Since the electrical field in CELIV experiments is not a constant value but it is ramping with time, the field at which the charge carrier mobility is measured is estimated from At_{max}/d (electric field at maximum extraction point t_{max}), since majority of carriers are extracted at this field.

Thick fullerene films (≈1–10 μm, in order to ensure surface photogeneration) were grown on ITO/glass substrates using physical vapor deposition [35]. Semitransparent, 30 nm thick aluminum electrode was vacuum deposited on top of the fullerene films. CELIV could only be measured down to 240 K in due to a phase transition and a peel off of the studied films. In both, CELIV and OFET experiments, the charge carrier mobility and its temperature dependencies were measured in a cryostat under vacuum (10^{-6} mbar). The measurements were conducted with a temperature step of 10 K, with a time delay of 1 h so that device got thermally stabilized. Studied devices were loaded in the Oxford cryostat under N_2 atmosphere inside the glove box to avoid exposure to ambient condition.

2.2. Charge carrier mobility measurements by organic field effect transistor (OFET)

Fig. 2 shows typical output characteristics of a FET device at different gate voltages and the corresponding transfer characteristics in the linear regime ($V_G \gg V_{DS}$, where V_G and V_{DS} are the gate and drain-source voltages correspondingly). In linear regime, the applied gate field is much larger than the in-plane drift field, which results in an approximately uniform density of charge carriers in the active channel. At these conditions source-drain current I_D increases linearly with V_G and is approximately described by the following equation:

$$I_D|_{V_{DS} \ll V_G} = \frac{W}{L} \mu \, C_i \, V_{DS}(V_G - V_{th}) \quad (4)$$

where L is the channel length, W is the channel width, C_i is the capacitance per unit area of the insulating layer, V_{th} is the threshold voltage.

By plotting I_D versus V_G at low V_{DS} and evaluating the slope of this plot, the carrier mobility μ can be calculated using Eq. (4). Similarly, mobility can also be determined in the saturation regime ($V_{DS} \geqslant V_G$), but due to pinch off in the channel, the mobility calculated in the saturated regime is not an option to study the charge carrier transport in FET devices, because it is deduced form an inhomogeneous distribution of the charge carriers in the conductive channel of the FET.

The charge carrier concentration n is estimated from the charge accumulated at the semiconductor/insulator interface by increasing V_G in metal–insulator-semiconductor (MIS) capacitor:

$$n = C_i \, V_G \frac{1}{ed}, \quad (5)$$

where e is the elementary charge, C_i is the geometric capacitance of the device with a 35 μm channel length and 2 mm channel width and d is the channel height.

Since the charge carrier transport is strongly dependent on the insulator and interface/surface treatment in OFETs [36], OFET devices were fabricated using indert divinyltetramethyldisiloxane-bis(benzocyclobutene) (BCB) as gate dielectric on ITO/glass substrates. Transistor channel length was 35 μm, width 2 mm and for concentration calculations we assumed the channel thickness on the interface of 10 nm (where most of the charge carriers are accumulated) [37]. Details of device fabrication steps were reported previously [38]. The transistor characteristics were recorded by Agilent 2000 SMU. Low V_{DS} (2, 4, 6, 8, 10 V) compared to high V_G (60 V) was used I the experiment in order to stay in the linear regime of OFET operation.

3. Results and discussion

In order to determine the charge transport properties of the studied C_{60} films, both CELIV and OFET measurements were employed. In order to compare the electron and hole mobility by CELIV, thick fullerene films were illuminated either through semitransparent Al or ITO electrode keeping the same applied voltage polarity [39]. Therefore, either electron (ITO illuminated with negative bias) or hole (Al illuminated with positive bias) transport can be measured in the film where the light absorption profile is much smaller than film thickness (surface photogeneration).

Fig. 3a shows CELIV transients for electron and hole transport. The extraction current is seen only for electron transport, whereas for hole transport the CELIV transients is indistinguishable with the dark response concluding that the electron mobility is much higher (>100 times) compared to hole mobility. Laser signal is well seen before the extraction pulse showing that the electrons and holes are photogenerated at the aluminum interface.

The current response for electron transport resembles a typical CELIV transient. The capacitive (displacement) charging current for dark transients is slightly increasing with time due to sum of both effects: increasing dielectric constant and carrier injection from electrode due to non-perfectly blocking contacts. Extraction maximum is seen only for electron transport, when negatively biased ITO electrode is illuminated with a laser.

The OFET transfer curve, shown in Fig. 3b, shows no significant hole injection into the channel when negative voltage is applied to the gate. Strong electron current is observed under positive gate bias. Therefore, both CELIV and OFET experiments confirm that electron mobility is much higher than hole in fullerene films. Further charge carrier transport studies in this work are shown for electron mobility.

Carrier mobility measurements as a function of carrier concentration at various temperatures is shown Fig. 4. In CELIV experiment (a) and (b) the transients were recorded at different t_{del}. The triangle voltage slope A was fixed, but the delay time between the laser and voltage pulse t_{del} was varied which changed carrier concentration. In OFET experiment (c) and (d) the transfer curves at different gate voltages are shown.

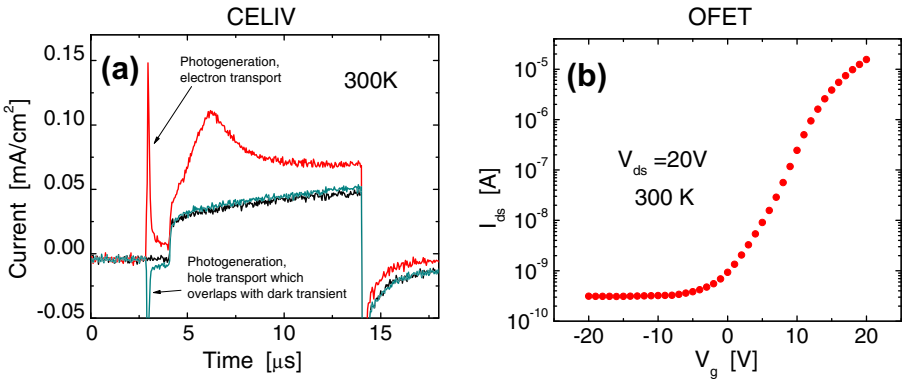

Fig. 3. CELIV transients (a) and OFET transfer curve (b) showing that the electron mobility is at least 100 times larger than hole mobility in C_{60}.

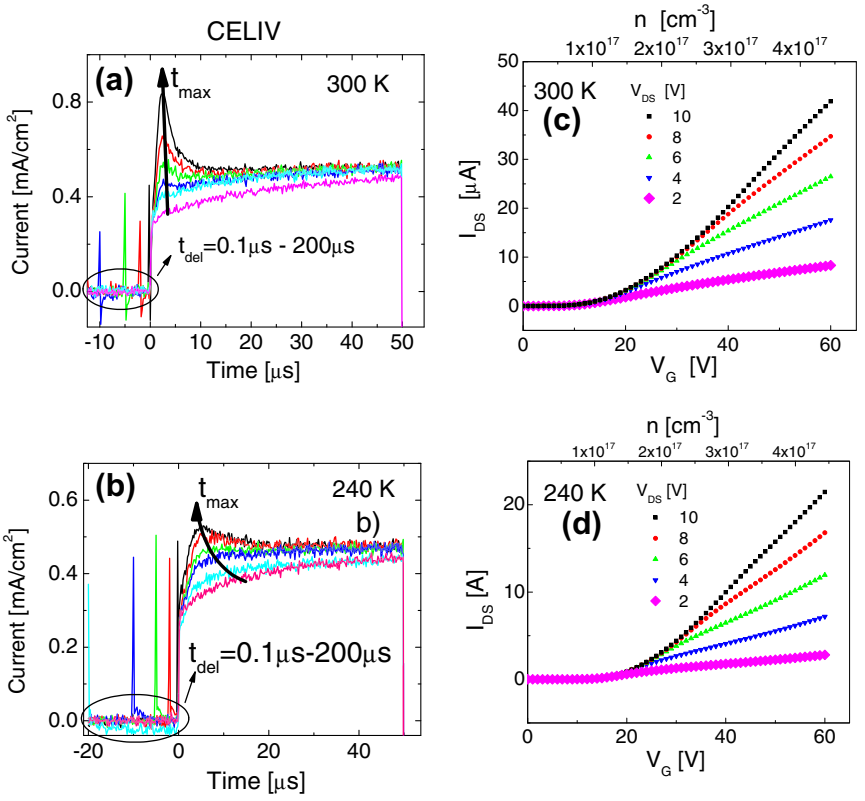

Fig. 4. CELIV current transients at various delay times t_{del} in (a) and (b) shown together with OFET transfer curves in (c) and (d) both at 300 K and 240 K, respectively. From CELIV transient time and concentration dependent carrier mobility as well as carrier density relaxation is measured. OFET curves (shown as thick points) are used to measure carrier concentration dependent electron mobility at different gate voltages.

CELIV transients are similar to the ones observed before only showing more dispersive extraction at lower temperatures. Stronger shift in extraction maximum, which is related to carrier mobility, can be seen at lower temperatures, directly showing that stronger concentration dependent carrier mobility at low temperatures. Charge carrier mobility dependence on time is calculated using Eq. (3) and plotted in Fig. 5a. Because the carrier extraction is not instantaneous and t_{max} is comparable delay time t_{del}, both times have to be taken into account. Therefore, the sum of t_{del} and t_{max} is plotted in Fig. 5 [40].

The charge carrier mobility decreases as a function of time due to the relaxation phenomena of photogenerated charge carriers (thermalization) within the density-of-states to deeper states (time-dependent mobility) as well as due to the charge carrier recombination during the de-

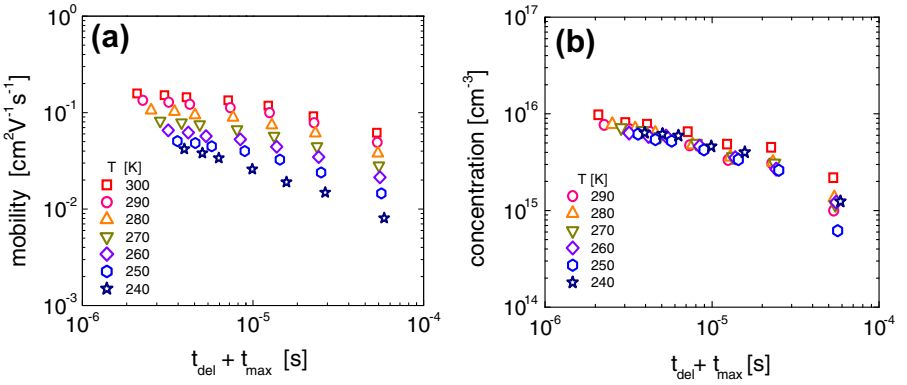

Fig. 5. Non-equilibrium time-dependent electron mobility (a) and density decay (b) in C60 films shown at various temperatures as measured from CELIV.

lay time t_{del} (concentration-dependent mobility) [40]. In the studied films charge transport is weakly dispersive especially at room temperatures, therefore only weak carrier mobility dependence on time is seen. Therefore, measured mobility dependence is attributed to carrier concentration.

By integrating the extraction photocurrent (dark current subtracted) of the CELIV transient over time, we estimate the amount of extracted charge which is proportional to charge carrier concentration in the film. Time-resolved decay of charge carrier concentration is measured and plotted in Fig. 5b. Charge carrier concentration is similar at all temperatures showing that appropriate experimental conditions were chosen to extract all photogenerated charge carriers which allow carrier concentration to be estimated from the photocurrent transients. In order to present the carrier mobility as a function of concentration, Fig. 5a and b are used to eliminate the time scale and plot carrier mobility at different concentrations. Carrier mobility values from OFET are estimated from Fig. 4 using Eq. (4) and plotted together with CELIV values comparatively in Fig. 6. Since the extraction maximum position changes with carrier concentration, so does the electric field at which carrier mobility is estimated. Therefore, non-constant electric field is present during CELIV measurements, but the change is insignificant (from 3000 to 1500 V/cm), whereas in OFET experiment the electric field is constant (500 V/cm).

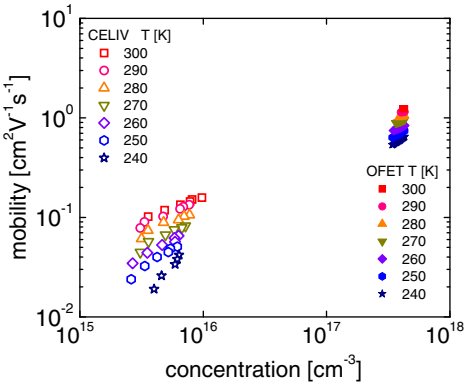

Fig. 6. Concentration dependent electron mobility in C_{60} films measured from CELIV and OFET. Electric field in CELIV experiment changes in the range from 3000 to 1500 V/cm, where in OFETs it is 500 V/cm.

Much lower charge carrier mobility values and stronger concentration dependence is seen in the bulk of the film from CELIV where carrier concentration is significantly lower. Weak dependence of carrier mobility on concentration observed in OFETs is attributed to the trap filling effect at high carrier concentrations which increases the effective transport energy in the DOS to higher values. This allows for carriers to reach higher energies where the mobility is larger and less dependent of concentration due to higher density of available states [41].

Arrhenius plots from both CELIV and OFET experiments are evaluated from the concentration dependent carrier mobility measurements. Fig. 7a and b shows the Arrhenius-type of charge carrier mobility replotted from the Fig. 6 as a function of temperature at different carrier concentrations from both CELIV and OFET experiments, respectively.

In both experiments carrier mobility follows Arrhenius type of dependence in contrast to typically observed non-Arrhenius dependence in π-conjugated polymers and molecularly doped polymer in which Bässler's model is used to describe the charge transport.[32,41] A common intersection point of extrapolated data lines allows the Meyer–Neldel parameters to be estimated. The charge carrier mobility becomes temperature and concentration independent at the isokinetic intersection point. MNR temperature obtained from CELIV is T_{MN} = 406 K and from OFET T_{MN} = 408 K which in both cases corresponds approximately to E_{MN} = 35 meV. Since the MNR energy E_{MN} is directly correlated with the level of disorder in the film quality and properties of DOS in which charge transport occurs [24,42,43], similar MNR energies obtained from CELIV and OFET suggest that charge carriers experience energetically similar landscape for charge transport in the bulk of the film and at the interface in studied devices. The absence of dipoles at the interface of fullerene and BCB forms the interface beneficial for charge transport which allows to reach high carrier mobility values. The MNR mobility

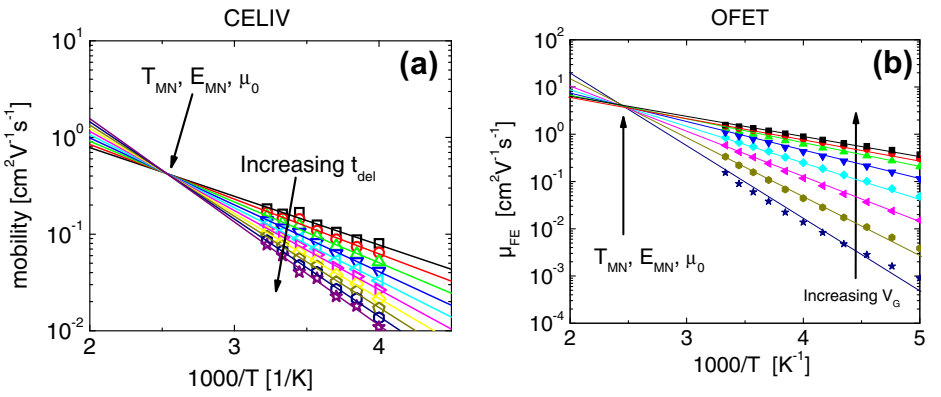

Fig. 7. Arrhenius plots of temperature dependent electron mobility at various concentrations measured from CELIV and OFET. Meyer-Neldel parameters from CELIV: T_{MN} = 406 K, E_{MN} = 35 meV, μ_{MN} = 0.4 $cm^2\,V^{-1}\,s^{-1}$; from OFET: T_{MN} = 408 K, E_{MN} = 35 meV, μ_{MN} = 4 $cm^2\,V^{-1}\,s^{-1}$.

prefactors (Eq. (2)) are μ_{MN} = 0.4 $cm^2\,V^{-1}\,s^{-1}$ from CELIV and μ_{MN} = 4 $cm^2\,V^{-1}\,s^{-1}$ from OFET. Obtained values are in good agreement with the results obtained in similar C_{60} devices in the past [10,24,42,43].

From Arrhenius plots the activation energies for electron transport are estimated from both CELIV and OFET measurements and plotted as a function of carrier concentration in Fig. 8a. Electric field at which concentration dependent carrier mobility was measured is different in both experiments. High voltage was used in CELIV to ensure the lowest error, whereas to satisfy linear regime conditions in OFET measurements, the smallest source-drain voltage was used. Despite a slight mismatch observed in Fig. 8a, the correct trend of activation energy is seen. At lower carrier concentrations larger activation energy is required for transport in disordered media.

We have estimated and plotted in Fig. 8b the mobility prefactor μ_0 as a function of activation energy using Eq. (1). Similar slopes show well matching MNR energies E_{MN} in both the bulk on the film and at the interface. The mobility prefactor μ_0 is order of magnitude higher in the OFET compared to transport in the bulk measured from CELIV, which well agrees with the difference in Meyer–Neldel mobility prefactor μ_{MN} as well as with difference in activation energies E_A.

A mismatch in μ_{MN}, μ_0 and E_A in diodes and OFETs can be caused by the nature of non-equilibrium measurements in CELIV compared to steady-state OFET measurements. Excess amount of energy available for photogenerated charge carriers might reduce the activation energy and be the reason for the observed mismatch. Further studies of concentration dependent activation energy at different electric fields is required in order to see the effect of electric field.

4. Conclusions

Carrier density and temperature dependent mobility is experimentally measured and compared in the bulk of the fullerene films and at the interface with insulator. Non-equilibrium mobility of photogenerated charge carriers measured using charge extraction by linearly increasing voltage (CELIV) technique as well as steady state mobility measured in organic field-effect transistors (OFET) is compared. Much higher electron mobilities (>100 times) as compared to hole mobilities are observed. Carrier concentration dependent electron mobility in both types of devices shows lower mobility values and stronger concentration dependence in diodes. Larger activation energy for electron transport is required at lower carrier

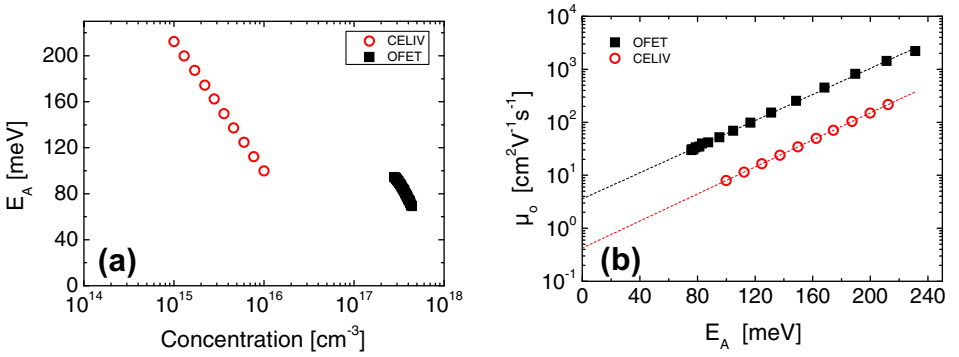

Fig. 8. (a) activation energy dependence on concentration. Electric field changes in the same range as specified in the caption of Fig. 6; (b) mobility prefactor μ_0 dependence on activation energy E_A shown for CELIV and OFET experiments.

concentrations. Arrhenius plots of temperature dependence of mobility at various concentrations demonstrate the presence of Meyer–Neldel rule (MNR). It is shown that MNR energy is the same in the bulk of the semiconductor and at the interface, suggesting similar levels of energetical disorder. Observed differences in charge transport in diodes and OFETs is proposed to be due to either different carrier concentrations or due to the nature of non-equilibrium charge carrier transport in CELIV compared to steady-state OFET measurements.

Acknowledgements

We thank Prof. I.I. Fishchuk and Prof. A.K. Kadashchuk for helpful scientific discussions. Austrian National Network (NFN S9711) funded by the Austrian Science Funds (FWF) is acknowledged.

References

[1] Paul M. Borsenberger, Mol. Cryst. Liquid Cryst. 228 (1993) 167.
[2] G. Juska, K. Genevicius, K. Arlauskas, R. Osterbacka, H. Stubb, Phys. Rev. B 65 (2002) 233208.
[3] A. Pivrikas, G. Juska, K. Arlauskas, M. Scharber, A. Mozer, N.S. Sariciftci, H. Stubb, R. Österbacka, Proc. SPIE 5938 (2005) 59380N.
[4] G. Juška, G. Sliauzys, K. Genevicius, K. Arlauskas, A. Pivrikas, M. Scharber, G. Dennler, N.S. Sariciftci, R. Österbacka, Phys. Rev. B 74 (2006) 115314.
[5] G. Juška, K. Arlauskas, G. Sliauzys, A. Pivrikas, A.J. Mozer, N.S. Sariciftci, M. Scharber, R. Österbacka, Appl. Phys. Lett. 87 (2005) 222110.
[6] G. Juška, K. Genevicius, G. Sliauzys, A. Pivrikas, M. Scharber, R. Österbacka, J. Appl. Phys. 101 (2007) 114505.
[7] R. Österbacka, K. Genevicius, A. Pivrikas, G. Juška, K. Arlauskas, T. Kreouzis, D.D.C. Bradley, H. Stubb, Synth. Met. 139 (2003) 811.
[8] W. Meyer, H. Neldel, Z. Tech. Phys. (Leipzig) 12 (1937) 588.
[9] P.W. Anderson, Absence of diffusion in certain random lattices, Phys. Rev. 109 (1958) 1492–1505.
[10] J.C. Wang, Y.F. Chen, Appl. Phys. Lett. 73 (1998) 948.
[11] Y. Lubianiker, I. Balberg, J. Non-Crystalline Solids 227–230 (1998) 180.
[12] S.K. Ram, S. Kumar, R. Vanderhaghen, P. Roca i Cabarrocas, J. Non-Crystalline Solids 411 (2002) 299–302.
[13] K.L. Ngai, Sol. Stat. Ionics 105 (1998) 231.
[14] K. Shimakawa, F. Abdel-Wahab, Appl. Phys. Lett. 70 (1997) 652.
[15] E.J. Meijer, M. Matters, P.T. Herwig, D.M. de Leeuw, T.M. Klapwijk, Appl. Phys. Lett. 76 (2000) 3433.
[16] R. Widenhorn, L. Mundermann, A. Rest, E. Bodegom, J. Appl. Phys. 89 (2001) 8179.
[17] J. Fortner, V.G. Karpov, M.L. Saboungi, Appl. Phys. Lett. 66 (1995) 997.
[18] M. Kondo, Y. Chida, A. Matsuda, J. Non-Crystalline Solids 178 (1996) 198–200.
[19] L. Pichon, A. Mercha, J.M. Routoure, R. Carin, O. Bonnaud, T. Mohammed-Brahim, Thin Solid Films 427 (2003) 350.
[20] H. Overhof, P. Thomas, Electronic Transport in Hydrogenated Amorphous Semiconductors, Springer, Berlin, 1989.
[21] G. Boisvert, L.J. Lewis, A. Yelon, Phys. Rev. Lett. 75 (1995) 469.
[22] A. Yelon, B. Movaghar, Phys. Rev. Lett. 65 (1990) 618.
[23] R. Widenhorn, A. Rest, E. Bodegom, J. Appl. Phys. 91 (2002) 6524.
[24] I.I. Fishchuk, A.K. Kadashchuk, J. Genoe, Mujeeb Ullah, H. Sitter, Th.B. Singh, N.S. Sariciftci, H. Bässler, Phys. Rev. B 81 (2010) 045202.
[25] R. Rawcliffe, D.D.C. Bradley, A.J. Campbell, Proc. SPIE 5217 (2003) 25.
[26] R. Rawcliffe, D.D.C. Bradley, A.J. Campbell, Proc. SPIE 5519 (2004) 89.
[27] J. Reynaert, V.I. Arkhipov, J. Genoe, G. Borghs, P. Heremans, Mater. Res. Soc. Symp. Proc. 846 (2005) DD6.8.1.
[28] M. Kotani, K. Kakinuma, M. Yoshimura, K. Ishii, S. Yamazaki, T. Kobori, H. Okuyama, H. Kobayashi, H. Tada, Chem. Phys. 325 (2006) 160.
[29] C. Tanase, E.J. Meijer, P.W.M. Blom, D.M. de Leeuw, Phys. Rev. Lett. 91 (2003) 216601.
[30] L. Li, G. Mellera, H. Kosina, Synth. Met. 157 (2007) 243.
[31] A.J. Mozer, G. Dennler, N.S. Sariciftci, M. Westerling, A. Pivrikas, R. Österbacka, G. Juška, Phys. Rev. B 72 (2005) 035217.
[32] A.J. Mozer, N.Se. Sariciftci, A. Pivrikas, R. Österbacka, G. Juška, L. Brassat, H. Bässler, Phys. Rev. B 71 (2005) 035214.
[33] G. Juska, K. Arlauskas, M. Viliunas, J. Kocka, Phys. Rev. Lett. 84 (2000) 4946.
[34] A. Pivrikas, R. Osterbacka, G. Juska, K. Arlauskas, H. Stubb, Synth. Met. 155 (2005) 242.
[35] H. Sitter, T. Nguyen Manh, D. Stifter, J. Cryst. Growth 174 (1997) 828.
[36] M. Shtein, J. Mapel, J.B. Benziger, S.R. Forrest, Appl. Phys. Lett. 81 (2002) 268.
[37] C. Tanase, E.J. Meijer, P.W.M. Blom, D.M. de Leeuw, Org. Electron. 4 (2003) 33.
[38] Mujeeb Ullah, D.M. Taylor, R. Schwödiauer, H. Sitter, S. Bauer, N.S. Sariciftci, Th.B. Singh, J. Appl. Phys. 106 (2009) 114505.
[39] A. Palmaerts, L. Lutsen, T.J. Cleij, D. Vanderzande, A. Pivrikas, H. Neugebauer, N.S. Sariciftci, Polymer 50 (2009) 5007.
[40] R. Osterbacka, A. Pivrikas, G. Juska, K. Genevicius, K. Arlauskas, H. Stubb, Current Appl. Phys. 4 (2004) 534.
[41] H. Bässler, Phys. Stat. Sol. B 175 (1993) 15.
[42] Mujeeb Ullah, T.B. Singh, H. Sitter, N.S. Sariciftci, Appl. Phys. A: Mater. Sci. Process 97 (2009) 521.
[43] Mujeeb Ullah, I.I. Fishchuk, A.K. Kadashchuk, P. Stadler, A. Pivrikas, C. Simbrunner, V.N. Poroshin, N.S. Sariciftci, H. Sitter, APL 96 (2010) 213306.

Organic Electronics 12 (2011) 169–178

Contents lists available at ScienceDirect

Organic Electronics

journal homepage: www.elsevier.com/locate/orgel

Revealing bipolar charge-transport property of 4,4′-*N*,*N*′-dicarbazolylbiphenyl (CBP) by quantum chemical calculations

Tomonori Yamada [a], Furitsu Suzuki [a], Atsushi Goto [a], Tohru Sato [b,c], Kazuyoshi Tanaka [b], Hironori Kaji [a,*]

[a] Institute for Chemical Research, Kyoto University, Uji, Kyoto 611-0011, Japan
[b] Department of Molecular Engineering, Graduate School of Engineering, Kyoto University, Kyoto 615-8510, Japan
[c] Fukui Institute for Fundamental Chemistry, Kyoto University, Takano-Nishihiraki-cho 34-4, Sakyo-ku, Kyoto 606-8103, Japan

ARTICLE INFO

Article history:
Received 8 August 2010
Received in revised form 18 October 2010
Accepted 31 October 2010
Available online 12 November 2010

Keywords:
Organic LED
Marcus theory
Charge transfer integral
Reorganization energy
Quantum chemical calculation

ABSTRACT

4,4′-*N*,*N*′-Dicarbazolylbiphenyl (CBP) has both the hole- and electron-transport ability, that is, bipolar charge-transport property, and has been widely used for organic light-emitting diodes (OLEDs). In this study, we explain the bipolar charge-transport property of CBP by quantum chemical calculations for the crystal. Both the reorganization energies and the charge transfer integrals were investigated, and charge-transfer rate constants were calculated based on Marcus theory. The hole- and electron-transfer rate constants thus calculated were found to be similar in magnitude. This is in sharp contrast with the case of a structurally similar but a poor electron-transport material, *N*,*N*′-diphenyl-*N*,*N*′-di(*m*-tolyl)benzidine (TPD), for which the hole-transfer rate constants were calculated to be much larger than the electron-transfer rate constants. From the detailed analysis of the charge transfer integrals for CBP, it was found that holes transfer through all the segments of the molecules, using the delocalized HOMO over the whole molecule as in the case of TPD. On the other hand, electrons transfer advantageously through the delocalized LUMO on the carbazole moieties of CBP, which have close intermolecular contacts. The LUMO of TPD localizes on the central biphenylene moiety, resulting in small electron transfer integrals. The results clearly show the difference of the electron-transport property between CBP and TPD.

© 2010 Elsevier B.V. All rights reserved.

1. Introduction

Organic light-emitting diodes (OLEDs) are promising devices for flat or flexible displays, and lighting equipments [1,2]. Fig. 1 shows widely known charge-transport materials for OLEDs, 4,4′-*N*,*N*′-dicarbazolylbiphenyl (CBP) [3–10] and *N*,*N*′-diphenyl-*N*,*N*′-di(*m*-tolyl)benzidine (TPD) [2,11–16]. The chemical structures of CBP and TPD are similar to each other, while the charge-transport properties are not. For CBP, both the hole and electron mobilities are on the order of 10^{-3} cm^2/Vs [7,8]. Conforming to the preceding studies [5,7–10], we should like to call CBP as a '*bipolar*' material on the basis of the comparable hole and electron mobilities. The latter, TPD, shows a similar hole-transport property with the mobility of $\sim 10^{-3}$ cm^2/Vs; however, the electron mobility is inferior, $<10^{-7}$ cm^2/Vs [14–16]. Understanding the origins of the different charge-transport properties between CBP and TPD is of importance not only for fundamental science but also for molecular designs with excellent performance.

Charge transports in organic materials have often been discussed based on Marcus theory [17,18], which describes the charge-transfer rate constant, k_{CT}, as Eq. (1).

$$k_{CT} = \frac{4\pi^2}{h} H_{AB}^2 \frac{1}{\sqrt{4\pi\lambda k_B T}} \exp\left(-\frac{\lambda}{4k_B T}\right) \quad (1)$$

* Corresponding author. Tel.: +81 774 38 3149; fax: +81 774 38 3148.
E-mail address: kaji@scl.kyoto-u.ac.jp (H. Kaji).

1566-1199/$ - see front matter © 2010 Elsevier B.V. All rights reserved.
doi:10.1016/j.orgel.2010.10.022

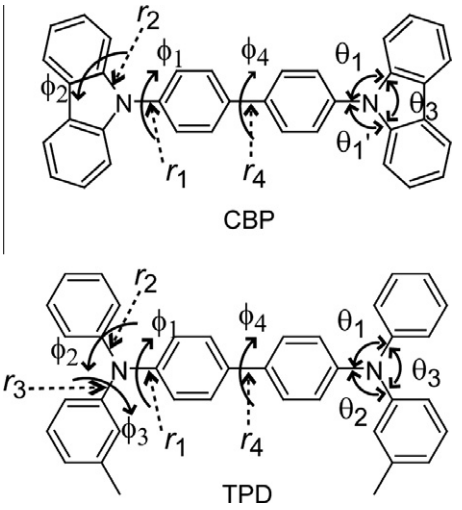

Fig. 1. The chemical structures of CBP and TPD. The θ, ϕ, and r represent bond angles, torsion angles, and bond lengths, respectively.

Here, λ is the reorganization energy, and H_{AB} is the charge transfer integral between the relevant two molecules. The temperature, T, is fixed at 300 K throughout this paper. The h and k_B are the Planck and Boltzmann constants, respectively. In some studies, for example, Refs. [19] and [20], reorganization energies were calculated to account for the charge-transport properties. The charge transfer integrals were assumed to be similar in these studies. The attempts were partly successful for the qualitative description of the charge-transport properties. However, it has been found that some experimental results cannot be explained by the simple consideration. For tris(8-hydroxyquinoline) aluminum(III) (Alq_3), for example, the difference between the hole- and electron-transport properties could not be explained by the consideration only of the reorganization energies. The charge transfer integrals were found to be a key factor [21].

Recently, we found that the hole transfer integrals in TPD crystals are several times larger than the electron transfer integrals [22]. The HOMO of TPD spreads over the molecule. Large intermolecular overlaps can be formed between the phenyl and/or tolyl rings, which have close intermolecular contacts in the crystals. In contrast, the LUMO of TPD is localized on the central biphenylene moiety, which results in small intermolecular overlaps (that is, small electron transfer integrals). Owing to both the small reorganization energies and the large charge transfer integrals for the hole transfers, the hole-transfer rate constants were calculated to be more than two orders of magnitude larger than the electron-transfer rate constants. In addition, there are effective hole-transport paths consisting of consecutive molecular pairs with large hole-transfer rate constants [22]. The results show the favorable hole-transport property of TPD.

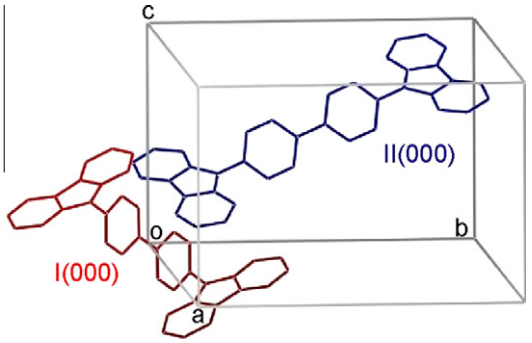

Fig. 2. The unit cell of CBP crystal and representations of molecules I and II. The cell parameters are as follows; a = 8.01 Å, b = 16.01 Å, c = 10.24 Å, $\alpha = \gamma = 90.0°$, and $\beta = 110.2°$.

On the other hand, the origins of the bipolar charge-transport property of CBP have been unclear, despite the practical importance as a host material of emitting layers in OLEDs. In this paper, we analyze the charge-transport property of CBP in the crystal as in the case of TPD. The reorganization energies and the charge transfer integrals are compared with those for TPD. The results explain the difference of charge-transport properties between CBP and TPD.

2. Computation

The structural optimizations were performed for neutral, cationic, and anionic CBP molecules by DFT method using the B3LYP functional [23–25] and the 6-31G(d) basis

Table 1
Structural parameters of a CBP molecule in the crystal, and those optimized by DFT method for the neutral, cationic, and anionic states. The parameters are defined in Fig. 1. As an initial structure for the optimizations, the crystalline structure was adopted. The parameters for the optimized TPD are also shown for comparison.

		Bond angle (°)			Torsion angle (°)				Bond length (Å)			
		θ_1	θ_2	θ_3	ϕ_1	ϕ_2	ϕ_3	ϕ_4	r_1	r_2	r_3	r_4
CBP												
Crystal[a]		125 ± 1	–	108	49 ± 3	9 ± 2	–	0	1.42	1.39 ± 0.01	–	1.49
Optimized	Neutral	126	–	108	53	2	–	0	1.42	1.40	–	1.49
	Cation	126	–	108	45	4	–	0	1.40	1.41	–	1.47
	Anion	126	–	108	70	1	–	0	1.43	1.39	–	1.44
TPD												
Optimized	Neutral	120	120	120	41	41	43	36	1.42	1.42	1.42	1.48
	Cation	121	121	118	26	49	49	21	1.39	1.43	1.43	1.46
	Anion	119	119	122	61	31	32	9	1.44	1.41	1.41	1.44

[a] The values are taken from Ref. [26].

set. The molecular structure in Ref. [26] was adopted as an initial structure for the optimizations. Using the DFT-optimized structures, the reorganization energies were calculated, according to Ref. [22]. The packing structure of the CBP crystal was also taken from Ref. [26]. Fig. 2 shows the unit cell. For all the pairs of two molecules in the identical and the neighboring cells, the charge transfer integrals were calculated by extended Hückel method from Eq. (2) [22,27,28].

$$H_{AB} = \frac{\beta - \frac{\alpha_A + \alpha_B}{2} S}{1 - S^2} \tag{2}$$

Here, $\alpha_A = \langle \Phi_A | \mathbf{H} | \Phi_A \rangle$, $\alpha_B = \langle \Phi_B | \mathbf{H} | \Phi_B \rangle$, $\beta = \langle \Phi_A | \mathbf{H} | \Phi_B \rangle = \langle \Phi_B | \mathbf{H} | \Phi_A \rangle$, $S = \langle \Phi_A | \Phi_B \rangle = \langle \Phi_B | \Phi_A \rangle$, and $\mathbf{H}$ is the electronic Hamiltonian. Φ_A and Φ_B are the HOMOs of isolated molecules, A and B, respectively, for the evaluations of hole transfer integrals. Also, for the evaluations of electron transfer integrals, they are the LUMOs of isolated molecules, A and B, respectively. Because the charge-transfer rate constant is a function of H_{AB}^2, the charge-transport property can be discussed by the absolute values of H_{AB} values. Hereafter, the charge transfer integrals are shown by the absolute values for simplicity. All of the quantum chemical calculations were performed by Gaussian 03 program [29] without the constraint of symmetry.

3. Results and discussion

3.1. Molecular structure and reorganization energy

The structural parameters of the crystalline CBP (Fig. 2) are shown in Table 1. Note that the parameters for the two molecules in Fig. 2 are equivalent with each other. The features are as follows. (1) The summation of the three ∠CNC

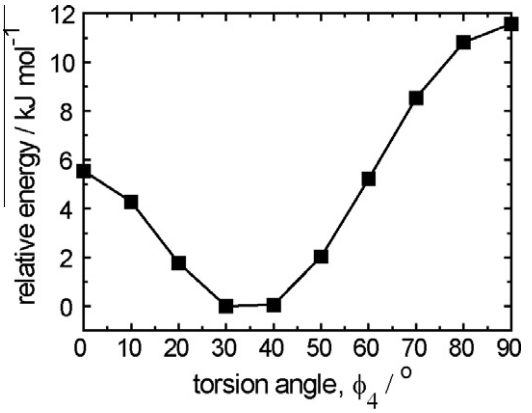

Fig. 3. The torsion angle ϕ_4 dependence of the SCF energy of a CBP molecule. The calculations were carried out with the interval of 10° and the energies are represented as relative values against the minimum energy, -3.93×10^6 kJ mol^{-1} ($\phi_4 = 30°$). The other structural parameters are fixed to the optimized values shown in Table 1. The calculations were performed by B3LYP/6-31G(d) level.

Table 2
The ratio of the maximum hole- and electron-transport rate constants, k_{CT}^+/k_{CT}^-, of CBP and TPD, based on Marcus theory.

	Calculation method for reorganization energy	k_{CT}^+/k_{CT}^{-a}	k_{CT}^+/k_{CT}^{-b}
CBP	Extended Hückel	3.3	1.7
	DFT	1.7×10	9.2
TPD	Extended Hückel	2.0×10	1.4×10^2
	DFT	2.7×10	1.9×10^2

[a] The ratios are obtained under the assumption that the hole and electron transfer integrals are equal.
[b] The ratios are obtained by considering both the reorganization energies and transfer integrals.

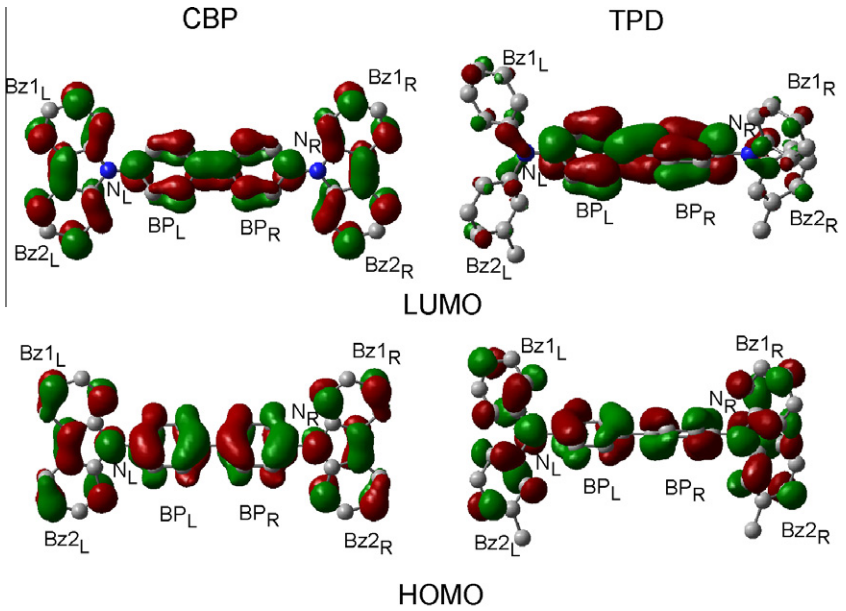

Fig. 4. The HOMO and LUMO of CBP calculated by extended Hückel method for the crystalline conformation. Those of TPD are also shown for comparison. The value for the surfaces is 0.02 a.u.

Table 3
Contributions of the nitrogen (N), biphenylene (BP), and the benzene rings in the carbazole moieties (Bz1, Bz2) of CBP to the HOMO and LUMO. The subscript of "L" or "R" indicates the left or right side of the molecule in Fig. 4. The values for TPD are also shown for comparison.

		N_L	N_R	BP_L	BP_R	$Bz1_L$	$Bz2_L$	$Bz1_R$	$Bz2_R$
CBP	HOMO	11	11	20	20	9	9	9	9
	LUMO	0	0	17	17	17	17	17	17
TPD	HOMO	15	15	18	18	9[a]	9[b]	9[a]	9[b]
	LUMO	1	1	43	43	4[a]	3[b]	4[a]	3[b]

[a] The values are for the phenyl group of TPD.
[b] The values are for the tolyl group of TPD.

bond angles around the nitrogen atom, $2\theta_1 + \theta_3$ (see Fig. 1), is almost 360°, meaning that the nitrogen atom and the three carbon atoms bonded to the nitrogen atom are in the same plane. This is similar to those for other triphenylamine compounds, including TPD. (2) The torsion angle of the central C–C bond in the biphenylene moiety, ϕ_4, is 0°, indicating that the biphenylene moiety has a planar structure in the CBP crystal. This feature is different from that for the TPD crystal, ϕ_4 = 34–37° [30,31]. The difference is considered to originate from a molecular packing effect, as discussed below.

Table 1 also shows the results of the structure optimizations by DFT method for CBP in the neutral, cationic, and anionic states. It must be noted that all of the CBP structures in Table 1 provide imaginary frequencies for a rotational fluctuation around the torsion angle, ϕ_4. Fig. 3 shows the torsion angle ϕ_4 dependence of the self-consistent field (SCF) energy for the optimized structure in the neutral state. The energetic minimum corresponds to ϕ_4 = 30–40°, not 0°. This indicates that the above optimized structure corresponds to a saddle point of the potential. The energetic difference from the potential minimum is about 6 kJ/mol. This result shows that the crystalline structure of CBP is different from the most stable conformation for an isolated molecule, probably due to the intermolecular packing effects in the crystal. In this study, we adopt the optimized structures in Table 1 to estimate the reorganization energies for the crystalline structure.

For the cationic and anionic structures, the torsion angles, ϕ_2 and ϕ_4, are almost comparable with those in the neutral structure. In contrast, the torsion angle ϕ_1 and bond length r_4 are different between the neutral and charged states. Based on these DFT-optimized structures, the reorganization energies were calculated by extended Hückel and DFT methods. The reorganization energies

Table 4
Molecular pairs in the CBP crystal. Pairs between a molecule in the cell (0 0 0) and another molecule in cells (a b c) (a, b, c = −1, 0, 1) are considered. They are classified into 25 types of relative geometries, A–Y. The geometrical types of A, B, and C are shown in boldface.

Molecular pair	a	b	c	Geometrical type	a	b	c	Geometrical type	a	b	c	Geometrical type
I(000)-I(abc)					1	0	0	G	−1	0	0	G
	0	0	1	H	1	0	1	D	−1	0	1	R
	0	0	−1	H	1	0	−1	R	−1	0	−1	D
	0	1	0	E	1	1	0	M	−1	1	0	F
	0	1	1	P	1	1	1	Q	−1	1	1	T
	0	1	−1	J	1	1	−1	V	−1	1	−1	**B**
	0	−1	0	E	1	−1	0	F	−1	−1	0	M
	0	−1	1	J	1	−1	1	**B**	−1	−1	1	V
	0	−1	−1	P	1	−1	−1	T	−1	−1	−1	Q
I(000)-II(abc)	0	0	0	**A**	1	0	0	**C**	−1	0	0	K
	0	0	1	O	1	0	1	I	−1	0	1	X
	0	0	−1	**A**	1	0	−1	K	−1	0	−1	**C**
	0	1	0	L	1	1	0	N	−1	1	0	S
	0	1	1	W	1	1	1	U	−1	1	1	Y
	0	1	−1	L	1	1	−1	S	−1	1	−1	N
	0	−1	0	**A**	1	−1	0	**C**	−1	−1	0	K
	0	−1	1	O	1	−1	1	I	−1	−1	1	X
	0	−1	−1	**A**	1	−1	−1	K	−1	−1	−1	**C**
II(000)-I(abc)					1	0	0	K	−1	0	0	**C**
	0	0	1	**A**	1	0	1	**C**	−1	0	1	K
	0	0	−1	O	1	0	−1	X	−1	0	−1	I
	0	1	0	**A**	1	1	0	K	−1	1	0	**C**
	0	1	1	**A**	1	1	1	**C**	−1	1	1	K
	0	1	−1	O	1	1	−1	X	−1	1	−1	I
	0	−1	0	L	1	−1	0	S	−1	−1	0	N
	0	−1	1	L	1	−1	1	N	−1	−1	1	S
	0	−1	−1	W	1	−1	−1	Y	−1	−1	−1	U
II(000)-II(abc)					1	0	0	G	−1	0	0	G
	0	0	1	H	1	0	1	D	−1	0	1	R
	0	0	−1	H	1	0	−1	R	−1	0	−1	D
	0	1	0	E	1	1	0	F	−1	1	0	M
	0	1	1	J	1	1	1	**B**	−1	1	1	V
	0	1	−1	P	1	1	−1	T	−1	1	−1	Q
	0	−1	0	E	1	−1	0	M	−1	−1	0	F
	0	−1	1	P	1	−1	1	Q	−1	−1	1	T
	0	−1	−1	J	1	−1	−1	V	−1	−1	−1	**B**

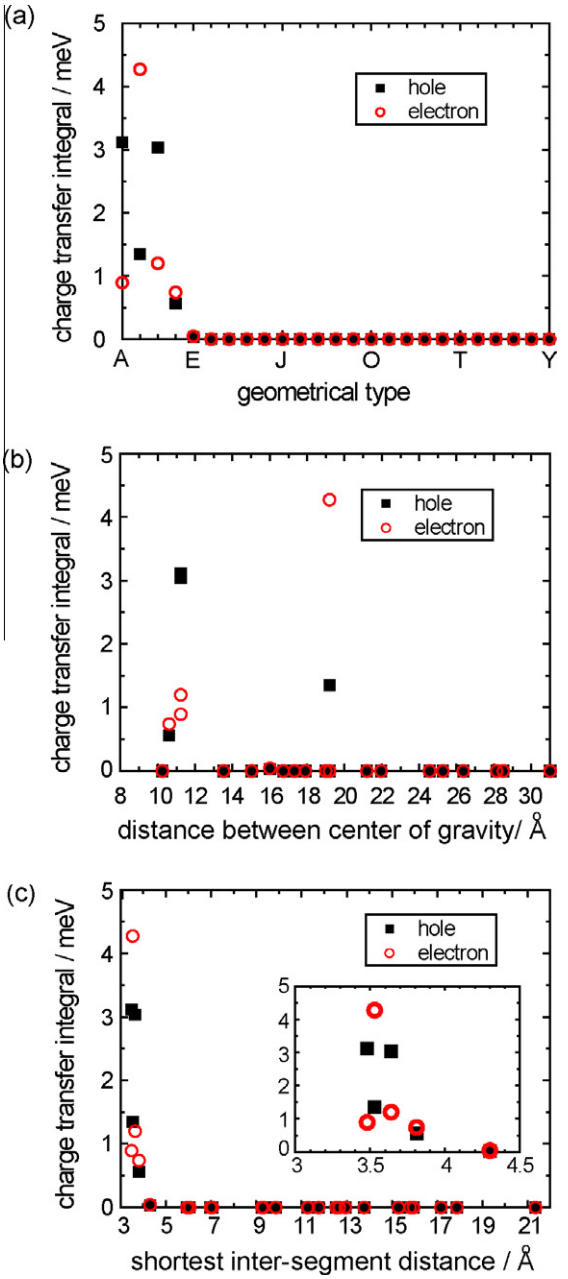

Fig. 5. The hole (filled square) and electron (open circle) transfer integrals for the geometrical types of A–Y in the CBP crystal. The values are shown (a) in order of A–Y, (b) as a function of intermolecular distance between the center of gravity of relevant two molecules, and (c) as a function of shortest inter-segment distance. The inset in (c) shows a expanded figure in the range of 3–4.5 Å.

obtained by extended Hückel method are 0.10 and 0.19 eV for hole and electron transfers, respectively. The value for electron transfer of CBP is found to be small, compared with the values for the electron transfer of TPD (0.15 and 0.40 eV for hole and electron transfers, respectively [22]).

The ratios of hole- and electron-transfer rate constants are summarized in Table 2. Assuming that the hole and electron transfer integrals are equivalent, the ratio of hole- and electron-transfer rate constants for CBP is calculated to be 3.3 from Eq. (1). A better electron-transport property is expected for CBP by comparing the ratio of 20 for TPD [22]. For TPD, the reorganization energies calculated by extended Hückel and DFT methods led the comparable values for the ratio of hole- and electron-transfer rate constants, under the assusmption that hole- and electron transfer integrals are the same (see Table 2 and Ref. [22]). This is not the case for CBP; the ratio of hole- and electron-transfer rate constants calculated by DFT method is larger than that calculated by extended Hückel method. Nevertheless, if both the reorganization energy and charge transfer integral are taken into account, the ratios of hole- and electron-transfer rate constants calculated by extended Hückel and DFT methods are in the same order of magnitude as shown in Table 2. For the following calculations, we use the reorganization energies by extended Hückel method, which has been accepted in Ref. [22].

3.2. Frontier orbital

Fig. 4 illustrates the HOMO and LUMO calculated by extended Hückel method for CBP. The HOMO and LUMO of TPD are also shown for comparison (HOMO−1 and LUMO+1 are shown in Fig. S1 with the orbital energies in the supplementary data). Table 3 summarizes, in percentage, the squares of the MO coefficients of respective segments of CBP, nitrogen (N), biphenylene (BP), and the two benzene rings in the carbazole moiety (Bz1 and Bz2). The subscripts of "L" and "R" mean left and right sides of the molecule, respectively (see Fig. 4). For the HOMO, all the contributions are from 9 to 20%, meaning that the MO is relatively delocalized over the molecule. Among them, the contributions from the biphenylene moieties are the largest (20% each for BP_L and BP_R), as in the case of TPD (see also Table 3). For the LUMO, contributions of the biphenylene moieties of CBP (17% each for BP_L and BP_R) are much smaller than those for TPD (43% each for BP_L and BP_R). Instead, contributions of the carbazole moieties of CBP (17% each for $Bz1_R$, $Bz1_L$, $Bz2_R$, and $Bz2_L$) are large, compared with the LUMO of TPD (3–4% each for $Bz1_R$, $Bz1_L$, $Bz2_R$, and $Bz2_L$). Fig. 4 clearly shows the difference between the LUMO of CBP and that of TPD, which is a critical point for electron transports as discussed later.

3.3. Molecular pair

As shown in Fig. 2, the unit cell of the CBP crystal contains two molecules. We refer to these molecules as I and II, respectively. The center of gravity of I locates on the origin of the cell, and that of II does on the center of the b-c plane. Defining that the cell in Fig. 2 as cell (0 0 0), neighboring cells at the +a, −a, +b, −b, +c, and −c directions are represented as (1 0 0), (−1 0 0), (0 1 0), (0 −1 0), (0 0 1), and (0 0 −1), respectively. Hereafter, a molecule X (X = I or II) in the cell (a b c) (a, b, c = −1, 0, or 1) is referred to as X(abc) as defined in our preceding paper [22]. For example, I(0 0 0) denotes molecule I in the cell (0 0 0).

Charge transfer integrals were investigated for all the molecular pairs between a molecule in the cell (0 0 0)

Table 5
The segmental β values for charge transfer and shortest inter-segment C–C, C–N, or N–N distances in the molecular pair I(0 0 0)–II(0 0 0), which corresponds to the geometrical type of "**A**". The segments are the nitrogen (N), biphenylene (BP), and benzene rings in the carbazole moieties (Bz1 and Bz2) in the left (L) and right (R) sides of CBP molecules as shown in Fig. 6a.

		II(0 0 0)							
		N_L	N_R	BP_L	BP_R	$Bz1_L$	$Bz2_L$	$Bz1_R$	$Bz2_R$
Segmental β for hole transfer (meV) (total β = −6.5 meV)									
I(0 0 0)	N_L	0.0	0.0	0.0	0.0	0.0	0.0	0.0	0.0
	N_R	0.0	0.0	0.0	0.0	−0.9	0.0	0.0	0.0
	BP_L	0.0	0.0	0.0	0.0	0.0	1.9	0.0	0.0
	BP_R	−4.9	0.0	0.5	0.0	2.2	−4.4	0.0	0.0
	$Bz1_L$	0.0	0.0	0.0	0.0	0.0	0.0	0.0	0.0
	$Bz2_L$	0.0	0.0	0.0	0.0	0.0	0.0	0.0	0.0
	$Bz1_R$	0.7	0.0	3.3	0.0	−7.9	0.0	0.0	0.0
	$Bz2_R$	0.0	0.0	0.0	0.0	3.1	0.0	0.0	0.0
Segmental β for electron transfer (meV) (total β = 1.4 meV)									
I(0 0 0)	N_L	0.0	0.0	0.0	0.0	0.0	0.0	0.0	0.0
	N_R	0.0	0.0	0.0	0.0	0.0	0.0	0.0	0.0
	BP_L	0.0	0.0	0.0	0.0	0.0	−2.0	0.0	0.0
	BP_R	0.1	0.0	0.1	0.0	−2.8	−1.8	0.0	0.0
	$Bz1_L$	0.0	0.0	0.0	0.0	0.0	0.0	0.0	0.0
	$Bz2_L$	0.0	0.0	0.0	0.0	0.0	0.0	0.0	0.0
	$Bz1_R$	−0.1	0.0	0.9	0.0	4.2	0.0	0.0	0.0
	$Bz2_R$	0.0	0.0	0.0	0.0	2.8	0.0	0.0	0.0
Shortest C–C, C–N, or N–N distance (Å)									
I(0 0 0)	N_L	9.7	16.2	10.2	12.9	9.9	6.8	17.4	15.6
	N_R	5.2	13.3	5.7	9.4	4.2	5.1	13.6	14.2
	BP_L	6.1	13.7	6.8	10.0	6.3	3.8	14.8	13.5
	BP_R	3.7	12.4	4.6	8.4	3.5	3.5	13.1	13.0
	$Bz1_L$	9.6	14.6	9.8	11.7	10.4	6.9	15.8	13.5
	$Bz2_L$	10.8	17.6	11.5	14.3	10.8	7.8	18.8	17.0
	$Bz1_R$	4.4	10.2	3.8	6.6	3.5	5.3	10.1	11.3
	$Bz2_R$	6.1	14.2	6.9	10.5	4.0	5.8	14.2	15.3

Table 6
The segmental β values for charge transfer and shortest inter-segment C–C, C–N, or N–N distances in the molecular pair I(0 0 0)–I(1 −1 1), which corresponds to the geometrical type of "**B**" (see Fig. 6b).

		I(1 −1 1)							
		N_L	N_R	BP_L	BP_R	$Bz1_L$	$Bz2_L$	$Bz1_R$	$Bz2_R$
Segmental β for hole transfer (meV) (total β = −3.1 meV)									
I(000)	N_L	0.0	0.0	0.0	0.0	0.0	0.0	0.0	0.0
	N_R	0.0	0.0	0.0	0.0	0.0	0.0	0.0	0.0
	BP_L	0.0	0.0	0.0	0.0	0.0	0.0	0.0	0.0
	BP_R	0.0	0.0	0.0	0.0	0.0	0.0	0.0	0.0
	$Bz1_L$	0.0	0.0	0.0	0.0	0.0	0.0	−0.6	0.0
	$Bz2_L$	0.0	0.0	0.0	0.0	0.0	0.0	−1.9	−0.6
	$Bz1_R$	0.0	0.0	0.0	0.0	0.0	0.0	0.0	0.0
	$Bz2_R$	0.0	0.0	0.0	0.0	0.0	0.0	0.0	0.0
Segmental β for electron transfer (meV) (total β = 6.5 meV)									
I(000)	N_L	0.0	0.0	0.0	0.0	0.0	0.0	0.0	0.0
	N_R	0.0	0.0	0.0	0.0	0.0	0.0	0.0	0.0
	BP_L	0.0	0.0	0.0	0.0	0.0	0.0	0.0	0.0
	BP_R	0.0	0.0	0.0	0.0	0.0	0.0	0.0	0.0
	$Bz1_L$	0.0	0.0	0.0	0.0	0.0	0.0	0.3	0.0
	$Bz2_L$	0.0	0.0	0.0	0.0	0.0	0.0	5.9	0.3
	$Bz1_R$	0.0	0.0	0.0	0.0	0.0	0.0	0.0	0.0
	$Bz2_R$	0.0	0.0	0.0	0.0	0.0	0.0	0.0	0.0
Shortest C–C, C–N, or N–N distance (Å)									
I(000)	N_L	19.2	9.5	15.1	10.9	19.4	20.2	6.2	7.7
	N_R	29.1	19.2	24.9	20.6	29.4	29.9	15.9	16.5
	BP_L	20.6	10.9	16.4	12.2	20.8	21.6	7.5	8.8
	BP_R	24.9	15.1	20.7	16.4	25.1	25.8	11.7	12.6
	$Bz1_L$	16.5	7.7	12.6	8.8	16.5	17.7	4.0	6.7
	$Bz2_L$	15.9	6.2	11.7	7.5	16.3	16.8	3.5	4.0
	$Bz1_R$	29.9	20.2	25.8	21.6	30.0	31.0	16.8	17.7
	$Bz2_R$	29.4	19.4	25.1	20.8	29.9	30.0	16.3	16.5

Table 7
The segmental β values for charge transfer and shortest inter-segment C–C, C–N, or N–N distances in the molecular pair I(0 0 0)–II(1 0 0), which corresponds to the geometrical type of "**C**" (see Fig. 6c).

		II(1 0 0)							
		N_L	N_R	BP_L	BP_R	$Bz1_L$	$Bz2_L$	$Bz1_R$	$Bz2_R$
Segmental β for hole transfer (meV) (total β = 7.0 meV)									
I(0 0 0)	N_L	0.0	0.0	0.0	0.0	0.0	0.1	0.0	0.0
	N_R	0.0	0.0	0.0	0.0	−0.6	0.0	0.0	0.0
	BP_L	0.0	0.0	0.0	0.0	0.0	0.8	0.0	0.0
	BP_R	0.0	0.0	0.0	0.0	6.4	−0.2	0.0	0.0
	$Bz1_L$	0.0	0.0	0.0	0.0	0.0	−2.7	0.0	0.0
	$Bz2_L$	0.0	0.0	0.0	0.0	0.0	0.0	0.0	0.0
	$Bz1_R$	0.0	0.0	0.0	0.0	3.2	0.0	0.0	0.0
	$Bz2_R$	0.0	0.0	0.0	0.0	0.0	0.0	0.0	0.0
Segmental β for electron transfer (meV) (total β = −1.8 meV)									
I(0 0 0)	N_L	0.0	0.0	0.0	0.0	0.0	0.0	0.0	0.0
	N_R	0.0	0.0	0.0	0.0	0.0	0.0	0.0	0.0
	BP_L	0.0	0.0	0.0	0.0	−0.2	−0.3	0.0	0.0
	BP_R	0.0	0.0	0.0	0.0	−0.2	−0.8	0.0	0.0
	$Bz1_L$	0.0	0.0	0.0	0.0	0.0	0.1	0.0	0.0
	$Bz2_L$	0.0	0.0	0.0	0.0	0.0	0.0	0.0	0.0
	$Bz1_R$	0.0	0.0	0.0	0.0	−0.4	0.0	0.0	0.0
	$Bz2_R$	0.0	0.0	0.0	0.0	0.0	0.0	0.0	0.0
Shortest C–C, C–N, or N–N distance (Å)									
I(0 0 0)	N_L	8.5	17.3	9.6	13.3	7.5	4.5	18.4	17.1
	N_R	7.9	16.4	9.0	12.5	4.3	7.0	16.4	17.6
	BP_L	6.6	15.9	7.9	11.8	4.5	3.7	16.8	16.2
	BP_R	6.4	15.5	7.6	11.5	3.6	4.2	15.9	16.3
	$Bz1_L$	7.4	15.0	8.0	11.5	7.1	3.7	16.3	14.4
	$Bz2_L$	9.7	18.6	10.9	14.7	8.7	5.7	19.8	18.4
	$Bz1_R$	6.8	13.8	7.5	10.4	3.8	6.6	13.4	15.0
	$Bz2_R$	9.2	17.7	10.3	13.9	5.5	8.3	17.5	18.9

and that in a cell (a b c) (a, b, c = −1, 0, or 1). The 105 pairs are listed in Table 4. Depending on the relative geometries, the pairs can be classified into 25 independent types, as indicated by geometrical types of A–Y in Table 4. For these 25 types of pairs, the charge transfer integrals were calculated, according to Eq. (2).

3.4. Hole transfer integral

The hole transfer integrals for the geometrical types of A–Y are shown in Fig. 5a. The types of A, B, and C have large values, 3.1, 1.4, 3.0 meV, respectively. The value for the type of D is 0.6 meV, and the values for the other types are less than 0.1 meV. In Fig. 5b, the hole transfer integrals are shown as a function of intermolecular distance between the center of gravity of each molecule. Also, in Fig. 5c, they are presented as a function of the shortest inter-segment distance. Here, we refer to the shortest internuclear distance between the relevant two molecules as the shortest inter-segment distance. Only the distances between carbon and/or nitrogen atoms are considered (hydrogen atoms are neglected), because hydrogen atoms hardly contribute to the frontier orbitals. It is found from these figures that the hole transfer integral strongly depends on the shortest inter-segment distance rather than the distance between the center of gravity.

Since the charge transfer integral in Eq. (2) is found to be almost proportional to β (this relation holds because $1 \gg S^2$ and $\beta \cong 1.75S(\alpha_A + \alpha_B)/2$ [32,33], as shown in Ref. [22]), the contribution of respective segments, N, BP, Bz1, and Bz2, to the charge transport integral can be investigated by separating the β value for the respective segments. The β values separated for the respective segments are called "segmental β values" as defined in Ref. [22]. The segmental β values are useful to understand which segments dominantly contribute to charge transfer integrals. Tables 5–7 show the segmental β values for the representative molecular pairs of the geometrical types of A, B, and C, respectively. The pairs are I(0 0 0)–II(0 0 0) (type A), I(0 0 0)–I(1−11) (type B), and I(0 0 0)–II(1 0 0) (type C) (see Fig. 6). The shortest inter-segment distances are also shown in the tables. Regarding I(0 0 0)–II(0 0 0), the geometrical type of A (Table 5), the following interaction are dominant for the total β value of −6.5 meV; $Bz1_R$–$Bz1_L$ (−7.9 meV), BP_R–N_L (−4.9 meV), and BP_R–$Bz2_L$ (−4.4 meV) (the left and right sides correspond to the segments in I(0 0 0) and II(0 0 0), respectively). All the types of the segments, N, BP, and Bz, contribute to the above interactions. The shortest inter-segment distance is a crucial factor for charge transfers; the distances for the above three segmental pairs are less than 3.8 Å, whereas the segmental β values are 0.0 meV when the distance is longer than 5.1 Å. For I(0 0 0)–I(1 −1 1), the geometrical type of B (Table 6), the segmental interaction between $Bz1_R$–$Bz2_L$ (−1.9 meV) is dominant for the total β value of −3.1 eV. This segmental interaction is smaller than the significant interactions for the types A and C in spite that the shortest inter-segment distance is as short as 3.5 Å. This suggests that the relative orientation of the relevant two molecules also affects the segmental β value as well as the

inter-segment distance. Lastly, the total β value is 7.0 meV for I(0 0 0)–II(1 0 0), the geometrical type of C (Table 7). The most significant interaction is obtained for the segmental pair of BP_R–$Bz1_L$; the segmental β value is 6.4 meV and the shortest inter-segment distance is 3.6 Å. Considering the geometrical types of A–C, holes are favorably transported through any of the segments, N, BP, and Bz.

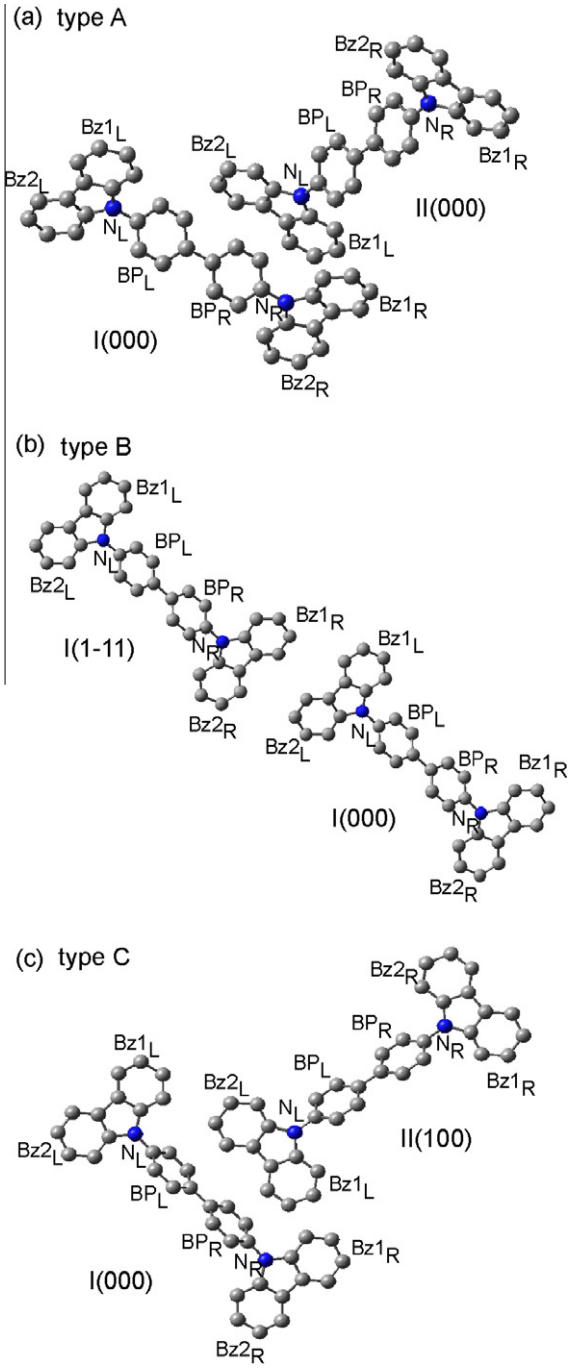

Fig. 6. Representations of the molecular pairs, (a) I(0 0 0)–II(0 0 0), (b) I(0 0 0)–I(1 −1 1), and (c) I(0 0 0)–II(1 0 0). The types of their relative geometries are A, B, and C, respectively.

3.5. Electron transfer integral

Fig. 5a also shows the electron transfer integrals for the geometrical types of A–Y. The geometrical type of B provides the largest value of the electron transfer integral, 4.3 meV. The values for the types of A, C, and D are 0.9, 1.2, and 0.7 meV, respectively. For the others, the values are less than 0.1 meV. In Fig. 5b and c, the electron transfer integrals are also shown as a function of the intermolecular distance between the center of gravity and the shortest inter-segment distance, respectively. As in the case of the hole transfer integral, the electron transfer integral strongly depends on the shortest inter-segment distance rather than the distance between the center of gravity.

The segmental β values of the electron transfer integrals for the geometrical types of A–C are also shown in Tables 5–7, respectively. For the pair of I(0 0 0)–II(0 0 0), the geometrical type of A (Table 5), the β value for $Bz1_R$–$Bz1_L$ with the shortest inter-segment distance of 3.5 Å is dominant, 4.2 meV. This indicates that the LUMO on the carbazole moieties, which have close intermolecular contacts, is advantageous for the large segmental β value. For I(0 0 0)–I(1 −1 1), the geometrical type of B (Table 6), the interaction between $Bz2_L$–$Bz1_R$ is significant, 5.9 meV, also indicating the importance of the carbazole moieties for electron transfers. For I(0 0 0)–II(1 0 0), the geometrical type of C (Table 7), the magnitudes of all the segmental β values are less than 0.8 meV, although the interaction between $Bz2_L$–BP_R is the largest. Considering the geometrical types of A–C, electrons are favorably transported through the carbazole moieties. The LUMO which spreads over the molecule, including the carbazole segments, would be an origin of the different electron-transport property between CBP and TPD. For TPD, the LUMO is localized on the central biphenylene moiety, which is unfavorable for providing large segmental β values.

Fig. 6 shows that only the carbazole moieties are in close intermolecular contact for the geometry of type B. However, this geometry provides the largest electron transfer integral, as shown in Fig. 5a. This result indicates that large transfer integrals can be obtained even if not all the segments are in close intermolecular contacts; only a partial contact is often enough.

3.6. Rate constant and paths for charge transfer

Fig. 7 shows the hole and electron-transfer rate constants for the geometrical types of A–H at 300 K, using the above reorganization energies and charge transfer integrals. For the other geometrical types, I–Y, the values are less than $10^1\ s^{-1}$. The hole-transfer rate constants for the types of A, B, and C are 2.0×10^{11}, 3.7×10^{10}, and $1.9 \times 10^{11}\ s^{-1}$, respectively. The value for the type of D is $6.4 \times 10^9\ s^{-1}$, and those for the rest types are less than $2.1 \times 10^7\ s^{-1}$. On the electron-transfer rate constants, large values are obtained for the types of A, B, and C; 4.8×10^9, 1.1×10^{11}, and $8.6 \times 10^9\ s^{-1}$, respectively. The value for the type D is $3.3 \times 10^8\ s^{-1}$, and those for the rest types are less than $1.2 \times 10^7\ s^{-1}$. The ratio of the maximum hole- and electron-transfer rate constants is 1.7. Compared with the orthorhombic crystal of TPD, for which the ratio is

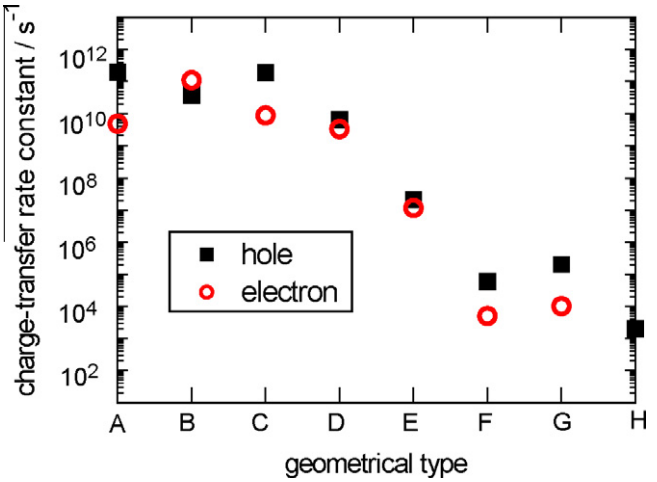

Fig. 7. The hole- (filled square) and electron-(open circle) transfer rate constants, k_{CT}, at 300 K calculated using the transfer integrals in Fig. 5. The rate constants smaller than 10^1 s^{-1} are not shown.

1.4×10^2, the bipolar charge-transport property of CBP is clearly presented.

In the TPD crystals, there are effective paths for the hole transport [22]. The paths consist of successive molecular pairs with large hole-transfer rate constants. Here, we investigate paths for the hole and electron transports in the CBP crystal. The molecular pairs of the geometrical types of A, B, and C, which are the most advantageous for both the hole and electron transports, are considered. As shown in Table 4, there are seven molecular pairs for the geometrical type of A. The pairs are illustrated in Fig. 8a. Through the pairs, both holes and electrons can be effectively transported in the b–c plane. In other words, effective percolation paths for charge transports are formed in the plane. For the geometrical type of B, four molecular pairs exist (see Table 4), which are presented in Fig. 8b. Through the periodic pairs of I(0 0 0)–I(1 −1 1) and I(0 0 0)–I(−1 1 −1), both holes and electrons are favorably transported along the [1 $\bar{1}$ 1] direction of the crystal. Also, they can be transported along the [1 1 1] direction by the periodic pairs of II(0 0 0)–II(1 1 1) and II(0 0 0)–I(−1 −1 −1). For the geometrical type of C, there are eight molecular pairs (see Table 4). The pairs are shown in Fig. 8c and d. The periodic pairs of I(0 0 0)–II(1 0 0)

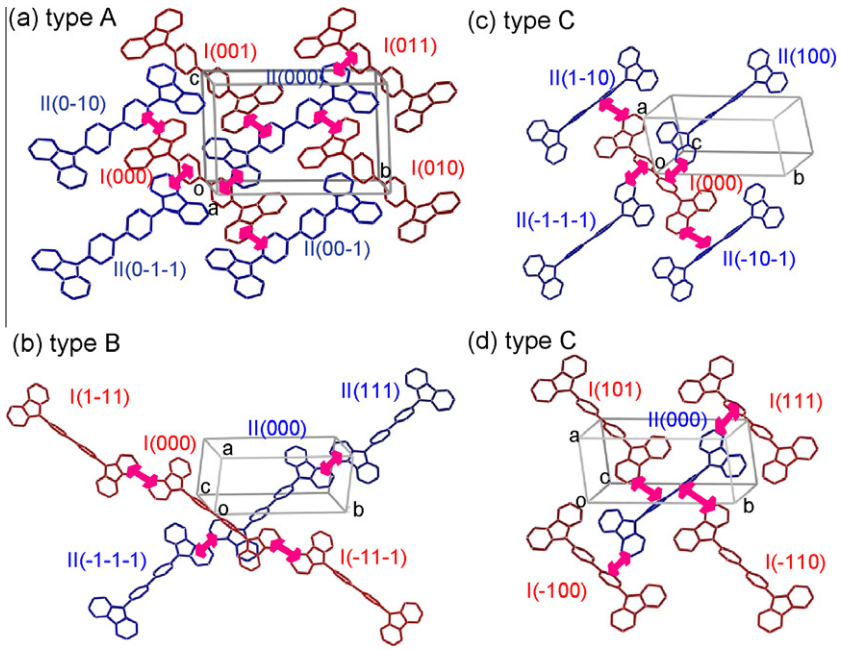

Fig. 8. Representations of percolation paths for both the hole and electron transports. The paths consist of the molecular pairs with large charge-transfer rate constants in the geometrical types of (a) A, (b) B, and (c, d) C.

and I(0 0 0)–II(−1 −1 −1), or II(0 0 0)–I(1 1 1) and II(0 0 0)–I(−1 0 0) can transport both holes and electrons along the [1 2 2] direction of the crystal. In addition, charges can be effectively transported along the [1 $\bar{2}$ 2] direction through the periodic pairs of I(0 0 0)–II(1 −1 0) and I(0 0 0)–II(−1 0 −1), or II(0 0 0)–I(1 0 1) and II(0 0 0)–I(−1 1 0). From the above discussion, effective paths exist for both the hole and electron transports in CBP, confirming the bipolar charge-transport property of CBP.

4. Conclusion

We have investigated the charge-transport property of CBP, based on Marcus theory. By investigating both the reorganization energies and charge transfer integrals, the hole- and electron-transfer rate constants were calculated to be similar in magnitude. In addition, effective paths for both the hole and electron transports exist in the CBP crystal, showing the bipolar charge-transport property of CBP. Through the delocalized HOMO over the CBP molecule, holes are conveyed via all the segments of molecules. In contrast, electrons favorably transfer through the carbazole moieties. This is in sharp contrast with TPD; the LUMO is localized on the central biphenylene moiety, which results in small electron transfer integrals.

Acknowledgements

This research was supported by the Japan Society for the Promotion of Science (JSPS) through its Funding Program for World-Leading Innovative R&D on Science and Technology (FIRST Program). The computation time was partly provided by the Academic Center for Computing and Media Studies (ACCMS), Kyoto University.

Appendix A. Supplementary data

Supplementary data associated with this article can be found, in the online version, at doi:10.1016/j.orgel.2010.10.022.

References

[1] C.W. Tang, S.A. VanSlyke, Appl. Phys. Lett. 51 (1987) 913.
[2] C. Adachi, S. Tokito, T. Tsutsui, S. Saito, Jpn. J. Appl. Phys. 27 (1988) L269.
[3] H. Kanai, S. Ichinosawa, Y. Sato, Synth. Met. 91 (1997) 195.
[4] B.E. Koene, D.E. Loy, M.E. Thompson, Chem. Mater. 10 (1998) 2235.
[5] C. Adachi, M.A. Baldo, S.R. Forrest, J. Appl. Phys. 87 (2000) 8049.
[6] C. Adachi, R. Kwong, S.R. Forrest, Org. Electron. 2 (2001) 37.
[7] N. Matsusue, Y. Suzuki, H. Naito, Jpn. J. Appl. Phys. 44 (2005) 3691.
[8] H. Matsushima, S. Naka, H. Okada, H. Onnagawa, Curr. Appl. Phys. 5 (2005) 305.
[9] Y. Wang, Y. Hua, X. Wu, L. Zhang, Q. Hou, F. Guan, N. Zhang, S. Yin, X. Cheng, Org. Electron. 9 (2008) 692.
[10] Y. Tao, Q. Wang, L. Ao, C. Zhong, J. Qin, C. Yang, D. Ma, J. Mater. Chem. 20 (2010) 1759.
[11] M. Stolka, J.F. Yanus, D.M. Pai, J. Phys. Chem. 88 (1984) 4707.
[12] J. Kido, M. Kimura, K. Nagai, Science 267 (1995) 1332.
[13] V. Bulović, G. Gu, P.E. Burrows, S.R. Forrest, M.E. Thompson, Nature 380 (1996) 29.
[14] H. Mattoussi, H. Murata, C.D. Merritt, Y. Iizumi, J. Kido, Z.H. Kafafi, J. Appl. Phys. 86 (1999) 2642.
[15] A. Kuwahara, S. Naka, H. Okada, H. Onnagawa, Appl. Phys. Lett. 89 (2006) 132106.
[16] P. Cusumano, S. Gambino, J. Electron. Mater. 37 (2008) 231.
[17] R.A. Marcus, J. Chem. Phys. 24 (1956) 966.
[18] R.A. Marcus, N. Sutin, Biochim. Biophys. Acta 811 (1985) 265.
[19] K. Sakanoue, M. Motoda, M. Sugimoto, S. Sakaki, J. Phys. Chem. A 103 (1999) 5551.
[20] B.C. Lin, C.P. Cheng, Z.P.M. Lao, J. Phys. Chem. A 107 (2003) 5241.
[21] B.C. Lin, C.P. Cheng, Z.Q. You, C.P. Hsu, J. Am. Chem. Soc. 127 (2005) 66.
[22] T. Yamada, T. Sato, K. Tanaka, H. Kaji, Org. Electron. 11 (2010) 255.
[23] A.D. Becke, Phys. Rev. A 38 (1988) 3098.
[24] A.D. Becke, J. Chem. Phys. 98 (1993) 5648.
[25] C.T. Lee, W.T. Yang, R.G. Parr, Phys. Rev. B 37 (1988) 785.
[26] P.J. Low, M.A.J. Paterson, D.S. Yufit, J.A.K. Howard, J.C. Cherryman, D.R. Tackley, R. Brook, B. Brown, J. Mater. Chem. 15 (2005) 2304.
[27] P.O. Löwdin, J. Chem. Phys. 18 (1950) 365.
[28] V. Coropceanu, J. Cornil, D.A. da Silva Filo, Y. Olivier, R. Silbey, J.L. Brédas, Chem. Rev. 107 (2007) 926.
[29] M.J. Frisch, et al., Gaussian 03, Revision E.01, Gaussian, Inc., Wallingford, CT, 2004.
[30] A.R. Kennedy, W.E. Smith, D.R. Tackley, W.I.F. David, K. Shankland, B. Brown, S.J. Teat, J. Mater. Chem. 12 (2002) 168.
[31] Z. Zhang, E. Burkholder, J. Zubieta, Acta Crystallogr., Sect. C 60 (2004) o452.
[32] M. Wolfsberg, L. Helmholz, J. Chem. Phys. 20 (1952) 837.
[33] R. Hoffmann, J. Chem. Phys. 39 (1963) 1397.

Organic Electronics 12 (2011) 179–184

Contents lists available at ScienceDirect

Organic Electronics

journal homepage: www.elsevier.com/locate/orgel

Air-stable polymer organic thin-film transistors by solution-processed encapsulation

Yu Fu, Feng-Yu Tsai *

Department of Material Science and Engineering, Nation Taiwan University, 1, Sec. 4, Roosevelt Road, Taipei, Taiwan, ROC

ARTICLE INFO

Article history:
Received 14 September 2010
Received in revised form 22 October 2010
Accepted 31 October 2010
Available online 12 November 2010

Keywords:
Organic field-effect transistors
Organic semiconductors
Passivation
Air stability

ABSTRACT

The air- and encapsulation-induced degradations of poly(3-hexylthiophene) (P3HT) organic thin-film transistors (OTFTs) encapsulated with solution-processed polymer films were systematically analyzed to realize air-stable devices. By studying the potential degradation-inducing factors from air–O_2, moisture, N_2, and light, we determined that device degradations could be eliminated by isolating the devices from two of the factors: moisture and light. In terms of encapsulation-induced degradations, we examined 10 types of encapsulating polymers and found that such degradations could be avoided with polymers containing low-polarity function groups, including poly(vinyl methyl ketone), poly(methyl vinyl ether), poly(methyl methacrylate), and polystyrene. Based upon the identified sources of degradations, we demonstrated an encapsulation approach that involved (1) using a low-polarity encapsulating polymer layer to serve as a moisture barrier and to avoid encapsulation-induced degradation, and (2) applying a light-blocking agent. The resultant OTFTs showed no encapsulation-induced degradation while maintaining stable device characteristics for >5500 h of storage in the ambient air.

© 2010 Elsevier B.V. All rights reserved.

1. Introduction

Organic thin-film transistors (OTFT) offer many advantages such as processability and mechanical flexibility over inorganic technologies [1–3] and have been developed for use in a wide range of applications including displays [4,5], sensors [6,7], and radio frequency identification [8,9]. Through the intensive research efforts of recent years, reasonably high device performance as well as manufacture-enabling processing techniques have been demonstrated for OTFTs [10,11]. Among the studied organic semiconductors, poly(3-hexylthiophene) (P3HT) is one of the more promising materials because of its solution processability, high charge carrier mobility, and commercial availability [4]. However, the practical application of P3HT-based OTFTs has been hindered by the susceptibility of P3HT to environment-induced degradations [12,13]. Such problem of poor stability is shared by many other types of organic semiconductors as well [14,15]. Therefore, an effective passivation or encapsulation method is paramount to the development of the OTFT technology. Previous research on the encapsulation of P3HT OTFTs has relied on the use of vapor-deposited films, taking advantages of the good gas-barrier performance of such films and the low contamination level of the vapor-deposition process [16], the latter of which is necessary to minimize encapsulation-induced degradations because of P3HT's high sensitivity to environmental factors. Despite the satisfactory results reported with such approaches, practical application of OTFTs calls for solution-processed encapsulation methods to reduce the cost and complexity of the encapsulation process as well as to improve the compatibility of the encapsulation process with the preceding and subsequent device fabrication processes. Solution-processed encapsulation method that can prevent both encapsulation- and air-induced degradations has not been reported for P3HT OTFTs.

* Corresponding author. Tel.: +886 2 33665302; fax: +886 2 2363 4562.
E-mail address: ftsai@ntu.edu.tw (F.-Y. Tsai).

1566-1199/$ - see front matter © 2010 Elsevier B.V. All rights reserved.
doi:10.1016/j.orgel.2010.10.021

In this work, we develop solution-processed encapsulation for P3HT OTFTs to achieve air-stable devices while avoiding encapsulation-induced degradations. We determine the sources of air-induced degradations by systematically studying the potential degradation-inducing factors including O_2, moisture, N_2, and light. To eliminate encapsulation-induced degradations, we investigate 10 types of encapsulating polymers as well as their solvents. Based on the obtained knowledge about the sources of degradations, we devise and demonstrate a solution-processed encapsulation method for P3HT OTFTs.

2. Materials and methods

P3HT (molecular weight 87K, region-regularity ratio = 98.5%) was purchased from Sigma–Aldrich co., and used as received. The substrates were heavily p-type doped silicon wafers with a 200 nm thermal oxide layer on the surface as the dielectric layer. The devices were of the bottom gate/bottom contact structure with 100 μm/1500 μm channel length/width (L/W). The device fabrication procedure was as follows: (1) a 100 nm gold layer was thermally evaporated onto the substrates as the bottom contact; (2) the gold layer was patterned with photolithography into the source and drain electrodes; (3) the substrate surface was treated with octadecyltrichlorosilane (OTS), which forms a self-assembled monolayer (SAM) on the SiO_2 dielectric layer [17]; (4) a 50 nm P3HT was spin-coated from a 1 wt.% P3HT solution in dichlorobenzene at 800 rpm for 30 s, followed by a 30 min bake at 130 °C. The I–V characteristics of the OTFTs were measured with a Keithley 4200-SCS Semiconductor Characterization System. Air-induced degradations of the OTFTs were studied by exposing the devices to pure N_2, O_2, or moisture at room temperature in a vacuum chamber equipped with a viewport, through which the devices could be illuminated with a 150 W halogen lamp. The device characteristics were measured in situ. The applied pressures were 760 torr for N_2, 760 torr for O_2, and 11 torr for H_2O. For encapsulation tests, an encapsulating polymer film was spin-coated onto the devices from a 15 wt.% polymer solution at 3000 rpm for 3 min, followed by a bake at 130 °C for 30 min. Ten encapsulating polymers were tested, including poly(vinyl methyl ketone) (PVMK) (solvent: methyl ethyl ketone), poly(methyl vinyl ether) (PMVE) (water), poly(methyl methacrylate) (PMMA) (methyl ethyl ketone), polystyrene (PS) (methyl ethyl ketone), poly(vinylidene chloride-co-vinyl chloride) (PVDC-co-PVC) (dimethyl sulfoxide), poly(vinyl chloride) (PVC) (dimethyl sulfoxide), poly(vinylidene fluoride) (PVDF) (dimethyl sulfoxide), polyacrylonitride (PAN) (dimethyl sulfoxide), poly(vinyl alcohol) (PVA) (water), poly(vinyl phenol) (PVP) (propylene glycol monomethyl ether acetate). The thickness of the encapsulating polymer films was 1–3 μm. The optimized encapsulation method used a PS film spin-coated with Sudan black B dye (Sigma–Aldrich co.). All device fabrication and encapsulation steps were performed in nitrogen-filled glove box except for the PVA and PMVE encapsulation steps, which were performed in air.

3. Results and discussion

3.1. Air-induced degradations

The device characteristics of the as-fabricated P3HT OTFTs were as follows: field-effect mobility = 0.008 cm^2/V, threshold voltage (V_{th}) = 20 V, on/off ratio = 4×10^4. Upon exposure to air at room temperature, the devices showed significant degradations (Fig. 1), as was consistent with previously reported results [12,13]. To investigate the sources of the degradations, the potential degradation-inducing factors from air—O_2, moisture, N_2, and light—were separately applied to the devices while the device characteristics were monitored. The findings were as follows: (1) in N_2, the devices did not noticeably degrade irrespective of the presence of light (see Supplementary materials); (2) in moisture, the devices degraded severely and rapidly (within 100 min) irrespective of the presence of light: the on current decreased, the off current increased and the V_{th} shifted to a more positive value (Fig. 2); notably, the degradations were fully recoverable upon thorough removal of moisture by evacuation, where the I–V curve became nearly identical to the pristine curve; (3) In

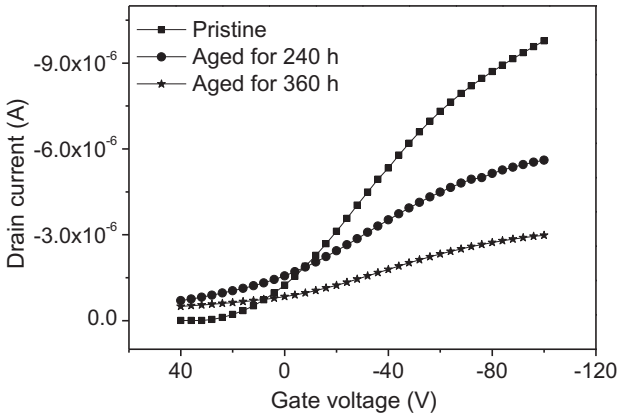

Fig. 1. IV characteristics of OTFTs before and after aging in air at room temperature.

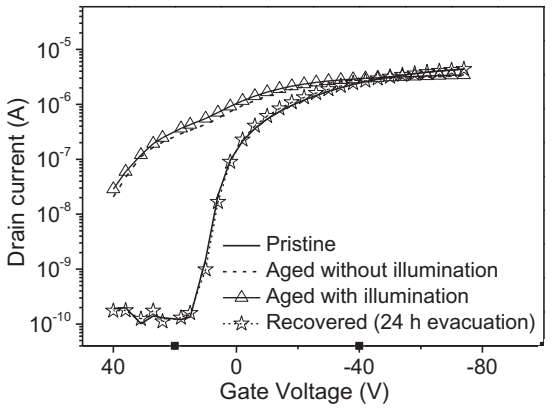

Fig. 2. Transfer characteristics of OTFTs before and after aging in moisture for 100 min with or without illumination. The source-to-drain bias was 60 V.

O_2 with illumination, upon 24 h of aging, the devices showed similar degradations to those caused by moisture (Fig. 3a), of which only the off current and the V_{th} could be recovered upon the removal of O_2 by heating in vacuum; but in the absence of light, the devices did not noticeably degrade for 500 h (Fig. 3b).

The moisture-induced degradations may be attributed to two mechanisms: (1) p-type doping, due to the polar interactions between P3HT and the hydroxyl group of H_2O, which upon the application of an external electric field (from the source/drain electrodes or the gate) induced holes in P3HT, thereby raising the off and on currents and shifting V_{th} to a more positive value [13,18]; (2) charge trapping, by the H_2O molecules absorbed in P3HT or adsorbed on the hydrophilic surface of the gate dielectric, which suppressed the charge mobility and therefore reduced the on current [15,19]. These mechanisms were consistent with the fact that the degradations were fully recoverable upon the removal of the applied moisture, as they involved only intermolecular forces and no chemical bonding. As for the O_2-induced degradations, the increased off current and positively-shifted V_{th} were also attributable to p-type doping, which is known to occur via O_2's complexing with organic semiconductors [20,21]. However, our observation that the degradations required light illumination revealed that such complexing for P3HT involved photo-excited states of P3HT and/or O_2. Importantly, such complexing was found to be reversible when the devices were evacuated for 24 h, upon which the off current and V_{th} returned to the original values (Fig. 3a). The reduced on current and charge mobility with illumination, which was not recoverable, was attributable to photo-oxidation of P3HT [12] (also see analyses in Supplementary materials).

3.2. Encapsulation-induced degradation

The encapsulating polymers, which directly contacted the P3HT layer in the OTFTs, were found to cause varying degrees of device degradation depending upon their functional groups, as shown in Figs. 4 and 5. It should be noted that the effects of the solvents used in casting the encapsulating films were verified to be negligible, provided that the encapsulating films were completely dried (see Supplementary materials). Of the 10 polymers tested, PVMK, PMVE, PMMA, and PS did not cause observable degradation, while the other six polymers—PVA, PVP, PAN, PVC, PVDC-co-PVC, and PVDF—induced strong p-type doping, i.e., increased off current (by 2–4 orders of magnitude), increased on current (by 2–7 folds), and reduced on/off ratio (by ~3 orders of magnitude). In other words, the P3HT layer encapsulated with the six doping-inducing polymers essentially became conductive, with conductivity rising from the pristine value of 1.1×10^{-5} S/cm to up to 1.6 S/cm. The strong p-type doping by the six polymers was attributable to their electron-withdrawing functional groups: –OH for PVA and PVP, –C≡N for PAN, and halogens for PVC, PVDC-co-PVC, and PVDF. The –OH, –C≡N, and halogen groups tend to induce holes in thiophene-based semiconductors through strong polar interaction aided by an external electric field [13,18,22–24]. A few trends were also observable from comparing the different degrees of p-doping effect induced by polymers with similar

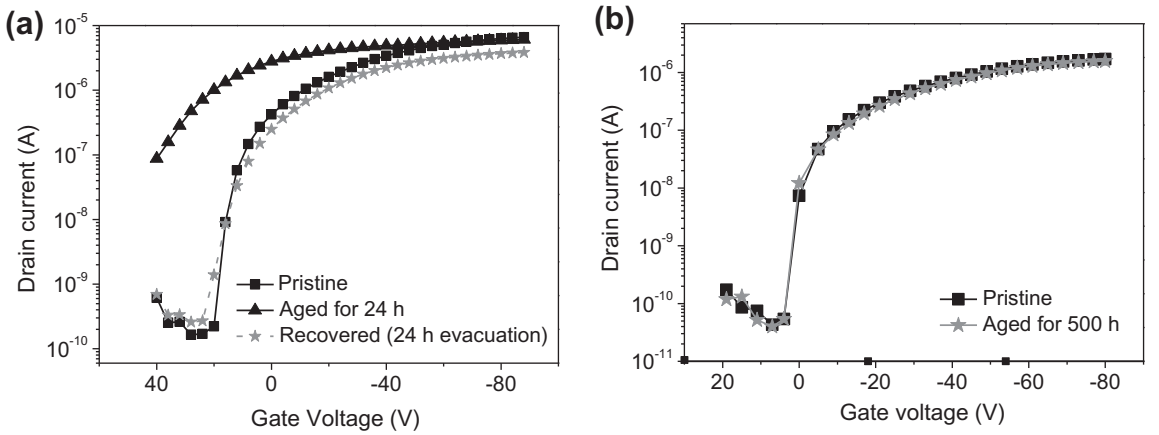

Fig. 3. Transfer characteristics of OTFTs before and after aging in O_2: (a) with illumination, and (b) without illumination. The source-to-drain bias was 60 V.

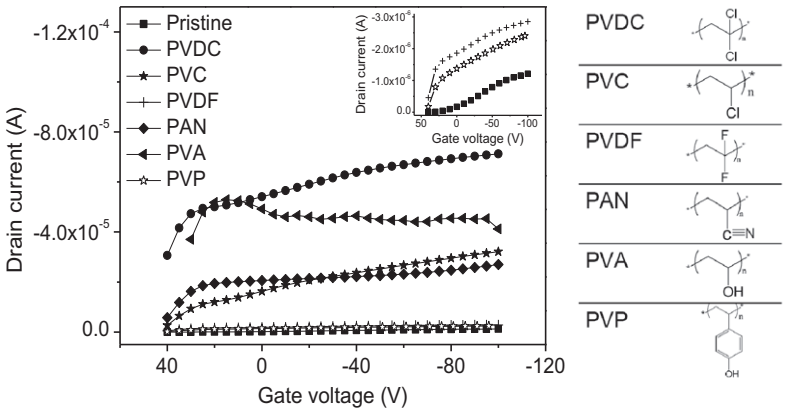

Fig. 4. Transfer characteristics of OTFTs before and after being encapsulated with 6 of the 10 encapsulating polymers tested. Inset shows the device characteristics with PVDF and PVP in smaller drain current range. The chemical structures of the polymers are also provided. The source-to-drain bias was 60 V.

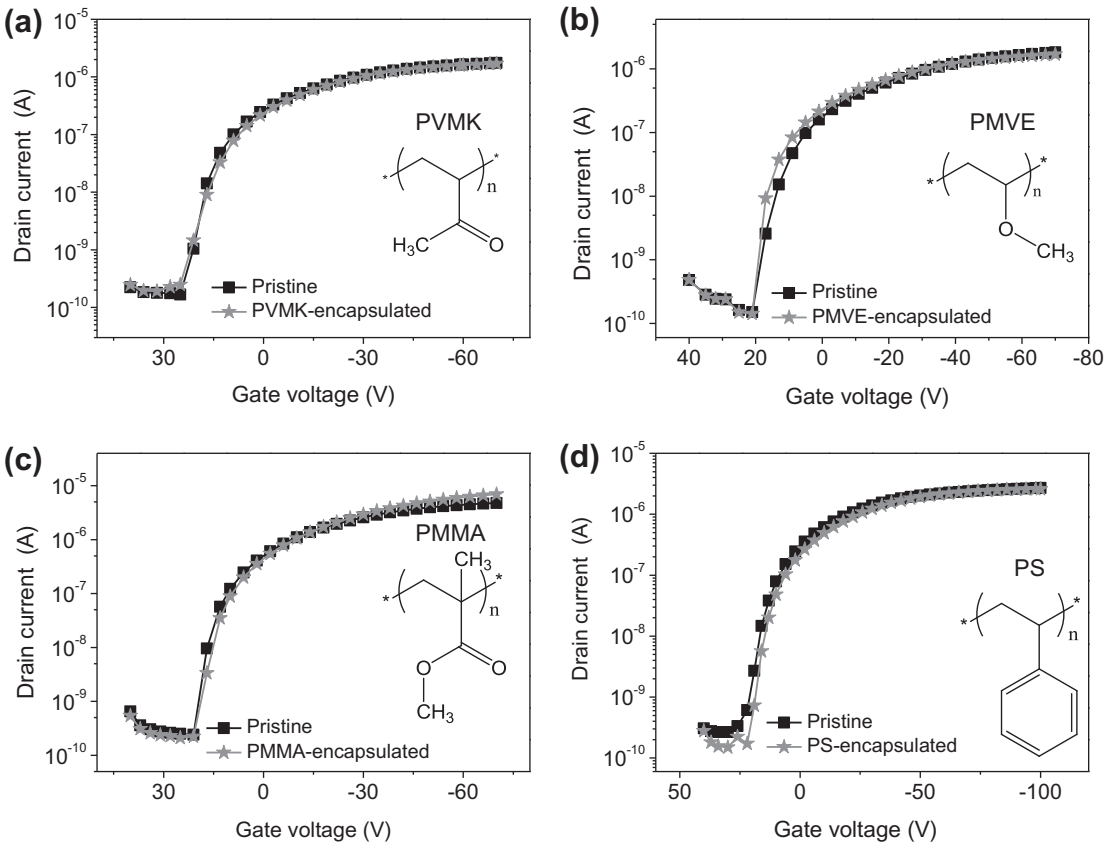

Fig. 5. Transfer characteristics of OTFTs before and after being encapsulated with (a) PVMK, (b) PMVE, (c) PMMA, and (d) PS. Insets show the chemical structures of the polymers. The source-to-drain bias was 60 V.

functional groups: (1) PVDC-co-PVC ≫ PVC, which was attributable to the greater number of Cl atoms on PVDC (two per repeating unit) than on PVC (one per repeating unit); (2) PVDC-co-PVC ≫ PVDF, which was due to the stronger dipole moment of the C–Cl bond than C–F, which would correspond to stronger polar interaction with P3HT [25]; (3) PVA ≫ PVP, which was attributable to PVP's greater steric hindrance (by the phenyl ring) against the –OH/P3HT interactions.

The observation that PVMK, PMVE, PMMA, and PS did not cause device degradation indicated that the functional groups on these polymers were not inducing charge-

displacing interactions with P3HT. This was attributable to the lack of electron-withdrawing group on PS and PMVE. On PVMK and PMMA, although there were the electron-withdrawing carbonyl groups, the absence of degradation suggested that the interactions between P3HT and the carbonyl groups may have been hindered by the alkyl groups adjacent to the carbonyl groups.

One interesting observation about the doping-inducing polymers was that, although the polymers' interactions with the P3HT film were limited to the polymer/P3HT interface with possibly a small intermixing region, their p-doping effects far exceeded those observed with moisture (Section 3.1), which could affect the bulk of the P3HT film upon absorption. The more pronounced effects of the polymers may be accounted for by the following mechanism. In the case of moisture, the high polarity (required for p-doping) of H_2O would limit its uptake in the low-polarity P3HT film, which in turn would limit the extent of doping. In the case the polymers, on the other hand, the connectivity of the polymer chains could bring a large number of the polar side groups into contact with the P3HT layer, thereby forming a heavily doped interfacial/intermixing layer, which could serve as a conduction path between the source and the drain electrodes.

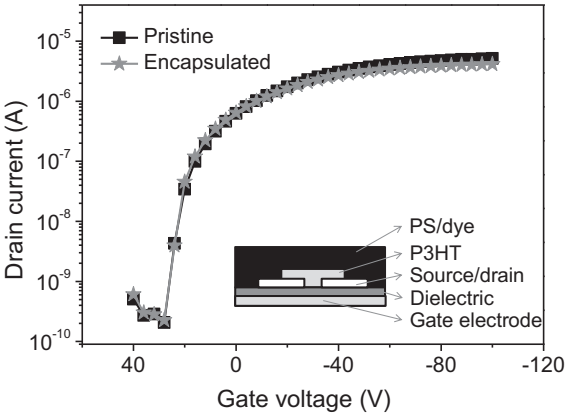

Fig. 6. Transfer characteristics of OTFTs before and after being encapsulated with the PS/dye approach. Inset shows a schematic drawing of the encapsulation approach. The source-to-drain bias was 60 V.

3.3. Device encapsulation

We determined our approach for encapsulating the P3HT OTFTs based on the findings discussed above, i.e. (1) O_2 does not cause degradation unless the devices are illuminated with light; (2) H_2O induces severe p-type doping and charge trapping; (3) encapsulation-induced degradation can be avoided with low-polarity encapsulating polymers, such as PVMK, PMVE, PMMA, and PS. Our approach involved using a combination of a low-polarity encapsulating polymer and a light-blocking agent (see Fig. 6 inset for a schematic illustration). The low polarity of the polymer was to prevent encapsulation-induced degradation and to block the permeation of moisture, while the light-blocking agent was to eliminate the effects of O_2, thereby removing the need for an O_2 barrier. We demonstrated this encapsulation approach with PS as the encapsulating polymer and a black dye as the light-blocking agent, and confirmed that this approach was indeed highly effective. As shown in Figs. 6 and 7, the encapsulated devices showed nearly identical device characteristics before and after encapsulation; moreover, the devices remained relatively stable for >5500 h of storage in air at room temperature. This long-term stability was a significant improvement over previously reported results with thiophene-based OTFTs [16,26–28], many of which used vacuum-deposited encapsulating films. The long lifetime of the encapsulated devices indicated that the water vapor permeability of the PS layer, at 9×10^{12} cm^3 cm/cm^2 s Pa [29], was sufficiently low for protecting the devices from moisture. It should be noted that devices encapsulated with the PS layer without the light-blocking agent showed rapid degradations due to photo-oxidation, as shown in Fig. 8. This was because PS is not a particularly good oxygen barrier owing to its lack of polar side groups [29]; and in the presence of light illumination, it allowed significant photo-oxidation to occur.

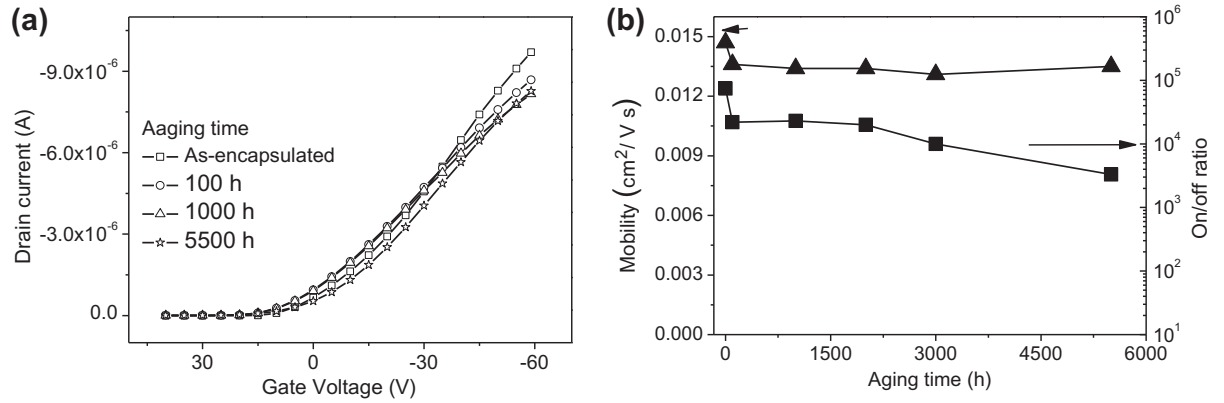

Fig. 7. (a) Transfer characteristics, and (b) field-effect mobility and on/off ratio, of the PS/dye-encapsulated devices as a function of aging time in air at room temperature. The source-to-drain bias in (a) was 60 V.

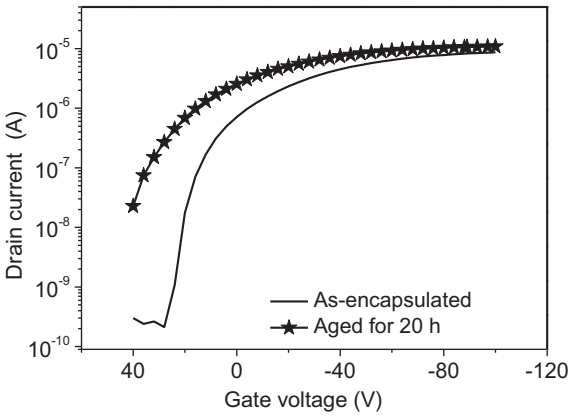

Fig. 8. Transfer characteristics of OTFTs passivated with only a PS layer before and after aging for 20 h in air at room temperature.

4. Conclusion

We demonstrated effective encapsulation of P3HT OTFTs using solution-processed polymer films via systematic analysis and elimination of the air- and encapsulation-induced degradations. In terms of air-induced degradations, moisture caused p-type doping (increased on and off currents with positive shift in V_{th}) and charge trapping (reduced on current) regardless of whether the devices were illuminated with light, and the degradations were fully recoverable upon removal of the applied moisture; on the other hand, oxygen exerted no effect without illumination, but caused pronounced p-type doping and irreversible photo-oxidation with illumination. Encapsulating the devices with a polymer film could result in significant degradations due to contact-doping of the P3HT layer by the encapsulating polymer film. By studying 10 encapsulating polymers, we found that such degradations were dependent upon the polarity of the polymers' functional groups: polymers with strong electron-withdrawing side groups—PVA, PVP, PAN, PVC, PVDC-co-PVC, and PVDF—induced various degrees of p-type doping depending upon the number and steric hindrance of the electron-withdrawing side groups, while those with low-polarity side groups—PVMK, PMVE, PMMA, and PS—caused no degradation. Taking into account the identified sources of degradation, we demonstrated an encapsulation approach that involved (1) using a low-polarity encapsulating polymer (polystyrene) layer to serve as a moisture barrier and to avoid encapsulation-induced degradation, and (2) applying a light-blocking dye to eliminate the effects of oxygen. The resultant OTFTs showed no encapsulation-induced degradation and maintained nearly constant device characteristics for >5500 h of storage in the ambient air.

Acknowledgements

This work was supported by Industrial Technology Research Institute's (ITRI) Electronics and Optoelectronics Research Laboratories (Project No. 8351AA5130), Ministry of Economic Affairs (Grant No. 97-EC-17-A-08-S1-015), National Science Council (Grants No. NSC 96-2221-E-002-143–MY3, 98-ET-E-002-007-ET, and 97-2218-E-002-012-), and Chung-Shan Institute of Science and Technology.

Appendix A. Supplementary data

Supplementary data associated with this article can be found, in the online version, at doi:10.1016/j.orgel.2010.10.021.

References

[1] S.R. Forrest, Nature 428 (2004) 6986.
[2] G.H. Gelinck, H. Edzer, A. Huitema, E. van Veenendaal, E. Cantatore, L. Schrijnemakers, J.B.P.H. van der Putten, T.C.T. Geuns, M. Beenhakkers, J.B. Giesbers, B. Huisman, E.J. Meijer, E.M. Benito, F.J. Touwslager, A.W. Marsman, B.J.E. van Rens, D.M. de Leeuw, Nat. Mater. 3 (2004) 106.
[3] A.C. Arias, S.E. Ready, R. Lujan, W.S. Wong, K.E. Paul, A. Salleo, M.L. Chabinyc, R. Apte, Robert A. Street, Y. Wu, P. Liu, B. Ong, Appl. Phys. Lett. 85 (2004) 3304.
[4] H. Sirringhaus, N. Tessler, R.H. Friend, Science 280 (1998) 1741–1744.
[5] L. Zhou, A. Wanga, S.-C. Wu, J. Sun, S. Park, T.N. Jackson, Appl. Phys. Lett. 88 (2006) 083502.
[6] J.W. Jeong, Y.D. Lee, Y.M. Kim, Y.W. Park, J.H. Choi, T.H. Park, C.D. Soo, S.M. Won, I.K. Han, B.K. Ju, Sens. Actuators B 146 (2010) 40–45.
[7] J. Huang, J. Miragliotta, A. Becknell, H.E. Katz, J. Am. Chem. Soc. 129 (2007) 9366–9376.
[8] E. Cantatore, T.C.T. Geuns, G.H. Gelinck, E. van Veenendaal, A.F.A. Gruijthuijsen, L. Schrijnemakers, S. Drews, D.M. de Leeuw, IEEE J. Solid-State Circ. 42 (2007) 84.
[9] K. Myny, S. Steudel, P. Vicca, M.J. Beenhakkers, N.A.J.M. van Aerle, G.H. Gelinck, J. Genoe, W. Dehaene, P. Heremans, Solid-State Electron. 53 (2009) 1220.
[10] C.D. Dimitrakopoulos, P.R.L. Malenfant, Adv. Mater. 14 (2002) 99.
[11] B.S. Ong, Y. Wu, Y. Li, P. Liu, H. Pan, Chem. Eur. J. 14 (2008) 4766.
[12] J. Ficker, H. von Seggern, H. Rost, W. Fix, W. Clemens, I. McCulloch, Appl. Phys. Lett. 85 (2004) 1377.
[13] S. Hoshino, M. Yoshida, S. Uemura, T. Kodzasa, N. Takada, T. Kamata, K. Yase, J. Appl. Phys. 95 (2004) 5088.
[14] P. Coppo, S.G. Yeates, Adv. Mater. 17 (2005) 3001–3005.
[15] Y. Qiu, Y. Hu, G. Dong, L. Wang, J. Xie, Y. Ma, Appl. Phys. Lett. 83 (2003) 1644.
[16] S. Ferrari, F. Perissinotti, E. Peron, L. Fumagalli, D. Natali, M. Sampietro, Org. Electron. 8 (2007) 407–414.
[17] L.A. Majewski, J.W. Kingsley, C. Balocco, A.M. Song, Appl. Phys. Lett. 88 (2006) 222108.
[18] P. Pacher, A. Lex, V. Proschek, H. Etschmaier, E. Tchernychova, M. Sezen, U. Scherf, W. Grogger, G. Trimmel, C. Slugovc, E. Zojer, Adv. Mater. 20 (2008) 3143–3148.
[19] D.H. Dunlap, P.E. Parris, V.M. Kenkre, Phys. Rev. Lett. 77 (1996) 542.
[20] M.S.A. Abdou, S. Holdcroft, Macromolecules 26 (1993) 2954–2962.
[21] J.-M. Zhuo, L.-H. Zhao, R.-Q. Png, L.-Y. Wong, P.-J. Chia, J.-C. Tang, S. Sivaramakrishnan, M. Zhou, E.C.-W. Ou, S.-J. Chua, W.-S. Sim, L.-L. Chua, P.K.-H. Ho, Adv. Mater. 21 (2009) 4747–4752.
[22] W.A. Sears, M.L. Hudolin, H.A. Jenkins, R.C. Mawhinney, C.D. Mackinnon, J. Coord. Chem. 61 (2008) 825–835.
[23] Z.-X. Wang, B.-S. Zheng, X.-Y. Yu, P.-G. Yi, J. Mol. Struct. (Theochem) 857 (2008) 13–19.
[24] M. Fourmigu, P. Batail, Chem. Rev. 104 (2004) 5379–5418.
[25] K.E. Riley, K.M. Merz, J. Phys. Chem. A 111 (2007) 1688–1694.
[26] Y. Fu, C. Lin, F.-Y. Tsai, Org. Electron. 10 (2009) 883–888.
[27] S.P. Tiwari, P. Srinivas, S. Shriram, N.S. Kale, S.G. Mhaisalkar, V. Rao, Thin Solid Films 516 (2008) 770–772.
[28] K.S. Ong, R.G.C. Ruey, E. Ou, Z. Zheng, D.L.M. Ying, Org. Electron. 11 (2010) 463–466.
[29] N.S. Sangaj, V.C. Malshe, Prog. Org. Coat. 50 (2004) 28–39.

Organic Electronics 12 (2011) 185–189

Contents lists available at ScienceDirect

Organic Electronics

journal homepage: www.elsevier.com/locate/orgel

Alternative resistive switching mechanism based on migration of charged counter-ions within conductive polymers

R. Sim [a,b,c], M.Y. Chan [b], A.S.W. Wong [c], P.S. Lee [a,*]

[a] School of Materials Science and Engineering, Nanyang Technological University, Block N4.1, Nanyang Avenue, Singapore 639798, Singapore
[b] GlobalFoundries Pte. Ltd., 60 Woodlands Industrial Park D, Street 2, Singapore 738406, Singapore
[c] Institute of Materials Research and Engineering, 3 Research Link, Singapore 117602, Singapore

ARTICLE INFO

Article history:
Received 8 July 2010
Received in revised form 2 November 2010
Accepted 6 November 2010
Available online 18 November 2010

Keywords:
PANI
Resistive switching
Electro-migration
Organic memory

ABSTRACT

In this paper, an alternative bi-stable resistive switching mechanism for non-volatile organic memory applications is reported. The memory device is formed from a sandwiched structure of Au/polyaniline:poly(4-styrenesulfonic acid) (PANI:PSSH)/ITO and operates via the migration of negatively charged counter-ions (PSS^-) within the polymer composite. The electro-statically bonded PSS^- within the polymer film segregates at the polymer's interface upon electrical biasing, serving to disrupt current conduction pathways through the polymer by influencing the resonance state of the conducting main chain. By relocation of this PSS^- layer at the polymer interface, electrical conductivity was modulated and an electrical bi-stable device was achieved. The resistive ratio between the ON/OFF states of the device is about 2–3 orders of magnitude, both of which can be read out for up to 500 times with negligible degradation.

© 2010 Elsevier B.V. All rights reserved.

1. Introduction

Organic electronics have attracted considerable attention in recent years due to their low cost, flexibility and easy-fabrication through solution processing. One aspect of the organic electrical circuit that has received considerable attention in recent years is the organic electronic memory. Resistive memories with two terminal cross-bar device structures are alternatives for up-coming non-volatile memory architectures. There are various organic materials that have shown resistive switching capabilities including polystyrene [1], polyethylene [2], poly(*N*-vinylcarbazole) (PVK) [3], 8-hydroxyquinoline [4], etc. There are also a large number of switching mechanisms responsible for switching behavior ranging from: filamentary switching due to device physical damage resulting in carbon-rich filaments from the local degradation of polymer materials [1]; space charge or traps either at the bulk or interface of the polymer, affecting carrier mobility and charge injection, respectively [3]; charge transfer effects between conjugated polymers and metal nano-particles [4]; tunneling related effects affecting the potential barriers [5]; conformational changes of molecules [6], etc. Till date, the continuous search for a robust and reliable resistive switching behavior has lead to many findings on various material combinations, device configurations and operating mechanisms.

With interest at hand to seek out a consistent memory source, an alternative operating mechanism for resistive switching application was discovered. This work describes the switching characteristics exhibited by a conjugated conductive polymer: polyaniline (PANI) doped with poly-(4-styrenesulfonic acid) (PSSH). PANI is advantageous due to the non-redox doping by protonic acids and easy modification of the oxidation states of its polymer chains. The alternative switching mechanism is based on migration related effects of charged counter-ions functioning to suppress one of the resonance/mesomeric states of the conduction parent chain, and serving as a barrier to charge translation along the polymer chains [7]. In this report, memory devices were fabricated in a simple two terminal

* Corresponding author. Tel.: +65 6790 6661; fax: +65 6790 9081.
E-mail address: pslee@ntu.edu.sg (P.S. Lee).

1566-1199/$ - see front matter © 2010 Elsevier B.V. All rights reserved.
doi:10.1016/j.orgel.2010.11.003

capacitor structure, using ITO coated glass substrates as bottom electrode and evaporated gold as top electrodes for electrical measurements. Compositional analysis of PANI:PSS was studied by X-ray photoelectron spectroscopy (XPS), time of flight-secondary ion mass spectroscopy (TOF-SIMS) and the device electrical characteristics were also measured.

2. Experimental section

2.1. Materials

Materials used for the synthesis of PANI:PSS are aniline, poly(4-styrenesulfonic acid) PSSH (18% water w/w), and ammonium persulfate (APS), purchased from Sigma–Aldrich.

2.2. Sample preparation/experimental procedures

PANI:PSS was synthesized by interfacial polymerization using aniline with ammonium persulfate in the presence of aqueous poly(styrenesulfonic acid) (PSSH) [8]. Aniline was added to PSS^- with a ratio of 1:2 in water followed by stirring at 0 °C for 30 min. Addition of ammonium persulfate was carried out over another 30 min at 10 min intervals, followed by stirring at 0 °C for 2 h and lastly stirring of the mixture at ambient conditions overnight.

ITO coated glass was cleaned prior to polymer deposition by immersing it in acetone, isopropyl alcohol and finally de-ionized water with ultrasonic cleaning for a duration of 10 min each. Deposition of the polymer film was done by two step spin-coating conducted, first at 500 rpm for 5 s, followed by another spin step at 2500 rpm for 20 s. The resultant polymer films were approximately 150 nm thick when measured using a surface step profilometer. For top electrical contact, 100 nm thick circular gold electrodes were deposited using electron-beam evaporator through a shadow mask, with electrode diameters ranging from 0.3 mm, 0.2 mm and 0.1 mm. For bottom electrical contact, the edge of the spin-on PANI:PSS film was removed with acetone to expose the underlying ITO substrate. During electrical characterization, grounding was applied at the ITO surface, and all electrical biasing was applied onto the Au top electrode, with all electrical characterization carried out using the Keithley 4200-SCS. Compositional analysis of the polymer film was studied by X-ray photoelectron spectroscopy (XPS) and time of flight-secondary ion mass spectroscopy (TOF-SIMS).

3. Results and discussion

PANI:PSS polymer films fabricated via the interfacial polymerization route were electrically conductive, as the presence of PSSH induced acid doping in PANI to a conductive emeraldine form [8,9], which resulted in the formation of protonated parent $PANI^+$ chains accompanied with electro-statically bonded PSS^- as counter-ions. Electrical transport occurs along the percolation pathways between $PANI^+$ chains throughout the film via hole conduction involving resonance translation of quinoidal structures [7,10], hence all the memory devices fabricated exhibits high electrical conductivity initially. Fig. 1a and b shows the current density–voltage (*J–V*) characteristics of the 0.3 mm diameter top electrode fabricated samples when swept from 0 to ±10 V.

It can be seen that the device displayed an initial high conductivity state (ON state) which was switched to a low conductive state upon application of a sufficient voltage/current density regardless of polarity. Subsequent sweeps showed stable current flow with three orders of magnitude lower (OFF state) than that of the initial conductive state. Application of opposite bias was unable to switch the devices back to its initial high conductive state, even when bias was applied up to 20 V in the opposite polarity (Fig. S1 in Supplementary data); suggesting

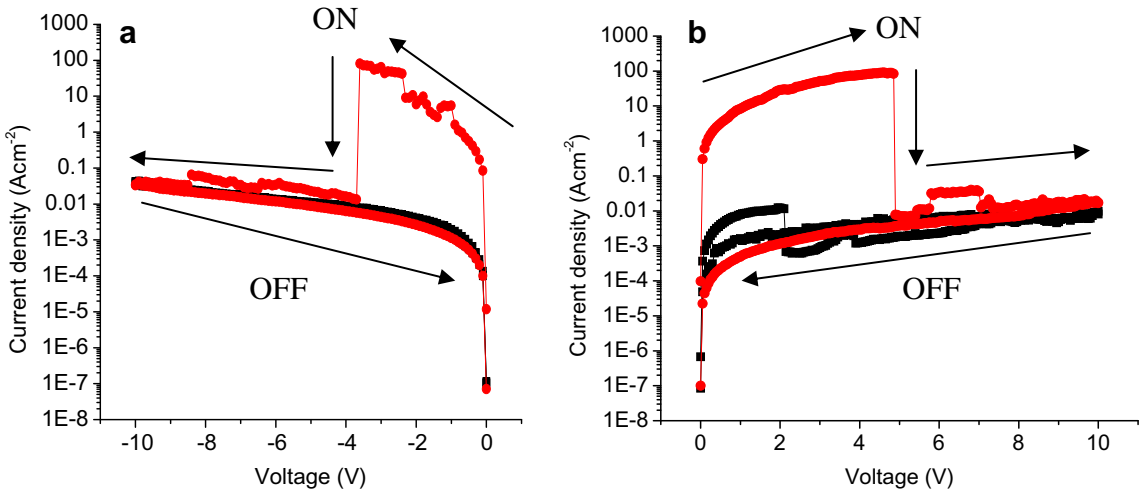

Fig. 1. *J–V* results of device demonstrating WORM memory characteristics in both polarities, when swept with voltages of 10 V magnitudes in both polarities. Red represents first initial sweep, and black represents second sweep. (a) Switching in negative polarity. (b) Switching in positive polarity. (For interpretation of the references to color in this figure legend, the reader is referred to the web version of this article.)

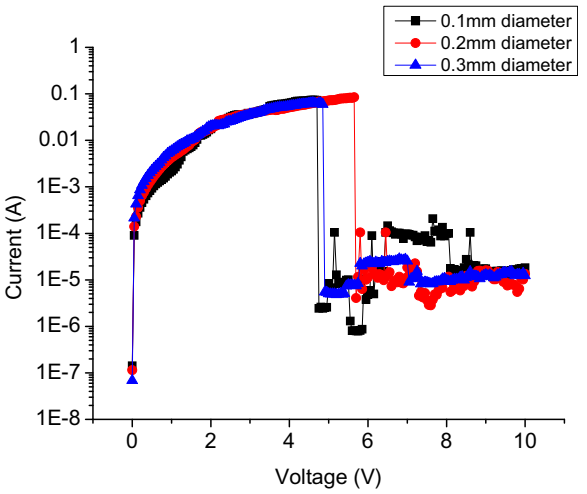

Fig. 2. *I–V* results for devices with 0.1 mm, 0.2 mm and 0.3 mm electrode sizes.

WORM (write once read many) memory characteristic similar to PEDOT:PSS in the literature [11]. Fig. 2 shows the current–voltage (IV) curve of devices with diameters 0.1 mm, 0.2 mm and 0.3 mm top electrodes. Comparison of switching characteristics between these devices suggests that the electrically induced conductivity drop only occurs when sufficient current was applied, with a current flow of approximately 1 A required before conductivity drop occurred. Comparing our results (PANI:PSS) to that exhibited by PEDOT:PSS [11], both the switching current density (10–100 A/cm^2) and voltage required (4 V) were of a similar magnitude, suggesting it to be electrical conditions required for migration of PSS^- to occur.

Though the memory device was unable to switch back to its initial conductive state by application of voltage sweeps alone; when current pulses were applied, conductivity changes were made possible. To demonstrate the conductivity changes achieved through current pulsing, the device was first switched to its low conductive state by a voltage sweep of 0–10 V. With the device in its low conductive state, another voltage sweep from 0 to 1 V was applied, serving as the conductivity baseline for further identification of any conductivity changes. Current pulses were then applied at magnitudes of ±0.1 A, for duration of 10 ms each; with 0.1 A serving to change the device from a low conductive state to a high conductive state, and −0.1 A switching back to a low conductive state. After application of each current pulse, a voltage sweep of 0–1 V was applied for identification of any conductivity changes. Fig. 3 shows the switching results after each current pulse, achieving a resistance ratio of 2–3 orders of magnitude before and after electrical pulsing. The inset in Fig. 3 demonstrates the stability of the two conductive states when undergoing a continuous readout at 0.2 V for 500 times with negligible degradation.

The switching mechanism responsible for the conductivity changes of the device is proposed to be related to the electro-migration of electro-statically bonded PSS^- counter-ions; which occurs upon the application of a voltage sweep. For the verification of migration related effects responsible for conductivity modulation, XPS was conducted on the polymer/gold interface before and after the initial 0–10 V voltage sweep, with nitrogen N_{1S} and sulphur S^{2P} peaks being monitored for the identification of PANI and PSS^-, respectively. This was done by peeling off the gold electrodes from the polymer after application of the voltage sweep. XPS was also conducted on the underside of the extracted gold electrodes which shows negligible nitrogen and sulphur contents (*Fig. S2*), suggesting that the peeling off process did not result in a removal of polymer surface layers. It was also noted that prior to any electrical biasing, the metal electrode could not be cleanly peeled off. This observation is also similar to the reported PEDOT:PSS and provides further evidence that interfacial changes has occurred as a result of the electrical biasing [11]. The result of the XPS analysis is shown in Fig. 4, a 15% increase in PSS^- concentration at the interface after application of voltage sweep was found. The XPS result also indicates a peak shift in the nitrogen N_{1S} peaks. The inset in Fig. 4 shows the deconvoluted N_{1S} contributions of

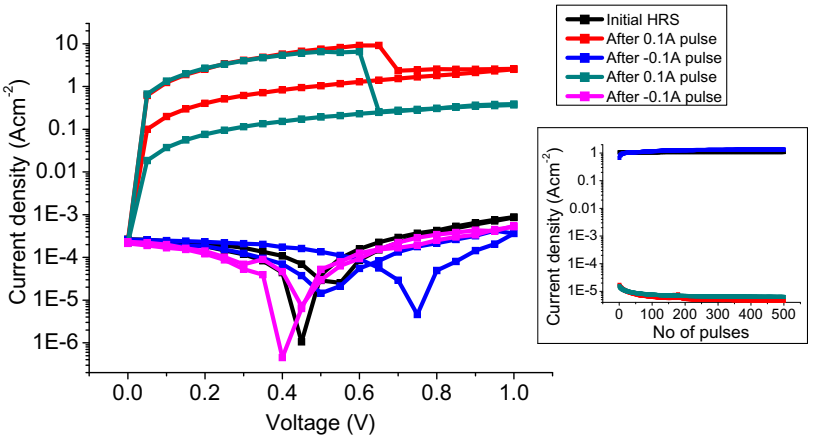

Fig. 3. *J–V* results demonstrating a resistance ratio of 2–3 orders of magnitude before and after current pulsing. Inset shows negligible degradation of conductivity states when undergoing continuous readouts at 0.2 V up to 500 times.

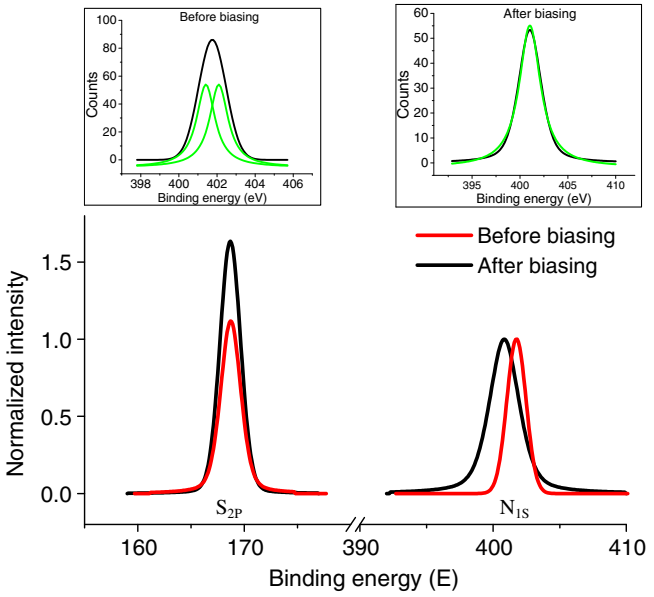

Fig. 4. XPS results on the PANI:PSS before and after electrical stimuli. The presence of PSS is represented by sulphur 2P peaks (168.5 eV) and the presence of PANI is represented by nitrogen 1S peaks (398.1–401.3 eV). Peak intensities of the XPS results were then normalized to the nitrogen peaks to compare the relative intensity difference of sulphur peaks. Black line represents peak intensity of PANI:PSS without electrical biasing applied and red line represents peak intensity of PANI:PSS after electrical biasing was applied. Inset shows the deconvoluted nitrogen 1S. (For interpretation of the references to color in this figure legend, the reader is referred to the web version of this article.)

401.1 eV and 402.6 eV, ascribing to the positively charged nitrogen: oxidized amine and protonated imine, respectively [12]. It was also noted that no nitrogen contributions attributed to quinoid di-imine and benzenoid diamine at 398.5 eV and 399.6 eV can be identified in the XPS readings, suggesting that all of the nitrogen components present within PANI were protonated.

The XPS result demonstrates that nitrogen contributions were altered as a result of the electrical biasing; from 50% oxidized amine and 50% protonated imine to almost 100% oxidized amine before and after biasing, respectively. This alteration is likely to have occurred due to the presence of excess PSS^- within the vicinity of the PANI main chain; as the ratio of protonated and charged nitrogen atoms has been reported to be related to the nature of counter-ions present [13]. Oxidized amine and protonated imine are representations of resonance/mesomerism demonstrated by acid doped polyaniline, and are believed to be accountable for the high charge carrier mobility demonstrated by the polymer [7,14]. Hence the absence of one of the mesomeric states (protonated imine) after electrical biasing is likely to render the polymer non-conductive.

To further examine the migration related effects of both voltage sweeps and current pulses, TOF-SIMS was conducted on the device before and after electrical biasing was done, with sulphur intensities used to map out the PSS^- content through the polymer film. Spectroscopy was carried out using a Cs source sputtering at 3 keV with a beam current of 15 nA over a $150 \times 150\ \mu m^2$ area, and the analysis were conducted on three electrodes: one without any electrical biasing in its pristine high conductive state; another after application of a voltage sweep, switching it to a low conductive state; and lastly one undergoing a voltage sweep to a low conductive state, followed by a current pulse, switching it back to a high conductive state. Results in Fig. 5 show a random distribution of PSS^- throughout the bulk polymer film before voltage application (curve (i) in Fig. 5), indicating no preferential positioning of the charged counter-ion within the polymer film. Application of a negative voltage sweep results in

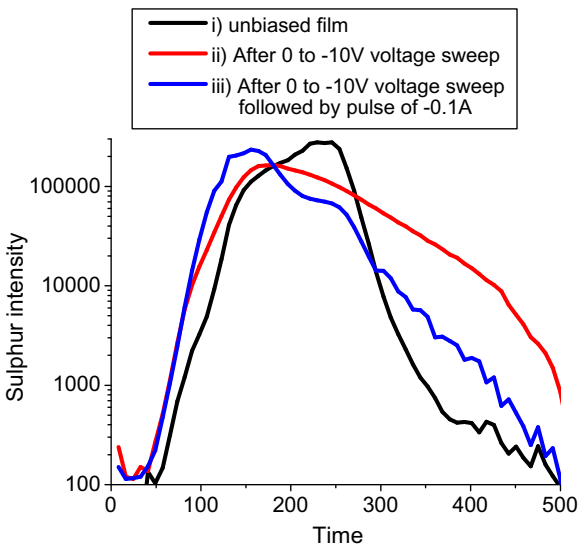

Fig. 5. Three SIMS curves showing the sulphur content in the polymer film (i) no bias applied, (ii) negative voltage sweep from 0 to −10 V, (iii) negative voltage sweep from 0 to +10 V followed by a current pulse at −0.1 A.

increasing the PSS^- content towards the bottom of the film due to the electro-static repulsion of the charged counter-ions with respect to the applied bias (curve (ii) in Fig. 5). This is in agreement with the previous XPS result, indicating that the drop in electrical conductivity is due to the increase in PSS^- at the bottom interface of the polymer. Effect of current pulse application was demonstrated in curve (iii) of Fig. 5, with a reduction in sulphur concentration at the bottom interface of the polymer film (previously high sulphur concentration due to the application of the voltage sweep); indicating reduction in PSS^- content at the polymer interface via back-migration. With this redistribution of negatively charged PSS^- content, the device switches back to a high conductive state; due to restoration of the resonance states of doped nitrogen species. Hence we have evidently demonstrated the modulation of electrical conductivity via migration of PSS^-, serving to alter the ratio of protonated and charged nitrogen atoms within the parent PANI chain; representing an alternative working mechanism for resistive switching application.

4. Conclusion

This is the first report of PANI:PSS displaying resistive switching characteristics. The conductivity of the polymer composite was altered by migration of electro-statically bonded PSS^- counter-ion, which functions to suppress one of the two resonance/mesomeric states of the proton doped polymer necessary for electrical conduction. Restoration of conductivity was achieved by relocation of previously segregated counter-ions. As the bi-stable memory states were brought about by solid state re-arrangement of composite components, this type of memory switching aims to provide a robust memory system not susceptible to memory loss. This work reveals an alternative switching mechanism for the operation of ReRAMs, which serves to supplement the family of switching mechanisms established for resistive switching applications.

Acknowledgments

This work was supported by Ministry of Education (MOE ARC 15/09 Grant No. M45070010), GlobalFoundries Pte. Ltd., Singapore, Nanyang Technological University and the Institute of Materials Research and Engineering (IMRE), Singapore.

Appendix A. Supplementary data

Supplementary data associated with this article can be found, in the online version, at doi:10.1016/j.orgel.2010.11.003.

References

[1] P.O. Sliva, G. Dir, C. Griffiths, Bistable switching and memory devices, J. Non-Cryst. Solids 2 (1970) 316–333.
[2] J. Gazso, Electrical behavior of thin-layer Au-polyethylene-Al sandwiches, Thin Solid Films 21 (1974) 43–49.
[3] Y. Sadaoka, Y. Sakai, Switching in poly(*N*-vinylcarbazole) thin-films, J. Chem. Soc.: Faraday Trans. II 72 (1976) 1911–1915.
[4] J.Y. Ouyang, C.W. Chu, R.J.H. Tseng, A. Prakash, Y. Yang, Organic memory device fabricated through solution processing, Proc. IEEE 93 (2005) 1287–1296.
[5] K. Seo, A.V. Konchenko, J. Lee, G.S. Bang, H. Lee, Electron transport processes in on/off states of a single alkyl-tailed metal complex molecular switch, J. Mater. Chem. 19 (2009) 7617–7624.
[6] A.K. Rath, A.J. Pal, Resistive switching in rose bengal and other xanthene molecules is a molecular phenomenon, Org. Electron. 9 (2008) 495–500.
[7] W.W. Focke, G.E. Wnek, Y. Wei, Influence of oxidation state, pH, and counterion on the conductivity of polyaniline, J. Phys. Chem. 91 (1987) 5813–5818.
[8] C.-W. Kuo, T.-C. Wen, Dispersible polyaniline nanoparticles in aqueous poly(styrenesulfonic acid) via the interfacial polymerization route, Eur. Polym. J. 44 (2008) 3393–3401.
[9] J.C. Chiang, A.G. Macdiarmid, Polyaniline–protonic acid doping of the emeraldine from to the metallic regime, Synth. Met. 13 (1986) 193–205.
[10] C.P.L. Rubinger, L.C. Costa, R. Faez, C.R. Martins, R.M. Rubinger, Hopping conduction on PAni/PSS blends, Synth. Met. 159 (2009) 523–527.
[11] X. Xu, R.A. Register, S.R. Forrest, Mechanisms for current-induced conductivity changes in a conducting polymer, Appl. Phys. Lett. 89 (2006) 3.
[12] S. Golczak, A. Kanciurzewska, M. Fahlman, K. Langer, J.J. Langer, Comparative XPS surface study of polyaniline thin films, Solid State Ionics 179 (2008) 2234–2239.
[13] C. Hennig, K.H. Hallmeier, R. Szargan, XANES investigation of chemical states of nitrogen in polyaniline, Synth. Met. 92 (1998) 161–166.
[14] H.A.M. van Mullekom, J.A.J.M. Vekemans, E.E. Havinga, E.W. Meijer, Developments in the chemistry and band gap engineering of donor–acceptor substituted conjugated polymers, Mater. Sci. Eng.: Rep. 32 (2001) 1–40.

Organic Electronics 12 (2011) 190–194

Contents lists available at ScienceDirect

Organic Electronics

journal homepage: www.elsevier.com/locate/orgel

Letter

Modeling the ultimate efficiency of polymer solar cell using Marcus theory of electron transfer

Dmitry Godovsky *

LG TCM, LG Electronics Ltd., Koroviy Val 7, Bldg.1, Moscow 119049, Russia
Institute of Elementoorganic Compounds, Russian Academy of Science, Vavilova, 28, Moscow, Russia

ARTICLE INFO

Article history:
Received 29 July 2010
Received in revised form 24 October 2010
Accepted 27 October 2010
Available online 11 November 2010

Keywords:
Polymer solar cell
Efficiency limit
Photoinduced charge transfer

ABSTRACT

Polymer solar cell operation is based on the photoinduced charge transfer between polymer donor and acceptor. Marcus theory of electron transfer was applied to calculate the upper limit of the polymer solar cell efficiency in no-recombination approximation. Such calculation becomes possible by optimizing the position of the acceptor LUMO for any band gap value, which in turn maximizes the multiplication product of photocurrent, calculated according to Marcus theory and V_{oc}, which is determined by the difference between the acceptor LUMO and the polymer HOMO. Ultimate efficiency of polymer solar cell critically depends on λ -parameter describing reorientation of neighbouring dipoles in Marcus theory. The model provides a method for selection of optimal acceptor molecules for use in the polymer solar cells.

© 2010 Elsevier B.V. All rights reserved.

1. Introduction

Polymer solar cells, based on heterojunction between polymers and various acceptors, introduced by team, headed by Alan Heeger [1] are broadly researched now and demonstrate quantum efficiencies better than 90% [2] and photovoltages up to 1,5 V [3]. The molecular engineering of conjugated polymers and acceptor molecules [4] allows to tailor properties like optical absorption and charge transfer; supramolecular assembly [5] helps to optimize device structures allowing to efficiently generate charge carriers, dissociate them into a photocurrent, transport and collect this photocurrent at electrodes. Design rules for efficient collection of energy from the solar spectrum would therefore be very worthwhile. A number of models with the approach to calculate polymer solar cells efficiency appeared during the last 10 years [6–9]. Most of these models [6–8] are devoted to the optimization of donor polymer Band Gap and absolute values of polymer HOMO and polymer LUMO levels in respect to acceptor LUMO position, which can maximize the energy conversion. Other model [9] uses standard Schockley–Queisser (S–Q) theory [10], applying it directly to polymer solar cell.

However, one should be very careful, from our point of view, applying S–Q theory to polymer solar cells based on donor–acceptor photoinduced charge transfer. The S–Q theory implies the radiative recombination of excited electron–hole pairs as a main factor, decreasing the efficiency from the ultimate upper limit. In case of donor/acceptor-based polymer solar cells the ultra-fast photoinduced charge transfer takes place with a time constants $\cong 10^{-14}$ s [1]. This is ~4 orders of magnitude faster, than the characteristic time for spontaneous emission from most of the polymers, used in solar cells. Thus, luminescence from the excited state is completely quenched in the presence of acceptor molecules in the neighbourhood, and the S–Q theory can not be applied directly. Also such photoinduced charge transfer is irreversible in it's nature, for the theoretical description of this irreversibility one should read the very good paper by Tributsch [11], so we will refer to this paper and will not explain, why the photoinduced charge transfer is irreversible.

* Tel.: +7 495 721 11 70; fax: +7 495 721 11 67.
E-mail address: dmigo@yandex.ru

1566-1199/$ - see front matter © 2010 Elsevier B.V. All rights reserved.
doi:10.1016/j.orgel.2010.10.015

Since the photoinduced charge transfer plays the key role in the photophysics, utilized in polymer solar cells, the model of solar cell efficiency should therefore include the photoinduced charge transfer. The description of latter is well known due to Rudolf Marcus, who first introduced a model [12] to describe the electron transfer in electrolytes, which was later generalized , covering almost all processes involving electron transfer in chemistry, including photoinduced charge transfer [13] (R.Marcus and S.Sutin). There were a number of successful attempts to describe the photoinduced charge transfer in donor–acceptor systems using Marcus theory of electron transfer, including possibility of multiply hopping in case of Donor-bridge-Acceptor molecules [14]. The main prediction from Marcus theory – existence of inverted region – was experimentally observed for photoinduced electron transfer in Ruthenium(II)–Polypyridine Complexes with Phenolate Ions [15]. The paper of W. Duncan [16] deals with peculiarity of photoinduced charge transfer on the interface between TiO_2 , dye and electrolyte applied in Graetzel cells, where it is found, that in such system Marcus theory also gives adequate description of the experimental photophysical data. Recently appeared review of V. Dyakonov and co-authors [17] provides the treatment of photoinduced charge transfer in Polymer Solar Cells, including intermediate Charge Transfer States (CTS) in terms of Marcus theory, providing some experimental results, supporting Marcus treatment of the photoinduced charge transfer process. Concluding, we would like to stress, that there are many examples of successful description of photoinduced charge transfer using Marcus theory, both theoretical and experimental.

The main equation of Marcus theory [12]:

$$k_{et} = \frac{2\pi}{\hbar}|H_{AB}|^2 \frac{1}{\sqrt{4\pi k_b T}} \exp\left(\frac{(\lambda + \Delta G)^2}{4\lambda k_b T}\right)$$

where $\triangle G$ - driving force of the process, namely the difference in free energy between the initial and the final state, H_{AB} - parameter, describing the intersection of the wave functions of the initial and the final state and λ - a parameter, describing the reorientation of the dipoles in the vicinity of electron final placement.

It is important that Marcus equation describes the rate of electron transfer, which is not a thermodynamic, but a kinetic parameter. The reason to switch to the kinetic approach from thermodynamic is the irreversible character of the photoinduced charge transfer which is followed by further charge separation in respect to light absorbance-luminescence. That is why the act of the photoinduced charge transfer will be described here in kinetic terms, as it was done by Marcus. If we treat the operation of the polymer solar cell as a photochemical reaction, we should use kinetic constants of stages, yields and conversion rates. Actually, the treatment of organic solar cell using Marcus theory was introduced already by S.-S.Sun [18], but from the author's point of view treatment of most of processes, taking place in organic solar cell using Marcus theory seems to be not exactly correct, since exciton decay is a process, having different nature from electron transfer described by Marcus model, as well the CT state recombination (ground state charge transfer) is the two-particle process, involving both electron and the hole, which is also out of limits of Marcus treatment. Also we will not try here, in distinction to S.-S.Sun, to include the kinetics of CT state recombination, since, as it will be described below, it does not correspond to ultimate efficiency case (no-recombination limit), which will be the main object of this paper.

2. Calculation

Writing down the main stages of this reaction, initiated by photon:

- $P + h\nu \leftarrow k_1, k_{-1} \rightarrow P_{exc}(I)$ absorption of photon leads to excited state
- $P_{exc} \leftarrow k_2, k_{-2} \rightarrow P^+F^-(II)$ charge separation occurs from excited state
- $P^+F^- \leftarrow k_3, k_{-3} \rightarrow PF + e + h(III)$ charge dissociation and transport to the electrodes

One can write the kinetic constant of the whole process as [11]:

$$K = \frac{k_1}{1 + [1 + \frac{k_{-2}}{k_3}] * \frac{k_{-1}}{k_2}}$$

Equivalent to: $K = \frac{k_3 k_2 k_1}{k_3 k_2 + k_{-2} k_{-1}}$ which can be rewritten as $\frac{1}{K} = \frac{1}{k_1} + \frac{k_{-2} k_{-1}}{k_3 k_2 k_1}$ where first term can be neglected due to it's incomparability with the second term (K_2>>K_1).

Since $\frac{k_{-1}}{k_1} = 1$, (Einstein), $K = \frac{k_3 k_2}{k_{-2}}$ where k_2/k_{-2} – the rate of Marcus Electron Transfer.

This confirms the fact that the rates of absorbance and luminescence are not influencing the rate of the overall process.

We can rewrite $k_3 = k_4 * k_5$, where $k_4 = k_d(F,T) = \frac{3\beta}{4\pi a^3} \exp(-\frac{E_{ch}}{kT})(1 + b + \frac{b^2}{3} + \frac{b^3}{18} + \frac{b^4}{180} + \ldots)$ Onsager dissociation rate [19] and $k_5 = \mu_e \mu_h / (\mu_e + \mu_h)$ charge transport rate.

The only term depending on the energy levels, shown at the Fig. 1 is the rate of Marcus process of photoinduced electron transfer. Rudolf Marcus in his Nobel lecture [20] has pointed out the fact that the polymer solar cells will

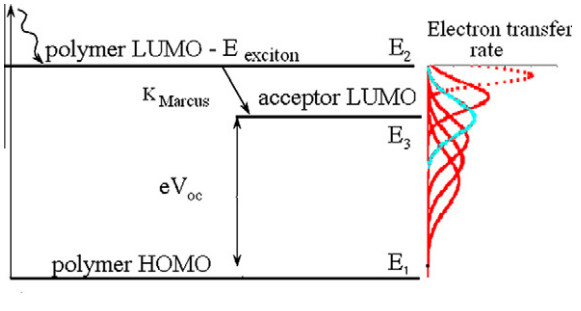

Fig. 1. The three-level diagram for donor–acceptor polymer photovoltaic cells, right side graph - dependence of Marcus rate of electron transfer from Energy level of Acceptor for different λ. Blue curve corresponds to Acceptor LUMO level, depicted at diagram. (For interpretation of the references to colour in this figure legend, the reader is referred to the web version of this article.)

work most optimally if $\Delta G = -\lambda$, since at these values the rate of electron transfer is maximal. The steepness of the dependence of kinetic constant from energy in vicinity of optimum Energy level (Fig. 1) determines the drastic downfall of kinetic rate for non-optimal E_{LUMO} values, to the point where kinetic rate of photoinduced charge transfer equals the luminescence rate, and the yield of the overall reaction (EQE) drops down to 50% and less.

In this paper we would like to determine the optimal position of the Acceptor LUMO level, as depicted at Fig. 1, giving the maximum power output. It should be noted also, that in distinction from S. S. Sun approach [18], where the optimum, maximizing the charge transfer rate is determined, we will determine the Optimum position of Acceptor LUMO, which maximizes the Energy Conversion Efficiency of a Polymer Solar Cell. Since we are calculating the ultimate efficiency of the cell, we can assume the Fill Factor = 1. The maximum power output is than: $P_{max} = V_{max} * I_{max}$.

V_{max} is determined by the difference $V_{max} \sim E_3 - E_1 \sim E_g + E_3 - E_2$ [6].

More accurately speaking, we should substitute E_g with $E_g - E_{\text{exciton binding}}$, which is of the order of 0.1–0.2 eV [3], so let us say that $E_2 - E_1 = E_g - E_{\text{exciton}}$, where $\sim$ means upper limit and then:

$$I_{max} = \frac{2\pi}{h} H^2 \frac{1}{\sqrt{4\pi\lambda kT}} \exp\left(-\frac{((E_3 - E_2) + \lambda)^2}{4\lambda kT}\right) \quad (1)$$

We can write than:

$$P_{max} = \frac{2\pi}{h} H^2 \frac{1}{\sqrt{4\pi\lambda kT}} \exp\left(-\frac{((E_2 - E_3) + \lambda)^2}{4\lambda kT}\right) \times (E_g + (E_3 - E_2)) \quad (2)$$

In order to find the P_{max} we have to take derivative of the expression (2) $P_{max}' = 0$. It gives us:

$$E_{LUMOptimal} = \frac{E_g - \lambda + \sqrt{(E_g - \lambda)^2 + 8\lambda kT}}{2} \quad (3)$$

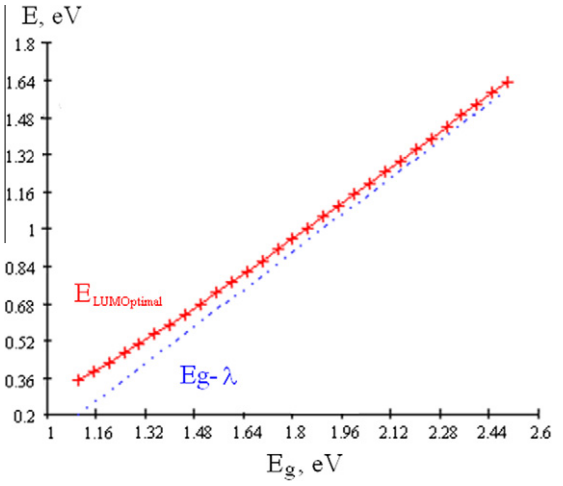

Fig. 2. Dependence of Optimal position of Acceptor LUMO level, maximizing the power output of the PV cell from the Band Gap Value for $\lambda = 0.9$. Solid line – $E_{LUMOptimal}$, dashed line – $E_g - \lambda$.

The position of $E_{LUMOptimal}$ from the E_g value can be seen from Fig. 2.

It can be seen that the optimal position of Acceptor LUMO is close to $E_g - \lambda$ value, but is higher in energy, and for the smaller band gaps this difference can be up to 0.2 eV.

Since we know the position of LUMO level of acceptor, which maximizes the power output, we can derive the expression for the Ultimate Efficiency of the polymer solar cell. Here we treat the Ultimate Efficiency in S–Q model sense, meaning that the cell with no radiative recombination losses lowering the efficiency is described, and also taking the ideal cell with Fill Factor = 1. This approximation describes the so-called no-recombination limit in S–Q model. Thus the expression for the Ultimate efficiency of the Solar Cell will be:

$$v = \frac{[\int_{E_g}^{\infty} N(h\omega)\alpha(h\omega)dh\omega] * eE_{LUMOptimal}}{\int_0^{\infty} N(h\omega)h\omega dh\omega} \quad (4)$$

Where $N(h\omega)$ the number of photons with corresponding energy, $\alpha(h\omega)$ Absorbance coefficient and $eE_{LUMOptimal}$ – ultimate limit of V_{oc}, in case of ideal device architecture, where $E_{LUMOptimal}$ is taken from (3).

It should be defined, which absorbance function we should use in expression (4). It seemed appropriate to model the Absorbance coefficient with the Heaviside step function:

$$H(x) \approx \frac{1}{2} + \frac{1}{2} tahn(E_g k) = \frac{1}{1 + e^{-2kE_g}} \quad (5)$$

Which is 0 for $E < E_g$ and 1 for $E > E_g$ and some transition curve whose steepness depends on the "k" value.

We believe (5) better corresponds to the Ultimate efficiency case, since the polymers which absorb all photons above the Band Gap are available [2] and (5) definitely corresponds to upper limit of efficiency. So we have used mentioned assumptions to calculate the Ultimate Efficiency and numerically calculated the integral (4), optimizing the E_{LUMO} for each taken Band Gap value. We modelled the Sun as black body with $T = 5800$ K, $T_{cell} = 320$ K, incident light perpendicular to the cell surface.

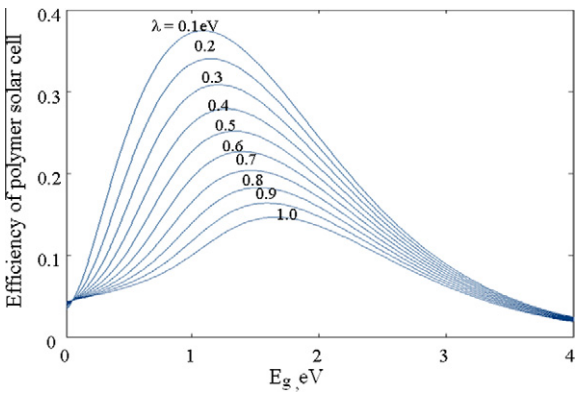

Fig. 3. Efficiency of the *D–A* based plastic solar cell depending on Band Gap energy for different values of λ parameter, obtained using equation (4).

The results of such modelling can be seen from Fig. 3. There are two facts, which result from the modelling: The ultimate efficiency for $\lambda = 0$ is the same, as in S–Q model [10], but as λ becomes higher, the absolute value of efficiency decreases and the maximum efficiency shifts to the higher E_g domain.

This result can be interpreted in Marcus theory terms: the polymer solar cell differs from inorganic one by the fact, that the dipole reorganization or intra-molecular reorganization takes place following the act of electron transfer. This reorganization is the heat dissipating process. Therefore the thermodynamic reversibility is impossible and the heat is evolving, thus lowering the ultimate solar cell efficiency. The larger the λ, the more energy is spent for reorganization, the lower is the upper limit of solar cell efficiency. Also the difference in E_2 and E_3 should be as high as ca. λ to allow the optimal power conversion. Marcus-based approach therefore describes the physics of operation of polymer solar cell, using kinetics, instead of thermodynamics, as in S–Q case.

It should be noted, that according to calculations even for smaller band gap values and even for E_g close to 0 we have non-zero efficiencies of the polymer solar cell. That is due to the fact, that, according to our model, for smaller band gaps the $E_{LUMOptimal}-E_{LUMOAcceptor}$ can be lower than polymer HOMO in energy. Even though it is counter-intuitive case, but in the frame of the given model, even in this case there will be power, generated in the external circuit. As it is assumed, upper limit of $V_{oc} = E_{LUMOAcceptor}-E_{HOMODonor}$ also equals to V_{BI} – built-in electric field in the polymer solar cell (in full accordance with C.Brabec et al. modelling [7]). If acceptor LUMO will be lower in energy than Donor HOMO we will still have the built-in field in the device: $V_{BI=}E_{HOMODonor}-E_{LUMOAcceptor.}$ This field, even though "inverse" in respect to usually met in polymer solar cell, will still be able to produce the energy by means of charge separation for every absorbed photon, equalling to $E = eV_{BI,}$ in the frame of the given model. That is why, even in such counter-intuitive case there will be non-zero efficiencies even for the small polymer band gaps, in limit approaching zero. Of course this should not be true for the point where $E_g = 0$, since at this point we have a metal-like and not a semiconductor-like polymer, therefore value corresponding to $E_g = 0$ should not be considered correct. This trend, appearing for small values of the polymer band gap, reflects the fact, that in polymer solar cells the built-in field, responsible for charge separation and for power output, is determined not by the E_g of the polymer, but by the difference $|E_{LUMOAcceptor}-E_{HOMODonor}|$. Whether this is just a model assumption or there is a deep physical meaning in it, is not clear.

The λ value for the fullerene molecule in different polymer matrices was calculated numerically [21], and was found to be ca. 0.6 eV. One can see the place of optimal band gap for conjugated polymer, blended with fullerene, and the maximum efficiency of PV cell with fullerene acceptor from Fig. 3. One design rule for acceptor moiety can be drawn from Fig. 3: the lower is the λ value, the higher is the efficiency of the solar cell. Author can express his own view, consisting in assumption, that due to rigidity of fullerene buckyball the restructuring of it, following the additional electron uptake, is quite low, comparing to other acceptor molecules, which are not so "rigid". So maybe the success of fullerene-like acceptors for polymer solar cells is due to their unique structure, giving low λ values in comparison with other acceptors.

It should be noted, that to calculate the real Fill Factor and Real V_{oc} values, one should take into consideration the radiative recombination, taking place between levels E_3 and E_1 (Ground state charge transfer). Such calculation was recently done and the results can be found in [22]. It should be stressed, that in our paper we treated the upper limit of efficiency (no-recombination limit) for the polymer solar cell. One can imagine the "ideal" polymer solar cell, where built-in field, caused by difference of two electrodes work functions is so high, that all separated electron–hole pairs are split, and radiative recombination does not take place. This "ideal" situation corresponds to upper limit in our terminology.

Even though our model does not give the exact expressions for V_{oc} and does not include the calculation of Fill Factor, which should be based on detailed treatment of three processes: Onsager dissociation of charge transfer states, caused by external field, competing with the ground state charge transfer, and secondly the recombination and resistive losses taking place during charge transport, it provides some sound clues on ultimate efficiency decrease in polymer solar cells due to the very nature of photoinduced charge transfer in organic media. Also calculating the upper limit, we do not treat the ohmic losses and recombination during charge transfer to electrodes. This detailed treatment is to follow. But even treating the no-recombination limit case we come to the sound results: upper limit is determined by λ of acceptor moiety, optimal band gap shifts with the change of λ and the optimal LUMO position is determined by expression (3). Also the fact that λ of acceptor should be as low as possible to maximize energy conversion efficiency gives a direction in search for new acceptors for polymer solar cells.

To check the validity of the model, one can take "classical" system in polymer solar cells, consisting of P3HT poly-3(hexylthiophene) and PCBM as an acceptor. In this system difference between LUMO of P3HT and LUMO of PCBM equals to 0.9 eV. If we take λ for PCBM similar to λ of fullerene (0.67 eV) and calculate $E_{LUMOptimal}$ according to expression (3), the difference will be 0.65 eV. Since one should take LUMO of P3HT – $E_{exciton}$, which is 0.15–0.2 eV for P3HT [17] it gives us 0.75–0.7 eV as real value versus 0.65 eV, obtained as a result from presented here modelling. It seems that, at least in first approximation, in P3HT-PCMB case the PCBM LUMO is pretty close to the optimal value, maximizing the Energy Conversion Efficiency, according to model presented here.

3. Conclusion

We used Marcus theory to model the ultimate efficiency of polymer solar cells in no-recombination sense. The main assumption, which is presented here, is the deviation of efficiency of polymer or organic solar cells from the standard S–Q theory, caused by absence of thermodynamic

equilibrium between photons, absorbed by solar cell, and photons emitted due to electron–hole pairs recombination. Such deviation is due to very nature of fast and irreversible photoinduced charge transfer from donor to acceptor, which destroys such equilibrium. Thus the main assumption here is, that polymer or organic solar cells operation is similar to photochemical reaction, where reagents are irreversibly converted to products under the action of photon flux. Modeling becomes possible by optimizing the relative position of acceptor molecule LUMO level in respect to polymer LUMO and polymer HOMO levels, which maximizes the power conversion efficiency of the polymer solar cell. The ultimate efficiency, calculated using such optimal acceptor LUMO level position, as it was found, critically depends on λ parameter, describing the reorientation of neighboring dipoles, or change of intra-molecular bonds, caused by photoinduced charge transfer of electron to acceptor molecule in accordance with Marcus theory. The presented model gives useful rules to choose or design the acceptor molecules for use in the polymer solar cells, basing on their LUMO level position and λ parameter, which can be calculated numerically [15] for any given polymer matrix, surrounding the acceptor moiety. It is possible, that the model can be applied not only to polymer, but also to small molecule organic solar cells, based on photoinduced charged transfer between the donor and the acceptor and Dye Type Solar Cells.

Acknowledgment

Author would like to thank Prof. Olle Inganaes for the support and many fruitful discussions at the beginning stage of this work.

References

[1] N.S. Sariciftci, David Braun, C. Zhang, V.I. Srdanov, A.J. Heeger, G. Stucky, F. Wudl, Semiconducting Polymer-Buckminsterfullerene Heterojunctions: Diodes, Photodiodes, and Photovoltaic Cells, Appl. Phys. Lett. 62 (6) (1993) 585–587.
[2] Y. Liang, Y. Wu, D. Feng, S.-T. Tsai, H.-J. Son, G. Li, L. Yu, Development of new semiconducting polymers for high performance solar cells, JACS 131 (2009) 56.
[3] C. Winder, N.S. Sariciftci, Low bandgap polymers for photon harvesting in bulk heterojunction solar cells, J. Mater. Chem. 14 (2004) 1077.
[4] M.M. Wienk, M.P. Struijk, R.A.J. Janssen, Low band gap polymer bulk heterojunction solar cells, Chem. Phys. Lett. 422 (2006) 1256.
[5] L. Chen, D. Godovsky, O. Inganäs, J.C. Hummelen, R.A.J. Janssen, M. Svensson, M.R. Andersson, Polymer photovoltaic devices from stratified multilayers of donor-acceptor blends, Adv. Mater. 12 (18) (2000) 1367.
[6] L.J.A. Koster, V.D. Mihailetchi, A.P.W.M. Blom, Ultimate efficiency of polymer/fullerene bulk heterojunction solar cells, Appl. Phys. Lett. 88 (2006) 093511.
[7] M. Scharber, D. Mühlbacher, M. Koppe, P. Denk, C. Waldauf, A. Heeger, C. Brabec, Design rules for donors in bulk-heterojunction solar cells-towards 10% energy-conversion efficiency, Adv. Mater. 18 (2006) 789.
[8] J. Gilot, M. Wienk, R.A.J. Janssen, On the efficiency of polymer solar cells, Nat. Mater. 6 (2007) 704.
[9] J. Nelson, J. Kirkpatrick, P. Ravirajan, Factors limiting the efficiency of molecular photovoltaic devices, Phys. Rev. B 69 (2004) 035337.
[10] W. Schockley, H. Queisser, Detailed Balance Limit of Efficiency of p-n Junction Solar Cells, J. Appl. Phys. 32 (3) (1961) 510.
[11] H. Tributsch, Kinetically determined Solar Cells, C. R. Chem. 9 (2006) 584–596.
[12] R.A. Marcus, Theory of oxidation-reduction reactions involving electron transfer, J. Chem. Phys. 24 (5) (1956) 966.
[13] R.A. Marcus, N. Sutin, Electron transfers in chemistry and biology, Biochim. Biophys. Acta. 811 (1985) 265.
[14] M.A. Smith, E. Prasad, K.R. Gopidas, Photoinduced Electron Transfer in Hydrogen Bonded Donor−Acceptor Systems. Free Energy and Distance Dependence Studies and an Analysis of the Role of Diffusion, J. Am. Chem. Soc. 123 (6) (2001) 1159–1165.
[15] P. Thanasekaran, T. Rajendran, S. Rajagopal, C. Srinivasan, R. Ramaraj, P. Ramamurthy, B. Venkatachalapathy, Marcus Inverted Region in the Photoinduced Electron Transfer Reactions of Ruthenium(II)−Polypyridine Complexes with Phenolate Ions, J. Phys. Chem. A 101 (44) (1997) 8195–8199.
[16] W.R. Duncan, O. Prezhdo, Theoretical studies of photoinduced electron transfer in dye-sensitized TiO_2, Annu. Rev. Phys. Chem. 58 (2007) 143–184.
[17] C. Deibel, T. Strobel, V. Dyakonov, Role of Charge Transfer States in Organic Donor-Acceptor Solar Cells, Adv. Mat. XX (2010) 1–15.
[18] S.S. Sun, Optimal energy offsets for organic solar cell containing Donor/Acceptor pair, Sol. Energy Mater. Sol. Cells 85 (2005) 261–267.
[19] L. Onsager, Deviations from Ohm's Law in Weak Electrolytes, J. Phys. Chem. 2 (1934) 599.
[20] http://nobelprize.org/nobel_prizes/chemistry/laureates/1992/marcus-lecture.html.
[21] Y. Wang, A. Suna, Fullerenes in photoconductive polymers charge generation and charge transport, J. Phys. Chem. B 101 (1997) 5627–5638.
[22] K. Vandewal, K. Tvingstedt, A. Gadisa, O. Inganäs, J.V. Manca, On the origin of the open-circuit voltage of polymer–fullerene solar cells, Nat. Mater. 8 (2009) 789.

Organic Electronics 12 (2011) 195–201

Contents lists available at ScienceDirect

Organic Electronics

journal homepage: www.elsevier.com/locate/orgel

Crystal order in pentacene thin films grown on SiO_2 and its influence on electronic band structure

R. Matsubara [a,*], M. Sakai [a], K. Kudo [a], N. Yoshimoto [b], I. Hirosawa [c], M. Nakamura [a]

[a] Department of Electrical and Electronic Engineering, Chiba University, 1-33 Yayoi-cho, Inage-ku, Chiba-shi, Chiba 263-8522, Japan
[b] Department of Materials Science and Engineering, Iwate University, 4-3-5 Ueda, Morioka-shi, Iwate 020-8551, Japan
[c] Japan Synchrotron Radiation Research Institute, 1-1-1 Kouto, Sayo-cho, Sayo-gun, Hyogo 679-5198, Japan

ARTICLE INFO

Article history:
Received 1 September 2010
Received in revised form 27 October 2010
Accepted 31 October 2010
Available online 11 November 2010

Keywords:
Pentacene
Grazing incidence X-ray diffraction
In-plane crystallite size
Electronic band structure
Organic thin-film transistor
HOMO-band-edge fluctuation

ABSTRACT

To clarify relationship between crystallographic and electronic structures in pentacene polycrystalline films grown on SiO_2, in-plane crystallite size and random strain of the films were analyzed by grazing incidence X-ray diffraction (GIXD) using synchrotron radiation source. The results indicate that the diffraction peak width is not determined by random strain but by crystallite size. The crystallite size remains constant within the range of 25–50 nm even when the size of polycrystalline domain, or crystal grain, increases more than tenfold by elevating the growth temperature. The crystallite size agrees well with characteristic periods of both HOMO-band-edge fluctuations in pentacene films, which was reported in our previous paper, and surface corrugation of the substrate. These facts strongly suggest that roughness of the SiO_2 surface limits the crystallite size and the interruption of long-range order in pentacene lattice introduces the HOMO-band-edge fluctuation.

© 2010 Elsevier B.V. All rights reserved.

1. Introduction

Organic thin-film transistors (OTFTs) are attracting significant research efforts to realize flexible RFID tags and flexible displays due to their ease of processing on polymer substrates and low cost of processing [1–4]. Around the year 2000, field-effect carrier mobility of pentacene, which is the most widely studied small-molecule organic semiconducting material, rapidly increased and became comparable to that of amorphous silicon [5–8]. However, the mobilities reported in literatures have been stagnating at around 1.0 $cm^2/V\,s$ for this decade. On the other hand, a mobility of 15–40 $cm^2/V\,s$ was reported for a field-effect transistor using a pentacene single-crystal active layer [9]. This value agrees well with the mobilities expected from band dispersion obtained by angle-resolved ultraviolet photoemission spectroscopy [10,11] and band calculations for single crystals [12]. Although these results may not indicate the final physical property of an ideal pentacene single crystal, 40 $cm^2/V\,s$ could be a target of the performance of pentacene TFTs at this stage. Accordingly, the disagreement between the real and the target values suggests that the apparent mobility of a practically important polycrystalline thin film is only less than 10% of that of a single crystal, and the material's true ability for carrier transport is not fully utilized.

It is widely believed that the reason for the mobility of polycrystalline films being lower than that of single crystals is the presence of energy barriers at morphological grain boundaries, which is easily observed by atomic force microscopy (AFM) [13]. Besides, we have reported that such energy barriers with a height of around 100 meV exist not only at the morphological grain boundaries but also at "polycrystalline domain" boundaries [14] which originate in the dendritic growth nature and divide the morphological grains typically into four parts [15]. Furthermore, by using AFM potentiometry (AFMP), we found that HOMO-band-edge fluctuations in the range of 10–20 meV_{rms} exist

* Corresponding authors. Tel./fax: +81 43 290 3516 (M. Nakamura).
E-mail addresses: matsubara@graduate.chiba-u.jp (R. Matsubara), nakamura@faculty.chiba-u.jp (M. Nakamura).

1566-1199/$ - see front matter © 2010 Elsevier B.V. All rights reserved.
doi:10.1016/j.orgel.2010.10.024

even within a "polycrystalline domain" formerly regarded as a single crystal [16]. There are two possible origins of these fluctuations. First, the "polycrystalline domain" itself is a single crystal in fact but contains random strains. Second, the "polycrystalline domain" is a mosaic of smaller crystallites and potential fluctuations are generated due to the crystallite boundaries. To determine a major cause of the band-edge fluctuation, the microstructures in pentacene thin films need to be precisely evaluated.

Some groups have reported about the correlation between out-of-plane crystallite sizes of pentacene films on SiO_2 and their mobility [17,18]. However, there have been a limited number of reports that mention the "in-plane" microstructures in pentacene thin films, even though they must be more important for carrier transport in a TFT channel rather than out-of-plane ones. This is mainly because crystallite sizes of organic polycrystalline materials tend to be larger than those of inorganic ones, which obliges us to use narrower-width slits or an analyzer crystal to measure very narrow full-width-at-half-maximum (FWHM) of the diffraction peaks, and also because organic materials are composed manly of light elements. Since both of them significantly weaken the intensity of diffracted X-ray, it is almost impossible to use a laboratory-scale grazing incidence X-ray diffraction (GIXD) instrument for this purpose. Therefore, to use very bright X-ray from a synchrotron radiation source is necessary for the GIXD analyses of in-plane microstructures. Natsume et al. reported a crystallite size in pentacene films grown by their special solution process [19], and Hong et al. reported that in pentacene films on Au electrodes [20]. However, none of these studies considered the random strain in crystals in their analyses, although such random strain also broadens the FWHM of diffraction peaks. Moreover, the in-plane microstructures of the vacuum-evaporated pentacene on SiO_2, which is the most popular OTFT combination of an active material and a gate insulator, has not been reported so far.

In this paper, we demonstrate that the influence of in-plane random strain on the FWHMs of in-plane GIXD peaks is negligible and that the crystallite sizes of pentacene polycrystalline films grown on SiO_2 substrates are in the range of 25–50 nm, which is at least one order of magnitude smaller than the polycrystalline domain size. Crystallite sizes were verified by also high-resolution frictional force microscopy (FFM). Contrary to conventional wisdom in thin-film growth, the crystallite size remains constant even when the apparent grain size increases tenfold by elevating the growth temperature. Our results demonstrate that it is highly probable that the mosaic structure of the polycrystalline domain causes the HOMO-band-edge fluctuation.

2. Experimental

2.1. Thin film growth

Pentacene films were deposited on Si wafers with 300 nm-thick silicon oxide. All samples were fabricated using the same method as in previous studies [15,16,21]. A heavily doped n-type silicon (1 0 0) wafer (Mitsubishi Materials, resistivity is less than 0.02 Ω cm) with thermally grown SiO_2 (300 nm) was used as the substrates. They were cleaned with acetone and UV/O_3 (200 °C, 30 min) to remove surface contamination. Pentacene with a purity of over 99.9% (Tokyo Chemical Industry, sublimation grade) were then deposited onto the substrates by molecular beam deposition in an ultra-high vacuum ($\approx 5 \times 10^{-8}$ Pa) [21]. The film thickness and deposition rate were controlled using a crystal thickness monitor. The growth rate was 0.3 nm/min, and the substrate temperature was varied in the range of 5–100 °C.

2.2. GIXD measurements

All GIXD measurements were performed using monochromated synchrotron radiation at the BL46XU beam line in SPring-8 with a goniometer manufactured by HUBER, which is specially designed for the characterization of thin films. The wavelength and incident angle of X-ray were 1 Å and 0.12°, respectively. All measurements were performed in a helium atmosphere. A lithium fluoride analyzer crystal was used for higher wavenumber resolution in the X-ray detection. GIXD peaks obtained in this work are however broadened to some extent due to the limit of angle resolution (instrumental function). GIXD patterns of the pentacene films were therefore fitted using a Voigt function whose width of the Gaussian component was fixed with that of the instrumental function and the width of the Lorentzian component was varied to analyze the true width of the diffraction from the pentacene film. The FWHM of the Gaussian instrumental function was estimated to be 0.047 nm^{-1} from (0 2 2) diffraction of Si(1 0 0) wafer.

2.3. Frictional force microscopy

FFM measurement was performed using an AFM (JEOL, JSPM-4200) in a nitrogen atmosphere just after the film growth. The AFM was operated in a contact (constant-height) mode by setting the force load as low as possible. Triangular-shaped silicon nitride cantilevers with a stiffness of 0.09 N/m (Olympus, OMCL-TR400 PB) were scanned in the perpendicular direction and torsion of the lever was corrected as the frictional signal. Using the triangular shape lever, all of the tip–sample force components in lateral directions were mixed due to the crosstalk between bending and torsional motion of the lever, which equalizes the sensitivities to parallel and perpendicular components of the frictional force and thereby molecular lattice images become relatively insensitive to the angle between the scanning direction and molecular crystals.

2.4. Atomic force microscope potentiometry

AFMP measurements were performed using an AC-mode AFM (JEOL, JSPM-5200) equipped with a conductive cantilever and a high-input impedance voltage-measurement circuit which is integrated in a cantilever holder. This technique is capable of accurately measuring the potential (voltage) distribution in working thin-film transistors

[16,22–24]. The spatial resolution of AFMP is estimated to be <10 nm and the potential resolution ~100 μV. All AFMP measurements were performed in nitrogen atmosphere with Pt-coated Si cantilevers.

3. Results

3.1. Film morphologies and GIXD patterns

Fig. 1 shows AFM height images of the pentacene films. By changing the growth temperature in the range of 5–100 °C, pentacene films with an average polycrystalline domain size (mean diameter of the area surrounded by 100 meV-order energy barriers, defined as half of the morphological grain size in the case of pentacene [15]) of 400–2.5 μm were prepared. Tall lamellar grains, in which the molecules lie flat [21], are seen in films grown at 5 and 20 °C. Although they strongly decrease the apparent mobility of the film grown at lower temperature [25], they are beyond the scope of the present work, and their volume is so small that they hardly appear in the GIXD pattern.

Fig. 2 shows GIXD patterns measured with the pentacene films. The FWHM of all the peaks are much wider than those of the instrumental function. Among many detectable in-plane diffraction peaks, these three peaks shown in the figure, corresponding to the thin-film phase [26,27], were selected for further analysis because they exhibited clear peak shapes with sufficient signal-to-noise ratios. It should be noted that the (0 2 0) and (1 2 0) peaks have asymmetric shoulders. By fitting two Voigt functions to these peaks, the lattice constant obtained from the major components was equal to that of the thin-film-phase pentacene, and the constant from the minor peaks was in between those of the thin-film and the bulk phases, of which composition ratio increases while increasing the thickness [28]. This suggests that the minor component is an intermediate state wherein the crystal structure of the pentacene changes from a thin-film phase to a bulk phase. In the structural analyses, we only use the major thin-film-phase components because the minor components is judged not to affect carrier transport in the film.

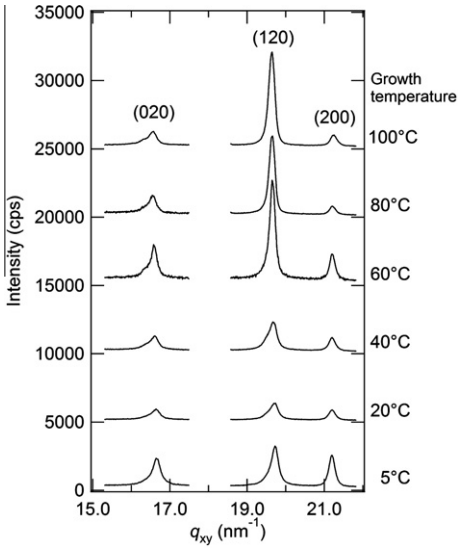

Fig. 2. In-plane GIXD patterns of pentacene thin films grown on SiO_2 substrates at various temperatures. The indexes of a thin-film phase pentacene crystal are labeled.

3.2. Analysis of GIXD peaks

As mentioned previously, the peak widths of XRD patterns are broadened not only by the size of crystallite but also by the random strain in the crystal structure. The Williamson–Hall (W–H) method can separate these two factors from the widths of the XRD peaks [29]. In this

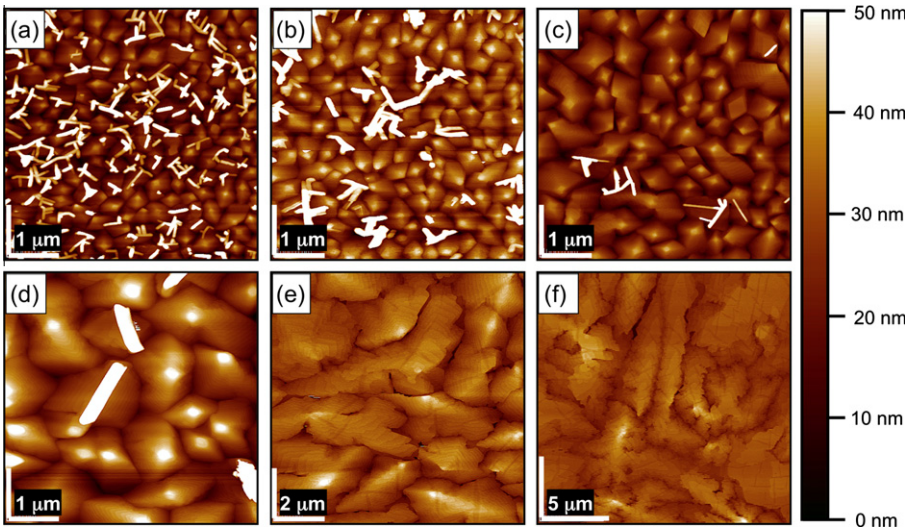

Fig. 1. AFM height images of pentacene thin films grown on SiO_2 substrates at (a) 5 °C, (b) 20 °C, (c) 40 °C, (d) 60 °C, (e) 80 °C, and (f) 100 °C. The displayed height range is evenly set to 50 nm.

method, the relationship between these structural parameters and peak width is described as follows:

$$\beta_q = \frac{2\pi K_s}{\langle D \rangle} + \varepsilon_{rms} q_{xy} \quad (1)$$

where β_q is the FWHM of a peak, K_S is the Scherrer constant, $\langle D \rangle$ is the average crystallite size, ε_{rms} is root mean square of the random strain, and q_{xy} is the scattering vector. The Scherrer constant is determined depending upon the composition and type of crystal. For organic crystals, values of 0.87–1.05 are frequently used [30–33]. In this work, we adopt $K_S = 0.95$ which is in middle of the range used for organic crystals. The error in crystallite size due to uncertainty in the Scherrer constant is less than 10% and does not influence the discussion in the present study. By fitting a straight line to the β_q versus q_{xy} plot, the random strain and crystallite size can be estimated from the positive slope and the positive intercept of the fitted line, respectively. In the case of the pentacene films studied in this work, there is no large anisotropy in the in-plane crystallite size as explained later. Therefore, we apply the W–H method to the three peaks from different diffraction planes, although it should be used for a series of higher-order diffraction peaks from the same diffraction plane as a general rule.

Fig. 3a shows W–H plots of all major peaks in Fig. 2. It is to be noted that no sample has a clear positive slope in its W–H plot. This result indicates that the FWHMs of the X-ray diffraction peaks from the pentacene films are determined by their finite crystallite sizes and the contribution of random strain is negligible. Therefore, hereafter, we only discuss the crystallite size estimated for each peak by the Scherrer equation

$$\langle D \rangle = \frac{2\pi K_s}{\beta_q}. \quad (2)$$

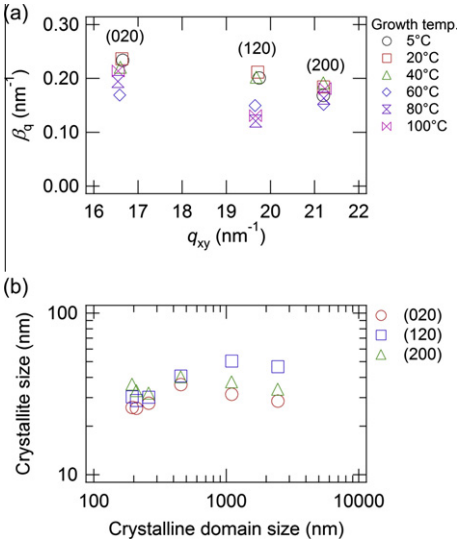

Fig. 3. (a) Williamson–Hall plot of the major GIXD peaks in Fig. 2. (b) Relationship between crystallite size estimated using the Scherrer equation and the polycrystalline domain size of the pentacene film. A Scherrer constant value of 0.95 was used to calculate the crystallite sizes.

In Fig. 3b, the crystallite size calculated from each peak is plotted against the polycrystalline domain size of the film. Although polycrystalline domain sizes are varied more than 10 times by changing the growth temperature, surprisingly, the crystallite sizes are unchanged. The estimated crystallite size is within the range of 25–50 nm and one- to two-orders-of-magnitude smaller than the domain size.

3.3. Comparison with molecular lattice image

To verify the small crystallite size estimated from GIXD, scanning probe microscopy is a good complementary technique. We observed molecular lattice images on flat terraces of a 5 nm-thick (three to four molecular layers) pentacene film using high-resolution frictional force microscopy (FFM), which is suitable for observations of lattice images of organic crystals [34,35]. Fig. 4 shows a 50×50 nm^2 FFM image along with a magnified one which indicates the unit cell structure of thin-film-phase pentacene. White rectangles denote directions of unit cells in each area. Shorter and longer sides correspond to a and b of the unit cell, respectively, and its direction was determined by period of the molecular rows. Judging from the direction of molecular lows, there exist at least three differently oriented crystallites within this area. Similar images were observed for many different terraces in different grains. In most of the same-sized images, at least one boundary between differently oriented crystallites was observed. No strongly anisotropic crystallite shape was seen. The FFM results strongly support the small (25–50 nm) crystallite size estimated by GIXD. Accordingly, a polycrystalline domain of pentacene considered to be a single crystal by many researchers is undoubtedly a mosaic crystal of several tens of nm-sized crystallites.

4. Discussion

4.1. Temperature independent crystallite size

As shown in Fig. 1, the size of a polycrystalline domain generally increases by elevating the growth temperature. This is explained by the decrease in the nucleation density due to the increased desorption rate of the molecules that form the nuclei. Since film growth of pentacene is strongly two-dimensional in this thickness range, the nucleation density at the initial stage of the growth, during the growth of the first or the second molecular layer, determines the polycrystalline domain size. On the other hand, the size of the crystallite is determined by the generation probability of stacking faults during horizontal crystal growth, which interrupts the coherency of the molecular lattice. The generation of stacking faults must be strongly influenced by the roughness of the substrate surface. Fig. 5a shows a fast-Fourier-transform (FFT) spectrum of the surface topography of the SiO_2 substrate used in this work. To improve the signal-to-noise ratio, the FFT spectrum is obtained by averaging eight FFT spectra calculated from line profiles at different positions. A dashed line shows a smoothing result of the FFT spectrum using the 5-point

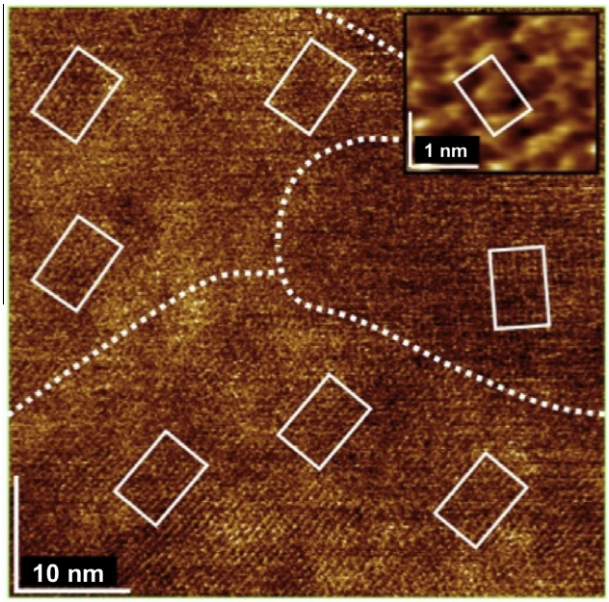

Fig. 4. A 50 × 50 nm^2 molecular lattice image obtained with an FFM on a flat molecular terrace of a pentacene film. The inset shows a magnified image to show a unit cell. Rectangles in the wide image show directions of unit cells in each area and the broken lines show boundaries between differently oriented domains.

Savitzky–Golay method [36]. A clear peak is seen within the range of the crystallite size (25–50 nm), while totally three peaks are prominent in the spectrum. Two peaks seen in the lower frequency side are components with double and quadruple period of the highest frequency one. Minor features in the higher frequency side also indicate the surface topography unless the period does not become smaller than the tip radius, less than 10 nm. Their amplitudes are, however, much smaller than those of the major peaks. Consequently, the highest spatial frequency of the characteristic surface corrugation of the substrate is at around 0.03 nm^{-1} (30 nm in period), which agrees well with the crystallite size. Based on the above discussion, it is highly probable that the crystallite size is regulated by the corrugation of the substrate surface, which induces stacking faults during the growth of the first or second layer [37]. Once these stacking faults are introduced, successive growth of the upper layers will follow the underlying crystallographic structure. Thus, crystallite size cannot be increased even by elevating the growth temperature.

4.2. Origin of HOMO-band-edge fluctuation

Single crystal pentacene exhibits band dispersion of HOMO with a bandwidth of a few hundred meV, and its carrier mobility reaches 40 cm^2/V s [9–12]. These characteristics are produced by high coherency of the molecular lattice and a relatively large transfer integral of the π orbitals. Under this condition, both random strain in the molecular lattice and disruption of lattice coherency lead to modulation of the band structure. According to the GIXD results in this work, the lattice coherency of the pentacene thin-film on SiO_2 is mainly disturbed by the small crystallite size rather than the random strain. Therefore, the mosaic structure of the polycrystalline domain with small crystallites would be the most probable cause of the band-edge fluctuation. To confirm the validity of this assumption, characteristic period of the band-edge fluctuation was also compared to the crystallite size. Inset of Fig. 5b shows a typical line profile of the band-edge fluctuation obtained with AFMP on a polycrystalline domain in a pentacene film grown at 60 °C [16] and Fig. 5b shows its corresponding FFT spectrum together with its smoothing result using the 5-point Savitzky–Golay method. Although AFMP measures a completely different physical property from the topography of the substrate, the FFT spectrum has similar prominent peaks as in Fig. 5a. Based on the same discussion as for Fig. 5a above, the highest spatial frequency of the characteristic band-edge fluctuation is concluded to be around 0.03 nm^{-1} (30 nm in period), which again agrees well with the crystallite size. The characteristic periods of the band-edge fluctuation were nearly constant among many pentacene films grown at different temperatures as in this work. Accordingly, it is highly probable that the mosaic structure with small crystallites causes the band-edge fluctuation. Detailed mechanism of the band-edge modulation is however still an open question. Further investigation using theoretical and computational studies is strongly desired to completely elucidate this issue.

4.3. Overview of HOMO-band-edge and crystallographic structures in pentacene thin films

Fig. 6 schematically summarizes the energy diagram and film structure of a pentacene polycrystalline film based on the results in this work and some previous stud-

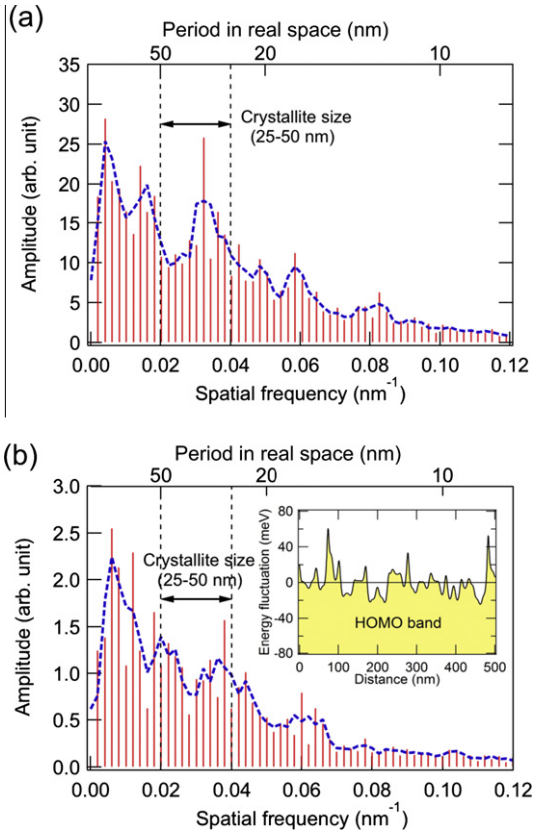

Fig. 5. FFT spectrums of (a) the surface topography of the SiO_2 substrate (average of eight spectra) and (b) the HOMO-band edge profile of the sample grown at 60 °C. Two pairs of dashed vertical lines show the range of crystallite size estimated in this work. Thick dashed lines are smoothing results of the FFT spectra using the 5-point Savitzky–Golay method. The inset in (b) is a typical HOMO-band-edge profile of the same sample taken on a flat terrace of pentacene.

ies [15,16,25]. A pentacene polycrystalline film consists of hierarchical structures, including (i) the micrometer-scale morphological grain, (ii) the polycrystalline domain surrounded by large energy barriers for carrier transport, (iii) the ten-nanometer-scale crystallite, (iv) the unit cell of the crystal, and (v) the molecule. A morphological grain of pentacene on SiO_2 has its nucleus at around the center and four branches grow from the nucleus toward four directions. Each branch finally becomes the polycrystalline domain (ii). During the film growth, they coalesce so as to form, in most cases, a smooth pyramid-shaped morphological grain (i) and the boundary of (ii) is invisible in an AFM image. The boundaries of (i) and (ii) are however almost equivalent and crucial limiting factors for carrier transport because their barrier height is more than 100 meV. Moreover, (ii) is still not a single crystal and the boundary of (iii) introduces 10 meV-scale fluctuations of the band edge. The barrier height at the boundary of (ii) is much higher than that of (iii) because crystal orientations are more different between two neighboring domains than between connected crystallites due to the different orientation of triclinic crystals. Overall apparent carrier mobility of the film is also reduced by the band-edge fluctuation by (iii) because it is proportional to the mobility in (ii) [15].

5. Conclusions

Crystallographic order in the most popular active layer material for OTFT, pentacene polycrystalline thin films grown on SiO_2, was analyzed using in-plane GIXD and FFM. The coherency of the molecular lattice was disturbed not by the random strain but by the size of the crystallites. The crystallite size was estimated to be 25–50 nm and remained almost constant even though the size of the polycrystalline domain was enlarged from 200 nm to 2.5 μm by elevating the growth temperature. A FFM molecular lattice image also indicated the presence of the small crystallite even within a flat molecular terrace. The crystallite size

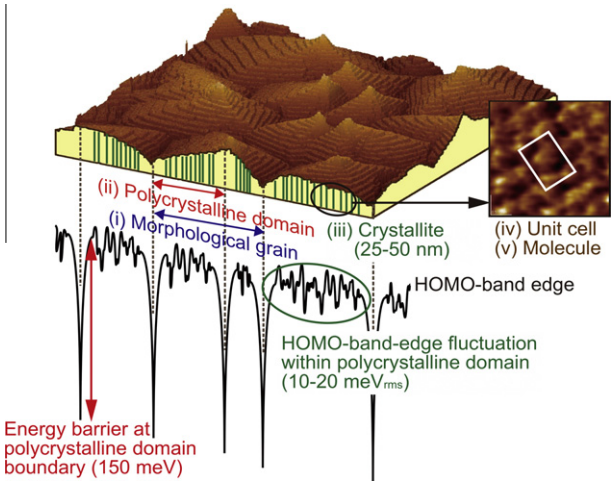

Fig. 6. Schematic illustration showing (top) crystallographic and (bottom) HOMO-band-edge structure in a pentacene polycrystalline film. A pentacene polycrystalline film consists of hierarchical structures, including (i) the micrometer-scale morphological grain, (ii) the polycrystalline domain surrounded by large energy barriers for carrier transport, (iii) the ten-nanometer-scale crystallite, (iv) the unit cell of the crystal, and (v) the molecule.

agreed well with the characteristic periods of both the corrugation of the substrate surface and the HOMO-band-edge fluctuation in a pentacene film. These facts suggest that the surface roughness of the substrate limits the crystallite size and thus band-edge fluctuation is introduced in the HOMO band of pentacene.

Acknowledgment

This work is supported in part by the Chiba University Global COE Program "Advanced School for Organic Electronics" and Grant-in-Aid for Scientific Research (No. 21350099). Synchrotron radiation experiments were performed in the SPring-8 with the approval of the Japan Synchrotron Radiation Research Institute (JASRI) (Proposal No. 2008A1813).

References

[1] V. Subramanian, P.C. Chang, J.B. Lee, S.E. Molesa, S.K. Volkman, IEEE Trans. Compon. Packag. Technol. 28 (2005) 742.
[2] E. Cantatore, T.C.T. Geuns, G.H. Gelinck, E. van Veenendaal, A.F.A. Gruijthuijsen, L. Schrijnemakers, S. Drews, D.M. de Leeuw, IEEE J. Solid-State Circuits 42 (2007) 84.
[3] L. Zhou, A. Wanga, S.-C. Wu, J. Sun, S. Park, T.N. Jackson, Appl. Phys. Lett. 88 (2006) 083502.
[4] A. Sugimoto, H. Ochi, S. Fujimura, A. Yoshida, T. Miyadera, M. Tsuchida, IEEE J. Sel. Topics Quantum Electron. 10 (2004) 107.
[5] M. Shtein, J. Mapel, J.B. Benziger, S.R. Forrest, Appl. Phys. Lett. 81 (2002) 268.
[6] D. Knipp, R.A. Street, A. Volkel, J. Ho, J. Appl. Phys. 93 (2003) 347.
[7] W.-Y. Chou, C.-W. Kuo, H.-L. Cheng, Y.-R. Chen, F.-Y. Yang, D.-Y. Shu, C.-C. Liao, Fu.-C. Tang, Jpn. J. Appl. Phys. 45 (2006) 7922.
[8] T.W. Kelley, L.D. Boardman, T.D. Dunbar, D.V. Muyres, M.J. Pellerite, T.P. Smith, J. Phys. Chem. B 107 (2003) 5877.
[9] O.D. Jurchescu, M. Popinciuc, B.J. van Wees, T.T.M. Palstra, Adv. Mater. 19 (2007) 688.
[10] H. Kakuta, T. Hirahara, I. Matsuda, T. Nagao, S. Hasegawa, N. Ueno, K. Sakamoto, Phys. Rev. Lett. 98 (2007) 247601.
[11] H. Yamane, E. Kawabe, D. Yoshimura, R. Sumii, K. Kanai, Y. Ouchi, N. Ueno, K. Seki, Phys. Stat. Sol. (b) 245 (2008) 793.
[12] K. Hummer, C. Ambrosch-Draxl, Phys. Rev. B 72 (2005) 205205.
[13] G. Horowitz, M.E. Hajlaoui, Adv. Mater. 12 (2000) 1046.
[14] S. Nishikata, G. Sazaki, J.T. Sadowski, A. Al-Mahboob, T. Nishihara, Y. Hujikawa, S. Suto, T. Sakurai, K. Nakajima, Phys. Rev. B 76 (2007) 165424.
[15] R. Matsubara, N. Ohashi, M. Sakai, K. Kudo, M. Nakamura, Appl. Phys. Lett. 92 (2008) 242108.
[16] N. Ohashi, H. Tomii, R. Matsubara, M. Sakai, K. Kudo, M. Nakamura, Appl. Phys. Lett. 91 (2007) 162105.
[17] W.Y. Chou, Y.S. Mai, H.L. Cheng, C.Y. Yeh, C.W. Kuo, F.C. Tang, D.Y. Shu, T.R. Yew, T.C. Wen, Org. Electron. 7 (2006) 445.
[18] O. Werzer, B. Stadlober, A. Haase, M. Oehzelt, R. Resel, Eur. Phys. J. B. 66 (2008) 455.
[19] Y. Natsume, T. Minakata, T. Aoyagi, Synth. Met. 159 (2009) 338.
[20] K. Hong, S.Y. Yang, C. Yang, S.H. Kim, D. Choi, C.E. Park, Org. Electron. 9 (2008) 864.
[21] H. Yanagisawa, T. Tamaki, M. Nakamura, K. Kudo, Thin Solid Films 464–465 (2004) 398.
[22] M. Nakamura, N. Goto, N. Ohashi, M. Sakai, K. Kudo, Appl. Phys. Lett. 86 (2005) 122112.
[23] M. Nakamura, H. Ohguri, H. Yanagisawa, N. Goto, N. Ohashi, K. Kudo, In Proc. Int. Symp. Super-Functionality Organic Devices, IPAP Conf. Ser. 6 (2005) 130.
[24] M.-S. Xu, A. Ohno, S. Aramaki, K. Kudo, M. Nakamura, Org. Electron. 9 (2008) 439.
[25] M. Nakamura, H. Ohguri, N. Goto, H. Tomii, M.-S. Xu, T. Miyamoto, R. Matsubara, N. Ohashi, M. Sakai, K. Kudo, Appl. Phys. A 95 (2009) 73.
[26] S.E. Fritz, S.M. Martin, C.D. Frisbie, M.D. Ward, M.F. Toney, J. Am. Chem. Soc. 126 (2004) 4084.
[27] T. Kakudate, N. Yoshimoto, Y. Saito, Appl. Phys. Lett. 90 (2007) 081903.
[28] I.P.M. Bouchoms, W.A. Schoonveld, J. Vrijmoeth, T.M. Klapwijk, Synth. Met. 104 (1999) 175.
[29] F. Williamson, W. Hall, Acta Metall. 1 (1953) 22.
[30] R. Hussain, D. Mohammad, Turk. J. Chem. 28 (2004) 725.
[31] Y. Iwanami, H. Kamiishi, K. Matsuura, A. Sano, S. Yokoyama, US Patent, 5002,714 (1991).
[32] H.S. Soliman, M.M. El Nahass, A.M. Farid, A.A.M. Farag, A.A. El Shazly, Eur. Phys. J. AP 21 (2003) 187.
[33] F.Y. Tsai, T.N. Blanton, D.R. Harding, S.H. Chen, J. Appl. Phys. 93 (2003) 3760.
[34] M. Nakamura, H. Tokumoto, Surf. Sci. 377–379 (1997) 85.
[35] M. Nakamura, H. Tokumoto, Surf. Sci. 398 (1998) 143.
[36] A. Savitzky, M.J.E. Golay, Anal. Chem. 36 (1964) 1627.
[37] V. Kalihari, E.B. Tadmor, G. Haugstad, C.D. Frisbie, Adv. Mater. 20 (2008) 4033.

Organic Electronics 12 (2011) 202–209

Contents lists available at ScienceDirect

Organic Electronics

journal homepage: www.elsevier.com/locate/orgel

Electrochromic and optical studies of solution processable benzotriazole and fluorene containing copolymers

Emine Kaya [a], Abidin Balan [a], Derya Baran [a], Ali Cirpan [a,c,*], Levent Toppare [a,b,c]

[a] Department of Chemistry, Middle East Technical University, 06531 Ankara, Turkey
[b] Department of Biotechnology, Middle East Technical University, 06531 Ankara, Turkey
[c] Department of Polymer Science and Technology, Middle East Technical University, 06531 Ankara, Turkey

ARTICLE INFO

Article history:
Received 4 October 2010
Received in revised form 1 November 2010
Accepted 3 November 2010
Available online 20 November 2010

Keywords:
Benzotriazole
Fluorene
Optoelectronic
Conjugated copolymers
Donor–acceptor

ABSTRACT

2-Dodecyl benzotriazole and 9,9-dioctylfluorene containing alternating copolymers poly((9,9-dioctylfluorene)-2,7-diyl-(2-dodecyl-benzo[1,2,3]triazole)) (**P1**), poly((9,9-dioctylfluorene)-2,7-diyl-(4,7-bis(thien-2-yl) 2-dodecyl-benzo[1,2,3]triazole)) (**P2**), poly((9,9-dioctylfluorene)-2,7-diyl-(4,7-bis(3-hexylthien-5-yl) 2-dodecyl-benzo[1,2,3]triazole)) (**P3**) were synthesized via Suzuki polycondensation. Electronic and optical properties of resulting polymers showed that all polymers are both p and n dopable and have multicolored electrochromic states. HOMO and LUMO values, band gaps and spectral response of polymers upon externally applied potential and trifluoro acetic acid (TFA) addition were given in detail.

© 2010 Elsevier B.V. All rights reserved.

1. Introduction

Conjugated polymers (CPs) have been extensively studied for their potentials as active materials in numerous industrial applications namely, electrochromics (ECDs) [1], light emitting diodes (OLEDs) [2], photovoltaic devices (OPVs) [3], and thin film transistors (OFETs) [4]. They combine the physical properties of polymers with those of semiconductors to obtain unique and novel materials. Since the small structural modifications on polymer backbone allow tuning of band gap and hence their optical and electronic properties, there have been several methods to obtain polymers with desired properties [5]. However, for optoelectronic applications, recent research interest have mainly focused on donor–acceptor (DA) type materials in which alternating electron rich and electron deficient groups are both present on the backbone [6]. Electronic and optical properties of these types of polymers are tuned efficiently by intramolecular charge transfer (ICT) [7]. In terms of electrochromic devices, the use of DA type CPs as active layers became more popular over the time due to their variation of optical properties via structural alternations [8]. Possibility for applications of CPs to large and flexible display devices makes their development significant for future display technologies [9].

Poly-9,9-dialkylfluorenes (**PFOs**) and their copolymers with different groups are considered as some of the most promising materials to be used in organic electronics and have been examined quite extensively up to date [10]. Combination of **PFOs** with an acceptor or a donor–acceptor–donor (DAD) group ensures that the band gap of the polymer can be modified according to device applications [8]. Alkylation of fluorene provides high solubility and stabilizes the carbon atom on 9-position; however, unsubstituted fluorenes form fluorenones which disturb effective conjugation on polymer backbone. These **PFO** copolymers, particularly benzothiadiazole (BTd) derivatives, were used in optoelectronic applications and inserting BTd units in **PFO** chains resulted in highly efficient OPVs, OLEDs and OFETs [11]. On the other hand, benzotriazole (BTz) was introduced to the **PFOs** in few studies where it was used as internal molecular additive [12].

* Corresponding author at: Department of Chemistry, Middle East Technical University, 06531 Ankara, Turkey. Tel.: +90 3122105103.
E-mail address: acirpan@metu.edu.tr (A. Cirpan).

1566-1199/$ - see front matter © 2010 Elsevier B.V. All rights reserved.
doi:10.1016/j.orgel.2010.11.001

However, properties of alternating copolymers with BTz groups with fluorene are yet lack of scientific inventory. We expect that the use of BTz may bring an improvement on the several properties of such devices.

Recently, BTz containing DAD type polymers has been received a great deal of attention in optoelectronic research due to their ease of synthesis and tremendous optical and electronic properties [13]. DAD type polymers of BTz with different donor units were shown to be multipurpose materials for device applications such as ECDs and OPVs with promising results [14].

Here, we report the synthesis and characterizations of benzotriazole and **PFO** containing alternating copolymers **P1**, **P2**, and **P3**. Electronic doping in thin film formed by externally applied potential revealed that polymers **P2** and **P3** are great candidates for multicolored electrochromic device applications. Furthermore, oxidative doping of polymers in toluene resulted in multi-colored solution phases due to varied oxidation states. Electronic and optical properties of new alternating fluorene–BTz copolymers and comparison of results with those of parent polymers (**PFO**, **PTBT**, and **PHTBT**) were given in detail.

2. Results and discussion

2.1. Synthesis

Synthetic pathway for polymers; poly((9,9-dioctylfluorene)-2,7-diyl-(2-dodecyl-benzo[1,2,3]triazole)) (**P1**), poly((9,9-dioctylfluorene)-2,7-diyl-(4,7-bis(thien-2-yl) 2-dodecyl-benzo[1,2,3]triazole)) (**P2**), poly((9,9-dioctylfluorene)-2,7-diyl-(4,7-bis(3-hexylthien-5-yl) 2-dodecyl-benzo [1,2,3] triazole)) (**P3**) is outlined in Scheme 1. The synthesis of 4,7-bis(thien-2-yl) 2-dodecyl-benzo[1,2,3]triazole (**TBT**) [13a] and 4,7-bis(3-hexylthien-5-yl) 2-dodecyl-benzo[1,2, 3]triazole (**HTBT**) [13b] was reported previously by our group.

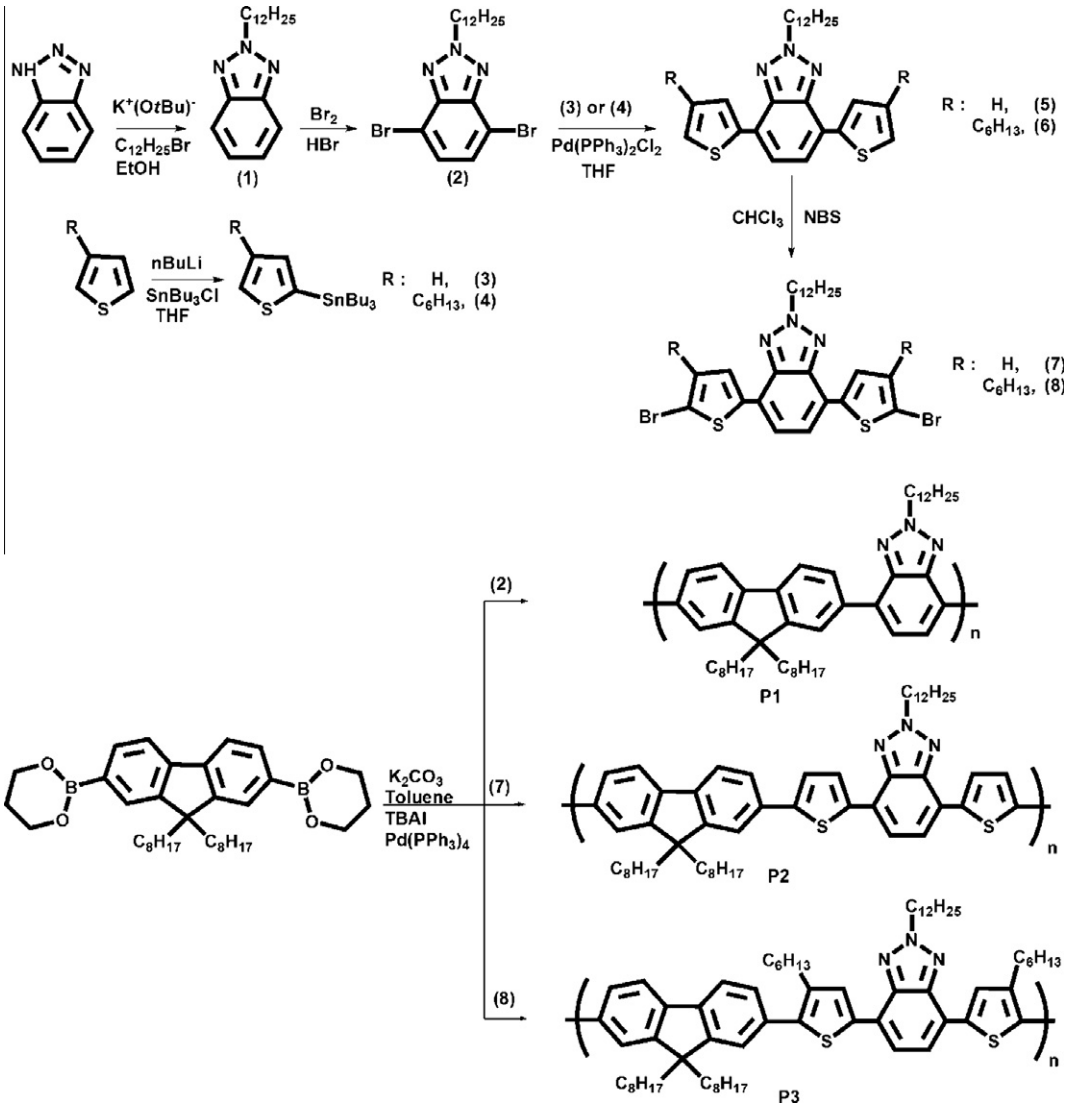

Scheme 1. Synthetic pathway for **P1**, **P2**, and **P3**.

TBT and **HTBT** were brominated by *N*-bromosuccinimide (NBS) in chloroform ($CHCl_3$). All polymers (**P1**, **P2**, and **P3**) were synthesized by Suzuki cross-coupling reactions [15]. Obtained polymers were purified by Soxhlet extraction using acetone and structurally characterized by ^1H NMR. All polymers are highly soluble in common organic solvents such as chloroform, dichloromethane, THF, and toluene. The average molecular weight (Mn) of **P1**, P2, and **P3** determined by gel permeation chromatography (GPC) using polystyrene as the standards is 5900, 6900, and45,000 g/mol, respectively, with relatively low polydispersity indexes. All the polymers showed excellent thermal stability with decomposition temperature (measured by TGA, 10 °C/min) of more than 350 °C. There was no transition observed up to 300 °C.

2.2. Cyclic voltammetry

For electrochemical characterization, polymers were dissolved in chloroform to a concentration of 5 mg/mL and spray coated on indium tin oxide (ITO) coated glass slides. The polymer films on ITO were subjected to cyclic voltammetry (CV) in ambient conditions to determine the redox potentials in 0.1 M tetrabutylammonium hexafluorophosphate ($TBAPF_6$)/acetonitrile (ACN) solutions at a scan rate of 50 mV/s. The potentials were swept between 1.5 and −2.4 V for **P1**, 1.4 and −2.3 for **P2** and 1.4 V and −2.1 V for **P3** versus Ag wire pseudo-reference electrode (50 mV versus Fc/Fc^+). Initially, polymer films were subjected to a repeated cycling to obtain electrochemically stable and reproducible doping–dedoping (Fig. 1).

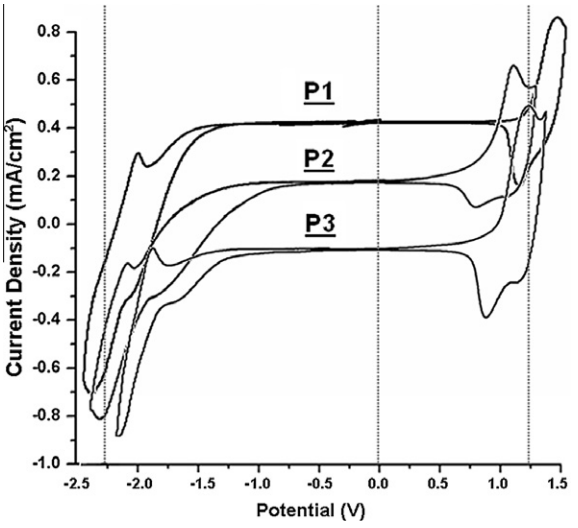

Fig. 1. Cyclic voltammograms for spray coated polymer films of **P1**, **P2**, and **P3** in ACN/$TBAPF_6$ solution at a scan rate of 50 mV/s.

P1 film revealed reversible redox couple at positive potentials pointed at 1.43 and 1.19 V versus Ag wire pseudo-reference electrode. Due to incorporation of electron donating thiophene rings in **P2** chains, polymer film showed lower redox potentials at (1.16 and 0.96 V) compared to those of **P1** versus the same reference electrode (Fig. 1). The highest oxidation potential was observed for **P1** among all as expected since it possesses electron poor structure relative to **P2** and **P3**.

True n-type doping properties of the polymers were investigated by CV which also enabled the determination of HOMO and LUMO levels for polymers electrochemically. Reversible doping/dedoping peaks confirmed that all polymers were both n-type dopable at negative potentials. Reduction of **P2** film was achieved at −2.17 V and the corresponding de-doping peak at −1.96 V which were −2.07/−1.8 V for **P3** and −2.35/−1.96 V for **P1**.

Due to their dual properties, HOMO/LUMO energy levels were calculated precisely from the onset potentials of p and n doping peaks from CV. The onset values were estimated by taking the intersection between the baseline and the tangent line drawn to the increasing part of the current. The reference electrode and all the results were subsequently calibrated to Fc/Fc^+ and the band energies were calculated relative to the vacuum level considering that the value of NHE is −4.75 eV versus vacuum. Table 1 summarizes the electrochemical data for polymers **P1**, **P2**, and **P3**. As seen from table, higher onset potentials for **P3** due to sharper p and n doping peaks than those of **P2** resulted in slightly higher HOMO energy and a wider electronic band gap. The electrochemical band gap values were calculated from the onset potentials as 2.56 and 2.68 eV for **P2** and **P3**, respectively. Calculated electrochemical band gaps were comparatively higher than the ones estimated from π–π^* transition due to the creation of free ions by means of applied potential [16].

In order to have a better understanding on structure–electronic properties relationship for **PFO** copolymers, they were compared with previously reported parent polymers **PFO**, **PTBT**, and **PHTBT** in terms of their HOMO/LUMO energy levels (Chart 1). π–π interaction between donor and acceptor determines the match between these units and plays a crucial role on the electronic properties of the resulting polymers since it influences the intramolecular charge transfer in these types of polymers [7a]. Fig. 2 shows that the addition of fluorene unit in **PTBT** did not

Table 1
Oxidation potentials and onset values for both p- and n-type doping, estimated HOMO–LUMO energies and band gaps of synthesized polymers **P1**, **P2**, and **P3**.

	Oxidation potential (V)		Reduction potential (V)		Band gap (eV)		Energy levels[a] (eV)	
	E_{ox}	E_{ox}^{onset}	E_{red}	E_{red}^{onset}	E_g^{ec}	E_g^{op}	HOMO	LUMO
P1	1.43	1.19	−2.35	−1.78	2.97	2.55	−5.94	−2.97
P2	1.16	0.96	−2.16	−1.60	2.56	2.16	−5.71	−3.15
P3	1.25	0.98	−2.10	−1.70	2.68	2.24	−5.73	−3.05

[a] Calculated from CV.

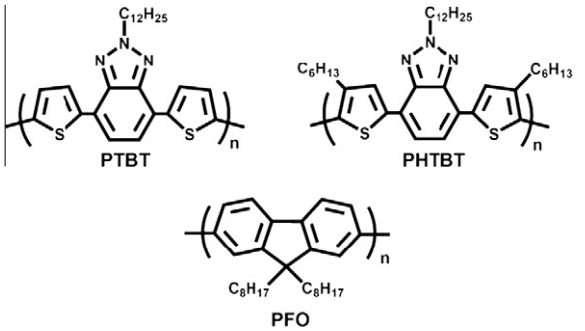

Chart 1. Chemical structures of related polymers.

significantly alter the electronic band gap of the resulting polymer **P2** (2.56 eV), but only lowered the HOMO–LUMO levels ca. 0.1 eV. Considering the energy levels of **P3**, LUMO level was intact upon addition of **PFO**, however; HOMO of the polymer was lowered due to the contribution of valence band (VB) of **PFO** and resulted in a higher electrochemical band gap (Fig. 2).

Although **PHTBT** has slightly lower band gap than **PTBT**, thiophene containing polymer **P2** revealed narrower band gap than that of its hexyl thiophene included analogue **P3**. This may be due to the steric interactions between the hexyl groups and the adjacent fluorene units. The same trend also is the case for benzothiadiazole bearing copolymers [18]. According to donor–acceptor approach, increasing donor strength should have raised the HOMO level while having less effect on LUMO energy. However, here both HOMO and LUMO levels were affected by incorporation of electron rich thiophene and hexyl thiophene units to **P1**.

2.3. Spectral properties

Neutral **P1**, **P2**, and **P3** films were spray coated on ITO coated glass slides from a solution of 3 mg/mL in chloroform. UV–vis–NIR spectra were recorded for corresponding polymer films in 0.1 M $TBAPF_6$/ACN solution upon gradually increased external bias. Coated films were subjected to subsequent redox cycling by CV to obtain electrochemical stability prior to spectroelectrochemical analysis. Fig. 4 exhibits that λ_{max} values for the π–π^* transitions for **P2** and **P3** were centered at 503 and 460 nm, respectively. Substitution of 9,9′-dioctyl fluorene units resulted in blue shifted absorption for polymers **P2** and **P3** compared to their previously studied parent polymers **PTBT** and **PHTBT**. Stepwise oxidation of the polymer films by applied external potentials resulted in a decrease in the π–π^* transitions and their lower energy transitions intensified at 715 and 1560 nm for both **P2** and **P3**. These absorbance bands in near-IR (NIR) region indicate the formation of lower energy charge carriers such as polarons and bipolarons. Visible polaronic absorbance for **P2** and **P3** allowed detection of different colored states upon stepwise oxidations. However, their electron poor homologue **P1** revealed blue shifted dominant wavelengths both in visible and in NIR regions (Fig. 3) which were consistent with electrochemical data. Electron deficient structure of **P1** complicated the formation of positive charge carriers on the polymer backbone upon oxidative doping. Thus, the neutral state absorption in the visible region (430 nm) did not reveal a significant depletion as **P2** and **P3** but hypsochromically shifted to 380 nm. Although the oxidation potential for **P1** was determined as 1.43 V, spectroelectrochemical data were recorded up to 1.3 V since at higher potentials no spectral change was observed. This indicates the limited formation of polaronic and bipolaronic bands for **P1** (Fig. 3).

Since neutral state absorptions for **P2** and **P3** are at around 400 nm and lower energy transition emerged at 700 nm, partially oxidized polymer films revealed green color for which these two absorption maxima are crucial. Further oxidation of polymer films resulted in blue color due to diminished π–π^* transition intensity.

Highly soluble polymers **P2** and **P3** were dissolved in toluene (8×10^{-3} mg/mL) and oxidatively doped by the stepwise addition of trifluoroacetic acid (TFA). TFA addition to solutions was continued until no spectral change was observed. As seen from the spectra (Figs. 4 and 5), initially neutral **P2** and **P3** have absorption maxima at 475 and 446 nm, respectively, in solution. Upon addition of

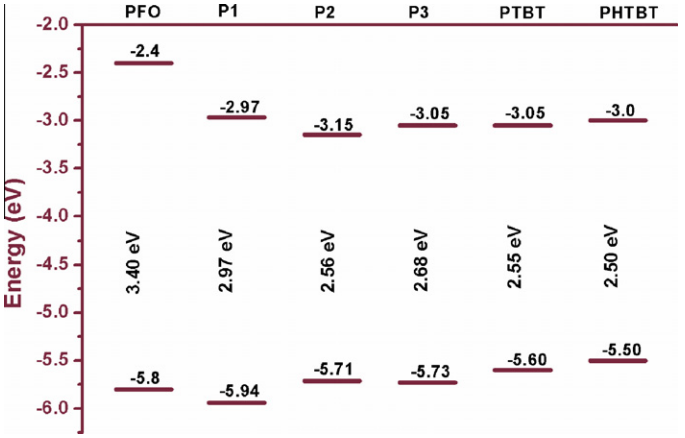

Fig. 2. HOMO/LUMO levels and band gaps of related polymers. Values for **PFO** [17], **PTBT** [13a], and **PHTBT** [13b] were taken from previous reports.

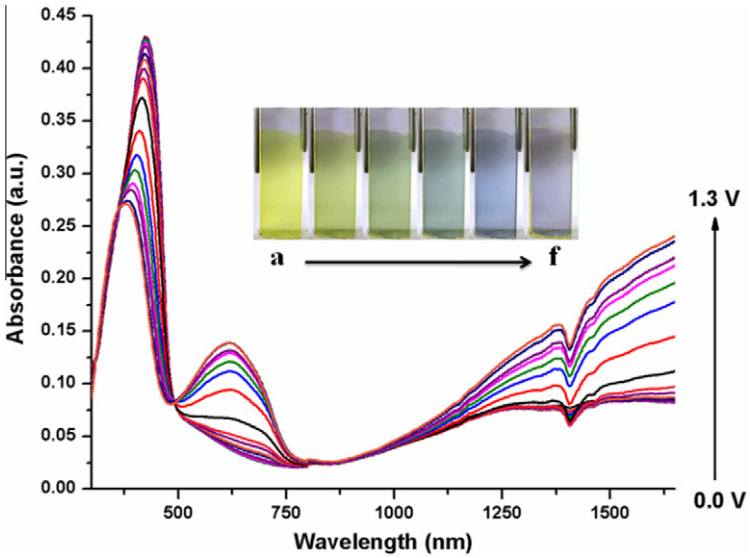

Fig. 3. Electrochemical p-type doping electronic absorption spectra of **P1** between 0.0 and 1.3 V with 0.1 V potential intervals.

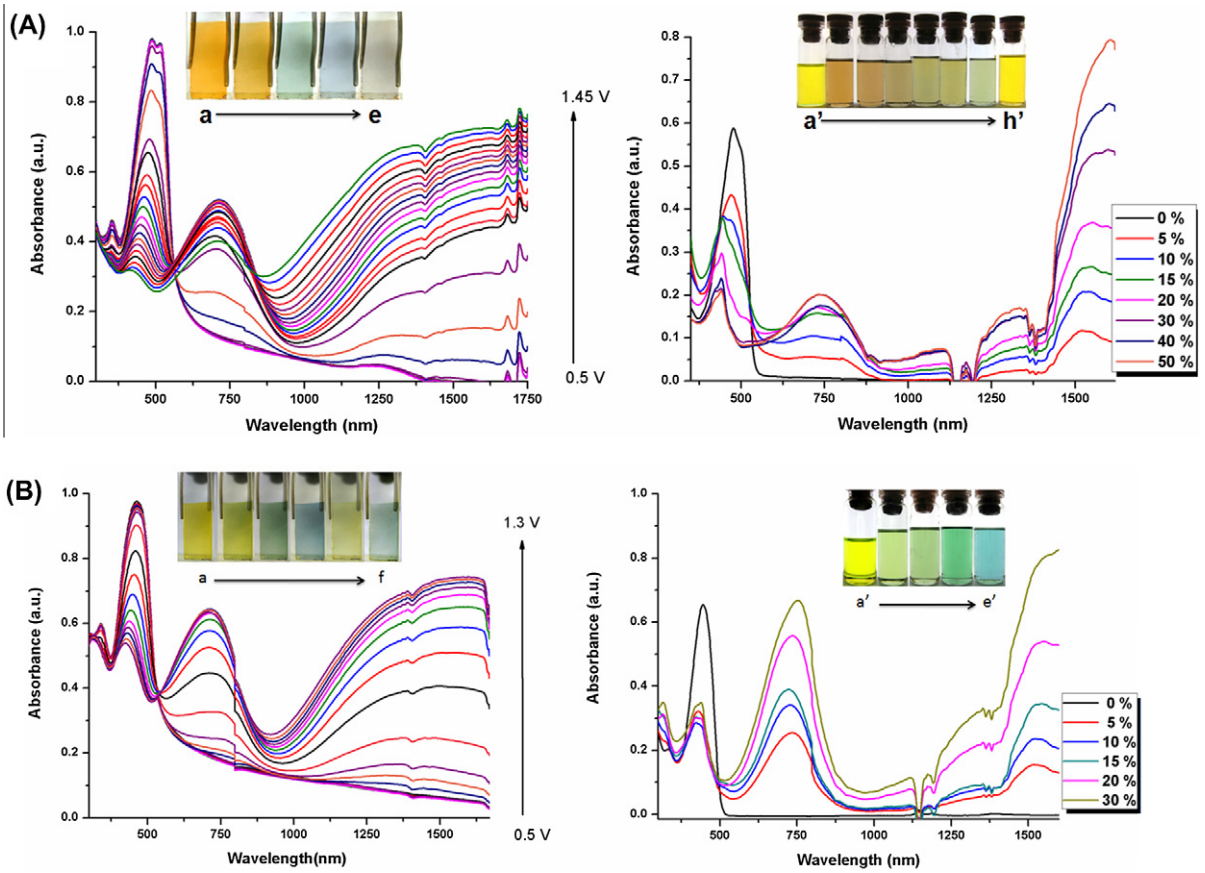

Fig. 4. (A) UV–vis–NIR spectra of **P2** in film form (left) and in toluene (right). (a) 0.5, (b) 0.8, (c)1.0, (d) 1.2, and (e) −2.16 V and (a′) 0%, (b′) 5%, (c′) 10%, (d′) 20%, (e′) 30%, (f′) 40% (g′) 50% TFA (v:v) and (h′) dedoped form with 1 mL TEA. (B) UV–vis–NIR spectra of **P3** in film form (left) and in toluene (right). (a) 0.5, (b) 0.8, (c) 1.0, (d) 1.2, (e) −2.0, and (f) −2.10 V and (a′) 0%, (b′) 5%, (c′) 10%, (d′) 20%, and (e′) 30% TFA (v:v).

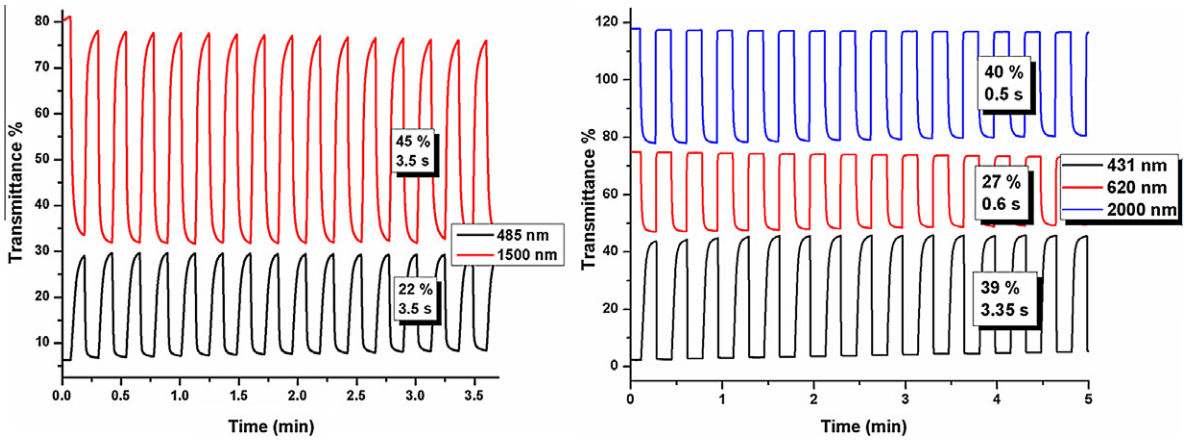

Fig. 5. Kinetic switching results in both visible and NIR regions for **P1** (right) and **P2** (left).

5% TFA (v:v) new absorption bands emerged at 750 and 1550 nm which are accompanied by a decrease in neutral state absorptions. The sharp peaks for the π–π^* transitions resulted in wider band gaps for polymers in solution than in film due to trapped dopant ions and the more dense polymer morphology in film form. The oxidative doping also resulted in color change in solutions. Neutral solutions of both polymers were yellow however upon the addition of TFA, the solution turned into green and blue as is shown as inset picture in Fig. 4[1] for **P2** and **P3**, respectively.

After doping, 1 mL of triethyl amine (TEA) was added to solutions which resulted in immediate appearance of the initial colors for both polymer solutions. This indicates the reversibility of solution doping process by adding TFA and pH responsive characters of polymers. It is worth noting that spectral responses of the polymers to stepwise oxidation were identical in both solution and thin film forms regardless of the doping or dopant type. Any color or spectral change was not observed by TFA addition to **P1** although reversible doping (both p and n) and de-doping were possible in thin film form electrochemically. This obviously indicates the effect of the presence of thiophene unit on solution doping process. Oxidation starts on electron rich thiophene heterocycle prior to charge transport along the conjugated polymer backbone (Fig. 4B).

Absorption spectra for **P2** revealed isosbestic point in thin film form which confirms the coexistence of discrete chromophores which is not taking place in solution. However, **P3** showed isosbestic point both in film and in solution indicating well-separated chromophores. That also eased the detection of different colors for **P3** solutions upon TFA addition in toluene.

The electrochemical stability as well as percent transmittance changes can be monitored by successive potential cycling of the polymer films in monomer-free solutions. Optical studies were carried out for polymers **P1** and **P2** in ACN/$TBAPF_6$ solution in order to observe the changes between their neutral and fully oxidized states upon applied external bias within 5 s time intervals. Percent transmittance changes were recorded for **P2** at its dominant wavelengths at 485 and 1500 nm. The polymer film revealed 22% optical contrast with a switching time of 3.5 s in visible region and 45% transmittance change (3.5 s) was recorded between doped and de-doped states in NIR region (Fig. 5). Although the switching times were relatively slow, the polymer film was stable upon repetitive cycles. Due to the high rigidity in **P3** films which stems from the long alkyl chains on both fluorene, thiophene and benzotriazole units, reasonable kinetic values could not be acquired. Since **P1** revealed a blue shift for high energy transition upon oxidation, it showed relatively high optical contrast for the one observed at 431 nm (Fig. 5).

3. Conclusion

Multicolored electrochromic alternating **PFO** and BTz copolymers **P1**, **P2** and **P3** were synthesized and investigated in terms of their electronic and optical properties. Convenient HOMO and LUMO levels, band gaps, and strong absorptions in the visible region suggest that they should be tested for various optoelectronic applications. Solution doping of **P2** and **P3** revealed multicolored solutions which make them pH responsive chromophores that may be used in different applications in due course. Reported properties prove that fluorene and BTz-based copolymers are multipurpose materials which will be subject of further research interest in near future.

4. Experimental

4.1. General

All chemicals were used without further purification as they were purchased from commercial sources. All reactions were carried out under argon atmosphere unless otherwise mentioned. Electrochemical studies were performed in a three-electrode cell consisting of an indium tin oxide doped glass slide (ITO) as the working electrode,

[1] For interpretation of color in Fig. 4, the reader is referred to the web version of this article.

platinum wire as the counter electrode, and Ag wire as the reference electrode under ambient conditions using a Voltalab 50 potentiostat. The value of normal hydrogen electrode (NHE) was taken as −4.75 eV [19]. ^{1}H and ^{13}C NMR spectra were recorded in $CDCl_3$ on Bruker Spectrospin Avance DPX-400 Spectrometer. Chemical shifts were given in ppm downfield from tetramethylsilane. Varian Cary 5000 UV–vis spectrophotometer was used to perform the spectroelectrochemical studies of the polymer. Average molecular weight was determined by gel permeation chromatography (GPC) using a Polymer Laboratories GPC 220. Differential scanning calorimetry (DSC) and thermal gravimetric analysis (TGA) were performed on Perkin Elmer Diamond DSC and Perkin Elmer Pyris 1 TGA. Trifluoroacetic acid (TFA) used for solution doping was 99%. 2-Dodecylbenzotriazole [13], 4,7-dibromo-2-dodecyl benzotriazole [13], tributyl(thiophen-2-yl) stannane [20], tributyl(4-hexylthiophen-2-yl)stannane [21], 4,7-bis(thien-2-yl) 2-dodecyl-benzo[1,2,3]triazole (TBT) [13a], 4,7-bis(3-hexylthien-5-yl) 2-dodecyl-benzo[1,2,3]triazole (**HTBT**) [13b] were synthesized according to previously published procedures.

4.2. Synthesis of 4,7-bis(5-bromothien-2-yl)-2-dodecylbenzo[1,2,3]triazole (7)

Two hundred milligrams of TBT (0.44 mmol) and 190 mg of *N*-bromosuccinimide (1.07 mmol) were stirred in 100 mL of $CHCl_3$ at room temperature by preventing the mixture from light exposure. After 12 h, solvent was removed under reduced pressure and crude product was filtered over silica by $CHCl_3$ to obtain 250 mg (93%) 7 as yellow solid. ^{1}H NMR (400 MHz, $CDCl_3$, δ): 7.72 (d, J = 5.6 Hz, 2H), 7.44 (s, 2H), 7.04 (d, J = 6.0 Hz, 2H), 4.72 (t, J = 7.0 Hz, 2H), 2.10 (m, 2H), 1.32–1.17 (m,18H), 0.80 (t, J = 6.9 Hz, 3H); ^{13}C NMR (100 MHz, $CDCl_3$-d_6, δ): 144.4, 142.2, 140.4, 127.3, 125.8, 123.9, 123.0, 57.1, 32.2, 30.3, 29.9, 29.8, 29.7, 29.6, 29.5, 29.3, 26.9, 22.9, 14.4. MS (m/z): 608 [M+].

4.3. Synthesis of 4,7-bis(5-bromo-4-hexylthien-2-yl)-2-dodecylbenzo[1,2,3]triazole (8)

Bromination of **HTBT** was performed with the same procedure explained for TBT above. Two hundred milligrams of **HTBT** (0.32 mmol) and 138 mg of *N*-bromosuccinimide (0.77 mmol) were used to obtain 235 mg (94.4%) 8 as yellow solid. ^{1}H NMR (400 MHz, $CDCl_3$, δ): 7.69 (s, 2H), 7.41 (s, 2H), 4.77 (t, J = 8.0 Hz, 2H), 2.61(t, J = 8.0 Hz, 4H) 2.16 (m, 2H), 1.65 (m, 4H), 1.41–1.24 (m, 26H), 0.91–0.85 (m, 9H); ^{13}C NMR (100 MHz, $CDCl_3$, δ): 143.1, 141.7, 139.2, 127.5, 123.0, 122.0, 110.1, 56.8, 32.0, 31.7, 30.0, 29.8, 29.7, 29.6, 29.5, 29.4, 29.1, 29.0, 26.7, 22.7 14.1. MS (m/z): 778 [M+].

4.4. General route for synthesis of *P1*, *P2,* and *P3*

Dibromo compound (1 mol equivalent), 2,2′-(9,9-dioctyl-9H-fluorene-2,7-diyl)bis(1,3,2-dioxaborinane) (1 mol equivalent), $Pd(PPh_3)_4$ (5 mol%), and tetrabutylammonium iodide ($N(Bu)_4I$, 1 mol%) were added into a degassed mixture of potassium carbonate (K_2CO_3, 2 M in H_2O), toluene (3:2 toluene:water). The mixture was refluxed at 115–120 °C for 48 h under argon. Solvent was removed and extracted with $CHCl_3$:H_2O twice to remove alkali solution. Combined organic layers were dried over anhydrous $MgSO_4$ and evaporated under reduced pressure. The crude product was washed with methanol and Soxhlet extracted by acetone to obtain corresponding polymer. **P1**: ^{1}H NMR (400 MHz, $CDCl_3$, δ): 8.20 (benzotriazole), 8.1 (fluorene), 7.9 (fluorene), 7.7 (fluorene), 4.8 (N–CH_2), 2.2 (C–CH_2), 1.6–0.7 (pendant alkyl chains). GPC: Mn: 5900, Mw: 10,600, PDI: 1.8, **P2**: ^{1}H NMR (400 MHz, $CDCl_3$, δ): 8.1 (benzotriazole), 8.8–8.5 (fluorene, thiophene), 7.4 (thiophene), 4.8 (N–CH_2), 2.2 (C–CH_2), 1.6–0.7 (pendant alkyl chains). GPC: Mn: 6900, Mw: 17,500, PDI: 2.5, **P3**: 1H NMR (400 MHz, $CDCl_3$, δ): 8.00 (benzotriazole), 7.8 (fluorene), 7.6 (fluorene), 7.4 (fluorene, thiophene), 4.9 (N–CH_2), 2.8 (CH_2), 2.2 (C–CH_2), 1.8–0.7 (pendant alkyl chains). GPC: Mn: 45,000, Mw: 183,000 PDI: 4.1.

Acknowledgements

The authors thank TUBA for financial support.

References

[1] (a) G. Sonmez, H.B. Sonmez, C.K.F. Shen, R.W. Jost, Y. Rubin, F. Wudl, A processable green polymeric electrochromic, Macromolecules 38 (2005) 669–675;
(b) M.A. Invernale, Y. Ding, D.M.D. Mamangun, G.A. Yavuz, Preparation of conjugated polymers inside assembled solid-state devices, Sotzing Adv. Mater. 22 (2010) 1379–1382;
(c) A.L. Dyer, M.R. Craig, J.E. Babiarz, K. Kiyak, J.R. Reynolds, Orange and red to transmissive electrochromic polymers based on electron-rich dioxythiophenes, Macromolecules 43 (2010) 4460–4467;
(d) P.M. Beaujuge, S.V. Vasilyeva, S. Ellinger, T.D. McCarley, J.R. Reynolds, Unsaturated linkages in dioxythiophene–benzothiadiazole donor–acceptor electrochromic polymers: the key role of conformational freedom, Macromolecules 42 (2009) 3694–3706;
(e) A. Durmus, G.E. Gunbas, P. Camurlu, L. Toppare, A neutral state green polymer with a superior transmissive light blue oxidized state, Chem. Commun. (2007) 3246–3248;
(f) G.E. Gunbas, A. Durmus, L. Toppare, Could green be greener? Novel donor–acceptor-type electrochromic polymers: towards excellent neutral green materials with exceptional transmissive oxidized states for completion of RGB color space, Adv. Mater. 20 (2008) 691–695.
[2] (a) A.C. Grimsdale, K.L. Chan, R.E. Martin, P.G. Jokisz, A.B. Holmes, Synthesis of light-emitting conjugated polymers for applications in electroluminescent devices, Chem. Rev. 109 (2009) 897–1091;
(b) H. Tsuji, C. Mitsui, Y. Sato, E. Nakamura, Bis(carbazolyl)benzodifuran: a high-mobility ambipolar material for homojunction organic light-emitting diode devices, Adv. Mater. 21 (2009) 3776–3779;
(c) S. Beaupre, P.T. Boudreault, M. Leclerc, Solar-energy production and energy-efficient lighting: photovoltaic devices and white light-emitting diodes using poly(2,7-fluorene), poly(2,7-carbazole), and poly(2,7-dibenzosilole) derivatives, Adv. Mater. 22 (2010) E6–E27;
(d) K.T. Kamtekar, H.L. Vaughan, B.P. Lyons, A.P. Monkman, S.U. Pandya, M.R. Bryce, Synthesis and spectroscopy of poly(9,9-dioctylfluorene-2,7-diyl-co-2,8-dihexyldibenzothiophene-*S*,*S*-dioxide-3,7-diyl)s: solution processable, deep-blue emitters with a high triplet energy, Macromolecules 43 (2010) 4481–4488;
(e) H.P. Rathnayake, A. Cirpan, P.M. Lahti, F.E. Karasz, Optimizing LED luminescent properties in 2,7-bis(phenylethenyl)fluorenes, Chem. Mater. 18 (2006) 560–566.
[3] (a) S. Gunes, H. Neugebauer, N.S. Sariciftci, Conjugated polymer-based organic solar cells, Chem. Rev. 107 (2007) 1324–1338;
(b) J.C. Bijleveld, A.P. Zoombelt, S.G.J. Mathijssen, M.M. Wienk, M. Turbiez, D.M. Leeuw, R.A.J. Janssen, Poly(diketopyrrolopyrrole–terthiophene) for ambipolar logic and photovoltaics, J. Am. Chem. Soc. 131 (2009) 16616–16617;
(c) S.H. Park, A. Roy, S. Beaupre, S. Cho, N. Coates, J.S.M.D. Moses, M. Leclerc, K. Lee, A.J. Heeger, Bulk heterojunction solar cells with

internal quantum efficiency approaching 100%, Nat. Photon. 3 (2009) 297–302;
(d) A.P. Zoombelt, M. Fonrodona, M.M. Wienk, A.B. Sieval, J.C. Hummelen, R.A.J. Janssen, Photovoltaic performance of an ultrasmall band gap polymer, Org. Lett. 11 (2009) 903–906;
(e) Samuel C. Price, Andrew C. Stuart, W. You, Low band gap polymers based on benzo[1,2-*b*:4,5-*b*′]dithiophene: rational design of polymers leads to high photovoltaic performance, Macromolecules 43 (2010) 4609–4612;
(f) Q. Zhang, A. Cirpan, T.P. Russell, T. Emrick, Novel donor–acceptor polythiophene–perylene diblock copolymers: synthesis and photovoltaic characterization, Macromolecules 42 (2009) 1079–1082.

[4] (a) S. Allard, M. Forster, B. Souharce, H. Thiem, U. Scherf, Organic semiconductors for solution-processable field-effect transistors (OFETs), Angew. Chem. Int. Ed. 47 (2008) 4070–4098;
(b) P.M. Beaujuge, W. Pisula, H.N. Tsao, S. Ellinger, K. Mullen, J.R. Reynolds, Tailoring structure–property relationships in dithienosilole–benzothiadiazole donor–acceptor copolymers, J. Am. Chem. Soc. 131 (2009) 7514–7515;
(c) I. McCulloch, M. Heeney, C. Bailey, K. Genevicius, I. MacDonald, M. Shkunov, D. Sparrowe, S. Tierney, R. Wagner, W. Zhang, M.L. Chabinyc, R.J. Kline, M.D. McGehee, M.F. Toney, Liquid-crystalline semiconducting polymers with high charge-carrier mobility, Nat. Mater. 5 (2006) 328–333;
(d) L.L. Chua, J. Zaumseil, J.F. Chang, E.C.W. Ou, P.K.H. Ho, H. Sirringhaus, R.H. Friend, General observation of n-type field-effect behaviour in organic semiconductors, Nature 434 (2005) 194–199.

[5] Y.J. Cheng, S.H. Yang, C.S. Hsu, Synthesis of conjugated polymers for solar cell applications, Chem. Rev. 109 (2009) 5868–5923.

[6] (a) U. Salzner, M.E. Kose, Does the donor–acceptor concept work for designing synthetic metals? 1. Theoretical investigation of poly(3-cyano-3′-hydroxybithiophene), J. Phys. Chem. B 106 (2002) 9214–9220;
(b) A. Berlin, G. Zotti, S. Zechinn, G. Schiavon, B. Vercelli, A. Zanelli, New low-gap polymers from 3,4-ethylenedioxythiophene-bis-substituted electron-poor thiophenes. The roles of thiophene, donor–acceptor alternation, and copolymerization in intrinsic conductivity, Chem. Mater. 16 (2004) 3667–3676;
(c) J. Roncali, Synthetic principles for bandgap control in linear pi-conjugated systems, Chem. Rev. 97 (1997) 173–206.

[7] (a) T. Yamamoto, Z.H. Zhou, T. Kanbara, M. Shimura, K. Kizu, T. Maruyama, Y. Nakamura, T. Fukuda, B.L. Lee, N. Ooba, S. Tomaru, T. Kurihara, T. Kaino, K. Kubota, S. Sasaki, π-Conjugated donor–acceptor copolymers constituted of π-excessive and π-deficient arylene units. Optical and electrochemical properties in relation to CT structure of the polymer, J. Am. Chem. Soc. 118 (1996) 10389–10399;
(b) S. Akoudad, J. Roncali, Electrogenerated poly(thiophenes) with extremely narrow bandgap and high stability under n-doping cycling, Chem. Commun. (1998) 2081;
(c) X. Zhang, S.A. Jenekhe, Electroluminescence of multicomponent conjugated polymers. 1. Roles of polymer/polymer interfaces in emission enhancement and voltage-tunable multicolor emission in semiconducting polymer/polymer heterojunctions, Macromolecules 33 (2000) 2069–2082;
(d) C.C. Liu, F.C. Tsai, C.C. Chang, K.H. Hsieh, J.J. Lin, W.C. Chen, Theoretical analysis on the electronic properties of coplanar conjugated poly(azomethines), Polymer 46 (2005) 4950–4957.

[8] P.M. Beaujuge, J.R. Reynolds, Color control in pi-conjugated organic polymers for use in electrochromic devices, Chem. Rev. 110 (2010) 268–320.

[9] F.C. Krebs, Electrochromic displays: the new black, Nat. Mater. 7 (2008) 766–767.

[10] (a) B. Friedel, C.R. McNeill, N.C. Greenham, Influence of alkyl side-chain length on the performance of poly(3-alkylthiophene)/polyfluorene all-polymer solar cells, Chem. Mater. 22 (2010) 3389–3398;
(b) R. Kroon, M. Lenes, J.C. Hummelen, P.W.M. Blom, B. Boer, Small bandgap polymers for organic solar cells (polymer material development in the last 5 years), Polym. Rev. 48 (2008) 531–582;
(c) P. Herguth, X. Jiang, M.S. Liu, A.K.Y. Jen, Highly efficient fluorene- and benzothiadiazole-based conjugated copolymers for polymer light-emitting diodes, Macromolecules 35 (2002) 6094–6100;
(d) P. Herguth, X. Jiang, M.S. Liu, A.K.Y. Jen, Poly(fluorene-co-benzothiadiazole)s: effect of structure, molecular weight and polydispersity on their performance in polymer light-emitting diodes, Proc. SPIE 4800 (2003) 138–147;
(e) A. Cirpan, L. Ding, F.E. Karasz, Optical and electroluminescent properties of polyfluorene copolymers and their blends, Polymer 46 (2005) 811–817;
(f) A. Cirpan, L. Ding, F.E. Karasz, Efficient light emitting diodes from polyfluorene copolymer blends, Synth. Met. 150 (2005) 195–198.

[11] (a) M.H. Chen, J. Hou, Z. Hong, G. Yang, S. Sista, L.M. Chen, Y. Yang, Efficient polymer solar cells with thin active layers based on alternating polyfluorene copolymer/fullerene bulk heterojunctions, Adv. Mater. 21 (2009) 4238–4242;
(b) F. Huang, L. Hou, H. Shen, J. Jiang, F. Wang, Hongyu. Zhen, Y. Cao, Synthesis, photophysics, and electroluminescence of high-efficiency saturated red light-emitting polyfluorene-based polyelectrolytes and their neutral precursors, J. Mater. Chem. 15 (2005) 2499–2507;
(c) S. Ko, R. Mondal, C. Risko, J.K. Lee, S. Hong, M.D. McGehee, J.L. Bredas, Z. Bao, Tuning the optoelectronic properties of vinylene-linked donor–acceptor copolymers for organic photovoltaics, Macromolecules 43 (2010) 6685–6698.

[12] (a) J.K. Lee, H.H. Fong, A.A. Zakhidov, G.E. McCluskey, P.G. Taylor, M.S. Berrios, H.D. Abruna, A.B. Holmes, G.G. Malliaras, C.K. Ober, Semiperfluoroalkyl polyfluorenes for orthogonal processing in fluorous solvents, Macromolecules 43 (2010) 1195–1198;
(b) M. Sun, Q. Niu, R. Yang, W. Yang, J. Peng, Y. Cao, Fluorene-based copolymers for color-stable blue light-emitting diodes, Eur. Polym. J. 43 (2007) 1916–1922.

[13] (a) A. Balan, D. Baran, G. Gunbas, A. Durmus, F. Özyurt, L. Toppare, One polymer for all: benzotriazole containing donor–acceptor type polymer as a multi-purpose material, Chem. Commun. (2009) 6768–6770;
(b) A. Balan, G. Gunbas, A. Durmus, L. Toppare, Donor–acceptor polymer with benzotriazole moiety: enhancing the electrochromic properties of the "Donor Unit", Chem. Mater. 20 (2008) 7510–7513;
(c) G.A. Çetin, A. Balan, A. Durmus, G. Gunbas, L. Toppare, A new p- and n-dopable selenophene derivative and its electrochromic properties, Org. Electron. 10 (2009) 34–41.

[14] (a) A. Balan, D. Baran, N.S. Sariciftci, L. Toppare, Electrochromic device and bulk heterojunction solar cell applications of poly 4,7-bis(2,3-dihydrothieno[3,4-b][1,4]dioxin-5-yl)-2-dodecyl-2H-benzo[1,2,3]triazole (PBEBT), Sol. Energy Mater. Sol. Cells 94 (2010) 1797–1802;
(b) D. Baran, A. Balan, S. Celebi, B.M. Esteban, H. Neugebauer, N.S. Sariciftci, L. Toppare, Processable multipurpose conjugated polymer for electrochromic and photovoltaic applications, Chem. Mater. 22 (2010) 2978–2987;
(c) Z. Zhang, B. Peng, B. Liu, C. Pan, Y. Li, Y. He, K. Zhou, Y. Zou, Copolymers from benzodithiophene and benzotriazole: synthesis and photovoltaic applications, Polym. Chem. 1 (2010) 1441–1447.

[15] N. Miyaura, A. Suzuki, Palladium-catalyzed cross-coupling reactions of organoboron compounds, Chem. Rev. 95 (1995) 2457–2483.

[16] C.Q. Ma, M. Fonrodona, M.C. Schikora, M.M. Wienk, R.A.J. Janssen, P. Bauerle, Solution-processed bulk heterojunction solar cells based on monodisperse dendritic oligothiophenes, Adv. Funct. Mater. 18 (2008) 3323–3331.

[17] S.A. Haque, S. Koops, N. Tokmoldin, J.R. Durrant, J. Huang, D.D.C. Bradley, E. Palomares, A multilayered polymer light-emitting diode using a nanocrystalline metal-oxide film as a charge-injection electrode, Adv. Mater. 19 (2007) 683–687.

[18] W. Li, R. Qin, M. Andersson, F. Li, C. Zhang, B. Li, Z. Liu, Z. Bo, F. Zhang, Tailoring side chains of low band gap polymers for high efficiency polymer solar cells, Polymer 51 (2010) 3031–3038.

[19] E.R. Kötz, H. Neff, K.J. Müller, A UPS, XPS and work function study of emersed silver, platinum and gold electrodes, Electroanal. Chem. 215 (1986) 331–344.

[20] S.S. Zhu, T.M. Swager, Conducting polymetallorotaxanes: metal ion mediated enhancements in conductivity and charge localization, J. Am. Chem. Soc. 119 (1997) 12568–12577.

[21] Q. Hou, Q. Zhou, Y. Zhang, W. Yang, R. Yang, Y. Cao, Synthesis and electroluminescent properties of high-efficiency saturated red emitter based on copolymers from fluorene and 4,7-di(4-hexylthien-2-yl)-2,1,3-benzothiadiazole, Macromolecules 37 (2004) 6299–6305.

Organic Electronics 12 (2011) 210–218

Contents lists available at ScienceDirect

Organic Electronics

journal homepage: www.elsevier.com/locate/orgel

A new approach to the Schiff base-substituted oligophenols: The electrochromic application of 2-[3-thienylmethylene]aminophenol based co-polythiophenes

İsmet Kaya *, Mehmet Yıldırım, Aysel Aydın

Çanakkale Onsekiz Mart University, Faculty of Sciences and Arts, Department of Chemistry, 17020 Çanakkale, Turkey

ARTICLE INFO

Article history:
Received 10 August 2010
Received in revised form 16 September 2010
Accepted 31 October 2010
Available online 18 November 2010

Keywords:
Electrocopolymerization
Electrochromism
Schiff base substituted
Oxidative polymerization
Polythiophene

ABSTRACT

Two new copolymers were synthesized by electrochemical polymerization of 2-[3-thienylmethylene]aminophenol (2,3-TMAP) and poly-2-[3-thienylmethylene]aminophenol (P-2,3-TMAP) with thiophene (Th) and the obtained thiophene copolymers were examined as electrochromic materials. Electro copolymerization reactions of the compounds were performed in acetonitrile (AN)/boron trifluoride ethyl etherate (BF_3EtE) solvent mixture (9:1, v/v) where $LiClO_4$ utilized as the supporting electrolyte. After electro copolymerization reaction, obtained electrochromic films deposited on ITO glass plates, 2,3-TMAP-co-Th and P-2,3-TMAP-co-Th, were investigated as spectroelectrochemically. The new electrochromic materials derived from Schiff base substituted-phenol/oligophenols are red colored at low potentials and blue colored at high potentials. Electro copolymerization mechanism was identified. Spectroelectrochemical monitoring showed good absorption recovery for P-2,3-TMAP-co-Th, while absorbance decrease was observed for 2,3-TMAP-co-Th during the repeated potential scans. Suitable potential range for operating the device from red to blue was found to be between 0 and +1.4 V. P-2,3-TMAP-co-Th showed 12–13% transmittance changes at applied potentials and the response times were 3.1 and 4.1 s for 476 and 800 nm, respectively. As a result P-2,3-TMAP-co-Th may be good candidate for electrochromic devices and can be thought as a feasible nominee for anodically coloring electrochromic layers in ECDs.

© 2010 Elsevier B.V. All rights reserved.

1. Introduction

Electrochromism is defined as reversible change in optical properties of a material like absorbance, transmittance, color, etc. [1]. Several kinds of electrochromic materials have been synthesized and characterized, so far [2]. A few SNS (thiophene–pyrrole–thiophene) derived electrochemical devices were also synthesized and improved as color-switching materials with different colors in oxidized and reduced states. Several color changes of SNS derivatives were observed like dark purple-blue [3], yellow-green-violet [4], and yellow-blue [5], etc. Polythiophene derivatives and its copolymer kinds have been widely chosen in improving such electrochromic devices. Polythiophenes are an important representative class of conducting polymers that can be used as electrical conductors [6]. Synthesis of new polythiophene derivatives with improved conductivity and processing properties is an important part of conducting polymer research [7]. Polythiophenes, a versatile class of conjugated polymers, are still of growing interest due to their potential applications in the development of new materials such as photovoltaics [8,9], electrochromic devices [10,11] and energy storage [12,13]. Processability and easy modification of monomer that alters properties of the conducting polymers (CP) have, therefore, attracted the attention of both academia

* Corresponding author. Tel.: +90 286 218 00 18; fax: +90 286 218 05 33.
E-mail address: kayaismet@hotmail.com (İ. Kaya).

1566-1199/$ - see front matter © 2010 Elsevier B.V. All rights reserved.
doi:10.1016/j.orgel.2010.10.020

and industries. Conducting polymers generally reveal an optical absorption band in the visible region due to their extended delocalization of the p electrons along the polymer backbone. Upon doping, charge carriers are formed in the conjugated backbone, namely polaron and bipolarons, which results in a change in the optical spectra [14]. One of the most important characteristics exhibited by the polymers of polythiophene family is their enhanced electrochromism upon application of a small voltage. A variety of conjugated polymers have colors both in the oxidized and reduced states since the band gap is in the visible region. After oxidation, the intensity of the π–π^* transition decreases, and two low energy transitions emerge to produce a second color. Therefore, there are many absorption changes in the visible region of the spectrum making them useful in the construction of electrochromic devices [15]. Polymers with imine (HC═N) linkages are isoelectronic with the HC═CH linked derivatives and result in significant difference in the electronic and opto electronic properties. Tsai et al. found that thiophene based poly(azomethine)s had lower band gaps than the phenylene based similar kinds [16]. Also, variation of the backbone ring and donor/acceptor side group on the phenylene ring significantly affected the electronic properties (like band gap) of the poly(azomethine)s. Schiff base substituted carbazole derivatives combined with thiophene moieties have been copolymerized electrochemically in the presence of thiophene and a clearly color change from yellow to green was observed when the potential increased from 0 up to 1.6 V [17]. Some kinds of imine coupled pyrrole monomers have been also employed as the comonomer agents to obtain new electrochromic materials via electrochemical copolymerization with pyrrole [18]. Ali et al. have investigated optical radio-chromic properties of polyaniline and found that imine (HC═N) linkages between the aniline units at the emeraldine form are responsible for the green color [19]. Other polyazomethine derivatives are still needed to examine as electrochromic materials. In all mentioned studies imine linkages were placed in polymer backbones. However, at the present study we synthesized new polythiophene derivatives with conjugated side phenylene/polyphenylene units bound with imine linkages. These conjugated side groups were expected to increase the conjugation length of polythiophene resulting in new electrochromic properties.

Oligophenol derivatives of Schiff bases have been previously synthesized and investigated as semi-conductive polymers by Kaya and co-workers [20–23]. Obtained Schiff base-substituted oligophenols were also found to be electroactive materials [24]. Also, obtained polymers have been studied with their optical and thermal properties as well as anti microbial activity [25]. However, their processibility as electrochromic devices are still interest. For this need we investigated the electrochromic application of newly synthesized imine-bounded phenol and oligophenol (2,3-TMAP and P-2,3-TMAP) containing electropolymerisable thiophene moiety as the side group. Electro copolymerization was carried out in the presence of thiophene. Potential range used in the experiments was 0–1.4 V. According to the obtained results the synthesized 2,3-TMAP and P-2,3-TMAP copolymers are red colored at 0 V and blue colored at 1.4 V. Resultantly, we demonstrated that Schiff base substituted oligophenol derivatives could also be used in construction of new electrochromic devices (ECDs).

2. Experimental

2.1. Chemicals

2-aminophenol, methanol, DMSO, KOH, acetonitrile (AN) and hydrochloric acid (HCl, 37%) were supplied from Merck Chemical Co. Thiophene-3-carboxyaldehyde and thiophene (Th) were supplied from Aldrich. Boron trifluoride ethyl etherate (BF_3EtE) and sodium hypo chloride (NaOCl) (30% aqueous solution) were supplied from Fluka and Paksoy Chemical Co. (Turkey), respectively.

2.2. Synthesis of 2-[3-thienylmethylene]aminophenol (2,3-TMAP)

2-[3-Thienylmethylene]aminophenol (2,3-TMAP) was prepared by the condensation of thiophene-3-carboxyaldehyde (1.22 g, 0.01 mol) with 2-aminophenol (1.37 g, 0.01 mol) in methanol (30 ml) achieved by boiling the mixture under reflux for 2 h (Scheme 1). The precipitated Schiff base was filtered, recrystallized from methanol and dried in a vacuum desiccator at 80 °C [20].

UV–vis (λ_{max}) (DMSO): 254, 268 and 343 nm. FT-IR (cm^{-1}): (OH aromatic) 3297; (C–H aromatic) 3083, 3035; (–CH═N–) 1615, (C═C phenyl) 1595, 1580, 1480; (C–S) 785. ^{1}H NMR (DMSO-d_6): δ ppm, 9.93 (s, 1H, –OH), 8.68 (s, 1H, –CH═N–), 7.81 (s, 1H, Ar–Ha), 7.69 (d, 1H, Ar–Hb), 7.02 (d, 1H, Ar–Hc), 7.25 (d, 1H, Ar–Hd), 7.19 (t, 1H, Ar–He), 6.90 (t, 1H, Ar–Hf), 7.39 (d, 1H, Ar–Hg).

2.3. Oxidative polymerization of 2,3-TMAP

P-2,3-TMAP was synthesized through oxidative polycondensation of 2-[3-thienylmethylene]aminophenol using NaOCl as the oxidant [23–25]. 2,3-TMAP (0.203 g, 0.001 mol) was dissolved in an aqueous solution of KOH (10%, 0.001 mol) and placed into a 50 ml three-necked round-bottom flask which was fitted with a condenser, thermometer, stirrer and an addition funnel containing 2 ml of NaOCl aqueous solution (30% by weight). After heating up to 60 °C, NaOCl was added drop by drop over about 20 min. Reaction was maintained for 5 h. Then, the reaction mixture was cooled at the room temperature, 0.001 mol HCl (37%) added for neutralization, and kept for 24 h at the room temperature for precipitation of the polymer. The mixture was filtered, washed with hot water (3×25 ml) and methanol (2×20 ml) to separate the mineral salts and unreacted monomers, respectively. The obtained polymer dried in a vacuum oven at 60 °C for 24 h. The reaction design is given in Scheme 2.

UV–vis (λ_{max}) (DMSO): 260, and 438 nm. FT-IR (cm^{-1}): (OH aromatic) 3228; (C–H aromatic) 3100; (–CH═N–) 1605, (C═C phenyl) 1566, 1516, 1497; (C–S) 747. ^{1}H NMR (DMSO-d_6): δ ppm, 10.02 (s, 1H, –OH), 9.20 (s, 1H,

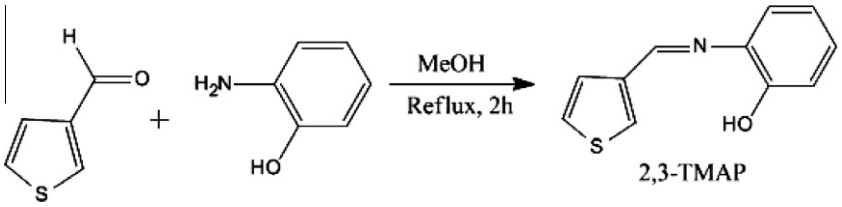

Scheme 1. Synthesis of 2-[3-thienylmethylene]aminophenol (2,3-TMAP).

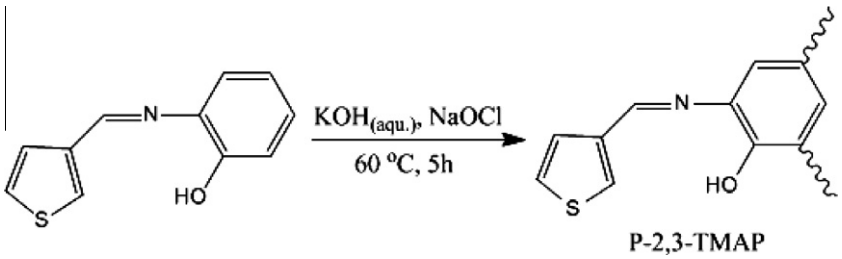

Scheme 2. Synthesis of poly-2-[3-thienylmethylene]aminophenol (P-2,3-TMAP).

–CH=N–), 8.79 (s, 1H, Ar–Ha), 8.61 (d, 1H, Ar–Hb), 7.62 (d, 1H, Ar–He), 7.33 (d, 1H, Ar–Hc), 6.88 (d, 1H, Ar–Hd).

2.4. Electrochemical copolymerization of 2,3-TMAP and P-2,3-TMAP with thiophene

Cyclic voltammetry (CV) measurements were carried out with a CHI 660 C Electrochemical Analyzer (CH Instruments, Texas, USA) at a potential scan rate of 200 mV/s. CV was employed in order to assay the electroactivity of the compounds and to determine the oxidation–reduction peak potentials. Electro polymerizations were carried out in the presence of thiophene. The system consists of a CV cell containing indium tin oxide (ITO)-coated glass plate as the working electrode, platinum wire as the counter electrode, and Ag wire as the reference electrode. The measurements were carried out in $LiClO_4$ (0.1 M)/acetonitrile (AN:BF_3EtE) (9:1, v/v) solvent mixture at the room temperature under argon atmosphere [5]. Electrocopolymerizations were carried out as follows: 2,3-TMAP or

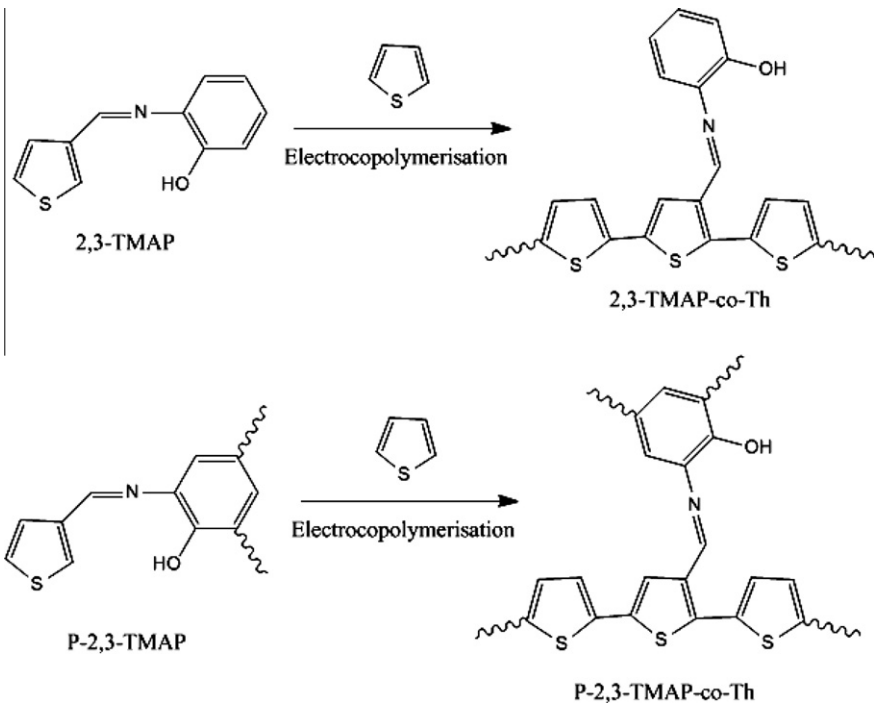

Scheme 3. Electro polymerization reaction of 2,3-TMAP and P-2,3-TMAP in the presence of thiophene (Th).

P-2,3-TMAP (1 g/L) was dissolved in 10 ml 0.1 M AN/$LiClO_4$:BF_3EtE (9:1, v/v) and placed into a CV cell. Four milligrams of thiophene was added into the cell. Electro polymerizations were run by repeated electrochemical scanning of the solutions between 0 and 1400 mV (scan rate: 200 mV/s; cycle number: 24 and 50 for 2,3-TMAP and P-2,3-TMAP, respectively). Resulting copolymer films were washed with AN to remove $LiClO_4$ and BF_3EtE. Polythiophene film was also deposited on ITO glass plate for comparison by similar method (cycle number: 9, scan rate: 200 mV/s) [26]. Electro polymerization reactions of 2, 3-TMAP and P-2,3-TMAP and their possible structures are given in Schemes 3 and 4, respectively.

2.5. Spectroelectrochemistry

In order to carry out the spectroelectrochemical experiments, the copolymer films were used which were electrochemically deposited on ITO-coated glasses. Spectroelectrochemical and electrochromic measurements were made in AN/$LiClO_4$ using Ag wire as the reference and a Pt wire as the auxiliary electrodes. The data obtained from the cyclic voltammetry measurements were used for spectroelectrochemical measurements of the copolymer films [27]. These measurements were carried out to consider absorption spectra of these copolymer films under applied voltages. The spectroelectrochemical cell includes a quartz cuvette, a Ag wire (RE), Pt wire counter electrode (CE) and polymer film coated ITO/glass as transparent working electrode (WE). These measurements were carried out in the 0.1 M $LiClO_4$ as supporting electrolyte in AN.

2.6. Solubility and characterization techniques

The solubility tests of 2,3-TMAP and P-2,3-TMAP were done in different solvents by using 1 mg sample and 1 ml solvent at 25 °C. 2,3-TMAP is completely soluble in organic solvents such as methanol, acetone, acetonitrile, THF, ethyl acetate, chloroform, DMSO, and H_2SO_4 but it was partly soluble in toluene. 2,3-TMAP was insoluble in heptane. P-2,3-TMAP was dark brown in powder form and was completely soluble in strong polar solvents like DMSO and H_2SO_4. However, P-2,3-TMAP was partly soluble in methanol, acetonitrile, toluene, acetone, ethyl acetate, chloroform, THF whereas insoluble in heptane.

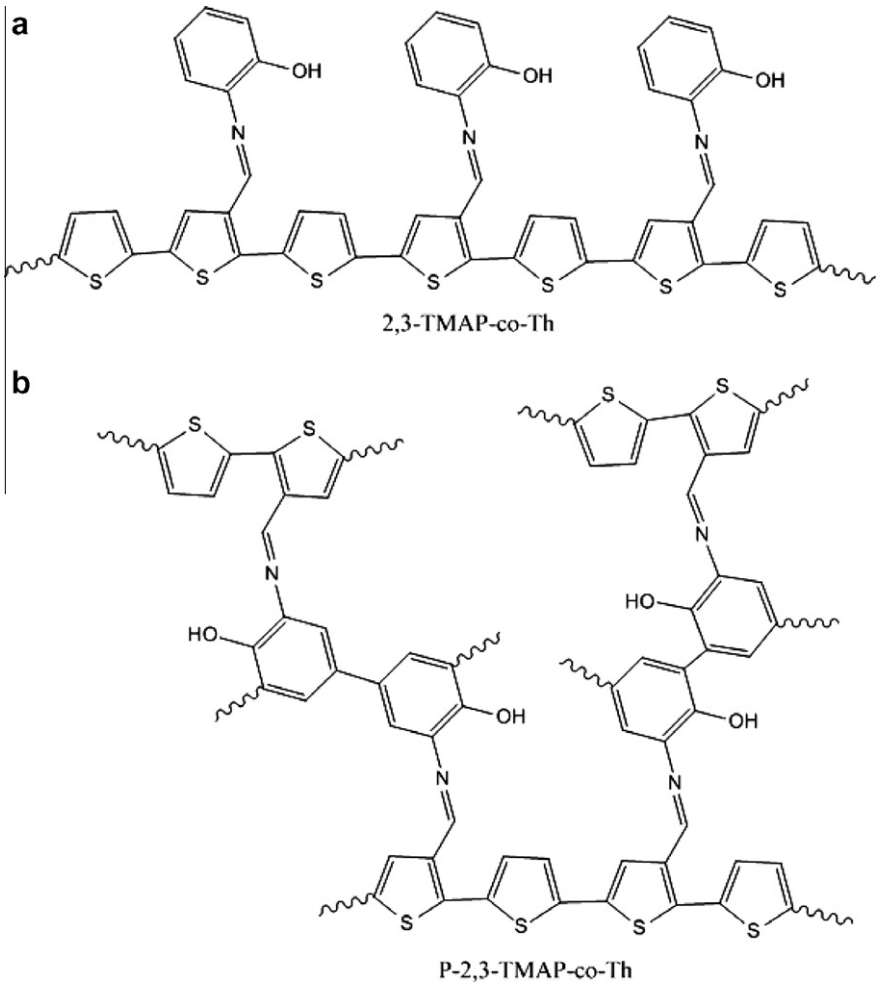

Scheme 4. Possible structure of 2,3-TMAP-co-Th (a) and P-2,3-TMAP-co-Th (b) including iminophenol as the side groups.

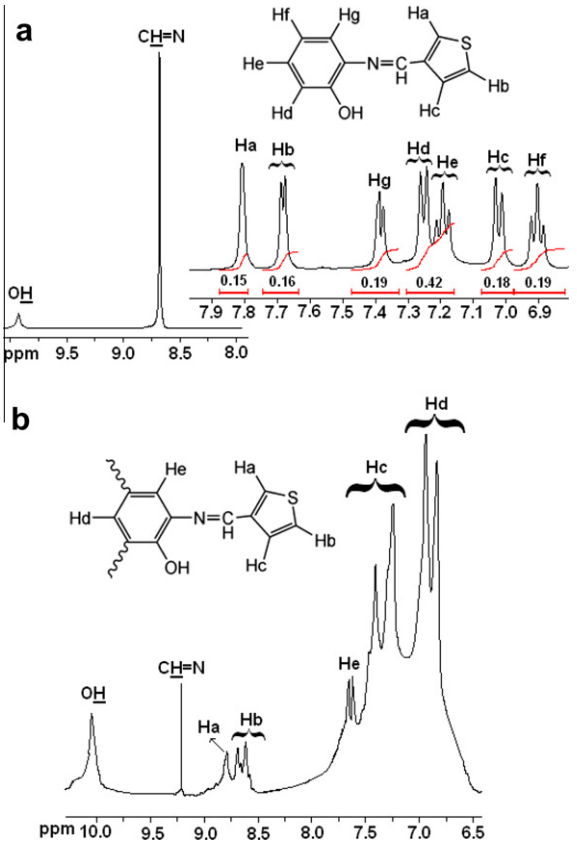

Fig. 1. ^{1}H NMR spectra of 2,3-TMAP (a) and P-2,3-TMAP (b).

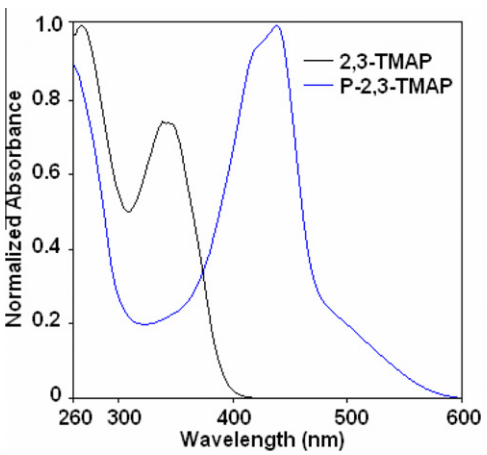

Fig. 2. Normalized absorption spectra of 2,3-TMAP and P-2,3-TMAP.

The infrared spectra were measured by Perkin Elmer FT-IR Spectrum one. The FT-IR spectra were recorded using universal ATR sampling accessory (4000–550 cm^{-1}). ^{1}H NMR spectra (Bruker AC FT-NMR spectrometer operating at 400 and 100.6 MHz, respectively) were also recorded by using deuterated DMSO-d_6 as a solvent at 25 °C. The tetramethylsilane was used as internal standard. The number-average molecular weight (M_n), weight-average molecular weight (M_w) and polydispersity index (PDI) were determined by size exclusion chromatography (SEC) techniques of Shimadzu Co. For SEC investigations a SGX (100 Å and 7 nm diameter loading material) 3.3 mm i.d. × 300 mm column was used; eluent: DMF (0.4 ml/min), polystyrene standards. A refractive index detector (RID) and UV detector were used to analyze the products at 25 °C.

3. Results and discussion

3.1. Structures of the synthesized compounds

The structures of the synthesized compounds are confirmed by FT-IR, UV–vis, and ^{1}H NMR analyses. According to the FT-IR spectra of 2,3-TMAP and P-2,3-TMAP imine bonds appear at 1615 and 1605 cm^{-1}, respectively. Also, phenolic O–H stretch and C–S stretch vibrations of thiophene rings are observed at 3297 and 785; and 3228 and 747 cm^{-1}, respectively. After the polycondensation reaction the peaks broaden and shift to lower wave number values. ^{1}H NMR spectra are given in Fig. 1. As seen in Fig. 1, at the NMR spectrum of P-2,3-TMAP the peaks indicating the aromatic protons broaden due to the polyconjugated structure [24]. At the ^{1}H NMR spectrum of 2,3-TMAP –OH and CH=N protons are observed at 9.93 and 8.68 ppm, respectively. These values shift up to 10.02 and 9.20 ppm at the ^{1}H NMR spectrum of P-2,3-TMAP, respectively. As compared of the both spectra, 2,3-TMAP polymerizes mainly by C–C coupling mechanism. Kaya et al. have been previously studied the coupling selectivity of the oligophenol derivatives. According to the mentioned studies phenol derivatives could be polymerized by C–O–C and/or C–C coupling mechanisms. Kaya et al. were determined the C–C/C–O–C coupling ratio using the integration area of imine and OH protons at the ^{1}H NMR spectra. The ^{1}H NMR results show that the polymerization of 2,3-TMAP mainly proceeds from *ortho* and *para* positions of phenolic –OH group by C–C coupling [24].

Normalized absorption spectra of the chemically synthesized compounds are shown in Fig. 2. R band of the absorption spectrum of 2,3-TMAP shifts from 342 to 439 nm, after the oxidative polymerization. Optical band

Table 1
The number-average molecular weight (M_n), weight-average molecular weight (M_w), polydispersity index (PDI), and % values of P-2,3-TMAP.

Detector	Molecular weight distribution parameters										
	Total			Fraction I				Fraction II			
	M_n	M_w	PDI	M_n	M_w	PDI	%	M_n	M_w	PDI	%
RI	17,460	18,810	1.077	59,790	60,390	1.010	18	8170	9680	1.185	82
UV	34,330	36,660	1.068	59,170	59,800	1.011	46	13,170	16,950	1.287	54

gap values are determined from the absorption edges as in the literature [28]. Optical band gaps of 2,3-TMAP and P-2,3-TMAP are calculated as 3.13 and 2.17 eV, respectively. These results clearly indicate that the polyphenol derivative of 2,3-TMAP has lower band gap than its monomer due to its polyconjugated structure.

According to the SEC chromatograms P-2,3-TMAP has two separate fractions and the results are given in Table 1. Total values of number-average molecular weight (M_n), weight-average molecular weight (M_w), and polydispersity index (PDI) of P-2,3-TMAP are calculated to be 17,460, 18,810 g mol^{-1}, and 1.077; and 34,300, 36,660 g mol^{-1}, and 1.068, using RI and UV detectors, respectively. According to the obtained results from RID P-2,3-TMAP has nearly 86–92 repeated units, whereas 168–180 repeated units according to the results obtained from UV detector. These values also confirm the polymer structure of P-2,3-TMAP.

3.2. Cyclic voltammetry

Thiophene derivatives readily undergo one-electron oxidation to form a radical cation (polaron) if the α-positions are unsubstituted. Continuous oxidation subsequently affords higher ordered oligomers by a radical coupling mechanism that ultimately results in polymer formation [29]. Cyclic voltammogram of P-2,3-TMAP in the presence of thiophene in AN/$LiClO_4$ solvent/electrolyte couple indicates two consecutive reversible oxidation peaks at 0.45 and 0.99 V which reverse at 0.26 V when the potential range between 0 and +1.3 V is scanned (Fig. 3c). Also, at the same potential scan range of 2,3-TMAP only one reversible oxidation peak at 0.95 V is observed that reverses at 0.56 V (Fig. 3b) [30]. Since the reduction potential values are sensitive to intramolecular and intermolecular electron transfer. Because of the same effect in the anodic area, reduction peak were also influenced by thiophene [17]. The formation of an electroactive film on the electrode is observed with the oxidation peaks combination at the potential of 0.61 V (see Fig. 3c). Upon consecutive cycle formation, a new oxidation peak appeared at 0.61 V due to the oxidation of the polymer. As the number of cycle increases, there is an increase in the intensity of the current. This is due to increase in the active area of the working electrode owing to electroactive polymer coating on the electrode [31].

Electrochemical homopolymerisations of 2,3-TMAP and P-2,3-TMAP without any active comonomer agent (like thiophene) in AN/$LiClO_4$ solvent/electrolyte mixture were also tried in various scan rates and concentrations. But the polymerizations failed. This means an electrochemically active comonomer agent is certainly needed. In order to investigate the CV behavior of the copolymer, we performed CV studies in the presence of thiophene. There is a drastic changes between the voltammograms of thiophene, 2,3-TMAP, and P-2,3-TMAP. As seen in Fig. 3, at the voltammogram of the polythiophene an increasing oxidation peak at the potential of 0.74 V is observed (Fig. 3a). However, at the voltammograms of 2,3-TMAP and P-2,3-TMAP new increasing oxidation peaks are at 0.95 and 0.61 V, respectively. Fig. 3 clearly presents the change in the anodic peak currents as a function of the potential [5]. The peak current increases are recorded during the

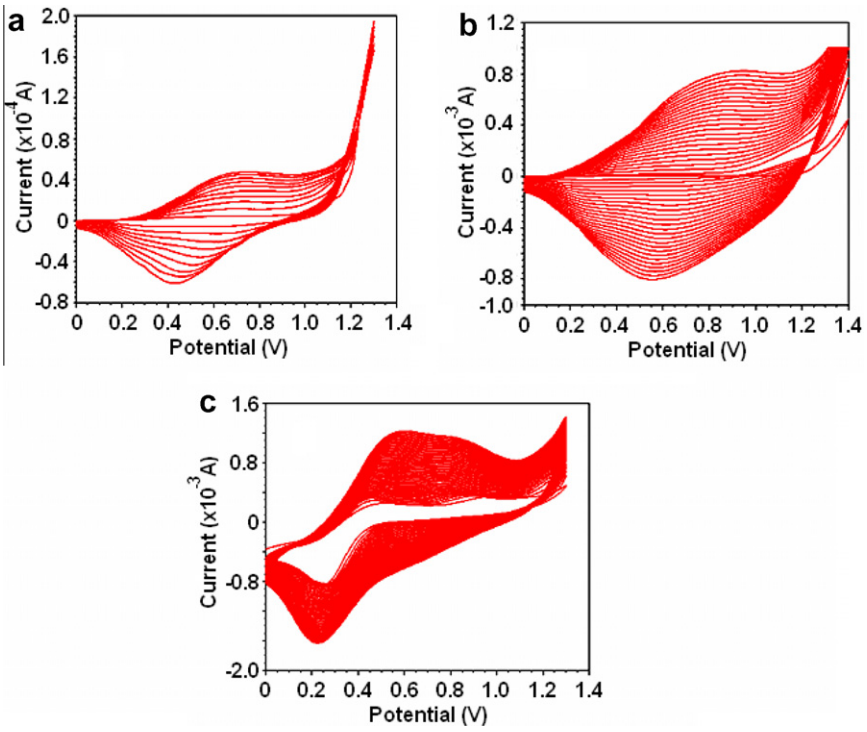

Fig. 3. Cyclic voltammograms of repeated potential scan of polythiophene (a), 2,3-TMAP (b), and P-2,3-TMAP (c) in the presence of thiophene (scan rate: 200 mV/s, cycle numbers: 9, 24, and 50, respectively).

formation of homo-polythiophene and the copolymers at the different potentials. This confirms the copolymer structures. The reaction mechanism of electro copolymerization of 2,3-TMAP with thiophene can be proposed as shown in Scheme 5 [32,33]. There are two different kinds containing electropolymerisable thiophene units in the electro

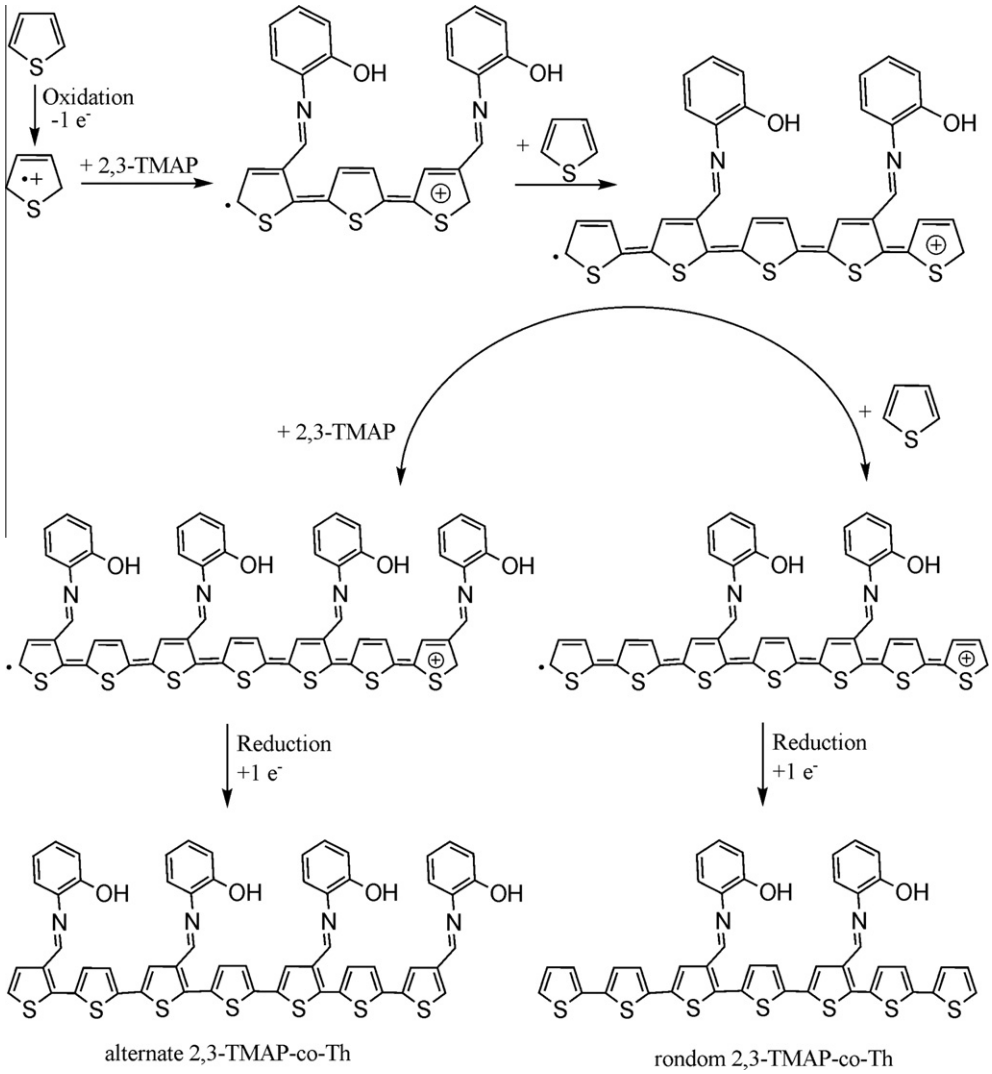

Scheme 5. Possible electro copolymerization mechanism of 2,3-TMAP in the presence of Th.

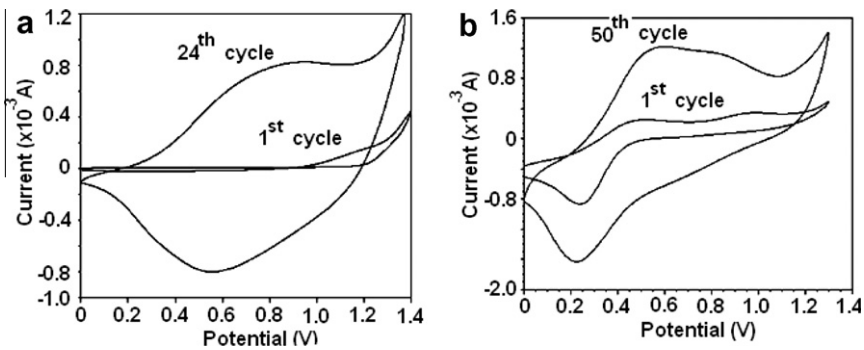

Fig. 4. The first and the last cycles of 2,3-TMAP (a) and P-2,3-TMAP (b) in the presence of thiophene.

polymerization cell: pure thiophene and thiophene substituted iminophenol/imino(polyphenol) (2,3-TMAP and P-2,3-TMAP). As examined the structures of 2,3-TMAP and P-2,3-TMAP the electronic attractive effect of azomethine on the thiophene ring increases the oxidation potential compared with that of thiophene. As a result, thiophene is expected to be firstly oxidized species and the polymerization starts by forming the polaron structure (radical cation) of thiophene. Moreover, the obtained polymer could have random or alternate copolymer structure (see Scheme 5). The first and the last cycles of 2,3-TMAP and P-2,3-TMAP are also given in Fig. 4a and b which is obtained by the electro copolymerization in the presence of thiophene.

3.3. Electro-optical properties

Spectroelectrochemistry is the best way of examining the changes in optical properties of a polymer on ITO upon applied potentials. It also provides information on the properties of conjugated polymers, such as band gap (E_g) and the intergap states that appear upon doping. Spectroelectrochemical measurements were carried out between the potential range of 0 V and +1.4 V in AN/$LiClO_4$ (0.1 M) solution. The λ_{max} for the π–π^* transitions in neutral states of 2,3-TMAP-co-Th and P-2,3-TMAP-co-Th at 0 V are found to be 437 and 476 nm, respectively. These λ_{max} values are higher than those of 2,3-TMAP and P-2,3-TMAP which indicate the higher conjugated-copolymer structures. Figs. 5a and 6a indicate the changes of the absorption spectra of 2,3-TMAP-co-Th and P-2,3-TMAP-co-Th at various applied potentials. The 3D optoelectrochemical spectrum of P-2,3-TMAP-co-Th between 0 and 1.4 V is also shown as insert figure of Fig. 6. As the copolymer devices get oxidized, the intensities of the π–π^* transitions decrease while the charge carrier bands at about 800–900 nm increase in intensities due to polaron formation [34].

3.4. Electrochromic switching and the stabilities

In order to carry out the spectrelectrochemical measurements a repeated scan mode of cyclic voltammetry coupled with optical spectroscopy method is used for 10 cycles scan. Potential scan range is 0–1.4 V which the colors clearly differ. Scan rate was chosen as 280 mV/s and the results were in cycle completions in a 10 s-time periods. The graphs are given in Figs. 5 and 6b. Measurements are carried out using two wavelengths in which the absorption intensities clearly change. For this purpose λ_{max} values of the copolymers and 800 nm are chosen. During the

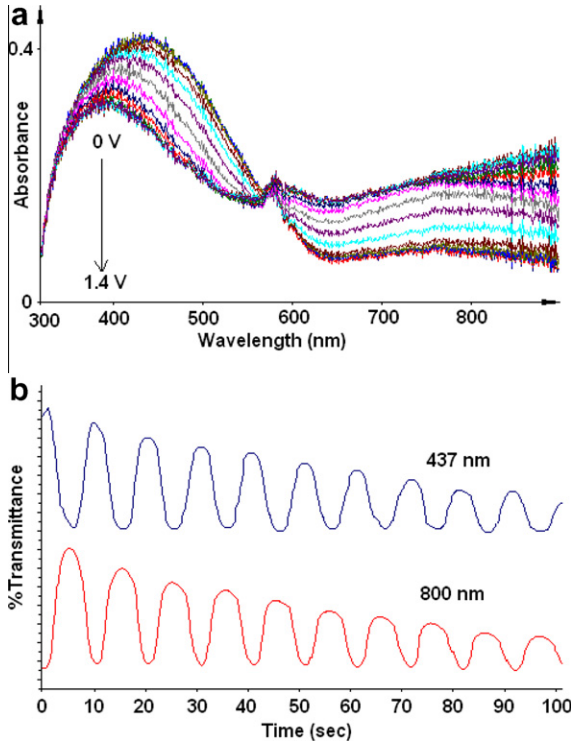

Fig. 5. (a) Optoelectrochemical spectrum of 2,3-TMAP-co-Th in the presence of 0.1 M $LiClO_4$ in AN and (b) electrochromic switching, optical absorbance monitored for 2,3-TMAP at 437 and 800 nm in the presence of 0.1 M $LiClO_4$ in AN.

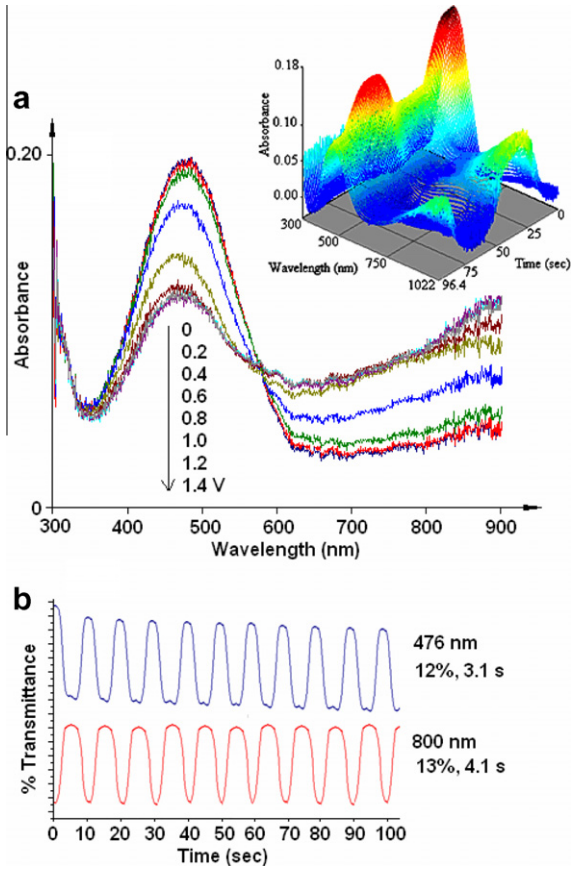

Fig. 6. (a) Optoelectrochemical spectrum of P-2,3-TMAP-co-Th in the presence of 0.1 M $LiClO_4$ in AN (insert: 3D optoelectrochemical spectrum of P-2,3-TMAP-co-Th at applied potentials between 0 and 1.4 V, scan rate: 100 mV/s) and (b) electrochromic switching, optical absorbance monitored for P-2,3-TMAP at 476 and 800 nm in the presence of 0.1 M $LiClO_4$ in AN.

switching experiment, the λ_{max} values are measured as 437 and 476 nm for the 2,3-TMAP-co-Th and P-2,3-TMAP-co-Th, respectively. The polymer film was deposited on ITO-coated glass slides under constant potential conditions, as mentioned above. The absorbances are then monitored at λ_{max} while the polymer and monomer are switched between 0 V and +1.4 V. As seen in Fig. 5b, during the repeated potential scan absorption intensities of 2,3-TMAP slowly decrease indicating the low absorption recovery at applied potentials. On the other hand, as seen in Fig. 6b P-2,3-TMAP-co-Th has good absorption recovery at applied potentials which indicates the percentage transmittance changes ($\Delta T\%$) of 12% and 13% for 476 and 800 nm, respectively. The stability between the redox states during the several scans is the most important property for an electroactive polymer to be useful in construction of new electrochromic devices [34]. Response time of P-2,3-TMAP-co-Th from the neutral (0.0 V) to oxidized (1.4 V) states are found to be 3.1 and 4.1 s for two wavelengths, respectively. For electrochromic applications, the ability of the material to exhibit a noteworthy color change is important. The synthesized electrochemical copolymers coated on ITO-glass exhibit red colors at the neutral states and blue colors at the oxidized states.

4. Conclusion

A new Schiff base and its oligophenol derivatives which contain electropolymerisable thiophene side groups were synthesized and characterized via FT-IR, ^{1}H NMR, UV–vis, and SEC analyses. Optical band gaps of 2,3-TMAP and P-2,3-TMAP were found as 3.13 and 2.17 eV. The copolymers of the synthesized materials were prepared in the presence of thiophene potentiostatically in AN:BF_3EtE (9:1, v/v) using $LiClO_4$ (0.1 M) as electrolyte. Electrocopolymerisation reactions were maintained by repeating potential scans between 0 and 1.4 V. Obtained electrochromic films deposited on ITO glass plates, 2,3-TMAP-co-Th and P-2,3-TMAP-co-Th, were investigated as spectroelectrochemically and monitored at two wavelengths in which the absorption intensities clearly change. For this purpose λ_{max} values of the copolymers (437 and 476 nm) and 800 nm were chosen. Obtained results showed that the new electrochromic materials derived from thiophene substituted-iminophenol/oligophenols were red colored at low potentials and blue colored at high potentials. However, on the contrary of P-2,3-TMAP-co-Th, spectroelectrochemical monitoring of 2,3-TMAP-co-Th showed an absorbance decrease during the repeated potential scans which may recover by changing the experimental conditions like copolymerization ratio. Suitable potential range for operating the device from red to blue was found to be between 0 and +1.4 V. Stable absorption recovery of P-2,3-TMAP-co-Th could make the new material appropriate for construction of novel electrochromic devices. P-2,3-TMAP-co-Th show 12–13% transmittance changes at applied potentials and the response times were 3.1 and 4.1 s for 476 and 800 nm, respectively.

References

[1] M.S. Ak, M. Ak, M. Güllü, L. Toppare, Eur. Polym. J. 43 (2007) 3452.
[2] E. Şahin, P. Çamurlu, L. Toppare, V.M. Mercore, I. Cianga, Y. Yagci, Polym. Int. 54 (2005) 1599.
[3] M. Ak, C. Tanyeli, I.M. Akhmedov, L. Toppare, Thin Solid Films 516 (2008) 4334.
[4] A. Cihaner, F. Algı, J. Electroanal. Chem. 614 (2008) 101.
[5] E. Yıldız, P. Çamurlu, C. Tanyeli, I. Akhmedov, L. Toppare, J. Electroanal. Chem. 612 (2008) 247.
[6] M. Krompiec, S. Krompiec, H. Ignasiak, M. Lapkowski, P. Kus, L. Stanek, R. Penczek, S. Lis, K. Staninski, M. Sajewicz, K. Gebarowska, Synth. Met. 158 (2008) 831.
[7] A. Iraqi, A. Irvin, J. Walton, J. Crayston, Synth. Met. 84 (1997) 377.
[8] S. Glenis, G. Horowitz, G. Tourillon, F. Garnier, Thin Solid Films 111 (1984) 93.
[9] H. Koezuka, A. Tsumura, T. Ando, Synth. Met. 18 (1987) 699.
[10] F. Garnier, G. Tourillon, M. Gazard, J.C. Dubois, J. Electroanal. Chem. 148 (1983) 299.
[11] K. Kaneto, K. Yoshino, Y. Inuishi, Jpn. J. Appl. Phys. Part 2 22 (1983) L412.
[12] K. Kaneto, K. Yoshino, Y. Inuishi, Jpn. J. Appl. Phys. Part 2 22 (1983) L567.
[13] T. Yamamoto, J. Chem. Soc. Chem. Commun. 4 (1981) 187.
[14] K. Fesser, A.R. Bishop, D.K. Campbell, Phys. Rev. B 27 (1983) 4804.
[15] P. Çamurlu, L. Toppare, J. Macromol. Sci. Pure Appl. Chem. 43 (2006) 449.
[16] F.C. Tsai, C.C. Chang, C.L. Liu, W.C. Chen, S.A. Jenekhe, Macromolecules 38 (2005) 1958.
[17] S. Koyuncu, İ. Kaya, F.B. Koyuncu, E. Özdemir, Synth. Met. 159 (2009) 1034.
[18] S. Tarkuc, E. Sahin, L. Toppare, D. Colak, I. Coanga, Y. Yagci, Polymer 47 (2006) 2001.
[19] M.A. Ali, E. Saion, A.A. Al-Zahrany, Y. Noorhana, K.M. Dahlan, A. Kassım, K.A. Rabaeh, M.H. Hamzah, J. Eng. Sci. Technol. 5 (2010) 244.
[20] İ. Kaya, A. Aydın, e-Polymers 071 (2008) 1.
[21] İ. Kaya, A. Bilici, Polimery 52 (2007) 827.
[22] İ. Kaya, A. Bilici, J. Appl. Polym. Sci. 104 (2007) 3417.
[23] İ. Kaya, M. Yıldırım, Eur. Polym. J. 43 (2007) 127.
[24] İ. Kaya, M. Yıldırım, M. Kamacı, Eur. Polym. J. 45 (2009) 1586.
[25] İ. Kaya, H.O. Demir, A.R. Vilayetoğlu, Synth. Met. 126 (2002) 183.
[26] O. Turkarslan, M. Ak, C. Tanyeli, I.M. Akhmedov, L. Toppare, J. Polym. Sci. Part A: Polym. Chem. 45 (2007) 4496.
[27] P. Wagner, P.H. Aubert, L. Lutsen, D. Vanderzande, Electrochem. Commun. 4 (2002) 912.
[28] K. Colladet, M. Nicolas, L. Goris, L. Lutsen, D. Vanderzande, Thin Solid Films 451 (2004) 7.
[29] S.A.P. Guarìn, W.G. Skene, Mater. Lett. 61 (2007) 5102.
[30] C. Begnn, J.V. Grazulevicius, P. Strohriegl, J. Simmerer, D. Haarer, Macromol. Chem. Phys. 195 (1994) 2353.
[31] M. Jadamiec, M. Lapkowski, M. Matlengiewicz, A. Brembilla, B. Henry, L. Rodehuser, Electrochim. Acta 52 (2007) 6146.
[32] T. Anjos, A. Charlton, S.J. Coles, A.K. Croft, M.B. Hursthouse, M. Kalaji, P.J. Murphy, S.J. Roberts-Bleming, Macromolecules 42 (2009) 2505.
[33] F. Alakhras, R. Holze, J. Appl. Polym. Sci. 107 (2008) 1133.
[34] A. Cihaner, F. Algı, Electrochim. Acta 54 (2008) 786.

Organic Electronics 12 (2011) 219–225

Contents lists available at ScienceDirect

Organic Electronics

journal homepage: www.elsevier.com/locate/orgel

Threshold voltage and turn-on voltage in organic transistors: Sensitivity to contact parasitics

L. Giraudet *, O. Simonetti

Université de Reims Champagne Ardenne, LMEN, Moulin de la Housse, BP1039, 51687 Reims Cedex 02, France

ARTICLE INFO

Article history:
Received 24 March 2010
Received in revised form 30 September 2010
Accepted 6 November 2010
Available online 18 November 2010

Keywords:
Organic transistors
Threshold voltage
Turn-on voltage
Non-linear injection
Modelling
Fermi level pinning

ABSTRACT

Threshold voltage and turn-on voltage of organic field effect transistors are very sensitive to the fabrication process. Their knowledge and control are required for design and fabrication of OFET based circuits. A simple gradual channel OFET model is not appropriate close to threshold, and even fails to describe turn-on voltage. Therefore a distributed model has been developed, based on a numerical calculation of the accumulated charge along the channel, allowing the calculation of the transistor output characteristics both below and above threshold. Also, uneven source contact carrier injection can be modelled, based on physical parameters. In the present work, in-depth analysis of contact influence is carried-out, both below and above threshold, and impact on threshold voltage and turn-on voltage is outlined. Besides, surface Fermi level pinning effects and influence of the semiconductor layer thickness is also discussed.

© 2010 Elsevier B.V. All rights reserved.

1. Introduction

Knowledge and control of threshold voltage (U_T) and turn-on voltage ($U_{TURN\text{-}ON}$) are mandatory for design and fabrication of organic field effect transistor (OFET) based circuits [1]. These two parameters are very sensitive to the device process, and their behaviour may appear difficult to understand. In a previous study, we outlined the influence of poor source contact on the OFET threshold voltage [2,3], using a self-consistent implementation of carrier injection phenomena. If the threshold voltage was proved to be very sensitive to uneven source contact, no such quantitative conclusion could be drawn on the turn-on voltage. Indeed, the model is based on the gradual channel approximation, except close to the source, using the usual $Q = C_i(U_{GC}\text{-}U_T)$ approximation [4,5]. This approach is convenient to describe the OFET behaviour above threshold (i.e. for gate voltage higher than U_T). However this equation is not valid below threshold, and the turn-on voltage remains out of reach. A numerical calculation of the accumulated charge along the channel appeared necessary, leading to a distributed model described in this work. Detailed discussion of threshold voltage and turn-on voltage behaviour is given.

2. Band diagram and accumulated mobile charge

A schematic transistor view is given in Fig. 1. In this work, the gate structure is a Au/SiO_2/organic semiconductor (OSC) stack. Material parameters and transistor dimensions are given in Table 1. The OSC is considered intrinsic, and single carrier transport is considered: here a p-type transistor is described. Although the electron concentration is calculated during the Poisson equation resolution, electrons are not considered to contribute to the channel conductivity: the accumulated mobile charge is restricted to the accumulated holes. This assumption leads to a floor in the accumulated mobile charge when a positive gate bias is applied (visible Fig. 3). This is likely to occur close to the drain contact, where the gate-to-channel bias can be highly positive, in particular in saturation regime.

* Corresponding author. Tel.: +33 0 326913326.
E-mail address: louis.giraudet@univ-reims.fr (L. Giraudet).

1566-1199/$ - see front matter © 2010 Elsevier B.V. All rights reserved.
doi:10.1016/j.orgel.2010.11.002

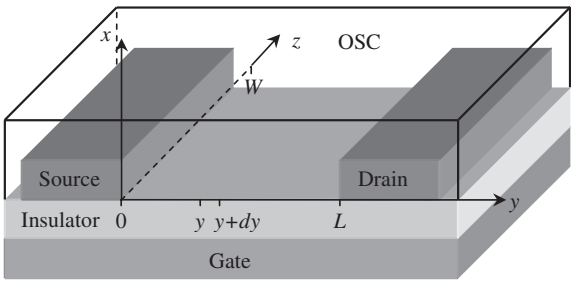

Fig. 1. Schematic view of the simulated OFET structure.

Neglecting any transverse field gradient, Poisson equation across the gate stack is simply given by:

$$\frac{\partial^2 V_y(x)}{\partial x^2} = \frac{(p(x) - n(x))}{\varepsilon_0 \varepsilon_r(x)} \tag{1}$$

Where $V_y(x)$ is the potential profile across the gate structure at a given channel position (y), $\varepsilon_0\varepsilon_r(x)$ the permittivity of a given layer, and $n(x)$ and $p(x)$ the free carrier concentration in this layer. This equation can be solved numerically using a 3D DOS and Fermi–Dirac statistics [4], as for example in [6]. A typical band diagram is given in Fig. 2 in reverse gate bias, together with free carrier concentrations across the structure. For comparison, a usual MOS-like band diagram is also shown in the figure, where the semiconductor bulk is intentionally n-type doped to allow inversion in the p-type channel. Resulting bands bending in both structures are quite different, due to the bulk semiconductor doping. In the intrinsic organic case, the Fermi level position at the semiconductor surface $(x = d)$ was arbitrarily fixed at its equilibrium position. However, both the semiconductor thickness and the surface Fermi level position will impact band bending and accumulated carrier concentrations. In the transistor structure considered here, a quantitative shift of the threshold voltage

Table 1
Transistor structure parameters.

Metal	SiO_2		OSC						Transistor		
W_m (eV)	d_i (nm)	ε_r	d (nm)	ε_r	E_G (eV)	χ (eV)	Nc (cm^{-3})	Nv (cm^{-3})	L (μm)	W (μm)	μ ($cm^2\,V^{-1}\,s^{-1}$)
5.1	100	3.9	500	3.0	2.5	3.5	5.10^{18}	5.10^{18}	10	1000	10^{-1}

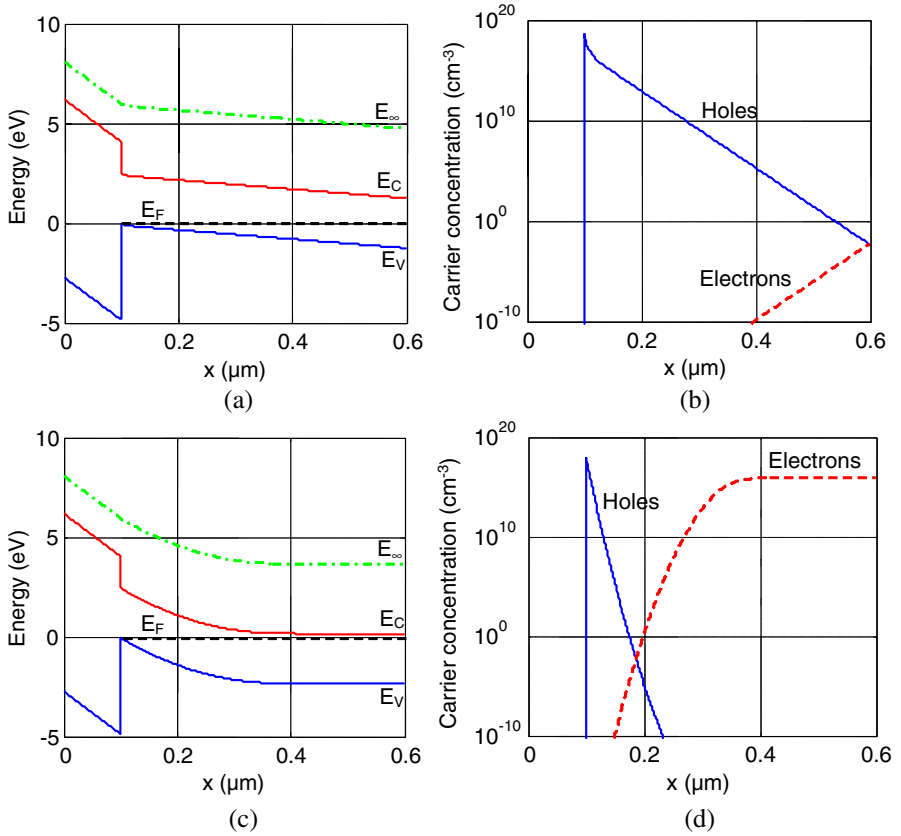

Fig. 2. Band diagram and carrier concentration for intrinsic (a) and (b) and 'MOS-like' (c) and (d) gate structure, respectively in accumulation and inversion mode. Only the bulk doping concentration was varied between these two simulations: null and 10^{16} cm^{-3} respectively, for intrinsic and n-type doping.

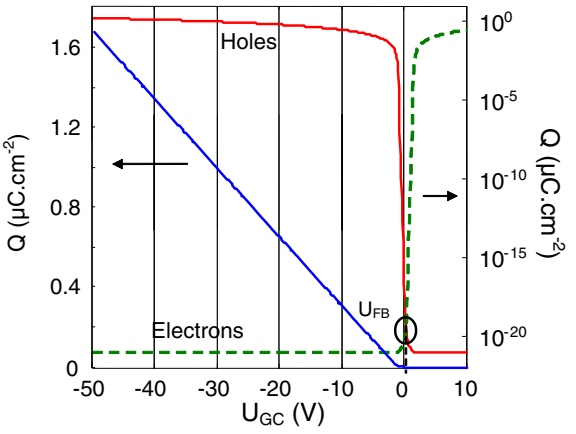

Fig. 3. Accumulated charge surface density versus applied gate-to-channel bias, in linear and logarithmic scale. Free electrons are only shown to locate the flat-band voltage, but not considered to contribute to the drain current.

and onset voltage with Fermi level position will occur for semiconductor thicknesses below 100 nm, as illustrated in the following sections. Such influence of the semiconductor interface opposite to the channel has been recently reported [7].

Traps in real organic field effect transistors play a major role [8,9]: significant shift of threshold voltage, turn-on voltage, or below threshold current slope can be observed. Traps may be located within the organic semiconductor, in the insulator, or at the various structure interfaces. Their concentration, energetic distribution, or location, are strongly dependent on material and technology. Although strongly impacting real devices, due to the numerous issues to be considered, and in order to clarify the impact of many contributions to the transistor behaviour, this work will not consider traps in order to focus on other phenomenon, such as indirect contact contributions, also very detrimental and so often observed. This is a first and necessary step to further analysis of more complex structures. The following results will give a figure of what one could expect from a trap free device with emphasis on contact contribution.

In order to carry on with the transistor current calculation, the accumulated hole concentration is integrated along the semiconductor thickness and stored for a range of positive to negative gate bias. An example is given in Fig. 3, where the surface charge density is plotted in linear and logarithmic scale. Despite not contributing to the transistor drain current, the electron surface density is also shown in order to locate the flat-band voltage.

3. Distributed OFET model

Considering only drift carrier motion with constant mobility, the transistor drain current I_{DS} can be written all along the channel as [4]:

$$I_{DS} = Q(U_{GC}(y))\mu\frac{\partial U_{GC}(y)}{\partial y} = \mu\frac{\partial U_{GC}(y)}{\partial y} q\int_0^d p(x,y)dx \qquad (2)$$

Where $U_{GC}(y)$ is the gate-to-channel voltage at a given channel position (y), $Q(U_{GC}(y))$ is the accumulated charge concentration (limited to the mobile holes), and μ is the hole drift mobility.

As shown in Fig. 1, in the distributed approach, the channel is divided along (y) into a number (N) of slices (y_i). Both $U_{GC}(y_0) = U_{GS}$ and $U_{GC}(y_N) = U_{GS} - U_{DS}$ are known. Starting from an initial drain current guess, the gate-to-channel voltage at position $(y_1 = y_0 + dy)$ can be obtained from Eq. (2). Then, in an iterative way the potential profile can be propagated through the N slices towards the drain contact. The drain bias $U_{GC}(y_N)$ can be compared to the applied bias, and the guess drain current is modified accordingly. Finally a simple algorithm allows calculating the drain current corresponding to a given bias point. The drain current can be obtained both below and above threshold, since the accumulated charge in the channel can be evaluated at any bias point.

The threshold voltage is usually extracted from the $\sqrt{I_{DS}} = f(U_{GS})$ characteristic in saturated regime. Unfortunately, uneven source contact behaviour, in particular non-linear injection, was demonstrated to shift the extracted value [2]. This complicates interpretation of threshold voltage variations with technological parameters since both the source contact and the gate structure determine the drain current near threshold. In order to study the source contact influence on below threshold OFET characteristics, source contact non-linear injection has been implemented in the distributed model as in [2], the physics of the injection model being discussed in [3]. In this model, an energetic barrier ϕ_B between the source contact and the organic semiconductor is responsible for a depleted region at the contact edge. All injection parameters at the source contact edge are evaluated within the drain current algorithm, in a self-consistent approach. These parameters are: the injecting field E_{inj} at the source edge, the potential drop U_{inj} across the depleted region, and the depleted region extension Y_{inj}.

An example of drain current characteristic is shown in Fig. 4, with a significant injection barrier $\Phi_B = 0.5$eV. Non-linear behaviour is clear, as frequently observed in

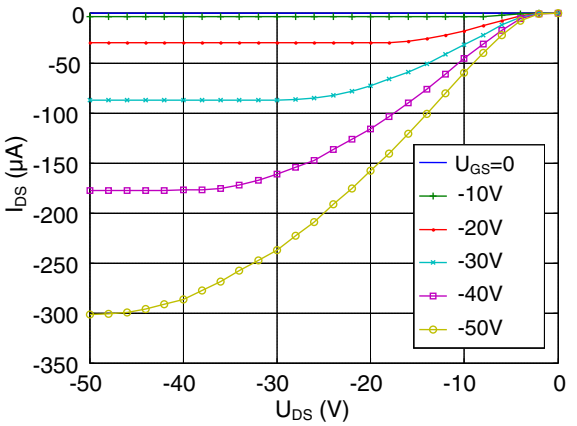

Fig. 4. Simulated I_{DS} characteristics: non-linearities observed at low drain bias are due to the carrier injection barrier at the source contact.

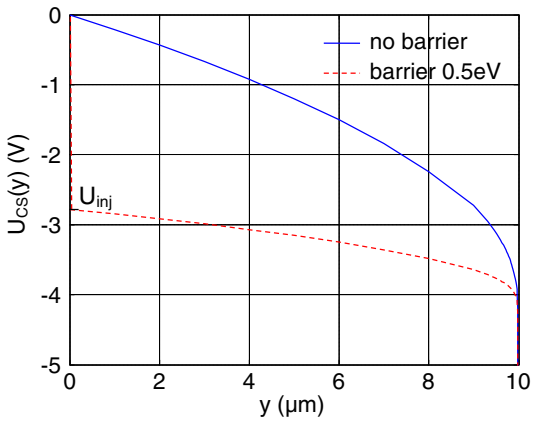

Fig. 5. Simulated potential profile along the channel without or with an injection barrier ($U_{DS} = -5$ V and $U_{GS} = -10$ V). The potential drop U_{inj} at the source ($y = 0$) is due to the injection barrier.

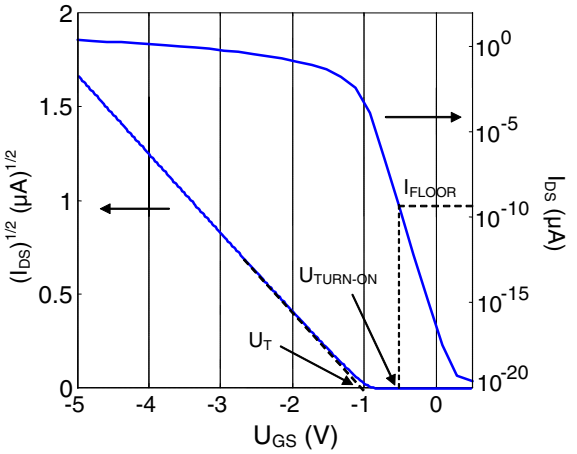

Fig. 6. Simulated $\sqrt{I_{DS}} = f(U_{GS})$ and $\log((I_{DS}) = f(U_{GS})$ characteristics, with extracted threshold voltage U_T and turn-on voltage $U_{TURN\text{-}ON}$.

published experimental results [10,11]. In Fig. 5, the potential profile along the channel is shown with or without injection barrier. At this bias point ($U_{GS} = -10$V and $U_{DS} = -5$V), due to the 0.5eV barrier height, the potential drop at the source contact edge is significant (as observed experimentally, see for example [12]), and represents more than half of the applied drain-source bias. The depleted zone extension (about 15 nm) is negligible compared to the channel length, and the potential drop at the source contact appears abrupt.

4. Threshold voltage and turn-on voltage

The threshold voltage U_T is usually obtained from the $\sqrt{I_{DS}} = f(U_{GS})$ characteristic, while the turn-on voltage $U_{TURN\text{-}ON}$ is extracted from the $\log(I_{DS}) = f(U_{GS})$ plot. Fig. 6 shows both plots, as obtained from the distributed model. Unfortunately, the threshold voltage cannot be calculated analytically in intrinsic organic FETs, as for their silicon MOSFET counterpart, since only accumulation occurs. For real device characterization, several extraction methods have been proposed for the threshold voltage, often derived from silicon devices [13]. For simulated device characteristics, we will consider here the previous straightforward method. To give a figure, one may consider the band diagram shown in Fig. 2 for organic FETs. For limited insulator thickness, one can see that the gate bias U_T required for accumulation to become significant should be about:

$$U_T \approx U_{FB} - qE_G/2 \tag{3}$$

Where U_{FB} is the flat-band voltage and E_G the OSC band gap.

Concerning the turn-on voltage $U_{TURN\text{-}ON}$, we will consider the intercept of the theoretical $\log(I_{DS}) = f(U_{GS})$ characteristic with a given floor current I_{FLOOR}, representing contributions such as gate leakage or surface leakage, not taken into account in the present model. Again to give a figure, a 10fA floor current is plotted (Fig. 6). This floor current is by far higher than the theoretical turn-on current (almost ten decades). Consequently, practical $U_{TURN\text{-}ON}$ will differ from the theoretical value, here by about a volt, depending on the actual transistor materials and gate structure. This shift is sensitive to the floor current, to the threshold slope, and in particular to traps. Note also that the theoretical $U_{TURN\text{-}ON}$ value will slightly differ from U_{FB}, as can be understood considering the hole surface density in Fig. 3. The floor charge is obtained for a gate bias above U_{FB}.

5. Surface Fermi level pinning

As mentioned, the surface Fermi level position, opposite to the accumulated charge interface, is usually unknown. To evaluate its influence, simulations have been performed for various semiconductor thicknesses and Fermi level positions, ±0.5 eV away from the intrinsic Fermi level. Free moving surface Fermi level cannot be simulated using the present model since this would prevent biasing the gate

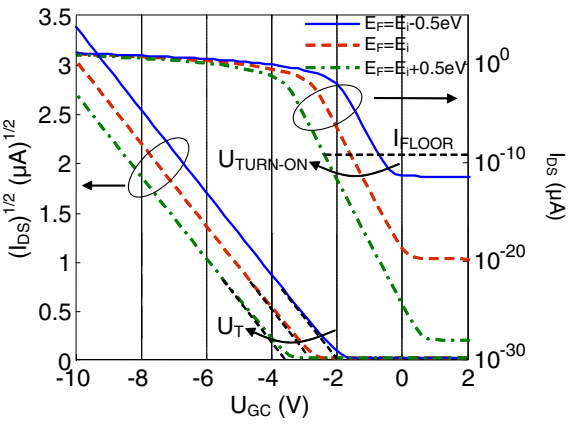

Fig. 7. Surface Fermi level pinning effect on threshold voltage and turn-on voltage.

structure. Results are shown in Fig. 7 for a 50 nm semiconductor thickness. No change in the threshold slope can be seen, but a significant shift of both the threshold voltage and the practical onset voltage is observed due to the Fermi level pinning, as well as a significant increase of the theoretical floor current. The surface Fermi level pinning may prevent the decrease of the hole concentration at positive gate bias, increasing the floor current. Above about 100 nm, the threshold voltage and the turn-on voltage are hardly affected by the surface Fermi level position. Only the theoretical floor current is shifted by almost the same amount. In the following, the Fermi level position is fixed to its intrinsic level.

6. Contact influence below and above threshold

To study indirect contact influence on threshold voltage and turn-on voltage, it appears necessary to distinguish between ohmic contributions (i.e. linear) and non-linear contributions. In Fig. 8, impact of linear contributions is shown. Ohmic series resistances have been varied from limited values to huge values (10 kΩ to 10 MΩ): reasonably no impact on threshold voltage nor onset voltage can be observed. In Fig. 9, non-linear effects due to an injection barrier have been illustrated. Obviously, the threshold voltage is significantly shifted towards higher values (more negative) when non-linear injection occurs, although the gate structure remains unchanged. Indeed, the gate-source voltage can be expressed as the sum of two contributions:

$$U_{GS} = U_{GC} + U_{CS} \tag{4}$$

where U_{GC} is the gate-channel voltage, depending on the gate structure, and U_{CS} is the source-channel voltage, depending on the source contact. The source contact and gate structure influences are additive. We get an intricate situation: practical analysis of its behaviour against technological parameters appears difficult, if not misleading.

In contrast, the transistor characteristic below threshold appears almost unaffected by the source contact. For reasonable contact barriers, within 0–0.7 eV, practical turn-on voltages are not be affected by the source contact: $U_{TURN\text{-}ON}$ remains a good indicator of the gate structure behaviour.

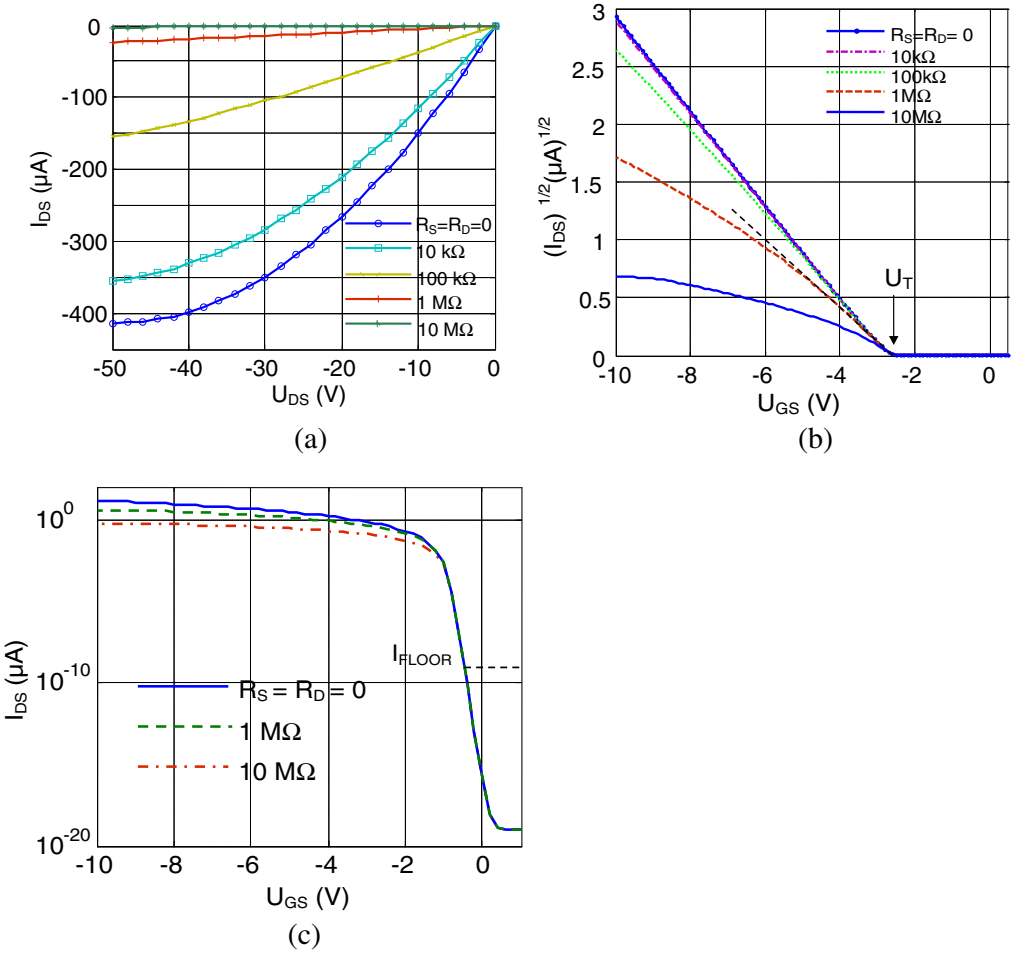

Fig. 8. Linear contact contribution: Ohmic contact impact on drain current (a), threshold voltage (b) and turn-on voltage (c).

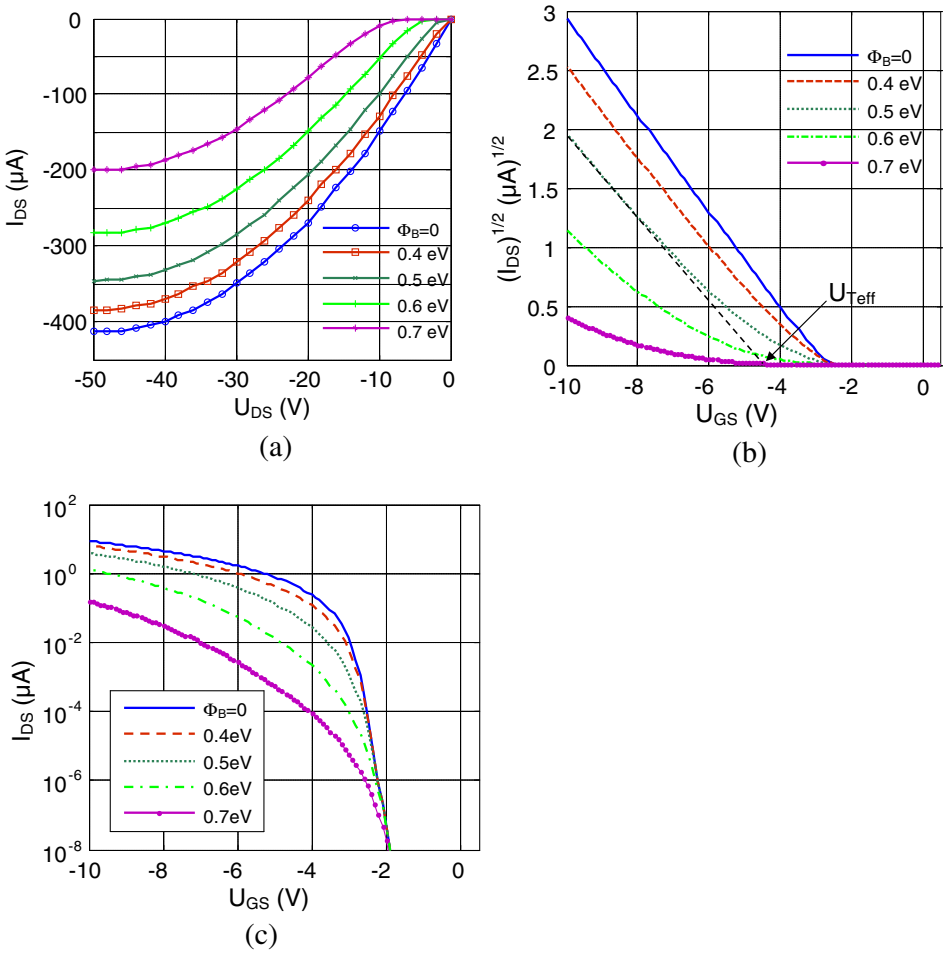

Fig. 9. Non linear contact contribution: Injection barrier impact on drain current (a), threshold voltage (b) and turn-on voltage (c).

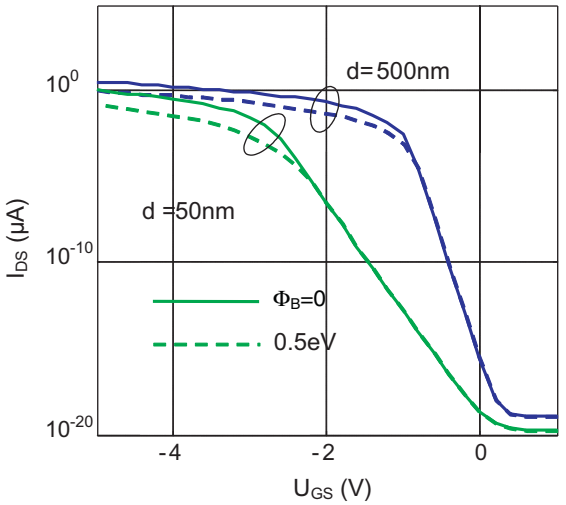

Fig. 10. Influence of the semiconductor layer thickness on below threshold $\log(I_{DS}) = f(U_{GS})$ characteristic, with or without a 0.5 eV injection barrier.

7. Semiconductor thickness

Following the above discussion, the below threshold part of the $I_{DS} = f(U_{GS})$ characteristic is a reliable indicator of the gate structure behaviour. In order to check the influence of the semiconductor thickness, simulations have been performed for 50 and 500 nm layers, with or without a significant injection barrier. The results, shown in Fig. 10, are in agreement with the previous statements: a reduction of the semiconductor thickness will impact the threshold slope, and will shift the turn-on voltage, which is consistent with a modification of the gate structure band diagram. However the source contact barrier will not impact the sub-threshold part of the characteristic.

8. Conclusions

A distributed model has been developed to study above and below threshold OFET drain current characteristics. Dependence of threshold voltage and turn-on

voltage on source contact misbehaviour has been studied, also considering surface Fermi level pinning and semiconductor thickness influence. Following a detailed discussion, it appears that the threshold voltage is unreliable to study the gate structure behaviour with technological parameters, since the source contact also strongly influence its value. On the other hand, the turn-on voltage and the threshold slope are not modified when uneven contacts are considered, and appear as much better indicators of the gate structure stack behaviour. Besides, pinning of the Fermi level is shown to shift both the threshold voltage and the turn-on voltage when thin organic semiconductor layers are considered, while the threshold slope appears sensitive mainly to the semiconductor thickness.

Acknowledgements

This work was supported by Region Champagne-Ardenne and French MESR through CPER project 'PEPITA'.

References

[1] S.G.J. Mathijssen, M. Cölle, H. Gomes, E.C.P. Smits, B. de Boer, I. McCulloh, P.A. Bobbert, D.M. De Leew, Adv. Mater. 19 (2007) 2785.
[2] O. Simonetti, L. Giraudet, T. Maurel, J.L. Nicolas, A. Belkhir, Org. Electron. 11 (2010) 1381.
[3] J.C. Scott, J. Vac. Sci. Technol. A 21 (2003) 521.
[4] S.M. Sze, Physics of Semiconductor Devices, third ed., John Wiley & Sons, 2007.
[5] G. Horowitz, Semiconducting Polymers, in: G. Hadziioannou (Ed.), Wiley-VCH, 2007.
[6] F. Hecht, A. Marrocco, E. Caquot, M. Filoche, COMPEL: Int. J. Comput. Math. Electr. Electron. Eng. 10 (1991) 425.
[7] D. Boudinet, M. Benwadih, S. Altazin, R. Gwoziecki, J.M. Verilhac, R. Coppard, G. Le Blevennec, I. Chartier, G. Horowitz, Org. Electron. 11 (2010) 291.
[8] S.G.J. Mathijssen, M. Kemerink, A. Sharma, M. Cölle, P.A. Bobbert, R.A.J. Janssen, D.M. De Leeuw, Adv. Mater. 20 (2008) 975.
[9] H. Sirringhaus, Adv. Mater. 17 (2005) 2411. and references therein.
[10] A. Petrovic, E. Pavlica, G. Bratina, A. Carpentiero, M. Tormen, Synth. Met. 159 (2009) 1210.
[11] B.H. Hamadani, D. Natelson, J. Appl. Phys. 97 (2005) 064508.
[12] L. Bürgi, T.J. Richards, R.H. Friend, H. Sirringhaus, J. Appl. Phys. 94 (2003) 6129.
[13] A. Ortiz-Conde, F.J. Garcia Sanchez, J.J. Liou, A. Cerdeira, M. Estrada, Y. Yue, Microelectron. Reliability 42 (2002) 583.

Organic Electronics 12 (2011) 227–233

Contents lists available at ScienceDirect

Organic Electronics

journal homepage: www.elsevier.com/locate/orgel

Heat transfer property of thin-film encapsulation for OLEDs

Jongwoon Park *, Hyokyun Ham, Cheolyoung Park

OLED Lighting Team, National Center for Nanoprocess and Equipment, Korea Institute of Industrial Technology, Gwangju 500-480, Republic of Korea

ARTICLE INFO

Article history:
Received 13 July 2010
Received in revised form 16 November 2010
Accepted 26 November 2010
Available online 7 December 2010

Keywords:
Organic light-emitting diodes
Thin-film encapsulation
Heat transfer

ABSTRACT

We investigate the heat transfer property of thin-film encapsulation (TFE) for organic light-emitting diodes (OLEDs). It is demonstrated that the TFE combined with a flexible heat sink shows better thermal performance, compared with the epoxy-filled glass encapsulation and the conventional glass encapsulation. By way of experiments and simulations, we verify that the multi-heterojunction configuration and the low thermal conductivity of the polymer layer in the TFE film have no impact on the thermal performance. Furthermore, we find through simulations that a significant temperature gradient appears inside the TFE layers only when the thermal conductivity of the polymer is lower than 1×10^{-3} W/m K. This enables us to perform design optimization of the TFE configuration with relaxed heat dissipation.

© 2010 Elsevier B.V. All rights reserved.

1. Introduction

Organic light-emitting diodes (OLEDs) have attracted much attention for their potential applications in flat panel lightings and backlight units of flat panel displays [1,2]. One of the key issues of OLEDs is to protect them from oxygen and moisture. To this end, various encapsulation techniques have been studied. The most commonly used method utilizes UV-cured epoxy along with a desiccant inside the glass-capped OLED device (hereinafter referred to as a glass encapsulation) [3]. Recently, many studies have been made on a thin-film encapsulation (TFE) [4–9]. It is required to have a water vapor transmission rate (WVTR) of below 10^{-6} g m^{-2} day^{-1} to achieve the lifetime of OLEDs above 10,000 h. Of many TFE methods, TFE based on vacuum based organic/inorganic multi-layers is very promising as a gas diffusion barrier [4,10,11].

Meanwhile, heat dissipation is another key issue for flat panel OLED lighting applications. In analogy to the conventional lighting sources such as bulbs, fluorescent lamps, and inorganic LEDs, flat panel OLED lightings generate a great deal of heat. Unlike inorganic LEDs that have a long heat transfer pathway due to the packaging issue, however, OLEDs have a very short one between the internal heat source (i.e., light-emitting active area) and the outer device surface; namely, the heat difference between them is very small. This facilitates heat dissipation of OLEDs without using a bulk heat sink. Even so, the Joule heating problem is always parasitic on the devices. Due to Joule heating induced by high current injection during operation, there arise a reduction of luminance, short lifetime, and large spectral shift of OLEDs. To suppress the thermal degradation of organic molecules, the use of a heat sink is inevitable. Such a heat sink is desirable to be slim in such a way as to show up the salient feature of ultra-thin OLEDs.

For bottom-emitting OLED lighting panels, heat transfers through the encapsulation layers to the heat sink. As such, encapsulation need allow high gas diffusion barrier while simultaneously meeting heat transfer requirements. The epoxy seal of the glass encapsulation may not be good moisture barrier. Besides, the glass encapsulation may show poor thermal performance as nitrogen gas resides inside the device, separating a heat sink from the OLED device without any contact involved between them. One may come up with an advanced glass encapsulation where a glass cover is filled with a thermally conductive epoxy through which a heat sink is in contact with the OLED device (hereinafter referred to as an epoxy-filled glass encapsulation). In this case, a significant temperature

* Corresponding author. Tel.: +82 62 600 6520; fax: +82 62 600 6509.
E-mail address: pjwup75@kitech.re.kr (J. Park).

1566-1199/$ - see front matter © 2010 Elsevier B.V. All rights reserved.
doi:10.1016/j.orgel.2010.11.023

Fig. 1. Schematic view of the layer structure of a thin-film encapsulated OLED.

gradient may appear if the thermal conductivity of epoxy is low [12]. In this respect, the TFE structure shown in Fig. 1 would be in good combination with a heat sink provided that its barrier property is satisfactory since the TFE layer is extremely thin (several μm). However, it still concerns us in respect that the TFE layer is composed of alternating organic/inorganic materials (namely, a multi-heterojunction is entailed) and furthermore organic (polymer) materials have relatively low thermal conductivity, which may degrade the heat transfer property. Though many researches on the encapsulation technologies are available in the open literature, yet not much has been reported on their thermal property.

This paper is written with the following objectives. We make a comparative analysis of those encapsulation methods in terms of the heat transfer property. In the presence of a flexible heat sink, it is addressed that the TFE shows the best thermal performance, followed by the epoxy-filled glass encapsulation and then the conventional glass encapsulation. We have also implemented a 1D numerical model and performed numerical simulations of OLEDs to study more systematically the thermal property of the TFE configuration. It is found that the multi-heterojunction of the TFE structure and the low thermal conductivity of a polymer material therein have no impact on the thermal performance.

2. Model

In this study, the OLED structure (Fig. 1) consists of a 150-nm-thick indium-tin-oxide (ITO) pre-coated on a glass substrate, 70-nm-thick N,N′-diphenyl-N,N′-bis(1-naphthyl)-1-1′biphenyl-4,4″diamine (α-NPD) for a hole transport layer (HTL), 45-nm-thick tris-(8-hydroxyquinoline) aluminum (Alq_3) for an electron transport layer (ETL), 1-nm-thick lithium fluoride (LiF) for an electron injection layer (EIL), and 150-nm-thick aluminum (Al) for cathode. The TFE layer is composed of alternating inorganic (50-nm-thick Al_2O_3)/organic (500-nm-thick polymer) multilayers. With attempt to capture the heat generation and transfer inside the OLED device, we have implemented a comprehensive 1D numerical model [13–16] in which Poisson's equation, drift–diffusion equation, and heat flow equation are coupled to one another.

2.1. Poisson's equation

$$\frac{\partial E(x,t)}{\partial x} = \frac{q}{\varepsilon_0 \varepsilon_r}\left(p(x,t) - n(x,t) + N_D - N_A\right) \tag{1}$$

where the variable E denotes the electric field, n and p the electron and hole densities, respectively, and N_D and N_A the donor and acceptor impurity concentrations, respectively.

2.2. Drift–diffusion equation

$$\begin{aligned}\frac{\partial n(x,t)}{\partial t} &= \frac{1}{q}\frac{\partial J_n(x,t)}{\partial x} - r(x,t)n(x,t)p(x,t)\\ \frac{\partial p(x,t)}{\partial t} &= -\frac{1}{q}\frac{\partial J_p(x,t)}{\partial x} - r(x,t)n(x,t)p(x,t)\end{aligned} \tag{2}$$

where

$$\begin{aligned}J_n(x,t) &= q\mu_n(x,t)n(x,t)E(x,t)\\ J_p(x,t) &= q\mu_p(x,t)p(x,t)E(x,t)\end{aligned} \tag{3}$$

with the variable μ_n defined as the electron mobility, and μ_p the hole mobility. The degree of disorder of the organic molecules is reflected in the field- and temperature-dependent carrier mobility expressed as [17,18]

$$\mu(E(x,t),T) = \mu_0(T)\exp\left(\sqrt{\frac{E(x,t)}{E_0(T)}}\right) \tag{4a}$$

where

$$\mu_0(T) = \mu_A \exp\left(-\frac{\Delta}{kT}\right) \tag{4b}$$

$$E_0^{-1/2}(T) = D_m\left(\frac{1}{kT} - \frac{1}{kT_0}\right) \tag{4c}$$

with $\mu_0(T)$ defined as the zero-field temperature-dependent mobility, μ_A a constant, Δ the activation energy, $E_0(T)$ the temperature-dependent characteristic field, and D_m and T_0 material-related constants. The recombination rate r is expressed in the Langevin form [19]

$$r(x,t) = q(\mu_n(x,t) + \mu_p(x,t))/\varepsilon_0\varepsilon_r. \tag{5}$$

2.3. Heat flow equation

$$C\frac{\partial T(x,t)}{\partial t} = \frac{\partial}{\partial x}\left(k(x,t)\frac{\partial T(x,t)}{\partial x}\right) + \left[\frac{J_n(x,t)^2}{q\mu_n(x,t)n(x,t)} + \frac{J_p(x,t)^2}{q\mu_p(x,t)p(x,t)}\right] \tag{6}$$

where C is the volumetric heat capacitance and k is the thermal conductivity. The second term in the right-hand side of Eq. (6) represents the Joule heating. The thermal conductivity is assumed to be independent of temperature. Dirichlet boundary condition has been applied at the air/heat sink interface. In the simulation, the ambient temperature was assumed to be 300 K. For simplicity, the thermoelectric effects such as the Seebeck effect and the Peltier effect are not considered in the model. The model is capable of capturing the temperature-dependent OLED behaviors by solving the equation governing the electrical behaviors and the heat flow equation, which are coupled to each other through the temperature-dependent carrier mobility (Eq. (4)). The solutions to the governing equations are obtained in a self-consistent manner. Table 1 lists the

Table 1
Material parameter values.

Layer	$\mu_{0,n}$ (cm^2/V s)	$\mu_{0,p}$ (cm^2/V s)	$E_{0,n}$ (V/cm)	$E_{0,p}$ (V/cm)
HTL (α-NPD)	1×10^{-8}	4.3×10^{-4}	1×10^{5}	1×10^{6}
ETL (Alq_3)	1.2×10^{-6}	0.12×10^{-6}	1959×10^{3}	1959×10^{3}

parameter values related to carrier mobilities [14], which are typical for such a device with the material system chosen.

3. Results and discussion

For experiments, we have employed a Polynetwork flexible heat sink (PN-FHB050N) [20] in the form of bonding sheet. It consists of a 50-μm-thick copper sheet and 35-μm-thick thermal radiation layer. The bonding sheet has the thermal conductivity of 0.86 W/m K. After depositing organic and cathode layers, we have formed alternating Al_2O_3/monomer layers using Barix™ thin-film encapsulation equipment. Alumina layers are deposited by reactive sputtering of an alumina target. Polymer layers are deposited by organic acrylate evaporation and condensation, followed by a UV cure. The alumina layers form the basis of the moisture and oxygen barrier. Alternating polymer layers provide a smooth surface to facilitate defect free alumina deposition. Shown in Fig. 2 is the scanning electron microscope (SEM) image where 5.5 dyads TFE layers are deposited. The Al_2O_3 and polymer layer thicknesses are measured to be about 44 and 590 nm, respectively.

To evaluate the barrier property of the TFE films, we have conducted a Ca test and estimated the WVTR. The Ca test has been done in the same manner presented in [6]. It is based on the corrosion of thin calcium films. We have carried out the Ca test at temperature of 20 °C and a common relative humidity of 50%. As presented in Table 2, we have achieved the WVTR as low as 2.7×10^{-6} g/m^2 day, which is acceptable for lighting applications.

We have then investigated the heat transfer property of the TFE film. To this end, we have fabricated three bilayers

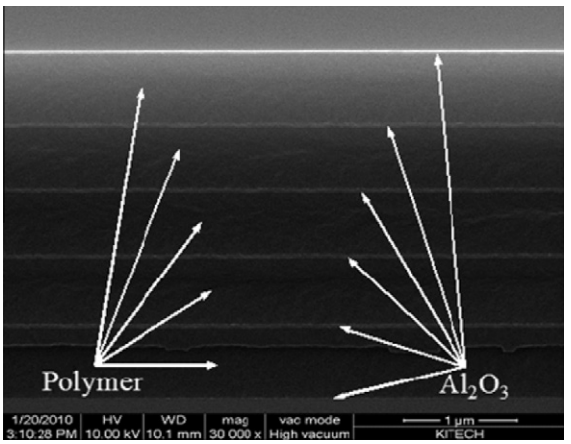

Fig. 2. SEM image of 5.5 dyads TFE layers fabricated with Vitex TFE equipment.

Table 2
Measured WVTR of the 5.5 dyads TFE film and sample images for different time slot.

Time (hr) \ Results	WVTR (g/m^2-day)	Sample
0		
100	2.17E-05	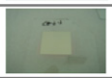
200	1.10E-05	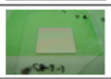
300	9.44E-06	
400	8.43E-06	
500	2.73E-06	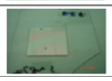

(HTL/ETL) OLEDs with different encapsulation structures (i.e., the conventional glass encapsulation, epoxy-filled glass encapsulation, and thin-film encapsulation) and made a comparative analysis of them in terms of the thermal performance. The emission area of the devices is 4.0 mm^2. Fig. 3 shows the measured *J–V* curve of the bilayer OLED, exhibiting the driving voltage of 4.7 V at 1000 cd/m^2 (21 mA/cm^2) and the luminance of 14,120 cd/m^2 at 7.5 V (378 mA/cm^2). For a comparison, we have measured the surface temperature of OLEDs without and with the flexible heat sink at a fixed voltage of 7.5 V using a thermal imager.

From Fig. 4, it is visible to the naked eye that there is no big difference in the surface temperature distribution between the glass encapsulated OLEDs with and without the heat sink. To quantify it, we have measured the transient variation of the maximum surface temperature. It is observed that the maximum surface temperature has been reduced by only 6 °C (from 55.5 °C to 49.6 °C) with the aid of the heat sink. Such a small reduction is due to the fact that there exists air (nitrogen gas) between the OLED device and the heat sink. Nitrogen gas has the thermal conductivity of 0.024 W/m K [12], which is much lower than that of glass. It hence results in poor heat transfer performance of the conventional glass encapsulation.

To eliminate nitrogen gas from the device, we have filled a thermally conductive epoxy resin (XNR 5570-B1, Nagase ChemteX Corp.) in the glass cover and then UV-cured it. Except for the epoxy-sealed area, the 0.7-mm-

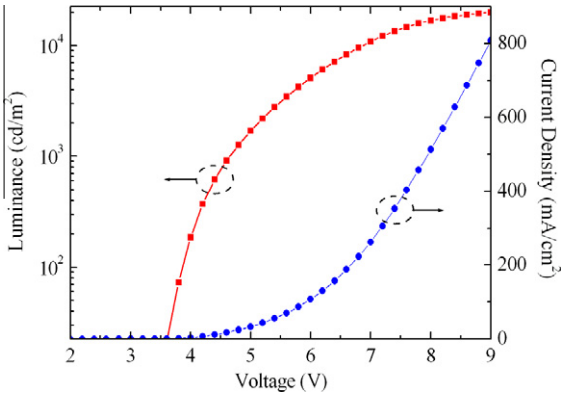

Fig. 3. Luminance and current density of the bilayer OLED as a function of bias voltage.

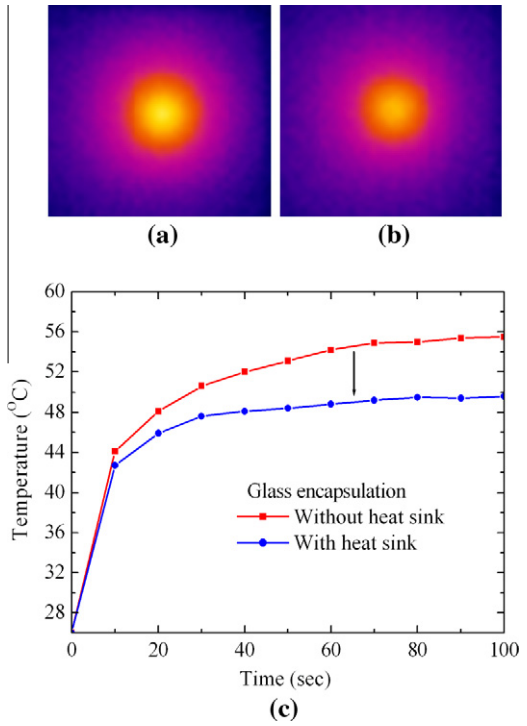

Fig. 4. Surface temperature distribution over the glass encapsulated OLED (a) without and (b) with heat sink, and (c) transient variation of the maximum surface temperature measured at 7.5 V.

thick glass cover is hollowed out such that its thickness becomes 0.35 mm and thus the epoxy resin can be filled therein. Just in case that epoxy causes any damage on the organic and cathode layers, we have inserted a buffer layer that consists of a 40-nm-thick NPB and 50-nm-thick LiF. For OLEDs with the epoxy-filled glass encapsulation, the maximum surface temperature is observed to be only 49 °C (Fig. 5) when the heat sink is not even involved, which is almost the same as that of the glass encapsulated OLED with the heat sink. It seems that heat transfers through the thermally conductive epoxy resin to the glass

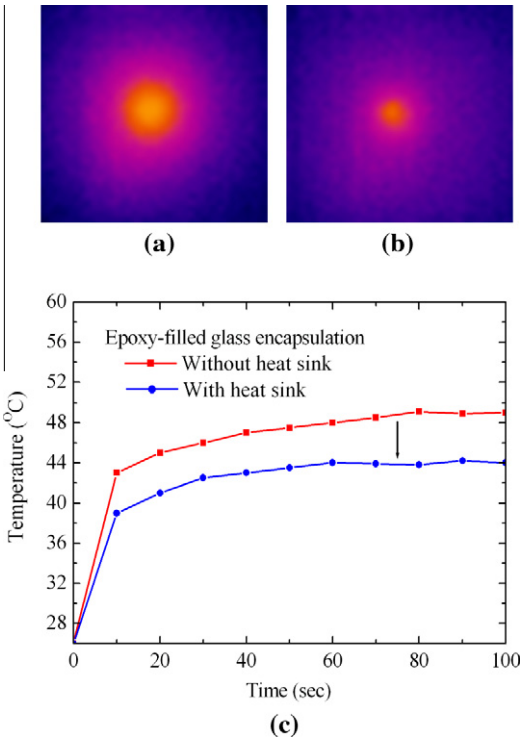

Fig. 5. Surface temperature distribution over the epoxy-filled glass encapsulated OLED (a) without and (b) with heat sink, and (c) transient variation of the maximum surface temperature measured at 7.5 V.

cover and then air. In fact, it is attributed that the thermal conductivity of epoxy is about 0.35 W/m K [12], which is much higher than that (0.024 W/m K) of nitrogen gas. Therefore, heat can be transferred to the surroundings even without the heat sink. However, the effect of the heat sink attached is likely to be little as the temperature reduction by the heat sink is only 5 °C (from 49 °C to 44 °C). It may be because the heat transfer pathway is very long and thus there appears a significant temperature gradient inside the thick (0.35 mm) epoxy layer, resulting from the fact that the thermal conductivity of epoxy is still low. There's plenty of room for improving its thermal performance. For instance, one may blend higher thermal conductivity materials (e.g., carbon nanotubes, Ag paste, etc.) with the epoxy. Meanwhile, the outgassing problem of this encapsulation scheme may be resolved by replacing the epoxy resin with a getter dryer such as a calcium oxide (CaO) powder.

We have then evaluated the thermal property of the thin-film encapsulated OLED. From Fig. 6, one can clearly see that the surface temperature is reduced to a great extent by the heat sink. It is observed to fall from 58 °C to 33 °C. Such a large reduction in temperature (25 °C) results from a short heat transfer pathway of the TFE structure. The total thickness of the TFE layer is only 3.2 μm. As such, heat generated in the emitting layer can be well transferred to the heat sink and dissipated by it. From this, one may jump into conclusion that the TFE structure combined with a heat sink shows the best heat transfer prop-

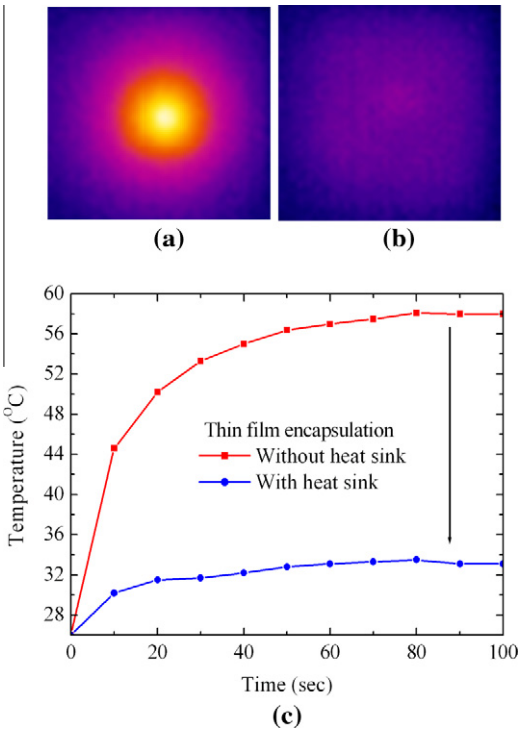

Fig. 6. Surface temperature distribution over the thin-film encapsulated (3.5 dyads) OLED (a) without and (b) with heat sink, and (c) transient variation of the maximum surface temperature measured at 7.5 V.

erty. Therefore, it is highly preferred for OLEDs provided that its oxygen barrier requirement is well met.

We have further investigated the positive effect of heat dissipation by the heat sink on the device performance of the thin-film encapsulated OLEDs. Shown in Fig. 7 are the power efficiency and luminance of thin-film encapsulated (3.5 dyads) OLEDs with and without heat sink as a function of bias voltage measured after 50 min of aging at 7.5 V (~10,000 nit). It is found that both devices exhibit a reduction of luminance and power efficiency because they were

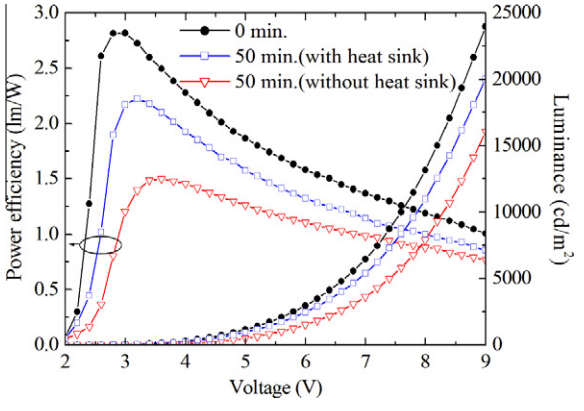

Fig. 7. Power efficiency and luminance of thin-film encapsulated (3.5 dyads) OLEDs with and without heat sink as a function of bias voltage measured after 50 min of aging at 7.5 V (~10,000 nit).

operated at high luminous intensity. However, less performance degradation appears in the device with heat sink due most likely to effective heat dissipation (Fig. 6). As such, it is desirable to employ a heat sink when OLEDs are operated at high luminance in order to reduce the unwanted Joule heating effect.

It is known that the heat transfer performance could be degraded if a multi-heterojunction is involved (namely, various different types of materials are interfaced) in the TFE structure and/or a polymer material used in the TFE film has low thermal conductivity. To verify it, we have simulated the heat transfer property of the TFE structure (Fig. 1) using the model introduced in Section 2. Summarized in Table 3 are the parameter values of thermal conductivity of those layer materials, which are required for simulations. The thermal conductivity of the polymer in the TFE film is assumed to be the same as that of the organic materials. For simplicity, we also make an assumption that the thermal conductivity of α-NPD is the same as that of Alq_3. By way of simulations, one can visualize where severe heat generation occurs inside the device. From Eqs. (3) and (6), the induced high carrier concentration along with the electric field is known to generate severe heat in the organic films. As presented in Fig. 8 showing the simulation results of the electric field and carrier density distributions inside the device, steep carrier accumulation takes place at the organic/organic interface and high electric field is induced near the interface inside the ETL layer, where severe heat is generated.

With attempt to investigate the effect of the thermal conductivity of the polymer layer on the heat transfer property, we have intentionally reduced its thermal conductivity from 0.107 W/m K to 0.107×10^{-3} W/m K and performed simulations of the spatial heat distribution without and with the heat sink. As shown in Figs. 9 and 10, when the thermal conductivity of the polymer is equal to 0.107 W/m K (i.e., it is close to the real value of the polymer conductivity), the simulation results of the surface temperature (61.7 °C without heat sink and 27.03 °C with heat sink) are very close to the measured ones (58 °C without heat sink and 33 °C with heat sink), validating our numerical calculations. It is observed that the temperature rises up with reduced thermal conductivity of the polymer. Consequently, there appears a significant temperature gradient inside the TFE layers. However, there will not arise a steep temperature gradient inside the TFE layers once the thermal conductivity of a polymer material is higher than 0.107×10^{-2} W/m K, which offers a wide choice of a polymer material. Since not many materials have such a low

Table 3
Thermal conductivity values.

Layer	k (W/m K)
Glass	1.05 [12]
ITO	12 [21]
α-NPD	0.107
Alq_3	0.107 [22]
Al	250 [12]
Al_2O_3	30 [12]
Polymer	0.107
Copper	401 [12]

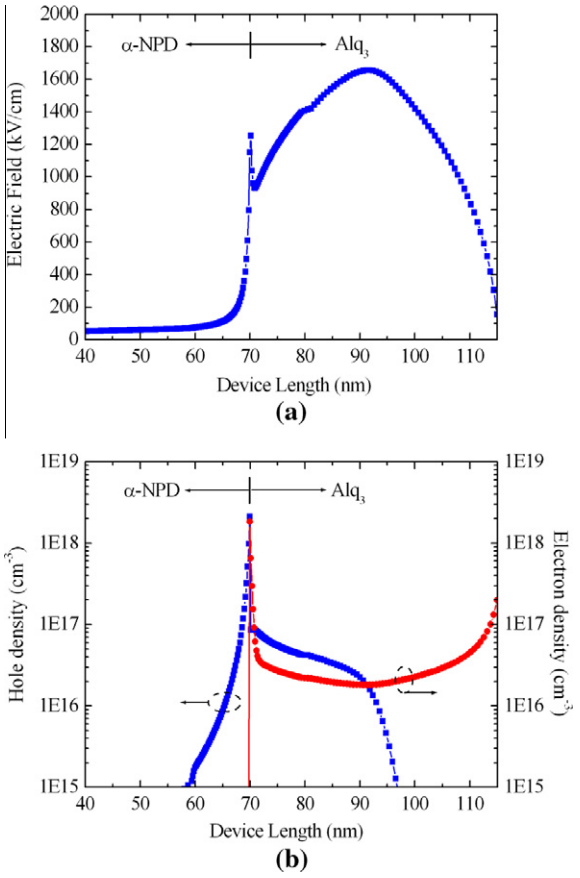

Fig. 8. Simulation results of (a) electric field and (b) carrier density distributions inside the bilayer OLED structure at 7.5 V.

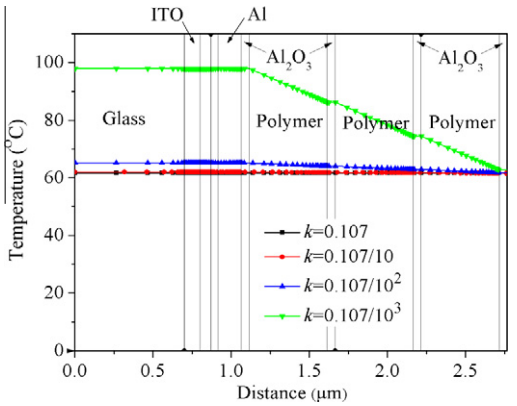

Fig. 9. Simulation results of temperature distribution over the thin-film encapsulated OLED without heat sink at 7.5 V.

thermal conductivity in reality, it can be concluded that the effect of a low thermal conductivity polymer material on the thermal performance of the TFE structure is negligible.

To find whether or not the multi-heterojunction configuration affects the thermal performance of the TFE film, we have further measured the maximum surface temperature

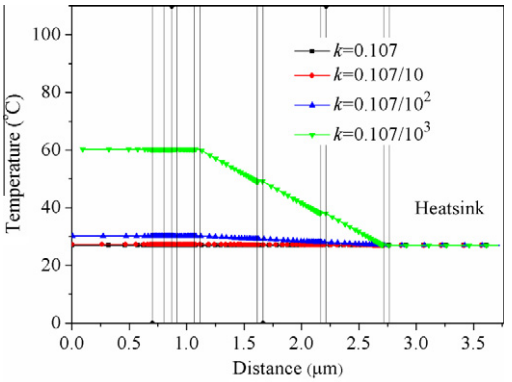

Fig. 10. Simulation results of temperature distribution over the thin-film encapsulated OLED with heat sink at 7.5 V.

Table 4
Measured and simulated maximum surface temperatures for different TFE structures without heat sink at 7.5 V.

	1.5 dyads	3.5 dyads	5.5 dyads
Measurement	59.1	58	58.7
Simulation	61.5	61.7	61.9

by varying the TFE structure. Namely, we have reduced the number of TFE dyads to 1.5 or increased it up to 5.5. As presented in Table 4, there is no big difference in the temperature. It means that though the TFE structure is based on the multi-heterojunction configuration, yet no significant degradation in the heat transfer performance is brought in since the overall thickness of the TFE film is very small, which is also supported by the simulation results in Table 4.

4. Conclusion

We have made a comparative analysis of the thermal performance of three different encapsulation schemes; namely, the conventional glass encapsulation, epoxy-filled glass encapsulation, and thin-film encapsulation. It has been found that, in the presence of a slim and flexible heat sink, the thin-film encapsulation shows the best thermal performance, followed by the epoxy-filled glass encapsulation and then the conventional glass encapsulation. By way of experiments and simulations, we have verified that the multi-heterojunction configuration and/or the low thermal conductivity of a polymer material in the TFE film have no impact on the thermal performance due to its extremely short heat transfer pathway.

Acknowledgement

This work was supported by the IT R&D program of MKE/IITA. (2009-F-016-01, Development of Eco-Emotional OLED Flat-Panel Lighting).

References

[1] S. Reineke, F. Lindner, G. Schwartz, N. Seidler, K. Walzer, B. Lüssem, K. Leo, Nature 4759 (2009) 234.

[2] Joerg Amelung, http://spie.org/x23960.xml
[3] P.E. Burrows, V. Bulovic, S.R. Forrest, L.S. Sapochack, D.M. McCarty, M.E. Thompson, Appl. Phys. Lett. 65 (1994) 2922.
[4] J.D. Affinito, M.E. Gross, C.A. Coronado, G.L. Graff, E.N. Greenwell, P.M. Martin, Thin Solid Films 290–291 (1996) 63.
[5] A.P. Ghosh, L.J. Gerenser, C.M. Jarman, J.E. Fornalik, Appl. Phys. Lett. 86 (2005) 223503-1.
[6] G. Nisato, M. Kuilder, P. Bouten, L. Moro, O. Philips, N. Rutherford, SID 00 Digest XXXIV, 2003, p. 88.
[7] J. Meyer, D. Schneidenbach, T. Winkler, S. Hamwi, T. Weimann, P. Hinze, S. Ammermann, H.-H. Johannes, T. Riedl, W. Kowalsky, Appl. Phys. Lett. 94 (2009) 233305-1.
[8] A.B. Chwang, M.A. Rothman, S.Y. Mao, R.H. Hewitt, M.S. Weaver, J.A. Silvernail, K. Rajan, M. Hack, J.J. Brown, X. Chu, L. Moro, T. Krajewski, N. Rutherford, Appl. Phys. Lett. 83 (2003) 413.
[9] F.L. Wong, M.K. Fung, S.L. Tao, S.L. Lai, W.M. Tsang, K.H. Kong, W.M. choy, C.S. Lee, S.T. Lee, J. Appl. Phys. 104 (2008) 014509-1.
[10] G.L. Graff, R.E. Williford, P.E. Burrows, J. Appl. Phys. 96 (2004) 1840.
[11] C. Charton, N. Schiller, M. Fahland, A. Hollander, A. Wedel, K. Noller, Thin Solid Films 502 (2006) 99.
[12] http://www.engineeringtoolbox.com/thermal-conductivity-d_429.html
[13] B. Ruhstaller, S.A. Carter, S. Barth, H. Riel, W. Riess, J.C. Scott, J. Appl. Phys. 89 (2001) 4575.
[14] B. Ruhstaller, T. Beierlein, H. Riel, S. Karg, J.C. Scott, W. Riess, IEEE J. Sel. Top. Quantum Electron. 9 (2003) 723.
[15] J.W. Park, Y. Kawakami, IEEE/OSA J. Display Tech. 2 (2006) 333.
[16] J.W. Park, Y. Kawakami, S.H. Park, IEEE/OSA J. Lightwave Technol. 25 (2007) 2828.
[17] P.W.M. Blom, M.J.M. de Jong, S. Breedijk, Appl. Phys. Lett. 71 (1997) 930.
[18] J.M. Lupton, I.D.W. Samuel, J. Phys. D: Appl. Phys. 32 (1999) 2973.
[19] G.G. Malliaras, J.C. Scott, J. Appl. Phys. 83 (1998) 5399.
[20] http://polynetwork.asia/eindex.html
[21] http://thinfilmproducts.umicore.com/pdf/datenblatt_ito.pdf
[22] M.W. Shin, H.C. Lee, K.S. Kim, S.H. Lee, J.C. Kim, Thin Solid Films 363 (2000) 244.

Organic Electronics 12 (2011) 234–238

Contents lists available at ScienceDirect

Organic Electronics

journal homepage: www.elsevier.com/locate/orgel

Dynamics study of electron extraction from 1D conjugated polymers to metal electrodes

Yue-Hua Zhou, Li-Ping Zhu, Yu Qiu *

Department of Physics, Zhejiang Normal University, Jinhua, Zhejiang 321004, China

ARTICLE INFO

Article history:
Received 28 September 2010
Received in revised form 31 October 2010
Accepted 23 November 2010
Available online 4 December 2010

Keywords:
Polymer/metal joint
Carrier mobility
Polaron dynamics

ABSTRACT

We simulate the processes of electron extraction from 1D conjugated polymers to metal electrodes in the presence of electric fields based on the Su–Schrieffer–Heeger (SSH) model extended to a polymer/electrode contact structure. From the simulation, we can obtain the lifetime of the process that a charged carrier known as polaron at the polymer chain end starts to dissociate and the released electron tunnels to the electrode immediately. An effective carrier mobility named interface mobility can be defined for this process and calculated from the lifetime. It is found that the interface mobility is independent on the external electric fields. However, this mobility increases with decreasing the work function of the electrode. By enhancing the coupling between the polymer and the electrode, the interface mobility is shown to increase. Kinetic energy of the electrons is also shown to favor the improvement of the mobility.

© 2010 Elsevier B.V. All rights reserved.

1. Introduction

In the past decades, organic moleculars and conjugated polymers have shown important applications in light-emitting diodes [1], field effect transistors [2] and photovoltaic devices [3,4]. In light-emitting diodes, charge injection process greatly affects the efficiency of electroluminescence. In photovoltaic devices, however, charge extraction from organic layers to electrodes is more important. The processes of charge injection and ejection in polymer/electrode structures is asymmetric because additional electron or hole in conjugated polymers results in discrete levels in the energy gap [5]. This asymmetry has been experimentally confirmed by the hysteretic current characteristic [6]. Despite many advances, further understandings of charge injection and extraction to and from organic materials are still necessary to improve the performance of organic-based electronic devices.

Carrier transport in organic layers has notorious effect on the efficiency of organic-based electronic devices [1–14]. Charge carrier mobility has been extensively studied and shown in close relevance with the performance of the devices [15–35]. Most of the studies show charge carrier mobility in organic materials depends closely on electric field and carrier density. It is well-known that in conjugated polymers, due to strong electron and lattice interactions, additional electrons or holes will induce self-localized excitations such as solitons [36], polarons [37] and bipolarons [38]. Many studies have been performed on polaron dynamics in 1D conjugated polymer chains [39–42]. The carrier mobility is shown relatively small and dependent on the strength of the applied electric fields [40]. In most devices, the organic layers as channels for charge carriers are usually connected with electrodes. Charge migration behavior is quite different within the polymer chain far from the interface from that near the interface due to the interface scattering effect [29]. Thus carrier mobility within the chain is also expected to differ from that near the interface. Experimentally obtained carrier mobility is essentially an incorporated result. Extensive researches have been carried on polaron dynamics and carrier mobility within polymer chains far from the chain ends [29,39,40]. However, polaron dynamics at the polymer/electrode joint has been

* Corresponding author.
E-mail address: yqiu@zjnu.cn (Y. Qiu).

1566-1199/$ - see front matter © 2010 Elsevier B.V. All rights reserved.
doi:10.1016/j.orgel.2010.11.022

less considered, which is an important aspect of functioning photovoltaic devices.

In the present work, we will focus on the electron extraction process at polymer/electrode joints and investigate the effects of electric field, kinetic energy of the electron, the work function of the electrode and the coupling strength between the electrode and the polymer on the electron extraction process. The model and the method employed in this work are described in the following section. The results are presented and discussed in Section 3. A summary of our findings is presented in Section 4.

2. Model and method

We consider a one dimensional polymer/metal structure. The conjugated polymer chain is described with SSH model [36–38] in which electron–phonon (e–p) interaction plays an important roll. The metal electrode is also described by SSH model, wherein however the e–p coupling is neglected [5,42,43]. Thus the Hamiltonian can be written as,

$$H = H_e + H_{latt} + H_F. \tag{1}$$

The electronic part is

$$H_e = -\sum_{n,s} t_n \left(c^\dagger_{n,s} c_{n+1,s} + c^\dagger_{n+1,s} c_{n,s} \right) + \mu \sum_{n,s} c^\dagger_{n,s} c_{n,s}, \tag{2}$$

where $c_{n,s}(c^\dagger_{n,s})$ denotes the electron annihilation (creation) operator at site n with spin $s(\uparrow,\downarrow)$. t_n is the hopping integral between sites n and $n+1$. For electrodes $t_n = t_0$, and for polymers $t_n = t_0 - \alpha(u_{n+1} - u_n) + (-1)^{n+1} t_e$, where u_n is the monomer displacement of site n and α the coefficient of electron–lattice coupling. t_e is introduced to lift the ground-state degeneracy for nondegenerate polymers [37]. $t_n = t_c$ represents the coupling between the sites connecting the organic molecule and the electrode. μ is the chemical potential. The lattice of the organic part is described by

$$H_{latt} = \frac{K}{2} \sum_n (u_{n+1} - u_n)^2 + \frac{M}{2} \sum_n \dot{u}_n^2, \tag{3}$$

where K is the elastic constant and M the mass of the repeat monomer. The first term on the righthand side of Eq. (3) describes the potential energy of the σ-bond, and the second term is the kinetic energy for the monomers. H_F describes the contribution from the external electric field,

$$H_F = \sum_{n,s} V_n \left(c^\dagger_{n,s} c_{n,s} - \frac{1}{2} \right), \tag{4}$$

V_n being site energies due to the applied field, $V_n = -|e|E[(n - n_0)a + u_n]$, with e being the electron charge, n_0 the first site of the polymer chain, a the lattice constant and E the uniform electric field.

For convenience, polymers are always assumed to be undoped. Thus the chemical potential μ of polymers is zero provided the virtual central level (VCL) of the gap is assigned to zero. For electrodes, if $\mu = 0$ the Fermi level and the VCL align. The electrode work function can be reduced by increasing the electrode chemical potential μ. The parameters in this model are those generally used in the SSH model without loss of universality [38]: $\alpha = 4.1$ eV/Å, $K = 21$ eV/Å^2, $M = 1349.14$ eV·fs^2/Å^2, $t_0 = 2.5$ eV, $t_e = 0.06$ eV and $a = 1.22$ Å. The interface coupling coefficient t_c is usually much smaller than t_0 indicating a relatively weak interchain charge transfer as compared to the intrachain transfer.

A nonadiabatic dynamics method has been used to study charge transfer across polymer/electrode contacts. The electronic wave functions evolve according to the Schrödinger equation,

$$i\hbar\dot{\psi}_i(n,t) = -t_{n-1}\psi_i(n-1,t) + V_n\psi_i(n,t) - t_n\psi_i(n+1,t), \tag{5}$$

where i is the index for the π-electrons. The lattice displacements of polymers are determined classically by the Newtonian equations,

$$M\ddot{u}_n = -K(2u_n - u_{n+1} - u_{n-1}) + 2\alpha[\rho_{n,n+1}(t) - \rho_{n,n-1}(t)] - |e|E[\rho_{n,n}(t) - 1] - \lambda M\dot{u}_n, \tag{6}$$

where the density matrix ρ is defined as $\rho_{n,m}(t) = \sum_i f_i \langle n|\psi_i(t)\rangle\langle\psi_i(t)|m\rangle$. $f_i(= 0, 1, 2)$ is the time independent distribution function determined by initial occupation number. λ is the damping coefficient introduced to give a realistic behavior of the system as a function of time [40]. $\lambda = 0.08$ fs^{-1} throughout the work. The coupled differential Eqs. (5) and (6) can be numerically solved by use of the same technique as in Refs. [40] and [42]. In our numerical simulations, fixed-end boundary condition [44] was employed because of the finite chain length character of the model. To avoid the numerical errors, we take the time step as small as 0.1 fs. In order to describe the configuration of the polymer lattice we define

$$y_n \equiv \frac{1}{2}(-1)^n(u_n - u_{n-1}). \tag{7}$$

3. Results

Due to strong electron and lattice interaction, an extra electron in conjugated polymer chain cannot stay steadily in the bottom of the conduction band. Instead, it induces surrounding lattice to deform. As a result, the deformed lattice constructs a new potential well and shallowly binds the electron. Under an external electric field, this electron can be pushed ahead towards the reverse direction of the field. The previously deformed lattice zone recovers to its normal state and the zone where the electron passes by is involved in a new distortion. Thus the carrier mobility in conducting polymers is usually small especially for cases of low electric field strength. However, if a relatively high electric field is applied the time the electron is injected into the polymer chain, the lattice deformation actually occurs near the chain end. In consequence, carrier mobility has a nonlinear enhancement in the strong field regime [29].

In order to simulate the process of electron transfer across the polymer/electrode interface, we consider 100 monomers in the polymer on the left side and 100 monomers in the electrode connected on the right side. Initially we have an electron appear at the polymer chain end near

the interface. Due to the strong electron and lattice interaction, a polaron is induced to form near the interface. An electric field, $\boldsymbol{E}$, of sufficient strength is then applied so that the electron can overcome the interface barrier and hop to the electrode. The lifetime T of the process of electron transfer from the polymer to the electrode can be numerically obtained. Although it is very difficult to define the thickness of the interface, the electron velocity v across the interface is proportional to the inverse of T,

$$v \sim \frac{1}{T}. \tag{8}$$

Thus we can define an effective carrier mobility for this charge transfer process as

$$v \equiv \frac{1}{T|\boldsymbol{E}|}. \tag{9}$$

We name this mobility as interface mobility (IM) in the following. By IM, the correlation of charge carrier transfer velocity particularly across the interface with electric field strength can be described.

Depicted in Fig. 1 is the evolution of the total charge on the polymer chain(line) and the metal electrode(dot) in the presence of an electric field of 3×10^4 V/cm with the electrode chemical potential $\mu = 0$. It can be seen the total charge on the polymer chain reduces with time, while the total charge on the metal electrode increases correspondingly. This indicates that the electron is being transferred from the polymer to the electrode. We can also find from the figure that the electron transfer process can be largely separated into two phases by the time of about 4800 fs. Before 4800 fs, although the total charge on the polymer reduces, it is more than 0.5. Thus in this period, the electron is actually still at the polymer chain end. The reduction in the quantity of the total charge suggests that the electron is breaking away from the binding of the lattice and preparing for the immediate charge tunneling process. After 4800 fs, the total charge on the electrode exceeds 0.5, which suggests that this is the charge extraction process. At about 9500 fs, the total charge of the polymer as well as of the electrode keeps almost invariant. The total charge of the electrode is very close to unit 1, which suggests that the electron has tunneled to the electrode. Thus the lifetime of the charge transfer process is T = 9500 fs. This process can also be recognized from Fig. 2 in which the dots describe a polaron initially rests at the right end of the polymer chain and the line describes the lattice configuration at 9500 fs. It is clear that at 9500 fs, the electron has hopped to the electrode and thus can the lattice recover to the dimerized state.

To discover the field effect on IM, we perform three other charge transfer simulations with field strengths of 2×10^4 V/cm, 4×10^4 V/cm and 5×10^4 V/cm, respectively, and with the chemical potential of the metal electrode being fixed to zero for all the cases. The result for effective charge tunneling velocity versus electric field is shown by the blocks in Fig. 3. The connecting lines are only the guides for eyes. We can see the four blocks are nearly lying in one line. If we extrapolate the line, it can be found that the line almost passes by the origin. Thus the slope of the curve actually describes the IM of the process. Interestingly the block-curve suggests that the IM is independent on electric field strength because the slope at each point is almost identical. This result is quite different from the field dependent carrier mobility within the polymer chain

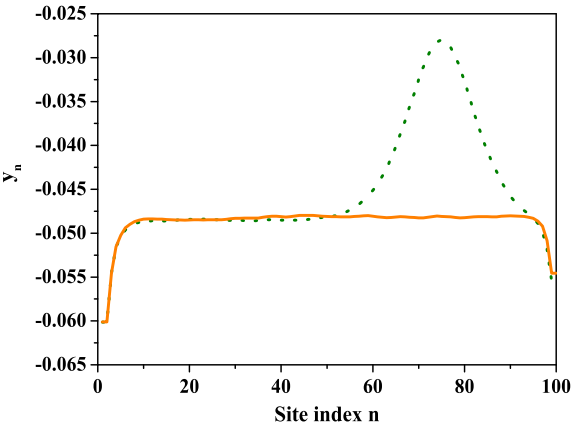

Fig. 2. Polymer lattice configuration at $t = 0$ (dot) and $t = 9500$ fs (line).

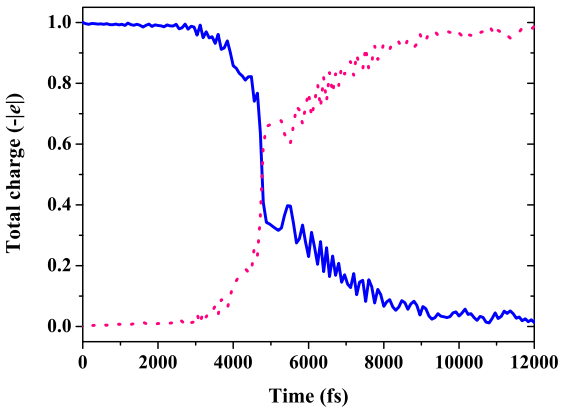

Fig. 1. Total charge evolution on the polymer chain(line) and the metal electrode(dot). Applied electric field is 3×10^4 V/cm.

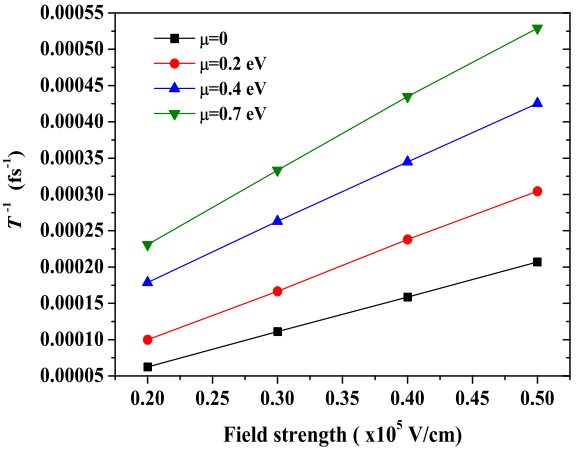

Fig. 3. Effective charge tunneling velocity with respect to electric field for various chemical potentials of the electrode $t_c = 1.0$ eV.

[40]. Thus we can conclude that the dependence of carrier mobility on electric fields is dominated by the intra-body behavior of charge carrier motion in polymers.

As is known, electrode work function has great impact on charge transfer between electrodes and organic layers. So it is necessary to investigate the influence of electrode work function on IM. In our model, the electrode work function is manipulated by changing the chemical potential μ of the metal electrodes. By increasing the electrode μ, the electrode work function is equivalently adjusted to a lower value. In order to readily observe the electron tunneling processes from the polymer to the electrode, we have the Fermi level of the electrodes always lower than the lowest unoccupied molecular orbital (LUMO) of the polymers. In Fig. 3 we show electronic velocity across the interface with respect to electric fields for four kinds of metal electrodes with various work functions. We can find that the triangles and the dots almost lie in a same line respectively like blocks. Moreover, the lines almost pass by the origin if extrapolated. Thus the slope of the lines represents the IM of the electron extraction processes. It is clear that the IM has no dependence on the applied electric fields in all the four cases. However, the IM increases with the chemical potential of the electrodes as indicated by the increasing slope of the curves. As the work function of the electrode decreases, the occupied level of the polymer has more and more correlation with the unoccupied levels of the electrode near the Fermi level because they gradually get access to each other in energy. Thus the correlation between the levels of electronic donor and acceptor stresses great effect on IM.

Typically, in electronic devices the property of polymer/electrode contacts can be markedly affected by chemisorptions or physisorptions in the preparation processes. In the present model, we have taken the polymer/electrode joint as a simple contact by introducing a coupling constant t_c to reflect the correlation between the electrodes and the polymers. In order to find out the influences of the joint character on IM, we carried out three groups of simulations for polaron transfer with three different interface coupling strengths. All the simulations are based on the same chemical potential of the electrode $\mu = 0.4$ eV. The results are shown in Fig. 4. One can find that the blocks, dots and triangles are almost lying in a same line respectively and the lines nearly pass by the origin if extrapolated. Thus it is clear that the correlation between the members of the contact has obvious effect on the electronic tunneling process. By increasing the correlation, both the IM and the electron tunneling velocity increase.

In real cases, migratory electrons do not have to be in the lowest energy state in polymers especially when thermal effect has to be taken into account. To this point, numerically we initially have the extra electron lying in an excited state (LUMO + 5 in the present work) in the polymer. It is different from the previous discussions where the extra electron is initially in the ground state (LUMO) and thus the charged carrier is polaron in the polymer that the extra electron in the excited state results in a delocalized charge carrier. The whole lattice is involved in vibrations due to the strong *e–p* coupling in the polymer. In order to compare with the previous results, we have the

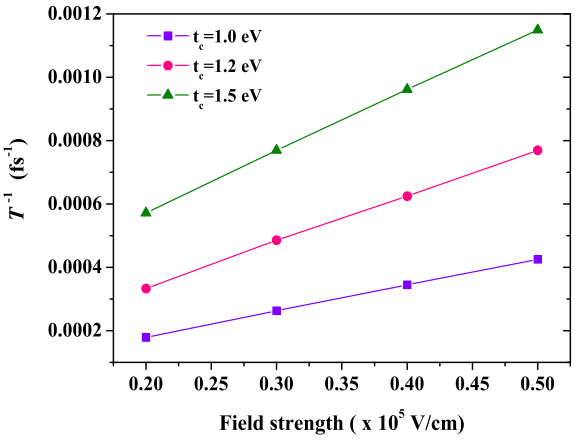

Fig. 4. Effective charge tunneling velocity with respect to electric field for various coupling strengths between the polymer and the metal electrode.

chemical potential of the electrode be zero and the charge tunneling simulation is performed under an electric field of the strength 3×10^4 V/cm. Fig. 5 gives the curves of total charge evolution of both the polymer(line) and the electrode(dot). It can be clearly seen that the lifetime of the charge transfer process is obviously reduced as compared to that shown in Fig. 1 where the charged carrier is localized polaron. This suggests that electrons of higher kinetic energy should have larger tunneling velocities. This point is more clearly shown in Fig. 6. The dots in this figure describe effective charge tunneling velocity versus electric field. The blocks of this figure are essentially the copies of the blocks in Fig. 3, only the scale of the ordinate is changed. Fig. 6 clearly shows that the electronic tunneling velocity is greatly increased for electrons with higher kinetic energy. By the comparison of the dots and the blocks of Fig. 6, it is also clear that the slope (or dv/dE) of these two cases are almost identical. However, since the dotted line does not pass by the origin, the IM of the dots are greater than that of the blocks. Thus we come to the conclusion that dv/dE is not impacted by the kinetic energy of the electrons although the electronic tunneling velocity as well as the IM is greatly enhanced.

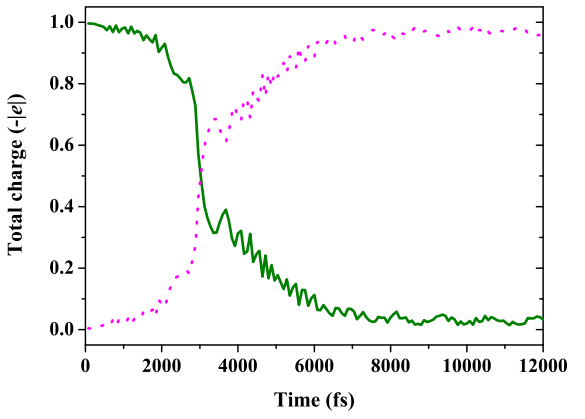

Fig. 5. Total charge evolution on the polymer chain(line) and the metal electrode(dot). Applied electric field is 3×10^4 V/cm.

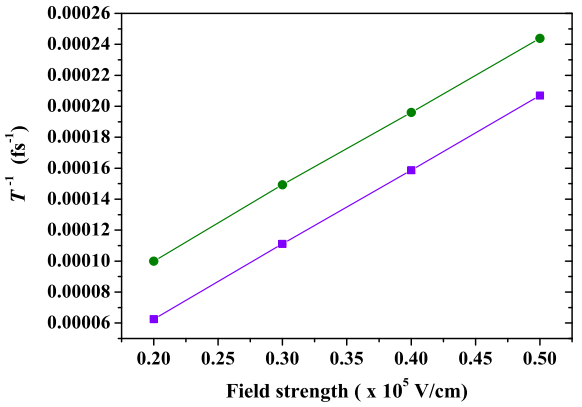

Fig. 6. Effective charge tunneling velocity with respect to electric field, with blocks for electrons initially lying in the ground state (LUMO) and dots for electrons initially lying in the excited state (LUMO + 5). For both cases the chemical potential of the metal electrode is 0.4 eV t_c = 1.0 eV.

From the previous discussions, we can find that the IM is essentially same as dv/dE if the charged carrier is polaron. As the electron is in an excited state and the charged carrier gets delocalized, the IM turns to be much large compared with dv/dE.

In the present work, the joint of the polymer and the electrode has been taken to be a simple contact. In real cases, however, the joint can be more complicated in both spacial organization and chemical ingredient. All the factors are important for practical device design task and will be studied in future work.

4. Summary

In conclusion, we have investigated electron transfer processes from polymers to metal electrodes through a dynamics method combined with an extended SSH model. We find that the IM is independent on the applied electric fields given the charged carriers being mainly composed of polarons. This suggests that the dependence of carrier mobility on electric fields is dominated by the intra-body behavior of the charged carrier in conducting polymers. In addition, we find that the IM closely depends on the work function of the electrode and the coupling of the polymer and the electrode. The IM can be obviously increased by decreasing the work function of the electrode or by increasing the correlation between the polymer and the electrode. We also find that the kinetic energy of the electrons in polymers does not affect dv/dE although it stresses great impact on electronic tunneling velocity as well as the IM.

Acknowledgements

This research is supported by the National Nature Science Foundation of China (Grants Nos. 20974101 and 10875106), the Scientific Research Foundation for the Returned Overseas Chinese Scholars, State Education Ministry, and the Program for Innovative Research Team in Zhejiang Normal University.

References

[1] J.H. Burroughes et al., Nature 347 (1990) 539.
[2] D. Gundlach, Y. Lin, T. Jackson, D. Schlom, Appl. Phys. Lett. 71 (1997) 3853.
[3] G. Yu, J. Gao, J.C. Hummelen, F. Wudl, A.J. Heeger, Science 270 (1985) 1789.
[4] N.S. Sariciftci, L. Smilowitz, A.J. Heeger, F. Wudl, Science 258 (1992) 1474.
[5] J.Y. Fu, J.F. Ren, X.J. Liu, D.S. Liu, S.J. Xie, Phys. Rev. B 73 (2006) 195401.
[6] H.X. He, J.S. Zhu, N.J. Tao, L.A. Nagahara, I. Amlani, R. Tsui, J. Am. Chem. Soc. 123 (2001) 7730.
[7] R.H. Friend et al., Nature 397 (1999) 121.
[8] Y. Cao, I.D. Parker, G. Yu, C. Zhang, A.J. Heeger, Nature 397 (1999) 414.
[9] M. Wohlgenannt, K. Tandon, S. Mazumdar, S. Ramasesha, Z.V. Vardeny, Nature 409 (2001) 494.
[10] E.S. Chen, S.H. Yeh, H.F. Meng, Phys. Rev. B 65 (2002) 235206.
[11] L. Zhou et al., J. Appl. Phys. 104 (2008) 114507.
[12] R. Meerheim et al., J. Appl. Phys. 104 (2008) 014510.
[13] D.D.C. Bradley, A.R. Brown, P.L. Burn, R.H. Friend, A.B. Holmes, A. Kraft, Electronc Properties of Polymers, Solid State Sciences, vol. 107, Springer, Heidelberg, 1992.
[14] R.N. Marks, D.D.C. Bradley, Synth. Met. 57 (1993) 4128.
[15] G.F. Neumark, Phys. Rev. B 1 (1970) 2613.
[16] C.P. Jarrett, R.H. Friend, A.R. Brown, D.M. de Leeuw, J. Appl. Phys. 77 (1995) 6289.
[17] P.W.M. Blom, M.C.J.M. Vissenberg, J.N. Huiberts, H.C.F. Martens, H.F.M. Schoo, Appl. Phys. Lett. 77 (2000) 2057.
[18] V.I. Arkhipov, P. Heremans, E.V. Emelianova, G.J. Adriaenssens, H. Bässler, Appl. Phys. Lett. 82 (2003) 3245.
[19] K. Tanaka, Y. Tsuchimura, K. Akabori, F. Ito, T. Nagamura, Appl. Phys. Lett. 89 (2006) 061916.
[20] D. Basu et al., Appl. Phys. Lett. 89 (2006) 242104.
[21] J. Li, J.X. Sun, C. Zhao, Synth. Met. 159 (2009) 1915.
[22] N. Rappaport, O. Solomesch, N. Tessler, Appl. Phys. Lett. 99 (2006) 064507.
[23] W.F. Pasveer, J. Cottaar, P.A. Bobbert, M.A.J. Michels, Synth. Met. 152 (2005) 157.
[24] D. Moses, A. Dogariu, A.J. Heeger, Chem. Phys. Lett. 316 (2000) 356.
[25] H. Sirringhaus et al., Synth. Met. 111–112 (2000) 129.
[26] S.V. Rakhmanova, E.M. Conwell, Appl. Phys. Lett. 76 (2000) 3822.
[27] J.A. Freire, Phys. Rev. B 72 (2005) 125112.
[28] Z.G. Xia, D.Y. Sun, M. Asta, J.J. Hoyt, Phys. Rev. B 75 (2007) 012103.
[29] Y. Qiu, L. Zhu, J. Chem. Phys. 131 (2009) 134901.
[30] K. Murata, S. Ciná, N.C. Greenham, Appl. Phys. Lett. 79 (2001) 1193.
[31] W.F. Pasveer et al., Phys. Rev. Lett. 94 (2005) 206601.
[32] Y. Roichman, N. Tessler, Synth. Met. 135-136 (2003) 443.
[33] R. Coehoorn, W.F. Pasveer, P.A. Bobbert, M.A.J. Michels, Phys. Rev. B 72 (2005) 155206.
[34] R. Coehoorn, Phys. Rev. B 75 (2007) 155203.
[35] R. Coehoorn, S.L.M. van Mensfoort, Phys. Rev. B 80 (2009) 085302.
[36] W.P. Su, J.R. Schrieffer, A.J. Heeger, Phys. Rev. Lett. 42 (1979) 1698.
[37] S.A. Brazovskii, N.N. Kirova, Sov. Phys. JETP 33 (1981) 4.
[38] A.J. Heeger, S. Kivelson, J.R. Schrieffer, W.P. Su, Rev. Mod. Phys. 60 (1988) 781.
[39] S.V. Rakhmanova, E.M. Conwell, Synth. Met. 110 (2000) 37.
[40] A.A. Johansson, S. Stafström, Phys. Rev. B 69 (2004) 235205.
[41] A. Johansson, S. Stafström, Phys. Rev. Lett. 86 (2001) 3602.
[42] C.Q. Wu, Y. Qiu, Z. An, K. Nasu, Phys. Rev. B 68 (2003) 125416.
[43] Z.G. Yu, D.L. Smith, A. Saxena, A.R. Bishop, Phys. Rev. B 59 (1999) 16001.
[44] S.J. Xie, J.H. Wei, L.M. Mei, S.H. Han, S.S. Lai, J. Phys.: Condens. Matter 10 (1998) 2291.

Organic Electronics 12 (2011) 239–243

Contents lists available at ScienceDirect

Organic Electronics

journal homepage: www.elsevier.com/locate/orgel

Photoconductivity and FET performance of an n-type porphyrazine semiconductor, tetrakis(thiadiazole)porphyrazine

Yasuhito Miyoshi [a], Takuya Fujimoto [a], Hirofumi Yoshikawa [a], Michio M. Matsushita [a], Kunio Awaga [b,*], Terufumi Yamada [c], Hiroshi Ito [c,*]

[a] Department of Chemistry, Nagoya University, Chikusa-ku, Nagoya 464-8602, Japan
[b] Research Center for Materials Science, Nagoya University, Chikusa-ku, Nagoya 464-8602, Japan
[c] Department of Applied Physics, Nagoya University, Chikusa-ku, Nagoya 464-8603, Japan

ARTICLE INFO

Article history:
Received 5 October 2010
Received in revised form 5 November 2010
Accepted 12 November 2010
Available online 24 November 2010

Keywords:
n-Type semiconductor
Photoconductivity
Field effect transistor
Tetrakis(thiadiazole)porphyrazine

ABSTRACT

Photoconductivity and field effect transistor (FET) performance of thin films of a thiadiazole-annulated porphyrazine compound, tetrakis(thiadiazole)porphyrazine (abbreviated as H_2TTDPz) were examined. The photocurrent-action spectra for ITO/H_2TTDPz/Au photocell exhibited symbatic and antibatic responses, depending on the bias polarity. This characteristic difference in photocurrent responses was interpreted as a filter effect in Schottky-type photocells; the dissociation of the excitons generated near the negative electrode can effectively produce photocurrent in n-type semiconductors. We also found n-type semiconductor behavior of H_2TTDPz in the thin-film FETs operated by the gates of an ionic liquid and SiO_2, and obtained a field effect mobility of 7.2×10^{-4} $cm^2 V^{-1} s^{-1}$ and an on/off ratio of 10^4.

© 2010 Elsevier B.V. All rights reserved.

1. Introduction

Organic semiconductors have attracted much attention due to their potential applications in organic electronics to field effect transistors (FETs), photovoltaic cells, light-emitting diodes, etc. Among organic semiconductors, porphyrazine compounds such as phthalocyanines (Pcs) have been extensively studied due to their excellent electrical and optical properties and to their chemical stability [1–3]. While most Pcs are p-type semiconductors, a very limited number of Pc analogs are known to exhibit n-type behavior [4,5]. Since, in general, n-type organic semiconductors are more unstable than p-type ones against oxygen and moisture, it is important to develop stable n-type semiconductors. The stable Pc family includes a halogen-substituted derivative, F_{16}CuPc, which exhibits n-type conduction in its FETs with a carrier mobility of 0.2 $cm^2 V^{-1} s^{-1}$ [6]. Introduction of such an electron-withdrawing group reduces the orbital energy of the lowest unoccupied molecular orbital of Pc and makes it close to the work functions of metal electrodes, providing an efficient electron injection from the electrodes to the LUMO [7].

Thiadiazole rings possess electron-withdrawing properties due to their electronegativity [8]. This chemical moiety was introduced to the molecular skeleton of Pc by the groups of Ercolani and Stuzhin through synthesis of the thiadiazole-ring annulated Pc, tetrakis(thiadiazole)porphyrazine (abbreviated as H_2TTDPz, see Fig. 1a) [9–12]. In our previous work, we have fabricated highly oriented thin films of H_2TTDPz and found a graphite-like structure: H_2TTDPz forms a 2D layer with an electrostatic side-by-side contact between the thiadiazole rings and the 2D layers stack perpendicular to substrates (see Fig. 1b) [13–15]. Furthermore, we have revealed the robustness of the thin films in electrochemical processes; the cyclic voltammogram of the H_2TTDPz thin film exhibited a repeatable reduction

* Corresponding authors. Tel.: +81 52 789 2487; fax: +81 52 789 2484 (K. Awaga); tel.: +81 52 789 5164; fax: +81 52 789 3712 (H. Ito).
E-mail addresses: awaga@mbox.chem.nagoya-u.ac.jp (K. Awaga), ito@nuap.nsagoya-u.ac.jp (H. Ito).

1566-1199/$ - see front matter © 2010 Elsevier B.V. All rights reserved.
doi:10.1016/j.orgel.2010.11.005

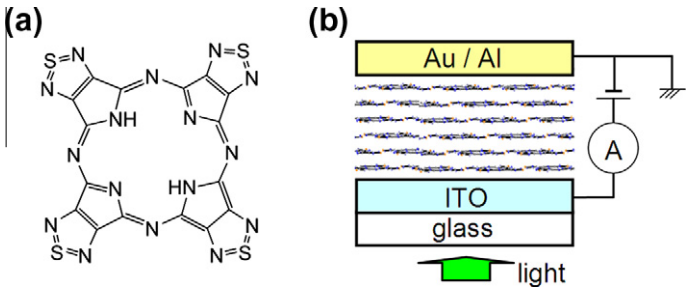

Fig. 1. H_2TTDPz molecule (a) and a schematic diagram for photoconductivity measurements (b).

peak at ca. −0.1 V *vs.* Ag/AgCl. This small negative value indicates a good electron-accepting ability of H_2TTDPz and its potential n-type semiconductor behavior. In the present report, we describe the photocurrent and the FET performance of the H_2TTDPz thin films, and present firm evidence for n-type transport.

2. Experimental

H_2TTDPz was prepared by the literature method [9]. We adopted sandwich cells (Fig. 1b) for the photocurrent measurements, and fabricated them as follows [16]. First, a thin film of H_2TTDPz was evaporated onto a glass substrate on which a 2 mm-width ITO electrode of thickness 100 nm was formed. Then a 2 mm-width Au or Al electrode with a thickness of 50 nm was evaporated onto the film perpendicular to the ITO electrode. The effective sample area was 0.04 cm^2. In order to avoid short circuiting, the thickness of H_2TTDPz was set to 200 nm, which was longer than the light penetration depth of 80 nm at the top of the Q-band.

The dc and ac photocurrent measurements were carried out with a 500-W halogen lamp [16]. The light intensity was calibrated with a Si photodiode. The monochromated light was allowed to illuminate the transparent ITO electrode, and the photocurrent was recorded under vacuum. To obtain the photocurrent-action spectra, the light was chopped with a frequency of 17–18 Hz, and the signals were detected by a two-phase lock-in amplifier [16]. The ac voltage appearing on a series resistance (1 MΩ) was measured under applied dc bias between two electrodes. The photocurrent-action spectra were then normalized in such a way that the incident photon number was constant ($10^{15}/cm^2$).

The FET performance of the H_2TTDPz thin films was examined using two kinds of gate materials, an ionic liquid, *N*,*N*-diethyl-*N*-methyl(2-methoxyethyl)ammonium bis(trifluoromethylsulfonyl)imide (abbreviated as DEME-TFSI), and SiO_2. Thin films of H_2TTDPz with a thickness of 100 nm were evaporated on interdigitated array electrodes (source and drain) with a channel width of W = 20 cm and a channel length of L = 10 μm, which are prepared by photolithography on surface-oxidized n-doped Si substrates (SiO_2: 300 nm). The ionic-liquid gate was prepared by putting a droplet of a commercial ionic liquid, DEME-TFSI, on the H_2TTDPz surface and inserting a Pt wire in it (see the inset of Fig. 6), while the surface-oxidized Si layer was used as gate in the SiO_2-gate FETs. The source and drain electrode materials were Pt and Au for ionic-liquid-gate and SiO_2-gate FETs, respectively. The performance of these FETs was examined under vacuum.

3. Results and discussion

3.1. Photocurrent

Fig. 2 shows the I–V characteristics of an (+)ITO/H_2TTDPz (200 nm)/Au(−) cell, shown in Fig. 1b. In the dark state, a clear rectifying behavior was observed (black curve), indicating the presence of a Schottky barrier, while, under illumination of white light, photocurrent was observed for both bias directions (red curve). The photocurrent quantum yield was calculated as approximately 0.1% under light illumination of 532 nm. Fig. 3 shows the photocurrent-action spectra with bias voltages of −2 (red), −1 (orange), 1 (green), and 2 V (blue), applied to the ITO electrode. This figure also shows the optical absorption spectrum of a 100-nm film of H_2TTDPz as a broken curve. When the ITO was negatively biased (red and orange), the photocurrent appeared in the range of photon energy above 1.4 eV, with a maximum of 1.8 eV. After passing through a minimum at 2.5 eV, the photocurrent increased again. These action spectra are nearly 'in phase' with the optical absorption, representing 'symbatic' behavior. When the ITO was positively biased (green and blue curves), however, the action spectra reached three maximums at

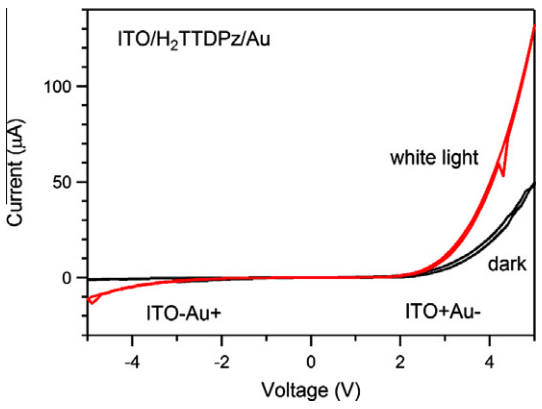

Fig. 2. I–V characteristics of the ITO/H_2TTDPz/Au photocell under dark and white light illumination.

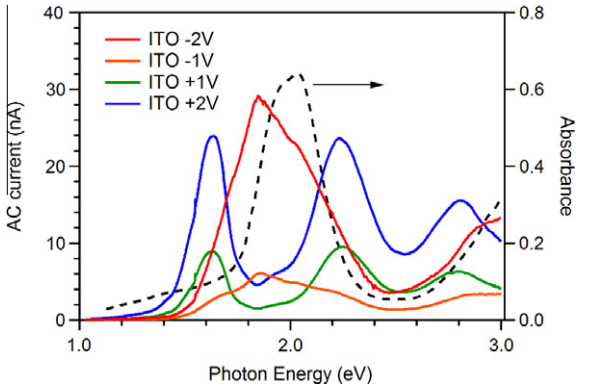

Fig. 3. Photocurrent-action spectra of the ITO/H_2TTDPz/Au photocell illuminated from ITO side under applied bias of −2 to +2 V. A broken line represents the optical absorption spectra.

1.6, 2.2, and 2.8 eV, being 'out of phase' with the photoabsorption ('antibatic' behavior).

Fig. 4 shows the photocurrent-action spectra of an (+)ITO/H_2TTDPz (200 nm)/Al(−) photocell under biases of −2 (red), −1 (orange), 1 (green), and 2 V (blue). When the Au anode was replaced with Al, the photocurrent became much smaller. In addition, the photocurrent always exhibited symbatic behavior under biases between 2 and −2 V.

The observed symbatic and antibatic behavior and the significant dependence on the anode metal can be explained as follows. Schottky-type photocells are known to exhibit a so-called filter effect in photocurrent-action spectra, in case in which the film thickness is larger than the light penetration depth [16–18]. More specifically, it is the light absorption near the Schottky contact that results in effective dissociation of excitons into free carriers because the electric field is concentrated on the barrier region [18]. The excitons far from the blocking contact cannot reach the barrier region, so they would recombine geminately without producing photocarriers.

Since the major carrier in n-type semiconductors is electrons, their photocurrent should be dominated by photocarriers generated near the negatively biased electrode, forming a Schottky contact with the n-type materials [19–22]. After charge separation near the negative electrode, the positive carriers or holes are easily absorbed into this electrode and electrons as negative carriers travel to the opposite positive electrode, producing photocurrent. Therefore, when the negative electrode is illuminated, the photocarrier yield is proportional to the light intensity and the photocurrent action spectrum coincides with the optical absorption spectrum of the semiconductor, resulting in 'symbatic' behavior. If the positive electrode is illuminated, however, the light intensity might attenuate before reaching the negative electrode at which the photocarriers are generated, due to a strong absorption in the organic semiconductors. Therefore, a larger photocurrent is expected at the absorption edges than at the absorption center, because such weakly absorbed light can reach the negative electrode and can induce charge separation there. The photocurrent action spectrum becomes out of phase with the optical absorption spectrum, resulting in 'antibatic' behavior.

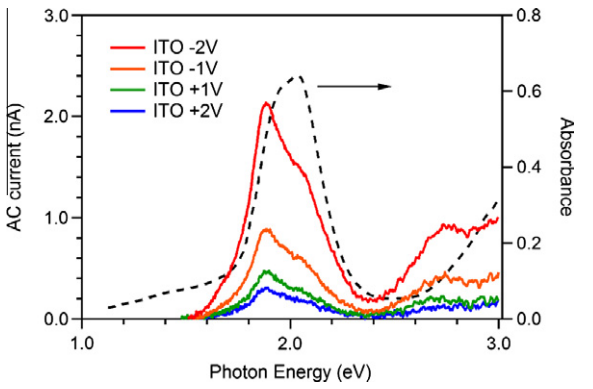

Fig. 4. Photocurrent-action spectra of the ITO/H_2TTDPz/Al photocell illuminated from ITO side under applied bias of −2 to +2 V. A broken line represents the optical absorption spectra.

Fig. 5a schematically shows the workfunctions of the ITO and Au electrodes as well as the HOMO and LUMO levels of H_2TTDPz. The expected charge separation region in the ITO/H_2TTDPz/Au photocell is indicated as a yellow oval. Photoelectron spectroscopy and photoabsorption spectroscopy on H_2TTDPz suggest that the LUMO and HOMO levels of H_2TTDPz are 4.6 and 6.6 eV, respectively, from the vacuum level [23]. Because these levels are far from the workfunctions of ITO (4.8–5.1 eV) and Au (5.1 eV), either ITO/H_2TTDPz or Au/H_2TTDPz contact would act as a blocking contact with a Schottky-type barrier when negatively biased. In contrast, the workfunction of Al (4.2 eV) is close to the LUMO level so that the Al contact probably forms an ohmic contact with H_2TTDPz. The symbatic and antibatic behavior and the strong electrode dependence of the ITO/H_2TTDPz/Au and ITO/H_2TTDPz/Al photocells are consistent with H_2TTDPz acting as an n-type semiconductor.

3.2. FET characteristics

In our previous work, we examined the solid-state electrochemical reduction of the H_2TTDPz thin films in an electrolyte solution, taking advantage of their robustness. In situ conductivity measurements for the thin films in NH_4Cl electrolyte revealed a conductivity enhancement on the order of 10^3, associated with penetration of the counter cations into the thin films. In the present work, we fabricated thin-film FETs of H_2TTDPz with an ionic liquid, DEME-TFSI, as a gate electrolyte (see the inset of Fig. 6). By using such an ionic liquid, high-density carrier accumulations were expected through an electric double layer (EDLs) formed on the H_2TTDPz surface in the gate electrolyte solution [24,25].

Fig. 6 shows the output characteristic, namely the source-drain current I_D *vs.* voltage V_D plots, measured in the dark under vacuum with the gate voltages V_G = 0.0, 0.2, 0.4 and 0.6 V. There is little deviation from zero current with an increase in V_G, indicating that current leakage through the dielectric is negligibly small.

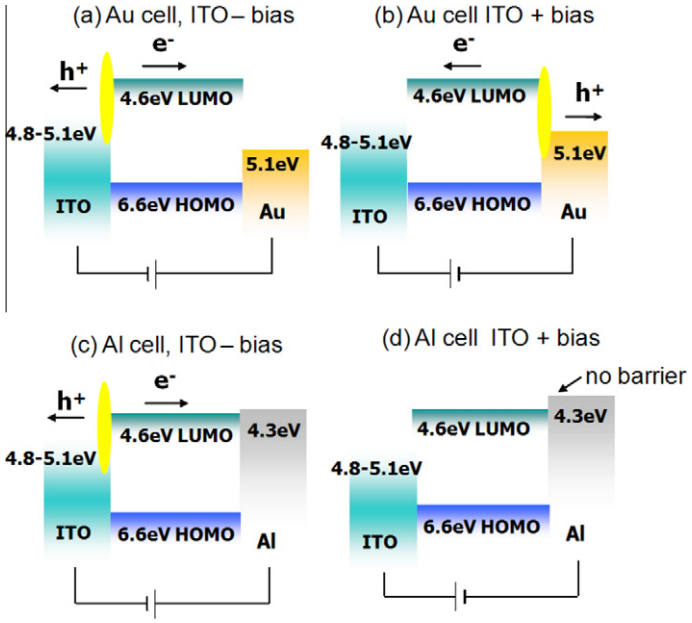

Fig. 5. Schematic energy diagram for ITO/H_2TTDPz/Au (a) and (b) and ITO/H_2TTDPz/Al (c) and (d) cells under negative (a) and (c) or positive (b) and (d) bias applied to the ITO electrode.

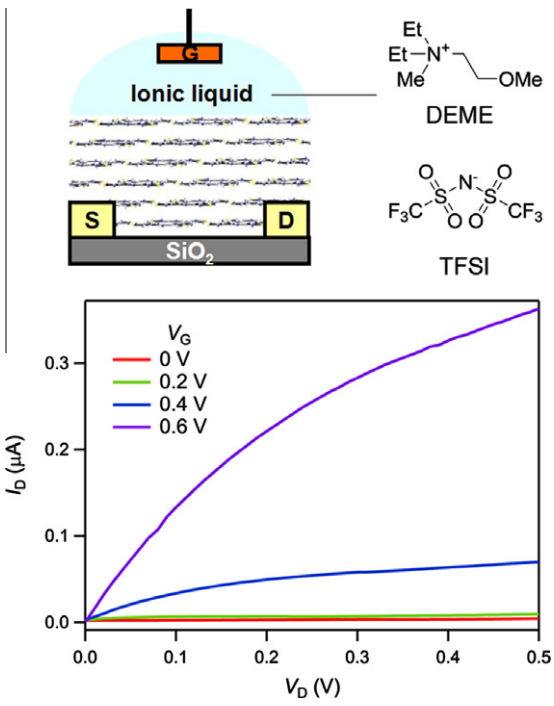

Fig. 6. Output characteristics of the ionic liquid-gate FET of H_2TTDPz. The inset shows a schematic illustration of the device configuration.

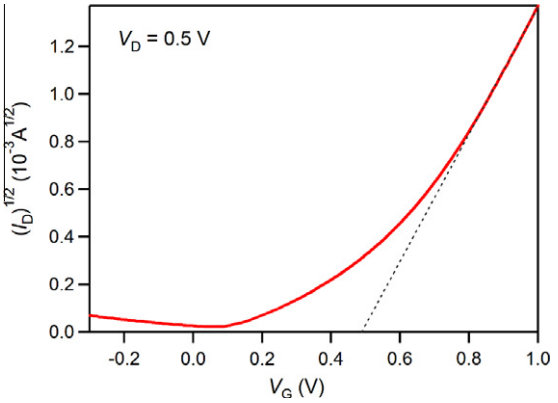

Fig. 7. Transfer characteristics of the ionic liquid-gate FET of H_2TTDPz.

Fig. 7 shows the transfer characteristic, namely the source-drain current $I_D^{1/2}$ *vs.* gate voltage V_G plots, measured in the dark under vacuum with a source-drain voltage of $V_D = 0.5$ V. The I_D value at $V_G = 0$ V is less than 1 nA, indicating that the present transistors are in normally off states. With an increase in V_G towards a positive value, I_D shows a quick increase above $V_G = 0.2$ V with an on/off ratio of ca. 10^4. This value is higher than the conductivity enhancement factor (10^3) obtained in solid-state electrochemistry [15]. In addition, the I_D *vs.* V_G curves showed a good reversibility, so that there should be no penetration of the counter cations in the present EDL-FET system.

This FET behavior clearly indicates that H_2TTDPz operates as an n-type semiconductor. The extrapolation of the $I_D^{1/2}$ *vs.* V_G curve from the large V_G range indicates a very low threshold voltage of $V_G^{th} = 0.5$ V. This type of low power operation is an advantage of ionic-liquid gate dielectrics transistors. The field effect mobility in the saturation regime is calculated as $\mu = 7.2 \times 10^{-4}$ cm^2 V^{-1} s^{-1}, using the equation $\mu = 2L/WC \cdot (\partial\sqrt{I_D}/\partial V_G)^2$, where L, W, and C are the channel length, the channel width, and the capacitance of the dielectric layer, respectively. The value of C for DEME-TFSI was obtained as 1 μF cm^{-2} in a separate measurement using a parallel plate capacitor of this

material. The μ value of H_2TTDPz is nearly comparable to that of F_{16}MPc [6]. We have also examined the performance of the SiO_2-gate thin-film FETs of H_2TTDPz. The results are shown in Supplementary Fig. S1, indicating $V_G^{th} = 10$ V, the on/off ratio = $\sim 10^2$, and $\mu = 1.3 \times 10^{-5}$ $cm^2\,V^{-1}\,s^{-1}$.

Although we found a slight improvement in μ by using wider gap electrodes, the obtained μ values for H_2TTDPz were not very high. This is perhaps because of a mismatch between the conduction pathway and the π stacking direction, as indicated in the inset of Fig. 6. Namely, the molecular planes of H_2TTDPz are parallel to substrates, so that the π stacking does not bridge the distance between the source and drain electrodes [15]. However, the n-type semiconductor behavior of H_2TTDPz indicates that p–n junctions between the series of Pc and H_2TTDPz would be highly possible, which are applicable to bulk heterojunction photovoltaic cells. Since porphyrazine has a good chemical stability and is useful in organic electronics, all porphyrazine-based organic devices would be promising.

4. Conclusion

We have performed photocurrent and FET performance measurements on the thin films of H_2TTDPz and have found firm evidence of n-type semiconductor behavior. The ITO/H_2TTDPz/Au cells exhibited symbatic and antibatic behavior, according to bias voltage direction, which was well-interpreted as a filter effect for the semiconductors. The thin film FET of H_2TTDPz also showed a typical feature of n-type semiconductors. The electron mobility was evaluated from the transfer characteristics as $\mu = 7.2 \times 10^{-4}\,cm^2\,V^{-1}\,s^{-1}$. Although this value is not very high, the chemical stability of H_2TTDPz as a porphyrazine derivative suggests the potential application of the M-TTDPz series in organic electronics as an n-type semiconductor.

Acknowledgment

This work was supported by a Grant-in-Aid for Scientific Research from the Ministry of Education, Culture, Sports, Science and Technology (MEXT).

Appendix A. Supplementary data

Supplementary data associated with this article can be found, in the online version, at doi:10.1016/j.orgel.2010.11.005.

References

[1] C.C. Leznoff, A.B.P. Lever, Phthalocyanines: Properties and Applications, vol. 4, VCH Publications, New York, 1996;
K.M. Kadish, K.M. Smith, R. Guilard, The Porphyrin Handbook. vols. 17 and 19, Academic Press, New York, 2003.
[2] H. Miyoshi, H. Ohya-Nishiguchi, Y. Deguchi, Bull. Chem. Soc. Jpn. 46 (1973) 2724;
K. Awaga, Y. Maruyama, Phys. Rev. B 44 (1991) 2589;
M. Matsuda, T. Asari, T. Naito, T. Inabe, N. Hanasaki, H. Tajima, Bull. Chem. Soc. Jpn. 76 (2003) 1935.
[3] C.G. Barraclough, R.L. Martin, S. Mitra, R.C. Sherwood, J. Chem. Phys. 53 (1970) 1643;
S. Mitra, A. Gregson, W. Hatfield, R. Weller, Inorg. Chem. 22 (1983) 1729;
M. Evangelisti, J. Bartolomé, L.J. Jongh, G. Filoti, Phys. Rev. B 66 (2002) 144410.
[4] P. Turek, P. Petit, J.-J. Andre, J. Simon, R. Even, B. Boudjema, G. Guillaud, M. Maitrot, J. Am. Chem. Soc. 109 (1987) 5119.
[5] Z. Bao, A.J. Lovinger, A. Dodabalapur, Appl. Phys. Lett. 69 (1996) 11.
[6] Z. Bao, A.J. Lovinger, J. Brown, J. Am. Chem. Soc. 120 (1998) 207.
[7] C.R. Newman, C.D. Frisbie, D.A. Da Silva Filho, J. Bredas, P.C. Ewbank, K.R. Mann, Chem. Mater. 16 (2004) 4436.
[8] M. Mamada, J. Nishida, D. Kumaki, S. Tokito, Y. Yamashita, Chem. Mater. 19 (2007) 5404.
[9] P.A. Stuzhin, E.M. Bauer, C. Ercolani, Inorg. Chem. 37 (1998) 1533.
[10] E.M. Bauer, D. Cardarrilli, C. Ercolani, P.A. Stuzhin, U. Russo, Inorg. Chem. 38 (1999) 6114.
[11] M.P. Donzello, C. Ercolani, A.A. Gaberkorn, E.V. Kudrik, M. Meneghetti, G. Marcolongo, C. Rizzoli, P.A. Stuzhin, Chem. Eur. J. 9 (2003) 4009.
[12] E.V. Kudrik, E.M. Bauer, C. Ercolani, A. Chiesi-Villa, C. Rizzoli, A. Gaberkorn, P.A. Stuzhin, Mendeleev Commun. 11 (2001) 45.
[13] M. Fujimori, Y. Suzuki, H. Yoshikawa, K. Awaga, Angew. Chem. Int. Ed. 42 (2003) 5863.
[14] Y. Suzuki, M. Fujimori, H. Yoshikawa, K. Awaga, Chem. Eur. J. 10 (2004) 5158.
[15] Y. Miyoshi, M. Kubo, T. Fujinawa, Y. Suzuki, H. Yoshikawa, K. Awaga, Angew. Chem. Int. Ed. 46 (2007) 5532.
[16] H. Ito, N. Nomura, T. Suzuki, S. Ukai, K. Marumoto, S. Kuroda, Collid. Surf. A 284–285 (2006) 613.
[17] K. Kaneto, K. Takayama, W. Takashima, T. Endo, M. Rikukawa, Jpn. J. Appl. Phys. 41 (2002) 675.
[18] A.K. Ghosh, T. Feng, J. Appl. Phys. 49 (1978) 5982.
[19] K. Yamashita, Y. Matsumura, Y. Harima, S. Miura, H. Suzuki, Chem. Lett. 13 (1984) 489.
[20] Y. Harima, H. Okazaki, Y. Kunugi, K. Yamashita, H. Ishii, K. Seki, Appl. Phys. Lett. 69 (1996) 1059.
[21] G.D. Sharma, M. Roy, M.S. Roy, Mater. Sci. Eng. B 104 (2003) 15.
[22] M.S. Roy, G.D. Sharma, S.K. Gupta, Thin Solid Films 310 (1997) 279.
[23] Y. Tanaka, K. Takahashi, T. Kuzumaki, Y. Yamamoto, K. Hotta, A. Harasawa, Y. Miyoshi, H. Yoshikawa, Y. Ouchi, N. Ueno, K. Seki, K. Awaga, K. Sakamoto, Phys. Rev. B 82 (2010) 073408.
[24] H. Shimotani, H. Asanuma, J. Takeya, Y. Iwasa, Appl. Phys. Lett. 89 (2006) 203501.
[25] T. Fujimoto, M.M. Matsushita, K. Awaga, Chem. Phys. Lett. 483 (2009) 81.

Organic Electronics 12 (2011) 244–248

Contents lists available at ScienceDirect

Organic Electronics

journal homepage: www.elsevier.com/locate/orgel

Influence of series resistance on the photocurrent analysis of organic solar cells

R.A. Street [a,*], K.W. Song [a], S. Cowan [b]

[a] Palo Alto Research Center, Palo Alto, CA 94304, United States
[b] Center for Polymers and Organic Solids, University of California, Santa Barbara,Santa Barbara, CA 93106, United States

ARTICLE INFO

Article history:
Received 30 July 2010
Received in revised form 19 October 2010
Accepted 14 November 2010
Available online 25 November 2010

Keywords:
Organic solar cell
Photoconductivity

ABSTRACT

The series resistance of a bulk heterojunction solar cell diode affects the measurement of the voltage dependence of the diode photocurrent, $P(V)$. An empirical model for the effect is described and shows that $P(V)$ can be significantly modified, particularly at high bias voltages. Experimental measurements on PCDTBT:PCBM solar cells with added series resistance demonstrate the effect and confirm the model. The model provides a method to correct the photoconductivity data using measured quantities.

© 2010 Elsevier B.V. All rights reserved.

1. Introduction

Organic solar cells are formed from a nanostructured composite of electron donor and acceptor domains with a bulk heterojunction (BHJ) diode structure [1]. Excitons which are optically excited in one or other domain are split by the band offset at the BHJ interface so that the electrons move in the acceptor and holes in the donor. The charge is collected by the internal voltage of the diode. The cell structure comprises metal contacts which are usually an indium tin oxide (ITO) anode and a suitable metal cathode, a hole contact layer which is typically poly(3,4-ethylenedioxythiophene):poly(styrenesulfonate) (PEDOT:PSS) and is principally in electrical contact with the donor, the BHJ diode and sometimes an additional optical spacer layer of TiO_x in electrical contact with the acceptor [2]. The diode built-in potential arises from the difference in the effective Fermi energy on either side of the diode.

The recombination of the electrons and holes is of great interest because it has a detrimental effect on the solar cells efficiency and because it is fundamentally interesting to understand the role of the nanostructure on the opto-electronic properties. There are several possible recombination mechanisms and considerable disagreement over which mechanism dominates in any particular cells [3–7]. A useful measure of the recombination is the voltage dependence of the cell photocurrent [7–9]. Barring contact injection or avalanche gain, both of which are negligible at low electric fields [10], the diode is limited to unity gain in reverse bias. Hence, the photocurrent normalized to the effective generation rate, $P(V)$, measures the fraction of carriers that reach the contacts, and $1 - P(V)$ is the fraction that recombine.

A knowledge of $P(V)$ therefore allows different recombination models for the BHJ diode to be tested. Since the recombination occurs at the interface in the BHJ structure, it is important that $P(V)$ correctly reflects the internal photocurrent of the diode and the electronic properties of the junction. The purpose of this paper is to point out that this is not necessarily the case. Generally it is expected that $P(V)$ will drop monotonically to zero when the applied voltage equals the built-in potential, V_{BI}, because at this voltage the internal field changes sign.

It is well known that a series resistance influences the current in a solar cell and reduces the fill factor as shown in BHJ cells by recent work [11]. The physical origin of the series resistance in any particular cell is not obvious

* Corresponding author. Tel.: +1 650 812 4165.
E-mail address: street@parc.com (R.A. Street).

1566-1199/$ - see front matter © 2010 Elsevier B.V. All rights reserved.
doi:10.1016/j.orgel.2010.11.012

because there are several possibilities. Most cells use an ITO transparent conductor and its resistance between the cell stack and the contact leads can be significant. Within the cell stack the PEDOT:PSS layer and the TiO_x (if used) have higher resistivity than the metal contacts, and could be the origin. Any of the junctions between the layers could also add resistance. For example, ITO and PEDOT:PSS have different work functions, and the alignment of the Fermi energy across the junction occurs by charge transfer at the interface. The resulting dipole layer at this or other junctions may introduce a series resistance. The internal resistance of carriers in the BHJ diode itself may also be the origin of the series resistance.

This paper describes how the resistance specifically affects the cell photocurrent. An empirical model is described that does not presuppose any specific physical origin of the series resistance. Indeed we show that some measured forms of $P(V)$ are a consequence of a series resistance that could be of any origin. Analytical expressions relating the experimentally measured and internal $P(V)$ are developed in Section 2 and compared to experimental data in Section 3.

2. Series resistance model

The photocurrent is the difference between the current measured under illumination, J_L, and the dark current, J_D,

$$J_L(V) = J_D(V) - e \cdot G \cdot P(V), \tag{1}$$

where G is the effective carrier generation rate (the concentration of optically excited excitons that are split at the BHJ interface), and the sign of the photocurrent is chosen so the $P(V)$ is positive under solar cell operating conditions. The diode dark current is described by [12,13],

$$J_D(V) = J_0 \exp\left(\frac{e(V - J_D(V)R_S)}{nkT}\right) = J_0 \exp\left(\frac{eV_{IDJ}}{nkT}\right), \tag{2}$$

where n is the diode ideality factor, R_S is the ohmic series resistance (in units of $\Omega\,cm^2$) and the shunt resistance is not included. $V_{IDJ} = V - J_D R_S$ is the internal diode junction voltage with the voltage drop across the resistance subtracted, and is the voltage that defines the diode junction. This conventional form of the dark current applies well to many BHJ solar cells at the voltages of interest [7,13]. Inserting Eq. (2) into Eq. (1) gives the experimentally measured $P_{EXP}(V)$,

$$eGP_{EXP}(V) = J_0 \exp\left(\frac{e(V - J_D(V)R_S)}{nkT}\right) - J_L(V) \tag{3}$$

$P_{EXP}(V)$ is the difference between the experimentally measured dark current and the experimentally measured current under illumination. However, inspection of Eq. (3) indicates that it cannot be the correct expression for the photocurrent, since the right side of the equation has the current J_L in one term and J_D in the other. The problem is that the voltage drop across the series resistance must reflect the current under illumination rather than the current in the dark. Consequently the photoconductivity derived experimentally from Eqs. (1) and (2) is not the correct internal photoconductivity when there is significant series resistance. The voltage drop across R_S has a different magnitude in the dark and under illumination and also changes sign with the current, and is therefore of opposite sign for the dark current and the photocurrent for $V < V_{OC}$.

There is a second related problem with the use of Eq. (3) to extract the internal $P(V)$. The term $(V - J(V)R_S)$ in the diode equation (Eq. (2)) arises because the internal voltage across the diode differs from the external applied voltage. The physically interesting $P(V)$ also reflects the internal diode voltage V_{IDJ}, rather than the external voltage. The internal diode photocurrent, $P_{INT}(V)$, is therefore described by Eqs. (1) and (2), in which V is replaced by V_{IDJ} in the expression for $P(V)$, which gives

$$eGP_{INT}(V_{IDJ}) = J_0 \exp(eV_{IDJ}/nkT) - J_L(V) \tag{4}$$

Inserting the value of V_{IDJ} gives,

$$eGP_{INT}(V - J_L(V)R_S) = J_0 \exp\left(\frac{e(V - J_L(V)R_S)}{nkT}\right) - J_L(V) \tag{5}$$

Combining Eqs. (3) and (5), relates the experimental and internal $P(V)$,

$$eGP_{INT}(V - J_L R_S) = eGP_{EXP}(V) - J_0 \times \exp\left(\frac{eV}{nkT}\right)\left[\exp - \frac{J_D(V)R_S}{nkT} - \exp - \frac{J_L(V)R_S}{nkT}\right] \tag{6}$$

or alternatively,

$$eGP_{INT}(V - J_L R_S) = J_D(V) \exp\left(\frac{eGP_{EXP}(V)R_S}{nkT}\right) - J_L(V) \tag{7}$$

The internal and experimental values of $P(V)$ are the same only when $J_L(V)R_S \ll V$ over the whole voltage range, otherwise they are different. The experimentally measured quantities are $J_L(V)$ and $J_D(V)$ from which $P_{EXP}(V)$ is obtained from Eq. (1). With the additional knowledge of R_S, which can be obtained from $J_D(V)$ using Eq. (2), $P_{INT}(V)$ can be deduced from these equations.

Calculations of $P_{EXP}(V)$ for a given $P_{INT}(V)$ with different series resistance and different illumination intensities were made to illustrate the effect. The parameters of the dark diode current calculation are chosen to correspond to the data for a PCDTBT/PCBM solar cell and we set $J_0 = 3 \times 10^{-12}$ A/cm^2, $n = 1.7$ and $V_{BI} = 0.86$ V. The internal $P_{INT}(V)$ in Eq. (7) is modeled by the charge collection equation used in Ref. [7], since it gives a good fit to the photoconductivity data but any suitable form could be used. The procedure for modeling the effect of series resistance to obtain $P_{EXP}(V)$ is to calculate the dark diode current from Eq. (2), the illuminated diode current, $J_L(V)$, from Eq. (5), and use these to calculate $P_{EXP}(V)$ from Eq. (3). The dark current is shown in the inset to Fig. 1, for a series resistance of 12 $\Omega\,cm^2$ and is a good fit to the data from Ref. [7].

Fig. 1 shows the calculated $P_{EXP}(V)$ for different series resistance at fixed generation rate and Fig. 2 shows the same as a function of the generation rate at fixed R_S. When the series resistance is zero, the internal and experimental $P(V)$ are identical. At low illumination levels, $P_{EXP}(V)$ differs from $P_{INT}(V)$ primarily at high forward voltages when $J_D(V)$ is large and $J_D(V)R_S$ is significant compared to V. At high

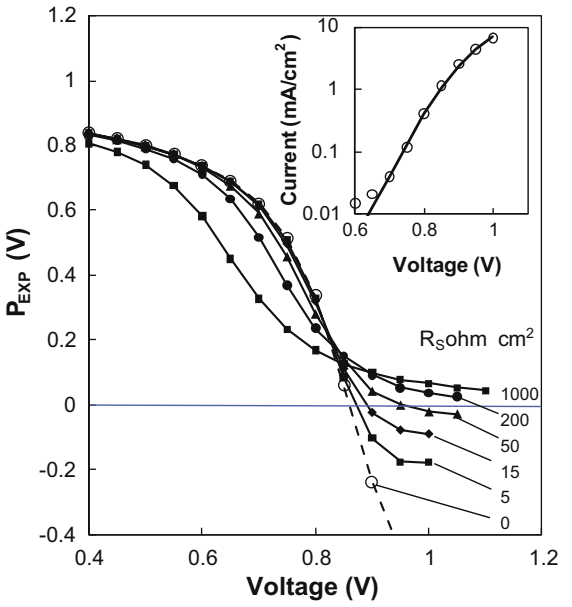

Fig. 1. Calculated $P_{EXP}(V)$ for fixed illumination and various series resistances as shown. The parameters of the calculation reflect data obtained for PCDTBT:PCBM cells, with V_{BI} = 0.86 V. $P_{INT}(V)$ is the dashed line. The illumination corresponds to a reverse saturation current of ~0.1 mA/cm^2. The inset shows the measured dark current for a PCBTBT:PCBM cell (data points), and the corresponding model (solid line) with R_S = 12 Ω cm^2, $J_0 = 3 \times 10^{-12}$ A/cm^2 and n = 1.7.

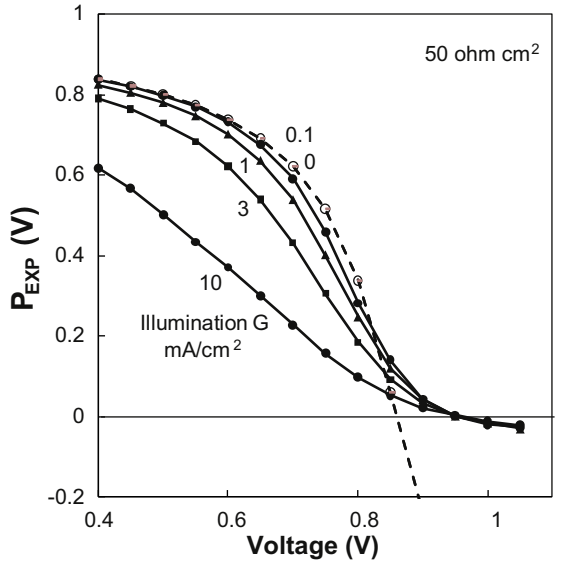

Fig. 2. Calculated $P_{EXP}(V)$ for a fixed series resistance and various illumination intensities as shown, with the same parameters as for Fig. 1.

light intensity $P_{EXP}(V)$ differs from $P_{INT}(V)$ over a wider range of voltages because $J_L(V)R_S$ is also large. Focusing on the high voltage behavior, there is an extended tail of $P_{EXP}(V)$ to high voltage, so that the zero crossing (the value of $V = V_X$ when $P_{EXP}(V_X) = 0$) moves to higher voltage with increasing R_S. Inspection of Eq. (6) shows that when $P_{EXP}(V_X)$ is zero, which occurs by definition, when $J_L = J_D$, then the right side of Eq. (6) is zero, so that $P_{INT}(V_X - J_L R_S)$ is also zero. This occurs when the internal voltage is the built-in potential, V_{BI}, so that,

$$V_X = V_{BI} + J_D(V_X)R_S \tag{8}$$

The voltage at which $P_{EXP}(V_X)$ crosses zero is therefore larger than V_{BI} and according to Eq. (8), should be independent of illumination, since none of the terms in the equation depend on the illumination intensity.

Further into forward bias than V_X, the increasing forward current results in a larger voltage drop across R_S, and the internal voltage is an increasingly small fraction of the applied voltage. $P_{EXP}(V > V_X)$ will therefore tend to a constant with absolute value <1 determined by the small residual internal voltage. Its value can be calculated from Eq. (3) and should decrease as R_S increases. If the series resistance is large enough to completely dominate the diode current, then $J_D \sim V_X/R_S$ and Eq. (8) has no solution. In this case $P_{EXP}(V_X)$ tends to zero asymptotically and never crosses zero, as is seen in the high resistance model calculations in Fig. 1.

The open circuit voltage V_{OC} occurs when $J_L(V_{OC}) = 0$, when from Eqs. (3) and (5),

$$eGP_{EXP}(V_{OC}) = J_0 \exp\left(\frac{e(V_{OC} - J_D(V)R_S)}{nkT}\right) \tag{9}$$

$$eGP_{INT}(V_{OC}) = J_0 \exp\left(\frac{eV_{OC}}{nkT}\right) \tag{10}$$

so that,

$$\frac{P_{INT}(V_{OC})}{P_{EXT}(V_{OC})} = \exp\left[-J_D(V_{OC})R_S/nkT\right] \tag{11}$$

Eq. (11) shows that $P_{INT}(V)$ is smaller than $P_{EXP}(V)$at V_{OC}, because the exponent is negative. However, at low illumination intensity and small V_{OC}, the right side of Eq. (11) becomes very close to unity.

3. Experimental measurements

To further illustrate the effects, we have measured $P_{EXP}(V)$ for BHJ solar cells in which an additional external series resistance is included. The cells are fabricated from a PCDTBT/$PC_{70}BM$ blend [14], and are similar to those used in the previous recombination studies [7]. Details of cell fabrication are given elsewhere [2]. The measurements are made using illumination chopped at 230 Hz, and a lock-in amplifier to record the photocurrent with the dark current automatically subtracted. The input to the lock-in amplifier is the voltage developed across a resistor, which was varied from R = 5 Ω–10 kΩ, and this resistor also acts as the added series resistance of the cell. The use of chopped illumination prevents possible effects of a temperature difference between measurements in the dark and under illumination.[15] The cell has an area of about A = 0.04 cm^2, and $R_S = R{\cdot}A$ for comparison with the model.

Fig. 3a shows the measurements of $P_{EXP}(V)$ for different added series resistance, and Fig. 3b shows measurements for different illumination intensities. The data also shows

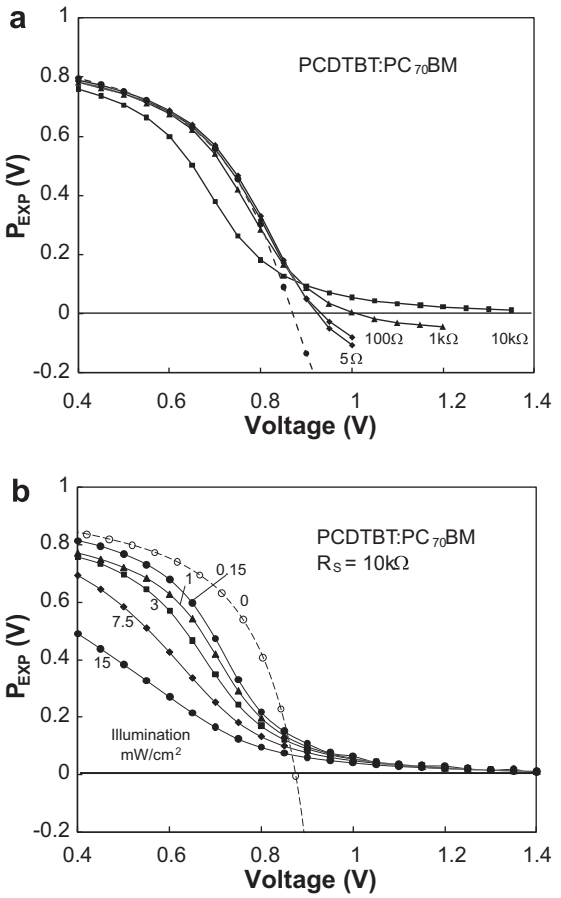

Fig. 3. (a) Measurements of $P_{EXP}(V)$ for a PCDTBT:PCBM solar cell with (a) added series resistance as shown and a constant light intensity, and (b) a fixed added series resistance of 10 kΩ, and for different light intensity, as shown. The measurements use a lock-in amplifier which automatically subtracts the dark current. The area of the cell is ~0.04 cm^2.

the charge collection model as used in the simulations of Figs. 1 and 2, with parameters chosen to fit the particular data set. Comparison of the data with the models in Figs. 1 and 2 shows qualitative and quantitative agreement. The change in shape of $P_{EXP}(V)$ for different resistance and light intensity is evident. The data shows no change in the $P_{EXP}(V)$ until R exceeds about 100 Ω ($R_S \sim 4\ \Omega\ cm^2$). The zero crossing voltage increases with series resistance, and at sufficiently large R, $P_{EXP}(V)$ remains positive and approaches zero asymptotically, as expected from the model. The data in Fig. 3a have a zero crossing at 0.92 V for the 5 Ω resistance and is almost the same for 100 Ω. The data in this voltage range deviate from the charge collection equation and have a higher zero crossing than we found previously (0.92 V versus 0.86 V). The curvature near the zero crossing indicates that there is a significant series resistance in this device even in the absence of the added resistance.

The variation with illumination intensity shown in Fig. 3b similarly agrees with the model, and demonstrates the expected decrease in $P_{EXP}(V)$ at lower voltages when G is sufficiently large. A large resistance was used for this experiment to accentuate the effects. The results illustrate that $P_{EXP}(V)$ can differ greatly from $P_{INT}(V)$.

The built-in potential and the corrected $P_{INT}(V)$ can be extracted from the measurement of $P_{EXP}(V_X)$ using set of equations given above. Fig. 4 shows measured $P_{EXP}(V_X)$ data for the PCDTBT/PCBM cell and the calculated $P_{INT}(V)$. The dark current, which is measured separately, provides a value of R_S, J_0 and n, and these parameters are shown in Fig. 4. The built-in potential can be obtained from the measured crossing point using Eq. (8). For the data in Fig. 4, the zero crossing voltage is 0.9 V and decreases to 0.87 V after the correction. The calculated $P_{INT}(V)$ in Fig. 4 differs from $P_{EXP}(V)$ mostly near the crossing point, and to a lesser extent at lower voltages, as expected. Cells with a much larger internal series resistance prove to be difficult to correct accurately, probably because R_S has a small voltage dependence rather than being constant, and the correction relies on an increasingly accurate model for J_D.

Previous data on similar PCDTBT cells had a zero crossing at 0.86 V and did not show significant curvature near the zero crossing [7]. The inset of Fig. 1 shows that the dark current data from Ref. [7] has a series resistance of 12 Ω cm^2 and the current at 0.86 V is about 1 mA/cm^2. The zero crossing voltage V_X is shifted by $J(V_X)R_S \sim 0.01$ V, which shows for that particular sample, that the measured P(V) is minimally affected by the series resistance. The cell in Fig. 4 has a larger internal resistance and hence a slightly different shape and crossing point. However the corrected values of the built-in potential for the two devices agree well.

The analysis of Fig. 4 shows that the series resistance measured in the dark leads to a function $P_{INT}(V)$ which is consistent with theoretical expectations and with measurements of $P_{EXP}(V)$ in similar devices with a lower resistance [7]. It is possible that the series resistance varies with light intensity in some solar cells [16]. In such cases the resistance can be treated as a free parameter and obtained from a best fit to any known property of $P_{INT}(V)$.

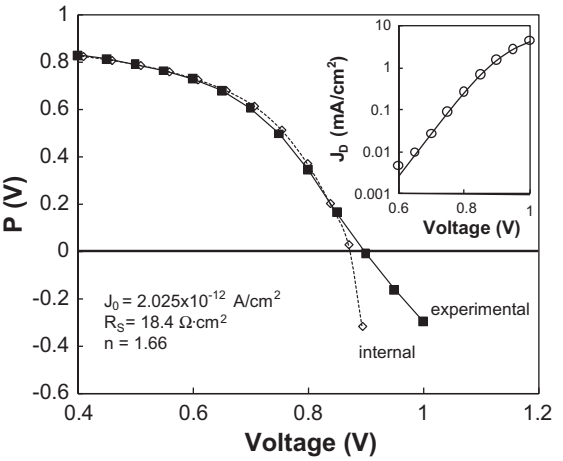

Fig. 4. Measurements of $P_{EXP}(V)$ for the same PCDTBT:PCBM cell as in Fig. 3, using dc illumination, and the calculation of $P_{INT}(V)$ as derived from Eq. (4). The series resistance and other diode parameters are obtained from the dark forward bias current, as shown in the inset (points are data and the line is the model). The reverse bias photocurrent is 0.7 mA/cm^2.

4. Discussion

The model and experiments show that $P(V)$ can be significantly modified by a series resistance. The data can be corrected to give the internal $P(V)$, provided that the series resistance can be determined and is not too large. The best test of whether there is a significant series resistance effect is to measure the dark forward bias characteristics, $J_D(V)$. If the exponential region of $J_D(V)$ continues up to at least the built-in potential, then the measured $P(V)$ is not influenced by series resistance at low illumination intensity, but otherwise will be increasingly distorted at high voltages. At high illumination intensity there is a series resistance effect whenever $J_L R_S$ is significant.

Other publications discuss the cell photoconductivity, $P(V)$, and exhibit a form of $P(V)$ that is similar to those that we demonstrate are influenced by series resistance. For example, Ooi et al. described P3HT/PCBM cells with a symmetric photocurrent response that is similar to the calculations in Fig. 1 and the data of Fig. 3 [16]. Ooi et al. correct for the possible change in temperature when the cell is illuminated which has a different effect on J_D and therefore on the experimental $P_{EXP}(V)$. The data by Ooi et al. show the same general shape as given by Fig. 1, as well as a zero crossing of $P_{EXP}(V)$ which is independent of illumination, and the saturation of $P_{EXP}(V)$ in forward bias at a value much lower than in reverse bias. Their data therefore closely follow the predictions expected for a cell with significant series resistance. Indeed the paper shows a forward current that is almost ohmic above $\sim$0.7 V, and a zero crossing at $\sim$0.9 V, which is much higher than other P3HT cells. Ooi et al. explain their results in terms of different extraction barriers at the two contacts, but a significant series resistance effect may be a more likely explanation.

Since our analysis of the series resistance is empirical, the effects described are independent of the physical mechanism that provides the series resistance. The shape of $P_{EXP}(V)$ can demonstrate that a series resistance effect is present, and the corrected value of $P_{INT}(V)$ provides insight into the photoconductivity of the cell diode, but neither measurement can give direct evidence for the origin of the series resistance, which requires additional experimental information.

5. Conclusions

The series resistance has a significant effect on the voltage dependence of the photocurrent, such that the measured result is different from the internal photocurrent of the diode. When the photocurrent is used to deduce the properties of the solar cell, it is important that the internal $P_{INT}(V)$ is determined. The presence of a significant series resistance effect can often be deduced from the form of $P_{EXP}(V)$ and the magnitude of the R_S can be obtained from the dark diode characteristics. It is possible to extract V_{BI} and $P_{INT}(V)$ from the experimental measurements, although the accuracy decreases with increasingly large values of the series resistance.

Acknowledgements

The authors are grateful to A. Heeger for enabling the collaboration to study BHJ solar cells. Research at UCSB was supported as part of the Center for Energy Efficient Materials, an Energy Frontier Research Center funded by the US Department of Energy, Office of Science, Office of Basic Energy Sciences under award Number DE-SC0001009. The materials used for the fabrication of the solar cells were provided by Dr. D. Waller of Konarka Technologies.

References

[1] H. Hoppe, N.S. Saraciftci, J. Mater. Res. 19 (2004) 1924.
[2] J.Y. Kim, K. Lee, N.E. Coates, D. Moses, T.Q. Nguyen, M. Dante, et al., Science 317 (2007) 222.
[3] V.D. Mihailetchi, L.J.A. Koster, J.C. Hummelen, P.W.M. Blom, Phys. Rev. Lett. 93 (2004) 216601.
[4] L.J.A. Koster, V.D. Mihailetchi, R. Ramaker, P.W.M. Blom, Appl. Phys. Lett. 86 (2005) 123509.
[5] D. Veldman, O. Ipek, S.C.J. Maskers, J. Sweelssen, M.M. Koetse, S.C. Veenstra, et al., J. Am. Chem. Soc. 130 (2008) 7721.
[6] J. Szmytkowski, Semicond. Sci. Technol. 25 (2010) 015009.
[7] R.A. Street, M. Schoendorf, A. Roy, J.H. Lee, Phys. Rev. B 81 (2010) 205307.
[8] H.H.P. Gommans, M. Kemerink, J.M. Kramer, R.A.J. Janssen, Appl. Phys. Lett. 87 (2005) 122104.
[9] V.D. Mihailetchi, H. Xie, B. de Boer, L.J.A. Koster, P.W.M. Blom, Adv. Funct. Mater. 16 (2006) 699.
[10] S.H. Park, A. Roy, S. Beaupre, S. Cho, N. Coates, J.S. Moon, et al., Nat. Photonics 3 (2009) 297.
[11] J.D. Servaites, S. Yeganeh, T.J. Marks, M.A. Ratner, Adv. Funct. Mater. 20 (2010) 97.
[12] S.M. Sze, Physics of Semiconductor Devices, Wiley, New York, 1981.
[13] P. Kumar, S.C. Jain, V. Kumar, S. Chand, R.P. Tandon, J. Appl. Phys. 105 (2009) 104507.
[14] PCDTBT is poly[N-9′-hepta-decanyl-2,7-carbazole-alt-5,5-(4′,7′-di-2-thienyl-2′,1′,3′-benzothiadiazole): $PC_{70}BM$ is [6-6]-phenyl C70-butyric acid methyl ester.
[15] Z.E. Ooi, R. Jin, J. Huang, Y.F. Loo, A. Sellinger, J.C. deMello, J. Mater. Chem. 18 (2008) 1644.
[16] G. Garcia-Belmonte, P.P. Boix, J. Bisquert, M. Sessolo, H.J. Bolink, Sol. Energy Mater. Sol. Cells 94 (2010) 366.

Organic Electronics 12 (2011) 249–256

Contents lists available at ScienceDirect

Organic Electronics

journal homepage: www.elsevier.com/locate/orgel

All inkjet-printed, fully self-aligned transistors for low-cost circuit applications

Huai-Yuan Tseng *, Vivek Subramanian

Department of Electrical Engineering and Computer Sciences, University of California, Berkeley, CA 94720-1770, USA

ARTICLE INFO

Article history:
Received 27 May 2010
Received in revised form 14 November 2010
Accepted 16 November 2010
Available online 30 November 2010

Keywords:
Inkjet printing
Self-alignment
Low-cost circuits

ABSTRACT

Layer-to-layer registration is a significant problem in printed electronics since parasitic overlap capacitances resulting from the poor registration of conventional printers substantially degrade device operating speeds. To overcome this, a novel inkjet printing process was utilized to demonstrate an all inkjet-printed and fully self-aligned transistor, as well as fully self-aligned inverters for the first time. Self-alignment of transistor source/drain electrodes to gates was achieved by a printed wetting-based roll-off process, resulting in an improved overlap capacitance as small as 0.14–0.23 pF mm^{-1}. Circuit building blocks including transistor arrays and inverters were demonstrated using a novel self-split source/drain and a self-aligned interconnect printing technique. Due to the substantial reduction in overlap capacitance, demonstrated inverters showed a propagation delay as low as 0.488 ms at a fan-out of 1, despite using materials with mobility of 0.01 cm^2 V^{-1} s^{-1}, thus showing a performance that is suitable for use in a range of low-cost electronics applications, realized using a simple, scalable process.

© 2010 Elsevier B.V. All rights reserved.

1. Introduction

Printing techniques have been industrialized and become an essential part of publishing and transaction printing for a century. In recent years, printed electronics has emerged as a candidate for the realization of low-cost and large area electronic systems. Unlike its conventional silicon counterpart, printed electronics reduces the major cost points of semiconductor manufacturing, including subtractive lithography and vacuum processing. Moreover, printing is compatible with flexible substrates and roll-to-roll processing, making it promising for use in such applications as low-cost printed radio frequency identification (RFID) tags and large-area flexible electronics and displays [1–3].

All printed passive devices [4,5] and active transistors [6] are maturing as printable materials have become widely available in recent years. Unfortunately, printed transistors typically suffer from degraded performance due to poor material quality, large channel length and very high overlap capacitance [7–9], limited by the coarse resolution of state-of-the-art printing techniques such as inkjet [10], rotogravure [11] and offset printing [12]. The material quality has been improved recently [13,14], resulting in devices with higher mobilities. Furthermore, printed transistors have been successfully downscaled to the range of 100 nm channel length by using self-aligned printing techniques to realize feature separation and definition in individual layers [15–17]. However, the poor layer-to-layer registration of printing techniques remains a tremendous bottleneck in printed devices. While some efforts have been made to realize self-aligned registration, these have necessitated the use of lithographic techniques [17–19], which are undesirable from a cost perspective, and could potentially damage the organic materials during back side exposure and photoresist developing processes.

Given this need, in this work, we demonstrated the self-alignment of the source and drain (*S*/*D*) to the gate

* Corresponding author. Address: 550 Sutardja Dai Hall, Berkeley, CA 94720-1770, USA. Tel.: +1 (510)664 4335; fax: +1 (510)642 2739.
E-mail address: hytseng@eecs.berkeley.edu (H.-Y. Tseng).

1566-1199/$ - see front matter © 2010 Elsevier B.V. All rights reserved.
doi:10.1016/j.orgel.2010.11.013

of fully-printed organic transistors using wetting-based roll-off techniques [20]. Using such techniques, we demonstrated fully self-aligned transistors and circuit elements in an all inkjet-printed process, without the need for any lithography or vacuum processing. We achieved a minimum overlap of 0.47 μm between the gate and *S*/*D*, contrasted to the >10 μm typically required in conventional printed transistors [19], resulting in an overlap capacitance as low as 0.14–0.23 pF mm^{-1}. As a result, the speed of the printed transistor is significantly enhanced since the overlap capacitances are minimized. We further extend this technique to demonstrate the self-alignment across circuits consisting of multiple devices, including the formation of transistors, interconnects, and vias to thus realize an extremely simple, high-performance fully-printed integrated circuit technology.

2. Results and discussion

In this work, printed transistors with a bottom gate and bottom contact structure were fabricated by four layers of inkjet printing (Fig. 1a; see Section 4). While the peak-process temperature used here was 200 °C, primarily because of the high-temperature anneal needed for the dielectric used in this work, the process will be applicable to sub-150 °C processing as well, as required for polyethylene terephthalate (PET) substrates, by using lower temperature sintering particles and dielectrics, which have been developed recently [21]. The general concept of wetting-based self-alignment was first introduced by Sirringhaus et al. [10,22] and applied to the formation of narrow-gap source–drain structures. In this work, the authors started with a lithographically patterned spacer as a hydrophobic mesa structure. Then, a conducting polymer poly(3,4-ethylenedioxythiophene) doped with polystyrene sulfonic acid (PEDOT/PSS) was inkjet printed onto the mesa structure. The hydrophilic PEDOT/PSS then dewetted the mesa structure and self-aligned the spacer to form *S*/*D* electrodes. The transistor was then completed by spin-coating of dielectric, semiconductor and inkjet-printed top gate. Herein, we apply the concept of wetting-based self-alignment to solve the critical issue of layer-to-layer alignment. We inkjet-printed silver as a bottom gate, followed by a PVP insulator, thus forming a mesa suitable for use in subsequent self-alignment. Fig. 1b illustrates the interfacial tension components of a source or drain drop on the side slope or the mesa-like structure of a printed transistor. Excluding the hydrostatic pressure, which is justified by the small drop volume of 10 pL [23], by Young's relation, the equilibrium of the drop is maintained by balancing the silver ink surface tension γ, poly(4-vinylphenol) (PVP)

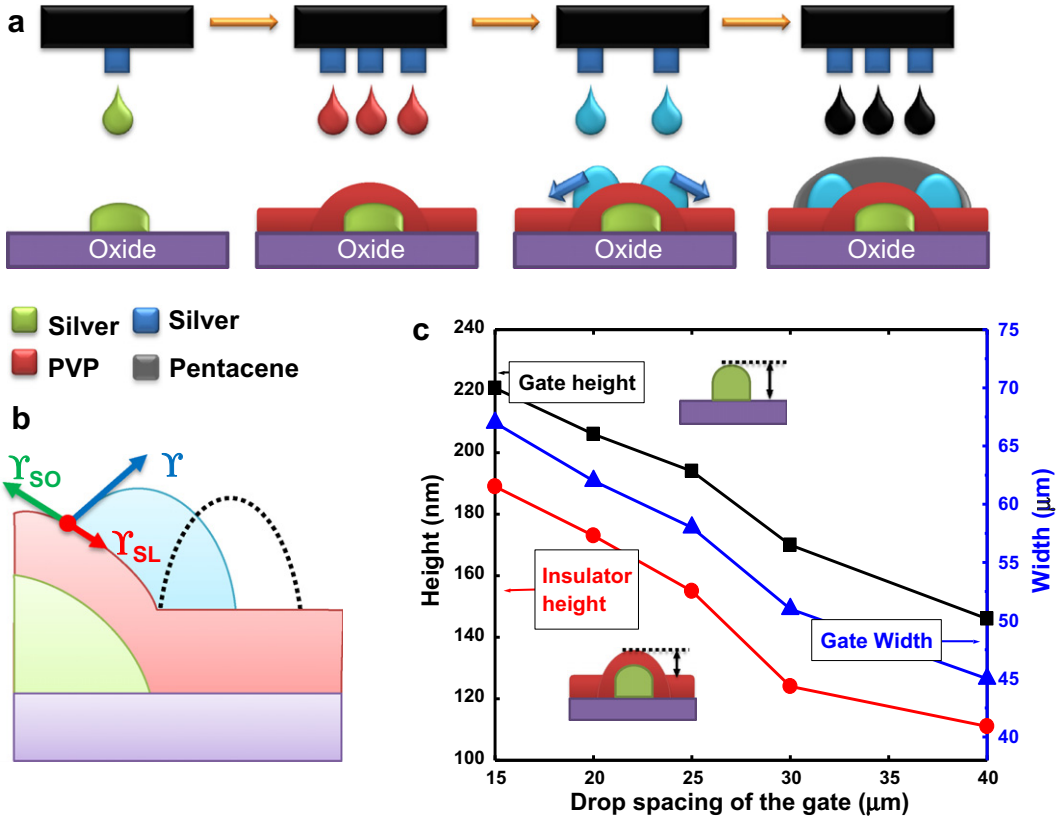

Fig. 1. Inkjet transistor process with self-aligned *S*/*D*. (a) Inkjet transistor process, consisting of four layers of printing. (b) Diagram showing the interfacial tension of a printed source or drain on the mesa structure. (c) Gate height, insulator height or mesa thickness and gate linewidth as a function of printed drop spacing of the gate.

surface energy γ_{SO} and a liquid–solid interaction γ_{SL}. To maximize the roll-off, it is, therefore, desirable to decrease γ_{SO}; unfortunately, the printed silver line integrity is often degraded by this decrease, causing the line to break into separate droplets. Therefore, to facilitate the roll-off of the printed *S*/*D*, we have optimized the inkjet process to achieve a roll-off without degrading the line morphology by (i) increasing the silver ink surface tension (ii) optimizing the PVP thickness, and (iii) increasing the step height. The silver ink, with a surface tension of 30 dyn cm^{-1}, consists of silver nanoparticles with an average size of 80 nm in an alcohol-based solvent (Supplementary information, Fig. S1a). This water miscible ink was diluted with water, with a surface tension of 70 dyn cm^{-1}, to increase the overall surface tension. Note that adding water reduces the ink viscosity, resulting in degraded jetting stability. Therefore, an upper bound of 15 vol.% water was added while maintaining the optimum viscosity of 10 cP in this work (Supplementary information, Fig. S1b). The step height of the mesa structure was naturally created by printing PVP atop the bottom gate. An outward convection flow driven by the coffee stain effect [24] occurred while the PVP solvent evaporated, resulting in a conformal coverage of the bottom gate and a mesa-like structure. As indicated by previous work [22], a thicker mesa structure promotes dewetting. On the other hand, thicker dielectrics degrade device performance due to poorer gate capacitive coupling. Therefore, PVP was kept as thin as possible to preserve the mesa geometry while maintaining good dielectric properties and device electrostatic integrity. Herein, 110 nm of PVP was printed. The mesa structure was thickened by increasing the gate height, achieved by reducing the printing drop spacing of the gate. Reducing drop spacing increases the deposited drop volume, resulting in a thicker gate profile. Fig. 1c shows the mesa structure thickening monotonically with increasing gate height due to the conformality of PVP. However, as indicated in Fig. 1c, line width increases simultaneously with step height, resulting in a slightly larger channel length. In order to obtain repeatable dewetting without compromising on the device speed through increased channel length, the gate line was printed with a 30 μm drop spacing throughout this work.

With the optimization, the printed *S*/*D* overlaps the gate initially, but starts to dewet gradually with time. Interestingly, dewetting mostly initiates at the head of the printed gate line as shown in the Supplementary information (Fig. S2a). This can be rationalized by the thicker mesa structure at the line head, which originated from the slightly more deposited drop volume (Supplementary information, Fig. S2b). Similar results showing a larger line head have been reported and modeled in detail in a previous work [25]. As a result, it is energetically favorable for the *S*/*D* to dewet starting at the head. Fig. 2a shows the optical micrographs of three post-*S*/*D*-sinter transistors, with different waiting times between printing and sintering. If sintered immediately after printing, the *S*/*D* remains overlapped over the gate; if 9 min of waiting are followed by sintering, the *S*/*D* partially dewets the gate. After 15 min, the *S*/*D* completely dewets and self-aligns to the gate. The overlap between the *S*/*D* and the gate was characterized using profilometry (Supplementary information, Fig. S2c and d). A minimum overlap of 0.47 μm was achieved, in contrast to a typical overlap of >10 μm in devices fabricated by printing. To demonstrate the overall improvement by self-alignment, overlap capacitance was measured (see Section 4). As shown in Fig. 2b, the overlap capacitance reduced with increasing waiting time and saturated after 15 min, matching the observation from Fig. 2a. An average overlap capacitance as low as 0.185 pF mm^{-1} with a standard deviation of 0.031 pF mm^{-1} was achieved purely by printing, substantially surpassing the results obtained by a previously reported lithography-reliant, semi-printing process [17]. As described above, the general mechanism of self-alignment is related to the roll-off from the gate, followed by pinning at the gate corner. There are several possible physical phenomena that govern the rolling-off behavior (1) the force gravity of the drop causes the *S*/*D* to minimize the potential energy by moving down the mesa structure. However, a calculation of the gravitational force from the volume and density of the ink indicates that the force is merely 5.9×10^{-7} dyn cm^{-1}, which is negligible when comparing to the ink surface tension and PVP surface energy. (2) The surface energy of PVP could be locally reduced due to the interactions with the underlying gate line, causing the *S*/*D* drop to minimize the energy by migrating to a much higher energy surface. However, we have found no specific evidence showing that the underlying gate alters the chemical structure of the PVP atop yet. (3) The geometry of the corner of the mesa structure could induce a capillary force to locally break the *S*/*D* drop into two parts. Subsequently, the ink located on the channel surface contracts upon evaporation, while the ink at the side of the mesa structure remained pinned. While this appears likely, and is consistent with the time-resolved optical micrographs of the self-alignment process, it is possible that the actual self-alignment is in fact a combination of these effects. A further study is required in the future to thoroughly understand the underlying physics. Overall, however, the self-aligned process is repeatable and has been used on a regular basis over more than 6 months of daily device and circuit printing, and has been found to be robust for printing transistors and circuits.

Fig. 2c and d shows the transfer and output characteristics of a printed self-aligned transistor with the channel width and length of 600 μm and 50 μm, respectively. The transistor shows an output characteristic without a contact barrier, implying that an ohmic contact is formed between the pentacene precursor-based channel and the silver electrodes, with the latter's work function adjusted through an interfacial dipole [26]. The average value of mobility, on/off ratio, threshold voltage and sub-threshold swing are 0.01 $cm^2 V^{-1} s^{-1}$, 1440, −1.5 V and 4.28 V $decade^{-1}$, respectively (see Supplementary information Fig. S3 for more statistical data). The degraded mobility, on/off ratio and the sub-threshold swing are likely caused by the annealing temperature of the pentacene precursor (150 °C), approaching the glass transition temperature of PVP (170 °C), resulting in degraded dielectric interfacial quality [27]. This can be improved in the future by using state-of-the-art inkjet printable organic semiconductor materials requiring low annealing temperatures, such as 6,13-bis(triisopropyl-silylethynyl)

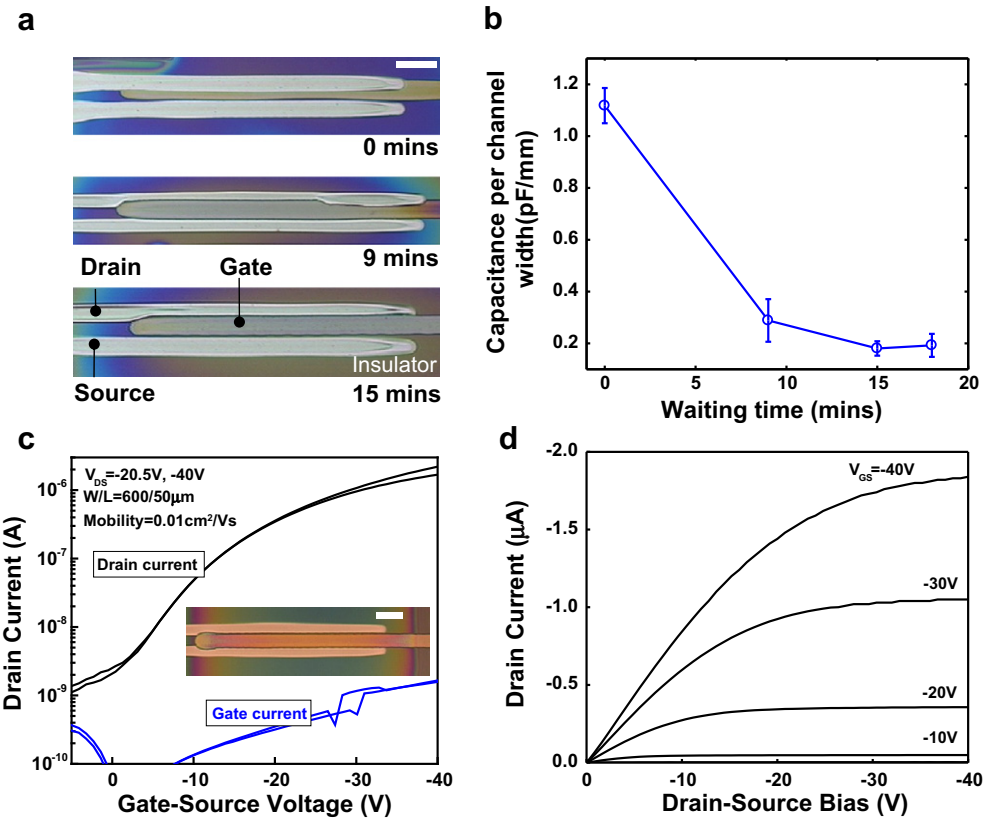

Fig. 2. Self-aligned *S*/*D* and electrical characteristics. (a) Optical micrographs of three post-*S*/*D*-sinter transistors, with three different waiting time between printing and sintering. (b) Measured overlap capacitance per channel width as a function of waiting time between printing and sintering. (c) Transfer characteristics of the printed self-aligned transistor. Inset shows the optical micrograph of the printed transistor. Top layer of printed pentacene was neglected for the clarity of the self-alignment. (d) Output characteristics of the printed self-aligned transistor. All scale bars represent 100 μm.

(TIPS) pentacene, which has been demonstrated to offer a high mobility and a low sub-threshold swing on PVP dielectrics [9,28,29]. Nevertheless, the printed transistors are reliable enough for the following circuit printing work.

The principle of dewetting the source and drain was extended beyond the single transistor level to entire circuit blocks, through a novel printing process – a self-split *S*/*D* device. The printing flow is illustrated in Fig. 3a, starting with the printing of gate, followed by the printing of PVP.

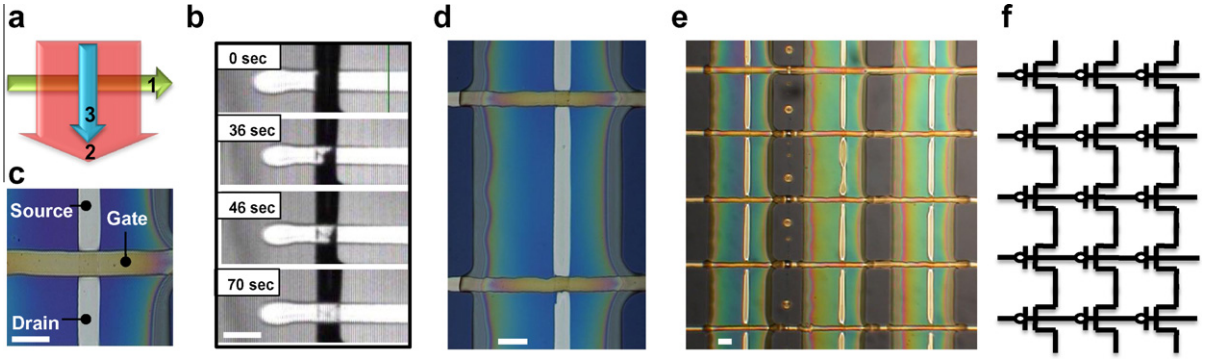

Fig. 3. Self-split *S*/*D* and transistor array. (a) Printing flow of a self-split transistor. (b) Time-lapse optical micrographs captured by the Dimatix printer showing the process of *S*/*D* self-splitting with time. (c) Optical micrograph of a printed self-split transistor. (d) Optical micrograph of an inverter structure printed using self-split *S*/*D*. (e) Optical micrograph of the printed self-split transistor array. (f) The equivalent circuit of the transistor array. All scale bars represent 100 μm.

The same optimization was performed on the gate, PVP and *S*/*D*. A perpendicular silver line was then printed across the gate line. The silver line self-split into *S*/*D* while simultaneously self-aligning the gate as shown in Fig. 3b. After sintering the *S*/*D*, as shown in Fig. 3c, a self-split transistor was then completed by printing the pentacene precursor on top. Similar electrical characteristics to our typical printed transistors are obtained (Supplementary information, Fig. S4a–c). The self-split technique is highly compatible with integrated circuit fabrication as illustrated in Fig. 3d. The line printed perpendicular to the gate self-splits into the *S*/*D* electrodes of the two transistors and provides the interconnect simultaneously in a single-printing pass. This is very promising for realizing a fully printed self-aligned Complementary Metal-Oxide-Semiconductor (CMOS) inverter in the near future, where pull-up and pull-down transistors have similar driving currents. Herein, however, we will demonstrate a fully printed inverter with more flexible sizing capability below. The self-split process was extended into the printing of a transistor array as shown in Fig. 3e, and the equivalent circuit in Fig. 3f. The array is completed in three passes of printing. An array printed by such a simple process is promising for realizing low-cost circuitry, such as disposable sensor arrays or tree-decoder applications.

To demonstrate more sophisticated printed circuits, the self-splitting technique has further been utilized for printing of an interconnection. Without a self-aligned interconnect, connecting discrete printed transistors becomes challenging. Short/open circuits caused by poor printing registration dramatically deteriorate fabrication yields. Herein, a self-split/self-align interconnect using the principal of selective wetting was demonstrated. Fig. 4a shows the time-lapse optical micrographs captured by the fiducial camera on Dimatix printer. A perpendicular interconnect was printed, intending to connect three adjacent printed post-*S*/*D*-sinter transistors. Instead of manually patterning the line into segments to align to the *S*/*D* pad of each transistor, a straight line was printed across all the three transistors. Similarly to the aforementioned self-split *S*/*D*, the silver dewets the channel of each transistor and spontaneously flows perpendicularly into the *S*/*D* electrodes, forming good contacts with no needed pad area. The resulting *S*/*D* electrodes completely split while three transistors are connected in a cascade scheme, resulting in borderless contacts with excellent alignment. A complete process module for interconnection requires a printable via technique to allow for interconnection between layers separated by a dielectric. The first printed via-hole was demonstrated by Sirringhaus et al., using a good solvent of isopropanol to dissolve PVP and form a crater-like via-hole [30]. Here, we demonstrated a novel semi-additive via process combining the printing of a via-hole with the printing of an interconnect line. Fig. 4b shows the optical micrograph of a printed contact chain demonstrating the connection of two metal layers through a sandwiched PVP insulator. The printing flow is illustrated in Fig. 4c, starting with the printing of two vertical silver lines, followed by sintering and the printing of a PVP insulator. Then, a horizontal silver line was printed prior

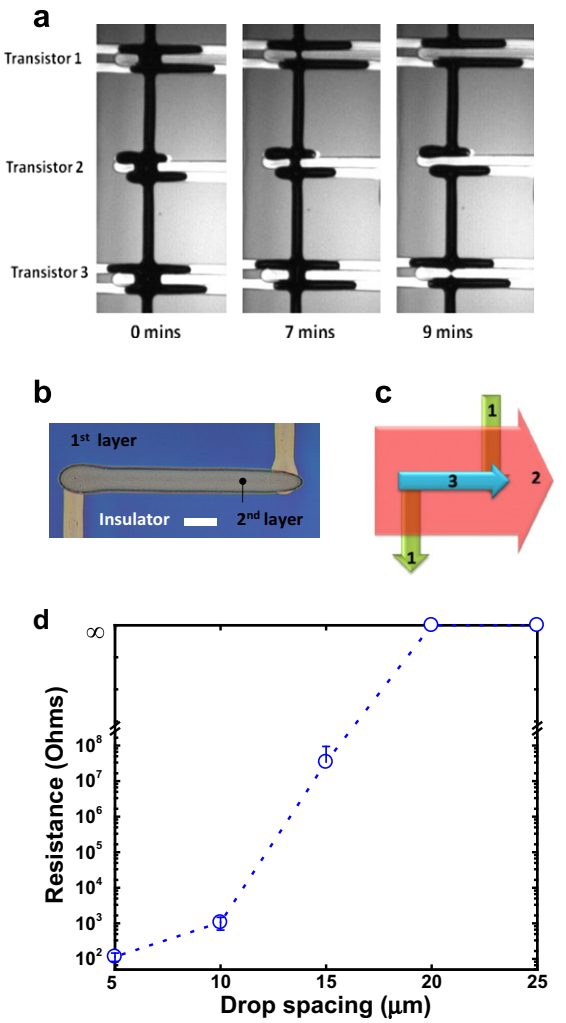

Fig. 4. Novel printed interconnect. (a) Time-lapse optical micrographs captured by the Dimatix printer, showing the process of self-split/self-aligned interconnect. (b) Optical micrograph of a printed contact chain. (c) Printing flow of the contact chain. (d) Resistance of the contact chain versus the drop spacing of the horizontal line. All scale bars represent 100 μm.

to cross-linking the PVP to dissolve the same and deposit silver nanoparticles simultaneously, followed by a single heating step to cross-link the PVP and sinter the silver. The horizontal line was printed with various drop spacing and the corresponding resistances of the contact chain are shown in Fig. 4d. Smaller drop spacing results in larger deposited solvent volume and silver concentration, and, therefore, the contact chain becomes conducting below drop spacing of 15 μm. The minimum resistance of 100 Ω, which is negligible comparing to the transistor resistance, is obtained at 5 μm drop spacing. The resistance of the contact chain is limited by the horizontal line, rather than the contact resistance between two metal layers.

Finally, a printed logic element–inverter was demonstrated using the self-aligned *S*/*D* and the interconnect introduced previously. Fig. 5a shows the circuit schematic

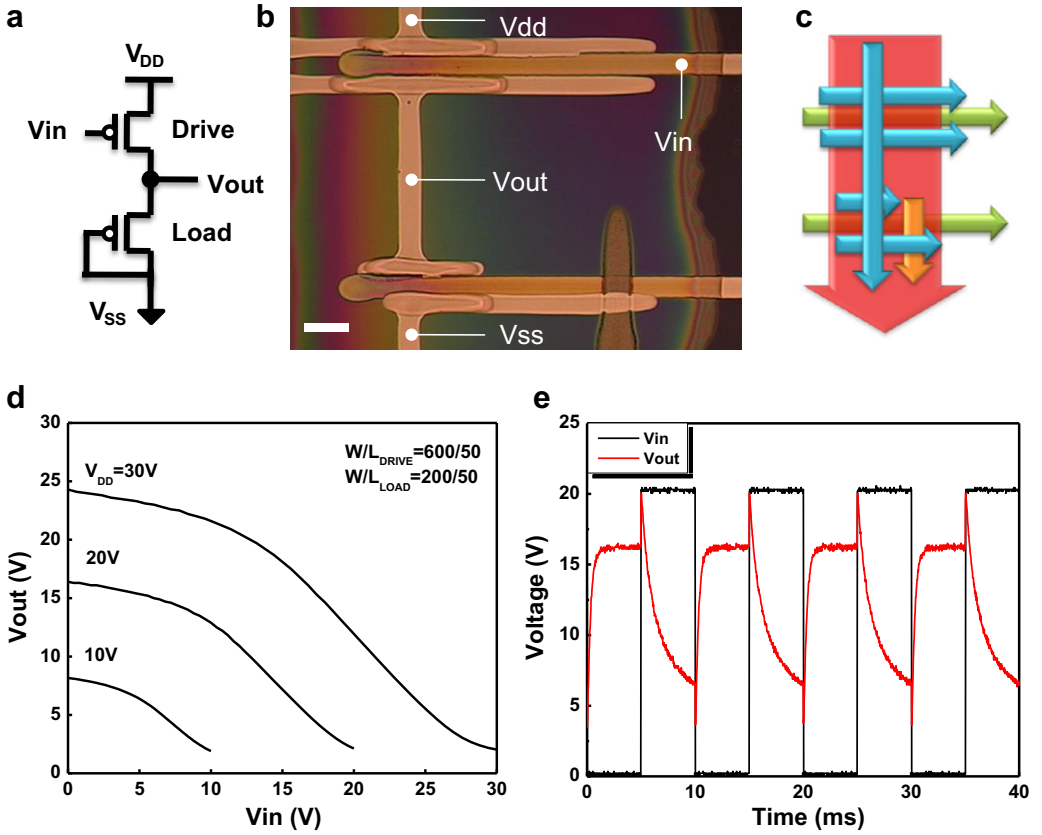

Fig. 5. Printed inverter. (a) The circuit schematic of the printed inverter. (b) Optical micrograph of the inverter. (c) Printing flow of the inverter. (d) Measured voltage transfer characteristic of the inverter with various V_{DD}. (e) Transient characteristics of the inverter. The scale bar represents 100 μm.

of the inverter using a diode connected transistor as a load device. The β ratio (the channel width ratio of the drive transistor to the load transistor) of 3 is chosen to enlarge the voltage gain and the output swing. The optical micrograph of the inverter shown in Fig. 5b was fabricated by the printing flow shown in Fig. 5c (see Section 4). The voltage transfer characteristic (VTC) of the printed inverter measured with various V_{DD} is shown in Fig. 5d. Maximum voltage gain of −1.46 was achieved under V_{DD} of 50 V (see Fig. 5a–c for detail inverter characteristics). The performance of the inverter was then determined by measuring the propagation delay time between an input square wave and the output waveform (see Section 4). As shown in Fig. 5e, a low-to-high delay of 0.3 ms and a high-to-low delay of 1.65 ms are measured at 10 V, resulting in an average propagation delay of 0.975 ms. Due to the extra loading caused by the parasitic capacitance between the output electrode and the bottom silicon wafer, the output load was equivalent to a fan-out of 2 ($C_{load}/C_{in} = 2$). Since propagation delay is proportional to the product of the equivalent resistance and the load capacitance ($T_p \sim R_{eq}C_{load}$), the inverter is expected to have a smaller propagation delay of 0.488 ms at a fan-out of 1 ($C_{load} = C_{in}$). While this performance level is suitable for many low-cost electronic applications, and is already competitive with the best fully printed circuits reported to date [31,32], the inverter gain can be further improved by enhancing the transistor performance and optimizing circuit design to maximize the product of gm (transconductance) and Rout (output resistance). The noise margin can also be improved by reducing the subthreshold leakage of the transistor. Furthermore, the gate delay is expected to be improved by downscaling of the channel length, improved mobility and the use of CMOS circuits in the future. Despite this, however, the benefits of self-alignment in terms of parasitic capacitance reduction are clear; the low parasitic capacitance achieved in this work will facilitate the realization of high-performance, high-yield fully printed circuits with simple printing processes.

3. Conclusions

We have demonstrated various novel printing techniques including self-aligned *S*/*D* to gate, self-split *S*/*D* and self-aligned interconnection for the first time. Using these, we demonstrate overlap capacitances as low as 0.14–0.23 pF mm^{-1} achieved by a purely printing process. We also demonstrated a fully printed inverter with a low propagation delay of 0.488 ms, despite the use of relatively low performance materials. Using such a simple process

formed entirely by printing with complete self-alignment, we are able to realize a robust integrated process suitable for use in a range of low-cost electronics applications.

4. Experimental

4.1. All inkjet-printed transistor process

An N-type silicon wafer with a thermally grown oxide of 100 nm was used as an underlying mechanical substrate. Silver nanoparticle ink (Suntronic U5603) was printed as a gate electrode with a drop spacing of 30 μm, and subsequently sintered at 200 °C for 10 min. Poly(4-vinylphenol) (PVP) (7.6 wt.%) dissolved in hexanol with 0.6 vol.% of cross linker poly(melamine-co-formaldehyde) was printed atop the gate and cross-linked at 200 °C for 10 min. Five nozzles were used simultaneously to print the PVP layer with a drop spacing of 30 μm, resulting in a dielectric thickness of 110 nm. Silver ink was then printed to form source and drain electrodes with a drop spacing of 20 μm. This was followed by a sintering step identical to that used for the gate electrode. The PVP surface was then treated with hexamethyldisilazane (HMDS) vapor to obtain a low energy channel-surface with a water contact angle in the range of 66°. Finally, 1.5 wt.% of pentacene precursor (Sigma–Aldrich) dissolved in anisole (Sigma–Aldrich, anhydrous, 99.7%) was printed as a p-type semiconductor. The precursor was annealed at 150 °C in a nitrogen ambient atmosphere with a 10 ppm oxygen level. All inkjetting was performed using a Dimatix DMP-2800 printer and a jetting frequency of 2 kHz was used at all times.

4.2. Measurement of overlap capacitance

An Agilent 4285A was used to measure capacitance. A small signal of 100 mV and 75 kHz was used as the input. Two co-axial probes that were connected to the 4285A were connected to the gate and drain electrodes, respectively. Before the measurement, calibration was performed to cancel out the parasitic components resulting from the cable and oxide substrate. The measurement was then performed on five to ten different devices and statistically consistent results were obtained.

4.3. Printing of an inverter

As shown in Fig. 5c, the process starts with the printing of silver as gate electrodes, followed by sintering at 200 °C for 10 min. PVP was then printed atop the gate as a gate insulator. Before cross-linking the PVP, a printed via and interconnect (step 3) was used to connect the gate and source of the load transistor to form a diode-connect configuration. A heating step of 200 °C was performed for 10 min to cross-link PVP and sinter the silver. *S*/*D* electrodes of both the drive and load transistors were then printed, self-aligning the gate, followed by sintering at 200 °C for 10 min. An interconnect was then printed to self-split and self-align the two transistors. Finally, a pentacene precursor was printed on the transistor channel, followed by an annealing step.

4.4. Electrical characterization of the transistor and the inverter

An Agilent 4156C semiconductor parameter analyzer was used to measure the transfer and output characteristics of the printed transistor and the voltage transfer characteristics of the printed inverter. The mobility was extracted from the slope of the extrapolated square-rooted drain current at a drain voltage of 40 V, and the threshold voltage was extracted from the *x*-intercept of the same fitting line. For the transient output measurement of the inverter, the 4156C was used to bias the circuit. The input square wave of 200 Hz was provided by an Interstate Electronics Corporation F34 function generator. The output was buffered by an operational amplifier Burr Brown OPA602BP and the waveform was measured using an Acute DS-1202 Oscilloscope.

Acknowledgements

We gratefully acknowledge Dimatix Fujifilm for the printer support and the Semiconductor Research Corporation and the World Class University Program at Sunchon National University for funding support.

Appendix A. Supplementary data

Supplementary data associated with this article can be found, in the online version, at doi:10.1016/j.orgel.2010.11.013.

References

[1] T. Someya et al., Conformable, flexible, large-area networks of pressure and thermal sensors with organic transistor active matrixes, Proc. Natl. Acad. Sci. USA 102 (2005) 12321–12325.
[2] T. Sekitani et al., A large-area wireless power-transmission sheet using printed organic transistors and plastic MEMS switches, Nat. Mater. 6 (2007) 413–417.
[3] T. Sekitani et al., Stretchable active-matrix organic light-emitting diode display using printable elastic conductors, Nat. Mater. 8 (2009) 494–499.
[4] D. Redinger, S. Molesa, S. Yin, R. Farschi, V. Subramanian, An ink-jet-deposited passive component process for RFID, IEEE Trans. Electron Devices 51 (2004) 1978–1983.
[5] N. Lim, J. Kim, S. Lee, N. Kim, G. Cho, Screen printed resonant tags for electronic article surveillance tags, IEEE Trans. Adv. Pack. 32 (2009) 72–76.
[6] V. Subramanian et al., Progress toward development of all-printed RFID tags: materials, processes, and devices, Proc. IEEE 93 (2005) 1330–1338.
[7] S.E. Molesa, S.K. Volkman, D.R. Redinger, A. de la Fuente Vornbrock, V. Subramanian, A high-performance all-inkjetted organic transistor technology, Int. Electron Device Meet. Tech. Dig. (2004) 784–787.
[8] W.S. Wong et al., Amorphous silicon thin-film transistors and arrays fabricated by jet printing, Appl. Phys. Lett. 80 (2002) 610.
[9] J. Kim et al., All-solution-processed bottom-gate organic thin-film transistor with improved subthreshold behaviour using functionalized pentacene active layer, J. Phys. D: Appl. Phys. 42 (2009) 115107.
[10] H. Sirringhaus et al., High-resolution inkjet printing of all-polymer transistor circuits, Science 290 (2000) 2123–2126.
[11] J.M. Ding, A. de la Fuente Vornbrock, C. Ting, V. Subramanian, Patternable polymer bulk heterojunction photovoltaic cells on plastic by rotogravure printing, Sol. Energy Mater. Sol. Cells 93 (2009) 459–464.

[12] D. Zielke et al., Polymer-based organic field-effect transistor using offset printed source/drain structures, Appl. Phys. Lett. 87 (2005) 123508–123510.
[13] I. McCulloch et al., Liquid-crystalline semiconducting polymers with high charge-carrier mobility, Nat. Mater. 5 (2006) 328–333.
[14] H. Yan et al., A high-mobility electron-transporting polymer for printed transistors, Nature 457 (2009) 679–686.
[15] C.W. Sele, T. von Werne, R.H. Friend, H. Sirringhaus, Lithography-free, self-aligned inkjet printing with sub-hundred-nanometer resolution, Adv. Mater. 17 (2005) 997–1001.
[16] N. Zhao et al., Self-aligned inkjet printing of highly conducting gold electrodes with submicron resolution, J. Appl. Phys. 101 (2007) 064513.
[17] Y.Y. Noh, N. Zhao, M. Caironi, H. Sirringhaus, Downscaling of self-aligned, all-printed polymer thin-film transistors, Nat. Nanotechnol. 2 (2007) 784–789.
[18] T. Arai et al., Self-aligned fabrication process of electrode for organic thin-film transistors on flexible substrate using photosensitive self-assembled monolayers, Jpn. J. Appl. Phys. 46 (2007) 2700–2703.
[19] W.S. Wong, E.M. Chow, R. Lujan, V. Geluz-Aguilar, M.L. Chabinyc, Fine-feature patterning of self-aligned polymeric thin-film transistors fabricated by digital lithography and electroplating, Appl. Phys. Lett. 89 (2006) 142118.
[20] H.Y. Tseng, V. Subramanian, All inkjet printed self-aligned transistors and circuits applications, Int. Electron Device Meet. Tech. Dig. (2009) 391–394.
[21] Y. Choi et al., Flexible complementary inverter with low-temperature processable polymeric gate dielectric on a plastic substrate, Org. Electron. 10 (2009) 1209–1216.
[22] J.Z. Wang, Z.H. Zheng, H.W. Li, W.T.S. Huck, H. Sirringhaus, Dewetting of conducting polymer inkjet droplets on patterned surfaces, Nat. Mater. 3 (2004) 171–176.
[23] P.G. de Gennes, F. Brochard-Wyart, D. Quere, A. Reisinger, Capillarity and Wetting Phenomena: Drops, Bubbles, Pearls, Waves, Springer, 2004 (Chapter 2).
[24] R.D. Deegan et al., Capillary flow as the cause of ring stains from dried liquid drops, Nature 389 (1997) 827.
[25] P.C. Duineveld, The stability of ink-jet printed lines of liquid with zero receding contact angle on a homogeneous substrate, J. Fluid Mech. 477 (2003) 175–200.
[26] D. Kim, S. Jeong, H. Shin, Y. Xia, J. Moon, Heterogeneous interfacial properties of ink-jet-printed silver nanoparticulate electrode and organic semiconductor, Adv. Mater. 20 (2008) 1–6.
[27] C. Kim, A. Facchetti, T.J. Marks, Polymer gate dielectric surface viscoelasticity strongly modulates pentacene transistor performance, Science 318 (2007) 76–80.
[28] J.A. Lim et al., Self-organization of ink-jet-printed triisopropyl-silylethynyl pentacene via evaporation-induced flows in a drying droplet, Adv. Funct. Mater. 18 (2008) 229–234.
[29] S.K. Park, T.N. Jackson, J.E. Anthony, D.A. Mourey, High mobility solution processed 6,13-bis(triisopropyl-silylethynyl) pentacene organic thin film transistors, Appl. Phys. Lett. 91 (2007) 063514.
[30] T. Kawase, H. Sirringhaus, R.H. Friend, T. Shimoda, Inkjet printed via-hole interconnections and resistors for all-polymer transistor circuits, Adv. Mater. 13 (2001) 1601–1605.
[31] M. Hambsch, K. Reuter, M. Stanel, G. Schmidt, H. Kempa, U. Fügmann, U. Hahn, A. Hübler, Uniformity of fully gravure printed organic field-effect transistors, Mater. Sci. Eng. B 170 (2010) 93–98.
[32] A. Knobloch, A. Manuelli, A. Bernds, W. Clemens, Fully printed integrated circuits from solution processable polymers, J. Appl. Phys. 96 (2004) 2286.

Organic Electronics 12 (2011) 257–262

Contents lists available at ScienceDirect

Organic Electronics

journal homepage: www.elsevier.com/locate/orgel

Simple routes for improving polythiophene:fullerene-based organic solar cells

T. Xiao [a,b,c], W. Cui [a,c], J. Anderegg [b], J. Shinar [b,c,d,*], R. Shinar [a,d,*]

[a] Microelectronics Research Center, Iowa State University, Ames, IA 50011, United States
[b] Ames Laboratory – USDOE, Iowa State University, Ames, IA 50011, United States
[c] Department of Physics and Astronomy, Iowa State University, Ames, IA 50011, United States
[d] Department of Electrical and Computer Engineering, Iowa State University, Ames, IA 50011, United States

ARTICLE INFO

Article history:
Received 9 September 2010
Accepted 14 November 2010
Available online 4 December 2010

Keywords:
Organic solar cells
PEDOT:PSS
P3HT:PCBM
Power conversion efficiency

ABSTRACT

Improved power conversion efficiency (PCE), by up to ~27%, of organic solar cells based on poly(3,4-ethylenedioxy-thiophene):poly(styrenesulfonate) (PEDOT:PSS)/poly(3-hexylthiophene):[6,6]-phenyl-C_{60}-butyric acid methyl ester (P3HT:PCBM) were obtained via simple modifications, widely applicable, in the fabrication of the spin-coated PEDOT:PSS layer. These included (i) further diluting the original PEDOT:PSS solution with deionized water, (ii) mixing the original PEDOT:PSS solution with ethylene glycol (EG), and (iii) spin coating EG over a PEDOT:PSS layer fabricated using the original solution. The optimal dilutions, spin coating rates, and durations were determined. Approach (iii) resulted in the best cell with a PCE of 4.7% as compared to 3.7% for the untreated PEDOT:PSS. To evaluate the origin of the improvements we monitored the PEDOT:PSS conductivity, external quantum efficiency of the devices, and their I–V curves that indicated an increase of ~16% in the short-circuit current I_{SC}. Other characteristics included the PEDOT:PSS layer thickness, its transmittance, P3HT:PCBM absorption spectra, its morphology, and surface chemical composition. The results indicate that in addition to the enhanced PEDOT:PSS conductivity (following some of the treatments) that improves charge extraction, enhanced PEDOT:PSS transmission and especially, enhanced P3HT:PCBM absorption contribute to improved solar cell performance, the latter by increasing I_{SC}. While the various treatments in the optimized devices had a minor effect on the PEDOT:PSS thickness, its morphology, and consequently that of the active layer, were affected. The surface roughness of the active layer increased significantly and, importantly, in devices with PEDOT:PSS/EG/P3HT:PCBM, PCBM aggregates were observed near the cathode. Such aggregates may also result in increased absorption and improved charge extraction.

© 2010 Elsevier B.V. All rights reserved.

Introduction

The development of organic solar cells is a fast-growing field as such devices have the advantage of being flexible, simple to fabricate, and potentially low cost [1–4]. Solar cells with a poly(3-hexylthiophene):[6,6]-phenyl-C_{60}-butyric acid methyl ester (P3HT:PCBM) active layer have been studied extensively with reports of typical power conversion efficiency (PCE) of ~3% to ~5% and fill factors (FF) of ~50% to 70% [4–11]. The PCE and FF depend on the starting materials, fabrication conditions and treatments at various stages of device fabrication. As an example, a PCE of 4.4% was obtained by varying the annealing conditions of the active layer [7,8]. The PCE was improved to 5.3% by replacing the PEDOT:PSS layer with NiO_2 [9]. A PCE of 5% was obtained for a single cell with TiO_x as an

* Corresponding authors. Addresses: Ames Laboratory – USDOE and Department of Physics and Astronomy, Iowa State University, Ames, IA 50011, United States. Tel.: +1 515 294 5442 (J. Shinar). Microelectronics Research Center and Department of Electrical and Computer Engineering, Iowa State University, Ames, IA 50011, United States. Tel.: +1 515 294 5898 (R. Shinar).

E-mail addresses: jshinar@iastate.edu (J. Shinar), rshinar@iastate.edu (R. Shinar).

1566-1199/$ - see front matter © 2010 Elsevier B.V. All rights reserved.
doi:10.1016/j.orgel.2010.11.008

optical spacer, and a two-unit tandem structure with 6.5% PCE was obtained by applying the TiO_x layer as an electron transport and collecting layer for the first unit and as a stable foundation to fabricate the second unit [10–12]. To obtain a good short-circuit current (I_{SC}), the active layer needs to have strong absorption of the solar spectrum, efficient exciton diffusion, good charge transfer, and sufficient charge extraction at the electrodes [13]. To achieve a high open-circuit voltage (V_{OC}), the offset between the highest occupied molecular orbital (HOMO) of the donor material and the lowest unoccupied molecular orbital (LUMO) of the acceptor material should be high, and ohmic contacts between the electrodes and the organics are required [13–16]. To get a high FF, the series resistance of the device should be low and the shunt resistance should be high. The polymer/electrode interfaces and the active layer properties play an important role in determining these parameters [17–19].

It is well known that the conductivity of PEDOT:PSS films is enhanced by over 100-fold by addition of organic materials, such as dimethyl sulfoxide (DMSO), *N*,*N*-dimethylformamide, tetrahydrofuran, sorbitol (with baking), glycerol, or ethylene glycol (EG) to the aqueous PEDOT:PSS solution [20–30]. Depending on the additive, the enhancement was related to the dielectric constant of the additive and to retention of some of the solvents used in the film [26], to reorientation of PEDOT chains with heat treatment [29], and to washing away of PSS [27]. For diethylene glycol addition, it was suggested that the particle size of the PEDOT:PSS reduces as the insulating, inter-particle excess PSS layer becomes very thin [28]. It was also shown that not only dilution of the PEDOT:PSS solution with EG enhances the conductivity, but also immersing the untreated PEDOT:PSS in EG solution for a few minutes [21]. It was reported that EG affects the solubility of the PEDOT:PSS film in water, suggesting, together with other measurements, that EG affects the conformation of the polymer chains with the surface becoming more hydrophobic. The conformational change of the PEDOT chains was attributed to the interaction between the dipole of one of the polar groups (only additives with two or more polar groups were found to enhance conductivity) of the organic additive and the dipoles or positive charges on the PEDOT [21]. It was also reported that the size of the PEDOT:PSS particles was increased by adding DMSO [23]. The increased conductivity was linked to the increased particles' size, due to reduced particle boundaries. Hence, there are still different fundamental explanations for the enhanced PEDOT:PSS conductivity upon addition of polar solvents.

Additives to PEDOT:PSS that enhance performance of solar cells were also evaluated. In addition to the effect of DMSO [23], for example, the substitution of ITO by PEDOT:PSS and PEDOT:PSS doped with glycerol or sorbitol was studied [22]. Glycerol and the surfactant ethylene glycol butyl ether at specific concentrations were also mixed with PEDOT:PSS for improved ink-printed solar cells [24]. The authors suggested that these additives may also affect the morphology of the ink-jet printed PEDOT:PSS, with a strong ionic interaction between the glycerol and the PEDOT, including with the addition of low-levels of the surfactant to enhance the conductivity. Improved device performance was attributed to surface morphology and enhanced conductivity that increase charge collection [24].

As every step in the fabrication of the solar cells affects device performance, this paper describes a systematic study of the effect of treatments of the PEDOT:PSS layer on the performance of the common P3HT:PCBM-based solar cells. Morphology variations of P3HT:PCBM were observed, with increased roughness, when PEDOT:PSS was treated in different ways. The treatments included (i) dilution of the as-received PEDOT:PSS solution with deionized (DI) water or (ii) with EG, and (iii) spin coating EG over the PEDOT:PSS layer. Among the various treatments that included optimization of the dilution and spin coating rate and duration, treatment (iii), namely the EG-treated PEDOT:PSS layer (following the fabrication of the latter from the original aqueous solution) exhibited the largest change in the P3HT:PCBM morphology, which is probably responsible for the observed largest improvement in the, I_{SC}, FF, and PCE. Importantly, small aggregates of PCBM, whose size depended on the anneal period of the EG-treated PEDOT:PSS layer, were observed at the surface of the active layer. These aggregates at the active layer/cathode interface may improve charge extraction and light absorption, and hence I_{SC}, FF, and PCE. Importantly, the conductivity of PEDOT:PSS exhibited a relatively minor contribution to the enhanced performance.

Experimental procedure

Materials

P3HT (P#200) was obtained from Rieke Metals and PCBM from nano-C; both materials were used without further purification. A solution of a 1:1 weight ratio of P3HT:PCBM in 1,2-dichlorobenzene, with a concentration of 30 mg/mL was used. The P3HT solution was filtered using a 0.22 μm Millex PTFE Filter before it was mixed with PCBM. The mixture was then stirred for 24 h before spin-coating. PEDOT:PSS was a Clevios™ P VP AI 4083 obtained from H.C. Starck. The PEDOT:PSS ratio was 1:6 by weight and the solid content 1.3–1.7%. EG was obtained from Fisher Scientific.

Procedures

The PEDOT:PSS layers (~40 nm thick) were baked for ~1 h at 120 °C under ambient conditions; they were then transferred into an argon-filled dual-sided MBraun glovebox. The oxygen level in the glovebox was ~30 ppm and that of water <0.1 ppm. Three different treatments of the PEDOT:PSS were evaluated in an attempt to improve the device performance. These treatments were: (i), diluting PEDOT:PSS with DI water (ii) mixing PEDOT:PSS with EG, and (iii) spin-coating EG following fabrication of the PEDOT:PSS layer. Each treatment was optimized by varying the spin-coating speed and duration as well as the dilution ratio as detailed above. The P3HT:PCBM solution was spin-coated on top of the PEDOT:PSS layer at the optimized 600 rpm rate for 60 s, and immediately placed under a petri dish for 2 h before baking at 110 °C for 12 min. The Ca

(25 nm)/Al (100 nm) were deposited on the P3HT:PCBM layer by low vacuum ($\sim 10^{-6}$ mbar) thermal evaporation. The active layers in all devices were fabricated under the same experimental conditions.

Measurements

The thickness of PEDOT:PSS layers was estimated with an AFM by using a sharp blade to generate ~9 μm wide cuts in the layer. In all cases a thickness of ~40 nm resulted in devices with the best performance, regardless of the treatment. I–V curves were obtained using a 100 mW/cm^2 ELH bulb. The EQE was measured at 0 V. AFM measurements were performed using a Digital Instruments system. SEM and Auger were measured with JEOL JAMP 7830F.

Results and discussion

Devices with an untreated PEDOT:PSS layer were optimized by varying the spin-coating rate, in the range of 1000–4000 rpm, and the spin duration, in the range of 60–120 s. The optimized condition for the untreated (prepared from the original solution) PEDOT:PSS was 3000 rpm for 60 s. Devices in which the PEDOT:PSS solution was further diluted with DI water (treatment (i)) were optimized by varying the volume ratio of PEDOT:PSS to water from 1:5 to 4:1, in combination with varying the spin-coating speed from 500 to 3000 rpm for each dilution. Optimized layers, as evaluated by the performance of the solar cells, were obtained for a volume ratio of 3:7 that was used to fabricate the PEDOT:PSS layers at 600 rpm for 60 s. Similarly to the dilution of the PEDOT:PSS with DI water, the volume ratio of the PEDOT:PSS to EG (treatment (ii)) varied from 10:3 to 3:7, and the spin-coating speed from 500 to 3000 rpm. The optimized condition for the EG-mixed PEDOT:PSS was obtained by using a 1:1 volume ratio and spin coating at 1000 rpm for 60 s. The performance of solar cells with the latter was similar to those based on the DI water dilution.

EG-treated devices were prepared also by spin-coating EG on top of the PEDOT:PSS layer (treatment (iii)). Different spin-coating speeds for both, the PEDOT:PSS layer and the EG, ranging from 500 to 3000 rpm, were tested. The best device was obtained by spin-coating the EG at 2000 rpm for 60 s on top of an untreated PEDOT:PSS layer prepared by spin-coating at 2000 rpm for 60 s.

All PEDOT:PSS layers were annealed at 120 °C for ~1 h. Following the application of the P3HT:PCBM, the samples were annealed at 110 °C for 12 min.

Fig. 1 shows the I–V curves of different, optimized P3HT:PCBM-based devices with PEDOT:PSS layers that underwent the different treatments, and Table 1 summarizes the values of V_{OC}, I_{SC}, FF and PCE for each device, including for devices prepared by spin coating EG at different rates for 60 s. As clearly seen, the treatments improved the cells' performance, in particular I_{SC} increased by up to 16% from 9.94 to 11.5 mA/cm^2 and PCE by up to ~27% from 3.7% to 4.7% for the device with the EG-treated PEDOT:PSS

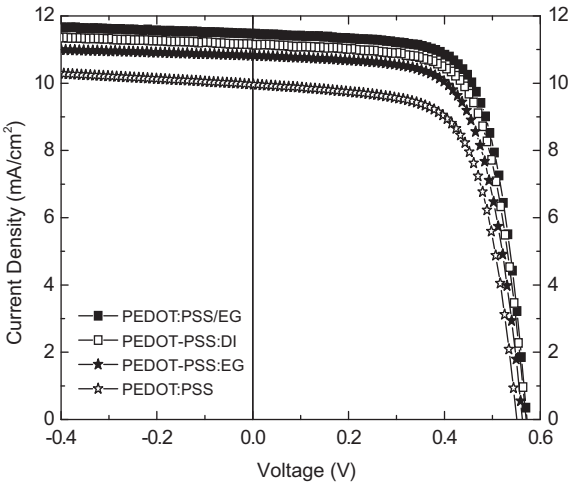

Fig. 1. I–V curves of optimized (see text) P3HT:PCBM-based solar cells, with the PEDOT:PSS layer generated by spin coating the original solution (open stars), the original solution diluted with EG (solid stars) or with DI water (open squares), and by spin coating EG on the untreated PEDOT:PSS layer (solid squares).

Table 1
Device characteristics of solar cells prepared with different treatments of the PEDOT:PSS layer. The data in the top three rows indicate EG solution spin coated over the PEDOT:PSS layer at various rates for 60 s.

Treatment	V_{OC} (V)	I_{SC} (mA/cm^2)	FF (%)	PCE (%)
EG 1000 rpm	0.571	10.7	71.8	4.39
EG 2000 rpm	0.573	11.5	71.3	4.70
EG 3000 rpm	0.566	11.2	70.3	4.46
PEDOT–PSS:DI (3:7 volume ratio)	0.571	11.2	69.5	4.44
PEDOT–PSS:EG (1:1 volume ratio)	0.563	10.8	69.3	4.21
Untreated PEDOT–PSS	0.551	9.94	67.6	3.70

in comparison to the untreated one. V_{OC} was unchanged at 0.55–0.57 V.

To elucidate the origin of the observed improvement in the device performance, various parameters described next were measured. The thickness of the PEDOT:PSS films, which may affect absorption, was measured by making fine cuts (~9 μm wide) on them with a sharp blade, and using scanning atomic force microscopy (AFM) with a scan size of 20 μm across the cuts to measure the films' thickness. The AFM results showed that the typical thickness of the optimized PEDOT:PSS layers of both treated and untreated samples is ~40 nm. This situation excludes a change in the PEDOT:PSS layer thickness as a major contributor to the observed enhancement.

The conductivity of the different PEDOT:PSS layers, which affects charge extraction and therefore, I_{SC} and FF, was also measured. The conductivity of the layer in the best performing devices, i.e., where EG was spin-coated on top of the PEDOT:PSS, was ~0.1 S/cm. It was ~10-fold larger than that of the untreated PEDOT:PSS film, but ~10-fold smaller than that of the PEDOT:PSS layer

prepared from the mixed solution of PEDOT:PSS and EG. The conductivity of the layer prepared from the solution diluted with DI water was comparable to that of the untreated film. Hence, the improved performance of the devices is not directly related to the enhanced conductivity. That is, the I_{SC} of the cell with the PEDOT:PSS layer with the highest conductivity (prepared from a mixture of PEDOT:PSS with EG) was inferior to that of the other devices with the treated PEDOT:PSS layer. And, the I_{SC} of the cell with the PEDOT:PSS layer prepared from further diluting the original solution with DI water was larger that of the device with the untreated layer, though their conductivities were comparable. Hence, and as shown below, other factors besides the conductivity play an important role in improving the performance of the solar cells.

Fig. 2 shows the external quantum efficiency (EQE) spectra of the four devices of Fig. 1. As seen, the EQE increased with PEDOT:PSS treatments, with a trend comparable to that shown in Fig. 1, as expected. The highest EQE, peaking at ~540 nm, was ~62%; it was observed for the device in which EG was spin coated at 2000 rpm for 60 s on top of the PEDOT:PSS prepared from the original solution at 2000 rpm for 60 s. The corresponding EQE for the optimized untreated device was ~50%.

In view of the above results, specifically the significant, reproducible increase in I_{SC} and EQE following modification of the PEDOT:PSS, the transmission of the different PEDOT:PSS layers and the absorption spectra of the different PEDOT:PSS/P3HT:PCBM structures were measured (Fig. 3). As seen in Fig. 3, the transmission of the DI water- and EG-treated PEDOT:PSS in the range 500–700 nm (which covers the main absorption region of the P3HT:PCBM) is slightly larger than that of the untreated layer. Similarly, the absorption spectra of PEDOT:PSS/P3HT:PCBM in the 400–700 nm range show that the absorption increases with the PEDOT:PSS treatments, with the largest absorption observed for the PEDOT:PSS over which EG was spin-coated.

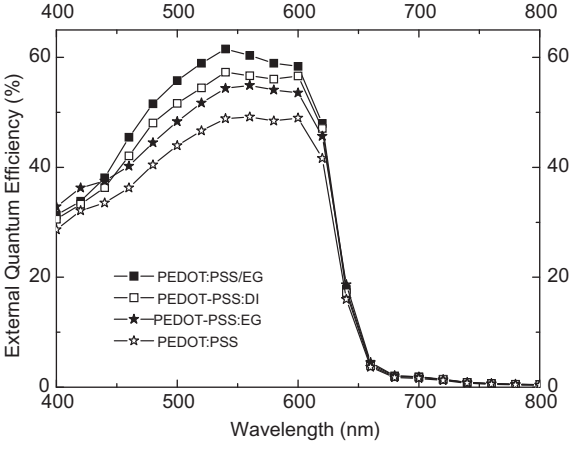

Fig. 2. External quantum efficiency vs wavelength for optimized devices with differently treated PEDOT:PSS layers, i.e., untreated – prepared using the original PEDOT:PSS solution (open stars), prepared by EG dilution of the original PEDOT:PSS solution (solid stars), prepared by DI water dilution (open squares), and EG-treated following PEDOT:PSS fabrication (solid squares). See text for details.

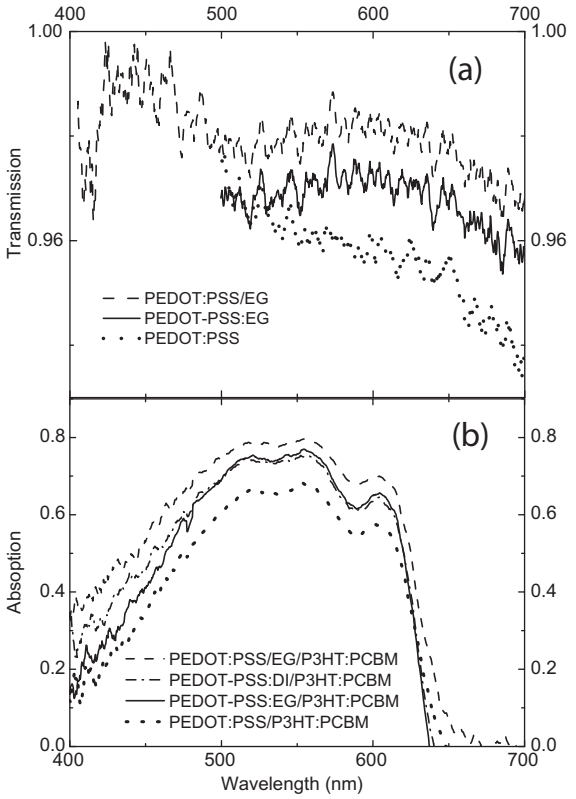

Fig. 3. (a) The transmission spectra of the PEDOT:PSS layer following different treatments. The PEDOT:PSS transmission at wavelengths <500 nm is comparable for all films and for clarity is shown only for one case. (b) The corresponding absorption spectra of the PEDOT:PSS/P3HT:PCBM structures: an untreated PEDOT:PSS film (dotted line), PEDOT:PSS film prepared from a volume dilution ratio of 3:7 PEDOT-PSS:DI water (solid line), PEDOT:PSS film prepared from a 1:1 PEDOT-PSS:EG volume ratio dilution (dashed-dotted line), and PEDOT:PSS film with post-fabrication EG spin coating (dashed line). In all spectra the transmission/absorption of the ITO/glass were subtracted.

To identify potential device characteristics that are responsible for the enhanced absorption and hence increased I_{SC} and EQE, the surface morphology of the PEDOT:PSS and P3HT:PCBM layers as well as the surface chemical composition of the P3HT:PCBM were monitored using AFM, SEM, and Auger electron spectroscopy.

The roughness of the PEDOT:PSS layer, as measured by AFM (Fig. 4) increased slightly from 2.8 nm RMS in the untreated layer and 2.7 nm RMS in the DI water-diluted solution to 3.4 nm in the PEDOT:PSS/EG film. Also, as seen, following the treatments, a more condensed packing of particles was observed. Specifically, the particles appeared smaller for the DI water- and EG-treated samples, in particular for the latter. The smaller particle size is in accordance to previous reports suggesting that the reduced size is due to removal of excess inter-particle PSS [21]. The slightly increased roughness of the PEDOT:PSS layer, and most importantly, the significantly increased "graininess" from untreated to DI water-diluted to EG-coated PEDOT:PSS likely increase the contact area between the PEDOT:PSS and the active layer, improving hole extraction to the anode.

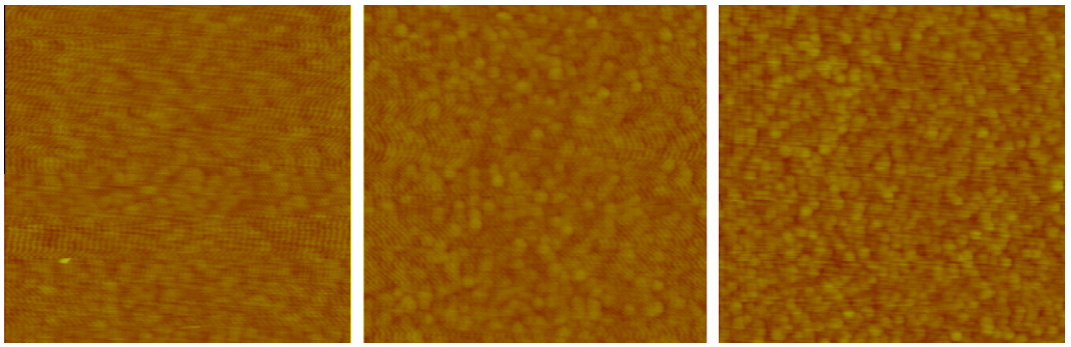

Fig. 4. AFM images of the morphology of PEDOT:PSS films differently treated: left-untreated, original PEDOT:PSS; center-additional dilution of 3:7 PEDOT-PSS:DI water volume ratio; right-EG-treated PEDOT:PSS following the fabrication of the latter. The full scale in each image is 5 μm.

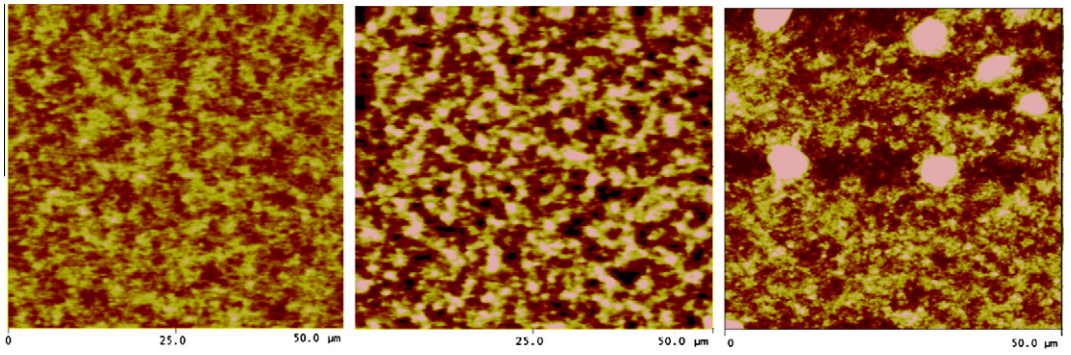

Fig. 5. Morphology AFM images of the P3HT:PCBM layers on top of the different PEDOT:PSS layers (full scale 50 μm). Left: untreated PEDOT:PSS; center: DI water diluted PEDOT:PSS; right: PEDOT:PSS layer with EG spun on top.

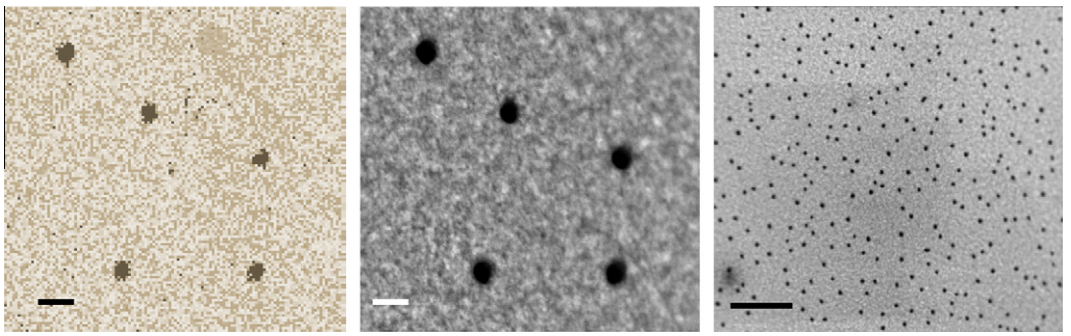

Fig. 6. Left: Auger carbon mapping of the surface of P3HT:PCBM spin-coated on top of the EG-treated PEDOT:PSS post-fabrication of the latter; the darker color indicates a higher concentration, center: the corresponding SEM image with 10 μm scale bar, and right: SEM image with 100 μm scale bar showing the distribution of the aggregates.

Significant morphology variations were observed in the P3HT:PCBM layers spin-coated on the differently-treated PEDOT:PSS layers, as seen in the AFM and SEM images of Figs. 5 and 6. The RMS surface roughness of P3HT:PCBM with the untreated PEDOT:PSS layer was 13.3 nm, that of the active layer with the PEDOT:PSS layer spun from DI water-diluted PEDOT:PSS (treatment (i)) was 28.5 nm, and the RMS of the active layer with the PEDOT:PSS layer on top of which EG was spin-coated (treatment (iii)) was 34.5 nm. Since all the P3HT:PCBM layers were prepared under the same experimental conditions, these changes in the surface roughness are obviously due to the various treatments and resulting graininess of the PEDOT:PSS layers. Rough surfaces may increase scattering of the incident light back into the active layer and hence lead to increased absorption. In addition, the larger roughness also enlarges the contact area between the active layer and the cathode, which may lead to better electron extraction.

As seen in Figs. 5 and 6, small aggregates, ~3 μm wide, were distributed across the surface of the P3HT:PCBM layer spin-coated on the EG-treated PEDOT:PSS layer. The dimensions of these aggregates, which are largely at the active layer/cathode interface, increased with anneal duration; this behavior is currently being investigated. We note that these features were not present if PEDOT:PSS annealing was performed for less than 30 min.

Auger surface mapping (Fig. 6) revealed a higher carbon (but no sulfur) concentration in those aggregates, which indicates that the aggregates were predominantly of PCBM. Increased PCBM level near the cathode following annealing of PEDOT:PSS/P3HT:PCBM is a known phenomenon, which facilitates electron extraction, improving the efficiency of the solar cells [31–33]. Similarly, the PCBM aggregates may result in an improved FF, since more of the acceptor molecules contact the metal cathode, resulting in more efficient charge collection. Moreover, the aggregates may also lead to light scattering into the active layer, and thus increased path of the light and consequently, its absorption.

Conclusions

Various treatments of the PEDOT:PSS layer in ITO/PEDOT:PSS/P3HT:PCBM/Ca/Al solar cells resulted in improved overall device performance. In particular, the use of a PEDOT:PSS film with spin coated EG on it post-fabrication resulted in an increase in the P3HT:PCBM absorption, and hence, an increase of ~16% in I_{SC} and a 27% increase in PCE, from 3.7% in the cell with the untreated PEDOT:PSS to 4.7% in the former. The FF increased to 71–72% (from ~68% in the untreated cell). Dilution of PEDOT:PSS with DI water, and not only with organic solvents, also improved device performance. Based on the above results, it appears that the improved devices result mostly from an increased surface roughness of the P3HT:PCBM associated with the treatment and consequently graininess of the PEDOT:PSS layers. The increased roughness generates a better contact with the metal electrode, which, possibly, together with the observed PCBM aggregates near the cathode improves charge extraction. The improved PEDOT:PSS transmission and PEDOT:PSS/P3HT:PCBM absorption, together with the improved PEDOT:PSS conductivity in some of the cases, improved the I_{SC} and the overall cell performance. This improvement is possibly also due to improved light scattering by the rougher surfaces that results in enhanced absorption in the active layer. The results do not indicate that a change in the thickness of the PEDOT:PSS films is a major contributor to the observed improvements, as optimized spin-coating conditions were employed in each case (untreated and treated PEDOT:PSS) and the optimized thicknesses of the different layers were comparable. Similarly, changes in the PEDOT:PSS conductivity did not correlate with the improved performance.

The simple routes that led to the significantly increased PCE are expected to be applicable to other organic-based solar cells.

Acknowledgements

This work was partially supported by the Iowa Power Fund and the Director for Energy Research, Office of Basic Energy Sciences, USDOE. Ames Laboratory is operated by Iowa State University for the US Department of Energy (USDOE) under Contract No. DE-AC 02-07CH11358.

References

[1] B.A. Gregga, M.C. Hanna, J. Appl. Phys. 93 (2003) 3605.
[2] H. Hoppea, N.S. Sariciftci, J. Mater. Res. 19 (2004) 1924.
[3] T.L. Benanti, D. Venkataraman, Photosynth. Res. 87 (2006) 73.
[4] C.J. Brabec, Sol. Energy Mater. Sol. Cells 83 (2004) 273.
[5] M. Reyes-Reyes, K. Kim, D.L. Carroll, Appl. Phys. Lett. 87 (2005) 083506.
[6] J.D. Servaites, S. Yeganeh, T.J. Marks, M.A. Ratner, Adv. Funct. Mater. 20 (2010) 97.
[7] G. Li, V. Shrotriya, J. Huang, Y. Yao, Tom Moriarty, K. Emery, Y. Yang, Nat. Mater. 4 (2005) 864.
[8] G. Li, V. Shrotriya, Y. Yao, Y. Yang, J. Appl. Phys. 98 (2005). 043704–1.
[9] M.D. Irwin, D.B. Buchholz, A.W. Hains, R.P.H. Chang, T.J. Marks, Proc. Nat. Acad. Sci. USA 105 (2008) 2783.
[10] J.Y. Kim, S.H. Kim, H.-H. Lee, K. Lee, W. Ma, X. Gong, A.J. Heeger, Adv. Mater. 18 (2006) 572.
[11] A. Roy, S.H. Park, S. Cowan, M.H. Tong, S. Cho, K. Lee, A.J. Heeger, Appl. Phys. Lett. 95 (2009). 013302–1.
[12] J.Y. Kim, K. Lee, N.E. Coates, D. Moses, T.-Q. Nguyen, M. Dante, A.J. Heeger, Science 317 (2007) 222.
[13] A. Moliton, J.-M. Nunzi, Polym. Int. 55 (2006) 583.
[14] Y. Shen, A.R. Hosseini, M.H. Wong, G.G. Malliaras, ChemPhysChem 5 (2004) 16.
[15] M.D. Perez, C. Borek, S.R. Forrest, M.E. Thompson, J. Am. Chem. Soc. 131 (2009) 9281.
[16] B.P. Rand, D.P. Burk, S.R. Forrest, Phys. Rev. B 75 (2007). 115327–1.
[17] J.D. Servaites, M.A. Ratner, T.J. Marks, Appl. Phys. Lett. 95 (2009). 163302–1.
[18] Dhritiman Gupta, Monojit Bag, K.S. Narayan, Appl. Phys. Lett. 92 (2008) 093301.
[19] Myung-Su Kim, Bong-Gi Kim, Jinsang Kim, ACS Appl. Mater. Interfaces 1 (2009) 1264.
[20] S. Timpanaro, M. Kemerink, F.J. Touwslager, M.M. De Kok, S. Schrader, Chem. Phys. Lett. 394 (2004) 339.
[21] J. Ouyang, Q. Xua, C.-W. Chua, Y. Yang, G. Li, J. Shinar, Polymer 45 (2004) 8443.
[22] F. Zhang, M. Johansson, M.R. Andersson, J.C. Hummelen, O. Inganas, Adv. Mater. 14 (2002) 662.
[23] S.-I. Na, S.-S. Kim, J. Jo, D.-Y. Kim, Adv. Mater. 20 (2008) 4061.
[24] S.H. Eom, S. Senthilarasu, P. Uthirakumar, S.Ch. Yoon, J. Lim, C. Lee, H.S. Lim, J. Lee, S.-H. Lee, Org. Electron. 10 (2009) 536.
[25] T. Ameri, G. Dennler, C. Waldauf, H. Azimi, A. Seemann, K. Forberich, J. Hauch, M. Scharber, K. Hingerl, C.J. Brabec, Adv. Funct. Mater. 20 (2010) 1592.
[26] J.Y. Kim, J.H. Jung, D.E. Lee, J. Joo, Synth. Met. 126 (2002) 311.
[27] S.K.M. Jönsson, J. Birgerson, X. Crispin, G. Greczynski, W. Osikowicz, A.W.D. van der Gon, W.R. Salaneck, M. Fahlman, Synth. Met. 139 (2003) 1.
[28] X. Crispin, S. Marciniak, W. Osikowicz, G. Zotti, A.W. Denier van der Gon, F. Louwet, M. Fahlman, L. Groenendaal, F. de Schryver, W.R. Salaneck, J. Polym. Sci. Pol. Phys. 41 (2003) 2561.
[29] L.A.A. Pettersson, S. Ghosh, O. Inganäs, Org. Electron. 3 (2002) 143.
[30] W.H. Kim, A.J. Mäkinen, N. Nikolov, R. Shashidhar, H. Kim, Z.H. Kafafi, Appl. Phys. Lett. 80 (2002) 3844.
[31] M. Campoy-Quiles, T. Ferenczi, T. Agostinelli, P.G. Etchegoin, Y. Kim, T.D. Anthopoulos, P.N. Stavrinou, D.D.C. Bradley, J. Nelson, Nat. Mater. 7 (2008) 158.
[32] S.S. Van Bavel, E. Sourty, G. De With, J. Loos, Nano Lett. 9 (2009) 507.
[33] A.J. Parnell, A.D.F. Dunbar, A.J. Pearson, P.A. Staniec, A.J.C. Dennison, H. Hamamatsu, M.W.A. Skoda, D.G. Lidzey, R.A.L. Jones, Adv. Mater. 22 (2010) 2444.

Organic Electronics 12 (2011) 263–268

Contents lists available at ScienceDirect

Organic Electronics

journal homepage: www.elsevier.com/locate/orgel

Direct imaging of conductivity in pentacene field-effect transistors by a near-field scanning microwave microprobe

Arsen Babajanyan [a], Harutyun Melikyan [a], Jongchel Kim [a], Kiejin Lee [a,*], Mitsumasa Iwamoto [b], Barry Friedman [c]

[a] Department of Physics and Basic Science Institute for Cell Damage Control, Sogang University, Seoul 121-742, Republic of Korea
[b] Department of Physical Electronics, Tokyo Institute of Technology, 2-12-1 O-Okayama, Meguro-ku, Tokyo 152-8552, Japan
[c] Department of Physics, Sam Houston State University, Huntsville, TX 77341, USA

ARTICLE INFO

Article history:
Received 1 September 2010
Received in revised form 12 October 2010
Accepted 21 November 2010
Available online 2 December 2010

Keywords:
Pentacene
OFET
Conductivity
Microwave reflection
Second harmonic

ABSTRACT

A near-field scanning microwave microprobe (NSMM) is employed to visualize the carrier distribution in the active layer of an organic field-effect transistor (OFET). Experiments using this technique with a pentacene OFET reveal changes of the conductivity profiles in the channel which arise from the development and exhaustion of an accumulated charge region. Electric field profiles that are visualized by using the electric field induced optical second harmonic generation (EFISHG) method, verify the results. NSMM is a powerful tool, and in combination with EFISHG will provide a way to directly probe carrier transport.

© 2010 Elsevier B.V. All rights reserved.

1. Introduction

Understanding carrier behaviors in materials is one of the most fundamental subjects in physics, material science, electronics, and electrical engineering. The study of carrier mobility and conductivity is important not only for device application [1], but also for understanding carrier transport, accumulation, charging, and trapping [2]. Interest in the dynamic behavior of carriers in organic material remains high due to possible application of organic devices, e.g., organic thin film transistors (OTFTs) [3], and organic electro-luminescent devices [4]. The recent research efforts to clarify the mechanism of OTFTs have been made to utilize efficiently organic materials [5], where probing the charge carrier is a key issue and many electrical measurements are being used [6,7]. Carrier trapping phenomena in OTFTs is generally observed by using electrical measurement [1,2,7], such as capacitance–voltage (C–V) and thermally simulated current measurements. Here the basic experimental concept is indirect characterization of charge storage using the C–V behaviors. The dynamical carrier motion has been explored using a variety of electrical techniques, e.g., the time-of flight (TOF) measurement [8]. The idea of these techniques is the indirect probing of the carrier motion and its related electrical phenomena through the current–voltage (I–V) characteristics. A Maxwell-displacement current pulse is recorded by electrical instruments and is analyzed in terms of the carrier motion [2,9]. Nevertheless, these techniques have drawbacks in discriminating carrier species, carrier-injection and carrier-transport processes. Direct probing and visualization of the carrier distribution can overcome these difficulties, and hence opens a new and fundamental way to discuss device operation [10].

In this paper, we demonstrate a direct probing of conductivity distribution in an organic thin film in terms of I–V characteristics, which relies on a near-field scanning microwave microprobe (NSMM) [11–14]. This is a direct

* Corresponding author. Tel.: +82 2 705 8429; fax: +82 2 715 8429.
E-mail address: klee@sogang.ac.kr (K. Lee).

1566-1199/$ - see front matter © 2010 Elsevier B.V. All rights reserved.
doi:10.1016/j.orgel.2010.11.016

observation method that allows visualizing conductivity profiles caused by injected carriers in a channel of OTFT. The near-field microwave reflection coefficient (S parameter) image from the organic thin film directly visualizes the conductivity dependence on bias voltages. This NSMM approach is based on nondestructive probing of a local electromagnetic near-field interaction between the probe tip and the organic materials, and can be used in exploring carrier behaviors in devices such as OTFTs. The results obtained with NSMM are confirmed by the complementally visualized profile of the electric-field distribution which is obtained by using an electric field induced optical second harmonic generation (EFISHG) method [15,16].

2. Experimental

In our design of NSMM experiments, the probe is simply a sharpened metal wire tip in which voltage oscillations are present at microwave frequencies. The tip is brought to a distance of 10 nm from the sample surface. Because tip-sample interactions take place over a distance of nanometers, much less than the microwave wavelength (~1 cm), these interactions occur under near-field conditions. If the sample is translated under the tip, changes in tip-sample coupling can be used to obtain images of the sample with submicron resolution. The resolution is governed by tip geometry rather than the diffraction limit. At its other end, the probe is inserted into a microwave resonance cavity, or "resonator", populated by standing microwaves. The resonator microwave fields drive the electronic oscillations in the probe and the microwaves are continually excited through an input wire line connected to an external source.

We designed a NSMM with a tuning fork distance control system to keep a constant distance between the sample and the tip [12,13]. The probe tip was made of tungsten wire with a diameter of 50 μm with tapered end size of 1 μm. The probe tip was oriented perpendicular to the sample surface and the other end of the tip was directly connected to a coupling loop in the resonator cavity. The resonance frequency of a given TE_{011} mode (4.1 GHz) was measured with a network analyzer (Agilent 8753ES). To drive the tuning fork, an AC voltage was applied to one contact on the tuning fork at its resonance frequency using the oscillator of a lock-in amplifier (Signal Recovery 7265). The output from the lock-in amplifier was fed into the feedback system to control the tip-sample distance (10 nm) using a piezo electric tube (PZT) that supports the sample stage. The general idea is that the tip-sample distance is modulated with the vibration amplitude of the quartz tuning-fork oscillator at the resonant frequency, and the modulated signal is used to control the separation of a few nanometers. As the probe tip is brought into close proximity of the sample surface, the amplitude and resonant frequency of the oscillation are changed by interactions between the probe tip and the sample. As result, the amplitude of the oscillation is a function of the distance at which this control can be performed: for smaller amplitude, a smaller control distance can be maintained. All NSMM measurements were done at the same tip-sample

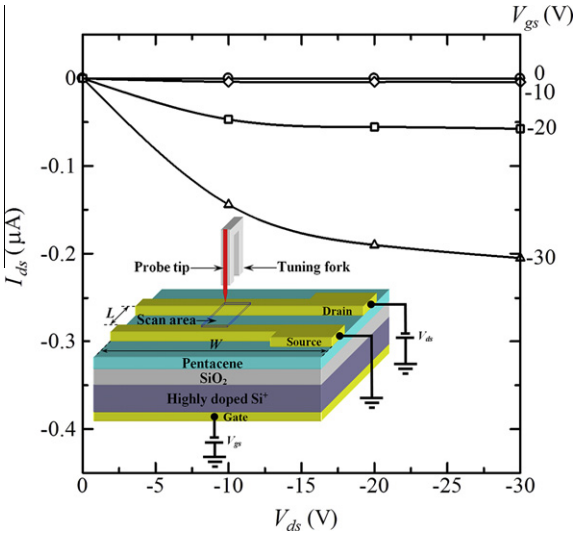

Fig. 1. I–V characteristics of the source–drain channel at the various negative gate biases obtained from the pentacene OFET. The inset shows the schematic diagram of the pentacene OFET with electrical connections and tuning fork attached probe tip for microwave scanning.

distance. The sample was mounted onto an x–y–z-translation stage for coarse adjustment which was driven by a computer-controlled microstepping motor with a resolution of 100 nm, whereas fine movement of the sample was controlled by a PZT tube with 10 nm resolution. The resulting spatial and lateral resolutions of mapping were about 2 μm and 5 μm, respectively, however, the NSMM incorporating with a commercial AFM probe-tip and 2D PZT scanner is able to map with an effective resolution of up to 50 nm [17].

The sample used in the experiments was a top-contact pentacene organic field-effect transistor (OFET) as schematically shown in the inset of Fig. 1. Before deposition of the pentacene, highly doped Si substrates were covered with a 500 nm thick SiO_2 insulating layer. The process pressure during deposition of the pentacene was kept at less than 10^{-4} Pa and the deposition rate were controlled at approximately 3 nm/min. After deposition of the pentacene, the top Au electrodes (source and drain electrodes) were deposited on the pentacene surface with a thickness of 100 nm. The channel length L and width W were 50 μm and 3 mm, respectively. For the field-effect transistor structure, a highly doped Si substrate was used as a gate electrode.

3. Results and discussion

The microwave reflection coefficient S_{11} measurements for a pentacene OFET reveal the changes of conductivity distribution in the OFET channel. That is, the electric conductivity distribution probed by NSMM depends on applied positive and negative drain–source (V_{ds}) and gate–source (V_{gs}) voltages. The electric conductivity distribution probed by NSMM during the off state obeys the Laplacian field. Here, this Laplacian field is the electric field caused

by the applied potentials on electrodes in the absence of any charge between the electrodes, and is formed when the pentacene shows the intrinsic nature of dielectric materials, e.g., low carrier density and lower conductivity [7,9]. On the other hand, electric-field distribution during the *on*-state deviates from this Laplacian field formed at the *off*-state, because excessive carriers injected from the source electrode makes a dominant contribution to the electric field formation, and regulates the carrier transport across the OFET channel, depending on the gate bias. By selecting an appropriate wavelength, the S_{11} signal could be localized in the various layers of the OFET due to the dependence of the penetration depth (so called skin depth: $\delta_s = (\pi\nu\mu\sigma/\lambda)^{-1/2}$, here ν is the speed of light, μ and σ are the permeability and the conductivity of the material) on the scanning wavelength, λ and material parameters, μ and σ [18].

NSMM is capable of imaging at submicron resolutions, is noncontact and nondestructive. This affordability stems in part from the use of microwave frequencies which do not require lens-based optics since the electromagnetic signals propagate along metal wire transmission lines. NSMM functions by sensing changes in electrostatic coupling between a near-field microwave probe and a sample [18,19]. An important feature of the present design, responsible for its high sensitivity, is that at the start of measurement the impedance of the cavity is equalized with that of the input line [20]. This tuning process consists of minimizing the complex reflection coefficient Γ given by assuming impedance matching between the probe and the microwave source [18].

$$\Gamma = \left|\frac{Z_{in} - Z_0}{Z_{in} + Z_0}\right|, \tag{1a}$$

where Z_0 is the characteristic impedance of the probe and Z_{in} is the modulus of the complex impedance of the OFET system. Analyzing the system as a four-layer model on the basis of transmission theory, we obtain [18,19]

$$Z_{in} = Z_a k_a t_{s^+}(1 - Z_g^R \sigma_p t_p) \tag{1b}$$

with Z_a and k_a (the impedance and wave number of free-space, respectively), t_{s^+} (the thickness of the n^+ doped silicon), Z_g^R (the real part of the complex impedance of the Au gate) and σ_p and t_p (the conductivity and thickness of the pentacene thin film, respectively). For a perfectly tuned system, $Z_{in} = Z_0$ and $\Gamma = 0$; in practice, we typically achieve $\Gamma \sim 10^{-3}$. Importantly, Z_{in} includes contributions from probe-sample interactions; therefore, tuning by necessity requires selection of a "reference state" for the sample. This is conveniently accomplished by using a surface region of known composition, for example one with zero coverage of molecules [20]. Minimization of Γ for the reference surface is analogous to subtraction of background in a fluorescence measurement.

The electrical property changes of active layer in pentacene OFET due to injected carriers, i.e., space charge generation, were investigated by measuring the changes of the reflection coefficient S_{11} ($S_{11} = 20\log|\Gamma|$). The S_{11} behavior depends on the V_{ds} and V_{gs} conditions. The behavior is due to injected charges into the OFET channel, hole injection is suppressed with $V_{gs} > 0$, whereas it is assisted with $V_{gs} < 0$. The changes of impedance of the pentacene films due to the accumulation of space charge are discussed based on how the changes in reflection coefficient depend on impedance changes.

The drain–source current, I_{ds} vs. V_{ds} characteristics at various negative gate voltages is shown in Fig. 1. The inset of Fig. 1 shows the sample structure and electrical connections for negative biases. The OFET shows typical *p*-type semiconductor characteristics. Let us briefly review the expected physics focusing on the operation of the *on*-state OFET. In OFETs, carrier transport is realized by charge accumulation and transport at the semiconductor/metal interface. A negative gate voltage, at zero drain bias, induces a uniform positive charge density, at the interface between the SiO_2 insulator and pentacene channel. This accumulated charge stems from the carriers injected from the source and drain electrodes, and its distribution is dependent on the V_{ds} and V_{gs}.

The situation is described by using a model that accounts for charge accumulation caused by the difference of dielectric relaxation times between the adjacent two materials (Maxwell–Wagner effect) [21], and carrier transport is described using macroscopic physical parameters, such as conductivity and electric field. In a *steady*-state, current flowing along the interface is always given by

$$j(x) = \sigma(x)E(x) = \text{const}, \tag{2}$$

where $\sigma(x)$, and $E(x)$ are the conductivity and electric field as a function of channel position x. In a three-electrode pentacene OFET system, charge transport is basically due to interface charging propagation by the accumulated charge on the semiconductor/insulator/gate interface. Injected carriers are excess charges and form a space charge field. The electric field profile $E(x)$ in the *on*-state is calculated by a transmission line model using an equivalent circuit consisting of infinitesimally small resistors and capacitors connected in series along the channel [22–24].

Transient analysis of the transmission line model gives a solution of the *steady*-state in the limit $t \to \infty$. In the *steady*-state, the potential distribution $V(x)$ ($V(0) = V_{gs} \cong V_g - V_s < 0$: source and $V(L) = V_{gs} - V_{ds}$: drain electrode) and electric-field distribution $E(x) = -\partial V(x)/\partial x$ are derived to be

$$V(x) = V_{ds}\sqrt{\frac{L-x}{L}} + V_{gs} - V_{ds}, \quad E(x) = \frac{V_{ds}}{2\sqrt{L(L-x)}}. \tag{3}$$

Note that $V(x)$ is a square root function of x, but it gives a linear potential profile in the region $x < L$, in the region of the source electrode side. In that region a gradual channel approximation is valid. Hole accumulation is created at the position x when the potential on the surface is attractive for holes, that is, $V(x) < 0$ while hole accumulation is not allowed when $V(x) > 0$ owing to the repulsive potential. Hence for $V_{ds} > V_{gs}$, charge accumulation is allowed over the entire region along the channel, whereas for $V_{ds} < V_{gs}$, the accumulated charge layer is established only in the region $0 \leqslant x \leqslant x_p$, and further charging is not allowed in the region $x_p \leqslant x$. Here $V(x_p) = 0$ and x_p is given by

$x_p = (1 - (1 - V_{gs}/V_{ds})^2)L$. In other words, x_p represents the maximum position where holes injected from the source are allowed to accumulate [21,22]. Note that the position x_p corresponds to the so-called "pinch-off" position [1], but it is different from the common use in semiconductor physics in that the position is determined by the potential caused by accumulation and propagation of injected holes. The potential $V(x)$ in Eq. (3) suggests that the carrier density profile is changing in proportion to $-C_g V(x)$, where C_g is the gate capacitance per unit area. Based on the above discussion, we find that when a negative bias ($V_{gs} < 0$) is applied to the gate under the condition $V_{ds} = 0$ (see Eq. (3)), firstly a uniform charge distribution is formed along the entire interface (channel formation), while when a negative drain bias V_{ds} is applied, a non-uniform charge distribution is created with lower density near the drain. When a more negative bias (more negative than the gate bias) is applied to the drain, an accumulated charge exhaustion layer is formed in the vicinity of the drain, i.e., an x_p position is created. Owing to the formation of this layer, the conductivity value is decreased and approaches the intrinsic one though the electric field is enhanced.

The NSMM probes the conductivity $\sigma(x)$ directly in the microwave frequency region, as follow from the relation in Eq. (1b). On the other hand, the EFISHG probes the static electric field $E(x)$ directly [21]. There is a reciprocal relationship between the conductivity $\sigma(x)$ and the static electric field $E(x)$ (see Eq. (2)). Hence the conductivity distribution mapped by the NSMM can be confirmed with the EFISHG profile.

Fig. 2 shows the 3D NSMM images from the channel of a pentacene OFET at various negative source–drain and gate bias voltages. Voltages are applied to the drain and gate electrodes with the source electrode grounded. As clearly shown in the images, the microwave reflection images correspond to the *I–V* characteristics. The change of microwave reflection coefficient traces the channel conductivity distribution. The conductivity along the pentacene channel is caused by accumulated charge and intrinsic carriers, and is given in the transmission line model by the expression

$$\sigma = \sigma_0 + \mu_p C_g \left[V_{ds} \left(1 - \sqrt{\frac{L - x}{L}} \right) - V_{gs} \right] \tag{4}$$

in the region $0 \leqslant x \leqslant x_p$, whereas in the region $x_p \leqslant x$, $\sigma = \sigma_0$. Here μ is the mobility of the carriers and σ_0 is the intrinsic conductivity of pentacene ($\mu_p = 5 \times 10^{-4}$ cm^2/Vs [25] and $\sigma_0 = 0.38 \times 10^{-6}$ S/cm [26]).

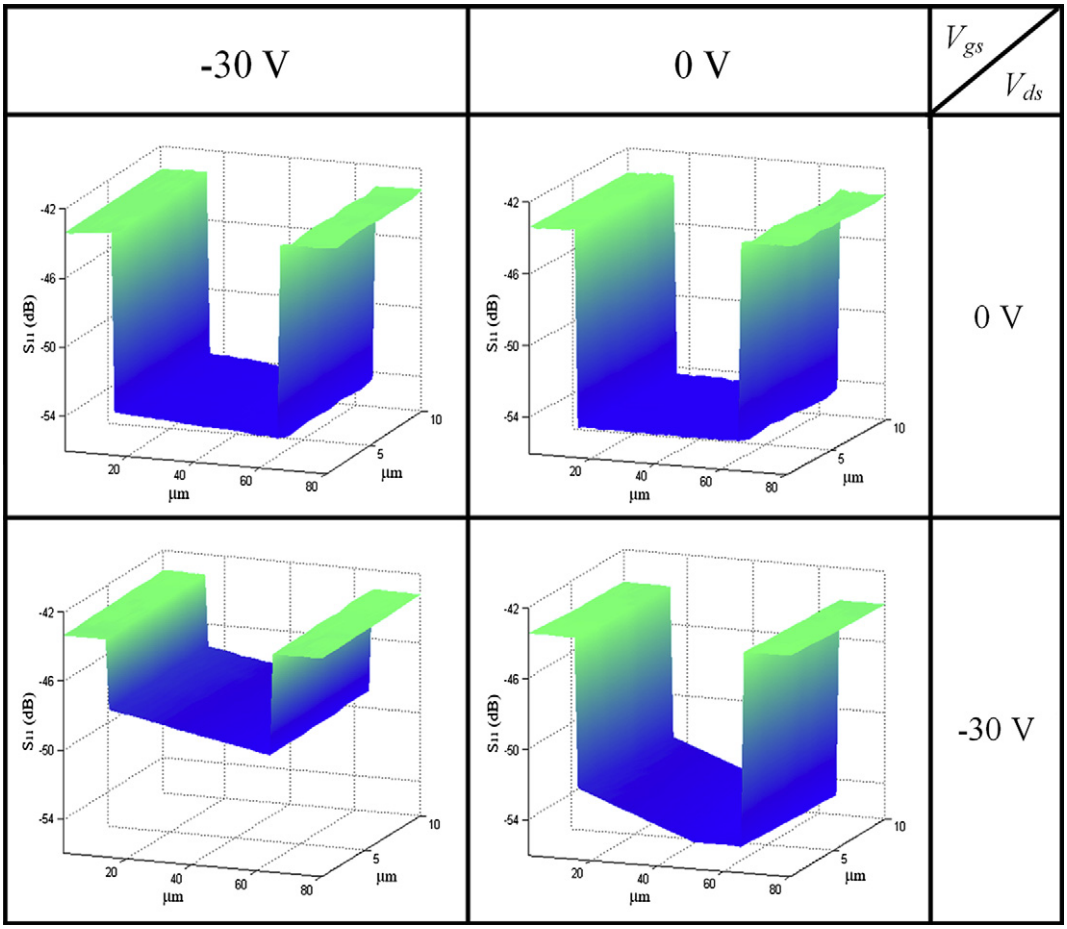

Fig. 2. 3D NSMM image of the pentacene OFET source–drain channel at the various negative gate biases.

Fig. 3 shows the relative change of estimated conductivity distribution in the pentacene OFET source–drain channel at $V_{ds} = -10$ V. The conductivity was estimated from measured microwave reflection coefficient S_{11} by using Eqs. (1a) and (1b) with empirical correlation of the experiment and the model [19]. As the magnitude of the negative gate bias increased the conductivity of the channel increased and a non-uniform conductivity distribution, with low density near the drain, was obtained. The inset of Fig. 3 shows the measured relative change of conductivity (from NSMM) vs. Eq. (4). Based on this good agreement, we conclude that the injection charges dominate in the conductivity. On the other hand, at $V_{gs} = 0$ V, a convex point x_p, corresponding to the boundary between charge accumulated and exhausted region, is seen. Eq. (4) accounts well for this result taking into account a threshold voltage $V_{th} = -10$ V, that is by replacing V_{gs} with $V_{gs} - V_{th}$. By increasing positively the biasing voltage V_{gs} ($V_{gs} > 0$), the conductivity decreased caused by hole depletion near the drain. In this situation, the role of the source and drain are converted into each other. Hence for analyzing the conductivity profiles using Eq. (4), we replace V_{ds} with $V_{sd} = -V_{ds}$, V_{gs} with $V_{gd} = V_{gs} - V_{sd} = V_{gs} + V_{ds}$, and x with $L - x$. Then the charge accumulation region is $L - x_p \leqslant x \leqslant L$. The convex point x_p shifts to the drain with increase of V_{gs} with $x_p = (V_{gs}/V_{ds})^2 L$, though we need to consider the contribution of V_{th} by replacing V_{gs} with $V_{gs} + V_{th}$.

To confirm our experiments with the NSMM, we probed the electric-field distribution along the OFET channel by using the reciprocal relationship between the NSMM and EFISHG. The system used for the EFISHG measurement was the same as in Ref. [10]. The EFISHG experiments were carried out in a manner as described in Ref. [27] at $V_{gs} = -100$ V, focusing on the electric field enhancement in the region where the conductivity is extremely low.

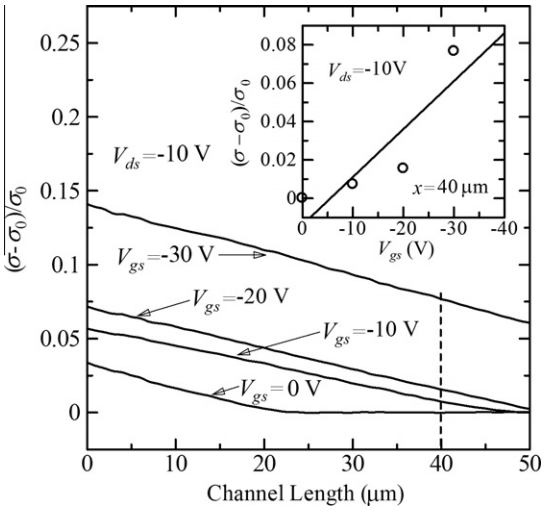

Fig. 3. The relative change of estimated conductivity distribution of the pentacene OFET source–drain channel at the various negative gate biases ($V_{gs} = 0$, -10, -20, -30 V). The inset shows the relative change of estimated conductivity (measured by NSMM), $(\sigma - \sigma_0)/\sigma_0$ vs. applied gate bias at a channel position of $x = 40$ μm and $V_{ds} = -10$ V. The solid line is a fit to Eq. (4) with $C_g = 7 \times 10^{-9}$ F/cm^2 and $\mu_p = 5 \times 10^{-4}$ cm^2/vs.

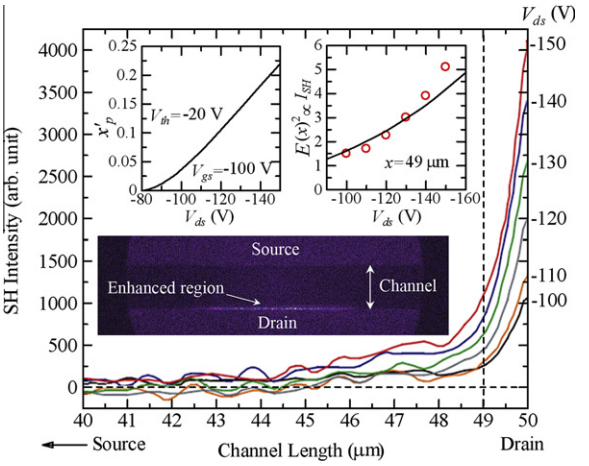

Fig. 4. SH intensity graph generated at various negative V_{ds} voltages. The gate bias was fixed at $V_{gs} = -100$ V. The upper left inset shows that $x_p' = 1 - x_p/L$ increases V_{ds} becomes more negative. The upper right inset shows that the calculated SH signal (see Eq. (3)) agrees well with the experimental data ($x = 49$ μm). The lower inset shows the EFISHG image of the pentacene OFET source–drain channel.

EFISHG is generated in proportion to square of electric field, $E^2(x)$. Fig. 4 shows a typical example of the experiments, in which we could see the second harmonic (SH) enhancement in the region where conductivity is low (lower inset of Fig. 4). That is, as the electric field is high in this region (see Eq. (2)), we could observe the enhanced EFISHG in proportion to $V_{ds}{}^2$ (see Eq. (3) and upper insets of Fig. 4). Note that EFISHG is a spectroscopic measurement, and the signal was selectively generated at a wavelength of 560 nm from the pentacene layer by the use of a incident laser with a wavelength of 1120 nm [10,26]. This supports the fact that EFISHG is probing carrier motion in the pentacene layer while the NSMM is probing the carrier distribution along the channel in the OFET. It is significant that the two experimental probes test the model in two different spatial regions of the interface; EFISHG works best where the electric field is high while NSMM works well in the high conductivity region (along the interface $j = E$ and so the regions are complementary). When we were carrying on the NSMM experiments shown in Fig. 2, we discovered the conductivity increased around the source with increase of V_{ds} ($V_{ds} < 0$) under the constant V_{gs} ($V_{gs} < 0$), though the fixed constant value $\sigma = \sigma_0 - \mu C_g V_{gs}$ (at $x = 0$) was suggested from Eq. (4). These results indicate the presence of hole injection from the source and transport via interfacial and bulk trapping states [12] caused by defects in the pentacene (otherwise the conductivity would not increase) [28–30].

4. Conclusions

The NSMM image clearly distinguishes the conductivity profiles caused by charge motion from source to drain. This is an advantage of direct observation by a NSMM. We anticipate that the use of this microwave method will be of great help for the understanding of carrier transport in organic materials, including bio-materials and molecules.

Further we should note that NSMM experiments in combination with EFISHG measurements could be an effective method for directly characterizing the *I–V* and *C–V* characteristics of materials on a microscopic scale. This study is a preliminary one and to clarify the details of the NSMM including the spatial and lateral resolution, dynamic range, etc., is our next work, but we may conclude from this study that NSMM provides a novel way to probe carrier behaviors in OFET.

Acknowledgements

This work was supported by Sogang University Special Research Grant (2010), the Seoul Research and Business Development Program (10816), the Korea Research Foundation Grant (KRF-2008-615-C00001), Basic Science Research Program through the National Research Foundation of Korea Grant (2010-0012037), and Priority Research Centers Program through the National Research Foundation of Korea (2010-0028291).

References

[1] S.M. Sze, Physics of Semiconductor Devices, second ed., John Wiley & Sons, New York, 1981.
[2] G.M. Sessler, Electrets, Springer, Berlin, 1980.
[3] G. Horowitz, Adv. Mater. 10 (1998) 365.
[4] C.W. Tang, S.A. Van Slyke, Appl. Phys. Lett. 51 (1987) 913.
[5] H. Sirringhaus, Adv. Mater. 17 (2005) 2411.
[6] D. Gracias, Nat. Photonics 1 (2007) 570.
[7] H. Meier, Organic Semiconductors: Dark- and Photoconductivity of Organic Solids, Chemie, Weinheim, 1974.
[8] R.G. Kepler, Phys. Rev. 119 (1960) 1226.
[9] M.A. Lampert, P. Mark, Current Injection in Solids, Academic, New York, 1970.
[10] T. Manaka, E. Lim, R. Tamura, M. Iwamoto, Nat. Photonics 1 (2007) 581.
[11] M. Abu-Teir, M. Golosovsky, D. Davidov, A. Frenkel, H. Goldberger, Rev. Sci. Instrum. 72 (2001) 2073.
[12] E. Lim, T. Manaka, M. Iwamoto, B. Friedman, A. Babajanyan, S. Kim, Y. Yoon, S. Kim, K. Lee, Thin Solid Films 516 (2008) 2573.
[13] J. Kim, M. Kim, K. Lee, J. Lee, D. Cha, B. Friedman, Meas. Sci. Technol. 14 (2003) 7.
[14] B. Knoll, F. Keilmann, A. Kramer, R. Guckenberger, Appl. Phys. Lett. 70 (1997) 2667.
[15] T. Manaka, E. Lim, R. Tamura, M. Iwamoto, Appl. Phys. Lett. 87 (2005) 222107.
[16] T. Manaka, E. Lim, R. Tamura, D. Yamada, M. Iwamoto, Appl. Phys. Lett. 89 (2006) 072113.
[17] H. Melikyan, T. Sargsyan, A. Babajanyan, S. Kim, J. Kim, K. Lee, B. Friedman, J. Magn. Magn. Mater. 321 (2009) 2483.
[18] D.M. Pozar, Microwave Engineering, Addison–Wesley, New York, 1990.
[19] A. Babajanyan, K. Lee, E. Lim, T. Manaka, M. Iwamoto, B. Friedman, Appl. Phys. Lett. 90 (2007) 182104.
[20] B. Friedman, M. Gaspar, S. Kalachikov, K. Lee, R. Levicky, G. Shen, H. Yoo, J. Am. Chem. Soc. 127 (2005) 9666.
[21] R. Tamura, E. Lim, T. Manaka, M. Iwamoto, J. Appl. Phys. 100 (2006) 114515.
[22] M. Weis, T. Manaka, M. Iwamoto, J. Appl. Phys. 105 (2009) 024505.
[23] G. Meller, T. Grasser, Organic Electronics, Springer, New York, 2010. p. 81.
[24] J.R. Burns, RCA Rev. 30 (1969) 13.
[25] E. Lim, T. Manaka, R. Tamura, M. Iwamoto, Jpn. J. Appl. Phys. 45 (2006) 3712.
[26] P. Parisse, M. Passacantando, S. Picozzi, L. Ottaviano, Org. Electron. 7 (2006) 403.
[27] D. Yamada, T. Manaka, E. Lim, R. Tamura, M. Iwamoto, J. Appl. Phys. 103 (2008) 084118.
[28] D.V. Lang, X. Chi, T. Siegrist, A.M. Sergent, A.P. Ramirez, Phys. Rev. Lett. 93 (2004) 076601.
[29] O.D. Jurchescu, J. Baas, T.T.M. Palstra, Appl. Phys. Lett. 87 (2005) 052102.
[30] E. Lim, D. Yamada, M. Weis, T. Manaka, M. Iwamoto, Chem. Phys. Lett. 477 (2009) 221.

Organic Electronics 12 (2011) 269–278

Contents lists available at ScienceDirect

Organic Electronics

journal homepage: www.elsevier.com/locate/orgel

Photoreactive low-bandgap 4*H*-cyclopenta[2,1-b:3,4-b′]dithiophene and 4,7-di(thiophen-2-yl)benzo[c][1,2,5]thiadiazole-based alternating copolymer for polymer solar cell

U Ra Lee [a], Tae Wan Lee [a], Mai Ha Hoang [a], Nam Su Kang [b], Jae Woong Yu [c], Kyung Hwan Kim [a], Kyung-Geun Lim [d], Tae-Woo Lee [d], Jung-Il Jin [a], Dong Hoon Choi [a,*]

[a] Department of Chemistry, Research Institute for Natural Sciences, Korea University, 5 Anam-dong, Sungbuk-gu, Seoul 136-701, Republic of Korea
[b] Korea Institute of Science & Technology, Center for Energy Materials Research, 39-1 Hawolkok-dong, Sungbuk-gu, Seoul 136-791, Republic of Korea
[c] Advanced Materials Engineering for Information and Electronics, Kyung Hee University, 1 Seocheon, Kiheung, Yongin, Kyungki 446-701, Republic of Korea
[d] Department of Materials Science and Engineering, Pohang University of Science and Technology, Pohang, Gyungbuk 790-784, Republic of Korea

ARTICLE INFO

Article history:
Received 29 July 2010
Received in revised form 20 November 2010
Accepted 22 November 2010
Available online 5 December 2010

Keywords:
Low-bandgap polymer
Photoreaction
Bulk heterojunction
Long-term stability
Polymer solar cell

ABSTRACT

Polymer solar cells (PSCs) are often fabricated using a well-known 4*H*-cyclopenta[2,1-b:3,4-b′]dithiophene and 4,7-di(thiophen-2-yl)benzo[c][1,2,5]thiadiazole-based polymer as a low-bandgap polymer. Further, PSCs are also fabricated by mixing methanofullerene [6,6]-phenyl C61-butyric acid methyl ester ($PC_{61}BM$) with the polymer. We prepared poly[4,4-bis(2-ethylhexyl)-4*H*-cyclopenta[2,1-b:3,4-b′]dithiophene-2,6-diyl-alt-4,7-bis(2-thienyl)-2,1,3-benzothiadiazole-5′,5″-diyl] after anchoring the penta-1,4-diene in the side chain of the cyclopentadithiophene and investigated the long-term performance stability of a photocrosslinked bulk heterojunction (BHJ) photovoltaic (PV) cell based on the polymer. The photocrosslinking reaction was monitored via infrared spectroscopy without the use of a photoinitiator, by carrying out a spontaneous radical coupling reaction. The polymer film has a broad absorption band extending from 300 to 850 nm with an optical bandgap as low as 1.52 eV. The polymer was employed to fabricate a PSC with $PC_{61}BM$. The resultant PSC device, which was treated by UV irradiation (λ = 254 nm, I = 40 mW/cm^2, 5 min), had good preliminary results with an open-circuit voltage of 0.62 V, a short-circuit current density of −5.37 mA/cm^2, a fill factor of 0.41, and an overall power conversion efficiency of 1.37%. All parameters of the UV-cured PSC device were more stable over the course of 300 h than those of P3HT-$PC_{61}BM$ devices, indicating the long-term stability of the polymer.

© 2010 Elsevier B.V. All rights reserved.

1. Introduction

Substantial progress has been made in the exploration of organic semiconductors as active elements in electronic devices such as light-emitting diodes, thin-film transistors (TFTs), and solar cells [1–7]. With regard to the application of organic semiconductors in electronic and optoelectronic devices, the organic photovoltaic (OPV) cell is expected to play an important role in developing devices to meet future energy requirements [8–15].

Bulk heterojunction (BHJ) PSCs have been shown to be the most promising devices for OPV cells. PSCs made of regioregular poly(3-hexylthiophene), poly[p-phenylene vinylene] and polyfluorene derivatives have been demonstrated with [6,6]-phenyl C (61 or 71) butyric acid methyl ester (PCBM) and exhibited quite promising power conversion efficiency (PCE) [16–22]. Since the photon flux of the solar emission has a maximum at 680 nm, many promising low-bandgap polymers have been designed and reported in the literatures [23–26].

* Corresponding author. Tel.: +82 2 3290 3140; fax: +82 2 924 3141.
E-mail address: dhchoi8803@korea.ac.kr (D.H. Choi).

1566-1199/$ - see front matter © 2010 Elsevier B.V. All rights reserved.
doi:10.1016/j.orgel.2010.11.021

The PCE value is often considered to evaluate device functionality and material properties in the PSC devices. The durability of PCEs, however, has not been much discussed. In fact, the lifetime of PSC is relatively short compared to silicon-based solar cells. In order to achieve good performance stability of PSC devices, the blend morphology of donor and acceptor materials should be sufficiently stable. Kim et al. emphasized the importance of the stability of the blend morphology in enabling the practical application of well-known BHJ PV devices, because any heat generated by solar emission can be detrimental to the performance of the devices. This damage is a result of the relatively low glass transition temperature (T_g) of the polymer blend and the miscibility of donor and acceptor materials in the photoactive layer [27]. Several useful methods for improving the performance stability of PSCs have been suggested in the literature, including the use of a proper compatibilizer and a fixation process involving two materials that stabilizes the two phases after nanophase separation [28]. Thermal crosslinking reactions have also been adopted to improve the stability of the blend morphology. However, thermal treatments used to induce crosslinking may be detrimental in that they prevent the annealing processes from being properly carried out [29–31]. Consequently, one of the major goals of this research is to control such "trade-off" problems.

In order to achieve this goal, we employed a photocrosslinking reaction to activate the thermal annealing process, followed by a separate photocrosslinking reaction. Considering all of the requirements for a photocrosslinkable BHJ, we designed a new copolymer based on a known low-bandgap polymer employing penta-1,4-diene, which undergoes a spontaneous photoreaction without the need for a photoinitiator. We hypothesized that the blend morphology would be tightly confined in three-dimensions following photocrosslinking as a result of volume shrinkage. The acceptor materials inside the polymer were expected to be more tightly caged by reducing the free volume through a lattice hardening mechanism. We also sought to control the stability of the interfacial contact between the materials by maintaining the semiconducting molecular nature and intrinsic electronic properties of the polymer.

The structures of the low-bandgap host polymers were designed such that the donor and acceptor moieties could be combined in the repeating unit in an alternating fashion. The electronic molecular energy levels (e.g., HOMO and LUMO levels) can be controlled through the intramolecular charge transfer (ICT) in D–A alternating copolymers.

In this study, we report the synthesis of the 4,7-di(thiophen-2-yl)benzo[c][1,2,5]thiadiazole (or 4,7-bis(thien-2-yl)-2,1,3-benzothiazole) and 4*H*-cyclopenta[2,1-b:3,4-b′]dithiophene-based copolymer using an alternating heteroarene-fused π-conjugated system containing bis(heptyl penta-1,4-dien-3-yl succinate) in the repeating unit. The feasibility of the polymer for fabricating PSC devices was investigated. In addition, the polymer was mixed with $PC_{61}BM$ to fabricate BHJ PSC devices. For comparative purposes, we also fabricated a control device, i.e., P3HT/$PC_{61}BM$ (1:2 w/w, η = 3.7–4.0%). The thermally annealed and UV-cured samples had an average PCE of 1.37% in OPV devices. The photocured BHJ PSC device fabricated using the new photoreactive polymer showed a significant improvement in stability relative to that of the BHJ fabricated with P3HT/$PC_{61}BM$ over a duration of 300 h.

2. Experimental

2.1. Materials

All commercially available starting materials and solvents were purchased from Aldrich, TCI, and ACROS Co. and used without further purification unless otherwise stated. HPLC grade toluene, methylene chloride (MC), Dimethylsulfoxide (DMSO) and tetrahydrofuran (THF) were purchased from J.T. Baker and distilled from CaH_2 immediately before use.

We synthesized 4*H*-cyclopenta[2,1-b:3,4-b′]dithiophene, **1** [32], 4,7-bis(2-bromo-5-thienyl)-2,1,3-benzothiazole, **5** [33] by following the literature method. Poly(3-hexylthiophene) and $PC_{61}BM$ was purchased from Rieke Metals and Nano-C, respectively.

2.2. Synthesis

2.2.1. (6-Bromohexyloxy)(tert-butyl)dimethylsilane (2)

6-Bromo-1-hexanol (11 g, 61 mmol), imidazole (12 g, 182 mmol), and 4-dimethylaminopyridine (DMAP, 0.74 g, 6.1 mmol) were mixed in 100 mL of MC under argon gas purging in a 250 mL three necked flask. *tert*-Butylchlorodimethylsilane (TBDMSCl, 18 g, 121 mmol) was added into the mother solution and the solution was allowed to stand for 3 h. Next, 10 mL of deionized water was added to quench the reaction. The mixture was extracted with MC (100 mL) and water (300 mL). The organic layer was collected and dried with sodium sulfate (Na_2SO_4). After concentrating the solution, the crude product was purified by silica gel column chromatography (eluent; ethyl acetate: *n*-hexane = 1:3). The reaction produced 14 g of product (**2**) (yield: 78%).

^{1}H NMR (300 MHz, CDC13): δ(ppm) 3.60 (t, J = 6.3, 2H), 3.40 (t, J = 6.9, 2H), 1.86 (q, J = 5.1, 2H), 1.54–1.35 (m, 6H), 0.89 (s, 9H), 0.04 (s, 6H) ^{13}C NMR (CDC13): δ(ppm) 63.0, 33.8, 32.8, 32.6, 27.9, 25.9, 25.0, 18.3, 5.3.

2.2.2. 4,4′-Bis(((tert-butyl)dimethylsilyloxy)hexyl)dicyclopenta[2,1-b:3,4-b′]dithiophene (3)

Compound (**1**) (1.5 g, 8.4 mmol) was dissolved in 70 mL dimethylsulfoxide (DMSO) at 0 °C and the solution was allowed to stir for 10 min under an argon atmosphere after the addition of KOH (1.5 g, 27 mmol) and KI (35 mg, 0.21 mmol). Compound (**2**) (6.2 g, 21 mmol) was added into the mother solution and the reaction was kept at 25 °C for 24 h. The reaction mixture was extracted with MC (100 mL) and water (300 mL). The organic layer was collected and dried with Na_2SO_4. The concentrated solution was purified by silica gel column chromatography (eluent; ethyl acetate: *n*-hexane = 1:3), yielding product **3**, 3.4 g (yield: 66%).

^{1}H NMR (300 MHz, CDC13): δ(ppm) 7.14 (d, J = 4.68 Hz, 2H), 6.91 (d, J = 4.68 Hz, 2H), 3.51 (t, J = 6.6, 4H), 1.81 (m, J = 5.1, 4H), 1.41–1.13 (m, 16H), 0.87 (s, 18H), 0.01 (s, 12H) ^{13}C NMR (CDC13): δ(ppm) 157.9, 136.4, 124.4, 121.5, 67.9, 63.2, 53.1, 37.6, 32.7, 29.7, 25.9, 24.4, 25.5, 18.3, 5.3.

EA analysis calcd. for C33H58O2S2Si2: C, 65.28; H, 9.63; S, 10.58; found: C, 65.37; H, 9.23; S, 10.90.

*2.2.3. 2,6-Di(tributyltin)-4,4′-bis((tert-butyl)dimethylsilyl)hexyl)dicyclopenta[2,1-b:3,4-b′]dithiophene (**4**)*

Compound (**3**) (3 g, 5 mmol) was dissolved in 70 mL of THF at 25 °C in a 250 mL round bottom flask and the solution was kept under an argon atmosphere. Next, *n*-butyllithium (2.5 M) in *n*-hexane (50 mL, 20 mmol) was added using a microsyringe. After the addition was completed, the reaction mixture was allowed to stir for 1 h, and then tributyltin chloride (6.4 g, 20 mmol) was added. After 6 h, the mixture was extracted with MC (200 mL) and water (400 mL). The organic layer was dried with Na_2SO_4 and the solution was concentrated. The crude product was purified by silica gel column chromatography treated with triethylamine (eluent; chloroform: *n*-hexane = 1:1) to produce 4.57 g of compound **4** (yield: 78%).

^{1}H NMR (300 MHz, CDC13): δ(ppm) 6.87 (s, 2H), 3.52 (t, J = 6.6, 4H), 1.72 (m, 4H), 1.10–1.50 (m, 24H), 0.80–1.00 (m, 30H), 0.87 (s, 9H), 0.01 (s, 6H) ^{13}C NMR (CDC13): δ(ppm) 160.1, 142.2, 135.8, 129.6, 63.2, 51.9, 37.7, 32.8, 29.8, 29.2, 28.9, 27.1, 25.9, 25.6, 24.6, 18.36, 13.6, 10.8, 8.7.

EA analysis calcd. for C57H110O2S2Si2Sn2: C, 57.76; H, 9.35; S, 5.41; found: C, 57.91; H, 9.07; S, 5.55.

*2.2.4. Polymer (**6**)*

Compound (**4**) (2.3 g, 1.9 mmol) and compound (**5**) (0.87 g, 1.9 mmol) were dissolved in 70 mL of toluene under an argon atmosphere. After adding $Pd(PPh_3)_4$ (0.11 g, 0.09 mmol), the reaction mixture was heated to 90 °C and stirred for 48 h. An End-capping reaction was performed by adding a toluene solution (5 mL) of tributyl tin thiophene (400 mg, 1.1 mmol). 2-Bromothiophene (800 mg, 4.9 mmol) in 5 mL of toluene was added dropwise into the mother solution. The reaction mixture was cooled to room temperature and was added dropwise into 60 mL of methanol to precipitate the crude solid product. The crude product was purified by Soxhlet extraction with methanol and acetone. The solid product was dissolved in 20 mL of chloroform and precipitation was performed in 300 mL of methanol again. The product was filtered and dried under vacuum for 48 h. Finally, 0.95 g of a dark blue solid powder (**6**) was obtained (yield: 53%).

^{1}H NMR (300 MHz, CDC13): δ(ppm) 7.89–6.98 (8H), 3.56 (s, br, 4H), 1.85 (s, br, 4H), 1.45–1.24 (m, 16H), 0.89 (s, 18H), 0.04 (s, 12H) GPC (THF): M_n = 3886 g/mol, M_w = 10,705 g/mol, PDI = 2.75 EA analysis calcd. for C47H64N2S5Si2: C, 62.34; H, 7.12; N, 3.09; S, 17.71; found: C, 62.88; H, 7.31; N, 3.55; S, 17.31.

*2.2.5. Polymer (**7**)*

Polymer **6** (0.4 g, 0.43 mmol) was dissolved in THF (70 mL) containing HCl (0.86 g, 8.6 mmol). The reaction was kept at room temperature for 48 h. After checking the progress of the reaction by thin layer chromatography, the reaction was neutralized with triethylamine. After concentrating the solution, the solution was dissolved into 300 mL methanol for precipitation. The crude product was filtered and dried under vacuum for 48 h. After drying, 0.25 g of a dark brown solid, compound (**7**), was obtained (yield: 83%).

EA analysis calcd. for C35H36N2O2S5: C, 62.09; H, 5.36; N, 4.14; S, 23.68; found: C, 62.92; H, 5.67; N, 3.80; S, 22.27.

2.2.6. Photoreactive polymer 8

Polymer **7** (0.2 g, 0.28 mmol) was dissolved in 80 mL of THF and 30 mL of MC. Dicyclohexyl carbodiimide (DCC, 0.15 g, 0.71 mmol) and DMAP (35 mg, 0.28 mmol) were added successively. 4-Oxo-4-(penta-1,4-dien-3-yloxy)butanoic acid (0.30 g, 1.4 mmol) was introduced into the mother solution and the solution was allowed to stand for 24 h. The residual hydroxyl group was protected with acetyl chloride. After the reaction was complete, the solid was purified by Soxhlet extraction with methanol and acetone successively. The solid was dissolved in chloroform again and precipitation was performed in methanol. The solid was filtered and dried under vacuum for 48 h. A dark blue solid polymer, compound **8**, was obtained (0.21 g, yield: 72%).

^{1}H NMR (300 MHz, CDC13): δ(ppm) 7.89–6.93 (8H), 5.79 (m, 4H), 5.70 (t, 2H), 5.23 (m, 8H), 4.02 (s, br, 4H), 2.63 (s, br, 8H), 1.92 (s, br, 4H), 1.27 (m, br, 16H) GPC (THF): M_n = 5991 g/mol, M_w = 20,431 g/mol, PDI = 3.41.

EA analysis calcd. for C53H56N2O8S5: C, 63.07; H, 5.59; N, 2.78; S, 15.88; found: C, 63.43; H, 5.33; N, 2.95; S, 15.06.

2.2.7. Instrumentation

^{1}H NMR spectra were recorded on a Varian Mercury NMR 300 MHz spectrometers using $CDCl_3$ purchased from Cambridge Isotope Laboratories, Inc. Elemental analyses were performed by the Center for Organic Reactions using an EA1112 (Thermo Electron Corp.) elemental analyzer. Thermal properties were studied under a nitrogen atmosphere on a Mettler DSC 821^e Instrument. Thermal gravimetric analysis (TGA) was conducted on a Mettler TGA50 (temperature rate 10 °C/min under N_2). The redox properties of synthesized polymers were examined by using cyclic voltammetry (Model: EA161 eDAQ). Thin films were coated on a platinum plate using methylene chloride as a solvent. The electrolyte solution employed was 0.10 M tetrabutylammonium hexafluorophosphate (Bu_4NPF_6) in a freshly dried methylene chloride (MC). The Ag/AgCl and Pt wire (0.5 mm in diameter) electrodes were utilized as reference and counter electrodes, respectively. The scan rate was at 50 mV/s. Fourier transformed-Infrared (FT-IR) spectra were recorded using a Nicolet 380 infrared spectrophotometer.

2.2.8. Absorption and PL spectroscopy

In order to study absorption behavior, the polymer film was fabricated on quartz substrates as follows. The solution (2.5 wt%) of polymer in monochlorobenzene was filtered through an acrodisc syringe filter (Millipore 0.2 μm) and subsequently spin-cast on the quartz glass.

The film was dried overnight at 80 °C for 12 h under vacuum. Absorption spectra of film samples were obtained using a UV–vis spectrometer (HP 8453, photodiode array type) in the wavelength range of 190–1100 nm.

When we investigate the PL spectral behavior, two emission spectra were recorded using the 488 nm line of a Ar^+ laser as the excitation light source. For PL measurements, the film specimen was mounted on the cold finger in the vacuum chamber (pressure < 10^{-5} Torr) of a closed cycle refrigerator. Emitted light was collected by a lens and analyzed using a single monochromator with 1 m focal length and a GaAs cathode photomultiplier. Standard lock-in detection techniques were used to maximize the signal-to-noise ratio. The diameter of incident laser beam was about 0.3 mm.

2.2.9. OTFT fabrication

Bottom-gate top-contact device geometry was employed for characterization of TFT performance. Spin-coated films (thickness ~40–50 nm) of polymer **8** were prepared on a heavily n-doped Si/SiO_2 substrate with monochlorobenzene (MCB) as solvent. Surface modification was carried out with octyltrichlorosilane (OTS) to give hydrophobic dielectric surfaces. The OTFTs were fabricated by directly spin-coating the polymer solution onto the dielectric substrate at 1200 rpm. The fabricated thin films were heated in air at 120 °C to remove the solvent and to anneal them thermally at 150 °C for 20 min. Then, the film was exposed to UV light for 5 min at 25 °C for inducing photocrosslink.

Source and drain electrodes were then thermally evaporated (t = 100 nm) through a shadow mask with a channel width and length of 1500 μm, and 100 μm, respectively. All the field effect mobilities were extracted in the saturation regime using the relationship $\mu_{sat} = (2I_{DS}L)/(WC(V_g - V_{th})^2)$, where I_{DS} is the a saturation drain current, C is the capacitance of the silicon oxide dielectric, V_g is the gate bias, and V_{th} is the threshold voltage. The device performance was evaluated in air using Keithley 4200-SCS semiconductor characterization system under ambient conditions.

2.2.10. PSC device fabrication

The hole collecting electrode was 300–400 nm thick indium tin oxide (ITO) coated glass with resistance of 19.5 Ω/cm. ITO glass was cleaned by boiling in chloroform, isopropyl alcohol, and acetone for 30 min in each solvent, sonification for 15 min in 50:50 isopropyl alcohol and acetone solution, and finally rinsed with de-ionized water. The cleaned ITO coated glass was treated with O_2 plasma and flattening ITO with a microwave-generated plasma reactor (Plasmatic Systems Inc., PLASMATIC-PREENII, 24 GHz) for 15 min. 30 nm thick PEDOT:PSS layer (Baytron P, 1 S cm^{-1}) was coated by spin coating stock solution at 2500 rpm for 30 s. PEDOT:PSS coating was heat treated in the glove box at 200 °C for 5 min.

The polymer and $PC_{61}BM$ were dissolved in anhydrous monochlorobenzene. The thickness of a resulting photoactive layer was ~80 nm. For inducing photocrosslinking, the film was exposed to UV light for 1 and 5 min. LiF (0.8 nm thick) which served as a buffer layer, was vacuum deposited on top of active layer and 150 nm thick aluminum was evaporated. Thickness of the photoactive film was measured with surface profiler (TENCOR®, P-10 α-step). Current–voltage characteristics were measures with Keithley 2400 source-measure unit. Xe lamp (300 W) was used as a light source to produce intensity of 100 mW/cm^2. To mimic sun light, AM 1.5 filter (Oriel) was used neutral density filter was used to reduce intensity as necessary. Intensity of incoming light power was measured with calibrated broadband optical power meter (Spectra Physics model 404).

3. Results and discussion

3.1. Synthesis and characterization

Scheme 1 illustrates the synthetic routes for the monomers and a π-conjugated D–A alternating copolymer having heteroaromatic-ring moieties as a repeating group. TBDMS-protected hexyl bromide was reacted with 4*H*-cyclopenta[2,1-b:3,4-b′]dithiophene to yield compound **3**. Compound **3** was then lithiated using *n*-butyllithium, with a reaction yield of 78%. Following lithiation, the tributyl tin groups were reacted with 4*H*-cyclopenta[2,1-b:3,4-b′]dithiophene in order to conduct Stille coupling polymerization. The 4,7-di(thiophen-2-yl)benzo[c][1,2,5]thiadiazole was synthesized following the method given in literature [33]. Bromination of 4,7-di(thiophen-2-yl)benzo[c][1,2,5]thiadiazole with *N*-bromosuccimide (NBS) yielded the dibromide monomer **5**. Eventually, the Stille coupling polymerization of monomer **5** was conducted with monomer **4** bearing tributylstannyl groups in the presence of a catalytic amount of $Pd(PPh_3)_4$ to afford polymer **6**. The TBDMS unit was then removed in the presence of hydrochloric acid at 25 °C. After removing the TBDMS groups from polymer **6**, the DCC esterification of polymer **7** and 4-oxo-4-(penta-1,4-dien-3-yloxy)butanoic acid produced polymer **8** in good yield (72%).

The identity and purity of the synthetic materials were confirmed by ^1H NMR, ^{13}C NMR, and elemental analysis. As solubilizing groups, tert-butyl(heptyloxy)dimethylsilane side chains were substituted in the dicyclopenta[2,1-b:3,4-b′]dithiophene groups in the polymer structures. The weight-average molecular weight (M_w) of **8** was determined by gel permeation chromatography (GPC) using a polystyrene standard and was found to be 20,431 (M_w/M_n = 3.41). The polymers **6**–**8** are soluble in various organic solvents including chloroform, xylene, MC, chlorobenzene, and THF, and they can be fabricated into smooth films by a spin-coating method.

The thermogravimetric analysis (TGA) measurements were conducted at a heating rate of 10 °C/min under nitrogen. The measurements revealed that the polymers were thermally stable having a decomposition temperature, T_d, of 325 °C (see Fig. 1A). The thermally induced phase transition behavior of polymer **8** was investigated with differential scanning calorimetry (DSC) under a nitrogen atmosphere. The glass transition temperature of the polymer was not detected but the melting temperature was determined to be 75 °C, indicating the semi-crystalline nature of the polymer.

FT-IR spectroscopy: An FT-IR investigation was carried out to confirm that photocrosslinking had occurred

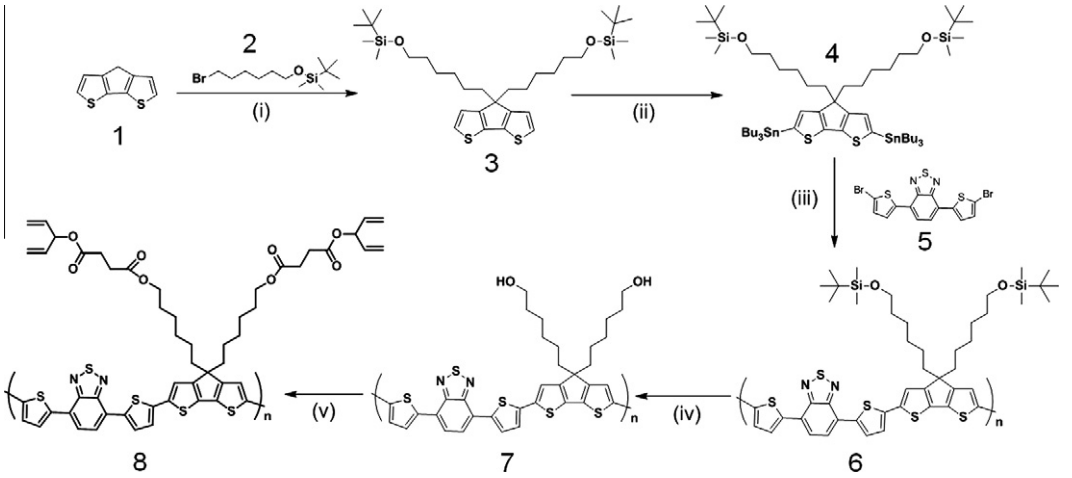

Scheme 1. Synthetic procedure for a photoreactive low-bandgap D–A alternating copolymer. (i) KOH, KI, DMSO, rt; (ii) Bu_3SnCl, *n*-BuLi, −78 °C; (iii) $Pd(pph_3)_4$, toluene, 90 °C; (iv) HCl, THF, rt; (v) 4-oxo-4-(penta-1,4-dien-3-yloxy)butanoic acid, DCC, DMAP, rt.

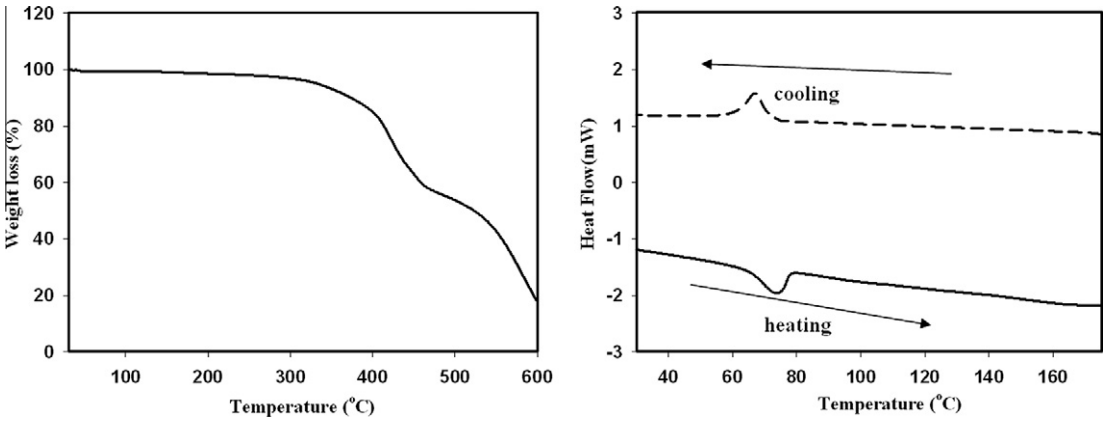

Fig. 1. TGA and DSC thermal analysis of the polymer. (A) TGA and (B) DSC.

between the pentadiene units. The film sample was prepared on a KBR window using the spin-coating method. Fig. 2 shows the FT-IR spectra of the polymer films before and after UV exposure (λ = 254 nm, I = 40.5 mW/cm^2). The characteristic absorption bands at 931, 985, and 1446 cm^{-1}, which can be unambiguously assigned to the pentadiene photoreactive groups, are labeled in the figure. The observed decrease in the intensity of the CH out-of-plane deformation in –CH=CH_2 at 985 and 931 cm^{-1} was clear evidence of the polymerization. Further verification of crosslinking was found from the slight decrease in the intensity of the in-plane deformation band of =CH at 1446 cm^{-1}.

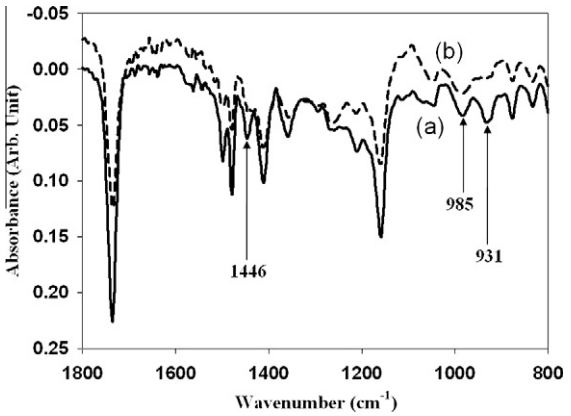

Fig. 2. FT-IR spectra of polymer **8** film before (a) and after (b) UV exposure.

3.2. Absorption and photoluminescence (PL) spectroscopy of polymer 8

The absorption spectra of polymer **8** in both dilute chloroform solution (conc. = 1 × 10^{-6} M) and thin solid films spin coated on a quartz substrate are illustrated in Fig. 3. The absorption maxima of polymer **8** and the other measured data are summarized in Table 1. In the solution state, polymer **8** exhibited absorption maxima at 657 and 446 nm and an absorption edge at 790 nm, indicating an optical

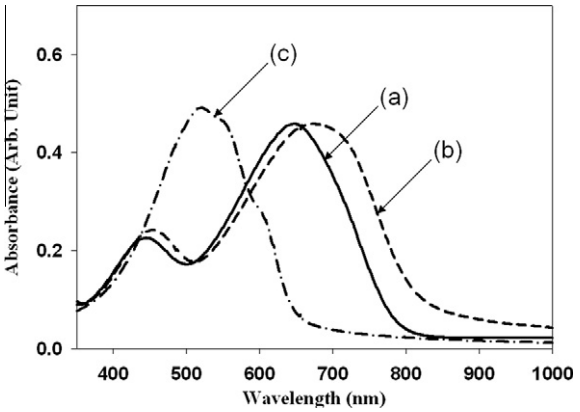

Fig. 3. Absorption spectra of polymer **8** in (a) solution and (b) film states. Spectrum (c) was obtained from P3HT film for comparison.

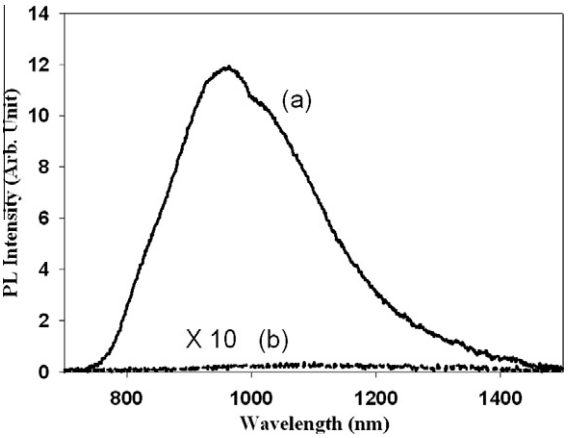

Fig. 4. PL spectra of the copolymer (a) and the blend sample with $PC_{61}BM$ (1:2 w/w) The PL intensity scale in spectrum (b) has been enlarged by 10 times.

bandgap energy of 1.52 eV. The low energy band is due to ICT between the donor and acceptor.

The absorption spectrum of the film of polymer **8** exhibits slight broadening and is red shifted by 10–12 nm compared to that of the solution state. This bathochromic shift results from strong intermolecular interactions in the solid state. The absorption maximum is hard to determine accurately, and the spectrum of the film floated over the base line, indicating the existence of scattering loss as a result of solid-state crystallization. Polymer **8** exhibits significant absorption throughout the visible region, extending into the NIR wavelength range. The optical spectrum of the film ranges from 300 to 850 nm, which can be fitted to the solar spectrum. The optical bandgap energy ($E_g^{opt.}$) in the film state was determined to be 1.52 eV, which is much smaller than that of the widely used regioregular poly(3-hexylthiophene) (P3HT) ($E_{HOMO} = -5.07$ eV, $E_{LUMO} = -3.24$ eV, $E_g^{opt.} = 1.83$ eV).

The photoluminescence (PL) spectra of the pristine film and blend film with $PC_{61}BM$ (1:2 w/w) were also acquired and are presented in Fig. 4. Because these polymers were expected to have an emission band in the near-IR region, a customized optical set-up was built to measure the emission spectrum generated by excitation at 488 nm with an Ar^+ laser. The wavelength of maximum emission is approximately 964 nm and the emission edge occurs in the region of 1500 nm, which is a typical emission spectrum for low-bandgap polymers, and corresponds to the long wavelength range of the absorption maximum.

As a representative example, the absorption spectrum of the blend sample with the copolymer and $PC_{61}BM$ (1:2 w/w) in the film state is illustrated. No emission was observed in the blended sample film (curve b) under 488 nm excitation. This PL quenching behavior can be explained by the aggregation-induced self-quenching of the excited polymer states and $PC_{61}BM$ units. The lack of emission might also be a result of intermolecular electron transfer from the photoexcited polymers to the $PC_{61}BM$ sensitizer. The photoinduced charge transfer in other conjugated molecular composites by PL quenching can be found in the literature, and is a prerequisite for efficient solar cells [34–36].

3.3. Electrochemical analysis

The electrochemical properties of the polymer were investigated by cyclic voltammetry and the scanned cyclic voltammogram is shown in Fig. 5. The HOMO and LUMO energies of the polymer are quite important for determining how to facilitate the photoinduced electron transfer in the BHJ OPV device after blending with $PC_{61}BM$. The voltammogram of a film sample was recorded and the potentials were obtained relative to an internal ferrocene reference (Fc/Fc^+).

The HOMO and LUMO levels of the polymer were estimated using the onset potentials of the oxidation and reduction waves. Polymer **8** showed one quasi-reversible oxidation peak and one quasi-reversible reduction peak. The HOMO and LUMO energy levels and electrochemical bandgap energy (E_g^{ec}) of the copolymer calculated from E_{ox}^{onset} and E_{red}^{onset} are listed in Table 1. The voltammogram

Table 1
Physical properties of polymer **8**.

	T_m (°C)	T_c (°C)	T_d (°C)	Solution		Film		E_{ox}^{onset} (V)/HOMO (eV)	E_{red}^{onset} (V)/LUMO (eV)	E_g^{ec} (eV)	E_g^{opt} (eV)
				λ_{max}^{abs} (nm)	$\lambda_{cut\text{-}off}$ (nm)	λ_{max}^{abs} (nm)	$\lambda_{cut\text{-}off}$ (nm)				
Polymer	74	67	325	446,657	785	453,669	815	0.51/−4.91	−0.85/−3.55	1.36	1.52

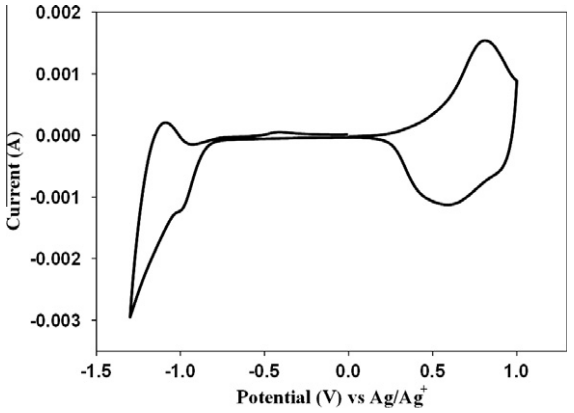

Fig. 5. Cyclic voltammogram of the polymer **8** film.

of the polymer in the film state showed that its lowest oxidative wave was at +0.51 eV. As shown in Table 1, polymer **8** has a HOMO level of −4.91 eV.

In addition, polymer **8** has a LUMO energy level of −3.55 eV. The electrochemical bandgap energy of the film sample was determined to be 1.36 eV, which is 0.06 eV less than the optical bandgap energy ($E_g^{opt.}$ = 1.52 eV). For comparison, the HOMO and LUMO levels of regioregular P3HT were also measured under identical conditions, and were found to have energies of −5.07 and −3.24 eV, respectively.

Although the HOMO level is too low to show low open-circuit voltage (V_{oc}), in the energy diagram (see Fig. 7) of the BHJ OPV devices, efficient photoinduced electron transfer between the host polymers and acceptor is expected on the basis of the PL quenching behavior.

3.4. Properties of OTFT made of polymer 8

A 40-nm-thin film of polymer **8** was deposited on OTS-SiO_2 by spin coating a 1 wt% solution of the polymer in monochlorobenzene. After spin coating the polymer solution onto the surface of the insulator, the thin-film layer (t = 70 nm) was annealed at 150 °C for 10 min and exposed to UV light (λ = 254 nm, I = 40 mW/cm^2). The gold electrodes were then deposited via thermal evaporation for the fabrication of thin-film transistors.

Fig. 6 shows the typical drain current (I_{DC}) versus source–drain voltage (V_{DS}) plots for various gate voltages

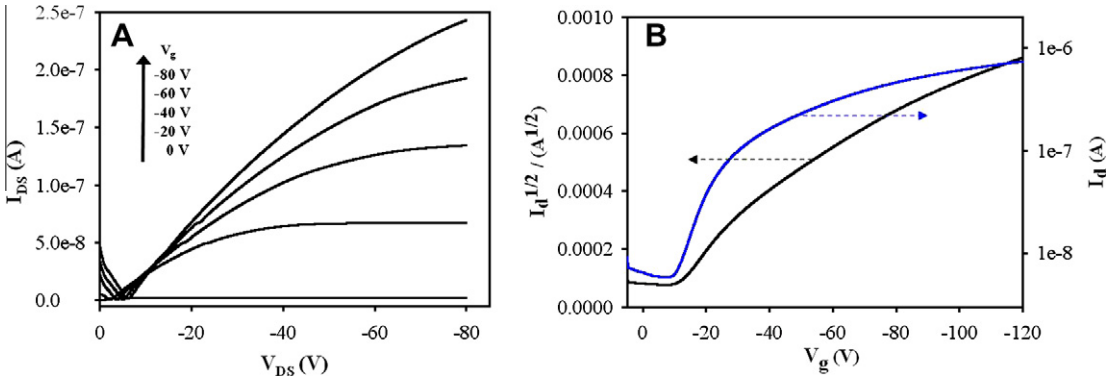

Fig. 6. Current–voltage characteristics (I_{DS} versus V_{DS}) at different gate voltages (V_g) (left) and I_{DS} and $(-I_{DS})^{1/2}$ versus V_g plots at V_{DS} of −100 V (right) for a top contact device (annealing at 150 °C, W = 1.5 mm, L = 100 μm). Insulator: OTS treated SiO_2.

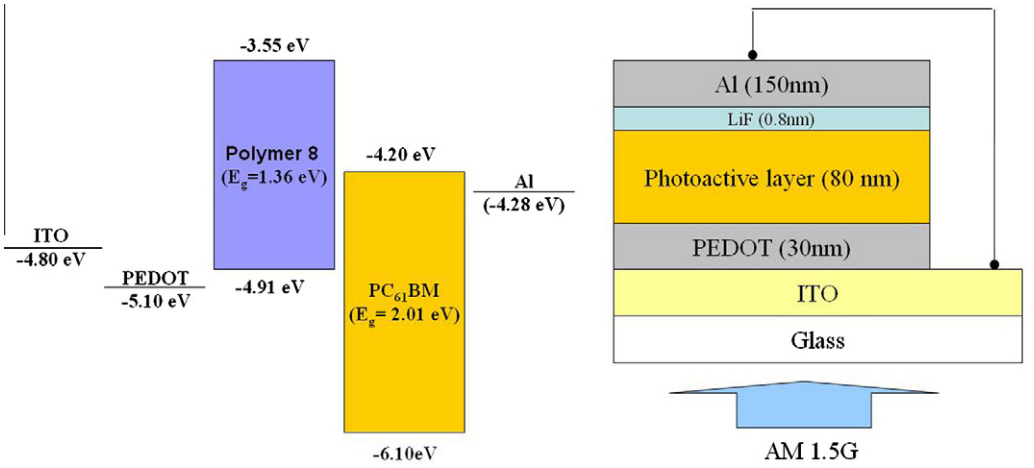

Fig. 7. Energy diagram of polymer photovoltaic cell (left). Device configuration of polymer solar cell (right).

in the accumulation mode of the polymer **8**-based TFTs. The output characteristics showed good saturation behaviors at low gate voltages, and clear saturation currents that were quadratic to the gate bias. The saturated field-effect mobilities, μ_{FET}, can be calculated from the amplification characteristics using the classical equations that describe field-effect transistors. The average mobility value obtained from five different devices equaled $(2.5 \pm 0.5) \times 10^{-3}$ cm^2/Vs with a current on/off ratio of approximately (1×10^2)–(3×10^2) and a threshold voltage, V_{th}, less than −15 V, under ambient conditions. The mobility value of the device fabricated using polymer **8** is comparable to those of D–A polymers for PSC, as reported in the literature [24].

The UV-induced photocrosslinking reaction is known to be detrimental to the semiconducting properties of the cell due to disruption of crystallization and molecular orderness [37]. It is noteworthy that a UV-induced crosslinked film of polymer **8** is very homogeneous and exhibits self-organization for uniform domains, which in turn enhances the ordered structure and charge transport in the thin film. Therefore, the mobility of the device made with the UV-cured film is comparable to that ($\mu = 3 \times 10^{-3}$ cm^2/Vs) of the device with unexposed film.

3.5. PSC device performances

PSC devices were fabricated by spin coating a solution of polymer **8**/$PC_{61}BM$ onto the PEDOT:PSS layer. After drying the blend film, the photocrosslinking reaction was induced using UV irradiation. The samples were exposed to UV light ($\lambda = 254$ nm, $I = 40$ mW/cm^2) for 20 min in order to cure the BHJ. The device configurations are as follows: ITO/PEDOT:PSS/polymer **8**:$PC_{61}BM$/LiF/Al (see Fig. 7).

Fig. 7 clearly illustrates the molecular energy levels and device configuration. First, PSC devices were fabricated using three polymer mixtures with $PC_{61}BM$ (1:1, 1:2, and 1:4 w/w). The characteristics of the device performances were determined under identical ambient conditions. The current density (J) versus voltage (V) curves of the PSCs are shown in Fig. 8. The devices **I**, **II**, and **III** contain photoactive layers with compositions of 1:1, 1:2, and 1:4 (polymer **8**:PCBM, w/w), respectively. The open-circuit voltage (V_{oc}), short-circuit current density (J_{sc}), fill factor (FF), and the PCE of the devices are summarized in Table 2. No significant change of the PCE was observed for the three different compositions, with all three samples displaying a PCE of almost unity ($\eta \approx 0.91$–1.08%). The effect of the annealing process on the device performances after annealing the samples at 80 °C followed by UV irradiation was also investigated. However, no significant annealing effects on the device performance accompanying the slight decrease of PCEs were observed. It appears that the photocuring effect is dominant over the thermal annealing effect, and manipulates the polymer structure toward the formation of ordered molecular structures in the PSCs. These preliminary experiments led us to select the blend ratio of 1:4 for further experiments to investigate the long-term stability of the PSCs.

In this experiment, the thermal annealing processes were excluded and the UV irradiation time was varied.

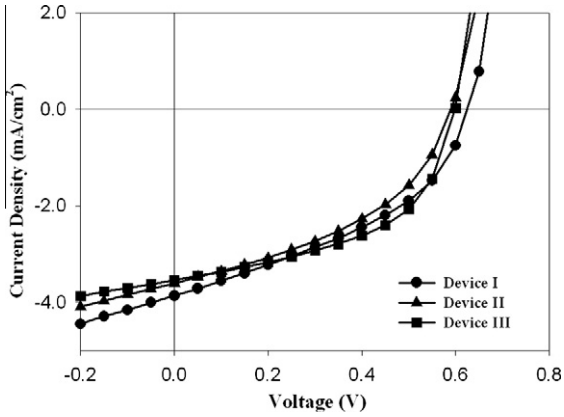

Fig. 8. Current density versus voltage curves of polymer **8**: $PC_{60}BM$ solar cells under AM 1.5G illumination. Circle: device **I**, triangle: device **II**, square: device **III**.

Table 2
Summary of polymer **8**-based PSC device performance.

Polymer **8**:PCBM (w/w)	J_{sc} (mA/cm^2)	V_{oc} (V)	FF	PCE (%)
1:1	−3.86	0.62	0.41	0.99
1:2	−3.61	0.59	0.43	0.91
1:4	−3.55	0.60	0.51	1.08

Fig. 9 shows the current density–voltage characteristics of the three devices under AM 1.5G illumination. The UV irradiation times were selected to be 0, 1, and 5 min at room temperature (see Table 3). Device **IV**, which was not UV irradiated ($t = 0$ min) demonstrated V_{oc}, J_{sc}, FF, and PCE values of 0.52 V, −3.35 mA/cm^2, 0.42, and 0.72%, respectively. The V_{oc} value (0.52 V) of device **IV** is smaller than the value shown in Fig. 8. For device **V**, in which the sample was exposed to UV light for 1 min, there was an increase in the J_{sc} value accompanied by an incremental increase in V_{oc}. The resultant PCE rose to 0.97% under these conditions. Finally, the sample that was irradiated for 5 min (device **VI**) had a PCE value of 1.37%, with increased J_{sc} and V_{oc} values relative to device **IV**. From the data, we concluded that a longer UV irradiation time leads to better device performance. In particular, the V_{oc} values varied with the irradiation time from 0.52 V for $t = 0$ min to 0.62 V for $t = 5$ min. In effect, the energy difference between the HOMO of the host polymer and the LUMO of the acceptor was found to most closely correlate with the V_{oc} value.

Theoretically, if the HOMO levels are identical, different devices having the same components should exhibit the same V_{oc} values regardless of the device conditions. These three samples exhibited inconsistent V_{oc} values, which could be attributed to the different surface morphological and interfacial properties between polymer **8** and $PC_{61}BM$, which could control the build-up potential.

In order to investigate the reason that device **III** showed the highest PCE value, the surface topographies of the blended films were observed using AFM microscopy. The AFM micrographs of the three samples are displayed in Fig. 10 along with the UV exposure time.

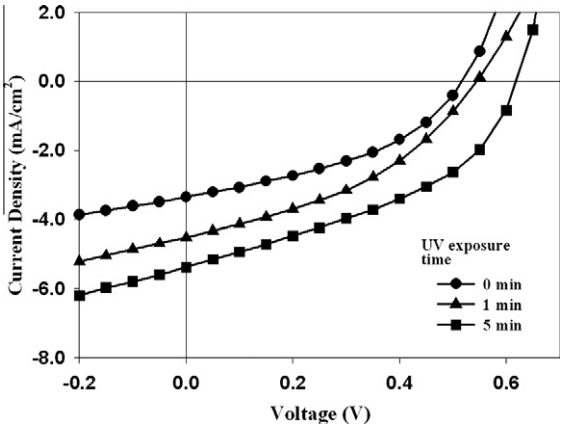

Fig. 9. Current density versus voltage curves of CP:$PC_{60}BM$ solar cells under AM 1.5G illumination. Device **IV**: pristine sample (circle); device **V**: UV exposure for 1 min (triangle); device **VI**: UV exposure for 5 min (square).

Table 3
Summary of polymer **8**-based PSC device performance with the UV exposure time.

Device	UV exposure time (min)	J_{sc} (mA/cm^2)	V_{oc} (V)	FF	PCE (%)
Device **IV**	0	−3.35	0.52	0.42	0.72
Device **V**	1	−4.52	0.54	0.39	0.97
Device **VI**	5	−5.37	0.62	0.41	1.37

From the three AFM images, it is easily noticeable that the surface topography changes with the UV exposure time. The pristine samples showed a surface roughness of 1.8–2.0 nm and contained a lot of large pinholes and dark areas. For longer irradiation times, the size of the pinholes significantly reduced and the surface became coarse. The sample exposed to UV light for 5 min has 8–10 nm surface roughness and the size of its pinholes is drastically reduced compared to the pristine sample. In principle, photopolymerization and the photocrosslinking reaction gave rise to the reduced volume of the polymer. It can be conjectured that under these conditions, the $PC_{61}BM$ domains were more tightly encompassed by polymer domains so that the interfacial contact could be highly improved. Therefore, more tightly bound polymer chains increase the short-circuit current (J_{sc}), resulting in increased PCE values. The reason for the increase in V_{oc} remains unclear in this study. A dense binary matrix has better interfacial contact that can reduce the build-up potential in the gap between the polymer and $PC_{61}BM$ domains.

Finally, we fabricated two devices; the first is the BHJ PSC cell made of P3HT and $PC_{61}BM$ (1:2 w/w), whereas the other is composed of polymer **8** and $PC_{61}BM$ (1:4 w/w). The latter was photocured by UV irradiation for 5 min under ambient conditions. The effect of photocrosslinking on the long-term stability of the devices was explored at 25 °C over a prolonged time period (t = 200 h). The decay behaviors of the PCEs are depicted in Fig. 11.

A P3HT:$PC_{61}BM$ (1:2 w/w) blended device was also prepared; it was not exposed to UV light and served as a control sample. The V_{oc}, J_{sc}, FF, and PCE values of the control sample were 0.60 V, 10.18 mA/cm^2, 0.60, and 3.79%, respectively. The photocured sample initially had V_{oc}, J_{sc}, FF, and PCE values of 0.65 V, 3.07 mA/cm^2, 0.47, and 0.97%, respectively. However, the photocured samples were quite different in terms of their long-term stability at ambient temperatures. The performance of the polymer **8**-based PSC devices treated with UV irradiation for 5 min were more stable in terms of device performance. In particular, the inset of Fig. 11 clearly showed slow decaying behavior of PCE of photocured sample in 40 h. Even after 200 h, the photocured devices retained more than 78% of the initial PCE. It was clearly observed in the inset of Fig. 11. In contrast, the device performance of the pristine-P3HT:$PC_{61}BM$ blend decreased rapidly to 25% of its initial efficiency value after 200 h. This result clearly shows that the photocrosslinking concept holds promise for thermally stable high-performance devices. All other evidence supports the efficacy of this synthetic strategy for improving the long-term stability of PSC device performance. Although we still observe a decreasing behavior for PSC device performance, the precise optimization of curing conditions and alternative methods for device fabrication may enhance the long-term stability of this polymer for fu-

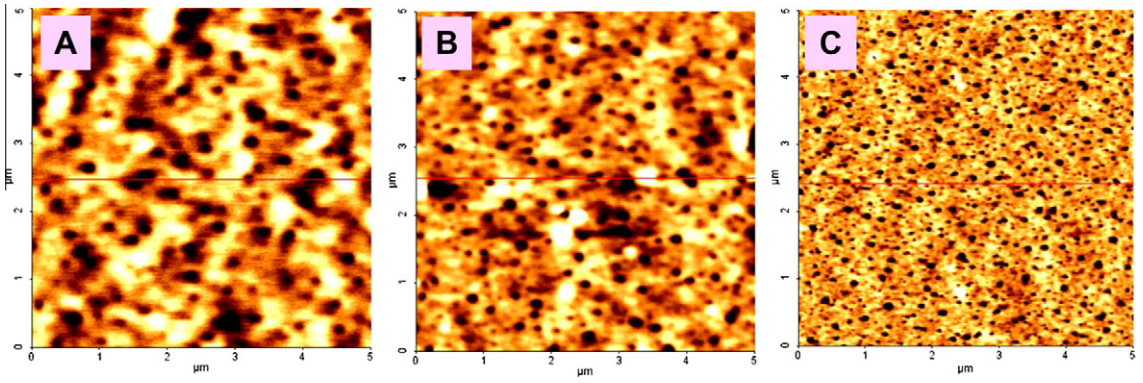

Fig. 10. AFM topographies of three film samples made of the polymer **8** deposited on PEDOT:PSS films. (A) Without UV exposure, (B) UV exposure for 1 min, (C) UV exposure for 5 min.

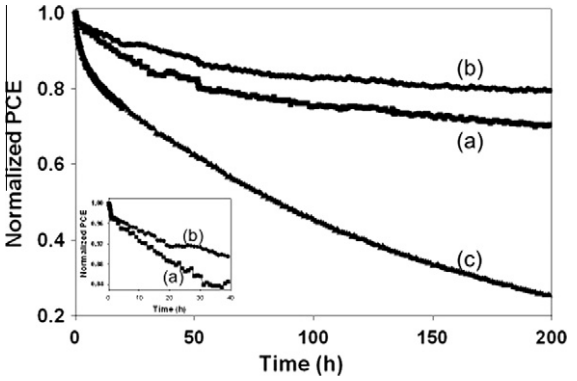

Fig. 11. Dynamic decaying behaviors of the PCE of PSCs under ambient conditions. (a) Polymer **8**:$PC_{61}BM$ before UV exposure, (b) polymer **8**:$PC_{61}BM$ after 5 min of UV exposure, and (c) P3HT:$PC_{61}BM$. Inset: expanded decaying behaviors of PCEs in 40 h.

ture use in practical applications. Our work unambiguously demonstrates that a photocrosslinkable and low-bandgap D–A alternating copolymer can be utilized for fabricating better PSC devices.

4. Conclusions

A soluble, photoreactive, low-bandgap D–A alternating copolymer based on cyclopentadithiophene and di(thiophen-2-yl)benzothiadiazole repeating units was synthesized by a palladium(0)-catalyzed Stille coupling reaction. The polymer contains pentadiene units in the side chain, which are reactive under UV exposure. A clear advantage of using the $PC_{61}BM$-containing polymer **8** in BHJ PSCs is that photocrosslinking can freeze the optimum internal morphology and long-term stability performance of the device can be achieved. Under optimized curing conditions, UV-cured polymer **8**-based PSC devices had a PCE of up to 1.37% under AM 1.5G illumination and the stability of PCE of photocured sample is better than the sample before UV exposure. BHJ solar cells based on the mixture of a D–A copolymer and $PC_{61}BM$ showed much improved long-term stability over long measuring periods as compared to conventional devices made of P3HT:$PC_{61}BM$.

These results can contribute to the design of photoreactive semiconducting π-conjugated polymers for practical applications in electronic and optoelectronic devices.

Acknowledgments

This research was supported by Korea Science and Engineering, (KOSEF R0120070001128402008) and by Priority Research Centers Program through the National Research Foundation of Korea (NRF) funded by the Ministry of Education, Science and Technology (NRF20100020209) Particularly, Prof. D.H. Choi thanks the financial support by the Seoul R&BD Program (10543, 2009–2010).

References

[1] M. Halik, H. Klauk, U. Zschieschang, G. Schmid, S. Ponomarenko, S. Kirchmeyer, W. Weber, Adv. Mater. 11 (2003) 917.
[2] J.A. Merlo, C.R. Newman, C.P. Gerlach, T.W. Kelley, D.V. Muyres, S.E. Fritz, M.F. Toney, C.D. Frisbie, J. Am. Chem. Soc. 127 (2005) 3997.
[3] H.E. Katz, Chem. Mater. 16 (2004) 4748.
[4] R.H. Friend, R.W. Gymer, A.B. Holmes, J.H. Burroughes, R.N. Marks, C. Taliani, D.D.C. Bradley, D.A.D. Santos, J.L. Bredas, M. Logdlund, W.R. Salaneck, Nature 397 (1999) 121.
[5] M.T. Bernius, M. Inbasekaran, J. O'Brien, W. Wu, Adv. Mater. 12 (2000) 1737.
[6] M.L. Chabinyc, A. Salleo, Y. Wu, P. Liu, B.S. Ong, M. Heeney, I. McCulloch, J. Am. Chem. Soc. 126 (2004) 13928.
[7] C.J. Brabec, N.S. Sariciftci, J.C. Hummelen, Adv. Funct. Mater. 11 (2001) 15.
[8] G. Yu, J. Gao, J.C. Hummelen, F. Wudl, A.J. Heeger, Science 270 (1995) 1789.
[9] L. Liu, C.-L. Ho, W.-Y. Wong, K.-Y. Cheung, M.-K. Fung, W.-T. Lam, A.B. Djurišić, W.-K. Chan, Adv. Funct. Mater. 18 (2008) 2824.
[10] H. Hoppe, N.S. Sariciftci, J. Mater. Chem. 16 (2006) 45.
[11] F.C. Krebs, H. Spanggaard, Chem. Mater. 17 (2005) 5235.
[12] J. Luo, Q. Hou, J. Chen, Y. Cao, Synth. Met. 156 (2006) 470.
[13] S.-P. Huang, J.-L. Liao, H.-E. Tseng, T.-H. Jen, J.-Y. Liou, S.-A. Chen, Synth. Met. 156 (2006) 949.
[14] D. Veldman, J.J.A.M. Bastiaansen, B.M.W. Langeveld-Voss, J. Sweelssen, M.M. Koetse, S.C.J. Meskers, R.A.J. Janssen, Thin Solid Films 511–512 (2006) 581.
[15] K. Chen, W.B. Caldwell, C.A. Mirkin, J. Am. Chem. Soc. 115 (1993) 1193.
[16] D.C. Coffey, O.G. Reid, D.B. Rodovsky, G.P. Bartholomew, D.S. Ginger, Nano Lett. 7 (2007) 738.
[17] M.M. Wienk, J.M. Kroon, W.J.H. Verhees, J. Knol, J.C. Hummelen, P.A.V. Hal, R.A.J. Janssen, Angew. Chem. Int. Ed. 42 (2003) 3371.
[18] G. Li, V. Shrotriya, J. Huang, Y. Yao, T. Moriarty, K. Emery, Y. Yang, Nat. Mater. 4 (2005) 864.
[19] W. Ma, C. Yang, X. Gong, K. Lee, A.J. Heeger, Adv. Funct. Mater. 15 (2005) 1617.
[20] S.A. Backer, K. Sivula, D.F. Kavulak, J.M.J. Fréchet, Chem. Mater. 19 (2007) 2927.
[21] J.Y. Kim, K. Lee, N.E. Coates, D. Moses, T.-Q. Nguyen, M. Dante, A.J. Heeger, Science 317 (2007) 222.
[22] M. Reyes-Reyes, K. Kim, D.L. Carroll, Appl. Phys. Lett. 87 (2005) 083506.
[23] J. Peet, J.Y. Kim, N.E. Coates, W.L. Ma, D. Moses, A.J. Heeger, G.C. Bazan, Nat. Mater. 6 (2007) 497.
[24] J. Hou, H.-Y. Chen, S. Zhang, G. Li, Y. Yang, J. Am. Chem. Soc. 130 (2008) 16144.
[25] J. Hou, H.-Y. Chen, S. Zhang, R.I. Chen, Y. Yang, Y. Wu, G. Li, J. Am. Chem. Soc. 131 (2009) 15586.
[26] Y. Liang, Z. Xu, J. Xia, S.-T. Tsai, Y. Wu, G. Li, C. Ray, L. Yu, Adv. Mater. 22 (2010) 1.
[27] B.J. Kim, Y. Miyamoto, B. Ma, J.M.J. Fréchet, Adv. Funct. Mater. 19 (2009) 2273.
[28] K. Sivula, Z.T. Ball, N. Watanabe, J.M.J. Fréchet, Adv. Mater. 18 (2006) 206.
[29] M. Drees, H. Hoppe, C. Winder, H. Neugebauer, N.S. Sariciftci, W. Schwinger, F. Schaffler, C. Topf, M.C. Scharber, Z. Zhu, R. Gaudiana, J. Mater. Chem. 15 (2005) 5158.
[30] Z. Zhu, S. Hadjikyriacou, D. Waller, R. Gaudiana, J. Macromol. Sci. Part A Pure Appl. Chem. 41 (2004) 1467.
[31] E. Zhou, Z.A. Tan, C. Yang, Y. Li, Macromol. Rapid Commun. 27 (2006) 793.
[32] H. Wynberg, A. Kraak, J. Org. Chem. 29 (1964) 2455.
[33] M. Jayakannan, P.A. Van Hal, R.A.J. Janssen, J. Poly. Sci. Part A: Poly. Chem. 40 (2002) 2360.
[34] H. Kim, J.Y. Kim, K. Lee, Y. Park, Y. Jin, H. Suh, Curr. App. Phys. 1 (2001) 139.
[35] M. Theander, A. Yartsev, D. Zigmantas, V. Sundström, W. Mammo, M.R. Andersson, O. Inganäs, Phys. Rev. B 61 (2000) 12957.
[36] F. Meng, J. Hua, K. Chen, H. Tian, L. Zuppiroli, F. Nuesch, J. Mater. Chem. 15 (2005) 979.
[37] I. McCulloch, W. Zhang, M. Heeney, C. Bailey, M. Giles, D. Graham, M. Shkunov, D. Sparrowe, S. Tierney, J. Mater. Chem. 13 (2003) 2436.

Organic Electronics 12 (2011) 279–284

Contents lists available at ScienceDirect

Organic Electronics

journal homepage: www.elsevier.com/locate/orgel

Effect of UV–ozone treatment on electrical properties of PEDOT:PSS film

Takahiro Nagata [a,*], Seungjun Oh [a,b], Toyohiro Chikyow [a], Yutaka Wakayama [a,b]

[a] Advanced Electric Materials Center, National Institute for Materials Science, 1-1 Namiki, Tsukuba, Ibaraki 305-0044, Japan
[b] Department of Chemistry and Biochemistry, Faculty of Engineering, Kyushu University, 1-1 Namiki, Tsukuba 305-0044, Japan

ARTICLE INFO

Article history:
Received 24 September 2010
Received in revised form 4 November 2010
Accepted 14 November 2010
Available online 25 November 2010

Keywords:
Organic conducting material
Conductive polymer
UV–ozone treatment
X-ray photoemission spectroscopy
Work function

ABSTRACT

We reveal the effect of UV–ozone treatment on the electrical properties of poly (styrenesulfonate) doped poly (3,4-ethylenedioxythiophene) (PEDOT:PSS) film by clarifying the respective roles of UV light irradiation and exposure to ozone gas. The UV–ozone treatment induced increases in both work function and resistivity. Furthermore, the film thickness was reduced at a rate of 0.13 nm/min. The ozone-exposed films also exhibited a marked increase in the work function. However, such variations were not observed in the resistivity and film etching. Angle resolved X-ray photoelectron spectroscopy revealed that the main role of the UV light was to decompose the chemical bonds in the PEDOT:PSS film, resulting in a resistivity increase and film etching. In contrast, the ozone and atomic oxygen were absorbed and oxidized the surface, which was responsible for the increase in the work function. Due to these different functions, UV–ozone treatment is capable of controlling the work function and resistivity of PEDOT:PSS film thus allowing them be adjusted to the device application.

© 2010 Elsevier B.V. All rights reserved.

1. Introduction

Poly (3,4-ethylenedioxythiophene) (PEDOT) is an electrochemically stable conjugated polymer that provides electrical conductivity with optical transparency. Polystyrenesulfonic acid (PSS) works as a charge balancing dopant giving PEDOT water solubility and high electrical conductivity. Thus, PEDOT:PSS has found a number of applications including as hole transport layers in polymer-based light-emitting diodes (LEDs) and in backlights for liquid crystal displays [1–5]. PEDOT:PSS has a high work function (~5.2 eV [2,6–8]), which is advantageous for opto-electronics applications such as a Schottky photo detector. Nakano et al. demonstrated a high quality Schottky contact on a zinc oxide (ZnO) single crystal [9]. The work function is critical to device performance, and so simple ways of tuning the work function to match the organic energy levels are technologically important. Some groups have increased the work function of PEDOT:PSS by employing UV-ozone treatment [10–12]. Benor et al. improved and controlled the device efficiency in phosphorescent organic light-emitting diodes with ultraviolet-ozone treatment, in which PEDOT:PSS was utilized as a hole injection layer [13–15]. They suggested that the changes in the PEDOT:PSS work function improved the external quantum efficiency of the phosphorescent organic light-emitting diodes. In these reports, two mechanisms of the work function increase have been proposed. Tengstedit et al. reported that UV–ozone treatment formed a surface dipole induced by surface oxidization [11]. In contrast, Helander et al. reported that the surface accumulation of residual Na^+ decomposed by UV–ozone treatment increased the work function [12]. However, the mechanism of the UV–ozone treatment of PEDOT:PSS has yet to be elucidated in detail. Understanding and controlling the UV–ozone treatment effect are both essential for practical device applications.

In this paper, the effects of UV–ozone treatment on the electrical properties of PEDOT:PSS film are examined using electrical measurements, surface observations, and angle resolved X-ray photoelectron spectroscopy (AR-XPS). All the measurements were carried out with and without UV light irradiation to distinguish the effect of ozone gas exposure from that of UV light.

* Corresponding author. Tel.: +81 29 860 4546; fax: +81 29 860 4916.
E-mail address: NAGATA.Takahiro@nims.go.jp (T. Nagata).

1566-1199/$ - see front matter © 2010 Elsevier B.V. All rights reserved.
doi:10.1016/j.orgel.2010.11.009

2. Experimental procedures

Glass substrates were employed to eliminate additional factors responsible for electrical properties. The substrates were cleaned at room temperature in organic solvents and a deionized water rinse, and this was followed by conventional UV–ozone cleaning (Filgen, UV253). The substrate surface was spin coated with a PEDOT:PSS aqueous solution (Sigma–Aldrich, 483095) and dried on a hot plate at 100 °C for 30 min in an ambient atmosphere. The rotation speed for the spin coating was set at 5000 rpm. The thickness of the PEDOT:PSS film was about 75 nm. The UV–ozone treatment was performed with a UV–ozone cleaner at UV wavelengths of 184.9 and 253.7 nm and an energy density of 33.3 mW/cm^3. For the ozone exposure, the samples were partly covered with a piece of aluminum foil to eliminate direct UV irradiation on the sample surface. The resistivity was measured with the four-point contact probe method (Napson, Model RG-80N), where the distance between each probe was 0.5 mm. The distance is much greater than the film thickness, and the obtained values can be regarded as bulk region resistivity. The work function was measured in air by employing photoelectron yield spectroscopy (Riken Keiki, AC-3) with a scan energy range of 4.0–7.0 eV and with an energy of 50 nW. The chemical bonding states were evaluated with XPS (Thermo, Theta Probe) using a monochromated Al Kα X-ray at an energy of 1486.6 eV. The samples were connected to the electrical ground of the system by using conductive copper tapes. The work function of the system was calibrated with reference to the Au $4f_{7/2}$ and Ag $3d_{5/2}$ peak positions. The total energy resolution was set at 700 meV. The depth profiles of the observed electronic states were examined with AR-XPS. The take off angles (TOA) of 0° and 76°, which are bulk-sensitive and surface-sensitive angles, respectively, correspond to average detection depths of 5.8 and 1.5 nm as calculated by the Tanuma–Powell–Penn (TPP-2M) equation (Ref. [16]). The film thickness was determined by X-ray reflection (XRR). The XRR measurement system had a 5-kW rotating anode Cu target (Bruker AXS, D8 Discover Super Speed with GADDS). For the XRR measurements, the glass substrates were replaced with c-plane sapphire substrates. This is because, to achieve reproducible high resolution measurements, the surface should be strictly aligned parallel to the traveling direction of the X-ray. The sapphire substrates were coated with PEDOT:PSS using the same procedure as that employed with the glass substrate, which had the same surface morphology and film thickness to the PEDOT:PSS film on glass substrate. The surface morphology was observed using atomic force microscopy (AFM; SII NanoTechnology, Inc., SPI4000 & E-sweep).

3. Results

3.1. Electrical properties

Fig. 1(a) shows the photoelectron yield spectra of the PEDOT:PSS films on glass substrates. The ionization energy of the polymer film is defined as the energy difference between the vacuum level and the extrapolated edge of the highest occupied molecular orbital (HOMO) [17]. Therefore the work function can be estimated by linearly extrapolating the edge of the square-root photoelectron yield to the baseline. The work function of the as-coated PEDOT:PSS film (denoted as as-PEDOT) was 5.16 eV, which is comparable to previously reported values (4.9–5.2 eV) [2,6–8]. Both the UV–ozone treatment and ozone exposure for 30 min caused shifts in the edge of the photoemission to a higher energy. The work functions were determined as 5.41 and 5.68 eV, respectively. These results suggest that both treatments affected the chemical states of the PEDOT:PSS film surface.

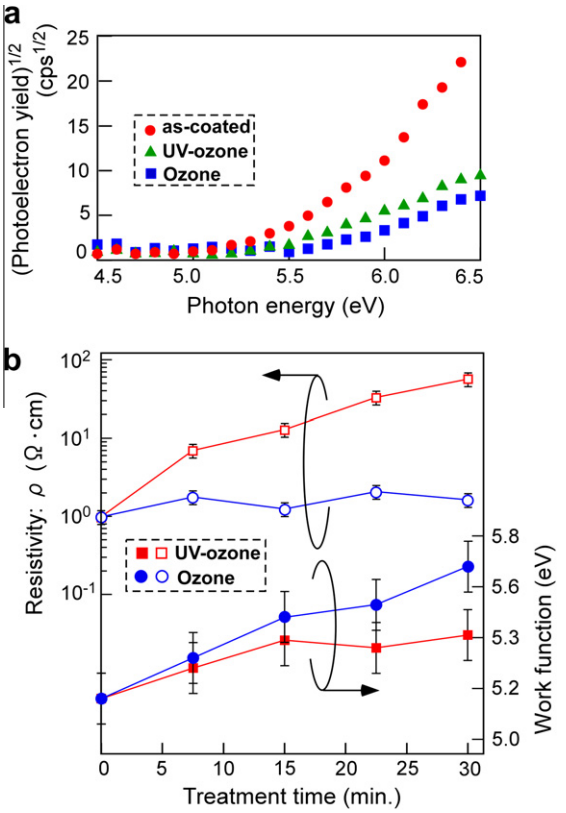

Fig. 1. (a) Photoelectron yield spectrum of as coated (circles), UV–ozone treated (triangles), and ozone exposed (squares) PEDOT:PSS films on glass substrates. (b) Treatment time dependence of resistivity (open symbols) and work function (solid symbols) of the PEDOT:PSS films with UV–ozone treatment (squares) and ozone exposure (circles).

The treatment time dependence of the resistivity and work function of the PEDOT:PSS films are summarized in Fig. 1(b). The variations in the resistivity differed noticeably with the respective treatments. The UV–ozone treated PEDOT:PSS film (denoted as UV–O_3–PEDOT) exhibited an almost two-order increase in resistivity. In contrast, the ozone exposed PEDOT:PSS film (denoted as O_3-PEDOT) exhibited a constant resistivity (~1.5 Ω cm). The work function increased with each treatment in a similar manner. However, a clear difference was observed after a treatment time of 15 min. The work function of the UV–O_3–PEDOT saturated around 5.4 eV, which is consistent with

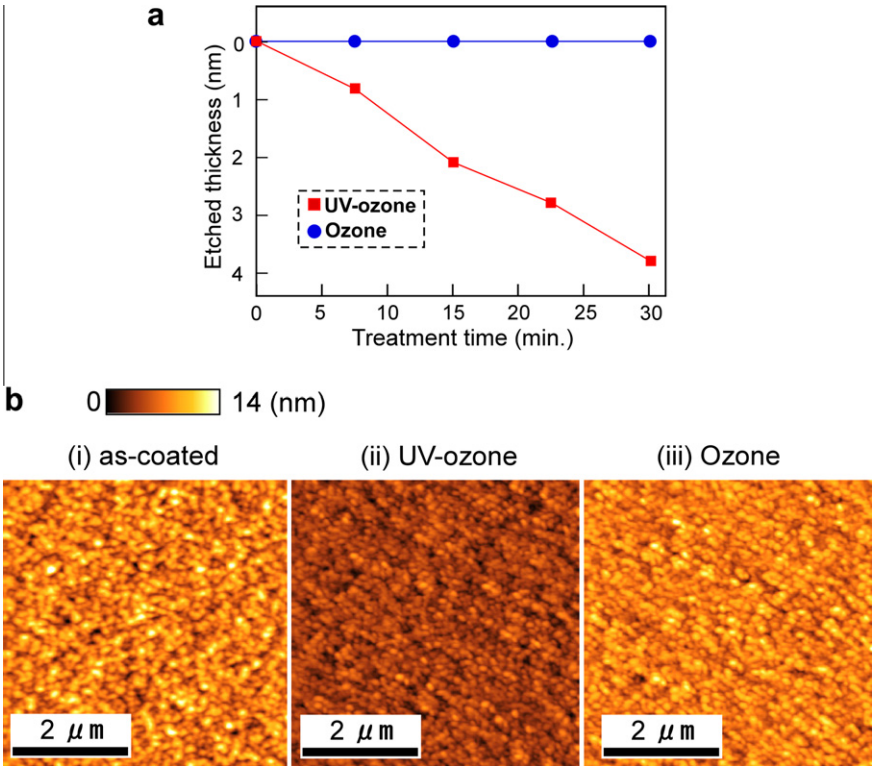

Fig. 2. (a) Relative etched film thickness of the UV–O_3–PEDOT (squares) and the O_3–PEDOT (circles) against the treatment time. (b) AFM images of (i) as-PEDOT, (ii) UV–O_3–PEDOT, and (iii) O_3–PEDOT.

a previous report [11]; the O_3–PEDOT exhibited a monotonic increase in the work function against exposure time.

3.2. Surface etching

The surface etching caused by the UV–ozone treatment was examined with XRR measurements and AFM observation. The O_3–PEDOT film thickness exhibited no significant change against the treatment time as shown in Fig. 2(a). In contrast, the UV–O_3–PEDOT film thickness decreased with an etching rate of approximately 0.13 nm/min. The etching effect on the UV–O_3–PEDOT was observed in the surface roughness as shown in Fig. 2(b). Although all the samples had similar small-grained surfaces, the surface roughness of the UV–O_3–PEDOT decreased. The root mean square roughness values of the as-PEDOT, UV–O_3–PEDOT, and O_3–PEDOT were 1.4 ± 0.1, 0.7 ± 0.1, and 1.3 ± 0.1 nm, respectively.

3.3. Chemical states

Representative S 2*p* core level spectra for the PEDOT:PSS films at the bulk sensitive TOA of 0° are shown in Fig. 3. To analyze the XPS spectra, we fitted all the spectra by the convolution of a Gaussian and a Lorentzian [18]. The background was subtracted by the Shirley method [19]. The S 2*p* core level consists of a spin-split component of S $2p_{1/2}$ and $2p_{3/2}$, whose reported energy difference and relative intensity are 1.18 eV and 1:2, respectively [13]. The peaks in the low binding energy peak around 164 eV correspond to the sulfur atoms in the thiophene rings of the PEDOT [13,20,21]. The higher binding energy peak around 169 eV corresponds to the sulfur atoms in the PSS. The contribution of PSS to the S *2p* peak is due to the doping ions PSS:H^+ (168.4 and 169.6 eV) and to the PSS:Na^+ salt (168.0 and 169.2 eV) [13,20,21]. Na^+ residues originate from the $Na_2S_2O_8$ oxidizing agent used for the polymerization of the PEDOT:PSS [22].

After the UV–ozone treatment, there was a pronounced binding energy peak at 168.7 eV, which corresponded to the sulfur atoms bonding with oxygen (PSS:O), as seen in Fig. 3(b), suggesting that the main effect of the UV–ozone treatment is to decompose and oxidize the PSS–Na^+ and –H^+ bonds. Although such bonding decomposition was not detected, a broadening of the PEDOT binding energies was observed in the O_3–PEDOT (Fig. 3(c)). This is because the positive charges are delocalized over the PEDOT chains, leading to a spread in the binding energies [23]. This charge distribution was affected by the oxidization of the PEDOT chain, resulting in the broad binding energy distribution of the sulfur atoms.

Fig. 4 summarizes the TOA dependence of the intensity ratio of PSS:O/PSS(–Na^+ and –H^+). The ratio for the UV–O_3–PEDOT exhibited a constant value of 0.3 through the TOAs, i.e., the decomposition and oxidization of PSS spread over the bulk region. The slight increase around the high TOAs (surface-sensitive angles) can be attributed to the native

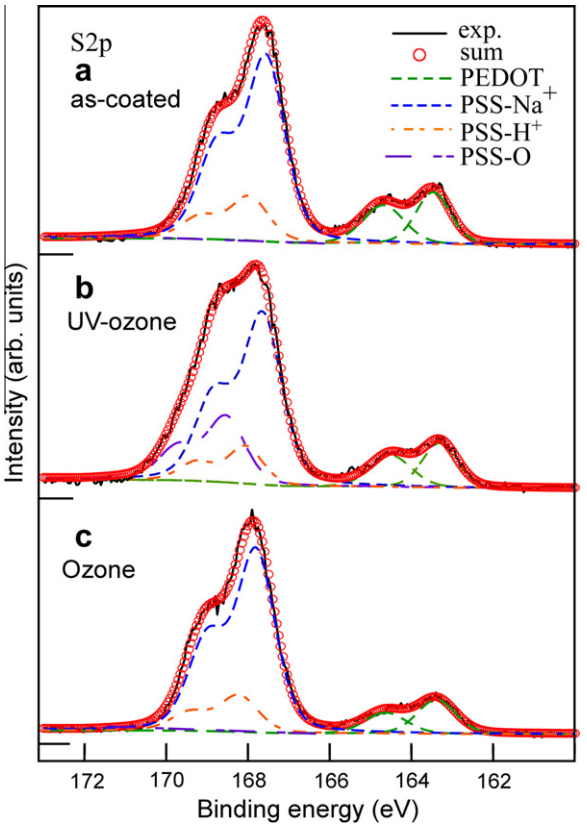

Fig. 3. S 2*p* core spectra of (a) as-PEDOT, (b) UV–O_3–PEDOT, and (c) O_3–PEDOT. The treatment time was 30 min. Solid lines and open circles show measured spectra and sum-fitted curves, respectively. Dashed lines are fitted curves for each bond: PEDOT, PSS–Na^+, PSS–H^+, and PSS–O.

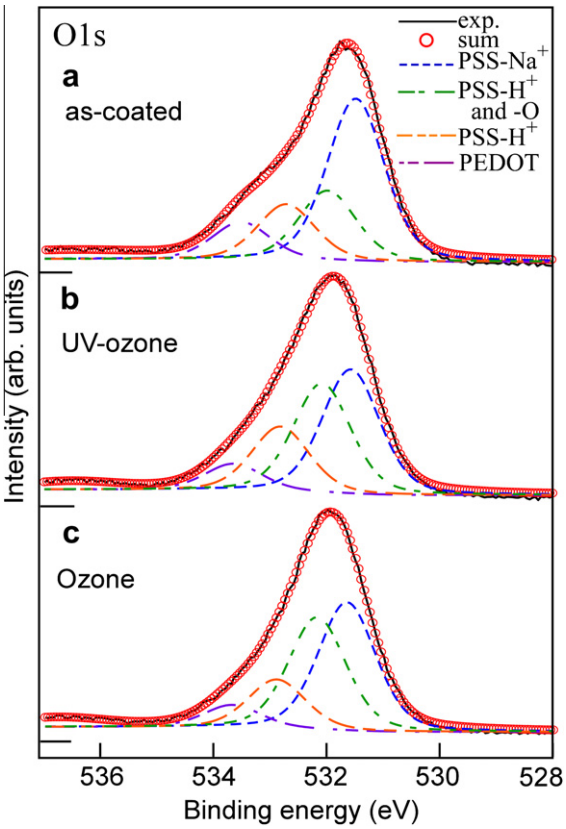

Fig. 5. O 1*s* core spectra of (a) as-PEDOT, (b) UV–O_3–PEDOT, and (c) O_3–PEDOT. The treatment time is 30 min. Solid lines and open circles show measured spectra and sum-fitted curves, respectively. Dashed lines are fitted curves for each bond: PEDOT, PSS–Na^+, and PSS–H.

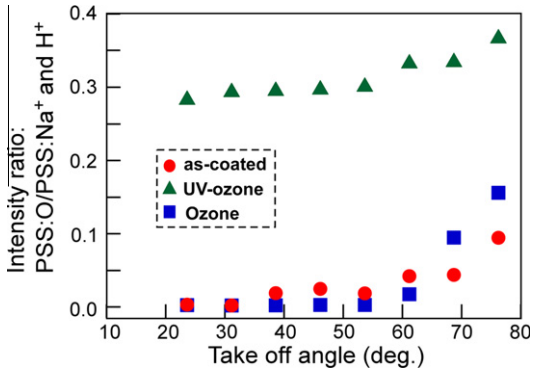

Fig. 4. TOA dependence of the intensity ratio between PSS–O and PSS–(Na^+ and H^+) for as-PEDOT (circles), UV–O_3–PEDOT (triangles), and O_3–PEDOT (squares).

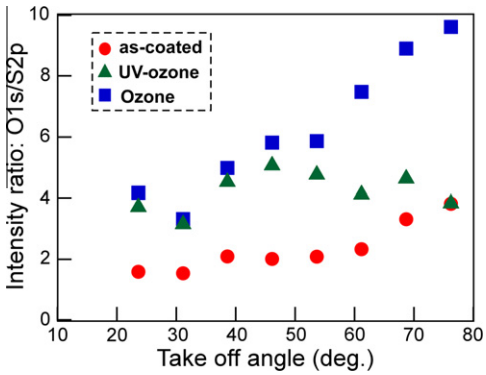

Fig. 6. TOA dependence of the intensity ratio between O 1*s* and S 2*p* for as-PEDOT (circles), UV–O_3–PEDOT (triangles), and O_3–PEDOT (squares).

oxidation as observed in the as-PEDOT. In contrast, no signals from PSS:O were detected with the shallow TOAs (bulk-sensitive angles) for the O_3–PEDOT as with the as-PEDOT. The distinction of the O_3–PEDOT can be ascribed to the steep increase in the ratio at high TOAs. These results indicate that ozone exposure induced a high concentration of absorbed oxygen only at the surface region.

The O 1*s* core spectra shown in Fig. 5 can be assigned as the convolution of four different components, namely 533.7 eV from PEDOT [13,20,21], 531.5 eV from PSS:Na^+, 532.1 and 532.85 eV from PSS:H^+ [23], and 532.1 eV from the adsorbed oxygen that overlaps with the PSS:H^+ signal.

The intensity ratios of O 1*s*/S 2*p* were plotted as a function of TOA in Fig. 6 to discuss the amount and distribution

of oxygen. After the UV–ozone treatment and the ozone exposure, the ratios at a TOA of 20° were double that of the as-PEDOT indicating that the total amounts of increased oxygen were the same for both UV–O_3–PEDOT and O_3–PEDOT. With respect to the TOA dependence, the O_3–PEDOT increased monotonically at a higher rate than the UV–O_3–PEDOT, indicating that the oxygen diffused into the PEDOT:PSS film on the UV–O_3–PEDOT. In contrast, the O_3–PEDOT surface had a higher concentration of oxygen than the bulk region and other PEDOT films. These results are consistent with the TOA dependence of the intensity ratio of PSS:O/PSS(–Na^+ and –H^+).

4. Discussion

The UV light from the low-pressure mercury lamp in the UV–ozone cleaner comprises two major wavelengths of 184.9 and 253.7 nm (denoted as 184.9-UV and 253.7-UV) [24,25]. The intensities of 184.9-UV and 253.7-UV are approximately 5% and 90%, respectively [26,27]. During the UV–ozone cleaning process, the 184.9-UV decomposes and activates oxygen molecules to form ozone gas. Furthermore the 253.7-UV decomposes the ozone and generates atomic oxygen that has strong oxidizability. The 253.7-UV also decomposes chemical bonds such as C–C, C–H, and C–OH bonds. The UV–ozone treatment cleans the sample surface by combining the oxidization and the decomposition of the chemical bonds. The energy (E) of UV light is given as [27]:

$$E = Nhc/\lambda \times 105(\mathrm{kJ/mol}), \quad (1)$$

where N, h, c and λ are Avogadro's number, Planck's constant, light speed and wavelength, respectively. The energy of 253.7-UV is 472 kJ/mol, which is higher than the bonding energy of single chemical bonds: C–C (347.7 kJ/mol), C–H (413.4 kJ/mol), C–O (351.5 kJ/mol), and C–S (370 kJ/mol) [28].

PEDOT has a two-ring structure as illustrated in Fig. 7(a) that consists of a π-conjugated thiophene ring and an ethylenedioxyl ring including C–O single bonds. The π-conjugated part, which is responsible for the conductivity of PEDOT, has a higher bonding energy than a single bond. Although PSS also has C=C double bonds (Fig. 7(b)), it does not form π-conjugated polymer chains. That is, the main role of the PSS is to provide carriers to the PEDOT, and it only contributes slightly to the conductivity. The 253.7-UV mainly decomposed the single bonds of PSS such as the C–C, S–H, and S–Na bonds, resulting in the functional inhibition of PSS as a dopant. Note that the energy of 184.9-UV is 647 kJ/mol, which is sufficiently high to decompose C=C double bonds [28]. However, the PEDOT decomposition is negligible because of the very low intensity of 184.9-UV.

According to the electrical measurements, surface observations, and AR-XPS results, the effects of ozone exposure and UV–ozone treatment on PEDOT:PSS films can be explained as follows.

(A) Ozone exposure (Fig. 7(c)): with ozone exposure, the atomic oxygen oxidized the film surface and was adsorbed thus forming oxygen molecules. The amount of adsorbed

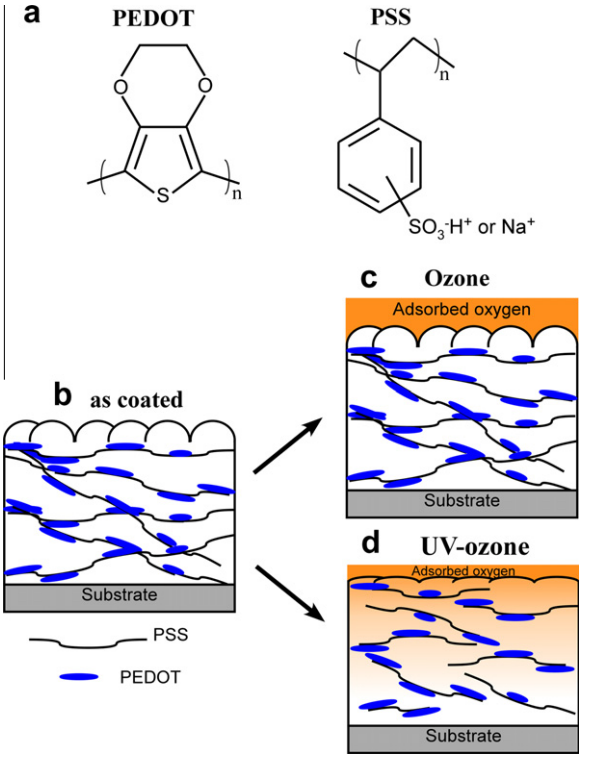

Fig. 7. (a) Chemical structure of PEDOT:PSS. Schematic structural illustrations of (b) as-PEDOT, (c) O_3–PEDOT, which has thick adsorbed oxygen on the surface, and (d) UV–O_3–PEDOT, which consists of decomposed PSS chains. The PEDOT structure maintains its initial state after both treatments.

oxygen increases with the treatment time. The absorbed oxygen molecules withdraw electrons from the PEDOT:PSS surface, because the electron affinity of oxygen is larger than that of PEDOT:PSS. Further oxygen adsorption makes the surface more negatively charged and forms a positive space–charge layer beneath the surface. As a result, dipoles are generated at the surface region lifting the HOMO level towards the high-binding energy. This is the main reason for the increase in the work function. In this process, the resistivity remains constant against the treatment time because the UV light was shadowed and decomposition of the chemical bonds was prevented.

(B) UV–ozone treatment (Fig. 7(d)): the decomposition of chemical bonds by UV light irradiation, resulting in the functional inhibition of PSS as a dopant, is promoted simultaneously with the oxidization and oxygen adsorption at the surface. The decomposed bonds are sufficiently reactive for further oxidization. Some of oxidized carbons were removed from the surface, resulting in the surface etching, which is conventional UV–ozone cleaning process. These are the reasons for the uniform distribution of oxygen across the entire film, and the increase in resistivity as well as the film etching. Furthermore, we assumed that the adsorbed oxygen could be re-activated by the UV light and be desorbed from the surface, leading the saturation of amount of adsorbed oxygen at the surface. As a result, the work function of UV–O_3 PEDOT increased at a slower rate than that of O_3 PEDOT and finally saturated.

5. Conclusion

We clarified the effect of UV–ozone treatment on the electrical properties of PEDOT:PSS films by distinguishing between the roles of UV light irradiation and ozone gas exposure. UV light was found to be responsible mainly for the decomposition of chemical bonds. On the other hand, ozone exposure caused dipoles to form on the film surface as a result of oxidization. This is the reason for the increase in the work function. In fact, the experimental data for the UV–O_3–PEDOT film showed the results of the overlap of both effects, namely a resistivity increase and surface etching, as well as an increase in the work function. Meanwhile, the O_3–PEDOT exhibited a variation only in the work function. In conclusion, a detailed understanding of these functions makes it possible to fine tune the electrical properties of PEDOT:PSS and improve device performance. Using UV–ozone treatment provide us to tune the electrical property of organic light-emitting diodes. In contrast, when we use PEDOT:PSS as a conductive electrode such as a Schottky electrode, ozone treatment should be better than UV–ozone treatment to eliminate the damage of PEDOT:PSS layer and to keep its conductivity.

Acknowledgments

This work was supported in part by the Bilateral Joint Project involving Hungary and Japan established by the Japan Society for the Promotion of Science (JSPS). A portion of this work was performed in the MANA foundry station, part of the World Premier International Research Center Initiative (WPI Program) established by the Ministry of Education, Culture, Sports, Science and Technology.

References

[1] F. Jonas, L. Schrader, Synth. Met. 41–43 (1991) 831.
[2] G. Heywang, F. Jonas, Adv. Mater. 4 (1992) 116.
[3] M. Dietrich, J. Heinze, G. Heywang, F. Jonas, J. Electroanal. Chem. 369 (1994) 87.
[4] I. Winter, C. Reese, J. Hormes, G. Heywang, F. Jonas, Chem. Phys. 194 (1995) 207.
[5] Q. Pei, G. Zuccarello, M. Ahlskog, O. Inganas, Polymer 35 (1994) 1347.
[6] N. Koch, A. Kahn, J. Ghijsen, J.J. Pireaux, J. Schwartz, R.L. Johnson, A. Elschner, Appl. Phys. Lett. 82 (2003) 70.
[7] J. Huang, P.F. Miller, J.S. Wilson, A.J. de Mello, J.C. de Mello, D.D.C. Bradley, Adv. Funct. Mater. 15 (2005) 290.
[8] N. Koch, A. Vollmer, A. Elschner, Appl. Phys. Lett. 90 (2007) 043512.
[9] M. Nakano, A. Tsukazaki, R.Y. Gunji, K. Ueno, A. Ohtomo, T. Fukumuraa, M. Kawasaki, Appl. Phys. Lett. 91 (2007) 142113.
[10] Y.-J. Lin, F.-M. Yang, C.-Y. Huang, W.-Y. Chou, J. Chang, Y.-C. Lien, Appl. Phys. Lett. 91 (2007) 092127.
[11] C. Tengstedt, A. Kanciurzewska, M.P. de Jong, S. Braun, W.R. Salaneck, M. Fahlman, Thin Solid Films 515 (2006) 2085.
[12] M.G. Helander, Z.B. Wang, M.T. Greiner, Z.W. Liu, K. Lian, Z.H. Lu, Appl. Phys. Lett. 95 (2009) 173302.
[13] A. Benor, S. Takizawa, P. Chen, C. Pérez-Bolívar, P. Anzenbacher Jr., Appl. Phys. Lett. 94 (2009) 193301.
[14] A. Benor, S. Takizawa, C. Pérez-Bolivar, P. Anzenbacher Jr., Org. Electron. 11 (2010) 938.
[15] A. Benor, S. Takizawa, C. Pérez-Bolivar, P. Anzenbacher Jr., Appl. Phys. Lett. 96 (2010) 243310.
[16] S. Tanuma, C.J. Powell, D.R. Penn, Surf. Interface Anal. 21 (1994) 165.
[17] J. Kido, H. Shionoya, K. Nagai, Appl. Phys. Lett. 67 (1995) 2281.
[18] S. Doniach, M. Šunjić, J. Phys. C 3 (1970) 285.
[19] D.A. Shirley, Phys. Rev. B 5 (1972) 4709.
[20] F. Petraki, S. Kennou, S. Nespurek, J. Appl. Phys. 103 (2008) 033710.
[21] G. Greczynski, T. Kugler, M. Keil, W. Osikowicz, M. Fahlman, W.R. Salanack, J. Electron Spectrosc. Relat. Phenom. 121 (2001) 1.
[22] J. Hwang, F. Amy, A. Khan, Org. Electron. 7 (2006) 387.
[23] G. Greczynski, T. Kugler, W.R. Salaneck, Thin Solid Films 354 (1999) 129.
[24] K. Burns, K.B. Adams, J. Longwell, J. Opt. Soc. Am. 40 (1950) 339).
[25] P.G. Wilkinson, K.L. Andrew, J. Opt. Soc. Am. 53 (1963) 710.
[26] Three Bond Technical News 17 (1987) 1.
[27] J. Vig, J. LeBus, IEEE Trans. Parts Hybrids Packag. 12 (1976) 365.
[28] Handbook of Chemistry, Basic, second ed., Chemical Society of Japan, Maruzen, Tokyo, Japan, 1966.

Organic Electronics 12 (2011) 285–290

Contents lists available at ScienceDirect

Organic Electronics

journal homepage: www.elsevier.com/locate/orgel

The effect of Ar plasma bombardment upon physical property of tungsten oxide thin film in inverted top-emitting organic light-emitting diodes

Joo Hyung Kim, You Jong Lee, Yoon Sung Jang, Jin Nyoung Jang, Doo Hyun Kim, Byung Chul Song, Dong Hyeok Lee, Soon Nam Kwon, MunPyo Hong *

Dept. of Display and Semiconductor Physics, Korea University, Chungnam, South Korea

ARTICLE INFO

Article history:
Received 27 May 2010
Received in revised form 19 October 2010
Accepted 31 October 2010
Available online 12 November 2010

Keywords:
OLED
Tungsten oxide
Plasma damage
HIL
Top emission
Inverted structure

ABSTRACT

This study examined the mechanism of performance degradation induced by the plasma sputtering process for the formation of the ITO top anode in inverted top-emitting organic light-emitting diodes (ITOLEDs) with WO_3 thin film as the hole injection layer (HIL) and the buffer layer. The degradation is mainly caused by the changes in the physical properties of the WO_3 thin film as well as the damages of organic layers, which are caused by the bombardment of energetic particles induced by the plasma sputtering process. The number of oxygen vacancies in the WO_3 thin film is increased with the increase of the bombardment energy of energetic particles such as Ar ions, resulting in the decrease in the work function and optical band gap and the dramatic increase in conductivity. Above all, the increase in the energy potential difference between WO_3 HIL and NPB HTL, which was attributed to the reduced work function of the WO_3 HIL, reduces the efficiency of carrier injection and dominantly affects the device performance. These results show that the plasma damage effect, induced by the sputtering process for ITO deposition, could not be effectively removed, even when the metal oxide thin film is used as the buffer layer in ITOLEDs.

© 2010 Elsevier B.V. All rights reserved.

1. Introduction

Top-emitting organic light-emitting diodes (TOLEDs) are quite attractive for their large aperture ratio and high pixel resolution [1–3]. In particular, TOLEDs with the inverted staggered structures, called as inverted TOLEDs (ITOLEDs), have been investigated actively because they are expected to be more suitable for n-type thin film transistors (TFTs) than the conventional TOLEDs [4,5].

To fabricate high performance ITOLEDs, the top anode of transparent conducting oxides (TCO), such as indium tin oxide (ITO) and indium zinc oxide (IZO), needs to be deposited on the hole injection layer by using the plasma sputtering process [6]. However, during the sputtering process, the underlying organic layers can be attacked easily by the bombardment of energetic particles (ions, electrons and neutralized particles), heating, and ultra violet (UV) radiation [7,8]. In particular, the energy of the charged particle bombardment is sufficiently high to break most of the carbon-based bonds in the organic layers [8]. If such breakage occurs because of the sputtering process, ITOLEDs will display degraded performance.

Over the past few years, many research groups have examined new sputtering technologies for depositing the TCO top anode, which would induce less damage to the underlying layers by reducing the energy of the particle bombardment [2,9,10]. Other groups have used a metal oxide hole injection layer (HIL) as a buffer layer to protect the organic layers from the energetic particle bombardment during the sputtering process. Recently, several transition metal oxides, such as tungsten oxide (WO_3),

* Corresponding author. Tel.: +82 10 7279 9601; fax: +82 41 865 0939.
E-mail address: goodmoon@korea.ac.kr (M. Hong).

1566-1199/$ - see front matter © 2010 Elsevier B.V. All rights reserved.
doi:10.1016/j.orgel.2010.10.023

molybdenum oxide (MoO_3), vanadium oxide (V_2O_5), rhenium oxide (ReO_3), and nickel oxide (NiO), have been evaluated as superior buffer layers with excellent HIL function [10–13]. Although these methods – new sputtering technologies and buffer layer – can somewhat reduce the plasma process-induced damage to the underlying layers, they still gave degraded device performance compared to the device not adopting sputtering deposition.

This study examined the changes in the physical properties of WO_3 thin films after Ar plasma irradiation to clarify the cause of the performance degradation in ITOLEDs with ITO top electrode formed by plasma sputtering. The correlation between the changes in the physical properties of the WO_3 thin film and device degradation was investigated by measuring various properties of the WO_3 thin films and the electro-optical characteristics of hole-only devices and OLED test devices. Moreover, the results suggested that under appropriate conditions, Ar plasma treatment can be used to obtain suitable physical properties of the WO_3 HIL for applications to high performance.

2. Experimental

Initially, to evaluate the plasma process-induced effect on ITOLEDs, we fabricated inverted bottom-emitting OLEDs (IBOLEDs) adopted with a 10 nm-thick top ITO electrode, which was deposited by the conventional DC magnetron sputtering process. The structure of the IBOLEDs in this study was the same as that in our previous work [2,4]; ITO (143 nm)/thin Al (3 nm)/8-hydroxyquinolatolithium (Liq) (0.9 nm)/tris (8-hydroxyquinoline) aluminum (Alq_3) (60 nm)/(*N*,*N*′-di-(naphthalene-1-yl)-*N*,*N*′-diphenyl-benzidine (NPB) (60 nm)/WO_3 (*x* nm)/ITO (10 nm)/Al (100 nm). The thickness of WO_3 was varied from 5 nm to 60 nm to investigate the buffering effect on the organic layers against the energetic particle bombardment generated by the DC magnetron sputter. The thin Al cathode layer was evaporated on a 143 nm-thick ITO coated glass (Shin–An SNP Co. Ltd.) with a sheet resistance of 11 Ω/square after cleaning the ITO coated glass in acetone and ethanol. All organic layers and the Al electrode layer were evaporated thermally in a high vacuum (under 1×10^{-6} Torr) chamber. The deposition rates of WO_3 and Liq were 0.01 nm/s and the evaporation rates of NPB, Alq_3 and Al ranged from 0.1 nm/s to 0.15 nm/s. All deposition rates were monitored by the in situ quartz oscillation thickness sensor. The DC magnetron sputtering deposition for top ITO was carried out with pure Ar gas at 3 mTorr for a 2×8 inch square ITO target. The distance between the substrate and target was 80 mm and the DC sputtering power was 40 W, which yielded a deposition rate of about 0.21 nm/s.

The changes in the physical properties of WO_3 thin films after Ar plasma irradiation were examined to determine the plasma bombardment effects on only the WO_3 HIL and not the organic layers. The WO_3 thin film was evaporated thermally with a WO_3 powder (99.99%) onto a bare glass after cleaning the glass by ultrasonification in acetone and ethanol. The sample was transferred to the reactive ion etching (RIE) chamber for Ar plasma treatment after vacuum break, and irradiated with Ar plasma at various power conditions of the radio frequency (RF) source, 40, 120, and 200 W, where the measured self bias (V_{self}) were −124, −267, and −348 V, respectively.

UV–Vis spectroscopy (Shimadzu, UV-3101PC) was used to measure the optical band gap. Atomic force microscopy (AFM) and electrostatic force microscopy (EFM) (Park system, XEP-100) were employed to determine the surface morphology and the work function in air environment. A source measure unit (HP, 4156C) and X-ray photoelectron spectroscopy (XPS) (Kratos, AXIS-NOVA) were used to examine the conductivity and binding energy, respectively. The electrical conductivity was calculated from the current–voltage data. For the XPS measurements, a monochromated Al Kα (150 W) X-ray source was used at 5.0×10^{-9} Torr and a charge neutralizer was turned onto exclude the charging effect. The XPS spectra were fitted with a combination of Gaussian and Lorentzian distributions after a Shirley background subtraction.

Hole-only devices and conventional bottom-emitting OLED test devices were fabricated to investigate the Ar plasma effect on the devices having WO_3 HIL. The structure of the hole-only device was ITO (143 nm)/WO_3 (5 nm)/NPB (60 nm)/Al (100 nm). The configuration of the conventional bottom emission OLED was ITO (143 nm)/WO_3 (5 nm)/NPB (60 nm)/Alq_3 (60 nm)/Liq (0.9 nm)/Al (100 nm). In the fabrication of both devices, after depositing the WO_3 HIL, the Ar plasma was irradiated under RF power conditions of 40, 120, and 200 W in the RIE chamber.

3. Results and discussion

In order to investigate the effect of the sputtering process for the deposition of ITO top electrode on the degradation of OLED performance, a 10 nm-thick ITO thin film was deposited by the DC plasma sputtering process and 100 nm-thick Al was deposited by thermal evaporation to produce the top anode in the IBOLED. To reduce the damage of the organic materials by the bombardment of energetic particles, induced by the sputtering process, WO_3 thin film was used as a buffer layer. The protection of the organic materials by the WO_3 thin film of various thicknesses, such as 5, 10, 20, and 60 nm was evaluated.

In the case of the IBOLED which did not undergo the sputtering process for ITO deposition, as shown in Fig. 1a, there were no serious differences in the *J*–*V*–*L* characteristics for various thicknesses of WO_3 thin film between 5 and 60 nm. In Fig. 1b, however, the *JV* characteristics of all of IBOLEDs that underwent the sputtering process indicated high leakage current from 10^{-2} mA/cm^2 to 10^{-1} mA/cm^2 in −8 V (Region I: reverse bias region). As reported by many researchers [9,14,15], the causes for the high leakage current are the damages in the underlying organic layers, which are generated by plasma sputtering process of ITO deposition. When energetic particles with high kinetic energy, such as Ar^+ ion, bombard the WO_3 HIL, the kinetic energy is transferred to organic layers. As a result, micro-current paths are induced by the local damages in the organic layers as well as the interface damages between the metal or metal oxide layer and organic layers [9,14].

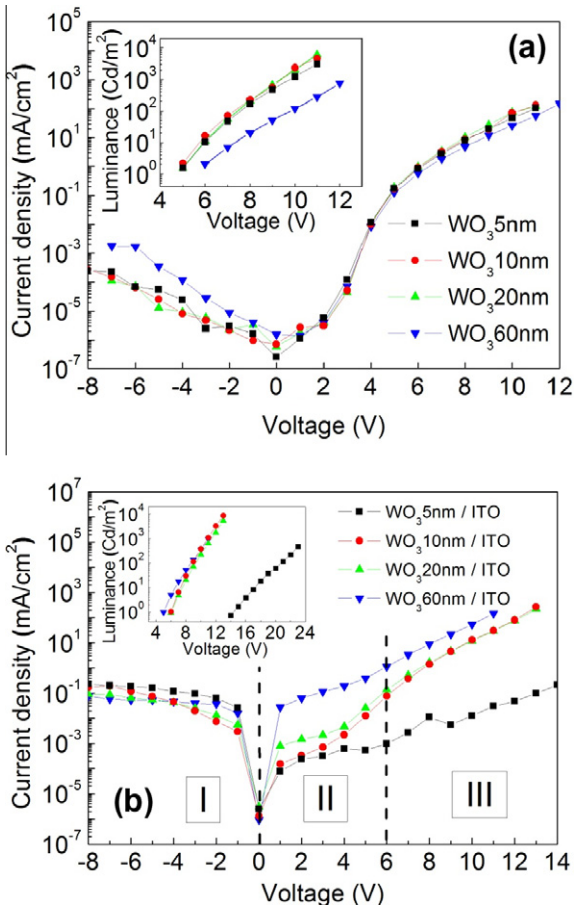

Fig. 1. Current density–voltage–luminance characteristics of (a) IBOLED without ITO sputtering deposition and (b) IBOLED with 5–60 nm-thick WO_3 buffer layer following deposition of top ITO by plasma sputtering process.

Unlike the results of Meyer et al. [15], however, the device with 60 nm WO_3 HIL shows high leakage current similar to other devices with much thinner WO_3 HIL.

In the forward bias region over 6 V (III region: typical space charge limited current (SCLC) region), the current density of the device with the 60 nm WO_3 HIL was increased to 4.75×10^1 mA/cm^2 at 10 V, which was 3700 times the current density of 1.3×10^{-2} mA/cm^2 in case of the device with a 5 nm WO_3 HIL. Moreover, while the IBOLEDs with a 5 nm-thick WO_3 HIL had a turn-on voltage of 14 V, the IBOLEDs with a thicker WO_3 HIL showed an improved turn-on voltage under 6 V. As reported by Meyer et al., the WO_3 buffer layer with the critical thickness could restrictively protect the organic layers from the bombardment of energetic particles [15].

In the forward bias region under 6 V (II region: strongly related with carrier injection properties), however, the devices with a thicker WO_3 HIL indicated higher current density. While the current density of the device with 5 nm-thick WO_3 was 3.12×10^{-4} mA/cm^2 in 3 V, the device with 60 nm-thick WO_3 indicated higher current density of 1.16×10^{-1} mA/cm^2. Unlike the analysis for "Region I", the higher current density of device with thicker WO_3 HIL could not be explained only by the mechanism of micro-current path induced by the local damages and be interpreted by a new mechanism, related with carrier injection properties.

In an actual DC magnetron sputtering process for ITO deposition, higher power density is needed than the power conditions of preceding studies [9,14,15]. As well as higher power density, energetic particles such as Ar^+, Ar, O_2, O, and In bombard the organic layers at much higher energy. Therefore, plasma sputtering process effects should be studied at high power density conditions, similar to actual sputtering process conditions.

To examine the degradation mechanism for the devices by ITO sputtering process, the physical properties of the WO_3 thin film subjected to energetic particles bombardment were analyzed, and the *J–V–L* characteristics of hole-only devices and conventional bottom OLEDs, which include the WO_3 HIL altered by plasma treatment under various conditions, were examined.

Initially, in order to investigate the Ar plasma-induced effect on the physical properties of WO_3 thin film, 50 nm-thick WO_3 thin films were thermally evaporated on glass substrates and were irradiated with the Ar plasma in the RIE chamber under RF powers of 40, 120, and 200 W. (The Ar ion bombardment energies corresponding to these powers were 124, 257, and 348 eV.)

Table 1 shows measured physical values, such as the work functions (Φ), optical band gaps (E_g) and conductivities (σ) of the as-deposited WO_3 thin film and WO_3 thin films with Ar plasma treatment. And some significant values were calculated, which are energy level difference between WO_3 and NPB ($\Delta\Phi$ (NPB–WO_3)) and between WO_3 and ITO ($\Delta\Phi$ (WO_3–ITO)). These values are directly related to the hole injection from anode to organic material. Detailed explanations about energy barrier are given in later part analyzing devices (Figs. 3 and 5). And atomic ratios of the W 6+ and 5+ states in the WO_3 thin films with various plasma treatments are calculated, also. We explain this value in depth with Fig. 2.

At RF power of 40, 120, and 200 W, the work function of the as-deposited WO_3 thin film decreased gradually from 5.2 to 4.8, 4.6, and 4.4 eV, respectively. In addition, the optical band gap slightly decreased from 4.08 to 4.02 eV after the plasma treatment. On the other hand, the conductivity drastically increased from 2.13×10^{-8} to 8.85 S/cm with increasing RF power.

However, from the AFM data, there were no remarkable changes in the surface roughness and grain size of the WO_3 thin films (0.02–0.1 nm), suggesting that Ar ion bombardment does not affect the surface and the generation of the crystallization of a WO_3 thin film.

XPS was used to determine the stoichiometry of WO_3 thin films before and after the Ar plasma treatment in order to investigate the theoretical mechanism for the changes in the physical properties of WO_3 thin films by Ar plasma treatment. As shown in Fig. 1a and b, the W4f core level of the as-deposited WO_3 thin film contained a well-resolved doublet of two symmetric peaks for W4f5/2 at 37.24 eV and W4f7/2 at 35.11 eV, with spin–orbit splitting (S.O.S.) of 2.14 eV and a peak ratio of 3:4. This is in good agreement with the data reported in the literature

Table 1
Physical values for the as-deposited WO_3 thin film and the WO_3 thin films after Ar plasma irradiation under various RF power conditions; the work functions (Φ) of the WO_3 thin films, energy level differences between WO_3 and NPB ($\Delta\Phi$ (NPB–WO_3)) and between WO_3 and ITO ($\Delta\Phi$ (WO_3–ITO)), optical band gaps (E_g), conductivities (σ), and atomic ratios of the W 6+ and 5+ states.

RF power (W)	Φ (eV)	$\Delta\Phi$ (NPB–WO_3) (eV)	$\Delta\Phi$ (WO_3–ITO) (eV)	E_g (eV)	σ (S/cm)	W 5+/W 6+ ratio
W O plasma treatment	5.2	0.2	0.4	4.08	2.13×10^{-8}	0.08
40	4.8	−0.6	0	4.07	4.18×10^{-4}	0.10
120	4.6	−0.8	−0.2	4.05	2.4×10^{-1}	0.14
200	4.4	−1.0	−0.4	4.02	8.85	0.13

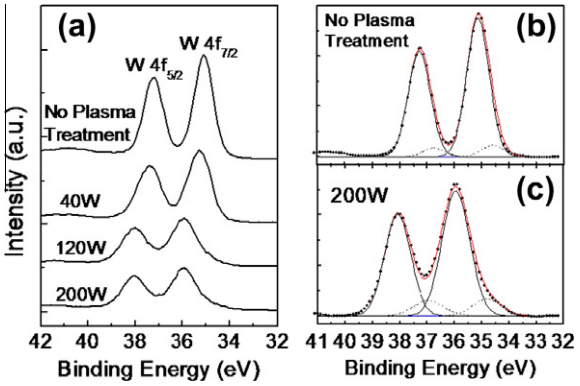

Fig. 2. (a) XPS spectra of W4f in WO_3 thin film surfaces after Ar plasma treatment at various RF power conditions. Peak fitting results of W4f core levels on WO_3 thin films (b) without and (c) with Ar plasma treatment (200 W RF power).

[12,13]. However, in the WO_3 thin films after Ar plasma treatment, the W4f doublet spectra decreased in intensity with increasing RF power and became broader due to the emergence of a shoulder peak at the lower binding energy region (Fig. 2a).

These results could be explained by the generation of oxygen vacancies in WO_3 thin film by Ar ion bombardment. The electronic structure of tungsten is [Xe]4f145d46s2 with empty 5d and 6s orbitals in its 6+ oxidation state close to the Fermi level [13]. Therefore, the XPS spectrum of the as-deposited WO_3 thin film showed a well-separated and sharp W4f doublet related mainly to the 6+ oxidation state, as shown in Fig. 2b.

However, energetic ion bombardment, which occurs on the surface of the WO_3 thin film during Ar plasma treatment, releases oxygen, creating a 5+ oxidation state of tungsten. Consequently, the spectra with the superposition of 6+ and 5+ oxidation states were observed. Fig. 2c shows the peak fitting result of the WO_3 thin film after the Ar plasma treatment at RF power 200 W (V_{self} = −348 V), indicating that the doublet of the 5+ oxidation state consists of W4f7/2 and W4f5/2 components positioned at the lower binding energies of 37 and 34.8 eV, respectively. In Table 1, the increasing atomic concentration ratio calculated with a spectrum area of 5+ and 6+ oxidation states confirms our hypothesis that Ar plasma treatment induces oxygen vacancies in WO_3 thin film. The creation of oxygen vacancies caused by Ar plasma treatment are similar to those caused by a range of different treatments for electrochromism reported by other, such as annealing at high temperature, UV radiation or X-ray exposure [12,16–22].

The changes in the work function, optical band gap and conductivity, as mentioned above (Table 1), can be explained by the more creation of oxygen vacancies. In the WO_3 thin film, which is a n-type semiconductor, the 5+ oxidation state was formed at a lower energy level than the 6+ oxidation state. Consequently, it moved the Fermi level upwards, as shown in Fig. 3. As a result, the work function and optical band gap decreased slightly. Furthermore, the conductivity increased dramatically because the upward shift in the Fermi level induced an increase in free electrons due to the electrons released from the 5d and 6s states.

Hole-only devices were fabricated and JV characteristics were examined to determine how the WO_3 HIL with altered properties affect the hole injection in the OLEDs (Fig. 4). The Ar plasma treatments at RF power 40, 120, and 200 W were carried out on WO_3 HIL prior to the deposition of NPB. While the current density of the hole-only device without the Ar plasma treatment was 108 mA/cm^2 at the operating voltage of 5.5 V, it decreased by 98% to 2.3 mA/cm^2 at 5.5 V in the case of the device subjected to 120 W Ar plasma treatment.

This result can be explained by the combination of the increased conductivity of the WO_3 thin films and the increased energy barrier between WO_3 HIL and NPB HTL. In other words, as shown in Table 1, the conductivity of WO_3 thin film that underwent Ar plasma treatment of 200 W was dramatically increased from 2.13×10^{-8} to 8.85 S/cm, which means improved conductance of the holes. However, the energy barrier between WO_3 HIL and

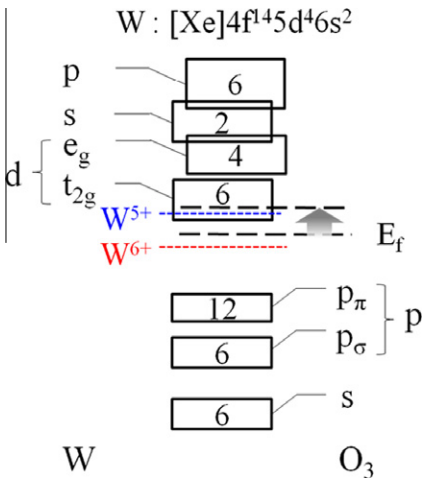

Fig. 3. Schematic band structure of WO_3. The numbers in the different bands define electron capacities.

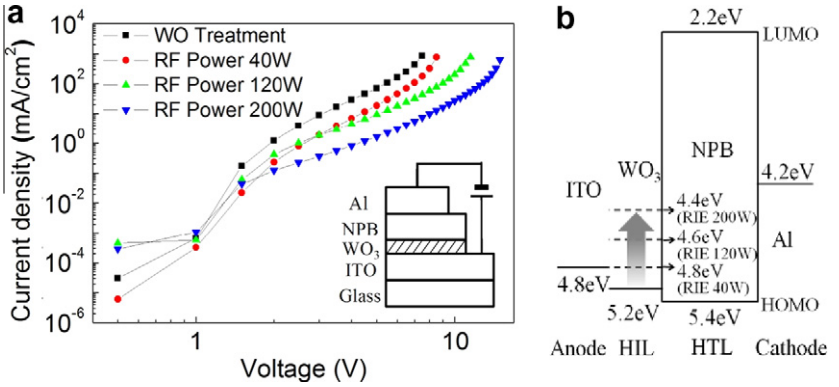

Fig. 4. (a) Current density–voltage characteristics (inset indicates the schematic structure of device) and (b) schematic energy level diagrams of hole-only devices without or with Ar plasma treatment.

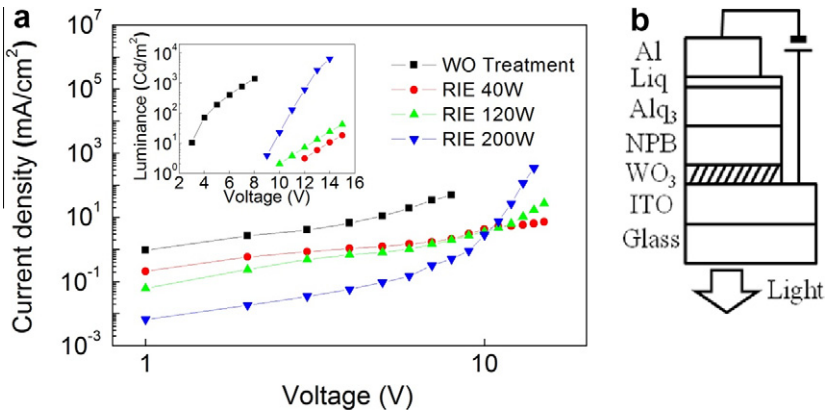

Fig. 5. Current density–voltage–luminance characteristics of (a) conventional OLEDs with plasma treatments for various conditions of WO_3 HIL and (b) schematic structures of devices.

NPB HTL was increased from 0.2 to 1.0 eV, degradation of hole injection can be expected (Fig. 4b).

From the decrease of the hole current in Fig. 4, we can know that the increase of the energy barrier between WO_3 HIL and NPB HTL more dominantly affected the *JV* characteristic than the increase of conductivity in WO_3 thin film did.

To investigate the effect of the altered physical properties of WO_3 thin film on the hole–electron recombination efficiency in OLEDs, the conventional bottom emission OLEDs with WO_3 HIL treated by Ar plasma at the same conditions as the hole-only devices were fabricated (Fig. 5).

The current density of the OLEDs in Fig. 5a decreased with increasing RF power because of the increased potential energy barrier between the WO_3 HIL and NPB HTL, similar to the case of the hole-only devices. The reduced hole-transfer from the HIL to HTL causes a decrease in hole–electron recombination in EML, which results in degradations of the luminance, current density and device efficiency.

At voltages over 10 V, however, current density was drastically increased and turn-on voltage was shifted to lower voltages with increasing RF power. This result can be explained as follows. High RF power reduces the work function of the WO_3 thin film. When a high bias is applied, band banding increases and more hole carriers are injected from ITO to NPB by the Poole–Frenkel effect. Therefore, the current density and hole–electron recombination increase and the turn-on voltage decreases.

Different from the report of Meyer et al. [15], when ITO thin film is deposited on WO_3 thin film by plasma sputtering process, the degradation of the *J–V–L* characteristics of OLEDs is affected by the changes of the physical properties on WO_3 thin film as well as by the damages of the organic layers.

On the other hand, the degradation effect on OLEDs by the bombardment of energetic particles could not be effectively removed even with the use of a metal oxide such as WO_3 as a buffer layer. Therefore, to adopt the plasma sputtering process in ITOLEDs fabrication, it is necessary to adopt the plasma damage free sputtering process, which can effectively control the energy of particle bombardment and deposit a TCO thin film of good quality. For this reason, we are also studying a novel method for ITO deposition that uses the hyper-thermal neutral beam (HNB) technology [2,23].

4. Conclusion

In summary, this paper reported a theoretical mechanism that relates the degradation of ITOLEDs subjected to

the sputtering process, which is used for the deposition of top ITO anode, to the changes in the physical properties of the WO_3 HIL as well as the damages on the organic layers. The number of oxygen vacancies in the WO_3 thin film increased with increasing bombardment energy of energetic particles, resulting in a decrease in work function and optical band gap and a dramatic increase in conductivity.

Above all, the increase in the potential energy difference between WO_3 HIL and NPB HTL, which was attributed to the reduced work function of WO_3, dominantly affected the device performance. In other words, although the metal oxide inorganic materials such as WO_3 was used as the buffer layer, the effect of the energetic particles bombardment induced by the plasma sputtering process on device performance could not be eliminated. In conclusion, it is necessary to study a new TCO deposition process which can control the bombardment energy of energetic particles effectively.

Acknowledgements

ITRC (Information Technology Research Center) support program supervised by the NIPA (National IT Industry Promotion Agency (NIPA-2010-C1090-1021-0004) and R&D Program through the National Fusion Institute of Korea (NFRI) funded by the Government funds.

References

[1] L.S. Hung et al., Appl. Phys. Lett. 74 (1999) 3209.
[2] Y.J. Lee et al., Thin Solid Films 517 (2009) 4019.
[3] H.W. Choi et al., Appl. Phys. Lett. 86 (2005) 012104.
[4] Y.J. Lee et al., Org. Electron. 9 (2008) 407.
[5] D.M. Mattox et al., J. Vac. Sci. Technol., A 7 (1989) 1105.
[6] H.K. Kim et al., Appl. Phys. Lett. 85 (2004) 4295.
[7] D.H. Kim et al., Jpn. J. Appl. Phys. 47 (2008) 5672.
[8] L. Sirghi et al., Thin Solid Films 515 (2006) 1334.
[9] H.K. Kim et al., Appl. Phys. Lett. 86 (2005) 1833503.
[10] H. You et al., J. Appl. Phys. 101 (2007) 026105.
[11] J. Meyer et al., Appl. Phys. Lett. 91 (2007) 113506.
[12] D.-S. Leem et al., Appl. Phys. Lett. 91 (2000) 0011113.
[13] I.M. Chan et al., Thin Solid Films 450 (2004) 304.
[14] T.H. Gil et al., Org. Electron. 11 (2010) 322.
[15] J. Meyer et al., Adv. Mater. 20 (2008) 3839.
[16] A. Siokou et al., Surf. Sci. 482 (2001) 294.
[17] S.F. Ho et al., J. Phys. Chem. 91 (1987) 4779.
[18] S. Tokito et al., J. Phys. D: Appl. Phys. 29 (1996) 2750.
[19] L.S. Liao et al., Appl. Phys. Lett. 75 (1999) 1619.
[20] Y. Shigesato et al., Appl. Surf. Sci. 33 (1988) 804.
[21] R. Sivkumar et al., Smart Mater. Struct. 15 (2006) 877.
[22] C.G. Granqvist, Sol. Energy Mater. Sol. Cells 32 (1994) 369.
[23] S.J. Yoo et al., Rev. Sci. Instrum. 79 (2008) 02C301.

Organic Electronics 12 (2011) 291–294

Contents lists available at ScienceDirect

Organic Electronics

journal homepage: www.elsevier.com/locate/orgel

Solution processed white phosphorescent organic light-emitting diodes with a double layer emitting structure

Kyoung Soo Yook, Jun Yeob Lee*

Department of Polymer Science and Engineering, Dankook University, Jukjeon-dong, Suji-gu, Yongin-si, Gyeonggi-do 448-701, Republic of Korea

ARTICLE INFO

Article history:
Received 11 July 2010
Received in revised form 15 November 2010
Accepted 22 November 2010
Available online 7 December 2010

Keywords:
Multilayer white device
High efficiency
Solution processed device
Alcohol soluble emitting

ABSTRACT

Solution processed multilayer white phosphorescent organic light-emitting diodes with a double layer emitting structure were developed using an alcohol soluble phosphorescent host and dopant materials. An alcohol soluble blue phosphorescent emitting layer was spin coated on a toluene soluble red/green emitting layer. A high current efficiency of 17.8 cd/A with a color coordinate of (0.31, 0.46) was obtained from the solution processed double emitting layer white phosphorescent organic light-emitting diodes. In addition, all solution processed multilayer white phosphorescent organic light-emitting diodes were also developed by using the two layer emitting structure.

© 2010 Elsevier B.V. All rights reserved.

1. Introduction

White organic light-emitting diodes (WOLEDs) hold great potential in display and lighting applications given their high efficiency and design versatility. In particular, solution processed WOLEDs are attractive because of lower material consumption and simple fabrication processes [1–5].

However, it is very difficult to improve the efficiency of soluble WOLEDs because the device structure cannot be diversified. While it is important to fabricate a multilayer stack structure to optimize WOLED device performance, realization of multilayer stack structures within WOLEDs is difficult [6–10]. An orthogonal film with no interlayer mixing between stacked organic layers has to first be formed to fabricate a multilayer structure in a soluble WOLED; however, most organic materials used in WOLEDs are soluble in similar solvents. Therefore, orthogonal film formation is difficult, although a double layer stack structure was reported using alcohol soluble polymer emitting material [6]. No WOLEDs with a double layer phosphorescent emitting layer structure have been reported. Our group has reported that an alcohol soluble blue phosphorescent emitting layer could be fabricated using a phosphine oxide-based host material and a fluorinated blue phosphorescent dopant [11].

In this work, WOLEDs with a double layer phosphorescent emitting layer were developed for the first time and the device performance of the WOLEDs were investigated. An alcohol soluble blue phosphorescent emitting layer was stacked onto a toluene soluble red/green phosphorescent emitting layer and the double layer phosphorescent emitting structure realized. All solution processed two emitting layer phosphorescent WOLEDs were demonstrated and a high efficiency of 17.8 cd/A was reported from the white phosphorescent organic light-emitting diodes (WPHOLEDs).

2. Experimental

A device configuration of indium tin oxide (ITO, 150 nm)/poly-3,4-ethylenedioxythiophene:polystyrenesulfonate(PEDOT:PSS, 60 nm)/poly(*N*-vinylcarbazole)(PVK): iridium(III) tris(2-phenylpyridine)(Ir(ppy)$_3$):iridium(III) bis(2-phenylquinoline) acetylacetonate(Ir(pq)$_2$acac) (15 nm, *x*%, 1%)/2,7-bis(diphenylphosphoryl)-9,9′-spirobi[fluorene] (SPPO13): iridium(III) bis(2-(4,6-difluorophenyl)-pyridinato-*N*,C^2)picolinate (FIrpic) (40 nm, 10%)/SPPO13

* Corresponding author. Tel.: +82 2 793 4102; fax: +82 2 709 2614.
E-mail address: leej17@dankook.ac.kr (J.Y. Lee).

1566-1199/$ - see front matter © 2010 Elsevier B.V. All rights reserved.
doi:10.1016/j.orgel.2010.11.020

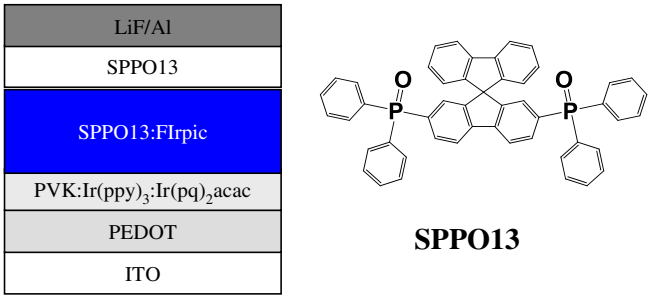

Fig. 1. Chemical structures of SPPO13 and device structure of WPHOLEDs fabricated in this work.

(30 nm)/LiF (1 nm)/Al (200 nm) was used to fabricate all phosphorescent soluble WPHOLEDs. The doping concentration of $Ir(ppy)_3$ was changed from 5% to 15%, while the doping concentration of the $Ir(pq)_2acac$ was fixed at 1.0%. Devices I, II, and III had $Ir(ppy)_3$ doping concentrations of 5%, 10%, and 15%, respectively. A representative device structure of the WPHOLEDs, and chemical structure of the SPPO13 are shown in Fig. 1. In addition, a device without the SPPO13 electron transport layer (device IV) was also fabricated. The device structure of the device IV was the same as that of device III except that SPPO13 was not deposited on the emitting layer. Red–green device and blue device were also fabricated for comparison. The device structure of the red–green device was ITO/PEDOT:PSS (60 nm)/PVK:$Ir(ppy)_3$:$Ir(pq)_2acac$ (40 nm, 5%:1%)/SPPO13 (30 nm)/LiF/Al and blue device had a device structure of ITO/PEDOT:PSS (60 nm)/PVK (10 nm)/SPPO13:FIrpic (40 nm, 10%)/SPPO13 (30 nm)/LiF/Al. The concentration of the PVK:$Ir(ppy)_3$:$Ir(pq)_2acac$ solution was 0.5 wt%, while the concentration of the SPPO13:FIrpic solution was 1.0 wt%. The PVK emitting layer was spin coated from toluene, while the SPPO13 emitting layer was deposited from a 2-propanol solution. Each emitting layer was baked at 80 °C for 10 min after spin coating. The SPPO13 electron transport layer was deposited by vacuum evaporation, followed by LiF/Al deposition. All devices were encapsulated with a glass lid and a getter after device fabrication. Device performances of the soluble WPHOLEDs were measured with a Keithley 2400 source measurement unit and CS 1000 spectroradiometer.

3. Results and discussion

Development of a multilayer emitting structure is paramount as various device structures can subsequently be fabricated and device performances improved [12–14]. In the case of vacuum evaporation-based small molecule WOLEDs, device performances were tuned by managing the stack structure of the emitting layers [12–15]. However, the stacked device structure was difficult to prepare in soluble WOLEDs because most emitting materials are soluble only in aromatic solvents, not polar. In particular, phosphorescent emitting materials are soluble only in aromatic solvents. However, our group reported alcohol soluble phosphorescent host and dopant materials that could be applied to fabricate multilayer emitting structures in soluble WPHOLEDs [11].

Fig. 2 shows the current density–voltage-luminance curves of the soluble WPHOLEDs with a two layer emitting structure. Red and green dopants were dispersed into the toluene soluble PVK layer and the blue dopant dispersed into the 2-propanol soluble SPPO13 layer. The doping concentration of the $Ir(ppy)_3$ was controlled from 5% to 15%. The current density of the WPHOLEDs was increased according to the doping concentration of the $Ir(ppy)_3$. It is well known that current density depends on the charge trapping and charge hopping effect of the dopant in the emitting layer [16]. In general, dopant is a trap site in the emitting layer and the use of the dopant reduces the current density at low doping concentration because of charge trapping by the dopant. However, the charge transport can be increased at high doping concentration due to the charge hopping effect. The trapped charges can be transported through hopping at high doping concentration. Therefore, the increase in the current density, according to the doping concentration, was due to the decreased hopping distance between dopant materials. Charge hopping between dopant materials was the main mechanism for the charge transport that was enhanced at high doping concentrations. The current density was even higher in the device IV without SPPO13 electron transport layer. The SPPO13 in the blue emitting layer played a role of an electron transport layer and the current density was not decreased. The high current density of the device IV is due to low thickness of the total organic layer. The luminance of the WPHOLEDs followed the same trend as the current density because the luminance depended on the current density and recombination efficiency.

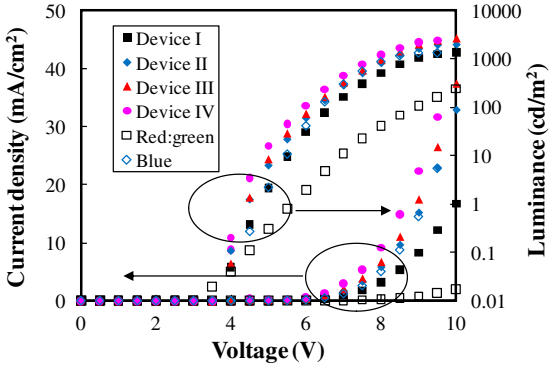

Fig. 2. Current density–voltage–luminance curves of WPHOLEDs.

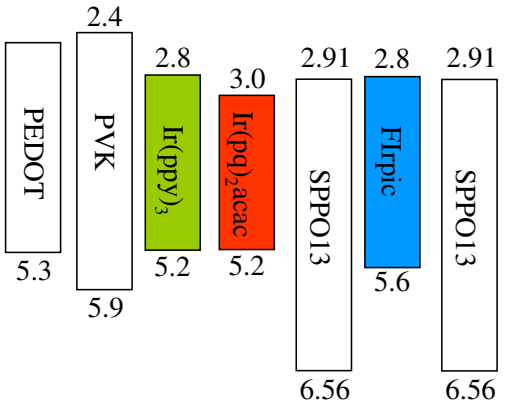

Fig. 3. Energy level diagram of the WPHOLED.

The current density–voltage and luminance–voltage curves of the red:green[1] and blue single layer devices are also shown in Fig. 2. The current density of the red:green device was much lower than that of the blue device. The charge trapping by the red and green dopants was significant in the red:green device due to the large energy level difference between the PVK host and red/green dopants (Fig. 3), leading to a low current density in the red:green single layer device.

The quantum efficiency–luminance and current efficiency–luminance curves of the WPHOLEDs are shown in Fig. 4. The quantum efficiency of the WPHOLEDs at 100 cd/m^2 was maximized at a Ir(ppy)$_3$ doping concentration of 5% and decreased according to the doping concentration. The quantum efficiency of device I at 100 cd/m^2 was 7.9%, compared with 7.2% and 6.9% for devices II and III. The high quantum efficiency of device I was due to the strong blue emission, compared with red and green emissions. As shown in the electroluminescence (EL) spectra in Fig. 5, device I showed stronger blue emissions than devices II and III. The quantum efficiency of the blue device was much higher than that of the red:green device, as shown in Fig. 4. Therefore, device I, with greater blue emission, showed a higher quantum efficiency than devices II and III with weak blue emissions.

Although the quantum efficiency at 100 cd/m^2 was high in device I, with a low doping concentration, the quantum efficiency at 1000 cd/m^2 was high in device III, with a 15% doping concentration. The high efficiency of device III at high luminance can be explained by the reduced triplet exciton quenching. The quantum efficiency of the blue single layer device sharply dropped at high luminance due to the triplet exciton quenching that originated from the narrow recombination zone. The contribution of the blue emission decreased in device III, resulting in less efficiency and a decrease at high luminance. Therefore, the efficiency at 1000 cd/m^2 was high in device III and low in device I. The device IV without any electron transport layer showed similar quantum efficiency to that of the device III. Although no electron transport layer was used in the device IV, the quantum efficiency was not degraded in the device IV. This is due to strong electron transport properties of the SPPO13. The emission is formed close to the interface between the red:green and blue emitting layers due to electron transport properties of the SPPO13 host, minimizing the triplet exciton quenching by the cathode. Therefore, the quantum efficiency was not degraded at all in the device IV. The device IV was fabricated by all solution process without any vacuum deposition process, indicating that all solution processed WPHOLEDs can show similar device performances to solution WPHOLEDs with vacuum deposited organic layers. The current efficiency of the WPHOLEDs is also shown in Fig. 4. The current efficiency of device I at 100 cd/m^2 was 17.8 cd/A, while devices II and III showed a current efficiency of 16.2 cd/A. Device IV without any electron transport layer showed as high current efficiency of 16.9 cd/A.

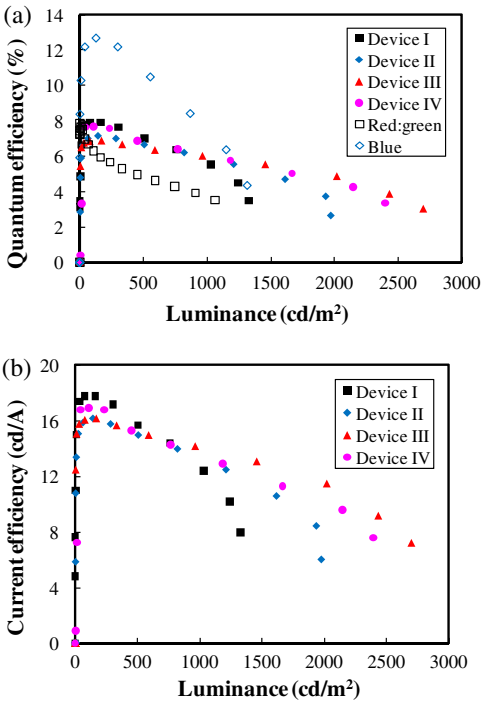

Fig. 4. Quantum efficiency and current efficiency of WPHOLEDs.

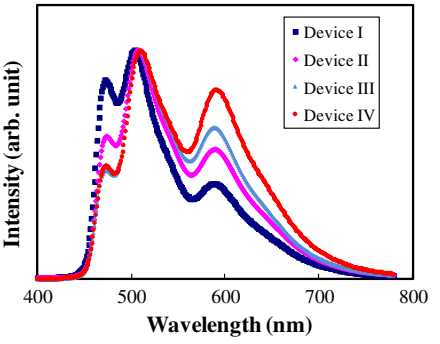

Fig. 5. Electroluminescence spectra of WPHOLEDs.

[1] For interpretation of colour in Figs. 2–5, the reader is referred to the web version of this article.

The EL spectra of the WPHOLEDs are shown in Fig. 5. All WPHOLEDs showed red, green, and blue emissions, and the relative emission intensity depended on the doping concentration. The blue intensity was strong in device I and decreased according to doping concentration. The decrease of the blue intensity at high doping concentration can be explained by the improved electron injection from the SPPO13:FIrpic layer into the PVK:$Ir(ppy)_3$:$Ir(pq)_2$acac layer. As explained in the current density–voltage curves, the charge transport was improved at high doping concentrations. In particular, the PVK is a hole transport type host material and the electron transport is limited by the host material. Electron transport was mainly determined by electron hopping through dopant materials and was improved by the $Ir(ppy)_3$ at high doping concentration due to a reduced electron hopping distance. Therefore, more electrons are injected from the blue emitting layer to the red:green-emitting layer, leading to the less blue emission intensity in device III. In addition, the blue emission was absorbed by the green emitting material and little blue emission was observed at high green doping concentrations. The red and green emission was even stronger in device IV due to more exciton generation in the red and green emitting layer.

The color coordinates of devices I, II, and III were (0.31, 0.46), (0.35, 0.47), and (0.39, 0.50). The coordinate was red-shifted according to the doping concentration because of increased green and red emissions. Therefore, the color coordinate of the soluble WPHOLEDs could be controlled by managing the doping concentration of the $Ir(ppy)_3$ in the red:green emitting layer. In general, the doping concentration of the green emitting material, in common soluble three color WPHOLEDs, was less than 1%, making color control difficult due to too low doping concentrations [17]. Slight changes of the doping concentration can result in large shifts in the color coordinate; the process margin for the white emission is too narrow. The process window for the doping concentration could be widened by using the double layer emitting structure developed in this work. There was only a 0.04 shift of the color coordinate by changing the doping concentration of the $Ir(ppy)_3$ from 10% to 15%, compared with the 0.04 shift of the color coordinate by changing the doping concentration by 1% in a single layer device. Therefore, control of the color in the stacked device structure proved simple as the blue and red:green layer gave separate emissions. The color coordinate of the device IV was (0.39, 0.47).

4. Conclusions

In conclusion, soluble WPHOLEDs with a double layer emitting structure were developed using an alcohol soluble blue phosphorescent emitting layer and a red:green phosphorescent emitting layer dissolved in an aromatic solvent. The color coordinate could be simply managed by changing the $Ir(ppy)_3$ doping concentration, with other parameters fixed, and a high current efficiency of 17.8 cd/A was achieved in the soluble WPHOLEDs. In particular, all solution processed two emitting layer WPHOLEDs could be fabricated for the first time. This double layer emitting structure can be useful in fabricating high efficiency soluble WPHOLEDs in display and lighting applications.

References

[1] F. Huang, P.-I. Shih, C.-F. Shu, Y. Chi, A.K.-Y. Jen, Adv. Mater. 21 (2009) 361.
[2] X. Gong, W. Ma, J.C. Ostrowski, G.C. Bazan, D. Moses, A.J. Heeger, Adv. Mater. 16 (2004) 615.
[3] Y.H. Xu, J.B. Peng, J.X. Jiang, W. Xu, W. Yang, Y. Cao, Appl. Phys. Lett. 87 (2005) 193502.
[4] H.A. Al Attar, A.P. Monkman, M. Tavasli, S. Bettington, M.R. Bryce, Appl. Phys. Lett. 86 (2005) 121101.
[5] P. Shih, C. Shua, Y. Tung, Y. Chi, Appl. Phys. Lett. 88 (2006) 251110.
[6] X. Niu, C. Qin, B. Zhang, J. Yang, Z. Xie, Y. Cheng, L. Wang, Appl. Phys. Lett. 90 (2007) 203513.
[7] S.O. Jeon, C.W. Joo, K.S. Yook, J.Y. Lee, Appl. Phys. Lett. 94 (2009) 093303.
[8] K.S. Yook, C.W. Joo, S.O. Jeon, J.Y. Lee, Org. Electron. 11 (2010) 184.
[9] S.R. Tseng, H.F. Meng, K.C. Lee, S.F. Horng, Appl. Phys. Lett. 93 (2008) 153308.
[10] J.D. You, S.R. Tseng, H.F. Meng, F.W. Yen, I.F. Lin, S.F. Horng, Org. Electron. 10 (2009) 1610.
[11] K.S. Yook, S.E. Jang, S.O. Jeon, J.Y. Lee, Adv. Mater. 22 (2010) 4479.
[12] B.W. D'Andrade, S.R. Forrest, Adv. Mater. 16 (2004) 1585.
[13] G. Schwartz, M. Pfeiffer, S. Reineke, K. Walzer, K. Leo, Adv. Mater. 19 (2007) 3672.
[14] S.-J. Su, E. Gonmori, H. Sasabe, J. Kido, Adv. Mater. 20 (2008) 4189.
[15] K.S. Yook, S.O. Jeon, C.W. Joo, J.Y. Lee, Appl. Phys. Lett. 93 (2008) 073302.
[16] J. Shen, J. Yang, J. Appl. Phys. 83 (1998) 7706.
[17] H.B. Wu, J.H. Zou, F. Liu, L. Wang, A. Mikhailovsky, G.C. Bazan, W. Yang, Y. Cao, Adv. Mater. 20 (2008) 696.

Organic Electronics 12 (2011) 295–299

Contents lists available at ScienceDirect

Organic Electronics

journal homepage: www.elsevier.com/locate/orgel

Density-functional theoretical study of fluorination effect on organic/metal interfaces

Kenji Toyoda [a,*], Ikutaro Hamada [b], Susumu Yanagisawa [c], Yoshitada Morikawa [c]

[a] Advanced Technology Research Laboratories, Panasonic Corporation, 3-4 Hikaridai, Seika-cho, Soraku-gun, Kyoto 619-0237, Japan
[b] WPI-Advanced Institute for Materials Research, Tohoku University, 2-1-1 Katahira, Aoba-ku, Sendai 980-8577, Japan
[c] Department of Precision Science and Technology, Graduate School of Engineering, Osaka University, 2-1 Yamada-oka, Suita, Osaka 565-0871, Japan

ARTICLE INFO

Article history:
Received 15 September 2010
Received in revised form 10 November 2010
Accepted 14 November 2010
Available online 25 November 2010

Keywords:
Density-functional theory
Organic/metal interface
van der Waals interactions
Vacuum level shift
Fluorination
Carrier injection

ABSTRACT

Density-functional theory with a semi-empirical dispersion correction was used to systematically examine how the number of fluorine (F) atoms affects atomic and electronic structures of fluorinated pentacene ($C_{22}F_nH_{14-n}$) adsorbed on Cu(1 1 1) surfaces. The fluorination effect on the carrier injection efficiency at organic/metal interfaces was investigated. We found that as the number of F atoms decreases, the electron affinity of isolated molecules decreases, suggesting that the molecule becomes less reactive. However, for adsorbed systems, as the number of F atoms decreases, molecular orbitals of $C_{22}F_nH_{14-n}$ strongly hybridize with the substrate states while retaining the n-type energy level alignment, resulting in lowering the barrier height of the carrier injection. Based on the calculation results, we propose using $C_{22}F_nH_{14-n}$ ($n \leqslant 8$) with Cu electrodes for efficient electron injection.

© 2010 Elsevier B.V. All rights reserved.

1. Introduction

Understanding the electronic structure at organic/metal interfaces is of great importance in developing organic devices [1,2]. The interface dipole at organic/metal interfaces induces vacuum level shift that modifies the barrier height of the carrier injection, which plays a decisive role in organic devices [1,2]. Therefore, accurate prediction and control of the interface dipole is crucial to designing the electrodes of organic devices.

Pentacene ($C_{22}H_{14}$, Pen) and perfluoropentacene ($C_{22}F_{14}$, PFP) are prototypical p-type [3] and n-type [4] organic semiconductors, respectively. Accordingly, the interactions of Pen and PFP with metal substrate have been studied extensively both experimentally and theoretically [5–20]. In particular, elucidation of the electronic properties of PFP on metal is crucial, because n-type organic/metal interfaces are not as well understood as p-type organic/metal interfaces [21,22]. Efficient n-type interfaces must be designed to fabricate complementary integrated circuits.

PFP is expected to lower the electron injection barrier height, because larger electron affinity makes the lowest unoccupied molecular orbital (LUMO) level closer to the Fermi energy of the electrode than that of Pen [23]. However, experimental reports have shown that the highest occupied molecular orbital (HOMO) state relative to the Fermi energy for PFP/Cu(1 1 1) is almost the same as that for Pen/Cu(1 1 1) [11], and moreover, that the PFP–substrate distance is larger than that for Pen/Cu(1 1 1) [16]. These indicate that the electron injection for PFP/Cu(1 1 1) is less efficient than that for Pen/Cu(1 1 1), because the overlap between the molecular orbitals and the substrate for PFP/Cu(1 1 1) becomes smaller than that for Pen/Cu(1 1 1). Our previous paper pointed out that the large PFP–Cu(1 1 1) distance originates from repulsion of F atoms by the substrate [10]. Therefore, it might be possible to modify the adsorption distance and electron injection barrier, by changing the number of F atoms in PFP.

* Corresponding author.
E-mail address: toyoda.kenji@jp.panasonic.com (K. Toyoda).

1566-1199/$ - see front matter © 2010 Elsevier B.V. All rights reserved.
doi:10.1016/j.orgel.2010.11.010

In this work, we have examined systematically how the number of F atoms affects the atomic and electronic structures of fluorinated pentacene ($C_{22}H_nF_{14-n}$) adsorbed on Cu(1 1 1) using density-functional theory (DFT) within the generalized gradient approximation (GGA) with a semi-empirical dispersion correction. We show that adsorption distance and hybridization of molecular orbitals of $C_{22}H_nF_{14-n}$ on Cu(1 1 1) are tunable by changing the number of F atoms, and we propose an optimal organic/metal interface for efficient electron injection.

2. Calculation method

Calculations were carried out using STATE [24], which implements a plane wave basis set and pseudopotentials [25,26]. The plane-wave kinetic-energy cutoff for the wave functions and augmented charge density were set to 25 and 225 Ry, respectively. The Perdew–Burke–Ernzerhof (PBE)-GGA [27] was adopted to describe the exchange–correlation functional. Because a semilocal GGA functional cannot correctly describe van der Waals (vdW) forces, which dominate the interaction between π conjugated molecules and metal surfaces [5,7–10,18,19,28–31], we used a semi-empirical dispersion correction proposed by Grimme [32] (DFT-D) for adsorption systems. DFT-D was shown to yield accurate adsorption distances of organic molecules on metal surfaces as well as the work-function changes [7,9,10].

In this work, we examined the following three $C_{22}F_nH_{14-n}$ molecules as shown in Fig. 1: 1, 2, 3, 4, 5, 7, 8, 9, 10, 11, 12, 14-dodecanefluoropentacene (F12), 1, 2, 3, 4, 8, 9, 10, 11-octafluoropentacene (F8), and 2, 3, 9, 10-tetrafluoropentance (F4). The numbers of F atoms in F12, F8, and F4 were 12, 8, and 4, respectively.

Isolated molecules were calculated in a $2 \times 1 \times 1$ nm^3 rectangular unit cell using the Γ point.

The Cu(1 1 1) surface was represented by a repeated slab model, in which one slab consisted of four Cu atomic layers. A vacuum region of ~2 nm was inserted in between slabs. A $C_{22}F_nH_{14-n}$ molecule was adsorbed on only one surface of the slab with its molecular plane parallel to the surface in a $\sqrt{43} \times 2\sqrt{3}$ surface unit cell, which is the same as that used in our previous calculation of PFP/metal systems [10]. A 2×4 **k**-point mesh was used to sample the surface Brillouin zone. The center of $C_{22}F_nH_{14-n}$ was assumed to be located at an hcp-hollow site on the Cu(1 1 1) surface with the long molecular axis aligned with close-packed metal atom rows as shown in Fig. 2. In the geometry optimization, we fixed the bottom layer of the substrate slabs at their respective bulk positions. The remaining degrees of freedom were optimized with the DFT-D method until the maximum force dropped below a threshold value of 0.2 nN. The work-function difference between the two surfaces of a slab was compensated for by using a dipole correction [33]. Work-functions were calculated from the difference between the Fermi energy of the system and the average electrostatic potential at the center of the vacuum region, and the vacuum level shifts were calculated from the work-function changes induced by the adsorption of $C_{22}F_nH_{14-n}$.

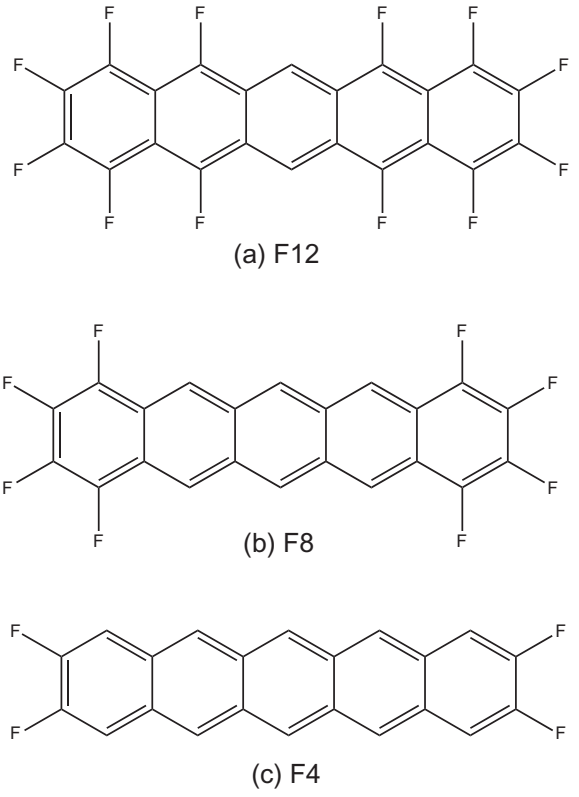

Fig. 1. The structural formula of (a) F12, (b) F8, and (c) F4.

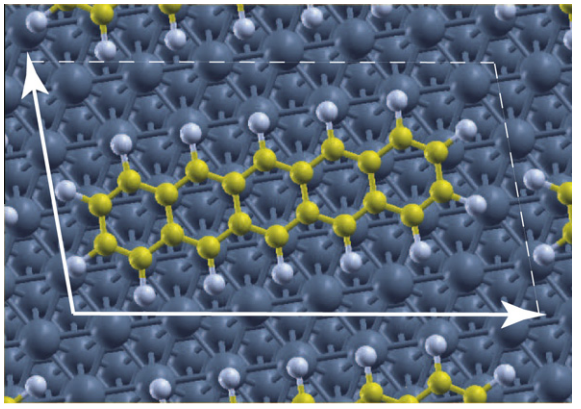

Fig. 2. Plan view of a $C_{22}F_nH_{14-n}$ molecule on Cu(1 1 1).

3. Results and discussion

3.1. Isolated molecules

First, we calculated the atomic and the electronic structures of isolated PFP, F12, F8, F4, and Pen molecules. The optimized molecular structures of F12, F8, and F4 are planar, similar to Pen and PFP. The ionization potential (IP) and electron affinity (EA) of PFP, F12, F8, F4, and Pen are summarized in Table 1. The IP and EA were estimated from

Table 1
IP and EA of PFP, F12, F8, F4, and Pen.

	PFP	F12	F8	F4	Pen
IP/eV	5.25	5.27	5.17	4.90	4.50
EA/eV	4.28	4.30	4.04	3.72	3.36

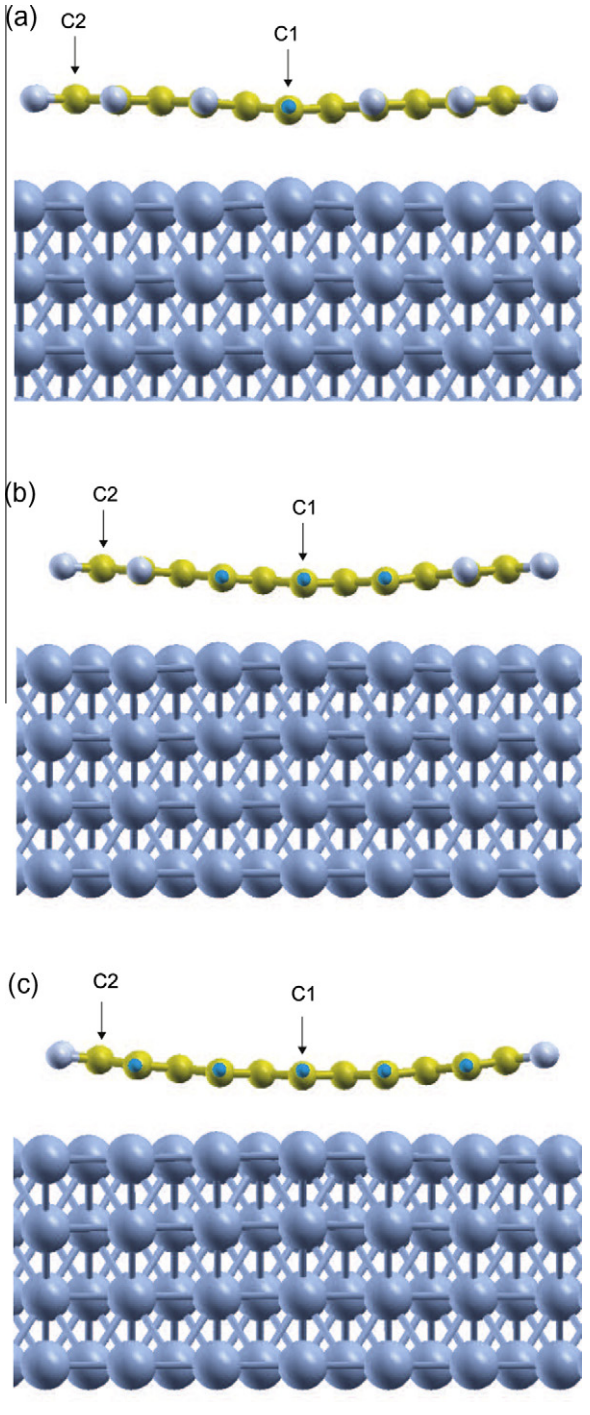

Fig. 3. Cross-sectional view of F12 (a), F8 (b), and F4 (c) on Cu(1 1 1).

the Kohn–Sham energy levels of the HOMO and LUMO relative to the vacuum level, respectively. We found that as the number of F atoms in $C_{22}F_nH_{14-n}$ decreases, the IP and EA of each molecule become small, suggesting that the molecule becomes less reactive. We also found that the IP and EA of F12 are almost the same as those of PFP.

3.2. Adsorbed systems

Next, we calculated the atomic geometries and the vacuum level shifts of PFP, F12, F8, F4, and Pen adsorbed on Cu(1 1 1) and then inspected the electronic structures of the adsorption systems.

3.2.1. Atomic geometries and vacuum level shifts

Fig. 3(a)–(c) depict a cross-sectional view of the atomic geometries of F12, F8, and F4 adsorbed on Cu(1 1 1). Table 2 summarizes the adsorption distances of C atoms depicted in Fig. 3 relative to the surface and the work-function change ($\Delta\phi$) for PFP, F12, F8, F4, and Pen adsorbed on Cu(1 1 1).

It turns out that as the number of F atoms decreases, the average adsorption distance of the C atoms becomes smaller (Fig. 3 and Table 2), even though decreasing the number of F atoms makes EA smaller, i.e., chemically less reactive. The results suggest that the adsorption distance is mainly determined by the number of F atoms rather than the reactivity of the molecule, because of the repulsion between F 2p and substrate states [10].

As seen in Fig. 3(a)–(c), the $C_{22}F_nH_{n-14}$ molecule is distorted when adsorbed on the surface, and the adsorption distance of an end C atom bonded to F (C1) is larger than that of the center C atom bonded to H (C2) (Table 2). The differences in adsorption distances of C1 and C2 for F12, F8, and F4 are almost the same (0.03–0.04 nm). The molecular distortion is attributed to (i) repulsion between F 2p and Cu substrate states and (ii) hybridization of the molecular orbitals with the substrate states [7]. When the number of F atoms is large (i.e., large distance), repulsion dominates and accordingly hybridization is small. On the other hand, when the number of F atoms is small, the adsorption distance becomes small (hence strong hybridization) because of the reduction of repulsion by F 2p. These effects compensate for each other depending on the distance, resulting in similar molecular distortion. Note that distortion caused by electron transfer is not significant [5,7].

Table 2
The average C adsorption distance (Z_C^{ave}), the adsorption distance of C1 and C2 in Fig. 3 (Z_{C1} and Z_{C2}, respectively), and the work-function change ($\Delta\phi$) for PFP, F12, F8, F4, and Pen adsorbed on Cu(1 1 1). Adsorption distances of C atoms are measured from the Cu surface.

	PFP	F12	F8	F4	Pen
Z_C^{ave}/nm	0.29[a]	0.29	0.27	0.26	0.24[b]
Z_{C1}/nm	–	0.27	0.25	0.24	–
Z_{C2}/nm	–	0.30	0.29	0.27	–
$\Delta\phi$/eV	−0.30[a]	−0.29	−0.41	−0.62	−0.97[b]

[a] Ref. [10].
[b] Ref. [7].

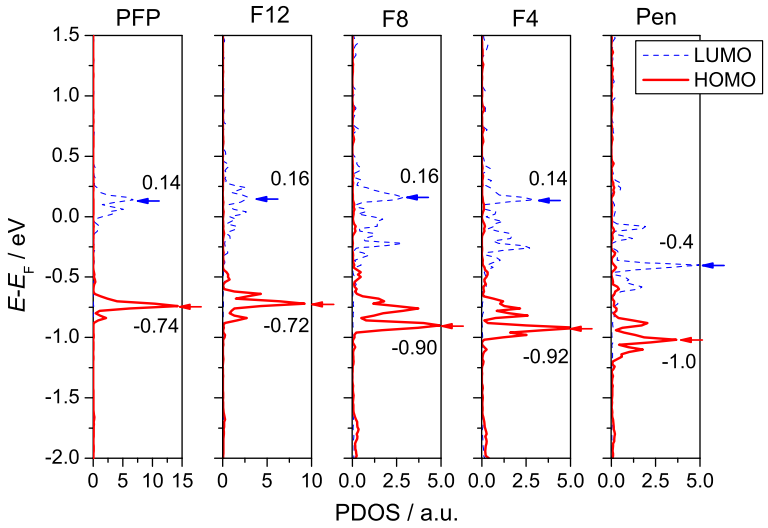

Fig. 4. The density of states projected (PDOS) onto molecular LUMO and HOMO for PFP, F12, F8, F4, and Pen on Cu(1 1 1). The arrows represent the peak positions of LUMO and HOMO states.

$\Delta\phi$ becomes smaller (i.e., larger $|\Delta\phi|$) as the number of F atoms decreases. Because the work-function changes caused by the molecular distortion are small (-0.04, -0.01, and 0.1 eV for F12, F8, and F4, respectively), we ascribe the change in $\Delta\phi$ mainly to the change in the adsorption distance.

3.2.2. Electronic structures

Fig. 4 shows the density of states projected (PDOS) onto molecular LUMO and HOMO for PFP, F12, F8, F4, and Pen on Cu(1 1 1). As shown in Fig. 4, the broadening of the molecular states (LUMO and HOMO) becomes larger as the number of F atoms decreases, as a result of stronger hybridization at a short distance. On the other hand, the PDOS for the molecular states of PFP and F12 are sharp, indicating weaker interaction of the adsorbate with the substrate. Although hybridization of the HOMO and LUMO states with the substrate depends significantly on the number of F atoms, their peak positions are almost unchanged, suggesting that n-type operation would be retained regardless of the number of F atoms. This is because the larger absolute value of $\Delta\phi$ cancels out the smaller EA of the isolated molecule as the number of F atoms decreases.

Our results indicate that the energy level alignment of $C_{22}F_nH_{14-n}$ ($n \geqslant 0$) adsorbed on Cu(1 1 1) is n-type, because a part of the LUMO state is below the Fermi energy. It should be noted that PBE-GGA has the well-known underestimation of the band gap [34–37] but can describe the LUMO and HOMO levels of an organic molecule adsorbed on a metal surface qualitatively [5,7,10].[1] Our results suggest that reducing the number of F atoms makes it possible to fabricate an optimal interface for carrier injection because of the strong hybridization. On the basis of our systematic study, we propose using $C_{22}F_nH_{14-n}$ ($0 \leqslant n \leqslant 8$) for efficient electron injection.

4. Conclusions

We have studied the fluorination effect on $C_{22}F_nH_{14-n}$/Cu(1 1 1) interfaces using density-functional calculations with the semi-empirical van der Waals (vdW) correction.

We found that although reducing the number of F atoms decreases the ionization potential and the electron affinity of the $C_{22}F_nH_{14-n}$ molecule (i.e., the molecule became less reactive), the adsorption distance of the molecule on the Cu(1 1 1) surface becomes smaller due to the reduction of repulsion between F 2p and the substrate states.

Calculated electronic structures show that the hybridization of the molecular orbitals with the substrate states becomes stronger, whereas the peak positions of the molecular states remains almost unchanged, retaining n-type interface as obtained with PFP, as the number of F atoms decreases. This suggests that electron injection is made efficient, and we therefore propose using $C_{22}H_nF_{14-n}$ ($n \leqslant 8$) to achieve efficient electron injection.

Our results indicate that controlling only the ionization potential and the electron affinity of isolated molecules is insufficient for designing an optimal organic/metal interface. We conclude that the energy level alignment at organic/metal interfaces is crucially governed by adsorption geometries which are quite flexible and are affected by a subtle balance between repulsive interaction due to Pauli repulsion and attractive interaction due to hybridization and vdW interactions.

Acknowledgments

The work was partly supported by Grant-in-Aid for Scientific Research from the Ministry of Education, Culture, Science, Sports, and Technology, Japan (Grant Nos.

[1] The gap underestimation tends to be compensated for by the error in the present GGA to describe the polarization of the metal surface, which reduces the band gap [38].

19054013 and 22241026). Numerical calculations were carried out at computer centers of Osaka University, the Institute for Solid State Physics of the University of Tokyo, and Tohoku University.

References

[1] W.R. Salaneck, K. Seki, A. Kahn, J.J. Pireaux (Eds.), Conjugated Polymer and Molecular Interfaces, Marcel Dekker, Inc., New York, Basel, 2002.

[2] H. Ishii, K. Sugiyama, E. Ito, K. Seki, Energy level alignment and interfacial electronic structures at organic/metal and organic/organic interfaces, Adv. Mater. 11 (8) (1999) 605–625.

[3] S. Lee, B. Koo, J. Shin, E. Lee, H. Park, Effects of hydroxyl groups in polymeric dielectrics on organic transistor performance, Appl. Phys. Lett. 88 (16) (2006) 162109-1–162109-3.

[4] Y. Inoue, Y. Sakamoto, T. Suzuki, M. Kobayashi, Y. Gao, S. Tokito, Organic thin-film transistors with high electron mobility based on perfluoropentacene, Jpn. J. Appl. Phys. 44 (6A) (2005) 3663–3668.

[5] K. Toyoda, Y. Nakano, I. Hamada, K. Lee, S. Yanagisawa, Y. Morikawa, First-principles study of the pentacene/Cu(1 1 1) interface: adsorption states and vacuum level shifts, J. Electron Spectrosc. Relat. Phenom. 174 (1–3) (2009) 78–84.

[6] K. Toyoda, I. Hamada, S. Yanagisawa, Y. Morikawa, Origin of surface-band dispersion at the pentacene/Cu interface, Appl. Phys. Express 3 (2010) 025701-1–025701-3.

[7] K. Toyoda, I. Hamada, K. Lee, S. Yanagisawa, Y. Morikawa, Density functional theoretical study of pentacene/noble metal interfaces with van der Waals corrections: vacuum level shifts and electronic structures, J. Chem. Phys. 132 (13) (2010) 134703-1–134703-9.

[8] K. Lee, J. Yu, Y. Morikawa, Comparison of the localized basis and planewave basis for density functional calculations of organic molecules on metals, Phys. Rev. B 75 (4) (2007) 045402-1–045402-5.

[9] K. Toyoda, I. Hamada, S. Yanagisawa, Y. Morikawa, Adsorption of benzene on noble metal surfaces studied by density functional theory with van der Waals correction, J. Nanosci. Nanotechnol., in press.

[10] K. Toyoda, I. Hamada, K. Lee, S. Yanagisawa, Y. Morikawa, Density functional theoretical study of perfluoropentacene/noble metal interfaces with van der Waals corrections: adsorption states and vacuum level shifts, unpublished.

[11] N. Koch, A. Gerlach, S. Duhm, H. Glowatzki, G. Heimel, A. Vollmer, Y. Sakamoto, T. Suzuki, J. Zegenhagen, J.P. Rabe, F. Schreiber, Adsorption-induced intramolecular dipole: correlating molecular conformation and interface electronic structure, J. Am. Chem. Soc. 130 (23) (2008) 7300–7304.

[12] A. Ferretti, C. Baldacchini, A. Calzolari, R.D. Felice, A. Ruini, E. Molinari, M.G. Betti, Mixing of electronic states in pentacene adsorption on copper, Phys. Rev. Lett. 99 (4) (2007) 046802-1–046802-4.

[13] H. Yamane, D. Yoshimura, E. Kawabe, R. Sumii, K. Kanai, Y. Ouchi, N. Ueno, K. Seki, Electronic structure at highly ordered organic/metal interfaces: pentacene on Cu(1 1 0), Phys. Rev. B 76 (16) (2007) 165436-1–165436-10.

[14] H. Yamane, E. Kawabe, D. Yoshimura, R. Sumii, K. Kanai, Y. Ouchi, N. Ueno, K. Seki, Intermolecular band dispersion in highly ordered monolayer and multilayer films of pentacene on Cu(1 1 0), Phys. Status Solidi B 245 (5) (2008) 793–798.

[15] N. Koch, I. Salzmann, R.L. Johnson, J. Pflaum, R. Friedlein, J. Rabe, Molecular orientation dependent energy levels at interfaces with pentacene and pentacenequinone, Org. Electron. 7 (6) (2006) 537–545.

[16] N. Koch, A. Vollmer, S. Duhm, Y. Sakamoto, T. Suzuki, The effect of fluorination on pentacene/gold interface energetics and charge reorganization energy, Adv. Mater. 19 (1) (2007) 112–116.

[17] N. Koch, Energy levels at interfaces between metals and conjugated organic molecules, J. Phys.: Condens. Matter 20 (18) (2008) 184008-1–184008-12.

[18] M. Simeoni, S. Picozzi, B. Delley, An ab-initio study of pentacene on aluminum (1 0 0) surface, Surf. Sci. 562 (1–3) (2004) 43–52.

[19] K. Lee, J. Yu, Ab initio study of pentacene on Au(0 0 1) surface, Surf. Sci. 589 (1–3) (2005) 8–18.

[20] D.G. de Oteyza, Y. Wakayama, X. Liu, W. Yang, P.L. Cook, F.J. Himpsel, J.E. Ortega, Effect of fluorination on the molecule–substrate interactions of pentacene/Cu(1 0 0) interfaces, Chem. Phys. Lett. 490 (1–3) (2010) 54–57.

[21] C.R. Newman, C.D. Frisbie, D.A. da Silva Filho, J.-L. Brédas, P.C. Ewband, K.R. Mann, Introduction to organic thin film transistors and design of n-channel organic semiconductors, Chem. Mater. 16 (23) (2004) 4436–4451.

[22] J. Zaumseil, H. Sirringhaus, Electron and ambipolar transport in organic field-effect transistors, Chem. Rev. 107 (4) (2007) 1296–1323.

[23] T. Yokoyama, C.B. Park, T. Nishimura, K. Kita, A. Toriumi, Oxygen-related degradation mechanisms for on- and off-states of perfluoropentacene thin-film transistors, Jpn. J. Appl. Phys. 47 (5) (2008) 3643–3646.

[24] Y. Morikawa, H. Ishii, K. Seki, Theoretical study of *n*-alkane adsorption on metal surfaces, Phys. Rev. B 69 (4) (2004) 041403-1–041403-4.

[25] N. Troullier, J.L. Martins, Efficient pseudopotentials for plane-wave calculations, Phys. Rev. B 43 (3) (1991) 1993–2006.

[26] D. Vanderbilt, Soft self-consistent pseudopotentials in a generalized eigenvalue formalism, Phys. Rev. B 41 (11) (1990) 7892–7895.

[27] J.P. Perdew, K. Burke, M. Ernzerhof, Generalized gradient approximation made simple, Phys. Rev. Lett. 77 (18) (1996) 3865–3868.

[28] S. Yanagisawa, Y. Morikawa, Important role of molecular permanent dipoles of the Alq_3/Al interface studied from first-principles, Chem. Phys. Lett. 420 (4–6) (2006) 523–528.

[29] L. Romaner, D. Nabok, P. Puschnig, E. Zojer, C. Ambrosch-Draxl, Theoretical study of PTCDA adsorbed on the coinage metal surfaces, Ag(1 1 1), Au(1 1 1) and Cu(1 1 1), New J. Phys. 11 (5) (2009) 053010-1–053010-26.

[30] K. Toyoda, Y. Nakano, I. Hamada, K. Lee, S. Yanagisawa, Y. Morikawa, First-principles study of benzene on noble metal surfaces: adsorption states and vacuum level shifts, Surf. Sci. 603 (18) (2009) 2912–2922.

[31] I. Hamada, K. Lee, Y. Morikawa, Interaction of water with a metal surface: important of van der Waals forces, Phys. Rev. B 81 (11) (2010) 115452-1–115452-6.

[32] S. Grimme, Semiempirical GGA-type density functional constructed with a long-range dispersion correction, J. Comput. Chem. 27 (15) (2006) 1787–1799.

[33] J. Neugebauer, M. Scheffler, Adsorbate–substrate and adsorbate–adsorbate interactions of Na and K adlayers on Al(1 1 1), Phys. Rev. B 46 (24) (1992) 16067–16080.

[34] J.B. Neaton, M.S. Hybertsen, S.G. Louie, Renormalization of molecular electronic levels at metal–molecule interfaces, Phys. Rev. Lett. 97 (21) (2006) 216405-1–216405-4.

[35] S. Kümmel, L. Kronik, Orbital-dependent density functionals: theory and applications, Rev. Mod. Phys. 80 (1) (2008) 3–60.

[36] T. Körzdörfer, S. Kümmel, N. Matom, L. Kronik, When to trust photoelectron spectra from Kohn–Sham eigenvalues: the case of organic semiconductors, Phys. Rev. B 79 (20) (2009) 201205-1–201205-4.

[37] K.S. Thygesen, A. Rubio, Renormalization of molecular quasiparticle levels at metal–molecule interfaces: trends across binding regimes, Phys. Rev. Lett. 102 (4) (2009) 046802-1–046802-4.

[38] J.M. Garcia-Lastra, C. Rostgaard, A. Rubio, K.S. Thygesen, Polarization-induced renormalization of molecular-levels at metallic and semiconducting surfaces, Phys. Rev. B 80 (2009) 245427-1–245427-7.

Organic Electronics 12 (2011) 300–305

Contents lists available at ScienceDirect

Organic Electronics

journal homepage: www.elsevier.com/locate/orgel

Charge transport and energetic disorder in polymer:fullerene blends

L. Mattias Andersson

Biomolecular and Organic Electronics, Department of Physics, Chemistry and Biology, Linköping University, SE-581 83 Linköping, Sweden

ARTICLE INFO

Article history:
Received 3 September 2010
Received in revised form 1 November 2010
Accepted 12 November 2010
Available online 25 November 2010

Keywords:
Polymer
Fullerene
Electrical transport
Mobility
Temperature dependence
Gaussian disorder model

ABSTRACT

Mobility versus temperature measurements on two different polymer:fullerene blends intended for solar cell applications have been evaluated in terms of the energetic disorder and how this varies with stoichiometry. The charge transport is shown to be confined to the intended phases in both cases, but with fundamentally different interaction properties. In one case the energetic disorder is a function of stoichiometry for the hole transport, while it is constant and equal to that of the pure fullerene for electrons, and in the other case it is the hole transport that has a stoichiometry independent energetic disorder. Transport site dilution is argued to be present in the fixed energetic disorder system and this is offered as a partial explanation to molecular weight dependent currents in solar cells. Determination of the glass transition temperature through the use of field effect transistors is also demonstrated.

© 2010 Elsevier B.V. All rights reserved.

1. Introduction

One of the more severe performance limitations in bulk heterojunction (BHJ) solar cells is their inability to both absorb light efficiently and transport the generated charge to the electrodes in the same device. Charge transport is typically not a big problem in devices less than 100 nm thick, but although the absorption in such a device is quite strong, it is far from sufficient [1]. Due to charge transport limitations there are many materials [1–3] that give optimum performance for thicknesses around the first optical interference maximum, which is device and material dependent, but usually in the 75–100 nm range. Despite very high incident photon to free charge efficiencies [4], peak external quantum efficiencies for good devices are usually only around 50%, but with values around 70% reported in thicker high band gap materials [5] with high extinction coefficients and favorable charge transport conditions.

Understanding charge transport thus goes a long way towards finding ways to improve BHJ solar cell efficiencies. Two promising, in the sense that they make good use of the available energy in terms of delivered voltage, materials are poly(2,7-(9,9-dioctyl-fluorene)-alt-5,5-(4′,7′-di-2-thienyl-2′,1′,3′-benzothiadiazole)) (APFO-3) [2] and poly(2,3-bis-(3-octyloxyphenyl)quinoxaline-5,8-diyl-*alt*-thiophene-2,5-diyl (TQ-1) [3]. Both materials are capable of efficient charge generation and high fill factors in solar cells with active layer thicknesses at the respective first interference induced absorption maximum.

Some polymers interact favorably with fullerenes of the [6,6]-phenyl-C_x-butyric acid methyl ester (PCBM) (where $x = 61$ for the C60 based [60]PCBM and $x = 71$ for the C70 based [70]PCBM) type in terms of mobility. Blend hole mobilities can be significantly higher than the corresponding pure polymer phase values [2,6] even at very high PCBM loading levels. The reason for this can actually be different for different systems. It will be shown here that the blend hole mobility in TQ-1:[70]PCBM is stoichiometry dependent and with variations due to changes in the energetic disorder induced by PCBM; and that the blend hole mobility in APFO-3:[60]PCBM is increased by a different type of interaction with a stoichiometry independent energetic disorder for hole transport.

Furthermore it will be shown that the hole transport is confined to the polymer phase and electron transport to the fullerene phase in both cases, and that molecular

E-mail address: matan@ifm.liu.se

1566-1199/$ - see front matter © 2010 Elsevier B.V. All rights reserved.
doi:10.1016/j.orgel.2010.11.007

weight becomes much more important in blends than in the pure phase, at least in APFO-3 type systems, due to charge transport site dilution. Site dilution is also offered as a partial explanation to why low molecular weight polymers tend to underperform in solar cells.

2. Experimental

Mobility evaluations have been done with field effect transistors (FET) from transfer characteristics and are maximum saturation values. Different gold electrode geometries with channel lengths in the 10–50 μm range and widths in the 2–20 mm range patterned by photolithography on top of 100 nm thick SiO_2 has been used as bottom contact transistor substrates in all measurements. The active layers were spin coated from a dichlorobenzene solution in air. Electrical characterization was done under high vacuum and illumination [7] using a parameter analyzer. Each measurement was cycled 10 times to allow the devices to settle in a quasi stable state, and the last acquisition was used to generate the presented data. A varying, but at least 15 min long, waiting time after changes in temperature was employed to ensure the correct temperature and to make sure that there was no influence from transient phenomena [2,7,8].

The energetic disorder is here taken to be in the context of the Gaussian disorder model (GDM) [9] with the characteristic energetic disorder parameter σ denoting the standard deviation of a Gaussian density of states through which the charge transport occurs.

Fundamentally the GDM assumes an activation energy that is proportional to $1/T$ based on the relaxation of carriers in the density of states. At high carrier concentrations, such as with FET, this is no longer true due to state filling effects [10] and the mobility temperature dependence will be reduced from its basic $1/T^2$ dependence. In addition to this, the hydrophilic nature of the SiO_2 means that there will be water present at the polymer-insulator interface during the measurements even under high vacuum conditions, which will be reflected in extracted energetic disorder parameters [8]. Supercooled water can also result in mobility-temperature hysteresis and prevent meaningful evaluation of low temperature data [11]. For measurements where extrinsic effects can be avoided and a wide temperature range used, such as in the absence of a hydrophilic interface or under ultra high vacuum conditions, it is possible to account for the carrier concentration effects and obtain accurate σ-values [12] provided, of course, that the charge transport is dominated by disorder and not polaronic effects. This is not possible here, but by using a narrow high temperature range, relative errors can be minimized since no water freezing will occur and carrier concentration effects are dependent on σ/kT [12]. A first order approach to data fitting will thus result in systematic errors in the absolute mobility and σ-values, but will, however, not influence the fundamental behavior as is evidenced by the very systematic data. Although a $1/T$ representation is possible due to the abovementioned effects, the mobility data is still plotted against $1/T^2$ to emphasize the disordered nature of the charge transport.

3. Results and discussion

Mobility versus temperature data for different stoichiometries and two different synthesis batches of TQ-1 are shown in Fig. 1. Each data set, i.e. temperature scan for a specific batch and stoichiometry, is done on a single transistor chosen at random and it may thus deviate from the statistical averages. There is sometimes a scatter in mobility between different devices and there are some uncertainties in stoichiometry due to blending of very small amounts of material, but the stoichiometry induced variations become clear as the number of characterized devices increase. Series resistance and current–voltage hysteresis [7] can have some small effect as the temperature and currents increase (seen as a slight downward bend in the temperature data). The data are nevertheless systematic overall, and any present errors are not significant with

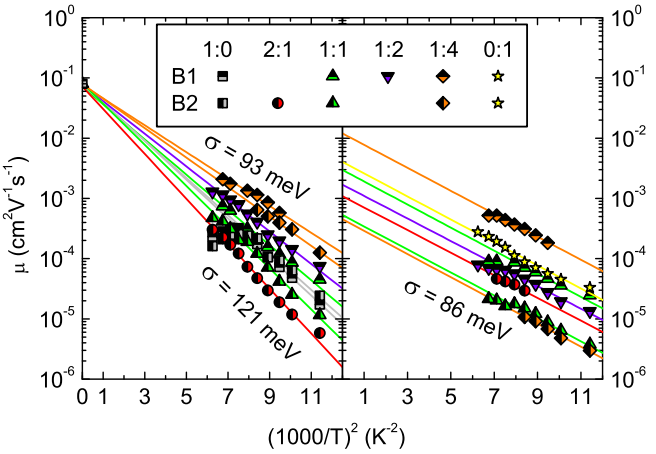

Fig. 1. Hole (left) and electron (right) mobility of TQ1:[70]PCBM blends from two different polymer synthesis batches (B1, B2) as a function of $1/T^2$ according to the GDM. The energetic disorder parameters (σ) do not accurately reflect the materials due to the extrinsic effects of water but is included for comparative purposes. The real σ-values are likely considerably smaller.

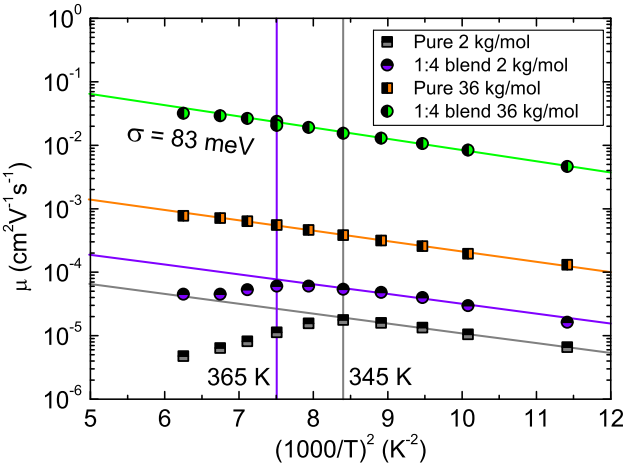

Fig. 2. Hole and electron mobility for two different molecular weights of pure APFO-3 and in 1:4 blends with [60]PCBM as a function of $1/T^2$ according to the GDM. The energetic disorder parameter (σ) is influenced by extrinsic effects of water and is in reality about 70 meV [20], but is included for comparative purposes. Also included in the figure are the glass transition temperatures of the low molecular weight APFO-3 and its [60]PCBM blend. The glass transition temperatures pertaining to the higher molecular weight are considerably higher and not clearly visible.

respect to the fundamental behavior. Occasionally devices break down during a temperature scan or there is too much contact-related noise in a particular measurement to prevent meaningful data evaluation and thus some data points are missing from Fig. 1. More data on these and several other batches have been collected and are considered in the discussion but not included in the figures to avoid heavy cluttering. Adding [70]PCBM to TQ-1 at fist increases the energetic disorder and concomitantly decreases the room temperature hole mobility. At roughly 30% [70]PCBM the energetic disorder starts to decrease and for loading levels above 50% the energetic disorder is less, and hole mobility higher, than in pure TQ-1. All in all the room temperature hole mobility varies on an order of magnitude scale.

Two striking things are immediately obvious from Fig. 1; that all of the hole mobility data seems to converge to a single point for infinite temperature, and that electron mobilities vary while pure [70]PCBM and all the blends share the same energetic disorder. From this it is possible to conclude that the charge transport is confined to the respective phase and that the stoichiometry induced hole mobility variations are due to changes in energetic disorder. The reasoning for this is as follows: pure TQ-1 and the blends share the same infinite temperature hole mobility. This would be extremely unlikely should the PCBM phase be involved actively in the hole transport. Furthermore, there is no trace of changing energetic disorder in the electron mobility data which, should the electron and hole charge transport occur in the same phase, would require vastly different behavior of the two involved energy bands. Considering the similarities in both energetic disorder and absolute mobility values between electrons and holes this is also extremely unlikely.

APFO-3 on the other hand, while still having a strongly stoichiometry dependent hole mobility, has a stoichiometry independent energetic disorder for the hole transport. The mechanism by which the hole mobility is influenced by the fullerene is thus different in APFO-3:[60]PCBM and TQ-1:[70]PCBM. Fig. 2 shows mobility as a function of temperature for pure APFO-3 and 1:4 [60]PCBM blends of two different APFO-3 molecular weights. The energetic disorder is always the same, as reflected in the temperature dependence. One important observation that can be made is that the mobility enhancement is considerably smaller, both relatively and absolutely, for the low molecular weight material. This appears to be a general trend; the hole mobility enhancement at high fullerene loading has a linear correlation to the molecular weight (at least for low to intermediate molecular weights). Interestingly enough, the enhancement is much more predictable than the absolute mobility values, which scatter strongly (order of magnitude) [13] for the available APFO-3 batches. Looking at mobility as a function of stoichiometry for the different molecular weights (Fig. 3) reveals that the hole mobility enhancement is universally about one order of magnitude independent of molecular weight, but that the mobility decreases with increasing fullerene content much faster for lower molecular weights. As has been pointed out elsewhere [2] and is further discussed below it is difficult to measure electron mobilites in APFO-3:[60]PCBM blends in a reliable way using FETs, but it can be shown that it increases monotonically with about one order of magnitude per 20 percentage points of [60]PCBM fraction [2]. Since the stoichiometry dependence of the electron and hole mobilities are opposite for a considerable stoichiometry range, and the energetic disorder is identical in pure APFO-3 and APFO-3:[60]PCBM blends it is possible to conclude that the hole transport in the APFO-3 blends is also confined to the polymer phase.

That the energetic disorder for hole transport is identical in the low and high molecular weight APFO-3 is quite remarkable. The low molecular weight APFO-3 has a degree of polymerization of 3 [13], which means that there are no effects on the transport site energetic distribution from delocalization beyond three or less repeat units.

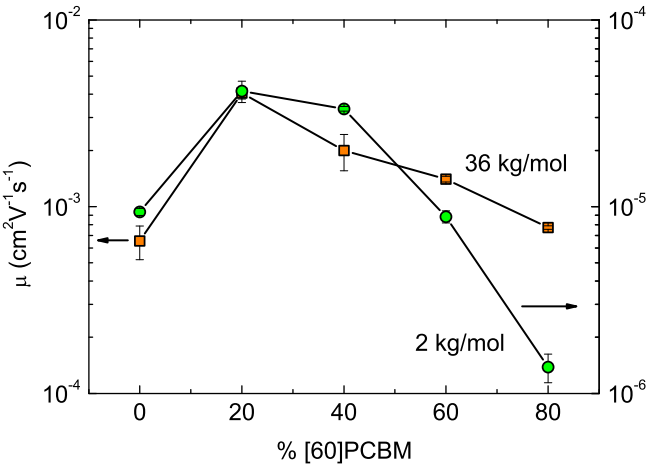

Fig. 3. Hole mobility as a function of stoichiometry for two different molecular weights of APFO-3 blended with [60]PCBM.

Depending on the particular theoretical framework used, different interpretations of the mobility enhancement and stoichiometry independent energetic disorder are possible, but in the context of a Miller–Abrahams type jump rate [9,14] the only explanation for the increased hole mobility in the APFO-3:[60]PCBM blends is an increased site density or an increase in the electronic wave function overlap. The decrease in blend hole mobility seen in Fig. 3 is likely due to site dilution which is quite plausible considering the high solubility of [60]PCBM in APFO-3 [15], and the initial increase in hole mobility should then be due to enhanced electronic coupling between sites.

There is a kink followed by a negative temperature dependence for some of the materials in Figs. 1 and 2. For hole mobilities in pure polymers, and presumably also for the APFO-3 based blends, this corresponds to the glass transition temperature. The glass transition temperature of the high molecular weight APFO-3 is too high to be observed in these measurements, but the low molecular weight values are included in Fig. 2. Interestingly enough, there is no trace of the glass transition temperature in the TQ-1:[70]PCBM blends. The pure TQ-1 glass transition temperature for the molecular weight range and layer thickness used in Fig. 1 is about 363 K, which is almost exactly at the kink in the hole mobility; while for instance a 1:1 blend has its transition close to 346 K where there is absolutely no trace of it in the electrical measurements.

Both TQ-1 and APFO-3 thus have the hole transport in PCBM blends confined to the polymer phase and show hole mobility enhancement upon the addition of PCBM for a relatively wide stoichiometry range. Physically, however, the nature of the enhancements are fundamentally different as it is due to induced ordering in the TQ-1 case, while it is due to some other form of interaction, quite possibly an increased inter-site coupling, in the APFO-3 case. One proposed mechanism for energetic disorder reductions in MDMO-PPV:[60]PCBM blends is through intercalation of PCBM in the polymer phase [16]. TQ-1, like MDMO–PPV, has a straight backbone and an asymmetric monomer unit, and the initially decreasing and then increasing energetic disorder upon the addition of increasing amounts of [70]PCBM to the system is consistent with a similar mechanism.

Although not necessarily obvious from Fig. 1, there seems to be systematic behavior beyond the energetic disorder also in the electron mobilities of TQ-1:[70]PCBM blends. The electron mobility has a maximum in the 50–60% PCBM range and the relative magnitude of this is always about one order of magnitude. On an absolute scale there are more than two orders of magnitude in electron mobility difference between blends based on different TQ-1 batches. That the electron mobilities in blends are dependent on the TQ-1 batch is surprising considering that the electron transport is confined to the [70]PCBM phase. Fundamentally however, there are many similarities between the hole transport in the APFO-3:[60]PCBM blends and the electron transport in the TQ-1:[70]PCBM blends since in both cases there is a predictable variation in mobility, pure material and blends share the same energetic disorder, and blends can exhibit higher mobilities than the pure materials. Even the stoichiometries of the mobility maxima are very similar for the two systems at about 40% [2] of the non transport participating phase.

Whether the absolute variations in electron mobilities of the TQ-1:[70]PCBM blends are real or some sort of measurement related artifact is an open question. There are no differences in the usually mobility sensitive fill factor between solar cells based on the different batches of TQ-1 and there are known issues with FETs that could be responsible for the observed behavior. Like other materials [17], these blends display active layer thickness dependent FET mobilities. For APFO-3 the typical blend behavior is shown in Fig. 4. It can be shown through the use of different solvents that this is unrelated to the spinodal decomposition that can occur in the APFO-3:[60]PCBM system [15]. The generally good correlation between FET hole mobility measurements on thick films and hole mobility measurements through other techniques indicate that, at least for the holes, reproducible results that accurately reflects properties like stoichiometry can be obtained. Electron mobilities are more difficult since there is no convergence to a specific number; the electron currents

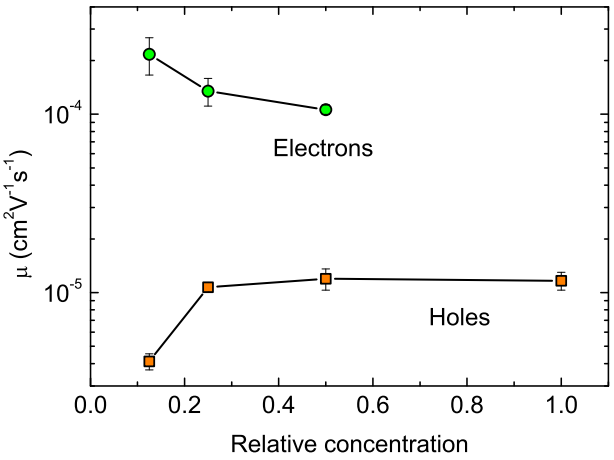

Fig. 4. Mobility versus spin-coating solution concentration for a 4:6 APFO-3:[60]PCBM blend. Higher concentrations give thicker films. The thickest films are close to 80 nm. The molecular weight, and thus hole mobility, is very low for this particular batch of APFO-3. For most molecular weights the hole mobility is higher than the electron mobility in this type of blend.

simply vanish as the thickness increases. This is the reason for the absence of APFO-3:[60]PCBM temperature dependence data and it might, but this is unlikely, explain the batch related variations in the TQ-1:[70]PCBM blends. Compared to APFO-3 there appears to be only very minor effects from the active layer thickness in TQ-1 based devices and electron currents are always visible. A more probable explanation is that there are some impurities present in TQ-1 that mainly influences electron conduction in the FET structure. All devices investigated here are intended to have a thick enough active layer to be in the regime where the thickness dependence is very weak. Different explanations for the active layer thickness dependence in FETs based on crystallization and morphology has been proposed [17], but so far fails to explain the behavior in Fig. 4.

Although it is difficult to measure electron mobilities with FETs in APFO-3:PCBM blends it can still be done in thin films. Such measurements are thickness sensitive and are hard to reproduce. Nevertheless, the available data agree well with an increase in electron mobility with increasing PCBM fraction just as observed with other techniques [2], and there is nothing that indicate that the electron mobility in APFO-3:[60]PCBM blends should depend on the particular batch of polymer. Again, just as for the hole transport, there is a pronounced difference between APFO-3 and TQ-1 based blends.

4. Conclusions

It has been shown that the electron and hole charge transport in the two investigated polymer:fullerene blends is confined to the respective expected and intended phases, and that several different mobility stoichiometry dependencies are possible; ordering induced variations, interaction with enhancement and site dilution, and a monotonous increase with increasing phase fraction. It has also been shown in the literature that simple site dilution without enhancement is possible [18].

These measurements represent a macroscopic average of the microscopic charge transport. Since the site dilution is macroscopically visible and influenced by molecular weight it is quite plausible that percolation problems might arise locally. For applications such as solar cells where charges are introduced everywhere throughout the active layer this might be a problem. A charge generated on a low mobility site will have a much higher probability of recombining without reaching the electrodes. The amount of low mobility sites is higher for low molecular weight materials and probably also for low molecular weight fractions in distributions. This might be one contribution to the decrease in performance with decreasing molecular weight that has been reported but not fully explained through absorption or charge separation [13,19]. Based on this it is possible that materials like TQ-1 in its [70]PCBM blend might be better suited for photovoltaic applications since there is no evidence of transport site dilution.

Acknowledgements

The author thanks S. Hellström, E. Wang and M.R. Andersson for the supply of TQ-1 and APFO-3, and C Müller for glass transition temperature determinations. The author would also like to thank O. Inganäs for fruitful discussions. This work was funded by the Swedish Energy Agency through the Morphoso project.

References

[1] D.J.D. Moet, P.d. Bruyn, J.D. Kotlarski, P.W.M. Blom, Organic Electronics 11 (2010) 1821.
[2] L.M. Andersson, F.L. Zhang, O. Inganas, Applied Physics Letters 91 (2007) 071108.
[3] E. Wang, L. Hou, Z. Wang, S. Hellström, F. Zhang, O. Inganas, M. R. Andersson, Adv. Mat., doi:10.1002/adma.201002225.
[4] K.G. Jespersen, F.L. Zhang, A. Gadisa, V. Sundstrom, A. Yartsev, O. Inganas, Organic Electronics 7 (2006) 235.
[5] M. Lenes, G.J.A.H. Wetzelaer, F.B. Kooistra, S.C. Veenstra, J.C. Hummelen, P.W.M. Blom, Advanced Materials 20 (2008) 2116.

[6] A. Gadisa, X.J. Wang, S. Admassie, E. Perzon, F. Oswald, F. Langa, M.R. Andersson, O. Inganas, Organic Electronics 7 (2006) 195.
[7] L.M. Andersson, O. Inganas, Organic Electronics 8 (2007) 423.
[8] L.M. Andersson, W. Osikowicz, F.L.E. Jakobsson, M. Berggren, L. Lindgren, M.R. Andersson, O. Inganas, Organic Electronics 9 (2008) 569.
[9] H. Bassler, Physica Status Solidi B – Basic Research 175 (1993) 15.
[10] Z.G. Yu, D.L. Smith, A. Saxena, R.L. Martin, A.R. Bishop, Physical Review Letters 84 (2000) 721.
[11] H.L. Gomes, P. Stallinga, M. Colle, D.M. de Leeuw, F. Biscarini, Applied Physics Letters 88 (2006) 082101.
[12] R. Coehoorn, W.F. Pasveer, P.A. Bobbert, M.A.J. Michels, Physical Review B 72 (2005) 155206.
[13] C. Muller, E.G. Wang, L.M. Andersson, K. Tvingstedt, Y. Zhou, M.R. Andersson, O. Inganas, Advanced Functional Materials 20 (2010) 2124.
[14] A. Miller, E. Abrahams, Physical Review 120 (1960) 745.
[15] S. Nilsson, A. Bernasik, A. Budkowski, E. Moons, Macromolecules 40 (2007) 8291.
[16] C. Melzer, E.J. Koop, V.D. Mihailetchi, P.W.M. Blom, Advanced Functional Materials 14 (2004) 865.
[17] X.Y. Tian, Z. Xu, S.L. Zhao, F.J. Zhang, G.C. Yuan, J. Li, Q.J. Sun, Y. Wang, X.R. Xu, Chinese Physics B 19 (2010) 018103.
[18] L.M. Andersson, O. Inganas, Applied Physics Letters 88 (2006) 082103.
[19] D.J.D. Moet, M. Lenes, J.D. Kotlarski, S.C. Veenstra, J. Sweelssen, M.M. Koetse, B. de Boer, P.W.M. Blom, Organic Electronics 10 (2009) 1275.
[20] A. Gadisa, F.L. Zhang, D. Sharma, M. Svensson, M.R. Andersson, O. Inganas, Thin Solid Films 515 (2007) 3126.

Organic Electronics 12 (2011) 306–311

Contents lists available at ScienceDirect

Organic Electronics

journal homepage: www.elsevier.com/locate/orgel

Organic thin film structures for high-sensitivity imaging of contact stress distributions

X.A. Cao *, Z.Y. Jiang, Y.Q. Zhang

Department of Computer Science and Electrical Engineering, West Virginia University, Morgantown, WV 26506, USA

ARTICLE INFO

Article history:
Received 25 October 2010
Received in revised form 20 November 2010
Accepted 21 November 2010
Available online 2 December 2010

Keywords:
Organic light-emitting diode
Tactile sensor
Electroluminescence
Piezoresistance

ABSTRACT

We studied the responses of the electrical and optical characteristics of organic light-emitting diodes (OLEDs) with green fluorescent and phosphorescent dyes doped in a polymer matrix to compressive stresses. The phosphorescent OLED converted stresses into measurable and reversible changes in both current density and electroluminescence (EL) intensity. The current showed a nearly linear characteristic response with sensitivity up to 205 μA kPa^{-1}, whereas EL decreased by over three orders of magnitude at 107 kPa. In contrast, the fluorescent OLED exhibited much smaller stress-induced modulations in current and light intensity, and the responses were saturated at stresses above 26 kPa. The discrepancy has been attributed to stress-enhanced back exciton energy transfer between guest and host molecules, which quenches the EL of the phosphorescent OLED, but has a much smaller impact on the performance of the fluorescent OLED.

© 2010 Elsevier B.V. All rights reserved.

1. Introduction

Tactile sensors have gained renewed interest as the level of sophistication in the applications of humanoid robotics and minimal invasive surgery increases [1–7]. Most robotic systems incorporate binary touch sensors that can distinguish between touch and no touch. To improve the manipulative capabilities of robotic hands, more sophisticated tactile sensors that can replicate the sensation of touch are needed [1]. That would require the development of a device that can be mounted on a curved surface and sense a distribution of contact stress as low as 10 kPa at a high spatial resolution of about 40 μm over a contact area of ~1 cm^2 [2]. Many technologies have been explored for tactile sensing, including conducting elastomers [3], piezoresistive materials [4,5], and micro-electro-mechanical systems [6]. However, their use in dexterous hands are hampered due to two limitations: (i) poor spatial resolution lagging by one order of magnitude compared to a human finger; and (ii) strain-induced nonuniform background signals in devices built on large curved surfaces due to the lack of flexibility. Recently, Maheshwari et al. [7] reported a new multilayer device structure consisting of metal and semiconducting nanoparticles. The device was capable of imaging stress distributions with a spatial resolution of ~40 μm, and showed significant promise for tactile sensing.

Organic materials are flexible and sensitive to external stresses. Upon compression, their resistivity may change dramatically due to reduced intermolecular distance and increased orbital overlap which lead to higher rates of electron transfer between neighboring molecules [8,9]. This sensitive piezoresistive response to deformation makes them a promising type of materials for pressure sensing applications [10]. In addition, many small-molecule organic materials have superior fluorescent or phosphorescent properties, and have been used to develop high-efficiency organic light-emitting diodes (OLEDs) [11–16]. The quantum efficiency of OLEDs is largely dependent upon carrier tunneling and energy transfer processes, whose rates are strong functions of the intermolecular distance [11–15]. Therefore, organic thin film structures may response to applied forces with changes in current density as well as

* Corresponding author. Tel.: +1 304 2939684; fax: +1 304 2938602.
E-mail address: xacao@mail.wvu.edu (X.A. Cao).

1566-1199/$ - see front matter © 2010 Elsevier B.V. All rights reserved.
doi:10.1016/j.orgel.2010.11.019

luminescent emission. Given these unique behaviors, along with easy fabrication and compatibility with flexible substrates, it is possible to use organic thin films to build a new type of tactile sensors capable of high-resolution imaging of stress distributions. In this work, we explore the applicability of fluorescent and phosphorescent OLED structures as tactile sensing devices by demonstrating their sensitive and repeatable responses to compressive stresses with changes in current density as well as electroluminescence (EL) intensity.

2. Experimental

The OLED structures were fabricated on glass substrates with pre-patterned indium-tin-oxide (ITO) (sheet resistance ~15 Ω/□). The substrates were first cleaned in sequence in acetone, ethanol, and de-ionized water, and then exposed to oxygen plasma for 5 min. The light-emitting layers (EML) were prepared by spin coating a mixture of phosphorescent fac-tris(2-phenylpyridinato-*N*, C2′) iridium(III) [Ir(ppy)$_3$] or fluorescent Tris(8-hydroxyquinolinato)aluminium (Alq$_3$), 4,4′-*N*, *N*′-dicarbazole-biphenyl (CBP), and polycarbonate (PC) dissolved in chloroform (10 mg mL^{-1}) at 3000 rpm for 1 min. Here CBP acts as a host material and PC is used as a polymer matrix to enhance the device robustness. The wt% ratio of the mixtures was 20:50:30. The thickness of the coated films was about 60 nm. The samples were then transferred to a high-vacuum thermal evaporation system with a base pressure of ~10^{-8}τ, and a 20 nm-thick 2,9-dimethyl-4,7-diphenylphenanthroline (BCP) hole blocking layer and 15 nm-thick Alq$_3$ electron transport layer were sequentially deposited at rates of ~0.1 nm s^{-1}. Finally, a 0.5 nm-thick LiF and 120 nm-thick Al cathode were deposited on the organic films through a shadow mask, which defined the active area of the OLEDs to be 3 × 3 mm^2. Under forward injection, the OLEDs exhibited green EL from Ir(ppy)$_3$ or Alq$_3$ with a brightness at 5 mA cm^{-2} of 184 and 169 cd m^{-2}, respectively. To characterize device responses to compression, forces were applied uniformly to the OLEDs through a 3 × 3 mm^2 Si sample placed atop the Al cathode using a probe tip attached to a micropositioner, and were measured by an electronic precision balance with 0.1 g readability. The current–voltage (I–V) characteristics of the OLEDs under different stresses were measured using an Agilent 4156C semiconductor parameter analyzer. The EL behaviors at different fixed currents or voltages were recorded in air from the glass side using an Ocean Optics spectrometer. The schematic diagram of the experimental apparatus is shown in Fig. 1. The maximum stress was limited to ~700 kPa, under which the deformation of the Si piece can be neglected.

3. Results and discussion

Fig. 2 shows the forward I–V characteristics of the Ir(ppy)$_3$-based phosphorescent OLED under different stresses. As seen, the current density increases with a remarkably high sensitivity as the stress is raised. A small stress of 16 kPa leads to an increase in the low-bias current by

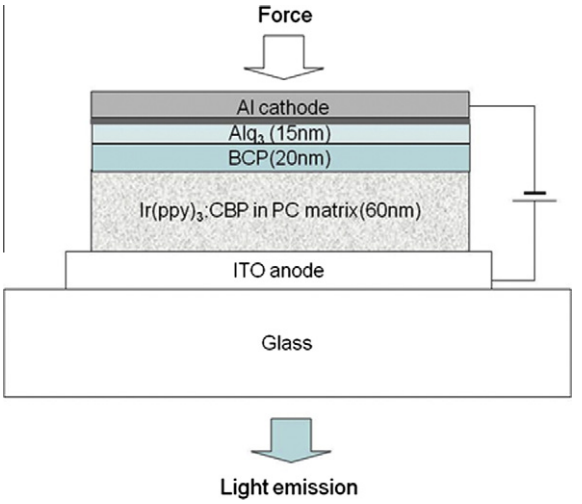

Fig. 1. Schematic diagram of the experimental apparatus for stress-sensing measurements.

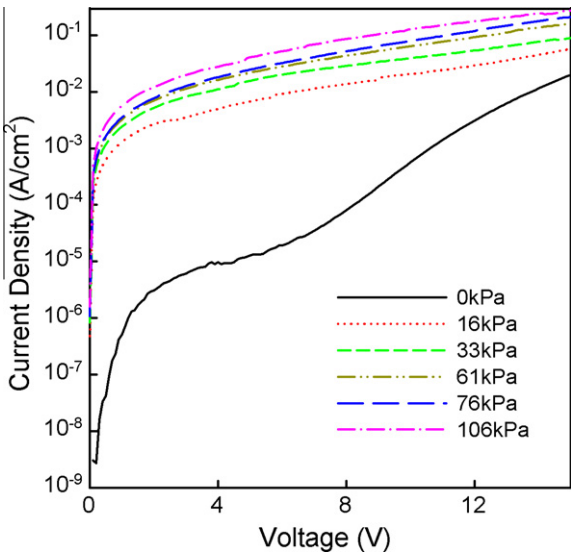

Fig. 2. Forward *I–V* characteristics of a green phosphorescent OLED under different compressive stresses.

more than two orders of magnitude. The influence of stress on the current density measured at three different fixed voltages is displayed in Fig. 3(a). At all voltages, the current shows a rapid and nearly linear increase with increasing stress over the entire range from 0 to 107 kPa. The current sensitivity varies from 94 to 205 μA kPa^{-1} as the voltage is changed from 10 to 14 V. The current response of the Alq$_3$-based fluorescent OLED is quite different, as seen in Fig. 3(b). At a constant bias, the current initially increases rapidly with increasing stress, but tends to saturate above 26 kPa. The current sensitivities in the low stress region are ~38–78 μA kPa^{-1}, which are still several times lower than that of the phosphorescent OLED. On the basis of the fact that two OLEDs with the same matrix/host materials

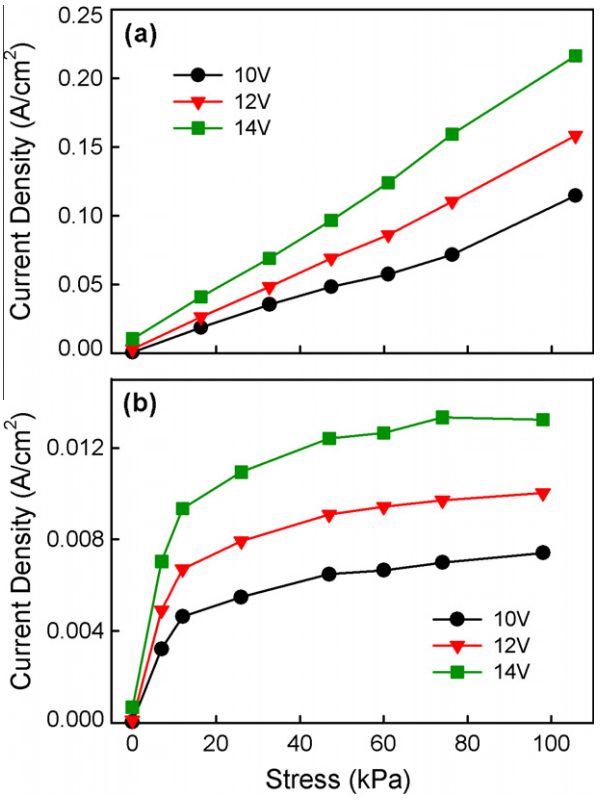

Fig. 3. Stress-dependent currents in (a) a green phosphorescent OLED and (b) a green fluorescent OLED measured at different fixed biases.

showed very different yet repeatable current responses to compression, we may rule out that localized shunt leakage paths are responsible for the current changes.

Since the applied stresses are relatively small, they can reduce the intermolecular spacing, but may not change the molecular geometry. Therefore, the stress-induced changes in the electronic states and energy levels should be minimal. This is supported by that fact that luminescence spectra of the OLEDs remained unchanged under compression. The observed current responses thus reflect changes in the electrical conductivity of the organic films rather than reduced barriers for charge injection. When a uniaxial stress is applied and the current flows along the same direction, the longitudinal piezoresistance coefficient π_l^σ can be defined as the relative change in electrical conductivity per unit stress:

$$\pi_l^\sigma = \frac{1}{X}\frac{\Delta\sigma}{\sigma_0} = \frac{1}{X}\frac{\Delta J}{J_0}$$

where σ_0 and J_0 are the conductivity and current density under zero stress, respectively, and X is the stress. π_l^σ for the phosphorescent OLED structure is found to be nearly independent of the stress and has a value of $\sim 2 \times 10^{-3}$ Pa^{-1} at 10 V. This value is more than two orders of magnitude greater than that of typical conjugated polymers [5] and five orders of magnitude greater than that of Si nanostructures [17]. We attribute the sensitive piezoresistive response to increased charge mobilities resulted from stronger intermolecular interaction in the compressed films. Young's moduli of PC and small molecular materials are on the order of GPa. Therefore, our results suggest that even a small percent of deformation may lead to a significant change in the rates of charge transfer between neighboring molecules through hopping. The stress of a human finger applies to sense texture and shape is typically on the order of 10–40 kPa. In our devices, an applied stress as low as 6 kPa can produce a noticeable current change, suggesting that the devices are capable of sensing touch on a par with a human finger. Compared to the fluorescent OLED, the phosphorescent OLED is clearly better suited for this application due to its high sensitivity over a wider stress range.

The EL of the phosphorescent OLED exhibited even more sensitive but opposite response to the applied forces. Fig. 4(a) illustrates the EL spectra measured at a fixed current of 6 mA from the OLED under various stresses. While the peak position and spectrum shape stay constant, the light intensity decreases sharply with increasing stress. A similar trend of EL evolution has been observed for the fluorescent OLED (Fig. 4(b)), though the magnitude of stress-induced quenching is much smaller. Fig. 5 plots the dependences of light intensity of the two OLEDs on stress at different currents. As with the current response, the EL of the phosphorescent OLED exhibits a much higher sensitivity upon compression. At 6 mA, the light intensity shows a monotonic decrease by over three orders of magnitude as the stress varies from 0 to 107 kPa. In contrast,

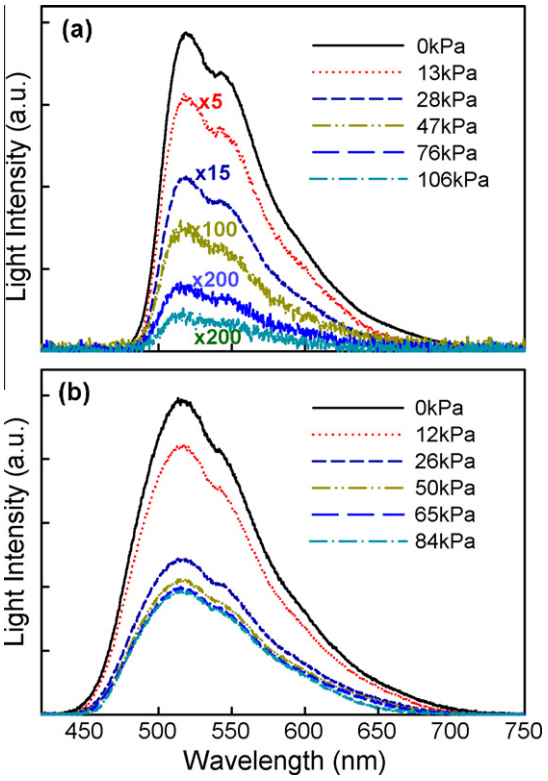

Fig. 4. EL spectra of (a) a green phosphorescent OLED and (b) a green fluorescent OLED recorded at 6 mA under different compressive stresses.

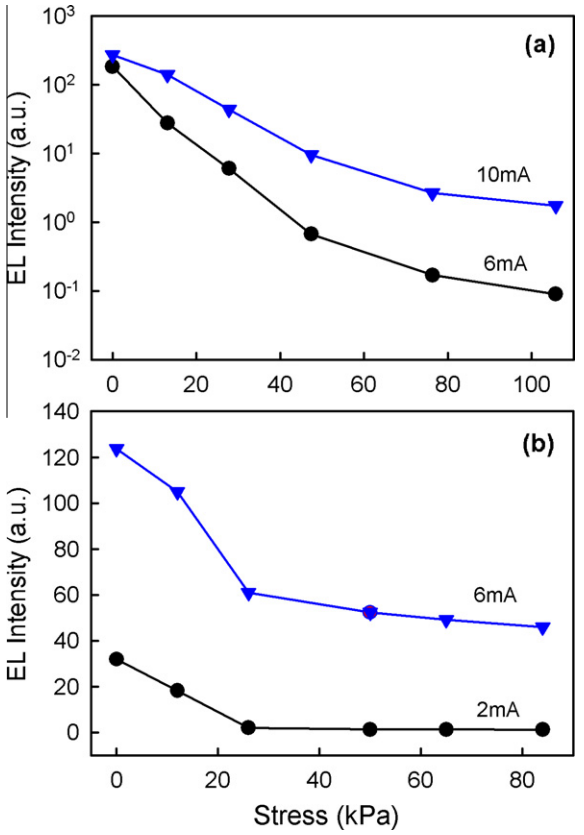

Fig. 5. Stress-dependent EL intensity of (a) a green phosphorescent OLED and (b) a green fluorescent OLED recorded at different fixed currents.

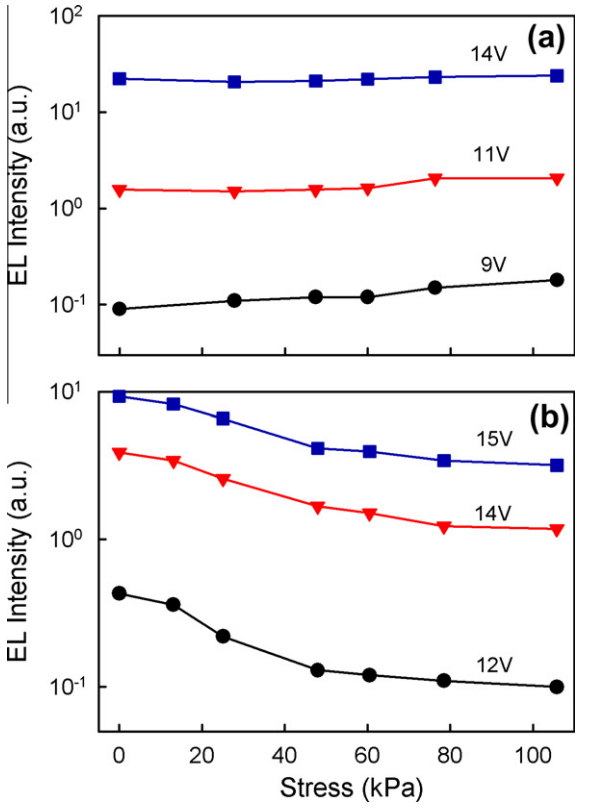

Fig. 6. Stress-dependent EL intensity of (a) a green phosphorescent OLED and (b) a green fluorescent OLED recorded at different fixed voltages.

the optical power of the fluorescent OLED drops by only 50% at 26 kPa and essentially stabilizes at higher stresses. These results suggest that the phosphorescent OLED may convert local stresses into both measurable electrical and optical signals with a high sensitivity, and is thus capable of direct imaging of contact stress distributions.

The stress-induced modulations in the EL intensity while fixing the voltage have also been measured. Interestingly, at a constant voltage, compression only causes small changes in the light intensity of the phosphorescent OLED, as seen in Fig. 6(a). Apparently, the EL quenching of the OLED under stress is largely offset by stress-induced increase of injection current at a constant bias. The light intensity of the fluorescent OLED under a constant bias decreases slightly with increasing stress, as seen in Fig. 6(b). In this device, EL quenching is a more dominant response to stress compared to the piezoresistance effect.

The vastly different optical responses of the two OLEDs to stress are believed to be associated with their different luminescent mechanisms. In the phosphorescent OLED, the excited singlet state of the $Ir(ppy)_3$ molecules is quickly and efficiently transferred to the triplet state via intersystem crossing. The EL originates from triplet excitons relaxing radiatively to the singlet ground state, whereas the radiative decay of singlets is negligible [11–16]. In contrast, despite that injection leads to the formation of both singlet and triplet states on Alq_3 molecules, the EL of the fluorescent OLED is limited to the radiative decay of singlet excitons that conserves spin symmetry [11,12]. Since the lifetime of the emitting triplet state of Ir(III) complexes is much longer than that of singlet excitons on fluorescent molecules, the EL of the phosphorescent OLED is expected to be much more sensitive to back energy transfer from triplets on the guest to triplets on the host molecules via a Dexter process. Dexter transfer is a short range process where excitons diffuse from donor to acceptor sites via intermolecular electron exchange [18]. The transfer rate is exponentially dependent on the donor–acceptor separation R_{DA}, and is proportional to the expression below [16]:

$$K_{ET} \propto \exp(-2R_{DA}/L),$$

where L is the sum of the van-der Waals radii of the donor and acceptor. Under normal conditions, the back energy transfer from $Ir(ppy)_3$ to CBP is insignificant due to relatively large R_{DA} as well as the fact that the process is endothermic given the higher energy of the host triplet ($E_{T,CBP}$ = 2.56 eV) compared to that of the guest triplet state ($E_{T,Ir(ppy)3}$ = 2.42 eV) [19]. However, as the intermolecular spacing is squeezed, its rate may increase substantially, leading to weaker confinement of excitons on the guest. When the film is further compressed, the back energy transfer followed by nonradiative decay at defects may become the major energy dissipation process. On the other hand, increased triplet–triplet back energy transfer has

no impact on the efficiency of the Alq_3 emission. Although Dexter transfer also permits singlet–singlet transfer, it only has a limited influence on the EL of the Alq_3 OLED due to the fast decay (~1 ns) of fluorescent dyes. To validate our hypothesis that back energy transfer is the physical origin of the dramatic EL quenching in the $Ir(ppy)_3$-based OLED, we characterized the performance of a phosphorescent OLED with 20 wt% Bis(1-(phenyl)isoquinolinato-*N*, C^2) iridium acetylacetonate [$Ir(piq)_2(acac)$], a red phosphorescent dye, doped in CBP. Its EL spectrum peaks at 632 nm with a brightness of 189 cd m^{-2} at 5 mA cm^{-2}. The triplet state energy of $Ir(piq)_2(acac)$ is 2.0 eV. It is therefore expected that the back energy transfer rate is much lower than that in the green phosphorescent OLED, leading to much weak responses to compression. Indeed, for stresses below 100 kPa, we observed little changes in current and EL intensity. The red OLED only exhibited noticeable yet moderate optical responses to stresses greater than 160 kPa at a constant current, as seen in Fig. 7.

Another factor which may contribute to the unexpected EL quenching in the phosphorescent OLED is the compression-enhanced concentration quenching effect. It is known that phosphorescent OLEDs suffer from self-quenching when the concentration of the phosphorescent molecules is high [12–15]. The efficiency of OLEDs with $Ir(ppy)_3$ doped in CBP peaks at ~6 wt% of $Ir(ppy)_3$ and decreases rapidly as the doping level is increased [12]. In OLEDs with a neat $Ir(ppy)_3$ EML, the maximum EL quenching magnitude is found to be ~90% [15]. Previous studies have suggested that the quenching effect originates from long-range Förster energy transfer between $Ir(ppy)_3$ molecules [13–15], whose rate is proportional to $(R_0/R)^6$, where R_0 is the Forster radius (on the order of several nanometers) and R is the intermolecular distance. Therefore, compressing the organic film could lead to increased concentration quenching of EL. If concentration quenching is indeed one of the underlying mechanisms of stress-induced EL quenching in the phosphorescent OLED, it would play a larger role as the $Ir(ppy)_3$ concentration is reduced to 6%, where EL is the most sensitive to changes in the dopant concentration resulted from compression. To test this assumption, we compared the responses of OLEDs with $Ir(ppy)_3$ doping of 6 and 20 wt% under the same applied stresses. As a result of reduced concentration quenching, the OLED with 6 wt% $Ir(ppy)_3$ is 5× brighter. Fig. 8 shows the current density at a fixed bias of 12 V and EL intensity at a constant current of 7 mA of the two OLEDs, as a function of stress. The OLED doped with 6 wt% $Ir(ppy)_3$ displays a similar linear current response with slightly lower sensitivity. Another finding is that the magnitudes of stress-induced EL quenching in the two OLEDs are comparable, indicating that concentration quenching may play a minimal role.

Since the device fabrication consists of simple spin casting and evaporation deposition, the phosphorescent OLED structure may be made on large curved surfaces of flexible substrates to replicate sensation of touch. The excellent flexibility of organic and polymer materials ensures a high spatial resolution of the OLEDs required for tactile sensing [7]. To test the robustness of this type of devices, we studied the stability of the OLED with 6 wt% $Ir(ppy)_3$ under fixed stresses and biases. Fig. 9(a) and (b) illustrates its current responses recorded at a fixed bias of 12 V over short testing periods under different constant stresses and a step-modulated stress of 55 kPa, respectively. Even though the measurements were carried out in air without device encapsulation, the current density in the deformed device at a fix bias was nearly constant. During the cycle testing, as the stress was alternatively applied and released, reversible changes in current were observed, suggesting that the deformation of the organic film is reversible with minimal hysteresis. The abrupt changes in current reflect rapid responses of the device to applied forces. These results demonstrate very good repeatability and stability of the phosphorescent OLED required for stress sensing applications.

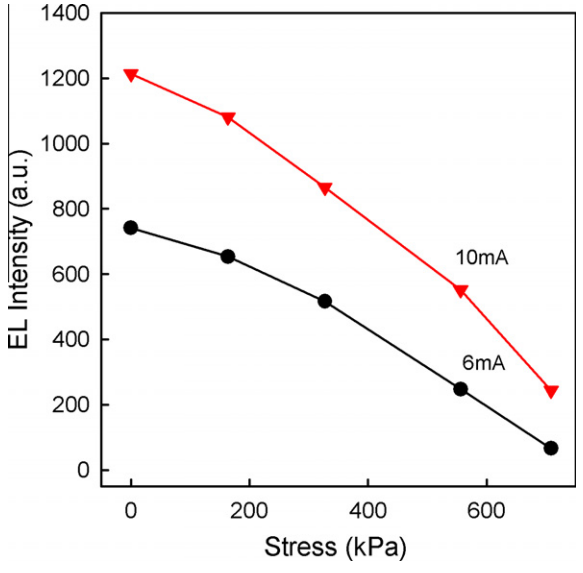

Fig. 7. Stress-dependent EL intensity of a red phosphorescent OLED recorded at different fixed currents.

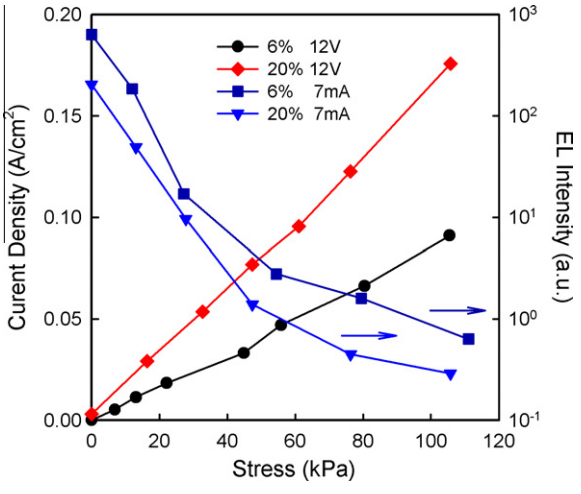

Fig. 8. Stress-dependent current density and light output power of green phosphorescent OLEDs doped with 6 and 20 wt% $Ir(ppy)_3$ measured at different fixed voltages or currents.

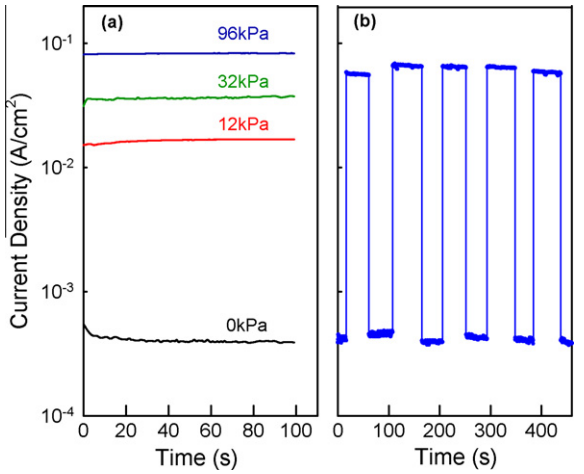

Fig. 9. Current responses of a green phosphorescent OLED recorded at a fixed bias of 12 V under (a) different constant stresses and (b) a step-modulated stress of 55 kPa.

4. Conclusion

In summary, we compared the responses of the electrical and optical characteristics of fluorescent and phosphorescent OLEDs with luminous dyes doped in a polymer matrix to compressive stresses. The phosphorescent OLED converted a stress as low as 6 kPa into measurable and reversible changes in both current density and EL intensity. The current showed a nearly linear characteristic response with sensitivity up to 205 μA kPa^{-1}, whereas EL decreased by over three orders of magnitude. In contrast, the stress-induced modulations in current and light intensity in the fluorescent OLED were much smaller and saturated at stresses above 26 kPa. The discrepancy has been explained by that stress-enhanced nonradiative back energy transfer between guest and host molecules severely quenches the EL of the phosphorescent OLED, but has a minimal impact on the performance of the fluorescent OLED. It is expected that similar phosphorescent OLEDs built on large curved surfaces may directly image stress distributions and sense touch on a par with a human finger.

Acknowledgment

This work was partially supported by a research seed grant from the NASA West Virginia EPSCoR Program.

References

[1] V. Maheshwari, R. Saraf, Angew. Chem. Int. Edit. 47 (2008) 7808.
[2] S.A. Mascaro, H.H. Asada, IEEE Trans. Robot. Autom. 17 (2001) 698.
[3] S.P. Lacour, C. Tsay, S. Wagner, IEEE Electron. Dev. Lett. 25 (2004) 792.
[4] D.D. Rossi, F. Carpi, E.P. Scilingo, Adv. Colloid Interface 116 (2005) 165.
[5] G.Y. Zhong, Y.Q. Zhang, X.A. Cao, IEEE Electron. Dev. Lett. 30 (2009) 1137.
[6] J. Engel, J. Chen, C. Liu, J. Micromech. Microeng. 13 (2003) 359.
[7] V. Maheshwari, R.F. Saraf, Science 312 (2006) 1501.
[8] M. Chandrasekhar, S. Guha, W. Graupner, Adv. Mater. 13 (2001) 613.
[9] H.G. Drickamer, C.W. Frank, Annu. Rev. Phys. Chem. 23 (1972) 39.
[10] G.Y. Zhong, Y. Liu, J. Song, Q. Zhao, Y.S. Li, F.Y. Li, J. Phys. D: Appl. Phys. 41 (2008) 205106.
[11] Z. Li, H. Meng (Eds.), Organic Light-Emitting Materials and Devices, Taylor and Francis, 2007 (Chapter 3).
[12] M.A. Baldo, S. Lamansky, P.E. Burrows, M.E. Thompson, S.R. Forrest, Appl. Phys. Lett. 75 (1999) 4.
[13] G.Y. Zhong, Y.Q. Zhang, X.A. Cao, Org. Electron. 11 (8) (2010) 1338.
[14] S. Reineke, G. Schwartz, K. Walzer, M. Falke, K. Leo, Appl. Phys. Lett. 94 (2009) 163305.
[15] Y.Q. Zhang, G.Y. Zhong, X.A. Cao, J. Appl. Phys. 108 (2010) 083107.
[16] W. Klopffer, in: J. Mort, G. Pfister (Eds.), Electronic Properties of Polymers, Wiley, New York, 1982 (Chapter 5).
[17] J.X. Cao, X.G. Gong, R.Q. Wu, Phys. Rev. B 75 (2007) 233302.
[18] D.L. Dexter, J. Chem. Phys. 21 (1953) 836.
[19] K. Goushi, R. Kwong, J.J. Brown, H. Sasabe1, C. Adachi, J. Appl. Phys. 95 (2004) 7798.

Organic Electronics 12 (2011) 312–321

Contents lists available at ScienceDirect

Organic Electronics

journal homepage: www.elsevier.com/locate/orgel

Realization of polymer charge pump circuits using polymer semiconductors

Senol Mutlu *, Iskender Haydaroglu, Ali Osman Sevim

Department of Electrical and Electronics Engineering, Bogazici University, 34342 Istanbul, Turkey

ARTICLE INFO

Article history:
Received 28 July 2010
Received in revised form 22 October 2010
Accepted 14 November 2010
Available online 2 December 2010

Keywords:
Charge pump circuit
AC–DC converter
Polymer diode
Poly(3-hexylthiophene)(P3HT)

ABSTRACT

Vertical diodes made of chromium/gold/poly(3-hexylthiophene) (P3HT)/aluminum are used to implement AC–DC charge pump circuits. A single stage polymer charge pump with 470 nF capacitors is able to supply 7.2 V DC to a load of 1 MΩ || 20 pF when an AC signal with a peak value of 10 V is applied. The circuit can be used up to 10 kHz. High turn-on voltages and internal resistances and capacitances of the diodes limit the DC output voltages. The ramp-up time of the circuit built with 10 nF capacitors is 9.4 ms for a 1 kHz, 10 V peak AC signal. Diodes are modeled and simulated in SPICE using space charge limited conduction model. The simulated charge pump circuit produces consistent results with measurements. Performances of air exposed vertical diodes deteriorate under vacuum, prolonged operation at atmospheric conditions and electrical bias stress resulting in blistering, emphasizing the importance of packaging the devices under inert atmosphere. The DC output voltage and the input impedance of the circuit can be adjusted by using multiple stages.

© 2010 Elsevier B.V. All rights reserved.

1. Introduction

Current electronic circuits made of polymer semiconductors may require very high supply voltages in the range of tens of volts [1]. Similarly, micromachined capacitive actuators require voltages in the same high levels [2]. Without a scheme to step up the supply voltages available from a commercial battery, portable applications of polymer semiconductor devices would be impractical. Furthermore, the potential for low cost and high volume fabrication makes polymer semiconductors attractive in a particular area, the polymer RFID tag. In this application, the power necessary for device operation needs to be transmitted wirelessly, in order not to include a battery that would drastically increase the cost of the device. Several approaches for the extraction of DC power from an RF signal are present, and a previous work shows a possible solution with two half-wave rectifiers to constitute the ground and supply rails of the RFID circuitry using diodes made out of pentacene [3]. This design confines the tag supply voltage to the peak-to-peak voltage of the RF signal picked up by the tag antenna, minus twice the turn-on voltage of the diodes, which tend to be high in current polymer electronics. The charge pump method has been evaluated favorably to the half-wave rectifier scheme in RFID applications [4], for the charge pump approach gives more flexibility to designer in many ways. Cascading multiple stages of charge pumps allows the designer to adjust the supply voltage levels as desired and compensate for the large voltage drops across diodes. In addition, the input impedance of a charge pump depends on the number of stages and the loading of the charge pump [5], which allows the designer to perform impedance matching to the antenna that feeds the charge pump, maximizing the extracted power [4]. This leads to the reasoning that charge pump circuits built with polymer semiconductors are worthwhile to explore.

Polymer and organic diode half-wave rectifiers were built in previous literature using P3HT [6,7], as well as other organic/polymer semiconductor materials such as PTAA [8], pentacene [3,9–11], and hybrid p–n junction organic diodes using n-ZnO/(PQT-12) [12], and their AC characteristics were demonstrated. For high performance

* Corresponding author. Tel.: +90 2123597442; fax: +90 2122872465.
E-mail address: senol.mutlu@boun.edu.tr (S. Mutlu).

1566-1199/$ - see front matter © 2010 Elsevier B.V. All rights reserved.
doi:10.1016/j.orgel.2010.11.006

organic semiconductors such as pentacene, 3-dB cut-off frequencies of 15 MHz [9] to 50 MHz [10] were reported for half-wave rectifier topologies, the latter publication demonstrating that organic diodes can be operated at the 13.56 MHz RFID frequency with acceptable performance levels [10]. Half-wave rectifiers fabricated using P3HT, which can be solution-processed at relatively low cost, exhibit lower AC performance on the other hand. Cut-off frequencies between 1–1.8 MHz [7] and 2 MHz [6] were reported for half-wave rectifiers fabricated using this material.

In this work, a charge pump circuit built using regioregular poly(3-hexylthiophene) (rr-P3HT) is investigated, the aim being to meet the demand for high supply voltages in electronic devices fabricated from polymer semiconductors, as well as the possible application of wireless power transmission to polymer electronic devices. The charge pump topology that is featured in this work is shown in Fig. 1. This is a more useful method in generating supply voltages from RF signals, since the design is scalable as opposed to supplying power from a single half-wave rectifier. The number of charge pump stages determines both the DC levels of the output voltage and the input impedance of the charge pump itself.

In the design of the charge pump circuits, an electrical model for fabricated vertical diodes has been used. After the diodes are fabricated, their electrical model parameters are extracted and used in a computer aided design tool, simulation program with integrated circuit emphasis (HSPICE), to investigate the operation of the charge pump circuit. In the models, the environmental effects on the characteristics of polymer diodes are also studied. Since in polymer semiconductor the performances of devices are deteriorated by environmental variables such as oxygen, humidity, ambient temperature [13–15] and electrical bias stress, the parameters of the model are also changed accordingly. Parameter fittings for the model have been done to the vertical diodes using the results of experiments that expose them to the mentioned environmental variables.

This paper is organized in five sections. Section 2 describes the fabrication of lateral and vertical polymer diodes and presents their current–voltage characteristics under various environmental conditions. Section 3 presents the theory and a model for the fabricated vertical diodes to be used in the charge pump circuits. Section 4 explains the operation of the charge pump circuit and gives experimental results for various conditions and compares them to the simulation results. Discussions and conclusion are given in Sections 5 and 6, respectively.

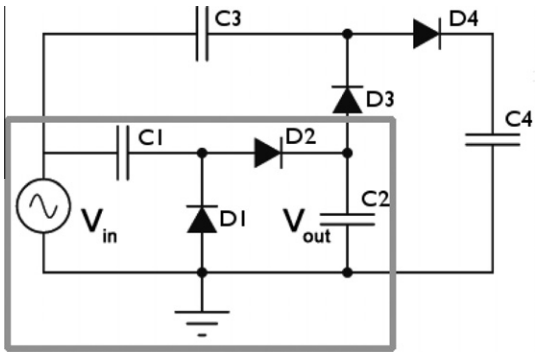

Fig. 1. Schematic representation of a multi-stage AC–DC charge pump. The gray box represents a single cell of a charge pump, the basic building block of a multi-stage design.

2. Polymer diodes

Polymer diodes are the main components of this work. They are fabricated, characterized and modeled before they are used in a charge pump circuit. Since polymer diodes are not stable under ambient conditions and they degrade, they are also tested for their changing performances under ambient conditions to check whether degradations can be modeled and predicted or tolerated in certain circuit applications. For this purpose, two types of diodes have been fabricated and tested; lateral and vertical diodes. The main purpose of the fabrication of the lateral diodes were to study the environmental effects on semiconductor polymers more easily since its active polymer is directly in contact with the environment. Its surface is not covered with a metal film.

2.1. Lateral diodes

2.1.1. Fabrication of lateral diodes

In fabricating lateral diodes, two electrodes of the diodes are fabricated in plane in an interdigitated manner. The aluminum cathode and the silver-epoxy anode are deposited on top of the glass substrate such that the diode, from the top view, resembles a system of interlocking fingers as drawn in Fig. 2. 90 nm thick aluminum is thermally evaporated on a glass substrate and patterned using lithography. Silver electrodes are formed by drop-casting a silver epoxy liquid and then cured on a hotplate at 110 °C. A sharp metal tip with a reservoir filled with silver epoxy is attached to a micromanipulator and is moved to make the silver electrodes between aluminum ones. This limited the gap size between electrodes to 300 μm. The total length of the diode formed by the interdigitated layout is measured to be 10.5 mm and the gap between the electrodes 300 μm. After the deposition of the electrodes, rr-P3HT (from Sigma–Aldrich) solution is deposited by drop-casting and annealed for one hour at 110 °C to evap-

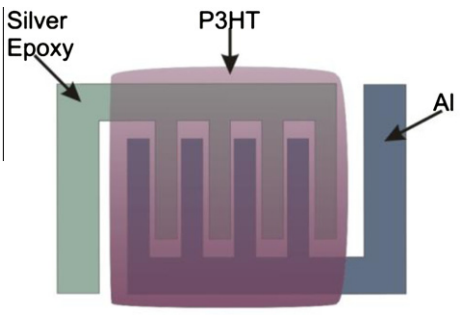

Fig. 2. Top view of the interdigitated lateral diode.

orate solvent. The polymer is dissolved in 1,2,4-trichlorobenzene with a weight concentration of 2.5 mg/ml and filtered through a 0.2 μm pore sized PTFE membrane syringe filter.

2.1.2. Experimental results of lateral diodes

Following fabrication, the lateral diodes stayed at ambient conditions for a day. Then, they are placed into a vacuum chamber and 30 mTorr vacuum is achieved inside the chamber before the characterization of the devices are initiated. DC voltage sweeps are conducted with Keithley semiconductor parameter analyzer (SCS4200) and the current through the diodes are measured at varying time intervals after the start of the vacuuming to investigate the effects of time under sustained vacuum on device performance. Results are summarized in Fig. 3. Vacuum treatment of the lateral diodes resulted in the decrease of both forward and reverse currents, indicating a drop in the parasitic conductivity. This is expected since the vacuum dedopes the semiconductor polymer by removing the atmospheric oxygen inside, which has been absorbed during the fabrication steps done at room conditions. Atmospheric oxygen is known to dope semiconductor polymer, thus create parasitic conductivity [1]. As the vacuum is maintained, reverse current diminishes more rapidly than the forward current, increasing the rectification ratio of the diode. The ratio of the diode's currents at a forward bias of 7 V and a reverse bias of 7 V is around 2 just before the vacuum started. This ratio increases to 240 after 4 h of vacuuming.

After vacuum tests, the chamber pressure is brought to 1 atm by releasing argon gas into the chamber. Being a noble gas, argon is used to eliminate the possibility of P3HT to react with doping agents such as oxygen and water vapor that would have been present had the experiment been conducted at atmospheric conditions. After the desired pressure is obtained, the diodes are heated to varying temperatures and current–voltage measurements are acquired after 5 min of maintaining the desired temperature. This waiting period is needed for the front surface of the glass wafer, where the diodes are, to reach the desired temperature. The results are shown in Fig. 4. Elevated temperatures resulted in a dramatic increase in forward current as well as the rectification ratio in lateral diodes. As theory suggests, the P3HT thin film, when formed, is an amorphous

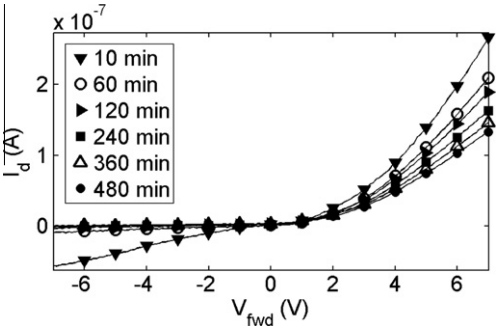

Fig. 3. Change in current–voltage characteristics for lateral diode under vacuum with elapsing time.

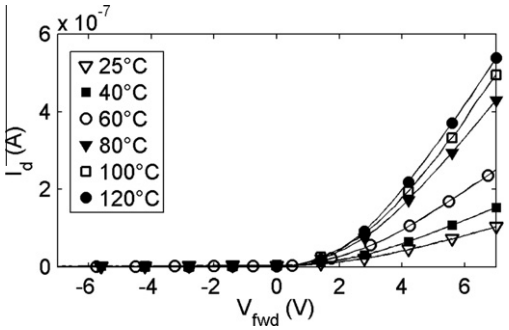

Fig. 4. Lateral diode current–voltage characteristics recorded at various temperatures.

composition of grains of polymer. The charges cannot hop between two neighboring grains unless the energy barrier constituted by the intergrain boundary, called a trap state, is overcome [15,16]. Elevated temperatures causes the excitation of a greater number of these trap states, which enables charges to move across the trap states. The end result is an increase in current density for a given voltage, increasing the performance of the diode. The improvement is not sustained after the temperature is reduced back to room temperature [17]. Therefore, it is determined that annealing of the thin film P3HT does not occur in lateral diodes in the applied temperature range of this work [18]. As a result of heating from 25 °C to 120 °C, the forward current increases from around 100 nA to 540 nA at 7 V forward bias. Similarly, rectification ratio of around 80 at 25 °C increases to 900 at 120 °C.

As observed in the vacuum tests, the rectification ratio of the lateral diode is improved by vacuum treatment, which can be preserved by an adequate packaging of the device following the vacuum treatment. The rectification ratio, which can also be referred to as the on–off ratio, is of vital importance in a charge pump application since a diode that leaks current when it is supposed to behave like an open circuit detracts from the efficiency of the charge pump. Despite the potential performance improvement, the lateral diode can provide small amounts of forward current (around 100 nA) since in this work electrode space is large, around 300 μm, forming a high parasitic resistance in series with the diode. This makes it ineligible for a charge pump application in which the charge pump acts as a current source for resistive current loads in need of about 10 μA. However, this electrode gap can be easily made to around 1 μm if another metal thin film such as Chromium (Cr)/Gold (Au) is evaporated and lithographically patterned. In that case it could conduct more current for the same voltage applied. Nevertheless, vertical diodes whose electrode gap between anode and cathode is the thickness of the polymer, would have less resistive parasitic and can supply more current than lateral diodes. However, one advantage of lateral diode may be that its semiconductor polymer is exposed to the environment directly. Since the semiconducting polymer is not capped with another thin film metal, it can be treated thermally or with vacuum much easily than the packaged one.

2.2. Vertical diodes

2.2.1. Fabrication of vertical diodes

The fabrication of the vertical diodes involves sandwiching the drop casted P3HT layer between two metal layers. While the bottom electrode is deposited by a high vacuum evaporator and patterned by lithography, the top electrode is formed by means of shadow mask evaporation. Alignment errors and the spread of the deposited metal in shadow masking cause deviations from designed device sizing.

The process sequence of the fabrication, as shown in Fig. 5, starts by lithographically patterning the thermally evaporated Cr/Au thin films to form bottom electrodes. Similar to the lateral diode fabrication, P3HT is dissolved in trichlorobenzene with a ratio of 2.5 mg/ml. This solution is drop-casted and is left to dry on the substrate at room conditions for 2 h, resulting in a film thickness of approximately 750 nm. For the deposition of the aluminum electrodes, a shadow mask is prepared from a 50 μm thick stainless steel (SS301) sheet. A photoresist mask is patterned on steel surface using lithography and then steel is isotropically etched using electrochemical etching in 1:7 HCl:DI water solution [19]. A vacuum chamber with a base pressure of 10^{-6} Torr is used to evaporate a 90 nm thick aluminum layer. The shadow mask is aligned perpendicular to the patterned Cr/Au electrodes and evaporation forms orthogonal aluminum electrodes resulting in diodes with active area of 2 mm × 0.5 mm.

2.2.2. Experimental results of vertical diodes

Similar to the lateral diode tests, vertical diodes are subjected to vacuum and elevated temperatures to determine the effects of atmospheric doping and thermal activation on them. Additionally, a set of diodes are operated under atmospheric exposure to observe the degradation of performance that is expected to happen as the P3HT thin film deteriorates.

Diodes tested under atmospheric conditions are kept at these conditions for a week before they are electrically tested. During tests, they continued to get exposed to atmospheric conditions. The results are presented in Fig. 6. The diodes continue to operate without much degradation in forward current up to 60 min after the start of the tests. Forward current is recorded to be around 1.2 mA at 8 V forward bias during this interval of time. The decline in forward current is discernible at 180 min, and after 420 min the forward current suffers drastically. This part of the experiment reveals that operation under atmospheric exposure causes the deterioration of device performance.

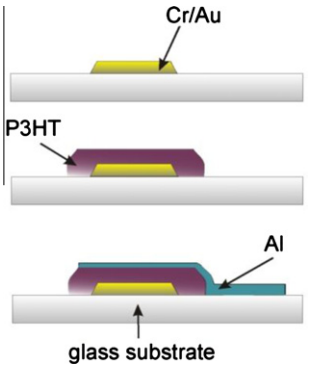

Fig. 5. Fabrication steps for polymer charge pump circuits, from top to bottom: evaporation of Cr/Au contacts, deposition of P3HT, followed by the evaporation of aluminum through a shadow mask.

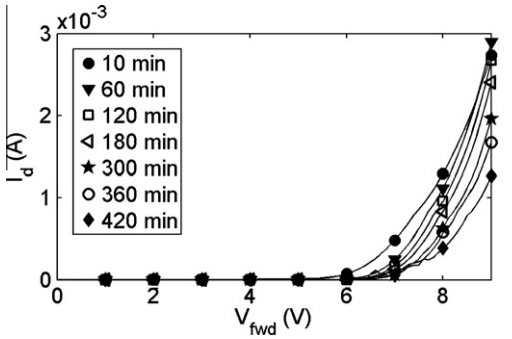

Fig. 6. Current–voltage characteristics of the vertical diode under atmospheric exposure with elapsing time.

Deterioration of the behavior of the diodes is correlated to changes in their physical appearance. The vertical diodes exhibited blistering under the top aluminum cathode of the diode as shown in Fig. 7. The existing bubbles and blisters are inflated with device operation, and new blisters emerge as tests are performed. Similar blistering was reported in P3HT-PEDOT systems [13] and in inkjet printed P3HT devices [14]. The explanation for this phenomenon was identified as the electrolysis of the atmospheric impurities such as water vapor that has dissolved inside the P3HT thin film with electrical bias stress. The resulting gases would try and escape the thin-film, but they would encounter the top electrode, where they form the observed blisters. Blistering mechanism might be a contributing factor in the decrease in diode forward current with time; since the bubbles break the integrity of the P3HT-Al interface where they form, thereby reducing device efficiency.

Vacuum treatment of the vertical diodes with the conditions mentioned at the lateral diode section reveals worse degradation than the atmospheric results. Current–voltage characteristics of the vertical diode just after vacuuming started are shown in Fig. 8. Diodes have been at atmospheric conditions for a day after their successful fab-

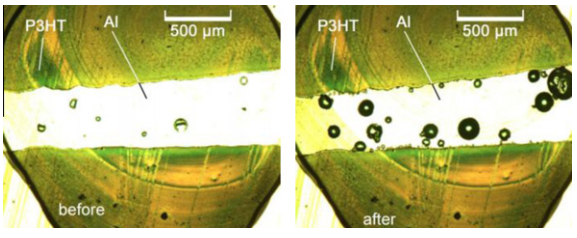

Fig. 7. Before (left) and after (right), operation of vertical diodes under atmospheric conditions.

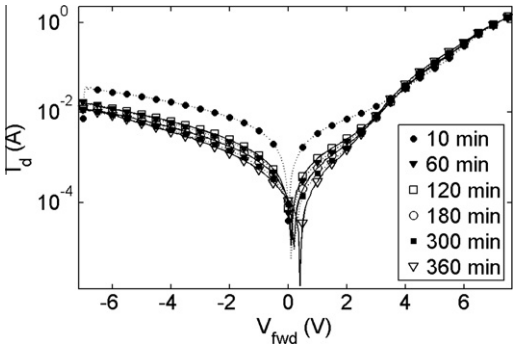

Fig. 8. Semilog plots for the current–voltage characteristics showing the effects of vacuum treatment on vertical diodes with elapsing time.

rication. At the beginning of the tests certain improvement in diode performance occur since the vacuum starts to extract the dopants inside the polymer, thus decreases the leakage currents in the reverse bias. However, the measured current–voltage curves deteriorate after some time. These deviations could be the result of an increasing number of blisters as the device is subjected to electrical bias stress. Severe deterioration on the aluminum surface due to vacuum and operation can be seen in Fig. 9. The blistering observed under vacuum treatment is extensive, resulting in comparatively smaller but far more numerous blisters beneath the top electrode, in contrast with devices tested under atmospheric conditions. A possible explanation for this is that the applied vacuum sucks out the dissolved impurities from the thin-film, collecting a portion of them under the top electrode through which they cannot diffuse away. The applied bias stress causes the electrolysis of these impurities, resulting in the blisters. Since vacuum drives a larger amount of impurities in comparison to the air exposed diodes, the blisters are numerous and cover the layer beneath the top electrode almost entirely. This also explains why these deteriorations are not observed on lateral diodes. Since the top of the lateral diode is not blocked by a thin metal film, vacuum treatment improves the diode performance with time steadily.

This situation for the vertical diodes may be avoided if a slower and gradual increase of vacuum is applied with thermal annealing to give a chance to dissolved impurities to leave the device surface without causing any deformation. Starting vacuum treatment at a lower vacuum value such as 150 Torr and then gradually and slowly increasing the vacuum while keeping the samples at elevated temperatures such as 90–110 °C may avoid blisters on the surface. During this time, the devices should not be operated. After this postfabrication treatment, the devices can be packaged under these conditions [20].

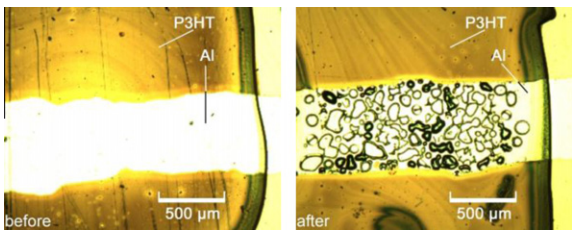

Fig. 9. Before (left) and after (right) operation of vertical diodes under vacuum.

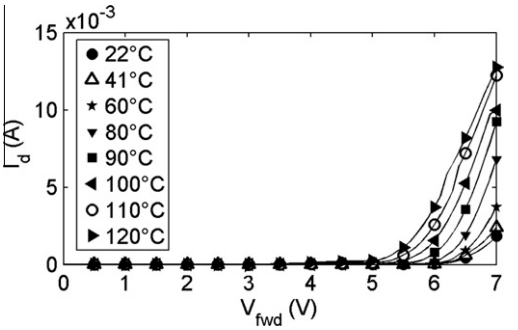

Fig. 10. Current–voltage characteristic of vertical diode at elevated temperatures.

A separate vertical diode is subjected to elevated temperatures under argon gas environment with the pressure maintained at around 1 atm. Before this test, the diode stayed at atmospheric conditions for a week. Similar to the performance improvement of lateral diodes at elevated temperatures, the vertical diodes are also observed to conduct more current at the same voltage values as the temperature is increased, as shown in Fig. 10. The thermal activation of the intergrain boundaries results in more carriers with enough energy to cross the trap states. As a result of heating, the forward current increases from around 2 mA to 12 mA at 7 V forward bias as the temperature increased from 22 °C to 120 °C. Lowering the temperature back to the initial temperature values does not sustain the improvement, leading to the conclusion that annealing of the thin-film did not occur in the process.

3. Polymer diode model

Simulation models for organic and polymer diodes have been reported, modeling the properties of various organic and polymer semiconductors with a voltage dependent mobility factor [21,22]. A more straightforward approach in modeling both organic [9] and organic–inorganic hybrid [12] diodes features two diodes connected in parallel but in reverse directions, one diode modeling the forward current component while the other modeling reverse current component. Both approaches produce good results in modeling the DC behavior of the measured characteristics; however it is found that the approach that makes use of voltage varying mobility produces a more accurate model of the charge pump operating at higher frequency ranges and for different values of peak amplitudes of input voltage.

Under high electric fields, (reported to be in the order of 10^5 V/cm for P3HT [22]) space charge limited conduction (SCLC) is dominant in polymer semiconductors such as P3HT [22]. In SCLC regime, current conduction is dominated by Mott–Gurney equation:

$$J = \frac{9}{8} \cdot \frac{\epsilon_0 \epsilon_r}{d^3} \cdot \mu \cdot V^2 \quad (1)$$

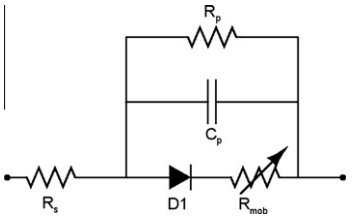

Fig. 11. Circuit model for the P3HT vertical diode.

where μ is the voltage dependent mobility, ϵ_0 is the electrical permittivity of air, ϵ_r is the dielectric constant of the polymer. V represents the voltage across the diode and d the thickness of the polymer film, estimated to be around 750 nm for this work. The voltage dependent mobility is expressed as follows:

$$\mu = \mu_0 \cdot e^{0.89\cdot\gamma\sqrt{V/d}} \tag{2}$$

where μ_0 is the zero-field mobility and γ is the electric field prefactor [22]. Including the voltage dependent mobility within the Mott–Gurney equation integrates the Frenkel effect into the model, emulating the effects of trap states within the polymer film. This yields a more accurate model since the rapid departures from the original Mott–Gurney equations, resulting from high electric field ranges, are now taken into account [23]. In low field regimes, current voltage characteristics of our device model, shown in Fig. 11, are dominated by the diode element, modeling the effects of Schottky contact. As the device enters SCLC regime, the current through the device is dominated by the modified Mott–Gurney equation that includes the Frenkel effect. This latter current regime is modeled by the voltage varying resistor R_{mob} in an approach similar to the work in [21].

The procedure for fitting the model to the measured data starts with fitting the model to the DC sweep measurements of the diode, which gives the reverse saturation current, *IS*, and the ideality factor, *N*, in the SPICE model of the diode element and series and parallel resistances, as well as field-dependent mobility parameters. Junction capacitance, *CJO*, in the SPICE model of the diode element is due to the depletion region caused by the Schottky contact between P3HT and aluminum. Junction capacitance value is estimated to be in the proximity of 100 pF based on the area of the diode and data reported in previous work on rr-P3HT/aluminum Schottky contact, which estimates the depletion width to about 170 nm for zero voltage bias [24]. The parasitic capacitance, C_p, is simply a parallel plate capacitor formed by the two metal electrodes and the polymer film in-between. It is set to 36 pF, based on the approximated polymer thickness of 750 nm, the relative permittivity of 3.0 [13], and an active device area of 1 mm^2. Transit time parameter, *TT*, in SPICE diode model, was also set to 150 μs to fit the model to the measurements. The model was simulated in HSPICE.

4. Charge pump circuits

Charge pump circuit is built using two of the fabricated vertical polymer diodes and two external capacitors. Its operation principle and the experimental results are given in the sections below.

4.1. Operation of the charge pump circuit

Assuming an alternating signal is applied as the input voltage to the charge pump circuit shown in Fig. 1, the negative cycle of the input switches diode D1 on while D2 remains turned off, allowing the capacitance C1 to charge up to the peak voltage of the applied signal. In this situation, D1 and C1 work as a clamper. The following positive cycle of the signal reverse biases D1 and forward biases D2. As a result, C2 is charged up to a positive peak voltage that is the sum of the peak voltage of the applied signal and the voltage stored in C1 from the previous cycle. In this situation, D2 and C2 form a half-wave rectifier. The two terminals of C2 can be used as a DC voltage source, yielding a DC level with some small ripple voltage superposed that is twice the peak voltage of the applied signal under ideal circumstances such as very small stray capacitances along with negligible diode turn on voltages. If a second stage is appended to the first stage, D3 would have its cathode connected to the DC output voltage of the prior stage, and the output voltage that is observed over C4 would be four times that of the peak amplitude of the applied signal.

A typical charge pump circuit given in Fig. 1 can have K stages. Each stage can have identical diodes with turn-on voltage of V_{on} and identical capacitors with capacitance of C. The output of this circuit, V_{out}, can be made to supply a current of I_{out} at the output when an AC signal with a frequency of f and a peak voltage of V_{peak} is applied to the input. Since there would also be stray capacitances, C_s, at the nodes that diodes are connected, a simple output equation for this charge pump circuit can be expressed as [5]:

$$V_{out} = 2\cdot K\cdot\left[\frac{C}{C+C_S}\cdot V_{peak} - V_{on} - \frac{I_{out}}{(C+C_S)\cdot f}\right] \tag{3}$$

It can be observed from this equation that the stray capacitances diminish the peak voltage on the output by sharing the stored charge within the charge pump capacitors, C. Eq. (3) fails to include the diminishing effects of the parasitic parallel plate capacitance, C_p, and the junction capacitance, *CJO*, of the diodes on the peak voltage. These parasitic capacitors must also be lumped to C_s to get a more accurate analytical result. Numerical results acquired from the simulations of HSPICE take the effects of these capacitors into account.

As a minimal requirement, the single stage polymer charge pump is designed to deliver 10 V DC when an oscilloscope probe is connected to its output node. The oscilloscope probe presents a 1 MΩ || 20 pF load to the charge pump. This load is similar to a load that is formed by multiple polymer transistors that we fabricate. Our typical polymer transistor passes a drain current of around 1 μA when a source-drain voltage of −40 V is applied to turn it on. The continuous, resistive current load provided by the oscilloscope brings down the DC output levels according to Eq. (3). The continuous resistive loading is a realistic model for a charge pump circuit driving multiple polymer transis-

tors, where current leakage is significant even if the devices are turned off.

4.2. Experimental results of charge pump circuits

Fabricated charge pumps are tested with external capacitors of 470 nF added on, soon after the completion of the fabrication of vertical diodes. Tests are conducted under argon environment after diodes have been exposed to atmosphere for about a week. These results are shown in Fig. 12. The frequency response of a single stage charge pump for different peak voltages of the input AC signal reveals that the device operates at reasonable output levels up to 1 kHz and it could possibly operate acceptably at around 10 kHz.

Simulation results for the charge pump circuit using the models developed for the vertical polymer diodes are also plotted in Fig. 12. In order to do this, first, the DC current–voltage characteristics of the vertical diodes are measured. Then, the DC parameters for the model described in Section 3 are extracted from these DC measurements. The measured DC current–voltage characteristics and the simulation results done with the extracted parameters are shown in Fig. 13. This figure shows a good match between them. Using these DC parameters, the AC characteristics of the model are also fit to the measurements, shown in Fig. 12.

The experimental and simulation results of the charge pump circuit in Fig. 12 are mostly in agreement. The observable mismatch between the experimental measurements and the simulation results, visible in the 7 V, 6 V and 5 V curves in Fig. 12, can be explained by the fact that the diodes are not under high enough electric fields at these voltage values to meet the SCLC condition that is assumed in this model [22]. For a peak voltage of 7.5 V and an estimated polymer thickness of 750 nm, the electric field becomes 10^5 V/cm, residing in the reported regime where SCLC becomes dominant for P3HT [22]. Above this voltage, i.e. for 8 V, 9 V and 10 V curves in Fig. 12, the featured SCLC model is highly accurate.

Following these tests, charge pump circuits using various capacitor sizes are built and tested. For different charge

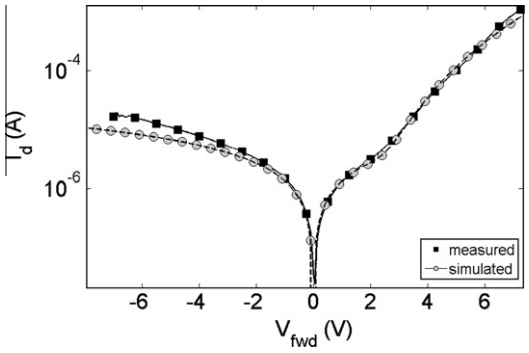

Fig. 13. Simulated and measured DC current–voltage characteristic of the fabricated vertical diodes.

pump capacitors, output voltages are measured as the frequency of the applied AC signal with a peak voltage of 10 V is changed. The results are summarized in Fig. 14. A drastic reduction in output voltage is observed as the pump capacitors are lowered from 68 nF to 10 nF, implying that the stray capacitance is relatively close to, but smaller than 10 nF, since the circuit can still operate with 10 nF capacitors. Simulation results using the diode model are also plotted on this figure.

It is observed that the model parameters fitted for diodes of the charge pump circuit with a fixed capacitor of 470 nF given in Fig. 12 do not fit accurately to the results of the output voltage measurements done using lower pump capacitors such as 68 nF and 10 nF shown in Fig. 14. Variances between the model parameters that are used to fit the former and latter measurements, the 470 nF and 10–68 nF cases, respectively, are reported in Table 1. *CJO*, *N* and *IS* are SPICE parameters defining the diode, and parameters *B* and u_0 belong to voltage dependent mobility element, electric field prefactor and zero-field mobility, respectively. This inaccuracy can be attributed to the degradation of the aluminum-P3HT interface with prolonged usage. The blisters that are induced due to electrical bias stress cause imperfections within the metal–semiconductor interface, where Schottky contact occurs. Since the initial measurements are made using

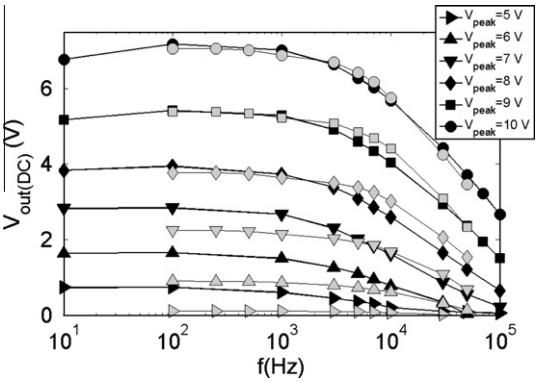

Fig. 12. V_{out} vs. frequency plots for various V_{peak} values of the AC input, C_{pump} = 470 nF. Simulation results are in grey and measurement data in black.

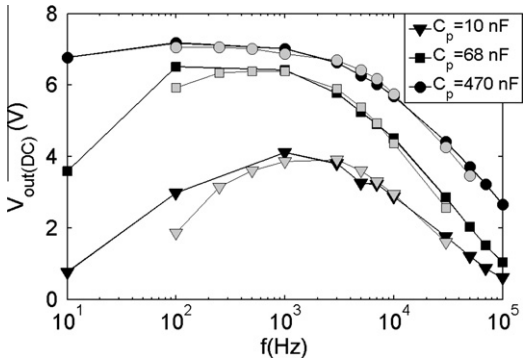

Fig. 14. V_{out} vs. frequency plots for various pump capacitors using AC signals with peak voltages of 10 V. Simulation results are in grey and measurement data in black.

Table 1
Varying model parameters used to fit two separate measurement runs; 470 nF and 68–10 nF cases.

Parameters	470 nF	10 nF & 68 nF
CJO	0.1n	0.5n
N	10.5	11.5
IS	2.5e−14	25e−14
B	1.25e−2	1.8e−2
u_0	1.75e−6	0.2e−6

470 nF capacitors, the model parameters that are required to fit the simulation results to the measurements are closer to the ideal than the latter charge pumps tested with 68 nF and 10 nF capacitors, using degraded diodes from previous use.

The expected effects from the increased number of defects due to the deterioration of the aluminum-P3HT interface include charge trapping within the defects and increased dependence of mobility on electric field. Charge trapping effects observed in similar vertical structures of aluminum-P3HT diodes have been modeled as capacitors parallel to depletion capacitor in the literature [25]. Trapping action due to the increased number of defect sites is incorporated into the junction capacitance in our model as an approximation, the reason being that the defects are occurring at the aluminum- P3HT interface where depletion capacitance also forms, increasing the overall junction capacitance in the deteriorated diode samples.

In addition to the measurements showing how the output voltage of the charge pump circuit changes with the frequency and the peak voltage value of the AC input, ramp-up times of charge pump circuits with various capacitor sizes are investigated. The operation of the charge pump may require a rapid rise time to the final output voltage value. For example in an RFID scenario, the reception of the RF signal must result in the power-up of an RFID tag as soon as possible or data might be lost during the process. Measured ramp-up times are shown in Fig. 15 for an input AC signal with a peak voltage of 10 V at 1 kHz frequency. The final output voltage is reached within 9.4 ms in charge pumps that used 10 nF, 32.5 ms for 68 nF and 205 ms for 470 nF designs. The ramp-up time for 470 nF case is much greater than 68 nF and 10 nF cases, and might be slow even for polymer electronics applications. The final DC levels reached in this figure are close to each other for the charge pump circuit with 470 and 68 nF capacitors, similar to the results in Fig. 14. However, charge pump circuit with 470 nF capacitors has smaller ripple voltages than the one with 68 nF.

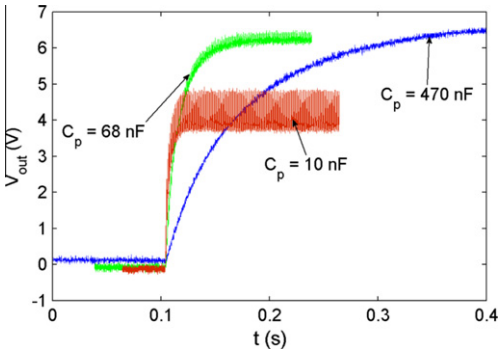

Fig. 15. Ramp-up waveforms for charge pumps built with various pump capacitors, with oscilloscope data for 470 nF, 68 nF and 10 nF cases superposed for comparison purposes. AC input signals are applied with a peak voltage of 10 V at frequency of 1 kHz.

5. Results and discussion

Experimental results from the lateral and vertical diodes reveal that the deterioration in their performance when operated under atmospheric conditions is drastic. This emphasizes the importance of packaging the devices under inert atmosphere, thus preserving the diodes in their best states. Considering that current–voltage characteristics that approximate an ideal switch is pivotal in the operation of the charge pump circuit, packaging process becomes as important as the design of the charge pump.

The thermal experiments reveal that both lateral and vertical diodes benefit from increased temperatures within a certain range. It is determined that the on/off ratios of the diodes improve invariably when the ambient temperature is raised from room temperature to 120 °C. This improvement in performance has been explained by the thermal activation of trap states formed by the boundaries between grains of polymer. Improvement in on-current is not sustained when the diodes are brought back to room temperature, therefore it is reasoned that thermal annealing does not take place within the temperature range that is used during the experiments.

The charge pump built using vertical polymer diodes in this work is considered to be the building block of larger charge pumps. The best case output voltage expected from the charge pump is, according to Eq. (3), twice the difference between AC input peak voltage and the turn-on voltage of the diodes. The output voltage can be improved by a peak voltage much larger than the turn-on voltage of the diode, which is roughly around 5 V in this work, and charge pump capacitors much greater than the stray capacitances, including the junction capacitances of the diodes. To ensure the best case condition in terms of capacitances, 470 nF capacitors are used, diminishing the effect of stray capacitances. For a peak voltage of 10 V, expecting an output load current of around 10 μA, the best case output voltage would be 9.6 V from this single stage charge pump. In meeting the above conditions, we have observed output voltages of 7.2 V between 100 Hz and 1 kHz frequency range, 75% of the calculated best case output voltage of the single stage charge pump under these conditions. The probable source of error is the parasitic internal resistances and capacitances of the diodes formed as a result of deterioration, which is caused by impurities inside under electrical bias stress. This causes the diodes to further deviate from the desired ideal switch behavior.

Another consideration is that the vertical diode with dimensions of 2 mm × 0.5 mm is able to adequately supply currents within milliampere range but only tens of microamperes is required by the following electronic circuit composed of polymer transistors. Excessive diode area does not help if the extra current is not used by the circuit

at the load. In fact an excessively wide device area introduces larger stray capacitances to the charge pump, shares the charge that would otherwise be stored entirely on the pump capacitors and reduces the high frequency performance of the design, as reported in the literature for P3HT rectifiers [7]. Therefore, a minimal diode area that satisfies the design objectives must be sought for, without neglecting some additional device area to safely meet any possible fabrication error.

Even though the output voltage of this circuit is lower than expected due to the high turn-on voltage of the diodes, internal diode resistances and capacitances that are the result of the deterioration of the exposed P3HT and high stray diode capacitances, cascading a number of stages of such cells would recover the loss in voltage in the expense of efficiency and frequency response. The cascading of multiple cells of charge pump is not preferable, but might be necessary for matching purposes [4]. The number of stages in a charge pump, as well as its loading and its operation frequency, controls its input impedance [4,5], and by adjusting the input impedance of the charge pump, impedance matching to the antenna that drives the charge pump can be achieved in an RFID application.

Simulation models based on SCLC theory are shown to be accurate under high electric field conditions, given that necessary adjustments to the model are made to adapt the models for the physical deterioration that can be observed after prolonged electrical bias stress. It is determined that by increasing the diode capacitance and the ideality factor of the diode, along with increasing the electrical prefactor (to make the diode current more dependent on the applied voltage) and decreasing the zero-field mobility, as expected when physical defects are introduced to the aluminum-P3HT interface, the degradation effects can be expressed within the SCLC model. DC current–voltage characteristics of P3HT diodes are modeled using a similar approach [22], and we demonstrate that the SCLC model featured in this work is also accurate and practical for the transient simulation of P3HT diodes at varying frequencies.

Along with their potential use in future polymer RFID tags, the charge pump is also attractive for other battery-powered, portable polymer electronics applications where very high voltages would be needed for device operation but supplying such amplitudes from conventional batteries would be impractical. In such devices, such as flexible polymer displays and micromachined capacitive actuators, polymer charge pumps could be implemented on plastic substrate without using additional, dedicated integrated charge pump chips or charge pumps built from discrete elements, which would cause the cost of such a system to rise noticeably. The frequency limitations of the multi-stage charge pump would become less of a problem in such systems since a steady DC voltage would be all that is needed, in contrast with the RFID data transmission problem.

6. Conclusion

Lateral and vertical polymer diodes have been fabricated using P3HT. Evaluations of the performances of the diodes were done under elevated temperature and vacuum/atmospheric exposure. Performances of air exposed lateral diodes improved continuously under vacuum since there was no metal film covering the polymer film. However, air exposed vertical diodes under vacuum and prolonged operation at atmospheric conditions showed deteriorated performances. Blistering of the vertical diodes was observed with electrical bias stress; and although the blistering was observed to be extensive under vacuum and air exposure, the performance of the devices operated under argon did not seem to suffer too much. Performances of both the lateral and vertical diodes under argon environment improved steadily when the ambient temperature was raised from room temperature to 120 °C. This was due to the thermal activation of trap states formed by the boundaries between grains of polymer. Improvement was not sustained when the diodes were brought back to room temperature indicating that thermal annealing did not take place. It was determined that protecting the device from atmospheric elements was necessary to preserve their current–voltage characteristics.

Circuit models have been developed for the vertical diodes. Transient simulations of P3HT diodes using SCLC model were demonstrated. Fabricated charge pumps using vertical diodes and various capacitors revealed similar results as the models predicted. Charge pump circuits were able to generate DC voltages from AC voltages in the frequency range from 100 Hz to 10 kHz. Generated DC voltage level was lower than ideal because of the high turn-on voltages of the diodes and their internal parasitic resistances and capacitances.

The simulation model was implemented in HSPICE and was practical to use. However, some modifications might be required to cover the smaller voltage amplitudes. Degradation effects that were observed under prolonged use of polymer diodes were incorporated into the model by modifying certain model parameters, which produced results consistent with experimental measurements.

Acknowledgement

This work is supported by the Scientific and Technological Research Council of Turkey (TUBITAK) under project EEEAG 106E013 and State Planning Organization of Turkey, TAM Project (2007K120610).

References

[1] D.M. Russell, T. Kugler, C.J. Newsome, S.P. Li, M. Ishida, T. Shimoda, Dedoping of organic semiconductors, Synthetic Metals 156 (2006) 769–772.
[2] E.T. Carlen, K.H. Heng, S. Bakshi, A. Pareek, C.H. Mastrangelo, High-aspect ratio vertical comb-drive actuator with small self-aligned finger gaps, Journal of Microelectromechanical Systems 14 (5) (2005) 1144–1155.
[3] K. Myny, S. Steudel, P. Vicca, J. Genoe, P. Heremans, An integrated double half-wave organic Schottky diode rectifier on foil operating at 13.56 MHz, Applied Physics Letters 93 (2008) 093305.
[4] D. Dobkin, The RF in RFID, Newnes, Oxford, 2008.
[5] F. Pan, T. Samaddar, Charge Pump Circuit Design, McGraw-Hill, New York, 2006.
[6] C.M. Kang, S. Kim, Y. Hong, C. Lee, Frequency analysis on poly(3-hexylthiophene) rectifier using impedance spectroscopy, Thin Solid Films 518 (2009) 889–892.

[7] S. Kim, H. Cho, Y. Hong, C. Lee, Effect of electrode area on high speed characteristics over 1 MHz of poly(3-hexylthiophene-2,5-diyl) diode with inkjet-printed Ag electrode, Molecular Crystals and Liquid Crystals 513 (2009) 256–261.
[8] K. Lilja, T.G. Bäcklund, D. Lupo, T. Hassinen, T. Joutsenoja, Gravure printed organic rectifying diodes operating at high frequencies, Organic Electronics 10 (2009) 1011–1014.
[9] B.N. Pal, J. Sun, B.J. Jung, E. Choi, A.G. Andreou, H.E. Katz, Pentacene-zinc oxide vertical diode with compatible grains and 15-MHz rectification, Advanced Materials 20 (2008) 1023–1028.
[10] S. Steudel, K. Myny, V. Arkhipov, C. Deibel, S. De Vusser, J. Genoe, P. Heremans, 50 MHz rectifier based on an organic diode, Nature Materials 4 (2005) 597–600.
[11] S. Steudel, K. Myny, P. Vicca, D. Cheyns, J. Genoe, P. Heremans, Ultra-high frequency rectification using organic diodes, Technical Digest International Electron Device Meeting – IEDS 2008, pp. 93–96
[12] J. Sun, B.N. Pal, B.J. Jung, H.E. Katz, Solution-processed hybrid p–n junction vertical diode, Organic Electronics 10 (1) (2009) 1–7.
[13] K. Rashmi, A. Kumar, U. Balakrishnan, V. Basu, Degradation process in organic thin film devices fabricated using P3HT, Pramana 68 (3) (2007) 489–498.
[14] S.P. Speakman, G.G. Rozenberg, K.J. Clay, W.I. Milne, A. Ille, I.A. Gardner, E. Bresler, J.H.G. Steinke, High performance organic semiconducting thin films: ink jet printed polythiophene [rr-P3HT], Organic Electronics 2 (2) (2001) 65–73.
[15] H. Klauk (Ed.), Organic Electronics Materials, Manufacturing and Applications, Wiley-VCH Verlag GmbH and Co., Weinheim, 2006.
[16] S. Mijalkovic, D. Green, A. Nejim, G. Whiting, A. Rankov, E. Smith, J. Halls, C. Murphy, Modeling of organic field effect transistors for technology and circuit design, in: Proceedings of the 26th International Conference On Microelectronics, 2008, pp. 469–476.
[17] S. Joshi, P. Pingel, S. Grigorian, T. Panzner, U. Pietsch, D. Neher, M. Forster, U. Scherf, Bimodal temperature behavior of structure and mobility in high molecular weight P3HT thin films, Macromolecules 42 (2009) 4651–4660.
[18] S. Cho, K. Lee, Thermal annealing-induced enhancement of the field-effect mobility of regioregular poly(3-hexylthiophene) films, Journal of Applied Physics 100 (2006) 114503.
[19] Y.D. Gokdel, B. Sarioglu, S. Mutlu, A.D. Yalcinkaya, Design and fabrication of two-axis micromachined steel scanners, Journal of Micromechanics and Microengineering 19 (7) (2009).
[20] A.O. Sevim, S. Mutlu, Post-fabrication electric field and thermal treatment of polymer light emitting diodes and their photovoltaic properties, Organic Electronics 10 (1) (2009) 18–26.
[21] A. Haldi, A. Sharma, W.J. Potscavage Jr., B. Kippelen, Equivalent circuit model for organic single-layer diodes, Journal of Applied Physics 104 (2008) 064503.
[22] M. Giulianini, E.R. Waclawik, J.M. Bell, N. Motta, Current–voltage characteristics of poly(3-hexylthiophene) diodes at room temperature, Applied Physics Letters 94 (2009) 083302.
[23] P.N. Murgatroyd, Theory of space-charge-limited current enhanced by Frenkel effect, Journal of Physics D: Applied Physics 3 (2) (1970) 151–156.
[24] A. Takshi, A. Dimopoulos, J.D. Madden, Depletion width measurement in an organic Schottky contact using a metal-semiconductor field-effect transistor, Applied Physics Letters 91 (2007) 083513.
[25] A. Takshi, J.D. Madden, Large apparent inductance in organic Schottky diodes at low frequency, Journal of Applied Physics 99 (2006) 084503.

Organic Electronics 12 (2011) 322–328

Contents lists available at ScienceDirect

Organic Electronics

journal homepage: www.elsevier.com/locate/orgel

Letter

Blue top-emitting organic light-emitting devices based on wide-angle interference enhancement and suppression of multiple-beam interference

Jun Xie [a], Chunyan Chen [a], Shufen Chen [a,*], Yang Yang [a], Ming Shao [a], Xu Guo [a], Quli Fan [b], Wei Huang [b]

[a] Institute of Advanced Materials (IAM), Nanjing University of Posts and Telecommunications, No. 9 Wenyuan Road, Nanjing 210046, China
[b] Key Laboratory for Organic Electronics and Information Displays (KLOEID), Nanjing University of Posts and Telecommunications, No. 9 Wenyuan Road, Nanjing 210046, China

ARTICLE INFO

Article history:
Received 24 June 2010
Received in revised form 29 October 2010
Accepted 21 November 2010
Available online 3 December 2010

Keywords:
OLED
Blue emission
Top-emitting
Multiple-beam interference
Wide-angle interference
PCR

ABSTRACT

Blue top-emitting organic light-emitting devices (TEOLEDs) based on blue phosphor iridium (III) bis[(4,6-difluorophenyl)-pyridinato-N,$C^{2\prime}$] picolinate (FIrpic) are demonstrated. Instead of using microcavity effects to obtain the blue top emission in conventional reports, the blue emission with a good chromaticity is achieved in this paper through the suppression of the multiple-beam interference by introducing a 2,9-dimethyl-4,7-diphenyl-1,10-phenanthroline light outcoupling layer onto the semitransparent Sm/Ag cathode. The electroluminescent performances of the blue emission is further improved based on the effective carrier transport and the consideration of the wide-angle interference at the emission peak of FIrpic with a maximum luminance of 8029 cd/m^2 and a luminous efficiency of 4.02 cd/A achieved at 14 V and 10 V, respectively. With a polarizer on the top cathode, a high pixel contrast ratio of 113:1 is realized under an ambient illumination of 140 lx and a pixel brightness of 1000 cd/m^2.

© 2010 Elsevier B.V. All rights reserved.

1. Introduction

Full-color organic light-emitting devices (OLEDs) can be constructed in different ways, e.g., patterning pixels with the three principle colors (blue, green, and red) or with the blue and orange–yellow complementary colors, white OLEDs with color filters [1,2], etc. It is obvious that blue light emission plays a key role in the manufacture of full-color displays [3]. Compared with the conventional bottom-emitting OLEDs (BEOLEDs), top-emitting OLEDs (TEOLEDs) are much more suitable for active matrix OLEDs applications, since the thin film transistors (TFTs) are buried below the bottom reflective anode and the light is extracted from the top semitransparent cathode. Besides, the TFTs can be largely increased without reducing the aperture ratio (AR) in TEOLEDs. However, due to the commonly used highly reflective metal as both cathode and anode, microcavity effects exit inevitably in TEOLEDs. The resonant wavelength corresponding to the major peak wavelength of blue emission is much thinner or thicker than that of red or green emission, which means it is easily broken down under a high bias or needs a high operating voltage. A common solution to this problem is fabricating blue TEOLEDs by introducing a thickness-adjustable ITO on the bottom reflective layer to fit the optical length of blue emission [4–7]. In our work, the blue TEOLEDs are obtained by using a suitable thickness of a 2,9-dimethyl-4,7-diphenyl-1,10-phenanthroline (BCP) layer as a light outcoupling layer onto the semitransparent top metal cathode, with which a low reflectivity of the top cathode is achieved with desirable suppression of multiple-beam interference in devices [8,9]. In addition, it is worth mentioning that the blue light electroluminescent (EL) performance can be further improved by optimizing the

* Corresponding authors.
E-mail addresses: iamsfchen@njupt.edu.cn (S. Chen), iamqlfan@njupt.edu.cn (Q. Fan), wei-huang@njupt.edu.cn (W. Huang).

1566-1199/$ - see front matter © 2010 Elsevier B.V. All rights reserved.
doi:10.1016/j.orgel.2010.11.018

thickness of the organic multilayer sandwiched between the emissive layer and the bottom reflective anode to satisfy wide-angle interference at the emission peak of iridium (III) bis[(4,6-difluorophenyl)-pyridinato-N,$C^{2\prime}$] picolinate (FIrpic). Furthermore, it is known that the high reflection of the metal cathode also leads to a strong reflection of ambient light with a result of a low pixel contrast ratio (PCR) in TEOLEDs [10,11]. In this paper, the PCR is obviously improved by using the BCP light outcoupling layer together with a polarizer.

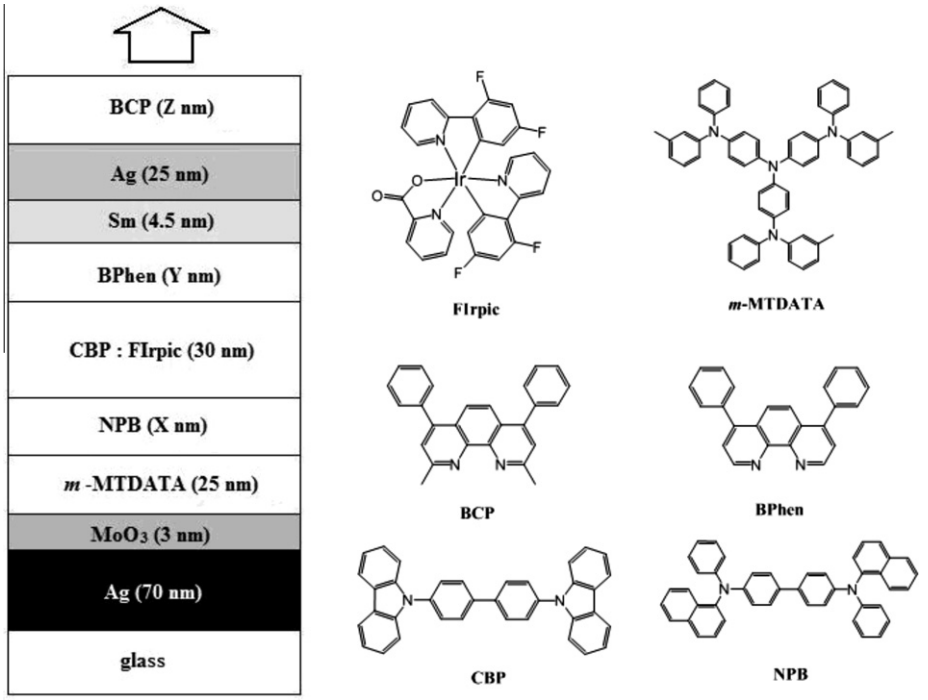

Fig. 1. Schematic configuration of TEOLEDs and chemical structures of materials used in this paper.

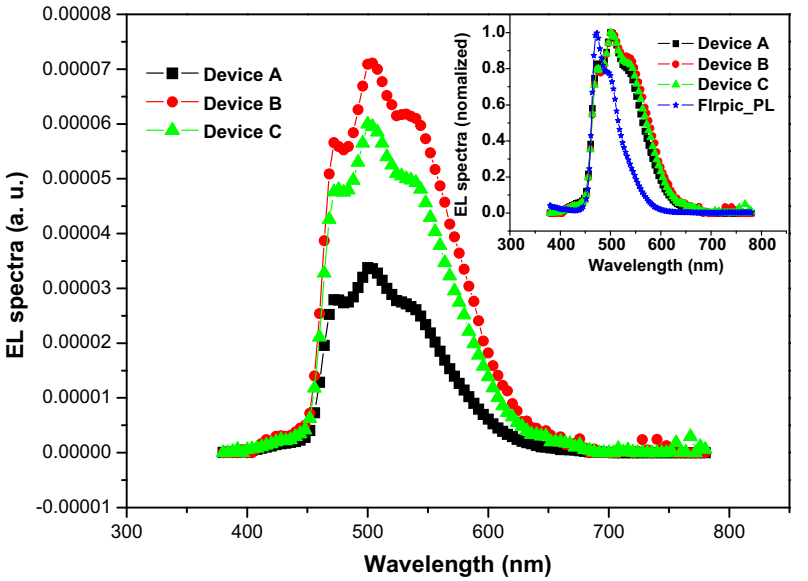

Fig. 2. The EL spectra of devices A, B, and C under the current density of 1 mA/cm^2. Inset: normalized EL spectra of devices A, B, and C at the same current density of 1 mA/cm^2, and the measured PL spectra of the blue phosphor FIrpic in a solid film state.

2. Theory calculation

The resonant wavelength that corresponds to multiple-beam interference satisfies Eq. (1) [12,13]:

$$\frac{2\pi}{\lambda}\sum 2n_m d_m \cos\theta - \Phi_1(\lambda) - \Phi_2(\lambda) = k2\pi. \quad (1)$$

Here, λ is the resonant wavelength, n_m and d_m are the refractive index and the thickness of the mth organic layer between the two electrodes, respectively, θ is an angle in the spacer layer (here, 0° is perpendicular to the electrode plane), $\Phi_1(\lambda)$ and $\Phi_2(\lambda)$ are the phase changes on reflection corresponding to the opaque anode/organic material and the organic material/semitransparent cathode, and k is the mode number.

In a TEOLED, when only the wide-angle interference is taken into account, Eq. (1) can be simplified by ignoring $\Phi_2(\lambda)$ and only the organic layers between the emission area and the reflective anode are under consideration.

The PCR of a device is calculated with Eqs. (2) and (3) [10,14]:

$$PCR = \frac{L_{on} + LR_L}{L_{off} + LR_L}, \quad (2)$$

and

$$R_L = \frac{\int_{\lambda_1}^{\lambda_2} V(\lambda)S(\lambda)R(\lambda)d\lambda}{\int_{\lambda_1}^{\lambda_2} V(\lambda)S(\lambda)d\lambda}. \quad (3)$$

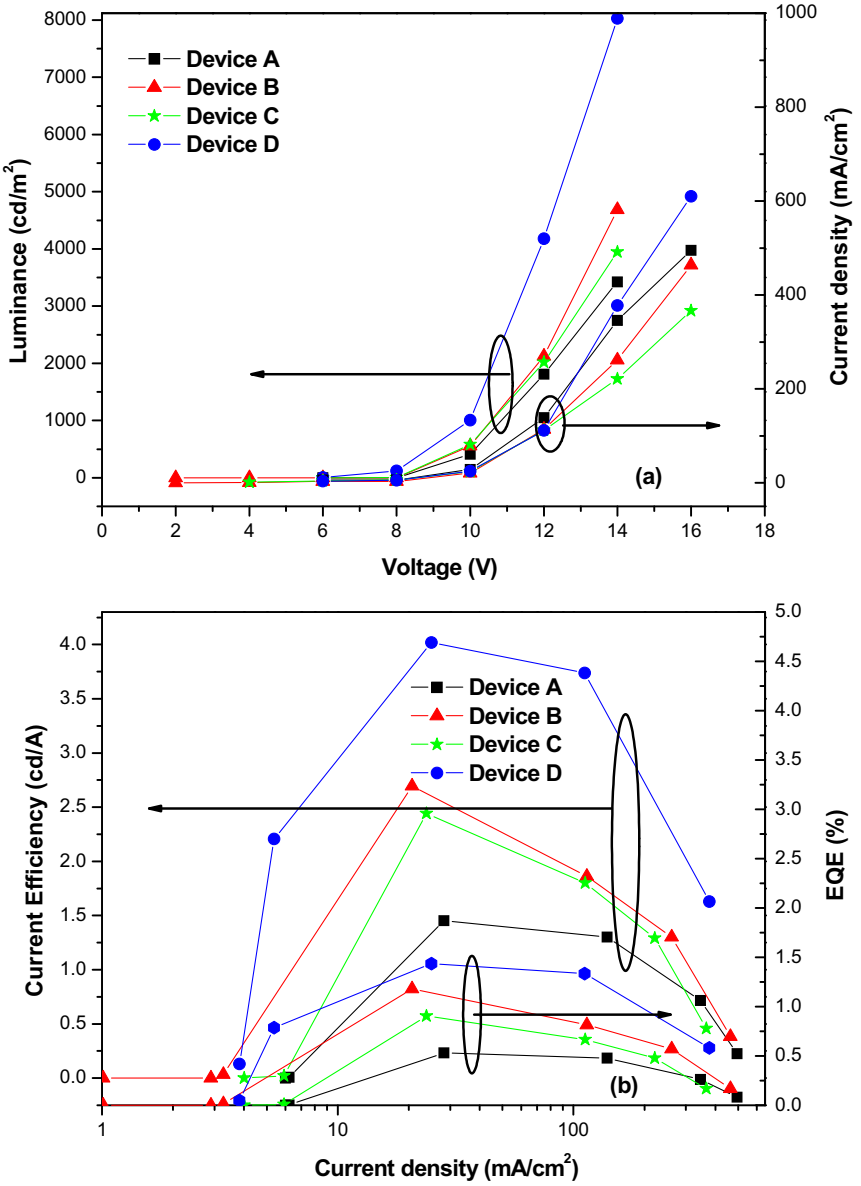

Fig. 3. *L–J–V* (a) and *η–EQE–J* (b) characteristics of devices A, B, C, and D.

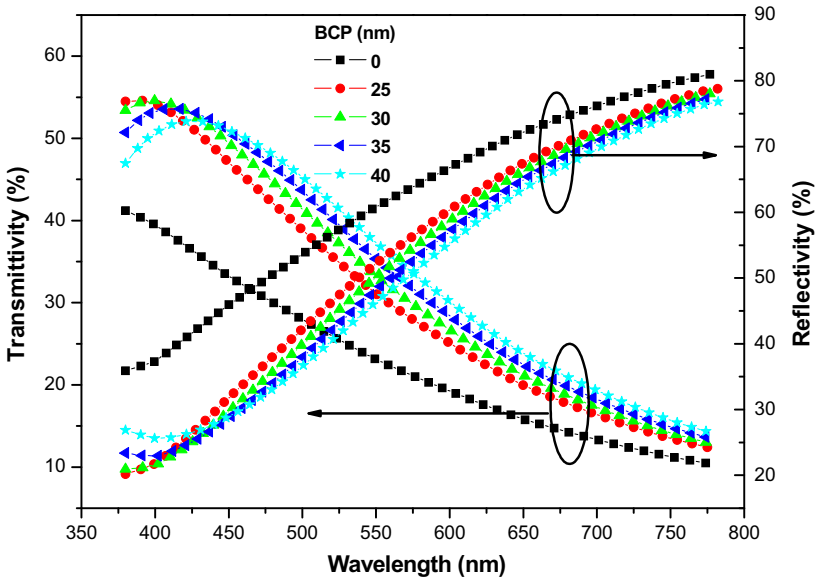

Fig. 4. Transmittivity and reflectivity characteristics of the CBP (25 nm)/BPhen (40 nm)/Sm (4.5 nm)/Ag (25 nm)/BCP/air multilayer system. Here, the thickness of the BCP layer is adjusted from 0 to 40 nm.

Here L_{on} and L_{off} are the brightness of a pixel at on- and off-state, respectively, L is the ambient illumination, R_L is the luminous reflectance, $V(\lambda)$ is the standard photometric curve, $R(\lambda)$ is the optical reflection of the device, and $S(\lambda)$ is the D65 light source.

3. Experimental

Our blue TEOLEDs were grown on glass substrates. Prior to the device deposition, the substrates were cleaned with acetone and ethanol by using an ultrasonic bath, rinsed with deionized water, and then dried in an oven. The TEOLED structure was glass/Ag (70 nm)/MoO_x (3 nm)/4,4′,4″-tris(3-methylphenylphenylamino)triphenylamine (*m*-MTDATA, 25 nm)/N,N′-bis(naphthalen-1-yl)-N,N′-bi (phenyl)-benzidine (NPB, X nm)/4,4′-bis(carbazol-9-yl)-biphenyl (CBP): FIrpic (7 wt.%, 30 nm)/4,7-diphenyl-1, 10-phenanthroline (Bphen, Y nm)/Sm (4.5 nm)/Ag (25 nm)/BCP (Z nm), as shown in Fig. 1. Here, *m*-MTDATA, NPB, CBP, FIrpic, BPhen, and BCP were utilized as a hole injection layer, a hole transport layer, a blue host, a blue phosphorescent guest, an electron injection and transport layer, and a light outcoupling layer, respectively, whose molecule structures were demonstrated in Fig. 1. Ag and MoO_x were utilized as the anode and the hole injection layer, respectively. The Sm/Ag bilayer was utilized as an effective cathode due to Sm's low work function of ~2.7 eV and relatively high transparence in the visible range and Ag's environmental stability. All depositions were finished in a high vacuum about 10^{-6} Torr with a rate of 0.1–0.3 nm/s. Current density–voltage–luminance characteristics of the devices were measured with a Keithley 2400 source measurement unit and a Photo-Research PR-655 SpectraScan Colorimeter in room-temperature air. The reflectivity characteristics of devices were measured with a Shimadzu UV3600 spectrometer at 25 °C. The photoluminescence (PL) spectra of the blue phosphor FIrpic were measured with a Shimadzu RF-5301PC.

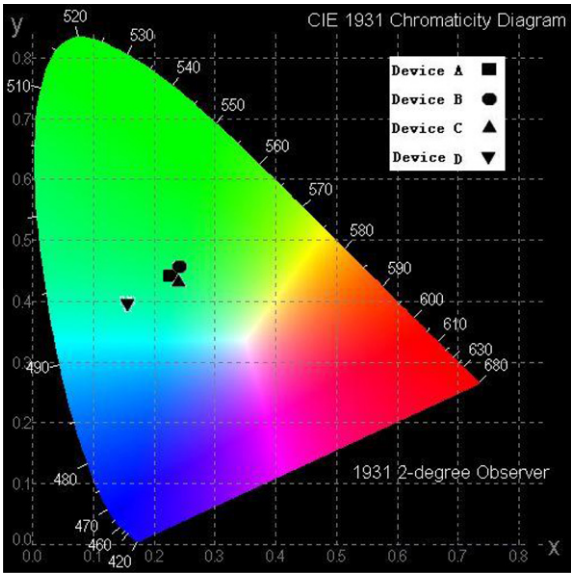

Fig. 5. CIE coordinates of devices A–D.

To realize wide-angle interference at the emission wavelength of FIrpic with a main peak wavelength of 472 nm, the total thickness of *m*-MTDATA and NPB is calculated with Eq. (1), where the exciton recombination zone is supposed at the NPB/CBP interface and the NPB thickness is adjustable. The total thickness of the organic multilayer keeps invariable and is fixed at 105 nm, so the BPhen layer thickness changes simultaneously accompanying with that of the NPB layer.

4. Results and discussion

In a cavity device, both wide-angle and multiple-beam interference have effects on the EL performances, especially for those devices when one electrode has a high reflectivity and the other has a low reflectivity. From Eq. (1), the calculated NPB thickness that satisfies the wide-angle interference at the blue emissive peak wavelength of FIrpic is 10 nm (Suppose that the excitons are generated at the NPB/CBP interface and the recombination area is just at the interface). Considering of the exciton diffusion, several devices are fabricated with different NPB thicknesses of 5 (Device A), 10 (Device B), and 15 nm (Device C). Fig. 2 demonstrates the EL spectra of devices A, B and C under the current density of 1 mA/cm^2, from which one can observe the EL intensity mainly caused by the wide-angle interference and balance of exciton formation. In the Fig. 2, which have a main peak of 502 nm with two shoulders of ~472 and ~540 nm is observed. The shoulder peak at 472 nm originates from native emission of FIrpic, while the other shoulder peak at 540 nm can be attributed to the multiple-beam interference, which is well matched with the calculated result of 542 nm. The main peak of 502 nm is resulted from the overlap of peak values of 472 and 540 nm together with the intrinsic minor shoulder of FIrpic at 500 nm (The PL spectra of FIrpic are in the inset of Fig. 2). The normalized EL spectra of device A, B, and C are shown in the inset of Fig. 2, from which we find device A exhibits the highest intensity at the peak value of 472 nm among all devices. Compared the experimental data with the theoretical one, we deduce the major exciton recombination area is not at the NPB/CBP interface, but in the CBP host and the site is 5 nm away from the interface (considering NPB and CBP have similar refractive indexes). In other words, it satisfies the wide-angle interference at the blue emissive peak wavelength of FIrpic in device A, which can be further proved by a better chromaticity (0.22, 0.45) in device A in the blue emission area, while the corresponding Commission International de L'Eclairage (CIE) coordinates (Fig. 5) for devices B and C are (0.24, 0.47) and (0.24, 0.46) at 10 V. Here, we conclude the exciton diffusion length in our blue emission devices is about 5 nm and we also find the wide-angle interference is weak although to some extent it affects the chromaticity coordinates. Moreover, from Fig. 2, we find the fact that the intensity of the EL spectra from device B is larger than those from devices A and C in the whole emission range, which indicates the thickness changes of NPB and BPhen influence the carrier transport. It exhibits a better transport ability in the structure of device B than those in devices A and C. As a result, both the carrier transport ability and the wide-angle interference affect the EL performances, where the former plays a more important role. The current density–luminance–voltage (J–L–V) and luminous efficiency–external quantum efficiency–current density (η–EQE–J) characteristics of devices A, B, and C shown in Fig. 3a and b also prove the result. Devices A, B, and C achieve their maximum luminance of 3420, 4687, and 3946 cd/m^2 at 14 V, and their maximum luminous efficiency are 1.45 (at 28.2 mA/cm^2), 2.69 (at 20.7 mA/cm^2), and 2.44 cd/A (at 23.8 mA/cm^2), respectively. Devices A, B, and C achieve their maximum EQE of 0.51% (at 29 mA/cm^2), 1.18% (at 21 mA/cm^2), and 0.905% (at 25 mA/cm^2), respectively. Device B demonstrates a best η–EQE–L performance among all the devices, mainly due to the effective transport of holes and electrons by adjusting the NPB and BPhen thickness and more excitons generation in device B.

The multiple-beam interference exists inevitably in devices A–C due to a relatively high reflectivity of the Sm/Ag cathode, as shown in Fig. 4, which results in the CIE coordinates apart from the blue light emission, as shown in Fig. 5. For further improvement of light outcoupling and reduction of the reflectivity of the Sm/Ag cathode, a BCP layer is introduced in the devices, aiming for suppressing

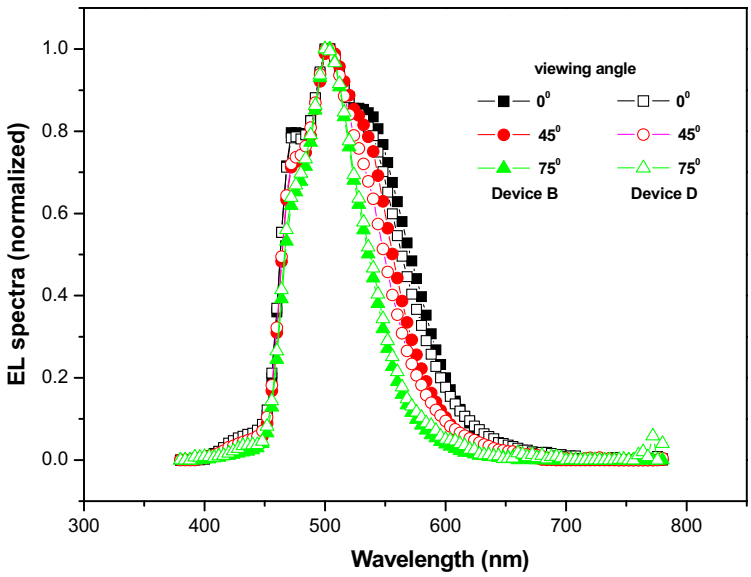

Fig. 6. EL spectra for devices B and D with viewing angles of 0°, 45° and 75°.

the multiple-beam interference in the devices. The optimization of the BCP layer thickness is based on device B with the NPB and BPhen thickness of 10 and 40 nm, respectively, since its EL performance is the best among all the devices. Since the exciton recombination and light generation takes place predominantly in the blue dopant layer and about 5 nm away from the NPB/CBP interface, light passes through the multilayer system of CBP (25 nm)/BPhen (40 nm)/Sm (4.5 nm)/Ag (25 nm)/BCP (if with) and then escapes from the Sm/Ag cathode of TEOLEDs, where the effect of the FIrpic dopant on refractive index of the CBP host is neglected. The transmittivity (T) and reflectivity (R) of the multilayer system with different thicknesses of the BCP layer are calculated with transfer matrix theory [15] and the transmittivity and reflectivity curves are shown in Fig. 4. Without a BCP layer, the *R* value is 49.3% at 472 nm (the emissive peak wavelength of FIrpic), while *T* value is 30%. The *R* value of the blue TEOLED gradually decreases and *T* increases with the increasing thickness of the BCP layer. Balancing the aspiration of achieving higher *T* and lower *R* simultaneously round 472 nm, the BCP thickness that we employ is chosen to be 35 nm.

Device D corresponding to device B is covered with another 35 nm-thick BCP light outcoupling layer, with which a low reflectivity of the cathode at the blue emission region can be achieved. As can be seen in Fig. 5, the CIE coordinates of device D show better chromaticity than those of device B without a BCP layer. The effective suppression of multiple-beam interference in device D, as shown in Fig. 5, leads to the blue shift of the CIE coordinates changing from (0.24, 0.47) to (0.17, 0.40), which is comparative to those of the blue BEOLEDs [16]. The EL spectra of devices

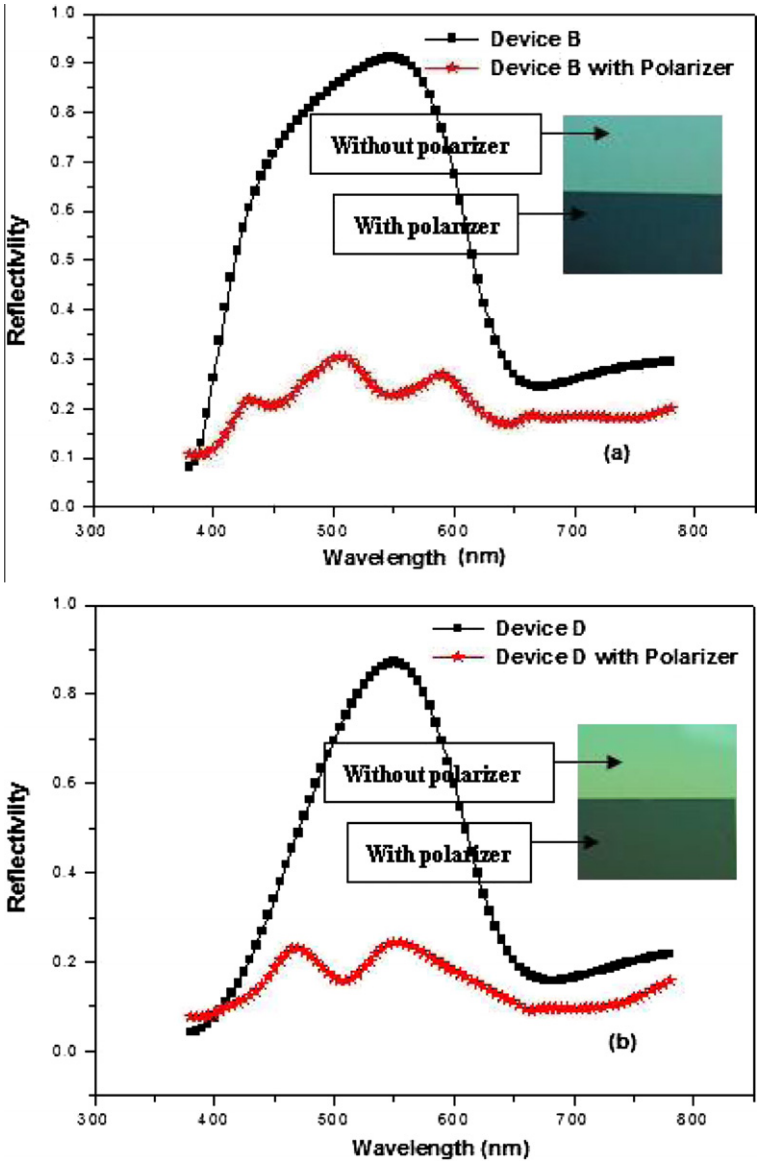

Fig. 7. Luminous reflectance of devices B (a) and D (b) with and without a polarizer. Inset: photographs of devices B and D with and without a polarizer under environmental lighting.

B and D with different viewing angles of 0°, 45°, and 75° are also compared in Fig. 6. From the figure we observe an obvious suppression of multiple-beam interference in device D until 75°. In addition, the utilization of an additional BCP layer results in 1.7 and 1.5 times improvement for L (Fig. 3a) and η (Fig. 3b) in device D, reaching 8029 cd/m^2 at 14 V and 4.02 cd/A at 25 mA/cm^2, respectively.

As an important parameter in full-color display applications, PCR is also explored in this paper. Fig. 7a and b gives the $R(\lambda)$ curves of devices B and D with or without a polarizer on the top cathode. With the on-state brightness and ambient illumination are 1000 cd/m^2 and 140 lx, respectively, the PCR of device D with the 35 nm-thick BCP layer is 32:1, which is almost the same with that of device B without a BCP layer (29:1). To enhance the PCR of the devices, we add a polarizer on the top cathode of the blue TEOLEDs. The PCRs increase to 92:1 and 113:1 for devices B and D, respectively, about 4 times of the corresponding devices without a polarizer layer. Such high-contrast TEOLEDs incorporated into active matrix OLED displays would possess a good readability under a strong ambient illumination.

5. Conclusion

In summary, we fabricate blue TEOLEDs based on the blue phosphor FIrpic. Through suppressing the multiple-beam interference with the utilization of a BCP light outcoupling layer and considering the wide-angle interference, an improved blue emission with a maximum luminance of 8029 cd/m^2 and a luminous efficiency of 4.02 cd/A is obtained. The better chromaticity of the blue emission in the TEOLED with the CIE coordinates (0.17, 0.40) is also achieved, which is comparative to those of the blue BEOLEDs. In addition, the device with a BCP light outcoupling layer shows a high PCR of 113:1 by adding a polarizer on the top of the device under an ambient illumination of 140 lx and a pixel brightness of 1000 cd/m^2. Such high-contrast TEOLEDs incorporated into active matrix OLED displays would possess a good readability under a strong ambient illumination.

Acknowledgments

The authors acknowledge financial support from the Ministry of Science and Technology (973 project, Grant No. 2009CB930600), NSFC (Grants No. 60907047, 20774043, 20704023, 20874048, 60706017, 60977024, and 60876010), the Key Project of Chinese Ministry of Education (Grants No. 104246, 208050, 707032), the Fok Ying-Tong Education Foundation (Grant No. 111051), the Research Fund for the Doctoral Program of Higher Education (Grant No. 20093223120003 and 20093223110003), NSF of Jiangsu Province (Grants No. BK2009423, BK2008453 and BK2008053), and NSF of the Education Committee of Jiangsu Province (Grants No. 08KJB510013, BK2008053, SJ209003, TJ209016, TJ209035, and TJ207035), The Pandeng Project of Nanjing University of Posts and Telecommunications under Grant No. NY 210015.

References

[1] D.Y. Kim, H.N. Cho, C.Y. Kim, Prog. Polym. Sci. 25 (2000) 1089–1139.
[2] T.C. Tsai, W.Y. Hung, L.C. Chi, K.T. Wong, C.C. Hsieh, P.T. Chou, Org. Electron. 10 (2009) 158–162.
[3] Q.J. Qi, X.M. Wu, Y.L. Hua, Q.C. Hou, M.S. Dong, Z.Y. Mao, B. Yin, S.G. Yin, Org. Electron. 11 (2010) 503–507.
[4] S.F. Hsu, C.C. Lee, A.T. Hu, C.H. Chen, Curr. Appl. Phys. 4 (2004) 663–666.
[5] S.F. Hsu, C.C. Lee, S.W. Hwang, H.H. Chen, C.H. Chen, A.T. Hu, Thin Solid Films 478 (2005) 271–274.
[6] J. Cao, X. Liu, M.A. Khan, W.Q. Zhu, X.Y. Jiang, Z.L. Zhang, S.H. Xu, Curr. Appl. Phys. 7 (2007) 300–304.
[7] B.D. Chin, J. Phys. D: Appl. Phys. 40 (2007) 5541–5546.
[8] Q. Huang, K. Walzer, M. Pfeiffer, V. Lyssenko, G.F. He, K. Leo, Appl. Phys. Lett. 88 (2006) 113515-1–113515-3.
[9] H. Riel, S. Karg, T. Beierlein, B. Ruhstaller, W. Riess, Appl. Phys. Lett. 82 (2003) 466–468.
[10] S.F. Chen, W.F. Xie, W. Huang, S.L. Liu, Opt. Express 16 (2008) 8868–8875.
[11] S.F. Hsu, C.C. Lee, S.W. Hwang, C.H. Chen, Appl. Phys. Lett. 86 (2005) 253508.
[12] B.Y. Jung, N.Y. Kim, C. Lee, C.K. Hwangbo, C. Seoul, Appl. Opt. 41 (2002) 3312–3318.
[13] S. Chen, X. Li, W. Huang, Org. Electron. 9 (2008) 1112–1117.
[14] Z.Y. Xie, L.S. Hung, Appl. Phys. Lett. 84 (2004) 1207–1209.
[15] S.F. Chen, W.F. Xie, Y.L. Meng, P. Chen, Y. Zhao, S.Y. Liu, J. Appl. Phys. 103 (2008) 054506.
[16] T.H. Zheng, W. Choy, Adv. Funct. Mater. 20 (2010) 648–655.

Organic Electronics 12 (2011) 329–335

Contents lists available at ScienceDirect

Organic Electronics

journal homepage: www.elsevier.com/locate/orgel

Charge transfer reactions in near IR absorbing small molecule solution processed organic bulk-heterojunction solar

Antonio Sánchez-Díaz [a], Roberto Pacios [b], Udane Muñecas [b], Tomás Torres [c,d], Emilio Palomares [a,e,*]

[a] Institute of Chemical Research of Catalonia (ICIQ), Avda Països Catalans 16, E-43007 Tarragona, Spain
[b] Department of Microsystems, IKERLAN S. Coop, Goiru 9, 20500 Arrasate, Spain
[c] Universidad Autónoma de Madrid, Departamento de Química Orgánica, E-28049 MD, Spain
[d] IMDEA-Nanociencia, Facultad de Ciencias, Ciudad Universitaria de Cantoblanco, 28049 Madrid, Spain
[e] InstitutCatalà de Recerca I EstudisAvançats (ICREA), Avda. Lluís Companys 23, E-80810 Barcelona, Spain

ARTICLE INFO

Article history:
Received 1 September 2010
Accepted 18 November 2010
Available online 1 December 2010

Keywords:
Organic solar cells
Solution processed
Small molecule solar cells
Recombination kinetics
Near IR absorption
Bulk heterojunction

ABSTRACT

We have measured the charge transfer processes on near IR small molecule solution processes solar cells under working conditions. The results show that there are two different behavior, for the device under working conditions, controlled by the intrinsic properties of the organic bulk-heterojunction phase to store charges at the different organic materials. Furthermore, our recombination kinetic studies show the origin of the photovoltage on these thin organic devices (80 nm thick) and the reason for the difference between the observed open circuit cell potential and the theoretical expected value based on the LUM-OPCBM–HOMO phthalocyanine difference.

© 2010 Elsevier B.V. All rights reserved.

1. Introduction

Solar cells based on organic molecular materials are currently undergoing intense research due to their expected low cost for the production of electrical energy [1–10]. Amongst the different molecular photovoltaic devices, small molecule organic solar cells (sMOSC) offers the possibility to be fabricated either by sublimation under high vacuum or by solution processing both techniques already implemented in commercially available optoelectronic devices [11–15]. However, solution processing allows the preparation by ink-jet printing or roll-to-roll coating, with the advantage of cover large area, and fine tuning of the morphology by changes on the solvent for example.

The best efficiencies of sMOSC reported to date contain a fullerene derivative as acceptor, the well known PCBM ([6,6]-phenyl-C61-butyric acid methyl ester). However PCBM contribution to the device light harvesting efficiency is rather small and hence a broad and intense absorption is a must from the donor material. Based on semi-empirical calculations organic photovoltaic devices based on PCBM as acceptor are predicted to have an efficiency of 10% [16]. Although attempts to increase the device photocurrent have been made by using C_{70} based PCBM as electron acceptor material the photocurrent generated is limited by the low molecular absorption extinction coefficient of the material [17]. Thus, the use of electron donor organic molecules with small band-gaps and high molecular absorption extinction coefficient are desirable for efficient photon harvesting in the near IR region of the solar spectrum with the subsequent increase in photocurrent

* Corresponding author at: Institute of Chemical Research of Catalonia (ICIQ), Avda Països Catalans 16, E-43007 Tarragona, Spain. Tel.: +34 977920200.
E-mail address: epalomares@iciq.es (E. Palomares).

1566-1199/$ - see front matter © 2010 Elsevier B.V. All rights reserved.
doi:10.1016/j.orgel.2010.11.014

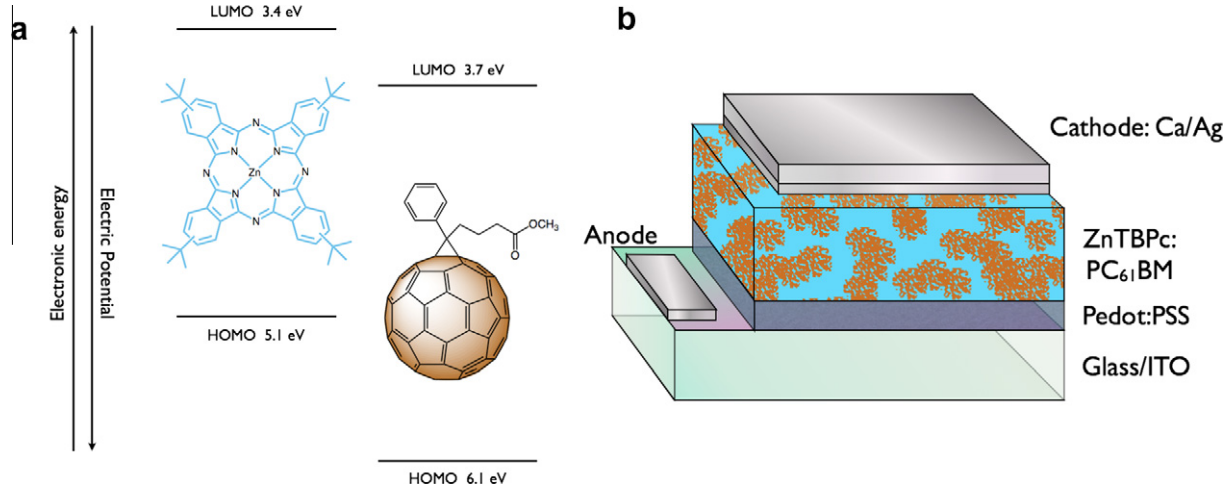

Scheme 1. (a) chemical structure of the donor Zinc phthalocyanine, ZnTBPc, and the acceptor PCBM. The energy of the band-gap edges were extracted from the cyclic voltammetry and converted to experimental values respect to vacuum. (b) The device architecture.

[18,19]. There are few studies using molecules with a strong absorption on the near IR and great efforts are currently being made to obtain low bandgap polymers with absorption spectra shifted towards the IR [20–22]. For example, Inganäs et al. published devices with light-to-energy conversion efficiencies of 0.3% using a polymer as electron donor material with light absorption close to 800 nm [20,23,24]. Cao and co-workers increased the efficiency to 0.7% in similar conditions [25], but the record was achieved by Heeger et al. with a 5.5% efficiency [26]. However, less attention have been focused on the use of phthalocyanines as electron donor materials in sMOSC [27,28]. Nevertheless, the use of Zinc phthalocyanines (ZnPc) in organic small molecular solar cells using high vacuum sublimation techniques has paved the way towards light-to-energy conversion efficiencies as high as 7.7% [29,30].

A recent result, using functionalized dendritic oligothiophene Ruthenium phthalocyanines with PCBM in bulk heterojunction devices [31], showed the potential of Ruthenium phthalocyanines as efficient electron donor for near IR sMOSC and fuelled our interest to investigate the possibility to obtain similar efficiencies with less synthetically demanding phthalocyanine based sensitizers. Thus, in this manuscript we aim to evaluate the use of a symmetrical Zinc phthalocyanine (Zinc 2,9,16,23-tetra-tert-butyl-29H,31H-phthalocyanine, (Scheme 1a) which have several advantages for sMOSC such as: (i) easy to synthesize and purify, (ii) possible to obtain in multi-kilogram scale and (iii) soluble in organic solvents with an intense absorption in the near IR [32]. Moreover, ZnPc molecules have a series of structural properties that favor their use as electron donor materials in sMOSC such as: (a) the formation of π–π stacking units which could lead to the formation of nanoscopic

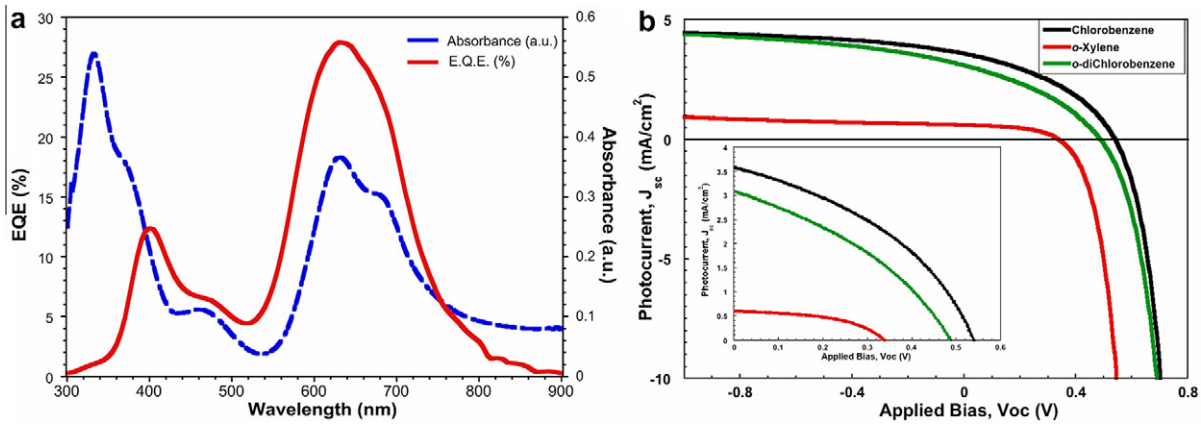

Fig. 1. (a) Absorption of ZnTBPc:PCBM blend film (dashed blue line) on top of PEDOT:PSS covered ITO substrate, prepared as for efficient devices and the external quantum efficiency, EQE, measurement (red line) of a complete device. (b) Characteristic photocurrent–voltage curves for our ZnTBPc/PCBM sMOSC when cast from different solvent solutions. The inset is a magnification of the first quadrant of the IV characteristics. (For interpretation of the references to color in this figure legend, the reader is referred to the web version of this paper.)

routes for the transport of polarons to the device metal contact, (b) the molecular symmetry, which promotes charge delocalization, thereby minimizing Coulombic repulsions, and (c) its ability to undergo oxidation at mild potentials to give a long lived radical cation. Furthermore, we measured and analyzed the interfacial charge transfer reactions in complete devices under working conditions to obtain additional information, which could be used for further device improvement. The ZnTBPc:PCBM film absorption spectrum, Fig. 1a, extends from the visible (λ = 400 nm) to the near IR region of the solar spectrum (λ = 800 nm) with a prominent maximum at a wavelength of λ_{max} = 630 with a molar extinction coefficient ε = 50,000 L mol^{-1} cm^{-1} [32]. For comparison purposes absorption spectrum is plotted with the measured external quantum efficiency (EQE), which refers to the efficiency of the device to convert absorbed light into free carriers and collect them at the device electrodes. It is clear that the EQE follows the same trend as the absorption spectrum and no ground state additional charge transfer bands are observed. We want to stress the fact that the sensitivity of our system might not be high enough to observe subgap charge transfer bands, which are typically low level signals [33–35]. The higher absorption in the 300–350 nm region of the spectrum is assigned to the transparent conducting glass based on Indium-doped Tin Oxide (ITO).

It is worthy to notice that, despite the thin film thickness of 60 nm, an EQE of ca. 30% is obtained, which corresponds to a theoretical photocurrent of 3.6 mA cm^{-2} when integrated using the 1.5 AM G solar spectrum as a reference for the device made using chlorobenzene as solvent. This thickness was found to be the optimum during the thickness optimization process, and is in agreement with the results found in ZnPc/C60 evaporated devices [36].

Fig. 1b illustrates the current density versus voltage (J–V) curve for the ZnTBPc/PCBM sMOSC upon illumination at 100 mW/cm^2 using sun-simulated light with the standard 1.5 AM G spectrum. The use of the correct organic solvent was critical to achieve the efficiency reported above. Table 1 shows the power conversion efficiencies for the devices made using different organic solvents. As can be observed, the use of chlorobenzene (CB) gives the best efficiency while *o*-Xylene (OX) shows very poor device performances. Table 1 shows the most relevant parameters for the different devices. The origin of this differences were evaluated by morphology measurements using Atomic Force Microscopy (AFM) Fig. 2. An apparent formation of homogeneously distributed holes in the film appear as a main feature when tapping mode was used to measure the surface morphology. The origin of this holes is intrinsic to the film formation, as they are also present in not thermally treated films. The poorer performance of devices prepared using *o*-dichloro benzene (ODCB) when compared to CB can be ascribed to a bigger hole formation, as better performance was obtained using CB. In the case of CB and OX the holes were significantly smaller than with ODCB. Also between the last two it can be seen that OX has a higher hole density, which might partially explain the poorer device performance when compared to CB. The solvents investigated herein were chosen because allow good solubility for both donor and acceptor molecules. As AFM only shows surface features, Differential Scanning Calorimetry (DSC) and Bright-field TEM were also used to investigate differences in crystallization of the films prepared with different solvents, respectively. For the DSC analysis, solutions of ZnTBPc/PCBM in different solvents were dried on the crucible where DSC was measured. The DSC results can be found at the Supporting information document Fig. S1. The results did not show significant differences at the crystallization temperature, with peaks at 110 °C. However the crystallization peak for the OX film was half intense than what it was obtained for the chlorinated solvents, which means a hindered crystallization after the annealing process. Therefore crystallization temperature in the film remains constant after the annealing step independently on the solvent used, but [37] not the final morphology which is indeed induced by the solvent selection and determines the output energy of the device. In-deep details of the crystallinity were also investigated using Bright-field TEM. The selected-area electron diffraction (SAED) patterns are consistent with our AFM and DSC results, and support our hypothesis that OX is less crystalline than CB and ODCB as it can be seen in the Supporting information Fig. S2, where less defined rings were obtained for the OX with respect to the CB and ODCB. The BF-TEM images show no segregation on the OX film, whereas for the chlorinated solvent prepared films an homogeneously distribution of aggregates are present, specially on the CB film where bigger domains were observed and from the IV-results such aggregates seems to be key for the overall device efficiency.

Once the characteristics of the blend and the device were analyzed we turned into the study of the interfacial charge recombination dynamics that limit the overall device efficiency. We focused only in the most efficiency device, which turns out to be the blend obtained by suing CB as solvent. The Fig. 3a illustrates the measured L-TAS spectrum of the film prepared using the same procedure as for complete devices. The spectrum taken 4 μs after the laser pulse excitation (λ_{ex} = 630 nm) exhibits an absorption peak at λ = 500 nm, which is assigned to the ZnTBPc radical cation species. The excitation at λ = 630 nm prevent direct excitation of the PCBM molecules [38].

Table 1
List of sMOSC J_{sc}–V_{oc} characteristics under 100 mW cm^{-2} 1.5 AM G simulated light.

Solvent	J_{sc} (mA cm^{-2})	V_{oc} (V)	Fill factor (%)	Efficiency (%)
Chlorobenzene	3.577 ± 0.005	0.539 ± 0.005	39.71 ± 0.05	0.765 ± 0.005
o-Xylene	0.602 ± 0.005	0.338 ± 0.005	48.68 ± 0.05	0.100 ± 0.005
o-Dichloro benzene	3.078 ± 0.005	0.489 ± 0.005	36.14 ± 0.05	0.543 ± 0.005

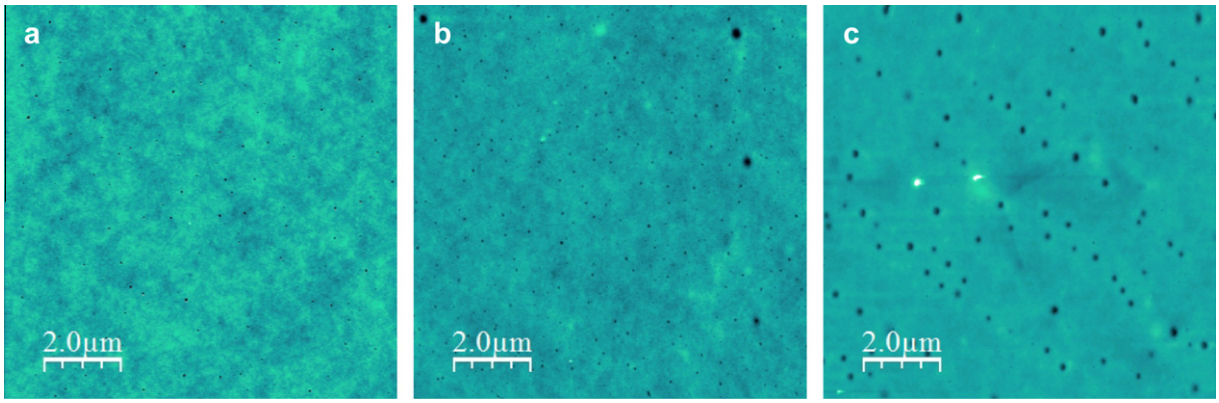

Fig. 2. AFM tapping mode images of annealed ZnTBPc/PCBM films cast from (a) chlorobenzene, (b) *o*-Xylene and (c) *o*-dichlorobenzene.

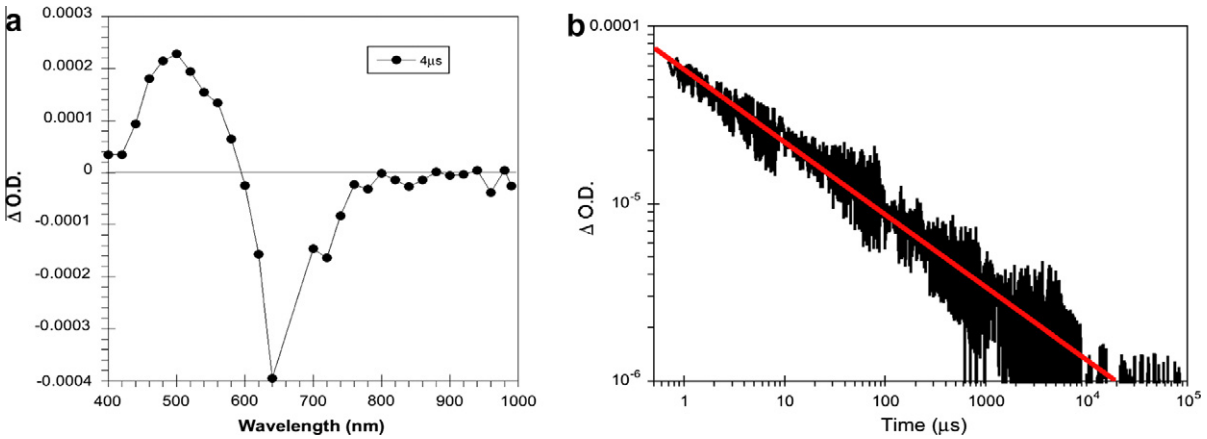

Fig. 3. (a) L-TAS spectrum upon excitation at 630 nm of a ZnTBPc/PCBM sMOSC after 4 μs. (b) Transient absorption decay obtained for a ZnTBPc/PCBM film (1:0.5 w.w. spin coated from chlorobenzene). The measured thickness was 50 nm after annealing at $T = 110\ ^{\circ}C$ for 10 min. Excitation wavelength was $\lambda = 630$ nm and the decay was monitored at $\lambda = 500$ nm. The solid line is the result of the fitting of the experimental data to a power-law exponential equation.

The time evolution of the transient signal optical density (ΔOD) at 500 nm was successfully fitted to a power equation of the form $\Delta OD = At^{-\alpha}$. The power-law decay Fig. 3b is characteristic of the bi-molecular charge recombination of long-lived, dissociated charged species in organic photovoltaic devices [39,40]. The exponent in the power equation was $\alpha = 0.5$ and the proportionality constant $A = 3.3 \times 10^{-8}$. The sub-unity value for α (α would be expected to equal 1 for ideal bimolecular recombination) has been discussed previously in terms of polaron trapping in a distribution of energetic traps at the tail of the Density of States (DOS) of the electron donor material and indicates the presence of bi-molecular charge recombination kinetics [39,41]. Yet, the presence of geminative recombination processes, that may also limit the device efficiency, cannot be discarded. The instrument response of our system did not allow us to measure kinetics faster than 500 ns.

To further verify a bimolecular recombination process, transient photovoltage measurements were carried out on complete devices. Both techniques allow the determination of charge densities and carrier lifetimes in working devices under standard operating conditions [42–44].

The total charge in the cell at V_{oc} was measured by "charge extraction" technique. In this method, a 1 sun white LED illumination source is turned off in <1 μs, while simultaneously, the cell is switched from open to short circuit. The resulting current, as the cell returns to $V = 0$ and $J = 0$, is integrated to give a direct measurement of the excess charge in the film. The number of charges measured is always smaller than real, given that some charges may recombine internally instead of traveling through the external circuit. This loss of charge will affect the magnitude of the curves, however the shape that is directly related with the DOS, will be the same, also previous studies showed an error lower than 10% when employing this technique on similar device structure [45,46]. Strikingly, the electron density rise linearly up to light biases of 500 mV Fig. 4a and from 500 mV to higher open circuit voltages (V_{oc}) an exponential increase is observed. Capacitance can also be measured by using $C = \Delta Q/\Delta V$. As observed in Fig. 4a, below 500 mV the capacitance is in

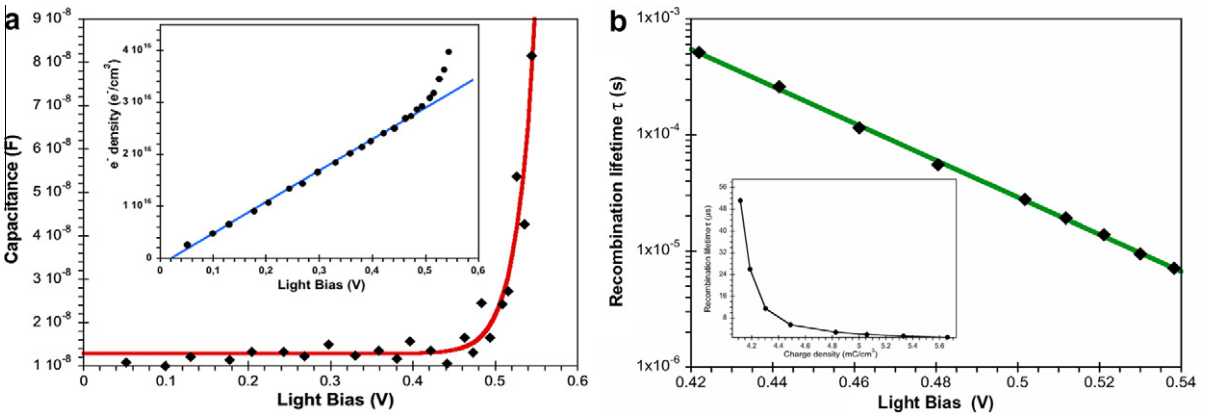

Fig. 4. (a) Capacitance of complete devices measured under standard operating conditions. The inset shows the electron density, measured with the charge extraction technique versus light bias induced open circuit voltage (V_{oc}). (b) Recombination lifetime at open circuit conditions extracted from fitting the transient photovoltage to a single exponential equation, the line corresponds to an exponential fit. The inset corresponds to small perturbation carrier lifetime as a function of charge density for V_{oc} from 570 to 420 mV, the solid line is a guide to eye.

the same range as the geometrical capacitance which is $\sim$15 nF cm^{-2}, calculated using $C = \varepsilon_r \varepsilon_0 A/d$ where $\varepsilon_r \approx 4.8$ is a suitable value for the relative static permittivity [47–50], $\varepsilon_0 \approx 8.854 \times 10^{-12}$ F m^{-1} is the dielectric permittivity of vacuum, A is the area of the device, and d is the active layer thickness. The capacitance curve suggests that below 500 mV there is no excess of charge accumulated in the device active layer and the capacitance obtained corresponds to the electrode capacitance. However, at light bias higher than 500 mV the capacitance is found to increase exponentially with increasing V_{oc} and it is assigned to a measure of charge carriers within the bulk of the device. Since the charge accumulation starts at potentials close to the V_{oc} observed in the I–V curve, the recombination lifetimes were measured at these potentials, in order to extract the limiting factors of the device under working conditions.

The recombination in complete devices was measured by transient photovoltage (TPV). For the TPV measurements, the devices were connected to the 1 MΩ input terminal of an oscilloscope, and illuminated with white light to set the light bias. A small optical perturbation was applied using a nitrogen pumped dye LASER as an excitation source with wavelength of 630 nm (frequency 1 Hz, pulse duration <1 ns), which resulted in a voltage transient with an amplitude of 2 mV. The intensity of the LASER pulse was attenuated as necessary using a circular neutral density filter. In open circuit conditions under white light an equilibrium is reached between charge formation and charge recombination, the pulsed small perturbation creates an excess of charges that will eventually recombine to reach the equilibrium set by the white light at the same rate determined by the equilibrium position.

The transients measured at different light bias were well fitted to a single exponential equation. In Fig. 4b is shown the recombination mean lifetime (τ) extracted from the fitting versus light induced open circuit voltage.

The charge carrier (τ) was found to be exponentially dependent on light bias,

$$\tau = \tau_0 e^{(-\beta V_{oc})}$$

where τ_0 corresponds to the lifetime at zero light bias and is $\sim 2.7 \times 10^5$ μs, β is the decay constant and it relates to the rate of decay, it was found to be $\sim$37. As the light intensity is increased, the lifetime decreases exponentially, reaching $\sim$10 μs at an approximate intensity of 1 sun.

The recombination lifetimes were plotted versus charge density to stress the relationship between charges stored in the device under working conditions and the charge recombination rate. In Fig. 4b is shown that as the charge density increases, the recombination lifetime decreases exponentially. This behavior implicates that the bimolecular recombination process, within the bulk, limits the device photocurrent in a way that at potentials close to the V_{oc}, the recombination is fast enough to directly compete with the charge extraction process at the electrodes. Therefore, according to this observation, we believe that the device open circuit voltage (V_{oc}) is limited by the bimolecular recombination process. The observed fast recombination kinetics under operating conditions (100 mW cm^{-2} sun-simulated light irradiation) has a direct influence over the materials Fermi level splitting hindering the charge occupancy of upper energetic levels that will lead to higher V_{oc} [51].

We have demonstrated that efficient near IR small molecule based solution processed bulk-heterojunction solar cells that incorporate a soluble Zinc phthalocyanine can be used as light harvester. When mixed with PCBM and sandwiched between selective electrodes, efficiencies at 100 mW cm^{-2} sun-simulated light reached 0.77%. The limiting factors in the device under working conditions were studied using time-resolved spectroscopic techniques, and we found a strong increase of the bimolecular recombination process at light-bias close to the device V_{oc} and above. The enlarged recombination kinetics can be directly correlated with the number of charges accumulated at the bulk and, moreover, we demonstrated that the faster recombination dynamics are one of the main factors limiting the device open circuit voltage. Therefore, strategies affecting such recombination kinetics must be applied in the synthesis of new phthalocyanines in order to improve the light-to-energy conversion efficiency of this type of solar cells.

2. Experimental

2.1. Photophysical characterization

Microsecond to millisecond LASER Transient Absorbance Spectra (L-TAS) employed 630 nm (1.97 eV) excitation pulses (frequency 1.5 Hz, duration <1 ns). The change in the sample transmission was monitored using a tungsten lamp with monochromators before and after the sample set at 540 nm. Data resulted from averaging 100–1000 laser shots. UV/visible spectra recorded before and after transient absorbance experiments did not indicate any sample degradation.

2.2. Device fabrication and characterization

Indium Tin Oxide (ITO) 4 Ω^2 covered glass substrates were first cleaned with acetone for the removal of the photo-protective layer with 5 min sonication. The glasses were then placed in an ultrasonic bath twice in 2-propanol (IPA) for 5 min. The ITO substrates were then treated in a UV ozone cleaner for 20 min followed by spin coating of poly(3,4-ethylenedioxythiophene) poly(styrenesulfonate) (PEDOT:PSS, Baytron P) (5000 rpm 30 s followed by 3500 rpm 10 s). The PEDOT:PSS film was dried at 100 °C inside a glove box for 10 min which yielded a film of 30 nm thick. A 15 (mg ml^{-1}) ZnTBPc and 7.5 (mg ml^{-1}) PCBM (Nano-C USA) solution in chlorobenzene was prepared inside a glove box and stirred for 12 h.

The spin coating of the photoactive layer was made inside a glove box and the conditions used were 1500 rpm during 20 s followed by 2000 rpm 30 s. These conditions gave thicknesses in the range of 60 nm.

Subsequently the devices were placed in a UHV chamber (1×10^{-6} mbar), and 10 nm of Calcium followed by 150 nm of Silver were deposited on top of the active layer through a shadow mask that leads 9 mm^2 devices.

Thermal annealing was carried out by directly placing the completed devices on a digitally controlled hotplate at 110 °C for 10 min inside the glove box.

The thickness of the films was measured with a stylus profilometer Ambios Tech. XP-1, from a scratch applied in the middle of the film to have accurate measurements.

Following fabrication, the films were maintained under a nitrogen atmosphere and stored in the dark until used.

The J_{sc}–V_{oc} characteristics measurement was carried out with a ABET 150 W Xenon light source equipped with the correct set of filters to achieve the solar spectrum 1.5 AM G. The light intensity was adjusted to 100 mW cm^{-2} using a calibrated Si photodiode. The applied potential and cell current were measured with Keithley model 2600 digital source meter. The current to voltage (I–V curve) was measured automatically with a home-built Labview© software.

Atomic Force Microscopy (AFM) of the samples was performed on tapping mode on a Molecular Imaging model Pico SPM II (pico +). Images were collected in air using silicon probes with a typical spring constant of 1–5 nN/m and a resonant frequency of 75 kHz.

TEM was performed on a JEOL JEM-1011 transmission electron microscope operated at an acceleration voltage of 100 kV. To quantitatively relate the diffraction intensity in SAED patterns to the crystallinity of the specimen investigated, all these SAED patterns were performed using a standard recording mode, i.e. fixed magnification, field-limiting apertura of 100 mm, current density of 0.6 pA cm^2 and exposure time of 11.0 s for SAED acquisition. Identical time and conditions were used for film development. All the negatives were digitalized using the same settings.

Acknowledgments

This work has been supported by the Spanish MICINN (CTQ-2008-00418BQU, CTQ2007-60746/BQU, CONSOLIDER 2010 CDS 2007-00010 Nanociencia Molecular, PLE2009-0070 and CONSOLIDER HOPE-CSD-0007-2007 and Project PSE-FotoMol). The Comunidad de Madrid Project Madridsolar-2 S2009/PPQ/1533 and the Generalitat de Cataluya DURSI-2009-SGR-207. A.S.D. acknowledges the ICIQ for pre-doctoral fellowship and E.P. thanks ICIQ and ICREA for financial support.

Appendix A. Supplementary data

Supplementary data associated with this article can be found, in the online version, at doi:10.1016/j.orgel.2010.11.014.

References

[1] N.S. Sariciftci, L. Smilowitz, A.J. Heeger, F. Wudl, Science 258 (1992) 1474.
[2] J.J.M. Halls, C.A. Walsh, N.C. Greenham, E.A. Marseglia, R.H. Friend, S.C. Moratti, A.B. Holmes, Nature 376 (1995) 498.
[3] G. Yu, J. Gao, J.C. Hummelen, F. Wudl, A.J. Heeger, Science 270 (1995) 1789.
[4] P. Peumans, S. Uchida, S.R. Forrest, Nature 425 (2003) 158.
[5] S. Günes, H. Neugebauer, N.S. Sariciftci, Chem. Rev. 107 (2007) 1324.
[6] B.C. Thompson, J.M.J. Fr_échet, Angew. Chem. Int. Ed. 47 (2008).
[7] F.C. Krebs, Sol. Energy Mater. Sol. Cells 93 (2009) 394.
[8] F.C. Krebs, Sol. Energy Mater. Sol. Cells 93 (2009) 465.
[9] G. Dennler, M.C. Scharber, C.J. Brabec, Adv. Mater. 21 (2009) 1.
[10] F.C. Krebs, Org. Electron. 10 (2009) 761.
[11] J.Y. Kim, K. Lee, N.E. Coates, D. Moses, T.-Q. Nguyen, M. Dante, A.J. Heeger, Science 317 (2007) 222.
[12] M.T. Lloyd, J.E. Anthony, G.G. Malliaras, Mater. Today (Oxford, United Kingdom) 10 (2007) 34.
[13] S. Pfuetzner, J. Meiss, A. Petrich, M. Riede, K. Leo, Appl. Phys. Lett. 94 (2009) 253303.
[14] S.H. Park, A. Roy, S. Beaupré, S. Cho, N. Coates, J.S. Moon, D. Moses1, M. Leclerc3, K. Lee, A.J. Heeger, Nat. Photonics 3 (2009) 297.
[15] S.E. Shaheen, C.J. Brabec, N.S. Sariciftci, F. Padinger, T. Fromherz, J.C. Hummelen, Appl. Phys. Lett. 78 (2001) 841.
[16] M.C. Scharber, D. Muehlbacher, M. Koppe, P. Denk, C. Waldauf, A.J. Heeger, C.J. Brabec, Adv. Mater. 18 (2006) 789.
[17] M.M. Wienk, J.M. Kroon, W.J.H. Verhees, J. Knol, J.C. Hummelen, P.A.V. Hal, R.A.J. Janssen, Angew. Chem. Int. Ed. 42 (2003) 3371.
[18] N.S. Sariciftci, Mater. Today 7 (2004) 36.
[19] A. Moliton, J.-M. Nunzi, Polym. Int. 55 (2006).
[20] X. Wanga, E. Perzon, J.L. Delgado, P.d.l. Cruz, F. Zhang, F. Langa, M. Andersson, O. Inganäs, Appl. Phys. Lett. 85 (2004).
[21] A. Tamayo, T. Kent, M. Tantitiwat, M.A. Dante, J. Rogers, A.T.-Q. Nguyen, Energy Environ. Sci. 2 (2009) 1180.
[22] A.B. Tamayo, B. Walker, T.-Q. Nguyen, J. Phys. Chem. C 112 (2008) 11545.
[23] X. Wang, E. Perzon, W. Mammo, F. Oswald, S. Admassie, N.-K. Persson, F. Langa, M.R. Andersson, O. Inganäs, Thin Solid Films 511–512 (2006) 576.
[24] A. Gadisa, X. Wang, S. Admassie, E. Perzon, F. Oswald, F. Langa, M.R. Andersson, O. Inganäs, Org. Electron. 7 (2006) 165.

[25] M. Sun, L. Wang, X. Zhu, B. Du, R. Liu, W. Yang, Y. Cao, Sol. Energy Mater. Sol. Cells 91 (2007) 1681.
[26] J. Peet, J.Y. Kim, N.E. Coates, W.L. Ma, D. Moses, A.J. Heeger, G.C. Bazan, Nat. Mater. 6 (2007) 497.
[27] M.A. Loi, P. Denk, H. Hoppe, H. Neugebauer, C. Winder, D. Meissner, C. Brabec, N.S. Sariciftci, A. Gouloumis, P. Vazquez, T. Torres, J. Mater. Chem. 13 (2003) 700.
[28] M.V. Martínez-Díaz, G. De la Torre, T. Torres, Chem. Commun. 46 (2010) 7090.
[29] J. Xue, B.P. Rand, S. Uchida, S.R. Forrest, Adv. Mater. 17 (2005) 66.
[30] <http://www.heliatek.com/en/page/index.php>.
[31] M.K.R. Fischer, I. López-Duarte, M.M. Wienk, M.V. Martínez-Díaz, R.A.J. Janssen, P. Bäuerle, T. Torres, J. Am. Chem. Soc. 131 (2009) 8669.
[32] C.G. Claessens, U. Hahn, T. Torres, Chem. Rec. 8 (2008) 75.
[33] D. Veldman, S.C.J. Meskers, R.A.J. Janssen, Adv. Funct. Mater. 19 (2009) 1.
[34] J.J. Benson-Smith, L. Goris, K. Vandewal, K. Haenen, J.V. Manca, D. Vanderzande, D.D.C. Bradley, J. Nelson, Adv. Funct. Mater. 17 (2007) 451.
[35] D. Veldman, Ö. Ipek, S.C.J. Meskers, J. Sweelssen, M.M. Koetse, S.C. Veenstra, J.M. Kroon, S.S.V. Bavel, J. Loos, R.A.J. Janssen, J. Am. Chem. Soc. 130 (2008) 7721.
[36] D. Gebeyehu, B. Maennig, J. Drechsel, K. Leo, M. Pfeiffer, Sol. Energy Mater. Sol. Cells 79 (2003) 81.
[37] J. Hou, H.-Y. Chen, S. Zhang, G. Li, Y. Yang, J. Am. Chem. Soc. 130 (2008) 16144.
[38] S. Cook, H. Ohkita, Y. Kim, J.J. Benson-Smith, D.D.C. Bradley, J.R. Durrant, Chem. Phys. Lett. 445 (2007) 276.
[39] J. Nelson, Phys. Rev. B 67 (2003) 155209.
[40] J. Nelson, S.A. Choulis, J.R. Durrant, Thin Solid Films 451–452 (2004) 508.
[41] A.F. Nogueira, I. Montanari, J. Nelson, J.R. Durrant, C. Winder, N.S. Sariciftci, C. Brabec, J. Phys. Chem. B 107 (2003) 1567.
[42] B.C. O'Regan, S. Scully, A.C. Mayer, E. Palomares, J. Durrant, J. Phys. Chem. B 109 (2005) 4616.
[43] C.G. Shuttle, B. O'Regan, A.M. Ballantyne, J. Nelson, D.D.C. Bradley, J.D. Mello, J.R. Durrant, Appl. Phys. Lett. 92 (2008).
[44] C.G. Shuttle, B. O'Regan, A.M. Ballantyne, J. Nelson, D.D.C. Bradley, J.R. Durrant, Phys. Rev. B 78 (2008).
[45] C.G. Shuttle, A. Maurano, R. Hamilton, B. O'Regan, J.C.D. Mello, J.R. Durran, Appl. Phys. Lett. 93 (2008).
[46] A. Maurano, R. Hamilton, C.G. Shuttle, A.M. Ballantyne, J. Nelson, B. O'Regan, W. Zhang, I. McCulloch, H. Azimi, M. Morana, C.J. Brabec, J.R. Durrant, Adv. Mater. 22 (2010) 4987.
[47] M. Pfeiffer, T. Fritz, J. Blochwitz, A. Nollau, B. Plönnigs, A. Beyer, K. Leo, Adv. Solid State Phys. 39 (1999) 77.
[48] A. Ahmad, R.A. Collins, Phys. Status Solidi (a) 123 (1991) 201.
[49] M.M. El-Nahass, A.F. El-Deeb, F. Abd-El-Salam, Org. Electron. 7 (2006) 261.
[50] B. Pevzner, A.F. Hebard, M.S. Dresselhaus, Phys. Rev. B 55 (1997) 16439.
[51] B.A. Gregg, J. Phys. Chem. B 107 (2003) 4688.

Organic Electronics 12 (2011) 336–340

Contents lists available at ScienceDirect

Organic Electronics

journal homepage: www.elsevier.com/locate/orgel

Letter

The effects of channel length and film microstructure on the performance of pentacene transistors

Franziska D. Fleischli [a,*], Katrin Sidler [b], Michel Schaer [a], Veronica Savu [b], Jürgen Brugger [b], Libero Zuppiroli [a]

[a] Laboratory of Optoelectronics of Molecular Materials, Ecole Polytechnique Fédérale de Lausanne (EPFL), 1015 Lausanne, Switzerland
[b] Microsystems Laboratory, Ecole Polytechnique Fédérale de Lausanne (EPFL), 1015 Lausanne, Switzerland

ARTICLE INFO

Article history:
Received 3 August 2010
Received in revised form 3 December 2010
Accepted 5 December 2010
Available online 17 December 2010

Keywords:
Organic thin-film transistor
Contact resistance
Pentacene film morphology

ABSTRACT

With the use of the stencil lithography, we fabricated pentacene thin-film transistors prepared directly on thermally oxidized silicon gates with channel lengths ranging from 2 to 600 μm. By performing 4-probe measurements or by using the transfer line method on these field-effect transistors, we were able to separate the respective contributions of the channel and the contacts to the transistor performance. The contact resistance depends strongly on the gate voltage and on the grain size and morphology; this behavior has been attributed to screening effects at the contact barriers. The low-field mobility in the channel is 0.5–0.6 cm^2/Vs in long-channel transistors and reaches mobility in the order of 10 cm^2/Vs in short-channel transistors consisting essentially of a single grain.

© 2010 Elsevier B.V. All rights reserved.

1. Introduction

The performance of an organic field-effect transistor is related to the microstructure and purity of the organic semiconductor [1,2], the degree of order at the interface [3], and the quality of the contacts. The need to miniaturize the organic electronic circuit and the use of standard lithographic methods has led to smaller and smaller channel lengths [4–7]. Several authors have observed that in such cases, the contact resistance dominates the device characteristics [8–11]. For very short channels ($L < 5$ μm), the Schottky barrier at the source and drain contacts dominates device performance [9]. For long channels ($L > 100$ μm), the contact resistance is not determined by the barrier at the metal–organic semiconductor interface, but rather by drift/diffusion of carriers close to this interface [12,13]. It has also been observed that the presence of a small concentration of residual carriers produced by doping the channel can decrease the contact resistance [3,14].

In the present work, we fabricated a series of pentacene thin-film transistors with channel lengths ranging from 2 to 600 μm. We have employed stencil technology, which is a one-step technique with high resolution down to the sub-100 nm range thus eliminating solvent-based processing steps [15]. In this large range of channel lengths, the transistor performance changes from contact limited to channel dominated. We investigated the influence of the pentacene film morphology on the contact and channel performance by separating their contributions; this was made possible using both 4-probes and transfer line methods.

2. Methods

The organic thin-film transistors (OTFTs) are based on pentacene as organic semiconductor and fabricated by high-vacuum deposition in top-contact configuration. Heavily *boron* doped *Si* wafers (resistivity of 0.1–0.5 Ω cm) were used as substrates and served also as gate contacts. The wafer was coated with a thermal SiO_2 layer (200 nm in thickness).

Pentacene was deposited by thermal evaporation in a high-vacuum chamber at a rate of about 1 nm/min ($p <$

* Corresponding author. Tel.: +41 21 693 33 80.
E-mail address: franziska.fleischli@epfl.ch (F.D. Fleischli).

1566-1199/$ - see front matter © 2010 Elsevier B.V. All rights reserved.
doi:10.1016/j.orgel.2010.12.004

10^{-7} mbar). The film thickness was 40 nm. The substrate temperature is either 20 °C (room temperature) or 55 °C. The growth processes lead to different grain sizes (small grains at RT, larger grains at 55 °C). The film morphology was imaged by AFM in semi-contact mode (*NT-MDT* with a *SMENA* scanner). Pentacene was purchased at *Fluka* and twice purified in a furnace with a temperature gradient.

The gold top contacts were deposited by thermal evaporation under high vacuum ($p < 10^{-7}$ mbar) and have a thickness of 25 nm. The substrate was cooled to the temperature of liquid nitrogen (−185 °C) during evaporation to avoid gold diffusion into pentacene.

OTFTs with different contact geometry were fabricated. Contacts for long-channel transistors were patterned by a metallic shadow mask. The channel has a length of 100, 200 and 600 μm, respectively, and a width of 6 mm. A stencil was used to define the contacts for short-channel transistors. The stencils are made of a low-stress *SiN* membrane supported by bulk silicon. The channel aspect ratio is 10 and includes the channel lengths of 2, 5, 10 and 20 μm, respectively.

The OTFTs were characterized by measuring output and transfer curves (*Keithley 4200 SCS*) under Argon atmosphere (after at least 4 h under vacuum). Drain and gate voltages were swept between +10 and −40 V while the drain and gate currents were measured. The apparent field effect mobility is calculated in the linear regime, from the slope of the conductance $g_D(V_G) = dI_D/dV_D|_{VD=0}$ as a function of the gate voltage V_G. The threshold voltage is the intercept between the gate voltage axis and the linear fit of the transfer curve for high negative gate voltages [3,16]. The results are shown in Table 1.

One of the main goals of the present work is to separate the resistance of the channel from the resistance of the contacts. This was achieved by using two different methods: the 4-probe measurements and the transfer line method.

By means of 4-probe measurements (*Keithley 236 source measure unit*), the channel resistance was determined independent of the contact resistance [17]. The contact resistance was then determined as the difference between the values obtained by the 2-probe and the 4-probe measurements.

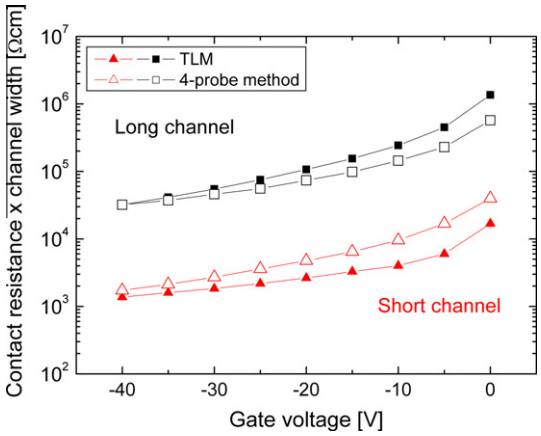

Fig. 1. Contact resistance (normalized to the channel width) measured by the 4-probe method (one transistor) and extrapolated by the transfer line method (5–6 transistors of the same batch). The long-channel transistors have a channel length of 100–600 μm and a channel width of 6 mm; the 4-probe measurements were done for a distance between the contacts of 600 μm. The short-channel transistors have a channel length of 2–20 μm and a channel width 10 times larger; the 4-probe measurements were done for a distance between the contacts of 10 μm. The pentacene film consists of large grains. The film thickness is 40 and 20 nm for long-channel and short-channel transistors, respectively.

The transfer line method uses transistors of the same batch but of different channel lengths. The contact resistance is obtained by extrapolating the resistance at zero channel length [18,19].

In Fig. 1, we compare the results of the 4-probe and the transfer line method for two different batches of transistors. The two measurements coincide within a factor of two at low gate fields and within 20% at large gate fields; the discrepancy is in large part due to the transfer line

Table 1
Characteristic values for OTFT with different channel lengths. The apparent mobility refers to the entire device and contains hidden contributions due to the contacts (see Table 2). The conductivity results from 4-probes measurements with a floating gate; they reflect the presence of a density of residual carriers in the channel.

	Apparent mobility (cm^2/Vs)	Conductivity (10^{-8} S □)	Threshold voltage (V)	Total resistance (MΩ)
Long channels, small grains (0.2–0.5 μm)				
600 μm	0.45	7.2	8.3	1.39
200 μm	1.04	14.3	1.0	0.23
100 μm	1.21	14.6	−1.1	0.12
Short channels, small grains (0.2–0.5 μm)				
20 μm	1.51	17.1	−1.4	0.58
10 μm	1.39	14.9	−4.3	0.67
5 μm	1.27	5.0	−6.3	2.0
2 μm	1.08	1.3	−5.1	8.0
Long channels, large grains (2–3 μm)				
600 μm	0.58	3.4	−2.7	2.92
200 μm	0.68	0.88	−12	3.78
100 μm	0.28	0.31	−12	5.36
Short channels, large grains (2–3 μm)				
20 μm	1.31	5.79	−4.8	1.73
10 μm	1.57	3.17	−10.8	3.15
5 μm	0.69	3.61	−3.3	2.77
2 μm	0.82	7.31	2.9	1.38

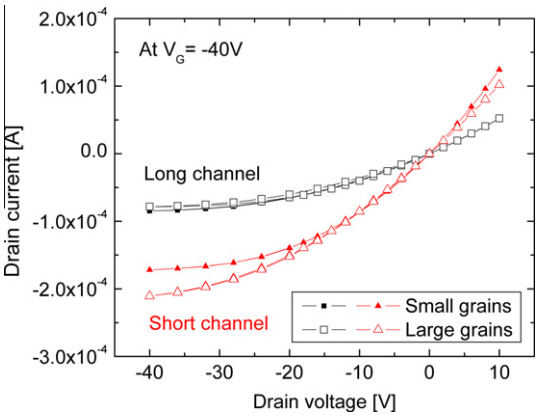

Fig. 2. Output curves of OTFTs with long and short channels (600 and 10 μm, respectively) and different film morphologies (small and large grains). The gate was polarized at a voltage of −40 V.

method which assumes a perfect homogeneity in the batch what is difficult to achieve in practice. As observed by other groups [12,13], the 4-probe method is also questionable when the potential of the inner electrodes is perturbed by the current flowing between the outer electrodes, especially for thick film when the electrodes do not penetrate enough in the channel region. But in the present work where large effects are observed and thin films are used (20 and 40 nm), the errors on the absolute value of the contact resistance are well below the measured variations.

3. Results

On the top of SiO_2, the morphology of the 40 nm thick pentacene film depends on the substrate temperature during pentacene deposition. At room temperature, the film has grown in submicron grains with a dendritic shape [20]. If the substrate temperature is 55 °C, the grains increase in size (2–3 μm in diameter) and become more compact.

The output curves in Fig. 2 show that all transistors have a linear regime around zero drain voltage and reach saturation. At a gate voltage of −40 V, the drain current through a transistor with a short channel (10 μm in length) is about twice as high as through a long-channel transistor (600 μm in length).

The transfer characteristics in Fig. 3 show that the short- and long-channel transistors behave differently.

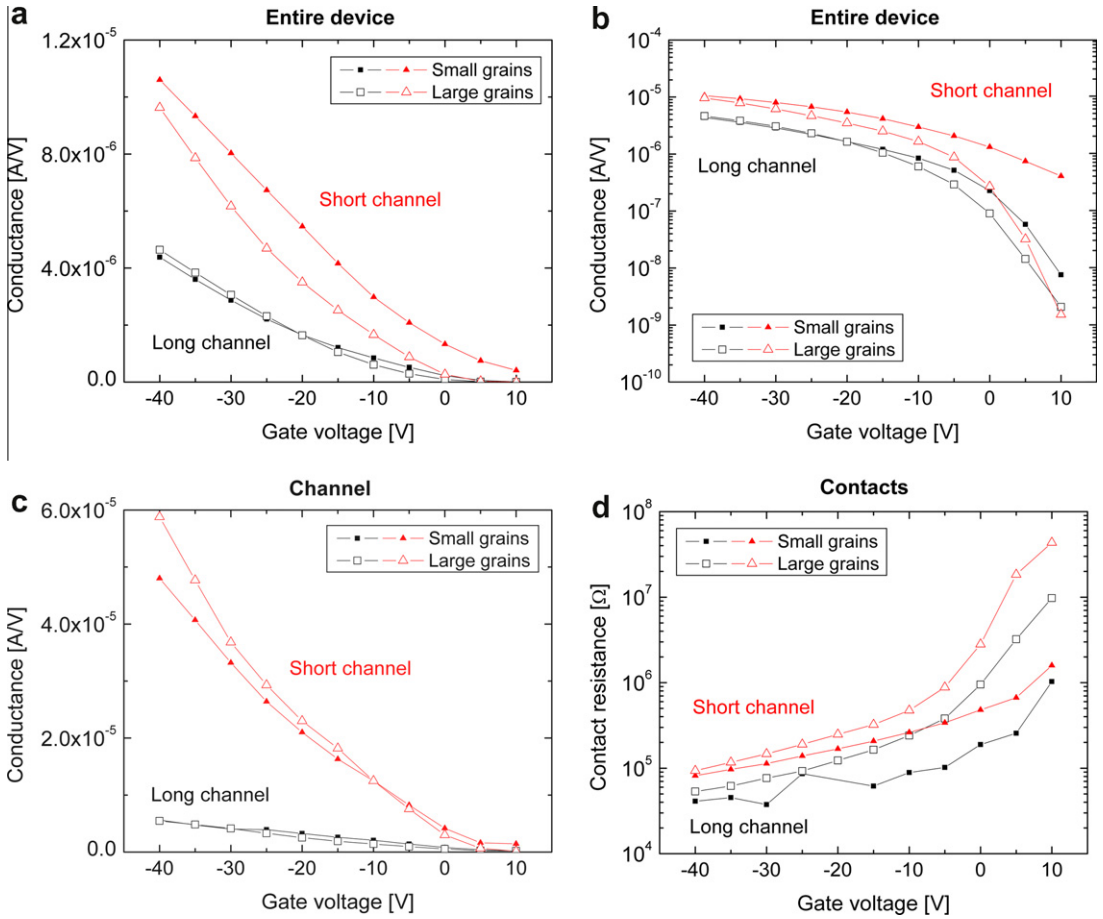

Fig. 3. Transfer curves (a) and (b) of the entire device and (c) of the channel, (d) contact resistance depending on the applied gate voltage for OTFTs with long and short channels (600 and 10 μm, respectively) and different film morphologies (small and large grains, respectively). The samples are the 4-probe devices of Table 2.

Table 2
Characteristic values for the entire device and the channel only. The density of residual carriers, P_{res}, can be derived from the following equation: $P_{res} = \sigma/(e\,\mu_{app})$, where σ is the conductivity, e the elementary charge, and μ_{app} the apparent mobility in the linear regime [17].

	Channel		Entire device		At floating gate			Residual carriers (cm^{-2})
	Apparent mobility (cm^2/Vs)	Threshold voltage (V)	Apparent mobility (cm^2/Vs)	Threshold voltage (V)	Total resistance (MΩ)	Channel resistance (MΩ)	Contact resistance (MΩ)	
Long channel (600 μm), small grains (0.2–0.5 μm)	0.59	7.3	0.45	8.3	1.39	1.26	0.14	1.0×10^{12}
Long channel (600 μm), large grains (2–3 μm)	0.74	−1.8	0.58	−2.7	2.92	2.11	0.81	3.7×10^{11}
Short channel (10 μm), small grains (0.2–0.5 μm)	7.42	−6.9	1.39	−4.3	0.67	0.23	0.44	6.7×10^{11}
Short channel (10 μm), large grains (2–3 μm)	10.2	−10.8	1.57	−10.8	3.15	0.33	2.82	1.3×10^{11}

The performance of long-channel transistors is dominated by the channel; this is shown in the small difference between the transfer curves of the entire device and the curve of the channel alone (see Fig. 3a–c). Consequently, the apparent and channel mobility do not differ significantly (from 0.45 to 0.74 cm^2/Vs, see Table 2).

In contrast, the transistors with a short channel (2–20 μm) are limited by the contacts. The channel conductance is approximately five times higher than the conductance of the entire device (see Fig. 3a–c). As expected, this behavior is reflected in the mobility values. While the apparent mobility of the entire device is in the range of 1.0–1.5 cm^2/Vs, the channel mobility is more than five times higher, and reaches 10 cm^2/Vs (see Table 2).

4. Discussion

The most important results of this work are those summarized in Fig. 3 and Table 2. Let us consider first the behavior of the pentacene channel resistance in a floating gate configuration. Table 2 shows that pentacene films made of small grains are always more conductive than films of the same length made of large grains; this fact demonstrates that grain boundaries do not act as simple barriers but also modify the trap distribution. In fact, some of the defects at the oxide surface act as traps (≡Si–H for instance) while others are recombination centers (the radical ≡Si–O· for example) inducing charge transfers by capturing electrons of the pentacene and leaving additional holes as residual carriers in the organic semiconductor film [3].

Apparently, small dendritic grains which lead to a higher density of grain boundaries in the film induce more charge transfers at the interface of the oxide than large grains. These charge transfer reactions explain why the devices do not show a clear off regime in the transfer curves. Fig. 3d shows that the contact resistance depends significantly on the gate voltage and also on the grain size and morphology. We attributed these effects to the concentration of charge carriers in the channel; the higher the charge carrier concentration is, the stronger are the screening effects at the contact barrier, and thus the contact resistance is smaller [14].

Gold films evaporated on small dendritic grains always give smaller contact resistances than the same films evaporated on large grains. To understand this result, the contact resistance has been plotted as a function of the residual carrier concentration in the channel (Fig. 4a). A clear correlation appears between these two quantities;

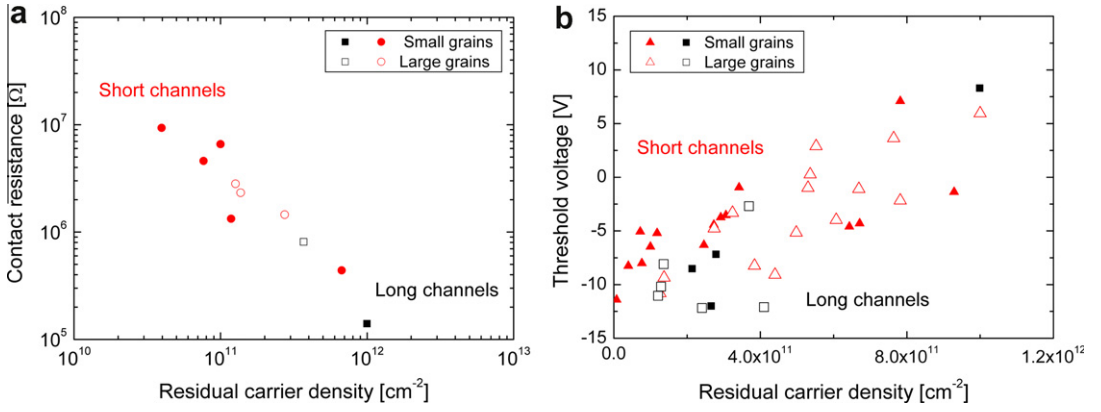

Fig. 4. (a) Contact resistance measured at floating gate (by the 4-probe method) versus residual carrier density for OTFTs with long and short channels (600, 10 and 20 μm, respectively) and (b) threshold voltage versus residual carrier density for OTFTs with long and short channels and different film morphologies (small and large grains, respectively).

residual carriers have a clear screening effect on the contact barriers [14]. The fact that small grains give smaller contact resistance than large ones is once again due to charge transfer reactions mainly occur at grain boundaries. For the same reason, a short-channel transistor with only a few grains in the channel exhibits larger contact resistance because of lower residual carrier concentration.

The threshold voltage of the transistors presented here varies from −10 to +10 V. The voltage also correlates with the residual carrier concentration (see Fig. 4b). The negative values reflect the distribution of dipolar traps at the oxide surface, while residual carriers in the channel push the voltage threshold towards positive values [17].

The transistors which were compared in this work have been fabricated with pentacene layers of 40 nm thickness. For the sake of clarity, the results obtained for 20 and 80 nm-thick pentacene layers are not presented here; however, we observed essentially the same behavior for all thicknesses. It is worth mentioning that the thickness of 40 nm represents a sort of optimum; the channel mobilities in both 20 and 80 nm transistors are 20% lower.

Some transistors have also been fabricated on aluminum oxide gate insulators. We have observed that the behavior of aluminum oxide is similar to that of silicon oxide; in particular, from the point of view of charge transfer reactions and residual carriers [3].

5. Conclusion

Pentacene thin-film transistors have given rise to a very large number of studies in the literature, which are not always consistent with each other. The use of the stencil technology together with 4-probe measurements has helped to clarify the surprising behavior of the apparent mobility with the pentacene grain size and the channel length. In fact, the contact resistance and the channel resistance are both gate voltage dependent and can vary in an opposite way with grain size and morphology. In pentacene transistors prepared directly on an oxide gate insulator, the interface traps and charge transfer centers dominate the transport. Although they belong essentially to the oxide, their activity is very often related to the presence of the grain boundaries of the pentacene dendritic grains. It is worth mentioning that a self-assembled monolayer (SAM) reduces the morphology and defect dependence by separating the interface traps and charge transfer centers from the pentacene film (surface passivation) [18,21]. When the passivation of the oxide by the SAM is efficient (number of residual carriers lower than 10^{11} per cm^2), then the mobility slowly increases with the grain size [22].

Acknowledgements

We thank Philippe Bugnon for the pentacene purification. This research was supported by the Swiss National Science Foundation through Grant SNSF 200020-121715.

References

[1] L.H. Jimison, A. Salleo, M.L. Chabinyc, D.P. Bernstein, M.F. Toney, Correlating the microstructure of thin films of poly[5,5-bis(3-dodecyl-2-thienyl)-2,2-bithiophene] with charge transport: effect of dielectric surface energy and thermal annealing, Phys. Rev. B 78 (2008) 125319.
[2] J. Rivnay, L.H. Jimison, J.E. Northrup, M.F. Toney, R. Noriega, S. Lu, T.J. Marks, A. Facchetti, A. Salleo, Large modulation of carrier transport by grain-boundary molecular packing and microstructure in organic thin films, Nat. Mater. 8 (2009) 952.
[3] S. Suarez, F.D. Fleischli, M. Schaer, L. Zuppiroli, From oxide surface to organic transistor properties: the nature and the role of oxide gate surface defects, J. Phys. Chem. C 114 (2010) 7153.
[4] A.C. Arias, J.D. MacKenzie, I. McCulloch, J. Rivnay, A. Salleo, Materials and applications for large area electronics: solution-based approaches, Chem. Rev. 110 (2010) 3.
[5] Y.L. Loo, I. McCulloch, Progress and challenges in commercialization of organic electronics, MRS Bull. 33 (2008) 653.
[6] L. Bürgi, T.J. Richards, R.H. Friend, H. Sirringhaus, Close look at charge carrier injection in polymer field-effect transistors, J. Appl. Phys. 94 (2003) 6129.
[7] P. Stallinga, Electrical Characterization of Organic Electronic Materials and Devices, 2009.
[8] I.N. Hulea, S. Russo, A. Molinari, A.F. Morpurgo, Reproducible low contact resistance in rubrene single-crystal field-effect transistors with nickel electrodes, APL 88 (2006) 113512.
[9] A. Molinari, I. Gutierrez, I.N. Hulea, S. Russo, A.F. Morpurgo, Bias-dependent contact resistance in rubrene single-crystal field-effect transistors, APL 90 (2007) 212103.
[10] A.S. Molinari, I. Gutierrez Lezama, P. Parisse, T. Takenobu, Y. Iwasa, A.F. Morpurgo, Quantitative analysis of electronic transport through weakly coupled metal/organic interfaces, APL 92 (2008) 133303.
[11] G.S. Tulevski, C. Nuckolls, A. Afzali, T.O. Graham, C.R. Kagan, Device scaling in sub-100nm pentacene field-effect transistors, APL 89 (2006) 183101.
[12] P.V. Pesavento, R.J. Chesterfield, C.R. Newman, C.D. Frisbie, Gated four-probe measurements on pentacene thin-film transistors: contact resistance as a function of gate voltage and temperature, J. Appl. Phys. 96 (2004) 7312.
[13] P.V. Pesavento, K.P. Puntambekar, C.D. Frisbie, J.C. McKeen, P.P. Ruden, Film and contact resistance in pentacene thin-film transistors: dependence on film thickness, electrode geometry, and correlation with hole mobility, J. Appl. Phys. 99 (2006) 094504.
[14] H. Ghoneim, J. Knoch, H. Riel, D. Webb, M.T. Björk, S. Karg, E. Lörtscher, H. Schmid, W. Riess, Suppression of ambipolar behavior in metallic source/drain metal-oxide-semiconductor field-effect transistors, Appl. Phys. Lett. 95 (2009) 213504.
[15] G.M. Kim, M.A.F. van den Boogaart, J. Brugger, Fabrication and application of a full wafer size micro/nanostencil for multiple length-scale surface patterning, Microelectron. Eng. 67 (2003) 609.
[16] G. Horowitz, Organic thin-film transistors: from theory to real device, J. Mater. Res. 19 (2004) 1946.
[17] M. Daraktchiev, A. von Mühlenen, F. Nüesch, M. Schaer, M. Brinkmann, M.N. Bussac, L. Zuppiroli, Ultrathin organic transistors on oxide surfaces, New J. Phys. 7 (2005) 133.
[18] A. Von Mühlenen, M. Castellani, M. Schaer, L. Zuppiroli, Controlling charge-transfer at the gate interface of organic field-effect transistors, Phys. Stat. Sol. B 245 (2008) 1170.
[19] C.S. Chiang, S. Martin, J. Kanicki, Y. Ugai, T. Yukawa, S. Takeuchi, Top-gate staggered amorphous silicon thin-film transistors: series resistance and nitride thickness effects, Jpn. J. Appl. Phys. 37 (1998) 5914.
[20] S. Pratontep, M. Brinkmann, F. Nuesch, L. Zuppiroli, Nucleation and growth of ultrathin pentacene films on silicon dioxide: effect of deposition rate and substrate temperature, Synth. Met. 146 (2004) 387.
[21] F.D. Fleischli, S. Suarez, M. Schaer, L. Zuppiroli, Organic thin-film transistors: the passivation of the dielectric–pentacene interface by dipolar self-assembled monolayers, Langmuir 26 (2010) 15044.
[22] H.S. Lee, D.H. Kim, J.H. Cho, M. Hwang, Y. Jang, K. Cho, Effect of the phase states of self-assembled monolayers on pentacene growth and thin-film transistor characteristics, J. Am. Chem. Soc. 130 (2008) 10556.

Organic Electronics 12 (2011) 341–347

Contents lists available at ScienceDirect

Organic Electronics

journal homepage: www.elsevier.com/locate/orgel

Analysis of chemical degradation mechanism within sky blue phosphorescent organic light emitting diodes by laser-desorption/ionization time-of-flight mass spectrometry

Ines Rabelo de Moraes [a,*], Sebastian Scholz [a,b], Björn Lüssem [a], Karl Leo [a]

[a] Institut für Angewandte Photophysik, Technische Universität Dresden, George-Bähr-Str. 1, 01062 Dresden, Germany
[b] Fraunhofer-Institut für Keramische Technologien und Systeme, Winterbergstraße 28, 01277 Dresden, Germany

ARTICLE INFO

Article history:
Received 20 August 2010
Received in revised form 5 November 2010
Accepted 9 November 2010
Available online 1 December 2010

Keywords:
FIrpic
LDI-TOF-MS
Intrinsic degradation
Blue phosphorescent OLEDs

ABSTRACT

We present an investigation of the intrinsic chemical degradation mechanisms of phosphorescent OLEDs based on the common sky blue emitter bis(2-(4,6-difluorophenyl)-pyridyl-*N*,C2′)iridium(III)picolinate (FIrpic). The OLEDs are investigated using the laser-desorption/ionization time-of-flight mass spectrometry. The comparison between the collected spectra for electrically aged and unaged OLEDs allows the identification of different reaction products, like fragments which are mainly related to the chemical dissociation of FIrpic molecules during the OLED operation. We present different reaction pathways of the blue emitter FIrpic. One proposed reaction indicates that the short lifetimes of the OLEDs may be related to the irreversible dissociation of the FIrpic molecule by the loss of carbon dioxide (CO_2) from the picolinate ligand. Additionally, the formation of chemical complexes between different fragments of the FIrpic molecules with their neighbour materials is visible. The cesium adducts of FIrpic formation indicate a possible contribution of the dopant to the OLED degradation process. Finally, we show rearrangement effects in the Cs doped electron transporting layer. This rearrangement is indicated by the presence of m/z signals of the BPhen dimer and adducts of the dimer with Cs.

© 2010 Elsevier B.V. All rights reserved.

1. Introduction

Organic Light Emitting diodes (OLEDs) have attracted much interest in the past years due to their potential application in next generation light sources and display technologies. OLEDs allow a thinner, lighter, and more flexible design, and are also quite efficient [1]. Unfortunately, apart from its current high manufacturing costs, lifetime is one of the major drawbacks of this technology. Although a remarkable improvement in efficiency and lifetime of *p-i-n* phosphorescent OLEDs have been reported recently [2–7], the short lifetime of blue emitting devices is still the major limitation for a broad application of this promising technology. For blue OLEDs, two different types of emitters can be used, phosphorescent [7] and fluorescent [8] molecules. These two types of emitters differ significantly in terms of light emission efficiency. In comparison to devices using fluorescent emitters, devices employing phosphorescent emitters can achieve higher external quantum efficiencies because they allow simultaneous harvesting of both singlet and triplet excitons [9]. Therefore, phosphorescent materials are ideal for use in both lightning and display devices.

Despite the importance of a detailed understanding of the intrinsic degradation mechanisms involved in the aging processes of blue phosphorescent OLEDs, only little information about the nature of the chemical reactions associated to the low stability of the blue emitters are known. For investigations of the degradation behavior of

* Corresponding author. Tel.: +49 351 46339189; fax: +49 351 46337065.
E-mail addresses: ines.rabelo.de.moraes@iapp.de (I.R.d. Moraes), karl.leo@iapp.de (K. Leo).

1566-1199/$ - see front matter © 2010 Elsevier B.V. All rights reserved.
doi:10.1016/j.orgel.2010.11.004

blue phosphorescent OLEDs, special attention has been paid to the phosphorescent emitter bis(2-(4,6-difluorophenyl)pyridyl-*N*,C2′)iridium(III)picolinate (FIrpic), unfortunately known to be relative unstable. The degradation processes of FIrpic based OLEDs have been previously analyzed by High Performance Liquid Chromatography coupled with a mass spectrometry (HPLC–MS) [10–12], and Laser-Desorption/Ionization Time-of-Flight Mass Spectrometry (LDI-TOF-MS) [13]. Within these investigations the degradation processes of the OLEDs has been attributed to different reaction mechanisms such as: (i) FIrpic molecule isomerization, as well as (ii) chemical dissociation of the FIrpic emitter by the cleavage of the picolinate ligand from the FIrpic molecule [10], (iii) chemical degradation of the materials used in the HTL and a further coupling reaction between its fragments and neighbouring molecules resulting in the formation of new products [11,12]. In previous work, we used the LDI-TOF-MS to discover the laser induced photochemical reaction mechanism of single FIrpic layers as well to investigate the possible reaction products in fully processed and aged OLEDs [13]. The excitation of the FIrpic molecule via laser light induces the formation of sodium and potassium adducts with FIrpic as well as the dissociation of the emitter molecule. This general reaction of dissociation may occur via two different chemical pathways. One of them is the reversible dissociation of the FIrpic molecule, where the picolinate ligand is removed and the second one is the irreversible loss of the carbon dioxide (CO_2) unit from the picolinate ligand with a further dissociation step to form a $Ir(F_2ppy)_2^+$ species, which may undergo further reactions. Although the reversible dissociation pathway could be observed in electrically driven OLEDs, the first hint of the irreversible pathway was obtained by creating a differential spectrum of an aged and an unaged OLED. In this differential spectra the m/z signal, which is related to the $[FIrpic\text{-}CO_2]^+$ fragment, was only poorly visible [13].

In this work we will present evidence that the FIrpic molecule may dissociate by two different reaction pathways, which occur during the OLED operation. Additionally, new degradation products, which may be associated to the short lifetime of the FIrpic based OLEDs, such as formation of chemical complexes between different fragments of the FIrpic molecules with their neighbour material like TPBi used as host and hole blocking layer, 4,7-diphenyl-1,10-phenanthroline (BPhen) dimerization, and adducts of the BPhen dimer with Cs will be presented as well.

2. Experimental

The OLEDs, as shown in the inset of Fig. 1(d), consist of a six-layer *p-i-n* organic structure, sandwiched between a 90 nm thick indium tin oxide (ITO) anode and a 100 nm thick aluminium top electrode. The devices are prepared by vacuum sublimation under a base pressure of 10^{-8} mbar (vacuum sublimation tool from the Kurt Lesker Co.). Immediately after preparation, the devices are encapsulated under a nitrogen atmosphere using epoxy glue and glass lids. The devices consist of a 20 nm thick

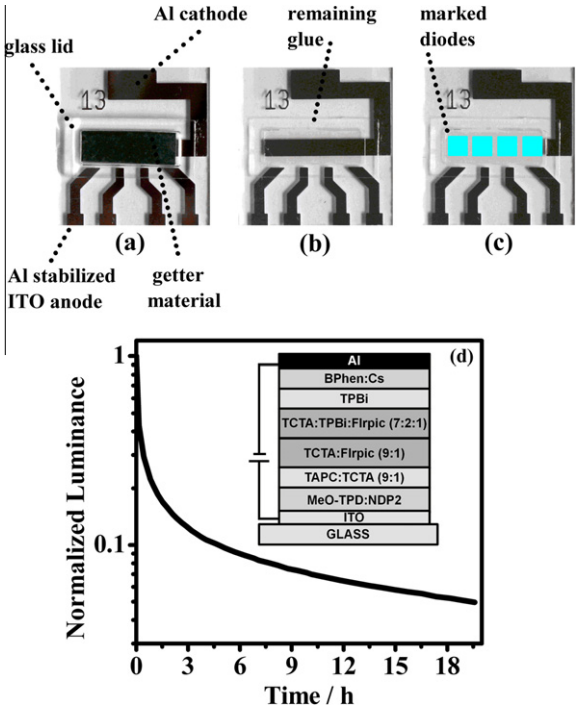

Fig. 1. OLED samples before (a), after removing the encapsulation (b), and after removing the Al cathodes from the samples (c). Typical lifetime characteristics of the FIrpic phosphorescent OLED aged under a constant current density of 30 $mAcm^{-2}$ corresponding to an initial luminance of $L_0 = 3623$ cdm^{-2} (d). The inset figure shows the structure of the blue sky phosphorescent OLED used in LDI-TOF-MS investigations.

hole injection and transport layer (HTL) from *N*,*N*,*N*′,*N*′-tetrakis 4-methoxyphenylbenzidine (MeO-TPD) doped with 4 mol% NDP-2 (Novaled AG) [14], a 10 nm thick electron blocking layer (EBL) composed by a mixture of 90 wt.% 1,1-bis(4-di-*p*-tolylaminophenyl)cyclohexane (TAPC) and 10 wt.% 4,4′,4″-tris(carbazol-9-yl)triphenylamine (TCTA), a double emission layer (D-EML) consisting of one 10 nm

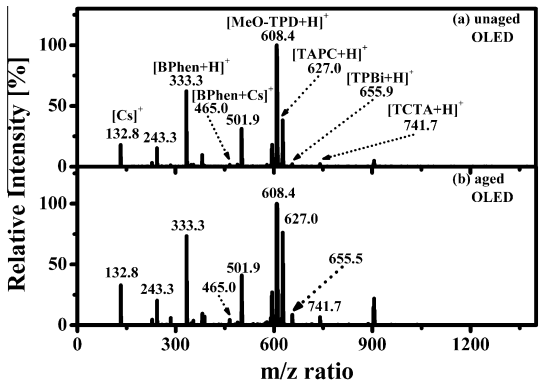

Fig. 2. LDI-TOF MS spectra collected in the positive mode of an unaged (a) and an aged (b) OLED sample. Both spectra show the signals of the materials $[Cs]^+$ at 132.8 amu, $[BPhen + H]^+$ at 333.3 amu, $[MeO\text{-}TPD+H]^+$ at 608.4 amu, $[TAPC + H]^+$ at 627.0 amu, $[TPBi + H]^+$ at 655 amu, and $[TCTA + H]^+$ at 741.7 amu used in the OLED stack. Additionally, some degradation products with very low signal intensities could also be detected and will be presented in the following enlarged figures.

thick layer of TCTA doped with 10 wt.% FIrpic and a layer of 10 nm of 70 wt.% TCTA, and 20 wt.% 1,3,5-tris(*N*-phenylbenzimidazol-2-yl)benzene (TPBi) doped with 10 wt.% FIrpic, a 10 nm thick hole blocking layer (HBL) TPBi, and finally an electron transport layer (ETL) of Cs doped BPhen (30 nm). The devices are aged under a constant current density of 30 $mAcm^{-2}$ corresponding to an initial luminance (L_0) of 3623 cdm^{-2}, until the emission decreased to about 5% of the initial luminance. Fig. 1(d) shows the normalized luminance decay, recorded during OLED operation. This aged sample is used for the LDI-TOF-MS investigation. Under the mentioned conditions, a half-lifetime ($t_{0.5}$) of only 13 min was observed. Although, a longer half-lifetime ($t_{0.5}$ = 13 h) was obtained for OLEDs driven at L_0 = 100 cdm^{-2}, this value is still far below the values required for most OLED applications. The aged and unaged OLEDs were analysed upon LDI in positive and negative detection mode, using the method of LDI-TOF-MS (Bruker Daltonics Autoflex TOF/TOF tandem mass spectrometer). Before mounting the OLEDs on a MALDI sample holder the encapsulation glasses (Fig. 1(a and b)), and the Al cathode (Fig. 1(b and c)) are removed from the samples under protective nitrogen. Removing the Al cathodes allows the analysis of the OLEDs at a very low laser intensity of about 120 μJ/pulse. The use of a low laser intensity during the spectra acquisition is important to avoid the formation of additional photochemical reactions during the analyzing process [15]. Transferring the samples into the LDI-TOF-MS set-up required less than 2 min in air. The samples are excited at a wavelength of 337 nm, where the maximum pulsed laser beam intensity can be set to 300 μJ/pulse (at 25 Hz). In total 180 single mass spectra from three different points of each sample are taken.

3. Results and discussion

Fig. 2(a), and (b) show the full scale LDI-TOF-MS spectra collected between 0 and 1400 amu for the unaged and aged

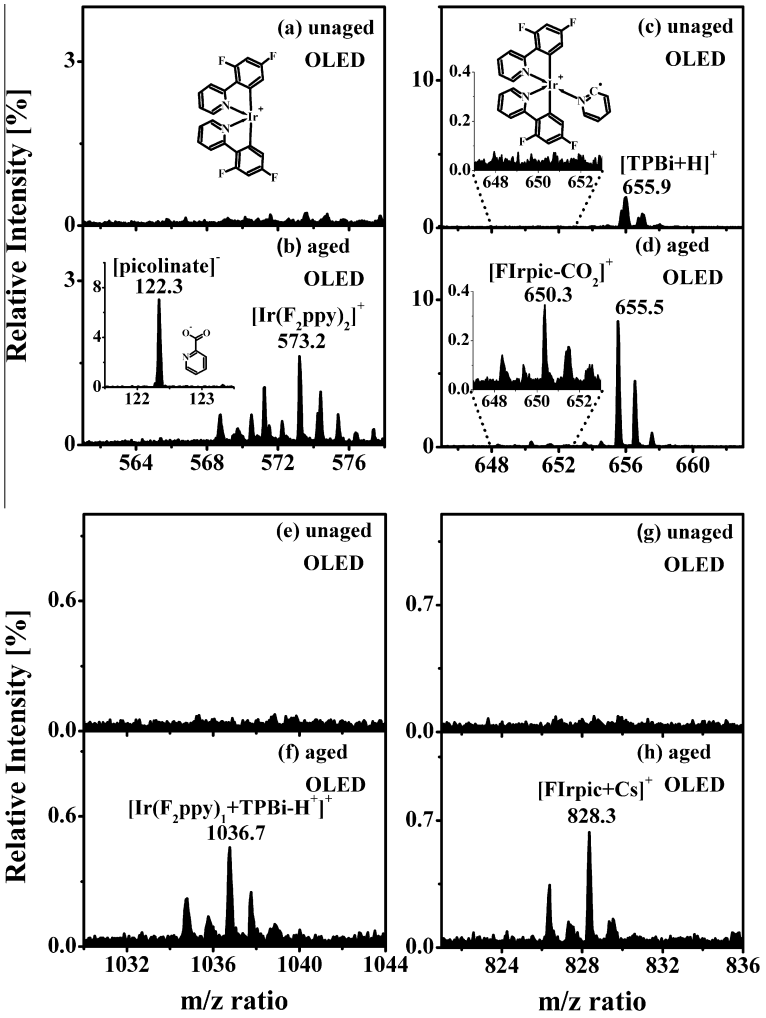

Fig. 3. Enlarged LDI-TOF-MS spectra of degradation products formed during the OLED aging process (b, d, f and h) in comparison to the spectra collected for unaged sample in the same m/z ratio range (a, c, e and g). The generated degradation products are related to $[Ir(F_2ppy)_2]^+$ at 573.2 amu, $[FIrpic–CO_2]^+$ at 650.3 amu, $[Ir(F_2ppy)_1 + TPBi\text{-}H^+]^+$ at 1036.7 amu, and $[FIrpic + Cs]^+$ at 828.3 amu. Inset Fig. 3(b) shows the spectrum of the negatively charged FIrpic fragment related to the $[picolinate]^-$ at 122.3 amu.

OLEDs, respectively. Both spectra show the expected mass/charge (m/z) signals of the materials $[Cs]^+$ at 132.8 amu, $[BPhen + H]^+$ at 333.3 amu, $[MeO\text{-}TPD]^+$ at 608.4 amu, $[TAPC + H]^+$ at 627.0 amu, $[TPBi + H]^+$ at 655 amu, and $[TCTA + H]^+$ at 741.7 amu. The presence of $[Cs]^+$ and $[BPhen + H]^+$ signals indicate that the ETL on top of the investigated samples has not been effected by the Al cathode removing procedure. The other signals at 243.3 and 501.9 amu correspond to the fragments of TCTA and MeO-TPD molecules, respectively. Additionally, a signal at 465 amu related to the laser induced degradation product $[BPhen + Cs]^+$ is observed in both samples analyzed. The signal present different relative intensities for the unaged (1.4%) and aged (4.5%) samples. One should be aware that the spectra are normalized using the $[MeO\text{-}TPD + H]^+$ signal, which is set to 100%. MeO-TPD itself undergoes some photochemical degradation reactions during the measurements as well. This may led to an influence on the relative intensities of the other signals, as observed in the case of the signal of $[BPhen + Cs]^+$. The comparison between LDI-TOF-MS spectra, collected for aged and unaged OLED samples, allows the identification of very low concentrations of reaction products and fragments which are mainly related to the chemical dissociation of FIrpic molecules during the OLED operation. Due to the low concentration of the degradation products formed during the OLED operation, the spectral analysis will be focused on the comparison of m/z signals at low signal intensities between the aged and unaged spectra.

3.1. Chemical degradation processes of FIrpic molecules

The spectrum in Fig. 3(b) shows the signal at 573.2 amu, which corresponds to the FIrpic molecule fragment $[Ir(F_2ppy)_2]^+$. The formation of such a fragment is an indication of the chemical dissociation of FIrpic by the loss of the picolinate ligand. To verify the dissociation reaction pathway of the FIrpic molecule during the OLED operation, a spectrum in negative mode was taken, which is displayed as inset in Fig. 3(b). In this spectrum a signal at 122.3 amu can be observed, which relates to the negatively charged picolinate ion. The enlarged spectrum inset Fig. 3(d) shows a second feature at 650.3 amu with a very low value of relative intensity, close to the more intense signal of $[TPBi + H]^+$ at 655.5 amu. This compound is the result of the dissociation of the FIrpic molecule by the loss of a carbon dioxide unit (CO_2). Although the signal $[FIrpic\text{-}CO_2]^+$ presents a very low intensity, it is difficult to correlate the signal intensity with the corresponding concentration as the LDI-TOF-MS is not a quantitative technique. This specie may exhibit lower ionization due to its instability. Even at higher concentrations of the fragment within the OLED, the fast fragmentation within the LDI experiment does not allow a quantitative characterization of the material at the LDI-detector. To interpret these results, we assume a dissociation reaction mechanism for FIrpic molecules as proposed in Fig. 4. According to this reaction mechanism, the FIrpic molecule is excited during the OLED operation and it is converted into an ionized form. The ionized FIrpic molecule may not be stable and can suffer further dissociation processes according to two different reaction pathways: a reversible (pathway 1) and/or an irreversible (pathway 2). In pathway 1 the FIrpic is reversibly dissociated by the scission of picolinate ligand from the FIrpic molecule with the formation of a [FIrpic–picolinate]$^+$ ion. A irreversible dissociation of FIrpic molecule is proposed in the pathway 2 by the loss of a neutral CO_2 molecule from the picolinate ligand accompanied by the

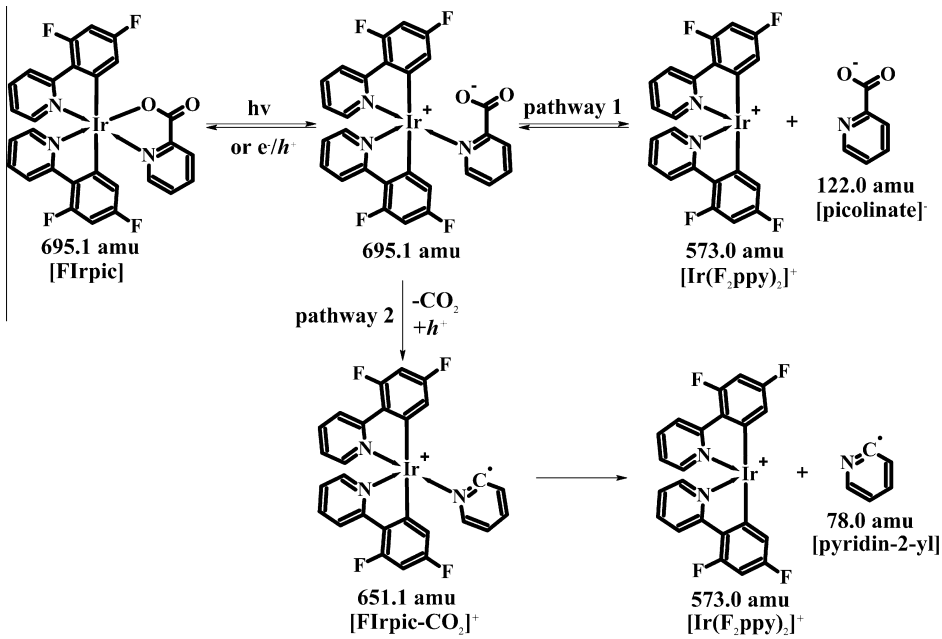

Fig. 4. Proposed dissociation reaction of the FIrpic molecule during the OLED operation according to two different dissociation pathways: a reversible (pathway 1), and/or an irreversible (pathway 2).

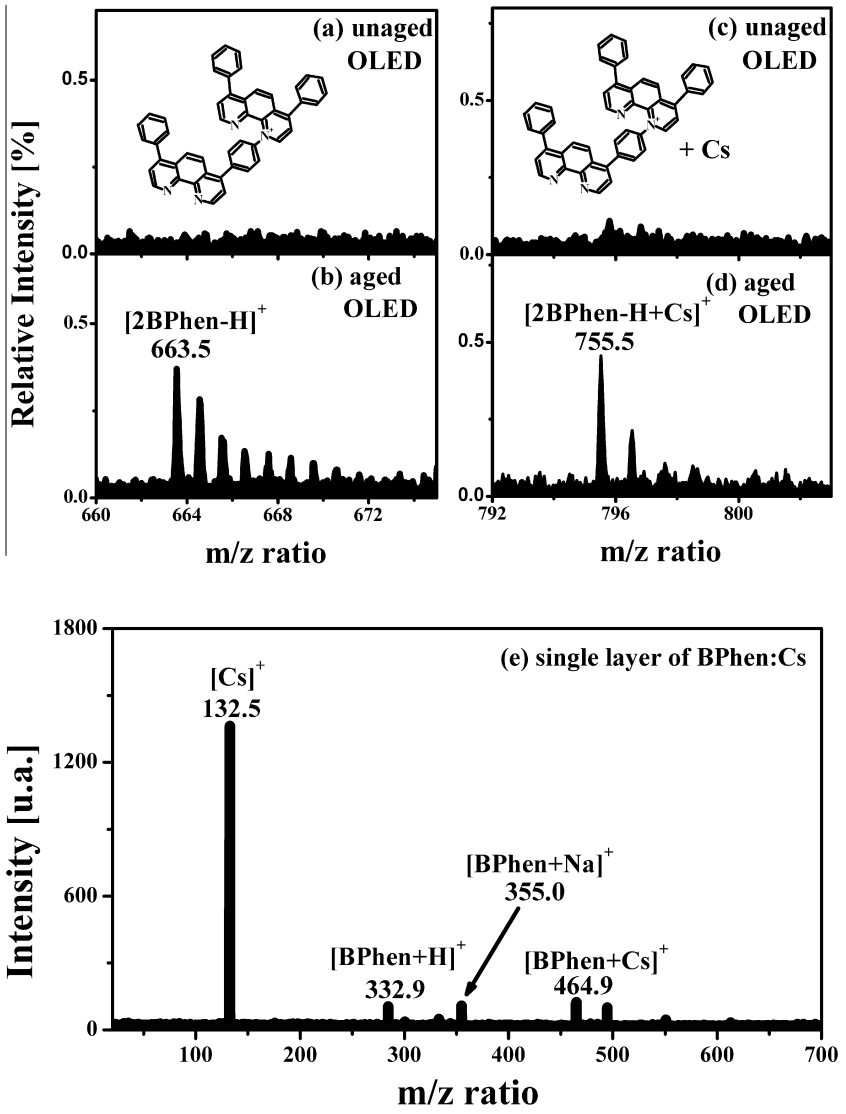

Fig. 5. LDI-TOF-MS spectra of single layers of BPhen doped with 10% cesium (10 nm) at 120 μJ/pulse. The spectrum shows that the doping of BPhen with Cs suppresses the formation of photo induced BPhen dimers and only the m/z signals related to $[Cs]^+$ at 132.5 amu, $[BPhen + H]^+$ at 332.9 amu, $[BPhen + Na]^+$ at 354.9 amu, $[BPhen + Cs]^+$ at 464.8 amu are observed.

formation of the $[FIrpic–CO_2]^+$ ion. The positively charged fragment $[FIrpic–CO_2]^+$ can suffer a further dissociation process with the formation of the positively charged fragment $[Ir(F_2ppy)_2]^+$ and pyridin-2-yl neutral radical. These findings are in agreement with the results of the photoinduced degradation process of a pure FIrpic layer in an LDI-TOF-MS investigation published by Scholz et al. [13]. We believe that the irreversible oxidation of the picolinate ligand may lead to a degradation of the FIrpic molecules and act as an exciton quencher during the OLED operation. To the best of our knowledge, this is the first time that a direct evidence of an irreversible dissociation process of the FIrpic occurring during OLED operation has been shown.

Fig. 3(f) and (h) show the spectra of two other degradation products presenting the characteristic iridium-complex isotopic pattern. Fig. 3(f) exhibits the signal at 1036.7 amu, which can be attributed to two possible reaction products; either to the interaction of the iridium fragment with surrounding TPBi, material used as host and HBL, or the interaction with the charged complex $[BPhen + Cs]^+$. Therefore the structure of degradation product can be described as $[Ir(F_2ppy)_1TPBi\text{-}H^+]^+$ or $[Ir(F_2ppy)_2BPhen\text{-}H + Cs]$ with a good agreement with the experimental value of the m/z signal. Although the formation of neither degradation products can be discarded we believe that the formation of $[Ir(F_2ppy)_1TPBi\text{-}H^+]^+$ seems more probable. The formation of the complex between TPBi and $[Ir(F_2ppy)]^{2+}$ may occur by the release of one proton from the $[Ir(F_2ppy)_1TPBi\text{-}H^+]^+$ complex like the mechanism proposed for the complexation of red triplet emitter iridium(III)bis(2-methyldibenzo-[f,h]quinoxaline)(acetylacetonate) $[Ir(MDQ)_2(acac)]$ frag-

ment with the TPBi molecule [15]. The formation of such iridium complexes, which are believed to act as non-radiative exciton quenchers, would cause a decreased photon emission during the OLED operation and therefore decrease the device lifetime. As already shown for highly stable red phosphorescent OLEDs containing [Ir(MDQ)$_2$(acac)], the dissociation behavior of the Ir-complex and the ability of its fragments to form chemically stable complexes with the neighbour materials such as TPBi have been directly correlated with the decrease of the devices lifetime [15–16]. However, the chemical structure of the [Ir(F$_2$ppy)$_1$TPBi-H$^+$]$^+$ is still unknown. Finally, the signal at 828.3 amu of [FIrpic + Cs]$^+$, shown in Fig. 3(h) indicates a possible contribution of the dopant to the OLED degradation process. The diffusion of the cesium into the emission layer with the formation of cesium adducts of FIrpic may act as non-radiative recombination centers as well.

3.2. Chemical reaction involving the BPhen molecule

In Fig. 5(b), and (d) the signals at 663.5 amu, and 795.5 amu are attributed to [2(BPhen)-H]$^+$ and [2(BPhen)-H + Cs]$^+$, respectively. The formation of chemically stable dimers of BPhen is well described in previous studies [17], where it has been suggested that the BPhen dimers form lower HOMO–LUMO gaps as compared to the unreacted BPhen and therefore they may act as trap states for charges and as quencher for excitons. Such a contribution to exciton quenching may be enhanced for wide band gap emitters compared to red emitting systems. The formation of BPhen dimers [15,16,18] as well as their cesium adducts [19] has been already observed, but only during the aging process of stable phosphorescent OLEDs with BPhen used as HBL. Our results show that the BPhen dimerization can occur even when a 10 nm layer of TPBi was used as HBL. The formation of such species may be induced by the unbalance of charge promoted by the dissociation process of the FIrpic molecules in the emitting layer and/or by the high current density applied during the OLED aging process.

To further investigate the reaction mechanism of the cesium BPhen dimer adduct, we performed a photo-induced experiment on a single BPhen layer doped with cesium by the LDI-TOF-MS method. The spectrum collected at 120 μJ/pulse for a 10 nm layer of BPhen doped with 10% of cesium is presented in Fig. 5(e), which shows the signals assigned to [Cs]$^+$ at 132.5 amu, [BPhen + H]$^+$ at 332.9 amu, [BPhen + Na]$^+$ at 354.9, and [BPhen + Cs]$^+$ 464.8 amu. The sodium adduct formation was forced by wetting the MALDI target with the solvent isopropanol without drying under a nitrogen stream in order to remain the alkaline impurities on the target. These results show clearly that the doping process of BPhen with cesium suppresses the BPhen dimerization. Therefore, we conclude that during the OLED degradation process, the BPhen dimer is the first species which is formed. Afterwards, in a further step it reacts with cesium. The role of the adducts between the BPhen dimer and the cesium on the performance and lifetime of OLED devices is still unclear and more investigations are needed in order to clarify these questions. The mechanism of the FIrpic degradation reveals a serious problem regarding the stability of the picoline containing emitters. In order to improve the stability of a blue phosphorescent dopant molecule it would be more appropriate to develop a molecule with three equivalent ligands, where an excitation (and therefore a metal–ligand-bond-opening) is statistically shared on all three ligands, which may promote an increase of the molecule lifetime. We are aware that due to the symmetry, such emitter molecules may show a decreased efficiency compared to other asymmetric species. Nevertheless the higher triplet gap has a major effect on the degradation effect due to the relative near to the dissociation state of any kind of molecules (even on the matrix [20]). Therefore the C–N binding energy is a critical parameter, e.g. for corresponding matrix materials as well.

4. Conclusion

In this contribution, we present an investigation of the intrinsic chemical degradation mechanisms of phosphorescent OLEDs based on the common sky blue emitter FIrpic by the use of the LDI-TOF-MS. The results show that LDI-TOF-MS is a powerful analytical technique to investigate fully processed OLEDs without the need to dissolve the OLED samples. The comparison between LDI-TOF-MS spectra collected for aged and unaged OLED samples allows the detection of different degradation products which may be associated to shorten the lifetime of the OLEDs. The analysis of the m/z signals and the shape of the isotopic pattern of individual spectra enabled us to identify some reaction products which are mainly related to the chemical dissociation of the FIrpic molecules used as phosphorescent emitter. Based on the FIrpic fragments observed only in the LDI-MS spectrum collected for the aged OLED sample a dissociation reaction pathway is proposed, which involve two different pathways: a reversible (pathway 1), involving the scission of the picolinate ligand from the FIrpic, and a second one related to the irreversible dissociation (pathway 2) of the FIrpic molecule by the loss of carbon dioxide (CO_2). Beside the chemical dissociation process of FIrpic, the formation of iridium complexes between different FIrpic fragments and surrounding materials as well as the formation of an adduct of FIrpic with cesium may also contribute to the degradation process of the OLED. Finally, the presence of m/z signals of BPhen dimers and adducts of BPhen dimers with cesium show a rearrangement of the ETL during the OLED operation.

Acknowledgments

This work has been funded by the BMBF under contract No. 13N 9872, project acronym "OPA". Additionally the authors wish to thank the Chemistry Department of the TU Dresden for providing access to their MALDI-TOF-MS device and NOVALED AG, Dresden for providing the HTL-dopant NDP-2.

References

[1] K. Walzer, B. Maennig, M. Pfeiffer, K. Leo, Chem. Rev. 107 (2007) 1233.
[2] R. Meerheim, K. Walzer, M. Pfeiffer, K. Leo, Appl. Phys. Lett. 89 (2006) 061111.

[3] J. Birnstock, T. Canzler, M. Hofmann, A. Lux, S. Murano, P. Wellmann, A. Werner, SID 07 Digest 38 (2007) 1193.
[4] J. Birnstock, T. Canzler, M. Hofmann, A. Lux, S. Murano, P. Wellmann, A. Werner, J. Soc. Inf. Disp. 16 (2008) 221.
[5] S. Madasamy, D. Pavicic, C. Rothe, S. Murano, J. Birnstock, J.B. Nimoth, S. Mladenovski, K. Neyts, M. Pfeiffer, Proc. SPIE 6999 (2008) 69991E.
[6] S. Reineke, F. Lindner, G. Schwartz, N. Seidler, K. Walzer, B. Lüssem, K. Leo, Nature 459 (2009) 234.
[7] N. Seidler, S. Reineke, K. Walzer, B. Lüssen, A. Tomkeviciene, J.V. Grazulevicius, K. Leo, Appl. Phys. Lett. 96 (2010) 093304/1.
[8] D. Gebeyehu, K. Walzer, G. He, M. Pfeiffer, K. Leo, J. Brandt, A. Gerhard, P. Stößel, H. Vestweber, Synth. Met. 148 (2005) 205.
[9] C. Adachi, M.A. Baldo, M.E. Thompson, S.R. Forrest, J. Appl. Phys. 90 (2001) 5048.
[10] V. Sivasubramaniam, F. Brodkorb, S. Hanning, H.P. Loebl, V. van Elsbergen, H. Boerner, U. Scherf, M. Kreyenschmidt, Cent. Eur. J. Chem. 4 (2009) 836.
[11] V. Sivasubramaniam, F. Brodkorb, S. Hanning, H.P. Loebl, V. van Elsbergen, H. Boerner, U. Scherf, M. Kreyenschmidt, J. Fluorine Chem. 130 (2009) 640.
[12] V. Sivasubramaniam, F. Brodkorb, S. Hanning, O. Buttler, H.P. Loebl, V. van Elsbergen, H. Boerner, U. Scherf, M. Kreyenschmidt, Solid State Sci. 11 (2009) 1933.
[13] S. Scholz, R. Meerheim, K. Walzer, K. Leo, Proc. SPIE 6999 (2008) 69991B.
[14] P. Wellmann, M. Hofmann, O. Zeika, A. Werner, J. Birnstock, R. Meerheim, G. He, K. Walzer, M. Pfeiffer, K. Leo, SID Int. Symp. Digest Tech. Papers 13 (2005) 393.
[15] R. Meerheim, S. Scholz, S. Olthof, G. Schwartz, S. Reineke, K. Walzer, K. Leo, J. Appl. Phys. 104 (2008) 014510.
[16] S. Scholz, R. Meerheim, B. Lüssem, K. Leo, SID 09 Digest 46 (2009) 681.
[17] S. Scholz, C. Corten, K. Walzer, D. Kuckling, K. Leo, Org. Electron. 8 (2007) 709.
[18] S. Scholz, K. Walzer, K. Leo, Adv. Funct. Mater. 18 (2008) 2541.
[19] S. Scholz, B. Lüssem, K. Leo, Appl. Phys. Lett. 95 (2009) 183309.
[20] D.Y. Kondakov, W.C. Lenhart, W.F. Nichols, J. Appl. Phys. 101 (2007) 024512.

Organic Electronics 12 (2011) 348–352

Contents lists available at ScienceDirect

Organic Electronics

journal homepage: www.elsevier.com/locate/orgel

Letter

High performance n-type organic–inorganic nanohybrid semiconductors for flexible electronic devices

Yerok Park [a], Kyu S. Han [a], Byoung H. Lee [a], Sangho Cho [a], Kwang H. Lee [b], Seongil Im [b], Myung M. Sung [a,*]

[a] Department of Chemistry, Hanyang University, Seoul 133-791, Republic of Korea
[b] Institute of Physics and Applied Physics, Yonsei University, Seoul 120-749, Republic of Korea

ARTICLE INFO

Article history:
Received 15 September 2010
Received in revised form 5 November 2010
Accepted 28 November 2010
Available online 16 December 2010

Keywords:
Organic–inorganic nanohybrid semiconductors
Molecular layer deposition
Atomic layer deposition
ZnO
Organic thin film transistors

ABSTRACT

We report a high-performance and air-stable flexible and invisible semiconductor which can be substitute for the n-type organic semiconductors. N-type organic–inorganic nanohybrid superlattices were developed for active semiconducting channel layers of thin film transistors at low temperature of 150 °C by using molecular layer deposition with atomic layer deposition. In these nanohybrid superlattices, self-assembled organic layers (SAOLs) offer structural flexibility, whereas ZnO inorganic layers provide the potential for semiconducting properties, and thermal and mechanical stability. The prepared SAOLs–ZnO nanohybrid thin films exhibited good thermal and mechanical stability, good flexibility, transparent in the visible range, and excellent field effect mobility (>7cm^2/V s) under low voltage operation (from −1 to 3 V). The nanohybrid semiconductor is also compatible with pentacene in p–n junction diodes.

© 2010 Elsevier B.V. All rights reserved.

1. Introduction

Flexible thin film transistors (TFTs) have been extensively studied over the past few decades because they have potential applications in low-cost displays, wearable devices, paper displays, and flexible electronics [1–6]. In particular, flexible semiconducting materials are considered essential elements for development of flexible TFTs. Organic semiconductors such as small organic molecules, conjugated oligomers, and conducting polymers are promising materials in electrical performance comparable to amorphous silicon (ca. 1 cm^2/V s) [7–10]. Most high-performance organic semiconductors are more likely to transport holes as charge carriers rather than electrons, leading to p-type semiconductors. In contrast, development of n-type organic semiconductors falls far behind p-type materials [11–15]. Compared to the field effect mobility (15 cm^2/V s) of p-type organic semiconductors such as single crystal rubrene, the highest reported electron mobility of n-type organic semiconductors is 1.83 cm^2/V s, which was obtained by employing thiazole derivatives [16,17]. This inferior electrical performance is caused by the inherent instability of organic anions (i.e. carbanions) which are known to react with oxygen and water in ambient conditions. Those factors also cause degradation of electrical performance in organic semiconductor devices [18–22]. Tuning electron affinity or modifying hydrophobic functionalities of n-type organic semiconductors can prevent the carbanions from reacting with oxygen and water under the normal operating conditions of devices. Despite the efforts of many research groups for over a decade, however, it is still difficult to enhance the field effect mobility of n-type organic semiconductor FETs to levels as high as p-type ones [23–27].

Organic–inorganic nanohybrid thin films provide both the stable and elegant optical, electrical, and magnetic properties of inorganic components and the structural flexibility of organic components [28–30]. Organic–inorganic hybrid superlattices are particularly attractive as flexible

* Corresponding author. Tel.: +82 2 2220 2555; fax: +82 2 2299 0762.
E-mail address: smm@hanyang.ac.kr (M.M. Sung).

1566-1199/$ - see front matter © 2010 Elsevier B.V. All rights reserved.
doi:10.1016/j.orgel.2010.11.026

semiconducting materials because they allow the combination of the excellent electrical and flexible properties of inorganic and organic components, respectively. Recently, we developed a new vapor phase deposition method of high quality self-assembled organic layers (SAOLs), called molecular layer deposition (MLD), in order to realize precisely controlled organic–inorganic nanohybrid superlattices [31–33]. MLD is a gas phase process analogous to atomic layer deposition (ALD), which is a potentially powerful method for preparing high quality multicomponent superlattices under vacuum conditions. Using the MLD method, high quality organic thin films can be quickly formed with monolayer precision under ALD conditions (temperature, pressure, etc.) [34–37]. The MLD method can be combined with ALD to take advantages of the possibility of obtaining organic–inorganic nanohybrid thin films [38–40].

Herein, we report a high-performance and air-stable flexible semiconductor which can be substituted for n-type organic semiconductors. We combined crystalline inorganic nanolayers with organic layers, leading to organic–inorganic nanohybrid semiconductors. The inorganic layer constitutes an extended framework bonded by powerful covalent or ionic interactions to furnish high carrier mobility and good thermal and mechanical stability. The organic layer adds mechanical flexibility to the inorganic framework. MLD combined with ALD (MLD–ALD) was applied to fabricate a new n-type organic (SAOLs)–inorganic (ZnO) nanohybrid semiconductor on flexible plastic substrates with accurate control of film thickness, large-scale uniformity, excellent conformality, good reproducibility, multilayer processing capability, sharp interfaces, and excellent film qualities at low temperature. The prepared SAOLs–ZnO nanohybrid thin films exhibited good thermal and mechanical stability, good flexibility, and excellent field effect mobility (>7 $cm^2/V{\cdot}s$) under low voltage operation (from −1 to 3 V). Furthermore, we also demonstrate the performance of p–n junction diodes prepared with the SAOLs–ZnO nanohybrid superlattices and pentacene.

2. Experimental section

2.1. Preparation of Si substrates

The flexible substrates employed in this study were cut from Glastic® polyethersulfone films (i-components Inc.). The polyethersulfone (PES) substrates were cleaned with methanol and de-ionized water, and blow-dried with nitrogen to remove contaminants. The Si substrates were cut from n-type (1 0 0) wafers (LG Siltron) with resistivity in the range of 1–5 Ω cm. The Si substrates were initially treated with a chemical cleaning process that involved degreasing, HNO_3 boiling, NH_4OH boiling (alkali treatment), HCl boiling (acid treatment), rinsing in deionized water, and blow-drying with nitrogen to remove contaminants and to grow a thin protective oxide layer on the surface [41]. The ITO-coated glass substrates were cleaned with acetone, methanol, de-ionized water, and blow-dried with nitrogen to remove contaminants.

2.2. Molecular layer deposition with atomic layer deposition (MLD–ALD)

The ZnO thin films were deposited onto the substrates at 150 °C using diethylzinc (Zn 52.0 wt.%, Aldrich) and H_2O as ALD precursors. Ar served as a carrier and purging gas at a rate of 50 sccm. The diethylzinc (DEZ) and water were evaporated at 20 °C. The cycle consisted of a 0.5 s exposure to DEZ, a 5 s Ar purge, a 1 s exposure to water, and a 5 s Ar purge. The vapor pressure of the Ar in the reactor was maintained at 300 mTorr. Alkene-terminated self-assembled organic layers (SAOLs) were formed by exposing the substrates to $[CH_2{=}CH(CH_2)_6SiCl_3]$ (Aldrich; 96%) with H_2O vapor at 150 °C in the ALD chamber. 7-Octenyltrichlorosilane (7-OTS) and water were evaporated at 100 and 20 °C, respectively. Exposure times in this process were 5 s for 7-OTS with water vapor and 10 s for the Ar purge. The reactor pressure during the process was about 300 mTorr. The terminal C=C groups of the SAOLs were converted to carboxylic acid groups with ozone treatment in the ALD chamber [31]. The ozone was generated by an ozone-generator and dosed to the 7-OTS coated samples for 30 s at 150 °C. The C=C groups of the SAOLs reacted with ozone to convert to carboxylic acid groups, which provided highly active adsorption sites for the anchoring of the next monolayer. The SAOLs–ZnO nanohybrid superlattices were grown using the cyclic MLD–ALD process.

2.3. Device fabrication

The 100 nm-thick Cr gate electrode of the TFT was formed on the PES substrates by radio frequency sputter through shadow masks (pressure: $\sim 10^{-8}$ Torr, temperature: room temperature, radio frequency power: 300 W). The 30 nm-thick SAOLs–Al_2O_3 dielectric layer was grown by MLD–ALD at 150 °C. The SAOLs–ZnO nanohybrid thin films as active channel layers were deposited by MLD–ALD through shadow masks in intimated contact with the substrates. The channel dimension was 50 μm(L) × 100 μm(W). The 100 nm-thick Al source and drain electrodes were deposited by thermal evaporation through shadow masks under a pressure of $\sim 1 \times 10^{-6}$ Torr. An inverted staggered structure was employed in TFT device fabrication. The 55 nm-thick SAOLs–ZnO nanohybrid n-type semiconducting layer was deposited on the ITO-coated glass by MLD–ALD. The pentacene (Aldrich; 99%) p-type semiconducting layer was fabricated on the SAOLs–ZnO layer through a shadow mask at room temperature by thermal evaporation. The deposition rate was fixed to 1 Å/s using an effusion cell (ALPHAPLUS Co., LTE-500S) in a vacuum chamber under a pressure of $\sim 1 \times 10^{-7}$ Torr. The thickness of the pentacene films was 50 nm as monitored by a quartz crystal oscillator and confirmed by ellipsometry. The 100 nm-thick Au dot electrodes (300 μm in diameter) were deposited by thermal evaporation in a vacuum chamber under a pressure of $\sim 1 \times 10^{-6}$ Torr.

2.4. Sample characterization

The samples were analyzed by JEOL-2100F transmission electron microscopy. Specimens for cross-sectional TEM

studies were prepared by mechanical grinding and polishing (~10 μm thick) followed by Ar-ion milling using a Gatan Precision Ion Polishing System (PIPSTM, Model 691). All current–voltage (I–V) properties of the TFTs and test structures were measured with a semiconductor parameter analyzer (HP 4155C, Agilent Technologies), and C–V measurements were made with a capacitance meter (HP 4284 LCR meter, Agilent Technologies, 1 MHz) in the dark and in an air ambient (relative humidity ~45%) at 20 °C.

3. Results and discussion

We fabricated an inverted staggered thin-film transistor (TFT) using an n-type organic–inorganic nanohybrid semiconducting superlattice on a polymer substrate. The inverted staggered TFT consists of an n-type organic–inorganic nanohybrid semiconducting channel and an organic–inorganic nanohybrid dielectric between the Cr bottom gate and Al source/drain electrodes on a polyethersulfone (PES) substrate, as shown in the device schematics of Fig. 1a. The n-type organic–inorganic nanohybrid semiconductor thin films were deposited on Cr gate-patterned PES substrates by molecular layer deposition combined with atomic layer deposition (MLD–ALD). The alkylsiloxane self-assembled organic layers (SAOLs) were grown by MLD, which is self-controlled and proceeds via layer-by-layer growth. ZnO inorganic nanolayers were grown by ALD using self-terminating surface reactions at 150 °C, followed by deposition of the SAOLs films using MLD at 150 °C: we named those organic–inorganic hybrid layers as SAOLs–ZnO (Fig. 1b). In these nanohybrid superlattices, SAOLs offer structural flexibility, whereas the ZnO inorganic layers provide the potential for semiconducting properties, as well as thermal and mechanical stability.

The SAOLs–ZnO nanolaminate films were grown on Si(1 0 0) substrates at 150 °C by repeating a cyclic MLD–ALD in the same deposition chamber, as shown in Fig. 2a. The Si substrates were first coated with a 10 nm-thick ZnO nanolayer by ALD and the top layer of each nanolaminate film was ZnO. The thicknesses of SAOLs and ZnO nanolayers in each sample were controlled by adjusting the number of MLD and ALD cycles with SAOLs and ZnO growth rates of about 11 and 1.5 Å/cycle, respectively. Fig. 2b shows a TEM image of SAOLs–ZnO active channel thin films with SAOLs–Al_2O_3 gate dielectric layers on the Si(1 0 0) substrates. The root mean square (RMS) roughnesses of the SAOLs–ZnO and the SAOLs–Al_2O_3 surfaces were about 6.0 and 3.0 Å, respectively, as measured by AFM. In comparison, the surface roughness of the initial cleaned Si substrate was about 2.1 Å. The SAOLs–ZnO layers appear to be relatively uniform despite polycrystallinity of the ZnO nanolayers. Fig. 2b suggests that flat and sharp interfaces enhance electrical performance of the TFTs which include organic–inorganic nanohybrid thin films grown by using MLD–ALD.

The unit TFT was fabricated on a PES substrate using the organic–inorganic hybrid superlattices. The SAOLs–ZnO hybrid films were approximately 32.2 nm-thick and consisted of three [SAOLs (1.1 nm)/ZnO (10 nm)] bilayer subunits. As shown in Fig. 3a, typical output (drain current–drain voltage: I_D–V_D) curves were obtained from our SAOLs–ZnO TFTs with SAOLs–Al_2O_3 dielectrics at low operating biases (−1 to 3 V). The maximum I_D level was around 8 μA under 3 V gate bias. According to the transfer characteristics (I_D–V_G) of Fig. 3b, a high field effect mobility of >7 $cm^2/V\,s$ was achieved in the saturation regime of V_D = 3 V along with an on/off ratio of $>10^6$ and a threshold voltage of 0.6 V. Gate leakage current (I_G) was below 10^{-11} A. Our device mobility is the highest among other n-type OTFTs with low threshold voltage. These SAOLs–ZnO TFTs could increase operating speed and decrease power consumption for flexible electronic devices operated under low operating biases. For comparison, a TFT was also fabricated on the PES substrate using a pure ZnO thin film grown by ALD at 150 °C. The mobility of the ZnO TFT (14 $cm^2/V\,s$) is higher than that of the SAOLs–ZnO while our operating voltage (3 V), on/off current ratio (10^6), and threshold voltage (0.6 V) are quite comparable.

The transfer characteristics of the SAOLs–ZnO TFTs before and after bending (bending direction across the channel) are presented in Fig. 3b. No significant loss in performance was observed when the devices were bent to a radius as small as 6 mm, as found in bending experiments performed on five randomly chosen devices that all exhibited similar behavior. The SAOLs–ZnO TFTs are also transparent in the visible range, as shown in Fig. 3c. These data demonstrate that our nanohybrid TFTs are potentially useful for flexible and invisible electronics.

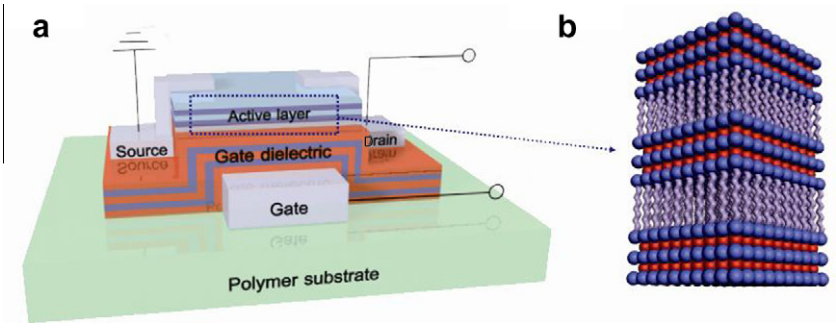

Fig. 1. (a) Schematic diagram of the TFTs with organic–inorganic nanohybrid active channel layers and gate dielectrics on flexible substrates. (b) Molecular structure of the SAOLs–ZnO organic–inorganic nanohybrid semiconducting thin films made by MLD–ALD.

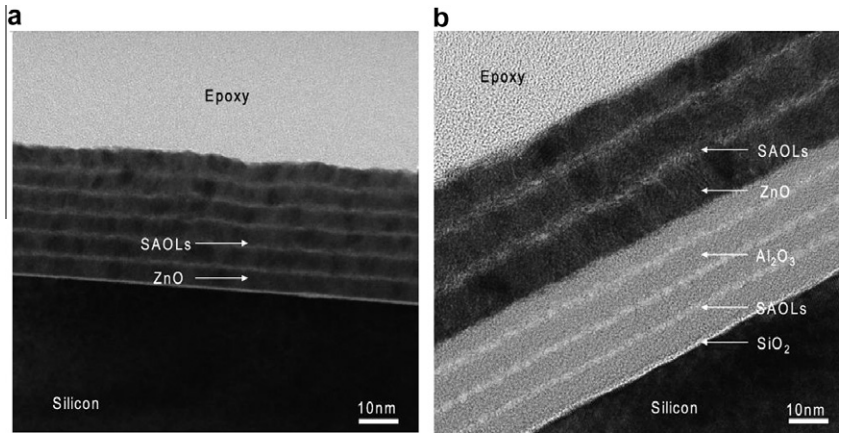

Fig. 2. (a) TEM image of SAOLs–ZnO nanohybrid superlattices made by MLD–ALD. (b) TEM image of SAOLs–ZnO nanohybrid superlattices on SAOLs–Al_2O_3 nanohybrid superlattices made by MLD–ALD.

We also estimated the stability and lifetime of the SAOLs–ZnO TFTs in air under controlled relative humidity and temperature. Our experiments were carried out in an environmental chamber, where relative humidity (±2%) and temperature (±1 °C) can be controlled simultaneously. Relative humidity and temperature were kept fixed in all experiments at 50% and 20 °C, respectively. After 6 months, this device still operated with constant field effect mobility and on-current, and slightly increased off-current, presumably due to light-generated oxygen vacancies and electrons.

To verify that our organic–inorganic superlattice is compatible with organic pentacene semiconductors, vertical p–n junction diodes were fabricated on ITO-coated glass. Pentacene was chosen as a p-type organic semiconductor because it is considered the benchmark material for maximum mobility in organic layers. A 55 nm-thick SAOLs–ZnO superlattice was grown on ITO-coated glass as the n-type semiconductor layer using MLD–ALD. A 50 nm-thick pentacene thin film was deposited on the SAOLs–ZnO layer by using a vacuum as the p-type semiconductor layer. In this diode, ITO and Au metals were used

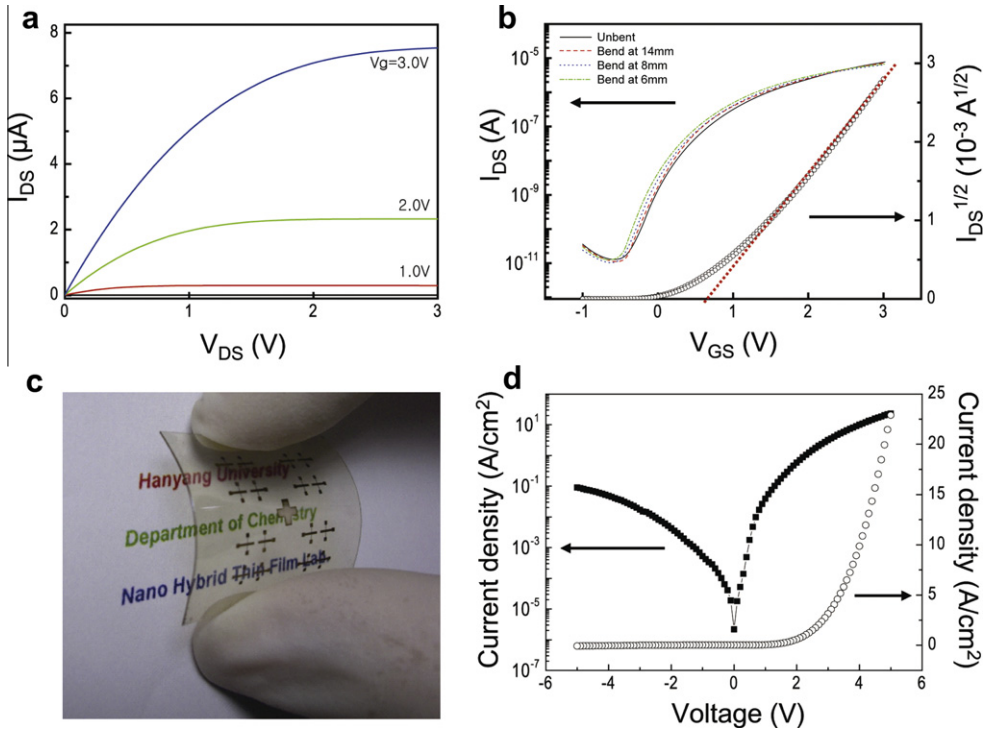

Fig. 3. (a) Drain current–drain voltage (I_{DS}–V_{DS}) output curves for our TFTs with the SAOLs–ZnO active channel layers. (b) Drain current–gate voltage (I_{DS}–V_{GS}) transfer curves of the TFTs unbent and bent at 14 mm, 8 mm, and 6 mm bending radius. (c) Photograph of our flexible TFT. (d) Current density–voltage characteristics (I–V) for the vertical p–n junction diodes with the SAOLs–ZnO nanohybrid and pentacene thin films.

as bottom and top electrodes, respectively. Fig. 3d shows *I–V* characteristics of the vertical p–n junction diodes. The current density at 5 V of the operating bias is 23 A/cm^2, which is comparable to that of other organic vertical diodes. The DC rectification ratio at ±5 V is more than 100. The forward turn-on voltage of the diode is approximately 2 V. The reverse breakdown voltage of the diodes is −17 V, eight times higher than the threshold voltage.

4. Conclusion

In conclusion, n-type organic–inorganic nanohybrid superlattices were developed for active semiconducting channel layers of TFTs at a low temperature of 150 °C by using MLD–ALD. SAOLs–ZnO TFTs on a flexible plastic substrate show a high field effect mobility of 7 cm^2/V·s, operating at 3 V with an on/off current ratio of 10^6 and also with a threshold voltage of 0.6 V. The ZnO inorganic component is a high-mobility n-type semiconductor and the SAOLs organic component provides structural flexibility. The stability and lifetime of the SAOLs–ZnO TFTs with good flexibility and excellent transparence in the visible range were tested under controlled relative humidity and temperature for 6 months. Field effect mobility of these TFTs was constant within measurement error range. Vertical p–n junction diodes were fabricated using the SAOLs–ZnO as the n-type semiconductor layer and pentacene as the p-type semiconductor layer, to verify that the organic–inorganic nanohybrid semiconductors can work with organic semiconductors.

Acknowledgements

This work was supported by the Korea Science and Engineering Foundation (KOSEF) funded by The Ministry of Education, Science and Technology (MEST) (No. 2009-0092807) and (No. 2010-0019125), and by Seoul R&BD program (ST090839) and by the IT R&D program of MKE/KEIT[10030559, Development of next generation high performance organic/nano materials and printing process technology] and by the Korea Research Foundation Grant funded by The Korea government (MOEHRD, Basic Research Promotion Fund) (KRF-2007-313-C00383).

References

[1] T. Someya, T. Sekitani, S. Iba, Y. Kato, H. Kawaguchi, T. Sakurai, Proc. Natl. Acad. Sci. USA 101 (2004) 9966.
[2] J.A. Rogers, Z. Bao, K. Baldwin, A. Dodabalapur, B. Crone, V.R. Raju, et al., Proc. Natl. Acad. Sci. USA 98 (2001) 4835.
[3] C.D. Dimitrakopoulos, P.R.L. Malenfant, Adv. Mater. 14 (2002) 99.
[4] G. Horowitz, Adv. Mater. 10 (1998) 365.
[5] R.H. Reuss, B.R. Chalamala, A. Moussessian, M.G. Kane, A. Kumar, D.C. Zhang, et al., Proc. IEEE 93 (2005) 1239.
[6] Z. Bao, J.A. Rogers, H.E. Katz, J. Mater. Chem. 9 (1999) 1895.
[7] S.R. Forrest, Nature 428 (2004) 911.
[8] Z. Bao, A. Dodabalapur, A.J. Lovinger, Appl. Phys. Lett. 69 (1996) 4108.
[9] M.M. Payne, S.R. Parkin, J.E. Anthony, C.C. Kuo, T.N. Jackson, J. Am. Chem. Soc. 127 (2005) 4986.
[10] H. Sirringhaus, N. Tessler, R.H. Friend, Science 280 (1998) 1741.
[11] B.S. Ong, Y. Wu, P. Liu, S. Gardner, J. Am. Chem. Soc. 126 (2004) 3378.
[12] M. Heeney, C. Bailey, K. Genevicius, M. Shkunov, D. Sparrowe, S. Tierney, et al., J. Am. Chem. Soc. 127 (2005) 1078.
[13] T.W. Kelley, D.V. Muyres, P.F. Baude, T.P. Smith, T.D. Jones, Mater. Res. Soc. Symp. Proc. 771 (2003) 169.
[14] B.A. Jones, M.J. Ahrens, M.H. Yoon, A. Facchetti, T.J. Marks, M.R. Wasielewski, Angew. Chem. Int. Ed. 43 (2004) 6363.
[15] M.H. Yoon, S.A. DiBenedetto, A. Facchetti, T.J. Marks, J. Am. Chem. Soc. 127 (2005) 1348.
[16] V.C. Sundar, J. Zaumseil, V. Podzorov, E. Menard, R.L. Willett, T. Someya, et al., Science 303 (2004) 1644.
[17] S. Ando, R. Murakami, J. Nishida, H. Tada, Y. Inoue, S. Tokito, et al., J. Am. Chem. Soc. 127 (2005) 14996.
[18] A.R. Murphy, J.M.J. Fréchet, Chem. Rev. 107 (2007) 1066.
[19] R.C. Haddon, A.S. Perel, R.C. Morris, T.T.M. Palstra, A.F. Hebard, R.M. Fleming, Appl. Phys. Lett. 67 (1995) 121.
[20] D.M. de Leeuw, M.M.J. Simenon, A.R. Brown, R.E.F. Einerhand, Synth. Met. 87 (1997) 53.
[21] J.H. Schön, Appl. Phys. Lett. 79 (2001) 4163.
[22] Ch. Pannemann, T. Diekmann, U. Hilleringmann, J. Mater. Res. 19 (2004) 1999.
[23] J.H. Burroughes, D.D.C. Bradley, A.R. Brown, R.N. Marks, K. Mackay, R.H. Friend, et al., Nature 347 (1990) 539.
[24] Z. Bao, A.J. Lovinger, J. Brown, J. Am. Chem. Soc. 120 (1998) 207.
[25] H.E. Katz, A.J. Lovinger, J. Johnson, C. Kloc, T. Siegrist, W. Li, et al., Nature 404 (2000) 478.
[26] H. Yan, S. Lu, Y. Zheng, P. Inagaki, A. Facchetti, T.J. Marks, Proc. SPIE 6658 (2007) 66580S.
[27] D. Song, H. Wang, F. Zhu, J. Yang, H. Tian, Y. Geng, et al., Adv. Mater. 20 (2008) 2142.
[28] C.R. Kagan, D.B. Mitzi, C.D. Dimitrakopoulos, Science 286 (1999) 945.
[29] L. Wang, M.H. Yoon, G. Lu, Y. Yang, A. Facchetti, T.J. Marks, Nat. Mater. 5 (2006) 893.
[30] L. Wang, M.H. Yoon, A. Facchetti, T.J. Marks, Adv. Mater. 19 (2007) 3252.
[31] B.H. Lee, M.K. Ryu, S.Y. Choi, K.H. Lee, S. Im, M.M. Sung, J. Am. Chem. Soc. 129 (2007) 16034.
[32] B.H. Lee, K.H. Lee, S. Im, M.M. Sung, Org. Electron. 9 (2008) 1146.
[33] B.H. Lee, K.K. Im, K.H. Lee, S. Im, M.M. Sung, Thin Solid Films 517 (2009) 4056.
[34] H.I. Shao, S. Umemoto, T. Kikutani, N. Okui, Polymer 38 (1997) 459.
[35] T. Yoshimura, S. Tatsuura, W. Sotoyama, Appl. Phys. Lett. 59 (1991) 482.
[36] A. Kim, M.A. Filler, S. Kim, S.F. Bent, J. Am. Chem. Soc. 127 (2005) 6123.
[37] Y. Du, S.M. George, J. Phys. Chem. C 111 (2007) 8509.
[38] K.H. Lee, J.M. Choi, B.H. Lee, K.K. Im, S. Lee, M.M. Sung, et al., Appl. Phys. Lett. 91 (2007) 123502.
[39] S.H. Cha, M.S. Oh, K.H. Lee, J.M. Choi, B.H. Lee, M.M. Sung, et al., IEEE Elect. Dev. Lett. 29 (2008) 1145.
[40] S.H. Cha, M.S. Oh, K.H. Lee, B.H. Lee, M.M. Sung, S. Im, Appl. Phys. Lett. 92 (2008) 023506.
[41] A. Ishizaka, Y. Shiraki, J. Electrochem. Soc. 133 (1986) 666.

Organic Electronics 12 (2011) 353–357

Contents lists available at ScienceDirect

Organic Electronics

journal homepage: www.elsevier.com/locate/orgel

Highly efficient inverted poly(3-hexylthiophene): Methano-fullerene [6,6]-phenyl C71-butyric acid methyl ester bulk heterojunction solar cell with Cs_2CO_3 and MoO_3

Yeon-Il Lee [a,b], Jun-Ho Youn [a,b], Mi-Sun Ryu [a], Jungho Kim [a], Hie-Tae Moon [b], Jin Jang [a,*]

[a] Advanced Display Research Center and Department of Information Display, Kyung Hee University Dongdaemoon-gu, Seoul 130-701, Republic of Korea
[b] Department of Physics, KAIST, Yuseong-gu, Daejeon 305-701, Republic of Korea

ARTICLE INFO

Article history:
Received 3 May 2010
Received in revised form 1 November 2010
Accepted 28 November 2010
Available online 10 December 2010

Keywords:
Organic solar cell
Inverted cell
Stable cell

ABSTRACT

We have studied the fabrication of an inverted P3HT:$PC_{71}BM$ bulk hetero-junction (IBHJ) solar cell using ultrathin cesium carbonate (Cs_2CO_3) and molybdenum trioxide (MoO_3) as the cathodic and anodic buffer layers, respectively. The influence of MoO_3 thickness on the performance of the IBHJ solar cells was investigated for thicknesses ranging from 0.75 to 3 nm and the optimum thickness was found to be 2 nm, which showed the highest power conversion efficiency of 4.01%. We also found that the power conversion efficiency of the IBHJ solar cells is relatively retained even in low temperature while that of BHJ solar cell rapidly decreased with decreasing temperature and the stability in air is also much better.

© 2010 Elsevier B.V. All rights reserved.

1. Introduction

Organic solar cells are of increasing interest because of their potential low cost manufacturing via simple processes [1,2]. Of particular interest are bulk hetero-junction (BHJ) solar cells, which have so far been regarded as having the promising structure for obtaining high internal quantum efficiency (IQE). Moreover, solution process-based BHJ solar cells with a blend of polymer and fullerene derivatives have emerged as promising candidates for flexible photovoltaic devices and a variety of large area applications [1–3]. Owing to the interpenetrating network between donor and acceptor materials, the BHJ structure, compared to the bi-layer structure of single junction solar cells, has a wider interface region that enhances the dissociation of excitons into mobile electrons and holes [4,5]. Using regio-regular poly(3-hexylthiophene) (rr-P3HT) and [6,6]-phenyl C71 butyric acid methyl ester ($PC_{71}BM$), conventional BHJ solar cells with high PCE above 3–5% have been reported.

Although the efficiency of BHJ solar cells is increasing steadily, stability remains as an obstacle to its commercialization. Since the conventional organic BHJ solar cell is composed of an *ITO/PEDOT:PSS/active layer/low work function metal cathode* structure, problems associated with the electrodes are common; a low work function metal is easily oxidized and PEDOT:PSS can degrade the ITO electrode due to its strong acidity [6]. To overcome these problems, PEDOT:PSS is often replaced by metal oxides such as MoO_3 [7], WoO_3 [8], NiO [9], as the anodic buffer layer in the conventional structure. It is also known that n-type metal oxides such as TiO_2 [10], ZnO [11], and low work function alkali metal compounds such as LiF [12], Cs_2CO_3 [13] can be used to improve electron extraction and device stability. The inverted structure, in which polarities of electrodes are converted using anodic/cathodic buffer layers such as metal oxides or alkali metal compounds have thus received more attention as a new device structure for high efficiency as well as good stability. Recently, the Y. Yang group demonstrated an efficient inverted solar cell with Cs_2CO_3 and V_2O_5 buffer layers [14] and introduced the concept of vertical phase separation [15]. According to this concept, an inverted structure would be an advantage for higher efficiency as well as stability.

* Corresponding author. Tel.: +82 2 961 0270; fax: +82 2 961 9154.
E-mail address: jjang@khu.ac.kr (J. Jang).

1566-1199/$ - see front matter © 2010 Elsevier B.V. All rights reserved.
doi:10.1016/j.orgel.2010.11.024

In this study, we demonstrate a stable inverted P3HT:$PC_{71}BM$ BHJ (IBHJ) solar cell with Cs_2CO_3 and MoO_3 buffer layers. IBHJ solar cells showed better stability and efficiency as compared with the conventional BHJ solar cells. We also investigated the influence of MoO_3 thickness to obtain an optimum layer thickness and studied the temperature dependency of the solar cell properties.

2. Experiment

The device structure of the solar cell studied in this work is an ITO (150 nm)/Cs_2CO_3 (0.5 nm)/Active layer (70 nm)/MoO_3 (*x* nm)/Al (100 nm). Fig. 1a shows the cross sectional view of the solar cell. The IBHJ solar cells were prepared according to the following procedure: A 0.1wt.% Cs_2CO_3 resolved in 2-ethoxy ethanol was spin coated at 4000 rpm on the patterned ITO glass substrate to form an ultra-thin layer. The Cs_2CO_3 layer was annealed at 150 °C for 20 min. The active solution was formed by a 1 wt.% of P3HT (Aldrich) and 1 wt.% of $PC_{71}BM$ (Aldrich), which were separately dissolved in 1, 2 dicholorobenzene and blended together in ratios of 1:0.6. The active solution was spin-casted at 700 rpm on the top of the ultra-thin Cs_2CO_3 layer. The fabricated active layer was then annealed at 130 °C for 30 min.

The thickness of active layer was ~70 nm, measured by a surface profiler (ET-3000 Kosaka. Lab. Ltd.). Following this, a MoO_3 layer was evaporated on the active layer and then a 100 nm Al layer was deposited without breaking the vacuum (~10^{-7} Torr, deposition rates (MoO_3: 0.01 nm/s; Al: 0.2–0.4 nm/s)). Without the post annealing, the cells were encapsulated with a glass cap and UV-resin. We used a current meter (Keithley 2400 LV) and a xenon lamp based solar simulator (MAX-302) to measure the solar cell properties under AM 1.5 (100mWcm^{-2}). External quantum efficiency (EQE) was measured by using a 300 W xenon light source with a monochromator (Oriel Cornerstone 130). The temperature dependence measurements were carried out in a cryostat system (JANIS CCS-450) having 10^{-3} mbar of vacuum.

3. Results and discussion

Fig. 1b shows the energy level diagram of an IBHJ solar cell. The deposition of an ultra-thin Cs_2CO_3 layer on ITO increases the contact angle and reduces its effective work function [14]. We changed the annealing temperature between 130 °C and 190 °C and the spin coating speed from 4000 rpm to 700 rpm. The optimum annealing temperature and spin speed were found to be 150 °C and 4000 rpm, respectively. The optimized fabrication condition of Cs_2CO_3 layer is similar to that of Liao's result [14]. At the optimum Cs_2CO_3 deposition condition, the MoO_3 thickness was varied from 0.75 to 3 nm.

Fig. 2 shows the *J*–*V* characteristics of the solar cells with different MoO_3 thickness under illumination. The optimized IBHJ (with MoO_3 of 2.0 nm) shows the highest J_{SC} of 10.1 mA/cm^2 and PCE of 4.01%. Note that the conventional BHJ solar cell having the structure ITO/PEDOT:PSS/Active layer (70 nm)/LiF/Al (100 nm) exhibited a J_{SC} of 8.8 mA/cm^2 and PCE of 3.63%. The device with MoO_3 of 0.75 nm shows unstable solar cell properties with high sheet resistance (R_S), poor fill factor (FF) and open circuit voltage (V_{OC}). The reason for this lies in the small MoO_3 intermolecular distance (~0.7 nm) and thus 0.75 nm is not enough to have full-coverage on the Al electrode; making the formation of islands more favorable compared to a thin layer [16]. With increasing MoO_3 thickness, the V_{OC}, FF

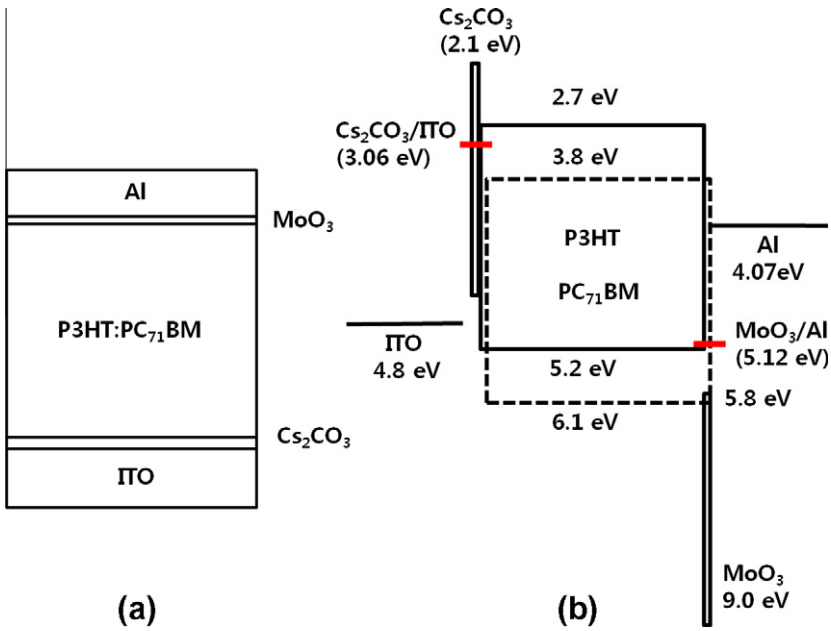

Fig. 1. (a) Device structure and (b) energy level diagram of an inverted BHJ solar cell. Red lines indicate the effective work functions of Cs_2CO_3/ITO and MoO_3/Al electrodes.(For interpretation of the references to colour in this figure legend, the reader is referred to the web version of this article.)

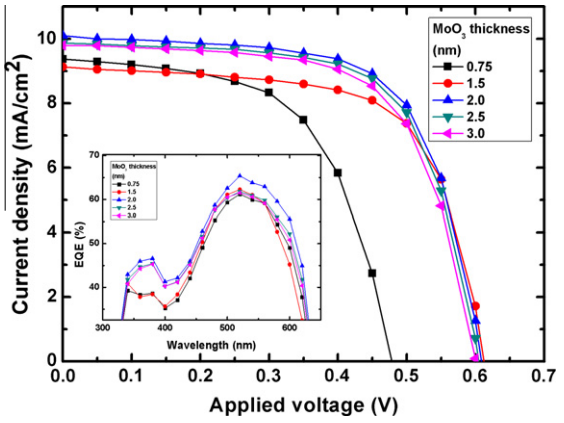

Fig. 2. The *J–V* characteristics of the inverted BHJ solar cells with different MoO_3 thicknesses under AM 1.5 illumination. The inset shows the EQE of the inverted BHJ solar cells with different MoO_3 thicknesses.

and R_S are thus improved, and in our case, up until 2 nm, after which the R_S increases due to the increased MoO_3 resistance.

A thin MoO_3 layer, with 1–3 atom layers, is able to convert the electrode polarity because MoO_3 has very deep LUMO (Lowest Unoccupied Molecule Orbital) and HOMO (Highest Occupied Molecule Orbital) levels of −5.8 and −9.0 eV [17], respectively. Such deep HOMO and LUMO levels results in easy formation of a strong dipole effect. Moreover, it was previously reported that a thin MoO_3 layer increases the work function of Al and thus reduces the hole injection barrier between Al and the p-type organic material by Fermi level pinning [18]. A MoO_3 thin layer would also modify the electronic structure of the P3HT/Al interface. The work function of the 2 nm MoO_3 on Al in our experiment was found to be 5.12 eV by ultraviolet photoelectron spectroscopy (UPS) measurement, and this value is very close to the HOMO of P3HT (5.2 eV). Therefore, hole extraction can be improved by inserting a MoO_3 layer on Al.

Table 1 summarizes the solar cell properties as a function of MoO_3 thickness. With increasing the MoO_3 thickness, the FF increased to the maximum and R_S decreased to the minimum at 2 nm. With further increase in the MoO_3 thickness (above 2.0 nm), the R_s increases slightly due to the resistance of MoO_3. A 2 nm MoO_3 anodic buffer layer induces a good ohmic contact to extract holes, resulting in high FF and low R_S.

The inset of Fig. 2 shows the external quantum efficiency (EQE) of the IBHJ solar cells with different MoO_3 thicknesses. The PCE accords with the enhancement of EQE. Even in the most dominant absorption range of conventional P3HT:$PC_{71}BM$ cells, which ranges from 480 to 550 nm, the EQE of IBHJ solar cell is ~18% higher. T. Ameri et al. previously reported this phenomena where an IBHJ solar cell with a TiO_x layer had a higher EQE than the conventional structure [19]. In our result, the main peak in EQE shifted slightly to the short wavelength region compared to that one of the conventional device. No wavelength shift was found in UV–Vis absorption measurement for the PEDOT/active and Cs_2CO_3/active layers. The shift of EQE indicates the modification of the optical field distribution due to total thickness variation of the device and may be related to the absence of the PEDOT:PSS layer. In our measurements, conventional PEDOT:PSS layers of several tens of nanometer thicknesses show around 95% transmittance and several hundreds of Ohm-centimeter resistivity values. This will lead to reduced efficiency due to optical absorption and inefficient carrier transport processes. On the other hand, since the Cs_2CO_3 layer is ultrathin, there is nearly 100% transmittance and thus no loss in efficiency.

Table 1
The solar cell performances of IBHJ devices with different MoO_3 thickness.

MoO_3 thickness (nm)	0.75	1.5	2.0	2.5	3.0
V_{OC} (V)	0.478	0.605	0.609	0.605	0.601
J_{SC} (mA/cm^2)	9.37	9.14	10.1	9.87	9.82
FF (%)	58.36	64.72	65.37	65.07	64.12
PCE (%)	2.62	3.58	4.01	3.89	3.79
R_S (Ω cm^2)	4.17	3.27	3.07	3.24	3.38

We also calculated the spatial distribution of the optical field in the IBHJ solar cells using the transfer matrix method [20]. Fig. 3 shows the comparison of the optical field distributions between inverted cells with a thin MoO_3 layer and PEDOT:PSS layer. The intensity is almost the same, but the optical field distribution in the active layer is better for the inverted structure with a thin MoO_3 layer compared to that with a PEDOT:PSS layer, because, in this structure, the field distribution is pushed towards the active layer.

In our result, the highest J_{SC} is also obtained for a MoO_3 thickness of 2 nm. To confirm the optical spacer effect as the MoO_3 layer thickness is varied from 0.75 to 3 nm, we calculated the spatial distribution of the optical field in IBHJ solar cells for each thickness. Considering the refractive index of ~2.4, there is a little effect on the absorption of the BHJ when the MoO_3 thickness is less than 3 nm. By increasing the MoO_3 thickness to 3 nm, the optical field distribution shifts slightly to the anodic buffer layer.

Fig. 4 shows the stability of an IBHJ solar cell in air. The IBHJ shows better stability than the conventional BHJ solar cell in ambient air at 295 K for 40 days. The PCE of the IBHJ solar cell drops to about 93.5% of the initial value, while that of BHJ solar cell decreases to 87.7%. This may be due to less damage to the ITO in the IBHJ because there is no PEDOT:PSS process and the improvement of carrier extraction due to the existence of a thin MoO_3. Therefore, IBHJ solar cell shows better stability and efficiency compared to conventional BHJ solar cells.

Fig. 5 shows the *J–V* characteristics of an IBHJ solar cell with a 2 nm MoO_3 layer at various temperatures. While the J_{SC} increases with increasing temperature up to 340 K and starts to decrease at temperatures $\geqslant$360 K, the V_{OC} decreases gradually with increasing temperature. The same tendency was previously reported for silicon-based inorganic solar cells [21,22]. As a result, the cells exhibited their maximum efficiency at ~300 K. Prolonged heating of the devices would induce irreversible reactions such as thermal oxidation, P3HT rearrangement and PCBM aggregation [23,6]. The degradation in efficiency observed at

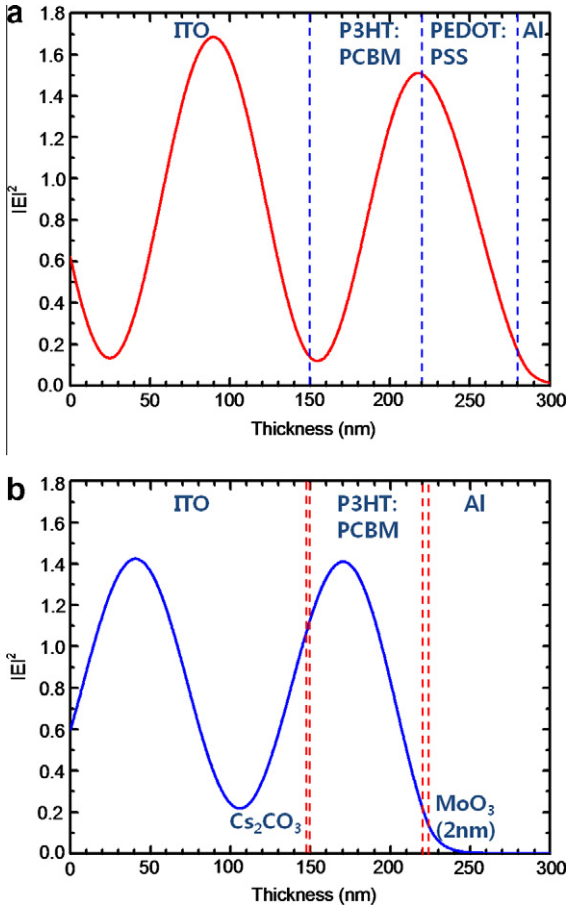

Fig. 3. The spatial distributions of optical field in inverted BHJ solar cells with (a) PEDOT:PSS layer and (b) Cs_2CO_3 and MoO_3 layer.

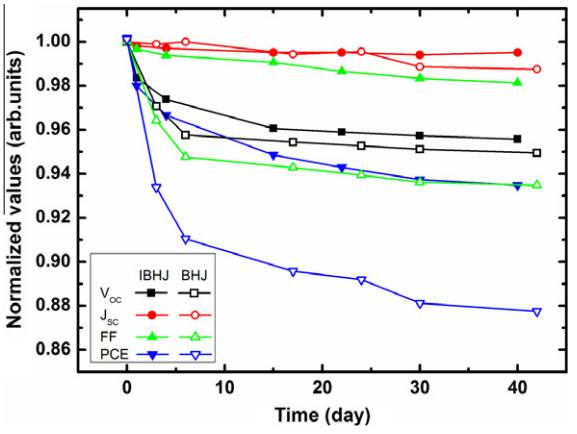

Fig. 4. Plot of solar cell parameters as a function of time in ambient air. The parameters are normalized to initial values. Solid symbols represent the parameters of inverted BHJ solar cell and open symbols represent that of conventional BHJ solar cell.

temperatures $\geqslant$360 K in both structures is due to this thermal effect. Fig. 6 shows the J–V characteristics of our conventional BHJ solar cell under AM 1.5 illumination at low

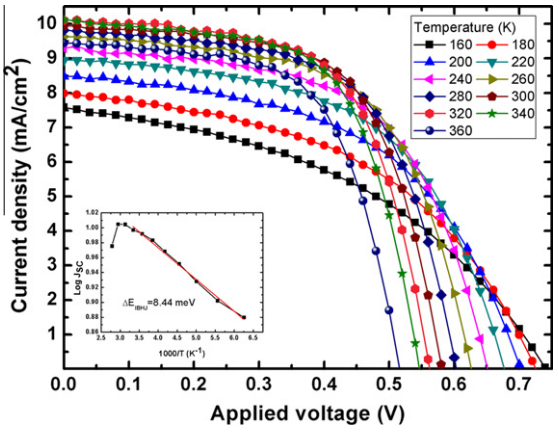

Fig. 5. The J–V characteristics of the inverted BHJ solar cells under AM 1.5 illumination with a 2.0 nm of MoO_3 layer at low temperatures. The inset shows the extraction of activation energy ΔE and J_0 under illumination.

temperatures. The insets of Figs. 5 and 6 show the extraction of activation energy ΔE and J_0 of both solar cells under illumination in the temperature range showing linearity between log J_{SC} and the inverse of absolute temperature.

J_{SC} has the temperature dependence behavior due to the thermally assisted hopping conduction in the disordered organic material. The activation energies of both structures are shown in the insets of Fig. 5 and 6. For the IBHJ solar cell with a 2.0 nm thick MoO_3 layer, an activation energy of 8.44 meV and J_0 of 13.63 mA/cm^2 are extracted using the following equation [21];

$$J_{SC}(T) = J_0 \exp(-\Delta E/kT), \tag{1}$$

where J_0 is a pre-exponential factor, ΔE is the activation energy, k is the Boltzmann constant, and T is an absolute temperature.

The IBHJ solar cells are more stable in ambient air and the reduction of efficiency at low temperature is much less as compared to conventional BHJ solar cell. The

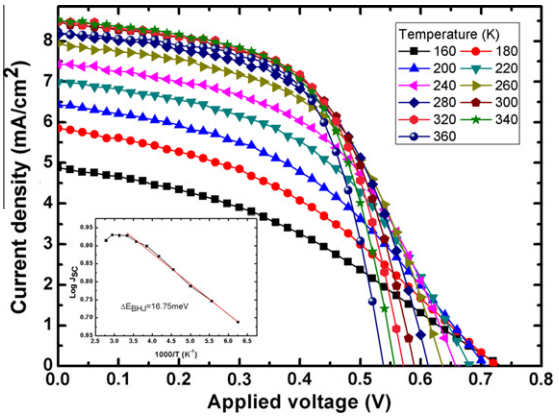

Fig. 6. The J–V characteristics of the conventional BHJ solar cells under AM 1.5 illumination at low temperatures. The inset shows the extraction of activation energy ΔE and J_0 under illumination.

variation in solar cell properties such as J_{SC}, FF, and PCE are relatively small with decreasing temperature. As the measurement temperature changes from 300 to 240 K, the PCE of the IBHJ solar cell decreases to 98% of the value at 300 K.

The activation energy of J_{SC} for the IBHJ solar cell is 8.44 meV which is much smaller than that (16.75 meV) of conventional BHJ solar cell, indicating that the efficiency lowering is much less for the IBHJ solar cell as compared to that of the conventional BHJ. The difference appears to be due to the different carrier extraction mechanisms for the same active layer in the two structures.

4. Conclusion

We have studied the fabrication of the inverted BHJ solar cells with Cs_2CO_3 and MoO_3 buffer layers. IBHJ solar cells show better performance due to the absence of the PEDOT:PSS layer and the existence of an efficient hole extraction mechanism through the MoO_3 layer. The cell using both the Cs_2CO_3 and MoO_3 layers has improved lifetime and conversion efficiency. The reduction in efficiency of the proposed IBHJ solar cell with decreasing temperature is also much lower than that of the conventional BHJ solar cell.

Acknowledgment

This work was supported by the Ministry of Knowledge Economy, Korea.

References

[1] N.S. Sariciftci, L. Smilowitz, A.J. Heeger, F. Wudl, Science 258 (5087) (1992) 1474.
[2] C.J. Brabec, Sol. Energy Mater. Sol. Cells 83 (2004) 273.
[3] S.E. Shaheen, C.J. Brabec, N.S. Sariciftci, F. Padinger, T. Fromherz, J.C. Hummelen, Appl. Phys. Lett. 78 (2001) 841.
[4] G. Yu, J. Gao, J.C. Hummelen, F. Wudl, A.J. Heeger, Science 270 (1995) 1789.
[5] J.J.M. Halls, C.A. Walsh, N.C. Greenham, E.A. Marsegila, R.H. Friend, S.C. Moratti, et al., Science 376 (1995) 498.
[6] M. Jorgensen, K. Norrman, F.C. Krebs, Sol. Energy Mater. Sol. Cells 92 (2008) 686.
[7] V. Shrotriya, G. Li, Y. Yao, C.W. Chu, Y. Yang, Appl. Phys. Lett. 88 (2006) 073508.
[8] M.D. Irwin, D.B. Buchholz, A.W. Hains, R.P.H. Chang, T.J. Marks, PNAS 105 (2008) 2783.
[9] K. Takanezawa, K. Tajima, K. Hashimoto, Appl. Phys. Lett. 93 (2008) 063308.
[10] S.H. Park, A. Roy, S. Beaupre, S. Cho, N. Coates, J.S. Moon, et al., Nat. Photonics 3 (2009) 297.
[11] S.K. Hau, H.L. Yip, H. Ma, A.K.Y. Jen, Appl. Phys. Lett. 92 (2008) 253301.
[12] C.J. Brabec, S.E. Shaheen, C. Winder, N.S. Sariciftci, Appl. Phys. Lett. 80 (2002) 1288.
[13] F.C. Chen, J.L. Wu, K.H. Hsieh, W.C. Chen, Shih.W. Lee, Org. Electron. 9 (2008) 1132.
[14] H.H. Liao, L.M. Chen, Z. Xu, G. Li, Y. Yang, Appl. Phys. Lett. 92 (2008) 173303.
[15] Z. Xu, L.M. Chen, G. Yang, C.H. Huang, H. Hou, Y. Wu, et al., Adv. Funct. Mater. 19 (2009) 1227.
[16] T. Aernouts, W. Geens, J. Poortmans, P. Heremans, S. Borghs, R. Mertens, Thin Solid Films 297 (2002) 403.
[17] J. Subbiah, D.Y. Kim, M. Hartel, F. So, Appl. Phys. Lett. 96 (2010) 063303.
[18] P. Jeon, K. Han, H. Lee, H.S. Kim, K. Jeong, K. Cho, Synth. Metals 159 (2009) 2502.
[19] T. Ameri, G. Dennler, C. Waldauf, P. Denk, K. Forberich, M.C. Scharber, et al., J. Appl. Phys. 103 (2008) 084506.
[20] L.A.A. Pettersson, L.S. Roman, O. Inganas, J. Appl. Phys. 86 (1999) 487.
[21] I. Riedel, J. Parisi, V. Dyakonov, L. Lutsen, D. Vanderzande, J.C. Himmelen, Adv. Funct. Mater. 14 (2004) 38.
[22] D. Chirvase, Z. Chiguvare, M. Knipper, J. Parisi, V. Dyakonov, J.C. Hummelen, J. Appl. Phys. 93 (2003) 3376.
[23] Y.-I. Lee, J.-H. Youn, M.-S. Ryu, J. Kim, J. Jang, H.T. Moon, J. Appl. Phys. 108 (2010) 054506.

Organic Electronics 12 (2011) 358–363

Contents lists available at ScienceDirect

Organic Electronics

journal homepage: www.elsevier.com/locate/orgel

Efficient blue organic light-emitting devices with a new bipolar emitter

Silu Tao [a,b,*], Yilan Jiang [a], Shiu-Lun Lai [b], Man-Keung Fung [b], Yechun Zhou [b], Xiaohong Zhang [c], Weiming Zhao [d], Chun-Sing Lee [b,*]

[a] School of Optoelectronic Information, University of Electronic Science and Technology of China (UESTC), Chengdu 610054, China
[b] Center of Super-Diamond and Advanced Films (COSDAF) & Department of Physics and Materials Science, City University of Hong Kong, Hong Kong SAR, China
[c] Nano-organic Photoelectronic Laboratory and Key Laboratory of Photochemical Conversion and Optoelectronic Materials, Technical Institute of Physics and Chemistry, Chinese Academy of Sciences, Beijing 100190, China
[d] Dongguan LITEWELL (OLED) Technology Incorporation, Dongguan 523656, China

ARTICLE INFO

Article history:
Received 2 October 2010
Received in revised form 2 December 2010
Accepted 3 December 2010
Available online 16 December 2010

Keywords:
OLED
Blue emitter
Bipolar emitter

ABSTRACT

A new multifunctional compound, 4,4′-di-(1-pyrenyl)-4″-[2-(9,9′-dimethylfluorene)]-triphenylamine (DPFA) has been designed, synthesized and applied respectively as host-emitter, electron- and hole-transporters in organic light-emitting devices (OLEDs). The compound exhibits good thermal stability with a glass transition temperature (T_g) of 161 °C and shows blue emissions in both solution and films. OLEDs with DPFA playing various roles have been fabricated and characterized. The results show that DPFA has efficient bipolar charge transport properties for both hole and electron. By using DPFA as a blue emitter in a typical three layer device with a configuration of ITO/NPB(50 nm)/DPFA(20 nm)/TPBI(30 nm)/LiF(0.5 nm)/MgAg, highly efficient blue emission with a maximum luminescence efficiency of 5.1 cd/A (5.3 lm/W) is obtained.

© 2010 Elsevier B.V. All rights reserved.

1. Introduction

White organic light-emitting devices (OLEDs) have drawn much attention due to their applications as backlights for liquid–crystal displays and for solid-state lightings [1–4]. For these applications, high efficiency and long life-time are important. Phosphorescent OLEDs have been shown to harvest 100% of the excitons generated by electrical injection, corresponding to a four times increase in efficiency compared to that achievable in singlet-harvesting fluorescent OLEDs [5]. For this reason, white OLED using phosphorescent emitters has been a focus of intense research. Meanwhile, one bottleneck for further enhancing the efficiency of white OLEDs is the performance of blue phosphorescent emitters, which is far behind those of green and yellow phosphorescent emitters. Although many blue phosphorescent emitters have been reported, Iridium(III)bis[(4,6-difluorophenyl)-pyridinato-N,$C^{2'}$]picolinate (FIrPic) is still the best and most widely used blue phosphorescent emitter [6–10]. However, FIrPic is in fact a blue–green emitter, with two peaks at 472 and 500 nm, respectively [11,12]. The color purity of the OLEDs based on FIrPic is thus compromised. Moreover, it is known that lifetime of FIrPic-based devices are often inadequate [2]. Till now, efficient blue phosphorescent emitters with a long lifetime have been scarce. Thus, more and more researchers have put efforts on white OLEDs which take advantages of red or yellow phosphorescent and blue fluorescence emitters. Therefore, high performance blue fluorescent emitters are expected to play an important role in white OLEDs.

On the other hand, keeping a good balance of electron and hole currents in OLEDs is known to be important for achieving a high efficiency [13]. One possible way to

* Corresponding authors. Address: Center of Super-Diamond and Advanced Films (COSDAF) & Department of Physics and Materials Science, City University of Hong Kong, Hong Kong SAR, China (S. Tao). Fax: +86 28 83201745 (S. Tao), +852 34420544 (C.-S. Lee).

E-mail addresses: silutao@uestc.edu.cn (S. Tao), apcslee@cityu.edu.hk (C.-S. Lee).

1566-1199/$ - see front matter © 2010 Elsevier B.V. All rights reserved.
doi:10.1016/j.orgel.2010.12.001

improve the charge balance in OLEDs is to use emitters with bipolar charge transporting properties. Till now, reported bipolar emitters are mostly emitting in longer wavelength and there are few bipolar blue emitters [14–19].

In this paper, we report the synthesis and characterization of a new compound, 4,4′-di-(1-pyrenyl)-4″-[2-(9,9'-dimethylfluorene)]-triphenylamine (DPFA). The compound exhibits good thermal stability with a glass transition temperature (T_g) of 161 °C and shows blue emission in both solution and films. It was found that in addition to giving a strong blue emission, DPFA can also efficiently transport both electrons and holes. A device with the configuration of ITO/NPB(50 nm)/DPFA(20 nm)/TPBI(30 nm)/LiF(0.5 nm)/MgAg shows a low turn-on voltage of 2.8 V and highly efficient blue emission with a maximum luminescence efficiency of 5.1 cd/A (5.3 lm/W).

2. Experimental

2.1. Material synthesis

All solvents were purified by routine procedures. Other reagents were used as received from commercial sources, unless otherwise stated.

4-[2-(9,9′-dimethylfluorene)]-triphenylamine (compound 1): 2-bromo-9,9′-dimethylfluorene (2.72 g), and triphenyl boronic acid (2.41 g), Pd $(PPh_3)_4$ (0.07 g), aqueous Na_2CO_3 (2.0 M, 15 mL), ethanol (10 mL), toluene (30 mL) were mixed in a flask. The mixture was degassed for several times and then the mixture was refluxed at 100 °C for 24 h under a nitrogen atmosphere. After cooling to room temperature, the solvent was evaporated under vacuum and the product was extracted with dichloromethane (CH_2Cl_2). The CH_2Cl_2 solution was washed with water and dried with $MgSO_4$. Evaporation of the solvent, followed by column chromatography on silica gel gives a white solid. Yield: 83%; MS (m/z): 437 (M^+); ^{1}H NMR ($CDCl_3$, 300 MHz): δ: 1.53 (*s*, 6H), δ: 7.01–7.06 (*t*, 2H), 7.13–7.18 (*m*, 6H), 7.24–7.26 (*d*, 2H), 7.27–7.38 (*m*, 4H), 7.43–7.46 (*d*, 1H), 7.52–7.56 (*m*, 3H), 7.57–7.63 (*d*, 1H), 7.72–7.78 (*t*, 2H).

4,4′-Dibromo-4″-[2-(9,9′-dimethylfluorene)]-triphenylamine (compound 2): compound 1 (2.18 g) was dissolved in 50 mL of DMF and then the solution was cooled by ice water. A solution of N-bromosuccinimide (NBS) in 30 mL of DMF was added drop-wise into the solution of compound 1. The reaction mixture was stirring for 3 h while kept cooled by ice water. Two hundred and fifty milliliters of cooled water was then added into the mixture to obtain a white precipitate. The precipitate was washed by plenty of water and further purified by column chromatography on silica gel to give a white solid. Yield: 86%; MS (m/z): 595 (M^+); ^{1}H NMR ($CDCl_3$, 300 MHz): δ: 1.53 (*s*, 6H), δ: 6.98–7.03 (*t*, 4H), 7.12–7.15 (*d*, 2H), 7.30–7.40 (*t*, 6H), 7.44–7.47 (*m*, 1H), 7.53–7.58 (*m*, 3H), 7.61–7.62 (*d*, 1H), 7.73–7.79 (*t*, 2H).

4,4′-Di-(1-pyrenyl)-4″-[2-(9,9′-dimethylfluorene)]-triphenylamine (DPFA): compound 2 (1.78 g), and pyrene boronic acid (2.46 g), Pd $(PPh_3)_4$ (0.05 g), aqueous Na_2CO_3 (2.0 M, 10 mL), ethanol (7 mL), toluene (20 mL) were mixed in a flask. The mixture was degassed several times and the mixture was then refluxed at 100 °C for 24 h under a nitrogen atmosphere. After cooling to room temperature, the solvent was evaporated under vacuum and the product was extracted with dichloromethane (CH_2Cl_2). The CH_2Cl_2 solution was washed with water and dried with $MgSO_4$. Evaporation of the solvent, followed by column chromatography on silica gel gives a white green solid. Yield: 62%; MS (m/z): 835 (M^+); ^{1}H NMR ($CDCl_3$, 300 MHz): δ: 1.56 (*s*, 6H), δ: 7.33–7.39 (*m*, 2H), 7.46–7.50 (*m*, 7H), 7.62–7.65 (*d*, 5H), 7.70–7.82 (*m*, 5H), 8.00–8.08 (*m*, 5H), 8.11 (*s*, 5H), 8.18–8.27 (*m*, 6H), 8.35–8.38 (*d*, 2H). Anal. Calcd. For $C_{65}H_{43}N$: C, 93.41; H, 5.15%; N, 1.44%. Found: C, 95.20; H, 5.14%; N, 1.49%.

Absorption and fluorescence spectra were recorded using a Perkin Elmer Lambda 2S UV–Vis spectrophotometer and a Perkin Elmer LS50B Luminescence spectrophotometer, respectively. Glass transition temperatures (T_g) were determined with a differential scanning calorimeter (DSC, TA instruments 2910MDSC) at a heating rate of 5 °C/min. Decomposition temperature (T_d) was obtained from TGA measurements using a TA instruments Q50 TGA with a heating rate of 20 °C/min. Highest occupied molecular orbital (HOMO) levels of the new compound were measured directly by using ultraviolet photoelectron spectroscopy (UPS), while the lowest unoccupied molecular orbital (LUMO) values were determined from the HOMO and the lowest energy absorption edge of the UV absorption spectra.

Device fabrication and measurement: OLEDs were fabricated by vacuum deposition on ITO glass substrates with a sheet resistance of 30 Ω/□. The emission area of each device was 10 mm^2. Before deposition, the ITO substrate was carefully cleaned, rinsed with deionized water several times, dried in an oven at 120 °C for an hour, and finally treated with UV–ozone. The ITO substrate was then loaded into a deposition chamber with a base pressure better than 3×10^{-6} mbar. The devices were fabricated by evaporating organic layers onto the ITO substrate sequentially at an evaporation rate of 2–4 Å/s. The Mg:Ag alloy cathode was prepared by co-evaporation of Mg and Ag at a volume ratio of 10:1. EL spectra and CIE color coordinates of unpackaged devices were measured with a Spectrascan PR650 photometer and the current–voltage–luminescence characteristics were measured with a computer-controlled Keithley 236 source meter under ambient condition.

3. Results and discussion

4,4′-Di-(1-pyrenyl)-4″-[2-(9,9′-dimethylfluorene)]-triphenylamine (DPFA) was synthesized according to the synthetic route in Scheme 1. The molecular structure of DPFA was confirmed by ^{1}H nuclear magnetic resonance, mass spectrometry and element analysis.

Thermal properties of DPFA were characterized by TGA and DSC measurements. DPFA is thermally stable up to 450 °C as shown by its high decomposition temperatures (T_d) in the TGA measurements. DPFA sample melted at 268 °C in the first run of the DSC measurement. As the melted sample was reheated on the second run, a glass transition was observed at 161 °C.

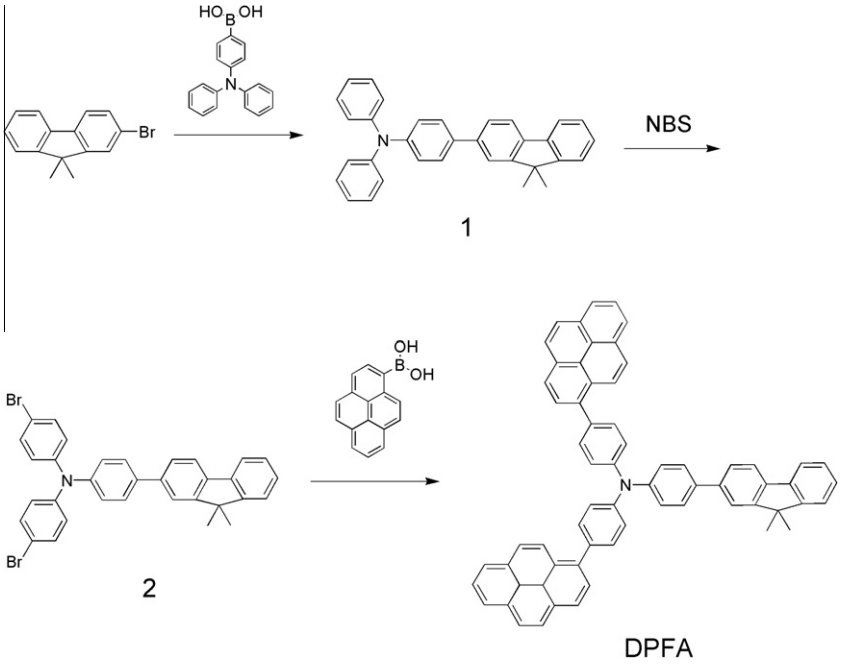

Scheme 1. The synthetic route of DPFA.

Fig. 1 shows absorption and photoluminescence (PL) spectra of DPFA in a dichloromethane solution and in a solid film. The PL spectrum of DPFA in solution shows a deep blue emission peak centered at 425 nm. The PL spectra in solution and in film are similar except for a red shift of 45 nm in the solid film. The fluorescence quantum yield of DPFA in a dichloromethane solution was measured to be 0.63. HOMO and LUMO energy levels of DPFA were determined to be 5.5 and 2.8 eV, respectively, by UPS and optical absorption.

To investigate the electroluminescence and charge transporting properties of DPFA, five devices were fabricated with active layers of,

I: DPFA(100 nm);
II: NPB(50 nm)/Alq_3(20 nm)/DPFA(30 nm);
III: DPFA(50 nm)/Alq_3(50 nm);
IV: DPFA(60 nm)/TPBI(30 nm) and
V: NPB(50 nm)/DPFA(20 nm)/TPBI(30 nm).

All the devices were sandwiched between an ITO anode and a composite cathode of LiF(0.5 nm)/Mg:Ag.

Device I is single layer device in which DPFA plays the role of emitter, hole- and electron-transporters. As shown in Fig. 2, the turn-on voltage (defined as the driving voltage required to give a brightness of 1 cd/m^2) of Device I is only 2.7 V, which is unexpectedly low for an OLED employ only one organic material. At 5 V the device can give a blue emission (peaked at 476 nm) of more than 100 cd/m^2 with CIE coordinates of $x = 0.17$ and $y = 0.29$. Similarity of the PL

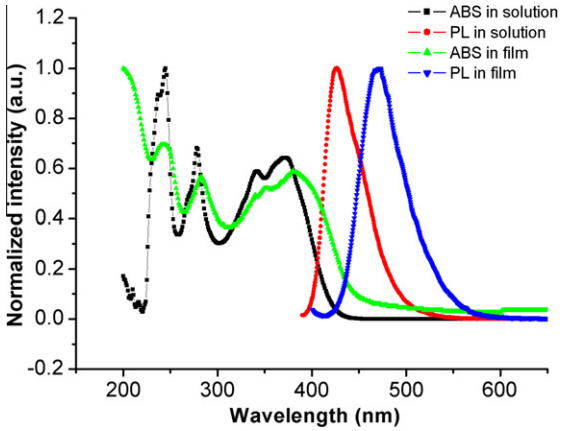

Fig. 1. Absorption and photoluminescence spectra of DPFA in solution and films.

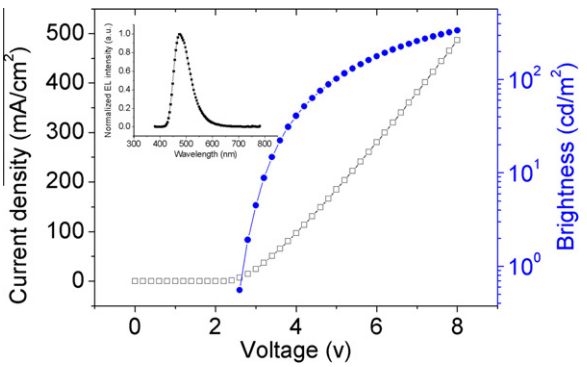

Fig. 2. *I–V–L* characteristics of device I. Inset is the EL spectrum of the device.

Table 1
Key performance data of the five devices.

Device	Turn-on voltage (V)	Maximum current efficiency (cd/A)	Maximum power efficiency (lm/W)	Maximum luminous peak (nm)	CIE coordinates (at 20 mA/cm^2)
I	2.7	0.07	0.03	476	0.17, 0.29
II	3.1	3.0	1.5	524	0.31, 0.54
III	2.5	3.9	3.2	518	0.29, 0.50
IV	2.9	4.3	4.5	472	0.14, 0.22
V	2.8	5.1	5.3	472	0.14, 0.24

I: ITO/DPFA(100 nm)/LiF(0.5 nm)/MgAg.
II: ITO/NPB(50 nm)/Alq_3(20 nm)/DPFA(30 nm)/LiF(0.5 nm)/MgAg.
III: ITO/DPFA(50 nm)/Alq_3(50 nm)/LiF(0.5 nm)/MgAg.
IV: ITO/DPFA(60 nm)/TPBI(30 nm)/LiF(0.5 nm)/MgAg.
V: ITO/NPB(50 nm)/DPFA(20 nm)/TPBI(30 nm)/LiF(0.5 nm)/MgAg.

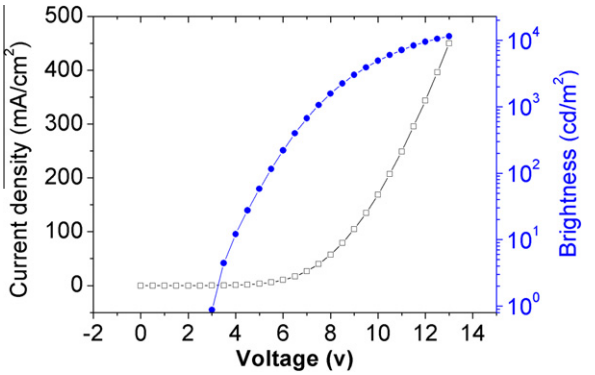

Fig. 3. *I–V–L* characteristics of device II.

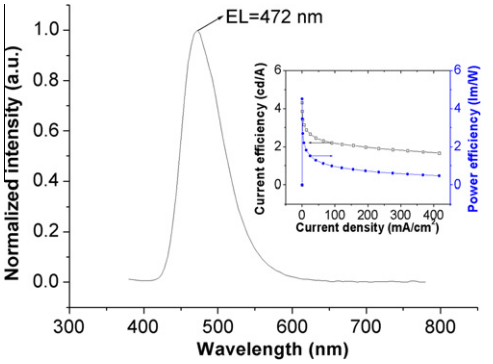

Fig. 5. An EL spectrum of device IV. Inset is the efficiency vs. current density.

and the EL spectra suggests that the EL can be attributed to the emission from the singlet excited state of DPFA. Table 1 lists key performance data of the device. While, the efficiency of device I is low, these results clear shown that DPFA can transport hole and electron and can be used as a host emitter.

To further explore the bipolar carrier transport properties of DPFA, devices II and III have been fabricated to use DPFA as electron and hole-transporter, respectively. In device II (NPB/Alq_3/DPFA) DPFA is used as the electron-transporter. The device turns on at 3.1 V (Fig. 3 and Table 1) and gives green Alq_3 emission peaked at 524 nm. It delivers a brightness of 11,490 cd/m^2 at 13 V and has a

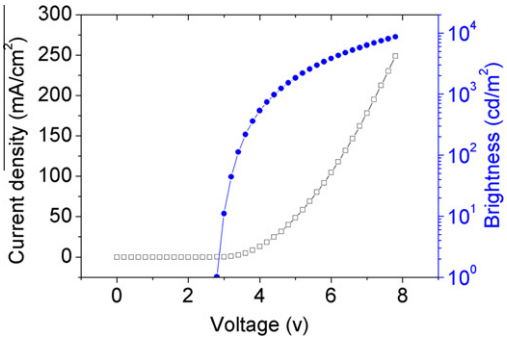

Fig. 6. *I–V–L* characteristics of device V.

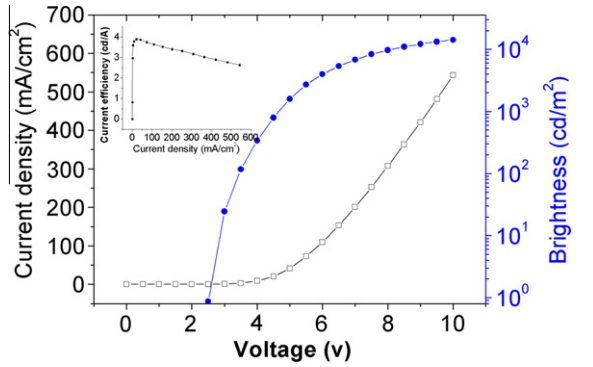

Fig. 4. *I–V–L* characteristics of device III. Inset is the efficiency vs. current density.

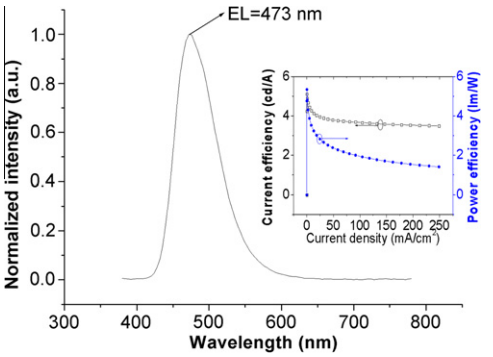

Fig. 7. EL spectrum of device V. Inset is the efficiency vs. current density of device V.

Table 2
Electroluminescence data of state-of-the-art OLEDs based on bipolar blue emitters.

Compound	Turn-on voltage (V)	Maximum current efficiency (cd/A)	Maximum power efficiency (lm/W)	Maximum luminous peak (nm)	CIE coordinates (at 20 mA/cm^2)	References
PhSPDPV	3	5.4	5.7	478	0.14, 0.22	[20]
TP-EPY	4.4	1.7	0.7	453	0.15, 0.07	[21]
CzThB	5.5	–	4.9	473	0.13, 0.21	[22]
DPF	3.3	6.0	3.6	470	0.15, 0.19	[14]
DPFA	2.8	5.1	5.3	472	0.14, 0.24	This work

maximum efficiency of 3.0 cd/A. As performance of this device is similar to that of a standard bilayer NPB/Alq_3 device, it can be reasonably expected the electron-transporting ability of DPFA is comparable with that of Alq_3.

Device III has a typically double layer structure (DPFA/Alq_3) in which DPFA functions as the hole-transporter; whereas Alq_3 is used as the emitter and electron-transporter. The device shows green Alq_3 emission peaked at 518 nm. As shown in Fig. 4, the turn on voltage of device III is just 2.5 V and the brightness is higher than 12,000 cd/m^2 at a voltage of 8 V. Device III has a maximum efficiency of 3.9 cd/A (3.2 lm/W), which is better than the performance of the standard NPB/Alq_3 device. The results suggest that DPFA is likely to have a better performance than NPB in terms of hole-transporting ability.

Device IV has a bilayer structure of DPFA/TPBI. Due to the low-lying HOMO of TPBI, it is commonly used a hole-blocker. Thus, in device IV, electrons and holes are expected to recombine in the DPFA layer. Therefore, DPFA functions as a hole-transporting emitter here. As shown in Fig. 5, the device shows a blue EL peak at 472 nm which can be attributed to the singlet emission of DPFA. A high maximum efficiency of 4.3 cd/A (4.5 lm/W) and CIE coordinates of $x = 0.14$ and $y = 0.22$ were observed. These results can firm that DPFA has good hole transporting properties and efficient blue emission.

While results from devices I–IV do show that DPFA has good electron and hole transporting properties, charge balance of electron and hole currents were not optimized due to mismatching of the energy levels between the organic layers and the electrodes in these devices. Thus, a typical three layers device with a configuration of NPB/DPFA/TPBI (device V) has been fabricated with DPFA as an emitter to improve device performance. *I–V–L* characteristics of device V are shown in Fig. 6. The turn-on voltage of the device is only 2.8 V and the device delivers bright blue emission with a maximum brightness of 8072 cd/m^2 at a voltage of 7.6 V and a current density of 230 mA/cm^2.

Fig. 7 shows an EL spectrum of device V. The EL spectrum centers at 472 nm and the CIE coordinates are $x = 0.14$, $y = 0.24$. Current and power efficiencies of the device are shown in the inset of Fig. 7. Device V has a maximum efficiency of 5.1 cd/A (5.3 lm/W).

For accessing the performance of DPFA, operation parameters of several state-of-the-art OLEDs based on bipolar blue-emitters are tabulated in Table 2. It can be seen that the efficiency of the device based on DPFA is among the best. With its highly efficient blue emission and bipolar charge transporting properties, DPFA can be a promising material for applications in both blue and white OLEDs.

In summary, a new multifunctional compound, 4,4′-di-(1-pyrenyl)-4″-[2-(9,9'-dimethylfluorene)]-triphenylamine (DPFA) has been synthesized and used respectively as a high efficiency blue emitter, a hole- and an electron-transporters in OLEDs. The compound exhibits good thermal stability with a glass transition temperature (T_g) of 161 °C. The results show that DPFA has efficient bipolar charge transporting properties for both hole and electron. A typical three layer device with a configuration of ITO/NPB(50 nm)/DPFA(20 nm)/TPBI(30 nm)/LiF(0.5 nm)/MgAg gives blue emission of high efficiency (5.1 cd/A or 5.3 lm/W) comparable or better than current state-of-art bipolar blue-emitters.

Acknowledgements

This work was supported by the Research Grants Council of Hong Kong (Grant No. CityU 101508). S. Tao would like to thank financial supports from the National Natural Science Foundation of China (NSFC Grant 21002011, 61006036), "the Fundamental Research Funds for the Central Universities" and "the Research Fund for the Doctoral Program of Higher Education of China (20100185120015)".

References

[1] J. Kido, M. Kimura, K. Nagai, Science 267 (1995) 1332.
[2] S. Reineke, F. Lindner, G. Schwartz, N. Seidler, K. Leo, Nature 459 (2009) 234.
[3] R.S. Sun, S.R. Forrest, Appl. Phys. Lett. 91 (2007) 263503.
[4] Y.R. Sun, N.C. Giebink, H. Kanno, B.W. Ma, M.E. Thompson, S.R. Forrest, Nature 440 (2006) 908.
[5] M.A. Baldo, D.F. O'Brien, Y. You, A. Shoustikov, S. Sibely, M.E. Thompson, S.R. Forrest, Nature 395 (1998) 151.
[6] C. Adachi, M.A. Baldo, M.E. Thompson, S.R. Forrest, J. Appl. Phys. 90 (2001) 5048.
[7] Y.C. Chiu, J.Y. Hung, Y. Chi, C.C. Chen, C.H. Chang, C.C. Wu, Y.M. Cheng, Y.C. Yu, G.H. Lee, P.T. Chou, Adv. Mater. 21 (2009) 2221.
[8] S.C. Lo, R.E. Harding, C.P. Shipley, S.G. Stevenson, P.L. Burn, I.D.W. Samuel, J. Am. Chem. Soc. 131 (2009) 16681.
[9] C.F. Chang, Y.M. Cheng, Y. Chi, Y.C. Chiu, C.C. Lin, G.H. Lee, P.T. Chou, C.C. Chen, C.H. Chang, C.C. Wu, Angew. Chem. Int. Ed. 47 (2008) 4542.
[10] N. Chopra, J. Lee, Y. Zheng, S.H. Eom, J. Xue, F. So, Appl. Phys. Lett. 93 (2008) 143307.
[11] S. Tokitoa, T. Iijima, Y. Suzuri, H. Kita, T. Tsuzuki, F. Sato, Appl. Phys. Lett. 83 (2003) 569.
[12] R.J. Holmes, S.R. Forrest, Y.J. Tung, R.C. Kwong, J.J. Brown, S. Garon, M.E. Thompson, Appl. Phys. Lett. 82 (2003) 2422.
[13] H. Aziz, Z.D. Popovic, N.X. Hu, A.M. Hor, G. Xu, Science 283 (1999) 1900.
[14] S.L. Tao, C.S. Lee, S.T. Lee, X.H. Zhang, Appl. Phys. Lett. 91 (2007) 013507.
[15] S.L. Tao, L. Li, J.S. Yu, Y.D. Jiang, Y.C. Zhou, C.S. Lee, S.T. Lee, X.H. Zhang, O. Kwon, Chem. Mater. 21 (2009) 1284.
[16] J.M. Hancock, A.P. Gifford, Y. Zhu, Y. Lou, S.A. Jenekhe, Chem. Mater. 18 (2006) 4924.

[17] T.H. Huang, J.T. Lin, L.Y. Chen, Y.T. Lin, C.C. Wu, Adv. Mater. 18 (2006) 602.
[18] Z.H. Li, M.S. Wong, H. Fukutani, Y. Tao, Org. Lett. 8 (2006) 4271.
[19] C.C. Wu, Y.T. Lin, K.T. Wong, R.T. Chen, Y.Y. Chien, Adv. Mater. 16 (2004) 61.
[20] C.C. Chi, C.L. Chiang, S.W. Liu, H. Yueh, C.T. Chen, J. Mater. Chem. 19 (2009) 5561.
[21] Y. Park, J.H. Lee, D.H. Jung, S.H. Liu, Y.H. Lin, L.Y. Chen, C.C. Wu, J. Park, J. Mater. Chem. 20 (2010) 5930.
[22] S.L. Lin, L.H. Chan, R.H. Lee, M.Y. Yen, W.J. Kuo, C.T. Chen, R.J. Jeng, Adv. Mater. 20 (2008) 3947.

Organic Electronics 12 (2011) 364–371

Contents lists available at ScienceDirect

Organic Electronics

journal homepage: www.elsevier.com/locate/orgel

A solution process for inverted tandem solar cells

Thue T. Larsen-Olsen, Eva Bundgaard, Kristian O. Sylvester-Hvid, Frederik C. Krebs *

Risø National Laboratory for Sustainable Energy, Technical University of Denmark, Frederiksborgvej 399, DK-4000 Roskilde, Denmark

ARTICLE INFO

Article history:
Received 18 August 2010
Received in revised form 12 November 2010
Accepted 21 November 2010
Available online 14 December 2010

Keywords:
Polymer solar cell
Solution processing
Tandem solar cell
Recombination layer
Inverted structure

ABSTRACT

Tandem solar cells with normal and inverted device geometries were prepared by a solution process. Both device types were based on the use of zinc(II)oxide as the electron transporting layer (ETL). The hole transporting layer (HTL) was either PEDOT:PSS for normal geometry tandem solar cells or vanadium(V)oxide in the case of inverted tandem cells. It was found that the inverted tandem solar cells performed comparable or better than the normal geometry devices, showing that the connection structure of vanadium(V)oxide, Ag nanoparticles and zinc(II)oxide functions both as a good recombination layer, ensuring serial connection, and as a solvent barrier, protecting the first photoactive layer from processing of the second layer. This successfully demonstrates a tandem solar cell fabrication process fully compatible with state-of-the-art solution based automated production procedures.

© 2010 Elsevier B.V. All rights reserved.

1. Introduction

Since the first reports of the polymer solar cell that presented power conversion efficiencies (PCEs) of less than 1% [1,2] the PCE has increased to above 8% that today represents the state-of-the-art [3]. To convincingly qualify as a photovoltaic technology with a potential to provide clean renewable energy polymer solar cells should have PCEs exceeding 10% in addition to low materials costs, ease of processing [4] and long-term stability under photovoltaic operation [5]. In terms of efficiency, several schemes of improving polymer solar cells have been proposed, the most successful ones being the use of low-band gap photo-active materials [6,7] and multi-junctions, i.e. tandem solar cell structures [8,9]. Efficiencies of 6.5% have been reported for tandem solar cells employing a combination of high- and low-band gap photo-active materials [10–17]. In the latter case the processing of the solar cell was an all-solution based process up to the point of depositing the Al back electrode, which was done by thermal evaporation. So far no viable route for printing an Al electrode has been found, and therefore normal geometry (Fig. 1A) solar cells requiring a cathode with a low work function (such as Al) are so far not realizable by all-solution and fully printable processes. To achieve an all printable solar cell one may reverse the polarity of the system (an inverted structure as shown in Fig. 1B) and employ a printable paste of Ag, now acting as the anode. Such inverted single junction solar cells have been shown to have similar photovoltaic characteristics compared to normal geometry devices employing an evaporated Al electrode [18].

Hence at this point it is clear that both the low-band gap and tandem polymer solar cell concepts have proven viable and that these most likely will be found in future incarnations of polymer solar cells, provided that the appropriate metal electrode can be deposited by printing. In the present study we describe a method for preparing inverted tandem solar cells which are compatible with an all printable process.

There are several challenges in the development of efficient tandem polymer solar cells which go beyond processing of a single junction cell. Firstly, the fabrication of a multi-layer stack involving more than one photo-active polymer layer is challenging since these polymers typically are processed from rather similar organic solvents. Hence, to protect the preceding photo-active layer from re-dissolving during the solution processing of a subsequent

* Corresponding author. Tel.: +45 46 77 47 99; fax: +45 46 77 47 91.
E-mail address: frkr@risoe.dtu.dk (F.C. Krebs).

1566-1199/$ - see front matter © 2010 Elsevier B.V. All rights reserved.
doi:10.1016/j.orgel.2010.11.017

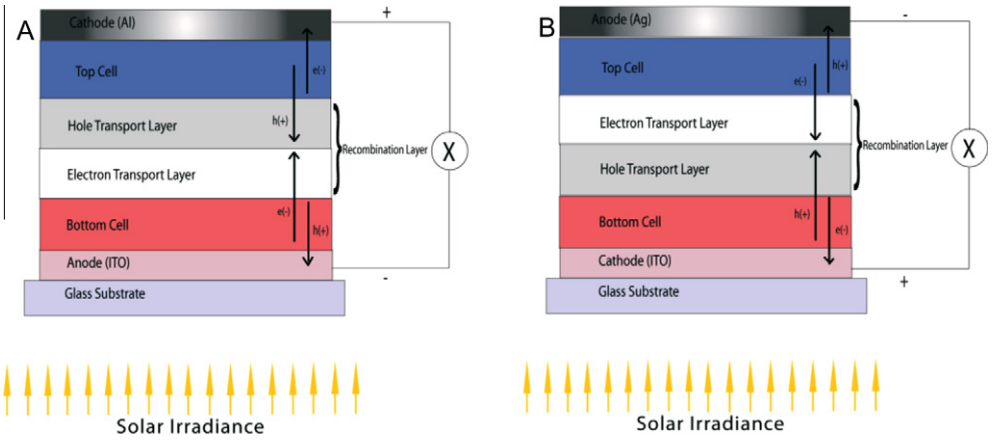

Fig. 1. Diagram of the two different tandem device geometries; (A) normal geometry, and (B) inverted geometry.

photo-active layer, the interlayer, the so called recombination layer, must be processed from an orthogonal solvent, typically some aqueous solution or suspension. Secondly, for two-terminal monolithic tandem solar cells the sub-cells are serially connected through the recombination layer which makes this part of the device critical to the operation of the tandem cell, since the layer must enable electron–hole recombination with as little potential drop as possible (otherwise the open circuit voltage is adversely affected) while also being optically transparent. Thirdly, for series connected tandem solar cells, the two (or more) sub-cells must be current matched, i.e. produce approximately the same current when subject to the respective and appropriate spectral ranges of the sun spectrum. The lack of current matching in the best case limits the current of the tandem solar cell to that of the sub-cell with the lowest current but may well limit it even further due to space charge build up at various interfaces. Finally, optical matching is important to ensure that complementary parts of the sun spectrum are harvested by the sub-cells, which in case of monolithic tandem solar cells with non-opaque layers may require optical simulations.

In this study we have a particular focus on finding a suitable solution processable recombination layer that will work for inverted tandem structures as depicted in Fig. 1B. Fully solution processable recombination layers for tandem solar cells have previously been realized by a sequence of either TiO_x [10] or ZnO [11] as electron transport layers (ETLs) and PEDOT:PSS or pH-neural PEDOT:PSS as hole transport layer (HTL). The pH neutrality is required to enable processing of aqueous PEDOT:PSS on top of previously deposited ZnO nanoparticles. In particular, the success of the ZnO/PEDOT:PSS recombination layer is derived from the fact that nanoparticles become insoluble after drying in both organic solvents and aqueous solutions. However, the polarity of these recombination layers suits only normal geometry tandem solar cell structures as shown in Fig. 1A.

Reversing the layer sequence of the recombination layer to match the polarity of an inverted tandem solar cell (Fig. 1B) has been attempted previously [12,29]. In the case of Hagemann et al. PEDOT:PSS/ZnO was interfacing an insoluble high-band gap polymer (P3CT) obtained by thermal cleaving of P3MHOCT and a low-band gap polymer (P3CTTP) obtained by thermal cleaving of P3TMDCTTP. Both sub cells employed zinc(II)oxide nanoparticles as electron acceptor and a printed back electrode. It presented a relatively low performance while showing stable operation in ambient air.

However, any efficient inverted tandem solar cell design should enable the use of high efficiency polymer materials, and in an all solution process this demands that a HTL is coated on top of the low surface energy polymer:fullerene photo-active layer. Aqueous PEDOT:PSS dispersions that present large surface tensions makes this challenging or very difficult.

A series of transition metal oxides have previously been demonstrated as suitable substitutes for PEDOT:PSS. In a recent paper, Chou et al. [29] realize PEDOT:PSS free, high efficiency inverted tandem cells, using evaporated MoO_3 as HTL and ZnO as ETL. Another interesting candidate is vanadium(V)oxide (V_2O_5) [19,20], and recently it was shown that V_2O_5 may also be solution processed as an efficient and nearly optically transparent HTL in inverted polymer solar cells [21] due to a high work function similar to that of PEDOT:PSS. Chou et al. [29] attempted the use of V_2O_5 as HTL, however the material was found incompatible with the subsequent processing of the ZnO layer. From this we expected that V_2O_5 could still function well as a HTL in a recombination layer, given an orthogonal ZnO formulation, and we present a work utilizing a V_2O_5 formulation based on isopropanol, and an orthogonal ZnO formulation based on methanol.

2. Materials and methods

Films were fabricated under ambient conditions only using a spin-coater and a digitally controlled oven, apart from the final electrode evaporated under vacuum. ITO patterned glass substrates, were cleaned by sonication for 10 min in both isopropanol and demineralized water, and blown dry with air.

First layer: For 'inverted' devices, the glass/ITO substrate was spin-coated with $Zn(OAc)_2{\cdot}2H_2O$, dissolved in methanol, at 3000 rpm for 30 s, followed by annealing for

Table 1
Photovoltaic parameters (AM1.5G, 1000 W m^{-2}, 85 ± 2 °C).

Cell description	PCE (%)	J_{sc} (mA/cm^2)	V_{oc} (V)	FF (%)
Front Cell Reference: ITO/ZnO/**P3HT:PCBM(75 nm)**/V_2O_5/PEDOT:PSS/Ag	1.3	−7.2	0.50	37
Back Cell Reference: ITO/ZnO/**PDTTDABT:PCBM(140 nm)**/PEDOT:PSS/Ag	1.2	−5.8	0.56	37
Back Cell Reference (T2): ITO/ZnO/**P3HT:PCBM(100 nm)**/PEDOT:PSS/Ag	2.1	−8.8	0.51	32
Inverted tandem cell (Ag nanoparticles): ITO/ZnO/**P3HT:PCBM(75 nm)**/V_2O_5/Ag-NP/ZnO/**PDTTDABT:PCBM(140 nm)**/PEDOT:PSS/Ag	1.0	−3.6	0.81	35
Inverted tandem cell (evaporated Ag): ITO/ZnO/**P3HT:PCBM(75 nm)**/V_2O_5/Ag-evap/ZnO/PDTTDAT:PCBM(140 nm)/PEDOT:PSS/Ag	1.1	−3.9	0.84	33
Inverted tandem cell (No Ag interlayer): ITO/ZnO/**P3HT:PCBM(75 nm)**/V_2O_5/ZnO/**PDTTDABT:PCBM(140 nm)**/PEDOT:PSS/Ag	0.94	−3.6	0.82	32
Inverted tandem cell (T2) (No Ag interlayer): ITO/ZnO/**P3HT:PCBM(75 nm)**/V_2O_5/ZnO/**P3HT:PCBM(100 nm)**/PEDOT:PSS/Ag	1.4	−5.1	0.80	36
Normal tandem cell (No Ag Interlayer): ITO/PEDOT:PSS/**P3HT:PCBM(75 nm)**/ZnO/PEDOT:PSS/**PDTTDABT:PCBM(140 nm)**/Al	0.53	−1.4	0.85	34

10 min at 140 °C, giving a layer thickness of 50 nm. For 'normal' devices the first layer was made by spin-coating of PEDOT:PSS (Aldrich) at 3000 rpm for 1 min followed by annealing for 5 min at 140 °C, leading to a layer thickness of 90 nm.

Second layer: This layer was processed under similar conditions for both device types, the active polymer blend for the bottom cell; P3HT(17 mg/ml):PCBM(15 mg/ml) dissolved in chlorobenzene, was spin-coated at 1500 rpm for 30 s leading to an approximate layer thickness of 75 nm, followed by annealing for 30 s at 140 °C and drying/cooling under ambient conditions for 5 min.

Third layer: For the 'inverted device' a solution of vanadium(V)-oxiisopropoxide diluted with isopropanol to a concentration of 50 mg/ml were prepared, and applied by spin-coating at 3000 rpm for 10 s, followed by annealing for 2 min at 140 °C, leading to a clear and slightly yellowish film, with a thickness of approximately 45 nm as determined by ellipsometry. For normal devices the layer was made by spin-coating the $Zn(OAc)_2{\cdot}2H_2O$/methanol solution at 3000 rpm for 30 s, followed by annealing for 6 min at 140 °C, giving an approximate layer thickness of 50 nm.

Intermediate silver layer: For some cells an intermediate silver layer was made; either by spin coating (3000 rpm, 1 min) a silver nanoparticle (100 ± 15 nm) solution prepared as described earlier [22] and further diluted in isopropanol to a final concentration of 10 mg/ml followed by annealing for 2 min at 140 °C, or by evaporating a thin Ag layer using the same procedure as for the final back electrode.

Fourth layer: For the 'inverted' device this was made by spin-coating the $Zn(OAc)_2{\cdot}H_2O$/methanol solution at 1000 rpm for 30 s, followed by annealing for 6 min at 140 °C, after which the procedure was performed for a second time. The two depositions are found necessary to best protect the cell against the second active layer deposition. This leads to a ZnO layer thickness of 160 nm, determined with AFM. For normal devices the layer was made by spin-coating of PEDOT:PSS (Aldrich) at 5000 rpm for 1 min, followed by annealing for 2 min at 140 °C.

Fifth layer: The active layer of the back cell for all device types was prepared from a blend of 15 mg/ml of PDTTDABT or P3HT mixed with 15 mg/ml of PCBM and dissolved in chlorobenzene, which was then spin-coated at 800 rpm for 1 min leading to an approximate layer thickness of 140 nm.

Sixth layer: For the inverted device this layer was made from PEDOT:PSS (Orgacon EL-P 5010 diluted with isopropanol 2:1 w/w) spin-coated at 3000 rpm for 1 min, followed by annealing for 2 min at 140 °C.

The final metal back electrode was applied with evaporation through a shadow mask in a vacuum chamber under a pressure of less than 3×10^{-6} mbar, the metal being Ag for inverted or Al for normal devices. The back electrode defines the active area of the cells to be 0.5 cm^2.

IV-characterization of the solar cells was carried out immediately after evaporation, under simulated sunlight at 1000 W m^{-2}, AM1.5G conditions, using a Keithley multiplexer setup.

3. Results and discussion

For the purpose of this study we constructed four different types of tandem solar cells, and descriptions of the different multilayer stacks can be found in Table 1 alongside the photovoltaic parameters from electrical characterization. Each of the tandem cells consists of two serially connected sub cells; a high band gap front cell and a low band gap back cell, utilizing P3HT:PCBM and PDTTDABT:PCBM, respectively, as photoactive layer (see Fig. 2).

In order to estimate the performance of the tandem cells, each of the constituent sub cells were also constructed as single junction reference cells (see Table 1). During this work several additional approaches were pursued based on the choice of zinc oxide (ZnO) as the ETL material, while various PEDOT:PSS types were employed as HTL material, but it was only when using vanadium oxide (V_2O_5) as HTL material that reliable tandem devices were realized.

3.1. The best performing tandem design

The most successful tandem cell design, retaining the all solution processing compatibility, is depicted in Fig. 3. The cell presents a novel recombination layer employing three sub layers; a HTL of V_2O_5, followed by a thin

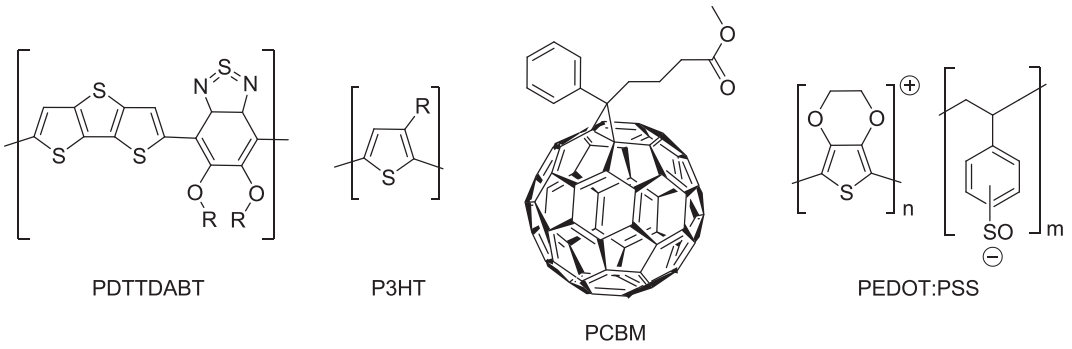

Fig. 2. Structure of PDTTDABT, P3HT, PCBM and PEDOT:PSS. $R_1 = C_{14}H_{29}$, $R_2 = C_6H_{13}$.

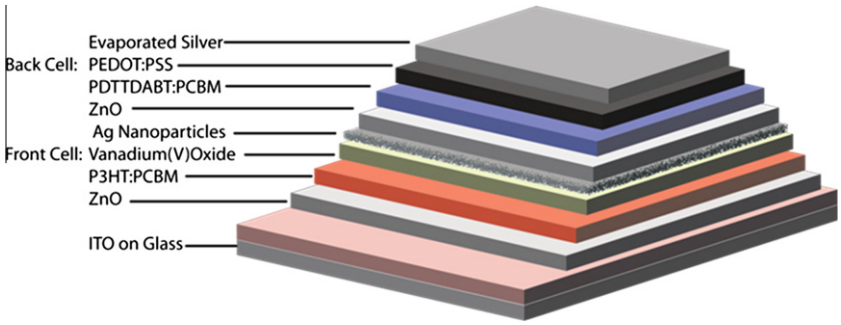

Fig. 3. The layer stack of the best performing inverted tandem solar cell.

transparent layer of Ag nanoparticles (Ag-NP) dispensed in isopropanol, and an ETL of ZnO. The *J–V* curves of the best device and corresponding reference sub cells are shown in Fig. 4.

The tandem cell yields a PCE of 1%. The open-circuit voltage (V_{oc}) is 0.81 V, corresponding to a voltage drop of 0.25 V with respect to the estimated ideal sum of the two reference sub cell voltages while the short circuit current density of 3.6 mA cm^{-2} is significantly lower than that the corresponding value of −5.8 mA cm^{-2} for the supposedly current limiting back cell reference. However significant, most of the loss in both current and voltage is probably explainable by losses due to the imperfect nature of the recombination layer, and poor current matching of the sub cells.

The issue of current matching is evident already from the difference between the currents produced in the reference sub cells (Table 1), and due to overlap of the absorption bands of P3HT and PDTTDABT (Fig. 5) and optical transmission losses across the recombination layer; it is likely that this current imbalance is further augmented in the actual tandem cell. This is investigated in the following section.

3.2. Estimating sub cell performance

To correctly quantify the problem of current matching in a tandem cell it is necessary to know the actual performance of the individual sub cells. And because the sub cells are in an environment hardly mimicked by a single junction reference cell, it would demand a three- or four terminal tandem architecture in order to do a proper *J–V* characterization. While such designs have been realized [13,14] this is not the goal of this study. Instead we utilize optical simulations based on the transfer matrix formalism [23,24] which can predict the number of photons absorbed in the active layers per unit time.

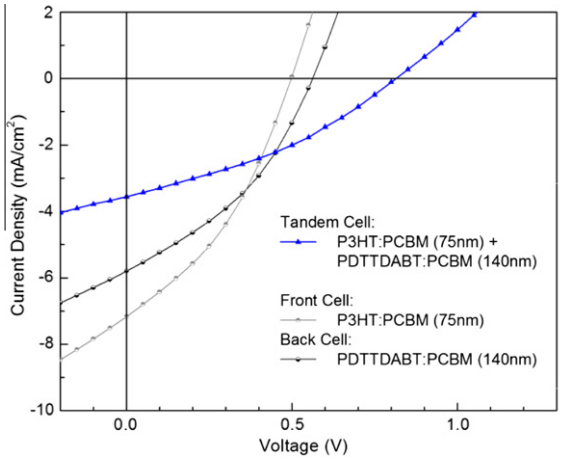

Fig. 4. *J–V* curve of the best performing tandem cell using a larger band gap polymer in the front cell (P3HT), and a lower band gap in the back cell (PDTTDABT).

The model takes as input the optical constants *n* and *k* for each layer, which are measured by ellipsometry, as well

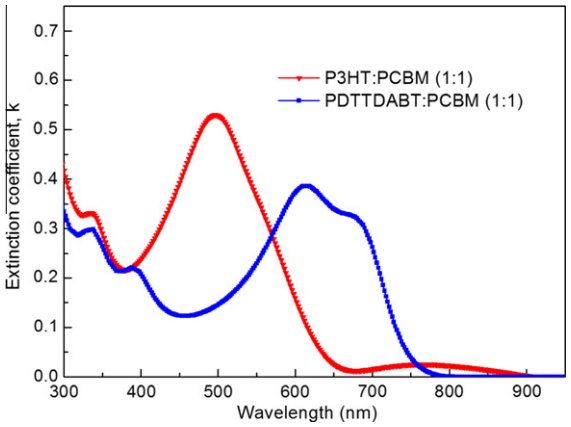

Fig. 5. The *k*-values for the P3HT:PCBM and PDTTDABT:PCBM blends, depicting their complementarily in terms of absorption.

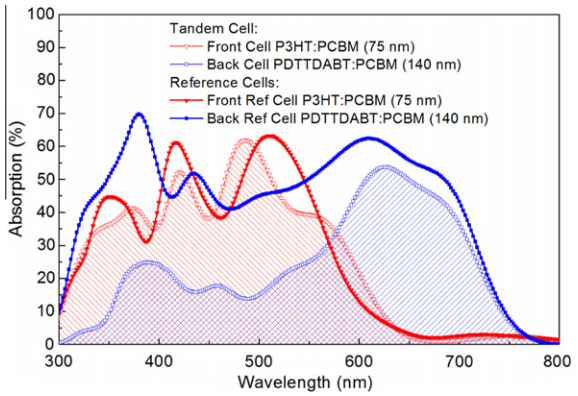

Fig. 6. The simulated absorption profiles for the sub cells of the tandem cell compared to the simulated absorption profiles of corresponding reference cells.

as the AM1.5G solar irradiance spectrum. In Fig. 6 we show the calculated absorption profiles for the sub cell photoactive layers and corresponding reference cells, illustrating the effect of the overlapping absorption bands. Key simulation parameters are summarized in Table 2, where $J_{\text{max-sim}}$ is the maximum available photocurrent density, supposing an internal quantum efficiency (IQE) of 100%, and

$$J^{\text{sub}}_{\text{sc-sim}} = \frac{J^{\text{reference}}_{\text{sc}}}{J^{\text{reference}}_{\text{max-sim}}} J^{\text{sub}}_{\text{max-sim}} = \text{IQE}_{\text{flat}} J^{\text{sub}}_{\text{max-sim}}$$

where IQE_{flat} infers an assumed constant IQE within the relevant spectrum of wavelengths. From the simulations we gather that the actual back cell probably delivers a J_{sc} closer to 4.2 mA cm^{-2} than the 5.8 mA cm^{-2} of the back cell reference, while the actual front cell is estimated to deliver equal to the reference current. According to these current estimates, only about 4 out of 7 holes from the front cell will be able to recombine with electrons from the back cell. We suspect that this significant current mismatch and resulting charge build-up at the recombination layer will compensate the build-in potentials across the sub cells, ideally leading to an equilibration of the tandem current density close to the limiting sub current density [25], which in this case would mean the estimated ~4.2 mA cm^{-2}. Moreover it should be noted that a complete understanding of the quantitative effect of current mismatch in a two terminal polymer tandem device is limited, and it is possible that charge pile-up at the less-than-perfect ohmic contact of the recombination layer will lead to further degrading effects of the photovoltaic performance such as lowering the effective V_{oc} [16] or fill-factor, in turn explaining the deviation from ideality that we observe. This will be further investigated in the following section.

Apart from estimating the sub cell current imbalance, the simulations shown in Fig. 6 also illustrates the potential of the tandem principle, where the complementary absorption bands of the two junctions provide ample amounts of current, meaning that the rather low efficiency of this tandem device is due to the low IQE of the PDTTTDABT:PCBM cell.

3.3. Current matching

To study the effect of current imbalance on the photovoltaic performance of the presented tandem device design, a tandem device having two P3HT:PCBM junctions was constructed. The front and back cell thicknesses were found with the aid of optical simulations, so as to deliver closer to the same amounts of photo current. The thickness of the front cell was kept at 75 nm while the back cell was given a thickness of approximately 100 nm. The *J*–*V* curves for the best P3HT-P3HT tandem device can be seen in

Table 2
Summary of simulation data.

Cell Description	Experimental	Simulation		
	J_{sc} (mA/cm^2)	$J_{\text{max-sim}}$ (mA/cm^2)	$J_{\text{sc-sim}}$ (mA/cm^2)	IQE_{flat} (%)
P3HT-PDTTDABT Tandem device:				
Front Cell Reference: P3HT:PCBM (75 nm)	−7.2	−9.4	–	75
Back Cell Reference: PDTTDABT:PCBM(140 nm)	−5.8	−15.8	–	37
Front Cell: P3HT:PCBM(75 nm)	–	−9.4	−7.2	75
Back Cell: PDTTDABT:PCBM(140 nm)	–	−11.5	−4.2	37
P3HT-P3HT Tandem device:				
Front Cell Reference: P3HT:PCBM (75 nm)	−7.2	−9.5	–	76
Back Cell Reference: P3HT:PCBM (100 nm)	−8.8	−11.3	–	78
Front Cell: P3HT:PCBM(75 nm)	–	−9.5	−7.2	76
Back Cell: P3HT:PCBM(100 nm)	–	−7.2	−5.6	78

Fig. 1, where it is compared to the tandem device having a PDTTDABT back cell. The photovoltaic parameters are summarized in Table 1, and as can be seen the efficiency has increased to 1.4%, most likely due to higher current of the P3HT back cell compared to the PDTTDABT back cell.

To investigate we performed the analysis based on optical simulations as described and done for the P3HT-PDTTDABT tandem, in Section 3.2. The results are summarized in Table 2. The simulations suggest that it is in fact a higher current from the P3HT back cell which drives the increased PCE. However the back cell is still the current limiting tandem device, having an estimated short circuit current density of $-5.6\ mA\ cm^{-2}$ against the estimated value of $-7.2\ mA\ cm^{-2}$ for the front cell, while the actually measured J_{sc} of the P3HT–P3HT tandem cell is $-5.2\ mA\ cm^{-2}$. The V_{oc} is 0.8 V which corresponds to a voltage drop of 0.21 V compared to the estimated ideal sum of the reference sub cells. These overall lower deviations from the ideal performance as compared to the P3HT–PDTTDABT tandem cell can be interpreted as an effect of the expected smaller current mismatch of the sub cells in the P3HT–P3HT tandem cell as shown in Fig. 7. However, these modest improvements do not suggest that a completely current matched tandem cell will exhibit ideal performance, thus it seems likely that losses associated with this particular recombination layer is expected. This is investigated in the following section.

3.4. Recombination layer

In this study we compared four different recombination layers; V_2O_5/ZnO, V_2O_5/Ag-NP/ZnO and V_2O_5/Ag(evap)/ZnO employed in the inverted geometry tandem cell (see Fig. 1), and ZnO/PEDOT:PSS used in the normal geometry cell.

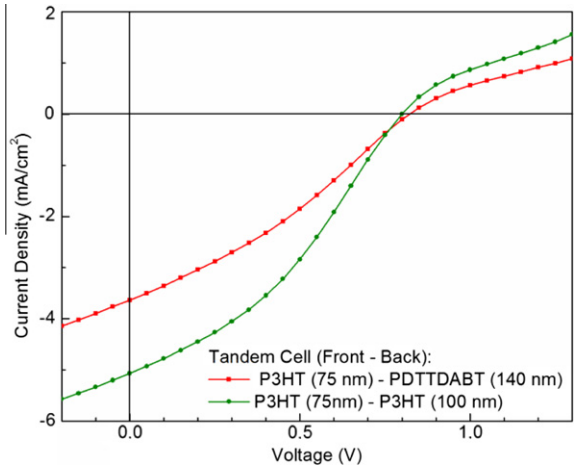

Fig. 7. Comparison of two inverted geometry tandem devices, having a different back cell, both without the silver interlayer added to the recombination layer. The P3HT back cell delivers more current than the PDTTDABT back cell, and thus increases the total current of the tandem device.

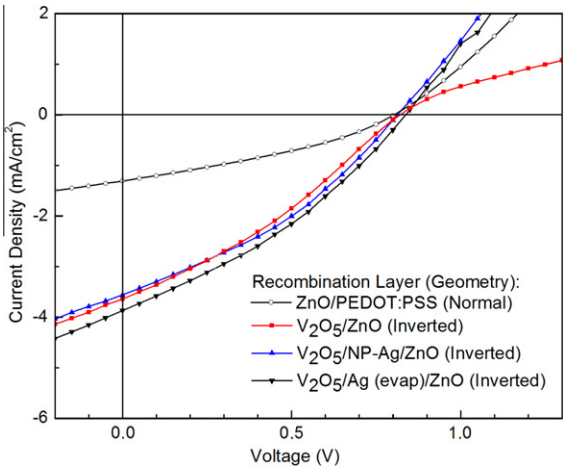

Fig. 8. Comparison of different recombination layers. For the inverted geometry tandem devices, applying a thin layer of Ag nano-particles (NP-Ag) or evaporated Ag to the recombination layer, seemingly has the effect of removing the inflection point.

First, we consider the cells having two-layered recombination structures, and representative *J–V* curves for these two types of tandem cells are presented in Fig. 8. As can be seen, the inverted type shows a significant inflection point in the *J–V* curve above short circuit, this phenomenon has been ascribed to low (majority) charge carrier concentrations in the recombination layer [11,17] leading to recombination inefficiency close to open circuit conditions. In the case of Gilot et al. [11] it was found that the inflection point was due to low charge carrier concentration in the ZnO ETL part of the recombination layer, a common problem in ZnO containing solar cells [22], resolved by exposure to UV-light triggering a photodoping process described elsewhere [26]. It can be seen that in our case no inflection point is observed in the *J–V* characteristics of the normal geometry tandem cell, having a recombination structure of ZnO/PEDOT:PSS, nor did the photovoltaic parameters improve under UV exposure. This leaves the V_2O_5 as potential bottle neck, and ways to improve the p-doping level of this material should be investigated further.

In order to certainly isolate the source of the inflection point to the recombination layer we pursued a method reported earlier [16,27] showing that such counter diodes can be counteracted by evaporating a thin metal interlayer, and in Fig. 8 the *J–V* curves for comparable tandem cell with and without an added Ag interlayer are presented. From this it is obvious that the addition of evaporated silver effectively removes the counter diode. In an attempt to avoid a vacuum demanding step, such as the evaporation of a thin Ag layer, and to keep the design compatible with solution based production-methods, the Ag nanoparticles were pursued as a remedy displaying a similar effect on the *J–V* characteristics. It is suggested that in both cases the silver forms an incomplete layer, where clusters act as recombination sites that due to their limited size will be aided by a coulomb charging effect [28]. However one

would suspect that the morphology of the two types of silver layers is quite different as the nano-particles are on the order of 100 nm while the evaporated layer is suspected to be less than 10 nm thick, nevertheless they induce a similar effect on the *J–V* characteristics, and further investigations of intermediate silver layers are warranted.

In summary, the addition of an intermediate silver layer between the HTL and ETL effectively removes the inflection point as seen in Fig. 8, but surprisingly the removal of the counter diode only seems to improve the photovoltaic performance minutely (Table 1), suggesting that the losses are not due to improper recombinatory properties of the recombination layer, rather we suspect that the significant sub cell current imbalance and possibly the low p-conductivity of V_2O_5, are causing the voltage drop and current losses, as compared to the ideal.

3.5. Future perspectives

A major perspective of this work lies in processing, and having described a process for inverted polymer tandem solar cells compatible with solution processing of all layers including the final electrode, the natural next step will be to transfer the method onto a roll-to-roll platform. In terms of optimizing the efficiency it is evident that the inefficient current generation of the low band-gap back cell is a limiting factor that should be resolved, whereby insights into the effect of current mismatch could be obtained. Also the materials of the recombination layer should be investigated and optimized, focusing on routes to improve the HTL. In this respect it would be interesting to improve the conductivity of V_2O_5 by possibly p-doping, or to investigate the usefulness of other metal oxides. It is believed that optimization of only a few of the mentioned parameters will lead to a tandem cell efficiency larger than the corresponding single junction cells, and in conjunction with the high throughput fabrication prospects this would conclusively demonstrate the importance and rigidness of the inverted tandem approach which do have significant processing requirements when compared to single junction cells.

4. Conclusion

We have presented a process for the fabrication of inverted tandem solar cells compatible with all solution processing of all layers, and demonstrated its usefulness by fabricating and characterizing inverted tandem solar cells utilizing a larger band gap P3HT:PCBM front cell serially connected with a lower band gap PDTTDABT:PCBM back cell, by means of a three layered solution processed recombination structure consisting of vanadium(V)oxide, Ag nanoparticles and zinc(II)oxide. The tandem cells yielded a PCE of 1%, mainly limited by a low IQE of the PDTTDABT:PCBM back cell, leading to poor current matching with the front cell, and a resultant low J_{sc} of the tandem cell. When preparing a similar tandem cell, having a P3HT:PCBM back cell, expected to deliver more current, the PCE increases to 1.4%, led by relative increases in J_{sc} and V_{oc} as compared to the expected ideal values, sustaining the idea of performance degrading effects from sub cell current mismatch. Normal geometry solar cells were also demonstrated, using the same photo active materials but with a two-layered recombination structure of zinc(II) oxide and PEDOT:PSS. The normal geometry cells exhibited a lower J_{sc}, while all tandem cells showed a V_{oc} just around 0.8 V which was about 0.2 V lower than the ideal. The findings suggest that although none of the trialed recombination layers are able to deliver perfect serial connection, vanadium(V)oxide is indeed a compatible substitute for PEDOT:PSS for the use as hole transporting material in cases where aqueous solutions cannot be used easily, such as the case for inverted polymer tandem solar cells.

Acknowledgements

This work was supported by the Danish Strategic Research Council (DSF 2104-05-0052 and 2104-07-0022) and EUDP (j. No. 64009-0050). We would like to thank Thomas Tromholt and Morten V. Madsen for ellipsometry measurements and Ole Hagemann for help with synthesis of the polymers.

References

[1] N.S. Sariciftci, L. Smilowitz, A.J. Heeger, F. Wudl, Science 258 (1992) 1474–1476.
[2] N.S. Sariciftci, D. Braun, C. Zhang, V.I. Srdanov, A.J. Heeger, G. Stucky, F. Wudl, Appl. Phys. Lett. 62 (1993) 585–587.
[3] Solarmer Energy, Inc., World Record: <www.solarmer.com>.
[4] F.C. Krebs, Sol. Energy Mater. Sol. Cells 93 (2009) 394–412.
[5] M. Jørgensen, K. Norrman, F.C. Krebs, Sol. Energy Mater. Sol. Cells 92 (2008) 686–714.
[6] E. Bundgaard, F.C. Krebs, Sol. Energy Mater. Sol. Cells 91 (2007) 954–985.
[7] R. Kroon, M. Lenes, J.C. Hummelen, P.W.M. Blom, B. De Boer, Polymer Rev. 48 (2008) 531–582.
[8] M. Hiramoto, M. Suezaki, M. Yokoyama, Chem. Lett. (1990) 327–330.
[9] T. Ameri, G. Dennler, C. Lungenschmied, C.J. Brabec, Energy Environ. Sci. 2 (2008) 347–363.
[10] J.Y. Kim, K. Lee, N.E. Coates, D. Moses, T.-Q. Nguyen, M. Dante, A.J. Heeger, Science 317 (2007) 222–225.
[11] J. Gilot, M.M. Wienk, R.A.J. Janssen, Appl. Phys. Lett. 90 (2007) 143512.
[12] O. Hagemann, M. Bjerring, N.Chr. Nielsen, F.C. Krebs, Sol. Energy Mater. Sol. Cells 92 (2008) 1327–1335.
[13] H.B. Yang, Q.L. Song, C.M. Li, Z.S. Lu, Energy Environ. Sci. 1 (2008) 389–394.
[14] A. Hadipour, B. de Boer, P.W.M. Blom, J. Appl. Phys. 102 (2007) 074506.
[15] A. Hadipour, P.W.M. Blom, Adv. Funct. Mater. 16 (2006) 1897–1903.
[16] F.-C. Chen, C.-H. Lin, J. Phys. D: Appl. Phys. 43 (2010) 025104.
[17] S. Sista, M.-H. Park, Z. Hong, Y. Wu, J. Hou, W.L. Kwan, G. Li, Y. Yang, Adv. Mater. 22 (2010) 380–383.
[18] F.C. Krebs, S.A. Gevorgyan, J. Alstrup, J. Mater. Chem. 19 (2009) 5442–5451.
[19] V. Shrotriya, G. Li, Y. Yao, C.-W. Chu, Y. Yang, Appl. Phys. Lett. 88 (2006) 073508.
[20] G. Li, C.-W. Chu, V. Shrotriya, J. Huang, Y. Yang, Appl. Phys. Lett. 88 (2006) 253504.
[21] J.-S. Huang, C.-Y. Chou, M.-Y. Liu, K.-H. Tsai, W.-H. Lin, C.-F. Lin, Org. Electron. 10 (2009) 1060–1065.
[22] F.C. Krebs, Org. Electron. 10 (2009) 761–768.
[23] L.A.A. Pettersson, L.S. Roman, O. Inganäs, J. Appl. Phys. 86 (1999) 487–496.
[24] P. Peumans, A. Yakimov, S.R. Forrest, Appl. Phys. Lett. 93 (2002) 3693–3723.
[25] A. Hadipour, B. de Boer, P.W.M. Blom, Org. Electron. 9 (2008) 617–624.
[26] F.C. Krebs, T. Tromholt, M. Jørgensen, Nanoscale 2 (2010) 878–886.

[27] B. Maennig, J. Drechsel, D. Gebeyehu, P. Simon, F. Kozlowski, A. Werner, F. Li, S. Grundmann, S. Sonntag, M. Koch, K. Leo, M. Pfeiffer, H. Hoppe, D. Meissner, N.S. Sariciftci, I. Riedel, V. Dyakonov, J. Parisi, Appl. Phys. A 79 (2004) 1–14.
[28] B.P. Rand, P. Peumans, S.R. Forrest, J. Appl. Phys. 96 (2004) 7519–7526.
[29] C.-H. Chou, W.L. Kwan, Z. Hong, L.-M. Chen, Y. Yang, Adv. Mater., in press.

Organic Electronics 12 (2011) 372–375

Contents lists available at ScienceDirect

Organic Electronics

journal homepage: www.elsevier.com/locate/orgel

Potassium doped Co phthalocyanine films: Charge transfer to the metal center and the ligand ring

V.Yu. Aristov [a,b], O.V. Molodtsova [c], M. Knupfer [a,*]

[a] ISSP, Russian Academy of Sciences, Chernogolovka, Moscow District 142432, Russia
[b] IFW Dresden, Postfach 270116, D-01171 Dresden, Germany
[c] Institut für Festkörperphysik, TU Dresden, D-01062 Dresden, Germany

ARTICLE INFO

Article history:
Received 12 November 2010
Received in revised form 2 December 2010
Accepted 5 December 2010
Available online 22 December 2010

Keywords:
CoPc
Electronic density of states
Transition metal complexes
Charge transfer

ABSTRACT

The electronic properties of potassium doped cobalt phthalocyanine (CoPc) films have been investigated using near-edge X-ray absorption fine structure measurements. Our results demonstrate that charge transfer to the CoPc molecules changes both the valence of the phthalocyanine ring as well as that of the central Co ion. The first electron transferred to the molecule occupies a Co 3d state, which is connected to a change of the magnetic moment of the molecule.

© 2010 Elsevier B.V. All rights reserved.

1. Introduction

Charge transfer, i.e. the addition or removal of charges to or from molecules in organic solids is one route to modify and control their electronic properties. There are prominent examples, where charge transfer is an essential ingredient in the control of the electronic properties of the respective material class. For instance, the formation of charge transfer compounds is accompanied by fascinating, and sometimes unexpected physical properties. Well-known examples are the so-called charge transfer salts (e.g. TTF-TCNQ) with low dimensional electronic behavior and very rich phase diagrams [1], or alkali doped fullerenes [2–6] and picene [7,8], which support superconductivity, or Mott insulating phases depending on the doping level. In addition, charge transfer induced by doping has been successfully applied to tune the electronic properties of organic semiconductor devices [9–13] or to tailor the spin functionality of hybrid metal–organic interfaces [14].

Recently, it has been demonstrated that selective charge transfer can be achieved by the formation of some well ordered phthalocyanine or porphyrine monolayers on noble metal surfaces (Au, Ag). Thereby, the charge is transferred from the metal substrate to a particular part of those molecules, the central transition metal ion. In other words, the formation of the corresponding monolayer is connected to valence changes of these transition metal centers [15–23], and in many investigated molecules, the transition metal center is Co. Moreover, this valence change is directly related to a change of the magnetic moment of the corresponding molecule, which represents an important aspect in view of the application of magnetic molecules in molecular or organic spintronic devices or the appearance of the Kondo effect in adsorbed molecules on surfaces [15].

The question now arises whether such valence and spin changes of the cobalt center in e.g. cobalt phthalocyanine (CoPc) upon charging are a consequence of the interface formation, or in a more general sense driven by charge

* Corresponding author. Tel.: +7 493514659 544; fax: +7 493514659 440.
E-mail address: M.Knupfer@ifw-dresden.de (M. Knupfer).

1566-1199/$ - see front matter © 2010 Elsevier B.V. All rights reserved.
doi:10.1016/j.orgel.2010.12.003

transfer independent of the presence of an interface and respective local interactions. In order to test this, we report here charge transfer to CoPc molecules in thin solid films that has been achieved by the addition of potassium. We demonstrate that selective charge transfer to the central Co ion not only occurs on metal surfaces but can also be realized by our doping procedure. Thereby, the first electron added to a CoPc molecule fills a metal 3d state, and in this way changes the orbital and magnetic ground state of the molecule.

2. Experimental

Our experiments using near-edge X-ray absorption fine structure (NEXAFS) were performed at the Berliner Speicherring für Synchrotronstrahlung (BESSY) using soft X-ray light emitted by the Russian–German high energy resolution dipole beam line. This type of beam line provides moderate-intensity radiation with a continuous distribution over a wide photon energy range (30–1500 eV). Therefore this beam line is well suited for the NEXAFS measurements and for organic materials, which are relatively fragile and potentially could be damaged under irradiation. The soft X-ray absorption spectra were recorded in the total electron yield mode and normalized to the incident photon flux. The resolution of the NEXAFS measurements is determined exclusively by the performance of the beam line and was about 80 meV full width at half maximum at the C 1s (283 eV) threshold, while it was about 100 meV for the Co 2p threshold (770 eV). In the NEXAFS experiments the photon incidence angle was selected to be 35 degrees relative to the sample surface normal. We have chosen this angle to explore simultaneously both excitations into π and σ derived states of the highly oriented molecules [24–26]. The pressure in the experimental system during data acquisition was always better than 2×10^{-10} Torr .

As substrate for CoPc film deposition we used the (100) surface of a gold single crystal. The surface was prepared by repeated sputtering and annealing cycles, after which a 5×20 surface reconstruction was observed using low energy electron diffraction, while no remaining contamination was detected in core level photoemission spectra. The CoPc film was deposited in a sample preparation chamber (base pressure of 2.5×10^{-10} Torr) directly connected to analyzer chamber. The CoPc deposition rate, monitored by a quartz microbalance, was 1–2 Å/min. The CoPc films used for our studies were about 70 Å thick. From previous studies it is known that CoPc films grown in this manner result in CoPc molecules that are arranged parallel to the substrate surface [24].

Potassium was evaporated onto the CoPc film at rates of 1–10 Å/min from a properly outgassed SAES alkali metal dispenser, without detectable pressure increase during deposition. The K concentration in the CoPc films was deduced from a comparison of the relative intensities of the K 2p and C 1s NEXAFS spectra. These relative intensities have been compared to previous core level excitation data at these edges from potassium doped molecular films of known stoichiometry ($K_6C_{60}, K_4C_{60}, K_4CuPc$) [6,27]. For more details about this procedure see Refs. [27,28].

3. Results and discussion

In Fig. 1 we show the evolution of the C 1s NEXAFS data upon potassium doping. The inset shows the data of the highest doped sample in a larger energy range including the excitations at the K 2p absorption edge. The C 1s excitation spectrum of undoped CoPc is characterized by a double peak feature at lowest excitation energy, labelled A′ and A, which is caused by excitations into the lowest unoccupied molecular orbital (LUMO) at either the benzene carbon atoms (A′) or those belonging to the pyrrole rings (A). The energy difference thereby is given by the different binding energies of the C 1s core levels due to different chemical environments (chemical shift). This shift can be directly seen in corresponding core level photoemission experiments [22,29]. The data for CoPc as presented here are very similar to the corresponding results for the related copper phthalocyanine material [30,31].

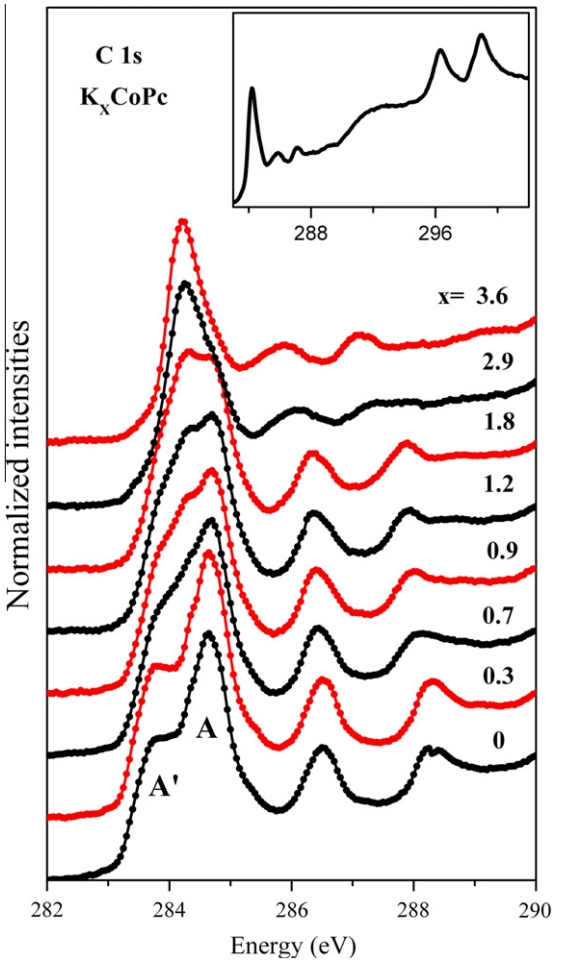

Fig. 1. C 1s X-ray absorption data of potassium doped CoPc films (K_xCoPc). The inset shows the data for the highest doping level including the K 2p absorption edge with maxima at 296.3 and 299 eV.

Upon increasing K content, one can see that the intensity of the peaks following the absorption threshold decreases. In analogy to K doped CuPc [32], we attribute this decrease to a filling of the LUMO of CoPc as a consequence of charge transfer of the outer s electron of potassium to the CoPc molecules. Furthermore, the fine structure of the C 1s spectra is smeared out upon potassium addition, which results in a broad excitation feature in the intermediate doping range before it narrows again at highest doping. The broadening and loss of fine structure has also been observed for K doped copper [32] and iron phthalocyanine [33] (CuPc and FePc) films, and there it has been ascribed to the appearance of a further, chemically shifted C 1s core level binding energy caused by the doping and the potential of the adjacent K^+ ions (see Refs. [32,33] for details). At highest doping the lowest excitation structure becomes narrower again, which most likely arises from a further filling of the LUMO level, and which indicates that the doping procedure renders the carbon atoms in the phthalocyanine molecule more similar in the sense of the chemical environment. An exact analysis of this behavior can only be achieved with the help of sophisticated calculations and detailed structural knowledge and is beyond the scope of this short contribution. However, from Fig. 1 it becomes clear that even at the highest doping level excitations into the LUMO are still possible, i.e. the LUMO level of the phthalocyanine ligand is not completely filled. Further, the remaining intensity implies that not all electrons donated by the introduced potassium are going to this ligand orbital, since in this case we would expect a lowest excitation feature with much lower spectral weight. We note that this is not due to the presence of unreacted (undoped) CoPc molecules in our sample. This will become clear in the discussion of the Co 2p absorption edge below, which clearly shows a complete change of these spectra upon doping with no indication for undoped CoPc. Finally, the absorption features at higher energies as depicted in Fig. 1 shift to lower energies with increasing potassium doping. This shift is caused by a relaxation of the molecular and electronic structure of CoPc while filling an antibonding molecular orbital, similar to what has been observed in other doped molecular films such as K_xC_{60}, K_xCuPc, or K_xFePc [6,27,32,33].

We are thus left with the question which further molecular state other than the LUMO arising from the phthalocyanine ligand is filled via the doping process? In order to clarify this question, we show in Fig. 2 the evolution at the Co 2p absorption edge induced by the potassium doping. We concentrate on the energy region of the Co $2p_{3/2}$ excitation edge as it reveals much more details on the different unoccupied Co 3d states [25]. For undoped CoPc the Co $2p_{3/2}$ excitation edge has been recently analyzed in detail as a function of polarization using NEXAFS and atomic multiplet calculations [25]. It is important for the discussion here that the lowest excitation feature at about 774.8 eV is due to excitations into unoccupied Co $3d_{3z^2-r^2}$ (in the following called $3d_{z^2}$) orbitals. The following excitations with maxima at 776.8 and 778 eV arise from a multiplet split feature related to excitations into the Co $3d_{x^2-y^2}$ orbital. Upon doping, Fig. 2 demonstrates clearly that the lowest excitation feature decreases in intensity until it

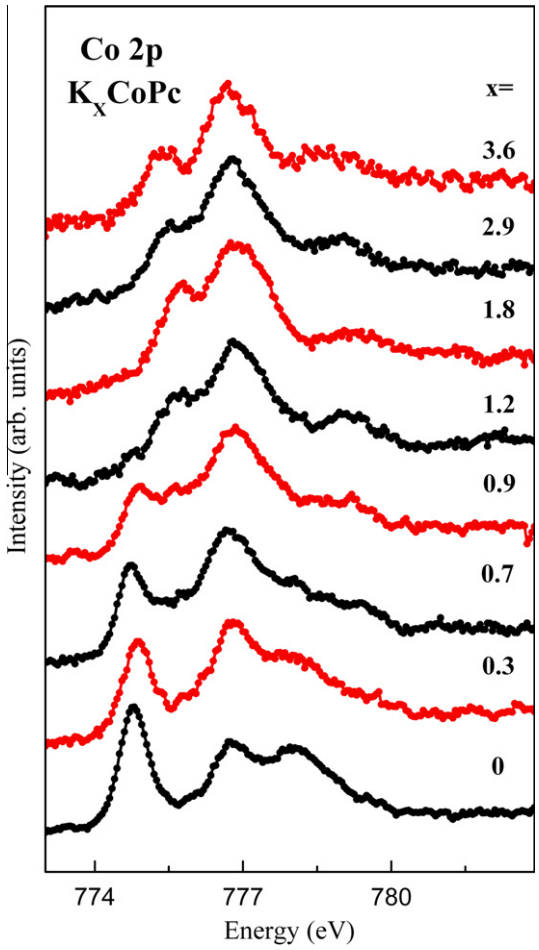

Fig. 2. Co $2p_{3/2}$ X-ray absorption edges of K_xCoPc films.

has vanished at a doping level of about $x = 1$ (K_xCoPc). This now indicates a predominant filling of the $3d_{z^2}$ orbital upon doping before ligand π derived states are charged. Increasing the doping level induces an energy shift of the remaining structures at the Co 2p excitation edge to lower energies but no further change in spectral shape can be observed. We again attribute this change to the relaxation of the molecule and thus also the molecular orbitals upon charging/filling state with antibonding character.

At this point it is important to notice that in the case of CuPc the Cu 2p absorption edge does not change at all upon doping with potassium [32]. In other words, while for CuPc a negative charging of the molecules does not affect the valence and spin of the central transition metal ion, this clearly is the case for CoPc studied here. At first glance, this looks surprising since many physical properties of CuPc and CoPc, such as their growth/orientation on metal surfaces [16,24,34,35], the energy position of the highest occupied ligand orbital [29] or the optical absorption spectra [29] are very similar. However, going from CuPc to CoPc the relative energy of the metal 3d levels and the π ligand orbitals changes mainly due to the different nucleus potentials of the transition metal

[36]. As a consequence, Co 3d levels are closer to the chemical potential in CoPc and can play a role in the low energy electronic behavior. Moreover, the metal 3d orbital filling is also different, $3d^9$ in CuPc and $3d^7$ in CoPc, which provides more orbitals for electron addition. From electrochemistry studies [37] it has been concluded that the first reduction state of CuPc is of pure ligand π character, while in CoPc there is evidence for a Co reduction to Co(I), similar to our observations.

In addition, the observed filling of the Co $3d_{z^2}$ orbital upon potassium addition demonstrates the formation of Co(I) centers, which is accompanied by a loss of the magnetic moment (spin zero). This now opens a way to deliberately change the magnetic properties of such molecules via charge transfer in thin films. It additionally has consequences for the charge transport behavior of CoPc films, since electrons injected into a film will occupy metal 3d rather than ligand π orbitals with a rather different wave function and hopping probabilities. The associated variation of the spin state of CoPc will also affect the spin scattering mechanisms in spin-dependent transport through CoPc films.

4. Summary

In conclusion, our studies show that a reduction of cobalt phthalocyanine via doping with potassium results in the formation of non-magnetic, charged Co(I)Pc molecules. The situation thus parallels that on noble metal surfaces where an equivalent Co reduction has been reported. This points to a general behavior of CoPc upon charge addition and might be of relevance for the use of this molecule in organic devices with spin functionalities.

Acknowledgements

We are grateful to R. Hübel, S. Leger and R. Schönfelder for technical assistance. Financial support by the Deutsche Forschungsgemeinschaft within the Forschergruppe FOR 1154 (Project KN393/14) and via KN393/15, as well as by the RFBR under Grant Nos. 08-02-01170 and 10-02-00269 are gratefully acknowledged.

References

[1] N. Toyota, M. Lang, J. Müller, Low-Dimensional Molecular Metals, Springer Series in Solid State Sciences, vol. 154, Springer, Berlin, 2007.
[2] O. Gunnarsson, Alkali Doped Fullerides, Narrow-Band Solids with Unusual Properties, World Scientific, Singapore, 2004 (and references therein).
[3] J.H. Weaver, D.M. Poirier, Solid State Physics 48, in: H. Ehrenreich, F. Saepen (Eds.), Academic, New York, 1994, p. 1.
[4] O. Gunnarsson, Rev. Mod. Phys. 69 (1997) 575 (and references therein).
[5] L. Forro, L. Mihaly, Rep. Prog. Phys. 64 (2001) 649 (and references therein).
[6] M. Knupfer, Surface Sci. Rep. 42 (2001) 1 (and references therein).
[7] R. Mitsuhashi, Y. Suzuki, Y. Yamanari, H. Mitamura, T. Kambe, N. Ikeda, H. Okamoto, A. Fujiwara, M. Yamaji, N. Kawasaki, Y. Maniwa, Y. Kubozono, Nature 464 (2010) 76.
[8] F. Roth, M. Gatti, P. Cudazzo, M. Grobosch, B. Mahns, B. Büchner, A. Rubio, M. Knupfer, New J. Phys. 12 (2010) 103036.
[9] M. Pfeiffer, A. Beyer, T. Fritz, K. Leo, Appl. Phys. Lett. 73 (1998) 3202.
[10] A. Nollau, M. Pfeiffer, T. Fritz, K. Leo, J. Appl. Phys. 87 (2000) 4340.
[11] X. Zhou, M. Pfeiffer, J. Blochwitz, A. Werner, A. Nollau, T. Fritz, K. Leo, Appl. Phys. Lett. 78 (2001) 410.
[12] W. Gao, A. Kahn, Org. Electronics 3 (2002) 53.
[13] P. Gargiani, A. Calabrese, C. Mariani, M.G. Betti, J. Phys. Chem. C 114 (2010) 12258.
[14] M. Cinchetti, S. Neuschwander, A. Fischer, A. Ruffing, S. Mathias, J.-P. Wüstenberg, M. Aeschlimann, Phys. Rev. Lett. 104 (2010) 217602.
[15] A. Zhao, Q. Li, L. Chen, H. Xiang, W. Wang, S. Pan, B. Wang, X. Xiao, J. Yang, J.G. Hou, Q. Zhu, Science 309 (2005) 1542.
[16] T.S. Ellis, K.T. Park, M.D. Ulrich, S.L. Hulbert, J.E. Rowe, J. Appl. Phys. 100 (2006) 093515.
[17] J. Xiao, P.A. Dowben, J. Phys.: Condens. Matter 21 (2009) 052001.
[18] Y. Bai, F. Buchner, I. Kellner, M. Schmid, F. Vollnhals, H.-P. Steinrück, H. Marbach, J.M. Gottfried, New J. Phys. 11 (2009) 125004.
[19] Y. Bai, M. Sekita, M. Schmid, T. Bischof, H.-P. Steinrück, J.M. Gottfried, Phys. Chem. Chem. Phys. 12 (2010) 4336.
[20] Z. Li, J. Yang, J.G. Hou, Acc. Chem. Res. 43 (2010) 954.
[21] P. Gargiani, M. Angelucci, C. Mariani, M.G. Betti, Phys. Rev. B 81 (2010) 085412.
[22] F. Petraki, H. Peisert, I. Biswas, T. Chasse, J. Phys. Chem. C 114 (2010) 17638.
[23] J.D. Baran, J.A. Larsson, R.A.J. Woolley, Y. Cong, P.J. Moriarty, A.A. Cafolla, K. Schulte, V.R. Dhanak, Phys. Rev. B 81 (2010) 075413.
[24] O.V. Molodtsova, M. Knupfer, Yu.A. Ossipyan, V.Yu. Aristov, J. Appl. Phys. 104 (2008) 083704.
[25] T. Kroll, V.Yu. Aristov, O.V. Molodtsova, Yu.A. Ossipyan, D.V. Vyalikh, B. Büchner, M. Knupfer, J. Phys. Chem. A 113 (2009) 8917.
[26] J. Stöhr, NEXAFS Spectroscopy, Springer Series in Surface State Sciences, vol. 25, Springer, Berlin, 1992.
[27] K. Flatz, M. Grobosch, M. Knupfer, J. Chem. Phys. 126 (2007) 214702.
[28] F. Roth, A. König, R. Kraus, M. Knupfer, J. Chem. Phys. 128 (2008) 194711.
[29] M. Grobosch, C. Schmidt, R. Kraus, M. Knupfer, Org. Electronics 11 (2010) 1483.
[30] O.V. Molodtsova, M. Knupfer, V.M. Maslyuk, D.V. Vyalikh, V.M. Zhilin, Yu.A. Ossipyan, T. Bredow, I. Mertig, V.Yu. Aristov, J. Chem. Phys. 129 (2008) 154705.
[31] H. Peisert, M. Knupfer, J. Fink, Surf. Sci. 515 (2002) 491.
[32] O.V. Molodtsova, M. Knupfer, V.Yu. Aristov, D.V. Vyalikh, V.M. Zhilin, Yu.A. Ossipyan, J. Appl. Phys. 103 (2008) 053711.
[33] V.Yu. Aristov, O.V. Molodtsova, V.V. Maslyuk, D.V. Vyalikh, T. Bredow, I. Mertig, A.B. Preobrajenski, M. Knupfer, Org. Electronics 11 (2010) 1461.
[34] T.S. Ellis, K.T. Park, S.L. Hulbert, M.D. Ulrich, J.E. Rowe, J. Appl. Phys. 95 (2004) 982.
[35] S. Stepanov, A. Mugarza, G. Ceballos, P. Moras, J.C. Cezar, C. Carbone, P. Gambardella, Phys. Rev. B 82 (2010) 014405.
[36] M.-S. Liao, S. Scheiner, J. Chem. Phys. 114 (2001) 9780.
[37] C.C. Leznoff, A.B.P. Lever, Phthalocyanines: Properties and Applications, VCH Publishers, New York, 1993.

Organic Electronics 12 (2011) 376–382

Contents lists available at ScienceDirect

Organic Electronics

journal homepage: www.elsevier.com/locate/orgel

Molecular migration behaviors in organic light-emitting diodes with different host structures

Chi-Ping Liu [a,c], Wei-Ben Wang [c], Cheng-Wei Lin [c], Wei-Chun Lin [a], Chia-Yi Liu [a], Che-Hung Kuo [a,b], Szu-Hsian Lee [a,b], Wei-Lun Kao [a,b], Guo-Ji Yen [a,b], Yun-Wen You [a], Hsun-Yun Chang [a], Jwo-Huei Jou [c,*], Jing-Jong Shyue [a,b,*]

[a] Research Center for Applied Sciences, Academia Sinica, Taipei 115, Taiwan, ROC
[b] Department of Materials Science and Engineering, National Taiwan University, Taipei 106, Taiwan, ROC
[c] Department of Materials Science and Engineering, National Tsing Hua University, Hsin-Chu 300, Taiwan, ROC

ARTICLE INFO

Article history:
Received 19 October 2010
Received in revised form 8 December 2010
Accepted 12 December 2010
Available online 23 December 2010

Keywords:
Organic light-emitting diode
Degradation
Molecular migration
Cluster ion beam
X-ray photoelectron spectrometry (XPS)

ABSTRACT

Over the past years, organic light-emitting diodes (OLEDs) have attracted increasing interest because of their great potential for use in high-quality flat-panel displays and solid-state lighting. One of the basic requirements in any emissive device is to provide adequate stability to ensure a sufficiently long lifetime. Recently, it was observed that small molecules migrate toward the ITO anode under a direct driving voltage while retaining their original structures. To prevent this bias-driven migration of small molecules, a chemical structure with a higher steric hindrance could be introduced as a blockade, thus molecular migration could be suppressed and the device half-life increased. In this work, OLED devices with different hosts, including CBP, mCP, SimCP2, and SimCP, with increasing steric hindrances are fabricated. The spatial distribution of the tracking molecules after operation for different lengths of time is examined by using X-ray photoelectron spectroscopy (XPS) with *in situ* high-energy C_{60}^{+} and low-energy Ar^{+} co-sputtering for depth profiling. It is found that the bias-driven molecular migration is suppressed and the device half-life prolonged as the steric hindrance of the host increases.

© 2010 Elsevier B.V. All rights reserved.

1. Introduction

Over the past decades, semiconductor development has proceeded at a rapid pace [1,2]. Inorganic semiconductors, such as Si and Ge, have several important applications. For example, silicon-based devices, like high performance chips [3–5], photodetectors [6], light-emitting diodes (LEDs) [7,8], have been widely used around the world. On the other hand, organic semiconductors, like organic light-emitting diodes (OLEDs), are also increasingly attracting interest because of their great potential as high-quality flat-panel displays and solid-state lighting [9–12]. For both inorganic and organic semiconductors, device reliability and lifetime are critical issues [13,14].

In silicon-based devices, the electro-migration of atoms [15] is known to degrade the device performance. Electrons flowing through the device can collide with atoms causing them to migrate from their original sites during operation [15]. As a result, the device structure changes, in turn leading to failure. Fortunately, the problem can be solved using heavier atoms like Cu, Pd, and Sc [15].

For organic semiconductors, there are many issues that may cause device degradation [16]. In terms of intrinsic degradation mechanisms, Franky So and Denis Kondakov found that the device degradation is because of the chemical transformations in the region nearby the recombination zone [17]. In addition, Karl Leo's group investigated the possible degradation products and dissociation of

* Corresponding authors. Tel.: +886 2 2789 8000x69.
E-mail addresses: jjou@mx.nthu.edu.tw (J.-H. Jou), shyue@gate.sinica.edu.tw (J.-J. Shyue).

1566-1199/$ - see front matter © 2010 Elsevier B.V. All rights reserved.
doi:10.1016/j.orgel.2010.12.005

molecules in an OLED aged by electrical driving [18,19]. In particular, it is proposed the FIrpic may dissociate irreversibly through the loss of CO_2 from the picolinate ligand. Furthermore, the migration of inorganic electron injection layers like Cs:BPhen [19], Li [20], and LiF [21] and migration of inorganic ITO anode [22] are also observed.

Recently, it was observed that in thin-film organic devices, like OLEDs, small molecules may also migrate from their original positions to other layers under direct DC bias operation [21]. Consequently, the distribution of molecules (namely electron-transporting materials) is significantly changed, while the chemical structure is retained. This phenomenon is very similar to the electro-migration of atoms reported before. However, the mechanism differs in that there are no quasi-free electrons in organic semiconductors that drive the molecules directly. Instead, the electrons hop between molecules and the molecules gain negative charge temporally. These charged molecules are then driven by the bias. Furthermore, small dopants tend to penetrate into other layers and thus change the composition and electrical properties [23]. Because the device structures that control the device performance are well designed at the beginning of the fabrication process, any change in the device structure, or the distribution, may affect the carrier-injection balance and lifetime significantly. To date, while the problem of electro-migration in inorganic semiconductor industry is well known and already solved, the similar phenomenon of bias-driven molecular migration in organic electronics is under-studied and there is no accepted method that solves the problem.

Because of the amorphous nature of OLED devices, the direct observation of the molecular distribution is known to be difficult [24]. X-ray photoelectron spectroscopy (XPS) is one of the most common techniques for studying the surface of materials due to its high surface sensitivity and the wealth of elemental and molecule information [21]. When combined with *in situ* cluster-ion (C_{60}^+) and Ar^+ ion co-sputtering, the depth distribution of materials close to the surface has been profiled successfully with nanometer resolution [25–27]. Because this technique provides a direct method for analyzing the distribution of materials in organic electronics with high depth-resolution, we use it to study bias-driven molecular migration in OLED devices.

2. Experimental

2.1. Fabrication of OLED devices

The details of the OLED fabrication processes and the properties are illustrated elsewhere [28]. In short, a 35-nm-thick hole-transporting layer (HTL) consisting of Baytron® Clevios P VP AI 4083, a composition of poly(ethylenedioxythiophene):poly(styrene sulfonic acid) (PEDOT:PSS) in a molar ratio of 1:4.5, was spin-coated on a 125-nm-thick layer of indium tin oxide (ITO) on glass. An emissive layer (EL, 40 nm thick) comprised of a host material, 4,4′-bis(carbazol-9-yl)biphenyl (CBP), doped with 14 wt.% bis(3,5-difluoro-2-(2-pyridyl)-phenyl)-(2-carboxypyridyl) iridium (III) (FIrpic) was spin-coated on the HTL. Other host materials, including 1,3-di(9*H*-carbazol-9-yl)benzene (mCP), bis(3,5-di(9*H*-carbazol-9-yl)phenyl) diphenylsilane (SimCP2), and 9,9′-(5-(triphenylsilyl)-1,3-phenylene)bis(9*H*-carbazole-9-yl) (SimCP), were also used and doped with 14 wt.% FIrpic as the guest material. An electron-transporting layer (ETL, 32 nm) consisting of 2,2′,2″-(1,3,5-benzenetriyl)-tris(1-phenyl-1-H-benzimidazole) (TPBi) was then thermally evaporated on the EL. An electron injection layer (EIL, 0.7 nm) of LiF and an Al cathode (150 nm) were also thermally evaporated on the top of the ETL. Beside of the use of different host materials, all other parameters are fixed so that the degradation mechanisms other than the effect of host materials make the same contribution to the device lifetime hence can be ignored. The luminescence area of each device was 2×2 mm, and each chip contained 4 OLED devices, which were separated by 2 mm.

2.2. XPS measurements

The experiments were performed on a PHI 5000 VersaProbe (Chigasaki, Japan) XPS system with a C_{60}^+ ion source (IOG C60-10, Ionoptika, UK). A micro-focused Al Kα X-ray (25 W, 100 μm) was used as the source, and the take-off angle of the photoelectron was 45°. The acceptance lens of the analyzer and the X-ray was rastered over an area of 500×500 μm and centered at the center of luminescence area of the OLED device. A dual-beam charge neutralizer, containing a 7 V Ar^+ beam and 30 V flooding electron beam, was used to compensate charge on the device surface during data acquisition. The Ar^+ sputter source was operated at 0.2 kV, 300 nA with an incident angle of 45°, and the C_{60}^+ ion-cluster source was operated at 10 kV, 10 nA with an incident angle of 70°. Both the Ar^+ and C_{60}^+ ion beams were rastered at the same time over an area of 2×2 mm. The beam currents were measured with the target current on an Au foil and were stable for at least 2 weeks of continuous operation. In addition, reference devices on the same chip were profiled to ensure steady sputtering conditions and to eliminate chip-to-chip variations between each profile. The as-fabricated devices were operated in a nitrogen atmosphere without encapsulation for the aging experiment. A power supply was used to provide a stable 5 V forward bias for 12, 24, 36, 72, and 120 h. Then the devices were measured and the depth in the profile was normalized to the relative thickness of the ETL and EL inside the device, which was defined by a vanishing Al cathode (relative thickness: 0) and the appearance of S in the PEDOT:PSS layer (relative thickness: 1).

2.3. Molecular structure

The molecular dipole moment was calculated with Gaussian 03 revision D.02 using the B3LYP density functional theory (DFT). The 6-31G basis set was employed for all atoms.

2.4. Device lifetime measurement (accelerated experiment)

For device reliability measurements, all of the studied devices with encapsulation were operated in a nitrogen atmosphere for accelerated experiments. In order to

examine the proposed field-driven migration of molecules, fixed driving force is desired. Therefore, a power supply was used to provide a constant forward bias (8.5 V) to the device to generate a constant electric field hence fixed driving force. The luminances of the resultant devices were measured with a Minolta CS-100 luminance meter and all the devices presented here has a similar luminance around $3–4 \times 10^3$ cd/m^2 and the current density is around 20–40 mA/cm^2 [28]. The time for the device to reach 50% initial luminance was reported. The emission area of all the resultant devices was 2×2 mm, and only the luminance in the forward direction was measured.

3. Results and discussion

Previously, we reported the direct observation of the OLED degradation process using XPS depth profiles. Fig. 1a shows the XPS depth profile of the CBP containing device before and after operating the device with a forward DC bias for different lengths of time in a nitrogen atmosphere. Initially, the difference in N intensity clearly delineated the TPBi (ETL, 11 at.% N and 89 at.% C) and CBP (EL, 5 at.% N, 95 at.% C) thin-film stack although it is noted that the observed atomic concentration is lower than expected owing to the implantation of C associated with C_{60}^+ sputtering [21,29]. Since TPBi has more N atoms, the intensity of N observed in XPS is higher than that in CBP layer. After 12 h of operation, the N distribution changed significantly. In short, the N intensity in the original ETL decreased and that in the EL increased. Such an obvious change in the N distribution can be attributed to the molecular migration of small TPBi molecules all the way into the PEDOT:PSS layer under DC bias [21]. We propose the following mechanism for the migration of the TPBi molecules (Fig. 1d). (1) The injected electrons hop on and between the disk-shaped TPBi molecules (Fig. 1c), and the molecules become temporarily charged (TPBi$^-$) and higher current density may lead to more charged molecules; (2) The negatively charged TPBi molecules migrate towards the anode in the electric field caused by the DC bias. In other words, the TPBi molecules are exposed to a driving force to push them from the cathode (Al) to the anode (ITO), and this force causes the TPBi molecules to migrate to the EL and HTL. It is noted that the joule heat generated during device operation may increase the mobility of molecules and assist the molecular migration.

The ease of TPBi (Fig. 1c) migration in CBP (Fig. 1b) may be related to the relative planarity of the host structure. This process significantly changes the device structure, leading to the failure of the device. To prolong the device lifetime, it is preferred to suppress the migration of the TPBi. One possible method is to replace the CBP host with other molecules that have stronger inter-molecular interactions or higher molecular weights. This change in

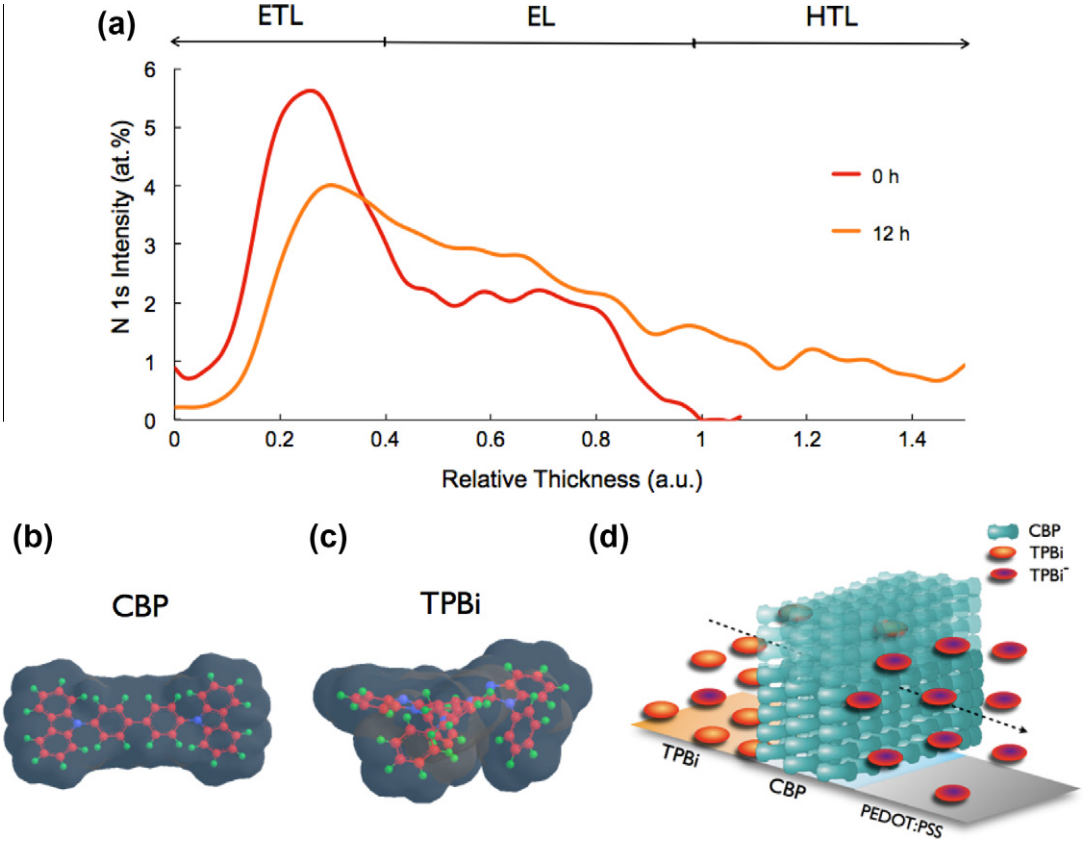

Fig. 1. (a) XPS N 1s depth profiles of the organic layers in the CBP devices operated at a 5 V forward bias for different lengths of time. (b) and (c) Molecular structure of CBP and TPBi (ETL), respectively. (d) A schematic illustration of the molecular migration through the CBP layer toward the anode.

materials can increase the energy barrier for the TPBi to move between the host molecules, and thus suppress the molecular migration inside the device. To examine this hypothesis, devices with mCP, SimCP2, and SimCP were fabricated using the same parameters as for those made with CBP and exposed to a constant 5 V bias (fixed driving force) for different lengths of time. The molecular distribution in these devices was then examined and compared with device half-life determined using an accelerated experiment at a constant 8.5 V operation.

The N distribution of the mCP-containing device after different operation times is shown in Fig. 2a. The mCP device could retain its stacking structure longer than the CBP device, as can be seen by comparing Figs. 1a and 2a. Because mCP molecules have a less symmetric molecular structure (Fig. 2b), the dipole moment of mCP is higher than that of CBP (Table 1). This higher dipole moment yields stronger van der Waals forces between molecules. Figs. 1d and 2c show schematic illustrations of the migration of TPBi through the EL. Although the mCP molecules are smaller than CBP molecules, the stronger inter-molecular interaction between them makes them harder to separate and hinders the migration of TPBi through the mCP layer. Hence, the energy barrier for TPBi to migrate through mCP is higher than that required to migrate through CBP. As a result, the TPBi molecules cannot migrate through mCP layer as easily as they can migrate through the CBP layer; therefore, the change in N distribution after 12 h operation is suppressed using mCP. Although mCP shows a better ability for suppressing the molecular migration of TPBi molecules than CBP, due to the stronger inter-molecular interactions, the molecular migration phenomenon is still apparent after prolonged operation. This limitation may be attributed to the small size of the mCP molecules and their low steric hindrances, which are not sufficient to block the TPBi for prolonged operation. To further improve the device lifetime by suppressing the migration of TPBi molecules, SimCP2, which has larger molecular weight and higher dipole moment, was selected as a host and blocking material.

Fig. 3a shows the XPS depth profiles of the SimCP2-containing device after operating device for different lengths of time. Comparing the SimCP2 with the mCP devices, SimCP2 devices show further retardation in the change of the N distribution during the first 24 h of forward bias. Due to the higher molecular weight, its bulky structure provides stronger steric hindrance that could be more efficient in preventing the TPBi molecules to migrate through (Fig. 3c). Furthermore, the asymmetrical structure (Fig. 3b) of SimCP2 yields higher dipole moment than mCP (Table 1) thus the van der Waals forces between molecules

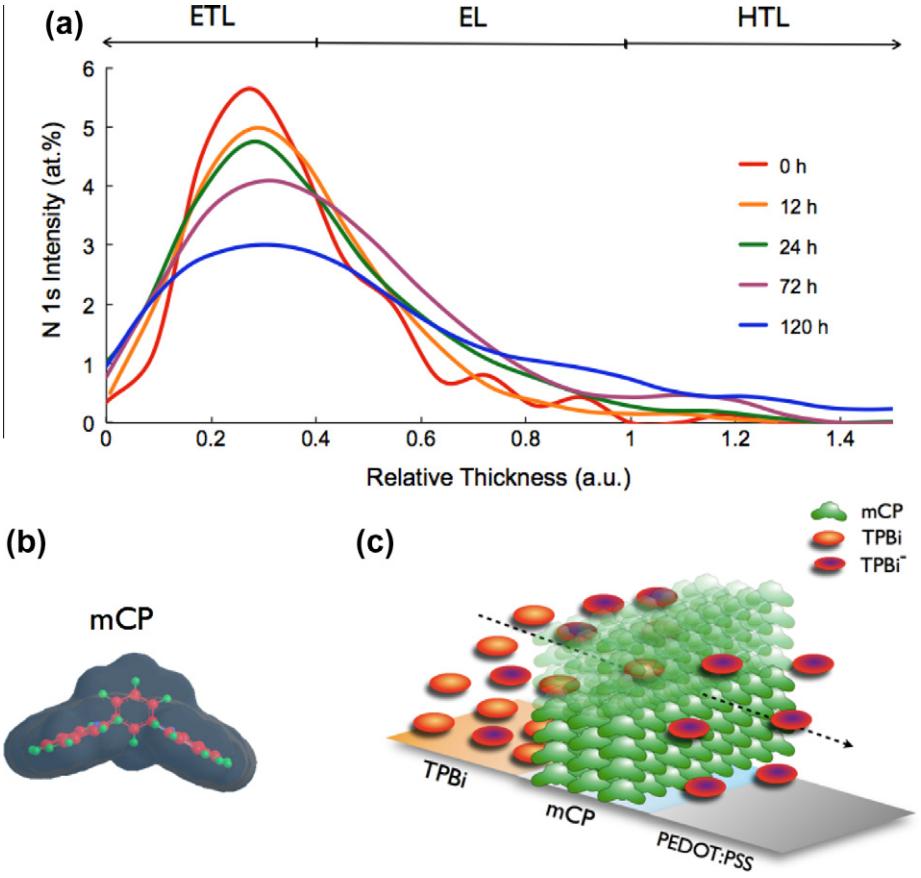

Fig. 2. (a) XPS N 1s depth profiles of the organic layers in the mCP devices operated at 5 V forward bias for different lengths of time. (b) Molecular structure of the mCP host. (c) A schematic illustration of the molecular migration through the mCP layer toward the anode.

Table 1
Physical properties of the four host materials.

	Density (g/cm^3)[a]	Molecular weight (g/mol)	Dipole moment (D)	Device half-life (min)[b]
CBP	1.28	484	0.00	4
mCP	1.25	408	1.34	6
SimCP2	0.80	997	2.40	9
SimCP	1.09	666	2.29	13

[a] The density was measured by using materials with a given weight and its displacement volume of hexane where materials does not dissolve.
[b] The device half-life were measured under 8.5 V forward bias (accelerated aging).

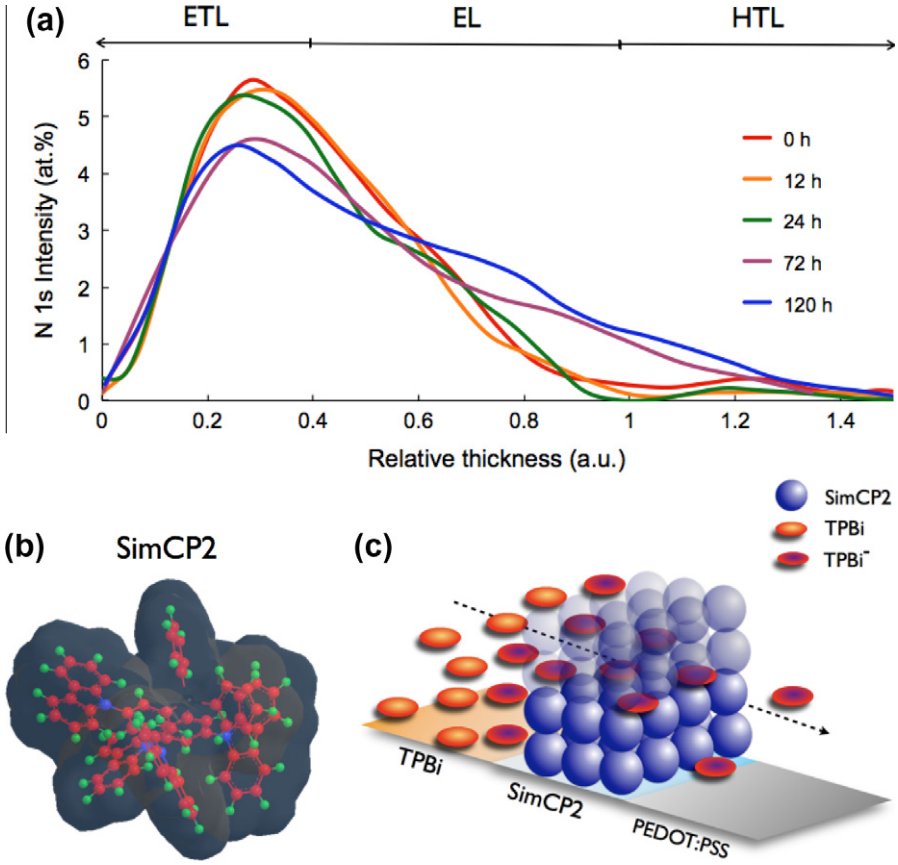

Fig. 3. (a) XPS N 1s depth profiles of the organic layers in the SimCP2 devices, operated at 5 V forward bias for different times. (b) Molecular structure of the SimCP2 host. (c) A schematic illustration of the molecular migration through SimCP2 layer toward the anode.

is stronger. As a result, the energy barrier for TPBi molecules to migrate through the SimCP2 is increased, and the bias-driven molecular-migration phenomenon is not clearly observed during the first 24 h of operation. However, after 72 h operation, the change in device structure due to the migration of TPBi toward the EL and HTL is still evident as the N distribution is broader than the original distribution.

It is found that the density of SimCP2 is significantly lower than other materials (Table 1). Such a low density suggests that the SimCP2 is not densely packed and there may be significant micro-pores in the solid due to its bulky structure. Although the high molecular weight serves as a blockade to TPBi migration and the stronger inter-molecular interaction increases the energy barrier for TPBi to migrate between SimCP2 molecules, these micro-pores provides a low-energy route for TPBi to pass through. In other words, there may be a compromise between the use of a bulky molecular structure and the existence of micro-pores. Therefore, SimCP, which has a similar dipole moment and higher density than SimCP2 (Table 1), was investigated as an alternative host material. Fig. 4a shows the XPS depth profile of the SimCP-containing device after operating for different lengths of time. It is clear that even after 120 h of device operation, the distribution of N-containing species did not change significantly from the initial distribution. This result indicated that the migration of TPBi molecules through the SimCP-containing EL is prevented. Although the molecular structure of SimCP (Fig. 4b) is smaller and

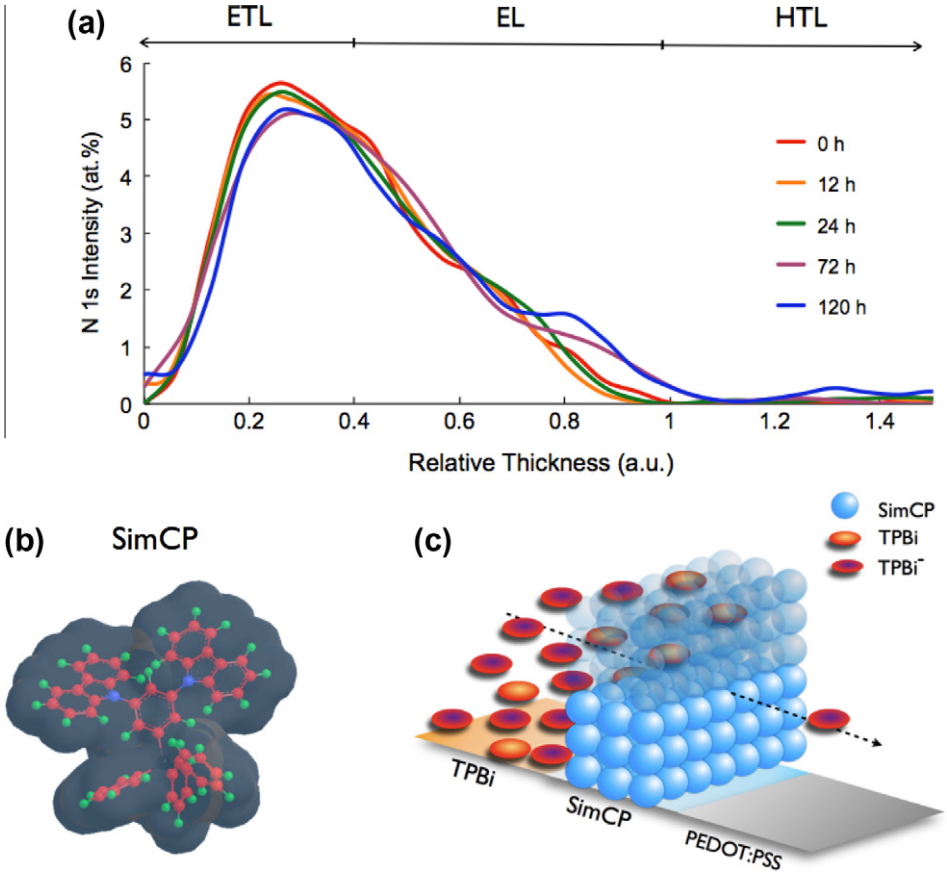

Fig. 4. (a) XPS N 1s depth profiles of the organic layers in the SimCP devices, operated at 5 V forward bias for different lengths of time. (b) Molecular structure of SimCP. (c) A schematic illustration of the molecular migration through the SimCP layer toward the anode.

more symmetrical than that of SimCP2 (Fig. 3b), the higher density of SimCP indicated that the molecules are packed closer than those in SimCP2, and hence it is more difficult for TPBi to pass through the SimCP layer (Fig. 4c).

To correlate the observed bias-driven molecular migration through different host materials and the device reliability, an accelerated experiment on the device lifetime was carried out. Table 1 shows the device half-life of different host materials. Although even under the nitrogen atmosphere, the device half-life is rather short due to the high bias, it was found that the half-life increased sequentially in CBP, mCP, SimCP2, and SimCP. This trend in device half-life is the same as the trend for the suppression of TPBi migration. In other words, by carefully designing a host material that can block the migration of electron-transporting materials toward the anode, the device lifetime can be enhanced.

4. Conclusion

Using *in situ* co-sputtering of high-energy C_{60}^{+} and low-energy Ar^{+} with XPS analysis, OLED devices (Al/LiF/TPBi/Hosts:FIrpic/PEDOT:PSS/ITO) with different hosts materials (CBP, mCP, SimCP2, and SimCP) were profiled to examine the distribution of molecules as a function of operation time. Under a forward bias, the TPBi molecules tend to migrate toward the ITO anode due to the electric field. This bias-driven molecular migration would affect device performance and lifetime reliability. To suppress the migration, organic materials with higher molecular weights, higher dipole moments, and thus stronger inter-molecular forces would increase the energy barrier for the change in device structure. Furthermore, organic materials with high thin-film packing densities can also efficiently suppress the migration. As a result, bias-driven molecular migration could be effectively suppressed by the design of host materials, thus enhancing device reliability.

Acknowledgment

The authors acknowledge sponsorship by Academia Sinica, the Department of Economic Affairs and the Taiwan National Science Council through grant nos. 98-2113-M-001-012-MY2 and 97-2120-M-002-014.

References

[1] M. Afzaal, P. O'brien, Recent developments in II–VI and III–VI semiconductors and their applications in solar cells, Journal of Materials Chemistry 16 (2006) 1597–1602.

[2] R. Bez, E. Camerlenghi, A. Modelli, A. Visconti, Introduction to Flash memory, Proceedings of the IEEE 91 (2003) 489–502.
[3] J. Welser, J.L. Hoyt, J.F. Gibbons, Electron-mobility enhancement in strained-Si N-type metal–oxide–semiconductor field-effect transistors, IEEE Electron Device Letters 15 (1994) 100–102.
[4] Y.A. Vlasov, X.Z. Bo, J.C. Sturm, D.J. Norris, On-chip natural assembly of silicon photonic bandgap crystals, Nature 414 (2001) 289–293.
[5] M.L. Lee, C.W. Leitz, Z. Cheng, A.J. Pitera, T. Langdo, M.T. Currie, G. Taraschi, E.A. Fitzgerald, D.A. Antoniadis, Strained Ge channel p-type metal–oxide–semiconductor field-effect transistors grown on Si1-xGex/Si virtual substrates, Applied Physics Letters 79 (2001) 3344–3346.
[6] E. Monroy, F. Omnes, F. Calle, Wide-bandgap semiconductor ultraviolet photodetectors, Semiconductor Science and Technology 18 (2003) R33–R51.
[7] A. Richter, P. Steiner, F. Kozlowski, W. Lang, Current-induced light-emission from a porous silicon device, IEEE Electron Device Letters 12 (1991) 691–692.
[8] F.A. Kish, F.M. Steranka, D.C. Defevere, D.A. Vanderwater, K.G. Park, C.P. Kuo, T.D. Osentowski, M.J. Peanasky, J.G. Yu, R.M. Fletcher, D.A. Steigerwald, M.G. Craford, V.M. Robbins, Very high-efficiency semiconductor wafer-bonded transparent-substrate (Alxga1-X)0.5in0.5p/Gap light-emitting-diodes, Applied Physics Letters 64 (1994) 2839–2841.
[9] J. Kido, M. Kimura, K. Nagai, Multilayer white light-emitting organic electroluminescent device, Science 267 (1995) 1332–1334.
[10] A.R. Duggal, J.J. Shiang, C.M. Heller, D.F. Foust, Organic light-emitting devices for illumination quality white light, Applied Physics Letters 80 (2002) 3470–3472.
[11] D. Mutaguchi, K. Okumoto, Y. Ohsedo, K. Moriwaki, Y. Shirota, Development of a new class of hole-transporting and emitting vinyl polymers and their application in organic electroluminescent devices, Organic Electronics 4 (2003) 49–59.
[12] B.W. D'andrade, S.R. Forrest, White organic light-emitting devices for solid-state lighting, Advanced Materials 16 (2004) 1585–1595.
[13] R.L. Hartman, B. Schwartz, M. Kuhn, Degradation and passivation of gap light-emitting diodes, Applied Physics Letters 18 (1971) 304.
[14] Y.C. Tsai, J.H. Jou, Long-lifetime, high-efficiency white organic light-emitting diodes with mixed host composing double emission layers, Applied Physics Letters 89 (2006) 243521.
[15] M. Hasunuma, H. Toyoda, H. Kaneko, Electromigration induced aluminum atom migration retarding by grain boundary structure stabilization and copper doping, Microelectronics Reliability 39 (1999) 1631–1645.
[16] H. Aziz, Z.D. Popovic, Degradation phenomena in small-molecule organic light-emitting devices, Chemistry of Materials 16 (2004) 4522–4532.
[17] F. So, D. Kondakov, Degradation mechanisms in small-molecule and polymer organic light-emitting diodes, Advanced Materials 22 (2010) 3762–3777.
[18] S. Scholz, K. Walzer, K. Leo, Analysis of complete organic semiconductor devices by laser desorption/ionization time-of-flight mass spectrometry, Advanced Functional Materials 18 (2008) 2541–2547.
[19] I.R.D. Moraes, S. Scholz, B. Lüssem, K. Leo, Analysis of chemical degradation mechanism within sky blue phosphorescent organic light emitting diodes by laser-desorption/ionization time-of-flight mass spectrometry, Organic Electronics (2010), doi:10.1016/j.orgel.2010.11.004.
[20] E.I. Haskal, A. Curioni, P.F. Seidler, W. Andreoni, Lithium–aluminum contacts for organic light-emitting devices, Applied Physics Letters 71 (1997) 1151–1153.
[21] W.C. Lin, W.B. Wang, Y.C. Lin, B.Y. Yu, Y.Y. Chen, M.F. Hsu, J.H. Jou, J.J. Shyue, Migration of small molecules during the degradation of organic light-emitting diodes, Organic Electronics 10 (2009) 581–586.
[22] S.T. Lee, Z.Q. Gao, L.S. Hung, Metal diffusion from electrodes in organic light-emitting diodes, Applied Physics Letters 75 (1999) 1404–1406.
[23] I. Bruder, S. Watanabe, J.Q. Qu, I.B. Muller, R. Kopecek, J. Hwang, J. Weis, N. Langer, A novel p-dopant with low diffusion tendency and its application to organic light-emitting diodes, Organic Electronics 11 (2010) 589–593.
[24] B.Y. Yu, W.C. Lin, W.B. Wang, S. Iida, S.Z. Chen, C.Y. Liu, C.H. Kuo, S.H. Lee, W.L. Kao, G.J. Yen, Y.W. You, C.P. Liu, J.H. Jou, J.J. Shyue, Effect of fabrication parameters on three-dimensional nanostructures of bulk heterojunctions imaged by high-resolution scanning ToF-SIMS, ACS Nano 4 (2010) 833–840.
[25] Y.Y. Chen, B.Y. Yu, W.B. Wang, M.F. Hsu, W.C. Lin, Y.C. Lin, J.H. Jou, J.J. Shyue, X-ray photoelectron spectrometry depth profiling of organic thin films using C-60 sputtering, Analytical Chemistry 80 (2008) 501–505.
[26] B.Y. Yu, Y.Y. Chen, W.B. Wang, M.F. Hsu, S.P. Tsai, W.C. Lin, Y.C. Lin, J.H. Jou, C.W. Chu, J.J. Shyue, Depth profiling of organic films with X-ray photoelectron spectroscopy using C-60(+) and Ar^+ co-sputtering, Analytical Chemistry 80 (2008) 3412–3415.
[27] W.C. Lin, Y.C. Lin, W.B. Wang, B.Y. Yu, S. Iida, M. Tozu, M.F. Hsu, J.H. Jou, J.J. Shyue, Effect of fabrication process on the microstructure and the efficiency of organic light-emitting diode, Organic Electronics 10 (2009) 459–464.
[28] J.H. Jou, W.B. Wang, S.Z. Chen, J.J. Shyue, M.F. Hsu, C.W. Lin, S.M. Shen, C.J. Wang, C.P. Liu, C.T. Chen, M.F. Wu, S.W. Liu, High-efficiency blue organic light-emitting diodes using a 3,5-di(9H-carbazol-9-yl)tetraphenylsilane host via a solution-process, Journal of Materials Chemistry 20 (2010) 8411–8416.
[29] W.-C. Lin, C.-P. Liu, C.-H. Kuo, H.-Y. Chang, C.-J. Chang, T.-H. Hsieh, S.-H. Lee, Y.-W. You, W.-L. Kao, G.-J. Yen, C.-C. Huang, J.-J. Shyue, The role of the auxiliary atomic ion beam in C_{60}^{+}–Ar^+ co-sputtering, Analyst (2011). (accepted).

Organic Electronics 12 (2011) 383–393

Contents lists available at ScienceDirect

Organic Electronics

journal homepage: www.elsevier.com/locate/orgel

Planar and textured heterojunction organic photovoltaics based on chloroindium phthalocyanine (ClInPc) versus titanyl phthalocyanine (TiOPc) donor layers

Weining Wang, Diogenes Placencia, Neal R. Armstrong *

Department of Chemistry, University of Arizona, Tucson, Arizona 85721, USA

ARTICLE INFO

Article history:
Received 2 July 2010
Received in revised form 15 November 2010
Accepted 18 November 2010
Available online 8 December 2010

Keywords:
Phthalocyanine
Organic solar cell
UV-photoemission
Near-IR
Heterojunction
Interface dipole

ABSTRACT

Planar and textured heterojunction solar cells (OPVs) are reported for vacuum deposited chloroindium phthalocyanine (ClInPc)/C_{60} heterojunctions, and their response compared to previously explored OPVs based on titanyl phthalocyanine (TiOPc)/C_{60} heterojunctions. As for TiOPc/C_{60} OPVs, the photoelectrical activity of ClInPc/C_{60} OPVs extends well into the near infrared, with good activity out to ca. 900 nm. As-deposited ClInPc films (Phase I) produce open-circuit photopotentials, V_{OC} as high as ca. 0.8 V (Phase I form of ClInPc), ca. 0.15 V larger than previously observed for Phase I TiOPc/C_{60} OPVs. The offsets in frontier orbital energies (E^{Pc}_{HOMO}–$E^{C_{60}}_{LUMO}$) revealed by UV-photoemission studies (UPS) are slightly smaller for ClInPc/C_{60} versus TiOPc/C_{60} heterojunctions, and the interface dipole contribution (shift in local vacuum level) to these offsets is in the opposite direction for ClInPc/C_{60} versus TiOPc/C_{60} heterojunctions, or missing altogether, suggesting differences in molecular interaction at the Pc/C_{60} interface. Higher V_{OC} values are correlated with lower reverse saturation currents, J_o, for ClInPc/C_{60}, versus other Pc or pentacene/C_{60} heterojunctions, suggesting weak intermolecular interactions at the ClInPc/C_{60} interface and large barriers to dark charge injection. Solvent annealing of the ClInPc films enhances the near-IR response, and textures the Pc film, enhancing the Pc/C_{60} interfacial contact area and the short-circuit photocurrent, J_{SC}. J_{SC} under AM 1.5 illumination conditions was estimated by integration of the incident photon current efficiency (IPCE) response, to compare relative power conversion efficiencies for the two different device types. The estimated efficiency of Phase I ClInPc/C_{60} OPVs is ca. 2.6%. The estimated AM 1.5 efficiency of ClInPc/C_{60} OPVs with solvent annealed Pc layers is estimated to be ca. 3.3%, arising from the extensive texturing achieved of the Pc layer, which nearly doubles J_{SC} for the Phase II versus Phase I Pc films.

© 2010 Elsevier B.V. All rights reserved.

1. Introduction

Organic photovoltaics (OPVs) based on "Type II" donor (D)/acceptor (A) heterojunctions [1], have been under investigation for over two decades, in either planar heterojunction (PHJ) or bulk heterojunction (BHJ) formats [2–20]. OPVs have recently achieved AM 1.5 efficiencies higher than 7% in both polymer BHJ formats [2,21], and in PHJ tandem OPVs [22–24]. Improving the efficiency of OPVs requires enhancing the short-circuit current (J_{SC}), utilizing materials with enhanced near-IR absorption, and nanotexturing of the donor/acceptor (D/A) interface, facilitating efficient exciton dissociation [15,18,20,25]. Such enhancements need to occur without sacrificing open-circuit voltage, V_{OC}, which is controlled by offsets in transport frontier orbital energies, E^{D}_{HOMO}–E^{A}_{LUMO} [1,26–30], and by the strength of intermolecular interactions at the D/A interface, and ultimately the magnitude of the reverse saturation current, J_o [8,12,31].

* Corresponding author. Tel.: +1 520 621 8242; fax: +1 520 621 8407.
E-mail address: nra@email.arizona.edu (N.R. Armstrong).

1566-1199/$ - see front matter © 2010 Elsevier B.V. All rights reserved.
doi:10.1016/j.orgel.2010.11.015

We show here that OPVs based on heterojunctions of C_{60} with planar and textured layers of the trivalent metal phthalocyanine chloroindium phthalocyanine (ClInPc) meet several of the criteria for good near-IR spectral overlap, high V_{OC} brought about by higher ionization potentials (IP) versus most other small molecule donors, and low values of J_o in the Pc/C_{60} heterojunction. Efficiencies of these ClInPc/C_{60} OPVs are higher than those we recently reported on using titanyl phthalocyanine (TiOPc) as the donor layer [14,15].

The tetravalent and trivalent metal phthalocyanines (titanyl and vanadyl phthalocyanines, TiOPc and VOPc, and the halo-aluminum, -gallium and -indium phthalocyanines, e.g. ClAlPc, ClGaPc, ClInPc) have been explored as xerographic photoreceptors and as photoelectrochemical energy conversion platforms, in both their as-deposited Phase I polymorph, or as Phase II or related polymorphs [11,14,32–41]. The ionization potentials (IP) of the tetravalent and trivalent metal Pcs are generally higher than seen in other Pc donors (e.g. CuPc, ZnPc), or pentacene and related polycyclic aromatic hydrocarbons [9,11,14,15,42–47]. For OPVs based on as-deposited (Phase I polymorph) TiOPc/C_{60} heterojunctions V_{OC} as high as 0.65 V has been observed [14]. Upon solvent annealing of these Pc films significant nano-texturing occurs during the formation of the Phase II polymorph along with a significant broadening of the *Q*-band absorbance out to ca. 900 nm. The increase in interfacial area between the Pc and C_{60} layers, along with the added near-IR absorbance, leads to a near doubling of power conversion efficiency as a result of these polymorphic transitions [15].

In this paper, we discuss planar and textured heterojunction OPVs based on ClInPc/C_{60} (Fig. 1), showing enhanced near-IR responses as for TiOPc OPVs, but with a larger V_{OC}. ClInPc demonstrates close to the same near-IR absorptivity (α, cm^{-1}) in its Phase I and Phase II polymorphs as seen in TiOPc polymorphs. As for TiOPc, ClInPc ohms per square is believed to have a high probability for triplet state formation [48], as has been hypothesized for OPVs based on thin films of other heavy metal phthalocyanines (e.g. SnPc) [49]. The trivalent and tetravalent Pcs, especially ClInPc films, can also be formed as well-ordered, epitaxial thin films, demonstrating layer-by-layer growth on ordered substrates, lending themselves to the formation of well-ordered organic/organic′ heterojunctions [50,51], amenable to characterization of their ionization potentials and interface dipole effects using UV-photoemission spectroscopies (UPS) [6].

We demonstrate here that OPVs based on Phase I ClInPc/C_{60} heterojunctions show values of V_{OC} nearly 0.2 V higher than their Phase I TiOPc/C_{60} counterparts. Estimated AM 1.5 efficiencies for the Phase I polymorph of ClInPc based OPVs are twice as those seen previously for Phase I TiOPc/C_{60} heterojunctions. Solvent annealing of the Phase I ClInPc films provides texturing of the Pc/C_{60} interface on ca. 100 nm length scales that enhances the short-circuit photocurrent, J_{SC}, with only small declines in V_{OC}, leading to estimated AM 1.5 efficiencies for heterojunctions based on the Phase II polymorph of ca. 3.3%. Improved efficiencies for OPVs based on textured Phase II and Phase III TiOPc films are reported elsewhere, but have also shown significant enhancements in efficiencies relative to our earlier reports [52].

The larger values of V_{OC} for OPVs based on ClInPc do not arise from larger $E^{Pc}_{HOMO}-E^{C_{60}}_{LUMO}$ offsets, estimated from UPS studies of ClInPc/C_{60} versus TiOPc/C_{60} heterojunctions, since these energy offsets are comparable for both donor layers. We show here that $E^{Pc}_{HOMO}-E^{C_{60}}_{LUMO}$ and the magnitude and sign of the interface dipole at the ClInPc/C_{60} heterojunction are dependent on the deposition rate of the Pc film, which likely controls the micro-crystallinity of these layers. Previous studies of organic heterojunctions of ClInPc with perylene-based acceptors have shown that interface dipoles seen at the O/O′ heterojunction are strongly dependent upon molecular architecture at this interface [6,18], as predicted by several other investigations [53–56]. We also observed much lower values of J_o for ClInPc/C_{60} heterojunctions, suggesting that apparently weaker intermolecular interactions at this interface are primarily responsible for enhanced values of V_{OC}.

2. Experimental methods

Commercial ITO was obtained from Colorado Concept Coating, LLC, with a sheet resistance of ca. 15 ohms per square. ITO substrates were cleaned with a micro-fiber cloth using 10% Triton-X100, followed by successive sonications in 10% Triton-X100 for 15 min, nanopure water for 5 min, and pure ethanol for 15 min. Prior to the deposition of organic thin films, substrates were dried under a

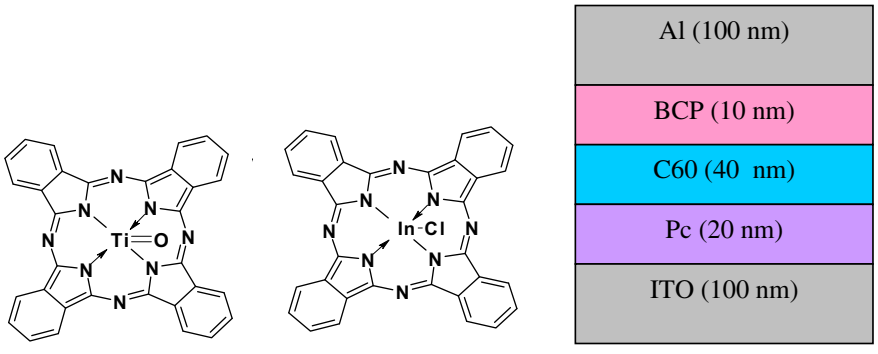

Fig. 1. Molecular structure of TiOPc and ClInPc, and OPV device structure, respectively.

stream of nitrogen and then etched via oxygen plasma cleaning (Harrick PDC-32G) for 15 min.

Titanyl phthalocyanine (TiOPc), chloroindium phthalocyanine (ClInPc), and bathocuproine (BCP) were purchased from Sigma–Aldrich. Fullerene (C_{60}) was obtained from MER. All chemicals were purified by multiple entrainer sublimation prior to use [57,58].

Organic thin-films were deposited via vacuum deposition (ca. 1 Å/s) at base pressures of ca. 10^{-7} Torr via Knudsen-type sublimation cells, monitored with a 10 MHz quartz crystal microbalance (QCM-Newark), and an Agilent Technologies frequency monitor (Model 53131A). Solvent-annealed TiOPc and ClInPc films were created by depositing the desired Pc film thickness, transfer of the film under nitrogen to an adjacent glovebox where it was placed in a sealed vessel adjacent to a reservoir of liquid chloroform for up to 5 h [15]. The Pc film was then returned to vacuum and the Pc/C_{60} OPV device completed. Aluminum top contacts were deposited at pressures no greater than 10^{-6} Torr at a deposition rate of 1–3 Å/s, monitored via a 6 MHz QCM (Tangidyne) and Inficon deposition monitor (Model 758-500-G1). These aluminum top contacts defined the device area, and we typically made from 9 to 26 devices for each deposition sequence, on ITO/glass substrates with dimensions approximately 2.5 × 2.5 cm. The region at the center of some of these substrates was left open to allow for absorbance spectra to be measured on the same films for which IPCE data was obtained.

Current–voltage (J/V) data was obtained for several OPVs for each ClInPc films composition, with areas of 0.019 cm^2. The J/V data presented here are representative of at least nine devices. IPCE data was obtained for devices with an area of 0.125 cm^2, apertured so as to minimize "edge effects" in the photocurrent response [15,59]. OPV testing was carried out in a N_2-filled double-glovebox (MBrawn Labmaster), with water and oxygen levels at less than 0.1 ppm. Current–voltage measurements were made with a Keithley 2400 source meter, while the data was acquired with in-house software created with *Labview* ver.8.2 (National Instruments). Scans ranged from −1.00 to 1.50 V using a 20 mV step starting from negative bias. A CUDA products light source with a 250 W quartz-halogen lamp (Model I-250) was used as the illumination source. The light was filtered with a 750 nm cutoff filter, along with a sand-blasted light diffuser (the spectral distribution for this filter set is shown in Supporting information). We adjusted the distance to the OPV device arrays to achieve an output of approximately 100 mW/cm^2 as measured with an Apogee PYR-S pyranometer.

Incident photon current efficiency (IPCE) measurements were carried out in atmosphere immediately after device fabrication. IPCE data were acquired after characterizing dark/light J/V behavior in the glovebox environment. IPCE measurements were made with a 500 W quartz-halogen lamp with a Mercron power stabilizer (Model TXC-500 120/120). The modulated light (250 Hz) was passed through a Jobin Yvon (Model H10/1200) monochromator. Spectra were acquired at 4 nm steps. Incident power through the monochromator was measured with a calibrated Hamamatsu photodiode acquired from Newport Optics (Model 818-SL). The bias for the OPV was maintained so as to obtain short-circuit current at each excitation wavelength. The current-to-voltage output was input to a EG&G (Model 5209) lock-in amplifier, and output into in-house software created with *Labview* ver.8.2 (National Instruments).

XPS/UPS measurements of Pc/C_{60} heterojunctions were carried out in a Kratos Axis-Ultra X-ray photoelectron spectrometer using an Al Kα source at 1486.6 eV for XPS measurements and a He(I) excitation source (21.2 eV) for UPS measurements. A −9.00 V bias was applied to the sample to further enhance the collection of lowest kinetic energy electrons [14,50,60]. For XPS data, the spot size was 300 × 700 μm, while for UPS, spot size ranged between 1 and 3 mm. A UHV organic deposition system attached to the Kratos spectrometer allowed for depositions of organic thin-films under conditions like those used to create OPVs. Thin-films were deposited (about 1 Å/s) on gold substrates (Alfa-Aesar) that were polished and etched with pirahna solution prior to the UPS studies [14,60]. Gold substrates were sputtered clean in vacuum to ensure that their effective work functions were 5.1 eV and to provide for measurement of the Fermi energy [60]. For the data shown in Fig. 6, photoemission from the Au Fermi level occurred at 32.0 eV for sputter-cleaned gold substrates and we made sure that this energy did not change during organic film deposition, which would have indicated charging effects [60]. For exploration of solvent-annealed ClInPc films, after the initial deposition and UPS characterization, the films were removed from vacuum into a nitrogen-filled glovebag and annealed as described above. Samples were then returned to vacuum, followed by subsequent UPS characterization.

Absorbance measurements were carried out with an Agilent Technologies UV/visible spectrophotometer (Model 8453) at 1 nm intervals with an integration time of 10 s and a range of 400–1100 nm. The morphology and root-mean-square (rms) roughness of ClInPc films were obtained from images collected using a Digital Instruments atomic force microscope (Dimension 3100). The images were collected in tapping mode with Mikromasch silicon cantilevers (Model TESP-7). Images were obtained in ambient air at a scan rate of 0.5 Hz with image sizes of 2.5 × 2.5 μm. SEM images were taken on a Hitachi 4800 FE-SEM (15 kV accelerating voltage) on as-prepared samples (i.e. no metallic over coating).

3. Results and discussion

3.1. Characterization of microstructure and thin film absorbance spectra and absorptivities

Figs. 1 and 2 show the schematics of the Pc donors, the OPV device configurations, and the field-emission (FE-SEM) images for ClInPc and TiOPc films of ca. 20 nm thickness, in as-deposited (Phase I) and solvent annealed (Phase II) form, on ITO. Fig. 3 (upper panel) shows the absorbance spectra of device-thickness TiOPc and ClInPc films (Phase I ClInPc films (20 nm), Phase I TiOPc films (18 nm), Phase II ClInPc films (22 nm) and Phase II TiOPc films (20 nm)). SEM and AFM images suggest that the Phase I TiOPc film is conformal, and reflects the structure of the underlying

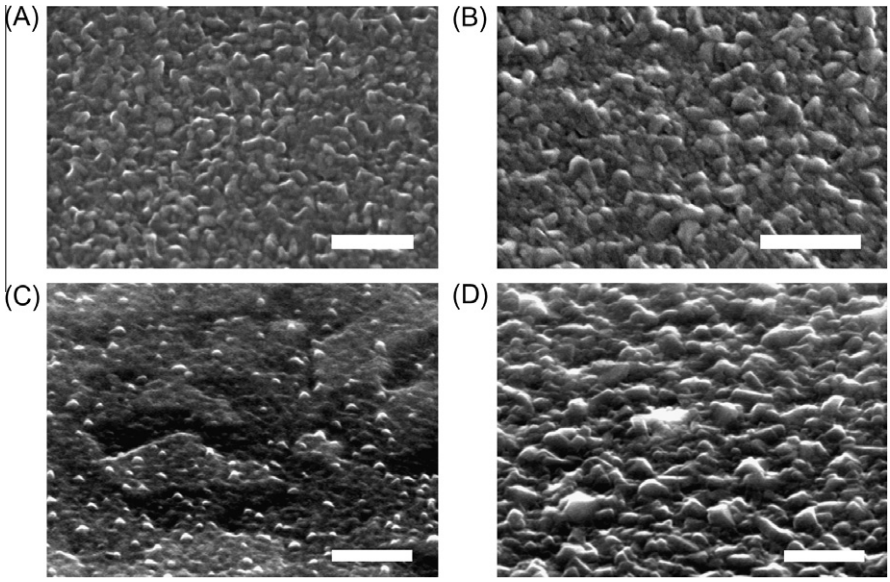

Fig. 2. SEM of ClInPc (A and B) and TiOPc (C and D) on ITO, in as-deposited, Phase I polymorph (A and C) and solvent annealed, Phase II polymorph (B and D) for 20 nm film thickness. Scale bar = 200 nm.

ITO [15]. The Phase I ClInPc film shows more texturing and surface roughness (rms roughness = 2.9 ± 0.6 nm) versus the Phase I TiOPc film (rms roughness = 0. 9 ± 0.03 nm, i.e. these Phase I TiOPc films were nearly conformal with the ITO substrate) (see AFM data in Supporting information).

After solvent annealing, which causes a change in Pc crystal structure from monoclinic (Phase I) to triclinic (Phase II) [34,38], both Phase II ClInPc and Phase II TiOPc films show greatly increased surface roughness (rms roughness = 5.0 nm for Phase II ClInPc and 6.6 for Phase II TiOPc), which subsequently leads to enhanced interfacial contact area between the Pc donor and C_{60} acceptor, coupled with greatly enhanced absorptivities in the near-IR, out to wavelengths of ca. 900 nm (we estimate that $\alpha \approx 1.5 \times 10^5\,cm^{-1}$ at the peak absorbance – Fig. 3). It has been proposed that this shift in the TiOPc *Q*-band absorbance is due to the formation of a charge-transfer-like state, owing to the much closer proximity of the opposed oxo-metal dipoles in these dyes, accompanying the shift in their crystal structures from monoclinic (Phase I) to triclinic (Phase II) [34,35,43–45,61–63]. We assume a similar situation may occur for the ClInPc system, although the internal dipole moment along the metal-halogen bond is not as large as along the metal-oxo bond in TiOPc [64–66]. We also note the similarity in structure of the polymorphic forms of this pigment, relative to those observed for TiOPc and VOPc [67,68]. Although there is substantial roughening of the Pc film, it should be noted that each asperity still has dimensions which exceed the presumed exciton diffusion length ($3 \times L_D$ in Pc films $\approx$ 18–22 nm) [20,69], so the kind of texturing needed to increase external quantum efficiencies (IPCE, see below) to greater than 0.85 (seen in polymer bulk heterojunction devices) [3,21], has not yet been achieved.

3.2. UPS studies of frontier orbital energy offsets for ClInPc/C_{60} versus TiOPc/C_{60} heterojunctions

Fig. 4 shows the UPS data used to characterize the frontier orbital energy offsets that set the upper limit for open-circuit photopotentials, V_{OC}, for Phase I ClInPc/C_{60} heterojunctions (upper panel) and Phase II ClInPc/C_{60} heterojunctions (lower panel). Figs. 5 and 6 show the energy level offsets inferred from these UPS data, and from estimates of LUMO levels from either optical absorbance data, or from inverse photoemission spectroscopic data for related Pcs and C_{60} [70,71]. The data shown in Fig. 4 were obtained by first depositing ClInPc thin films on clean Au substrates (work function $\approx$ 5.1 eV), followed by the deposition of C_{60} layers in small thickness increments. Using those UPS data in Fig. 5 and previously described analysis protocols [14,50,72–75], we determined the ionization potential (IP) for both Phase I ClInPc and Phase II ClInPc to be ca. 5.4 eV. A shift of ca. −0.3 eV in the local vacuum level (interface dipole effect) was observed as C_{60} was deposited onto Phase I ClInPc, while a vacuum level shift of −0.2 eV was observed for Phase II ClInPc/C_{60} heterojunctions. No difference in the photoemission features for C_{60} were observed for the last two incremental depositions of C_{60}, indicating that it had reached its bulk electronic properties. The IP of C_{60} in these heterojunctions was estimated to be ca. 6.4 eV.

Those IP values and vacuum level shift derived from the UPS data are used to estimate the frontier orbital energy offsets for the ClInPc/C_{60} junctions. The band diagrams are then compared with those for the TiOPc/C_{60} heterojunction in Fig. 5 (Phase I Pc/C_{60} junctions) and Fig. 6 (Phase II Pc/C_{60} junctions) [14,15,18]. The LUMO energies were estimated from combinations of absorbance spectroscopy, inverse photoemission spectroscopy (IPES), solution electrochemistry,

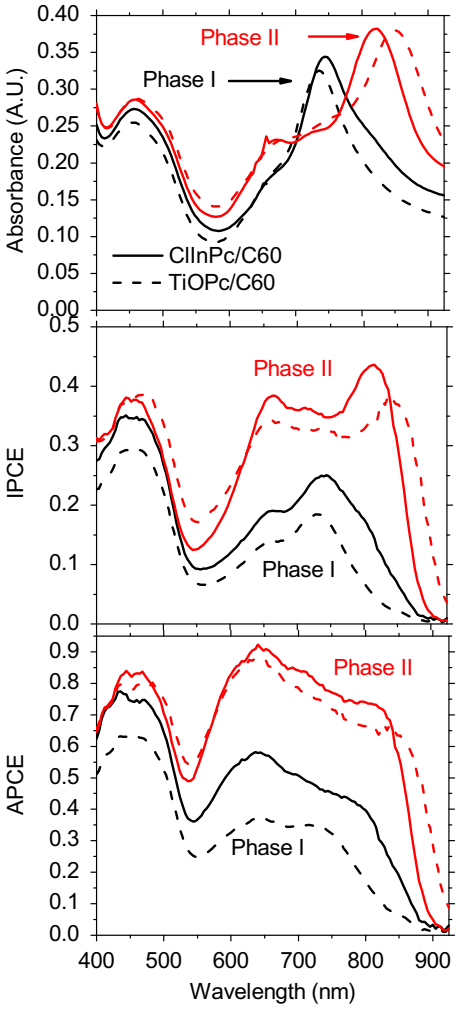

Fig. 3. (Upper panel) Absorbance spectra, (middle panel) incident photon to current conversion efficiency (IPCE) and (bottom panel) absorbed photon to current conversion efficiency (APCE) plots for Phase I TiOPc (18 nm)/C_{60} (40 nm)/BCP (10 nm) (dark dashed line), Phase I ClInPc (20 nm)/C_{60} (40 nm)/BCP (10 nm) (dark solid line), Phase II TiOPc (20 nm)/C_{60} (40 nm)/BCP (10 nm) (red dashed line), Phase II ClInPc (22 nm)/C_{60} (40 nm)/BCP (10 nm) (red solid line). (For interpretation of the references to color in this figure legend, the reader is referred to the web version of this article.)

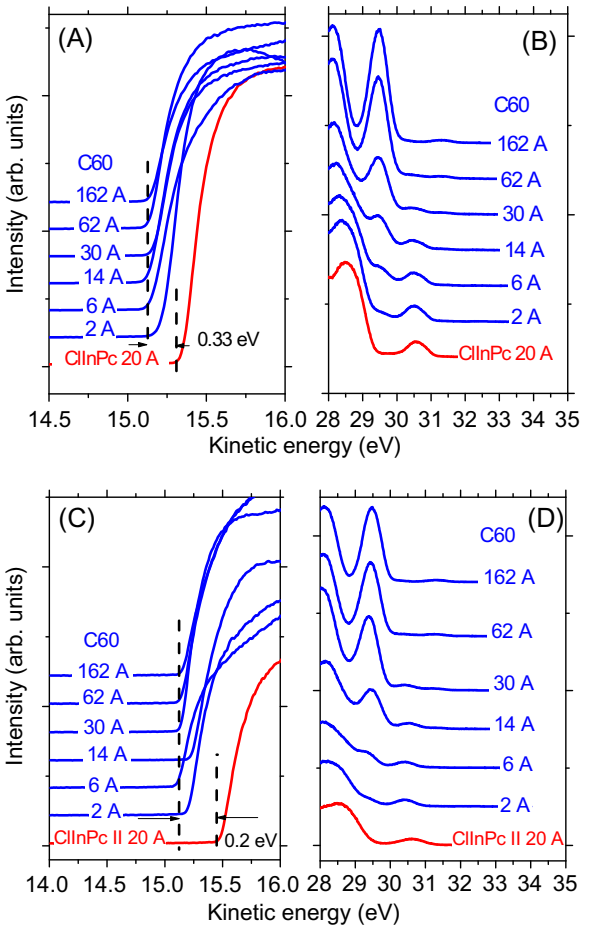

Fig. 4. He (I) UPS spectra for C_{60} deposited, in small thickness increments, on Phase I ClInPc at low kinetic energy cutoff edge (A) and at high kinetic energy cutoff region (B); and for C_{60} deposited, in small thickness increments, on Phase II ClInPc at low kinetic energy cutoff edge (C) and at high kinetic energy cutoff region (D).

and scanning tunneling spectroscopic (STS) data for other Pc systems and for other studies of C_{60} [9,15,50,70,76–78]. We note that LUMO energies and electron affinities estimated from IPES data can be much smaller than those estimated from absorbance data in the Pc films, owing to the significant exciton binding energy for donor layers like the Pcs, and there is additional uncertainty in determining the LUMO energy to less than ±0.2 eV in IPES experiments, owing to the resolution of that data [70]. For comparison of otherwise quite similar Pc/C_{60} heterojunctions the uncertainties in these estimates of LUMO energy, which can be ±0.3 eV, are not of concern.

We note that $E^{Pc}_{HOMO}-E^{C_{60}}_{LUMO} \approx 1.0$ eV for Phase I ClInPc/C_{60} junction versus Phase I TiOPc/C_{60} where $E^{Pc}_{HOMO}-E^{C_{60}}_{LUMO} \approx 1.3$ eV (the absolute values of these offsets are larger if we use transport LUMO levels estimated from other IPES data) [70], suggesting that V_{OC} should be larger for Phase I TiOPc/C_{60} heterojunctions. As shown below, we actually see larger values of V_{OC} in ClInPc/C_{60} OPVs. In addition to these difference in $E^{Pc}_{HOMO}-E^{C_{60}}_{LUMO}$ the shift in local vacuum level for ClInPc/C_{60} heterojunction (−0.33 eV) is opposite in sign to that observed at the TiOPc/C_{60} heterojunctions (0.2 eV). Interface dipoles observed for previously explored Pc/C_{60} heterojunctions have been greater than zero, including Phase I TiOPc/C_{60} (0.2 eV), CuPc/C_{60} (0.3 eV) and SubPc/C_{60} (0.5 eV) [14,15,79].

We have recently observed, however, interface dipoles of −0.3 eV for both ClInPc and ClAlPc films in heterojunctions with electron acceptors such as perylenetetracarboxylicdianhydride (PTCDA), which has a slightly higher electron affinity than C_{60}. These different interactions may be attributable to variations in packing structures and the local density of these trivalent metal Pcs, which impacts on the density of local dipoles from the metal-halogen bond, which in turn is dependent upon deposition rate, and the molecular nature of the donor/acceptor

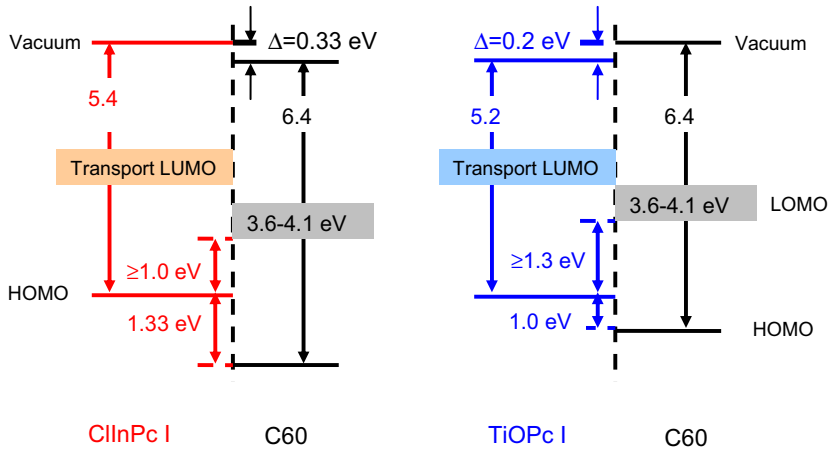

Fig. 5. Frontier orbital offset energies for ClInPc/C_{60} and TiOPc/C_{60} heterojunctions. The UPS data used to obtain these energies for ClInPc/C_{60} junction is summarized in Fig. 4. The UPS data used to obtain the energies for TiOPc/C_{60} junction is from previously published work [14,15]. For Phase I ClInPc/C_{60} heterojunction, an inverse interface dipole (−0.33 eV) was observed, suggesting a different kind of structure and polarizability the ClInPc I/C_{60} interface, comparing with Phase I TiOPc/C_{60} heterojunction with a positive interface dipole of 0.2 eV. After correction for vacuum level shifts for each heterojunction, we conclude that the critical energy differences which form the upper limit for V_{OC} in OPVs, $E^{Pc}_{HOMO}-E^{C_{60}}_{LUMO}$, is lower for Phase I ClInPc/C_{60} than for Phase I TiOPc/C_{60} heterojunctions. The energetic driving force for exciton dissociation, however, is higher for Phase I ClInPc/C_{60} heterojunctions, versus Phase I TiOPc/C_{60} heterojunctions, consistent with the higher photocurrent from the Phase I ClInPc/C_{60} heterojunctions.

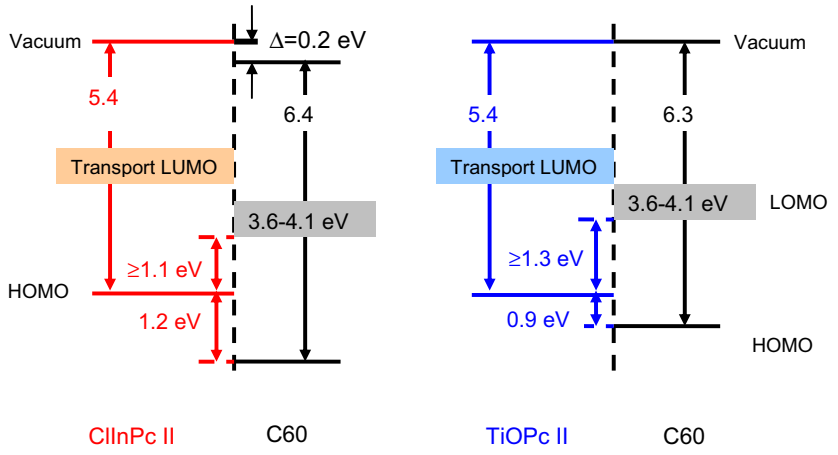

Fig. 6. Frontier orbital offset energies for Phase II ClInPc/C_{60} and Phase II TiOPc/C_{60} heterojunctions. The UPS data used to obtain these energies is summarized in Fig. 4. The UPS data used to obtain the energies for TiOPc/C_{60} junction is from previously published studies [15]. For Phase II ClInPc/C_{60} heterojunction, an inverse interface dipole (−0.2 eV) was observed, suggesting a different kind of reaction at the ClInPc II/C_{60} interface, comparing with Phase II TiOPc/C_{60} heterojunction with no interface dipole. After correction for vacuum level shifts for each heterojunction, we conclude that the critical energy differences which form the upper limit for V_{OC} in OPVs, $E^{Pc}_{HOMO}-E^{C_{60}}_{LUMO}$, are slightly lower for Phase II ClInPc/C_{60}, versus Phase II TiOPc/C_{60} heterojunctions. The energetic driving force for exciton dissociation, however, is higher for Phase I ClInPc/C_{60} heterojunctions, versus Phase I TiOPc/C_{60} heterojunctions, consistent with the higher photocurrent from the Phase I ClInPc/C_{60} heterojunctions.

interface formed. Jones and coworkers [80], have recently shown that the interface dipole at ClAlPc/C_{60} heterojunction is −0.1 eV at low deposition rates of ClAlPc films, and that as the deposition rate of ClAlPc increases, and the molecular density decreases, the interface dipole at the ClAlPc/C_{60} heterojunction changes from −0.1 to 0.2 eV. We have observed similar differences in UPS-derived interface dipoles, dependent upon ClInPc deposition rate. For ClInPc films deposited at 2–3 Å/s (a factor of 3× larger than used for OPV heterojunction formation) we saw no interface dipole upon formation of the Pc/C_{60} heterojunction, and larger $E^{Pc}_{HOMO}-E^{C_{60}}_{LUMO}$ offsets (see Fig. SI-1, Supporting information).

We also explored Phase II ClInPc/C_{60} heterojunctions (Fig. 6). Similar to Phase I Pc/C_{60} heterojunction in Fig. 5, we observed lower value of $E^{Pc}_{HOMO}-E^{C_{60}}_{LUMO}$ ($\geqslant$1.1 eV) for the Phase II ClInPc/C_{60} junction than for Phase II TiOPc/C_{60} junction ($\geqslant$1.3 eV). An inverse interface dipole (−0.2 eV) is again observed at the ClInPc/C60 heterojunction, while no interface dipole is observed at the TiOPc/C_{60} heterojunction. Despite these uncertainties in energy levels, it does appear that for both Phase I and Phase II

Table 1
Device parameters for OPVs based on ClInPc/C_{60} and TiOPc/C_{60} heterojunctions.

Type of Pc/C_{60} heterojunction (and Pc film thickness); C_{60} thickness in all cells = 40 nm	V_{OC} (V)[a]	J_{SC} (mA/cm^2)[b]	Fill factor	n_o[c]	η (%)[d]	J_o (mA/cm^2)[e]	$E^{Pc}_{HOMO}-E^{C_{60}}_{LUMO}$ (eV)
Phase I – ClInPc (20 nm)	0.79	−11.1	0.58	2.3	2.6	1.0×10^{-5}	1.0
Phase I – TiOPc (18 nm)	0.61	−8.1	0.53	2.3	1.3	1.7×10^{-4}	1.3
Phase II – ClInPc (22 nm)	0.68	−15.9	0.50	2.3	3.3	4.8×10^{-5}	1.1
Phase II – TiOPc (20 nm)	0.57	−15.1	0.53	2.5	3.0	7.1×10^{-4}	1.3

[a] Open-circuit photovoltage.
[b] Short-circuit photocurrent.
[c] Ideality factor calculated from fitting the dark *J–V*.
[d] AM 1.5 power conversion efficiency [(V_{OC}·J_{SC}·*FF*)/P_{IN}].
[e] Reverse saturation current – estimated from lowest dark current (log plots).

ClInPc polymorphs the estimated $E^{Pc}_{LUMO}-E^{C_{60}}_{LUMO}$ energy offsets, which control the exciton dissociation efficiency [8,9], are larger for ClInPc/C_{60} versus TiOPc/C_{60} heterojunctions. The expectation is that for equivalent thickness and textured Pc films, the short circuit photocurrent for ClInPc OPVs will be larger, which is born out in the *J*/*V* data for equivalent devices described below.

3.3. ClInPc/C_{60} photovoltaic device performance

ClInPc/C_{60} OPVs based on optimized thicknesses of Phase I ClInPc film and Phase II ClInPc donor films are compared to Phase I and Phase II TiOPc/C_{60} OPVs, created as described previously (device configuration in Fig. 1 and data in Figs. 2 and 3) [15]. Table 1 summarizes the device parameters for these OPVs.

We first compare Phase I TiOPc/C_{60} and ClInPc/C_{60} OPVs. Fig. 7 shows the dark and illuminated *J–V* characteristics for ITO/Phase I TiOPc (18 nm)/C_{60} (40 nm)/BCP (10 nm)/Al and ITO/Phase I ClInPc (20 nm)/C_{60} (40 nm)/BCP (10 nm)/Al. Optimum OPV performance was obtained for Pc film thicknesses of ca. 18 nm (TiOPc) and ca. 20 nm (ClInPc). For Phase I TiOPc OPVs $J_{SC}=-8.1$ mA/cm^2; $V_{OC}=0.6$ V; $FF=0.53$, while for Phase I ClInPc OPVs $J_{SC}=-11.1$ mA/cm^2, $V_{OC}=0.8$ V, $FF=0.58$. There was a significant increase (almost 0.2 V) in V_{OC} as the donor layer was changed from TiOPc to ClInPc. J_{SC} was also improved for the ClInPc OPVs (Fig. 3 – upper panel), correlating with the enhanced light absorption for these films in the near-IR. We found that we could produce optimum response in ClInPc OPVs with 22 nm Pc layers (versus 20 nm thickness for TiOPc devices – see Table 1). For both Pcs the estimated absorptivity, $\alpha=1.5\times10^5$ cm^{-1} at the *Q*-band absorbance maximum, suggesting that other factors lead to improved performance of the ClInPc OPVs, such as enhanced exciton diffusion lengths, and/or enhanced charge mobilities [81,82]. The estimated AM 1.5 power conversion efficiency, η, was doubled for Phase I ClInPc versus TiOPc OPVs. Comparable values of V_{OC} have recently been reported for "Phase I" ClAlPc/C_{60} OPVs, where thin molecular interlayers (PTCDA) were used at the ITO interface to "template" the growth of ordered ClAlPc layers, and/or add a hole-selectivity to this interface [83,84]. Li and Forrest have also recently reported OPVs based on textured Phase I ClAlPc layers with a V_{OC} of ca. 0.8 V [16,25].

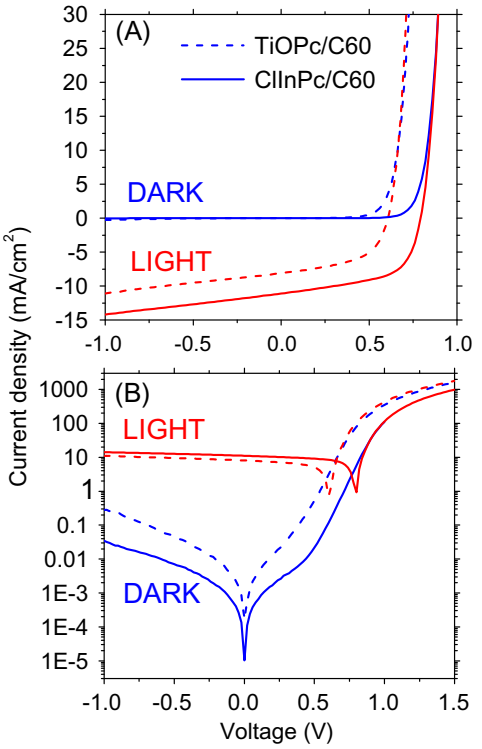

Fig. 7. The *J–V* characteristics for Phase I TiOPc (18 nm)/C_{60} (40 nm)/BCP (10 nm) (dashed lines) and for Phase I ClInPc (20 nm)/C_{60} (40 nm)/BCP (10 nm) (solid lines) in the dark (blue lines) and under illumination (red lines). (A) Linear *J–V*; (B) semi-log *J–V*. At 140 mW/cm^2 for the TiOPc/C_{60} solar cell, $J_{SC}=8.12$ mA/cm^2; $V_{OC}=0.61$ V; $FF=0.53$; for the ClInPc/C_{60} solar cell, $J_{SC}=11.11$ mA/cm^2; $V_{OC}=0.79$ V; $FF=0.58$. Device area = 0.019 cm^2. (For interpretation of the references to color in this figure legend, the reader is referred to the web version of this article.)

Fig. 8 shows the *J–V* characteristics for Phase II ClInPc (22 nm)/C_{60} (40 nm)/BCP (10 nm) and Phase II TiOPc (20 nm)/C_{60} (40 nm)/BCP (10 nm), in the dark and under illumination. For the Phase II TiOPc OPVs $J_{SC}=15.10$ mA/cm^2; $V_{OC}=0.57$ V; $FF=0.53$, while for Phase II ClInPc OPVs, $J_{SC}=15.86$ mA/cm^2; $V_{OC}=0.68$ V; $FF=0.50$. Both devices have comparable J_{SC} and *FF*, but V_{OC} for Phase II ClInPc solar cell is higher than for Phase II TiOPc solar cell, although lower than seen in the Phase I OPV, still leading, however, to substantially higher efficiency for Phase II ClInPc OPVs.

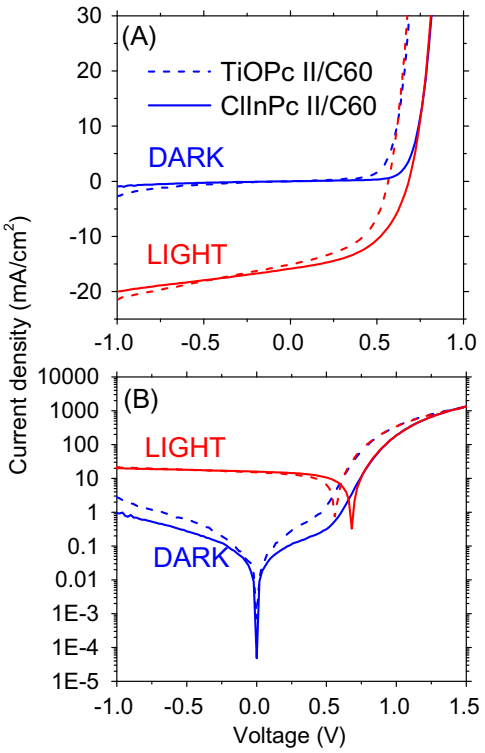

Fig. 8. The *J–V* characteristics for Phase II TiOPc (20 nm)/C_{60} (40 nm)/BCP (10 nm) (dashed lines) and for Phase II ClInPc (22 nm)/C_{60} (40 nm)/BCP (10 nm) (solid lines) in the dark (blue lines) and under illumination (red lines). (A) Linear *J–V*; (B): semi-log *J–V*. At 140 mW/cm^2 for the TiOPc/C_{60} solar cell, J_{SC} = 15.10 mA/cm^2; V_{OC} = 0.57 V; *FF* = 0.53; for the ClInPc/C_{60} solar cell, J_{SC} = 15.86 mA/cm^2; V_{OC} = 0.68 V; *FF* = 0.50. Device area = 0.019 cm^2. (For interpretation of the references to color in this figure legend, the reader is referred to the web version of this article.)

3.4. Incident photon and absorbed photon current efficiencies (IPCE and APCE)

Incident photon current efficiency (IPCE) and absorbed photon current efficiency (APCE) data for OPVs based on Phase I ClInPc films (20 nm), Phase I TiOPc films (18 nm), Phase II ClInPc films (22 nm) and Phase II TiOPc films (20 nm) are shown in Fig. 3 (middle and lower panels, respectively). As described elsewhere [15], IPCE data were obtained for OPVs with a device area of 0.125 cm^2, with a metal aperture used to eliminate "edge effects" in the photocurrent response [59]. APCE data was calculated using the IPCE data and the absorbance (transmittance) spectra for the solar cell under test, in a region near the OPV, but away from the opaque contacts.

For both the Phase I and Phase II Pc/C_{60} OPVs ClInPc-based devices outperform the TiOPc-based OPVs throughout the entire *Q*-band spectral region. The spectral shift in the *Q*-band is not as large for the Phase I → Phase II transition for ClInPc versus TiOPc (the absorption peak for Phase II ClInPc is at 820 nm, while the maximum absorbance seen for Phase II TiOPc is at 850 nm), however, the shapes of the IPCE curves are comparable for both Phase II Pc/C_{60} heterojunctions. For both device types some of the enhanced OPV response can be attributed to this enhanced *Q*-band spectral response and the corresponding integrated increase in IPCE at wavelengths above 750 nm, however, the texturing of the Pc/C_{60} heterojunction via the solvent-annealing process also accounts for a significant enhancement in J_{SC} and IPCE [15]. Normalizing IPCE by the actual absorbance (transmittance) for these Pc/C_{60} heterojunctions gives the APCE which reaches its maximum at ca. 620 nm, gradually decreases out to ca. 850–900 nm for both Phase I and Phase II heterojunctions, and then sharply declines in spectral regions where there is still appreciable optical density. APCE is a reflection of the efficiency of photocurrent production per absorbed photon, and might be expected to be constant at all wavelengths in the *Q*-band region for either the Phase I or Phase II Pc films.

The integration of the IPCE data in Fig. 3 over the spectral irradiance of the filtered light source provides estimates of J_{SC} close to the observed J_{SC} values seen in Figs. 7 and 8. Subsequently integrating the IPCE responses in Fig. 3 over the standard AM 1.5G spectrum, we predict a $J_{SC} = -5.7$ mA/cm^2 for OPVs based on Phase I (20 nm) ClInPc films, while we predict a $J_{SC} = -9.7$ mA/cm^2 for OPVs based on Phase II (22 nm) ClInPc films under such illumination conditions. Using the fill-factors and V_{OC} values obtained from Figs. 7 and 8 and Table 1, we predict an AM 1.5G power conversion efficiency for devices based on Phase I ClInPc films $\eta = 2.6\%$ (comparing with Phase I devices based on TiOPc films, $\eta = 1.3\%$), while for Phase II ClInPc films $\eta = 3.3\%$ (comparing with Phase I devices based on TiOPc films, $\eta = 3.0\%$). Examining the IPCE plots of Fig. 3 we conclude that a significant fraction of the increased efficiency of ClInPc/C_{60} versus TiOPc/C_{60} OPVs is due to enhanced V_{OC}, not predicted from the estimated values of E^{Pc}_{HOMO}–$E^{C_{60}}_{LUMO}$.

As seen in Table 1 V_{OC} in these OPVs has an inverse correlation with the observed reverse saturation current J_o. The Phase I ClInPc/C_{60} solar cell with the highest V_{OC} (0.8 V) has the lowest J_o (1.0×10^{-5} mA/cm^2), consistent with expectations from the Shockley equation [12]:

$$V_{OC} = \frac{n_o k_B T}{e} \ln\left(\frac{J_{ph}}{J_o} + 1\right)$$

where J_{ph} is the photocurrent, n_o is the ideality (quality) factor, k_B is the Boltzmann constant, T is the absolute temperature, and e is the charge of an electron. Several different studies have recently suggested that the strength of intermolecular interaction at the D/A interface plays a key role in determining the magnitude of J_o, and thus the maximum obtainable V_{OC} [8,12,31,85]. Kippelen and coworkers, exploring the temperature dependence of J_o, have proposed that J_o is controlled by the energy barrier to dark charge injection, which favors donor layers with high IPs, such as TiOPc, over donor layers such as pentacene or CuPc [12]. Ingannas and coworkers have suggested that, for polymer bulk heterojunction OPVs, the spectral position of a charge-transfer band, which depends mainly on E^{D}_{HOMO}–E^{A}_{LUMO}, can cause exponential changes in J_o, and thus changes in V_{OC}. The theoretical maximum V_{OC} can be obtained by eliminating all non-radiative pathways, resulting in maximum charge-carrier lifetime [31]. In the case of

ClInPc OPVs we see one of the largest values for V_{OC} seen for small molecule systems, and a value that is ca. 0.2 V below the maximum predicted built-in potential, limited by the size of $E^{Pc}_{HOMO}-E^{C_{60}}_{LUMO}$, because of these low values for J_o (see Table 1 for summary). Using these values of J_o, ideality factor n, J_{SC} (see Table 1), and the Shockley equation, the difference in V_{OC} between ClInPc/C_{60} and TiOPc/C_{60} solar cell are predicted to be 0.19 V for Phase I and 0.11 V for Phase II cells, respectively, consistent with the observed increase in values of V_{OC} for those solar cells.

4. Conclusions

ClInPc/C_{60} heterojunctions are an attractive materials combination as a small molecule OPV. With proper film processing to form the Phase II polymorph, the photoelectrical activity extends well into the near infrared, retaining a reasonably large V_{OC}. As a result of the large $E^{Pc}_{HOMO}-E^{C_{60}}_{LUMO}$ offsets, and the low J_o values for ClInPc/C_{60} heterojunctions, V_{OC} is larger, and the AM 1.5 efficiency of Phase I ClInPc/C_{60} OPVs is twice as that of Phase I TiOPc/C_{60} solar cell (2.6% versus 1.3%). For textured Phase II ClInPc/C_{60} heterojunctions improved efficiencies arise from both improved absorptivities in the near IR, and the increased Pc/C_{60} interfacial area. It is encouraging that IPCE values for our best ClInPc/C_{60} heterojunctions investigated to date maximize at ca. 0.45, suggesting that much greater improvements in efficiency will be achievable as texturing of the Pc/C_{60} interface allows feature sizes to approach $3 \times L_D$, providing that J_o can simultaneously be kept low (and V_{OC} high), by minimizing intermolecular interactions at the Pc/C_{60} interface leading to dark charge injection processes [13,86]. It is clear that if IPCE could be doubled to 0.9, through texturing of the Pc/C_{60} interface to create features comparable in size to $3 \times L_D$, keeping V_{OC} and FF constant, power conversion efficiencies near 6% might be achievable for single heterojunction ClInPc/C_{60} OPVs. Studies are underway to explore texturing approaches which would produce those kinds of efficiencies, and to create side chain modified forms of these tetravalent and trivalent metal Pcs which provide the advantages of near-IR absorbing phases, coupled with solution processability.

Acknowledgments

This research has been supported by the Office of Naval Research, and the National Science Foundation through the Science and Technology Center, Materials and Devices for Information Technology (DMR-0120967).

Appendix A. Supplementary data

Supplementary data associated with this article can be found, in the online version, at doi:10.1016/j.orgel.2010.11.015.

References

[1] C.W. Tang, 2-Layer organic photovoltaic cell, Appl. Phys. Lett. 48 (1986) 183–185.
[2] H.Y. Chen, J.H. Hou, S.Q. Zhang, Y.Y. Liang, G.W. Yang, Y. Yang, L.P. Yu, Y. Wu, G. Li, Polymer solar cells with enhanced open-circuit voltage and efficiency, Nat. Photonics 3 (2009) 649–653.
[3] G. Dennler, M.C. Scharber, C.J. Brabec, Polymer–fullerene bulk-heterojunction solar cells, Adv. Mater. 21 (2009) 1323–1338.
[4] C.N. Hoth, P. Schilinsky, S.A. Choulis, C.J. Brabec, Printing highly efficient organic solar cells, Nano Lett. 8 (2008) 2806–2813.
[5] C.J. Brabec, J.R. Durrant, Solution-processed organic solar cells, MRS Bull. 33 (2008) 670–675.
[6] D.M. Alloway, N.R. Armstrong, Organic heterojunctions of layered perylene and phthalocyanine dyes: characterization with UV-photoelectron spectroscopy and luminescence quenching, Appl. Phys. A: Mater. Sci. Process. 95 (2009) 209–218.
[7] E.I.M. Peter, I. Djurovich, Stephen R. Forrest, Mark E. Thompson, Measurement of the lowest unoccupied molecular orbital energies of molecular organic semiconductors, Org. Electron. 10 (2009) 515–520.
[8] M.D. Perez, C. Borek, S.R. Forrest, M.E. Thompson, Molecular and morphological influences on the open circuit voltages of organic photovoltaic devices, J. Am. Chem. Soc. 131 (2009) 9281–9286.
[9] B.P. Rand, D.P. Burk, S.R. Forrest, Offset energies at organic semiconductor heterojunctions and their influence on the open-circuit voltage of thin-film solar cells, Phys. Rev. B 75 (2007) 11537.
[10] D. Venkataraman, S. Yurt, B.H. Venkatraman, N. Gavvalapalli, Role of molecular architecture in organic photovoltaic cells, J. Phys. Chem. Lett. 1 (2010) 947–958.
[11] R.F. Bailey-Salzman, B.P. Rand, S.R. Forrest, Near-infrared sensitive small molecule organic photovoltaic cells based on chloroaluminum phthalocyanine, Appl. Phys. Lett. 91 (2007).
[12] W.J. Potscavage, S. Yoo, B. Kippelen, Origin of the open-circuit voltage in multilayer heterojunction organic solar cells, Appl. Phys. Lett. 93 (2008) 3.
[13] W.J. Potscavage, A. Sharma, B. Kippelen, Critical interfaces in organic solar cells and their influence on the open-circuit voltage, Acc. Chem. Res. 42 (2009) 1758–1767.
[14] M. Brumbach, D. Placencia, N.R. Armstrong, Titanyl phthalocyanine/C-60 heterojunctions: band-edge offsets and photovoltaic device performance, J. Phys. Chem. C 112 (2008) 3142–3151.
[15] D. Placencia, W. Wang, R.C. Shallcross, K.W. Nebesny, M. Brumbach, N.R. Armstrong, Organic photovoltaic cells based on solvent-annealed, textured titanyl phthalocyanine/C60 heterojunctions, Adv. Funct. Mater. 19 (2009) 1913–1921.
[16] N. Li, B.E. Lassiter, R.R. Lunt, G. Wei, S.R. Forrest, Open circuit voltage enhancement due to reduced dark current in small molecule photovoltaic cells, Appl. Phys. Lett. 94 (2009) 3.
[17] D.Y. Kim, G. Sarasqueta, F. So, SnPc:C-60 bulk heterojunction organic photovoltaic cells with MoO3 interlayer, Sol. Energy Mater. Sol. Cells 93 (2009) 1452–1456.
[18] N.R. Armstrong, W.N. Wang, D.M. Alloway, D. Placencia, E. Ratcliff, M. Brumbach, Organic/organic′ heterojunctions: organic light emitting diodes and organic photovoltaic devices, Macromol. Rapid Commun. 30 (2009) 717–731.
[19] N.R. Armstrong, P.A. Veneman, E. Ratcliff, D. Placencia, M. Brumbach, Oxide contacts in organic photovoltaics: characterization and control of near-surface composition in indium-tin oxide (ITO) electrodes, Acc. Chem. Res. 42 (2009) 1748–1757.
[20] F. Yang, S.R. Forrest, Photocurrent generation in nanostructured organic solar cells, ACS Nano 2 (2008) 1022–1032.
[21] S.H. Park, A. Roy, S. Beaupre, S. Cho, N. Coates, J.S. Moon, D. Moses, M. Leclerc, K. Lee, A.J. Heeger, Bulk heterojunction solar cells with internal quantum efficiency approaching 100%, Nat. Photonics 3 (2009) 297–302.
[22] R. Timmreck, S. Olthof, K. Leo, M.K. Riede, Highly doped layers as efficient electron-hole recombination contacts for tandem organic solar cells, J. Appl. Phys. 108 (2010).
[23] R. Schueppel, R. Timmreck, N. Allinger, T. Mueller, M. Furno, C. Uhrich, K. Leo, M. Riede, Controlled current matching in small molecule organic tandem solar cells using doped spacer layers, J. Appl. Phys. 107 (2010).
[24] D. Wynands, B. Mannig, M. Riede, K. Leo, E. Brier, E. Reinold, P. Bauerle, Organic thin film photovoltaic cells based on planar and mixed heterojunctions between fullerene and a low bandgap oligothiophene, J. Appl. Phys. 106 (2009) 5.
[25] N. Li, S.R. Forrest, Tilted bulk heterojunction organic photovoltaic cells grown by oblique angle deposition, Appl. Phys. Lett. 95 (2009) 3.
[26] S.E. Gledhill, B. Scott, B.A. Gregg, Organic and nano-structured composite photovoltaics: an overview, J. Mater. Res. 20 (2005) 3167–3179.
[27] B.A. Gregg, Excitonic solar cells, J. Phys. Chem. B 107 (2003) 4688–4698.

[28] M. Riede, T. Mueller, W. Tress, R. Schueppel, K. Leo, Small-molecule solar cells – status and perspectives, Nanotechnology 19 (2008) 12.
[29] S. Günes, H. Neugebauer, N.S. Sariciftci, Conjugated polymer-based organic solar cells, Chem. Rev. 107 (2007) 1324–1338.
[30] M.C. Scharber, D. Wuhlbacher, M. Koppe, P. Denk, C. Waldauf, A.J. Heeger, C.L. Brabec, Design rules for donors in bulk-heterojunction solar cells – towards 10% energy-conversion efficiency, Adv. Mater. 18 (2006) 789–794.
[31] K. Vandewal, K. Tvingstedt, A. Gadisa, O. Inganas, J.V. Manca, On the origin of the open-circuit voltage of polymer–fullerene solar cells, Nat. Mater. 8 (2009) 904–909.
[32] T.J. Klofta, J. Danziger, P. Lee, J. Pankow, K.W. Nebesny, N.R. Armstrong, Photoelectrochemical and spectroscopic characterization of thin-films of titanyl phthalocyanine – comparisons with vanadyl phthalocyanine, J. Phys. Chem. 91 (1987) 5646–5651.
[33] T.D. Sims, J.E. Pemberton, P. Lee, N.R. Armstrong, Comparison of supramolecular aggregate structure and spectroscopic and photoelectrochemical properties of tetravalent and trivalent metal phthalocyanine thin films, Chem. Mater. 1 (1989) 26–34.
[34] J. Mizuguchi, G. Rihs, H.R. Karfunkel, Solid-state spectra of titanylphthalocyanine as viewed from molecular distortion, J. Phys. Chem. 99 (1995) 16217–16227.
[35] Z.D. Popovic, M.I. Khan, S.J. Atherton, A.M. Hor, J.L. Goodman, Study of carrier generation in titanyl phthalocyanine (TiOPc) by electric-field-induced quenching of integrated and time-resolved fluorescence, J. Phys. Chem. B 102 (1998) 657–663.
[36] S. Yamaguchi, Y. Sasaki, Primary process of photocarrier generation in Y-form titanyl phthalocyanine studied by electric-field-modulated picosecond time-resolved fluorescence spectroscopy, J. Phys. Chem. B 103 (1999) 6835–6838.
[37] S. Yamaguchi, Y. Sasaki, Primary carrier-generation process in Y-form and phase I titanyl phthalocyanines, Chem. Phys. Lett. 323 (2000) 35–42.
[38] M. Brinkmann, J.C. Wittmann, M. Barthel, M. Hanack, C. Chaumont, Highly ordered titanyl phthalocyanine films grown by directional crystallization on oriented poly(tetrafluoroethylene) substrate, Chem. Mater. 14 (2002) 904–914.
[39] K. Walzer, T. Toccoli, A. Pallaoro, A. Pallaoro, R. Verucchi, T. Fritz, K. Leo, A. Boschetti, S. Iannotta, Morphological and optical properties of titanyl phthalocyanine films deposited by supersonic molecular beam epitaxy (SuMBE), Surf. Sci. 573 (2004) 346–358.
[40] T. Dienel, R. Forker, K. Leo, T. Fritz, Optical differential reflectance spectroscopy of molecular thin films on a metal: evidence for strong oscillator strength increase, J. Phys. Chem. C 111 (2007) 14593–14596.
[41] N. Coppede, T. Toccoli, A. Pallaoro, F. Siviero, K. Walzer, M. Castriota, E. Cazzanelli, S. Iannotta, Polymorphism and phase control in titanyl phthalocyanine thin films grown by supersonic molecular beam deposition, J. Phys. Chem. A 111 (2007) 12550–12558.
[42] H. Fukagawa, S. Kera, T. Kataoka, S. Hosoumi, Y. Watanabe, K. Kudo, N. Ueno, The role of the ionization potential in vacuum-level alignment at organic semiconductor interfaces, Adv. Mater. 19 (2007) 665–668.
[43] H. Fukagawa, T. Kataoka, S. Hosourni, S. Kera, N. Ueno, Estimation of the electric dipole moment, polarizability and dielectric constant in organic monolayer system using UPS, J. Electron Spectrosc. Relat. Phenom. 156 (2007) 37.
[44] S. Kera, H. Yamane, H. Fukagawa, T. Hanatani, K.K. Okudaira, K. Seki, N. Ueno, Angle resolved UV photoelectron spectra of titanyl phthalocynine monolayer film on graphite, J. Electron Spectrosc. Relat. Phenom. 156 (2007) 135–138.
[45] H. Fukagawa, H. Yamane, S. Kera, K.K. Okudaira, N. Ueno, Experimental estimation of the electric dipole moment and polarizability of titanyl phthalocyanine using ultraviolet photoelectron spectroscopy, Phys. Rev. B 73 (2006) (2006).
[46] P. Palmgren, T. Claesson, A. Onsten, B. Agnarsson, M. Mansson, O. Tiernberg, M. Gothelid, Band bending and structure dependent HOMO energy at the ZnO(0 0 0 1)–titanyl phthalocyanine interface, Surf. Sci. 601 (2007) 4222–4226.
[47] S. Kera, Y. Yabuuchi, H. Yamane, H. Setoyama, K.K. Okudaira, A. Kahn, N. Ueno, Impact of an interface dipole layer on molecular level alignment at an organic–conductor interface studied by ultraviolet photoemission spectroscopy, Phys. Rev. B 70 (2004).
[48] X.F. Zhang, Y. Wang, L.H. Niu, Titanyl phthalocyanine and its soluble derivatives: highly efficient photosensitizers for singlet oxygen production, J. Photochem. Photobiol. A: Chem. 209 (2010) 232–237.
[49] B.P. Rand, J.G. Xue, F. Yang, S.R. Forrest, Organic solar cells with sensitivity extending into the near infrared, Appl. Phys. Lett. (2005) 87.
[50] R. Schlaf, B.A. Parkinson, P.A. Lee, K.W. Nebesny, N.R. Armstrong, HOMO/LUMO alignment at PTCDA/ZnPc and PTCDA/ClInPc heterointerfaces determined by combined UPS and XPS measurements, J. Phys. Chem. B 103 (1999) 2984–2992.
[51] M.L. Anderson, V.S. Williams, T.J. Schuerlein, G.E. Collins, C.D. England, L.K. Chau, P.A. Lee, K.W. Nebesny, N.R. Armstrong, RHEED and optical charcterization of ordered multilayers of phthalocyanine/C60 and phthalocyanine-tetracarboxylicaciddianydride (PTCDA), Surf. Sci. 309 (1994) 551–558.
[52] D. Placencia, W.W. Jeremy Gantz, Judith L. Jenkins, N.R. Armstrong, Titanyl phthalocyanine polymorphs as textured donor layers in organic solar cells, J. Phys. Chem. C, submitted for publication.
[53] D. Steffen, S. Ingo, H. Georg, O. Martin, H. Anja, L.J. Robert, P.R. Jurgen, K. Norbert, Controlling energy level offsets in organic/organic heterostructures using intramolecular polar bonds, Appl. Phys. Lett. 94 (2009) 033304.
[54] I. Salzmann, S. Duhm, R. Opitz, R.L. Johnson, J.P. Rabe, N. Koch, Structural and electronic properties of pentacene–fullerene heterojunctions, J. Appl. Phys. 104 (2008) 11.
[55] N. Koch, A. Gerlach, S. Duhm, H. Glowatzki, G. Heimel, A. Vollmer, Y. Sakamoto, T. Suzuki, J. Zegenhagen, J.P. Rabe, F. Schreiber, Adsorption-induced intramolecular dipole: correlating molecular conformation and interface electronic structure, J. Am. Chem. Soc. 130 (2008) 7300–7304.
[56] S. Duhm, G. Heimel, I. Salzmann, H. Glowatzkl, R.L. Johnson, A. Vollmer, J.P. Rabe, N. Koch, Orientation-dependent ionization energies and interface dipoles in ordered molecular assemblies, Nat. Mater. 7 (2008) 326–332.
[57] M. Brumbach, in: Chemistry, Ph.D. Dissertation, University of Arizona, Tucson, 2007.
[58] D.M. Alloway, Ph.D. Dissertation, University of Arizona, 2008.
[59] V. Shrotriya, G. Li, Y. Yao, T. Moriarty, K. Emery, Y. Yang, Accurate measurement and characterization of organic solar cells, Adv. Funct. Mater. 16 (2006) 2016–2023.
[60] D.M. Alloway, M. Hofmann, D.L. Smith, N.E. Gruhn, A.L. Graham, R. Colorado, V.H. Wysocki, T.R. Lee, P.A. Lee, N.R. Armstrong, Interface dipoles arising from self-assembled monolayers on gold: UV-photoemission studies of alkanethiols and partially fluorinated alkanethiols, J. Phys. Chem. B 107 (2003) 11690–11699.
[61] M. Tsushima, Y. Motojima, N. Ikeda, H. Yonehara, H. Etori, C. Pac, T. Ohno, Excitons and a charge-separated pair in thin crystals of oxotitanium(IV) phthalocyanine as revealed by femtosecond time-resolved absorption and time-correlated single photon counting, J. Phys. Chem. A 106 (2002) 2256–2264.
[62] K. Nakai, K. Ishii, N. Kobayashi, H. Yonehara, C. Pac, Theoretical calculations of the electronic absorption spectra of oxotitanium(IV) phthalocyanine in the solid state, J. Phys. Chem. B 107 (2003) 9749–9755.
[63] N. Coppede, M. Castriota, E. Cazzanelli, S. Forti, G. Tarabella, T. Toccoli, K. Walzer, S. Iannotta, Controlled polymorphism in titanyl phthalocyanine on mica by hyperthermal beams: a micro-Raman analysis, J. Phys. Chem. C 114 (2010) 7038–7044.
[64] M. Durmus, T. Nyokong, Synthesis, photophysical and photochemical properties of tetra- and octa-substituted gallium and indium phthalocyanines, Polyhedron 26 (2007) 3323–3335.
[65] V. Chauke, M. Durmus, T. Nyokong, Photochemistry, photophysics and nonlinear optical parameters of phenoxy and tert-butylphenoxy substituted indium(III) phthalocyanines, J. Photochem. Photobiol. A: Chem. 192 (2007) 179–187.
[66] Y. Chen, Y. Araki, D. Dini, Y. Liu, O. Ito, M. Fujitsuka, The steady-state and time-resolved photophysical properties of a dimeric indium phthalocyanine complex, Mater. Chem. Phys. 98 (2006) 212–216.
[67] K.J. Wynne, Crystal and molecular-structure of chloro(phthalocyaninato)gallium(III), Ga(Pc)Cl, and chloro(phthalocyaninato)aluminum(III), Al(Pc)Cl, Inorg. Chem. 23 (1984) 4658–4663.
[68] W. Hiller, J. Strahle, W. Kobel, M. Hanack, Synthesis and properties of new one-dimensional conductors. 14. Polymorphism, conductivity and crystal-structure of oxo-phthalocyaninato titanium(IV), Z. Kristallogr. 159 (1982) 173–183.
[69] F. Yang, M. Shtein, S.R. Forrest, Controlled growth of a molecular bulk heterojunction photovoltaic cell, Nat. Mater. 4 (2005) 37–41.
[70] D.R.T. Zahn, G.N. Gavrila, M. Gorgoi, The transport gap of organic semiconductors studied using the combination of direct and inverse photoemission, Chem. Phys. 325 (2006) 99–112.
[71] J. Hwang, A. Wan, A. Kahn, Energetics of metal–organic interfaces: new experiments and assessment of the field, Mater. Sci. Eng.: R: Rep. 64 (2009) 1–31.
[72] A. Kahn, W. Zhao, W.Y. Gao, H. Vazquez, F. Flores, Doping-induced realignment of molecular levels at organic–organic heterojunctions, Chem. Phys. 325 (2006) 129–137.

[73] D. Cahen, A. Kahn, Electron energetics at surfaces and interfaces: concepts and experiments, Adv. Mater. 15 (2003) 271–277.
[74] J. Hwang, E.G. Kim, J. Liu, J.L. Bredas, A. Duggal, A. Kahn, Photoelectron spectroscopic study of the electronic band structure of polyfluorene and fluorene–arylamine copolymers at interfaces, J. Phys. Chem. C 111 (2007) 1378–1384.
[75] H. Ishii, K. Sugiyama, E. Ito, K. Seki, Energy level alignment and interfacial electronic structures at organic metal and organic organic interfaces, Adv. Mater. 11 (1999) 605.
[76] J.H. Weaver, J.L. Martins, T. Komeda, Y. Chen, T.R. Ohno, G.H. Kroll, N. Troullier, R.E. Haufler, R.E. Smalley, Electronic-structure of solid C60 – experiment and theory, Phys. Rev. Lett. 66 (1991) 1741–1744.
[77] X.H. Kong, M. Wang, S.B. Lei, Y.L. Yang, C. Wang, Electronic sensory behavior of titanylphthalocyanine revealed by scanning tunneling spectroscopy and cyclic voltammetry methods, J. Mater. Chem. 16 (2006) 4265–4269.
[78] L.K. Chau, C.D. England, S.Y. Chen, N.R. Armstrong, Visible absorption and photocurrent spectra of epitaxially deposited phthalocyanine thin-films – interpretation of exciton coupling effects, J. Phys. Chem. 97 (1993) 2699–2706.
[79] S.W. Cho, L.F.J. Piper, A. DeMasi, A.R.H. Preston, K.E. Smith, K.V. Chauhan, P. Sullivan, R.A. Hatton, T.S. Jones, Electronic structure of C60/phthalocyanine/ITO interfaces studied using soft X-ray spectroscopies, J. Phys. Chem. C 114 (2010) 1928–1933.
[80] S.W. Cho, L.F.J. Piper, A. DeMasi, A.R.H. Preston, K.E. Smith, K.V. Chauhan, P. Sullivan, R.A. Hatton, T.S. Jones, Electronic structure of C-60/phthalocyanine/ITO interfaces studied using soft X-ray spectroscopies, J. Phys. Chem. C 114 (2010) 1928–1933.
[81] S.R. Forrest, The limits to organic photovoltaic cell efficiency, MRS Bull. 30 (2005) 28–32.
[82] L.J.A. Koster, V.D. Mihailetchi, P.W.M. Blom, Ultimate efficiency of polymer/fullerene bulk heterojunction solar cells, Appl. Phys. Lett. 88 (2006).
[83] V. Chauhan, R. Hatton, P. Sullivan, T. Jones, S.W. Cho, L. Piper, A. deMasi, K. Smith, Elucidating the factors that determine the open circuit voltage in discrete heterojunction organic photovoltaic cells, J. Mater. Chem. 20 (2010) 1173–1178.
[84] K.V. Chauhan, P. Sullivan, J.L. Yang, T.S. Jones, Efficient organic photovoltaic cells through structural modification of chloroaluminum phthalocyanine/fullerene heterojunctions, J. Phys. Chem. C 114 (2010) 3304–3308.
[85] K. Vandewal, K. Tvingstedt, A. Gadisa, O. Inganas, J.V. Manca, Relating the open-circuit voltage to interface molecular properties of donor:acceptor bulk heterojunction solar cells, Phys. Rev. B 81 (2010) 8.
[86] S. Yoo, B. Domercq, B. Kippelen, Intensity-dependent equivalent circuit parameters of organic solar cells based on pentacene and C-60, J. Appl. Phys. 97 (2005) 9.

Organic Electronics 12 (2011) 394–403

Contents lists available at ScienceDirect

Organic Electronics

journal homepage: www.elsevier.com/locate/orgel

Calculation of solid state molecular ionisation energies and electron affinities for organic semiconductors

P.E. Schwenn [a], P.L. Burn [b], B.J. Powell [a,*]

[a] Centre for Organic Photonics and Electronics, School of Mathematics and Physics, University of Queensland, QLD 4072, Australia
[b] Centre for Organic Photonics and Electronics, School of Chemistry and Molecular Biosciences, University of Queensland, QLD 4072, Australia

ARTICLE INFO

Article history:
Received 31 October 2010
Received in revised form 23 November 2010
Accepted 26 November 2010
Available online 9 December 2010

Keywords:
Density functional theory
Polarizable continuum model
Ionisation energy
Electron affinity
Cancellation of errors

ABSTRACT

Energy level engineering has become one of the central ideas in organic optoelectronics; particularly in the field of organic photovoltaics. However, this paradigm has led to significant ambiguities and errors in the literature. To investigate and address these issues we calculate solid state ionisation energies and electron affinities of a range of organic molecular semiconductors from density functional theory and the polarizable continuum model. We show that the differences between these results and measurements from (inverse) photoemission are on the same scale as the differences between the measured values reported by different groups. We compare our results with *in vacuo* calculations and estimates of the ionisation energies and electron affinities from the eigenvalues of the Kohn–Sham equations. *In vacuo* calculations overestimate the ionisation energies measured in the solid state, but underestimate solid state electron affinities. However, the Kohn–Sham eigenvalues predict the measured ionisation energies nearly as well as the full calculation. However, we show that the apparent accuracy of the Kohn–Sham eigenvalues is fortuitous and arises from the cancellation of the errors due to the use of Kohn–Sham molecular orbital energies as predictions of ionisation energies and electron affinities and the neglect of the polarizable solid state environment. These results stress the importance of descriptions based on molecular states rather than molecular orbitals when designing and characterising materials for organic electronic and optoelectronic devices.

© 2010 Elsevier B.V. All rights reserved.

1. Introduction

Devices based on the optoelectronic and electronic properties of organic molecules are rapidly coming to market. Yet despite the maturity of the experimental and technological aspects of the field [1] the theoretical understanding of the electronic and optoelectronic properties of organic molecular semiconductors is far from complete. The lack of predictive power in current models of such materials is a major hurdle in the goal of rationally designing new compounds for organic electronic and photonic applications. Thus, most improvements in organic electronic materials have been brought about by a combination of empirical rules and trial and error. This should be contrasted with the state-of-play in inorganic electronics, where the deep theoretical underpinnings of Fermi liquid theory and band structure [2] have lead to important design criteria from the very beginning of the field [3–5].

Empirical design rules in organic electronics are often based on the concept of engineering the energy levels of the frontier molecular orbitals, particularly the highest occupied molecular orbital (HOMO) and lowest unoccupied molecular orbital (LUMO) [6]. Establishing a firm theoretical basis for these empirical rules is somewhat problematic as molecular orbitals are an abstraction from molecular orbital theories [7]. Molecular orbitals are not well defined once electronic correlations are included, and it is well known that electronic correlations are

* Corresponding author.
E-mail address: bjpowell@gmail.com (B.J. Powell).

1566-1199/$ - see front matter © 2010 Elsevier B.V. All rights reserved.
doi:10.1016/j.orgel.2010.11.025

extremely important in organic molecules [7]. In particular, it is important to stress that one cannot measure molecular orbital energies, even in principle. Rather, one can for example measure the oxidation or reduction potential, ionisation energy (IE), electron affinity (EA), optical absorption or emission spectra of molecules. Outside of the very simplest molecular orbital theories one does not expect any of these properties to equal any other; with the differences resulting from electronic correlations [7].

It is easy to understand, on a purely physical basis, why electronic correlations mean that the electron affinity is not the same as molecular orbital energies. When an electron is added to the system, one does not only have to account for the energy of that electron; that electron now interacts with all of the other electrons in the molecule. Further, this changes the details of the correlations between the other electrons. Similarly, when an electron is removed one must also account for all the interactions that are no longer there. These effects can be very large in organic molecules that form electronically active materials [8,9]. Further, the geometry of a molecule will typically relax once an electron is added/removed, further changing the energy [10].

In practice, further complications arise because the quantities of interest, such as the IE and EA, depend strongly on the environment surrounding the molecule [11]. This means that the electrochemical measurements of the oxidation or reduction potential in solution will typically differ from measurements of the solid state IE by, say, ultraviolet photoemission spectroscopy (UPS) and the solid state EA using inverse photoemission spectroscopy (IPES). Furthermore, these differences are typically on the scale of changes one wants to control to optimise material design [12], for example, the offset in the energy between a donor–acceptor pair required for so-called 'exciton dissociation' in bulk heterojunction solar cells. Therefore, any theoretical approach should include a description of the environment sufficient to capture these effects.

There have been a number of recent studies where density functional theory (DFT) was used to predict the IE or EA for broad ranges of the molecules used in organic electronics [13–16]. The choice of DFT is motivated because it is computationally much cheaper than more accurate methods, yet still provides reasonable accuracy. The cost of the computational method is important if we are to eventually screen large numbers of molecules for an application. We have therefore limited our approach below to low cost computational methods. Both Djurovich et al. [13] and Nayak et al. [14,15] treated density functional theory as a semi-quantitative approach and, by studying a large selection of molecules, demonstrated correlations between their calculations and experimental measurements. In principle such correlations, once established, could be used to rescale calculated data to make quantitative predictions, although this would be rather unsatisfactory unless one has a clear understanding of when such a rescaling is likely to work and when it should be expected to fail. Alternatively, one could also ask how well the absolute values predicted by DFT compare with experiment. This has clear advantages, but the inherent limitations of the approximations in currently available functionals may mean that accurate predictions are not possible.

The accurate calculation of IEs and EAs from molecular orbital energies is a particular problem for DFT. This long-standing problem is closely related to the 'band gap problem' in solid state physics [17]. To understand the root of this problem a brief discussion of the foundations of DFT [18] is required. The twin foundations of DFT are the Hohenberg–Kohn theorem, which proves that the ground state energy of a molecule or solid can be expressed as a functional of the electron density, and the Kohn–Sham scheme, which provides a practical framework to calculate the electron density and hence the total energy. To do this Kohn and Sham introduced a set of differential equations, know as the Kohn–Sham equations, that have a strong mathematical resemblance to the approximate form of the Schrödinger equation obtained from the Hartree–Fock (molecular orbital) approximation [18].

It is therefore tempting to treat the solutions of the Kohn–Sham equations as molecular orbitals (in molecular systems) or bands (in periodic structures). However, there is no theoretical justification for this interpretation of the Kohn–Sham equations [19]. Nevertheless, this interpretation is frequently employed and has been used to, at least semi-quantitatively, describe materials in a broad range of contexts [16,18]. However, this additional approximation (on top of those already inherent in approximating the exchange-correlation functional) significantly reduces the accuracy of DFT. A classic example is the band structure of Si. The eigenvalues of the Kohn–Sham equations do reproduce, qualitatively, what is known experimentally about the band structure of Si, such as the indirect gap and the locations of the valence band maxima and conduction band minima; but, the band gap calculated is $\sim$50% larger than that measured experimentally [17]. Similar problems are found in calculating the IEs and EAs and optical gaps in molecular systems [18,20].

An important result about the density functional formalism is Janak's theorem [21], which proves that the exact functional could be used to calculate the Lagrange multiplier associated with conservation of particle number. In a solid this corresponds to the chemical potential and in a molecule it is the IE, [22,23]. This suggests that the Kohn–Sham HOMO energy should predict the IE, although this is, of course, approximate for approximate functionals. However, there is no theoretical basis for this for other orbitals, and in particular the Kohn–Sham LUMO is not required to correspond to the EA even for the exact functional. It is well known that, in practice, electron affinities estimated from Kohn–Sham LUMO eigenvalues are less accurate than the corresponding ionisation energies estimated from the Kohn–Sham HOMO energies [16,17,24]. Nevertheless, this approach has found widespread application in the organic electronics literature [13,16].

In this paper we consider eleven molecules with application in organic electronics (shown in Fig. 1). We calculate their IE and EA by three different DFT-based methods: (i) from the Kohn–Sham eigenvalues; (ii) directly from the ground state energies of the relevant charge states and (iii) by method (ii), but including the polarizable

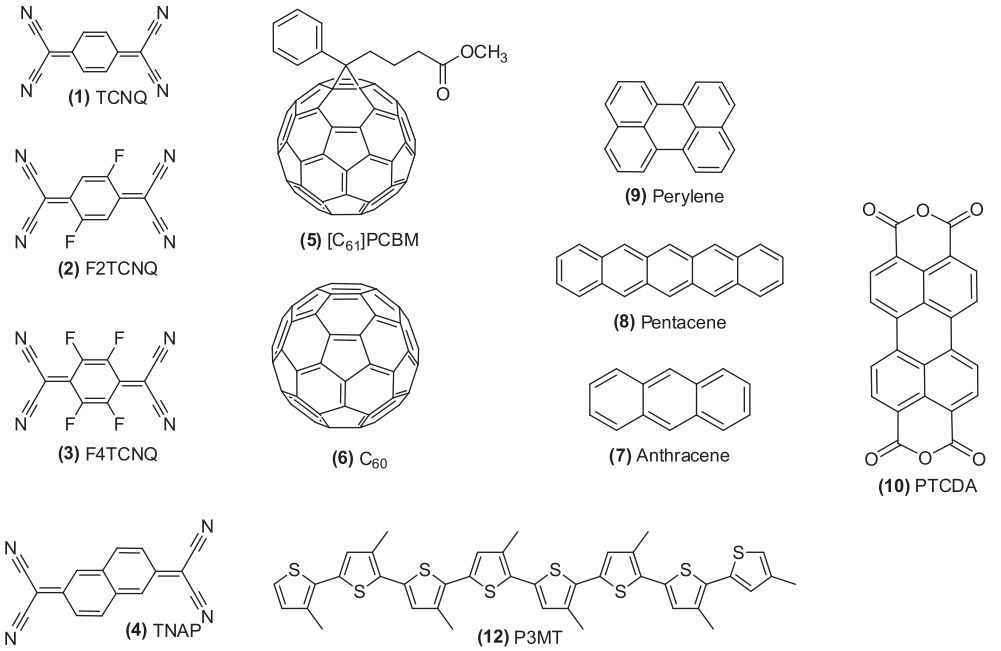

Fig. 1. The molecules studied in this paper: (1) tetracyanoquinodimethane (TCNQ); (2) difluoro-tetracyanoquinodimethane (F2TNCQ); (3) tetrafluoro-tetracyanoquinodimethane (F4TCNQ); (4) tetracyanonaphthoquinodimethane (TNAP); (5) [6,6]-phenyl-C_{61}-butyric acid methyl ester (PCBM); (6) Buckminsterfullerene (C_{60}); (7) anthracene; (8) pentacene; (9) perylene (or dibenzanthracene); (10) perylenetetracarboxylic acid dianhydride (PTCDA); (11) poly-(3-methylthiophene) (P3MT), which is a model compound for poly(3-n-hexylthiophene) (P3HT).

environment of the solid state via the polarizable continuum model (PCM). Method (iii) reproduces both the trends and absolute values found in experiments accurately. However, surprisingly, method (i) performs almost as well as method (iii) and significantly outperforms method (ii). We show that this is because of a cancellation of errors, specifically those due to the approximation that molecular orbital energies approximate ionisation energies and electron affinities and the neglect of the environment.

2. Methods

All density functional calculations were performed in the GAMESS-US software package [25] with the B3LYP hybrid functional [26,27] in the 6−31+G basis set. This, relatively small, basis set was chosen for compatibility with future studies of larger numbers of molecules and larger molecules. Diffuse functions were used to better represent the loosely held extra charges in anions [28,29]. Extensive benchmarking on C_{60} showed that, despite its small size, this basis set gave good agreement with larger basis sets and with literature calculated and measured values of the IE and EA [30–34]. The geometries of the molecules were optimised in DFT so as to keep the procedure independent of experimental data.

The PCM [35] assumes that a cavity made of a continuous solvent surrounds each 'solute' molecule. In the case of a single component amorphous molecular solid, which we consider here, the 'solute' and 'solvent' molecules are the same species. However, this does not increase the complexity of the problem as the solvent is simply described by its dielectric constant, ε, and radius, R. The charges on the solute molecule inside the cavity interact with this dielectric medium, causing it to polarize. This induced polarization in the solvent medium then interacts back on the wavefunction of the solute. The energy of the resultant interaction is minimized self consistently.

The geometry of the molecule and ion were optimised at the B3LYP/6−31+G level *in vacuo*. ChemDraw 3D Ultra version 12.0 was used to calculated the Connolly molecular area (CMA) of the neutral molecule. The CMA is determined by the contact surface created when a spherical probe (with a standard radius of 1.4 Å) representing the solvent molecule is rolled over the molecular model [36]. This area defines a sphere of the same surface area. The radius of this sphere, $R = \sqrt{A/4\pi}$, was used to define the 'radius' of the solvent molecule.

The Clausius–Mossotti equation [2] can be solved for ε, which yields

$$\varepsilon = \left(1 + \frac{8\pi\bar{\alpha}}{3v}\right)\left(1 - \frac{4\pi\bar{\alpha}}{3v}\right)^{-1}, \quad (1)$$

where v is volume occupied by a single molecule, which we take as the Connolly molecular volume (CMV), the volume of a sphere with an area equal to the CMA, $\bar{\alpha}$ is the isotropic component of the molecular polarizability, $\bar{\alpha} = \frac{1}{3}\sum_i \alpha_{ii}$, and the α_{ii} are the diagonal matrix elements of the first order polarizability tensor. The polarizability was calculated for each molecule from DFT. A sequence of fields were applied to the molecule and the polarizabilities extracted [37]. The step size for the applied field strength was 0.001 in atomic units. Four layers of points

were chosen on successive fused van der Waals spheres. The sum of fitted atomic charges were constrained to reproduce the total molecular charge.

3. Results and discussion

3.1. Kohn–Sham eigenvalues

The Kohn–Sham HOMO energies ($HOMO_{KS}$) and the ionisation energies measured by ultraviolet photoemission spectroscopy (I_{UPS}) are listed in Table 1 and compared in Fig. 2. A linear regression analysis (to the form $I_{UPS} = c - m \times HOMO_{KS}$) resulted in a slope $m = 0.91 \pm 0.10$ and intercept $c = 0.5 \pm 0.7$ with a linear least squares correlation co-efficient $r^2 = 0.89$, which show that this approach correctly predicts the trends observed across this series of molecules. Note that in Fig. 2 (and, indeed, Figs. 3–7) we do not show the line of best fit, rather the line indicates perfect agreement between the prediction and experiment. The root mean squared deviation (RMSD) of $HOMO_{KS}$ from the I_{UPS} was 0.4 eV or equivalently the mean absolute deviation (MAD) was 4.1%. Considering the extremely low computational cost of these calculations this is rather encouraging accuracy, which has been noted previously on the basis of similar calculations [13,16].

In Fig. 3 a similar comparison is made for the energies of the lowest unoccupied Kohn–Sham molecular orbital ($LUMO_{KS}$) and the electron affinity measured by inverse photoemission spectroscopy (A_{IPES}). The data are listed in Table 2. A linear regression results in a slope $m = 0.80 \pm 0.09$, intercept $c = 0.6 \pm 0.4$ and $r^2 = 0.89$. The correlation is clearly not as strong as that between the $HOMO_{KS}$ and I_{UPS}. Further, the slope is further from unity, the intercept is further from the origin, and the RMSD (0.50 eV) and the MAD (13%) are both significantly larger than for the data shown in Fig. 2. Thus, it is clear that the calculations of the $LUMO_{KS}$ predict A_{IPES} less accurately than calculations of $HOMO_{KS}$ predict the I_{UPS}. While the qualitative trends are reasonable, the quantitative accuracy is not sufficient to describe the subtle changes needed to design molecules for organic electronic applications. This is, of course, consistent with what one expects from the foundations of DFT [17,21] and several decades of DFT literature [16,17,20]. The level of accuracy of prediction of electron affinities provided by the Kohn–Sham energies may be sufficient for some purposes, but a more accurate method would be a significant advantage. In particular, the RMSD, 0.50 eV, is rather large considering the scale on which one would like to tune interactions to design better materials for organic electronic and optoelectronic applications.

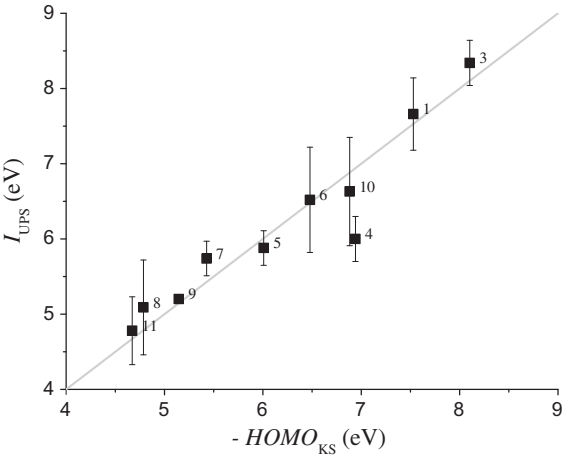

Fig. 2. Comparison of the ionisation energy measured by UPS, I_{UPS}, (see Section 3.5 and Table 1 for references and error analysis) with the Kohn–Sham HOMO, $HOMO_{KS}$, for the compounds shown in Fig. 1 where the experimental data exists in the literature. Surprisingly good agreement is found between theory and experiment. The line is $-HOMO_{KS} = I_{UPS}$.

Table 1
Comparison of the literature values of ionisation energies measured by ultraviolet photoemission spectroscopy (UPS) to the calculated energies of the Kohn–Sham HOMOs ($HOMO_{KS}$), gas phase and solid state vertical (I_g^v, I_s^v) and adiabatic (I_g^a, I_s^a) ionisation energies. All values in eV. Quoted errors on the experimental data indicate two standard deviations in the range of the literature values. The absence of errors indicates that we were only able to identify one reported experimental value. We were unable to identify any reports of the ionization energy for F2TCNQ.

Molecule	I_{UPS} (eV)	References	$HOMO_{KS}$	I_g^v	I_g^a	I_s^v	I_s^a
TCNQ (1)	7.7 ± 0.5	[38–40]	7.5	9.0	9.0	7.3	7.3
F2TCNQ (2)	–	–	7.8	9.3	9.3	7.6	7.6
F4TCNQ (3)	8.3	[41]	8.1	9.6	9.5	7.9	7.8
TNAP (4)	6.0	[38]	6.9	8.3	8.2	6.6	6.6
PCBM (5)	5.9 ± 0.2	[42,43]	6.0	7.1	7.0	6.2	6.2
C_{60} (6)	6.5 ± 0.7	[42,30,44,43,45–48,30,49,31,50]	6.5	7.7	7.6	6.3	6.2
Anthracene (7)	5.7 ± 0.2	[38,39,51–57]	5.4	7.0	7.0	5.8	5.7
Pentacene (8)	5.1 ± 0.6	[38,58–60]	4.8	6.1	6.0	5.0	5.0
Perylene (9)	5.2	[38]	5.1	6.6	6.5	5.5	5.4
PTCDA (10)	6.6 ± 0.7	[61–69]	6.9	8.2	8.1	6.7	6.7
P3MT (11)	4.8 ± 0.45[a]	[43,70–76]	4.7	5.5	5.4	4.9	4.8
		RMSD[b]	0.35	1.4	1.3	0.32	0.32
		MAD[c]	4.1%	22%	20%	4.1%	3.9%

[a] For P3HT.
[b] Root mean square deviation, RMSD = $\sqrt{\frac{\sum (I_{DFT} - I_{UPS})}{N}}$
[c] Mean absolute deviation, MAD = $\frac{1}{N}\sum |\frac{I_{UPS} - I_{DFT}}{I_{UPS}}| \times 100\%$

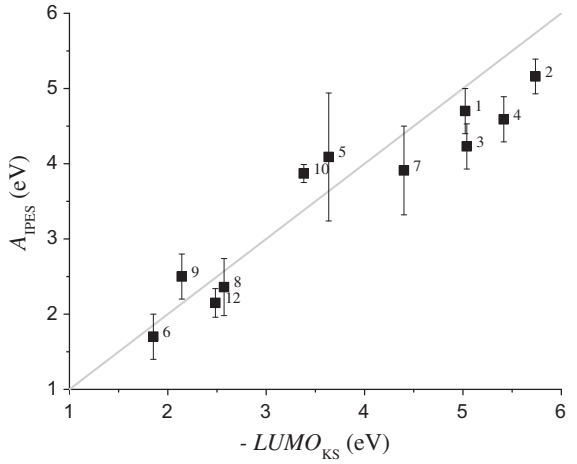

Fig. 3. Comparison of electron affinity measured by IPES, A_{IPES}, (see Section 3.5 and Table 2 for references and error analysis) with Kohn–Sham LUMO ($LUMO_{KS}$) for the compounds shown in Fig. 1 where the experimental data exists in the literature. The agreement with experiment is not as strong as that seen in Fig. 2, but qualitative trends are reproduced, as is indicated by a linear regression analysis, $r^2 = 0.89$ (not shown). The line is $-LUMO_{KS} = A_{IPES}$.

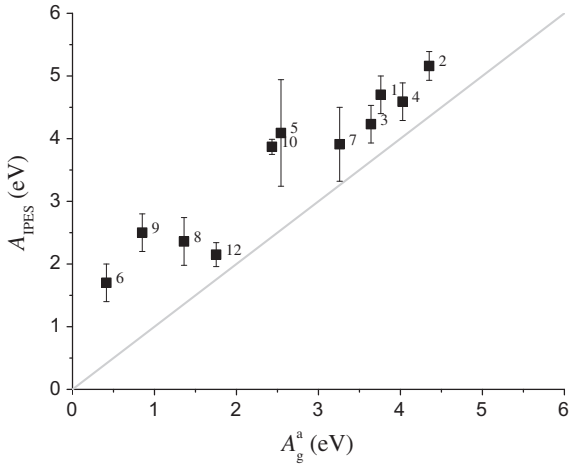

Fig. 5. Comparison of experimental electron affinities measured by IPES, A_{IPES}, (see Section 3.5 and Table 2 for references and error analysis) and calculated *in vacuo* electron affinities, A^a_g. A^a_g consistently underestimates A_{IPES}, as one would expect from Eq. 2b, as the polarizable solid state environment, which stabilises the anion, is not accounted for in the calculation. The line is $A^a_g = A_{IPES}$.

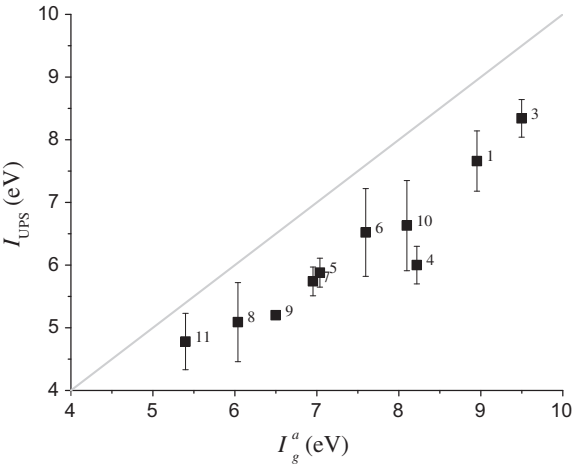

Fig. 4. Comparison of experimental ionisation energies measured by UPS, I_{UPS}, (see Section 3.5 and Table 1 for references and error analysis) and calculated *in vacuo* ionisation energies, I^a_g. I^a_g consistently overestimates I_{UPS}, as one would expect from Eq. 2a, as the polarizable solid state environment, which stabilises the cation, is not accounted for in the calculation. The line is $I^a_g = I_{UPS}$.

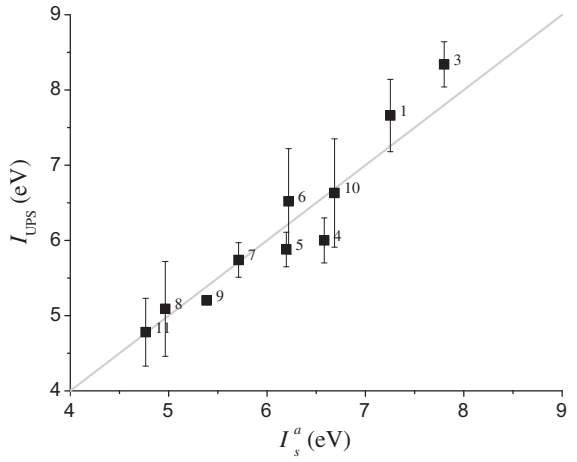

Fig. 6. Comparison of experimental ionisation energies measured by UPS, I_{UPS}, (see Section 3.5 and Table 1 for references and error analysis) and calculated solid state ionisation energies, I^a_s. I^a_s provides a consistently accurate prediction of I_{UPS}. The line is $I^a_s = I_{UPS}$.

3.2. Direct calculation of the ionisation energy and electron affinity

Although, density functional formalism does not imply any correspondence between the Kohn–Sham eigenvalues and, say, the electron affinity, the ionisation energy, I, and the electron affinity, A, are defined in terms of the differences between the *ground state* energies of different charge states, specifically,

$$I \equiv E_0(+1) - E_0(0) \tag{2a}$$

$$A \equiv E_0(0) - E_0(-1), \tag{2b}$$

where $E_0(q)$ is the ground state energy of the molecule with charge q. Ground state energies are what we do have general expectations of calculating in DFT and what DFT gives most accurate answers for. Therefore, a natural way to improve the accuracy of the DFT calculation is to directly calculate $E_0(q)$ for the relevant charge states. This approach has recently been applied to organic molecules that form strongly correlated molecular metals, Mott insulators and superconductors [8,9]. One subtlety in this calculation is whether one considers the vertical ionisation energy, I^v_g (where the molecular geometry is kept fixed in the neutral ground state geometry irrespective of the charge on the molecule) or the adiabatic ionisation energy, I^a_g (where the geometry is relaxed in the ionic state). Similarly, one

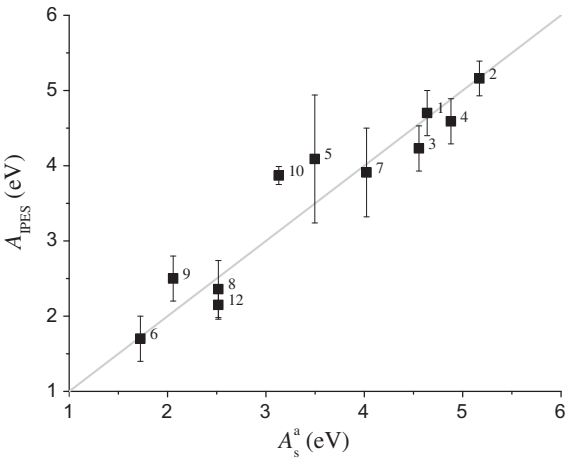

Fig. 7. Comparison of experimental electron affinities measured by IPES, A_{IPES}, (see Section 3.5 and Table 2 for references and error analysis) and calculated solid state electron affinities, A_s^a. For the most part A_s^a provides an accurate prediction of A_{IPES}: outliers are discussed in Section 3.3. The line is $A_s^a = A_{IPES}$.

can calculate either the vertical electron affinity, A_g^v, or the adiabatic electron affinity, A_g^a. However, as can be seen in Tables 1 and 2, the differences between the vertical and adiabatic energies are relatively small compared to the other uncertainties in the problem. Therefore we will focus primarily of the adiabatic energies.

We carried out direct calculations of the IE and EA for the molecules shown in Fig. 1. The calculated ionisation energies and electron affinities are listed in Tables 1 and 2, respectively. Comparisons with the experimentally measured ionisation energies and electron affinities are presented Figs. 4 and 5, respectively. What is immediately evident from these figures is that the calculated EA and IE give significantly worse predictions of experimental results than a naive interpretation of the Kohn–Sham eigenvalues. For the IE there is a MAD ≈20% while for the EA this increases to >30%. These correspond to RMSDs in excess of 1 eV, meaning the direct comparison of the calculated IE/EA is too inaccurate to be of any real value. However, it is interesting to note that the correlation between the calculated and measured IEs/EAs is significant: a linear regression gives $r^2 > 0.89$ ($m = 0.84 \pm 0.10$, $c = 0.0 \pm 0.7$) for the IE and $r^2 > 0.89$ ($m = 0.83 \pm 0.09$), $c = 1.4 \pm 0.3$) for the EA, showing that this method also captures the overall trends seen experimentally.

It is important to stress that the direct calculation of the IE/EA is known from the foundations of density functional theory to be an improvement over the values taken from the Kohn–Sham eigenvalues. Therefore, the finding that the Kohn–Sham eigenvalues are much closer to the experimentally measured values than the direct calculation suggests that this agreement is fortuitous and presumably results from some uncontrolled cancellation of errors.

The direct calculations overestimate the IE and underestimate EA. Note that all of the calculations reported above are for molecules *in vacuo*. However, the measurements were performed in the solid state. The solid provides a polarizable environment for the molecule, which will stabilise the ionic species, lowering the IE and increasing the EA (cf. Eq. (2)). Thus, one expects the *in vacuo* IE to overestimate the solid state IE and the *in vacuo* EA to underestimate the solid state EA. Thus, at least qualitatively, the direct calculation of the IE and EA is consistent with expectations, whereas the values from the Kohn–Sham eigenvalues are not! In order to address the complication of the solid state environment we repeated the calculations above with the environment included via the PCM.

3.3. Solvation effects in the solid state

The PCM requires the knowledge of the dielectric constant, ε, and the effective radius of the molecule. In order to keep our methodology viable as an approach to screen large numbers of candidate molecules we have calculated ε from first principles even where experimental values are available. In Table 3 we report the calculated molecular polarizabilites, the CMA, the CMV, the permittivities calculated from Eq. 1 and, where available, the measured permittivities, ε_{exp}, for each of the molecules in Fig. 1. For all

Table 2
Comparison of the literature values of electron affinities experimentally measured by inverse photoemission spectroscopy (IPES) to the calculated Kohn–Sham energies ($LUMO_{KS}$), gas phase and solid state vertical (A_g^v, A_s^v) and adiabatic (A_g^a, A_s^a) electron affinities. All values in eV. Quoted errors on the experimental data indicate two standard deviations in the range of the literature values. The absence of errors indicates that we were only able to identify one reported experimental value.

Molecule	A_{IPES} (eV)	References	$LUMO_{KS}$	A_g^v	A_g^a	A_s^v	A_s^a
TCNQ (1)	4.2	[77]	5.0	3.5	3.6	4.4	4.6
F2TCNQ (2)	4.6	[77]	5.4	3.9	4.0	4.8	4.9
F4TCNQ (3)	5.2 ± 0.2	[41,77]	5.7	4.2	4.4	5.0	5.2
TNAP (4)	4.7	[77]	5.0	3.6	3.8	4.5	4.6
PCBM (5)	3.9 ± 0.1	[42,43,77]	3.4	2.3	2.4	3.0	3.1
C_{60} (6)	3.5 ± 0.9	[42,43,77,46,31]	3.6	2.5	2.5	3.4	3.5
Anthracene (7)	1.7	[78]	1.9	0.3	0.4	1.6	1.7
Pentacene (8)	2.4 ± 0.4	[60]	2.6	1.3	1.4	2.5	2.5
Perylene (9)	2.5	[79]	2.1	0.8	0.8	2.0	2.1
PTCDA (10)	3.9 ± 0.6	[63,64]	4.4	3.1	3.3	3.9	4.0
P3MT (11)	2.2 ± 0.2[a]	[43,71]	2.5	1.7	1.8	2.4	2.5
		RMSD	0.50	1.2	1.1	0.38	0.36
		MAD	13%	34%	31%	8.5%	8.6%

[a] For P3HT.

Table 3
Parameters for the polarization continuum model for the molecules shown in Fig. 1. The static molecular polarizability is $\bar{\alpha}$. The relative dielectric constants (ε) were calculated from Eq. 1. Experimentally determined values for the dielectric constant (ε_{exp}) are listed where available.

Molecule	$\bar{\alpha}$ (Å^3)	CMA (Å^2)	CMV (Å^3)	ε	ε_{exp}
TCNQ (1)	33.0	191.9	249.9	4.7	
F2TCNQ (2)	33.9	198.6	263.2	4.5	
F4TCNQ (3)	35.0	204.9	275.8	4.4	
TNAP (4)	49.7	233.8	336.1	5.9	
PCBM (5)	102.8	534.7	1162.6	2.8	3.9 [80]
C_{60} (6)	79.1	366.5	659.6	4.0	4.1 [81]
Anthracene (7)	26.0	184.0	234.7	3.6	2.5–4 [82][a]
Pentacene (8)	48.8	268.2	413.0	3.9	4.0 [83][b]
Perylene (9)	37.3	232.7	333.8	3.6	2–4.5 [84][a]
PTCDA (10)	53.7	291.5	468.1	3.8	3.6 [85]
P3MT (11)	169.5	658.8	1590.0	3.4	3 [86][c]

[a] Variation due to crystal anisotropy.
[b] Quoted in [87].
[c] For P3HT, measured with photo-charge extraction in a linearly increasing voltage.

bar one of the molecules for which there are measurements of the permittivity we find that the calculation gives excellent agreement with experiment. The exception is PCBM, where the calculated permittivity is only about 70% the literature experimental value. It is interesting to note that the calculation predicts rather different values of ε for PCBM and C_{60}, whereas experimentally the two molecules have similar permittivities. This may indicate that the 'tail' of the molecule leads to an overestimation of CMV – recall that the CMV is defined by a sphere with surface area defined by CMA.

It is natural to extend the notation of IEs and EAs to the solid state. Thus, we define the solid state ionisation energy as

$$I_s \equiv E_0^{(s)}(+1) - E_0^{(s)}(0) \tag{3a}$$

and the solid state electron affinity as

$$A_s \equiv E_0^{(s)}(0) - E_0^{(s)}(-1), \tag{3b}$$

where $E_0^{(s)}(q)$ is the ground state energy of the molecule with charge q *in the solid state environment*. We report the vertical and adiabatic IEs and EAs calculated from Eq. 3 in the PCM in Tables 1 and 2. In Fig. 6 we compare the calculated solid-state adiabatic IE, I_s^a, to I_{UPS} and in Fig. 7 we compare the calculated solid-state adiabatic EA, A_s^a, to A_{IPES}. Both data sets show excellent agreement between theory and experiment. The PCM solid state correction to the IE produces a RMSD between the calculated solid state value and that from the UPS measurements of only 0.32 eV, corresponding to a 3.9% MAD. This result is a significant improvement over the gas phase calculations and yields predictions that are of a similar accuracy to the $HOMO_{KS}$ approximation. However, whereas the $LUMO_{KS}$ does not provide a good estimate of A_{IPES}, cf. Fig. 3, A_s^a does. The PCM reduces the RMSD between A_{IPES} and A_s^a to 0.36 eV, which corresponds to a MAD of 8.6%.

Thus we see that by calculating the IE/EA directly from DFT with the solid state environment included via the PCM one is able to give a qualitatively accurate account of the experiments. The errors in this method are now approximately the same as the experiment uncertainty, therefore it is not possible to use comparison with experiments to judge the efficacy of further refinements (cf. Section 3.5).

3.4. Charge transport

The type of calculation reported above can straightforwardly be extended to determine a number of additional properties that are important for the design of organic photovoltaic devices.

The so-called 'transport gap', E_t, is defined as the difference between the ionisation energy and electron affinity in the solid state and represents the minimum energy needed to completely separate an electron and hole in the solid,

$$E_t = I_s - A_s. \tag{4}$$

Physically, the transport gap represents the energy difference between the ground state of the system and the state where two charges have been taken to infinity. Thus, this number can give some insights into the energetics of charge transfer in monocomponent systems.

Table 4 lists the experimental transport gap E_t^{exp} derived from the difference between I_{UPS} and A_{IPES} energies (Eq. 4). The transport gap was also calculated from the Kohn–Sham orbital energies, $E_t^{KS} \equiv LUMO_{KS} - HOMO_{KS}$, the gas phase ionic energies, $E_t^g \equiv I_g^a - A_g^a$, and the solid state IE and EA, $E_t^s \equiv I_s^a - A_s^a$. Error analyses of the transport gaps follow as one would expect given the discussion above and provide no new information.

In a donor–acceptor system an important quantity is

$$V = I_s^D - A_s^A, \tag{5}$$

where I_s^D is the solid state ionisation energy of the donor and A_s^A is the solid state electron affinity of the acceptor. V is the energy require to take two charges too infinity and is therefore strongly correlated with the maximum open circuit voltage achievable in this type of organic solar cell [88].

Understanding the energetics of charge transport is a key first step to understand the performance of organic photovoltaic devices. However, kinetics are probably at least as important [89]. Thus, it is also important to understand the reorganisation energy, which includes an internal part, λ_i – the difference between adiabatic and vertical IE/EA, and terms arising from the polarizability of the crystalline environment. In Marcus–Hush theory [90] the greatest charge transfer rate is achieved when the total reorganisation energy is equal and opposite to the energy difference between the initial and final states.

In molecular solids ionic states are characterized by strong coupling of the localized charge to the polarizable environment. The energetics of this coupling are characterized by the polarization energies,

$$P_+ = I_g^a - I_s^a \tag{6a}$$

$$P_- = A_s^a - A_g^a. \tag{6b}$$

Therefore, understanding the trends in the polarisation energies across large ranges of molecules is a key step towards the ability to design new materials.

The polarization energies calculated from Eq. (6) and the internal reorganisation energies are also reported in Table 4. Experimental data for negative polarization energies are lacking and the reported values for the positive polarization energies can vary widely. Therefore, P_+ and P_- are usually assumed equal, however the results in Table 4 show that this assumption is not generally valid. A similar conclusion has previously been argued for on experimental grounds [91].

In order to fully examine the charge transfer rates one also needs to consider the relaxation rates and energetics of the relevant transition states. These will be discussed in a forthcoming publication. Nevertheless, Marcus–Hush theory gives a clear design principle for organic photovoltaics: matching the reorganisation energy to energy difference between ionic and neutral configurations will allow one to optimise for the desired reaction pathways, leading to more efficient photovoltaic devices. The calculations above, when extended to all of the additional transition states, will provide a computationally cheap method to explore these effects.

3.5. Experimental uncertainties

Given that the RMSD deviations between experiment and the IEs/EAs calculated from the PCM + DFT approach the of order of the uncertainty in experiments, a brief discussion of those uncertainties is required.

Photoemission spectroscopy is very sensitive to surface conditions. In the analysis of photoemission spectra, the threshold energy is believed to provide a better characterisation of the ionisation energy than the peak [38,92]. This difference adds uncertainty to the reported values found in the literature which can vary by as much as 1 eV [38] – three times the RMSD between our calculations and the experimental values!

There are also great difficulties in making IPES measurements on organic materials [92,93]. Again the onset is believed to represent the solid state electron affinities [92]. But this poorly defined IPES threshold value further adds to the variation between different reported experimental EAs.

Finally, note that experimental issues, such as sample thickness, sample charging and substrate workfunction, have profound effects on the measured polarization energy, and can vary the experimental value by nearly 1 eV [94–96]. Therefore, to guard against the temptation to cherry pick the literature, we carried out a systematic literature search using ISI Web of Science. In Tables 1 and 2 we report the mean values of the standard deviations in this literature data. Where only one measurement has been reported in the literature we have estimated an error of ±0.3 eV in Figs. 2–7, which is typical of the errors found in the literature data. Similar or larger errors have been estimated by previous authors [12,13]. Note that, for the solvated calculations the RMSD from experiment compares favourably with the deviation between different experiments.

Table 4
Calculated and experimental transport gaps and polarization energies. Vertical values were calculated using the geometry of the neutral molecule whereas the adiabatic values were derived from optimised geometry for the ionic species. E_t^{exp} are the experimental values from the literature. E_t^{KS}, E_t^g and E_t^s represent the transport gaps calculated from the $HOMO_{KS} - LUMO_{KS}$ gap, gas phase energies and PCM, respectively. P_+ and P_- correspond to the polarization energies calculated for the relevant ionic species. Here, $\lambda_i^{s,I} \equiv I_s^v - I_s^a$ is the internal reorganisation in the solid state following ionisation. Similarly, $\lambda_i^{s,A} \equiv A_s^v - A_s^a$.

Molecule	E_t^{exp}	E_t^{KS}	E_t^g	E_t^s	P_+	P_-	$\lambda_i^{s,I}$	$\lambda_i^{s,A}$
TCNQ (1)	3.4	2.5	5.3	2.7	1.7	0.9	0.05	0.13
F2TCNQ (2)	–	2.4	5.2	2.7	1.4	0.8	0.06	0.12
F4TCNQ (3)	3.2	2.4	5.1	2.6	1.7	0.8	0.06	0.13
TNAP (4)	1.3	1.9	4.5	1.9	1.6	0.9	0.03	0.11
PCBM (5)	2.0	2.6	4.6	3.1	0.8	0.7	0.05	0.08
C_{60} (6)	2.4	2.8	5.1	2.7	1.4	1.0	0.06	0.06
Anthracene (7)	4.0	3.6	6.5	4.0	1.2	1.3	0.07	0.10
Pentacene (8)	2.7	2.2	4.7	2.5	1.1	1.2	0.05	0.06
Perylene (9)	2.7	3.0	5.6	3.3	1.1	1.2	0.07	0.08
PTCDA (10)	2.7	2.5	4.8	2.7	1.4	0.8	0.03	0.16
P3MT (11)	2.6	2.2	3.6	2.3	0.6	0.8	0.11	0.10

4. Conclusions

We have seen that the Kohn–Sham orbitals provide a qualitative and even semi-quantitative prediction of the IE and EA in organic molecular semiconductors. However, the Kohn–Sham HOMO predicts the IE far more accurately than the Kohn–Sham LUMO predicts the EA.

The calculated *in vacuo* IE and EA do not accurately predict the solid state IE and EA. Qualitative trends *are* reproduced, but the IE is consistently overestimated and the EA is consistently underestimated with respect to their measured values. As the polarizable solid state environment will stabilise the ionic species and the measurements are made in the solid state, this difference is expected (cf. Eqs. 3 and 6).

Including the effects of the solid state environment via the PCM gives an accuracy comparable to experiment: the RMSD between the calculated and measured IEs and EAs is comparable to or smaller than the deviation between different measurements in the literature. Importantly, this agreement is found for both the IEs and the EAs. The agreement between theory and experiment for the EAs is significantly better for the PCM approach than for simply considering Kohn–Sham LUMOs.

We are now in a position to understand why the Kohn–Sham eigenvalues gave fortuitously good agreement with experiment. Beyond the approximations in the B3LYP functional and the finite basis set used, there are two sources of error in the Kohn–Sham calculation: (i) the approximation that the Kohn–Sham eigenvalues represent the IE and EA and (ii) the neglect of the polarizable solid state environment. When the former approximation is not made, the agreement with experiment is worsened, but in the direction we would expect from a simple analysis of the energetics of ions. Therefore, we conclude that these two errors approximately cancel and that this leads to the apparent success of the Kohn–Sham approach. We stress the common maxim that one cannot rely on approaches that give the right answer for the wrong reason, as one does not know when these approaches might fail dramatically. Therefore, a proper calculation of the ionic energet-

ics, including the polarizable medium, is required to understand charge transfer processes in organic electronics.

The relatively small variation in $P_+ + P_-$ explains the correlation between calculated *in vacuo* IE and EA and the measured solid state IE and EA. However, the variation in $P_+ + P_-$ is large enough to significantly reduce the correlation between *in vacuo* results and experiment relative to the correlation between the PCM calculations and experiment.

Nevertheless excellent accuracy was achieved at the relatively cheap $6-31+G/B3LYP$ level of theory. The accuracy is comparable to that which can be achieved experimentally by UPS or IPES and the theoretical values can be obtained far more cheaply. This suggests that this method will have an important role to play in screening target molecules in the design of new materials for organic electronic and photonic applications.

Most importantly, these results stress the importance of descriptions based on molecular states rather than molecular orbitals when designing and characterising materials of organic electronic and optoelectronic devices.

Acknowledgements

We thank Seth Olsen and Arthur Smith for helpful conversations. All calculations were performed on the National Computer Infrastructure National Facility. This work was funded by the Australian Research Council (ARC). PLB is supported by an ARC Federation Fellowship (FF0668728) and BJP is supported by an ARC Queen Elizabeth II Fellowship (DP0877875).

References

[1] A.J. Heeger, N.S. Sariciftci, E.B. Namdas, Semiconducting and Metallic Polymers, Oxford University Press, 2010.
[2] N. Ashcroft, N. Mermin, Solid State Physics, Holt, Rinehart and Winston, 1976.
[3] J. Bardeen, W.H. Brattain, The transistor, a semi-conductor triode, Phys. Rev. 74 (1948) 230–231.
[4] J. Bardeen, W.H. Brattain, Physical principles involved in transistor action, Phys. Rev. 75 (1949) 1208–1225.
[5] L. Hoddeson, V. Daitch, True genius: the life and science of John Bardeen: the only winner of two Nobel Prizes in Physics, Joseph Henry Pr, 2002.
[6] S. Braun, W. Salaneck, M. Fahlman, Energy-level alignment at organic/metal and organic/organic interfaces, Adv. Mater. 21 (2009) 1450–1472.
[7] P. Fulde, Electron Correlations in Molecules and Solids, Springer, 1995.
[8] E. Scriven, B.J. Powell, Toward the parametrization of the hubbard model for salts of bis(ethylenedithio)tetrathiafulvalene: a density functional study of isolated molecules, J. Chem. Phys. 130 (2009) 104508.
[9] E. Scriven, B.J. Powell, Effective coulomb interactions within BEDT–TTF dimers, Phys. Rev. B 80 (2009) 205107.
[10] I.B. Bersuker, The Jahn–Teller Effect, Cambridge University Press, 2006.
[11] I.G. Hill, A. Kahn, Z.G. Soos, R.A. Pascal Jr., Charge-separation energy in films of [pi]-conjugated organic molecules, Chem. Phys. Lett. 327 (2000) 181–188.
[12] B.W. D'Andrade, S. Datta, S.R. Forrest, P. Djurovich, E. Polikarpov, M.E. Thompson, Relationship between the ionization and oxidation potentials of molecular organic semiconductors, Org. Electron. 6 (2005) 11–20.
[13] P.I. Djurovich, E.I. Mayo, S.R. Forrest, M.E. Thompson, Measurement of the lowest unoccupied molecular orbital energies of molecular organic semiconductors, Org. Electron. 10 (2009) 515–520.
[14] P.K. Nayak, N. Periasamy, Calculation of electron affinity, ionization potential, transport gap, optical band gap and exciton binding energy of organic solids using 'solvation' model and DFT, Org. Electron. 10 (2009) 1396–1400.
[15] P. Nayak, N. Periasamy, Calculation of ionization potential of amorphous organic thin-films using solvation model and DFT, Org. Electron. 10 (2009) 532–535.
[16] J.C. Rienstra-Kiracofe, G.S. Tschumper, H.F. Schaefer, S. Nandi, G.B. Ellison, Atomic and molecular electron affinities: photoelectron experiments and theoretical computations, Chem. Rev. 102 (2002) 231–282.
[17] R.O. Jones, O. Gunnarsson, The density functional formalism, its applications and prospects, Rev. Mod. Phys. 61 (1989) 689–746.
[18] W. Koch, M. Holthausen, M. Holthausen, A Chemist's Guide to Density Functional Theory, Wiley Online Library, 2000.
[19] L.J. Sham, W. Kohn, One-particle properties of an inhomogeneous interacting electron gas, Phys. Rev. 145 (1966) 561–567.
[20] P. Politzer, F. Abu-Awwad, A comparative analysis of Hartree–Fock and Kohn–Sham orbital energies, Theor. Chem. Acc. 99 (1998) 83–87.
[21] J.F. Janak, Proof that $\frac{\partial e}{\partial n_i} = \epsilon$ in density-functional theory, Phys. Rev. B 18 (1978) 7165–7168.
[22] C.-O. Almbladh, U. von Barth, Exact results for the charge and spin densities, exchange-correlation potentials, and density-functional eigenvalues, Phys. Rev. B 31 (1985) 3231.
[23] J.P. Perdew, R.G. Parr, M. Levy, J.L. Balduz, Density-functional theory for fractional particle number: derivative discontinuities of the energy, Phys. Rev. Lett. 49 (1982) 1691.
[24] A. Cohen, P. Mori-Sanchez, W. Yang, Insights into current limitations of density functional theory, Science 321 (2008) 792.
[25] M.W. Schmidt, K.K. Baldridge, J.A. Boatz, S.T. Elbert, M.S. Gordon, J.H. Jensen, S. Koseki, N. Matsunaga, K.A. Nguyen, S. Su, T.L. Windus, M. Dupuis, J.A.M. Jr, General atomic and molecular electronic structure system, J. Comput. Chem. 14 (1993) 1347–1363.
[26] A.D. Becke, Density-functional thermochemistry. iii. the role of exact exchange, J. Chem. Phys. 98 (1994) 5648–5652.
[27] P.J. Stephens, F. Devlin, C. Chabalowski, M. Frisch, Ab initio calculation of vibrational absorption and circular dichroism spectra using density functional force fields, J. Chem. Phys. 98 (1994) 11623–11627.
[28] E. Lewars, Computational Chemistry: Introduction to the Theory and Applications of Molecular and Quantum Mechanics, Springer, 2003.
[29] P. Warner, Ab initio calculations on heteroatomic systems using density functional theory and diffuse basis functions, J. Org. Chem. 61 (1996) 7192–7194.
[30] N. Sato, Y. Saito, H. Shinohara, Threshold ionization energy of C_{60} in the solid state, Chem. Phys. 162 (1992) 433–438.
[31] R. Schwedhelm, L. Kipp, A. Dallmeyer, M. Skibowski, Experimental band gap and core-hole electron interaction in epitaxial C_{60} films, Phys. Rev. B 58 (1998) 13176–13180.
[32] V. de Coulon, J.L. Martins, F. Reuse, Electronic structure of neutral and charged c_{60} clusters, Phys. Rev. B 45 (1992) 13671–13675.
[33] M.R. Pederson, A.A. Quong, Polarizabilities, charge states, and vibrational modes of isolated fullerene molecules, Phys. Rev. B 46 (1992) 13584–13591.
[34] R.L. Martin, J.P. Ritchie, Coulomb and exchange interactions in c_{60}^{n-}, Phys. Rev. B 48 (1993) 4845–4849.
[35] J. Tomasi, M. Persico, Molecular interactions in solution: an overview of methods based on continuous distributions of the solvent, Chem. Rev. 94 (1994) 2027–2094.
[36] M. Connolly, The molecular surface package, J. Mol. Graph. 11 (1993) 139–141.
[37] H. Kurtz, J. Stewart, K. Dieter, Calculation of the nonlinear optical properties of molecules, J. Comput. Chem. 11 (1990) 82–87.
[38] N. Sato, K. Seki, H. Inokuchi, Polarization energies of organic solids determined by ultraviolet photoelectron spectroscopy, J. Chem. Soc. Faraday Trans. 2 (77) (1981) 1621–1633.
[39] P. Nielsen, A. Epstein, D. Sandman, Photoemission studies of TCNQ compounds, Solid State Commun. 15 (1974) 53–58.
[40] R. Murdey, W. Salaneck, Charge injection barrier heights across multilayer organic thin films, Jpn. J. Appl. Phys. 44 (2005) 3751.
[41] W. Gao, A. Kahn, Electronic structure and current injection in zinc phthalocyanine doped with tetrafluorotetracyanoquinodimethane: Interface versus bulk effects, Org. Electron. 3 (2002) 53–63.
[42] K. Akaike, K. Kanai, H. Yoshida, J. Tsutsumi, T. Nishi, N. Sato, Y. Ouchi, K. Seki, Ultraviolet photoelectron spectroscopy and inverse photoemission spectroscopy of [6,6]-phenyl-c_{61}-butyric acid methyl ester in gas and solid phases, J. Appl. Phys. 104 (2008) 023710.
[43] Z. Guan, J. Kim, H. Wang, C. Jaye, D. Fischer, Y. Loo, A. Kahn, Direct determination of the electronic structure of the poly (3-

hexylthiophene): phenyl-[6, 6]-C61 butyric acid methyl ester blend, Org. Electron. 11 (2010) 1779.
[44] J. Seo, S. Kang, C. Kim, S. Cho, K. Yoo, C. Whang, Energy level alignment between C_{60} and Al using ultraviolet photoelectron spectroscopy, Appl. Surf. Sci. 252 (2006) 8015–8017.
[45] F. Zhang, A. Vollmer, J. Zhang, Z. Xu, J. Rabe, N. Koch, Energy level alignment and morphology of interfaces between molecular and polymeric organic semiconductors, Org. Electron. 8 (2007) 606–614.
[46] W. Zhao, A. Kahn, Charge transfer at n-doped organic–organic heterojunctions, J. Appl. Phys. 105 (2009) 123711.
[47] Y. Ge, J. Whitten, Energy level alignment between sexithiophene and buckminsterfullerene films, Chem. Phys. Lett. 448 (2007) 65–69.
[48] M. Ruckman, B. Xia, S. Qiu, Adsorption of C_{60} on Ta(110): Photoemission and C K-edge studies, Phys. Rev. B 48 (1993) 15457.
[49] J. Weaver, J. Martins, T. Komeda, Y. Chen, T. Ohno, G. Kroll, N. Troullier, R. Haufler, R. Smalley, Electronic structure of solid C_{60}: experiment and theory, Phys. Rev. Lett. 66 (1991) 1741.
[50] A. Maxwell, P. Brühwiler, D. Arvanitis, J. Hasselström, N. Mårtensson, C 1s ionisation potential and energy referencing for solid C_{60} films on metal surfaces, Chem. Phys. Lett. 260 (1996) 71–77.
[51] L. Lyons, G. Morris, 1000. Photo-and semi-conductance in organic crystals. Part VIII. Photo-emission of electrons from crystals of aromatic hydrocarbons, J. Chem. Soc. 1960 (1960) 5192–5199.
[52] R. Katoh, M. Kotani, External photoemission by singlet-exciton photoionization in an anthracene single crystal, Chem. Phys. Lett. 174 (1990) 537–540.
[53] S. Hino, T. Hirooka, H. Inokuchi, Photoemission from anthracene and compounds containing anthracene-ring systems, Bull. Chem. Soc. Jpn. 50 (1977) 620–625.
[54] F.I. Vilesov, D.A. Sukhov, Soviet Physics-Solid State 13 (1971) 2300.
[55] A.P. Marchetti, D.R. Kearns, Photoelectron emission from aromatic and metallooraganic hydrocarbons, Soviet Physics-Solid State 6 (1970) 299.
[56] N. Karl, N. Sato, K. Seki, H. Inokuchi, UV photoelectron spectroscopy of several one-and two-component organic photoconductors, J. Chem. Phys. 77 (1982) 4870.
[57] A. Zakhidov, K. Yoshino, Polarization double barriers at the interfaces in organic multilayered structures and superlattices, Synth. Met. 64 (1994) 155–165.
[58] N. Sato, K. Seki, H. Inokuchi, Y. Harada, Photoemission from an amorphous pentacene film, Chem. Phys. 109 (1986) 157–162.
[59] H. Fukagawa, H. Yamane, T. Kataoka, S. Kera, M. Nakamura, K. Kudo, N. Ueno, Origin of the highest occupied band position in pentacene films from ultraviolet photoelectron spectroscopy: hole stabilization versus band dispersion, Phys. Rev. B 73 (2006) 245310.
[60] F. Amy, C. Chan, A. Kahn, Polarization at the gold/pentacene interface, Org. Electron. 6 (2005) 85–91.
[61] Y. Hirose, W. Chen, E.I. Haskal, S.R. Forrest, A. Kahn, Band lineup at an organic-inorganic semiconductor heterointerface: perylenetetracarboxylic dianhydride/GaAs(100), Appl. Phys. Lett. 64 (1994) 3482–3484.
[62] N. Karl, N. Sato, UV-photoelectron spectroscopy of one-and two component organic crystals, Mol. Cryst. Liq. Cryst. 218 (1992) 79–84.
[63] D.R. Zahn, G.N. Gavrila, M. Gorgoi, The transport gap of organic semiconductors studied using the combination of direct and inverse photoemission, Chem. Phys. 325 (2006) 99–112.
[64] N. Sato, H. Yoshida, K. Tsutsumi, Unoccupied electronic structure in organic thin films studied by inverse photoemission spectroscopy, J. Mater. Chem. 10 (2000) 85–89.
[65] J. Sauther, J. Wüsten, S. Lach, C. Ziegler, Gas phase and bulk ultraviolet photoemission spectroscopy of 3,4,9,10-perylene-tetracarboxylic dianhydride, 1,4,5,8-naphthalene-tetracarboxylic dianhydride, and 1,8-naphthalene-dicarboxylic anhydride, J. Chem. Phys. 131 (2009) 034711.
[66] H.-Y. Chen, J. Hou, S. Zhang, Y. Liang, G. Yang, Y. Yang, L. Yu, Y. Wu, G. Li, Polymer solar cells with enhanced open-circuit voltage and efficiency, Nat. Photon 3 (2009) 649–653.
[67] R. Schlaf, P.G. Schroeder, M.W. Nelson, B.A. Parkinson, P.A. Lee, K.W. Nebesny, N.R. Armstrong, Observation of strong band bending in perylene tetracarboxylic dianhydride thin films grown on SnS_2, J. Appl. Phys. 86 (1999) 1499–1509.
[68] S. Duhm, A. Gerlach, I. Salzmann, B. Bröker, R. Johnson, F. Schreiber, N. Koch, PTCDA on Au (111), Ag (111) and Cu (111): correlation of interface charge transfer to bonding distance, Org. Electron. 9 (2008) 111–118.
[69] H. Yamane, S. Kera, K. Okudaira, D. Yoshimura, K. Seki, N. Ueno, Intermolecular energy-band dispersion in PTCDA multilayers, Phys. Rev. B 68 (2003) 33102.
[70] W. Osikowicz, M. de Jong, W. Salaneck, Formation of the interfacial dipole at organic–organic interfaces: C_{60}/polymer interfaces, Adv. Mater. 19 (2007) 4213–4217.
[71] K. Kanai, T. Miyazaki, H. Suzuki, M. Inaba, Y. Ouchi, K. Seki, Effect of annealing on the electronic structure of poly (3-hexylthiophene) thin film, Phys. Chem. Chem. Phys. 12 (2010) 273–282.
[72] Y. Sohn, J. Stuckless, Characteristics of photoexcitations and interfacial energy levels of regioregular poly (3-hexythiophene-2, 5-diyl) on gold, ChemPhysChem 8 (2007) 1937–1942.
[73] J.E. Lyon, A.J. Cascio, M.M. Beerbom, R. Schlaf, Y. Zhu, S.A. Jenekhe, Photoemission study of the poly(3-hexylthiophene)/Au interface, Appl. Phys. Lett. 88 (2006) 222109.
[74] A.J. Cascio, J.E. Lyon, M.M. Beerbom, R. Schlaf, Y. Zhu, S.A. Jenekhe, Investigation of a polythiophene interface using photoemission spectroscopy in combination with electrospray thin-film deposition, Appl. Phys. Lett. 88 (2006) 062104.
[75] D. Schmeißer, Valence states of poly (3-hexyl-thiophene) as probed by photoelectron spectra at resonant excitation, Synth. Met. 138 (2003) 135–140.
[76] M. Onoda, K. Tada, A. Zakhidov, K. Yoshino, Photoinduced charge separation in photovoltaic cell with heterojunction of p-and n-type conjugated polymers, Thin Solid Films 331 (1998) 76–81.
[77] K. Kanai, K. Akaike, K. Koyasu, K. Sakai, T. Nishi, Y. Kamizuru, T. Nishi, Y. Ouchi, K. Seki, Determination of electron affinity of electron accepting molecules, Appl. Phys. A: Mater. Sci. Process. 95 (2009) 309–313.
[78] P. Yannoulis, K.-H. Frank, E.-E. Koch, Electronic structure and orientation of anthracene on Ag(111), Surf. Sci. 241 (1991) 325.
[79] K.H. Frank, P. Yannoulis, R. Dudde, E.E. Koch, Unoccupied molecular orbitals of aromatic hydrocarbons adsorbed on Ag(111), J. Chem. Phys. 89 (1988) 7569–7576.
[80] V. Mihailetchi, J. van Duren, P. Blom, J. Hummelen, R. Janssen, J. Kroon, M. Rispens, W. Verhees, M. Wienk, Electron transport in a methanofullerene, Adv. Funct. Mater. 13 (2003) 43–46.
[81] P.C. Eklund, A.M. Rao, Y. Wang, P. Zhou, K.-A. Wang, J.M. Holden, M.S. Dresselhaus, G. Dresselhaus, Optical properties of C_{60}- and C_70-based solid films, Thin Solid Films 257 (1995) 211–232.
[82] P. Cummins, D. Dunmur, The electric permittivity of crystalline anthracene, J. Phys. D: Appl. Phys. 7 (1974) 451.
[83] T. Li, J.W. Balk, P.P. Ruden, I.H. Campbell, D.L. Smith, Channel formation in organic field-effect transistors, J. Appl. Phys. 91 (2002) 4312–4318.
[84] D.Y. Zang, F.F. So, S.R. Forrest, Giant anisotropies in the dielectric properties of quasi-epitaxial crystalline organic semiconductor thin films, Appl. Phys. Lett. 59 (1991) 823–825.
[85] F.F. So, S.R. Forrest, Evidence for exciton confinement in crystalline organic multiple quantum wells, Phys. Rev. Lett. 66 (1991) 2649–2652.
[86] K.B. Krueger, personal communication, unpublished data (2010).
[87] S.P. Park, S.S. Kim, J.H. Kim, C.N. Whang, S. Im, Optical and luminescence characteristics of thermally evaporated pentacene films on Si, Appl. Phys. Lett. 80 (2002) 2872–2874.
[88] J.-L. Brédas, J.E. Norton, J. Cornil, V. Coropceanu, Molecular understanding of organic solar cells: the challenges, Acc. Chem. Res. 42 (2009) 1691–1699.
[89] J. Cornil, V. Lemaur, M.C. Steel, H. Dupin, A. Burquel, D. Beljonne, J.-L. Bredás, in: S.S. Sun, N.S. Sariciftci (Eds.), Organic Photovoltaics: Mechanism, Materials, and Devices, CRC.
[90] R.A. Marcus, Electron transfer reactions in chemistry. theory and experiment, Rev. Mod. Phys. 65 (1993) 599–610.
[91] N. Sato, H. Inokuchi, E.A. Silinsh, Reevaluation of electronic polarization energies in organic molecular crystals, Chem. Phys. 115 (1987) 269–277.
[92] S. Krause, M. Casu, A. Schöll, E. Umbach, Determination of transport levels of organic semiconductors by UPS and IPS, New J. Phys. 10 (2008) 085001.
[93] N. Smith, Inverse photoemission, Rep. Prog. Phys. 51 (1988) 1227–1294.
[94] E. Tsiper, Z. Soos, W. Gao, A. Kahn, Electronic polarization at surfaces and thin films of organic molecular crystals: PTCDA, Chem. Phys. Lett. 360 (2002) 47–52.
[95] S. Tadayyon, H. Grandin, K. Griffiths, L. Coatsworth, P. Norton, H. Aziz, Z. Popovic, Reliable and reproducible determination of work function and ionization potentials of layers and surfaces relevant to organic light emitting diodes, Org. Electron. 5 (2004) 199–205.
[96] I. Hill, A. Kahn, J. Cornil, D. dos Santos, J. Bredas, Occupied and unoccupied electronic levels in organic π-conjugated molecules: comparison between experiment and theory, Chem. Phys. Lett. 317 (2000) 444–450.

Organic Electronics 12 (2011) 405–410

Contents lists available at ScienceDirect

Organic Electronics

journal homepage: www.elsevier.com/locate/orgel

Letter

Wavelength sensitive photodiodes in the visible based on J-type aggregated films patterned by inkjet method

Yu Yang [a,*], Soichiro Omi [a], Ryo Goto [a], Masayuki Yahiro [b], Masanao Era [c], Hirofumi Watanabe [a], Yuji Oki [a]

[a] Department of Electronics, Graduate School of Information Science and Electrical Engineering, Kyushu University, Fukuoka 819-0395, Japan
[b] Institutes of Systems, Information Technologies and Nanotechnologies, Fukuoka 814-0001, Japan
[c] Department of Chemistry and Applied Chemistry, Faculty of Science and Engineering, Saga University, 1 Honjo, Saga 840-8502, Japan

ARTICLE INFO

Article history:
Received 7 July 2010
Received in revised form 28 October 2010
Accepted 14 November 2010
Available online 25 November 2010

Keywords:
Organic photodiodes
J-type aggregate
Inkjet
Cyanine dye
Open-circuit voltage

ABSTRACT

In this study, a kind of disposable and miniaturized organic photodiodes in the visible has been developed based on the J-type aggregated cyanine dyes films by the drop-on-demand inkjet method. Wavelength sensitivity has been found by measuring the open-circuit voltage (Voc) of the organic photodiodes under the excitation of laser pulses at various wavelengths and high spectral resolution around the absorption peak of each cyanine dye J-aggregates can be obtained, where a sharp decrease on the Voc and a Voc in reverse direction are observed. The mechanism responsible for the sharp decrease and reverse Voc are discussed and the feasibility of using the laser output from a solid-state dye laser waveguide as the excitation source for the organic photodiodes which may be possibly integrated together onto the flow-cytometry chips in the future are also demonstrated.

© 2010 Elsevier B.V. All rights reserved.

1. Introduction

During the past several years, inkjet printing has generated extensive research interests as a direct patterning technique for the cost-effective fabrication of organic optoelectronic devices such as organic light-emitting diodes (OLEDs) [1–4], organic field-effect transistors (OFETs) [5–7], and organic solar cells (OSCs) [8–10], and so on [11,12]. As compared with other film deposition techniques of organic chemicals, inkjet method is highly preferable due to the concerns on versatility, miniaturization, and high precision patterning. And also, inkjet printing such as the drop-on-demand has the advantages such as being fast and simple with high throughput. The consumption of materials can be reduced to an extremely low level of picoliter of each droplet in volume, providing a low cost, mask free, and non-contact printing approach [1]. Based on this knowledge, it is suggested that the drop-on-demand inkjet printing may be one of the most suitable technical pathway for the fabrication of some optical electrical elements on the disposable integrated flow-cytometry chips, which has been proposed in our previous studies [13–15]. So, as one of the latest application of inkjet method in our group, in this work, organic photodiodes in the visible region have been developed by the inkjet printing technique, which we suggest, may monitor the laser output from the tunable solid-state dye laser waveguides or the laser induced fluorescence from the micro fluid channel on the integrated cytometry chips [15,16]. And it should also be noted that for the fabrication of this kind of disposable and miniaturized organic photodiodes on the flow-cytometry chips, other techniques such as spin-coating is not applicable because of the complicated structures of the flow-cytometry chips, risk of contamination, and the infeasibility to integrate photodiodes in various spectral region on one single chip.

As considering the suitable materials for the photodiodes printed by inkjet method, cyanine dyes dissolved in aqueous solutions are suggested to be the best candidates

* Corresponding author. Tel.: +81 92 802 3742; fax: +81 92 802 3739.
E-mail address: yuyang@laserlab.ed.kyushu-u.ac.jp (Y. Yang).

1566-1199/$ - see front matter © 2010 Elsevier B.V. All rights reserved.
doi:10.1016/j.orgel.2010.11.011

because of their self-aggregation tendency due to the hydrophobic nature of the molecular structures, which have been investigated widely in recent years as wideband semiconductors, information recording materials, nonlinear optical materials, and fluorescence indicator in biological researches [17–20]. Depending on the angle between the transition dipoles and molecular axis of the aggregate, the aggregates of cyanine dyes can be classified into J- or H-type aggregates, with an intense red-shifted or broad hypsochemically shifted absorption spectrum, respectively, as compared with their monomer counterparts [21,22]. Recently, J-aggregate cyanine dye films have been fabricated by inkjet method and the influence on J-aggregate formation by inkjet parameters has been investigated [23]. Herein we report, as a new attempt to the best of our knowledge, the disposable and miniaturized organic photodiodes based on the J-type aggregation of cyanine dye films printed by inkjet method, which are wavelength sensitive because of the J-aggregate formation of each cyanine dye.

2. Experimental details

To make photodiodes in the visible region, three kinds of cyanine dyes NK-3989, NK-1952, and NK-2203, which correspond to the blue, green and red spectral regions, respectively, are dissolved into the solution of a conductive polymer, poly(3,4-ethylenedioxythiophene) poly(styrene sulfonate) (PEDOT:PSS, Sigma–Aldrich, 2.8 wt% in H_2O solution) respectively, and applied to the drop-on-demand piezoelectric inkjet system as the ink for printing. Details on the inkjet printing process of J-aggregated cyanine dye/PEDOT:PSS films can be found elsewhere [23]. The cyanine dyes, NK-3989, NK-1952, and NK-2203 (Hayashibara Biochemical Laboratories) and PEDOT:PSS are used as received without further purification. First, 17.5 mg of cyanine dye is mixed with 0.175 wt% of PEDOT:PSS and DI water and the dye/polymer ratio is kept at 10:1 by weight. After ultrasonic treatment to prompt the totally dissolution of the cyanine dye, the viscous cyanine dye/PEDOT:PSS solutions are filtered (Whatman filter GF/B 1.0 μm).

A piezoelectric inkjet system (Microjet IJK-200s) is adopted in this work. The indium tin oxide (ITO) coated polyethylene terephthalate (PET) film is used as the substrate for printing, which has been etched by 10% of aqua regia (120 s) with masks to obtain designed patterns. UV exposure (172 nm, 10 mW/cm^2, Ushio UER20-172) on the ITO substrate before the inkjet printing is applied to make it hydrophilic and reduce the contact angle of cyanine dye/PEDOT:PSS solutions on ITO substrates. The nozzle size of the piezoelectric inkjet is 70 μm and the pulse voltage and pulse duration is 75 V and 67 μs, respectively. Large area patterned films can be made by delicately overlapping neighboring spots. In order to avoid the environmental turbulence interference on the droplet, the distance between the jet nozzle and the ITO substrate is kept to less than 1 mm. The absorption spectra of the printed films are measured with a UV–vis-NIR absorption spectrometer (Shimadzu UV-160A).

A thin Al layer is vapor deposited on the top of cyanine dye films after the inkjet printing (ULAC, 6×10^{-3} Pa). The resistance between the cathode and anode is typically ~1.6 MΩ. A tunable pico-second laser with the pulse duration of 36 ps and maximum output energy of 130 μJ is used as the excitation source and the output wavelength is monitored by a multi-channel spectroscope (Ocean Optics HR4000). The Voc between the cathode and anode of inkjet printed photodiodes is measured by oscilloscope (Tetronix, TDS 3032) with 10^3 times of amplification on the signal. To verify the feasibility of using the organic photodiodes as the detectors for the solid-state dye laser media, which have been investigated widespread in recent years [24–26], the laser output from a Rhodamine 6G (R6G) doped Poly(methyl methacrylate) (PMMA) film is also used as the excitation source for the organic photodiodes and the pump source for the solid-state dye laser film is a passively-Q-switched and frequency-doubled Nd:YAG laser (0.5 ns, 532 nm) with a beam expander and cylindrical lens to focus the pump beam onto the sample surface with the size of 15 × 0.3 mm. The pump energy and repetition rate was 30 μJ/pulse and 500 Hz, respectively. Details on the fabrication process of the R6G doped PMMA film can be found elsewhere [24,27,28].

3. Results and discussion

The typical size of the inkjet printed cyanine/PEDOT:PSS spots on the ITO substrates is ~300 μm in diameter and 20 nm in average thickness, as shown in Fig. 1(a). Large area films with desired patterns are made by delicately overlapping neighboring spots, although just one single spot is also suggested to have sufficient absorption as localized monitoring in the practical applications. The architecture of the photodiodes is shown in Fig. 1(b), with NK-1952 as an example. With the ITO as the anode, while the thin Al layer deposited on the top of NK-1952/PEDOT:PSS films as the cathode, the photodiode behaves as a bulk heterojunction [29]. The lowest unoccupied molecular orbital (LUMO) and highest occupied molecular orbital (HOMO) energy levels of each chemical and workfunctions of the electrodes are summarized in Fig. 1(c) [30–32].

The absorption spectra of the three kinds cyanine dye/PEDOT:PSS films printed by inkjet method are shown in Fig. 2, in which the red-shifted, sharp and narrow absorption peaks at ~466, 542 and 594 nm can be observed from NK-3989, NK-1952 and NK-2203, respectively, indicating the J-aggregate formation of each dye, as compared with the broad absorption bands of their monomers, for instance, the 502 nm absorption band of NK-1952. So, wavelength resolution can be expected around the peak wavelengths.

With the photodiodes made through above process, the Voc between anode and cathode under various pumping wavelength is measured. As shown in Fig. 3, with the 0.04 ns pulse duration and from 430 to 670 nm tunable range of incident probe beam, the Voc from the photodiode base on NK-1952 doped PEDOT:PSS film increases significantly with the increase of the probe wavelength from 470 to 532 nm, which corresponds well with the

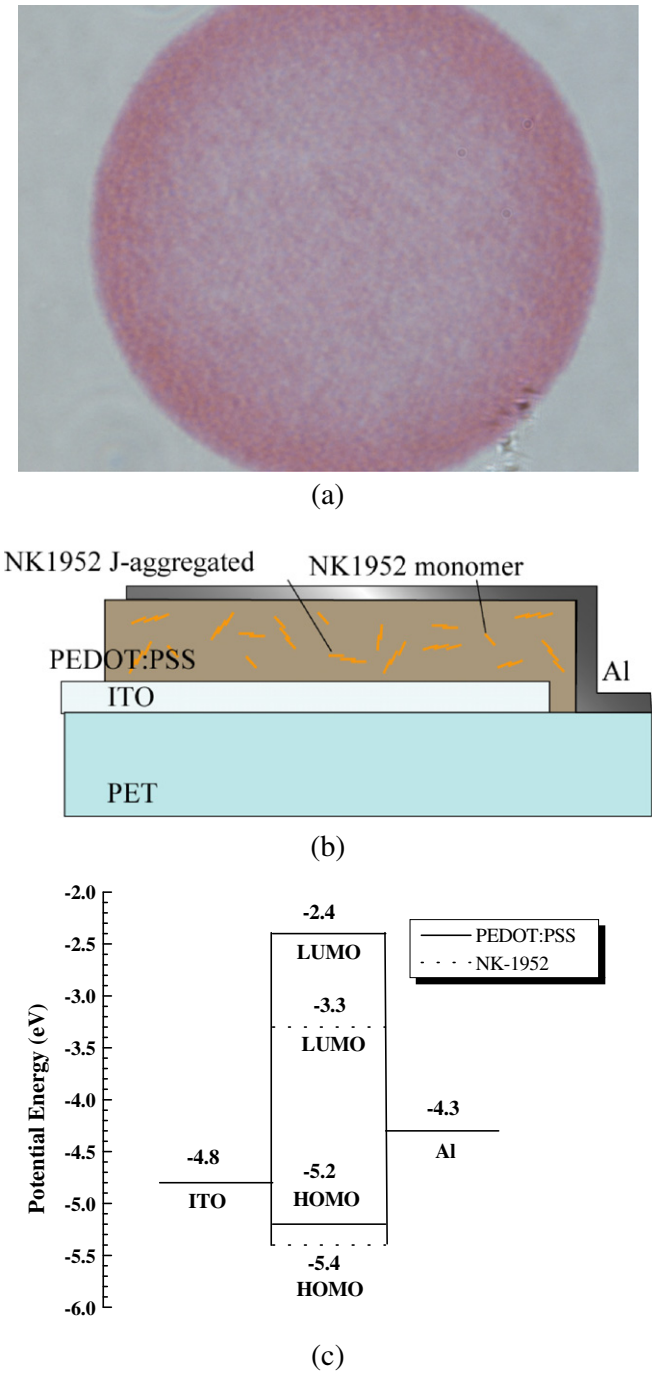

Fig. 1. (a) Image of inkjet printed NK-2203/PEDOT:PSS spot, (b) Architecture of the inkjet printed photo-diodes, (c) the HOMO and LUMO energy levels, and the workfunctions of electrodes.

absorption spectrum of the film. The pulse duration of Voc is ~2 μs, as shown in Fig. 4. However, increasing the probe wavelength around the absorption peak results in a sharp decrease on the voltage, and it can provide relatively high wavelength resolution. In addition, further increase in wavelength makes negative Voc around 550 nm, indicating the possibility of employing this photodiode as the wavelength sensitive detector at this spectral region. To explain the inversed slope and the negative voltage, the vertical inhomogeneous distribution of NK-1952 dye molecules in different J-aggregation degree in the inkjet printed spots is assumed to be responsible. As has be revealed by other cyanine dye based photovoltaic devices, excitons are induced after the absorption of photons by the cyanine dyes

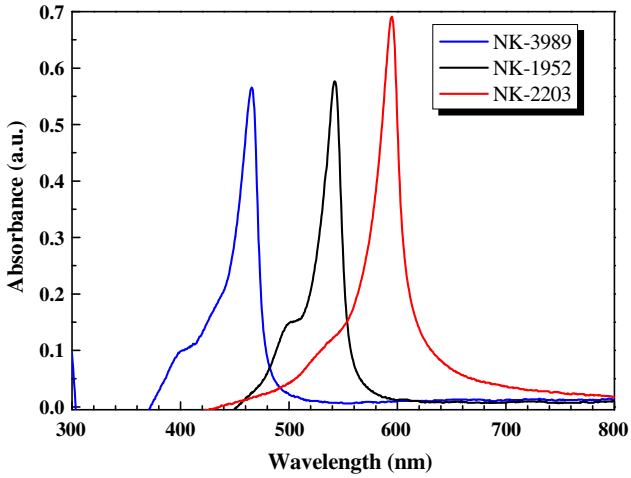

Fig. 2. Absorption spectra of cyanine dye NK3989, NK-1952 and NK-2203 doped into PEDOT:PSS films by inkjet method.

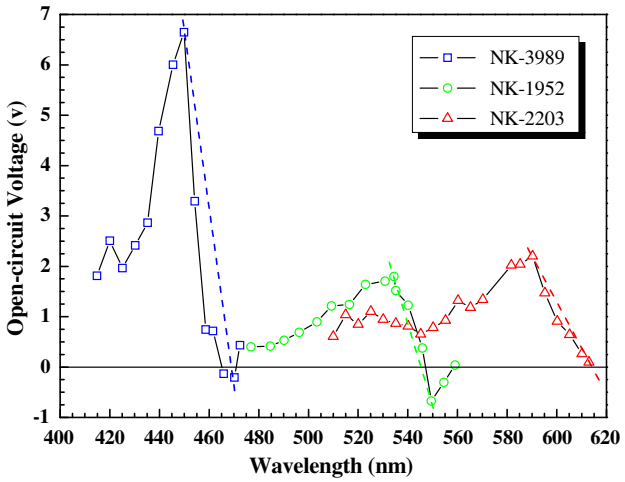

Fig. 3. The open-circuit voltage of photodiodes based on NK-3989, NK-1952 and NK-2203 under various excitation wavelength.

molecules and then separated into electron–hole pairs at the interface between NK-1952 and PEDOT:PSS, which acts as the hole transporting materials [30–32]. So, the Voc increases with the increase of extinction coefficient of NK-1952 J-aggregate from 470 to 532 nm. However, a concentration gradient of the J-aggregated cyanine dye in the inkjet printed spots is assumed during the evaporation of solvent in droplets and J-aggregate formation process. So, further increase the probe wavelength, only NK-1952 dye molecules with the largest J-aggregation degree can absorb the photons. However, as considering the average thickness of ~20 nm, which corresponds to the stack of ~40 molecules [30], the migration distance of electrons from the bottom of spots to the Al cathode is relatively long and an aggregation of electrons at the ITO surface may occur, resulting in the recombination with holes from the ITO anode and thus the reverse Voc can be observed. It is suggested that other mechanisms may also be responsible for the reverse Voc at 550 nm, for instance, the photocurrent in a schottky junction at an interface between ITO/PEDOT:PSS:NK-1952 arised from a space charge [33]. For detailed explanation, this research is now underway.

Similar results are obtained from the photodiodes based on NK-3989, as shown in Fig. 3. With the increase of probe wavelength from 410 to 450 nm, the Voc also increases. The inversed slope of 0.34 V/nm is observed around 465 nm and a small negative Voc is also confirmed. The quantum yield of the NK-3989 based photodiode at 450 nm is estimated to be $\sim 10^{-6}$, which is low as a photovoltaic device [29–32]. It is suggested that the sensitivity of this kind of photodiode can be improved by optimizing the photodiode architecture and materials composition [31,32], for instance, introducing the hole-transport and electron-transport layers between the active cyanine layer and electrodes respectively, or increasing the difference in workfunctions between the anode and cathode. And this is work is now underway. However, as a wavelength sensitive photodiodes, the spectral resolution, which is a much

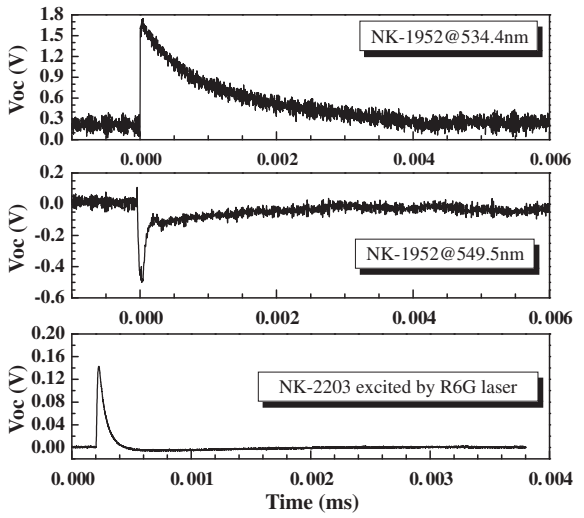

Fig. 4. The waveform of open-circuit voltage of the NK-1952 based photodiode under various excitation wavelength and that of NK-2203 based photodiode under the excitation of laser output from a R6G doped polymeric waveguide laser.

more important performance parameter, can be expected to reach the level of 0.1 nm due to the inversed slope of 0.34 V/nm in the Voc at around 465 nm, with the photodiodes based on NK-3989, indicating the nm-resolved laser spectrum monitor device, for such as integrated waveguide solid state dye lasers, can be realized.

To monitor wavelength around 600 nm, which is a typical wavelength of the waveguide dye lasers [24–28], the Voc of photodiodes based on NK-2203 is also investigated, as shown in Fig. 3. The peak Voc is obtained at the wavelength of ~590 nm, and inversed slope of 0.08 V/nm is confirmed, which is in correspondence with the absorption spectrum of the J-aggregated NK-2203 dye. Based on this result, ~2 μJ of amplified spontaneous emission (ASE) from a R6G doped PMMA film at ~580 nm is coupled into the photodiode based on NK-2203, and ~150 mV of Voc has been obtained, as shown in Fig. 4, indicating the enough sensitivity of this kind of photodiodes for the application on the integrated cytometry chips.

At last, it should also be noted that in this work, overlapped films in the size of $9 * 9$ mm are made, which normally consist of ~900 spots. In our other experiment, smaller films in the size of $1 * 1$ mm can also be made and used as organic photodiodes, which consist of ~16 spots. It is suggested that the advantages of the organic photodiodes made by inkjet printing may be better demonstrated by the smaller size of photodiodes, or in the extreme case, single spot photodiodes, which cost less spots and area size. However, there exist two main problems for this kind of single spot photodiodes. First, the capacity of the photodiodes is decided by the size of the films. Thus, by decreasing the size of the films and numbers of spots needed, a shorter and fast response Voc pulse may be expected while the photodiodes are more easily to be saturated. Second, to make the single spot photodiodes, the precise printing of the ink jet and a new ITO pattern are needed to avoid any contact between the electrodes which causes shortcut. In this work, because of the concerns on the saturation and relatively shorter lifetime of the single spot photodiodes, the large area films are made and used as the first characterisation for the organic photodiodes made by ink jet printing. However, single spot photodiodes can also be fabricate by using a thin polymer film printed by the same ink jet nozzle onto the ITO patterned substrates as the blocking layer to avoid the possible shortcut between the electrodes. Under the excitation of a 532 nm laser beam, ~0.43 V of Voc and much shorter pulse duration have been observed. After overcoming the problems of easy saturation and relatively shorter lifetime, for instance, utilizing several inkjet printed spots which are isolated to each other, it is suggested that this kind of organic photodiodes can be integrated to the flow-cytometry chips. This work is now underway.

4. Conclusion

In conclusion, in this work, disposable and miniaturized photodiodes in the visible based on the J-aggregated cyanine dye films printed by inkjet method have been realized. Wavelength sensitivity of these organic photodiodes has been observed with a sharp decrease and reverse Voc around the absorption peak of each J-aggregated dye and mechanism involved have been suggested. The detection of output from a solid-state dye laser film by the inkjet printed photodiode has been demonstrated, indicating the promise of applying this kind of photodiodes on the integrated cytometry chips.

Acknowledgements

This study was supported by Industrial Technology Research Grant Program in 2007 from the New Energy and Industrial Technology Development Organization in Japan.

Appendix A. Supplementary data

Supplementary data associated with this article can be found, in the online version, at doi:10.1016/j.orgel.2010.11.011.

References

[1] Y. Yoshioka, P.D. Calvert, G.E. Jabbour, Macromol. Rapid Commun. 26 (2005) 238.
[2] Y. Yoshioka, G.E. Jabbour, Adv. Mater. 18 (2006) 1307.
[3] E. Tekin, E. Holder, D. Kozodaev, U.S. Schubert, Adv. Funct. Mater. 17 (2007) 277.
[4] S.-C. Chang, J. Liu, J. Bharathan, Y. Yang, J. Onohara, J. Kido, Adv. Mater. 11 (1999) 734.
[5] J.A. Lim, W.H. Lee, H.S. Lee, J.H. Lee, Y.D. Park, K. Cho, Adv. Funct. Mater. 18 (2008) 229.
[6] H. Sirringhaus, T. Kawase, R.H. Friend, T. Shimoda, M. Inbasekaran, W. Wu, E.P. Woo, Science 290 (2000) 2123.
[7] W.Y. Park, J.S. Park, T.-D. Kim, K.-S. Lee, H.S. Lim, J.S. Lim, C. Lee, Org. Electron. 10 (2009) 1028.
[8] C.N. Hoth, P. Schilinsky, S.A. Choulis, C.J. Brabec, Nano Lett. 8 (2008) 2806.
[9] C.N. Hoth, S.A. Choulis, P. Schilinsky, C.J. Brabec, Adv. Mater. 19 (2007) 3973.
[10] Y. Xia, R.H. Friend, Macromolecules 38 (2005) 6466.
[11] B. de Gans, S. Hoeppener, U.S. Schubert, Adv. Mater. 18 (2006) 910.

[12] T.H.J. van Osch, J. Perelaer, A.W.M. de Laat, U.S. Schubert, Adv. Mater. 20 (2008) 343.
[13] Y. Oki, Y. Ogawa, K. Yamashita, M. Miyazaki, M. Maeda, Mol. Cryst. Liq. Cryst. 463 (2007) 131.
[14] Y. Oki, S. Kataoka, N. Kamogawa, H. Watanabe, K. Yamashita, M. Miyazaki, Proc. Advance Solid-State Photonics (2008). MB3.
[15] Y. Yang, S. Kataoka, N. Kamogawa, H. Watanabe, K. Yamashita, M. Miyazaki, Y. Oki, Proc. CLEO/QELS 1 (9) (2008) 1258.
[16] C.-M. Chang, S.-K. Hsiung, G.-B. Lee, Jpn. J. Appl. Phys. 46 (2007) 3126.
[17] C. Chen, X. Qi, B. Zhou, J. Photochem. Photobiol. A 109 (1997) 155.
[18] K.S. Min, H.T. Chung, O.K. Cho, G.Y. Kim, K.Y. Park, Mol. Cryst. Liq. Cryst. Sect. A 247 (1994) 161.
[19] K.D. Belfield, M.V. Bondar, F.E. Hernandez, O.V. Przhonska, S. Yao, Chem. Phys. 320 (2006) 118.
[20] B. Becher, J. Clapper, K.R. Harkins, J.A. Olson, Anal. Biochem. 221 (1994) 78.
[21] F. Würthner, S. Yao, Angew. Chem. Int. Ed. 39 (2000) 1978.
[22] C. Ouyang, S.J. Chen, B. Che, G. Xue, Colloids Surf. A 301 (2007) 346.
[23] Y. Yang, H. Hajime, K. Yamashita, N. Kamogawa, H. Watanabe, M. Miyazaki, Y. Oki, Jpn. J. Appl. Phys. 49 (2010) 010204.
[24] Y. Oki, K. Ohno, M. Maeda, Jpn. J. Appl. Phys. 37 (1998) 6403.
[25] A. Costela, I.G. Moreno, L. Cerdan, V. Martin, O. García, R. Sastre, Adv. Mater. 21 (2009) 4163.
[26] W. Holzer, A. Penzkofer, T. Pertsch, N. Danz, A. Bräuer, E.B. Kley, H. Tillmann, C. Bader, H.-H. Hörhold, Appl. Phys. B 74 (2002) 333.
[27] Y. Oki, K. Aso, D. Zuo, N.J. Vasa, M. Maeda, Jpn. J. Appl. Phys. 41 (2002) 6370.
[28] Y. OkiT. Yoshiura, Y. Chisaki, M. Maeda, Appl. Opt. 41 (2002) 5030.
[29] G. Yu, J. Gao, J.C. Hummelen, F. Wudl, A.J. Heeger, Science 270 (1995) 1789.
[30] S. Saito, E. Aminaka, T. Tsutsui, M. Era, J. Lumin. 60–61 (1994) 902.
[31] B. Fan, R. Hany, J.-E. Moser, F. Nüesch, Org. Electron. 9 (2008) 85.
[32] T. Geiger, S. Kuster, J.-H. Yum, S.-J. Moon, M.K. Nazeeruddin, M. Gratzel, F. Nüesch, Adv. Funct. Mater. 19 (2009) 2720.
[33] L.G. Hu, Y. Noda, H. Ito, H. Kishida, A. Nakamura, K. Awaga, Appl. Phys. Lett. 96 (2010) 243303.

Organic Electronics 12 (2011) 411–418

Contents lists available at ScienceDirect

Organic Electronics

journal homepage: www.elsevier.com/locate/orgel

Ambipolar thin-film transistors and an inverter based on pentacene/self-assembled monolayer modified ZnO hybrid structures for balanced hole and electron mobilities

Chanwoo Yang [a], Youngjin Kwack [b], Se Hyun Kim [a], Tae Kyu An [a], Kipyo Hong [a], Sooji Nam [a], Mijeong Park [a], Woon-Seop Choi [b], Chan Eon Park [a,*]

[a] POSTECH Organic Electronics Lab, Polymer Research Institute, Department of Chemical Engineering, Pohang University of Science and Technology, Pohang 790-784, Republic of Korea
[b] School of Display Engineering, Hoseo University, Asan-City, Chungnam 336-795, Republic of Korea

ARTICLE INFO

Article history:
Received 30 September 2010
Received in revised form 19 November 2010
Accepted 12 December 2010
Available online 23 December 2010

Keywords:
Ambipolar thin-film transistor
Organic–inorganic hybrid transistor
Complementary-like inverter
Organic semiconductor
Oxide semiconductor
Pentacene
ZnO

ABSTRACT

We have fabricated high performance ambipolar thin-film transistors (TFTs) and an inverter based on organic–inorganic bilayer structures composed of an upper pentacene layer and a lower atomic-layer-deposited zinc oxide (ZnO) layer. The insertion of a dodecanoic acid (DA) self-assembled monolayer (SAM) into the interface between pentacene and ZnO results in an improvement in the morphology of the pentacene layer and in well-balanced ambipolarity with hole and electron mobilities of 0.34 and 0.38 $cm^2V^{-1}s^{-1}$, respectively. The ambipolar TFTs with DA-treated ZnO exhibit a hole to electron mobility ratio of approximately 0.90, which is higher by a factor of ~2.8 than that of ambipolar TFTs with untreated ZnO. We also tested the introduction of a perfluorooctyltriethoxysilane (PFOTES) SAM; the effects of the permanent dipole fields of the SAMs on the electrical and ambipolar characteristics of the hybrid TFTs were investigated.

© 2010 Elsevier B.V. All rights reserved.

1. Introduction

Thin-film transistors (TFTs) based on organic semiconductors [1] or metal oxide semiconductors [2–6] have been intensively studied as potential alternatives to transistors based on conventional silicon technologies for electronic applications requiring low cost, flexibility, large area, and transparency. The charge carrier mobilities of TFTs based on these two classes of semiconductors have been shown to be superior to those of *a*-Si:H-based TFTs. TFTs based on organic semiconductors are generally used as unipolar devices, and exhibit mostly *p*-type semiconducting behavior. Although high-performance unipolar devices have been achieved with TFTs based on *p*-type organic semiconductors, the use of TFTs based on *n*-type organic semiconductors in complementary logic circuits has been limited by their instability in the presence of atmospheric water and oxygen. TFTs based on metal oxide semiconductors, such as zinc oxide (ZnO), indium zinc oxide, zinc tin oxide and indium gallium zinc oxide, exhibit mostly *n*-type semiconducting behavior, and have the advantages of high charge mobility, excellent environmental stability and high transparency [2–6].

Ambipolar TFTs have also been intensively studied because of their applications in complementary logic circuits, which can be used to overcome the limitations of integrated circuits that use only unipolar logic [5–13]. In addition, the fabrication of complementary circuits based on ambipolar TFTs requires reduced process complexity and manufacturing cost [7]. Ambipolar TFTs based on organic semiconductors with various types of layer structures such as bilayer [8,13], blend [10], and single-component type

* Corresponding author. Tel.: +82 54 279 2269; fax: +82 54 279 8298.
E-mail addresses: wschoi@hoseo.edu (W.-S. Choi), cep@postech.ac.kr (C.E. Park).

1566-1199/$ - see front matter © 2010 Elsevier B.V. All rights reserved.
doi:10.1016/j.orgel.2010.12.008

[9–12] have been reported by many groups. In particular, ambipolar TFTs with an organic–inorganic bilayer structure composed of a *p*-type organic semiconductor and an *n*-type metal oxide semiconductor have been reported; these TFTs make use of both classes of semiconductors [5,6]. Nakanotani et al. reported high-performance ambipolar TFTs based on an organic–inorganic hybrid structure containing an indium zinc oxide and pentacene bilayer, which was found to exhibit ambipolar TFT characteristics with hole and electron mobilities of 0.14 and 13.8 $cm^2V^{-1}s^{-1}$, respectively [5]. Pal et al. reported pentacene/ZnO bilayer TFTs that exhibit well-balanced hole and electron mobilities of 6.3×10^{-3} and 7.6×10^{-3} $cm^2V^{-1}s^{-1}$, respectively [6]. However, these hybrid bilayer ambipolar TFTs do not exhibit well-balanced hole and electron mobilities and a high charge carrier mobility at the same time due to poor compatibility between pentacene and the oxide semiconductor at their interface. In this paper, we report high-performance ambipolar TFTs and an inverter with well-balanced hole and electron mobilities; this balance is obtained by inserting a self-assembled monolayer (SAM) between pentacene and the ZnO active layer to enhance their compatibility at the interface. We also varied the dipole moment of the interface between the pentacene and ZnO layers by testing various SAMs, and investigated the effects of the permanent dipoles on the ZnO surface on the ambipolar characteristics of these pentacene/ZnO hybrid TFTs.

2. Experiments

Heavily doped *n*-type silicon wafers (n++ Si) with 300 nm thick thermally grown silicon dioxide (SiO_2) layers were used as gate substrates. Each ZnO thin film used as an *n*-type channel material was deposited on a cleaned gate substrate by using atomic layer deposition (ALD) at a temperature of 150 °C. Diethylzinc was used as the source of zinc. Oxygen plasma was used as the oxygen source for ZnO fabrication. The reactor pressure was maintained at 0.7 Torr with argon gas purging at 100 sccm. During the reaction, diethylzinc and the oxygen plasma were sequentially injected into the reactor chamber to produce a ZnO monolayer on the substrate. The thickness of the ZnO layer was 20 nm, which was patterned by using photolithography. A schematic diagram of the device structure of an *n*-type unipolar TFT with a ZnO active layer is shown in the inset in Fig. 1a. The source-drain electrodes of each unipolar TFT were defined on the ZnO active layer by thermally evaporating gold (Au) through a shadow mask. The channel length (L) and width (W) were 150 and 1500 μm, respectively. A schematic diagram of an ambipolar TFT based on a bilayer hybrid structure composed of an upper pentacene layer and a lower SAM-modified ZnO layer is shown in Fig. 2. After the ZnO layer was ultraviolet–ozone-treated for 15 min, the SAMs were then deposited on the ZnO surface by using spin-coating or a dipping process. Two different SAMs, dodecanoic acid (DA) and perfluorooctyltriethoxysilane (PFOTES) were chosen based on their dipole and terminal groups, as shown in Fig. 2. 1 mM of DA in ethanol was spin-coated onto the ZnO film, resulting in the formation of a monolayer of DA through the chemical bonding between carboxylic acid and ZnO [14–17]. The DA-treated ZnO was spin-coated again using pure ethanol to remove physically absorbed DA molecules. In the preparation of the PFOTES SAM, the ZnO sample was dipped into a 1 mM toluene solution of PFOTES with 0.01 vol.% *n*-butylamine as a catalyst. After treating the sample at 45 °C for 90 min, the PFOTES-treated ZnO sample was removed from solution and rinsed with toluene in order to remove excess PFOTES molecules. After drying, 50 nm thick pentacene films were deposited onto the SAM-treated ZnO samples held at room temperature, under a

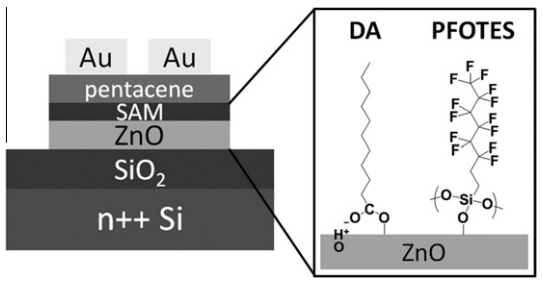

Fig. 2. Device architecture of the ambipolar TFT based on a pentacene/ZnO hybrid structure, and the modification of the interface between pentacene and ZnO by the insertion of a DA or PFOTES SAM, and their chemical structures on the ZnO active layer.

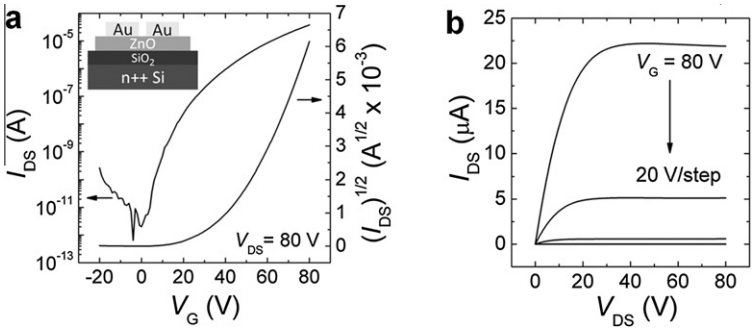

Fig. 1. (a) Saturated (V_{DS} = 80 V) transfer and (b) output characteristics of a unipolar TFT based on an atomic-layer-deposited 20 nm thick ZnO film as the *n*-type active layer. The inset shows a schematic diagram of the TFT structure.

vacuum pressure of $\sim 10^{-6}$ Torr with a deposition rate of 0.2 Ås^{-1}. In the case of the bare sample, the pentacene film was deposited onto the ZnO film without SAM treatment. Finally, 80 nm thick Au source-drain electrodes were deposited though a shadow mask. The channel length L and width W were 100 and 1500 μm, respectively. In particular, Al source-drain electrodes were deposited onto the SAM-treated ZnO without a pentacene layer by using the same shadow mask to fabricate the n-type unipolar TFT shown in the inset in Fig. 5b. We measured the electrical characteristics of the TFTs in air at room temperature by using Keithley 2400 and 236 source/measurement units. The capacitance was measured with an HP 4284A Precision *LCR* meter. The secondary electron emission (SEE) spectra of the bare surface and the DA-treated and PFOTES-treated ZnO on n++ Si substrates were obtained with ultraviolet photoemission spectroscopy (UPS) (Escalab 220IXL) by using the He I emission at 21.2 eV. During the UPS measurements, a −5.0 eV bias was applied to improve the transmission of low kinetic energy electrons and ensure the determination of the low kinetic energy edge.

3. Results and discussion

First, we measured the unipolar TFT characteristics by using a 20 nm thick ZnO film as an n-type channel material with top Au contact source-drain electrodes. Fig. 1 shows the transfer and output characteristics of the unipolar ZnO TFT, which are those of typical n-type TFT operation. The charge carrier mobility (μ) was extracted from the slope of a plot of the square root of the drain-source current (I_{DS}) versus gate voltage (V_G) in the saturation regime by using the following equation:

$$I_{DS} = \mu C_i \frac{W}{2L}(V_G - V_T)^2, \quad (1)$$

where V_T is the threshold voltage. The measured capacitance, C_i, was 10 nFcm^{-2} at 1 kHz. V_G was scanned from −20 to 80 V at a constant V_{DS} of 80 V. The transfer characteristics are those of a good TFT device: a μ value of 0.56 cm^{2}V^{-1}s^{-1}, a current on–off ratio (I_{on}/I_{off}) of $\sim 10^7$, and a V_T value of 44.8 V. These values are comparable to those of previously reported ALD-processed ZnO TFTs [4].

Fig. 2 shows a schematic diagram of an ambipolar TFT based on an organic–inorganic hybrid structure composed of pentacene as the upper p-type layer and ZnO as the lower n-type layer. Balanced hole and electron mobilities are preferred in ambipolar TFT applications. In order to fabricate a high-performance ambipolar TFT based on a pentacene/ZnO bilayer structure with balanced hole and electron mobilities and a high hole mobility (μ_h), the crystallinity of the pentacene layer must be well ordered, but usually only inferior growth of pentacene crystals can be obtained on inorganic oxide films with rough surfaces and high surface energies [17–21]. Therefore, we chose an ALD-processed ZnO film as the underlying n-type active layer because it has a very smooth surface ($R_q \sim 0.59$ nm, Fig. 3a) when compared to those obtained with other methods [3,6]. To improve μ_h further, we introduced DA as an alkyl SAM at the interface between the pentacene and ZnO layers, as shown in Fig. 2. The preparation of alkyl SAMs such as octadecyltrichlorosilane on SiO_2 gate dielectrics is a very effective method for improving the μ_h values of organic TFTs because the crystallinity and the morphology of organic semiconducting films on gate dielectrics are enhanced by the presence of alkyl SAMs [22–24]. In addition, a ZnO layer was modified with a PFOTES SAM, which

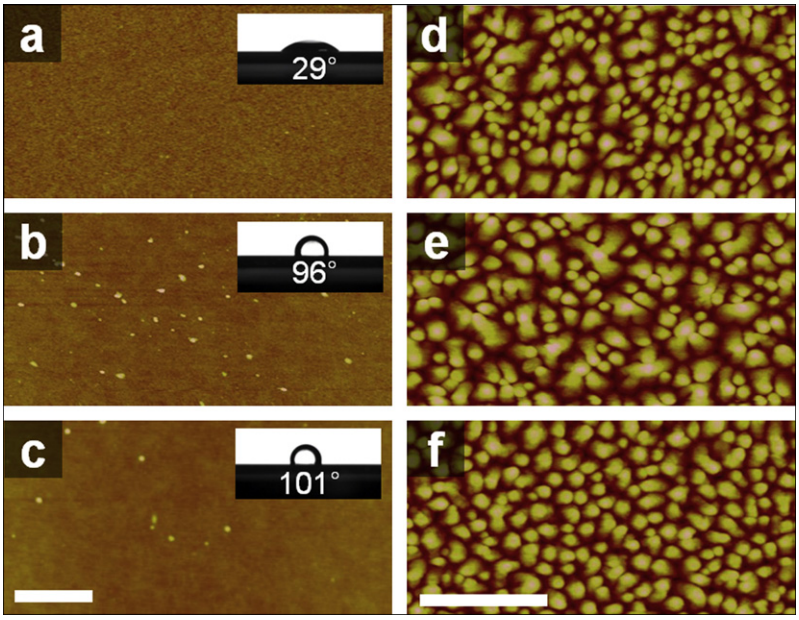

Fig. 3. AFM topographic images of (a) bare ZnO, (b) DA-treated ZnO, and (c) PFOTES-treated ZnO surfaces. The R_q values of the ZnO surfaces are (a) 0.59 nm, (b) 0.90 nm, and (c) 0.68 nm. The AFM images in (d–f) show the morphologies of 50 nm thick pentacene films on surfaces (a), (b), and (c), respectively. The insets show images of droplets on the ZnO surfaces and the corresponding water contact angles (θ_{water}). The scale bars are 1 μm.

contains an electron-withdrawing group, to investigate the effects of permanent dipoles on the electrical characteristics of ambipolar TFTs.

To examine the effects of the SAM treatment on the surface properties of the ZnO layer, we investigated the surface roughness of each sample by using tapping-mode atomic force microscopy (AFM) and measured its water contact angle (θ_{water}). The spin coating of DA onto the ZnO layer was found to result in a hydrophobic surface ($\theta_{water} \sim 98°$) with an rms roughness (R_q) of approx. 0.90 nm, as shown in Fig. 3b, which is higher than the surface roughness of the bare ZnO layer. When ZnO is treated with PFOTES, R_q increases slightly to 0.68 nm, resulting in the most hydrophobic surface ($\theta_{water} \sim 101°$) of the samples, as shown in Fig. 3c. Fig. 3d–f show AFM topographic images of pentacene films on bare, DA-treated, and PFOTES-treated ZnO, respectively. The grain size of the pentacene film on DA-treated ZnO is higher than that on bare ZnO even though R_q increases from 0.59 to 0.90 nm. This increase in grain size despite the increased ZnO surface roughness is due to the hydrophobic surface obtained through the formation of a DA monolayer; variations of the hydrophobic surface roughness within ~1.5 nm have little effect on the grain size, the degree of crystallinity, and the carrier mobility of pentacene [25]. In contrast, the pentacene film on PFOTES-treated ZnO, which has a very low surface energy, formed in the three-dimensional (3D) island growth mode and thus contains small grains (~100 nm) and has a high grain-boundary density, as shown in Fig. 3f.

Fig. 4a shows the current–voltage transfer behaviors (linear regime, V_{DS} = ±10 V) of the ambipolar TFTs containing pentacene on bare, DA-treated, and PFOTES-treated ZnO surfaces; their electrical characteristics are summarized in Table 1. The electron and hole mobilities and V_T values were obtained from the slopes of plots of I_{DS} versus V_G in the linear regime by using the following equation:

$$I_{DS} = \mu \frac{C_i W}{L}(V_G - V_T)V_{DS}. \quad (2)$$

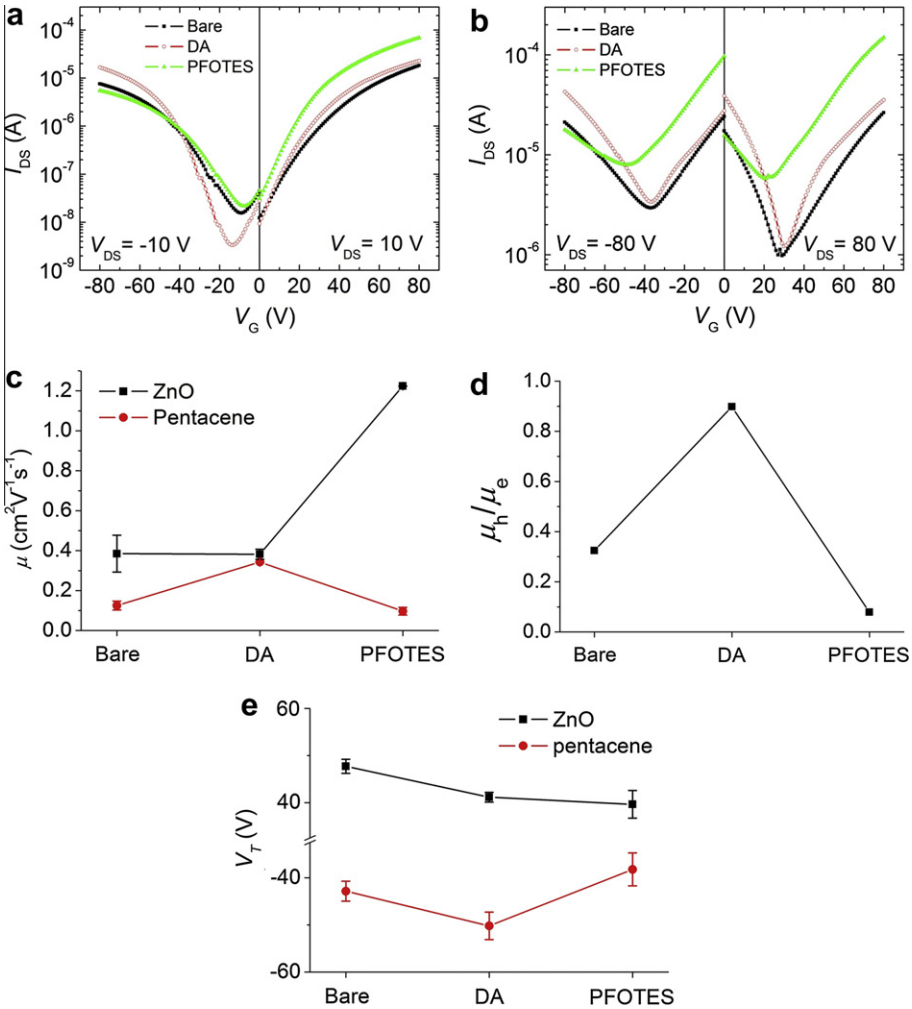

Fig. 4. Transfer characteristics of ambipolar TFTs containing pentacene on bare, DA-treated, and PFOTES-treated ZnO surfaces in (a) the linear regime (V_{DS} = ± 10 V) and (b) the saturation regime (V_{DS} = ± 80 V). The variations in the linear regime of the ambipolar TFTs in (c) the hole and electron mobilities, (d) the hole to electron mobility ratio (μ_h/μ_e), and (e) the threshold voltage.

Table 1
Electrical characteristics in the linear regime of the ambipolar TFTs based on organic–inorganic hybrid structures consisting of pentacene as the *p*-type layer and untreated (bare) or DA-treated ZnO or PFOTES-treated ZnO as the *n*-type layer.

Device	n-Type (ZnO)					p-Type (pentacene)					μ_h/μ_e
	C_i (nF/cm^2)	μ_e (cm^2 v^{-1} s^{-1})	I_{on}/I_{off}	V_T (V)	S (V/decade)	C_i (nF/cm^2)	μ_h (cm^2 v^{-1} s^{-1})	I_{on}/I_{off}	V_T (V)	S (V/decade)	
Bare	10	0.385	10^3	47.7	12.7	9.94	0.125	10^2	−42.8	11.1	0.32
DA	10	0.382	10^4	41.2	12.0	9.82	0.343	10^3	−50.2	7.50	0.90
PFOTES	10	1.224	10^3	39.6	11.0	9.88	0.097	10^2	−38.2	12.7	0.08

The electron mobility (μ_e) of the ambipolar TFT containing bare ZnO as the *n*-type layer is 0.385 ± 0.092 cm^{2}V^{-1}s^{-1}, I_{on}/I_{off} is approx. 10^3, and V_T is 47.7 ± 1.5 V. In DA-treated ZnO, the bonding between DA and ZnO arises when carboxylic acid (–COOH) groups react with hydroxyl groups on ZnO to form carboxylate anions (–COO$^-$), which are electron donors and can provide electrons to ZnO [15,26]; as a result, in the *n*-type operation of the ambipolar TFT based on DA-treated ZnO I_{DS} increases and V_T is shifted negatively, even though the direction of the dipole field from the electron-donating alkyl groups in the DA molecules disturbs the injection of electrons at the source (S) electrode. The ambipolar TFTs based on PFOTES-treated ZnO exhibit an average μ_e of 1.224 cm^{2}V^{-1}s^{-1}, which is higher by a factor of ~3.2 than that of the ambipolar TFT based on bare ZnO, and a negative shift in V_T, as shown in Figs. 4a, 4c, and 4e. These changes in μ_e and V_T in the *n*-type operation of the PFOTES device result from the easy electron injection from the source electrode that arises because of the electron-withdrawing PFOTES SAM, which also induces the increase of the charge density due to a charge transfer at the interface between the ZnO and the PFOTES molecules [27].

The μ_h value of the ambipolar TFTs based on bare ZnO is 0.125 ± 0.022 cm^{2}V^{-1}s^{-1}, I_{on}/I_{off} is approx. 10^2, V_T is −42.8 ± 2.11 V, and the subthreshold slope (S) is 11.1 V/decade. In the *p*-type operation of the ambipolar TFT based on DA-treated ZnO, μ_h is 0.343 cm^{2}V^{-1}s^{-1}, V_T is shifted negatively with respect to that of the bare device, and S is 7.50 V/decade. The low grain-boundary density that results from the increase in the grain size of pentacene on DA-treated ZnO reduces the number of interface-trap states, and thus leads to improvements in the μ_h and the S values, as indicated in Table 1. The improvement in μ_h leads to better balance between the hole and electron mobilities with a hole and electron mobility ratio (μ_h/μ_e) of approx. 0.90, which is much better than that of the bare device ($\mu_h/\mu_e \sim 0.32$), as shown in Fig. 4d. In contrast, in the case of the PFOTES device, the low value of μ_h (0.097 cm^{2}V^{-1}s^{-1}), which is due to the formation of an inferior pentacene film on PFOTES-treated ZnO, and the high electron mobility result in poorly balanced hole and electron mobilities; μ_h/μ_e is approx. 0.08. Kwak et al. reported that the μ_h value of a pentacene film on a fluorinated surface with a very low surface energy ($\theta_{water} \sim 103°$) was degraded by the large number of grain boundaries [28]. The reduction in the grain size, i.e. the high grain-boundary density, of the pentacene film on PFOTES-treated ZnO induces an increase in the number of interface-trap states, as shown in the value of S, which can be used as an indicator for estimating the maximum trap density (N_{trap}) at the interface between the semiconductor and the dielectric according to the following equation [24]:

$$N_{trap} \approx \left[\frac{qS\log(e)}{kT} - 1\right]\frac{C_i}{q}, \quad (3)$$

where q is the electronic charge, k is Boltzmann's constant, and T is the temperature. With this equation, we estimated the interface-trap densities of the devices containing bare ZnO, DA-treated ZnO, and PFOTES-treated ZnO to be 1.2×10^{13}, 7.9×10^{12}, and 1.3×10^{13} cm^{-2}, respectively. These results indicate that the electrical characteristics of *p*-type operation of the ambipolar TFTs are in agreement with the results for the morphologies of the pentacene films.

Fig. 4b shows the transfer characteristics for positive and negative gate biases in the saturation regime (V_{DS} = ± 80 V) of the ambipolar TFTs containing pentacene on bare, DA-treated, and PFOTES-treated ZnO. The dependences in the saturation regime of the electrical parameters μ, V_T, and S on the treatment of ZnO are similar to those in the linear regime. When $|V_G - V_T| < |V_{DS}|$, both the source and drain electrodes inject their respective charge carriers and thus both holes and electrons are present in the channel, so this is the ambipolar regime [7–9]. At a V_G of 0 V, I_{DS} increases markedly in contrast with the linear regime, which is explained for *p*-type operation by the injection of opposite carriers at the drain (D) electrode induced by the positive V_G in the ZnO active channel layer, and for *n*-type operation by the negative V_G in the pentacene active channel layer. In particular, a high I_{DS} value (~0.1 mA) was obtained at a V_G of 0 V in the *p*-type operation of the PFOTES device because of the permanent dipole of the PFOTES-treated ZnO surface.

The formation of a permanent dipole in the SAM layer is induced by the charge distribution within the functional groups of the SAM molecule [29]. The permanent dipole in the SAM layer on ZnO influences the secondary electron emission (SEE) onset for the active layers. The changes in the SEE onset on the SAM-treated ZnO surfaces thus indicate the relative strength of the SAM's electron-donating or electron-withdrawing character, and can be determined from the SEE spectra [30]. We determined the relative strengths of the permanent dipoles of the bare and SAM-treated ZnO layers from the changes in SEE onset obtained from their SEE spectra. Fig. 5a shows the SEE spectra of the bare, DA-treated, and PFOTES-treated ZnO. The SEE onset was determined by extrapolating two solid lines from the

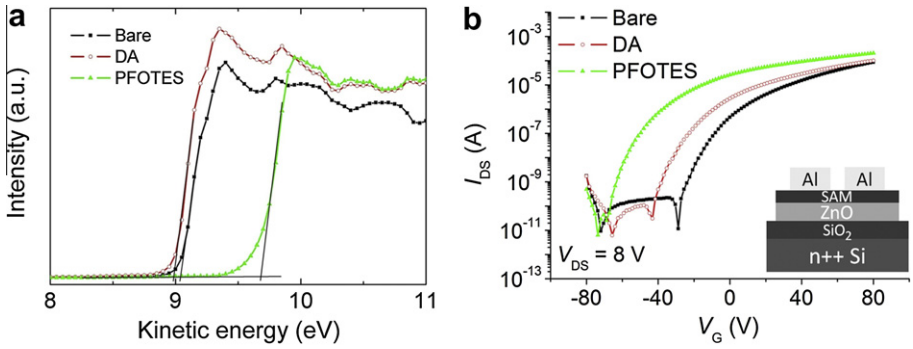

Fig. 5. (a) Secondary electron emissions (SEEs) of the three samples: bare ZnO (closed black rectangles), DA-treated ZnO (open red circles), and PFOTES-treated ZnO (closed green triangles). (b) Transfer characteristics in the linear regime (V_{DS} = 8 V) of *n*-type unipolar TFTs without pentacene based on bare ZnO, DA-treated ZnO, and PFOTES-treated ZnO. Inset: a schematic diagram of a unipolar TFT.

background and the straight onset in each spectrum. The SEE onset for DA-treated ZnO was found to be at a kinetic energy (8.99 eV) that is a little lower (by 0.05 eV) than that of bare ZnO. In contrast, the onset for PFOTES-treated ZnO is higher by 0.64 eV than that of the bare ZnO. The large shift of the SEE onset for PFOTES-treated ZnO originates from the presence of the fluorine-induced strongly negative surface dipole moments of the PFOTES SAM, which is strongly electron withdrawing. The electron-donating alkyl groups of the DA SAM with weakly positive surface dipole moments mean that the DA-treated ZnO has a slightly shifted the SEE onset. These differences influence the density of hole carriers in *p*-type operation, the injection of charge carriers at the S/D electrodes, and the ambipolar characteristics.

For the pentacene films on SAM-treated ZnO, the permanent dipole field demonstrated by the change in the SEE onset (Fig. 5a) modifies the surface potential and the electronic structure of the interface between the pentacene and ZnO layers, and thus results in a change in the carrier density and a shift in V_T [31,32]. In the *p*-type operation of the PFOTES device, the electron-withdrawing properties of the PFOTES SAM on ZnO leads to the formation of a permanent dipole field under the pentacene film. As a result, electrons from the pentacene film are attracted by the PFOTES SAM leaving the more mobile holes in the channel and therefore V_T is shifted more positively, as shown in Fig. 4e [31]. In the case of the DA device, on the other hand, a negative shift in V_T is observed since the dipole field and negative interface charges that originate from the electron-donating DA SAM modify the surface potential, which has the same effect as applying a positive gate bias.

The V_G–I_{DS} transfer characteristics of *n*-type unipolar TFTs without a pentacene layer based on bare, DA-treated, and PFOTES-treated ZnO and a schematic diagram of the device structure are shown in Fig. 5b; the transfer characteristics can be used to investigate the effects of the permanent dipole field of the SAMs on the injection behavior at the source electrode. Inserting the PFOTES SAM between the Al electrodes and the ZnO active layer means that the turn-on voltage (V_{on}) is dramatically shifted from −28.8 to −68.8 V and that I_{DS} increases markedly over that of the TFT without SAM treatment. These differences can be attributed to the easy charge (electrons in this case) injection from the Al electrode to the ZnO active layer that arises because the direction of the permanent dipole field of the PFOTES SAM enhances electron injection at the source electrode [33,34]. Furthermore, the PFOTES SAM with a strong electron-withdrawing ability on the ZnO layer can produce the mobile charges in the channel due to charge transfer at the interface between the ZnO and the PFOTES molecules [27]. For the DA-treated ZnO device, V_{on} is also shifted negatively to −43.2 V despite the disturbance of the electron injection at the source electrode that results from the direction of the permanent dipole field of the DA SAM. This result means that the effects on the TFT transfer characteristics of the electron donation of the carboxylate anions (–COO^-) in the DA SAM to ZnO are greater than those of the weak permanent dipole field of the DA SAM. These effects of the SAMs on the transfer characteristics of the *n*-type unipolar TFTs without a pentacene layer also contributed equally to the *n*-type operation of the ambipolar TFTs shown in Fig. 4.

Fig. 6 shows the output and ambipolar characteristics of the hybrid TFTs based on the pentacene/ZnO bilayer structures illustrated in the insets. The bare device without SAM treatment exhibits typical ambipolar output characteristics (Fig. 6a) similar to those of previously reported ambipolar TFTs [5–10,13]. When $|V_G| \leqslant 40$ V and $|V_{DS}|$ is increased, divergent I_{DS}–V_{DS} behavior is observed, indicating abrupt electron injection (in the case of *p*-type operation) or hole injection (in the case of *n*-type operation) from the drain electrode, which is typical of ambipolar operation in TFTs [5–10,13].

For the ambipolar TFT based on DA-treated ZnO and a positive gate bias, typical *n*-channel characteristics were observed for positive drain-source voltages with $|V_{DS}| \leqslant |V_G - V_T| = |V_{G,eff}|$, where $V_{G,eff}$ is the effective gate voltage. When $|V_{DS}|$ is increased, the additional hole current that originates from the abrupt hole injection at the drain electrode increases when compared with that of the bare device, as shown in Fig. 6b. The negative interface charge produced by the permanent dipole field of the DA SAM attracts additional holes in the channel from the drain electrode and thus results in an increase in the additional hole current [8]. For the DA device with a negative gate

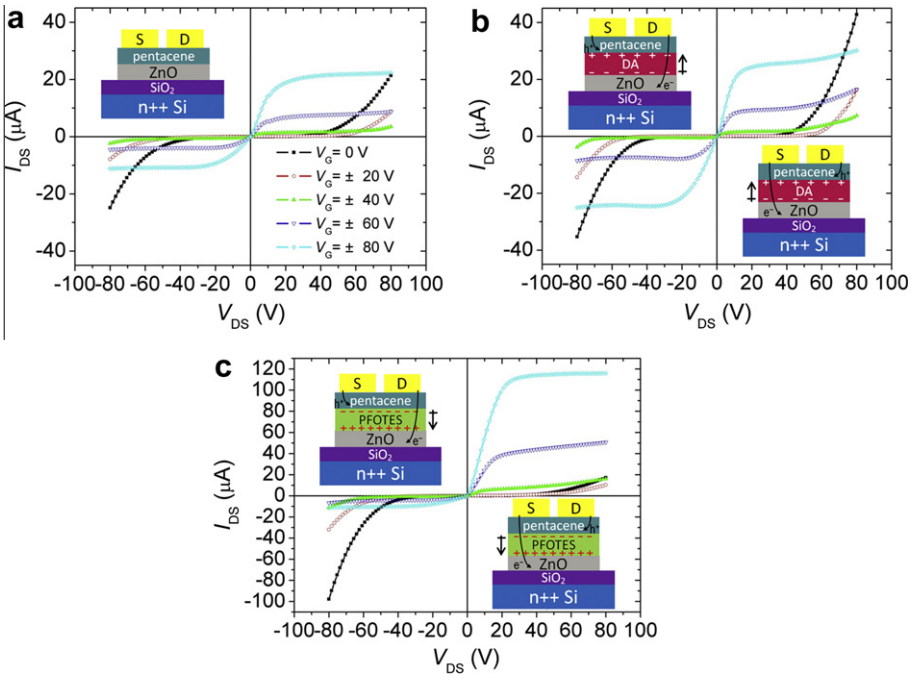

Fig. 6. Output characteristics of ambipolar TFTs containing *p*-/*n*-type layers based on (a) pentacene/bare ZnO, (b) pentacene/DA-treated ZnO, and (c) pentacene/PFOTES-treated ZnO. The *p*- and *n*-type operations were carried out under negative and positive V_G biases, respectively. Insets: schematic cross-sections of the ambipolar TFTs, schematic diagrams of the injection behaviors of electrons (e^-) and holes (h^+) at the source (S) and drain (D) electrodes, and the directions of the permanent dipole fields of the SAMs.

bias, i.e. *p*-type operation, an increase in the drain-injected additional electron current is also observed even though the direction of the permanent dipole field of the DA SAM interrupts the electron injection from the drain electrode to the ZnO, as shown in the schematic diagram in the inset in Fig. 6b. This result means that the weak surface dipole moment of the DA SAM does not affect electron injection from the drain electrode significantly. When in the *p*-type operation of the DA device $|V_{G,eff}|$ decreases due to the negative shift in V_T, a shift of the onset of the drain-injected electron current to lower $|V_{DS}|$ can result in an increase in the additional electron current [8]. The output characteristics of the DA device show that the drain-source current levels of the *p*- and *n*-type operations are almost symmetric due to the well-balanced hole and electron mobilities, as shown in Fig. 6b.

In the output characteristics of the device with pentacene/PFOTES-treated ZnO (Fig. 6c), typical *n*-type operation is observed for positive V_G with a dramatically increased drain-source current (e.g. $I_{DS} \sim 120$ μA at a V_G of 80 V), which results from the improvement in μ_e ($1.224\ cm^2V^{-1}s^{-1}$) that results from treatment with the PFOTES SAM. When the V_G was 0 or 20 V and the V_{DS} was greater than ~40 V, a decrease in the drain-injected hole current with respect to that of the bare device was observed; this decrease can be explained as follows: the positive interface charge produced by the permanent dipole field of the PFOTES SAM repels additional holes in the channel from the drain electrode [8]. In the *p*-type operation of the PFOTES device, on the other hand, a decrease in the saturation current and an increase in the drain-injected additional electron current were observed, as shown in Fig. 6c. The decrease in the saturation current arises because of the low value of μ_h ($0.095\ cm^2V^{-1}s^{-1}$), which is due to the increase in the number of interface-trap states that results from the high grain-boundary density of the pentacene film on PFOTES-treated ZnO, and thus an unbalanced hole and electron saturation current is observed. The increase in the drain-injected electron current results from the direction of the fluorine-induced strongly negative surface dipole field of the PFOTES SAM, which induces easy electron injection from the drain electrode to the ZnO active layer. Thus a high I_{DS} (~0.1 mA) at a V_G of 0 V in the transfer characteristics (saturation regime) was also observed, as shown in Fig. 4b. These unbalanced ambipolar behaviors of the PFOTES device in the *p*- and *n*-type operations produce asymmetric output characteristics.

In addition, we fabricated a complementary-like inverter through the integration of two identical pentacene/ZnO ambipolar TFTs employing DA SAMs. As mentioned above, the presence of the DA SAM between the pentacene and ZnO layers means that μ_h and μ_e of the ambipolar TFT are better balanced than is the case for the other surface treatment layer investigated here, and thus results in the optimization of ambipolar charge transport. Fig. 7 shows the typical voltage transfer characteristics of the resulting inverter; the inset shows a schematic diagram of the inverter structure. The supply voltage (V_{DD}) of 40 V was biased to the inverter, so the output voltage (V_{out}) varied from high to low in response to the swing of the input voltage (V_{in}) from low to high, and a sharp inversion of V_{in} is found near 15.5 V. The voltage gain (defined as the absolute value

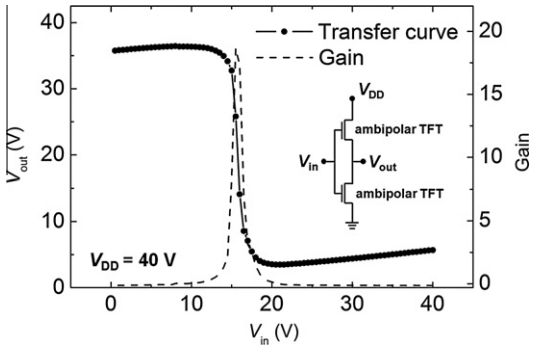

Fig. 7. Voltage-transfer characteristics of a complementary-like inverter comprised of two identical pentacene/ZnO ambipolar TFTs (L = 100 μm, W = 1500 μm) employing a DA SAM. The inset shows a schematic circuit diagram of the inverter.

of dV_{out}/dV_{in}), the noise margin, and the output voltage swing (defined as $V_{out}^{max} - V_{out}^{min}$) were calculated from the voltage transfer curves. The maximum voltage gain reaches a maximum value of 18.6, and the values of the noise margin and the output voltage swing are approx. 4.5 V and 33 V, respectively. The voltage gain of our inverter surpasses recently reported values for complementary-like inverters with ambipolar transistors [10–13], and those of unipolar inverters, in particular those employing pentacene transistors [35,36].

4. Conclusions

We have demonstrated high performance ambipolar TFTs and a complementary-like inverter based on an organic–inorganic hybrid structure composed of pentacene and ZnO as the semiconducting *p*-type and *n*-type layers, respectively. A simple method was developed to modify the interface of the *p*-type and *n*-type layers by the introduction of a SAM between the pentacene and ZnO layers. We achieved well-balanced hole and electron mobilities in the pentacene/DA-treated ZnO ambipolar TFT with a μ_h value of $\sim$0.34 $cm^2V^{-1}s^{-1}$ and a μ_e value of $\sim$0.38 $cm^2V^{-1}s^{-1}$. This modification of the interface between the pentacene and ZnO layers was found to enable the control of the surface energy and the permanent dipole field at the interface, which influences the electrical and ambipolar characteristics such as the hole and electron mobilities, the threshold voltage, and the injection behavior of charge carriers at the S/D electrodes. The optimized interface between the *p*- and *n*-type active layers that is obtained through treatment with a DA SAM produces well balanced ambipolar behavior and thus enables the realization of a high performance complementary-like inverter.

Acknowledgments

This work was supported by a Korea Science and Engineering Foundation (KOSEF) grant funded by the Korea government (MEST) (2010-0000809) and a Basic Science Research Program grant funded through the NRF by the Ministry of Education, Science and Technology (2010-0005187).

References

[1] D. Braga, G. Horowitz, Adv. Mater. 21 (2009) 1473.
[2] K. Nomura, H. Ohta, A. Takagi, T. Kamiya, M. Hirano, H. Hosono, Nature 432 (2004) 488.
[3] C. Yang, K. Hong, J. Jang, D.S. Chung, T.K. An, W.-S. Choi, C.E. Park, Nanotechnology 20 (2009) 465201.
[4] S. Kwon, S. Bang, S. Lee, S. Jeon, W. Jeong, H. Kim, S.C. Gong, H.J. Chang, H. Park, H. Jeon, Semicond. Sci. Technol. 24 (2009) 035015.
[5] H. Nakanotani, M. Yahiro, C. Adachi, K. Yano, Appl. Phys. Lett. 90 (2007) 262104.
[6] B.N. Pal, P. Trottman, J. Sun, H.E. Katz, Adv. Funct. Mater. 18 (2008) 1832.
[7] J. Zaumseil, H. Sirringhaus, Chem. Rev. 107 (2007) 1296.
[8] G. Paasch, Th. Lindner, C. Rost-Bietsch, S. Karg, W. Riess, S. Scheinert, J. Appl. Phys. 98 (2005) 084505.
[9] E.C.P. Smits, T.D. Anthopoulos, S. Setayesh, E. van Veenendaal, R. Coehoorn, P.W.M. Blom, B. de Boer, D.M. de Leeuw, Phys. Rev. B 73 (2006) 205316.
[10] E.J. Meijer, D.M. de Leeuw, S. Setayech, E. van Veenendaal, B.-H. Huisman, P.W.M. Blom, J.C. Hummelen, U. Scherf, T.M. Klapwijk, Nat. Mater. 2 (2003) 678.
[11] T.D. Anthopoulos, D.M. de Leeuw, E. Cantatore, S. Setayesh, E.J. Meijer, C. Tanase, J.C. Hummelen, P.W.M. Blom, Appl. Phys. Lett. 85 (2004) 4205.
[12] B. Singh, P. Senkarabacak, N.S. Sariciftci, A. Tanda, C. Lackner, R. Hagelauer, G. Horowitz, Appl. Phys. Lett. 89 (2006) 033512.
[13] M.-J. An, H.-S. Seo, Y. Zhang, J.-D. Oh, J.-H. Choi, Appl. Phys. Lett. 97 (2010) 023506.
[14] N.H. Moreira, A.L. da Rosa, T. Frauenheim, Appl. Phys. Lett. 94 (2009) 193109.
[15] X. Tian, J. Xu, W. Xie, J. Phys. Chem. C 114 (2010) 3973.
[16] H.-L. Yip, S.K. Hau, N.S. Baek, A.K.-Y. Jen, Appl. Phys. Lett. 92 (2008) 193313.
[17] D. Knipp, R.A. Street, A.R. Völkel, Appl. Phys. Lett. 82 (2003) 3907.
[18] D. Knipp, R.A. Street, A.R. Völkel, J. Ho, J. Appl. Phys. 93 (2003) 347.
[19] S. Steudel, S.D. Vusser, S.D. Jonge, D. Janssen, S. Verlaak, J. Genoe, P. Heremans, Appl. Phys. Lett. 85 (2004) 4400.
[20] S.E. Fritz, T.W. Kelley, C.D. Frisbie, J. Phys. Chem. B 109 (2005) 10574.
[21] H. Yang, C. Yang, S.H. Kim, M. Jang, C.E. Park, ACS Appl. Mater. Interfaces 2 (2010) 391.
[22] Y.-Y. Lin, D.J. Gundlach, S.F. Nelson, T.N. Jackson, IEEE Electron Device Lett. 18 (1997) 606.
[23] D.J. Gundlach, J.A. Nichols, L. Zhou, T.N. Jackson, Appl. Phys. Lett. 80 (2002) 2925.
[24] M. McDowell, I.G. Hill, J.E. McDermott, S.L. Bernasek, J. Schwartz, Appl. Phys. Lett. 88 (2006) 073505.
[25] K. Shin, C. Yang, S.Y. Yang, H. Jeon, C.E. Park, Appl. Phys. Lett. 88 (2006) 072109.
[26] C. Lao, Y. Li, C.P. Wong, Z.L. Wang, Nano Lett. 7 (2007) 1323.
[27] M.F. Calhoun, J. Sanchez, D. Olaya, M.E. Gershenson, V. Podzorov, Nat. Mater. 7 (2008) 84.
[28] S.-Y. Kwak, C.G. Choi, B.-S. Bae, Electrochem. Solid-State Lett. 12 (2009) G37.
[29] I.H. Campbell, S. Rubin, T.A. Zawodzinski, J.D. Kress, R.L. Martin, D.L. Smith, Phys. Rev. B 54 (1996) 014321.
[30] H. Ishii, K. Sugiyama, E. Ito, K. Seki, Adv. Mater. (Weinheim, Ger.) 11 (1999) 605.
[31] K.P. Pernstich, S. Haas, D. Oberhoff, C. Goldmann, D.J. Gundlach, B. Batlogg, A.N. Rashid, G. Schitter, J. Appl. Phys. 96 (2004) 6431.
[32] Y. Jang, J.H. Cho, D.H. Kim, Y.D. Park, M. Hwang, K. Cho, Appl. Phys. Lett. 90 (2007) 132104.
[33] J.H. Seo, A. Gutacker, B. Walker, S. Cho, A. Garcia, R. Yang, T.-Q. Nguyen, A.J. Heeger, G.C. Bazan, J. Am. Chem. Soc. 131 (2009) 18220.
[34] J.H. Park, S.W. Cho, S.H. Park, J.G. Jeong, H.J. Kim, Y. Yi, M.-H. Cho, Synth. Met. 160 (2010) 108.
[35] J.B. Koo, C.H. Ku, S.C. Lim, S.H. Kim, J.H. Lee, Appl. Phys. Lett. 90 (2007) 133503.
[36] S.H. Kim, J. Jang, H. Jeon, W.M. Yun, S. Nam, C.E. Park, Appl. Phys. Lett. 92 (2008) 183306.

Organic Electronics 12 (2011) 419–423

Contents lists available at ScienceDirect

Organic Electronics

journal homepage: www.elsevier.com/locate/orgel

Three-dimensional integrated circuit using printed electronics

A.C. Hübler, G.C. Schmidt *, H. Kempa, K. Reuter, M. Hambsch, M. Bellmann

Institute of Print- and Media Technology at Chemnitz University of Technology, 09107 Chemnitz, Germany

ARTICLE INFO

Article history:
Received 1 November 2010
Received in revised form 10 December 2010
Accepted 14 December 2010
Available online 30 December 2010

Keywords:
Printed electronics
Three-dimensional circuits
Organic field-effect transistors
Multilayer interconnects

ABSTRACT

A fully printed ring oscillator circuit is reported, which has not only horizontally arranged parts, but inverter stages stacked vertically on top of each other in four through-connected substrate layers. For the preparation of the inverters exclusively gravure and flexographic printing were used. Characteristics of the stacked ring oscillator are similar to planar circuits. A very interesting path of development for printed electronics is opened with this approach, because three-dimensional circuits become possible.

© 2010 Elsevier B.V. All rights reserved.

1. Introduction

Stacking and vertical interconnecting of several circuit layers has been studied in the past within the framework of conventional microelectronics in order to overcome technological barriers that arise with the ongoing increase of integration density [1]. Most importantly, global length of interconnects and thereby signal delay as well as power consumption are expected to be reduced [2]. Although several approaches for the realization of three-dimensional circuits exist, a breakthrough has so far been hindered by technological difficulties limiting three-dimensional integration to a few layers [3]. However, truly three-dimensional arrangement of electronic components, as it is realized for example in the biological brain, would allow for an extremely enhanced complexity of interconnects and thus enable a new way of improving the functionality of integrated circuits [4]. It should be noted that multilayers are state of the art in printed circuit board technology, where dozens of layers can be interconnected [5]. An approach for three-dimensional integration was combining organic and inorganic materials in order to stack numerous circuit layers directly on top of each other, whereby definition of patterns and preparation of interconnects was done by means of mask-based processes such as photolithography [6].

Beside classical silicon electronics, printed electronics is seen as a complementary technology for the manufacture of integrated circuits. Printable inks can be prepared from electronically functional polymers or nanoparticles, which can be used to print electronic devices, e.g. transistors, as well as complete circuits on flexible substrates such as PET-foil [7]. Although nowadays inkjet printing is very often used in printed electronics (for reviews see [8,9]), especially high-volume rotary printing methods, namely offset, gravure and flexographic printing, have an interesting economic potential due to their high productivity [10]. Transistors [11] and ring oscillator circuits [12] realized in unipolar (PMOS-equivalent) logic by means of these methods have been demonstrated already some time ago. Meanwhile, printable n-type semiconductors have become available [13,14], allowing for CMOS-equivalent circuitry [15–17], while at the same time alternative approaches emerge like ambipolar transistors [18] and charged dielectrics [19].

Nevertheless, for further development of printed digital circuits principal challenges exist. Especially the limited homogeneity and topology of printed films limits the

* Corresponding author. Tel.: +49 371 531 35175; fax: +49 371 531 835175.
E-mail address: georg.schmidt@mb.tu-chemnitz.de (G.C. Schmidt).

1566-1199/$ - see front matter © 2010 Elsevier B.V. All rights reserved.
doi:10.1016/j.orgel.2010.12.010

possibilities for straight-forward reduction of feature sizes as well as for enhancement of lateral integration density; hence new paths of development are to be explored. The idea presented here is to use established post-press methods like folding and cutting in order to enable three-dimensional circuitry. Flexible substrate layers printed with electronic devices are supposed to be accurately stacked on top of each other and individual devices to be interconnected in vertical direction throughout the layers. In order to validate this approach, a stacked ring oscillator circuit consisting of five inverter stages was realized (see Fig. 1h for circuitry). Two of the inverter stages were located in the first substrate layer, while the other three were located in separate layers. With the transistors thereby arranged in a truly three-dimensional pattern, a three-dimensional integrated circuit was created.

2. Experimental

A ring oscillator was chosen for the demonstration of a three-dimensional circuit because possible performance variations due to the stacked arrangement in comparison with the planar setup can be easily detected using this kind of circuit. All necessary components were prepared using exclusively gravure and flexographic printing in an identical way for the planar and for the three-dimensional device. Details of printing processes used for manufacturing of integrated circuits have been reported several times [11,12,20]. Here, a 100 μm thick PET-foil (Melinex 400 of DuPont Teijin Films) was used as substrate for printing of transistors in top-gate configuration. Source/drain structures were firstly printed from an adapted formulation of the conductive polymer poly(3,4-ethylenedioxythiophene):poly(styrenesulfonate) (PEDOT:PSS, Clevios P of H.C. Starck) by means of a recently developed technique, called "Cyflex" [21]. The semiconductor used was the p-type liquid crystalline polymer poly(9,9-dioctylfluorene-co-bithiophene) (F8T2 of Evonik), which was gravure printed on top of the source/drain structures from a 0.5 wt.% solution in a 1:1 mixture of toluene and tetrahydrofurane. Subsequently, a dual film dielectric was gravure printed as well, where a thin film of a proprietary butylene copolymer (P105 of Merck) forms the interface with the semiconductor and a poly(methyl methacrylate) film (PMMA of Aldrich, molecular weight = 996,000 g/mol) from a 7.5% solution in ethyllactate/butylacetate serves as gate insulator. In order to ensure good insulation, three successive printing runs of PMMA were conducted. The printing steps described so far were performed on a laboratory roll-to-roll printing machine with a web width of 35 mm and with process speeds between 0.5 and 1 m/s. Finally gate electrodes and contact pads for the source/drain

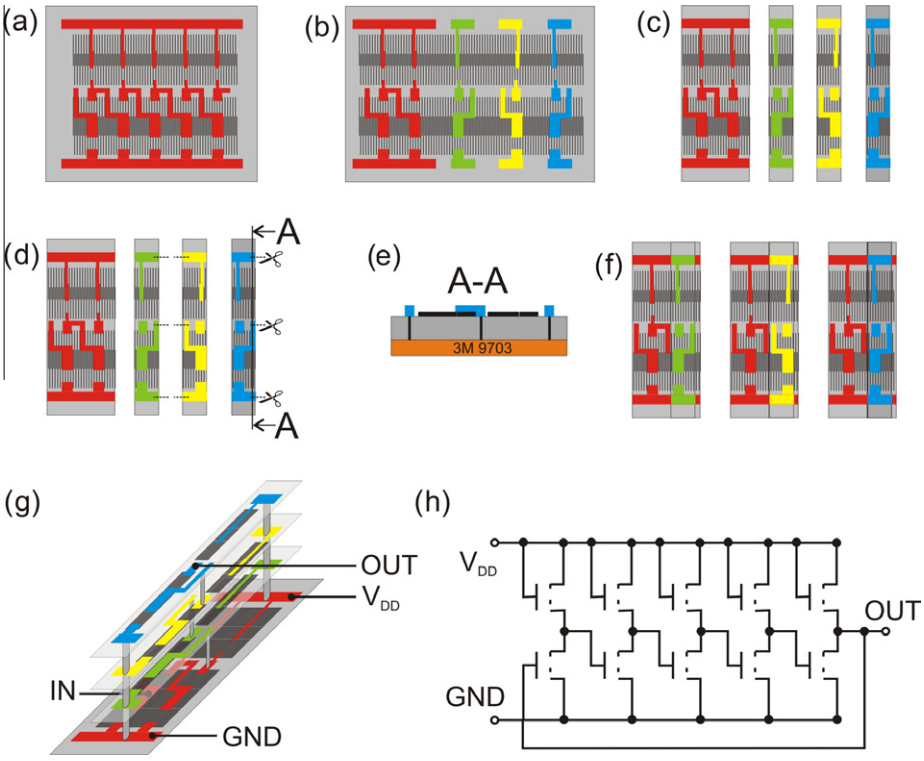

Fig. 1. (a) Schematic representation of a printed planar ring oscillator circuit. (b) Schematic representation of printed components of a stacked ring oscillator. Grey color represents the substrate, black color represents source/drain electrodes, other colors represent gate electrodes. Semiconductor and dielectrics are omitted for clarity. (c) Inverter stages 3, 4 and 5 are separated from stages 1 to 2 and from each other. (d) Small cuts are made at the contacts. (e) Cuts are filled with PEDOT:PSS and anisotropic conductive two-side adhesive tape is attached to the backside. (f) These inverter stages are subsequently sticked to stage 2. (g) Exploded scheme of the stacked ring oscillator. (h) Circuitry of a five-stage ring oscillator (For interpretation of the references to color in this figure legend, the reader is referred to the web version of this article).

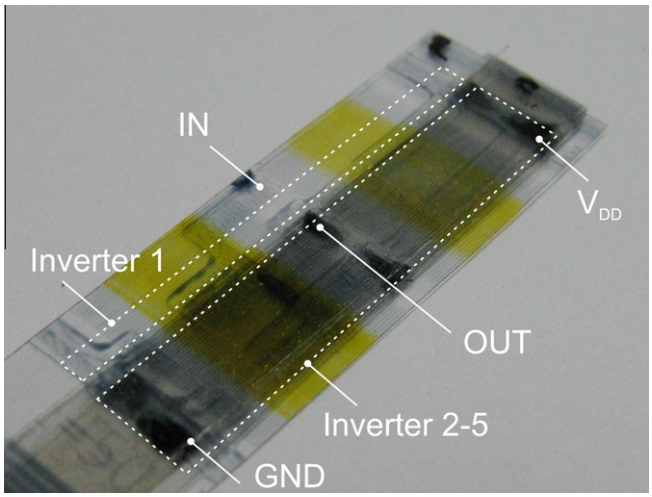

Fig. 2. Photograph of a fully mass printed and stacked ring oscillator.

electrodes were printed from an adapted formulation of Clevios P on a flexographic test printing device (Flexiproof 100 of RK Print).

The experiment reported here was not aimed at the preparation of structures with particular high resolution. In contrast, safely printable and reproducible results were targeted in order to compare the three-dimensional arrangement with the conventional setup. Printed transistors had a channel length (i.e. the distance between source and drain electrodes) of 45 μm, the width of single electrode fingers being 105 μm. Each inverter stage consisted of two transistors, one so-called drive transistor with a channel-width-to-length-ratio of 666 and one so-called load transistor with a ratio of 120. Complete planar ring oscillators (Fig. 1a) were printed together with separated inverter stages with the input contact situated on one of two adjacent sides (Fig. 1b). The latter ones were used for the preparation of the stacked ring oscillator, which thus could be compared with a planar one prepared under identical experimental conditions. The first substrate layer of the stacked ring oscillator consisted of two interconnected inverter stages in order to allow for later contacting, while three more inverter stages were situated in layers two, three and four, respectively. Due to the alternating position of the output contact each of them was positioned so that it could be connected with the input contact of the following one by a vertical interconnect (Fig. 1c).

Vertical interconnects were prepared manually for maximum process control in this basic experiment. Fig. 1d–g illustrates the method. It has been shown, however, that through-connections in printed circuits on foil can be mechanically realized by preparing holes using perforation devices or lasers, which are subsequently overprinted with conductive inks [22]. This process was simulated by cutting into the substrate of the inverter stages three, four and five on a length of approx. one milimeter at the positions of the input and supply voltage contacts. By applying a drop of the gate material (PEDOT:PSS) on the cut from each side of the substrate, a through connection was established. Subsequently these layers were stacked on top of inverter stage two using an anisotropic conductive two-sided adhesive tape (acrylate with embedded silver-coated nickel particles, 9703 of 3 M) for mechanical and electrical connection between adjacent layers. The adhesive tape covered the whole area of the layers so that the mechanical connection was very stable, while for a safe electrical connection with a contact resistance <1Ω an overlap of the adjacent contacts larger than 3 mm^2 is necessary according to the technical data sheet. Fig. 2 shows a photographic image of the stacked ring oscillator.

3. Results and discussion

The contact resistance of the vertical interconnects was determined on a series of samples of two interconnected layers to be 5–6 kΩ, which can be attributed to the through-connection using PEDOT:PSS. This value is in accordance with the total resistance over three interconnects, measured at the conducting path of the supply voltage of the stacked ring oscillator from the first to the fifth inverter stage, which was approx. 21 kΩ. The same conducting path without vertical interconnects in the planar circuit had a resistance of approx. 10 kΩ. In spite of shorter interconnection length, the resistance of interconnects turns out to be larger in the case of the stacked circuit compared to the planar one due to the resistance of through-connections. However, the resistance values of through-connections can be largely reduced when more suitable materials are used. In preliminary experiments with mechanical perforation and a silver ink, resistances of a few Ω have been realized.

The electrical properties were characterized using a two-channel source measure unit (Keithley 2612) controlled by a computer. Fig. 3a shows the static characteristics of the inverter stages of the planar as well as of the stacked circuit, which are typical for unipolar printed

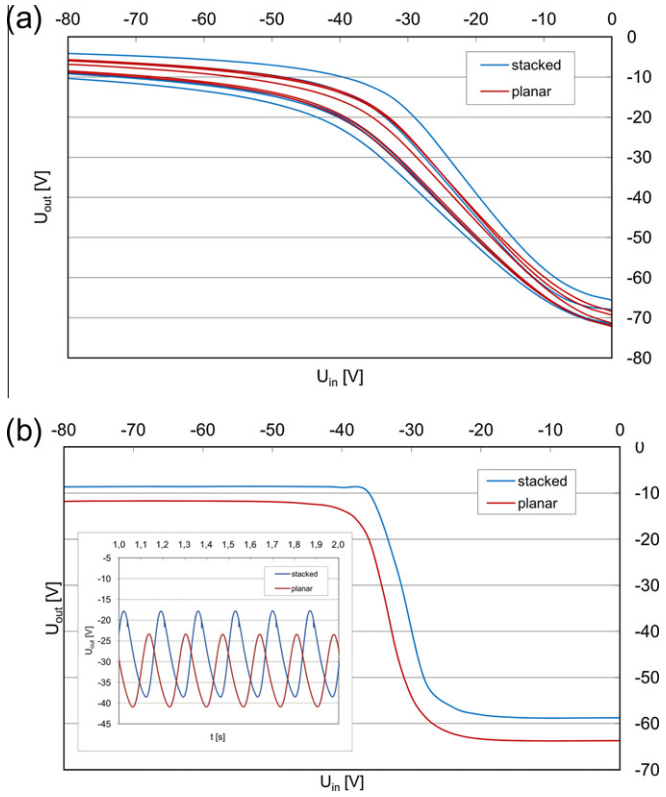

Fig. 3. (a) Static output characteristic of single inverter stages (for stacked and planar ring oscillator) at $V_{DD} = -80$ V. (b) Static output characteristic of 5-stage ring oscillators (stacked and planar) at $V_{DD} = -80$ V. Inset: oscillation of stacked and planar ring oscillator.

inverters. Within the variation of the individual characteristics there is no difference between the two circuits apart from a slightly larger variation in the case of the stacked ring oscillator, which is accidental. The static characteristics of five inverter stages connected in series of the planar and the stacked circuit, respectively, are plotted in Fig. 3b. The voltage swings are 52 V for the planar and 50 V for the stacked circuit, which is an insignificant difference. There is, however, a small shift of a few volts in both directions in between the curves, which can be attributed to the variations among the inverter stages. When the output signal of the last inverter stage is fed back into the input of the first stage, the ring oscillator delivers an oscillating signal. This is the case for both of the configurations; the frequencies of the oscillations, 6.0 Hz for the planar circuit and 5.9 Hz for the stacked circuit at a supply voltage of −80 V, are nearly identical. From these results we conclude that the characteristics of the ring oscillator circuit are not significantly affected by the vertical configuration. Generally alternate stacking of even and odd inverter stages is expected to have a positive effect on parasitic capacitances because of identical charge polarity of adjacent electrode layers (gate of even stage vs. source/drain of odd stage and vice versa) during operation. This "bootstrapping" effect probably compensates for parasitics introduced by vertical interconnects and is thereby responsible for the similar performance of stacked circuits as compared to planar ones.

4. Conclusions

Despite of the poor performance of printed transistors, the improvement of which is subject to investigations not considered here, the reported approach opens a new path for the enhancement of the lateral integration density and the complexity of interconnections in the field of printed electronics. In conventional printing technology it is state of the art to accurately stack and join hundreds of layers. Although technical requirements are different for the case of electronic circuits, there is no basic reason why an integrated printing and post-press processing of electronics should not be possible as well. Thereby the limitations of printed electronics in terms of minimum feature size and lateral integration density could be overcompensated: (a) lateral integration density is growing proportional to the number of layers; (b) interconnect lengths become shorter; (c) qualitatively new degrees of freedom in terms of circuitry emerge, because a significantly larger number of interconnects can be connected to a single contact point.

The path of future development of printed electronics might not be the quest for smaller devices and higher integration density in-plane, but printing of electronic structures on large areas which are converted to a batch of hundreds of layers, using post-press methods like folding and cutting. An interesting model for this kind of circuits is the biological brain. Individual neurons are poorly per-

forming in comparison with silicon transistors in terms of size, switching frequency etc. Instead, the superior performance of the system results from three-dimensional integration and neuronal circuitry. A similar type of circuitry might turn out to be suitable for printed electronics as well.

Acknowledgements

Part of the reported work was financially supported by the German Federal Ministry of Education and Research (BMBF) under Grant No. 03WKW04C. Technical support by U. Fügmann, B. Meier, M. Stanel and K. Weigelt is gratefully acknowledged.

References

[1] J.A. Davis, R. Venkatesan, A. Kaloyeros, M. Beylansky, S.J. Souri, K. Banerjee, K.C. Saraswat, A. Rahman, R. Reif, J.D. Meindl, Interconnect limits on gigascale integration (GSI) in the 21st century, Proc. IEEE 89 (2001) 305–324.
[2] S.F. Al-Sarawi, D. Abbott, P.D. Franzon, A review of 3-D packaging technology, IEEE Trans. Comp. Pack. Man. Tech. B 21 (1998) 2–14.
[3] A.W. Topol, D.C. La Tulipe, L. Shi, D.J. Frank, K. Bernstein, S.E. Steen, A. Kumar, G.U. Singco, A.M. Young, K.W. Guarini, M. Ieong, Three-dimensional integrated circuits, IBM J. Res. Dev. 50 (2006) 491–506.
[4] F.M. Dias, A. Antunes, A.M. Mota, Artificial neural networks: a review of commercial hardware, Engin. Appl. Artif. Intell. 17 (2004) 945–952.
[5] E. Beyne, Multilayer thin-film technology enabling technology for solving high-density interconnect and assembly problems, Nucl. Instr. Meth. Phys. Res. A 509 (2003) 191–199.
[6] J.H. Ahn, H.S. Kim, K.J. Lee, S. Jeon, S.J. Kang, Y.G. Sun, R.G. Nuzzo, J.A. Rogers, Heterogeneous three-dimensional electronics by use of printed semiconductor, Science 314 (2006) 1754–1757.
[7] S.R. Forrest, The path to ubiquitous and low-cost organic electronic appliances on plastic, Nature 428 (2004) 911.
[8] M. Singh, H.M. Haverinen, P. Dhagat, G.E. Jabbour, Inkjet printing – process and its applications, Adv. Mater. 22 (2010) 673–685.
[9] V. Subramanian, J.M.J. Frechet, P.C. Chang, D.C. Huang, J.B. Lee, S.E. Molesa, A.R. Murphy, D.R. Redinger, Progress toward development of all-printed RFID tags: materials, processes, and devices, Proc. IEEE 93 (2005) 1330–1338.
[10] J.M. Xu, Plastic electronics and future trends in microelectronics, Synth. Met. 115 (2000) 1–3.
[11] D. Zielke, A.C. Hubler, U. Hahn, N. Brandt, M. Bartzsch, U. Fugmann, T. Fischer, J. Veres, S. Ogier, Polymer-based organic field-effect transistor using offset printed source/drain structures, Appl. Phys. Lett. 87 (2005) 123508–123510.
[12] A.C. Huebler, F. Doetz, H. Kempa, H.E. Katz, M. Bartzsch, N. Brandt, I. Hennig, U. Fuegmann, S. Vaidyanathan, J. Granstrom, S. Liu, A. Sydorenko, T. Zillger, G. Schmidt, K. Preissler, E. Reichmanis, P. Eckerle, F. Richter, T. Fischer, U. Hahn, Ring oscillator fabricated completely by means of mass-printing technologies, Org. Electr. 8 (2007) 480–486.
[13] H.E. Katz, A.J. Lovinger, J. Johnson, C. Kloc, T. Siegrist, W. Li, Y.Y. Lin, A. Dodabalapur, A soluble and air-stable organic semiconductor with high electron mobility, Nature 404 (2000) 478–481.
[14] H. Yan, Z.H. Chen, Y. Zheng, C. Newman, J.R. Quinn, F. Dotz, M. Kastler, A. Facchetti, A high-mobility electron-transporting polymer for printed transistors, Nature 457 (2009) 679–686.
[15] B. Crone, A. Dodabalapur, Y.Y. Lin, R.W. Filas, Z. Bao, A. LaDuca, R. Sarpeshkar, H.E. Katz, W. Li, Large-scale complementary integrated circuits based on organic transistors, Nature 403 (2000) 521–523.
[16] H. Klauk, U. Zschieschang, J. Pflaum, M. Halik, Ultralow-power organic complementary circuits, Nature 445 (2007) 745–748.
[17] D. Bode, C. Rolin, S. Schols, M. Debucquoy, S. Steudel, G.H. Gelinck, J. Genoe, P. Heremans, Noise-margin analysis for organic thin-film complementary technology, IEEE Trans. Electr. Dev. 57 (2010) 201.
[18] N. Benson, M. Schidleja, C. Melzer, R. Schmechel, H. von Seggern, Complementary organic field effect transistors by ultraviolet dielectric interface modification, Appl. Phys. Lett. 89 (2006) 182105.
[19] K. Reuter, H. Kempa, K.D. Deshmuk, H.E. Katz, A.C. Hübler, Full-swing organic inverters using a charged perflourinated electret fabricated by means of mass-printing technologies, Org. Electr. 11 (2010) 95.
[20] M. Hambsch, K. Reuter, M. Stanel, G. Schmidt, H. Kempa, U. Fügmann, U. Hahn, A.C. Hübler, Uniformity of fully gravure printed organic field-effect transistors, Mater. Sci. Eng. B 170 (2010) 93–98.
[21] G.C. Schmidt, M. Bellmann, B. Meier, M. Hambsch, K. Reuter, H. Kempa, A.C. Hübler, Modified mass printing technique for the realization of source/drain electrodes with high resolution, Org. Electr. 11 (2010) 1683–1687.
[22] G. Schmidt, M. Bellmann, C. Scholz, M. Clair, B. Keiper, A.C. Hübler, J. Hänel, Vias and interconnections for printed electronics, mst-news 4 (2009) 38.

Organic Electronics 12 (2011) 424–428

Contents lists available at ScienceDirect

Organic Electronics

journal homepage: www.elsevier.com/locate/orgel

Enhanced photovoltaic performance of ZnO nanoparticle/poly(phenylene vinylene) hybrid photovoltaic cells by semiconducting surfactant

Insun Park [a], Younhee Lim [a], Sangtaik Noh [a], Donggu Lee [b], Michael Meister [c], Jason J. Amsden [a,b], Frédéric Laquai [c], Changhee Lee [b,*], Do Y. Yoon [a,*]

[a] Department of Chemistry, Seoul National University, Seoul 151-747, South Korea
[b] School of Electrical Engineering and Computer Science, Seoul National University, Seoul 151-744, South Korea
[c] Max Planck Institute for Polymer Research, Ackermannweg 10, Mainz D-55128, Germany

ARTICLE INFO

Article history:
Received 11 October 2010
Received in revised form 2 December 2010
Accepted 5 December 2010
Available online 16 December 2010

Keywords:
ZnO nanoparticles
MDMO-PPV
Surfactants
Hybrid photovoltaic cells
Bulk heterojunction

ABSTRACT

Hybrid films of ZnO nanoparticles and poly[2-methoxy-5-(3′,7′-dimethyloctyloxyl)-1,4-phenylene vinylene] (MDMO-PPV) were investigated as a model hybrid bulk heterojunction (HBHJ) photovoltaic cell which combines the simple processability and excellent electrical characteristics of inorganic nanoparticle acceptors and conjugated polymer donors. Improved photovoltaic performance was observed when the ZnO nanoparticles were stabilized with a new semiconducting surfactant, 2-(2-ethylhexyl)-1,3-dioxo-2,3-dihydro-1H-benzo[de]isoquinoline-6,7-dicarboxylic acid (BQ). We found that using the BQ surfactant increased the power conversion efficiency (1.23%) while a typical insulating surfactant, oleic acid (OA), decreased the efficiency (0.65%) despite the improvement of the ZnO dispersion, as compared to the HBHJ films prepared without a surfactant (0.75%). The underlying mechanism was delineated by hybrid-morphology study, photoluminescence spectroscopy, and photo-induced absorption spectroscopy.

© 2010 Elsevier B.V. All rights reserved.

1. Introduction

In recent years, polymer-based bulk heterojunction (BHJ) solar cells exhibiting promising power conversion efficiencies (PCE) up to 8% have been reported with fullerene derivatives, [6,6]-phenyl C61 butyric acid methyl ester ($PC_{61}BM$) or [6,6]-phenyl C71 butyric acid methyl ester ($PC_{71}BM$), as the electron acceptor [1–3]. Alternatively, inorganic semiconducting nanoparticles, such as TiO_2 [4,5], ZnO [6–10], and CdSe [11,12], have also been investigated as electron acceptors due to their higher electron mobility and lower cost as compared with PCBM. However, despite the high electron mobility, the photovoltaic performance of hybrid bulk heterojunction (HBHJ) photovoltaic cells prepared with inorganic semiconducting nanoparticles and p-type conjugated polymers is significantly lower than the BHJ photovoltaic cells prepared with PCBM. A maximum PCE of 3% was demonstrated for CdSe based HBHJ solar cells [13] and 2% was achieved for metal-oxide based HBHJ solar cells [4,9,12]. The severe aggregation of n-type inorganic nanoparticles in p-type organic polymers is considered to be the main reason for the poor efficiency because the hybrid morphology critically affects the charge separation, charge transport, and recombination in the HBHJ solar cells.

Many groups have been trying to improve the hybrid morphology of inorganic nanoparticles dispersed in polymer matrix by employing various methods such as surfactant addition or in situ HBHJ preparation from the deposited film containing a reactive precursor of inorganic nanoparticles [4–9,11,14]. Although the application of surfactants has become critical to suppressing the severe aggregation of inorganic nanoparticles, previous works mostly employed traditional surfactants such as oleic acid (OA), that are electrical insulators and thus block charge

* Corresponding authors. Tel.: +82 2 880 6648; fax: +82 2 877 6814 (D.Y. Yoon).
E-mail addresses: chlee7@snu.ac.kr (C. Lee), dyyoon@snu.ac.kr (D.Y. Yoon).

1566-1199/$ - see front matter © 2010 Elsevier B.V. All rights reserved.
doi:10.1016/j.orgel.2010.12.002

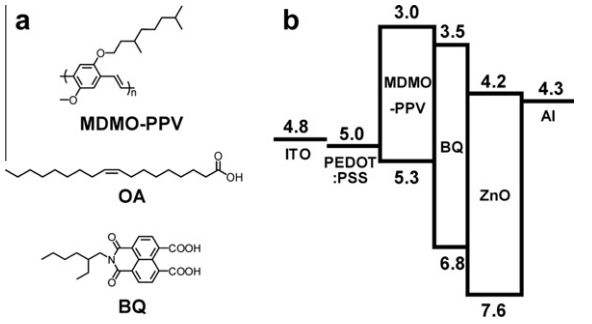

Fig. 1. A schematic diagram shows (a) the structure of MDMO-PPV, OA surfactant, and BQ surfactant, and (b) the energy level diagram of the materials comprising the HBHJ solar cell.

transport. Therefore, the advantage of using surfactants to improve the hybrid morphology was offset by the resultant decrease in charge mobility in the nanoparticle–polymer and nanoparticle–nanoparticle interfaces that are critical to the charge separation and transport in HBHJ solar cells. Although the surfactants could partly be removed from the HBHJ devices, this process also causes poor interfacial contact, and hence degrades the charge separation and transport. Therefore, in order to improve the efficiency of HBHJ cells, it is very desirable to employ non-removable surfactants with semiconducting characteristics of electron mobility and an appropriate energy level of the lowest unoccupied molecular orbital (LUMO). They will help not only with achieving a desired hybrid morphology of nanoparticles dispersed in polymer matrix, but also with intimate electronic contact and transport at the nanoparticle–polymer and nanoparticle–nanoparticle interfaces.

In this study, we investigated how the performance characteristics of HBHJ solar cells are affected by the application of different surfactants. For the n-type inorganic acceptor, we chose zinc oxide (ZnO) nanoparticles due to their easy synthesis and high electron mobility [15–18]. Among the many promising p-type semiconducting polymers, we selected poly[2-methoxy-5-(3′,7′-dimethyloctyloxyl)-1,4-phenylene vinylene] (MDMO-PPV) (Fig. 1a) that was shown to readily form HBHJ films with ZnO nanoparticles [10]. Two kinds of surfactants were investigated: insulating oleic acid (OA) and semiconducting 2-(2-ethylhexyl)-1,3-dioxo-2,3-dihydro-1H-benzo[de]isoquinoline-6,7-dicarboxylic acid (BQ) (Fig. 1a). The hybrid film morphology was studied by transmission electron microscopy (TEM) and atomic force microscopy (AFM), and the device performance was determined from J–V curve analysis. The effects of surfactants on the photoexcited states of ZnO/MDMO-PPV hybrid films were investigated using steady-state photoluminescence (PL) and quasi steady-state photo-induced absorption (PIA) spectroscopy.

2. Experimental details

2.1. Materials

MDMO-PPV which is known to have its glass transition temperature around 25–50 °C [19] was purchased from COVION (now Merck KGaA), with molecular weights of M_n 150,000, polydispersity index of 4.7. Poly(3,4-ethylene-dioxythiophene):poly(styrenesulfonate) (PEDOT:PSS, CLEVIOS™ P VP AI 4083) was purchased from CLEVIOS. Zinc acetate dihydrate ($Zn(Ac)_2{\cdot}2H_2O$, >98% purity) and potassium bromide (KBr, 99+%, FTIR grade) were obtained from Sigma–Aldrich. Potassium hydroxide (KOH, GR reagent) was obtained from Duksan Pharmaceutical Co. Ltd. All solvents used in this work are of analytical grade or purer. All chemicals mentioned above were used without further purification.

2.2. Synthesis of ZnO nanoparticles

The synthesis of ZnO nanoparticles was accomplished using minor modification of the procedure previously described in the literature [15]. The synthesis is carried out under N_2 atmosphere. At first, 1.23 g of $Zn(Ac)_2{\cdot}2H_2O$ was dissolved in 55 mL of methanol at room temperature. Then, 25 mL of a methanol solution containing 0.48 g of KOH is added dropwise over a 20 min time interval at 60 °C with magnetic stirring. After the KOH solution is added, the solution is stirred at 60 °C for 2 h. The product appears as a white precipitate. After collecting by centrifugation, this white precipitate is washed three times with methanol until it transforms to a gel-like precipitate. Each washing process includes dispersion into methanol by sonication and subsequent centrifugation. Finally, the gel-like precipitate is redispersed in chlorobenzene and 10 vol.% of propanol is added for stabilization. The resulting ZnO surface was stabilized with each surfactant and stored as a colloidal solution because of its inability to be redispersed after the complete removal of the solvent.

2.3. Photovoltaic cell fabrication and measurements

Photovoltaic devices were fabricated on cleaned indium tin oxide (ITO) patterned glass substrates. First a 40 nm layer of PEDOT:PSS was deposited on top of the ITO by spin coating and annealing at 120 °C for 30 min. Then the active layer was spun from a ZnO nanoparticle/MDMO-PPV (2:1 ratio by mass) solution using chlorobenzene:propanol (10 vol.%) as the solvent. The thickness of the resulting hybrid film is around 110 (±10) nm, as determined by AFM. After spin coating, 0.5 nm of LiF and 100 nm of Al are deposited onto the active layer by thermal evaporation. All the current density–voltage (J–V) characteristics of the photovoltaic devices were measured in ambient conditions using a computer-controlled Keithley 237 source measure unit; the measurements in vacuum showed practically the same results. The active device area was 0.20 cm^2 and the device performance was measured with 100 mW cm^{-2} AM 1.5G illumination using a commercial solar simulator (Newport91160A). To avoid direct optical excitation of ZnO nanoparticles, a 435 nm long pass UV filter was inserted between light source and device, which slightly decreased the final illumination power to 95 mW cm^{-2}. The EQE measurements were performed using chopped monochromatic light and lock-in detection. A homebuilt setup, utilizing a 300 W Xenon lamp (Müller Elektronik–Optik) and a monochromator (SpectraPro-150, Acton Research Corp.), was used for the light source. The

incident light was chopped at 113 Hz with an optical chopper (model 651, EG&G Instruments). The sample photocurrent was acquired at 0 V bias with DSP lock-in amplifier (model 7265, Signal Recovery). The monochromatic light was focused on the sample using optical lens with 3 mm diameter. The light power versus wavelength was measured with a calibrated silicon photodiode (Hamamatsu Corp.). These measurements were performed without bias illumination.

To obtain UV–Vis, PL, PIA spectra, and AFM images, the same conditions for photovoltaic cell fabrication were used with the exception of thermal evaporation of electrodes. For TEM measurements, thinner film thickness (40 nm) was prepared by controlling the concentration with the same weight ratio of MDMO-PPV and ZnO nanoparticles and then the prepared film was floated onto the surface of deionized water and picked up by a copper grid. The images were acquired with a Hitachi H-7600 transmission electron microscope operated at an acceleration voltage of 100 kV. The AFM images were obtained with PSIA XE-100 atomic force microscope at non-contact tapping mode. UV–Vis spectra were recorded using a JASCO V-530 UV–Vis spectrophotometer. Photoluminescence (PL) spectra were measured using a JASCO FP-6500 spectrofluorometer. PIA spectra were measured at 80 K with excitation at 530 nm wavelength by a LED light source, ca. 100 mW cm^{-2} intensity and a modulation frequency of 317 Hz. The resulting change in transmission was monitored at each wavelength with a dispersed tungsten-halogen light source as a probe and using Si and Ge detectors and with lock-in detection. Cyclic voltammetry was performed using Pt electrodes as the working and counter electrodes, and Ag/Ag^+ as the reference electrodes on a CHI 700C electrochemical instrument at a scan rate of 100 mV s^{-1}. Tetrabutylammonium hexafluorophosphate (0.1 M) in tetrahydrofuran was the electrolyte. The redox potentials (E_{ox} and E_{red}) were calibrated by using ferrocene (Fc) as the standard, whose HOMO energy level is −4.8 eV.

3. Results and discussion

The solvent-stabilized ZnO nanoparticles employed in this work were synthesized by hydrolysis and condensation method [15] with some minor modifications (see Section 2 for details). The estimate of ZnO nanoparticle size from $\lambda_{1/2}$ of the UV–Vis absorption spectrum of the nanoparticles in solution yielded an average particle diameter of 3.2 nm [20], in agreement with the size estimated by TEM image. (Figure S1).

We employed two different surfactants in our study, namely, oleic acid (OA) which is a conventional insulating surfactant and a newly synthesized semiconducting surfactant with a reasonable electron mobility, 2-(2-ethylhexyl)-1,3-dioxo-2,3-dihydro-1H-benzo[de]isoquinoline-6,7-dicarboxylic acid (BQ) (Fig. 1a). The details of the synthetic procedure are shown in the Supplementary Material [21]. OA is a typical surfactant adopted for improving the dispersion properties of inorganic nanoparticles in polymers [11]. BQ has two carboxylic acid groups that can attach to the surface of ZnO nanoparticles and the benzoisoquinoline aromatic group with 2-ethylhexyl side chain, which should be miscible with conjugated polymers. The energy levels of BQ were determined from the cyclic voltammetry and UV–Vis spectra and appear to be appropriate for electron transfer from MDMO-PPV to ZnO nanoparticles when compared with other materials of the HBHJ solar cells (Fig. 1b). Furthermore, the electron mobility of BQ was estimated by the time-of-flight technique to be approximately 10^{-7} cm^2/Vs. (See Supplementary Material for the detailed characteristics of BQ).

The absorbance and the PL spectra of ZnO/MDMO-PPV hybrid films, shown in Fig. 2, were measured on quartz substrates coated with poly(3,4-ethylenedioxythiophene): poly(styrenesulfonate) (PEDOT:PSS) hole transport layer. The UV–Vis spectrum of MDMO-PPV had the maximum absorption peak at 495 nm. It remained unchanged upon addition of ZnO nanoparticles, regardless of the type of added surfactant. The PL emission of the MDMO-PPV was significantly quenched by the addition of ZnO nanoparticles. Moreover, the quenching efficiency of PL spectra of the hybrid films showed a large difference depending upon the added surfactant. The highest PL quenching was achieved in samples prepared with BQ as the stabilizing surfactant of ZnO nanoparticles, while the hybrid films prepared with OA-stabilized ZnO nanoparticles exhibited a reduced quenching efficiency as compared to the hybrid films prepared without a surfactant. Therefore, these PL results show that the semiconducting surfactant BQ resulted in increasing the electron transfer from the excitons of MDMO-PPV to ZnO while the insulating surfactant OA resulted in decreased electron transfer, compared to the hybrid films prepared without any surfactant.

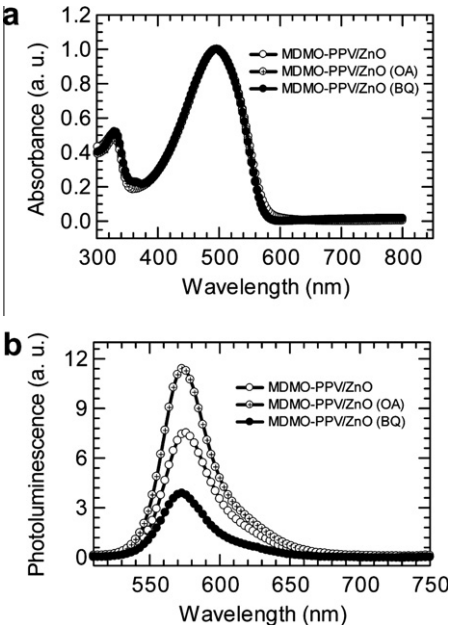

Fig. 2. Normalized (a) UV–Vis, and (b) photoluminescence (excited at 500 nm wavelength) spectra of the ZnO/MDMO-PPV hybrid films spin-coated from ZnO nanoparticles, without a surfactant (open circle), stabilized with OA (open circle with cross), and stabilized with BQ (closed circle).

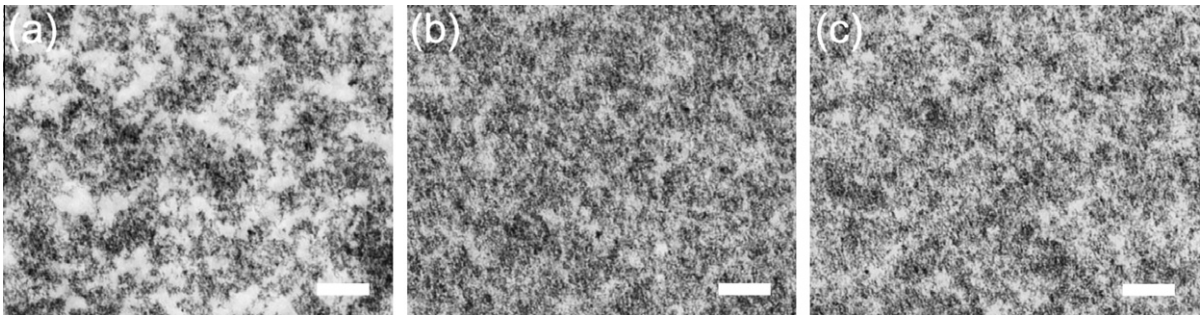

Fig. 3. TEM images of the ZnO/MDMO-PPV hybrid films prepared without a surfactant (a), with OA (b), and with BQ (c). The scale bar indicates 100 nm.

Morphological investigation of the ZnO/MDMO-PPV hybrid films was performed by TEM and AFM. ZnO/MDMO-PPV hybrid films prepared without any surfactant showed a root mean square (RMS) roughness of 4.3 nm by AFM. Applying surfactants to stabilize the nanoparticles in solutions improved the hybrid morphology due to better dispersion of ZnO nanoparticles in the polymer matrix, resulting in an RMS roughness of 2.8 nm for OA and 3.2 nm for BQ. Corresponding changes in the internal microstructure investigated by TEM are shown in Fig. 3. The TEM results clearly showed that both surfactants significantly suppressed the aggregation of ZnO nanoparticles in the MDMO-PPV matrix.

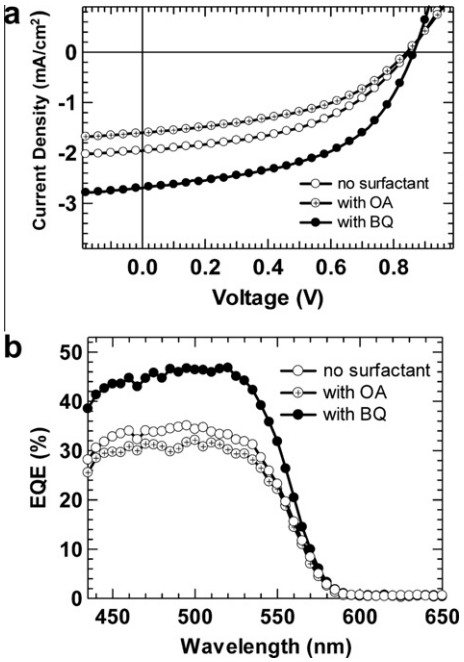

Fig. 4. (a) J–V characteristics, and (b) external quantum efficiency (EQE) of ZnO/MDMO-PPV HBHJ solar cells, prepared without a surfactant (open circle), with OA (open circle with cross), and with BQ (closed circle).

The J–V curves of the ZnO/MDMO-PPV (2:1 ratio by mass) HBHJ devices were measured to investigate the photovoltaic performance. A high open circuit voltage (V_{oc}) of 0.88 V was achieved as expected due to the low HOMO energy level of MDMO-PPV. Together with a short circuit current (J_{sc}) of 1.83 mA cm^{-2} and a fill factor (FF) of 0.44, the power conversion efficiency (PCE) reached 0.75% without any thermal/solvent processing treatment (Fig. 4a and Table 1). This result is somewhat lower than the value reported by Beek et al. [10], but this may be a result of slightly different device preparation and measurement conditions. An increased PCE of 1.23% was observed when approximately 3% (relative to ZnO by mass) BQ surfactant was used for the stabilization of ZnO nanoparticles, with V_{oc} = 0.86 V, J_{sc} = 2.86 mA cm^{-2}, and FF = 0.48. The main reason for the improved efficiency derives from an enhanced J_{sc} when BQ is used as a surfactant. The external quantum efficiency (EQE) was measured and found to reflect the trend in J_{sc} with a maximum EQE over 45% with BQ surfactant (Fig. 4b). On the other hand, applying the same amount of OA surfactant to stabilize the ZnO nanoparticles reduced the J_{sc} and resulted in a decreased PCE of 0.65%, although the OA surfactant significantly improved the dispersion of ZnO nanoparticles, as shown in Fig. 3. The values of the series resistance R_s, also shown in the table, clearly show that the short circuit current is limited by the charge transport at the interface.

To further investigate the surfactant effects on PCE, quasi steady-state photo-induced absorption (PIA) spectra of various ZnO/MDMO-PPV hybrid films were measured

Table 1
Summary of photovoltaic properties of the ZnO/MDMO-PPV HBHJ solar cells prepared with different surfactants[†].

	J_{sc} (mA cm^{-2})	V_{oc} (V)	FF	PCE_{avg} (%)	R_s (Ω cm^2)
Without surfactant	1.83	0.88 (±0.03)	0.44 (±0.04)	0.75 (±0.18)	90.5
With OA	1.56	0.88 (±0.06)	0.45 (±0.02)	0.65 (±0.23)	112
With BQ	2.86	0.86 (±0.07)	0.48 (±0.03)	1.23 (±0.23)	35.7

[†] Uncertainty in the typical device characteristics is estimated by one standard deviation from the mean obtained from over 15 devices and five batches of ZnO preparations. The standard deviation in PCE mainly results from the batch to batch variation of ZnO nanoparticle preparation/handling conditions, while it is much smaller within each batch. The standard deviations in J_{sc} and R_s track the trend in PCE.

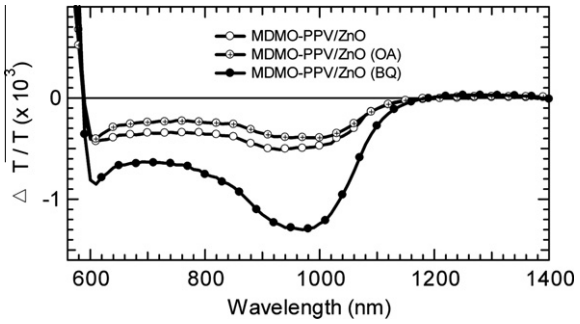

Fig. 5. Normalized photo-induced absorption spectra of ZnO/MDMO-PPV hybrid films, prepared without a surfactant (open circle), with OA (open circle with cross), and with BQ (closed circle), recorded at 80 K with excitation at 530 nm wavelength, ca. 100 mW cm^{-2} intensity and modulation frequency of 317 Hz.

(Fig. 5). The spectra were measured from 600 to 1400 nm at 80 K with excitation from a 530 nm LED light source (see Section 2), and the signal intensity was corrected for the absorption of the films. The PIA of the MDMO-PPV cations is clearly observed at 970 nm. The highest steady-state concentration of MDMO-PPV cations, i.e., the most intense PIA signal, was observed for the hybrid film prepared with BQ stabilized ZnO nanoparticles, while films prepared with OA stabilized ZnO nanoparticles showed a lower concentration of MDMO-PPV cations as compared to the films prepared without a surfactant. Clearly, the PIA results are in line with the trend in PCE observed for the various HBHJ devices. These results are also consistent with the observed PL quenching efficiency and demonstrate that improved electron transfer from MDMO-PPV to the ZnO nanoparticles is the main reason for the enhanced PCE as a consequence of the improved hybrid morphology. Although the OA surfactant also improved the morphology, the electron transfer from MDMO-PPV to the ZnO nanoparticles was partly blocked by the insulating nature of OA surfactant.

4. Conclusions

In conclusion, the dispersion morphology of hybrid bulk heterojunction films from ZnO nanoparticles and MDMO-PPV was significantly improved upon applying two different surfactants, insulating OA and semiconducting BQ. However, the larger interfacial area obtained by the better dispersion of ZnO nanoparticles led to an improved PCE of HBHJ solar cells only when the semiconducting BQ surfactant was used due to its appropriate energy level and electron mobility (10^{-7} cm^2/Vs) which facilitates efficient electron transfer. Devices using the newly synthesized BQ surfactant showed an enhanced photovoltaic efficiency up to 1.23%, nearly 60% increase over the surfactant-free device, as a consequence of an enhanced short circuit current resulting from more efficient charge separation and transport. Therefore, developing novel n-type semiconducting surfactants with appropriate energy levels and electron mobility could open a very promising avenue for significantly improving the efficiency of hybrid bulk heterojunction photovoltaic cells.

Acknowledgements

Financial support from International Research Training Group (IRTG), co-funded by the German Research Foundation (DFG) and the National Research Foundation of Korea (NRF), and the Division of Chemistry and Molecular Engineering Program of the Brain Korea 21 Project is gratefully acknowledged. The authors thank S. Noh for the time-of-flight measurements.

Appendix A. Supplementary data

Supplementary data associated with this article can be found, in the online version, at doi:10.1016/j.orgel.2010.12.002.

References

[1] G. Dennler, M.C. Scharber, C.J. Brabec, Adv. Mater. 21 (2009) 1323–1338.
[2] J.Y. Kim, K. Lee, N.E. Coates, D. Moses, T.-Q. Nguyen, M. Dante, A.J. Heeger, Science 317 (2007) 222–225.
[3] Y. Liang, Z. Xu, J. Xia, S.T. Tsai, Y. Wu, G. Li, C. Ray, L. Yu, Adv. Mater. 22 (2010) E135–E138.
[4] Y.-Y. Lin, T.-H. Chu, S.-S. Li, C.-H. Chuang, C.-H. Chang, W.-F. Su, C.-P. Chang, M.-W. Chu, C.-W. Chen, J. Am. Chem. Soc. 131 (2009) 3644–3649.
[5] C. Goh, S.R. Scully, M.D. McGehee, J. Appl. Phys. 101 (2007) 114503.
[6] P. Ravirajan, A.M. Peiró, M.K. Nazeeruddin, M. Graetzel, D.D.C. Bradley, J.R. Durrant, J. Nelson, J. Phys. Chem. B 110 (2006) 7635–7639.
[7] T.C. Monson, M.T. Lloyd, D.C. Olson, Y.J. Lee, J.W.P. Hsu, Adv. Mater. 20 (2008) 4755–4759.
[8] D.J.D. Moet, L.J.A. Koster, B. de Boer, P.W.M. Blom, Chem. Mater. 19 (2007) 5856–5861.
[9] S.D. Oosterhout, M.M. Wienk, S.S. Van Bavel, R. Thiedmann, L. Jan Anton Koster, J. Gilot, J. Loos, V. Schmidt, R.A.J. Janssen, Nat. Mater. 8 (2009) 818–824.
[10] W. Beek, M. Wienk, R. Janssen, Adv. Mater. 16 (2004) 1009–1013.
[11] J. Chen, J.L. Song, X.W. Sun, W.Q. Deng, C.Y. Jiang, W. Lei, J.H. Huang, R.S. Liu, Appl. Phys. Lett. 94 (2009) 153115.
[12] B. Sun, E. Marx, N.C. Greenham, Nano Lett. 3 (2003) 961–963.
[13] S. Dayal, N. Kopidakis, D. Olson, D. Ginley, G. Rumbles, Nano Lett. 10 (2010) 239–242.
[14] J. Liu, T. Tanaka, K. Sivula, A.P. Alivisatos, J.M.J. Fréchet, J. Am. Chem. Soc. 126 (2004) 6550–6551.
[15] C. Pacholski, A. Kornowski, H. Weller, Angew. Chem. Int. Ed. 41 (2002) 1188–1191.
[16] H. Faber, M. Burkhardt, A. Jedaa, D. Kalblein, H. Klauk, M. Halik, Adv. Mater. 21 (2009) 3099–3104.
[17] E.M.C. Fortunato, P.M.C. Barquinha, A.C.M.B.G. Pimentel, A.M.F. Goncalves, A.J.S. Marques, R.F.P. Martins, L.M.N. Pereira, Appl. Phys. Lett. 85 (2004) 2541–2543.
[18] B.J. Norris, J. Anderson, J.F. Wager, D.A. Keszler, J. Phys. D: Appl. Phys. 36 (2003) L105–L107.
[19] L. Lutsen, P. Adriaensens, H. Becker, A.J. Van Breemen, D. Vanderzande, J. Gelan, Macromolecules 32 (1999) 6517–6525.
[20] E.A. Meulenkamp, J. Phys. Chem. B 102 (1998) 5566–5572.
[21] V. Gorteau, G. Bollot, J. Mareda, A. Perez-Velasco, S. Matile, J. Am. Chem. Soc. 128 (2006) 14788–14789.

Organic Electronics 12 (2011) 429–434

Contents lists available at ScienceDirect

Organic Electronics

journal homepage: www.elsevier.com/locate/orgel

Letter

Tuning on threshold voltage of organic field-effect transistor with a copper oxide layer

Guozheng Nie, Junbiao Peng *, Linfeng Lan, Ruixia Xu, Jianhua Zou, Yong Cao

Institute of Polymer Optoelectronic Materials and Devices, Key Laboratory of Special Functional Materials of the Ministry of Education, South China University of Technology, Guangzhou 510640, PR China

ARTICLE INFO

Article history:
Received 25 September 2010
Received in revised form 10 December 2010
Accepted 20 December 2010
Available online 4 January 2011

Keywords:
Field-effect transistors
CuO embedded layer
Tuning of threshold voltage
Electron trapping

ABSTRACT

Organic field-effect transistors (OFETs) based on the pentacene semiconductor with an embedded thin layer of copper oxide (CuO) were investigated. The drain current of OFETs with a thin CuO layer embedded in pentacene increases more than three times compared to that of traditional OFETs without the CuO layer, and the threshold voltage shifts from −17.5 V to −7.9 V. A possible mechanism for OFETs with the CuO layer was discussed via analysis of electron transfer near the contact between CuO and pentacene. OFETs with the CuO layer exhibit an interesting result of a systematic tuning of threshold voltage by controlling the initial voltage of gate-to-source upon scanning transfer curves.

© 2011 Elsevier B.V. All rights reserved.

1. Introduction

Organic field-effect transistors (OFETs), as the critical component of organic integrated circuits (ICs), have attracted considerable attention due to their low cost, easy processability, flexibility, and applicability in large-area devices [1,2]. Nowadays, great efforts have been devoted to design and synthesize organic semiconductors as well as to fabricate OFETs with high performance, high stability and low cost [3–5]. However, there are still many challenges of restricting their practical applications in organic ICs, such as wide range tuning of the threshold voltage (V_{TH}). So far, the works on tuning of V_{TH} to control OFETs at low-power modes have made a progress [6–11]. For example, the V_{TH} of OFETs can be tuned by using polar self-assembled monolayers [6], depositing an additional layer of organic acceptor on the top of channel [7], and using ferroelectric gate dielectrics [8] or ion-dispersed gate dielectrics [9,10]. In addition, the shift of threshold voltage could be observed in a single OFET with molybdenum trioxide (MoO_3) covered on the surface of p-bis [(p-styry1) styry1] benzene single crystal [11]. However, these methods are slightly complicated to systematically control V_{TH} in a wide range. In inorganic FETs, doping in the active channel was used to accurately control the V_{TH} of the devices [12]. For organic semiconductors, we found an efficient way to systematically tune V_{TH} in OFETs by embedding a copper oxide acceptor layer in the semiconductor layer.

Copper oxide was normally used for hole injection layer in the OFETs [13] or organic light-emitting diodes (OLEDs) [14,15]. In this paper, we significantly improved both V_{TH} and mobility of the OFETs by embedding a thin CuO layer inside the pentacene semiconductor. Furthermore, a systematic tuning of threshold voltage of the OFETs can be realized by controlling the initial scanning voltage upon measurement of transfer curves. A possible mechanism for the results is discussed.

2. Experimental

The OFETs were fabricated with a top contact configuration (Fig. 1) by using a heavily-doped n-type silicon wafer

* Corresponding author. Address: Institute of Polymer Optoelectronic Materials and Devices, South China University of Technology, 381 Wushan Road, Guangzhou 510640, PR China. Tel.: +86 20 87114535; fax: +86 20 87110606.
E-mail address: psjbpeng@scut.edu.cn (J. Peng).

1566-1199/$ - see front matter © 2011 Elsevier B.V. All rights reserved.
doi:10.1016/j.orgel.2010.12.012

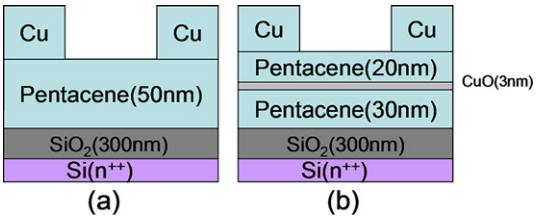

Fig. 1. Cross section of the OFETs, (a) pentacene-based OFET (b) CuO-embedded OFET.

with a 300 nm thick layer of thermally oxided SiO_2 (C_i = 10nF), serving as the gate electrode and gate insulator, respectively. The wafers were cleaned with deionized water, acetone and isopropanol for 10 min in sequence. Pentacene and CuO were thermally deposited at rate of 0.5 Å/s and 0.3 Å/s, respectively, in a vacuum chamber under a pressure of 3×10^{-4} Pa. The 3 nm thick CuO is sandwiched in the pentacene layer with a distance of 30 nm apart from the interface of SiO_2 and pentacene. The total thickness of the pentacene is 50 nm. The Cu source and drain electrodes (40 nm-thick) were then thermally evaporated through a shadow mask. The length (L) and width (W) of the channel were 100 μm and 10,000 μm, respectively. Fig. 1a and b shows the schematic structures of pure pentacene OFET (pentacene-based OFET) and CuO layer embedded pentacene OFET (CuO-embedded OFET). The electrical characteristics of OFETs were measured by using a semiconductor parameter analyzer (Agilent 4155C) at room temperature. The absorption spectra were recorded by using a UV–Vis spectrophotometer (HP 8453). The XPS spectra were measured by using Mutil-photoelectron spectroscopy (Kratos AXis Ultra (DLD)).

3. Results and discussion

Output and transfer characteristics of pentacene-based OFET and CuO-embedded OFET, are shown in Fig. 2 and in Fig. 3, respectively. Obviously, a great increase in saturation current (I_D) of CuO-embeded OFET was observed. The field-effect mobility of OFET in the saturation region can be calculated from the following equation [16].

$$I_D = \frac{W\mu C_i}{2L}(V_{GS} - V_{TH})^2 \quad (1)$$

where C_i is the capacitance of per unit area of the gate insulator, V_{GS} is the gate-to-source voltage, and V_{TH} is the threshold voltage. The mobility, V_{TH} , and current on/off ratio of the pentacene-based OFET are obtained from Eq. (1) to be 0.06 $cm^2 V^{-1} S^{-1}$, −17.5 V, and 4.5×10^4, respectively, while the corresponding parameters of CuO-embedded OFET are 0.18 $cm^2 V^{-1} S^{-1}$, −7.9 V, and 1.4×10^4, respectively. The results show that both hole mobility and V_{TH} are much improved in the CuO-embedded OFET.

3.1. Function of CuO embedded layer

The V_{TH} shift of OFET was usually originated from the following two reasons: (1) slow polarization of the gate dielectric [17]; (2) charge trapping at the interface between dielectric and semiconductor [18] or in the organic semiconductor [19]. Since the polarization of SiO_2 dielectric was hardly occurred in this case, we prefer to the second reason as stated below. In order to clarify the V_{TH} shift mechanism, time domain measurement was carried out in ambient air. This method was often used to determine the type of charge trapping in OFETs [20]. At the beginning, a gate-to-source voltage (denoted as V_{GS0}) was constantly applied for 100 s (for gaining clear signal), and then abruptly stepped to a constant gate-to-source voltage of V_{GS1} (−20 V) for another 100 s. The source-drain current (I_D) was measured under source-to-drain voltage (V_{DS}) at −10 V. Fig. 4a and b shows $-I_D$ versus time (t) curves of applied voltages for both CuO-embedded and pentacene-based OFETs under different V_{GS0}, respectively.

For the p-type CuO-embedded OFET, when the V_{GS} switched from V_{GS0} with negative values (−30 V or −50 V) to V_{GS1} (−20 V), the current ($-I_D$) was slightly decreased and then fixed in the value of about 2.0×10^{-5} A. However, when the V_{GS} switched from V_{GS0} with positive values (30 V or 50 V) to V_{GS1} (−20 V), the current ($-I_D$) was remarkably enhanced. The results of CuO-embedded OFETs suggest that positive V_{GS0} could induce extra hole accumulation in the OFET channel, resulting in current increase under polar change of V_{GS} from positive V_{GS0} to negative V_{GS1}. The production of extra holes was considered to be due to electron trapping in the active layer at a positive V_{GS0} [21]. However, the negative V_{GS0} could not induce any extra charged carriers in p-type OFET. So the $-I_D$ was fixed to a constant value after V_{GS} switched from negative V_{GS0} to

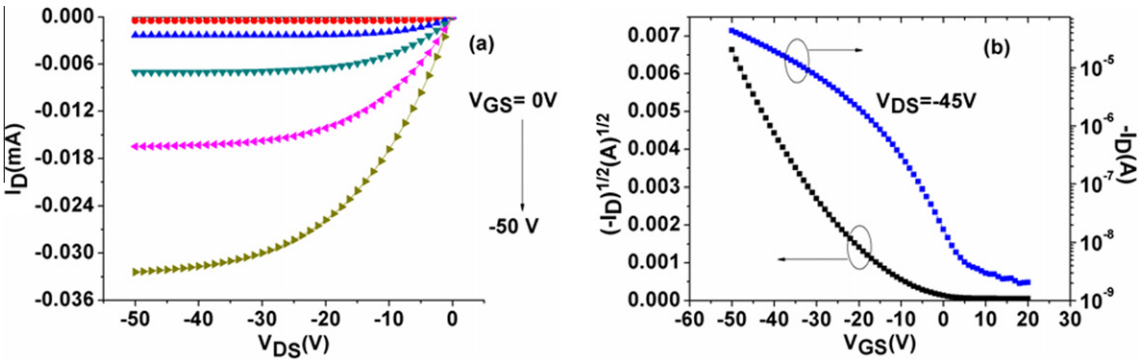

Fig. 2. Output characteristics (a) and transfer characteristics (b) of pentacene-based OFET.

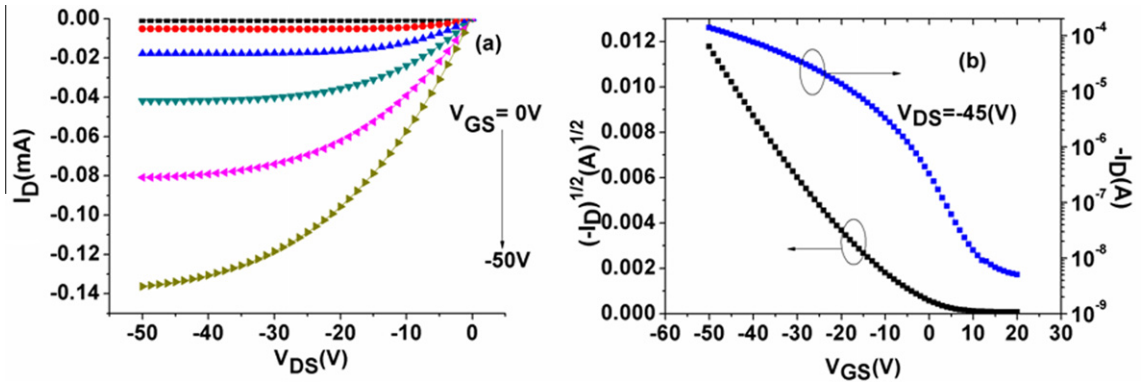

Fig. 3. Output characteristics (a) and transfer characteristics (b) of CuO-embedded OFET.

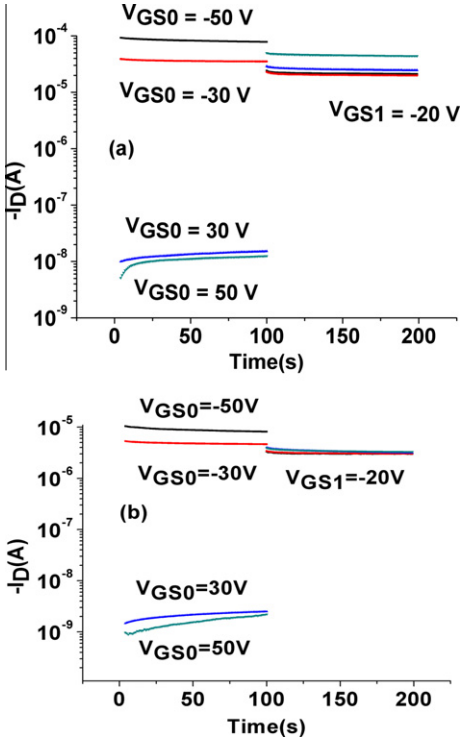

Fig. 4. Time domain measurements of the OFETs (a) CuO-embedded OFET, (b) pentacene-based OFET, in ambient air at different V_{GS0} (V_{GS0} = −50,−30,30,50 V), and V_{GS1} = −20 V, V_{DS} = −10 V.

V_{GS1} (−20 V). In addition, when V_{GS0} was applied at positive value, the larger the V_{GS0} value, the higher the value of $-I_D$ was obtained after switching V_{GS} from positive V_{GS0} to V_{GS1} (−20 V). For example, $-I_D = 2.5\text{x}10^{-5}$ A for V_{GS0} = 30 V, while $-I_D = 4.5 \times 10^{-5}$ A for V_{GS0} = 50 V (see Fig. 4a). The data suggests that electron trapping population could increase with increasing the positive value of V_{GS0}. No such phenomenon was observed from pentacene-based OFETs (see Fig. 4b), hence it was further confirmed that the CuO layer could trap electrons and induce holes in pentacene. The detailed discussion for the roles of the embedded CuO layer is given below.

The capability of CuO accepting electrons could result in electron transfer from pentacene to CuO and formation of charge transfer (CT) complexes between CuO and pentacene, as confirmed by the absorption spectra [22] (see Fig. 5a). The absorption spectrum of the CuO-doped pentacene film shows the additional absorption peaks at around 423 nm and 1000 nm, indicating the electron transfer from pentacene to high work-function CuO (5.3 eV [23]). In addition, X-ray photoelectron spectra (XPS) can also confirm electron transfer at the interface between pentacene and CuO layers, as shown in Fig. 5b. The Cu $2p_{3/2}$ peak shifts to higher energies as shown in the XPS spectra of sample (E). Since a negatively charged atom has a higher binding energy of electrons [24], the peak shift further verifies electron transfer from pentacene to CuO and formation of CT complexes at their interface. The CT complexes could push the Fermi level of pentacene toward its highest occupied molecular orbital (HOMO), because it is p-type doping system [25,26]. The shift of Fermi level can reduce bulk hole trap density in pentacene [26,27] and enhance the bulk hole injection [27]. Therefore, the improvement of field-effect mobility of CuO-embedded OFETs could be attributed to the formation of CT complexes at the CuO/pentacene interfaces. The holes supplied from the CT complexes enhance the drain current and result in the threshold voltage shift from −17.5 V to −7.9 V (see Figs. 2 and 3). Additionally, the field-effect mobility of the CuO-embedded OFET does not vary with V_{GS0} after time domain measurements, as shown from the almost unchangeable slopes of the $(-I_D)^{1/2}$ versus V_{GS} curves in Fig. 6. In this case, similar to the V_2O_5 [28] and MoO_3 layers [29], the embedded CuO layer could act as a charge-generation layer when a positive V_{GS0} was applied. In CuO layer, electrons and holes were dissociated under positive V_{GS0}, and the generated electrons were trapped at the interface between pentacene and CuO due to the poor electron-transporting ability of pentacene and electron traps of CuO surface. The trapped electrons can induce holes in pentacene semiconductor. The larger the V_{GS0} value, the more electron–hole pairs were generated in CuO layer, leading to the higher source-drain current ($-I_D$) (see Fig. 4a). Therefore, the trapped electron population in CuO could be controlled by adjusting of positive V_{GS0}.

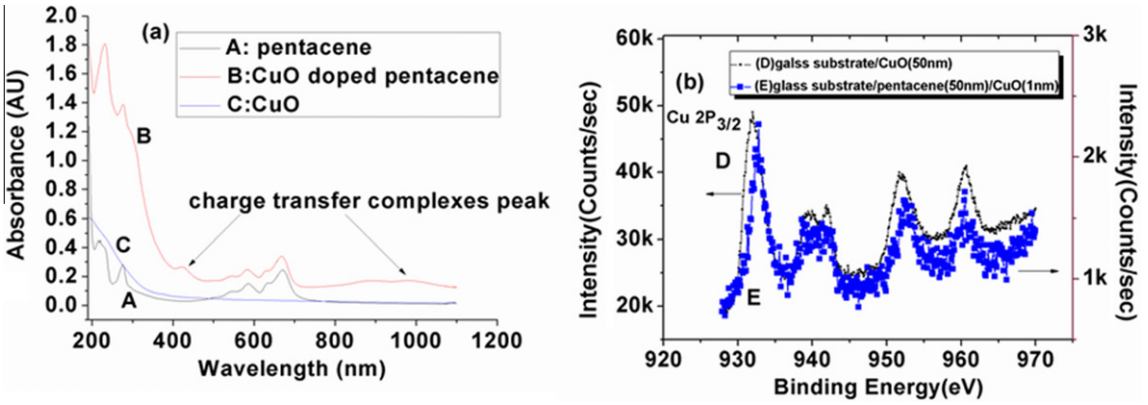

Fig. 5. (a) UV–Vis absorption spectra of samples of (A) pentacene, (B) CuO-doped pentacene and (C) pure CuO films on quartz substrate. (b) XPS spectra: Cu $2p_{3/2}$ peak observed in the samples of (D): glass substrate/CuO (50 nm), and (E): glass substrate/pentacene (50 nm)/CuO (1 nm).

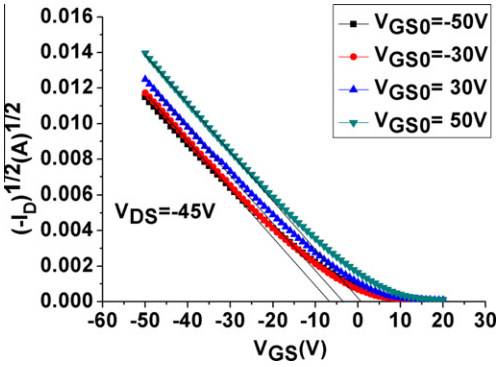

Fig. 6. $(-I_D)^{1/2}$ versus V_{GS} transfer curves for the CuO-embedded OFET after the time domain measurements at different V_{GS0} (V_{GS0} = −50, −30,30,50 V), respectively.

3.2. Tuning of V_{TH}

The shift of V_{TH} is related to trapped charges in OFETs according to the following equation [30].

$$Q_{trap} = -\Delta V_{TH} C_i \quad (2)$$

where Q_{trap} is the amount of trapped charge, ΔV_{TH} the shift of V_{TH}, and C_i the capacitance of per unit area of the gate insulator. If the trapped electrons can be controlled, the V_{TH} of OFETs can be strictly tuned. So the V_{TH} of CuO-embedded OFET depended on the trapped electron population in CuO, and could be changeable with the positive V_{GS0}. The induced holes could act as a floating gate voltage that can influence the threshold voltages. When adjusting

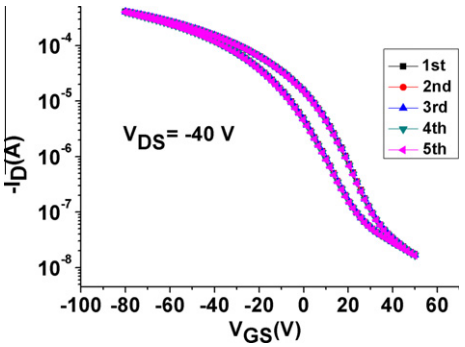

Fig. 8. I_D–V_{GS} transfer curves at V_{DS} = −40 V measured for five times. Each transfer curve is double-swept, V_{GS} scans from 50 V to −80 V then back to 50 V.

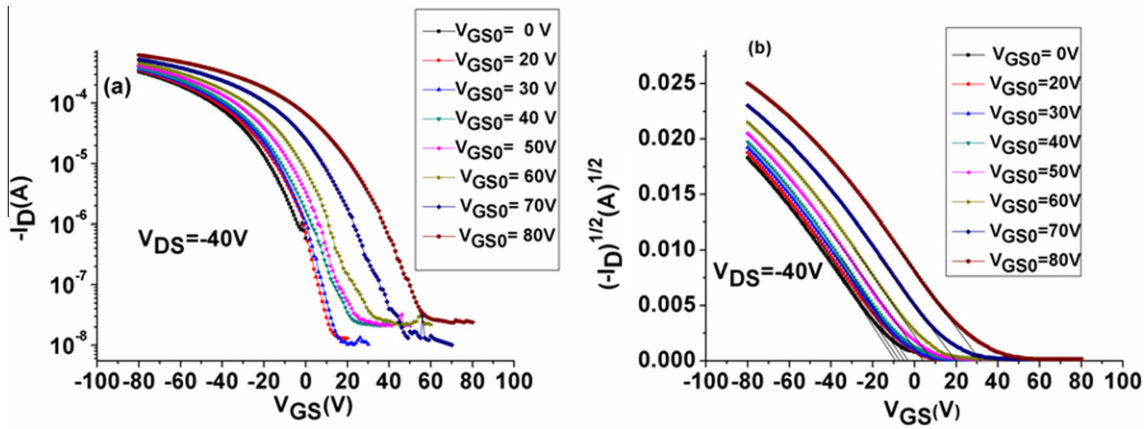

Fig. 7. (a) Log plots of $-I_D$ versus V_{GS} and (b) $(-I_D)^{1/2}$ versus V_{GS} transfer curves for CuO-embedded OFET with different V_{GS0}: 80, 70, 60, 50, 40, 20 and 0 V.

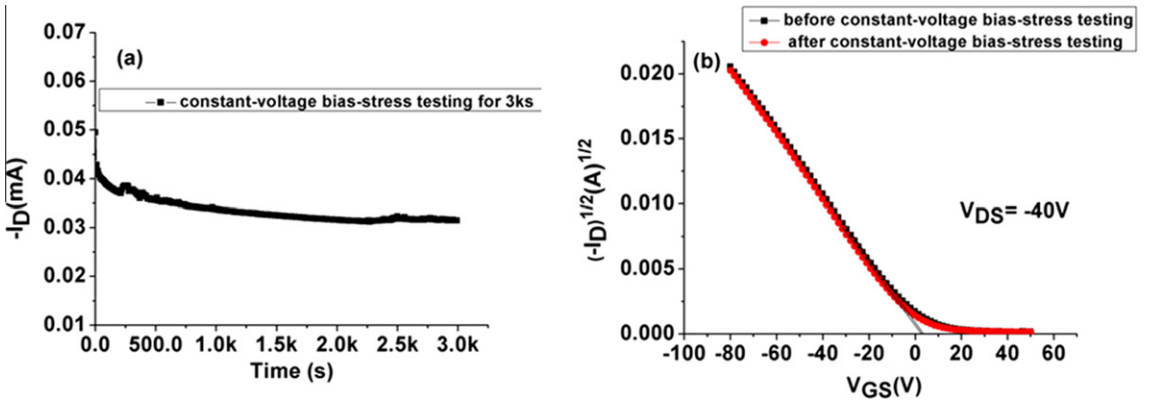

Fig. 9. (a) Drain current as a function of stress time over a period of 3×10^3 s for a constant voltage-bias stress testing, the time interval is 10 s, and the drain current was measured at $V_{GS} = -30$ V and $V_{DS} = -30$ V. (b) $(-I_D)^{1/2}$–V_{GS} transfer curves with $V_{DS} = -40$ V before and after constant-voltage bias-stress testing over a period of 3×10^3 s, respectively.

positive V_{GS0}, trapped electrons in CuO could be changed as discussed (see Fig. 4a). In the transfer curves, when changing the starting gate-to-source voltages (V_{GS0}) in positive range, systematic tuning of the V_{TH} of the CuO-embedded OFET can be realized. For example, when V_{GS0} varies from 0 V to 80 V, the transfer curves regularly shift from negative voltage to positive voltage, and the V_{TH} shifts from −9.5 V to 32.5 V (as shown in Fig. 7a and b). The shift of threshold voltage was not observed in pentacene-based OFET (data is not shown here). Therefore, the systematic tunable V_{TH} in our device can be ascribed to the fact that V_{GS0} influenced the trapped electron population at the interface between CuO and pentacene layers.

3.3. Stability of V_{TH}

To investigate the stability of the tuned V_{TH}, the transfer curves with V_{GS0} at 50 V were repeatedly measured in five times, and exhibited a good repeatability (see Fig. 8). On the other hand, the drain current was measured with $V_{GS} = -30$ V and $V_{DS} = -30$ V at the mode of constant-voltage bias-stress testing for 3×10^3 s (as shown in Fig. 9a), exhibiting a very small decrease of the drain current. The $(-I_D)^{1/2}$ versus V_{GS} transfer curves were then measured at V_{GS0} of 50 V, exhibiting almost unchangeable V_{TH} after constant-voltage bias-stress testing over a period of 3×10^3 s, as shown in Fig. 9b. The results suggest that the trapped electrons at the interface between CuO and pentacene layers are not easily released and the tuned V_{TH} is stable.

4. Conclusion

An organic field-effect transistor based on pentacene with an embedded CuO layer was investigated. With the thin CuO layer embedded in the pentacene semiconductor, the drain current was increased and the threshold voltage shifted from −17.5 V to −7.9 V. The interesting results are attributed to the formation of CT complexes at the interface of CuO and pentacene. Electrons trapped in CuO can induce holes in pentacene. The induced holes act as a floating gate voltage that influences the threshold voltages. The regular tuning on threshold voltages of CuO-embedded OFET is achieved by scanning the transfer curves with different starting positive gate-to-source voltage (V_{GS0}) because the population of trapped electrons can be changed by setting the V_{GS0}. The threshold voltages are stable under stress of source-to-drain and gate-to-source voltages.

Acknowledgements

The authors are grateful to National "863" Project of China (Grant No. 2008AA03A335), National "973" Project of China (Grant No. 2009CB623604), the National Natural Science Foundation of China (under the Grant Nos. 610,36,007, 50573024 and 50433030), the project of Guangdong province (Grant No. 20081202) and Key Project of Chinese Ministry of Education (Grant No. 104208).

Reference

[1] C.D. Dimitrakopoulos, P.R.L. Malenfant, Adv. Mater. 14 (2002) 99.
[2] B.K. Crone, A. Dodabalapur, R. Sarpeshkar, et al., J. Appl. Phys. 89 (2001) 5125.
[3] Y.L. Wu, Y.N. Li, S. Gardner, B.S. Ong, J. Am. Chem. Soc. 127 (2005) 614.
[4] A.L. Briseno, M. Roberts, M.M. Ling, H. Moon, E.J. Nemanick, Z. Bao, J. Am. Chem. Soc. 128 (2006) 3880.
[5] C.A. Di, G. Yu, Y.Q. Liu, X.J. Xu, D.C. Wei, Y.B. Song, Y.M. Sun, Y. Wang, D.B. Zhu, J. Liu, X.Y. Liu, D.X. Wu, J. Am. Chem. Soc. 128 (2006) 16418.
[6] K.P. Pernstich, S. Haas, D. Oberhoff, C. Goldmann, D.J. Gundlach, B. Batlogg, A.N. Rashid, G. Schitter, J. Appl. Phys. 96 (2004) 6431.
[7] Y. Abe, T. Hasegawa, Y. Takahashi, T. Yamada, Y. Tokura, Appl. Phys. Lett. 87 (2005) 153506.
[8] C.A. Nguyen, P.S. Lee, S.G. Mhaisalkar, Org. Electron. 8 (2007) 415.
[9] H. Sakai, Y. Takahashi, H. Murata, Appl. Phys. Lett. 91 (2007) 113502.
[10] H. Sakai, K. Konno, H. Murata, Appl. Phys. Lett. 94 (2009) 073304.
[11] H. Nakanotani, M. Saito, H. Nakamura, C. Adachi1, Appl. Phys. Lett. 95 (2009) 103307.
[12] S.M. Sze, K.K. Ng, Physics of Semiconductor Devices (Chapter 6), third ed., Wiley, Hoboken, 2007. pp. 346.
[13] J.W. Park, K.J. Baeg, J. Ghim, S. Ju, K.J.H. Park, D.Y. Kim, Electrochem. Solid-State Lett. 10 (2007) H340.
[14] G.B.M. Greiner, M.G. Helander, Z.B. Wang, Z.H. Lu, Appl. Phys. Lett. 93 (2008) 083309.
[15] S. Kim, K. Hong, K. Kim, et al., J. Electrochem. Soc. 157 (2010) J147.
[16] S.M. Sze, Physics of Semiconductor Devices, second ed., Wiley, New York, 1981.
[17] G. Nunes Jr., S.G. Zane, J.S. Meth, J. Appl. Phys. 98 (2005) 104503.
[18] J.W.H. Smith, I.G. Hill, J. Appl. Phys. 101 (2007) 044503.
[19] T.P.I. Saragi, J. Londenberg, J. Salbeck, J. Appl. Phys. 102 (2007) 046104.

[20] G. Gu, M.G. Kane, S.C. Mau, J. Appl. Phys. 101 (2007) 014504.
[21] G. Gu, M.G. Kane, Appl. Phys. Lett. 92 (2008) 053305.
[22] J.H. Lee, D.S. Leem, H.J. Kim, J.J. Kim, Appl. Phys. Lett. 94 (2009) 123306.
[23] F.P. Koffyberg, F.A. Benko, J. Appl. Phys. 53 (1982) 1173.
[24] T. Matsushima, Y. Kinoshita, H. Murata, Appl. Phys. Lett. 91 (2007) 253504.
[25] K. Walzer, B. Maennig, M. Pfeiffer, K. Leo, Chem. Rev. 107 (2007) 1233.
[26] B. Maennig, M. Pfeiffer, A. Nollau, X. Zhou, K. Leo, P. Simon, Phys. Rev. B 64 (2001) 195208.
[27] T. Minari, T. Miyadera, K. Tsukagoshi, Y. Aoyagi, H. Ito, Appl. Phys. Lett. 91 (2007) 053508.
[28] M. Terai, K. Fujita, T. Tsutsui, Jpn. J. Appl. Phys., Part 2 44 (2005) L1059.
[29] X.F. Qi, N. Li, S. Forrest, J. Appl. Phys. 107 (2010) 014514.
[30] S.M. Sze, K.K. Ng, Physics of Semiconductor Devices, Wiley, New York, 2007.

Organic Electronics 12 (2011) 435–441

Contents lists available at ScienceDirect

Organic Electronics

journal homepage: www.elsevier.com/locate/orgel

The influence of substrate heating on morphology and layer growth in C_{60}:ZnPc bulk heterojunction solar cells

Steffen Pfuetzner [a,*], Christine Mickel [b], Jens Jankowski [a], Moritz Hein [a], Jan Meiss [a], Christoph Schuenemann [a], Chris Elschner [a], Alexandr A. Levin [a], Bernd Rellinghaus [b], Karl Leo [a], Moritz Riede [a]

[a] Institut für Angewandte Photophysik, Technische Universität Dresden, D-01062 Dresden, Germany
[b] Leibniz-Institut für Festkörper und Werkstoffforschung, D-01171 Dresden, Germany

ARTICLE INFO

Article history:
Received 1 September 2010
Received in revised form 3 December 2010
Accepted 10 December 2010
Available online 28 December 2010

Keywords:
Solar cell
Organic
Small molecules
C_{60}
ZnPc
Morphology

ABSTRACT

The change of morphology in mixed layers due to different substrate temperature T_{sub} of organic solar cells containing C_{60} and zinc phthalocyanine (ZnPc) is studied. Heating the substrate during deposition of the bulk heterojunction C_{60}:ZnPc leads to a significant improvement of solar cell performance, mainly due to an increase in photocurrent and fill factor (*FF*). This is attributed to improved charge carrier percolation pathways within the C_{60}:ZnPc blend. Using atomic force microscopy, scanning electron microscopy, transmission electron microscopy, organic field effect transistor, X-ray diffraction, and absorption measurements, we observe aggregation, cluster-like, and polycrystalline growth of the heated bulk layer. This provides better transport percolation paths by inducing a phase separation of the molecules. Heated blend layer with thickness of 60 nm shows high performance without loss in *FF*. When heating the substrate to the optimum temperature of 110 °C, a power conversion efficiency of 3.0% is achieved, compared to 1.4% for an identical device prepared on a substrate held at room temperature.

© 2010 Elsevier B.V. All rights reserved.

1. Introduction

Since the first copper phthalocyanine/perylene derivative-based flat heterojunction organic solar cell (OSC) by Tang [1], OSCs have attracted considerable interest as a potential cost-efficient alternative to current inorganic solar cells. However, a drawback of flat heterojunction OSC is that the photoactive layer thickness is usually limited by the exciton diffusion length L_D, i.e. the average distance that the excitons diffuse before recombination. Typical values of L_D are in the range of 5–30 nm [2]. This limitation can partially be overcome by the concept of bulk heterojunctions (BHJ) [3–6], consisting of a mixture of donor and acceptor molecules, e.g. fullerene C_{60}:zinc phthalocyanine (ZnPc). Thicker BHJ layers can lead to increased photon harvesting due to higher absorbance and efficient dissociation of photogenerated excitons at the distributed donor–acceptor interface throughout the bulk. A challenge associated with BHJ is that during film deposition, isolated clusters of donor or acceptor molecules can form which have no direct charge carrier percolation path towards an electrode. These clusters or dead ends act as recombination sites, reducing photocurrent and fill factor *FF*. Furthermore, the charge carrier mobilities are also limited due to higher molecular disorder in an amorphous BHJ compared to a pristine crystalline layer [27]. In order to achieve higher photocurrent, it is necessary to control morphology and properties of the BHJ, e.g. by heating, as shown by Suemori et al. [7]. It is desirable to improve the percolation network to reduce isolated clusters and trap sites.

In this contribution, we show improved morphology of a C_{60}:ZnPc BHJ and the formation of percolation paths due to controlled substrate heating, leading to efficient OSC with blend layers of 60 nm.

* Corresponding author.
E-mail address: steffen.pfuetzner@iapp.de (S. Pfuetzner).

1566-1199/$ - see front matter © 2010 Elsevier B.V. All rights reserved.
doi:10.1016/j.orgel.2010.12.007

Despite thicker layers than a standard C_{60}:ZnPc cell with a 30 nm thick BHJ [8], reasonable *FF* of over 55% are achieved. Combined with a photocurrent increase by over 40%, the power conversion efficiency (η) is increased from 1.4% to 3.0%.

The correlation between substrate temperature T_{sub} and OSC performance for 150 nm thick C_{60}:ZnPc blend layers has recently been studied by us [12]. There, the temperature was varied in-situ during evaporation of the organic C_{60} and ZnPc layers between room temperature (RT) and 130 °C. An optimum substrate temperature for this absorber system was found at 110 °C.

In this work we investigate in more detail the mechanism that determine the correlation of substrate temperature and device characteristics. Different characterization tools, e.g. atomic force microscopy (AFM), scanning electron microscopy, transmission electron microscopy (TEM), and organic field effect transistors are applied to gather, information for our studies.

2. Experimental

The solar cells are fabricated in a custom-made multichamber ultrahigh vacuum (UHV) evaporation system (BESTEC, Germany) at a base pressure of 10^{-8} mbar. As substrate, pre-structured tin-doped indium oxide (ITO)-coated glass (Thin Film Devices, USA) is used. The substrates are cleaned in ultrasonic baths with detergent, acetone, ethanol, and iso-propanol prior to processing.

For sample heating during deposition, an additional fully ITO-coated glass substrate is put beneath the sample. The substrate temperature (T_{sub}) is controlled by resistive heating of the ITO layer and is monitored by a thermocouple as depicted in Fig. 1.

The OSC stack consists of ITO, followed by 5 nm of C_{60} and a blend layer of 60 nm co-evaporated C_{60} and ZnPc (volume ratio 1:1). The subsequent layer system consists of 5 nm *N*,*N*′-di(4-(2,2-diphenyl-ethen-1-yl)-phenyl)–*N*,*N*′-di(4-methylphenylphenyl)benzidine (PV-TPD, Sensient), 20 nm of PV-TPD [9] doped with 3.2 wt% of a p-type dopant NDP2 (Novaled AG, Dresden, Germany) [10], and 10 nm of 4.4 wt% p-doped ZnPc. These layers are used as hole transport layers and as electron and exciton blocker, to place the maximum of the optical field within the photoactive layer, and to ensure low energy barriers for good hole extraction to the Au electrode [11]. Finally, a 40 nm reflective Au back contact is deposited.

All organic materials except for the p-dopant had been purified at least twice by vacuum gradient sublimation to remove contaminations. The typical solar cell area is nominal ≈6.4 mm^2, defined by the overlap of ITO and Au.

J(*V*)-characteristics are recorded using a source measurement unit 236 SMU (Keithley) and an AM 1.5G sun simulator (Hoenle AG). All short-circuit current densities (J_{SC}) shown in this work are normalized to 100 mW/cm^2 with respect to a calibrated Si reference diode; the data are not corrected for spectral mismatch. The intensity loss due to the additional ITO glass substrate is taken into account with an average transmission of 85% in the spectral range 350–900 nm [12]. The morphology is analyzed using atomic force microscopy (AFM Nanoscope 3, Digital Instruments), scanning electron microscopy (SEM, Zeiss DSM 982 Gemini), transmission electron microscopy (TEM, Tecnai), and wide-angle X-ray diffraction (WAXRD, URD-6 X-ray powder diffractometer, Seifert FPM GmbH; designed in Bragg–Brentano geometry; monochromatized Cu-Kα radiation). To identify lattice planes by WAXRD reflection positions the Cambridge Structural Database (CSD) [21] is used. For the TEM measurements a 10–15 nm carbon-coated nickel grid and an accelerating voltage of 200 kV are used. Absorption measurements are made using a spectrometer (Perkin-Elmer) Lamda 900 UV/VIS/NIR. Mobilities are determined using organic field effect transistors (OFETs). The OFETs consist of a silicon gate and silicon oxide. The OFET substrates with pre-structured source and drain Au contacts and a channel length in the range of 2.5–20 µm are purchased from the Fraunhofer IPMS (Dresden). C_{60}, ZnPc, and C_{60}:ZnPc (unheated and heated at 110 °C) layers of 30 nm are deposited on the OFET substrates. For the substrate heating during evaporation a heatable copper block is used and the temperature is monitored by a thermal couple glued onto the substrate with silver paste. OFET-characteristics are recorded using source measurement units 236 SMU (Keithley).

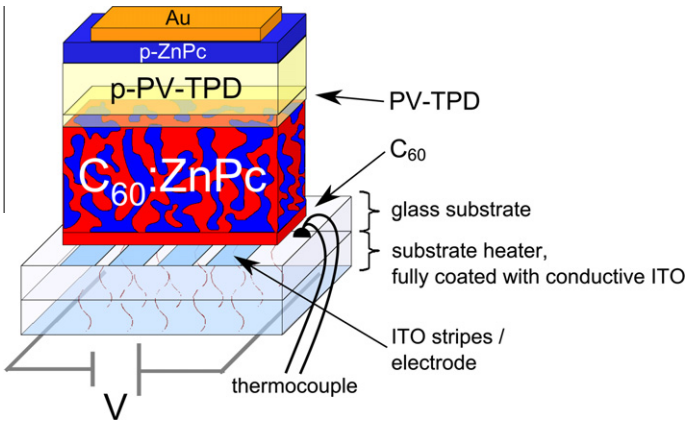

Fig. 1. p-i-i solar cell stack on a fully coated ITO substrate, which is used as resistive substrate heater. A thermocouple for temperature control is glued with silver paste on the deposition face.

3. Results and discussion

3.1. J(V)-characteristics of heated bulk heterojunction solar cells

Here, we use 60 nm instead of 150 nm C_{60}:ZnPc blend layer due to a more distinct heating effect and better processability. This can be attributed to less recombination losses due to shorter transport paths in the bulk to the adjacent charge transport layers. The probability to form then percolation paths without dead ends is higher for thinner blend layers. Furthermore, series resistance and charge carrier mobilities also have to be considered as limiting parameters. This means that for thicker blend layers, the probability for charge carrier recombination is increased even if perfect percolation paths are formed.

Therefore, the solar cell performance is further improved with respect to *FF* and saturation $S = (J(-1V)/J_{SC})$. *J*(*V*) curves under simulated sunlight, see Fig. 2, and in the dark (Fig. 2, inset) are shown for samples processed at RT and T_{sub} = 110 °C. The characteristics of the complete devices are summarized in Table 1.

Generally, a low *FF* hints at charge carrier recombination within the solar cell, in particular for samples with injection or extraction barriers [13], unbalanced charge carrier mobilities, disturbed transport paths, and trap states in the blend layer [14]. It is observed that heating leads to improved, lower saturation *S* and series resistance. The saturation changes from 1.3 at room temperature to 1.1 for 110 °C substrate temperature. The better saturation suggests a better charge carrier separation and transport in the blend layer to the respective electrode. For the heated blend layer the charge carriers can more easily be extracted out of the blend layer before they recombine. In case of the unheated blend layer a higher electric field in backward direction is required to extract the photogenerated charge carriers due to poor transport paths. While at 0 V the difference of J_{SC} between heated and unheated solar cell is 41%, at −1.5 V the photo current differs only by 15%. Since only the blend layer is deposited during substrate heating, no influence of heating on other layers, or changes in energy level alignment are expected. Thus, the improved series resistance of 7.8 Ω cm^2 compared to 28.9 Ω cm^2 is an additional hint at better charge transport through the blend layer in forward bias. V_{OC} is comparable for both devices. Saturation factors are positively influenced by heating, while the most decisive improvements which ultimately lead to the increased η are *FF* and J_{SC}.

Table 1
Solar cell parameters (J_{SC}, V_{OC}, *FF*, $(J(-1V)/J_{SC})$, and η) for substrate temperatures T_{sub} = RT and 110 °C. J_{SC} is normalized to 100 mW/cm^2 with respect to calibrated Si reference.

T_{sub} (°C)	J_{SC} (mA/cm^2)	V_{OC} (V)	*FF* (%)	$J(-1V)/J_{SC}$	η (%)
RT	7.2	0.53	36	1.39	1.4
110	10.3	0.52	57	1.09	3.0

Values of *FF* = 36.4% and J_{SC} = 7.2 mA/cm^2 for the device processed at RT are achieved, whereas *FF* of 56.6% and J_{SC} of 10.3 mA/cm^2 are measured for T_{sub} = 110 °C. Absorption measurements are performed of C_{60} (5 nm)/C_{60}:ZnPc (20 nm, 1:1) samples deposited on quartz glass at RT and 110 °C. No significant enhancement in absorption (Fig. 4b) of the heated layer is observed, which might have explained the increased J_{SC} in the OSC. The slight change in absorption in particular for the ZnPc peak around 625 nm is discussed in Section 3.1.1. Both improvements in *FF* of over 55% and J_{SC} of over 43% lead to an increase of η by a factor of two. Due to an additional thermal energy supply to the molecules evaporated onto the substrate by substrate heating, the molecules can diffuse over a larger area before adsorption. We attribute the solar cell improvement

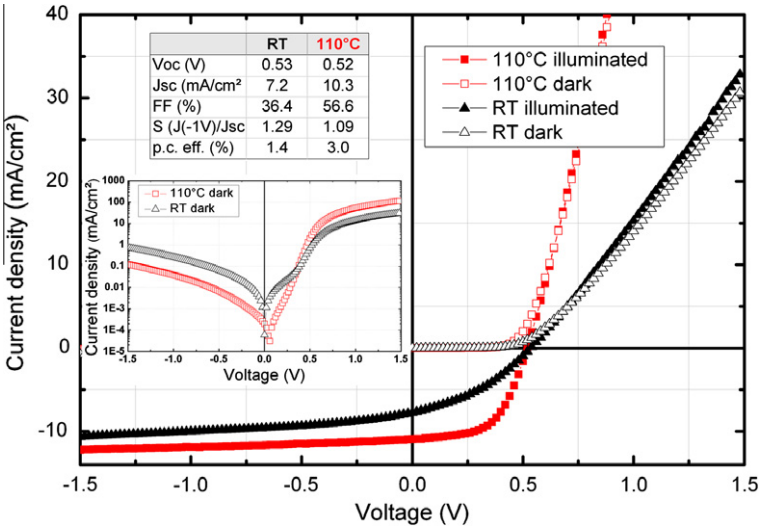

Fig. 2. *J*(*V*)-characteristics of (ITO/C_{60} (5 nm)/C_{60}:ZnPc (60 nm, 1:1)/PV-TPD (5 nm)/p-PV-TPD (40 nm, 4.4 wt%)/p-ZnPc (10 nm, 3.2 wt%)/Au) samples processed at RT and T_{sub} = 110 °C. Short current density J_{SC}, open circuit voltage V_{OC}, fill factor *FF*, saturation $(J(-1V)/J_{SC})$, and power conversion efficiency η are given. J_{SC} is normalized to 100 mW/cm^2 with respect to the Si reference.

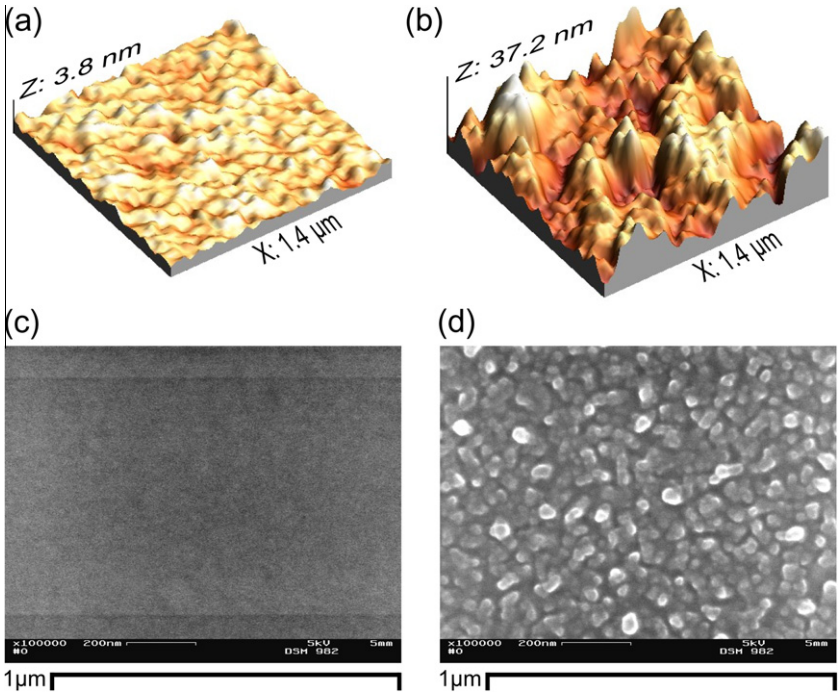

Fig. 3. AFM (a and b) and SEM (c and d) measurements of ITO/C_{60} (5 nm)/C_{60}:ZnPc (30 nm, 1:1) the first two layers of the solar cell stack: (a) unheated blend layer with RMS roughness of 0.5 nm; (b) blend layer deposited at T_{sub} = 110 °C with RMS roughness of 6.4 nm; (c) unheated blend layer; (d) blend layer deposited at T_{sub} = 110 °C.

to a change in BHJ layer morphology. It is estimated that the interaction energies between nearest neighbors are 0.87 eV (CuPc–CuPc) [15], 1.5 eV (C_{60}–C_{60}) [16,17], and 0.44 eV (CuPc–C_{60}) [18], respectively. Similar values for ZnPc are assumed, because CuPc and ZnPc have similarities concerning molecular structure, optical properties, and energy levels. These high interaction energies suggest a preferential aggregation of like molecules. If sufficient thermal energy for diffusion is supplied, formation of interconnected ZnPc and C_{60} networks occurs, which results in an improved percolation network and thus increased charge carrier mobility. To check the preferential aggregation due to heating, the morphology of the bulk layers is investigated by AFM, SEM, TEM, WAXRD, absorption, and photoluminescence measurements.

3.1.1. AFM and SEM measurements

For AFM and SEM investigations, the first two layers of the solar cell C_{60} (5 nm)/C_{60}:ZnPc (30 nm; volume ratio 1:1) are deposited at ambient conditions and T_{sub} = 110 °C, on ITO, respectively. While the unheated device forms a smooth amorphous surface with peak heights of 4 nm and a root mean square (RMS) roughness of 0.5 nm, the heated device shows a rough surface with peak heights of 37 nm and RMS roughness of 6.4 nm, as shown in Fig. 3a and b, respectively. Island and cluster-like growth can also clearly be seen in the SEM picture (Fig. 3d) for the heated structure, while for the unheated structure no such features are observed (Fig. 3c). Clusters on the heated sample have diameters in the range of 20 nm. Bright spots correspond to high peaks on the surface.

3.1.2. Absorption measurements

Maennig et al. [19] have shown absorption measurements (Fig. 4a) of ZnPc prepared at different substrate temperatures: the RT sample was prepared while the substrate was held at 25 °C. The low temperature (LT) sample was prepared while the substrate was cooled to −150 °C. They obtained for the RT sample discrete diffraction spots using transmission electron microscopy due to the polycrystalline morphology of the phthalocyanine, while for the LT sample no such features were observed, which hints at a stable amorphous phase. From the absorption measurements (Fig. 4a) it is concluded that in the solid state, the electronic excitation of ZnPc splits up in to two parts because of the molecular interactions [20]. The positions of the peaks are at 625 and 710 nm for the RT sample and at 635 and 688 nm for the LT sample, respectively. The peak separation is smaller for the amorphous than for the polycrystalline sample. This is a strong hint at a lower interaction of the molecules of the LT sample, which fits well with the lower degree of order.

To check whether polycrystalline domains of ZnPc in the heated blend layers are present, absorption measurements are carried out for C_{60} (5 nm)/C_{60}:ZnPc (20 nm) made at RT and T_{sub} = 110 °C, see Fig. 4b. The peak positions of the RT sample are at 631 and 688 nm and hint at amorphous growth, as reported by Maennig et al. [19]. We conclude that the polycrystalline growth of ZnPc is suppressed in the unheated C_{60}:ZnPc blend layer. A peak shift which might have indicated polycrystalline domains in the heated blend layer is not observed. Anyway, another feature is the peak ratio dependency of ZnPc for amor-

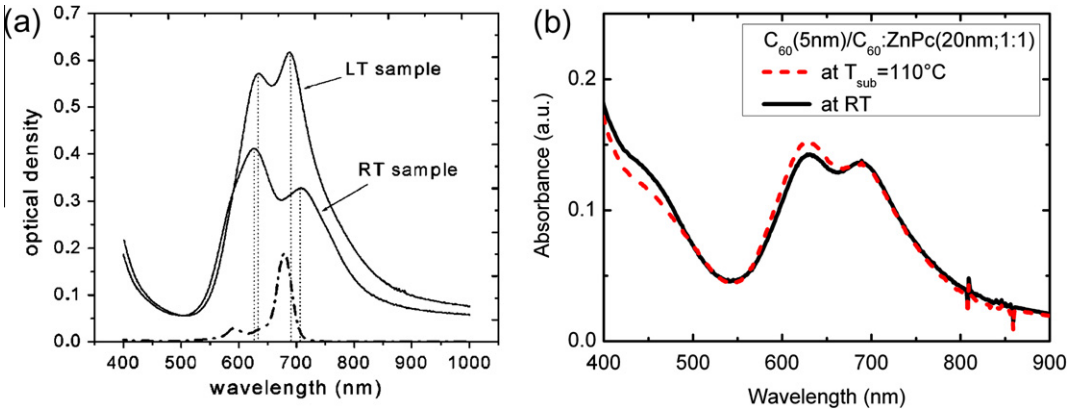

Fig. 4. Absorption spectra of (a) ZnPc layers (50 nm thick) with permission taken from Ref. [19]: the RT sample was prepared at 25 °C substrate temperature and the low temperature (LT) sample at −150 °C substrate temperature. The dotted line shows schematically the absorption of ZnPc dissolved in 1-chloronaphthalene; (b) C_{60} (5 nm)/C_{60}:ZnPc (20 nm; volume ratio 1:1) made at RT (black solid line) and T_{sub} = 110 °C (red dashed line). (For interpretation of the references to color in this figure legend, the reader is referred to the web version of this article.)

phous and polycrystalline layer. In Fig. 4a it can be seen that for the amorphous layer (LT sample) the first peak is smaller than the second one and vice versa for the polycrystalline layer (RT sample) [19]. Such a peak ratio shift is also observed for the blend layer, see Fig. 4b. For the sample at RT, both peaks have almost the same height, while for the heated samples, the first peak is increased compared to the second one. This suggests at least a certain amount of polycrystalline domains of ZnPc in the heated blend layer.

3.1.3. WAXRD measurements

For the WAXRD measurements, a layer sequence of C_{60} (5 nm)/C_{60}:ZnPc (50 nm) volume ratio 1:1 is deposited on silicon at ambient conditions and T_{sub} = 100 °C, respectively. To check whether the cluster formation is also present when using a silicon substrate instead of ITO, additional SEM measurements of these samples are carried out and show similar aggregation and cluster assembly. Measuring over diffraction angle diapazon of 2θ (2–28 °), no characteristic WAXRD reflections indicating at nanocrystalline growth for ZnPc and C_{60} are observed in the blend layer, see Fig. 5. Additionally, pristine 25 nm thick C_{60} and ZnPc layers deposited on heated silicon substrate (T_{sub} = 90 °C) are investigated by WAXRD. In contrast to the heated C_{60}:ZnPc blend layer, nanocrystalline growth is observed, in heated pristine ZnPc indicated by a set of WAXRD reflections. For C_{60} only a very weak reflection is seen in Fig. 5. Probably, the nanocrystalline growth of ZnPc in the blend is reduced resulting in a material that is at least X-ray amorphous. According to Crystal Structure Database (CSD) [21], the reflections detected for the thin ZnPc film can be attributed to modifications, which are isomorphous with triclinic (space group $P\bar{1}$) [22] and monoclinic (space group $C2/n$) [23] α-polymorphs of CuPc. They are characterized by similar molecular structure, molecular weight, and atomic radii of metal elements, Zn and Cu. The observed reflection positions of heated ZnPc, 2θ = 6.89°, 13.76°, and 27.66° correspond, respectively, to the reflections 100 (theoretical 2θ = 6.86°), 200 (13.73°), and 400 (27.67°) of the triclinic modification, or to the reflections 200 (6.73°), 400 (13.45°), and 800 (27.15°) of the monoclinic phase. Note that in both cases, the ZnPc film exhibits a preferred orientation along the [100] crystallographic direction of the corresponding crystalline lattice.

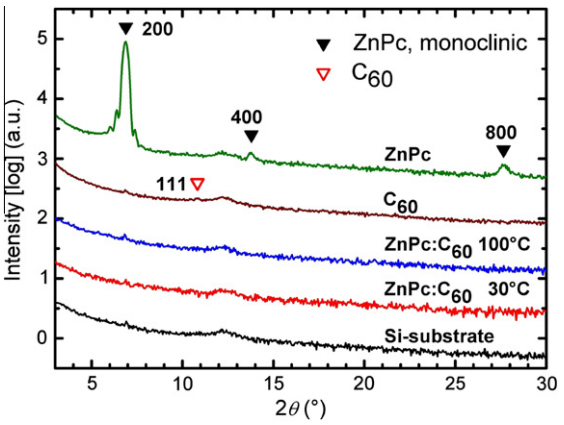

Fig. 5. WAXRD patterns of silicon/C_{60} (5 nm)/C_{60}:ZnPc (50 nm, 1:1) samples of unheated (T_{sub} = 30 °C), heated (T_{sub} = 100 °C) blend layer, heated (T_{sub} = 90 °C) 25 nm thick pristine C_{60}, and ZnPc layers deposited at silicon substrate. For comparison WAXRD pattern of Si substrate is shown at bottom of Fig. 5. The thickness fringes for ZnPc (200) reflection at Bragg angles 2θ = 6.02°, 6.38°, 6.89°, and 7.42° appear due to diffraction at thin layer, and are resolved in the reflection profile. The Miller indices of observed ZnPc reflections are indicated according to possible monoclinic α-polymorphs. The Miller indices of the C_{60} phase are indicated for cubic (space group $Fm\bar{3}m$) structure model [24]. For better visualization the WAXRD patterns are shifted vertically.

3.1.4. TEM measurements

The methods used before show a tendency of molecular phase separation and polycrystalline growth of ZnPc, but could not confirmed yet. To further investigate the blend layer morphology, TEM measurements are performed. The 5 nm of C_{60} of the stack C_{60} (5 nm)/C_{60}:ZnPc (30 nm, 1:1) are deposited at RT while the mixed layers are depos-

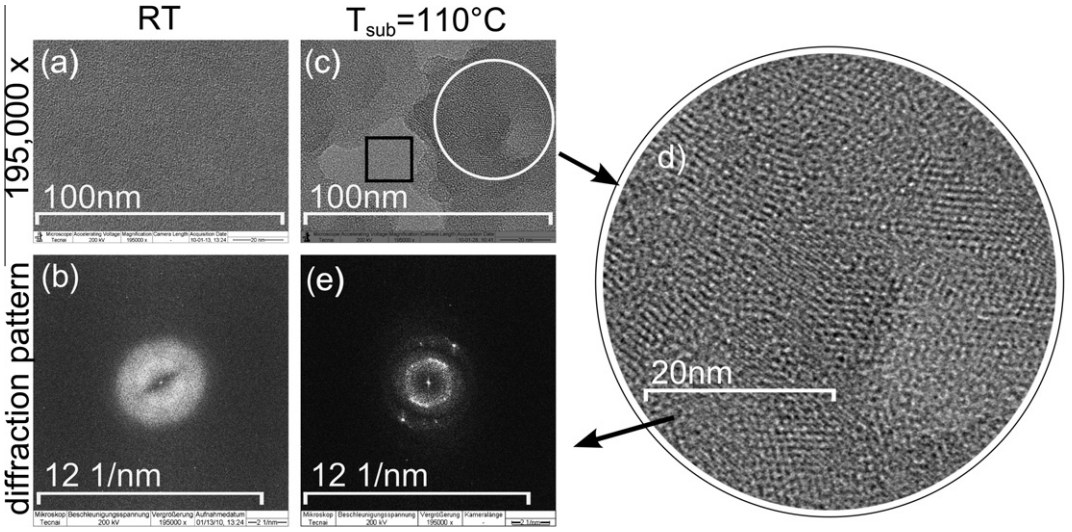

Fig. 6. TEM images at a magnification of 195,000 of C_{60} (5 nm)/C_{60}:ZnPc (30 nm, 1:1) stacks deposited on carbon-coated nickel grids are shown. (a) Blend layer processed at RT; (b) diffraction pattern (a); (c) processed at T_{sub} = 110 °C; (d) region marked by the white circle is enlarged for a better view; (e) diffraction pattern of (d).

ited at RT and T_{sub} = 110°C, respectively. The TEM results are shown in Fig. 6 for a magnification of 195,000. For the sample made at RT (Fig. 6a) only a homogeneous gray area is observed. It indicates amorphous layer growth. This is confirmed by the Fourier transformation as shown in image b, where a pattern with a halo ring typical for amorphous growth can be seen.

In the TEM images of the 110 °C heated sample (Fig. 6c and d), bright and dark regions are observed. The dark regions can be related to thicker layers or molecules with a higher scattering factor, caused by, e.g. Zn with a higher atomic number of Z = 30 compared to Z = 6 for C. It means that phase separation occurs due to heating, and a rougher surface is formed, which was already observed in the AFM measurements.

The dark regions are framed by a white circle and the bright regions by a black rectangle. Polycrystalline structures (white circle) in Fig. 6c are observed, which is not the case for the bright regions (black rectangle). The region of the white circle in Fig. 6c is enlarged and is shown in Fig. 6d. Large polycrystalline domains with lateral diameters of 50 nm are obtained, while the lateral crystal sizes are in the range of 10 nm. A Fourier transformation (Fig. 6e) of this region exhibits a mixture of polycrystalline (diffraction spots) and amorphous (halo ring) domains. Fifteen of such images are taken at different sample positions and evaluated using Fourier transformation to investigate the polycrystalline structure with respect to its composition, either to ZnPc or C_{60}. The same data from the CSD [21], which had already been utilized for the WAXRD measurements are taken. The correlation between theoretical lattice plane spacing d_{hkl} from CSD and the theoretical lattice planes of ZnPc and C_{60} are summarized in Table 2. Only very few crystals can be attributed to C_{60} (1 1 1) atomic planes. Some of the observed lattice plane spacings d_{hkl} are around 8.0 Å and cannot clearly be referred to C_{60} (d_{hkl} = 8.175 Å) or ZnPc (7.882 Å). However, the majority of assigned reflections is attributed to monoclinic ZnPc [23] and consist of 003, 403, and 005 reflections. Usually they are forbidden for space group $C2/n$ due to extinction laws. Evidently, the appearance of the forbidden reflections is related to strong dynamic interaction of the electron beam and crystalline lattice [25,26] of the monoclinic ZnPc in the thin blend layers. Aside from weak intensities of the forbidden reflections, the small scattering volume of the crystalline ZnPc prevents the observation of the ZnPc reflections in the WAXRD measurements.

Table 2
Correlation between the theoretical lattice spacing (d_{hkl}) from CSD and lattice planes (h k l) for monoclinic ZnPc [23] and C_{60} [24]. Measured d_{hkl} are sorted and related to the theoretical lattice planes.

T_{sub} = 110 °C	Lattice plane spacing (d_{hkl}) (Å)	Lattice plane (h k l)
ZnPc monoclinic, space group $C2/n$	7.88	(0 0 3)[a]
	4.87	(4 0 3)[a]
	4.73	(0 0 5)[a]
C_{60}, space group $Fm\bar{3}m$	8.19	(1 1 1)

[a] Forbidden reflections (lattice planes) according to extinction law.

3.1.5. Mobility measurements

To check whether the mobilities are positively influenced by the formation of polycrystals due to substrate heating, OFET measurements in the saturation regime of unheated and heated blend layers are carried out. Using the OFET method, where the silicon oxide sublayer is the same for all devices, a reliable comparison of the mobilities of different samples is possible. Similar aggregation of heated C_{60}:ZnPc on silicon oxide compared to C_{60} is observed by SEM. The hole mobility μ_h of neat ZnPc of 6.5×10^{-4} cm^2/Vs is decreased in a blend layer with C_{60} (volume ratio 1:1) to 5.1×10^{-5} cm^2/Vs. This might be attributed to a smaller overlap of the π-orbitals of ZnPc due to a higher disorder in the blend [27] and to the reduction of the effective channel width by a factor of two. Sim-

ilar observations are made for the electron mobility μ_e of C_{60}. For the neat layer, $\mu_e = 9.2 \times 10^{-3}$ cm^2/Vs and for the blend layer, $\mu_e = 5.2 \times 10^{-3}$ cm^2/Vs is measured. The heated sample shows a clear tendency to higher μ_h of ZnPc. Values of 2.2×10^{-4} cm^2/Vs are achieved due to polycrystalline growth of ZnPc. In case of C_{60}, no improvement of μ_e is determined for the heated sample compared to the unheated, both are on the order of 5.0×10^{-3} cm^2/Vs. This fits to the observations in TEM that no or only very few C_{60} crystals are formed, which would lead to an improvement of the mobility. Furthermore, the increase of μ_h for ZnPc closer to the mobility of C_{60} positively influences the charge carrier balance within the blend layer and leads to less charge carrier recombination and therefore to a higher *FF* [14]. Not only the formation of percolation paths caused by molecular phase separation, but also the increased mobility lead to the improved performance of heated solar cells.

4. Conclusion

In summary, we have shown that controlled in-situ substrate heating during evaporation of a blend consisting of 60 nm C_{60}:ZnPc with volume ratio 1:1 can positively influence the OSC efficiency by a factor of two. The main reasons are that J_{SC} rises by over 40%, and *FF* by over 55%. The observed effects are investigated by AFM, SEM, TEM, and OFET measurements. While X-ray diffraction measurements show no polycrystalline growth in the heated blend layer both for C_{60} and ZnPc, probably due to at least X-ray amorphous material, in the TEM measurements polycrystalline domains of 50 nm are observed and are mainly attributed to ZnPc. The hole mobility of ZnPc is improved by one order of magnitude, probably caused by the formation of percolation paths, while the mobility of C_{60} remains unchanged. Well established percolation networks within the BHJ due to molecular phase separation and polycrystalline growth leads to improved charge carrier extraction and solar cell performance.

Acknowledgments

This work is supported by the Bundesministerium für Bildung und Forschung in the framework of the OPA-project (# 13N9872). We thank A. Petrich for the material purification and E. Kern from the Institute of Chemistry and Food Chemistry, Technische Universität Dresden, Germany, for the SEM measurements.

References

[1] C.W. Tang, Appl. Phys. Lett. 48 (1986) 183.
[2] P. Peumans, A. Yakimov, S.R. Forrest, J. Appl. Phys. 95 (2004) 2938.
[3] M. Hiramoto, H. Fujiwara, M. Yokoyama, Appl. Phys. Lett. 58 (1991) 1062.
[4] D. Meissner, J. Rostalski, Synth. Met. 121 (2001) 1551.
[5] G. Yu, J. Gao, J.C. Hummelen, F. Wudl, A.J. Heeger, Science 270 (1995) 5243.
[6] J.J.M. Halls, C.A. Walsh, N.C. Greenham, E.A. Marseglia, R.H. Friend, S.C. Moratti, A.B. Holmes, Nature 376 (1995) 498.
[7] K. Suemori, T. Miyata, M. Hiramoto, M. Yokoyma, Jpn. J. Appl. Phys. 43 (2004) 1014.
[8] S. Pfuetzner, J. Meiss, A. Petrich, M. Riede, K. Leo, Appl. Phys. Lett. 94 (2009) 223307.
[9] S. Pfuetzner, A. Petrich, C. Malbrich, J. Meiss, M. Koch, M. Riede, K. Leo, Proc. SPIE 6999 (2008) 69991M.
[10] S. Reineke, F. Lindner, G. Schwartz, N. Seidler, K. Walzer, B. Luessem, K. Leo, Nature 459 (2009) 234.
[11] J. Blochwitz, T. Fritz, M. Pfeiffer, K. Leo, D.M. Alloway, P.A. Lee, N.R. Amstrong, Org. Electron. 2 (2001) 97.
[12] S. Pfuetzner, J. Meiss, A. Petrich, M. Riede, Karl Leo, Appl. Phys. Lett. 94 (2009) 253303.
[13] W. Tress, K. Leo, M. Riede, Adv. Funct. Mater., submitted for publication.
[14] L.J.A. Koster, V.D. Mihailetchi, P.W.M. Blom, Appl. Phys. Lett. 88 (2006) 052104.
[15] D.-J. Liu, R.L.B. Selinger, J.D. Weeks, J. Chem. Phys. 105 (1996) 4751.
[16] V.P. Antropov, O. Gunnarsson, O. Jepsen, Phys. Rev. B 46 (1992) 13647.
[17] R.W. Lof, M.A. van Veenendaal, B. Koopmans, H.T. Jonkman, G.A. Sawatzky, Phys. Rev. Lett. 68 (1992) 3924.
[18] M. Fendrich, T. Wagner, M. Stohr, R. Moller, Phys. Rev. B 73 (2006) 115433.
[19] B. Maennig, M. Pfeiffer, A. Nollau, X. Zhou, K. Leo, Phys. Rev. B 64 (2001) 195208.
[20] M. Hoffmann, K. Schmidt, T. Fritz, T. Hasche, V.M. Agranovich, K. Leo, Chem. Phys. Lett. 258 (2000) 73.
[21] F.H. Allen, Acta Crystallogr. B 58 (2002) 380. Cambridge Structural Database (CSD), Release 2009, Cambridge Crystallographic Data Centre (CCDC), UK.
[22] A. Hoshino, Y. Takenaka, H. Miyaji, Acta Crystallogr. B 59 (2003) 622. CCDC Code 219250.
[23] P. Erk, H. Hengelsberg, M.F. Haddow, R. van Gelder, CrystEngComm 6 (2004) 474. CCDC Code 241066.
[24] H.-B. Bürgi, R. Restori, D. Schwarzenbach, Acta Crystallogr. B 49 (1993) 832. Inorganic Crystal Structure Database (ICSD) Code 73661.
[25] A. Jain, K. Vijayan, Bull. Mater. Sci. 27 (2004) 47.
[26] R.W. Vook, J. Appl. Phys. 32 (1961) 2475.
[27] M. Bronner, A. Opitz, W. Brütting, Phys. Status Solidi 205 (2008) 549.

Organic Electronics 12 (2011) 442–446

Contents lists available at ScienceDirect

Organic Electronics

journal homepage: www.elsevier.com/locate/orgel

Letter

Standing and flat lying α-6T molecules probed by imaging photoelectron spectroscopy

Thorsten Wagner *, Daniel Roman Fritz, Peter Zeppenfeld

Johannes Kepler University Linz, Altenberger Straße 69, 4040 Linz, Austria

ARTICLE INFO

Article history:
Received 16 October 2010
Received in revised form 25 November 2010
Accepted 15 December 2010
Available online 30 December 2010

Keywords:
Photoelectron-emission microscopy (PEEM)
Local photoelectron spectroscopy (PES/UPS)
Nanocrystallites
Electronic structure
α-sexithiophene
Ag(110)

ABSTRACT

Photoelectron-emission microscopy (PEEM) is a very versatile tool for studying dynamic processes like growth and phase transitions on surfaces. But besides the real time characterization of the morphology it can provide local spectroscopic information on a sub-μm scale. To this end we have combined a conventional PEEM setup with a He-discharge lamp delivering high energy photons for electron excitation. The setup thus allows probing the electronic structure of individual crystallites of α-sexithiophene on Ag(110). Upon growth of this organic semiconductor on the surface held at 370 K, needles consisting of flat lying molecules and platelets containing near upright standing molecules are formed. Both types of crystallites can not only be distinguished by their shape but also by their photoelectron emission spectra. We also identify a wetting layer consisting of flat lying molecules which have essentially the same spectroscopic signature as the molecules in the needles.

© 2010 Elsevier B.V. All rights reserved.

1. Introduction

The deposition of thick films of organic molecules on surfaces leads often to a variety of crystalline structures because of the polymorphism of the organic material. By tuning the lattice constant and/or the chemical composition of the surface it is possible to favour a particular structure and crystalline orientation with a well defined epitaxial relationship. For instance, on a well prepared TiO_2 substrate α-sexithiophene molecules (α-6T, see Fig. 1) lie flat on the surface with their long molecular axis parallel to the [001] direction. However, if the surface is "disordered", e.g., after sputtering and insufficient annealing, the molecules adsorb in a near upright fashion [1]. Similar results were reported for α-6T on Ag(111) and on Ag(111) pre-covered by α,ω-dihexyl-sexithiophene (DH6T) [2]. In both cases, the different orientation of the molecules leads to characteristic changes in the electronic and optical properties. Besides these changes due to the molecular alignment, the authors also argue that the different facets of a given crystallographic structure will have different ionization potentials due to different molecular states determining the electronic structure of the facets. For inorganic materials like silver this is well known [3,4].

For ultrathin films of other organic materials like phthalocyanines [5,6] ionization potentials (*IP*s) depending on the molecular orientation are observed, but it is not clear to what extend these *IP*s and the associated shift of the molecular electronic levels are merely due to the modified substrate surface or intrinsic to the different phases of the molecular film. To further explore these issues, photoelectron-emission microscopy (PEEM) in combination with imaging photoelectron spectroscopy, which allows to study the properties of different types of crystallites on the very same surface, was applied to the system α-6T on Ag(110). As a result, this method does not only provide information on the local morphology and polymorphism, but also on the associated characteristic electronic structure.

The fundamentals of the PEEM technique were described in the literature already in the early 1930's [7,8].

* Corresponding author. Tel.: +43 732 2468 8505; fax: +43 732 2468 8509

E-mail addresses: thorsten.wagner@jku.at (Th. Wagner), drf@inode.at (D.R. Fritz), peter.zeppenfeld@jku.at (P. Zeppenfeld).

URL: http://www.exphys.jku.at/aop/ (P. Zeppenfeld).

1566-1199/$ - see front matter © 2010 Elsevier B.V. All rights reserved.
doi:10.1016/j.orgel.2010.12.011

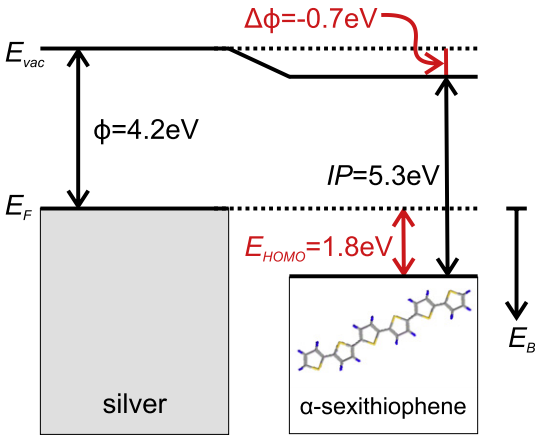

Fig. 1. Schematic of the energy level alignment between the silver surface and the α-6T layer. Substrate and molecules have a common Fermi-level E_F and an interface dipole $\Delta\phi$ is formed. The indicated values are taken from Grobosch and Knupfer for a polycrystalline silver surface [10]. The work function of a Ag(110) surface is slightly higher, namely $\phi = 4.25$ eV [4].

A bright light source, usually a mercury arc discharge lamp (Hg lamp), excites photoelectrons from the sample surface. By means of an electrostatic lens system the emitted electrons are imaged by a combination of a multichannel plate and a fluorescence screen. For most metal surfaces, the excitation energy of 4.9 eV provided by an Hg lamp is sufficient to emit enough electrons for imaging. For instance, the work function of the bare Ag(110) surface is 4.25 eV [4]. Besides the lateral variation of the work function, field enhancement due to the topography of the sample also contributes to the contrast in PEEM [9].

In the case of semiconducting materials, not the work function – defined as the difference between the vacuum level E_{vac} and the Fermi energy E_F – but the ionization potential determines whether electrons can be excited over the vacuum barrier via the photoelectric effect. Since for semiconductors the Fermi-level lies within the band gap, the ionization potential for semiconducting molecular films is larger than their respective work function. Fig. 1 shows qualitatively the alignment of the different energy levels involved in the experiments of α-sexithiophene on Ag(110) [10]. Due to the formation of an interface dipole $\Delta\phi$, the vacuum level of α-6T is lower than that of the substrate. Yet, the ionization potential of α-6T is 5.3 eV which is larger than the energy of the photons from the Hg lamp. Therefore, one expects that no photons are emitted from the α-6T layer under illumination with an Hg lamp. Nevertheless, the PEEM image shown in Fig. 2a reveals a clear contrast between the wetting layer (bright) and the thick α-6T crystallites (dark). Moreover, the wetting layer appears brighter in PEEM than the clean Ag(110) surface. This can be explained by the interface dipole $\Delta\phi = -0.7$ eV formed within the first layer of α-6T on Ag(110) as depicted in Fig. 1. This effectively lowers the energy barrier for the electron emission from the underlying Ag(110) substrate. Although the emission intensity from the substrate is attenuated by the α-6T wetting layer, the overall effect is an increased emission intensity for the α-6T wetting layer as compared to the bare Ag(110) surface. In addition, Grobosch and Knupfer suggest the formation of an interface state for α-6T on silver which would further increase the emission probability. A detailed discussion of similar intensity variations during growth is found in Ref. [11] for para-sexiphenylene on Cu(110)–(2×1)O and in Ref. [12] for pentacene on Si(001). In this work we do not want to discuss the contrast of different layers but different polymorphes of the same organic material, namely α-sexithiophene grown on Ag(110).

2. Experimental setup

The experiments were carried out in an ultra high vacuum system housing a Focus IS-PEEM with a retarding field energy analyzer [13]. The PEEM is equipped with an integrated sample stage with a high mechanical stability allowing a lateral resolution of about 50 nm. The vacuum system has a base pressure of less than 5×10^{-10} mbar.

Besides the standard Hg lamp (Focus GmbH) for the excitation of the photoelectrons the same port can be used to mount a D_2 lamp (Hamamatsu Photonics). Due to the optical parts of the vacuum system the spectrum of the deuterium lamp is limited to a photon energy of 6.4 eV. Another port is used to mount a He lamp (Focus HIS 13, 21.2 eV). For all excitation sources, the angle of incidence of the light beam with respect to the surface normal is about 65°. The angle between excitation source and detector in the PEEM experiment is comparable to that in a usual UPS setup. In contrast to an angular resolved UPS experiment the PEEM detector, however, collects electrons over a larger angular range around the surface normal.

The emitted photoelectrons are imaged by an electrostatic lens system onto a fluorescence screen. The images are acquired with a 12 bit CCD camera (PCO AG, Pixelfly). For spectroscopic measurements the dynamic range of the camera is not sufficient. Therefore, we either use a customized ImageJ software [14] plug-in which automatically adjusts the exposure time or we manually increase the voltage of the multichannel plate with increasing retarding voltage. To maintain a constant energy resolution of the retarding field analyzer we apply a variable voltage to the sample while the retarding field analyzer before the imaging unit remains at a constant potential. As a result, there is a little defocusing of the images while ramping the sample voltage.

The energy scale was calibrated using a Ag(110) sample as shown in the bottom panel of Fig. 3. The half height of the Fermi edge was used to define $E_B = 0$. From this we derive a work function of the Ag(110) surface of $\phi = 4.25 \pm 0.1$ eV, which is in good agreement with Ref. [4].

3. Sample preparation

The substrate used is a Ag(110) single crystal (Mateck GmbH) with a nominal surface miscut of less than 0.1°. The surface was cleaned by repeated cycles of Ar^+ ion sputtering (0.9 kV, 3.6 μA/cm^2, 60 min) and subsequent annealing at 600 K until no impurities could be detected by Auger electron spectroscopy.

The commercially available α-sexithiophene was prepurified by gradient sublimation before inserting it into a Ta-crucible. The α-6T films were prepared within the PEEM while monitoring the intensity integrated over the whole image (using the Hg lamp for photoelectron excitation). The maximum of the intensity was identified with the completion of the monolayer – similar to the case of p-6P on Cu(1 1 0)–(2 × 1)O [11]. The sample temperature during α-6T deposition was 370 K.

4. Results and discussion

In Fig. 2a several dark structures with different shapes can be distinguished which match different types of α-6T crystallites. Most of the crystallites appear as elongated, thin needles which are typically observed for α-6T grown on well ordered substrates [15]. Within these needles, the molecules are orientated parallel to the surface [16]. In addition, more compact islands (platelets) can be observed. The crystallites appear darker than the wetting layer because the electrons emitted from the silver/α-6T interface have to pass through a much thicker organic layer. According to [17] and [18], the inelastic mean free path of the electrons excited by the Hg light from the silver substrate into the organic layer can be estimated to be about 1.5 nm. Therefore, the probability for electrons to pass through more than 5 layers of flat lying α-6T molecules should be negligible. Later on, we will show that the average height of the needles might even exceed 300 monolayers. The electrons are also efficiently attenuated by the more compact two-dimensional α-6T islands (platelets) found on the right side of Fig. 2a. As will be shown later, these platelets have a lower height than the needles and consist of upright standing molecules.

The very same spot on the sample was also imaged by using a D_2 and a He lamp which provide photons of higher energies. If photons with an energy of $h\nu = 21.2$ eV (He I) are used (see Fig. 2c), needles and platelets are both imaged brighter than the wetting layer. As the photon energy is much higher than the ionization potential of the molecules, electrons can easily be emitted from the α-6T molecules. The fact that the wetting layer has now a lower intensity than the crystallites illustrates that α-6T is a dye and acts as an efficient optical absorber for light above a certain threshold energy. In fact, the photoelectron emission from the needles is slightly lower than that from the platelets. The difference in intensity between the needles and the platelets is even more pronounced if the D_2 lamp with a photon energy $h\nu = 6.4$ eV is used (Fig. 2b). In this case, some side facets of the needles appear darker than the top face of the needles. Nevertheless, not all facets show this behaviour and the brightness strongly depends on the direction of the illumination: As the needles are very high compared to their width, there is a strong shadowing effect. Indeed, the facets, which are not facing the light impinging from the top of the image in Fig. 2b, appear darker. The width of the needles ranges between 1 and 3 μm and is definitely large enough to absorb most of the incoming light. The height of the needles can not be measured directly by means of PEEM but it can be estimated from the average film thickness (about 33 monolayers) and the area in the image which is covered by needles and platelets (roughly 10%). This results in an average height of the crystals (needles and platelets) of 320 monolayers. Assuming flat lying molecules this corresponds to a mean height larger than 100 nm.

Taking a closer look at Fig. 2b and the platelets in the lower right of the image, one finds that there is no pronounced shadowing effect. We thus conclude that the platelets have a much lower height as compared to the needles. This is in agreement with our experience of bringing the needles and the platelets into the focus of the PEEM: For the needles – as they are quite high – it is hard to determine an exact focus point, whereas the range for which the platelets are sharply imaged is much smaller.

The top panel of Fig. 3 depicts energy filtered images for three selected values of the retarding field. Note that by using a retarding field analyzer the images are high pass filtered with respect to the kinetic energy E_{kin}, such that only those electrons with a binding energy E_B below a given threshold can be detected:

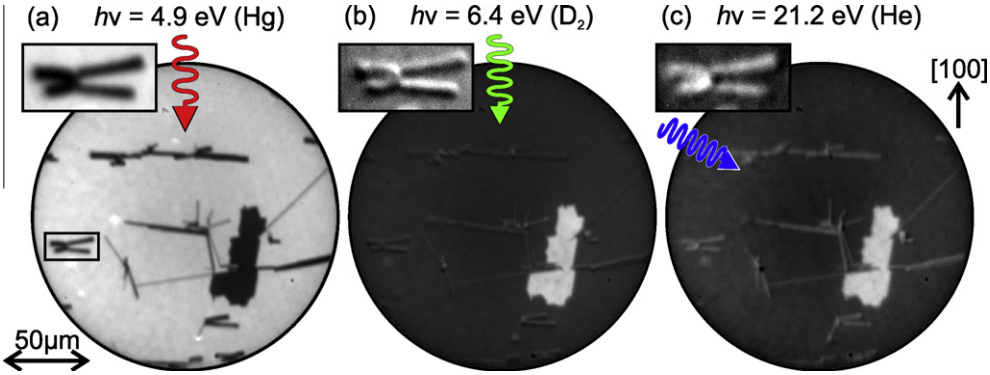

Fig. 2. PEEM images of a 33 monolayer thick film of α-6T grown at 370 K on Ag(1 1 0) using different light sources for electron excitation. The field of view is about 180 μm. The direction and the wavelength of the incoming light are indicated by the coloured arrows. The insets show an enlarged crystallite which consists of several needles arranged into a cross-like structure. The crystallite appears homogenous if the Hg lamp is used for excitation, whereas, under the illumination with the D_2 or the He lamp the contrast of the structure is not uniform. (For interpretation of the references to colour in this figure legend, the reader is referred to the web version of this article.)

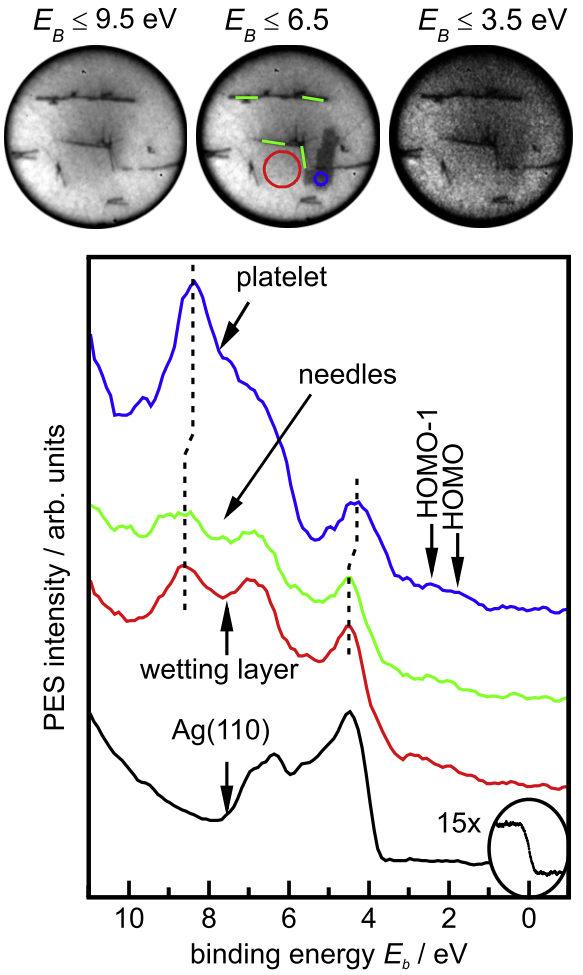

Fig. 3. The top shows three energy filtered PEEM images with different retarding fields applied. The energy ranges indicated correspond to the binding energies which contribute to the image. The contrast of the images was adapted to optimize the visibility; the area imaged is the same as in Fig. 2. The bottom panel shows the photoelectron spectra derived from the energy filtered images for selected regions indicated in the top panel. The arrows indicate two weak features which can be attributed to the lowest occupied states of the organic thin film. For comparison also the spectrum of the clean Ag(1 1 0) surface is shown. The inset in the circle shows a high resolution scan of the Fermi edge. (For interpretation of the references to colour in this figure legend, the reader is referred to the web version of this article.)

$$E_{kin} = h\nu - \phi - E_B - E_{ret} \geqslant 0 \qquad (1)$$

In this equation and in the following, $E_B = 0$ refers to the Fermi level of the silver substrate. The energy indicated above the images corresponds to the allowed binding energy range of the emitted electrons. The images in Fig. 3 are taken from exactly the same spot of the α-6T covered Ag(1 1 0) sample as the unfiltered ones ($E_{ret} = 0$) displayed in Fig. 2. In Fig. 2c, all electrons with $E_B < (21.1\ \text{eV} - IP)$ contribute to the image. For this range of binding energies both the platelets and the needles have a higher intensity than the thinner wetting layer. In Fig. 3, the range of the binding energy contributing to the images is smaller. As a result, the contrast for the images in Fig. 3 is inverted so that the needles now appear darker than the wetting layer. On the other hand, for binding energies $E_B < 9.5$ eV and $E_B < 3.5$ eV, the platelets have the same intensity as the wetting layer, whereas for $E_B < 6.5$ eV the platelets appear darker.

From a series of images recorded with different E_{ret}, the local spectroscopic information can now be obtained from the (numerical) derivative of the intensity curves $I(E_{ret})$ at any given location, in particular those areas covered by the wetting layer (red), needles (green) and the platelet (blue) as indicated in the central image of Fig. 3. The so derived local photoelectron spectra are shown in the lower panel of Fig. 3 in corresponding colours. For comparison and calibration also the spectrum of the bare Ag(1 1 0) surface is presented. As far as the spectroscopic information is concerned, the spectra in Fig. 3 can be compared to traditional UV photoelectron spectra (UPS) data. However, in contrast to conventional UPS, which averages over a large surface area, the spectra obtained by PEEM based imaging spectroscopy are spatially resolved with a lateral resolution of less than 100 nm. The spectra recorded from different molecular structures with the main features at 4.4, 7.0, and 8.5 eV are quite similar to the UPS data shown, e.g., in Fig. 4 of Ref. [1] recorded at normal emission from α-6T layers on "ordered" and "disordered" TiO_2, respectively. The highest occupied molecular orbital (HOMO) are expected at binding energies E_{HOMO} of 1.8 and 2.4 eV (see Fig. 1 and Ref. [10]). Indeed, in Fig. 3 there are two very weak features marked by arrows at the expected positions. The stronger signatures at higher binding energies mainly stem from anti-bonding and nonbonding-orbitals [1,19].

Note that the red and the green curve in Fig. 3, representing the spectra of the wetting layer and the needles, respectively, are essentially the same. This confirms that (i) the area between the crystallites is covered by a wetting layer of α-6T molecules and that (ii) the electronic structure of the molecules in the wetting layer and in the needles is very similar. Since the latter are known to consist of flat lying molecules, we infer that the orientation of the molecules in the wetting layer should also be nearly parallel to the surface. This result is in agreement with previous studies by X-ray absorption (NEXAFS) and scanning tunnelling microscopy [16,20,21].

The correspondence of the two spectra also indicates that local charging does not play an important role. As the wetting layer consists of only two layers of α-6T and the first layer, at least, is strongly coupled to the substrate, we assume that there is no charging effect for the wetting layer. As discussed before, the needles have a height of several hundred layers of flat lying α-6T molecules. The low conductivity may give rise to a charging of the needles. In this case, the local potential of the needles would deviate from that of the wetting layer and, therefore, the spectrum of the needles shown in Fig. 3 should be shifted with respect to the one of the wetting layer. This is obviously not the case and we thus conclude that there is no charging effect for the needles.

The spectrum recorded from a platelet (blue curve) again reveals three main contributions (at 4.3, 6.9, and 8.4 eV), but their relative intensity is considerably different

from that of the needles and the wetting layer. In particular, the feature around 8.4 eV is now most pronounced. In addition, a systematic shift to the lower binding energy of the order of 0.1–0.2 eV for all three major peaks can be noticed.

As mentioned before, a very similar spectrum as the blue curve displayed in Fig. 3 has been obtained by conventional UPS for the growth of α-6T on "disordered" TiO_2 where α-6T forms crystallites in which the molecules align in a near upright standing fashion [1]. We thus ascribe the platelets to α-6T crystallites of near upright standing molecules. This assignment is also consistent with the more compact shape of the platelets [22]. Duhm et al. [2] have used a spacing layer of α,ω-dihexyl-sexithiophene (DH6T) between a thick layer of α-6T and Ag(111) to switch between the growth of flat lying and near upright standing molecules. They also support their experimental data by DFT calculations. In both cases a shift of 0.6 eV for the *IP* was found between flat lying and standing molecules. While we cannot reliably determine the shift of the HOMO level from Fig. 3 but only that of the energetically lower orbitals, our value for the peak shift might actually be lower. This could be due to he fact that we – in contrast to the previous studies – have characterized platelets and needles coexisting on the very same substrate surface, i.e., without modification of the surface. In any case, the *IP* of the standing molecules is definitely lower than that of the flat lying ones. The direction of the shift is opposite to what would be expected if the platelets were positively charged upon photoelectron emission.

Koller et al. [23] have pointed out that the orientation of the π-stacked molecules with respect to the electrodes of a device has an important effect on its performance in organic field effect transistors (OFETs) or organic light emitting diodes (OLEDs). Whereas for the first kind of device a film consisting of upright standing molecules should be preferred for optimum electron transport, flat lying molecules should give the higher photon emission in the direction perpendicular to the film as desired in OLEDs. Therefore, the control of the orientation of the molecular stacking is crucial. In addition, this study shows that besides the macroscopic conductivity along certain crystallographic axes, also the local electronic interface to the vacuum or the electrodes depends on the orientation of the molecules. This has to be taken into account when designing a device.

5. Summary

In summary, our results show that there are two kinds of α-6T crystallites present on the Ag(110) surface – elongated needles of flat lying α-6T molecules and two-dimensional platelets consisting of near upright standing molecules. Both kinds of crystallites grow on a uniform wetting layer. By applying imaging photoelectron emission spectroscopy the differences of the electronic structure can be resolved down to the scale of the individual crystallites. Between needles consisting of flat lying molecules and platelets formed by near upright standing α-6T grown on the very same substrate a distinct shift of the binding energies and different relative emission intensities are evidenced.

Acknowledgements

We gratefully acknowledge the fruitful discussion with Michael Schicketanz and Matthias Escher from Focus GmbH. We also thank Alexander "Sandy" Fleming and Mike Ramsey from the TU Graz for sharing their experience on PEEM.

References

[1] J. Ivanco, T. Haber, J.R. Krenn, F.P. Netzer, R. Resel, M.G. Ramsey, Sexithiophene films on ordered and disordered TiO_2(110) surfaces: electronicstructural and morphological properties, Surf. Sci. 601 (2007) 178–187.
[2] S. Duhm, G. Heimel, I. Salzmann, H. Glowatzki, R.L. Johnson, A. Vollmer, J.P. Rabe, N. Koch, Orientation-dependent ionization energies and interface dipoles in ordered molecular assemblies, Nat. Mater. 7 (2008) 326–332.
[3] M. Chelvayohan, C.H.B. Mee, Work function measurements on (110), (100) and (111) surfaces of silver, J. Phys. C 15 (1982) 2305–2312.
[4] W.Y. Li, K. Goto, R. Shimizu, PEEM is a suitable tool for absolute work function measurements, Surf. Interface Anal. 37 (2005) 244–247.
[5] W. Chen, H. Huang, S. Chen, Y.L. Huang, X.Y. Gao, A.T.S. Wee, Molecular orientation-dependent ionization potential of organic thin films, Chem. Mater. 20 (2008) 7017–7021.
[6] T. Toader, G. Gavrila, W. Braun, J. Ivanco, D.R.T. Zahn, Valence band fine structure of copper phthalocyanine thin films: effect of molecular orientation, Phys. Status Solidi B 246 (2009) 1510–1518.
[7] E. Brüche, Elektronenmikroskopische Abbildung mit lichtelektrischen Elektronen, Z. Phys. 86 (1933) 448–450.
[8] J. Pohl, Z. Tech. Phys. 15 (1934) 579.
[9] J. Stöhr, S. Anders, X-ray spectro-microscopy of complex materials and surfaces, IBM Res. Dev. 44 (2000) 535–552.
[10] M. Grobosch, M. Knupfer, Energy level alignment and interface states at α-sexithiophene/Ag interfaces, Org. Electron. 8 (2007) 625–630.
[11] A.J. Fleming, F.P. Netzer, M.G. Ramsey, Nucleation and 3D growth of para-sexiphenyl nanostructures from an oriented 2D liquid layer investigated by photoemission electron microscopy, J. Phys. Condens. Matter 21 (2009) 445003.
[12] F.-J. Meyer zu Heringdorf, M.C. Reuter, R.M. Tromp, Growth dynamics of pentacene thin films, Nature 412 (2001) 517–520.
[13] M. Merkel, M. Escher, J. Settemeyer, D. Funnemann, A. Oelsner, C. Ziethen, O. Schmidt, M. Klais, G. Schönhense, Microspectroscopy and spectromicroscopy with photoemission electron microscopy using a new kind of imaging energy filter, Surf. Sci. 480 (2001) 196–202.
[14] W.S. Rasband, ImageJ, U.S. National Institutes of Health, Bethesda, Maryland, USA, 1997–2010. Available from: <http://rsb.info.nih.gov/ij/>.
[15] F. Balzer, H.-G. Rubahn, Dipole-assisted self-assembly of light-emitting p-nP needles on mica, Appl. Phys. Lett. 79 (2001) 3860–3862.
[16] G. Yoshikawa, M. Kiguchi, S. Ikeda, K. Saiki, Molecular orientations and adsorption structures of α-sexithienyl thin films grown on Ag(110) and Ag(111) surfaces, Surf. Sci. 559 (2004) 77–84.
[17] M. Grobosch, M. Knupfer, Electronic properties of the interface between the organic semiconductor α-sexithiophene and polycrystalline palladium, Org. Electron. 9 (2008) 767–774.
[18] M.P. Seah, W.A. Dench, Quantitative electron spectroscopy of surfaces: a standard data base for electron inelastic mean free paths in solids, Surf. Interface Anal. 1 (1979) 2–11.
[19] H. Fujimoto, U. Nagashima, H. Inokuchi, K. Seki, Y. Cao, H. Nakahara, J. Nakayama, M. Hoshino, K. Fukuda, Ultraviolet photoemission study of oligothiophenes: π-band evolution and geometries, J. Chem. Phys. 92 (1990) 4077–4092.
[20] H. Inoue, G. Yoshikawa, K. Saiki, Molecular chain structure of α-sexithienyl on Ag(110) observed by scanning tunneling microscopy, Jpn. J. Appl. Phys. 45 (2006) 1794–1796.
[21] T. Yokoyama, Self-assembled templating for the growth of molecular nanodots, Appl. Phys. Lett. 96 (2010) 063101.
[22] L. Kankate, F. Balzer, H. Niehus, H.-G. Rubahn, Organic nanofibers from thiophene oligomers, Thin Solid Films 518 (2009) 130–137.
[23] G. Koller, S. Berkebile, J. Ivanco, F. Netzer, M. Ramsey, Device relevant organic films and interfaces: a surface science approach, Surf. Sci. 601 (2007) 5683–5689.

Organic Electronics 12 (2011) 447–452

Contents lists available at ScienceDirect

Organic Electronics

journal homepage: www.elsevier.com/locate/orgel

Influence of structural properties on environmental stability of pentacene thin film transistors

D. Simeone, M. Rapisarda, G. Fortunato, A. Valletta, L. Mariucci *

CNR-IMM, Via del fosso del cavaliere 100, 00133 Roma, Italy

ARTICLE INFO

Article history:
Received 14 June 2010
Received in revised form 17 November 2010
Accepted 23 December 2010
Available online 6 January 2011

Keywords:
Pentacene TFTs
Environmental stability
Moisture effects
Aging effects

ABSTRACT

We studied environmental stability of top contact pentacene TFTs with active layer evaporated at different growth rates. We measured the transfer characteristics in vacuum and in air and after storing the devices in oxygen for several days. Different pentacene growth rates result in different grain size of active layer. This morphology difference influences the hysteresis of transfer characteristics induced by water absorption. On the contrary, aging effects on the transfer characteristics of pentacene O-TFTs, induced by oxygen diffusion into the active layer, are not related to structural characteristics of pentacene film.

© 2011 Elsevier B.V. All rights reserved.

1. Introduction

The environmental stability of electrical characteristics of devices is a fundamental requirement for organic thin film transistor (O-TFTs) applications. On the other hand, it has been shown that the exposure of these devices to air is in general detrimental for their performance [1–15]. Two main effects of environment have been identified in pentacene TFTs: hysteresis of transfer characteristics [1–7], when the devices are measured in air, and variation of transfer characteristics after exposure to air for a long time [8–15]. These phenomena are attributed to the diffusion of water molecules and/or oxygen into pentacene active layer.

The hysteresis of transfer characteristics is usually related to the effect of water and it has been explained in terms of different microscopic mechanisms. A possible explanation of the hysteresis effect is that the diffusion of water molecules into pentacene induces slow trapping of carriers in the device active layer [1,2] or at the semiconductor/insulator interface [7], with a consequent shift of threshold voltage during measurement. Charge injection into the gate insulator has been also considered as origin of hysteresis [6,16]. In particular, the mechanism proposed by Sharma et al. [16], that explains the bias-stress effect in terms of exchange of holes with protons in the presence of water at the semiconductor/insulator interface and the subsequent migration of protons into the oxide, could also explain the hysteresis phenomenon. Water diffusion has been also considered responsible of a variation of energy barrier at pentacene/metal interface [4] and a reduction of field-effect mobility [4,5]. It has been generally observed that the hysteresis is reversible and disappears almost completely when the devices are stored in vacuum or dry atmosphere. This seems related to a weak interaction between adsorbed H_2O and pentacene molecules [3,8], allowing an easy removal of the water molecules from the active layer.

A permanent variation of transfer characteristics has been observed when the device are exposed to air for a long time [8–15]. In this case all the main electrical parameters (field-effect mobility, threshold voltage and subthreshold swing) are degraded, while the hysteresis remains unaffected [9,12]. Although some studies [4,5] have shown that also moisture can play a role in the aging of pentacene O-TFTs, this effect has been mainly attributed

* Corresponding author.
E-mail addresses: luigi.mariucci@cnr.it, luigi.mariucci@imm.cnr.it (L. Mariucci).

1566-1199/$ - see front matter © 2011 Elsevier B.V. All rights reserved.
doi:10.1016/j.orgel.2010.12.013

to the diffusion of oxygen into pentacene layer that induces new gap states located at about 0.2–0.3 and 0.6 eV above the valence band [12–14]. Experimental results are in good agreement with theoretical calculations that consider defects in pentacene molecules induced by oxygen [15].

It has been shown that it is possible to reduce environmental sensitivity of pentacene TFTs by using opportune gate dielectrics [7] or by device passivation through barrier layers in order to reduce the molecule diffusion [11]. On the other hand, also the structure of the pentacene active layer seems to play a role on the environmental stability of pentacene O-TFTs [4,10]. Growth rate, substrate characteristics and deposition temperature have been shown to be key parameters in controlling the nucleation density [17–19] and, therefore, the pentacene film characteristics (grain size and grain boundary density). In this work we have investigated the influence of the morphology of pentacene film, deposited at different growth rates, on the stability of electrical characteristics of O-TFTs, measuring the transfer characteristics in vacuum and in air and after storing the devices in oxygen.

2. Material and methods

Top-contact (TC) bottom gate devices were fabricated using a highly doped-Si substrate as a large area gate with a 90 nm thermal oxide as gate dielectric. Before pentacene deposition a buffer layer of PMMA (5 nm thick) was spin coated and annealed at 70 °C for 15 min. It has been shown that a thin PMMA buffer layer improves the performance of pentacene O-TFTs both in bottom contact (BC) and TC configurations [20], improving the interface quality between pentacene and both Au contacts (in BC-TFTs) and SiO_2 gate dielectric (in BC and TC-TFTs). Pentacene active layers (30 nm thick) were evaporated, with the substrate at room temperature (RT), by using a Radak evaporation source, with growth rates r = 0.01, 0.03 and 0.07 nm/s.

Atomic force microscopy analysis, performed by a PSIA XE100 system in non-contact mode, of the pentacene layers deposited at different growth rates are shown in Fig. 1. As can be seen the film exhibits the typical morphology of highly ordered polycrystalline pentacene, with a characteristic "terrace" structure with 1.6 nm steps, corresponding to the height of one molecular layer. The analysis shows that, as already reported in literature [17,18,21], the deposition conditions influence the morphology of pentacene film. Indeed, whereas pentacene films grown at low rate show grain size up to 2 μm and a very compact structure, pentacene films grown at a faster rate have smaller grain size (less than 1 μm for sample deposited at a growth rate of 0.07 nm/s) and more pronounced grain boundaries. This results in a higher density of grain boundaries for samples deposited at higher growth rates.

Source and drain contacts were formed by evaporating gold (30 nm thick) after pentacene deposition and defined through a shadow mask. Device electrical characteristics were measured in a MMR cryostat using a Keythley 236 source/measure unit and a Keythley 2635 source-meter. In order to evaluate the hysteresis of transfer characteristics, measurements have been performed sweeping the gate voltage, sequentially, from off-to-on and from on-to-off (between 5 and −30 V). Field-effect mobility has been calculated considering the maximum of the transconductance relative to off-to-on curve.

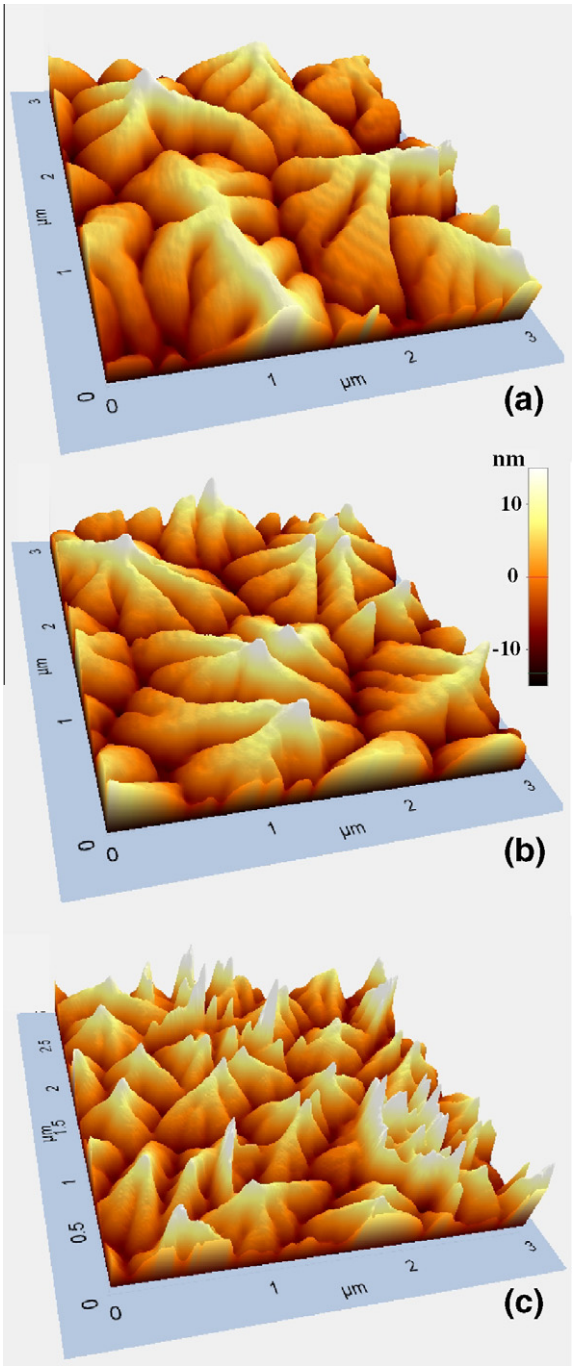

Fig. 1. AFM images of pentacene films deposited at different evaporation rates, (a) 0.01 nm/s (b) 0.03 nm/s and (c) 0.07 nm/s.

Aging effects have been investigated by storing in dark the pentacene O-TFTs in air and in pure oxygen

atmosphere and performing at selected aging time intervals measurements of transfer characteristics in vacuum.

3. Results and discussion

3.1. Water related instability

Fig. 2 shows typical transfer characteristics, measured in vacuum, of TC pentacene O-TFTs fabricated with active layers deposited at different growth rates. As can be seen, the differences of pentacene morphology observed by AFM analysis do not result in major differences in the electrical transfer characteristics. Indeed, transfer characteristics appear quite similar for all devices, with field-effect mobility, μ_{FE}, ranging between 0.3 and 0.4 cm^2/Vs and subthreshold slope of about 0.6 V/dec. It can be also noted that hysteresis of transfer characteristics, measured in vacuum, is very small for all samples. On the contrary, when the measurements are carried out in air (with a relative humidity of 50%) (see Fig. 3) the transfer characteristics measured from off-to-on and from on-to-off are different, resulting in a counter-clockwise hysteresis. As evident in Fig. 3, the differences in the pentacene morphology influence the device electrical characteristics measured in air: whereas only a small increase of hysteresis observed in the low growth-rate devices, high growth-rate O-TFTs exhibit an evident sensitivity to environmental conditions. Also shown in Fig. 3 are the transfer characteristics of a TC pentacene O-TFT fabricated without PMMA buffer layer and with pentacene active layer deposited at a growth rate of 0.07 nm/s. Lower field-effect mobility is observed in such devices, probably related to the different interface quality between pentacene and gate oxide and confirming the beneficial role of the PMMA. On the other hand, the hysteresis remains comparable with the devices with

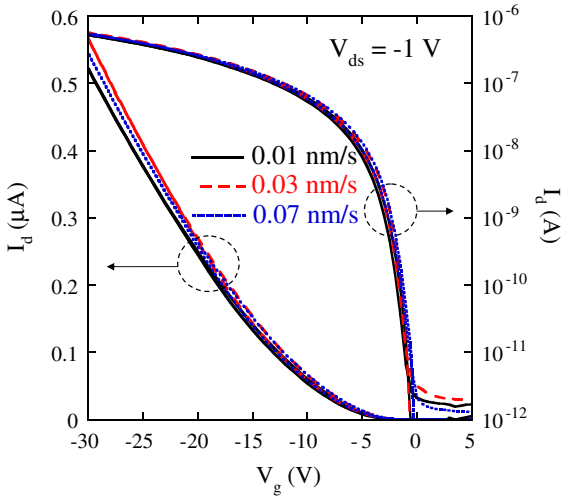

Fig. 2. Transfer characteristics, measured in vacuum, of TC pentacene O-TFTs with active layers deposited at different growth rates (as shown in the legend). The O-TFTs have channel length $L = 100$ μm and channel width $W = 200$ μm. The transfer characteristics are measured sweeping the gate voltage, sequentially, from off-to-on and from on-to-off. Only a small counter-clockwise hysteresis can be observed for all devices.

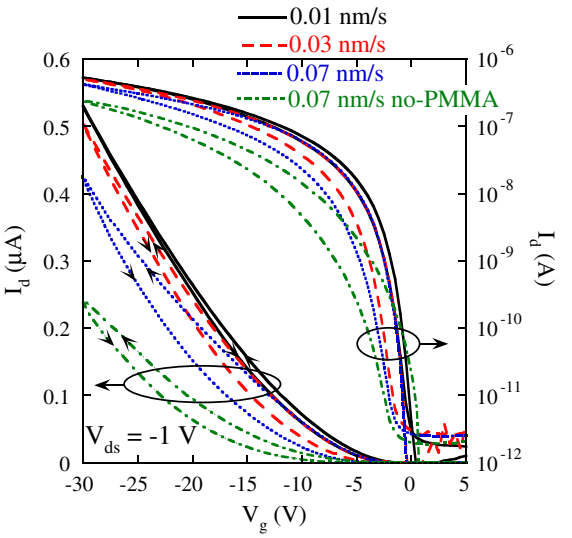

Fig. 3. Transfer characteristics, measured in air, of TC pentacene O-TFTs with active layers deposited at different growth rates. Also shown are the transfer characteristics of a device fabricated without PMMA buffer layer (dot-dashed curve). As in Fig. 2, off-to-on and on-to-off sweeps are sequentially measured and a counter-clockwise hysteresis is observed, dependent on pentacene growth-rate.

PMMA buffer layer and active layer deposited at the same growth rate. This implies that the PMMA layer does not increase the sensitivity of pentacene O-TFTs to moisture and suggests that the hysteresis is unlikely related to the pentacene/gate dielectric interface or to trapping into the gate dielectric.

By analyzing in more detail the experimental data shown in Figs. 2 and 3, we can observe that the off-to-on sweep of characteristics measured in air coincides with the curves measured in vacuum in the subthreshold regime, whereas in the on-regime (above threshold voltages) a current reduction is observed, both in the off-to-on and on-to-off sweeps. This reduction is induced by the progressive shift of threshold voltage and can be related to charge trapping occurring during the off-to-on sweep above threshold voltage [2]. It can be also noted that the on-to-off curve measured in air is almost parallel to the characteristics measured in vacuum, showing that in our devices the field-effect mobility is not influenced by the water diffusion into pentacene active layer, as sometimes observed in literature [4,5].

In order to quantitatively evaluate the hysteresis of the transfer characteristics we can consider, for a given current level, the voltage difference between the transfer characteristics measured in vacuum and in air, as shown in the inset of Fig. 4 for the device with the active layer grown at $r = 0.07$ nm/s. The average voltage shifts, evaluated considering as reference current the drain currents measured in air at $V_g = -30$ V and averaged over more than 12 devices, are reported in Fig. 4. As can be seen, whereas devices with pentacene active layer deposited at low growth rate (0.01 nm/s) show a very small hysteresis, a voltage shift as high as 4 V is observed in devices fabricated at higher growth rate and the hysteresis monotonically

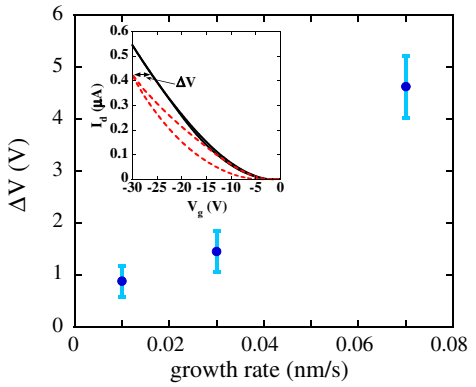

Fig. 4. Average voltage shifts (evaluated according to the method illustrated in the inset) of TC pentacene O-TFT transfer characteristics induced by water absorption in pentacene layers deposited at different growth rates. Average values and standard deviation were obtained from a set of >12 device measurements.

increases with increasing the growth rate. Considering that the hysteresis of transfer characteristics measured in air is related to the diffusion of H_2O into pentacene active layer [1,2], our results suggest that the diffusion takes place mainly at the grain boundaries, being enhanced by a higher density of grain boundaries and a less compact structure of pentacene layer.

3.2. Aging effects

In order to clarify the main cause of degradation of transfer characteristics when pentacene TFTs are exposed to air for a long time, we stored two BC TFTs, fabricated in the same run, in air and in pure oxygen, measuring their electrical characteristics during several days. As can be seen in Fig. 5, both devices show a current degradation mainly related to field-effect mobility reduction. However, as shown in Fig. 6, while the reduction of field-effect mobility of O-TFTs stored in air after 3 weeks is about 45%, a larger degradation (more than 90%) was observed in the devices stored in pure oxygen. These results clearly point out that the main cause of aging in pentacene TFTs is related to the diffusion of oxygen into pentacene film.

We then evaluated the aging effects for devices fabricated with different pentacene growth rates storing the devices in pure oxygen for 10 days and measuring the transfer characteristics of O-TFTs at different aging times. Fig. 7 shows typical transfer characteristics, measured in vacuum, of TC pentacene TFTs fabricated with active layers deposited at different growth rates before and after 10 days in oxygen. Control devices, stored in vacuum for the same aging period, did not show any variation of the transfer characteristics. As for BC TFTs shown in Fig. 5, the transfer characteristics of TC pentacene TFTs show

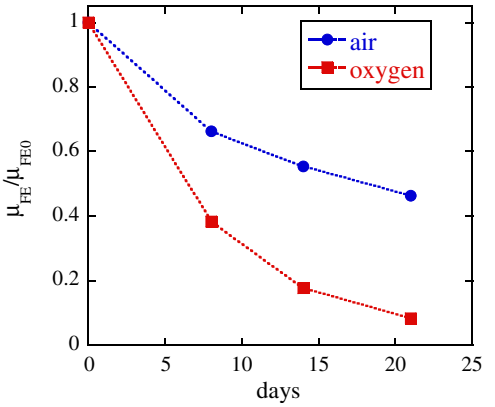

Fig. 6. Relative field-effect mobility variations, calculated from the transfer characteristics shown in Fig. 5, vs aging time for devices stored in air (dot) and oxygen atmosphere (square).

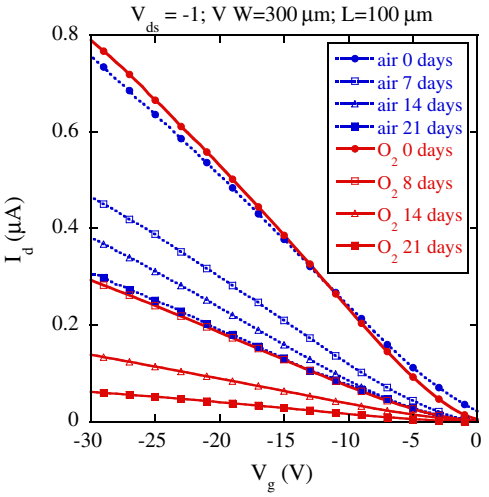

Fig. 5. Transfer characteristics of BC pentacene O-TFTs before and after storing the devices in air (dot lines) and oxygen atmosphere (solid lines) for several days (as shown in the legend).

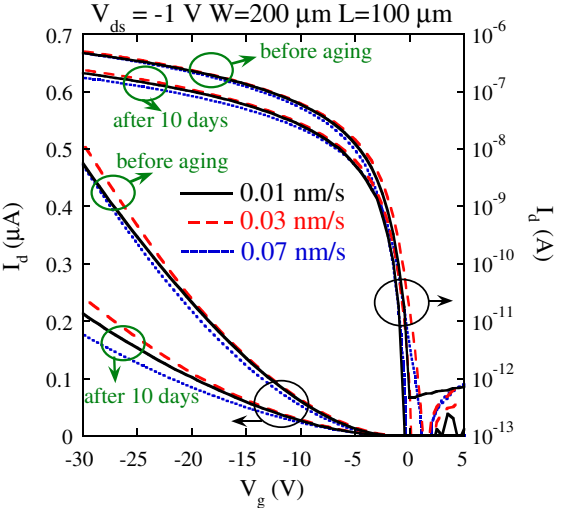

Fig. 7. Transfer characteristics of TC pentacene O-TFTs, with active layers deposited at different growth rates, before and after storing the devices in oxygen atmosphere for 10 days. The measurements are carried out in vacuum.

during the aging period a reduction of the on-current, mainly related to the reduction of field-effect mobility, confirming previous results. The relative variations of the field-effect mobility, averaged over more than 12 O-TFTs, during the aging time are reported in Fig. 8. As can be seen, the field-effect mobility reduction is similar, within the parameter variations observed for different O-TFTs, for devices fabricated at different growth rates, with a reduction of about 50% of the initial field-effect mobility values after 10 days. The average threshold voltage, V_{th}, variation (Fig. 9) during aging time seems not to be correlated to the structure of pentacene active layer. However, the large variation of the V_{th} values prevents to define a clear trend with aging time. It can be noted that the electrical characteristics variation induced by oxygen is not recovered after storing the sample in vacuum at room temperature for several days.

These results suggest that the aging induced by the oxygen is not correlated to the morphology of pentacene film. As a consequence the diffusion of oxygen into the film does not seem to occur at the grain boundaries but it appears to take place through the entire film. In addition, the decrease of field-effect mobility and the stability of subthreshold slope suggest that the effect of the oxygen can be attributed to the creation of defect states near the valence band, according to what observed in Ref. [9,12], while deep states seem to play a minor role.

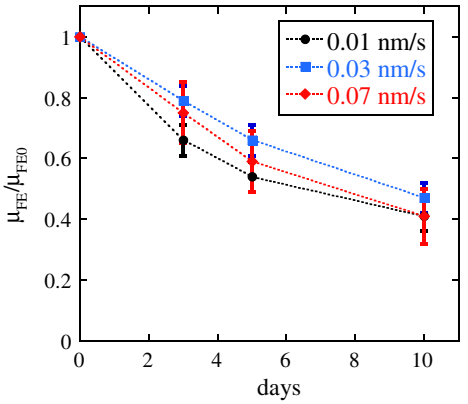

Fig. 8. Relative field-effect mobility variations (average values and standard deviation were obtained from a set of >12 device measurements) vs aging time in oxygen atmosphere for pentacene O-TFTs with active layers deposited at different growth rates.

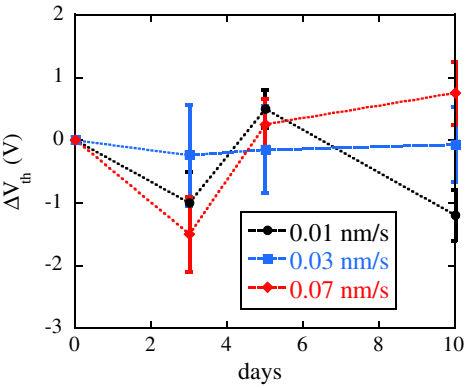

Fig. 9. Threshold voltage variations (average values and standard deviation were obtained from a set of >12 device measurements) vs aging time in oxygen atmosphere for pentacene O-TFTs with active layers deposited at different growth rates.

4. Conclusions

The environmental stability of pentacene TFTs with different active layer structure has been investigated. Higher hysteresis of transfer characteristics has been observed in devices with small grain pentacene films, deposited at high growth rate. This is evidence that a higher density of grain boundaries contributes to a higher sensitivity to moisture, probably due to an enhanced diffusion of water molecules in the pentacene film through the grain boundaries. The water molecules can be trapped at the grain boundaries or incorporated in the film affecting the transport properties of pentacene O-TFTs, probably inducing lattice distortion and polarization that generate slow traps for holes [2].

We showed that long term stability of transfer characteristics of pentacene TFTs is related to interaction with oxygen that induces appreciable degradation of field-effect mobility. The long term stability appears not to be influenced by the pentacene structure and, therefore, by the number of grain boundaries present in the channel, indicating that the diffusion of oxygen takes place through the entire pentacene active layer.

The present results indicate that an improvement of pentacene layer structural properties can reduce the sensitivity of devices to water, reducing the need of a water barrier layer, whereas an oxygen barrier layer is required in order to avoid aging effects of pentacene O-TFTs.

References

[1] G. Gu, M.G. Kane, Appl. Phys. Lett. 92 (2008) 053305.
[2] L. Mariucci, S. Cipolloni, D. Simeone, M. Cuscunà, L. Maiolo, A. Minotti, A. Pecora, A. Valletta, G. Fortunato, J. Korean Phys. Soc. 54 (2009) 505.
[3] K.-J. Lee, K. Ihm, T.-H. Kang, S. Chung, Surf. Sci. 603 (2009) 3445.
[4] D. Knipp, A. Benor, V. Wagner, T. Muck, J. Appl. Phys. 101 (2007) 044504.
[5] A. Petrović, G. Bratina, Appl. Phys. Lett. 94 (2009) 123301.
[6] C.-A. Lee, D.-W. Park, S.-H. Jin, I.-H. Park, J.-D. Lee, B.-G. Park, Appl. Phys. Lett. 88 (2006) 252102.
[7] S.-H. Kim, H. Yang, S.-Y. Yang, K. Hong, D. Choi, C. Yang, D.-S. Chung, C.E. Park, Org. Electron. 9 (2008) 673.
[8] L. Tsetseris, S.T. Pantelides, Phys. Rev. B 75 (2007) 153202.
[9] F. De Angelis, S. Cipolloni, L. Mariucci, G. Fortunato, Appl. Phys. Lett. 88 (2006) 193508.
[10] Y. Hu, G. Dong, Y. Hu, L. Wang, Y. Qiu, J. Phys. D: Appl. Phys. 39 (2006) 4553.
[11] H. Jung, T. Lim, Y. Choi, M. Yi, J. Won, S. Pyo, Appl. Phys. Lett. 92 (2008) 163504.
[12] W.L. Kalb, K. Mattenberger, B. Batlogg, Phys. Rev. B 78 (2008) 035334.
[13] A. Benor, D. Knipp, J. Northrup, A.R. Völkel, R.A. Street, J. Non-Cryst. Solids 354 (2008) 2875.
[14] V. Nádaždy, R. Durný, J. Puigdollers, C. Voz, S. Cheylan, K. Gmucová, Appl. Phys. Lett. 90 (2007) 092112.
[15] J.E. Northrup, M.L. Chabinye, Phys. Rev. B 68 (2003) 041202(R).
[16] A. Sharma, S.G.J. Mathijssen, M. Kemerink, D.M. de Leeuw, P.A. Bobbert, Appl. Phys. Lett. 95 (2009) 253305.
[17] S. Pratontep, M. Brinkmann, F. Nüesch, L. Zuppiroli, Phys. Rev. B 69 (2004) 165201.

[18] B. Stadlober, U. Haas, H. Maresch, A. Haase, Phys. Rev. B 74 (2006) 165302.
[19] P.R. Ribič, V. Kalihari, C.D. Frisbie, G. Bratina, Phys. Rev. B 80 (2009) 1115307.
[20] F. De Angelis, S. Cipolloni, L. Mariucci, G. Fortunato, Appl. Phys. Lett. 86 (2005) 086521.
[21] T. Itoh, N. Yamauchi, Appl. Surf. Sci. 253 (2006) 6196.

Organic Electronics 12 (2011) 453–460

Contents lists available at ScienceDirect

Organic Electronics

journal homepage: www.elsevier.com/locate/orgel

Letter

Microwires and microtwists from X-shaped conjugated molecules as low-loss, long distance photo waveguide materials

Ting Lei [a], Hai-Bo Chen [a], Jie Yin [a], Shan Huang [b], Xing Zhu [b,*], Jian Pei [a,*]

[a] The Key Laboratory of Bioorganic Chemistry and Molecular Engineering and of Ministry of Education, College of Chemistry and Molecular Engineering, Peking University, Beijing 100871, China
[b] The State Key Laboratory for Mesoscopic Physics, School of Physics, Peking University, Beijing 100871, China

ARTICLE INFO

Article history:
Received 6 October 2010
Received in revised form 25 December 2010
Accepted 27 December 2010
Available online 8 January 2011

Keywords:
Microwires
Chiral structure
Conjugated molecules
Photo waveguide
Solution process

ABSTRACT

Single crystalline microwires and polycrystalline microtwists were self-assembled from X-shaped conjugated molecules through solution process in high yield. The excellent long-range optical waveguide ability and efficient light transfer between wires made the as-prepared microwires potential building blocks for complex optical devices at micrometer scale. By slight structural change, well-dispersed polycrystalline microtwists were also successfully obtained. We further demonstrated that such chiral structures could also be used as optical waveguiding materials. The investigation of photo waveguide property in the well-dispersed single microtwist is the first demonstration of chiral microstructures in the application of optical waveguide, which opens the possibility of coupling the chirality of material to that of light.

© 2011 Elsevier B.V. All rights reserved.

1. Introduction

Due to the quantum effects of electrons, traditional integrated circuits are facing serious challenges when the device size goes down to tens of nanometers. Therefore, it is important to exploit novel optical materials and technologies for information transmission and processing in the next generation information and communication systems. Most recently, considerable attention has been paid to the preparation and fabrication of semiconducting nanomaterials due to their potential applications as active materials in miniaturized optoelectronic devices [1–8]. Among all kinds of functional optoelectronic materials, submicrometer photo waveguide materials play an important role in integrated light-based devices [9–11]. They can be used to control the efficient delivery of light at nano or micrometer scale, indicating the possibility of high-speed and low-loss integrated circuit. One dimensional single crystal inorganic nanowires for active photo waveguide materials have been obtained through chemical vapor deposition (CVD) or physical vapor deposition (PVD) method, and their photo waveguide properties, including the optical cavity effect and lasing, have been extensively studied [12–16]. Very recently, nano- or micro- architectures (mostly 1D structures) self-assembled from conjugated organic molecules through solution process have been attracting increased interest in this field [3–8]. They might serve as better media to generate or propagate light in a predefined way, due to their flexibility, easy optical tunability, strong luminescence efficiency [17–30]. However, waveguiding behavior has been observed only in few organic materials. Hence, the challenge of fabricating organic nanowires, which could provide photo waveguide devices with enhanced performance and more functionality, is a subject of significant scientific interest and technological importance.

Herein, we report the photo waveguiding behaviors of single crystalline microwires and polycrystalline microtwists fabricated by solution process from a new kind of X-shaped π-conjugated molecules synthesized by us recently [31]. These ultralong microstructures provide us

* Corresponding authors. Tel.: +86 10 6275 8145; fax: +86 10 6275 1708.
E-mail addresses: zhuxing@pku.edu.cn (X. Zhu), jianpei@pku.edu.cn (J. Pei).

1566-1199/$ - see front matter © 2011 Elsevier B.V. All rights reserved.
doi:10.1016/j.orgel.2010.12.016

much convenience in the fabrication of optical and electronic devices. Fluorescence microscope and scanning near-field optical microscope (SNOM) show that our 1D microstructures can serve as long-distance active optical waveguides, which allow locally excited photoluminescence to propagate along the 1D structure and out-couple at the tip. We further observed excellent coupling between the as-synthesized organic wires, which is an important element in the construction of complex optical circuits. The ability to change the direction of light would be of great interest for real application in miniaturized complex photonic devices [9–11]. By slight change in chemical structure, we have obtained well-dispersed single microtwist and further demonstrated that such chiral structures could also be used as optical waveguiding materials. Our microtwist is the first chiral structure for waveguide research and opens the possibility of coupling the chirality of material to that of light.

2. Materials and methods

X-shaped molecules were synthesized in our recently published paper [31]. Absorption spectra were recorded on PerkinElmer Lambda 35 UV–vis Spectrometer. Photoluminescent (PL) spectra were carried out on PerkinElmer LS55 Luminescence Spectrometer. Thermal gravity analyses (TGA) were carried out on a TA Instrument Q600 analyzer and differential scanning calorimetry (DSC) analyses were performed on a METTLER TOLEDO Instrument DSC822e calorimeter. Scanning electron microscopy (SEM) was performed on a Philips XL30W/TMP operating at 1 kV. Transmission electron micrographs (TEM) were recorded on a Philips model Tecnai F20 electron microscope operating at 120 kV. Powder X-ray diffraction was recorded on a D/max-RA High Power Rotating Anode 12KW X-ray Diffractometer. Refractive index was measured on a HORIBA JOBIN YVON spectroscopic ellipsometer. The fluorescence images were taken on a DMLS fluorescence microscope (Leica, Germany). The optical waveguide properties were measured with a scanning near-field optical microscope composed of a NSOM-100 near field scanning tip (Nanonics Co.), SPM-100 (RHK Co.) controller and SPEX 0.34 fluorescence optical spectrometer.

3. Results and discussion

Scheme 1 illustrates the chemical structure of our X-shaped molecules. Fig. 1 shows the absorption and photoluminescence (PL) spectra of **1a** in CH_2Cl_2 solution and in the crystalline state. The monomer exhibits two resolved absorption peaks at 300 and 327 nm, and a relative weak shoulder peak at about 350 nm. All absorption peaks slightly red-shifted after the molecules self-assembled into microwires, and the intensity of the shoulder peak increases considerably. In the dissolved state, **1a** exhibits a single emission peak at about 414 nm. In the solid state, a small red-shift of the photoluminescence peak was observed. The small red-shifts in absorption and fluorescence spectra on going from solution to solid state indicated that the π–π stacking interactions among the molecules are not very strong in the microwires. The photophysical properties of **1b** are almost the same as that of **1a** due to the same skeleton.

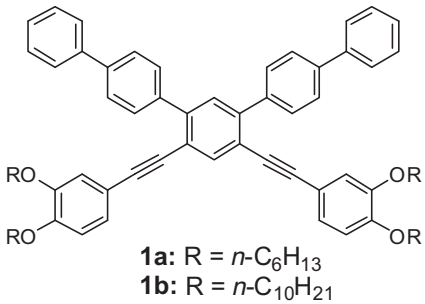

Scheme 1. Chemical structure of X-shaped molecule **1a** and **1b**.

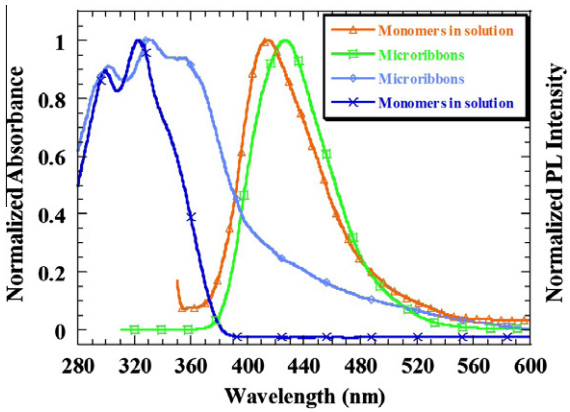

Fig. 1. Normalized absorption and emission spectrum of **1a** in dilute CH_2Cl_2 solution (1×10^{-6} M) and in single-crystalline microribbons.

A facile method that combines reprecipitation and self-assembly techniques [5] was developed to fabricate the single-crystalline microribbons. Experimentally, the microstructures were prepared by dissolving the molecule **1a** in mixed solvents of CH_2Cl_2 and EtOH (1:1.5, V/V) at a concentration of 1 mg/mL and stay with slow evaporation of the solvents. The slow crystallization process results in the formation of ribbon-shaped aggregates from the self-assembly of the molecules. Fig. 2 shows typical scanning electron microscopy (SEM) and fluorescence microscope images of the microribbons. Large-area SEM images of an EtOH suspension of self-assembled **1a** through slow crystallization process on silica substrate showed a uniform fibrous structure (Fig. 2a). Most of the microribbons are hundreds of micrometers long and 1–4 μm wide. Small area SEM image (Fig. 2b) demonstrated that each single ribbon has a fixed size along its entire length. The cross-sections of the microribbons are rectangular (see Fig. 2c), which is a propitious condition to realize the fluorescence out-coupling at the end of the ribbons compared with the microstructures with irregular tips. Some thinner nanowires with length of tens of micrometers and width of 200–400 nm were also found. The selected area electron diffraction (SAED) pattern indicated that the

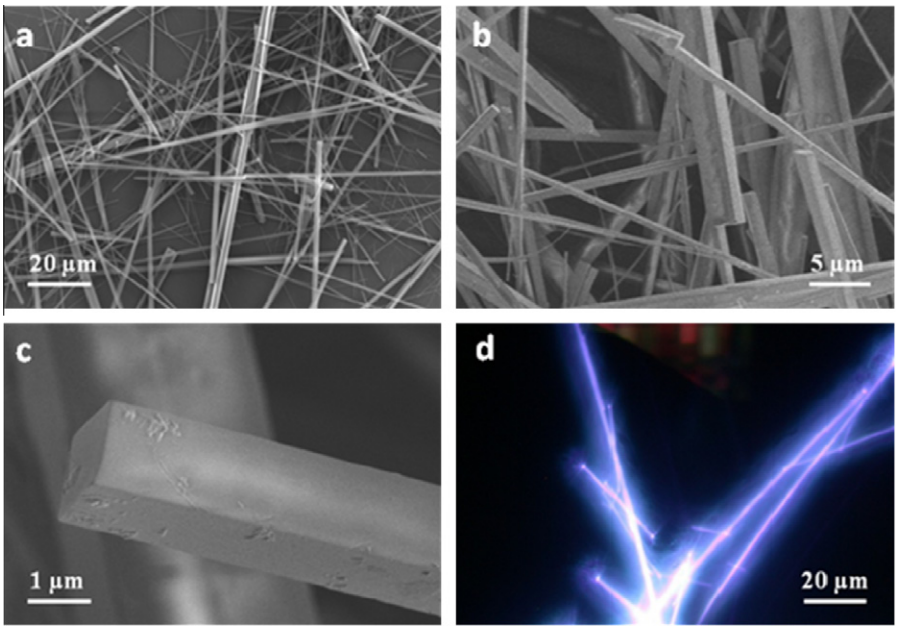

Fig. 2. Morphologies of the microribbons. (a) Large-area; (b) small-area and (c) further amplified SEM image of single-crystalline microribbons prepared from **1a** (1 mg/mL). (d) Photoluminescence images of the microribbons.

ribbon-shaped 1D morphology was single crystalline [31]. Fig. 2d shows a PL microscopy image of the microribbons on glass substrate. The microribbons were transferred onto the substrate by spin casting and were directly observed by using a PL microscope. The PL image shown in Fig. 2d indicates that the microribbons exhibit blue emission, with very bright luminescence spots at both tips and relatively weaker emission from the bodies of the ribbons. This is a typical characteristic of an optical waveguide material.

Photoluminescence images of the microribbons on a glass substrate reveal that they are suitable for long-range optical waveguide materials. To study the detailed wave-guiding properties of the microribbons, we employed a continuous laser focused down to the diffraction limit (~5 μm) with a wavelength of 325 nm according to the absorption spectrum of the microribbon. The local emission of light from each single microribbon under laser excitation was so strong that it could be imaged clearly with a color CCD. Fig. 3a shows the micro area fluorescence microscopy image of a single microribbon obtained from scanning near-field optical microscopy (SNOM) in bright field, indicating that the ribbons are suitable single wire long range photo waveguide materials. Guided PL was emitted from both ends of the microribbons irrespective of the excited position. No emission was detected other than the tips and the excited area. It can be supposed that due to a large enough diameter of the crystallite (larger than excitation and fluorescence wavelength), luminescence excited on the ribbon surface spreads out inside the ribbon by means of total internal reflection [22].

A SNOM collection tip was placed stationary at one of the ribbon ends to detect the out-coupled fluorescence. As shown in Fig. 3b, the PL spectra collected at different transmitted distance are very similar, with only a slight red-shift due to self-absorption at low wavelength. The process of light traveling along the wire can be investigated by moving the laser along the ribbon, as shown in Fig. 4. The distance-dependent photoluminescence spectra, showing propagation of light through single microribbons, were also measured with a SNOM. The PL intensity at 424 nm decreases with increasing the guided distance, without any change in outcoupled position (Fig. 3c). The optical loss mainly comes from the reabsorption during propagation of light and coupling between the ribbons and the substrates. Another possible source for the optical loss is the Rayleigh scattering arising from defects and roughness, which will result in the local variation in the refractive index along the length of the ribbons.

$$\alpha = -10 \times \log(I_{out}/I_{in}) \times L^{-1} \quad (1)$$

The optical loss coefficient of guided fluorescence in the microribbons can be calculated by the following Eq. (1). I_{out} and I_{in} are the intensities of incidence and out-coupled light, and L is the propagation distance [30]. The loss coefficients at 424 nm in the microribbons is determined to be 4.9 dB/100 μm, which is much lower than those of many 1D organic nanomaterials reported before [28–30]. This indicated that the microribbons are excellent candidate for low-loss, long-distance optical waveguide material. The PL of the microribbons at 424 nm displays linear losses (Fig. 3d) with increasing propagation length. Hence, by using the loss coefficient and the value of I_{in} from the spectrum of L = 40 μm in Fig. 3d, one could calculate the theoretical intensity of PL at different wavelengths guided through different distance (L) along the microribbons.

The transition from spontaneous PL to stimulated emission is significantly influenced by the size and length of the

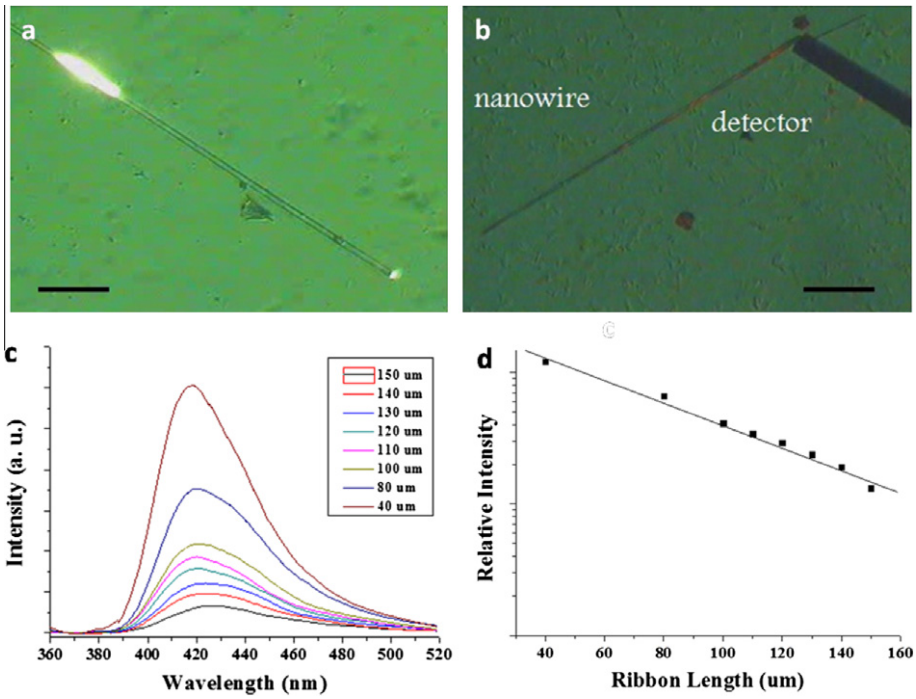

Fig. 3. (a) Micro area fluorescence microscopy image of an excited single microribbon in bright field. (b) The detection of the out-coupled fluorescence: a SNOM collection tip was placed stationary at one of the ribbon ends. (c) The distance-dependent photoluminescence spectra of propagated light through single microribbon measured with an SNOM detection tip. (d) The logarithmic plot of relative intensities of PL peak at 500 nm. Scale bars: (a) 20 μm, (b) 40 μm.

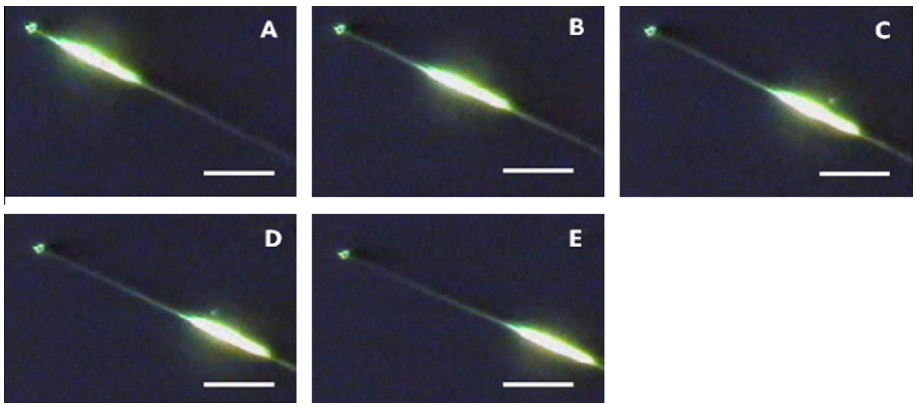

Fig. 4. Selected images of an excited microwire with different guided distance. (A) 40 μm; (B) 80 μm; (C) 100 μm; (D) 110 μm and (E) 120 μm.

microribbons. For example, for thinner ribbons with a width of 300–400 nm, no emission was detected at the tip of the ribbon (Fig. 5). It has been demonstrated that light can only propagate within the transverse magnetic (TM) modes of microribbon waveguides [24], whereby the number of possible modes, m, is restricted by

$$m < \frac{2a}{\lambda} \cdot \frac{n_{\perp}}{n_{\parallel}} \cdot \sqrt{n_{\parallel}^2 - n_s^2} \qquad (2)$$

with a being the width of the ribbon; $\lambda \approx 424$ nm, the wavelength of the propagated light, $n_{\parallel}$ and $n_{\perp}$, the refractive indices along and perpendicular to the microribbon, respectively, and $n_S = 1.46$, the refractive index of the quartz substrate. Here, we assume that both $n_{\parallel}$ and $n_{\perp}$ are close to the value of the bulk material (≈1.62), which was measured using a spectroscopic ellipsometer (as shown in Fig. 6). According to the Eq. (2), the minimum width required for light propagation at 424 nm is approximately 302 nm as given by $m = 1$. This is consistent with the experimental observations that thinner ribbons with a width of 300 nm exhibit no long-range optical waveguide properties. The maximum mode (m) that a microwire with width of 2 μm could propagate is 6.

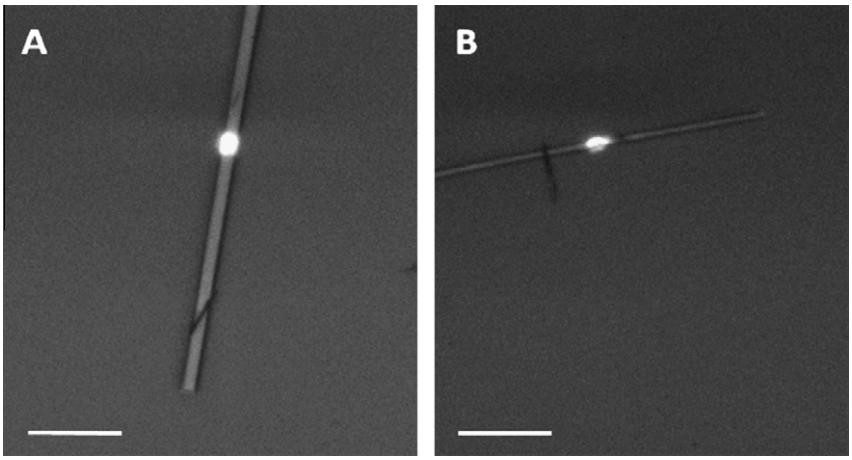

Fig. 5. SNOW image of a single wire with a width of about 300 nm: No emission was detected at the tip of the wire. Scale bars: (A) 2 μm and (B) 5 μm.

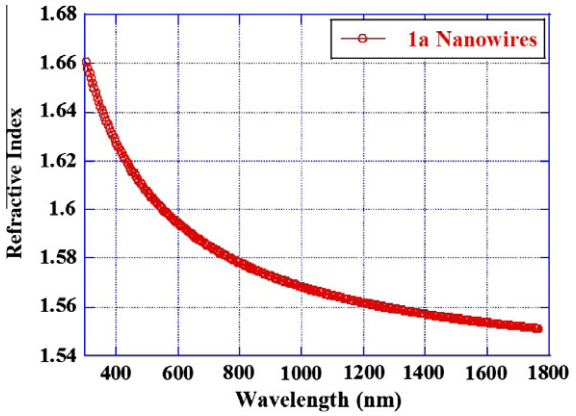

Fig. 6. The wavelength-dependent refractive index of the microwires measured with an HORIBA JOBIN YVON spectroscopic ellipsometer.

The cutoff wavelength above which no propagating mode can exist can be given as follows:

$$\lambda_{\text{cutoff}} = 2a\sqrt{n_{\parallel}^2 - n_s^2} \tag{3}$$

By using the above values of $n_{\parallel}$, $n_{\perp}$ and $n_{S,}$ the λ_{cutoff} is calculated to be 421 and 1402 nm when $a = 300$ and 1000 nm, respectively. This mode analysis implies that due to the cutoff effect, the ribbons with a width of about 300 nm may exhibit an significant increase in the optical loss for $\lambda >$ 421 nm. The cutoff effect can be observed only for ribbons with a relatively narrow width because λ_{cutoff} is out of the wavelength range of the emission band for fibers wider than 650 nm. In our case, most of the ribbons were 1–4 μm along the 1D direction, so the cutoff effect has negligible influence on the out-coupling fluorescence at 424 nm.

Excellent coupling effect (Fig. 7) was found in the system of two or more ribbons from molecule **1a**, which was unusual in organic micrometer scale photo waveguide materials. In Fig. 7a and b, both the right ends of ribbons A and B emitted luminescence as long as any one of the left ends was excited by the laser. This observation suggested that part of the light is transferred from one ribbon to another, and the residual light propagated along the same ribbon. Similar coupling behavior could also be observed for 3 or more microwires, as shown in Fig. 7c and d. The left end of ribbon C emitted intrinsic luminescence of the microribbon if the right end of ribbon A was excited, showing the transfer of light among three ribbons, which was never reported before. This phenomenon is common in our material. We tentatively proposed that the transfer of the light took place at the contact point of the two fibers where the difference of the refractive index disappeared. The surface condition of the fibers at the contact point is an important factor for the transfer of the light. As an example, in Fig. 7b, 46% of the light intensity transfer into ribbon A from ribbon B at the contacting point according to the known loss constant (Fig. 8). The unique feature of the microfibers provides us a convenient way to control the direction and distribution of the fluorescence, indicating the potential in building complex optical system in micrometer or submicrometer scale.

Usually, waveguiding materials have simple geometric shapes such as wire and ribbon. We wondered whether complex microstructure could also used to transport light and whether such materials would give new physical phenomena. As we reported recently, by simply changing the length of peripheral alkoxy groups, well-dispersed, regular microtwists were easily obtained [31]. Such a large change in morphology was remarkable. We ascribed such change to different crystal growth kinetics of **1a** and **1b**. In short, the imbalance in the growth rate between the center and the edge part of a growing front provided the driving force for twist growth in **1b** [31]. In the preparation of the manuscript, Luis Sánchez and coworkers also reported a similar system for the growing of chiral one-dimensional microstructures. However, in our system, the chirality of the microwires was not induced by the chirality of the side alkyl chains but by the intrinsic crystal packing [32]. Fig. 9a shows a SEM image of the microtwists prepared at 15 °C through solution process. The fluorescence microscope image of the microtwist on glass substrate (Fig. 9b and inset)

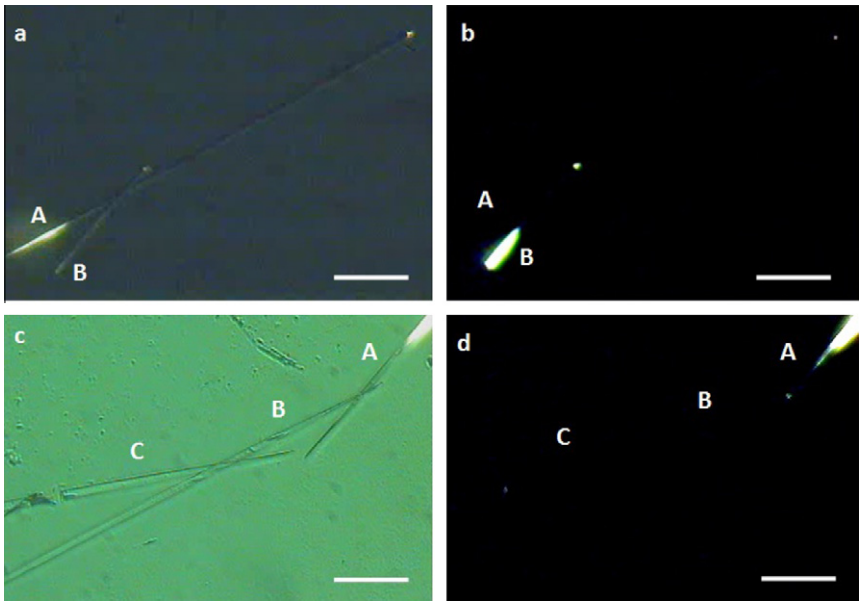

Fig. 7. Coupling effect in the microribbons. (a) Coupling effect in a two-ribbon system in bright field, excitation position: left end of microribbon A. (b) A corresponding picture of the two-ribbon system in dark field, excitation position: left end of microribbon B. (c) Coupling effect in a three-ribbon system in bright field, excitation position: right end of microribbon A. (d) A corresponding picture of the three-ribbon system in dark field, excitation position: right end of microribbon A. Scale bars: (a) 20 μm, (b) 20 μm, (c) 10 μm and (d) 10 μm.

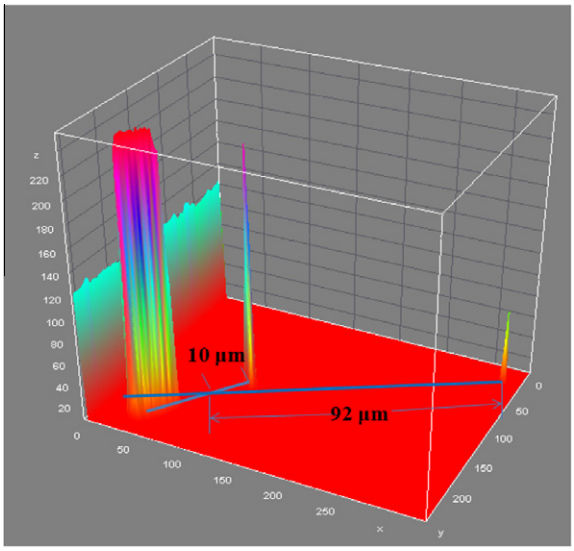

Fig. 8. The calculation of the transfer efficiency in Fig. 7b.

indicates that such chiral structure could also serve as optical waveguide materials. The distance-dependent photoluminescence spectra along a single microtwist were also measured with a SNOM. Fig. 9d shows the logarithmic plot of relative intensities of PL peak of the microtwists with a pitch of 1 μm. The microtwist showed photo waveguide properties similar to that of the microwire. Although its loss coefficient is systematically higher (8.3 dB/100 μm with a pitch of 1 μm according to Eq. (1)), the loss coefficient is still lower than many other organic photo waveguide materials [30]. The comparatively higher performance of the microribbons can be attributed to two factors: first, as demonstrated by SAED experiment [31], the microribbons are single crystalline while the microtwists are relative polycrystalline. Single crystalline materials are known to have superior device performance due to less grain boundaries and scattering. Second, the dramatic curvature change at the groove of the twists might constitute many scattering sites, which further increased the optical loss. The scattered strength should be strongly dependent on the size of the scattering center; further investigation is undergoing focused on these problems. In general, the loss coefficient increased with the decrease of the pitch, which is a result of the lower crystallinity and more scattering sites. Nevertheless, the ability of realizing single twist device with definite chirality allowed us to explore the interesting possibility of chirality-coupled optical devices. We are currently examining this possibility in a single left-handed or right-handed twist.

4. Conclusion

In summary, we have demonstrated a series of 1D microstructure which can be used as optical waveguide materials. 1D microwires and microtwists were prepared from X-shaped conjugated molecules through simple solution process in high yield, which provides us a convenient and low-cost fabrication method for functional organic microstructures. The as-prepared microwires demonstrated excellent properties in low-loss long-distance (4.9 dB/100 μm, >200 μm) photo waveguide in single wire as well as the transfer of light between the wires, showing the potential as building blocks in complex optical devices

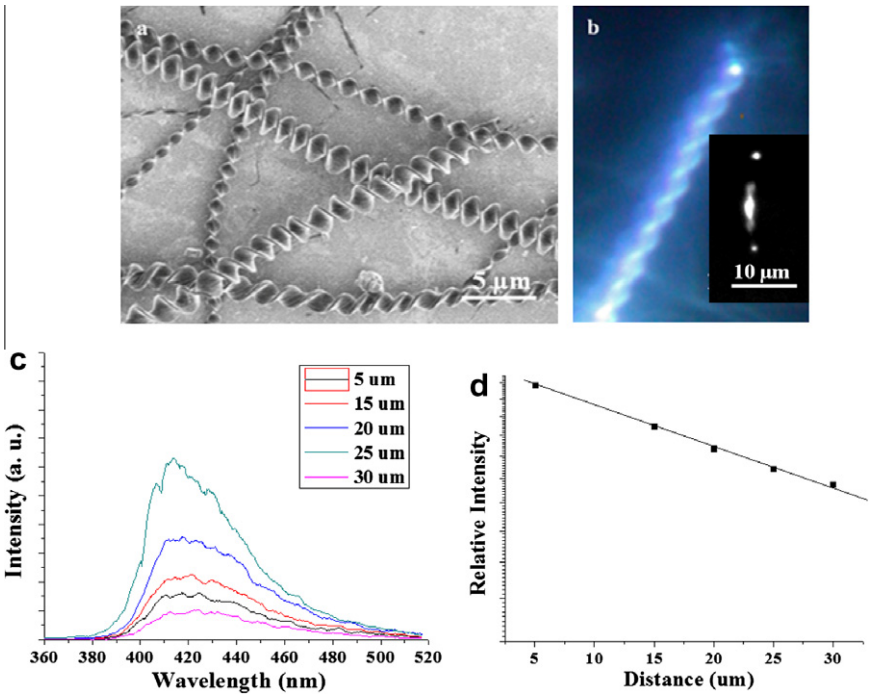

Fig. 9. (a) SEM image of the microtwists prepared at 15 °C. (b) Photoluminescence images of a single microtwist. Inset: the photo waveguiding behavior of the microtwist. (c) The distance-dependent photoluminescence spectra of propagated light through single microtwist measured with an SNOM detection tip. (d) The logarithmic plot of relative intensities of PL peak at 424 nm.

at micrometer scale. On the other hand, we were also able to greatly change the morphology of the microstructure by a slight change in the chemical structure. Our microtwist is the first chiral material that shows waveguiding properties. Despite the medium performance (8.3 dB/100 μm), realization of photo waveguiding in chiral materials suggest many interesting possibilities for novel devices. Further efforts would be made to control the distribution of PL between two wires, and to reveal the relationship between the coupling efficiency and the surface condition of the wires at the contact point. Also, we are further developing microtwists with pitch comparable to the wavelength of guided light in order to check whether the chirality of the materials would influence its interaction with light.

Acknowledgments

This work was supported by the Major State Basic Research Development Program (Nos. 2006CB921602 and 2009CB623601) from the Ministry of Science and Technology and National Natural Science Foundation of China.

References

[1] J. Hu, T.W. Odom, C.M. Lieber, Acc. Chem. Res. 32 (1999) 435.
[2] Y. Xia, P. Yang, Y. Sun, Y. Wu, B. Mayers, B. Gates, Y. Yin, F. Kim, H. Yan, Adv. Mater. 15 (2003) 353.
[3] Y.S. Zhao, H. Fu, A. Peng, Y. Ma, D. Xiao, J. Yao, Adv. Mater. 20 (2008) 2859.
[4] R. Li, W. Hu, Y. Liu, D. Zhu, Acc. Chem. Res. 43 (2010) 529.
[5] L. Zang, Y. Che, J.S. Moore, Acc. Chem. Res. 41 (2008) 1596.
[6] V.K. Praveen, S.S. Babu, C. Vijayakumar, R. Varghese, A. Ajayaghosh, Bull. Chem. Soc. J. 81 (2008) 1196.
[7] Y. Zhou, W.J. Liu, Y. Ma, H. Wang, L. Qi, Y. Cao, J. Wang, J. Pei, J. Am. Chem. Soc. 129 (2007) 12386.
[8] E. Ahmed, A.L. Briseno, Y. Xia, S.A. Jenekhe, J. Am. Chem. Soc. 130 (2008) 1118.
[9] X.F. Duan, Y. Huang, R. Agarwal, C.M. Lieber, Nature 421 (2003) 241.
[10] C.J. Barrelet, A.B. Greytak, C.M. Lieber, Nano Lett. 4 (2004) 1981.
[11] R. Agarwal, C.J. Barrelet, C.M. Lieber, Nano Lett. 5 (2005) 917.
[12] D.J. Sirbuly, M. Law, H.Q. Yan, P.D. Yang, J. Phys. Chem. B 109 (2005) 15190.
[13] J.C. Johnson, H.-J. Choi, K.P. Knutsen, R.D. Schaller, P. Yang, R.J. Saykally, Nat. Mater. 1 (2002) 106.
[14] J.C. Johnson, H. Yan, P. Yang, R.J. Saykally, J. Phys. Chem. B 107 (2003) 8816.
[15] J.Y. Kim, F.E. Osterloh, J. Am. Chem. Soc. 127 (2005) 10152.
[16] A. Pan, R. Liu, Q. Yang, Y. Zhu, G. Yang, B. Zou, K. Chen, J. Phys. Chem. B 109 (2005) 24268.
[17] Y. Qi, J. Ding, M. Day, J. Jiang, C.L. Callender, Chem. Mater. 17 (2005) 676.
[18] K. Takazawa, Chem. Mater. 19 (2007) 5293.
[19] K. Takazawa, J. Phys. Chem. C 111 (2007) 8671.
[20] D. O'Carroll, I. Lieberwirth, G. Redmond, Nat. Nanotech. 2 (2007) 180.
[21] D. O'Carroll, I. Lieberwirth, G. Redmond, Small 3 (2007) 1178.
[22] H. Yanagi, T. Morikawa, Appl. Phys. Lett. 75 (1999) 187.
[23] H. Yanagi, T. Ohara, T. Morikawa, Adv. Mater. 13 (2001) 1452.
[24] F. Balzer, V.G. Bordo, A.C. Simonsen, H.-G. Rubahn, Phys. Rev. B 67 (2003) 115408.
[25] K. Takazawa, Y. Kitahama, Y. Kimura, G. Kido, Nano Lett. 5 (2005) 1293.
[26] A.N. Lebedenko, G.Y. Guralchuk, A.V. Sorokin, S.L. Yefimova, Y.V. Malyukin, J. Phys. Chem. B 110 (2006) 17772.
[27] S. Kanazawa, M. Ichikawa, T. Koyama, Y. Taniguchi, ChemPhysChem 7 (2006) 1881.
[28] Y.S. Zhao, A. Peng, H. Fu, Y. Ma, J. Yao, Adv. Mater. 20 (2008) 1661.
[29] Y.S. Zhao, J. Xu, A. Peng, H. Fu, Y. Ma, L. Jiang, J. Yao, Angew. Chem. Int. Ed. 47 (2008) 7301.

[30] Q. Liao, H. Fu, J. Yao, Adv. Mater. 21 (2009) 4153.
[31] H.B. Chen, Y. Zhou, J. Yin, J. Yan, Y. Ma, L; Wang, Y. Cao, J. Wang, J. Pei, Langmuir 25 (2009) 5459.
[32] F. Garcıá, F. Aparicio, M. Marenchino, R. Campos-Olivas, L. Sánchez, Org. Lett. 19 (2010) 4264.

Organic Electronics 12 (2011) 461–471

Contents lists available at ScienceDirect

Organic Electronics

journal homepage: www.elsevier.com/locate/orgel

Enhanced charge transport by incorporating additional thiophene units in the poly(fluorene-thienyl-benzothiadiazole) polymer

Zhuoying Chen [a,1], Junfeng Fang [b,1], Feng Gao [a], Thomas J.K. Brenner [a], Kulbinder K. Banger [a], Xingzhu Wang [b], Wilhelm T.S. Huck [b,c,*], Henning Sirringhaus [a,*]

[a] Cavendish Laboratory, Department of Physics, University of Cambridge, CB3 0HE, United Kingdom
[b] Melville Laboratory for Polymer Synthesis, Department of Chemistry, University of Cambridge, CB2 1EW, United Kingdom
[c] Radboud University Nijmegen, Institute for Molecules and Materials, Heyendaalseweg 135, 6525 AJ Nijmegen, The Netherlands

ARTICLE INFO

Article history:
Received 3 November 2010
Accepted 12 December 2010
Available online 23 December 2010

Keywords:
Conjugated polymers
Ambipolar transport
Field-effect transistors
Solar cells

ABSTRACT

We report a comparative study of optical properties, structure and morphology, field-effect transistor (FET) and solar cell performance between poly(4-(3,4′-dihexyl-2,2′-bithiophen-5-yl)-7-(5′-(9,9-dioctyl-9*H*-fluoren-2-yl)-3,4′-dihexyl-2,2′-bithiophen-5-yl)benzo[*c*][1,2,5]-thiadiazole) (F8TTBTT), and its predecessor poly((9,9-dioctylfluorene)-2,7-diyl-alt-[4,7-bis(3-hexylthien-5-yl)-2,1,3-benzothiadiazole]-2′,2″-diyl) (F8TBT). Compared to F8TBT, F8TTBTT has two more thiophene units incorporated in its monomer structure. Such a modification leads to a reduced optical band gap, improved charge injection and significantly enhanced ambipolar field-effect mobilities reaching 5×10^{-2} $cm^2 V^{-1} s^{-1}$ for holes and 4×10^{-3} $cm^2 V^{-1} s^{-1}$ for electrons. The enhanced carrier mobilities are most likely a result of an increased backbone planarization and interchain interaction. As a consequence of ambipolar transport, light-emission was observed from the transistor channel during operation. The reduced band gap and improved charge transport make F8TTBTT an interesting candidate also for solar cell applications. Unoptimized solar cells based on F8TTBTT:PCBM blends were found to exhibit power conversion efficiency under AM 1.5 illumination of ~1.54%.

© 2011 Published by Elsevier B.V.

1. Introduction

Solution-processed semiconducting conjugated polymers have attracted extensive interest in recent years in applications such as organic field-effect transistors (FETs) and organic photovoltaics (OPV) [1–4]. This class of materials combines several appealing characteristics such as low-cost synthesis, tunable optical and transport properties, high absorption coefficients, physical flexibility, and large-scale industrial processing. For FET applications, recent synthetic progress has demonstrated impressive field-effect mobility values in between 0.1 and 0.8 $cm^2 V^{-1} s^{-1}$ in some conjugated polymer systems [5–7]. Yet the charge transport properties of polymers are often extremely sensitive to their morphology and crystallinity [1,8,9]. Many amorphous polymers synthesized to-date, while demanding less processing control over semicrystalline systems, still have field-effect mobilities lower than 0.01 $cm^2 V^{-1} s^{-1}$ [4,10–12]. Much research efforts are currently being addressed to achieve improved transistor performance by understanding material synthesis, microstructure, processing, and device architecture. Furthermore, ambipolar charge transport with balanced electron and hole mobilities has been discovered to be an intrinsic property of many organic semiconductors [4,11]. This has opened up exciting opportunities for application of organic materials in new device architectures. These

* Corresponding authors. Address: Radboud University Nijmegen, Institute for Molecules and Materials, Heyendaalseweg 135, 6525 AJ Nijmegen, The Netherlands (W.T.S. Huck).
E-mail addresses: wtsh2@cam.ac.uk (W.T.S. Huck), hs220@cam.ac.uk, hs220@phy.cam.ac.uk (H. Sirringhaus).
[1] These authors contributed equally to this work.

1566-1199/$ - see front matter © 2011 Published by Elsevier B.V.
doi:10.1016/j.orgel.2010.12.009

architectures include complementary-like voltage inverters with a single semiconducting material [13,14] and light-emitting FETs [15–17], which combine the switching behavior of transistors and the light-emitting behavior of light-emitting diodes (LEDs). In terms of scientific understanding there are still subtle differences between electron and hole mobilities in many polymer families and better understanding of how these depend on the molecular structure of the polymer is needed. This requires classes of materials where ambipolar transport properties can be correlated with targeted modifications of chemical structure.

For solar cell applications new conjugated polymers having efficient charge transport of electrons and holes and good absorption properties are required [2]. In organic bulk heterojunction solar cells, the photocurrent is governed by two main factors: (1) the amount of absorbed photons in the active layer under a fixed total flux of photons; (2) the internal quantum efficiency defined by the fraction of collected carriers per absorbed photon, which contains the efficiencies in both exciton dissociation and carrier transport toward collecting electrodes. Approaches to rationally increase carrier mobilities in conjugated polymers and extend their absorption ranges to cover a larger portion of the solar spectrum, while maintaining efficient charge generation at the donor–acceptor heterojunction, are currently under intensive research [2,18].

Among many conjugated polymer systems reported recently, the poly((9,9-dioctylfluorene)-2,7-diyl-alt-[4,7-bis(3-hexylthien-5-yl)-2,1,3-benzothiadiazole]-2′,2″-diyl) (F8TBT) system and similar derivatives without side chains on the thiophene units (often labeled as APFO-3 or PFDTBT) have received much research attention in LED, solar cell and FET studies [16,19–25]. Compared to other polyfluorene derivatives such as poly(9,9-dioctylfluorene) (F8) and poly(9,9-di-*n*-octylfluorene-*alt*-benzothiadiazole) (F8BT) [11,12], F8TBT has a higher HOMO level and a smaller band gap [19,22]. Due to the electron-withdrawing benzothiadiazole (BT) moiety and the relative small band gap, F8TBT FETs exhibit good ambipolar transport characteristics with gold as injection electrodes [16]. Even though the hole and electron mobilities in such ambipolar F8TBT FETs are imbalanced, red light emission during device operation was observed. On the other hand, because F8TBT shows larger absorption range in the solar spectrum compared to other polyfluorene derivatives, it has also shown potential for use in solar cells [21–23]. Due to its ambipolar nature, efficient solar cells have been demonstrated based on the use of F8TBT as an electron donor (in polymer/small molecule blends) [21–23] and an electron acceptor (in polymer/polymer blends) [2,21–24]. P3HT-F8TBT polymer blend solar cells are currently among the best performing non-fullerene based organic solar cells [26]. Based on the chemical structure of F8TBT, a recent study showed that increasing the number of thiophene rings in the repeating units of this donor–acceptor type of polymers can effectively red-shift the absorption spectra [25]. Even though enhanced solar cell performance was shown, the charge transport properties in these new systems containing more thiophene units have not yet been studied.

In this work, through a systematic comparison between F8TBT and poly(4-(3,4′-dihexyl-2,2′-bithiophen-5-yl)-7-(5′-(9,9-dioctyl-9*H*-fluoren-2-yl)-3,4′-dihexyl-2,2′-bithiophen-5-yl)benzo[*c*][1,2,5]thiadiazole) (F8TTBTT), we present a comprehensive study aiming to understand the effect of these additional thiophene units on electronic structure, optical properties, structure and morphology, charge transport in FETs and solar cell performance. In particular, by comparison to other previously reported polyfluorene derivatives, we find that F8TTBTT demonstrates enhanced field-effect mobility for hole transport, while extending its absorption range due to its reduced band gap. Combined improvements in both carrier mobility and absorption range make this new material an interesting system for its further optimization and application in FETs and solar cells.

2. Experimental section

2.1. Synthesis

All commercial chemical reagents were obtained from Aldrich and used as received. 4,7-Dibromo-2,1,3-benzothiadiazole, 3-hexylthiophene and fluorene were purchased form Aldrich for precursor synthesis. 2,7-bis(1,3,2-dioxaborolan-2-yl)-9,9-dioctylfluorene, 4,7-bis(5-bromo-4-hexylthiophen-2-yl)benzo[*c*][1,2,5]thiadiazole (Br–TBT–Br), 4,7-bis(5′-bromo-3,4′-dihexyl-[2,2′-bithiophen]-5-yl)benzo[*c*][1,2,5]thiadiazole (Br–TTBTT–Br) were prepared following the already published procedures [20,27]. Synthetic pathways are described in Scheme 1. For step (i), $PdCl_2(PPh_3)_2$ was added to a solution of tributyl(4-hexylthiophen-2-yl)stannane and Br–TBT–Br in tetrahydrofuran (THF). The mixture was refluxed under a nitrogen atmosphere for 6 h before solvent removal and purification. For step (ii), TTBTT was dissolved in THF under a nitrogen flow and then *N*-bromosuccinimide (NBS) was added. The reaction mixture was stirred at 0 °C for 2 h before product extraction. Details of these steps can be found in previous reports [20,27].

2.1.1. 4,7-Bis(3,4′-dihexyl-[2,2′-bithiophen]-5-yl)benzo[c][1,2,5]thiadiazole (TTBTT)

0.06 mmol $Pd(PPh_3)_4$ was added to a solution of 1 mmol 4,7-bis(5′-bromo-3,4′-dihexyl-[2,2′-bithiophen]-5-yl)benzo[*c*][1,2,5]thiadiazole (TBT) and 2.5 mmol tributyl-(4-hexyl-2-thienyl)stannane in THF under nitrogen. The mixture was refluxed under a nitrogen atmosphere for 12 h. The reaction solution was cooled to room temperature. After the removal of most of the solvent at a reduced pressure, the residue was purified by column chromatography on silica gel (eluent CH_2Cl_2/hexane) to yield pure product (TTBTT) with a yield of 90%. ^{1}H NMR (400 MHz, $CDCl_3$). δ (ppm): 7.90 (s, 2H), 7.75 (s, 2H), 7.00 (s, 2H), 6.87 (s, 2H), 2.79–2.75 (m, 4H), 2.58–2.54 (m, 4H). 1.70–1.56 (m, 8H), 1.37–1.24 (m, 24H), 0.85–0.81 (m, 12H). ^{13}C NMR (100 MHz, $CDCl_3$). δ (ppm): 153.00, 144.15, 140.65, 137.01, 136.06, 133.30, 130.99, 127.82, 125.88, 125.59, 120.69, 32.09, 31.01, 30.92, 30.82, 29.91, 29.71, 29.42, 23.05, 23.03, 14.50.

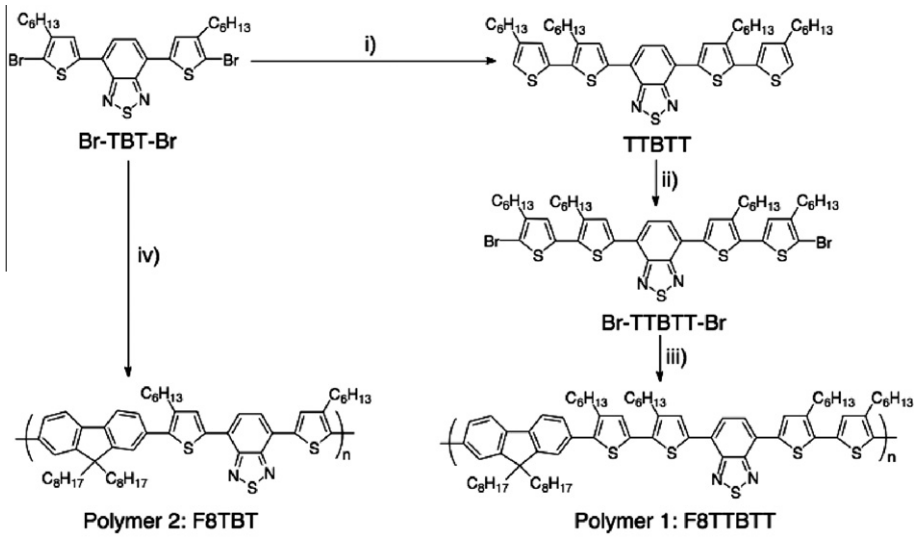

Scheme 1. Synthetic pathways to precursors and the structures of the two polymers studied in this work: F8TTBTT and F8TBT.

2.1.2. 4,7-Bis(5′-bromo-3,4′-dihexyl-[2,2′-bithiophen]-5-yl)-benzo[c][1,2,5]thiadiazole (Br–TTBTT–Br)

4,7-Bis(3,4′-dihexyl-[2,2′-bithiophen]-5-yl)benzo[*c*][1,2,5]thiadiazole (TTBTT) was dissolved in THF under a nitrogen flow at 0 °C. After complete dissolution of the solid, 2.05 equal *N*-bromosuccinimide (NBS) was added. The reaction mixture was stirred at 0 °C for 5 h and warmed to room temperature for 10 h. The reaction solution was extracted with ether, and the organic layer was washed with brine for three times and dried over anhydrous sodium sulfate. The solvent was removed at a reduced pressure to give the product as a red solid. The crude solid was purified by column chromatography on silica gel (yield: 80%); ^{1}H NMR (400 MHz, $CDCl_3$). δ (ppm): 7.83 (s, 2H), 7.67 (s, 2H), 6.83 (s, 2H), 2.72–2.68 (t, 4H), 2.52–2.48 (t, 4H), 1.65–1.53 (m, 8H), 1.35–1.27 (m, 24H), 0.85–0.81 (m, 12H). ^{13}C NMR (100 MHz, $CDCl_3$). δ (ppm): 152.86, 142.96, 141.05, 135.92, 130.87, 127.19, 125.75, 125.54, 109.37, 32.08, 32.05, 31.00, 30.08, 29.98, 29.91, 29.70, 29.35, 23.06, 23.02, 14.50.

2.1.3. Polymerization of F8TTBTT (step iii of (Scheme 1))

2,7-Bis(1,3,2-dioxaborolan-2-yl)-9,9-dioctylfluorene (0.5 mmol, 265.18 mg), 4,7-bis(5′-bromo-3,4′-dihexyl-[2,2′-bithiophen]-5-yl)benzo[*c*][1,2,5]thiadiazole (Br–TTBTT–Br) (0.5 mmol, 478.08 mg) and $(PPh_3)_4Pd$ (8 mg) were dissolved in a mixture of toluene and aqueous 2 M K_2CO_3 under nitrogen flow. The solution was refluxed under vigorous stirring for 72 h under a nitrogen atmosphere. The mixture was then poured into methanol. The precipitate was recovered by filtration and was extracted by acetone, methanol for 24 h separately to remove oligomers and catalyst residues. The resulting polymer was dried under vacuum to afford the polymer (420 mg, 70%) as a black powder. ^{1}H NMR (400 MHz, $CDCl_3$). δ (ppm): 7.95 (m, 2H), 7.79 (m, 2H), 7.71–7.69 (m, 2H), 7.45–7.40 (m, 4H), 7.11 (m, 2H), 2.84–2.86 (m, 4H), 2.68–2.66 (m, 4H), 2.05–1.95 (m,4H), 1.73–1.64 (m, 8H), 1.48–1.03 (m, 48H), 0.85–0.73 (m,18H). Element Anal. Calcd for $C_{75}H_{100}N_2S_5$: C, 75.70; H, 8.47; N, 2.35. Found: C, 75.26; H, 8.39; N, 2.37.

2.1.4. F8TBT (step iv)

For comparison we also synthesized F8TBT following the already published procedure [20]. The polymerization procedure was the same as described for F8TTBTT except using 4,7-bis(5-bromo-4-hexylthiophen-2-yl)benzo[*c*][1,2,5]thiadiazole as the reactant instead of 4,7-bis(5′-bromo-3,4′-dihexyl-[2,2′-bithiophen]-5-yl)benzo[*c*][1,2,5]thiadiazole.

2.2. Material characterizations

The number-averaged molecular weight (M_n) and molecular weight distribution (M_w/M_n) were measured using a gel permeation chromatography (GPC) instrument. GPC was carried out using THF as the eluent (1.0 mL/min) at 35 °C on two PLGel 5 μm mixed-C columns from Polymer Laboratories (with pore size ranging from 10 to 10^5 Å), connected in series with a SPD M20A prominence diode array detector (Shimadzu) and a differential refractometer/viscometer model 200 (Viscotek) calibrated by polystyrene standard. AFM images were obtained using a Digital Instruments Dimension 3100 AFM in tapping mode. UV–Visible absorption spectra were measured in air using a Hewlett–Packard HP845× Visible–UV spectrometer (using quartz Spectrosil B substrates for polymer films and quartz cuvettes for solutions). The ionization potential (HOMO level) was measured by photoelectron spectroscopy with a Riken AC-2 spectrometer. Photoluminescence (PL) and photoluminescence quantum efficiency (PLQE) measurements were carried out at room temperature with a nitrogen-purged integrating sphere using polymer films on quartz Spectrosil B substrates. The 515 nm line of an argon-ion laser (Coherent Innova305) was used as the excitation source and a cooled CCD camera (Oriel Instaspec IV) was used for photon detection. The PLQE value was calcu-

lated as described by de Mello et al. [28]. For optical experiments (UV–Vis, AC-2 and PL/PLQE), thin films were spin-coated from 1,2,4-trichlorobenzene solutions. The θ–2θ X-ray diffraction data was obtained using a Pan-Analytical diffractometer with the X-ray wavelength to be 1.54 Å (CuKα). A TA Instruments DSC Q1000 was used in the modulated differential scanning calorimetry (MDSC) mode with a heating/cooling rate of 5 °C/min. Film thickness was measured using a Veeco Dektak 6 M stylus profilometer. Raman spectra were obtained using a WITec Raman microscope with a 785 nm excitation (Starbright diode laser system, ~0.6 mW) focused through a ×100 normal microscope objective. For Raman samples, film thickness ranging from 100 nm to 300 nm were investigated for F8TTBTT and F8TBT and no significant thickness dependence was found. For F8TTBTT and F8TBT Raman samples, we used different substrates, including quartz Spectrosil B substrates and glass substrates with 30-nm-thick gold evaporated on top. Besides the polymers synthesized in this work we also include in Fig. 3 a reference Raman spectrum measured on a F8BT thin film (~100 nm thick, on quartz Spectrosil B substrate). F8BT was obtained from Cambridge Display Technology Ltd. and its molecular weight M_n was 62 kg/mol.

2.3. Thin film field-effect transistors (FETs) fabrication and measurements

The polymer dielectric and all solvents used in device fabrications were used as purchased without further purification. We used poly(methyl methacrylate) (PMMA) as the gate dielectric (M_w = 319 kg/mol, polydispersity index (PDI) of 1.25, Polymer Source Inc.). The anhydrous solvent used to dissolve the semiconducting polymers was 1,2,4-trichlorobenzene (TCB, from Romil), and the solvent used to dissolve PMMA was *n*-butyl acetate (Aldrich). The top-gate/bottom-contact (TGBC) FET configuration was used for all transistors studied in this work. The gold source and drain bottom electrodes (with Cr as the adhesion layer) were patterned by photolithography and a double-layer lift-off process on low-sodium glass (Corning 7059) substrates. The semiconducting polymers were dissolved in TCB at 10 mg/mL by heating at 100 °C for 30 min. Polymer solutions were then deposited onto substrates by spin-coating with film thicknesses of ~30–50 nm. The as-spun films for FETs were dried at 100 °C for more than five hours to ensure residual solvent removal. For further annealing FET samples were placed on a hotplate (preheated to the annealing temperature) for 30 min before cooling down to room temperature. PMMA solution (45 mg/mL in *n*-butyl acetate) was then spin-coated onto the semiconducting polymer resulting in a dielectric layer of 500–600 nm thickness. After spin-coating the dielectric layer, samples were further dried at 80 °C for 30 min to remove any residual *n*-butyl acetate. A layer of semi-transparent gold (8.5 nm-thick) was then evaporated through a shadow mask onto the dielectric layer as the gate electrode by a thermal evaporator integrated into the glovebox. The transistors were characterized with an Agilent 4155B semiconductor parameter analyzer (SPA). In order to apply higher voltage (>100 V) we used a dual channel Keithley 2636A system sourcemeter. The dielectric capacitance (C_i) was determined with separate capacitor structures using a HP 4192A impedance analyzer. Light emission during FET operation was measured with a silicon photodiode (Hamamatsu, S1133-01) mounted directed above the gold top gate of the FETs. The sensitivity of the silicon photodiode is 0.39 A W^{-1} at λ = 670 nm, and 0.43 A W^{-1} at λ = 714 nm. To record electroluminescence (EL) spectra during FET operations, an Ocean Optics USB 2000 spectrometer was mounted directly on top of the gold top gate. Starting from the step of making the semiconductor polymer solution to the final step of FET measurements, all procedures/measurements were carried out inside a dry nitrogen glovebox.

2.4. Solar cell fabrication and measurements

[6,6]-Phenyl-C_{61}-butyric acid methyl ester (PCBM) was purchased from Nano-C. F8TTBTT:PCBM blend solutions were prepared with a weight ratio of 1:1, 1:2, 1:3, and 1:4 and heated at 100 °C to dissolve in anhydrous chlorobenzene (Romil). Blend solutions were then spin-coated onto PEDOT:PSS-coated indium-tin oxide substrates. Two kinds of active layer (blend film) thickness were experimented by controlling the spin rate (6000 rpm for thickness ~100 nm, and 8000 rpm for ~80 nm). Device were completed by evaporation of 100 nm of aluminum deposited at a vacuum lower than 2×10^{-6} mbar. For annealed solar cells, after the aluminum evaporation, samples were placed onto a hotplate (preheated to 150 °C) for 30 min before cooling down to room temperature. As-spun and annealed solar cell devices were then encapsulated before removal from the glovebox for testing in air. Device external quantum efficiency (EQE) was evaluated as a function of wavelength at intensities $\leqslant$1 mW cm^{-2}, with short-circuit current measured by a Keithley 237 source measure unit (SMU). Current–voltage (*I*–*V*) characteristics were recorded in the dark and under monochromatic light source λ = 550 nm using Keithley 237 SMU. For optimized devices, *I*–*V* characteristics were also recorded under simulated solar conditions (100 mW cm^{-2} air mass AM 1.5 global spectrum) from an Oriel 81160-1000 solar simulator calibrated to a silicon reference cell.

3. Results and discussion

3.1. Material characterization

The chemical structures of the two polymers examined in this study are shown in Scheme 1. UV–Vis absorption experiments on F8TTBTT and F8TBT solutions and spin-coated thin films reveal characteristic "camel-back"-shape [19,29] absorption spectra (Fig. 1a). In the case of F8TBT, using semi-empirical quantum-chemical method, the "camel-back" absorption spectrum was previously attributed to one charge transfer state at lower energy localized on the TBT unit and one delocalized excitonic state at higher energy corresponding to the π-conjugated segment of the polymer backbone [29]. Based on the similarities previously found between F8BT and F8TBT, we speculate that

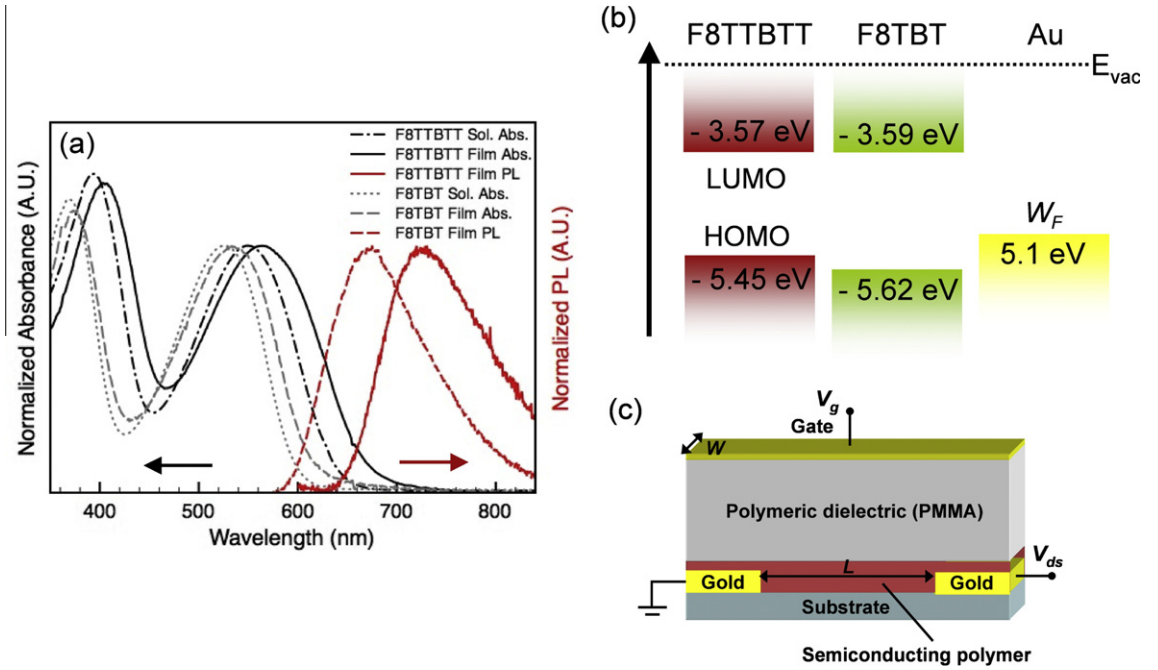

Fig. 1. (a) Room-temperature UV–Visible absorption and photoluminescence of F8TTBTT and F8TBT solutions and as-spun thin films (solvent: TCB). PL excitation was at 515 nm. (b) Schematic energy level diagram of F8TTBTT and F8TBT thin films in relation to Au assuming vacuum level alignment. The HOMO levels were determined by AC-2 photoelectron spectroscopy. The LUMO level of each material was estimated from the HOMO level by adding the optical band gap. The work function (W_f) of gold was taken from the literature [33]. (c) Schematic diagram of the top-gate/bottom-contact organic field-effect transistor structure.

the nature of electronic states in the F8TTBTT is qualitatively the same as in F8TBT. In thin films, the onset of absorption in F8TTBTT is ~660 nm (1.88 eV), while F8TBT thin films start to absorb at higher energy ~610 nm (2.03 eV). This reflects the reduced optical band gap in F8TTBTT compared to F8TBT as a result of the incorporation of additional thiophene units. For both systems, a notable red shift can be observed comparing solution and thin film absorptions. This indicates that as the polymer goes into the solid state a certain extent of either interchain delocalization or chain planarization occurs [30]. This effect is stronger in the case of F8TTBTT compared to F8TBT, i.e., the solution-to-film absorption red shift is larger in F8TTBTT (Fig. 1a). Room-temperature PL and PLQE measurements reveal red emission in both F8TTBTT and F8TBT thin films, centered at ~730 nm and 675 nm respectively. We observed a lower PLQE (~11%) in F8TTBTT films compared to F8TBT films (~22%). The reduced PLQE observed in F8TTBTT may be attributed to the existence of impurities, defects, different molecular packing, and/or the increased conjugation length (and reduced localization of excited states) associated to the addition of thiophene units in the polymer main chain. Using photoelectron spectroscopy (with a Riken AC-2 spectrometer) we determined the ionization potential (IP) of F8TTBTT and F8TBT to be about 5.45 eV and 5.62 eV, respectively (AC-2 measurement spectra see Supplementary Data Fig. S1). Using the measured IP and optical band gap values, we estimated the HOMO and LUMO levels in these two systems (Fig. 1b). These energy level values for the F8TBT system are in excellent agreement with those previously reported [24]. The reduced band gap in F8TTBTT mainly originates from the destabilization of the HOMO levels while the LUMO levels stay similar as F8TBT. For FET applications with gold source and drain electrodes (Fig. 1c), we therefore expect improved hole injections in F8TTBTT.

θ–2θ X-ray diffraction (XRD) experiments on both as-spun F8TTBTT and F8TBT thin films reveal no observable diffraction peak, indicating an amorphous microstructure in these polymer films. Absence of any crystalline order in either pristine or annealed F8TBT has been previously reported [31]. In order to identify any possible phase transitions, we performed modulated differential scanning calorimetry (MDSC) experiments on polymer powders, which can characterize not only the total heat flow but also the heat capacity and non-reversing (kinetic) components. For both F8TTBTT and F8TBT, no melting or any clear phase transition was observed upon heating to 300 °C. Upon cooling we identified the glass transition temperature (T_g) of F8TTBTT and F8TBT to be located at approximately 110 °C (see Supplementary Data Fig. S2). In both polymers similar morphology displaying nodule-like structures was observed using atomic force microscopy (AFM) on films of either as-spun or annealed (above T_g) conditions (Fig. S3). Summary of the material characteristics of F8TTBTT and F8TBT in terms of molecular weight, optical properties, thermal behavior and microstructure is tabulated in Table 1.

Table 1
Summary of molecular weight and polydispersity index, thin film optical characteristics from AC-2, UV–Vis, PLQE measurements, thermal characteristics from modulated differential scanning calorimetry (MDSC), and thin film structural characteristics from θ–2θ X-ray diffraction.

Material	M_n (g/mol)	M_w/M_n	HOMO (eV)	$E_{g,\ optical}$ (nm)	PLQE (%)	T_{glass} (°C)	θ–2θ XRD
F8TTBTT	33,000	1.93	−5.45	660	11	113	Amorphous
F8TBT	167,000	1.2	−5.62	610	22	111	Amorphous

3.2. Thin film field-effect transistor characterization

We employed a top-gate/bottom-contact (TGBC) device configuration with lithographically patterned gold source/drain electrodes for all FETs studied in this work (Fig. 1c). Such a device structure has been shown to lower contact resistance and allows greater flexibility to use different dielectric to reduce charge trapping [14,32]. The unipolar parts of the transfer characteristics were used to extract threshold voltages V_{th} and saturation field-effect mobilities μ [16,33], by applying

$$I_d^{sat} = \frac{WC_i}{2L}\mu_h(V_g - V_{th,h})^2 \text{ for holes} \quad (1)$$

$$I_d^{sat} = \frac{WC_i}{2L}\mu_e((V_g - V_{ds}) - V_{th,e})^2 \text{ for electrons} \quad (2)$$

Here, W is the channel width, L the channel length, I_d^{sat} the source–drain current in saturation, V_g the gate voltage, and C_i the capacitance per unit area of the gate dielectric. PMMA ($\varepsilon = 3.6$) was used as the dielectric for all FETs studied in this work since it contains very few electron-trapping groups thus allowing ambipolar charge transport [14,16,33].

FETs fabricated from as-spun F8TTBTT showed clear ambipolar characteristics exhibiting saturation hole mobility $\mu_h \sim 2 \times 10^{-2}$ cm^2 V^{-1} s^{-1} and electron mobility μ_e in the range of 1×10^{-3}–4×10^{-3} cm^2 V^{-1} s^{-1} for devices of channel length $L = 20$ or 40 μm (Fig. 2a and b). The highest μ_h was observed to be 5×10^{-2} cm^2 V^{-1} s^{-1} on a $L = 10$ μm as-spun F8TTBTT-based FET (device characteristics see Fig. S4). In comparison, as-spun F8TBT FETs (Fig. 2b) studied in this work showed much lower field-effect mobilities (μ_h up to 1.5×10^{-3} cm^2 V^{-1} s^{-1}, and μ_e up to 4×10^{-5} cm^2 V^{-1} s^{-1}), in good agreement with those previously reported for F8TBT FETs [16]. This is in spite of the higher molecular weight and lower PDI of the F8TBT polymer, which should have a tendency to increase the electron and holes mobilities [34]. Previous studies on as-spun and annealed F8BT FETs suggested that annealing polymer films close to or above their melting temperature in the range of 250–290 °C can significantly improve the ambipolar transistor performance and reduce threshold voltages [33]. In this work we also studied FETs fabricated from polymer films annealed at 260 °C. As shown in Fig. 2b, FET performances based on annealed F8TTBTT films are qualitatively the same as FETs fabricated by as-spun films. On the other hand, annealing F8TBT films at 260 °C did significantly improve the electron mobility and electron threshold voltage compared to the as-spun case. The mobility and threshold voltage values of as-spun/annealed F8TTBTT and F8TBT FETs are summarized in Table 2.

From Table 2 it is evident that the polymer F8TTBTT shows much enhanced ambipolar field-effect mobilities compared to F8TBT (in either as-spun or annealed condition). In fact, compared to various reported polyfluorene derivatives [4], F8TTBTT FETs exhibit a remarkably high hole mobility, even without undertaking additional efforts to induce chain alignment. This mobility improvement compared to F8TBT can be understood considering the following factors:

(1) For *p*-channel operation, improvement of hole injection is apparent when comparing the output characteristics of FETs from these two material systems (Fig. 2c and e). Besides the overall increased output current levels, the drain current of F8TTBTT FETs is less suppressed at low source–drain voltages in the output characteristics, indicating reduced contact resistance. This improvement can be understood as a result of the reduced difference between the HOMO level and the work function of gold in F8TTBTT compared to F8TBT (Fig. 1b). In addition, as previously discussed in the cases of F8BT and F8TBT [12,16,29], holes are expected to delocalize along the polymer backbone whereas electrons are largely localized on the BT unit. Besides charge injection, by adding thiophene units on the polymer backbone in F8TTBTT, the conjugation length for hole transport is further increased and this is likely to contribute to the observed, more efficient hole transport.

(2) For *n*-channel operation, a priori, we had expected less efficient electron transport in F8TTBTT compared to F8TBT due to the increased distance between BT units, on which the electron wavefunction is likely to be localized, but the opposite situation was observed. One potential reason for this is suggested by comparing the output characteristics (Fig. 2d and f). The electron contact resistance in F8TTBTT FETs seems to be slightly better than in F8TBT FETs. As the LUMO levels between these two materials are approximately the same, the slight improvement in electron injection in F8TTBTT may be due to a different polymer microstructure at the polymer–metal interface [35] or a slightly different extent of LUMO localization between the two materials. A second factor for the improved electron mobility could be an increased backbone planarity, leading to somewhat lower degree of electron localization on the BT unit, and enhanced interchain interactions and more compact packing of the polymer chains in F8TTBTT. These aspects are further studied below using Raman spectroscopy. We note that the enhanced mobility is observed in spite of a larger electron threshold voltage of F8TTBTT, which is most likely due to more electron trapping by impurity and/or chain-end defects, as suggested by the molecular weight of F8TTBTT studied in this work, which is at present still lower than that achieved by the more optimized synthesis of F8TBT.

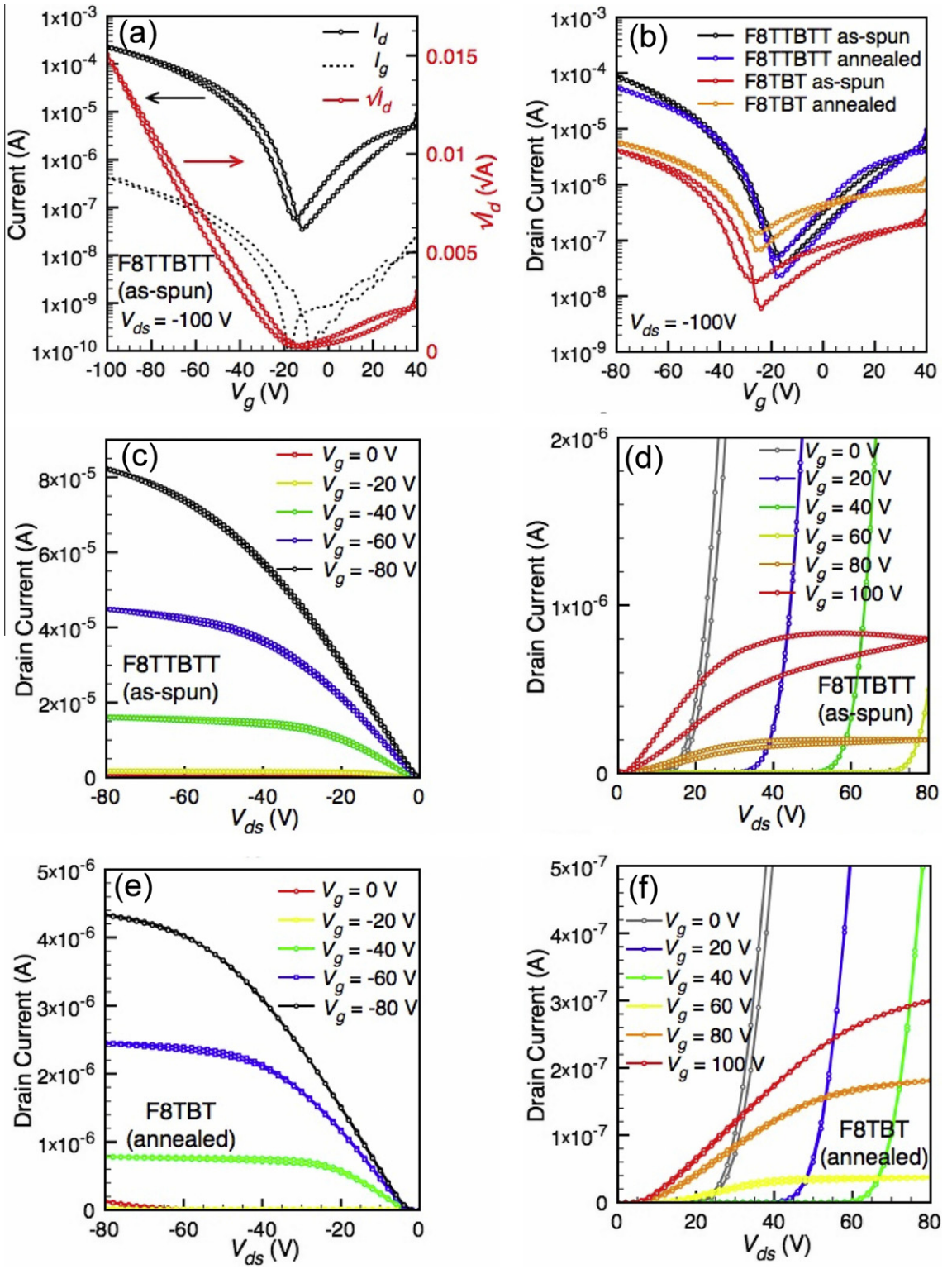

Fig. 2. (a) Transfer characteristics of an as-spun F8TTBTT FET (drain current: I_d, leakage current: I_g, and the square root of drain current: $\sqrt{I_d}$, W/L = 500, L = 20 μm). (b) Comparison of the transfer characteristics of as-spun and annealed (at 260 °C) F8TTBTT and F8TBT FETs (W/L = 500, L = 40 μm). (c, d) Output characteristics of an as-spun F8TTBTT FET (the same FET as shown in (b)). (e, f) Output characteristics of an annealed F8TBT FET (the same device as shown in (b)). All FETs in this figure were fabricated with ~550 nm-thick PMMA as the gate dielectric (capacitance C_i = 6.2 nF cm^{-2}).

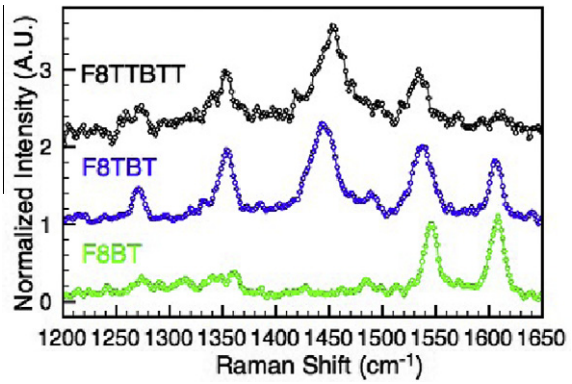

Fig. 3. Normalized Raman spectra (785 nm excitation) of as-spun films of F8TTBTT, F8TBT and F8BT. Spectra have been offset for clarity.

3.3. Raman spectroscopy

In order to gain further insight into the understanding of the enhanced mobilities in F8TTBTT compared to F8TBT, we used Raman spectroscopy to probe the vibrational modes in these materials and study their conformations. For this purpose, Raman spectroscopy is a powerful technique and has been widely used in many conjugated polymer systems [12,36–39]. In particular, combined with density functional theory (DFT) calculations, increased conformational planarization in F8BT (induced by pressure effects) has been shown to result in an increased I_{1545}/I_{1608} Raman intensity ratio [38], where the 1545 cm^{-1} peak corresponds to the BT ring-stretching mode and 1608 cm^{-1} to the ring-stretching mode for the F8 units [12,36,38].

Fig. 3 shows the Raman spectra obtained from approximately 100 nm-thick films of as-spun F8TTBTT and F8TBT on gold-coated glass substrates (gold layer thickness ~30 nm). Experiments on quartz spectrosil substrates revealed identical spectra (Fig. S5) but the use of gold-coated substrates provides a better signal-to-noise ratio due to signal enhancement. For a better comparison, we also include a Raman spectrum obtained from an approximately 100 nm-thick film of F8BT (Fig. 3). The F8BT spectrum is in very good agreement with previously reported Raman spectra for this material [12,36,38,39]. In all three spectra shown in Fig. 3 we can assign the 1545 cm^{-1} peak to the BT ring-stretching mode and the 1608 cm^{-1} peak to the ring-stretching mode of the F8 units. The peak around 1450 cm^{-1}, clearly present in F8TTBTT and F8TBT but not in F8BT, is due to the C=C stretching of the thiophene [37,40]. In the wave number region between 1250 and 1400 cm^{-1}, in F8BT there should be four peaks around 1280, 1315, 1342, and 1358 cm^{-1} as previously reported [12,39]. The peak around 1280 cm^{-1} may be due to the C–C stretch between phenylene rings [41]. The 1315 and 1342 cm^{-1} peaks have been previously assigned to C–C and C–H stretches within the F8 unit, whereas the 1358 cm^{-1} peak can be attributed to the C–C stretch involving the two carbon atoms common to the benzene ring and the thiadiazole unit in the BT. However, we were not able to resolve these four peaks clearly in our F8BT reference film. For F8TTBTT and F8TBT there are two more easily resolved peaks in this spectral range, centered around 1280 cm^{-1} and 1353 cm^{-1}, respectively.

As shown in Fig. 3, a notable increased intensity ratio of I_{1545}/I_{1608} was observed in F8TTBTT compared to F8TBT and F8BT. Similar increased intensity ratio of the BT ring-stretching mode (at 1545 cm^{-1}) over the ring-stretching mode for the F8 units (1608 cm^{-1}) was previously experimentally observed in F8BT thin films upon application of pressure [38]. A decreased F8-BT torsional angle and the resultant increased coupling of the BT ring-stretching mode to the electronic HOMO–LUMO transition in the planar structure were identified as the origin for this on the basis of theoretical calculations. In analogy to this study on F8BT, our Raman results suggest that the incorporation of more thiophene units on the polymer backbone of F8TBT also leads to increased planarization of the polymer backbone.

Furthermore, the peak corresponding to the C=C stretching of the thiophene at around 1450 cm^{-1} is slightly shifted to higher frequency ($\Delta \sim 5$ cm^{-1}) in F8TTBTT compared to F8TBT. Previous Raman studies in oligothiophene reported two mechanisms to explain the frequency shift of this mode [37]. On one hand, conformational ordering and longer conjugation length will cause a red-shift in this C=C stretching mode. On the other hand, increased intermolecular interactions (e.g. due to smaller intermolecular distance) will result a blue-shift in this mode. When both situations are simultaneously present, the effect from intermolecular interactions was found to be dominating [37]. Similar blue-shift in this Raman mode due to increased intermolecular interactions was observed in sexithiophene single crystals with applied pressure [42]. An analogous dependence was also observed in polyacetylene with increasing pressure [43,44]. Studies of *in situ* heated oligothiophene thin films reported a red-shift in this Raman mode due to *decreased* intermolecular interactions (upon lattice expansion) compared to room-temperature samples [37]. Therefore, our Raman results also suggest stronger intermolecular interactions and more compact chain-packing in F8TTBTT compared to F8TBT.

The Raman results are overall consistent with our optical and field-effect mobility measurements in F8TTBTT and

Table 2
Summary of saturation field-effect mobilities μ and threshold voltages of F8TTBTT and F8TBT FETs studied in this work.

Materials	μ_h (cm^2 V^{-1} s^{-1})	μ_e (cm^2 V^{-1} s^{-s})	$V_{th,h}$ (V)	$V_{th,e}$ (V)
F8TTBTT[a]	2×10^{-2}–5×10^{-2}	1×10^{-3}–4×10^{-3}	~−20	~65
F8TBT (as-spun)	1×10^{-3}–1.5×10^{-3}	3×10^{-5}–4×10^{-5}	~−22	~55
F8TBT (annealed)	1.5×10^{-3}–2×10^{-3}	1×10^{-4}–2×10^{-4}	~−20	~30

[a] No clear difference in terms of mobilities and threshold voltages was observed between F8TTBTT FETs fabricated from as-spun films and annealed films at 260 °C (see Fig. 2b). Thus their characteristics are not tabulated separately.

F8TBT. The increased conformational planarization in F8TTBTT leads to more extended conjugation length for holes transport. Since electron transport in both systems is likely to rely mainly on interchain hopping, the increased intermolecular interactions in F8TTBTT will result in more efficient electron transport as well. Note that a previous study in semi-crystalline F8BT speculated that worse electron transport might result if backbone planarization is associated with a change in packing geometry, i.e., in the relative positions of BT units between adjacent chains [12]. However, our current systems of F8TTBTT and F8TBT are both amorphous, and it appears unlikely that backbone planarization could result in a specific packing geometry unfavorable for electron transport. Instead, we believe that the dominant effects is that more compact chain-packing in F8TTBTT facilitates interchain hopping and enhances both electron and hole transport.

3.4. Light-emission during the F8TTBTT FET operation

As a consequence of efficient ambipolar charge transport, F8TBT has been shown to emit red light during transistor operation [16,23]. Similarly, we also expect light emission from F8TTBTT FETs due to its ambipolar characteristics. Employing a very thin semi-transparent gold gate in the same FET structure shown in Fig. 1c, we were able to observe a deep-red light emission during the operation of F8TTBTT FETs (Fig. 4a and b). Due to the imbalanced hole and electron mobility and the relatively large electron threshold voltage, the light-emission zone is very close to the electron-injecting electrode for a wide range of bias conditions. By placing an optical fiber connected to a spectrometer directly on top of the metal top gate, we recorded the electroluminescence from F8TTBTT, which is slightly blue-shifted from its PL (Fig. 4c). This mismatch may be due to interference effects, and/or polaron absorption below the band gap. By placing a silicon photodiode directly on top of the FET metal gate, we measured the photocurrents I_{ph} simultaneously with the transfer I–V curve (Fig. 4d). From the ratio between the photocurrent and the drain current, taking into account the photodiode sensitivity [45], we estimated the EQE of F8TTBTT light-emitting transistors to be up to ~0.2% (Fig. 4d). The EQE values from the F8TTBTT FETs are within the same order of magnitude but slightly lower than those reported in F8TBT (up to ~0.4%) [16], which can be understood as the combined consequence from the relatively lower PLQE, imbalanced ambipolar mobilities, and larger electron threshold voltage found in F8TTBTT.

3.5. F8TTBTT:PCBM blend bulk heterojunction (BHJ) solar cells

Since F8TTBTT shows much higher field-effect mobility for hole transport compared to F8TBT and an absorption range further extended to lower energy, it can be potentially interesting for photovoltaic applications. We fabricated BHJ solar cells by blending F8TTBTT (as the hole transporting phase) with PCBM (as the electron transporting phase). In this work the best solar cell performance was obtained from a F8TTBTT:PCBM blend of 1:4 weight ratio and a ~80 nm-thick active layer. Fig. 5 shows the EQE (recorded at low light intensity) and current–density–voltage (J–V) characteristics (under 100 mW/cm^2 simulated AM 1.5 global illumination) of as-spun and annealed F8TTBTT:PCBM devices. As-spun solar cells exhibit decent photovoltaic operation, demonstrating ~25% in EQE (at 550 nm) and 1.54% in power conversion efficiency (PCE). Our current result is comparable to the solar cell performance recently reported on polymers of similar structure but different side-chains [25]. Detailed summary of the F8TTBTT:PCBM solar cell J–V characteristics is shown in Table 3.

Previous solar cell reports on other material systems often reported improved performance by post-annealing (annealing after electrode evaporation) [2,23]. Such improvements may be due to either improving the transport properties of the active material by annealing or inducing more favorable blend morphology, for example, by inducing more efficient percolation pathways. Attempts to anneal our solar cells led to significantly worse performance (Fig. 5). As presented above, as-spun F8TTBTT already showed relatively high field-effect mobilities which

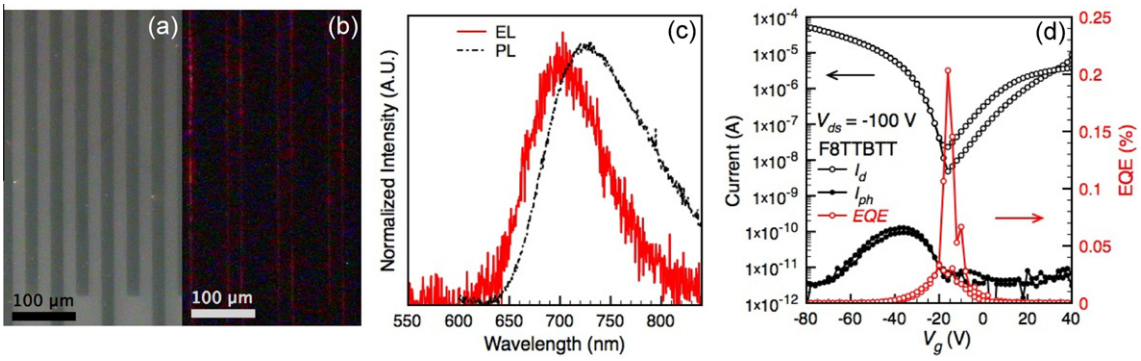

Fig. 4. (a) Digital camera image of an F8TTBTT FET under illumination showing source and drain electrodes (W/L = 500, L = 20 μm). (b) The digital camera image of the same FET at the same position as (a) recorded in the dark and under the bias condition of V_{gs} = −200 V, V_{ds} = −300 V. (c) Electroluminescence (EL) spectra of a light-emitting F8TTBTT FET recorded under the bias condition of V_{gs} = −100 V, V_{ds} = −200 V. (d) Transfer characteristics of an light-emitting F8TTBTT FET and corresponding photocurrent measured with a photodiode mounted on top of the device and the calculated external quantum efficiencies (EQE).

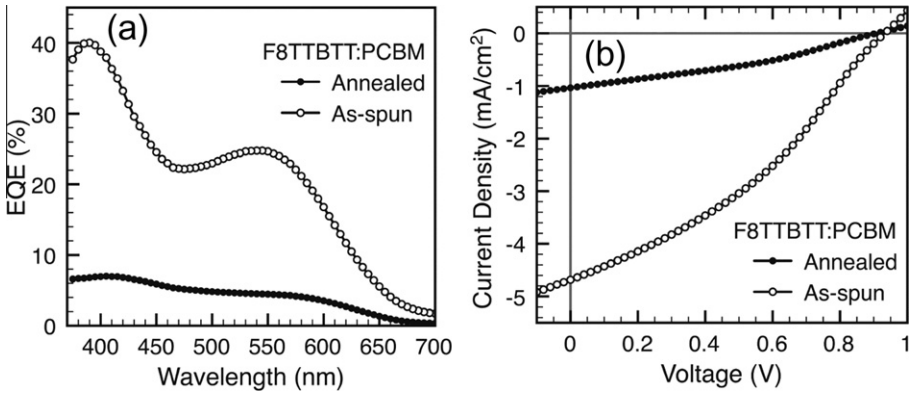

Fig. 5. (a) External quantum efficiency (EQE) and (b) current–voltage characteristics (under 100 mW/cm^2 simulated AM1.5G illumination) of F8TTBTT:PCBM-based solar cells for as-spun and annealed (150 °C) conditions.

Table 3
Summary of the current–voltage characteristics of the F8TTBTT:PCBM solar cells under illumination from solar simulator (AM 1.5 global, 100 mW/cm^2).

Conditions	J_{sc} (mA/cm^2)	V_{oc} (V)	Fill factor	PCE (%)
As-spun	4.7	0.93	0.35	1.54
Annealed[a]	1.1	0.87	0.34	0.32

[a] Annealing was performed after aluminum electrode evaporation and annealing temperature was 150 °C.

did not further increase with annealing. As annealing will not lead to more efficient charge transport, even a slight grain coarsening upon annealing would lead to reduced performance because fewer interfaces are available for exciton dissociation.

Reports on F8TBT:PCBM solar cells presented power conversion efficiency (under AM 1.5 illumination) ranging from 1.25% to 2.8% [22,23,46,47]. Even though not yet fully optimized, the overall performance of our as-spun F8TTBTT:PCBM solar cells are comparable to that reported for F8TBT:PCBM solar cells. Further performance optimization is likely to be achievable through the use of different solvents to optimize blend morphology, other electrodes for more efficient charge collections and F8TTBTT polymers with higher molecular weight and reduced PDI. Moreover, since F8TTBTT exhibits good ambipolar charge transport characteristics with enhanced electron mobilities over F8TBT, it also appears as a promising acceptor phase in polymer:polymer blend solar cells.

4. Conclusion

We have studied the comparison between two donor–acceptor polymers F8TTBTT and F8TBT in terms of optical properties, structure and morphology and ambipolar field-effect transistor performance. The incorporation of more thiophene units on the polymer backbone leads to smaller optical band gap (by destabilization of HOMO levels) and a more planar backbone conformation. Compared to F8TBT, F8TTBTT exhibits more efficient charge injection due to the reduced ionization potential and improved ambipolar mobilities, most likely as a result of the more planar backbone configuration and more compact chain-packing. Ambipolar F8TTBTT FETs exhibit deep-red light emission from within the transistor channel. Even though not fully optimized, F8TTBTT:PCBM solar cells were demonstrated to show comparable performance to F8TBT:PCBM devices.

Acknowledgements

This work was partly funded by The EPSRC Nanotechnology Grand Challenges: Energy programme (EP/F056702/1), The Basic Technology Research Grant Initiative COSMOS (EP/D04894X/1), and by the EU through the EC FP7 ONE-P large-scale collaborative project no. 212311. Z.C. is grateful to the help of Dr. J. Oguma (Cambridge Display Technology Ltd.) in AC-2 photoelectron spectroscopy measurements and helpful discussions. We acknowledge the assistance of Cambridge Display Technology Ltd. for the F8BT polymer used in our Raman study.

Appendix A. Supplementary data

Supplementary data associated with this article can be found, in the online version, at doi:10.1016/j.orgel.2010.12.009.

References

[1] I. McCulloch, M. Heeney, M. Chabinyc, L.D. DeLongchamp, J. Kline, R.M. Cölle, W. Duffy, D. Fischer, D. Gundlach, B. Hamadani, R. Hamilton, L. Richter, A. Salleo, M. Shkunov, D. Sparrowe, S. Tierney, W. Zhang, Semiconducting thienothiophene copolymers: design, synthesis, morphology, and performance in thin-film organic transistors, Adv. Mater. 21 (2009) 1091–1109.
[2] C.R. McNeill, N.C. Greenham, Conjugated-polymer blends for optoelectronics, Adv. Mater. 21 (2009) 3840–3850.
[3] J. Peet, M.L. Senatore, A.J. Heeger, G.C. Bazan, Heterojunction solar cells: the role of processing in the fabrication and optimization of plastic solar cells, Adv. Mater. 21 (2009) 1521–1527.
[4] J. Zaumseil, H. Sirringhaus, Electron and ambipolar transport in organic field-effect transistors, Chem. Rev. 107 (2007) 1296–1323.
[5] H. Pan, Y. Li, Y. Wu, P. Liu, B. Ong, S. Zhu, G. Xu, Synthesis and thin-film transistor performance of poly(4, 8-didodecylbenzo[1, 2-b:4, 5-b]dithiophene), Chem. Mater. 18 (2006) 3237–3241.

[6] D.M. DeLongchamp, R.J. Kline, Y. Jung, D.S. Germack, E.K. Lin, A.J. Moad, L.J. Richter, M.F. Toney, M. Heeney, I. McCulloch, Controlling the orientation of terraced nanoscale "ribbons" of a poly(thiophene) semiconductor, ACS Nano 3 (2009) 780–787.
[7] H. Yan, Z. Chen, Y. Zheng, C. Newman, J.R. Quinn, F. Dötz, M. Kastler, A. Facchetti, A high-mobility electron-transporting polymer for printed transistors, Nature 457 (2009) 679–687.
[8] H. Sirringhaus, R.J. Wilson, R.H. Friend, M. Inbasekaran, W. Wu, E.P. Woo, M.D. Grell, D.C. Bradley, Mobility enhancement in conjugated polymer field-effect transistors through chain alignment in a liquid-crystalline phase, Appl. Phys. Lett. 77 (2000) 406–408.
[9] S. Shaked, S. Tal, Y. Roichman, A. Razin, S. Xiao, Y. Eichen, N. Tessler, Charge density and film morphology dependence of charge mobility in polymer field-effect transistors, Adv. Mater. 15 (2003) 196–913.
[10] J. Veres, S.D. Ogier, S.W. Leeming, D.C. Cupertino, S.M. Khaffaf, Insulators as the choice of dielectrics in organic field-effect transistors, Adv. Funct. Mater. 13 (2003) 199–204.
[11] L.L. Chua, J. Zaumseil, J.F. Chang, E.C.W. Ou, P.K.H. Ho, H. Sirringhaus, R.H. Friend, General observation of N-type field-effect behaviour in organic semiconductors, Nature 434 (2005) 194–199.
[12] C.L. Donley, J. Zaumseil, J.W. Andreasen, M.M. Nielsen, H. Sirringhaus, R.H. Friend, J.S. Kim, Effects of packing structure on the optoelectronic and charge transport properties in poly(9,9-di-n-octylfluorene-alt-benzothiadiazole), J. Am. Chem. Soc. 127 (2005) 12890–12899.
[13] T.D. Anthopoulos, D.M. de Leeuw, E. Cantatore, S. Setayesh, E.J. Meijer, C. Tanase, J.C. Hummelen, P.W.M. Blom, Organic complementary-like inverters employing methanofullerene-based ambipolar field-effect transistors, Appl. Phys. Lett. 85 (2004) 4205–4207.
[14] Z. Chen, H. Lemke, S. Albert-Seifried, M. Caironi, M.M. Nielsen, M. Heeney, W. Zhang, I. McCulloch, H. Sirringhaus, High mobility ambipolar charge transport in polyselenophene conjugated polymers, Adv. Mater. 22 (2010) 2371–2375.
[15] J.S. Swensen, C. Soci, A.J. Heeger, Light emission from an ambipolar semiconducting polymer field-effect transistor, Appl. Phys. Lett. 87 (2005) 3.
[16] J.C. Zaumseil, R. McNeill, M. Bird, D.L. Smith, P.R. Ruden, M.M. Roberts, M.J. McKiernan, R.H. Friend, H. Sirringhaus, Quantum efficiency of ambipolar light-emitting polymer field-effect transistors, J. Appl. Phys. 103 (2008) 064517.
[17] R. Capelli, S. Toffanin, G. Generali, H. Usta, A. Facchetti, M. Muccini, Organic light-emitting transistors with an efficiency that outperforms the equivalent light-emitting diodes, Nat. Mater. 9 (2010) 496–503.
[18] Y. Cheng, J.S. Yang, H.C. Hsu, Synthesis of conjugated polymers for organic solar cell applications, Chem. Rev. 109 (2009) 5868–5923.
[19] Q. Hou, Y. Xu, W. Wang, M. Yuan, J. Peng, Y. Cao, Novel red-emitting fluorene-based copolymers, J. Mater. Chem. 12 (2002) 2887–2892.
[20] Q. Hou, Q. Zhou, Y. Zhang, W. Yang, R. Yang, Y. Cao, Synthesis and electroluminescent properties of high-efficiency saturated red emitter based on copolymers from fluorene and 4,7-di(4-hexylthien-2-yl)-2,1,3-benzothiadiazole, Macromolecules 37 (2004) 6299–6305.
[21] M. Svensson, F. Zhang, S.C. Veenstra, W. Verhees, J.C. Hummelen, J.M. Kroon, O. Inganäs, M.R. Andersson, High-performance polymer solar cells of an alternating polyfluorene copolymer and a fullerene derivative, Adv. Mater. 15 (2003) 988–991.
[22] O. Inganäs, M. Svensson, F. Zhang, A. Gadisa, N.K. Persson, X. Wang, M. Andersson, Low bandgap alternating polyfluorene copolymers in plastic photodiodes and solar cells, Appl. Phys. A 79 (2004) 31–35.
[23] C.R. McNeill, A. Abrusci, J. Zaumseil, R. Wilson, M.J. McKiernan, J.H. Burroughes, et al., Dual electron donor/electron acceptor character of a conjugated polymer in efficient photovoltaic diodes, Appl. Phys. Lett. 90 (2007) 193506.
[24] B. Friedel, C.R. McNeill, N. Greenham, Influence of alkyl side-chain length on the performance of poly(3-alkylthiophene)/polyfluorene all-polymer solar Cells, Chem. Mater. 22 (2010) 3389–3398.
[25] E. Wang, M. Wang, L. Wang, C. Duan, J. Zhang, W. Cai, C. He, H. Wu, Y. Cao, Donor polymers containing benzothiadiazole and four thiophene rings in their repeating units with improved photovoltaic performance, Macromolecules 42 (2009) 4410–4415.
[26] X. He, F. Gao, G. Tu, D. Hasko, S. Hüttner, U. Steiner, et al., Formation of nanopatterned polymer blends in photovoltaic devices, Nano Lett. 10 (2010) 1302–1307.
[27] M. Ranger, D. Rondeau, M. Leclerc, New well-defined poly(2,7-fluorene) derivatives: photoluminescence and base doping, Macromolecules 30 (1997) 7686–7691.
[28] J.C. de Mello, H.F. Wittmann, R.H. Friend, An improved experimental determination of external photoluminescence quantum efficiency, Adv. Mater. 9 (1997) 230–232.
[29] K.G. Jespersen, W.J.D. Beenken, Y.A. Zaushitsyn, A. Yarsev, M. Andersson, T. Pullerits, V. Sundström, The electronic states of polyfluorene copolymers with alternating donor-acceptor units, J. Chem. Phys. 121 (2004) 12613–12617.
[30] T.Q. Nguyen, V. Doan, B.J. Schwartz, Conjugated polymer aggregates in solution: control of interchain interactions, J. Chem. Phys. 110 (1999) 4068–4078.
[31] C. Müller, E. Wang, M.L. Andersson, K. Tvingstedt, Y. Zhou, M.R. Andersson, O. Inganäs, Influence of molecular weight on the performance of organic solar cells based on a fluorene derivative, Adv. Funct. Mater. 20 (2010) 2124–2131.
[32] R.A. Street, A. Salleo, Contact effects in polymer transistors, Appl. Phys. Lett. 81 (2002) 2887–2889.
[33] M.C. Gwinner, S. Khodabakhsh, H. Giessen, H. Sirringhaus, Simultaneous optimization of light gain and charge transport in ambipolar light-emitting polymer field-effect transistors, Chem. Mater. 21 (2009) 4425–4433.
[34] J.R. Kline, M.D. Mcgehee, E.N. Kadnikova, J. Liu, J.M.J. Fréchet, M.F. Toney, Dependence of regioregular poly(3-hexylthiophene) film morphology and field-effect mobility on molecular weight, Macromolecules 38 (2005) 3312–3319.
[35] X. Cheng, Y.Y. Noh, J. Wang, M. Tello, J. Frisch, R.P. Blum, A. Vollmer, J.P. Rabe, N. Koch, H. Sirringhaus, Controlling electron and hole charge injection in ambipolar organic field-effect transistors by self-assembled monolayers, Adv. Funct. Mater. 19 (2009) 2407–2415.
[36] J.S. Kim, P.K.H. Ho, C.E. Murphy, R.H. Friend, Phase separation in polyfluorene-based conjugated polymer blends: lateral and vertical analysis of blend spin-cast thin films, Macromolecules 37 (2004) 2861–2871.
[37] A. Milani, L. Brambilla, M.D. Zoppo, G. Zerbi, Raman dispersion and intermolecular interactions in unsubstituted thiophene oligomers, J. Phys. Chem. B 111 (2007) 1271–1276.
[38] J.P. Schmidtke, J.S. Kim, J. Gierschner, C. Silva, R.H. Friend, Optical spectroscopy of a polyfluorene copolymer at high pressure: intra- and intermolecular interactions, Phys. Rev. Lett. 99 (2007) 167401.
[39] J.M. Winfield, C.L. Donley, R.H. Friend, J.S. Kim, Thin-film morphology of conjugated polymers by Raman spectroscopy, J. Appl. Phys. 107 (2010).
[40] M. Trznadel, M. Zagórska, M. Lapkowski, G. Louarn, S. Lefrant, A. Pron, UV–VIS–NIR and Raman spectroelectrochemistry of regioregular poly(3-octylthiophene): comparison with its non-regioregular analogue, J. Chem. Soc., Faraday Trans. 92 (1996) 1387–1393.
[41] M. Ariu, D.G. Lidzey, D.D.C. Bradley, Influence of film morphology on the vibrational spectra of dioctyl substituted polyfluorene (PFO), Synth. Met. 111-112 (2000) 607–610.
[42] M.A. Loi, Q. Cai, H.R. Chandrasekhar, M. Chandrasekhar, W. Graupner, G. Bongiovanni, A. Mura, C. Botta, F. Garnier, High pressure study of the intramolecular vibrational modes in sexithiophene single crystals, Synth. Met. 116 (2001) 321–326.
[43] Y. Yacoby, S. Roth, Resonant Raman scattering in polyacetylene under hydrostatic pressure, Solid State Commun. 56 (1985) 319–322.
[44] N.M. Balzaretti, C.A. Perottoni, J.A.H. de Jornada, High-pressure Raman and infrared spectroscopy of polyacetylene, J. Raman Spectrosc. 34 (2003) 259–263.
[45] J.F. Chang, M. Gwinner, C.M. Caironi, T. Sakanoue, H. Sirringhaus, Conjugated-polymer-based lateral heterostructures defined by high-resolution photolithography, Adv. Funct. Mater. 26 (2010). Published online, doi:10.1002/adfm.201000436.
[46] C. Shi, Y. Yao, Y. Yang, Q. Pei, Regioregular copolymers of 3-alkoxythiophene and their photovoltaic application, J. Am. Chem. Soc. 128 (2006) 8980–8986.
[47] F. Zhang, K.G. Jespersen, C. Björström, M. Svensson, M.R. Andersson, V. Sundström, K. Magnusson, E. Moons, A. Yartsev, O. Inganäs, Influence of solvent mixing on the morphology and performance of solar cells based on polyfluorene copolymer/fullerene blends, Adv. Funct. Mater. 16 (2006) 667–674.

Organic Electronics 12 (2011) 472–476

Contents lists available at ScienceDirect

Organic Electronics

journal homepage: www.elsevier.com/locate/orgel

Close-packed hemispherical microlens arrays for light extraction enhancement in organic light-emitting devices

Sang-Hyun Eom, Edward Wrzesniewski, Jiangeng Xue *

Department of Materials Science and Engineering, University of Florida, Gainesville, FL 32611-6400, USA

ARTICLE INFO

Article history:
Received 11 August 2010
Received in revised form 26 December 2010
Accepted 31 December 2010
Available online 13 January 2011

Keywords:
Microlens
Soft lithography
Organic light-emitting diode
Light extraction efficiency

ABSTRACT

Close-packed hemispherical microlens arrays have been fabricated using a soft lithography method and used to enhance the light extraction efficiency in organic light-emitting devices (OLEDs). A close-packed monolayer of polystyrene microspheres was used to produce a soft template of polydimethylsiloxane for fabricating microlens arrays from a photopolymerizable optical adhesive. The microlens contact angle and array fill-factor increase with the polystyrene microsphere size, reaching (85° ± 5°) and (85 ± 3)% for 100 μm size microspheres, respectively. Attaching such a large-area (2 cm in diameter) microlens array on the glass substrate of an OLED leads to up to 70% efficiency enhancement, which also shows dependencies on the area and detailed structure of the OLED.

© 2011 Elsevier B.V. All rights reserved.

1. Introduction

Organic light-emitting devices (OLEDs) have important application in flat-panel displays and as solid-state lighting sources [1]. Many advances in material development and device structure innovations have led to the demonstration of high efficiency and long-lived monochromatic or white OLEDs [2–5]. A significant issue limiting the further improvement in device efficiency lies in the relatively low light extraction or outcoupling efficiency, η_{out}, which is typically ~20% due to the total internal reflection (TIR) losses at multiple interfaces of planar OLEDs [6]. Several different methods have been reported in order to improve η_{out}, such as using a photonic crystal [7], embedded low-index grids [8], or a resonant cavity [9]. However, these methods typically require complicated and expensive fabrication processes, modification of active layer structure, and/or insertion of additional layers between the substrate and the transparent indium-tin oxide (ITO) anode. Microlens arrays directly deposited on the light-emitting surface of the glass substrate can be more easily integrated with the OLED fabrication, offering a potentially effective, yet low cost light extraction enhancing mechanism. There have been several previous reports on microlens array fabrication, such as using photolithography and wet-etching of silicon substrate for microlens mold [10], melting self-assembled polystyrene (PS) spheres on a pre-patterned substrate [11], liquid crystal droplet microlens [12], three-dimensional diffuser lithography for microlens mold [13], and ink-jet printed microlens [14]. Although Sun et al. recently improved the imprint lithography method obtaining η_{out} enhancement of (1.68 ± 0.09) [8,15], high-cost and complicated photolithography and wet-etching processes are considered as the inefficient fabrication steps for making a reproducible microlens mold.

Here, we demonstrate the fabrication of large-area (several square inches), close-packed hemispherical polymer microlens arrays using a soft lithography method, and the application of such microlens arrays for enhancing the light extraction efficiency in OLEDs. A close-packed monolayer of polystyrene (PS) microspheres was formed using a convective and capillary assembly [16], which was employed to generate a polydimethylsiloxane (PDMS) concave template for the fabrication of transparent microlens arrays based on a Norland optical adhesive (NOA). Similar templating methods have been previously used to produce microlens arrays from monolayer of sub-micron

* Corresponding author. Tel.: +1 352 846 3775; fax: +1 352 846 3355.
E-mail address: jxue@mse.ufl.edu (J. Xue).

1566-1199/$ - see front matter © 2011 Elsevier B.V. All rights reserved.
doi:10.1016/j.orgel.2010.12.021

or a few micron size PS spheres prepared by spin-coating, leading to microlenses with contact angles (θ_c) < 45° [17–18]. Here, we found that θ_c increases with the PS microsphere size (ϕ_{PS}), approaching hemispherical shape ($\theta_c \sim 85° \pm 5°$) for ϕ_{PS} = 100 μm. While close-packed monolayer of PS microspheres with such large sizes cannot be achieved over a large-area by spin-coating due to the strong centrifugal force, we have achieved that using the convective and capillary assembly method we employed here [16].

2. Experimental

Fig. 1 illustrates the fabrication procedures for the microlens arrays. PS microspheres in an aqueous solution were dispersed on a pre-cleaned [19] UV-ozone treated glass or SiO_2 substrate. Three different sizes of PS microspheres (ϕ_{PS} = 5, 20, and 100 μm, from Thermo Scientific) were used. A PS monolayer covering several square inches could be easily formed for 20 and 100 μm size PS microspheres, whereas it was much more challenging to generate a uniform, large-area monolayer using 5 μm size PS microspheres due to the increased domination of the capillary force. For a reproducible soft template of microlens arrays, PDMS (Sylgard 184, Dow Corning) was prepared with a 10:1 mixing ratio (base polymer:curing agent) and poured above the PS monolayer. Following thermal curing of PDMS for 2 h at 60 °C in a vacuum oven, the substrate was separated from the cured PDMS, and the PS microspheres embedded in PDMS was subsequently removed using scotch tapes leading to a concave PDMS mold. We used a NOA 61 (refractive index ~1.56 for the cured polymer) as the microlens material. With a few drops of NOA 61 on the concave surface of PDMS mold, the glass substrate of an OLED was placed on top without any additional pressure. After curing for 3 min under UV-light (365 nm, 200 mW/cm^2), the PDMS mold was then released leaving behind convex microlens arrays on the glass substrate of the OLED. The PDMS mold could be reused for many times without any breakage. Optical microscopy and scanning electron microscopy (SEM, JOEL 6335F) were used to characterize the geometry and surface topology of the PS microsphere array, the PDMS stamp, and the microlens array.

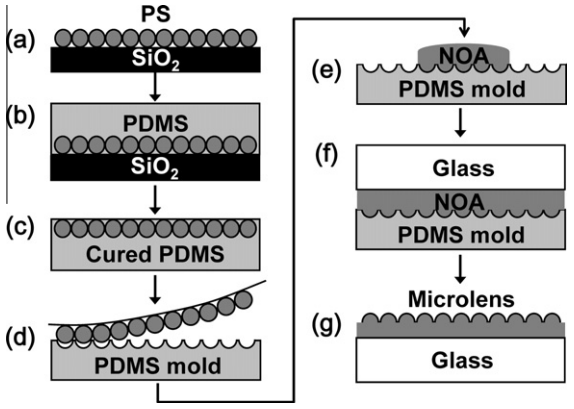

Fig. 1. Schematic illustration of fabrication procedures for hemispherical microlens arrays. See text for details.

Microlens arrays (fabricated from 20 or 100 μm PS spheres) covering a circle of approximately 2 cm in diameter were attached to the glass surface of OLEDs to examine light extraction efficiency enhancement. Both fluorescent and phosphorescent OLEDs (FOLEDs and PHOLEDs, respectively) have been fabricated on glass substrates commercially precoated with an indium-tin oxide (ITO) transparent anode (sheet resistance ~20 Ω/square). The FOLED structure was glass/ITO/N, *N*′-bis(naphthalen-1-yl)-*N*,*N*′-bis(phenyl)-benzidine (NPB, 60 nm)/tris(8-hydroxy-quinolinato) aluminum (Alq_3, 60 nm)/Cs_2CO_3(1 nm)/Al(100 nm), and the PHOLED structure was glass/ITO/NPB (40 nm)/8.0 wt.% *fac*-tris-(phenylpyridine) iridium [$Ir(ppy)_3$] doped 4,4′-*N*,*N*′-dicarbazole-biphenyl (CBP) (20 nm)/bathocuproine (BCP, 20 nm)/Alq_3 (40 nm)/Cs_2CO_3(1 nm)/Al(100 nm). The organic and cathode layers were sequentially evaporated in a custom-made vacuum thermal evaporator with a base pressure ~3×10^{-7} Torr. Two different sizes of OLEDs (small-area = 2×2 mm^2, large-area = 12×12 mm^2) in cross-bar electrode geometry were fabricated following procedures published elsewhere [3,19].

The η_{out} enhancement factor, *f*, was obtained using two different measurement methods. First, OLEDs (with and without microlens arrays) are aligned and attached to the entrance port of a Newport integrating sphere (819D 3-Port) and an Ocean Optics Jaz spectrometer is connected to the outlet port to measure the total luminous flux in the forward direction from the OLEDs, excluding the emission from the glass substrate edge. Only the light-emitting device area is opened toward the inside of an integrating sphere, while all the other non-emitting areas are completely blocked. The second method involves the direct measurement of the near-field emission intensity at the normal direction. An optical fiber (diameter = 400 μm) was positioned vertically within 1 mm of the light-emitting surface of the glass substrate, and the near-field optical intensity was recorded by the Ocean Optics Jaz spectrometer. The angular distribution of the luminous intensity for the OLEDs was also measured using a small-area Si spot photodetector at 10 cm away from the device (corresponding to a half angle of ~0.5°).

3. Results and discussion

Using 20 and 100 μm size PS microspheres, close-packed domains with size ranging from a few mm to over 1 cm can be observed and the total area could easily cover a few square inches. As shown in Fig. 2(a), there are imperfections at the domain boundaries and occasionally inside individual domains. A top-view of the concave PDMS mold (with ϕ_{PS} = 100 μm) near the edge of the array under the SEM is shown in Fig. 2(b), whereas the cross-sectional image in the inset of Fig. 2(b) clearly shows the hemispherical concave shape of the PDMS mold.

Fig. 3(a) shows an optical image of a hexagonally close-packed microlens array of ϕ_{PS} = 100 μm, and the smooth microlens surface is also revealed by the SEM image shown

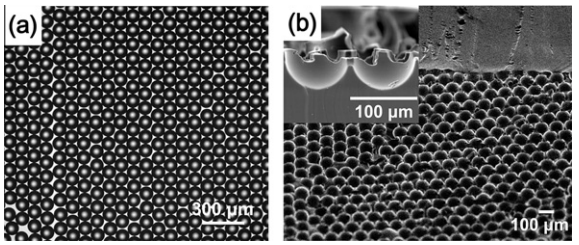

Fig. 2. (a) Optical microscope image of a part of a large-area polystyrene (PS) monolayer fabricated using 100 μm PS spheres. (b) Tilted scanning electron microscope (SEM) image of a concave PDMS template for 100 μm microlens arrays. PS spheres were completely removed by a scotch-tape. Inset: cross-sectional SEM image of the concave PDMS mold.

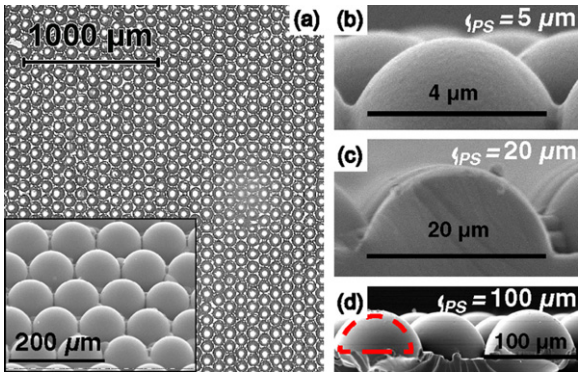

Fig. 3. (a) Optical microscope image of a part of a large-area microlens array fabricated using 100 μm PS spheres. Inset: tilted-view of the microlens array using a scanning electron microscope (SEM). Cross-sectional SEM images of microlenses with varying size of polystyrene spheres (ϕ_{PS}) are shown in (b–d). In (d), a semi-circle (dashed line) is drawn just inside the microlens contour for comparison.

in the inset of Fig. 3(a) (sample tilted). The measured fill factor (*FF*) of the microlens array is (85 ± 3)%, which is very close to the ideal *FF* of two-dimensional hexagonally close-packed spheres (91%). The same microlens fabrication method could be applied to different sizes of PS microspheres, however, θ_c of the microlenses is dependent on ϕ_{PS} as shown in the cross-sectional SEM images of Fig. 3(b)–(d). Here, θ_c was averaged over more than 10 microlenses, and summarized in Table 1 along with the average base size of the microlenses and the array fill factor. We obtained $\theta_c = (45° \pm 5°)$ with ϕ_{PS} = 5 μm, which is similar to previous reports [17–18]. As the ϕ_{PS} was increased to 20 and 100 μm, θ_c was increased to (65° ± 5°) and (85° ± 5°), respectively. From the cross-sectional SEM images shown in the Fig. 3(d) in which a semi-circle is drawn just inside the microlens contour, clearly hemispherical microlenses were achieved with ϕ_{PS} = 100 μm. We believe that this size dependence for θ_c is related to the mechanical robustness of the PDMS mold. When PDMS was poured onto the PS microspheres in order to make a concave template, it could completely cover the PS microspheres, penetrating all the way down to the SiO_2 surface through the interstitials among the microspheres, which after curing form columns connecting PDMS below and above the PS microspheres. For ϕ_{PS} = 100 μm, these columns are mechanically robust, and are broken at the narrowest neck area (corresponding to the horizontal plane through the center of the PS microspheres, see Fig. 1(d)) when the PS microspheres were removed from the thermally-cured PDMS using scotch tapes, resulting in hemispherical concave shapes on the PDMS mold. However, for smaller PS microspheres, the narrower PDMS columns were more easily torn off away from the narrowest neck area, resulting in concave shapes on the PDMS mold with height less than the PS microsphere radius, and in turn less than 90° contact angles for the microlenses. The smaller microlens base size (see Table 1) than the corresponding ϕ_{PS} also corroborates the above explanation.

Attaching microlens arrays to the glass substrates of OLEDs does not change the current density–voltage (*J–V*) characteristics, however, it does increase the total luminous flux (or luminance) at a given voltage. For small-area FOLEDs, for example, the peak external quantum efficiency η_{EQE} at J = 100 mA/cm^2 is increased from 0.75% for a bare device (without a microlens array attached) to 0.94% or 1.01% when 20 or 100 μm microlens array is attached to the OLED, respectively. This corresponds to a light extraction enhancement factor (*f*) of (1.25 ± 0.04) and (1.35 ± 0.04), respectively. It should be noted that *f* is virtually independent of the OLED operating condition (*J–V* characteristics), suggesting that the light extraction enhancement mechanism is purely attributed to the optical effect.

Table 1 also summarizes the different light extraction enhancements when microlens arrays were attached to the OLEDs in various situations, as obtained from the integrating sphere measurement method. Comparing microlens arrays for ϕ_{PS} = 20 and 100 μm, we have found that the larger PS microspheres lead to a higher *f* for the corresponding OLEDs in all cases. This is most likely attributed to the higher lens contact angle for ϕ_{PS} = 100 μm as the fill

Table 1
Comparison of the light extraction efficiency enhancement factor (*f*) for small-area (2 × 2 mm2) and large-area (12 × 12 mm^2) fluorescent and phosphorescent OLEDs (FLOEDs and PHOLEDs, respectively) using microlens arrays fabricated from different sizes of polystyrene microspheres (ϕ_{PS}). The actual microlens base diameter (ϕ_{lens}), contact angle (θ_C), and array fill-factor (*FF*) are also listed.

ϕ_{PS} (μm)	ϕ_{lens} (μm)	θ_C (°)	*FF* (%)	*f*		
				FOLEDs		PHOLEDs
				Small-area	Large-area	Large-area
5	4.6 ± 0.1	45 ± 5	–	–	–	–
20	18.4 ± 0.4	65 ± 5	77 ± 3	1.25 ± 0.04	1.45 ± 0.05	1.44 ± 0.05
100	98 ± 2	85 ± 5	85 ± 3	1.35 ± 0.04	1.70 ± 0.07	1.56 ± 0.06

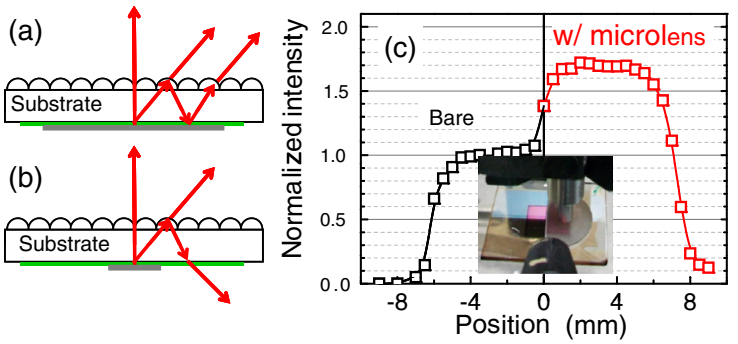

Fig. 4. Schematic illustrations for light extraction in a large-area (a) and a small-area (b) OLED with a microlens array attached to the glass substrate. (c) The normalized near-field optical intensity profile across a large-area fluorescent OLED, half of which was covered with a microlens array while the other half was bare (a picture of the device is shown in the inset). (For interpretation of the references to colour in this figure legend, the reader is referred to the web version of this article.)

factors for the two microlens arrays are relatively close, although optical simulation may be needed to identify the relative contribution of these two factors.

Moreover, we have also observed greater outcoupling enhancement in larger size devices. For small-area FOLEDs with microlens arrays based on 20 and 100 μm PS spheres, we obtained $f = (1.25 \pm 0.04)$ and (1.35 ± 0.04), respectively. However, for large-area FOLEDs, f is significantly improved to (1.45 ± 0.05) and (1.70 ± 0.07), respectively, resulting in peak $\eta_{EQE} = 1.28\%$ at $J = 100\ \mathrm{mA/cm^2}$ when 100 μm microlens array is attached to the glass surface of the large-area FOLED. Such a device size dependence is attributed to the larger Al cathode size allowing for more effective re-direction of light into the forward-viewing direction, as illustrated in Fig. 4(a). For a small-area device, as shown in Fig. 4(b), light that is reflected back towards the cathode from the microlens/air interface may travel to outside the cathode area due to the ~1 mm thick glass substrate, and not be re-directed to forward-viewing directions.

The light extraction enhancement factor due to microlens arrays attached to FOLEDs was also confirmed from the near-field optical intensity measurement with an optical fiber. As shown in the inset of Fig. 4(c), a large-area FOLED was partially covered with a microlens array ($\phi_{PS} = 100$ μm). As the optical fiber was scanned perpendicularly to the boundary between the bare side and the side covered with the microlens array, the near-field optical intensity was recorded in the spectrometer attached to the optical fiber. Fig. 4(c) shows that the intensity on the microlens covered side is $(69 \pm 4)\%$ higher than the bare side, in excellent agreement with the integrating sphere measurement for large-area FOLEDs.

For the large-area PHOLED, the enhancement factor is somewhat lower, $f = (1.56 \pm 0.06)$ (see Table 1), compared with that for the FOLED based on the near-field optical intensity measurement. We attribute this difference to the multi-layered structure of PHOLEDs which can generate more significant confinement of the optical modes in the emissive layer, particularly considering that the CBP emissive layer in the PHOLED has a higher index of refraction at the OLED emission wavelength than the Alq_3 emissive layer in the FOLED, 1.83 vs. 1.75 as measured by ellipsometry.

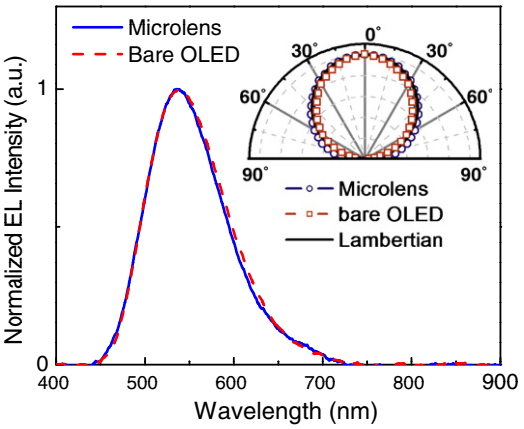

Fig. 5. Normalized electroluminescence (EL) spectra of the fluorescent OLED with and without a microlens array attached to the glass substrate. Inset shows the normalized luminous intensity as a function of the viewing angle from the substrate normal for a bare fluorescent OLED (red open squares) and the same OLED with a hemispherical microlens attached (blue open circles), as well as that for a Lambertian source (solid line). (For interpretation of the references to colour in this figure legend, the reader is referred to the web version of this article.)

Fig. 5 shows the normalized electroluminescence (EL) spectra of the FOLED with or without a microlens array attached. Negligible changes in the emission spectrum, with a 4 nm blue shift in the peak wavelength and a 3 nm reduction in the full width at half maximum, were observed after the microlens array was attached. The inset of Fig. 5 compares the angular emission pattern of the FOLED with or without a microlens array along with that for a Lambertian source. The attachment of the microlens array only slightly modified the angular emission profile, slightly enhancing luminous intensities at larger angles. Note that Sun et al. demonstrated enhanced luminous intensities at larger angles (especially at >50°) using 7 μm microlens arrays [15], which is consistent with what we observed with our microlens array. This could be attributed to the broadened

light-emission area with microlens arrays, creating a blurred pixel image.

4. Conclusions

In conclusion, we have demonstrated large-area, close-packed hemispherical microlens arrays using a simple and low-cost fabrication method. Different contact angles of the microlens are achieved by varying the size of PS microspheres, reaching (85° ± 5°) with 100 μm PS microspheres. The measured fill factor of lens array is as high as (85 ± 3)%. The attachment of such microlens arrays to OLEDs can improve the light outcoupling efficiency by up to 70%, which only slightly modifies the angular emission pattern. The light extraction efficiency depends on the lens contact angle, device area, and the detailed layered device structure of the OLED. The technique described here could have important applications to OLED-based device systems, especially for lighting applications where large-area devices instead of small pixels are sought after.

Acknowledgements

The authors gratefully acknowledge financial supports from the US Department of Energy Solid State Lighting Program (Award # DE-EE0000990) and the Florida Energy Systems Consortium. S.H.E. also acknowledges a fellowship from Samsung SDI. Co., Ltd.

References

[1] S.R. Forrest, Nature 428 (2004) 911.
[2] S.-H. Eom, Y. Zheng, E. Wrzesniewski, J. Lee, N. Chopra, F. So, J. Xue, Appl. Phys. Lett. 94 (2009) 153303.
[3] S.-H. Eom, Y. Zheng, E. Wrzesniewski, J. Lee, N. Chopra, F. So, J. Xue, Org. Electron. 10 (2009) 686.
[4] J. Fang, P. Matyba, L. Edman, Adv. Funct. Mater. 19 (2009) 2671.
[5] T. Matsushima, H. Murata, J. Appl. Phys. 104 (2008) 034507.
[6] H. Benisty, H.D. Neve, C. Weisbuch, IEEE J. Quantum Electron. 34 (1998) 1612.
[7] Y.-J. Lee, S.-H. Kim, J. Huh, G.-H. Kim, Y.-H. Lee, S.-H. Cho, Y.-C. Kim, Y.R. Do, Appl. Phys. Lett. 82 (2003) 3779.
[8] Y. Sun, S.R. Forrest, Nat. Photonics 2 (2008) 483.
[9] T. Shiga, H. Fujikawa, Y. Taga, J. Appl. Phys. 93 (2003) 19.
[10] S. Moller, S.R. Forrest, J. Appl. Phys. 91 (2002) 3324.
[11] Y. Lu, Y.D. Yin, Y.N. Xia, Adv. Mater 13 (2001) 34.
[12] C.C. Cheng, C.A. Chang, J.A. Yeh, Opt. Express 14 (2006) 4101.
[13] S.I. Chang, J.B. Yoon, Opt. Express 12 (2004) 6366.
[14] R. Danzebrink, M.A. Aegerter, Thin Solid Films 392 (2001) 223.
[15] Y. Sun, S.R. Forrest, J. Appl. Phys. 100 (2006) 073106.
[16] L. Malaquin, T. Kraus, H. Schmid, E. Delamarche, H. Wolf, Langmuir 23 (2007) 11513.
[17] H. Yabu, M. Shimomura, Langmuir 21 (2005) 1709.
[18] H.J. Nam, D.-Y. Jung, G.-R. Yi, H. Choi, Langmuir 22 (2006) 7358.
[19] S.-H. Eom, Y. Zheng, N. Chopra, J. Lee, F. So, J. Xue, Appl. Phys. Lett. 93 (2008) 133309.

Organic Electronics 12 (2011) 477–485

Contents lists available at ScienceDirect

Organic Electronics

journal homepage: www.elsevier.com/locate/orgel

Analysis of the hysteresis in organic thin-film transistors with polymeric gate dielectric

Emanuele Orgiu [a,b,*], Simone Locci [a,b,c], Beatrice Fraboni [d], Erika Scavetta [e], Paolo Lugli [c], Annalisa Bonfiglio [a,b]

[a] Dipartimento di Ingegneria Elettrica e Elettronica, Università di Cagliari, Piazza d'Armi, 09123 Cagliari, Italy
[b] INFM-CNR Centre S3 "nanoStructures and bioSystems at Surfaces", via Campi 213/A, I-41100 Modena, Italy
[c] Institute for Nanoelectronics, Technische Universität München, Arcisstraße 21, 80333 München, Germany
[d] Dipartimento di Fisica, Università di Bologna, viale Berti Pichat 6/2, 40127 Bologna, Italy
[e] Dipartimento di Chimica Fisica e Inorganica, Università di Bologna, viale Risorgimento 4, 40127 Bologna, Italy

ARTICLE INFO

Article history:
Received 13 June 2010
Received in revised form 2 December 2010
Accepted 23 December 2010
Available online 6 January 2011

Keywords:
Polymeric dielectrics
Hysteresis
Leakage current
Poly(vinyl alcohol)
Organic thin-film transistors
Device simulation

ABSTRACT

Controlling threshold voltage (V_{TH}) and field-effect mobility (μ_{FET}) in organic thin-film transistors (OTFTs) is of primary importance to attain reliable devices that can be harnessed in more complicated circuits and eventually commercialized. In particular hysteresis in OTFT transfer curves is an issue that has to be better understood and analyzed. In this regard, even if the interface between organic dielectric and organic semiconductor seems to play an important role, our study shows that a further and relevant factor is played by the transport of charges across the bulk of the dielectric layer. Here, an analytical approach is applied to identify and understand the different components that give rise to the hysteresis in the transfer curves of pentacene-based OTFTs using poly(vinyl alcohol) (PVA) and poly(-vinyl alcohol) cross-linked with ammonium dichromate (PVAad) as the (polymeric) gate dielectric. Transfer curves simulations which include charge transport in the PVA show a hysteretic behavior in good agreement with the experimental data. Moreover, the hysteresis measured in OTFTs can be reduced by the insertion of an underlying dielectric layer of SiO_2 that blocks the above-mentioned effect. The residual contribution to the hysteresis is then analyzed by investigating the chemistry nature of both PVA and PVAad, which show different electron trapping efficiency at the interface with the pentacene layer. Therefore, a consistent explanation of how the polymeric dielectric is able to impact the transfer curves requires considering all mentioned factors.

© 2011 Elsevier B.V. All rights reserved.

1. Introduction

Organic thin-film transistors (OTFTs) have been attracting an increasing interest for 20 years as promising technology candidates for large area, low-cost applications which can be eventually implemented on cheap, low-temperature, flexible and unconventional substrates [1–3]. Recent advances in organic semiconductor performances pave the way towards commercialization of OTFTs [4,5]. In addition these devices are widely used as tools for studying material properties on the device scale [6]. In particular, drain current vs. gate voltage (I_d–V_g) curves, also called *transfer characteristics*, are a very powerful means for analyzing the behavior of a field-effect device since threshold voltage (V_{TH}), field-effect mobility (μ_{FET}), I_{on}/I_{off} can be extracted from these curves [7,8]. Transfer curves are traced at a fixed value of the drain voltage, which can be set in the linear range ($V_d < V_g - V_{TH}$) of the transistor current, i.e. with mobile charges

* Corresponding author. Present address: Institut de Science et d'Ingénierie Supramoléculaires, Université de Strasbourg, 8, allée Gaspard Monge, 67083 Strasbourg, France.
E-mail address: orgiu@unistra.fr (E. Orgiu).

1566-1199/$ - see front matter © 2011 Elsevier B.V. All rights reserved.
doi:10.1016/j.orgel.2010.12.014

accumulated along the whole distance between source and drain or, alternatively, in the so-called saturation regime ($V_d > V_g - V_{TH}$), i.e. with mobile charges accumulated only between the source electrode and the pinch-off point (whose potential difference referred to the gate is equal to the threshold voltage, V_{TH}). In the latter case the drain current curve exhibits not a linear but rather a quadratic dependence from the gate voltage. Consequently, Sqrt(I_d) vs. V_g rather than I_d vs. V_g has to be plotted and fitted linearly in order to extract both threshold voltage and field-effect mobility values in the saturation regime [9]. Transfer characteristics hold the potential to reveal charge trapping effects. In particular, trap states may give rise to hysteresis when the gate voltage is swept forward and backward in the working range of the device. Information on trapping mechanisms can be therefore derived from the magnitude and sign of the threshold voltage shifts [10]. As mentioned, hysteresis appears when the input voltage V_g is swept forward and backward; hence, two different values of the threshold voltage are derived whenever the forward and the backward branch of the drain current curve differ. In addition, transfer curves affected by hysteresis usually have different slopes which consequently result in significantly different values of the extracted mobility. Unpredictable threshold voltage shifts represent a major problem for the applicability of these devices as they introduce uncertainty about the capability of the device switching between two different values of the input voltage. Furthermore, they degrade the amplification ability of the device when used in an amplifying configuration as they modify its transconductance. In addition to that, the threshold voltage values usually shift further with aging. So, ideally, for being successfully harnessed in a circuit, a field-effect device should not show any unpredictable hysteresis. A marked, stable and repeatable threshold voltage shift could be in fact exploited for using the device as a memory, in which a voltage step could be used to permanently "write" information on the device. For these reasons it would be extremely interesting to understand the mechanisms that cause the hysteresis effect to appear, in order to finely control it and achieve an ideal transistor behavior or, alternatively, obtain a permanent memory effect.

This picture becomes even more complicated when polymeric gate dielectrics are used for the fabrication of field-effect transistors. They feature optical transparency, flexibility and a wide range of dielectric constants. Despite the fact that some ultrathin polymeric gate dielectrics featuring low leakage values have been put forward [11–13], organic dielectrics generally suffer from not always having good insulating properties i.e. they usually require thick film thicknesses to minimize the gate current (I_g).

In this paper we investigate how hysteresis is related to the properties of the gate insulating layer in devices using polymeric dielectrics. In particular, we used poly(vinyl alcohol) (PVA) and poly(vinyl alcohol) cross-linked with ammonium dichromate (PVAad). The former is commonly believed to give rise to a large hysteresis and it is therefore used in non-volatile memory applications [14,15].

Up to now, hysteresis in transistors using polymeric gate dielectrics has been largely attributed to different mechanisms such as semiconductor–dielectric interface effects, residual dipole-induced effects and moisture [16,17]. In the following, we will show a number of experimental observations that aim to clarify a key factor that heavily affects the hysteretic device behavior i.e. the current flowing through the bulk of the gate dielectric layer as well as the role of the semiconductor–insulator interface. It has been previously observed that the hysteresis in OTFTs is influenced by the current flowing through the bulk of polymeric dielectrics but this current contribution has been never measured or analyzed quantitatively [18]. In our study the hysteresis was found to be much larger in devices having only a polymeric film as the insulating layer rather than a double one, formed by an organic dielectric on a Si/SiO_2 substrate which shields any possible transport occurring between polymeric dielectric and gate electrode.

Our results show that: (i) the current flowing through the dielectric in metal–insulator–metal (MIM) capacitors at typical OTFTs' operation voltages follows a Space–Charge Limited Current (SCLC) trend [19]; (ii) modeling of the charge transport across the polymeric dielectric as well as numerical simulations of transfer curves were found to be in good agreement with the experimental data; (iii) the transport and the trapping mechanisms at the interface between the semiconductor and the dielectric layer, also affecting the I_d–V_g curve, must be interpreted only after considering and possibly removing the contribution of the leakage current through the dielectric.

2. Experimental

Organic thin-film transistors and metal–insulator–metal (MIM) structures were assembled on the same glass substrate, or, alternatively on heavily doped silicon substrates with a 500 nm thick layer of silicon dioxide (Fig. 1). PVA (Mowiol® 40-88) with an average molecular weight of 120,000 (Sigma–Aldrich) was used as received. PVA solution (10% weight in bi-distilled water) was spun at 600 rpm for 60 s and successively baked in an oven at 100 °C for 24 h. Cross-linked PVA solution was composed of PVA (10% in water), ammonium dichromate (Sigma–Aldrich) (1.4% weight) as a cross-linking agent and bi-distilled water as a solvent. PVAad solutions were spun at the same conditions as PVA (600 rpm for 60 s). Spin-coated PVAad films were cross-linked by UV irradiation (5′) and then baked at 100 °C for 24 h. Glass and silicon substrates (oxide nominal thickness 500 nm) were both cleaned through ultrasonic baths first in acetone (15 min) and successively in isopropanol (15 min).

Pentacene (Sigma–Aldrich, 98%) films with a nominal thickness of 30 nm were grown by thermal evaporation at a nominal deposition rate of about 0.5–1 Å s^{-1}. Gold source and drain contacts ($W/L = 100$) were thermally evaporated onto the semiconducting layer (top-contact configuration) through a shadow mask. Employed polymeric gate layers were 3 μm thick in all of the tested devices as estimated from capacitance–frequency measurements performed on the corresponding MIM structures.

Drain current (I_d) measurements were carried out at room temperature, in dark, in an inert nitrogen environ-

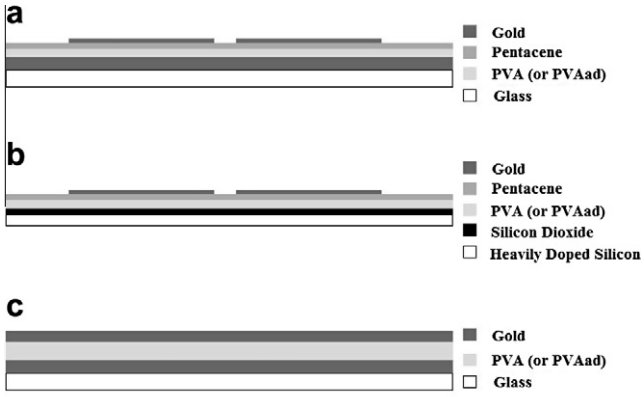

Fig. 1. Schematic illustration of the tested devices: (a) transistor in bottom-gate top-contact configuration assembled on a glass substrate (single dielectric layer); (b) transistor in bottom-gate top-contact configuration assembled on silicon/silicon dioxide (double dielectric layer); (c) Metal–Insulator–Metal (MIM) capacitor (thermally evaporated gold plates) with a single polymeric dielectric layer, assembled on glass.

ment (glove box). Agilent HP 4155 Semiconductor Parameter Analyzer, provided with gold tips for contacting the electrodes, was used to supply both the gate voltage (V_g) and the drain voltage (V_d) (the source being the common ground) and to measure the gate (I_g) and the drain (I_d) currents. All transfer curves reported in the main manuscript were acquired at a gate sweep rate of 13.3 V/s. Measurements with varying the gate sweep rate are reported in the Supplementary Data.

Space–Charge Limited Current (SCLC) measurements were carried out with a Keithley 6517 Electrometer, at room temperature, in vacuum. Capacitance–frequency as well as quasi-static capacitance–voltage measurements were acquired in inert environment (glove box) by using a 4284A precision LCR meter.

FT-IR spectra were recorded with a Nicolet Nexus 470 spectrometer, configured with a Nicolet Continuum microscope and a MCT/B liquid-nitrogen-cooled detector. Spectra were collected in ATR (Attenuated Total Reflectance) mode through a Cassegrain objective (14×), reaching a spatial resolution of ~100 μm^2 on PVA and PVA ad films deposited on glasses slides from 10% water solutions. The spectra were recorded (as sum of 256 scans with a resolution of 4 cm^{-1}) in the spectral region of the medium infrared (800–4000 cm^{-1}). Sixteen spectra (recorded with a nominal resolution of 4 cm^{-1}) were averaged to improve the signal-to-noise ratio.

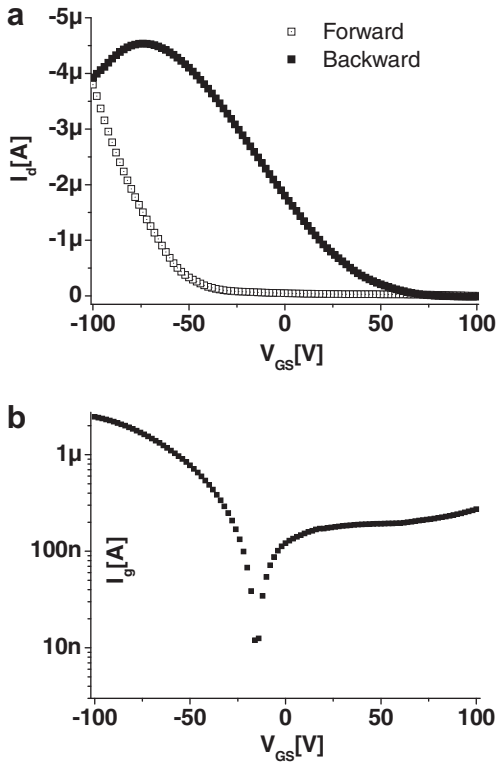

Fig. 2. (a) Transfer curve (I_d vs. V_g) recorded on a transistor in top-contact bottom-gate configuration having PVA as the dielectric layer (C_i = 2.95 nF cm^{-2}, L = 50 μm, W/L = 100) during a double sweep of V_g swept from +100 V to −100 V, V_d = −100 V (saturation regime); (b) I_g vs. V_g curve measured on the same device (V_g swept from +100 V to −100 V, V_d = −100 V, saturation regime).

3. Results and discussions

The following sections will show the results of a systematic study performed on pentacene-based OTFTs with thermally evaporated gold source and drain electrodes in top-contact bottom-gate configuration, having either glass (Fig. 1a) or silicon/silicon dioxide (Fig. 1b) as the substrate, and PVA or alternatively PVAad as a gate dielectric. In addition MIM capacitors (Fig. 1c) were fabricated and tested in order to investigate the conduction mechanisms through the dielectric layer.

3.1. Analysis of the hysteresis in transistors employing PVA as the gate dielectric

In Fig. 2a and b, we report a couple of typical curves taken on a pentacene-based transistor assembled on glass with PVA as the gate dielectric. These graphs show respectively (a) the I_d vs. V_g recorded during a double sweep of V_g

between +100 and −100 V, being the drain voltage (V_d) set to −100 V (saturation regime) and (b) the gate current (I_g) collected at the electrode. In Fig. 2a is shown a large hysteresis (with a clockwise direction) which appears on the drain current curve, leading to a big shift in the threshold voltage values extracted from the I_d–V_g curve. According to the well-known equation

$$I_d = \frac{1}{2}\mu_{SAT} C_i \frac{W}{L}(V_{GS} - V_{TH})^2 \quad (1)$$

which adequately models the drain current in the saturation regime [7], threshold voltage values were calculated by plotting the Sqrt|I_d| vs. V_g curve and then extracting the intercept with the voltage axis of the line which fits the linear part of the curve.

Consistently with this method, two remarkably different values were extracted, respectively $V_{TH,forward} = -30$ V and $V_{TH,backward} = +75$ V which produce a huge overall voltage threshold shift (ΔV_{TH}) of 105 V. Gate sweep rate was found not to sensibly affect the hysteresis or induce threshold voltage shifts as reported in Figs. S1 and S2.

In agreement with Eq. (1) field-effect mobility can be calculated as

$$\mu_{SAT,p} = 2\frac{\left(\frac{\partial\sqrt{I_d}}{\partial V_{GS}}\right)^2}{C_i \frac{W}{L}} \quad (2)$$

Being $\mu_{SAT,p}$ the saturation mobility value for a transistor working in accumulation mode, where holes are the majority carriers, and $C_i = 2.95$ nF cm^{-2} the capacitance of the PVA layer measured through capacitance–frequency measurements on MIM capacitors. The width-to-length ratio was 100. The dielectric permittivity of PVA was set to 8, as reported in literature [15]. The forward and backward curve (Fig. 2a) differ in slope and this leads to a slope difference also on the Sqrt|I_d| vs. V_g curves. In view of that, two different field-effect mobility values are extracted, respectively $\mu_{forward} = 5.4 \times 10^{-3}$ cm^2 V^{-1} s^{-1} and $\mu_{backward} = 1.8 \times 10^{-3}$ cm^2 V^{-1} s^{-1}. The same mobility and threshold voltage values were found by measuring tens of devices made using the same technological steps and device parameter (W/L, C_i) and biased with the same gate, source and drain voltages.

Though threshold voltage and field-effect mobility values could be easily extracted, the straight interpretation as well as the physical meaning of the discrepancy among them is still an issue that needs to be addressed. A correlation between hysteresis and charge trapping is commonly invoked to explain this data inconsistency [20]. Although it has been previously reported that leakage current may affect OTFTs performance and it has therefore to be minimized [21,22], the relationship between the current flowing through the bulk of polymeric gate dielectrics and the hysteresis appearing on the transistor curves has not yet been directly addressed and is not actually being taken into account when evaluating the FET device performances.

As a matter of fact, Fig. 2b reveals that a large current flows through the PVA layer and is collected at the gate electrode. In particular, the I_g follows the same trend as the transfer curves, thus indicating a dependance from I_d,

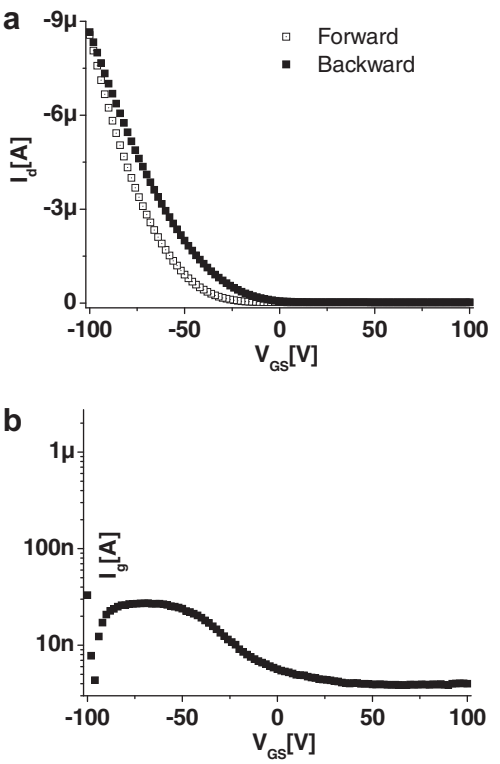

Fig. 3. (a) Transfer curve (I_d vs. V_g) recorded on a transistor in top-contact bottom-gate configuration having PVA/SiO_2 as the dielectric layer ($C_{TOT} = 2.1$ nF cm^{-2}, $L = 50$ μm, $W/L = 100$) during a double sweep of V_g swept from +100 V to −100 V, $V_d = -100$ V (saturation regime); (b) I_g vs. V_g curve measured on the same device (V_g sweeping from +100 V to −100 V, $V_d = -100$ V, saturation regime).

reaching larger current values at negative gate voltages. It is therefore necessary to get rid of this relevant current contribution before commenting on possible source of drain current hysteresis due to other mechanisms.

Interestingly, to completely remove this undesired contribution (and discard possible interferences of the leakage current with different phenomena as trapping) one should use PVA (or any other "leaky" dielectric) only as a surface layer deposited on another not leaky dielectric, as for instance SiO_2.

This is clearly shown in Fig. 3a, showing I_d vs. V_g current recorded on device having a double PVA/SiO_2 dielectric layer, where a remarkable reduction on the hysteresis in the transfer curves due to the insertion of a silicon dioxide layer (see Fig. 1b) is highlighted. The polymeric gate dielectric in these devices was around 3 μm thick, as the one in the devices assembled on glass (see Fig. 1a), which only used PVA as the dielectric layer.

The same equations as above were used to extract threshold voltage and field-effect mobility, except for the capacitance value. When a double dielectric is employed the resulting capacitive contribute to the device is equivalent to the series of two capacitors, C_{PVA} and C_{SiO2} in this case.

Consequently the total capacitance of the double dielectric layer will be given by Eq. (3)

$$C_{TOT} = \frac{C_{PVA} C_{SiO_2}}{C_{PVA} + C_{SiO_2}} \quad (3)$$

where C_{PVA} and C_{SiO2} are respectively 2.95 nF cm^{-2} and 6.9 nF cm^{-2} (as measured from several capacitance–frequency measurements on MIM structures) and the total capacitive contribute is therefore C_{TOT} = 2.1 nF cm^{-2}. After replacing C_{TOT} with C_i in Eq. (2) the field-effect mobility can be properly calculated.

The threshold voltage values extracted from Sqrt$|I_d|$ vs. V_g curve are $V_{TH,forward}$ = −25 V and $V_{TH,backward}$ = −5 V (both of them having the same sign) which gives place to an associated overall threshold voltage shift (ΔV_{TH}) far lower than in the case of Fig. 2a. The extracted mobility values, $\mu_{forward} = 1.4 \times 10^{-2}$ cm^2 V^{-1} s^{-1} and $\mu_{backward} = 0.9 \times 10^{-2}$ cm^2 V^{-1} s^{-1}, are higher and their values match better than in the case of devices using only PVA as the gate insulator; this is also clearly evidenced by the I_d–V_g curve slope change as a consequence of the insertion of a further shielding dielectric layer (Fig. 3a). These results point out that (1) the hysteresis phenomenon is largely reduced due to the strong reduction in leakage current (now only being 0.1% of I_d) through the dielectric (compare Fig. 3b with Fig. 2b), (2) the extracted mobility values relative to the hole transport in pentacene-based transistor with PVA as the gate dielectric can now be considered reliable for studying the charge transport.

3.2. Modeling and simulation of transfer curves in OTFTs having PVA as the polymeric gate dielectric

To assess the possible influence of transport mechanisms across the dielectric in the transistor curves, we performed a numerical simulation in which a transistor with charge transport occurring in the bulk of the dielectric is considered. The simulated device is a pentacene-based thin-film transistor in top-contact bottom-gate configuration. Pentacene and dielectric thickness was set to 30 nm and 3 μm, respectively. The width-to-length ratio was set to 100.

We used the Sentaurus program by Synopsys, which is a well-known tool for semiconductor device modeling, to simulate the hysteresis of the device [23]. The Poisson equation coupled with the current continuity equations was solved:

$$\begin{cases} \nabla^2 V = \frac{q}{\varepsilon}(n - p - N + n_t - N_t) \\ \nabla \cdot \boldsymbol{J}_n = -qR + \frac{\partial n}{\partial t} \\ -\nabla \cdot \boldsymbol{J}_p = -qR + \frac{\partial p}{\partial t} \end{cases} \quad (4)$$

where q is the elemental charge, V is the electrostatic potential, ε is the dielectric permittivity, n is the density of electrons, p is the density of holes, N is the doping profile, N_t is the density of trap states, if present, n_t the density of occupied traps; R is the recombination factor. We model the current with the drift diffusion equations, therefore

$$\begin{cases} \boldsymbol{J}_n = q\mu_n n\mathbf{E} + qD_n \nabla n \\ \boldsymbol{J}_p = q\mu_p p\mathbf{E} - qD_p \nabla p \end{cases} \quad (5)$$

for the current of electrons and holes, respectively. μ_n and μ_p are the carrier mobilities, $D_n = \mu_n kT/q$ and $D_p = \mu_p kT/q$ are the diffusivities.

For the pentacene, the following properties were set up: band gap $E_g = 2.5$ eV, electron affinity $q\chi = 2.6$ eV, density of states $N_C = N_V = 2 \times 2.9 \times 10^{21}$ cm^{-3} [24]. The hole mobility in agreement with the experimental data was set to $\mu_p = 1.7 \times 10^{-3}$ cm^2 V^{-1} s^{-1}, whereas the mobility for electrons was supposed to be negligible $\mu_n = 10^{-11}$ cm^2 V^{-1} s^{-1}. Source and drain contacts, realized in gold, had a metal work-function $q\phi_m = 5.1$ eV.

On the other hand, PVA cannot be modeled as an ideal insulator, because current flows through it. A fully detailed description of the current physics is still under investigation [25]; however, we will assume that carriers follow Eqs. (4) and (5). This hypothesis has already been used to simulate ion channels with drift–diffusion simulators [26]. We will also suppose that the boundary conditions for the gate electrode define charge neutrality at the interface, therefore Dirichlet boundary conditions hold [27].

The intrinsic carrier density in the PVA was set to an arbitrary small value. We assumed a density of donor traps $N_t = 10^{17}$ cm^{-3}, with an energy, estimated by fitting the transfer curves of the transistors, $E_{tr} = E_V + 0.3$ eV. The mobility of the carriers were determined as fitting parameters: $\mu_n = 10^{-11}$ cm^2 V^{-1} s^{-1}, $\mu_p = 10^{-10}$ cm^2 V^{-1} s^{-1}. The order of magnitude of the carrier mobility used in the simulation of the PVA is in agreement with the value extracted from the SCLC measurements on MIM capacitors using PVA as the insulator.

Using the same sweep times of the experimental measurements, we obtained the curve reported in Fig. 4, which shows a very good qualitative agreement with the experimental data, for both magnitude and sign of the hysteresis. The large hysteresis is determined by the carriers in the PVA, whose slow motion in the dielectric, due to the electric field, affects the threshold voltage of the device; the traps in the dielectric further contribute to the change in threshold voltage and, therefore, to the hysteresis.

To increase the agreement with the experimental data, a more in-depth description of the pentacene/PVA interface should be achieved, including details about the band-gap of the dielectric and the energy distribution of possible trap states at the interface. The carrier transport in the PVA itself could be better described, if the physical nature of the current across the dielectric layer could be described in detail. These points are currently under investigation, and will be addressed in future publications.

3.3. SCLC characterization of PVA and PVAad/analysis of trapping at the semiconductor-polymeric dielectric interface

Following the previous considerations, the current through the polymeric dielectric layer seems to play a major role on both performance and characteristic parameters of the device. To further investigate the transport mechanisms across the dielectric layer, current vs. voltage measurements were performed on MIM structures as shown in Fig. 5a and b. This electrical behavior can be described in the framework of the Lampert and Mark model for trap-controlled electrical transport in semi-insulating materials [19]. Three different regimes can be resolved in the I–V curves: a linear (ohmic) regime at low voltages, a quadratic regime named "space–charge limited current"

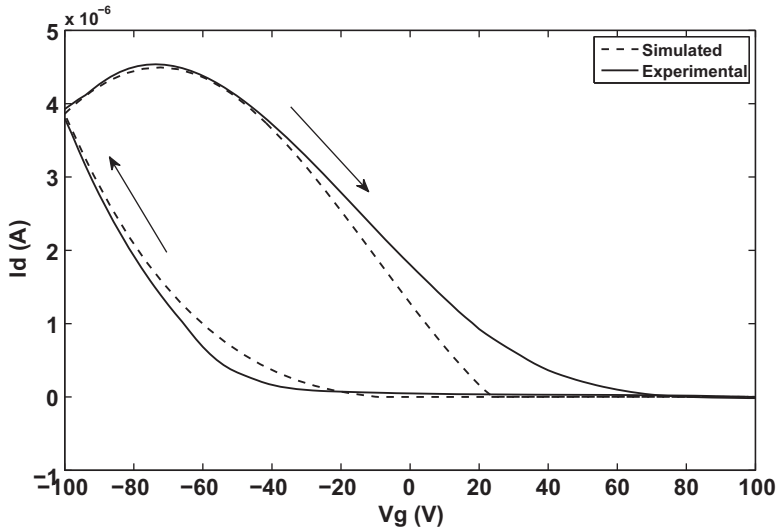

Fig. 4. Simulation and fitting of the I_d–V_g curve reported in Fig. 2a. The simulated device is a pentacene-based thin-film transistor in top-contact bottom-gate configuration with a single polymeric gate dielectric layer. Here only the charge transport occurring in the bulk of the polymeric gate dielectric is considered. The simulation is in good agreement with the experimental data, revealing that charge transport across the dielectric layer represents the major contribution to the hysteretic behavior.

(SCLC) at higher voltages and the so-called "trap filled limited" (TFL) region characterized by the steep increase of the current. The charge carrier mobility μ can be estimated from the equation describing the SCLC curve in a trap-free semi-insulator (Mott–Gurney law) $\mu = \frac{8JL^3}{9\varepsilon V^2}$ for $V = V_{TFL}$, where J is the current density at the beginning of the trap-free region, ε the dielectric constant and L is the separation between the contacts (the dielectric thickness). We can also estimate the density of traps from the voltage V_{TFL}, where the trap-free region starts, using the relation $N_t = \frac{\varepsilon V_{TFL}}{eL^2}$, where e is the electron charge. In particular, significant current flows through the dielectric layer (Fig. 5a) at voltage values that are typical of transistor operation. Only after the V_{TFL} (Trap Filled Limit Voltage) is reached, the material behaves as a trap free insulator following the Mott–Gurney quadratic law. From the V_{TFL} value, majority carrier mobility (10^{-10} cm^2 V^{-1} s^{-1}) and trap density (10^{17} cm^{-3}) can be estimated [19].

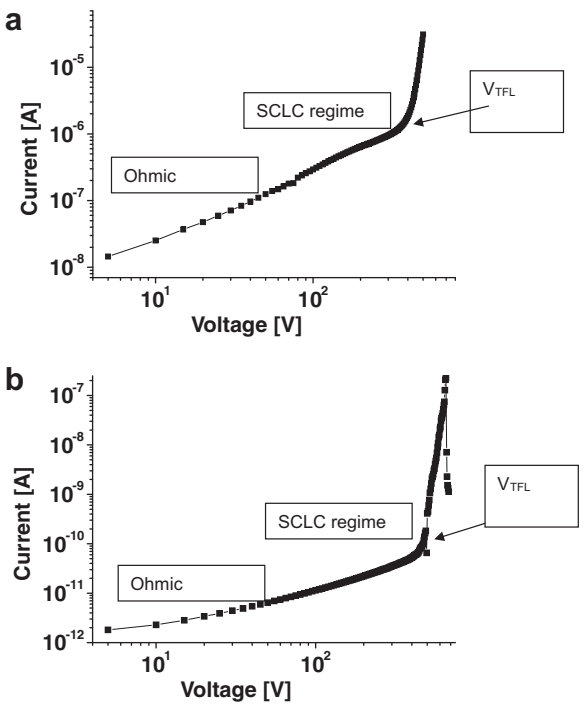

Fig. 5. I vs. V (logarithmic scale) curves of (a) a PVA-based MIM capacitor and (b) a PVAad-based MIM capacitor (in vacuum).

With the purpose of investigating the relationship between transport and leakage current into a polymeric gate dielectric, current vs. voltage measurements were performed also on PVAad. Surprisingly, I–V curves (Fig. 5b) show that SCLC regime occurs later in voltage than for PVA, which means that PVAad has a much lower ability than PVA to transport injected charges (in the operational voltage range of transistor). Thanks to the consequent low leakage currents through the dielectric (the leakage current being respectively three orders of magnitude lower than I_d, Fig. 6b, and four orders of magnitude lower than I_d, Fig. 6d), hysteresis is almost negligible on PVAad-based FET devices when they are assembled both on glass (Fig. 6a) and silicon dioxide (Fig. 6c). These results partially differ from what Park et al. highlighted in their work where residual hysteresis still appears when using PVAad together with silicon dioxide (100 nm thick) as the gate dielectric layer [18]. This is probably due to the fact that a thicker both silicon dioxide layer (500 nm) and polymeric insulating layer (3 μm) was used in our study thus shielding more efficiently this parasitic contribute to the hysteresis.

At this point, the residual and not negligible hysteresis on PVA-based devices assembled on silicon/silicon dioxide

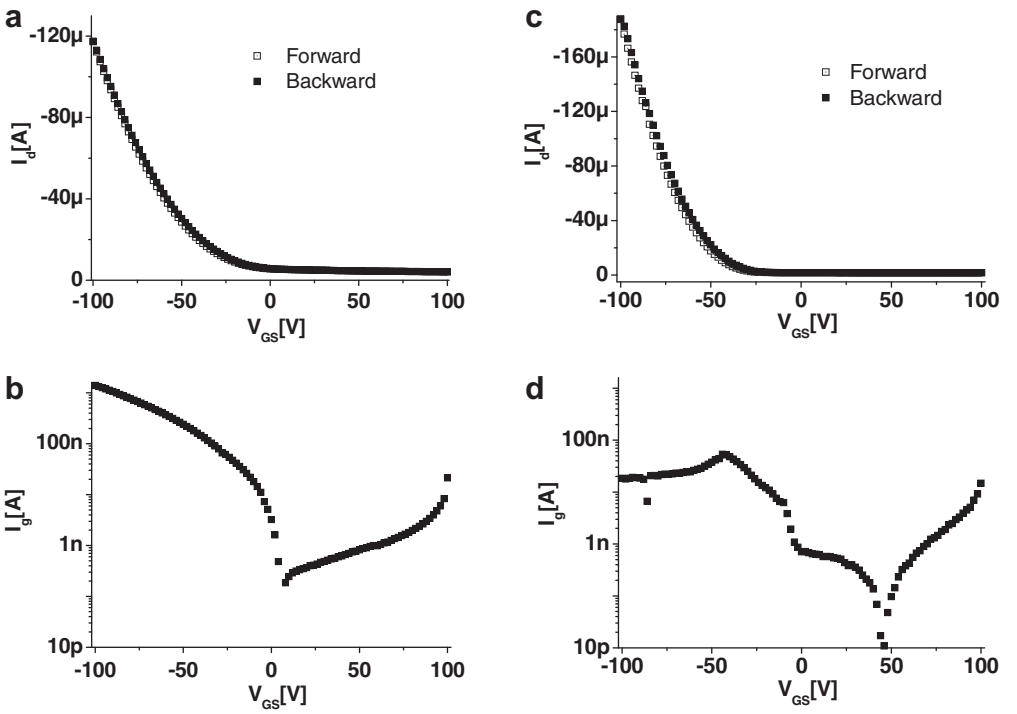

Fig. 6. (a) Transfer curve (I_d vs. V_g) recorded on a transistor in top-contact bottom-gate configuration having PVAad as the dielectric layer (C_{TOT} = 2.1 nF cm^{-2}, L = 50 μm, W/L = 100) during a double sweep of V_g swept from +100 V to −100 V, V_d = −100 V (saturation regime); (b) I_g vs. V_g curve measured on the same device in Fig. 6a (V_g sweeping from +100 V to −100 V, V_d = −100 V, saturation regime); (c) transfer curve (I_d vs. V_g) recorded on a transistor in top-contact bottom-gate configuration having PVAad/SiO_2 as the dielectric layer during a double sweep of V_g swept from +100 V to −100 V, V_d = −100 V (saturation regime); (d) I_g vs. V_g curve measured on the same device in Fig. 6c (V_g sweeping from +100 V to −100 V, V_d = −100 V, saturation regime).

(Fig. 3a) has to be further investigated. Residual hysteresis can be attributed to (a) dipole-induced effect due to slow polarization of dipole groups (inside the dielectric bulk) that can be slowly reoriented by an applied electric field or (b) trapping at the semiconductor/dielectric interface due to the chemical nature of the gate dielectric.

Slow polarization mechanism has been widely proved on organic transistors with poly (vinyl 4-phenol) (PVP) as a gate dielectric [28–30]. In particular, OH groups inside the dielectric are considered possible source of hysteresis on transfer curves. Hysteresis was reduced by exposing PVP to cross linking reaction with polymelamine-co-formaldehyde. This condensation reaction led to a dielectric layer having minimal density of hydroxyl groups and internal impurities, but does not actually affect the surface groups of the dielectric and consequently not changing the semiconductor/insulator interface [29]. In order to minimize the possible presence of residual dipoles (water molecules) into the dielectric film, our dielectric layers were baked for 24 h at 100 °C (as described in the experimental session) before pentacene and source and drain electrodes deposition. Capacitance–frequency measurements recorded at different bias voltages were performed on MIM structures having double dielectric (PVA and silicon dioxide) to verify the existence of slow polarization coming from slow dipoles. PVA layers were as thick as the ones used as the gate dielectrics in the transistor device. Results are shown in Fig. 7 where a comparison between two different measurements (using different bias voltage) is shown; no significant effect due to a bias voltage application was observed over all the used range of frequencies. This means that a slow polarization effect due to residual immobile dipoles in the insulating PVA layer can be considered negligible and cannot actually represent the major contribute to hysteresis on transfer curves.

Even by using different experimental conditions than ours, other authors have observed hysteresis in organic

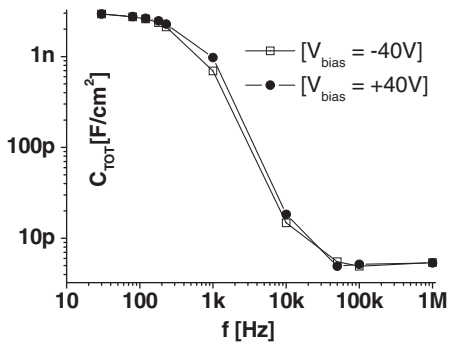

Fig. 7. Capacitance vs. frequency curves at V_{bias} = −40 V and V_{bias} = +40 V recorded on a MIM capacitor having PVA and silicon dioxide as a double dielectric layer. The curve shows that there is no evidence (at any frequency) for a slow polarization effect due to residual immobile dipoles in the insulating PVA layer.

thin-film transistors employing only a PVA layer as the gate insulator [25]. This phenomenon was ascribed to ionic impurities which moved in the dielectric bulk of the transistor. Such evidence is in accordance with the outcome of our study where the presence of charge motion in the polymeric dielectric layer was attributed to low mobility charges as consistently modeled in the simulations.

Examining the organic/dielectric interface is therefore crucial to draw conclusions on hysteresis. The chemical nature of polymeric gate dielectric/semiconductor interface has been found to play a key role for deeply understanding transport behavior and electrical performances in OTFTs [31–33]. In particular, a different electron trapping efficiency depending on the terminal side chains of the polymeric dielectrics has been suggested by Yoon et al. [34].

To assess the chemical end-groups on the both PVA and PVAad, FT-IR analyses were performed (Fig. 8). The reaction of PVA with ammonium dichromate results in the oxidation of hydroxyl groups. We can notice a considerable increase of the two bands at 1702 and 1560 cm^{-1} which, in agreement with the literature, can be attributed to C=O stretching vibrations of ketones and carboxylate groups respectively. Furthermore we observe the decrease of the OH stretching vibration band and two new absorption bands at 1658 and 1620 cm^{-1} which are quite characteristic of amide groups. The formation of these two bands might be due to some interaction between the starting NH_4 and chromium(VI), that would react with residual ester groups, leading to amide functions [35]. PVA is thus a hydroxyl-terminated dielectric, while PVAad contains a higher amount of ketone functionalities as already reported [36]. Ketone groups are known to be more effective electron traps than hydroxyls [34]. Therefore, the interface chemistry indicates that in both cases electron traps could play a major role and that, possibly, charge (electron) trapping should be even more efficient in PVAad based devices. The fact that PVAad does only show negligible hysteresis can be ascribed to either the presence of a few trap states or to the ability of these trap sites to trap and retain charge for times that are much longer than the measurement time. The possibility of strong electrostatic interaction with charge carriers due to polar carbonyl groups has been also recently pointed out [37].

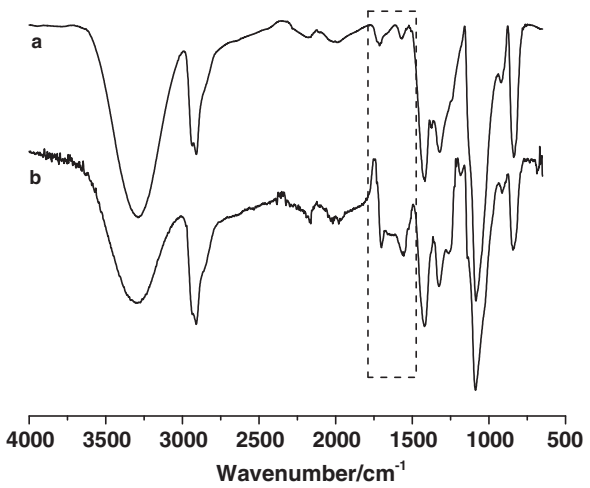

Fig. 8. FTIR Spectrum of (a) PVA and (b) PVA cross-linked with ammonium dichromate.

In the case of PVA (Fig. 3a), electron traps act by subtracting electrons while gate voltage is swept from positive to negative values (forward) but also, passing from positive to negative voltages, re-emit electrons which recombine with holes, thus lowering the drain current value. Analogously, when the gate voltage is swept backward since all of the electrons are likely to having been re-emitted, the hole population will be no longer (or much less) influenced by the presence of electrons so that the net amount of measured current will be higher. This explains the clockwise hysteresis loop observed on the I_d–V_g curves in devices using PVA and silicon dioxide as the insulating layer. On the other hand, if we assume that in devices using PVAad electron traps are much more effective than in PVA, as suggested by the chemistry of ketone and hydroxyl groups, it can be inferred that electron re-emission does not happen in the timeframe of the measurement. The forward curve does not therefore differ significantly from the backward curve. As further evidence, I_d–V_g curves were acquired on PVAad transistors at various gate sweep rate to explore the possible charge carriers re-emission, but negligible dependance on this parameter was observed (see Supplementary Data, Fig. S3).

In addition, these observations shed light on why n-type behavior has been never observed onto devices using PVAad as the gate dielectric whilst n-type transport has been widely reported on PVA-based transistors [32,38,39].

4. Conclusions

We have found that the charge transport across the bulk of a polymeric dielectric layer exerts a strong influence on the performances of the organic field-effect transistors. In particular it gives place to a large hysteresis on the transfer curves which impacts the extraction and the straight interpretation of major device parameters such as the field-effect mobility and the threshold voltage. This charge contribution was highlighted through space-charge limited current measurements carried out on MIM capacitors having a polymeric dielectric as the insulating layer. The extracted parameters were employed first to model and then to simulate the transfer curves of a pentacene-based thin-film transistor using PVA as the gate dielectric. The simulations confirmed the experimental data showing that the charge transport in the dielectric is the main responsible for the hysteresis that arises in the electrical measurements. The undesired contribution was blocked by the insertion of a silicon dioxide layer underlying the polymeric dielectric. The residual hysteretic behavior was analyzed and ascribed to the trapping effects occurring at the interface between the organic semiconductor and the polymeric dielectric. In this regard, the impact of the trapping efficiency due to the different chemical nature between PVA and PVAad was assessed: the increase of carbonyl groups in PVAad supports the idea of a stronger trapping

effect that could in fact lead to longer carrier emission times and reduced hysteresis in the I_d–V_g curves. From a practical perspective our work clearly shows that organic thin-film transistors should use organic dielectric layers in which this undesired charge contribution is blocked. In addition, this work points out the importance of the transistor device as a tool for investigating material properties and, on the other hand, it underlines that the extracted charge carrier mobility and threshold voltage values might not only depend on the chemical nature of the semiconductor/dielectric interface as widely shown in the past.

Acknowledgements

European Commission and the Italian Ministry of Research (MIUR) are acknowledged for funding this activity respectively under the Programme IST-IP, VI FP Integrated Project No. 26987 "PROETEX" and under PRIN 2006 ("Ion sensitive field effect devices on flexible films").

Appendix A. Supplementary data

Supplementary data associated with this article can be found, in the online version, at doi:10.1016/j.orgel.2010.12.014.

References

[1] Y.-Y. Noh, N. Zhao, M. Caironi, H. Sirringhaus, Nat. Nanotechnol. 2 (2007) 784.
[2] C.D. Dimitrakopoulos, P.R.L. Malenfant, Adv. Mater. 14 (2002) 99.
[3] M. Maccioni, E. Orgiu, S. Locci, P. Cosseddu, A. Bonfiglio, Appl. Phys. Lett. 89 (2005) 143515.
[4] H. Usta, C. Risko, Z. Wang, H. Huang, M.K. Deliomeroglu, A. Zhukhovitskiy, A. Facchetti, T.J. Marks, J. Am. Chem. Soc. 131 (2009) 5586.
[5] I. McCulloch, M. Heeney, C. Bailey, K. Genevicius, I. Macdonald, M. Shkunov, D. Sparrowe, S. Tierney, R. Wagner, W.M. Zhang, M.L. Chabinyc, R.J. Kline, M.D. McGehee, M.F. Toney, Nat. Mater. 5 (2006) 328.
[6] M. Morana, P. Koers, C. Waldauf, M. Koppe, D. Muehlbacher, P. Denk, M. Scharber, D. Waller, C. Brabec, Adv. Funct. Mater. 17 (2007) 3274.
[7] G. Horowitz, R. Hajlaoui, H. Bouchriha, R. Bourguiga, M. Hajlaoui, Adv. Mater. 10 (1998) 923.
[8] A.R. Brown, C.P. Jarrett, D.M. de Leeuw, M. Matters, Synth. Met. 88 (1997) 37.
[9] IEEE Std 1620™-2004, IEEE Standard Test Methods for the Characterization of Organic Transistors and Materials, 2004.
[10] K.P. Pernstich, S. Haas, D. Oberhoff, C. Goldmann, D.J. Gundlach, A.N. Rashid, G. Schitter, B. Batlogg, J. Appl. Phys. 96 (2004) 6431.
[11] Y.-Y. Noh, H. Sirringhaus, Org. Electron. 10 (2009) 174.
[12] U. Zschieschang, K. Amsharov, R.T. Weitz, M. Jansen, H. Klauk, Synth. Met. (2009) 159.
[13] T. Sekitani, Y. Noguchi, U. Zschiensang, H. Klauk, T. Someya, PNAS 105 (2008) 4976.
[14] T.B. Singh, N. Marjanovic, G.J. Matt, N.S. Sariciftci, Appl. Phys. Lett. 85 (2004) 5409.
[15] T.B. Singh, N. Marjanovic, P. Stadler, M. Auringer, G.J. Matt, N.S. Sariciftci, J. Appl. Phys. 97 (2005) 83714.
[16] D.K. Hwang, M.S. Oh, J.M. Hwang, J.H. Kim, S. Im, Appl. Phys. Lett. 92 (2008) 13304.
[17] S.H. Kim, H. Yang, S.Y. Yang, K. Hong, D. Choi, C. Yang, D.S. Chung, C.E. Park, Org. Electron. 9 (2008) 673.
[18] D. Park, C.A. Lee, K. Jung, B. Park, H. Shin, J.D. Lee, Appl. Phys. Lett. 89 (2006) 263507.
[19] M.A. Lampert, P. Mark, In Current Injection in Solids, Academic Press, New York, 1970.
[20] G. Gu, M.G. Kane, J.E. Doty, A.H. Firester, Appl. Phys. Lett. 87 (2005) 243512.
[21] R.W.I. De Boer, N.N. Iosad, A.F. Stassen, T.M. Klapwijk, A.F. Morpurgo, Appl. Phys. Lett. 86 (2005) 0321031.
[22] Y. Yun, C. Pearson, C. Petty, J. Appl. Phys. 105 (2009) 034508.
[23] Web source: <www.synopsys.com>.
[24] T. Li, J.W. Balk, P.P. Ruden, I.H. Campbell, D.L. Smith, J. Appl. Phys. 91 (2002) 4312.
[25] M. Egginger, M. Irimia-Vladu, R. Schwoediauer, A. Tanda, I. Frischauf, S. Bauer, N.S. Sariciftci, Adv. Mater. 20 (2008) 1018.
[26] K. Hess, U. Ravaioli, M. Gupta, N. Aluru, T. Van Der Straaten, R.S. Eisenberg, VLSI Des. 13 (2001) 179.
[27] C.M. Snowden (Ed.), Introduction to Semiconductor Device Modelling, World Scientific Pub. Co., Inc., 1987.
[28] D.K. Hwang, M.S. Oh, J.M. Hwang, J.H. Kim, S. Im, Appl. Phys. Lett. 92 (2008) 013304.
[29] D.K. Hwang, K. Lee, J.H. Kim, S. Im, J.H. Park, E. Kim, Appl. Phys. Lett. 89 (2006) 093507.
[30] H. Klauk, Organic Electronics, Wiley-VCH Verlag GmbH and Co., KGaA, New York, 2006. pp. 132–162, (Chapter 6).
[31] L. Chua, J. Zaumseil, J. Chang, E. Ou, P. Ho, H. Sirringhaus, R.H. Friend, Nature 434 (2005) 194.
[32] T.B. Singh, F. Meghdadi, S. Gunes, N. Marjanovic, G. Horowitz, P. Lang, S. Bauer, N.S. Sariciftci, Adv. Mater. 17 (2005) 2315.
[33] J. Veres, S. Ogier, G. Lloyd, D. De Leeuw, Chem. Mater. 16 (2004) 4543.
[34] M. Yoon, C. Kim, A. Facchetti, T.J. Marks, J. Am. Chem. Soc. 128 (2006) 12851.
[35] F. Djouani, Y. Israeli, L. Frezet, A. Rivaton, R.A. Lessard, M. Bolte, J. Polym. Sci. Polym. Chem. 44 (2006) 1317.
[36] L. Grimm, K.-J. Hilke, E. Scharrer, J. Electrochem. Soc. 130 (1983) 1767.
[37] N.G. Martinelli, M. Savini, L. Muccioli, Y. Olivier, F. Castet, C. Zannoni, D. Beljonne, J. Cornil, Adv. Funct. Mater. 19 (2009) 1.
[38] M. Schidleja, C. Melzer, H. von Seggern, Appl. Phys. Lett. 94 (2009) 123307.
[39] S. Takebayashi, S. Abe, K. Saiki, K. Ueno, Appl. Phys. Lett. 94 (2009) 083305.

Organic Electronics 12 (2011) 486–491

Contents lists available at ScienceDirect

Organic Electronics

journal homepage: www.elsevier.com/locate/orgel

Room temperature lifetime of triplet excitons in fluorescent host/guest systems

Marcus Lehnhardt [a], Thomas Riedl [b], Torsten Rabe [a,*], Wolfgang Kowalsky [a]

[a] Institut für Hochfrequenztechnik, Technische Universität Braunschweig, 38106 Braunschweig, Germany
[b] Institute of Electronic Devices, Bergische Universität Wuppertal, Rainer-Gruenter Str. 21, 42119 Wuppertal, Germany

ARTICLE INFO

Article history:
Received 12 November 2010
Accepted 27 December 2010
Available online 8 January 2011

Keywords:
Triplet–triplet annihilation
Host/guest system
Fluorescent OLED
Organic solid state laser

ABSTRACT

We studied the triplet decay dynamics in the fluorescent polymer–polymer host/guest system F8BT/MEH-PPV and in the small molecule host/guest system Alq_3/DCM. The triplet lifetime was determined by a highly sensitive time-resolved measurement of the triplet state absorption via a pump and probe experiment in a waveguide structure. We were able to identify triplet–triplet annihilation as a major decay mechanism of triplet states in the pristine amorphous organic materials at room temperature (rate constant: $k_{TT} \approx 10^{-12}\,cm^3\,s^{-1}$). On the contrary, the host/guest systems showed a significantly increased triplet lifetime caused by a reduced triplet–triplet annihilation rate which we attribute to a substantially lowered mobility of the localized triplet excitons. Our results are expected to be of paramount importance for organic light emitting devices based on fluorescent emitters (e.g. organic lasers and organic light emitting diodes).

© 2011 Elsevier B.V. All rights reserved.

1. Introduction

Fluorescent organic materials are widely used in organic light emitting diodes (OLEDs) and organic lasers. Systems consisting of an emitter doped into a wider energy band gap host material generally increase the device performance compared to neat materials. Organic devices like OLEDs or lasers using these host/guest systems show higher efficiencies [1], a lower lasing threshold, or a wider tuning range [2]. In OLEDs, singlet and triplet excitons are generated by charge carrier recombination at a ratio of 1:3. In fluorescent materials, the emission from triplet states is very weak because the triplet energy is efficiently converted to heat. This limits the internal efficiency in fluorescent OLEDs to less than 25%. Nevertheless, triplet–triplet annihilation (TTA) can be used in fluorescent OLEDs to generate additional singlet states from otherwise useless triplet excitons [3–6], which leads to very high efficiencies, even exceeding the classical theoretical limit [7,8]. This is particularly important for lighting applications, where elevated luminance levels are required. Today, highly efficient OLEDs commonly use triplet emitters which suffer from a strong decrease in efficiency at high current densities (''roll off'') [9]. Here, fluorescent OLEDs using the TTA to generate additional singlet excitons may be promising alternatives especially for the blue spectral region. On the other hand, triplet excitons can also reduce the device performance by singlet–triplet annihilation [10] or by the triplet state absorption. These effects are especially relevant for organic lasers [11,12], where the triplet absorption is predicted to be a major obstacle preventing electrically driven lasing [11,13].

In view of the importance of triplet related processes in both OLEDs and organic lasers, information about the TTA rate at room temperature and the lifetime of triplet excitons is a key to the understanding and the design of efficient devices. Based on the approach presented in this paper, we are able to assess these quantities and study the triplet dynamics in organic host/guest systems.

The TTA rate is related to the triplet diffusion coefficient since the triplet mobility directly relates to the probability that two triplet excitons meet. Giebink et al. demonstrated

* Corresponding author. Fax: +49 531 391 2008.
E-mail address: torsten.rabe@ihf.tu-bs.de (T. Rabe).

1566-1199/$ - see front matter © 2011 Elsevier B.V. All rights reserved.
doi:10.1016/j.orgel.2010.12.017

a reduced triplet diffusion in 4,4′-bis(*N*-carbazolyl)biphenyl (CBP) by blending with *p*-bis(triphenylsilyl)benzene (UGH2) [14]. They attributed this observation to the higher triplet energy of UGH2 which forms an energy barrier for CBP triplets. In commonly used fluorescent host/guest systems, the wide-band-gap host might support the localization of triplets on the guest molecules in a similar way and thereby hinder their diffusion. In this case, one has to be careful by simply using the often reported TTA rates for pristine materials for fluorescent host/guest devices without change. To our knowledge, this important effect has not been studied for fluorescent systems so far, mainly due to the difficulties in the observation of the predominantly non-radiative nature of triplet states at room temperature.

In this paper we study the triplet lifetime in the polymer–polymer host/guest system *poly*[(9,9-di-*n*-octylfluorenyl-2,7-diyl)-alt-(benzo[2,1,3]thiadiazol-4,8-diyl)] (F8BT) and *poly*[2-methoxy-5-(2-ethylhexyloxy)-1,4-phenylene-vinylene (MEH-PPV) and the small molecule host/guest system tris(8-hydroxyquinoline)aluminium(III) (Alq_3) and 4-(dicyanomethethylene)-2-methyl-6-[*p*-(di-methyl-amino)styryl]-4H-pyran (DCM). The triplet lifetime is determined by measuring the time resolved triplet absorption at room temperature in amorphous thin films. A waveguide structure is used to achieve a highly sensitive measurement [15]. We determined the triplet decay in the host/guest systems as well as in the corresponding pristine materials. As a result, we found a significantly longer triplet lifetime in the host/guest systems due to a reduced TTA rate, which we attribute to a decreased diffusion constant for triplet excitons, whereas in pristine materials the TTA is dominating the decay mechanism at triplet densities relevant for OLEDs.

2. Experimental

The triplet lifetime measurement was carried out as shown in Fig. 1. The organic layers form a waveguide structure for the light generated by the pump and the probe pulse. Both pulses were separated spatially and temporally to exclusively measure the triplet absorption. Specifically, the edge emission of the waveguide is detected with spectral and temporal resolution. For the determination of the triplet lifetime, the wave guided emission generated by excitation with the probe pulse has to pass the region, where the previous excitation by the pump pulse has led to the creation of triplet excitons. Therefore, the intensity of the edge emission, detected for different delay times between pump and probe pulse, will be directly related to the absorption due to triplets in this region of the waveguide. All measurements are carried out at room temperature.

The organic layers were deposited on silicon wafers covered with 2 μm silicon dioxide. The 180 nm thick polymer layers were spincast from chlorobenzene solution and dried at 60 °C for ten minutes on a hotplate. The 200 nm thick small molecule thin films were prepared by thermal evaporation in ultra high vacuum (base pressure 10^{-8} mbar). The organic layer thicknesses were chosen to build up a waveguide structure on top of the silicon

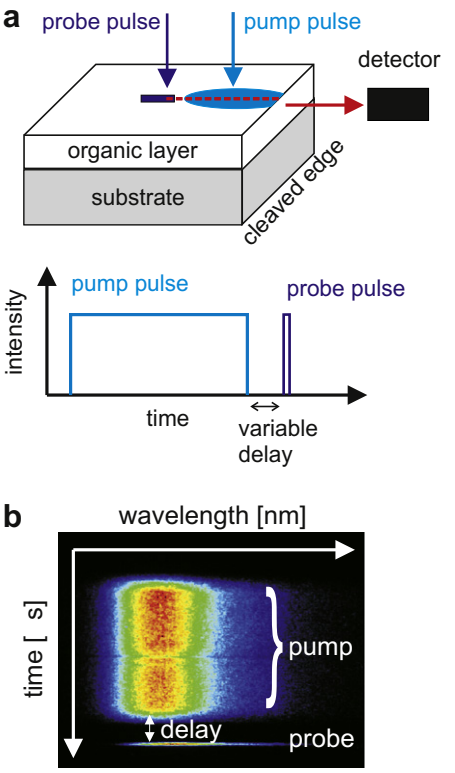

Fig. 1. (a) Measurement setup for triplet lifetime determination. (b) Streak camera image of the detection signal.

dioxide which enables only the propagation of the first transverse electrical mode (TE_0). To simulate the optical mode a transfer matrix algorithm [17] was used taking the dispersion of the refractive index into account. As a pump source for triplet generation via ISC we used two InGaN based laser diodes ($\lambda = 445$ nm and $\lambda = 405$ nm) provided by Nichia Chemical (NBD7112, NDHV220APAE1). If not mentioned explicitly the laser diode emitting at $\lambda = 445$ nm was used in the experiments. The laser diodes were driven with a pulse width of 10 μs and a repetition rate of 2 kHz. The multimode output of the diode is focussed on a spot of around 0.77×0.18 mm^2 with a pump pulse energy density of 600–900 μJ/cm^2.

As a source for the probe pulse we used a Q-switched, frequency-tripled, diode pumped solid-state (DPSS) laser emitting at $\lambda = 355$ nm. The pulse width and repetition rate were 700 ps and 2 kHz, respectively. The probe pulse is focussed on a stripe of 27 μm width and an adjustable length of approximately 0.5 mm. During the optical measurements, the samples were mounted in a nitrogen purged chamber. The probe pulse is positioned 0.1 mm behind the pump pulse with respect to the sample edge, as shown in Fig. 1. This spatial separation excludes singlet–triplet annihilation [12]. The probe pulse follows the pump pulse with a variable time delay of 200 ns to 488 μs. A minimum delay of 200 ns assures that all singlets generated by the pump pulse are decayed. The edge emission is detected by a streak camera (Hamamatsu C4334) to allow spectral and temporal resolution (Fig. 1b)). The light generated by

the probe pulse is monitored against the delay between pump and probe pulse. By using waveguide simulations the triplet induced material absorption is calculated with the optical confinement factor Γ in a spectral region where the principal waveguide loss (without triplet absorption) is sufficiently low [16]. The following spectral regions are used for the calculation of the average material absorption shown in the following: F8BT 557–687 nm; MEH-PPV: 627–657 nm; F8BT/MEH-PPV: 642–727 nm; Alq_3: 517–642 nm; Alq_3/DCM: 632–657 nm.

3. Results

3.1. Triplet generation via intersystem crossing

In this study we use a laser diode pump pulse to generate triplet states. The incident light of the pump pulse is absorbed in the organic material and produces excited singlet states. Triplet states can be formed via intersystem crossing (ISC) from the singlets [18]. The process is described below:

$$S_0 + h\nu \rightarrow S_1 \overset{k_{ISC}}{\rightarrow} T_1 \quad (1)$$

S_0 denotes a molecule in the ground state, S_1 the lowest excited singlet state and T_1 the lowest excited triplet state. The efficiency of this process is determined by the intersystem crossing rate k_{ISC} or by the quantum yield $\Phi = k_{ISC}\tau_S$ (τ_S = singlet lifetime). For F8BT quantum yields of $\Phi = 0.02$ [19,20] and for MEH-PPV $\Phi = 0.0125$–0.025 [21,22] have been published, respectively. Alq_3 showed quantum yields of $\Phi = 0.12$–0.24 [23,24]. During the pump pulse triplets accumulate, whereas the singlets decay relatively fast [20,23]. As we will show later, we achieve triplet densities in the order of 10^{17} cm^{-3}, which is close to typical triplet densities in OLEDs [25] where the triplet states are generated efficiently by charge recombination. In our case high triplet densities are achieved in spite of the less efficient ISC process by using long excitation pulses and a high excitation density.

Beside their intrinsic decay, triplets can decay via TTA determined by the rate constant k_{TT} as described below in detail

$$T_1 + T_1 \overset{k_{TT}}{\rightarrow} S_0 + T_n \rightarrow T_1 + S_0 \quad (2)$$
$$S_n + S_0 \rightarrow S_1 + S_0$$

After the annihilation of two triplet excitons, a highly excited triplet state T_n is populated. Some fraction converts to the S_n state and then, after relaxation, the fluorescence from S_1 can be detected (delayed fluorescence) [26]. In the case of Alq_3 we observed delayed fluorescence at 12 K after excitation with the pump pulse (not shown here), which indicates the occurrence of the discussed triplet–triplet interaction [27]. Note that our subsequent measurements are not influenced by the delayed fluorescence because of its very low intensity at room temperature. To calculate the generated triplet density we will use the triplet absorption cross section σ_T taken from literature data to derive the triplet density.

3.2. Triplet lifetime in F8BT/MEH-PPV

Initially, we studied the pristine material F8BT. In Fig. 2a the absorption spectrum is shown for varied delay times between pump and probe pulse. For the smallest delay time triplet related absorption causes an almost 50% decay of the signal. For longer delay times the triplet density becomes smaller and the signal is less attenuated. The spectral characteristics are in good agreement with previous publications of the triplet absorption spectra [28]. For wavelengths shorter than 540 nm the ground state absorption of F8BT limits the short wavelength site of the measurement. At long wavelengths the measurement is limited by the photoluminescence spectrum of F8BT. Further details concerning the spectral characteristics of triplet absorption and the generation of triplet states via laser diode excitation have been published before for F8BT, MEH-PPV and F8BT/MEH-PPV [12]. From our measurements (Fig. 2a) the triplet induced material absorption is calculated by a simulation of the light propagating in the waveguide. The results are displayed in Fig. 2b (to minimize the impact of noise the average absorption for a reasonable spectral region is taken). The fit is calculated according to the model described below.

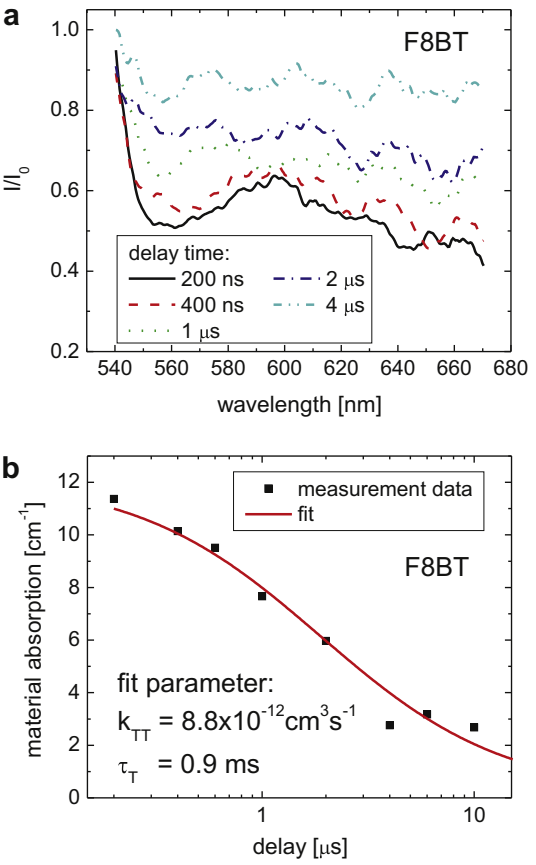

Fig. 2. (a) Spectrally resolved intensity of light generated by the probe pulse (I) for different delays to the pump pulse in comparison to the signal without a pump pulse (I_0). The spectra are shown for the material F8BT. (b): Average material absorption calculated for (a) and fit according to formula (3).

Hale et al. showed that TTA is a major de-excitation mechanism for photo excited triplet excitons in MEH-PPV [29]. In order to express the triplet decay dynamics we used the following model [30]:

$$\frac{dn_T}{dt} = n_0 - \frac{n_T}{\tau_T} - \frac{1}{2}k_{TT} \times n_T^2 \quad (3)$$

Here, aside from the intrinsic decay (intrinsic lifetime τ_T) the TTA rate k_{TT} is included as a further decay mechanism. The triplet density is described by n_T. The initial triplet density n_0 is generated by the pump pulse.

Fig. 3 shows that in the host/guest system F8BT/MEH-PPV (16 wt.%) a significantly slower decay is measured than for pristine MEH-PPV.

It should be noted that a simple mono exponential model which disregards the TTA does not sufficiently describe our observations.

As mentioned above n_0 is calculated straight forward by using the triplet absorption cross section σ_T. For F8BT a cross section of $\sigma_T = 1 \times 10^{-16}$ cm^2 in the spectral region around 600 nm is assumed according to previous reports [19,28,31,32]. For MEH-PPV a cross section of $\sigma_T = 5 \times 10^{-16}$ cm^2 in the spectral region around $\lambda = 680$ nm is taken for the calculation [33]. A higher absorption cross section for PPV in comparison to F8BT has been theoretically predicted by Ford et al. [19]. In case of the host/guest system the same σ_T is assumed as that used for MEH-PPV [12]. The measurement data are fitted with k_{TT} and τ_T as fitting parameters.

For F8BT an annihilation rate of $k_{TT} = 8.8 \times 10^{-12}$ cm^3 s^{-1} and for MEH-PPV of $k_{TT} = 5.4 \times 10^{-12}$ cm^3 s^{-1} is obtained. According to the results of our experiment, TTA is the major decay mechanism in the pristine materials under our experimental conditions. The triplet lifetime τ_T is fitted best with a value of 0.4 ms for MEH-PPV and 0.9 ms for F8BT, respectively. Due to the dominating influence of TTA on the decay, the fitted lifetime τ_T is subject to a relatively large uncertainty. Nevertheless, the determined values of 0.9 ms for F8BT and 0.4 ms for MEH-PPV are in good agreement with earlier reports. For F8BT a triplet lifetime of 0.98 ms has been reported at low temperatures of 10 K where TTA is insignificant [19]. For MEH-PPV in solution triplet lifetimes in the order of 0.1 ms have been reported [22,33].

In case of the host/guest system, the measurement data are favorably simulated with $k_{TT} = 6.2 \times 10^{-13}$ cm^3 s^{-1}, which is nearly one order of magnitude lower than in the pristine materials. Interestingly the intrinsic lifetime τ_T is determined to be 0.4 ms, which is similar to that of pristine MEH-PPV. Disregarding the TTA a mono exponential fit leads to a time constant of $\tau_{mono.exp.} = 138$ µs.

3.3. Triplet lifetime in Alq_3/DCM

In the second experiment, we studied the triplet decay in the archetype small molecule based host/guest system Alq_3/DCM (2 vol.%). The spectrally resolved triplet related absorption for pristine Alq_3 and for the doped system is shown in Fig. 4. As mentioned in the experimental, the observable spectral region is limited by the edge emission spectrum of the sample. For Alq_3 we found an triplet

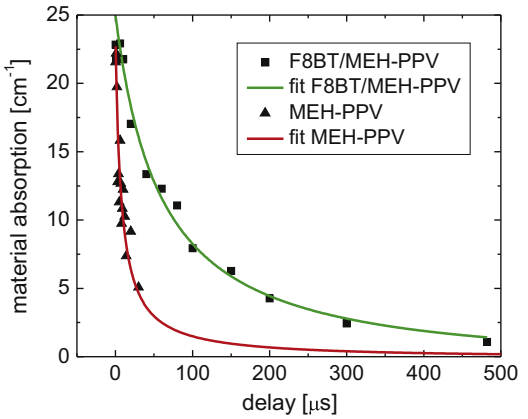

Fit parameter:

Material	k_{TT}[cm^{3}s^{-1}]	τ_T[ms]
F8BT	8.8x10^{-12}	0.9
MEH-PPV	5.4x10^{-12}	0.4
F8BT:MEH-PPV	6.2x10^{-13}	0.4

Fig. 3. Material absorption of the MEH-PPV and F8BT/MEH-PPV vs. the delay time between pump and probe pulse. Fits are according to (3).

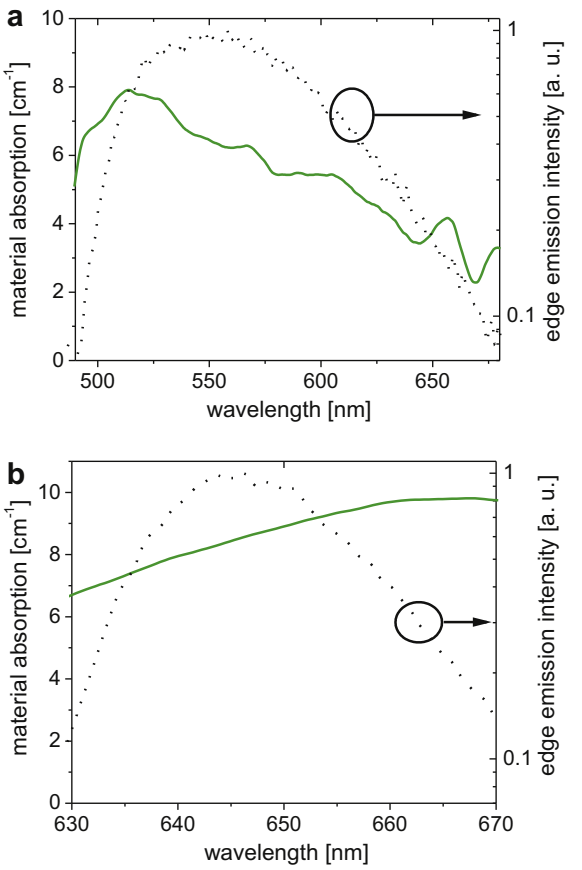

Fig. 4. Triplet absorption spectra and edge emission spectra for Alq_3 (a) and Alq_3/DCM (b).

absorption maximum around 515 nm which is in good agreement with former publications [23,24]. In the doped system we measured increasing triplet absorption from 630 nm to 670 nm which has also been observed for pristine DCM [34].

The triplet dynamics are fitted by the model described above. For Alq_3 a triplet absorption cross section of $\sigma_T = 1.27 \times 10^{-17}$ cm^2 is used for the calculation [24]. The host/guest system is fitted with $\sigma_T = 3.4 \times 10^{-17}$ cm^2 as reported for DCM [34]. The results are displayed in Fig. 5. We observed dramatically slower triplet decay in the host/guest system compared to that in pristine Alq_3. Referring to our model the TTA is dominating the decay in pristine Alq_3 with a rate constant of $k_{TT} = 2.2 \times 10^{-12}$ cm^3 s^{-1}. In contrast to this TTA is insignificant in Alq_3/DCM corresponding to very low annihilation rate of $k_{TT} \approx 1 \times 10^{-15}$ cm^2. Zhang et al. proposed a similar rate of $k_{TT} = 2.2 \times 10^{-15}$ cm^{-3} s^{-1} for Alq_3/DCM in OLEDs [10]. In our experiments the decay in the host/guest system is favorably fitted with a triplet lifetime of $\tau_T = 1.55$ ms, which is significantly longer than published for pristine DCM [34,35].

For pristine DCM we observed no triplet induced absorption for a minimal delay time between pump and probe pulse of 100 ns and excitation densities below 1 mJ/cm^2. Also no photoluminescence quenching due to singlet–triplet annihilation was observed in our experiments (details about the used measurement technique have been reported elsewhere [12]). Assuming a triplet absorption cross section of $\sigma_T = 3.4 \times 10^{-17}$ cm^2 (630–670 nm) the triplet density must be lower than 1×10^{16} cm^{-3}, to fall below the detection limit of our technique. A possible cause for these observations is an inefficient generation of triplet excitons by the pump pulse or a very fast triplet decay. Both effects lead to low densities of triplet excitons. For DCM a low quantum yield for triplet generation via ISC has been published ($\Phi \leqslant 3 \times 10^{-3}$) [34,36]. Furthermore, it has been shown that pristine DCM films suffer from strong concentration quenching which obviously influences triplet excitons as well [37].

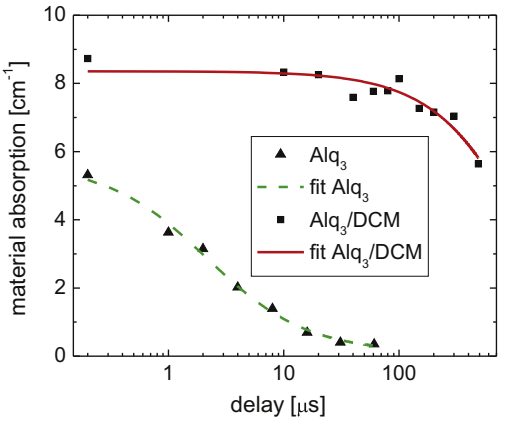

Fit parameter:

Material	k_{TT}[cm^{3}s^{-1}]	τ_T[ms]
Alq_3	2.2×10^{-12}	0.17
Alq_3/DCM	1×10^{-15}	1.55

Fig. 5. Triplet absorption decay in Alq_3 ($\lambda_{pump} = 405$ nm) and Alq_3 doped with 2 vol.% DCM. Fit parameters are shown in the table.

4. Discussion

Our experimental results have shown a high TTA rate in the pristine materials in the order of 10^{-12} cm^3 s^{-1} at room temperature. In comparison to our results for the pristine F8BT and Alq_3 former publications carried out at low temperatures showed 2–3 orders of magnitude lower TTA rates for pristine fluorescent materials [19,39]. The obvious discrepancy in the TTA rates can be explained by blocked triplet diffusion at extremely low temperatures [26,38].

In contrast to the pristine materials, we observed strongly reduced (by 1–3 orders of magnitude) TTA in both the polymer host/guest system and the small molecule host/guest system. This effect can be explained by assuming a deep trap for the triplet excitons on the guest site. This leads to a strong stabilization of triplet excitons, yielding in low TTA rates similar to TTA rates obtained by low temperature measurements as mentioned above. It has been shown that the diffusion of triplets depends exponentially on the energy difference between the interacting (neighboring) molecules [40–42]. However, Staroske et al. showed that TTA can take place even for low mobility triplet excitons and attributed this to a long range Förster-type energy transfer between the guest molecules [9] yielding in a lower limit for the TTA rate.

Due to the spectral characteristics of the triplet absorption and the efficient energy transfer from the host to the guest molecules we can assume that the majority of triplets are located on the guest. To understand the triplet diffusion in host/guest systems, the triplet energies of the host and the guest as well as the position to each other must be considered. For MEH-PPV a triplet energy of 1.27 eV and a S_1–T_1 splitting of 1.1 eV have been published [22]. Köhler et al. reported on an almost constant S_1–T_1 splitting of 0.7 eV in a large number of conjugated polymers [18]. Assuming a similar S_1–T_1 splitting for F8BT, the triplet excitons on the guest (MEH-PPV) have a significantly lower energy than the triplet states of the host. This energy difference forms a barrier which reduces the triplet diffusion and therefore explains our observation of a strikingly lowered TTA rate. For Alq_3 a triplet energy around 2.1 eV [24,43] and a S_1–T_1 splitting of 0.64 eV [43] was measured. Chang et al. reported on the triplet level of DCM and found a lower T_1 level than S_1 like it is the case in the materials discussed above [44]. As above, the different triplet energies of guest and host form an energy barrier which might hinder the triplet diffusion from the dopant. The non-dispersive triplet diffusion coefficient D_T is proportional to the TTA rate. In case of our polymer–polymer system the reduced TTA rate corresponds to a triplet mobility one order of magnitude lower than of the pristine guest. The extremely low annihilation rate in Alq_3/DCM correlates with a very low diffusion of DCM triplet excitons. As mentioned before we could not study triplets in pristine DCM thin films due to severe concentration quenching of excitons.

In the polymer host/guest system F8BT/MEHPPV we observed a much weaker stabilization of the triplets (corresponding to a weaker decrease of the TTA rate) than in the small molecule host/guest system Alq_3/DCM. In case of the polymer system efficient triplet transfer along the polymer chain can take place [41,42], which is not frustrated by the blending into the host.

5. Conclusion

In summary we measured the triplet decay in the fluorescent host/guest systems F8BT/MEH-PPV and Alq_3/DCM. The measurements were performed using a highly sensitive pump and probe experiment in a waveguide structure. This technique allows studying triplets in amorphous thin films of fluorescent organic materials at room temperature; under conditions relevant for organic devices. For the pristine materials the following TTA rates were calculated: F8BT: $k_{TT} = 8.8 \times 10^{-12}$ cm^3 s^{-1}, MEH-PPV: $k_{TT} = 5.4 \times 10^{-12}$ cm^3 s^{-1} and Alq_3: $k_{TT} = 2.2 \times 10^{-12}$ cm^3 s^{-1}. On the contrary, the host/guest systems showed a triplet lifetime orders of magnitude larger. Based on our model, we attribute this phenomenon to a strongly reduced TTA rate. We determined TTA rates for F8BT/MEH-PPV of $k_{TT} = 6.2 \times 10^{-13}$ cm^3 s^{-1} and for Alq_3/DCM of $k_{TT} = 1 \times 10^{-15}$ cm^3 s^{-1}, respectively. We believe that our findings for these model systems are of a general character and will be of substantial importance for the understanding, the design and optimization of fluorescent organic opto-electronic devices.

Acknowledgements

This work was financially supported by the German Federal Ministry for Education and Research BMBF (FKZ 13N8166A).

References

[1] C.W. Tang, S.A. VanSlyke, C.H. Chen, J. Appl. Phys. 65 (1989) 3610.
[2] D. Schneider, T. Rabe, T. Riedl, T. Dobbertin, M. Kröger, E. Becker, H. Johannes, W. Kowalsky, T. Weimann, J. Wang, P. Hinze, Appl. Phys. Lett. 85 (2004) 1886.
[3] C. Ganzorig, M. Fujihira, Appl. Phys. Lett. 81 (2002) 3137.
[4] D.Y. Kondakov, J. Appl. Phys. 102 (2007) 114504.
[5] Y. Luo, H. Aziz, Adv. Func. Mater. 20 (2010) 1285.
[6] Z.D. Popovic, H.J. Aziz, Appl. Phys. 98 (2005) 013510.
[7] J. Kido, T. Matsumoto, Appl. Phys. Lett. 73 (1998) 2866.
[8] K. Okumoto, H. Kanno, Y. Hamaa, H. Takahashi, K. Shibata, Appl. Phys. Lett. 89 (2006) 063504.
[9] W. Staroske, M. Pfeiffer, K. Leo, M. Hoffmann, Phys. Rev. Lett. 98 (2007) 197402.
[10] Y. Zhang, M. Whited, M.E. Thompson, S.R. Forrest, Chem. Phys. Lett. 495 (2010) 161.
[11] N.C. Giebink, S.R. Forrest, Phys. Rev. B 79 (2009) 073302.
[12] M. Lehnhardt, T. Riedl, T. Weimann, W. Kowalsky, Phys. Rev. B 81 (2010) 165206.
[13] C. Gärtner, C. Karnutsch, U. Lemmer, C. Pflumm, J. Appl. Phys. 101 (2007) 023107.
[14] N. Giebink, Y. Sun, S. Forrest, Org. Electron. 7 (2006) 375.
[15] T. Rabe, P. Görrn, M. Lehnhardt, M. Tilgner, T. Riedl, W. Kowalsky, Phys. Rev. Lett. 102 (2009) 137401.
[16] T. Rabe, S. Hamwi, J. Meyer, P. Görrn, T. Riedl, H. Johannes, W. Kowalsky, Appl. Phys. Lett. 90 (2007) 151103.
[17] R.E. Smith, S.N. Houde-Walter, G.W. Forbes, IEEE J. Quantum Electron. 28 (1992) 1520.
[18] A. Köhler, D. Beljonne, Adv. Func. Mater. 14 (2004) 11.
[19] T.A. Ford, I. Avilov, D. Beljonne, N.C. Greenham, Phys. Rev. B 71 (2005) 125212.
[20] J. Yu, R. Lammi, A.J. Gesquiere, P.F. Barbara, J. Phys. Chem. B 109 (2005) 10025.
[21] H.D. Burrows, J.S. de Melo, C. Serpa, L.G. Arnaut, A.P. Monkman, I. Hamblett, S. Navaratnam, J. Chem. Phys. 115 (2001) 9601.
[22] A.P. Monkman, H.D. Burrows, M. da G. Miguel, L. Hamblett, S. Navaratnam, Chem. Phys. Lett. 307 (1999) 303.
[23] S. Watanabe, A. Furube, R. Katoh, J. Phys. Chem. A 110 (2006) 10173.
[24] H.D. Burrows, M. Fernandes, J. Seixas de Melo, A.P. Monkman, S. Navaratnam, J. Am. Chem. Soc. 125 (2003) 15310.
[25] S. Reineke, T.C. Rosenow, B. Lüssem, K. Leo, Adv. Mater. 22 (2010) 3189.
[26] A. Köhler, H. Bässler, Mater. Sci. Eng. R 66 (2009) 71.
[27] M. Cölle, C. Gärditz, J. Lumin. 110 (2004) 200.
[28] C. Lee, X. Yang, N.C. Greenham, Phys. Rev. B 76 (2007) 245201.
[29] G.D. Hale, S.J. Oldenburg, N.J. Halas, Phys. Rev. B 55 (1997) R16069.
[30] M.A. Baldo, C. Adachi, S.R. Forrest, Phys. Rev. B 62 (2000) 10968.
[31] H. Ohkita, S. Cook, T. Ford, N.C. Greenham, J.C. Durrant, J. Photochem. Photobiol. A 182 (2006) 225.
[32] S. Westenhoff, I.A. Howard, J.M. Hodgkiss, K.R. Kirov, H.A. Bronstein, C. Williams, N.C. Greenham, R.H. Friend, J. Am. Chem. Soc. 130 (2008) 13653.
[33] L.P. Candeias, G. Padmanaban, S. Ramakrishnan, Chem. Phys. Lett. 349 (2001) 394.
[34] M. Meyer, J.C. Mialocq, B. Perly, J. Phys. Chem. 94 (1990) 98.
[35] A. Barbon, E.D. Bott, M. Brustolon, M. Fabris, B. Kahr, W. Kaminsky, P.J. Reid, S.M. Wong, K.L. Wustholz, R. Zanré, J. Am. Chem. Soc. 131 (2009) 11548.
[36] J.C. Mialoq, M. Meyer, Laser Chem. 10 (1989) 277.
[37] F.P. Schäfer, Dye Lasers, Springer-Verlag, 1990.
[38] J.C. Ribierre, A. Ruseckas, I.D.W. Samuel, S.V. Staton, P.L. Burn, Phys. Rev. B 77 (2008) 085211.
[39] C. Rothe, H.A. Al Attar, A.P. Monkman, Phys. Rev. B 72 (2005) 155330.
[40] I.I. Fishchuk, A. Kadashchuk, L. Sudha Devi, P. Heremanns, H. Bässler, A. Köhler, Phys. Rev. B 78 (2008) 045211.
[41] L. Sudha Devi, M.K. Al-Suti, C. Dosche, M.S. Khan, R.H. Friend, A. Köhler, Phys. Rev. B 78 (2008) 045210.
[42] D. Hertel, H. Bässler, R. Guentner, U. Scherf, J. Chem. Phys. 115 (2001) 10007.
[43] R.L. Martin, J.D. Kress, I.H. Campbell, D.L. Smith, Phys. Rev. B 61 (2000) 15804.
[44] C. Chang, Y. Kao, E.W. Diau, Chem. Phys. Lett. 374 (2003) 110.

Organic Electronics 12 (2011) 492–496

Contents lists available at ScienceDirect

Organic Electronics

journal homepage: www.elsevier.com/locate/orgel

Letter

Efficient green OLED devices with an emissive layer comprised of phosphor-doped carbazole/bis-oxadiazole side-chain polymer blends

Sung-Jin Kim [a,1], Yadong Zhang [b], Carlos Zuniga [b], Stephen Barlow [b], Seth R. Marder [b], Bernard Kippelen [a,*]

[a] Center for Organic Photonics and Electronics (COPE) and School of Electrical and Computer Engineering, Georgia Institute of Technology, Atlanta, GA 30332, USA
[b] Center for Organic Photonics and Electronics (COPE) and School of Chemistry and Biochemistry, Georgia Institute of Technology, Atlanta, GA 30332, USA

ARTICLE INFO

Article history:
Received 1 October 2010
Received in revised form 10 December 2010
Accepted 11 December 2010
Available online 23 December 2010

Keywords:
Organic light-emitting diodes
Electroluminescence
Bis-oxadiozole polymer

ABSTRACT

High-efficiency organic light-emitting devices (OLEDs) were fabricated in which solution-processed ambipolar blends of hole- and electron-transport polymer hosts doped with a green-emitting iridium complex are sandwiched between a photocrosslinked hole-transporting layer and a vacuum-deposited electron-transporting layer. The ambipolar host blends consist of blends of bis-oxadiazole-functionalized poly(norbornene) electron-transport materials and poly(*N*-vinylcarbazole). For the best device examined, an external quantum efficiency of 13.6% and a maximum luminous efficiency of 44.6 cd/A at 1000 cd/m^2 with a turn-on voltage of 5.9 V were obtained.

© 2011 Elsevier B.V. All rights reserved.

Considerable research has been directed toward the synthesis of organic light-emitting diodes (OLEDs) with respect to their illumination applications and potential to be used to cover surfaces, or to be placed on objects of various shapes [1–5]. Current OLEDs have achieved significant luminous efficiencies at brightness levels that are compatible with portable flat-panel display technologies [6–8]. In particular, efficient OLEDs based on phosphorescent emitters have been demonstrated by either co-evaporation of guest and host molecules from the vapor phase [2,3], or by doping a semiconducting polymer with transport molecules and phosphor emitters [1]. However, a concern with these guest/host approaches is the stability of the resulting material. Another approach of interest is the blending of semiconducting polymers together, where one possesses good hole-transport properties and another possesses good electron-transport properties and provide for a blended ambipolar host for the emissive layer. The polymer blend may be a more challenging approach than the doping of a polymer with small molecules because it can result in materials phenomena, such as vertical phase segregation [9,10], that can decrease device efficiency and lifetime. While blends of conjugated polymers in OLEDs have been widely studied [11] with external quantum efficiencies as high as 6% [12], reports on blends of side-chain polymers are scarce [13] with external quantum efficiencies below 0.1%.

The literature on oxadiazole-type small molecules used for OLEDs demonstrates their use for improvement of electron transporting properties in polymer OLEDs based on polyfluorenes [14–16]. They have also been shown to have effective electron injection and transport functionality [17,18], in addition to hole-blocking properties [19], and their use as hosts for phosphorescent polymeric OLEDs has also been explored [20]. We have therefore, synthesized poly(norbornene)s functionalized with bis-oxadiazole side chain groups for electron-transport application. In order to balance hole and electron transport in the host based on bis-oxadiazole polymers, an additional material with hole transport properties is desirable. This can be achieved by adding a molecular compound or a hole transporting polymer.

* Corresponding author. Tel.: +1 404 385 5163; fax: +1 404 385 5170.
E-mail addresses: kippelen@ece.gatech.edu, kippelen@gatech.edu (B. Kippelen).
[1] Present address: College of Electrical and Computer Engineering, Chungbuk National University, Cheongju 361-763, Korea.

1566-1199/$ - see front matter © 2011 Elsevier B.V. All rights reserved.
doi:10.1016/j.orgel.2010.12.006

Here, we report on some surprising results on green phosphorescent devices based on an emitting layer that is formed by blending an electron transporting polymer and hole transporting polymer together and by doping the blend with the phosphor $Ir(ppy)_3$ [21,22] or $Ir(pppy)_3$ [23]. In this work, the polymer blends are comprised of PVK and one of two bis-oxadiazole polymers. PVK was used as a hole transporting functional moiety and bis-oxadiazole side chain polymers based on a poly(norbornene) backbone were used as a electron-transport component.

Fig. 1 shows the molecular structures of the materials used for this study. The photo-crosslinkable hole-transporting polymer (P-TPD-F) was obtained from corresponding methacrylate monomers via radical initiation polymerization and insolubilized by photocrosslinking as previously described [24]. The poly(norbornene)-based electron-transport polymers with bis-oxadiazole side chains were synthesized by ROMP polymerization using Grubbs ruthenium initiators [25]. These polymers are soluble in common organic solvents and form uniform films when cast from solution. Fig. 2 shows an energy level diagram based on the estimated solid-state ionization energy (IE) and electron affinity (EA) of each of the compounds used [26]; the values for both the PVK and both oxadiazole polymers (OP**1** and OP**2**) relative to those of $Ir(ppy)_3$ should allow for efficient hole and electron trapping on the green phosphorescent dopant.

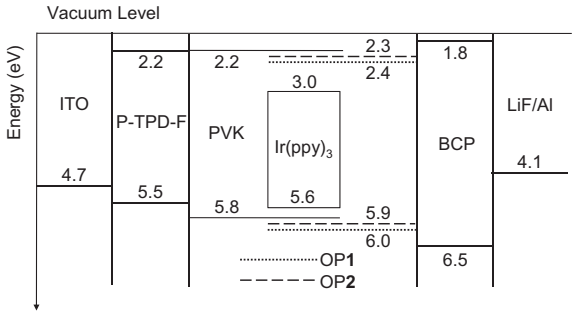

Fig. 2. Energy level diagram showing the estimated IE and EA levels for materials investigated in this work [26].

All of the devices were fabricated on glass substrates coated with indium tin oxide (ITO). The substrates were first cleaned in sequential ultrasonic baths of detergent, deionized water, acetone, and isopropanol. A section of the ITO with a sheet resistance of 20 Ω/□ (Colorado Concept Coatings, L.L.C.) was covered with SiO_x to define the anode and substrates were treated by oxygen-plasma (Plasma-preen II-862, Plasmatic Systems) for 3 min. The holes transport material P-TPD-F was spin-coated from toluene onto the oxygen plasma treated ITO-coated glass substrates and yielded 35 nm-thick films. These films were crosslinked using a standard broad-band UV light with a

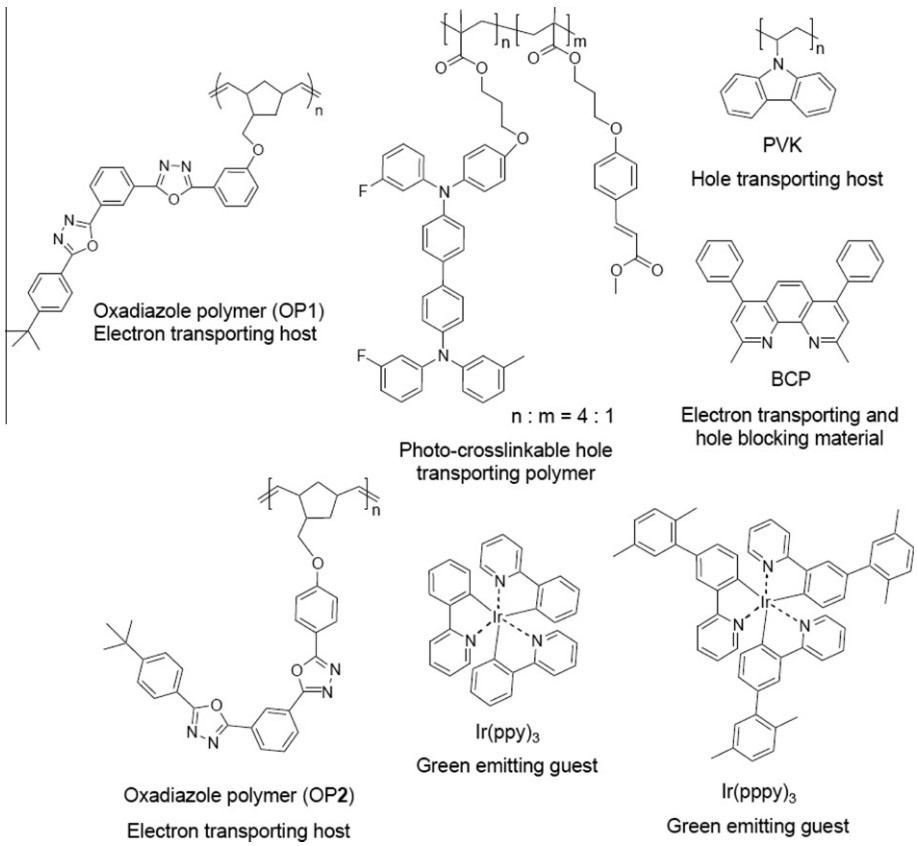

Fig. 1. Chemical structures of the employed materials.

0.7 mW cm^{-2} power density for 1 min. Subsequently, 1% concentration solutions were prepared by dissolving 10 mg of oxadiazole polymer – either OP**1** (device **A**) or OP**2** (devices **B** and **C**), 8.8 mg of PVK, and 1.2 mg of Ir(ppy)$_3$ (devices **A**, **B**) or Ir(pppy)$_3$ (device **C**) in 2 ml of chlorobenzene. All solutions were prepared under inert atmosphere and were stirred overnight. For the hole-blocking and electron-transport layer, a 40 nm-thick 2,9-dimethyl-4,7-diphenyl-1,10-phenanthroline (BCP) was vacuum deposited. Finally, 2.5 nm of lithium fluoride as an electron-injection layer and a 200 nm-thick aluminum cathode were vacuum deposited at a pressure below 1×10^{-6} Torr and at rates of 0.1 Å/s and 2 Å/s, respectively. A shadow mask was used for the evaporation of the metal to form five devices with an area of 0.1 cm^2 per substrate. Luminance–current density–voltage (*L*–*J*–*V*) characteristics of the devices were measured using a Keithley 2400 source meter for current voltage measurements. The devices were tested inside a nitrogen-filled glovebox with O_2 and H_2O levels <20 and <1 ppm, respectively.

Fig. 3 shows the current density (*J*–*V*) and luminance–voltage (*L*–*V*) characteristics of devices **A** and **B**, which differ in the oxadiazole polymer used. Both devices possess a rather high luminance of ca. 7550 cd/m^2 and ca. 7340 cd/m^2 (Fig. 2b, d), respectively.

Device **A** compared to device **B** exhibits lower leakage current as illustrated by the lower current density (<10^{-5} A/cm^2) observed at low voltage (<3 V) before the diode turns on. This lower leakage current directly affects the external quantum efficiency of the devices, especially at applied voltages below 10 V. The leakage current is generally associated with the quality of the films that are formed during device fabrication. The better quality of devices fabricated with OP**1** is tentatively attributed to a better wetting of the photo-crosslinked hole-transport layer by the polymer blend layer. The turn-on voltage (defined as the voltage required to obtain a brightness of 10 cd/m^2) of device **B** (6.1 V) is slightly lower than that of device **A** (6.8 V). At a luminance of 1000 cd/m^2, device **A** shows a maximum external quantum efficiency (EQE) of 9.6% and a current efficiency of 31.6 cd/A, while device **B** shows efficiencies of 10.1% and 32.7 cd/A, respectively.

Devices with emissive layers based on a composite blend of bis-oxadiazole polymer (OP**2**) and PVK with another iridium(III) complex, the more soluble Ir(pppy)$_3$ [23] with the same device geometry were also demonstrated (device **C**). The devices exhibit high current density and an EQE of 13.6% at a luminance of 1000 cd/m^2 and efficiencies of 44.6 cd/A, as shown in Fig. 3. Furthermore, the turn-on voltage of 5.9 V is significantly lower than those of other polymeric electrophosphorescent OLEDs [27]. Electroluminescence spectra of OLEDs based on blended ambipolar host are shown in inset of Fig. 4. The spectra show maxima at 516 and 540 nm, which correspond to the triplet emission of Ir(pppy)$_3$ [23]. The higher EQE observed for device **C** vs. device **B** may be due to decreased aggregation and self-quenching of the more soluble and bulkier phosphors in the former device.

In summary, we have demonstrated efficient green phosphorescent devices based on an emitter layer that is formed by blending two polymers together and by doping the blends with the phosphors Ir(ppy)$_3$ and Ir(pppy)$_3$. The

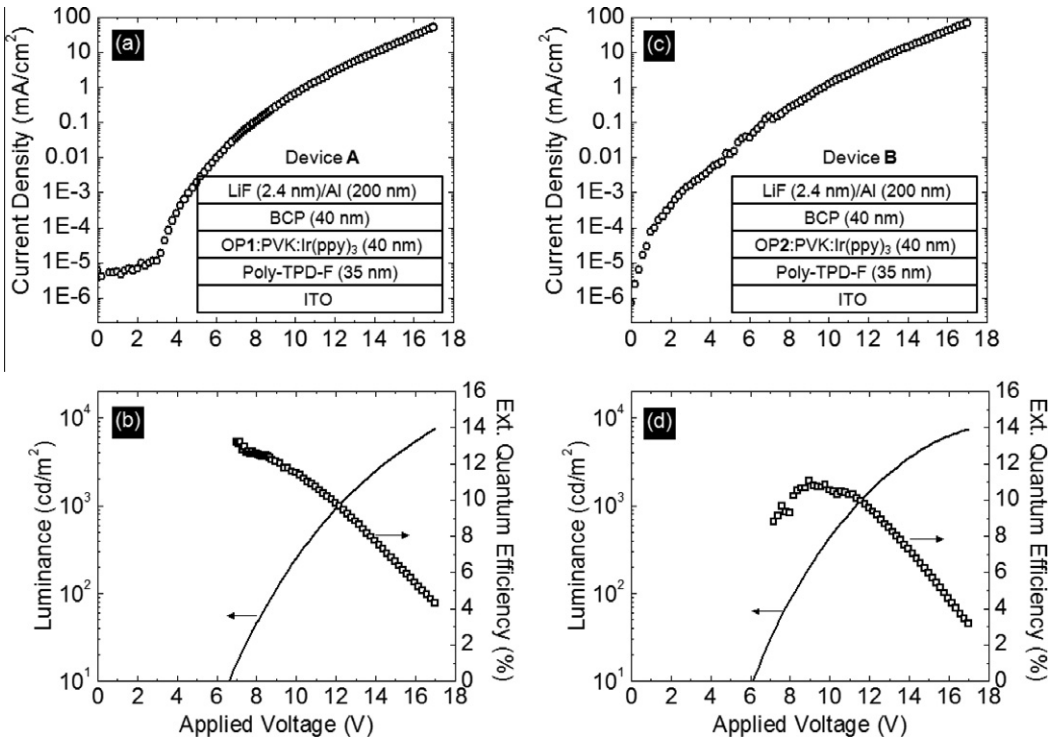

Fig. 3. Current density–voltage characteristics of devices **A** (a) and **B** (c); Luminance and external quantum efficiency as a function of applied voltage for devices **A** (b) and **B** (d). Insets: device structures.

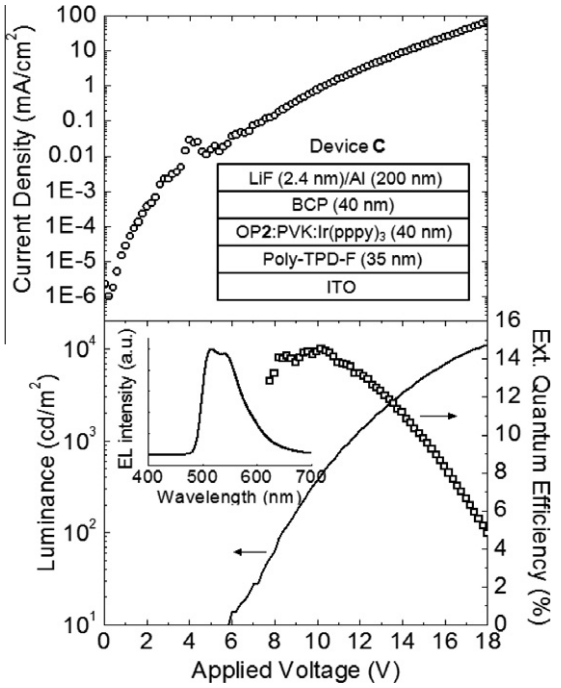

Fig. 4. Current density, luminance, and external quantum efficiency as a function of applied voltage for a device **C**. Insets: The device structure (top) and normalized electroluminescence spectra of OLED **C** at a luminance of 100 cd/m^2 (bottom).

polymer blends are comprised of two side-chain polymers, namely PVK and a poly(norbornene) with a bis-oxadiazole electron-transporting side chain. Devices show highly efficient light output and low turn-on voltage. Our work suggests that highly efficient solution processed phosphorescence OLEDs can be achieved by finding a combination of polymers with hole and electron transport properties and by doping the blend with a phosphorescent emitter. With an external quantum efficiency of 13.6% and a maximum luminous efficiency of 44.6 cd/A at 1000 cd/m^2 these devices exhibit a performance level that exceeds by several orders of magnitude the performance of previously reported OLEDs based on mixtures of side-chain polymers with a non-conjugated polymer backbone [13]. To the best of our knowledge, the efficiency of these devices (13.4%) also exceeds that of the best OLEDs based on mixtures of fluorescent conjugated polymers (6%) [12] and that of OLEDs based on a mixture of PVK with a fluorene-type conjugated polymer and a phosphorescent emitter (8.4%) [28] .

Acknowledgments

This material is based upon work supported by Solvay SA and in part by The STC Program of The National Science Foundation under Agreement number DMR-0120967.

References

[1] C.-L. Lee, K.B. Lee, J.-J. Kim, Polymer phosphorescent light-emitting devices doped with tris(2-phenylpyridine) iridium as a triplet emitter, Appl. Phys. Lett. 77 (2000) 2280–2282.
[2] C. Adachi, M.A. Baldo, M.E. Thompson, S.R. Forrest, Nearly 100% internal phosphorescence efficiency in an organic light-emitting device, J. Appl. Phys. 90 (2001) 5048.
[3] J.H. Burroughes, D.D.C. Bradley, A.R. Brown, R.N. Marks, K. Macay, R.H. Friend, P.L. Burns, A.B. Holmes, Light-emitting diodes based on conjugated polymers, Nature 347 (1990) 539.
[4] R.H. Friend, R.W. Gymer, A.B. Holmes, J.H. Burroughes, R.N. Marks, C. Taliani, D.D.C. Bradley, D.A.D. Santos, J.L. Bredas, M. Logdlund, W.R. Salaneck, Electroluminescence in conjugated polymers, Nature 397 (1999) 121–128.
[5] C.W. Tang, S.A. VanSlyke, C.H. Chen, Electroluminescence of doped organic thin films, J. Appl. Phys. 65 (1989) 3610–3616.
[6] Y.-C. Chiu, J.-Y. Hung, Y. Chi, C.-C. Chen, C.-H. Chang, C.-C. Wu, Y.-M. Cheng, Y.-C. Yu, G.-H. Lee, P.-T. Chou, En route to high external quantum efficiency (12%), organic true-blue-light-emitting diodes employing novel design of iridium (iii) phosphors, Adv. Mater. 21 (2009) 2221–2225.
[7] L. Wang, Y. Jiang, J. Luo, Y. Zhou, J. Zhou, J. Wang, J. Pei, Y. Cao, Highly efficient and color-stable deep-blue organic light-emitting diodes based on a solution-processible dendrimer, Adv. Mater. 21 (2009) 4854–4858.
[8] Y. Fang, B. Tong, S. Hu, S. Wang, Y. Meng, J. Peng, B. Wang, A highly efficient tris-cyclometalated iridium complex based on phenylphthalazine derivative for organic light-emitting diodes, Org. Electron. 10 (2009) 618–622.
[9] J.J.M. Halls, A.C. Arias, J.D. MacKenzie, W. Wu, M. Inbasekaran, E.P. Woo, R.H. Friend, Photodiodes based on polyfluorene composites: influence of morphology, Adv. Mater. 12 (2000) 498.
[10] Y. Xia, R.H. Friend, Phase separation of polyfluorene-based blend films and its influence on device operations, Adv. Mater. 18 (2006) 1371.
[11] A.C. Grimsdale, K.L. Cahn, R.E. Martin, P.G. Jokisz, A.B. Holmes, Synthesis of light-emitting conjugated polymers for applications in electroluminescent devices, Chem. Rev. 109 (2009) 897–1091.
[12] J.L. Huang, G.E. Wu, Q. Xu, Y. Yang, Achieving high-efficiency polymer white-light-emitting devices, Adv. Mater. 18 (2006) 114–117.
[13] S. Dailey, W.J. Feast, R.J. Peace, I.C. Sage, S. Tilla, E.L. Wooda, Synthesis and device characterisation of side-chain polymer electron transport materials for organic semiconductor applications, J. Mater. Chem. 11 (2001) 2238.
[14] F.I. Wu, D.S. Reddy, C.F. Shu, Novel oxadiazole-containing polyfluorene with efficient blue electroluminescence, Chem. Mater. 15 (2003) 269.
[15] F.I. Wu, P.I. Shih, C.F. Shu, Highly efficient light-emitting diodes based on fluorene copolymer consisting of triarylamine units in the main chain and oxadiazole pendent groups, Macromolecules 38 (2005) 9028.
[16] X.W. Zhan, Y.Q. Liu, X. Wu, S. Wang, D.B. Zhu, New series of blue-emitting and electron-transporting copolymers based on fluorene, Macromolecules 35 (2002) 2529.
[17] C. Adachi, T. Tsutsui, S. Saito, Blue light-emitting organic electroluminescent devices, Appl. Phys. Lett. 56 (1990) 799.
[18] G. Hughes, M.R. Bryce, Electron-transporting materials for organic electroluminescent and electrophosphorescent devices, J. Mater. Chem. 15 (2005) 94.
[19] M. Ichikawa, T. Kawaguchi, K. Kobayashi, T. Miki, K. Furukawa, T. Koyama, Y. Taniguchi, Bipyridyl oxadiazoles as efficient and durable electron-transporting and hole-blocking molecular materials, J. Mater. Chem. 16 (2006) 221.
[20] M.K. Leung, C.C. Yang, J.H. Lee, H.H. Tsai, C.F. Lin, C.Y. Huang, Y.O. Su, C.F. Chiu, The unusual electrochemical and photophysical behavior of 2,2'-bis(1,3,4-oxadiazol-2-yl)biphenyls, effective electron transport hosts for phosphorescent organic light emitting diodes, Org. Lett. 9 (2007) 235.
[21] M.A. Baldo, M.E. Thompson, S.R. Forrest, High-efficiency fluorescent organic light-emitting devices using a phosphorescent sensitizer, Nature 403 (2000) 750.
[22] R.C. Kwong, S. Lamansky, M.E. Thompson, Organic light-emitting devices based on phosphorescent hosts and dyes, Adv. Mater. 12 (2000) 1134.
[23] P. Stössel, H. Spreitzer, I. Bach, patent application WO/2004/037836.
[24] R.D. Hreha, Y.D. Zhang, B. Domercq, N. Larribeau, J.N. Haddock, B. Kippelen, S.R. Marder, Synthesis of photo-crosslinkable hole-transport polymers with tunable oxidation potentials and their use in organic light-emitting diodes, Synthesis 9 (2002) 1201.
[25] S.R. Marder, S. Barlow, Y. Zhang, S. Pal, B. Kippelen, B. Domercq, A. Haldi, M. Weck, A. Kimyonok, patent application WO/2009/0807797.

[26] The EAs of OP**1** and OP**2** were estimated from the electrochemical reduction potentials of the corresponding monomers, while the IP values were obtained from the EA estimate and the optical gap and, therefore, are likely to be underestimates due to the neglect of exciton binding energy.

[27] X. Yang, D.C. Müller, D. Neher, K. Meerholz, Highly efficient polymeric electrophosphorescent diodes, Adv. Mater. 18 (2006) 948.

[28] D.H. Yu, O.O. Park, J.H. Park, Optimization of polymeric host composition for polymer-based electrophosphorescent devices, J. Lumin. 129 (2009) 496–500.

Organic Electronics 12 (2011) 497–503

Contents lists available at ScienceDirect

Organic Electronics

journal homepage: www.elsevier.com/locate/orgel

Water soluble poly(1-vinyl-1,2,4-triazole) as novel dielectric layer for organic field effect transistors

Mamatimin Abbas [a,*], Gulbeden Cakmak [b], Nalan Tekin [c], Ali Kara [d], Hasan Yuksel Guney [b], Elif Arici [a], Niyazi Serdar Sariciftci [a]

[a] Linz Institute for Organic Solar Cells (LIOS), Physical Chemistry, Johannes Kepler University Linz, Altenbergerstr. 69, 4040 Linz, Austria
[b] Department of Physics, Kocaeli University, Eski Istanbul Yolu 10. km, 41380 Umuttepe, Turkey
[c] Department of Chemistry, Kocaeli University, Eski Istanbul Yolu 10. km, 41380 Umuttepe, Turkey
[d] Department of Chemistry, Uludag University, Gorukle Kampusu 16059, Turkey

ARTICLE INFO

Article history:
Received 11 October 2010
Received in revised form 21 December 2010
Accepted 31 December 2010
Available online 13 January 2011

Keywords:
Polyvinyl triazole
Dielectric
Organic field effect transistor
Pentacene
C_{60}

ABSTRACT

Water soluble poly(1-vinyl-1,2,4-triazole) (PVT) as a novel dielectric layer for organic field effect transistor is studied. Dielectric spectroscopy characterization reveals it has low leakage current and rather high breakdown voltage. Both n-channel and p-channel organic field effect transistors are fabricated using pentacene and fullerene as active layers. Both devices show device performances with lack of hysteresis, very low threshold voltages and high on/off ratios. Excellent film formation property is utilized to make AlO_x and thin PVT bilayer in order to decrease the operating voltage of the devices. All solution processed ambipolar device is fabricated with simple spin coating steps using poly(2-methoxy-5-(2-ethyl-hexyloxy)-1,4-phenylenevinylene) (MEH–PPV) end capped with polyhedral oligomeric silsesquioxanes (POSS) as active layer. Our investigations show that PVT can be a very promising dielectric for organic field effect transistors.

© 2011 Elsevier B.V. All rights reserved.

1. Introduction

Organic optoelectronic devices fabricated using organic, polymeric materials possess huge application potential in consumable electronics due to their easy processability and low cost. Moreover, realizing future all plastic electronics relies on the development of efficient organic electronic components. Organic field effect transistors (OFETs) are being extensively studied as basic constituents of such devices [1]. In OFETs, the dielectric insulating layer greatly affects device characteristics. Low hysteresis of the transfer characteristics (source-drain current I_{DS} versus the gate voltage V_{GS}) and a trap free dielectric/semiconductor interface are required for stable working OFETs with comparable performance as those of inorganic ones such as amorphous silicon. One of the major problems in OFETs is their high voltage operation because organic semiconductors, as active layers, generally have relatively low charge carrier mobilities. However, dielectric layer can be optimized to achieve lower operation voltage. One of the approaches is using high dielectric constant metal oxides to obtain high capacitance [2]. Passivation of the metal oxide surface is necessary in order to decrease intrinsic traps at the oxide/semiconductor interface. This can be done by self-assembled monolayers (SAMs) onto the oxide surface [3]. Another approach is to cast an organic insulator thin film on top of the gate. To obtain similar capacitance as of the oxide layer, this passivation layer has to be fairly thin (in submicrometer regime). Therefore, good film formation property is prerequisite for such bi-layer dielectric structures. Most of the polymeric semiconductors are soluble in nonpolar organic solvents. In solution processed devices, to avoid the dissolution of the underlayer, we need organic dielectrics which are well soluble in polar solvents, such as water, with bad solubility in the nonpolar organic solvents.

* Corresponding author. Tel.: +43 732 2468 8854; fax: +43 732 2468 8770.
E-mail address: mamatimin.abbas@jku.at (M. Abbas).

1566-1199/$ - see front matter © 2011 Elsevier B.V. All rights reserved.
doi:10.1016/j.orgel.2010.12.023

Poly(vinyl alcohol) (PVA) is one of the most extensively studied water soluble polymers with high dielectric constant and excellent film formation properties [4–8]. Hysteresis had been an issue quite for a while in PVA based OFETs [5,7,8]. Although non-volatile hysteresis behaviour can be implemented for memory elements [5], OFETs should have hysteresis free characteristic in logic circuit applications. Hysteresis mechanism has been investigated in detail and charge trapping as well as mobile ions are ascribed to be the factors [7,8]. Dialysis process can minimize the hysteresis effects in PVA based OFETs and result in good device characteristics for n-channel OFET devices [8]. However, intrinsic OH groups in PVA induce potential electron traps at the dielectric semiconductor interface hindering n-channel electron mobility and ambipolar behaviour of the devices [9]. Therefore, new water soluble polymeric dielectrics need to be explored.

Poly(1-vinyl-1,2,4-triazole) (PVT) was reported to be a non-toxic, biocompatible, thermally stable and easily soluble in water or polar organic solvents [10,11]. Monomers of PVT were first obtained by vinylation of 1,2,4-triazole with acetylene [12]. Later, radical polymerization was realized [13]. Since then, PVT or copolymers have found a wide range of applications in medicine and agriculture such as preparation of soft contact lenses, biosynthetic activation of connective tissue cells, clarification or stabilization of juices and wines [14–16]. Application for nanotechnology was proposed by incorporation of nanoparticles in the polymer matrix [17,18]. PVT based salts are shown to be reliable binders in propellant and explosives as energetic polymers [19]. Recently, acid doped PVTs were studied as promising proton conducting polymer electrolytes in proton exchange membrane fuel cells [20,21].

In his work we investigated the dielectric property of PVT for OFETs. Dielectric spectroscopy measurements show low leakage current and very high breakdown voltage (around 4 MV cm^{-1}). Excellent film formation and smooth surfaces of the PVT films are observed by using atomic force microscopy. We used pentacene as p-channel and C_{60} as n-channel semiconductor layers. Both types of devices based on PVT revealed hysteresis free transfer characteristics with relatively high on/off ratios (>1000) and low threshold voltages. Solution processed ambipolar OFET device was realized using simple spin coating steps. All these technical properties suggest PVT as an excellent polymer dielectric for OFETs.

2. Experimental

2.1. Materials

Vinyl-triazole monomer was bought from Sigma–Aldrich and polymerized using Free radical polymerization technique. Azobisisobutyronitrile was used as radical initiator, benzene as solvent and CCl_4 as chain transfer agent. Pentacene (normal grade, carbon $\geqslant$93.5%) and C_{60} (sublimation grade, 99.9%) were purchased from Sigma–Aldrich and MER corporation, respectively. They were used as received. MEH–PPV–POSS was purchased from American Dye Source Inc. It was purified by repeated precipitation. Device preparation: PVT was dissolved in high resistant ultra-pure water in a weight ratio of 7%. The solution was filtered and spin-coated on glass substrate with evaporated Al gate contact. The films were dried in vacuum oven overnight at a temperature of 50 °C. For AlO_x/PVT bi-layer dielectric, Al gate contacts were partially anodized as described in references [24,25]. In ultra-pure water and citric acid solution (0.01 M), constant current density of 6 mA cm^{-2} was applied between Al contact and stainless steel counter electrode. Final anodization voltage was set to 50 V with anodization ratio around 1.3 nm V^{-1}, which

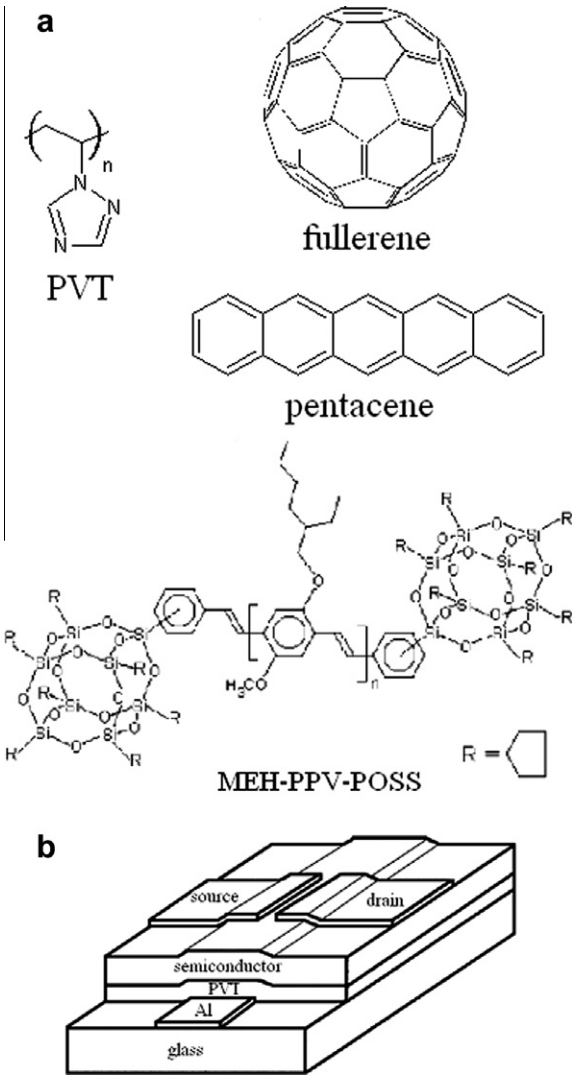

Fig. 1. (a) Molecular structure of poly(1-vinyl-1,2,4-triazole) (PVT), fullerene (C_{60}), pentacene and MEH–PPV–POSS; (b) Device structure of the bottom gate, top contact OFETs structure used. Al gate contact was partially anodized to make AlO_x layer for low voltage operation devices. Pentacene as p-channel semi-conducting layer has Au source/drain contacts, whereas C_{60} as n-channel semi-conducting layer has LiF/Al source/drain contacts. Channel length is 0.06 mm, and channel width is 2 mm. For ambipolar OFET with MEH–PPV–POSS as active layer, Ca/Au asymmetric contacts were angle evaporated. Channel length is 0.05 mm and channel width is 3 mm.

gives around 65 nm thickness of AlO_x layers. They were dried in vacuum oven at 120 °C overnight. On top of it, low concentration PVT solution (1.5% weight ratio) was spin-coated (1500 rpm for 40 s). The films were dried in vacuum oven overnight at a temperature of 50 °C. For dielectric characterization, Al contact was evaporated through shadow mask to make MIM structure. Electrode contact area is 4.84 mm^2. Two different thickness films were spin coated using 2000 rpm and 3000 rpm for 30 s, and thicknesses were measured using AFM. For OFETs, 7% weight ratio PVT solution was spin coated (1500 rpm for 40 s and 2000 rpm for 20 s) on glass substrate with evaporated Al gate contact. Pentance (100 nm) and C_{60} (100 nm) films were thermally evaporated in UNIVEX system. Substrate was kept at room temperature. Evaporation rate is around 0.5 nm s^{-1}. Au (100 nm) for pentance films and LiF(0.6 nm)/Al(100 nm) for C_{60} films as sources/drain contacts were evaporated thermally through shadow mask to complete the bottom gate, top contact OFET devices. Channel length is 0.06 mm and channel width is 2.0 mm. MEH–PPV–POSS was dissolved in Cholorobenzene (15 mg/ml) and spin coated (1500 rpm for 40 s and 2000 rpm for 20 s) directly on top of PVT. Ca (50 nm) and Au (50 nm) asymmetric contacts were angle evaporated using thick shadow mask. Channel length is 0.05 mm and channel width is 3.0 mm. Characterization: PVT film morphology and thickness are investigated with Atomic Force Microscopy (Digital Instruments Dimension 3100) in tapping mode. Images are analysed using WSxM software [26]. For MIM structures, dielectric spectroscopy was obtained with a Novocontrol Alpha Analyzer. Leakage DC current was measured using Keithley 230 unit. I–V characterizations were performed using Agilent E5273A. All the characterizations were carried out in nitrogen glove box or sealed box with nitrogen gas.

3. Results and discussions

Chemical structure of PVT is given in Fig. 1a). Electron rich nitrogen atoms in triazole ring can form hydrogen bonds with water molecules, which is an exothermic dissolution process.

Spin coating of PVT films results in very homogeneous film. AFM images of the films with 720 nm and 960 nm thicknesses are shown in Fig. 2a and b. Both give very low root-mean-square roughness of about 0.2 nm. We have made metal–insulator–metal (MIM) structure of PVT films sandwiched between evaporated Al electrodes for dielectric characterization, results of which are shown in Fig. 3. The contact area is 4.84 mm^2, and film thicknesses are 720 nm and 960 nm as measured by AFM. Frequency dependence of the capacitance is given in Fig. 3a. From

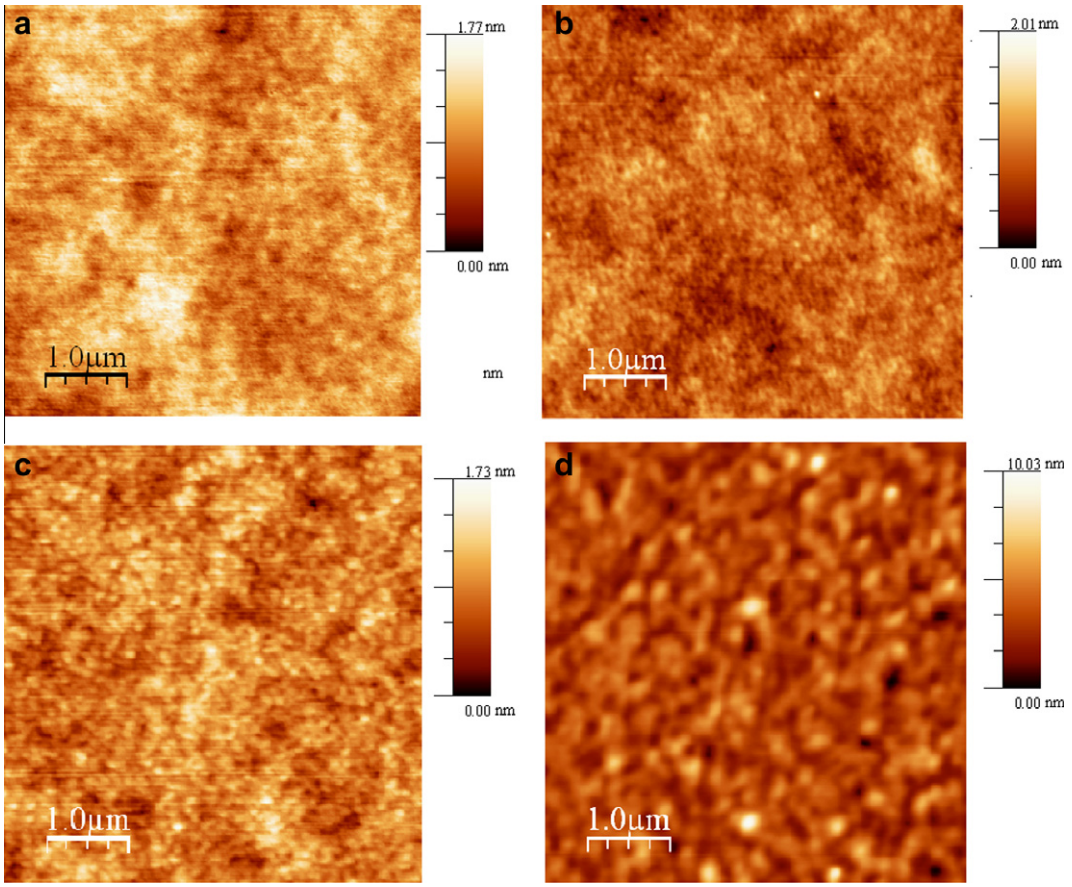

Fig. 2. AFM images of spin coated PVT films on Al gate with glass substrate: (a) 720 nm; (b) 960 nm; (c) 90 nm; (d) 90 nm film on anodized AlO_x surface.

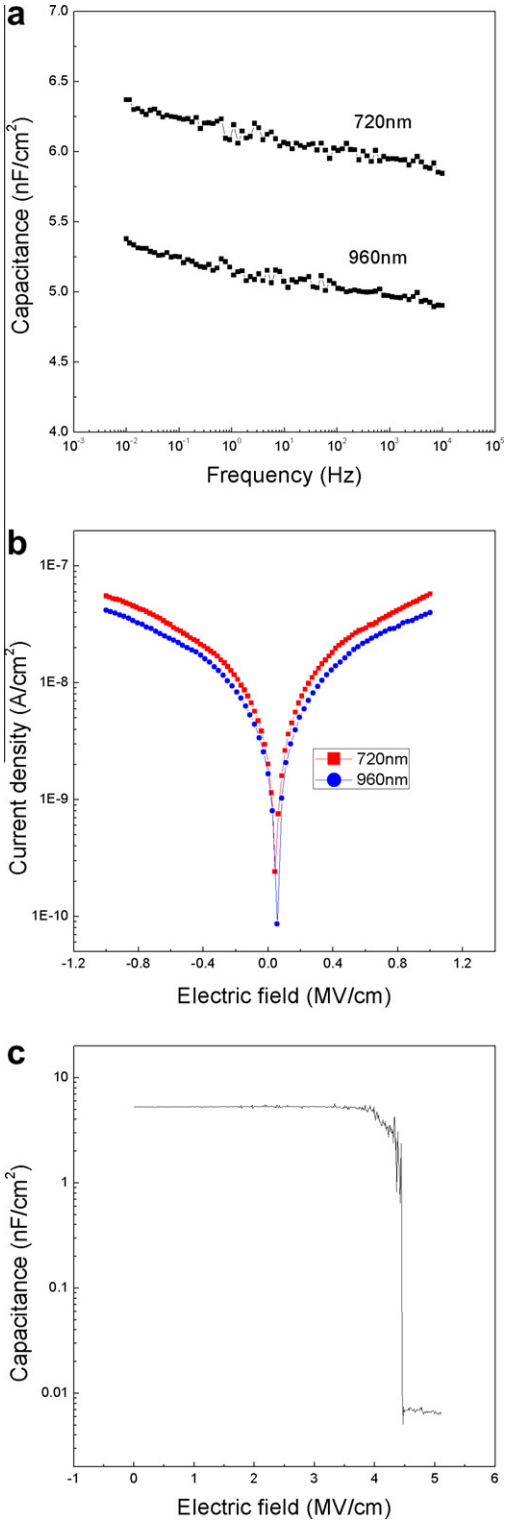

Fig. 3. Dielectric characterization of PVT films (720 nm and 960 nm) as in Al/PVT/Al structure: (a) frequency dependence of the capacitance; (b) leakage current versus applied DC voltage; (c) capacitance versus applied electric field at 10 Hz for the sample with the thickness of 720 nm.

0.01 Hz to 10 kHz, the capacitances of the films show dispersionless behaviour with rather low variance. Capacitance values at 10 Hz is used to determine the dielectric constant k, as given by $C_i = \varepsilon_0 k/d$, where C_i represents capacitance per unit area and d is the thickness of the dielectric layer. Linear fitting of the capacitance values versus different thicknesses yields dielectric constant of 5.1. Low leakage current is necessary to achieve high on/off ratio from an OFET. Leakage current versus applied electric field is shown in Fig. 3b. DC voltage is applied within ±110 V. At an electric field of 1 MV cm^{-1}, we have observed a leakage current density of around 5×10^{-8} A cm^{-2}. Dielectric strength of an insulator can be represented by the breakdown electric field, i.e. the sustainable voltage maximum before it loses its insulating character. It's a crucial parameter in achieving high capacitance by decreasing the thickness of the dielectric. Breakdown electric field of PVT is higher than 4 MV cm^{-1} as shown in Fig. 3c for the 720 nm thick sample, where capacitance were measured by ramping up the applied voltage at a frequency of 10 Hz.

Fig. 4a shows typical transfer characteristics of PVT in a p-channel device with pentacene as active layer. Gate leakage current is about −0.2 nA at −15 V. No hysteresis is observed with forward and reverse gate voltage sweep for the transfer curve. In the gradual channel approximation, drain current dependence on the gate voltage can be given by the following equation in saturation regime (given mobility is independent of the gate voltage):

$$I_{DS} = (W/2L)\mu_{sat}C_i(V_{GS} - V_{th})^2$$

where I_{DS} is the drain current; μ_{sat} is the mobility; V_{GS} is the gate voltage; V_{th} is the threshold voltage; W is the channel width and L is the channel length. The square root of drain current versus gate voltage of the saturation curve can be linearly extended to the "off" current to determine the threshold voltage. Rather low threshold voltage of −2.2 V is obtained. Considering the flat band potential of Al gate and pentacene work function, and also quite low dielectric capacitance of around 5 nF cm^{-2}, this value implies very low trap density. We have estimated the total trap density of 2.3×10^{10} cm^{-2} using $N_{trap} = C_i|V_{th} - V_{to}|/e$, where C_i is the capacitance per unit area; V_{th} is threshold voltage as determined above; V_{to} is the turn-on voltage which refers to applied gate voltage at the onset of the drain current [22]. Sub-threshold swing of 1.75 V dec^{-1} is derived. It reflects "turning on" speed of the device and correlates to the interface trap capacitance C_{it} through the equation [2]: $S = (K_B T/e)\ln(10)(1 + C_{it}/C_i)$. On/off ratio is higher than 10^3. The device sustained −200 V gate voltage without breakdown and further scaled up on/off ratio. Good linear and saturation behaviour is observable from the output curves (Fig. 4b). Mobility can be estimated from the linear regime where the charge carriers are uniformly distributed as given in the equation below:

$$I_{DS} = W/L\mu_{lin}C_i(V_{GS} - V_{th})V_{DS}$$

where V_{DS} is the drain voltage. Calculated hole mobility is 0.002 cm^2 V^{-1} s^{-1}. Dielectrics are more critical for the performance of n-channel OFETs, as the hydroxyl groups in organic dielectrics tend to trap electrons easily. However, it is essential for the dielectric to perform in an equal manner for both p- and n-channel devices if ambipolar and light

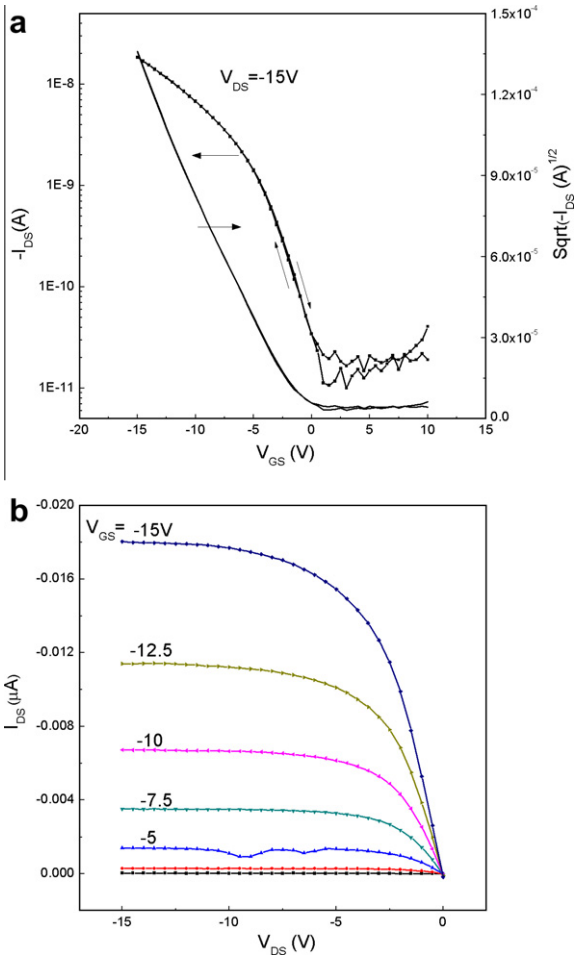

Fig. 4. Transfer (a) and output (b) characteristics of pentacene as p-channel OFET device with PVT dielectric layer. Au source/drain contacts were used with channel length of 0.06 mm and channel width of 2 mm.

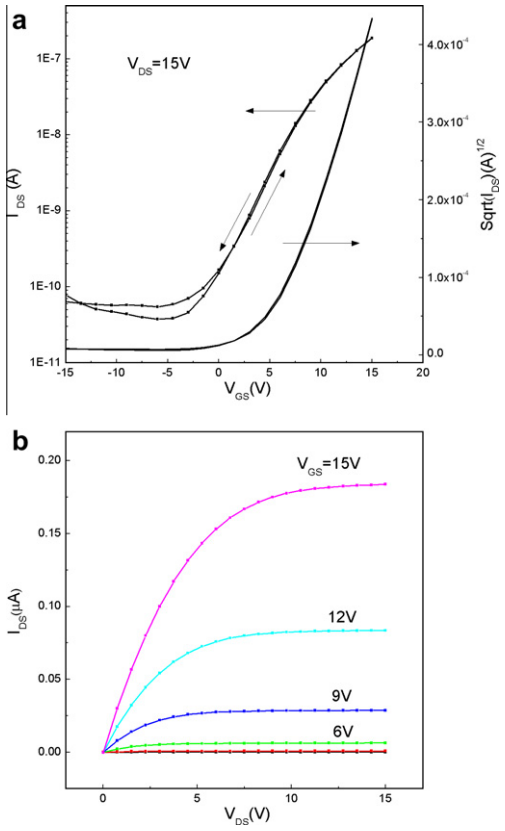

Fig. 5. Transfer (a) and output (b) characteristics of fullerene as n-channel OFET device with PVT dielectric layer. LiF/Al source/drain contacts were used with channel length of 0.06 mm and channel width of 2 mm.

emitting OFETs are pursued for various purposes. We investigated PVT in n-channel OFET, where C_{60} is used as active layer. Fig. 5a shows typical transfer characteristics of such an OFET device. Transfer curve again shows almost hysteresis free behaviour with forward and reverse gate voltage sweep. Slightly higher off currents can be due to the higher conductivity of C_{60} at drain voltage of 15 V as compared to the pentacene device. On/off ratio is higher than 10^3 and further scaling up is possible without breaking the dielectric. Gate leakage current is about 0.9 nA at 15 V. Derived threshold voltage is around 5.5 V. Comparing to p-channel OFET, this value suggests total trap states for electrons are slightly higher. Estimated total trap density from the difference between threshold voltage and turn-on voltage is about 6.6×10^{10} cm^{-2}. Compared to the C_{60} n-channel OFET based on dialysis grade PVA [8], using PVT as dielectric gives superior parameters. Sub-threshold swing is about 3.2 V dec^{-1}. Again, clear linear and saturation behaviour is observable from the output curves (Fig. 5b). Estimated electron mobility from the linear regime is 0.02 cm^2 V^{-1} s^{-1}.

Low voltage operation of OFETs is required for their practical application. Increasing capacitance of the dielectric layer is a direct approach. By decreasing the thickness of the film, one can obtain higher capacitance, thus lower operating voltage. Main problems can be that polymer dielectrics may not form homogenous films when solution concentration is lowered; leakage current may be comparable to the drain current or it can be easily breakdown. Cross linking of the thin polymer dielectrics is a viable approach. However, it will introduce additional processing step and impurities left from the cross linking agents might affect the performance of the devices. AFM study evidenced very good film formation property of PVT. When thinner films are prepared with low solution concentration, PVT still forms homogeneous films without defects or pinholes (see Fig. 2c). We attempted to fabricate n-channel OFET devices with dielectric thickness as low as 90 nm (capacitance around 50 nF cm^{-2}). Among more than 16 devices, almost all the devices worked below 1 V, with two orders of magnitude on/off ratio and well defined linear-saturation behaviours. Despite such a high yield, when gate voltage is applied more than 1 V to achieve comparable on/off ratios, leakage current becomes higher than those of the devices with thick PVT layer. In order to realize similar performance as of the thick PVT films, we fabri-

cated anodized AlO_x/PVT bi-layer dielectric to control the leakage current. Sixty-five nanometer AlO_x with capacitance around 120 nF cm^{-2} and 90 nm PVT with capacitance of 50 nF cm^{-2} yields a total capacitance of 35 nF cm^{-2}. Roughness of the film increased slightly due to the anodized AlO_x layer (see Fig. 2d) with root-mean-square roughness of about 1 nm. Fig. 6a shows the transfer characteristic of pentacene p-channel OFET based on such a bi-layer dielectric. At applied voltage of −3 V, the device performed in similar fashion as the thick PVT film based device. Gate leakage current is −0.4 nA at gate voltage of −3 V. Threshold voltage is about −1.5 V. Sub-threshold swing of 360 mV dec^{-1} is comparable to state of art low voltage operation OFET devices and direct result of low interface trap states. Linear and saturation trends in the output curves are evident (Fig. 6b). More impressive performance is attained in the C_{60} n-channel devices. Fig. 7a shows typical transfer curve. At applied voltage of 2 V, the device performed in a similar way as the thick PVT film based device with comparable on/off drain current ratio. Gate leakage current is 0.6 nA at gate voltage of 2 V. Threshold voltage is about 0.6 V and sub-threshold swing shows a very low value of 230 mV dec^{-1}. Output curves are shown in Fig. 7b.

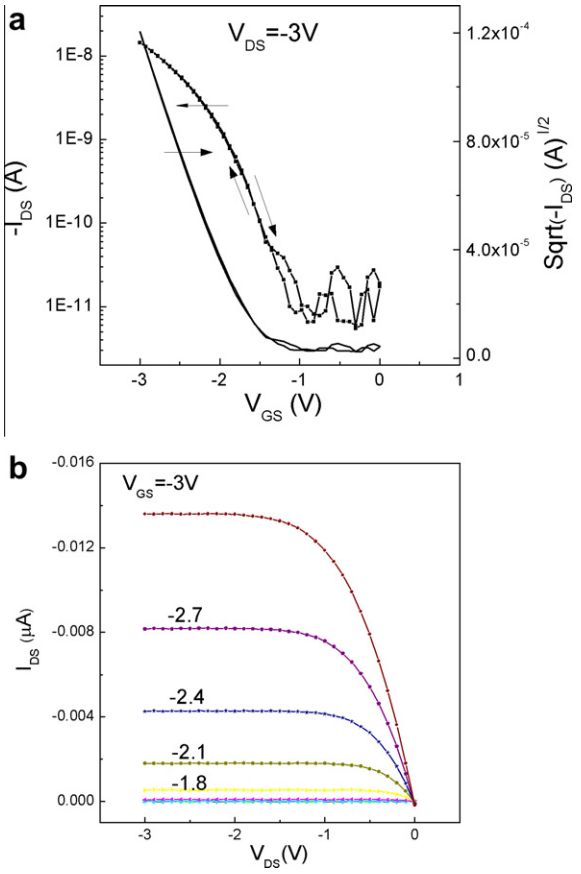

Fig. 6. Transfer (a) and output (b) characteristics of pentacene as p-channel OFET device with AlO_x (65 nm) and PVT (90 nm) dielectric bi-layer. Au source/drain contacts were used with channel length of 0.06 mm and channel width of 2 mm.

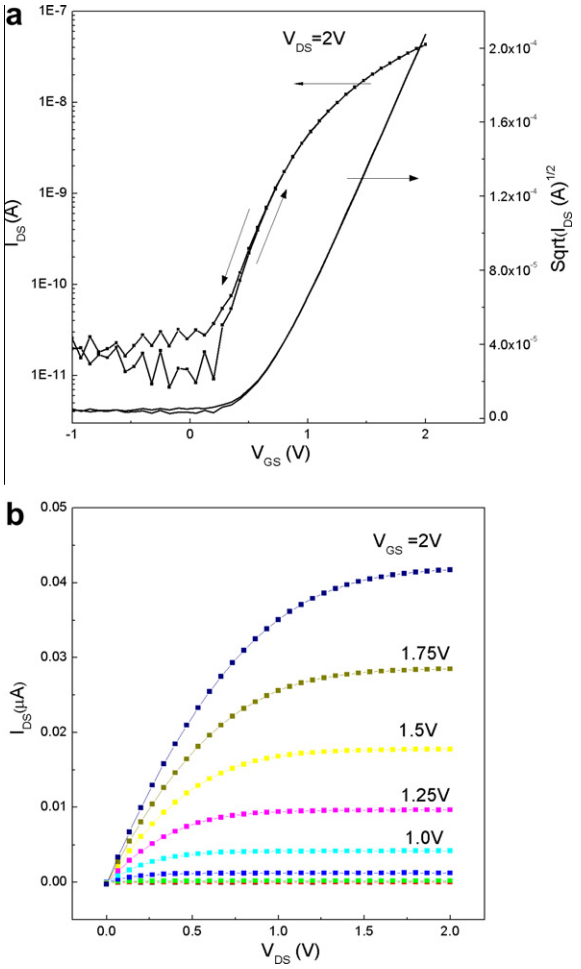

Fig. 7. Transfer (a) and output (b) characteristics of fullerene as n-channel OFET device with AlO_x (65 nm) and PVT (90 nm) dielectric bi-layer. LiF/Al source/drain contacts were used with channel length of 0.06 mm and channel width of 2 mm.

For all solution processed device, PVT, as a water soluble polymer dielectric, is suitable for most of the organic semiconductors. Here we used poly(2-methoxy-5-(2-ethylhexyloxy)-1,4-phenylenevinylene) (MEH–PPV) end capped with polyhedral oligomeric silsesquioxanes (POSS) as the active layer. Although its lower charge carrier mobility has not been appreciated for organic transistors, comparatively high photoluminescence efficiency is very promising for efficient light emission from organic transistor device. POSS renders relatively high air stability for the polymer without changing its absorption and photoluminescence [23]. MEH–PPV–POSS was directly spin coated on top of the PVT dielectric. Ca and Au source/drain electrodes were angle evaporated for efficient electron and hole injection. Typical transfer characteristics of such an ambipolar OFET device are shown in Fig. 8a. Both electron and hole enhancement is observed. This can also be confirmed by the output curves as displayed in Fig. 8b, where pronounced increase of drain current can be observed at low or reverse gate bias, a typical ambipolar current behaviour.

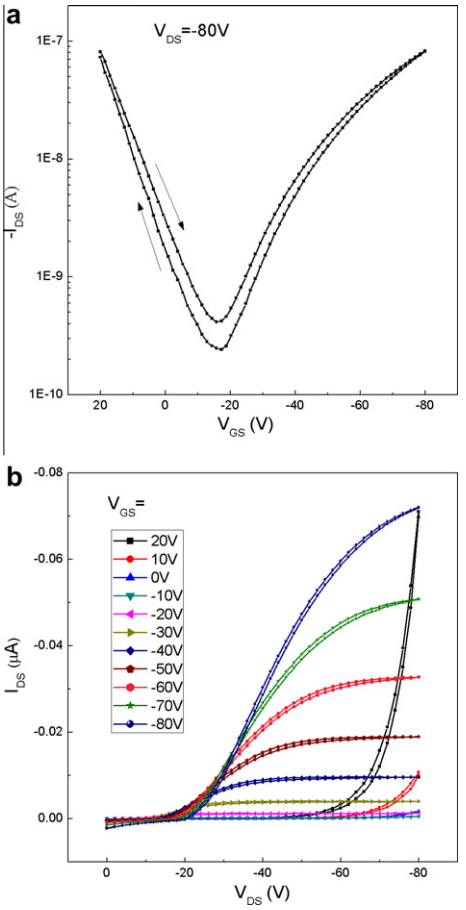

Fig. 8. Transfer (a) and output (b) characteristics of ambipolar OFET device with MEH–PPV–POSS active layer and PVT dielectric layer. Ca/Au asymmetric source/drain contacts were angle evaporated. Channel length is 0.05 mm and channel width is 3 mm.

4. Conclusions

In summery, we have investigated the dielectric property of PVT and its application for OFETs. PVT films showed considerably high breakdown voltage and low leakage current. Both n-channel and p-channel OFET devices are fabricated. Excellent performances are observed in both devices, with hysteresis free and very low threshold voltages. Owing to its good film formation property, using anodized AlO_x/PVT bi-layer dielectrics, both p-channel and n-channel OFET devices operated in low voltages with low threshold voltage and sub-threshold swing. Solution processed ambipolar device is fabricated with simple spin coating steps. Typical ambipolar characteristics were observed. Our results show that PVT can be a very promising polymer dielectric for OFET devices, especially for ambipolar and light emitting OFETs. Moreover, its solubility in water allows for a wide range of solution processed polymer based OFET devices directly fabricating layer by layer. Biocompatibility of PVT is another advantage of its application for bio-electronic devices.

Acknowledgements

We are grateful for the useful discussions with Dr. Martin Egginger and Dr. A. Montaigne Ramil. The work is financially supported by FWF project of AMBIPOL (No. P20724-N20).

References

[1] J. Zaumseil, H. Sirringhaus, Chem. Rev. 107 (2007) 1296.
[2] R.P. Ortiz, A. Facchetti, T.J. Marks, Chem. Rev. 110 (2010) 205.
[3] L.-L. Chua, J. Zaumseil, J.-F. Chang, E.C.-W. Ou, P.K.-H. Ho, H. Sirringhaus, R.H. Friend, Nature 434 (2005) 194.
[4] R. Parashkov, E. Becker, G. Ginev, T. Riedl, H.-H. Johannes, W. Kowalsky, J. Appl. Phys. 95 (2004) 1594.
[5] Th.B. Singh, N. Marjanovic, G.J. Matt, N.S. Sariciftci, R. Schwödiauer, S. Bauer, Appl. Phys. Lett. 85 (2004) 5409.
[6] T.B. Singh, F. Meghdadi, S. Gunes, N. Marjanovic, G. Horowitz, P. Lang, S. Bauer, N.S. Sariciftci, Adv. Mater. 17 (2005) 2315.
[7] C.A. Lee, D.W. Park, S.H. Jin, H. Park, J.D. Lee, B.-G. Park, Appl. Phys. Lett. 88 (2006) 252102.
[8] M. Egginger, M. Irimia-Vladu, R. Schwodiauer, A. Tanda, I. Frischauf, S. Bauer, N.S. Sariciftci, Adv. Mater. 20 (2008) 1018.
[9] M.-H. Yoon, C. Kim, A. Facchetti, T.J. Marks, J. Am. Chem. Soc. 128 (2006) 12851.
[10] Yu.S. Bulyshev, I.M. Kashirskii, V.V. Sinitskii, G.F. Myatchina, T.G. Ermakova, V.A. Lopyrev, Phys. Stat. Sol. (A) 70 (1982) 139.
[11] M.V. Kurik, G.F. Myachina, T.G. Ermakova, Mol. Cryst. Liq. Cryst. 468 (2007) 669.
[12] L.P. Makhno, T.G. Ermakova, E.S. Dommina, L.A. Tatarova, G.G. Skvortsov, V.A. Lopyrev, USSR Inventor's Certificate 1975, No. 464584, Byull. Izobret., No. 11.
[13] L.A. Tatarova, T.G. Yermakova, A.A. Berlin, Y.F. Razvodovskii, L.A. Lopyrev, N.F. Kedrina, N.S. Yenikopolopyan, Vysokomol. Soedin. Ser. A 24 (1982) 2205.
[14] T.G. Ermakova, N.P. Kuznetsova, Nauka-Proizvod.-Stvu. 6 (2003) 55.
[15] L.A. Mansurova, A.B. Skornyakova, N.A. Sevastyanova, L.A. Tatarova, T.G. Ermakova, V.A. Lopyrev, V.B. Kazimirovskaya, L.I. Slutskii, Khim.-Farm Zh. 25 (1991) 22.
[16] V.I. Zinchenko, A.S. Makarov, V.A. Lopyrev, T.G. Ermakaova, L.A. Tatarova, Pivo Napitki 4 (1999) 58.
[17] G.F. Myachina, S.A. Korzhova, T.G. Ermakova, B.G. Sukhov, B.A. Trofimov, Doklady Chem. 420 (2008) 123.
[18] G.F. Myachina, T.V. Konkova, S.A. Korzhova, T.G. Ermakova, A.S. Pozdnyakov, B.G. Sukhov, K.Yu. Arsentev, E.V. Likhoshvai, B.A. Trofimov, Doklady Chem. 431 (2010) 63.
[19] H. Xue, H.X. Gao, J.M. Shreeve, J. Polym. Sci. Part A-Polym. Chem. 46 (2008) 2414.
[20] S.U. Celik, A. Aslan, A. Bozkurt, Solid State Ionics 179 (2008) 683.
[21] A. Aslan, S.U. Celik, U. Sen, R. Haser, A. Bozkurt, Electrochim. Acta 54 (2009) 2957.
[22] K.P. Pernstich, S. Haas, D. Oberhoff, C. Goldmann, D.J. Gundlach, B. Batlogg, A.N. Rashid, G. Schitter, J. Appl. Phys. 96 (2004) 6431.
[23] S. Xiao, M. Nguyen, X. Gong, Y. Cao, H. Wu, D. Moses, A. Heeger, Adv. Funct. Mater. 13 (2003) 25.
[24] L.A. Majewski, M. Grell, S.D. Ogier, J. Veres, Org. Elect. 4 (2003) 27.
[25] L.A. Majewski, R. Schroeder, M. Grell, Adv. Mater. 17 (2005) 192.
[26] I. Horcas, R. Fernandez, J.M. Gomez-Rodriguez, J. Colchero, J. Gomez-Herrero, A.M. Baro, Rev. Sci. Instrum. 78 (2007) 013705.

Organic Electronics 12 (2011) 504–508

Contents lists available at ScienceDirect

Organic Electronics

journal homepage: www.elsevier.com/locate/orgel

pH-neutral PEDOT:PSS as hole injection layer in polymer light emitting diodes

Sha Wu, Shaohu Han, Yina Zheng, Hua Zheng, Nanliu Liu, Lei Wang, Yong Cao, Jian Wang *

Institute of Polymer Optoelectronic Materials and Devices, South China University of Technology, Key Laboratory of Specially Functional Materials, Ministry of Education, Guangzhou 510640, China

ARTICLE INFO

Article history:
Received 11 November 2010
Received in revised form 23 December 2010
Accepted 28 December 2010
Available online 11 January 2011

Keywords:
Polymer light emitting diode
PEDOT:PSS
Hole injection layer
Hole injection barrier
Solution process

ABSTRACT

In the application of polymer light emitting diodes (PLEDs), to prevent etching of ITO by the acidic poly(3,4-ethylenedioxythiophene):poly(styrene sulfonate) (PEDOT:PSS), the pH-neutral PEDOT:PSS was introduced as the hole injection layer (HIL). For the double layer PEDOT:PSS HIL, the pH-neutral PEDOT:PSS on top of ITO stops the indium migration into the polymer, while the regular acidic PEDOT:PSS beneath the light emitting layer keeps the efficient hole injection. The performance of the double layer HIL PLEDs is comparable to or even better than that of the single layer HIL light emitting device. To use pH-neutral PEDOT:PSS as a single layer HIL, the neutral PEDOT:PSS layer was treated by UV and oxygen plasma. Such treatments reduced the hole injection barrier between the HIL and the light emission layer to improve the hole injection, leading to a device performance better than that of the regular acidic PEDOT:PSS HIL device.

© 2010 Elsevier B.V. All rights reserved.

1. Introduction

Polymer light emitting diodes (PLEDs) generally have a bi-layer device structure, consisting of a hole injection layer (HIL) on top of an ITO coated glass substrate, and an electroluminescent (EL) layer between the HIL and low work function cathode [1–4]. The HIL helps the holes injected from the anode into the EL layer to radiatively recombine with the injected electrons from the cathode. So far, the most successful HIL material for the PLED devices is poly(3,4-ethylenedioxythiophene):poly(styrene sulfonate) (PEDOT:PSS). With PEDOT:PSS as HIL, the PLED devices show dramatically increased performances in terms of efficiency, brightness, lifetime, etc. [5,6] H.C. Starck GmbH offers two kinds of commercial PEDOT:PSS: Clevios™ P Al 4083 (4083) for PLED application and Clevios™ P CH 8000 (8000) for passive matrix display application [7]. Both PEDOT:PSS have a pH value between 1 and 3 at 20 °C, which make the interface between ITO and PEDOT:PSS unstable [8–10]. The instability comes from the fact that In_2O_3 has a relatively high solubility in acidic solution [11]. During the coating process, PEDOT:PSS can etch ITO causing indium migration into the PEDOT:PSS layer. The presence of indium in PEDOT:PSS could increase the hole injection barrier for PLED operation [12], and be responsible for device degradation [8]. Moreover, if indium diffused into the EL layer, as a quenching center for exciton, it would significantly reduce the luminous efficiency [13,14].

Recently, to lower the cost of the transparent electrodes in the display industry, zinc oxide based transparent conducting oxide (TCO), such as gallium-doped zinc oxide (GZO) and aluminum-doped zinc oxide (AZO), has progressed steadily in order to replace the expensive indium oxide based TCO, i.e. ITO [15–18]. Since ZnO has a higher solubility in the acid than In_2O_3 [11], it is anticipated that the acidic PEDOT:PSS 4083 and 8000 will etch ZnO based TCO even more. Therefore, finding the right HIL materials becomes necessary for the success of the PLED technology.

Different approaches have been attempted to protect the organic layers from indium contamination, including the insertion of a self-assembly monolayer between ITO anode and HIL to stop indium from penetrating into HIL

* Corresponding author. Tel.: +86 (20)8711 4525; fax: +86 (20)8711 0606.
E-mail address: jianwang@scut.edu.cn (J. Wang).

1566-1199/$ - see front matter © 2010 Elsevier B.V. All rights reserved.
doi:10.1016/j.orgel.2010.12.015

[10,19], the mixture of a silane material with PEDOT:PSS to block the indium dissolution in PEDOT:PSS [20,21], and the introduction of an interlayer between PEDOT:PSS and EL layer to prevent indium's diffusion into the EL layer [22,23]. In this contribution, first, we introduced a thin layer of pH-neutralized PEDOT:PSS before the deposition of the acidic PEDOT:PSS to make a double layer HIL for PLED application. The double layer HIL not only stops the etching of indium species due to the pH-neutral layer on top of ITO, but also retains the PLED performance due to the regular PEDOT:PSS beneath the EL layer. Second, we utilized the pH-neutral PEDOT:PSS without any acidic PEDOT:PSS as the single layer HIL. By applying the surface UV and plasma treatment on the pH-neutral PEDOT:PSS HIL, the PLED's performance is improved 10-fold than the device without any HIL treatment due to the reduction of the hole injection barrier. The performance is even better than the device with the regular acidic PEDOT:PSS HIL. As expected, the neutral PEDOT:PSS stops the etching of indium species protecting both the ITO anode and the EL layer. In addition, the utilization of pH-neutral PEDOT:PSS keeps the solution processability of the PLED device, which is regarded as a low cost process compared to the vacuum evaporation process.

2. Experimental

2.1. XPS measurements

The pH-neutralized version of PEDOT:PSS with a pH value of 5–8 at 20 °C is Clevios™ P Jet N (Jet N), developed by H.C. Starck GmbH for the printing of conductive patterns and particularly designed for the use in ink-jet-processes [7]. No application of Jet N in PLED has ever been reported. The three types of PEDOT:PSS, i.e. Jet N, 4083, and 8000, have the same chemical structure as shown in Fig. 1(a).

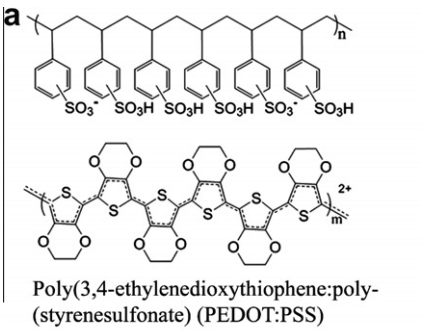

Fig. 1. Chemical structures of: (a) PEDOT:PSS and (b) P-PPV.

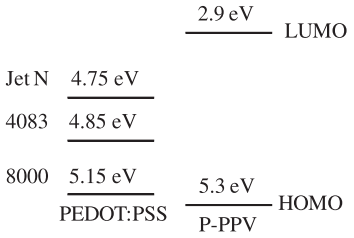

Fig. 2. Schematic illustration of the work function of different kinds of PEDOT:PSS, and the LUMO and HOMO energy levels of P-PPV.

The PEDOT to PSS ratio in those PEDOT:PSS is 1:2.5, 1:6, and 1:20, respectively [7], leading to different work functions of each kind of PEDOT:PSS (schematically illustrated in Fig. 2), i.e. $W_{8000}(5.15\ \text{eV}) > W_{4083}(4.85\ \text{eV}) > W_{\text{Jet N}}(4.75\ \text{eV})$ [24]. To investigate the etching effects of PEDOT:PSS, X-ray photoelectron spectroscopy (XPS) measurements were carried out on PEDOT:PSS coated ITO glass substrate and SiO_2/Si substrate.

Prior to the deposition of PEDOT:PSS, the ITO glass and SiO_2/Si substrates were thoroughly cleaned in sequence in an ultrasonic bath of acetone, isopropyl alcohol, detergent, de-ionized water, isopropyl alcohol, and went through O_2 plasma for 20 min. PEDOT:PSS was spin-cast in air followed by 10 minutes' baking at 200 °C in nitrogen. Five different devices were prepared: single layer Jet N and 4083 on both ITO glass and SiO_2/Si, plus UV and plasma treated Jet N film on ITO glass. The thickness of Jet N film, 4083 film, and UV and plasma treated Jet N film is 20 nm, 40 nm, and 10 nm, respectively, determined by a surface profiler (VEECO-D150). After the completion of the devices, all the devices and a bare ITO glass substrate were loaded into an ultrahigh vacuum chamber for XPS experiment. XPS was performed with a base pressure in the range of 10^{-9} mbar, using Mg Kα radiation (1253.6 eV) with the energy resolution of 0.48 eV. The X-ray survey spectra were acquired in the 0–1110 eV binding energy region at the power of 75 W (15 kV, 5 mA), with a pass energy of 160 eV. Narrow scans of C 1s, O 1s, N 1s, S 2p, Na 1s, In 3d, Sn 3d were obtained at 40 eV pass energy.

2.2. PLED fabrication

To fabricate the PLED devices, green light emitting conjugated polymer poly[2-(4-(3′,7′-dimethyloctyloxy)-phenyl)-p-phenylenevinylene] (P-PPV) (chemical structure in Fig. 1(b), purchased from Canton OLedking Optoelectric Materials Co., Ltd.) was used as the light emission material. Six different HIL structures were made: (A) single layer Jet N; (B) single layer 8000; (C) single layer 4083; (D) double layer Jet N/8000; (E) double layer Jet N/4083; and (F) UV and plasma treated single layer Jet N. The optimal HILs' thickness are, respectively: (A) 10–20 nm; (B) 10–40 nm; (C) 40 nm; (D) 15/40 nm; (E) 15/40 nm; and (F) 5–10 nm. Three single layer HIL devices A, B, and C were prepared following the procedures described early. To make the double layer HIL devices D and E, the second PEDOT:PSS (8000 or 4083) layer was spin-coated on top of the Jet N layer immediately after the baking of Jet N. Directly

afterwards, the double layer HIL was baked at 200 °C for 10 min in nitrogen. For UV and plasma treated single layer Jet N HIL device F, the Jet N film was prepared by the process as same for device A, followed by 5 min exposure under a 120 W UV lamp, and five minutes' oxygen plasma treatment with a power of 80 W at 150 sccm oxygen flow (Shenyang Tiancheng Vacuum Technology Co., Ltd.).

After the completion of HILs, the EL polymer layer was prepared by spin-casting P-PPV solutions in *p*-xylene with the concentration of 8 mg/ml on top of the HIL. The resulted P-PPV layer was about 80 nm thick. The cathode layer consisting of 3 nm barium (Ba) and 200 nm aluminum (Al) was thermally evaporated on top of the organic layers in vacuum at a pressure below 1×10^{-6} Torr. The device performances were characterized in a nitrogen filled glove box by a Keithley 236 source meter and a silicon photodiode calibrated by a Chroma Meter CS-200 (Konica Minolta).

3. Results and discussion

Table 1 summarizes the XPS testing results, and the XPS spectra are shown in Fig. 3. For the bare ITO substrate, the indium atomic concentration reaches 34.7%, which is predictably the highest among all the devices. For PEDOT:PSS on Si/SiO_2 substrate, as expected, there is no In detected, since Si/SiO_2 substrate does not have any indium composition. However, 0.13% In is observed in the device of 4083 on ITO glass, while in the device of Jet N on ITO glass, only 0.02% In is found. The results clearly show that by replacing the acidic PEDOT:PSS with a neutral one, the ITO etching effect is dramatically reduced by a factor of 6.5, which will lead to the long operation stability of PLED. After the UV and oxygen plasma treatment, 0.05% In content is detected in the Jet N on the ITO device. The reason why In content doubles after UV and plasma treatment is not clear at the current stage. Lau's group reported an In concentration of 1.7% in acidic PEDOT:PSS coated ITO glass [10]. The difference is explained by the film preparation method. In Lau's work, the film was dried slowly at room temperature in nitrogen, while in our work, the film was hard baked at high temperature (200 °C) in nitrogen. Using a similar fast-drying method, de Jong's group observed an indium content of 0.02% via Rutherford backscattering spectrometry [9]. The fact that different PEDOT:PSS film preparation methods leading to different In concentrations, verifies that the main ITO etching mechanism is coming from the dissolution of In_2O_3 in an acidic solution. The prolonged PEDOT:PSS drying process in PLED fabrication is detrimental to the PLED performance and stability.

Table 1
Atomic concentration of indium in PEDOT:PSS by XPS analysis.

Type	Atomic concentration (%) by XPS						
	C 1s	O 1s	N 1s	S 2p	Na 1s	In 3d	Sn 3d
ITO glass	10.85	51.71	0.00	0.00	0.00	34.70	2.74
ITO/4083	72.27	17.92	3.47	5.15	1.06	0.13	0.00
ITO/Jet N	71.54	18.99	2.72	4.94	1.79	0.02	0.00
SiO_2/Jet N	65.64	21.67	2.65	8.63	1.41	0.00	0.00
SiO_2/4083	66.44	21.08	2.59	8.44	1.46	0.00	0.00
ITO/UV-plasma-Jet N	62.45	25.84	4.32	5.73	1.60	0.05	0.00

Though it effectively stops the indium diffusion, Jet N does not succeed as a single layer HIL in PLED application. Fig. 4(a) shows the current density (*J*)–bias (*V*)–luminance (*L*) characteristics and (b) shows the luminous efficiency (LE) vs. the current density. Among the three single layer HIL devices A, B, and C, the 8000 device exhibits the best performance, while the single layer Jet N device A exhibits the worst performance with the turn-on voltage of 4 V, the maximum luminance of 14,942 cd/m^2, and the highest LE of 2.24 cd/A. It demonstrates that Jet N is a rather poor HIL material. As shown in Fig. 2, the hole injection barrier between Jet N and P-PPV is substantially larger than that between 8000 and P-PPV, which may be responsible for the difference in the devices' performance.

By applying the regular PEDOT:PSS on top of Jet N, double layer HIL devices D and E greatly improve the device

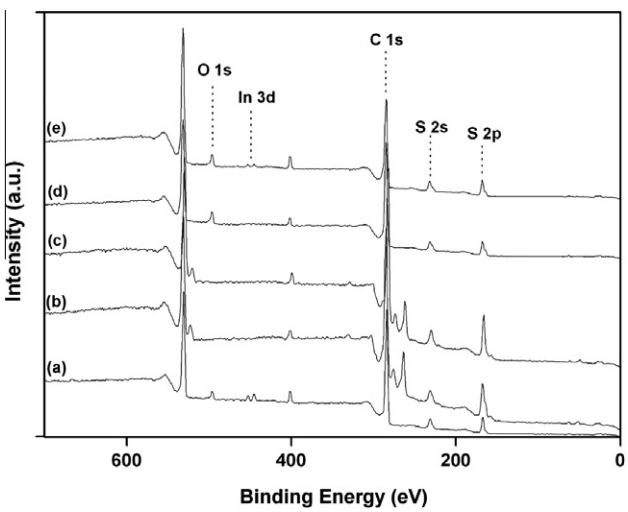

Fig. 3. XPS spectra of (a) ITO/4083, (b) ITO/Jet N, (c) SiO_2/Jet N, (d) SiO_2/4083, and (e) ITO/UV-plasma-Jet N.

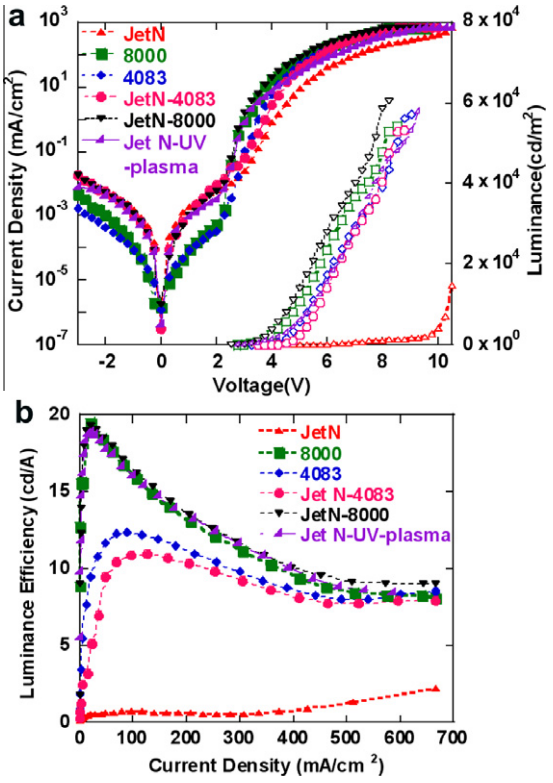

Fig. 4. (a) *J–V–L* characteristics, and (b) EL efficiency vs. current density of PLEDs with different HIL.

performances to the level comparable to or even better than the single acidic PEDOT:PSS HIL devices B and C. For example, the Jet N/8000 double HIL device D displays the highest LE of 19.3 cd/A at a current density of 19.1 mA/cm^2 with a luminance of 3685 cd/m^2. At the same current density, the 8000 single HIL device B has the same LE of 19.3 cd/A with a luminance of 3682 cd/m^2. In addition, the maximum brightness of device D reaches 60,374 cd/m^2, better than that of device B, which is 54,111 cd/m^2. Comparing Jet N/4083 double layer HIL device with 4083 single HIL device, the 4083 device has a maximum LE of 12.4 cd/A and a maximum luminance of 57,337 cd/m^2, while the Jet N/4083 device has a maximum LE of 11.0 cd/A and a maximum luminance of 53,128 cd/m^2. All the devices' performance is summarized in Table 2.

By using the double layer PEDOT:PSS HIL device structure, we successfully deal with the ITO/HIL interface via the pH-neutral PEDOT:PSS, and the HIL/light emitting polymer interface through the acidic PEDOT:PSS. However, adding another layer of HIL complicates the device fabrication process. It is desirable that a single layer HIL could not only prevent the ITO etching, but also retain the PLED performance. As demonstrated earlier, Jet N is a poor HIL material for PLED. Some groups reported that the work function of the acidic PEDOT:PSS could be tuned by UV and/or oxygen plasma treatment [25,26]. To modify the interface between Jet N and the EL layer, we applied the UV and the oxygen plasma treatment to the Jet N layer. After the treatments, the device performance was enhanced to a level even better than the regular PEDOT:PSS device. As shown in Fig. 4 and listed in Table 2, the UV and plasma treated Jet N HIL device F exhibits the highest LE of 18.8 cd/A at a current density of 20.3 mA/cm^2 with a luminance of 4462 cd/m^2. At the same current density, the 8000, 4083, Jet N HIL devices' LE are 19.5 cd/A, 9.5 cd/A, and 0.56 cd/A with a luminance of 3942 cd/m^2, 1932 cd/m^2, and 110 cd/m^2, respectively. In addition, the maximum brightness of the UV and plasma treated device reaches 57,855 cd/m^2, better than those of the 8000, and the 4083 devices, which are, respectively, 54,111 cd/m^2, and 57,335 cd/m^2. Another important feature of the UV and plasma treated device is that it has a turn-on voltage of 2.75 V, even lower than that of the 4083 device, which is 3.25 V.

To further understand the functions of the treated Jet N HIL, hole only device was fabricated with the device structure of ITO/treated Jet N/P-PPV/Au. The *J–V* characteristics are depicted in Fig. 5. It is revealed that with the UV and

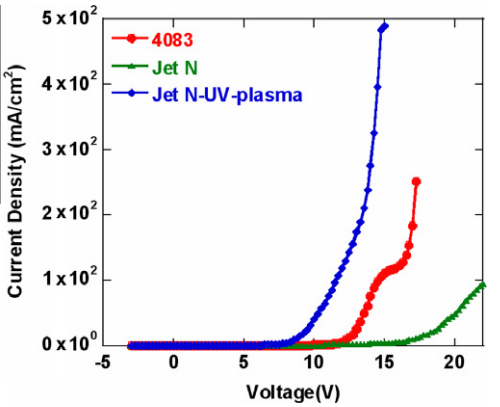

Fig. 5. *J–V* characteristics of hole-only devices with different HIL.

Table 2
Performance of PLED with different HIL.

HIL	Turn-on voltage (V)	*L* (max) (cd/m^2)	LE (max) (cd/A)	Performance at 19.1 mA/cm^2		
				V	*L*	LE
Jet N	4.00	14,942	2.24	5.6	106	0.5
8000	2.75	54,111	19.5	4.2	3682	19.3
4083	3.25	57,337	12.4	4.4	1900	9.4
Jet N/4083	3.50	53,128	11.0	4.7	1155	5.5
Jet N/8000	2.50	60,374	19.3	4.0	3685	19.3
UV-plasma-Jet N	2.75	57,855	18.9	4.7	4462	18.8

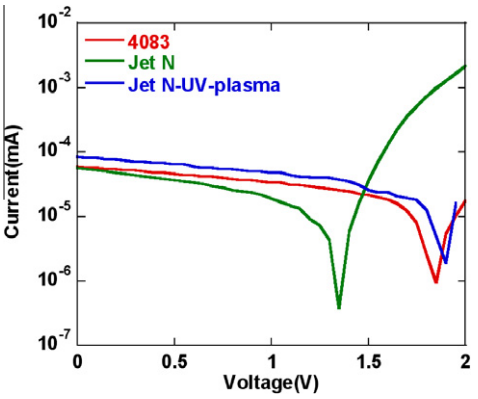

Fig. 6. Photovoltaic characteristics of the PLED devices with different HIL.

plasma treatment, Jet N device shows much higher hole current and lower turn-on voltage than both the device without the treatment and the regular 4083 device. The data demonstrates that the pH-neutral PEDOT:PSS with the UV and plasma treatment serves better as HIL in PLED than the acidic species.

The hole injection improvement is probably due to the reduction of the hole injection barrier between the HIL and the EL layer. Photovoltaic measurement is a direct measurement of the built-in potential, which scales with the hole injection barrier height on the anode side, when the cathode and the organic layers are same for all the devices [27]. Fig. 6 shows the Current (I)–Voltage (V) characteristics of the devices with different HIL under white-light illumination (80 mW cm^{-2}). The open-circuit voltage (V_{OC}) increased from 1.35 V for the non-treated Jet N device to 1.90 V for the treated Jet N device. For comparison, V_{OC} of the 4083 device is 1.85 V. The significant enhancement of V_{OC} confirms that the hole injection barrier is substantially lowered by Jet N HIL after treatment. Reducing hole injection barrier helps hole injections and makes electron and hole density balanced inside the device, therefore, improving the device performance.

4. Conclusions

We have demonstrated the utilization of pH-neutral PEDOT:PSS as the hole injection layer in the PLED devices. In a double layer HIL device structure, the neutral PEDOT:PSS on top of ITO prevents the acidic PEDOT:PSS from etching ITO, while the acidic PEDOT:PSS beneath the EL layer keeps the efficient hole injection from the anode to the light emission layer for the PLED operation. The double layer HIL structure not only reduces the ITO etching effect by a factor of 6.5, but also stops the indium penetration into the polymer layer. The performance of such a device is comparable to or even better than that of the single layer HIL device.

To simplify the double layer HIL structure, the neutral PEDOT:PSS as a single layer HIL in PLED was successfully achieved. Through the UV and the oxygen plasma treatment, the hole injection barrier between the HIL and the EL layer is reduced to improve the hole injection. The performance of the single layer Jet N HIL device is better than that of the regular acidic PDDOT:PSS HIL device. Furthermore, neutralized PEDOT:PSS serving as HIL has a process advantage over inorganic HIL. While the application of inorganic HIL generally requires high vacuum, the solution processability of the PEDOT:PSS retains the simplicity of the PLED process.

Acknowledgments

This work was supported by Ministry of Science and Technology of China (973 Program 2009CB623604, 2009CB930604, and 863 Program 2008AA03A311).

References

[1] R.H. Friend, R.W. Gymer, A.B. Holmes, J.H. Burroughes, R.N. Marks, C. Taliani, D.D.C. Bradley, D.A. Dos Santos, J.L. Brédas, M. Löqdlund, W.R. Salaneck, Nature 397 (1999) 121.
[2] Y. Yang, E. Westerweele, C. Zhang, P. Smith, A.J. Heeger, J. Appl. Phys. 77 (1995) 694.
[3] Y. Cao, G. Yu, C. Zhang, R. Menon, A.J. Heeger, Synth. Met. 87 (1997) 171.
[4] Y. Cao, G. Yu, L.D. Parker, A.J. Heeger, J. Appl. Phys. 88 (2000) 3618.
[5] J.S. Kim, M. Granström, R.H. Friend, N. Johansson, W.R. Salaneck, R. Daik, W.J. Feast, F. Cacialli, J. Appl. Phys. 84 (1998) 6859.
[6] A. Elschner, F. Bruder, H.-W. Heuer, F. Jonas, A. Karbach, S. Kirchmeyer, S. Thurm, R. Wehrmann, Synth. Met. 111–112 (2000) 139.
[7] Product Information. Available from: <http://www.clevios.com>.
[8] S.J. Jo, C.S. Kim, J.B. Kim, S.Y. Ryu, J.H. Noh, H.K. Baik, Y.S. Kim, S.J. Lee, J. Appl. Phys. 103 (2008) 114502.
[9] M.P. de Jong, L.J. van Ijzendoorn, M.J.A. de Voigt, Appl. Phys. Lett. 77 (2000) 2255.
[10] K.W. Wong, H.L. Yip, Y. Luo, K.Y. Wong, W.M. Lau, K.H. Low, H.F. Chow, Z.Q. Gao, W.L. Yeung, C.C. Chang, Appl. Phys. Lett. 80 (2002) 2788.
[11] D.R. Lide, CRC Handbook of Chemistry and Physics, 83rd ed., CRC, Florida, 2002.
[12] C.H. Chang, S.A. Chen, Appl. Phys. Lett. 91 (2007) 103514.
[13] A.R. Schlatmann, D. Wilms Floet, A. Hilberer, F. Garten, P.J.M. Smulders, T.M. Klapwijk, G. Hadziioannou, Appl. Phys. Lett. 69 (1996) 1764.
[14] S.T. Lee, Z.Q. Gao, L.S. Hung, Appl. Phys. Lett. 75 (1999) 1404.
[15] J.J. Berry, D.S. Ginley, P.E. Burrows, Appl. Phys. Lett. 92 (2008) 193304.
[16] L. Wang, D.W. Matson, E. Polikarpov, J.S. Swensen, C.C. Bonham, L. Cosimbescu, J.J. Berry, D.S. Ginley, D.J. Gaspar, A.B. Padmaperuma, J. Appl. Phys. 107 (2010) 043103.
[17] H. Kim, C.M. Gilmore, J.S. Horwitz, A. Piqué, H. Murata, G.P. Kushto, R. Schlaf, Z.H. Kafafi, D.B. Chrisey, Appl. Phys. Lett. 76 (2000) 259.
[18] J.Q. Zhao, S.J. Xie, S.H. Han, Z.W. Yang, L.N. Ye, T.L. Yang, Synth. Met. 114 (2000) 251.
[19] J.E. Malinsky, G.E. Jabbour, S.E. Shaheen, J.D. Anderson, A.G. Richter, T.J. Marks, N.R. Armstrong, B. Kippelen, P. Dutta, N. Peyghambarian, Adv. Mater. 11 (1999) 227.
[20] J.Y. Lee, Synth. Met. 156 (2006) 537.
[21] J.Y. Lee, Chem. Phys. Lett. 393 (2004) 260.
[22] J.Y. Lee, Synth. Met. 156 (2006) 852.
[23] T.P. Nguyen, S.A. de Vos, Appl. Surf. Sci. 221 (2004) 330.
[24] N. Koch, A. Elschner, J.P. Rabe, R.L. Johnson, Adv. Mater. 17 (2005) 330.
[25] A. Benor, Shin-ya Takizawa, César Pérez-Bolívar, P. Anzenbacher Jr., Org. Electron. 11 (2010) 938.
[26] B.J. Chen, X.W. Sun, B.K. Tay, L. Ke, S.J. Chua, Appl. Phys. Lett. 86 (2005) 063506.
[27] C.J. Brabec, A. Cravino, D. Meissner, N.S. Sariciftci, T. Fromherz, M.T. Rispens, L. Sanchez, J.C. Hummelen, Adv. Funct. Mater. 11 (2001) 374.

Organic Electronics 12 (2011) 509–515

Contents lists available at ScienceDirect

Organic Electronics

journal homepage: www.elsevier.com/locate/orgel

An ambipolar to n-type transformation in pentacene-based organic field-effect transistors

Jer-Wei Chang [a], Po-Wei Liang [a], Min-Wei Lin [a], Tzung-Fang Guo [a,*], Ten-Chin Wen [b], Yao-Jane Hsu [c]

[a] Institute of Electro-Optical Science and Engineering, Advanced Optoelectronic Technology Center, National Cheng Kung University, Tainan, Taiwan 701, Republic of China
[b] Department of Chemical Engineering, National Cheng Kung University, Tainan, Taiwan 701, Republic of China
[c] National Synchrotron Radiation Research Center, Hsinchu, Taiwan 300, Republic of China

ARTICLE INFO

Article history:
Received 27 September 2010
Received in revised form 25 November 2010
Accepted 30 December 2010
Available online 12 January 2011

Keywords:
Pentacene
Organic field-effect transistors
Aluminum
Ambipolar
n-Type

ABSTRACT

We report an ambipolar to n-type transformation in pentacene-based organic field-effect transistors (OFETs) of aluminum (Al) source–drain electrodes. The hole currents of the ambipolar OFETs were decreased by over two orders of magnitude within 24 h after the device fabrication, but the electron currents remained unchanged, which makes the devices present n-type only characteristics. The transformation is correlated with the interfacial interactions between Al electrodes and pentacene, as characterized by analyzing near-edge X-ray absorption fine structure spectra and Micro-Raman spectra. This study highlights the importance of metal/organic interfaces in the performance of OFETs, and demonstrates decent n-type pentacene-based OFETs with electron mobility of 0.1 $cm^2/V/s$ with proper annealing treatment.

© 2011 Elsevier B.V. All rights reserved.

A significant progress has been achieved in materials, device architectures, and fabrication processes of organic field-effect transistors (OFETs) [1,2]. Pentacene is one of the most promising materials for high performance p-type OFETs [3]. Besides p-type, the ambipolar [4–6] and n-type [7–9] conduction of pentacene-based OFETs were also observed when metal electrodes of low work function and trap-free dielectrics are used. Ambipolar OFETs could be deployed in organic circuits, such as inverters, oscillators, logic circuits, [10,11] and even organic light-emitting field-effect transistors recently [12,13].

In consideration of charge injection barriers, aluminum (Al) is a suitable metal as source–drain (S–D) electrodes in ambipolar pentacene-based OFETs, because the energy barriers for the injection of electrons and holes from Al S–D electrodes to pentacene are comparable. Therefore, the studies of ambipolar pentacene-based OFETs using Al S–D electrodes were reported [5,6]. However, we recently disclosed the pentacene-based OFETs of Al S–D electrodes only perform the decent n-type performance [8]. In this paper, the output characteristics of the OFETs were ambipolar initially. Within 24 h after the device fabrication, the hole currents decreased by over 2 orders of magnitude, but the magnitude of the electron currents remained the same. We attributed the time-dependent ambipolar to n-type transformation in pentacene-based OFETs of Al S–D electrodes to the specific interfacial interaction at the Al–pentacene junction, which presumably functioned as the hole blocking layer and was characterized by the near-edge X-ray absorption fine structure (NEXAFS) spectra and Micro-Raman spectra.

The device configuration, as shown in the inset of Fig. 1(d), is composed of the indium-tin-oxide (ITO) (as gate electrode) glass substrate/poly(3,4-ethylenedioxythiophene): polystyrenesulfonate (PEDOT:PSS)/crosslinked poly(4-vinyl phenol) (PVP) (as bottom dielectric)/polystyrene (PS) (as top dielectric)/pentacene (as active layer)/Al (as source and drain electrodes). The fabrication details

* Corresponding author. Tel.: +886 6 2757575; fax: +886 6 2095040.
E-mail addresses: guotf023@hotmail.com, guotf@mail.ncku.edu.tw (T.-F. Guo).

1566-1199/$ - see front matter © 2011 Elsevier B.V. All rights reserved.
doi:10.1016/j.orgel.2010.12.018

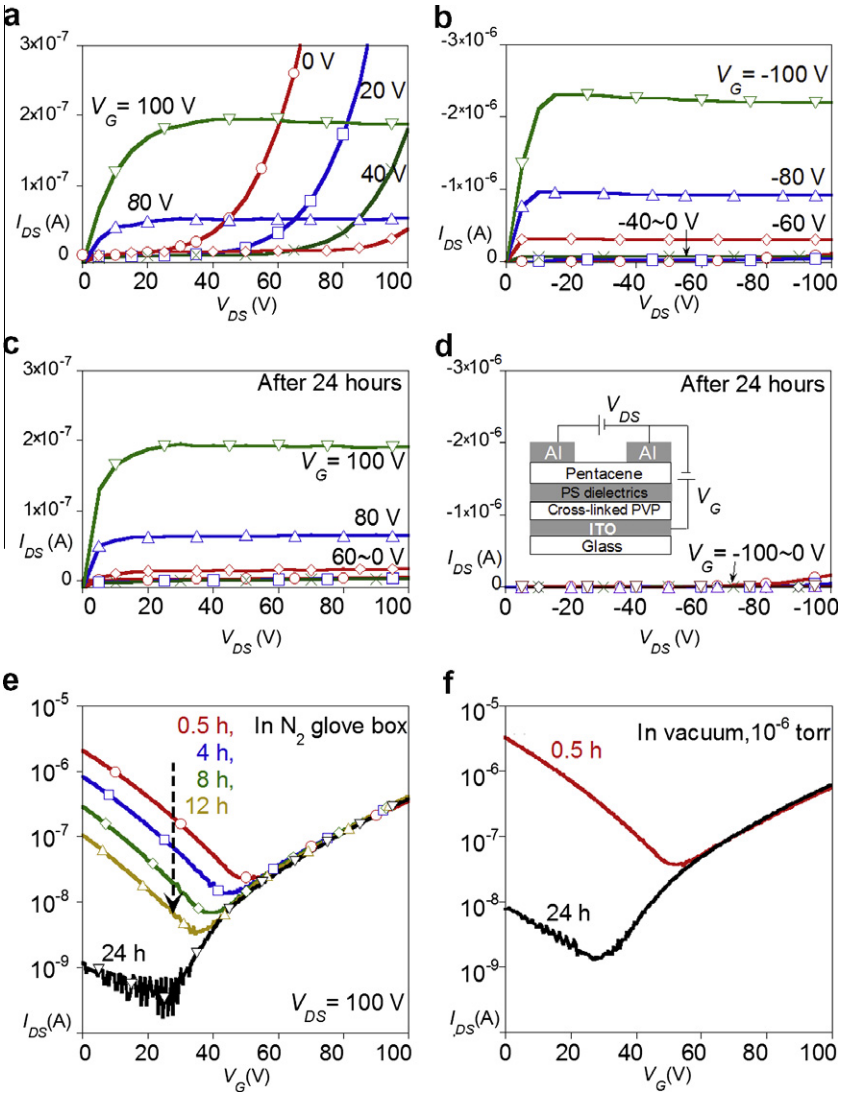

Fig. 1. The output characteristics of I_D vs. V_{DS} plot of pentacene-based OFETs with Al source–drain electrodes, (a) measured at 0.5 h after the fabrication of OFETs at V_G of (○) 0 V, (□) 20 V, (×) 40 V, (◇) 60 V, (△) 80 V, and (▽) 100 V in n-type operation regime (b) measured at 0.5 h at V_G of (○) 0 V, (□) −20 V, (×) −40 V, (◇) −60 V, (△) −80 V, and (▽) −100 V in p-type operation regime, (c) measured at 24 h in n-type operation regime, and (d) measured at 24 h in p-type operation regime. The inset is the structure of a pentacene-based OFET used in this study. (e) Transfer characteristics (I_{DS} vs. V_G) in nitrogen-filled glove box at (○) 0.5, (□) 4, (◇) 8, (△) 12, and (▽) 24 h and (f) in vacuum of 10^{-6} torr after fabrication at V_{DS} = 100 V.

were reported in a previous study [9]. PS was dissolved in toluene at a concentration of 5.0 wt.% and then spun on the substrate as top layer dielectric. The thicknesses of cross-linked PVP, PS dielectric, and pentacene layer were 160, 120, and 80 nm, respectively. The channel length (L) and width (W) were 100 and 1000 μm, respectively. The completed OFETs were stored in nitrogen-filled glove box at the oxygen and moisture level <1 ppm, or in vacuum at 10^{-6} torr. The output electrical characteristics were measured inside the glove box using HP4145B semiconductor parameter analyzer. The NEXAFS spectra were taken in radiation normal to sample substrates at the X-ray photoemission electron microscopy station with an energy resolution of 100 meV at the K-edge in National Synchrotron Radiation Research Center (NSRRC), Hsin-Chu, Taiwan. The Micro-Raman scattering spectra were recorded in backscattering configuration using Bruker SENTERRA Raman Microscope at room temperature through 50× objective with excitation by a 532 nm laser. The height images of atomic force microscopy (AFM) were taken by Veeco D5000 in tapping mode.

The output characteristics and transfer characteristics of pentacene-based OFETs with Al S–D electrodes are measured from originally ambipolar to n-type in 24 h. Fig. 1(a) plots the output characteristics, S–D current (I_{DS}) vs. S–D voltage (V_{DS}) of one device operated at positive gate voltage (V_G) from 0 to +100 V, n-channel accumulation regime, at 0.5 h after the fabrication. When V_G was from 0 to 60 V, the output currents did not exhibit the output characteristics of a transistor, but of a diode. These diode-like output

currents were decreased as positive V_G was increased which are contributed by hole carriers. When V_G was from 80 to 100 V, the curves presented saturated S–D output currents were increased as positive V_G was increased which are dominated by electron carriers. Fig. 1(b) shows the output characteristics of the same device operated at negative V_G of p-channel accumulation regime. It shows this device is p-type of output characteristics under negative V_G bias. In comparison of Fig. 1(a) and (b), the ambipolar conduction of the device is valid in both n-type and p-type operations with clear saturated electron currents and hole currents. Electron mobility and hole mobility are calculated as 2.43×10^{-3} and 2.18×10^{-2} $cm^2/V/s$ respectively in saturation region. Fig. 1(c) shows the output characteristics of the same device after 24 h of storage in nitrogen-filled glove box (oxygen and moisture level <1 ppm). The diode-like currents which are shown in Fig. 1(a) were not detected, but the saturated currents were remained. In Fig. 1(d), the p-type saturated currents are decreased about to the noise level of measurement system. According to the data of Fig. 1(c) and (d), the electron mobility after 24 h remains 2.43×10^{-3} $cm^2/V/s$, but the hole mobility is too low to be calculated correctly. Fig. 1(e) displays the evolution of transfer characteristics measured at 0.5 to 24 h after the fabrication of OFETs in a nitrogen-filled glove box. The I_{DS} of OFETs illustrates the ambipolar characteristics with hole current of 10^{-6} amp at $V_G = 0$ V and electron current of 10^{-7} amp at $V_G = 100$ V at 0.5 h. As the storage time increases, the hole current decreases to 10^{-9} amp after 24-h of storage, but the magnitude of the electron current remains unchanged. The originally ambipolar pentacene-based OFET becomes a n-type device in the inert atmosphere at the oxygen and moisture levels <1 ppm without any post treatment.

In order to find the origins of this phenomenon of the decreased hole currents, storage environments, annealing effect, gate dielectrics, metals of S–D electrodes, and the contact of S–D electrodes and pentacene layer were investigated systemically. By comparing Fig. 1(e) and (f), the hole current of the device stored in a vacuum of 10^{-6} torr is still decreased by over two orders of magnitude within 24 h. Although the oxygen and moisture inside the glove box and a vacuum of 10^{-6} torr is very low, we still cannot completely exclude the possible influence of the residual atmosphere to the device performance. When OFETs fabricated in this study were exposed to the air atmosphere or dry oxygen gas in 0.5 h, both the hole current and the electron current were decreased remarkably by few orders of magnitude. Full details of environmental experiments are presented in the Supporting Information S1. According to the results, oxygen and moisture in ambient atmosphere damage both n-type and p-type operations, but the levels of oxygen and moisture inside the glove box or a vacuum of 10^{-6} torr did not cause the decreasing of electron currents in Al pentacene-based OFETs.

To clarifying the correlation of this transformation and annealing effect on pentacene, annealing of 100 °C 0.5 h right after the device fabrication was applied. Fig. 2 presents the transfer curves of one annealed device measured at 0.5 and 24 h after the fabrication. The inset is the output characteristics of the device at 24 h. Firstly, the hole current of 10^{-6} amp at $V_G = 0$ V still existed right after annealing. Secondly, the hole current was decreased by over two orders of magnitude within 24 h. Thirdly, the electron current of the annealed device at $V_G = 100$ V was increased over 1.5 orders of magnitude, and its calculated electron mobility in saturation region is improved, up to 0.1 $cm^2/V/s$. The influence of annealing treatment of pentacene-based OFETs has been studied by several groups. Annealing effects include improving mobility as increasing crystallinity [14–16], keeping durability under continuous bias stress [15], and causing a shift in threshold voltages of the ambipolar pentacene OFETs [17]. As a result of this experiment, annealing treatment improves the electron currents of the Al pentacene-based OFET, and the phenomenon of decreased hole currents with time remains regardless of applying annealing treatment or not.

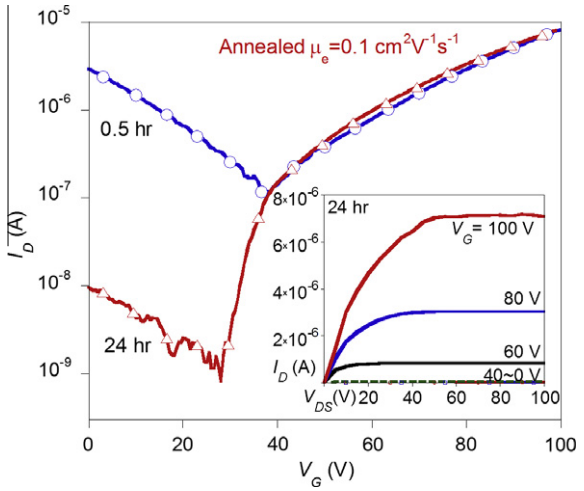

Fig. 2. Transfer characteristics of one pentacene-based OFET with Al S–D electrodes with annealing of 100 °C 0.5 h, then measured at (○) 0.5 and (△) 24 h after the fabrication. The inset is the output characteristics of the device at 24 h.

The influence of gate dielectrics such as poly(methyl methacrylate) (PMMA), PVP, polyvinyl alcohol (PVA), and PS, were surveyed which affects the morphologies of pentacene films. Fig. 3(a) presents the normalized hole currents at $V_G = 0$ V and $V_{DS} = 100$ V vs. time from 0.5 to 24 h for devices of different gate dielectrics. The hole currents for all pentacene-based OFETs of Al S–D electrodes comprising different gate dielectrics are decreased with time. Noted that the pentacene-based OFETs of Al S–D electrodes have the maximum decline in hole current after 24 h of fabrication, when PS is used as the gate dielectric. The variations in the decline of hole currents for OFETs of different gate dielectrics are probably related to the interfacial morphologies between different pentacene films and Al electrodes. The root-mean-square (rms) roughness as characterized by AFM of 80 nm thick pentacene films on PMMA, PVP, PVA, and PS are 15.5, 16.3, 10.4, and 7.6 nm, respectively. The difference of surface topography for 80 nm thick pentacene films on PMMA and PS can be identified by AFM height images as shown in Fig. 3(b).

Fig. 3(a) also summarizes the normalized hole currents vs. time for OFETs made of Au and Ag, as S–D electrodes to

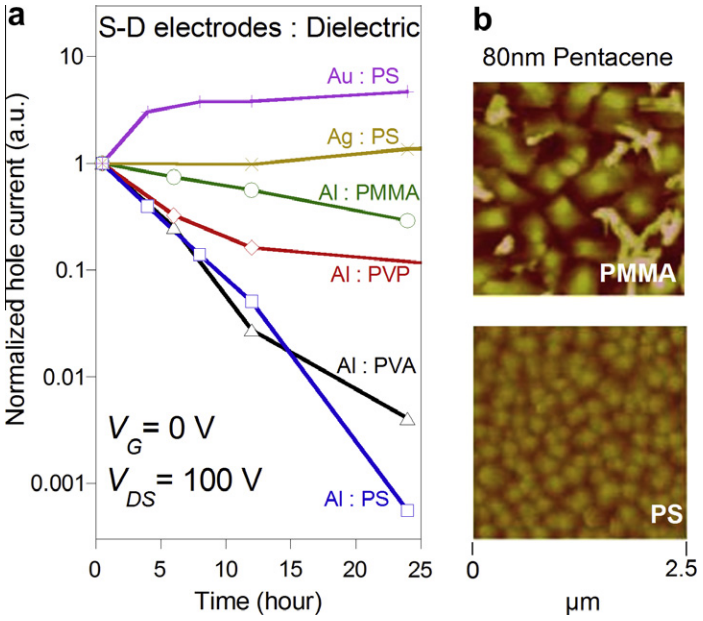

Fig. 3. (a) The normalized hole currents as a function of storage time (hours) in pentacene-based OFETs of (+) Au, (×) Ag S–D electrodes with PS as gate dielectric, and Al S–D electrodes with (○) PMMA, (◇) PVP, (△) PVA, and (□) PS as gate dielectrics at V_{DS} = 100 V and V_G = 0 V. (b) AFM height images (2.5 × 2.5 μm) of pentacene films (80 nm) on PMMA and on PS dielectrics.

investigate the correlations of the decreased hole currents with metal S–D electrodes. When Au was applied as S–D electrodes, the hole current increased initially, and it became stable after 4 h. Such an initial increase was attributed to the defect healing effect of pentacene-based OFETs at room temperature as reported by Kalb et al. [18]. The hole current of the OFET with Ag as S–D electrodes is also slightly increased. The marked decrease in the hole current can only be observed for OFETs of Al S–D electrodes. As a result, Al metal S–D electrodes are critical to the decline of hole currents, and the Al-pentacene interface should be characterized essentially.

To investigate the contact of S–D electrodes and pentacene layer, two approaches were utilized. One was S–D contact resistance by the transmission line model (TLM), and the other was the separation of Al and pentacene by inserting a buffer layer. First, TLM is a useful approach to identify the variation of hole currents on the S–D contact region or on the field-effect channel region by deriving contact resistance (R_C) and channel resistance (R_{Ch}) [19–21]. The total resistance (R_T) is equal to the sum of R_C and R_{Ch} according to

$$R_T = \left.\frac{\partial V_{DS}}{\partial I_{DS}}\right|_{V_{DS\to 0}}^{V_G} = R_{Ch} + R_C = \frac{L}{W\mu C(V_G - V_T)} + R_C, \qquad (1)$$

where L, μ, and V_T are the channel length, mobility, and threshold voltage, respectively. The R_C is given by the intercept of the total resistance, R_T, vs. L plot at L = 0, and is the sum of contact resistance of the source and the drain.

To apply TLM approach, the S–D total resistances of hole currents are measured at V_G = −100 V and V_{DS} = −1 V, and those of electron currents are measured at V_G = +100 V and V_{DS} = +1 V for OFETs made of different channel length L, 50, 100, 150, and 200 μm. From 0.5 to 48 h, the total resistance of hole currents increases by 2 orders of magnitude regardless of channel lengths. Accordingly, the contact resistance of hole currents dominates the total resistance, which was increased at the range from 6×10^6 to 10^9 Ω approximately as the storage time of OFETs was increased from 0.5 to 48 h. For the resistance of electron currents from 0.5 to 48 h, the contact resistance is slightly decreased from 8×10^6 to 5×10^6 Ω, and the channel resistance is also decreased from 3.3×10^6 Ω per 10 μm to 1.3×10^6 Ω per 10 μm, according to Eq. (1). More detail results on TLM approach are presented in the Supporting Information S2. The variations of the contact and channel resistance of electron currents are relatively small as compared to the increase in the contact resistance of hole currents. Therefore, the decrease of hole currents is a result of the increase of contact resistance at the Al–pentacene junction which determines the injection of charge carriers.

The second approach to investigate the contact of S–D electrodes and pentacene layer is inserting a buffer layer to prevent the direct contact of Al and pentacene without influencing the injection of charge carriers. Fig. 4(a–c) compare the transfer characteristics of one original pentacene-based OFET, with a buffer layer of molybdenum trioxide (MoO_3) which favors the injection of holes [22], and with lithium fluoride (LiF) layer which favors the injection of electrons and the blocking of holes [6,23]. Fig. 4(a) shows one pentacene-based OFET without a buffer layer inserted between pentacene and Al, which is the same device shown in Fig. 1(e), for comparison with those inserted a buffer layer. When the MoO_3 layer of 10 nm thickness was applied, it shows both hole and electron currents keep the same level within 24 h without the significant decreas-

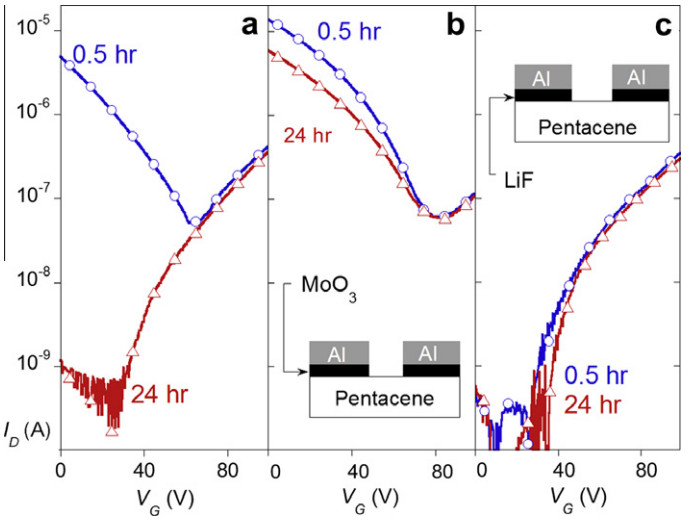

Fig. 4. Transfer characteristics of (a) one pentacene-based OFET with Al S–D electrodes, (b) one with MoO_3 of 10 nm thickness, and (c) one with LiF of 5 nm thickness as a buffer layer between pentacene layer and Al electrodes.

ing of hole currents in Fig. 4(b). When the buffer layer was replaced by LiF of 5 nm thickness, hole currents are blocked in the level of 10^{-9} A without delay in Fig. 4(c). Therefore, when Al and pentacene are separated, the time-dependant decreasing of hole currents does not happen. It indicates the main cause of the decreased hole currents is presumably the junction of Al and pentacene.

The injection barrier heights of hole carriers are examined by Fowler–Nordheim (FN) tunneling theory [24,25] $I \propto F^2 \exp(-\kappa/F)$, where I is the current of a diode, F is the electric field under bias V, and κ is a parameter which is related to the shape of the barrier height (φ). Fig. 5(a) shows the decrease of hole currents with time for a diode of ITO/PEDOT:PSS/pentacene/Al configuration at hole-dominated operation regime. For the matching of energy levels of hole transport, PEDOT:PSS/pentacene interface is considered as an Ohmic contact, but pentacene/Al interface is as a Schottky contact. The diode in this configuration is one hole-dominated device. The tunneling of hole carriers is mainly attributed at pentacene/Al interface. Fig. 5(b) presents the FN plots of $\ln(I/F^2)$ vs. $1/F$ for the same device. The slope of FN curves, κ, is proportional to $\varphi^{3/2}$. The increased slopes of FN curves in positive voltage with time probably suggest the barrier height of hole carriers through the tunneling process at Al–pentacene junction was increased due to the interfacial interaction, which block hole carriers and results a time-dependent output characteristics. There is no change in PEDOT:PSS/pentacene interface according to the similarity of the slopes of FN curves in negative voltage region in 48 h shown in Supporting Information S3.

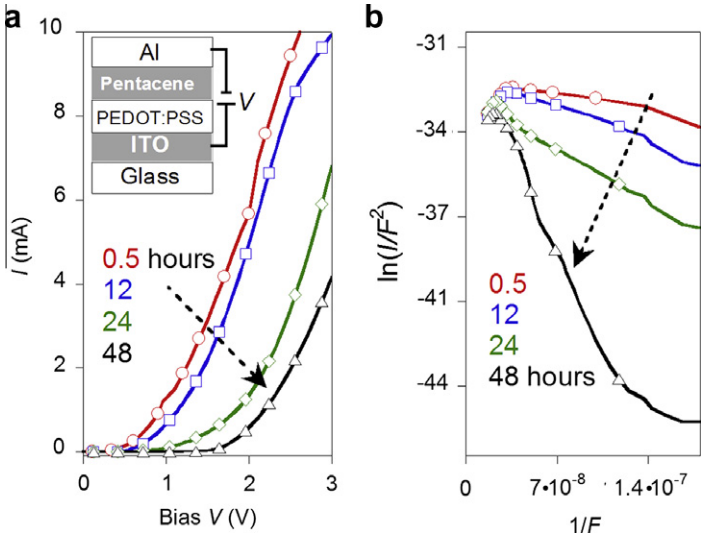

Fig. 5. (a) I–V characteristics for a diode of ITO/PEDOT:PSS/pentacene/Al configuration from 0.5 to 48 h after fabrication and (b) Fowler–Nordheim plots, $\ln(I/F^2)$ vs. $1/F$, for the same diode. F is the electric field under bias V.

Fig. 6(a) shows the NEXAFS spectra of pentacene films covered with ultra thin metals, such as Al and Ag. In Fig. 6(a) the signals of LUMO (282–283.7 eV) and LUMO + 1 (283.7–285.5 eV) groups of pristine pentacene in the π^*-transition region were apparent and the signal of σ^* (C–H)/Rydberg resonances region (287–288 eV) was very small [26,27]. The spectrum of the pentacene film deposited with 3 nm Ag was almost identical to that of pristine pentacene film in Fig. 6(a). The spectra of the pentacene film deposited with 1 nm Ag, 1 nm Au, and 3 nm Au are the same (not shown here). However, in the spectra for pentacene deposited with 1- and 3-nm-thick Al, the intensities of LUMO and LUMO + 1 were decreased and the signal of σ^* (C–H) was markedly enhanced with the thickness of Al. These results suggest that the change from carbon double bonds into carbon–hydrogen-like single bond is due to the deposition of Al on pentacene. The σ^* signal regarding the Al-related carbon single bond indicates the existence of Al–pentacene interactions.

The affected vibration mode of the Al–pentacene interactions is observed in Raman spectroscopy. Fig. 6(b) shows Raman spectra of a 10-nm-thick pentacene film and a 10-nm-thick pentacene film deposited with 8-nm-thick Al. The 1596 cm^{-1} Raman signal is enhanced in the as deposited 8-nm-thick Al over pentacene, which corresponds to a quadrant stretching mode of benzene rings. The relative intensity of the peak at 1596 cm^{-1} to the one at 1533 cm^{-1} was enhanced from 0.2 ($I_{1596\ cm^{-1}}/I_{1533\ cm^{-1}}$) for pristine pentacene film to 0.9 for one covered with Al. There are few possible mechanisms to change the quadrant stretching mode of pentacene molecules, such as the variation of the orientation of pentacene molecules [28] and the formation of humidity-induced pentacene–water interaction [29]. In our experiment, we suggest that the changes of 1596 cm^{-1} quadrant stretching mode are correlated with the specific Al–pentacene interfacial interactions as characterized in NEXAFS spectra. Although a time-dependent chemical analysis of Al–pentacene interface to examine the detailed hole blocking mechanism is still in progress currently, the decrease of hole currents in pentacene-based OFETs associated with the Al–pentacene interactions is quite apparent in our studies.

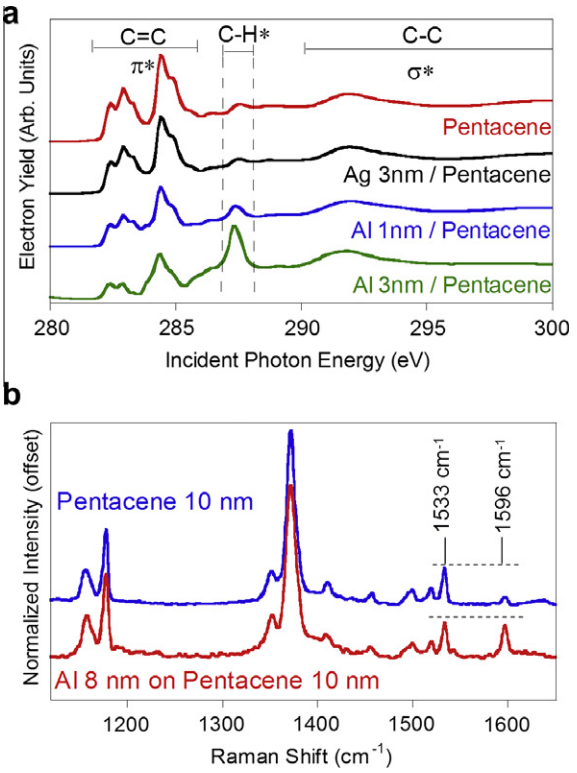

Fig. 6. (a) NEXAFS spectra of a pristine 200 nm thick pentacene film, and ones deposited with 3 nm Ag, 1 nm Al, and 3 nm Al. (b) Raman spectra of a pristine 10 nm pentacene film and one deposited with 8 nm Al.

In summary, we fabricated ambipolar pentacene-based OFETs with Al S–D electrodes initially, but the output characteristics of devices are transformed from ambipolar into n-type within 24 h. This transformation is due to the decrease of hole currents and correlated with the markedly increased contact resistance of hole currents. It is suggested that the interface at the Al–pentacene junction, after storing the OFETs in inert environment for 24 h, functions as an effective hole blocking layer to interfere the injection of the hole currents in ambipolar OFETs. This study highlights the importance of metal/organic material interface in the output performance of OFETs and indicates that Al S–D electrodes are suitable for the fabrication of decent n-type pentacene-based OFETs with electron mobility of 0.1 $cm^2/V/s$ with proper annealing treatment. The time-dependent *in situ* chemical analysis of the Al–pentacene interactions with the OFETs performance is currently in progress.

Acknowledgements

The authors would like to thank the National Science Council (NSC) of Taiwan (NSC99-2113-M-006-008-MY3) and the Asian Office of Aerospace Research and Development (AOARD-10-4054) for financially supporting this research. AFM measurements in National Chung Cheng University, Prof. Yean-Ren Jeng's laboratory are highly appreciated.

Appendix A. Supplementary data

Supplementary data associated with this article can be found, in the online version, at doi:10.1016/j.orgel.2010.12.018.

References

[1] B. Crone, A. Dodabalapur, Y.Y. Lin, R.W. Filas, Z. Bao, A. LaDuca, R. Sarpeshkar, H.E. Katz, W. Li, Nature 403 (2000) 521.
[2] H. Klauk, U. Zschieschang, J. Pflaum, M. Halik, Nature 445 (2007) 745.
[3] Y.Y. Lin, D.J. Gundlach, S.F. Nelson, T.N. Jackson, IEEE Trans. Electron Devices 44 (1997) 1325.
[4] Th.B. Singh, F. Meghdadi, S. Günes, N. Marjanović, G. Horowitz, P. Lang, S. Bauer, N.S. Sariciftci, Adv. Mater. 17 (2005) 2315.
[5] C.-Y. Yang, S.-S. Cheng, C.-W. Ou, Y.-C. Chuang, M.-C. Wu, Dhananjay, C.-W. Chu, J. Appl. Phys. 103 (2008) 094519.
[6] C.-Y. Yang, Dhananjay, S.-S. Cheng, C.-W. Ou, Y.-C. Chuang, M.-C. Wu, C.-W. Chu, Appl. Phys. Lett. 92 (2008) 253307.

[7] M. Ahles, R. Schmechel, H. von Seggern, Appl. Phys. Lett. 85 (2004) 4499.
[8] T.-F. Guo, Z.-J. Tsai, S.-Y. Chen, T.-C. Wen, C.-T. Chung, J. Appl. Phys. 101 (2007) 124505.
[9] J.-W. Chang, W.-L. Hsu, C.-Y. Wu, T.-F. Guo, T.-C. Wen, Org. Electron. 11 (2010) 1613.
[10] Th.B. Singh, P. Senkarabacak, N.S. Sariciftci, A. Tanda, C. Lackner, R. Hagelauer, G. Horowitz, Appl. Phys. Lett. 89 (2006) 033512.
[11] T.D. Anthopoulos, S. Setayesh, E. Smits, M. Cölle, E. Cantatore, B. de Boer, P.W.M. Blom, D.M. de Leeuw, Adv. Mater. 18 (2006) 1900.
[12] A. Hepp, H. Heil, W. Wiese, M. Ahles, R. Schmechel, H. Von Seggern, Phys. Rev. Lett. 91 (2003) 157406.
[13] J. Zaumseil, C.L. Donley, J.S. Kim, R.H. Friend, H. Sirringhaus, Adv. Mater. 18 (2006) 2708.
[14] S.J. Kang, M. Noh, D.S. Park, H.J. Kim, C.N. Whang, C.-H. Chang, J. Appl. Phys. 95 (2004) 2293.
[15] T. Sekitani, S. Iba, Y. Kato, Y. Noguchi, T. Someya, T. Sakurai, Appl. Phys. Lett. 87 (2005) 073505.
[16] D. Guo, S. Ikeda, K. Saiki, H. Miyazoe, K. Terashima, J. Appl. Phys. 99 (2006) 094502.
[17] T. Takenobu, K. Watanabe, Y. Yomogida, H. Shimotani, Y. Iwasa, Appl. Phys. Lett. 93 (2008) 073301.
[18] W.L. Kalb, F. Meier, K. Mattenberger, B. Batlogg, Phys. Rev. B 76 (2007) 184112.
[19] S. Luan, G.W. Neudeck, J. Appl. Phys. 72 (1992) 766.
[20] J. Zaumseil, K.W. Baldwin, J.A. Rogers, J. Appl. Phys. 93 (2003) 6117.
[21] P.V. Necliudov, M.S. Shur, D.J. Gundlach, T.N. Jackson, Solid-State Electron. 47 (2003) 259.
[22] C.-W. Chu, S.-H. Li, C.-W. Chen, V. Shrotriya, Y. Yang, Appl. Phys. Lett. 87 (2005) 193508.
[23] L.S. Hung, C.W. Tang, M.G. Mason, Appl. Phys. Lett. 70 (1997) 152.
[24] I.D. Parker, J. Appl. Phys. 75 (1994) 1656.
[25] R.H. Fowler, L. Nordheim, Proc. R. Soc. London Ser. A 119 (1928) 173.
[26] W.S. Hu, Y.T. Tao, Y.J. Hsu, D.H. Wei, Y.S. Wu, Langmuir 21 (2005) 2260.
[27] M. Alagia, C. Baldacchini, M.G. Betti, F. Bussolotti, V. Carravetta, U. Ekström, C. Mariani, S. Stranges, J. Chem. Phys. 122 (2005) 124305.
[28] Y. Hosoi, D.M. Deyra, K. Nakajima, Y. Furukawa, Mol. Cryst. Liq. Cryst. 491 (2008) 317.
[29] F. De Angelis, G. Das, E. Di Fabrizio, Chem. Phys. Lett. 462 (2008) 234.

Organic Electronics 12 (2011) 516–519

Contents lists available at ScienceDirect

Organic Electronics

journal homepage: www.elsevier.com/locate/orgel

Letter

Photopatternable, highly conductive and low work function polymer electrodes for high-performance n-type bottom contact organic transistors

Kipyo Hong [a], Se Hyun Kim [a], Chanwoo Yang [a], Tae Kyu An [a], Hyojung Cha [a], Chanjun Park [b], Chan Eon Park [a,*]

[a] Polymer Research Institute, Department of Chemical Engineering, Pohang University of Science and Technology, Pohang 790-784, Republic of Korea
[b] Department of Mechanical Engineering, Seoul National University of Science and Technology, Seoul 139-743, Republic of Korea

ARTICLE INFO

Article history:
Received 25 November 2010
Received in revised form 21 December 2010
Accepted 31 December 2010
Available online 14 January 2011

Keywords:
n-Type organic field-effect transistor
Low work function
Conductive polymer
Source/drain electrodes

ABSTRACT

We demonstrate the use of n-type *N*,*N*′-ditridecyl-3,4,9,10-perylenetetracarboxylic diimide (PTCDI-C13) bottom contact organic field-effect transistors that employ photopatternable highly conductive poly(3,4-ethylenedioxythiophene):tosylate (PEDOT:Tos) source/drain electrodes characterized by a very low work function (4.3 eV). Due to the low work function of this material, the electron injection barrier between PTCDI-C13 and PEDOT:Tos was 0.25 eV lower than that between PTCDI-C13 and gold. The low injection barrier reduced the contact resistance, yielding a high field effect mobility in transistors based on PEDOT:Tos (0.145 cm^2/Vs); the field effect mobility was 16 times higher than that in transistors based on gold (0.009 cm^2/Vs).

© 2011 Elsevier B.V. All rights reserved.

Organic field-effect transistors (OFETs) have attracted considerable attention in recent years due to their potential applications in low-cost, flexible, and light-weight electronic integrated circuits used in portable displays, disposable radio frequency identification tags, and smart cards [1,2]. In logic circuit designs, complementary metal-oxide semiconductor-like logic elements consisting of p-type and n-type organic transistors are preferred due to their very low power consumption and the simplifications they bring to the logic circuits. Metals with a low work function, such as calcium (2.9 eV) and aluminum (4.3 eV), have been used as source/drain (S/D) electrode materials in n-type OFETs because their work functions match the lowest unoccupied molecular orbital (LUMO) energy level of the semiconductor, leading to a lower electron injection barrier between n-type organic semiconductors and the electrodes. However, metals are easily oxidized in air, which degrades the performance of OFETs. Therefore, the use of metals is limited to micron-scale logic circuits fabricated by photolithographic process in air. Despite the high work function of gold (5.1 eV), it is widely used due to its good air stability [3,4]. However, gold is not appropriate for organic devices because fabrication via vacuum deposition methods has a high associated cost, and the opaqueness and high contact resistance between gold and n-type semiconductors in OFETs are not favorable.

Poly(3,4-ethylenedioxythiophene) (PEDOT) is a promising electrode material for use in OFETs due to its high optical transparency in the visible region, its flexibility, low fabrication cost, and high conductivity [5]. PEDOT doped with the polyelectrolyte poly(4-styrene sulfonate) (PSS) has a conductivity that can vary from 0.03 to 900 S/cm [6]. Many reports have demonstrated good device performances of p-type OFETs based on PEDOT:PSS S/D electrodes due to the material's high work function, between 4.75 and 5.15 eV [7,8]. Recent reports have shown that vapor-polymerized PEDOT doped with the monomeric arylsulfonate, tosylate (Tos), has a very high conductivity of

* Corresponding author. Tel.: +82 54 279 2269; fax: +82 54 279 8298.
E-mail address: cep@postech.ac.kr (C.E. Park).

1566-1199/$ - see front matter © 2011 Elsevier B.V. All rights reserved.
doi:10.1016/j.orgel.2010.12.022

up to 4500 S/cm, comparable with that of indium tin oxide electrodes [9]. The studies also reported a work function of 4.30 eV, which is one of the lowest values among conductive polymers [10]. This work function is sufficiently low that the material may be used in S/D electrodes in n-type OFETs. In this letter, we describe n-type *N,N′*-ditridecyl-3,4,9,10-perylenetetracarboxylic diimide (PTCDI-C13) bottom contact OFETs using photopatterned PEDOT:Tos as S/D electrodes. We found that the electron field effect mobility of transistors based on PEDOT:Tos S/D electrodes was 16 times higher than that of devices composed of gold S/D electrodes. The mechanism underlying this higher device performance was examined by characterizing the crystallinity of PTCDI-C13 on electrodes at the interface between the channel and the electrodes, and the electron injection barrier between the electrodes and PTCDI-C13.

Bottom contact OFETs were fabricated on heavily doped silicon wafers covered with thermally grown 300 nm thick silicon dioxide layers. Polystyrene (Aldrich, Mw ≈ 192,000) was spin-coated onto silicone oxide substrates (to a thickness of 150 nm). Fe (III)-tosylate (FTS, 40 wt.%) was dissolved in 1-butanol, and the basic inhibitor, imidazole, was added to the solution at a concentration of 0.048 g/g, which enhanced the conductivity of PEDOT [5]. The solution was spin-coated onto the substrate. The coated substrate was subsequently exposed to UV light (λ = 255 nm, power = 50 W) (G15T8, Sankyo Denki) through a photomask for 5 min. Within the area exposed to UV light, the oxidant Fe^{3+} became Fe^{2+} by the photo-Fenton reaction [11]. Because Fe^{2+} does not oxidize 3,4-ethylenedioxythiophene (EDOT), oxidative polymerization of PEDOT did not occur [12]. By contrast, Fe^{3+} in the unexposed areas oxidized EDOT, leading to oxidative polymerization (Fig. 1a). Thus, the substrate was exposed to EDOT vapor for 3 min in a closed jar with heating at 60 °C, followed by rinsing with methanol to obtain S/D patterned PEDOT:Tos substrates (Fig. 1b). The PEDOT:Tos could be photopatterned with a spatial resolution of 50 μm in our laboratory, and the conductivity of the fabricated PEDOT:Tos film was about 600 S/cm. A 50 nm thick PTCDI-C13 (Aldrich) film was then deposited as the active layer. Fig. 1c shows a schematic representation of the fabrication process. In order to compare with transistors based on PEDOT:Tos, we prepared transistors composed of gold S/D electrode deposited on PS-coated substrates by thermal evaporation with a shadow mask.

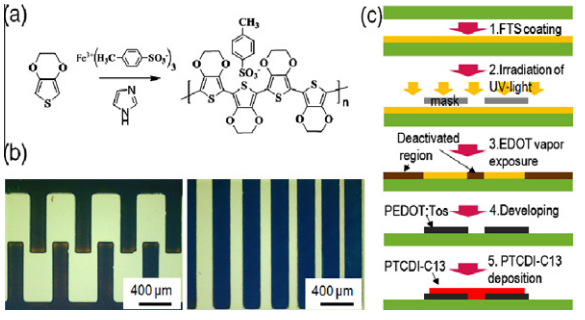

Fig. 1. (a) Polymerization scheme for producing poly(3,4-ethylenedioxythiophene):tosylate (PEDOT:Tos); (b) optical microscopy images of the photopatterned PEDOT:Tos electrodes, and (c) schematic representation of the photopatterning of PEDOT:Tos.

Fig. 2b and c shows the transfer and output characteristics, respectively of the fabricated OFETs, shown schematically in Fig. 2a. The electron mobility was calculated in the linear regime using the slope of a plot of the drain current versus gate voltage by fitting the data to the following equation: $I_D = (WC_i/L)\mu(V_G - V_{th})V_D$, where I_D is the drain current, μ is the carrier mobility, V_G is the gate voltage, V_{th} is the threshold voltage, and V_D is the drain voltage (6 V) [13]. The measured capacitance, C_i, was 6.4 nF/cm^2. The channel length (L) and width (W) were 150 and 1000 μm, respectively. The average electron mobility of twenty PTCDI-C13 transistors composed of PEDOT:Tos was 0.145 ± 0.017 cm^2/Vs, which was 16 times higher than that of devices containing gold S/D electrodes (0.009 ± 0.001 cm^2/Vs). As shown in Fig. 2c, ohmic contact behavior was observed for the devices based on PEDOT:Tos electrodes. Transistors based on gold exhibited non-ohmic contact characteristics, indicating a high contact resistance in these devices. Fig. 1d shows the width-normalized total resistance, *RW*, of transistors fabricated using gold and PEDOT:Tos S/D electrodes. *RW* is the sum of the channel resistance and the contact resistance as a function of V_G, at a V_D of 6 V. *RW* is given by

$$RW = R_C W + \frac{L}{\mu C_i (V_G - V_{th})}$$

where $R_C W$ is the width-normalized contact resistance [14]. When V_G was varied from 0 to 20 V, the *RW* of the device fabricated with gold decreased because the channel resistance decreased (channel resistance is inversely proportional to V_G). However, beyond a V_G of 20 V, *RW* became nearly constant, despite further increases in V_G, because $R_C W$ was too large and therefore the changes in channel resistance as a function of V_G were negligible compared to $R_C W$. Therefore, the transistor showed typical contact-limited device performance, and the average value of $R_C W$ was approximately 7×10^6 Ω cm at a V_G of 60 V. In contrast, *RW* for the device containing PEDOT:Tos decreased consistently during the sweep across V_G, from 0 to 60 V, indicating that *RW* was dominated by the channel resistance rather than by $R_C W$. For this device, $R_C W$ was less than 6×10^4 Ω cm at a V_G of 60 V. Thus, the higher performances of devices composed of PEDOT:Tos arose from a contact resistance that was smaller than that of transistors based on gold.

Atomic force microscopy (AFM) images of PEDOT:Tos and gold surfaces (Fig. 3a and b) showed that the surface of PEDOT:Tos was much rougher (surface roughness of 5.04 nm) than that of gold (surface roughness of 0.81 nm). Despite the pronounced differences between the two surfaces, the morphology of PTCDI-C13 on PEDOT:Tos was not distinctly different from that of gold (Fig. 3c and d). Most likely, the strong interactions between gold and PTCDI-C13 and the largely rough surface of PEDOT:Tos significantly hindered crystallization of PTCDI-C13, yielding 100 nm-sized small PTCDI-C13 grains on either surface [15,16]. The in-plane GIXD patterns shown in Fig. 3e were used to derive the coherence length in the

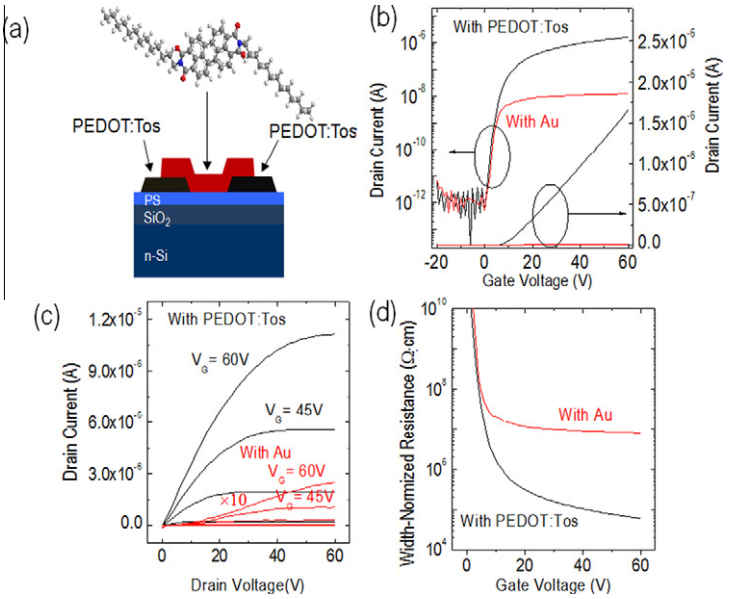

Fig. 2. (a) Schematic diagram of a bottom-contact PTCDI-C13 OFET fabricated using PEDOT:Tos; (b) transfer characteristics in the linear regime (V_D = 6 V) for OFETs prepared using PEDOT:Tos and gold; (c) output characteristics of OFETs with PEDOT:Tos and gold; (d) width-normalized total resistance, including channel and contact resistances, in an OFET as a function of gate voltage.

PTCDI-C13 films (i.e., the distance over which order was maintained). In the (1 0 0) direction, this length was determined to be 28 nm on the gold substrate and 32 nm on the PEDOT:Tos surface. The coherence lengths were determined from the half-widths of the (1 0 0) peaks using Scherrer's formula (Fig. 3f) [17]. Given that the coherence length is proportional to the size of the crystallites over which structural order is maintained, the PEDOT:Tos surface crystallites were only slightly larger than on the gold substrate, representing that the crystallinity of PTCDI-C13 on PEDOT:Tos was almost the same as that on the gold, consistent with the AFM results.

Fig. 4a shows the ultraviolet photoemission spectra (UPS, He(I): 21.2 eV) of PEDOT:Tos and gold, and Fig. 4b shows the C K-edge near-edge X-ray absorption fine structure (NEXAFS) spectra of 6.4 nm thick PTCDI-C13 films on PEDOT:Tos and gold. During the UPS measurements, a bias of −5.0 eV was applied to improve the transmission of low-kinetic-energy electrons and to ensure determination of the energy of the low-kinetic-energy edge. Angle-independent NEXAFS spectra of PTCDI-C13 were obtained using a fixed photon incidence angle of 55° from the surface normal (approximately equal to the magic angle of 54.7°). These spectra allowed calculation of the work function of each electrode and the relative position of the LUMO, as summarized in Fig. 3c [19,20]. The work function of PEDOT:Tos was 4.30 eV, which was 0.72 eV smaller than that of gold (5.02 eV). Owing to this low work function of PEDOT:Tos, the electron injection barrier between PTCDI-C13 and PEDOT:Tos was 0.25 eV lower than that between PTCDI-C13 and gold. The differences between the work functions (0.72 eV) and between the electron injection barriers (0.25 eV) is likely due to the larger downward vacuum level shift between gold and PTCDI-C13. The vacuum

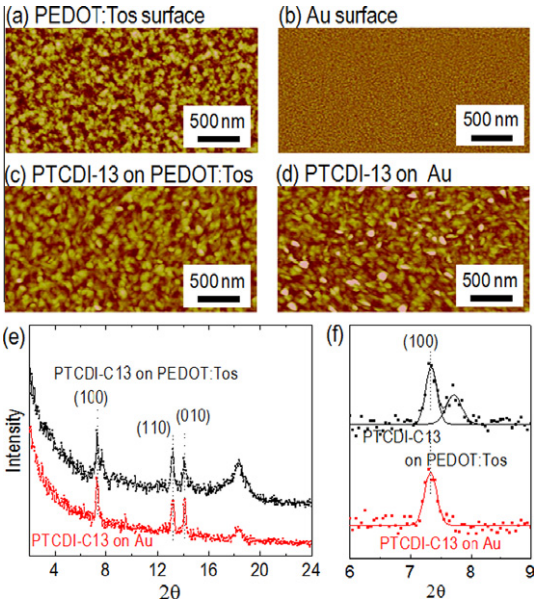

Fig. 3. (a) AFM images (3 × 3 μm) of the PEDOT:Tos surface and (b) gold surface. AFM images of 50 nm thick PTCDI-C13 films deposited on (c) a PEDOT:Tos surface and (d) a gold surface. (e) In-plane GIXD patterns of a 50 nm thick PTCDI-C13 film deposited on a PEDOT:Tos surface and on gold (λ = 1.075 Å). (f) The (100) peaks are shown in greater detail (the baselines of the GIXD pattern were subtracted and the peaks were fit to a Gaussian distribution). The peak at 7.7° corresponded to a diffraction peak (2 0 0) of the PEDOT [18].

level shift can be explained in terms of the high induced density of the interface states of PTCDI-C13 at the interface between gold and PTCDI-C13, which originates from the strong local orbital exchange and the potential correlations between the metal and the semiconductor [16,21].

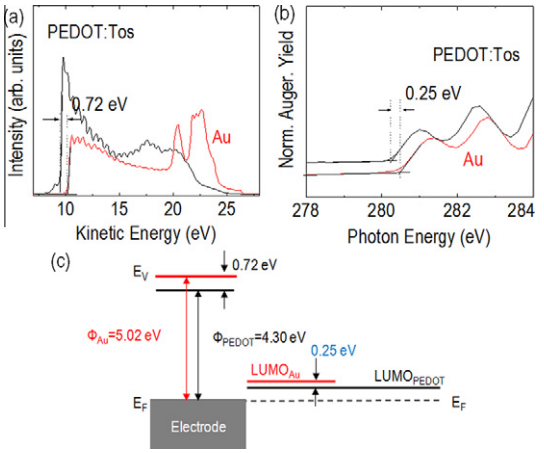

Fig. 4. (a) ultraviolet photoemission spectra of PEDOT:Tos and gold, (b) NEXAFS spectra of 6.4 nm thick PTCDI-C13 films on gold and PEDOT:Tos, and (c) band diagrams of the interface between gold and PTCDI-C13 and between PEDOT:Tos and PTCDI-C13.

In organic transistors, low electron injection barriers and highly crystalline organic semiconductor structures at the interface between the channel and S/D electrodes lead to a lower contact resistance [16]. AFM, GIXD, UPS and NEXAFS results demonstrated that the crystallinity of PTCDI-C13 on PEDOT:Tos was almost the same as that on gold, but the electron injection barrier between PTCDI-C13 and PEDOT:Tos was 0.25 eV lower than that between PTCDI-C13 and gold. Therefore, the lower contact resistance of OFETs based on PEDOT:Tos can be attributed to the lower electron injection barrier, which originates from the low work function of PEDOT:Tos.

We fabricated n-type PTCDI-C13 organic transistors by applying photopatternable highly conductive PEDOT:Tos S/D electrodes. Because PEDOT:Tos has a very low work function of 4.30 eV, the electron injection barrier between PTCDI-C13 and PEDOT:Tos was 0.25 eV lower than that between PTCDI-C13 and gold, leading to a reduced contact resistance in the transistor. The reduced contact resistance resulted in a high field effect mobility in transistors based on PEDOT:Tos (mobility of 0.145 cm^2/Vs) that was much greater than that in transistors based on gold (0.009 cm^2/Vs).

Acknowledgements

This work was supported by a grant from the Korea Science and Engineering Foundation (KOSEF) grant, funded by the Korea government (MEST) (Grant No. 2010-0000809). The authors thank the Pohang Accelerator Laboratory for providing the 4B1 (PES II) and 10C1 (XRS II) beamlines used in this study.

References

[1] R.A. Street, W.S. Wong, S.E. Ready, M.L. Chabinyc, A.C. Arias, S. Limb, A. Salleo, R. Lujan, Mater. Today 9 (2006) 32.
[2] S.R. Forrest, Nature (London) 428 (2004) 911.
[3] B. Yoo, T. Jung, D. Basu, A. Dodabalapur, B.A. Jones, A. Facchetti, M.R. Wasielewski, T.J. Marks, Appl. Phys. Lett. 88 (2006) 082104.
[4] P.R.L. Malenfant, C.D. Dimitrakopoulos, J.D. Gelorme, L.L. Kosbar, T.O. Graham, A. Curioni, W. Andreoni, Appl. Phys. Lett. 80 (2002) 2517.
[5] B.L. Groenendaal, F. Jonas, D. Freitag, H. Pielartzik, J.R. Reynolds, Adv. Mater. 12 (2000) 481.
[6] <http://www.hcstarck.com/>.
[7] D. Li, L.J. Guo, Appl. Phys. Lett. 88 (2006) 063513.
[8] H. Sirringhaus, T. Kawase, R.H. Friend, T. Shimoda, M. Inbasekaran, W. Wu, E.P. Woo, Science 290 (2000) 2123.
[9] J.-Y. Kim, M.-H. Kwon, Y.-K. Min, S. Kwon, D.-W. Ihm, Adv. Mater. 19 (2007) 3501.
[10] N. Koch, A. Elschner, J.P. Rabe, R.J. Johnson, Adv. Mater. 17 (2005) 330.
[11] R. Bauer, Chemosphere 29 (1994) 1225.
[12] M.S. Lee, H.S. Kang, H.S. Kang, J. Joo, A.J. Epstein, J.Y. Lee, Thin Solid Films 477 (2005) 169.
[13] S. Sze, Semiconductor Devices: Physics and Technology, second ed., Wiley, New York, 1981.
[14] D. Gamota, P. Brazis, K. Kalyanasundaram, J. Zhang, Printed Organic and Molecular Electronics, first ed., Kluwer Academic Publishers, Boston, 2004.
[15] K. Shin, S.Y. Yang, C. Yang, H. Jeon, C.E. Park, Org. Electron. 8 (2007) 336.
[16] K. Hong, S.Y. Yang, C. Yang, S.H. Kim, D. Choi, C.E. Park, Org. Electron. 9 (2008) 864.
[17] R. Ruiz, A.C. Mayer, G.G. Malliaras, Appl. Phys. Lett. 85 (2004) 4926.
[18] K.E. Aasmundtveit, E.J. Samuelsen, O. Inganäs, L.A.A. Pettersson, T. Johansson, S. Ferrer, Synth. Met. 113 (2000) 93.
[19] R. Mitsumoto, T. Araki, E. Ito, Y. Ouchi, K. Seki, K. Kikuchi, Y. Achiba, H. Kurosaki, T. Sonoda, H. Kobayashi, O.V. Boltalina, V.K. Pavlovich, L.N. Sidorov, Y. Hattori, N. Liu, S. Yajima, S. Kawasaki, F. Okino, H. Touhara, J. Phys. Chem. A 102 (1998) 552.
[20] D. Cahen, A. Kahn, Adv. Mater. 15 (2003) 271.
[21] H. Vazquez, R. Oszwaldowski, P. Pou, J. Ortega, R. Perez, F. Flores, A. Kahn, Europhys. Lett. 65 (2004) 802.

Organic Electronics 12 (2011) 520–528

Contents lists available at ScienceDirect

Organic Electronics

journal homepage: www.elsevier.com/locate/orgel

Interfacial charge transfer and charge generation in organic electronic devices

Toshinori Matsushima, Guang-He Jin, Yoshihiro Kanai, Tomoyuki Yokota, Seiki Kitada, Toshiyuki Kishi, Hideyuki Murata *

School of Materials Science, Japan Advanced Institute of Science and Technology, 1-1 Asahidai, Nomi, Ishikawa 923-1292, Japan

ARTICLE INFO

Article history:
Received 5 July 2010
Received in revised form 9 December 2010
Accepted 2 January 2011
Available online 13 January 2011

Keywords:
Organic light-emitting diodes
Hole-only devices
Interfacial charge transfer and generation
Organic hole-transport materials and layers
Molybdenum trioxide

ABSTRACT

We have recently proposed that improvement of device performance using a buffer layer of molybdenum trioxide (MoO_3) originates from interfacial charge generation at an interface of MoO_3 and an organic hole-transport layer [17]. However, there is no clear experimental evidence enough to support the charge generation in our recent report. In this study, from comparison of current density–voltage characteristics of organic hole-only devices and ultraviolet/visible/near-infrared absorption spectra of composite films, we can conclude that the interfacial charge generation surly occurs to realize space-charge-limited currents of a wide variety of organic hole-transport layers. Moreover, a drastic increase in current density of a bilayer device of *n*-type C60 and *p*-type *N*,*N*′-diphenyl-*N*,*N*′-bis(1-naphthyl)-1,1′-biphenyl-4,4′-diamine (α-NPD) by using a MoO_3 layer can provide the evidence of the charge generation.

© 2011 Elsevier B.V. All rights reserved.

1. Introduction

Large charge injection barriers are frequently present at electrode/organic heterojunction interfaces in organic electronic devices, making precisely clarifying charge transport mechanisms of organic thin films difficult because observed current density–voltage (*J*–*V*) characteristics are controlled by both charge injection and transport processes [1–3]. Also, the charge injection barriers are problematic for overall performance of organic electronic devices [4,5]. To solve the injection barrier problem, transition metal oxide, molybdenum trioxide (MoO_3) has been used as a buffer layer between a metal electrode and an organic layer in organic electronic devices, such as organic light-emitting diodes (OLEDs) [6,7], organic solar cells [8,9], and organic thin-film transistors [10,11]. Previously, we have demonstrated that use of a MoO_3 buffer layer with a specific thickness of 0.75 nm between an anode layer of indium tin oxide (ITO) and a hole-transport layer (HTL) of *N*,*N*′-diphenyl-*N*,*N*′-bis(1-naphthyl)-1,1′-biphenyl-4,4′-diamine (α-NPD) leads to an increase in current density by about four orders of magnitude and appearance of a space-charge-limited current (SCLC) of α-NPD [12], indicating that the injection barrier at the ITO/α-NPD interface is completely negligible. This specific MoO_3 thickness of 0.75 nm is much smaller than those previously used for OLEDs. Power consumption and operational lifetimes of OLEDs are markedly improved by using the 0.75 nm MoO_3 buffer layer as well [5]. Thus, the very thin MoO_3 buffer layer is useful for establishing fundamental physics of charge transport in organic films and for developing the organic electronic devices.

Electronic states of multilayer films and composite films of organic and MoO_3 have been intensively investigated using ultraviolet photoelectron spectroscopy, inverse photoelectron spectroscopy, and X-ray photoelectron spectroscopy [13–16]. These leading papers have shown that: (1) charge transfer between electrode/MoO_3/organic interfaces induces large vacuum level shifts, minimizing a hole injection barrier height, (2) gap states are generated inside band gaps of α-NPD and MoO_3, and (3) a vacuum-deposited

* Corresponding author. Tel.: +81 761 51 1531; fax: +81 761 51 1149.
E-mail address: murata-h@jaist.ac.jp (H. Murata).

1566-1199/$ - see front matter © 2011 Elsevier B.V. All rights reserved.
doi:10.1016/j.orgel.2011.01.001

MoO_3 layer works as an electron conductor due to donating electrons from gap states to a conduction band. We have recently proposed that the improved device characteristics originate from interfacial charge generation at a MoO_3/HTL interface [17]. However, there is no clear experimental evidence enough to support the charge generation in our recent report. In this study, from comparison of *J*–*V* characteristics of organic hole-only devices and ultraviolet/visible/near-infrared (UV–vis–NIR) absorption spectra of composite films, we can conclude that the interfacial charge generation surly occurs to realize SCLCs of a wide variety of organic HTLs. Moreover, a drastic increase in current density of a bilayer device of *n*-type C60 and *p*-type α-NPD by using a MoO_3 layer can provide the evidence of the charge generation.

The interfacial charge generation mechanism we have recently proposed [17] is composed of (i) electron transfer from a lower-ionization-energy HTL to a higher-work-function MoO_3 layer to form electron–hole pairs at the MoO_3/HTL interface, (ii) separation of the electron–hole pairs under an external electric field, (iii) transit of resultant electrons and holes to corresponding electrodes through a conduction band (or gap states) of MoO_3 and a hole-transport level of α-NPD, and repetition of the charge transfer (i), the charge separation (ii), and the charge transit (iii) for steady-state current flow (Fig. 1). For a well-known standard hole injection mechanism without a MoO_3 buffer layer, HTL-to-ITO electron extraction (transfer) under a local high electric field and separation of electron–hole pairs are repeated in a manner almost similar to the charge generation mechanism mentioned above [15]. The difference between the charge generation and the charge injection is whether the charge transfer occurs or not under no electric field condition. Using the charge generation mechanism, a well-known charge injection barrier is no longer considered important and *J*–*V* characteristics are controlled by a SCLC. Since the HTL-to-MoO_3 electron transfer characteristics are expected to be related to a difference between an ionization energy of an HTL and a work function of a MoO_3 layer, a relationship between *J*–*V* characteristics and electron transfer characteristics is investigated in this study when ionization energies of HTL materials are systematically changed (see Fig. 2).

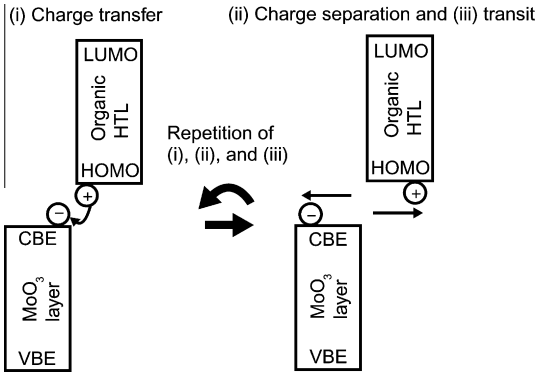

Fig. 1. Illustrations of energy-level diagrams showing charge generation mechanism, which is composed of (i) charge transfer, (ii) charge separation, and (iii) charge transit. These processes (i), (ii), and (iii) are repeated for steady-state current flow. CBE, VBE, HOMO, and LUMO stand for conduction band edge, valence band edge, highest occupied molecular orbital, and lowest unoccupied molecular orbital, respectively.

2. Experimental

HTL materials used in this study are 4,4′,4″-tris(*N*-3-methylphenyl-*N*-phenyl-amino)triphenylamine (m-MTDATA), *fac*-tris(2-phenylpyridinato)iridium(III) [Ir(ppy)$_3$], 4,4′,4″-tris(*N*-2-naphthyl-*N*-phenyl-amino)triphenylamine (2-TNATA), *N*,*N*′-di(m-tolyl)-*N*,*N*′-diphenyl benzidine (TPD), rubrene, α-NPD, 2,4,6-tricarbazolo-1,3,5-triazine (TRZ-2), and 4,4′-bis(carbazol-9-yl)-2,2′-biphenyl (CBP) (the chemical structures of the HTL molecules are shown in Fig. 2). Hole-only device structures and bilayer device structures of C60 and α-NPD are glass substrate/ITO anode (150 nm)/MoO_3 buffer layer (*X* nm)/m-MTDATA, Ir(ppy)$_3$, 2-TNATA, TPD, rubrene, α-NPD, TRZ-2, or CBP HTL (100 nm)/MoO_3 electron-blocking layer (EBL) (10 nm)/Al cathode (100 nm) and glass substrate/ITO anode (150 nm)/*n*-type C60 layer (30 nm)/MoO_3 buffer layer (0 or 5 nm)/*p*-type α-NPD HTL (100 nm)/MoO_3 EBL (10 nm)/Al cathode (100 nm), respectively. Source materials of m-MTDATA (Luminescence Technology), 2-TNATA (Luminescence Technology), rubrene (Aldrich), TRZ-2 (Luminescence Technology), and C60 (Materials Technologies Research) were purchased and purified twice using a vacuum train sublimation technique prior to evaporation. High-purity source materials of Ir(ppy)$_3$ (Nippon Steel Chemical), TPD (Tokyo Chemical Industry), α-NPD (Nippon Steel Chemical), CBP (Nippon Steel Chemical), MoO_3 (Mitsuwa Chemicals), and Al (Nilaco) were purchased and used as-received. The glass substrates coated with the 150 nm ITO anode layer with a sheet resistance of 10 Ω sq^{-1} (SLR grade) were purchased from Sanyo Vacuum Industries and the ITO layers were patterned by conventional photolithography. The substrates were cleaned using ultrasonication in acetone, followed by ultrasonication in detergent, pure water, and isopropanol. Then, the substrates were placed in an UV-ozone treatment chamber for 30 min. After the cleaning, the substrates were set in an evaporation chamber. The chamber was evacuated to a base pressure of $\approx 10^{-4}$ Pa. The layers of the MoO_3 and the organic materials were thermally deposited on the ITO surface from an alumina crucible (MoO_3) and individual carbon crucibles (organic materials). To complete the devices, the Al cathode layer was thermally deposited from a tungsten basket through a shadow mask with openings. The deposition rates were precisely controlled at 0.05 nm s^{-1} (MoO_3), 0.1 nm s^{-1} (organic materials), and 0.5 nm s^{-1} (Al) using a calibrated quartz crystal microbalance. The active device area was defined at 4 mm^2 by the overlapped area of the ITO layer and the Al layer. The completed devices were transferred to a nitrogen-filled glove box (O_2 and H_2O levels are less than 2 ppm) without exposing the devices to ambient air and encapsulated using a glass cap and an UV curing epoxy resin together with a desiccant sheet. The steady-state *J*–*V* characteristics of the devices were measured using a semiconductor characterization system (SCS4200, Keithley) at room tempera-

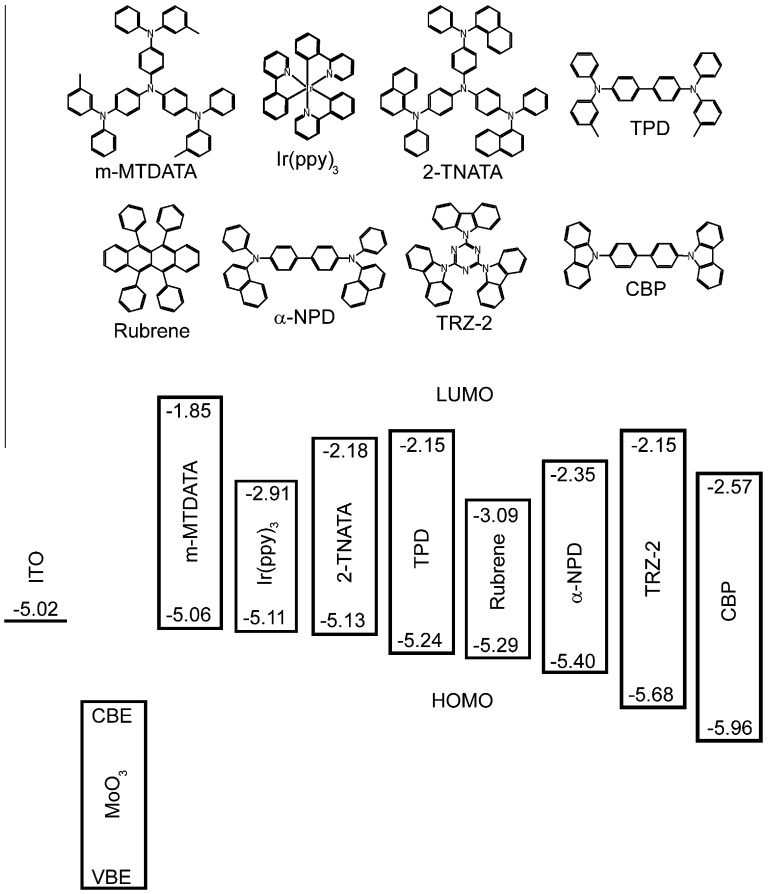

Fig. 2. Chemical structures of organic molecules and energy-level diagrams.

ture when the MoO_3 thicknesses (X) and the HTL materials are systematically changed. Since no electroluminescence was observed during the J–V measurements, it was confirmed that holes are dominant charge carriers in our devices.

A 50 nm organic layer, a 50 nm MoO_3 layer, and a 50 nm Al layer were thermally deposited on the cleaned ITO substrates using the preparation conditions described above. The ionization energies and the work functions of the layers were measured using an UV photoelectron spectrometer in air (AC-2, Riken Keiki). The work function of ITO was measured from the UV–ozone-treated bare ITO surface using the AC-2. The electron affinities of the organic layers were estimated by subtracting their absorption onset energies from the ionization energies.

Devices with a structure of glass substrate/Al electrode (100 nm)/organic layer (200 nm)/Al layer (100 nm) were fabricated using the preparation conditions described above. To calculate the relative permittivities, the capacitance of the organic layers was measured using an LCR meter (4284A, Agilent). The input voltage and the amplitude of the input signal were set at 0.1 V and ±0.005 V, respectively. No current flow was confirmed under the capacitance measurements. The capacitance of the organic layers remained constant in a frequency range from 20 Hz to 100 kHz.

Fifty nanometer intrinsic organic films and 50 nm composite films of organic and MoO_3 were thermally deposited on cleaned quartz substrates. The deposition ratio of organic to MoO_3 was controlled at 1:1 by mol using a calibrated quartz crystal microbalance. The total deposition rate was fixed at $\approx$0.1 nm s^{-1}. The UV–vis–NIR absorption spectra of the intrinsic films and the composite films were measured using an absorption spectrometer (V670, JASCO).

3. Results and discussion

3.1. Current density–voltage characteristics

The ionization energies of the HTL materials are measured as summarized in Table 1. The work functions of ITO, MoO_3, and Al are also measured respectively to be 5.02 ± 0.02, 5.68 ± 0.03, and 3.58 ± 0.02 eV. The work function of MoO_3 corresponds to a difference between a vacuum level and a Fermi level right below a conduction band edge [16]. The ionization energies and the work functions we measured here may be slightly different from actual values because they are measured in air [18]. In fact, the work function of a fresh Al surface has been measured to be $\approx$4.0 eV in an ultra-high vacuum condition [19]. The corresponding energy-level diagram with these values is shown in Fig. 2.

Table 1
Ionization energies (IE), relative permittivities (ε_r), zero field hole mobilities (μ_0), and field dependence parameters (β) of HTLs with thickness of 200 nm.

HTL material	IE (eV)	ε_r	SCLC		TOF	
			μ_0 ($cm^2\ V^{-1}\ s^{-1}$)	β ($cm^{0.5}\ V^{-0.5}$)	μ_0 ($cm^2\ V^{-1}\ s^{-1}$)	β ($cm^{0.5}\ V^{-0.5}$)
m-MTDATA	5.06 ± 0.02	2.76 ± 0.02	$2.2 \pm 0.2 \times 10^{-6}$	$4.3 \pm 0.4 \times 10^{-3}$	1.6×10^{-5} [23]	1.8×10^{-3} [23]
$Ir(ppy)_3$	5.11 ± 0.02	3.35 ± 0.05	$2.2 \pm 0.2 \times 10^{-8}$	$1.0 \pm 0.1 \times 10^{-2}$	No data reported	
2-TNATA	5.13 ± 0.02	2.77 ± 0.04	$6.8 \pm 0.5 \times 10^{-6}$	$3.1 \pm 0.2 \times 10^{-3}$	1.8×10^{-5} [22]	2.0×10^{-3} [22]
TPD	5.24 ± 0.02	3.38 ± 0.03	$1.4 \pm 0.1 \times 10^{-4}$	$2.0 \pm 0.2 \times 10^{-3}$	6.6×10^{-4} [24]	1.0×10^{-3} [24]
Rubrene	5.29 ± 0.01	2.78 ± 0.03	$2.5 \pm 0.2 \times 10^{-4}$	$1.1 \pm 0.2 \times 10^{-3}$	4.9×10^{-3} [25]	1.8×10^{-3} [25]
α-NPD	5.40 ± 0.01	3.42 ± 0.02	$3.3 \pm 0.3 \times 10^{-4}$	$8.0 \pm 0.6 \times 10^{-4}$	4.0×10^{-4} [24]	1.1×10^{-3} [24]
TRZ-2	5.68 ± 0.02	3.24 ± 0.05	No SCLC observed			
CBP	5.96 ± 0.02	2.62 ± 0.03	No SCLC observed			

If an Ohmic contact is formed at an electrode/organic interface and a free charge density is negligible in comparison to an injected charge density, a SCLC with field-dependent mobilities is expressed as the equation [20]:

$$J = \frac{9}{8}\varepsilon_r\varepsilon_0\mu_0 \exp\left(0.89\beta\frac{V^{0.5}}{L^{0.5}}\right)\left(\frac{V^2}{L^3}\right) \quad (1)$$

where ε_r is the relative permittivity, ε_0 is the vacuum permittivity, μ_0 is the zero field mobility, β is the field dependence parameter, and L is the film thickness. The relative permittivities of the HTLs are determined as summarized in Table 1 by measuring their capacitance. By fitting the obtained J–V characteristics with the SCLC Eq. (1), the zero field hole mobilities and the field dependence parameters can be determined at the same time.

The J–V characteristics of m-MTDATA, $Ir(ppy)_3$, and 2-TNATA are independent of the MoO_3 thicknesses X and are well fitted with the SCLC Eq. (1) (Figs. 3a–c), indicating that the J–V characteristics are controlled by the SCLCs and the junctions of ITO/m-MTDATA, ITO/$Ir(ppy)_3$, and ITO/2-TNATA are already Ohmic contacts without the MoO_3 buffer layer. We assume that the small barrier heights less than ≈0.1 eV no longer affect the J–V characteristics. Indeed, it has been shown that ITO forms ideal hole-injecting contacts with m-MTDATA [21] and 2-TNATA [22], which agree with our results.

On the other hand, the J–V characteristics of TPD, rubrene, and α-NPD are markedly dependent upon the MoO_3 thicknesses X (Figs. 3d–f). The current densities at the MoO_3 thickness of 0 nm are very small due to the relatively large hole injection barrier heights ranging from ≈0.2 to ≈0.4 eV. The current densities increase $\approx 10^4$ times and then decrease $\approx 10^1$ times as the MoO_3 thicknesses are increased. Details of the changes in the J–V characteristics have been discussed in our recent paper [17]. The optimized MoO_3 thicknesses are 1.0 nm for rubrene and 0.75 nm for TPD and α-NPD, which provide the highest current densities for the devices. Since the electron transfer from these HTLs to the MoO_3 layer can be confirmed (the electron transfer characteristics will be discussed later), the marked increase in current density by using the MoO_3 buffer layer is attributable to the interfacial charge generation mechanism as illustrated in Fig. 1. The J–V characteristics at the optimized thicknesses can be fitted with the SCLC Eq. (1).

The J–V characteristics of TRZ-2 and CBP slightly shift to higher current densities by using the MoO_3 buffer layer maybe due to a reduction in hole injection barrier height caused by the high-work-function MoO_3, but cannot be fitted with the SCLC Eq. (1) (Figs. 3g and h), indicating that the J–V characteristics are still controlled by injection-limited currents. Since the ionization energies of TRZ-2 (≈5.68 eV) and CBP (≈5.96 eV) are equal to or higher than the work function of MoO_3 (≈5.68 eV), no charge transfer and no charge generation occur at the HTL/MoO_3 interfaces.

The J–V characteristics of the hole-only devices with various HTL thicknesses (L) ranging from 50 to 800 nm are investigated (see Fig. 4). The optimized MoO_3 thicknesses (X) are used for the devices (0 nm for m-MTDATA, $Ir(ppy)_3$, and 2-TNATA, 0.75 nm for TPD and α-NPD, and 1 nm for rubrene). The J–V characteristics of all the devices can be fitted with the SCLC Eq. (1) when the field dependence parameters summarized in Table 1 are used for the SCLC fitting. The zero field hole mobilities estimated from the SCLC regions are plotted versus the HTL thicknesses in Fig. 5. The zero field hole mobilities are found to gradually increase as the thicknesses of the HTLs are increased.

The zero field mobilities and the field dependence parameters estimated from the SCLC regions are compared with those of m-MTDATA [23], 2-TNATA [22], TPD [24], rubrene [25], and α-NPD [24] measured using a time-of-flight (TOF) technique (Table 1). In this table, we summarize the zero field hole mobilities and the field dependence parameters of the 200 nm HTLs because the zero field hole mobilities are dependent on the film thicknesses and the mobility of the 100 nm α-NPD HTL does not still reach a saturation value. While the SCLC field dependence parameters are almost similar to the TOF field dependence parameters, the SCLC zero field mobilities are about one order of magnitude lower than the TOF zero field mobilities. It has been shown that electron mobilities of tris(8-hydroxyquinoline)aluminum (Alq_3) [26] and 4,7-diphenyl-1,10-phenanthroline (Bphen) [27] and hole mobilities of α-NPD [3] and 2-TNATA [28] depend on their film thicknesses. Chu and Song have attributed the thickness-dependent mobilities to a change in hole trap concentration in organic films [3].

While the J–V characteristics of TPD, rubrene, and α-NPD are dependent upon the MoO_3 thicknesses, the J–V characteristics of m-MTDATA, $Ir(ppy)_3$, and 2-TNATA

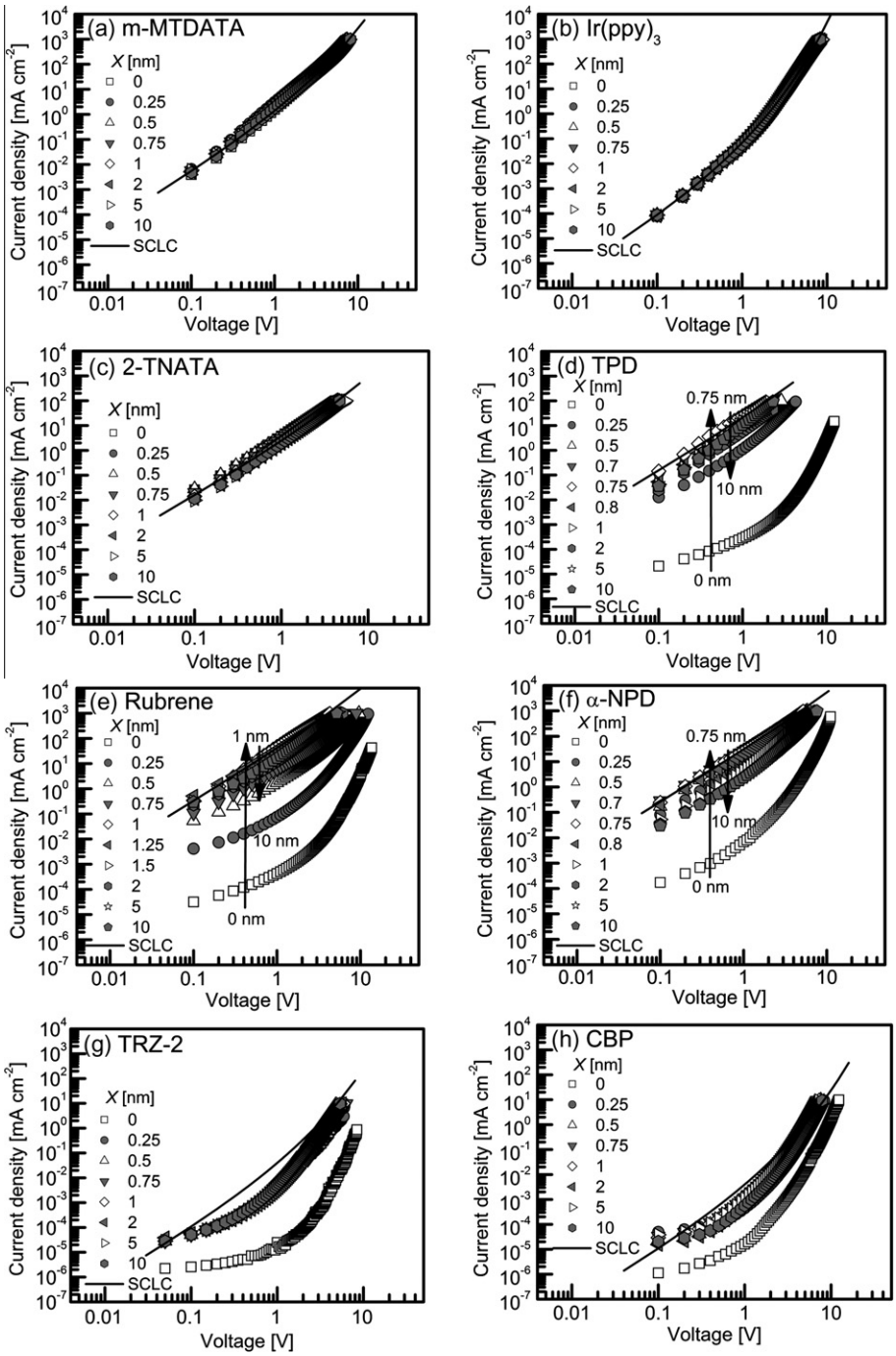

Fig. 3. *J–V* characteristics of hole-only devices, where 100 nm HTL layers are changed from (a) m-MTDATA, (b) $Ir(ppy)_3$, (c) 2-TNATA, (d) TPD, (e) rubrene, (f) α-NPD, (g) TRZ-2, and (h) CBP and MoO_3 thicknesses (*X*) are changed from 0 to 10 nm. Solid lines represent SCLCs.

are independent of the MoO_3 thicknesses as shown in Fig. 3. One possible explanation for the independent and dependent *J–V* characteristics is a difference in hole mobility between the organic layers. The layers of m-MTDATA, $Ir(ppy)_3$, and 2-TNATA have lower hole mobilities than the other layers of TPD, rubrene, and α-NPD have as summarized in Table 1. Thus, the *J–V* characteristics of m-MTDATA, $Ir(ppy)_3$, and 2-TNATA are strongly limited by a bulk hole transport process due to their lower mobilities, thereby obscuring the dependency of the *J–V* characteristics of m-MTDATA, $Ir(ppy)_3$, and 2-TNATA.

Built-in potential (a difference between Fermi levels of an anode and a cathode) sometimes makes difficult to analyze charge injection and transport characteristics of or-

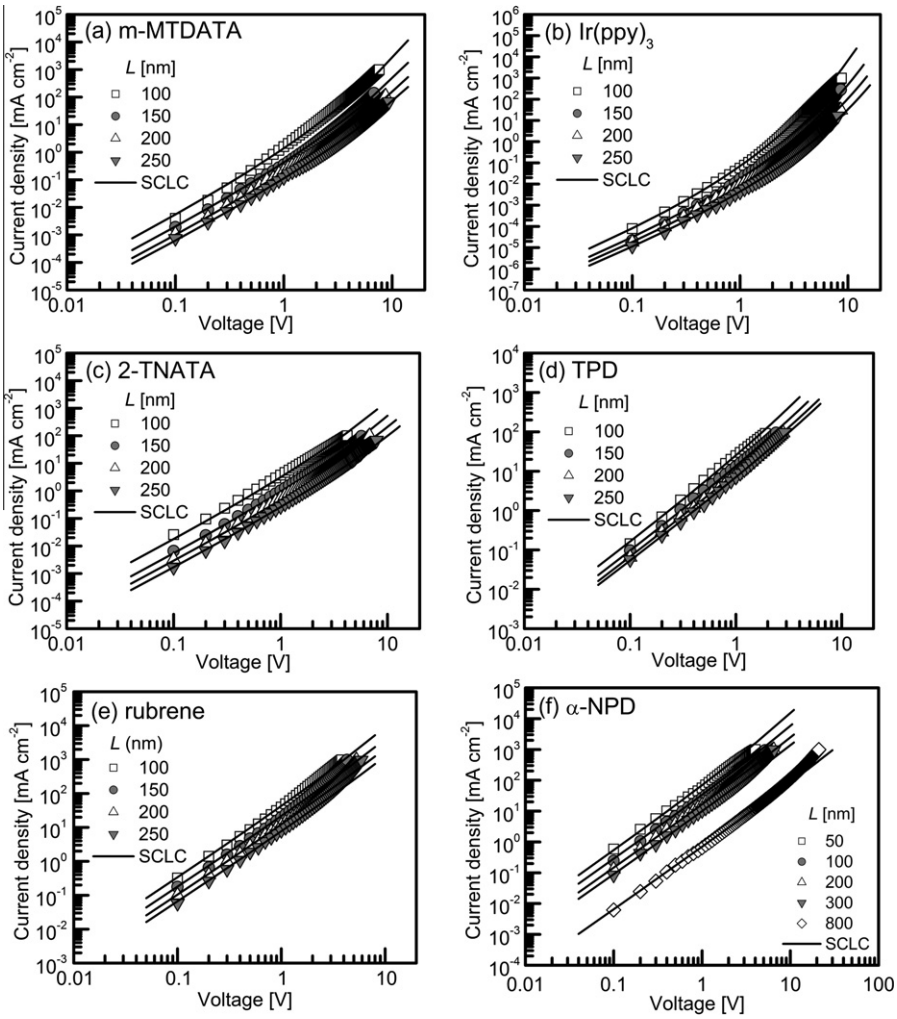

Fig. 4. *J–V* characteristics of hole-only devices with structures of glass substrate/ITO anode (150 nm)/MoO_3 buffer layer (*X* nm)/(a) m-MTDATA, (b) Ir(ppy)$_3$, (c) 2-TNATA, (d) TPD, (e) rubrene, or (f) α-NPD HTL (*L* nm)/MoO_3 EBL (10 nm)/Al cathode (100 nm). HTL thicknesses (*L*) are changed in range from 50 to 800 nm. Optimized MoO_3 thicknesses (*X*) are used (0 nm for m-MTDATA, Ir(ppy)$_3$, and 2-TNATA, 0.75 nm for TPD and α-NPD, and 1 nm for rubrene). Solid lines represent SCLCs. Field dependence parameters (β) summarized in Table 1 are used for SCLC fitting. Estimated zero field hole mobilities are shown in Fig. 5.

ganic electronic devices [29,30]. To investigate whether the built-in potential is present or not in our devices, the *J–V* characteristics of the hole-only devices with the structures of glass substrate/ITO anode (150 nm)/2-TNATA HTL (100 nm)/MoO_3 EBL (0 or 10 nm)/Al cathode (100 nm) are compared in the forward and reverse bias directions (Fig. 6). The reverse biased ITO/2-TNATA/Al device has much smaller current densities than the other devices have due to large charge injection barriers for both electrons and holes. No current flow is observed in a low voltage region of the forward biased ITO/2-TNATA/Al device due to the presence of the built-in potential. The built-in potential is roughly estimated to be ≈1.0 eV from a difference between the work functions of ITO (5.02 ± 0.02 eV) and Al (≈4.0 eV [19]). However, the estimated value is larger than the observed turn-on voltage (≈0.6 V), perhaps resulting from that actual built-in potential is slightly changed by a vacuum level shift [19].

Otherwise, the *J–V* characteristics of the forward and reverse biased ITO/2-TNATA/MoO_3/Al devices are completely overlapped and well explained with the SCLC Eq. (1), indicating that the influence of the built-in potential on the *J–V* characteristics is completely negligible by using the MoO_3 EBL. We assume that a Fermi level of MoO_3 is pinned near a hole-transport level of 2-TNATA due to the electron transfer from the 2-TNATA HTL to the MoO_3 layer, resulting in the completely overlapped *J–V* characteristics in both bias directions.

3.2. Electron transfer characteristics

To confirm the HTL-to-MoO_3 electron transfer under no electric field, the UV–vis–NIR absorption spectra of the 50 nm intrinsic organic films and the 50 nm composite films of organic:MoO_3 (1:1 by mol) on the quartz substrates are measured (Fig. 7). The absorption peaks appear

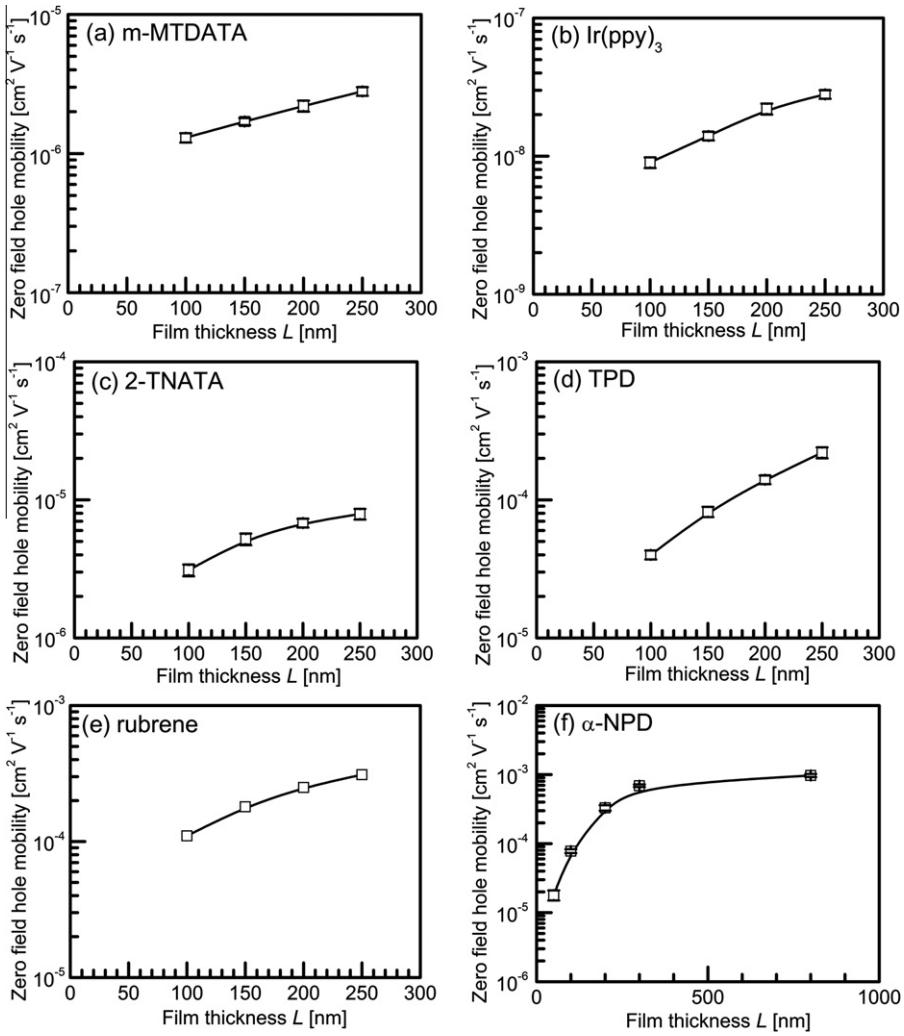

Fig. 5. Zero field hole mobility (μ_0)–film thickness (L) characteristics of (a) m-MTDATA, (b) Ir(ppy)$_3$, (c) 2-TNATA, (d) TPD, (e) rubrene, and (f) α-NPD. Zero field hole mobilities of HTLs are estimated by fitting J–V characteristics shown in Fig. 4 with SCLC Eq. (1).

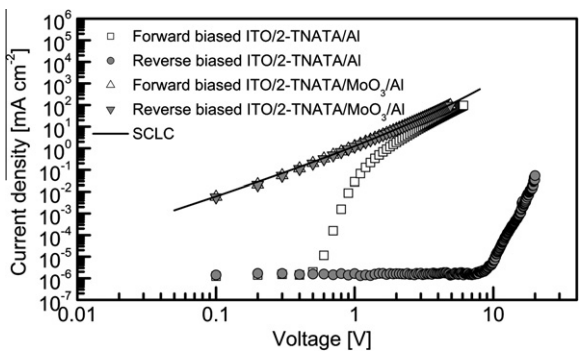

Fig. 6. J–V characteristics of 2-TNATA hole-only devices in forward and reverse bias directions. Solid line represents SCLC.

in the NIR region for the composite films (m-MTDATA, Ir(ppy)$_3$, 2-TNATA, TPD, rubrene, and α-NPD) when compared with their intrinsic films. The NIR peaks are attributable to generation of radical cations of HTL molecules, resulting from the electron transfer [31,32]. On the other hand, there is no absorption peak in the NIR region for the other composite films (TRZ-2 and CBP). These results indicate that the ionization energies of the HTLs must be lower than the work function of MoO_3 to induce the HTL-to-MoO_3 electron transfer.

A reduction in hole injection barrier height by using a MoO_3 buffer layer has been reported by analyzing electronic structures of electrode/MoO_3/organic interfaces using photoelectron spectroscopy [13–16] although it is still difficult to estimate actual hole injection barrier heights under operation of devices. Thus, the standard hole injection mechanism from the ITO anode to the HTL through the MoO_3 layer cannot be ruled out. However, since the electron transfer characteristics (Fig. 7) are in good agreement with the SCLC characteristics (Figs. 3 and 4), the interfacial charge generation mechanism surely occurs in addition to the hole injection mechanism. Since the charge generation rate is found to be high enough to real-

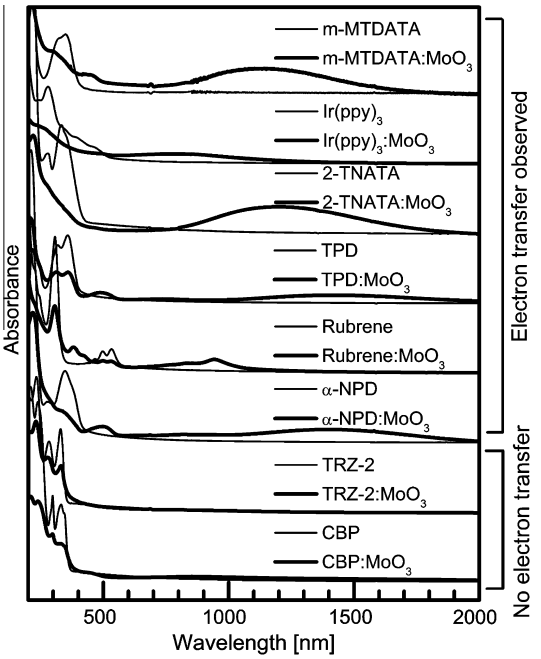

Fig. 7. UV–vis–NIR absorption spectra of intrinsic organic films and composite films of organic and MoO_3 (1:1 by mol).

ize the SCLCs (this evidence will be presented in the next section), we are able to conclude that the charge generation is a more dominant mechanism than the hole injection when the MoO_3 buffer layer is used.

The work functions of MoO_3 reported thus far are in a wide range from 5.3 to 6.86 eV [11,12,14–16,33]. Also, CBP-to-MoO_3 electron transfer has been confirmed from photoelectron spectroscopy under an ultra-high vacuum condition [14], which is in contrast to no CBP-to-MoO_3 electron transfer observed here. It has been shown that a major molecular species vaporizing is polymeric, $(MoO_3)_n$ [15,34] and oxygen vacancy defects are present in the resulting oxide films [16,33,35]. We assume that preparation conditions of the oxide films (such as a deposition rate and a partial pressure of oxygen inside a vacuum evaporator) affect degrees of the clustering and the oxygen vacancy defects, which further affect the work functions and the electron transfer characteristics. It has been shown that the amount of the oxygen vacancy defects are changed by annealing the oxide films in a vacuum [16] and exposing the oxide films to ambient air [35]. Also, Meyer et al. have reported that contamination by air exposure of the oxide film reduces its work function by about 1 eV [36]. We suggest that the charge generation is possible for the higher-ionization-energy materials (such as TRZ-2 and CBP) if the preparation conditions are favorably controlled and/or other higher-work-function metal oxide is used (such as WO_3 (6.4 eV) [37]).

3.3. Interfacial charge generation

To obtain the evidence of the interfacial charge generation, the *J–V* characteristics of two types of the devices are measured and compared (glass substrate/ITO anode (150 nm)/*n*-type C60 layer (30 nm)/MoO_3 buffer layer (0 or 5 nm)/*p*-type α-NPD HTL (100 nm)/MoO_3 EBL (10 nm)/Al cathode (100 nm)) (Fig. 8). Although it has been reported that a thin C60 layer (2.5 nm) improves hole injection from ITO [3], the use of the thick C60 layer (30 nm) between the ITO layer and the α-NPD layer extremely lowers the current densities of the C60/α-NPD device (Fig. 8a) due to effective blocking of hole injection from the ITO layer to the high-ionization-energy C60 layer (Fig. 8b). Surprisingly, the current densities markedly increase by inserting the MoO_3 layer between the C60 layer and the α-NPD layer. This increase in current density originates from the interfacial charge generation mechanism, which is composed of α-NPD-to-MoO_3 electron transfer to form electron–hole pairs, separation of the electron–hole pairs under an electric field, and transit of electrons and holes to corresponding electrodes through a conduction band (or gap states) of MoO_3, an electron-transport level of C60, and a hole-transport level of α-NPD (see Fig. 8b). A similar phenomenon has been observed in stacked OLEDs with a charge generation layer consisting of alkali metal and transition metal oxide [33,38,39]. Since there is negligible hole injection from the ITO layer for these devices, it

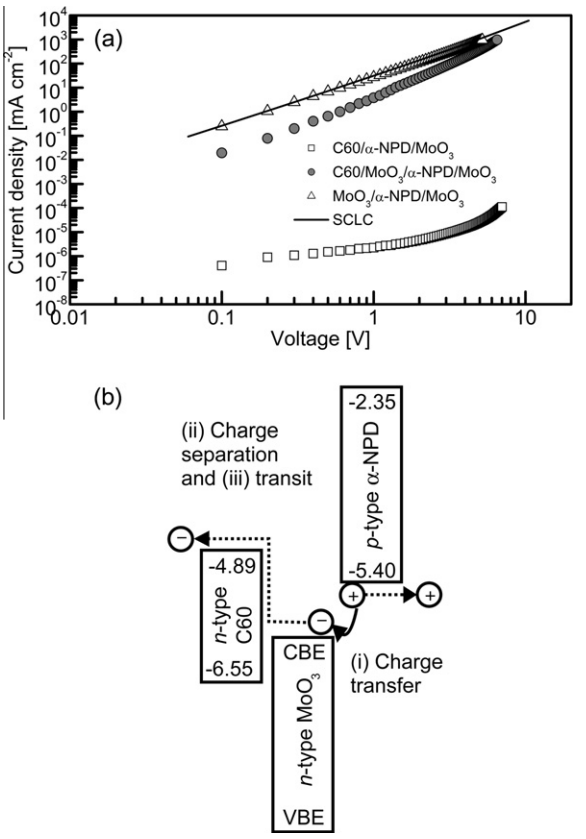

Fig. 8. (a) *J–V* characteristics of devices based on C60 and α-NPD. Solid line represents SCLC. (b) Energy-level diagrams showing charge generation mechanism of this device. Electron injection barrier at C60/MoO_3 interface is roughly estimated to be ≈0.79 eV from difference between electron affinity of C60 (≈4.89 eV) and work function of MoO_3 (≈5.68 eV).

is suggested that the charge generation rate is high enough to realize the SCLC. The current densities of the C60/MoO_3/α-NPD device are slightly lower than a SCLC level observed in the α-NPD device with the optimized MoO_3 thickness (glass substrate/ITO anode (150 nm)/MoO_3 buffer layer (0.75 nm)/α-NPD HTL (100 nm)/MoO_3 EBL (10 nm)/Al cathode (100 nm)). The lower current densities would be due to the presence of an electron injection barrier at the C60/MoO_3interface as shown in Fig. 8b.

4. Conclusions

J–V characteristics of organic hole-only devices having a MoO_3 buffer layer and UV–vis–NIR absorption spectra of composite films of organic and MoO_3 are investigated when HTL materials with different ionization energies are systematically changed. We find that SCLCs of a wide variety of HTLs are observed and their hole mobilities can be estimated using a SCLC analysis when ionization energies of HTLs are lower than a work function of MoO_3. From comparison of the *J–V* characteristics and the UV–vis–NIR absorption spectra, the HTL-to-MoO_3 electron transfer is crucial to realizing the SCLCs. Thus, we can attribute the observation of the SCLCs by using the MoO_3 buffer layer to an interfacial charge generation mechanism (composed of charge transfer, separation, and transit as shown in Fig. 1). Finally, we would like to mention that the interfacial charge generation is a versatile technique used to eliminate an influence of hole injection barriers on *J–V* characteristics of organic electronic devices.

Acknowledgements

This work is supported by Grants-in-Aid for Scientific Research (Nos. 21760005, 20241034, and 20108012). Part of this work is based on "Development of the Next Generation Large-scale Organic Electroluminescence Display Basic Technology (Green IT Project)" with New Energy and Industrial Technology Development Organization (NEDO).

References

[1] M. Abkowitz, J.S. Facci, J. Rehm, J. Appl. Phys. 83 (1998) 2670.
[2] G.G. Malliaras, J.C. Scott, J. Appl. Phys. 83 (1998) 5399.
[3] T.-Y. Chu, O.-K. Song, Appl. Phys. Lett. 90 (2007) 203512.
[4] I.D. Parker, J. Appl. Phys. 75 (1994) 1656.
[5] T. Matsushima, G.-H. Jin, H. Murata, J. Appl. Phys. 104 (2008) 054501.
[6] S. Tokito, K. Noda, Y. Taga, J. Phys. D: Appl. Phys. 29 (1996) 2750.
[7] C.-W. Chen, Y.-J. Lu, C.-C. Wu, E.H.-E. Wu, C.-W. Chu, Y. Yang, Appl. Phys. Lett. 87 (2005) 241121.
[8] V. Shrotriya, G. Li, Y. Yao, C.-W. Chu, Y. Yang, Appl. Phys. Lett. 88 (2006) 073508.
[9] Y. Kinoshita, R. Takenaka, H. Murata, Appl. Phys. Lett. 92 (2008) 243309.
[10] G.L. Frey, K.J. Reynolds, R.H. Friend, Adv. Mater. 14 (2002) 265.
[11] C.-W. Chu, S.-H. Li, C.-W. Chen, V. Shrotriya, Y. Yang, Appl. Phys. Lett. 87 (2005) 193508.
[12] T. Matsushima, Y. Kinoshita, H. Murata, Appl. Phys. Lett. 91 (2007) 253504.
[13] H. Lee, S.W. Cho, K. Han, P.E. Jeon, C.-N. Whang, K. Jeong, K. Cho, Y. Yi, Appl. Phys. Lett. 93 (2008) 043308.
[14] M. Kröger, S. Hamwi, J. Meyer, T. Riedl, W. Kowalsky, A. Kahn, Org. Electron. 10 (2009) 932.
[15] M. Kröger, S. Hamwi, J. Meyer, T. Riedl, W. Kowalsky, A. Kahn, Appl. Phys. Lett. 95 (2009) 123301.
[16] K. Kanai, K. Koizumi, S. Ouchi, Y. Tsukamoto, K. Sakanoue, Y. Ouchi, K. Seki, Org. Electron. 11 (2010) 188.
[17] T. Matsushima, H. Murata, Appl. Phys. Lett. 95 (2009) 203306.
[18] Y. Kawamura, H. Sasabe, C. Adachi, Jpn. J. Appl. Phys. 43 (2004) 7729.
[19] H. Ishii, K. Sugiyama, E. Ito, K. Seki, Adv. Mater. 11 (1999) 605.
[20] P.N. Murgatroyd, J. Phys. D: Appl. Phys. 3 (1970) 151.
[21] C. Giebeler, H. Antoniadis, D.D.C. Bradley, Y. Shirota, Appl. Phys. Lett. 72 (1998) 2448.
[22] C.H. Cheung, K.C. Kwok, S.C. Tse, S.K. So, J. Appl. Phys. 103 (2008) 093705.
[23] S.W. Tsang, S.K. So, J.B. Xu, J. Appl. Phys. 99 (2006) 013706.
[24] S. Naka, H. Okada, H. Onnagawa, Y. Yamaguchi, T. Tsutsui, Synth. Met. 111–112 (2000) 331.
[25] H.H. Fong, S.K. So, W.Y. Sham, C.F. Lo, Y.S. Wu, C.H. Chen, Chem. Phys. 298 (2004) 119.
[26] S.C. Tse, H.H. Fong, S.K. So, J. Appl. Phys. 94 (2003) 2033.
[27] W. Xu, Khizar-ul-Haq, Y. Bai, X.Y. Jiang, Z.L. Zhang, Solid State Commun. 146 (2008) 311.
[28] O.J. Weiß, R.K. Krause, A. Hunze, J. Appl. Phys. 103 (2008) 043709.
[29] T.M. Brown, J.S. Kim, R.H. Friend, F. Cacialli, R. Daik, W.J. Feast, Appl. Phys. Lett. 75 (1999) 1679.
[30] T.M. Brown, R.H. Friend, I.S. Milard, D.J. Lacey, T. Butler, J.H. Burroughes, F. Cacialli, J. Appl. Phys. 93 (2003) 6159.
[31] X. Zhou, J. Blochwitz, M. Pfeiffer, A. Nollau, T. Fritz, K. Leo, Adv. Funct. Mater. 11 (2001) 310.
[32] D.-S. Leem, H.-D. Park, J.-W. Kang, J.-H. Lee, J.W. Kim, J.-J. Kim, Appl. Phys. Lett. 91 (2007) 011113.
[33] H. Kanno, N.C. Giebink, Y. Sun, S.R. Forrest, Appl. Phys. Lett. 89 (2006) 023503.
[34] J. Berkowitz, M.G. Inghram, W.A. Chupka, J. Chem. Phys. 26 (1957) 842.
[35] C.H. Cheung, W.J. Song, S.K. So, Org. Electron. 11 (2010) 89.
[36] J. Meyer, A. Shu, M. Kröger, A. Kahn, App. Phys. Lett. 96 (2010) 133308.
[37] J. Meyer, S. Hamwi, T. Bülow, H.-H. Johannes, T. Riedl, W. Kowalsky, Appl. Phys. Lett. 91 (2007) 113506.
[38] T. Tsutsui, M. Terai, Appl. Phys. Lett. 84 (2004) 440.
[39] J. Meyer, M. Kröger, S. Hamwi, F. Gnam, T. Riedl, W. Kowalsky, A. Kahn, Appl. Phys. Lett. 96 (2010) 193302.

Organic Electronics 12 (2011) 529–533

Contents lists available at ScienceDirect

Organic Electronics

journal homepage: www.elsevier.com/locate/orgel

Electroluminescence enhancement of the phosphor dispersed in a polymer matrix using the tandem structure

Jin-Young Kim [a,1], Min Jong Bae [b,c,1], Shang Hyeun Park [b,*], Taewon Jeong [b], Sunjin Song [b], Jeonghee Lee [b], Intaek Han [b], Ji Beom Yoo [c], Donggeun Jung [a], SeGi Yu [d,*]

[a] Department of Physics, BK 21 Physics Research Division, Sungkyunkwan University, Suwon 440-746, South Korea
[b] Materials Research Lab, Samsung Advanced Institute of Technology, Yongin 446-712, South Korea
[c] SKKU Advanced Institute of Nanotechnology (SAINT), Sungkyunkwan University, Suwon 440-746, South Korea
[d] Department of Physics, Hankuk University of Foreign Studies, Yongin 449-791, South Korea

ARTICLE INFO

Article history:
Received 7 September 2010
Received in revised form 1 December 2010
Accepted 31 December 2010
Available online 13 January 2011

Keywords:
Electroluminescence
Inorganic
Tandem structure
ZnS

ABSTRACT

An alternating current driven electroluminescence (EL) device consisting of a phosphor dispersed in a polymer matrix device was fabricated as a tandem structure. This structure can be formed by duplicating the emitting and conducting layers. The EL device with the tandem structure, particularly the device with the triple emitting layer, was six times brighter than (1460 cd/m^2 at an alternating voltage application of 50 V) the structure with a single emitting layer. This tandem structure plays important roles by increasing the chance of electron–hole tunneling into the phosphor with leading to an increase in brightness by combining the light emitted from several emitting layers in a device. In addition, the adoption of a spin-coating method for the deposition of an emitting layer can allow the production of a dielectric part on the lower-lying emitting phosphor powder particles. The implementation of a dielectric part and emitting part by one spin-coating procedure simplifies the overall fabrication process, particularly for the tandem structure. The significant increase in brightness with each additional emitting layer as well as a facile fabrication process would help to make the EL device a competitive candidate in future displays and lightings.

© 2011 Elsevier B.V. All rights reserved.

1. Introduction

Recently, considerable research effort has been poured into future potential flat panel displays [1–5] beyond liquid crystal displays and plasma display panels, which are both commercially available. Among these candidates, alternating current (AC) thick-film powder electroluminescence (EL) devices have attracted interest owing to their low cost and a simple fabrication process with the ability for mass production [6–9]. This EL structure is composed of a top electrode, an emitting layer, a dielectric layer, and a transparent electrode. Since AC EL is light emission under a high electric field, a dielectric layer is needed to prevent catastrophic dielectric breakdown in the device. Despite the merits of EL devices, such as an easy fabrication process and scalability to a large size for EL displays, the practical applications of AC thick-film EL devices are currently limited to backlighting in cellular phones. This is mainly due to the insufficient brightness of EL devices compared to other types of flat panel displays. More research on materials and structures for these devices will help overcome the key issues in EL, such as low brightness, relatively short lifetime and high operation voltages [10–13].

In this paper, we propose a tandem structure for an AC thick-film EL device with a multiple emitting layer. This tandem structure can help overcome one of the main weak

* Corresponding authors. Tel.: +82 31 280 8167 (S.H. Park), +82 31 330 4398 (S. Yu).
E-mail addresses: sh100.park@samsung.com (S.H. Park), segiyu@hufs.ac.kr (S. Yu).
[1] These authors contributed equally to this work.

1566-1199/$ - see front matter © 2011 Elsevier B.V. All rights reserved.
doi:10.1016/j.orgel.2010.12.020

points of the EL device, i.e., low brightness. This structure enhances the brightness of an EL device by combining the light emitted from several emitting layers (in this study up to three layers), which is similar to semiconductor multiple quantum wells or tandem solar cells [14,15]. In addition, since the capacitance of a device is increased by the parallel connection of the component emitting layers, the tandem structure would increase the chance of electron–hole tunneling in the phosphor leading to an increase in brightness. To simplify the fabrication process, a spin-coating method was also used to deposit the emitting layer. Since the dielectric part was formed on the phosphor powder particles during spin-coating, the spin-coating method can reduce the fabrication process to a single processing step instead of the two steps generally required [16].

2. Experimental

Fig. 1 shows the structure of the tandem EL device. The emitting layers are multiply stacked and the transparent conducting electrode layers are sandwiched between the adjacent emitting layers. The fabrication process for the tandem structure is as follows. An emitting layer was spin-coated on an indium doped tin oxide (ITO)-coated glass substrate at 1000 rpm for 40 s using the emitting paste composed of ZnS:Cu,Cl EL green phosphor powder (Sylvania, GG44) and an organic binder (EL-Korea, ELPR530) as a polyvinylidene fluoride (PVDF) based polymer [17]. The phosphor to binder weight ratio is 1/2. The spin-coated emitting layer was dried at 130 °C for 30 min, which yielded two separate layers by gravitation. The organic-based dielectric part was positioned on the emitting part, which was composed of phosphor particles. This spin-coating process simplified the fabrication of a tandem structure which will be explained later. An ITO transparent conducting layer was sputtered on top of the emitting layer. For a tandem structure, the coating process for the emitting and conducting layers was carried out repetitively. In this study, three different tandem structures were prepared – one, two, and three emitting layer(s). After forming the multiple emitting layer, an aluminum thin film as a top electrode was deposited on it by DC sputtering.

The light emission characteristics of the three different structured EL devices were measured under ambient conditions by varying the applied AC voltage and frequency.

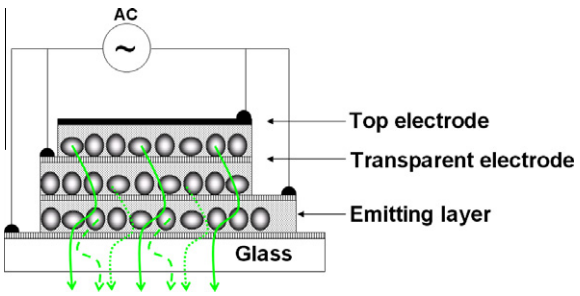

Fig. 1. Schematic diagram of an EL device with a triple emitting layer. The component emitting layers were connected to a power supply in parallel.

Fig. 1 shows the measurement system providing the electrical power to the device. In the tandem structure, the electrical wiring was connected in parallel to each emitting layer. The middle transparent electrode was shared by the neighboring upper and lower emitting layers. A sinusoidal AC voltage generated by the combination of a conventional function generator (Agilent, 33250A) and amplifier (Trek, P0610B-K) was applied to the device. An oscilloscope (Hewlett–Packard, 400D) was used to monitor the applied voltage. All AC readings are the peak-to-peak values. The absolute brightness was measured using a luminance colorimeter (Topcon, BM-7). After measuring the light emission, the morphology of the tandem structure of the emitting layers and intervening conducting layers was examined by field emission scanning electron microscopy (FE-SEM, Hitachi S-4200).

3. Results and discussion

The spin-coating method allows the deposition of two parts (an emitting phosphor part and a dielectric part in an emitting layer) in only one spin-coating because the tandem structure inherently requires the deposition of many component layers compared to the conventional single emitting layered EL structure. After spin-coating and consecutive drying of the emitting layer, most of the remaining organic binder, which would become an organic-based dielectric part, was located on and beside the phosphor powder particles due to the low viscosity of the emitting paste. However, virtually no organic binder was located under the phosphor powder particles due to the difference in density between the powder (4.1 g/cm^3) and binder (1.8 g/cm^3) during the spin-coating process. As shown in Fig. 2, this separation yielded the simultaneous formation of a phosphor-based emitting layer part at the low region and an insulating dielectric layer part at the upper region. Therefore, the deposition of a dielectric layer can be omitted when this spin-coating process is used. This omission is difficult to obtain using the screen-printing method because the high-viscosity nature of the emitting paste for printing results in incomplete coverage over the phosphor particles. This incompleteness in coverage leads to the formation of pinholes in the emitting layer, which is a serious failure mechanism in EL devices [3]. This can be explained by the fact that the paste for the spin-coating method is thinner, i.e., lower viscosity, than that for the screen-printing method due to the difference in the film deposition mechanism. The screen-printing method has practical problems for the fabrication of a tandem structure because many deposition processes are necessary for the deposition of dielectric layers. Furthermore, a transparent electrode can be broken easily by the squeeze pressure during the deposition of emitting and dielectric layers in the screen-printing method. Consequently, the spin-coating is a suitable method for the tandem structure of an EL device.

In AC thick-film EL devices, the total thickness of the emitting and dielectric layers is important because it determines the intensity of the electric field for a given voltage. Since the brightness of an EL device is a function

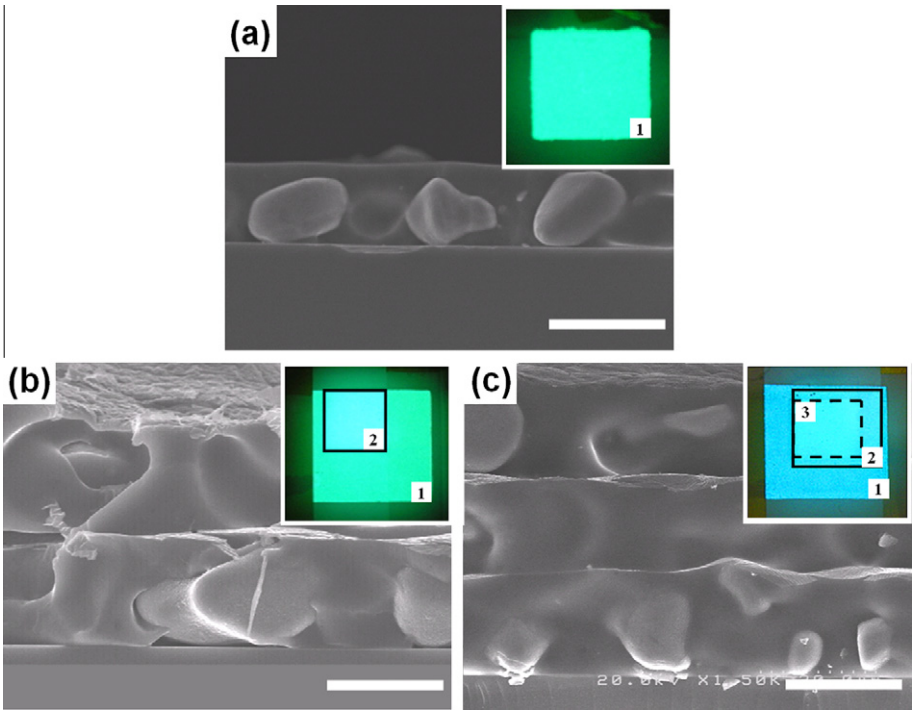

Fig. 2. SEM images of (a) single-, (b) double-, and (c) triple-layered structures on an ITO substrate by the spin-coating method. The scaling bars in the lower part of three SEM images correspond to 20 μm. The insets show optical images of light emission for the single-, double-, and triple-layered structure taken by a digital camera, where the Arabic numeral corresponds to the number of emitting layers. Although the emission colors of the EL device were taken by a digital camera, they have the same color (505 nm). This was caused by the automatic settings in the digital camera, which failed to match the precise color.

of the applied electric field, the brightness can be strongly affected by the layer thickness [18,19]. This suggests that using small phosphor powder particles, i.e., reduced thickness of the emitting layer, would result in high brightness. For this reason, an emitting layer as thin as possible was fabricated, i.e. one monolayer of phosphor particles. Fig. 2(a) shows a cross-sectional SEM image of the single emitting layer structure, where the mean thickness of the layer was approximately 15 μm. The average thickness of the two components in the emitting layer, i.e., the phosphor particles part and dielectric part, which was formed mostly on and beside the phosphor particles, were approximately 13.5 and 1.5 μm, respectively (see Fig. 2). The same AC voltage was applied to each emitting layer of the EL device due to the *parallel* electrical wiring to the layers, as shown in Fig. 1, despite the serial geometric stacking of the layers. Therefore, the brightness of a tandem structure was the combination of the similar brightness of each emitting layer. The insets in Fig. 2 show emission images of a single, double and triple emitting layered structure taken by a digital camera. The emission images of Arabic numerals 1, 2 and 3 are for the single-layered, double-layered (regions marked by the solid line in Fig. 2(b) and (c)) and triple-layered structure (region marked by the dotted line in Fig. 2(c)), respectively. The brighter image comes out from the structure with an additional layer (see the insets in Fig. 2), which is explained quantitatively in Fig. 3.

Fig. 3 shows a plot of the brightness as a function of the voltage (the frequency) at a fixed frequency (voltage) at 400 Hz (50 V) for the tandem structures. Although the brightness of the single-layered structure was 100 cd/m^2, that of the double- and triple-layered structures was 170 and 230 cd/m^2, respectively, at 150 V and 400 Hz, as shown in Fig. 3(a). This does not follow the increase in brightness with increasing number of emitting layers precisely. This may be caused by the fact that the light was absorbed or scattered by other components when the light passed through the other component layers. However, when the operation of the tandem structures moved to a high frequency of 12 kHz, the brightness increased substantially to 830 cd/m^2 (1460) for the double- (triple-) layered structure, even at a low voltage of 50 V (see Fig. 3(b)). In contrast, the single-layered structure showed a brightness of only 230 cd/m^2, indicating a more than threefold increase for the tandem structure. Since the emission mechanism in ZnS:Cu,Cl phosphor is different at low and high frequencies [20–23], this might affect the different multiple increases in brightness of the tandem structure. At the low frequency, a green emission (520 nm) transition occurred from Cl on a S site (Cl_S) to Cu on a Zn site (Cu_{Zn}) [6]. However, at high frequency, a blue transition (440 nm) occurred from Cl_S to interstitial Cu (Cu_i) [23].

All the devices in Fig. 4(a) showed a decrease in capacitance, as measured using a LCR meter at 0.1 V, with increasing frequency. The magnitude of the capacitance at the actual driving voltage of the EL device ranged from 30 to 150 V, which might be different from the measured

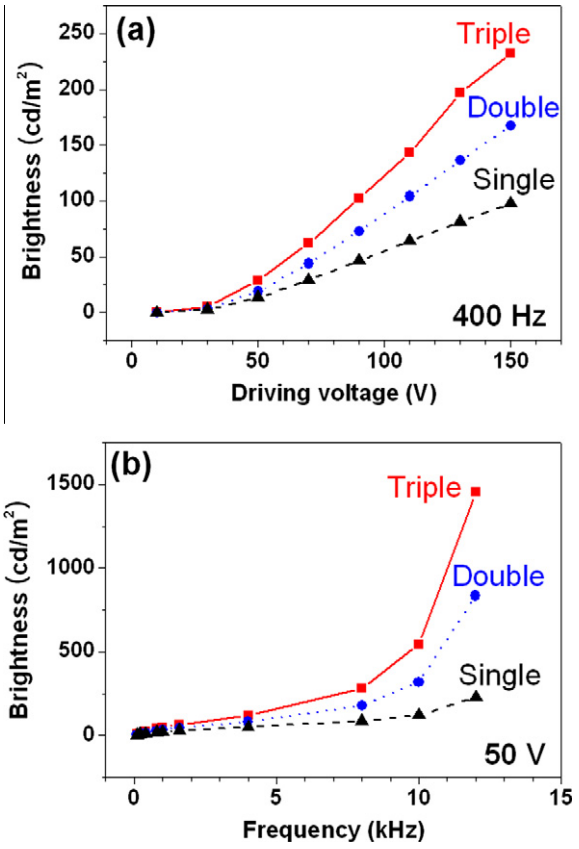

Fig. 3. (a) Brightness vs. voltage and (b) brightness vs. frequency curves of the tandem EL device using the emitting paste.

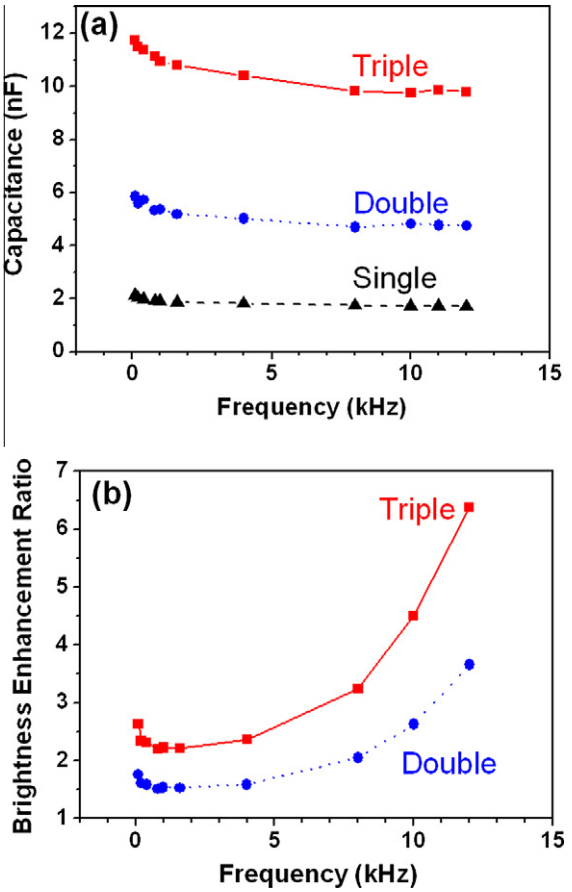

Fig. 4. (a) Capacitance vs. frequency curves of the tandem EL device at 0.1 V. (b) The ratio of brightness enhancement vs. frequency curve using the single to double and single to triple ratios in the tandem EL device.

capacitance at 0.1 V. However, it is reasonable to assume that the tendency of the measured capacitance reflects the qualitative behavior of the actual capacitance among the devices operated at 30–150 V. The capacitance of the single, double and triple emitting layer at a frequency of 12 kHz was 1.7, 4.7 and 9.8 nF, respectively. This can be explained by considering the capacitive characteristics of the emitting layer in the EL device. The capacitance was increased by the emitting layer due to their parallel connection in the electrical wiring. Fig. 4(b) presents the brightness enhancement ratios of the double-layered (circular line) and triple-layered (square line) structures to the single-layered structure. At frequencies <1 kHz, the enhancement ratio was decreased slightly, where the range of brightness enhancement of the single-layered to double- (triple-) layered structures was 1.5–1.7 (2.1–2.6). The ratios of the brightness enhancement increased at frequencies >1 kHz (the range of double to single: 2.1–3.7 and triple to single: 3.2–6.3). The brightness enhancement of the tandem structured EL device at the high capacitance and frequency can be interpreted as follows. In the ZnS:Cu,Cl phosphor, Cu_xS conducting needles are formed by the Cu concentration exceeding the solubility limit in ZnS. Electrons and holes are injected into the host lattice (ZnS) at opposite ends of each Cu_xS needle in the ZnS–Cu_xS interface by the high local electric field [24,25]. Electrons are trapped in the shallow Cl_S donor site, whereas holes are trapped by the Cu recombination centers. When the electric field is reversed, the emitted electrons recombine with the trapped holes to produce light. Therefore, the increase in capacitance of the tandem EL device led to a high probability of tunneling charge carriers at the interface between the ZnS–Cu_xS interface. This large charge density due to the increased capacitance based on the equation of charge, $Q = CV$, would increase the brightness of an EL device. Furthermore, the high frequency applied to an EL device would increase the chance of electron–hole pair recombination because light emission from an EL device normally occurs at the moment of the field reversal [3]. As a result, the brightness of the tandem EL devices is proportional to the capacitance by the increased electron–hole tunneling and recombination at a high frequency of 12 kHz. This would lead to large increase in the brightness of the tandem EL devices. The ratio of the increment brightness of single-layered to double- (triple-) layered structure was 3.6 (6.3) at a frequency of 12 kHz. At the same frequency, the ratio of the increment capacitance of the single-layered to double- (triple-) layered structure was 2.8 (5.7).

The capacitive reactance, X_C, was calculated to further examine the dependency of the brightness on the

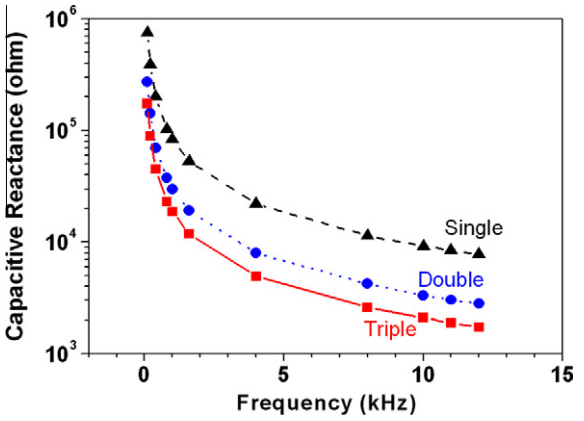

Fig. 5. Capacitive reactance vs. frequency curve with the *y*-log scale for the tandem EL device.

capacitance and frequency in the tandem structure. X_C can be written as $X_C = 1/(2\pi fC)[\Omega]$, where f is the frequency of an applied voltage and C is the capacitance of an EL device. This X_C value has a strong influence on the brightness of an EL device [10]. A decrease in X_C (high capacitance and frequency) can lead to an increase in the tunneling charge carriers at the ZnS–Cu_xS contact. Fig. 5 shows the capacitive reactance as a function of the various frequencies at a fixed voltage of 50 V. X_C for the single, double, and triple emitting layer was found to be 7.8×10^3, 2.8×10^3, and $1.7 \times 10^3\,\Omega$, respectively, at a frequency of 12 kHz. Figs. 3(b) and 5 show that the brightness increased rapidly with a substantial decrease in X_C. Similar results were reported in Ref. [10]. The EL device suggests that a low X_C value generally results in high brightness. The enhancement in the brightness of the double and triple emitting layer along with the simple lamination process of the spin-coating has potential for EL devices in flat panel displays.

4. Conclusion

A tandem structure for powder EL devices was fabricated by spin-coating an emitting paste composed of ZnS:Cu,Cl green phosphor powder particles and a PVDF based organic binder. Three different structures were prepared with one, two, and three emitting layer(s). The capacitance of the tandem EL device increased due to their parallel connection in the electrical wiring. This tandem structure EL device increases the probability of electron–hole tunneling into ZnS lattice and recombination electron–hole, and combines the light emission from each emitting layer. An approximately six fold increase in brightness for triple emitting layer was obtained at the high frequency regime. In addition, the tandem EL device was fabricated using a fast and simple process because the emitting phosphor part and dielectric part in the emitting layer were deposited by a single spin-coating process. This tandem structure can be a potential candidate for flat panel EL displays.

Acknowledgements

This work was supported in part by the National Research Foundation of Korea [NRF 2010-0011894] and in part by Hankuk University of Foreign Studies Research Fund of 2010. D. Jung was supported by the Priority Research Centers Program under Grant NRF-20090094025. J.-Y.K. is a recipient of the Seoul Science Fellowships of the Seoul Metropolitan Government.

References

[1] C.-H. Chang, H.-C. Cheng, Y.-J. Lu, K.-C. Tien, H.-W. Lin, C.-L. Lin, C.-J. Yang, C.-C. Wu, Org. Electron. 11 (2010) 247.
[2] S. Yu, S. Jin, W. Yi, J. Kang, T. Jeong, Y. Choi, J. Lee, J. Heo, N.S. Lee, J.-B. Yoo, J.M. Kim, Jpn. J. Appl. Phys. 40 (2001) 6088.
[3] Y.A. Ono, Electroluminescent Displays, World Scientific, Singapore, 1995, pp. 7–25.
[4] T. Tstusui, J. Korean Phys. Soc. 39 (2001) S356.
[5] V.P. Singh, D.C. Morton, IEEE T. Electron Dev. 39 (1992) 1331.
[6] S. Shionoya, W.M. Yen, Phosphor Handbook, CRC Press, Boca Raton, 1999, pp. 581–612.
[7] G. Destriau, J. Chim. Physique 34 (1937) 117.
[8] M.J. Kim, D.W. Shin, J.-Y. Kim, S.H. Park, I.T. Han, J.B. Yoo, Carbon 47 (2009) 3461.
[9] J.-Y. Kim, S.H. Park, T. Jeong, M.J. Bae, S. Song, J. Lee, I.T. Han, D. Jung, S. Yu, IEEE T. Elect. Dev. 57 (2010) 1470.
[10] T. Satoh, T. Nakatsuta, K. Tsuruya, Y. Tabata, T. Tamura, Y. Ichikawa, H. Tango, J. Mater. Sci.: Mater. Electron. 18 (2007) S239.
[11] T. Satoh, M. Kobayashi, S. Kawamura, T. Uchida, Electron. Lett. 43 (2007) 1047.
[12] N. Miura, Proc. 14th Int'l Workshop on Inorganic and Organic Electroluminescence, Sep. 2008, pp. 427.
[13] V. Wood, J.E. Halpert, M.J. Panzer, M.G. Bawendy, V. Bulovic, Nano Lett 9 (2009) 2367.
[14] S. Yu, K.W. Kim, M.A. Stroscio, G.J. Iafrate, J.-P. Sun, G.I. Haddad, J. Appl. Phys. 82 (1997) 3363.
[15] J.Y. Kim, K. Lee, N.E. Coates, D. Moses, T.-Q. Nguyen, M. Dante, A.J. Heeger, Science 317 (2007) 222.
[16] S.-D. Han, I. Singh, D. Singh, Y.-H. Lee, G. Sharma, C.-H. Han, J. Lumin. 115 (2005) 97.
[17] The brand name of product is ELPR530, and the detail information on this product can be found from the company webpage (http://www.el-korea.co.kr).
[18] A. Abu-Dayah, J.F. Wager, S. Kobayashi, J. Appl. Phys. 74 (1993) 5575.
[19] P.D. Rack, A. Naman, P.H. Holloway, S.-S. Sun, R.T. Tuenge, MRS Bull. 82 (1996) 49.
[20] J. Ibanez, E. Garcia, L. Gil, M. Mollar, B. Mari, Displays 28 (2007) 112.
[21] K. Manzoor, S.R. Vadera, N. Kumar, T.R.N. Kutty, Appl. Phys. Lett. 84 (2004) 284.
[22] M. Warkentin, F. Bridges, S.A. Carter, M. Anderson, Phys. Rev. B 75 (2007) 075301.
[23] J. Stanley, Y. Jiang, F. Bridges, S.A. Carter, L. Ruhlen, J. Phys.: Condens. Matter 22 (2010) 055301.
[24] A.G. Fischer, J. Electrochem. Soc. 110 (1963) 733–748.
[25] Y.-T. Nien, I.-G. Chen, C.-S. Hwang, S.-Y. Chu, J. Electroceram. 17 (2006) 299.

Organic Electronics 12 (2011) 534–540

Contents lists available at ScienceDirect

Organic Electronics

journal homepage: www.elsevier.com/locate/orgel

Mechanism of the Fermi level pinning at organic donor–acceptor heterojunction interfaces

Hong Ying Mao [a], Fabio Bussolotti [c], Dong-Chen Qi [b], Rui Wang [b], Satoshi Kera [c], Nobuo Ueno [c], Andrew Thye Shen Wee [b], Wei Chen [a,b,*]

[a] Department of Chemistry, National University of Singapore, 3 Science Drive 3, Singapore 117543, Singapore
[b] Department of Physics, National University of Singapore, 2 Science Drive 3, Singapore 117542, Singapore
[c] Graduate School of Advanced Integration Science, Chiba University, Chiba, Japan

ARTICLE INFO

Article history:
Received 31 October 2010
Received in revised form 27 December 2010
Accepted 6 January 2011
Available online 19 January 2011

Keywords:
Organic heterojunction
Energy level alignment
Ultraviolet photoelectron spectroscopy

ABSTRACT

We investigate the energy level alignment and the Fermi level pinning mechanism at organic donor–acceptor heterojunctions interfaces by using the model organic–organic heterojunctions (OOHs) with well-defined molecular orientation of the standing copper (II) phthalocyanine (CuPc) and zinc phthalocyanine (ZnPc) films on the standing copper-hexadecafluoro-phthalocyanine (F_{16}CuPc) thin films on SiO_2. We identify two distinct regions for the energy level alignment by *in situ* ultraviolet photoelectron spectroscopy investigation. In region (I) where the work function (WF) of the underlying substrate is larger than the ionization potential (IP) of the top organic layers, the substrate Fermi level is pinned at the leading edge of the HOMO peak accompanied by a decreasing of the WF; in region (II) where the WF is smaller than the IP of the top organic layers, a downward shift of both the HOMO and vacuum level is observed. In connection with the defect induced gap states, we provide a detailed explanation for this thickness dependent energy level alignment and Fermi level pinning mechanism at the organic donor–acceptor OOH interface.

© 2011 Elsevier B.V. All rights reserved.

1. Introduction

Understanding the energy level alignment at organic–organic heterojunction (OOH) interfaces is crucial for organic electronic devices, such as OOH-based organic photovoltaic cells (OPVs), organic photodiodes and organic light-emitting diodes (OLEDs). It is of key importance for determining the electron and hole injection barriers in OLEDs or open circuit voltages and charge collection in OPVs [1–6]. Intensive research efforts have been devoted to establishing a general mechanism that governs the energy level alignment at these interfaces with limited success [4–14]. Various models, including the integer charge transfer (ICT) [10] model and the induced density of interface states (IDIS) [8,15] model, have been proposed. It is also argued that the tiny density of gap states, which is induced by defects and/or disorder in the molecular packing structure, determine the interfacial energy level alignment as well as the position of the highest-occupied-molecular-orbital (HOMO) with respect to the Fermi level [8,12,16,17]. Moreover, the highly anisotropic nature of π-conjugated organic molecules leads to the orientation dependent charge transport, as well as the electronic structures of highly ordered organic thin films, such as ionization potential (IP) of organic films and the interfacial dipole formation at the donor–acceptor OOH interfaces [18–22]. These can further complicate the understanding of the energy level alignment at the OOH interfaces. Therefore, it is necessary to carry out detailed investigation to understand the energy level alignment mechanism at the OOHs with well-defined supramolecular arrangement or molecular orientation.

* Corresponding author at: Department of Chemistry, National University of Singapore, 3 Science Drive 3, Singapore 117543, Singapore.
E-mail address: phycw@nus.edu.sg (W. Chen).

1566-1199/$ - see front matter © 2011 Elsevier B.V. All rights reserved.
doi:10.1016/j.orgel.2011.01.003

Using well-oriented polar phthalocyanine (Pc) monolayers on graphite surface to control the substrate work function, Fukagawa et al. [12] have demonstrated the role of the IP in vacuum-level alignment at organic semiconductor interfaces. When work function of substrate is smaller than the IP of the standing pentacene films, the vacuum-level alignment can be observed; whereas for substrate work functions exceed the IP of the pentacene films, the Fermi level of the substrate is pinned with the HOMO of the pentacene films due to spontaneous electron transfer under thermodynamic equilibrium. Similar pinning effect relative to the substrate Fermi level was also observed by Koch et al. [23] for pentacene on several polymer substrates with different work functions, due to a charge transfer reaction between neutral pentacene molecules and poly(3,4-ethylenedioxythiophene)/poly(styrenesulfonic acid) (PEDT/PSS) substrate cations in the presence of sulfonate moieties. However, in both cases the thickness of the pentacene thin films is no more than 2.0 nm corresponding to one or two monolayer of the standing

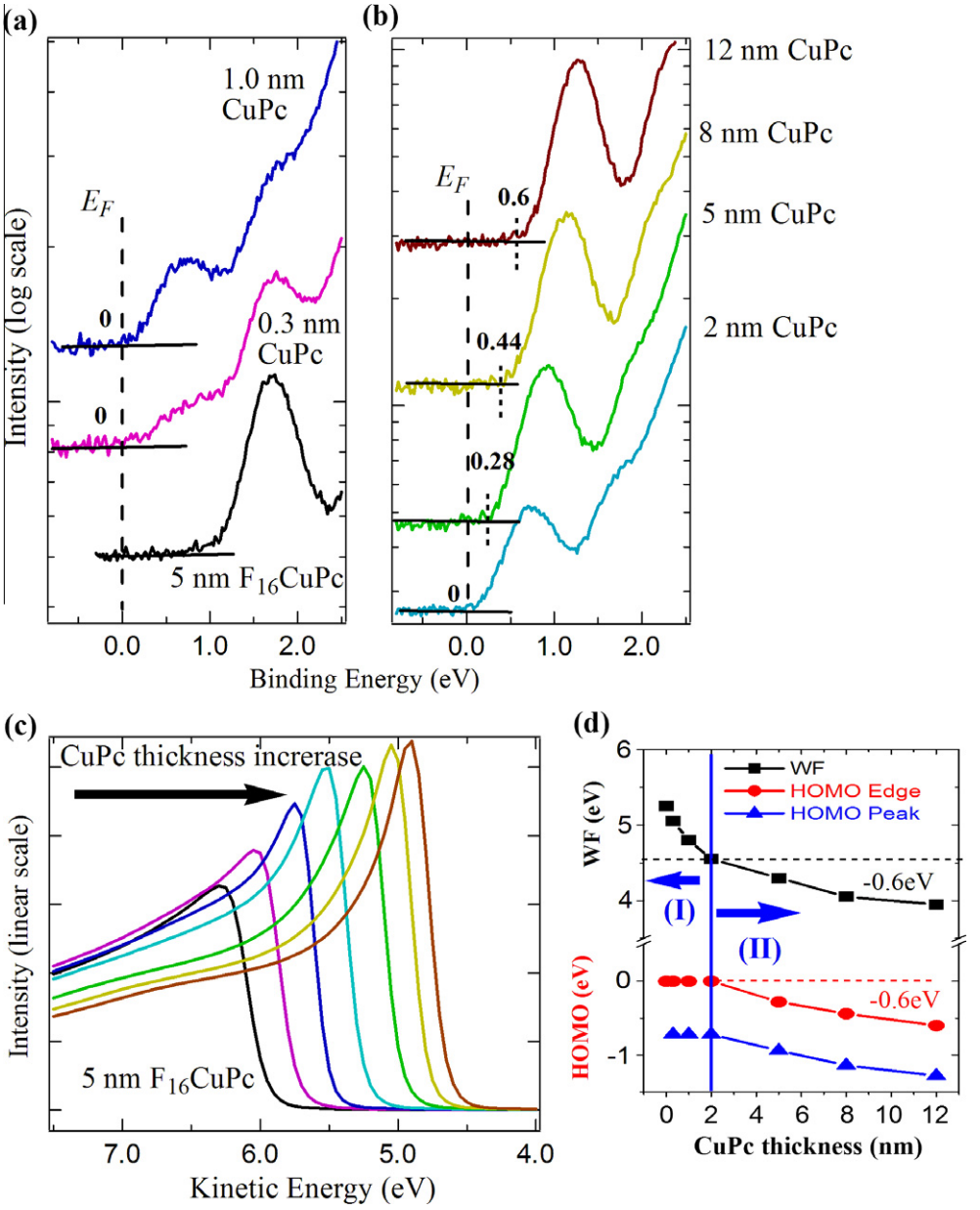

Fig. 1. Synchrotron-based UPS spectra for the deposition of CuPc on F_{16}CuPc film on SiO_2 at (a and b) the low-binding energy part near the E_F region (the intensity is on a log scale) and (c) at the low-kinetic energy region (secondary electron cut-off and the intensity is in linear scale) with a sample bias of −5 V. (d) Plot showing the change of the work function, CuPc HOMO edge and HOMO peak maximum as a function of CuPc thickness. All spectra are measured with photon energy of 60 eV. All binding energy are relative to the Fermi level position of the electron analyzer.

Table 1
Summary of sample energetics derived from UPS measurement: sample work function (WF), the energy position of CuPc HOMO edge and HOMO peak maximum with respect to the substrate Fermi level, and ionization potential (IP) of CuPc top layers. The errors are within 0.02 eV for all values.

	WF (eV)	HOMO edge (eV)	HOMO peak maximum (eV)	IP (eV)
5 nm F16CuPc on SiO_2	5.25	–	–	–
0.3 nm CuPc	5.05	0	0.72	5.05
1.0 nm CuPc	4.80	0	0.72	4.80
2.0 nm CuPc	4.55	0	0.72	4.55
5.0 nm CuPc	4.30	0.28	0.94	4.58
8.0 nm CuPc	4.05	0.44	1.14	4.49
12.0 nm CuPc	3.95	0.60	1.28	4.55

pentacene films. On the other hand, according to the ICT model [10], with the increasing thickness of the organic thin films (bulk structure, more than 10 nm), the Fermi level of the substrate is found to be pinned with the positive (negative) integer charge transfer states, which usually lies a few hundred meV above (below) the HOMO (LUMO) edge. In this article, in order to answer this discrepancy, we use *in situ* high resolution ultraviolet photoelectron spectroscopy (UPS) to study the energy level alignment mechanism at selected donor–acceptor OOH interfaces with different thickness, including the model OOHs with well-defined molecular orientation of the standing copper (II) phthalocyanine (CuPc) and zinc phthalocyanine (ZnPc) films on the standing copper-hexadecafluoro-phthalocyanine (F_{16}CuPc) thin film on SiO_2.

2. Experiment

Synchrotron-based *in situ* UPS experiments were carried out at the SINS beamline of the Singapore Synchrotron Light Source (SSLS) [24]. Vacuum level (VL) shifts were determined from UPS spectra at the low-kinetic energy onset (secondary electron cut-off) using photon energy of 60 eV with −5 V sample bias. Vacuum-sublimation purified F_{16}CuPc, CuPc and ZnPc molecules were thermally evaporated onto a substrate of Si(1 1 1) with native oxide (referred as SiO_2) held at room temperature in the growth chamber. The experimental details can be found elsewhere [24,25]. In order to better resolve the weak density of states near Fermi level, a novel high-precision and low-background UPS system with an electron energy analyzer (MBS, A-1) and a monochromatic Xe Iα source ($h\upsilon$ = 8.437 eV) were employed, while for UPS spectra at the low-kinetic energy onset, −7 V sample bias was applied [16,17]. All the UPS measurements were carried out at normal electron emission mode with the sample held at room temperature.

3. Results and discussion

As previously reported, the CuPc/F_{16}CuPc OOH (on SiO_2) can be considered as a standing OOH, where both CuPc and F_{16}CuPc molecules adopt a standing-up configuration with their molecular π-planes oriented nearly perpendicular to the substrate surface [22]. The evolution of the UPS spectra of CuPc on 5 nm standing F_{16}CuPc film on SiO_2 as a function of CuPc nominal thickness is shown in Fig. 1 for the HOMO (Fig. 1(a) and (b)) and VL (Fig. 1(c)) regions. In order to better reveal the weak density of states near the Fermi level, we plot the valence band spectra on a log intensity scale as displayed in Fig. 1(a) and (b). It is clear that the Fermi level is pinned at the leading edge of the CuPc HOMO for the CuPc thickness below 2 nm. This is accompanied by a downward shift of VL by 0.7 ± 0.02 eV or the reduction of the substrate work function (WF) from 5.25 ± 0.02 to 4.55 ± 0.02 eV, as shown in Fig. 1(c). Above the CuPc thickness of 2 nm, this Fermi pinning is no longer observed and the HOMO peak moves towards the higher binding energy together with a further downward shift of the VL with increasing thickness of CuPc films. As compared to the 2 nm CuPc coverage, both VL and CuPc HOMO edge show downward shift by 0.6 ± 0.02 eV and saturate when the thickness reaches to 12 nm. Similar behaviors have been reported by Hwang et al. previously, who demonstrated that the interface position of molecular levels with respect to the substrate Fermi level can be different from the position deeper in the bulk of the layer. This is attributed to states extending into the organic band gap [26]. The substrate WF, binding energy of CuPc HOMO edge and HOMO peak maximum, and IP (sum of WF and HOMO edge binding energy) of CuPc top layers are summarized in Table 1. Their changes as a function of CuPc nominal thickness are also plotted in Fig. 1(d).

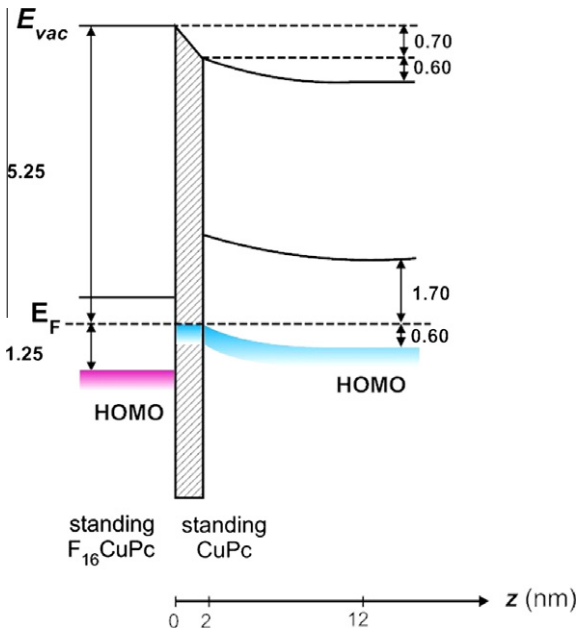

Fig. 2. The energy diagram of the CuPc/F_{16}CuPc interface.

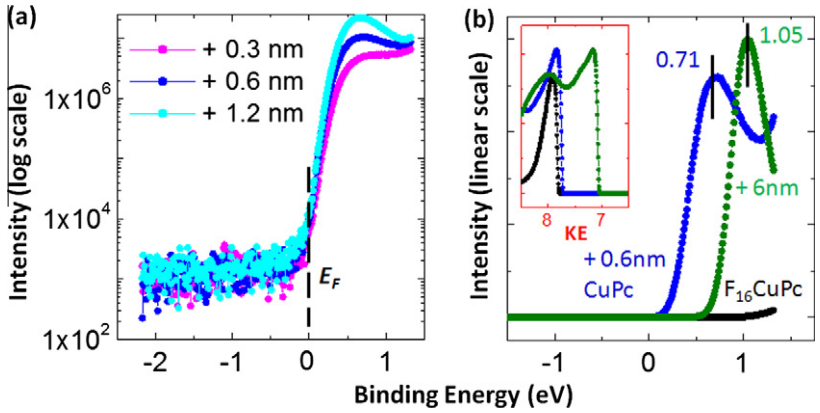

Fig. 3. (a and b) High-precision and low-background UPS spectra with monochromatic Xe Iα source (8.437 eV) during the deposition of CuPc on F_{16}CuPc film on SiO_2 at the low-binding energy part near the E_F region. The intensity in panel (a) is plotted on a log scale to better reveal the HOMO reaching the Fermi edge, while panel (b) is plotted in linear scale. The inset in panel (b) showing the corresponding UPS spectra at the low-kinetic energy region with a sample bias of −7 V.

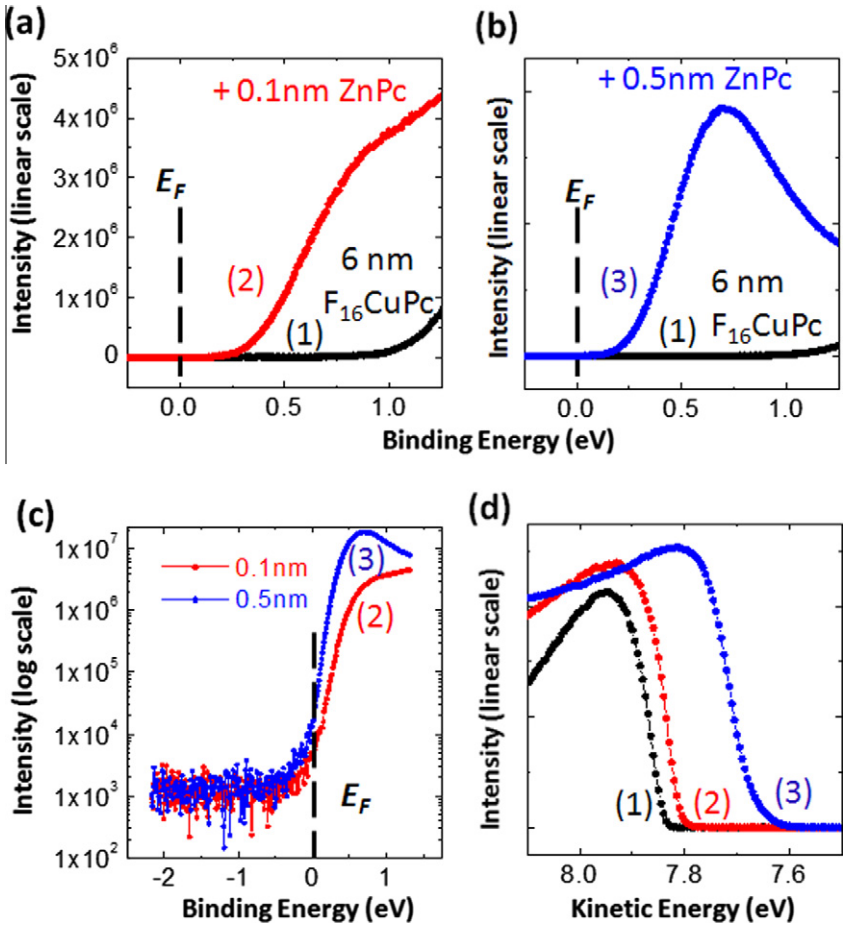

Fig. 4. UPS spectra during the deposition of 0.1 and 0.5 nm ZnPc on F_{16}CuPc film on SiO_2 at (a–c) the low-binding energy part near the E_F region and (d) at the low-kinetic energy part (secondary electron cut-off and the intensity is on a linear scale) with sample bias of −7 V. The intensity in panels (a) and (b) is plotted on a linear scale, while the intensity in panel (c) is plotted on a log scale to better reveal the HOMO reaching the Fermi edge. All spectra are measured with monochromatic Xe Iα source (8.437 eV).

As shown in Fig. 1(d), the energy level alignment at the CuPc/F_{16}CuPc interface can be divided into two regions. Region (I) represents the initial formation stage of the CuPc/F_{16}CuPc heterojunction with the CuPc thickness no more than 2 nm. In this region, the substrate WF is larger than the IP of the standing CuPc film (~4.55 eV) [21,22].

If assuming that the vacuum level is aligned at the heterojunction interface, this leads the HOMO of CuPc lies above the Fermi level, thereby facilitating a spontaneous charge (electron) transfer from CuPc top layer to the substrate Fermi level. This results in a downward shift of the substrate VL or reduction of substrate WF due to the interfacial charge transfer; while at the same time, the substrate Fermi level is pinned at the CuPc HOMO edge. In region (II) where the CuPc thickness is above 2 nm, the substrate WF is smaller than the IP of the standing CuPc film. We observe a downward shift for VL, CuPc HOMO edge and HOMO peak maximum at higher CuPc thickness, i.e., a "band-bending like" feature. For better illustration, the energy level diagram at the interface of CuPc/F_{16}CuPc heterojunction is shown in Fig. 2.

To better demonstrate the pinning of the Fermi level to the CuPc HOMO edge at low CuPc thickness, we used an ultrahigh sensitive and ultralow background UPS system to investigate this OOH [16,17]. Fig. 3(a) shows the UPS spectra with low CuPc coverage (0.3, 0.6 and 1.2 nm, in region (I)) near the E_F region on a log intensity scale. It clearly reveals the Fermi level pinning at the CuPc HOMO edge. By increasing the CuPc coverage to 6 nm (region (II)), the CuPc HOMO peak shifts to the higher binding energy from 0.71 ± 0.02 eV (0.6 nm CuPc coverage) to 1.05 ± 0.02 eV, as shown in Fig. 3(b), which is consistent with our observation of the energy level alignment at the OOH interface in Fig. 1(d).

Similar pinning behavior can be also found for the OOH of ZnPc on the standing F_{16}CuPc film on SiO_2 as shown in Fig. 4. After the deposition of 0.1 nm (Fig. 4(a)) and 0.5 nm (Fig. 4(b)) ZnPc, the substrate WF is 5.20 ± 0.02 and 5.05 ± 0.02 eV (Fig. 4(d)), respectively. It is reported that the IP for ZnPc thin film on C_{60} is 4.79 eV [27]. This

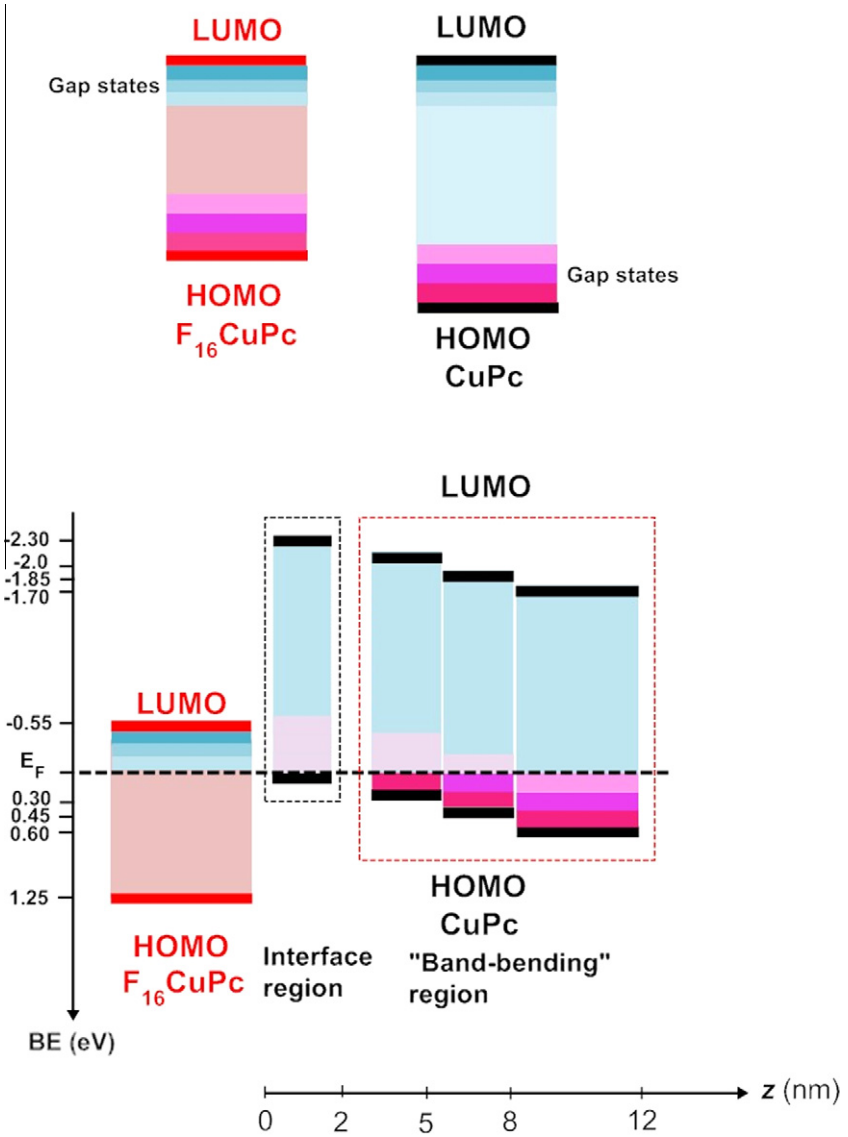

Fig. 5. Schematic illustration of the Fermi level pinning mechanism and the "band-bending" like feature at the CuPc/F_{16}CuPc heterojunction interface.

is smaller than the substrate work function of the standing F_{16}CuPc film on SiO_2. Compared to the experimental results for standing CuPc on F_{16}CuPc, the substrate Fermi level should be pinned at the ZnPc HOMO leading edge, in consistent with our experimental observations as shown in Fig. 4(a) and (b). This pinning effect can be seen more clearly in Fig. 4(c) using the plot on a log intensity scale. As such, we can conclude that the Fermi level will be pinned at the organic HOMO edge if the substrate work function is larger than the IP of the molecule at the OOH interfaces.

Recently, Kalb et al. examined the defects induced gap states extending from the valence-band edge into the band gap for small organic molecules as derived from electrical characteristics of organic field-effect transistors or from space-charge-limited current measurements [28]. Such gap or trap states exist not only in poly-crystalline films but also in crystalline thin films [29–32], even in molecular single crystals [33–35]. For the thermally evaporated CuPc thin films in the present work, there is no doubt that such defects induced gap states exist in the film, as shown by the schematic in the top panel in Fig. 5. The density of these gap states (DOGS) decays exponentially as a function of the energy from the HOMO, i.e., the larger the energy, the weaker the DOGS. It is found that these gap states have a significant effect on the energy level alignment at the OOH interface. As shown in the bottom panel in Fig. 5, when the thickness of CuPc thin films is below 2.0 nm (region I: WF > IP), the work function of the F_{16}CuPc substrate is larger than the ionization potential of the CuPc film. As a result, electrons from the CuPc layer (gap states + HOMO electrons) spontaneously transfer to the underlying F_{16}CuPc layer upon contact. When the integrated electrons over all occupied gap states of the CuPc layer are not sufficient to achieve the thermodynamic equilibrium, electrons in the HOMO of the CuPc layer are also transferred to the F_{16}CuPc layer until the thermodynamic equilibrium is achieved. As the density of states (DOS) of the HOMO is very large and increases steeply with energy near the HOMO leading edge, the Fermi level looks pinned at the HOMO edge after the depletion of all the gap states. It is worthy noting that the Fermi level is actually not pinned at a discrete energy level, but looks pinned at the HOMO leading edge relying on the energy dependence of the DOS. The Fermi level can move but only very slightly with increase in thickness (below 2 nm).

With increasing CuPc thickness above 2 nm (region II: WF < IP), upper part of the gap states of the newly deposited CuPc still locates above the Fermi level, allowing the electron transfer from the upper gap states to the underlying film. However, the degree of the charge transfer is weaker compared to that at the interface region (region I, CuPc thickness below 2 nm). In this case, the integration (or depletion) of a necessary smaller energy range of the occupied gap states can be sufficient for the thermodynamic equilibrium at the interface. As shown in the bottom panel in Fig. 5, the Fermi level can thus be pinned (or located) at an energy position in DOGS above the CuPc HOMO. Further increasing CuPc thickness, the interfacial charge transfer is even weaker, hence the integration of the DOGS over a much smaller energy range is enough to provide necessary electrons to reach the thermodynamic equilibrium at the interface, which result in the Fermi level location/pinning at a position even further away from the HOMO. As a result, the Fermi level moves in the band gap of the CuPc film depending on the distance from the CuPc/F_{16}CuPc interface as shown in Fig. 5. This can well explain the Fermi level pinning observed for the CuPc thickness below 2 nm (region I) and the "band-bending like phenomenon" above 2 nm (region II).

4. Conclusion

Organic donor heterojunctions of CuPc and ZnPc on F_{16}CuPc films on SiO_2 have been used as model systems to understand the interfacial energy level alignment mechanism. By using *in situ* high-resolution UPS measurements, we identify two regions for the interfacial energy level alignment: in region I (low thickness) where the WF of the underlying film is larger than the IP of the top organic layers, the Fermi level is pinned at the HOMO peak leading edge of CuPc or ZnPc and the WF is decreased due to the interfacial charge transfer; in region II (large thickness) where the WF is smaller than the IP of the top organic layers, a downward band-bending like feature is observed at the OOH interface. This observed thickness-dependent Fermi pinning behavior could account for the discrepancies on the Fermi pinning energy often found in literatures (i.e., integer charge transfer state *vs*. tailing gap states), as they essentially were looking into different thickness of the organic films. In connection with the defect induced gap states, we provide a detailed explanation for this thickness dependent energy level alignment and Fermi level pinning mechanism at the organic donor–acceptor OOH interface. The present study can help better understand the energy level alignment mechanism at various OOH interfaces, and hence facilitate the practical applications of organic heterojunction based electronic devices, such as organic light-emitting diodes, bipolar organic field transistors and organic photovoltaic cells.

Acknowledgments

Authors acknowledge the support from Singapore ARF Grants R-143-000-392-133, R-143-000-406-112, R143-000-440-112, NUS YIA Grant R143-000-452-101, NRF-CRP Grant "Graphene and Related Materials and Devices" and G-COE program at Chiba University (G-03, MEXT). W. Chen thanks the support from JSPS-NUS SEP program.

References

[1] G. Malliaras, R. Friend, Phys. Today 58 (2005) 53.
[2] S.R. Forrest, MRS Bull. 30 (2005) 28.
[3] Y.G. Wen, Y.Q. Liu, Adv. Mater. 22 (2010) 1331.
[4] (a) H. Ishii, K. Sugiyama, E. Ito, K. Seki, Adv. Mater. 11 (1999) 605;
(b) Y.L. Gao, Mat. Sci. Eng. R – Rep. 68 (2010) 39.
[5] N. Koch, ChemPhysChem 8 (2007) 1438.
[6] (a) F. Zhu, H.B. Wang, D. Song, K. Lou, D.H. Yan, Appl. Phys. Lett. 93 (2008) 103308;
(b) J. Wang, H.B. Wang, X.J. Yan, H.C. Huang, D. Jin, J.W. Shi, Y.H. Tang, D.H. Yan, Adv. Funct. Mater. 16 (2006) 824;
(c) J. Wang, H.B. Wang, X.J. Yan, H.C. Huang, D.H. Yan, Appl. Phys. Lett. 87 (2005) 093507;

(d) F. Zhu, J.B. Yang, D. Song, C.H. Li, D.H. Yan, Appl. Phys. Lett. 94 (2009) 143305.
[7] A. Kahn, N. Koch, W.Y. Gao, J. Polym. Sci., Part B: Polym. Phys. 41 (2003) 2529.
[8] J. Hwang, A. Wan, A. Kahn, Mat. Sci. Eng. R – Rep. 64 (2009) 1.
[9] N. Koch, J. Phys.: Condens. Matter 20 (2008) 184008.
[10] (a) S. Braun, W.R. Salaneck, M. Fahlman, Adv. Mater. 21 (2009) 1450;
(b) W. Osikowicz, M.P. de Jong, W.R. Salaneck, Adv. Mater. 19 (2007) 4213;
(c) S. Braun, X. Liu, W.R. Salaneck, M. Fahlman, Org. Electron. 11 (2010) 212.
[11] (a) J.X. Tang, C.S. Lee, S.T. Lee, J. Appl. Phys. 101 (2007) 064504;
(b) K.M. Lau, J.X. Tang, H.Y. Sun, C.S. Lee, S.T. Lee, D.H. Yan, Appl. Phys. Lett. 88 (2006) 173513.
[12] H. Fukagawa, S. Kera, T. Kataoka, S. Hosoumi, Y. Watanabe, K. Kudo, N. Ueno, Adv. Mater. 19 (2007) 665.
[13] M. Brumbach, D. Placencia, N.R. Armstrong, J. Phys. Chem. C 112 (2008) 3142.
[14] S.W. Cho, L.F.J. Piper, A. DeMasi, A.R.H. Preston, K.E. Smith, K.V. Chauhan, P. Sullivan, R.A. Hatton, T.S. Jones, J. Phys. Chem. C 114 (2010) 1928.
[15] H. Vazquez, F. Flores, A. Kahn, Org. Electron. 8 (2007) 241.
[16] T. Sueyoshi, H. Fukagawa, M. Ono, S. Kera, N. Ueno, Appl. Phys. Lett. 95 (2009) 183303.
[17] T. Sueyoshi, H. Kakuta, M. Ono, K. Sakamoto, S. Kera, N. Ueno, Appl. Phys. Lett. 96 (2010) 093303.
[18] P. Sullivan, T.S. Jones, A.J. Ferguson, S. Heutz, Appl. Phys. Lett. 91 (2007) 233114.
[19] K.V. Chauhan, P. Sullivan, J.L. Yang, T.S. Jones, J. Phys. Chem. C 114 (2010) 3304.
[20] S. Duhm, G. Heimel, I. Salzmann, H. Glowatzki, R.L. Johnson, A. Vollmer, J.P. Rabe, N. Koch, Nat. Mater. 7 (2008) 326.
[21] W. Chen, H. Huang, S. Chen, Y.L. Huang, X.Y. Gao, A.T.S. Wee, Chem. Mater. 20 (2008) 7017.
[22] (a) W. Chen, S. Chen, H. Huang, D.C. Qi, X.Y. Gao, A.T.S. Wee, Appl. Phys. Lett. 92 (2008) 063308;
(b) W. Chen, S. Chen, S. Chen, Y.L. Huang, H. Huang, D.C. Qi, X.Y. Gao, J. Ma, A.T.S. Wee, J. Appl. Phys. 106 (2009) 064910.
[23] N. Koch, A. Elschner, J.P. Rabe, R.L. Johnson, Adv. Mater. 17 (2005) 330.
[24] X.J. Yu, O. Wilhelmi, H.O. Moser, S.V. Vidyaraj, X.Y. Gao, A.T.S. Wee, T. Nyunt, H.J. Qian, H.W. Zheng, J. Electron Spectrosc. Relat. Phenom. 144 (2005) 1031.
[25] W. Chen, D.C. Qi, X.Y. Gao, A.T.S. Wee, Prog. Surf. Sci. 84 (2009) 279.
[26] J. Hwang, E.G. Kim, J. Liu, J.L. Brédas, A. Duggal, A. Kahn, J. Phys. Chem. C 111 (2007) 1378.
[27] S.H. Park, J.G. Jeong, H.J. Kim, S.H. Park, M.H. Cho, S.W. Cho, Y.J. Yi, M.Y. Heo, H. Sohn, Appl. Phys. Lett. 96 (2010) 013302.
[28] W.L. Kalb, S. Haas, C. Krellner, T. Mathis, B. Batlogg, Phys. Rev. B 81 (2010) 155315.
[29] W.L. Kalb, K. Mattenberger, B. Batlogg, Phys. Rev. B 78 (2008) 035334.
[30] F. De Angelis, S. Cipolloni, L. Mariucci, G. Fortunato, Appl. Phys. Lett. 88 (2006) 193508.
[31] W.L. Kalb, F. Meier, K. Mattenberger, B. Batlogg, Phys. Rev. B 76 (2007) 184112.
[32] F. De Angelis, S. Cipolloni, L. Mariucci, G. Fortunato, Appl. Phys. Lett. 86 (2005) 203505.
[33] D.V. Lang, X. Chi, T. Siegrist, A.M. Sergent, A.P. Ramirez, Phys. Rev. Lett. 93 (2004) 086802.
[34] W.Y. So, D.V. Lang, V.Y. Butko, X. Chi, J.C. Lashley, A.P. Ramirez, J. Appl. Phys. 104 (2008) 054512.
[35] V.Y. Butko, X. Chi, D.V. Lang, A.P. Ramirez, Appl. Phys. Lett. 83 (2003) 4773.

Organic Electronics 12 (2011) 541–546

Contents lists available at ScienceDirect

Organic Electronics

journal homepage: www.elsevier.com/locate/orgel

Carbazole–pyrene derivatives for undoped organic light-emitting devices

S.L. Lai [a], Q.X. Tong [b,c,*], M.Y. Chan [d], T.W. Ng [a], M.F. Lo [a], C.C. Ko [e], S.T. Lee [a], C.S. Lee [a,*]

[a] Center of Super-Diamond and Advanced Films (COSDAF) and Department of Physics and Materials Science, City University of Hong Kong, Hong Kong Special Administrative Region
[b] Department of Chemistry, Shantou University, Guangdong 515063, China
[c] Jiangsu Key Laboratory for Carbon-Based Functional Materials & Devices, Soochow University, Suzhou, China
[d] Department of Chemistry, The University of Hong Kong, Pokfulam Road, Hong Kong Special Administrative Region
[e] Department of Biology and Chemistry, City University of Hong Kong, Hong Kong Special Administrative Region

ARTICLE INFO

Article history:
Received 29 October 2010
Received in revised form 29 December 2010
Accepted 31 December 2010
Available online 13 January 2011

Keywords:
Small-molecule
Organic light-emitting diode
Electroluminescence
Undoped
Carbazole
Pyrene

ABSTRACT

Two carbazole–pyrene derivatives, namely 3,6-dipyrenyl-9-(4′-*tert*-butylphenyl) carbazole (BPyC) and 3,6-dipyrenyl-9-(4′-pyrenylphenyl) carbazole (TPyC), have been designed and synthesized for application in organic light-emitting devices (OLEDs). While the two compounds have similar chemical structures and photoluminescent properties, OLEDs based on them show distinct electroluminescence (EL) spectra. The BPyC-based devices show a single peak saturated blue emission with CIE coordinates of (0.15, 0.18); whereas the TPyC-based devices exhibit two emission peaks at blue and yellow hues with CIE coordinates of (0.22, 0.29). The difference in their EL spectra is attributed to the substitution of the *t*-butyl unit of BPyC with a pyrenyl group to form TPyC, which effectively increases the electron-donating property and results in exciplex formation at its interface with the electron-accepting TPBI. A high external quantum efficiency of 3.11% is achieved in the TPyC-based devices. Influences of chemical structure and fluorescent quantum yield on the efficiency of exciplex emission are discussed.

© 2011 Elsevier B.V. All rights reserved.

1. Introduction

Organic light-emitting device (OLED) is emerging as a leading next generation technology for full-color flat-panel displays and ambient illumination sources because of its huge market potential and excellent performance in terms of brightness, operating voltage and color gamut. Incorporation of extrinsic dyes into conductive hosts is an effective way to customize emitting color of OLEDs that is particularly useful for fabricating white OLEDs with two complementary or three primary colors [1,2]. Electroluminescence (EL) in terms of Commission Internationale de L'Eclairage (CIE) coordinates can be fine-tuned and optimized through precise control of dopant concentration and thickness for each light-emitting layer (EML). However, this approach would complicate device configuration as well as fabrication process, and inevitably increases the total manufacturing cost. In addition, the shortened device lifetime due to morphological phase separation caused by operation induced heating is another challenge for doped OLEDs.

Recent studies [3–9] have demonstrated a simple way to tailor the emitting color via interfacial excited-state charge-transfer complex (termed exciplex) formation to control emission peak location and/or intensity by using different binary combinations of electron-donor/hole-transporting materials (HTMs) and electron-acceptor/electron-transporting materials (ETMs), i.e., $h\nu_{\text{exciplex}} = E_{\text{LUMO}}$ (ETM) $- E_{\text{HOMO}}$ (HTM), ignoring the band bending at the organic/organic interface [10]. In the equation, E_{HOMO} and E_{LUMO} are the energies of the highest occupied molecular orbital (HOMO) and the lowest unoccupied molecular orbital (LUMO), respectively. However, only certain combinations of materials were reported to be capable of giving

* Corresponding authors. Address: Department of Chemistry, Shantou University, Guangdong 515063, China (Q.X. Tong).
E-mail addresses: qxtong@gmail.com (Q.X. Tong), apcslee@cityu.edu.hk (C.S. Lee).

1566-1199/$ - see front matter © 2011 Elsevier B.V. All rights reserved.
doi:10.1016/j.orgel.2010.12.026

exciplex emission and their external quantum efficiencies (η_E) are usually low (e.g., m-MTDATA/Alq_3 (0.22%) [4], 2-TNATA/Alq_3 (0.30%) [5] and TPD/PBD (1.10%) [6]). Thus, the appearance of exciplex is often considered as one of the main reasons responsible for poor device performance. On the other hand, Palilis et al. recently reported exciplex-based OLEDs using NPB/PPSPP, and achieved an exceptionally high η_E of 3.40% [7]. Later, our group demonstrated the TPyPA/BPhen based exciplex emitting devices with η_E as high as 3.93% [8]. It is proposed that matched carrier mobilities, high photoluminescence quantum yield (Φ_{PL}), and suitable electron energy levels of organic materials are the prerequisites for efficient exciplex-based OLEDs [8]. These findings provide guidelines for designing organic materials with desirable physical properties to facilitate high efficiency exciplex emission.

In addition to triphenylamine [4,5,8], both pyrene [8,11] and carbazole [9,12] and their derivatives have also been employed for exciplex emission, owing to their excellent luminescence characteristics, structural stabilities, and particularly their strong electron-donating tendencies when contacting with different electron-acceptors. However, the influences on how the chemical structures of organic materials affecting the nature of exciplex emission have seldom been studied. In this work, two carbazole-based compounds end-capped with one *t*-butyl and two pyrene groups, namely 3,6-dipyrenyl-9-(4′-*tert*-butylphenyl) carbazole (BPyC) and three pyrene groups, namely, 3,6-dipyrenyl-9-(4′-pyrenylphenyl) carbazole (TPyC) have been synthesized. While the two compounds have very similar structures and photoluminescent spectra, OLEDs using them as host emitters show distinct EL characteristics. Particularly, the BPyC-based devices (η_E = 2.21%) show only a single blue emission peak while the TPyC-based devices show two emission peaks with higher maximum η_E of 3.11%. Reason for these differences is attributed to the higher degree of electron-donating property with increasing number of pyrene groups. This results in the formation of the yellow exciplex emission which shifts the EL spectrum from saturated blue (BPyC) to near white (TPyC). It is worth noting that both carbazole derivatives have Φ_{PL} of about 95%, which are much higher than that of our previously reported triphenylamine TPyPA (Φ_{PL} = 80%) [8]. This results in a higher maximum η_E of the TPyC-based devices, as compared to that of a similarly structured TPyPA-based OLED (η_E = 2.83%). Based on these results the influences of chemical structures and Φ_{PL} on the efficiency of exciplex emission are discussed.

2. Experimental

2.1. Materials and instruments

All reagents and solvents for the synthesis of BPyC and TPyC were purchased from either Sigma–Aldrich or Acros Organics and used as received without further purification. ^{1}H NMR spectra were recorded with the use of a Bruker DPX-400 spectrometer (400 MHz). Mass spectrometry was performed on a PE SCIEX LC/MS spectrometer. Elemental analyses were carried out on a Vario EL Elementar by the Flash EA 1112 method. Modulated differential scanning calorimetry (MDSC) and thermogravimetric analysis (TGA) were performed under a nitrogen atmosphere at a heating rate of 10 °C min^{-1} on a TA Instruments MDSC 2910 and TGA Q50, respectively. Solution Φ_{PL} were determined by using the method of Demas and Crosby [13] with a degassed aqueous solution of quinine sulfate as a reference. Optical absorption and photoluminescence (PL) spectra were measured with a Perkin-Elmer Lambda 2S UV/vis spectrometer and a Perkin-Elmer LS 50B luminescence spectrometer, respectively. Ultraviolet photoelectron spectroscopic (UPS) studies were performed in a VG ESCALAB 220i-XL surface analysis system with an unfiltered He I (21.22 eV) gas discharge lamp under a base vacuum of 10^{-10} Torr.

2.2. Fabrication and characterization of OLEDs

Transparent indium tin oxide (ITO) pre-coated and patterned glass slides with a sheet resistance of 30 Ω square^{-1} were used as anodic substrates. Prior to successive film deposition, they were thoroughly cleaned with Decon 90, rinsed in de-ionized water, dried in an oven, and finally treated in an ultraviolet–ozone cleaner. OLEDs consisting of a hole-transporting layer (HTL) of *N*,*N*′-diphenyl-1,1′-biphenyl-4,4′-diamine (NPB), a hole-transporting light-emitter of BPyC or TPyC, an electron-transporting layer (ETL) of 1,3,5-tris(*N*-phenylbenzimidazol-2-yl) benzene (TPBI) or 4,7-diphenyl-1,10-phenanthroline (BPhen), and a LiF/Al cathode. All films were thermally deposited sequentially without vacuum break in an evaporation chamber under a base pressure of ~10^{-6} Torr. Deposition rates were monitored with quartz oscillation crystals and controlled at a rate of 0.1–0.2 nm s^{-1} for both organic and metal layers. A shadow mask was used to define the cathode and to make four 0.1 cm^2 devices on each substrate. Current density–voltage–luminance (*J*–*V*–*L*) characteristics, EL spectra, and CIE coordinates were measured simultaneously with a programmable Keithley model 237 power source and a Photoresearch PR650 spectrometer. All measurements were carried out at room temperature under ambient atmosphere without any encapsulation.

3. Results and discussion

3.1. Material syntheses

Molecular structures of BPyC and TPyC and their synthetic routes are shown in Scheme 1. Incorporation of the 9-phenylcarbazole group is expected to enhance hole-transporting properties of the two compounds. BPyC and TPyC can be easily prepared with high yields using typical Suzuki coupling reactions from 3,6-dibromo-9-(4-*tert*-butylphenyl)-9*H*-carbazole [14], 3,6-dibromo-9-(4-bromophenyl)-9*H*-carbazole [15], and commercial starting material pyrene-1-boronic acid, respectively, according to reported procedures [16]. Molecular structures of the final compounds were confirmed by ^{1}H nuclear magnetic resonance, mass spectrometry, and elemental analysis.

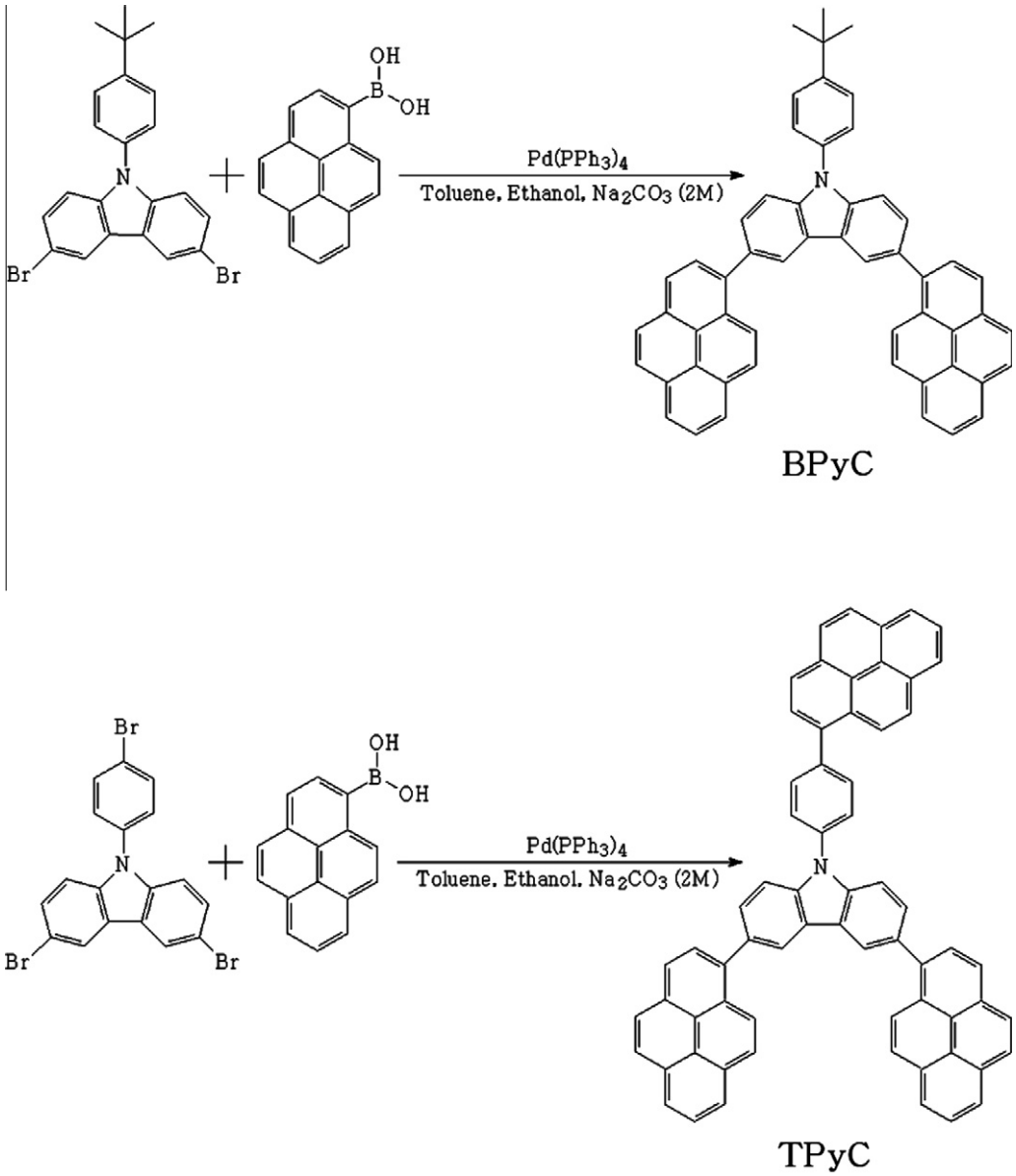

Scheme 1. Synthetic routes and molecular structures of 3,6-dipyrenyl-9-(4′-*tert*-butylphenyl) carbazole (BPyC) and 3,6-dipyrenyl-9-(4′-pyrenylphenyl) carbazole (TPyC).

3.2. Chemical and photophysical properties

The rigid molecular structures in the two carbazole derivatives are beneficial to thermal stability, as manifested by their high decomposition temperatures (T_d) of 496 and 516 °C, and melting temperatures (T_m) of 293 and 245 °C for BPyC and TPyC, respectively (T_d corresponds to 5% weight loss in the TGA measurements whereas T_m was determined by MDSC) although no obvious glass transitions were observed.

Optical absorption and PL spectra of BPyC and TPyC vacuum-deposited solid thin-films on quartz plates are depicted in Fig. 1. The longest wavelength absorption maxima ($\lambda_{abs,\,max}$) appear at 358 and 369 nm for BPyC and TPyC, respectively, while the PL spectra show intense blue emissions peaked at 443 nm (BPyC) and 465 nm (TPyC) under excitation at 385 nm. It is well recognized that an increase in conjugation length would generally result in red-shifts in both λ_{abs} and PL. Indeed, the addition of a pyrene arm (from BPyC to TPyC) does red-shift the absorption and PL peaks by respectively 11 and 22 nm. From the PL quantum yield measurement, Φ_{PL} of BPyC and TPyC in solution are 94.8% and 95.0%, respectively. These high Φ_{PL} values may be attributed to large Stoke shifts (difference between positions of band maxima of the absorption and emission spectra) in both organic materials that can effectively avoid re-absorption of the emitted photons during the PL process.

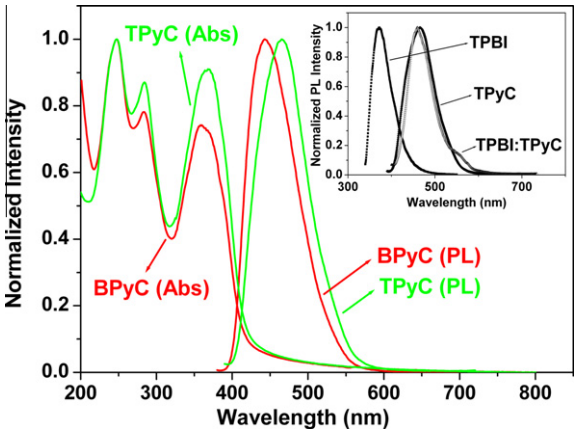

Fig. 1. Optical absorption (Abs) and photoluminescence (PL) spectra of BPyC and TPyC solid thin-films on quartz substrates. Inset: PL spectra of 10% TPBI:TPyC, TPBI, and TPyC thin-films, respectively.

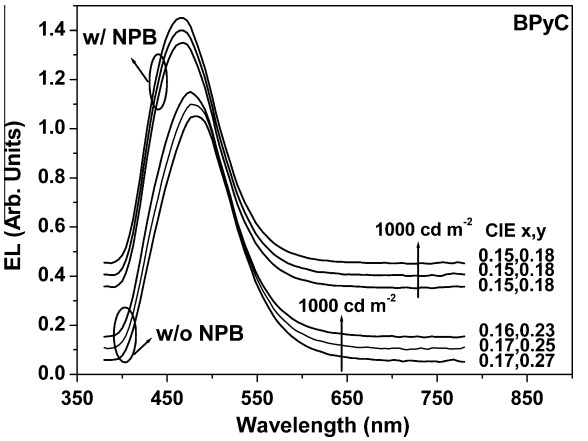

Fig. 2. Electroluminescence spectra of the BPyC-based OLEDs without (lower) and with (upper) NPB viewed in the normal direction at the luminance of 10, 100, and 1000 cd m^{-2}, respectively.

UPS was employed to measure the E_{HOMO} values of the carbazole derivatives, in which they are found to be 5.57 and 5.67 eV for BPyC and TPyC, respectively. By subtracting from the optical band gaps determined from long wavelength onsets of the absorption bands, E_{LUMO} are estimated to be 2.58 eV (for BPyC) and 2.71 eV (for TPyC). Table 1 summarizes the thermal and photophysical data of BPyC and TPyC.

3.3. Device characteristics

Devices with the structures of ITO/EML (100 nm)/TPBI (20 nm)/LiF (0.5 nm)/Al (100 nm) (w/o NPB) and ITO/NPB (70 nm)/EML (30 nm)/TPBI (20 nm)/LiF (0.5 nm)/Al (100 nm) (w/NPB) were fabricated to evaluate the properties of BPyC or TPyC as hole-transporting EML. Fig. 2 depicts EL spectra of the BPyC-based OLEDs with (upper) and without (lower) the NPB layer viewed in the normal direction at the luminance of 10, 100, and 1000 cd m^{-2}. Both devices exhibit similar pure blue emissions with mild change in CIE coordinates of (0.17, 0.25) (Device w/o NPB) and (0.15, 0.18) (Device w/NPB) over a wide range of luminance from 10 to 1000 cd m^{-2}. This suggests that the hole and electron recombination is well confined within the emissive BPyC layer. In addition, these undoped blue-emitting devices show high efficiencies (as shown in Fig. 3) and low operating voltages (as shown in Fig. 4) in which current and power efficiencies (η_C and η_P), and η_E and operating voltage at 20 mA cm^{-2} are 4.3 cd A^{-1}, 4.5 lm W^{-1}, 2.49%, and 3.7 V for device without NPB, and are 2.9 cd A^{-1}, 2.7 lm W^{-1}, 2.21%, and 3.5 V for device with NPB. After

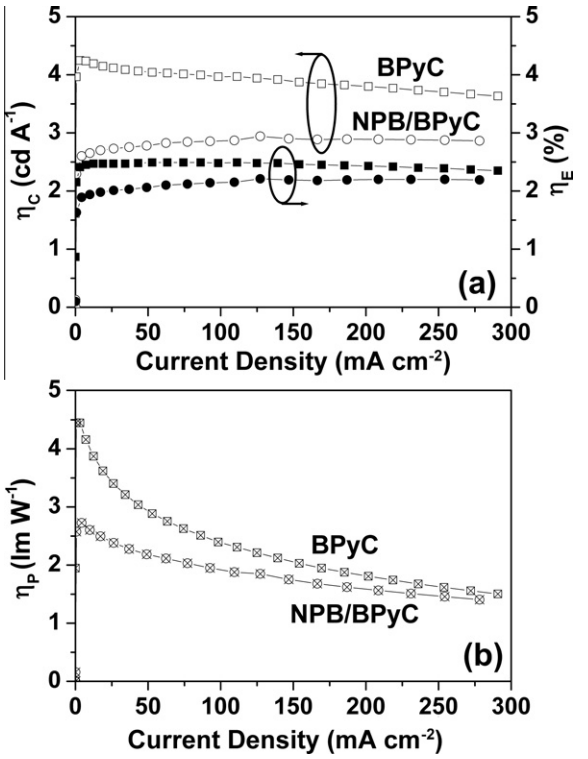

Fig. 3. (a) Current efficiency (η_C), external quantum efficiency (η_E) and (b) power efficiency (η_P) as a function of current density. Device configurations: ITO/BPyC (100 nm)/TPBI (20 nm)/LiF (0.5 nm)/Al (100 nm); ITO/NPB (70 nm)/BPyC (30 nm)/TPBI (20 nm)/LiF (0.5 nm)/Al (100 nm).

Table 1
Thermal and photophysical properties of BPyC and TPyC. T_d and T_m were determined by thermogravimetric analysis (TGA) and modulated differential scanning calorimetry (MDSC) measurements at a same heating rate of 10 °C min^{-1} under a nitrogen atmosphere whereas T_d corresponds to 5% weight loss. λ_{abs} and λ_{PL} were measured with solid thin-film. E_{opt} was estimated from the long wavelength onset of the absorption band. E_{HOMO} was defined by ultraviolet photoelectron spectroscopy (UPS) while E_{LUMO} was estimated by $E_{LUMO} = E_{HOMO} - E_{opt}$. Φ_{PL} was measured in solution.

Compound	T_m/T_d (°C)	$\lambda_{abs,\ max}$ (nm)	λ_{PL} (nm)	Stokes shift (nm)	$\lambda_{abs,\ onset}$ (nm)/E_{opt} (eV)	E_{HOMO}/E_{LUMO} (eV)	Φ_{PL} (%)
BPyC	293/496	358	443	85	415/2.99	5.57/2.58	94.8
TPyC	245/516	369	465	96	419/2.96	5.67/2.71	95.0

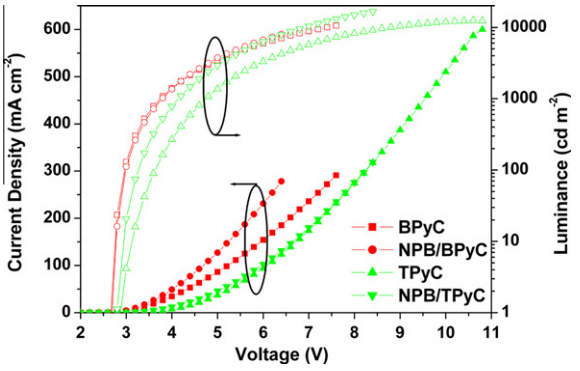

Fig. 4. Current density and luminance characteristics as a function of voltage in various devices. Device configurations: ITO/TPyC (100 nm)/TPBI (20 nm)/LiF (0.5 nm)/Al (100 nm); ITO/NPB (70 nm)/TPyC (30 nm)/TPBI (20 nm)/LiF (0.5 nm)/Al (100 nm); ITO/BPyC (100 nm)/TPBI (20 nm)/LiF (0.5 nm)/Al (100 nm); ITO/NPB (70 nm)/BPyC (30 nm)/TPBI (20 nm)/LiF (0.5 nm)/Al (100 nm).

insertion of NPB at the ITO/BPyC interface, the E_{HOMO} of NPB can function as a stepping-stone for hole-injection, similar to the case of ITO/m-MTDATA/NPB [17]. This improvement for hole-injection definitely reduces the driving voltage. It is believed that the amounts of hole and electron are balanced inside the device w/o NPB. However, the excess of holes in the device w/NPB eventually reduces the device efficiency. Nevertheless, these relatively high device efficiencies and low driving voltage are comparable or even better than current state-of-the-art undoped emitters with saturated blue fluorescence [18–20].

Unexpectedly, the extra pyrene arm in TPyC leads to large difference in EL properties. Fig. 5 depicts EL spectra of the TPyC-based OLEDs with (middle) and without (lower) NPB viewed in the normal direction at the luminance of 10, 100, and 1000 cd m^{-2}. In contrast with the PL spectrum of neat thin-film, both devices demonstrate two broad emission peaks at ca. 475 and 558 nm. The blue emission peak at 475 nm is contributed from the TPyC emission,

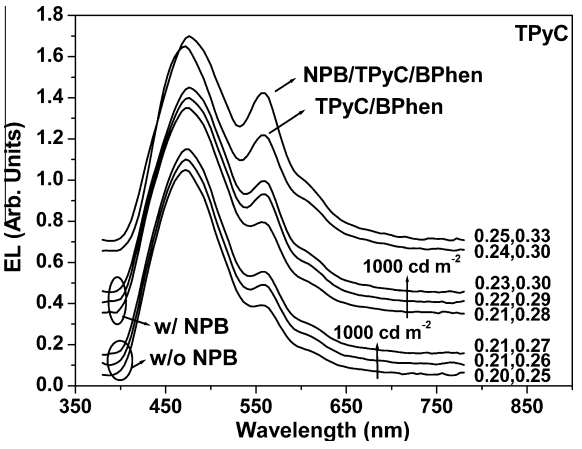

Fig. 5. Electroluminescence spectra of the TPyC-based OLEDs without (lower) and with (middle) NPB viewed in the normal direction at the luminance of 10, 100, and 1000 cd m^{-2}, respectively. Electroluminescence spectra for devices with the structures of ITO/TPyC/BPhen/LiF/Al and ITO/NPB/TPyC/BPhen/LiF/Al (upper) are also inserted.

whereas the red-shifted band centered at 558 nm appears to be arising from the exciplex emission formed at the TPyC/TPBI interface. This can be confirmed with the PL spectrum of the TPBI:TPyC blended film as shown in the inset of Fig. 1. It is considered that coupling between the strong electron-donating TPyC and the strong electron-accepting TPBI results in exciplex emission at their interface. Combining with the intrinsic blue emission at 475 nm, near white light emission with CIE coordinates of (0.21, 0.26) and (0.22, 0.29) were obtained for the devices without and with the NPB layer, respectively. In fact, the CIE coordinates change even closer to white emission of (0.24, 0.30) and (0.25, 0.33) when the ETL (i.e., TPBI) is replaced by BPhen (as shown in the two top-most spectra of Fig. 5).

Fig. 6 demonstrates efficiencies of the TPyC-based devices as a function of current density. With the insertion of NPB layer, η_C, η_P, and η_E dramatically increase to 6.4 cd A^{-1}, 5.3 lm W^{-1}, and 3.11%, respectively, much higher than those of device without the NPB layer (3.8 cd A^{-1}, 3.3 lm W^{-1}, and 2.01%). More importantly, the η_E of TPyC-based device is considerably higher than that of our previously reported triphenylamine TPyPA-based device (η_E = 2.83%) with the same device configuration. One possible explanation for this difference is that the Φ_{PL} of TPyC (95%) is much higher than that of TPyPA (80%). It should be noted that as Φ_{PL} of both TPyC and TPyPA materials are very high in solution, various solid-state quenching effects could be much more important than the yields in solution. The exact solid-state quenching effects in both

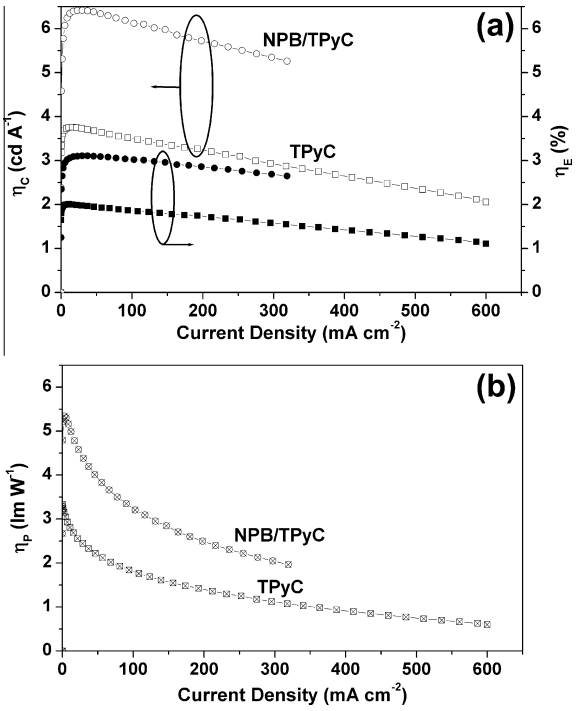

Fig. 6. (a) Current efficiency (η_C), external quantum efficiency (η_E) and (b) power efficiency (η_P) as a function of current density. Device configurations: ITO/TPyC (100 nm)/TPBI (20 nm)/LiF (0.5 nm)/Al (100 nm); ITO/NPB (70 nm)/TPyC (30 nm)/TPBI (20 nm)/LiF (0.5 nm)/Al (100 nm).

Table 2
Electroluminescence performance of BPyC and TPyC-based devices. Device configurations: ITO/BPyC (100 nm)/TPBI (20 nm)/LiF (0.5 nm)/Al (100 nm); ITO/NPB (70 nm)/BPyC (30 nm)/TPBI (20 nm)/LiF (0.5 nm)/Al (100 nm); ITO/TPyC (100 nm)/TPBI (20 nm)/LiF (0.5 nm)/Al (100 nm); ITO/NPB (70 nm)/TPyC (30 nm)/TPBI (20 nm)/LiF (0.5 nm)/Al (100 nm).

Device	$V_{turn\text{-}on}$ (V)	V at 20 mA cm^{-2} (V)	η_C (cd A^{-1})	η_P (lm W^{-1})	η_E (%)	CIE (x, y)
BPyC	2.7	3.65	4.25	4.45	2.49	0.17, 0.25
NPB/BPyC	2.7	3.48	2.94	2.72	2.21	0.15, 0.18
TPyC	2.9	4.58	3.76	3.34	2.01	0.21, 0.26
NPB/TPyC	2.8	4.34	6.42	5.34	3.11	0.22, 0.29

thin-films are now under investigation. Nevertheless, the discrepancy of Φ_{PL} on the device performance is in consistent with our previous study [8] and underscores the importance of high Φ_{PL} in organic materials for achieving highly efficient exciplex-based OLEDs. Characteristics of all BPyC- and TPyC-based devices are summarized in Table 2.

It is interesting to note that, in our previous study, the use of a better ETL (i.e., BPhen) would effectively increase the intensity of exciplex emission and, in turns, results in a better balanced white emission. In particular, the CIE coordinates change from (0.18, 0.25) for devices with TPBI as ETL to (0.31, 0.35) for the BPhen-based TPyPA device. In addition, the replacement of BPhen results in a high η_E of 3.93%, much higher than that of the TPBI-based device (2.83%). These enhancements have been attributed to the different carrier mobility of BPhen and TPBI. Indeed, the intensity of exciplex emission is determined by the charge accumulation densities, which in turns depends on the relative hole mobility and electron mobility in HTL and ETL. In particular, the use of ETL with higher electron mobility would lead to higher exciplex emission intensity. As the electron mobility in TPBI is two orders of magnitude lower than that in BPhen, the relatively small electron mobility in TPBI would inevitably reduce the number of electron–hole pairs formed for exciplex emission, and in turns leads to a weak exciplex emission. However, it is not the case in our present study, in which there is only a mild shift on the CIE coordinates from (0.22, 0.29) to (0.25, 0.33) and a small increase on η_E from 3.11% to 3.16% when the ETL is replaced by BPhen. Such minor device performance improvement for the TPyC-based devices may be ascribed by the lower mobility in TPyC than that in TPyPA. Particularly, it is expected that the hole mobility of TPyC is much lower than that of TPyPA, and thus the use of better electron-transporting materials, e.g., BPhen, would not result in a dramatic increase on the interfacial charge accumulation density at the HTL/ETL interface. It is also the reason for the larger driving voltage for the TPyC-based devices. For instance, to generate a current density of 20 mA cm^{-2}, the driving voltages of the TPyC-based device with TPBI or BPhen as ETL are 4.34 and 3.76 V, respectively, while those of the TPyPA-based device with TPBI or BPhen as ETL are 3.60 and 3.31 V, respectively [8].

4. Conclusions

We have designed and synthesized two carbazole–pyrene based fluorophores, namely BPyC and TPyC, to investigate how chemical structures of organic materials affecting exciplex emission. By employing the carbazole derivatives as emitters in contact with the electron-transporting TPBI, both devices exhibit distinct EL properties. Particularly, the TPyC-based devices display two emission peaks with CIE coordinates of (0.22, 0.29); while the BPyC-based devices show a single blue emission peak with CIE coordinates of (0.15, 0.18). More importantly, a relatively high η_E of 3.11% can be obtained for the TPyC-based device. This discrepancy on the device performance is attributed to the substitution of *t*-butyl unit of BPyC with a pyrenyl group, resulting in an increase on the degree of electron-donating property and hence the presence of exciplex emission at the HTL/ETL heterojunction.

Acknowledgments

This work was supported by the Research Grants Council of the Hong Kong Special Administrative Region, China (Project No. CityU 101508). Q.X. Tong thanks his financial supports from the National Science Foundation of China (No. 91027041) and the Key Laboratory of Photochemical Conversion and Optoelectronic Materials, TIPC, CAS.

References

[1] S. Reineke, F. Lindner, G. Schwartz, N. Seidler, K. Walzer, B. Lüssem, K. Leo, Nature (London) 459 (2009) 234.
[2] M.H. Ho, S.F. Hsu, J.W. Ma, S.W. Hwang, P.C. Yeh, C.H. Chen, Appl. Phys. Lett. 91 (2007) 113518.
[3] S. Chen, Z. Wu, Y. Zhao, C. Li, J. Hou, S. Liu, Org. Electron. 6 (2005) 111.
[4] C. Giebeler, H. Antoniadis, D.D.C. Bradley, Y. Shirota, J. Appl. Phys. 85 (1999) 608.
[5] K. Okumoto, Y. Shirota, J. Lumin. 87 (2000) 1171.
[6] Y. Kawabe, J. Abe, Appl. Phys. Lett. 81 (2002) 493.
[7] L.C. Palilis, A.J. Mäkinen, M. Uchida, Z.H. Kafafi, Appl. Phys. Lett. 82 (2003) 2209.
[8] S.L. Lai, M.Y. Chan, Q.X. Tong, M.K. Fung, P.F. Wang, C.S. Lee, S.T. Lee, Appl. Phys. Lett. 93 (2008) 143301.
[9] J. Thompson, R.I.R. Blyth, M. Mazzeo, M. Anni, G. Gigli, R. Cingolani, Appl. Phys. Lett. 79 (2001) 560.
[10] G. Li, C.H. Kim, Z. Zhou, J. Shinar, K. Okumoto, Y. Shirota, Appl. Phys. Lett. 88 (2006) 253505.
[11] R.D. Fossum, M.A. Fox, J. Phys. Chem. B 101 (1997) 6384.
[12] S.L. Lin, L.H. Chan, R.H. Lee, M.Y. Yen, W.J. Kuo, C.T. Chen, R.J. Jeng, Adv. Mater. (Weinheim, Ger.) 20 (2008) 3947.
[13] J.N. Demas, G.A. Crosby, J. Phys. Chem. 75 (1971) 991.
[14] J.F. Ambrose, L.L. Carpenter, R.F. Nelson, J. Electrochem. Soc. 122 (1975) 876.
[15] G.L. Feng, S.J. Ji, W.Y. Lai, W. Huang, Synlett 17 (2006) 2841.
[16] N. Miyaura, A. Suzuki, Chem. Rev. 95 (1995) 2457.
[17] Y. Shirota, Y. Kuwabara, H. Inada, T. Wakimoto, H. Nakada, Y. Yonemoto, S. Kawami, K. Imai, Appl. Phys. Lett. 65 (1994) 807.
[18] S. Tao, Z. Peng, X. Zhang, P. Wang, C.S. Lee, S.T. Lee, Adv. Funct. Mater. 15 (2005) 1716.
[19] W.J. Shen, R. Dodda, C.C. Wu, F.I. Wu, T.H. Liu, H.H. Chen, C.H. Chen, C.F. Shu, Chem. Mater. 16 (2004) 930.
[20] K.C. Wu, P.J. Ku, C.S. Lin, H.T. Shih, F.I. Wu, M.J. Huang, J.J. Lin, I.C. Chen, C.H. Cheng, Adv. Funct. Mater. 18 (2008) 67.

Organic Electronics 12 (2011) 547–555

Contents lists available at ScienceDirect

Organic Electronics

journal homepage: www.elsevier.com/locate/orgel

White organic light-emitting devices with ultra-high color stability over wide luminance range

Chih-Hung Hsiao [a], Yi-Hsin Lan [a], Pei-Yu Lee [b], Tien-Lung Chiu [b], Jiun-Haw Lee [a,*]

[a] Graduate Institute of Photonics and Optoelectronics, and Department of Electrical Engineering, National Taiwan University, No. 1, Sec. 4, Roosevelt Road, Taipei, Taiwan, ROC
[b] Department of Photonics Engineering, Yuan Ze University, Taiwan, ROC

ARTICLE INFO

Article history:
Received 18 July 2010
Received in revised form 28 December 2010
Accepted 31 December 2010
Available online 15 January 2011

Keywords:
White organic light-emitting devices
Color stability
Selectively doped profile

ABSTRACT

A white organic light-emitting device (WOLED) with ultra-high color stability was achieved by introducing an appropriate emitting layer (EML) structure with a spacer, and engineering a blue EML (B-EML) with a selectively doped profile. The advantage of the selectively doped profile over the conventional, uniformly doped profile was to minimize direct exciton formation on dopants with lower exciton energies to suppress electroluminescence (EL) spectrum variations. The recombination zone was found to be located at the spacer/B-EML interface, with a width of 4.5 nm. With the selectively doped profile, the WOLED exhibited ultra-high color stability, with the CIE coordinates shifting from (0.399, 0.483) to (0.395, 0.479) as the luminance increased from 145 to 12,100 cd/m^2 and from (0.401, 0.481) to (0.400, 0.479) as the luminance increased from 1240 to 4850 cd/m^2, the practical luminance range for display and lighting applications. In addition to the small CIE coordinates variation of (−0.004, −0.004) over the broad luminance range of about two orders of magnitude, we also achieved a high device efficiency of 34.1 cd/A, which stayed larger than 30 cd/A below 2000 cd/m^2.

© 2011 Elsevier B.V. All rights reserved.

1. Introduction

Owing to almost three decades of development, the power efficiency of organic light-emitting devices (OLEDs) has leapfrogged to several lm/W for monochromatic emission and over one hundred lm/W for white emission [1–5]. In addition to the marked improvement in the efficiency, which is obviously an important breakthrough as well as a prerequisite for practical applications, another issue concerning the user experience has been attracting attention, namely the color performance. For a monochromatic OLED, its color performance under different driving conditions is of less concern since only one kind of emitting sites is responsible for the emission. However, for a broadband white OLED (WOLED), its color performance, as quantified by factors such as the Commission Internaionale de l'Eclairage (CIE) coordinates and color rendering index (CRI), is of utmost importance because typically more than two different types of emitting sites are involved in the light generation. In this case, different dopants can conceivably compete with one another under different driving conditions due to differences in the exciton energy and shifts in the recombination zone [6–11]. As a result, the color performance will vary with different driving conditions, luminance levels and degrees of device degradation. This phenomenon inevitably presents additional difficulties for lighting applications and down-conversion displays with backlight units of WOLED and color filters. For lighting applications, CIE coordinates variation during operation will distort the color of the illuminated object. For down-conversion displays, the panel will suffer from distortions of the pixel emitting color and non-uniform color distribution over the panel under the same driving conditions. Therefore, for the sake of competitiveness in the

* Corresponding author. Tel.: +886 2 3366 3650; fax: +886 2 2367 7467.
E-mail address: jhlee@cc.ee.ntu.edu.tw (J.-H. Lee).

1566-1199/$ - see front matter © 2011 Elsevier B.V. All rights reserved.
doi:10.1016/j.orgel.2010.12.019

Table 1
Device structures of the OLED. R, G, and B are representatives of $Ir(phq)_3$, $Ir(ppy)_3$, and FIrpic, respectively. The unit for layer thickness is nm.

Device	NPB	G:mCP	mCP			B:mCP				BPhen
A1		30				18				
		RG:mCP				B:mCP				
A2	50	30	4.5			18				30
		RG:mCP				RB:mCP				
A3		30				18				
Device	NPB	G:mCP	mCP							BPhen
P1				RB:mCP (4.5)			B:mCP (13.5)			
P2	50	30	4.5	B:mCP (4.5)	RB:mCP (4.5)		B:mCP (9)			30
P3				B:mCP (9)			RB:mCP (4.5)		B:mCP (4.5)	
P4					B:mCP (13.5)				RB:mCP (4.5)	
Device	NPB	RG:mCP	mCP							BPhen
B1					B:mCP (13.5)				RB:mCP (4.5)	
B2	50	30	4.5	B:mCP (9)			RB:mCP (9)			30
B3				B:mCP (4.5)			RB:mCP (13.5)			
Device	NPB	G:mCP	mCP	B:mCP	RB:mCP					BPhen
C1						13.5				30
C2	50	30	4.5	4.5		18				40
C3										50

R = $Ir(phq)_3$; G = $Ir(ppy)_3$; B = FIrpic; RB:mCP = 0.5% R:9% B:mCP; RG:mCP = 0.5% R:9% G:mCP; B:mCP = 9% B:mCP; G:mCP = 9% G:mCP.

market, WOLED must be developed with high color stability, on top of high efficiency.

To suppress the CIE coordinates variation, the use of a single dopant to generate broadband emission for white light through bimolecular interactions holds promise as a viable solution, due to the absence of competition among the different kinds of dopants [12,13]. However, the difficulty lies in finding such organic materials. In contrast, stacking different EMLs or mixing different dopants in the same EML to yield white EML is a simpler way to generate white emission and obtain efficient devices. Direct stacking without introducing additional functional organic layers usually leads to electroluminescent (EL) spectral variations due to differences in the electric field dependence of carrier mobilities in different EMLs and saturation of the emitting sites as the injected carriers increase in number [6,7,10,14,15]. This directly stacked EML structure also results in lower efficiency as compared to its reference monochromatic OLED, since exciton competition will obviously arise due to the different exciton energies of the different emitting dopants. To ease the energy difference induced exciton competition, position control methods by which the recombination zone is deliberately allocated in the appropriate region have been suggested [4,16–24]. The crux of the approach is that excitons with lower energies are fed via energy transfer or diffusion from regions with high energies. Since the energy transfer is nearly independent of the carrier and exciton concentration, the EL spectrum is also independent of the driving conditions and luminance level. In this paper, we demonstrate how a spacer and a selective doping method were applied to achieve an ultra-high color stability WOLED, which exhibited a rather slight CIE coordinates variation of $(-0.004, -0.004)$ from 145 to 12,100 cd/m^2. Within the luminance range of lighting or backlight applications, this WOLED exhibited a negligible CIE coordinates variation of $(-0.001, -0.002)$ from 1240 to 4850 cd/m^2. This optimal WOLED further achieved peak efficiencies of 34.1 cd/A and 26 lm/W.

2. Experiments

The OLED fabrication and encapsulation followed similar procedures as outlined in our previous studies [24]. In our carrier transporting system, *N*,*N*′-diphenyl-*N*,*N*′-bis(1-napthyl)-1,1′-biphenyl-4,4′-diamine (NPB) was used as a hole-transporting layer (HTL) and 4,7-diphenyl-1,10-phenanthroline (BPhen) as an electron-transporting layer (ETL) beneath a LiF/Al cathode. An EML sandwiched between the HTL and ETL consisted of red-emitting tris(2-phenyl-1-quinoline)iridium(III) ($Ir(phq)_3$) [25], green-emitting tris(phenylpyridine)iridium ($Ir(ppy)_3$) and blue-emitting [(4,6-di-fluoropheny)-pyridinato-*N*,$C^{2'}$]picolinate (FIrpic), which were doped in the same host of *N*,*N*′-dicarbazolyl-3,5-benzene (mCP). The device structures under investigation were listed in Table 1. The current density–voltage (*J*–*V*) characteristics and EL spectrum were measured and recorded by a testing setup comprising of a Keithley 2400 source-meter and a Minolta CS-1000 spectrometer.

3. Results and discussions

3.1. Uniformly doped profile in EML

Although devices with thinner EML structures exhibited improved power efficiencies [22], the efficiencies of these devices nonetheless dropped rapidly at higher luminance levels due to more severe triplet–triplet annihilation (TTA) [23]. Therefore, thicker EML structures were proposed for high luminance applications as investigated in this study [24]. By deliberately manipulating the exciton distribution and energy transfer, we arrived at a backbone EML structure of 9% $Ir(ppy)_3$:mCP (30 nm) (G-EML)/mCP (4.5 nm)/9% FIrpic:mCP (18 nm) (B-EML) which exhibited a high color stability, with the adoption of an appropriate layer thickness to suppress the sensitivity of the electric field dependent carrier injection and transport [24].

A WOLED following this EML structure could be implemented by doping red-emitting molecules such as Ir(phq)$_3$. Naturally, the next question to be addressed is where to dope the red dopants in order to inherit the high color stability of the OLED with the backbone of G + B EML. In previous study [24], the Ir(phq)$_3$ was uniformly doped in the G-EML. To lessen the effect on the performance of the backbone EML, the Ir(phq)$_3$ was lightly doped to avoid obvious exciton catching events by this low-energy dopant, instead of the desired Ir(ppy)$_3$. Excitons caught by the Ir(phq)$_3$ would result in lower color stability, since a saturation of the emitting sites with an increase in the number of injected carriers would occur and alter the exciton relaxation paths.In addition to the G-EML, the Ir(phq)$_3$ could be also doped in the B-EML. However, doping the low-energy molecules in the main recombination zone (e.g. B-EML) will increase the probability of direct exciton formation on the Ir(phq)$_3$, thereby compounding the drawback of large EL spectrum variation. A device with the backbone of G + B EML was referred as to Device A1 as listed in Table 1. Devices with 0.5% Ir(phq)$_3$ doped throughout the G-EML and both the G- and B-EML were labeled as Devices A2 and A3, respectively. Fig. 1(a) shows the *J*–*V* and external quantum efficiency (EQE) versus *J* characteristics of Devices A1–A3. These three devices exhibited similar *J*–*V* characteristics, suggesting that the low concentration of Ir(phq)$_3$ had little impact on the electrical properties. On the other hand, with the introduction of the high-efficiency red dopants, the EQE were improved in Devices A2 and A3. The EQE of A3 was higher than that of A2 because the emission efficiency of the FIrpic is lower than that of the Ir(ppy)$_3$ [10,26]. Fig. 1(b)–(d) shows the spectra under different driving voltages for Devices A1, A2, and A3, respectively. It should be noted that the spectra were very stable in Devices A1 and A2 although there was a small increase in the red emission with increasing voltage for Device A2. In Device A3, the red emission was stronger than the green and blue emission, because the red dopants were doped in the main recombination zone. Contrary to the case of Device A2, the spectral variation was obvious, and the blue and green emission increased with increasing driving voltage in Device A3. Since the CIE is a measure of both the EL spectrum and human eye sensitivity, a more straightforward parameter is required to quantify the differences in the EL spectra without taking into consideration the human eye sensitivity. For this purpose, we have defined an EL spectrum area variation ratio (Ψ) as $\frac{\sum |P_{H(\lambda)} - P_{L(\lambda)}|}{\sum P_{L(\lambda)}}$, where $P_{H(L)}(\lambda)$ is the power distribution of the EL spectrum, normalized to its total radiation power and driven by a higher (lower) applied voltage. The newly defined Ψ without involving the human eye sensitivity will likely provide a more precise indicator for determining what really transpires in a high color stability OLED.

The electrical and optical performances of Devices A1–A3 were summarized in Table 2. Here, $P_L(\lambda)$ was chosen to be the EL spectrum at 4.5 V as a common reference level for Devices A1–A3 since these devices exhibited similar

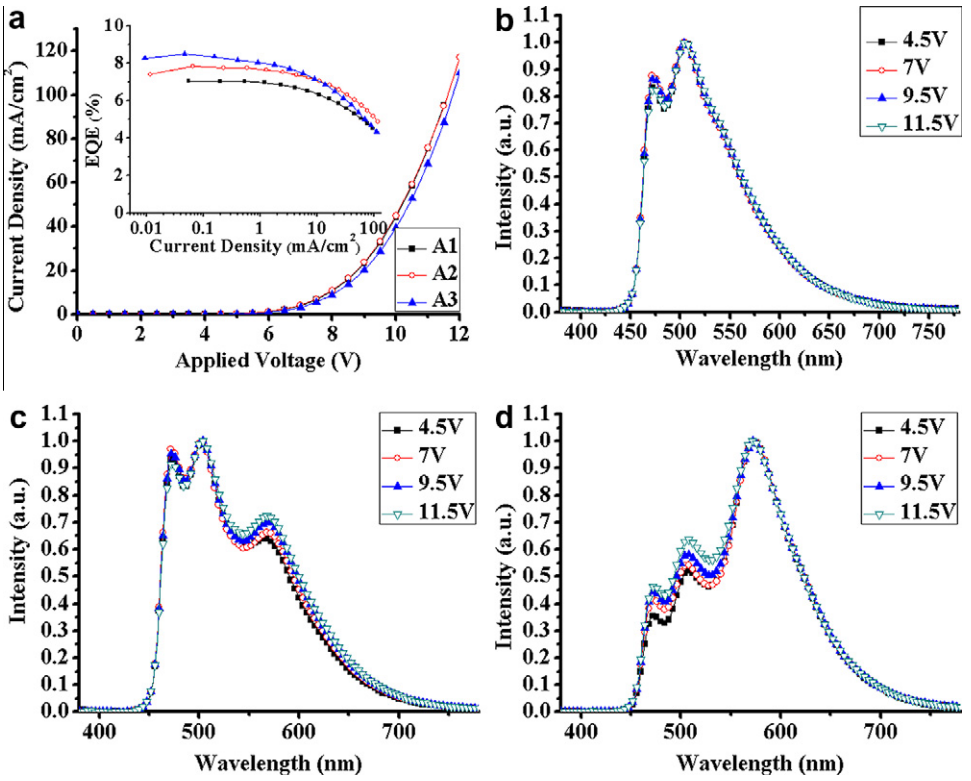

Fig. 1. *J*–*V* characteristics (a) and EQE (Inset in (a)) of Devices A1–A3, and EL spectra of Devices A1(b), A2(c), and A3(d) under applied voltage of 4.5, 7, 9.5, and 11.5 V. Emissions around 470, 520, 575 nm were generated by FIrpic, Ir(ppy)$_3$, Ir(phq)$_3$, respectively.

electrical characteristics (driving voltage variation within 0.5 V at 100 mA/cm^2, as can be seen from Fig. 1(a)). This suggested that light red dopant concentration did not dramatically alter the carrier transporting properties regardless of the regions doped.

Within the range from 4.5 to 11.5 V, the maximum Ψ values were 2.8%, 7.12%, and 8.96% for Devices A1, A2, and A3, respectively. The stable EL spectrum for Device A1 was ascribed to its mCP spacer and the low sensitivity of the electric field to carrier injection and transport [24]. For Device A3, doping Ir(phq)$_3$ in the entire B-EML further raised the Ψ value since the location of the main recombination zone within the B-EML made the saturation-induced EL spectrum variation more significant.

For extracting information on exciton behaviors in the different EMLs, the spectra of the WOLEDs were decomposed into their red (R, Ir(phq)$_3$), green (G, Ir(ppy)$_3$) and blue (B, FIrpic) emission components, respectively, as shown in Table 3 [24]. The different variations of the emission components in the EL spectra at different driving voltages for Devices A2 and A3 suggested that the EL spectral shifts were dominated by different mechanisms. For Device A2, as the applied voltage was increased from 4.5 to 11.5 V, the R component increased from 20.46% to 23.92%, while the B component decreased from 52.84% to 49.45%. The growth of the R component was likely due to the extension of the minor recombination zone, which could in turn be attributed to electron leakage out of the B-EML. On the other hand, the reduction of the B component could result from typical TTA in the B-EML, by which the FIrpic excitons in the main recombination zone were quenched. For Device A3 with the Ir(phq)$_3$-doped B-EML, the composition variation was reversed. In this case, the R component decreased from 55.27% to 48.80%, while the B component increased from 23.02% to 27.71%. In the main recombination zone, the Ir(phq)$_3$, with lower exciton energy than the FIrpic, made itself a preferred exciton formation site in the B-EML. As the number of injected carrier increased, the low concentration of Ir(phq)$_3$ was unable to provide sufficient exciton formation sites, and became saturated. Once the increasing number of carriers exceeded this saturation level, the number of excitons formed and released from the higher energy FIrpic would increase. Accordingly, the compositional variation in the EL spectra for Device A3 was a function of the degree of saturation of the Ir(phq)$_3$ molecules.

3.2. Selectively doped profile in EML

For Device A3, doping Ir(phq)$_3$ in the entire B-EML further raised the Ψ value since the main recombination zone was located in the B-EML. In order to increase the color stability, the selective doping method could be applied to modify this R:B-EML [16,21]. The prerequisite for applying the selective doping method was to ascertain the location of the maximum recombination zone.

Therefore, the P-series devices listed in Table 1 were designed to investigate the location of the recombination zone. By analyzing the EL spectra, it was possible to understand the exciton formation and diffusion characteristics [27–29]. Fig. 2 showed the red and green percentage and EL spectrum area variation ratio (Ψ) of the four devices (P1–P4). The green component was nearly the same, so the (blue + red) component was also nearly constant. Red component was highest at P1, with red dopant within 4.5 nm from the spacer/B-EML interface. And it decreased and then reached another local maximum within 4.5 nm from the B-EML/ETL interface. The Ψ value was very high for P1 device, which was due to serious carrier trapping of red dopant at the main recombination zone. Then it reached minimum at P2 and slightly increased toward P4. Although the red component in P4 was 8.8%, which was only slightly lower than that in P1 (11.7%), the Ψ value was greatly reduced from 19.79% (P1) to 5.79% (P4). Because the exciton lifetime in phosphorescent OLED was typically long, excitons might diffuse to the B-EML/ETL interface and be blocked (and partially quenched) by BPhen. When red dopants were inserted at this interface, energy would be transferred to red emitters for stable light emission, with significant reduction of Ψ value compared with P1. We can also note that green emission in P4 was slightly lower than P1–P3. Actually, it came from the stronger red emission near B-EML/ETL interface, which was transferred from blue emission. It provided another radiative pathway for light emission and decreased the BPhen quenching. Hence, the (red + blue) components increased, and the green percentage decreased. From discussion above, the major recombination zone should be located was within 4.5 nm from the spacer/B-EML interface, which resulted in a strong red emission, accompanying large spectral variation with different driving voltages in Device P1.

In the B-series devices shown in Table 1, the 0.5% Ir(phq)$_3$:mCP EML (R:B-EML) extended from the BPhen ETL. As long as this doped region extended toward and encompassed the recombination zone, an increasingly red emission would be observed [29]. In addition, a distinct EL variation with voltage would be observed [21]. As can be seen in Fig. 3, the red emission component from the Ir(phq)$_3$ in the EL spectrum increased as the selectively doped Ir(phq)$_3$ region extended to the spacer/B-EML

Table 2
Performances of Devices A1–A3.

Device	[a]Driving voltage (V)	Max. efficiency			CIE coordinate		Max. Ψ (%)
		lm/W	cd/A	EQE (%)	[b]Low luminance	[c]High luminance	
A1	11.6	17.4	24.9	7.05	(0.259, 0.468) (13.5 cd/m^2)	(0.259, 0.468) (15,200 cd/m^2)	2.80
A2	11.31	19.8	26.4	7.82	(0.305, 0.447) (16.9 cd/m^2)	(0.321, 0.451) (16,600 cd/m^2)	7.12
A3	11.77	22	28.7	8.50	(0.423, 0.476) (13.2 cd/m^2)	(0.404, 0.475) (13,700 cd/m^2)	8.96

Measurement conditions: [a]100 mA/cm^2; [b]4.5 V; [c]11.5 V.

Table 3
$Ir(phq)_3$ (R), $Ir(ppy)_3$ (G), and FIrpic (B) emission percentages of the EL spectra at 4.5 and 11.5 V.

Device	Driving voltage (V)	R (%)	G (%)	B (%)
A1	4.5		39.40	60.60
	11.5		39.86	60.14
A2	4.5	20.46	26.70	52.84
	11.5	23.92	26.63	49.45
A3	4.5	55.27	21.71	23.02
	11.5	48.80	23.49	27.71
B1	4.5	28.57	23.98	47.45
	11.5	31.53	24.63	43.84
B2	4.5	33.17	24.04	42.79
	11.5	34.93	23.92	41.15
B3	4.5	43.41	21.98	34.61
	11.5	44.13	22.35	33.52

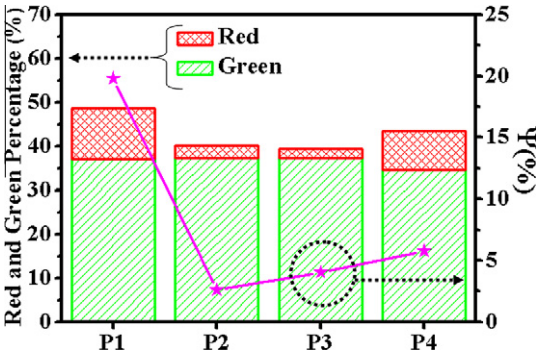

Fig. 2. Red and green percentage and EL spectra variations (Ψ values) of devices P1–P4. (For interpretation of the references to color in this figure legend, the reader is referred to the web version of this article.)

interface from the ETL. Therefore, this suggested that the recombination zone was located primarily at the spacer/B-EML interface. It also illustrated that the FIrpic molecules (2.9 eV), with similar LUMO to the BPhen (3.1 eV), could provide an electron injection pathway at the B-EML/BPhen interface to avoid electron accumulation and thus carrier recombination at this interface.

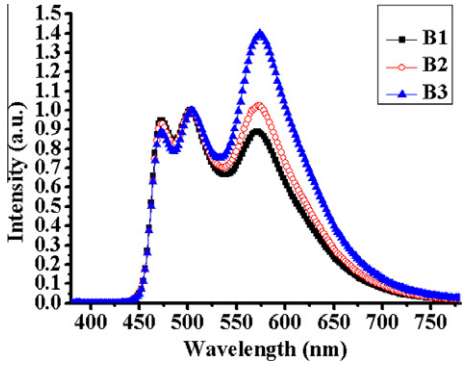

Fig. 3. EL spectra, measured at an injected current density of 2.5 mA/cm^2 and normalized to the green emission peak at 520 nm, of Devices B1–B3. (For interpretation of the references to color in this figure legend, the reader is referred to the web version of this article.)

As shown in Fig. 4(a), Devices B1–B3 exhibited similar electrical characteristics (with driving voltage variation within 0.5 V at 100 mA/cm^2), suggesting that the $Ir(phq)_3$ had little effect on the carrier transporting properties in the B-EML. The EQE values of B1, B2, B3, and A3 were similar because of the presence of the efficient red dopants. Fig. 4(b)–(d) illustrates the behaviors of EL spectrum variations under different voltages for the B-series devices, from which Ψ could be calculated. Under similar driving conditions, from 4.5 to 11.5 V, as listed in Table 4, the maximum Ψ values for Devices B1, B2, and B3 were 5.57%, 4.02% and 3.77%, respectively, all below that of Device A3 (Ψ: 8.96%) with a conventional, uniformly doped R:B-EML. In the B-series devices, the $Ir(phq)_3$ in the B-EML was located some distance away from the spacer/B-EML interface. In this regard, the emitting site saturation of the $Ir(phq)_3$ in the B-EML was automatically averted since the excitons were formed on the mCP or FIrpic in the absence of the $Ir(phq)_3$, and part of the excitons were sequentially diffused out or transferred to the $Ir(phq)_3$ to complete the EL spectrum. Since the energy transfer is nearly independent of the driving voltage and number of injection carriers, the EL spectra was expected to be stable under different driving conditions, thereby leading to lower Ψ values for the B-series devices as compared to the reference Device A3. According to the high color stability (lower Ψ) of Device B3, we inferred that the recombination zone was within 4.5 nm from the spacer/B-EML interface.

For the composition variations of the B-series devices (shown in Table 3), their B components decreased as the applied voltage was increased. This phenomenon could be a result of typical TTA in phosphorescent devices such as Device A2. In addition, according to the different extents of B component reduction among the B-series devices, we could infer that the $Ir(phq)_3$-doped EML played an important role in the TTA process. Since TTA is related to the exciton lifetime and rate constant of the TTA process [30], the behaviors of the TTA in B-EML (9% Firpic:mCP), R:B-EML (0.5% $Ir(phq)_3$:9% FIrpic:mCP), and even different combinations of both B-EML and R:B-EML may be different. According to similar TTA behaviors indicated by small B composition reductions for Devices B2 (42.79–41.15%) and B3 (34.61–33.52%), we postulated that the R:B-EMLs in these two devices were within the energy transfer radius of the FIrpic dopants, which therefore led to similar influence on the TTA. In Device B1, with the red doped region situated away from the recombination zone, the influence of the $Ir(phq)_3$ on the TTA in the B-EML was relatively weak due to the absence of $Ir(phq)_3$ within the energy transfer radius of the FIrpic dopants, thereby leading to a larger B component reduction (47.45–43.84%). In Ref. [24], we found that the TTA affected the color stability in G + B OLED (e.g. Device A1). Here, we found that the different $Ir(phq)_3$-doped regions altered the color balance between the red and blue emission in the B-EML/R:B-EML. If the energy transfer from the FIrpic to $Ir(phq)_3$ were efficient, as in the cases with Devices B2 and B3, the exciton concentration of the FIrpic emitting sites would not be as high as that in Device B1, thus alleviating the TTA events of FIrpic excitons. However, for Device B1, the energy transfer from the FIrpic to $Ir(phq)_3$ was not efficient

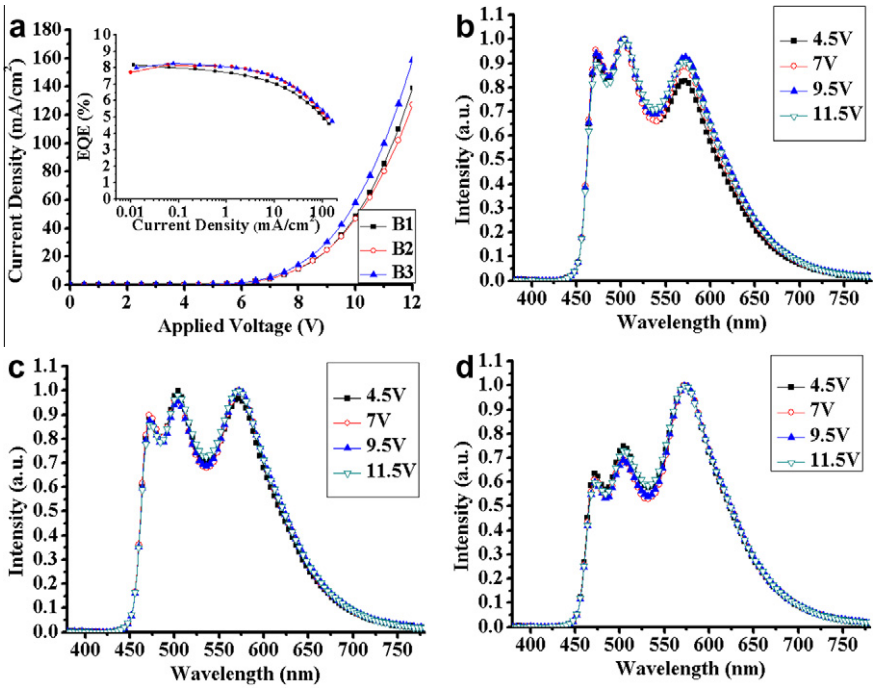

Fig. 4. *J–V* characteristics (a) and EQE (inset of (a)) of Devices B1–B3; EL spectrum variations of Devices B1(b), B2(c), and B3(d) from 4.5 to 11.5 V.

Table 4
Performances of Device B1–B3. Driving voltage was measured at current density of 100 mA/cm^2.

Device	Driving voltage (V)	Max. efficiency			CIE coordinate		Max. Ψ (%)
		lm/W	cd/A	EQE (%)	Low luminance	High luminance	
B1	11.3	21.4	27.5	8.15	(0.335, 0.449) (17.4 cd/m^2)	(0.346, 0.455) (18,700 cd/m^2)	5.57
B2	11.46	21.1	28.2	8.18	(0.353, 0.456) (17 cd/m^2)	(0.359, 0.459) (18,500 cd/m^2)	4.02
B3	11	22	28.7	8.24	(0.387, 0.461) (22.1 cd/m^2)	(0.390, 0.465) (22,500 cd/m^2)	3.77

(outside the energy transfer radius of the FIrpic) due to the large spacing between the recombination zone and R:B-EML. In this regard, the FIrpic dopants would be rapidly occupied by excitons and hence suffer from TTA at lower current densities, as can be seen from its EQE performance in the inset of Fig. 3(a). As compared with Device A2 with the absence of Ir(phq)$_3$ in B-EML, the B-series devices exhibited lower Ψ values since the presence of Ir(phq)$_3$ would prevent FIrpic excitons from being quenched by TTA. For the most color-stable Device B3, its CIE coordinates over the wide luminance range of 204–12,200 cd/m^2 varied from (0.389, 0.459) to (0.394, 0.462) with CIE coordinates variation of (0.005, 0.003). In addition, over the practical luminance range of 1430–5040 cd/m^2 for display and lighting applications, Device B3 exhibited a rather low CIE variation of (0.002, 0.001). Therefore, the replacement of a single R:B-EML by a two layer structure of B-EML/R:B-EML successfully led to satisfactory red emission and high color stability.

Before further optimization to achieve high efficiency and high color stability WOLED, the energy transfer paths of Device B3 with EML should be discussed. According to the previous study [24] and discussions above, the main recombination zone of Device B3 was located within the B-EML in the B-EML/R:B-EML region as indicated in Fig. 5, while a minor recombination zone was found in the R:G-EML. As illustrated in Fig. 5, excitons were first formed on mCP and FIrpic molecules in the B-EML, and subsequently on the Ir(ppy)$_3$ and Ir(phq)$_3$ molecules in the R:G-EML. The function of the spacer was to stabilize the emission ratio of B-EML to R:G-EML by interrupting the Dexter energy transfer of FIrpic to Ir(ppy)$_3$ and FIrpic to Ir(phq)$_3$, as indicated by the dashed lines in Fig. 5, in a way of separating the two different dopants in the spatial domain because Dexter energy transfer results from electronic orbital coupling. The Förster energy transfer ($D^{3*} + A^1 \rightarrow D^1 + A^{3*}$) path of the dashed lines were originally prohibited by spin conservation. A portion of the excitons on the mCP in the B-EML diffused out to either the R:G-EML or R:B-EML due to the relatively higher triplet exciton concentration in the main recombination zone. Therefore, in the R:G-EML, the Ir(phq)$_3$ emission was attributed to either direct exciton formation or energy transfer from higher energy molecules. In contrast, in the EML of the B-EML/R:B-EML, the Ir(phq)$_3$ emission originated purely from the energy transfer from the mCP and

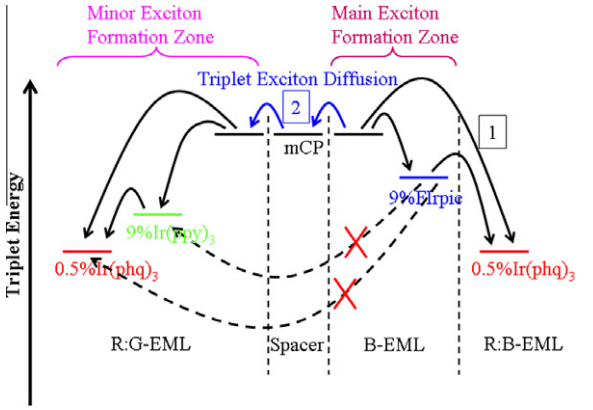

Fig. 5. Energy transfer diagram of molecules in R:G-EML/spacer/B-EML/R:B-EML structure. Main exciton formation zone was within B-EML while minor recombination zone was within R:G-EML and close to the spacer interface. Solid (dashed) lines indicate allowed (forbidden) energy transfer paths.

FIrpic in the B-EML. Since the $Ir(phq)_3$ in the R:B-EML were not located in the main recombination zone, direct exciton formation on the $Ir(phq)_3$ was technically prohibited. This absence of direct exciton formation on the $Ir(phq)_3$ in the B-EML resulted in the stable EL spectra in our WOLED devices.

Analysis of Devices A2, A3, B1, B2, and B3 revealed the role of the $Ir(phq)_3$ molecules in the B-EML. As shown in Fig. 6, Ψ decreased as the R:B-EML extended from the BPhen ETL until the red dopants were fully doped in the B-EML, as was the case with Device A3. In Device A2, the EL variation was attributed to the extension of the recombination zone toward the R:G-EML and TTA in the B-EML. For Device A3 with the single R:B-EML, the higher Ψ value arose from the saturation of the red emitters. Among the B-series devices, the competition between paths 1 and 2 in Fig. 5 led to lower Ψ values than that in Device A2.

Increasing the efficiency of the energy transfer via path 1 decreased the exciton diffusion toward the R:G-EML via path 2. In this regard, the main contributor to the exciton source supplying the R:G-EML was the recombination zone

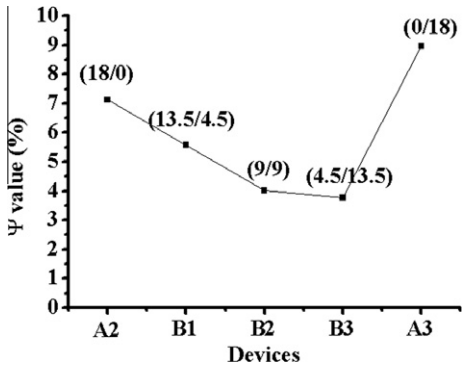

Fig. 6. EL spectra variations (Ψ values) of Devices A2, A3, B1, B2, and B3. Different EML structures between the spacer and BPhen ETL were indicated in parentheses as (B-EML thickness/R:B-EML thickness).

extension. For instance, the larger number of mCP excitons transferred to the $Ir(phq)_3$ in Devices B2 and B3 than that in Device B1 due to the closer spacing between the R:B-EML and recombination zone suppressed the mCP exciton diffusion via path 2, thereby lowering Ψ values as compared with Devices B1 and even A2.

3.3. Optimization of WOLED

As can be seen in Fig. 4(d), the 0.5% $Ir(phq)_3$-doped B-EML enabled significant red emission. Therefore, red-emitting $Ir(phq)_3$ in the R:G-EML (e.g. the B-series devices) could be removed (e.g. Device C1) to further simplify the device fabrication. Based on Device C1, the thickness of B-EML/R:B-EML and ETL were made thicker in Devices C2 and C3 (listed in Table 1) for the purposes of alleviating the TTA in the B-EML/R:B-EML, reducing metal quenching by the cathode, and adjusting the charge balance. For even thicker EMLs, increases in the driving voltage would lead to lower power efficiencies. After ascertaining the proper ETL thickness to avoid metal quenching and improve the charge balance, a WOLED structure optimized for high efficiency (e.g. Device C1 in Table 1) and with thicker layers of 0.5% $Ir(phq)_3$:9% FIrpic:mCP (18 nm) and BPhen (40 nm) was obtained. Fig. 7 shows the electrical and optical characteristics of Devices C2 and C3. Improvement in the efficiency due to the microcavity effect was ruled out, since the EL spectra for Devices C2 and C3 were almost identical.

In terms of efficiency as shown in Fig. 7(b), Device C2 exhibited the maximum efficiency of 26 lm/W and 34.1 cd/A, which stayed >30 cd/A until 2000 cd/m^2. As shown in Table 5, the maximum quantum efficiency of Device C3 was 9.93%, still lower than 10%. In terms of maximum quantum efficiency, this value was not high under similar phosphorescent dyes [22]. In our experiment, BPhen was used as ETL due to its comparable carrier mobility with NPB [24]. In this case, we could possibly achieve better charge balance and lower driving voltage. Although higher electron mobility could shift the recombination zone away from the B-EML/ETL interface, the excitons were able to diffuse to the ETL interface. Therefore, lower triplet exciton state (2.6 eV) of BPhen than that (2.7 eV) of FIrpic leaded to the occurrence of exciton quenching at this interface [31,32]. In order to avoid this exciton quenching, ETL with sufficiently higher triplet states were introduced [33,34]. Similar situation happened at the HTL/G-EML interface. The triplet state of NPB was 2.4 eV, and that of $Ir(ppy)_3$ was also 2.4 eV [31,35]. The almost equal triplet states of these two materials could make $Ir(ppy)_3$ transfer to NPB, thus leading to the fact that emitting triplet excitons were quenched by HTL. To well confine excitons in EML, 4,4′,4″-tris-(*N*-carbazolyl)-triphenylamine (TCTA), for example, with higher triplet state (2.8 eV) was inserted in between HTL and EML [34,36]. As for the blue-emitting material system, the host of FIrpic was continuously developed to extract more photons from FIrpic [33,34,37]. Since these adverse factors (exciton quenching at two interfaces of HTL and ETL, and inefficient blue host materials) in our material system, the EQE of our devices were below the level 10%. The main purpose of this study was to propose a methodology to manage EML for

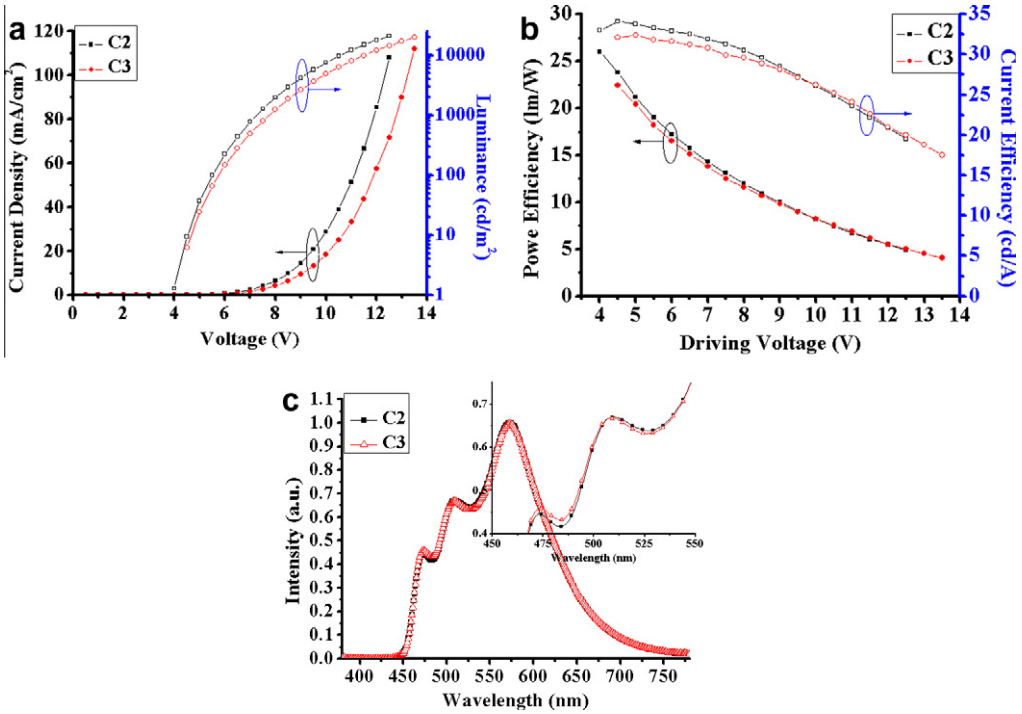

Fig. 7. The electrical and optical performances of optimized Devices C2 and C3. (a) *B–J–V* characteristic. (b) Current and power efficiency. (c) Normalized EL spectra measured at an injected current density of 2.5 mA/cm^2.

Table 5
Performance of Devices C1–C3. Driving voltage was measured at current density of 100 mA/cm^2.

Device	Driving voltage (V)	Max. efficiency			CIE coordinate		Max. Ψ (%)
		lm/W	cd/A	EQE (%)	Low luminance	High luminance	
C1	11.36	21	29.4	8.52	(0.355, 0.481) (19.1 cd/m^2)	(0.354, 0.487) (10,400 cd/m^2)	4.22
C2	12.35	26	34.1	9.93	(0.399, 0.485) (9.37 cd/m^2)	(0.404, 0.484) (12,100 cd/m^2)	4.41
C3	13.20	22.4	32.4	9.83	(0.401, 0.486) (24.1 cd/m^2)	(0.395, 0.479) (12,100 cd/m^2)	3.19

achieving white OLEDs with stable CIE coordinates by using commercial organic materials and suitable carrier mobility. Here, high electron mobility for ETL and not-too-high hole mobility for HTL were mostly desired. Transporting layer materials with higher triplet energy together with better host material in the EML would be most desired for further boosting up the OLED efficiency.

The efficiency roll-off beyond 2000 cd/m^2 was a typical phenomenon of triplet exciton quenching possibly due to increasing triplet excitons and polarons, leakage of charges, and non-radiative recombination at the transporting layers. Reineke et al. showed that triplet-polaron annihilation (TPA) only quenched excitons by ~20% at 200 mA/cm^2 [38] and the rate constant of TPA was 10 times lower than that of TTA [39] in Ir(ppy)$_3$-doped devices. Leakage of charges and non-radiative recombination at the transporting layers would lead to unstable EL spectrum at different injection conditions [24]. However, the performance of stable EL spectrum in our devices naturally ruled out these two factors. As a consequence, we suggested TTA dominated the efficiency roll-off in our cases. The stable EL spectra (maximum Ψ = 4.41% from 4.5 to 11 V) under different driving conditions suggested that the recombination zone was located in the same region as in Devices B3 and C1. As for the CIE coordinates so crucial to display and lighting applications, Device C2 exhibited a slight variation from (0.396, 0.484) at 100 cd/m^2, to (0.406, 0.483) at 5670 cd/m^2, finally approaching (0.404, 0.484) at 12,100 cd/m^2. Over the practical luminance range for backlight and lighting applications, Device C2 exhibited an ultra-high color stability, namely, a more or less fixed CIE coordinates from 1270 cd/m^2 with (0.403, 0.483) to 5670 cd/m^2 with (0.406, 0.483). Device C3, with 50 nm BPhen as the ETL, exhibited a slightly lower efficiency (shown in Fig. 7(b) and Table 5) than Device C2, but also a higher color stability (maximum Ψ = 3.19% from 5 to 12 V). In Device C3, the CIE coordinates shifted from (0.399, 0.483) at 145 cd/m^2, to (0.401, 0.481) at 1240 cd/m^2, finally reaching (0.395, 0.479) at 12,100 cd/m^2. The maximum δ was (−0.004, −0.004) over a wide luminance variation of about two orders of magnitude. In the practical luminance range, we observed almost unchanged CIE

coordinates, (0.401, 0.481) and (0.400, 0.479) for 1240 and 4850 cd/m^2, respectively. As compared with Device C2, the reduced EL spectrum and CIE coordinates variation could be attributed to the decreased sensitivity of the electric field to the carrier injection and transport as discussed in Ref. [24], since the thicker BPhen ETL (50 nm) would result in a greater voltage drop. The larger voltage drop across the thicker BPhen ETL possibly resulted in the lower voltage drop across the B-EML/R:B-EML, thereby lowering the electric field. In this regard, the electrons could not obtain sufficient energy to traverse the mCP spacer and leak to the G-EML. The result of the carrier confinement was the increasingly blue emission, as shown in Fig. 7(c).

4. Conclusion

The WOLED with ultra-high color stability both in the practical and over a rather wide luminance range was implemented by the selection of an appropriate EML layer thickness to reduce the sensitivity of electric field to the carrier injection and transport, a spacer to implement the desired exciton dynamics, and a selectively doped profile to generate red emission via complete energy transfer from the blue excitons. The combined effects of the abovementioned efforts were that the WOLED exhibited a rather small CIE coordinates variation of (−0.004, −0.004) over hundred-time luminance variation and an ultimately negligible variation of (−0.001, −0.002) in a commonly used luminance range for display and lighting applications. The efficiency reached a maximum value of 34.1 cd/A (26 lm/W) and stayed >30 cd/A until 2000 cd/m^2.

Acknowledgement

This work was supported by the National Science Council of Taiwan, under Grant Nos. NSC 98-2221-E-002-038-MY3, 99-2622-E-155-010-CC3, 99-2221-E-155-092, and NSC 99-2218-E-155-003.

References

[1] C.W. Tang, S.A. VanSlyke, Appl. Phys. Lett. 51 (1987) 913.
[2] C. Adachi, R. Kwong, S.R. Forrest, Org. Electron. 2 (2001) 37.
[3] B.C. Krummacher, V.-E. Choong, M.K. Mathai, S.A. Choulis, F. So, F. Jermann, T. Fiedler, M. Zachau, Appl. Phys. Lett. 88 (2006) 113506.
[4] Y. Sun, N.C. Giebink, H. Kanno, B. Ma, M.E. Thompson, S.R. Forrest, Nature 440 (2006) 908.
[5] S. Reineke, F. Lindner, G. Schwartz, N. Seidler, K. Walzer, B. Lüssem, K. Leo, Nature 459 (2009) 234.
[6] B.W. D'Andrade, R.J. Holmes, S.R. Forrest, Adv. Mater. 16 (2004) 624.
[7] D. Berner, F. Nuesch, E. Tutiš, C. Ma, X. Wang, B. Zhang, L. Zuppiroli, J. Appl. Phys. 95 (2004) 3749.
[8] C.-H. Chen, H.-F. Meng, Appl. Phys. Lett. 86 (2005) 201102.
[9] X.-M. Yu, H.-S. Kwok, W.-Y. Wong, G.-J. Zhou, Chem. Mater. 18 (2006) 5097.
[10] Y. Sun, S.R. Forrest, Appl. Phys. Lett. 91 (2007) 263503.
[11] J.-H. Jou, M.-H. Wu, S.-M. Shen, H.-C. Wang, S.-Z. Chen, S.-H. Chen, C.-R. Lin, Y.-L. Hsieh, Appl. Phys. Lett. 95 (2009) 013307.
[12] E.L. Williams, K. Haavisto, J. Li, G.E. Jabbour, Adv. Mater. 19 (2007) 197.
[13] Q.-X. Tong, S.-L. Lai, M.-Y. Chan, J.-X. Tang, H.-L. Kwong, C.-S. Lee, S.-T. Lee, Appl. Phys. Lett. 91 (2007) 023503.
[14] S.H. Kim, J. Jang, J.Y. Lee, Appl. Phys. Lett. 91 (2007) 123509.
[15] G. Schwartz, M. Pfeiffer, S. Reineke, K. Walzer, K. Leo, Adv. Mater. 19 (2007) 3672.
[16] C.-H. Hsiao, C.-F. Lin, J.-H. Lee, J. Appl. Phys. 102 (2007) 094508.
[17] C.-L. Ho, M.-F. Lin, W.-Y. Wong, W.-K. Wong, C.H. Chen, Appl. Phys. Lett. 92 (2008) 083301.
[18] K.S. Yook, S.O. Jeon, C.W. Joo, J.Y. Lee, Org. Electron. 10 (2009) 384.
[19] K.S. Yook, S.O. Jeon, C.W. Joo, J.Y. Lee, M.S. Kim, H.S. Choi, S.J. Lee, C.-W. Han, Y.H. Tak, Org. Electron. 10 (2009) 681.
[20] K.S. Yook, S.O. Jeon, J.Y. Lee, K.H. Lee, Y.S. Kwon, S.S. Yoon, J.H. Yoon, Org. Electron. 10 (2009) 1378.
[21] C.H. Hsiao, J.H. Lee, J. Appl. Phys. 106 (2009) 024503.
[22] Q. Wang, J. Ding, D. Ma, Y. Cheng, L. Wang, F. Wang, Adv. Mater. 21 (2009) 2397.
[23] Q. Wang, C.-L. Ho, Y. Zhao, D. Ma, W.-Y. Wong, L. Wang, Org. Electron. 11 (2010) 238.
[24] C.H. Hsiao, S.W. Liu, C.T. Chen, J.H. Lee, Org. Electron. 11 (2010) 1500.
[25] K. Saito, N. Matsusue, H. Kanno, Y. Hamada, H. Takahashi, T. Matsumura, Jpn. J. Appl. Phys. 43 (2004) 2733.
[26] X. Ren, J. Li, R.J. Holmes, P.I. Djurovich, S.R. Forrest, M.E. Thompson, Chem. Mater. 16 (2004) 4743.
[27] S.H. Kim, J. Jang, K.S. Yook, J.Y. Lee, Thin Solid Films 517 (2009) 4464.
[28] C.H. Hsiao, J.H. Lee, C.A. Tseng, Chem. Phys. Lett. 427 (2006) 305.
[29] C.W. Tang, S.A. VanSlyke, C.H. Chen, J. Appl. Phys. 65 (1989) 3610.
[30] M.A. Baldo, C. Adachi, S.R. Forrest, Phys. Rev. B 62 (2000) 10967.
[31] M.E. Kondakova, T.D. Pawlik, R.H. Young, D.J. Giesen, D.Y. Kondakov, C.T. Brown, J.C. Deaton, J.R. Lenhard, K.P. Klubek, J. Appl. Phys. 104 (2008) 094501.
[32] V.I. Adamovich, S.R. Cordero, P.I. Djurovich, A. Tamayo, M.E. Thompson, B.W. D'Andrade, S.R. Forrest, Org. Electron. 4 (2003) 77.
[33] K.R. Wee, W.S. Han, H.J. Son, S. Kwon, S.O. Kang, J. Phys. D: Appl. Phys. 42 (2009) 235107.
[34] S.J. Su, E. Gonmori, H. Sasabe, J. Kido, Adv. Mater. 20 (2008) 4189.
[35] M.A. Baldo, S.R. Forrest, Phys. Rev. B 62 (2000) 10958.
[36] J.H. Lee, C.L. Huang, C.H. Hsiao, M.K. Leung, C.C. Yang, C.C. Chao, Appl. Phys. Lett. 94 (2009) 223301.
[37] T. Tsuboi, S.W. Liu, M.F. Wu, C.T. Chen, Org. Electron. 10 (2009) 1372.
[38] S. Reineke, K. Walzer, K. Leo, Phys. Rev. B 75 (2007) 125328.
[39] S. Reineke, G. Schwartz, K. Walzer, K. Leo, Appl. Phys. Lett. 91 (2007) 123508.

Organic Electronics 12 (2011) 557–561

Contents lists available at ScienceDirect

Organic Electronics

journal homepage: www.elsevier.com/locate/orgel

Enhanced conversion efficiency of polymeric photovoltaic cell by nanostructured antireflection coating

W.C. Luk [a], K.M. Yeung [a], K.C. Tam [a], K.L. Ng [a], K.C. Kwok [a], C.Y. Kwong [a,*], A.M.C. Ng [b], A.B. Djurišić [b]

[a] Nano and Advanced Materials Institute Ltd., Unit 608–609, Lakeside 2, Hong Kong Science Park, Shatin, Hong Kong
[b] Department of Physics, The University of Hong Kong, Pokfulam Road, Hong Kong

ARTICLE INFO

Article history:
Received 6 October 2010
Received in revised form 31 December 2010
Accepted 31 December 2010
Available online 25 January 2011

Keywords:
Nano-silica
Antireflection
Organic photovoltaic
Organic solar cell
Omnidirectional
Self-assembly method

ABSTRACT

A nanostructured antireflection coating has been fabricated on glass side of an indium tin oxide (ITO) coated glass by self-assembling a monolayer of nano-silica spheres. Significant reduction in the weighted reflectance from 10.2% to 7.2% at 5° incident angle is observed. At 60° incident angle, the weighted reflectance of ITO glass with antireflection coating is still about 3% lower than that of bare ITO glass. This nanostructured antireflection coating has been applied on the glass surface of the ITO substrate in a polymer photovoltaic cell. Improvement in the power conversion efficiency from 1.80% to 2.05% at normal incidence has been demonstrated. The relative enhancement in the conversion efficiency is almost independent of the incident angles.

© 2011 Elsevier B.V. All rights reserved.

1. Introduction

Polymer photovoltaic technology has been getting more important nowadays due to the low cost and simple manufacturing process, and its compatibility to low cost plastic substrates. A lot of research has been conducted around the world [1–10]. Most of the works have been devoted to novel materials development [1–4] and process optimization [5–9]. However, investigations on the optical confinement and antireflection coatings for polymer photovoltaics have been scarce [10–13].

Various light trapping techniques are available for inorganic solar cells such as texturing [14,15]. Textured surfaces enhance scattering and, thus, the light is trapped in the device. Normally, the features of the conventional textured transparent conductive oxide is in the range of several hundreds nanometers, which are comparable or larger than the usual thickness of an active layer in a polymer photovoltaic cell (~100 nm). These large features would generate defects in polymer photovoltaic cells and degrade its performance and yield. Different new methods have been investigated to confine the photons within a thin polymer active layer. Rim et al. [12] proposed to fabricate the polymer solar cell on a V-shape indium tin oxide (ITO) substrate. They demonstrated an efficiency improvement by 52%. However, shunt defects might be generated from the sharp V-shape substrate, which have been discussed by Leo et al. [11]. Nanostructured polymer active layer was investigated for the light trapping in polymer solar cells [10]. By using nano imprint process, they replicated the pattern with nano-scale features on the polymer layer, poly(3-hexylthiophene) (P3HT): poly((9,9-dioctylfluorene)-2,7-diyl-alt-[4,7-bis(3-hexylthien-5-yl)-2,1,3-benzothiadiazole] -2′,2″-diyl). They observed that the power conversion efficiency was increasing by decreasing the sizes of nanodots. The best efficiency was 1.85%, obtained with 25 nm nanodot pattern [10]. The efficiency was just comparable to the polymer solar cell fabricated with the representative materials consisted of P3HT and

* Corresponding author.
E-mail address: cykwong@gmail.com (C.Y. Kwong).

1566-1199/$ - see front matter © 2011 Elsevier B.V. All rights reserved.
doi:10.1016/j.orgel.2010.12.024

[6,6]-phenyl-C_{61}-butyric acid methyl ester (PCBM). Ko et al. [13] suggested using photonic crystal structure to trap light in a polymer active layer. Their photonic crystal structure was fabricated in the polymer active layer by Pattern Replication in Nonwetting Templates. The power conversion efficiency was improved, although the efficiency was still below 1% [13]. In their method, the photonic crystal polymer layer had to be thermally cured [13]. Therefore, not all polymer materials are compatible to this method. The choice of materials may be one of the reasons for the relatively low efficiency even after the incorporation of the photonic crystal. The pattern replication also increases the complexity of the device structure and the fabrication process.

In this work, we have used a simple method to fabricate antireflection coating on a polymer photovoltaic cell without any addition step involved before the completion of polymer photovoltaic cell fabrication. Our process is kept in room temperature, so that most of the polymer materials are compatible. Using this antireflection coating, we have demonstrated a 13% relative improvement in power conversion efficiency of a polymer photovoltaic cell.

2. Experimental details

2.1. Fabrication of polymer photovoltaic cell

The polymer photovoltaic cell was fabricated on a thoroughly cleaned ITO glass substrate. The structure of the polymer photovoltaic cell is ITO/poly(3,4-ethylenedioxythiophene) poly(styrenesulfonate) (PEDOT:PSS, 70 nm)/P3HT:PCBM (1:1, 100 nm)/Al (100 nm). PEDOT:PSS and P3HT:PCBM thin films were fabricated by spin coating, while Al was thermally evaporated under high vacuum. Finally, the device with active area of 16 mm^2 was encapsulated in a nitrogen box with desiccant and encapsulation glass.

2.2. Fabrication of nanostructured antireflection coating

After completion of the polymer photovoltaic cell, the glass side of the ITO coated glass was then cleaned by rubbing with acetone and ethanol. Then nanostructured antireflection coating (nano-ARC) was fabricated on glass side of ITO glass of the polymer photovoltaic cell at room temperature by self-assembly 100 nm nano-silica spheres supplied by Nissan Kagaku, Japan. The completed device was immersed in 1% v/v 3-aminopropyltrimethyoxysilane (APTMS), in anhydrous toluene solution at room temperature for 30 min and rinsed with deionized water [16,17]. Then the glass surface was silanized. It was then immersed into the negatively charged mono-dispersed nano-silica colloidal solution (MP1040 with ~126 nm in diameter, supplied by Nissan Kagaku, Japan) for 5 min, rinsed with deionized water twice and blow dried. The nano-silica spheres were self-assembled on the glass surfaces of the polymer photovoltaic cell. Detailed description of the preparation procedure and properties of the coatings with different sphere sizes are given in Ref. [17].

2.3. Characterization

SEM was used to characterize the morphology of the nano-ARC. Si wafer with native oxide was used as the substrate due to its better conductivity. The direct transmittance and the specular reflectance were measured by Perkin Elmer Lambda 750 UV/Vis/NIR Spectrophotometer. The polymer photovoltaic cell was characterized by current–voltage (J–V) measurement under air mass (AM) 1.5 conditions (100 mW/cm^2). The J–V curve of polymer photovoltaic cell with the nano-ARC was measured first. Then the nano-ARC was removed by rubbing with clean room tissue. The J–V curve of the same polymer photovoltaic cell was measured again. The efficiency data were compared.

3. Results and discussion

Fig. 1 shows the SEM images of the nano-ARC coating on glass. The monolayer of nano-silica spheres are self-assembled in a random non-close packed manner, which is in agreement with previous work [17,18]. The direct transmittance, specular reflectance and weighted reflectance of ITO coated glass with and without nano-ARC are shown in Fig. 2.

Fig. 2a shows the transmittance of ITO glasses with or without nano-ARC and the absorption of P3HT:PCBM. The transmittance is enhanced in the whole spectrum for glass with nano-ARC compared to that of the bare glass, which is beneficial to our polymer photovoltaic cells with absorption in the visible region. The peak transmittance of

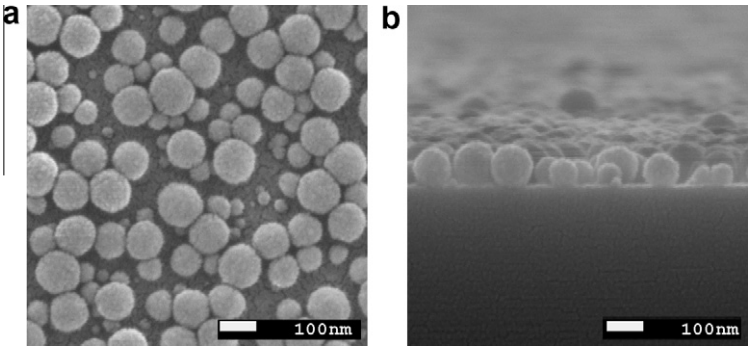

Fig. 1. SEM images show the morphology of nano-ARC (a) top view and (b) corresponding cross-sectional image.

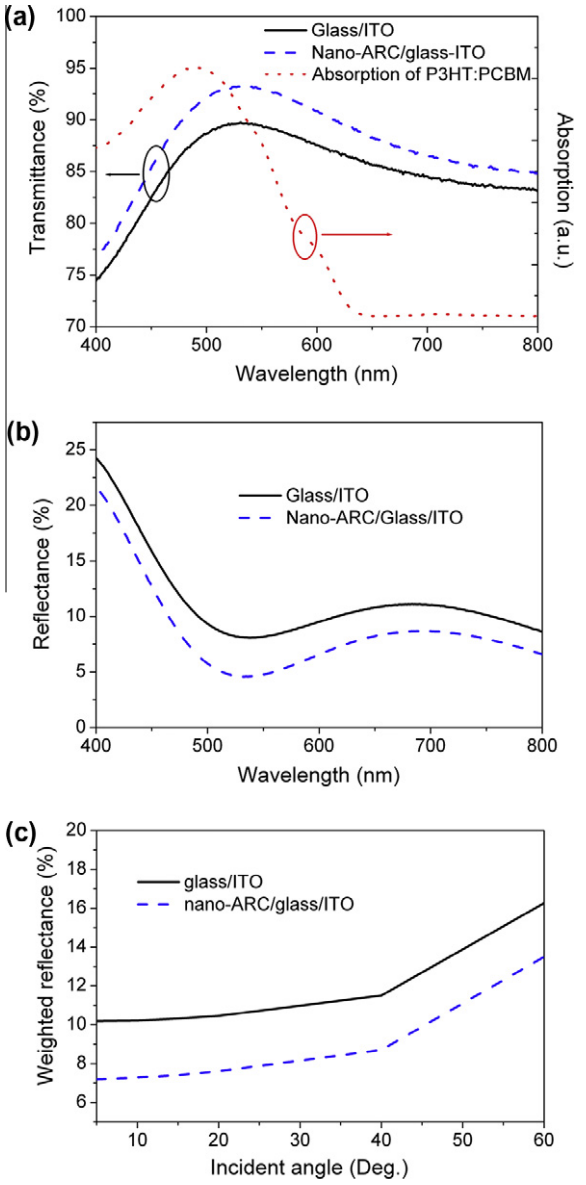

Fig. 2. (a) Transmission spectra and absorption spectrum of P3HT:PCBM, (b) spectral reflectance, and (c) angular dependent weighted reflectance of nano-ARC coated ITO and bare ITO glass.

93.3% is obtained at 532 nm for nano-ARC ITO glass, while it is 89.6% for ITO glass.

The reflectance spectra shown in Fig. 2b and c are measured by Perkin Elmer Lambda 750 UV/Vis/NIR Spectrophotometer. The spectral reflectance is measured at 5° incident angle. For angular dependent reflectance measurements, the samples are mounted in vertical plane and the reflectance are measured at 20°, 40°, and 60°. For the best reduction in reflectance, the refractive index of the antireflection coating should be equal to $\sqrt{n_{air} n_{glass}}$. In our work, the refractive index of the glass is 1.47. Therefore, for the best antireflection properties, the refractive index of the nano-ARC should be $n_{nano\text{-}ARC} = 1.21$. We have attempted to control the coverage percentage of nano-silica spheres to control the refractive index of the nano-ARC. Fig. 2b shows the reflectance measured at 5°. It can be seen that the reflectance of nano-ARC coated ITO glass is decreased compared to that of the bare ITO glass in the whole spectrum from 400 to 800 nm. The minimum reflectance is occurred at around 530 nm. The reduction in the reflectance could be attributed to the lower effective refractive index of the nano-ARC, which is about 1.38 calculated by effective medium theory with 74.5% coverage of nano-silica [19,20]. The optical thickness of the nano-ARC for the minimum reflectance at 532 nm should be equal to $\lambda/4$ (~133 nm). This value is in consistent with the diameter of the nano-silica (~126 ± 13 nm). Fig. 2c shows the weighted reflectance at different incident angles calculated according to Eq. (1).

$$R_w = \int_{400}^{800} R(\lambda) I(\lambda) d\lambda / \int_{400}^{800} I(\lambda) d\lambda \quad (1)$$

where R_w is the weighted reflectance, R is the reflectance from 400 to 800 nm, and $I(\lambda)$ is the intensity of light at particular wavelength, and measured $R(\lambda)$ is the reflectance at particular wavelength. The weighted reflectance of nano-ARC ITO glass is 3% below that of the bare ITO glass. The reduction in the weighted reflectance is almost constant for any incident angle, due to the omnidirectional antireflection properties at the air/nano-ARC/glass interface. The reduction in reflectance over the wide range of incident angles might be attributed to both the lower effective refractive index and the graded-index profile due to the spherical shape of the silica [21–27]. Similar independency of antireflection properties against incident angles was reported by other research groups [26,28,29]. Chang et al. reported that the reflectance of ITO nanocolumns on top of a silicon wafer was independent on the incident angles due to the gradient of refractive index [26]. Zhou et al. also studied the fabrication of various microstructures as antireflection coating on a solar cell. They found that microspheres on top of the substrate can results in significantly reduction in reflectance up to 60° due also to the gradient in the refractive index, and spherical nature of the micro-size silica [29]. Comparing to our previous work on double-side nano-ARC on glass substrate, the reflectance increases more sharply for a single side nano-ARC ITO glass [17]. The reason is the additional planar ITO thin film, which causes addition reflection at the glass/ITO interface and ITO/air interface, especially at large incident angle. Nevertheless, the reduction in reflectance or the enhancement in transmittance at any incident angle is particular important in photovoltaic applications.

Table 1 summarizes the performances of the polymer photovoltaic cells with and without nano-ARC measured under AM1.5G one-sun condition. It is obvious that only

Table 1
Comparison of the polymer photovoltaic performance with and without nano-ARC under AM1.5G irradiation at normal incidence.

	V_{OC} (V)	J_{SC} (mA/cm^2)	FF	η (%)
Without nano-ARC	0.45	12.64	0.32	1.80
Nano-ARC	0.46	13.83	0.33	2.05

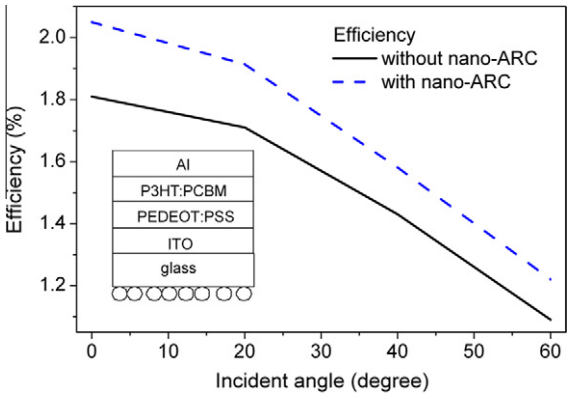

Fig. 3. Angular dependent power conversion efficiency of a polymer photovoltaic cell with and without nano-ARC, the inset shows the structure of polymer photovoltaic cell with nano-ARC.

short circuit current density has been affected by the antireflection coating, which agrees well with the Ref. [30]. It is simply because the fabrication of our nano-ARC does not modify any fabrication process nor the device structure. Therefore, it is reasonable that only short circuit current density is increased due to the increase in the light coupling into the solar cell [30]. The current density has been improved to 13.83 mA/cm^2 from 12.64 mA/cm^2 at normal incidence. This results in an improvement of power conversion efficiency to 2.05% from 1.80%. We have also measured the power conversion efficiency at different incident angles, which is shown in Fig. 3. Upon increasing the incident angles, the relative conversion efficiency improvement drops slightly from 13.3% at normal incident to 12.0% at 60°. The trend of efficiency enhancement disagrees with the reference [30], in which they obtained larger efficiency enhancement at larger incident angle for the omnidirectional antireflection coating. One possible reason may be due to the different in the device structure. Their device structure is antireflection coating/ITO/amorphous silicon, while our device structure is nano-ARC/glass/ITO/polymer. The higher number of planar interfaces in our device structure may result in larger reflectance at larger incident angle, which results in decrease in efficiency enhancement with increasing incident angles. Nevertheless, the power efficiency enhancement is quite obvious from 0° to 60° due to the omnidirectional antireflection properties of the nano-ARC, which could be attributed to the gradient of refractive index of the antireflection coating and the spherical nature of our nano-silica [29].

4. Conclusion

In summary, broadband nanostructured antireflection coating has been fabricated by a simple self-assembly method on a glass substrate of a polymer photovoltaic cell. The fabrication process is fully compatible with any polymer photovoltaic cell, which does not involve any additional fabrication step prior to the completion of the polymer solar cell. The reflectance of the nano-ARC coated ITO glass has been reduced in a broad spectrum from 400 to 800 nm. The weighted reflectance of nano-ARC coated ITO glass has been reduced by 3% at incident angle from 5° to 60°. With the broadband antireflection property, the power conversion efficiency of the polymer photovoltaic cell with nano-ARC increases to 2.05% from 1.80% of the polymer photovoltaic cell without nano-ARC at normal incidence. Due to the omnidirectional property, the relative enhancement of the power conversion efficiency with the nano-ARC is almost independent of the light incident angles.

Acknowledgements

This work has been supported by HKSAR Innovation and Technology Fund (ITP/030/09NP) and Strategic Research Theme, University Development Fund, and Small Project Grant of the University of Hong Kong.

References

[1] J.S. Kim, Y.M. Lee, J.H. Lee, J.H. Park, J.K. Kim, K.W. Cho, High-efficiency organic solar cells based on end-functional-group-modified poly(3-hexylthiophene), Adv. Mater. 22 (2010) 1355.
[2] X.Z. Wang, Q.W. Wang, L. Yan, W.Y. Wong, K.Y. Cheung, A.N. Ng, A.B. Djurišić, W.K. Chan, Very-low-bandgap metallopolyynes of platinum with a cyclopentadithiophenone ring for organic solar cells absorbing down to the near-infrared spectral region, Macromol. Rapid Commun. 31 (2010) 861.
[3] W.Y. Wong, X.Z. Wang, Z. He, A.B. Djurišić, C.T. Yip, K.Y. Cheung, H. Wang, C.S.K. Mak, W.K. Chan, Metallated conjugated polymers as a new avenue towards high-efficiency polymer solar cells, Nat. Mater. 6 (2007) 521.
[4] H. Jung, J.Y. Yu, E.J. Jeong, J.S. Kim, S.C. Kwon, H.Y. Kong, K.H. Lee, H.Y. Woo, H.K. Shim, Synthesis and photovoltaic properties of cyclopentadithiophene-based low-bandgap copolymers that contain electron-withdrawing thiazole derivatives, Chem. Eur. J. 16 (2010) 3743.
[5] W.H. Baek, M.J. Choi, T.S. Yoon, H.H. Lee, Y.S. Kim, Use of fluorine-doped tin oxide instead of indium tin oxide in highly efficient air-fabricated inverted polymer solar cells, Appl. Phys. Lett. 96 (2010) 133506.
[6] C.Y. Kwong, W.C.H. Choi, A.B. Djurišić, P.C. Chui, K.W. Cheng, W.K. Chan, Poly(3-hexylthiophene):TiO2 nanocomposites for solar cell applications, Nanotechnology 15 (2004) 1156.
[7] C.Y. Kwong, A.B. Djurišić, P.C. Chui, K.W. Cheng, W.K. Chan, Influence of solvent on film morphology and device performance of poly(3-hexylthiophene):TiO_2 nanocomposite solar cells, Chem. Phys. Lett. 384 (2004) 372.
[8] P.M. Sirimanne, B.W. Jensen, H.C. Weerasinghe, Y.B. Cheng, Towards an all-polymer cathode for dye sensitized photovoltaic cells, Thin Solid Films 518 (2010) 2871.
[9] M. Girtan, M. Rusu, Role of ITO and PEDOT:PSS in stability/degradation of polymer: fullerene bulk heterojunctions solar cells, Sol. Energy Mater. Sol. Cells 94 (2010) 446.
[10] X.M. He, F. Gao, G.L. Tu, D. Hasko, S. Hüttner, U. Stenier, N.C. Greenham, R.H. Friend, W.T.S. Huck, Formation of nanopatterned polymer blends in photovoltaic devices, Nano Lett. 10 (2010) 1302.
[11] M. Niggemann, M. Riede, A. Gombert, K. Leo, Light trapping in organic solar cells, Phys. Status Solidi 205 (2008) 2862.
[12] S. Rim, S. Zhuo, S. Scully, M.D. Mc Gehee, M.D. Peumans, An effective light trapping configuration for thin-film solar cells, Appl. Phys. Lett. 91 (2007) 243501.
[13] D.H. Ko, J.R. Tumbleston, L. Zhang, S. Williams, J.M. DeSimone, R. Lopez, E.T. Samulski, Photonic crystal geometry for organic solar cells, Nano Lett. 9 (2009) 2742.
[14] I.A. Krasnov, Light scattering by textured transparent electrodes for thin-film silicon solar cells, Sol. Energy Mater. Sol. Cells 94 (2010) 1648.
[15] S. Chattopadhyay, Y.F. Huang, Y.J. Jen, A. Granguly, K.H. Chen, L.C. Chen, Anti-reflecting and photonic nanostructures, Mater. Sci. Eng. R-Rep 69 (2010) 1.
[16] C.W. Tse, K.Y.K. Man, K.W. Cheng, C.S.K. Mak, W.K. Chan, C.T. Yip, Z.T. Liu, A.B. Djurišić, Layer-by-layer deposition of rhenium-containing

hyperbranched polymers and fabrication of photovoltaic cells, Chem. Eur. J. 13 (2007) 328.
[17] K.M. Yeung, W.C. Luk, K.C. Tam, C.Y. Kwong, M.A. Tsai, H.C. Kuo, A.M.C. Ng, A.B. Djurišić, 2-step self-assembly method to fabricate broadband omnidirectional antireflection coating in large scale, Sol. Energy Mater. Sol. Cells 95 (2011) 699.
[18] X.T. Zhang, O. Sato, M. Taguchi, Y. Einaga, T. Murakami, A. Fujishima, Self-cleaning particle coating with antireflection properties, Chem. Mater. 17 (2005) 696.
[19] W.H. Southwell, Pyramid-array surface-relief structures producing antireflection index matching on optical surfaces, J. Opt. Soc. Am. A 8 (1991) 549.
[20] B.T. Liu, W.D. Yeh, Reflective properties of nanoparticle-arrayed surfaces 518 (2010) 6015.
[21] C.C. Chen, D.J. Lin, T.M. Don, F.H. Huang, L.P. Cheng, Preparation of organic–inorganic nano-composites for antireflection coatings, J. Non-Cryst. Solids 354 (2008) 3828.
[22] D.J. Poxson, M.F. Schubert, F.W. Mont, E.F. Schubert, J.K. Kim, Broadband omnidirectional antireflection coatings optimized by genetic algorithm, Opt. Lett. 34 (2009) 728.
[23] M.L. Kuo, D.J. Poxson, Y.S. Kim, F.W. Mont, J.K. Kim, E.F. Schubert, S.Y. Lin, Realization of a near-perfect antireflection coating for silicon solar energy utilization, Opt. Lett. 33 (2008) 2572.
[24] V.C. Coffey, SOLAR CELLS: 'Near perfect' antireflection coating boosts solar-cell efficiency, Laser Focus World 45 (2009) 20.
[25] S. Chhajed, M.F. Schubert, J.K. Kim, E.F. Schubert, Nanostructured multilayer graded-index antireflection coating for Si solar cells with broadband and omnidirectional characteristics, Appl. Phys. Lett. 93 (2008) 251108.
[26] C.H. Chang, P. Yu, C.S. Yang, Broadband and omnidirectional antireflection from conductive indium-tin-oxide nanocolumns prepared by glancing-angle deposition with nitrogen, Appl. Phys. Lett. 94 (2009) 051114.
[27] W.L. Min, P. Jiang, B. Jiang, Large-scale assembly of colloidal nanoparticles, fabrication of periodic subwavelength structures, Nanotechnology 19 (2008) 475604.
[28] X. Li, J. Gao, L. Xue, Y. Han, Porous polymer films with gradient-reflective-index structure for broadband and omnidirectional antireflection coatings, Adv. Funct. Mater. 20 (2010) 259.
[29] W. Zhou, M. Tao, L. Chen, H. Yang, Microstructured surface design for omnidirectional antireflection coatings on solar cells, J. Appl. Phys. 102 (2007) 103105.
[30] Y. Wang, R. Tummala, L. Chen, L.Q. Guo, W. Zhou, M. Tao, Solution-processed omnidirectional antireflection coatings on amorphous silicon solar cells, J. Appl. Phys. 105 (2009) 103501.

Organic Electronics 12 (2011) 562–565

Contents lists available at ScienceDirect

Organic Electronics

journal homepage: www.elsevier.com/locate/orgel

Improvements of electron injection efficiency using subphthalocyanine mixed with lithium fluoride in cathode structures of organic light emitting diodes

Yu-Hung Chen [a], Yu-Jen Cheng [a], Guan-Ru Lee [a], Chih-I Wu [a,*], Tun-Wen Pi [b]

[a] Department of Electrical Engineering and Graduate Institute of Photonics and Optoelectronics, National Taiwan University, Taipei 10617, Taiwan, ROC
[b] National Synchrotron Radiation Research Center, Hsinchu 30077, Taiwan, ROC

ARTICLE INFO

Article history:
Received 7 May 2010
Received in revised form 22 November 2010
Accepted 8 January 2011
Available online 22 January 2011

Keywords:
OLED
Photoemission
Interfaces

ABSTRACT

The improvement of current injection efficiency in organic light emitting diodes is demonstrated with incorporation of lithium fluoride (LiF) mixed with subphthalocyanine (SubPc) as electron injection layers. The photoemission spectra indicate that the lithium released from LiF would remove chlorine atoms from SubPc molecules and create large density of gap states at the interfaces. These gap states, resulted from the addition of SubPc in conventional aluminum/LiF/ tris-(8-Hydroxyquinoline)-aluminum (Alq_3) cathode structures, further enhance the electron injection efficiency in OLEDs. The results demonstrate a relatively unique feature of SubPc which can be used to improve both electron and hole injection efficiency.

© 2011 Elsevier B.V. All rights reserved.

1. Introduction

Thin film organic light-emitting diodes (OLEDs) have attracted huge attentions in both academic research and industrial development due to their potential applications for future display and lighting [1]. However, the unbalanced carrier mobilities for electrons and holes in organic materials lead to the carrier accumulation at the organic-organic interfaces and device instability [2,3]. In general, the current efficiency can be improved by insertion of electron injection layers (EILs), such as lithium fluoride (LiF) between aluminum cathodes and electron transport layers (ETLs) [4,5]. The chemical reaction mechanism of such a cathode structure has been studied extensively [6–8]. In this letter, we reports an effective cathode structure consisting of a mixture of chlorosubphthalocyaninato boron(III) (SubPc) [9,10] and LiF as electron injection layers and an aluminum cathode, which improves the electron injection current by an order of magnitude as compared to the conventional LiF/Al cathode. The molecular structure of SubPc is shown in Fig. 1. It has already been reported that SubPc can be used as a hole injection layer or be mixed with *N*,*N*′-di(naphthalene-1-yl)-*N*,*N*′-diphenyl-benzidene (NPB) to improve the hole injection efficiency [11,12]. These results demonstrate a rather unique feature of SubPc, which can be used to improve carrier injection efficiency for both holes and electrons in OLEDs. The electronic structures of SubPc/LiF at the cathode interfaces were also studied via photoemission spectroscopy and quantum chemistry calculation to understand the mechanisms leading to the carrier injection improvements.

2. Experimental

Photoemission spectroscopy experiments, including valence band and core level spectra, were carried out at the National Synchrotron Radiation Research Center (NSRRC). The detail specifications of the experimental setups at NSRRC are described in the previous report [13]. The OLEDs investigated in this study were fabricated with the following procedures. The glass substrate coated with ITO

* Corresponding author.
E-mail address: chihiwu@cc.ee.ntu.edu.tw (C.-I Wu).

1566-1199/$ - see front matter © 2011 Elsevier B.V. All rights reserved.
doi:10.1016/j.orgel.2011.01.006

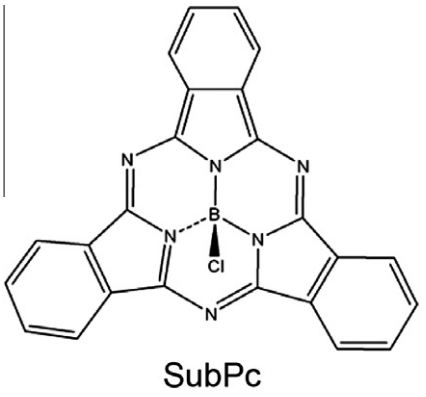

Fig. 1. Molecular structures of SubPc.

was cleaned with acetone, methanol, and UV ozone, sequentially, before being loaded into a thermal evaporation chamber. The deposition rate and thickness of the films were monitored by quartz crystals calibrated with depth profilers. The thermal evaporation chamber was designed to enable mask-change *in situ* so that the devices can be fabricated without exposure to ambient environment in order to minimize the contamination at the electrode-organic interfaces. Furthermore, the sample holder was rotated with constant speed during deposition to ensure good uniformity of films. The current density–voltage (*J*–*V*) characteristics were measured by a Keithley 2400 source-meter. Theoretical simulations with density functional theory (DFT) methods [14] were used to compute density of states. The optimized geometric structures were obtained with the method of B3LYP [15,16] using the basis set of 6-31G, and the single-point energy was then applied to retrieve the detail information of molecular energy using Gaussian03 software [17]. The simulated valence band spectra were extracted via GaussSum [18] with full-width-at-half-maximum of 0.4 eV [19].

3. Results and discussion

To investigate the efficiency of electron injections, a set of multilayer devices consisting of SubPc, LiF, or LiF mixed with SubPc (1:1 ratio) as EILs were fabricated in our customized evaporation chamber. The device structures are indium tin oxide (ITO)/NPB (80 nm)/Alq_3 (80 nm)/EIL (1 nm)/Al (150 nm). Fig. 2(a) shows the current density versus voltage (*J*–*V*) characteristics of the OLEDs with combinations of SubPc and LiF as the EILs. With SubPc inserted in the devices as an EIL between Alq_3 and Al, the current density at operation voltages is only slightly better than that of the device without an injection layer, but is much lower than that of the conventional device with LiF as an EIL. When the 1:1 mixture of SubPc and LiF is used to replace LiF as an EIL, however, the current density of the devices is improved as compared to that of the devices using just LiF as an EIL. The optimized percentages of SubPc in the mixture layers are about 25% to 50% and the device performances are similar when the mixture ratios are in this range. The luminance–voltage (*L*–*V*) data shown in Fig. 2(b) also

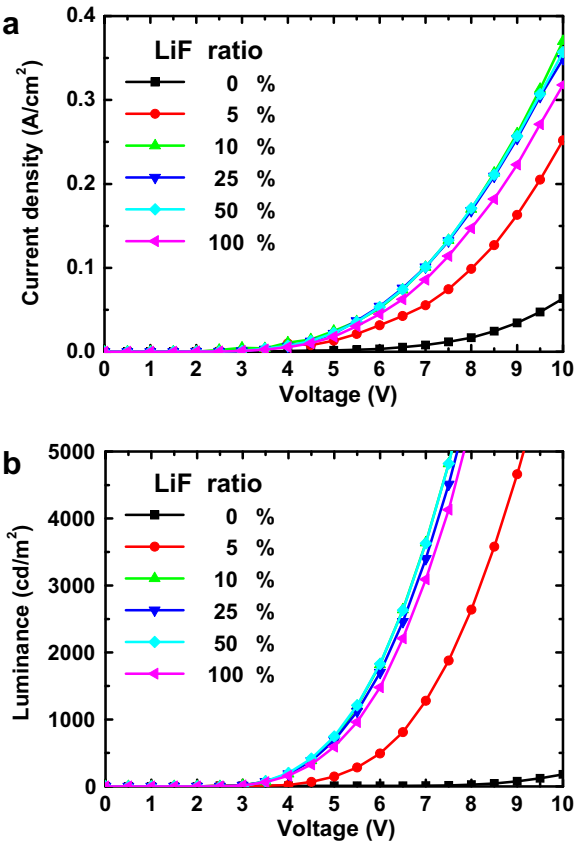

Fig. 2. (a) The *J*–*V* characteristics and (b) the *L*–*V* characteristics of the devices with SubPc and LiF of different ratios as EILs.

demonstrate similar improvement. These results show that LiF:SubPc mixtures are more efficient than the conventional LiF as EILs. Since the cathode structures only consist of EILs about 1 nm between the electron transport layers and cathodes, the electronic structures and the chemical interaction at the Al/LiF:SubPc/Alq_3 interface would be the origins related to the performance improvement of the devices and were therefore further investigated.

It is well known that in Al/LiF/Alq_3 cathode structures chemical reactions between aluminum and LiF lead to the release of lithium from LiF to Alq_3 matrix at the interfaces [5]. In this study with cathode structures consisting of Al/LiF:SubPc/Alq_3, the interactions between SubPc and lithium were investigated via photoemission spectroscopy. Fig. 3 shows the valence band spectra of SubPc with incremental deposition of lithium. The valence band shifts to lower binding energy with very low lithium coverage of 0.2 Å. More importantly, there are new states emerging in the forbidden gap and extending to the Fermi level. These new states close to the Fermi level reaches the maximum intensity at about 2.5 Å of lithium coverages and disappears when the valence band spectra are dominated by lithium with thickness of 10 Å. The result demonstrates that these gap states only appear at the interfaces of lithium and SubPc. The formations of the gap states were further investigated via core level photoemission spectroscopy.

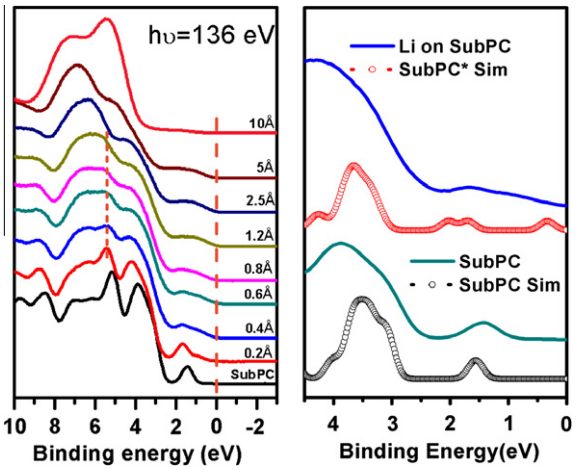

Fig. 3. The valence band spectra of SubPc with incremental deposition of lithium on the surfaces.

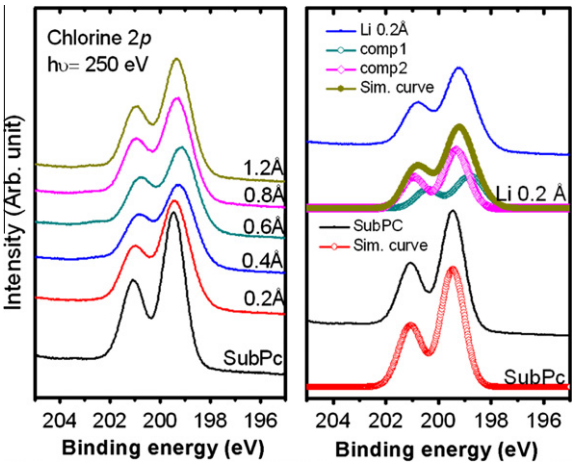

Fig. 5. The chlorine 2p core level spectra of SubPc with incremental deposition of lithium on the surfaces. The figure on the right hand side is the deconvolution of chlorine 2p core levels.

Fig. 4 shows the boron 1s core-level spectra of SubPc with incremental deposition of lithium. It is clear that a new component of boron 1s emerges at the lower binding energy when lithium is mixed with SubPc. The spectra of SubPc with 0.2 Å coverage of lithium is decomposed and shown on the right hand side of Fig. 4. The full-width-at-half-maxima (FWHM) of all the decomposed components are about 1 eV. The new component of the boron 1s core level is at the binding energy of 191 eV. This emerging peak at lower binding energy of boron 1s core level spectra implies that chlorine atoms are detached from the boron in SubPc molecules with the presence of lithium at the interfaces [11].

The core-level spectrum of chlorine 2p was also investigated with excitation photon energy of 250 eV. As shown in Fig. 5, the binding energies of chlorine 2p core levels in pristine SubPc are 199.45 eV for $2p_{3/2}$ and 201.05 eV for $2p_{1/2}$. When lithium is mixed with SubPc, the chlorine core-level spectra are broadened and there is a new feature appearing at the lower binding energy. To clearly identify the energy of the new components, the spectra of pristine SubPc and SubPc with lithium of 0.2 Å are decomposed and shown on the right hand side of Fig. 5. The new features are located at 198.8 and 200.4 eV for chlorine $2p_{2/3}$ and $2p_{1/2}$ core levels, respectively, which are the binding energies of chlorine 2p core-levels in lithium chloride [20]. Fig. 6 shows the Li 1s core level spectra on SubPc films with incremental deposition of lithium. In Fig. 6, at low coverage of Li, the binding energy of Li 1s peak is about 56 eV, which is consistent with the binding energy of Li 1s electron in LiCl [21]. The metallic Li peak begins dominating at high coverage. These results indicate that lithium would take away chlorine atoms from SubPc molecules and form a new radical SubPc*, i.e. SubPc molecules with chlorine atoms detached.

From DFT calculation, SubPc would react with lithium and the products are SubPc* and LiCl and the heat of formation of this reaction is about −27 kcal/mol, which is about the same as the reaction heat of $Alq_3 + Li \rightarrow Li+ Alq_3^-$. The simulated valence band spectra of SubPc and

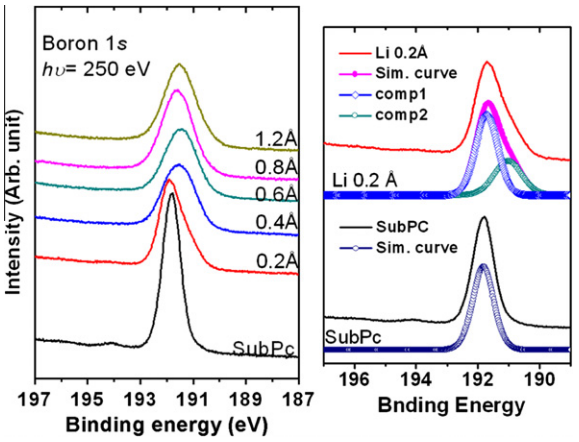

Fig. 4. The boron 1s core level spectra of SubPc with incremental deposition of lithium on the surfaces. The figure on the right hand side is the deconvolution of boron 1s core levels.

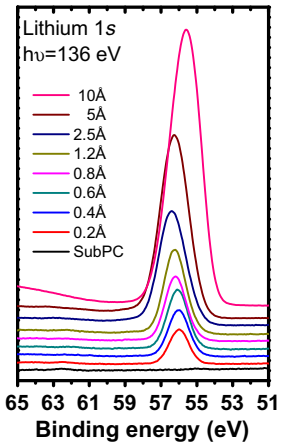

Fig. 6. The lithium 1s core level spectra of SubPc with incremental deposition of lithium on the surfaces.

SubPc* are shown on the right hand side of Fig. 3, which agree fairly well with the experimental spectra. The results indicate that the gap states shown in Fig. 3 are derived from the SubPc* radical. It is known that LiF can react with Al and release lithium atoms. Therefore with SubPc being added in the Al/LiF/Alq_3 cathode structures, other than forming a complex with Alq_3 and resulting *n*-doped Alq_3, lithium could also react with SubPc and create gap states at the interfaces. As a result, the electron injection efficiency would be improved through not only the lowering of injection barriers but also the formation of gap states with SubPc:LiF as EILs, which is consistent with the device characteristics shown in Fig. 2(a).

4. Conclusion

In summary, the improvement of current injection efficiency in organic light emitting diodes is demonstrated with incorporation of LiF:SubPc as electron injection layers. The photoemission spectra indicate that the lithium released from LiF would remove chlorine atoms from SubPc molecules and create large density of gap states at the interfaces. These gap states, resulted from the addition of SubPc in conventional aluminum/LiF/Alq_3 cathode structures, further enhance electron injection efficiency in OLEDs. Combined with the previous report showing SubPc as an efficient hole injection layer, the results demonstrate a unique feature of SubPc which can be used to improve both electron and hole injection efficiency.

Acknowledgments

This work is supported by National Science Councils (NSC 98-2112-M-002-016-MY3 and NSC 98-3114-E-002-001) and "Aim for Top University Project" from the Ministry of Education, Republic of China.

References

[1] C.W. Tang, S.A. Vanslyke, Appl. Phys. Lett. 51 (1987) 913–915.
[2] X. Zhou, J. He, L.S. Liao, M. Lu, X.M. Ding, X.Y. Hou, X.M. Zhang, X.Q. He, S.T. Lee, Adv. Mater. 12 (2000) 265–269.
[3] H. Aziz, Z.D. Popovic, N.X. Hu, A.M. Hor, G. Xu, Science 283 (1999) 1900–1902.
[4] L.S. Hung, C.W. Tang, M.G. Mason, P. Raychaudhuri, J. Madathil, Appl. Phys. Lett. 78 (2001) 544–546.
[5] M.G. Mason, C.W. Tang, L.S. Hung, P. Raychaudhuri, J. Madathil, D.J. Giesen, J. Appl. Phys. Lett. 89 (5) (2001).
[6] C.I. Wu, G.R. Lee, T.W. Pi, Appl. Phys. Lett. 87 (2005).
[7] H.W. Choi, S.Y. Kim, W.K. Kim, J.L. Lee, Appl. Phys. Lett. 87 (2005).
[8] G. Parthasarathy, C. Shen, A. Kahn, S.R. Forrest, J. Appl. Phys. 89 (2001) 4986–4992.
[9] B. Del Rey, U. Keller, T. Torres, G. Rojo, F. Agullo-Lopez, S. Nonell, J. Am. Chem. Soc. 120 (49) (1998) 12808–12817.
[10] C.G. Claessens, D. Gonzalez-Rodriguez, T. Torres, Chem. Rev. 102 (3) (2002) 835–853.
[11] Y.H. Chen, J.H. Chang, G.R. Lee, I.W. Wu, J.H. Fang, C.I. Wu, T.W. Pi, Appl. Phys. Lett. 95 (2009) 133302.
[12] Y.H. Chen, Y.J. Cheng, G.R. Lee, J.H. Chang, I.W. Wu, J.H. Fang, S.H. Hsu, S.W. Liu, C.I. Wu, T.W. Pi, Org. Electron. 11 (2010) 445–449.
[13] T.W. Pi, T.C. Yu, C.P. Ouyang, J.F. Wen, H.L. Hsu, Phys. Rev. B 71 (2005).
[14] W. Kohn, L.J. Sham, Phys. Rev. 140 (1965) A1133–A1138.
[15] C. Lee, W. Yang, R.G. Parr, Phys. Rev. B 37 (1988) 785–789.
[16] D. Axe1, J. Becke, Chem. Phys. 98 (7) (1993) 5648–5652.
[17] M.J. Frisch et al., Gaussian 03 Revision E.01, Gaussian Inc., Wallingford, CT, 2004.
[18] Noel M. O'boyle, Adam L. Tenderholt, Karol M. Langner, J. Comput. Chem. 29 (5) (2008) 839–845.
[19] M.H. Chen, Y.J. Lu, Y.J. Cheng, C.C. Wu, C.I. Wu, Electrochem. Solid-State Lett. 13 (6) (2010) 203–205.
[20] A.G. Wren, R.W. Phillips, L.U. Tolentino, J. Colloid Interf. Sci. 70 (1979) 544–557.
[21] Handbook of X-ray photoelectron spectroscopy, published by Perkin Elmer Inc., ISDN:09627026-2-5.

Organic Electronics 12 (2011) 566–574

Contents lists available at ScienceDirect

Organic Electronics

journal homepage: www.elsevier.com/locate/orgel

ITO-free flexible polymer solar cells: From small model devices to roll-to-roll processed large modules

Matthieu Manceau, Dechan Angmo, Mikkel Jørgensen, Frederik C. Krebs *

Risø National Laboratory for Sustainable Energy, Technical University of Denmark, P.O. Box 49, DK-4000 Roskilde, Denmark

ARTICLE INFO

Article history:
Received 16 December 2010
Received in revised form 7 January 2011
Accepted 9 January 2011
Available online 22 January 2011

Keywords:
Polymer solar cells
ITO-free
Roll-to-roll processing
P3HT:PCBM
Monolithic
Chromium/Aluminum

ABSTRACT

Manufacturing of flexible ITO-free polymer solar cell modules by roll-to-roll methods (R2R) is described. Inverted devices with top illumination were built on a Kapton foil and an Aluminum/Chromium bi-layer system was used as electron contact. The layer structure was Kapton/Al/Cr/P3HT:PCBM/PEDOT:PSS/Ag (printed) and devices were encapsulated. Small area cells (3 cm^2 active area) were first carefully optimized investigating the influence of a number of discrete parameters on performance. A maximum power conversion efficiency of 1.4% was achieved under 1 sun illumination (AM 1.5G, 1000 W m^{-2}). Optimized lab-scale single devices were then transferred to a full R2R process combining slot-die coating and screen printing. All the layers were processed from solution under ambient conditions. Two different concepts were explored: (i) serially connected stripe modules (to reduce the Ohmic losses) and (ii) monolithic modules (to achieve high geometric fill factor and increase the flexibility of the process). For this second concept, the only layer that needs to be patterned is the silver grid electrode and the grid pattern design can then be readily tuned. As an example, four different patterns were used and the resultant performances compared. Modules comprising 16 serially connected cells gave total area efficiencies up to 0.5% (235 cm^2 – 1% on the active area) while the best monolithic ones gave 0.35% (100 cm^2 – 0.4% on the active area). The freshly prepared devices consistently showed an inflection point in the *IV* curve indicative of a rather poor photovoltaic behavior. Upon light exposure and repeated *IV* scans the inflection point partially disappeared, and performance significantly increased.

© 2011 Elsevier B.V. All rights reserved.

1. Introduction

Polymer solar cells (PSC) are emerging as a very promising alternative for solar energy conversion. They ideally present a unique combination of attractive features (low-cost, light weight, flexibility etc.) and are characterized by an incomparable ease of processing [1]. The current state-of-the-art devices rely on a photoactive layer sandwiched between a transparent ITO-based bottom electrode deposited on glass and an evaporated metallic back contact [2]. These so-called "normal geometry" cells are successfully prepared on the lab scale and efficiencies greater than 8% have been reported [3]. As encouraging as these results are, such devices fail to meet most of the prerequisites for a commercially viable device. This is mainly due to the fact that requirements regarding upscaling of fabrication are not taken into consideration. For example, the low-cost potential of PSC is based on high production speeds. This is anticipated to be accomplished by roll-to-roll processing, which totally excludes the use of rigid glass substrates. Vacuum-free processing also seems beneficial as each vacuum step is likely to be cost-increasing unless very high speeds can be accomplished. This point can be addressed by switching from "normal" to "inverted geometry" devices that allow for the use of a solution-processed back electrode. Such devices can be manufactured on a large

* Corresponding author. Tel.: +45 46 77 47 99; fax: +45 46 77 47 91.
E-mail addresses: frederik.krebs@risoe.dk, frkr@risoe.dtu.dk (F.C. Krebs).

1566-1199/$ - see front matter © 2011 Elsevier B.V. All rights reserved.
doi:10.1016/j.orgel.2011.01.009

scale under ambient conditions following a full solution R2R process [4,5]. This has already led to various demonstration projects confirming the feasibility of the approach [6–8]. Detailed cost analysis of these projects interestingly revealed that ITO is one of the major cost-driving factors [9] and because of the cost of Indium and its scarcity, alternative solutions are highly desirable. This has motivated some attempts to prepare PSC without the use of ITO and different ITO-free working concepts have already been described [10–15]. The replacement of ITO by a highly conductive pure PEDOT:PSS layer or by a composite electrode associating PEDOT:PSS and a metal grid has for instance been investigated [10,11]. Inverted geometries employing a multi-layer system (metal/metal or metal/oxide) as electron contact have also been reported [12–15]. Efficiencies up to 3.1% and excellent stability have for example been obtained by Zimmerman et al. using a Chromium/Aluminum/Chromium stack (hereafter referred to as the Fraunhofer-approach) [13].

In this manuscript, the transfer of the suitably modified Fraunhofer-type approach from the lab scale to a full R2R process is presented. An Aluminum/Chromium bottom electrode deposited on a Kapton foil is used in conjunction with a printed silver grid as the top electrode (Fig. 1). The performances of small model devices were first optimized and a new R2R process was then developed where all the layers except the electron contact were processed from solutions under ambient conditions. Both serially connected modules and monolithic solar cells were prepared. This second approach greatly simplifies the processing as the only patterning requirement concerns the top grid [14].

2. Materials and methods

2.1. Materials

Poly(3-hexylthiophene) was purchased as Sepiolid P200 from BASF and [60]PCBM was purchased from Solenne BV (purity of 99%). PEDOT:PSS was purchased as Orgacon EL-P 5010 from Agfa and was diluted with isopropanol until a viscosity of 270 mPa s was obtained. The silver ink was a heat curable one (Dupont PV410) and used as received. The barrier foil was purchased from Amcor.

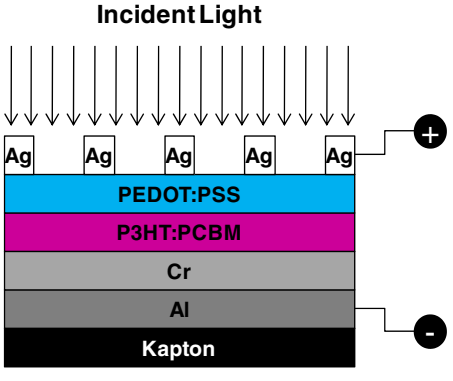

Fig. 1. Illustration of the device architecture employed in this study.

2.2. R2R processing of the electron contact

Kapton foil was purchased from Skultuna Flexibles AB (Sweden) and trimmed to a web of 290 mm. It was chosen owing to its higher thermal stability and better mechanical properties. Deposition of the Aluminum/Chromium stack was performed using a roll-to-roll evaporator. The bare foil was introduced into a R2R sputtering system employing two DC magnetrons with two different targets (Aluminum and Chromium). After pumping down, 100 nm of Aluminum were first sputtered then followed by 15 nm of Chromium on the next target. The web speed was 1 cm min^{-1}. The Al/Cr stack on top of Kapton was obtained either as 16 stripes, each 13-mm-wide and separated from each other by a 2-mm-wide gap (hereafter referred to as striped foil) or as a 200-mm wide band (hereafter referred to as plain foil). The two different patterns are pictured in Fig. 2. Two different kinds of plain foil were also prepared changing the pumping time preceding the stack deposition. The respective sheet resistances of the foils used within this study are collected in Table 1.

2.3. Model devices preparation

Small pieces of the plain foils were first cut manually (25 × 50 mm) and 15 mm of the electrode was then removed from one end by dipping the sample into a 1 M NaOH solution. The as-obtained substrates were rinsed with deionized water and isopropanol. A P3HT:PCBM layer was spin-coated at 600 rpm from a chlorobenzene solution (polymer:fullerene weight ratio 15:10, 30:20, 21:14, 21:18.5 or 21:21 mg/mL of chlorobenzene). The active layer surface was wetted with isopropanol and a PEDOT:PSS layer was then spin-coated at 700, 1000, 1250, 1400 or 2000 rpm. A 5 min thermal annealing was subsequently performed either at 110 or 140 °C on a hot plate. The silver grid was printed using a small laboratory screen printer and dried immediately after printing for 3 min at 140 °C on a hot plate. Finally, the devices were manually encapsulated. All preparative steps were carried out in air and the device active area was 3 cm^2.

2.4. R2R processing

2.4.1. Geometrical considerations

2.4.1.1. 16-Stripe modules. Fig. 3 shows the principle whereby the Al/Cr bilayer is patterned into endless stripes. All the stripes are then serially connected via the ensuing silver printing process.

2.4.1.2. Monolithic modules. In principle, devices as wide as 200 mm could have been made, but here we chose to work on 85 mm wide stripes so that two monolithic modules can fit on the width of the foil.

2.4.2. R2R slot-die coating of P3HT:PCBM and PEDOT:PSS

The R2R slot-die coating was performed on a BC30 basecoater from Solarcoating Machinery GmbH (Germany). The equipment has already been extensively described elsewhere [16]. The active layer was coated from a chlorobenzene solution having the following composition:

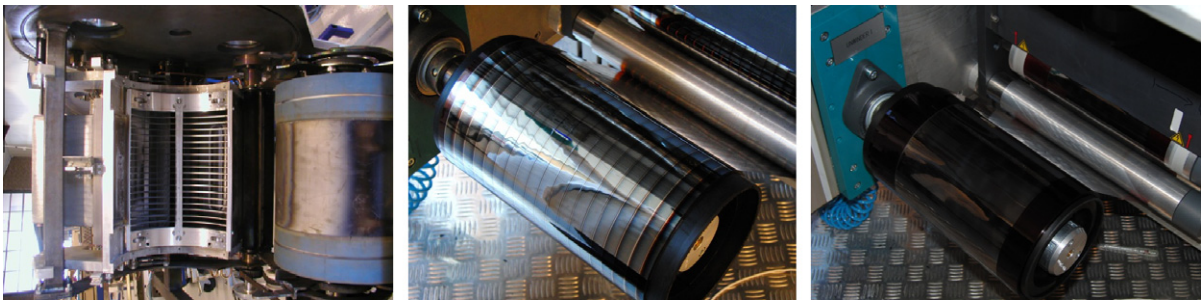

Fig. 2. Photograph of the R2R evaporator setup showing the drum and the mask in front of the two targets (Al and Cr). Courtesy of Susanne Libergreen (left). The two different electron contact patterns are also shown as the striped pattern (middle) and the plain foil (right).

Table 1
Characteristics of the foils employed in this study.

Foil	Pumping time (h)	Sheet resistance (Ω square^{-1})
Stripes	15	0.5
Plain A	2	10–15
Plain B	15	0.5

21 mg mL^{-1} for P3HT and 18.5 mg mL^{-1} for PCBM (Fig. 4). The typical coating speed was 2 m min^{-1} and the active layer was subsequently dried at 90 °C with a residence time in the oven of around 30 s. The wet and dry layer thicknesses were about 8 μm and 300 nm, respectively. The PEDOT:PSS solution was then slot-die coated at a typical speed of 0.3 m min^{-1} and the material was dried at 110 °C with a residence time in the oven of around 3 min. The wet layer thickness was about 70 μm and the dry one about 20 μm. To avoid dewetting of the PEDOT:PSS layer prior to drying, the active layer was wetted with isopropanol immediately before coating.

In the case of the striped foil, P3HT:PCBM was coated as 16 13-mm-wide stripes on top of the Al/Cr stripes with a 1-mm offset allowing for contact between the printed silver and the Al/Cr in the serial connection. Sixteen stripes of PEDOT:PSS were coated on top of the active layer with a 1-mm offset to avoid contact with the Al/Cr layer.

As for the plain foil, two 96-mm wide P3HT:PCBM stripes were coated on top of the Al/Cr (Fig. 4). The two stripes were separated by a 20-mm wide gap allowing for final contacting of the Al/Cr electrode. Two 94-mm wide PEDOT:PSS stripes were coated on top of the active layer with a 1-mm offset to avoid contact with the Al/Cr system.

2.4.3. R2R screen printing of the silver back electrode

This step was carried out on a flat bed R2R screen printer from Alraun [5]. The printing speed of the squegee was 550 mm s^{-1} and the web speed was 1 m min^{-1}. The drying was carried out immediately after printing in a hot air oven. The temperature was set to 140 °C and the total drying time was around 1.2 min (oven length 120 cm). The printed silver pattern used for the 16-stripes modules has already been described elsewhere [5]. In the case of the monolithic devices, four different patterns were employed (Figs. 5 and 6). Four monolithic modules were thus made in one print, each of them having a different silver grid pattern.

2.4.4. R2R lamination

Device encapsulation was achieved on both sides of the completed solar cells by cold lamination of the barrier foil carrying an adhesive. The barrier on the top side was made such that a part of the printed silver electrode was exposed ensuring reliable contact with the electrodes during electrical characterization. The modules were finally cut manually into individual devices prior to electrical characterization. The illuminated area and active area of the final modules are reported in Table 2 for both approaches. For monolithic devices the active area corresponds to the illuminated area minus the silver electrode area (shadow loss).

2.5. Devices characterization

IV-characteristics were recorded under illumination with a Keithley 2400 source-measure unit. The illumination was provided by a KHS575 solarkonstant from Steuernagel Lichttechnik (AM 1.5G, 1000 W m^{-2}) and the intensity regularly controlled. The temperature was 72 ± 2 °C. Photo-annealing studies were also performed by light-soaking the devices under simulated sunlight (AM 1.5G, 1000 W m^{-2}, 72 ± 2 °C) and recording *IV*-curves at fixed interval over an extended period of time.

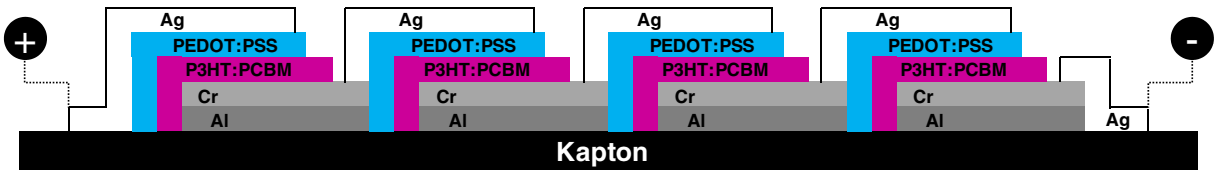

Fig. 3. Schematic cross section of the device showing the layers stacking and their position (view along the stripes).

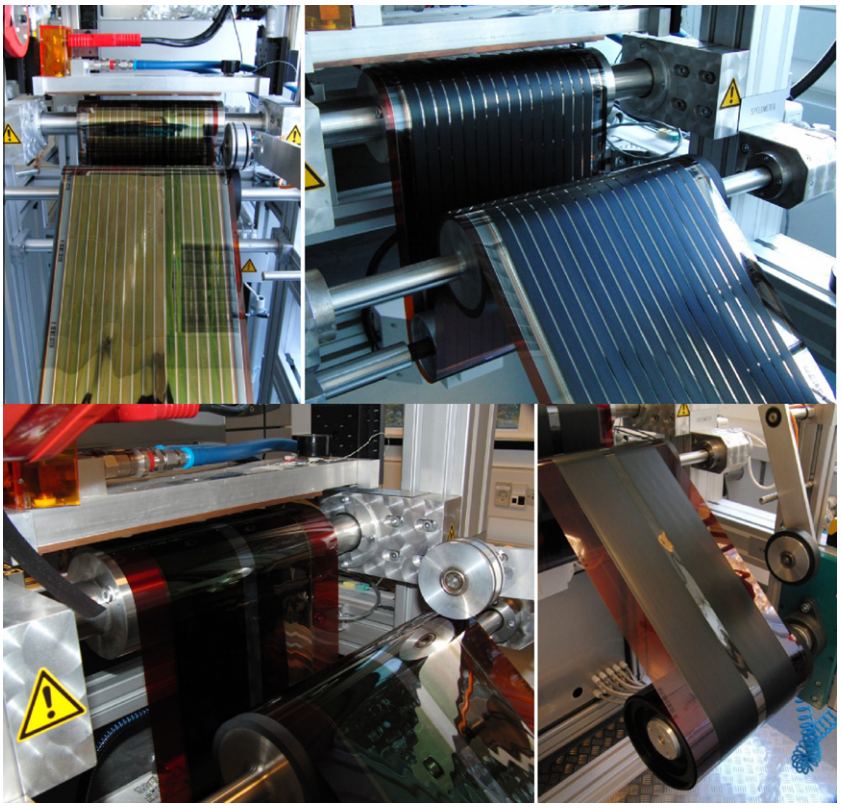

Fig. 4. The slot-die coating of P3HT:PCBM (left) and PEDOT:PSS (right) using the striped foil (top) or the plain foil (bottom).

Light Beam Induced Current (LBIC) experiments were carried out using a custom made setup previously described [17].

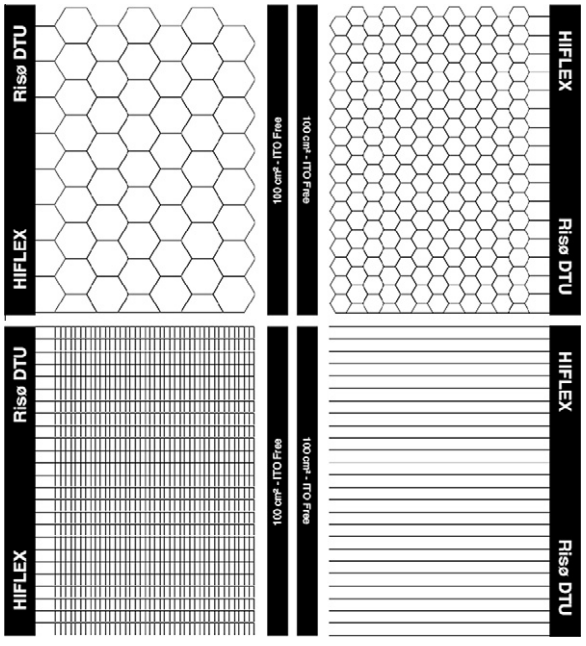

Fig. 5. Drawings of the four silver patterns used for the monolithic devices. Large honey-comb (top left), small honey-comb (top right), grid (bottom left) and simple comb (bottom right).

3. Results and discussion

3.1. Model devices (3 cm^2)

Before preparing the large modules, initial studies were performed on small area model devices. This was done both to evaluate the potential of the approach and to optimize a range of discrete parameters. All the results are collected in the Table 3, together with the experimental details. All the values reported are obtained from an average of four photovoltaic cells.

3.1.1. Influence of the active layer composition

A first series of devices have been fabricated to optimize the solution concentration. The various P3HT concentrations tested were 15, 21 and 30 mg mL^{-1} while the P3HT:PCBM ratio was set to 1.5:1 (w/w). In these conditions, the highest performances were obtained with the intermediate P3HT concentration (21 mg mL^{-1}). A second set of experiments was performed to investigate the influence of the P3HT:PCBM ratio. Three compositions were used – 21:14, 21:18.5 and 21:21 mg mL^{-1} – and very similar performances were recorded. This is not completely surprising as a recent study evidenced that a relatively broad range of P3HT:PCBM mixing ratio affords the optimal device performances [18]. The optimized devices gave V_{OC} = 0.37 V, J_{SC} = −7.3 mA cm^{-2}, and a fill factor (FF) of 0.30, resulting in an aperture efficiency of 0.8% (average value). An inflection point was systematically observed in

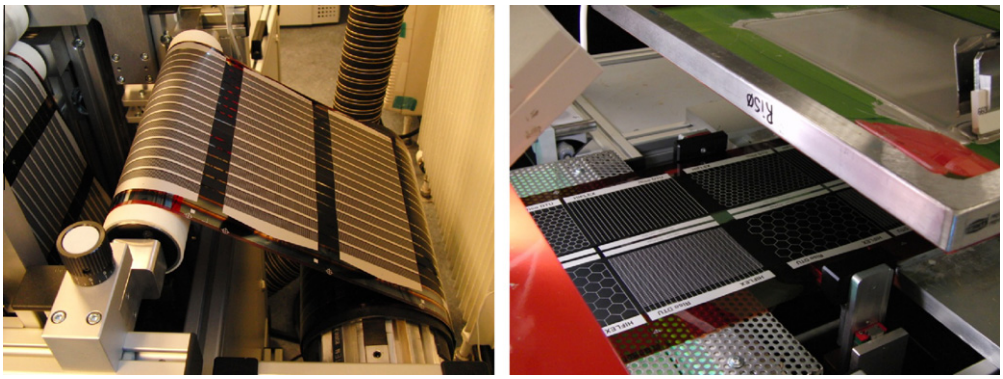

Fig. 6. Silver screen printing for the 16-stripes devices (left) and the monolithic devices (right).

Table 2
Illuminated and active area of the different modules prepared in this study.

Module types	Total illuminated area (cm^2)	Active area (cm^2)	Ratio active/total
16-Stripes	235	160	68.1
Monolithic	100		
Comb		95.8	95.8
Grid		87.8	87.8
Honey comb		94.7	94.7
Large honey comb		97.3	97.3

Table 3
Overview of processing of small area model devices together with the corresponding photovoltaic properties.

Foil	P3HT:PCBM (mg mL^{-1})	PEDOT:PSS		V_{oc} (V)	J_{sc} (mA cm^{-2})	FF	PCE (%)
		Spinning speed (rpm)	Drying				
A	15:10	1000	5 min/110 °C	0.35	3.9	0.31	0.42
	21:14			0.35	5.9	0.35	0.72
	30:20			0.32	3.4	0.24	0.26
	21:21			0.36	7.4	0.3	0.8
	21:18.5			0.37	7.3	0.3	0.8
B	21:18.5	1000	5 min/110 °C	0.43	8.0	0.3	1
			5 min/140 °C	0.39	5.4	0.31	0.65
		700	5 min/110 °C	0.41	6.4	0.35	0.9
		1250		0.4	7.7	0.36	1.1
		1400		0.4	8.0	0.33	1.1
		2000		–	–	–	–

the *IV*-curves of the devices explaining the low fill factor (Fig. 7, dashed curved). This behavior has been frequently observed in a wide range of devices and is generally attributed to poor carrier transport in one of the layers or interfaces [19].

3.1.2. Influence of the electron contact preparation

The influence of Al/Cr deposition conditions was then studied. Two kinds of foils were used (Table 1) and the resultant performances of the devices were compared (Table 3). As expected, the best results were obtained with the low resistance foil as a 25% efficiency increase was recorded using it. The optimized device gave V_{OC} = 0.43 V, J_{SC} = −8.0 mA cm^{-2}, a fill factor (FF) of 0.30 and an aperture efficiency of 1% (on average).

3.1.3. Influence of the PEDOT:PSS

Further experiments were then conducted to optimize the thickness and the drying conditions of the hole-transporting layer. PEDOT:PSS thickness is especially critical as the use of non-transparent substrate imposes to illuminate the device through the PEDOT:PSS layer. The use of a too thick layer leads to low current densities because of significant transmission loss. In principle, reducing the layer thickness increases transmission of light and subsequently the current density. However, a too thin layer has already been shown to lead to short circuit, a phenomenon ascribed to the destruction of the active layer by the solvent of the silver paste [4]. Increasing the layer thickness solves this problem as solvent diffusion is then prevented. A good balance has thus to be found to get working devices that

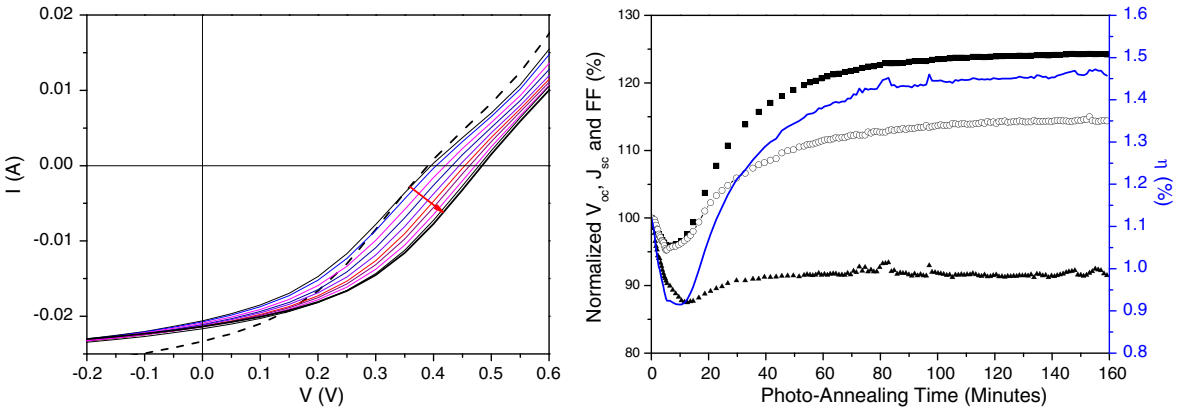

Fig. 7. (Left) *IV*-curve typical evolution during photo-annealing of an encapsulated model device at 1000 W m^{-2}, 72 ± 2 °C (- - -) as-produced (–) after photo-annealing. The curves corresponding to the first phase are omitted; (right) evolution of the photovoltaic parameters versus photo-annealing time (■) V_{oc}, (▲) J_{sc}, (○) FF and (–) η. Device was processed using foil B and PEDOT:PSS was spin-coated at 1250 rpm.

remain as efficient as possible. To adjust the PEDOT:PSS layer thickness, different spinning speeds were employed (700, 1000, 1250, 1400 and 2000 rpm, see Table 3). A practical optimum was obtained processing the PEDOT:PSS in the range 1000–1400 rpm as efficiencies around 1.1% were achieved in these conditions. Lower spin speed yielded lower current while higher spin speed led to reduced voltage.

A last series of experiments were made to study the influence of the drying conditions on the device efficiency. The PEDOT:PSS layer was dried either at 70, 90, 110 or 140 °C. The two lower ones were proved to be practically irrelevant as the time needed to complete a proper drying was extremely long (>45 min at 70 °C). It was also observed that annealing at 140 °C causes a significant efficiency decrease (ca 35%) and 110 °C consequently appeared to be the best drying temperature.

3.1.4. Device photo-annealing

The effects of illumination on the cells photovoltaic properties were studied by measuring the electrical properties of encapsulated devices all along ageing. An instantaneous but rather limited decrease in efficiency was initially observed and immediately followed by a drastic performance increase. A characteristic experiment is shown in Fig. 7. V_{oc}, J_{sc} and FF data have been normalized by their respective initial values for the sake of clarity. One can clearly observe the progressive removal of the inflection point in the *IV*-curve that leads to a sharp increase in the fill factor (FF) and the open-circuit voltage (V_{oc}) while the short-circuit current density is reduced by ca. 10%. A very similar behavior has already been observed and recently described in the case of inverted devices including a ZnO layer [19]. In our case, for the best performing devices a 30% increase was observed and final efficiency as high as 1.4% was obtained (Table 4). This peculiar behavior was systemically observed, but the maximum efficiency varied considerably with the PEDOT:PSS processing conditions (Table 4). Indeed, for devices comprising a thicker PEDOT:PSS layer, the efficiency of photo-aged devices remained inferior to their initial one. This places further evidence on the critical influence of the PEDOT:PSS layer thickness.

Table 4
Overview of the initial and final power conversion efficiencies for different PEDOT:PSS processing conditions.

PEDOT:PSS spinning speed (rpm)	η As-produced (%)	η After photo-annealing (%)
700	0.9	0.85
1000	1	1.2
1250	1.1	1.4
1400	1.1	1.35

3.2. R2R devices

Once the lab-scale experiments completed, the next step was to transfer the optimized devices to a full R2R process allowing for large area modules production. Whatever the module geometry – 16-stripes or monolithic – active layer and PEDOT:PSS were slot-die coated and the silver grid was screen-printed. Of course, when going from spin-coating to slot-die coating some adjustments have to be made (e.g. the active layer has to be dried). But, to the best of our ability, we tried to limit them as much as possible. There was no particular wetting problem of the P3HT:PCBM ink on the electron contact and the active layer coating proceeded well. After isopropanol pre-washing, the PEDOT:PSS was slot-die coated on top of the active layer and subsequently dried. Here again, no particular technical difficulty was encountered during this step.

3.2.1. 16-Stripe modules (235 cm^2)

In this first case, the total length of the material processed was 6 m, giving 20 print repetitions, corresponding to a total of 40 cells. The screen printing of the silver grid being a non continuous process – as opposed to the slot-die coating – it is possible to adjust the position of the mask only between two prints. One prerequisite to making a good print is that all the stripes are perfectly straight and regularly spaced, at least over the repetition length of the

print. Otherwise, some stripes could be shorted after silver printing which of course reduces the module voltage. Unfortunately, this requirement was not always satisfied and difficulties were encountered during the printing step. These alignment problems resulted in strong variations of modules voltage. According to the results obtained with the model devices and assuming that all the stripes perform equally, a V_{oc} as high as 6.4 V could have been expected while the highest voltage achieved was around 5.2 V. The average properties of the devices showing a V_{oc} > 3.5 V (21 devices out of 40) are reported in Table 5 together with the characteristics of the best device. The fill factor is very close to the one reached with model devices whereas the current density is much lower by a factor 5-6. LBIC analysis was performed and revealed that in each module, some of the stripes were performing poorly (Fig. 8) thus limiting the whole efficiency. As observed on Fig. 8, seven out of the 16 stripes show no or limited photovoltaic behavior. This clearly explains the efficiency difference between the lab-scale and the R2R processed devices.

The effects of photo-annealing on the device properties were also examined. As observed for the model cells, large modules required light soaking for some time to reach the optimum performance (Fig. 9). While the fill factor remained almost unchanged, both the short-circuit current density and the open-circuit voltages largely increased. The efficiency recorded after light-soaking was more than doubled and the top performance reached was 0.5%.

Table 5
Overview of the results obtained for the 16-stripes modules showing a V_{oc} > 3.5 V. The highest performance obtained are indicated in brackets.

	V_{oc} (V)	J_{sc} (mA cm^{-2})	FF	η (%)
As-prepared	4.3 (5.1)	0.12 (0.14)	0.35 (0.41)	0.19 (0.29)
After photo-annealing	5.9 (6.1)	0.17 (0.21)	0.41 (0.41)	0.41 (0.53)

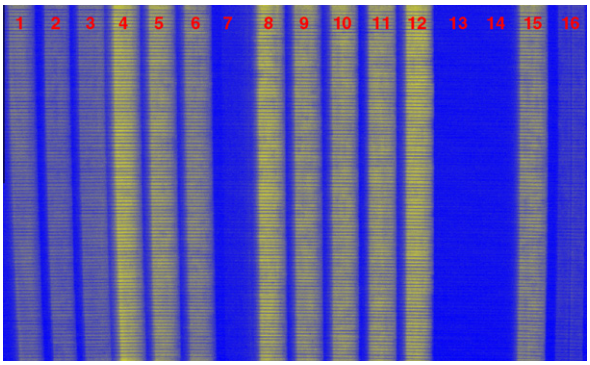

Fig. 8. LBIC image of a typical 16-stripe module where bright yellow represents the highest absolute current extracted while blue represents the lowest current. Stripes nos. 7, 13 and 14 exhibit no photovoltaic behavior. (For interpretation of the references in colour in this figure legend, the reader is referred to the web version of this article.)

3.2.2. Monolithic devices (100 cm^2)

When a process is up-scaled and large-area solar modules produced, large electrical currents are encountered that have to be extracted. When ITO is used, the distance over which the current can be efficiently transported – i.e. without significant Ohmic loss – is strongly limited by the non negligible electrode sheet resistivity (>5 Ω square^{-1} minimum). The situation is even more problematic when ITO is deposited on flexible polymeric substrates where the sheet resistivity is often much higher (around 60 Ω square^{-1}). It is then necessary to pattern the ITO into stripes that can be serially connected. In this way, Ohmic losses are reduced but this is achieved at the expense of the active area (Table 2). In addition, some extra processing steps are needed and this also implies that a great part of the initial amount of ITO is lost [9]. It thus seems attractive to use a high conductivity metal bottom electrode allowing for the processing of large area monolithic devices [14]. Another advantage of this approach is that there is no requirement as for a patterning of the active layer or the PEDOT:PSS. The only patterning constraints reside in the front grid, but this can be easily varied. The whole processing is then simplified to a great extent as this approach does not rely on an extremely accurate patterning which can be a serious issue otherwise, as exemplified in the former paragraph.

Ten meters of Al/Cr foil were processed and a total of 200 cells were obtained. As expected, it was necessary to light-soak the modules in order to reach the highest efficiency. The results obtained for the four different grid patterns are collected in Table 6. From these data it is clear that the grid pattern provides the best results as it provides the highest current density and consequently the maximum performance after light-soaking was 0.36% (0.4% on the active area). This finding is due to the higher surface coverage of this pattern (Table 2 and Fig. 5). Indeed, the rather low conductivity of the PEDOT:PSS limits the distance over which the holes can be transported. If this distance is increased – i.e. if the "density" of the grid is reduced – some of the holes are not extracted and the collected current is lowered. Of course, the grid density must be limited as well. Because of the shadow losses, the amount of light reaching the active layer diminishes when the grid density increases. At some point, this second effect would overbalance the former leading to an efficiency decrease.

One can notice that in comparison to model devices, the efficiency of these cells is strongly limited by a low fill factor (ca 0.25) and a reduced current density (ca. −3 mA cm^{-2}) while the voltage is close to the one obtained for the small devices (ca 0.4–0.45 V). Modules were finally characterized by LBIC and two examples are given below (Fig. 10). From these pictures it is clear that current is collected from the whole device area and one can easily see the shape of the grid.

3.3. Comments and outlook

While ITO has accompanied the PSCs development from the very beginning of the field and is now used worldwide in almost all the devices, its alleviation is commonly seen

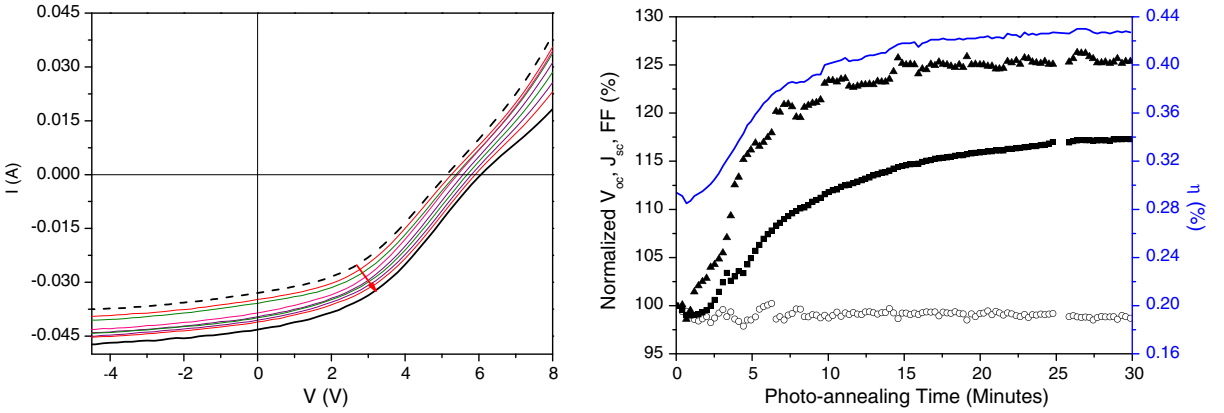

Fig. 9. (Left) *IV*-curve typical evolution during photo-annealing of an encapsulated 16-stripe module at 1000 W m^{-2}, 72 ± 2 °C (- - -) as-produced (–) after photo-annealing; (right) evolution of the photovoltaic parameters versus photo-annealing time (■) V_{oc}, (▲) J_{sc}, (○) FF and (–) η.

Table 6
Overview of the results obtained for the monolithic devices. The highest performance obtained for each kind of modules is shown in brackets.

		V_{oc} (V)	J_{sc} (mA cm^{-2})	FF (%)	η (%)
Comb	As-prepared	0.18 (0.19)	1.01 (1.29)	24.1 (24.8)	0.04 (0.06)
	After photo-annealing	0.32 (0.33)	2.25 (2.6)	25.6 (25.3)	0.18 (0.22)
Grid	As-prepared	0.31 (0.36)	1.94 (2.28)	24.5 (23.6)	0.15 (0.19)
	After photo-annealing	0.44 (0.45)	3.2 (3.30)	24.4 (24.4)	0.34 (0.36)
Honey comb	As-prepared	0.20 (0.23)	1.10 (1.24)	24.6 (24.5)	0.05 (0.07)
	After photo-annealing	0.34 (0.34)	2.35 (2.6)	25.2 (24.7)	0.20 (0.22)
Large honey comb	As-prepared	0.25 (0.3)	1.02 (1.13)	23.8 (23.3)	0.06 (0.08)
	After photo-annealing	0.42 (0.43)	2.01 (2.30)	24.2 (24.1)	0.20 (0.24)

as a prerequisite for commercially viable devices. This is of course very challenging as it requires developing totally different approaches that lie outside the trotted path. To the best of our knowledge, very few studies have been published where processes enabling large-scale R2R manufacture of ITO-free solar cells are described [14,15]. In a context where new concepts are highly sought, the efforts reported here are then valuable. The achievability of the approach we followed has indeed been demonstrated even if it implies a significant sacrifice in performance in comparison to the state-of-the-art [8]. It is obvious that new strategies allowing for the removal of ITO can only be successful if they solve more problems than they create. From this point of the view, two main shortcomings can already be pointed out in this work. The use of Kapton is a first drawback owing to its cost alone (40 times more expensive than PET). However, as there is no need for a transparent substrate, solar modules could potentially be built on any flexible substrate. The vacuum-deposition of the metallic electron contact is a second negative aspect, although it is completely feasible to do it on a large scale using R2R methods (cf. the example of the food packaging industry). Solution-processed electrodes are much more attractive as they can be prepared in higher cadence and potentially with a reduced cost. Besides, a successful attempt has already been reported where PSCs were prepared using a process free from ITO and vacuum coating steps [15].

4. Conclusion

In this work, the preparation of large area ITO-free flexible polymer solar cells has been described. The device structure comprised Kapton/Al/Cr/P3HT:PCBM/PEDOT:PSS/Ag with illumination through the top electrode. The performances of small area model cells were first optimized and the efficiency that could be reached was 1.4% as tested under standard conditions (AM 1.5G, 1000 W m^{-2}). The process was subsequently up-scaled using full roll-to-roll processing and two different concepts were developed: (i) serially connected stripe modules and (ii) monolithic modules. The feasibility of both approaches has been demonstrated and their respective photovoltaic properties presented. Efficiencies up to 0.5% were achieved with the 16-stripe modules (total area 235 cm^2) while the best monolithic ones gave 0.35% (100 cm^2). This second approach provides strong additional advantages in terms of processing as the module shape can be chosen when the silver grid – i.e. the last layer – is printed. Finally, the current limitations of the strategy we followed were outlined. First of all, while the problem of the use of ITO is addressed, a sacrifice in performance was also observed. In addition the upscaling to larger area devices brings along with it challenges in alignment of layers during coating and printing leading to large defective areas (stripes) limiting the performance. More control over the coating and printing process is thus warranted before detailed physical insight can be gained. Other shortcomings are the vacuum coating of Aluminum and Chromium and the use of Kapton. Possible solutions to these hindrances were finally discussed.

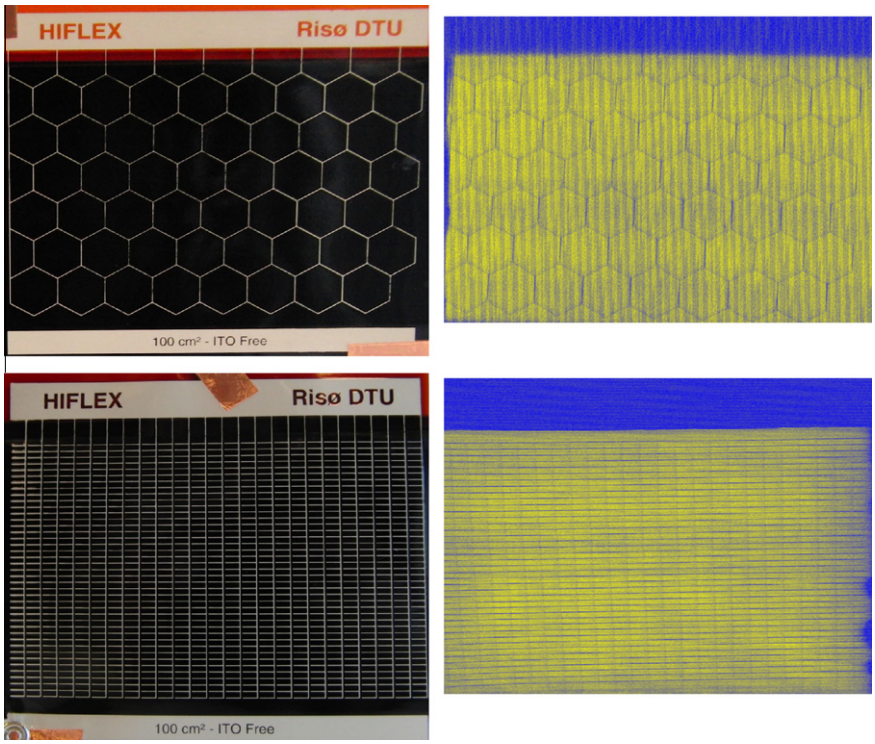

Fig. 10. Picture of a large honey comb (top left) and a grid device (bottom left) together with the corresponding LBIC clichés (top right and bottom right).

Acknowledgements

This work has been supported by the European Commission as part of the Framework 7 ICT 2009 collaborative project HIFLEX (Grant No. 248678). The authors thank Dr Birger Zimmermann (Fraunhofer ISE, Germany) for fruitful discussions about the Kapton/Al/Cr concept and Dr Yulia Galagan (Holst Centre, The Netherlands) for her help in calculations of surface coverage.

References

[1] F.C. Krebs, Sol. Energy Mater. Sol. Cells 93 (2009) 394–412.
[2] C.J. Brabec, S. Gowrisanker, J.J.M. Halls, D. Laird, S. Jia, S.P. Williams, Adv. Mater. 22 (2010) 3839–3856.
[3] <http://www.solarmer.com/; http://www.konarka.com/>.
[4] F.C. Krebs, S.A. Gevorgyan, J. Alstrup, J. Mater. Chem. 19 (2009) 5442–5451.
[5] F.C. Krebs, T. Tromholt, M. Jørgensen, Nanoscale 2 (2010) 873–886.
[6] F.C. Krebs, M. Jørgensen, K. Norrman, O. Hagemann, J. Alstrup, T.D. Nielsen, J. Fyenbo, K. Larsen, J. Kristensen, Sol. Energy Mater. Sol. Cells 93 (2009) 422–441.
[7] F.C. Krebs, T.D. Nielsen, J. Fyenbo, M. Wadstrøm, M.S. Pedersen, Energy Environ. Sci. 3 (2010) 512–525.
[8] F.C. Krebs, J. Fyenbo, M. Jørgensen, J. Mater. Chem. 20 (2010) 8994–9001.
[9] N. Espinosa, R. García-Valverde, A. Urbina, F.C. Krebs, Sol. Energy Mater. Sol. Cells. doi:10.1016/j.solmat.2010.08.020.
[10] Y. Galagan, J.-E.J.M. Rubingh, R. Andriessen, C.-C. Fan, P.W.M. Blom, S.C. Veenstra, J.M. Kroon, Sol. Energy Mater. Sol. Cells doi:10.1016/j.solmat.2010.08.011.
[11] T. Aernouts, P. Vanlaeke, W. Geens, J. Poortmans, P. Heremans, S. Borghs, R. Mertens, R. Andriessen, L. Leenders, Thin Solid Films 451–452 (2004) 22–25.
[12] B. Zimmermann, M. Glatthaar, M. Niggemann, M.K. Riede, A. Hinsch, A. Gombert, Sol. Energy Mater. Sol. Cells 91 (2007) 374–378.
[13] B. Zimmermann, U. Würfel, M. Niggemann, Sol. Energy Mater. Sol. Cells 93 (2009) 491–496.
[14] F.C. Krebs, Sol. Energy Mater. Sol. Cells 93 (2009) 1636–1641.
[15] F.C. Krebs, Org. Elec. 10 (2009) 761–768.
[16] F.C. Krebs, Sol. Energy Mater. Sol. Cells 93 (2009) 465–475.
[17] F.C. Krebs, R. Søndergaard, M. Jørgensen, Sol. Energy Mater. Sol. Cells. doi:10.1016/j.solmat.2010.11.007.
[18] J. Alstrup, M. Jørgensen, A.J. Medford, F.C. Krebs, A.C.S. Appl, Mater. Interfaces 2 (2010) 2819–2827.
[19] M.R. Lilliedal, A.J. Medford, M.V. Madsen, K. Norrman, F.C. Krebs, Sol. Energy Mater. Sol. Cells 94 (2010) 2018–2031.

Organic Electronics 12 (2011) 575–581

Contents lists available at ScienceDirect

Organic Electronics

journal homepage: www.elsevier.com/locate/orgel

Efficient carrier- and exciton-confining device structure that enhances blue PhOLED efficiency and reduces efficiency roll-off

Wen-Yi Hung [a,*], Zhong-Wen Chen [a], Hong-Wei You [a], Fu-Chuan Fan [b], Hsiao-Fan Chen [b], Ken-Tsung Wong [b,*]

[a] Institute of Optoelectronic Sciences, National Taiwan Ocean University, Keelung 202, Taiwan
[b] Department of Chemistry, National Taiwan University, Taipei 106, Taiwan

ARTICLE INFO

Article history:
Received 16 November 2010
Received in revised form 11 January 2011
Accepted 11 January 2011
Available online 31 January 2011

Keywords:
Phosphorescent OLEDs
Device structure
Time-of-flight
Charge mobility

ABSTRACT

In this study we used a known host material diphenylbis[4-(9-carbazoyl)phenyl]silane (SiCa) to realize a highly efficient bis[4,6-(difluorophenyl)-pyridinato-N,$C^{2'}$]picolinate (FIrpic)–based blue phosphorescent device exhibiting high efficiencies of up to 18.3%, 41.5 cd/A, and 31 lm/W in a carrier- and exciton-confined device structure. At a practical brightness of 1000 cd/m^2, the device performance (η_{ext}) remained as high as 16.7%. The enhanced efficiency and reduced roll-off resulted mainly from the introduction of (a) DTAF as an HTL that efficiently blocked and confined excitons within the FIrpic-doped emissive layer, and (b) a thin layer of DPPS between the EML and TAZ, serving as an exciton- and hole-blocking layer to suppress exciton quenching by FIrpic at the EML–ETL interface. In addition, we incorporated a red phosphorescent dopant ($Mpq_2Iracac$) into the blue device to fabricate a white phosphorescent organic light-emitting device, which exhibited satisfactory efficiencies (11.6%, 21.2 cd/A, 14.2 lm/W) with the Commission Internationale de L'éclairage (CIE) coordinates of (0.35, 0.38).

© 2011 Elsevier B.V. All rights reserved.

1. Introduction

Phosphorescent organic light-emitting devices (PhOLEDs) featuring emissive layers comprising transition metal–centered dyes doped into appropriate host materials are attracting much research attention because they can achieve internal efficiencies as high as 100% [1]. Unlike the reported efficient green- and red-PhOLEDs, the realization of highly efficient blue PhOLEDs remains a great challenge because the triplet energy (E_T) of host molecules must be sufficiently high (i.e., $E_T \geqslant 2.7$ eV) to confine the triplet excitons within the emitting layer [2–5]. In addition, the tendency of triplet excitons to diffuse into the nonradiative levels of the neighboring hole transport layer (HTL) and/or electron transport layer (ETL) must also be avoided. In this regard, Zheng et al. demonstrated highly efficient blue PhOLEDs using 1,1-bis[(di-4-tolylamino)phenyl]cyclohexane (TAPC) as the HTL, obtaining a maximum external quantum efficiency (η_{ext}) of 18.1%, which is approximately 50% higher than the value obtained (12%) for a previously reported device featuring bis[*N*-(1-naphthyl)-*N*-phenylamino]biphenyl (NPB) as the HTL [6]. The Kido group recently reported several ETLs exhibiting hole-blocking ability that improve the performance of bis[4,6-(difluorophenyl)-pyridinato-N,$C^{2'}$]picolinate (FIrpic)–based blue PhOLEDs [7–9]. For example, a device incorporating diphenylbis[4-(pyridin-3-yl)phenyl]silane (DPPS) as the ETL provided a maximum value of η_{ext} of 22%, which is much higher than the value obtained (15.3%) when using 3-(4-biphenylyl)-4-phenyl-5-(4-*tert*-butylphenyl)-1,2,4-triazole (TAZ) as the ETL [9]. It appears that achieving highly efficient blue PhOLEDs requires improvements in the charge recombination efficiency by

* Corresponding authors. Tel.: +886 2 24622192x6718; fax: +886 2 24634360 (W.-Y. Hung).
E-mail addresses: wenhung@mail.ntou.edu.tw (W.-Y. Hung), kenwong@ntu.edu.tw (K.-T. Wong).

1566-1199/$ - see front matter © 2011 Elsevier B.V. All rights reserved.
doi:10.1016/j.orgel.2011.01.012

using efficient charge-transporting materials to maintain the charge balance as well as to confine the generated triplet excitons within the emissive layer. The neighboring hole- and electron-transport materials (HTMs and ETMs) require: (a) the higher triplet energy than that of blue dye to suppress the triplet exciton quenching of the emitter, (b) the carrier blocking ability to confine the carriers within EML and (c) the high carrier transport/injection property to reduce the driving voltage of devices.

Among the many silicone-based wide-bandgap host materials that have been developed, tetraphenylsilane-functionalized ultrahigh-energy-gap hosts (UGHs) are particularly useful for fabricating deep blue PhOLEDs [3,10,11]. Unfortunately, tetraphenylsilane has an undesirably low glass transition temperature (T_g), which limits its practical applicability. To solve this problem, Kim et al. developed a new host material, diphenylbis[4-(9-carbazoyl)phenyl] silane (SiCa) [12], by appending carbazole moieties through their 9-positions (i.e., the nitrogen atom) to a tetraphenylsilane core. The design of SiCa was based on the fact that both tetraphenylsilane and carbazole possess large triplet energy gaps (3.5 and 3.0 eV, respectively) [10,13]. The tetrahedral Si center serves as an effective spacer that blocks the π-conjugation of the carbazole substituents, thereby maintaining a high triplet energy (E_T = 3.0 eV) and enhancing the thermal stability (T_g = 109 °C). These values suggest that SiCa might be a promising host material for blue electrophosphorescent devices. Unfortunately, the use of SiCa as a host for tris[(3,5-difluoro-4-cyanophenyl)pyridine]iridium (FCNIr) [12,14] resulted in a low quantum efficiency (4.9% at 300 cd/m^2), presumably because of poor energy transfer in the host/guest system, poor triplet exciton confinement, and/or unbalanced charge recombination in the emitting layer.

In this report, we demonstrate that high efficiency can be achieved in a carrier- and exciton-confined device structure. Indeed, we achieved a maximum value of η_{ext} of 18.3% when using the well-established blue phosphorescent iridium complex FIrpic as the dopant dispersed in SiCa by using efficient charge-transporting materials (DTAF and DPPS) to maintain the charge balance as well as to confine the generated triplet excitons within the emissive layer. These results can provide the basic guidelines for the device design of FIrpic-based OLEDs. We have also used SiCa in conjunction with a red phosphorescent dopant ($Mpq_2Iracac$) [15] to fabricate a white PhOLED that exhibited satisfactory efficiency (11.6%, 21.2 cd/A, 14.2 lm/W) with the Commission Internationale de L'éclairage (CIE) coordinates of (0.35, 0.38).

2. Results and discussion

We adopted two approaches to improve the performance of the previously reported device incorporating SiCa as the blue host: (1) employing a dopant material having a lower triplet energy and (2) optimizing the device structure so that it featured charge transport layers with high triplet energies [16]. Because the triplet energy of SiCa (E_T = 3.0 eV) is 0.2 eV higher than that of FCNIr (E_T = 2.8 eV), it should serve as a host for FCNIr, except that the neighboring charge transport layers – bis[*N*-(1-naphthyl)-*N*-phenylamino]biphenyl (NPB) and 2,9-dimethyl-4,7-diphenyl-1,10-phenanthroline (BCP) with low triplet energies are strong quenchers of the blue phosphorescence of FCNIr. We anticipated that selecting the popular blue emitter FIrpic, which has a lower triplet energy (E_T = 2.62 eV) [2], as the dopant would prevent back energy transfer from the dopant to the adjacent functional layers. Therefore, we employed the phosphor FIrpic to replace FCNIr in the emitting layer having the original structure reported by Kim [12]. By changing the doping concentration of FIrpic, we prepared three devices (**A1–3**) having the following configuration: indium tin oxide (ITO)/ *N*,*N*′-diphenyl-*N*,*N*′-bis-[4-(phenyl-m-tolyl-amino)-phenyl]-biphenyl-4,4′-diamine (DNTPD, 60 nm)/NPB (30 nm)/SiCa:FIrpic (**A1**: 5%; **A2**: 10%; **A3**: 15%) (30 nm)/BCP (5 nm)/tris(8-hydroxyquinoline) aluminium (Alq_3, 20 nm)/LiF (1 nm)/Al (200 nm). Fig. 1 presents the current

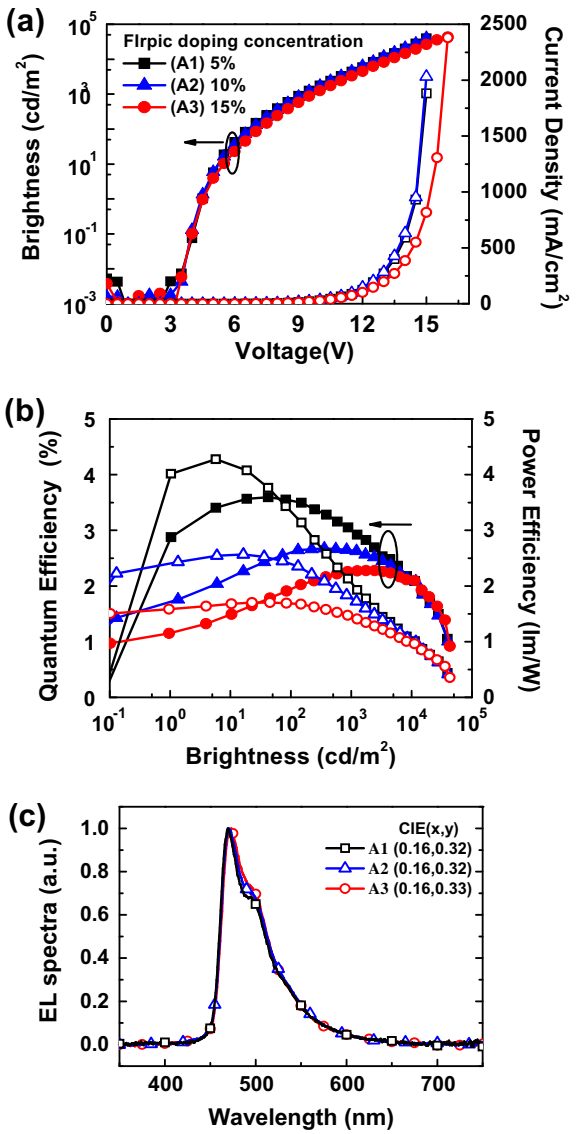

Fig. 1. (a) Current density–voltage–luminance (*I*–*V*–*L*) characteristics, (b) external quantum (η_{ext}) and power (η_p) efficiencies plotted as a function of brightness, and (c) EL spectra of devices **A1–3**.

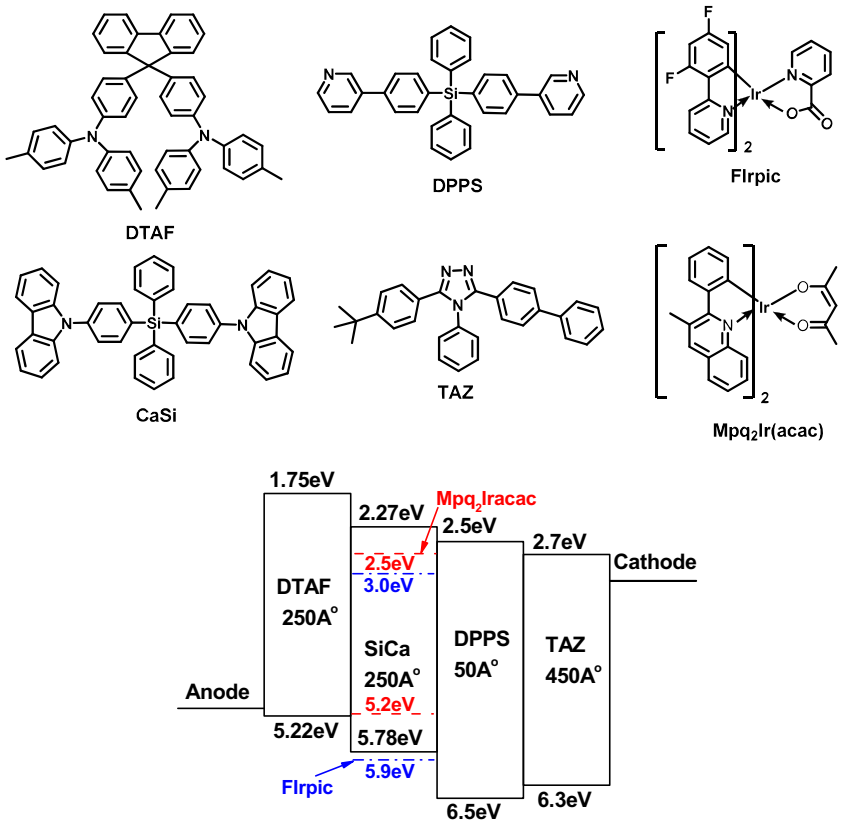

Fig. 2. Energy level diagram and molecular structures of the materials used in device **D1**.

density–voltage–luminance (*I–V–L*) characteristics and EL efficiencies of devices **A1–3**. Notably, the brightnesses (39,400–43,100 cd/m^2) and current densities (1880–2380 mA/cm^2) of our devices were significantly higher than those reported previously [12], suggesting that SiCa is capable of effectively confining the triplet energy of FIrpic. Nevertheless, the EL efficiencies (3.6–2.3% or 4.3–1.7 lm/W) of devices **A1–3** were low relative to those reported previously, presumably because we used NPB, which has a low triplet energy (E_T = 2.3 eV), as the HTL [17], which could not efficiently prevent exciton diffusion.

To improve the EL efficiencies of devices **A1–3**, we used 1,1-bis[(di-4-tolylamino)phenyl]-9,9′-fluorene (DTAF) to replace NPB as the HTL [18,19]. The molecular design of DTAF endows it with several advantageous properties: (1) high morphological and thermal stability (T_g = 124 °C); (2) an appropriate HOMO energy level (−5.22 eV) to provide a low hole injection barrier from the anode and a low-lying LUMO energy level (−1.75 eV) to block electrons injected from the cathode; (3) high hole transport properties ($\mu_h > 10^{-3}$ cm^2/Vs); and (4) a high triplet energy gap (E_T = 2.87 eV) relative to that of NPB, allowing triplet excitons to be confined in the EML. In addition, we adopted a 5-nm-thick layer of diphenylbis[4-(pyridin-3-yl)phenyl]silane (DPPS), inserted between the EML and the ETL (TAZ), to serve as an exciton- and hole-blocking layer (HBL) for suppressing the FIrpic exciton quenching at the EML–ETL interface. Chemical structures of related compounds and their energy levels are shown in Fig. 2, in which HOMO levels of compounds in films are determined here by Riken AC-2 photoemission spectrometer while the HOMO levels of DPPS and TAZ are taken from the literature [9]. The LUMO levels of all compounds are derived by subtracting the HOMO levels from the optical energy gaps.

To evaluate the feasibility of using DTAF as an HTL and DPPS as an HBL, we designed three different devices **B1–3** having the following configuration: ITO/poly(3,4-ethylenedioxythiophene)/poly(styrenesulfonic acid) (PEDOT:PSS) (30 nm)/HTL (25 nm)/SiCa:12 wt% FIrpic (25 nm)/ETL (50 nm)/LiF (0.5 nm)/Al (100 nm). In device **B1**, NPB (20 nm)/TCTA (5 nm) was used as the HTL; in devices **B2** and **B3**, DTAF (25 nm) was employed as the HTL. In addition, TAZ (50 nm) was employed as the ETL in devices **B1** and **B2**, whereas DPPS (5 nm)/TAZ (45 nm) was adopted in device **B3** as the ETL. In device **B1**, we inserted a thin layer of 4,4′,4″-tri(*N*-carbazolyl)triphenylamine (TCTA, 5 nm), which has a high triplet energy (E_T = 2.76 eV) [20], between NPB and the EML to serve as the exciton-blocking layer. In device **B3**, we inserted a 5-nm-thick layer of DPPS, which has a HOMO energy level of 6.5 eV, between the EML and TAZ to bolster the hole-blocking capability of TAZ (HOMO = 6.3 eV) and to confine the excitons within the EML.

Fig. 3 displays the electroluminescence (EL) characteristics of devices **B1–3** featuring this new device structure;

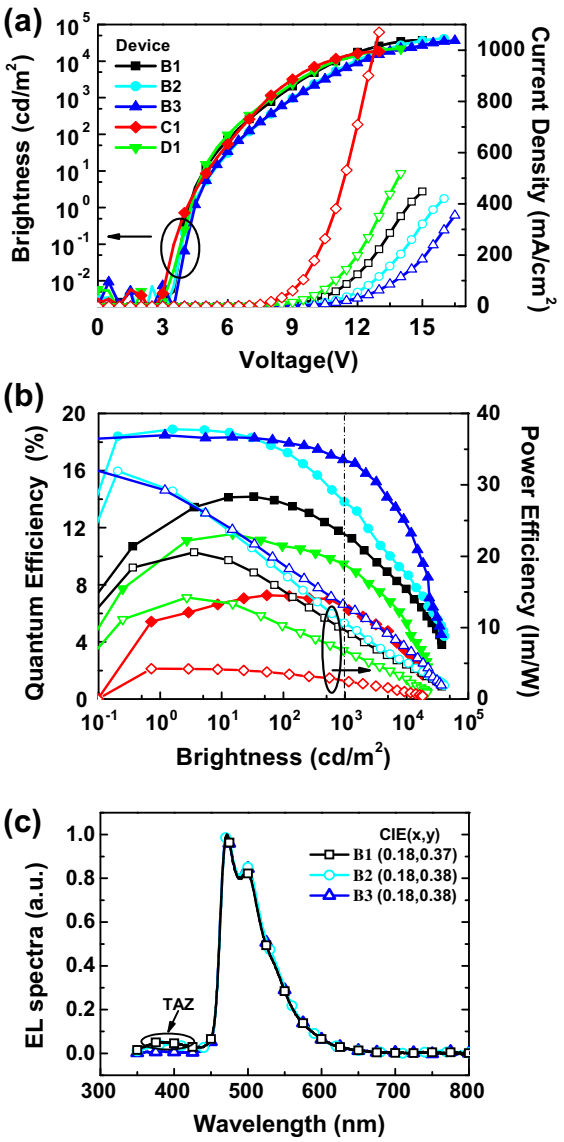

Fig. 3. (a) Current density–voltage–luminance (*I–V–L*) characteristics, (b) external quantum (η_{ext}) and power (η_p) efficiencies plotted as a function of brightness, and (c) EL spectra of devices.

Table 1 summarizes the data. Although devices **B1–3** exhibited similar turn-on voltages (ca. 3.5 V) and similar brightnesses (37,300–40,900 cd/m^2) relative to those of devices **A1–3**, the current densities (360–450 mA/cm^2) had obviously decreased. The *I–V* characteristics revealed that the device **B2** incorporating DTAF as HTL exhibited a slightly lower current density at high voltage relative to device **B1** incorporating NPB/TCTA as HTLs. The lower current density may be due to a large barrier of 0.5 eV between DTAF/CaSi. (see the schematic energy level diagram in Fig. 2). The large energy mismatch should enable a lot of holes accumulate at the HTL/EML interface and lead to a direct trap of charge carriers by FIrpic. In addition, the high triplet energy of DTAF (E_T = 2.87 eV) also enables the efficient confinement of excitons within the EML. Combining these effects together, the DTAF-based device **B2** exhibited efficiencies [a maximum η_{ext} of 18.9% (41.7 cd/A) and a value of η_P of 30 lm/W] that were much higher than those of the traditional NPB/TCTA-based device **B1** (14.2%, 31 cd/A, and 20.6 lm/W, respectively; Fig. 3b). These results indicate that the exciton-confined ability is more crucial than hole injection, because of the greater number of holes than electrons in the OLED. Therefore, the charge balance in the DTAF-based device **B2** might be better than that of the NPB/TCTA-based device **B1**, and results in a higher charge-recombination efficiency.

Careful analysis of the electroluminescence (EL) spectra of devices **B1** and **B2** revealed the presence of short wavelength (λ = 360–410 nm) emissions (Fig. 3c), which presumably arose from a portion of the holes that overcame the barrier at the EML–TAZ interface recombining with electrons in TAZ. Thus, we inserted a 5-nm-thick layer of DPPS between the EML and TAZ in device **B3** to serve as the exciton- and hole-blocking layer to prevent exciton quenching and hole leakage into the TAZ. Obviously, the emission of device **B3** occurred only from FIrpic, without any other emission from its neighboring materials. The quantum efficiency roll-off of device **B3** was suppressed after the introduction of the 5-nm-thick DPPS layer (Fig. 3b). When the brightness reached 1000 cd/m^2, the value of η_{ext} of device **B3** remained as high as 16.7%, with an efficiency roll-off as low as 9%. This result indicates that DPPS can be more effectively blocked the holes within the EML, owing to the wider energy gap, that is, the HOMO level (6.5 eV) is greater than that of TAZ. To gain further insight into the emission mechanisms, three testing devices with doping in only a portion of the 25 nm SiCa emitting layer under B3 device structure (device B3a: doping 8 nm next to DTAF; device B3b: doping 8 nm at the center;

Table 1
EL performances of devices.

	V_{on}[a] [V]	L_{max} [cd/m^2]	I_{max} [mA/cm^2]	η_{ext} [%]	η_l [cd/A]	η_p [lm/W]	L = 1000 nit [%, lm/W]	CIE [x, y]
A1	3.5	39,400 (15 V)	1880	3.6	7.2	4.3	3, 2.1	0.16, 0.32
A2	3.5	40,400 (15 V)	2030	2.7	5.3	2.6	2.6, 1.8	0.16, 0.32
A3	3.5	43,100 (16 V)	2380	2.3	4.5	1.7	2.3, 1.5	0.16, 0.33
B1	3.5	37,300 (15 V)	450	14.2	31	20.6	11.5, 9.5	0.18, 0.37
B2	3.5	40,900 (16 V)	420	18.9	41.7	30	13.8, 10.6	0.18, 0.38
B3	3.5	36,400 (16.5 V)	360	18.3	41.5	31	16.7, 13.2	0.18, 0.38
C1	3	18,200 (13 V)	1070	7.3	7.3	4.2	6.3, 2.5	0.66, 0.34
D1	3	21,600 (14 V)	520	11.6	21.2	14.2	9.5, 6.8	0.37, 0.38

[a] Defined as the voltage at which the EL is rapidly enhanced.

device B3c: doping 8 nm next to DPPS) were also fabricated and tested. Although all three devices showed emission dominantly from FIrpic, device B3b showed much lower quantum efficiency (4%) than devices B3a and B3c (7.8% and 8.7%, respectively). The results indicate that the emitting zone mainly takes place near the HTL/EML and EML/ETL interfaces. The holes accumulate at the HTL/EML interface due to a large barrier of 0.5 eV between DTAF/CaSi. FIrpic is an emitting ET material [21], therefore, localization of excitons on FIrpic can occur through direct charge trapping at the HTL/EML interface. The emitting zone also takes place near the EML/ETL interface, where electrons inject either onto CaSi or directly onto FIrpic.

We confirmed this hypothesis by exploring the carrier transport properties of SiCa, probed using time-of-flight (TOF) techniques [22]. The device used for TOF measurement was prepared through vacuum deposition with the structure ITO glass/SiCa (2.1 μm)/Ag (150 nm) and then it was placed inside a cryostat under vacuum. Fig. 4a display representative TOF transients for holes measured at ambient temperature under an applied field of 9.7×10^4 V/cm. The observed photocurrents did not display any distinct constant current plateaus; instead, the current decayed significantly, resulting in *dispersive* charge transport. This result suggests that the charge carriers in SiCa were trapped and could not attain dynamic equilibrium while migrating across the sample. We obtained the transit times (t_T) from the intersection points of two asymptotes in the double-logarithmic representations (insets to Fig. 4a). The hole mobility was determined using the equation $\mu = d^2/Vt_T$ where d is the thickness of the organic film, V is the applied voltage, and t_T is the transit time. Fig. 4b plots the calculated field-dependent hole mobility of SiCa as a function of $E^{1/2}$. The hole mobilities exist in the range from 1.2×10^{-4} to 5.4×10^{-4} cm^2/Vs for fields varying from 9.7×10^4 to 5.3×10^5 V/cm. Conversely, the electron mobility of SiCa was too low to be measured. The preferential hole mobility of SiCa agrees with the results observed for devices.

In addition to acting as a blue host, SiCa can also be used as the host for red phosphorescent dopants. Using the structure of device **B3**, we introduced $Mpq_2Iracac$ [15] as a red phosphorescent emitter to obtain device **C1**, which exhibited a maximum brightness of 18,200 cd/m^2 at 1070 mA/cm^2 with CIE coordinates of (0.66, 0.34). The *I–V* characteristics of device **C1** revealed a higher current density (1070 mA/cm^2 at 13 V) than that of device **B3** (Fig. 3a). This result can be rationalized by considering that the HOMO energy level of $Mpq_2Iracac$ is close to that of DTAF, thereby reducing the hole injection barrier at the interface. Notably, however, device **C1** provided relatively low values of η_{ext}, η_l, and η_P (7.3%, 7.3 cd/A, and 4.2 lm/W, respectively), due to the intrinsic lower quantum yield of red triplet emitter.

To take advantage of the double confinement strategy used in device **B3**, we fabricated a white PhOLED (device **D1**) by doping the emitting layer in device **B3** with the red phosphor $Mpq_2Iracac$. The CIE coordinates of device **D1** (Fig. 5a) reveal the complementary nature of these

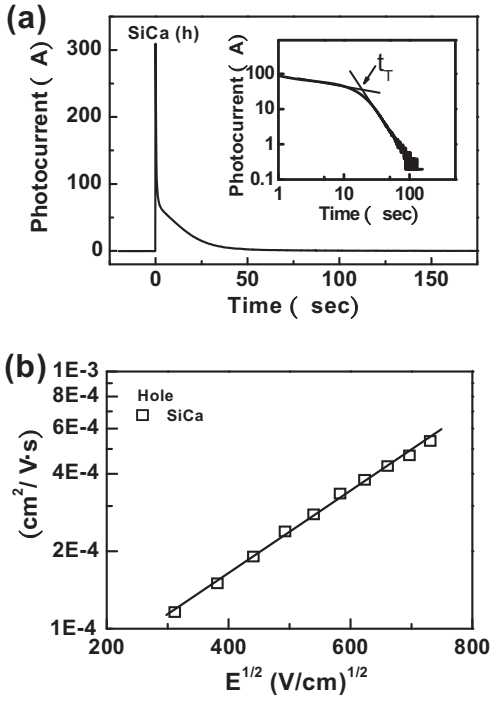

Fig. 4. (a) Representative TOF transients for holes of SiCa (d = 2.1 μm) at a value of E of 9.4×10^4 V/cm. (b) Hole mobility plotted with respect to $E^{1/2}$ at ambient temperature.

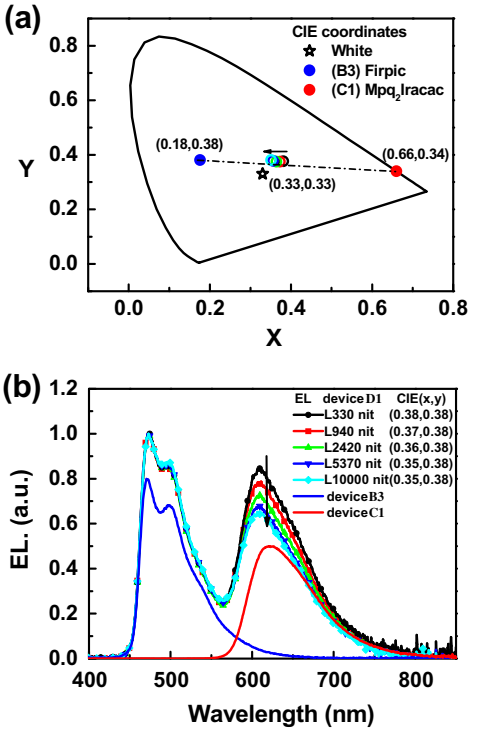

Fig. 5. (a) Chromaticity diagram (CIE coordinates), and (b) EL spectra of devices **B3** (blue), **C1** (red), and **D1** (white) at various luminance (For interpretation of the references to colour in this figure legend, the reader is referred to the web version of this article).

two phosphors for white light emission. White emission with CIE coordinates close to (0.33, 0.33) could be achieved if appropriate combinations were made [23–25]. For the two-dopant single-EML device, the EL was strongly influenced by the ratio of the two dopants. Through systematic tuning of the dopants' concentrations, we fabricated a white light-emitting device **D1** incorporating 12 wt% of FIrpic and 0.2 wt% of $Mpq_2Iracac$ doped into the host SiCa. The proportion of red dopant required to produce balanced emission in this device is relatively low because the red emission occurred from the combined effects of efficient energy transfer from the blue phosphor and exciton formation by charge trapping on the red dopant. The maximum brightness of 21,600 cd/m^2 was achieved at 14 V, with maximum efficiencies (η_{ext}, η_l, and η_p) of 11.6%, 21.2 cd/A, and 14.2 lm/W. Fig. 5b displays the EL spectra of device **D1** recorded at various brightnesses. The relative intensity of the red emission decreased slightly when the brightness increased, leading to a slight shift in the CIE coordinates from (0.38, 0.38) at a value of L of 330 cd/m^2 to (0.35, 0.38) at 10,000 cd/m^2. This color shift originated from the shifting of the recombination zone upon increasing the applied voltage and from the easier formation of high-energy excitons at higher voltage [26]. Compared with multi-EML white organic light emitting diodes (WOLEDs) [27–29,24], our two-dopant single-EML device exhibits higher color stability, which we attribute to the more-uniform distribution of the two dopants in the EML [30].

3. Experimental

We study of carrier-transport properties in the organic materials by the time-of-flight (TOF) transient photocurrent technique. The samples for the TOF measurement were prepared by vacuum deposition using the structure: ITO glass/SiCa (2.1 μm)/Ag (150 nm), and then placed inside a cryostat and kept under vacuum. The thickness of organic film was monitored in situ with a quartz crystal sensor and calibrated by a Thin Film Thickness Measurement (K-MAC ST2000). A pulsed nitrogen laser was used as the excitation light source through the transparent electrode (ITO) induced photogeneration of a thin sheet of excess carriers. Under an applied dc bias, the transient photocurrent was swept across the bulk of the organic film toward the collection electrode (Ag), and then recorded with a digital storage oscilloscope. Depending on the polarity of the applied bias, selected carriers (holes or electrons) are swept across the sample with a transit time of t_T. With the applied bias V and the sample thickness D, the applied electric field E is V/D, and the carrier mobility is then given by $\mu = D/(t_T E) = D^2/(Vt_T)$, in which the carrier transit time, t_T, can be extracted from the intersection point of two asymptotes to the plateau and the tail sections in double-logarithmic plots.

The PHOLEDs were fabricated on a clean glass substrate precoated with an ITO layer having a sheet resistance of 20 Ωsq. Prior to use, the substrate was degreased with solvents and cleaned in a UV-ozone chamber. To improve the hole injection from the anode, PEDOT:PSS was spun onto the pre-cleaned substrate to form a 30-nm-thick polymer buffer layer. The other organic layers were sequentially deposited onto the substrate without breaking vacuum at a pressure of ca. 10^{-6} torr. All materials were purified by train sublimation prior to used. The I–V–L characteristics of the devices were measured simultaneously in a glovebox using a Keithley 6430 source meter and a Keithley 6487 picoammeter equipped with a calibration Si-photodiode. EL spectra were measured using a photodiode array (OTO SD1000).

4. Conclusion

We have fabricated a highly efficient FIrpic-based blue PhOLED, exhibiting a decreased efficiency roll-off that possesses a carrier-balanced and exciton-confined device structure. This device exhibited a maximum external quantum efficiency (η_{ext}) of 18.3% (41.5 cd/A) and a power efficiency of 31 lm/W; the quantum efficiency roll-off was minimal: the value of η_{ext} remained as high as 16.7% at a brightness of 1000 cd/m^2. The enhanced efficiency and reduced roll-off resulted mainly from the introduction of (a) DTAF as an HTL that efficiently blocked the injected electrons and confine excitons within the FIrpic-doped emissive layer, and (b) a thin layer of DPPS between the EML and TAZ, serving as an exciton- and hole-blocking layer to suppress exciton quenching by FIrpic at the EML–ETL interface. By incorporating a red phosphorescent dopant ($Mpq_2Iracac$) into the blue device, we fabricated a white PhOLED that exhibited satisfactory efficiencies (11.6%, 21.2 cd/A, 14.2 lm/W) with CIE coordinates of (0.35, 0.38).

Acknowledgment

This study was supported financially by the National Science Council of Taiwan.

References

[1] M.A. Baldo, D.F. O'Brien, Y. You, A. Shoustikov, S. Sibley, M.E. Thompson, S.R. Forrest, Nature (London) 395 (1998) 151.
[2] R.J. Holmes, S.R. Forrest, Y.-J. Tung, R.C. Kwong, J.J. Brown, S. Garon, M.E. Thompson, Appl. Phys. Lett. 82 (2003) 2422.
[3] R.J. Holmes, B.W. D'Andrade, S.R. Forrest, X. Ren, J. Li, M.E. Thompson, Appl. Phys. Lett. 83 (2003) 3818.
[4] S. Tokito, T. Iijima, Y. Suzuri, H. Kita, T. Tsuzuki, F. Sato, Appl. Phys. Lett. 83 (2003) 569.
[5] I. Tanaka, Y. Tabata, S. Tokito, Chem. Phys. Lett. 400 (2004) 86.
[6] Y. Zheng, S.-H. Eom, N. Chopra, J. Lee, F. So, J. Xue, Appl. Phys. Lett. 92 (2008) 223301.
[7] S.J. Su, T. Chiba, T. Takeda, J. Kido, Adv. Mater. 20 (2008) 2125.
[8] H. Sasabe, E. Gonmori, T. Chiba, Y. Li, D. Tanaka, S.J. Su, T. Takeda, Y. Pu, K. Nakayama, J. Kido, Chem. Mater. 20 (2008) 5951.
[9] L. Xiao, S.-J. Su, Y. Agata, H. Lan, J. Kido, Adv. Mater. 21 (2009) 1271.
[10] X. Ren, J. Li, R.J. Holmes, P.I. Djurovich, S.R. Forrest, M.E. Thompson, Chem. Mater. 16 (2004) 4743.
[11] R.J. Holmes, S.R. Forrest, T. Sajoto, A. Tamayo, P.I. Djurovich, M.E. Thompson, J. Brooks, Y.-J. Tung, B.W. D'Andrade, M.S. Weaver, R.C. Kwong, J.J. Brown, Appl. Phys. Lett. 87 (2005) 243507.
[12] S.H. Kim, J. Jang, S.J. Lee, J.Y. Lee, Thin Solid Films 517 (2008) 722.
[13] V. Adamovich, J. Brooks, A. Tamayo, A.M. Alexander, P.I. Djurovich, B.W. D'Andrade, C. Adachi, S.R. Forrest, M.E. Thompson, New J. Chem. 26 (2002) 1171.
[14] K.S. Yook, S.O. Jeon, C.W. Joo, J.Y. Lee, Org. Electron. 10 (2009) 170.
[15] W.-Y. Hung, T.-C. Tsai, S.-Y. Su, K.-T. Wong, L.-C. Chi, Phys. Chem. Chem. Phys. 10 (2008) 5822.
[16] S.-J. Su, E. Gonmori, H. Sasabe, J. Kido, Adv. Mater. 20 (2008) 4189.
[17] K. Goushi, R. Kwong, J.J. Brown, H. Sasabe, C. Adachi, J. Appl. Phys. 95 (2004) 7798.

[18] W.-Y. Hung, L.-C. Chi, W.-J. Chen, Y.-M. Chen, S.-H. Chou, K.-T. Wong, J. Mater. Chem. 20 (2010) 10113.
[19] M.-T. Kao, W.-Y. Hung, Z.-H. Tsai, H.-W. You, H.-F. Chen, Y. Chi, K.-T. Wong, J. Mater. Chem. 21 (2011) 1846.
[20] Y. Kuwabara, H. Ogawa, H. Inada, N. Noma, Y. Shirota, Adv. Mater. 6 (1994) 677.
[21] V.I. Adamovich, S.R. Cordero, P.I. Djurovich, A. Tamayo, M.E. Thompson, B.W. D'Andrade, S.R. Forrest, Org. Electron. 4 (2003) 77.
[22] P.M. Borsenberger, D.S. Weiss, Organic Photoreceptors for Imaging Systems, Marcel Dekker, New York, 1993.
[23] S.H. Kim, J. Jang, J.Y. Lee, Appl. Phys. Lett. 91 (2007) 123509.
[24] X.-M. Yu, H.-S. Kwok, W.-Y. Wong, G.-J. Zhou, Chem. Mater. 18 (2006) 5097.
[25] C.-H. Chang, C.-C. Chen, C.-C. Wu, C.-H. Yang, Y. Chi, Org. Electron. 10 (2009) 1364.
[26] Y. Shao, Y. Yang, Appl. Phys. Lett. 86 (2005) 073510.
[27] Y.Z. Wang, R.G. Sun, F. Meghdadi, G. Leising, A.J. Epstein, Appl. Phys. Lett. 74 (1999) 3613.
[28] C.-H. Kim, J. Shinar, Appl. Phys. Lett. 80 (2002) 2201.
[29] G. Lei, L. Wang, Y. Qiu, Appl. Phys. Lett. 88 (2006) 103508.
[30] B. Ma, P.I. Djurovich, S. Garon, B. Alleyne, M.E. Thompson, Adv. Funct. Mater. 16 (2006) 2438.

Organic Electronics 12 (2011) 582–588

Contents lists available at ScienceDirect

Organic Electronics

journal homepage: www.elsevier.com/locate/orgel

Dependence of carrier recombination mechanism on the thickness of the emission layer in green phosphorescent organic light emitting devices

Dandan Song [a,b,c], Qi Wang [a], Suling Zhao [b,c], Hany Aziz [a,*]

[a] Department of Electrical and Computer Engineering, University of Waterloo, 200 University Avenue West, Waterloo, Ontario, Canada N2L 3G1
[b] Key Laboratory of Luminescence and Optical Information (Beijing Jiaotong University), Ministry of Education, Beijing 100044, PR China
[c] Institute of Optoelectronics Technology, Beijing Jiaotong University, Beijing 100044, PR China

ARTICLE INFO

Article history:
Received 3 November 2010
Received in revised form 17 December 2010
Accepted 8 January 2011
Available online 22 January 2011

Keywords:
Phosphorescent
Emission layer
Carrier recombination
Carrier transport
Delayed electroluminescence

ABSTRACT

Delayed EL measurements are used to elucidate carrier recombination and light emission mechanism in phosphorescent organic light emitting devices (PhOLEDs) based on 4,4′-bis(9-carbazolyl)-1,1′-biphenyl (CBP) and fac-tris(2-phenylpyridine) iridium ($Ir(ppy)_3$) host:guest system. The results show that changing the thickness of the emitting layer (EML) leads to marked changes in charge-trapping and host–host triplet–triplet-annihilation (TTA) patterns, suggesting that carrier transport and recombination processes change depending on EML thickness. The results suggest a change in carrier recombination and exciton formation mechanism, depending on EML thickness, from a scenario (for EMLs <20 nm) in which recombination occurs mostly on the guest rather than the host thus creating excitons directly on the guest, and hence is not strongly influenced by host-to-guest energy transfer; to another scenario (for EMLs >20 nm) where carrier recombination and exciton creation on the host is not negligible, and hence also the role of host-to-guest energy transfer.

© 2011 Elsevier B.V. All rights reserved.

1. Introduction

Phosphorescent materials are widely used in organic light emitting devices (OLEDs) for their capacity to realize higher efficiencies [1–4]. These phosphorescent materials are usually used in the emitting layer (EML) of a device in the form of a guest doped into a host, the latter typically a fluorescent material. A higher device efficiency favors that the recombination of electrons and holes will occur directly on the phosphorescent guest rather than on the host material [5], and therefore requires that the guest sites act as carrier recombination centers within the EML [5]. This, in turn, requires that the EML will be able to transport both carriers within its bulk; a role that is believed to be generally taken by the host material rather than the guest, owing to the higher carrier mobility of the earlier. Understanding carrier transport and recombination processes in phosphorescent OLEDs (PhOLEDs) utilizing these host:guest systems is therefore crucial for optimizing their performance.

Fac-tris(2-phenylpyridine) iridium ($Ir(ppy)_3$) is a widely used phosphorescent emitter and is considered to be the benchmark emitter for green PhOLEDs. In these devices, 4,4′-bis(9-carbazolyl)-1,1′-biphenyl (CBP) is usually the material of choice for the host, owing to their demonstrated superior performance. Despite their wide utilization, the carrier transport and recombination processes in CBP: $Ir(ppy)_3$ remain not very well understood. For example, the superior efficiency performance of CBP: $Ir(ppy)_3$ is widely attributed to CBP's bipolar charge transport characteristics and efficient energy transfer to $Ir(ppy)_3$ [1,2,6,7]. However, some studies show that light emission in CBP: $Ir(ppy)_3$-based PhOLEDs originates primarily from excitons that are directly created on $Ir(ppy)_3$ sites by the recombination of electrons transported on CBP lowest unoccupied molecular orbitals (LUMO) and holes injected and transported on $Ir(ppy)_3$ highest occupied molecular orbitals

* Corresponding author.
E-mail address: hany.aziz@ecemail.uwaterloo.ca (H. Aziz).

1566-1199/$ - see front matter © 2011 Elsevier B.V. All rights reserved.
doi:10.1016/j.orgel.2011.01.008

(HOMO) [10]; entailing that the light emission mechanism should not strongly depend on host-to-guest energy transfer. Furthermore, time of flight studies reveal that holes have much lower mobility in CBP: $Ir(ppy)_3$ in comparison to electrons [8,9] indicating that transport is not bipolar, and suggesting that the transport of holes via hopping between $Ir(ppy)_3$ [10] sites can not be efficient.

In this work, we study and compare prompt and delayed electroluminescence (EL) from CBP: $Ir(ppy)_3$ PhOLEDs of various architectures to elucidate charge transport and recombination mechanisms. The results show that changing the EML thickness leads to marked changes in charge-trapping and host–host TTA patterns, suggesting that carrier transport and recombination processes change depending on EML thickness.

2. Experimental

In this study, two series of PhOLEDs in two different structures and various layer configurations are investigated. The general device structures are:

Series I: ITO/NPB (40 nm)/CBP: 4 wt% $Ir(ppy)_3$ (x nm)/BPhen (30 nm)/Mg/Ag.
Series II: ITO/NPB (40-y nm)/TAPC (y nm)/CBP: 4wt% $Ir(ppy)_3$ (x nm)/CBP(40-x nm)/BPhen (30 nm)/Mg/Ag.

where NPB represents *N*,*N*′-di(naphthalene-1-yl)-*N*,*N*′-diphenyl-benzidine and is used as a hole transport material; BPhen represents 4,7-diphenyl-1,10-phenanthroline and is used as a hole blocking and electron transport material; and TAPC represents 1,1′-bis(di-4-tolylaminophenyl) cyclohexane, and is used as a hole transport and electron blocking material. ITO and Mg/Ag are employed as the anode and cathode, respectively. "x" represents the thickness of the EML, and ranges from 5 to 40 nm, as is typically the case in PhOLEDs. In series II devices, "y" represents the thickness of the TAPC layer, and is either 0 or 10 nm. All devices are fabricated by the deposition of organic materials and metals at a rate of 1–2 Å/s by using thermal evaporation in vacuum at a base pressure of about 5×10^{-6} Torr on UV ozone-cleaned ITO-coated glass substrates. Current–Voltage–Luminance (J–V–L) measurements are carried out using Agilent 4156C and Minolta Chroma Meter CS-100. The setup for delayed EL measurements is as described in our previous work [11–12]. The devices are kept in a nitrogen atmosphere during all tests.

3. Results and discussions

First, we measure the J–V–L characteristics in series I devices of various EML thicknesses. Fig. 1a shows the dependence of driving voltage on EML thickness whereas Fig. 1b shows the dependence of current efficiency (in cd/A) on current density for the different devices. As expected, for any given current, the driving voltage increases with EML thickness. The dependence of current efficiency on current density in the low current (<20 mA/cm^2), on the other hand, displays different trends in thin (<20 nm) versus thick (>20 nm) EMLs regime, displaying, in case of thin EMLs, an initial increase in efficiency with current density before the expected efficiency roll-off trend is attained.

In order to obtain some insights about the change in current efficiency trends with EML thickness, we carried out delayed EL measurements on the same devices. In this technique, the devices are driven using a square pulse driving scheme, with a forward bias pulse width of 0.5 ms, which is sufficiently long for prompt EL to reach its steady-state intensity. A photomultiplier tube is used to collect any persistent (i.e. delayed) electroluminescence from the devices that persists after the end of the forward bias. An optical chopper allows signal collection to begin only after a delay of about 0.3 ms following the end of the forward bias pulse, which is significantly longer than host singlet lifetime (typically <20 ns) and $Ir(ppy)_3$ triplet lifetime ($\sim$1 μs), to ensure the absence of any contributions from prompt EL (i.e. from the relaxation of excitons created *during* the forward bias pulse) in the collected signal. Fig. 2a shows a schematic diagram of the driving and signal collection timing scheme, whereas Fig. 2b shows the delayed EL signal collected from the devices versus time elapsed from the end of the forward bias pulse. As can be seen from the figure, the intensity of delayed EL collected from the devices varies significantly depending on the thickness of the EML, where PhOLEDs with the thicker EMLs (i.e. 30–40 nm) produce 2–3 times stronger delayed EL than their counterparts with the thinner EMLs (i.e. 5–10 nm). It should be pointed out that, like prompt EL, delayed EL arises from $Ir(ppy)_3$ triplet state, evidenced in the essentially identical delayed and prompt EL spectra (Fig. 2b inset). It is noteworthy to point out that the relative intensities of delayed EL do not correlate with the prompt EL intensities (Table 1) measured at the same current density, indeed proving that they must have different origins, and that there are no significant contributions from the prompt EL in the collected delayed EL signal as maintained above.

In general, prompt EL arises from the radiative decay of $Ir(ppy)_3$ triplet excitons produced by the recombination of electrons and holes *during* electrical excitation either directly on $Ir(ppy)_3$ sites, or on CBP sites followed by host to guest energy transfer. In this regard, its intensity is primarily governed by the carrier recombination efficiency on the guest in case of the former, or on the concentration of excitons (both singlet and triplet) on the host as well as the efficiency of their transfer to the guest in case of the latter. In comparison, the delayed EL can be the product of one or several of the following processes [11–13]: (i) recombination of trapped charges that get released after the end of the forward bias pulse; (ii) slow migration of host triplet excitons that are generated during the electrical excitation and their late arrival to the proximity of guest sites where energy transfer to the guest can take place; and (iii) triplet–triplet-annihilation (TTA), which in this case will be primarily due to the fusion of host triplet excitons (i.e. host–host TTA). Unlike in fluorescent OLEDs, any contributions from guest–guest TTA to delayed EL in the milliseconds time frame, as is used in our measurements here, will be insignificant in case of PhOLEDs. This is due to the much shorter lifetime of phosphorescent guest triplet excitons, (because of the efficient intersystem crossing),

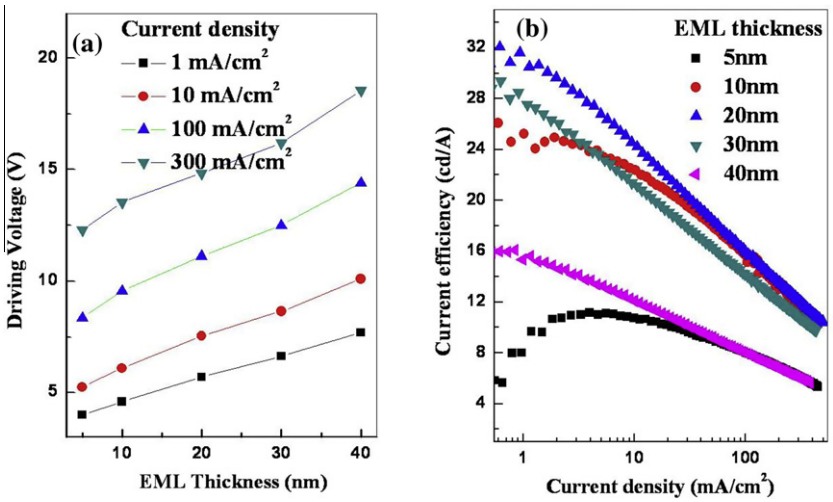

Fig. 1. Dependence of operating voltage on EML thickness from devices in series I with a device structure of ITO/NPB (40 nm)/CBP: 4wt% $Ir(ppy)_3$ (x nm)/BPhen (30 nm)/Mg/Ag.

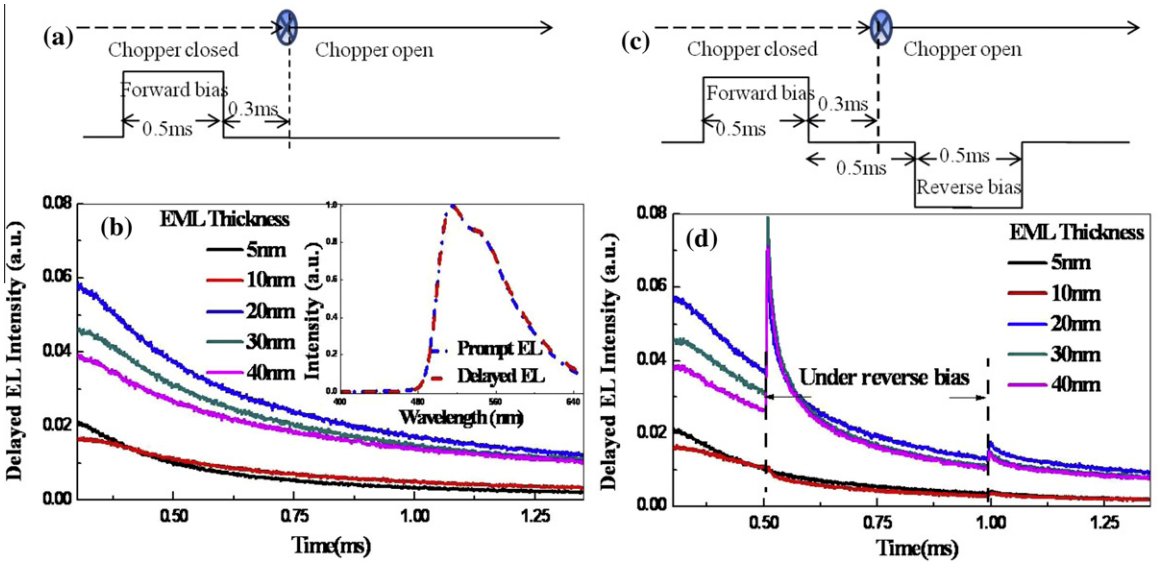

Fig. 2. (a) A schematic time setup of delayed EL measurement. A forward current density of 20 mA/cm² was removed at t = 0 ms and at t = 0.3 ms, the optical chopper open and the emission was recorded. (b) The time evolution of delayed EL emission from devices in series I. Inset: spectral distribution of prompt and delayed EL emission. (c) A schematic time setup of delayed EL measurement with reverse bias. At t = 0.5 ms, a reverse bias of −8 V was applied for another 0.5 ms and removed at t = 1 ms. (d) The time evolution of delayed EL emission from devices in series I with reverse bias.

Table 1
Prompt and delayed EL intensity at different EML thicknesses.

EML thickness	5 nm	10 nm	20 nm	30 nm	40 nm
Brightness (in cd/m²) at 20 mA/cm²	2050	4100	4500	3750	2180
Delayed EL intensity (normalized to delayed EL of PhOLED with 20 nm EML)	0.363	0.284	1	0.789	0.660

which requires that any such processes must occur in a much shorter time scale (i.e. <1 ms). Therefore, the intensity of delayed EL strongly correlates with the concentrations of trapped charges and CBP triplet excitons. Processes (ii) and (iii) can generally be described by the following multi step mechanistic schemes [13]:Process ii:

$$H_3^* + G_o \rightarrow H_o + G_3^* \text{(Energy transfer)} \quad \text{(ii-1)}$$

$$G_3^* \rightarrow G_o + h\nu \text{ (Phosphorescence)} \quad \text{(ii-2)}$$

Process iii:

$$H_3^* + H_3^* \rightarrow H_1^* + H_o \text{(Host—host TTA)} \quad \text{(iii1)}$$

$$H_1^* + G_o \rightarrow H_o + G_1^* \text{(Energy transfer)} \quad \text{(iii2)}$$

$$G_1^* \rightarrow G_3^* \text{ (Intersection crossing)} \quad \text{(iii3)}$$

$$G_3^* \rightarrow G_o + h\nu \text{ (Phosphorescence)} \quad \text{(iii4)}$$

where H_1^*, H_3^*, G_1^*, G_3^*, H_o and G_o denote host singlet exciton, host triplet exciton, guest singlet exciton, guest triplet exciton, host ground state and guest ground state, respectively.

In order to differentiate between these processes, a 0.5 ms reverse bias pulse is applied on the devices during the delayed EL signal collection, and subsequent changes in delayed EL characteristics are recorded. Fig. 2c shows a schematic diagram of the driving and signal collection timing scheme used in this case, whereas Fig. 2d shows the delayed EL characteristics under these conditions. As can be seen from the figure, the application of the reverse bias leads to the appearance of a strong spike followed by a decrease in delayed EL intensity in devices with 20–40 nm EML, and a subsequent partial recovery at the end of the pulse. In contrast, the reverse bias pulse has negligible effect on delayed EL from the devices with the thinner EMLs (5–10 nm). The observed spike at the beginning of the reverse bias is an indication of a sudden release of trapped charges by the reverse bias field, after which they recombine producing the delayed EL spike [11,12]. The observations therefore indicate that the number of trapped charges increases with EML thickness, suggesting it is a bulk effect, and that only thick (i.e. $\geqslant$20 nm) EMLs contain a significant number of trapped charges. The partial recovery in delayed EL at the end of the reverse bias pulse, on the other hand, is indicative of host–host TTA [13], as the fusion of two triplet excitons can lead to the production of a singlet intermediate (entity H_1^* in step iii-1 in the above scheme) that can be easily dissociated by the electric field, hence its susceptibility to quenching by the reverse bias. It should be noted that in contrast to singlet excitons, triplet excitons are much less susceptible to electric field induced quenching [11,12], due to their lower energy, and therefore do not themselves contribute to the quenching effect of the reverse bias aside from their role in creating singlets through the TTA process. The partial recovery in delayed EL at the end of the reverse bias pulse in Fig. 2d in case of thicker EML is therefore indicative of significant host–host TTA, suggesting the concentration of host triplet excitons must be significantly higher in these devices for efficient TTA to occur. The results in Fig. 2d therefore indicate that the higher delayed EL intensity in devices with thicker EMLs (Table 1) arises from higher concentrations of trapped charges and host triplet excitons in these devices.

From an energy levels standpoint, $Ir(ppy)_3$ sites can be expected to act as traps for carriers in a CBP: $Ir(ppy)_3$ EML, especially for holes. This is due to the differences between CBP and $Ir(ppy)_3$ HOMO and LUMO levels (CBP HOMO and LUMO are 6.0 and 2.9 eV, respectively, $Ir(ppy)_3$ HOMO and LUMO are 5.6 and 3.0 eV, respectively [14]), which suggest that $Ir(ppy)_3$ should efficiently trap holes in a CBP: $Ir(ppy)_3$ mixture. To test if this is indeed the case, we compare J–V characteristics of devices with or without $Ir(ppy)_3$ dopant. Fig. 3a shows J–V characteristics from standard devices of structure as shown in the inset. It can be seen that the device with $Ir(ppy)_3$ doping displays lower current density for a given driving voltage in comparison to the device with the neat CBP layer (i.e. without the dopant), suggesting that $Ir(ppy)_3$ indeed acts as charge traps. However, as the transport of electrons is known to be efficient in a CBP host, and therefore may strongly influence the J–V characteristics, it is important to rule out possible variations in electron currents among these devices. We therefore also test hole-only devices that include a CBP layer with or without $Ir(ppy)_3$, following the general approach adopted by Murata et al. [15]. In these devices, the CBP layer is sandwiched between two NPB layers, rendering it a hole-only device due to the limited electron injection capacity of NPB/Mg:Ag interface. The J–V characteristics from these devices and the device structure are depicted in Fig. 3b. As can be seen, hole currents at a given voltage are significantly lower in device with $Ir(ppy)_3$ doping, convincingly verifying the hole trapping role of $Ir(ppy)_3$ in a CBP host. Therefore, the increase in the delayed EL spike intensity with EML thickness in Fig. 2d can be readily explained in terms of the larger number of $Ir(ppy)_3$ sites in the thicker layers, which would expectedly increase the number of trapped charges. To explain the marked differences between the thin (5–10 nm) versus thick (30–40 nm) EMLs in terms of the amount of trapped charges and the magnitude of host–host TTA (hence the concentration of triplets on CBP), we propose the following as a possible charge transport and recombination model, which is also depicted, pictorially, in Fig. 4.

Due to the small difference in energy between BPhen and CBP LUMO levels ($\sim$0.1 eV), electrons are easily injected from the BPhen electron transport layer into the LUMO of CBP, and are transported mostly on CBP sites (processes 1 and 2 on the diagram) [13,16]. On the other hand, due to the relatively large barrier ($\sim$0.6 eV) for hole injection from NPB to CBP, the injection of holes onto CBP is difficult [17], and therefore, the majority of holes are injected directly into $Ir(ppy)_3$ sites (process 3 on the diagram) [6]. When the EML is thin (5–10 nm), (the scenario depicted in Fig. 3a), electrons transported onto the LUMOs of CBP will be able to drift across the EML rather quickly, thereby reaching the hole transport layer (HTL)/EML interface, where they recombine with the holes on $Ir(ppy)_3$ sites. As a result, the excitons are formed mainly directly on $Ir(ppy)_3$ sites in this case, and the CBP host will be deficient in holes and excitons, hence the absence of the host–host TTA characteristic "finger print" (i.e. the partial recovery in delayed EL at the end of the reverse bias pulse in Fig. 2d). However, in case of the thicker EMLs (the scenario depicted in Fig. 4b), the electrons will take longer times to drift across the EML (the electron mobility of CBP is only about 10^{-3} cm^2 V^{-1} s^{-1} [8]). As such, holes will have the time to drift from the HTL/EML interface deep into the EML bulk. Although the transport of holes in the EML can proceed via hopping between $Ir(ppy)_3$ sites (process

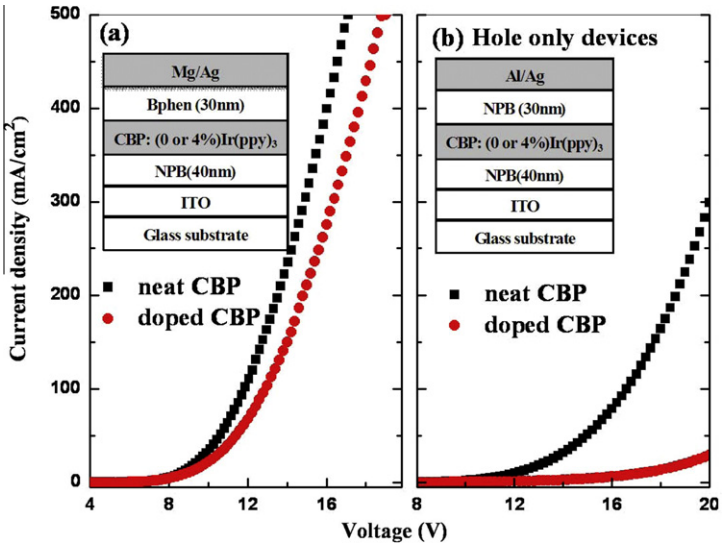

Fig. 3. (a) J–V characteristics from devices with 40 nm neat CBP EML and CBP: 4%Ir(ppy)$_3$ EML, respectively. (b) J–V characteristics from hole-only devices with 40 nm neat CBP EML and CBP: 4%Ir(ppy)$_3$ EML, respectively. Insets: the schematic device structures.

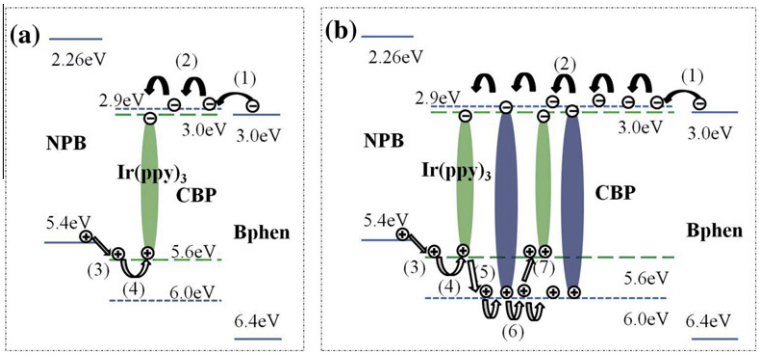

Fig. 4. Schematic energy level diagram of charge carrier injection and transport for electrons and holes in thinner EML (a) and thicker EML (b), respectively. (1) Electron injection from ETL into CBP and Ir(ppy)$_3$, (2) Electron transport through LUMO of CBP, (3) hole injection from HTL into Ir(ppy)$_3$, (4) direct hopping of holes between Ir(ppy)$_3$ sites, (5) hole injection from HOMO of Ir(ppy)$_3$ to that of CBP, (6) hole transport through HOMO of CBP, and (7) hole trapping at Ir(ppy)$_3$ sites. Values for HOMO and LUMO levels are taken from references [14,16,17].

4 on the diagram), the large intermolecular distances between the guest sites makes this process inefficient [8,18], and allows for a fraction of the holes to be injected onto CBP where they can be transported more easily via CBP HOMOs (processes 5 and 6 on the diagram), where their mobility can be higher (about 10^{-2} cm^2 V^{-1} s^{-1} [8]). With the increase in the hole population on CBP, electron–hole recombination on the host rather than the guest becomes increasingly prominent, hence the larger concentration of CBP triplet excitons, evident from the clear host–host TTA "finger print" observed in only the thick EMLs. As, in case of the thin EMLs, holes recombine with electrons very close to the HTL/EML interface, only very few holes will penetrate deeper into the EML where they may become trapped on Ir(ppy)$_3$ sites, hence the absence of the characteristic "trapped charges" spike in these devices on Fig. 2d. The results are therefore consistent with a charge transport and recombination mechanism that depends on the EML thickness, and can change from a scenario (for EMLs <20 nm) in which carrier recombination occurs mostly on the guest rather than the host thus creating excitons directly on the guest, and hence is not strongly influenced by host-to-guest energy transfer; to another scenario (for EMLs >20 nm) where carrier recombination and exciton creation on the host is not negligible, and hence also the role of host-to-guest energy transfer. In this regard, the initial increase in the current efficiency with current observed only in case of the PhOLEDs with the thin EMLs (Fig. 1b) can be attributed to improved charge balance with increasing the bias, which alleviates the higher initial concentration of electrons in the recombination zone (due to the facile transport of electrons across the thin EML as pointed to above).

Although the above model can fully explain the experimental results described above, it necessitates that the injection of holes from Ir(ppy)$_3$ HOMO to CBP HOMO (pro-

cess 5 on Fig. 4b) is non negligible in the thicker EMLs, a process whose likelihood could be questionable due to the significant hole injection barrier, as is also suggested by some reports [8]. Therefore, in order to see if injection of holes from $Ir(ppy)_3$ to CBP can indeed be significant, we fabricate and test a second series of devices (series II). In these devices, only one part of the EML (the one adjacent to the HTL interface) is doped with $Ir(ppy)_3$, whereas the other part comprises neat CBP. The total thickness of the EML is maintained at 40 nm in all devices, but the thickness of the doped part is varied from 5 to 40 nm (the latter being a fully doped EML, hence is the same as in series I above). Fig. 5 shows the normalized prompt EL spectra, respectively, collected from these devices. Clearly, both sets of spectra show the $Ir(ppy)_3$ characteristic emission (the 514 and 540 nm bands, where the small variations in the 540–514 nm relative intensities are due to the known micro-cavity effects [14] resulting from variations in the distance between the emission zone and the reflective metal cathode due to differences in the thickness of the neat CBP part). Aside from $Ir(ppy)_3$ emission, the prompt EL spectra show some weak blue emission in the blue range, with bands peaking at around 400 and 450 nm. Introducing a thin layer of TAPC at the HTL/EML interface leads to the disappearance of the 450 nm band, indicating it arises from NPB emission. As the 400 nm band coincides with CBP singlet emission, is only visible in devices with a neat CBP layer, and its intensity increases with the thickness of the neat CBP layer, it must be due to CBP singlet emission from the neat layer [19]. Obviously, the detection of CBP emission from the neat layer indicates that the injection of holes from the $Ir(ppy)_3$-doped part of the EML to the neat CBP part is possible, proving that the injection of holes from $Ir(ppy)_3$ to CBP can indeed take place. In fact, the ability to detect emission from the neat part indicates that some of the underlying CBP singlets do not undergo complete energy transfer to $Ir(ppy)_3$, suggesting they must be created at least a few molecular monolayers into the neat part, away from the interface with the $Ir(ppy)_3$-doped part.

Fig. 6 shows normalized time resolved delayed EL characteristics of the same devices (i.e. of the same type II devices described in the previous paragraph), under the driving scheme depicted in Fig. 2c (i.e. with the additional reverse bias component). As can be seen from the figure, the height of the spike at the beginning of the reverse bias pulse increases with the thickness of CBP:$Ir(ppy)_3$ layer, similar to series I devices (Fig. 2a) despite the fact that the thickness of the entire EML remains the same in all the devices. These results show that the trapped charges are mainly present in the $Ir(ppy)_3$-doped part, confirming our earlier supposition that they are indeed mostly trapped on $Ir(ppy)_3$ sites. As can also be seen from the figure, the partial recovery at the end of the pulse also increases with the thickness of CBP:$Ir(ppy)_3$ layer in this case. This suggests that most of the host–host TTA still occurs in the $Ir(ppy)_3$-doped part of the EML. This may perhaps be due to the easier transport of holes across the neat CBP layer, which would cause their capture cross section to electrons to be smaller, hence leads to a lower electron–hole recombination rate, and, as a result, a lower exciton concentration in the neat CBP.

4. Conclusions

In conclusion, delayed EL measurements are used to elucidate carrier recombination and light emission mechanism in PhOLEDs based on CBP: $Ir(ppy)_3$. The results show that changing the EML thickness leads to marked changes in charge-trapping and host–host TTA patterns, suggesting that carrier transport and recombination processes change depending on EML thickness. The results suggest a change in carrier recombination and exciton formation mechanism, depending on EML thickness, from a scenario (for EMLs <20 nm) in which recombination occurs mostly on

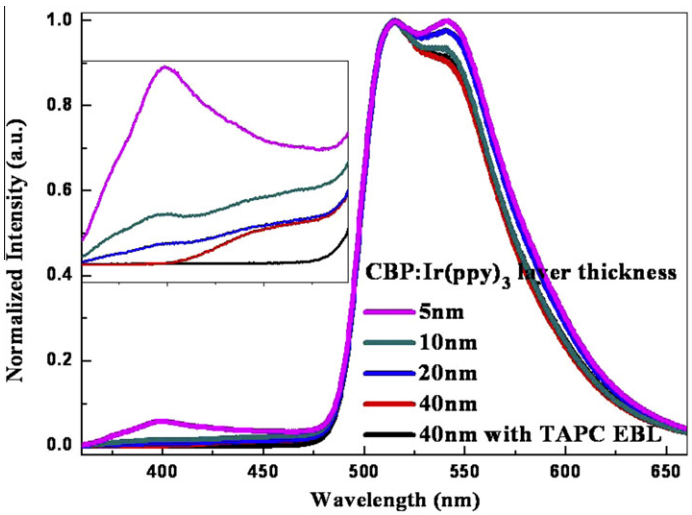

Fig. 5. The prompt EL spectra from devices in series II with a device structure of ITO/NPB (40-*y* nm)/TAPC (*y*nm)/CBP: 4wt% $Ir(ppy)_3$ (*x* nm)/CBP(40-*x* nm)/BPhen (30 nm)/Mg/Ag. Inset: magnification of spectra in the range from 365 to 475 nm.

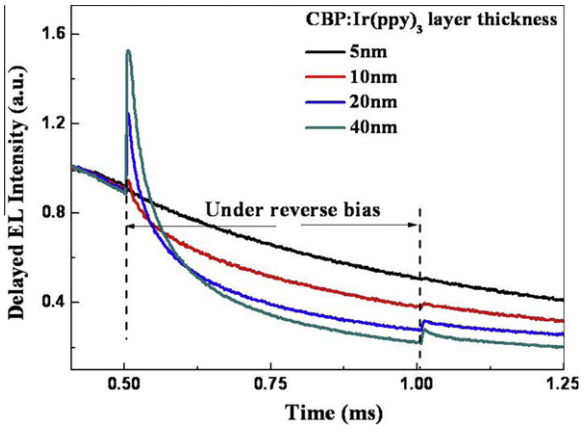

Fig. 6. The time evolution of delayed EL emission from devices in series II. The forward voltages are the values under a current of 20 mA/cm^2 and the reverse bias is −4 V.

the guest rather than the host thus creating excitons directly on the guest, and hence is not strongly influenced by host-to-guest energy transfer; to another scenario (for EMLs >20 nm) where carrier recombination and exciton creation on the host is not negligible, and hence also the role of host-to-guest energy transfer.

Acknowledgements

Partial support by DALSA Corporation and the Natural Science and Engineering Research Council of Canada is acknowledged. D.S. also acknowledges support from the State Scholarship Fund provided by PR China.

References

[1] M.A. Baldo, D.F. O'Brien, Y. You, A. Shoustikov, S. Sibley, M.E. Thompson, S.R. Forrest, Nature (London) 395 (1998) 151.
[2] C. Adachi, M. Baldo, M.E. Thompson, S.R. Forrest, J. Appl. Phys. 90 (2001) 5048.
[3] G. He, M. Pfeiffer, K. Leo, M. Hofmann, J. Birnstock, R. Pudzich, J. Salbeck, Appl. Phys. Lett. 85 (2004) 3911.
[4] M.E. Kondakova, T.D. Pawlik, R.H. Young, D.J. Giesen, D.Y. Kondakov, C.T. Brown, J.C. Deaton, J.R. Lenhard, K.P. Klubek, J. Appl. Phys. 104 (2008) 094501.
[5] I.H. Campbell, B.K. Crone, Appl. Phys. Lett. 89 (2006) 172108.
[6] Z.W. Liu, M.G. Helander, Z.B. Wang, Z.H. Lu, Appl. Phys. Lett. 94 (2009) 113305.
[7] Y. Sun, N.C. Giebink, H. Kanno, B. Ma, M.E. Thompson, S.R. Forrest, Nature (London) 440 (2006) 908.
[8] N. Matsusue, S. Ikame, Y. Suzuki, H. Naito, Appl. Phys. Lett. 85 (2004) 4046.
[9] C. Lee, H. Baek, J. Kwak, J.Y. Kim, B.D. Chin, Proc. SPIE 7051 (2008) 70510M.
[10] B.D. Chin, M.C. Suh, M.H. Kim, S.T. Lee, H.D. Kim, H.K. Chung, Appl. Phys. Lett. 86 (2005) 133505.
[11] Z.D. Popovic, H. Aziz, J. Appl. Phys. 98 (2005) 013510.
[12] Y. Luo, H. Aziz, Adv. Funct. Mater. 1285 (2010) 20.
[13] D. Song, S. Zhao, Y. Luo, H. Aziz, Appl. Phys. Lett. 97 (2010) 243304.
[14] H. Baek, C. Lee, J. Appl. Phys. 103 (2008) 054510.
[15] H. Murata, C.D. Merritt, Z.H. Kafafi, IEEE J. Select. Top. Quantm. Electr. 4 (1998) 119.
[16] G.F. He, M. Pfeiffer, K. Leo, M. Hofmann, J. Birnstock, R. Pudzich, J. Salbeck, Appl. Phys. Lett. 85 (2004) 3911.
[17] C.H. Cheng, Z.Q. Fan, S.K. Yu, W.H. Jiang, X. Wang, G.T. Du, Y.C. Chang, C.Y. Ma, Appl. Phys. Lett. 88 (2006) 213505.
[18] N. Matsusue, Y. Suzuki, H. Naito, Jpn. J. Appl. Phys. 44 (2005) 3691.
[19] A. Ruseckas, J.C. Ribierre, P.E. Shaw, S.V. Staton, P.L. Burn, I.D.W. Samuel, Appl. Phys. Lett. 95 (2009) 183305.

Organic Electronics 12 (2011) 589–594

Contents lists available at ScienceDirect

Organic Electronics

journal homepage: www.elsevier.com/locate/orgel

Mechanism of enhanced mobility and conductivity at donor–acceptor organic interfaces

V.R. Nikitenko [a,*], A.R. Tameev [b], A.V. Vannikov [b]

[a] National Research Nuclear University "MEPhI", Kashirskoe sh. 31, Moscow 115409, Russia
[b] A.N. Frumkin Institute of Physical Chemistry and Electrochemistry, RAS, Leninsky Prosp. 31, Moscow 119991, Russia

ARTICLE INFO

Article history:
Received 20 September 2010
Received in revised form 18 December 2010
Accepted 17 January 2011
Available online 1 February 2011

Keywords:
Organic semiconductors
Donor–acceptor interface
Integer charge transfer
Energy level alignment
Charge delocalization
Charge carrier transport

ABSTRACT

The model of metallic type or enhanced hopping conductivity with reduced activation energy at the donor–acceptor interface formed by organic dielectrics is suggested. High density of electrons and holes at the interface arises due to the integer charge transfer from donor to acceptor molecules. Significant part of charge carriers can avoid thermal activation and tunneling in course of their transport if the interfacial energy barrier is low enough. The critical value of an interfacial energy barrier, density of free electrons, the values of two-dimensional mobility and conductivity of charge carriers are estimated by numerical modeling and compared with experimental data.

© 2011 Elsevier B.V. All rights reserved.

1. Introduction

Electric conduction along organic interfaces attracts much attention since electronic processes at organic–organic and organic–metal interfaces can differ from those in the bulk of organic layers, and interfacial properties have a profound impact on device performance [1–4]. High conductivity is required to maintain superior device characteristics. Electronic transport at organic interfaces, as well as in organic layers, is known to be restricted typically by localization and low concentration of mobile charge carriers [5]. Typically, improvement results from electrochemical doping [6,7] and field effect [7–9]. The latter increases concentration of carriers and their mobility within a thin ($\cong$ 1 nm) layer at the polymer–gate interface due to filling of deep fraction of localized states.

High mobility and conductivity in organic structures involving interface of electron donor (D) and acceptor (A) materials has been recently reported (see, for examples, [10–13]). In original materials, conductivity was found to be lower by several orders of magnitude than that in the interface structure. An important result of Ref. [11] was the saturation of conductivity with thickness of the top A-layer as soon as its thickness exceeded ca. 2 nm in the course of formation of D–A interface. The Hall mobility of both electrons and holes above 1 $cm^2\ V^{-1}s^{-1}$ was measured, suggesting the sheet density of *delocalized* charge carriers up to $5 \times 10^{10}\ cm^{-2}$ at the copper phthalocyanine (CuPc)/copper hexadecafluoro phthalocyanine ($F_{16}CuPc$) interface. In those experiments [13], the conductivity was trap-controlled hence thermoactivated one. In [10], two-dimensional (2D) conductivity above the minimal metallic level, e^2/h, characterized by metallic temperature dependence, along the interface formed by two organic crystals of tetrathiofulvalene (TTF) and 7,7,8,8-tetracyanoquinodimethane (TCNQ) has been demonstrated and attributed to the formation of 2D electronic gas, resulting from electron transfer from TTF to TCNQ. The question about the occurrence of *complete* (integer) or *partial* charge transfer at the concrete donor–acceptor organic interface is under debate. The complete electron transfer at the interface between two dielectrics, including organic ones, is known for a rather long time; in particular, this effect

* Corresponding author. Tel./fax: +7 4953247476.
E-mail address: vladronik@yandex.ru (V.R. Nikitenko).

1566-1199/$ - see front matter © 2011 Elsevier B.V. All rights reserved.
doi:10.1016/j.orgel.2011.01.017

is responsible for the charging of dye particles in a mixture of powders used in xerography [14]. Recent work on modeling of organic–metal and organic–organic interfaces has been summarized in the review [15]. Obviously, none of the existing models describe the whole variety of organic–organic interfaces. However, strong arguments has been reported, that integer electron transfer from donor to acceptor molecule occurs at the organic–organic interface, if (i) chemical interaction of these molecules is rather weak in order to prevent considerable hybridization of electronic molecular orbitals and (ii) this transfer is profitable energetically, i.e. the energy of highest occupied molecular orbital (HOMO) of a donor lies high enough relative to the position of lowest unoccupied molecular orbital (LUMO) of an acceptor. In particular, integer charge transfer in the structure involving TTF and TCNQ has been approved. On the other hand, many experimental and theoretical works have pointed to partial charge transfer at organic–organic interfaces, including TTF–TCNQ interface (see, for example, [16]). Perhaps, the reason of this uncertainty is the dependence of the relative energetic positions of electrons and holes at the interface on the choice of the conductive substrate (electrode) [15]. In this work, we assume that an integer charge transfer is the case for the analyzed interface, because this case (weak chemical intermolecular interaction), which is typical for organics, seems to be most questionable in view of 2D-electronic gas formation.

The primary step in this case is the formation of an electron–hole (e–h) pair in which the charges are separated by the distance ca. 1 nm and localized by mutual Coulomb interaction. Formation of 2D e-gas needs in rather high area density of pairs, in order to delocalize charge carriers by means of interaction with charges from adjacent pairs. However, the microscopic nature of the huge enhancement of conductivity along the D–A interface with respect to the bulk conductivity of the materials remains unclear. One has to clarify the mechanism of 2D e-gas formation at such an interface and quantify the critical parameters of the interface. The mechanism of conductivity exploited for the interfaces of perovskite transition metal oxides ABO_3 [17] seems to be not appropriate for the organic structures, in which sequential polar layers are absent.

The concept of sequence of charge carrier transfers from charge-transfer states (CTSs) to the neighboring unpaired charge (“Coulomb hole”) was suggested earlier to explain the sharp increase in the bulk conductivity of electrochemically doped polymers [18] and the electronic switching in polymers [19]. In the present paper, we show that the concept provides a mechanism describing both enhanced hopping conductivity with reduced activation energy and metallic conductivity along the D–A interface. We quantify the conditions of 2D e-gas formation as well.

2. Model

The integer charge transfer of an electron from donor to acceptor molecule produces a pair of positive (donor) and negative (acceptor) CTSs, having energies E^+_{ICT} and E^-_{ICT}, respectively. The energy $E^+_{ICT}(E^-_{ICT})$ is defined as the energy required to withdraw an electron (respectively, the energy gained when an electron is added to the molecule) producing a fully relaxed state, i.e. both electronic and geometrical relaxation and interaction of charges are taken into consideration. These energies differ from respective energies of neutral HOMO and LUMO states [15]. The electron donated at the interface is transferred to the nearby molecule of an acceptor enabling significant Coulomb interaction with the energy $U_a = e^2/4\pi\varepsilon\varepsilon_0 a$, where e is the elementary charge, ε is an effective permittivity, ε_0 is the electric constant and a is the mutual electron–hole distance. Thus, the recombination of an (isolated) electron–hole pair at the interface is suppressed by the energy barrier $\Delta E = U_a + E^{don} - E^{acc}$, where E^{don} and E^{acc} are the energies of an electron, being located at donor and acceptor molecules, respectively (see Fig. 1). Charge transfer can be energetically beneficial, i.e. $\Delta E > 0$, even if $E^{don} < E^{acc}$, due to Coulomb interaction of the pair. An electron (e) and a hole (h) in an isolated pair should be localized by this interaction.

Yet, an e–h pair is not isolated at interface. If the distance between the neighboring pairs is comparable with the spacing of charges inside the pair, it is necessary to take into account the interaction of charges with the environment consisting of dipoles (e–h pairs), “vacancies” (pairs of neutral molecules) formed due to the recombination of a fraction of e–h pairs, and unpaired charges of both signs (i.e. dissociated pairs). The random arrangement of e–h pairs, vacancies and unpaired charges produces the potential fluctuations around each e–h pair. In average, the energy barrier ΔE is compensated by the drop of the electrostatic energy ΔU in equilibrium state, hence the energy level alignment of integer CTSs, E^+_{ICT} and E^-_{ICT}, is established at the interface [15] (see Fig. 1).

One has to note that organic–organic interface is a complex of interacting molecules of both materials. Hence, the morphology of the interface can differ from the morphology in the bulk of both materials. We perform model calculations under the simplifying assumption that the pairs of molecules of both materials at the interface form a square lattice with the parameter $b \geqslant a$, and all pairs of molecules

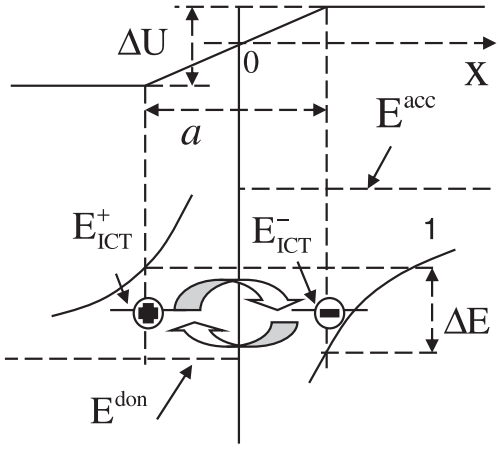

Fig. 1. Energy diagram of the interface between two organic materials. Curve 1 shows the function $E^{acc} - e^2/4\pi\varepsilon\varepsilon_0 x$.

are able to form e–h pairs. Vacancies, e–h pairs and dissociated pairs of charges were randomly arranged over the sites of a square lattice filling a square with dimensions $m \geqslant 20$ in any direction from the given pair with the relative concentrations $n_{\pm}$, n_0 and n, respectively. The contribution of distant electrons and holes was taken into account in the approximation of point dipoles forming a square lattice with the effective lattice parameter $b_{eff} = b/\sqrt{1-n_0}$. Relative concentrations of e–h pairs and vacancies are equal [20,21], because rates of separation and recombination of pairs seems to be equal under the presumed condition $E^{+}_{ICT} = E^{-}_{ICT}$, hence the normalizing condition $n_0 + n + n_{\pm} = 1$ yields

$$n_0 = n_{\pm} = (1-n)/2. \tag{1}$$

The spatial profile of the Coulomb energy of electron interaction with surrounding electrons and holes is calculated as follows,

$$U(x,y) = -\chi^{+}_{00}U_C(x,y,a/b) + \sum_{r_{ij}\neq 0}\left[\chi^{-}_{ij}U_C(x-i,y-j,0) - \chi^{+}_{ij}U_C(x-i,y-j,a/b)\right], \tag{2}$$

where $U_C(x,y,z) = U_b/\sqrt{x^2+y^2+z^2}$ is the energy of Coulomb repulsion, $U_b = e^2/4\pi\varepsilon\varepsilon_0 b$, $r_{ij} = \sqrt{i^2+j^2}$; x, y and z are coordinates in units of b (an electron is located at the zero point), the z axis is orthogonal to the interface; equations $z = 0$ and $z = a/b$ define the "plane of electrons" and "plane of holes", respectively. The pair of integers $\{i,j\}$ gives the position of a site (i.e. a pair of molecules) in the x–y plane, and χ^{+}_{ij}, χ^{-}_{ij} are random numbers. These numbers take the values 1 or 0, if the site is occupied or not occupied by positive and negative charge, respectively. A combination $\chi^{+}_{ij} = \chi^{-}_{ij} = 1$, i.e. an e–h pair, is realized with the probability $n_{\pm}$; a combination $\chi^{+}_{ij} = 0$ and $\chi^{-}_{ij} = 1$, i.e. an unpaired electron, occurs with the probability $n/2$, ets. Eq. (2) shows that the random spatial profile of electron potential energy, U/U_b, is affected by the unique parameter b/a. It is instructive to relate this parameter and the energy offset Δ, $\Delta = E^{don} - E^{acc}$ (the value of Δ is negative on Fig. 1). Taking into account the energies of electron's interaction with surrounding electrons and holes, namely

$$E^{+}_{ICT} = E^{don} + U^{don},\ E^{-}_{ICT} = E^{acc} + U^{acc} - U_a, \tag{3}$$

$$U^{don} = U_b\sum_{r_{ij}\neq 0}\left[\chi^{-}_{ij}/\sqrt{r_{ij}^2 + (a/b)^2} - \chi^{+}_{ij}/r_{ij}\right], \tag{4a}$$

$$U^{acc} = U_b\sum_{r_{ij}\neq 0}\left[\chi^{-}_{ij}/r_{ij} - \chi^{+}_{ij}/\sqrt{r_{ij}^2 + (a/b)^2}\right], \tag{4b}$$

one obtains the following equation from Eqs. (3) to (4) and from the condition $E^{+}_{ICT} = E^{-}_{ICT}$,

$$\frac{\Delta}{U_b} = -\frac{b}{a} + \sum_{r_{ij}\neq 0}\left(\chi^{+}_{ij} + \chi^{-}_{ij}\right)\left(\frac{1}{r_{ij}} - \frac{1}{\sqrt{r_{ij}^2 + (b/a)^{-2}}}\right), \tag{5}$$

Eq. (5) connects the ratio b/a with the energetic characteristic of an interface, i.e. the dimensionless energy Δ/U_b. It is instructive to relate Δ and such measurable values as energies of HOMO and LUMO states, E^{don}_{HOMO} and E^{acc}_{LUMO}. These energies include a "molecular" term which can be measured as ionization potential, I_G, and electron affinity, A_G, in gaseous phase, and energy of polarization of surrounding molecules by an electron (a hole), P_e (P_h): $E^{don}_{HOMO} = -I^{don}_G + P^{don}_h$, $E^{acc}_{LUMO} = -A^{acc}_G - P^{acc}_e$. It is conventional to consider the terms I, A, P as positive values [22]. The contribution of polarization energy at the interface differs from that in the bulk of both materials because ca. half of surrounding molecules belongs to another material. Therefore, one-can estimate the energies as following: $E^{don} = -(I^{don}_G - 0.5P^{don}_h - 0.5P^{acc}_h)$, $E^{acc} = -(A^{acc}_G - 0.5P^{acc}_e - 0.5P^{don}_e)$. Consequently,

$$\Delta = \left(E^{don}_{HOMO} - E^{acc}_{LUMO}\right) + 1/2\left(P^{acc}_h - P^{acc}_e\right) + 1/2\left(P^{don}_e - P^{don}_h\right). \tag{6}$$

Thus, the energy offset Δ can be equal to the difference of donor HOMO energy and acceptor LUMO energy at the interface, $\Delta = E^{don}_{HOMO} - E^{acc}_{LUMO}$, in the typical case of symmetry of polarization caused by electrons and holes, $P_h = P_e$ [22].

The result of numerical solution of Eq. (5) is a distribution function of the ratio $p = b/a$ for the definite value of Δ/U_b because of the random arrangement of a given e–h pair. The distribution is well fitted by Gaussian function,

$$\Phi(p) = \exp\left[-(p - \langle p\rangle)^2/2\sigma^2\right]/\sqrt{2\pi\sigma^2}, \tag{7}$$

where the mean value $\langle p\rangle = \langle b/a\rangle$ is well fitted by the universal (i.e. the parameter less) function of Δ/U_b in the investigated interval $-0.4 < \Delta/U_b < 0.8$:

$$\langle b/a\rangle = 0.57 + \exp[-(\Delta/U_b)/2.75]. \tag{8}$$

The variance σ is practically independent on the energy Δ, $\sigma = 0.11 \pm 0.01$, and both the values $\langle b/a\rangle$ and σ are practically independent on the relative concentration n, $0 \leqslant n \leqslant 1/3$.

The mechanism of thermally non-activated dissociation of e–h pairs is important for consideration of metal-type conductivity. Interaction of a pair with neighboring "vacancy", i.e. the process $n_0 + 2n_{\pm} \rightarrow n + n_{\pm}$ (Fig. 2a) has been analyzed previously [20,21]. The process is cooperative. For example, the shift of an electron toward the right

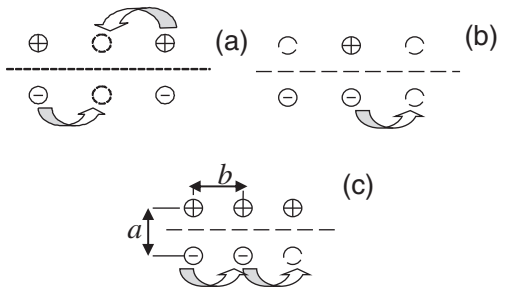

Fig. 2. Schematics of processes at the interface (broken lines): (a) Dissociation of e–h pairs by interaction with a "vacancy"; (b) dissociation by interaction with neighboring unpaired charge; and (c) transport of a "Coulomb hole".

stimulates the hopping of a hole in the opposite direction (Fig. 2a). This process, however, becomes inefficient if $b/a > 1.2$, that seems to be a typical case [20,21]. In such a case, dissociation of an e–h pair caused by Coulomb repulsion of one of the charges from neighboring unpaired charge, which is injected from an electrode or photogenerated (Fig. 2b), is the most likely process. An electron, being injected, can produce a lot of dissociated pairs in the course of its motion towards counter electrode. The value of n is limited by the reverse process, i.e. recombination. Using the steady-state relation $n = \varphi_{dis} n_{\pm}$ and Eq. (1) one obtains

$$n = \varphi_{dis}/(2 + \varphi_{dis}), \tag{9}$$

where the dissociation probability, φ_{dis}, is calculated by Monte–Carlo simulation as the ratio of the number of dissociation events to the total number of attempts, providing that the configuration shown in Fig. 2b is realized. The results of the simulation are exhibited in Table 1.

It is assumed that dissociation event occurs provided that the minimum of electron potential energy (see Eq. (2)) is shifted from the point {0,0} by more than $b/2$ in the x–y plane due to both the dynamic character of the interaction and the possibility of cooperative processes. This criterion yields the probability of dissociation which is free from thermal activation and from tunneling possibly. Condition for the latter is discussed below.

3. Results and discussion

The value of φ_{dis} depends only on the ratio $p = b/a$ because only this parameter affects the profiles of potential energy, see Eq. (2). Numerical simulations of φ_{dis} and Eq. (9) yield the value of n for a given p. It is important that (i) the values of p are distributed in accordance with Eq. (7) and (ii) random potential of dipoles and unpaired charges produces energetic disorder. Really, it is correlated disorder, i.e. charge carriers in neighboring states tends to obtain similar energies [23]. Therefore, the value of n should be calculated as the average of $n(p)$ values which are determined by *local* values of p:

$$n = \langle n \rangle = \int n(p)\Phi(p)dp \tag{10}$$

Practically, the value of $\langle n \rangle$ is estimated as a sum of the products $n(p_i)\Phi(p_i)\Delta p_i$ by the use of Eqs. (7)–(9) and the values of $\varphi_{dis}(p_i)$, see Table 1. The result is as following: $\langle n \rangle = 0.04$, $\Delta/U_b = 0.2$, and $\langle n \rangle = 0.02$, $\Delta/U_b = 0.0$. Eventually, the value of n is determined by the normalized energy offset Δ/U_b. The value of n is critical for the mechanism of charge carrier transport as it is shown below.

Table 1
Results of numerical modeling.

Δ/U_b	$\langle b/a \rangle$	φ_{dis}	φ	$\bar{\varphi}$ (0.2)
0.8	1.32	0.18	0.61	0.44
0.4	1.44	0.03	0.58	0.35
0.2	1.5	0.01	0.55	0.33
0.0	1.57	0.005	0.52	0.26
−0.4	1.73	<0.001	0.45	0.15

Energy of an electron at the interface, both paired and unpaired, is the subject of random temporal (as well as spatial) fluctuations which are related to variations of numbers χ_{ij}^{+}, χ_{ij}^{-} because of the recombination and dissociation events. Therefore, the electron energy is uncertain. We calculated the distribution function of the energy of paired and unpaired electrons ($E_{\pm}$ and E_0, respectively) in order to estimate the uncertainty. The energies $E_{\pm}$ and E_0 are calculated as $U(0,0)$ from Eq. (2), providing that $\chi_{00}^{+} = 1$ and $\chi_{00}^{+} = 0$ in the former and the latter case, respectively. One obtains the Gaussian distribution functions in both cases, see examples in the Fig. 3. The energy offset Δ and the relative concentration of dissociated pairs, n, are considered as independent variable parameters, operationally. One obtains that the mean energies, $\langle E_{\pm} \rangle$ and $\langle E_0 \rangle$, are independent of n, see Fig. 3, while their mutual displacement increases slightly with the decrease of Δ ($\langle E_0 \rangle - \langle E_{\pm} \rangle = 1.31$, $\Delta = 0.8$, and $\langle E_0 \rangle - \langle E_{\pm} \rangle = 1.57$, $\Delta = 0.0$, in units of U_b). Vice versa, the Gaussian variances, $\sigma_{\pm} \approx \sigma_0$, are independent of Δ and increases strongly with the increase of n, see Fig. 4:

$$\sigma_{\pm}/U_b \approx 5 \cdot n^{0.55}, 0.01 \le n \le 0.33. \tag{11}$$

Their values are minimal if $n = 0$: $\sigma_{\pm} \approx \sigma_0 \approx 0.06U_b$. Strictly speaking, the calculation of energies is complicated by the Gaussian energy disorder that is caused by interactions of the charge with molecular dipole moments [5,23]. However, one can neglect this disorder if the respective variance does not exceed the value which is predicted by Eq. (11).

Two different physical situations arises at small and large ($n \ge 0.02$) concentration of unpaired charges. In the latter case, energy bands of paired and unpaired charge carriers are broad and effectively overlapped, see Fig. 3. The band width, $\sqrt{2}\sigma_{\pm}$, exceeds 0.8 relative to U_b. Providing $b \approx 1$ nm and $\varepsilon = 3.5$, one obtains $U_b \approx 0.4$ eV, hence $\sqrt{2}\sigma_{\pm} \ge 0.3$ eV. The latter value is comparable with the band width of organic conductor TTF–TCNQ, 0.5 eV [24]. The intersite transfer time is $t_0 \cong \hbar/\sqrt{2}\sigma_{\pm} \approx 10^{-15}$ s, that is not larger than typical time of electronic polarization in organics. One can consider nb^{-2} as the area density of

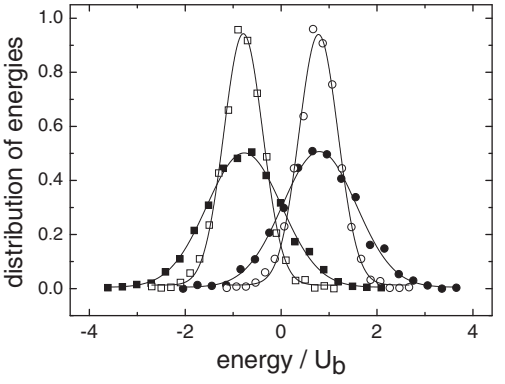

Fig. 3. Distribution functions of energy of an electron, which belongs to e–h pair (squares) and the same of a single electron (circles). Gaussian fits are also shown. $\Delta = 0.0$. The relative concentration of dissociated pairs, n, is 0.03 (filled symbols) and 0.01 (open symbols).

free (delocalized) charge carriers (2D e-gas). The critical concentration of unpaired charges, $n \approx 0.02$, corresponds to $\Delta \approx 0$, as mentioned above. This value seems to be reasonable for the TTF–TCNQ interface (the offset of energy levels in the bulk, $E^{don}_{HOMO} - E^{acc}_{LUMO} = -0.2$ eV [24], yet this value can be reduced due to quantum splitting of energy levels at the interface [25]). Recently, the energy level alignment, $E^{+}_{ICT} = E^{-}_{ICT}$, has been reported for TTF–TCNQ D–A interfaces [15,26], hence $\Delta E = \Delta U$. Basing on the value of an interfacial electrostatic energy from the Ref. [26], $\Delta U = 0.6$ eV, and providing that, again, $U_b \approx 0.4$ eV and $b/a \approx 1.5$, one obtains $\Delta = \Delta E - U_a \approx 0$.

In order to approve the possibility of metal-type conductivity, we calculated the probability φ (by means of the same criteria which was used in calculations of φ_{dis}) of thermal activation- and tunneling- free electron's transfer caused by an adjacent unpaired hole (see Fig. 2c). If $\varphi \geq 0.5$, that relates to $\Delta/U_b \geq 0.0$, see Table 1, each unpaired charge can initiate sequential transfers of opposite charge (motion of a "Coulomb hole") [20,21] because the number of "open bonds" in a 2D square lattice exceeds two, hence the criterion of percolation is fulfilled [27]. One can estimate the mobility, μ, and the surface (2D) conductivity, $\sigma_{2D} = e\mu n b^{-2}$, as follows: $\mu = (e/kT)b^2/t_0$, $\sigma_{2D} = (e^2/kT)n/\ t_0$, where T is the temperature, and k is the Boltzmann constant. The value of σ_{2D} exceeds the threshold of metallic 2D conductivity [28], $\sigma_{\min} \approx e^2/h \approx 0.4 \cdot 10^{-4}$ S at $T \leq 300$ K, provided that $n \geq 0.02$ (hence $t_0 \leq 10^{-15}$ s^{-1}), and $b \leq 1$ nm: $\sigma_{2D} \geq 10^{-4}$ S. This value is in good agreement with the experimental result of Alves et al. $\sigma_{2D} \leq 10^{-3}$ S [10].

If the concentration of dissociated pairs is rather small, $n \leqslant 0.01$, energy bands of paired and unpaired charge carriers are narrow (<0.05 eV) and separated by energy gap. Charge carriers are localized on molecules, and the transport of "Coulomb holes" occurs via hopping in this case. However, Coulomb interaction between oppositely charged carriers from adjacent pairs can substantially reduce activation energy of hops and hence increase mobility. Table 1 shows the probability $\tilde{\varphi}$ that potential drop on the distance b compensates energy difference of initial and final localized states, which is more than $0.2 \cdot U_b \cong 0.1$ eV. The reciprocal value, $\tilde{\varphi}^{-1}$, yields the frequency of attempts of the hops relative to typical frequency of fluctuations of potential. The latter seems to be the typical frequency of recombination of the e–h pairs, i.e. the frequency of non-activated tunnel charge transfers.

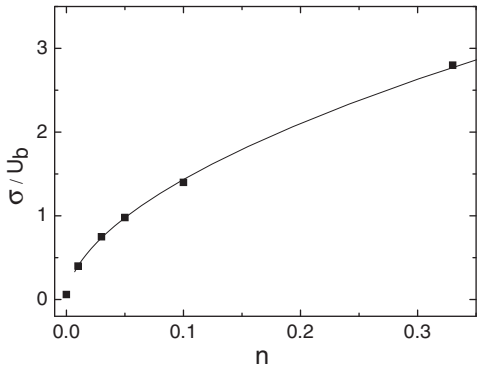

Fig. 4. Gaussian variances of electron's energy distributions, see Fig. 3, in dependence of the relative concentration of dissociated pairs, n. Solid curve shows the fit by Eq. (11).

As an example of the above reasoning one can consider the charge carrier transport in polymer composites based on either poly-N-vinylcarbazole (PVK) or aromatic polyimide derivative (API) incorporating either carbon single-walled nanotubes (SWNT) or nanocrystals of J-aggregated cyanine dye molecules (CD) [29–32]. In the polymer composites, one of the components (anthracene moiety in API, carbazole in PVK) acts as an electron donor and another one (carbocyanine core in J-aggregate, semiconducting SWNT) exhibits electron-acceptor behavior. The difference of energy levels between donor HOMO and acceptor LUMO (−5.8 and −4.8 eV [33], for the case of PVK/SWNT composite; −5.2 [34] and −3.7 eV [32] for the case of API/CD composite, respectively) is much higher than those for TTF and TCNQ. However, the formation of D–A interface is reasonable even if the barrier is as high as 1 eV [12]. The transport is shown to exhibit a similar behavior in the mentioned composites, namely: (1) the drift mobility of charge carriers in the composite is higher than that in the undoped polymer by 1–1.5 order of magnitude although the SWCNT or CD concentration is below that of percolation threshold; (2) the mobility of electrons is higher than that of holes, vice versa than in the pristine polymers; (3) the field dependence of the mobility is linear in Poole–Frenkel coordinates. The third feature is a manifestation of hopping transport [5,23], while the second one can be an evidence of transport by mean of "Coulomb holes".

4. Conclusion

Integer charge transfer over D–A organic interface can produce a high area density ($\cong 10^{14}$ cm^{-2}) of strong and fluctuating dipoles (pairs of CTSs). Moreover, the high density of single electrons and holes arises due to dissociation of the pairs, if $\Delta/U_b \geq 0.0$. Strong Coulomb interaction results in intermolecular transfer time of charge carriers which is less than the time of electron polarization. Hence, metal-type band transport along the interface, at least through some fractal areas, is achieved. If the density of CTSs is too low (e.g., the D–A interface is not perfect, or HOMO–LUMO barrier is too high), an increase of mobility can originate from the reduction of the energy barrier for hopping of "Coulomb holes" by Coulomb attraction.

Acknowledgement

The work was supported by the International Science and Technology Centre (Project 3718) and Russian Foundation for Basic Research (Projects 09-03-00616 and 10-03-92005).

References

[1] K. Seki, A. Kahn, J.-J. Pireaux, in: W.R. Salaneck (Ed.), Conjugated Polymer and Molecular Interfaces: Science and Technology for Photonic and Optoelectronic Applications, Marcel Dekker, New York, 2002.

[2] R.H. Friend, R.W. Gymer, A.B. Holmes, J.H. Burroughes, R.N. Marks, C. Taliani, D.D.C. Bradley, D.A. Dos Santos, J.L. Brédas, M. Lögdlund, W.R. Salaneck, Nature 397 (1999) 121.
[3] C. Deibel, T. Strobel, V. Dyakonov, Phys. Rev. Lett. 103 (2009) 036402.
[4] V.R. Nikitenko, O.V. Salata, H. Bässler, J. Appl. Phys. 92 (2002) 2359.
[5] H. Bässler, Phys. Status Solidi B 175 (1993) 15.
[6] Jing-Mei Zhuo, Li-Hong Zhao, Perg-Jon Chia, Wee-Sun Sim, R.H. Friend, P.K.H. Ho, Phys. Rev. Lett. 100 (2008) 186601.
[7] H. Shimotani, G. Diguet, Y. Iwasa, Appl. Phys. Lett. 86 (2005) 022104.
[8] M.J. Panzer, C.D. Frisbie, Adv. Funct. Mat. 16 (2006) 1051.
[9] S. Fratini, H. Xie, I.N. Hulea, S. Ciuchi, A.F. Morpurgo, New J. Phys. 10 (2008) 033031.
[10] H. Alves, A.S. Molinari, H. Xie, A.F. Morpurgo, Nat. Mater. 7 (2008) 574.
[11] T. Sakanoue, T. Irie, C. Adachi, J. Appl. Phys. 105 (2009) 114502.
[12] J.H. Kim, A. Watanabe, J.W. Chung, Y. Jung, B.-K. An, H. Tada, S.Y. Park, J. Mater. Chem. 20 (2010) 1062.
[13] F. Zhu, H. Wang, D. Song, K. Lou, D. Yan, Appl. Phys. Lett. 93 (2008) 103308.
[14] L.B. Shein, M. LaHa, D. Novotny, Phys. Lett. A 167 (1992) 79.
[15] S. Braun, W.R. Salaneck, M. Fahlman, Adv. Mater. 21 (2009) 1450.
[16] I. Avilov, V. Geskin, J. Cornil, Adv. Funct. Mater. 19 (2009) 624.
[17] S.A. Pauli, P.R. Willmott, J. Phys.: Condens. Matter 20 (2008) 264012.
[18] V.I. Arkhipov, E.V. Emelianova, P. Heremans, H. Bässler, Phys. Rev. B 72 (2005) 235202.
[19] V.R. Nikitenko, A.R. Tameev, A.V. Vannikov, A.N. Lachinov, H. Bässler, Appl. Phys. Lett. 92 (2008) 153307.
[20] V.R. Nikitenko, A.R. Tameev, A.V. Vannikov, Tech. Phys. Lett. 35 (2009) 823.
[21] V.R. Nikitenko, A.R. Tameev, A.V. Vannikov, Semiconductors 44 (2010) 211.
[22] E. Siliņš, V. Čapek, Organic.Molecular. Crystals, Interaction, Localization, and Transport Phenomena, AIP Press, New York, 1994.
[23] S.V. Novikov, D.H. Dunlap, V.M. Kenkre, P.E. Parris, A.V. Vannikov, Phys. Rev. Lett. 81 (1998) 4472.
[24] T. Mori, J. Phys.: Condens. Matter 20 (2007) 184010.
[25] M.C. Petty, Molecular Electronics: From Principles to Practice, Wiley, Chichester, 2007.
[26] S. Braun, X. Liu, W.R. Salaneck, M. Fahlman, Org. Electron. 11 (2010) 212–217.
[27] B.I. Shklovskii, A.L. Efros, Electronic Properties of Doped Semiconductors, Springer, Heidelberg, 1984.
[28] N.F. Mott, E.A. Davis, Electron Processes in Non-crystalline Materials, Clarendon Press, Oxford, 1979.
[29] A.R. Tameev, A.V. Vannikov, H.F.M. Schoo, Thin Solid Films 451–452 (2004) 109.
[30] L. Licea-Jimenes, A.D. Grishina, L.Ya. Pereshivko, T.V. Krivenko, V.V. Savelyev, R.W. Rychwalski, A.V. Vannikov, Carbon 44 (2006) 113.
[31] A.R. Tameev, A.A. Kozlov, E.I. Mal'tsev, D.A. Lypenko, V.V. Bobinkin, A.V. Vannikov, Proc. SPIE – Int. Soc. Opt. Eng. 4105 (2001) 443.
[32] E.I. Mal'tsev, D.A. Lypenko, V.V. Bobinkin, B.I. Shapiro, A.R. Tameev, J. Wright, V.I. Berendyaev, B.V. Kotov, A.V. Vannikov, Mol. Cryst. Liq. Cryst. 361 (2001) 217.
[33] S. Kazaoui, N. Minami, N. Matsuda, H. Kataura, Y. Achiba, Appl. Phys. Lett. 78 (2001) 3433.
[34] F.I. Vilesov, A.A. Zagrubskii, D.Z. Garbuzov, Sov. Phys.-Solid State 5 (1964) 1460.

Organic Electronics 12 (2011) 595–601

Contents lists available at ScienceDirect

Organic Electronics

journal homepage: www.elsevier.com/locate/orgel

New blue host materials based on anthracene-containing dibenzothiophene

Lei Wang [a,b,*], Zhi-Yong Wu [a], Wai-Yeung Wong [b,c,*], Kok-Wai Cheah [d], Hong Huang [a], Chin H. Chen [b,*]

[a] Wuhan National Laboratory for Optoelectronics, School of Optoelectronic Science and Engineering, Huazhong University of Science and Technology, Wuhan 430074, PR China
[b] Department of Chemistry and Centre for Advanced Luminescence Materials, Hong Kong Baptist University, Waterloo Road, Hong Kong, PR China
[c] Institute of Molecular Functional Materials, Areas of Excellence Scheme, University Grants Committee, Hong Kong, PR China
[d] Department of Physics and Centre for Advanced Luminescence Materials, Hong Kong Baptist University, Waterloo Road, Hong Kong, PR China

ARTICLE INFO

Article history:
Received 8 November 2010
Received in revised form 4 January 2011
Accepted 5 January 2011
Available online 25 January 2011

Keywords:
Blue material
Anthracene
Dibenzothiophene
Organic light-emitting devices

ABSTRACT

A series of novel host blue-emitting materials based on anthracene have been synthesized and investigated in which, a π-electron-rich dibenzothiophene moiety was introduced as a side group to fine adjust the HOMO/LUMO levels of the anthracene and enhance the ability of hole-transport and electron-injection. These materials exhibit good film-forming capabilities, and display strong blue fluorescence in solution. To explore the electroluminescent properties of these materials, sky blue devices of 2-TNATA (60 nm)/NPB (10 nm)/Host: BUBD-1 (40 nm)/Alq_3 (15 nm)/LiF (1 nm)/Al (150 nm) were fabricated. For the device with 9, 10-bis(dibenzothiophen-4-yl)anthracene as the host, an electroluminescence efficiency of 13.14 cd/A and 6.76 lm/W at 20 mA/cm^2 and 6.09 V were achieved, with Commission Internationale d'Eclairage ($CIE_{x,y}$) color coordinates of (x = 0.15, y = 0.30).

© 2011 Elsevier B.V. All rights reserved.

1. Introduction

Organic light emitting diodes (OLEDs) have been a subject of intense academic and industrial research for the last decades due to their potential application in displays and solid state lighting [1–3]. Until now, among the three primary colors, green and red phosphorescent material have been studied intensively, and high efficiency and long lifetime red and green devices have been obtained [4–7]. However, it is very difficult to get high efficiency and long lifetime blue phosphorescent devices in spite of many relevant studies related to blue phosphorescent devices. Therefore, blue fluorescent material is still of prime importance for application in full-color flat-panel displays. To date, several derivatives of anthracene [8], binaphthol [9,10], spirobifluorene-linked bianthracene [11] and biaryl have been developed and subsequent attempts were made to improve their electroluminescent (EL) properties.

Among them, anthracene derivatives are one of the earliest luminescent materials reported [9] and they emit violet light both in the solid state and in solution. Derivatives such as 9, 10-di-2-naphthylanthracene (**ADN**) and 2-*tert*-butyl-9, 10-di-2-naphthylanthracene (**m-ADN**) have been used successfully as blue emitters in commercial OLED products (Scheme 1). Recently, Park et. al have reported anthracene derivatives bearing bulky side groups with an excellent external quantum efficiency (EQE) of 7.18% and Commission Internationale d'Eclairage (CIE) coordinates of (0.156, 0.088) [12]. Char and coworkers reported anthracene derivatives bearing non-planar diarylsilyl groups exhibiting high external quantum efficiency (EQE) (6.3%)

* Corresponding authors. Address: Wuhan National Laboratory for Optoelectronics, School of Optoelectronic Science and Engineering, Huazhong University of Science and Technology, Wuhan 430074, PR China. Tel./fax: +86 27 87793032 (L. Wang), Institute of Molecular Functional Materials, Areas of Excellence Scheme, University Grants Committee, Hong Kong, PR China. Tel.: +852 34117074; fax: +852 34117348 (W.-Y. Wong), tel.: +852 34117257 (C.H. Chen).

E-mail addresses: wanglei@mail.hust.edu.cn (L. Wang), rwywong@hkbu.edu.hk (W.-Y. Wong), fredchen@hkbu.edu.hk (C.H. Chen).

1566-1199/$ - see front matter © 2011 Elsevier B.V. All rights reserved.
doi:10.1016/j.orgel.2011.01.002

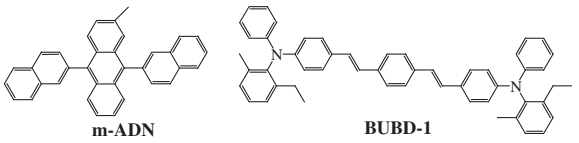

Scheme 1. The molecular structure of **m-ADN** and **BUBD-1**.

and good CIE coordinates (0.142, 0.149) [13]. Additionally, it was found that the introduction of *m*-dibenzothiophene into the polyfluorene backone could effectively suppress the long-wavelength emission [14]. Furthermore, dibenzothiophene-S, *S*-dioxide was incorporated into the small molecules owing to its high fluorescence efficiency and electron affinity energy [15]. However, to our knowledge, there is no report on the blue-emitting materials based on anthracene with dibenzothiophene as the wing to increase the charge transporting properties.

In this work, a series of high efficiency blue-emitting dibenzothiophenyl-anthracene derivatives were designed and synthesized. The design concept is to attach the π-electron-rich dibenzothiophene moiety to the 9, 10 positions of anthracene and therefore to facilitate the ready manipulation of its electronic structure (HOMO/LUMO levels) and tune the resulting physical properties. We anticipated that these new anthracene derivatives would reconstitute the properties of the **ADN** derivatives for the following two reasons: (1) The π-electron-rich benzothiophene substitution would offer the resulting new molecule with better hole transport properties. (2) The introduction of sterically hindered dibenzothiophene group at the side of anthracene would reduce the LUMO of the anthracene, which will be beneficial for the injection of electrons. At the same time, the PL emission of these benzothiophene derivatives will be blue-shifted as compared to **m-ADN**.

Because the use of sky blue light represents an efficient way to obtain the favorable white light [16,17], multilayered sky blue OLEDs were fabricated using these new blue host materials and BUBD-1 as the dopant (BUBD-1 = (*N*-(4-((1*E*,8*E*)-4-((*E*)-4-((2-ethyl-6-methylphenyl)(phenyl) amino)styryl)styryl)phenyl)-2-ethyl-6-methyl-*N*-phenylbenzenamine)) in investigating the EL properties of these materials (Scheme 2). As will be demonstrated below, devices using materials **2S-ADN** exhibited highly efficient sky blue emissions.

2. Experimental section

2.1. Material and methods

All reagents and solvents were used as purchased from Aldrich and were used without further purification. ^{1}H and ^{13}C NMR spectra were recorded on a Bruker-AF301 AT 400 MHz NMR spectrometer. Mass spectra were obtained on a Finnigan MAT SSQ-710 in FAB (positive) mode. Fluorescence spectra were obtained on a Perkin-Elmer LS55 luminescence spectrometer. The differential scanning calorimetry (DSC) and thermal gravimetric analysis (TGA) experiments were performed under a nitrogen atmosphere on a TA Instruments DSC 2920 or DSCQ2000. Elemental

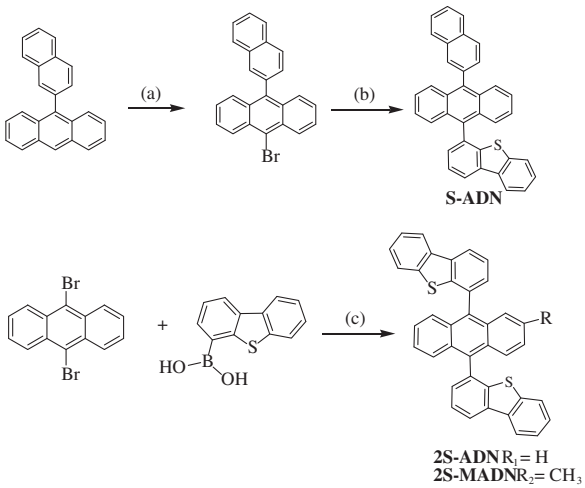

Scheme 2. Synthesis of compounds **S-ADN**, **2S-ADN** and **2S-MADN**. Conditions: (a) hυ, NBS, CH_2Cl_2; (b) $PdCl_2(PPh_3)_2$, toluene, 2 M K_2CO_3, 4-dibenzolthiophene boronic acid; (c) $Pd(PPh_3)_4$, toluene, 2 M K_2CO_3.

analyses were determined by a Finnigan FLASH 1112 SERIES EA elemental autoanalyzer. Cyclic voltammetric measurements were carried out in a conventional three electrode cell using a Pt button working electrode of 2 mm in diameter, a platinum wire counter electrode, and a SCE reference electrode on a computer-controlled EG&G Potentiostat/Galvanostat model 283 at room temperature. Reduction of all compounds was performed in dichloromethane containing Bu_4NPF_6 (0.1 M) as the supporting electrolyte.

9-(2-naphthyl)anthracene and 9-(2-naphthyl)-10-(bromo)-anthracene were prepared by the process reported in the literature [18]. Suzuki coupling reaction was conducted under a nitrogen atmosphere in the absence of light exposure.

2.2. Preparation of compounds

2.2.1. Synthesis of 9-(2-naphthyl)anthracene

It was synthesized by the method reported in the literature [18]. Yield: 89%. ^{1}H NMR (400 MHz, $CDCl_3$): δ 8.52 (s, 1H, Ar), 7.99–8.09 (m, 4H, Ar), 7.88–7.93 (m, 2H, Ar), 7.66–7.69 (m, 2H, Ar), 7.54–7.61 (m, 3H, Ar), 7.44–7.49 (m, 2H, Ar), 7.29–7.34 (m, 2H, Ar).

2.2.2. Synthesis of 9-(2-naphthyl)-10-(bromo)anthracene

It was synthesized by the method reported in the literature [18]. Yield: 91%. ^{1}H NMR (400 MHz, $CDCl_3$): δ 8.61–8.63 (d, 2H, Ar), 7.99–8.075 (m, 2H, Ar), 7.84–7.89 (m, 2H, Ar), 7.64–7.66 (d, 2H, Ar), 7.56–7.60 (m, 4H, Ar), 7.50–7.52 (m, 1H, Ar), 7.32–7.35 (m, 2H, Ar).

2.2.3. 4-(10-(Naphthalen-2-yl)anthracen-9-yl) dibenzothiophene (***S-ADN***)

A mixture of 4-dibenzothiophene boronic acid (2 mmol, 456 mg), 9-(2-naphthyl)-10-(bromo)anthracene(**2**) (2 mmol, 760 mg), $PdCl_2$ $(PPh_3)_2$ (0.06 mmol), toluene (30 mL), and K_2CO_3 (10 mL, 2 M) was flushed with N_2 for 10 min under

stirring. The reaction mixture was heated at 120 °C for 12 h under a N_2 atmosphere. After cooling to room temperature, the organic layer was evaporated to dryness under reduced pressure. The residue was purified by flash column chromatography on silica gel using CH_2Cl_2: hexane = 1:3 (v/v). Yield: 85%. ^{1}H NMR (400 MHz, $CDCl_3$) δ 8.36–8.36 (m, 1H, Ar), 8.28–8.30 (m, 1H, Ar), 8.0–8.11 (m, 3H, Ar), 7.91–7.96 (m, 1H, Ar), 7.59–7.78 (m, 10H, Ar), 7.47–7.51 9 (m, 1H, Ar), 7.39–7.43 (m, 1H, Ar), 7.26–7.33 (m, 4H, Ar). ^{13}C NMR ($CDCl_3$) δ 141.83, 139.96, 138.0, 136.5, 136.47, 136.43, 135.94, 135.76, 134.52, 133.41, 133.37, 132.79, 130.3, 130.23, 129.56, 129.48, 128.15, 128.09, 127.98, 127.95, 127.92, 127.90, 127.31, 126.85, 126.47, 126.45, 126.38, 126.26, 125.57, 125.31, 124.94, 124.43, 122.87, 121.86, 120.97 (Ar). FAB-MS: 486.1 (*m/z*), calcd for $C_{36}H_{22}S$: 486.6. Anal.calcd for $C_{36}H_{22}S$: C 88.85, H 4.56, S 6.59; found: C 88.80, H 4.58, S 6.51.

*2.2.4. 9, 10-Bis(dibenzothiophen-4-yl)anthracene (**2S-ADN**)*

The compound was synthesized using a similar procedure as for compound **S-ADN**. Yield: 80%. ^{1}H NMR (400 MHz, $CDCl_3$): 8.36–8.39 (m, 2H, Ar), 8.29 (d, 2H, Ar), 7.59–7.76 (m, 10H, Ar), 7.44–7.52 (m, 2H, Ar), 7.40–7.44 (m, 2H, Ar), 7.27–7.29 (m, 4H, Ar). ^{13}C NMR ($CDCl_3$) δ 142.0, 140.3, 136.2, 136.0, 134.0, 129.9, 129.7, 127.1, 126.0, 125.1, 124.7, 123.2, 123.1, 122.1, 121.3 (Ar). FAB-MS: 543.2 (*m/z*), calcd for $C_{38}H_{22}S_2$: 542.7. Anal.calcd for $C_{38}H_{22}S_2$: C 84.10, H 4.09, S 11.82; found: C 84.0, H 4.15, S 11.72.

*2.2.5. 2-Methyl-10-bis(dibenzothiophen-4-yl)anthracene (**2S-MADN**)*

The compound was synthesized using a similar procedure as for compound **S-ADN**. Yield: 76% ^{1}H NMR (400 MHz, $CDCl_3$): δ 8.37–8.40 (m, 2H, Ar), 8.29–8.32 (m, 2H, Ar), 7.74–7.79 (m, 2H, Ar), 7.48–7.69 (m, 9H, Ar), 7.42–7.45 (m, 2H, Ar), 7.37 (s, 1H, Ar), 7.25–7.28 (m, 2H, ar), 7.12–7.15 (m, 1H, Ar), 2.3 (s, 3H, Ar). ^{13}C NMR ($CDCl_3$): 141.78, 140.01, 139.96, 135.91, 135.84, 135.78, 135.53, 135.28, 134.38, 134.0, 133.92, 129.95, 129.80, 129.63, 129.57, 129.13, 128.65, 128.30, 126.83, 126.82, 126.60, 126.50, 125.65, 125.32, 124.98, 124.94, 124.70, 124.43, 122.87, 121.86, 120.96, 120.94, 22.06 (Ar). FAB-MS: 557.4 (*m/z*), calcd for $C_{39}H_{24}S_2$: 556.7. Anal.calcd for $C_{38}H_{24}S_2$: C 84.14, H 4.35, S 11.52; found: C 84.12, H 4.39, S 11.42.

2.3. Device fabrication

The device structure used for the evaluation of **S-AND**, **2S-ADN**, and **2S-MADN** as a host material was indium-tin-oxide (ITO)/2-TNATA (60 nm)/NPB (10 nm)/Host: BUBD-1 (40 nm)/Alq_3 (15 nm)/LiF (1 nm)/Al (150 nm) and the energy level diagram is shown in Fig. 4. Prior to the deposition of organic materials, the indium-tin-oxide (ITO)/glass was cleaned with a routine cleaning procedure and pretreated with UV-ozone. Devices were fabricated under a base vacuum of about 10^{-6} torr in a thin-film evaporation coater following a published protocol [19]. The current density–voltage–luminance characteristics of the devices were measured with a diode array rapid scan system using a Photo Research PR650 spectrophotometer and a computer-controlled, programmable, direct-current (DC) source.

Table 1
Crystallographic data for compounds **S-ADN** and **2S-AND**.

Compound	**S-ADN**	**2S-ADN**
Formula	$C_{36}H_{25}O1.5S$	$C_{38}H_{22}S_2$
Formula weight	513.62	542.68
Crystal size/nm	0.30 × 0.26 × 0.24	0.32 × 0.25 × 0.22
Crystal system	Monoclinic	Monoclinic
Space group	*C*2/*c*	$P2_1/n$
a/Å	34.197(4)	16.086(2)
b/Å	8.634(1)	9.074(1)
c/Å	25.340(3)	19.466(2)
α/°	90	90.00
β/°	131.011(2)	105.458(2)
γ/°	90	90.00
V/Å^3	5645(1)	2738.5(5)
F(000)	2152	1128
Z	8	4
D_{calc}/g cm^{-3}	1.209	1.316
Absorption coefficient/ mm^{-1}	0.143	0.221
Reflections collected	12,672	15,346
Independent reflections (R_{int})	4736 (0.062)	6487 (0.0522)
Observed reflections ($I > 2\sigma(I)$)	2692	3421
*R*1, *wR*2 ($I > 2\sigma(I)$)	0.0871, 0.1732	0.0779, 0.1352
*R*1, *wR*2 (all data)	0.1504, 0.2177	0.1450, 0.1544
Goodness-of-fit on F^2	0.815	1.032

2.4. X-ray crystallography

Pertinent crystallographic data and other experimental details are summarized in Table 1. Diffraction data were collected at 293 K using graphite monochromated Mo Kα radiation (λ = 0.71073 Å) on a Bruker Axs SMART 1000 CCD diffractometer. The collected frames were processed with the software SAINT+ [20] and an absorption correction (SADABS) [21] was applied to the collected reflections. The structure was solved by the Direct methods (SHELXTL) [22] in conjunction with the standard difference Fourier techniques and subsequently refined by full-matrix least-squares analyses on F^2. All non-hydrogen atoms were refined anisotropically. Hydrogen atoms were generated in their idealized positions and allowed to ride on their respective parent carbon atoms. CCDC reference numbers 794330 and 794331.

3. Results and discussion

The chemical structures and synthetic routes of the three new compounds are shown in Scheme 2. They were synthesized by the Pd-catalyzed Suzuki cross-coupling of the 4-dibenzothiopheneboronic acid and the corresponding bromide with high yields. All of the newly synthesized compounds were fully characterized with ^{1}H-NMR spectroscopy and FAB-MS spectrometry and found to be in good agreement with their structures.

In order to look into the conformation of the benzothiophene-substituted derivatives, the crystal structure of **S-ADN** and **2S-ADN** were determined. As shown in Fig. 1

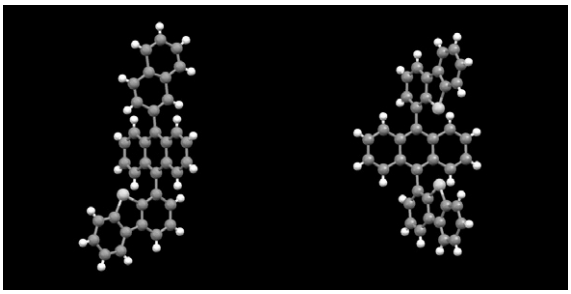

Fig. 1. The ORTEP drawings of **S-ADN** (left), and **2S-AND** (right).

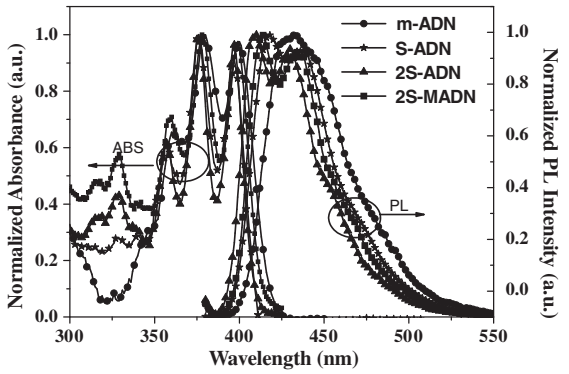

Fig. 2. Photoluminescence (PL) (λ_{ex} = 376 nm) and absorption spectra of compounds **m-ADN**, **S-ADN**, **2S-ADN**, and **2S-MADN** in toluene.

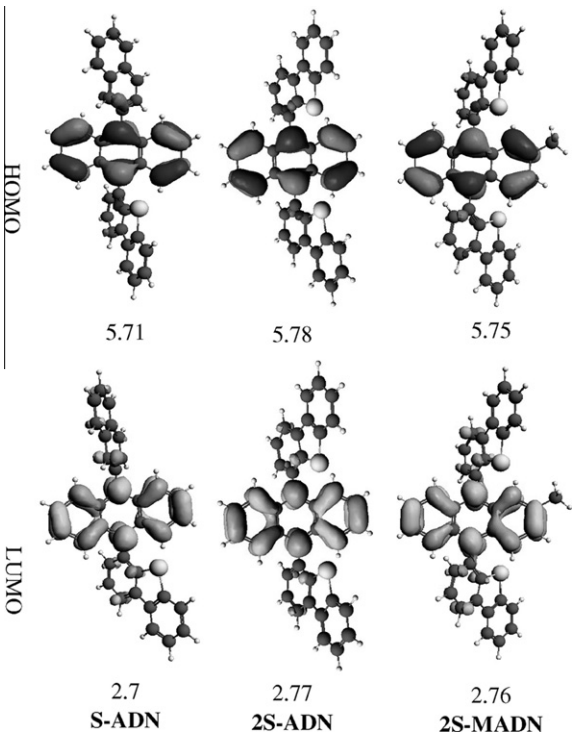

Fig. 3. The B3LYP/6-31-G calculated HOMOs and LUMOs for **S-ADN**, **2S-ADN**, **2S-MADN**.

(left), the twisted angle between the anthracene main core and the dibenzothiophene side unit is 86.55°, whereas the twisted angle between 2-naphthyl and anthracene is 77.02°. For the compound **2S-ADN**, the corresponding twist angles between the dibenzothiophene and anthracene groups are 74.14° and 76.45°. The results suggest that the obtained **2S-ADN** has a non-coplanar structure which bears bulky substituents for the purpose of disrupting the intermolecular interaction and suppressing the problematic recrystallization that would eventually reduce self-aggregation, which in turn, improves the morphological stability of the thin film of the OLED devices.

Thermal properties of these new blue host materials were studied using DSC and TGA. In Table 2, the glass transition temperature (T_g) and onset decomposition temperature (T_d) of the compounds are given. The compounds **S-ADN**, **2S-ADN,** and **2S-MADN** posses high (T_g's) at 177 °C, 115 °C and 149 °C in the DSC heating cycle, respectively. As we know, the high T_g will be beneficial for the performance of OLED device. TGA measurements showed that all the compounds exhibit high T_d (5% weight loss) at 411, 437, and 454 °C, respectively. It means that these materials are stable enough to endure the temperature of the vacuum vapor deposition.

Absorption and photoluminescence (PL) spectra of **S-ADN**, **2S-ADN**, **2S-MADN**, and **m-ADN** were recorded to compare the photophysical properties of the three blue-emitting host materials. Fig. 2 shows the UV absorption and PL spectra of **S-ADN**, **2S-ADN**, **2S-MADN**. In the toluene solution, the peak positions of UV absorption spectra of the three compounds are similar to anthracene except for a new peak at 329 nm. The new peak can be ascribed to the absorption of dibenzothiophene. From **S-ADN** to **2S-ADN** and **2S-MADN**, the intensity of the new peak increased with the number of dibenzothiophene. The absorption band in the 330–400 nm region is assigned to the $S_1 \leftarrow S_0$ transition of the anthracene moiety [23,24]. On irradiation at 376 nm in toluene, all of the compounds show intense blue fluorescence, with an emission peak centred at 410–440 nm. There is a distinct blue shift in the PL maxima emission of **S-ADN**, **2S-ADN** and **2S-MADN** as compared to **m-ADN**, and this is likely due to a decrease

Table 2
The optical, photophysical and thermal properties of **S-ADN**, **2S-ADN**, and **2S-MADN**.

	λ_{max}/nm (abs)	λ_{max}/nm (PL)	E_{gap}/eV	HOMO/LUMO	T_d/T_g (°C)	Φ_f
m-ADN	360, 380, 399	432	2.96	−5.49/−2.53	397/120	1
S-ADN	328, 356, 376, 396	418, 436	2.95	−5.50/−2.55	411/177	0.78
2S-ADN	329, 357, 376, 397	410, 430	3.03	−5.67/−2.64	437/115	0.74
2S-MADN	329, 360, 378, 398	414, 434	3.0	−5.61/−2.61	454/149	0.87

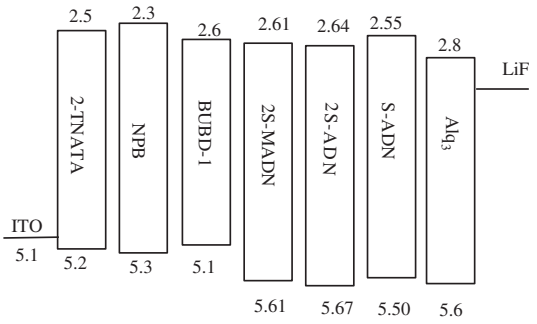

Fig. 4. Configuration and energy level diagram of blue-doped device.

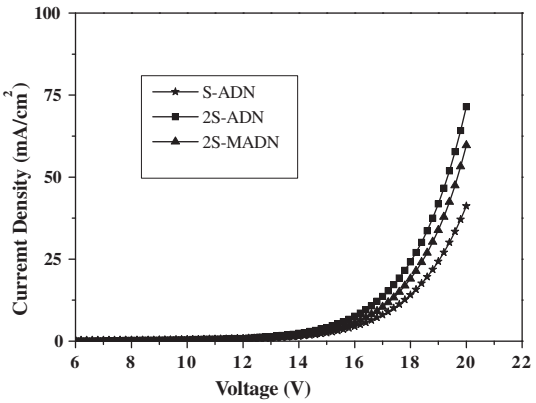

Fig. 6. Current density–voltage (*J*–*V*) curve of hole-only device for **S-ADN**, **2S-ADN**, and **2S-MADN** in device ITO/2-TNATA (40 nm)/blue host (20 nm)/Al (150 nm).

in conjugation because of a higher steric hindrance of the dibenzothiophene ring. The fluorescent quantum yields (0.78, 0.74, and 0.87, respectively) of **S-ADN**, **2S-ADN** and **2S-MADN** are listed in Table 2, which are measured using **m-ADN** as the reference. The optical and photophysical properties of **S-ADN**, **2S-ADN**, and **2S-MADN** are also summarized in Table 2.

The electrochemical behavior of **S-ADN**, **2S-ADN** and **2S-MADN** were investigated by cyclic voltammetry. From the electrochemical data and optical band gap (E_{gap}), the HOMO and LUMO energies were calculated as −5.50 and −2.55 eV for **S-ADN**, −5.67 and −2.64 eV for **2S-ADN**, −5.61 and −2.61 eV for **2S-MADN**. In our design, we introduce the dibenzothiophene group to reduce the LUMO level of **ADN**, and it is clear that the LUMO of **2S-ADN** is 0.09 eV lower than that of **S-AND**. As we know, the lower LUMO level will favor the injection of electron. The band gap, HOMO and LUMO of **S-ADN**, **2S-ADN**, and **2S-MADN** were calculated from the absorption spectra and cyclic voltammetric measurements. The E_{gap} are 2.95 eV for **S-ADN**, 3.0 eV for **2S-MADN** and 3.03 eV for **2S-ADN**. The increase of E_{gap} can be attributed to the larger torsional angle between anthracene and the attached side group. The effect of the dibenzothiophene side group in fine adjusting the photophysical properties and the HOMO/LUMO level of anthracene is clear.

In order to investigate the origin of this observation, molecular simulations of **S-ADN**, **2S-ADN** and **2S-MADN** were carried out to understand their physical properties at the molecular level. Ab initio calculations were performed using a suite of Gaussian programs, and the chemical structures of **S-ADN**, **2S-ADN**, and **2S-MADN** were fully optimized by density functional theory (DFT) using PBE ADF2009. The optimized structures and the HOMO/LUMO orbitals for **S-ADN**, **2S-ADN** and **2S-MADN** are shown in Fig 3. The HOMO and LUMO orbitals of these compounds are mostly distributed over the anthracene unit and the dibenzothiophene group only plays an accessory role. The calculated HOMO/LUMO values are in the range of 5.71–5.78 eV/2.7–2.77 eV, which also correlate well with the experimental data considering the approximations employed. By the way, in the compounds **S-ADN**, the two dihedral angles between the 2-naphthyl unit and the adjacent anthracene ring as well as dibenzothiophene unit and anthracene ring are 73.1° and 83°, respectively, which are close to the experimental values of 77.02°/86.55° obtained from the single-crystal X-ray structural analysis. The larger dihedral angles will shift the emission peak toward the blue, (see Fig. 2).

To investigate the performance of **S-ADN**, **2S-ADN** and **2S-MADN** as a blue host emitting material, the relevant OLED devices were fabricated. The device configuration

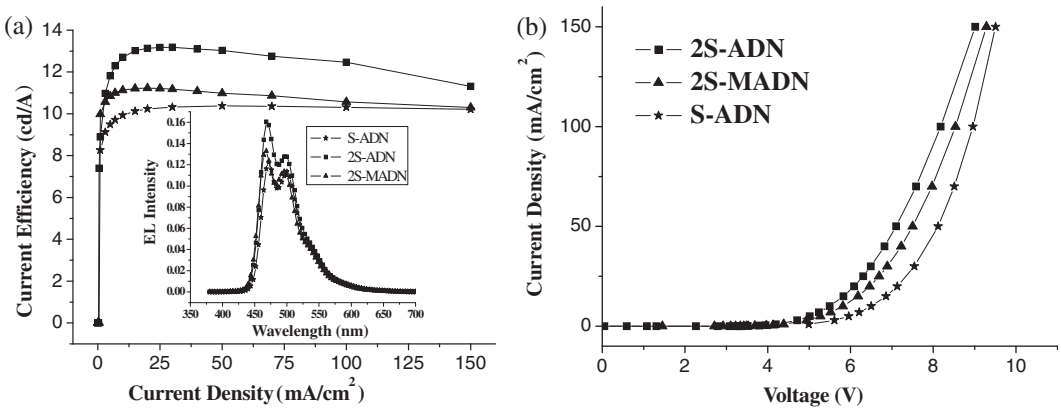

Fig. 5. (a) Dependence of the current efficiency on the drive current density for **S-ADN**, **2S-ADN**, and **2S-MADN** based devices (Insert: The EL spectrum of the device at 20 mA/cm^2). (b) Current density–voltage (*J*–*V*) curve.

Table 3
The EL performance of **S-AND, 2S-AND** and **2S-MADN** in the tri-layer device[a].

	Voltage (V)	Current density (mA/cm^2)	CE (cd/A)	PE (lm/W)	EQE (%)	CIE
S-ADN	7.13	20	10.24	4.51	5.01	(0.18, 0.31)
2S-ADN	6.09	20	13.14	6.76	6.86	(0.152, 0.304)
2S-MADN	6.40	20	11.24	5.51	5.70	(0.15, 0.312)

[a] CE = current efficiency, PE = power efficiency, EQE = external quantum efficiency.

used for the blue host material test was ITO/2-TNATA (60 nm)/NPB (10 nm)/Blue Host: BUBD-1 (40 nm)/Alq_3 (15 nm)/LiF (1 nm)/Al (150 nm). In the device, 4,4′,4″-*tris* [*N*-(1-naphthyl)-*N*-phenylamino]triphenylamine (2-TNATA), *N*,*N*′-bis-(1-naphthyl)-*N*,*N*′-diphenyl,1,1′-biphenyl-4,4′-diamine (NPB), tris(8-quinolino-lato)aluminium (Alq_3) and LiF were used as the hole injection, hole transport and electron transport materials, respectively. The emission layer consists of a sky blue styrylamine-type fluorescent material, BUBD-1, uniformly doped in the new blue host material [25,26]. Devices at different dopant concentrations have been fabricated (see SFig. 1), and the optimal BUBD-1 concentration in these hosts is 5%.

The current efficiency of **S-ADN**, **2S-ADN** and **2S-MADN** devices was plotted against current density in Fig. 5(a). The current efficiency increased in turn with **S-ADN**, **2S-MADN**, and **2S-ADN**, which can be ascribed to the increased hole-transporting and electron injection ability. Meanwhile, their EL spectra showed a slight blue-shift, which can be ascribed to the larger steric hindrance of dibenzothiophene. For the **2S-ADN**, an EL efficiency of 13.14 cd/A and 6.76 lm/W at 20 mA/cm^2 and 6.09 V was observed, with $CIE_{x,y}$ coordinates of (x = 0.15, y = 0.30), which is amongst the best sky-blue emitting devices reported so far in the current available literature. Fig. 5(b) shows the current density–voltage curves of **S-ADN**, **2S-ADN**, and **2S-MADN** devices. At the same driving voltage, the current density of **2S-ADN** is higher than that of **S-ADN**, which may be ascribed to the better charge injection and transport properties of the added dibenzothiophene. For **2S-MADN**, the current density is between those of **S-ADN** and **2S-MADN**, and it is a manifestation of the methyl substituent in the 2-position in increasing the distance between molecules and reducing the transport properties as compared to **2S-ADN**. In order to corroborate this prediction, the hole-only devices of these materials were fabricated. The device configuration was ITO/2-TNATA (40 nm)/blue host (20 nm)/Al (150 nm). From the current density–voltage (J–V) curve (Fig. 6), it is obviously that the charge injection of **2S-ADN** is the best, and at the same current density, the voltage increased in turn from **2S-ADN**, **2S-MADN** to **S-ADN**. The EL properties of sky blue devices based these new materials are summarized in Table 3, with all devices showing good sky blue light.

4. Conclusions

Some anthracene-based blue light-emitting materials, composed of anthracene as the main unit and dibenzothiophene group as side wings were developed and characterized. The introduced rigid and dibenzothiophene wings inhibited intermolecular interactions and increased the hole transport ability. Single-crystal diffraction analysis has shown that the obtained material has a non-coplanar structure, which results in high PL efficiency, thin film of a high quality, and high thermal stability with a high T_g. In the guest/host emitting system, the sky blue devices 2-TNATA (60 nm)/NPB (10 nm)/Host: BUBD-1 (40 nm)/Alq_3 (15 nm)/LiF (1 nm)/Al (150 nm) were fabricated for the **2S-ADN**, achieving an EL efficiency of 13.14 cd/A and 6.76 lm/W at 20 mA/cm^2 and 6.09 V, with $CIE_{x,y}$ color coordinates of (x = 0.152, y = 0.30).

Acknowledgements

This work was supported by the central allocation grant from Dong hu New & High Technology Development Zone of Wuhan City and the Research Grants Council of Hong Kong SAR (GHP/057/05) and Faculty Research Grant (FRG/05-06/II-43) of HKBU. W.-Y.W. also thanks a grant from Areas of Excellence Scheme, University Grants Committee, Hong Kong (Project No. [AoE/P-03/08]) and Analytical and Testing Centre of Huazhong University of Science and Technology for providing the facilities to carry out measurements.

Appendix A. Supplementary data

Supplementary data associated with this article can be found, in the online version, at doi:10.1016/j.orgel.2011.01.002.

References

[1] C.W. Tang, S.A. VanSlyke, Appl. Phys. Lett. 51 (1987) 913.
[2] S.J. Su, E. Gonmori, H. Sasabe, J.J. Kido, Adv. Mater. 20 (2008) 4189.
[3] T.F. Guo, T.C. Wen, Y.S. Huang, M.W. Lin, C.C. Tsou, C.T. Chung, Opt. Express. 23 (2009) 21205.
[4] Z.Q. Jiang, Y.H. Chen, C.L. Yang, Y. Cao, Y.T. Tao, J.G. Qin, D.G. Ma, Org. Lett. 11 (2009) 1503.
[5] Z.Q. Jiang, Y.H. Chen, C. Fan, C.L. Yang, Q. Wang, Y.T. Tao, Z.Q. Zhang, J.G. Qin, D.G. Ma, Chem. Commun. (2009) 77.
[6] S.L. Gong, Y.B. Zhao, C.L. Yang, C. Zhao, J.G. Qin, D.G. Ma, J. Phys. Chem. C 114 (2010) 5193.
[7] H.H. Chou, C.H. Cheng, Adv. Mater. 13 (2010) 2468.
[8] P.I. Shih, C.Y. Chuang, C.H. Chien, E.W.G. Diau, C.F. Shu, Adv. Funct. Mater. 17 (2007) 3141.
[9] J. Shi, C.W. Tang, Appl. Phys. Lett. 80 (2002) 3201.
[10] B. Wei, J.Z. Liu, Y. Zhang, J.H. Zhang, H.N. Peng, H.L. Fan, Y.B. He, X.C. Gao, Adv. Funct. Mater. 20 (2010) 2448.
[11] H. Benmansour, T. Shioya, Y. Sato, G.C. Bazan, Adv. Funct. Mater. 13 (2003) 883.
[12] S.K. Kim, B. Yang, Y. Ma, J.H. Lee, J.W. Park, J. Mater. Chem. 18 (2008) 3376.
[13] Y.T. Lyu, J. Kwak, O. Kwon, S.H. Lee, D. Kim, C. Lee, K. Char, Adv. Mater. 20 (2008) 2720.
[14] W. Shen, R. Dodda, C. Wu, F. Wu, T. Liu, H. Chen, C. Chen, C. Shu, Chem. Mater. 16 (2004) 930.
[15] T.H. Huang, J.T. Lin, L.Y. Chen, Y.T. Lin, C.-C. Wu, Adv. Mater. 18 (2006) 602.
[16] S.H. Yang, B.C. Hong, S.F. Huang, J. Electro. Soc. 156 (2009) 41.

[17] Y. Kim, D. Shin, S. Kim, C. Ko, H. Yu, Y. Chae, S. Kwon, Adv. Mater. 13 (2001) 1690.
[18] L. Wang, W.-Y. Wong, M.F. Lin, W.-K. Wong, H.L. Tam, K.W. Cheah, C.H. Chen, J. Mater. Chem. 18 (2008) 4529.
[19] S.A. Van Slyke, C.H. Chen, C.W. Tang, Appl. Phys. Lett. 69 (1996) 2160.
[20] SAINT+, ver. 6.02a, Bruker, Analytical X-ray System Inc., Madison, WI, 1998.
[21] G.M. Sheldrick, SADABS Empirical Absorption Correction Program, University of Göttingen, Germany, 1997.
[22] G.M. Sheldrick, SHELXTL™, Reference Manual, ver. 5.1, Madison, WI, 1997.
[23] T. Nakabayashi, B. Wu, T. Morikawa, T. Iimori, M.B. Rubin, S. Speiser, N. Ohta, J. Photochem. Photobio. A: Chem. 178 (2006) 236.
[24] L. Wang, M.F. Lin, W.-K. Wong, H.L. Tam, K.W. Cheah, C.H. Chen, Appl. Phys. Lett. 91 (2007) 183504.
[25] C.-L. Ho, M.-F. Lin, W.-Y. Wong, W.-K. Wong, C.H. Chen, Appl. Phys. Lett. 92 (2008) 083301.
[26] M.F. Lin, L. Wang, W.-K. Wong, H.L. Tam, K.W. Cheah, C.H. Chen, Appl. Phys. Lett. 89 (2006) 121913.

Organic Electronics 12 (2011) 602–608

Contents lists available at ScienceDirect

Organic Electronics

journal homepage: www.elsevier.com/locate/orgel

Odd–even modulation of electrode work function with self-assembled layer: Interplay of energy barrier and tunneling distance on charge injection in organic light-emitting diodes

Yu-Tai Tao [a,*], Kun-Yang Wu [b], Ko-Hui Huang [c], Tsong-Ping Perng [b]

[a] Institute of Chemistry, Academia Sinica, Taipei 115, Taiwan, ROC
[b] Department of Materials Science and Engineering, National Tsing Hua University, Hsin-chu 300, Taiwan, ROC
[c] Department of Chemistry, National Taiwan Normal University, Taipei 113, Taiwan, ROC

ARTICLE INFO

Article history:
Received 4 November 2010
Received in revised form 3 January 2011
Accepted 8 January 2011
Available online 22 January 2011

Keywords:
Work function
Organic light-emitting diodes
Self-assembled monolayer
Odd-even effect

ABSTRACT

In this study, a series of trifluoromethyl-terminated alkanethiols with different chain length ($CF_3(CH_2)_nSH$, n = 5, 6, 10, 11, 12 and 13), were used to form self-assembled monolayers(SAMs) on silver and gold surfaces. The SAM modulates the metal work function as a result of the different orientation of the terminal dipolar CF_3 group due to different chain tilt of the SAM on Au and Ag surfaces, respectively. The SAM-modified Ag and Au were used as the anode in the fabrication of hole-only devices as well as top-emitting organic light-emitting diodes (TOLEDs) with different hole-transporting layers. The correlation between current density/luminous efficiency and the SAM chain length/work function were analyzed to provide information on charge balance. Thus with NPB as the hole-transporting layer, where little difference between the HOMO energy level and the work function of the SAM-modified electrode, the charge injection is modulated by the chain length (tunneling distance-dependent) of the SAM used for modification, decreasing with increasing chain length. With BPAPF as the HTL, where a barrier is present, the charge injection is modulated more by the work function (injection barrier-dependent), which shows an odd–even alternation.

© 2011 Elsevier B.V. All rights reserved.

1. Introduction

A metal/organic (M/O) interface is involved in most of organic electronic devices, including organic light-emitting diodes (OLEDs), organic solar cells, and organic field-effect transistors. In general, these interfaces involve an abrupt shift of the vacuum level between materials, i.e. an interface dipole barrier (Δ), usually with negative charges on the metal side and positive charges on the organic side, due to different carrier density between metal and organic materials. In addition, a barrier may also exist due to different alignment of the metal work function and the molecular orbital energy level. The magnitude of these barriers determines how efficient the charges can across the interface, which in turn influences the device performance in a major way. For example, the hole/electron charge balance is one important contributing factor in the current efficiency in a light-emitting device [1]. An understanding and further modulating the barrier is of great interest in fabricating various devices.

Considerable efforts have been devoted to reducing the charge injection barrier in order to improve the current density in organic electronic devices. These include various surface treatments and/or adsorption of specific species to create a new dipolar layer for better charge injection [2]. Among these, self-assembled monolayers [3] (SAMs) provide a systematic way of modulating the M/O interfacial barrier by varying the functional group and/or the chain length of the molecule [4]. The size and direction of the

* Corresponding author. Tel.: +886 2 27898580; fax: +886 2 27831237.
E-mail address: ytt@chem.sinica.edu.tw (Y.-T. Tao).

1566-1199/$ - see front matter © 2011 Elsevier B.V. All rights reserved.
doi:10.1016/j.orgel.2011.01.004

molecular dipole introduced by the SAM adsorption lead to change in the work function of the metal on which it is adsorbed [5]. Improvement in charge injection can be achieved with a proper work function modification. Nevertheless, increasing the current density by reducing injection barrier does not always lead to improved luminous efficiency because increasing carriers which is already in excess will reduce the recombination ratio and thus the luminous efficiency [6]. Besides introducing an oriented dipole, the SAM also imposes a tunneling barrier through which the charges have to pass to reach the organic layer. It was demonstrated that within the same series of SAM-forming molecules (alkyl chain carrying the same terminal molecular dipole) modifying the anode, the current injection decreases with increasing chain length. The corresponding trend in luminous efficiency provides insights to the charge balance situation in an organic light-emitting device [7]. Thus in the case of a hole-dominating device, increasing the chain length (and thus decreasing the hole injection) would improve the hole/electron charge balance and results in increasing luminous efficiencies. Whereas in the case of a hole-deficient device, increasing the chain length would further the charge imbalance and results in decreasing luminous efficiency [7]. However, the work function and the molecular chain length may have different impact on the charge injection, depending on the energy level of the organic material in contact with the electrode.

In this work, we use a series of dipole-carrying ω-trifluoromethylalkanethiols of different chain length as modifiers and focus on the effect of the dipole direction due to odd–even chain length alternation on the work function and charge injection in an organic light-emitting device. The efficiency of charge injection and device performance in hole-only diodes and top-emitting organic light-emitting diodes (TOLEDs) were analyzed to show that depending on the electrode (Au or Ag) and the hole-transporting material used (and thus the injection barrier involved), different current responses were observed. This can shed light on the charge balance picture in a device and help in looking for strategy to improve the luminous efficiency.

2. Experimental

The silver or gold substrates were prepared by thermally evaporating 150 nm of silver or gold on a 2-inch silicon wafer primed with 10 nm chromium. The substrates were immersed in a 1 mM ethanolic solution containing various alkanethiols ($CF_3(CH_2)_nSH$, n = 5, 6, 10, 11, 12 and 13, designated as CF_3C5, CF_3C6, CF_3C10 and so on) for 2 h. The substrates were then removed from the solution, rinsed with absolute ethanol, acetone, and finally spun-dried on a spinner. Reflection–absorption IR spectra were taken with a Biorad FTS-60 Infrared spectrometer equipped with a DTGS detector, and a custom-designed optics unit with 86° incidence angle and p-polarized light were employed. Plasma-cleaned gold was used as reference for all spectra. Contact angle was taken with a GBX DIGIDROP Goniometer, and Teflon-coated needles were used to dispense water and hexadecane as the contacting liquids onto the surface of the monolayers. Atomic force microscopy (AFM) measurements were carried out under ambient conditions using a Digital Instruments Nanoscope IIIa microscope. Topography images were captured by tapping mode with silicon tip at 300 kHz frequency.

For device fabrication, the anodes were prepared by thermally evaporating 150 nm of Ag or Au on the soda glass primed with 10 nm chromium, with the area (4 mm^2) defined by a shadow mask. The Au or Ag substrates modified with SAMs of various alkanethiols were placed in a custom-designed rotating substrate holder in a vacuum chamber for device fabrication. Layers of naphthylphenylbiphenyldiamine (NPB) or 9,9-bis{4-[di-(p-biphenyl)aminophenyl]}fluorene (BPAPF) [8] as the hole-transporting layer (HTL), tris-(8-hydroxyquinoline) aluminum (Alq) as emitting and electron transporting layer (ETL), and the cathode were deposited sequentially in the same vacuum to give either the hole-only devices of metal/SAM/NPB(120 nm)/Al or TOLED devices of metal/SAM/NPB or BPAPF (50 nm)/Alq (50 nm)/LiF (1 nm)/Al (2 nm)/Ag (25 nm). The devices were encapsulated with UV-cured epoxy glue "*in situ*" before property measurement. The luminance–current density–voltage characteristics (L–J–V) of the devices were measured by a computer-controlled Keithley 2400 Source meter connected with a PR650 spectrometer. The work functions of SAM-modified metal electrodes were measured by a photoelectron spectrometer (AC-2, RIKEN KEIKI, Japan) in ambient with a UV source.

3. Results and discussion

3.1. Odd–even effect on the structure of orientated SAMs on Au and Ag surface

n-Alkanethiols are known to form well-ordered and closely packed monolayers on both Au and Ag surfaces, with a slight structural difference in that a higher chain tilt is obtained on Au (~30°) than on Ag (~11°) because of different binding lattices on the two metals [6]. An odd–even effect in the infrared absorption intensity was observed for the terminal methyl group as a result of orientation alternation between odd and even chain length [9]. An odd–even effect in the wetting property was also observed due to the different interaction of the very outer surface with wetting liquids [10]. When the terminal methyl group is changed to a strongly dipolar group of CF_3, the dipole component along the surface normal direction is expected to alternate between odd and even chain thiols (Fig. 1), which may contribute to the work function modulation. Vibration signatures in the reflection absorption IR spectra of SAMs of CF_3-terminated alkanethiol on Au and Ag surfaces (Fig. 2) provide the evidences for the alternation in the orientation of terminal CF_3 group. The absorption peak intensities of CF_3 group (at ~1170 and ~1385 cm^{-1} for ν_{as} and $\nu_{as\ ip}$, respectively, and ~1265 cm^{-1} for ν_s [11]) alternate clearly depending on the chain length (odd versus even) for SAM on Au (Fig. 2a), but less so for SAM on Ag, presumably due to a lower chain tilt in SAMs on Ag surface (Fig. 2b). However, the $\nu_{as}(CF_3)$ and $\nu_{as\ ip}(CF_3)$ are stronger for odd chain, which is opposite to that of *n*-alkanethiol, where

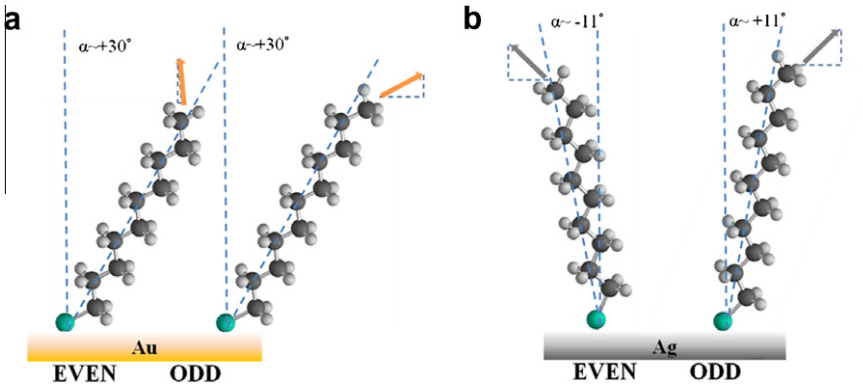

Fig. 1. Schematic diagram of monolayer of *n*-alkanethiol on (a) Au and (b) Ag surfaces.

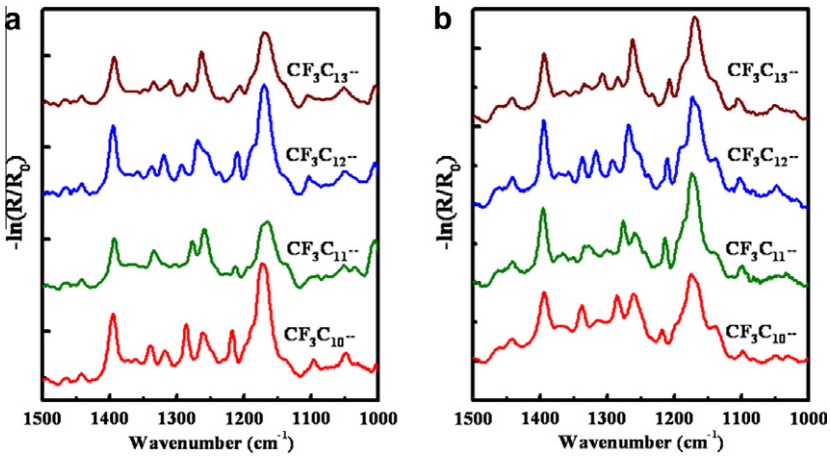

Fig. 2. Reflection adsorption IR spectra of ω,ω,ω-trifluoroalkanethiol on (a) Au and (b) Ag surfaces.

$\nu_{as}(CH_3)$ and $\nu_{as\ ip}(CH_3)$ are stronger for even chains [9]. Contact angle measurement on the SAMs using water and hexadecane as wetting liquids also showed different trends for the SAMs on different metal surfaces. On Au surface, both water contact angle and hexadecane contact angle show alternation with the chain length (Fig. 3), presumably due to different dispersive and polar interaction of the wetting liquid with the terminal CF_3 groups pointing at different directions for odd chain and even chain. Again the contact angle values are slightly higher for odd chain than on even chain. This is also opposite to that for *n*-alkanethiol on Au [9]. It is noted that an opposite odd–even trend in contact angle was observed for polar liquids on such series of thiols on Au was observed [12]. Whereas on Ag surface, little alternation was observed for the same series of SAMs, again due to a lower chain tilt in the SAMs on Ag. This is in corroboration with the IR results.

The effect of adsorbed dipole on work function ($\Delta\Phi$) is related [13] to $N\mu_\perp/\varepsilon_0\kappa$, where the N is the density of dipoles, $\mu_\perp$ is the dipole moment along the surface normal on the substrate, ε_0 is the permittivity of free space, κ is the dielectric constant of the SAM. Assuming same surface density and dielectric constant for the same series of SAM, the work function will be sensitive to the orientation of the dipole. The work function ω measured on SAM-modified

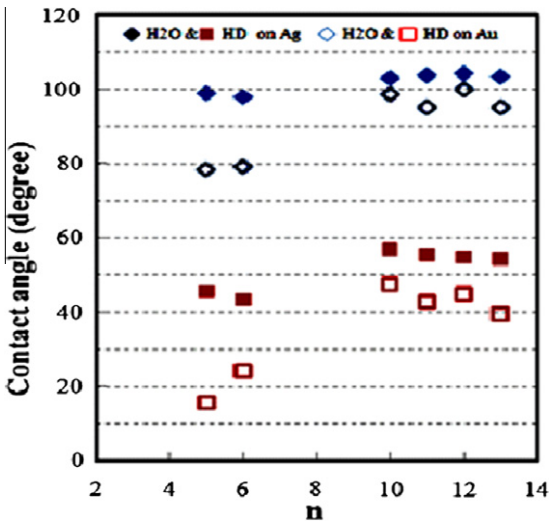

Fig. 3. The contact angles on ω,ω,ω-trifluoroalkanethiol-modified Ag and Au surfaces.

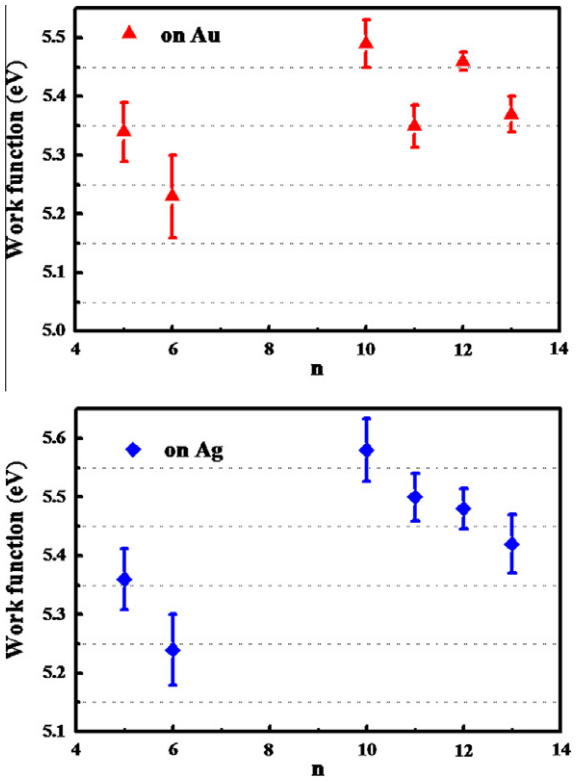

Fig. 4. The work function of ω,ω,ω-trifluoroalkanethiol-modified Ag and Au surfaces.

Au exhibits a clear odd–even effect (Fig. 4) for chain length longer than C11, presumably due to the alternating direction of the terminal CF_3 group of the monolayer. Yet there is no clear alternating trend for work function measured on Ag. It is noted that the odd chain length ($n + 1$ is odd-numbered) produces higher effective work function than the even chain length, which is in contrast with the trend expected based on Fig. 1, where a bond angle of Au–S–C of ~110° is depicted and the odd chain should have CF_3 group pointing away from the surface normal. The trend observed here is similar to the trend observed by UPS for chain length from C10–C18 [14]. It is known that *n*-alkanethiol on Au and Ag exhibit opposite odd–even alternation trend in contact angles and IR peak intensities. Different binding angle for sulfur atom at the surface was suggested: bent Au–S–C angle (~110°) on Au and linear Au–S–C angle on Ag (180°).[15] In the current case, the CF_3-terminated alkanethiols result in an opposite trend could imply a different binding angle for sulfur at the Au surface due to the perturbation of the polar CF_3 group. This bond angle change also can explain the opposite odd–even trend observed for IR intensity and contact angle above. It is also noticed that the data for short chain ones like CF_3C5 and CF_3C6 fall off the line and the trend. We assume these short chain SAMs are disordered and the CF_3 group is too close to the substrate to be free from influence from the underlying substrate.

The SAM-modified Ag and Au appear to give work functions of similar range even though the bare metals have very different work function (4.3 and 5.2 eV, respectively) [2c,4c]. Similar observation for SAM-modified metal substrates was reported [16]. This can be a collective result of the packing density, chain tilt in the SAM, as well as the metal-sulfur bond dipole, which are all different on Au and Ag surfaces. All these factors contribute to the overall interfacial dipole. It is also noted that while the same work function was extracted for the SAM-modified Ag metal and SAM-modified Au (for example, ~5.5 eV for CF_3C11-modified Ag and CF_3C10-modified Au), the Ag metal gives off more electron density than Au, as reflected in the slope of electron yield upon UV-irradiation (Fig. 5). The roughness of the two metals are also quite different (Fig. 6a and b). It is suggested that the electron fluxes from different metal surfaces depend not only on the work function, but also on the effective area of electrode (roughness).

Hole-only devices with SAM-modified Ag or Au as anode and NPB as HTL, Al as cathode were fabricated. The *I–V* characteristics are shown in Fig. 7(a and b). The devices based on SAM-modified Au gave much lower currents. With both electrodes, similar trend in that the current density decreased with increasing alkyl chain length was observed. No odd–even effect was detected for devices with Au as anode, even though the ω value showed odd–even alternation. It is suggested that the modified surfaces (Ag or Au) have Fermi level similar or lower than the HOMO level of NPB (~5.2 eV) [17] so that there is no energy barrier and the hole injection is influenced mainly by the chain length, which imposes a tunneling distance for charges to overcome. The shorter the monolayer chain length, the higher the current. Hole-only devices with SAM-modified Au as anode and BPAPF as the HTL exhibited a very different *I–V* trend, as shown in Fig. 7(c). The currents decrease in the order of $CF_3C10 > CF_3C12 > CF_3C11 > CF_3C13 > CF_3C5 > CF_3C6$, which parallels to the trend of work function approximately: higher work function anodes gave higher currents. For the pair of odd chain (and even chain), the shorter chain gave higher currents. BPAPF has a lower-lying HOMO level (5.62 eV) than NPB does. A substantial injection barrier exists in the M/O interface and the charge injection is influenced mainly by the work function (with a

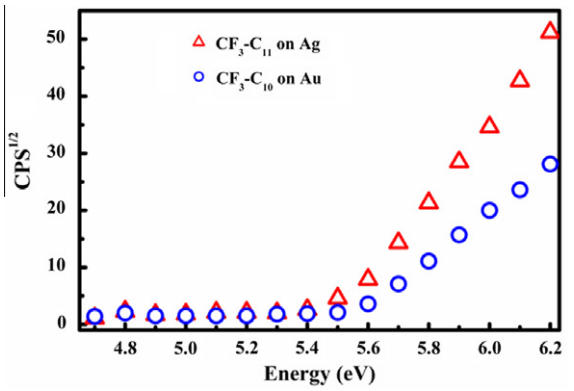

Fig. 5. The photoemission spectra of CF_3C11-SAM-modified Ag and CF_3C10-SAM-modified Au by AC2 photoelectron spectrometer.

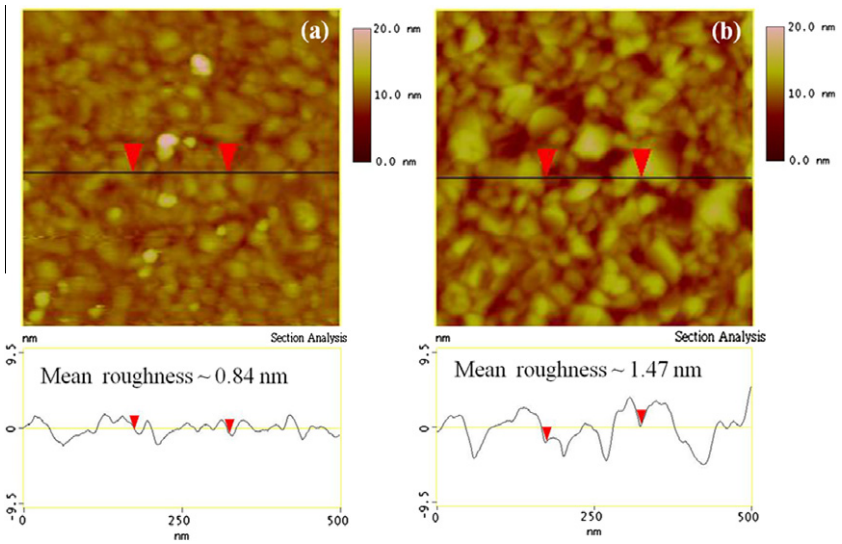

Fig. 6. AFM topograhphs of (a) CF_3C11-SAM-modified Au and (b) CF_3C10-SAM-modified Ag surfaces.

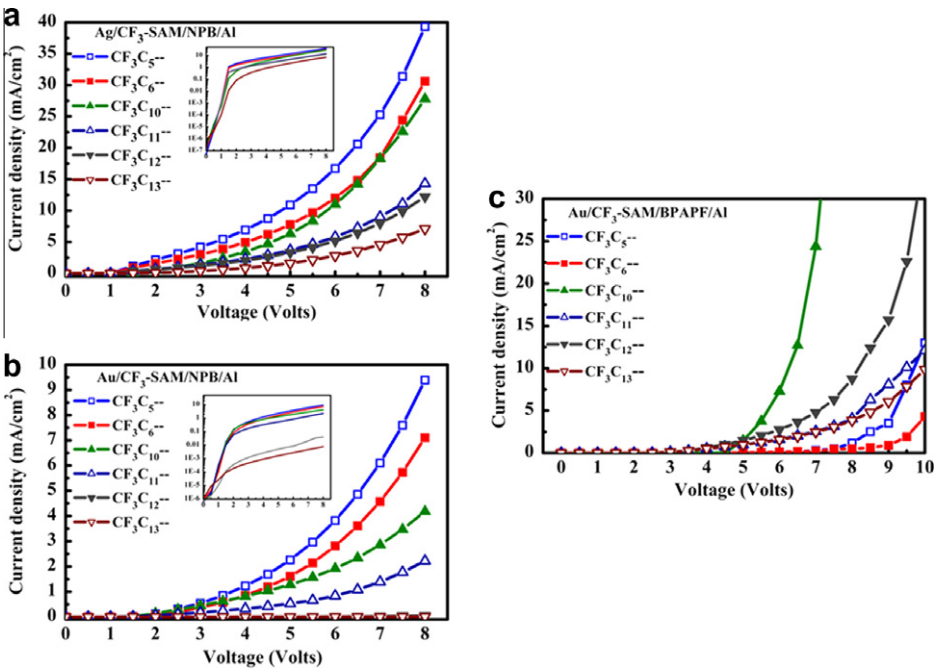

Fig. 7. *I–V* characteristics of hole-only devices with NPB as the HTL and (a) Ag as the anode; (b) Au as the anode; and (c) with Au as the anode and BPAPF as the HTL.

minor effect from chain length), which shows an odd–even effect.

The TOLEDs with NPB as HTL and SAM-modified Ag as anode showed similar trend in current as in the hole-only devices in that the longer chain SAM-modified anodes result in lower currents (Fig. 8a). The luminous efficiency, on the other hand, showed a monotonous yet opposite trend in that the higher the current density, the lower the luminous efficiency (Fig. 8b). This is ascribed to the hole-dominating nature of these devices. The hole/electron carriers are imbalanced, with hole charges in excess. Diminishing the hole charges by imposing a longer insulating organic layer improves the charge balance (or alleviate the imbalance) and thus enhances the luminous efficiency.

TOLEDs with BPAPF as HTL and SAM-modified Au as anodes were also fabricated. The *I–V* characteristics (Fig. 9) showed similar chain length-dependence as in hole-only devices, that is, the current is higher for odd chain

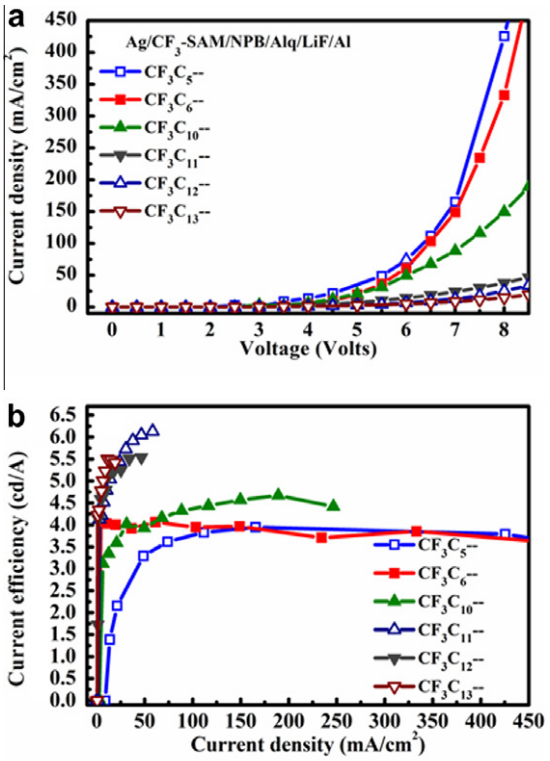

Fig. 8. (a) *I–V* characteristics and (b) current efficiency for TOLEDs using NPB as the HTL and SAM-modified Ag as the anode.

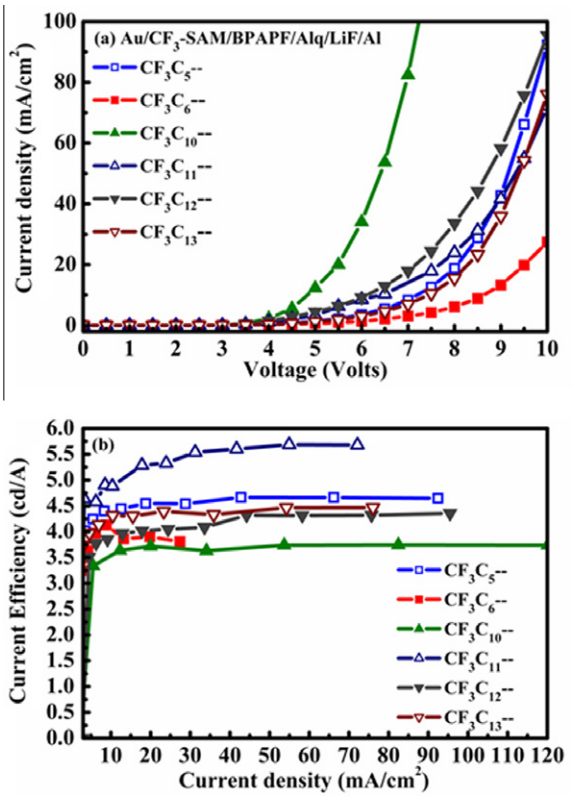

Fig. 9. (a) *I–V* characteristics and (b) current efficiency for TOLEDs using BPAPF as the HTL and SAM-modified Au as anode.

derivatives than for even chain derivatives. However, the luminous efficiency varies in a non-monotonous fashion: the device with the highest current (and the hole injection, i.e. CF_3C10) yielded the lowest efficiency (~3.6 cd/A). Decreasing the current (CF_3C12) enhanced the efficiency. Further decrease in current (CF_3C11) gave a maximum (~5.6 cd/A). Then the efficiency decreased again with further decrease in current (CF_3C13, CF_3C6, CF_3C5). It is suggested that in the current device, a switch in charge balance occurred, from hole-dominating to more balanced carriers and then to electron-dominating as a result of the systematic variation in the hole injection. Thus in order to balance the electron charges from the LiF/Al cathode into Alq, a specific work function and injection barrier exist. Further decreasing the barrier and increasing the hole current will not help the luminous efficiency. It should be noted that the power efficiency (lumen/watt) of the devices have different trend as the luminous efficiency. At a reduced current density to reach a balanced charge, a higher voltage is needed to reach similar brightness. This will reduce the power efficiency.

4. Conclusions

In summary, it is demonstrated here that both dipole moment and chain length of the monolayer can be used to modulate the charge injection. The importance of either depends on the energy barrier between the M/O interfaces. Where there is little energy gap between the metal and the HOMO of organic layer, the current is influenced by the chain length of the SAM (tunneling distance-dependent). Where there is a barrier between the metal and the HOMO of organic layer, the current is dominated by the work function (injection barrier-dependent). The trend in the current efficiency provides further information regarding the charge balance in the devices. It is demonstrated that excessive charge injection does not necessarily benefit the luminous efficiency. This will help in approaching the charge balance through proper interfacial modification and improve the device efficiency.

Financial support of this work from the National Science Council, Taiwan, the Republic of China is gratefully acknowledged.

References

[1] W. Brütting, S. Berleb, A.G. Mückl, Org. Electron. 2 (2001) 1.
[2] (a) H. Ishii, K. Sugiyama, E. Ito, K. Seki, Adv. Mater. 11 (1999) 972;
(b) H. Ishii, N. Hayashi, E. Ito, Y. Washizu, K. Sugi, Y. Kimura, M. Niwano, Y. Ouchi, K. Seki, Phys. Status Solidi A 201 (2004) 1075;
(c) C.W. Chen, P.Y. Hsieh, H.H. Chiang, C.L. Lin, H.M. Wu, C.C. Wu, Appl. Phys. Lett. 83 (2003) 5127.
[3] A. Ulman, Chem. Rev. 96 (1996) 1533.
[4] (a) I.H. Campbell, S. Rubin, T.A. Zawodzinski, J.D. Kress, R.L. Martin, D.L. Smith, Phys. Rev. B 54 (1996) 14321;
(b) R.W. Zehner, B.F. Parsons, R.P. Hsung, L.R. Sita, Langmuir 15 (1999) 1121;
(c) W. Chen et al., J. Phys. Chem. B 110 (2006) 26075.
[5] X. Crispin, V. Geskin, A. Crispin, J. Cornil, R. Lazzaroni, W.R. Salaneck, J.L. Bredas, J. Am. Chem. Soc. 124 (2002) 8131.

[6] K.Y. Wu, S.Y. Yu, Y.T. Tao, Langmuir 25 (2009) 6232.
[7] K.Y. Wu, Y.T. Tao, H.W. Huang, Appl. Phys. Lett. 90 (2007) 241104.
[8] C.W. Ko, Y.T. Tao, Synth. Met. 126 (2002) 37.
[9] P.E. Laibinis, G.M. Whitesides, D. L Allara, Y.T. Tao, A.N. Parikh, R.G. Nuzzo, J. Am. Chem. Soc. 113 (1991) 7152.
[10] Y.T. Tao, J. Am. Chem. Soc. 115 (1993) 4350.
[11] (a) J.F. Kang, S. Liao, R. Jordan, A. Ulman, J. Am. Chem. Soc. 120 (1998) 9662;
(b) Peaks assignments were also defined and simulated by PC-Spartan
[12] M. Graupe, M. Takenaga, T. Koini, R. Colorado Jr., T.R. Lee, J. Am. Chem. Soc. 121 (1999) 3222.
[13] B.D. Boer, A. Hadipour, M.M. Mandoc, T.V. Woudenbergh, P.W.M. Blom, Adv. Mater. 17 (2005) 621.
[14] D.M. Alloway, M. Hofmann, D.L. Smith, N.E. Gruhn, A.L. Graham, R. Colorado Jr., V.H. Wysocki, T.R. Lee, P.A. Lee, N.R. Armstrong, J. Phys. Chem. B 107 (2003) 11690.
[15] (a) S.C. Chang, I. Chao, Y.T. Tao, J. Am. Chem. Soc. 116 (1994) 6792;
(b) M.M. Walczak, C. Chung, S.M. Stole, C.A. Widrig, M.D. Porter, J. Am. Chem. Soc. 113 (1991) 2370.
[16] C.D. Zangmeister, L.B. Picraux, R.D. Van Zee, Y. Yao, J.M. Tour, Chem. Phys. Lett. 442 (2007) 390.
[17] S.T. Lee, Y.M. Wang, X.Y. Hou, C.W. Tang, Appl. Phys. Lett. 74 (1999) 670.

Organic Electronics 12 (2011) 609–613

Contents lists available at ScienceDirect

Organic Electronics

journal homepage: www.elsevier.com/locate/orgel

The encapsulation of an organic light-emitting diode using organic–inorganic hybrid materials and MgO

Yun Cheol Han [a], Cheol Jang [a], Kuk Joo Kim [a], Kyung Cheol Choi [a,*], KyungHo Jung [b], Byeong-Soo Bae [b]

[a] Department of Electrical Engineering, KAIST, Daejeon, Republic of Korea
[b] Department of Materials Science and Engineering, KAIST, Daejeon, Republic of Korea

ARTICLE INFO

Article history:
Received 9 November 2010
Received in revised form 6 January 2011
Accepted 8 January 2011
Available online 22 January 2011

Keywords:
OLED
Encapsulation
Multi-barrier
Hybrid materials
Sol–gel
Ca test

ABSTRACT

The characteristics of organic–inorganic multi-barriers were investigated in this study. Polymerized cycloaliphatic epoxy hybrid materials (hybrimers), synthesized by a sol–gel method and MgO were used as an organic and inorganic material, respectively. We performed a Ca test at 30 °C and 90% R.H. A multi-barrier of 6 dyads on 100 μm thick PET resulted in a water vapor transmission rate (WVTR) of 4.9×10^{-5} g/m^2 day and optical transmittance of 81.8% in the visible region (350–850 nm). We suggested relatively simple passivation method with a solution process involving an organic material coupled with low temperature deposition of MgO using an electron beam evaporator. Due to the solution process of the organic layer, the OLEDs were passivated without dark spots or an additional protective layer. After driving of 740 h with a constant current source under ambient conditions, a half-life time of 15,000 h was estimated by the stretched exponential decay (SED) model with an initial luminance value L_0 = 1000 cd/m^2.

© 2011 Elsevier B.V. All rights reserved.

1. Introduction

Organic light-emitting diodes (OLEDs) have great potential for use in next-generation flat-panel displays due to their many advantages, such as their fast response, low power consumption and potential for use with flexible displays. However, reliability issues remain as a major challenge for mass production at present. The organic materials used in OLEDs are very sensitive to oxygen and water vapor. The water vapor transmission rate (WVTR) requirements in organic electronics are stricter than those of any other packaging application [1]. In an OLED, the WVTR must be less than 10^{-6} g/m^2 day. To reduce the weight of the device and realize a full potential of OLEDs, a technology that replaces glass encapsulation is indispensable. Although polymers have been considered as promising candidates for these substrates, the enormously rapid permeation of this setup is known to be a major obstacle [2]. Therefore, a barrier-coating technique is essential before the great potential of OLEDs can be realized. The permeation properties of multi-barriers were discussed by Graff et al. using classical Fickian diffusion models [3]. The effective diffusion path was increased using an alternating layer design.

The lifetime and electroluminescence of OLEDs are directly affected by the formation of non-emitting areas known as dark spots, which accelerate with continuous operation. Various mechanisms of the dark spots have been studied. Crystallization of the organic material by Joule heating and local decomposition of the ITO/organic interface have been reported as possible origins of the dark spots [4,5]. It was also revealed by Liew et al. that cathode delamination is a primary factor in the growth of the dark spots [6]. The growth of the dark spots due to external factors can be blocked by a reliable encapsulation method. Research in relation to the multi-barrier encapsulation

* Corresponding author. Tel.: +82 42 350 3482; fax: +82 42 350 8082.
E-mail address: kyungcc@ee.kaist.ac.kr (K.C. Choi).

1566-1199/$ - see front matter © 2011 Elsevier B.V. All rights reserved.
doi:10.1016/j.orgel.2011.01.007

method has been done in which a vacuum process was utilized. Atomic layer deposition (ALD) and chemical vapor deposition (CVD) have also been shown to provide a high-quality layer [7,8]. However, a vacuum-based deposition process requires considerable time and lowers the price competitiveness. Although a multi-barrier design provides high performance with low WVTR values, encapsulation without dark spots is quite challenging. A protective layer for passivation using a vacuum process is crucial for avoiding damage during the passivation process [9].

In this work, we report a simpler multi-barrier encapsulation method for OLEDs involving the use of a solution process, prepared UV-curable epoxy hybrid materials and the low-temperature deposition of MgO. Directly coated hybrid materials on top of the devices serve as a protective layer in the passivation process. They also function as permeation barrier. A passivated device using the multi-barrier design showed no dark spots. It also demonstrated performance identical to that of glass-lid encapsulation devices.

2. Experimental setup

2.1. Preparation of organic–inorganic hybrid materials

In an earlier study, we prepared a UV-curable epoxy hybrid material (hybrimer) in a sol–gel method [10]. Cycloaliphatic-epoxy oligosiloxane resins were synthesized in a condensation reaction between [2-(3,4-epoxycyclohexyl)ethyl]trimethoxysilane (ECTS, Fluka, USA) and diphenylsilanediol (DPSD, Gelest, USA). Polyethylene glycol methyl ether acetate (PGMEA, Aldrich, USA) and arylsulfonium hexafluorophosphate salt (Aldrich, USA) were used as a solvent and a photo initiator respectively.

The characteristics of the cycloaliphatic-epoxy oligosiloxane resins were also studied [11]. The WVTR value was affected by the siloxane and epoxy network density, and the surface energy of the coating. Higher packing density, greater transparency and lower surface energy were obtained in accordance with increasing the DPSD content of the hybrimer. An optimized hybrimer applicable to the passivation of an OLED was used for the multi-barriers.

2.2. Organic–inorganic multi-barrier coating

In the multi-barrier structure, polymerized cycloaliphatic epoxy hybrid materials (hybrimers) and MgO were used as an organic and inorganic material, respectively. A diluted cycloaliphatic-epoxy oligosiloxane solution with a predetermined amount of solvent (PGMEA) was spin-coated at 2000 rpm for 15 s to create a 1 μm thick layer on 100 μm PET. The coated film was cured by I-line UV light ($\lambda = 365$ nm, optical power density = 11 mW/cm^2) for 360 s. Following this process, thermal curing at 60 °C was conducted in a vacuum chamber for 1.5 h to remove the remaining solvent. 100 nm thick MgO was then deposited using an electron beam evaporator at 2×10^{-6} torr. To prevent the deformation of the film and thermal degradation of the organic materials, a low temperature of 60 °C was maintained, throughout the MgO deposition process. These processes were successively repeated to create the organic–inorganic multi-barrier structure.

2.3. Device fabrication

The OLED was fabricated on a glass substrate coated with indium tin oxide (ITO) in a bottom-emission type. After an O_2 plasma treatment, the 150 nm thick ITO had a sheet resistance of 10 Ω/□. The OLED device had a configuration of ITO(150 nm)/2-TNATA(60 nm)/NPB(30 nm)/Alq$_3$-MADN doped with DCJTB (35 nm)/Alq$_3$(30 nm)/LiF(0.8 nm)/Al(150 nm), wherein 4,4′,4″-tris(2-naphthylphenyl–phenylamino)-triphenylamine (2-TNATA) and *N*,*N*′-bis(1-naphthyl)-*N*,*N*′-diphenyl-1,1′-biphenyl-4,4′-diamine (NPB) independently functioned as a hole injection layer (HIL) and a hole transport layer (HTL). The emitting layer was co-deposited with tris(8-hydroxyquinolinato)aluminum (Alq3) of 20% and 2-methyl-9,10-di(2-naphthyl) anthracene (MADN) of 80% as the co-host materials, and this was doped with 4-(dicyanomethylene)-2-t-butyl-6-(1,1,7,7-tetramethyl-juloli-dyl-9-enyl)-4*H*-pyran (DCJTB) of 2% as a red dopant. Alq$_3$ was subsequently used as an electron transport layer (ETL), and LiF/Al was used as a cathode [12]. Each layer was deposited by a thermal evaporator at 8×10^{-8} torr. Following the fabrication process, the organic–inorganic layers were coated alternatively for passivation via an identical multi-barrier coating method. After the passivation process, silver paste was used to ensure contact. The photograph in Fig. 5 (iii) shows the passivated device.

3. Results and discussion

The WVTR measurements were carried out in a Ca test using the electrical corrosion method involving a Ca sensor at 30 °C and 90% R.H [13]. 100 μm PET was employed as a substrate for the film. A 1.5 cm^2 area of the 250 nm Ca was encapsulated by barrier-coated film with a UV sealant. Al at a thickness of 100 nm was used as an electrode (Fig. 2(a)-(i)). For greater accuracy, a four-point probe system was also utilized during the Ca test. The WVTR value was determined using the following equation:

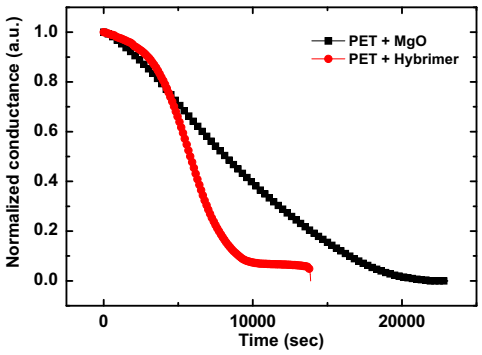

Fig. 1. The permeation test results for the single layer of 1 μm hybrimer and 100 nm MgO on PET substrate.

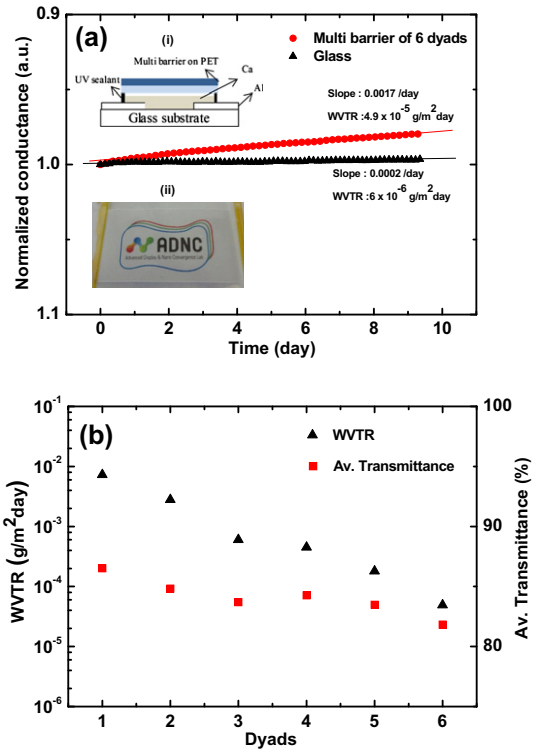

Fig. 2. (a) The results of the Ca test for the 6-dyad multi-barrier on 100 μm PET and glass. Inset: (i) Schematic diagram of the Ca test. (ii) Photograph of a logo image under the 6-dyad multi-barrier on PET. (b) Change in the WVTR and optical transmission (350–850 nm) of the multi-barriers on a 100 μm PET substrate after an increase in the number of dyads.

$$P = -n\left(\frac{1}{R_0}\right)\frac{\mathrm{M}(\mathrm{H_2O})}{\mathrm{M}(Ca)}\delta\rho\frac{l}{b}\frac{d(R_0/R)}{dt}$$

Here, n is the molar equivalent of the degradation reaction, $\mathrm{M}(\mathrm{H_2O})$ and $\mathrm{M}(\mathrm{Ca})$ are the molar masses of H_2O and Ca, respectively. Additionally, δ is the density of the Ca, ρ is the Ca resistivity, l is the length and b is the width of the Ca layer. The slope of the conductance curve R_0/R could be extracted by a Ca test and R_0 is the initial resistance.

Fig. 1 shows the normalized conductance curve of the 1 μm of hybrimer and the 100 nm of MgO on the PET substrate. A WVTR value of 0.79 g/m^2 day for the 1 μm hybrimer and 0.46 g/m^2 day for the single layer of 100 nm MgO was obtained. These WVTR values do not meet requirements of OLED passivation. The WVTR value can be effectively reduced by applying organic–inorganic multi-barriers. Because the permeability is controlled by defects, the diffusion path of oxygen and water vapor can be increased by alternating the layers. To achieve a low WVTR value, each single layer was coated, alternatively, to make a multi-barrier structure.

The Ca test was conducted in accordance with the number of dyads. For the 6-dyad multi-barrier and the glass, the change in the normalized conductance of the Ca sensor is shown in Fig. 2(a). A 1.7% change of the conductance and a WVTR value of 4.9×10^{-5} g/m^2 day were recorded for the multi-barrier. The glass was tested with an identical sealing method. The WVTR value was 6×10^{-6} g/m^2 day with a 0.2% change in the conductance after 10 days. Fig. 2(b) illustrates the performance of the multi-barrier for a set of hybrimer (1 μm)/MgO (100 nm) layers. The WVTR values of multi-barriers, from 1 to 5 dyads, were determined to be 0.0073, 0.0028, 0.0006, 0.00045, and 0.00018 g/m^2 day, respectively. Suppression of the permeation was verified by increasing the number of pairs of layers. The optical transmission of the film was measured using a Shimadzu spectrophotometer (UV-2550). An average transmittance of 81.8% was obtained with 6 dyads on PET in the visible region (350–850 nm) with air used for the baseline. As shown in Fig. 2(a)-(ii), the logo image shows that the transparency of the barrier-coated film is comparable to that of the glass.

Fig. 3 depicts a scanning electron microscope (SEM) image of an individual layer. The cross-section image was taken by a Hitachi instrument (S-4800). A Si wafer was used as the substrate. The film is composed of 100 nm of MgO and 1 μm of hybrimer. Each layer is well defined in the barrier structure. Due to the quality of the spin-coating process, the error range in the thickness of the hybrimer was observed to range from 924 to 1050 nm. However, the effect of the errors did not significantly influence the performance of overall barrier system compared to a 6.6 μm perfect film.

Fig. 4(a) shows the I–V–L characteristics of the multi-barrier passivated OLED and a glass-lid encapsulated device with a desiccant. A 4 mm^2 active area of the devices is defined with an insulator (inset Fig. 4) to eliminate the edge effect by the mask. After encapsulation, the I–V–L results were automatically accumulated by a measurement system with a source meter (Keithley 2400) and a spectrophotometer (TOPCON BM7-A). The maximum luminance of the thin-film passivated OLED showed a luminance value of 33205 cd/m^2 at 24.5 mA according to a dc-current sweep measurement (Fig. 4(b)). These results indicate that no significant differences exist between the two devices.

To evaluate the performance of the multi-barrier, a lifetime test was carried out. The devices were driven by a constant current source of 0.76 mA. The measurements started with an initial luminance value of L_0 = 1000 cd/m^2 under ambient conditions, as shown in Fig. 5. After driving

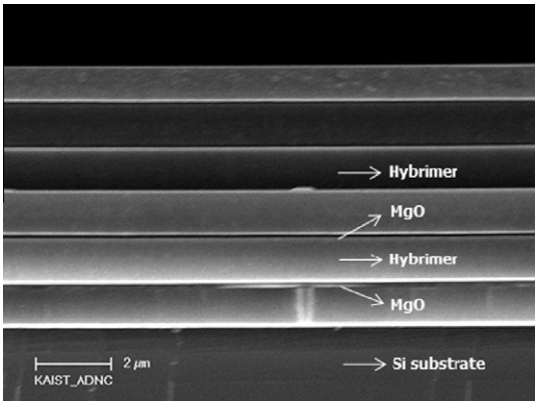

Fig. 3. Cross-sectional SEM image of MgO (100 nm)/hybrimer (1 μm) on a Si substrate.

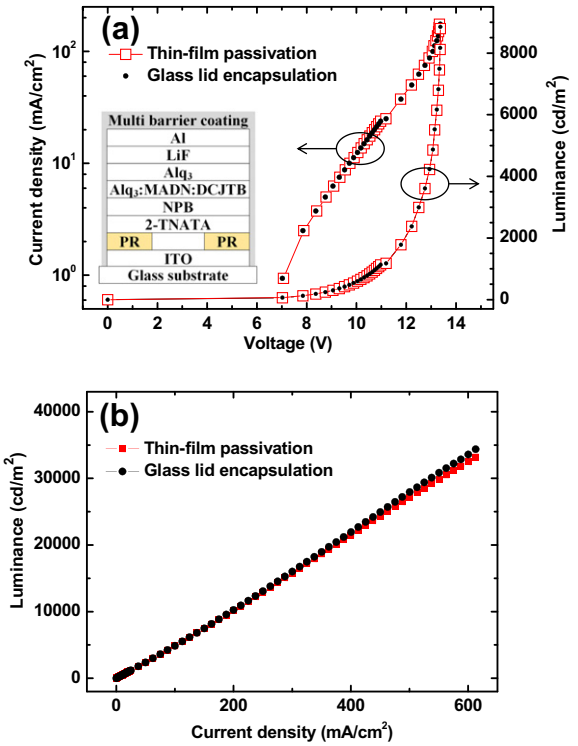

Fig. 4. (a) A comparison of I–V–L characteristics of the encapsulated OLEDs. Inset: Structure of the device. (b) Plot of the luminance versus current density.

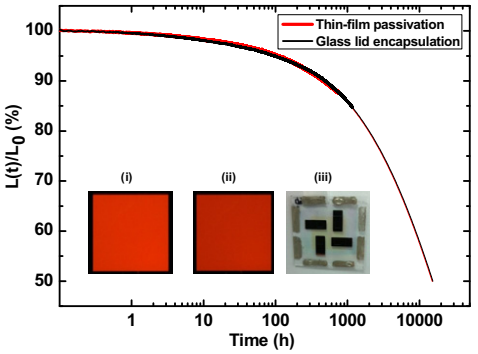

Fig. 5. Half-life time of devices with an initial luminance value $L_0 = 1000$ cd/m^2. The bold lines are the experimental data and the other lines are the exponential fitting data. The inset shows the 4 mm^2 active areas. (i) Before driving, (ii) After driving, (iii) The passivated device. There was no damage during the passivation process and during actual operation.

of 740 h for the thin-film passivated device and at 1182 h for the glass-lid encapsulated device, the lifetime was fitted using the stretched exponential decay (SED) model to consider the half-life time [14,15]. It is known that the luminance of OLEDs decreases exponentially over time. The lifetime was fitted using following equation:

$$L(t) = L_0 \exp\left[-\left(\frac{t}{\tau}\right)^{\beta}\right]$$

In this equation, $L(t)$ is the luminance at time t, L_0 is the initial luminance, and β and τ were obtained from the experimental data. The luminance of the OLEDs decreased to 87.8% of the initial value after operation for 740 h. The lifetime was extrapolated to 15,000 h for the multi-barrier passivation and 15,300 h for the glass-lid encapsulation, respectively, using a constant value for $\beta = 0.556$. In the case of the non-passivated device, the half-decay time was only 5.7 h (not shown in the figure). The microscope image shown in the inset of Fig. 5(i) and (ii) reveals that the OLED did not degrade during the passivation process or during its operation test. The OLED was seriously degraded during the inorganic deposition vacuum process without a protecting layer. When MgO was deposited on top of the device, no light emission was observed. The first layer should serve as a buffer layer during the passivation process. The hybrimer was sufficient to protect the OLED from damage. Due to the solution process of the hybrimer layer, a low-cost and relatively simple OLED passivation process was achieved. The surface roughness of the hybrimer had a RMS value of 0.5 nm in a previous work. We believe that, for the MgO/Hybrimer multi-barrier structure, the MgO surface was planarized in each step. Consequently, the possibility of the formation of the defects and pinholes was reduced effectively at the organic–inorganic interface.

4. Conclusion

We demonstrated the performance of the multi-barriers composed of MgO and UV-curable epoxy hybrid materials (hybrimers). A low WVTR value for the 6-dyad multi-barrier is adequate for encapsulation of the OLED to protect it from water vapor and oxygen. Due to the spin-coated hybrimer layers and the use of MgO deposited at a low temperature, the device was encapsulated without dark spots. The passivated OLED showed stable operation and feasible I–V–L characteristics comparable to those of the glass-lid encapsulated devices. Furthermore, the optimization processes of the barrier structure and composition are practical for application to flexible displays with high transmittance in the visible region. This can be applied to other fields, for instance, to organic thin-film transistors and organic solar cells.

Acknowledgment

This research was supported by Basic Science Research Program through the National Research Foundation of Korea (NRF) funded by the Ministry of Education, Science and Technology (CAFDC-20100009890).

References

[1] P.E. Burrows, G.L. Graff, M.E. Gross, P.M. Martin, M.K. Shi, M. Hall, E. Mast, C. Bonham, W. Bennett, M.B. Sullivan, Displays 22 (2001) 65–69.
[2] M.C. Choi, Y. Kim, C.S. Ha, Progress in Polymer Science 33 (2008) 581–630.
[3] G.L. Graff, R.E. Williford, P.E. Burrows, Journal of Applied Physics 96 (2004) 1840.
[4] S.Y. Kim, K.Y. Kim, Y.H. Tak, J.L. Lee, Applied Physics Letters 89 (2006) 132108.

[5] P. Melpignano, A. Baron-Toaldo, V. Biondo, S. Priante, R. Zamboni, M. Murgia, S. Caria, L. Gregoratti, A. Barinov, M. Kiskinova, Applied Physics Letters 86 (2005) 041105.
[6] Y.F. Liew, H. Aziz, N.X. Hu, H.S.O. Chan, G. Xu, Z. Popovic, Applied Physics Letters 77 (2000) 2650.
[7] A.P. Ghosh, L.J. Gerenser, C.M. Jarman, J.E. Fornalik, Applied Physics Letters 86 (2005) 223503.
[8] K. Yamashita, T. Mori, T. Mizutani, Journal of Physics D: Applied Physics 34 (2001) 740.
[9] F.L. Wong, M.K. Fung, S.L. Tao, S.L. Lai, W.M. Tsang, K.H. Kong, W.M. Choy, C.S. Lee, S.T. Lee, Journal of Applied Physics 104 (2008) 014509.
[10] K.H. Jung, B.S. Bae, Journal of Applied Polymer Science 108 (2008) 3169–3176.
[11] K.H. Jung, J.Y. Bae, S.J. Park, S.H. Yoo, B.S. Bae, Journal of Materials Chemistry (2010).
[12] Y.G. Lee, H.N. Lee, S.K. Kang, T.S. Oh, S. Lee, K.H. Koh, Applied Physics Letters 89 (2006) 183515.
[13] R. Paetzold, A. Winnacker, D. Henseler, V. Cesari, K. Heuser, Review of Scientific Instruments 74 (2003) 5147.
[14] C. Fery, B. Racine, D. Vaufrey, H. Doyeux, S. Cina, Applied Physics Letters 87 (2005) 213502.
[15] B. Racine, C. Fery, A. Bettinelli, H. Doyeux, S. Cina, T.R.D. France, Organic Thin-Film Electronics 34 (1) (2005) 12–34.

Organic Electronics 12 (2011) 614–622

Contents lists available at ScienceDirect

Organic Electronics

journal homepage: www.elsevier.com/locate/orgel

Triphenylamine-containing linear D-A-D molecules with benzothiadiazole as acceptor unit for bulk-heterojunction organic solar cells

Dan Deng [a,b], Yang Yang [a], Jing Zhang [a,b], Chang He [a], Maojie Zhang [a,b], Zhi-Guo Zhang [a], Zhanjun Zhang [b,*], Yongfang Li [a,*]

[a] Beijing National Laboratory for Molecular Sciences, Institute of Chemistry, Chinese Academy of Sciences, Beijing 100190, China
[b] Graduate University of Chinese Academy of Sciences, Beijing 100049, China

ARTICLE INFO

Article history:
Received 2 November 2010
Received in revised form 10 January 2011
Accepted 12 January 2011
Available online 31 January 2011

Keywords:
Organic solar cells
Conjugated organic molecules
Organic semiconductors
Solution processability
Organic photovoltaic materials

ABSTRACT

Three solution-processable triphenylamine (TPA)-containing low band gap D-A-D molecules with benzothiadiazole (BT) as acceptor unit and TPA-(4-hexyl)thiophene (TPA-HT), TPA-(4-hexyl)thieno[3,2-b]thiophene (TPA-HTT) and bis(octyloxy)TPA-(4-hexyl)thieno[3,2-b]thiophene (boTPA-HTT) as donor units, TPA-HT-BT, TPA-HTT-BT and boTPA-HTT-BT, have been designed and synthesized for the application in the bulk-heterojunction organic solar cells (OSCs). The molecules show broad absorption band in the visible range and appropriate HOMO energy levels for the donor materials in OSCs. The OSC devices were fabricated with the molecules as donor and $PC_{70}BM$ as acceptor. The power conversion efficiencies of the OSCs based on TPA-HT-BT, TPA-HTT-BT and boTPA-HTT-BT reached 1.44%, 1.44% and 0.75%, respectively, under the illumination of AM.1.5, 100 mW/cm^2.

© 2011 Elsevier B.V. All rights reserved.

1. Introduction

Solution-processable organic small molecules have attracted much interest recently for the applications as donor in bulk-heterojunction organic solar cells (OSCs) [1–16], because they exhibit the advantages of high purity and definite molecular weight in comparison with polymers, and low-cost solution processability in comparison with common vacuum-deposition of organic molecules. The organic molecules reported in literatures include branched oligothiophenes [4,5], linear D-A molecules [2,3,10–14] and triphenylamine (TPA)-containing molecules [14–22]. Nguyen et al. synthesized a series of linear D-A-D molecules with oligothiophenes as donor and diketopyrrolopyrrole (DPP) as acceptor unit. The molecules show narrow band gap of ca. 1.8 eV and broad visible absorption. The power conversion efficiency (PCE) of the bulk-heterojunction OSCs based on the molecules as donor and PCBM as acceptor reached 3–4% [12,13]. TPA-containing organic molecules possess good solution-processibility because of its 3-dimensional spatial structure. Therefore, the TPA-containing molecules have been designed and synthesized for the application in solution-processed organic light-emitting diodes (OLEDs) and OSCs in recent years. Our group has reported various TPA-containing D-A structured organic molecules as donor materials, and the highest PCE reached 3% [22].

For further study of the relationship of the molecular structure and photovoltaic properties of the solution-processable organic photovoltaic materials, we synthesized three new TPA-containing linear D-A-D molecules with benzothiadiazole (BT) as acceptor unit and TPA-(4-hexyl)thiophene (TPA-HT), TPA-(4-hexyl)thieno[3,2-b]thiophene (TPA-HTT) and bis(octyloxy)TPA-(4-hexyl)thieno[3,2-b]thiophene (boTPA-HTT) as donor units, TPA-HT-BT, TPA-HTT-BT and boTPA-HTT-BT. The design of the molecular structure was from the following consider-

* Corresponding authors. Fax: +86 10 62559373.
E-mail address: liyf@iccas.ac.cn (Y. Li).

1566-1199/$ - see front matter © 2011 Elsevier B.V. All rights reserved.
doi:10.1016/j.orgel.2011.01.013

ations: (1) the D-A-D structure of the molecules is to reduce the band gap of the materials for improving the absorption; (2) (4-hexyl)thieno[3,2-b]thiophene is introduced in TPA-HTT-BT and boTPA-HTT-BT for enhancing the hole mobility and improving absorption of the compounds, because fused thiophenes usually show larger π-conjugation and higher hole mobility [23–25]; (3) the terminal alkoxy group in boTPA-HTT-BT is to strengthen the electron donating effects of TPA unit to make the absorption broader. TPA-HT-BT, TPA-HTT-BT and boTPA-HTT-BT films show broad absorption band in the range of 350–700 nm, lower band gap and good thermal stability. The solution processed bulk-heterojunction OSC devices based on the blend of TPA-HT-BT or TPA-HTT-BT as donor and $PC_{70}BM$ as acceptor (the weight ratio of donor/acceptor is 1:3), reached 1.44% under the illumination of A.M. 1.5 G, 100 mW/cm^2, which indicates that TPA-HT-BT and TPA-HTT-BT are promising organic donor photovoltaic materials.

2. Experimental section

2.1. Chemicals

Triphenylamine, 3-hexylthiophene, *n*-butyllithium (2.5 mol/L in hexane), tri-*n*-butyltin chloride, 4,7-dibromo-2,1,3-benzothiadiazole, $Pd(PPh_3)_2Cl_2$, methyltriphenylphosphonium bromide, tetrabutylammonium bromide, sodium acetate, palladium acetate and *N,N*-dimethyl formamide (DMF) were purchased from Acros Organics. Tetrahydrofuran (THF) was dried over Na/benzophenoneketyl and freshly distilled prior to use. Thieno[3,2-b]thiophene and 1-*n*-octyloxy-4-iodobenzene, 4-Formyltriphenylamine (1), monomer C were synthesized as reported in the literatures [26–29]. Other chemicals were common commercial level and were used as received.

2.2. Synthesis of compounds

2.2.1. Monomer (A)

N,N-Diphenyl-N-(4-vinylphenyl)amine(A): To a solution of methyltriphenylphosphonium bromide (7.19 g, 20 mmol) in dry THF (250 ml) at −78 °C was added *n*-butyllithium (8 ml, 2.5 M, 20 mmol) by syringe. The mixture was warmed to room temperature slowly. Compound 1 (5 g, 18 mmol) in dry THF (50 ml) was added dropwise to the mixture, and the resulted mixture was kept at room temperature for 12 h. The mixture was poured into water and extracted into dichloromethane (3 × 150 ml). The combined organic extracts were washed with brine and dried by anhydrous magnesium sulfate. After evaporation of the solvent, the crude product was purified by column chromatography (hexane) to get monomer A as white solid. Yield 4.33 g (87%). ^{1}H-NMR ($CDCl_3$, 400 MHz, δ/ppm): 7.30–7.25 (m, 6H), 7.23 (d, 4H), 7.03 (d, 4H), 6.67 (q, 1H), 5.62 (d, 1H), 5.14 (d, 1H). MS: m/z = 271 (M^+).

2.2.2. Monomer (B)

N,N-Di(n-octyloxyphenyl)-pheneylamine (2): 1-*n*-Octyloxy-4-iodobenzene (13 g, 39 mmol), phenylamine (1.65 g, 17.7 mmol), cuprous chloride (0.142 g, 1.42 mmol), phenanthroline (0.257 g, 1.42 mmol) and potassium hydroxide (17.44 g, 311 mmol) were dissolved in toluene (28 ml) and refluxed for 24 h. The reaction mixture was poured into ice water. The product was extracted into dichloromethane (5 × 150 ml) and the combined organic extracts were washed by brine and dried by anhydrous magnesium sulfate. The crude product was purified by column chromatography (petroleum) to give compound 2 as colorless liquid. Yield 3.75 g (39.14%). ^{1}H-NMR ($CDCl_3$, 400 MHz, δ/ppm): 7.28 (q, 1H), 7.17 (t, 2H), 7.04 (d, 4H), 6.94 (d, 2H), 6.82 (d, 4H), 3.95 (t, 4H), 1.78 (m, 4H), 1.43 (m, 4H), 1.31 (m, 16H), 0.90 (t,6H). MS: m/z = 501 (M^+).

N,N-Di(n-octyloxyphenyl)-4-(formylphenyl)amine (3): Phosphorus oxychloride (11.1 ml, 121 mmol) was added dropwise into a stirred *N,N*-dimethyl formamide (18.6 ml, 242 mmol), under argon at 0 °C. After addition, the reaction mixture was stirred at 0 °C for 1 h and at room temperature for 1 h. Compound 2 (10 g, 19.9 mmol) in 1,2-dichloroethane was added dropwise to the mixture and the resulted mixture was kept at 90 °C over night. The reaction mixture was cooled to room temperature, poured into ice water and neutralized with sodium hydroxide (2 M). The product was extracted into dichloromethane (5 × 150 ml) and the combined organic extracts was washed with brine and dried by anhydrous magnesium sulfate. The crude product was purified by column chromatography (petroleum:ethyl acetate, 5:1) to give compound 3 as yellow liquid. Yield 6.6 g (66.2%). ^{1}H-NMR ($CDCl_3$, 400 MHz, δ/ppm): 9.74 (s, 1H), 7.63 (d, 2H), 7.10 (d, 4H), 6.88 (m, 6H), 3.88 (t, 4H), 1.79 (m, 4H), 1.44 (m, 4H), 1.33 (m, 16), 0.90 (t, 6H). MS: m/z = 529 (M^+).

N,N-Di(n-octyloxyphenyl)-4-(vinylphenyl)amine (B): To a solution of methyltriphenylphosphonium bromide (4.1 g, 11.5 mmol) in anhydrous THF (250 ml) at −78 °C was added *n*-butyllithium (4.6 ml, 2.5 M, 11.5 mmol) by syringe. The mixture was warmed to room temperature slowly. Compound 3 (5 g, 9.5 mmol) in anhydrous THF (100 ml) was added dropwise to the mixture, and the resulted mixture was kept at room temperature for 12 h. The mixture was poured into water and extracted into dichloromethane (5 × 100 ml). The combined organic extracts were washed with brine and dried by anhydrous magnesium sulfate. After evaporation of the solvent, the crude product was purified by column chromatography (hexane) to get monomer B as yellow liquid. Yield 4.85 g (97%). ^{1}H-NMR ($CDCl_3$, 400 MHz, δ/ppm): 7.21 (d, 2H), 7.04 (d, 4H), 6.88(d, 2H), 66.84 (d, 4H), 6.66 (m, 1H), 5.60 (d, 1H), 5.10 (d, 1H), 3.92 (t, 4H), 1.80 (m, 4H), 1.49 (m, 4H), 1.29–1.34 (m, 16H), 0.89 (t, 6H). MS: m/z = 527 (M^+).

2.2.3. Monomer (D)

4,7-Di(6-hexyl-thieno[3,2-b]thiophen-2-yl)-2,1,3-benzothiadiazole (5): *n*-Butyllithium (17.8 ml, 2.5 M in hexane, 44.6 mmol) was added dropwise to a stirred solution of 3-hexylthieno[3,2-b]thiophene (10 g, 44.6 mmol) in anhydrous THF (200 ml), under argon at 0 °C. The reaction mixture was maintained under these conditions for a further 2 h before tri-*n*-butyltin chloride (12 ml, 44.6 mmol) was added dropwise. The mixture was allowed to warm to room temperature and stirred for another 6 h. 4,7-bib-

romo-2,1,3-benzothiadiazole (5.9 g, 20.3 mmol) and $PdCl_2(PPh_3)_2$ (853 mg, 1.2 mmol) were added to the stirring mixture. After the solution was stirred for 12 h at 80 °C, hydrochloric acid (3%, 50 ml) was added to the solution to quench the reaction. The product was extracted into dichloromethane (3 × 150 ml) and the combined organic extracts were washed with brine and dried by anhydrous magnesium sulfate. The crude product was purified by column chromatography (petroleum) to give compound 5 as red powder. Yield 8.2 g (69%). ^{1}H-NMR ($CDCl_3$, 400 MHz, δ/ppm): 8.45 (s, 2H), 7.88 (s, 2H), 7.06 (s, 2H), 2.78 (t, 4H), 1.87–1.54 (m, 4H), 1.35 (m, 12H), 0.90(t, 6H). MS: m/z = 580 (M^+).

4,7-Di(5-bromo-6-hexyl-thieno[3,2-b]thiophen-2-yl)-2,1,3-benzothiadiazole (D): To a solution of compound 5 (3 g, 5.17 mmol) in 100 mL anhydrous DMF was added NBS (1.93 g, 10.8 mmol) in one portion at room temperature and stirred for 24 h. The precipitate was filtered and washed with methanol and water to give monomer D as dark red powder. Yield 2 g, 63%. ^{1}H-NMR ($CDCl_3$, 400 MHz, δ/ppm): 8.15 (s, 2H), 7.6 (s, 2H), 2.53 (t, 4H), 1.53 (m, 4H), 1.09 (m, 12H), 0.65 (t, 6H). MALDI-TOF MS: 738.1, calcd for $C_{30}H_{30}Br_2N_2S_5$ 738.71.

2.2.4. TPA-HT-BT

Monomer C (1 g, 1.6 mmol), monomer A (0.95 g, 3.52 mmol), palladium (II) acetate (10 mg), tetra-*n*-butylammonium bromide (161 mg, 0.5 mmol), and sodium acetate anhydrous (2.62 g, 32 mmol) were dissolved and kept in degassed *N*,*N*-dimethyl formamide (30 ml) under argon at 100 °C for 24 h. The mixture was poured into water (30 ml). The precipitate was filtered, washed with water and dissolved in dichloromethane, then dried by anhydrous sodium sulfate. After evaporation of the solvent, the residue was purified by column chromatography (petroleum/dichloromethane, 1:1). Yield 600 mg (37%). ^{1}H-NMR ($CDCl_3$, 400 MHz, δ/ppm): 7.68 (s, 2H), 7.55 (s, 2H), 7.13 (d, 4H), 7.01 (t, 8H), 6.87 (t, 8H), 6.78 (t, 8H), 6.73 (d, 4H), 2.48 (t, 4H), 1.43 (m, 4H), 1.08 (m, 12H), 0.64 (t, 6H). MALDI-TOF MS: 1006.8, calcd for $C_{66}H_{62}N_4S_3$ 1006.41. Anal. Calcd for $C_{66}H_{62}N_4S_3$: C, 78.88; H, 5.98; N, 5.58. Found: C, 78.02; H, 6.32; N, 5.36.

2.2.5. TPA-HTT-BT

Monomer D (1 g, 1.3 mmol), monomer A (808 mg, 2.98 mmol), palladium (II) acetate (15 mg), tetra-*n*-butylammonium bromide (140 mg, 0.43 mmol), and sodium acetate anhydrous (2.2 g, 27 mmol) were dissolved and kept in degassed *N*,*N*-dimethyl formamide (30 ml), under argon at 100 °C for 24 h. The mixture was poured into water (30 ml). The precipitate was filtered, washed with water and dissolved in dichloromethane, then dried by anhydrous sodium sulfate. After evaporation of the solvent, the residue was purified by column chromatography (petroleum/dichloromethane, 1:1). Yield 500 mg (33%). ^{1}H-NMR ($CDCl_3$, 400 MHz, δ/ppm): 8.45 (s, 2H), 7.81 (s, 2H), 7.37 (d, 4H), 7.29 (t, 2H), 7.21 (d, 2H), 7.13 (d, 10H), 7.06 (t, 10H), 6.93 (d, 4H), 2.94 (t, 4H), 1.78 (m, 4H), 1.43 (m, 4H), 1.35 (m, 8H), 0.92 (t, 6H). MALDI-TOF MS: 1118.5, calcd for $C_{70}H_{62}N_4S_5$ 1118.36. Anal. Calcd for $C_{70}H_{62}N_4S_5$: C, 75.1; H, 5.54; N, 5.0. Found: C, 73.53; H, 5.82; N, 4.54.

2.2.6. boTPA-HTT-BT

Monomer D (1 g, 1.3 mmol), monomer B (1.57 g, 2.98 mmol), palladium (II) acetate (15 mg), tetra-*n*-butylammonium bromide (140 mg, 0.43 mmol), and sodium acetate anhydrous (2.2 g, 27 mmol) were dissolved and kept in degassed *N*,*N*-dimethyl formamide (30 ml), under argon at 100 °C for 24 h. The mixture was poured into water (30 ml). The precipitate was filtered, washed with water and dissolved in dichloromethane, then dried by anhydrous sodium sulfate. After evaporation of the solvent, the residue was purified by column chromatography (petroleum/dichloromethane, 1:1). Yield 490 mg (28%). ^{1}H-NMR ($CDCl_3$, 400 MHz, δ/ppm): 8.36 (s, 2H), 7.81 (s, 2H), 7.31 (d, 4H), 7.16 (d, 2H), 7.06 (d, 8H), 6.99 (d, 4H), 6.84 (d, 10H), 3.95 (t, 8H), 2.83 (s, 4H), 1.82 (m, 12H), 1.46 (m, 12H), 1.34 (m, 40H), 0.91 (t, 18H). MALDI-TOF MS: 1631.2, calcd for $C_{102}H_{126}N_4O_4S_5$ 1632.44. Anal. Calcd for $C_{102}H_{126}N_4O_4S_5$: C, 75.18; H, 7.62; N, 3.43. Found: C, 75.16; H, 7.92; N, 3.29.

2.3. Measurements and instruments

Nuclear magnetic resonance (NMR) spectra were taken on a Bruker DMX-400 spectrometer. MALDI-TOF spectra were recorded on a Bruker BIFLEXIII. Absorption spectra were taken on a Hitachi U-3010 UV-vis spectrophotometer. The film on quartz used for UV measurements was prepared by spin-coating with 1% chloroform solution. The TGA measurement was performed on a Perkin-Elmer TGA-7 apparatus. The electrochemical cyclic voltammograms were obtained using a Zahner IM6e electrochemical workstation in a 0.1 mol/L tetrabutylammonium hexafluorophosphate (Bu_4NPF_6) acetonitrile solution. A Pt electrode coated with the sample film was used as the working electrode; a Pt wire and Ag/Ag^+ (0.01 M $AgNO_3$ in acetonitrile) were used as the counter and reference electrodes respectively.

2.4. Fabrication and characterization of organic solar cells

Organic solar cells (OSCs) were fabricated in the configuration of the traditional sandwich structure with an ITO positive electrode and a metal negative electrode. Patterned ITO glass with a sheet resistance of 30 Ω sq^{-1} was purchased from CSG Holding Co. Ltd (China). The ITO glass was cleaned in an ultrasonic bath of acetone and isopropanol, and treated by UVO (ultraviolet ozone cleaner, Jelight Company, USA). Then a thin layer (30 nm) of PEDOT:PSS (poly(3,4-ethylenedioxythiophene):poly(styrene sulfonate)) (Baytron PVP AI 4083, Germany) was spin-coated on the ITO glass. Subsequently, the photosensitive layer was prepared by spin-coating the blend solution of the linear molecules and $PC_{70}BM$ (1:3 w/w) on the top of the PEDOT:PSS layer (ca. 60 nm thickness) and baked at 80 °C for 0.5 h. The concentration of the solution was 10 mg/mL in chlorobenzene. The thickness of the photoactive layer was measured using an Ambios Technology XP-2 profilome-

ter. Finally, Al electrode (ca. 120 nm) was vacuum evaporated on the photoactive layer under a shadow mask in the vacuum of ca. 10^{-4} Pa. The active area of the devices is 4 mm^2. The current–voltage (I–V) measurement of the devices was conducted on a computer-controlled Keithley 236 Source Measure Unit. A xenon lamp coupled

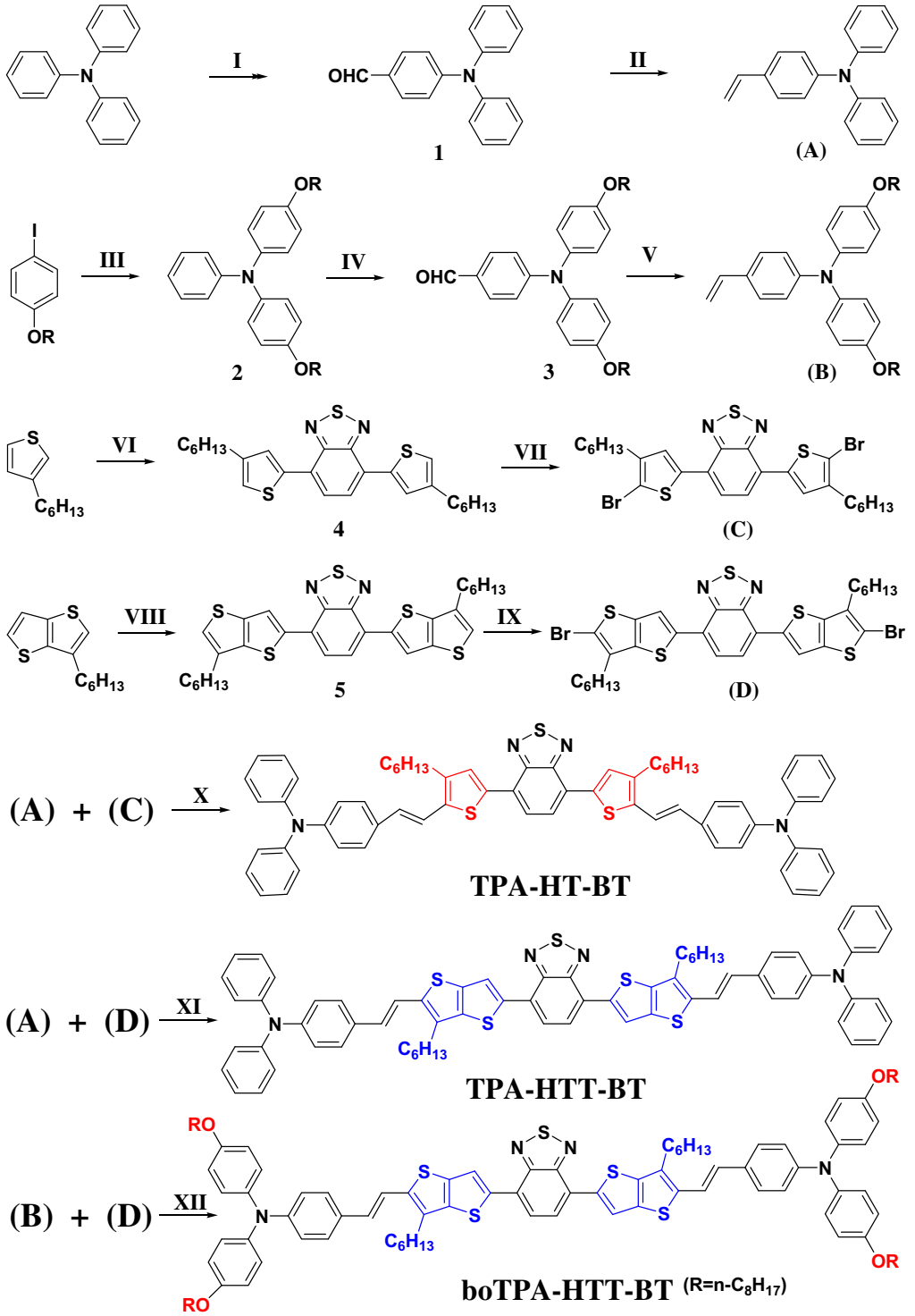

Scheme 1. Synthetic route of TPA-HT-BT, TPA-HTT-BT and boTPA-HTT-BT. (I, IV) $POCl_3$, DMF, under N_2; (II, V) *n*-BuLi, DMF, THF, under N_2; (III) Phenanthroline, KOH, CuCl, toluene, reflux for 24 h; (VI, VIII) *n*-BuLi, THF, tri-*n*-butyltin chloride, $PdCl_2(PPh_3)_2$, under N_2; (VII) NBS, $CHCl_3$, 25 °C for 24 h; (IX) NBS, DMF, 25 °C for 24 h; (X, XI, XII) $Pd(OAc)_2$, NaOAc, *n*-Bu_4NBr, DMF, under N_2, 100 °C for 24 h.

with A.M. 1.5 solar spectrum filters was used as light source, and the optical power at the sample was ca. 100 mW/cm^2.

3. Results and discussion

3.1. Synthesis and thermal stability of the molecules

The three linear molecular materials were synthesized by the route shown in Scheme 1. Monomer A reacted with C or D, B reacted with D by a palladium-catalyzed Heck reaction to get linear molecules of TPA-HT-BT, TPA-HTT-BT and boTPA-HTT-BT, respectively [15,17].

The three linear compounds are soluble in common organic solvents, such as $CHCl_3$, THF, chlorobenzene and toluene. The thermal stability of the compounds was investigated by thermogravimetric analysis (TGA). The temperatures with 5% weight loss are at 367, 338 and 378 °C for TPA-HT-BT, TPA-HTT-BT and boTPA-HTT-BT respectively, as shown in Fig. 1. The thermal stability of the materials is good enough for the application in optoelectronic devices. As compared to TPA-HT-BT, TPA-HTT-BT, the char yield of boTPA-HTT-BT is much lower, which should be attributed to the thermally instable alkoxy groups in boTPA-HTT-BT (Fig. 1).

3.2. Absorption spectra

Fig. 2 shows the UV-vis absorption spectra of TPA-HT-BT, TPA-HTT-BT and boTPA-HTT-BT in chloroform solution and film state. The optical absorption maxima (λ) were summarized in Table 1. Benefited from their D-A molecular structures, the absorption spectra of the three linear molecules in chloroform solutions exhibit strong absorption in the wavelength range from 300 to 700 nm. And because the similar structure of the three linear molecules, the absorption spectra of them are similar with three peaks. By comparing the λ_{max} of the similar molecules in our previous work [15,17,21], the two peaks at ca. 310 nm and at ca. 410 nm correspond to the $\pi-\pi*$ transition absorption of the molecules, and the visible absorption peak located at longer wavelength centered at ca. 580 nm could be assigned to the intramolecular charge transfer transition between the TPA donor moiety and the BT acceptor unit.

For all of the three linear molecules, in comparison with absorption spectra of their dilute solutions, the three absorption peaks of the films red-shifted a little, which indicates some aggregation of the molecules in the film state exists. The absorption spectra of TPA-HTT-BT and boTPA-HTT-BT solutions and films are broader than that of TPA-HT-BT, due to the planar and larger π-conjugation of the thieno[3,2-b]thiophene unit in TPA-HTT-BT and boTPA-HTT-BT than the thiophene unit in TPA-HT-BT. This phenomenon was also observed in literature [23]. In addition, benefitted from the electron-donating alkoxy groups on the TPA unit in boTPA-HTT-BT, the three absorption peaks of boTPA-HTT-BT solution and film red shifted a little in comparison with TPA-HTT-BT. The absorption edge of TPA-HT-BT, TPA-HTT-BT and boTPA-HTT-BT films are at ca. 715, ca. 754, and ca. 766 nm, corresponding to the band gap of 1.73, 1.64 and 1.61 eV, respectively.

3.3. Electrochemical properties and electronic energy levels

Electrochemical cyclic voltammetry was carried out for TPA-HT-BT, TPA-HTT-BT and boTPA-HTT-BT films on Pt electrode, in order to estimate their HOMO and LUMO energy levels. Fig. 3 shows the cyclic voltammograms of TPA-HT-BT, TPA-HTT-BT and boTPA-HTT-BT films. The HOMO energy level, the LUMO energy level, and the electrochemical band gaps (E_g^{ec}) of the polymers were calculated from onset oxidation potentials (E_{onset}^{ox}) and onset reduction potentials (E_{onset}^{red}) according to the following equations [30]: $E_{HOMO} = -e\ (E_{onset}^{ox} + 4.71 + 4.71)$ (eV), $E_{LUMO} = -e\ (E_{onset}^{red} + 4.71)$(eV) and $E_g^{ec} = E_{LUMO} - E_{HOMO}$. The detailed results of electrochemical measurement of the three compounds were listed in Table 1. The calculated HOMO and LUMO energy levels of TPA-HT-BT are −5.14 and −3.37 eV, respectively, which is similar to that of TPA-th-TPA [15]. The HOMO levels of TPA-HTT-BT and boTPA-

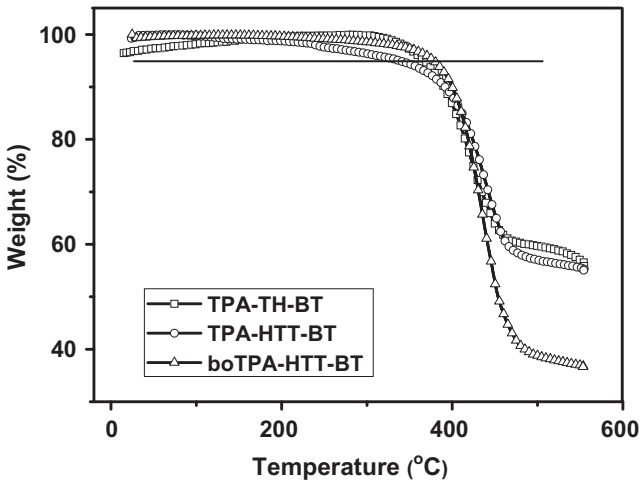

Fig. 1. TGA plots of TPA-HT-BT, TPA-HTT-BT and boTPA-HTT-BT.

HTT-BT are 0.04 and 0.09 eV higher than that of TPA-HT-BT respectively, which could result from the planar and large π-conjugation of the thieno[3,2-b]thiophene unit in the molecules. The further up-shift of the HOMO of boTPA-HTT-BT than TPA-HTT-BT should be due to the electron-donating alkoxy groups attached to TPA in boTPA-HTT-BT. Compared with the HOMO and LUMO energy levels (−5.87 and −3.91 eV respectively [31]) of $PC_{70}BM$, the three compounds are suitable to be used as the photovoltaic donors blended with $PC_{70}BM$ as acceptor in bulk-heterojunction OSCs.

3.4. AFM morphology and hole mobility

Morphology of the photoactive layer is very important for the photovoltaic performance of OSCs [32,33]. We used atomic force microscopy (AFM) to investigate the morphology of the linear molecules: $PC_{70}BM$ (1:3, w/w) blend films. All of the AFM images of the blend films exhibit typical amorphous morphology without any crystalline domains, as shown in Fig. 4. We can see intuitively that the interpenetrating network was formed on the surface of the blend films of TPA-HT-BT/$PC_{70}BM$ and TPA-HTT-BT/$PC_{70}BM$,

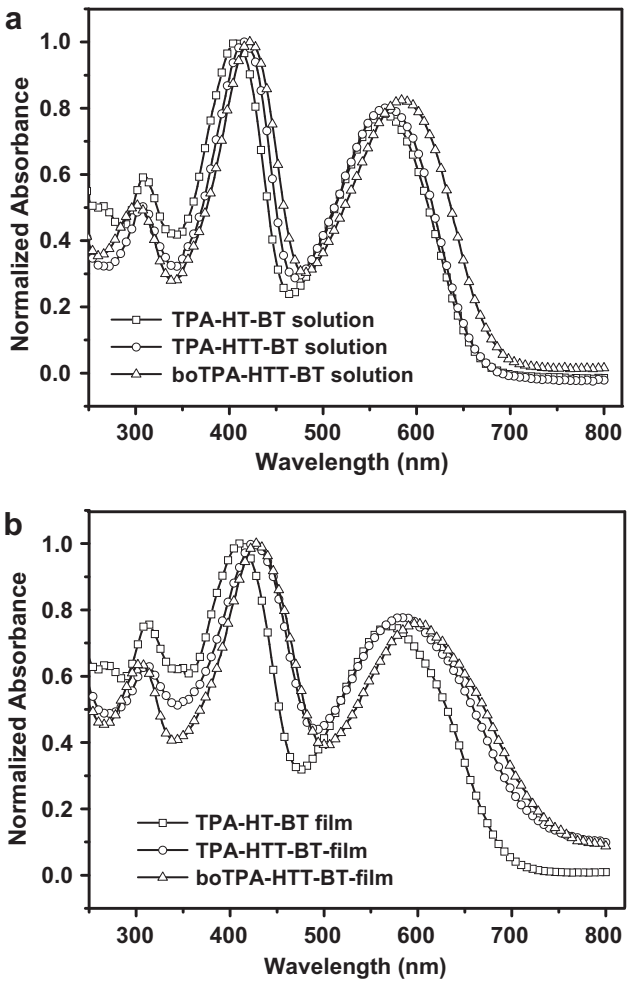

Fig. 2. UV-vis absorption spectra of TPA-HT-BT, TPA-HTT-BT and boTPA-HTT-BT in chloroform solutions (a) and in film state (b).

Table 1
Absorption and electrochemical properties, HOMO and LUMO energy levels of TPA-HT-BT, TPA-HTT-BT and boTPA-HTT-BT.

Compounds	$\lambda_{solution}$(nm)	λ_{film}(nm)	λabs_{edge} (nm)	E_g^{opt}(eV)	E_{onset}^{ox}(V[a])/HOMO (eV)	E_{onset}^{red}(V[a])/LUMO(eV)	E_g^{ec} (eV)
TPA-HT-BT	308/405/564	311/409/569	715	1.73	0.43/−5.14	−1.34/−3.37	1.77
TPA-HTT-BT	306/414/568	311/425/581	754	1.64	0.39/−5.10	−1.29/−3.42	1.68
boTPA-HTT-BT	300/420/585	305/428/596	766	1.61	0.30/−5.01	−1.35/−3.36	1.65

[a] Reference electrode is Ag/Ag^+.

which should be beneficial to the charge separation and charge transport in the OSC devices. However, the blend film of boTPA-HTT-BT/$PC_{70}BM$ exhibit rougher morphology and big aggregates, which could lead to decrease in the D-A interfacial area for efficient charge separation [34,35], and result in lower short circuit current in the OSCs with boTPA-HTT-BT/$PC_{70}BM$ as active layer.

Hole mobility of the molecules was measured by space-charge-limited-current (SCLC) method with the device structure of ITO/PEDOT:PSS/linear molecule film/Au. The hole mobilities of TPA-HT-BT, TPA-HTT-BT and boTPA-HTT-BT are 1.04×10^{-4}, 1.48×10^{-4} and 2.78×10^{-5} $cm^2\ V^{-1}\ s^{-1}$ respectively. Obviously, replacement of the thiophene unit in TPA-HT-BT by thienothiophene unit in TPA-HTT-BT increased the hole mobility, but the four alkoxy groups in boTPA-HTT-BT decreased the hole mobility significantly which could be related to its poorer morphology mentioned above.

3.5. Photovoltaic properties

Bulk-heterojunction OSCs were fabricated by using the three linear molecules as donor materials, $PC_{70}BM$ as acceptor materials [36–38] and Al as the negative electrode. The device structure is ITO/PEDOT: PSS/photoactive layer (60 nm)/Al. The photoactive layers are composed of the blend of the linear molecule and $PC_{70}BM$. For the donor/acceptor weight ratios in the photoactive layers, the optimized weight ratio is 1:2 [20,22] or 1:3 [17,21] in our previous papers for the TPA-containing molecule donors. To determine the optimized weight ratio for the three linear molecules, the blend of TPA-HT-BT/$PC_{70}BM$ was investigated with different weight ratios of 1:1, 1:2 and 1:3. Table 2 lists the photovoltaic performance of the OSCs. It can be seen from Table 2 that the OSC with the TPA-HT-BT/$PC_{70}BM$ weight ratio of 1:3 shows the best photovoltaic performance with I_{sc} of 5.71 mA/cm^2 and power conversion efficiency (PCE) of 1.44%.

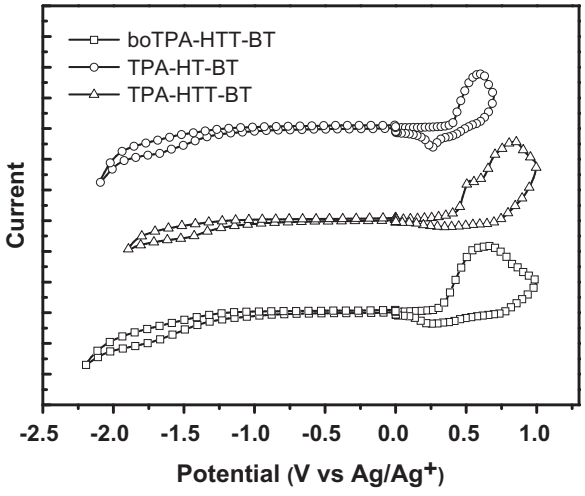

Fig. 3. Cyclic voltammograms of TPA-HT-BT, TPA-HTT-BT and boTPA-HTT-BT films on Pt electrode in an acetonitrile solution of 0.1 mol/L Bu_4NPF_6 (Bu = butyl) with a scan rate of 100 mV/s.

Based on the above optimization of weight ratio, we studied the photovoltaic properties of the three linear molecules by fabricating the OSCs with the donor/acceptor weight ratio of 1:3. Fig. 5 shows the typical current–voltage curves of the OSCs based on the linear molecules/$PC_{70}BM$ (1:3, w/w) at dark and under the illumination of

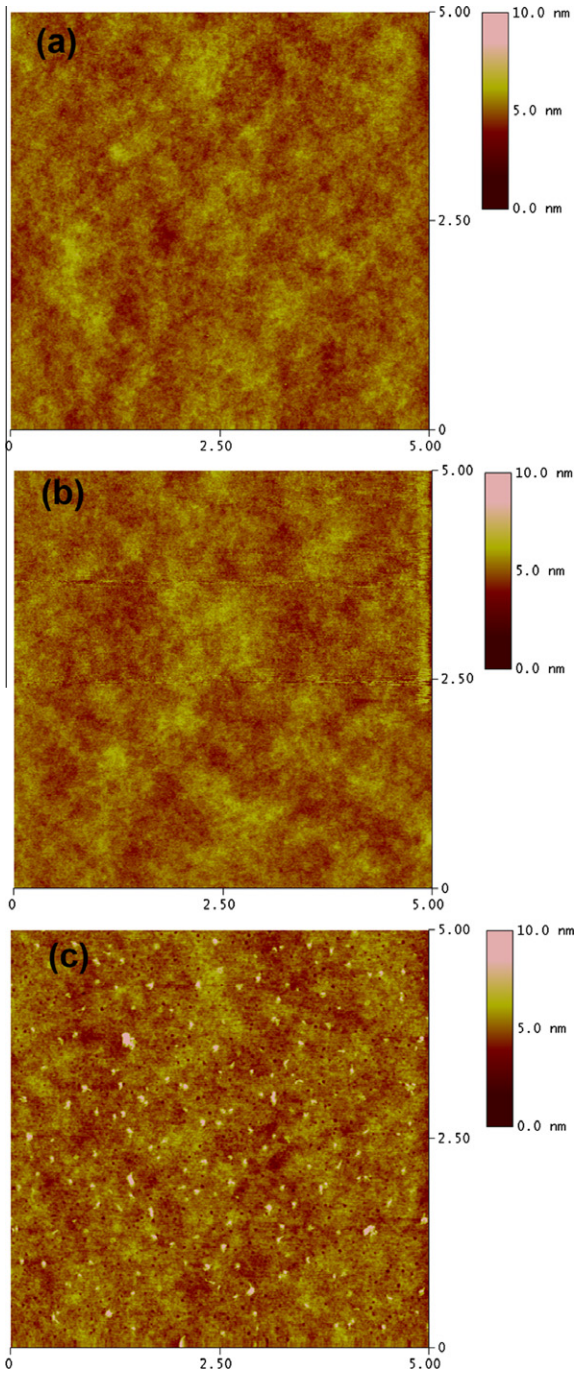

Fig. 4. AFM images of linear molecules: $PC_{70}BM$ films spin-coated from the blend solutions: (a) TPA-HT-BT/$PC_{70}BM$, (b) TPA-HTT-BT/$PC_{70}BM$, (c) boTPA-HTT-BT/$PC_{70}BM$. All films were spin-coated on ITO/PEDOT: PSS substrates and the scan size for all images is 5 μm × 5 μm.

Table 2
Photovoltaic performance of the OSCs based on TPA-HTT-BT: $PC_{70}BM$ with different weight ratios under the illumination of AM 1.5, 100 mW/cm^2.

TPA-HTT-BT:PC70BM	Voc (V)	Isc (mA/cm2)	FF (%)	η (%)
1:1	0.79	1.68	29	0.40
1:2	0.71	4.78	36	1.22
1:3	0.74	5.71	34	1.44

AM 1.5, 100 mW/cm^2. The photovoltaic performance data of the OSCs, including the open circuit voltage (V_{oc}), short circuit current (I_{sc}), fill factor (FF) and power conversion efficiency (PCE) values, are summarized in Table 3. V_{oc} of the OSC based on TPA-HT-BT reached 0.79 V, which should be benefitted from the lower HOMO energy level of the compound. V_{oc} value of 0.61 V for the OSC based on boTPA-HTT-BT is much lower than that of TPA-HT-BT (0.79 V) and TPA-HTT-BT (0.74 V), which should mainly result from its higher HOMO level (see Table 1), since V_{oc} is proportional to the difference of the LUMO of the acceptor (PCBM) and the HOMO of the donor [30]. The replacement of (4-hexyl) thiophene (HT) in TPA-HT-BT with TPA-(4-hexyl)thieno[3,2-b]thiophene (HTT) in TPA-HTT-BT enhanced the I_{sc} value from 4.84 to 5.71 mA/cm^2, which is consistent with the broader absorption of TPA-HTT-BT in visible region and higher hole mobility mentioned above. PCE values of the OSCs based on TPA-HTT-BT is 1.44% which is the same with that of TPA-HT-BT because of its lower V_{oc}. The OSC based on boTPA-HTT-BT exhibited lower I_{sc} and lower PCE than that of TPA-HTT-BT, due to the poorer morphology (as shown in Fig. 4) which could result from the introduction of terminal alkoxy groups on TPA.

Table 3
Photovoltaic performance of the OSCs with the device structure of ITO/PEDOT: PSS/Liner molecules: $PC_{71}BM$ (1:3, w/w)/Al under the illumination of AM 1.5, 100 mW/cm^2.

Donor Compounds	V_{oc} (V)	I_{sc} (mA/cm^2)	FF (%)	PCE (%)
TPA-HT-BT	0.79	4.84	37.5	1.44
TPA-HTT-BT	0.74	5.71	34	1.44
boTPA-HTT-BT	0.61	3.61	34.2	0.75

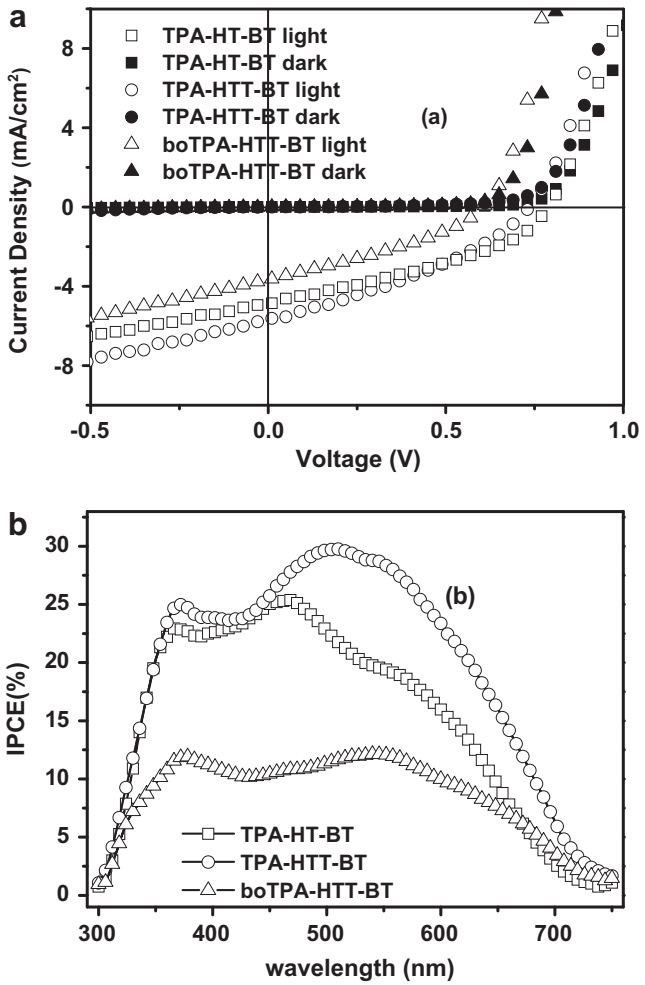

Fig. 5. (a) Current density–voltage characteristics of the OSC devices based on the blends of liner molecules/$PC_{70}BM$ (1:3, w/w) with Al as the negative electrode at dark and under the illumination of AM 1.5, 100 mW/cm^2; (b) IPCE spectra of the OSC devices.

Higher HOMO level, poorer miscibility with $PC_{70}BM$ and lower hole mobility should be the main reasons for the lower PCE value of the OSCs based on boTPA-HTT-BT. The results indicate that the introduction of the terminal alkoxy groups to the TPA seems not a good strategy in the molecular design for high performance photovoltaic molecules.

The incident photon-to-converted current efficiency (IPCE) spectra (see Fig. 5b) shows similar shapes as those of the absorption spectra of the three linear molecules, indicating that all the visible light absorption of TPA-HT-BT, TPA-HTT-BT and boTPA-HTT-BT contributed to the photovoltaic conversion. The maximum IPCE value of the OSC based on TPA-HTT-BT reached 30%, which is higher than those of the devices based on TPA-HT-BT and boTPA-HTT-BT. The higher IPCE value of TPA-HTT-BT agrees with the higher I_{sc} of the OSC based on it. The significant decrease of the IPCE values from TPA-HTT-BT to boTPA-HTT-BT should result from inefficient charge transfer due to the poor miscibility of boTPA-HTT-BT with $PC_{70}BM$ as explained above.

4. Conclusions

A series of TPA-containing linear D-A-D structured molecules with BT as acceptor unit and TPA-HT, TPA-HTT or boTPA-HTT as donor unit, were synthesized through palladium-catalyzed Heck reaction for the application in bulk-heterojunction OSCs. TPA-HT-BT, TPA-HTT-BT and boTPA-HTT-BT films show broad absorption band in the range of 350–700 nm, lower band gap at 1.6–1.7 eV and good thermal stability. The OSC devices were fabricated by spin-coating the blend solution of the three linear molecules as donor and $PC_{70}BM$ as acceptor. The OSC devices based on TPA-HT-BT/$PC_{70}BM$ (1:3, w/w) exhibited a V_{oc} of 0.79 V, an I_{sc} of 4.84 mA/cm^2, and a PCE of 1.44%, under the illumination of AM.1.5, 100 mW/cm^2. The devices based on TPA-HTT-BT/$PC_{70}BM$ (1:3, w/w) show a higher I_{sc} of 5.71 mA/cm^2 but lower V_{oc} of 0.74 V, leading to the same PCE of 1.44%. The results indicate that broadening the absorption with remaining the lower HOMO energy level should be considered in the design of high performance organic photovoltaic donor materials.

Acknowledgment

This work was supported by NSFC (Nos. 50633050, 50803071, 20874106 and 50933003) and the Chinese Academy of Sciences.

References

[1] J. Cremer, P. Bauerle, J. Mater. Chem. 16 (2006) 874;
Y. Shirota, H. Kageyama, Chem. Rev. 107 (2007) 953.
[2] J.A. Mikroyannidis, A.N. Kabanakis, S.S. Sharma, Anil Kumar, G.D. Sharma, Organic Electronics 11 (2010) 1631;
J.A. Mikroyannidis, A.N. Kabanakis, S.S. Sharma, Anil Kumar, G.D. Sharma, Organic Electronics 11 (2010) 311.
[3] Y. Liu, X. Wan, B. Yin, J. Zhou, G. Long, S. Yin, Y. Chen, J. Mater. Chem. 20 (2010) 2464.
[4] C.Q. Ma, E. Mena-Osteritz, T. Debaerdemaeker, M.M. Wienk, R.A.J. Janssen, P. Bauerle, Angew. Chem. Int. Ed. 46 (2007) 1679.
[5] C.Q. Ma, M. Fonrodona, M.C. Schikora, M.M. Wienk, R.A.J. Janssen, P. Bauerle, Adv. Funct. Mater. 18 (2008) 3323.
[6] S. Roquet, A. Cravino, P. Leriche, O. Aleveque, P. Frere, J. Roncali, J. Am. Chem. Soc. 128 (2006) 3459.
[7] A. Cravino, S. Roquet, O. Aleveque, P. Leriche, P. Frere, J. Roncali, Chem. Mater. 18 (2006) 2584.
[8] S. Roquet, R. de Bettignies, P. Leriche, A. Cravino, J. Roncali, J. Mater. Chem. 16 (2006) 3040.
[9] J. Roncali, P. Leriche, A. Cravino, Adv. Mater. 19 (2007) 2045.
[10] M.L. Sun, L. Wang, X.H. Zhu, B. Du, R. Liu, W. Yang, Y. Cao, Solar Energy Materials & Solar Cells 91 (2007) (1681).
[11] A.B. Tamayo, B. Walker, T.Q. Nguyen, J. Phys. Chem. C 112 (2008) 11545.
[12] A.B. Tamayo, X.D. Dang, B. Walker, J. Seo, T. Kent, T.Q. Nguyen, Appl. Phys. Lett. 94 (2009) 103301.
[13] B. Walker, A.B. Tomayo, X.D. Dang, P. Zalar, J.H. Seo, A. Garcia, M. Tantiwiwat, T.Q. Nguyen, Adv. Funct. Mater. 19 (2009) 3063.
[14] L.L. Xue, J.T. He, X. Gu, Z.F. Yang, B. Xu, W.J. Tian, J. Phys. Chem. C 113 (2009) 12911;
(b) Y.W. Li, Q. Guo, Z.F. Li, J.N. Pei, W.J. Tian, Energy & Environmental Science 3 (2010) 1427.
[15] C. He, Q.G. He, Y.J. He, Y.F. Li, F.L. Bai, C.H. Yang, Y.Q. Ding, L.X. Wang, J.P. Ye, Solar Energy Materials & Solar Cells 90 (2006) 1815.
[16] C. He, Q.G. He, X.D. Yang, G.L. Wu, C.H. Yang, F.L. Bai, Z.G. Shuai, L.X. Wang, Y.F. Li, J. Phys. Chem. C 111 (2007) 8661.
[17] C. He, Q.G. He, Y.P. Yi, G.L. Wu, F.L. Bai, Z.G. Shuai, Y.F. Li, J. Mater. Chem. 18 (2008) 4085.
[18] G.J. Zhao, G.L. Wu, C. He, F.Q. Bai, H.X. Xi, H.X. Zhang, Y.F. Li, J. Phys. Chem. C 113 (2009) 2636.
[19] G.L. Wu, G.J. Zhao, C. He, J. Zhang, Q.G. He, X.M. Chen, Y.F. Li, Solar Energy Materials & Solar Cells 93 (2009) 108.
[20] Y. Yang, J. Zhang, Y. Zhou, G.J. Zhao, C. He, Y.F. Li, M. Andersson, O. Inganas, F.L. Zhang, J. Phys. Chem. C 114 (2010) 3701.
[21] J. Zhang, Y. Yang, C. He, Y.J. He, G.J. Zhao, Y.F. Li, Macromolecules 42 (2009) 7619.
[22] J. Zhang, D. Deng, C. He, Y. J. He, M. J. Zhang, Z.-G. Zhang, Z. J. Zhang, Y. F. Li, Chem. Mater., 2010, doi:10.1021/cm102077j.
[23] Y.J. He, W.P. Wu, G.J. Zhao, Y.Q. Liu, Y.F. Li, Macromolecules 41 (2008) 9760.
[24] N.S. Baek, S.K. Hau, H.L. Yip, O. Acton, K.S. Chen, A.K.Y. Jen, Chem. Mater. 20 (2008) 5734.
[25] W.H. Tang, S.P. Singh, K.H. Ong, Z.K. Chen, J. Mater. Chem. 20 (2010) 1497.
[26] M.Q. He, F.X. Zhang, J. Org. Chem. 72 (2007) 442.
[27] L. Valentini, D. Bagnis, A. Marrocchi, M. Seri, A. Taticchi, J.M. Kenny, Chem. Mater. 20 (2008) 32.
[28] S.-J. Chung, K.-S. Kim, T.-C. Lin, G.S. He, J. Swiatkiewicz, P.N. Prasad, J. Phys. Chem. B. 103 (1999) 10741.
[29] J. Huang, C. Li, Y.-J. Xia, X.–H. Zhu, J. Peng, Y. Cao, J. Org. Chem. 72 (2007) 8581.
[30] Q.J. Sun, H.Q. Wang, C.H. Yang, Y.F. Li, J. Mater. Chem. 13 (2003) 800.
[31] Y.J. He, G.J. Zhao, B. Peng, Y.F. Li, Adv. Funct. Mater. 20 (2010) 3383.
[32] W.L. Ma, C.Y. Yang, X. Gong, K. Lee, A.J. Heeger, Adv. Funct. Mater. 15 (2005) 1617.
[33] G. Li, V. Shrotriya, J.S. Huang, Y. Yao, T. Moriarty, K. Emery, Y. Yang, Nature Materials 4 (2005) 864.
[34] H. Hoppe, M. Niggemann, C. Winder, J. Kraut, R. Hiesgen, A. Hinsch, D. Meissner, N.S. Sariciftci, Adv. Funct. Mater. 14 (2004) 1005.
[35] H. Hoppe, N.S. Sariciftci, J. Mater. Chem. 16 (2006) 45.
[36] M.M. Wienk, J.M. Kroon, W.J.H. Verhees, J. Knol, J.C. Hummelen, P.A. van Hal, R.A.J. Janssen, Angew. Chem. Int. Ed. 42 (2003) 3371.
[37] F.B. Kooistra, V.D. Mihailetchi, L.M. Popescu, D. Kronholm, P.W.M. Blom, J.C. Hummelen, Chem. Mater. 18 (2006) 3068.
[38] B.C. Thompson, J.M.J. Frechet, Angew. Chem. Int. Ed. 47 (2008) 58.

Organic Electronics 12 (2011) 623–633

Contents lists available at ScienceDirect

Organic Electronics

journal homepage: www.elsevier.com/locate/orgel

Time dependence and freezing-in of the electrode oxygen plasma-induced work function enhancement in polymer semiconductor heterostructures

Thomas M. Brown [a,*], G. Mattia Lazzerini [b], Lisa J. Parrott [b], V. Bodrozic [b], Lukas Bürgi [c], Franco Cacialli [b,*]

[a] Centre for Hybrid and Organic Solar Energy (CHOSE), Department of Electronic Engineering, University of Rome – Tor Vergata, via del Politecnico 1, 00133 Rome, Italy
[b] Department of Physics and Astronomy, London Centre for Nanotechnology, University College London, Gower Street, London WC1E 6BT, UK
[c] Sensirion AG, Laubisrütistrasse 50, 8712 Stäfa, Switzerland

ARTICLE INFO

Article history:
Received 4 November 2010
Received in revised form 13 January 2011
Accepted 15 January 2011
Available online 1 February 2011

Keywords:
Organic semiconductors
Plasma treatment
Energy level alignment
Contacts
Conjugated polymer devices

ABSTRACT

Indium tin oxide (ITO), Au and Pt are materials of interest as high work function contacts for organic semiconductor devices. In this paper the relative energy level line-up of these materials is investigated both as bare surfaces or part of a polymer/conductor interface. Kelvin probe (KP) measurements show that the estimated work function for Au and Pt surfaces, evaporated under normal high vacuum (HV) fabrication conditions and measured in air, can be significantly lower (by ~0.2 to 0.9 eV) than those of clean surfaces evaporated and measured in the more demanding and clean ultra high vacuum (UHV), that are often used as reference values. The work function of all surfaces increases significantly (from ~0.4 to >1 eV) after an oxygen plasma, but then decreases upon air exposure, with different rates for different materials. The effect of the plasma wears off most rapidly for Au whilst it is more resilient for ITO. Most interestingly, via KP and electroabsorption measurements of the built-in potential on polymer/conductor and conductor/polymer/conductor structures, we demonstrate that a plasma-induced enhancement of the work function is "frozen in" by the application of a polymer semiconductor layer over the plasma-treated surfaces and can be made to last for years by proper device encapsulation. These results have strong implications on the understanding, fabrication, design and stability of organic semiconductor devices.

© 2011 Elsevier B.V. All rights reserved.

1. Introduction

Fabrication of efficient organic semiconductor optoelectronic devices often requires the identification and development of high work function conducting materials for use as electrical contacts. The relative energy level alignment [1–6], and the matching of the work function of these materials with the highest occupied molecular orbitals (HOMOs) or polaron levels of the active semiconductor layer is important to improve hole injection in light-emitting diodes (LEDs) and (p-type) thin film transistors (TFTs), and to increase the built-in potential and carrier extraction in photodiodes and photovoltaic cells. To obtain an ohmic contact it is necessary to minimise injection barriers. Since the ionisation potential of many organic semiconductors is $\geqslant 5$ eV, contact materials with a work function close to or higher than 5 eV are often sought.

The work function is a parameter that depends very strongly on the condition of the surface it relates to: namely, on different deposition conditions, treatments and environments it is subjected to. Prevalent reference values for the work function of mono-atomic metals [7],

* Corresponding authors.
E-mail addresses: thomas.brown@uniroma2.it (T.M. Brown), f.cacialli@ucl.ac.uk (F. Cacialli).

1566-1199/$ - see front matter © 2011 Elsevier B.V. All rights reserved.
doi:10.1016/j.orgel.2011.01.015

including high work function metals such as Au and Pt, are typically extracted from samples that are as close as possible to ideal, prepared and measured under ultra high vacuum (UHV). However, the conditions used in the fabrication of conjugated polymer devices are often far from these. For example, evaporation of contacts occurs mainly in the high vacuum range (10^{-7}–10^{-5} mbar) rather than in UHV (<10^{-9} mbar). Furthermore, for bottom contacts, the deposition of the overlaying organic semiconductor often occurs after the contact surface has seen a glove-box environment or air at some stage of the fabrication process. Processing in air is attractive commercially since fabrication costs are greatly reduced. However, contact with air over time, as we confirm, can reduce the work function considerably.

In the case of transparent anodes, typically indium tin oxide (ITO), the work function of the untreated surface is initially a few tenths of electron volts below 5 eV. As we show in this manuscript, the work functions of evaporated Au and Pt surfaces exposed to air are also below 5 eV. It becomes therefore often necessary to increase the work function of the contact after its deposition. Different strategies have been developed, including treating the surface with self assembled monolayers [8–13], overlaying a hole-injecting layer [14,15] like poly(3,4-ethylene dioxythiophene):poly(styrene sulfonate) PEDOT:PSS, that has a high work function [16] or subjecting the electrode to an oxygen plasma or ozone treatments which is also used as a cleaning procedure [17–29]. The latter two procedures, which also clean the surfaces from contaminants, have now become a common strategy in a wide variety of organic semiconductor device heterostructures.

In this work we investigate three different surfaces that have been widely used as anodic contacts: ITO, Au and Pt. Using a Kelvin probe (KP) we have monitored the enhancement of the work function of the contacts as a result of exposure to oxygen plasma. We see that the enhancement is not permanent but decreases over time if the surface is left bare in air. Via a combination of Kelvin probe and electroabsorption (EA) measurements on polymer/conductor and conductor/polymer/conductor sandwich heterostructures, we give direct evidence that the effect of increasing the work function, is made to last considerably longer by depositing a conjugated semiconducting polymer over the contact soon after it has been subjected to the plasma treatment. Furthermore, with an effective encapsulation of the diodes, EA results show that this O_2 plasma effect on the energy levels endures stably over the time scale of the over two years of our investigation. These results have strong implications on the understanding, fabrication, design and stability [30,31], of organic semiconductor devices.

2. Experimental

The results presented here are the outcome of KP and EA investigations of three different sample batches: (1) Au, Au* study, (2) Pt, Pt* study and (3) ITO, ITO* study. The symbol "*" here denotes a surface that has been subjected to an oxygen plasma. ITO was provisioned commercially on glass substrates. Au and Pt were thermally evaporated as detailed below. The samples prepared include bare conducting electrode surfaces, polymer-semiconductor/electrode and full electrode/semiconductor/electrode device structures.

Contact potential difference (CPD) measurements were carried out using a gold mesh Kelvin probe (Besocke Delta-Phi) in air. Description of the EA apparatus used for this experiment can be found in reference [32]. The sample fabrication details were the following.

2.1. Au/Au* study

Fifty nanometer films of Au were thermally evaporated on 12.5 mm × 12.5 mm glass substrates previously ultrasonically cleaned in acetone and propan-2-ol(IPA) and blow dried in N_2. Two sets were prepared: Au(1) evaporated at ~1×10^{-6} mbar and Au(2) evaporated at 4–5 × 10^{-6} mbar. Evaporation rates were 0.03–0.05 nm/s. After evaporation the samples were kept in a plastic box in air for over 12 h before measurement. After a first set of Kelvin probe measurements on untreated surfaces, the samples underwent an oxygen RF plasma treatment and a new series of KP measurements were carried out. The plasma was created in a Harrick plasma cleaner (PDC-002) at pressures of 4–7 × 10^{-2} mbar for 5 min and at a plasma power of 100 W.

A third sample, equivalent to Au(1), was covered with a 75 nm film of poly(9,9-dioctylfluorene), F8, spun from a 2% (wt.) xylene solution at 1500 rpm for 180 s, straight (i.e. ~2 min) after completion of the plasma treatment. The samples see air after completion of the plasma. The symbol "*" after Au (and the other surfaces) indicates that the surface has been subjected to an oxygen plasma.

2.2. Pt, Pt* study

2.2.1. Surfaces

The first sample of this set, (i), consisted of a bare ITO surface (on glass substrate) provisioned from Asahi. A second sample, (ii), had a 1 nm-thick semitransparent Pt layer evaporated onto the ITO layer. A third sample (iii) was the same as sample (ii), after the surface was treated with an oxygen plasma. We made sample (ii) and (iii) semitransparent as EA measurements require a (semi)transparent contact. For work function measurements we also prepared a fourth sample (iv), consisting of a thicker opaque Pt layer (several nm thick) evaporated on a glass substrate. A fifth sample (v) consisted of sample (iv) after being treated with an oxygen plasma (i.e. Pt*). The final sample (vi) had a Au layer evaporated on it at pressures in the 10^{-6} mbar range. The ITO substrates were subjected to the wet cleaning procedure of two successive ten minute ultrasonic baths in acetone and in IPA, and were then dried with nitrogen: before measurement for sample (i) and before deposition of Pt for sample (ii). Thermal evaporation of Pt was realized by winding a Pt wire around a tungsten filament heated by the Joule effect. Although great care was taken in cleaning the chamber to avoid degassing of contaminants, the pressures during thermal evaporation went up to 1×10^{-5} mbar due to the high temperatures necessary to evaporate Pt (melting temperature of Pt is 1768 °C compared to 1064 °C for Au and the vapour pressure for Pt is

0.0312 Pa at 2045 K and 0.000237 Pa at 1337 K for Au. Heat of vaporization is 510 kJ/mol for Pt and 334.4 kJ/mol for Au).

2.2.2. Diodes

Single-layer sandwich structures were also fabricated using bottom contacts equivalent to (i), (ii), and (iii) described above; a 120 nm layer of poly(dioctyfluorene-alt-benzothiadiazole), F8BT, was subsequently spun over these semitransparent electrode surfaces. The diodes were completed by thermally evaporating 14 mm^2 and 15 nm-thick gold top electrodes at a pressure in the $\sim 1 \times 10^{-6}$ mbar range.

2.3. ITO/ITO∗ study

2.3.1. Surfaces

One hundred nanometer thick ITO-covered glass substrates were obtained from Merck KGaA. The substrates were cleaned in two 10-min ultrasound baths (acetone and IPA) before undergoing KP measurements. After the first set of measurements, the samples underwent an oxygen plasma treatment in a Harrick plasma cleaner (PDC-002) at pressures of $\sim 1 \times 10^{-1}$ mbar for 5 and 10 min. Plasma powers used were 60 W and 100 W. Varying these treatment conditions (time and power) does not lead to variations in the results greater than the reproducibility. Here, we show two representative results over a set of measurements: it is likely that the variations shown in the work function of the ITO soon after plasma treatment between samples are due to the difficulty in maintaining a constant and reproducible pressure in the plasma chamber. An oxygen-plasma treated-ITO sample (5 min, 60 W power, 1×10^{-1} mbar) was covered by a 75 nm F8 film [spun at 1500 rpm from a 2% (wt.) xylene solution] 2 min after completion of the plasma treatment.

2.3.2. Diodes

Indium tin oxide (ITO) substrates were cleaned in acetone and isopropanol. One of them was treated with oxygen plasma. Subsequently, the substrates were transferred in a nitrogen glove-box for all subsequent processing steps. A 70 nm thick layer of a polyfluorene-based blue-emitting polymer was spin coated over the substrates from a xylene solution [33,34]. The cathode was Al (400 nm) evaporated at pressures between 10^{-6} and 10^{-7} mbar. The finished devices were encapsulated with metal cans and epoxy resin, and contact pins were attached to allow characterization outside the glove-box.

3. Results

We utilised the Kelvin probe technique [35,36] to measure the contact potential difference (CPD), or work function difference, between the gold mesh of the experimental apparatus and the conductive surface samples we prepared (i.e. (1) Au, Au∗; (2) Pt, Pt∗; (3) ITO, ITO∗ where "∗" is an oxygen-plasma treated sample).

In the literature, the reported gold work function values vary between 4.2 eV and 5.4 eV, depending strongly on the environment and state of its surface [7,37,38]. We chose a freshly cleaned (10 min acetone + 10 min IPA ultrasound rinse) ITO substrate as our daily reference for all KP measurements as the readings are stable over that time period (and even longer as we show in Fig. 1) and is more practical than dismounting the gold mesh and cleaning it before each measurement. This is evident from Fig. 1 in which we have plotted the work function of 100 nm thick ITO/glass substrates (Merk KGaA) treated in ultrasonic baths of acetone and IPA and blow dried with nitrogen. The absolute value of the work function of the ITO samples was extracted by also measuring the CPD of a surface of highly oriented pyrolytic graphite, HOPG, monochromator grade ZYH (supplied by GE advanced ceramics) for each data point. The work function was monitored over a time span of 10 weeks. HOPG surfaces are customarily utilised for calibration of work function values since its own work function (4.475 ± 0.005 eV) is known to be reliable and sufficiently stable as measured against standard calomel electrodes (SCE) [39]. Over the 10 week time span the mean value of the ITO sample was 4.70 with a standard deviation of 0.05 V (also equivalent to the CPD difference measurement error) with a minimum (maximum) reading of 4.62 eV (4.76 eV). A second sample (2 min baths in acetone and IPA) showed similar behaviour over the 10 week timeframe with a mean work function of 4.74 eV (standard deviation of 0.04 eV).

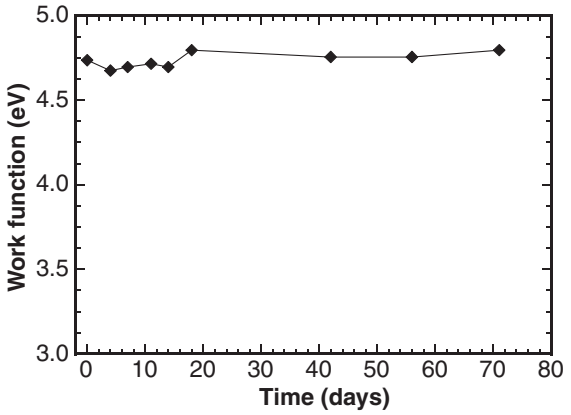

Fig. 1. Work function of ITO/glass sample cleaned in 5 min baths of acetone and IPA prior to each measurement calibrated utilizing a highly oriented pyrolytic graphite surface (Kelvin probe contact potential difference measurements). The mean value is 4.70 eV with a standard deviation of 0.05 eV.

Thus, in order to report measurements that can be compared with the energy levels of a variety of organic semiconductors and of other conductor surfaces, we have converted experimental CPD measurements to a work function (ϕ) using the following equation: $\phi(\text{sample}) = e{\cdot}\text{CPD} + \phi(\text{ITO})$, where we assigned: $\phi(\text{ITO}) = 4.7$ eV. Photoelectron spectroscopy is usually utilised to measure absolute values for work functions (see for example distinctions compared to the KP technique in reference [40]). Work function values for ITO are typically between 4.6 and 4.8 eV [16,40] depending also on the ITO supplier. We found that the ITO substrates from the particular

batches in our possession gave the same KP readings within 0.05–0.1 V (differences may be higher between different ITO materials/suppliers). We consider ϕ(ITO) = 4.7 eV to be a satisfactory estimate as this value is also supported by EA measurements of the built-in potential [16,41]. Note however that irrespective of the choice of reference surfaces, work function differences are independent of any reference value used. Furthermore, the original CPD difference (referenced to the reference ITO sample) can be traced back from the work function data reported here by subtracting 4.7 eV. Due to error propagation, the experimental error on the reported work function values we present here, apart from that on the HOPG reference and the oscillations in the CPD (±0.05 eV), will have to include the variability between ITO substrates giving an estimated total error of 0.1–0.15 eV.

In this manuscript we report KP measurements not only on bare conducting surfaces, but also on conducting surfaces covered by either a F8 or F8BT polymer overlayer. F8 and F8BT are polyfluorenes employed in the fabrication of efficient optoelectronic devices [42]. Here they were chosen mainly for their high purity and high ionisation potential (HOMO(F8) = 5.8 eV [43], HOMO(F8BT) = 5.9 eV [44]) so that space charge in the semiconductor, band bending and/or strong pinning of the conductor Fermi level occurring at the HOMO (bi)polaronic levels of the semiconductor [45] would not occur. Polyfluorenes have in fact been shown to be high purity materials devoid of significant charge over the film thicknesses $\leqslant$100 nm under consideration [32,41,46]. No evidence for band bending in pristine polymer layers was detected for distances as long as 110 nm from the interface [32]. Thus, for fresh samples, we are confident that CPD measurements probe the work function of the contact/polymer structure, which to a first approximation is the sum of the work function of the underlying conductor and any interfacial dipole contribution at the conductor/polymer interface. All KP measurements reported here were taken in air.

Electroabsorption spectroscopy measures the normalized variation of the transmission of light ($\Delta T/T$) through a sample upon application of a periodic electric field of frequency ω. As described by Campbell and coworkers [45], the signal measured at the fundamental frequency ω:

$$\Delta T/T(\omega) \propto \xi(h\nu) \times V_0 V_{AC} \cos(\omega t) \propto (V_{DC} - V_{BI}) V_{AC} \cos(\omega t), \quad (1)$$

can be used to extract the built in potential (V_{BI}) by monitoring at which applied bias (V_{DC}) the EA response is zero.

The built-in potential originates from the equilibration of the Fermi level throughout the heterostructure. Without significant charge (extrinsic or intrinsic) accumulation inside the polymer film, the electric field is essentially uniform in the bulk of the polymer layer. As shown in Fig. 2, EA can be a powerful tool as it can provide a direct measurement of V_{BI} enabling to gauge the energy level alignment of different contacts by measuring the V_{BI} on a series of diodes that differ only by the anode material (keeping the cathode and polymer layer unaltered). Further and more detailed considerations on the EA technique can be found in references [32,47].

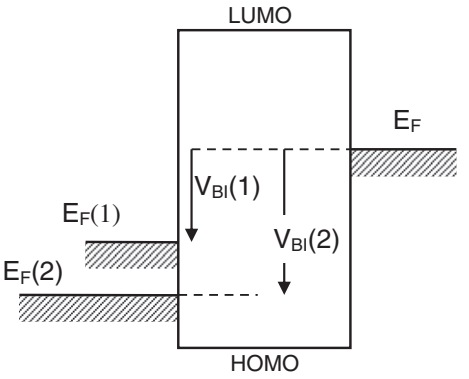

Fig. 2. Schematic diagram of the energy levels of a diode structure at flat band. The distance between the Fermi levels of the two electrodes will generate a built-in potential at equilibrium. In the case of two heterostructures having the same cathode and semiconductor and differing only by the anode material (1) and (2), V_{BI} becomes a useful quantitative measure of the relative alignment of the two electrodes. A positive and higher V_{BI} extracted from electroabsorption data indicates that the Fermi level of the bottom electrode (2) lies closer to the HOMO level of the semiconductor resulting in a lower barrier to hole injection.

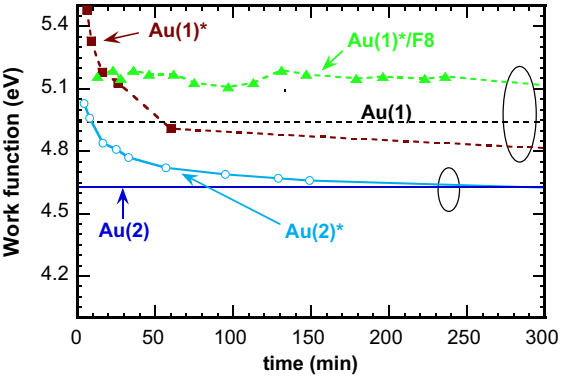

Fig. 3. Kelvin probe work function measurements in air over the first 5 h of: (1) a gold surface evaporated at a pressure of <1.8 × 10^{-6} mbar before [Au(1) – dashed line] and after an O_2 plasma [Au(1)* – squares]; 2) a gold surface evaporated at a pressure of 4–5 × 10^{-6} mbar before [Au(2) – full line] and after an O_2 plasma [Au(2)* – circles]; 3) Au(1) surface evaporated at a pressure of <1.8 × 10^{-6} mbar and subjected to an O_2 plasma and covered by an F8 polymer semiconductor overlayer spun cast 3 min after completion of the plasma treatment (triangles). The plot lines connect data points (some with data points located beyond the 300 min shown in the figure). The symbol "*" indicates that the surface has been subjected to an oxygen plasma.

3.1. Au, Au* study

Fig. 3 shows the work function of the two gold surfaces we evaporated, Au(1) and Au(2), obtained by measuring the CPD with the Kelvin probe and referencing the result to the work function of the reference ITO sample (ϕ = 4.7 eV). The straight horizontal lines correspond to the work function of the two surfaces measured after having rested in air for a period between 12 and 24 h after evaporation.

The dashed horizontal line represents the work function of Au(1) which was evaporated at pressures of 1 × 10^{-6} mbar.

The CPD of Au(1) is 0.24 V higher than the reference ITO sample giving an estimated work function of ϕ[Au(1)] = 4.94 eV. The continuous horizontal line represents the work function of Au(2) which was evaporated at (4–5) $\times$ 10^{-6} mbar. The CPD of Au(2) (relative to the ITO surface) is -0.07 V, yielding ϕ[Au(2)] = 4.63 eV. We have seen that although the CPD reading (vs. the ITO reference) of untreated Au surfaces in air can stray by a more than a tenth of a volt on the time scale of several weeks, it stays constant (±0.05 eV) on the time scale of a day and has hence been represented as horizontal lines in Fig. 3.

After the initial set of KP measurements represented by the horizontal lines of Fig. 3, both Au(1) and Au(2) were subjected to an oxygen plasma as described in the experimental section. The samples were then taken out of the etcher and their work function measured in air with the Kelvin probe. A significant enhancement in the work function of both surfaces was measured. The work function of the gold surfaces, with respect to their initial untreated values, increased by 0.54 eV for Au(1) (first measurement taken 6 min after completion of the O_2 plasma treatment) and by 0.40 eV for Au(2) (first measurement taken 4.5 min after the plasma treatment). We then continued monitoring the CPD of the plasma treated Au surfaces over time while left resting in air. We found that the plasma effect on the work function is not permanent in these conditions: the work function decreases appreciably with time (Au(1)$*$ and Au(2)$*$ in Fig. 3) when the surfaces are left in air. Not only does ϕ reach its initial value (prior to the plasma treatment) within an hour for Au(1) and 4 h for Au(2), but it tailors off to values which are even lower than the initial ones.

The work function for the third gold sample [Au$*$/F8], which was covered by a 75 nm-thick F8 film 2 min after completion of the oxygen plasma treatment, is ϕ = 5.15 eV, This corresponds to an increase of 0.2 eV with respect to the initially untreated surface, a value that remains constant (within experimental error) over the period of 5 h shown in Fig. 3.

3.2. Pt, Pt$*$ study

3.2.1. Surfaces

Table 1 reports CPD measurements and work function values taken in air of the electrodes (i)–(v), described in the experimental section: (i) ITO, (ii) ITO/Pt, (iii) ITO/Pt$*$, (iv) Pt, (v) Pt$*$ and (vi) Au. Untreated Pt, samples (ii) and (iv), show the same work function as ITO. The work function of sample (vi) Au is 0.2 eV lower than that of ITO. After the oxygen plasma treatment, the work function of both Pt surfaces (iii) and (v) increases by a large amount (by 0.8–0.9 eV) yielding a value of ϕ = 5.5–5.6 eV. Table 1 also shows that the work function of the thinner ($\sim$1 nm) semi-transparent (ii)–(iii) and thicker opaque (iv)–(v) Pt layers coincide within 0.1 eV.

The evolution of the Pt$*$ CPD over time in air showed a 0.3 eV decrease between a measurement taken at t = 15 min after the plasma treatment and the last measurement at t = 120 min.

Table 1
The values of contact potential difference (CPD) relative to an ITO reference sample measured with the Kelvin probe in air. The work function, ϕ, can be estimated by adding 4.7 eV to e·CPD. Fabrication details of the surfaces can be found in the experimental section. The symbol "$*$" indicates that the surface has been subjected to an oxygen plasma.

Surface	(i)	(ii)	(iii)	(iv)	(v)	(vi)
Materials	ITO	ITO/Pt	ITO/Pt$*$	Pt	Pt$*$	Au
[CPD ± 0.1]V	–	0	0.8	0	0.9	−0.2

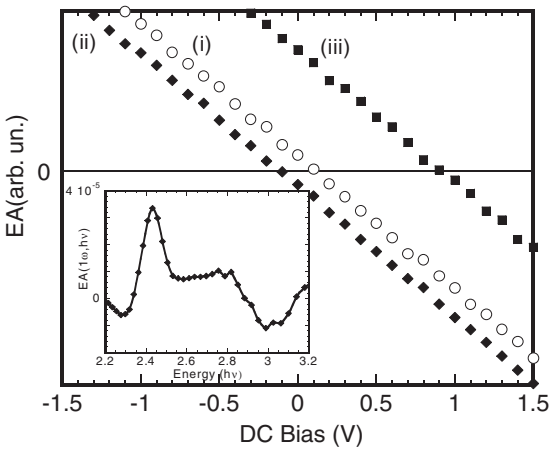

Fig. 4. Electroabsorption response at hν = 2.41 eV and V_{AC} = 0.5 V as a function of applied bias for: (i) ITO/F8BT/Au, (ii) ITO/Pt/F8BT/Au and (iii) ITO/Pt$*$/F8BT/Au diode structures. The spectral dependence of the EA signal, originating from F8BT, is shown in the inset. The large shift ($\sim$1 V) in curve (iii) compared to curve (ii) indicates that the plasma treatment on the platinised surface (ITO/Pt$*$) has pulled the anode's work function closer to the F8BT's HOMO by an equivalent amount ($\sim$1 eV) as schematised in Fig. 2.

3.2.2. Diodes

Electroabsorption measurements on diodes consisting of contact/F8BT/Au [bottom contact $\equiv$ (i) ITO, (ii) ITO/Pt or (iii) ITO/Pt$*$] are reported in Fig. 4. The EA spectrum (Eq. (1)) at the fundamental frequency of the F8BT, sandwiched between the two contacts, is shown in the inset. The latter shows a prominent peak at $\sim$2.43 eV. The absorption spectrum of F8BT can be found in Ref. [42]. In order to measure the built-in potential across the F8BT diode structures, the photon energy (hν = 2.41 eV) and the amplitude (V_{AC} = 0.5 V) were kept fixed and the dependence of the EA signal upon DC bias was monitored. The results for the three devices, (i), (ii) and (iii), are shown in the

Table 2
The values of the built-in potential for the three different F8BT-based diode structures measured with electroabsorption (extracted from Fig. 4). A positive V_{BI} is an indication that the Fermi level of the bottom electrode lies lower than that of Au (i.e. further away from the vacuum level) at flat band as shown in Fig. 2. The symbol "$*$" indicates that the surface has been subjected to an oxygen plasma.

Device	(i)	(ii)	(iii)
Top electrode	Au	Au	Au
Bottom electrode	ITO	ITO/Pt	ITO/Pt$*$
V_{BI}	0.1 V	−0.1 V	0.9 V

main panel of Fig. 4. The values at which the electroabsorption signals of Fig. 4 intersect the zero axis correspond to V_{BI}. These values are reported in Table 2. (i) V_{BI} = 0.1 V for the ITO/F8BT/Au diode; (ii) V_{BI} = −0.1 V for ITO/Pt/F8BT/Au; (iii) V_{BI} increases very significantly (V_{BI} = +0.9 V) when the Pt surface is subjected to an oxygen plasma prior to the deposition of the organic semiconductor, i.e. for ITO/Pt∗/F8BT/Au. As discussed earlier the use of a material with such a deep HOMO (∼5.9 eV below vacuum) as F8BT ensures that hole injection is negligible in the LEDs during electroabsorption experiments in the range of applied DC voltages used here.

3.3. ITO, ITO∗ study

3.3.1. Surfaces

Emission KP measurements of the ITO surfaces are reported in Fig. 5. The work function of the untreated surface was set at 4.7 eV and is shown as a horizontal dashed line. After plasma treatment, the CPD measured by the KP increases by ∼1.3–1.6 eV. Two ITO∗ surfaces are included in Fig. 5 to show that the reproducibility of the CPD enhancement due to the plasma treatment, just after its completion, is within a few tenths of an eV. Once the ITO∗ surfaces are left in air, the CPD decreases quite rapidly (within 100–400 min) by ∼0.7–1 V towards a more stable value. Note that this plateau in the work function is still 0.5–0.7 eV higher than the work function of the initial untreated surface. The work function (t > 1000 min, not shown) actually continues to decrease slowly with time. Indeed, after four months (right panel of Fig. 5), the work function of both ITO∗ surfaces has reached, within 0.05 eV, its "initial" value (i.e. CPD ≅ 0 V, i.e. ϕ = 4.7 eV, before either surface was subjected to an ITO plasma).

Also shown in Fig. 5 is the ITO surface which was covered with a 75 nm film of F8 two minutes after being

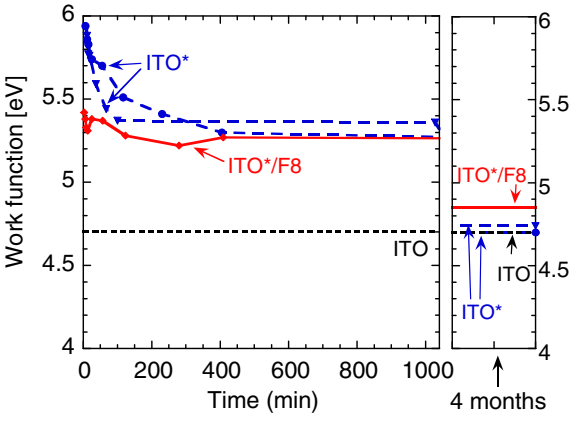

Fig. 5. Left panel: Kelvin probe work function measurements of two oxygen-plasma treated ITO surfaces (ITO∗) as a function of time after completion of the plasma treatment (dashed curves, diamond and circles treated for 5 and 10 min, respectively). Also shown are the results for an oxygen-plasma treated sample covered by a 75 nm film of F8 (continuous curve). Measurements were taken in air. Right panel: work function of the same samples after they were left in air for four months. The horizontal line at 4.7 eV represents the work function of the ITO surface before plasma treatment.

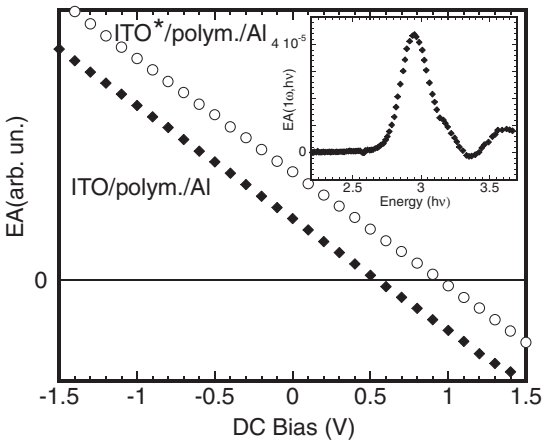

Fig. 6. Electroabsorption (EA) response at hν = 2.9 eV and V_{AC} = 1 V as a function of applied bias for the following encapsulated diodes: ITO/polymer/Al (left, black diamonds, V_{BI} = 0.51 V), and ITO∗/polymer/Al (right, circles, V_{BI} = 0.99 V). The difference in V_{BI} between the two samples is a direct verification that the Fermi energy level of the plasma treated ITO* sample is 0.48 eV closer to the HOMO level of the semiconductor compared to the untreated surface. The measurements (only one shown for each heterostructure) were taken shortly (0 months) and repeated 20 months and 25 months after fabrication and encapsulation of the diodes, with no appreciable change in the EA response. The spectral dependence of the EA signal is shown in the inset.

treated with the oxygen plasma. Here the initial CPD enhancement due to the plasma is still significant (0.6–0.7 V) but reduced compared to the "free" ITO∗ surface. There is also some CPD evolution – an overall small decrease (0.1–0.15 V) within the first 400 min. The work function tends to a plateau value ∼0.5 eV higher than the untreated ITO surface before decreasing further after 4 months (CPD = 0.15 eV).

3.3.2. Diodes

The inset of Fig. 6 shows the EA spectrum of the ITO/polymer/Al device described in the experimental section. The energy of the incident photon was kept at 2.9 eV and the EA signal monitored as a function of the applied bias for both the ITO/polymer/Al and the ITO∗/polymer/Al encapsulated devices. The zero crossing of the plots are: V_{BI} = 0.51 V for ITO/polymer/Al diode; V_{BI} = 0.99 V for the ITO∗/polymer/Al diode. Note that the electroabsorption measurements of V_{BI} were taken straight after fabrication (∼0 months) and then repeated 20 and 25 months (left idle – i.e. without being driven) after the devices were fabricated and encapsulated in nitrogen atmosphere, without any noticeable change in the V_{BI} over this entire period.

4. Discussion

4.1. Au, Au∗ study

Fig. 3 shows clearly that both the gold surfaces under study Au(1) and Au(2), in an air environment, possess a work function that can be significantly lower than that of a gold surface formed and measured in ultra high vacuum (despite even the tendency of photoemission techniques to

provide smaller values than KP [40]). Typically, ϕ [Au] $\geqslant$ 5.1 eV in UHV [7]. Adventitious species that are adsorbed on (or co-evaporated with) the gold surfaces in the evaporation chamber [21] (in high vacuum conditions rather than UHV) and when the surfaces are left resting in air [20], are the reported causes of the lower work function we measured: ϕ = 4.94 eV for Au(1) and ϕ = 4.63 eV for Au(2). Au(1) was evaporated at pressures of $<1.8 \times 10^{-6}$ mbar and Au(2) at higher pressures $\leqslant 5 \times 10^{-6}$ mbar. We believe that the lower work function for Au(2) is caused by a higher partial pressure of hydrocarbons [7,18,21,22,48,49] and other contaminants [50], present in the evaporation chamber (in which a variety of other materials are also routinely evaporated).

The O_2 plasma treatment initially increases the work function of the Au surfaces by 0.4–0.54 eV (Fig. 3). Chemically sensitive techniques such as photoemission spectroscopy [3,51,52] would be required to gauge the chemistry of the Au* surface (although outside the scope of this work), but the enhancement in work function may be in part ascribed to the plasma ablation of adventitious adsorbed contaminant layers, as also occurs, at least partially, in less chemically stable surfaces such as ITO [18,20–22,24,48,49] and also to the adsorption or chemisorption of more reactive species such as oxygen [27,53]. Leaving the plasma treated Au surfaces in air ambient causes the work function to decrease in time to values that are even lower than those of the same surfaces prior to the plasma (Fig. 3). While there are a number of possible explanations, this behaviour may mean that the plasma creates a more reactive surface (through the generation of reactive chemical surface species) which then attracts a higher concentration of adsorbed hydrocarbons and contaminants from the air environment, over the time scale of hundreds of minutes. The above results confirm that Au is not a good standard in air [38,39] since its work function depends strongly on the evaporation conditions and on the environment it sees before and during measurement.

Beierlein et al. [20] have reported that the reduction of the work function of metals upon exposure to air may be strongly mitigated by putting samples in an inert atmosphere. In Fig. 3 we show that by overlaying an F8 film over the O_2 plasma-functionalised Au surface (Au*/F8), the enhancement in the work function is "frozen-in". The fact that this enhancement is stabilised at a lower value compared to the equivalent work function of the bare plasma treated surface (cf. Fig. 3 squares) may potentially be ascribed to a significantly large dipole forming at the Au/F8 interface [2,3,6], and/or to the fact that the more reactive (but unstable) species that may be produced initially by the plasma on the gold surface are then passivated/eliminated by the spin coating of the film; a partial contribution from band bending cannot be excluded. However, since the polymers utilised in this work are of high purity, we believe this effect to be marginal in this case, as also confirmed by subsequent EA measurements on diodes; recent photoemission studies on polymer/Au interfaces by Osikowicz et al. [54] have related this effect to a compression of the metal electron density tail in the presence of an organic layer. Fig. 3 shows that the work function of the Au*/F8 sample is constant (±0.05 eV) over the time scales of the 10^2–10^3 min under study and is $\phi \cong 5.15$ eV: a significant value in that it is very close to the ones reported for Au formed and measured in UHV (i.e. a clean surface). Note that although in principle strong pinning of the anode work function (and thus V_{BI}) cannot be excluded as recent photoemission experiments show instead a large relaxation energy for the polaronic energy levels (placed at ~5.2 eV [55] that can pin the Fermi level, here it is improbable as in the results using F8BT (see next section) which has an IP similar to that of F8, the built-in potential measured is greater than would be expected if strong pinning were occurring at a polaronic energy level with a relaxation energy of 0.4–0.7 eV. In previous EA experiments pinning was shown to occur closer to the ionization potential of F8, i.e. 5.8 eV) [56]; photoemission studies and EA techniques may inherently give rise to differences [33], for reasons similar to those encountered when comparing photoemission studies to KP measurements [40].

4.2. Pt, Pt* study

4.2.1. Surfaces

Table 1 shows that the work function of evaporated Pt layers (i) and (iv) measured in air is 4.7 eV. An oxygen plasma treatment brings the work function of the Pt surfaces to ϕ = 5.5–5.6 eV. This value corresponds to the work function of a UHV clean Pt surface [7]. The ϕ of the untreated Pt is much lower because of species adsorbed in air but also because of the relatively elevated pressures reached in the evaporation chamber during the thermal evaporation (1×10^{-5} mbar) which can contaminate [20,21] the surface with species degassing from the crucible and chamber.

The increase in work function after the plasma suggests that it is the surface contamination that is removed by the plasma although there may also be a contribution from oxygen adsorbed or chemisorbed on the Pt surface [53]. The reduction in the work function of 0.3 eV over the time period of 2 h (measured 15 min and 2 h 15 min after the plasma treatment in air) confirms that bare clean Pt may have a similar (although improved) [21] stability trend compared to the Au surface. It is also interesting to note that the thin Pt layers where a contribution from the underlying ITO* sample (island growth) may also be present give the same result as the thicker opaque Pt layers.

4.2.2. Diodes

Fig. 4 and Table 2 show that the V_{BI} of the diode with a plasma treated Pt contact (ITO/Pt*/F8BT/Au) is ~1 eV higher compared to the device with an untreated Pt anode (ITO/Pt/F8BT/Au) (see Fig. 4 and Table 2). This means that the barrier to hole injection from the anode into the F8BT has been reduced by a similar amount (see Fig. 2). This O_2 plasma-induced enhancement in V_{BI} is ~ equal (within ± 0.1 eV) to that in the work function, ϕ, of the bare platinum surface (Table 1). The ensuing barrier height lowering of the same magnitude (see Fig. 2) is responsible for the improvement in hole injection in diodes with ITO/Pt anodes as reported by Shen et al. [57]. Note that among the ITO*/polymer, Au*/polymer and the Pt*/polymer samples, it is the latter that yields the largest increase in ϕ or V_{BI}. Also, unlike the Au*/F8 case, where a significant dipole

may have formed at the metal/semiconductor interface, the remarkable consistency between the V_{BI} of Table 2 and the work function data of Table 1 indicates that: (a) the Schottky–Anderson model for the interface between F8BT and Pt (ii) and (iii), and also ITO (i), constitutes a good approximation in describing the energy level alignment at these electrode–polymer interfaces, (b) the plasma is not likely to generate a significant concentration of unstable reactive species at the Pt∗ surface, (c) that the zero crossing voltage difference can be utilised to gauge the variation on barrier height (NB ionisation potential of F8 > estimated work function of anode) [32,58]. It is interesting to note that the case of Pt is in contrast to Au for which the original work function enhancement due to the plasma is reduced by spinning an organic overlayer on top. Furthermore, the F8BT film of the LEDs of Table 2 was spun minutes after completion of the plasma treatment of the anode, but the EA measurements were taken over 24 h later. Thus, on this timescale, overlaying a polymer layer over an oxygen-plasma treated Pt surface "preserves" the V_{BI}, and thus the original work function of the surface.

Finally, we consider that the gold interface with F8BT for all the diodes of Fig. 4 and Table 2, is evaporated directly over the polymer film in vacuum and has thus never seen air. V_{BI} for sample (i) ITO/F8BT/Au is −0.1 V. This implies that, at flat band, the Fermi level of the Au top-contact is 0.1 eV closer to the vacuum level than that of ITO (Fig. 2); if the Schottky–Anderson vacuum-level alignment model ruled, the work function of the Au would be 4.6 eV [ϕ (ITO) = 4.7 eV]. This is far lower than the expected work function of Au in a good vacuum [7], indicating that estimates of charge injection barriers based on the work function of atomically clean gold surfaces can lead to errors as also outlined in recent photoemission experiments by Osikowicz et al. [54] for which a decrease of the vacuum energy levels of Au in contact with a polymer layer is consistently observed and due to the compression of the metal electron density tail in the presence of an organic contact layer. Note also that the Au contact of Table 2, evaporated over the conjugated polymer, may give rise to quantitatively different energy level alignment compared to the situation in which the organic layer is spun over a previously deposited (and cleaned) Au surface.

4.3. ITO, ITO∗ study

4.3.1. Surfaces

The work function of the plasma treated ITO surface (Fig. 5) has a similar time dependence to that of the Au surfaces of Fig. 3 with two main differences: (a) the increase and absolute value for ITO* are significantly higher just after the plasma treatment and (b) the decrease with time when the surfaces are left in air reaches an initial plateau after 100–400 min which is still sizeably higher than the initial untreated ITO.

Although higher than that of the untreated ITO, the work function of the ITO∗/F8 sample is lower (by ∼0.5 eV) than that of the ITO∗ shortly after the plasma treatment (but before F8 deposition). This suggests that either: (a) a simple Schottky vacuum-level alignment does not occur and a significant dipole (that shifts the levels by 0.5 eV) is formed at the ITO∗/F8 interface, and/or (b) that any reactive chemical species [27] present on the ITO∗ surface after the oxygen-plasma, which could induce a work function increase, are quenched much more rapidly by application of the polymer layer, and/or (c) that the polymer film causes a reduction of the electron tail density that extends outside the metal surface [54]. A partial contribution from band bending cannot be excluded. However, since the polymers utilised in this work are of high purity, we believe this to be low in this case as also confirmed by subsequent EA measurements on diodes, and by the perfect linearity of the EA vs. V_{DC} characteristics. Fig. 5 shows that any chemical, physical and electronic process or interaction between F8 and ITO∗ continue even some time (∼200 min) after deposition of the polymer overlayer. Although in previous work [18,22,24,29,49,59] the increase of the ITO work function upon plasma treatment has mainly been ascribed to the removal of surface contaminants such as hydrocarbons and to chemical modification (e.g. oxidation) of the ITO, recently Kim et al. [27] proposed that a dipole layer of O^- ions is formed on the ITO surface, which increases the work function of the ITO. We consider that the role of reactive, unstable species left on the surface after an oxygen plasma and the evolution of these in time has received little attention, and that would deserve a dedicated investigation with chemistry-sensitive techniques such as X-ray photoelectron spectroscopy (XPS).

A consideration that arises when analysing these results is that the time elapsed between the completion of the plasma treatment and the deposition of F8 can be crucial in determining the energy level alignment, since a dipole that actually decreases the separation of the semiconductor HOMO and the Fermi level of the high work function conductor are rare [6]. It thus becomes important to overlay the organic semiconductor before the work function of the underlying contact has decreased much beyond the ionization potential of the semiconductor in order to minimise the hole injection barrier.

Although the effect of the plasma is longer lasting in the case of ITO compared to gold surfaces, Fig. 5 shows that the work function of the ITO∗ surfaces has returned to its initial value after leaving the samples 4 months idle in air. Even the work function of the ITO∗/F8 sample has decreased very sizeably, although it remains 0.15 eV higher than untreated ITO surface. The F8 layer carries out some protective action on the electronic properties of the underlying interface, but not on the time scale of months. This large decrease in the KP reading over time can either be ascribed to chemical/electronic variations at the electrode/polymer interface (as seen in electrically stressed PLEDs with a PEDOT:PSS anodes for example) [60], and/or polymer/air interface and/or polymer/air interface and/or in the bulk of the semiconductor. Either way, this will have a strong and detrimental impact on the performance and lifetime of any device built with these materials and is mainly due to molecules from the air environment diffusing into and through the semiconducting polymer.

4.3.2. Diodes

Very significantly, however, proper encapsulation of the diodes results in a dramatic improvement on the lifetime

of the plasma-induced work function enhancement (Fig. 6). EA measurements were taken soon after fabrication and also 20 and 25 months after fabrication and encapsulation of the samples (no getter included). No change during this time period of over two years was detected in the V_{BI} for either ITO/polymer/Al or ITO∗/polymer/Al samples. The relative energy levels have therefore remained unaltered over this time. Using the top Al electrode as the reference and assuming a work function of 4.2 eV (and a Schottky type alignment at the Al/polymer interface as determined in a previous paper) [32], the Fermi level of the untreated ITO sample would lie 0.5 eV (V_{BI} = 0.51 V) higher than Al (see Fig. 2), i.e. at 4.7 eV from the vacuum level. This value also coincides with the measured value for ITO (see Fig. 1) meaning that Schottky–Anderson vacuum-level alignment is valid at this ITO/polymer interface as well. For the ITO∗ anode, V_{BI} = 0.99 V. This is a direct verification, on a working diode structure, that the Fermi energy level of the ITO∗ sample is 0.48 eV closer to the HOMO level of the semiconductor compared to the untreated surface (i.e. ϕ(ITO∗) ≈.5.18 eV). The resulting barrier lowering leads to improved injection of holes in organic semiconductor diodes as detailed in a number of studies [17,24,61].

The above results also shed some light on the issue of poor reproducibility that can affect the fabrication of organic semiconductor devices. The electronic properties of an interface, including the energy level positioning and formation of interfacial dipoles, depend obviously and critically on the choice of contact and semiconductor materials. Not only do they depend on the different fabrication processes, conditions, and environments, but also on more subtle and sometimes less controllable parameters such as variations in the chamber pressure during evaporation and the time elapsed between the treatment of the contacts and the actual deposition of the semiconducting layers.

5. Conclusions

Evaporating films of Au and Pt in high vacuum conditions and leaving the samples in an air environment leads to a work function that can be considerably lower than the equivalent reference surfaces formed and measured in UHV conditions. For Au and Pt surfaces, it is desirable to keep the pressures in the evaporation chambers as low as possible ($\leqslant 1 \times 10^{-6}$ mbar) as higher pressures lead to a lowering of the work function which can be detrimental to the operation of optoelectronic devices.

We have shown that treating Au, Pt and ITO surfaces with an oxygen plasma can increase their work function by up to over 1 eV. This enhancement is however not permanent when the samples are left in air as the work function starts to decrease when exposed to air. For Au surfaces the work function can fall back to the pre-treated value (and lower) within a few tens of minutes. For ITO there is a similar initial reduction but the work function plateaus (on the time scale of 10^3 min) to a value which is still considerably higher than its initial one. This difference compared to the metallic Au electrode suggests that for the ITO surface the plasma has not only a superficial effect (e.g. removing hydrocarbons, impurities and adding adsorbed species (e.g. O^-)) but also more lasting chemical modifications. Ultimately however, after 4 months we see that the work function of ITO has gone back to its initial untreated value, ϕ (ITO) = (4.7 ± 0.1 eV), as measured utilizing a highly oriented pyrolytic graphite surface for calibration.

By spinning a semiconductor polymer layer over the plasma treated Au, Pt, and ITO surfaces, we show that the enhancement of the work function brought about by the plasma is at least partially preserved even in air: in its entirety for the Pt∗ surface covered with F8BT (which suggests a vacuum-level alignment); somewhat reduced for the Au∗ and ITO∗ surfaces when covered with an F8 film, which may indicate that a significant dipole has formed at those semiconductor/electrode contacts or that the more reactive species generated by the plasma have been removed/passivated by the film. Nevertheless, for all the plasma-treated surfaces (Au, Pt and ITO), the Fermi level of the conductor has been brought closer to the HOMO levels of the semiconducting polymers decreasing the barrier to hole injection significantly, by between 0.2 eV and 1 eV. The electroabsorption results on complete diode structures confirm this. The estimated "effective" work functions (∼ ± 0.15 eV) of these plasma treated electrodes are 5.15 eV for Au∗, 5.18 eV for ITO∗ and 5.6 eV for Pt∗. For the untreated surfaces the initial values in air are much lower: 4.5–4.9 eV for Au, 4.7 eV for ITO (the reference sample) and 4.6–4.7 eV for evaporated Pt.

Although the polymer overlayer keeps the work function of plasma-treated surfaces steady over the times scale of a day, it does not preserve it on the time scale of a few months with detrimental effects on the lifetime of a device. On the other hand, if devices are properly encapsulated in inert atmosphere, we have also proven that the relative energy level alignment of the contact and semiconductor materials (and thus of the ensuing injection barriers) is completely and firmly frozen over the time scale of the 25 months of our study.

Although it would be desirable to offer a more detailed analysis of the underlying mechanisms for the measured work-function deepening, recovery and stabilisation, this would require a number of studies which fall beyond the scope of this communication, owing to their complexity and length. An obvious explanation of the stabilisation may be the suppression of diffusion of polar atmospheric contaminants to the metal/polymer interface. However, the identification of the nature of the contaminants that are likely to be adsorbed and responsible for the observed effects is a particularly demanding task, which requires a separate and dedicated study.

While these results have been obtained with a particular class of materials (polyfluorenes) that are significantly stable, we consider that the results are more general to well – encapsulated electrode/organic-semiconductor/electrode devices. For example, recently devices with a different class of materials, have currently been reported with optical and electroluminescent properties that are stable over a period of ∼10 years when stored in the dark [13]. We suggest therefore that our results have strong implications

for the understanding, design, fabrication strategies, processing timings, and lifetimes of un-encapsulated surfaces and electrode-organic heterostructures and ultimately of completely encapsulated devices. For the latter, the fact that the high work function electrode/semiconductor alignment stays constant on the timescale of years contributes in explaining the observations of correspondingly long shelf lives and lifetimes seen in organic semiconductor devices including OLEDs [62–66], TFTs [67], and photovoltaic cells [68–73].

Acknowledgements

The Pt, Pt∗ investigation was carried out at the Cavendish Laboratory, Cambridge University. The ITO, ITO∗ diodes were fabricated at Cambridge Display Technology. TMB wishes to thank MIUR for a "Incentivazione alla mobilità di studiosi residenti all'estero" fellowship and financial support "Polo Solare Organico Regione Lazio" from Regione Lazio. We also thank the EC Marie Curie RTN-THREADMILL (MRTN-CT-2006-036040) and ITN-SUPERIOR (PITN-GA-2009-238177), EPSRC, the EC FP7 ONE-P large-scale project N. 212311 for financial support.

References

[1] S. Braun, W.R. Salaneck, M. Fahlman, Energy-level alignment at organic/metal and organic/organic interfaces, Advanced Materials 21 (2009) 1450–1472.
[2] N. Koch, A. Kahn, J. Ghijsen, J.J. Pireaux, J. Schwartz, R.L. Johnson, A. Elschner, Conjugated organic molecules on metal versus polymer electrodes: demonstration of a key energy level alignment mechanism, Applied Physics Letters 82 (2003) 70–72.
[3] H. Ishii, K. Sugiyama, E. Ito, K. Seki, Energy level alignment and interfacial electronic structures at organic/metal and organic/organic interfaces, Advanced Materials 11 (1999) 605–625.
[4] N. Koch et al., Applied Surface Science 166 (2000) 354–362.
[5] I.G. Hill, D. Milliron, J. Schwartz, A. Kahn, Stability and characterization of large area polymer light-emitting diodes over extended periods, Applied Surface Science 166 (2000) 354–362.
[6] A. Kahn, N. Koch, W. Gao, Electronic structure and electrical properties of interfaces between metals and pi-conjugated molecular films, Journal of Polymer Science: B 41 (2003) 2529–2548.
[7] H.B. Michaelson, The work function of the elements and its periodicity, Journal of Applied Physics 48 (1977) 4729–4733.
[8] I.H. Campbell, S. Rubin, T.A. Zawodzinski, J.D. Kress, R.L. Martin, D.L. Smith, N.N. Barashkov, J.P. Ferraris, Controlling Schottky energy barriers in organic electronic devices using self-assembled monolayers, Physical Review B 54 (1996) 14321–14324.
[9] S.F.J. Appleyard, S.R. Day, R.D. Pickford, M.R. Willis, Organic electroluminescent devices: enhanced carrier injection using SAM derivatized ITO electrodes, Journal of Materials Chemistry 10 (2000) 169–173.
[10] B. de Boer, A. Hadipour, M.M. Mandoc, T. van Woundenbergh, P.W.M. Blom, Tuning of metal work functions with self-assembled monolayers, Advanced Materials 17 (2005) 621–625.
[11] J. Morgado, N. Barbagallo, A. Charas, M. Matos, L. Alcacer, F. Cacialli, Self-assembly surface modified indium-tin oxide anodes for single-layer light-emitting diodes, Journal of Physics D: Applied Physics 36 (2003) 434–438.
[12] G. Latini, M. Wykes, R. Schlapak, R. Howorka, F. Cacialli, Self-assembled monolayers of protonated poly(amidoamine) dendrimers on indium-tin oxide, Applied Physics Letters 92 (2008) 013511.
[13] G. Winroth, S. Brovelli, R. Daik, W.J. Feast, F. Cacialli, Stability of optical and electroluminescence properties of a semiconducting polymer over a decade, Organic Electronics 11 (2010) 1445–1448.
[14] G. Gustafsson, Y. Cao, G.M. Treacy, F. Klavetter, N. Colaneri, A.J. Heeger, Flexible light-emitting diodes made from soluble conducting polymers, Nature 357 (1992) 477–479.
[15] S.A. Carter, M. Angelopoulos, S. Karg, P.J. Brock, J.C. Scott, Polymeric anodes for improved polymer light-emitting diode performance, Applied Physics Letters 70 (1997) 2067–2069.
[16] T.M. Brown, J.S. Kim, R.H. Friend, F. Cacialli, R. Daik, W.J. Feast, Built-in field electroabsorption spectroscopy of polymer light-emitting diodes incorporating a doped poly(3,4-ethylene dioxythiophene) hole injection layer, Applied Physics Letters 75 (1999) 1679–1681.
[17] J.S. Kim, M. Granström, R.H. Friend, N. Johansson, W.R. Salaneck, R. Daik, W.J. Feast, F. Cacialli, Indium-tin oxide treatments for single- and double-layer polymeric light-emitting diodes: the relation between the anode physical chemical and morphological properties and the device performance, Journal of Applied Physics 84 (1998) 6859–6870.
[18] J.S. Kim, P.K.H. Ho, D.S. Thomas, R.H. Friend, F. Cacialli, G.-W. Bao, S.F.Y. Li, X-ray photoelectron spectroscopy of surface-treated indium-tin oxide thin films, Chemical Physics Letters 315 (1999) 307–312.
[19] H.W. Choi, S.Y. Kim, K.-B. Kim, Y.-H. Tak, J.-L. Lee, Enhancement of hole injection using O_2 plasma-treated Ag anode for top-emitting organic light-emitting diodes, Applied Physics Letters 86 (2005) 012101–012104.
[20] T.A. Beierlein, W. Bruetting, H. Riel, E.I. Haskal, P. Mueller, W. Riess, Kelvin probe investigations of metal work functions and correlation to device performance of organic light-emitting devices, Synthetic Metals 111–112 (2000) 295–297.
[21] S.M. Tadayyon, K. Griffiths, P.R. Norton, C. Tripp, Z. Popovic, Work function modification of indium-tin-oxide used in organic light emitting devices, Journal of Vacuum Science and Technology A 17 (1999) 1773–1778.
[22] P. He, S.D. Wang, W.K. Wong, L.F. Cheng, C.S. Lee, S.T. Lee, S.Y. Liu, Vibrational analysis of oxygen-plasma treated indium tin oxide, Chemical Physics Letters 370 (2003) 795–798.
[23] H. Kim, J. Lee, C. Park, Y. Park, Surface characterization of O_2-plasma-treated indium-tin-oxide (ITO) anodes for organic light-emitting-device applications, Journal of the Korean Physical Society 41 (2002) 395–399.
[24] C.C. Wu, C.I. Wu, J.C. Sturm, A. Kahn, Surface modification of indium tin oxide by plasma treatment: an effective method to improve the efficiency, brightness and reliability of organic light emitting devices, Applied Physics Letters 70 (1997) 1348–1350.
[25] M. Ishii, T. Mori, H. Fujikawa, S. Tokito, Y. Taga, Improvement of organic electroluminescent device performance by in situ plasma treatment of indium-tin-oxide surface, Journal of Luminescence 87-9 (2000) 1165–1167.
[26] L. Burgi, T.J. Richards, R.H. Friend, H. Sirringhaus, Close look at charge carrier injection in polymer field-effect transistors, Journal of Applied Physics 94 (2003) 6129–6137.
[27] K.P. Kim, A.M. Hussain, D.K. Hwang, S.H. Woo, H.K. Lyu, S.H. Baek, Y. Jang, J.H. Kim, Work function modification of indium-tin oxide by surface plasma treatments using different gases, Japanese Journal of Applied Physics 48 (2009).
[28] M.G. Mason, L.S. Hung, C.W. Tang, S.T. Lee, K.W. Wong, M. Wang, Characterization of treated indium-tin-oxide surfaces used in electroluminescent devices, Journal of Applied Physics 86 (1999) 1688–1692.
[29] J. Xue, S.R. Forrest, Journal of Applied Physics 95 (2004) 15.
[30] F. Cacialli, R.H. Friend, S.C. Moratti, A.B. Holmes, Characterization of properties of polymeric light-emitting-diodes over extended periods, Synthetic Metals 67 (1994) 157–160.
[31] G. Winroth, O. Fenwick, M.A. Scott, D. Yip, S. Howorka, F. Cacialli, Interfacial dipole dynamics of light-emitting diodes incorporating a polyamidoamine dendrimer monolayer, Applied Physics Letters 97 (2010).
[32] T.M. Brown, R.H. Friend, I.S. Millard, D.J. Lacey, T. Butler, J.H. Burroughes, F. Cacialli, Electronic line-up in light emitting diodes with alkali-halide/metal cathodes, Journal of Applied Physics 93 (2003) 6159–6172.
[33] V. Bodrozic, T.M. Brown, S. Mian, D. Caruana, M. Roberts, J.J. Halls, I. Grizzi, J.H. Burroughes, F. Cacialli, The built-in potential in blue polyfluorene-based light-emitting diodes, Advanced Materials 20 (2008) 2410–2415.
[34] V. Bodrozic, M. Roberts, N. Phillips, J.H. Burroughes, S. Mian, F. Cacialli, The influence of subgap features in the electromodulation and built-in voltage measurements of polyfluorene blue light-emitting diodes with anodic charge injection layers, Journal of Applied Physics 101 (2007).
[35] K. Besocke, S. Berger, Piezoelectric driven Kelvin probe for contact potential difference studies, Review of Scientific Instruments 47 (1976) 840–842.

[36] H.O. Jacobs, H.F. Knapp, A. Stemmer, Practical aspects of Kelvin probe force microscopy, Review of Scientific Instruments 70 (1999) 1756–1760.
[37] G.F. Saville, P.M. Platzman, G. Brandes, R. Ruel, R.L. Willet, Feasibility study of photocathode electron projection lithography, Journal of Vacuum Science and Technology B 13 (1995) 2184–2188.
[38] W.N. Hansen, K.B. Johnson, Work function measurement in gas ambient, Surface Science 316 (1994) 373–382.
[39] W.N. Hansen, G.J. Hansen, Standard reference surfaces for work function measurements in air, Surface Science 481 (2001) 172–184.
[40] J.S. Kim, B. Lagel, E. Moons, N. Johansson, I. Baikie, W.R. Salaneck, R.H. Friend, F. Cacialli, Kelvin probe ultraviolet photoelectron spectroscopy measurements of indium tin oxide workfunction: a comparison, Synthetic Metals 111–112 (2000) 311–314.
[41] T.M. Brown, Ph.D. Thesis, Cambridge University, 2001.
[42] Y. He, S. Gong, R. Hattori, J. Kanicki, High performance organic polymer light-emitting heterostructure devices, Applied Physics Letters 74 (1999) 2265–2267.
[43] S. Janietz, D.D.C. Bradley, M. Grell, C. Giebeler, M. Inbasekaran, E.P. Woo, Electrochemical determination of the ionization potential electron affinity of poly(9,9-dioctylfluorene), Applied Physics Letters 73 (1998) 2453–2455.
[44] R. Riehn, R. Stevenson, J.J.M. Halls, D.R. Richards, D.-J. Kang, M. Blamire, F. Cacialli, Near-field photoconductivity imaging of a conjugated polymer blend, Advanced Functional Materials 16 (2006) 469–476.
[45] I.H. Campbell, T.W. Hagler, D.L. Smith, J.P. Ferraris, Direct measurement of conjugated polymer electronic excitation energies using metal/polymer/metal structures, Physical Review Letters 76 (1996) 1900–1903.
[46] G. Greczynski, M. Fahlman, W.R. Salaneck, Electronic structure of hybrid interfaces of poly(9,9-dioctylfluorene), Chemical Physics Letters 321 (2000) 379–384.
[47] T.M. Brown, F. Cacialli, Internal fields and electrode interfaces in organic semiconductor devices: noninvasive investigations via electroabsorption, in: T. Skotheim, J. Reynolds (Eds.), Handbook of Conducting Polymers, CRC Press – Taylor and Francis, New York, 2007, pp. 19.11–19.49.
[48] S.M. Tadayyon, H.M. Grandin, K. Griffiths, L.L. Coatsworth, P.R. Norton, H. Aziz, Z.D. Popovic, Reliable and reproducible determination of work function and ionization potentials of layers and surfaces relevant to organic light emitting diodes, Organic Electronics 5 (2004) 199–205.
[49] Y.-H. Liau, N.F. Scherer, K. Rhodes, Nanoscale electrical conductivity and surface spectroscopic studies of indium-tin oxide, Journal of Physical Chemistry B 105 (2001) 3282–3288.
[50] J.M. Gottfried, K.J. Schimdt, S.L.M. Schroeder, K. Christmann, Adsorption of carbon monoxide on Au, Surface Science 536 (2003) 206–224.
[51] J. Bigerson, M. Fahlman, P. Broms, W.R. Salaneck, Conjugated polymer surfaces and interfaces: a mini review and some new results, Synthetic Metals 80 (1996) 125–130.
[52] W.R. Salaneck, S. Stafström, J.-L. Brédas, Conjugated Polymer Surfaces and Interfaces: Electronic and Chemical Structure of Interfaces for Polymer Light Emitting Devices, Cambridge University Press, Cambridge, 1996.
[53] M. Berdau, S. Moldenhauer, A. Hammoudeh, J.H. Block, K. Christmann, Interaction of oxygen with Pt(210): formation of new oxygen states at higher exposures, Surface Science 446 (2000) 323–333.
[54] W. Osikowicz, M.P. de Jong, S. Braun, C. Tengstedt, M. Fahlman, W.R. Salaneck, Energetics at Au top and bottom contacts on conjugated polymers, Applied Physics Letters 88 (2006).
[55] M. Fahlman, A. Crispin, X. Crispin, S.K.M. Henze, M.P. de Jong, W. Osikowicz, C. Tengstedt, W.R. Salaneck, Electronic structure of hybrid interfaces for polymer-based electronics, Journal of Physics – Condensed Matter 19 (2007).
[56] P.A. Lane, P.J. Brewer, J.S. Huang, D.D.C. Bradley, J.C. deMello, Elimination of hole injection barriers by conducting polymer anodes in polyfluorene light-emitting diodes, Physical Review B 74 (2006) 125320.
[57] Y. Shen, D.B. Jacobs, G.G. Malliaras, G. Koley, M.G. Spencer, A. Ioannidis, Modification of indium tin oxide for improved hole injection in organic light emitting diodes, Advanced Materials 13 (2001) 1234–1238.
[58] R.J. de Vries, S.L.M. van Mensfoort, R.A.J. Janssen, R. Coehoorn, Relation between the built-in voltage in organic light-emitting diodes and the zero-field voltage as measured by electroabsorption, Physical Review B 81 (2010).
[59] K.H. Lee, H.W. Jang, K.-B. Kim, Y.-H. Tak, J.-L. Lee, Mechanism for the increase of indium-tin-oxide work function by O_2 inductively coupled plasma treatment, Journal of Applied Physics 95 (2004) 586–590.
[60] R.U.A. Khan, D.D.C. Bradley, M.A. Webster, J.L. Auld, A.B. Walker, Degradation in blue-emitting conjugated polymer diodes due to loss of ohmic hole injection, Applied Physics Letters 84 (2004) 921–923.
[61] A.J. Campbell, D.D.C. Bradley, H. Antoniadis, M. Inbasekaran, W.S.W. Wu, E.P. Woo, Transient and steady-state space-charge-limited currents in polyfluorene copolymer diode structures with ohmic hole injecting contacts, Applied Physics Letters 76 (2000) 1734–1736.
[62] P.E. Burrows, V. Bulovic, S.R. Forrest, L.S. Sapochak, D.M. McCarty, M.E. Thompson, Reliability and degradation of organic light-emitting devices, Applied Physics Letters 65 (1994) 2922–2924.
[63] B. Chalamala, G. Nisato, Y. Ohmori, Introduction to the issue on organic light-emitting diodes, IEEE Journal of Selected Topics in Quantum Electronics 10 (2004) 1–2.
[64] R.E. Gill, P. van de Weijer, C.T.H. Liedenbaum, H.F.M. Schoo, A. Berntsen, J.J.M. Vleggaar, R.J. Visser, Stability and characterization of large area polymer light-emitting diodes over extended periods, Optical Materials 12 (1999) 183–187.
[65] J.C. Carter, I. Grizzi, S.K. Heeks, D.J. Lacey, S.G. Latham, P.G. May, O.R. delospanos, K. Pichler, C.R. Towns, H.F. Wittmann, Operating stability of light-emitting polymer diodes based on poly(p-phenylene vinylene), Applied Physics Letters 71 (1997) 34–36.
[66] K. Fehse, S. Olthof, K. Walzer, K. Leo, R.L. Johnson, H. Glowatzki, B. Broker, N. Koch, Energy level alignment of electrically doped hole transport layers with transparent and conductive indium tin oxide and polymer anodes, Journal of Applied Physics 102 (2007).
[67] J. Ficker, A. Ullmann, W. Fix, H. Rost, W. Clemens, Stability of polythiophene-based transistors and circuits, Journal of Applied Physics 94 (2003) 2638–2641.
[68] P. Schilinsky, C. Waldauf, J. Hauch, C.J. Brabec, Polymer photovoltaic detectors: progress and recent developments, Thin Solid Films 451 (2004) 105–108.
[69] G. Yu, G. Srdanov, H.L. Wang, Y. Cao, A.J. Heeger, High performance polymer photovoltaic cells and photodetectors, in: Z.H. Kafafi (Ed.), Organic Photovoltaics, 2000, pp. 48–56.
[70] G. Dennler, C. Lungenschmied, H. Neugebauer, N.S. Sariciftci, M. Latreche, G. Czeremuszkin, M.R. Wertheimer, A new encapsulation solution for flexible organic solar cells, Thin Solid Films 511 (2006) 349–353.
[71] C. Lungenschmied, G. Dennler, H. Neugebauer, S.N. Sariciftci, M. Glatthaar, T. Meyer, A. Meyer, Flexible, long-lived, large-area, organic solar cells, Solar Energy Materials and Solar Cells 91 (2007) 379–384.
[72] S.K. Hau, H.L. Yip, N.S. Baek, J.Y. Zou, K. O'Malley, A.K.Y. Jen, Air-stable inverted flexible polymer solar cells using zinc oxide nanoparticles as an electron selective layer, Applied Physics Letters 92 (2008).
[73] B. Zimmermann, U. Wurfel, M. Niggemann, Longterm stability of efficient inverted P3HT:PCBM solar cells, Solar Energy Materials and Solar Cells 93 (2009) 491–496.

Organic Electronics 12 (2011) 634–640

Contents lists available at ScienceDirect

Organic Electronics

journal homepage: www.elsevier.com/locate/orgel

Improved performance uniformity of inkjet printed n-channel organic field-effect transistors and complementary inverters

Kang-Jun Baeg [b,c], Dongyoon Khim [b], Ju-Hwan Kim [b], Minji Kang [b], In-Kyu You [c], Dong-Yu Kim [b], Yong-Young Noh [a,*]

[a] Department of Chemical Engineering, Hanbat National University, 16-1 Dukmyung-dong, Yuseong-gu, Daejeon 305-719, Republic of Korea
[b] Heeger Center for Advanced Materials, Department of Nanobio Materials and Electronics, Gwangju Institute of Science and Technology (GIST), 261 Cheomdan-gwagiro (Oryong-dong), Buk-gu, Gwangju 500-712, Republic of Korea
[c] Convergence Components and Materials Research Laboratory, Electronics and Telecommunications Research Institute (ETRI), 218 Gajeongno, Yuseong-gu, Daejeon 305-700, Republic of Korea

ARTICLE INFO

Article history:
Received 14 September 2010
Received in revised form 13 January 2011
Accepted 17 January 2011
Available online 1 February 2011

Keywords:
Organic field-effect transistors
Inkjet printing
Conjugated molecule

ABSTRACT

In the present study, we demonstrate inkjet-printed n-type organic field-effect transistors (OFETs) and their complementary inverters with high performance uniformity, using soluble *N*,*N*′-bis(*n*-octyl)-(1,7&1,6)-dicyanoperylene-3,4:9,10-bis(dicarboximide) (PDI8-CN_2). The device performance and uniformity were improved by ink-jet printing a PDI8-CN_2 solution onto a heated substrate (60 °C). The printed features, which were discontinuous crystalline films at RT, were uniform films when the substrate temperature was increased to 60 °C. Optimized n-channel PDI8-CN_2 FETs showed a high field-effect mobility of 0.05–0.06 cm^2/Vs, a high on/off ratio of $\sim 10^6$, and a high uniformity that was within 10% with a bottom-gate/bottom-contact device configuration. Inkjet-printed organic complementary inverters were constructed by direct inkjet-printing of n-channel (PDI8-CN_2) and p-channel (6,13-bis(triisopropyl-silylethynyl)-pentacene or poly(3-hexylthiophene)) organic semiconductors onto silicon dioxide gate dielectrics. The inkjet-printed organic complementary inverters exhibited a high voltage gain of more than 15 and small standard deviation of inverting voltage and gain of ±0.95 V and ±0.56, respectively, for measuring 12 samples from four difference batches.

© 2011 Elsevier B.V. All rights reserved.

1. Introduction

Complementary metal–oxide–semiconductor (CMOS) inverters, which are composed of both p-type and n-type transistors, are fundamental logic circuits in current microprocessors and most advanced integrated circuits. The advantages of CMOS inverters include both higher noise immunity and lower static power consumption than n-type-only or p-type-only MOS inverters [1–3]. Currently, solution-processible organic field-effect transistors (OFETs) and complementary circuits are being developed to realize large-area flexible electronics, such as digital processors in radio-frequency identification (RFID) tags and driver circuits in full color flexible displays, via cost-effective graphic art printing techniques [4–6]. To achieve these low-cost and high-speed organic complementary circuits, high performance n- and p-channel OFETs that have well-balanced charge carrier mobility must be realized by direct printing methods. Earlier studies that aimed to develop soluble conjugated molecules as the active layer of OFETs were focused mainly on high-performance p-type organic semiconductors because of their facile chemical synthesis [7–10]. These previous studies resulted in the development of state-of-the-art, soluble p-type organic small molecules and polymers that exhibit field-effect mobilities, μ_{FET} ($\sim$1 cm^2/Vs), comparable to those of amorphous silicon transistors [9,10]. In recent years, research has focused on the development of high-performance and air-stable n-type conjugated molecules [6,11].

* Corresponding author.
E-mail address: yynoh@hanbat.ac.kr (Y.-Y. Noh).

1566-1199/$ - see front matter © 2011 Elsevier B.V. All rights reserved.
doi:10.1016/j.orgel.2011.01.016

Inkjet-printing is a promising patterning method for the formation of active layers in OFETs and their integrated circuits. Inkjet-printing, which is an alternative to conventional photolithography, was recently applied in various processes required for the manufacture of microelectronic devices, such as formation of the color filter of a liquid crystal display and patterning of a luminescent polymer for an organic light-emitting display [12]. The direct-write ability and precise production of droplets with a constant volume enables to decrease device manufacturing costs due to simplification of the patterning process and minimization of material waste and contamination. Several groups have demonstrated inkjet-printed OFETs and inverters using conjugated small molecules or polymers [4–6,13]. OFETs fabricated by inkjet-printing of these small molecules typically have slightly superior μ_{FET} compared with conjugated polymers because highly crystalline films are readily formed. Inkjet-printing of one prototype molecule, 6,13-bis(triisopropyl-silylethynyl) pentacene (TIPS-pentacene), resulted in a μ_{FET} as high as >1 cm^2/Vs [2,13]. The ability to control the features of the inkjet-printed film is very important for microelectronic applications, including OFETs, since the device functionality depends on well-defined and highly uniform deposits. For example, OFETs inkjet-printed with small molecules suffer from large differences in device performance due to non-uniform semiconducting films. The most common causes of non-uniform films are the relatively lower viscosity of the semiconducting ink and inhomogeneous drying of liquid droplets on a non-absorbing substrate, e.g., the coffee-ring effect [14]. Consequently, the conjugated solute localized near the boundary of the inkjet-printed deposits. The coffee-ring effect is typically minimized by using a mixture of high- and low-boiling-point solvents with different surface tension energies, which reduces the rate of evaporation at the boundary of the liquid deposit. Alternatively, increasing the substrate temperature also reduces the coffee-ring effect [15,16]. Lim et al. used the solvent-mixture approach to improve the performance and uniformity of inkjet-printed TIPS-pentacene OFETs [13]. However, this method was effective only for transistor channels with an abnormal circular geometry and is difficult to apply for poor solubility molecules to various organic solvents. Indeed organic semiconductors typically have poor solubility in low-surface-tension solvents.

Here, we report highly uniform OFETs that were inkjet-printed with an n-channel small molecular semiconductor, *N*,*N*′-bis(*n*-octyl)-(1,7&1,6)-dicyanoperylene-3,4:9,10-bis(dicarboximide) (PDI8-CN_2). The performance and uniformity were improved by inkjet-printing a PDI8-CN_2 solution onto a substrate that had been heated to 60 °C to enhance solvent evaporation. The printed features were changed from a discontinuous film composed of crystals of PDI8-CN_2 at room temperature (25 °C) to a uniform film as a result of heating the substrate. Optimized n-channel PDI8-CN_2 OFETs with a bottom-gate/bottom-contact (TG/BC) device configuration showed a reasonably high μ_{FET} of 0.05–0.06 cm^2/Vs with a gold source and drain electrode and a high uniformity within 10%. In addition, inkjet-printed organic complementary inverters were constructed by direct inkjet-printing of n-channel (PDI8-CN_2) and p-channel {small molecule (TIPS-pentacene) or polymer (poly(3-hexylthiophene), P3HT} organic semiconductors onto silicon dioxide gate dielectrics. The inkjet-printed organic complementary inverters using PDI8-CN_2 and P3HT showed a high voltage gain of more than 15 and small standard deviation of inverting voltage and gain of ±0.95 V and ±0.56, respectively, for measuring 12 samples from four difference batches.

2. Experimental

The soluble n-channel organic semiconducting material, PDI8-CN_2 (Polyera, ActivInk N1200), was used as received. The chemical structure of PDI8-CN_2 is shown in Fig. 1. The PDI8-CN_2 was dissolved in anhydrous chlorobenzene (CB) and 1,2-dichlorobenzene (DCB) to obtain a concentration of ca. 2–5 mg/ml, and the solution was filtered using a 0.2 μm PTFE syringe filter. By using a piezoelectric-type inkjet head (50 μm orifice diameter, Microfab, Inc.), uniformly sized droplets of the PDI8-CN_2 solution were made by controlling the voltage pulses at an operating frequency of 1 kHz. The formation of inkjet droplets was verified using a built-in CCD camera. Silicon wafers with a 300 nm-thick thermal oxide layer were used as substrates after cleaning in an ultrasonic bath using a series of solvents: de-ionized water, acetone, and isopropanol for 10 min each. The gold/nickel (Au/Ni) patterns for the source and drain (S/D) electrodes (Ni, adhesion layer) were fabricated using a conventional lift-off photolithography technique. The PDI8-CN_2 solutions were inkjet-printed onto the as-cleaned substrate at a temperature of 25, 40, 50, 60, or 70 °C in air. The substrate temperature (T_s) means the temperature of SiO_2 surface measured by a digitalized thermo-couple type thermometer. The inkjet-printed PDI8-CN_2 films were annealed at 110 °C for 20 min in a nitrogen-filled glove box with low oxygen and moisture levels (<5 ppm) to remove any residual

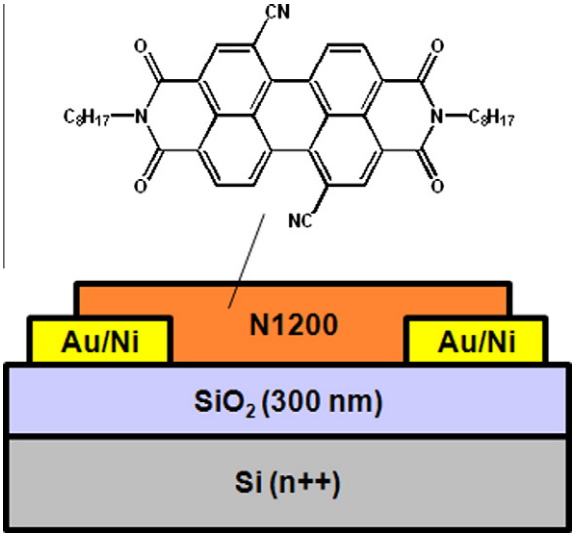

Fig. 1. Molecular structure of PDI8-CN_2 and a schematic diagram of a bottom-gate/ bottom-contact organic field-effect transistor.

solvent and obtain an ordered crystalline morphology, which were verified by optical microscopy. The electrical characteristics were measured using a Keithley 4200-SCS in a nitrogen-filled glove box. The transistor parameters, such as the μ_{FET} and threshold voltage (V_{Th}) were calculated in the saturation regime using the standard formula for FETs.

3. Results and discussion

The formation of stable and uniform droplets with no satellite drops is the first step in the fabrication of OFETs by inkjet-printing. Fig. 2a shows captured images of PDI8-CN_2 droplets with chlorobenzene (CB) solvent at propagation delay times of 80 μs. The diameter, volume, and velocity of the PDI8-CN_2 droplets were measured as ca. 30–35 μm, 15–20 pl and 3.0–3.6 m/s, respectively. It is worth noting that selection of the appropriate PDI8-CN_2 solvent for use in inkjet-printing is the key to obtaining uniform printed features. PDI8-CN_2 showed good solubility in chloroform, which is not a suitable solvent for inkjet-printing due to its very low boiling point (BP) (61 °C). PDI8-CN_2 dissolved in high BP solvents, such as CB or 1,2-dichlorobenzene (DCB) at a low concentration (2–5 mg/ml). As shown in Fig. 2b, when a high BP and high surface tension energy solvent (DCB, BP = 161 °C, surface tension = 33.6 mN/m at 20 °C) was used, the crystalline feature of the printed single drops were well defined. Although the printed single drops using DCB appeared to have a crystalline domain with, typical crystal sizes (on average a few μm in diameter) were not large enough to permit their direct use as the active channel area. The typical channel length of the OFETs in the present study was ca. 2–20 μm. Therefore, uniform single lines, or overlapped inkjet-printed lines, are more desirable for complete interconnectivity between the S/D electrodes. Multi-drop inkjet-printing of the PDI8-CN_2 DCB solution at T_s = 25 °C created stacked single crystals with diameters of a few μm (Fig. 2c). It was very interesting that the organic single crystals formed immediately after dropping the PDI8-CN_2 solution onto the SiO_2/Si(n+) substrate. Presumably this happened because of the slow evaporation rate of the solvent and because the solubility of PDI8-CN_2 in DCB is only marginal (up to ca. 2 mg/ml). The PDI8-CN_2 single crystals are expected to show excellent performance in n-channel OFETs with high μ_{FET}. Although we are investigating inkjet-printed single crystalline PDI8-CN_2 FETs using DCB solvent, currently it is difficult to use the individual crystals as an active layer of OFETs, because sizes of single crystals are a relatively smaller than channel length. Therefore, we changed DCB to CB solvent providing more uniform and continuous PDI8-CN_2 films due to a relatively lower BP (131–132 °C) and better solubility.

Continuous and uniform inkjet-printed PDI8-CN_2 lines and films were obtained by using CB solvent Fig. 2d on a heated substrate (T_s = 40–70 °C). Fig. 3a and b show the typical output and transfer characteristics of an inkjet-printed PDI8-CN_2 OFET with a Au S/D electrode (channel width/length = 1 mm/20 μm). The transistor parameters, such as the μ_{FET} and the threshold voltage (V_{Th}), were calculated in the saturation or linear regime using the standard formula for FETs [17]. The best device, which was constructed using a substrate heated to 60 °C and no

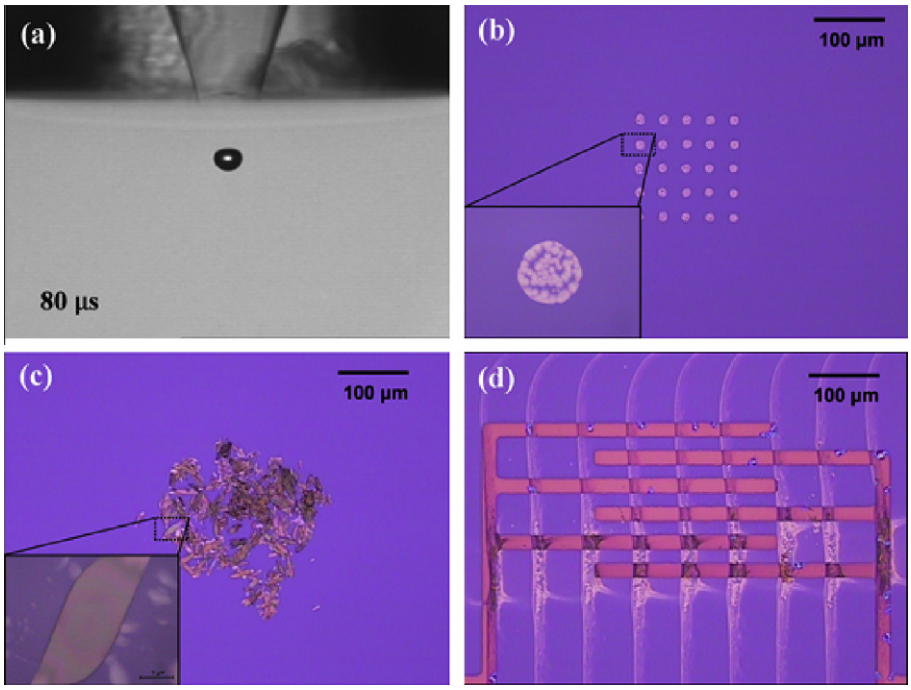

Fig. 2. (a) High-speed CCD camera images of inkjet droplet formation at a delay time (τ_d) of 80 μs for solution of PDI8-CN_2 in CB. Optical microscopy images of PDI8-CN_2 film inkjet-printed on a SiO_2/Si(n+) substrate at room temperture (RT = 25 °C) or 60 °C. (b) A single drop of PDI8-CN_2 in DCB at RT, (c) multi-drop printing of PDI8-CN_2 in DCB at RT, and (d) line printing of PDI8-CN_2 in CB at 60 °C. Inset shows magnified images of selected parts of the figures.

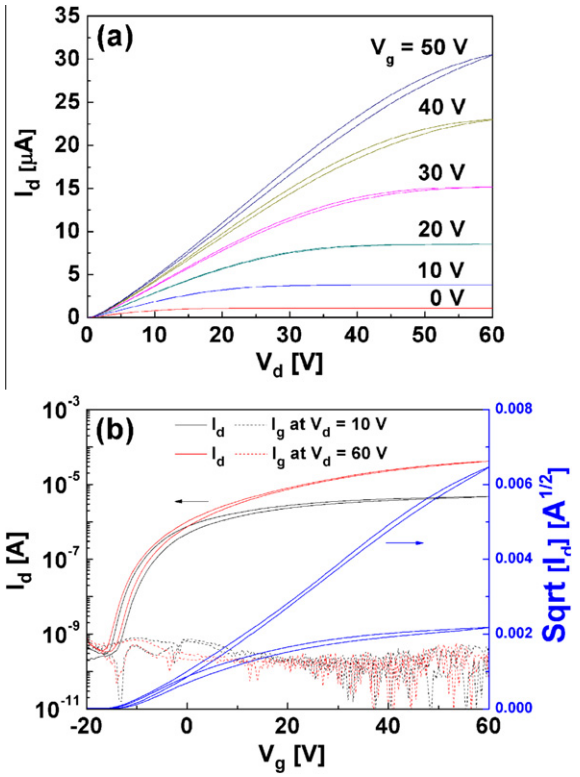

Fig. 3. (a) Output and (b) transfer characteristics of inkjet-printed PDI8-CN_2 transistors (W/L = 1 mm/20 μm). PDI8-CN_2 films were printed with CB solvent at T_s = 60 °C.

hydrophobic surface treatment, showed a high saturation μ_{FET} of 0.05–0.06 cm^2/Vs and a high on/off-current ratio of ~10^6. The device parameters are summarized in Table 1. The transfer curve showed a small bias hysteresis between forward and backward sweep which may be resulted from trapping of electrons in hydroxyl groups of SiO_2 surface and polycrystalline morphology of printed PDI8-CN_2 films. The gate leakage current was a few orders of magnitude smaller than unpatterned spin-coated devices due to patterned PDI8-CN_2 films by ink-jet printing.

In bottom-gate/bottom-contact (BG/BC) OFETs, the charge injection is highly dependent on the contact resistance (R_c), which includes the injection resistance of the charge (R_{inj}) at the metal–semiconductor interface and the bulk resistance (R_{bulk}) of the semiconductor [18]. R_{inj} is a function of the injection barrier height, which is primarily determined by the difference between the work-function of the injecting metal and the electron affinity/ionization potential of the semiconductor. R_{bulk} is largely determined by the local conductivity of the organic semiconducting film at the metal–semiconductor interface [4,19]. Therefore, the slightly reduced performance of a BG/BC device is mainly due to both the large electron injection barrier height (~0.7 eV) between work-function of gold electrode and lowest unoccupied molecular orbital (LUMO) energetic level of PDI8-CN_2 and the smaller charge injection area of a coplanar OFET compared with that of a staggered configuration. The slight deviation from linear for the BG/BC PDI8-CN_2 OFETs in the typically linear region of the output characteristics indicates a large R_c (Fig. 3a). Device performance can be improved by insertion of a specific self-assembly monolayer, which decreases the work-function of the injection electrode [20,21].

Fig. 4a shows the plot of μ_{FET} versus channel length (L) at various substrate temperatures (T_s) between 40 and 70 °C. All devices showed better μ_{FET} at the devices with L > 10 μm than devices with L < 10 μm due to the aforementioned decrease in the R_c between charge injection

Table 1
Device parameters of the inkjet-printed OFET at various substrate temperatures (T_s). The field-effect mobilities were calculated in the saturation region (drain voltage = ±60 V) using a standard device formula [5].

Active (device)	L (μm)	Mobility (cm_2/Vs)	Threshold voltage (V)	On/off ratio	Subthreshold swing (V/dec.)
PDI8-CN_2	20	0.025	−4.0	~10^5	2.1
T_s = 40 °C		(±0.015)	(±0.4)		(±0.6)
	10	0.019	−3.6	~10^5	2.8
		(±0.011)	(±0.9)		(±0.5)
PDI8-CN_2	20	0.050	−2.0	~5 × 10^5	1.6
T_s = 50 °C		(±0.004)	(±1.4)		(±0.5)
	10	0.040	−2.2	~5 × 10^5	1.8
		(±0.005)	(±0.4)		(±0.3)
PDI8-CN_2	20	0.055	−3.4	~5 × 10^5	1.5
T_s = 60 °C		(±0.003)	(±1.6)		(±0.5)
	10	0.056	−1.4	~10^6	1.3
		(±0.002)	(±0.6)		(±0.6)
PDI8-CN_2	20	0.041	−7.0	~10^5	1.9
T_s = 70 °C		(±0.005)	(±0.4)		(±0.6)
	10	0.045	−5.0	~10^5	2.0
		(±0.005)	(±1.2)		(±0.4)
TIPS-Pent.	20	0.007	−21.1	~5x10^4	−4.6
T_s = 60 °C		(±0.004)	(±2.3)		(±1.2)
P3HT	20	1.3 × 10–3	−10.9	~5x10^4	−2.1
T_s = RT		(±0.001)	(±1.1)		(±0.9)

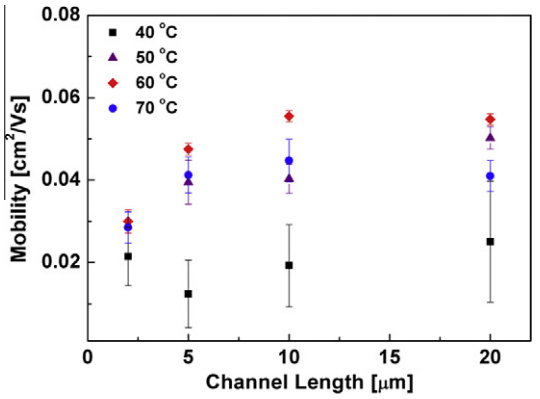

Fig. 4. Field-effect mobility versus channel length at various substrate temperatures.

electrode and PDI8-CN_2. The relationship between the resistances of a FET and L is given by;

$$R_{on}(L) = R_{ch}(L) + R_p = \frac{L}{W\mu Ci(V_G - V_T)} + R_p \quad (1)$$

where R_{on}, R_{ch}, and R_p are the total, channel, and parasitic resistance of a transistor, respectively. W is the channel width, C_i is the gate capacitance per unit area. The parasitic resistance (R_p), which is mainly composed of R_c, exceeds R_{ch} and dominates R_{on} when L is small. Therefore, PDI8-CN_2 transistors showed inferior μ_{FET} when $L < 5$ μm. The threshold at which L has a significant impact on R_c is between 5 and 10 μm. The best PDI8-CN_2 device, which was achieved at $T_s = 60$ °C, showed very high performance uniformity with only a 10% deviation from the average μ_{FET} obtained for 50 measured devices with four different substrates and showed 100% yield. Although printed PDI8-CN_2 lines showed the coffee-ring effect at $T_s = 60$ °C as shown in Fig. 2d, devices showed very uniform characteristics since charges mainly transport through one and two monolayers placed at embedded semiconductor-SiO_2 dielectric interface not uneven top surfaces of printed films. The high performance uniformity might be attributed to the uniform printed features at the high T_s. By contrast, devices with an active layer that was inkjet-printed at low T_s showed a lower μ_{FET} with a large deviation in performance uniformity due to the inhomogeneous drying of the liquid droplets. The low rate of solvent evaporation resulted in the formation of micro-sized crystals (Fig. 2b). However,

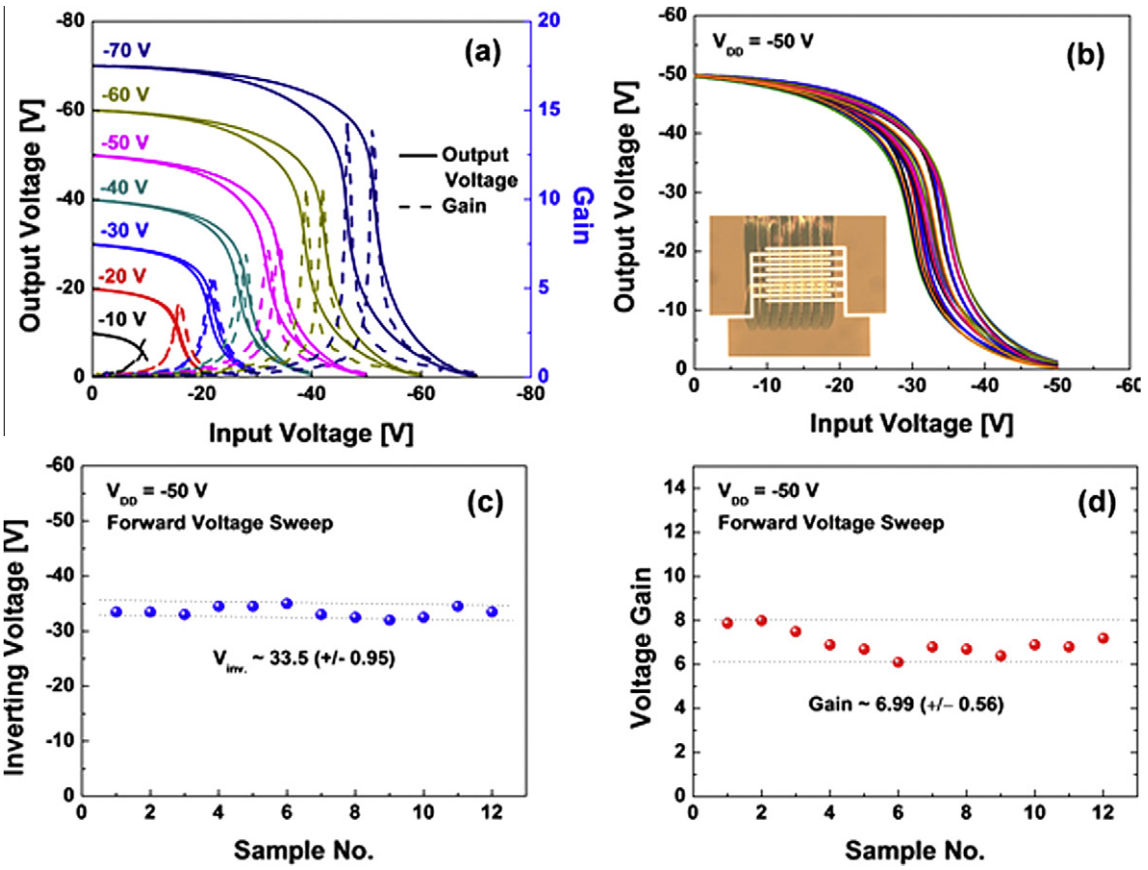

Fig. 5. Complementary organic inverter characteristics using the inkjet-printed PDI8-CN_2 and P3HT [SiO_2 300 nm, $L = 20$ μm, $W_n/W_p = 1$ mm/10 mm]. PDI8-CN_2 and P3HT were inkjet-printed at $T_s = 60$ °C and RT, respectively. (a) Voltage transfer characteristics (VTC) curves at various supplied voltages (V_{DD}) from −10 V to −70 V. Statistical characteristics of the organic inverters, (b) VTC curves [inset: optical microscope image of inkjet-printed P3HT film feature], (c) inverting voltages, and (d) voltage gains at the $V_{DD} = -50$ V during forward voltage scan.

device performance did not increase further when higher T_s were used (>70 °C), because too rapid evaporation of the solvent caused poor crystallinity in the semiconducting film.

The PDI8-CN_2 FETs were incorporated with different types of p-channel semiconductors {soluble small molecule (TIPS-pentacene) or polymer (P3HT)} into complementary inverters. TIPS-pentacene and P3HT were used as-received and were dissolved in anhydrous toluene (10 mg/ml) and CB (5 mg/ml), respectively. TIPS-pentacene and P3HT solutions were inkjet-printed onto a clean SiO_2/Si(n++) substrate at T_s = 60 °C and RT, respectively, followed by a thermal annealing at 110 °C for 20 min in N_2. The TIPS-pentacene transistors (0.005–0.01 cm^2/Vs) typically showed a higher μ_{FET} and better balanced performance with PDI8-CN_2 than those of P3HT (ca. 1×10^{-3} cm^2/Vs). The TIPS-pentacene/PDI8-CN_2 inverters showed a high voltage gain as high as 30 and had the inverting voltage (V_{int}) near half point of the supplied voltage (½V_{DD}) (not shown here) after adjustment of W/L ratio to 5:1 for those p- and n-type transistors. However, it was observed that the relatively large standard deviation of the V_{int} (±1.9 V) and voltage gains (±4.78) was induced mainly from TIPS-pentacene OFETs, which showed a large bias hysteresis and μ_{FET} and V_{Th} fluctuation presumably due to less optimized film morphology of the inkjet-printed p-type small molecular semiconductor.

Statistical characteristics and its standard deviation of the inkjet-printed organic complementary inverters can be improved by using p-channel polymer semiconductors, since polymer semiconductors typically exhibited better device-to-device printed-film uniformity (see inset in Fig. 5b) than those of small molecules. Inkjet-printed P3HT OFETs showed lower μ_{FET} (ca. 1.3×10^{-3} cm^2/Vs) than TIPS-pentacene, as shown in Fig. 5a, so that voltage transfer characteristics curve of the PDI8-CN_2/P3HT inverters still shifted from ½V_{DD} in the negative direction even after adjustment of W/L ratio of p-type and n-type transistors up to 10:1. The voltage gain was up to 15 by proportional to increase in the V_{DD}. Statistical characteristics of complementary inverters exhibited much improved by reduction of standard variation of the p-channel transistor properties. PDI8-CN_2/P3HT CMOS inverters showed average inverting voltage ($V_{inv.}$) and voltage gains of −33.5 V and 6.99 with the small standard deviation of ±0.95 V and ±0.56, respectively, for measuring 12 samples from four difference batches. Consequently, this inkjet-printed n-type OFETs can be utilized in a variety of organic electronic applications, such as drivers for display backplanes, digital or analog circuits in printed RFID tag, organic memory, and sensors [22–26].

4. Conclusion

In conclusion, we have demonstrated high performance inkjet-printed n-type organic transistors and their complementary inverters. The device performance and uniformity were improved by inkjet-printing a PDI8-CN_2 solution onto a heated substrate (60 °C) and by selection of the optimal organic solvent (CB). The inkjet-printed features, which were initially discontinuous crystalline domains at RT, were converted to continuous films when the substrate temperature was increased to 60 °C. When we measured more than 50 n-type OFETs, those devices showed highly uniform μ_{FET} and V_{Th} within 10% standard deviation. The optimized n-channel PDI8-CN_2 FETs were integrated into inkjet-printed organic complementary inverters in combination with TIPS-pentacene or P3HT OFETs. The inkjet-printed PDI8-CN2/P3HT inverters exhibited a high voltage gain of more than 15 and small standard deviation of inverting voltage and gain of ±0.95 V and ±0.56, respectively, for measuring 12 samples from four difference batches.

Acknowledgements

This research was financially supported by following: Development of Next Generation RFID Technology for item-level applications (2008-F052-01) funded by The Ministry of Knowledge Economy (MKE) of Korea; the 2nd stage Brain Korea 21 (BK21) program funded by The Ministry of Education, Science and Technology (MEST) of Korea; Development of New Materials and Solution Processes for LCD Backplanes funded by ISTK; the Regional Innovation Center for Industrialization of Advanced Chemical Materials (TIC04-05-42, Hanbat National Univ.); Development of printing ink for touch panel and OLED lighting funded by The Ministry of Knowledge Economy (MKE) and Daedeok innopolis (A2010D-D006); Basic Science Research Program through the National Research Foundation of Korea (NRF) funded by The Ministry of Education, Science and Technology (2010-0023180).

References

[1] H. Klauk, U. Zschieschang, J. Pflaum, M. Halik, Ultralow-power organic complementary circuits, Nature 445 (2007) 745.
[2] S.K. Park, T.N. Jackson, J.E. Anthony, D.A. Mourey, High mobility solution processed 6, 13-bis (triisopropyl-silylethynyl) pentacene organic thin film transistors, Appl. Phys. Lett. 91 (2007) 063514.
[3] T.N. Ng, S. Sambandan, R. Lujan, A.C. Arias, C.R. Newman, H. Yan, A. Facchetti, Electrical stability of inkjet-patterned organic complementary inverters measured in ambient conditions, Appl. Phys. Lett. 94 (2009) 233307.
[4] Y.-Y. Noh, N. Zhao, M. Caironi, H. Sirringhaus, Downscaling of self-aligned, all-printed polymer thin-film transistors, Nat. Nanotechnol. 2 (2007) 784.
[5] K.-J. Baeg, D. Khim, D.-Y. Kim, S.-W. Jung, J.B. Koo, I.-K. You, H. Yan, A. Facchetti, Y.-Y. Noh, High speeds complementary integrated circuits fabricated with all-printed polymeric semiconductors, J. Poly. Sci. Part B: Poly. Phys. 49 (2011) 62.
[6] H. Yan, Z. Chen, Y. Zheng, C. Newman, J.R. Quinn, F. Dotz, M. Kastler, A. Facchetti, A high-mobility electron-transporting polymer for printed transistors, Nature 457 (2009) 679.
[7] B.S. Ong, Y.L. Wu, P. Liu, S. Gardner, High-performance semiconducting polythiophenes for organic thin-film transistors, J. Am. Chem. Soc. 126 (2004) 3378.
[8] M. Heeney, C. Bailey, K. Genevicius, M. Shkunov, D. Sparrowe, S. Tierney, I. McCulloch, Stable polythiophene semiconductors incorporating thieno[2,3-b]thiophene, J. Am. Chem. Soc. 127 (2005) 1078.
[9] I. McCulloch, M. Heeney, C. Bailey, K. Genevicius, I. Macdonald, M. Shkunov, D. Sparrowe, S. Tierney, R. Wagner, W.M. Zhang, M.L. Chabinyc, R.J. Kline, M.D. McGehee, M.F. Toney, Liquid-crystalline semiconducting polymers with high charge-carrier mobility, Nat. Mater. 5 (2006) 328.
[10] B. Lim, K.-J. Baeg, H.-G. Jeong, J. Jo, H. Kim, J.-W. Park, Y.-Y. Noh, D. Vak, J.-H. Park, J.-W. Park, D.-Y. Kim, A new poly (thienylenevinylene) derivative with high mobility and oxidative

stability for organic thin-film transistors and solar cells, Adv. Mater. 21 (2009) 2808.
[11] M. Caironi, C. Newman, J.R. Moore, D. Natali, H. Yan, A. Facchetti, H. Sirringhaus, Efficient charge injection from a high work function metal in high mobility n-type polymer field-effect transistors, Appl. Phys. Lett. 96 (2010) 183303.
[12] S. Seki, M. Uchida, T. Sonoyama, M. Ito, S. Watanabe, S. Sakai, S. Miyashita, Current status of printing OLEDs, SID Symp. Dig. 40 (2009) 593.
[13] J.A. Lim, W.H. Lee, H.S. Lee, J.H. Lee, Y.D. Park, K. Cho, Self-organization of ink-jet-printed triisopropylsilylethynyl pentacene via evaporation-induced flows in a drying droplet, Adv. Funct. Mater. 18 (2008) 159.
[14] J. Perelaer, P.J. Smith, E. Van den Bosch, S.S.C. van Grootel, P.H.J.M. Ketelaars, U.S. Schubert, The spreading of inkjet-printed droplets with varying polymer molar mass on a dry solid substrate, Macromol. Chem. Phys. 210 (2009) 495.
[15] E. Tekin, B.-J. de Gans, U.S. Schubert, Ink-jet Printing and Microwave Sintering of Conductive Silver Tracks, Adv. Mater. 18 (2006) 2101.
[16] H. Hu, R.G. Larson, Marangoni effect reverses coffee-ring depositions, J. Phys. Chem. B 110 (2006) 7090.
[17] S.M. Sze, Physics of Semiconductor Devices, Wiley, New York, USA, 1981.
[18] A. Hoppe, D. Knipp, B. Gburek, A. Benor, M. Marinkovic, W. Wagner, Scaling limits of organic thin film transistors, Org. Electron. 11 (2010) 626–631.
[19] T.J. Richards, H. Sirringhaus, Analysis of the contact resistance in staggered, top-gate organic field-effect transistors, J. Appl. Phys. 102 (2007) 094510.
[20] B. de Boer, A. Hadipour, M.M. Mandoc, T. van Woudenbergh, P.W.M. Bolm, Tuning of metal work functions with self-assembled monolayers, Adv. Mater. 17 (2005) 621.
[21] X. Cheng, Y.-Y. Noh, J. Wang, M. Tello, J. Frisch, R.-P. Blum, A. Vollmer, J.P. Rabe, N. Koch, H. Sirringhaus, Controlling electron and hole charge injection in ambipolar organic field-effect transistors by self-assembled monolayers, Adv. Funct. Mater. 19 (2009) 2407.
[22] K.-J. Baeg, Y.-Y. Noh, J. Ghim, S.-J. Kang, H. Lee, D.-Y. Kim, Organic non-volatile memory based on pentacene field-effect transistors using polymeric gate electret, Adv. Mater. 18 (2006) 3179.
[23] K.-J. Baeg, Y.-Y. Noh, J. Ghim, B. Lim, D.-Y. Kim, Polarity effects of polymer gate electrets on non-volatile organic field-effect transistor memory, Adv. Funct. Mater. 18 (2008) 3678.
[24] H. Marien, M. Steyaert, E. van Veenendaal, P. Heremans, Analog techniques for reliable organic circuit design on foil applied to an 18 dB single-stage differential amplifier, Org. Electron. 11 (2010) 1357–1362.
[25] K.-J. Baeg, Y.-Y. Noh, H. Sirringhaus, D.-Y. Kim, Controllable shifts in threshold voltage of top-gate polymer field-effect transistors for applications in organic nano floating gate memory, Adv. Funct. Mater. 20 (2010) 224.
[26] G. Gelinck, P. Heremans, K. Nomoto, T.D. Anthopoulos, Organic transistors in optical displays and microelectronic applications, Adv. Mater. (2010) 3778–3798.

Organic Electronics 12 (2011) 641–647

Contents lists available at ScienceDirect

Organic Electronics

journal homepage: www.elsevier.com/locate/orgel

Enhanced performances of hybrid polymer solar cells with *p*-methoxybenzoic acid modified zinc oxide nanoparticles as an electron acceptor

Shuyan Shao, Fengmin Liu, Gang Fang, Baohua Zhang, Zhiyuan Xie *, Lixiang Wang

State Key Laboratory of Polymer Physics and Chemistry, Changchun Institute of Applied Chemistry, Graduate School of Chinese Academy of Sciences, Chinese Academy of Sciences, Changchun 130022, PR China

ARTICLE INFO

Article history:
Received 13 October 2010
Received in revised form 7 January 2011
Accepted 12 January 2011
Available online 3 February 2011

Keywords:
Hybrid polymer solar cell
Surface modification
p-Methoxybenzoic acid
Zinc oxide nanocrystal

ABSTRACT

Enhanced performances of hybrid polymer solar cells based on a blend of poly[2-methoxy-5-(2′-ethyl-hexyloxy)-1,4-phenylene vinylene] (MEH-PPV) and *p*-methoxybenzoic acid (MBA) modified zinc oxide (ZnO) nanoparticles were reported. Both the short-circuit current and open-circuit voltage of solar cells were improved by using MBA modified ZnO nanoparticles as electron acceptor. The overall power conversion efficiency was increased from 1.09% to 1.52% under AM 1.5 G 100 mW/cm^2 illumination after ZnO was modified with MBA at 0.1 wt.%. It was found that modification of ZnO with 0.1 wt.% of MBA did not affect electron and hole transport properties of the active layer. However, a fine phase separation between MEH-PPV donor and MBA-modified ZnO acceptor was obtained. The fine phase separation enhanced the exciton dissociation efficiency and hence the power conversion efficiency of solar cells.

© 2011 Elsevier B.V. All rights reserved.

1. Introduction

Hybrid solar cells using conjugated polymers as electron donors and inorganic semiconductor nanocrystals as electron acceptors have attracted a lot of attention in recent years due to the combined merits of both materials: solution processability of conjugated polymers, high electron mobility and low-cost fabrication of inorganic semiconductor nanocrystals. By far, several kinds of hybrid polymer solar cells have been reported using CdSe [1–5], CdS [6], TiO_2 [7–12] and ZnO nanocrystals [13–17] as electron acceptors. Efficient hybrid solar cells with power conversion efficiency (PCE) over 2% have been obtained by using CdSe and TiO_2 nanocrystals as electron acceptors [5,9]. However, CdSe nanocrystal has high toxicity and TiO_2 nanocrystal has high crystallization temperature. ZnO nanocrystal is a more promising candidate for electron acceptor due to its non-toxicity and low crystallization temperature properties.

Because of short exciton diffusion length (less than 10 nm) in semiconducting polymers, only excitons generated within 10–20 nm distance from the donor/acceptor interface can diffuse to the interface and dissociate into free carriers [18–20]. Therefore, a bulk heterojunction structure with nanoscale donor–acceptor phase separation is required to realize efficient exciton dissociation [21]. The main challenge for hybrid polymer solar cells is the large phase separation between polymer donors and inorganic semiconductor acceptors due to the high surface polarity of inorganic nanocrystals [22,23]. Studies have been done to achieve hydrophobic surfaces of inorganic semiconductor nanocrystals via surface modification with conductive ligands to reduce the polymer/inorganic nanocrystal phase separation in hybrid polymer solar cells [24,25]. However, few result has been reported on simultaneously reducing the phase separation and enhancing the PCE of ZnO-based hybrid polymer solar cell. Ravirajan et al. reported enhanced charge separation yield in hybrid polymer solar cell

* Corresponding author.
E-mail address: xiezy_n@ciac.jl.cn (Z. Xie).

1566-1199/$ - see front matter © 2011 Elsevier B.V. All rights reserved.
doi:10.1016/j.orgel.2011.01.011

based on poly(3-hexylthiophene) (P3HT) and amphiphilic ruthenium complex (Z907) modified ZnO nanorods, whereas the PCE of the cell was only 0.2% [26]. Said et al. reported recently a hybrid solar cell based on P3HT and porphyrin-modified ZnO nanorods in which the phase separation between P3HT and ZnO nanorods was increased, the short-circuit current (J_{sc}) and PCE were reduced [27].

In this work, we report enhanced performances of hybrid polymer solar cells using poly[2-methoxy-5-(2′-ethyl-hexyloxy)-1,4-phenylene vinylene] (MEH-PPV) as donor and *p*-methoxybenzoic acid (MBA) modified ZnO nanoparticles as acceptor. MBA was selected as the ZnO surface modifier because its small size may not influence the charge transport between ZnO nanocrystals. Moreover, the MBA may possess good compatibility with MEH-PPV since both of them have alkoxy groups. Compared to the control solar cell based on MEH-PPV: as-prepared ZnO blend, solar cells with MBA-modified ZnO showed improvements on both the J_{sc} and open-circuit voltage (V_{oc}) and the resulted 50% increasing on PCE. The effect of MBA modification on the film morphologies and the charge transport properties of the MEH-PPV:ZnO composite film was discussed in detail.

2. Experimental section

The MEH-PPV (Fig. 1) was purchased from Canton OLEDKING Optoelectronic Materials Co., Ltd. and used as received. ZnO nanocrystal with a diameter of about 5 nm was prepared according to the literature [16]. Zinc acetate dihydrate (2.95 g, >99%) was dissolved in methanol (120 mL) at 60 °C under vigorous stirring. 1.48 g of KOH (>85%) was dissolved in methanol (60 mL). The KOH solution was dropped into the zinc acetate dihydrate solution in 10 min under vigorous stirring. The solution temperature was held at 60 °C and stirred for 4 h, and then the heating and stirring were removed to allow particles to precipitate for additional 12 h. The precipitate was cleaned by centrifugation of the dispersion and washed twice with 50 mL of methanol. The washed ZnO nanoparticles were dissolved in 5 mL of chlorobenzene and were formed ZnO solution with a concentration of 120 mg mL^{-1}. The surface modification of ZnO was done by adding quantitative MBA into ZnO chlorobenzene solution.

The hybrid polymer solar cells with a structure of indium–tin oxide (ITO) anode/PEDOT:PSS/MEH-PPV:ZnO/Al cathode were prepared as shown in Fig. 1. The ITO-coated glass substrate with a sheet resistance of 10 Ohm/square was cleaned with detergent and deionized water in sequence and then dried at 120 °C for 30 min. The ITO substrate was treated with UV ozone cleaner for 10 min. A 40-nm-thick PEDOT:PSS layer was spin-coated onto the ITO substrate and baked at 120 °C for 30 min in ambient. A solution comprising MEH-PPV and ZnO nanocrystal (with or without MBA modification) with a weight ratio of 1:3.3 in chlorobenzene was spincoated on top of the PEDOT:PSS layer to produce a 100-nm-thick active layer. Finally, the device was completed by depositing a 100 nm Al cathode on top of the active layer in vacuum chamber under a base pressure of 4×10^{-4} Pa. The illuminated current density–voltage (*J–V*) characteristics of the solar cells were tested using a Keithley 236 source meter under AM 1.5 G 100 mW/cm^2 illumination from a calibrated solar simulator filtered with GG420 filter to remove UV irradiation. The external quantum efficiency (EQE) was measured under short-circuit condition with a lock-in amplifier (SR830, Stanford Research System) at a chopping frequency of 280 Hz during illumination with the monochromatic light from a Xenon lamp.

Fourier transformed infrared (FTIR) spectroscopy in absorption mode was recorded with a BRUKER Vertex 70 FTIR spectrometer using pressed KBr tablets. The samples for FTIR analysis were obtained by drying the ZnO nanoparticles just after the washing process (as-prepared ZnO) or surface modification procedure (2% MBA-modified ZnO is used due to the detecting sensitivity of the FTIR spectrometer). Water contact angle test was performed on a DSA10 Control UNIT. Transmission electron microscopy (TEM) of the MEH-PPV:ZnO blend films was conducted on a JEM-1011 transmission electron microscope operated at an acceleration voltage of 100 kV. The samples for TEM observation were obtained by stripping the active layer off the underlying PEDOT:PSS layer and then transferred onto a carbon-coated copper grid. Ultraviolet photo-

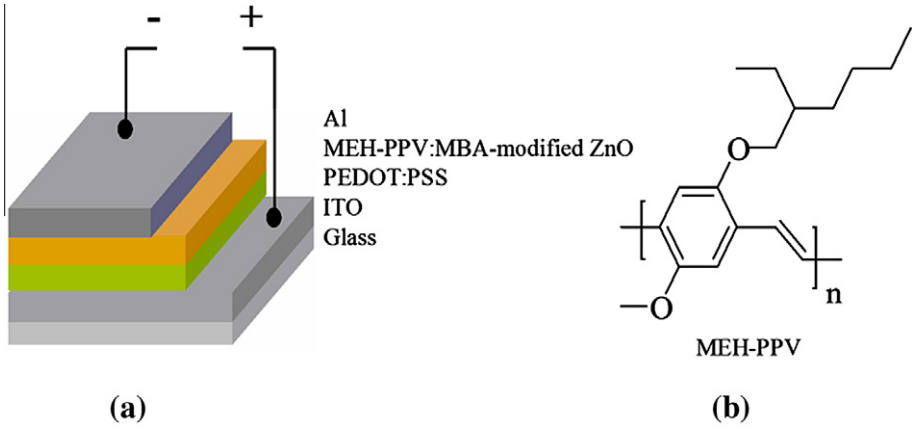

Fig. 1. (a) The device configuration of MEH-PPV:MBA-modified ZnO hybrid solar cell and (b) the chemical structure of MEH-PPV.

electron spectroscopy (UPS) measurement of as-prepared and 0.1% MBA-modified ZnO were performed on Thermo ESCALAB 250 with HeI (21.2 eV) as monochromatic light source. The absorption spectra of as-prepared and 0.1% MBA-modified ZnO were measured using a Perkin–Elmer 35UV–vis spectrophotometer on quartz substrates.

3. Results and discussion

To verify the adsorption of MBA ligand onto the ZnO surface, FTIR spectroscopy of the MBA-modified and as-prepared ZnO samples was recorded in absorption mode. Fig. 2 showed the FTIR spectra of the MBA, as-prepared ZnO and 2% MBA-modified ZnO. The main bands and their assignments for MBA were as follows: stretching vibration of the aromatic ring ν(C=C)/ν(C–C) at 1603 and 1516 cm^{-1}, the symmetric and asymmetric stretch of CO in OCH_3 group ν_s(C–O) at 1261 cm^{-1} and ν_{as}(C–O) at 1027 cm^{-1}, the ν(C=O) stretch in COOH at 1686 cm^{-1}, the bending vibration of CH in aromatic ring γ(C–H) at 845 and 773 cm^{-1}, and the ν(O–H) in COOH at 2500–3000 cm^{-1}. For the as-prepared ZnO sample, the band at 441 cm^{-1} was attributed to the stretching vibration of ZnO. The $\nu_{as}(COO^-)$ at 1582 cm^{-1} and $\nu_s(COO^-)$ at 1416 cm^{-1} were characteristics for a carboxylic group being coordinated to a metal. They were assigned to the acetates adsorbed on ZnO surface. The stretch ν(O–H) at 3420 cm^{-1} was assigned to hydroxyl group of methanol adsorbed on ZnO surface. In the case of the MBA-modified ZnO sample, the stretching vibration of the aromatic ring ν(C=C)/ν(C–C) at 1608 and 1512 cm^{-1}, the ν_s(C–O) and ν_{as}(C–O) of OCH_3 group at 1257 and 1032 cm^{-1}, the γ(C–H) of aromatic ring at 853 and 785 cm^{-1} were observed. However, the characteristic bands of carboxylic group, namely, ν(C=O) stretch at 1686 cm^{-1}, and the wide band located around 2500–3000 cm^{-1} of the ν(O–H) in COOH disappeared. The asymmetric stretch, $\nu_{as}(COO^-)$ at 1561 cm^{-1}, and symmetric stretch, $\nu_s(COO^-)$ at 1421 cm^{-1} were presented, indicating

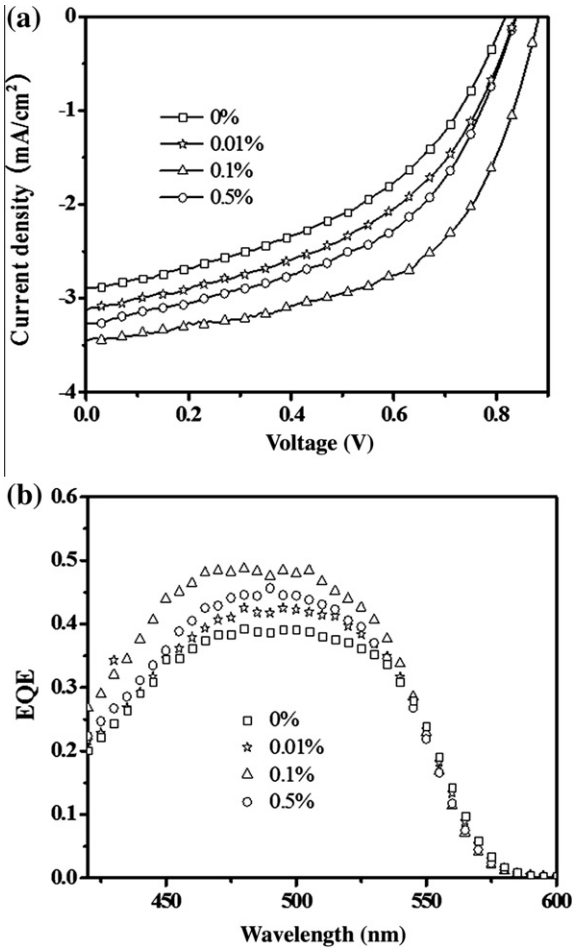

Fig. 3. (a) The illuminated *J–V* characteristics and (b) EQE curves of MEH-PPV:MBA-modified ZnO (1:3.3 in weight ratio) hybrid solar cells with different weight ratios of MBA to ZnO.

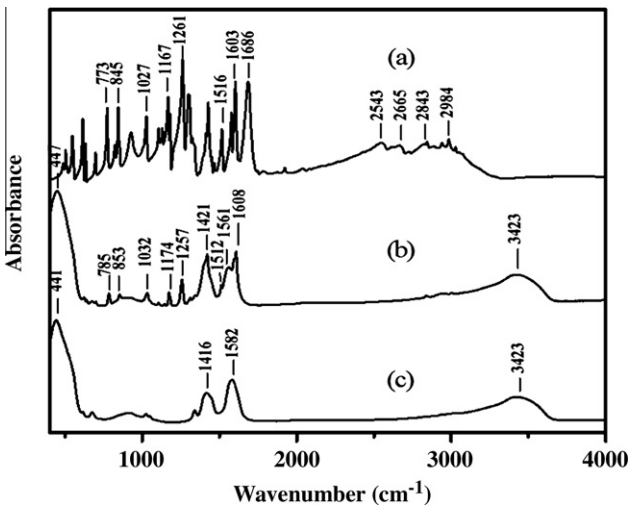

Fig. 2. FTIR spectra of (a) MBA, (b) 2% MBA-modified ZnO nanocrystal and (c) ZnO nanocrystal without modification.

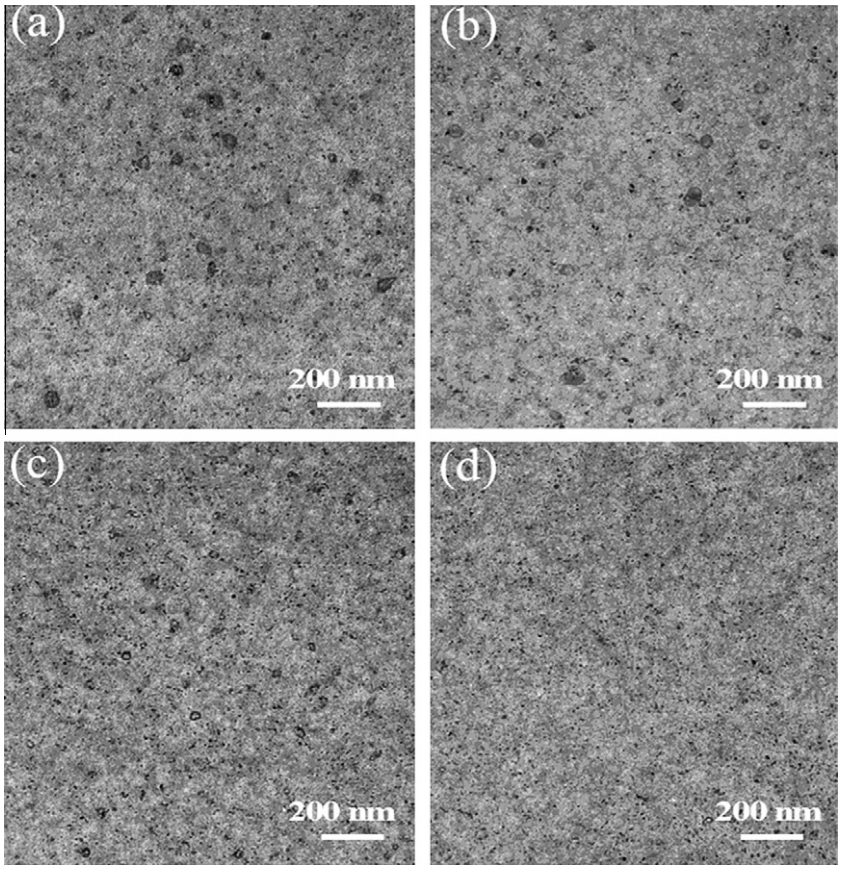

Fig. 4. TEM images of the MEH-PPV:MBA-modified ZnO composite (1:3.3 in weight ratio) films with different weight ratios of MBA to ZnO: (a) 0%, (b) 0.01%, (c) 0.1% and (d) 0.5%.

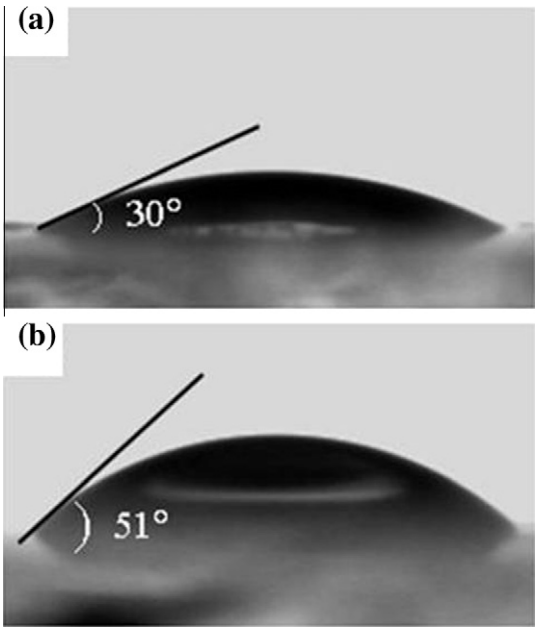

Fig. 5. Water contact angles of (a) non-modified and (b) 0.5% MBA-modified ZnO nanocrystal films.

that the carboxylic group in MBA was coordinated to ZnO nanocrystals and formed carboxylate complexes.

The illuminated *J–V* characteristics of the hybrid polymer solar cells based on MEH-PPV:MBA-modified ZnO composites with different weight ratios of MBA to ZnO (0%, 0.01%, 0.1% and 0.5%) are shown in Fig. 3a. The MEH-PPV: ZnO solar cell shows a V_{OC} of 0.82 V, a J_{SC} of 2.89 mA cm^{-2}, and a fill factor (*FF*) of 0.46, respectively. The overall PCE of this cell is about 1.09%. It is noted that the MEH-PPV:MBA modified ZnO solar cells show enhanced V_{OC}, J_{SC} and *FF* compared to the MEH-PPV: as prepared ZnO control cell. Interestingly, the J_{SC} of the solar cells based on MEH-PPV:MBA-modified ZnO blends increases initially at low content of MBA and then decreases at high content of MBA. The highest J_{SC} of 3.45 mA cm^{-2} is achieved for the MEH-PPV: 0.1 wt.% MBA modified ZnO solar cell. This cell also shows a V_{OC} of 0.88 V and an *FF* of 0.5, leading to a maximum PCE of 1.52%. When the weight percentage of MBA is increased to 0.5%, the J_{SC} of the resulted solar cell drops but the V_{OC} keeps unchanged. The EQE curves of the hybrid solar cells are shown in Fig. 3b. The MEH-PPV:0.1% MBA-modified ZnO solar cell shows a maximum EQE of 49%, much higher than 39% of the MEH-PPV:ZnO solar cell.

To understand the variation in J_{SC}, the effect of MBA surface modification of ZnO on the morphology of

MEH-PPV:ZnO composites was studied. TEM images of the MEH-PPV:MBA-modified ZnO composite films with various weight ratios of MBA to ZnO are shown in Fig. 4. The dark regions in the images are assigned to ZnO-rich domains and the bright regions are assigned to MEH-PPV-rich domains based on larger mass density of ZnO nanocrystal than that of MEH-PPV. It can be seen that the MEH-PPV:MBA-modified ZnO composite films show smaller ZnO aggregates than those in the MEH-PPV:ZnO composite film. It may be attributed to reduced surface polarity of ZnO nanocrystals by MBA modification. This is also supported by the water contact angle results of the as-prepared and 0.5 wt.% MBA-modified ZnO films as shown in Fig. 5. It can be seen that the water contact angle of ZnO nanocrystal film is increased from 30° to 51° after MBA surface modification. The result demonstrates that a more hydrophobic ZnO surface has formed. As mentioned before that the exciton diffusion length in conjugated polymers is merely about 10 nm, the fine phase separation between the MEH-PPV donor and ZnO acceptor is favorable for efficient exciton dissociation and for enhancement of J_{SC}. Thus, it is understandable that the MEH-PPV:0.01 wt.% MBA-modified ZnO solar cell only shows a slightly increased J_{SC} due to insignificant improvement of the MEH-PPV:ZnO composite morphology. The maximum J_{SC} is obtained in the MEH-PPV:0.1 wt.% MBA-modified ZnO solar cell, although the MEH-PPV:0.5% MBA-modified ZnO composite film demonstrates a more uniform phase separation at nanoscale.

To gain further insight into the variation in J_{SC}, the charge transport characteristics in MEH-PPV:ZnO composite films was investigated by single carrier devices. Fig. 6 shows the experimental dark J–V curves of the electron-only and hole-only devices. For electron-only devices, Al

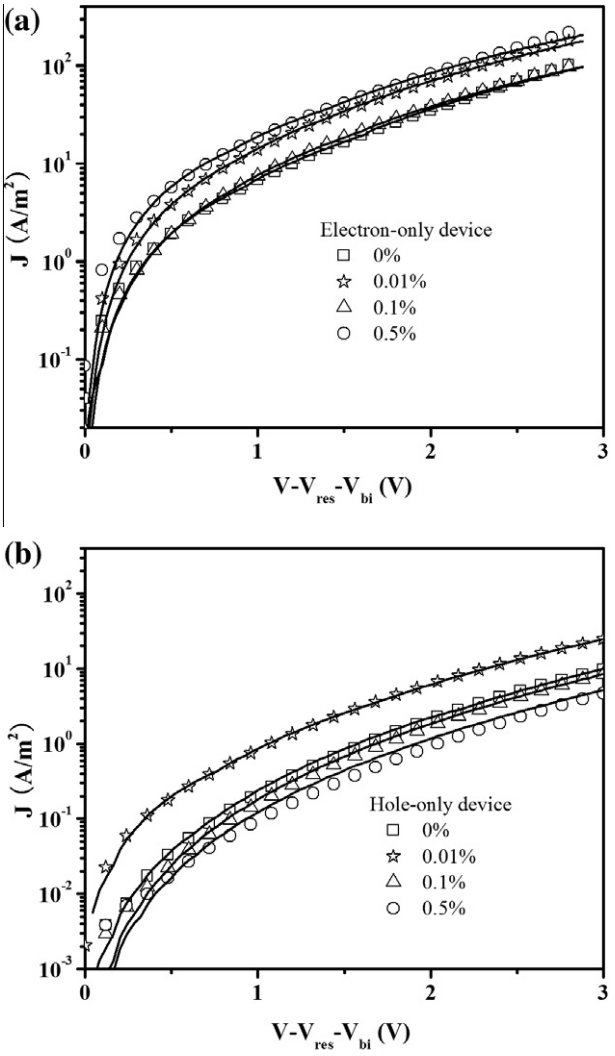

Fig. 6. The dark J–V characteristics, corrected for built-in voltage (V_{bi}) and series resistance (V_{res}), of the electron- and hole-only devices: (a) electron-only devices with a structure of Al/MEH-PPV:ZnO (x_1 nm)/Al, where x_1 equals 210, 165, 210 and 150 nm for devices based on 0%, 0.01%, 0.1% and 0.5% MBA-modified ZnO and (b) hole-only devices with a structure of ITO/PEDOT:PSS/MEH-PPV:ZnO (x_2 nm)/MoO_3/Al, where x_2 equals 170, 150, 170 and 160 nm for devices based on 0%, 0.01%, 0.1% and 0.5% MBA-modified ZnO. The experimental data are fitted (shown by solid lines) with a space–charge-limited current.

was used as bottom electrode to suppress hole injection into the MEH-PPV:ZnO active layer. For hole-only devices, the top cathode Al was replaced by MoO_3/Al to suppress electron injection. The electron and hole mobilities in MEH-PPV:ZnO composite films are calculated by space-charge-limited current (SCLC) in the hole- and electron-only devices [28]:

$$J_{e(h)} = \frac{9}{8}\varepsilon_r\varepsilon_0\mu_0\frac{V^2}{L^3}\exp\left(0.89\beta\sqrt{\frac{V}{L}}\right) \quad (1)$$

where $J_{e(h)}$ is the electron (hole) current density, μ_0 the zero-field mobility of electron (hole), β is the field activation factor, ε_0 is the permittivity of free space, ε_r is the relative permittivity of the material, and L is the thickness of the active layer. The experimental data in Fig. 6 were fitted using Eq. (1) and the results were shown by the solid lines. Electron mobilities of 1.06×10^{-9}, 1.15×10^{-9}, 1.02×10^{-9}, 1.6×10^{-9} $m^2\,V^{-1}\,s^{-1}$ and hole mobilities of 8.7×10^{-11}, 9.2×10^{-11}, 7.2×10^{-11} and 1.9×10^{-11} $m^2\,V^{-1}\,s^{-1}$ were obtained for the MEH-PPV:MBA (0%, 0.01%, 0.1% and 0.5%)-modified ZnO composite films. It was noted that the electron mobility in the MEH-PPV: 0.5 wt.% MBA-modified ZnO composite film was slightly higher than electron mobility in other devices. This was attributed to smaller ZnO aggregates in that composite film, which reduced the distance between ZnO aggregates and led to favorable electron hopping between them. It also indicated that low content of MBA ligands did not hinder the electron transport between ZnO aggregates. The average numbers of MBA molecule attached to each ZnO nanoparticle were calculated to be 0.13, 1.3, 6.5 for 0.01, 0.1 and 0.5 wt.% of MBA, respectively. It corresponded to a coverage of 0.04%, 0.4% and 2% of ZnO surface by MBA molecules, assuming a perpendicular orientation of MBA molecules relative to ZnO surface and an occupied surface area of 0.25 nm^2 [29]. Although electron hopping between ZnO aggregates had not been hindered by MBA ligands, the hole mobility in MEH-PPV:0.5 wt.% MBA-modified ZnO composite film was reduced to about one fifth of that in MEH-PPV: as prepared ZnO composite film. The decreasing of hole mobility may be attributed to the restrained packing of MEH-PPV polymer chains in ZnO dispersed matrix. Hence, it was concluded that the decreased J_{SC} for the solar cell based on MEH-PPV:0.5% MBA-modified ZnO composite film resulted from the decreasing of hole mobility. The highest J_{SC} of the MEH-PPV:0.1 wt.% MBA-modified ZnO solar cell was resulted from a tradeoff between the exciton dissociation and charge collection in MEH-PPV:ZnO composite film.

In addition to the enhanced J_{SC}, the V_{OC}s of the MEH-PPV:MBA-modified ZnO solar cells were also improved compared to the MEH-PPV:ZnO solar cell. In order to clarify the origin of the increased V_{OC}, both absorption and UPS experiments were carried out to determine the effect of MBA modification on ZnO electronic energy levels. The absorption spectra for both ZnO and 0.1% MBA-modified ZnO (the inset of Fig. 7a) showed the same absorption onset at 360 nm, indicating an unchanged band gap of 3.44 eV. The UPS spectra for ZnO and 0.1 wt.% MBA-modified ZnO displayed the same spectrum width of 13.53 eV

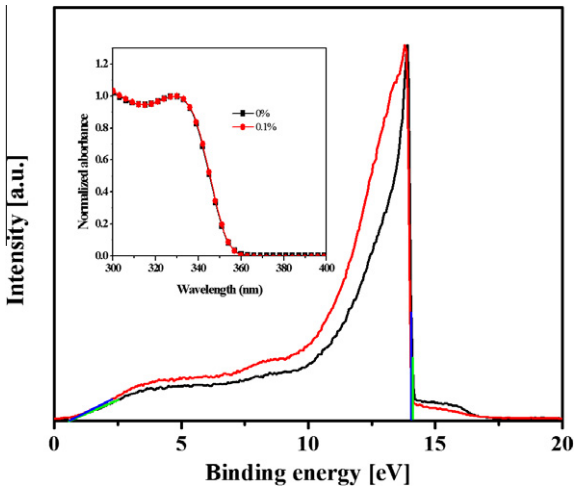

Fig. 7. UPS spectra for ZnO and 0.1% MBA-modified ZnO samples. The inset shows normalized absorption spectra for ZnO and 0.1% MBA-modified ZnO.

(Fig. 7). The same highest occupied molecular orbital (HOMO) of 7.67 eV and the same lowest unoccupied molecular orbital (LUMO) level of 4.23 eV were estimated for ZnO and 0.1% MBA-modified ZnO. Vandewal et al. reported that V_{OC} of polymer-fullerene solar cells scaled linearly with the band gap of charge-transfer state ($E_{eff,g}$, effective bandgap of donor and acceptor blends) which was determined by the difference between the HOMO energy level of donor and LUMO energy level of acceptor [30]. They pointed out that $E_{eff,g}$ was influenced by the active layer morphology for a given donor and acceptor blends with constant composition ratio. In our case, the packing of MEH-PPV chains was restrained by improved dispersion of MBA modified ZnO in matrix. The restrained packing of polymer chains may lower the HOMO energy level of MEH-PPV and thus resulted in increasing of V_{OC}.

4. Conclusions

In summary, hybrid polymer solar cells using MBA-modified ZnO nanocrystal as electron acceptor are fabricated. The poor compatibility between MEH-PPV and ZnO is well resolved via ZnO surface modification by MBA. The methoxyl group in MBA molecule renders ZnO surface more hydrophobic that improves the dispersion of ZnO nanocrystals in MEH-PPV matrix. The electron transport between ZnO aggregates is not influenced by MBA surface modification of ZnO, while the hole transport in MEH-PPV domains is reduced with high content of MBA. The highest J_{SC} can be achieved by coordinately optimizing the composite film morphology and charge transport properties. The power conversion efficiency of the hybrid solar cell with MBA-modified ZnO has increased up to 50% compared to solar cell with as-prepared ZnO.

Acknowledgments

The authors acknowledge financial support from the National Natural Science Foundation of China (Nos.

50873100, 20834005 and 20621401) and 973 Project of Ministry of Science and Technology of China (2009CB930603).

References

[1] W.U. Huynh, J.J. Dittmer, A.P. Alivasatos, Science 295 (2002) 2425.
[2] B.Q. Sun, E. Marx, N.C. Greenham, Nano Lett. 3 (2003) 961.
[3] L. Gur, N.A. Fromer, C.P. Chen, A.G. Kanaras, A.P. Alivasatos, Nano Lett. 7 (2007) 409.
[4] S. Dayal, N. Kopidakis, D.C. Olson, D.S. Ginley, G. Rumbles, Nano Lett. 10 (2010) 239.
[5] B.Q. Sun, N.C. Greenham, Phys. Chem. Chem. Phys. 8 (2006) 3557.
[6] L. Wang, Y.S. Liu, X. Jiang, D.H. Qin, Y. Cao, J. Phys. Chem. C 111 (2007) 9538.
[7] Y.Y. Lin, T.H. Chu, S.S. Li, C.H. Chuang, C.H. Chang, W.F. Su, C.P. Chang, M.W. Chu, C.W. Chen, J. Am. Chem. Soc. 131 (2009) 3644.
[8] D.A.R. Barkhouse, H.E. Bishop, B.M. Henry, G.R. Webster, Org. Electron. 11 (2010) 649.
[9] R. Zhu, C.Y. Jiang, B. Liu, S. Ramakrishna, Adv. Mater. 21 (2009) 994.
[10] C.Y. Kwong, A.B. Djurišić, P.C. Chui, K.W. Cheng, W.K. Chan, Chem. Phys. Lett. 384 (2004) 372.
[11] K.M. Coakley, Y.X. Liu, M.D. McGehee, K.L. Frindell, G.D. Stucky, Adv. Funct. Mater. 13 (2003) 301.
[12] C. Goh, S.R. Scully, M.D. McGehee, J. Appl. Phys. 101 (2007) 114503.
[13] W.J.E. Beek, M.M. Wienk, A.J.R. Janssen, Adv. Mater. 16 (2004) 1009.
[14] D.J.D. Moet, L.J.A. Koster, B. de Boer, P.W.M. Blom, Chem. Mater. 19 (2007) 5856.
[15] W.J.E. Beek, M.M. Wienk, A.J.R. Janssen, Adv. Funct. Mater. 16 (2006) 1112.
[16] S.Y. Shao, F.M. Liu, Z.Y. Xie, L.X. Wang, J. Phys. Chem. C 114 (2010) 9161.
[17] J.W. Zhou, D.H. Qin, C. Luo, L.L. Han, Y. Cao, Vcacuum Cryogenics 12 (2006) 9.
[18] W.Z. Cai, X. Gong, Y. Cao, Sol. Energy Mater. Sol. Cells 94 (2010) 114.
[19] K.M. Coakley, McGehee, Appl. Phys. Lett. 83 (2003) 3380.
[20] T.J. Savenije, J.M. Warman, A. Goossens, Chem. Phys. Lett. 287 (1998) 148.
[21] G. Yu, J. Gao, J. Hummelen, F. Wudl, A.J. Heeger, Science 270 (1995) 1789.
[22] A.C. Arango, S.A. Carter, P.J. Brock, Appl. Phys. Lett. 74 (1999) 1698.
[23] J.S. Salafsky, W.H. Lubberhuizen, R.E.I. Schropp, Chem. Phys. Lett. 290 (1998) 297.
[24] L.Q. Tang, B. Zhou, Y.M. Tian, H. Bala, Y. Pan, S.X. Ren, Y. Wang, X.T. Lv, M.G. Li, Z.C. Wang, Coll. Surf. A 296 (2007) 92.
[25] J.C. Liu, W.L. Li, H.Z. Yu, Z.L. Wu, J.B. Peng, Y. Cao, Sol. Energy Mater. Sol. Cells 92 (2008) 1403.
[26] P. Ravirajan, A.M. Peiro, M.K. Nazeeruddin, M. Graetzel, D.D.C. Bradley, J.R. Durrant, J. Nelson, J. Phys. Chem. B 110 (2006) 7635.
[27] A.J. Said, G. Poize, C . Martini, D. Ferry, W. Marine, S. Giorgio, F. Fages, J. Hocq, J. Bouclé, J. Nelson, J.R. Durrant, J. Ackermann, J. Phys. Chem. C 114 (2010) 11273.
[28] V.D. Mihailetchi, H.X. Xie, B. de Bober, L.J.A. Koster, P.W.M. Blom, Adv. Funct. Mater. 16 (2006) 699.
[29] M. Bruenling, E. Moons, D.Y. Marcovich, D. Cahen, J. Libman, A. Shanzer, J. Am. Chem. Soc. 116 (1994) 2972.
[30] K. Vandewal, A. Gadisa, W.D. Oosterbaan, S. Bertho, F. Banishoeib, I.V. Severen, L. Lutsen, T.J. Cleij, D. Vanderzande, J.V. Manca, Adv. Funct. Mater. 18 (2008) 2064.

Organic Electronics 12 (2011) 648–653

Contents lists available at ScienceDirect

Organic Electronics

journal homepage: www.elsevier.com/locate/orgel

Letter

Roughening the white OLED substrate's surface through sandblasting to improve the external quantum efficiency

Junhong Zhou, Na Ai, Lei Wang, Hua Zheng, Chan Luo, Zhixiong Jiang, Shufu Yu, Yong Cao, Jian Wang *

Institute of Polymer Optoelectronic Materials and Devices, Key Lab of Specially Functional Materials of Ministry of Education, South China University of Technology, Guangzhou 510640, PR China

ARTICLE INFO

Article history:
Received 14 September 2010
Received in revised form 11 January 2011
Accepted 22 January 2011
Available online 4 February 2011

Keywords:
Sandblasting
Output coupling efficiency
External quantum efficiency
Organic light-emitting diodes
Solid-state lighting

ABSTRACT

A simple, low cost, and scalable process based on sandblasting to modify the OLED substrate's surface, has been successfully developed. The rough surface produced by sandblasting efficiently suppressed the internally generated photons' waveguide mode, and enhanced the white OLED's EQE from 9% to 11.6% without changing the emission spectrum and the Lambertian emitter property. The improvement of the EQE was found to monotonically decrease with the surface roughness within the roughness range from around 1 μm to 3 μm. The white OLED's luminous efficiency was increased from 15.5 cd A^{-1} to 20 cd A^{-1}. Furthermore, the realization of rough surface on a 3.5 inch white lighting panel not only improved the 9-point uniformity from 80% to 90%, but also demonstrated the manufacturing scalability of the sandblasting technique.

© 2011 Elsevier B.V. All rights reserved.

1. Introduction

Due to their promising applications in full-color flat-panel displays, backlights for liquid-crystal displays (LCD), and solid-state lighting sources, organic light-emitting diodes (OLED) have attracted considerable interests since their discoveries [1–5]. Through collective efforts by world-wide researchers, and heavy investments by display companies, OLED technology has been commercialized in the display industry in the past decade. Recently, the development of white OLEDs (WOLEDs) for the application in the solid-state lighting became the focus of OLED researches. The power efficiency (PE) of WOLEDs based on small molecules has been reported to reach 90 lm W^{-1} [6], while the PE of WOLEDs based on semiconducting conjugated polymers has exceeded 20 lm W^{-1} [7,8], for the devices without any substrate's surface modifications. Since the internal quantum efficiency almost reached 100% [9–11], how to improve the external quantum efficiency is critical for WOLEDs' success in the lighting industry.

The relationship between the internal quantum efficiency (IQE) defined as the number of generated photons per injected carrier, and the external quantum efficiency (EQE) defined as the number of photons emitted into the viewing direction per injected carrier [12], is expressed in the following equation:

$$\eta_{EQE} = \eta_{IQE} \times \eta_{OUT} \quad (1)$$

where η_{OUT} is the light output coupling efficiency. As schematically illustrated in Fig. 1a, a large portion of internally generated lights can not exit the OLED devices' forward viewing side, due to the total reflection at the interface between the air and the transparent device substrate which generally has a high refraction index value. The light output coupling efficiency determines how much lights can escape from the device in the forward viewing direction. For a smooth plane device surface, the η_{OUT} is given by [13]:

$$\eta_{OUT} = 1 - \frac{3}{4}\left\{\sqrt{1-\frac{1}{n^2}} + \frac{1}{3}\left(1-\frac{1}{n^2}\right)^{\frac{3}{2}}\right\} \approx 0.75n^{-2} \quad (2)$$

* Corresponding author. Tel.: +86 20 8711 4525; fax: +86 20 8711 0606.
E-mail address: jianwang@scut.edu.cn (J. Wang).

1566-1199/$ - see front matter © 2011 Elsevier B.V. All rights reserved.
doi:10.1016/j.orgel.2011.01.018

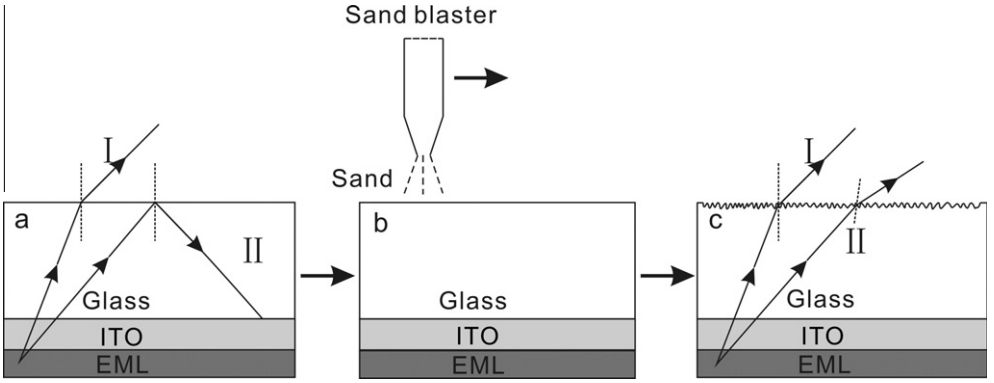

Fig. 1. Schematics of (a) the propagation of lights from an OLED device with smooth surface substrate. I represents the escaped lights, and II represents the trapped lights; (b) sandblasting process; and (c) the propagation of lights from an OLED device with rough surface substrate. Both lights I and II can escape from the OLED surface.

where n is the refraction index of the substrate. Taking the refraction index of the glass ($n \sim 1.5$), the η_{OUT} is only 0.33, meaning that two thirds of the generated lights are trapped inside.

To address the output coupling issue, two directions are generally considered: lowering the substrate's refraction index, or modifying the light's incident angle at the substrate–air interface. Tsutsui's group used silica aerogel with n around 1 as the device substrate to double the EQE [14]. However, the fragility and porosity of the silica aerogel prevents its use in real applications. To modify the light's incident angle, various approaches have been attempted, such as mesa structures [15], spherical substrate [6,16,17], microlens array [18], Bragg grating [19–21], corrugated structures [22–24], textured surface [25,26], and so on. However, all the methods aforementioned required complicated substrate process, including precise photolithography [15,18–23,25,26], lamination [6,16], stamping [18,24], self assembly [17], etc. Moreover, some of the device structures like spherical substrate, or mesa structure are impractical in the application of large area, plane light source. It's clear that a simple, scalable, and low cost process suitable for large size substrate in the industrial manufacturing facility is critical for the success of WOLED as solid-state lighting source.

In our contribution, we developed a novel process to roughen the substrate surface via sandblasting. The sandblasting technique, was first mentioned by Prof. Baldo's group [27], and was realized in a green small moledule OLED by Prof. Kwok's group [28]. The rough surface on OLED device will change the emitted lights' incident angle at the substrate–air interface, leading to more escaped photons in the forward viewing direction as illustrated in Fig. 1(c). By employing the sandblasting method, the maximum brightness of the WOLED was enhanced 42.5%, and the external quantum efficiency was increased 28.9%. Through the accurate control of the surface roughness, we found a linear dependence of the EQE improvement on the surface roughness in the roughness range from around 1 μm to 3 μm. The successful demonstration of the sandblasting technique on a 3.5 inch WOLED lighting panel shows the great potential of such technology in real manufacturing.

2. Experiments

To demonstrate the rough surface effects on the external quantum efficiency, solution processed WOLEDs with the device configuration of ITO/poly(ethylendioxythiophene):poly(styrene sulfonic acid) (PEDOT:PSS)(50 nm)/poly(*N*-vinylcarbazole) (PVK)(40 nm)/light emitting layer (60 nm)/Ba(4 nm)/Al(200 nm) were fabricated. The white light emission was achieved by doping a blue emitting conjugated dendrimer G0 with phosphorescent green emitter Ir(mppy)$_3$, and red emitter Ir(piq)$_2$acac. The blue light device was made with G0 only, while the red and green devices were obtained by doping PVK with Ir(piq)$_2$acac and Ir(mppy)$_3$, respectively. The molecular structures of the materials and the device structures are detailed in our early publication [29,30]. All chemicals and materials were purchased and used as received. PVK was purchased from Aldrich. Ir(piq)$_2$acac and Ir(mppy)$_3$ were purchased from American Dyes Sources. PEDOT:PSS was CleviosTM P Al 4083 from H. C. Starck GmbH. G0 was provided by Prof. Jian Pei in Peking University, Beijing, China [29]. Device fabrication followed well-established processes that have been described elsewhere [30]. The current density (J)-voltage (V)-luminance (L) characteristics were obtained using a Keithley 236 source meter and a silicon photodiode calibrated by a Chroma Meter CS-200 (Konica Minolta). The EL spectra and CIE coordinates were recorded by a PR-705 SpectraScan Spectrophotometer (Photo Research). The EQEs were obtained in an integrating sphere (IS-080, Labsphere). To measure the forward viewing EQE, the edges of the devices were covered by the black ink. No lights escaped from the device edges.

Sandblasting is one of the abrasive blasting techniques, which uses high-pressure air to blow a stream of sands against a surface. It's widely used for refurnishing buildings, creating art works, cleaning surfaces, etc. In display industry, as a low cost and scalable process, sandblasting is adopted for making barrier ribs on the rear panel of the plasma display panel. Fig. 2 shows the three dimensional pictures of the glass substrate's surface before and after sandblasting. The glass surface became textured from smooth after sandblasting. To characterize the rough

surface topology, Average Roughness, universally called Ra, is the standardized parameter. It is defined as arithmetic mean of the departures of the profile from the mean line over a given length [31]. In the following experiments, Ra is specified and measured by a confocal laser scanning microscope (OLYMPUS-OLS3100) for the roughness characterization.

Sandblasting provides a variety ways to modify the surface morphology, for example: the sand injection pressure, the blasting frequency, the size of the sand, the spraying angle, the distance between the spray nozzle and the substrate, etc. In our experiment, we set the distance from the nozzle to the glass substrate at 10 cm, the spraying angle at zero degree (perpendicular to the substrate surface), the sand injection pressure at 3.92×10^4 Pa, and the blasting frequency at 1 Hz. While fixing all the other parameters, we changed the size of the white corundum sand (from 20 μm to 60 μm) to obtain different but reproducible surface roughness. The sandblasting machine is Model 6090B from Jichuan International (Hong Kong) Co., Ltd. The sands were purchased from Zhengzhou Fengda Abrasive Materials (China) Co., Ltd.

3. Results and discussion

The WOLED device with smooth substrate surface (W1) has a peak PE of 9.0 lm W^{-1} at 5.0 V, and a peak luminous efficiency (LE) of 15.5 cd A^{-1} at the current density of 0.334 mA cm^{-2}. The maximum luminance reaches 30,151 cd m^{-2}. By introducing the rough surface substrate with Ra = 1.266 μm, the device performance is significantly enhanced. As summarized in Table 1, the WOLED device with rough substrate surface (W2) has a peak PE of 11.1 lm W^{-1} at 5.25 V, a peak LE of 20 cd A^{-1} at the current density of 0.654 mA cm^{-2}, and a maximum brightness of 42,978 cd m^{-2}. The performance improvements in terms of PE, LE and brightness are 23.3%, 29% and 42.5%, respectively. More important, the EQE is enhanced by 28.9%, from 9% to 11.6%.

By carefully examining the *J–V–L* characteristics of the two WOLED devices (Fig. 3a), it's clear that the EQE enhancement by the rough surface is totally due to the optical output coupling efficiency, because the electrical properties (*J–V* curves) of W1 and W2 are identical. It's worth to note that the turn-on voltage (defined as the operation voltage at which 1 cd m^{-2} is collected in the forward viewing direction) of W2 is 0.25 V lower than that of W1, which also confirms that more lights pass through the rough surface than the smooth surface. Under the operation brightness of 3000 cd m^{-2}, W2 has a smaller current density of 18.6 mA cm^{-2}, and a lower operation voltage of 8.5 V, compared to those of W1 which are 21.7 mA cm^{-2} and 8.75 V, respectively. As a result, rough surface device W2 has a higher PE of 6 lm W^{-1} at the operation brightness, leading to reduced power consumption. The comparison of the two devices' LE and PE's dependence on the current density are shown in Fig. 3b and c.

Table 1
The device performance of WOLEDs. W1: smooth surface device. W2: rough surface device.

Device	CIE [X, Y]	Turn-on voltage [V]	Max L [cd/m^2]	Max LE [cd/A]	Max EQE [%]	Max PE [lm/W]
W1	0.340, 0.366	4.5	30,151	15.5	9	9.1
W2	0.326, 0.362	4.25	42,978	20	11.6	11

To study the rough surface's influence on the emitting spectrum, the spectra of W1 and W2 under the same current density of 6.7 mA cm^{-2}, are collected and normalized to the W2 spectrum's peak value. As revealed in Fig. 3d, Device W2 shows intensity enhancement across the whole visible spectrum, which suggests that at the roughness of Ra = 1.266 μm, all the primary color emissions, i.e. red, green, and blue, have more outputs than at zero roughness (smooth surface). However, the blue (432 nm) and green (512 nm) peaks have big increases of 17.5% and 16.6%, respectively, while the red light (618 nm) exhibits only 2.8% intensity increase. To investigate why the blue and green peaks have more pronounced improvement than the red peak, we made individual red, green, and blue devices based on the material set of the white device to guarantee the same emission peaks as those from the white, i.e. red (PVK doped with $Ir(piq)_2acac$), green (PVK doped with $Ir(mppy)_3$), and blue (G0). At the roughness of 1.219 μm, the EQE improvements for red, green, and blue devices

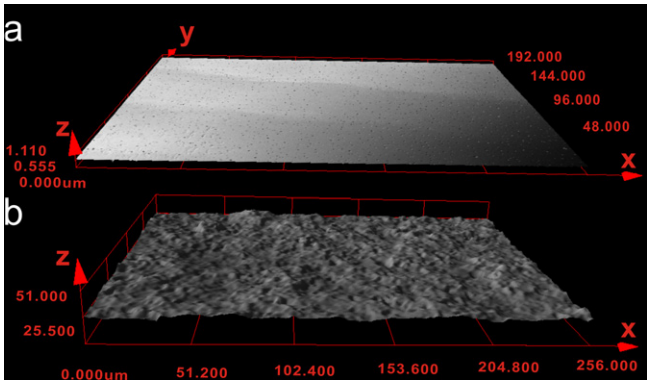

Fig. 2. Three dimension pictures of (a) smooth surface, and (b) rough surface obtained by Confocal Laser Scanning Microscope (OLYMPUS-OLS3100).

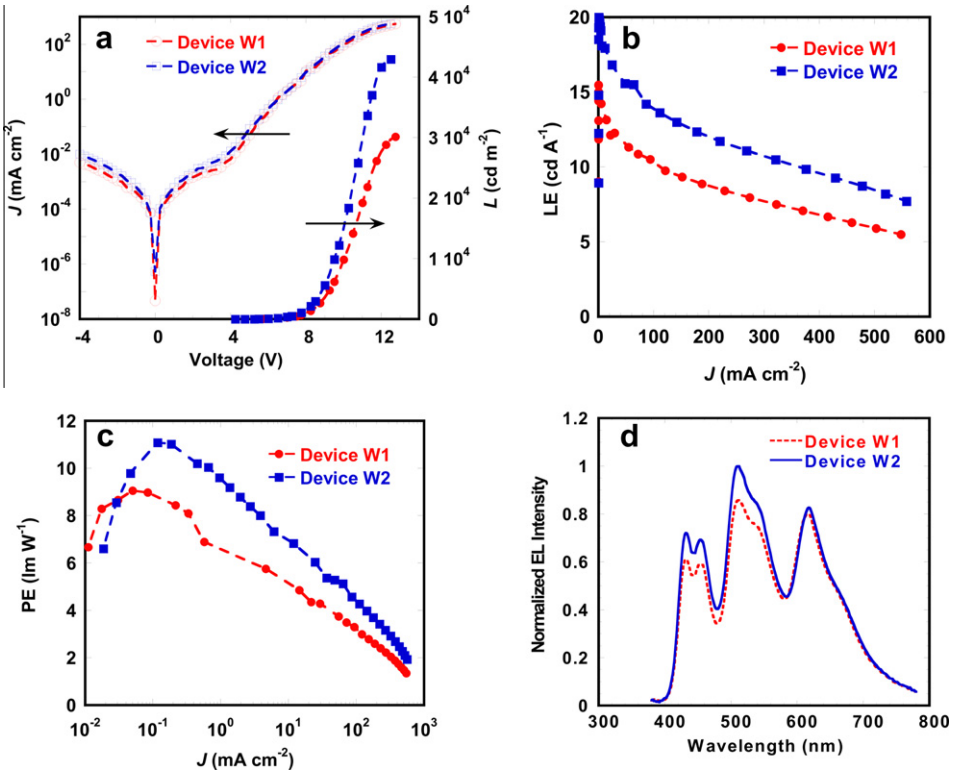

Fig. 3. Device W1's and W2's: (a) *J–V–L* characteristics; (b) the dependence of luminous efficiency on the current density; (c) the dependence of the power efficiency on the current density; (d) the normalized EL spectra.

are 8.46%, 42.3%, and 36.4%, respectively, among which the improvement of red device is the lowest, consistent with the findings in the white color device. The underlying mechanism on why the same surface roughness have different effects on different color is currently under investigation.

It's known that when the trichromatic color mixture has the same color coordinates and the same brightness as the equal-energy radiator Illuminant E does, the brightness ratio of the three standard primary colors emitters is $\tilde{r} : \tilde{g} : \tilde{b} = 1.0000 : 4.5907 : 0.0601$ [32]. The equation reveals that the green emission counts more in producing a white light [33], since the human eyes are most sensitive to the green color. The big increase of the green portion in Device W2 is preferable in improving the white light efficiency. Unfortunately, the uneven light intensity improvements among the three primary emissions shift the color coordinates from (0.340, 0.346) to (0.326, 0.362). Nonetheless, the color coordinates are still in the center of the white light region specified in the CIE 1931 Chromaticity Diagram [32].

For the lighting application, either solid-state lighting source, or backlights panel in LCD, Lambertian emitter is always required. Plane structure OLED with smooth substrate surface is theoretically-proven ideal Lambertian emitter [13]. After the surface was modified by sandblasting, it's important to test if the Lambertian emission still remains. The angular dependence of the light intensity of Device W2 is plotted in Fig. 4a. The zero degree denotes the viewing direction normal to the substrate plane as illustrated in Fig. 4a inset. The light intensity is normalized to the intensity at zero degree. The dashed line is the plot of an ideal Lambertian emitter's normalized light intensity vs. the viewing angle, following the equation [34]:

$$L(\theta) = L_0 \cos\theta \tag{3}$$

where L_0 is the light intensity at zero degree. The superposition of the experimental data and the theoretical curve demonstrates that the rough surface WOLED is a perfect Lambertian emitter.

It's important to optimize the surface roughness of the WOLED substrate to achieve the highest external quantum efficiency. Though it is a simple technology, sandblasting provides a variety ways to modify the surface morphology (Section 2). The dependences of the EQE improvement on the surface roughness is illustrated in Fig. 4b. In the roughness range from around 1 μm to 3 μm, the smaller the roughness, the higher the EQE. Since the smallest roughness is 0 meaning smooth surface, it suggests that the EQE will have a peak value between 0 and 1 μm. Some works by other groups demonstrated that when the surface scattering medium has the size of half the light wavelength, the EQE has its largest value [25]. For our white emission with three primary colors, it's therefore, expected that when the roughness of the substrate approaches 256 nm, the EQE will reach its maximum. To produce sub-micrometer roughness, special sandblasting machine equipped with much smaller sands is needed.

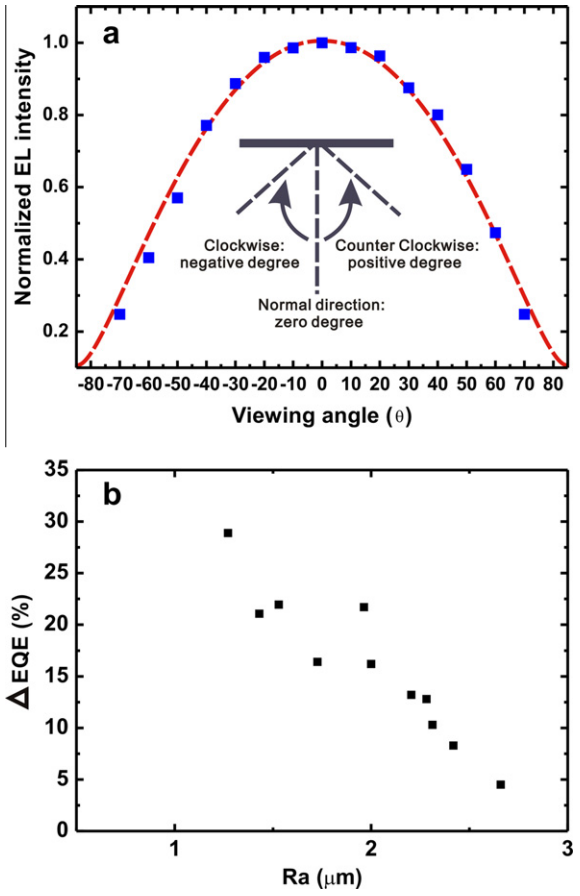

Fig. 4. (a) The dependence of luminance on the viewing angle. Square: the normalized luminance from a rough surface WOLED. Dashed line: the theoretical plot of an ideal Lambertian emitter. Inset: the illustration of the measurement. (b) The dependence of the EQE improvement on the surface roughness Ra.

For large size plane light source, the uniformity is a crucial parameter. Since the rough surface scattered the internally generated photons out of the surface randomly as schematically illustrated in Fig. 1c, the roughness is expected to improve the uniformity of the large area plane light source. To confirm the uniformity improvement and demonstrate the manufacturing scalability of the sandblasting technique, a 3.5 inch diagonal white lighting panel was fabricated. The 3.5 inch substrate is 2.7 inch long, and 2.2 inch wide. On the ITO surface, a group of Cr lines with the width of 40 μm were patterned using standard photolithography. The Cr lines help conduct the current from the edge to the center. The white emission of the panel was achieved by doping G0 with the green emitting conjugated polymer poly [2-(4-(3′,7′-dimethyloctyloxy)-phenyl)-*p*-phenylenevinylene] (P-PPV), and orange emitting polymer poly[2-methoxy-5-(2′-ethyl-hexyloxy)-1,4-phenylenevinylene] (MEH-PPV), which were purchased from Canton OLedking Optoelectric Materials Co., Ltd. The lighting panel with smooth surface has a 9-point uniformity [35] of 80%, while after sandblasting the substrate, the uniformity improves to 90%. The panel picture is shown in Fig. 5.

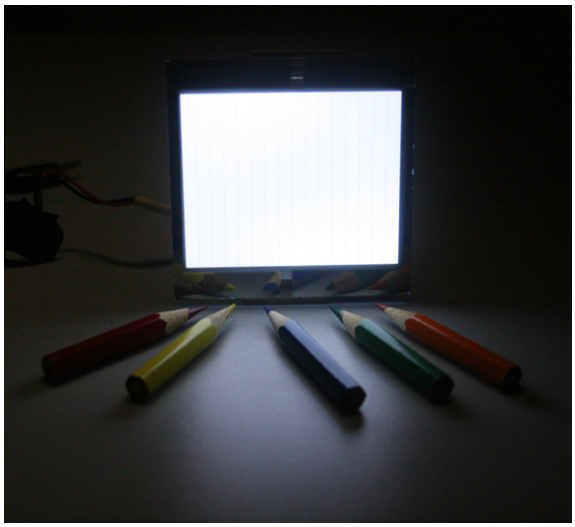

Fig. 5. The picture of a 3.5 inch white light panel.

4. Summary

In summary, we have successfully developed a simple, low cost, and scalable process to modify the WOLED substrates' surface. The rough surface created by the sandblasting technique efficiently suppressed the optical waveguide mode of the internally generated photons, and significantly enhanced the output coupling efficiency. For a white emission OLED, the EQE was improved from 9% to 11.6%. The surface roughness can be accurately controlled and reproduced. In the roughness range between about 1 μm and 3 μm, the EQE improvement is inversely proportional to the surface roughness. Moreover, neither the emission spectrum, nor the angular dependence of the light intensity, were altered by the rough surface. The realization of rough surface on a 3.5 inch white lighting panel not only improves the 9-point uniformity from 80% to 90%, but also demonstrates the feasibility of sandblasting technique in real manufacturing.

Acknowledgements

The authors are deeply grateful to the Ministry of Science and Technology (973 Program 2009CB623604, 2009CB930604, and 863 Program 2008AA03A311), and the National Natural Science Foundation of China (U0634003) for their financial supports. The authors thank Prof. Jian Pei in Peking University, Beijing, China, for providing the blue material G0.

References

[1] C.W. Tang, S.A. VanSlyke, Appl. Phys. Lett. 51 (1987) 93.
[2] J.H. Burroughes, D.D.C. Bradley, A.R. Brown, R.N. Marks, K. Mackay, R.H. Friend, P.L. Born, A.B. Holmes, Nature 347 (1990) 539.
[3] J. Kido, M. Kimura, K. Nagai, Science 267 (1995) 1332.
[4] B.W. D'Andrade, S.R. Forrest, Adv. Mater. 16 (2004) 1585.
[5] A. Misra, P. Kumar, M.N. Kamalasanan, S. Chandra, Semicond. Sci. Technol. 21 (2006) R35.

[6] S. Reineke, F. Lindner, G. Schwartz, N. Seidler, K. Walzer, B. Lüssem, K. Leo, Nature 459 (2009) 234.
[7] H.B. Wu, G.J. Zhou, J.H. Zou, C.-L. Ho, W.-Y. Wong, W. Yang, J.B. Peng, Y. Cao, Adv. Mater. 21 (2009) 4181.
[8] F. Huang, P.-I. Shih, C.-F. Shu, Y. Chi, A.K.-Y. Jen, Adv. Mater. 21 (2009) 361.
[9] M.A. Baldo, D.F. O'Brien, Y. You, A. Shoustikov, S. Sibley, M.E. Thompson, S.R. Forrest, Nature 395 (1998) 151.
[10] C. Adachi, M.A. Baldo, M.E. Thompson, S.R. Forrest, J. Appl. Phys. 90 (2001) 5048.
[11] E.L. Williams, K. Haavisto, J. Li, G.E. Jabbour, Adv. Mater. 19 (2007) 197.
[12] S.R. Forrest, D.D.C. Bradley, M.E. Thompson, Adv. Mater. 15 (2003) 1043.
[13] J.-S. Kim, P.K.H. Ho, N.C. Greenham, R.H. Friend, J. Appl. Phys. 88 (2000) 1073.
[14] T. Tsutsui, M. Yahiro, H. Yokogawa, K. Kawano, M. Yokoyama, Adv. Mater. 13 (2001) 1149.
[15] G. Gu, D.Z. Garbuzov, P.E. Burrows, S. Venkatesh, S.R. Forrest, M.E. Thompson, Opt. Lett. 22 (1997) 396.
[16] C.F. Madigan, M.-H. Lu, J.C. Sturm, Appl. Phys. Lett. 76 (2000) 1650.
[17] T. Yamasaki, K. Sumioka, T. Tsutsui, Appl. Phys. Lett. 76 (2000) 1243.
[18] S. Moller, S.R. Forrest, J. Appl. Phys. 91 (2002) 3324.
[19] J.M. Ziebarth, M.D. McGehee, J. Appl. Phys. 97 (2005) 064502.
[20] J.M. Lupton, B.J. Matterson, I.D.W. Samuel, M.J. Jory, W.L. Barnes, Appl. Phys. Lett. 77 (2000) 3340.
[21] J.M. Ziebarth, A.K. Saafir, S. Fan, M.D. McGehee, Adv. Funct. Mater. 14 (2004) 451.
[22] B.J. Matterson, J.M. Lupton, A.F. Safonov, M.G. Salt, W.L. Barnes, I.D.W. Samuel, Adv. Mater. 13 (2001) 123.
[23] P.A. Hobson, S. Wedge, J.A.E. Wasey, I. Sage, W.L. Barnes, Adv. Mater. 14 (2002) 1393.
[24] W.H. Koo, S.M. Jeong, F. Araoka, K. Ishikawa, S. Nishimura, T. Toyooka, H. Takezoe, Nat. Photon 4 (2010) 222.
[25] I. Schnitzer, E. Yablonovitch, C. Caneau, T.J. Gmitter, A. Scherer, Appl. Phys. Lett. 63 (1993) 2174.
[26] R. Windish, P. Heremans, A. Knobloch, P. Kiesel, G.H. Döhler, Appl. Phys. Lett. 74 (1999) 2256.
[27] C.L. Mulder, K. Celebi, K.M. Milaninia, M.A. Baldo, Appl. Phys. Lett. 90 (2007) 211109.
[28] S.M. Chen, H.S. Kwok, Opt. Express 18 (2010) 37.
[29] Y. Jiang, J.-Y. Wang, Y. Ma, Y.-X. Cui, Q.-F. Zhou, J. Pei, Org. Lett. 8 (2006) 4287.
[30] L. Wang, Y. Jiang, J. Luo, Y. Zhou, J.H. Zhou, J. Wang, J. Pei, Y. Cao, Adv. Mater. 21 (2009) 4854.
[31] ANSI B46.1 "Surface Texture (Surface Roughness Waviness and Lay)" 2002, American Society of Mechanical Engineers.
[32] R.W.G. Hunt, Measuring Colour, 2nd ed., Ellis Horwood, New York, 1991. Chapter 2.
[33] Y. Xiong, L. Wang, W. Xu, J. Zou, H. Wu, Y. Xu, J. Peng, J. Wang, Y. Cao, G. Yu, Org. Electron. 10 (2009) 857.
[34] M.H. Freeman, C.C. Hull, Optics, 11th ed., Butterworth–Heinemann, New York, 2003. Chapter 10.
[35] Flat Panel Display Measurements Standard, Version 2.0, Video Electronics Standards Association.

Organic Electronics 12 (2011) 654–659

Contents lists available at ScienceDirect

Organic Electronics

journal homepage: www.elsevier.com/locate/orgel

Rigorous S-matrix approach to the modeling of the optical properties of OLEDs

A.A. Shcherbakov [a,b], A.V. Tishchenko [a,b], D.S. Setz [c,*], B.C. Krummacher [c]

[a] University of Lyon, Laboratory Hubert Curien, UMR CNRS 5516, Saint-Etienne, France
[b] Moscow Institute of Physics and Technology, Laboratory of Nanooptics and Femtosecond Electronics, Dolgoprudny, Russia
[c] OSRAM Opto Semiconductors GmbH, OLED-Lighting, Regensburg, Germany

ARTICLE INFO

Article history:
Received 6 October 2010
Received in revised form 20 December 2010
Accepted 21 January 2011
Available online 5 February 2011

Keywords:
Organic light-emitting diodes
Optical simulation
Loss-channel analysis

ABSTRACT

A new approach for the simulation of OLEDs based on a plane wave field expansion is proposed. Exact general formulae are given that allow for the calculation of their optical characteristics including losses in all layers in an arbitrary OLED structure. The S-matrix approach is used which ensures numerical stability of the algorithm. A simple way is proposed to take into consideration non-coherent reflections in a thick substrate. The validity of the model is demonstrated by comparing with experimental data.

© 2011 Elsevier B.V. All rights reserved.

1. Introduction

The development of light-emitting devices and displays based on organic light-emitting diodes (OLEDs) is an important area of modern optics since such devices have important advantages in comparison with their conventional inorganic analogs [1]. Usually an OLED structure is composed of a stack of plane layers, whose thickness and optical properties crucially influence the behavior of the whole device. The properties include the external efficiency, color, spectral and angular distribution of the emission. The manufacturing of experimental samples is an involved and expensive technological process therefore, it is important to first carry out an optimization of an OLED structure by means of rigorous modeling.

A number of models have been proposed for the description of the optical behavior of OLED devices. Considering only those which implement a rigorous electromagnetic analysis, one can divide these models into two groups. The models of the first group are based on field decomposition into a set of cylindrical harmonics [2,3], and the second group includes models which are based on a plane wave representation of the electromagnetic field [4–6]. Note that both groups of approaches use the dipole emission rate calculation in a plane layered medium. The first approach was proposed in [7] and further developed for an arbitrary multilayer system in [8]. Regarding the dipole emission in a layered structure described in terms of plane waves, important developments were made in [9,10] where also the links can be found to papers concerning the wave propagation in a plane layered media.

All the models elaborated for the calculation of the electromagnetic properties of OLED structures are aimed at estimating both the internal fields and waves outgoing from a structure. The capability of an exact calculation of the electromagnetic fields in all layers of a device, and hence the power flux and losses inside, is a prerequisite for the optimization of the performance of a device. The mentioned approaches as they are usually presented suffer however from a lack of a clear, simple and precise way of calculation of these physical quantities. Simplified equations solving this problem were given in [3] for the model using a cylindrical harmonic representation. For the plane-wave-representation approach, authors usually give only

* Corresponding author. Tel.: +49 9418502338.
E-mail address: daniel-steffen.setz@osram-os.com (D.S. Setz).

1566-1199/$ - see front matter © 2011 Elsevier B.V. All rights reserved.
doi:10.1016/j.orgel.2011.01.019

the expressions for the energy flux outside the layers to calculate the emission from the whole structure [11,12]. Reference [13] might have given the required solution, but the authors place dipoles at the interfaces between different media which cannot be justified neither from physical nor from mathematical points of view.

The present work aims at giving exact formulae in the frame of the plane-wave approach that describes in the most general way the power flux inside an OLED device containing an arbitrary number of emitting layers. To complete the model, an S-matrix propagation algorithm (instead of T-matrices) is used for sake of numerical stability [14] and a simple way of accounting for non-coherent reflections in a thick substrate is introduced.

2. Plane wave expansion model

Before giving the details of the method it is necessary to define the considered structure. A conventional OLED is composed of a stack of plane layers comprising a metal cathode and several lossy dielectric layers: an active layer, an anode and possibly electron/hole transport and blocking layers [15]. The sketch representing the general structure of the device can be seen in Fig. 1. The numeration of all layers starts from the semi-infinite medium under the cathode. Each layer is considered to be homogeneous of complex dielectric permittivity ε_i and thickness h_i. All plane layers and interfaces are parallel to the plane XOY in a Cartesian system XYZ.

Dealing with plane wave propagation seems to be the most natural way when describing a plane layered structure. The field emitted by a point source is decomposed into a set of plane harmonics. As usual, the active layer is represented as an infinite layer with point dipoles. Note that while studying propagation of plane harmonics found by decomposition of a point source field we implicitly deal with an infinite plane layer of sources instead of a single dipole. Additionally, no absorption is supposed in the surrounding dipole medium since the dipole field tends to infinity in the vicinity of the dipole. However the medium can absorb at some nonzero distance from the dipole.

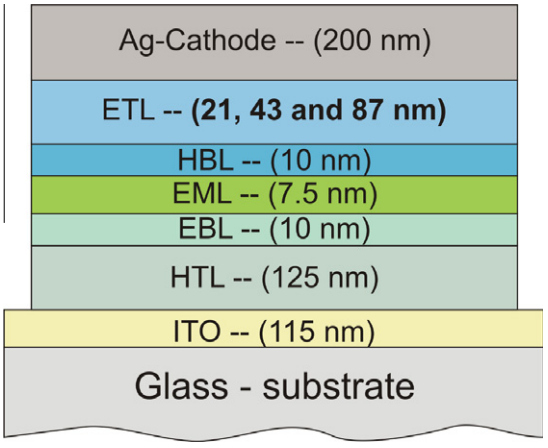

Fig. 1. Structure of the green-emitting electrophosphorescent OLEDs used in this study.

3. Dipole emission in a homogeneous medium

Consider first a monochromatic point Dirac dipole with polarization amplitude $\mathbf{p}_0$ located at point $\mathbf{r}_0 = (x_0, y_0, z_0)$ in a homogeneous medium of permittivity ε_p:

$$\mathbf{p}(\mathbf{r}, t) = \mathbf{p}_0 \delta(\mathbf{r} - \mathbf{r}_0) \exp(-i\omega t) \tag{1}$$

Monochromatic source (1) is considered as a Fourier decomposition of a real broadband source whose spectrum has to be integrated to obtain the final temporal response. All the fields produced by source (1) are proportional to the term $\exp(-i\omega t)$ which will be omitted hereunder for sake of brevity.

Denote the wavevector of a plane harmonic as

$$\mathbf{k}_i^{\pm} = (k_x, k_y, \pm k_{zi}) \tag{2}$$

where

$$k_{zi} = \sqrt{k_i^2 - k_x^2 - k_y^2} \tag{3}$$

is the wavenumber in the i-th layer $k_i = \omega\sqrt{\mu_0 \varepsilon_i}$ and signs "plus" and "minus" correspond to the waves propagating in half-spaces $z > z_0$ and $z < z_0$, respectively. Introduce also an in-plane wavevector modulus $\gamma = \sqrt{k_x^2 + k_y^2}$. Then the amplitudes of TE and TM polarized harmonics of the field propagating upwards and downwards with respect to the z axis write (see, for example [13]):

$$a_{TE}^{(S)\pm} = \frac{i\omega^2 \mu_0 k_0^2}{8\pi^2 \gamma k_{pz}} (k_y p_{0x} - k_x p_{0y}) \tag{4}$$

$$a_{TM}^{(S)\pm} = \frac{i\omega k_0^2}{8\pi^2 \gamma k_{pz}} (\mp k_x k_{pz} p_{0x} \mp k_y k_{pz} p_{0y} + \gamma^2 p_{0z}) \tag{5}$$

Here the factor k_0^2 is introduced to keep the same dimension of the real field and of the plane harmonic amplitudes. Note that in derivation of Eqs. (4) and (5) we have used the following relation between field components and the amplitudes of TE- and TM-polarized waves:

$$E_x^{\pm} = \frac{k_y}{\gamma} a_{TE}^{\pm} \mp \frac{k_x k_z}{\omega \varepsilon_i \gamma} a_{TM}^{\pm};\ E_y^{\pm} = -\frac{k_x}{\gamma} a_{TE}^{\pm} \mp \frac{k_y k_z}{\omega \varepsilon_i \gamma} a_{TM}^{\pm};$$
$$E_z^{\pm} = \frac{\gamma}{\omega \varepsilon_i} a_{TM}^{\pm} \tag{6}$$

$$H_x^{\pm} = \pm \frac{k_x k_z}{\omega \mu_0 \gamma} a_{TE}^{\pm} + \frac{k_y}{\gamma} a_{TM}^{\pm};\ H_y^{\pm} = \pm \frac{k_y k_z}{\omega \mu_0 \gamma} a_{TE}^{\pm} - \frac{k_x}{\gamma} a_{TM}^{\pm};$$
$$H_z^{\pm} = -\frac{\gamma}{\omega \mu_0} a_{TE}^{\pm} \tag{7}$$

The power flux through any interface parallel to XY plane is found as the real part of the Poynting vector z-projection. In terms of the TE and the TM amplitudes $a_{TE}^{\pm}$ and $a_{TM}^{\pm}$ it has the form:

$$S_z(k_x, k_y) = \begin{bmatrix} \frac{1}{2}\left\{\frac{\mathrm{Re}(k_z)}{\omega\mu_0} \left|a_{TE}^{+}\right|^2 + \mathrm{Re}\left(\frac{k_z}{\omega\varepsilon_m}\right)\left|a_{TM}^{+}\right|^2\right\}, & z > z_0 \\ -\frac{1}{2}\left\{\frac{\mathrm{Re}(k_z)}{\omega\mu_0} \left|a_{TE}^{-}\right|^2 + \mathrm{Re}\left(\frac{k_z}{\omega\varepsilon_m}\right)\left|a_{TM}^{-}\right|^2\right\}, & z < z_0 \end{bmatrix} \tag{8}$$

Therefore, the total power emitted by the dipole into a given harmonic is found as:

$$I_d(k_x,k_y) = \lim_{z\to z_0+0} S_z(k_x,k_y) + \lim_{z\to z_0-0} S_z(k_x,k_y)$$
$$= \frac{1}{2}\left\{\frac{\mathrm{Re}(k_z)}{\omega\mu_0}\left(\left|a_{TE}^{(S)+}\right|^2 + \left|a_{TE}^{(S)-}\right|^2\right)\right.$$
$$\left. + \mathrm{Re}\left(\frac{k_z}{\omega\varepsilon_m}\right)\left(\left|a_{TM}^{(S)+}\right|^2 + \left|a_{TM}^{(S)-}\right|^2\right)\right\} \quad (9)$$

Eqs. 4, 5, 8, and 9 lie in the core of the model. They allow for the calculation of all electromagnetic properties of the OLED structure including losses in layers and the effective source emission.

4. Plane wave propagation in a multilayer stack

As was stated in the introduction the S-matrix propagation algorithm was implemented to trace and relate fields in all layers of a structure instead of the T-matrices. Consider a plane structure perpendicular to the z axis and suppose that the reflection and transmission coefficients are found for it. Denoting by $a_1^{\pm}$ the plane wave amplitudes below the structure and by $a_2^{\pm}$ above the structure the S-matrix relates them as follows:

$$\begin{pmatrix} a_1^- \\ a_2^+ \end{pmatrix} = S\begin{pmatrix} a_1^+ \\ a_2^- \end{pmatrix} = \begin{pmatrix} S_{11} & S_{21} \\ S_{12} & S_{22} \end{pmatrix}\begin{pmatrix} a_1^+ \\ a_2^- \end{pmatrix} \quad (10)$$

Further, we need to specify explicitly two elementary types of S-matrices. The first one is an S-matrix of an interface between two media of permittivities ε_1 and ε_2. It consists of the Fresnel reflection and transmission coefficients and depends on the polarization:

$$S_{TE} = \begin{pmatrix} \frac{k_{1z}-k_{2z}}{k_{1z}+k_{2z}} & \frac{2k_{2z}}{k_{1z}+k_{2z}} \\ \frac{2k_{1z}}{k_{1z}+k_{2z}} & \frac{k_{2z}-k_{1z}}{k_{1z}+k_{2z}} \end{pmatrix} \quad (11)$$

$$S_{TM} = \begin{pmatrix} \frac{\varepsilon_2 k_{1z}-\varepsilon_1 k_{2z}}{\varepsilon_2 k_{1z}+\varepsilon_1 k_{2z}} & \frac{2\varepsilon_1 k_{2z}}{\varepsilon_2 k_{1z}+\varepsilon_1 k_{2z}} \\ \frac{2\varepsilon_2 k_{1z}}{\varepsilon_2 k_{1z}+\varepsilon_1 k_{2z}} & \frac{\varepsilon_1 k_{2z}-\varepsilon_2 k_{1z}}{\varepsilon_2 k_{1z}+\varepsilon_1 k_{2z}} \end{pmatrix} \quad (12)$$

where $k_{z1,2}$ are defined by (3) for lower and upper media, respectively. The second type is an S-matrix of a homogeneous layer of permittivity ε_l and thickness h_l. It contains only the exponential factors expressing the plane wave propagation and regardless of polarization writes

$$S = \begin{pmatrix} 0 & \exp(ik_{lz}h_l) \\ \exp(ik_{lz}h_l) & 0 \end{pmatrix} \quad (13)$$

Note that in the case of a homogeneous layer both exponents in (13) have the "plus" sign. Such property is quite opposite to that of T-matrix and leads to the numerical stability of S-matrices.

We define next the basic S-matrix relations that give means to calculate the field amplitudes at any point of the structure. If a plane layered structure consists of two substructures characterized by S-matrices $S^{(L)}$ and $S^{(U)}$ (the first corresponds to the lower substructure and the second – to the upper one) then one can find the resulting S-matrix S of the whole structure by applying the following multiplication rule:

$$\begin{aligned} S_{11} &= S_{11}^{(L)} + S_{12}^{(L)}S_{11}^{(U)}(I - S_{11}^{(U)}S_{22}^{(L)})^{-1}S_{21}^{(L)} \\ S_{12} &= S_{12}^{(L)}(I - S_{11}^{(U)}S_{22}^{(L)})^{-1}S_{12}^{(U)} \\ S_{21} &= S_{21}^{(L)}(I - S_{11}^{(U)}S_{22}^{(L)})^{-1}S_{21}^{(U)} \\ S_{22} &= S_{22}^{(U)} + S_{21}^{(U)}S_{22}^{(L)}(I - S_{11}^{(U)}S_{22}^{(L)})^{-1}S_{12}^{(U)} \end{aligned} \quad (14)$$

By successively applying Eq. (14) one can obtain the S-matrix components for a whole stack containing any number of layers.

5. Dipole emission in a layer

We proceed with considering a dipole source placed between two structures characterized by S-matrices $S^{(L)}$ and $S^{(U)}$. When the source emits plane waves of amplitudes $a_s^{\pm}$ the effective wave amplitudes differ from those of emitted waves because of the interference with reflected waves. This effect is very important since it describes the modifications in a spectrum emitted by a source placed in a layered structure.

Denote the z coordinates of two interfaces that bound a layer containing a dipole by z_1 and z_2, and the dipole position by z_s as shown in Fig. 2. The harmonic amplitudes emitted by the dipole $a_s^{\pm}$ are found in accordance with (4) and (5). The effective amplitudes $a^{\pm}(z_s)$ in the plane of the source are different from $a_s^{\pm}$. They are found as a result of the interference of all emitted and reflected waves:

$$\begin{aligned} a^+(z_s) &= (I - S_{22}^{(L)}S_{11}^{(U)})^{-1}(S_{22}^{(L)}a^{(S)-} + a^{(S)+}) \\ a^-(z_s) &= (I - S_{11}^{(U)}S_{22}^{(L)})^{-1}(S_{11}^{(U)}a^{(S)+} + a^{(S)-}) \end{aligned} \quad (15)$$

At any plane $z = const$ that does not coincide with the layer of dipoles the amplitudes of both up- and down-propagating harmonics are then found $a_{TE,TM}^{\pm}(z)$ and the correspondent power flux writes

$$S_z(k_x,k_y,z) = \frac{1}{2}\left\{\frac{\mathrm{Re}(k_z)}{\omega\mu_0}\left(\left|a_{TE}^+\right|^2 - \left|a_{TE}^-\right|^2\right)\right.$$
$$\left. + \mathrm{Re}\left(\frac{k_z}{\omega\varepsilon_m}\right)\left(\left|a_{TM}^+\right|^2 - \left|a_{TM}^-\right|^2\right)\right\}$$
$$- \frac{\mathrm{Im}(k_z)}{\omega\mu_0}\mathrm{Im}(a_{TE}^+ a_{TE}^{-*}) - \mathrm{Im}\left(\frac{k_z}{\omega\varepsilon_m}\right)\mathrm{Im}(a_{TM}^+ a_{TM}^{-*}) \quad (16)$$

The latter relation follows directly from (8). The effective power emitted by a dipole source layer located in the plane $z = z_s$ is found from (16) by substituting the corresponding field amplitudes in the vicinity above and under the layer:

$$I_s = \lim_{z\to z_s+0} S_z + \lim_{z\to z_s-0} S_z$$
$$= \frac{1}{2}\left\{\frac{\mathrm{Re}(k_z)}{\omega\mu_0}\left(|a_{TE}^+(z_s)|^2 - |a_{TE}^+(z_s) - a_{TE}^{(S)+}|^2 + |a_{TE}^-(z_s)|^2\right.\right.$$
$$\left. - |a_{TE}^-(z_s) - a_{TE}^{(S)-}|^2\right) + \mathrm{Re}\left(\frac{k_z}{\omega\varepsilon_m}\right)\left(|a_{TM}^+(z_s)|^2 - |a_{TM}^+(z_s)\right.$$
$$\left.\left. - a_{TM}^{(S)+}|^2 + |a_{TM}^-(z_s)|^2 - |a_{TM}^-(z_s) - a_{TM}^{(S)-}|^2\right)\right\}$$
$$- \frac{\mathrm{Im}(k_z)}{\omega\mu_0}\mathrm{Im}[a_{TE}^{+*}(z_s)a_{TE}^{(S)-} + a_{TE}^{-*}(z_s)a_{TE}^{(S)+}]$$
$$- \mathrm{Im}\left(\frac{k_z}{\omega\varepsilon_m}\right)\mathrm{Im}[a_{TM}^{+*}(z_s)a_{TM}^{(S)-} + a_{TM}^{-*}(z_s)a_{TM}^{(S)+}] \quad (17)$$

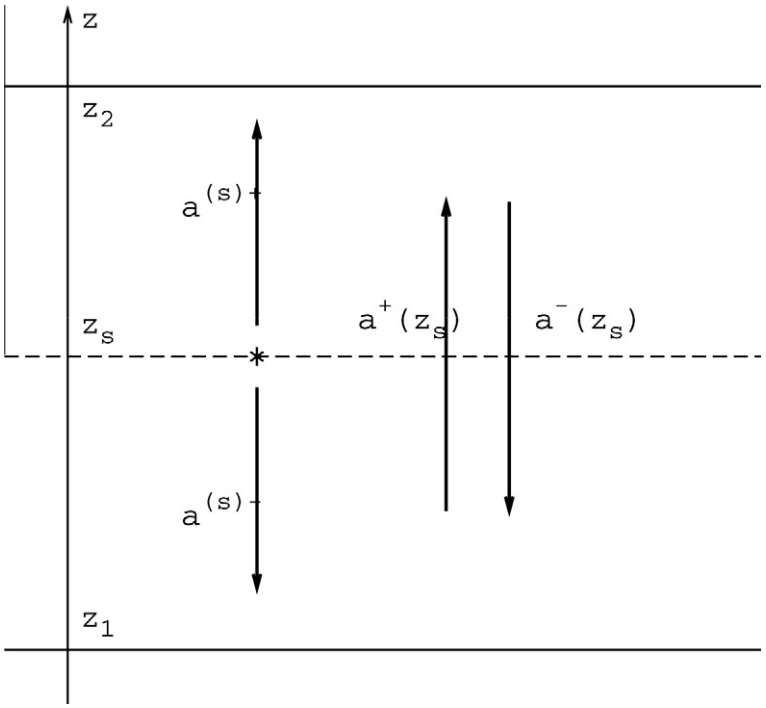

Fig. 2. Schematic picture of a layer with emitting dipole.

The "asterisk" indicates complex conjugation. The last two terms of expression (17) represent the power flux in the evanescent components of the emission of point sources. Finally the power emitted (or lost if there is no sources) in a layer is found as

$$I_l = \left| \lim_{z \to z_u - 0} S_z - \lim_{z \to z_d + 0} S_z - I_s \right| \tag{18}$$

An important practical significance of this formula is that it gives losses in a layer regardless of the presence of sources inside it.

The only thing left is the definition of unknown amplitudes in (16) and (17). Equations (13) allow for obtaining output amplitudes from the whole structure:

$$\begin{aligned} a^-(z_1) &= S^A_{12} a^-(z_s) = S^A_{12}(I - S^B_{11} S^A_{22})^{-1}(S^B_{11} a^{(S)+} + a^-_s) \\ a^+(z_2) &= S^B_{21} a^+(z_s) = S^B_{21}(I - S^A_{22} S^B_{11})^{-1}(S^A_{22} a^{(S)-} + a^+_s) \end{aligned} \tag{19}$$

In order to trace the fields in different layers we use the solution to the following problem. Given a structure composed of two elements characterized by S-matrices $S^{(L)}$ and $S^{(U)}$ and two incident plane waves with amplitudes $a^+(z_1)$ and $a^-(z_2)$ (under and above the structure), the incident waves have the same temporal and spatial frequencies, therefore, wave amplitudes $a^{\pm}(z_3)$, $z_1 < z_3 < z_2$ between elements are found as result of the interference between all transmitted and reflected waves:

$$\begin{aligned} a^+(z_3) &= (I - S^{(U)}_{11} S^{(L)}_{22})^{-1}[S^{(L)}_{21} a^+(z_1) + S^{(L)}_{22} S^{(U)}_{12} a^-(z_2)] \\ a^-(z_3) &= (I - S^{(U)}_{11} S^{(L)}_{22})^{-1}[S^{(U)}_{11} S^{(L)}_{21} a^+(z_1) + S^{(U)}_{12} a^-(z_2)] \end{aligned} \tag{20}$$

Formulae (15)–(20) are sufficient for the description of plane wave emission and propagation in an arbitrary plane layered structure. By using them one can find the energy flux and losses at every point of the structure.

6. External reflections and non-coherent return of light

In many cases, the light is extracted from the structure to the air through a substrate. The substrate is too thick to preserve light coherence and therefore waves reflected back from the air-substrate interface do not interfere with emitted waves. A correct analysis of such situation includes the calculation of light emission to the substrate by means of the techniques developed in the previous sections. Then, the air-substrate interface is introduced which modifies the intensities.

The presence of the air-substrate interface leads to two main consequences: first, all waves with in-plane wave vector projection $\gamma \geqslant k_{air}$ will be totally reflected back and guided in the substrate; secondly, in the case $\gamma \leqslant k_{air}$, the emitted waves will be partially reflected at the interface resulting in decreasing output efficiency. Let R_a and T_a be the reflection and transmission power coefficients at the air-substrate interface

$$R_{aTE} = \left|\frac{k_{sz} - k_{az}}{k_{sz} + k_{az}}\right|^2,\ R_{aTM} = \left|\frac{\varepsilon_a k_{sz} - \varepsilon_s k_{az}}{\varepsilon_a k_{sz} + \varepsilon_s k_{az}}\right|^2,\ T_a = 1 - R_a \tag{21}$$

The reflection coefficient $R_s$from the structure is found as the square modulus of element $S_{22}$of the structure's

S-matrix. Then, the total intensity transmitted into the air after N reflections is found

$$I_a = I \cdot T_a \frac{1-(R_a R_s)^N}{1-R_a R_s} = I \cdot (1-R_a)\frac{1-(R_a R_s)^N}{1-R_a R_s} \quad (22)$$

where I is the intensity calculated in the absence of the air-substrate interface. The intensity lost due to re-absorption in the structure is

$$I_l = I \cdot R_a(1-R_s)\frac{1-(R_a R_s)^N}{1-R_a R_s} \quad (23)$$

The rest of intensity is "guided" by the substrate:

$$I_s = I - I_a - I_l = I \cdot (R_a R_s)^N \quad (24)$$

The effective number of reflections N depends on the structure geometry and on the wave vector projections k_x, k_y which determine the angles of wave propagation in the substrate.

7. Calculation examples

To demonstrate the functioning of the model we compared the experimental data on the spectral and angular characteristics of OLED devices with corresponding results obtained with numerical simulation. For this study three green bottom-emitting devices with an active area of 1.6 cm^2 and 4 mm^2 were fabricated. The structure of the devices was glass-substrate/115 nm indium tin oxide (ITO)/125 nm hole transporting layer (HTL)/10 nm electron blocking layer (EBL)/7.5 nm green emitting layer (EML) consisting of host and a green dye/10 nm hole blocking layer (HBL)/electron transporting layer (ETL)/200 nm Ag-cathode. The stack was fabricated with three different ETL thicknesses (21, 43 and 87 nm). Using standard evaporation techniques the organic layers were deposited on an ITO coated glass substrate. For better electron and hole transport, doped ETL and HTL were used. The dopant was applied by co-evaporation. This technique was also used for depositing the green dye inside the host. The evaporation rate was 0.5 Å/s at a base pressure of 10^{-7} mbar. After the evaporation of the Ag-cathode the devices were encapsulated with a glass lid and getter. The scheme of the stack is shown in Fig. 1.

The measurements were performed with a Keithley 2400 Source-Measurement Unit and an Instrument Systems fiber spectrometer (CAS 140) on a rotational stage for measurements at different angles.

For determination of the integral spectrum the measurements were performed in an integrating sphere, which was connected to the Keithley 2400 Source-Measurement Unit and the Instrument Systems fiber spectrometer. Prior to the measurement a calibration with a halogen lamp was performed with and without device in order to obtain the absorption spectra of the OLED. The substrate edges were blackened in order to avoid an influence of the side emission. For the measurement of the light trapped in the substrate an index matched half-ball lens with a diameter of 25 mm was optically coupled with an index matching gel from Cargille laboratories. The lens has a refractive index of $n = 1.52$, matching the substrate refractive index exactly. For these measurements the devices with an active area of 4 mm^2 were used.

In order to ensure accurate simulation the complex refractive indices as a function of wavelength were determined by means of reflection-transmission spectroscopy of single supported films for all used materials [16]. The emission spectrum of the phosphorescent dye in free space has been extracted from the electroluminescence (EL) spectrum emitted in the direction normal to the substrate (zero angle) by applying optical simulations based on [7] on the measured data. We first simulated the zero angle emission spectra from the OLED using a white spectrum (constant intensity over all wavelengths) and subsequently multiplied the outcome by the measured EL-spectrum.

Fig. 3 shows devices spectra measured at zero angle. Very good agreement is seen not only in the curves shape but also in the relative positions of the curves corresponding to the different devices on the whole visible spectrum. Next, angular properties of the emitted radiation are presented in Fig. 4 demonstrating dependence of the color coordinates from the viewing angle with angle step 5°. Both in experimental and theoretical characterization color coordinates were obtained with the CIE coefficients 1931 standard observer via known power flux of emitted radiation in different directions. The shape of the simulated curve well suites to the experimental one, their positions however slightly differ, this can be explained by the finite size of the detector aperture and relatively fast decrease of the emitted light intensity at high viewing angles. To demonstrate the influence of the substrate on the decrease of the external efficiency there were measured integral spectra of the usual device and the device with an optically coupled half-ball lens placed atop the substrate. Collection of the radiation from the OLED with the half-ball lens gives the total power emitted into the substrate. The results of measurement and simulation for the device with an ETL-thickness of 87 nm are shown in Fig. 5. It can be seen that the radiation in air and in the substrate can be calculated very well. The power emitted to the substrate and to the air can be also compared with theoretically calculated total effective emitted power and power losses in layers. This is done via expressions (17), (18) and the resulting spectral

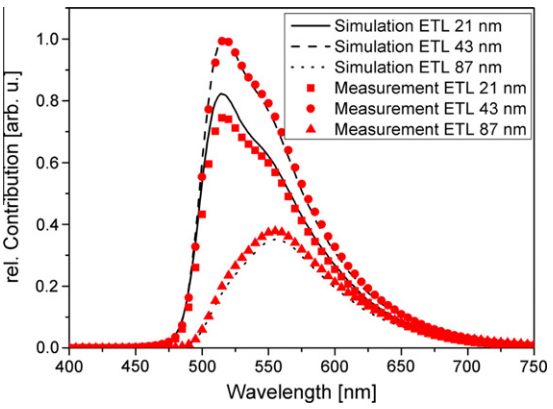

Fig. 3. Zero-angle spectra for the three devices as a function of wavelength.

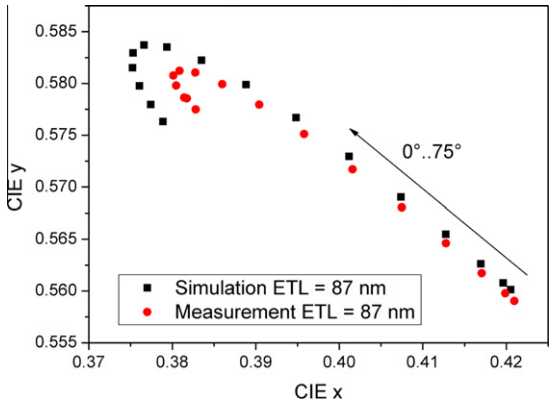

Fig. 4. Angular dependent Color coordinates of the device with an ETL-thickness of 87 nm.

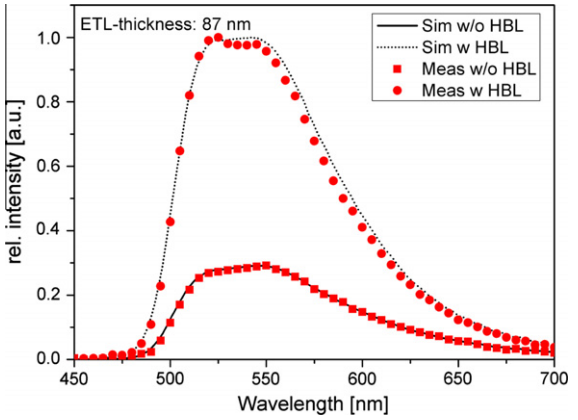

Fig. 5. Spectra with and w/o Half-Ball Lens measured in an integrating sphere as a function of wavelength.

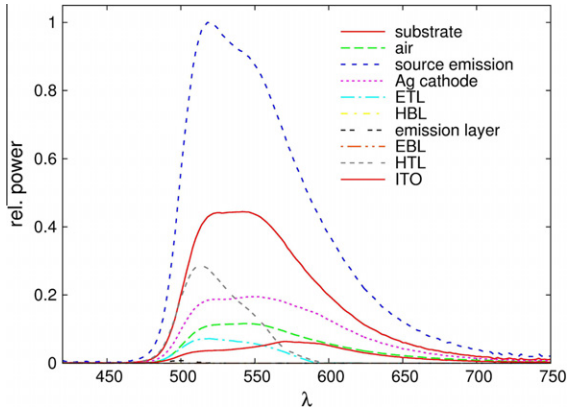

Fig. 6. Effective emission, outgoing power and losses in each layer.

dependencies are shown in Fig. 6. The analysis of losses in each layer of the structure presented in Fig. 6 may be very important in general for optimization of OLED structures. It immediately shows the layers with main losses in different parts of the spectrum, and allows the accurate tuning of the output efficiency.

8. Conclusions

The plane wave propagation model of OLEDs was revised and its ability to rigorously simulate all electromagnetic properties of devices was demonstrated. The important exact relationships for the power flux and losses in OLED layers were given. The presence of a substrate was accounted for via non-coherent reflection and transmission. The applicability of this model was confirmed by a comparison with the experimental data obtained by the measurement of the optical properties of fabricated green OLEDs.

Acknowledgements

This work was supported in part by the Russian Foundation for Basic Research (Grants No. 09-07-00285 and 09-07-12144-ofi_m) and the Russian Ministry of Education and Science (Contract No. 02.740.11.5058), and the German Federal Ministry of Education and Research (Contract No. 13N10474 (TOPAS2012)).

References

[1] M.T. Bernius, M. Inbaserkaran, J. O'Brien, W. Wu, Progress with light-emitting polymers, Adv. Mater. 23 (12) (2000) 1737–1750.
[2] V. Bulovic, V.B. Khalfin, G. Gu, P.E. Burrows, D.Z. Garbuzov, S.R. Forrest, Weak microcavity effects in organic light-emitting devices, Phys. Rev. B 58 (7) (1998) 3730–3740.
[3] K. Celebi, T.D. Heidel, M.A. Baldo, Simplified calculation of dipole energy transport in a multilayer stack using dyadic Green's functions, Opt. Exp. 15 (4) (2007) 1762–1772.
[4] K.A. Neyts, Simulation of light emission from thin film microcavities, J. Opt. Soc. Am. A 15 (4) (1998) 962–971.
[5] J.A.E. Wasey, W.L. Barnes, Efficiency of spontaneous emission rates from planar microcavities, J. Mod. Opt. 47 (4) (2000) 275–741.
[6] J.A.E. Wasey, A. Safonov, I.D.W. Samuel, W.L. Barnes, Effects of dipole orientation birefringence on the optical emission from thin films, Opt. Commun. 183 (2000) 109–121.
[7] R.R. Chance, A. Prock, R. Silbey, Molecular fluorescence and energy transfer near interfaces, Adv. Chem. Phys. 37 (1987) 1–65.
[8] N. Danz, R. Waldhausl, A. Brauer, R. Kowarschik, Dipole lifetime in stratified media, J. Opt. Soc. Am. B: Opt. Phys. 19 (3) (2002) 412–419.
[9] W. Lukosz, Theory of optical-environment-dependent spontaneous-emission rates for emitters in thin layers, Phys. Rev. B 22 (6) (1980) 3030–3038.
[10] O.H. Crawford, Radiation from oscillating dipoles embedded in a layered system, J. Chem. Phys. 89 (10) (1988) 6017–6027.
[11] K.B. Kahen, Rigorous optical modeling of multilayer organic light-emitting diodes, Appl. Phys. Lett. 78 (12) (2001) 1649–1651.
[12] X.-W. Chen, W.C.H. Choy, S. He, Efficient and rigorous modeling of light emission in planar multilayer organic light-emitting diodes, J. Display Technol. 3 (2) (2007) 110–117.
[13] L. Polerecky, J. Hamrle, B.D. MacCraith, Theory of the radiation of dipoles placed within a multilayer system, Appl. Opt. 39 (22) (2000) 3968–3977.
[14] T.W. Preist, J.R. Sambles, Periodic multilayer gratings of arbitrary shape, J. Opt. Soc. Am. A 12 (1995) 1740.
[15] J. Shinar, Organic light emitting devices: a survey, Springer-Verlag Inc., New York, 2004.
[16] M. Flämmich, N. Danz, D. Michaelis, A. Bräuer, M.C. Gather, J.H.-W.M. Kremer, K. Meerholz, Dispersion-model-free determination of optical constants: application to materials for organic thin film devices, Appl. Opt. 48 (8) (2009) 1507–1513.

Organic Electronics 12 (2011) 660–665

Contents lists available at ScienceDirect

Organic Electronics

journal homepage: www.elsevier.com/locate/orgel

Measuring the current density – voltage characteristics of individual subcells in two-terminal polymer tandem solar cells

Jan Gilot, Martijn M. Wienk, René A.J. Janssen *

Molecular Materials and Nanosystems, Eindhoven University of Technology, P.O. Box 513, 5600 MB Eindhoven, The Netherlands

ARTICLE INFO

Article history:
Received 14 November 2010
Received in revised form 11 January 2011
Accepted 15 January 2011
Available online 3 February 2011

Keywords:
Polymer solar cell
Tandem configuration
Conjugated polymer
Fullerene

ABSTRACT

Measuring the current density to voltage (*J–V*) characteristics of the separate subcells in two-terminal polymer tandem solar cells enables assessing the individual contributions of the two subcells to the total performance. We present two different methods to determine the *J–V* characteristics of the subcells in a two-terminal tandem cell without interfering with the light incoupling of the cell. The first method employs an extra proximity metal electrode that acts as a voltage probe. The proximity electrode is in contact with the recombination layer that separates the two subcells, but is positioned outside the illuminated area of the tandem cell. The second method uses bias-dependent external quantum efficiency measurements of two-terminal tandem solar cells and subsequent integration with the solar spectrum to determine the *J–V* curves of the subcells. The methods show good mutual agreement. For a 4.7% efficient solution processed two-terminal polymer tandem cell, based on PFTBT:PCBM as wide band gap and pBBTDPP2:PCBM as small band gap layer, we find that the subcells contribute with efficiencies of 2.9% and 1.8%.

© 2011 Elsevier B.V. All rights reserved.

1. Introduction

Employing wide and small band gap semiconductors in a tandem solar cell reduces the energy losses inherent to single junction cells. The wide band gap subcell lowers the thermalization losses associated with absorption of high energy photons in a small band gap cell and on the other hand the small band gap subcell absorbs the low energy photons for which a wide band gap cell is not sensitive. Hence in a tandem solar cell the photon energy can be better preserved. Recently semiconducting organic molecules and polymers are being considered for tandem solar cells, resulting in power conversion efficiencies over 5% [1–14]. Most organic and polymer tandem solar cells use a series connection in which the two subcells are electrically connected via a thin metallic interlayer or a stack of doped organic, polymer, or metal oxide electron and hole transporting layers.

The performance of a tandem cell can be determined from the current density to voltage (*J–V*) characteristics under (simulated) solar illumination but this does not allow obtaining a deeper insight in the functioning of individual layers in the tandem cell. Measuring the *J–V* characteristics of the subcells can provide better understanding of the interplay of the two subcells and assess their individual contributions. Such measurements have been demonstrated in three-terminal devices, where an intermediate metallic contact is available [6,10,15,16]. Also polymer tandem solar cells connected in a parallel configuration allow determining the *J–V* characteristics of the subcells [17,18].

A solution processed intermediate contact is, however, commercially the most interesting cell configuration because printing techniques are less time and energy consuming and eventually allow roll-to-roll processing [19]. Recently, polymer tandem solar cells with electron transporting (ET) and hole transporting (HT) layers processed from solution in a two-terminal configuration have been reported [8,9,11,12]. The conductivity of the solution

* Corresponding author. Tel.: +31 40 2473597
E-mail address: r.a.j.janssen@tue.nl (R.A.J. Janssen).

1566-1199/$ - see front matter © 2011 Elsevier B.V. All rights reserved.
doi:10.1016/j.orgel.2011.01.014

processed intermediate contact, or recombination ET–HT layer, parallel to the surface is, however, too low to use it for external *J–V* measurements.

Here, we present two methods to measure the *J–V* characteristics of the subcells of a polymer tandem solar cell with an electrically inaccessible intermediate contact. We apply these to a solution processed polymer tandem solar cell that we described recently [12]. Both methods preserve the exact layout of the tandem cell such that the optical electric field inside the device remains identical. In the first method an extra metal proximity electrode (Fig. 1a and b), located just outside of the active area, is evaporated between the ET and HT layers creating a pseudo three-terminal device that allows assessing the voltage difference between the intermediate contact and one of the two terminal electrodes. The second technique exploits bias-dependent external quantum efficiency (*EQE*) measurements of the polymer tandem solar cell in a two-terminal device as described recently [20]. Varying the bias voltage over the tandem cell allows determining the *J–V* curve of the subcells under appropriate bias illumination.

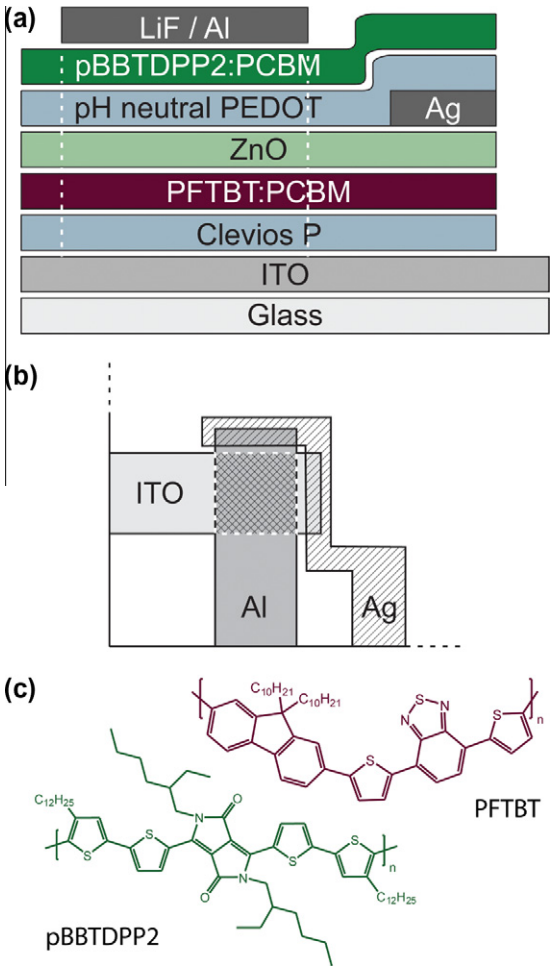

Fig. 1. Schematic side (a) and top (b) view of the device structure for a polymer tandem solar cell with an accessible intermediate contact situated just outside of the active area. The layer thickness is 180 nm for PFTBT:PCBM, 30 nm for ZnO, 15 nm for pH neutral PEDOT, and 115 nm for PBBTDPP2:PCBM. The active area, defined by the overlap of the ITO and LiF/Al electrodes, is 3×3 mm^2 and indicated by white dashed lines. The lateral distance of the Ag electrode to the actual device is 0.5 mm and the Ag layer is 30 nm thick. Panel (c) shows the chemical structures of the two polymers used.

2. Experimental

The tandem cell studied is based on poly[2,7-(9,9-didecylfluorene)-alt-5,5-(4′,7′-di-2-thienyl-2′,1′,3′-benzothiadiazole)] (PFTBT) as wide band gap polymer and poly[3,6-bis(4′-dodecyl-[2,2′]bithiophenyl-5-yl)-2,5-bis(2-ethylhexyl)-2,5-di-hydropyrrolo[3,4-]pyrrole-1,4-dione] (pBBTDPP2) as small band gap polymer (Fig. 1c), both in combination with [6,6]-phenyl-C_{61}-butyric acid methyl ester ([60]PCBM or PCBM in short) [12,20]. The recombination layer that separates the two subcells consists of a 30 nm ET layer of ZnO nanoparticles and a 15 nm HT layer of pH neutral PEDOT:PSS, both deposited from solution on the wide band gap photoactive layer [8]. When sandwiched between a ITO/PEDOT:PSS bottom electrode and a LiF/Al top electrode the entire tandem structure with a 180 nm thick PFTBT:PCBM front cell and a 115 nm thick pBBTDPP2:PCBM back cell resulted in an overall efficiency of 4.7% under simulated AM1.5G (global air mass 1.5, 100 mW/cm^2) solar light. The fabrication and optimization of these devices have been described in detail in Ref. [12]. Fig. 2 shows the AM1.5G spectrum together with the normalized absorption spectra of the two active layers and the lamp spectrum used in this study.

For the accessible intermediate contact, 30 nm Ag was evaporated through a shadow mask on top of the ZnO layer prior to the deposition of the pH neutral PEDOT. The mask was designed such that the Ag layer was placed 0.5 mm from the 3×3 mm^2 active area of the cell defined by the overlap of ITO and LiF/Al electrodes (Fig. 1b). *J–V* measurements were performed under simulated AM1.5G solar light from a tungsten-halogen lamp filtered by a Schott GG385 UV filter and a Hoya LB120 daylight filter using a Keithley 2400 source meter. Illumination was done through a mask

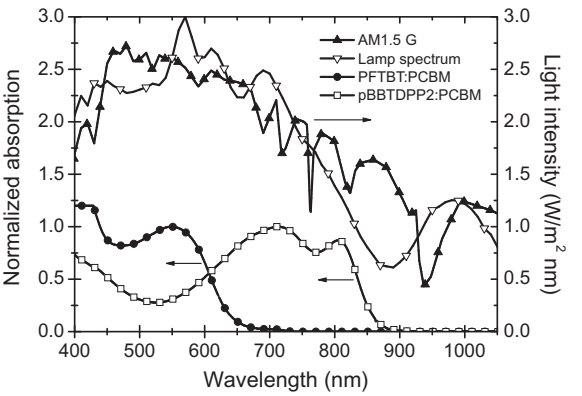

Fig. 2. Normalized absorption spectra of the two active layers (PFTBT:PCBM and pBBTDPP2:PCBM) together with the AM1.5G spectrum and the lamp spectrum of the solar simulator used in the present investigation.

with an aperture of 3×3 mm^2 that is equal to the nominal device area defined by the overlap of the ITO and LiF/Al electrodes to avoid parasitic photocurrents. The voltage difference between the accessible intermediate contact and one of the two electrodes was determined with a Keithley 6512 programmable electrometer. The high input resistance (200 TΩ) of the Keithley 6512 exceeds the lateral series resistance of the recombination layer to the Ag contact of <10 MΩ that can be inferred from the measured lateral conductivity of the pH neutral PEDOT:PSS of 0.2 S/cm and the dimensions of the device layout.

The *EQE* measurements were done in a home-built setup [20]. Modulated monochromatic (Oriel Cornerstone 130 1/8 m, Newport) probe light (Halotone halogen lamp, Philips) was mechanically chopped at a frequency of 165 Hz with an optical chopper (SR 540, Stanford Research). The bias illumination was provided by a 532 nm (B&W, Tek Inc., 30 mW) and 780 nm (B&W, Tek Inc., 21 mW) solid state laser. The sample was stored in a nitrogen filled container during the measurements and illuminated through a circular aperture of 2 mm which is slightly smaller than the device area to avoid errors. This aperture was used for the sample cell and for the calibrated Si reference cell used in the measurements. The measurements were executed with a lock-in-amplifier (SR 830, Stanford Research) over a load of 50 Ω. All data were recorded by a Labview program on a computer. The electrical bias over the tandem cell was provided by the lock-in-amplifier. Details of the measurement procedure of the *EQE* of polymer tandem solar cells have been described in detail recently [20].

3. Results and discussion

3.1. Method 1: tandem cell configuration with a proximate middle electrode

In the first method a Ag proximity electrode is evaporated after the deposition of the ZnO ET layer and prior to deposition of the pH neutral PEDOT HT layer just outside of the active area of the solar cell defined by the geometrical overlap between the patterned indium tin oxide and evaporated Al electrode (Fig. 1a and b) to create a three-terminal device. In this layout the light incoupling in the stack of the layers is not disturbed and the additional middle contact does not affect the performance of a device with optimal active layer thicknesses [12].

Measuring a *J–V* curve directly with this intermediate Ag proximity contact is not possible due to the low conductivity of the ET and HT layers parallel to the surface, which makes it impossible to pass a lateral current through the intermediate contact without significant resistance losses. However, this set-up does allow for measuring the voltage difference between the intermediate contact and one of the two electrodes. The internal impedance of the measuring unit is preferentially large to minimize current and voltage losses in the tandem cell (see Section 2). By sweeping the voltage over the entire tandem cell and recording the current density of the tandem cell and the voltage difference between the intermediate contact and one of the two electrodes, one can determine the *J–V* characteristics of the subcells in a tandem cell (Fig. 3). Apart from ensuring that the lateral series resistance is small compared to the input resistance of the voltmeter, this method only requires that there is no voltage drop at the recombination layer.

From these measurements the contribution of both subcells to the performance of the tandem cell can easily be deduced. The power density of the tandem cell in the maximum power point (*MPP*) is 4.7 mW/cm^2. For the current density corresponding to the *MPP* of the current tandem cell, the power densities of the subcells are 2.9 and 1.8 mW/cm^2 for the front and back cell, respectively. These power densities are very close to the *MPPs* of the two subcells in the tandem device (3.0 and 1.7 mW/cm^2), but in general this need not to be true. We note that Method I works best for subcells that provide rather similar current densities under illumination, because the limiting subcell sets the maximum current that can be achieved in the device. As a result, the *J–V* curve of the nonlimiting subcell cannot be measured beyond this value. This is shown in Fig. 3 where *J–V* curve of the back cell is only accessible down to −0.35 V.

3.2. Method 2: electrical bias sweep in the EQE measurement

The extra proximity contact requires an additional evaporation step during the processing of the device. The second method exploits the spectral response measurement of the polymer tandem solar cell without the need for additional processing or contacts. To allow direct comparison, the second technique has been performed on the same device as used for the first method. We have recently shown that the exact determination of the *EQE* of the subcells requires, besides a specific optical bias illumination, a forward electrical bias on the entire cell to measure the

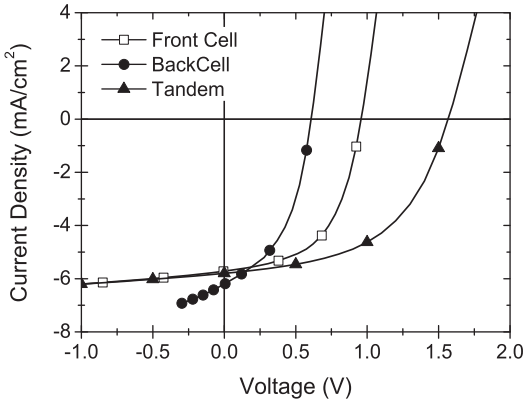

Fig. 3. Method 1. *J–V* characteristics of the front, back, and tandem cell measured with an intermediate contact situated just outside of the active area under simulated solar light. In the experiment the voltage over the tandem cell was set by the source unit and the voltage over the back cell was measured between the intermediate Ag contact and the LiF/Al contact. The data for the front cell were calculated from the two measured curves. Virtually identical results were obtained when the voltage over the front cell was measured directly between the ITO contact and the intermediate Ag contact in a separate experiment.

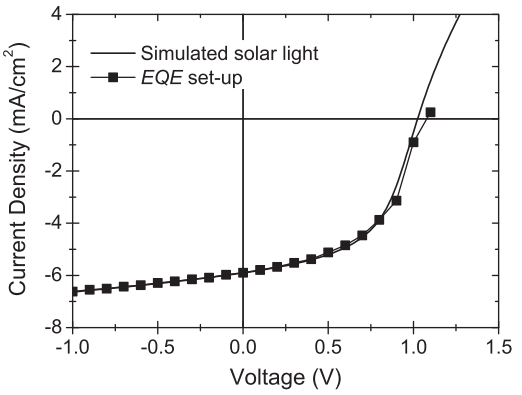

Fig. 4. Comparison of J_{photo}–V characteristics of a single junction PFTBT:PCBM solar cell measured under simulated solar light and after integration of the *EQE*, measured at different electrical bias, with the AM1.5G solar spectrum.

subcell under short-circuit conditions [20]. To correctly determine the amount of optical and voltage bias in the *EQE* measurement, the refractive index and extinction coefficient of all layers must be known as function of wavelength together with the thickness of each individual layer and the behavior of the corresponding single junction cells as function of light intensity. Integration of the experimental *EQE* at the correct bias voltage with the AM1.5G solar spectrum results in the J_{sc} of the subcell in the tandem cell.

The second methods relies on measuring the *EQE* of the subcell at variable bias voltages *V*. Integration of the resulting *EQE*(*V*) with the AM1.5G solar spectrum for each value of *V* corresponds to measuring the *J*–*V* characteristics of the subcells under simulated solar light. This is first demonstrated by measuring the *J*–*V* characteristics of a single junction PFTBT:PCBM solar cell. The *J*–*V* curve measured under simulated solar light and the *J*–*V* curve obtained from the *EQE* with varying electrical bias showed a good correspondence for the single junction cell (Fig. 4). In an *EQE* measurement only the photocurrent is determined as the response of the cell to modulated light is measured. Therefore, the J_{photo}–V curve obtained from $J_{photo} = J_{light} - J_{dark}$ measured under simulated solar light is compared to the curve from the *EQE* measurement. We note that the relation $J_{photo} = J_{light} - J_{dark}$ is only approximate because the different light intensities used in measuring J_{light} and J_{dark} cause temperature differences in the active layer [21].

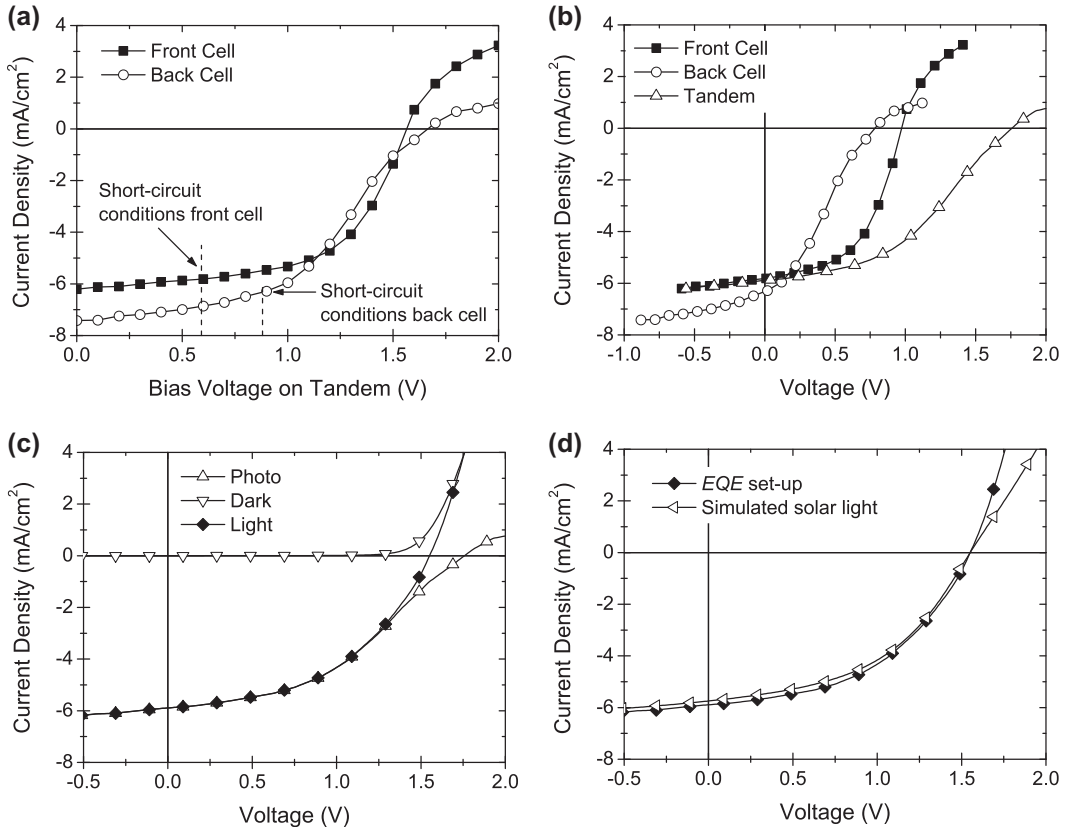

Fig. 5. Method 2. (a) Current density vs. bias voltage on the polymer tandem solar cell of the front and back cell obtained from the *EQE* measurement after integration of the *EQE* with the AM1.5G solar spectrum. The dotted line represents the electrical bias required for measuring under short-circuit conditions. (b) J_{photo}–V characteristics of the front and back cell. The J_{photo}–V curve of the tandem cell is the addition of photo *J*–*V* curves of the subcells. (c) The photo, dark, and light *J*–*V* curve of the tandem cell. (d) Comparison between the constructed *J*–*V* curve obtained from *EQE* measurements and the measured *J*–*V* curve under simulated solar light after the series of *EQE* measurements.

Table 1
Performance parameters of the front, back, and tandem cell measured with a proximity electrode (Method 1) and measured via the EQE measurement of the subcells (Method 2).

Cell	J_{sc} (mA/cm^2)	V_{oc} (V)	*FF* (–)	*MPP* (mW/cm^2)
Method 1				
Front cell (PTFBT:PCBM)	5.7	0.96	0.54	3.0
Back cell (pBBTDDP2:PCBM)	6.3	0.61	0.46	1.7
Measured tandem cell	5.8	1.57	0.52	4.7
Method 2				
Front cell (PTFBT:PCBM)	5.8	0.94	0.53	2.9
Back cell (pBBTDDP2:PCBM)	6.3	0.58	0.39	1.4
Constructed tandem cell	5.9	1.55	0.47	4.3
Measured tandem cell	5.7	1.55	0.48	4.2

The lower temperature in the dark measurement may cause an overestimation of J_{photo}. This effect is mainly present at $V > V_{oc}$ where J_{dark} steeply increases and can be seen as small deviation of the two curves in Fig. 4.

This experiment was also performed for the tandem cell used in the experiments of the first technique. For the PFTBT:PCBM front cell, all *EQE* curves at the different electrical biases were measured under a 780 nm bias illumination that ensures that the small band gap cell is not current limiting. The *EQE* was subsequently mathematically corrected for the sub-linear light intensity dependence of the current. Without this correction, the *EQE* would be overestimated because it is measured at low monochromatic light intensity. The necessity for the correction strongly depends on the light intensity (I) dependence of the short-circuit current. For many polymer solar cells this can be described by $J_{sc} = I^{\alpha}$, with the exponent α being in the range of 0.95–1.00. For example when $\alpha = 0.98$ and the monochromatic light intensity is 1% of AM1.5G intensity, the error in J_{sc} can be as large as 10%. In the Ref. [20] we have shown that for the PFTBT:PCBM cell and the present *EQE* setup the required correction factor is about 0.93.

For determining the *EQE* of the pBBTDPP2:PCBM back cell, the sample was illuminated by 532 nm light, which serves simultaneously as flood light for the back cell and as bias illumination for the front cell during the measurements. Under these conditions, the short-circuit condition in the subcells was obtained at an applied electrical bias of 0.59 V and 0.88 V for the front and back cell, respectively. This resulted in a $J_{sc} = 5.8$ mA/cm^2 for the front cell and $J_{sc} = 6.3$ mA/cm^2 for the back cell.

After integration of the *EQE* with the AM1.5G solar spectrum for variable electrical bias, the current densities of front and back cell were plotted vs. the bias voltage on the tandem cell (Fig. 5a). These curves were rectified with the appropriate forward bias voltage on the tandem cell, shifting the curves, so that the short-circuit current densities end up at 0 V (Fig. 5b). The *J–V* curves of the subcells were summed using Kirchhoff's law to obtain the *J–V* curve of the tandem cell (Fig. 5b). Addition of this photocurrent curve of the tandem cell to the measured dark curve ($J_{light} = J_{photo} + J_{dark}$) led to the *J–V* curve of the tandem cell under illumination (Fig. 5c). This *J–V* curve obtained from the *EQE* of the subcells in the tandem shows an excellent agreement with the *J–V* curve measured under simulated solar light, recorded after completing the series of spectral response measurements (Fig. 5d).

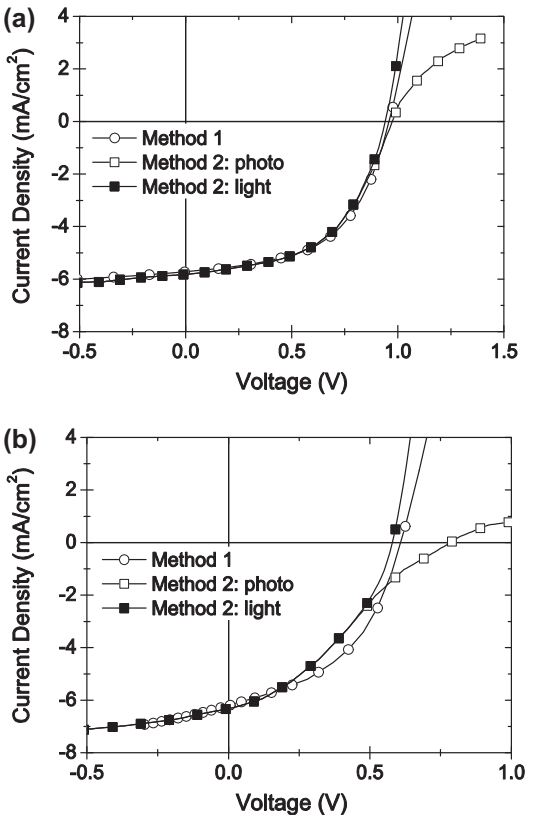

Fig. 6. Comparison between the *J–V* characteristics determined by Method 1 and Method 2 for the PFTBT:PCBM front cell (a) and the pBBTDPP2:PCBM back cell (b) in the polymer tandem solar cell. The light curve for Method 2 is defined as $J_{light} = J_{photo} + J_{dark}$, see text.

3.3. Comparison of the J–V curves of the subcells from methods 1 and 2

The two methods both allow determining the *J–V* characteristics of the subcells in a polymer tandem solar cell with a solution processed intermediate contact. Fig. 6 plots the *J–V* curves of the front and back cell obtained using the proximity electrode (Method 1) and via the *EQE* measurement (Method 2). The performance parameters of the subcells are summarized in Table 1. For the determination of the V_{oc} of the subcells in Method 2, the photocurrent curve is summed with a measured dark curve of a single junction 'dummy' cell, identical to the subcell.

For the PFTBT:PCBM front cell, the *J–V* curves of the two methods match well (Fig. 6a). On the other hand, the *J–V* curves of the pBBTDPP2:PCBM back cell diverge slightly in the region of 0.2–0.5 V (Fig. 6b). Only the fill factor (*FF*) of the back cell deviates. Because this subcell is not current-limiting, this has little to no influence on the performance of the tandem cell. The main reason for the difference is the stability of the tandem cell during the

spectral response measurements. Table 1 shows that the tandem cell has degraded from 4.7% to 4.2% as a result of the long (several hours) and intense illumination (up to 3 sun bias illumination for the PFTBT:PCBM cell) during the bias dependent *EQE* measurements.

4. Conclusions

We have developed two methods to measure the *J–V* curves of the subcells in a solution processed tandem polymer solar cell. In these devices a third middle contact that extracts current cannot be used because the conductivity parallel to the surface in the intermediate recombination layer is too limited. In the first method an additional Ag electrode was evaporated between the ET and HT layers that form the recombination layer. The Ag electrode was positioned just outside of the active area to prevent interference with the optical electric field in the stack. This extra proximity contact allows the determination of the voltage difference between the intermediate contact and one of the two electrodes. The second method employs the *EQE* measurement of the subcells in the tandem configuration and varying the electrical bias over the tandem cell. After integration with the AM1.5G solar spectrum, the current density as a function of the voltage over the tandem cell is determined for both subcells and can be transformed in the *J–V* curves of the subcells of the tandem cell. The results of the two methods are in mutual agreement and enable characterizing the individual cells in the tandem stack.

Acknowledgements

We thank Frank Louwet and Dirk Bollen (Agfa Gevaert NV) for providing a sample of the pH neutral Orgacon PEDOT. We acknowledge Jörgen Sweelssen (Dutch Organization for Applied Scientific Research, TNO) and Mathieu Turbiez (BASF) for the synthesis of PFTBT and pBBTDPP2, respectively. This work has been financially supported by the Senter/Novem in the EOS project Zomer (EOSLT03026). The research was further supported by the "Europees Fonds voor Regionale Ontwikkeling" (EFRO) in the Interreg IV-A project Organext.

References

[1] T. Ameri, G. Dennler, C. Lungenschmied, C.J. Brabec, Organic tandem solar cells: a review, Energy Environ. Sci. 2 (2009) 347–364.
[2] A. Hadipour, B de Boer, P.W.M. Blom, Organic tandem and multi-junction solar cells, Adv. Funct. Mater. 18 (2008) 169–181.
[3] B. Maennig, J. Drechsel, D. Gebeyehu, P. Simon, F. Kozlowski, A. Werner, F. Li, S. Grundmann, S. Sonntag, M. Koch, K. Leo, M. Pfeiffer, H. Hoppe, D. Meissner, N.S. Sariciftci, I. Riedel, V. Dyakonov, J. Parisi, Organic *p–i–n* solar cells, Appl. Phys. A 79 (2004) 1–14.
[4] J. Xue, S. Uchida, B.P. Rand, S.R. Forrest, Asymmetric tandem organic photovoltaic cells with hybrid planar-mixed molecular heterojunctions, Appl. Phys. Lett. 85 (2004) 5757–5760.
[5] J. Drechsel, B. Männig, F. Kozlowski, M. Pfeiffer, K. Leo, H. Hoppe, Efficient organic solar cells based on a double *p–i–n* architecture using doped wide-gap transport layers, Appl. Phys. Lett. 86 (2005) 244102/1–244102/3.
[6] A. Hadipour, B. de Boer, J. Wildeman, F.B. Kooistra, J.C. Hummelen, M.G.R. Turbiez, M.M. Wienk, R.A.J. Janssen, P.W.M. Blom, Solution-processed organic tandem solar cells, Adv. Funct. Mater. 16 (2006) 1897–1903.
[7] G. Dennler, H.-J. Prall, R. Koeppe, M. Egginger, R. Autengruber, N.S. Sariciftci, Enhanced spectral coverage in tandem organic solar cells, Appl. Phys. Lett. 89 (2006) 073502/1–3.
[8] J. Gilot, M.M. Wienk, R.A.J. Janssen, Double and triple junction polymer solar cells processed from solution, Appl. Phys. Lett. 90 (2007) 143512/1–143512/3.
[9] J.Y. Kim, K. Lee, N.E. Coates, D. Moses, T.-Q. Nguyen, M. Dante, A.J. Heeger, Efficient tandem polymer solar cells fabricated by all-solution processing, Science 317 (2007) 222–225.
[10] A. Hadipour, B. de Boer, P.W.M. Blom, Solution-processed organic tandem solar cells with embedded optical spacers, J. Appl. Phys. 102 (2007) 074506/1–074506/6.
[11] S. Sista, M.-H. Park, Z. Hong, Y. Wu, J. Hou, W.L. Kwan, G. Li, Y. Yang, Highly efficient tandem polymer photovoltaic cells, Adv. Mater. 22 (2009) 380–383.
[12] J. Gilot, M.M. Wienk, R.A.J. Janssen, Optimizing polymer tandem solar cells, Adv. Mater. 22 (2010) E67–E71.
[13] R. Schueppel, R. Timmreck, N. Allinger, T. Mueller, M. Furno, C. Uhrich, K. Leo, M. Riede, Controlled current matching in small molecule organic tandem solar cells using doped spacer layers, J. Appl. Phys. 107 (2010) 044503/1–044503/6.
[14] D. Cheyns, B.P. Rand, P. Heremans, Organic tandem solar cells with complementary absorbing layers and a high open-circuit voltage, Appl. Phys. Lett. 97 (2010) 033301/1–033301/3.
[15] V. Shrotriya, E.H.-E. Wu, G. Li, Y. Yao, Y. Yang, Efficient light harvesting in multiple-device stacked structure for polymer solar cells, Appl. Phys. Lett. 88 (2006) 064104/1–064104/3.
[16] H.B. Yang, Q.L. Song, C.M. Li, Z.S. Lu, New architecture for accurate characterization of the behavior of individual sub-cells within a tandem organic solar cell, Energy Environ. Sci. 1 (2008) 389–394.
[17] X. Guo, F. Liu, W. Yue, Z. Xie, Y. Geng, L. Wang, Efficient tandem polymer photovoltaic cells with two subcells in parallel connection, Org. Electron. 10 (2009) 1174–1177.
[18] S. Sista, Z. Hong, M.-H. Park, Z. Xu, Y. Yang, High-efficiency polymer tandem solar cells with three-terminal structure, Adv. Mater. 22 (2010) E77–E80.
[19] Y. Galagan, I.G. de Vries, A.P. Langen, R. Andriessen, W.J.H. Verhees, S.C. Veenstra, J.M. Kroon, Technology development for roll-to-roll production of organic photovoltaics, Chem. Eng. Process. (2010), doi:10.1016/j.cep.2010.07.012.
[20] J. Gilot, M.M. Wienk, R.A.J. Janssen, Measuring the external quantum efficiency of two-terminal polymer tandem solar cells, Adv. Funct. Mater. 20 (2010) 3904–3911.
[21] Z.E. Ooi, R. Jin, J. Huang, Y.F. Yoo, A. Sellinger, J.C. De Mello, On the pseudo-symmetric current–voltage response of bulk heterojunction solar cells, J. Mater. Chem. 18 (2008) 1644–1651.

Organic Electronics 12 (2011) 666–676

Contents lists available at ScienceDirect

Organic Electronics

journal homepage: www.elsevier.com/locate/orgel

Arylvinylene phenanthroline derivatives for electron transport in blue organic light emitting diodes

Poopathy Kathirgamanathan *, Sivagnanasundram Surendrakumar, Raghava Reddy Vanga, Seenivasagam Ravichandran, Juan Antipan-Lara, Subramaniam Ganeshamurugan, Muttulingham Kumaraverl, Gnanamoly Paramaswara, Vincent Arkley

Organic Electronics, Wolfson Centre, Brunel University, Kingston Lane, Uxbridge UB 8 3PH, UK

ARTICLE INFO

Article history:
Received 3 September 2010
Received in revised form 26 November 2010
Accepted 31 December 2010
Available online 25 January 2011

Keywords:
Phenanthrolines
Electron transporters
OLEDs
Blue materials
Device fabrication

ABSTRACT

A series of novel arylvinylene substituted phenanthroline derivatives has been synthesised and their application as electron transporting materials in organic light emitting diodes (OLEDs) has been investigated. One particular derivative, namely, 2,9-bis-(2-thiophen-2-yl-vinyl)-[1,10]phenanthroline (C-4) shows significantly lower operating voltage (36% reduction) and increase of power efficiency of up to 83% compared to tris (8-quinolinolato)aluminium (III) (Alq_3). C4 also shows substantially longer (nearly 6-fold) life-time than bathophenanthroline (BPhen) in blue devices. Doping of C4 with electron donors such as m-MTDATA, α-NPB and lithium quinolinolate (Liq) further reduces the turn-on voltage and operating voltage.

© 2011 Elsevier B.V. All rights reserved.

1. Introduction

Organic light emitting diode (OLED) based displays have become one of the significant flat panel display technologies as evidenced by the production of active matrix OLEDs for mobile phones by Samsung SDI and the introduction of 11″ AM-OLED TV (XEL-1) to the market by Sony. Recent announcement by Samsung of its intention to invest US Dollars 2.2 billion into active matrix OLED Television (AM-OLED) to bring them into mainstream TV market has given considerable impetus to the scientists developing materials for the OLED devices [1–9].

Since Tang et al. reported an organic light emitting device (OLED) using tris (8-quinolinolato)aluminium (III) (Alq_3) as an electron transporting material (ETM) in 1987, Alq_3 has widely been employed both in commercial production and research because of its low cost and acceptable life-time [2]. However, Alq_3 has three disadvantages: (i) poor mobility, therefore high operating voltage and reduced luminous efficiency. (ii) It leaves behind considerable amount of residue and ash under production condition (during vacuum thermal evaporation). (iii) Perceived toxicological properties of aluminium compounds. Considerable research effort has been expended to develop high mobility materials which would reduce the operating voltage without diminishing the efficiency and life-time [8,9]. In addition to metal quinolates, oxadiazole(s), oxazole(s), thiazole(s), imidazole(s), pyridyl compounds, silole(s), perfluorinated oligophenylene(s), phenanthroline(s), pyrimidone(s) and triazine(s) have been reported by several authors [3–8,10–14,19,28–31].

Amongst the phenanthroline derivatives, bathophenanthroline (BPhen), bathocuproine (BCP) have been extensively studied because of their high mobility (1×10^{-4} $cm^2 V^{-1} s^{-1}$) compared to that of Alq_3 (1×10^{-6}–1×10^{-7} $cm^2 V^{-1} s^{-1}$) [6–7] and deep HOMO levels (typically, −6 eV to −6.9 eV) which make them excellent hole blockers. However, both virgin BCP and BPhen give significantly poorer life time compared to other hole blockers. The former tends to crystallize (BCP films crystallize upon

* Corresponding author. Tel.: +44 1895 265094; fax: +44 1895 269737.
E-mail address: p.kathir@brunel.ac.uk (P. Kathirgamanathan).

1566-1199/$ - see front matter © 2011 Elsevier B.V. All rights reserved.
doi:10.1016/j.orgel.2010.12.025

storage) and the latter has a very low T_g of 62 °C [9,15–17]. Both BCP and BPhen were found to give acceptable life-time if they are doped or mixed with electron donors such as low work function metals (e.g. Li and Cs) or their complexes [10–13]. Kim and Im [15] reported that their devices with pristine BCP or BPhen lasted only a few hours even at an initial luminance of 150 cd m^{-2}. Another potential candidate, 1,3,5-tris(phenyl-2-benzimidazolyl)benzene (TPBI), has similar crystallisation problem [21].

Yan-Jun Li et al. recently reported some phenanthroline derivatives with superior performance to Alq_3 [11] for their device structure ITO/α-NPB (50 nm)/Alq_3 (40 nm)/ETL (30 nm)/LiF (1 nm)/Al where their best ETM gave a 21% reduction in operating voltage at 1000 cd m^{-2} and 32% increase in power efficiency (lm/W) compared to Alq_3 based devices. However, no life-time information was reported.

A good electron transporter (et) should have the following characteristics [7]: (i) high electron affinity to match with the workfunction (W.F.) of the cathode, thus reducing the energy barrier; (ii) high electron mobility ($\mu_e > 1 \times 10^{-5}$ cm^2 V^{-1} s^{-1}) to aid the transport of electrons into the emissive layer and efficiently confine the excitons in this layer; (iii) a reversible electrochemical reduction with a sufficiently high reduction potential;(iv) a high ionisation potential (I.P.) to serve as a hole blocker (I.P. > 6 eV); (v) a high glass transition temperature and melting point; (vi) thermal stability up to at least 250 °C (high $T_g/T_m/T_d$); (vii) stability under evaporation conditions for a period of at least 144 h if vacuum processing is employed as the manufacturers would like to run their production equipment at least for 6 days in a row without interruption; (viii) good stability to moisture and oxygen; (ix) capable of forming amorphous film so that crystallisation induced degradation is avoided; (x) photostability; (xi) if phosphorescent emitters are used, the triplet energy level of the et should be higher than that of the phosphorescent emitters; (xii) processability to produce uniform and pinhole-free films either by evaporation (small molecules) or by solution casting.

We have been interested in developing electron transporters cum hole blockers which would give long life-times. Here, we report the synthesis of some selected 2,9 substituted phenanthrolines, their physical properties and their performance as ETMs in blue OLEDs [14].

2. Experimental

2.1. Synthesis

The compounds were synthesized according to the general method as shown in Scheme 1. All the compounds were purified by double sublimation.

2.1.1. 2,9-Bis(styryl)-[1,10]-phenanthroline [C-1]

A mixture of neocuproine hydrate (5.0 g; 0.024 mol) and benzaldehyde (5.4 g; 5.2 mL; 0.050 mol) was refluxed

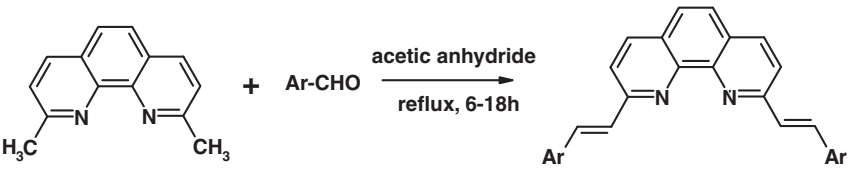

Scheme 1. Ar = phenyl (*C*-1), 4-trifluoromethylphenyl (*C*-2), 4-cyanophenyl (*C*-3) and thienyl (*C*-4).

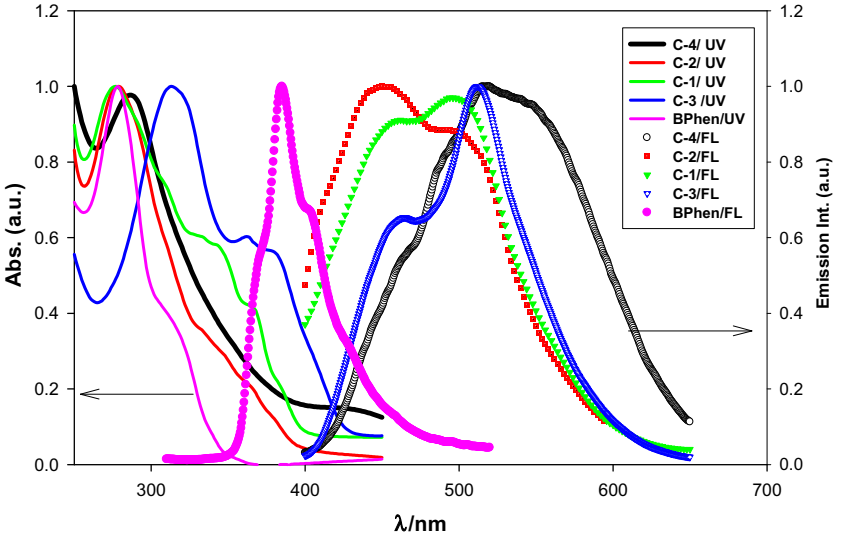

Fig. 1. Thin film UV–Vis absorption and fluorescence spectra of C-1, C-2, C-3, C-4 and BPhen. Excitation wavelengths: C-1 (360 nm), C-2 (360 nm), C-3 (350 nm), C-4 (350 nm) and BPhen (350 nm).

in acetic anhydride (20 mL) for 6 h and the cooled reaction mixture was poured into ice-cold water. The product was extracted into ethyl acetate. The organic phase was washed with water, dried over anhydrous magnesium sulphate and then the solvent removed. To the residue con. HCl was added and the yellow solid that obtained was again taken into dichloromethane and extracted with 5% NaOH solution. The organic phase was washed well with water, dried over anhydrous magnesium sulphate and solvent removed to give a yellow solid. The product was purified by column chromatography on silica gel (eluent: CH_2Cl_2–MeOH 49:1). The eluents containing the product was evaporated and by addition of ether and petroleum ether gave an analytically pure material 4.8 g (52%). *Anal.* Calc. for $C_{28}H_{20}N_2$: C, 87.47; H, 5.24; N, 7.28. Found: C, 87.14; H, 5.15; N, 7.20%. ^{1}H NMR ($CDCl_3$): 7.33(t, J = 7.4 Hz, H-1), 7.42(t, J = 7.4 Hz, H-2), 7.70(d, J = 8.3 Hz, H-3), 7.78(d, J = 16 Hz, H-4), 7.73(d, J = 16 Hz, H-5), 7.89(d, J = 8.4 Hz, H-6), 8.16(d, J = 8.4 Hz, H-8), 7.68 (s, H-8 and H-9).

2.1.2. 2,9-Bis(4,4′-trifluoromethylphenyl)vinyl-[1,10]-phenanthroline [C-2]

A mixture of neocuproine hydrate (5.0 g; 0.024 mol) and 4-(trifluoromethyl)benzaldehyde (8.8 g; 0.050 mol) was refluxed in acetic anhydride (20 mL) for 6 h and then allowed to cool for 18 h to give light pinkish crystals. Methanol and small amounts of water were added and the crystals were collected by suction filtration. The product was then washed thoroughly with methanol, water and diethyl ether before dried under vacuum at 80 °C for several hours to give (7.9 g; 63%) of product. Finally, the product was purified by sublimation (270 °C at 10^{-6} Torr) to give an analytically pure material as a light yellow solid, m.p. 279 °C (DSC, onset); 285 °C (DSC, peak). *Anal.* Calc. for $C_{30}H_{18}N_2F_6$: C, 69.23, H, 3.49; N, 5.38. Found: C, 69.54, H, 3.39, N, 5.40%; ^{1}H NMR (d-DMF): 7.88(d, J = 8 HZ, H-3, 4H), 7.93 (d, J = 16 Hz, H-5), 8.02 (s, H-9), 8.03 (s, H-8), 8.11(d, J = 8 Hz, H-2, 4H), 8.20 (d, J = 8.3 Hz, H-6), 8.26 (d, J = 16 Hz, H-4), 8.58 (d, J = 8.3 Hz, H-7).

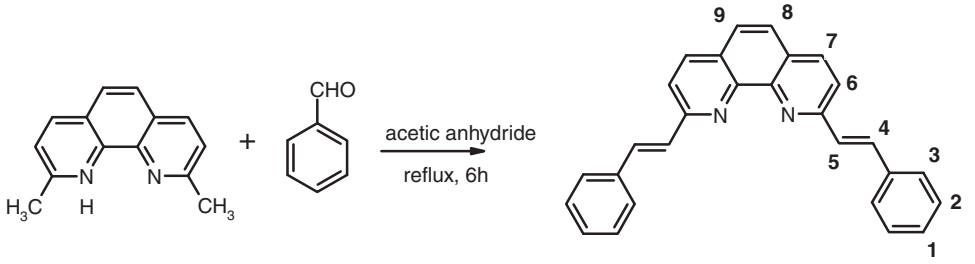

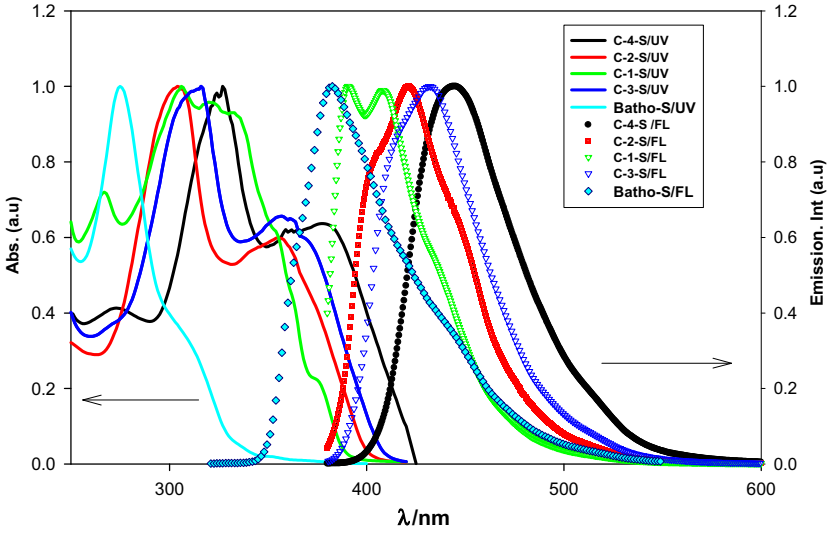

Fig. 2. UV–Vis absorption and fluorescence spectra of C-1 (4.16×10^{-5} M), C-2 (3.84×10^{-5} M), C-3 (5.06×10^{-5} M), C-4 (4.03×10^{-5} M) and BPhen (6.0×10^{-5} M) in CH_2Cl_2. Excitation wavelengths: C-1, C-2, C-3, C-4 (all 350 nm) except BPhen (300 nm).

Table 1
Physical properties of compounds, C-1–C-4 Compared with Alq_3 and bathophen.

Compound	M.p. (°C) (a)	T_g (°C) (a)	T_d (°C) (b)	HOMO (eV) (c)	LUMO (eV) (c)	UV (λ_{max}/nm, absorption) Thin film	FL (λ_{max}/nm, emission) Thin film	Comments
C-1	192	69	300	−5.8	−2.8	277 (m), 340 (sh))	453, 493	Decomposes on sublimation
C-2	279	(d)	337	−5.9	−2.8	279 (m), 345 (sh)	451, 491 (sh)	Stable in OLED production conditions
C-3	289	(d)	130	−5.9	−3.0	313 (m), 362 (sh)	461 (sh), 512	Decomposes on sublimation. So, no device fabricated
C-4	298	111	345	−6.0	−3.0	329(m), 385 (sh)	520	Stable in OLED production conditions
Bathophen (BPhen)	218	62	287	−6.4	−3.0	278 (m), 314 (sh)	385, 402 (sh)	Stable in OLED production conditions. Poor life-time due to low T_g
Alq_3	415	172	352	−5.7	−2.9	265, 393	520	Stable in OLED production conditions

a: Determined by DSC; b: from TGA for 1% mass loss; c: determined from cyclic voltammetry; d: not observed; sh: shoulder.

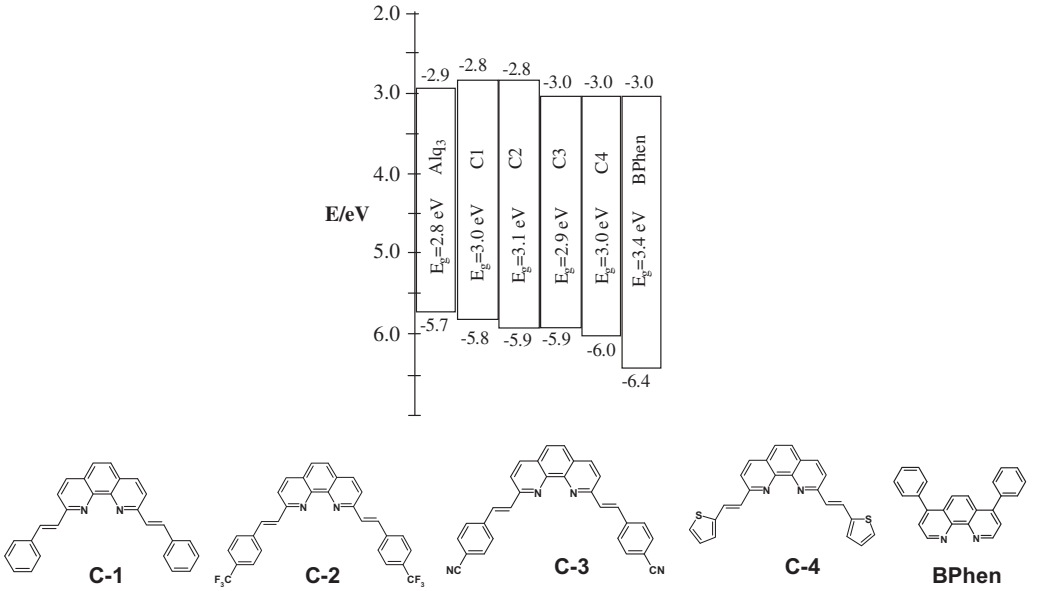

Fig. 3. HOMO–LUMO levels of Alq_3, C-1, C-2, C-3, C-4 and bathophenanthroline (BPhen).

2.1.3. 2, 9-Bis(4,4′-cyanophenyl)vinyl-[1,10]-phenanthroline [C-3]

A mixture of neocuproine hydrate (5.0 g; 0.024 mol) and 4-cyanobenzaldehyde (6.6 g; 0.050 mol) was refluxed in acetic anhydride (30 mL) for 18 h under nitrogen and then allowed to cool to room temperature to give a yellow orange solid. The product was filtered off under suction and washed with petroleum ether (40–60 °C), methanol and finally with diethyl ether. The product was dried under vacuum at 80 °C to give a light yellow solid (7.9 g; 76%). Finally, the crude product was purified by sublimation (at 280 °C; 10^{-6} Torr) to give an analytically pure material, m.p. 289 °C (DSC, onset). *Anal.* Calc. for $C_{30}H_{18}N_4$: C, 82.93; H, 4.18; N, 12.82. Found: C, 82.67; H, 4.07; N, 12.82%. The compound was so insoluble in most of the organic solvents that ^1H NMR could not be carried out.

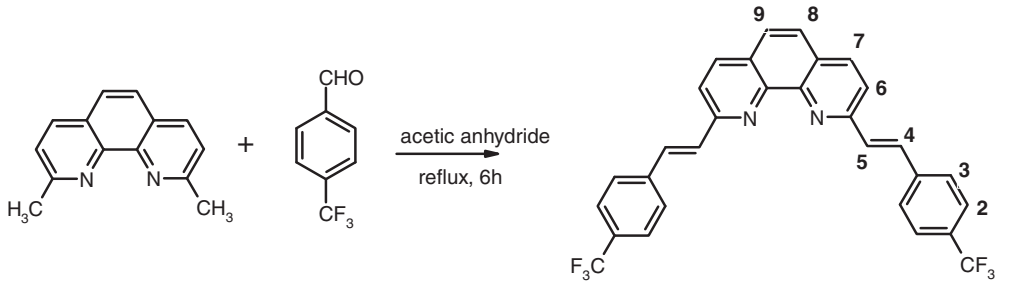

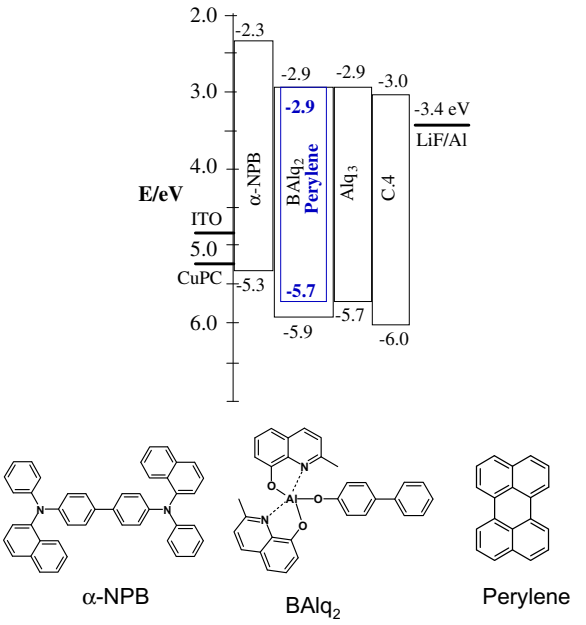

Fig. 4. Energy level diagram for the device: ITO/CuPc(50 nm)/a-NPB (75 nm)/$BAlq_2$ + perylene(50:0.1 nm)/ETL(20 nm)/LiF(0.5 nm)/Al where the ETL is either Alq_3 or C-4.

2.1.4. 2,9-Bis-(2-thiophen-2-yl-vinyl)-[1,10]phenanthroline [C-4]

A mixture of neocuproine hydrate (50 g; 0.24 mol) and 2-thiophene carboxaldehyde (46.5 mL; 0.50 mol) was refluxed in acetic anhydride (90 mL) for 6 h and then allowed to cool to room temperature over 20 h. Water (20 mL) and methanol (130 mL) were added to the reaction mixture and the product was collected by suction filtration to give a light yellow brown solid. The solid was washed with petroleum ether (40–60 °C), methanol followed by diethyl ether and dried under vacuum at 80 °C for several hours (>10 h) to give (46 g; 48%) of product . Finally, the product was further purified by sublimation (at 260 °C; 10^{-6} Torr) to give a golden yellow solid, m.p. 298 °C (DSC, onset); T_g 111 °C. *Anal.* Calc. for $C_{24}H_{16}N_2S_2$: C, 72.70; H, 4.07; N, 7.06; S, 16.17. Found: C, 72.85; H, 4.12: N, 7.10; S, 16.17%; ^{1}H NMR (d-DMF): 7.21(dd, H-2), 7.45 (d, J = 16 Hz, H-5), 7.52 (d, J = 3.5 Hz,H-3), 7.67 (d, J = 5 Hz, H-1), 7.95(S, H-8, 9), 8.15 (d, J = 8.3 Hz, H-6), 8.32 (d, J = 16 Hz, H-4), 8.49 (d, J = 8.3 Hz, H-7). MS (m/z) (%): 419 (100) (M^++Na), also peaks appeared at m/z 435, 472 and 499.

3. Characterisation

UV–Vis absorption spectroscopy (Shimadzu, UV-1601) and fluorescent spectroscopy (Perkin–Elmer LS55) were performed on evaporated thin films on quartz (spectrosil) and in dichloromethane solutions. The decomposition characteristics were examined under nitrogen atmosphere on a TGA equipment (Rheometric Scientific) and the Differential Scanning calorimetry was performed on Perkin Elmer (Pyris 6 DSC). Band gap was estimated from absorption spectroscopy of thin films produced by vacuum thermal evaporation.

HOMO–LUMO levels were determined by cyclic voltammetry (computer controlled potentiostat PAR 273 or CHI 600D, analyte = 0.5 mM, supporting electrolyte (tetrabutyl ammonium tetrafluoroborate = 10 mM in dichloromethane as the solvent). The working, counter and reference electrodes were Pt foil, Pt wire and Ag/AgCl electrodes, respectively.

The HOMO/LUMO levels were determined from the equation in the reference [26]:

$$\text{HOMO/LUMO} = -(E_{1/2}\text{vs.NHE} + 4.40)\ \text{eV} \quad (1)$$

(NHE: normal hydrogen electrode)

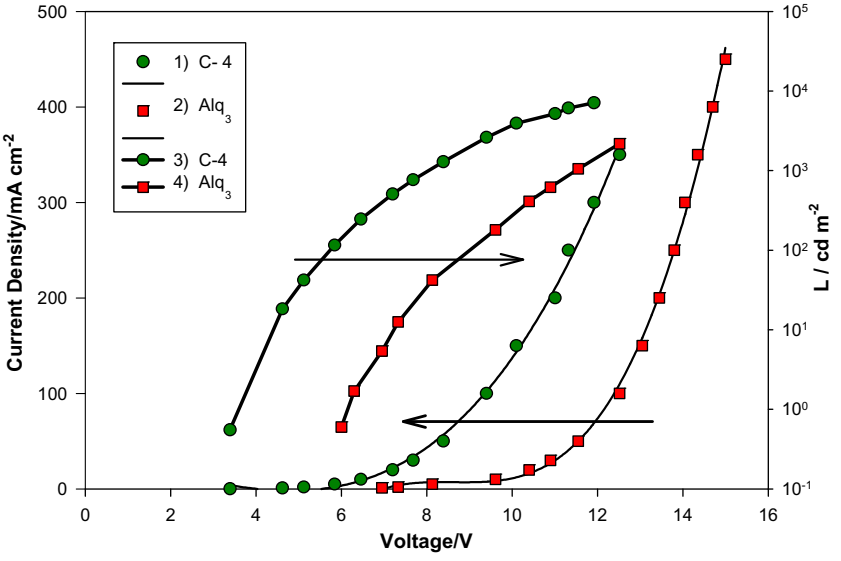

Fig. 5. Current density–voltage–luminance characteristics of ITO/CuPc(50 nm)/a-NPB(75 nm)/$BAlq_2$ + perylene(50:0.1 nm)/ETL(20 nm)/LiF(0.5 nm)/Al where the ETL is either Alq_3 or C-4.

Table 2
Performance of blue devices (Set A).

ETM	Turn-on voltage (V)	V_{op}/V at 1000 cd m^{-2}	V at 100 mA cm^{-2}	Eff./cd A^{-1} at 100 cd m^{-2}	Eff./lm W^{-1} at 100 cd m^{-2}	Eff./cd A^{-1} at 1000 cd m^{-2}	Eff./lm W^{-1} at 1000 cd m^{-2}	EQE (%)	Life-time ($t_{1/2}$)/h) initial luminance 100 cd m^{-2}
Alq_3 (a)	6.0	11.0	12.5	1.2	0.5	2.2	0.6	1.54	7200
C-4 (a)	3.5	7.0	8.0	2.3	1.2	2.5	1.1	1.61	3000

(a): ITO/CuPC (50 nm)/α-NPB (75 nm)/$BAlq_2$ + perylene (50: 0.1 nm)/ETL (20 nm)/LiF (0.5 nm)/Al.

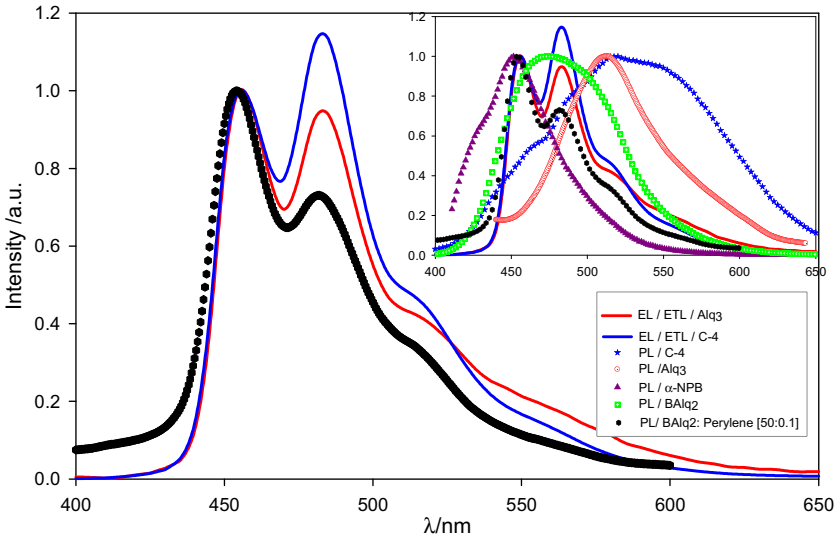

Fig. 6. EL spectra (solid lines) of ITO/CuPc(50 nm)/a-NPB(75 nm)/$BAlq_2$ + perylene (50:0.1 nm)/ETL(20 nm)/LiF(0.5 nm)/Al where the ETL is either Alq_3 or C-4. Thin film PL spectra of C-4, Alq_3, a-NPB, $BAlq_2$ and perylene (50:0.1).

The $E_{1/2}$ employed here were determined from the derivative of the cyclic voltammograms.

3.1. Device fabrication

Electroluminescent devices were fabricated by thermal evaporation method using a multi-chamber OLED pilot plant machine (Solciet, manufactured by ULVAC, Japan). The devices were fabricated on a patterned (pixelated ITO substrate (40 Ω per square surface resistance), Hitachi High Tech., Japan), cleaned with deionised water, acetone, isopropyl alcohol and water (in that order), then dried at 150 °C for 20 min and then subjected to ozone cleaning (UV irradiation, 185 nm) at 150 °C for 10 min. The substrate was then plasma cleaned in the presence of oxygen for 25 s and moved into the vacuum chamber from which the hole injector (copper phthalocyanine, CuPC), hole transporter [*N*,*N*′-bis-(1-naphthalenyl)-*N*,*N*′-bis-phenyl-(1,1′-biphenyl)-4,4′-diamine (α-NPB)]], host ($BAlq_2$ or BH-3)):dopant (perylene or BD-3), electron transporter (20 nm) were sequentially deposited under vacuum. The evaporation rates of CuPc, α-NPB, $BAlq_2$, perylene, BH-3, BD-3, Alq_3 and C-4 were 0.7, 1.5, 1, 0.002, 1, 0.1, 1 and 1 Å s^{-1}, respectively.

An electron injection layer (LiF, 0.5 nm) was deposited on top of the ETM before depositing the top contact (Al, 150 nm). All the devices were encapsulated with a UV curable adhesive (Nagase, Japan) with glass backplates in a glovebox under nitrogen atmosphere. The electrical and optical measurements were carried out by computer controlled Keithley 2400 Source Meter and Minolta (CS-1000) spectrometer, respectively. Life time measurements were carried out on encapsulated devices under constant current.

4. Results and discussion

4.1. Physical properties

The thin film absorption and fluorescence spectra of the compounds C-1-C-4 and bathophenanthroline (BPhen) are compared in Fig. 1. The absorbance and fluorescence in dichloromethane are shown in Fig. 2. All the compounds were found to be fluorescent, light blue as thin films and dark blue in solutions.

Table 1 summarises the physical properties of the compounds C-1, C-2, C-3 and C-4. All the compounds were purified by double sublimation.

HOMO–LUMO data are shown in Fig. 3. On substituting the phenyl ring of C-1 with electron withdrawing groups such as CF_3 (C-2), the HOMO level is depressed by 0.1 eV whilst LUMO level is unchanged. In contrast, both HOMO

and LUMO levels are lowered by 0.1 eV on substituting C-1 with the CN group (C-3). This is consistent with the postulation by Bredas and Heeger [20].

4.2. Device performance

As C-1 and C3 decompose on sublimation, they were not suitable for device fabrication under vacuum thermal evaporation. We report here the blue device performance of only compound 4 as our preliminary results showed that C4 was superior to C2 in terms of operating voltage, efficiency and life-time [22] with green OLEDs. Thus, we fabricated two sets of OLEDs. One (Set A), light blue based on $BAlq_2$ as host and perylene as dopant and the other (Set B) dark blue [(CIE (x, y): (0.15, 0.14)] based on host BH-3 (Kodak) and dopant BD-3 (Kodak).

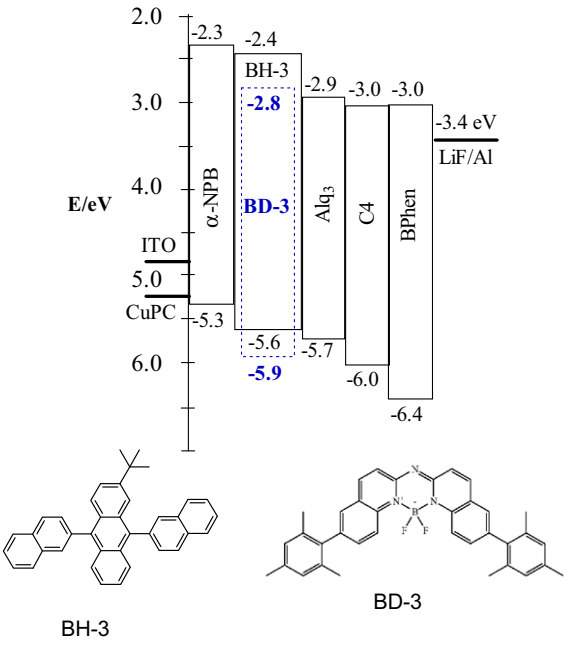

Fig. 7. Energy level diagram for ITO/CuPc (10 nm)/a-NPB(50 nm)/BH-3 + BD-3 (30:0.5 nm)/ETL (20 nm)/LiF(0.5 nm)/Al where the ETL is either Alq_3, C-4 or BPhen.

4.2.1. Device Set A

The device architecture of Set A is ITO/CuPC (50 nm)/α-NPB (75 nm)/$BAlq_2$ + perylene (50:0.1 nm)/ETL (20 nm)/LiF (0.5 nm)/Al where the ETL is either Alq_3 or C-4. The energy level diagram for the device under zero bias is shown in Fig. 4.

Fig. 5 shows the luminance vs. voltage and the current density vs. voltage plots for the Set A. From Fig. 5, it is obvious that the current injection and transport are much more efficient in the case of C-4 as opposed to Alq_3 as evidenced by the lower operating voltage presented by C-4 at any given luminance or current density. For example, the voltage required for devices with Alq_3 as ETM to give a luminance of 1000 cd m^{-2} was 11 V as opposed to those with C-4 was only 7 V, a reduction of nearly 36% in operating voltage. Correspondingly, the power efficiency for devices with Alq_3 as ETL was 0.6 lm/W and those with Compound C-4 was 1.1 lm/W at 1000 cd m^{-2}, representing an increase of 83% in efficiency. The device data are also summarised in Table 2. The colour co-ordinates obtained for devices with Alq_3 [(CIE (x, y): (0.173, 0.252)] and that for the devices with C4 is (0.150, 0.233). This is consistent with our expectation that the mobility of C-4 is much greater than that of Alq_3 and hence the electron/hole recombination would take place closer to the α-NPB interface for the devices with C-4 and hence more saturated blue colour co-ordinates. Fig. 6 compares the EL spectra of the devices

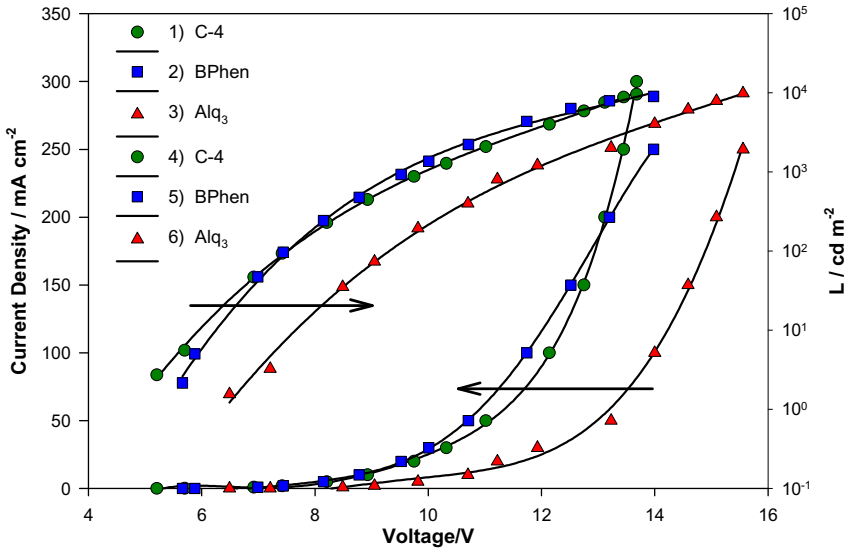

Fig. 8. Current density–voltage–luminance characteristics of ITO/CuPc (10 nm)/a-NPB(50 nm)/BH-3 + BD-3 (30:0.5 nm)/ETL (20 nm)/LiF(0.5 nm)/Al where the ETL is either Alq_3, C-4 or BPhe.

with C-4 and the Alq_3 as ETL and the PL of α-NPB, $BAlq_2$, a mixture of $BAlq_2$ with perylene (50:0.1) and Alq_3 and C-4. It is clear from Fig. 6 that the peak positions of the EL spectra and the PL of mixture of $BAlq_2$ and perylene are identical, but the relative ratios of the intensity of emission are slightly different. The second peak at 483 nm from the EL of the devices with C-4 as the ETL is slightly more intense than the first peak at 455 nm when compared with the EL from devices where Alq_3 is ETL. The EL spectra of devices with Alq_3 has a longer emission tail than the EL spectra of devices with C-4 as the ETL. This explains the differences in colour co-ordinates obtained here. Furthermore, the relative intensity differences could be due to the slight differences in the concentration of perylene in the host as the control of concentration at such a low level (0.2% of perylene) is not easy under the co-evaporation conditions.

The life-time of the devices with Alq_3 as ETM has significantly longer life-time than C-4. We attribute this to the high Tg (172 °C of Alq_3) as compared to C-4 (111 °C) and the fact that Alq_3 is a mixture of at least two isomers thus retaining a high degree of amorphicity [27].

It is well known that the nature of current injection of an electron transporter is dependent on its interfacial characteristics with the adjacent layer, namely, host + dopant.

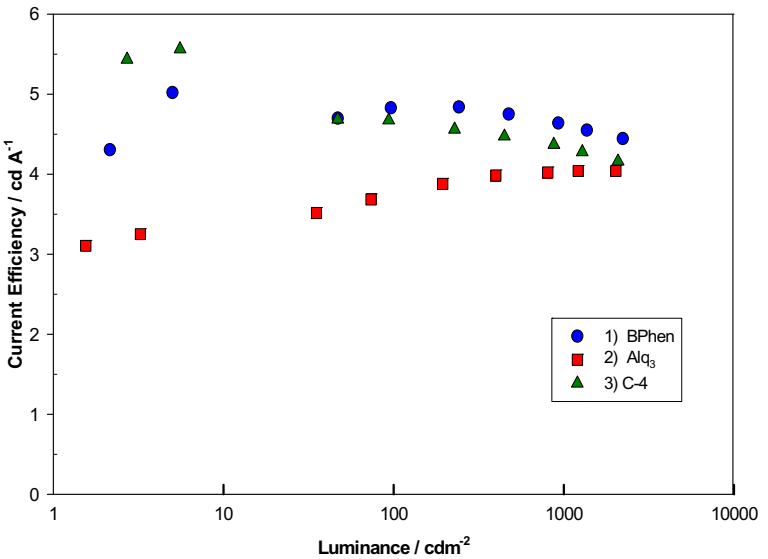

Fig. 9. Current efficiency vs. luminance characteristics of ITO/CuPc (10 nm)/a-NPB (50 nm)/BH-3 + BD-3 (30 + 0.5 nm)/ETL (20 nm)/LiF (0.5 nm)/Al, where the ETL is either Alq_3, C-4 or BPhen.

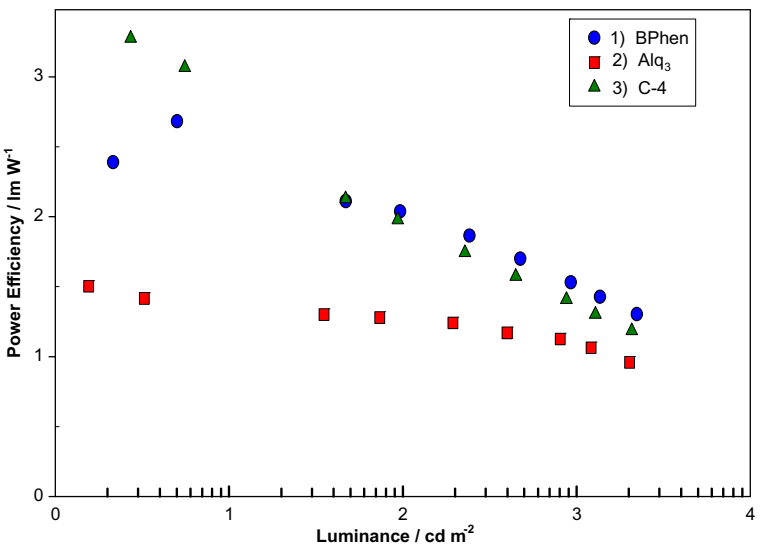

Fig. 10. Power efficiency vs. luminance characteristics of ITO/CuPc (10 nm)/a-NPB (50 nm)/BH-3 + BD-3 (30 + 0.5 nm)/ETL (20 nm)/LiF (0.5 nm)/Al, where the ETL is either Alq_3, C-4 or BPhen.

Table 3
Performance for Blue Devices from Set B.

ETM	Turn-on voltage (V)	V_{op}/V at 1000 cd m^{-2}	V at 100 mA cm^{-2}	Eff./cd A^{-1} at 100 cd m^{-2}	Eff./ lm W^{-1} at 100 cdm^{-2}	Eff./cd A^{-1} at 1000 cd m^{-2}	Eff./lm W^{-1} at 1000 cd m^{-2}	CIE (x, y) at 1000 cd m^{-2}	EQE(%)	Life-time ($t_{1/2}$) at 1000 cd m^{-2}
Alq_3	6.0 ± 0.2	11.5 ± 0.2	14.0	3.5	1.3	4.0	1.2	(0.152, 0.145)	3.3	1500
BPhen	5.0 ± 0.2	9.5 ± 0.2	12.0	4.5	2.0	4.4	1.4	(0.147, 0.157)	3.4	40
C-4	4.3 ± 0.2	9.5 ± 0.2	12.0	4.6	2.0	4.4	1.6	(0.151, 0.144)	3.6	250

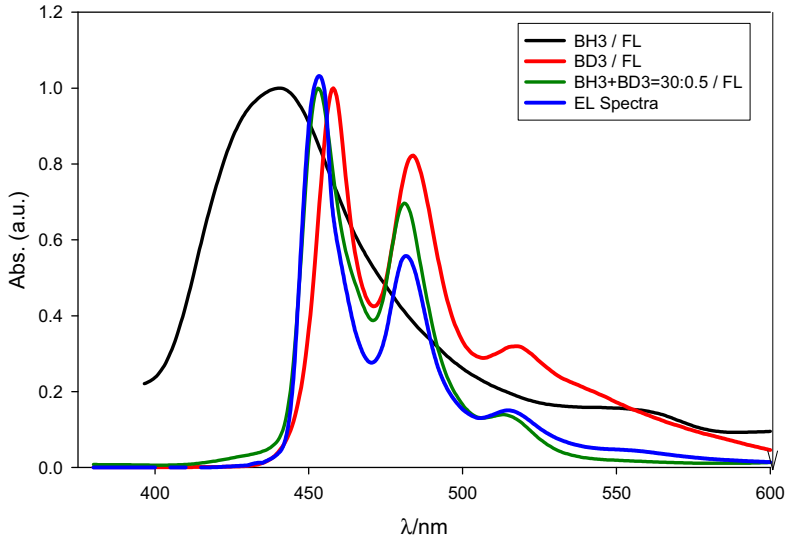

Fig. 11. Fluorescence and EL spectra of ITO/CuPc (10 nm)/ a-NPB (50 nm)/BH-3 + BD-3 (30 + 0.5 nm)/C-4 (20 nm)/LiF (0.5 nm)/Al.

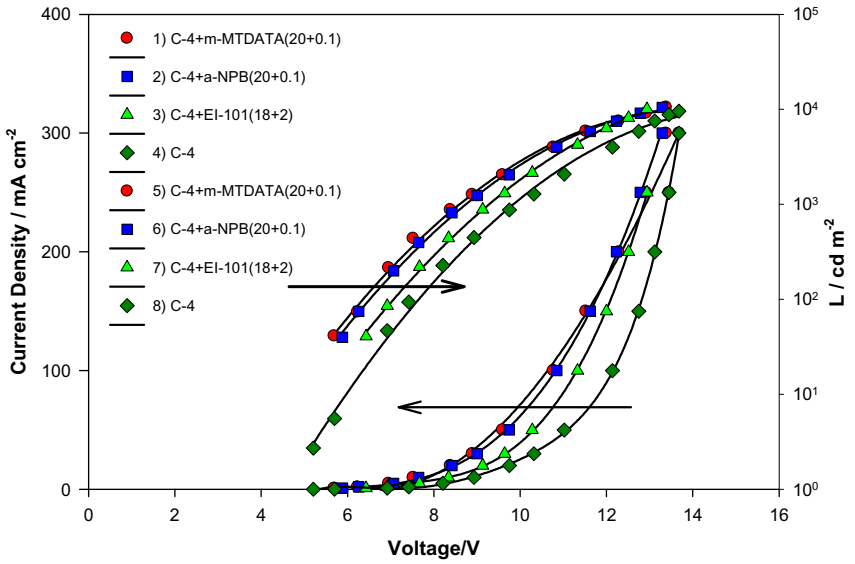

Fig. 12. Current density vs. voltage vs. luminance for ITO/CuPc (10 nm)/a-NPB (50 nm)/BH-3 + BD-3 (30 + 0.5 nm)/C-4 (20 nm)/LiF (0.5 nm)/Al where C-4 was doped with m-MTDATA (0.5%), a-NPB (0.5 %) and Liq (10%).

The question is whether C-4 would perform well in another system. Further, the comparison of the electron transporter, C-4 with Alq_3 alone is not sufficient as it is known that bathophenanthroline (BPhen) has much higher electron mobility and deeper HOMO level than Alq_3, any new ETM has to be compared with BPhen as well. Thus, we designed the device structure Set B to compare C-4 with BPhen and Alq_3.

4.2.2. Device Set B

ITO/CuPc (10 nm)/α-NPB (50 nm)/BH-3 + BD-3 (30:0.5 nm)/ETL (20 nm)/LiF (0.5 nm)/Al where the ETL is either Alq_3, C-4 or BPhen. The energy level diagram for the devices in Set B is shown in Fig. 7.

Figs. 8–10 show the luminance vs. voltage, current density vs. voltage, current efficiency (cd/A) vs. luminance and power efficiency (lm/W) vs. luminance for Set B. Reduction in operating voltage with C-4 is again substantial. The turn-on voltage for the devices with C-4, BPhen and Alq_3 are 4.3, 5.0 and 6.0 V, respectively (Table 3). A 17% reduction in operating voltage and 33% increase in power efficiency has been achieved by replacing Alq_3 with C-4 at 1000 cd m^{-2}. The current injection from C-4 is similar to that of BPhen.

We attribute the low turn-on voltage and operating voltage of C-4 to its high mobility. The EL and PL spectra of BH-3, BD-3 and a mixture of BH-3 and BD-3 (30.0:0.5) are shown in Fig. 11. The PL spectra of the mixture is blue shifted by 4 nm compared to virgin BD-3 as expected. The EL spectra of the devices in Set B are identical to the PL of the mixture. Thus, the same excited state is involved in both the cases.

It has to be stressed that interfacial effects dominate OLED performance and the electron transporter/host + dopant interface is no exception. Thus, a good electron transporter for one particular system may not be as good in another system even if the mobilities of the ETM's are high. What is required is a balanced injection of electrons and holes.

The life time at 1000 cd m^{-2} for C-4 is 6.25 times longer than that for BPhen as ETL. We attribute the enhanced life-time from devices with C-4 to its higher T_g of 111 °C as opposed to the lower T_g of 62 °C for BPhen.

Though, the life-time of devices with C-4 is longer than that with BPhen, they are not as long as Alq_3. It is general practice to dope the electron transporters with lithium quinolinolate (Liq) to improve the life time of devices [23]. Okumoto and Kanno reported that doping of the electron transporters with hole transporters such as m-MTDATA, α-NPB resulted in reduction in operating voltage and increased life-time [18]. We fabricated devices of the Type C (ITO/CuPc (10 nm)/ α-NPB (50 nm)/BH-3 + BD-3 (30:0.5 nm)/C-4 (20 nm)/LiF (0.5 nm)/Al) where the compound 4 is doped with m-MTDATA (0.5%), α-NPB (0.5%) and Liq (10%) and found that the turn-on voltage and the operating voltages are indeed reduced (Fig. 12). The performances of the devices are summarised in Table 4.

We found that m-MTDATA as the dopant was most effective in reducing the operating voltage, then α-NPB and Liq. However, there was no significant gain in either the current efficiency or power efficiency.

Fig. 13 shows the energy level diagram for device Type C. The turn-on voltage of the doped systems simply follow the energy difference between LUMO level of the dopants and LUMO level of the host ETM (C-4), The difference of energy between the LUMO levels of the dopants, m-MTDATA, α-NPB and Liq and C-4 are 1.1, 0.7 and 0.5 eV which correlate with the turn on-voltage of 3.8, 4.1 and 4.2 V, respectively. The diminution of the turn on voltage and operating voltage could be attributed to charge transfer from the donor molecules to the acceptor (C-4), thereby increasing the conductivity [24,25]. Life-time measurements of the doped systems are on going and will be reported elsewhere.

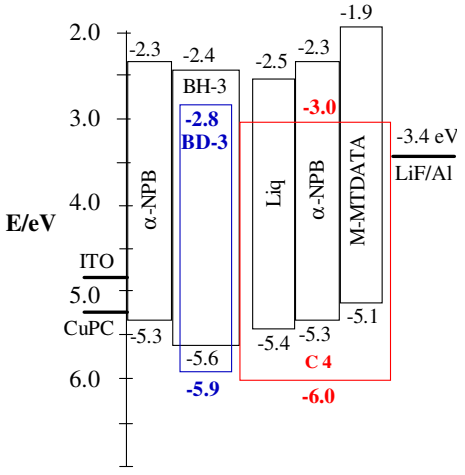

Fig. 13. Energy level diagram for ITO/CuPc (10 nm)/a-NPB (50 nm)/BH-3 + BD-3 (30 + 0.5 nm)/C-4 (20 nm)/LiF (0.5 nm)/Al where C-4 was doped with m-MTDATA (0.5%), a-NPB (0.5%) and Liq (10%).

Table 4
Device Performance of C-4 with m-MTDATA, α-NPB and Liq as dopants.

ETM	Turn-on voltage (V)	V_{op}/V at 1000 cd m^{-2}	V at 100 mA cm^{-2}	Eff./cd A^{-1} at 100 cd m^{-2}	Eff./lm W^{-1} at 100 cd m^{-2}	Eff./cd A^{-1} at 1000 cd m^{-2}	Eff./lm W^{-1} at 1000 cd m^{-2}	EQE (%)	CIE (x, y) at 1000 cd m^{-2}
Compound 4 (C-4)	4.3	9.5	12.0	4.6	2.0	4.4	1.6	3.6	(0.151, 0.144)
C-4 + m-MTDATA (0.5%)	3.8	8.7	10.5	4.8	2.4	4.6	1.7	3.6	(0.152, 0.155)
C-4 + α-NPB (0.5%)	4.1	8.7	10.5	4.0	2.2	4.2	1.6	3.5	(0.146, 0.139)
C-4 + Liq (10%)	4.2	9.0	11.5	4.3	1.8	4.4	1.6	3.6	(0.148, 0.143)

5. Conclusion

We have demonstrated that it is possible to produce phenanthroline derivatives for example, 2,9-bis-(2-thiophen-2-yl-vinyl)-[1,10]phenanthroline (C-4) which can act as good electron transporters and hole blockers with reasonably long life-times even in their virgin form. Further synthetic work is in progress to identify phenanthroline derivatives which would give much longer life-time than Alq_3 or doped BPhen.

Acknowledgements

We thank Drs. T. Yuki and Mr. S. Nakajima (Pioneer, Japan), Dr. C. Domoto (Kyocera), Dr. H. Ogawa (Kyocera) and Dr. C.H. Lee , Dr. J.H. Lee and J.H. Shin (Samsung Displays, Korea) for stimulating discussions. We also thank Dr. H.H.-Y. Oh (LG Displays, Korea) for fruitful discussions. We also thank Professor C.H. Chen (Shanghai Jiao Tong University) for thought provoking questions and Dr. David R. Rosseinsky of Exeter University for constant encouragement.

We are grateful for the support from Brunel University and encouragement from Professors C. Jenks, M. Sarhadi, G. Rodgers and J. Silver.

References

[1] T. Matsushima, C. Adachi, Appl. Phys. Lett. 89 (2006) 253506.
[2] C.W. Tang, S.A. Van Slyke, Appl. Phys. Lett. 51 (1987) 913.
[3] H. Sasabe, T. Chiba, S.J. Su, Y.-J. Pu, K. Naayama, J. Kido, Chem. Commun. (2008) 5821.
[4] M. Ichikawa, N. Hiramatsu, N. Yokoyama, T. Miki, S. Narita, T. Koyama, Y. Taniguchi, Phys. Status Solidi RRL 1 (1) (2006) R37.
[5] P. Kathirgamanathan, WO 00/32717 (08-06-2000).
[6] T. Sano, M. Fujita, T. Fujii, Y. Nishio, Y. Hamada, US Patent 5456988 (10-10-1995).
[7] A.P. Kulkarni, C.J. Tonzole, A. Babel, S.A. Jeneke, Chem. Mater. 16 (2004) 4556.
[8] D. Tanaka, T. Takeda, T. Chiba, S. Watanabe, J. Kido, Chem. Lett. 36 (2007) 262.
[9] P. Kathirgamanathan, V. Arkley, S. Surendrakumar, Y.-F. Chan, S. Ravichandran, S. Ganeshamurugan, M. Kumaraverl, J. Antipan-Lara, G. Paramaswara, V.R. Reddy, SID Digest 32.2 (2010) 465.
[10] S. Reinnke, F. Lindner, G. Schwartz, N. Seidler, K. Walzer, B. Lussem, K. Leo, Nature 459 (2009) 234.
[11] Y.-J. Li, H. Sasabe, S.-J. Su, D. Tanaka, T. Takeda, Y.-J. Pu, J. Kido, Chem. Lett. 38 (2009) 712.
[12] S.R. Forrest, V. Bulovic, P. Peumans, US Patent 6451,415 B1 (17-09-2002).
[13] H.W. Lee, J.-G. An, H.-K. Yoon, H. Jang, N.G. Kim, Y. Do, Bull. Korean Chem. Soc. 26 (2005) 1569.
[14] P. Kathirgamanathan, S. Surendrakumar, PCT Patent WO 2008/078115 A1 (03-07-2008).
[15] V. Kim, W.B. Im, Phys. Status Solidi A 201 (2004) 2148.
[16] C.H. Hsiao, S.W. Liu, C.T. Chen, J.H. Lee, Org. Electron. 11 (2010) 1500.
[17] S. Naka, H. Okada, H. Onnegawa, T. Tsutsui, Appl. Phys. Lett. 76 (2000) 197.
[18] K. Okumoto, H. Kanno, US Patent 2006/0051563A1 (09-03-2006).
[19] J.P. Chen, X.C. Li, US Patent 6713,781 B1 (30-03-2009).
[20] J.L. Bredas, A.J. Heeger, Chem. Phys. Lett. 217 (1994) 507.
[21] N. Li, P. Wang, S.L. Lai, W. Liu, C.S. Lee, S.T. Lee, Z. Liu, Adv. Mater. 22 (2010) 527.
[22] P. Kathirgamanathan, S. Surendrakumar, S. Ravichandran, V.R. Reddy, J. Antipan-Lara, S. Ganeshamurugan, M. Kumaravel, G. Paramaswara, V. Arkley, Chem. Lett. 39 (11) (2010) 1222.
[23] E. Bohm, C. Pflumm, F. Voges, M. Flammich, H. Heil, A. Busing, A. Parham, R. Fortte, T. Mijica, in: IDW' 09 Proceedings, Miyazaki, Japan, 2009, p. 431.
[24] P. Kathirgamanathan, D.R. Rosseinsky, J. Chem. Soc., Chem. Commun. (1980) 306.
[25] D. Fox, M.M. Labes, A. Weissberger (Eds.), Physics and Chemistry of the Organic Solid State, Interscience Publishers, New York, 1967.
[26] B.W. D'Andrade, S. Datta, S.R. Forrest, P. Djurovich, E. Polikarpov, M. Thompson, Org. Electron. 6 (2005) 11.
[27] M. Cole, W. Brutting, Physics of Organic Semiconductors, Wiley-VCH Verlag GmBH, ISBN-13:978-3-527-40550-3, 2005, pp. 95–128.
[28] H.Y. Chen, W.Y. Lam, J.D. Luo, Y.L. Ho, B.Z. Tang, D.B. Zhu, M. Wong, H.W. Kwok, Appl. Phys. Lett. 81 (4) (2002) 574.
[29] H.F. Chen, S.J. Yang, Z.H. Tsai, W.Y. Hung, T.C. Wang, K.T. Wong, J. Mater. Chem. 19 (2009) 8112.
[30] Z. Ge, T. Hayakawa, S. Ando, M. Ueda, T. Akiike, H. Miyamoto, T. Kajita, M. Kakimoto, Org. Lett. 10 (3) (2008) 421.
[31] S.J. Su, H. Sasabe, Y.J. Pu, K. Nakayama, J. Kido, Adv. Mater. 22 (2010) 3311.

Organic Electronics 12 (2011) 677–681

Contents lists available at ScienceDirect

Organic Electronics

journal homepage: www.elsevier.com/locate/orgel

Top-emitting white organic light-emitting diodes with a color conversion cap layer

Shuming Chen, Hoi-Sing Kwok *

Center for Display Research, Department of Electronic and Computer Engineering, The Hong Kong University of Science and Technology, Clear Water Bay, Kowloon, Hong Kong

ARTICLE INFO

Article history:
Received 25 October 2010
Received in revised form 3 January 2011
Accepted 8 January 2011
Available online 22 January 2011

Keywords:
White organic light-emitting diodes
Top-emitting
Color conversion
Color stability

ABSTRACT

We report top-emitting white organic light-emitting diodes (WOLEDs) by thermally evaporating non-doped (4-(4-(1,2,2-triphenylvinyl)phenyl)-7-(5-(4-(1,2,2-triphenylvinyl)phenyl) thiophen-2yl)benzo[c][1,2,5]thiadiazole) (BTPETTD) as a color conversion cap layer on top-emitting blue OLEDs. With a 240 nm cap layer, 74.5% of the blue photon energy are absorbed and converted to red emission with a conversion efficiency of 40%. By mixing the unabsorbed blue emission and red emission, the resulting top-emitting WOLEDs exhibit a broad band spectra with CIE coordinates of (0.34, 0.35), high color stability over a wide range of driving voltages, and peak efficiency of 17.7 cd/A and 8.7 lm/W.

© 2011 Elsevier B.V. All rights reserved.

1. Introduction

White organic light-emitting diodes (WOLEDs) are of considerable interests in recent years due to their potential applications in full color display and solid-state lighting [1–16,19]. Theoretically, the white color can be generated by additive mixing of three primary colors or two complementally colors. Thus, WOLEDs is mainly constructed by combining multiple color light emissive layers [1,2], or employing a single emissive layer doped simultaneously with different color dopants [3,4], as well as stacking several OLED units with each unit emitting different colors [5,6]. Although efficient and bright WOLEDs have been realized of adopting these methods, the fabrication process is somewhat complicated. The exciton distribution profile and the doping concentration should be carefully tuned to achieve a balanced exciton distribution in each emissive layer or among the light emitting dopants [7,8]. Furthermore, such WOLEDs suffer low color stability, i.e., the white spectra change with driving voltages and/or operation times, which is probably due to the shifting of the recombination zone and/or differential aging of different emitting materials [9,10].

WOLEDs by combining blue OLEDs with a color down conversion layer (CCL) have been proposed to simplify the fabrication process and achieve high color stability [11–16]. However, most reports focused on bottom-emitting WOLEDs, in which the CCL, typically composed by a host layer doped with an organic/inorganic dye, is spin-coated/laminated on the back glass side [11–14], or deposited as an internal hole-injection and conversion layer for the bottom-emitting blue OLEDs [15]. It is desirable to develop top-emitting WOLEDs since they promise large aperture ratio and can be fabricated on opaque substrates such as silicon and metal. Moreover, the combination of top-emitting blue OLEDs with CCL can easily yield broad band spectra, which is difficult to achieve in conventional top-emitting structures mainly due to the well-known microcavity effect [19].

To construct the top-emitting WOLEDs, the CCL should be thermally evaporated on top of top-emitting blue OLEDs in order not to damage the underneath OLEDs. Thus conventional CCL [11–14], which require spin-coating technique and/or thicker layer (~10 μm) are impractical. Ji

* Corresponding author.
E-mail address: eekwok@ust.hk (H.-S. Kwok).

1566-1199/$ - see front matter © 2011 Elsevier B.V. All rights reserved.
doi:10.1016/j.orgel.2011.01.005

et al. employed thermal evaporated phosphors DPPO deposited on top-emitting blue OLEDs to construct top-emitting WOLEDs [16], but the efficiencies of the resulting WOLEDs are low. Tien et al. proposed color tunable double-emitting OLEDs by capping Alq_3: DCJTB/rubrene on the metal cathode to recycle a portion of the energy trapped by surface plasmon polariton [22]. In this work, we show that 4-(4-(1,2,2-triphenylvinyl)phenyl)-7-(5-(4-(1,2,2-triphenylvinyl)phenyl)thiophen-2yl)benzo[c][1,2,5]thiadiazole (BTPETTD) with aggregation-induced-emission (AIE) characteristics is an ideal CCL for top-emitting blue OLEDs. By thermally evaporating 240 nm BTPETTD on top of top-emitting blue OLEDs, 74.5% of the blue photon energy are absorbed and subsequently converted to red emission by photoluminescence (PL) with a conversion efficiency of 40%. Combining with the unabsorbed blue emission, the resulting top-emitting WOLEDs exhibit broad band spectra with 1931 Commision International de L'Eclairage (CIE) coordinates of (0.34, 0.35), demonstrate high color stability over a wide range of driving voltages, and perform peak efficiencies of 17.7 cd/A and 8.7 lm/W.

2. Experimental

The top-emitting blue OLEDs were fabricated in a multi-source vacuum chamber with a base pressure of around 5×10^{-7} Torr with structure glass/Al (100 nm)/MoO_3 (8 nm)/NPB 25 nm/TcTa 10 nm/CDBP:Firpic 12 wt.%, 20 nm/TAZ 10 nm/BPhen 20 nm/Yb 5 nm/Ag 20 nm, where Al, MoO_3 and NPB functions as reflective anode, hole-injection and hole-transporting layer, respectively, Firpic doped CDBP works as blue light-emitting layer, TcTa and TAZ servers as exciton-blocking layer, Bphen, Yb and Ag acts as electron-transporting, electron-injection layer and semi-transparent cathode, respectively. A 190 nm or 240 nm BTPETTD layer was further deposited on the top-emitting blue OLEDs without breaking vacuum as a non-doped CCL. The synthesized method and AIE characteristics of the BTPETTD were reported elsewhere [17]. The schematic illustration of the device structure is shown in the inset of Fig. 2(a). The current density–voltage–luminance characteristics of the devices were measured by the HP4145B semiconductor parameter analyzer and a calibrated UDT PIN-25D silicon photodiode. The electroluminescent (EL) spectra were obtained with the PR650 spectrophotometer.

3. Results and discussion

Fig. 1(a) shows the refractive index n and extinction coefficient k of BTPETTD as measured by spectroscopic ellipsometer. The molecular structure of BTPETTD is also shown in Fig. 1(a). The calculated absorption spectra based on the measured k value agree well with the measured absorption spectra as shown in Fig. 1(b). The absorption peak at 470 nm matches well with the EL spectra of the top-emitting blue OLEDs, signifying that BTPETTD may absorb the blue photon energy and convert to red emission effectively via the PL process. To verify this assumption, two devices, one with 190 nm and the other with 240 nm BTPETTD layer were fabricated; the EL spectra of the devices are shown in Fig. 2(a). The top-emitting blue OLEDs exhibit a single peak at 472 nm; however, by introducing a 240 nm BTPETTD cap layer, a secondary peak at 610 nm appeared, confirming that some of the blue photons are absorbed and converted to red photons by the cap layer. Interestingly, the devices with a 190 nm cap layer exhibit a secondary peak at 550 nm, which is neither the intrinsic emission of Firpic nor the PL emission of BTPETTD. This peak is likely due to the microcavity effect, since in top-emitting OLEDs, the thickness of the cap layer can alter the optical properties of the OLED film stacks and hence shift the resonant wavelength of the cavity [18,19].

To verify this assertion, we used a rigorous classical electromagnetic method to model the interference effect of the top-emitting blue OLEDs with different cap layer thicknesses [20,21]. The simulated spectra are shown in Fig. 2(a). They agree well with the experimental results, confirming the accuracy of the model. Based on the model, the emission of Firpic at 550 nm is enhanced by introducing a 190 nm cap layer, and thus the combination of the modified blue emission with PL emission of BTPETTD

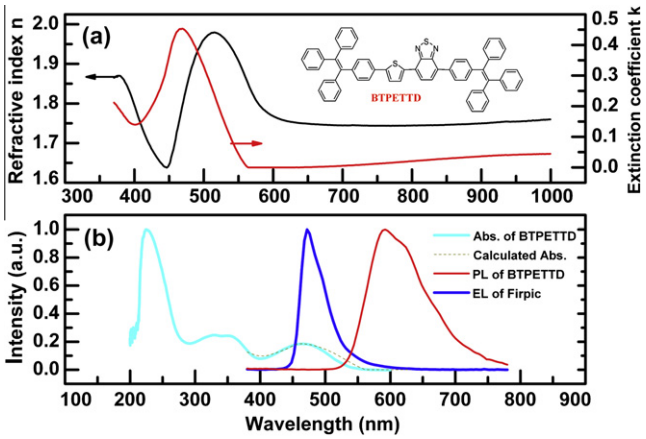

Fig. 1. (a) Refractive index n and extinction coefficient k of BTPETTD, inset: molecular structure of BTPETTD; (b) measured and calculated absorption spectra, PL spectra of BTPETTD, and EL spectra of top-emitting blue OLEDs based on Firpic emitter.

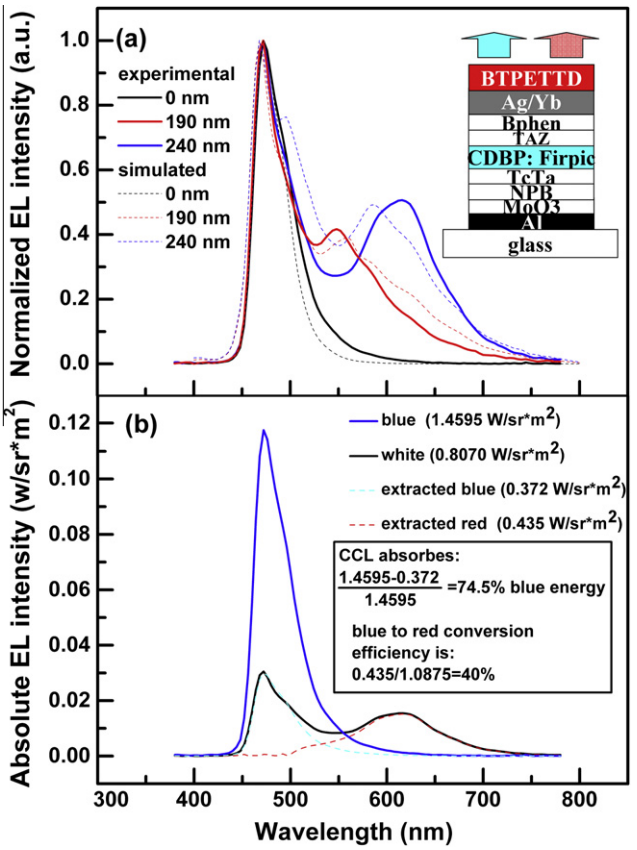

Fig. 2. (a) Normalized EL spectra of the devices with different thickness cap layer, inset: device structure; (b) absolute EL intensity of the devices without and with 240 nm cap layer.

exhibits a secondary peak at 550 nm. While with 240 nm cap layer, the resonant wavelength of the cavity is set equal to the peak intrinsic emission of Firpic, and hence the combination of the intrinsic emission of Firpic with PL emission of BTPETTD results in a secondary peak at 610 nm, similarly with the PL peak of BTPETTD. Therefore, to obtain pure white emission, the thickness of the cap layer should be carefully tuned to set the resonant wavelength equal to the peak intrinsic emission of Firpic, as well as to generate appropriate red emission intensity. As shown in Fig. 2(a), the mixture of the unabsorbed intrinsic blue emission of Firpic and the red PL emission of the 240 nm cap layer yields a white emission with CIE coordinates of (0.34, 0.35).

To evaluate the conversion efficiency of the cap layer, the absolute EL spectra of the top-emitting blue OLEDs without and with a 240 nm cap layer, operating at a driving current of 5 mA/cm^2 and luminance of 1165 cd/m^2, 857 cd/m^2, respectively, were tested. As shown in Fig. 2(b), the output blue emission intensity without cap layer is 1.4595 W/sr m^2, obtained by integrating the blue spectra. By introducing a 240 nm cap layer, the intensity is reduced to 0.8070 W/sr m^2 white emission, which can further be decomposed to 0.3720 W/sr m^2 unabsorbed blue emission intensity and 0.4350 W/sr m^2 red emission intensity by integrating the extracted blue and red spectra, respectively. Thus the cap layer absorbs 1.4595–0.3720 = 1.0875 W/sr m^2 (74.5%) blue emission and subsequently converts it to 0.4350 W/sr m^2 red emission. Therefore the blue to red watt to watt conversion efficiency can be calculated as 0.4350/1.0875 = 40%. Taking account the output red photon energy at 600 nm is ~80% of the input blue photon energy at 472 nm, the quantum efficiency of the cap layer is about 40%/80% = 50%, which agree well with 55% as measured by integrated sphere [17]. Obviously, to enhance the conversion efficiency, CCL with higher quantum yield should be employed.

Fig. 3(a) shows the EL spectra of the devices with 240 nm cap layer under different driving voltages. Obviously, no significant EL spectra change can be observed as the driving voltages increased from 6 V to 10 V, indicating that the top-emitting WOLEDs demonstrated here have excellent color stability. Fig. 3(b) shows the EL spectra normalized to 472 nm under different viewing angles. By setting the resonant wavelength equal to the peak intrinsic emission of Firpic, the blue emission shows minimal blue shift with increased viewing angles. While the red emission exhibits a slightly blue shift, with its peak changing from 610 nm at normal viewing angle to 584 nm at 60° viewing angle. Interestingly, the red emission is enhanced significantly as increased of viewing angles, which may be likely due to the light at oblique angles experiencing

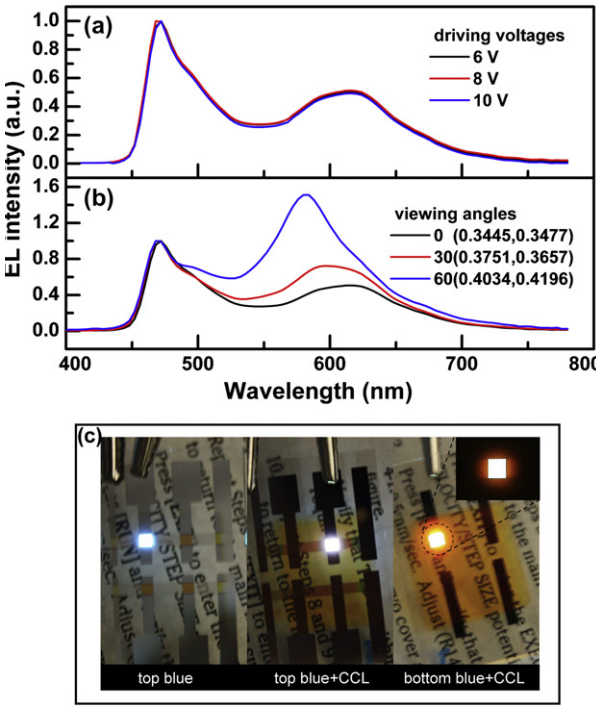

Fig. 3. (a) EL spectra under different driving voltages; (b) EL spectra under different view angles; (c) photos of the devices.

thicker CCL than its counterpart at normal angle; hence more blue photon energy are absorbed, resulting in an enhanced red emission and a shifting of CIE coordinates. As shown in Fig. 3(c), by depositing a 240 nm cap layer on top of top-emitting blue OLEDs, the blue emission has been modified as a uniform white emission. The photo of the bottom-emitting blue OLED with its back glass side covered by BTPETTD is also shown for comparison. Unlike the top-emitting WOLEDs with uniform white emission, the bottom-emitting WOLEDs are surrounded by a red ring, indicating that all the blue emission in the edges is absorbed and converted to red emission completely. Such phenomena may be mainly due to the light diffusing effect induced by thick glass substrate, resulting in a weak edges blue emission. The weak edges blue emission is subsequently converted to red emission by the CCL completely. To eliminate this effect, the CCL should be directly deposited on the blue OLEDs. Thus the combination of top-emitting blue OLEDs with CCL cap is superior to the bottom-emitting blue OLEDs with external CCL in terms of white lighting qualities.

Fig. 4 shows the luminance-voltage-current density and external quantum efficiency–luminance–power efficiency characteristics of the devices with different cap layer thickness. All devices show identical current density–voltage characteristics since the cap layer does not alter the electrical characteristics of the devices. Due to conversion loss, the luminance decreases as increased of cap layer thickness; for example, at a driving current of 5 mA/cm^2, the luminance decreases from 1165 cd/m^2 to 914 cd/m^2, 857 cd/m^2, corresponding to a external quantum efficiency of 10% (23 cd/A, 10 lm/W), 6.8% (18.3 cd/A, 7.2 lm/W) and 6% (17.1 cd/A, 6.6 lm/W), for the devices with 0 nm, 190 nm and 240 nm cap layer, respectively. The efficiency of the top-emitting WOLEDs can be further enhanced by developing efficient top-emitting blue OLEDs, employing high quantum yield CCL, as well as adopting light out-coupling techniques.

4. Summary

In summary, we have demonstrated an easily fabricated top-emitting WOLEDs by thermally evaporating a non-doped BTPETTD cap layer on top of top-emitting blue OLEDs. By carefully tuning the cap layer thickness, the top-emitting WOLEDs emit pure white light emission with CIE coordinates of (0.34, 0.35), exhibit extremely high color

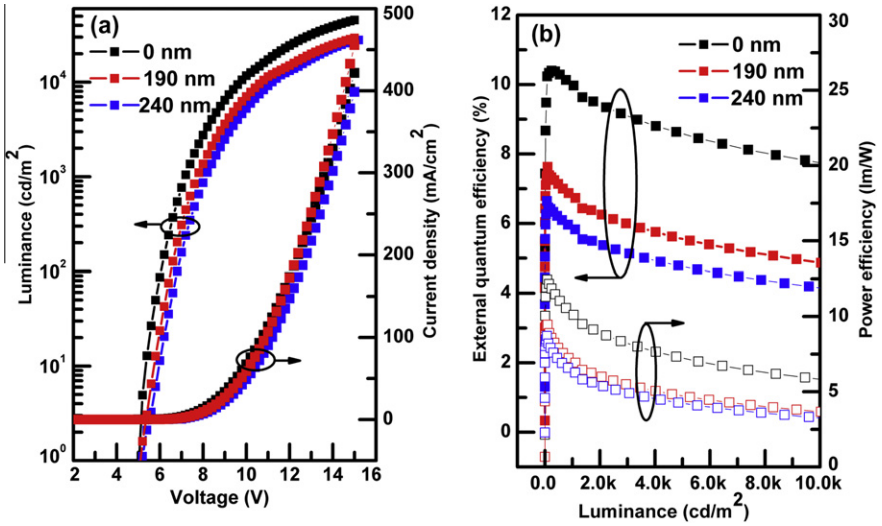

Fig. 4. (a) Luminance–voltage–current density; (b) external quantum efficiency–luminance–power efficiency characteristics of the devices.

stability over a wide range of driving voltages, and perform a peak efficiency of 6.6%, 17.7 cd/A and 8.7 lm/W.

Acknowledgments

The authors thank Dr. Zujin Zhao and Prof. Ben Zhong Tang for providing the BTPETTD. This work was supported by the Hong Kong Government Research Grants Council Grant Number AOE/P0308PG2.

References

[1] S. Reineke, F. Lindner, G. Schwartz, N. Seidler, K. Walzer, B. Lüssem, K. Leo, Nature 459 (2009) 234.
[2] Y. Sun, S.R. Forrest, Appl. Phys. Lett. 91 (2007) 263503.
[3] Q. Wang, J. Ding, D. Ma, Y. Cheng, L. Wang, F. Wang, Adv. Mater. 21 (2009) 2397.
[4] Q. Wang, J. Ding, D. Ma, Y. Cheng, L. Wang, Appl. Phys. Lett. 94 (2009) 103503.
[5] X. Qi, M. Slootsky, S. Forrest, Appl. Phys. Lett. 93 (2008) 193306.
[6] T.-W. Lee, T. Noh, B.-K. Choi, M.-S. Kim, D.W. Shin, Appl. Phys. Lett. 92 (2008) 043301.
[7] J.H. Seo, I.H. Park, G.Y. Kim, K.H. Lee, M.K. Kin, S.S. Yoon, Y.K. Kim, Appl. Phys. Lett. 92 (2008) 183303.
[8] U.S. Bhansali, H. Jia, M.A.Q. Lopez, B.E. Gnade, W.-H. Chen, M.A. Omary, Appl. Phys. Lett. 94 (2009) 203501.
[9] C.-H. Kim, J. Shinar, Appl. Phys. Lett. 80 (2002) 2201.
[10] M.C. Gather, R. Alle, H. Becker, K. Meerholz, Adv. Mater. 19 (2007) 4460.
[11] A.R. Duggal, J.J. Shiang, C.M. Heller, D.F. Foust, Appl. Phys. Lett. 80 (2002) 3470.
[12] B.C. Krummacher, V.-E. Choong, M.K. Mathai, S.A. Choulis, F. So, F. Jermann, T. Fiedler, M. Zachau, Appl. Phys. Lett. 88 (2006) 113506.
[13] Y.B. Yuan, S. Li, Z. Wang, H.T. Xu, X. Zhou, Opt. Express 17 (2009) 1577.
[14] S.-H. Cho, J.R. Oh, H.K. Park, H.K. Kim, Y.-H. Lee, J.-G. Lee, Y.R. Do, Opt. Express 18 (2010) 1099.
[15] C. Li, M. Ichikawa, B. Wei, Y. Taniguchi, Opt. Express 15 (2007) 608.
[16] W. Ji, L. Zhang, R. Gao, L. Zhang, W. Xie, H. Zhang, B. Li, Opt. Express 16 (2008) 15489.
[17] Z. Zhao, J.W.Y. Lam, B.Z. Tang, Curr. Org. Chem. 14 (2010) 2109.
[18] H. Riel, S. Karg, T. Beierlein, B. Ruhstaller, W. Rieß, Appl. Phys. Lett. 82 (2003) 466.
[19] M. Thomschke, R. Nitsche, M. Furno, K. Leo, Appl. Phys. Lett. 94 (2009) 083303.
[20] W. Lukosz, R.E. Kunz, J. Opt. Soc. Am. 67 (1977) 1607.
[21] H. Benisty, H.D. Neve, C. Weisbuch, IEEE J. Quantum Electron. 34 (1998) 1612.
[22] K.-C. Tien, M.-S. Lin, Y.-H. Lin, C.-H. Tsai, M.-H. Shiu, M.-C. Wei, H.-C. Cheng, C.-L. Lin, H.-W. Lin, C.-C. Wu, Org. Electron. 11 (2010) 397.

Organic Electronics 12 (2011) 682–685

Contents lists available at ScienceDirect

Organic Electronics

journal homepage: www.elsevier.com/locate/orgel

Letter

All ink-jet printed polyfluorene photosensor for high illuminance detection

Leah Lucas Lavery *, Gregory Lewis Whiting, Ana Claudia Arias [1]

Palo Alto Research Center, 3333 Coyote Hill Road, Palo Alto, CA 94304, USA

ARTICLE INFO

Article history:
Received 7 August 2010
Received in revised form 11 December 2010
Accepted 26 January 2011
Available online 23 February 2011

Keywords:
Ink-jet
Photosensor
PFB:F8BT

ABSTRACT

An all-printed photosensor based on polyfluorene derivatives has been developed for high illuminance range detection (>100 klux). The active layer is a blend of hole-accepting poly(9,9′-dioctylfluorene-co-bis-*N*,*N*′-(4-butylphenyl)-bis-*N*,*N*′-phenyl-1,4-phenylenediamine) (PFB) and electron-accepting poly(9,9′-dioctylfluorene-co-benzothiadiazole) (F8BT). A top-absorbing architecture was used with poly(3,4-ethylenedioxythiophene):poly(styrenesulfonate) (PEDOT:PSS) as the transparent electrode. The surface energy of the PEDOT:PSS ink was modified in order to allow printing directly onto the hydrophobic surface of the PFB:F8BT blend layer, placing the transparent electrode at the top of the light sensor structure. The all-printed photosensor shows a linear response over multiple measurements within the illuminance range of (100–400) klux.

© 2011 Elsevier B.V. All rights reserved.

High intensity light sensors are needed in order to monitor working environmental conditions and assist with the diagnosis of blast-related injuries [1] which include traumatic brain injury (TBI) [2]. Light-emitted from blasts or explosions can be of very high illuminance [3] (greater than 100 klux) and cause photo-stress, temporary blindness and disorientation [4]. We have been developing a monitoring system that could be worn by soldiers to collect daily information that can be incorporated as part of their medical record. This device is designed to be disposable, inexpensive and adhered directly to objects (including non-planar surfaces). This requires the development of light sensors with transparent top electrodes, high light intensity response and process compatibility with flexible substrates. In our approach we use ink-jet printing as a deposition and patterning technique and use solution processible materials such as conjugated polymers and metal nanoparticles as active layers in the device. Ink-jet printing has been previously used to print the active layers of photovoltaics [5], organic light emitting diodes [6], field effect transistors [7] and display backplanes [8].

Typically organic-based light sensors are fabricated on glass substrates with a sputtered layer of indium tin oxide (ITO) as the transparent anode [9], with light being absorbed through the glass. As described above, our application requires a top-absorbing device architecture with the transparent conductor deposited directly on top of the semiconducting material, which can sometimes damage the organic layer. The surface of the organic photoactive layer is hydrophobic and presents a challenge when fabricating top-absorbing devices from solution. We have been able to address this fabrication challenge by employing a modified conductive polymer ink as the transparent electrode in order to improve wetting and printing characteristics onto the photoactive layer.

A cross-sectional view of the all-printed light sensor is shown in Fig. 1. Poly(3,4-ethylenedioxythiophene):poly(styrenesulfonate) (PEDOT:PSS from H.C. Starck) was used as the transparent anode as an alternative to conventional sputtered-ITO and ITO nanodispersions [10]. As illustrated in Fig. 1a, light absorption occurs directly through the top electrode PEDOT:PSS layer. The sessile drop contact angle of conventional PEDOT:PSS solution on the polyfluorene blend (photoactive layer) surface was $\theta = 104 \pm 5°$ (Fig. 1b). The surface tension of PEDOT:PSS ink was modified by mixing Zonyl fluorosurfactant (0.1–0.2 wt%) to the original formulation. This new ink composition reduced the contact angle to $\theta = 22 \pm 4°$

* Corresponding author.
E-mail addresses: leah.lavery@parc.com (L.L. Lavery), acarias@eecs.berkeley.edu (A.C. Arias).
[1] Current address: Department of Electrical Engineering and Computer Sciences, University of California, Berkeley, Berkeley, CA 94720-1770, USA.

1566-1199/$ - see front matter © 2011 Elsevier B.V. All rights reserved.
doi:10.1016/j.orgel.2011.01.023

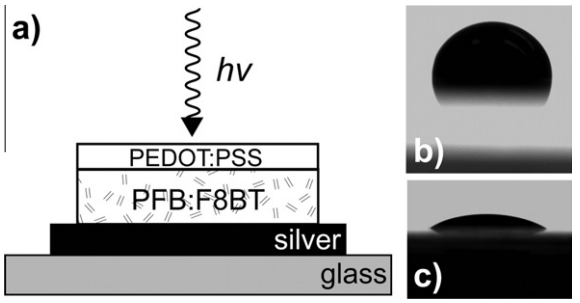

Fig. 1. (a) Cross-sectional view of the all-printed polyfluorene PFB:F8BT photosensor. Illumination is through the PEDOT:PSS top electrode layer. (b) PEDOT:PSS droplet on PFB:F8BT semiconducting film. (c) Modified PEDOT:PSS droplet with addition of Zonyl fluorosurfactant on a PFB:F8BT film.

(Fig. 1c) allowing printing of PEDOT:PSS (film thickness 25–30 nm) directly onto the semiconducting film surface. While making the PEDOT ink compatible with other layers of devices, the addition of the surfactant did not alter the PEDOT:PSS conductivity. The measured conductivity of films with and without the fluorosurfactant was 29 ± 4 and 31 ± 6 S/cm, respectively. The printed PEDOT:PSS electrode area defines the active area of the light sensor, and it varied from 6 to 9 mm^2 in the experiments described here.

The organic photoactive layer was composed of a blend of electron accepting poly(9,9′-dioctylfluorene-co-benzothiadiazole) (F8BT) and the electron donor poly(9,9′-dioctylfluorene-co-bis-*N*,*N*′-(4-butylphenyl)-bis-*N*,*N*′-phenyl-1,4-phenylenediamine) (PFB). The molecular weights of PFB and F8BT were 46 and 27 K, respectively. The PFB:F8BT blend layer was ink-jet printed, in air, from a 1:1 weight ratio solution in dichlorobenzene atop a printed silver nanoparticle electrode [8] using a previously described custom-built system [7]. Our printer system consists of a piezoelectric print head, translation stages, substrate holder and alignment camera. The printed silver nanoparticle electrode (Cabot Corporation) was annealed at 130 °C for 10 min, typically ≈50 nm thick. The printed PFB:F8BT layers were optically smooth thin films of ≈35 mm^2 area and thicknesses of 0.8–1.0 μm. We have adopted this thickness to ensure high yield and reproducibility in our fabrication process. As we are printing all layers in the device and PEDOT:PSS directly onto the photoactive blend layer, we need to take into account the roughness of the printed silver electrodes. This blended system has been used previously in polymer based photovoltaics [11], and it has been shown that the degree of phase separation of the polymer components influences the resulting morphology and device performance [11,12]. Methods used to vary the thin film phase separation include altering: polymer component ratio [11], selection of solvent based on boiling point [12], substrate temperature [12], molecular weight [13], and the formation of polymer nanospheres from a miniemulsion process [14]. These methods alter the domain size from nanometers to microns when observed by atomic force microscopy (AFM) or fluorescence microscopy. Compositional mapping via synchrotron-based scanning X-ray [15], scanning near-field optical [16], and electrostatic force microscopies [17] have shown that these micron-sized domains are not composed of a single phase but contain proportions of both PFB and F8BT. Using synchrotron-based scanning X-ray microscopy [15], McNeill et al. have mapped the composition of the enclosed domains to be PFB-rich (70 ± 3 wt%) and the surrounding majority phase to be F8BT-rich (95 wt%).

Ink-jet printing can also be used as a method to vary the thin film morphology that has lead to improved device performance over other processing methods such as spin-coating [18]. Xia and Friend observed increased external quantum efficiency (EQE) in ink-jet printed devices attributed to improved charge transport compared to spin-coated devices [18]. The external quantum efficiency of the printed PFB:F8BT photosensor is shown in Fig. 2. EQE was calculated by

$$\mathrm{EQE} = \frac{hcJ_{SC}}{e\lambda P} \tag{1}$$

where λ is the incident wavelength, J_{SC} is the short-circuit photocurrent density, e is the elementary charge, h is the Planck constant, c is the speed of light, and P is the incident light power. Spectral response was measured under zero bias using an Oriel Cornerstone Monochromator with Oriel Instruments Quartz Tungsten Halogen lamp (100 W). Photoresponsivity was at wavelengths below 550 nm and EQE reaches a maximum of 5.9% at 400 nm. The photocurrent increases at higher excitation energy, which has been explained by the theoretical analysis of the nature of excited states in PPV [19] and applied to the PFB:F8BT system [11], namely that excitons at higher excitation energies have smaller binding energies and greater number of delocalized wavefunctions, making disassociation more probable. For comparison, the absorption spectra measured by UV–vis spectroscopy of a printed blend layer (∼220 nm thickness) is also plotted in Fig. 2. The photoaction spectrum of the blend devices was mostly symbatic with the absorption curves for excitation energies below ∼3.75 eV.

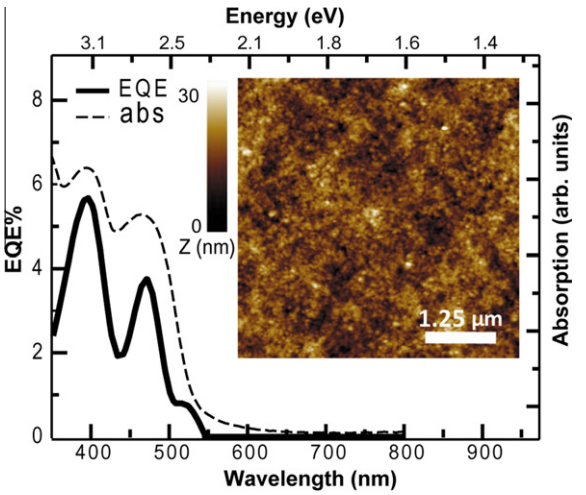

Fig. 2. External quantum efficiency (EQE) and UV–vis absorption spectra for printed PFB:F8BT photosensor. Atomic force micrograph (inset) of ink-jet printed film. *Z*-height scale is 30 nm and scale bar is 1.25 μm.

Examination of the printed surface topology by AFM (Veeco Dimension 3100) revealed a fine phase separation of the polyfluorene components as shown in the inset of Fig. 2. The ink-jet printed features are on the nanometer-scale measuring ≈60–150 nm in size. Xia and Friend observed device improvements and finer phase separation in ink-jet printed devices compared to spin-coated devices [18]. They observed little change in the photoluminescence (PL) efficiency between devices with micron-sized domains to nanometer-sized domains indicating almost no change due to charge dissociation and therefore attributed the improvement in EQE of their ink-jetted devices to improved charge transport. Ink-jet printed devices likely have finer phase separation because solvent drying rates are more rapid in ink-jet printing due to the small volumes of liquid (≈100 pL) being dispensed, allowing for less time for the polyfluorene blend components to phase-separate.

The printed high light intensity sensors were tested under illumination provided by a Newport 1600W solar simulator (Xenon short arc lamp). The illuminance was varied from 100 to 400 klux which was achieved by changing the vertical distance between the photosensor and the vertex of the light source since *illuminance* = I/d^2, where d is the distance from the sample to the illumination source and I is the intensity of the illumination source. Illuminance was measured by an Extech EA30 light meter. Fig. 3 shows current–voltage (I–V) characteristics for the all-printed sensor measured by a Keithley 6487 electrometer. The dark current at −1 V was 1 nA/cm^2. The photocurrent (measured at −1 V) increases linearly with light intensity and no current saturation is observed (Fig. 3 inset). For all sensors, the open circuit voltage (V_{oc}) was within the range of 0.1–0.2 V, however, for an individual sensor, the V_{oc} did not shift as illuminance increased. Previous researchers [20] observed a logarithmic increase in the V_{oc} in PFB:F8BT bilayer devices from increasing Argon-ion laser intensity (based on 458 nm line), but for those measurements, the V_{oc} saturated at radiometric intensities above 0.7 mW/cm^2, which is significantly lower than the testing conditions used in the experiments described here.

Further examination of the printed PFB:F8BT photosensors was completed under short illumination pulses. Light exposure from a explosion or blast was simulated by exposing the PFB:F8BT photosensor to light from the solar simulator for only 0.5–0.75 s, by toggling the mechanical shutter of the Newport solar simulator open and closed. The change in voltage was recorded by a Tektronix TDS2014B digital oscilloscope at different illuminance levels. The signal from the PFB:F8BT photosensor at zero bias was amplified by a Keithley 427 current amplifier (gain 10^7 V/A) and the oscilloscope was triggered using a calibrated silicon photodiode (Newport) from a secondary input channel. An example of the oscilloscope voltage readout of the PFB:F8BT photosensor is shown in Fig. 4a. Plotting the change of voltage (ΔV) from the initial background voltage ($V_o \approx 0$) versus illuminance (Fig. 4b) shows that the photosensor voltage increased ≈0.3 V per 100 klux, and linear photoresponse as a function of illuminance over multiple measurements. Future experiments will further examine the transient photocurrent response as well as device reliability, which is necessary to understand the dynamics of charge transport and charge separation at these high illuminance values.

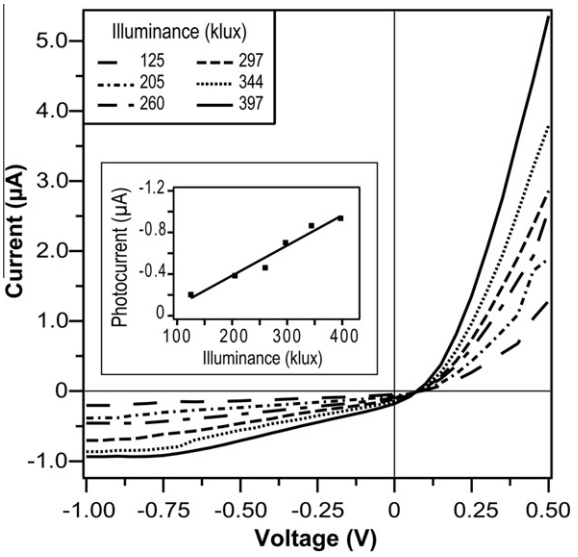

Fig. 3. Current–voltage (I–V) characteristics for the printed polymer blend photosensor collected at increasing illuminance values (inset legend, measured in klux, photocurrent measured at −1 V).

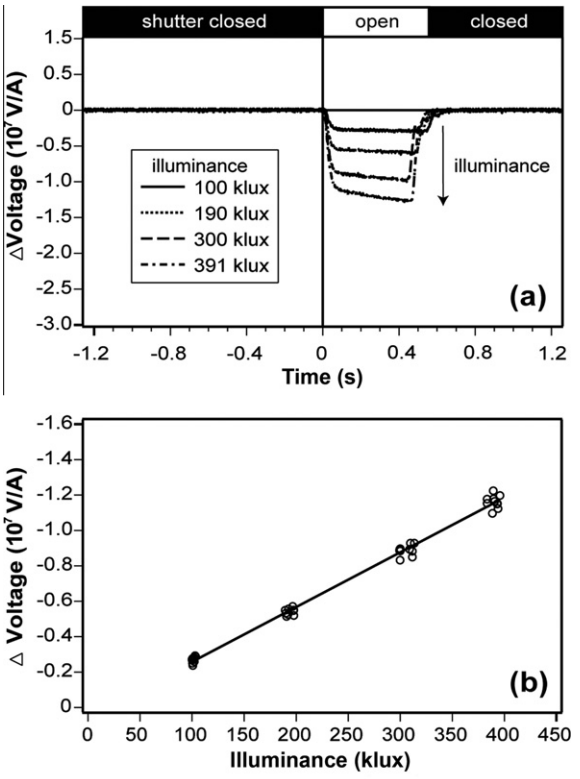

Fig. 4. (a) Change in voltage (ΔV) as the photosensor is exposed to ≈0.5 s of illumination from solar simulator at varying levels of illuminance (see inset legend). (b) Change in voltage (ΔV) from (a) plotted as a function of illuminance for multiple measurements.

In summary, we have demonstrated an all ink-jet printed top-absorbing photosensor fabricated from printed layers of a PFB:F8BT polymer blend, and Ag nanoparticles and PEDOT:PSS electrodes. Ink-jet printing of the PEDOT:PSS top electrode directly onto the hydrophobic PFB:F8BT layer was made possible by the addition of a fluorosurfactant to the PEDOT:PSS ink. The photosensors were examined under short illumination pulses (0.5–0.75 s), and showed good linearity in photoresponse over multiple measurements at high illuminance values of 100–400 klux.

Acknowledgments

The authors thank T.N. Ng, B. Russo and B. Krusor for assistance with experiments and helpful discussions. The authors wish to thank A. Kalio for use of solar simulator and N. Johnson and R.A. Street for use of monochromator equipment. This work is partially supported by Sensor Tape Program of the Defense Advanced Research Projects Agency (DARPA) under contract W81XWH-08-0065. Approved for Public Release Distribution Unlimited.

References

[1] R.G. DePalma, D.G. Burris, H.R. Champion, M.J. Hodgson, N. Engl. J. Med. 352 (13) (2005) 1335.
[2] K.H. Taber, D.L. Warden, R.A. Hurley, J. Neuropsychiatry Clin. Neurosci. 18 (2) (2006) 141.
[3] C.P. Butler, Science 138 (3539) (1962) 483.
[4] R.M. Pivovar, A.S. Snurnikov, J. Opt. Technol. 67 (9) (2000) 781.
[5] C.N. Hoth, P. Schilinsky, S.A. Choulis, C.J. Brabec, Nano Lett. 8 (9) (2008) 2806.
[6] T.R. Hebner, C.C. Wu, D. Marcy, M.H. Lu, J.C. Sturm, Appl. Phys. Lett. 72 (5) (1998) 519.
[7] A.C. Arias, S.E. Ready, R. Lujan, W. Wong, K.E. Paul, A. Salleo, M.L. Chabinyc, R. Apte, R.A. Street, Y. Wu, P. Liu, B. Ong, Appl. Phys. Lett. 85 (2004) 3304.
[8] A.C. Arias, J. Daniel, B. Krusor, S. Ready, V. Sholin, R.A. Street, J. Soc. Inform. Disp. 5 (7) (2007) 485.
[9] P. Schilinsky, C. Waldauf, C.J. Brabec, Appl. Phys. Lett. 81 (20) (2002) 3885.
[10] T.N. Ng, W.S. Wong, M.L. Chabinyc, S. Sambandan, R.A. Street, Appl. Phys. Lett. 92 (21) (2008) 213303.
[11] J.J.M. Halls, A.C. Arias, J.D. MacKenzie, W.S. Wu, M. Inbasekaran, E.P. Woo, R.H. Friend, Adv. Mater. 12 (7) (2000) 498.
[12] A.C. Arias, J.D. MacKenzie, R. Stevenson, J.J.M. Halls, M. Inbasekaran, E.P. Woo, D. Richards, R.H. Friend, Macromolecules 34 (17) (2001) 6005.
[13] H.J. Snaith, R.H. Friend, Thin Solid Films 451 (2004) 567.
[14] T. Kietzke, D. Neher, M. Kumke, R. Montenegro, K. Landfester, U. Scherf, Macromolecules 37 (13) (2004) 4882.
[15] C.R. McNeill, B. Watts, L. Thomsen, H. Ade, N.C. Greenham, P.C. Dastoor, Macromolecules 40 (9) (2007) 3263.
[16] R. Stevenson, R.G. Milner, D. Richards, A.C. Arias, J.D. Mackenzie, J.J.M. Halls, R.H. Friend, D.J. Kang, M. Blamire, J. Microsc. 202 (2) (2001) 433.
[17] D.C. Coffey, D.S. Ginger, Nat. Mater. 5 (9) (2006) 735.
[18] Y.J. Xia, R.H. Friend, Macromolecules 38 (15) (2005) 6466.
[19] A. Kohler, D.A. dos Santos, D. Beljonne, Z. Shuai, J.L. Bredas, A.B. Holmes, A. Kraus, K. Mullen, R.H. Friend, Nature 392 (6679) (1998) 903.
[20] C.M. Ramsdale, J.A. Barker, A.C. Arias, J.D. MacKenzie, R.H. Friend, N.C. Greenham, J. Appl. Phys. 92 (8) (2002) 4266.

Organic Electronics 12 (2011) 686–693

Contents lists available at ScienceDirect

Organic Electronics

journal homepage: www.elsevier.com/locate/orgel

Low-temperature formation of self-assembled 1,5-diaminoanthraquinone nanofibers: Substrate effects and field emission characteristics

Kuo-Jung Huang [a], Yu-Sheng Hsiao [b,*], Wha-Tzong Whang [a,*]

[a] Department of Materials Science and Engineering, National Chiao Tung University, Hsinchu 30010, Taiwan, ROC
[b] Research Center for Applied Sciences, Academia Sinica, Taipei 11529, Taiwan, ROC

ARTICLE INFO

Article history:
Received 11 October 2010
Received in revised form 11 January 2011
Accepted 12 January 2011
Available online 23 February 2011

Keywords:
DAAQ
Self-assemble
Nanofibers
Small organic molecules
Field emission

ABSTRACT

In this study, we used thermal evaporation with a low sublimation temperature (42 °C) to deposit 1,5-diaminoanthraquinone (DAAQ) in various morphologies—including nanorods, nanocornerstones, and nanofibers—onto various substrates. Three major factors influenced the growth of vertically aligned DAAQ nanofibers on the electrodes: a low water contact angle (WCA) for the substrate and intermolecular hydrogen bonding and π–π interactions between the DAAQ molecules. On Au and Ti substrates (low-WCA), the DAAQ nanofibers **DAAQ-Au** and **DAAQ-Ti**, respectively, possessed great verticality and high aspect ratios; they also exhibited field emission characteristics, with maximum emission current densities of 0.31 and 0.65 mA/cm^2, respectively, at an applied electric field of 12 V/μm. The turn-on electric fields for producing a current density of 10 μA/cm^2 were 8.5 V/μm for **DAAQ-Au** and 8.25 V/μm for **DAAQ-Ti**. From the slopes of Fowler–Nordheim plots, we calculated the field enhancement factors (β) of **DAAQ-Au** and **DAAQ-Ti** to be 447 and 831, respectively. Field emission stability studies revealed that the DAAQ nanofibers possessed outstanding anti-degrading capability. The emission current did not decrease, but rather increased slightly, after 3000 s. Given the advantages of this simple low-temperature process and the impressive anti-degrading field emission characteristics, such DAAQ nanofibers have great potential for use in various electronics applications (e.g., as organic field emitters).

© 2011 Elsevier B.V. All rights reserved.

1. Introduction

Nanostructures based small organic molecules have become the focus of intensive research efforts because of their unique applications in nanoscale devices [1–3]. One-dimensional (1D) organic nanostructures, including nanorods, nanofibers, nanowires, and nanotubes, can be fabricated using a wide range of methods; they often exhibit unique material properties that make them suitable for use in organic electronics applications (e.g., solar cells [4–7], chemical vapor sensors [8], field emitters [9–15]) and in various optoelectronic devices [16–19]. Recently, several small organic molecules, including tris(8-hydroxyquinolinato) aluminum (Alq_3) [9,13,16,19], anthracene (AN), perylene (PY) [20], coronene [10], copper phthalocyanine (CuPc) [11], and 1,5-diaminoanthraquinone (DAAQ) [8], have been prepared in form of various nanostructures under conditions milder than those used to prepare related nanostructures from inorganic compounds. Because of their suitability for use in inexpensive, low temperature-processed, highly flexible optoelectronic devices, increasing attention is being drawn to the development of nanostructures of small-molecule organic materials.

Several fabrication methods have been reported for the preparation of organic 1D nanostructures [1–3,21]. Nanowires and nanorods have been prepared through thermal evaporation (solid state chemical reactions) [20]

* Corresponding authors. Tel.: +886 2 27898000-21; fax: +886 2 27826680 (Y.S. Hsiao), tel.: +886 35 731873; fax: +886 35 724727 (W.T. Whang).
E-mail addresses: yshsiao@gate.sinica.edu.tw (Y.-S. Hsiao), wtwhang@mail.nctu.edu.tw (W.-T. Whang).

1566-1199/$ - see front matter © 2011 Elsevier B.V. All rights reserved.
doi:10.1016/j.orgel.2011.01.010

at high temperatures (up to 280 °C). Solution processing of nanorods has been employed using a microemulsion route assisted by surfactants [19]. Self-polymerization and self-assembly process has been developed for production of supramolecular nanomaterials [22]. Thermal evaporation of nanotubes and nanotube junctions onto metal catalysts has been performed at 340 °C under a flow of Ar gas [23]. Vapor condensation has been used to prepare nanowires [9] and nanoparticles [24] under Ar atmospheres at temperatures of over 400 °C with the substrate placed under a N_2-cooled trap. Zhao et al. applied neutral aluminum oxide (or silica gel) in the adsorbent-assisted physical vapor deposition of nanoribbons and nanowires [25,26]. Vacuum sublimation, a form of vapor-phase deposition, has also been applied to the preparation of nanostructures, particularly for fabricating 1D organic nanofibers for organic field emission devices [10–12]. We have previously applied high vacuum processing to fabricate nanostructures with highly uniform distributions on targeting substrates, without the need for catalysts or high temperatures. Such simple one-step approaches not only eliminate the effects of impurities but also potentially lower the fabrication temperature.

Recent investigations of DAAQ-based optoelectronic devices, such as chemical sensors [8], optical waveguides [27], and organic solar cells [28], have led to a rapid development of DAAQ fabrication technologies. Zhao et al. [27] recently reported that this organic dye prefers to undergo vertical deposition on substrates having high surface energies (SEs) and hydrophilic domains. In this present study, we synthesized 1D DAAQ nanofibers through vacuum sublimation on selected substrates. We characterized these 1D DAAQ nanofibers using scanning electron microscopy (SEM) and high-resolution transmission electron microscopy (HRTEM). From investigations of the morphologies of DAAQ thin films formed on different substrates, we selected electrodes suitable for the vertical deposition of DAAQ nanofibers. To determine the practicality of employing DAAQ nanofibers as cathode materials in field emission devices, we evaluated their field emission characteristics using a vacuum emission measurement (VEM) system.

Stabilized by intermolecular hydrogen bonding and π–π interactions, DAAQ self-assembles onto substrates to form vertically out-of-plane nanostructures. Analogous to organic vapor-phase deposition (OVPD), the vacuum sublimation of small organic molecules is also a vapor-solid (VS) process. Because sublimation proceeds at lower temperatures in higher vacuums, relative to those used for OVPD, its use opens up a new area of study and potentially increases the applications of organic small molecules in flexible electronic devices.

2. Experimental

Commercially available DAAQ powder (purity: 92%; Tokyo Chemical Industry) and 1,1,1,3,3,3-hexamethyldisilazane (HMDS; Lancaster), for Si surface treatment, were used as received without further purification.

DAAQ films were deposited on various substrates (Ag, Al, Au, Ni, Si, Ti) using a thermal evaporator operated at a base pressure of 6×10^{-6} torr. The metal substrates were prepared by depositing metal films onto Si (1 0 0) substrates using an electron beam (E-beam) evaporator. Prior to E-beam evaporation of each metal thin film, a Ti layer (thickness: 200 Å) was deposited on the bare Si substrate as an adhesion layer. Without breaking the vacuum, a thin layer of Ag, Al, Au, Ni, or Ti (thickness: 1000 Å) was then deposited. The entire Si substrate was treated with HMDS vapor and then cured at 160 °C for 0.5 h, and the surface chemistry of the Si substrate was modified through the formation of a self-assembled monolayer of HMDS.

DAAQ nanostructure films were formed on the various substrates while maintaining the substrate temperature at 25 °C. The sublimation of DAAQ was performed at a temperature of 42 °C; the corresponding deposition rate, controlled by a quartz crystal microbalance, was 0.5 Å/s.

Top and cross-sectional views of the morphologies of the DAAQ nanostructure films were surveyed using a JEOL JSM-6500F scanning electron microscope. Ultraviolet–visible (UV–Vis) spectra (250–900 nm) were recorded using a Shimadzu UV-3600 spectrophotometer. Contact angles (CAs) and SEs were determined on each substrate using a Krüss universal surface tester (model GH-100), the geometric mean approximation, and three standard liquids: water (H_2O), diiodomethane (CH_2I_2), and ethylene glycol [$C_2H_4(OH)_2$]. The profiles and fine structure of nanofibers were imaged and analyzed using a JEOL-2010 high-resolution transmission electron microscope and an internal charge-coupled device (CCD) camera. The crystalline of DAAQ nanofibers was characterized by GIXRD, using Bruker D8 system and Cu Kα radiation. The incident angle of the X-ray beam was fixed at 0.2°. The field emission characteristics of the DAAQ nanofibers were determined under a base pressure of 8×10^{-6} torr. Indium tin oxide (ITO) plate glasses were used as anodes, positioned above the substrate surfaces at a distance of 80 μm. The field emission instrument featured a plate-to-plate geometry; the cathode comprised DAAQ nanofibers deposited on Au and Ti substrates (area: 0.06 cm^2). Current density–electric field (J–E) curves of the field emission devices were measured using a Keithley 237 instrument (accuracy: 10^{-13} A). The emission currents of the DAAQ nanofibers were monitored as a function of the sweep bias.

3. Results and discussion

Fig. 1(a) displays the molecular structure of DAAQ. Assemblies of DAAQ molecules feature both intramolecular charge transfer [29] and intermolecular hydrogen bonding [23]. Intramolecular charge transfer occurs between the amino (NH_2) and carbonyl (C=O) groups of the anthraquinone ring; intermolecular hydrogen bonding occurs between the oxygen atoms of the C=O group in one DAAQ molecule and the hydrogen atoms of the NH_2 group in another. For the nonpolar molecule coronene [10] to form 1D nanofibers, molecular stacking occurs mainly through π–π and van der Waals interactions. In the stacking of DAAQ molecules, we suspected that both intra- and intermolecular hydrogen bonds would coexist. In addition to π–π interactions and van der Waals contacts between

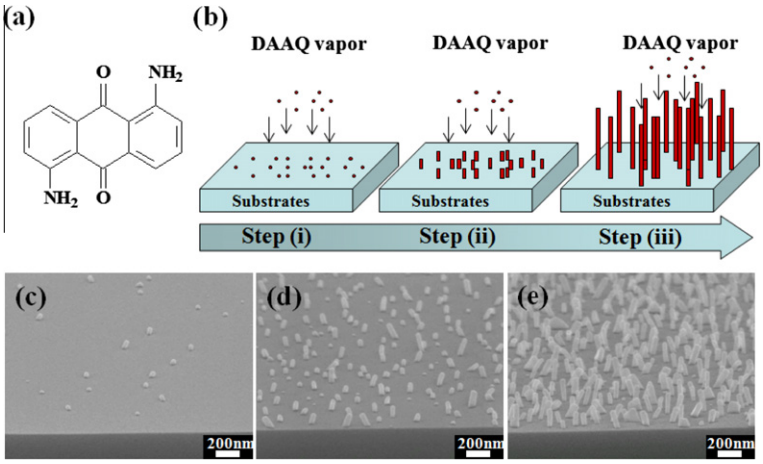

Fig. 1. (a) Chemical structure of DAAQ. (b) Schematic representation of the growth of 1D DAAQ nanofibers through vacuum sublimation. SEM images (cross-sectional view) of DAAQ thin films grown on a Si substrate for (c) 6 s, (d) 10 s, and (e) 60 s at a deposition rate of 0.5 Å/s.

stacking molecules, intermolecular hydrogen bond also plays an important role in 1D self-assembly.

The major advantage of vacuum sublimating DAAQ nanostructure films is the simplicity and accessibility of the process. No catalyst is used and no droplets of catalyst are found at the tips of the nanofibers; therefore, the growth mechanism of DAAQ nanostructure films is presumed to be similar to that of the physical vapor transport method [27]. One strategy for achieving 1D structures, reported by Xia et al. [30], is the use of various templates with 1D morphologies to direct the assembly process. The growth mechanism normally involves three steps (Fig. 1(b)) (i) as the concentration of DAAQ increases, the molecular building blocks begin to aggregate into small nuclei; (ii) these nuclei become seeds for the anisotropic packing of DAAQ molecules; (iii) with a continuous supply of DAAQ, vapor molecules self-assemble to form 1D morphologies with vertically aligned nanostructures on the substrates. In this study, we used vacuum sublimation of DAAQ to construct 1D nanostructures on selected substrates. We investigated the growth mechanism of these DAAQ thin films to develop guidelines for the design of suitable structures for field emitters. Fig. 1(c–e) present cross-sectional SEM images of the early stage (6, 10, and 60 s of deposition at a rate of 0.5 Å/s, respectively) products of the DAAQ nanofibers on a Si wafer. We observe a layer of vertically self-assembled and elongated nanoparticles, which acted as seeds for the anisotropic overgrowth of the nanofibers into columnar structures. Furthermore, varying the deposition time allowed us to adjust the length of the nanofibers on the substrates.

Fig. 2 presents SEM images (top and cross-sectional views) of the DAAQ nanostructure films formed on the Ag, Al, Au, Ni, Si, and Ti substrates. Clearly, the nature of the substrate influenced the morphology of its DAAQ thin film. Fig. 2(a and d) reveal entangled, in-plane, rod-like morphologies for the DAAQ films formed on the Ag and Ni substrates, respectively. In the top-view SEM images in Fig. 2(b, c and e, f) we observe that most of the DAAQ nanofibers grew perpendicularly (slightly slanting) from the substrates to form quasi-arrays. Repulsive forces among nuclei can result in a parallel-displaced conformation, leading to a tilted columnar structure [10,31]. In Fig. 2(c, e, and f), the high-density packing morphologies of the DAAQ nanofibers on the Si and Ti substrates are similar to those on the Au surface. The densities of these nanostructures on all of the substrates ranged from 10^8 to 10^9 cm^{-2} (Table 1). The DAAQ thin films deposited on the Ag and Ni substrates both possessed tilted out-of-plane and in-plane nanorod morphologies, as revealed in their cross-sectional SEM images (insets to Fig. 2(a and d), respectively). The short, tilted nanorods on the Ag surface had a mean radius of 48 nm and a mean length of 226 nm; those on the Ni substrate, however, had larger dimensions (90 and 843 nm, respectively). The DAAQ nanostructures deposited on the Al substrate (inset to Fig. 2(b)) had the largest average radius (100 nm) and length (883 nm); we suspect these oversized nanostructures comprised three or four nanofibers aggregated together in the form of nanocornerstones. In contrast, the DAAQ molecules packed on the Au, Si, and Ti substrates to present an out-of-plane morphology with uniform arrangement; these nanofibers had average lengths of 427, 794, and 587 nm, respectively (insets to Fig. 2(c, e, and f), respectively). The mean radii of these nanofibers, featuring smooth surfaces, ranged from 27 to 35 nm. The lengths of the nanofibers on these substrates could be adjusted by varying the deposition time. Table 1 summarizes the mean lengths (L), radii (r_m), and nanostructural types of the DAAQ assemblies deposited on the various substrates. The aspect ratios (ARs), defined as

$$\mathrm{AR} = L/r_m \tag{1}$$

of the 1D DAAQ nanofibers deposited on the Au, Si, and Ti substrates were 12.6, 29.4, and 16.8, respectively. The high ARs of these DAAQ nanofibers suggest that they are potentially applicable nanostructures for use as organic field emitters.

The selective growth of vertical DAAQ nanowires generally occurs through preferential deposition on geometrical

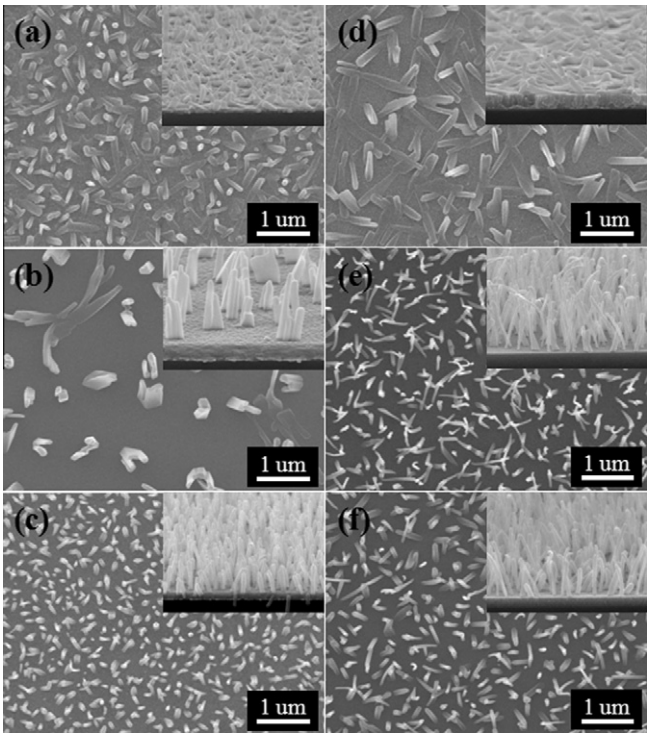

Fig. 2. SEM images (top view) of DAAQ thin films deposited on (a) Ag, (b) Al, (c) Au, (d) Ni, (e) Si, and (f) Ti substrates. Insets are the cross-sectional SEM images.

Table 1
Mean lengths (L), mean radii (r_m), ARs, nanostructure types, and distributions for the DAAQ thin films deposited on various substrates.

Substrate	Mean length (nm)	Mean radius (nm)	AR	Nanostructure type	Distribution (1/cm^2)
Ag	226	48	4.7	Nanorod	2.4×10^9
Al	883	100	8.8	Nanocornerstone	2.1×10^8
Au	427	34	12.6	Nanofiber	2.5×10^9
Ni	843	90	9.4	Nanorod	5.8×10^8
Si	794	27	29.4	Nanofiber	1.6×10^9
Ti	587	35	16.8	Nanofiber	1.6×10^9

chemically modified surfaces; for example, substrates featuring sharp tips or edges, silica beads, or hydrophilic domains [27]. To realize the effects of CAs and to select appropriate metals for use as electrodes for potential applicability in organic field emission, we selected Ag, Au, Al, Ni, Si, and Ti as substrates and investigated the morphologies of the DAAQ nanostructure films formed on these surfaces. Table 2 summarizes the CAs of the various substrates and their SEs, calculated using the Owens and Wendt method [32]. The water contact angles (WCAs) of the Ag, Al, and Ni substrates were 96.1°, 96.7°, and 100.9°, respectively, making them hydrophobic substrates. The majority of DAAQ molecules deposited on these substrates formed flat and entangled structures. In contrast, the DAAQ molecules deposited on the Au, Si, and Ti surfaces extended perpendicularly from the substrates, which had WCAs of 81.8°, 59.7°, and 78.8°, respectively (i.e., hydrophilic substrates). Therefore, it appears that the preferred growth of 1D vertical DAAQ nanofibers requires hydrophilic, rather than hydrophobic, surfaces. This result is similar to those reported by Zhao et al. [27] who studied the effect using UV–Vis absorption spectroscopy. Next, we performed surface treatment of the Si substrate to confirm our

Table 2
CAs and SEs of various substrates.

Substrate	CA (°)			SE[b] (mJ/m^2)
	H_2O	CH_2I_2	$C_2H_4(OH)_2$	
Ag	96.1	52.7	66.5	34.8
Al	96.7	49.5	72.8	35.0
Au	81.8	19.9	56.2	45.1
Ni	100.9	39.5	69.9	46.4
Si	59.7	48.1	38.2	41.3
Ti	78.8	33.5	57.0	39.0
SiH[a]	88.5	58.5	69.9	27.6

[a] Sample obtained after the bare Si substrate had been treated with HMDS vapor and annealed at 160 °C for 30 min.
[b] Calculated using the Owens method from the geometric mean approximation (GMA) measurements of the static CAs of H_2O, CH_2I_2, and $C_2H_4(OH)_2$.

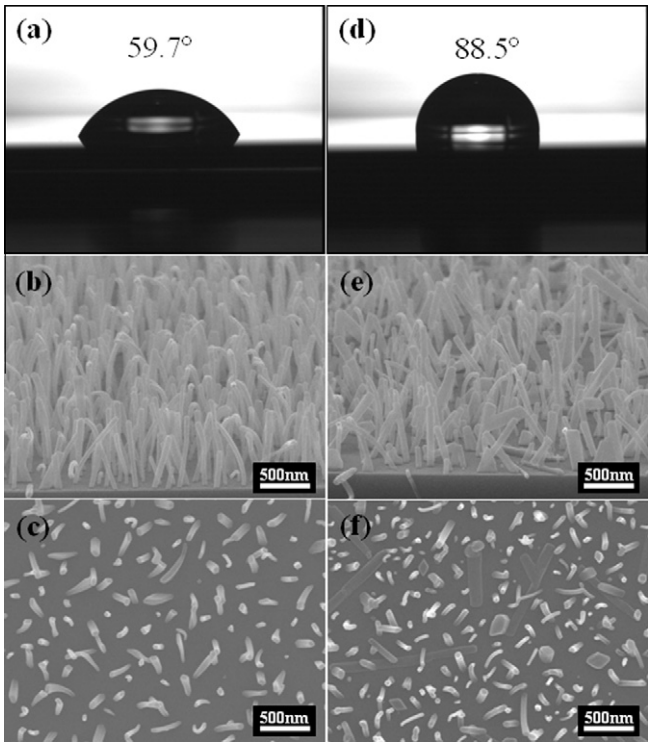

Fig. 3. (a, d) Photographs of water droplets on the (a) bare Si substrate (WCA: 59.7°) and (d) HMDS-treated SiH substrate (WCA: 88.5°). (b, c, e, f) SEM images of the DAAQ structures formed on the (b, c) bare Si and (e, f) SiH substrates; (b, e) cross-sectional views; (c, f) top views.

hypothesis. Fig. 3(a and d) present images of water droplets on the surfaces of bare Si and HMDS-treated Si (SiH), respectively; the WCAs were 59.7° and 88.5°, respectively. We suspect that the greater WCA for the SiH substrate resulted from a reduction in the density of interfacial trapping states and a lowering of the SE. Fig. 3(b and c) display SEM images of the DAAQ thin films deposited on the bare Si surface; as before, the structures extend away from the substrate. In contrast, some of the DAAQ nanofibers were deposited in-plane and entangled on the SiH substrate (Fig. 3(e and f)). This finding confirms that a low-WCA surface endows a preference for vertical deposition of 1D DAAQ nanofibers.

Fig. 4(a and c) present TEM images of the DAAQ nanofibers formed on the Au and Ti substrates, respectively; these nanofibers were very smoothly faceted and uniform in length. High-resolution TEM images of single nanofibers revealed (Fig. 4(b and d)) indistinct lattice fringe spacing. We suspect that the DAAQ molecules were oriented in short-range order at the edges of the nanofibers, but entangled randomly within the nanofibers. The selected area electron diffraction (SAED) pattern in the inset to Fig. 4(a) features only amorphous rings, rather than distinct diffractive spots, suggesting that an insignificant degree of crystallinity was responsible for the isotropic and randomly oriented molecules. Similarly, the electron diffraction pattern in the inset to Fig. 4(c) also reveals the amorphous features of the DAAQ molecules deposited on the Ti substrates. In addition, these HRTEM images do not reveal the presence of any metal catalysts at the tips of the fibers, confirming that the growth mechanism was different from that of carbon nanotubes (CNTs) [33]. In order to understand the lattice differences in our system, the XRD patterns of the DAAQ commercial powders and nanofiber arrays were used to further study (Fig. 4(e)). Although the DAAQ nanofiber arrays feature lower peak intensity than the commercial powders, the relative percentages of (1 0 0), (1 0 2) and (1 1 2) lattice planes show some changes. Comparison of our results with the previous report of DAAQ nanowires [8], the DAAQ nanofiber arrays (formed by vacuum sublimation in low-temperature process) also prefer to grow in the orientation of (1 0 0) lattice plane.

To determine the differences in energy levels between the electrodes and the DAAQ materials for potential field emission applications, we used photoelectron spectroscopy in air (PESA; Fig. 5(a)) and UV–Vis spectroscopy (Fig. 5(b)) to measure the energy levels of DAAQ. When we bombarded our surface materials under a slowly increasing amount of UV light, photoelectrons were emitted from the surface (from a depth of several to hundred angstroms) at a certain energy level, due to the photoelectron effect. These emitted photoelectrons were then counted by a detector and open counter. Using this approach, the valence band [highest occupied molecular orbital (HOMO)] of DAAQ obtained through linear fitting from the PESA data was 5.60 eV relative to the vacuum level. The UV–Vis absorption spectra of the DAAQ films revealed an absorption band in the region 300–800 nm. From the on set wavelength at 614 nm, we derived an energy gap

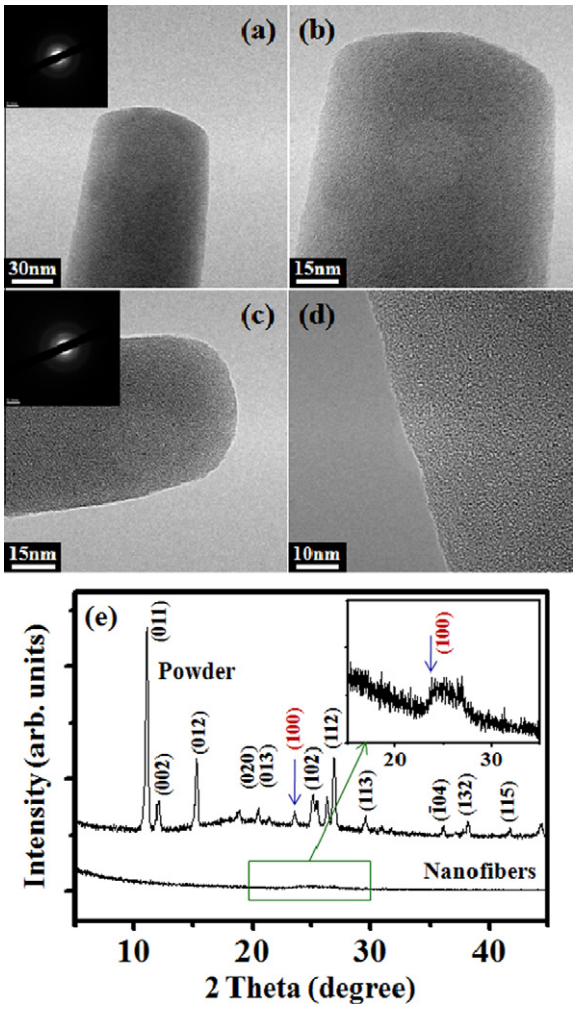

Fig. 4. (a) HRTEM image of a single DAAQ nanofiber formed on the Au substrate; inset: corresponding SAED pattern. (b) Magnified image of the nanofiber in (a). (c) HRTEM image of a single DAAQ nanofiber formed on the Ti substrate; inset: corresponding SAED pattern. (d) HRTEM image of the smooth surface of a single nanofiber. (e) XRD patterns of DAAQ commercial powder (top) and nanofiber arrays (bottom). Inset: magnified XRD pattern of DAAQ nanofiber arrays.

for the DAAQ of 2.02 eV. From this value, we estimated the energy of the conduction band [lowest unoccupied molecular orbital (LUMO)] to be 3.58 eV. Fig. 5(c and d) provide a schematic energy level diagram; the HOMO and LUMO states of DAAQ were 5.60 eV and 3.58 eV, respectively; the work functions of Au and Ti, for use as cathode substrates, were 5.1 and 4.33 eV, respectively. Therefore, electrons injected from the Au substrate into the LUMO state of the DAAQ layer must conquer a larger energy gap than those injected from the Ti substrate.

We examined the field emission properties of the DAAQ nanofibers using a parallel-plate configuration with the spacing of 80 μm in a vacuum chamber at a pressure of 8×10^{-6} torr. The anode ITO glass was connected to the source monitor unit (SMU) of a Keithley 237 instrument; the cathode of Au and Ti substrates were grounded. Fig. 6 displays the field emission characteristics (J–E curve) of the DAAQ nanofibers deposited on the Au (**DAAQ-Au**) and Ti (**DAAQ-Ti**) substrates. The turn-on fields (defined as the applied field required for a current density of 10 μA/cm^2) of **DAAQ-Au** and **DAAQ-Ti** were 8.5 and 8.25 V/μm, respectively; at an applied field of 12 V/μm, the maximum current densities were 0.31 and 0.65 mA/cm^2, respectively. The dependence of the emission current of a field emitter on the applied field is described by the Fowler–Nordheim (FN) equation [34]:

$$ln\left(\frac{J}{E^2}\right) = \ln\left(\frac{A\beta^2}{\phi}\right) + \left(\frac{-B\phi^{3/2}}{\beta}\right)\left(\frac{1}{E}\right) \quad (2)$$

where A and B are constants (1.54×10^{-6} A eV/V^2 and 6.83×10^3 V/eV$^{3/2}$/μm, respectively), J is the current density, E is the applied field, and ϕ is the local work function of the emitter material. By plotting $\ln(J/E^2)$ versus $1/E$, the slope of the line of best fit can be used to deduce the field enhancement factor (β):

$$\beta = -\frac{B\phi^{3/2}}{S} \quad (3)$$

where S is the slope of the FN plot. According to FN theory, β is strongly dependent on the geometric structure of the field emitter. The linear FN plots in the insets to Fig. 6(a and b) reveal that the J–E characteristics of the DAAQ nanofibers followed the FN field emission mechanism. The slopes of FN plots for **DAAQ-Au** and **DAAQ-Ti** were −103.5 and −55.67, respectively. Because the LUMO energy level (ϕ) of DAAQ was 3.58 eV, we estimated the values of β of **DAAQ-Au** and **DAAQ-Ti** to be 447 and 831, respectively. To understand why these values of β differed so dramatically, we must consider the effect of the geometry of the nanofibers. Tarntair et al. [35] reported that the field enhancement factor β could be approximated by the length-to-radius ratio of the 1D nanostructure, expressed as

$$\beta = \frac{l}{r} \quad (4)$$

where r is the radius of curvature of the tip and l is the length of the nanofiber. This equation suggests that emitters having longer lengths and smaller radii, resulting in larger values of β, would have better field emission characteristics. Because our low-WCA surfaces (Au and Ti) favored DAAQ molecules self-assembling into standing nanofibers and because the value of β of **DAAQ-Ti** was greater than that of **DAAQ-Au**, we suspected that the higher AR of the DAAQ nanofibers deposited on Ti would be superior, to those formed on Au, for use in field emission devices. Cho et al. [36] reported the effective radius (r_e) of an effective area at the tips of their Alq_3 nanostructural thin film; the calculated radius (r_e = 2.07 nm) was smaller than the measured radius (r_m = 40 nm). The DAAQ nanofibers of **DAAQ-Au** and **DAAQ-Ti** had effective radii of 0.96 and 0.7 nm, respectively (Table 3). From the differences between the values of r_m (34 nm for **DAAQ-Au**; 35 nm for **DAAQ-Ti**) and r_e, we suspect that the electrons were emitted from a localized area at the tip of a nanofiber, rather than from the entire measured area of the nanofiber. From the viewpoint of the energy levels, Fig. 5(c and d) reveal

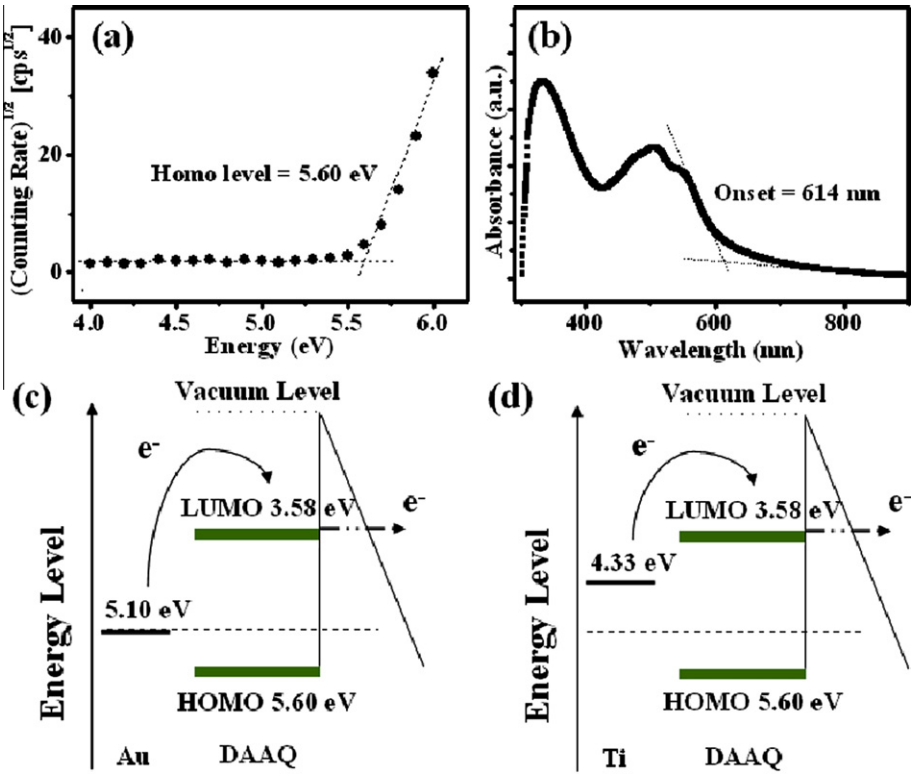

Fig. 5. (a) PESA analysis of the DAAQ thin films. (b) UV–Vis absorption spectra of DAAQ thin films. (c, d) Schematic representations of the energy levels and electrons field emitting through the DAAQ nanofibers of the (c) Au-DAAQ and (d) Ti-DAAQ contacts.

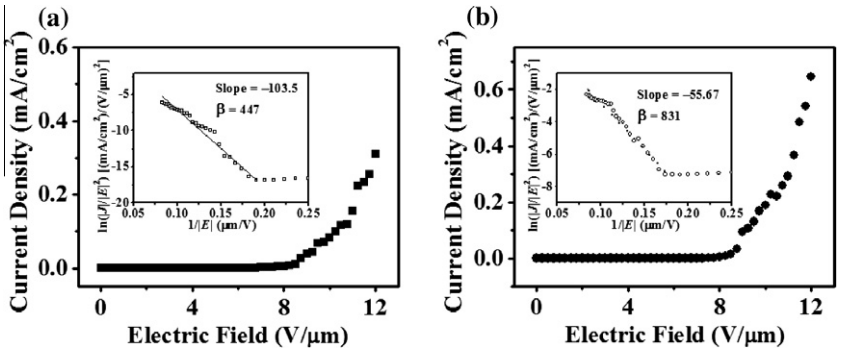

Fig. 6. Field emission *J*–*E* curves of (a) **DAAQ-Au** and (b) **DAAQ-Ti**. Insets: Corresponding FN plots.

Table 3
Values of $E_{turn\text{-}on}$, slopes of FN plots, field emission enhancement factors (β), and effective radii (r_e) for the DAAQ nanofibers.

Substrate	$E_{turn\text{-}on}$ (V/μm)	Slope	β	r_e (nm)
Au	8.50	−103.50	447	0.96
Ti	8.25	−55.67	831	0.70

that the work function (5.1 eV) of Au was much higher than that (4.33 eV) of Ti; therefore, the energy barrier (1.52 eV) at the Au-DAAQ interface was larger than that (0.75 eV) at the Ti-DAAQ contact. These energy barriers limited the injection of electrons from the conducting substrates to organic nanofibers; consequently, a higher applied field was required to reach the same level of emission current.

We performed stability tests of our DDAQ nanofibers under an applied field of 11 V/μm for 3000 s. The calculated mean current densities were ca. 0.07 mA/cm^2 for **DAAQ-Au** (Fig. 7(a)) and 0.19 mA/cm^2 for **DAAQ-Ti** (Fig. 7(b)), with perturbations of less than one order. In addition, we observed a slowly increasing **DAAQ-Ti** emission current over time and two apparent increasing **DAAQ-Au** emission currents from 150 to 250 s and from

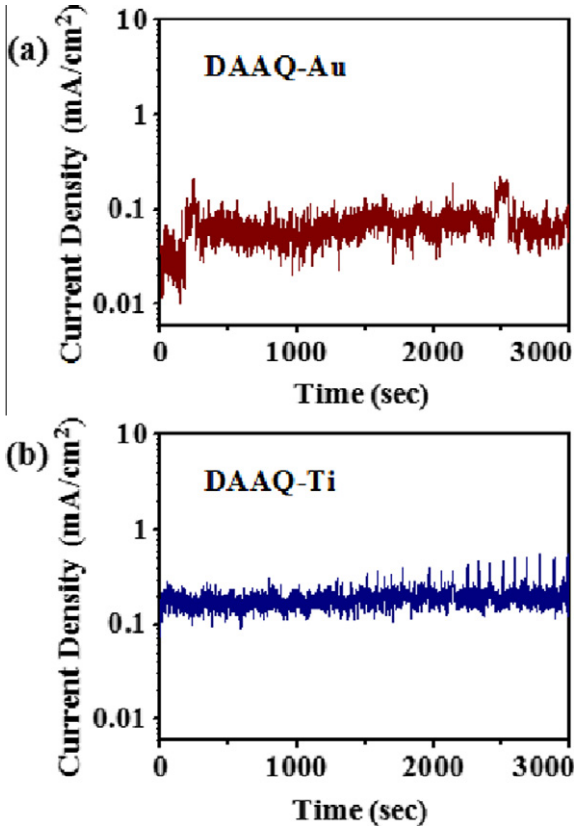

Fig. 7. Emission current stability plots recorded at a constant voltage for 3000 s: (a) **DAAQ-Au**; (b) **DAAQ-Ti**.

2440 to 2540 s. The latter presumably arose from a training effect [37,38]; that is, contaminants were expelled from the nanofibers after an adapted biasing on the nanofibers for a period of time. Thus, the organic semiconductor sustained a stable field emission current, without any decay, during the measurement period, demonstrating that DAAQ organic nanofibers have great potential for use in cold field electron-emitting devices.

4. Conclusions

By using DAAQ as a starting material, we prepared vertical organic nanofibers through low-temperature (42 °C) vacuum sublimation. The morphologies of the structures formed from the DAAQ molecules were controlled by the surface properties of the substrates, with vertically aligned 1D DAAQ structures growing preferentially on low-WCA surfaces, such as Au, Si, and Ti. The DAAQ nanofibers exhibited unique field emission characteristics and followed FN behavior. The maximum emission current densities of **DAAQ-Au** and **DAAQ-Ti** were 0.31 and 0.65 mA/cm^2 when biased at 960 V (E = 12 V/μm), respectively. The field enhancement factors β of the DAAQ nanofibers on the Au and Ti substrates were 447 and 831, respectively. In field emission stability tests, the field emission current was stable, without any decay, during the duration of the measurements. The stability of the emission current and the simplicity of the synthetic process suggest that this method of fabricating vertically aligned DAAQ nanofibers is suitable for application in the fabrication of electron-emitting devices.

Acknowledgment

We thank for National Science Council (Project NSC 98-2221-E-009-021-MY3), ROC, for financial support.

References

[1] A.B. Djurišić, A.M.C. Ng, K.Y. Cheung, M.K. Fung, W.K. Chan, J. Mater. Sci. Technol. 24 (2008) 563.
[2] Y.S. Zhao, H. Fu, A. Peng, Y. Ma, D. Xiao, J. Yao, Adv. Mater. 20 (2008) 2859.
[3] Y.S. Zhao, H. Fu, A. Peng, Y. Ma, Q. Liao, J. Yao, Acc. Chem. Res. 43 (2010) 409.
[4] F. Yang, M. Shtein, S.R. Forrest, J. Appl. Phys. 98 (2005) 014906.
[5] F. Yang, S.R. Forrest, Adv. Mater. 18 (2006) 2018.
[6] R.R. Lunt, J.B. Benziger, S.R. Forrest, Appl. Phys. Lett. 90 (2007) 181932.
[7] Y.S. Hsiao, W.T. Whang, S.C. Suen, J.Y. Shiu, C.P. Chen, Nanotechnology 19 (2008) 415603.
[8] Y.S. Zhao, J. Wu, J. Huang, J. Am. Chem. Soc. 131 (2009) 3158.
[9] J.J. Chiu, C.C. Kei, T.P. Perng, W.S. Wang, Adv. Mater. 15 (2003) 1361.
[10] S.C. Suen, W.T. Whang, B.W. Wu, Y.F. Lai, Appl. Phys. Lett. 84 (2004) 3157.
[11] S.C. Suen, W.T. Whang, F.J. Hou, B.T. Dai, Org. Electron. 7 (2006) 428.
[12] S.C. Suen, W.T. Whang, F.J. Hou, B.T. Dai, Org. Electron. 8 (2007) 505.
[13] C.P. Cho, T.P. Perng, Org. Electron. 11 (2010) 115.
[14] H. Liu, Q. Zhao, Y. Li, Y. Liu, F. Lu, J. Zhuang, S. Wang, L. Jiang, D. Zhu, D. Yu, L. Chi, J. Am. Chem. Soc. 127 (2005) 1120.
[15] S. Cui, Y. Li, Y. Guo, H. Liu, Y. Song, J. Xu, J. Lv, M. Zhu, D. Zhu, Adv. Mater. 20 (2008) 309.
[16] J.J. Chiu, W.S. Wang, C.C. Kei, C.P. Cho, T.P. Perng, P.K. Wei, S.Y. Chiu, Appl. Phys. Lett. 83 (2003) 4607.
[17] Y.S. Zhao, J. Xu, A. Peng, H. Fu, Y. Ma, J. Yao, Adv. Mater. 20 (2008) 1661.
[18] Y.S. Zhao, H. Fu, F. Hu, A.D. Peng, J. Yao, Adv. Mater. 19 (2007) 3554.
[19] W. Chen, Q. Peng, Y. Li, Adv. Mater. 20 (2008) 2747.
[20] H. Liu, Y. Li, S. Xiao, H. Gan, T. Jiu, H. Li, L. Jiang, D. Zhu, D. Yu, B. Xiang, Y. Chen, J. Am. Chem. Soc. 125 (2003) 10794.
[21] S. Cui, H. Liu, L. Gan, Y. Li, D. Zhu, Adv. Mater. 20 (2008) 2918.
[22] H. Gan, H. Liu, Y. Li, Q. Zhao, Y. Li, S. Wang, T. Jiu, N. Wang, X. He, D. Yu, D. Zhu, J. Am. Chem. Soc. 127 (2005) 12452.
[23] H. Liu, Y. Li, S. Xiao, H. Li, L. Jiang, D. Zhu, B. Xiang, Y. Chen, D. Yu, J. Phys. Chem. B 108 (2004) 7744.
[24] J.J. Chiu, W.S. Wang, C.C. Kei, T.P. Perng, Appl. Phys. Lett. 83 (2003) 347.
[25] Y.S. Zhao, C.A. Di, W. Yang, G. Yu, Y. Liu, J. Yao, Adv. Funct. Mater. 16 (2006) 1985.
[26] Y.S. Zhao, D. Xiao, W. Yang, A. Perng, J. Yao, Chem. Mater. 18 (2006) 2302.
[27] Y.S. Zhao, P. Zhan, J. Kim, K. Sun, J. Huang, ACS Nano 4 (2010) 1630.
[28] H. Derouiche, V. Djara, Sol. Energy Mater. Sol. Cells 83 (2004) 125.
[29] G. Suganthi, C. Meenakshi, V. Ramakrishnan, J. Fluoresc. 20 (2010) 95.
[30] Y.N. Xia, P.D. Yang, Y.G. Sun, Y.Y. Wu, B. Mayers, B. Gates, Y.D. Yin, F. Kim, H.Q. Yan, Adv. Mater. 15 (2003) 353.
[31] J.D. Wright, Molecular Crystals, second ed., Cambridge University Press, 1995. p. 22.
[32] D.K. Owens, R.C. Wendt, J. Appl. Polym. Sci. 13 (1969) 1741.
[33] V. Vinciguerra, F. Buonocore, G. Panzera, L. Occhipinti, Nanotechnology 14 (2003) 655.
[34] R. Fowler, L.W. Nordheim, Proc. R. Soc. London 119 (1928) 173.
[35] F.G. Tarntair, C.Y. Wen, L.C. Chen, J.J. Wu, K.H. Chen, P.F. Kuo, S.W. Chang, Y.F. Chen, W.K. Hong, H.C. Cheng, Appl. Phys. Lett. 76 (2000) 2630.
[36] C.P. Cho, T.P. Perng, Nanotechnology 18 (2007) 125202.
[37] J.M. Bonard, N. Weiss, H. kind, T. Stöckli, L. Forró, K. Kern, A. Châtelain, Adv. Mater. 13 (2001) 184.
[38] S.K. Patra, G.M. Rao, J. Appl. Phys. 100 (2006) 024319.

9,10-di(2-naphthyl)anthracene (AND) [11], which is designed to be used as a host material because it also has the anthracene structure identical to the dopants. Here, both the host and guest contain the anthracene moieties which are supposed to increase the compatibility between guest and host as to have well-dispersed dopants in the host matrix, and lead to an increase in the emission efficiency.

The dopants (with sample code) for OLEDs fabrication were N,N,N′,N′-tetraphenyl-anthracene-9,10-diamine (TAD), N,N,N′,N′-tetra-*m*-tolyl- anthracene-9,10-diamine (T*m*AD), N,N,N′,N′-tetra-*p*-tolyl-anthracene-9,10-diamine (T*p*AD) and N,N,N′,N′-tetrakis-(3,4-dimethyl-phenyl)-anthracene-9,10-diamine (T*mp*AD). Among these compounds, the physical properties and device performances of TAD and T*p*AD were already reported as the host emitters [12]. Here, we present the first reported case in which the *N*-diaryl amino anthracenes were used as green dopant in ADN host system for OLED devices. We are reporting on the synthesis, characterization, fabrication and performance of OLED devices that incorporate the four dopant molecules described above in the emitting layer. The effects of substituted methyl group at different positions of aromatic *N*-aryl-substituted anthracene-9,10-diamine have been compared based on both materials and solid device evaluation. Moreover, the device performance of the dimethyl-substituted dopants/AND-based devices was also compared to a general guest/host system based on coumarin (C545T) as dopant and Alq_3 as host [13]. The improvement effect of guest/host both based on anthracence derivatives could be observed in this study.

2. Experimental

2.1. Materials and Instrumentations

Sodium tert-butoxide (*t*-BuONa, Merck), Tri-tert-butylposphine (P(t-Bu)$_3$, Strem), Palladium(II) acetate ($Pd(OAc)_2$, Strem), Tris(dibenzylideneacetine)dipalladium ($Pd_2(dba)_3$, Strem), 9,10-Dibromoanthracene (98%, Alfa), Diphenylamine (98%, Alfa), Di-*m*-tolyl-amine (98%, Alfa), Di-*p*-tolyl-amine (97%, Adrich), 4-Bromo-*o*-xylene (98%, Alfa), Benzylamine (99%, Acros), Palladium (10% on carbon, Alfa), Anthracene (98%, Acros), Ethanol (Merck), n-Hexane (Merck), Methanol (Merck) were used as received without further purification. Tetrahydrofuran (THF, Merck), Toluene (SHOWA), Dichloromethane (CH_2Cl_2, Merck) were dried and distilled under standardard procedure (THF and Toluene dried using Na/Ph_2CO; CH_2Cl_2 dried using CaH_2) and stored under nitrogen. For device fabrication, 9,10-di(2-naphthyl)anthracene (ADN), copper phthalocyanine (CuPc), N,N′-bis(naphthalene-1-yl)-N,N′-bis(phenyl)benzidine (NPB), 2,3,6,7-tetrahydro-1,1,7,7,-tetramethyl-1*H*,5*H*,11*H*-10(2-benzothiazolyl)quinolizine- [9,9a,1gh] coumarin (C545T), tris(8-hydroxyquinoline)aluminum (Alq_3) were received from a commercial source (Summit-Tech Co., Ltd.) and purified by a temperature programmated sublimation system. Tungsten boat (Summit-Tech Co., Ltd.), Alumina (Alfa) and LiF (Alfa) were used as received from commercial sources. Indium tin oxide (ITO)-coated glass subtrates with surface resistance 15 Ω/□ were bought from Ritek Co., Ltd.

The synthesized compounds were characterized by Nuclear Magnetic Resonance (NMR) and Mass spectrometer. NMR measurements were made using Bruker AMX 400 and 500 NMR spectrometer. Mass spectra were obtained with a MAT-95XL HRMS mass spectrometer. The UV–visible spectra were recorded using a Perkin Elmer Lambra 35 UV–visible spectrophotometer. Fluorescence spectra were recorded using a Hitachi F-4500 fluorescence spectrophotometer. Photo-electron spectra were obtained by a Riken Keiki Photo-electron Spectrometer model AC-2. Quantum yields were recorded using an integrating sphere and a HAMAMATSU photonic multi-channel analyzer C10027. All data were averaged from at least five raw data to ensure statistical significance. Device properties were monitored using a Keithley 2400 power supply with a 400 nm cut-off filter. An optical meter of model PR705 was used in this study. All of the products were purified by sublimation method with a temperature programmed condition using an upper opened sublimation system made by ULVAC. The high vacuum evaporation system was made by Branchy Technology Co., Ltd. for organic thin film deposition. Thin films were prepared by vacuum evaporation at a base pressure of 2×10^{-5} Torr or lower. The film thickness was measured with a calibrated quartz-crystal microbalance during deposition.

2.2. General procedure for the synthesis of diaryl-anthracene-9,10-diamine derivatives

The structure of as-synthesized diaryl-anthracene-9,10-diamine derivatives are illustrated in Fig. 1 with compound code TAD, T*m*AD, T*p*AD and T*mp*AD, respectively. The diaryl-anthracene-9,10-diamine derivatives were prepared in high yields, by palladium-catalyzed C–N cross-coupling [12,14–16] of the 9,10-Dibromoanthracence with the amine (Diphenylamine, Di-*m*-tolyl-amine, Di-*p*-tolyl-amine or Bis-(3,4-dimethyl-phenyl)-amine). 9,10-Dibromoanthracence (1 equiv.), $Pd(OAc)_2$ or $Pd_2(dba)_3$ (1 mol%), *t*-BuONa (2.5 equiv.), the amine (Diphenylamine, Di-*m*-tolyl-amine, Di-*p*-tolyl-amine or Bis-(3,4-dimethyl-phenyl)-amine) (2.4 equiv.) were weighted into a 500 ml double-neck round-bottom flask connected with a condenser under nitrogen. Dry toluene (200 mL) was then added under nitrogen with stirring to give a homogeneous mixture. A solution containing P(*t*-Bu)$_3$ (5 mol%) and dry toluene (3.4 mol%) was then added to the mixture and reacted under nitrogen for some hours at 130 °C. The endpoint of reaction was monitored by thin-layer chromatography. After complete consumption of starting materials, the resulting solution was cooled to room temperature; and *n*-hexane was added to precipitate the products. The products were collected by filtering and then dried under vacuum for overnight at 100 °C. The crude products were purified by sublimation method under the programmated condition (e.g. 280 °C for 90 min, 300 °C for 90 min, 320 °C for 90 min and then 100 °C). The detailed synthetic procedures of compounds TAD, T*m*AD, T*p*AD and T*mp*AD were described as follows:

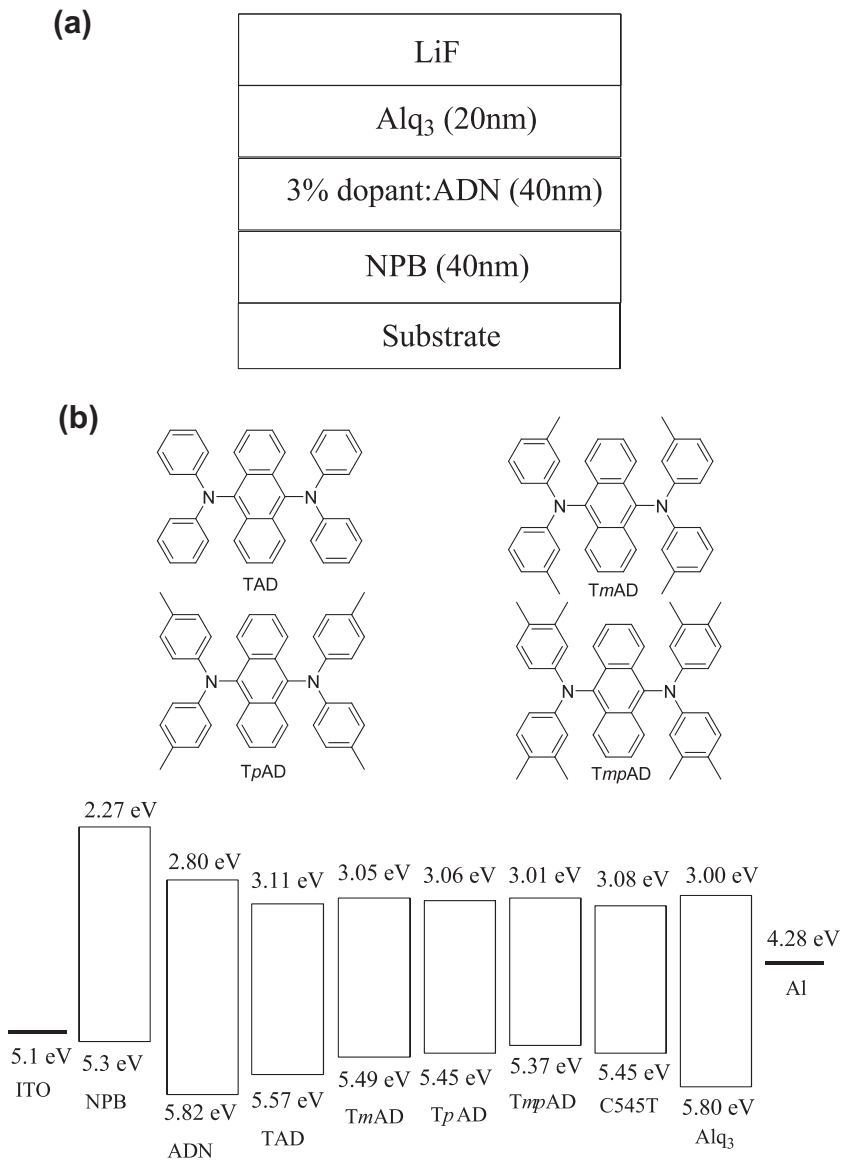

Fig. 1. (a) Schematic OLED device setup. (b) Molecular structure of as-synthesized dopants and relative energy diagram of materials used in all the devices.

2.2.1. N,N,N′,N′-tetraphenyl-anthracene-9,10-diamine (TAD)

From 9,10-Dibromoanthracence (10 g, 29.8 mmol) and Diphenylamine (12.09 g, 71.4 mmol), compound TAD was obtained as a yellow solid. The crude product was purified twice by sublimation to afford compound TAD in 78% yield. ^{1}H NMR (400 MHz, $CDCl_3$): δ = 6.89–6.92 (*t*, *J* = 3.2 Hz, *J* = 7.2 Hz, 4 H), 7.10–7.12 (*d*, *J* = 4.4 Hz, 8 H), 7.18–7.22 (*t*, *J* = 7.2 Hz, *J* = 8.4 Hz, 8 H), 7.33–7.36 (*q*, *J* = 3.2 Hz, 4 H), 8.17–8.20 (*q*, *J* = 3.2 Hz, 4 H); ^{13}C NMR (100 MHz, $CDCl_3$): δ = 120.3, 121.4, 125.1, 126.8, 129.3, 131.8, 137.4, 147.7; EI MS (m/e): 512 (M^+).

2.2.2. N,N,N′,N′-tetra-m-tolyl-anthracene-9,10-diamine (TmAD)

From 9,10-Dibromoanthracence (5 g, 14.9 mmol) and Di-*m*-tolyl-amine (7.05 g, 35.7 mmol), compound T*m*AD was obtained as a yellow solid. The crude product was purified twice by sublimation to afford compound T*m*AD in 79% yield. ^{1}H NMR (400 MHz, $CDCl_3$): δ = 2.19 (s, 12 H), 6.70–6.72 (*d*, *J* = 7.2 Hz, 4 H), 6.86–6.88 (*d*, *J* = 9.84 Hz, 4 H), 6.94 (s, 4 H), 7.04–7.08 (*t*, *J* = 8.0 Hz, *J* = 7.6 Hz, 4 H), 7.33–7.34 (*q*, *J* = 3.2 Hz, 4 H), 8.17–8.17 (*q*, *J* = 3.2 Hz, 4 H); ^{13}C NMR (100 MHz, $CDCl_3$): δ = 21.6, 117.7, 120.9, 122.1, 125.1, 126.6, 129.0, 131.9, 137.5, 138.9, 147.9; EI MS (m/e): 568 (M^+).

2.2.3. N,N,N′,N′-tetra-p-tolyl-anthracene-9,10-diamine (TpAD)

From 9,10-Dibromoanthracence (5 g, 14.9 mmol) and Di-*p*-tolyl-amine (7.05 g, 35.7 mmol), compound T*p*AD was obtained as a yellow solid. The crude product was purified twice by sublimation to afford compound T*p*AD

in 82% yield. ^{1}H NMR (500 MHz, $CDCl_3$): δ = 2.24 (s, 12 H), 6.98–6.99 (*d*, *J* = 1.2 Hz, 16 H), 7.30–7.34 (m, 4H), 8.16–8.19 (m, 4H); ^{13}C NMR (125 MHz, $CDCl_3$): δ = 20.6, 120.1, 121.1, 126.6, 129.8, 130.3, 131.9, 137.5, 145.6; EI MS (m/e): 568 (M^+).

2.2.4. N,N,N′,N′-tetrakis-(3,4-dimethyl-phenyl)-anthracene-9,10-diamine (TmpAD)

For the synthesis of T*mp*AD, the Bis-(3,4-dimethyl-phenyl)-amine was first synthesized as the following procedure: 4-Bromo-*o*-xylene (2 g, 10.8 mmol), Benzylamine (2.54 g, 23.7 mmol), $Pd_2(dba)_3$ (0.1 g, 1 mol%), *t*-BuONa (2.4 g, 2.3 equiv.) were weighted into a 250 ml double-neck round-bottom flask connected with a condenser under nitrogen. About 50 mL of toluene was added and then stirred to give a homogeneous mixture. A solution of 5 mol% P(*t*-Bu)$_3$ in toluene (2.6 mL) was then added to the mixture and reacted at 130 °C. After overnight, the resulting solution was cooled to room temperature, and the solution was evaporated to dryness to afford a powder, which was adsorbed onto 4 g of silica gel and chromatographed with hexane to give 2 g (yield: 80%) of Benzyl-bis-(3,4-dimethyl-phenyl)-amine as a red-brown liquid. The as-prepared Benzyl-bis-(3,4-dimethyl-phenyl)-amine was further reduced to form Bis-(3,4-dimethyl-phenyl)-amine. A mixed solvent of ethanol and THF was added to a 100 mL double-neck round-bottom flask which contained Benzyl-bis-(3,4-dimethyl-phenyl)-amine (2 g, 6.34 mmol) and Pd/C (0.025 g, 2 mol%) and stirred under nitrogen. After the starting materials had dissolved, hydrogen gas was then bubbled into the solution and further reacted overnight. The reaction was monitored by thin-layer chromatography. After the reaction had completed, the resulting brown solution was evaporated to dryness to afford 0.83 g (yield: 58%) of Bis-(3,4-dimethyl-phenyl)-amine as a brown solid which was used as the starting material for the synthesis of compound T*mp*AD. Compound Benzyl-bis-(3,4-dimethyl-phenyl)-amine was identified by ^{1}H NMR (400 MHz, $CDCl_3$): δ = 2.08–2.19 (m, 12 H), 4.30 (s, 2 H), 6.40–6.43 (*q*, *J* = 2.4 Hz, 2H), 6.49–6.50 (*d*, *J* = 2.0 Hz, 2H), 6.93–6.95 (*d*, *J* = 80 Hz, 2H), 7.25–7.38 (m, 5H). Compound bis-(3,4-dimethyl-phenyl)-amine was identified by ^{1}H NMR (400 MHz, $CDCl_3$): δ = 2.19–2.20 (d, 12 H), 5.43 (s, 1 H), 6.78–6.82 (m, 4 H), 6.99–7.01 (d, 2H).

From 9,10-Dibromoanthracence (5 g, 14.9 mmol) and Bis-(3,4-dimethyl-phenyl)-amine (8.05 g, 35.7 mmol), compound T*mp*AD was obtained as an orange solid. The crude product was purified twice by sublimation to afford compound T*mp*AD in 81% yield. ^{1}H NMR (400 MHz, $CDCl_3$): δ = 2.11 (s, 12 H), 2.15 (s, 12H), 6.77–6.80 (*q*, *J* = 2.4 Hz, 4 H), 6.91–6.93 (m, 8 H), 7.31–7.33 (*q*, *J* = 3.2 Hz, 4 H), 8.17–8.19 (*q*, *J* = 3.2 Hz, 4 H); ^{13}C NMR (100 MHz, $CDCl_3$): δ = 18.9, 20.1, 117.8, 121.4, 125.2, 126.4, 129.0, 130.2, 132.0, 137.2, 137.5, 145.96; EI MS (m/e): 624 (M^+).

2.3. OLED fabrication

Indium tin oxide (ITO)-coated glass substrates were thoroughly cleaned and treated with oxygen plasma. OLEDs were fabricated by using a multiple source thermal evaporation system at a base pressure of 2×10^{-5} Torr or lower. The deposition rate was 1 Å/s for all organic films. The LiF film, with thickness of 15 Å, was evaporated at a rate of 0.1 Å/s. The Al cathode, with thickness of 200 nm, was deposited at a rate of 5 Å/s.

3. Results and discussion

3.1. Photo-physics studies

The photo-physics properties of as-synthesized methyl groups substituted N-aryl anthracene-9,10-diamine derivatives TAD, T*m*AD, T*p*AD and T*mp*AD were studied by UV–visible and fluorescence spectrophotometer. The absorption and emission spectra as illustrated in Fig. 2a and Table 1 show that these compounds in form of solid film have major absorption bands with wavelength maxima (λ_{max}) within 258–268, 296–297, 360–380 and 470–490 nm. The potoluminence (PL) emission band has λ_{max} located around 519–532 nm. As a result, compound TAD and T*m*AD have similar emission spectra with $\lambda_{max} \sim 520$ nm in solid state, whereas there are obvious bathochromic shift observed at $\lambda_{max} \sim 530$ nm for compound T*p*AD and T*mp*AD. The compound T*mp*AD, with methyl groups substituted in both *para*/*meta* position, also has similar emission spectra to that of T*p*AD. The result indicates the methyl group substituted at the *para* position of aromatic phenyl diamine has a greater electronic effect than *meta* position on the anthracene moiety. There is a strong solvent effect for these anthracene materials as illustrated in Fig. 2b and Table 1. Basically the emission color of these compounds exhibit a green color in non-polar solvents, i.e., toluene, and red shift to yellow-green color in polar solvents, i.e., CH_2Cl_2, for compound with methyl substuents. The solvent effect indicates there is an observable dipole moment between phenyl diamine and anthracene moieties. The dipole moment is strongly dependent on the position of methyl groups at the phenyl diamine, especially for the compound T*p*AD and T*mp*AD. The effects of methyl substituents for the comparison of λ_{em} in solvent phase showed the following sequence of T*mp*AD, T*p*AD and then T*m*AD.

A photoelectron spectrometer was used to evaluate the energy of the highest occupied molecular orbital (HOMO). The energy gap (E_g) was calculated by the formula: E_g (eV) = $hc/\lambda_{onset} = \sim 1241/\lambda_{onset}$, where h is Planck's constant and c is speed of light. The wavelength onset, λ_{onset}, was obtained by absorption spectra as illustrated in Table 1. The lowest unoccupied molecular orbital (LUMO) was derivated from the values of HOMO and E_g, and the data are listed in Table 1. The relative energy diagram of materials used for devices fabrication is compared in Fig. 1 The compound T*mp*AD has relatively the smallest value of HOMO, i.e. 5.37 eV, due to its higher donor ability than others. The delocalization degree of anthracene relatively decreased along with the donor ability of phenyl diamine moiety, and the energy band gaps become smaller. The energy band gaps follow the sequence: compound TAD > T*m*AD > T*p*AD > T*mp*AD, where the E_g values are 2.46, 2.44, 2.39 and 2.36 eV, respectively.

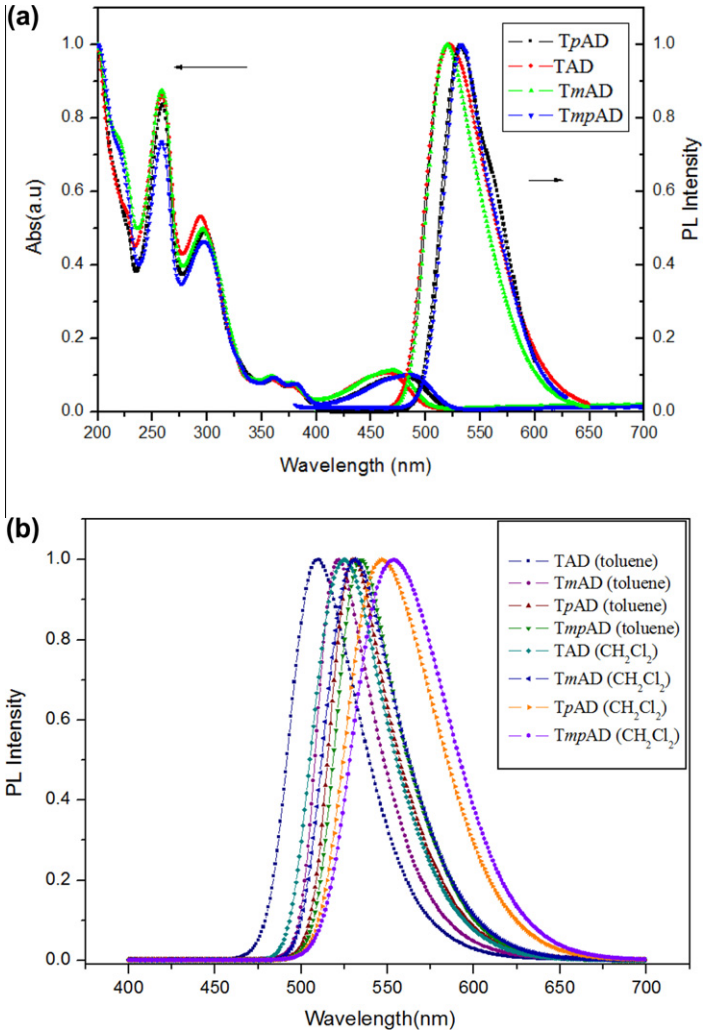

Fig. 2. (a) The absorption and PL spectra of TAD, T*m*AD, T*p*AD, and T*mp*AD in solid film. (b) Solvent effect studies of PL spectra for compound TAD, T*m*AD, T*p*AD and T*mp*AD in toluene and CH_2Cl_2.

Table 1
Relationship of the as-prepared anthracene-9,10-diamine derivatives TAD, T*m*AD, T*p*AD, and T*mp*AD with the λ_{abs}, λ_{onset}, λ_{em}, Q.Y., HOMO, LUMO and Band Gap measured by UV–vis spectrophotometer, fluorescence spectrophotometer, photoelectron spectrometer.

Sample code	λ_{abs} (nm) Film	λ_{onset} (nm) Film	λ_{em} (nm)			Q.Y.[a]	HOMO (eV)	LUMO (eV)	Band Gap (eV)
			Film	Toluene	CH_2Cl_2				
TAD	259, 297, 360, 379, 480	504	520	510	524	0.95	5.57	3.11	2.46
T*m*AD	258, 296, 360, 379, 469	509	519	521	530	0.92	5.49	3.05	2.44
T*p*AD	258, 296, 360, 379, 486	519	531	530	546	0.94	5.45	3.06	2.39
T*mp*AD	268, 296, 360, 379, 486	526	532	535	553	0.82	5.37	3.01	2.36

[a] Measured in a CH_2Cl_2 solution by using a HAMAMATSU Photonic multi-channel analyzer C10027.

3.2. Devices fabrication

The as-prepared anthrancene-9,10-diamine materials TAD, T*m*AD, T*p*AD, and T*mp*AD were used as dopants of the emitting layer for the application of organic electroluminescent devices. Before device fabrication, compound T*p*AD was used as a dopant for doping concentration tests with devices fabricated as follows: ITO/CuPc (15 nm)/NPB (40 nm)/T*p*AD:AND (40 nm)/Alq_3 (20 nm)/LiF (1.5 nm)/Al (200 nm), where the doping concentration of T*p*AD was changed between 1 and 4 mol%. It can be seen that the luminance efficiency and brightness of devices were relatively increased by changing the concentration from 1 to 4 mol% as the curves show in Fig. 3. The results show that

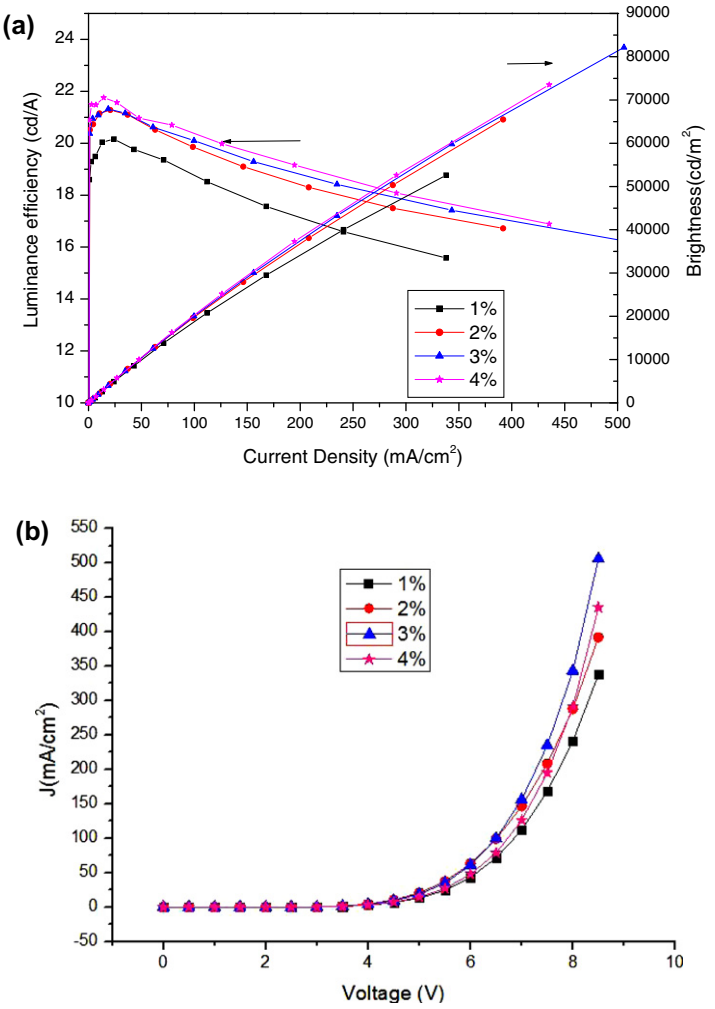

Fig. 3. The doping concentration test with devices fabricated as: ITO/CuPc (15 nm)/NPB (40 nm)/T*p*AD:AND (40 nm)/Alq_3 (20 nm)/LiF (1.5 nm)/Al (200 nm), where the concentration of T*p*AD is changed between 1 and 4 mol%.

the devices have good luminance efficiency below a current density of 100 mA/cm^2. As the current density increased, the optimized concentration of T*p*AD doping in AND could be compared and selected, where the doping concentration of 3 mol% was the optimum value for considering the driving voltage, luminance efficiency and brightness over a wide range of current density. The result could be observed from the *J*–*V* curves for the doping concentration test as shown in Fig. 3b, in which 3 mol% of dopant shows relatively lower driving voltage, when compared at the same current density. Therefore, in this study, a series of solid state devices were fabricated by using 3 mol% dopant for the comparison in the effects of methyl substituents on the dopants.

The structure of devices using the as-prepared anthracene-9,10-diamine derivatives as dopants was designed and fabricated as ITO/NPB (40 nm)/3% dopant:AND (40 nm)/Alq_3 (20 nm)/LiF (1.5 nm)/Al (200 nm) and schematic shown as Fig. 1 Herein, NPB was used as the hole transport layer (HTL). The wide band gap material of AND, which has a high energy band gap of 3.02 eV, was used as the host material because it might restrict the electron and hole in the emitting layer and was expected to improve the efficiency of emission during recombination. Moreover, the same structure of anthracene moieties for both dopant and the host AND was expected to have more compatible properties and be suitable as a good guest/host combination for the emitting layer. The electron transport layer (ETL) was tris(8-hydroxyquinoline)aluminum (Alq_3).

3.3. Devices properties studies

A comparative device based on a general guest/host system with coumarin (C545T)/Alq_3-based emitting layer was fabricated and named as device 1, which has the structure of ITO/NPB (40 nm)/2% C545T:Alq_3 (40 nm)/Alq_3 (20 nm)/LiF (1.5 nm)/Al (200 nm). The devices based on the as-prepared compound TAD, T*mp*AD, T*m*AD, and T*p*AD were fabricated and named as device 2, device 3, device 4 and device 5, respectively. The device properties are summarized in Table 2. As the results show, device 3 exhibits the best performance with maximal external quantum

efficiency (E.Q.E.) reached to 8.2%. The E.Q.E. values of devices 1–5, which evaluated at 100 mA/cm^2, follow the sequence: device 3 > device 5 > device 4 > device 2 > device 1, where the E.Q.E. values are 6.91%, 6.37%, 5.40%, 5.33% and 3.52%, respectively. The effects of substituted methyl group at both *para/meta* positions of aromatic *N*-aryl-methyl-substituted 9,10-diaminoanthracene by fabricating the device using the T*mp*AD/AND based guest/host system have been observed with the power efficiency of 9.24 lm/W and current efficiency of 28.17 cd/A, evaluated at luminance of 10,000 cd/m^2. All of the devices have color coordinates located at the green region in the Commission internationale de l'éclairage (CIE) chromaticity diagram. The electroluminescent spectra of devices 1–5 are shown in Fig. 4. Evidently, the trends of emission for these devices are similar to that of solid films as shown in Fig. 2a. For the devices 1–5, the relationships of luminance (B) versus current density (*J*) are shown in Fig. 5. As shown in *B–J* curves, the brightness of devices using the dopants with methyl groups at both *para/meta* or *para* positions of *N*-aryl-methyl-substituted 9,10-diaminoanthracene, i.e., the devices 3 and 5, were better than that at *meta* position or non-substituted, i.e., devices 4 and 2. However, all of these developed devices based on the anthracene-9,10-diamine derivatives/AND based guest/host system were greatly enhanced in brightness as compared at the same current density to the system based on coumarin (C545T)/Alq_3 of device 1. Furthermore, as we study the current efficiency (cd/A) or power efficiency (lm/W) related to luminance (cd/m^2), we can find that the curve trends show the device efficiency as follows: device 3 is better than device 5, device 5 is better than devices 4 and 2; device 1 is the worst, as shown in Fig. 6. The improvement in optoelectronic properties of the guest/host system based on anthracene-9,10-diamine derivatives/9,10-di(2-naphthyl)anthracene (AND) as compared to the coumarin (C545T)/Alq_3 is obvious. In addition, the dopant T*mp*AD illustrated the effect of methyl groups substituted at both the *para/meta* positions could greatly improve in device performance. This may be attributed to the relative amorphous property of the emission film and the reduction of the self-quenching phenomena. The steric effect of the two methyl groups substituted at the *meta* and *para* position of phenyl diamine may make the molecules relatively difficult to aggregate with each other. Therefore the emission efficiency can be improved by developing these serials of 9,10-diaminoanthracene derivatives as the dopant T*mp*AD. However, the methyl substituents may decrease the carrier mobility and lead to a higher driving voltage as compared with the current density (mA/cm^2) versus driving voltage (*V*) curves of the fabricated devices as shown as Fig. 7. The driving voltage of device 1 is lower than device 2–5 because of the relatively lower energy barrier between the host

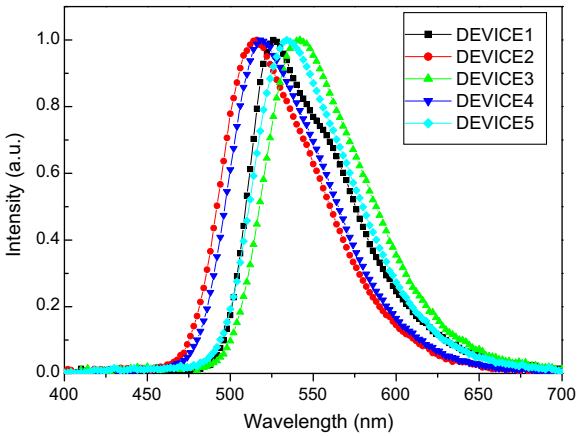

Fig. 4. The electroluminescent spectra of devices fabricated in this study, where device 2–5 with structure of ITO/NPB (40 nm)/dopants: AND (40 nm)/Alq_3 (20 nm)/LiF (1.5 nm)/Al (200 nm), and device 1 (as a compared device) with structure of ITO/NPB (40 nm)/C545T: Alq_3(40 nm)/Alq_3 (20 nm)/LiF (1.5 nm)/Al (200 nm). The dopant of device 2, TAD; device 3, T*mp*AD; device 4, T*m*AD; Device 5, T*p*AD.

Table 2
The device properties of the as-synthesized anthracene-9,10-diamine derivatives acted as the dopants in the device structure of device 2–5: ITO/NPB (40 nm)/3% dopant:ADN (40 nm)/Alq_3 (20 nm)/LiF (1.5 nm)/Al (200 nm); and compared with the device 1: ITO/NPB (40 nm)/2% C545T:Alq_3 (40 nm)/Alq_3 (20 nm)/LiF (1.5 nm)/Al (200 nm).

	Device 1	Device 2	Device 3	Device 4	Device 5
Dopant	C545T	TAD	T*mp*AD	T*m*AD	T*p*AD
E_L, nm	526	514	542	518	534
CIE (*x*, *y*)	(0.34, 0.62)	(0.26, 0.61)	(0.38, 0.59)	(0.29, 0.62)	(0.35, 0.61)
fwhm, nm	66	69	71	68	68
V^a, volt	9.90	10.27	10.49	9.93	10.23
B^a, cd/m^2	13,190	17,048	24,991	19,955	23,378
$E_p{}^a$, lm/W	4.19	5.21	7.48	6.31	7.18
$E_c{}^a$, cd/A	13.19	17.05	24.99	19.95	23.38
E.Q.E.^{a} (%; V)	3.52; 9.90	5.33; 10.27	6.91; 10.49	5.4; 9.93	6.37; 10.23
E.Q.E.^{b} (%; V)	4.12; 8.0	6.94; 9.0	8.20; 9.0	5.82; 9.0	6.93; 9.0
I^c,mA/cm^2	74.41	51.81	35.5	49.01	39.63
$E_p{}^c$, lm/W	4.45	6.22	9.24	6.96	8.48
$E_c{}^c$, cd/A	13.44	19.30	28.17	20.41	25.23

B, luminance; *I*, current density; *V*, driving voltage; E_p, power efficiency; E_c, current efficiency; fwhm, full width at half maximum; E.Q.E., external quantum efficiency.

[a] evaluated at a current density of 100 mA/cm^2.

[b] the maximum value of E.Q.E.

[c] evaluated at luminance of 10,000 cd/m^2.

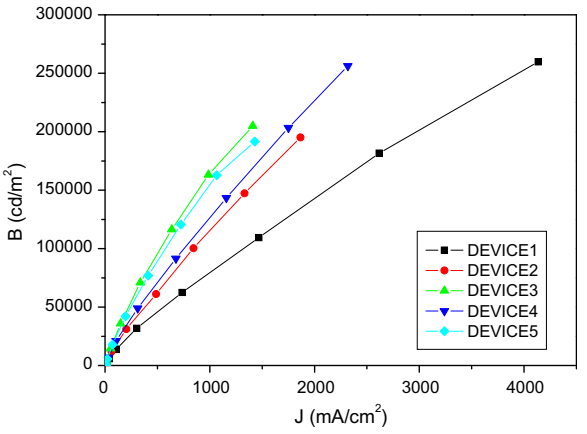

Fig. 5. The relationships of luminance (B) versus current density (J) for the fabricated devices.

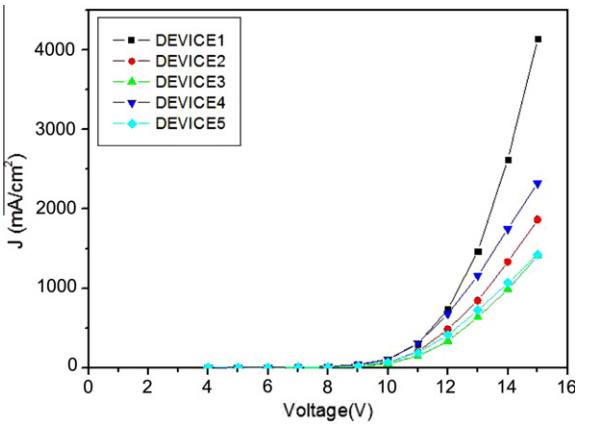

Fig. 7. The current density (mA/cm^2) versus driving voltage (V) measured from the fabricated devices.

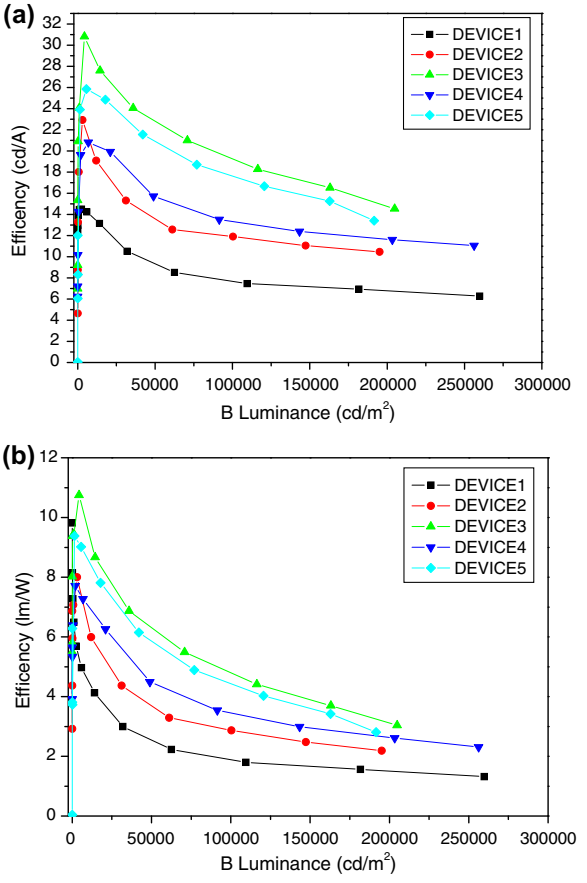

Fig. 6. The relationships of (a) current efficiency (cd/A) and (b) power efficiency (lm/W) relate to luminance (cd/m^2) for the fabricated devices.

emitter layer and the electron transport layer (ETL) as illustrated in Fig. 1. Device 1 has both a host emitter layer and an ETL using material of Alq_3, while devices 2–5 had been fabricating the host emitter by using AND as to improve the properties of the organic devices. However, a little higher driving voltage is acceptable as compared to the voltages illustrated in Table 2, e.g., 10.23 volt of device 5 as compared to 9.9 V of device 1.

From the discussion above, we demonstrate the as-prepared compound TAD, T*m*AD, T*p*AD, and T*mp*AD, especially T*mp*AD, could be used as good dopants in the AND based host material for OLEDs fabrication, with excellent electroluminescent properties. In general, their performances are better than coumarins/Alq_3 based devices, although the driving voltage is a little worse. The methyl substituents on the aromatic ring of phenyl diamine also induce the emission red-shift to closer to the range of eye sensitive wavelength near 550 nm, e.g., 542 nm for T*mp*AD. Therefore, these methyl-substituted dopants are suitable when used as highly efficient green dopant materials for OLEDs.

As compared with device 2 for the effects of methyl substituents in devices efficiency, current efficiency was promoted about 2.9, 6.33, and 7.94 cd/A for dopants with the substituted methyl groups at *meta*, *para and both meta/para* position, for device 4, 5 and 3, respectively. In addition, the power efficiency was also significantly increased with 0.74, 2.26 and 3.02 lm/W for device 4, 5, and 3, respectively. When comparing the results, device 3, fabricated by T*mp*AD/AND-based emitter system, exhibits the best E.Q.E., luminance efficiency, power efficiency, and the most saturated green with CIE $x = 0.038$; $y = 0.59$ for OLED applications. We demonstrate that the as-prepared compound TAD, T*m*AD, T*p*AD and T*mp*AD, especially T*mp*AD, could be used as good dopants in the AND based host material for OLEDs fabrication, with excellent electroluminescent properties. In general, their performances are better than coumarins/Alq_3 based devices.

4. Conclusions

The methyl substuents on the *N*-diarryl rings of anthracene-9,10-diamine showed obvious effects in emission spectra as demonstrated in photo-studies, which observed a significant bathochromic shift followed by the sequence of compound T*mp*AD, T*p*AD, and T*m*AD as compared to TAD. The energy band gaps are relatively decreased as

the methyl groups substituted at the *N*-diarryl rings, especially significant for both on *para*/*meta* positions of compound T*mp*AD. Here we demonstrate the as-prepared compound TAD, T*m*AD, T*p*AD, and T*mp*AD, especially T*mp*AD, could be used as good dopants in the wide band gap AND based emitting layers for OLEDs farication, which have excellent performances better than coumarins/Alq_3 based devices. The effect of methyl groups substituted at both the *para*/*meta* positions of the *N*-diarryl rings of anthracene-9,10-diamine could show great improvement in device performance as compared to the non-substituent compound TAD.

Acknowledgements

The financial support of this research by the NSC-96-2622-E-267-001-CC3 is gratefully acknowledged. We thank Professor Ken-Tsung Wong and Miss Shu-Hua Chou at Department of Chemistry of National Taiwan University for the measurement of quantum yields.

References

[1] C.W. Tang, S.A.V. Slyke, Appl. Phys. Lett. 51 (1987) 913.
[2] L.S. Liao, K.P. Klubek, C.W. Tang, Appl. Phys. Lett. 84 (2004) 167.
[3] J. Kalinowski, Organic Light Emitting Diodes: Principles, Characteristics, and Processes, Marcel Dekker, New York, 2005.
[4] J. Kido, Y. Iizumi, Appl. Phys. Lett. 73 (1998) 2721.
[5] M.T. Lee, C.K. Yen, W.P. Yang, H.H. Chen, C.H. Liao, C.H. Tsai, C.H. Chen, Org. Lett. 6 (2004) 1241.
[6] X.-Y. Jiang, Z.-L. Zhang, X.-Y. Zheng, Y.-Z. Wu, S.-H. Xu, Thin Solid Films 401 (2001) 251.
[7] J.-W. Park, P. Kang, H. Park, H.-Y. Oh, J.-H. Yang, Y.-H. Kim, S.-K. Kwon, Dyes Pigm. 85 (2010) 93.
[8] K.H. Lee, J.N. You, S. Kang, J.Y. Lee, H.J. Kwon, Y.K. Kim, S.S. Yoon, Thin Solid Films 518 (2010) 6253.
[9] Y.-J. Pu, A. Kamiya, K.-I. Nakayama, J. Kido, Org. Electron. 11 (2010) 479.
[10] W.J. Jo, K.-H. Kim, H.C. No, D.-Y. Shin, S.-J. Oh, J.-H. Son, Y.-H. Kim, Y.-K. Cho, Q.-H. Zhao, K.-H. Lee, H.-Y. Oh, S.-K. Kwon, Synth. Met. 159 (2009) 1359.
[11] H. Tang, X. Wang, Y. Li, W. Wang, R. Sun, Displays 29 (2008) 502.
[12] M.-X. Yu, J.-P. Duan, C.-H. Lin, C.-H. Cheng, Y.-T. Tao, Chem. Mater. 14 (2002) 3958.
[13] Khizar-ul Haq, Liu Shan-peng, M.A. Khan, X.Y. Jiang, Z.L. Zhang, Jin Cao, W.Q. Zhu, Curr. Appl. Phys. 9 (2009) 257.
[14] J.F. Hartwig, Synlett (1997) 329.
[15] B.H. Yang, S.L.J. Buchwald, Organomet. Chem. 576 (1999) 125.
[16] A.R. Muci, S.L. Buchwald, Top. Curr. Chem. 219 (2002) 131.

Organic Electronics 12 (2011) 703–709

Contents lists available at ScienceDirect

Organic Electronics

journal homepage: www.elsevier.com/locate/orgel

Patterning of pinhole free small molecular organic light-emitting films by ink-jet printing

Zicheng Ding, Rubo Xing *, Qiang Fu, Dongge Ma *, Yanchun Han

State Key Laboratory of Polymer Physics and Chemistry, Changchun Institute of Applied Chemistry, Chinese Academy of Sciences and Graduate University of the Chinese Academy of Sciences, 5625 Renmin Street, Changchun 130022, PR China

ARTICLE INFO

Article history:
Received 26 September 2010
Received in revised form 30 November 2010
Accepted 29 January 2011
Available online 23 February 2011

Keywords:
Ink-jet printing
Small molecular organic light-emitting diodes
Dewetting

ABSTRACT

Small molecular organic light-emitting diodes (SMOLEDs) were fabricated with an ink-jet printed film of 2-(*t*-butyl)-9,10-bis (20-naphthyl) anthracene (TBADN) doped with 4,4′-bis[2-{4-(*N*,*N*-diphenylamino)phenyl vinyl] (DPAVBi) as emitting layer. Dewetting behavior of ink-jet printed TBADN/DPAVBi solutions were restrained by adding cyclohexylbenzene or α-chloronaphthalene to the main solvent chlorobenzene. The high boiling point and high viscosity of cyclohexylbenzene and α-chloronaphthalene has increased the thickness of liquid films and the viscosity, which restrained the dewetting from thermodynamics and kinetics aspect. Uniform TBADN/DPAVBi films obtained by ink-jet printing from chlorobenzene/cyclohexylbenzene solution have been used in the fabrication of matrix display of SMOLEDs. The OLEDs has a turn-on voltage of 5.5 V, the maximum luminance of 289 cd/m^2 and the maximum current efficiency of 0.71 cd/A.

© 2011 Elsevier B.V. All rights reserved.

1. Introduction

Organic light-emitting diodes (OLEDs) have drawn much attention in flat-panel displays (FPD) because of their high brightness, low power consumption, wide viewing angle and good contrast [1–4]. Ink-jet printing provides an opportunity to gain large-area full color displays of OLEDs by high efficiency and low-cost process [5–7]. A lot of light-emitting polymers have been patterned by ink-jet printing and were used in full color display devices [8–13]. The ink-jetting behavior of polymer solutions has also been studied [14–17]. Recently solution-processed small molecular organic light-emitting diodes (SMOLEDs) have attracted more attention because of the simple film forming process and good performance of devices [18–20]. Printable phosphorescent organic light-emitting devices have been demonstrated to be able to exhibit high performance and long lifetime [21,22].

To gain a high-performance and long-lifetime device by wet-processing, a good film-forming property of the materials is necessary. But the small molecular materials usually have poor film-forming properties. The liquid films covered on the substrates can dewet from the substrate surface and cannot form continuous uniform films during the solidification. There are ways to improve the film-forming properties of the solution. Materials with large molecular volume and long alkyl-chain are properly designed and synthesized to improve the solubility and film-forming property [23,24]. Small molecular materials can also be mixed with polymers to form films [25,26]. Ultra-high molecular weight polystyrene (UHMW-PS) has been added to the small molecular solution to provide good film-forming characteristics and advantageous mechanical properties [27].

The film formation can also be improved by localizing the dewetting in the chemical or physical patterned substrates. Sirringhaus et al. gained high-resolution polymer electrodes through inkjet printing of water-based conducting polymer solution on hydrophilic glass with hydrophobic polyimide pattern [28]. Hendriks et al. produce silver tracks by ink-jet print nanoparticle ink on the

* Corresponding authors. Tel.: +86 431 85262267/85262357; fax: +86 431 85262126.
E-mail addresses: rbxing@ciac.jl.cn (R. Xing), mdg1014@ciac.jl.cn (D. Ma).

1566-1199/$ - see front matter © 2011 Elsevier B.V. All rights reserved.
doi:10.1016/j.orgel.2011.01.027

hot-embossed structure, where ink can imbibe the corner of the channel as a consequence of the capillary forces when the contact angel is small [29]. However, the influences of the solvents on the film-forming properties of the small molecular materials are rarely investigated though binary solvents system have been used to gain uniform film morphology in ink-jet printing of organic semiconductor films [30–32].

In this paper, we choose the 2-(*t*-butyl)-9,10-bis (20-naphthyl) anthracene (TBADN) doped with 4,4′-bis [2-{4-(*N*,*N*-diphenylamino)phenyl vinyl] (DPAVBi) system to reveal the solvent effects on the film-forming property of the small molecular materials. The spin-coated films of TBADN doped with DPAVBi from toluene and chlorobenzene solutions have been used as emitting layer. The solution-processed devices have a high performance which is comparable with the vacuum-deposited ones [19]. The film forming property of ink-jet printed TBADN/DPAVBi solutions from different solutions were investigated on the substrate with low surface energy separators. We found that the solvents have great effects on the film-forming properties of TBADN/DPAVBi system. And an probable film-forming mechanism of the liquid film from different solvents were given. With the ink-jet printed pin-hole free film as emitting layer, a passive matrix display has been fabricated and the performance of the matrix was characterized.

2. Experimental

2.1. Materials

The positive photoresist was purchased from Suzhou Ruihong Electronic Chemical Co., Ltd., China. Polystyrene (PS, Mw: ~31600, PDI: ~2.02, T_g = 103 °C) and poly (4-vinylpyridine) (P4VP, Mw: ~60,000, PDI: ~2.96, T_g = 137 °C) were purchased from Aldrich. Polydimethylsiloxane (PDMS, Sylgard™ 184) was purchased from Dow Corning. ITO glass (glass slide with indium-tin-oxide films) was purchased from Chinese South Glass Holding (CSC) Co., Ltd. The hole-injection material of poly (styrene sulfonic acid)-doped poly (3,4-ethylenedioxythiophene) (PEDOT: PSS, Baytron P VP.AI4083) was purchased from H.C. Starck GmbH. 2-(*t*-Butyl)-9,10-bis (20-naphthyl) anthracene (TBADN) as the emitting host material and 4,4′-bis[2-{4-(*N*,*N*-diphenylamino)phenyl vinyl] (DPAVBi) as the dopant material were purchased from LumTech Corporation. α-Chloronaphthalene (ClNaph) and cyclohexylbenzene (CHB) were purchased from Aldrich without further purifying. The chlorobenzene (CB) and o-dichlorobenzene (oDCB) were purchased from Beijing Chemical Reagent Co. Ltd., China and were purified by reflux distillation in N_2 for 12 h.

2.2. Ink-jet printing of organic light-emitting films

The substrates with low surface energy separators are prepared from the method used in our previous work [12]. Transfer printed PS pattern was used as mask to realize selective deposition and patterning of Au/Ni metal film on P4VP/photoresist films. The metal film can be used as mask of photolithography to realize the patterning of photoresist and form separator with T shape cross-section. After self-assembling monolayer of fluorinated mercaptan on the patterned metal film, low surface energy separators were obtained.

The PEDOT:PSS served as the hole-injection layer was spin-coated on the substrate to give a thickness of 45 nm and then baked at 80 °C for 30 min in vacuum. TBADN doped with DPAVBi (95/5 wt/wt) was dissolved in CB or mixed solvents. The mixed solvents were obtained with a mixture of 70% CB and 30% other solvents by weight, such as CB and oDCB, CB and ClNaph, CB and CHB, etc. The solutions were ink-jet printed into the grooves between the separators by a home-built ink-jet printer to form films, as shown in Fig. 1a. The ink-jet printer was equipped with a piezoelectric print head to form and eject drops, an X–Y stage to move the substrate. The spatial and repeatable resolution of the stage is 10 and 5 μm. The print head with nozzle diameter of 70 μm was manufactured by Microdrop Technique GmbH. The spin-coated films from CB and CB/CHB solutions were also prepared. All the films were put into a vacuum oven at room temperature for 20 min and then at 80 °C for 2 h to remove the solvents.

2.3. Fabrication of OLEDs

The light-emitting layer of TBADN/DPAVBi (80 nm) from CB/CHB solutions were deposited by spin-coating or ink-jet printing. After removing the solvents in the vacuum oven, the electron-transporting layer TPBI (20 nm) and LiF (1 nm)/Al (100 nm) cathode were deposited by thermal evaporation with pressure of less than 4×10^{-4} Pa without breaking the vacuum.

2.4. Characterization of films and SMOLEDs

The ink-jet printed films were observed by Optical Microscopy (Leica DMLP, Leica Microsystems Ltd., Germany). The surface morphology of the films were investigated by Atomic Force Microscopy (SPA 300HV with a SPI 3800N Probe Station, Seiko Instruments Inc., Japan) in tapping model. The current–luminance–voltage characteristics were acquired through a Keithley source measurement unit (Keithley 2400) with a calibrated silicon photodiode. The PL spectra were recorded using a Perkin–Elmer LS 50B spectrofluorometer and the EL spectra were measured using a PR650 spectra colorimeter. The thickness profiles of the films were investigated by a Veeco Dektak 6M Stylus Profilometer.

3. Results and discussion

3.1. Film-forming property

For wet-processing procedure, the solvents have a great effect on the quality of the films, which leads to different performance of the devices. In spin-coating process, the solvents can influence the microstructure and the morphology of the films [19,33]. In the ink-jet printing process, coffee ring can be effectively prevented by using a

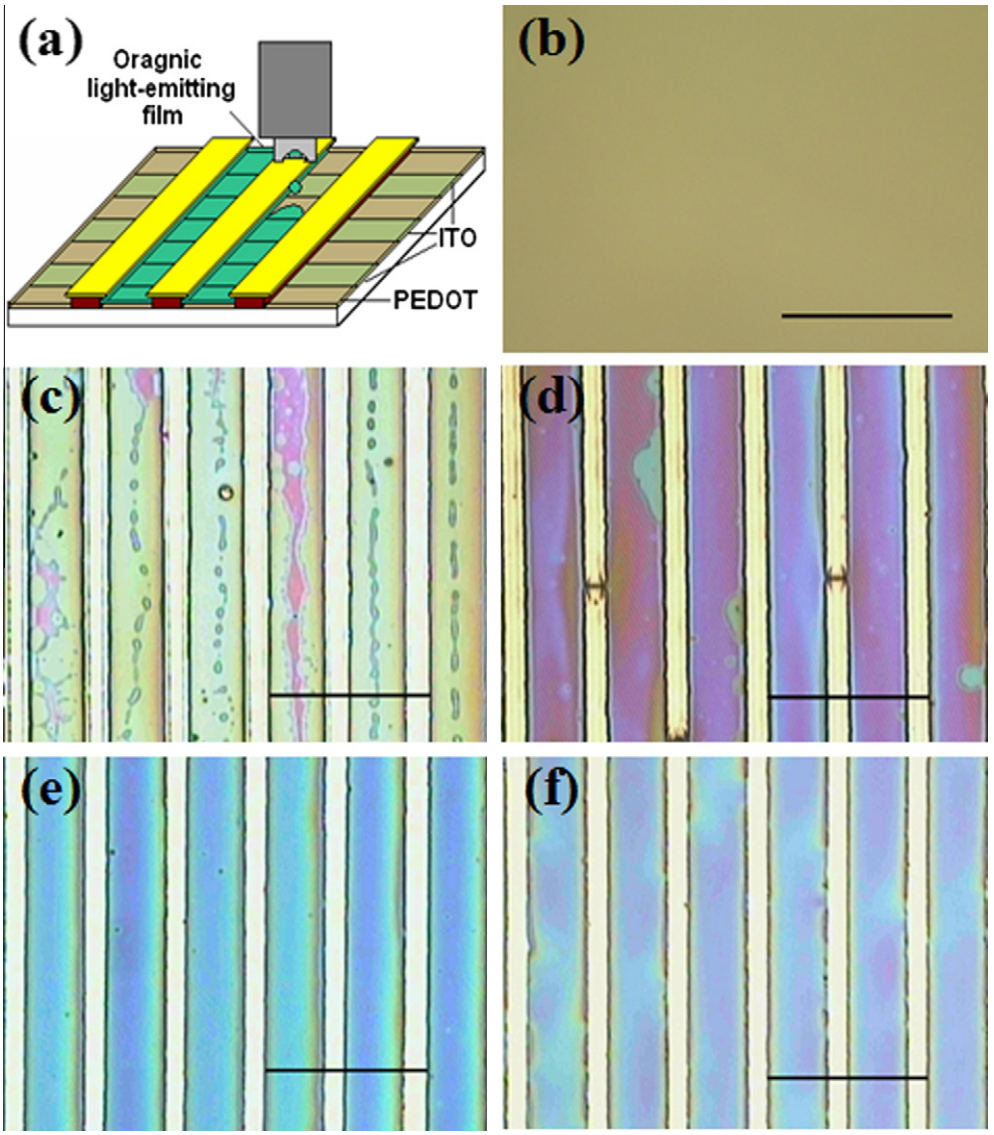

Fig. 1. (a) The schematic process of ink-jet printing. The optical images of TBADN/DPAVBi (95/5, w/w) films (b) spin-coated from CB and ink-jet printed from (c) CB, (d) CB/oDCB, (e) CB/ClNaph and (f) CB/CHB, respectively. The scale bar is 500 μm.

mixture of two solvents with great difference in boiling points and uniform films can be gained [30–32].

And the properties of the solvents can also influence the film-forming properties of the small molecular materials. The optical images of TBADN/DPAVBi (95/5, w/w) films by ink-jet printing from CB solution, CB/oDCB solution, CB/ClNaph solution and CB/CHB solution are shown in Fig. 1c–f. When only CB is used, each groove of the substrate is only partially covered by TBADN/DPAVBi films. As shown in Fig. 1c, discontinuous dots are dispersed at the middle of the grooves and most area of the substrate is not coated well by the films. But when CB solution is deposited by spin-coating, the TBADN/DPAVBi film is uniform in the vast, as shown in Fig. 1b. When oDCB is added to CB by 30% in weight, most area is covered by the film but there are a few holes as shown in Fig. 1d. The holes in the film can cause electrical shorts when voltage is applied. Fig. 1e and f shows the ink-jet printed films from CB/ClNaph and CB/CHB solutions, where all the grooves are fully coated by the emitting materials and uniform films are obtained.

3.2. Mechanism for restraining dewetting

The different film-forming behaviors of the same small molecular materials should result from the different properties of the solvents. The basic properties of the solvents used in our work are shown in Table 1. All the solvents are with relative high boiling points to prevent the clogging of nozzle of the print head during ink-jet printing process. As examples, we discuss the film forming

Table 1
The boiling point, viscosity and surface tension of the solvents.

Solvent	Boiling point (°C)	Viscosity (mPa s)	Surface tension (mN/m)
CB	131.7	0.730	32.93
oDCB	180.5	1.322	36.63
ClNaph	259.3	2.927	39.23
CHB	240.1	2.685	33.29

Data compiled from Yaws' Handbook of Thermodynamic and Physical Properties of Chemical Compounds© 2003 Knovel.

behaviors of the small molecular materials from CB and CB/CHB solutions by two aspects.

On the one hand, the thickness of the solution film reduces fast because of the evaporation of solvent. According to the dewetting theory, the rupture of a thin liquid film is initiated only when the film thickness is smaller than a certain value, namely the critical dewetting thickness e_c. The critical thickness e_c can be given by the equation $e_c = 2\kappa^{-1}\sin(\frac{\theta_E}{2})$, where κ^{-1} is the capillary length and θ_E is the static contact angle. The capillary length is defined by the equation $\lambda_{cap} = \sqrt{\gamma_{lv}/\rho g}$ [34,35], where γ_{lv} is the liquid/vapor surface tension and ρ the density of the liquid. Smaller than the critical dewetting thickness, molecular forces dominate over gravitational forces and the film may dewet [36,37]. The rupture, which may be initiated by the heterogeneous nucleation mechanism, would firstly take place on the areas where the thickness of liquid film is smaller and reaches the critical value firstly. Then the dewetted liquid flows away exposing the underlying substrate, as shown in Stages I and II in Fig. 2a. When the solvent with high boiling point, such as CHB, is used, the evaporating velocity will be slower. When the time scale for liquid droplet evaporation is much less than the time scale for solutes near the contact line to meet each other, the solutes have sufficient time to migrate to the contact line and form a monolayer to maintain a pinned contact line [38], thus the liquid film can evaporate without receding and cover the substrate well. Since low volatility of CHB, liquid films with relatively higher thickness will be stayed on the substrate in the ink-jet printing process. The thicker film is beneficial for preventing the dewetting behavior of the solution deposited in the grooves, as shown in Stages I and II in Fig. 2b. The improved film-forming property of CB/oDCB and CB/ClNaph solutions are the same reason.

On the other hand, the dewetting velocity of ink-jet printed liquid films is affected by the properties of the solvents. Solutions contained small molecular materials, in which there is not any inter-chain entanglement as polymers, belong to Newtonian fluids and can retain their initial viscosity as the solvents [21]. Eq. (1) shows the dewetting velocity of the ideal Newtonian fluids [39,40]:

$$V = \frac{dR}{dt} = k\frac{\gamma}{\eta}\theta e^3 \tag{1}$$

In which, V is the dewetting velocity, R is the radius of the rim and t is the time, γ is the surface tension, η is the viscosity and θ_e is the contact angle in the equilibrium state. When only CB is used, the solution cannot form continuous film in every groove. This may be due to the large value (~45.11) of $\frac{\gamma}{\eta}$, which results in a high dewetting velocity. When the CHB/CB solvent is used, the concentration of CHB in the solution will increase in the drying process because of its high boiling point and low volatility. Compared with CB, the value (~12.40) of $\frac{\gamma}{\eta}$ for CHB is much smaller. Thus the viscosity and surface tension of the solution will change and the value of $\frac{\gamma}{\eta}$ decreases. At last, the dewetting velocity of the liquid film will be much lower for the CB/CHB solution during the drying process. Combined with drying in vacuum condition, which reduce

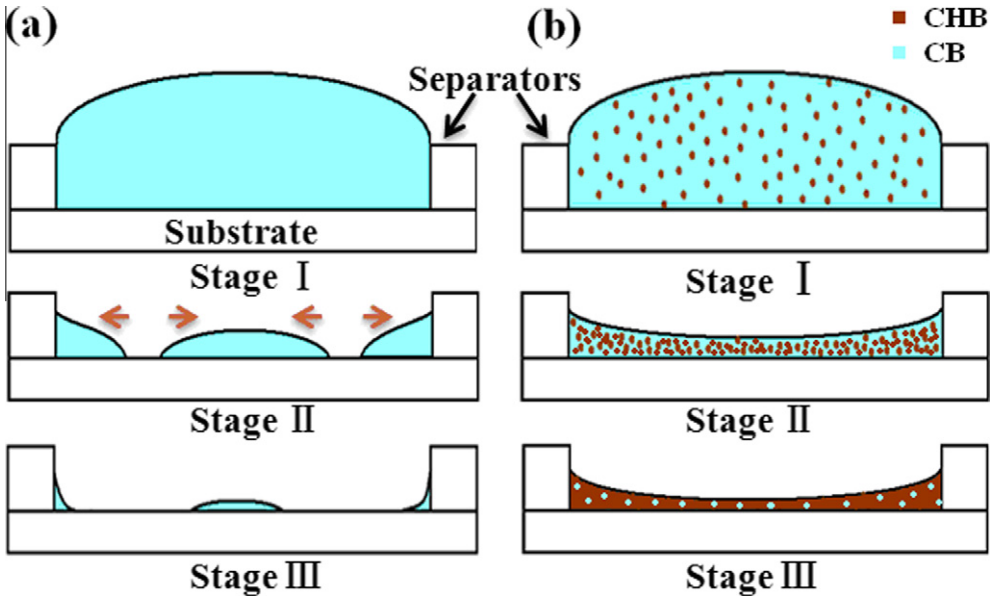

Fig. 2. The schematic process of solvent evaporating of the liquid films between the separators from different solution: (a) CB, and (b) CB/CHB (70/30, w/w).

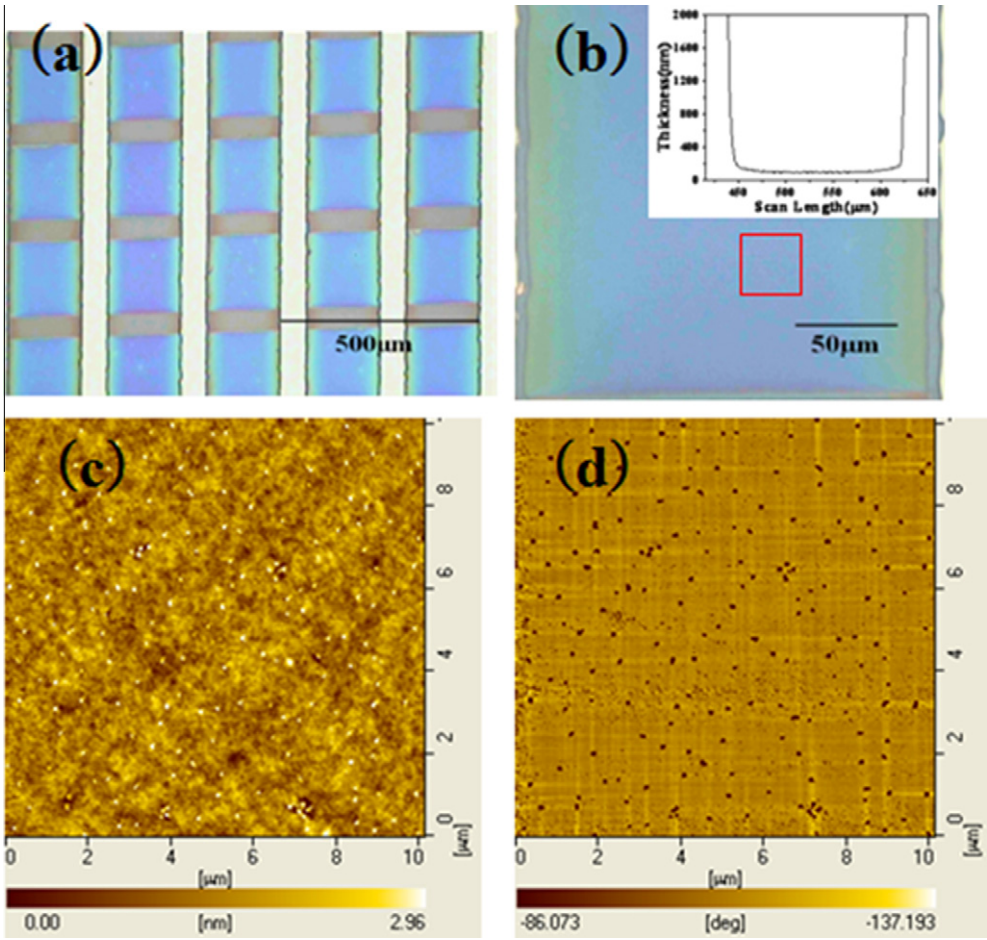

Fig. 3. The optical images of the ink-jet printed TBADN/DPAVBi film from CB/CHB (70/30, w/w) solution: (a) pixel array, (b) a single pixel and the inset is the thickness profile of the single pixel, (c) AFM height image of the center area (part of the selected area in (b)) of the ink-jet printed TBADN/DPAVBi film (RMS = 0.43 nm), and (d) AFM phase image of (c).

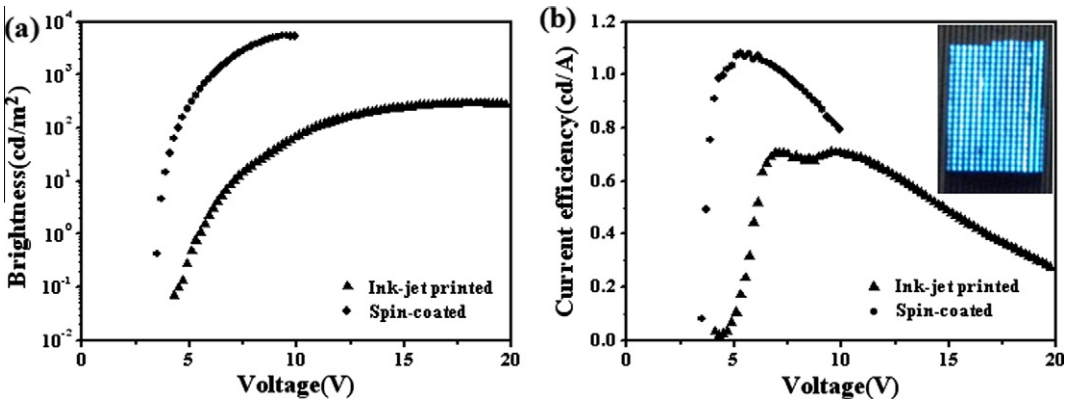

Fig. 4. (a) Luminance–voltage curve and (b) current efficiency–voltage curve of the ink-jet printed and spin-coated SMOLEDs from the CB/CHB solution. The inset in (b) is the optical image of matrix of the ink-jet printed SMOLEDs.

the drying time of deposited solution, the dewetting of liquid film is restrained effectively. At last, pinhole-free solid films were obtained by ink-jet printing, as shown in Fig. 1f. Likewise, we can know that the dewetting velocity from different solutions as following: $V_{CB/CHB} < V_{CB/ClNaph} < V_{CB/oDCB} < V_{CB}$.

3.3. Fabrication and performance of OLEDs

The device structure of the OLEDs is ITO/PEDOT:PSS (45 nm)/TBADN doped with DPAVBi (80 nm)/TPBI (20 nm)/LiF/Al. The films of TBADN doped with DPAVBi deposited on the substrates with low energy separators by ink-jet printing from CB/CHB solution were served as emitting layer. The low energy separators have a width of 50 μm with a space of 200 μm. The patterned ITO stripes have a width of 200 μm with a space of 50 μm. So the dimension of the light-emitting region in every pixel of the passive matrix was 200 × 200 μm. By comparison, a device with an 80 nm-thick emitting layer of TBADN doped with DPAVBi by spin-coating from CB/CHB solution also was fabricated.

The optical images of the ink-jet printed pixel array and a single pixel from CB/CHB (70 w/30 w) solution are shown in Fig. 3a and b. All the pixels are similar to each other in the whole. Most of the area in the single pixel is uniform from the Fig. 3b. The inset of Fig. 3b shows the profile of cross section of the ink-jet printed film. The thickness is a little higher at the edge than that at the center. It may be caused by the pinning of the solvent contact line and the faster evaporation at the edge than the center, as coffee-ring effect [41–43]. Fig. 3c and d shows the surface morphology of the ink-jet printed TBADN/DPAVBi film from CB/CHB (70/30, w/w). The RMS roughness value of the center area of the ink-jet printed TBADN/DPAVBi films is 0.43 nm, which indicates that the film is very smooth and without pinholes. But there are some aggregations in the film, which show a different phase from the bulk area as it shows in Fig. 3d. When TBADN only solution at the same condition is ink-jet printed, the aggregations are also observed (not show in the paper). So the aggregations are consisted of TBADN molecules.

Fig. 4a and b shows the brightness and current efficiency of the ink-jet printed and the spin-coated devices. For the ink-jet printed devices, the turn-on voltage (at 1 cd/m^2) is 5.5 V, the maximum luminance is 289 cd/m^2 and the maximum current efficiency is 0.71 cd/A. While the performance of the spin-coated devices is better than the ink-jet printed ones. In spin-coated OLEDs, the turn-on voltage is 3.7 V, the maximum luminance is 5400 cd/m^2 and the maximum current efficiency is 1.08 cd/A. The reason for the lower performance of the ink-jet printed devices need to be further investigated. The inset of Fig. 4b shows optical image of the matrix of ink-jet printed SMOLEDs. There is only one dead pixel which may come from the defect caused from the fabricating process. The ratio of the light-emitting area to the pixel area is high. So it is feasible to fabricate SMOLEDs by ink-jet printing.

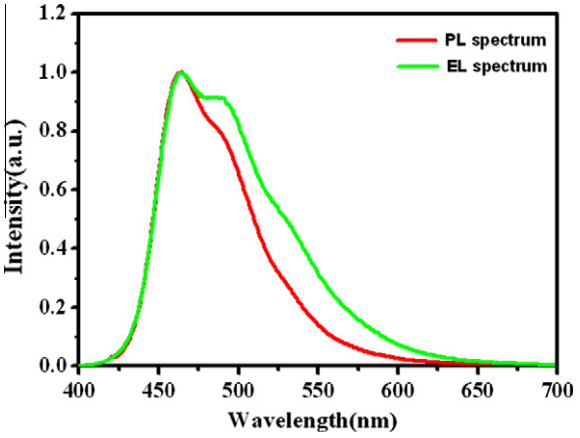

Fig. 5. The PL spectrum of spin-coated DPAVBi doped TBADN film and EL spectrum of SMOLED based on the ink-jet printed film under a bias of 7 V.

The color purity can be recognized from the EL spectrum of the device. Fig. 5 shows the PL spectrum of the ink-jet printed TBADN/DPAVBi film and EL spectrum of the SMOLEDs. It shows that films emit only at 464 and 483 nm from DPAVBi [44]. There is no emission of TBADN at all. It proves the energy transfer between host and dopant is complete. On the other hand, it indicates that the consistency property of TBADN and DPAVBi is good. And the aggregation behavior of TBADN molecules in the films has little influence on the energy transfer.

4. Conclusion

In conclusion, we have improved film-forming property of ink-jet printed small molecular materials by mixing chlorobenzene with α-chloronaphthalene or cyclohexylbenzene, a solvent with higher boiling point and higher viscosity. The mechanisms of the film-forming process from different solutions were also given. Higher boiling point of the solvent stays liquid films with higher thickness which restrains the dewetting of ink-jet printed films from thermodynamics aspect. Then the higher viscosity restrained the dewetting of ink-jet printed liquid films from kinetics aspect. Uniform and pinhole free TBADN/DPAVBi films were patterned by ink-jet printing from chlorobenzene/cyclohexylbenzene solution. The matrix display device of SMOLEDs was fabricated after deposition of electron-transport layer and cathode on the patterned films. The performance of the ink-jet printed devices is lower than the spin-coated ones in our experiments. Aiming to improve the performance of ink-jet printed devices, the techniques are under optimization and the reason need to be further investigated.

Acknowledgments

This work was subsidized by the National Natural Science Foundation of China (20621401, 51003102) and the Ministry of Science and Technology of China (2009CB930603, 2009CB623604).

References

[1] C.W. Tang, S.A. Vanslyke, Organic electroluminescent diodes, Applied Physics Letters 51 (1987) 913–915.
[2] M.A. Baldo, D.F. O'Brien, Y. You, A. Shoustikov, S. Sibley, M.E. Thompson, S.R. Forrest, Highly efficient phosphorescent emission from organic electroluminescent devices, Nature 395 (1998) 151–154.
[3] Y. Sun, N.C. Giebink, H. Kanno, B.W. Ma, M.E. Thompson, S.R. Forrest, Management of singlet and triplet excitons for efficient white organic light-emitting devices, Nature 440 (2006) 908–912.

[4] S. Reineke, F. Lindner, G. Schwartz, N. Seidler, K. Walzer, B. Lussem, K. Leo, White organic light-emitting diodes with fluorescent tube efficiency, Nature 459 (2009) 234–238.
[5] J. Bharathan, Y. Yang, Polymer electroluminescent devices processed by inkjet printing: I. Polymer light-emitting logo, Applied Physics Letters 72 (1998) 2660–2662.
[6] S.-C. Chang, J. Liu, J. Bharathan, Y. Yang, J. Onohara, J. Kido, Multicolor organic light-emitting diodes processed by hybrid inkjet printing, Advanced Materials 14 (1999) 734–737.
[7] T. Shimoda, K. Morii, S. Seki, H. Kiguchi, Inkjet printing of light-emitting polymer displays, MRS Bulletin 28 (2003) 821–827.
[8] E. Tekin, E. Holder, V. Marin, B.J. de Gans, U.S. Schubert, Ink-jet printing of luminescent ruthenium- and iridium-containing polymers for applications in light-emitting devices, Macromolecular Rapid Communications 26 (2005) 293–297.
[9] Y.J. Xia, R.H. Friend, Polymer bilayer structure via inkjet printing, Applied Physics Letters 88 (2006) 163508.
[10] E. Fisslthaler, S. Sax, U. Scherf, G. Mauthner, E. Moderegger, K. Landfester, E.J.W. List, Inkjet printed polymer light-emitting devices fabricated by thermal embedding of semiconducting polymer nanospheres in an inert matrix, Applied Physics Letters 92 (2008) 183305.
[11] Q.L. Niu, Y.X. Shao, W. Xu, L. Wang, S.H. Han, N.H. Liu, J.B. Peng, Y. Cao, J. Wang, Full color and monochrome passive-matrix polymer light-emitting diodes flat panel displays made with solution processes, Organic Electronics 9 (2008) 95–100.
[12] R. Xing, T. Ye, Y. Ding, D. Ma, Y. Han, Formation of low surface energy separators with undercut structures via a full-solution process and its application in inkjet printed matrix of polymer light-emitting diodes, Organic Electronics 10 (2009) 313–319.
[13] Y.J. Xia, R.H. Friend, Controlled phase separation of polyfluorene blends via inkjet printing, Macromolecules 38 (2005) 6466–6471.
[14] Y. Christanti, L.M. Walker, Surface tension driven jet break up of strain-hardening polymer solutions, Journal of Non-Newtonian Fluid Mechanics 100 (2001) 9–26.
[15] B.J. de Gans, E. Kazancioglu, W. Meyer, U.S. Schubert, Ink-jet printing polymers and polymer libraries using micropipettes, Macromolecular Rapid Communications 25 (2004) 292–296.
[16] J.Z. Wang, Z.H. Zheng, H.W. Li, W.T.S. Huck, H. Sirringhaus, Dewetting of conducting polymer inkjet droplets on patterned surfaces, Nature Materials 3 (2004) 171–176.
[17] B.J. de Gans, L.J. Xue, U.S. Agarwal, U.S. Schubert, Ink-jet printing of linear and star polymers, Macromolecular Rapid Communications 26 (2005) 310–314.
[18] Y. Hino, H. Kajii, Y. Ohmori, Efficient low-molecule phosphorescent organic light-emitting diodes fabricated by wet-processing, Organic Electronics 5 (2004) 265–270.
[19] T.W. Lee, T. Noh, H.W. Shin, O. Kwon, J.J. Park, B.K. Choi, M.S. Kim, D.W. Shin, Y.R. Kim, Characteristics of solution-processed small-molecule organic films and light-emitting diodes compared with their vacuum-deposited counterparts, Advanced Functional Materials 19 (2009) 1625–1630.
[20] D.D. Wang, Z.X. Wu, X.W. Zhang, B. Jiao, S.X. Liang, D.W. Wang, R.L. He, X. Hou, Solution-processed organic films of multiple small-molecules and white light-emitting diodes, Organic Electronics 11 (2010) 641–648.
[21] T. Sonoyama, M. Ito, S. Seki, S. Miyashita, S. Xia, J. Brooks, K.O. Cheon, R.C. Kwong, M. Inbasekaran, J.J. Brown, Ink-jet-printable phosphorescent organic light-emitting-diode devices, Journal of the Society for Information Display 16 (2008) 1229–1236.
[22] S. Xia, K.O. Cheon, J.J. Brooks, M. Rothman, T. Ngo, P. Hett, R.C. Kwong, M. Inbasekaran, J.J. Brown, T. Sonoyama, M. Ito, S. Seki, S. Miyashita, Printable phosphorescent organic light-emitting devices, Journal of the Society for Information Display 17 (2009) 167–172.
[23] Z.Q. Fan, C.H. Cheng, S.K. Yu, K.Q. Ye, R.S. Sheng, D.C. Xia, C.Y. Ma, X. Wang, Y.C. Chang, G.T. Du, Red and near-infrared electroluminescence from organic light-emitting devices based on a soluble substituted metal-free phthalocyanine, Optical Materials 31 (2009) 889–894.
[24] F. Liu, C. Tang, Q.Q. Chen, S.Z. Li, H.B. Wu, L.H. Xie, B. Peng, W. Wei, Y. Cao, W. Huang, Pyrene functioned diarylfluorenes as efficient solution processable light emitting molecular glass, Organic Electronics 10 (2009) 256–265.
[25] X. Gong, J.C. Ostrowski, G.C. Bazan, D. Moses, A.J. Heeger, Red electrophosphorescence from polymer doped with iridium complex, Applied Physics Letters 81 (2002) 3711–3713.
[26] X. Gong, J.C. Ostrowski, D. Moses, G.C. Bazan, A.J. Heeger, Electrophosphorescence from a polymer guest–host system with an iridium complex as guest: Forster energy transfer and charge trapping, Advanced Functional Materials 13 (2003) 439–444.
[27] N. Stingelin-Stutzmann, E. Smits, H. Wondergem, C. Tanase, P. Blom, P. Smith, D. De Leeuw, Organic thin-film electronics from vitreous solution-processed rubrene hypereutectics, Nature Materials 4 (2005) 601–606.
[28] H. Sirringhaus, T. Kawase, R.H. Friend, T. Shimoda, M. Inbasekaran, W. Wu, E.P. Woo, High-resolution inkjet printing of all-polymer transistor circuits, Science 290 (2000) 2123–2126.
[29] C.E. Hendriks, P.J. Smith, J. Perelaer, A.M.J. Van den Berg, U.S. Schubert, "Invisible" silver tracks produced by combining hot-embossing and inkjet printing, Advanced Functional Materials 18 (2008) 1031–1038.
[30] J.A. Lim, W.H. Lee, H.S. Lee, J.H. Lee, Y.D. Park, K. Cho, Self-organization of ink-jet-printed triisopropylsilylethynyl pentacene via evaporation-induced flows in a drying droplet, Advanced Functional Materials 18 (2008) 229–234.
[31] E. Tekin, B.-J. de Gans, U.S. Schubert, Ink-jet printing of polymers – from single dots to thin film libraries, Journal of Materials Chemistry 14 (2004) 2627–2632.
[32] B.-J. de Gans, U.S. Schubert, Inkjet printing of well-defined polymer dots and arrays, Langmuir 20 (2004) 7789–7793.
[33] Z.J. Zhao, S.M. Chen, X.Y. Shen, F. Mahtab, Y. Yu, P. Lu, J.W.Y. Lam, H.S. Kwok, B.Z. Tang, Aggregation-induced emission, self-assembly, and electroluminescence of 4,4′-bis(1,2,2-triphenylvinyl)biphenyl, Chemical Communications 46 (2010) 686–688.
[34] F.B. Wyart, J. Daillant, Drying of solids wetted by thin liquid-films, Canadian Journal of Physics 68 (1990) 1084–1088.
[35] R. Seemann, S. Herminghaus, C. Neto, S. Schlagowski, D. Podzimek, R. Konrad, H. Mantz, K. Jacobs, Dynamics and structure formation in thin polymer melt films, Journal of Physics-Condensed Matter 17 (2005) S267–S290.
[36] P.G. Degennes, Wetting – statics and dynamics, Reviews of Modern Physics 57 (1985) 827–863.
[37] F. Brochard, C. Redon, F. Rondelez, Dewetting: the gravity controlled regime, Comptes Rendus de l Academie des Sciences Series II Mecanique, Physique, Chimie, Sciences de l'univers, Sciences de la Terre 306 (1988) 1143–1146.
[38] X.Y. Shen, C.M. Ho, T.S. Wong, Minimal size of coffee ring structure, Journal of Physical Chemistry B 114 (2010) 5269–5274.
[39] C. Redon, F. Brochardwyart, F. Rondelez, Dynamics of dewetting, Physical Review Letters 66 (1991) 715–718.
[40] F.B. Wyart, P. Martin, C. Redon, Liquid–liquid dewetting, Langmuir 9 (1993) 3682–3690.
[41] R.D. Deegan, O. Bakajin, T.F. Dupont, G. Huber, S.R. Nagel, T.A. Witten, Capillary flow as the cause of ring stains from dried liquid drops, Nature 389 (1997) 827–829.
[42] R.D. Deegan, O. Bakajin, T.F. Dupont, G. Huber, S.R. Nagel, T.A. Witten, Contact line deposits in an evaporating drop, Physical Review E 62 (2000) 756–765.
[43] R.D. Deegan, Pattern formation in drying drops, Physical Review E 61 (2000) 475–485.
[44] J.H. Lee, S.W. Liu, C.C. Teng, J.H. Lin, T.C. Lin, C.C. Yang, Device performance and carrier dynamics in blue mixing host organic light-emitting devices, Light-Emitting Diode Materials and Devices 5632 (2005) 1–6.

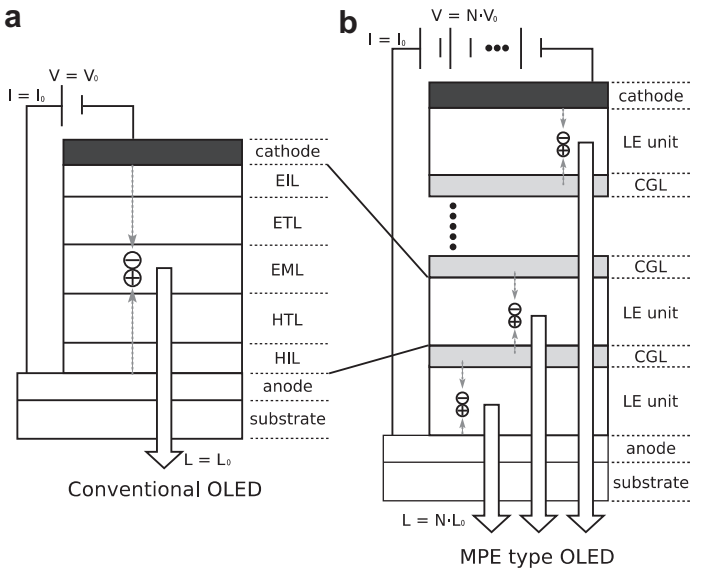

Fig. 1. Device structure. (a) Conventional OLED and (b) MPE-type OLED.

however, ITO results in sputtering damage to an organic layer, and its high conductivity causes crosstalk between each emitting pixels in display applications. On the other hand, CGL consisting of an electron-accepting and an electron-donating layer can be used as an intermediate layer, and its conductivity is enough low and almost insulating. In general, the electron-accepting components of CGL are metal oxides such as V_2O_5 [3,6], MoO_3 [7,9,11,16,19], WO_3 [8,14,15,21,22], and Lewis acids such as tetracyanoquinodimethane (TCNQ) [10,13], and the electron-donating components are arylamine derivatives. However, metal oxides also have some disadvantages such as high deposition temperature, resulting in complicated production line. Recently, the organic acceptor compound, 1,4,5,8,9,11-hexaazatriphenylene hexacarbonitrile (HAT-CN_6), was reported as a substitute of metal oxide in the CGL of MPE devices [17,20]. HAT-CN_6 has no absorption in visible range and has a deep lowest unoccupied molecular orbital (LUMO) level. Because of such a low LUMO level, HAT-CN_6 can accept one electron from highest occupied molecular orbital (HOMO) level of an adjacent donor compound such as *N*,*N*′-di(naphthalene-1-yl)-*N*,*N*′-diphenylbenzidine (NPD).

In this letter, we report the charge-generation characteristics of MPEs fabricated with organic CGLs that are free of metal oxides. These organic CGLs consist of the organic acceptor material HAT-CN_6 and the organic donor materials NPD or 1,1-bis-(4-bis(4-tolyl)-aminophenyl)cyclohexene (TAPC). The LUMO level of HAT-CN_6 is very deep, which makes it difficult for electrons, accepted from NPD, to be injected into the LUMO of adjacent ETL. To resolve this problem, we use a stack consisting of an ultra-thin 1 nm layer of the alkali halide LiF and of Al as an electron-injection layer (EIL). We applied this combination of LiF/Al as EIL and HAT-CN_6/NPD or TAPC as CGL to a fluorescent yellow MPE–OLED resulting in high luminance and a long operational lifetime, simultaneously, and to a phosphorescent green MPE–OLED resulting in an extremely high current efficiency over 250 cd/A.

2. Experimental

All organic materials were purified by temperature-gradient sublimation in vacuum. HOMO energy levels were estimated by the photoelectron yield spectroscopy (Sumitomo Heavy Industries, Ltd.) under atmospheric pressure of N_2 [23]. LUMO energy levels were calculated from the HOMO energy levels and the lowest-energy absorption edges of the UV–vis absorption spectra. Electrochemistry was performed using an BAS Electrochemical Analyzer 660B. All measurements were made at room temperature on samples dissolved in dry benzonitrile with 0.1 M tetra-*n*-butylammonium tetrafluoroborate as the electrolyte. The sample concentration was 1 mM, and a platinum working electrode, platinum counter electrode in 0.1 M tetra-*n*-butylammonium tetrafluoroborate in the same solvent as used for the sample, and a Ag/0.1 M $AgNO_3$ in acetonitrile reference electrode were used. The scan rate was 100 mV/s. The solutions were deoxygenated with argon. The ferricenium/ferrocene couple was used as standard. All potentials are quoted relative to the ferricenium/ferrocene couple. All devices were grown on glass substrates pre-coated with a ~110 nm thick layer of indium tin oxide (ITO) having a sheet resistance of 15 Ω/square. The substrates were cleaned with ultra-purified water and organic solvents, and then dry-cleaned for 30 min by exposure to an UV-ozone ambient. The organic compounds were deposited onto the ITO substrate under the vacuum (~10^{-5} Pa), successively. LiF and Al were patterned using a shadow mask with an array of 2 mm × 2 mm openings without breaking the vacuum (~10^{-5} Pa). All devices were encapsulated immediately after preparation under a nitrogen atmosphere using epoxy glue and glass lids. The EL

spectra were taken using an optical multichannel analyzer Hamamatsu Photonics PMA-11. The current density–voltage and luminance–voltage characteristics were measured using a Keithley source measure unit 2400 and a Minolta CS200 luminance-meter, respectively. External quantum efficiencies were calculated from the front luminance, current density, and EL spectrum. The device lifetimes were measured under a constant current density of 50 mA/cm^2.

3. Results and discussion

The CGL-only devices were fabricated to investigate charge generation of CGLs and electron injection from CGL to ETL (Fig. 2). In case of device A, which has no CGL, showed no current response under forward bias, which is an indication of the excellent ability of Alq_3 to block holes from the anode and of NPD to block electrons from the cathode. However, device B, which has the organic electron acceptor HAT-CN_6 between the Alq_3 and NPD layers exhibit a current response. The HOMO of HAT-CN_6 was estimated from 7.5 eV of the ionization potential (Ip), measured by the photoelectron yield spectroscopy of the thin film (50 nm) on ITO. The LUMO level was tentatively estimated to be 4.4 eV from the difference between Ip and optical energy gap from the absorption edge of the UV–vis spectra. In cyclic voltammetry measurement, redox potential of NPD, corresponding to the HOMO level, was 0.32 V. On the other hand, redox potential of HAT-CN_6, corresponding to the LUMO level, was −0.53 V. There was 0.85 V of the difference in the redox potentials, and this difference suggest that HAT-CN_6 cannot oxidize NPD in a solution environment. However, the LUMO level, 4.4 eV, was smaller than the reported value, 5.6 eV, from UPS measurement [24,25]. Further detailed discussion of interface between HAT-CN_6 and NPD will be necessary to understand the charge generation mechanism under electric filed. These results demonstrate that the CGLs HAT-CN_6/NPD internally generate current in response to an applied voltage and that the organic CGL HAT-CN_6/NPD may be used instead of an inorganic metal oxide. In device C, the thin Al layer did not act as CGL because the energy difference between the NPD HOMO and the work function of Al is too large to allow charge generation. We also investigated the influence of the electron-injection barrier between the LUMO of HAT-CN_6 in CGL and the adjacent Alq_3 layer. Thin layers of LiF and Al were used as the EIL to assist electron injection from CGL in device D. The EIL consisting of LiF and Al dramatically reduces the driving voltage. In conventional OLEDs, alkali halides such as LiF are widely used as efficient EILs and Al, deposited successively, is essential to activate the LiF in order to enhance electron injection [26]. In order to discuss the effect of LiF/Al in detail, we used a thin Al or LiF layer, independently, as EIL in devices E and device F, respectively. The current response of these device was much smaller than that of device D, having both of LiF and Al in EIL.

Based on a thin LiF/Al EIL and a HAT-CN_6/NPD CGL, we investigated the device lifetime of the fluorescent MPE device fabricated with NPD as a hole transporting layer, rubrene as a dopant, and Alq_3 as a host and an electron-transporting layer (Fig. 3(a)). A thin LiF/Al EIL was used, along with an HAT-CN_6/NPD CGL. Fig. 3(b) shows the EL spectra of conventional device and MPE device at a current density of 20 mA/cm^2. The narrower spectra of MPE device was due to optical interference between each emissions from each stacked LE unit. At a current density of 30 mA/cm^2, the driving voltage and luminance of the conventional (i.e. single-unit) device are 7.9 V and 2240 cd/m^2, respectively, whereas the driving voltage and luminance of the 2-unit MPE device are 13.4 V and 4111 cd/m^2, respectively, which are about twice that of the single-unit device (Fig. 4(a)). The current efficiencies of the 2-unit MPE device are also almost twice those of the single-unit device (Fig. 4(b)). At a luminance of 100 and 1000 cd/m^2, the 2-unit MPE device exhibited a current efficiency of 20.2 and 16.8 cd/A, respectively, which are two times higher than those of the single-unit device. In other words, to achieve a luminance of 1000 cd/m^2, 12.0 mA/cm^2 is required for the

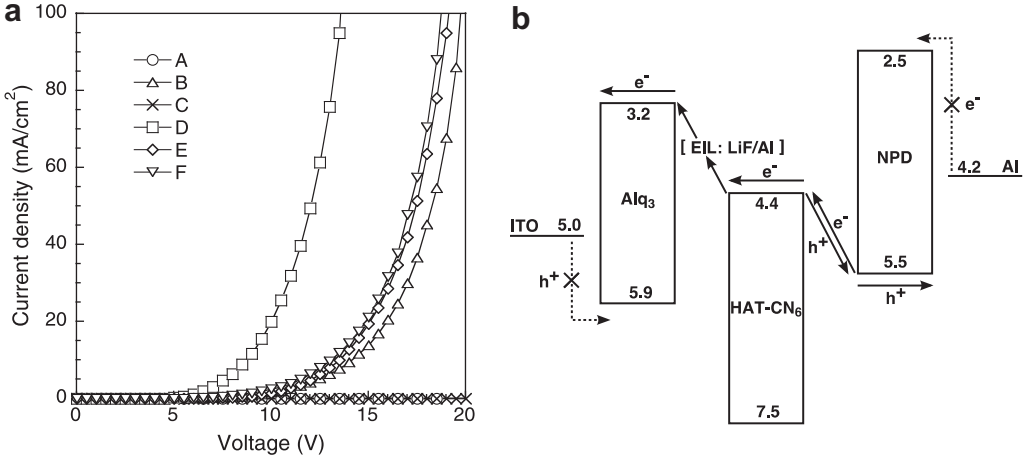

Fig. 2. Current density–voltage characteristics of the CGL-only devices and the energy-level diagram of the CGL-only device. (A): ITO/Alq_3 (100)/NPD (90)/Al, (B): ITO/Alq_3 (100)/HAT-CN_6 (10)/NPD (90)/Al, (C): ITO/Alq_3 (100)/Al (1)/NPD (100)/Al, (D): ITO/Alq_3 (100)/LiF (1)/Al (1)/HAT-CN_6 (10)/NPD (100)/Al, (E): ITO/Alq_3 (100)/Al (1)/HAT-CN_6 (10)/NPD (90)/Al, and (F): ITO/Alq_3 (100)/LiF (1)/HAT-CN_6 (10)/NPD (90)/Al. The numbers in parentheses are thickness (nm).

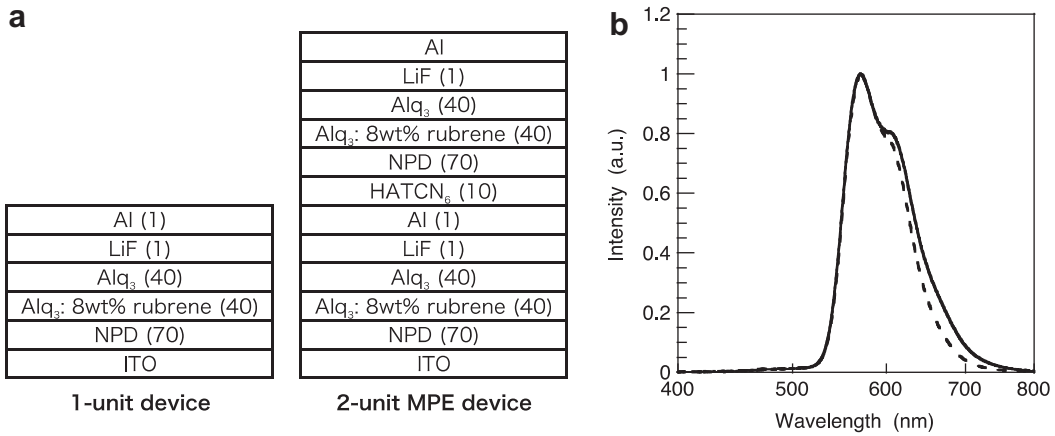

Fig. 3. (a) Device structure of the conventional fluorescent device and 2-unit MPE device. The numbers in parentheses are thickness (nm). (b) EL spectra of the conventional device (solid line) and 2-unit MPE device (dashed line).

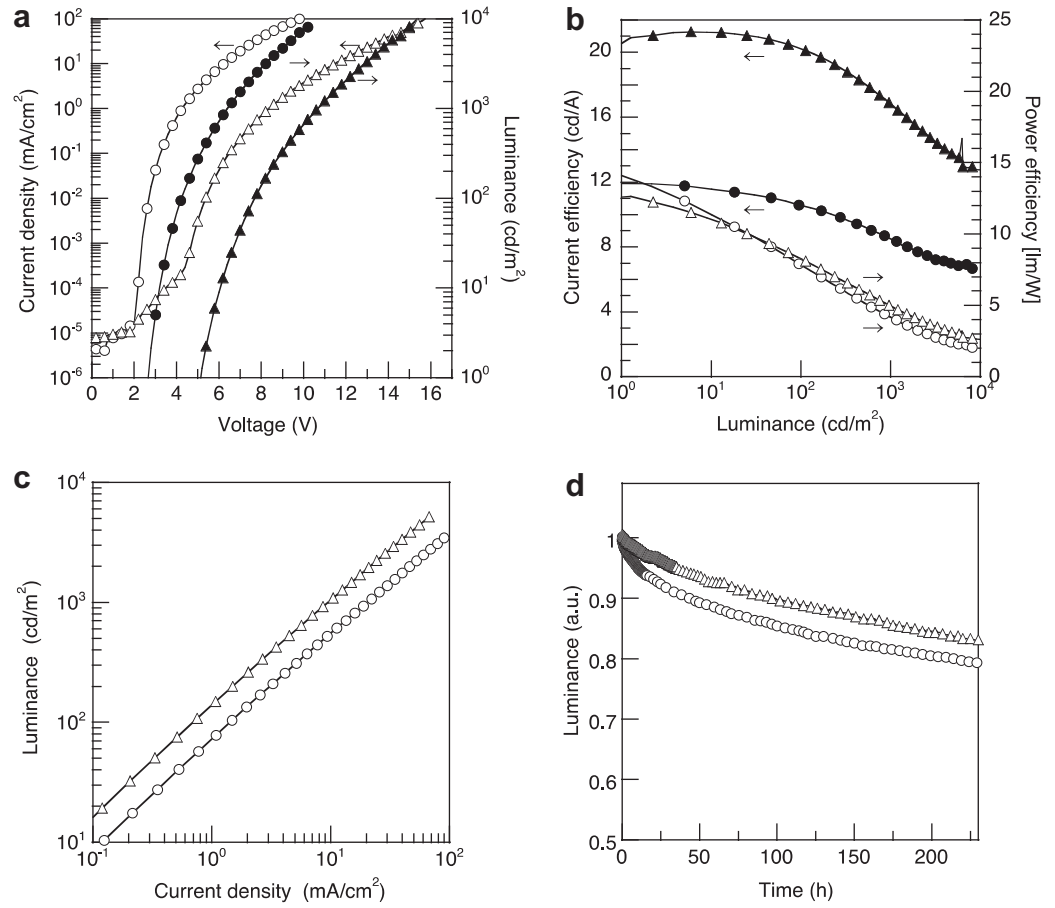

Fig. 4. Characterization of the fluorescent devices (the 1-unit: circles and 2-unit: triangles). (a) Current density- and luminance–voltage characteristics. (b) Current efficiency and power efficiency characteristics. (c) Luminance–current density characteristics. (d) Operational stability. In the lifetime measurement, the constant current density was 50 mA/cm^2 and the initial luminances were 3410 cd/m^2 in the 1-unit device and 6600 cd/m^2 in the 2-unit device.

single-unit device, whereas only half that (i.e. 6.04 mA/cm^2) is required for the 2-unit MPE device (Fig. 4(c)).

The device lifetimes was measured at a current density of 50 mA/cm^2 (Fig. 4(d)). The lifetime at 85% of degradation

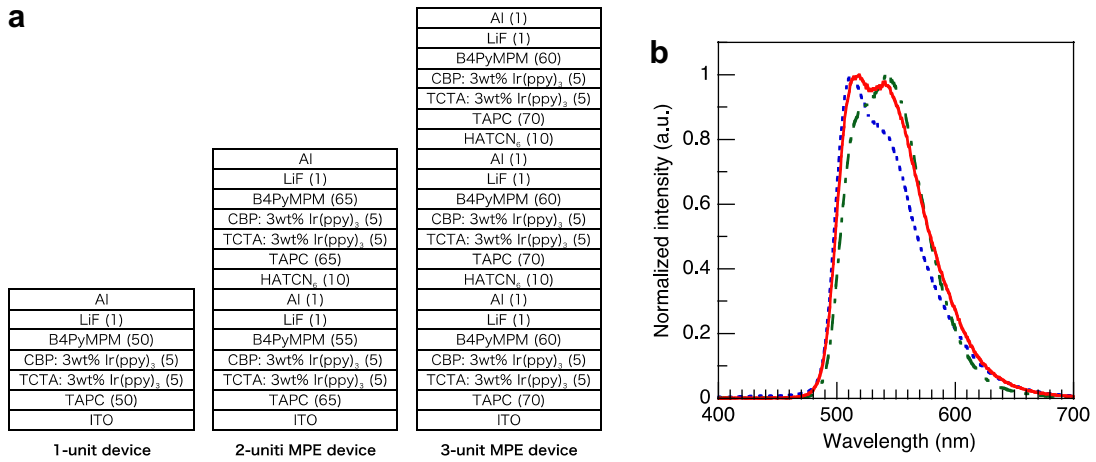

Fig. 5. (a) Device structure of the phosphorescent devices. The numbers in parentheses are thickness (nm). (b) EL spectra of the 1-unit (blue dotted line), 2-unit (red solid line) and 3-unit (green dashed line) devices at 20 mA/cm^2. (For interpretation of the references to colour in this figure legend, the reader is referred to the web version of this article.)

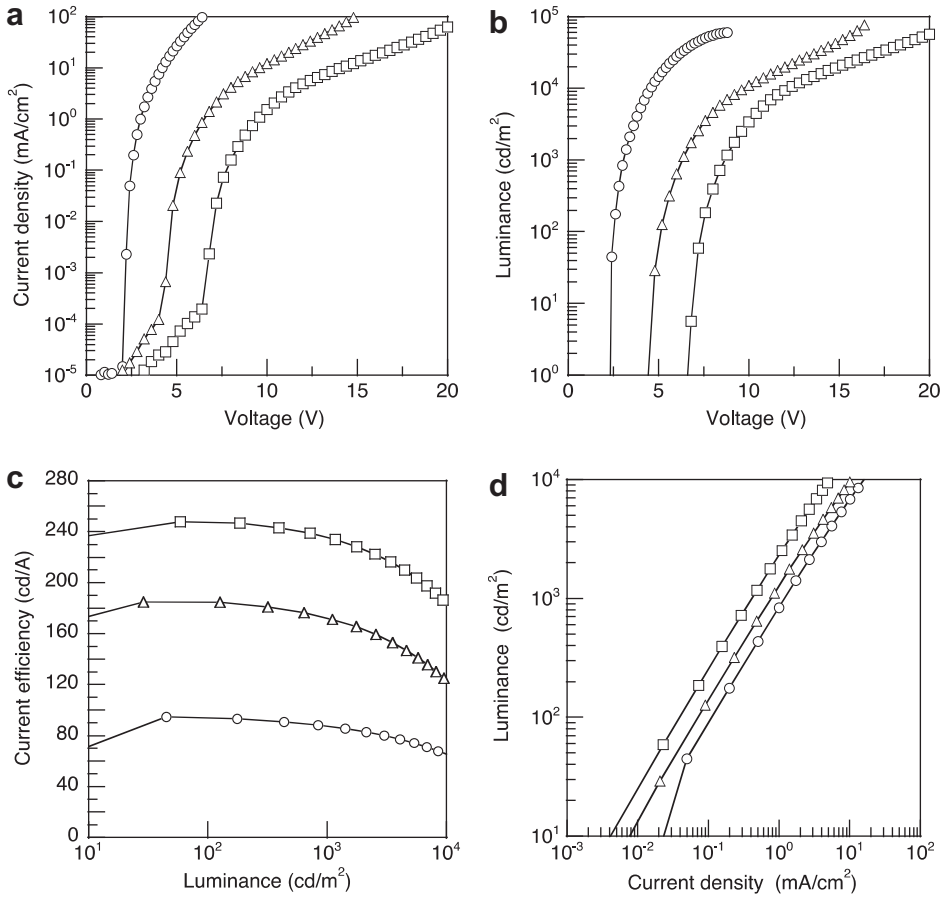

Fig. 6. Characterization of the phosphorescent devices (the 1-unit: circles, 2-unit: triangles, and 3-unit: squares). (a) Current density–voltage characteristics. (b) Luminance–voltage characteristics. (c) Current efficiency–luminance characteristics. (d) Luminance–current density characteristics.

($T_{85\%}$) of the conventional single-unit device, which began with a luminance of 3410 cd/m^2, was 98 h. Although the initial luminance of the 2-unit MPE device is twice 6600 cd/m^2 that of the single-unit device at the same

current density, the 2-unit MPE device $T_{85\%}$ was 190 h. This result demonstrates that, by exploiting the reduced current density in an MPE device, higher-luminance OLEDs can be achieved without deteriorating the device lifetime. The longer lifetime of the 2-unit MPE device than that of the single-unit device is considered to be resulted from the better stability of electron and hole injection from CGL into adjacent LE unit than the injections from electrode in the single device. Furthermore, power efficiencies (lm/W) of both conventional and MPE OLEDs are similar, which means that this new MPE structure does not suffer any penalties in terms of power consumption (Fig. 4(b)).

We also fabricated ultra-high efficiency green phosphorescent MPE devices based on a thin LiF/Al EIL and a HAT-CN_6/TAPC CGL with two or three LE units (Fig. 5(a)). The complex *fac*-tris(2-phenylpyridine) iridium [$Ir(ppy)_3$] was used as green phosphorescent dopant and TAPC was used as the HTL. The hole-transporting host material 4,4′,4″-tris(*N*-carbazolyl)triphenylamine (TCTA) and the bipolar host material, 4,4′-(*N*-carbazolyl)biphenyl (CBP) were used in the double emitting layers. Bis-4,6-(3,5-di-4-pyridylphenyl)-2-methylpyrimidine (B4PYMPM) [27] was used as an electron-transporting and hole-blocking layer. In the EL spectra (Fig. 5(b)) of the green phosphorescent MPE devices at a current density of 20 mA/cm^2, the peak on the shoulder of the spectrum near 542 nm increases in comparison with what is observed with a conventional single-unit device, because of optical interference between the emissions from each stacked unit. Fig. 6(a) and (b) shows the voltage–current–density and luminance characteristics of the devices. At the current density of 2.0 mA/cm^2, the conventional single-unit device requires a driving voltage of 3.26 V, whereas the 2- and 3-unit MPE devices require driving voltages of 7.19 and 10.35 V, which are 2.2 and 3.2 times that of the single-unit device, respectively. Simultaneously, the single-unit-device luminance is 1600 cd/m^2, whereas the luminances of the 2- and 3-unit MPE devices are 3100 and 4300 cd/m^2, which are 1.9 and 2.7 times that of the single-unit device, respectively. These linear increases in driving voltage and luminance with respect to the number of stacked LE units are important parameters that demonstrate that charges are efficiently generated in CGLs and injected into adjacent LE units in the MPE device. Fig. 6(c) shows current efficiency as a function of luminance for the three devices. At a luminance of 100 cd/m^2, the 2- and 3-unit MPE devices exhibit extremely high current efficiencies of 181 and 256 cd/A, which are 2.0 and 2.8 times the current efficiency of 90 cd/A measured for the single-unit device, respectively. Even at the high luminance of 1000 cd/m^2, high current efficiencies of 171 and 244 cd/A are achieved in the 2- and 3-unit MPE devices, which are 2.1 and 2.9 times the 83 cd/A of the single-unit device, respectively. These ultra-high current efficiencies result in low driving currents for these OLEDs. In the 3-unit MPE device, only one-third of the current density (i.e. 0.0395 and 0.404 mA/cm^2) is required to get 100 and 1000 cd/m^2 of luminance, respectively (Fig. 6(d)).

4. Conclusions

We investigated the effect of charge generation and electron injection characteristics of intermediate layer, based on a thin LiF/Al EIL and a HAT-CN_6/NPD CGL, for a stacked OLED. The EIL consisting of LiF and Al dramatically reduces the driving voltage, which are due to enhance of electron injection. This EIL–CGL combination was applied to an orange-emitting fluorescent MPE device and that exhibited a high luminance and a long operational lifetime. We also fabricated green phosphorescent MPE devices that exhibited extremely high current efficiency of over 250 cd/A. This intermediate layer can be a powerful tool for improvement MPE device performance.

Acknowledgement

T. Chiba acknowledges Grant-in-Aid for Scientific Research from the Japan Society for the Promotion of Science.

References

[1] R. Meerheim, K. Walzer, M. Pfeiffer, K. Leo, Appl. Phys. Lett. 89 (2006) 061111.
[2] J. Kido, J. Endo, S. Nakata, K. Mori, K. Yokoi, T. Marsumoto, 49th Annual Meeting of the Japan Society of Applied Physics, March 2002, 27p-YL-3.
[3] T. Matsumoto, T. Nakada, J. Endo, K. Mori, N. Kavamura, A. Yokoi, J. Kido, SID 03 Digest, 2003, p. 979.
[4] L.S. Liao, K.P. Klubek, C.W. Tang, Appl. Phys. Lett. 84 (2004) 167.
[5] T. Tsutsui, M. Terai, Appl. Phys. Lett. 84 (2004) 440.
[6] F.W. Guo, D.G. Ma, Appl. Phys. Lett. 87 (2005) 173510.
[7] C.W. Chen, Y.J. Lu, C.C. Wu, E.H.E. Wu, C.W. Chu, Y. Yang, Appl. Phys. Lett. 87 (2005) 241121.
[8] C.C. Chang, J.F. Chen, S.W. Hwang, C.H. Chen, Appl. Phys. Lett. 87 (2005) 253501.
[9] H. Kanno, N.C. Giebink, Y.R. Sun, S.R. Forrest, Appl. Phys. Lett. 89 (2006) 023503.
[10] C.W. Law, K.M. Lau, M.K. Fung, M.Y. Chan, F.L. Wong, C.S. Lee, S.T. Lee, Appl. Phys. Lett. 89 (2006) 133511.
[11] H. Kanno, R.J. Holmes, Y. Sun, S. Kena-Cohen, S.R. Forrest, Adv. Mater. 18 (2006) 339.
[12] H. Kanno, Y. Hamada, K. Nishimura, K. Okumoto, N. Saito, H. Ishida, H. Takahashi, K. Shibata, K. Mameno, Jpn. J. Appl. Phys. 45 (2006) 9219.
[13] M. Terai, T. Tsutsui, Appl. Phys. Lett. 90 (2007) 083502.
[14] M.H. Ho, T.M. Chen, P.C. Yeh, S.W. Hwang, C.H. Chen, Appl. Phys. Lett. 91 (2007) 233507.
[15] M.Y. Chan, S.L. Lai, K.M. Lau, M.K. Fung, C.S. Lee, S.T. Lee, Adv. Func. Mater. 17 (2007) 2509.
[16] T.W. Lee, T. Noh, B.K. Choi, M.S. Kim, D.W. Shin, J. Kido, Appl. Phys. Lett. 92 (2008) 043301.
[17] L.S. Liao, K.P. Klubek, Appl. Phys. Lett. 92 (2008) 223311.
[18] D.S. Leem, J.H. Lee, J.J. Kim, J.W. Kang, Appl. Phys. Lett. 93 (2008) 103304.
[19] X.F. Qi, M. Slootsky, S.R. Forrest, Appl. Phys. Lett. 93 (2008) 193306.
[20] L.S. Liao, W.K. Slusarek, T.K. Hatwar, M.L. Ricks, D.L. Comfort, Adv. Mater. 20 (2008) 324.
[21] S. Hamwi, J. Meyer, M. Kroger, T. Winkler, M. Witte, T. Riedl, A. Kahn, W. Kowalsky, Adv. Funct. Mater. 20 (2010) 1762.
[22] J. Meyer, M. Kroger, S. Hamwi, F. Gnam, T. Riedl, W. Kowalsky, A. Kahn, Appl. Phys. Lett. 96 (2010) 193302.
[23] Y. Nakayama, S. Machida, D. Tsunami, Y. Kimura, M. Niwano, Y. Noguchi, H. Ishii, Appl. Phys. Lett. 92 (2008) 153306.
[24] Y.-K. Kim, J.W. Kim, Y. Park, Appl. Phys. Lett. 94 (2009) 063305.
[25] S.M. Park, Y.-H. Kim, Y. Yi, H.-Y. O, J.W. Kim, Appl. Phys. Lett. 97 (2010) 063308.
[26] Y.-J. Pu, M. Miyamoto, K. Nakayama, T. Oyama, Y. Masaaki, J. Kido, Org. Electron. 10 (2009) 228.
[27] D. Tanaka, H. Sasabe, Y.J. Li, S.J. Su, T. Takeda, J. Kido, Jpn. J. Appl. Phys. 46 (2007) L10.

microscopy, transmission electron microscopy, optical microscopy, and light-induced electron spin resonance (LESR) [11–17]. On the basis of these studies, it is now well established that the growth of PCBM clusters leads to the formation of percolation paths for electron carriers. On the other hand, the well-known lamellar structure of P3HT gradually disappears with increasing PCBM fraction. However, almost all previous research was focused only on bulk or surface morphology and not on the interfacial structure between active layers and insulators. In order to understand the fundamental properties of the accumulation and transport of charge carriers in FETs, it is necessary to develop a method suitable for the characterization of interfacial molecular structures.

Recently, we have developed a new method for studying organic field-effect devices, such as metal–insulator-semiconductor (MIS) diodes and FETs, that employs field-induced electron spin resonance (FI-ESR), and we were able to reveal microscopic properties of charge carriers at the device interface, including spin states, spatial extent of their wave functions, and charge carrier concentration, in regioregular poly(3-alkylthiophene) [18–22] and pentacene [23]. In addition, we also successfully observed field-induced ambipolar charge carriers in P3HT/C_{60} [24] and PCBM composites [25] using MIS diodes. It should be noted that FI-ESR is a powerful tool to investigate the interfacial molecular structure because the molecular orientation can be directly determined by the angular variation of FI-ESR signals through the anisotropic g-value and hyperfine-determined linewidth of unpaired π-electrons [18–23,26]. Moreover, FETs with controlled in-plane chain orientation have also been fabricated using Langmuir–Blodgett (LB) techniques by co-spreading liquid crystal molecules with P3HT [26]. Consequently, we have been able to directly determine orthorhombic anisotropies of g-values and hyperfine couplings of P3HTs for the first time. The use of such orthorhombic anisotropies makes it possible to precisely analyze the interfacial molecular orientations of P3HT and also complex composites of P3HT and PCBM.

In this study, in order to investigate interfacial molecular orientations of P3HT domains modulated by the introduction of PCBM molecules, we performed FI-ESR measurements on MIS devices using P3HT/PCBM composites with various PCBM mixing ratios as active layers, parylene as a gate insulator, and gold (Au) as top electrodes. In the case of pure P3HT devices, by applying a negative gate bias, clear FI-ESR signals were observed around $g = 2.0031$ with the external magnetic field normal to the substrate plane, where the g-value agrees well with that along the inter-lamellar direction [18–22,26]. This indicates that positive polarons localize at the domain of edge-on orientations of the P3HT lamellar structure. In the case of higher PCBM mixing ratios, on the other hand, a new additional peak was observed at $g = 2.0022$, which is characteristic of the $p\pi$-orbital axis, indicating the occurrence of flat-on structures. The intensity of this peak increased with increasing PCBM fraction above 50 wt.%. Using ESR spectrum simulations with anisotropic g-values, the fractions and orientation distributions of both edge-on and flat-on domains at the interface were determined. Ambipolar charge transport was also clearly observed in FETs using P3HT/PCBM. With increasing PCBM fraction from 0 to 100 wt.%, the field-effect mobility of holes decreased, while, that of electrons increased. These results demonstrate that the flat-on orientation strongly reduces charge carrier transport of holes because two-dimensional charge transport assisted by π–π interaction is interrupted by the presence of the flat-on structure.

2. Experimental

P3HT (Fig. 1a; regioregularity 98.5%) and PCBM (Fig. 1b; purity 99.5%) were purchased from Aldrich and Frontier Carbon Co., respectively. A schematic illustration of the MIS device with the P3HT/PCBM composite used in the present study is shown in Fig. 1c. Aluminum (Al) gates were patterned by vacuum deposition on polyethylenenaphthalate (PEN) films as substrates. The thickness of the PEN and Al gates were about 0.25 mm and 50 nm, respectively. Parylene insulator was deposited by chemical vapor deposition using a PDS 2010 LABCOTER (Speciality Coating System Inc.) [27]. The thickness and capacitance of the parylene were evaluated to be 850 nm and 3.4 nF/cm^2, respectively. We confirmed that the quality factor (Q-factor) of the ESR cavity does not decrease with the parylene insulator. The active semiconductor layer of P3HT/PCBM was deposited by drop-casting of chloroform solution with a concentration of 0.5 wt.%. We prepared devices with different mixing fractions of PCBM (0, 22, 50, 67 wt.%). The thickness of the active layer was about 0.5 μm. 30 nm-thick Au top electrodes were vacuum-deposited formed an effective area of 0.44 cm^2. Our previous studies showed that the Au electrode was not suitable for efficient injection of ambipolar carriers, in particular electrons, because of the energy level mismatch between PCBM LUMO (3.7 eV) and Au (5.1 eV) [4,25]. In this study, however, we did employ Au electrodes in order to specify

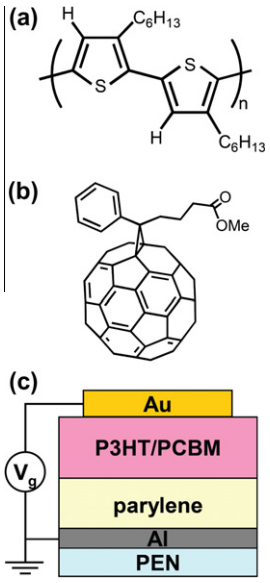

Fig. 1. Chemical structures of (a) P3HT and (b) PCBM. (c) Schematic illustration of the MIS device used in this work with a P3HT/PCBM composite and parylene insulator.

and characterize the accumulated holes at the interface between the active layers and insulators. FET devices with Au source and drain electrodes were fabricated on the same parylene insulator with a channel length (L) and width (W) of 100 μm and 2.2 mm, respectively. FET characteristics were measured under vacuum using Keithley 2400 and 6487 source meters with application of a gate voltage (V_g) and a drain-source voltage (V_{ds}), respectively. All the devices were annealed under a He atmosphere at 125 °C for 10 min before the measurements.

All ESR measurements were performed using a Bruker E500 X-band spectrometer at room temperature. ESR signals were obtained by subtracting the background ESR signal at V_g = +40 V. It should be noted that ESR signals from PCBM are observable only at low temperatures because the spin–lattice relaxation time is too short at higher temperatures [25]. Thus, the present FI-ESR signals describe those of hole carriers (polarons) in P3HT.

3. Results and discussion

3.1. Field-induced ESR of P3HT/PCBM composites

Fig. 2a shows the dependence of FI-ESR signals on the PCBM mixing ratio. All FI-ESR signals were measured by applying V_g of −60 V and an external magnetic field (H) perpendicular to the substrate at room temperature, except for the dotted plots shown at the top of Fig. 2a, where H was applied parallel to the substrate. The observed g-value ($g \sim 2.00310$), determined from the resonance field, and the peak-to-peak linewidth ($\Delta H_{PP} \sim 1.1$ G) of the field-induced signal for lower PCBM mixing fractions (up to 22 wt.%) with H perpendicular to the substrate agree well with those reported in our previous studies for pure P3HT MIS devices on SiO_2 and Al_2O_3 gate insulators [18–22,24–26]. The observed anisotropic spectra are consistent with an edge-on orientation as schematically shown in Fig. 3a. Here, the errors for the g-value and ΔH_{PP} are estimated to be ±0.00005 and ±0.05 G, respectively. This result indicates that the injected charge carriers are positive polarons of P3HT.

On the other hand, FI-ESR signals for higher PCBM fractions (above 50 wt.%) drastically changed with increasing PCBM fraction. The FI-ESR signal split into two components with different g-values (around 2.0030 and 2.0022). The signal is considered to originate not from PCBM anions but from polarons of P3HT, because the spin–lattice relaxation time for PCBM anions is short at room temperature [24,25]. In the case of our previous LESR study of cast films of the same composite system, LESR signals due to polarons on P3HT, which are generated in the bulk composites, never showed such splitting [17]. Thus, the splitting

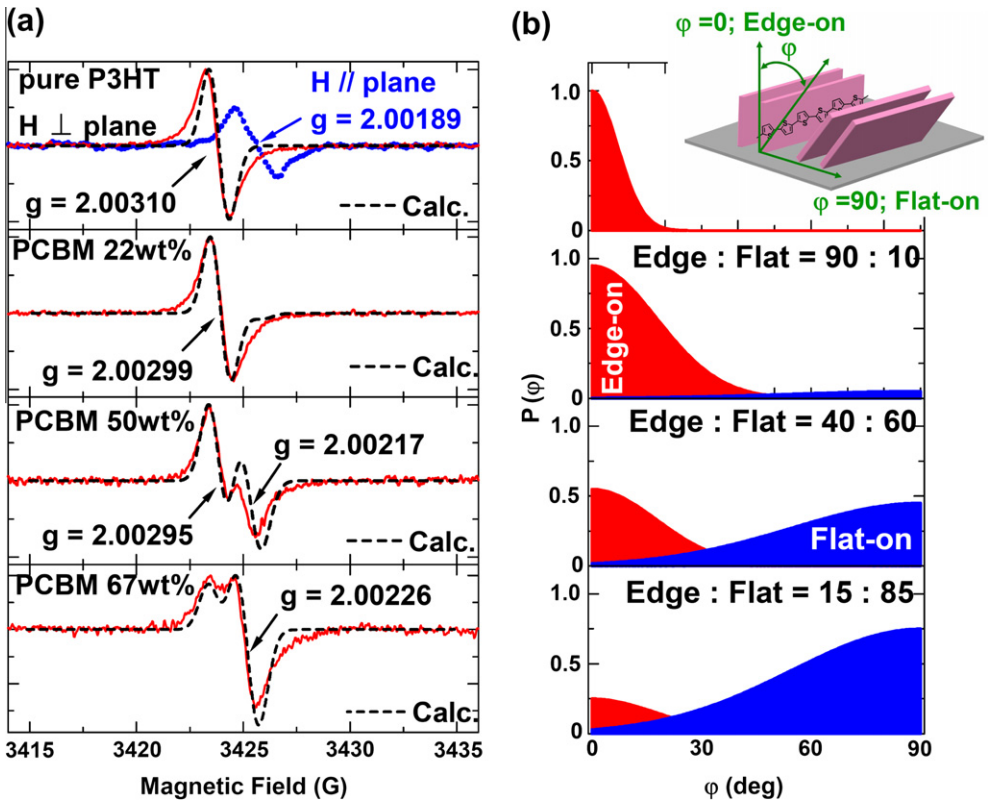

Fig. 2. (a) Dependence of FI-ESR signals on the PCBM mixing ratio. PCBM mixing fractions of 0, 22, 50, and 67 wt.% were used, as shown from the top to the bottom plots, respectively. All ESR signals were measured with a microwave power of 6.3 mW at 293 K. The solid and dotted lines represent FI-ESR signals with H perpendicular and parallel to the substrate, respectively. Dashed lines show the calculated spectra obtained by simulation with the distribution function $P(\varphi)$, whose angular distributions are shown in (b). The inset in (b) shows a schematic diagram of the ordered lamellar structure of P3HT. Alkyl-side chains are omitted. φ denotes the tilt angle between the short axis of the π-conjugated plane and the normal direction of the substrate, i.e., the edge-on and flat-on orientations correspond to φ = 0 and 90°, respectively.

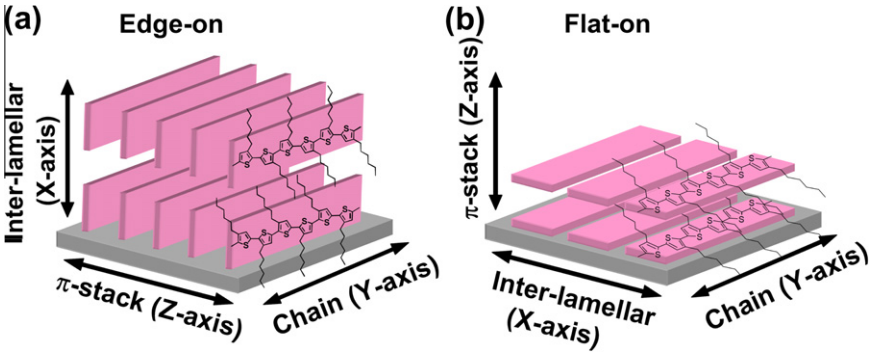

Fig. 3. Schematic illustrations of (a) edge-on and (b) flat-on orientations. In the actual devices, the chain axes are randomly oriented in both cases.

phenomenon can be considered to be a unique feature in FI-ESR measurements, which specifically detect the interfacial structure.

As mentioned in the introduction section, orthorhombic anisotropy of g-values and hyperfine-determined ESR linewidths have been directly determined using FI-ESR techniques on ultrathin-film FETs with controlled in-plane chain orientations [26]. According to this result, the anisotropy of g-values and ΔH were determined to be: $g_X = 2.00310$, $g_Y = 2.00152$, $g_Z = 2.00203$ and $\Delta H_X = 1.09$ G, $\Delta H_Y = 1.41$ G, $\Delta H_Z = 1.21$ G, respectively, where the X-, Y-, and Z-axes correspond to the directions of the inter-lamellar, polymer main-chain, and π-stack, respectively (see definitions in Fig. 3(a and b)). The observed g-value of around 2.0022 at a higher magnetic field is very close to the g_Z ($p\pi$-orbital) component, suggesting that the splitting of the FI-ESR signals could be caused by flat-on components at the interface, where the $p\pi$-axis is normal to the plane direction, as shown in Fig. 3b. These direct comparisons of the g-values suggest that FI-ESR signals obtained for a lower PCBM fraction (22 wt.%) originate from edge-on components ($H//X$-axis, that is, inter-lamellar direction) and splitting of FI-ESR originates in the co-existence of edge-on and flat-on components. This result indicates that mixing PCBM molecules could modulate the polymer orientation into a flat-on structure at the interface. We note that observations of such flat-on orientations in thin films of P3HT have been reported using X-ray diffraction measurements, which are considered to be related to substrate conditions and the degree of regioregularity [28–30]. Introducing PCBM molecules is considered to be a factor to provide poor regioregularity due to the molecular interactions between P3HT and PCBM domains, resulting in such unique co-existence of edge-on and flat-on regions. Thus, the differences in the film microstructure observed in this work may be the origin of charge transport properties of FET devices.

We also confirmed that the intensities of FI-ESR linearly increase with the application of a negative V_g up to −60 V. It should be noted that the number of injected charge carriers calculated by capacitance measurements was consistent with that of injected spins in the case of composite MIS devices at lower $|V_g|$. This result strongly suggests that all the injected charge carriers have spin 1/2 and accumulate at the insulator interface [18–22,24–26]. However, at a higher $|V_g|$ of 80 V, the intensities of these spectra tended to saturate, where the number of injected spins reached $\sim 3 \times 10^{12}$ spins/cm^2 and the spin concentration (doping level) was evaluated to be 0.3% per thiophene monomer unit. The observed spin saturation agrees well with our previous values for the onset of spin saturation [18–22, 24,25]. Such spin saturation strongly suggests the formation of a doubly charged spinless state, such as bipolarons or polaron-pairs.

3.2. Angular dependence of FI-ESR signals for composite MIS devices

Fig. 4a shows the angular dependence of FI-ESR signals of a PCBM composite (22 wt.%) MIS device, where θ denotes the angle between H and the normal to the substrate. The angular dependence of both g-values and FI-ESR linewidths are shown in Fig. 4b, representing circles and squares, respectively. As reported previously, FI-ESR signals of pure P3HT MIS devices show clear angular variations of g-values and ΔH_{PP} [18–22,24,25]. The observed g-anisotropy is well explained by that of π-electrons of a P3HT chain ($g_X > g_Y, g_Z$) having edge-on orientation due to the formation of a lamellar structure [18–22,24–26]. The angular dependence of FI-ESR signals thus shows the same behavior as that for pure P3HT MIS devices. This suggests that the edge-on orientation is still maintained for PCBM fractions of up to 22 wt.%.

In the case of higher PCBM mixing devices, the angular dependence of FI-ESR signals is clearly different from the above cases, reflecting the presence of the flat-on component. The case of the device with 67 wt.% mixing fraction is shown in Fig. 5. The solid and dashed curves represent peaks originating from edge-on and flat-on orientations, respectively, shown as guides to the eye. FI-ESR signals around $\theta = 0°$ show clear splitting of peaks. With increasing θ, to a mid-angle around 40–60°, the FI-ESR signal approaches a single component line and finally splits again around $\theta = 90°$. These behaviors provide evidence for the above assignment of edge-on and flat-on components through g-value anisotropy; smaller g-value gives higher magnetic field and *vice versa* [19]. The peak at the lower magnetic field for the FI-ESR signal obtained at $\theta = 0°$ seems to shift to a higher magnetic field, *i.e.* shifting from g_X to the averaged value between g_Y and g_Z, with increasing

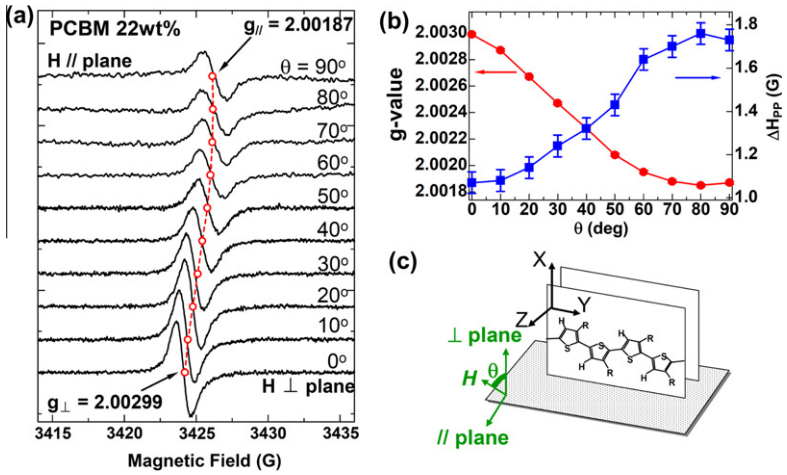

Fig. 4. (a) Angular dependence of the FI-ESR signal due to polarons for the PCBM composite (22 wt.%) MIS device. θ denotes the angle between H and the normal to the substrate, as defined in (c). Open circles represent the obtained g-values. (b) Angular dependence of the g-value and peak-to-peak linewidth (ΔH_{PP}) of the FI-ESR signals, denoted by circles and squares, respectively. (c) Schematic of the ordered lamellar structure of P3HT on the substrate. The X, Y, and Z axes are the principal axes of the g-value and linewidth due to proton-hyperfine coupling of a π-electron.

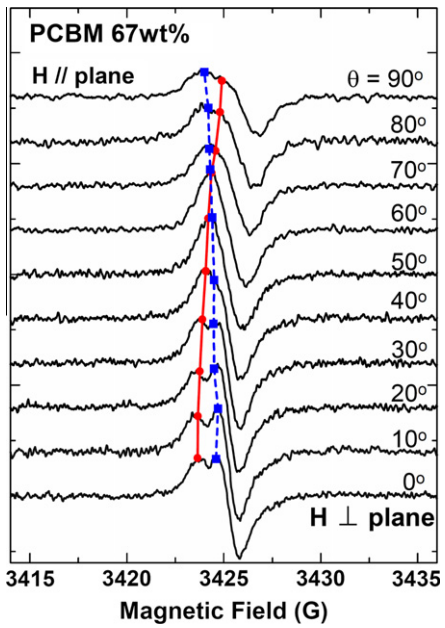

Fig. 5. Angular dependence of FI-ESR signals due to polarons for a PCBM composite (67 wt.%) MIS device. The angle is between H and the normal to the substrate. Solid and dashed curves are guides to the eye for the two peaks of the FI-ESR signals.

θ (solid line in Fig. 5). This indicates that the peak originates from the edge-on structure because the shift follows the anisotropy in the g-value ($g_X > g_Y$, g_Z). On the other hand, the other peak at $\theta = 0°$ with a higher magnetic field, ascribed to be the flat-on orientation, tends to shift to lower magnetic field, *i.e.* shifting from g_Z to the averaged value between g_X and g_Y, with increasing θ (see dashed line in Fig. 5). This is also consistent with g-anisotropy ($g_Z < (g_X + g_Y)/2$) and suggests that the peak originates from the flat-on structure. Thus these peak shifting and exchanging behaviors can be reasonably explained by considering g-anisotropy, consequently, we can assign these peaks as edge-on and flat-on components. Thus, the angular dependence of FI-ESR signals also provides clear evidence of the co-existence of both edge-on and flat-on structures.

3.3. ESR spectrum simulation for PCBM composite MIS devices

The observed dependence of the FI-ESR signals for various PCBM mixing ratios, shown in Fig. 2a, provides the basis for identifying the relative fractions of edge-on and flat-on components and their detailed molecular orientations. This can be achieved by an ESR spectrum simulation method, as described below. In this method, the ESR spectrum of either single or split peaks is calculated by employing a molecular orientation distribution function $P(\varphi)$ and convoluting a single Gaussian-type line-shape function $G[g(\varphi), \Delta H(\varphi)]$ centered at $g = g(\varphi)$ with linewidth $\Delta H(\varphi)$. The ESR spectrum $I(H)$ can be described by

$$I(H) = \int_0^{\pi/2} P(\varphi) G[g(\varphi), \Delta H(\varphi)] d\varphi \quad (1)$$

Here, $g(\varphi)$ and $\Delta H(\varphi)$ are given as,

$$g(\varphi) = \sqrt{g_X^2 \cos^2(\varphi) + g_Z^2 \sin^2(\varphi)} \quad (2)$$

$$\Delta H(\varphi) = \sqrt{\Delta H_X^2 \cos^2(\varphi) + \Delta H_Z^2 \sin^2(\varphi)} \quad (3)$$

where g_X, g_Z, ΔH_X, and ΔH_Z represent the X and Z components of the g-value and linewidth, respectively, whose values were also determined from previous studies [26]. Here, we limit ourselves to the calculation of the ESR spectrum with H perpendicular to the substrate because splitting of FI-ESR signals due to the two orientations are most clearly resolved along this direction. We also assume that the contribution of the Y-axis (chain-direction)

component is negligible in the calculation because the *Y*-axis is likely to be confined in the substrate plane. Indeed, corresponding peak of *Y*-component, which should be observed at a higher magnetic field given by g_Y, is not resolved, thus excluding the significant contribution of the *Y*-axis along the normal direction of the substrate. For the molecular orientation distribution function of $P(\varphi)$, the following form is adopted,

$$P(\varphi) = P^{\mathrm{Edge}} \exp\left\{-\left(\frac{\varphi}{\delta^{Edge}}\right)^2\right\} + P^{Flat} \exp\left\{-\left(\frac{\varphi - \pi/2}{\delta^{Flat}}\right)^2\right\} \quad (4)$$

where φ is the tilt angle between the *Z*-axis and the normal direction, (i.e., perfect edge-on and flat-on orientations correspond to $\varphi = 0$ and 90°, respectively; see the definition in the inset in Fig. 2b). P^{Edge} and P^{Flat} are the amplitudes of the edge-on and flat-on orientations, which determine the ratio between the edge-on and flat-on components. δ^{Edge} and δ^{Flat} are the widths of the orientation distribution of the molecules. It is reasonable to use this molecular orientation function (Eq. (4)) in the ESR spectrum simulation because single component ESR spectra for pure P3HT MIS devices are well reproduced with this simple function, as shown at the top of Fig. 2b. In this case, the distribution width is assumed to be ~10° at the maximum. Considering the surface roughness of the parylene insulator (root mean square: RMS ~ 10 nm), this value is reasonable [19,22,26].

It is noted that a little deviation of the line-shape from Gaussian is seen at wings of each signal. This may be ascribed to the fact that the ESR spectra exhibit certain extent of motional narrowing due to the thermal motion of carriers at room temperature, giving the intermediate line-shape between Gaussian and Lorentzian [19]. This is most clearly recognized from the fact that the spectrum of pure P3HT case at the top of Fig. 2 a already shows a deviation of the wings from Gaussian, where the y-axis is well-confined in the substrate plane, as is evidenced from ESR simulation and X-ray structural analyses. It should be also mentioned that the observed spectra with two split peaks in the composite case shown in Fig. 2a can not be well-reproduced by any other line-shape function such as pure Lorentzian. Therefore, applying single Gaussian line-shape is approximately reasonable.

The obtained molecular orientation distributions at each PCBM mixing ratio in this work are shown in Fig. 2b. By assuming these orientation functions, the split ESR spectra are well reproduced (see dashed lines in Fig. 2a). At a low PCBM mixing ratio (22 wt.%), the experimentally obtained *g*-value was slightly smaller than that for the pure P3HT device (shifted to a higher magnetic field) due to the broadening of ΔH_{pp}. This trend could be traced to the increasing distribution width δ^{Edge} (~20°) and the introduction of flat-on components, indicating that almost all molecular orientations of P3HT maintain the original edge-on structure. On the other hand, for higher PCBM mixing ratio, for example 67 wt.%, the split ESR spectrum is well reproduced by using the parameters δ^{Edge} of 25°, δ^{Flat} of 45°, P^{Edge} of 0.25, and P^{Flat} of 0.75, yielding a ratio between the edge-on and flat-on orientations of 15:85. This result indicates that the split ESR spectra, especially the peak obtained at a higher magnetic field, originated from spins localized on polymers with a flat-on orientation.

According to previous studies on X-ray structural analyses of bulk heterojunction solar cells of the P3HT/PCBM composites system, with increasing PCBM mixing fraction, the edge-on component of the P3HT lamellar structure gradually decreases and is interrupted by microcrystalline domains for a PCBM fraction above 70–80 wt.% [13,14]. In contrast to these structural analyses on the bulk or surface, FI-ESR revealed that some fractions of the edge-on orientation were maintained even at higher PCBM mixing ratios above 50–67 wt.%, consistent with results obtained by optical measurements [12–14] and LESR [17]. This indicates that highly-crystalline domains of the P3HT lamellar structure still remain even though phase separation between P3HT and PCBM is drastically enhanced. However, microcrystals of PCBM may strongly modulate P3HT lamellar domains into unique orientations at the device interface, where both the fraction and distribution width of such flat-on orientations increases up to around 85% and 45°, respectively, in the case of the higher PCBM mixing ratio (67 wt.%). Such flat-on orientations are a unique feature occurring only at the device interface, which has been revealed by using FI-ESR that can selectively observe interfacial orientations. The co-existence of two such components is regarded as a kind of disordering of the original P3HT lamellar orientations caused by mixing PCBM molecules. Therefore, the field-effect mobility for holes may be decreased within such a disordered structure [28].

3.4. Ambipolar characteristics of field-effect transistors using P3HT/PCBM composites

Finally, ambipolar operations of FET devices on a parylene insulator are discussed. Fig. 6 shows the transfer characteristics of FET devices with application of a (a) negative and (b) positive bias. Circles, squares, and triangles represent FET devices for pure P3HT, composite (67 wt.% PCBM), and pure PCBM, respectively. Clear *p*-type and *n*-type operations for pure P3HT and PCBM devices are observed on the parylene insulator with a relatively high on/off ratio above 10^3. The field-effect mobility (μ) was estimated by gradual channel approximation in the linear region. In the case of pure P3HT and pure PCBM FET, the mobilities for both holes and electrons were evaluated to be 7.6×10^{-4} and 4.9×10^{-3} cm^2/Vs, respectively. The transfer characteristics for PCBM composite (67 wt.%) devices were obtained for both hole and electron enhancement modes (squares in Fig. 6(a and b)). The mobilities of holes and electrons were evaluated to be 3.1×10^{-6} and 4.2×10^{-4} cm^2/Vs, respectively. We also observed ambipolar behavior for the 50 wt.% PCBM devices.

Fig. 7 shows the mobilities of both holes and electrons for various PCBM mixing ratios, represented by circles and squares, respectively. The two dashed lines in Fig. 7 are shown as guides to the eye. With increasing PCBM mixing fraction, the electron mobilities drastically increased (about two orders of magnitude) because percolation paths

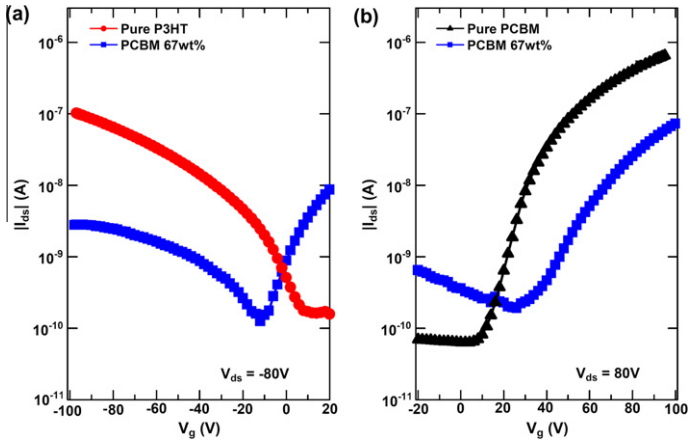

Fig. 6. Transfer characteristics of pure P3HT, pure PCBM, and PCBM composite (67 wt.%) devices, represented by circles, triangles, and squares, respectively. (a) p-type operation mode ($V_{ds} = -80$ V) and n-type operation mode ($V_{ds} = 80$ V).

for electrons grew at the interface. On the other hand, the hole mobility remained in the 10^{-4} cm^2/Vs range with increasing PCBM mixing fraction up to 22 wt.%, where only the edge-on component, though with higher distribution width, was seen. However, at higher PCBM mixing ratios, over 50 wt.%, the hole mobility steeply decreased to the 10^{-6} cm^2/Vs range. These shifts of both mobilities associated with mixing PCBM are consistent with previous reports [5,6,31,32]. In these studies, the decrease of hole mobility for higher PCBM mixing ratio has been ascribed to the decrease of percolation path of P3HT. On the other hand, FI-ESR measurements can spectroscopically reveal interfacial molecular orientations at lower PCBM mixing ratios (<50 wt.%) maintain well-known edge-on structures and at higher ratios (>50 wt.%) are gradually modulated to flat-on structures, although some fraction of the edge-on component still remains. Since the FI-ESR method gives the information about the sites where the carriers actually accumulate, such changes of molecular orientation will also correlate with the charge carrier mobility. Indeed, flat-on structure of P3HT gives smaller hole mobility than the case of edge-on structure [28].

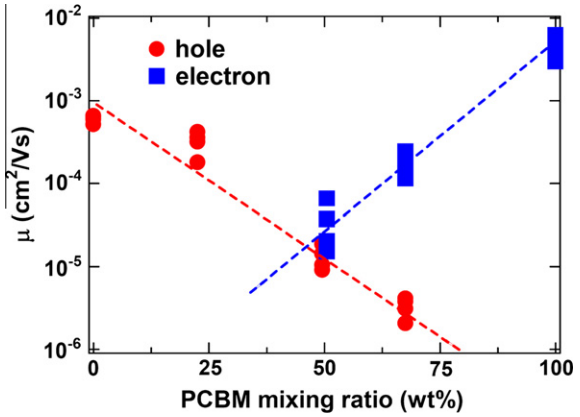

Fig. 7. PCBM mixing ratio dependence of hole and electron mobilities, represented by circles and squares, respectively. The dashed lines are shown as a guide to the eye.

The demonstrated flat-on structure may strongly reduce charge carrier transport for holes because two-dimensional charge transport assisted by overlap of π–π interaction on the edge-on structure is interrupted by the presence of flat-on structures. Indeed, it has been found that anisotropy of mobility between intra-chain and inter-chain (π-stack) is relatively small for P3HT, which has been confirmed from the mobility studies of in-plane oriented P3HT film combined with the detailed determination of in-plane orientations using ESR [25]. This means that charge carrier transport for P3HT can be supposed to be two-dimensional transport. Such two-dimensional charge transports can be reduced by flat-on orientations. Thus, the decrease of mobility within P3HT domain might be possibly crucial for hole transport as well as percolations.

4. Conclusions

In this study, FI-ESR measurements were performed on MIS devices using P3HT/PCBM composites with various PCBM mixing ratios on a parylene insulator. In the case of pure P3HT devices, a clear FI-ESR signal was observed around $g = 2.0031$ with H perpendicular to the substrate plane, indicating that positive polarons localize at the domain of edge-on orientations of the P3HT lamellar structure, as shown in previous studies on P3HT devices. The edge-on orientation of P3HT is maintained below 20 wt.% PCBM fraction. On the other hand, FI-ESR signals due to positive polarons clearly split into two components with $g = 2.0030$ and 2.0022 with increasing PCBM mixing fraction above 50 wt.%. The latter g-value is characteristic of the $p\pi$-orbital axis, indicating the occurrence of flat-on orientations, which was further confirmed by angular dependence of the FI-ESR signals. By ESR spectrum simulations using anisotropic g-values, the fractions and orientation distributions of both edge-on and flat-on domains at the interface were determined. We also observed clear ambipolar charge transport in field-effect transistors of P3HT/PCBM on parylene insulators. With increasing PCBM fraction, the field-effect mobility of holes decreased, while that

of electrons increased. A systematic study of both interfacial molecular orientation and charge transport properties demonstrates that the interfacial molecular orientation, such as edge-on and flat-on, strongly correlates with charge carrier transport properties in ambipolar field-effect devices.

Acknowledgements

This work was partially supported by Grants-in-Aid for Scientific Research (Grant Nos. 21740224 and 22340080) from the Ministry of Education, Culture, Sports, Science and Technology of Japan. One of the authors (S.W.) was also supported by a JSPS Research Fellowship for Young Scientists.

References

[1] E.J. Meijer, D.M. De Leeuw, S. Setayesh, E. Van Veenendaal, B.H. Huisman, P.W.M. Blom, J.C. Hummelen, U. Sherf, T.M. Klapwijk, Nat. Mater. 2 (2003) 678.
[2] J. Zaumseil, H. Sirringhaus, Chem. Rev. 107 (2007) 1296.
[3] T. Yasuda, T. Goto, K. Fujita, T. Tsutsui, Appl. Phys. Lett. 85 (2004) 2098.
[4] S. Cho, J. Yuen, J.Y. Kim, K. Lee, A.J. Heeger, Appl. Phys. Lett. 89 (2006) 153505.
[5] M. Shibao, T. Morita, W. Takashima, K. Kaneto, Jpn. J. Appl. Phys. 46 (2007) L 123.
[6] J.Y. Kim, C.D. Frisbie, J. Phys. Chem. C 112 (2008) 17726.
[7] T.D. Anthopoulos, D.M. De Leeuw, E. Cantatore, S. Setayesh, E.J. Meijer, C. Tanase, J.C. Hummelen, P.W.M. Blom, Appl. Phys. Lett. 85 (2004) 4205.
[8] J. Zaumseil, R.H. Friend, H. Sirringhaus, Nat. Mater. 5 (2006) 69.
[9] S.Z. Bisri, T. Takenobu, Y. Yomogida, H. Shimotani, T. Yamano, S. Hotta, Y. Iwasa, Adv. Funct. Mater. 19 (2009) 1728.
[10] J.Y. Kim, K. Lee, N.E. Coates, D. Moses, T.-Q. Nguyen, M. Dante, A.J. Heeger, Science 317 (2007) 222.
[11] G. Li, V. Shrotriya, Y. Yao, J. Huang, Y. Yang, J. Mater. Chem. 17 (2007) 3216.
[12] T. Erb, U. Zhokhavets, G. Gobsh, S. Raleva, B. Stühn, P. Schilinsky, C. Waldauf, C.J. Brabec, Adv. Funct. Mater. 15 (2005) 1193.
[13] A. Swinnen, I. Haeldermans, P. Vanlaeke, J. D'haen, J. Poortmas, M. D'Olieslaeger, J.V. Mance, Eur. Phys. J. Appl. Phys. 36 (2007) 251.
[14] D. Chirvase, J. Parisi, J.C. Hummelen, V. Dyakonov, Nanotechnology 15 (2004) 1317.
[15] U. Zhokhavets, T. Erb, H. Hoppe, G. Gobsch, N.S. Sariciftci, Thin Solid Films 496 (2006) 679.
[16] M. Campoy-Quiles, T. Ferenczi, T. Agostinelli, P.G. Etchegoin, Y. Kim, T.D. Anthopoulos, P.N. Stavrinou, D.D.C. Bradley, J. Nelson, Nat. Mater. 7 (2008) 158.
[17] H. Tanaka, Y. Yokoi, N. Hasegawa, S. Kuroda, T. Iijima, T. Sato, T. Yamamoto, J. Appl. Phys. 107 (2010) 083708.
[18] K. Marumoto, Y. Muramatsu, S. Ukai, H. Ito, S. Kuroda, J. Phys. Soc. Jpn. 73 (2004) 1673.
[19] K. Marumoto, Y. Muramatsu, Y. Nagano, T. Iwata, S. Ukai, H. Ito, S. Kuroda, Y. Shimoi, S. Abe, J. Phys. Soc. Jpn. 74 (2005) 3066.
[20] S. Watanabe, K. Ito, H. Tanaka, H. Ito, K. Marumoto, S. Kuroda, Jpn. J. Appl. Phys. 46 (2007) L792.
[21] H. Tanaka, S. Watanabe, H. Ito, K. Marumoto, S. Kuroda, Appl. Phys. Lett. 94 (2009) 103308.
[22] S. Kuroda, S. Watanabe, K. Ito, H. Tanaka, K. Marumoto, Appl. Magn. Reson. 36 (2009) 357.
[23] K. Marumoto, S. Kuroda, T. Takenobu, Y. Iwasa, Phys. Rev. Lett. 97 (2006) 256603.
[24] K. Marumoto, T. Sakamoto, S. Watanabe, H. Ito, S. Kuroda, Jpn. J. Appl. Phys. 46 (2007) L1191.
[25] S. Watanabe, H. Tanaka, H. Ito, K. Marumoto, S. Kuroda, Synth. Met. 159 (2009) 893.
[26] S. Watanabe, H. Tanaka, S. Kuroda, A. Toda, S. Nagano, T. Seki, A. Kimoto, J. Abe, Appl. Phys. Lett. 96 (2010) 173302.
[27] Y. Furukawa, J. Yamamoto, D.-C. Cho, T. Mori, Macromol. Symp. 205 (2004) 9.
[28] H. Sirringhaus, P.J. Brown, R.H. Friend, M.M. Nielsen, K. Bechgaard, B.M.W. Langeveld-Voss, A.J.H. Spiering, R.A.J. Janssen, E.W. Meijer, P. Herwig, D.M. de Leeuw, Nature 401 (1999) 685.
[29] M. Brinkmann, P. Rannou, Adv. Funct. Mater. 17 (2007) 101.
[30] Y.D. Park, J.A. Lim, H.S. Lee, K. Cho, Mater. Today 10 (2007) 46.
[31] E. Von Hauff, J. Parisi, V. Dyakonov, J. Appl. Phys. 100 (2006) 043702.
[32] J. Nakamura, K. Murata, K. Takahashi, Appl. Phys. Lett. 87 (2005) 132105.

quired to develop OBLED which can be processed in solution and have multilevel luminance control performance over wide luminance range. The luminance range which can be controlled in OBLED was around 100 cd/m^2.

In this work, a solution processed organic multistable light-emitting diode (OMLED) with nonvolatile multilevel luminance switching performances was developed. The integration of the solution processed OLED and solution processed OBD was carried out by a metal interlayer using a tandem structure and a stamp transfer printing of a common polyphenylenevinylene (PPV) based polymer. A high on/off ratio over 1000, a wide range luminance control over 300 cd/m^2 and four level luminance switching were demonstrated from the solution processed tandem OMLED.

2. Experimental

The device structure of the OMLED was indium tin oxide (ITO, 150 nm)/polyethylene-3,4-dioxythiophene:polystyrenesulfonate (PEDOT:PSS, 60 m)/PPV (50 nm)/LiF (1 nm)/Al (100 nm)/PPV (70 nm)/Al (100 nm). The ITO substrate was cleaned in deionized water and 2-propanol in ultrasonic bath for 30 min to remove particles on the substrate followed by cleaning in boiling 2-propanol to remove organic contaminants. After drying, the cleaned ITO substrate was exposed to ultraviolet/O_3 to modify the work function of the ITO. PEDOT:PSS was spin coated from water dispersion at a spin speed of 2000 rpm to obtain 60 nm thick PEDOT:PSS film. The PEDOT:PSS layer was baked at 200 °C for 10 min to remove residual solvent. The PPV layer on PEDOT:PSS was spin-coated from 0.7 wt.% toluene solution at a spin speed of 2000 rpm. The PPV layer on the Al was coated by spin-coating or stamp transfer printing. The spin-coating of the PPV layer was carried out at a spin speed of 1000 rpm from 0.7 wt.% toluene solution. The stamp transfer printing of the PPV layer was performed by transferring the PPV film spin-coated on Si wafer at a thickness of 70 nm. The PPV film on Si susbstrated was transferred to the polydimethylsiloxane (PDMS) stamp and the PPV film on the PDMS stamp was transferred on the Al electrode at 120 °C. The device structure of the OBD was Al (100 nm)/PPV (70 nm)/Al (100 nm) and the PPV was coated by the stamp transfer printing. The device structure of the OLED was ITO (150 nm)/PEDOT:PSS (60 nm)/PPV (50 nm)/LiF (1 nm)/Al (100 nm). The PPV was spin-coated from toluene solution.

Current density–voltage curves of the OBD, OLED and OMLED were obtained using a Keithley 2400 source measurement unit and the luminance performances were measured with CS 1000 spectroradiometer (Minolta Co.). The cross-section of the fabricated device was analyzed by transmission electron microscopy (TEM, model JEM-2100F, Jeol Co.) after sampling using a focused ion beam method. The stability of the luminance over cycles was measured using a Si photodiode.

3. Results and discussion

The OLED and the OBD units were integrated using a tandem device structure by connecting the two devices

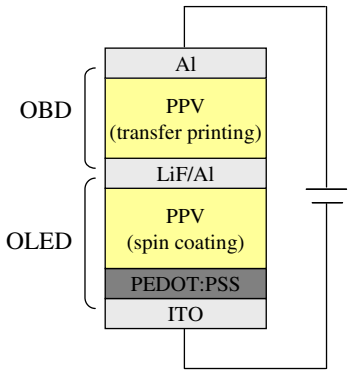

Fig. 1. Device structures of the OMLED.

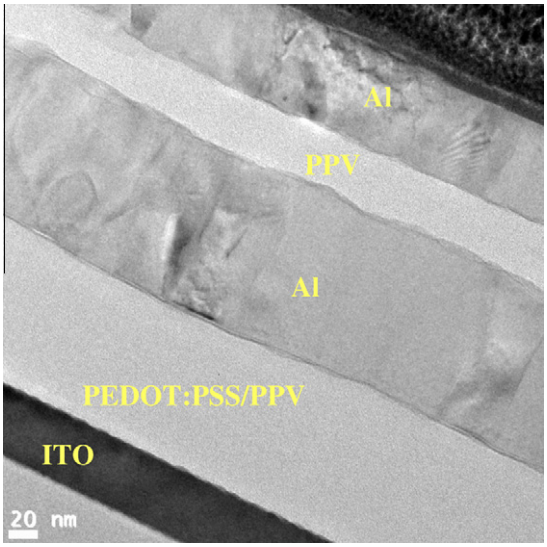

Fig. 2. Transmission electron microscopic pictures of the cross-section of the OMLED fabricated by the stamp transfer printing.

in series with a metal interlayer. Compared with the typical structure reported in earlier work [11–14], the tandem device structure with the metal interlayer is advantageous because two device units can function independently. In earlier work, the OBD unit was introduced as a layer inside the OLED unit and it was difficult to manage the OBD and OLED performances at the same time. In this work, the Al interlayer separates the OLED and OBD units and they can function separately. The device architecture of the OMLED is shown in Fig. 1. The OBD unit was stacked on the electrode of the OLED unit using the electrode as the interlayer. The PPV polymer was coated on the LiF/Al electrode of the OLED unit and the Al electrode of the organic memory unit was deposited on the PPV. Two devices with different PPV coating processes, spin coating and stamp transfer printing, were fabricated. The spin coating method is a conventional film coating method, but the solution can permeate through the pin hole of the Al electrode to the active layer of the OLED. Therefore, a stamp transfer printing method was also used to make the PPV active layer film of the memory unit. The stamp transfer printing method is a

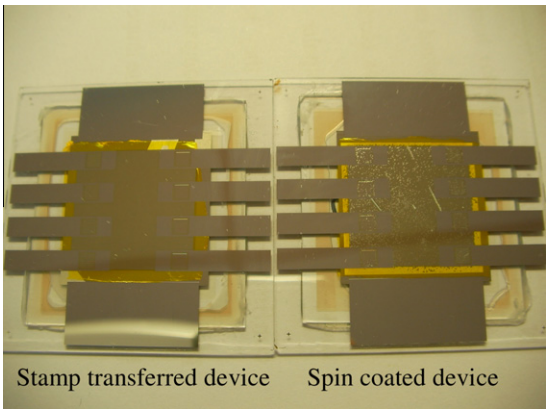

Fig. 3. Device pictures of the spin coated and stamp transfer printed device.

dry patterning method and does not affect the PPV active layer of the OLED unit and LiF/Al electrode [15–17]. Fig. 2 shows the transmission electron microscope (TEM) pictures of the OMLED prepared by the stamp transfer printing of the PPV active layer. In the case of the spin coated device, the spin coated PPV active layer penetrated into the LiF/Al cathode through the pin hole of the thermally evaporated Al as shown in Fig. 3. The active layer was damaged in the device with the spin coated PPV on LiF/Al. Compared with the spin coated device, the stamp transfer printed device showed clear boundary between the Al and the stamp transfer printed PPV film. Therefore, solution processed tandem OMLEDs with stable morphology could be fabricated using the stamp transfer printing process instead of the spin coating. Device pictures of the spin coated and stamp transfer printed tandem devices are shown in Fig. 3. It can be clearly seen from the picture that the PPV layer contaminated the active layer of the OMLED in the spin coating case, while the PPV layer did not affect the active layer of the OMLED in the stamp transfer printing case. Therefore, the active layer of the OBD in the OMLED was fabricated by stamp transfer printing process in this work, while the PPV layer of the OLED unit was spin coated. Detailed stamp transfer printing process was already reported in previous work [17].

Nonvolatile bistable switching performances of the memory unit are important for the nonvolatile bistable luminance control of the integrated OMLEDs as the OBD unit is directly connected to the OLED unit in the tandem structure. Therefore, the bistable behavior of the PPV memory device was investigated. Fig. 4**a** shows the current density–voltage curves of the OBD with the PPV active layer. PPV was stamp transfer printed on the Al electrode. The device structure of the OBD was Al/PPV/Al. The OBD exhibited bistable current state depending on the applied voltage to the device. The high current state (on state) was induced by applying 3 V (writing voltage), while the low current state (off state) was induced by applying a voltage above 5 V (erasing voltage). The bistable switching behavior of the PPV based OBD was already reported in other works and negative differential resistance (NDR) was observed [18,19]. It was reported that the bistable

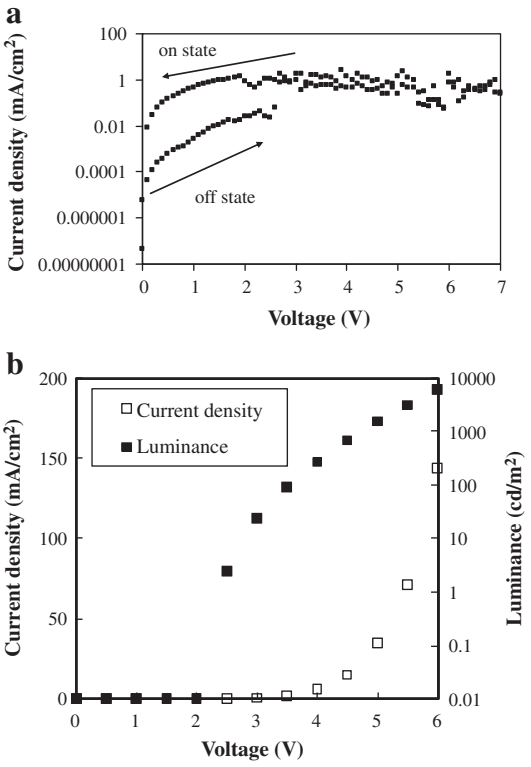

Fig. 4. Current density–voltage curves of the OBD (a) and current density–voltage–luminance curves of OLED (b).

stable switching behavior of the PPV OLED was originated from the electron trapping and freeing through the metal nanoclusters at the interface between the active layer and Al cathode [18]. Other than this, filament mechanism based on the aluminum oxide formation at the interface was also proposed as the origin of the bistability of the PPV based OBDs [19]. Aluminum oxide was generated during the deposition process of the OBD and it was responsible for the bistability of the device. Similar data were obtained in the PPV OBD fabricated in this work. A sharp increase of the current was observed at 2.7 V during forward scan from 0 to 7 V at low conductance state. The high conductance state could be maintained during reverse scan from 7 to 0 V. The high conductance state can return to the low conductance state by applying a voltage higher than 5 V. Therefore, the OBD showed bistable current state between 0 and 2.7 V. The on/off ratio of the OBD was over 100 and the on/off ratio was kept stable during multiple switching. The writing voltage of the OBD could be set as 3 V and the erasing voltage could be set as >5 V.

Current density–voltage-luminance performances of the OLED unit are also presented in Fig. 4b. The PPV based OLED showed typical light-emitting performances of the OLED. The turn-on voltage was 2.5 V and the voltage at 100 cd/m^2 was 3.6 V. Comparing the current level of the OBD and OLED, the current level of the OLED was higher than that of the OBD above 4 V, while it was lower than that of the OBD below 4 V. This indicates that the OBD has lower resistance than the OLED in the writing voltage

range and the OBD has higher resistance than the OLED in the erasing voltage range. This affects the bistable switching performances of the OMLED as the voltage applied to the OLED and OBD units is determined by the resistance of each device. The relative ratio of the resistance of the OLED and OBD at 3 V was R_{OLED}: R_{OBD} (2:1). Therefore, it can be expected that the voltage range for the bistable current state is widened compared with that of the OBD.

Fig. 5 shows the current density–voltage and luminance-voltage curves of the integrated OMLEDs. The integrated OMLED showed typical current density–voltage curves of the nonvolatile OBDs. The current density was sharply increased from 6 to 8.5 V and NDR characteristics of the OBD were observed at high voltage. The current density at high conductance state was higher than that at low conductance state below 8.5 V and similar NDR curve was obtained above 8.5 V. The on/off ratio of the OMLED was over 1000 at 6 V and it showed good device performances as the memory device. The bistability of the OMLED is due to the bistability of the OBD integrated into the device. The voltage range for the bistability of the OBD was from 0 to 2.7 V. The bistable voltage range was expanded in the OMLED as the voltage was applied both to the OBD and OLED units. At high conductance state, the current density was the same as that of the low conductance state up to 1.5 V, but high current density was obtained from 1.5 to 8.5 V. Therefore, the bistability was observed between 1.5 and 8.5 V although the on/off ratio was dependent on the reading voltage of the OMLED. The on state was induced at a writing voltage of 9 V and the off state was induced at an erasing voltage of 15 V. Therefore, the integrated OLBED device could play a role of the OBD over wide voltage range.

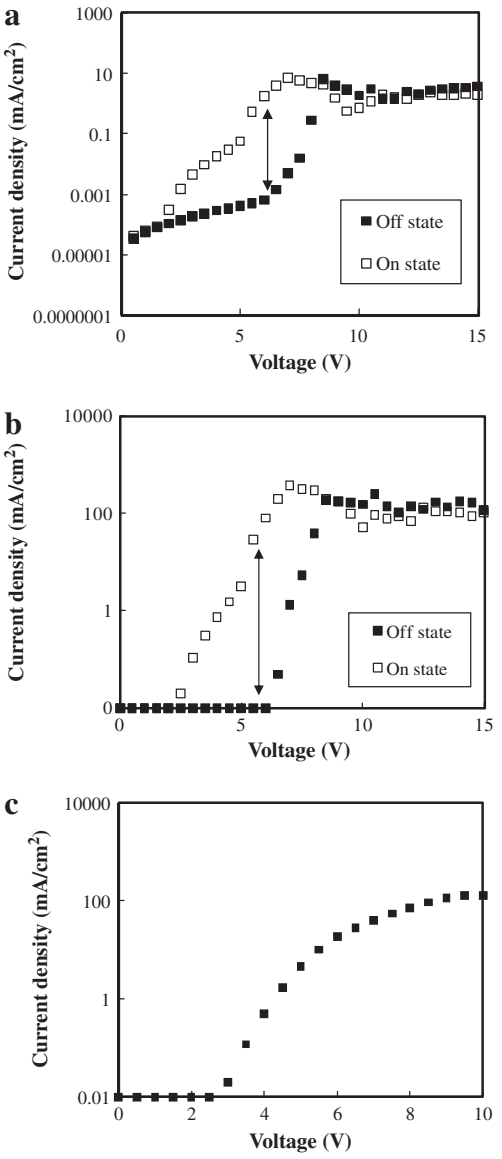

Fig. 5. Current density–voltage (a) and lumimance–voltage (b) curves of the OMLED at off state and on state. The erasing voltage for the off state was 15 V and the writing voltage for the on state was 9 V. Luminance–voltage (c) curve of the spin coated device is also shown.

As the current density was different depending on the applied voltage to the OMLED, it is expected that the luminance of the OMLED may be changed according to the switching voltage of the OMLED. As expected, the luminance of the OMLED was dependent on the switching voltage of the device. Within the bistable voltage range, the bitable luminance control of the OMLED was realized. The OMLED at low conductance state was not turned on until 6 V, while the OMLED was turned on from 2.5 V at high conductance state. The luminance of the OMLED at high conductance state at 6 V was 78 cd/m^2 compared with 0 cd/m^2 at low conductance state. The difference of the luminance was even higher at 7 V. The luminance at high conductance state was 369 cd/m^2, while that at low conductance state was only 1.3 cd/m^2. There was almost 300 times increase of the luminance at 7 V by changing the writing voltage of the OMLED. As the luminance is mainly determined by the charge density in the emitting layer, the increase of the current density increased the luminance of the OLED. The luminance of the OMLED at high and low conductance states was kept stable and the same luminance was obtained at the same voltage before applying different writing voltage. Therefore, nonvolatile bistable luminance switching behavior could be achieved in the tandem OMLED fabricated in this work. In the case of the spin coated device, no nonvolatile luminance switching behavior was observed and very low luminance level was observed. Luminance data of the spin coated device are shown in Fig. 5.

It is important to manage the current state at several levels to achieve multilevel luminance control in OMLED. Therefore, multilevel current control performance of the OMLED was investigated. Fig. 6 shows the current density of the OMLED depending on the writing voltage of the OMLED. The writing voltage of the OMLED was changed from 8 to 15 V to induce the multilevel current state in the OMLED. The reading voltage of the OMLED was 7 V. The OMLED showed low current level at a writing voltage of 8 V and high current level at a writing voltage of 9 V. Intermediate current level was observed at a writing voltage of 10 and 12 V. Therefore, four different current levels were clearly observed at different writing voltages.

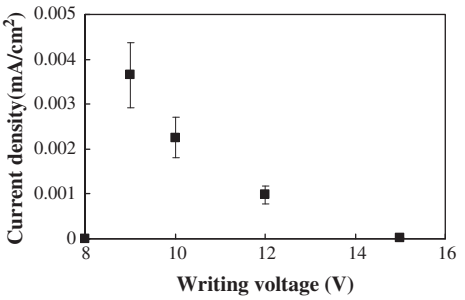

Fig. 6. Multilevel current density data of the OMLED according to the writing voltage.

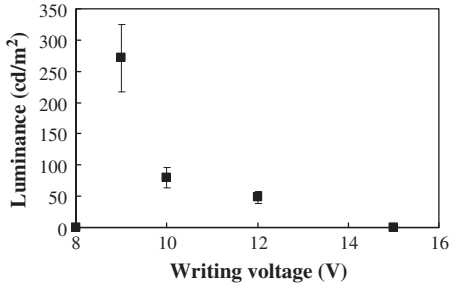

Fig. 7. Multilevel luminance data of the OMLED according to the writing voltage.

Multilevel luminance test of the tandem OMLED was carried out and test result is shown in Fig. 7. The writing voltage was controlled to manage the luminance of the OMLED and the reading voltage of the OMLED was 7 V. The OMLED was not turned on at a writing voltage below 9 V and the luminance was reduced by increasing the writing voltage. Intermediate luminance level between the off and on luminance levels was obtained at the writing voltage of 10 and 12 V. Although there was some scattering of the luminance data, four different luminance levels could be achieved in the OMLED. The average luminance of the OMLED at a writing voltage of 9 V was 270 cd/m^2, while it was 48 cd/m^2 at a writing voltage of 12 V. The OMLED was turned off at a writing voltage of 15 V and the average luminance level was 0.1 cd/m^2. Therefore, it was possible to control the luminance of the OMLED at the same driving voltage by just simply changing the writing voltage of the OMLED. The luminance of the OMLED could be kept stable before changing the writing voltage of the OMLED. Therefore, nonvolatile luminance switching of the OMLED could be achieved in the OMLED with tandem structure of OBD and OLED.

The pictures of the OMLED at a reading voltage of 7 V are presented in Fig. 8. The writing voltage of the OMLED was 9 V at on state and it was 15 V at off state. Low luminance level of 1.5 cd/m^2 can be clearly seen in the figure at off state, while high luminance level of 350 cd/m^2 was obtained at on state. Therefore, it can be proved that the nonvolatile multistable luminance state can be induced in the OMLED fabricated by the stamp transfer printing process.

The stability of the nonvolatile luminance state was evaluated by measuring the photocurrent of the Si photodiode. Writing voltages of 9 and 15 V were applied alternatively and the current was measured at 7 V. Fig. 9 shows the photocurrent of the OMLED at 7 V depending on the applied voltage. The OMLED was cycled 100 times and it can be seen that the high and low luminance states were maintained stable over 100 times. This proves that the OMLED shows reproducible luminance state. The high and low current states were maintained stable before applying writing or erasing voltage.

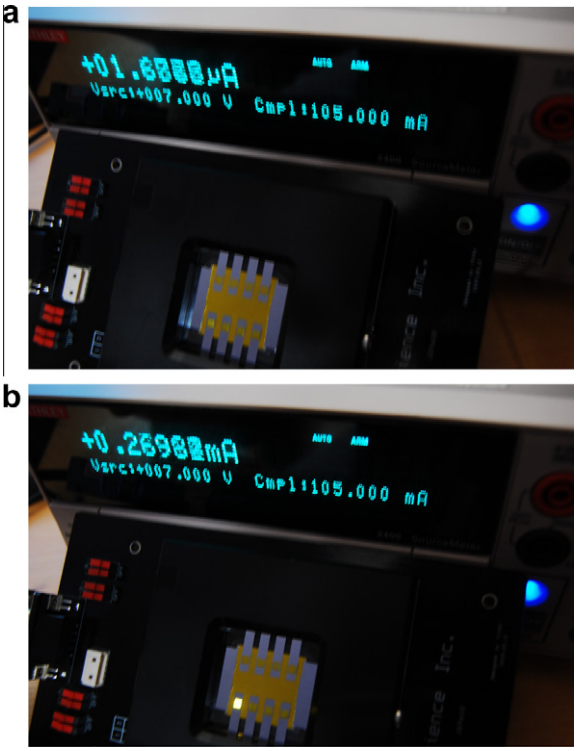

Fig. 8. Pictures of the OMLED at off (a) and on (b) state. The reading voltage was 7 V. The erasing voltage was 15 V and the writing voltage was 9 V.

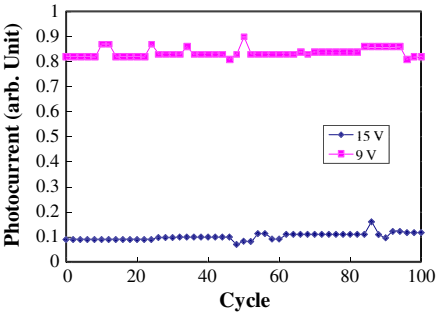

Fig. 9. Long term stability data of the OMLED through multiple cycling test.

4. Conclusions

In conclusion, solution processed tandem type OMLED with nonvolatile luminance switching over wide lumi-

nance range, four level luminance control, bipolar switching performances was successfully fabricated using a stamp transfer printing method. A high on/off ratio over 1000 was achieved in the tandem OMLED and the luminance could be managed over 300 cd/m^2 at the same voltage. The tandem structure of different device units and the stamp transfer process for the polymer film formation can be effectively used in future development of multifunctional organic electronic devices.

References

[1] C.W. Tang, S.A. VanSlyke, Appl. Phys. Lett. 51 (1987) 913.
[2] J.H. Burroughes, D.D.C. Bradley, A.R. Brown, R.N. Marks, K. Mackay, R.H. Friend, P.L. Burns, A.B. Holmes, Nature 347 (1990) 539.
[3] C.W. Tang, Appl. Phys. Lett. 48 (1986) 183.
[4] J.H. Burroughes, C.A. Jones, R.H. Friend, Nature 335 (1988) 137.
[5] L.P. Ma, J. Liu, Y. Yang, Appl. Phys. Lett. 80 (2002) 2997.
[6] K.S. Yook, S.O. Jeon, C.W. Joo, J.Y. Lee, S.H. Kim, J. Jang, Org. Electron. 10 (2009) 48.
[7] A. Cravino, P. Leriche, O. Alévêque, S. Roquet, J. Roncali, Adv. Mater. 18 (2006) 3033.
[8] A.K. Pandey, J.-M. Nunzi, Adv. Mater. 19 (2007) 3613.
[9] A. Hepp, H. Heil, W. Weise, M. Ahles, R. Schmechel, H. von Seggern, Phys. Rev. Lett. 91 (2003) 157406.
[10] C. Rost, S. Karg, W. Riess, M.A. Loi, M. Murgia, M. Muccini, Appl. Phys. Lett. 85 (2004) 1613.
[11] L. Ma, J. Liu, S. Pyo, Y. Yang, Appl. Phys. Lett. 80 (2002) 362.
[12] S.H. Kang, T. Crisp, I. Kymissis, V. Bulovic, Appl. Phys. Lett. 85 (2004) 4666.
[13] X. Gao, D. Zou, K. Fujita, T. Tsutsui, Appl. Phys. Lett. 81 (2002) 4508.
[14] S.H. Kim, K.S. Yook, J.Y. Lee, J. Jang, Appl. Phys. Lett. 93 (2008) 053306.
[15] B.D. Gates, Q.B. Xu, M. Stewart, D. Ryan, C.G. Willson, G.M. Whitesides, Chem. Rev. 105 (2005) 1171.
[16] L. Chen, P. Degenaar, D.D.C. Bradley, Adv. Mater. 20 (2008) 1679.
[17] C.W. Joo, S.O. Jeon, K.S. Yook, J.Y. Lee, Org. Electron. 10 (2009) 372.
[18] M. Lauters, B. McCarthy, D. Sarid, G.E. Jabbour, Appl. Phys. Lett. 89 (2006) 013507.
[19] M. Colle, M. Buchel, D.M. de Leeuw, Org. Electron. 7 (2006) 305.

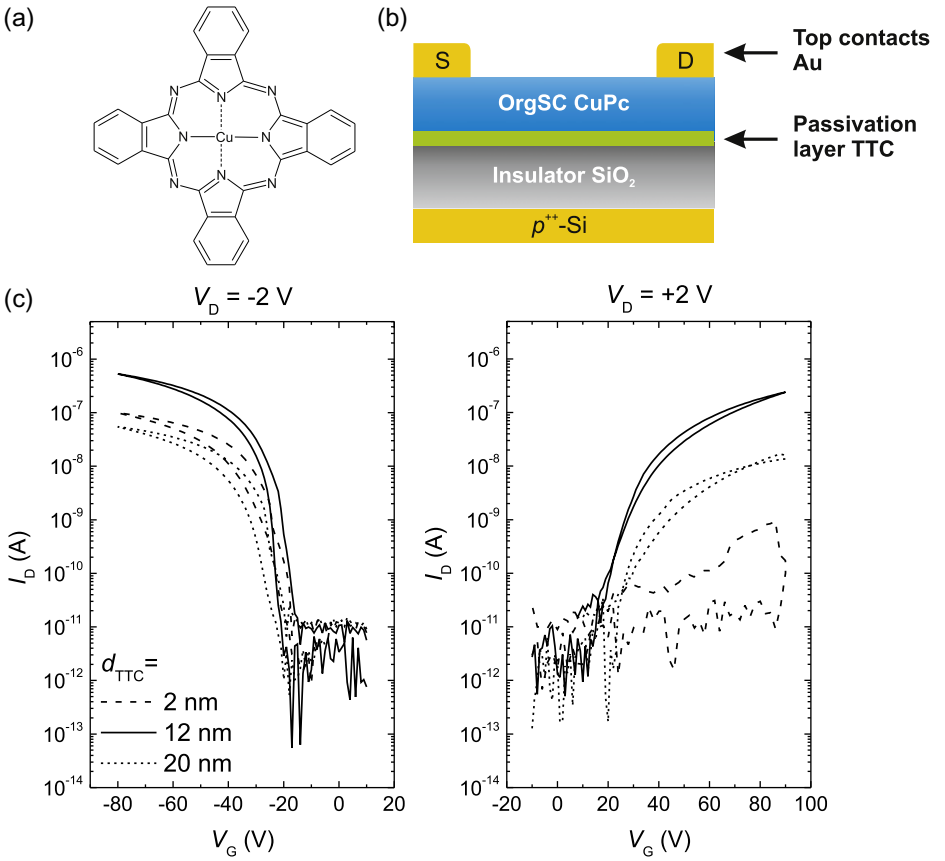

Fig. 1. (a) Chemical structure of the organic semiconductor (OrgSC) CuPc, (b) schematic layout of top-contact OFETs and (c) transfer characteristics of devices with channel length $L = 50$ μm, channel width $W = 3.0$ mm and TTC thicknesses d_{TTC} of 2 nm, 12 nm and 20 nm.

2. Experimental

We fabricated top-contact bottom-gate organic field-effect transistors with varying TTC thickness and 25 nm of CuPc on heavily *p*-doped silicon wafers with 310 nm thermally grown SiO_2 acting as gate dielectric. TTC, CuPc and the gold top contacts were fabricated by thermal evaporation. TTC layers are highly hydrophobic with a water contact angle of approximately 105°. We determined a dielectric constant of $\varepsilon_{TTC} \approx 2.5$ by capacitance measurements. A systematic sketch of the sample can be seen in Fig. 1b. On each substrate, there are six individual transistors with channel length ranging from 50 μm to 130 μm and a channel width of 3.0 mm. A detailed description of the fabrication and analysis of the OFETs is given elsewhere [9]. We found that the transistor characteristics depend strongly on the thickness and the post-deposition treatment of the TTC passivation layer. We note that the TTC thicknesses of the investigated devices are nominal thicknesses obtained from the deposited amount on the quartz monitor during evaporation, but not taking into account film roughness (see below).

3. Growth of CuPc on TTC

In Fig. 1c transfer characteristics of samples with 2, 12 and 20 nm of TTC are displayed. The sample with 2 nm TTC shows unipolar hole transport, whereas all other samples are ambipolar. The sample with 12 nm TTC reveals the best characteristics, while the 20 nm sample has a significantly reduced performance. In order to understand this behavior the TTC morphology was analyzed. As already known from previous work TTC forms crystalline terraces where the molecules are standing upright [9]. The height of one terrace (i.e. one individual TTC layer) is approximately 5 nm which agrees with the length of the molecule. For the following analysis of the charge carrier transport three thickness regimes are relevant. Fig. 2a shows atomic force microscopy (AFM) images of 2, 6 and 14 nm of TTC on SiO_2 being representative for each of these three regimes. Region I, TTC thickness lower than one monolayer, corresponds to the growth of islands of TTC on SiO_2 which are not connected to each other. On some islands even the formation of a second layer can already be seen. Region II represents TTC thicknesses between one and about three monolayers. Here, the SiO_2 is covered completely and additional TTC layers are being formed. In region III, i.e. layer thickness larger than about three monolayers, very high columns of TTC appear [10]. For a nominal thickness of 14 nm some of these columns can reach a height of 100 nm. Thus, the growth of TTC on SiO_2 can be described by a Stranski–Krastanov scenario. To determine the influence of these different growth regimes on charge carrier transport we fabricated OFETs with TTC thicknesses

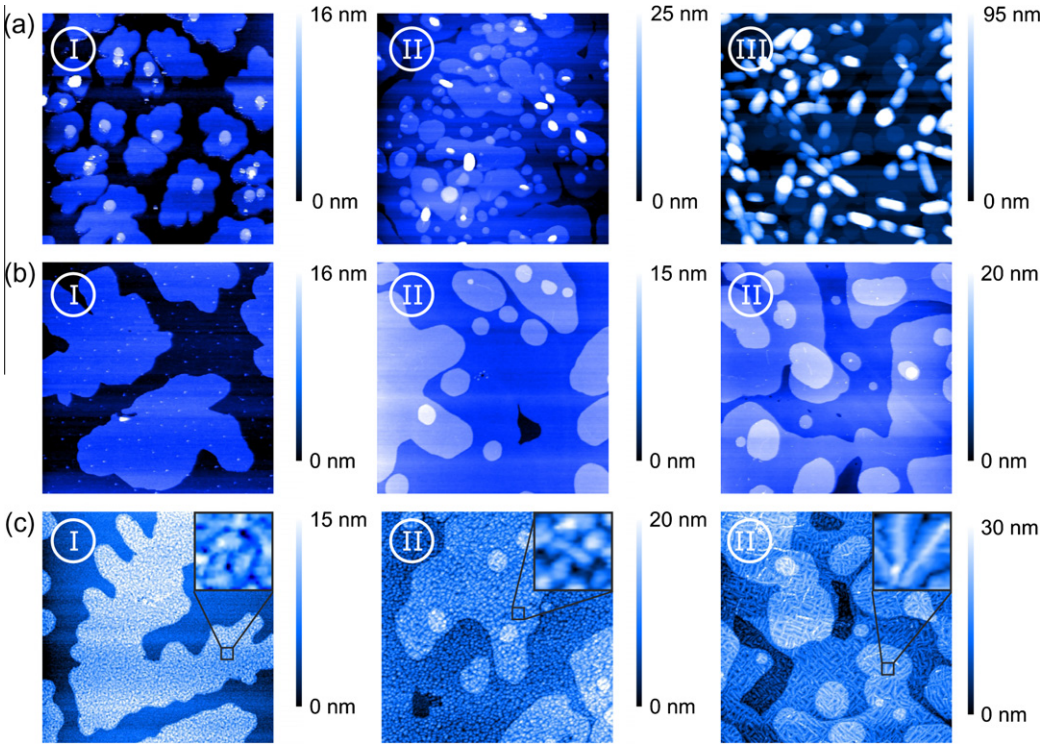

Fig. 2. (a) AFM images of nominally 2 nm (left), 6 nm (center) and 14 nm (right) TTC on SiO_2 and (b) the same as (a) but with TTC annealed at 60 °C for 2 h. Black colored areas in the 2 nm and 6 nm images of (a) and (b) symbolize bare SiO_2. (c) AFM images of 5 nm of CuPc on TTC layers prepared as in case (b) (all sizes $5 \times 5\ \mu m^2$). The numbers in circles represent the transport regimes described in the text. The insets show zoomed areas ($0.25 \times 0.25\ \mu m^2$) of the CuPc crystallites on the first TTC layer (I), on the second layer (II) and on the third layer (II*).

between 0 and 22 nm. Charge carrier mobilities were evaluated in the linear regime using the so-called transmission line method (TLM) [11]. The corresponding charge carrier mobilities are shown in Fig. 3a.

The three growth regimes can be correlated very well with three distinct transport regimes. Fig. 3c explains schematically the transport processes in the individual regimes I, II and III. In regime I the TTC layer is not fully closed. This leads to the presence of electron traps on bare SiO_2, so that there is no electron transport below roughly one complete monolayer of TTC. For 4 nm TTC there is already a percolation path for electrons, which leads to the onset of electron transport but with rather low mobility. Hole mobility is increasing with TTC thickness from around $2 \times 10^{-4}\ cm^2/Vs$ on bare SiO_2 to approximately $2 \times 10^{-2}\ cm^2/Vs$ for 8 nm TTC due to the larger grain size of CuPc on TTC as compared to SiO_2 [9]. Larger grains lead to less grain boundaries, which are a key limiting factor for charge carrier transport [12,13]. In regime II the TTC layer is fully closed and hole and electron mobilities remain relatively constant, however, the electron mobility is by a factor of 2 lower than the hole mobility. In regime III the high columns of insulating TTC begin to hinder the charge carrier transport along the interface. A larger nominal TTC thickness leads to an increase of the area occupied by these columns. Thus, electron and hole mobility decrease again with increasing TTC thickness due to a reduction of the effective area available for the transport channel at the insulator-semiconductor interface, resulting in a decrease of the current [14].

4. Effects of annealed TTC layers

From these results it can be concluded that the morphology of the TTC–CuPc interface is limiting the charge carrier transport and needs to be improved. Therefore we fabricated a series of TTC-covered SiO_2 substrates and annealed them prior to the deposition of CuPc in an oven at 60 °C for 120 min in N_2 atmosphere. Fig. 2b shows the corresponding AFM images of nominally 2, 6 and 14 nm of annealed TTC on SiO_2. For 2 nm, there are also TTC islands with a height of one monolayer, like in the non-annealed case. However, the area of the islands is larger and no second layer is formed. In the 6 nm picture, significant changes to the non-annealed samples occur: the height distribution becomes more homogeneous and the TTC terraces are enlarged. This effect is much more pronounced in the case of 14 nm and at even larger thicknesses: the previous extremely high TTC columns in the non-annealed case disappear completely and large, flat TTC terraces of constant height are being formed. We fabricated OFETs using annealed TTC passivation layers with a TTC thickness in the range from 2 to 28 nm. The rest of the fabrication was identical to the samples described above. The resulting field-effect mobilities can be seen in Fig. 3b and, again, be distinguished in

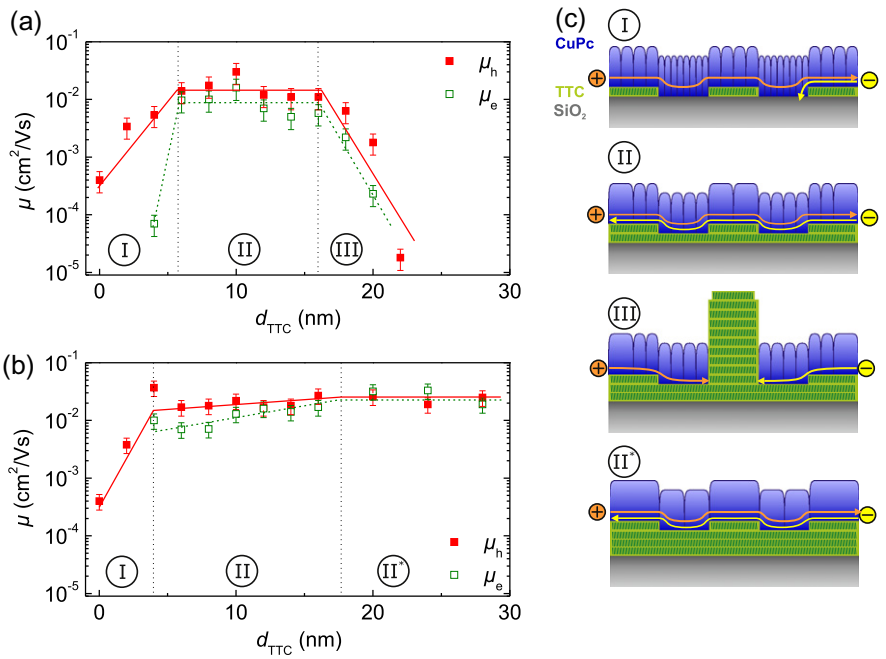

Fig. 3. (a) Field-effect mobility determined by TLM for holes (closed symbols) and electrons (open symbols) as a function of TTC thickness for as-deposited TTC layers and (b) for TTC layers annealed at 60 °C for 2 h (the lines are guides for the eye). (c) Schematic sketches of the charge carrier transport regimes.

three regimes: In regime I, 0–4 nm, there is only hole transport with increasing mobility and no electron transport. In regime II, for TTC thicknesses between 4 and 16 nm, the hole mobility increases very slowly until it reaches its maximum value ($\mu_{ho} \approx 2.0 \times 10^{-2}$ cm^2/Vs), whereas the increase of the electron mobility up to comparable values is more pronounced. In contrast to the non-annealed case there is no regime III with diminishing charge carrier transport for large TTC thicknesses. Instead, for a thickness larger than 18 nm TTC – regime II* – electron and hole mobility are equal at $\mu \approx 2.0$–3.0×10^{-2} cm^2/Vs and stay constant with increasing TTC thickness. We note that this is the highest reported value for electron mobility in CuPc and comparable to the highest reported hole mobilities in thin-film transistors with heated CuPc layers and silanization of SiO_2 surfaces [14] but still lower than the hole mobility in single-crystals ($\mu_{sc,ho} \approx 0.5 - 1$ cm^2/Vs) [15,16]. Ambipolar transport has been reported for single-crystal FETs but hole mobilities were significantly lower than other values reported for single-crystals ($\mu_{sc,ho} \approx 10^{-3}$–$10^{-1}$ cm^2/Vs) and electron mobilities were even lower than in our thin-film devices ($\mu_{sc,el} \approx 10^{-5} - 10^{-3}$ cm^2/Vs) [7]. The fact that the mobilities do not decrease for large TTC thicknesses can be explained very well with the disappearance of the high TTC columns. However, this model cannot explain why the electron mobility still increases in the range from 4 to 18 nm TTC. AFM images show that TTC forms a closed film already for 6 nm annealed TTC so that all electron traps should be passivated. Thus, the reason must be another effect on the insulator-semiconductor interface, namely in the CuPc. To investigate the effects of increasing TTC thickness on the transport channel in CuPc we performed AFM measurements with only 5 nm CuPc on nominally 2, 6 and 14 nm annealed TTC films. The results are shown in Fig. 2c. CuPc forms polycrystalline layers where the CuPc grains are very well visible and the TTC terraces can still be identified. Details about the crystalline structure of CuPc on TTC have been reported elsewhere [9]. It can clearly be seen that the CuPc grain size increases steadily with the thickness of the underlying TTC layer. On the first TTC monolayer CuPc forms round grains with an average diameter of 100 nm. On thicker TTC layers the grains become more and more elongate, e.g. on 14 nm TTC the CuPc grains have an average length of 200–230 nm. We observed a saturation of the grain size for TTC thicknesses beyond 16–18 nm with crystallite lengths up to 300 nm. This high degree of crystallinity shows that the growth of CuPc on TTC can be considered as some kind of "pseudoepitaxial" growth [9]. The reason for the increase of the crystallite size is not yet fully understood. It is imaginable that TTC grows in a slightly distorted way on SiO_2 and needs some three or four monolayers to relax to its original crystal structure, which then promotes optimum CuPc growth. Or, as indicated by preliminary X-ray diffraction measurements (not shown here), a different CuPc phase, that exhibits larger crystals, could be formed on upper TTC layers. The increase and the subsequent saturation of the CuPc grain size are coincident with the behavior of the electron mobility in the annealed devices. This effect is illustrated in Fig. 3c (II*).

The CuPc films in the presented devices are clearly polycrystalline. This limits the charge carrier transport [12,13] and explains why the mobilities in these devices are smaller than the reported values in single crystal OFETs [15,16]. Due to our simultaneous analysis of electron and hole

transport in the same device a differentiation for the two charge carrier types is possible. Levinson et al. suggested a model to analyze the grain boundary trap density in polycrystalline films which can also be applied for organic semiconductors [18,19]. In our case the temperature dependent analysis for samples with 14 nm (regime II) and 28 nm (regime II*) annealed TTC lead to electron trap densities at the grain boundaries of about 2.6×10^{12} cm^{-2} for both devices. The trap density for holes is by a factor of 1.6 lower than the trap density of electrons (see the Supplementary information for a detailed analysis). These observations can explain that there is a general difference between electron and hole transport but cannot explain the difference between regime II and II*. A difference in the mobility prefactor is observed which is related to a larger scattering rate for electrons at the grain boundaries or to a lower electron mobility inside the crystalline grains [18]. This could be an indication for a different electrostatic interaction between the charge carriers and the SiO_2 interface. Thereby, the interaction of the charge carriers in the organic semiconductor to induced polarization in the oxide insulator or to interface traps at the oxide surface, can be different for electrons and holes since the traps can be charged and thus affect electrons and holes differently. Additionally, the effective mass of the polaron can be different for negative and positive charges. Both effects will decrease with increasing distance between SiO_2 and CuPc [17]. Further investigations concerning the growth behavior and the electronic interaction are required to quantify these effects.

5. Summary

In summary, the influence of the morphology of an insulating TTC interlayer on the morphology of a semiconducting CuPc layer deposited on top and the charge carrier transport in this CuPc layer was analyzed. The insulating interlayer is free of electron traps and leads to a CuPc layer with large grain size up to 300 nm when the film thickness of the low-temperature annealed TTC film is larger than three monolayers. At room temperature the contact resistance-corrected mobilities for electrons and holes are equal and as high as the hole mobility reported for heated CuPc films. The transport is limited by the polycrystalline nature of the semiconducting film which exhibits a slight asymmetry between electrons and holes due to a difference in the grain boundary trap density for both charge carrier types. The possibility of rather high electron and hole mobilities in thin-film devices and their ambipolar nature should be considered when CuPc is used as donor in solar cells or as *p*-type semiconductor in field-effect transistors or diodes. Additionally, balanced electron and hole mobilities are also crucial for the realization of organic light-emitting field-effect transistors or complementary organic inverters based on one single active material [14,20,21].

Acknowledgment

We thank the Deutsche Forschungsgemeinschaft (DFG) for financial support through SFB 484 and Br 1728/8.

Appendix A. Supplementary data

Supplementary data associated with this article can be found, in the online version, at doi:10.1016/j.orgel.2011.02.001.

References

[1] N. Karl, in: O. Madelung, M. Schulz, H. Weiss (Eds.), Landolt–Boernstein (New Series), Updated Edition, vol. 41E, Springer, Berlin, 2000. Ch. Organic Semiconductors, Group III.
[2] T. Yasuda, T. Tsutsui, Organic field-effect transistors based on high electron and ambipolar carrier transport properties of copper-phthalocynanine, Chem. Phys. Lett. 402 (2005) 395.
[3] M. Ahles, R. Schmechel, H. von Seggern, n-Type organic field-effect transistor based on interface-doped pentacene, Appl. Phys. Lett. 85 (2004) 4499.
[4] L.L. Chua, J. Zaumseil, J.F. Chang, E.C.W. Ou, P.K.H. Ho, H. Sirringhaus, R.H. Friend, General observation of n-type field-effect behaviour in organic semiconductors, Nature 434 (2005) 194.
[5] R. Schmechel, M. Ahles, H. von Seggern, A pentacene ambipolar transistor: experiment and theory, J. Appl. Phys. 98 (2005) 084511.
[6] A. Opitz, M. Kraus, M. Bronner, J. Wagner, W. Brütting, Bipolar transport in organic field-effect transistors: organic semiconductor blends versus contact modification, New J. Phys. 10 (2008) 065006.
[7] R.W.I. de Boer, A.F. Stassen, M.F. Craciun, C.L. Mulder, A. Molinari, S. Rogge, A.F. Morpurgo, Ambipolar Cu- and Fe-phthalocyanine single-crystal field-effect transistors, Appl. Phys. Lett. 86 (2005) 262109.
[8] S. Ogawa, Y. Kimura, M. Niwano, H. Ishii, Trap elimination and injection switching at organic field effect transistor by inserting an alkane ($C_{44}H_{90}$) layer, Appl. Phys. Lett. 90 (2007) 033504.
[9] M. Kraus, S. Richler, A. Opitz, W. Brütting, S. Haas, T. Hasegawa, A. Hinderhofer, F. Schreiber, High-mobility copper-phthalocyanine field-effect transistors with tetratetracontane passivation layer and organic metal contacts, J. Appl. Phys. 107 (2010) 094503.
[10] Please note that the AFM images of non-annealed TTC substrates shown in Ref. [9] are only 2×2 μm^2 and are selected areas between high columns. The detailed analysis we performed for the present work showed that only on annealed TTC-covered substrates it is possible to obtain reproducibly good 5×5 μm^2 images.
[11] D.J. Gundlach, L. Zhou, J.A. Nichols, T.N. Jackson, P.V. Necliudov, M.S. Shur, An experimental study of contact effects in organic thin film transistors, J. Appl. Phys. 100 (2006) 024509.
[12] G. Horowitz, M. Hajlaoui, Grain size dependent mobility in polycrystalline organic field-effect transistors, Synth. Met. 122 (2001) 185.
[13] P. Lugli, C. Erlen, A. Pecchia, F. Brunetti, L. Latessa, A. Bolognesi, G. Csaba, G. Scarpa, A. di Carlo, The simulation of molecular and organic devices: a critical review and look at future developments, Appl. Phys. A: Mater. Sci. Process. 87 (2007) 593.
[14] M. Bronner, A. Opitz, W. Brütting, Ambipolar charge carrier transport in organic semiconductor blends of phthalocyanine and fullerene, Phys. Stat. Sol. (A) 205 (2008) 549.
[15] R. Zeis, T. Siegrist, C. Kloc, Single-crystal field-effect transistors based on copper phthalocyanine, Appl. Phys. Lett. 86 (2005) 022103.
[16] K. Yamada, J. Takeya, K. Shigeto, K. Tsukagoshi, Y. Aoyagi, Y. Iwasa, Charge transport of copper phthalocyanine single-crystal field-effect transistors stable above 100 °C, Appl. Phys. Lett. 88 (2006) 122110.
[17] I.N. Hulea, S. Fratini, H. Xie, C.L. Mulder, N.N. Iossad, G. Rastelli, S. Ciuchi, A.F. Morpurgo, Tunable Fröhlich polarons in organic single-crystal transistors, Nature Mater. 5 (2006) 982.
[18] J. Levinson, F.R. Shepherd, P.J. Scanlon, W.D. Westwood, G. Este, M. Rider, Conductivity behavior in polycrystalline semiconductor thin film transistors, J. Appl. Phys. 53 (1982) 1193.
[19] S.H. Jin, K.D. Jung, H. Shin, B.-G. Park, J.D. Lee, Grain size effects on contact resistance of top-contact pentacene TFTs, Synth. Met. 156 (2006) 196.
[20] A. Hepp, H. Heil, W. Weise, M. Ahles, R. Schmechel, H. von Seggern, Light-emitting field-effect transistor based on a tetracene thin film, Phys. Rev. Lett. 91 (2003) 157406.
[21] J. Zaumseil, H. Sirringhaus, Electron and ambipolar transport in organic field-effect transistors, Chem. Rev. 107 (2007) 1296.

Oxidation of the low work function cathode appears to be the main efficiency-limiting mechanism in unencapsulated OPVs in dark, similar to the case of organic light-emitting diodes (OLED), and generally, no alteration of the photoactive blend is reported in this condition [9,10,15–17]. Moisture and oxygen are demonstrated to diffuse through pinholes and edges of the cathode leading to oxidation of the metal only at the organic/metal interface; even delamination of the cathode is observed in some cases [17,18]. This degradation severely hinders charge extraction in the oxidized regions resulting in increased series resistance and reduced short-circuit current [17]. Several strategies have been proposed to overcome the rapid failure in ambient conditions, such as addition of a metal oxide layer between the active layer and the metal cathode, and/or the implementation of an inverted device architecture that avoids the need for a low work function metal entirely [19–22].

Even though PEDOT:PSS is commonly used as a hole transport layer in conventional polymer-based solar cells, its impact on device degradation remains controversial and not widely investigated [17,23–25]. Kawano et al. concluded that humidity induces formation of an insulating layer at the PEDOT:PSS/blend interface leading to device failure [23]. Norrman et al. equally observed the reaction of PSS in the presence of air, while Lloyd et al. reported that PEDOT:PSS seemed to have a negligible impact on the degradation rate of P3HT:PCBM devices with Ca/Al electrode [17,24]. In contrast, Yamanari et al. demonstrated that replacement of PEDOT:PSS by MoO_3 considerably enhances air stability of similar devices with an Al cathode, suggesting that PEDOT:PSS might accelerate the degradation [25]. Despite the fact that in these studies similar devices, aged in comparable conditions, exhibited qualitatively identical device degradation, in each case the complementary experiments led to different conclusions.

Here, we report a series of experiments to elucidate the main degradation mechanism in polymer-based solar cells in ambient atmosphere and shelf-life conditions. A combination of electrical and optical measurements allows to confirm that only charge extraction is hindered in degraded devices, whereas other steps in the photo-generation process remain unchanged. By altering device interfaces and materials, we conclude that cathode oxidation is the main degradation mechanism, and decay rate is greatly accelerated by PEDOT:PSS. To gain further insight into the mechanism, we evaluate the impact of PEDOT:PSS acidity on device degradation and show that, in fact, only its hygroscopic nature is detrimental. Consequently, ambient humidity seems to be the dominating stress factor for polymer solar cells in air, which we confirm by experiments in a controlled-humidity environment. Moreover, we evaluate device lifetime at different humidity levels at room temperature, in an effort to establish an adapted accelerated testing for OPVs subjected to these conditions. Finally, we show that humidity infiltration can also be visually observed in our devices, and this reveals further details of the degradation mechanism. While the purpose of this paper is to explain the role of PEDOT:PSS in the failure of polymer solar cells, it has broader implications since PEDOT:PSS is also used in several other organic electronics devices.

2. Experimental

2.1. Sample preparation and characterization

We prepared a variety of device architectures in this study, here we describe the preparation of standard cells and deposition of other layers which were used additionally or alternatively. We prepared standard solar cells on glass samples coated with patterned indium-tin-oxide (ITO) purchased from Kintec, with a sheet resistance of 15 Ω/□. Samples were thoroughly cleaned in a sequence of sonication in detergent, deionized water, acetone and isopropanol, and finally treated with ultraviolet-ozone. First, filtered PEDOT:PSS (HC Starck, Baytron P VPAl4083 with pH 2) was spin-coated at 3000 rpm for 60 s, giving a 35 nm thick layer. Then, samples were entered in a nitrogen filled glovebox (with H_2O and O_2 both below 1 ppm), where they were annealed at 130 °C for 10 min to remove excess water. Variation of the PEDOT:PSS thickness achieved by using spin-coating speeds between 500 and 6000 rpm. Neutral pH PEDOT:PSS purchased from Agfa (Gen5pH5 and Gen5pH7) was spin-coated and treated similar to the acidic PEDOT:PSS. Alternatively, 15 nm of molybdenum trioxide was evaporated at $\sim 10^{-7}$ mbar at a deposition rate of 2 Å/s. All further steps of processing were carried out in an inert nitrogen atmosphere. P3HT (Rieke Metals) and PCBM (Solenne bv.) were used as purchased to prepare a solution of 3 wt.% in ortho-dichlorobenzene in a 1:1 wt.% ratio. The solution was stirred inside the glovebox at 80 °C overnight and filtered with a 5 μm PTFE filter prior to use. The active layer was spin-coated at 1000 rpm for 60 s. The samples were subsequently heated at 130 °C for 10 min to achieve an optimal morphology. Standard samples were transferred to a metal evaporation chamber where 40 nm of Yb and 150 nm of Al were deposited at 10^{-7} mbar with 1.5 Å/s deposition rate, without breaking vacuum. Alternatively 40 nm Ca and 150 nm Al was evaporated in similar conditions. The metals evaporated through a shadow mask defined twelve 0.134 cm^2 on each substrate. The device area is scaled by changing the area of the metal shadow mask or even additionally decreasing the size of the ITO. On a few samples, 5 nm of C_{60} was deposited over the whole substrate prior to the metal cathode evaporation. C_{60} was sublimated at 10^{-6} mbar with a 1 Å/s deposition rate.

Photovoltaic characteristics were measured at regular intervals in ambient atmosphere with a Keithley 2602A in two-wire configuration under a Lot Oriel 1000 W Xenon arc lamp filtered by OD0.8 Newport neutral density to obtain 100 mW/cm^2 illumination intensity and AM1.5G spectrum. The lamps intensity was calibrated with an ISE Fraunhofer certified Si photodiode. Characterization of one substrate, 12 devices, requires a total illumination of ~40 s resulting in a cumulated illumination of ~5–10 min over the lifetime study. Optical microscope images are observed and recorded with Olympus AX70 at 5× magnification. Layer thicknesses were measured by a Dektak D150.

2.2. Degradation conditions

Samples were aged in ambient conditions, in dark. The ambient temperature was constantly 20 °C, while humidity varied slightly from 30% to 40% RH between experiments. Controlled atmosphere was achieved by either placing the samples in presence of (previously dried) silica gel or a saturated salt solution in a hermetically sealed chamber, which only opened for device characterization. Humidity level of 11% RH, 33% RH, 53% RH, 75% RH and 84% RH were achieved at 20 °C by using saturated solution of LiCl, $MgCl_2$, $Mg(NO_3)_2$, NaCl, and KCl, respectively [26].

2.3. Photo-induced absorption spectroscopy

Near steady-state photo-induced absorption (PIA) spectra were recorded between 2 and 1 eV by excitating with 2.54 eV photons from a mechanically modulated (275 Hz) Ar^+ laser source. The resulting change in transmission of a tungsten–halogen probe beam through the device after reflection at the back electrode (ΔR) was recorded with a phase sensitive lock-in amplifier after dispersion with a monochromator and detection using Si and InGaAs detectors. The pump power was 100 mW with a beam diameter of 2 mm. The PIA signal ($\Delta R/R$) was corrected for the photoluminescence, which was recorded in a separate experiment. The devices were held at short circuit during the measurements, at room temperature and in N_2 atmosphere, using a Oxford Optistat continuous flow cryostat.

2.4. TEM and SEM characterization

Analysis by transmission electron microscopy (TEM) is performed in a Tecnai F30 at 300 kV. Cross-sectional specimens are prepared by focused ion beam (FIB) in a Strata400S by the internal lift-out method. In case no metal is present on the surface, an Al cap layer is evaporated on the samples to protect the surface during the ion beam milling. The samples are transferred to the FIB system in nitrogen boxes and the thinned TEM specimens are analyzed as soon as possible to avoid long air exposure. Compositional analysis is done in parallel by energy dispersive X-ray spectroscopy (EDS) and electron energy loss spectroscopy (EELS) in scanning transmission electron microscopy (STEM) mode. STEM images are acquired in high angle annular dark field (HAADF) mode.

Characterization of the films by scanning electron microscopy (SEM) was performed with a Philips XL30 S SEM (5 kV acceleration voltage, spot size 3, and a typical working distance between 4 and 6 mm).

3. Results and discussion

3.1. Degradation of reference devices in ambient conditions

The device structure consists of indium tin oxide (ITO)/ PEDOT:PSS (35 nm)/ P3HT:PCBM (~300 nm)/Yb (40 nm)/ Al (150 nm) with an initial efficiency of 3.6 ± 0.1%, measured under 100 mW/cm^2 AM1.5G simulated solar illumination where the short-circuit current density (J_{SC}) is 9.8 ± 0.2 mA/cm^2, the open-circuit voltage (V_{OC}) is 581 ± 3 mV and the fill factor (FF) is 63 ± 0.3%. The evolution of photovoltaic device characteristics of these reference devices stored in air is shown in Fig. 1. The electrical parameters of the solar cells are normalized to their initial values to facilitate comparison. Unless stated otherwise, all samples in this study are stored at 20 °C, in dark and ambient conditions with a relative humidity (RH) level of 30–40%. Samples are briefly illuminated only during regular measurements in air. Initially, we verified that neither the illumination nor the electrical biasing induces significant additional degradation (see Fig. S1 in the Supporting information). The efficiency degradation in these devices is uniquely determined by a two-stage decrease of the J_{SC}, while the V_{OC} and FF remain constant, in agreement with previous reports [17,25]. This two-stage degradation consists of a fast, initial drop followed by a slow, almost linear degradation. Even though the series resistance increases in degraded cells, it does not follow the same kinetics as the decrease in photocurrent: it remains low during the first phase and only increases during the second stage. One could also remark that performance variation among devices increases with time. Furthermore, we found that the degradation is entirely irreversible in contrast to reports where degradation in dry air could be partially recovered [12,13].

First, we could exclude that the drop in J_{SC} stems from a loss in absorption as determined by absorption and external quantum efficiency spectrum (EQE) measurements (shown in Fig. S2a,b in the Supporting information). The EQE spectrum is evenly lowered over the whole wavelength range indicating that neither change in absorption, nor morphology reorganization occurs in the devices [27]. Furthermore, current density–voltage measurements up to high reverse bias show that the initial photocurrent density could be recovered, even in considerably aged devices by a suitably high reverse bias (Fig. 2). This indicates

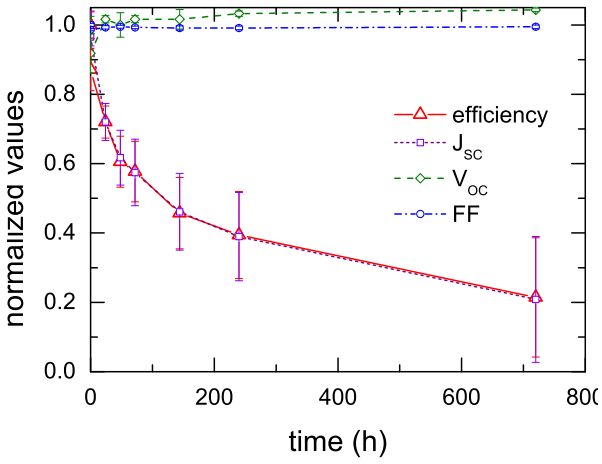

Fig. 1. Normalized solar cell parameters extracted from regular measurements under 100 mW/cm^2 AM1.5G simulated solar illumination. Devices consisting of ITO/PEDOT:PSS/P3HT:PCBM/Yb/Al were stored in shelf-life conditions, in ambient atmosphere. The values correspond to mean values and the error bars are standard deviations calculated from 12 identical devices on a single substrate.

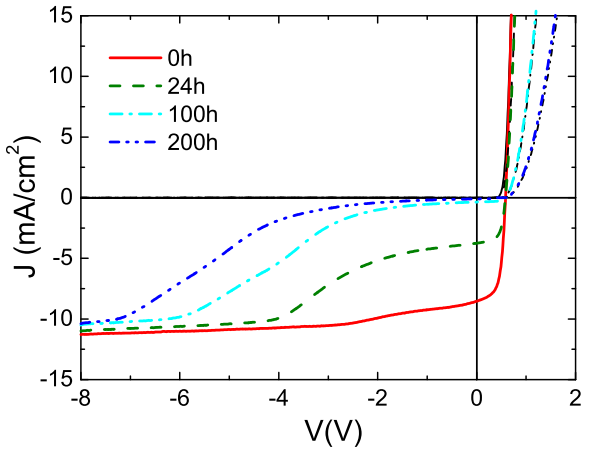

Fig. 2. Dark and illuminated current density–voltage (*JV*) measurements of reference devices stored in shelf-life conditions under ambient atmosphere.

that exciton generation is unaltered in degraded cells. Moreover, the voltage dependent photocurrent could be the signature of various loss mechanisms; the most probable ones include reduced geminate pair dissociation or hindered charge transfer at organic-electrode interfaces.

Next, we performed near-steady-state photo-induced absorption spectroscopy (PIA) measurements on fresh and degraded cells in reflection geometry to investigate the efficiency of exciton dissociation with a contactless technique. The signal that is recorded is proportional to the near-steady-state photogenerated charge carrier density. As illustrated in Fig. 3, the bands characteristic of radical cations of regio-regular P3HT, namely 1.25 and 1.7 eV, remain unchanged even after 44 h exposure to air [28]. Hence, we can conclude that charge generation also remains unaltered in devices exposed to air.

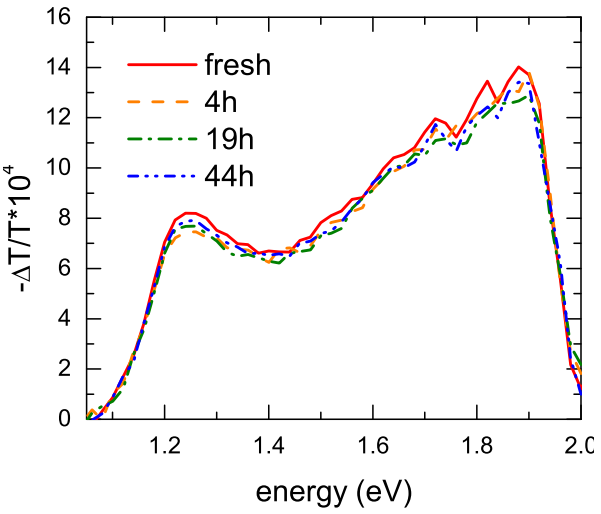

Fig. 3. Near-steady-state photo-induced absorption spectroscopy in reflection mode on devices exposed to ambient air for 0, 4, 19 and 44 h.

3.2. Impact of hole transport layers on device degradation

Further understanding of the degradation mechanism could be obtained by comparing the degradation in solar cells with the same active layer and different electrodes. In the first series we employed two different hole transport layers (HTL) in four different devices, all capped with Yb/Al cathode. We compared PEDOT:PSS, MoO_3, the stack of these two materials, as well as a sample without HTL. Except the sample without a HTL, which presents a lower initial FF (42% versus 63%), all samples yielded comparable initial efficiencies of 3.6%. Since all device parameters, except J_{SC}, remain constant during the test, we solely compared this evolution in Fig. 4. Exclusion or replacement of the PEDOT:PSS layer considerably reduced the initial degradation of J_{SC}, while the pace of the linear decay remains similar for all devices. More precisely, samples with PEDOT:PSS exhibited a lifetime of ~10 h compared to ~600 h obtained for devices employing MoO_3. Device lifetime in our study is defined as the time to reach 80% of the initial efficiency (T80). Furthermore, deposition of MoO_3 on the PEDOT:PSS layer reduced the decay rate of J_{SC} compared to only PEDOT:PSS sample. As the fast degradation is not completely impeded, the conclusion is not straightforward, but it clearly implies that direct reaction between the active layer and the PEDOT:PSS is not the cause of the degradation. It seems that MoO_3 acts as a protective layer here, either to oxygen and humidity diffusion in the PEDOT:PSS layer or diffusion from the PEDOT:PSS towards other layers/interfaces in the device.

Exchanging the Yb/Al cathode with a Ca/Al stack, which is known to be even more reactive towards atmospheric gases, led to both qualitatively and quantitatively the same J_{SC} degradation as Yb/Al (Fig. 4) [26]. Even though the degradation in current density is similar, devices with Ca/Al electrode also exhibit a linear degradation of the FF over time, unlike cells with Yb/Al (see Fig. S13 in the Supplementary information). This discrepancy might be explained by the difference in the properties of their oxide,

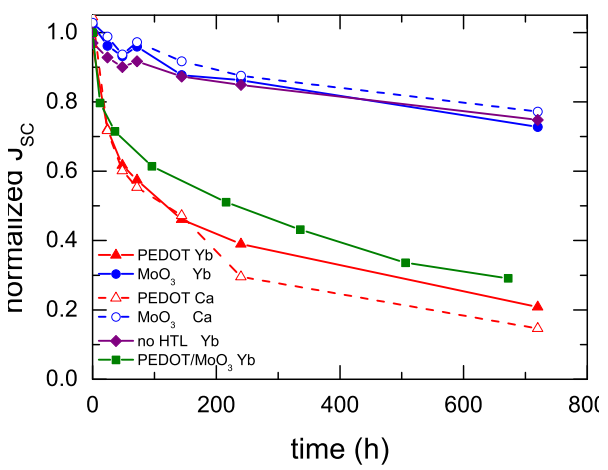

Fig. 4. Normalized current density degradation recorded on devices with identical P3HT:PCBM active layer and different hole transport layers (full lines) or metal cathodes (dashed lines) as indicated in the legend.

but further investigation of this property is out of scope of this paper.

Although these results initially suggest the degradation of the hole transport layer, low work function metals are also known to be inherently unstable in ambient conditions. Thus in an effort to elucidate the exact degradation mechanism, we continued by investigating the degradation of the metal cathode in a complete device stack by delaminating and subsequently re-depositing the electrode. Since the adhesion between the organic and metal layer proved to be strong, delamination of the electrodes with simple peeling process with tape was impossible. Therefore, we inserted a thin layer of C_{60} between the organic and the metal layer, which considerably reduces the adhesion of the metal resulting in a clean delamination process. In a control experiment we verified that the insertion of the C_{60} layer does not impact the device degradation (see Fig. S4 in the Supporting information). Then, by the re-deposition of a fresh electrode on the aged device stack, we could fully recover J_{SC} and the series resistance of the device as presented in Fig. 5. We also confirmed that the recovered performance is not due to outgasing of the aged organic layers in vacuum during the fresh electrode deposition. Therefore, this result proves that the hindered charge extraction in these devices stems from the oxidation of the low work function metal cathode and its subsequent contact with the underlying organic layers, while degradation of the hole transport layer can be excluded.

To further confirm the previous results, we exposed the ITO/PEDOT:PSS and ITO/PEDOT:PSS/P3HT:PCBM stacks to ambient conditions prior to the deposition of the subsequent layers. As the metal cathode provides a barrier to oxygen and humidity diffusion, the uncapped samples experience accelerated ageing conditions. Nevertheless, in both stacks the J_{SC} remains 8–9 mA/cm^2, even after prolonged exposure (see Fig. S5 in the Supporting information).

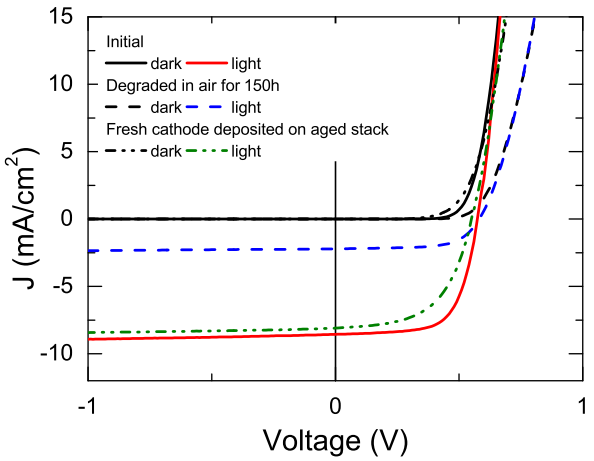

Fig. 5. Current density–voltage measurement of ITO/PEDOT:PSS/P3HT:PCBM/C_{60}/Yb/Al device stack as produced (red full), degraded in ambient conditions for 150 h with the original cathode (blue dashed) and with a fresh cathode (green dash-dot). On the degraded device stack, the cathode (Yb/Al) was delaminated and a fresh one was evaporated. (For interpretation of the references to color in this figure legend, the reader is referred to the web version of this article.)

This series of experiment confirms that the low work function metal cathode oxidation is the primary cause of degradation and, perhaps more importantly, that the hole transport layer extensively determines the pace of this degradation. Consequently, our conclusions differ from previous reports as we demonstrated that the PEDOT:PSS layer and its associated interfaces are not the main cause of degradation [23,24]. These electrical measurements are also supported by cross-sectional analysis of the device stack with transmission electron microscopy (TEM). We observed a 10–15 nm thick Yb_2O_3 layer at the metal–organic interface but clearly no sign of delamination at the interface, contrary to devices with Ca/Al cathodes [17]. This can be explained by the nature of Yb_2O_3, which forms a dense oxide layer with a comparable volume as the metal, while oxidized Ca has a significantly reduced volume resulting in void formation [26]. Furthermore, these TEM images do not show any alteration of the anode-HTL or HTL-active layer interface (see Fig. S6 in the Supporting information).

3.3. Impact of humidity on device degradation

To elucidate a detailed mechanism of the cathode oxidation accelerated by PEDOT:PSS, we pursued our investigation by focusing on different properties of PEDOT:PSS, namely the impact of its acidity and hygroscopic nature. The high acidity of the commonly used PEDOT:PSS has long been assumed to be harmful, it is surmised to etch the ITO layer resulting in Indium (In) leaching into the organic layers [29,30]. In contrast, Kok et al. reported no improvement in OLEDs lifetime with the neutralization of the PEDOT:PSS [30]. To assess the impact of PEDOT:PSS acidity, we used modified PEDOT:PSS with pH 5 and pH 7 as substitute in the reference device architecture. Devices with identical PEDOT:PSS thickness yielded similar initial efficiencies and presented comparable device degradation both for standard PEDOT:PSS and its neutral version (results shown in Fig. S7 in the Supporting information). Thus, the acidity of the PEDOT:PSS does not appear to be a contributing factor. Furthermore, energy dispersive X-ray spectroscopic (EDS) analysis on a degraded cell with the standard, acidic PEDOT:PSS only detected 2–7 at.% of Na^+ cations, while no traces of In were observed (see Fig. S6c in the Supporting information). The Na^+ cation is a residual product of the synthesis [31], and its potential impact on device degradation is unknown. This result is also in agreement with the previous experiment where we could completely recover device performance with a re-deposited cathode.

Another problem associated with PEDOT:PSS is its hygroscopic nature, meaning that in the presence of moisture it takes up water [31,32]. The impact of the hygroscopic nature of the PEDOT:PSS is investigated by ageing devices both with PEDOT:PSS and MoO_3 HTLs in dry air. The initial fast decrease of the J_{SC} of reference devices with PEDOT:PSS under ambient conditions is entirely impeded in the dry air and they exhibit identical degradation as the samples with MoO_3 shown in Fig. 6. This indicates that the hygroscopy of PEDOT:PSS clearly accelerates device degradation in the first phase of the degradation.

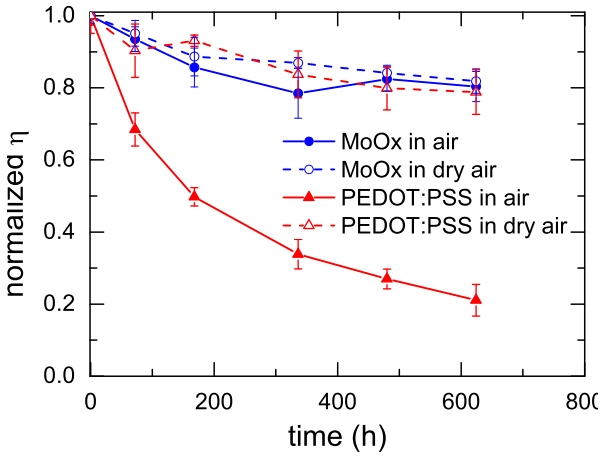

Fig. 6. Normalized efficiency degradation of devices with either PEDOT:PSS (red triangles) or MoO_3 (blue circles) as hole transport layer in ambient conditions (∼35% RH) and dry air (⩽5% RH). (For interpretation of the references to color in this figure legend, the reader is referred to the web version of this article.)

Additionally, the negligible difference of the presence of humidity on the samples with MoO_3 proves the stability of the active layer and the metal cathode even in presence of moisture. Krebs et al. similarly observed that standard devices degrade faster in presence of humidity, while inverted devices interestingly behave opposite [33,34].

As a conclusion of these experiments we can extend the description of the degradation mechanism: the hygroscopic PEDOT:PSS attracts ambient humidity and enables its diffusion under the electrodes. The release of this absorbed water towards the highly reactive metal cathode leads to the rapid oxidation of the cathode. In addition, low work function metals are known to be more reactive towards humidity than oxygen. Without this additional pathway for moisture diffusion, the metal cathode oxidizes at a considerably lower pace, as the thick Al layer proves to be a good barrier.

3.4. Edge diffusion

Interestingly, humidity infiltration can be visually observed in our devices as shown in the pictures of Fig. 7a. Optical microscope images observed through the glass substrate show the intersection of the ITO lines with the Yb/Al cathodes. We distinguish a progressive color change from the edges towards the inner regions. The inner regions, with a darker color, are the electrically active zones, while the outer brighter regions do not contribute to the current, as shown by illumination masking. This visual aspect of the degradation permits to correlate the degradation in J_{SC} to the decrease in active area. As presented in Fig. 7a, the J_{SC} degradation is directly proportional to the shrinking area. In devices without PEDOT:PSS, a similar color change is observed from the edges at a considerably lower progression rate. Alteration of the device stacks color can be ascribed to different origins: oxidation of the metal cathode, change in the optical properties of the organic layers or humidity infiltration. We could exclude the first reason by detecting a similar color change in samples with Au/Al cathode. Furthermore UV–vis absorption did not allow us to detect any alteration of the transmission of the organic layers exposed to air. Another reason to this color change could be the de-doping of the PEDOT:PSS layer, but we neither observe the degradation of its electrical properties nor arousal of a characteristic absorption peak around 620 nm [35]. Direct proof of humidity infiltration from the edges was found by biasing the samples at high reverse voltage: indeed, this treatment resulted in bubble formation in the outer region of the active areas, exactly where the color change occurred (see Figs. S8 and S9 in the Supplementary information). Such bubble formation was reported in OLEDs to be due the electrolysis of water leading to gas formation, which then diffused to the organic/metal interface and formed dome-like structures [36,37].

These visual observations prove that the metal cathode is an effective barrier to humidity diffusion, with most entering via the edges. Therefore, increasing the perimeter

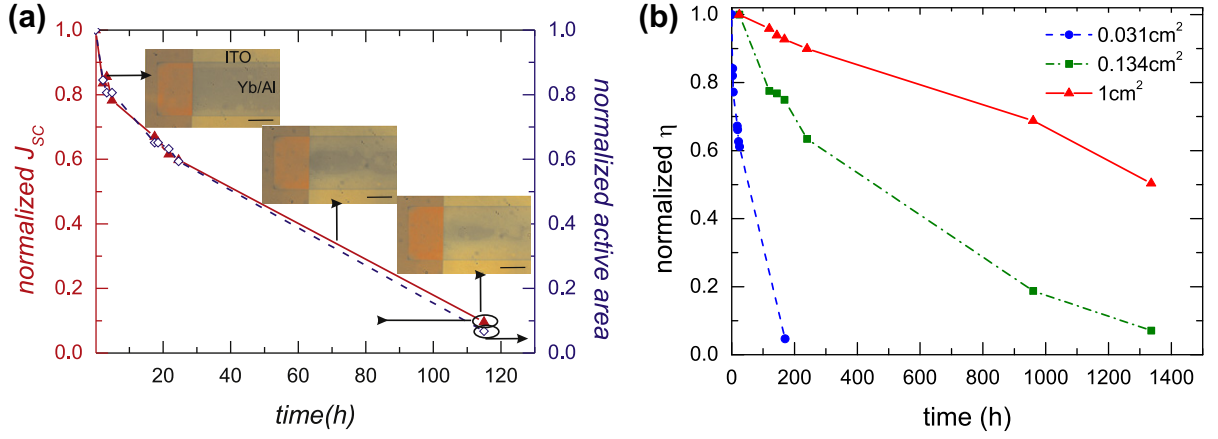

Fig. 7. (a) Normalized current density (red triangles) degradation on standard devices with 0.031 cm^2 active area, correlated with simultaneous active area degradation (blue diamonds). The scale bars correspond to 0.5 mm on the optical microscope images. The active area degradation is estimated from the microscope images, where the inner darker region is the electrically active zone. (b) Normalized efficiency degradation on standard devices with three different active areas: 0.031 cm^2 (blue circles), 0.134 cm^2 (green squares) and 1 cm^2 (red triangles) in ambient conditions. (For interpretation of the references to color in this figure legend, the reader is referred to the web version of this article.)

versus active area ratio can considerably enhance device lifetime as presented in Fig. 7b. Identical reference devices are fabricated, where the active device area is scaled by varying the size of the metal cathode and the ITO lines. Device lifetime increases from a few hours to hundreds of hours by simply scaling the device area from 0.03 to 1 cm^2. Furthermore, one should also note that infiltration through pinholes is not fully negligible; hence particle-free processing is also indispensable for reproducibly enhanced device stability. Moreover, this detailed assessment of the most relevant processing and experimental parameters on device degradation can also explain the origin of the variations in lifetime reported on similar devices by different research groups.

3.5. Accelerated shelf-life test

The in-depth understanding of the degradation mechanism in these conditions not only enables stability improvements, but also the definition of adequate accelerated testing conditions. For example, the ageing conditions applied in this study could be well-suited for separate evaluation of device encapsulation. Indeed, there is a direct correlation between the lifetime of standard samples exposed to ambient atmosphere in dark and the quality of the encapsulation against water vapor ingress. Our standard samples stored in nitrogen exhibit a lifetime of over 4000 h at room temperature [38]. As humidity proves to be the dominant stress factor, we investigated its impact on device lifetime. Standard samples were placed in a closed container in presence of saturated salt solutions imposing a precise humidity level. As presented in Fig. 8. Device lifetime decays exponentially with the humidity level at ambient temperature for both PEDOT:PSS and MoO_3 as HTLs. We assume that the water vapor ingress that explains the reduced lifetime with increasing humidity for MoO_3 HTL is to be located at the organic/metal interface

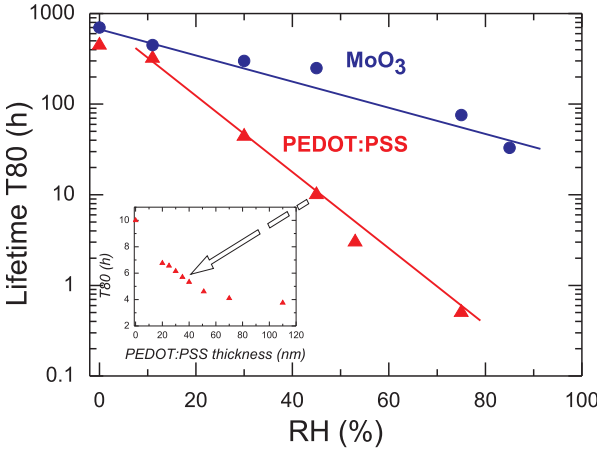

Fig. 8. Lifetime (T80) of reference samples at different humidity levels is extracted from degradation curves for devices both with PEDOT:PSS (red triangles) and MoO_3 (blue circles). The lines serve as guide to the eye. Inset: Lifetime as a function of the PEDOT:PSS layer thickness in standard devices at 42% RH. (For interpretation of the references to color in this figure legend, the reader is referred to the web version of this article.)

and to some pinholes in the metal cathode. At very low humidity levels ($\leqslant$10%), solar cells with PEDOT:PSS HTLs exhibit comparable results as MoO_3-based HTLs. At higher humidity levels, an additional diffusion mechanism seems to be activated in the case of PEDOT:PSS HTL, which is the penetration of water vapor through this HTL as shown in the previous sections. We obtained further proof of this additional pathway by scanning transmission electron microscopy (STEM) coupled with electron energy-loss spectroscopy (STEM–EELS), as an increased oxygen atom concentration was reproducibly detected only in samples that contained PEDOT:PSS and were previously exposed to air. Although the EELS data cannot distinguish between oxygen in water or other bonded state, we suppose it is a signature of the incorporation of water. To control this observation, we also analyzed samples with PEDOT:PSS and MoO_3 stored in nitrogen and in air, respectively, but none of them contained oxygen in the organic layers.

The above quantitative analysis establishes humidity as an acceleration factor for the shelf-life of devices having a low work function cathode, in our case OPV cells. Moreover, derived from the detailed understanding of the degradation mechanism, we equally identified PEDOT:PSS thickness as an acceleration factor. As presented in the inset of Fig. 8, on identical devices where only the thickness of PEDOT:PSS is varied the lifetime increases from 3 to 7 h when the thickness is scaled from 100 to 20 nm. A sample without HTL layer is represented as reference value at 0 nm. This trend obviously implies that the thickness of the PEDOT:PSS layer should be minimized, if it is not replaced by another material.

4. Conclusions

We found that the short-circuit current density degradation in devices exposed to air stems from hindered charge extraction at the cathode-organic interface. This conclusion is drawn from a set of experiments including delamination of the cathode of a degraded device and subsequent redeposition of a fresh one, in which case the initial electrical performance could be recovered. We further relate the degradation primarily to oxidation of the low work function metal cathode and we could exclude the degradation of the PEDOT:PSS layer and its associated interfaces. However, PEDOT:PSS greatly accelerates cathode oxidation due to its hygroscopic nature and it is found to promote infiltration of humidity from the device edges. Consequently this HTL layer renders conventional polymer solar cells extremely sensitive to moisture. We established an exponential relation between device lifetime and increasing humidity levels.

This detailed understanding of the degradation mechanism of OPVs in ambient atmosphere has several major implications. First, it guides further device and material optimization. Here we presented a vacuum deposited MoO_3 as an alternative HTL to enhance device stability, but recently introduced solution processed oxide layers seem also promising alternatives [39,40]. It further indicates that selection of low work function metals whose oxide is semiconducting with a conduction band close to the lowest unoccupied molecular orbital of the PCBM

may also lead to improved device stability [41,42]. Second, we propose adapted accelerated testing conditions to evaluate barrier layers and device encapsulation. The high sensitivity of the conventional device structure to moisture even at room temperature makes this ageing condition better suited than damp heat tests, where several mechanisms are activated simultaneously.

Acknowledgements

The authors acknowledge D. Cheyns, B.P. Rand and T. Aernouts for helpful discussion. P. Favia and H. Bender for TEM analysis. The work of Daniele Di Nuzzo is part of the research programme of the Dutch Polymer Institute (DPI, Project 631).

Appendix A. Supplementary data

Supplementary data associated with this article can be found, in the online version, at doi:10.1016/j.orgel.2011.01.025.

References

[1] S.E. Shaheen, D.S. Ginley, G.E. Jabbour, Organic-based photovoltaics: toward low-cost power generation, MRS Bull. 30 (2005) 10–15.
[2] C.J. Brabec, S. Gowrisanker, J.A.M. Halls, D. Laird, S. Jia, S.P. Williams, Polymer–fullerene bulk-heterojunction solar cells, Adv. Mater. 22 (2010) 3839–3856.
[3] D. Cheyns, B.P. Rand, P. Heremans, Organic tandem solar cells with complementary absorbing layers and a high open-circuit voltage, Appl. Phys. Lett. 97 (2010) 033301.
[4] C. Girotto, D. Moia, B.P. Rand, J. Genoe, P. Heremans, Highly efficient organic solar cells with sprayed hole-transport and active layers, Adv. Funct. Mater. 21 (2011) 64–72.
[5] F.C. Krebs, Fabrication and processing of polymer solar cells: a review of printing and coating techniques, Sol. Energy Mater. Sol. Cells 93 (2009) 394–412.
[6] M. Jorgensen, K. Norrman, F.C. Krebs, Stability/degradation of polymer solar cells, Sol. Energy Mater. Sol. Cells 92 (2008) 686–714.
[7] J. Lewis, Material challenges for flexible organic devices, Mater. Today 9 (2006) 38–45.
[8] C. Brabec, V. Dyakonov, U. Scherf (Eds.), Organic Photovoltaics, Wiley-VCH Verlag, 2008. volume Chapters 17 and 18.
[9] A. Rivaton, S. Chambon, M. Manceau, J.L. Gardette, N. Lamaitre, S. Guillerez, Light-induced degradation of the active layer of polymer-based solar cells, Polym. Degrad. Stab. 95 (2010) 278–284.
[10] M. Manceau, A. Rivaton, J.L. Gardette, S. Guillerez, N. Lemaitre, The mechanism of photo- and thermooxidation of poly(3-hexylthiophene) (p3ht) reconsidered, Polym. Degrad. Stab. 94 (2009) 898–907.
[11] J. Schafferhans, A. Baumann, A. Wagenpfahl, C. Deibel, V. Dyakonov, Oxygen doping of p3ht:pcbm blends: influence on trap states charge carrier mobility and solar cell performance, Org. Electron. 11 (2010) 1693–1700.
[12] A. Seemann, J.H. Egelhaaf, C.J. Brabec, J.A. Hauch, Influence of oxygen on semi-transparent organic solar cells with gas permeable electrodes, Org. Electron. 10 (2009) 1424–1428.
[13] H.H. Liao, C.M. Yang, C.C. Liu, S.F. Horng, H.F. Meng, J.T. Shy, Dynamics and reversibility of oxygen doping and de-doping for conjugated polymer, J. Appl. Phys. 103 (2008) 104506.
[14] M. Reese, A.M. Nardes, B.L. Rupert, R.E. Larsen, D.C. Olson, M.T. Lloyd, S.E. Shaheen, D.S. Ginley, G. Rumbles, N. Kopidakis, Photoinduced degradation of polymer and polymer–fullerene active layers: experiment and theory, Adv. Funct. Mater. 20 (2010) 3476–3483.
[15] F. So, D. Kondakov, Degradation mechanisms in small-molecule and polymer organic light-emitting diodes, Adv. Mater. 22 (2010) 3762–3777.
[16] M. Schaer, F. Nuesch, D. Berner, W. Leo, L. Zuppiroli, Water vapor and oxygen degradation mechanisms in organic light emitting diodes, Adv. Funct. Mater. 11 (2001) 116–121.
[17] M.T. Lloyd, D.C. Olson, P. Lu, E. Fang, D.L. Moore, M.S. White, M.O. Reese, D.S. Ginley, J.W.P. Hsu, Impact of contact evolution on the shelf life of organic solar cells, J. Mater. Chem. 19 (2009) 7638–7642.
[18] K. Norrman, S.A. Gevorgyan, F.C. Krebs, Water-induced degradation of polymer solar cells studied by h2o-o18 labeling, ACS Appl. Mater. Interfaces 1 (2009) 102–112.
[19] K. Lee, J. Kim, S. Park, S. Kim, S. Cho, A. Heeger, Air-stable polymer electronic devices, Adv. Mater. 19 (2007) 2445–2449.
[20] S.K. Hau, H.-L. Yip, N.S. Baek, J. Zou, K. O'Malley, A.K.-Y. Jen, Air-stable inverted flexible polymer solar cells using zinc oxide nanoparticles as an electron selective layer, Appl. Phys. Lett. 92 (2008) 253301.
[21] F.C. Krebs, Air stable polymer photovoltaics based on a process free from vacuum steps and fullerenes, Sol. Energy Mater. Sol. Cells 92 (2008) 715–726.
[22] T. Kuwabara, T. Nakayama, K. Uozumi, T. Yamaguchi, K. Takahashi, Highly durable inverted-type organic solar cell using amorphous titanium oxide as electron collection electrode inserted between ITO and organic layer, Sol. Energy Mater. Sol. Cells 92 (2008) 1476–1482.
[23] K. Kawano, R. Pacios, D. Poplavzkyy, J. Nelson, D.C. Bradley, J.R. Durrant, Degradation of organic solar cells due to air exposure, Sol. Energy Mater. Sol. Cells 90 (2006) 3520–3530.
[24] F.C. Krebs, J.E. Carl, N. Cruys-Bagger, M. Andersen, M.R. Lilliedal, M.A. Hammond, S. Hvidt, Lifetimes of organic photovoltaics: photochemistry, atmosphere effects and barrier layers in ITO-MEHPPV:PCBM-aluminium, Sol. Energy Mater. Sol. Cells 86 (2005) 499–516.
[25] T. Yamanari, T. Taima, J. Sakai, J. Tsukamoto, Y. Yoshida, Effect of buffer layers on stability pf polymer-based organic solar cells, Jpn. J. Appl. Phys. 49 (2010) 01AC02.
[26] D.R. Liede (Ed.), CRC Handbook of Chemistry and Physics, 85th ed., CRC Press, 2004.
[27] P.J. Brown, S.D. Thomas, A. Köhler, J.S. Wilson, J.-S. Kim, C.M. Ramsdale, H. Sirringhaus, R.H. Friend, Effect of interchain interactions on the absorption and emission of poly(3-hexylthiophene), Phys. Rev. B 67 (2003) 064203.
[28] R. sterbacka, C.P. An, X.M. Jiang, Z.V. Vardeny, Two-dimensional electronic excitations in self-assembled conjugated polymer nanocrystals, Science 287 (2000) 839–842.
[29] M.P. Jong, L.J. van Ijzendoorn, M.J.A. de Voigt, Stability of the interface between indium-tin-oxide and poly(3,4-ethylenedioxythiophene)/poly(styrenesulfonate) in polymer light-emitting diodes, Appl. Phys. Lett. 77 (2000) 2255.
[30] M.M. de Kok, M. Buechel, S.I.E. Vulto, P. van de Weijer, E.A. Meulenkamp, S.H.P.M. de Winter, A.J.G. Mank, H.J.M. Vorstenbosch, C.H.L. Weijtens, V. van Elsbergen, Modification of PEDOT:PSS as hole injection layer in polymer LEDs, Phys. Status Solidi A 201 (2004) 1342–1359.
[31] Clevios website: <http://www.clevios.com/pages/985/chemical_properties_clevios_20080314.pdf>.
[32] K. Fehse, R. Meerheim, K. Walzer, K. Leo, W. Lovenisch, A. Elschner, Lifetime of organic light emitting diodes on polymer anodes, Appl. Phys. Lett. 93 (2008) 083303.
[33] F.C. Krebs, S.A. Gevorgyan, J. Alstrup, A roll-to-roll process to flexible polymer solar cells: model studies, manufacture and operational stability studies, J. Mater. Chem. 19 (2009) 5442–5451.
[34] F.C. Krebs, S.A. Gevorgyan, J. Alstrup, Degradation patterns in water and oxygen of an inverted polymer solar cell, J. Am. Chem. Soc. 132 (2010) 16883–16892.
[35] J.S. Kim, P.K.H. Ho, C.E. Murphy, N. Baynes, R.H. Friend, Nature of non-emissive black spots in polymer light-emitting diodes by in-situ micro-Raman spectroscopy, Adv. Mater. 14 (2002) 206–209.
[36] B.C. de Brito, E.C.P. Smits, P.A. van Hal, T.C.T. Geuns, B. de Boer, C.J.M. Lasance, H.L. Gomes, D.M. de Leeuw, Ultralow power microfuses for write-once read-many organic memory elements, Adv. Mater. 20 (2008) 3750–3753.
[37] S.C. Luo, H.H. Chung, E.T. Pashuck, E.P. Douglas, P.H. Holloway, Formation of bubbles on electrical contacts to polymer light-emitting diode devices, Thin Solid Films 478 (2005) 326–331.
[38] E. Voroshazi, B. Verreet, T. Aernouts, P. Heremans, Long-term operational lifetime and degradation analysis of P3HT:PCBM photovoltaic cells solar energy materials and solar cells, Sol. Energy Mater. Sol. Cells (2010) (early view).
[39] M.Y. Lin, C.y. Lee, S.C. Shiu, I.J. Wang, J.Y. Sun, W.H. Wu, Y.H. Lin, J.S. Huang, C.F. Lin, Sol–gel processed CuOx thin film as an anode interlayer for inverted polymer solar cells, Org. Electron. 11 (2010) 1828–1834.

[40] F. Liu, S. Shao, X. Guo, Y. Zhao, Z. Xie, Efficient polymer photovoltaic cells using solution-processed MoO_3 as anode buffer layer, Sol. Energy Mater. Sol. Cells 94 (2010) 842–845.
[41] M. Wang, Q. Tang, J. An, F. Xie, J. Chen, S. Zheng, K.Y. Wong, Q. Miao, J. Xu, Performance and stability improvement of P3HT:PCBM-based solar cells by thermally evaporated chromium oxide (CrOx) interfacial layer, ACS Appl. Mater. Interfaces 2 (2010) 2699–2702.
[42] B. Zimmermann, U. Wurfel, M. Niggemann, Longterm stability of efficient inverted P3HT:PCBM solar cells, Sol. Energy Mater. Sol. Cells 93 (2009) 491–496.

the sputter-patterned ITO edges. Such an insulating organic molecule is preferred to have low carrier (both electron and hole) mobility. It is demonstrated that the reverse current density of OLEDs based on this scheme is comparable to that of photolithography-patterned ITO-based OLEDs.

2. Results and discussion

For a comparative study, we have used two different ITO-coated glass substrates. One was purchased from Shinan SNP Co. Ltd., showing the sheet resistance of 12 Ω/□. The other one was fabricated using a sputtering deposition system (SUNICOAT-IS3000, SUNIC SYSTEM) under the DC power of 500 W and at the substrate heater temperature of 250 °C. The sputtered ITO at the rate of 2.3 Å/s exhibits the sheet resistance of 17 Ω/□. The commercial ITO was patterned using the standard photolithography process with or without a patterned polyimide insulation layer (TORAY, Photoneece™ DL-1602). In this paper, a device fabricated based on this method is referred to as a photolithography-patterned and insulator-coated (or insulator-uncoated) ITO-based OLED (PP/IC-OLED or PP/IU-OLED). Meanwhile, the sputtered ITO was patterned using a metal open mask during deposition. To make a comparison with PP/IC- and PP/IU-OLEDs, the sputter-patterned ITO edges were covered with the patterned polyimide insulation layer (Fig. 1(a)). A device fabricated based on this method is named as a sputter-patterned and insulator-coated ITO-based OLED (SP/IC-OLED), whereas a device fabricated based on this method with the insulator excluded is named as a sputter-patterned and insulator-uncoated ITO-based OLED (SP/IU-OLED) (Fig. 1(b)). In replacement of the polyimide insulation layer, thermally evaporated insulating organic molecules can be employed to cover the sputter-patterned ITO edges. A device fabricated based on this method is referred to as a sputter-patterned ITO-based and insulator-evaporated OLED (SP/IE-OLED) (Fig. 1(c)). In the SP/IE-OLED configuration, the insulating organic layer can be evaporated either right on the ITO edges or right before the cathode layer. It is noted that the insulating organic molecule evaporated right on the ITO edges should have low hole mobility (i.e., blocking hole injection), whereas it should have low electron mobility when evaporated right before the cathode (i.e., blocking electron injection).

We have fabricated phosphorescent green OLED devices that consist of a 10-nm-thick LG-101 for a hole injection layer (HIL), 25-nm-thick 4,4′-bis[*N*-(1-nathyl)-*N*-phenylamino]biphenyl (NPB) for a hole transport layer (HTL), 25-nm-thick 4,4′-*N*,*N*′-dicarbazolylbiphenyl (CBP) doped with tris(2-phenylpyridinate) iridium(III) ($Ir(ppy)_3$, 8 wt.%) for an emitting layer (EML), 10-nm-thick m-bis-(triphenylsilyl)benzene (UGH3) for a hole/exciton blocking layer (HBL), 30-nm-thick (2,9-dimethyl-4, 7-diphenyl-1, 10-phenanthroline) (Bphen) for an electron transport layer (ETL), 1-nm-thick lithium fluoride (LiF) for an electron injection layer (EIL), and 100-nm-thick aluminum (Al). In SP/IE-OLEDs, NPB is used as an insulating material, which has very low electron mobility ($\sim 1 \times 10^{-8}$ cm^2/Vs) [13]. The sheet resistance, surface roughness, and cross-sectional image of ITO were measured by aging package (Mcscience Polaronix, M6101), atomic force microscopy (AFM, XE-200 system, PSIA), and field emission scanning electron microscope (FE-SEM, Quanta 200FEG, FEI Co.), respectively.

As depicted in Fig. 1, the width of the photolithography- and sputter-patterned ITOs is 4 mm. The Al cathode has the same width as the patterned ITO anode. Insulator-coated ITO-based OLEDs (PP/IC- and SP/IC-OLEDs) have the emission area of 2×2 mm. Meanwhile, insulator-uncoated ITO-based OLEDs (PP/IU- and SP/IU-OLEDs) have the emission area of 4×4 mm. As such, the leakage

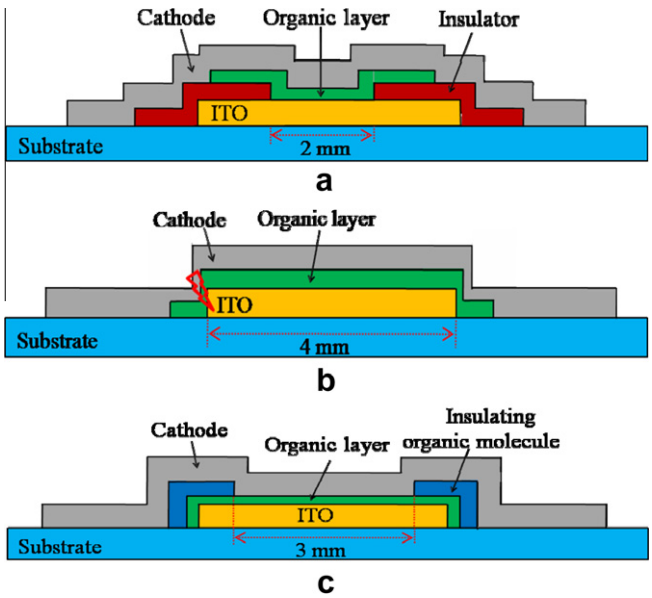

Fig. 1. Cross-sectional view of (a) SP/IC-OLED, (b) SP/IU-OLED, and (c) SP/IE-OLED structures.

current is expected to occur on the slope of the ITO edges. In SP/IE-OLEDs, the insulating NPB layer is deposited before the Al cathode, with the width of 1 mm centered at the ITO edges and with the length of 5 mm. Therefore, the emission area of SP/IE-OLEDs is as large as 3×4 mm. It is noteworthy that as the emission area of those devices is all different, a direct comparison should be made at the same current density or the current density instead of the current should be considered.

Shown in Fig. 2(a)–(c) are the images of green light emission from those devices (SP/IC-, SP/IU-, and SP/IE-OLEDs) when the current density is 10 mA/cm^2. It is clearly seen to the naked eye that the SP/IE-OLED has smaller emission area (3×4 mm) than the SP/IU-OLED (4×4 mm), indicating that the insulating organic molecule prevents the current flow effectively near the ITO edges. Fig. 2(d) shows the current efficiency of those devices as a function of the current density. Summarized in Table 1 are the luminance and current efficiency of those devices at a current density of 10 mA/cm^2. As expected, the PP/IC-OLED is shown to have the highest luminance (6114 cd/m^2) and current efficiency (54 cd/A). A small reduction (2 cd/A) in the current efficiency appears on the PP/IU-OLED due possibly to increased leak channels. Though the emission area is increased four times, yet the leakage current is little increased for photolithography-patterned ITO-based OLEDs. Meanwhile, the SP/IC-OLED shows slightly lower current efficiency (51.2 cd/A at 10 mA/cm^2) than the PP/IC-OLED. It may arise from the fact that the sheet resistance (17 Ω/□) of the sputtered ITO is higher than that (12 Ω/□) of the commercial ITO. However, the current efficiency is substantially reduced (39.6 cd/A at 10 mA/cm^2) in the SP/IU-OLED. Considering that the emission area of the SP/IU-OLED is the same as that of PP/IU-OLED, such a large

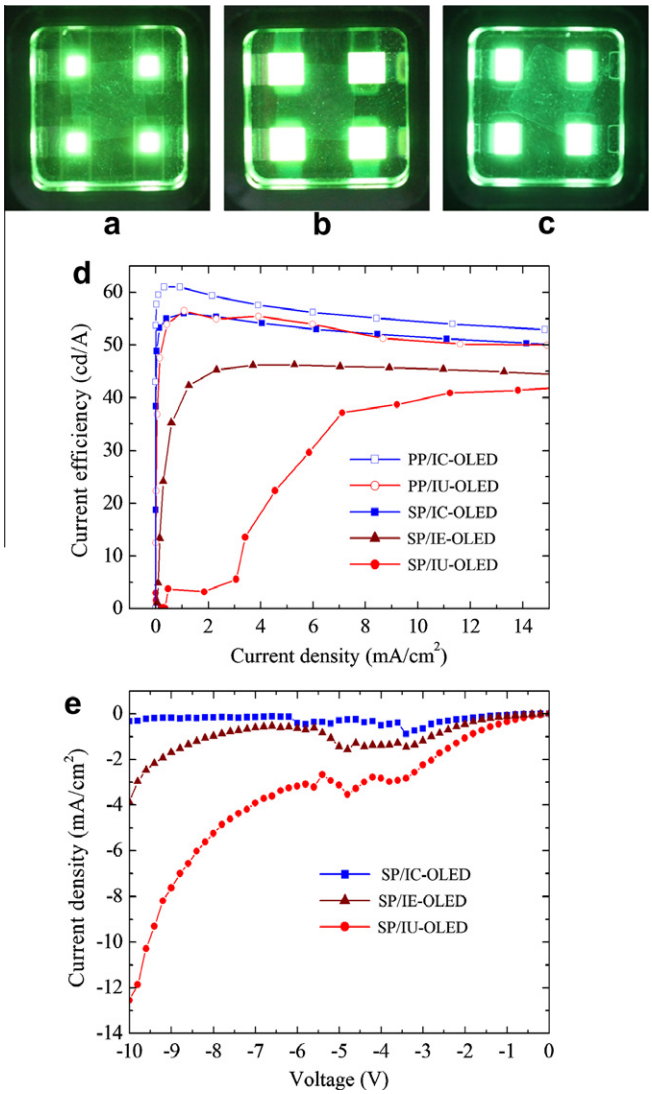

Fig. 2. Images of green light emission from (a) SP/IC-OLED, (b) SP/IU-OLED, and (c) SP/IE-OLED at 10 mA/cm^2, (d) measured current efficiency versus current density, and (e) reverse current density versus bias voltage. The insulating organic (NPB) layer of SP/IE-OLED is as thick as 50 nm.

Table 1
Measured luminance and current efficiency of those devices at a current density of 10 mA/cm^2.

@10 (mA/cm^2)	PP/IU OLED	PP/IC OLED	SP/IU OLED	SP/IC OLED	SP/IE OLED
Luminance (cd/m^2)	5837	6114	4062	5685	4983
Current efficiency (cd/A)	52	54	39.6	51.2	45.4

reduction (52 cd/A → 39.6 cd/A) in the current efficiency is due most likely to the rough surface state of the ITO edges. From the results in Fig. 2(d), we can see that the leakage current can be suppressed to a great extent by evaporation of insulating organic molecules (SP/IE-OLED), especially at low current density (<10 mA/cm^2) or below the luminance of 5000 cd/m^2.

The leakage current is further demonstrated by measuring the current density of those devices under the reverse

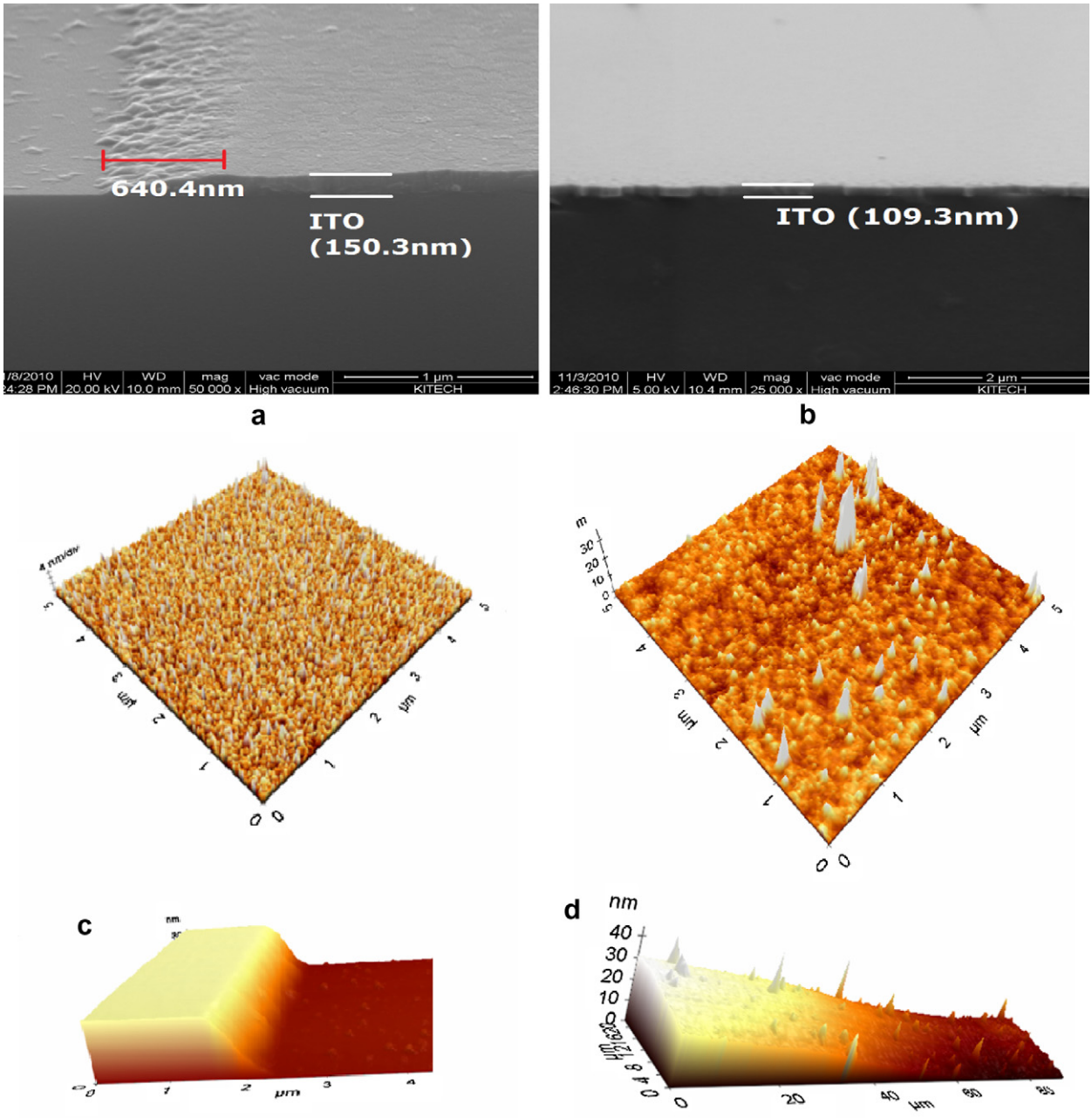

Fig. 3. FE-SEM images of (a) photolithography-patterned ITO and (b) sputter-patterned ITO and AFM images of (c) photolithography-patterned ITO and (d) sputter-patterned ITO (scanning area of 5 × 5 μm).

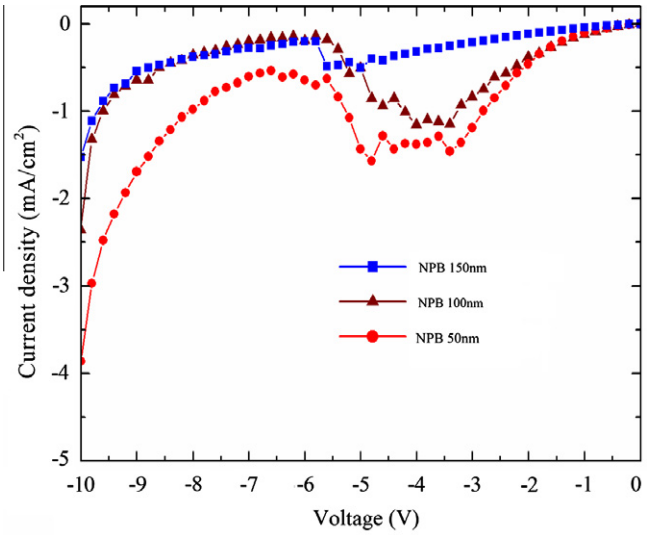

Fig. 4. Measured reverse current density of SP/IE-OLEDs for different thicknesses of insulating NPB molecule.

bias condition (from 0 V to −10 V). As shown in Fig. 2(e), significant leakage current occurs in the SP/IU-OLED device. Such leakage current is substantially suppressed in the SP/IE-OLED device. The reverse current density of SP/IC-OLED, SP/IE-OLED, and SP/IU-OLED is measured to be 118 μA/cm^2, 537 μA/cm^2, and 3.6 mA/cm^2, respectively, at the reverse bias voltage of 6.6 V. Within the range between 0 V and −7 V, the reverse current density of SP/IE-OLED is comparable to that of SP/IC-OLED, indicating that the insulating organic molecule prevents the flow of leakage current as effectively as the polyimide insulation material.

It appears that the leakage current is highly related with the surface morphology of ITO, especially on the slope of the ITO edges. To investigate it, we have measured the cross-sectional image and the surface morphology of the patterned ITOs and presented the results in Fig. 3. It was observed that the photolithography-patterned ITO has a very steep slope (the slope length is about 0.64 μm), whereas the sputter-patterned ITO has a very gentle slope (the slope length is about 400 μm). The gentle slope of the sputter-patterned ITO edges is induced by the spatial distance (5.5 cm) between the metal open mask and the substrate in the in-line sputter. The slope length could be reduced further by placing them more closely. Due to their gentle slope, we are capable of measuring the surface morphology of the sputter-patterned ITO on the slope of the ITO edges, though the whole ITO slope cannot be measured by FE-SEM. The SEM image in Fig. 3(b) was measured on the sputter-patterned ITO slope. It is likely that the ITO thickness (109.3 nm) measured on the slope is a little smaller than that (150 nm) on the flat surface. Meanwhile, we have measured the surface morphology of the photolithography-patterned ITO near the ITO edges. From Fig. 3(c) and (d), grain structure of ITO surfaces are clearly confirmed. It is evident that many rugged regions appear on the sputter-patterned ITO slope during the sputtering process. While the surface morphology of the photolithography-patterned ITO is good, with a root mean square roughness (R_{rms}) of 1.13 nm and peak to valley roughness (R_{pv}) of 10.01 nm, the surface roughness of the sputter-patterned ITO is poor, with R_{rms} of 1.837 nm and R_{pv} of 39.028 nm. A high R_{pv} indicates the existence of spikes. In Fig. 3(d), several spikes that have very large height were observed. Spike-like surface induces more injection of holes into the device, which may increase the chance of causing a short-circuit problem. It is known that R_{pv} rather than R_{rms} directly affects a leakage current under reverse bias condition [14,15]. Therefore, more leakage current appears in SP/IU-OLEDs due to high R_{pv}. In other words, non-emissive current component exists at the rugged edges of the electrode. Another cause for the occurrence of more leakage current in SP/IU-OLEDs lies in the gentle slope of the patterned ITO edges (i.e., broader spiky surface). Since the surface morphology of the photolithography-patterned ITO is relatively good, it was found that the current efficiency of the PP/IU-OLED was comparable to that of the PP/IC-OLED (Table 1).

With attempt to investigate further the effect of the insulating organic layer on the leakage current of SP/IE-OLEDs, we have varied its thickness and measured the reverse leakage current. As shown in Fig. 4, less leakage current occurs with increasing insulating organic layer thickness. It indicates that thicker insulating organic layer prevents more effectively the flow (or injection) of electrons through (into) the slope of the ITO edges. It is noteworthy that any organic molecules such as hole injecting, hole transporting, and electron transporting materials can be used as an insulating material given that their electron or hole mobility is low enough to suppress leakage current. Ideally, organic molecules that have both low electron and hole mobility are preferred. This scheme allows us to implement an in-line type organic evaporation system that does not require any photolithography process, thereby bringing in a reduction of a tact time and fabrication cost.

3. Conclusion

We have shown that, without a standard photolithography process, ITO can be patterned by a sputtering deposition and thermal evaporation of an insulating organic molecule. OLEDs based on this scheme exhibit much less leakage current, which is even comparable to that of photolithography-patterned ITO-based OLEDs. The most salient feature of this technique is that it is applicable to in-line type organic evaporation system, a reduction of fabrication cost by which is feasible.

References

[1] K. Leo, Science 310 (2005) 1762.
[2] Y. Sun, N. Giebink, H. Kanno, B. Wa, M.E. Thompson, S.R. Forrest, Nature (London) 440 (2006) 908.
[3] J. Kido, SID 08 (2008) 931.
[4] Joerg Amelung, <http://spie.org/x23960.xml>.
[5] LEDs Magazine, December 2007. <http://www.ledsmagazine.com/news/4/12/30>.
[6] B. D'Andrade, J. Esler, C. Lin, M. Weaver, J. Brown, SID08 Digest (2008) 940.
[7] <http://www.oled-display.net>.
[8] C.C. Wu, C.I. Wu, J.C. Sturm, A. Kahn, Appl. Phys. Lett. 70 (1997) 1348.
[9] F. Nuesch, E.W. Forsythe, Q.T. Le, Y. Gao, L.J. Rothberg, J. Appl. Phys. 87 (2000) 7973.
[10] H.-C. Hsieh, S.-C. Chang, Y.-M. Tsai, SID'03 Digest Tech. (2003) 498.
[11] Z. Wang, S. Naka, Hiroyuki, Thin Solid Films 518 (2009) 497.
[12] C. Jonda, A.B.R. Mayer, U. Stolz, A. Elschner, A. Karbach, J. Mater. Sci. 35 (2000) 5645.
[13] J.W. Park, IEEE/OSA J. Lightwave Tech. 28 (2010) 2873.
[14] Y.H. Tak, K.B. Kim, H.G. Park, K.H. Lee, J.R. Lee, Thin Solid Films 411 (2002) 12.
[15] K.B. Kim, Y.H. Tak, Y.S. Han, K.H. Baik, M.H. Yoon, M.H. Lee, Jpn. J. Appl. Phys. 42 (2003) L439.

and biological sensing has been demonstrated by an integrated semiconductor device consists of an excitation source, a photo detector (PD), and a sensing unit [8]. So far, the integrated semiconductor devices were used to detect glucose [9] and oxygen [8,10]. A sensor specific to NO has not been realized mainly because there is no sensing film for NO. In our recent work, a NO sensing hydrogel film was demonstrated possessing high selectivity, sensitivity, and stability in various pH values which could be used as the sensing unit for NO [11]. But so far no trial has been done to use the NO sensing film as the sensing unit. Besides, to miniaturize the integrated semiconductor device, a small-sized organic light-emitting diode (OLED) was used in glucose [9] and oxygen [8,10] sensor. However, the NO sensing film was characterized with a solid-state laser diode module as an excitation source, and no work has been done to show the NO sensing characteristics using OLED as an excitation source. Furthermore, unlike the laser with narrow emission spectrum, the emission spectrum of the OLED excitation light is broad, and hence the separation of reflected excitation light and the emission of the sensing unit is important in order to reduce the influence of the tail of excitation light on the emission of the sensing unit. However, optical filters based on glass substrate is conventionally used which is expensive and occupies volumes [8–10]. Light separation was never achieved in an easy way.

In this work, a NO sensor is realized for the first time by integrating a sensing hydrogel film specific to NO with a top-emitting polymer light-emitting diode (PLED), silicon (Si) PD, and two organic filters as shown in Fig. 1(a). The top-emitting PLED is used to excite the sensing hydrogel film, and the small-sized Si PD is used to detect the photoluminescence (PL) of the sensing hydrogel film. The influence of the tail of excitation light on the emission of the sensing unit is reduced by using two organic filters. Filter 1 is deposited above the transparent cathode of the top-emitting PLED to filter out the wavelength of the excitation light around the emission peak of the sensing hydrogel film. Filter 2 is placed in front of the Si PD to remove the light other than the sensing hydrogel film. The sensing film specific to NO developed in our group [11] is utilized as the sensing unit. The PL of the NO sensing hydrogel film changes after adsorbing NO, and such change in PL can be monitored by Si PD. Light signal is therefore transformed into electric signal for recording. Real-time and indicator-free detection of NO is demonstrated. All components except the NO sensing film can be sealed inside a water-proof container with electrical feedthroughs for driving PLED and monitoring photocurrent outputs from Si PD. The photocurrent response with response time within 5 min is demonstrated. In practice, after each usage, the sensing hydrogel film is the only component that needs to be replaced.

2. Experimental

Top-emitting PLED is fabricated on cleaned glass substrate. Schematic device structure and the image of the top-emitting PLED under forward bias are shown in Fig. 1(b) and (c), respectively. Aluminium (Al)/molybdenum oxide (MoO_3)/poly(3,4-ethylenedioxythiophene):

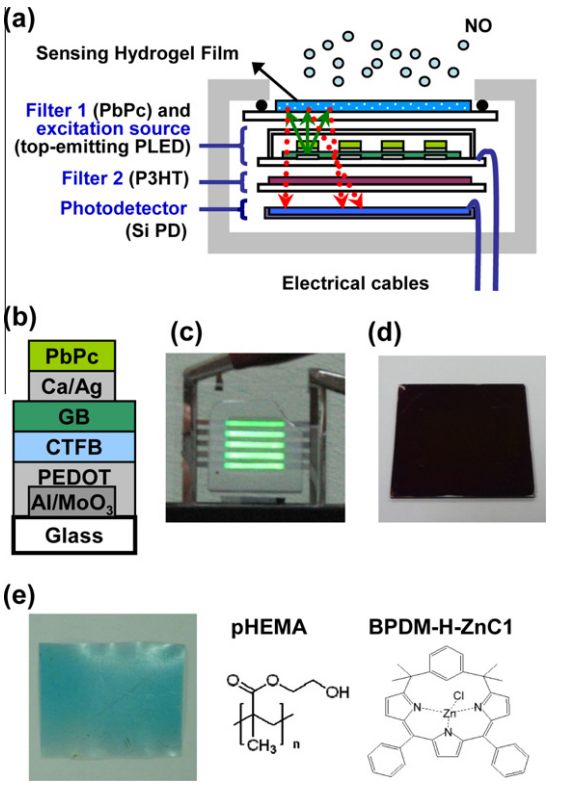

Fig. 1. (a) The schematic structure of the sensor integrated with a sensing hydrogel film, a top-emitting PLED, a Si PD, and two organic filters. (b) Device structure of the top-emitting PLED. PbPc is deposit on transparent cathode serving as filter. (c) Photograph of the top-emitting PLED. (d) Photograph of the P3HT filter. (e) Photograph of the sensing hydrogel film composed of pHEMA and BPDM–H–ZnC1. Molecule structures of pHEMA and BPDM–H–ZnC1 are also shown.

poly(styrenesulfonate) (PEDOT:PSS) is used as an opaque anode. A striped-type shadow mask is used for preparing Al (100 nm) and MoO3 (3 nm). PEDOT:PSS (CLEVIOS^{TM} P VP AI 4083) of 40 nm is then spin coated and annealed at 200 °C for 15 min. On top of the PEDOT:PSS surface, the PLED structure is cross-linkable TFB (20 nm)/Green B (65 nm)/Ca (10 nm)/Ag (15 nm)/PbPc (200 nm). The hole transport layer of cross-linkable poly[(9,9-dioctylfluorenyl-2,7-diyl)-co-(4,4′-(*N*-(p-butylphenyl))diphenylamine)] (CTFB) (in toluene) is formed by spin coating and then baked at 180 °C for 60 min. The emitting layer is also formed by spin coating polyfluorene derivative LUMATION Green B (GB) by Dow Chemical (in toluene) and then baking at 130 °C for 30 min. The transparent cathode Ca/Ag and lead phthalocyanine (PbPc) are deposited with striped-type shadow mask. Each active area is about 1 mm × 10 mm, and the width of gap between each active area is 1 mm. During the real-time detection, the luminescence of the top-emitting PLED is kept at 1600 cd/m^2. Fig. 1(d) shows 250 nm poly(3-hexylthiophene) (P3HT) Filter 2 prepared by drop casting P3HT dichlorobenzene solution on glass substrate. The sensing hydrogel film is a blend of host polymer poly(2-hydroxyethyl methacrylate) (pHEMA) and fluorescent probe 11,16-bisphenyl-6,6,21,21-tetramethyl-*m*-benzi-6,21-porphodimetheno-chloro-Zinc(II)

(BPDM–H–ZnCl). The image of the sensing hydrogel film and molecular structures of pHEMA and BPDM–H–ZnCl are shown in Fig. 1(e). BPDM–H–ZnCl (2 mg) is first dissolved in a mixture (10 ml) of 2-hydroxyethyl methacrylate (HEMA), ethylene glycol dimethacrylate (EGDMA), and azobisisobutyronitrile (AIBN), and then the blending solution is poured into a Teflon cell and annealed at 80 °C for 10 min to form a film of 180 micrometer. HEMA is used as a hydrophilic monomer, EGDMA is used as a hydrophobic cross-linker, and AIBN (1%) is used as thermal initiator. HEMA is blended with EGDMA in the weight ratio 12:1. BPDM–H–ZnCl is synthesized from *m*-benziporphodimethene based molecule.[12] The real-time detection of NO is carried out with a polydimethylsiloxane (PDMS) microfluidic system.[13] The dimension of the channel is $30 \times 15 \times 1$ mm (length × width × height). The PDMS with a sheet of sensing hydrogel film in the channel is sealed with a glass slide. Fluid inlet and outlet are located at two ends of the channel. NO bubbled water is prepared by bubbling 1000 ppm NO (in N_2 carrier gas) into DI water for 1 h. The electroluminescence (EL) spectra and current–luminance–voltage (*I–L–V*) characteristics of top-emitting PLED are measured by a Photo Research PR650 spectrophotometer integrated with Keithley 2400 multi-meter. Absorption spectra are recorded by Hewlett–Packard 845X UV–visible system. Emission spectrum of sensing hydrogel film is monitored by high resolution fiber optic spectrometer (EPP2000, StellarNet). Si PD (S2387, Hamamatsu Photonics), sensitive from visible light to infrared light, is biased at −10 V by Keithley 2400 multi-meter to monitor the photocurrent. In some experiment, 405 nm laser diode (Power Technology) is used to excite sensing hydrogel film.

3. Results and discussion

The selectivity of BPDM–H–ZnC1 is demonstrated in Fig. 2(a) and (b). Various gases are bubbled into 2×10^{-6} M BPDM–H–ZnC1 acetonitrile solution for 2 min. No dramatic difference in PL spectrum can be observed after bubbling oxygen (O_2), carbon dioxide (CO_2), and carbon monoxide (CO). A decrease in PL is observed only after bubbling NO. BPDM–H–ZnC1 is specific to NO and it does not react with O_2 and CO_2 in the atmosphere and another important signalling molecule CO. In addition, since nitrate (NO_3^-) and nitrite (NO_2^-) are end products of NO metabolism, nitrate donor (PPN(NO_2)) (PPN: bis(triphenylphosphine)iminium) and nitrite donor (PPN(NO_3)) are added into BPDM–H–ZnCl solution to test the influence of nitrate and nitrite on the PL intensity. Hydrogen peroxide (H_2O_2), another free radical in human body, is also tested. *S*-nitroso-*N*-acetylpenicillamine (SNAP) is used as NO donor. The molecule structures of SNAP, PPN(NO_2) and PPN(NO_3) are shown in Fig. 2(c). Concentrations of donors are all 10^{-3} M. Except the SNAP, no one can induce continuing decrease in PL as shown in Fig. 2(b). This demonstrates the BPDM–H–ZnCl is highly selective which makes it a reliable reagent for future applications in biological systems.

As shown in Fig. 3(a), NO sensing characteristics of the hydrogel film are first demonstrated by using a microfluidic system and 405 nm laser as excitation source. The sensing hydrogel film is initially settled in deionized (DI) water in the microfluidic channel with stable PL at 675 nm. The PL spectrum of the sensing hydrogel film is similar to the one of BPDM–H–ZnC1 solution which means BPDM–H–ZnCl probe functions well even after being trapped in pHEMA. Dramatic decrease in PL of the sensing hydrogel film can be observed when the NO bubbled water is injected into the microfluidic channel at 16th and 51st minute. The changing in PL stops after refilling the channel with DI water at 36th and 66th minutes. These characteristics show that the sensing hydrogel film is suitable for real-time and indicator-free detection.

To separate excitation light and the emission light, the first step is to filter the EL of the top-emitting PLED to form

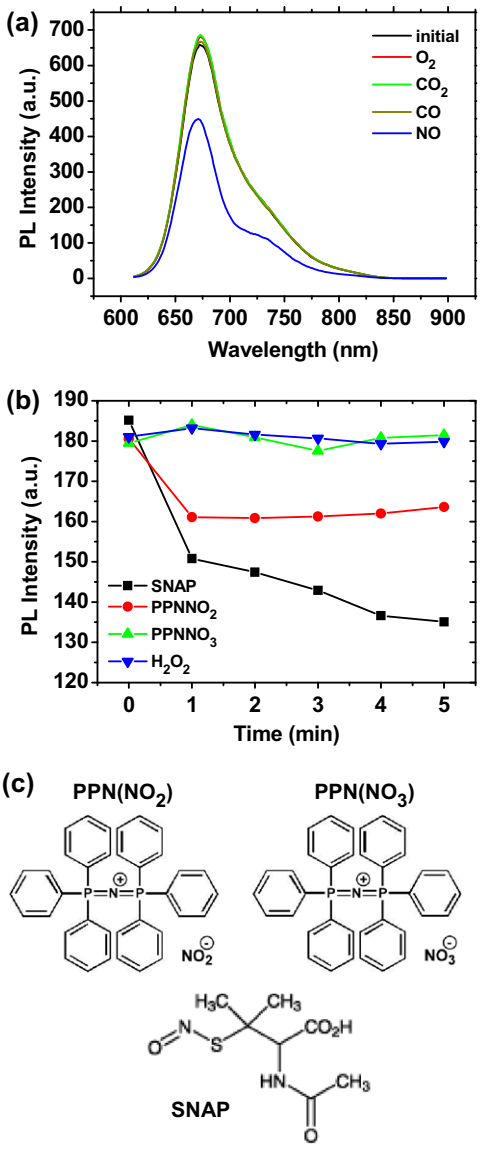

Fig. 2. (a) The PL spectra after bubbling different gases. (b) The PL intensities at 675 nm vary with time after adding different molecules. (c) The molecule structures of SNAP, PPN(NO_2) and PPN(NO_3).

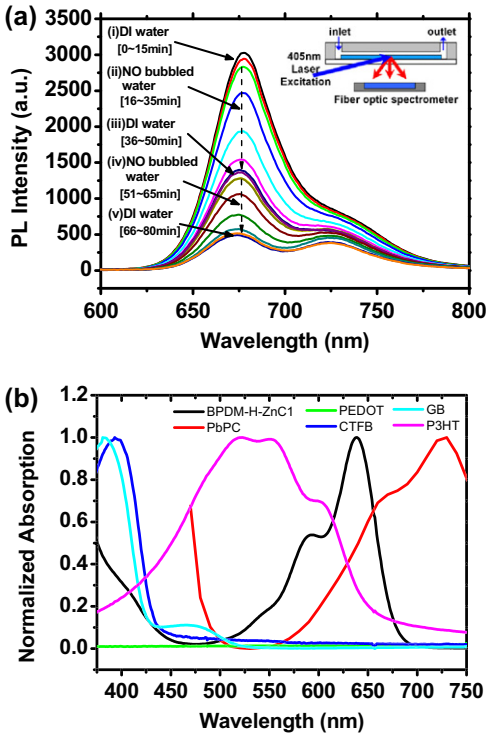

Fig. 3. (a) The PL spectra of the sensing hydrogel film placed in microfluidic channel. The inset shows the experimental setup. DI water or NO bubbled water is injected into microfluidic channel at different time. (b) Normalized absorption spectra of BPDM–H–ZnC1, PbPc, PEDOT, CTFB, GB, and P3HT.

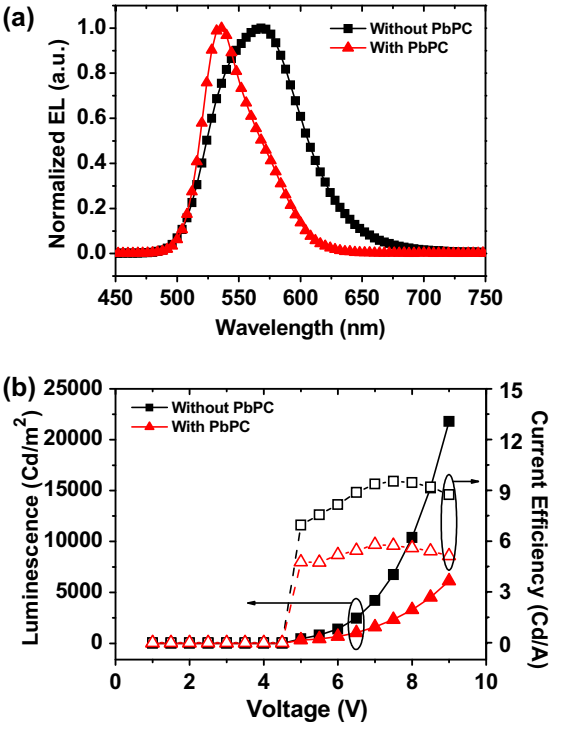

Fig. 4. (a) Normalized EL spectra and (b) luminescence and current efficiency of top-emitting PLED with or without PbPc on top of the transparent cathode.

an excitation light without the wavelength overlaps the emission of the sensing hydrogel film. Organic material PbPc is therefore deposited on top-emitting PLED as Filter 1 since it absorbs light above 600 nm with an absorption peak at 730 nm as shown in Fig. 3(b). Besides, PbPc is almost transparent for the light between 500 and 570 nm, and the emission of top-emitting PLED with PbPc on transparent cathode in that range can pass PbPc for excitation without large light intensity attenuation. Fig. 4(a) shows the EL spectra of top-emitting PLED with or without covering PbPc. The EL spectrum of the top-emitting PLED without PbPc ranges from 500 to 700 nm. Deposition of 200 nm PbPc on top-emitting PLED narrows its spectrum range and almost no emission around 675 nm can be observed. This ensures the 675 nm light that Si PD received comes mostly from the BPDM–H–ZnC1 fluorescent NO probe in the sensing hydrogel film. The luminescence and current efficiency of the top-emitting PLED with or without PbPc are shown in Fig. 4(b). Although both luminescence and current efficiency are decreased for the top-emitting PLED with PbPc filter because part of the emission is absorbed, stable current efficiency with maximum of 5.8 cd/A at 7 V can still be obtained. The luminescence at 7 V is 1600 cd/m^2 which is enough for this integrated semiconductor device.

The second step to separate excitation light and the emission light is to remove the rest of excitation light. As shown in Fig. 5(a), the spectrum shows two apparent peaks at 535 nm and 680 nm as P3HT Filter 2 is absent. Since each material used in top-emitting PLED does not have apparent absorption above 500 nm, the PL of the sensing film as well as the reflected excitation light can pass though the gaps between active areas of top-emitting PLED and received by Si PD without large light intensity attenuation. Except the PL of the sensing hydrogel film, the reflected excitation light can also be detected. In the presence of P3HT Filter 2 which absorbs most of the visible light below 650 nm, the reflected excitation light can be removed. However, the absorption of P3HT filter above 650 nm is not zero, and hence the emission from sensing hydrogel film also decreased a little but still detectable. The P3HT filter used in this work is deposited on a glass substrate and placed in front of Si PD to demonstrate its function. In practice, the P3HT filter can be deposited on Si PD or on the bottom of the PLED glass substrate for space saving.

After the separation of the excitation light and emission of the sensing hydrogel film is achieved, the change in photocurrent outputs from Si PD may represent mostly the change in PL of the sensing hydrogel film. Fig. 5(b) shows the real-time and indicator-free detection of NO by an integrated semiconductor device consisting of a sensing hydrogel film, a top-emitting PLED with PbPc filter, and a Si PD covered with P3HT filter. The photocurrent curve is smoothed by taking the average of 40 data points around each point as shown in Fig. 5(c). The photocurrent output from Si PD remains at almost the same value until the NO bubbled water is injected into the microfluidic channel. The photocurrent ceases to descend as DI water is refilled

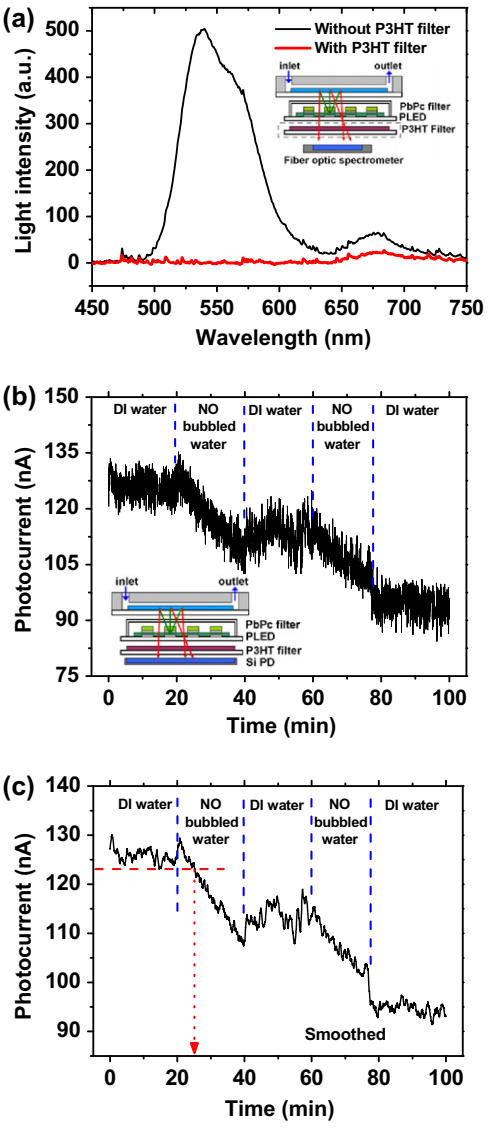

Fig. 5. (a) Spectra of the light received by Si PD with or without P3HT filter placed in front of it. (b) The photocurrent response to different environment. (c) The photocurrent response is smoothed for clarity.

into the microfluidic channel. The decrease in photocurrent corresponds to the decrease in PL intensity of the sensing hydrogel film as shown in Fig. 3(a). This is the first time that aqueous NO can be detected by an integrated solid-state optoelectronic sensor in a real-time and indicator-free manner. The NO concentration is estimated to be in the order of 10^{-3} M since it has been reported that NO solubility in oxygen-free water is 1.9 mM at 25 °C [7]. It has been demonstrated in our previous work that a higher NO concentration leads to a larger PL variation in the same time interval [11]. The slopes of the photocurrent obtained from the photocurrent vs. time plot are different for various NO concentrations. The slope of the photocurrent is therefore used to indicate the NO concentration, and the response time is the time needed for the slope of the photocurrent changes to another value and the photocurrent exceeds the noise level. Although immediate slope change is observed within few seconds after injecting NO bubbled water as shown in Fig. 4(c), the response time is still estimated to be 5 min which is determined by the time needed for the PD to output an photocurrent lower than the noise level. The response time can be improved by increasing the signal-to-noise ratio and enhancing the fluorescence of the NO probe. Increasing the surface area of the sensing film may also help. The realization of this integrated optoelectronic sensor makes the real-time and indicator-free detection of NO possible for the first time. Such a small-sized sensor is suitable for long-term and portable detection of NO, and it is a help to understand the relation between NO and physiological changes.

4. Conclusion

In conclusion, real-time and indicator-free detection of nitric oxide is achieved by an integrated semiconductor optoelectronic device consisting of a sensing film, an excitation source, and a photodetector. The influence of the excitation light on the output current of the photodetector is diminished by utilizing two organic filters. One filter is deposited above a top-emitting PLED to produce an excitation light without overlapping the emission maximum of the sensing hydrogel film. The other filter is placed in front of photodetector to prevent the excitation light get into the photodetector. The photocurrent changes as NO enters the environment and the response time is 5 min. Such integrated solid-state device is compact, small-size, and portable which can be used in fundamental research and clinical diagnosis.

Acknowledgement

This work is supported by the National Science Council of Taiwan (NSC99-2628-M-009-001-), Academia Sinica (AS-100-TP-B03), and the Veterans General Hospitals and University System of Taiwan Joint Research Program (VGHUST100-G5-1-1). Authors are grateful to members in biomimetic system research center, National Chiao Tung University.

References

[1] D.S. Bredt, S.H. Snyder, Annu. Rev. Biochem. 63 (1994) 175.
[2] S. Moncada, R.M. Palmer, E.A. Higgs, Pharmacol. Rev. 43 (1991) 109.
[3] R.M.J. Palmer, A.G. Ferrige, S. Moncada, Nature 327 (1987) 524.
[4] C. Bogdan, Nature Immunol 2 (2001) 907.
[5] L.L. Thomsen, D.W. Miles, L. Happerfield, L.G. Bobrow, R.G. Knowles, S. Moncada, Br. J. Cancer 72 (1995) 41.
[6] R.S. Clark, P.M. Kochanek, M.A. Schwarz, J.K. Schiding, D.S. Turner, M. Chen, T.M. Carlos, S.C. Watkins, Pediatr. Res. 39 (1996) 784.
[7] T. Nagano, Chem. Rev. 102 (2002) 1235.
[8] V. Savvate'ev, Z. Chen-Esterlit, J.W. Aylott, B. Choudhury, C.-H. Kim, L. Zou, J.H. Friedl, R. Shinar, J. Shinar, R. Kopelman, Appl. Phys. Lett. 81 (2002) 4652.
[9] B. Choudhury, R. Shinar, J. Shinar, J. Appl. Phys. 96 (2004) 2949.
[10] Z. Zhou, R. Shinar, A.J. Allison, J. Shinar, Adv. Funct. Mater. 17 (2007) 3530.
[11] Y.C. Chao, S.D. Yeh, H.W. Zan, G.F. Chang, H.F. Meng, C.H. Hung, T.C. Meng, C.S. Hsu, S.F. Horng, Appl. Phys. Lett. 96 (2010) 223702.
[12] C.H. Hung, G.F. Chang, A. Umar, G.F. Lin, L.Y. Luo, W.M. Ching, E.W.G. Diau, Chem. Comm. (2008) 978.
[13] F. Patolsky, G. Zheng, C.M. Lieber, Nat. Protoc. 1 (2006) 1711.

need of further improvements. Hence, phosphorescent organic emitters are typically employed to efficiently utilize the triplet excitons and thus increase the radiative recombination [4]. Compared with fluorescent emitters, due to the short range of the Dexter energy transfer, phosphorescent emitters are present in much higher concentrations (~10%) in the host material, a fact which may significantly alter the carrier injection, carrier transport, and recombination process in the emitting layer (EML) [5]. With regards to the electrical properties, dopants may: (1) serve as the injection channel from the hole-transporting layer (HTL) and/or electron-transporting layer (ETL) for reducing the driving voltage [6], (2) trap carriers and decrease the carrier mobility [7–9], and (3) exhibit transport characteristics such as carrier hopping among the dopant sites, especially at high dopant concentrations [6–10]. Further, the electroluminescence (EL) mechanisms can be categorized into energy transfer from host to dopant, or carrier trapping at the dopant sites [11,12]. Due to the short carrier lifetime of the triplet excitons, triplet–triplet (TT) annihilation occurs when the charge carrier concentration is high (under high voltage driving). Hence, sometimes the phosphorescence of an OLED will reach a maximum before decreasing sharply with increasing current driving [13]. Such an efficiency roll-off sometimes hampers the use of white OLEDs in real applications. With a bipolar host, mixing host, or double emitting layer (DEML) structure, an OLED can effectively broaden its recombination zone, reduce the TT annihilation, and maintain high efficiency under reasonably high luminance levels (say, 1000 cd/m^2) [14–20]. Another popular concept is the fluorescence-interlayer-phosphorescence, which utilizes fluorescent emitters to accelerate the exciton generation, and phosphorescent emitters to convert the excitions into photons, thereby sustaining the efficiency at high injection levels [21].

Generating a broadband white light typically requires two or three types of emitters, which adds to the complications involved in material selection and device design [22,23]. In addition to considering the interplay among the host(s) and dopants materials and reducing the efficiency roll-off, two other important issues are achieving a high color rendering index (CRI) and maintaining a stable EL spectrum. In general, OLEDs with three types of emitters are preferred for high CRI applications [24]. Although it is possible to adjust the emission color by tuning the driving voltage [25], it is often preferable to achieve a white OLED emission independent of the driving conditions. To fulfill this requirement, one will need to design a device structure which can: (1) effectively confine the carriers, (2) effectively confine the excitons, and (3) maintain the energy transfer path and/or trapping conditions without saturation of the emitter sites within the driving range [26]. Typically, a blocking layer is incorporated to confine the carriers and excitons [27,28]. By sandwiching the low bandgap emitter between two high bandgap emitters, it is also possible to achieve a high level of confinement with high color stability [29]. One may also utilize a very thin EML to ensure that the recombination zone is fixed [30]. Another successful approach is the DEML. By doping emitters with different hole and electron transport properties in EML1 and EML2, respectively, carrier confinement is automatically achieved, thereby stabilizing the EL emission [31]. One potential issue for this kind of device structure is the material selection of the electron transporting host [32]. Typically, the highest occupied molecular orbital (HOMO) value of such a host is high, which results in a high driving voltage [31]. To reduce the driving voltage and manage the carriers and excitons, a hole-transporting material can be mixed into the electron-transporting host [33–35].

In this paper, we demonstrated a white OLED with a DEML configuration. The electron-transporting host was 2,2′-bis[5-phenyl-2-(1,3,4)oxadazolyl]biphenyl (OXD), which has been proven to be a suitable host for the green phosphorescent emitters, fac-tris(phenylpyridine) iridium [Ir(ppy)$_3$], in our previous study [36,37]. It was also demonstrated that the Ir(ppy)$_3$ doped OXD exhibits bipolar transport characteristics, and can be regarded as an electron-rich bipolar EML. On the other hand, the hole-transporting host was *N*,*N*-dicarbazolyl-3,5-benzene (mCP) doped with 9% iridium(III)bis[4,6-di-fluorophenyl-pyridinato-N,C2]picolinate (FIrpic). From EL spectral analysis, it was demonstrated that the recombination zone was also broad in this hole-transporting EML, because the mCP exhibited certain electron-transport characteristics. Hence, it can be regarded as a hole-transporting bipolar EML. Combining the hole- and electron-transporting EMLs with blue and green emission for the backbone of the white OLED, carrier confinement was achieved with a broad recombination zone, so that both color stability and high efficiency can be achieved with a reduction in the efficiency roll-off. Compared with single EML cases of mCP- and OXD-based OLEDs, the external quantum efficiency (EQE) improved by 33.1% and 168.6% at 2.5 mA/cm^2, respectively. Further, the color coordinates shift from 100 to 10,000 cd/m^2 was reduced from (−0.029, −0.052) and (−0.014, −0.029) to (−0.013, 0.002). Last but not least, 0.5% tris(2-phenylquinoline)iridium(III) [Ir(2-phq)$_3$] red dopants were doped in EML1 and EML2, respectively, for white light generation. Ir(2-phq)$_3$ doping resulted in almost no change in the EQE of EML2 but a boost in the EQE of EML1 to 10.49% at 2.5 mA/cm^2 due to the higher internal quantum efficiency of Ir(2-phq)$_3$ than that of FIrpic. The maximum current efficiency and power efficiency of the WOLED obtained were 35.8 cd/A and 20.5 lm/W, respectively. When the luminance increased from 100 to 10,000 cd/m^2, the variations in the Commission Internationale de l'Eclairage (CIE) coordinates were only 0.014 and 0.004.

2. Experiments

Table 1 illustrates the device structures of the OLEDs with monochromatic, bi-chromatic and white-light emissions used in this study. The hole transport layer (HTL) and electron transport layer (ETL) materials were *N*,*N*′-diphenyl-*N*,*N*′-bis(1-napthyl)-1,1′-biphenyl-4,4′-diamine (NPB) and 4,7-diphenyl-1,10-phenanthroline (BPhen), with a thickness of 50 and 40 nm, respectively. Due to the higher triplet energy of FIrpic (T_1 = 2.7 eV), we inserted a 10 nm exciton

Table 1
Device structures of OLEDs. (Unit:nm).

Device	HTL	EBL	EML		ETL
	50	10	15	13	40
D1			9% Fipic:mCP	9% $Ir(ppy)_3$:OXD	
D2			9% Fipic:mCP	OXD	
D3			mCP	9% $Ir(ppy)_3$:OXD	
D4			mCP	OXD	
S1	NPB	mCP	9% Fipic:mCP	9% $Ir(ppy)_3$:mCP	BPhen
S2			9% Fipic:OXD	9% $Ir(ppy)_3$:OXD	
S3			9% Fipic:(mCP:OXD = 1:1)	9% $Ir(ppy)_3$:(mCP:OXD = 1:1)	
W1			9% Fipic:mCP	0.5% $Ir(2\text{-phq})_3$:9% $Ir(ppy)_3$:OXD	
W2			0.5% $Ir(2\text{-phq})_3$:9% Fipic:mCP	9% $Ir(ppy)_3$:OXD	

blocking layer (EBL) to prevent exciton diffusion from the EML to the HTL. The main host materials in the EML were *N*,*N*-dicarbazolyl-3,5-benzene (mCP) and 2,2′-bis[5-phenyl-2-(1,3,4)oxadazolyl]biphenyl (OXD), both of which exhibited bipolar characteristics. Typically, Poole-Frankel model with the form $\mu = \mu_0 \exp(\beta\sqrt{E})$ was used to describe the carrier mobility (μ) in organic thin films. μ_0 represents the zero-field carrier mobility, β describes the electric field dependence of the mobility, and E is the applied electrical field. Zero-field mobility of mCP for hole is 1.2×10^{-4} cm^2/V s, which is three times higher than that of electron (4×10^{-5} cm^2/V s) [26]. β value of the hole and electron mobility of mCP was 0.00254 and 0.00426, respectively. So, that means the hole mobility is higher than electron under low electric field. With increasing driving voltage (electric field), electron mobility increases faster than holes, which may shift recombination zone toward anode direction. For the OXD case, although we did not measure the mobility values, we have fabricated OXD with different thicknesses sandwiched by HTL and ETL materials [36]. When OXD layer was thin (40 nm), both HTL and ETL emission were both observed, which meant OXD layer can support hole and electron transport. When increasing the OXD layer to 90 nm, only HTL emission was observed. That meant the electron transport dominated. Hence, in OXD we concluded that the electron mobility is higher than that of hole one. The phosphorescent dopants for the red, green, and blue emission were tris(2-phenylquinoline)iridium(III) [$Ir(2\text{-phq})_3$], fac-tris(phenylpyridine) iridium [$Ir(ppy)_3$] and iridium(III)bis[4,6-di-fluorophenyl-pyridinato-N,C2]picolinate (FIrpic), respectively. The chemical structures and the energy diagrams of all the organic materials are shown in Fig. 1a and b, respectively.

First, we utilized the mCP/OXD (15/13 nm) DEML structure with different doping profiles for studying the carrier injection, transport, and recombination characteristics, and denoted the devices as D1 to D4, as shown in Table 1. Device D1 was a bi-chromatic OLED with 9% FIrpic doped in the mCP and 9% $Fir(pic)_3$ in the OXD. The dopants in the OXD and mCP were removed for Devices D2 and D3, which exhibited blue and green emission, respectively. In Device D4, there were no dopants in either the mCP or OXD. In the second part of the experiments, devices with the mCP, OXD, and their mixture (mCP:OXD = 1:1) as a single host of the EML were fabricated, and denoted as S1, S2, and S3, respectively, for comparison with the OLED with the DEML structure (D1). Lastly, red dopants [$Ir(2\text{-phq})_3$] were co-doped with $Ir(ppy)_3$ (Device W1) and FIrpic (Device W2) for white light generation.

3. Results and discussion

3.1. Carrier injection and transport in blue–green OLED

Fig. 2a shows the *J*–*V* characteristics of the OLEDs with different doping profiles, D1–D4, respectively, on a linear scale. One can see that the Device D1, with both green and blue dopants (denoted as B/G in Fig. 2a), exhibited the lowest driving voltage of 10.6 V at 50 mA/cm^2, as shown in Table 2. On the other hand, the driving voltage of Device D4 (denoted as U/U in Fig. 2a, where "U" means "undoped") without any dopants was the highest (12.1 V at 50 mA/cm^2), implying that the presence of the dopant helped to reduce the driving voltage. Comparing the effects of the blue and green dopants on the driving voltage, one can see that Device D2, with only the blue dopants (FIrpic), exhibited a lower driving voltage than Device D3, with only the green dopants ($Ir(ppy)_3$). To further understand the mechanism behind the dopant-induced voltage reduction in our OLEDs, we replotted the *J*–*V* characteristics on a double log scale, as shown in Fig. 2b. Here, three regions of the *J*–*V* curves can be clearly distinguished. For unipolar organic thin films, the trap-charge-limited-current equation is typically used:

$$j_{TCLC} \propto V^{l+1} \tag{1}$$

where j_{TCLC} is the current density, V is the voltage, and l is the parameter derived from the trap distribution. With a higher trap density, the l-value will be larger. If $l = 0$, we have ohmic conduction. Although our OLEDs possessed a multilayer structure with double carrier transportation, this equation can still be used for qualitative comparisons. At low voltage (Region 1), in what is typically known as the ohmic region, the current conduction is effected by the thermally activated carriers, and the l-value for the four devices, D1–D4, were quite similar, ranging from 1.17 to 1.27, as shown in Table 3. For Region 2, a typical TCLC region, Device D1, with both green and blue dopants, exhibited the highest l-value of 13.8, whereas the corresponding value for the undoped Device D4 was $l = 9.78$. The l-value of Device D2 was slightly higher than that of Device D3. These values implied that the dopants in our OLEDs served

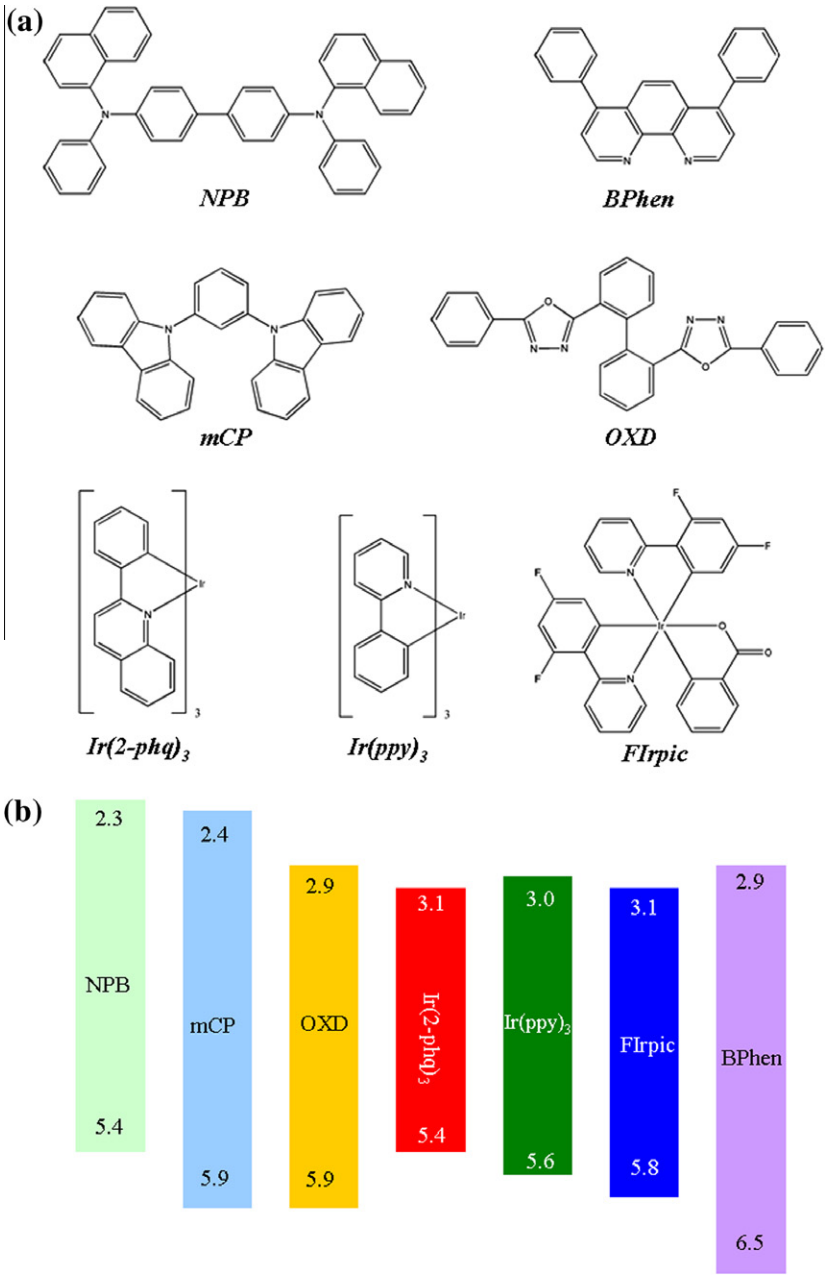

Fig. 1. (a) Chemical structures of organic materials, and (b) energy diagrams.

as trapped sites where the recombination process took place. The recombination current increased the current density, which in turn reduced the driving voltage [38]. At high injection conditions (Region 3), the traps were filled and possibly formed some space charges, provided that the recombination rate was not exceedingly high or that the electron-hole concentration was not matched in the spatial domain. This reduced the carrier mobility and also reduced the *l*-value [39]. One can also note that in Region 1 (low bias condition), the current density was the highest in the undoped device, which also implied that the dopants acted as traps, and that the free carrier concentration was the highest in the absence of dopants.

Fig. 2c shows the EL spectra of Device D1 at different driving voltages, which can be decomposed to those of Device D2 and D3, also shown as the dash lines in the figure. One can see that the EL spectral variation was quite small, with only a slight decrease in the green emission with increasing driving voltage. This suggested that the carrier confinement effected by the mCP/OXD interface was rather stable. Additionally, the recombination zone shifted slightly toward the FIrpic doped mCP layer, which resulted

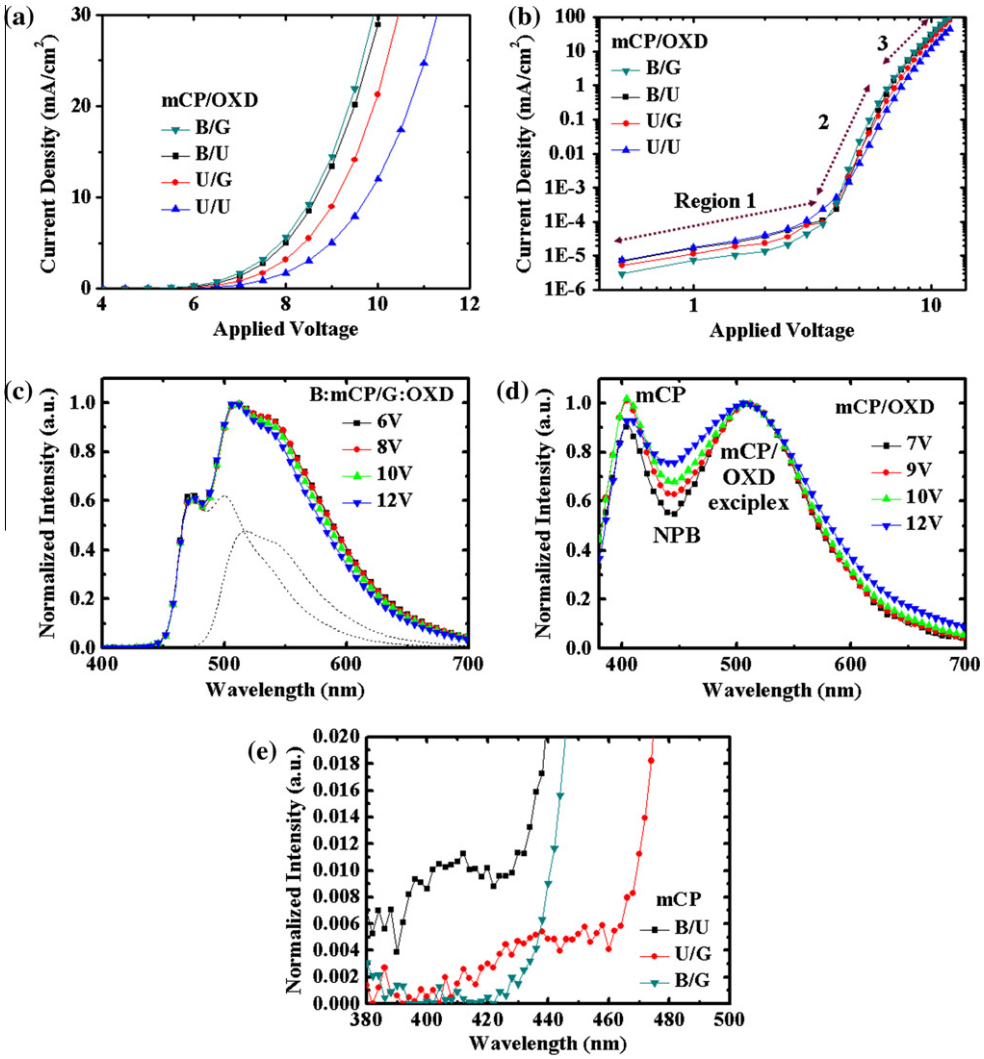

Fig. 2. *J–V* characteristics of devices D1, D2, D3, and D4 in (a) linear and (b) double log scale. B, G, and U: blue-emitter (FIrpic) doped, green $(Irppy)_3$ doped, and undoped EMLs. (c) EL spectra at different driving voltages of D1. Dashed lines shows EL spectra of D2 and D3 at 12 V. (d) EL spectra at different driving voltage of D4. (e) Zoom-in spectra at short wavelength region (<500 nm) of D1, D2, and D3 at 12 V. (For interpretation of the references to colour in this figure legend, the reader is referred to the web version of this article.)

in the slight decrease in the green emission. To further investigate the emission process, we measured the EL spectrum of Device D4, as shown in Fig. 2d. There were two main peaks at 402 and 510 nm, from the exciton emission of the mCP and the exciplex emission at the mCP/OXD interface, respectively. When the driving voltage was increased from 7 to 9 V, the mCP peak increased accordingly, meaning that the recombination zone had shifted from the interface into the mCP. When the driving voltage was further increased to 10 and 12 V, the mCP peak dropped. However, the dip around 432–444 nm, from the NPB emission, increased. This suggested that the recombination zone had been extended into the NPB layer, a clue that the recombination zone in the mCP layer was rather broad. Fig. 2e shows the EL spectra in the short wavelength region of Devices D1, D2, and D3. For Device D1, there was no leakage from the EBL (mCP) or HTL (NPB). Interestingly, for Device D2, with no green dopants ($Ir(ppy)_3$) in the OXD but FIrpic in the mCP, one can detect a miniscule amount of mCP emission (400–420 nm), which came from the EBL, implying that the recombination zone had shifted toward the anode side where there were no $Ir(ppy)_3$ dopants. From our previous study, we can deduce that the $Ir(ppy)_3$ doped in the OXD served as electron traps to retard the electron transport, and also provided another hopping channel for the holes [36]. Another conclusion we may draw was that the recombination zone was truly broad in the FIrpic-doped mCP layer, making it possible to observe the emission from the EBL in Device D2. In the EL spectrum of Device D3, we can discern a low mCP emission (if any at all) and a rather obvious NPB emission, meaning that the recombination had taken place further inside the HTL. Therefore, both dopants (FIrpic and $Ir(ppy)_3$) acted as electron traps and shifted the recombination zone

Table 2
Performances of OLEDs.

Device	[a]Driving voltage (V)	Current efficiency (cd/A)	Power efficiency (lm/W)	[b]CIE coordinates shift	CIE at cd/m^2	100 [c]EQE (%)
D1	10.6	32.1 at 6 V, 0.302 mA/cm^2	18.7 at 5 V, 0.0232 mA/cm^2	(−0.013, 0.002)	(0.311, 0.506)	9.16
D2	10.8	13.4 at 7.5 V, 2.73 mA/cm^2	6.38 at 6 V, 0.183 mA/cm^2	[1](0.009, 0.005)	(0.181, 0.398)	5.45
D3	11.2	31.7 at 6 V, 0.125 mA/cm^2	18.1 at 5 V, 0.0104 mA/cm^2	(−0.004, −0.001)	(0.320, 0.619)	7.20
D4	12.1	0.618 at 7.5 V, 0.883 mA/cm^2	0.269 at 7 V, 0.403 mA/cm^2	L always below 100 cd/m^2	L always below 100 cd/m^2	0.20
S1	11.0	36.5 at 5.5 V, 0.0189 mA/cm^2	20.9 at 5.5 V, 0.0189 mA/cm^2	(−0.029, −0.052)	(0.287, 0.605)	6.88
S2	11.0	16.8 at 5.5 V, 0.0453 mA/cm^2	10.2 at 5 V, 0.0101 mA/cm^2	(−0.014, −0.029)	(0.268, 0.550)	3.41
S3	8.0	28.9 at 5.5 V, 0.935 mA/cm^2	17.3 at 5 V, 0.201 mA/cm^2	(0.031, 0.070)	(0.206, 0.473)	6.88
W1	10.8	27.7 at 6 V, 0.347 mA/cm^2	16.5 at 5 V, 0.0287 mA/cm^2	(−0.008, 0.001)	(0.360, 0.444)	9.04
W2	10.8	35.8 at 6.5 V, 0.643 mA/cm^2	20.5 at 5 V, 0.0203 mA/cm^2	(−0.014, 0.004)	(0.435, 0.482)	10.49

[1]L from 100 to 5000 cd/m^2.
[a] Measured at 50 mA/cm^2.
[b] Measured from 100 to 10,000 cd/m^2.
[c] Measured at 2.5 mA/cm^2.

Table 3
l-value of D1–D4.

	Region 1	Region 2	Region 3
D1	1.17	13.8	7.65
D2	1.24	12.2	7.65
D3	1.14	11.9	8.43
D4	1.27	9.78	8.63

towards the cathode sides, consistent with the conclusions derived from the *J–V* characteristics.

Fig. 3 shows a schematic diagram we proposed to characterize the carrier transport in the blue/green devices. Holes were injected from the anode, HTL, and EBL into EML1 (FIrpic doped mCP). It was a hole-rich EML, and holes were subsequently piled up at the mCP/OXD interface, due to the difference in the hole mobilities of the mCP and OXD. The OXD is a bipolar material with a higher electron mobility than hole mobility, and the doped Ir(ppy)3 inside the OXD opened a new hole-transporting channel. Therefore, EML2, the Ir(ppy)3 doped OXD, became an electron-rich EML. On the other hand, the electrons were injected from the cathode, ETL (HBL) into EML2. The Ir(ppy)3 captured some of the electrons and recombined with the holes. In EML2, the electrons were majority carriers. Therefore, the recombination was limited by the number of holes transported into EML2. Some of the electrons might accumulate at the mCP/OXD interface, and then become injected into EML1 and then trapped by the FIrpic. In this picture, the recombination current enhancement (driving voltage reduction) corresponded to the minor carrier concentration. As we can see from Fig. 2a, Device D2 exhibited a lower driving voltage (higher recombination current) than Device D3, which indicated that the main recombination zone was located in the EML1 and that the entire recombination zone was broad.

3.2. Comparison between OLEDs with single- and double-EML

Fig. 4a shows the *J–V* curves of Devices D1, S1, S2, and S3 for comparing the electrical characteristics between OLEDs with single- and double-EMLs. The mCP and OXD

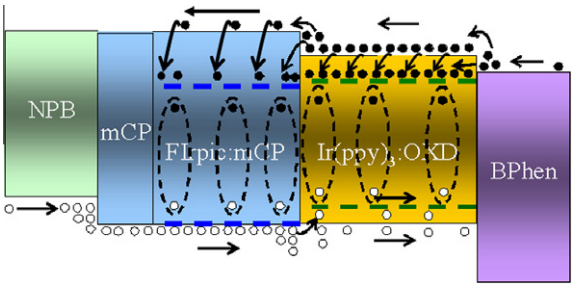

Fig. 3. Illustration of carrier injection and transport behavior in doped DEML–OLED (D1).

were hole- and electron-rich bipolar EMLs. Hence, electrons and holes were not balanced in these two cases (S1 and S2). With a DEML configuration (D1), the charge balance condition was satisfied, which reduced the driving voltage to 0.4 V at 50 mA/cm^2. By mixing mCP and OXD (1:1) as the host of the EML (S3), bipolar transport can be also achieved for the whole EML which significantly decreased the driving voltage to 8 V at 50 mA/cm^2, compared to S1 and S2.

Fig. 4b shows the EL spectra of Device S1 (with a mCP single host) at different driving voltages. One can see that the spectral variation was severe, which was due to the shift in the recombination zone. Additionally, the blue emission was rather weak, because energy was transferred from the FIrpic to Ir(ppy)$_3$. With increasing driving voltage, the blue emission increased. The insertion of an extra spacer is typically used to confine the carrier and excitons for stabilizing the color coordinates and increasing the blue emission [27]. Fig. 4c shows the EL spectra in the short wavelength regions of Devices D1 and S1. There was no leakage to the HTL side for Device S1, because the mCP was hole-rich and the main recombination zone was located near the EML/HBL interface. With increasing driving voltage, the recombination zone was shifted toward the HTL side, which increased the recombination from the FIrpic molecules with stronger blue emission.

Fig. 4d shows the EL spectra of Device S2 (with an OXD single host) at different driving voltages. Compared with the case of Device S1, the blue peak of Device S2 was

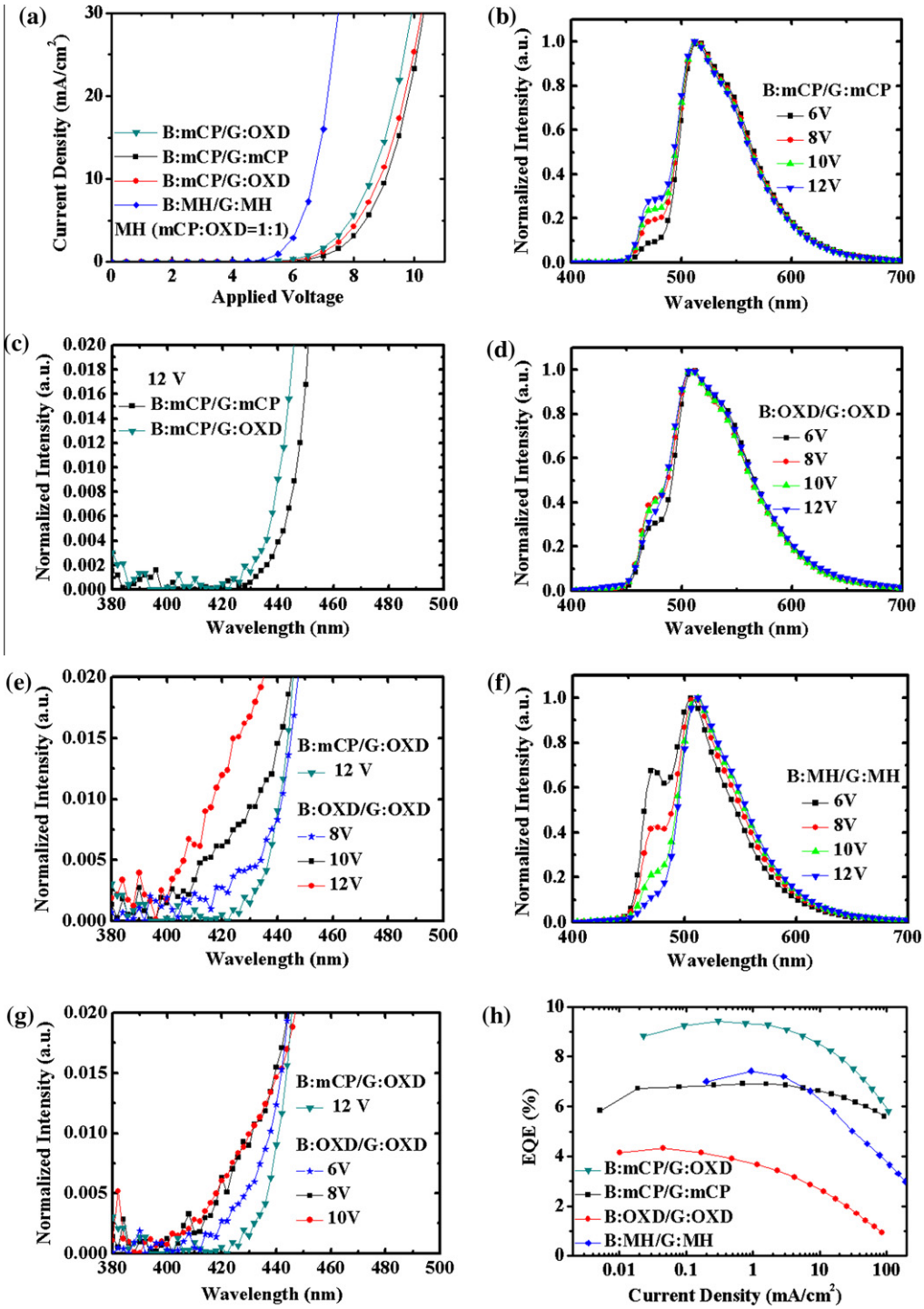

Fig. 4. (a) *J–V* characteristics of devices D1, S1, S2, and S3. (b) EL spectra at different driving voltages of S1. (c) Zoom-in spectra at short wavelength region (<500 nm) of D1 and S1 at 12 V, respectively. (d) EL spectra at different driving voltages of S2. (e) zoom-in spectra at short wavelength region (<500 nm) of D1 (at 12 V) and S2 (at 8, 10, and 12 V), respectively. (f) EL spectra at different driving voltages of S3. (g) zoom-in spectra at short wavelength region (<500 nm) of D1 (at 12 V) and S3 (at 6, 8, and 10 V), respectively. (h) EQE at different current density of D1, S1, and S2.

stronger and more stable. In this case, with the electron-rich EML, the main recombination zone was located at the EBL/EML interface, and a strong leakage from the HTL was observed, as shown in Fig. 4e. Although the main recombination zone was located in the FIrpic-doped region, the blue emission of Device S2 was still lower than

that of Device D1, because the energy transfer from the OXD to the FIrpic was less efficient than that from the mCP to the FIrpic. The blue emission increased with increasing driving voltage, which meant that the recombination zone had penetrated into the HTL. Fig. 4e shows the leakage emission in the short wavelength region. As the driving voltage was increased from 8 to 12 V, one can see that the leakage emission of the OXD-based OLED increased significantly, signifying a shift of the recombination zone toward the HTL side.

Fig. 4e and f shows the EL spectra of mixed-host OLED (Device S3) and their zoom-in spectrum at short wavelengths region, respectively. One can see that the spectral variation in mixed-host OLED was more severe than that in pure mCP (Device S1) and pure OXD (Device S2) cases. The trend of blue and green emission variation under different driving voltages for mixed-host OLED is contrary to the cases in S1 and S2. The blue emission decreased (rather than increased) rapidly with increasing driving voltage. Under low driving voltage, saying 6 V, the blue emission was even higher compared with pure mCP, pure OXD, and D EML OLEDs. To generate enough blue emission, one may need to have enough electron-hole recombination at the blue dopant region (EML close to the EBL), together with efficient host material. In our case, mCP was a better choice than OXD as the host material of FIrpic. In mixed-host case (Device S3), both electrons and mCP molecules were sufficient at the EBL/EML interface, which resulted in high blue emission under low driving voltage. As shown in Fig. 4f, there were still NPB emission (around 430 nm) due to the electron leakage into HTL. It also increased with increasing driving voltage, because the recombination peak penetrated deeper into the HTL, which was also explained previously for the pure OXD case (Device S2). In a mixed-host OLED, electrons and holes transported through their most energy favorable paths (OXD and mCP in our cases), respectively, and it was also the main reason accounting for the significant voltage reduction. So there may be some electrons accumulated at the EBL/EML interface, as shown in Fig. 4f. Similarly, holes hop through mCP molecules may transport all the way to the EML/ETL interface. And the recombination took place in the whole EML [40]. With increasing driving voltage, electrons and holes may be driven toward the EBL and ETL. Clear evidence of the electron part is the increasing NPB emission with increasing driving voltage as shown in Fig. 4f. It reduced the blue emission efficiency under high voltage driving, similar to the pure OXD cases (device S2). On the other hand, for the hole case, BPhen is a good hole-blocking layer and block the hole at the EML/HTL interface for efficient recombination with electrons supplied from cathode. With increasing driving voltage, holes were accumulated at EML/ETL interface for efficient green emission. At the same time, blue emission decreased a lot because the penetration of electrons into HBL and HTL. It may be a possible reason accounting for the severe spectral variation in mixed-host blue/green OLED. However, more evidence should be provided. Besides, optimization of mixing ratios, doping concentrations and locations should be made for boosting up efficiency and stabilizing the spectrum of the mixed-host OLED and it is out of the scope of this paper. As shown in Table 2, due to the excellent carrier confinement of the DEML structure, the CIE coordinates of Device D1 shifted only (−0.013, 0.002) in the luminance range from 100 to 10,000 cd/m^2, a drastic improvement in comparison to Devices S1 (−0.029, −0.052), S2 (−0.014, −0.029), and S3 (0.031, 0.070), respectively.

Fig. 4h shows the EQE of Devices D1, S1, S2, and S3 at different current densities. It is not surprising that the D-EML OLED exhibited a higher efficiency than the single emitting layer devices, due to better carrier confinement and charge balance. For the mCP-based OLED (S1), one can see that the efficiency was rather stable under different driving conditions, which meant that the entire recombination zone was broad and that TT annihilation was not a significant factor. On the other hand, for the OXD-OLED (S2), the efficiency dropped significantly with increasing driving current density. When the current density was 20.4 mA/cm^2, the EQE was reduced to half the maximum value (2.17%). This suggested that the OXD-EML was not as "bipolar" as the mCP device and that the recombination region was narrower. For the D-EML case, the TT annihilation was just between S1 and S2, and the EQE was reduced to half its maximum value over 100 mA/cm^2.

3.3. White OLED with red-doped B/G-DEML structure

In order to fabricate high performance WOLEDs, high efficiency dopants for red emission were doped in the EML. As shown in Table 1, the phosphorescent red emitter Ir(2-phq)$_3$ with 0.5% was co-evaporated in the Ir(ppy)$_3$:OXD and FIrpic:mCP layers, respectively for two devices, denoted as W1 and W2 [41]. Fig. 5a shows the *J–V* curves of Devices D1, W1, and W2 for comparing the electrical characteristics between dichromatic (green/blue) and white OLEDs. The addition of the low concentration red dopants increased the trap density (both for the electron and holes) and slightly increased the driving voltage by about 0.2 V at 50 mA/cm^2. Fig. 5b and c show the EL spectra at different driving current densities of Devices W1 and W2, respectively. When the red emitter was doped in the green region (W1) as shown in Fig. 5b, the relative green emission decreases for red light emission, compared with the dichromatic OLED (D1) in Fig. 2c. On the other hand, in the case of Device W2, the red emitter was doped in the blue region, and hence the blue emission decreases for red emission (by comparing Figs. 5c and 2c). For the spectral shifts, obvious drops in the red emission were observed, both in Fig. 5b and c, from the saturation or trap-filling of the low-concentration red dopant materials [42,43].

Considering the EQE shown in Fig. 5d, one can see that the efficiency of Device W1 was nearly identical to that of Device D1. When red emitters were doped in the green region, the emission efficiency of Ir(2-phq)$_3$ and Ir(ppy)$_3$ were comparable, and had little effect on the EQE. On the other hand, when Ir(2-phq)$_3$ was added into the FIrpic, the maximum EQE increased because the emission efficiency of blue emitter was lower than that of the red emitter. As shown in Fig. 6, the maximum current efficiency and power efficiency of Device W2 were 35.8 cd/A with EQE 10.73% at 6.5 V and 20.5 lm/W at 5 V, respectively.

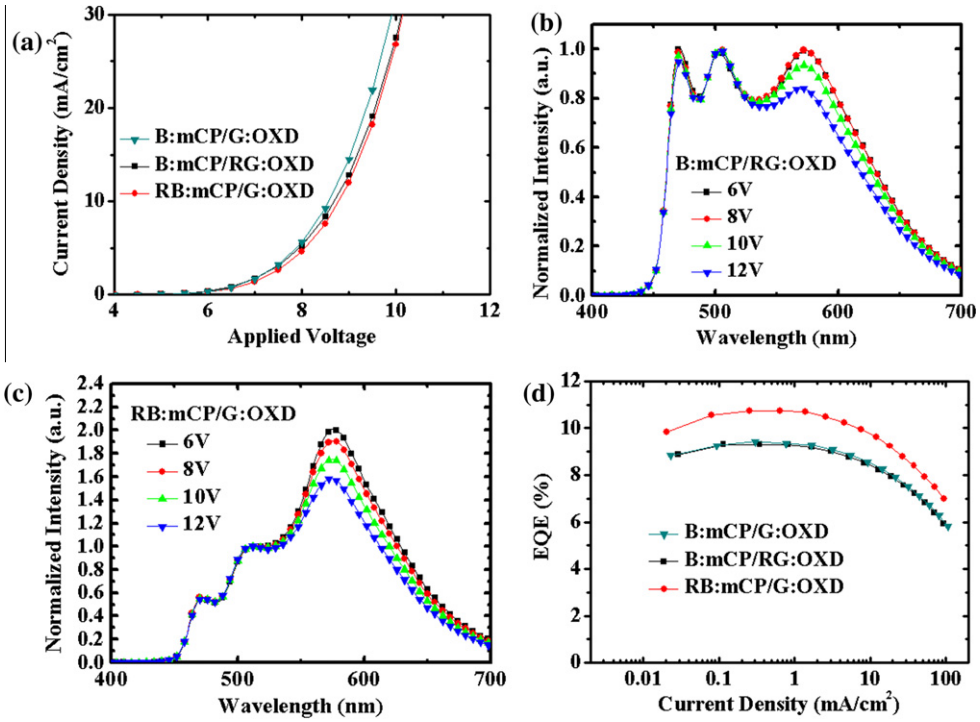

Fig. 5. (a) *J–V* characteristics of devices D1, W1, and W2. (b and c) EL spectra at different driving voltages of W1 and W2, respectively. (d) EQE at different current density of D1, W1, and W2.

The measurements of all devices were summarized in Table 2. Compared with other high efficiency white OLEDs with maximum efficiency of 19.5% and 25% in Refs. [44] and [45], respectively, our efficiency was quite low. One key point was the design of the EML. To have higher maximum quantum efficiency, one may use a thinner EML (both 10 nm in these two references), to localize the electron and hole concentrations at the same position. Although the maximum efficiency was high, however, in an OLED with thin EML, it may often result in a severe reduction in efficiency with increasing driving current due to triplet–triplet annihilation. On the other hand, our EML was 28 nm, which was much thicker, and relief the triplet–triplet annihilation effect. Besides, in fabricating our OLEDs, organic materials were purchased from the vendor and use without further purification (except that the OXD was synthesized by ourselves). Here, we purified FIrpic (only FIrpic and purify only once) and duplicate the device in D2. Amazingly, just purified once of FIpic, 50.7% improvements of cd/A was achieved. It is reasonable to expect that when all organic materials were well purified, higher maximum external quantum efficiency can be achievable. The low maximum external quantum efficiency in our device (10.73%) may come from: (1) the device configuration (thicker EML was adopted for reducing triplet–triplet annihilation), and (2) non-purification of the organic materials.

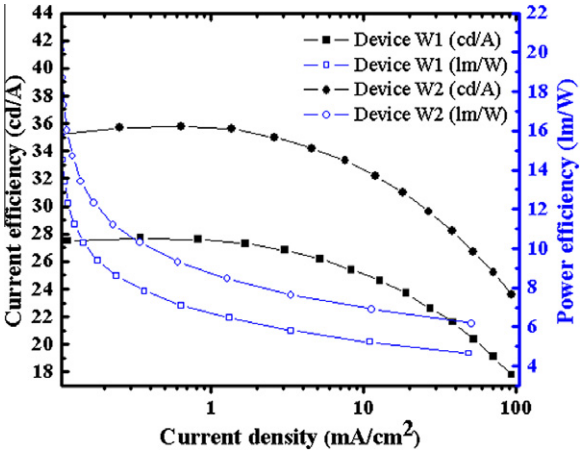

Fig. 6. Current efficiency (solid dots) and power efficiency (open dots) versus current density of W1 and W2.

We also conducted the lifetime test of Devices W2 and D3 under constant DC current driving at 50 mA/cm^2. Unfortunately, operation lifetime, which was defined as the elapsed time of luminance decreasing to its initial value, were quite short (21 and 5.3 mins for Devices W2 and D3, respectively) upon such high current stress. Interestingly, when there was no dopants in the EML1 (mCP) in Device D3 case, operation lifetime was greatly reduced compared with the white OLED (Device W2). For the EL process, input of electrical power converted to radiative light emission or heat dissipation. The latter not only had no contribution for EL, but also generated heat, which may increase temperature and deteriorate the organic material. Here, Device W2 exhibited a lower driving

voltage and higher efficiency compared with Device D3. That means lower heat was generated and the lifetime is hence elongated in Device W2 [46,47]. Checking the organic materials used in our device, one of the main bottlenecks accounting for such a short lifetime may be the use of low Tg (62 °C) organic material, BPhen, as the ETL. Here, BPhen was chosen due to its superior electron mobility, which helped to reduce voltage drop [26,48]. With replacement of other ETL materials with high Tg [49–51], elongation of operation lifetime may be possible. Comparing the normalized EL spectra of Device W2 before and after aging process (not shown here), it was found that the percentage of blue emission was reduced after aging due to its lower lifetime [52]. Because red emission was basically transferred from blue emitter, the luminance decay was more serious compared with that of green one.

4. Conclusions

In this paper, we discussed the electrical and optical characteristics of OLEDs with a DEML structure and multiple emitters. Phosphorescent green and blue dopants in the EML served as the carrier trapping and recombination centers and helped to reduce the driving voltage. Light leakage outside the EMLs was studied by EL analysis at short wavelengths, indicating that the recombination zone was broad (over the entire EML) and would become too broad (outside the EML region) without the green or blue dopants. Compared with the single EML cases (mCP and OXD), the DEML dichromatic OLED exhibited a lower driving voltage, higher EQE, and lower color shift, because the D-EML balanced the charges and confined the carriers at the mCP/OXD interface. By doping a low concentration (0.5%) red emitter in the FIrpic:mCP layer, we successfully fabricated a high efficiency WOLED with high color stability and alleviated the efficiency roll-off. The maximum current efficiency was 35.8 cd/A at 6.5 V. The EQE reached 10.49% at 2.5 mA/cm^2, and decreased to half its maximum value over 100 mA/cm^2. The CIE shifts were $(-0.014, 0.004)$ across the luminance levels from 100 to 10,000 cd/m^2.

Acknowledgements

This work was supported by the National Science Council of Taiwan, under Grant Nos. NSC 98-2221-E-002-038-MY3, NSC 98-2221-E-259-003, NSC 98-2622-E-259-001-CC3, NSC 98-2119-M002-006-MY3, and NSC 99-2218-E-155-003.

References

[1] C.W. Tang, S.A. VanSlyke, Appl. Phys. Lett. 51 (1987) 913.
[2] C.W. Tang, S.A. Vanslyke, C.H. Chen, J. Appl. Phys. 65 (1989) 3610.
[3] S. Reineke, F. Lindner, G. Schwartz, N. Seidler, K. Walzer, B. Lüssem, K. Leo, Nature 459 (2009) 234.
[4] M.A. Baldo, D.F. O'Brien, Y. You, A. Shoustikov, S. Sibley, M.E. Thompson, S.R. Forrest, Nature 395 (1998) 151.
[5] H.A. Al Attar, P. Monkman, Adv. Funnct. Mater. 16 (2006) 2231.
[6] C. Adachi, R. Kwong, S.R. Forrest, Org. Electron. 2 (2001) 37.
[7] N. Matsusue, S. Ikame, Y. Suzuki, H. Naito, J. Appl. Phys. 97 (2005) 123512.
[8] N. Matsusue, S. Ikame, Y. Suzuki, H. Naito, Appl. Phys. Lett. 85 (2004) 4046.
[9] S. Noh, C.K. Suman, Y. Hong, C. Lee, J. Appl. Phys. 105 (2009) 033709.
[10] W.H. Choi, C.H. Cheung, S.K. So, Org. Electron. 11 (2010) 872.
[11] X. Zhang, F. Wei, X. Liu, W. Zhu, X. Jiang, Z. Zhang, Thin Solid Films 518 (2010) 7119.
[12] Y.S. Seo, D.G. Moon, J. Phys. D. 43 (2010) 305101.
[13] C. Adachi, M.E. Thompson, S.R. Forrest, IEEE J. Sel. Top. Quan. Electron. 8 (2002) 372.
[14] K.S. Yook, S.O. Jeon, C.W. Joo, J.Y. Lee, M.S. Kim, H.S. Choi, S.J. Lee, C.W. Han, Y.H. Tak, Org. Electron. 10 (2009) 681.
[15] M.E. Kondakova, T.D. Pawlik, R.H. Young, D.J. Giesen, D.Y. Kondakov, C.T. Brown, J.C. Deaton, J.R. Lenhard, K.P. Klubek, J. Appl. Phys. 104 (2008) 094501.
[16] N. Chopra, J.S. Swensen, E. Polikarpov, L. Cosimbescu, F. So, A.B. Padmaperuma, Appl. Phys. Lett. 97 (2010) 033304.
[17] J. Lee, J.I. Lee, J.Y. Lee, H.Y. Chu, Appl. Phys. Lett. 94 (2009) 193305.
[18] X. Qiao, Y. Tao, Q. Wang, D. Ma, C. Yang, L. Wang, J. Qin, F. Wang, J. Appl. Phys. 108 (2010) 034508.
[19] X. Zhou, D.S. Qin, M. Pfeiffer, J. Blochwitz-Nimoth, A. Werner, J. Drechsel, B. Maennig, K. Leo, M. Bold, P. Erk, H. Hartmann, Appl. Phys. Lett. 81 (2002) 4070.
[20] G. He, M. Pfeiffer, K. Leo, M. Hofmann, J. Birnstock, R. Pudzich, J. Salbeck, Appl. Phys. Lett. 85 (2004) 3911.
[21] T. Zheng, W.C.H. Choy, Adv. Funnct. Mater. 20 (2010) 648.
[22] S.L. Lai, S.L. Tao, M.Y. Chan, T.W. Ng, M.F. Lo, C.S. Lee, X.H. Zhang, S.T. Lee, Org. Electron. 11 (2010) 1511.
[23] Y. Sun, N.C. Giebink, H. Kanno, B. Ma, M.E. Thompson, S.R. Forrest, Nature 440 (2006) 908.
[24] Y.W. Park, Y.M. Kim, J.H. Choi, T.H. Park, H.J. Choi, M.J. Cho, U.R. Lee, D.H. Choi, B.K. Ju, Electrochem. Solid-State Lett. 13 (2010) J81.
[25] J.H. Jou, M.H. Wu, S.M. Shen, H.C. Wang, S.Z. Chen, S.H. Chen, C.R. Lin, Y.L. Hsieh, Appl. Phys. Lett. 95 (2009) 013307.
[26] C.H. Hsiao, S.W. Liu, C.T. Chen, J.H. Lee, Org. Electron. 11 (2010) 1500.
[27] C.H. Hsiao, J.H. Lee, J. Appl. Phys. 106 (2009) 024503.
[28] H. Baek, C. Lee, J. Appl. Phys. 103 (2008) 124504.
[29] S.H. Kim, J. Jang, J.Y. Lee, Appl. Phys. Lett. 91 (2007) 123509.
[30] Q. Wang, J. Ding, D. Ma, Y. Cheng, L. Wang, F. Wang, Adv. Funct. Mater. 21 (2009) 2397.
[31] K.S. Yook, J.Y. Lee, Synth. Met. 159 (2009) 1636.
[32] H. Baek, C. Lee, J. Appl. Phys. 103 (2008) 054510.
[33] K.S. Yook, S.O. Jeon, J.Y. Lee, Thin Solid Films 518 (2010) 5827.
[34] S.H. Kim, J. Jang, J.Y. Lee, Appl. Phys. Lett. 91 (2007) 083511.
[35] S.H. Kim, J. Jang, K.S. Yook, J.Y. Lee, Appl. Phys. Lett. 92 (2008) 023513.
[36] J.H. Lee, H.H. Tsai, M.K. Leung, C.C. Yang, C.C. Chao, Appl. Phys. Lett. 90 (2007) 243501.
[37] J.H. Lee, C.L. Huang, C.H. Hsiao, M.K. Leung, C.C. Yang, C.C. Chao, Appl. Phys. Lett. 94 (2009) 223301.
[38] C.H. Hsiao, J.H. Lee, C.A. Tseng, Chem. Phys. Lett. 427 (2006) 305.
[39] Md.K. Nazeeruddin, R. Humphry-Baker, D. Berner, S. Rivier, L. Zuppiroli, M. Graetzel, J. Am. Chem. Soc. 125 (2003) 8790.
[40] C.H. Hsiao, Y.H. Chen, T.C. Lin, C.C. Hsiao, J.H. Lee, Appl. Phys. Lett. 89 (2006) 163511.
[41] K. Saito, N. Matsusue, H. Kanno, Y. Hamada, H. Takahashi, T. Matsumura, Jpn. J. Appl. Phys. 43 (2004) 2733.
[42] C.H. Chen, H.F. Meng, Appl. Phys. Lett. 86 (2005) 201102.
[43] Q. Wang, J. Ding, D. Ma, Y. Cheng, L. Wang, X. Jing, F. Wang, Adv. Funct. Mater. 19 (2009) 84.
[44] J.H. Seo, S.J. Lee, B.M. Seo, S.J. Moon, K.H. Lee, J.K. Park, S.S. Yoon, Y.K. Kim, Org. Electron. 11 (2010) 1759.
[45] S.J. Su, E. Gonmori, H. Sasabe, J. Kido, Adv. Mater. 20 (2008) 4189.
[46] J.H. Lee, J.J. Huang, C.C. Liao, P.J. Hu, Y. Chang, Chem. Phys. Lett. 402 (2005) 335.
[47] J.H. Lee, Y.H. Ho, T.C. Lin, C.F. Wu, J. Electrochem. Soc. 154 (2007) J226.
[48] C.H. Hsiao, Y.H. Lan, P.Y. Lee, T.L. Chiu, J.H. Lee, Org. Electron. 12 (2011) 547.
[49] S.W. Liu, C.C. Lee, C.F. Lin, J.C. Huang, J.H. Lee, C.T. Chen, J. Mater. Chem. 20 (2010) 7800.
[50] T. Matsushima, M. Takamori, Y. Miyashita, Y. Honma, T. Tanaka, H. Aihara, H. Murata, Org. Electron. 11 (2010) 16.
[51] J.H. Lee, M.H. Wu, C.C. Chao, H.L. Chen, M.K. Leung, Chem. Phys. Lett. 416 (2005) 234.
[52] K.S. Yook, S.O. Jeon, C.W. Joo, J.Y. Lee, Thin Solid Films 518 (2010) 4462.

by choosing electron-withdrawing substituents on the cyclometalated ligands to stabilize the highest occupied molecular orbital (HOMO) or electron-donating substituents on the ancillary ligands to destabilize the lowest unoccupied molecular orbital (LUMO), thus can lead to a wider HOMO–LUMO gap, as demonstrated in neutral iridium complexes [7–9]. However, for those cationic iridium complexes containing 2,2′-bipyridine(bpy)-type ancillary ligands, due to the intrinsically narrowed energy gap of bpy-type ligands [10], it is very difficult to tune the emission color into the blue region and most of the emission is still peaked at blue-green region. Therefore, the electronic properties of the ancillary ligand become the decisive factors in shifting the emission color of the cationic iridium complex toward blue region. Compared with the bpy-type ancillary ligand, the anionic N-based heterocyclic rings have attracted much research interests [5,11,12] since the electron denoting N atom of the ancillary ligand can strongly destabilize the LUMO, thus can increase the energy gap and result in a blue-shifted emission in the cationic iridium complex. Recently, Qiu and co-workers [11] demonstrated that by using ancillary ligands involving electron-donating nitrogen, 2-(1*H*-pyrazol-1-yl)pyridine (pzpy), the emission of the obtained cationic iridium complex can be successfully tuned to blue region, despite that the EQE of the LECs is only 0.28% due to the severe excited-state quenching of the complexes in the light-emitting layer.

Compared with the pzpy, triazole-pyridine ancillary ligand has even more stronger electron-donating capability to realize a blue emission from cationic iridium complex due to the strong σ-donor properties of the triazole ring [13]. Despite their successful application in neutral iridium complexes [9,14–20], however, a few about employing triazole-pyridine ancillary ligand in the cationic iridium complexes were reported. De Cola and co-workers [19,21,22] demonstrated the blue emission in LEC devices recently, in which 1,2,3-triazole as ancillary ligand was used [23]. In this paper, 1,2,4-triazole-pyridine was used as ancillary ligand in the cationic complex to tune the emission into the blue region. Moreover, it was found that cyanogen group in the alkyl chain has a significant impact on the device performances.

2. Experimental section

2.1. Materials and analytical instruments

All reactants and solvents purchased from commercial sources and used as received unless otherwise stated. All reactions were performed under an argon atmosphere. ^{1}H NMR spectra of compounds were collected on a 300 MHz spectrometer at room temperature. Photo-physical characteristics of complexes were collected at room temperature in dichloromethane (DCM) solution of 10^{-3} M, which were carefully purged with nitrogen prior to measurements. UV–vis absorption spectra were recorded on a HP 8453 spectrophotometer. PL spectra were measured with a cooled charge coupled device (CCD) coupled to a monochromator using the 325-nm line of the He-Cd laser as the excitation. Elemental analyses were performed on a Vario EL elemental analysis instrument (Elementar Co.). Thermogravimetric analyses (TGA) were performed on a Netzsch TG 209 at a heating rate of 20 °C/min. DSC measurements were performed on a Netzsch DSC 204 under N_2 flow at the heating rate of 15 °C/min. Cyclic voltammetry (CV) was performed on a CHI660A electrochemical workstation at a scan rate of 100 mV/s at room temperature under argon protection in CH_3CN solution of 10^{-3} M with tetrabutylammonium hexafluorophosphate of 0.1 mol/L as the supporting electrolyte. A platinum electrode was used as the working electrode, and a Pt wire as the counter electrode, and a calomel electrode as the reference electrode. The energy level and energy gap were calculated from the empirical formula [24]: $E_{HOMO} = -e(E_{ox} - E_{1/2,ferrocene}) + (-4.8)$ eV; $E_{LUMO} = -e(E_{red} - E_{1/2}) + (-4.8)$ eV; $E_{gap} = E_{HOMO} - E_{LUMO}$; E_{HOMO} is the energy level of the highest occupied molecular orbital; E_{LUMO} is the energy level of the lowest unoccupied molecular orbital; E_{gap} is the energy gap; E_{ox} is the oxidation potential; E_{red} is the reduction potential.

2.2. Synthesis

2.2.1. 2,2-Dimethyl-6-(3-methyl-5-(pyridin-2-yl)-4H-1,2,4-triazol-4-yl) hexanenitrile (trzpy-cn)

The compound 5-methyl-3-(pyridin-2-yl)-4*H*-1,2,4-triazole (hptz) was synthesized according to the literature [25] with a yield of 60%. The ancillary ligand 2,2-dimethyl-6-(3-methyl-5-(pyridin-2-yl)-4*H*-1,2,4-triazol-4-yl) hexanenitrile (trzpy-cn) was synthesized from hptz and 6-bromo-2,2-dimethylhexanenitrile by following procedure. Hptz (1.11 g, 7.6 mmol), 6-bromo-2,2-dimethylhexanenitrile (1.87 g, 12 mmol), and potassium carbonate (3.72 g, 11 mmol) were dissolved in acetone (40 mL). The solution was refluxed under an argon atmosphere for 48 h and then cooled to room temperature. The solvent was removed under vacuum and the residue was extracted with dichloromethane (150 mL). The product was then obtained by column chromatography on silica gel (200–300 mesh) first with petroleum ether/ethyl acetate (4:1) as the eluent, then with the ethanol to yield a white solid (1.15 g, 5.2 mmol). Yield: 68%. ^{1}H NMR ($CDCl_3$, 300 MHz), δ (ppm): 8.73 (s, 1H, ArH), 8.10 (d, 1H, J = 7.92 Hz, ArH), 7.78 (t, 1H, J = 6.27 Hz, ArH), 7.30 (d, 1H, J = 6.45 Hz, ArH), 4.18 (t, 2H, J = 6.87 Hz, –N–CH_2–), 2.55 (s, 3H), 2.0–2.1 (m, 2H), 1.52–1.58 (m, 4H), 1.33 (s, 6H).

2.2.2. [Ir(dfppy)$_2$(trzpy-cn)]PF$_6$ (**C1**)

In a round-bottomed flask, 0.200 g dichloro-bridged iridium dimer $[Ir(dfppy)_2Cl]_2$ and 2.2 equiv the ancillary ligand trzpy-cn are mixed together in 25 mL ethylene glycol. The solution was then heated to reflux (150 °C) under an inert atmosphere with constant stirring for 15 h. Upon cooling to room temperature, a 10 mL aqueous ammonium hexafluorophosphate solution (1.0 g in 10 mL deionized water) was added to the reaction mixture, producing a yellow-green powder. The precipitate was filtered and washed with deionized water, and then was dried under vacuum at 70 °C for 12 h. The crude product was purified by column chromatography on neutral alumina with CH_2Cl_2 as the eluent, yielding a light-yellow powder. Yield:

77%. ^{1}H NMR (300 MHz, $CDCl_3$) δ (ppm): 8.49 (d, 1H, J = 8.04 Hz, ArH), 8.33 (d, 3H, J = 8.52 Hz, ArH), 7.81–7.93 (m, 4H, ArH), 7.49–7.56 (m, 2H, ArH), 7.21–7.24 (m, 2H, ArH), 6.50–6.60 (m, 2H, ArH), 5.64–5.68 (m, 2H, ArH), 4.72–4.89 (m, 2H), 2.10–2.15 (m, 2H), 1.78 (s, 3H), 1.44–1.48 (m, 4H), 1.34 (s, 6H). ESI: m/z 856.3 $(M-PF_6)^+$. Anal. Found (%): C 45.52, H 3.46, N 9.17. Anal. Calcd for $C_{38}H_{33}N_7$ $PF_{10}Ir$: C 45.61, H 3.30, N 9.80.

*2.2.3. [Ir(mppy)$_2$(trzpy-cn)]PF$_6$ (**C2**)*

The synthesis was similar to that of **C1** except that the dichloro-bridged diiridium complex $[Ir(dfppy)_2Cl]_2$ was replaced with $[Ir(mppy)_2Cl]_2$. Yield: 70%. ^{1}H NMR (300 M Hz, $CDCl_3$) δ (ppm): 8.31 (d, 1H, J = 7.92 Hz, ArH), 7.98–8.08 (m, 2H, ArH), 7.73–7.89 (m, 5H, ArH), 7.55 (t, 2H, J = 6.15 Hz, ArH), 7.43 (d, 1H, J = 5.79 Hz, ArH), 7.30–7.37 (m, 2H, ArH), 6.95 (t, 1H, J = 7.14 Hz, ArH), 6.83 (t, 2H, J = 7.98 Hz, ArH), 6.14 (s, 1H, ArH), 6.05 (s, 1H, ArH), 4.10–4.32 (m, 2H), 2.10 (s, 6H), 2.02–2.09 (m, 2H), 1.89 (s, 3H), 1.50–1.52 (m, 4H), 1.31 (s, 6H). ESI: m/z 812.3 $(M-PF_6)^+$. Anal. Found (%): C 50.11, H 4.35, N 9.30. Anal. Calcd for $C_{40}H_{41}N_7$ PF_6Ir: C 50.2, H 4.31, N 10.2.

*2.2.4. [Ir(dfppy)$_2$(trzpy-hx)](PF$_6$) (**C3**) and [Ir(mppy)$_2$-(trzpy-hx)](PF$_6$) (**C4**)*

Compounds **C3** and **C4** were synthesized according to the similar methods with that of **C1** and **C2**, respectively. Compound **C3**: Yield: 65%. ^{1}H NMR (300 MHz, $CDCl_3$) δ (ppm): 8.33–8.35 (m, 2H, ArH), 8.27 (d, 1H, J = 9.21 Hz, ArH), 8.04–8.14 (m, 2H, ArH), 7.79–7.85 (m, 3H, ArH), 7.40–7.46 (m, 3H, ArH), 7.07 (t, 1H, J = 6.12 Hz, ArH), 6.49–6.61 (m, 2H, ArH), 5.71–5.75 (m, 1H, ArH), 5.61–5.65 (m, 1H, ArH), 4.10–4.29 (m, 2H), 1.96 (s, 3H), 1.23–1.44 (m, 12H), 0.88 (t, 3H, J = 7.08 Hz). ESI: m/z 854.3 $(M-PF_6)^+$. Anal. Found (%): C 46.21, H 3.99, N 8.18. Anal. Calcd for $C_{38}H_{36}N_6$ $PF_{10}Ir$: C 46.10, H 3.61, N 8.40.

Compound **C4**: Yield: 67%. ^{1}H NMR (300 MHz, $CDCl_3$) δ (ppm): 8.29 (d, 1H, J = 7.74 Hz, ArH), 7.95–8.04 (m, 2H, ArH), 7.70–7.89 (m, 5H, ArH), 7.55 (t, 2H, J = 7.50 Hz, ArH), 7.44 (d, 1H, J = 5.73 Hz, ArH), 7.34–7.38 (m, 2H, ArH), 6.93–6.97 (m, 1H, ArH), 6.78–6.86 (m, 2H, ArH), 6.15 (s, 1H, ArH), 6.05 (s, 1H, ArH), 4.13–4.15 (m, 2H), 2.12 (s, 3H), 1.85 (s, 6H), 1.23–1.26 (m, 12H), 0.88 (t, 3H, J = 7.11 Hz). ESI: m/z 810.2 $(M-PF_6)^+$. Anal. Found (%): C 50.9, H 4.52, N 8.31. Anal. Calcd for $C_{40}H_{44}N_6PF_6Ir$: C 50.8, H 4.60, N 8.80.

2.3. Fabrication and characterization of LEC devices

LEC devices were fabricated by spin-coating the mixed solutions of complexes on indium-tin-oxide coated glass substrates to form a 100-nm thick film, followed by thermal evaporation of a 150 nm Al top contact (cathode). $BMIM^+(PF_6)^-$ was added to provide additional anions, which shortened the device response time. The electrical and emission characteristics of LECs were measured under constant bias voltages. The current density–time–luminance characteristics were collected using a Keithley 236 source measurement unit and a calibrated silicon photodiode. The luminance was calibrated by a PR-705 SpectraScan Spectrophotometer (Photo Research) with simultaneous acquisition of the EL spectra and CIE coordinates, driven by a Keithley model 2400 vague-current source, and all of the device fabrication and measurements were performed in the glove box filled with nitrogen. The alternating current (ac) impedances were measured using a HP4192A impedance analyzer in the frequency (f) range from 100 Hz to 5 MHz at room temperature, with an ac drive amplitude of 30 mV. The impedance results in the paper are expressed as: $Z = Z' - jZ''$, where Z' and Z'' are the real part and the imaginary part of the impedance, respectively.

3. Results and discussion

3.1. Synthesis and characterization

The synthetical routes of the ligands and complexes are shown in Scheme 1. **C1** refers to $[Ir(dfppy)_2(trzpy\text{-}cn)]^+(PF_6)^-$, and **C2** to $([Ir(mppy)_2(trzpy\text{-}cn)]^+(PF_6)^-$, where dfppy is 2-(2,4-difluorophenyl)pyridine, trzpy-cn is 2,2-dimethyl-6-(3-methyl-5 -(pyridin-2-yl)-4*H*-1,2,4-triazol-4-yl) hexanenitrile). The ancillary ligand trzpy-cn was easily synthesized from 5-methyl-3-(pyridin-2-yl)-4*H*-1,2,4-triazole (hptz) and 6-bromo-2,2-dimethylhexanenitrile by alkylation reaction. Compounds **C1** and **C2** were then synthesized by reacting dimeric iridium intermediates with trzpy-cn, following by ion exchange from Cl^- to PF_6^-. Compounds **C3** and **C4,** in which the cyanogen group is absent in the alkyl chain were synthesized with the similar methods to **C1** and **C2**, respectively, except that the 6-bromo-2,2-dimethylhexanenitrile was replaced with the 1-bromooctane.

3.2. Thermal and electrochemical properties

The thermal properties of the complexes ware investigated by the thermogravimetric (TGA) and differential scanning calorimetry (DSC). TGA curves of the complexes are shown in Fig. 1. The decomposition temperatures (T_d, corresponding to 5 wt.% loss) and the glass transition temperature (T_g) for complexes are shown in Table 1. The decomposition temperatures for **C1**, **C2**, **C3** and **C4** are as high as 370, 358, 360 and 351 °C, respectively. Compared with **C4**, the higher T_d of **C2** suggests that cyanogen group have the ability to increase the thermal stability of the complex. On the other hand, the highest T_d of **C1** could be attributed to the presence of fluorine atom and cyanogen group. The T_gs for **C2**, **C3** and **C4** are 131, 113, and 118 °C, respectively. The high T_g and T_d are important for the complexes to be used in LECs applications, which would be expected to retain stable film morphology during the device operation. The morphologies of **C1** and **C2** film were investigated by AFM (Fig. 2) spin-coated from acetonitrile solvent, which forms homogeneous film with very low average surface roughness (0.683 nm for **C1** and 0.381 nm for **C2**).

The electrochemical properties of the complexes were investigated by cyclic voltammetry (Fig. 3) and the data are summarized in Table 1. As shown in Fig. 3, the complexes exhibit reversible oxidation and reduction processes in CH_3CN solution. The redox reversibility of the complexes indicates that both holes (upon oxidation) and electrons

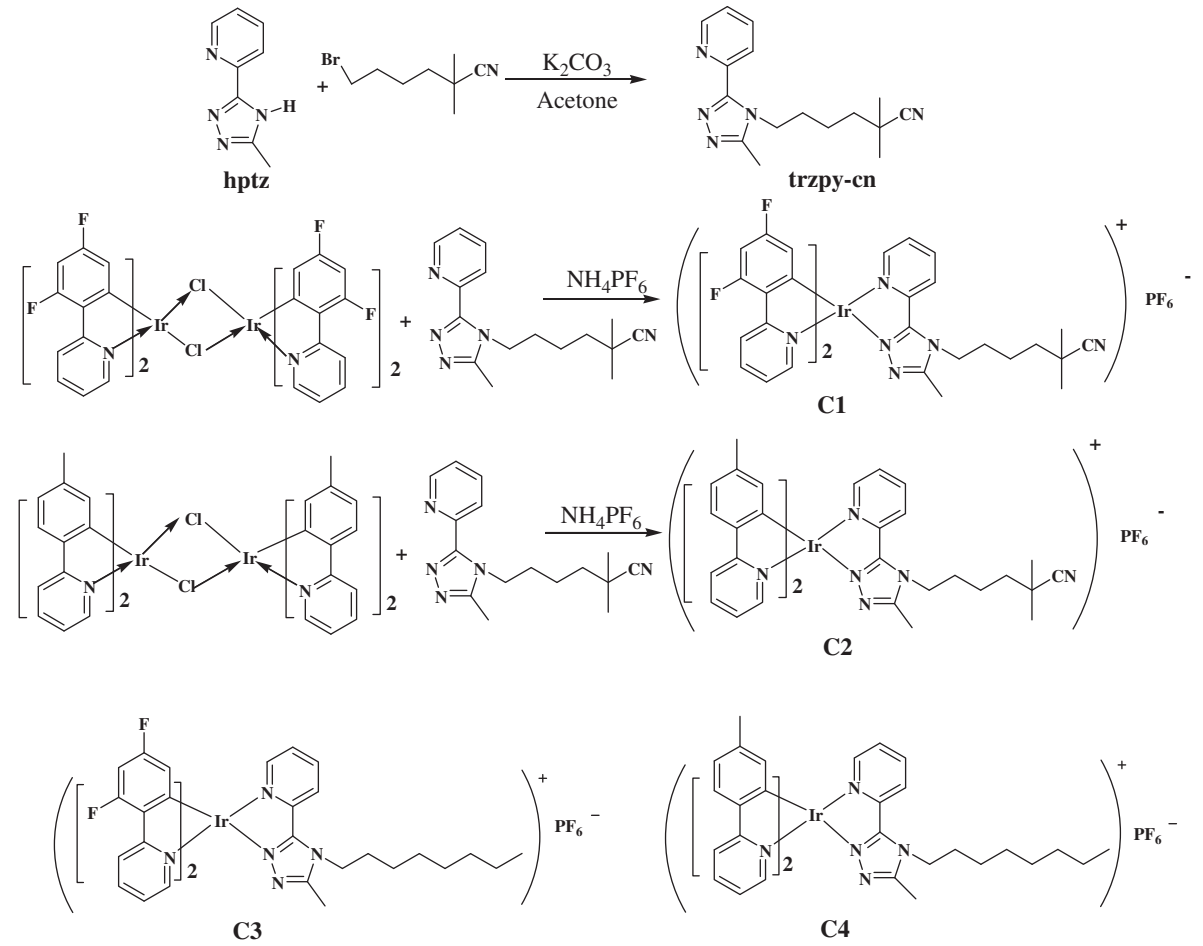

Scheme 1. The synthetic routes of the complexes.

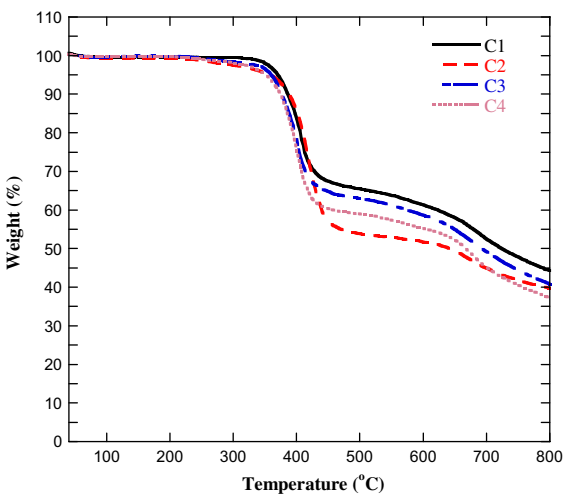

Fig. 1. TGA curves of the complexes at a heating rate of 20 °C/min in nitrogen.

(upon reduction) can be transported, therefore efficient LECs can be constructed based on these complexes. The measured oxidation potentials for **C1** and **C2** were 1.14 and 0.74 V as referred to ferrocene, respectively, which can be mainly assigned to the oxidation of Ir(**III**) cationic site to Ir(**IV**), with a minor contribution from the cyclometalated ligand. The higher oxidation potential of **C1** can be attributed to the strong electron-withdrawing fluorine substituents in the complex, which decrease the electron density in the phenylpyridines, thus make the complex more difficult to be oxidized [3,26,27].

The measured reduction potentials for **C1** and **C2** are −1.92 and −1.99 V, respectively, which are mainly assigned to the reduction of ancillary ligand. The slightly lower reduction potentials of **C1** can be attributed to the fluorine atom which also makes the complex more electrophilic and decrease the reduction potential as described in the literature [28]. The higher LUMO of **C1** (−2.88 eV) and **C2** (−2.81 eV) respect to $[Ir(ppy)_2(dtb\text{-}bpy)]PF_6$ [10] indicate that the LUMO are significantly destabilized by the ancillary ligand trzpy-cn due to the strong electron-donating triazole ring. The HOMO–LUMO gap of **C1** and **C2** are 3.05 and 2.73 eV, respectively. A wider energy gap observed in **C1** than that in **C2** thus can suggest a blue-shifted emission. The electrochemical properties of **C3** and **C4** are almost identical with that of **C1** and **C2**, respectively, as referred in Table 1.

Table 1
The physical properties of the complexes.

Complex	UV (nm)	PL (nm)	E_{ox} (V)	E_{red} (V)	HOMO (eV)	LUMO (eV)	E_{gap} (eV)	T_d[a] (°C)	T_g (°C)
C1	249, 366	454, 485	1.14	−1.92	−5.93	−2.88	3.05	370	–
C2	257, 388	480, 512	0.74	−1.99	−5.54	−2.81	2.73	358	131
C3	249, 367	453, 485	1.15	−1.98	−5.92	−2.82	3.10	360	113
C4	256, 387	479, 512	0.75	−2.03	−5.55	−2.77	2.78	351	118

[a] Corresponding to 5 wt.% loss.

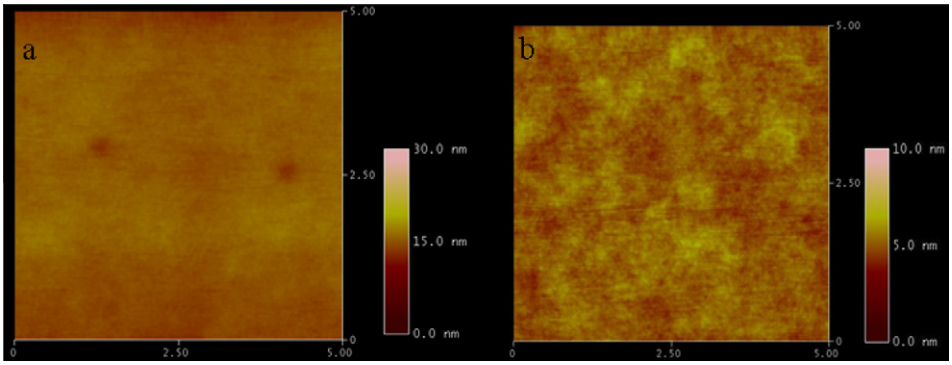

Fig. 2. AFM images (5 μm × 5 μm) of **C1** (a) and **C2** (b) spin-coated in acetonitrile solution onto ITO substrates.

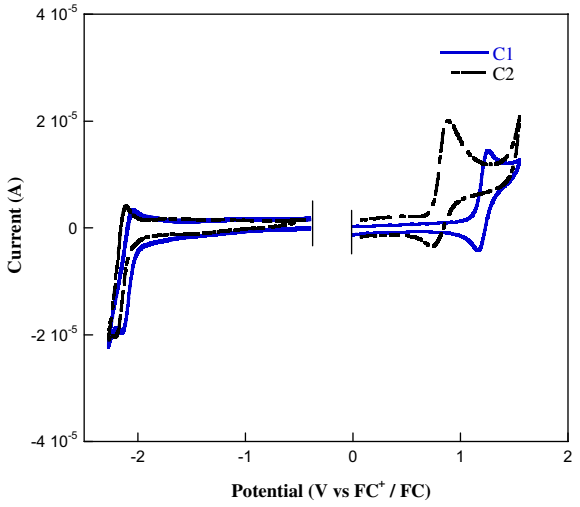

Fig. 3. Cyclic voltammograms of **C1** and **C2** in CH_3CN solution of 10^{-3} M, potentials recorded versus Fc^+/Fc (ferrocene).

3.3. Photophysical properties

The UV–vis absorption and photoluminescence (PL) spectra of the complexes in CH_2Cl_2 solution as well as in film are shown in Fig. 4. The intense absorption bands in the region of 230–350 nm can be ascribed to spin-allowed $^1\pi$–π ligand-centered (LC) transitions. The relatively weak absorption bands range between 350 nm and the visible region correspond to metal-to-ligand charge-transfer transitions (^{3}MLCT) of the complexes. As compared with **C2**, the absorption of the **C1** shows a blue-shift of 30 nm due to the electron-withdrawing fluorine atom in the ligand.

The photo-physical characteristics of the obtained complexes are summarized in Table 1. The PL spectra of **C1** and **C2** in solution are peaked at 452 nm and 479 nm, located in the blue and blue-green region, respectively. The PL spectra of **C1** are significantly blue-shifted about 80 nm with respect to the ionic iridium complexes used bpy as the ancillary ligand, such as $[Ir(dfppy)_2(dtb\text{-}bpy)](PF_6)$(534 nm) [29]. The results clearly demonstrate that the trzpy-cn ancillary ligand has a favorable capability to tune the emission color of the cationic iridium complex to blue region.

As compared with that in solution, the PL spectra of **C1** and **C2** in film are only a little broaden, implying a weak excited-state quenching of the complexes in solid-state, which is very important toward highly efficiency non-doping single-layer LECs. Of which, the emission of **C1** peaked at 454 nm in film is one of the shortest wavelength for cationic iridium complex reported up to now [26,30,31].

3.4. Electroluminescent properties

LECs with device structure of indium tin oxide (ITO)/poly(3,4-ethylenedioxy-thiophene): poly(styrene sulfonate)(PEDOT:PSS)/(complex:$BMIM^+(PF_6^-)$ 14 wt.%)/Al was fabricated, where the PEDOT:PSS layer is inserted as anode buffer layer to smoothen the anode surface and facilitate hole injection, while ionic liquid $BMIM^+(PF_6^-)$ (1-butyl-3-methylimidazolium hexafluorophosphate) is introduced into the emissive layer to reduce the response time of these devices.

Electroluminescent spectra of the complexes are shown in Fig. 5. The device based on **C1** emits sky-blue light with CIE coordinates of (0.21, 0.33), which is, to our knowledge, one of the bluest light emission for LECs from ionic complexes reported so far [4,5,8,11,26]. The device based on

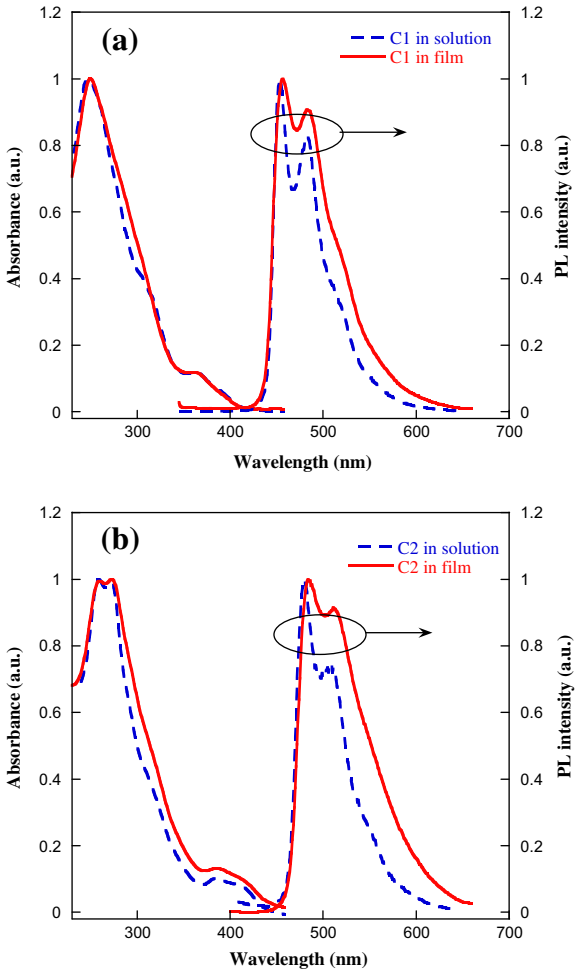

Fig. 4. Absorption spectra and fluorescence spectra of **C1** (a) and **C2** (b) in dilute CH_2Cl_2 solution and in film.

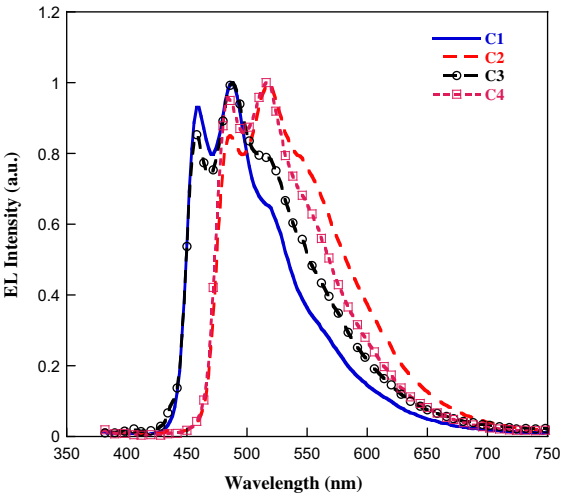

Fig. 5. Electroluminescent spectra of **C1**–**C4** with the device configuration of ITO/PEDOT:PSS/complex:$BMIMPF_6$/Al.

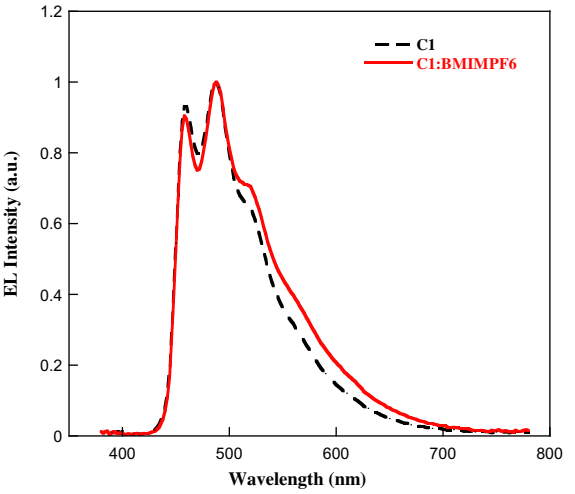

Fig. 6. Electroluminescent spectra of complex **C1** with and without $BMIMPF_6$.

C2 emits blue-green light with CIE coordinates of (0.31, 0.53). In addition, the devices from **C3** and **C4** exhibit almost the similar EL spectra with that of **C1** and **C2**, respectively. Unlike other reports [11], EL spectra of the complexes are almost identical with and without $BMIM^+(PF_6^-)$ (Fig. 6), which suggest that the emissive excited state of complexes are very stable even in the $BMIM^+(PF_6^-)$ blended film [32].

The device performances are shown in Table 2. The device from **C1** exhibit a LE of 2.6 cd/A (corresponding to an EQE of 2.7%), comparable with the best in literatures [11,26,30]. The LE of **C1** (2.6 cd/A) is 10 times of that of the **C3** (0.26 cd/A). Similarly, the LE of the **C2** device is found to be 4 times over that of **C4** device (6.8 cd/A vs. 1.7 cd/A). Fig. 7a shows the current density–luminance–time characteristics of LECs based on **C1** and **C3** under a constant bias of 5.0 V. We note that the device of **C1** exhibits much faster turn-on time (23 min vs. 45 min), higher current density, and higher brightness compared with the **C3** device. The similar results also can be found in **C2** and **C4** devices(Fig. 7b), in which **C2**/**C4** devices show faster turn-on time (4 min for **C2**, 12 min for **C4**) than **C1**/**C3** device. The results show that the cyanogen group in the alkyl chain of the complexes has a significant impact on the response time and the efficiency of LEC device.

Underlying mechanism responsible for the enhanced performances in **C1**/**C2** devices was further investigated by using alternating current (ac) impedance spectroscopy [33,34]. Fig. 8 shows Cole–Cole plots of the devices at several different bias voltages based on **C2** and **C4**. As can be clearly seen, under the same applied voltage studied, **C2** device shows much smaller electrical impedance than **C4** device, implying a higher ion mobility in the former device as expected from differential form of Ohm law. Therefore, the faster motion of the ions in the **C1**/**C2** devices can ensure the faster turn-on time and the higher current density observed in the devices as mentioned above. So

Table 2
Electrical characteristics of LECs at different bias voltages.

Materials[a]	Bias Voltage (v)	Turn-on time[b] (min)	Maxima			EL λ (nm)	CIE (x, y)
			Brightness (cd/m2)	Efficiency (cd/A)	EQE%		
C1	4	52	5.3	2.6	2.7	(458, 488)	(0.21, 0.33)
	4.5	35	20.2	2.2	2.3		
	5	23	48.1	2.3	2.4		
C2	4	4.5	97	3.5	1.4	(484, 517)	(0.31, 0.53)
	4.5	1.5	308	6.8	2.8		
	5	1.0	430	3.8	1.5		
C3	4.5	140	4.5	0.26	0.27	(457, 486)	–
	5	45	10.5	0.27	0.28		
C4	4.5	5.0	175	1.7	0.67	(483, 515)	–
	5	2.6	228	2.9	1.1		

[a] The device structures of ITO/PEDOT:PSS/complex:BMIMPF$_6$ (1:0.14)/Al.
[b] Time required to reach 1.0 cd/m^2.

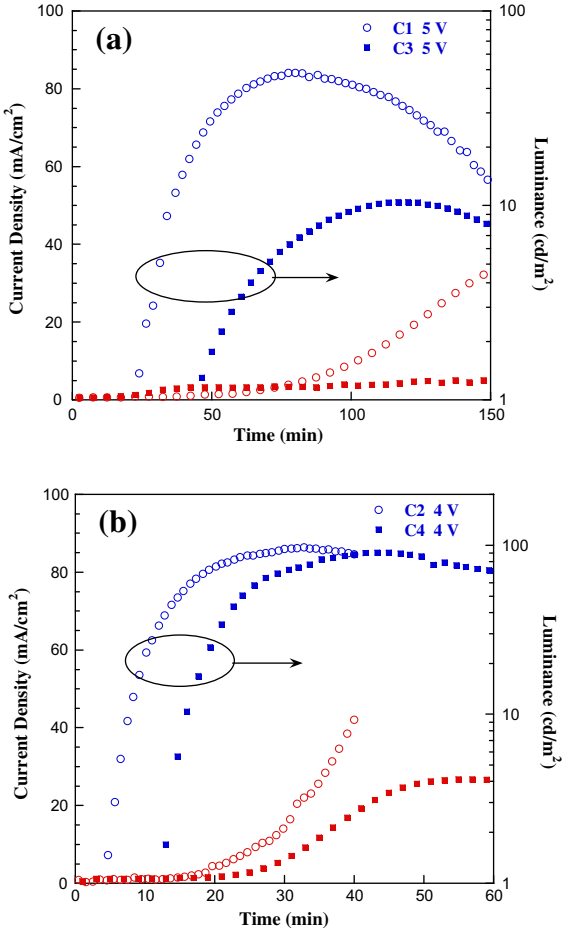

Fig. 7. Time-dependent curves of current density and brightness of **C1**, **C3** (a), and **C2**, **C4** (b), with the device structure of ITO/PEDOT:PSS/C:BMIMPF$_6$ (1:0.14 wt.)/Al.

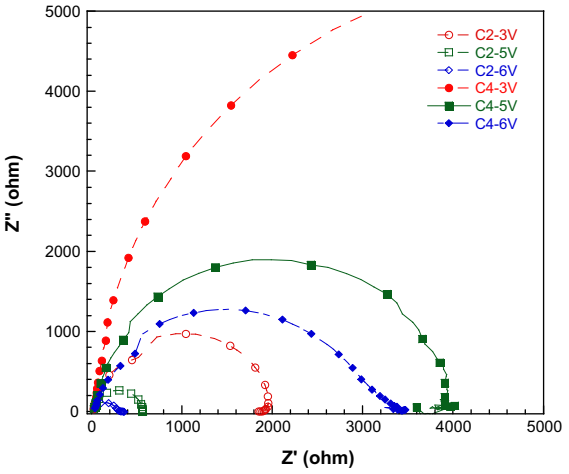

Fig. 8. Cole–Cole plots of the devices based on **C2** and **C4** at different bias voltages.

far, the observed higher ion mobilities in the **C1**/**C2** devices could be attributed to the interaction between the cyanogen group in the alkyl chain of the complexes and the electrodes, and hence lead to smaller electrical impedances and improved device efficiencies.

4. Conclusions

Four novel sky-blue and blue-green emitting cationic iridium complexes with triazole-pyridine as the ancillary ligand were prepared and characterized. The emission of these cationic iridium complexes can be tuned and blue-shifted by using triazole-pyridine ancillary ligand. Upon the cyanogen group in the side alkyl chain of the ancillary ligand, the device efficiencies were significantly improved. Single layer LECs based on **C1** and **C2** show a high luminous efficiency of 2.6 cd/A with CIE coordinate of (0.21, 0.33), and a LE of 6.8 cd/A with a CIE coordinate of (0.31, 0.53), respectively.

Acknowledgements

W.Y. thanks the State Key Basical Research Project of China (Nos. 2009CB623602 and 2009CB930604), the National Nature Science Foundation of China (Nos. U0634003 and 21074038) and H.B.W. thanks the Fundamental Research Funds for the Central Universities for the financial support.

References

[1] Q. Pei, G. Yu, C. Zhang, Y. Yang, A.J. Heeger, Science 269 (1995) 1086.
[2] Q. Pei, G. Yu, C. Zhang, Y. Yang, A.J. Heeger, J. Am. Chem. Soc. 118 (1996) 3922.
[3] J.D. Slinker, C.Y. Koh, G.G. Malliaras, M.S. Lowry, S. Bernhard, Appl. Phys. Lett. 86 (2005) 173506.
[4] H.J. Bolink, L. Cappelli, E. Coronado, A. Parham, P. Stossel, Chem. Mater. 18 (2006) 2778.
[5] A.B. Tamayo, S. Garon, T. Sajoto, P.I. Djurovich, I.M. Tsyba, R. Bau, M.E. Thompson, Inorg. Chem. 44 (2005) 8723.
[6] C. Rothe, C.J. Chiang, V. Jankus, K. Abdullah, X.S. Zeng, R. Jitchati, A.S. Batsanov, M.R. Bryce, A.P. Monkman, Adv. Funct. Mater. 19 (2009) 2038.
[7] I. Avilov, P. Minoofar, J. Cornil, L. De Cola, J. Am. Chem. Soc. 129 (2007) 8247.
[8] D. Di Censo, S. Fantacci, F. De Angelis, C. Klein, N. Evans, K. Kalyanasundaram, H.J. Bolink, M. Gratzel, M.K. Nazeeruddin, Inorg. Chem. 47 (2008) 980.
[9] E. Orselli, G.S. Kottas, A.E. Konradsson, P. Coppo, R. Frohlich, R. Frtshlich, L. De Cola, A. van Dijken, M. Buchel, H. Borner, Inorg. Chem. 46 (2007) 11082.
[10] J.D. Slinker, A.A. Gorodetsky, M.S. Lowry, J. Wang, S. Parker, R. Rohl, S. Bernhard, G.G. Malliaras, J. Am. Chem. Soc. 126 (2004) 2763.
[11] L. He, L. Duan, J. Qiao, R. Wang, P. Wei, L. Wang, Y. Qiu, Adv. Funct. Mater. 18 (2008) 2123.
[12] L. He, J. Qiao, L. Duan, G.F. Dong, D.Q. Zhang, L.D. Wang, Y. Qiu, Adv. Funct. Mater. 19 (2009) 2950.
[13] S. Fanni, T.E. Keyes, C.M. O'Connor, H. Hughes, R.Y. Wang, J.G. Vos, Coord. Chem. Rev. 208 (2000) 77.
[14] S.J. Yeh, M.F. Wu, C.T. Chen, Y.H. Song, Y. Chi, M.H. Ho, S.F. Hsu, C.H. Chen, Adv. Mater. 17 (2005) 285.
[15] P. Coppo, E.A. Plummer, L. De Cola, Chem. Commun. (2004) 1774.
[16] T. Sajoto, P.I. Djurovich, A. Tamayo, M. Yousufuddin, R. Bau, M.E. Thompson, R.J. Holmes, S.R. Forrest, Inorg. Chem. 44 (2005) 7992.
[17] C.J. Chang, C.H. Yang, K. Chen, Y. Chi, C.F. Shu, M.L. Ho, Y.S. Yeh, P.T. Chou, Dalton Trans. (2007) 1881.
[18] X.J. Zhang, C.Y. Jiang, Y.Q. Mo, Y.H. Xu, H.H. Shi, Y. Cao, Appl. Phys. Lett. 88 (2006) 051116.
[19] S. Stagni, S. Colella, A. Palazzi, G. Valenti, S. Zacchini, F. Paolucci, M. Marcaccio, R.Q. Albuquerque, L. De Cola, Inorg. Chem. 47 (2008) 10509.
[20] E. Orselli, R.Q. Albuquerque, P.M. Fransen, R. Frohlich, H.M. Janssen, L. De Cola, J. Mater. Chem. 18 (2008) 4579.
[21] C.H. Yang, J. Beltran, V. Lemaur, J. Cornil, D. Hartmann, W. Sarfert, R. Frohlich, C. Bizzarri, L. De Cola, Inorg. Chem. 49 (2010) 9891.
[22] M. Felici, P. Contreras-Carballada, J.M.M. Smits, R.J.M. Nolte, R.M. Williams, L. De Cola, M.C. Feiters, Molecules 15 (2010) 2039.
[23] M. Mydlak, C. Bizzarri, D. Hartmann, W. Sarfert, G. Schmid, L. De Cola, Adv. Funct. Mater. 20 (2010) 1812.
[24] J.L. Bredas, R. Silbey, D.S. Boudreaux, R.R. Chance, J. Am. Chem. Soc. 105 (1983) 6555.
[25] H.Y. Zhen, J. Luo, W. Yang, Q.L. Chen, L. Ying, J.H. Zou, H.B. Wu, Y. Cao, J. Mater. Chem. 17 (2007) 2824.
[26] M.S. Lowry, J.I. Goldsmith, J.D. Slinker, R. Rohl, R.A. Pascal, G.G. Malliaras, S. Bernhard, Chem. Mater. 17 (2005) 5712.
[27] C. Adachi, R.C. Kwong, P. Djurovich, V. Adamovich, M.A. Baldo, M.E. Thompson, S.R. Forrest, Appl. Phys. Lett. 79 (2001) 2082.
[28] J. Brooks, Y. Babayan, S. Lamansky, P.I. Djurovich, I. Tsyba, R. Bau, M.E. Thompson, Inorg. Chem. 41 (2002) 3055.
[29] F. Lafolet, S. Welter, Z. Popovic, L.D. Cola, J. Mater. Chem. 15 (2005) 2820.
[30] M.K. Nazeeruddin, R.T. Wegh, Z. Zhou, C. Klein, Q. Wang, F. De Angelis, S. Fantacci, M. Gratzel, Inorg. Chem. 45 (2006) 9245.
[31] L. He, L. Duan, J. Qiao, D.Q. Zhang, G.F. Dong, L.D. Wang, Y. Qiu, Org. Electron. 10 (2009) 152.
[32] H.J. Bolink, L. Cappelli, S. Cheylan, E. Coronado, R.D. Costa, N. Lardies, M.K. Nazeeruddin, E. Orti, J. Mater. Chem. 17 (2007) 5032.
[33] Y.F. Li, J. Gao, G. Yu, Y. Cao, A.J. Heeger, Chem. Phys. Lett. 287 (1998) 83.
[34] S.-C. Chang, Y. Yang, F. Wudl, G.F. He, Y.F. Li, J. Phys. Chem. B. 105 (2001) 11419.

1. Introduction

Organic semiconducting materials open the way of low-cost, flexible, and large-scale solar cells. Recently, power conversion efficiencies (PCEs) above 5% and to 6.1% have been reported for bulk-heterojunction (BHJ) solar cells [1–3]. These solar cells comprising interpenetrating networks of an organic donor (D) and a fullerene derivative acceptor (A) such as [6,6]-phenyl-C61-butyric acid methyl ester (PCBM) constitute a promising technology because they are easy to fabricate by solution processing and are predicted theoretically to yield PCEs of up to 10–15% if a suitable low band gap donor material is discovered [4]. Although considerable research effort has been expended to develop such low band-gap donor materials [5], the highest reported efficiencies have been dominated by conjugated polymers such as poly(3-hexylthiophene) (P3HT) [6–9]. This system has been explored thoroughly for the past decade. The high efficiency of P3HT–fullerene devices can be explained by the ability of the blend to phase separate and crystallize into desirable BHJ morphologies after processing, allowing for efficient charge separation and transport [10,11]. The current effort in this area was focused on developing the low band gap polymers to harvest the near infrared light [12]. However, polymers have problems of poor reproducibility, difficulty in purification, and poor controllability in the molecular weight. Thus efforts have been laid on developing solution processable low band gap organic SM donors, because they offer advantages of easy synthesis and purification and mono-dispersion in the molecular weight, which greatly improve the reproducibility in the performance of the devices.

Most of the researchers related to BHJ solar cells have focused on polymeric donor materials, since they generally have better film-forming properties than non-polymeric materials [13]. Small-molecule (SM) donor materials can also form useable BHJ solar cells by solution processing, although it is more challenging to obtain high-quality films. The highest reported efficiencies for such devices have remained lower relative to solution processed solar cells using polymeric donor materials. SM materials, however, offer advantages over polymeric materials in terms of ease of synthesis and purification, which greatly improve fabrication reproducibility, as well as possessing a greater tendency to self assemble into ordered domains, which leads to high charge carrier mobilities [14,15]. SMs do not suffer from batch to batch variations, broad molecular-weight distributions, end-group contamination, or difficult purification methods, which can be significant problems for polymeric materials. These considerations make SMs a promising class of donor material for BHJ solar cell applications [16–24]. The PCE of solution processable SMs has steadily improved up to in the range 2.0–4.4% [25], due to considerable efforts towards the development of new SMs having low band gap and semiconducting property. Particularly, significant progress has been made in the synthesis and processing of donor–acceptor (D–A) SMs. Theoretical and experimental progresses in organic solar cells (OSCs) have demonstrated that such D–A SMs and polymers have great potential to be one class of promising materials for OSCs. D–A SMs can be considered as efficient donor materials for OSCs because of the fact that the absorption spectrum of theses molecules can be extended towards longer wavelengths by intra-molecular charge transfer (ICT) transition between donor and acceptor inside molecules [21] and the energy level can be easily controlled by introducing various electron donating or acceptor groups into the molecules.

On the other hand, a number of polyfluorenes and their derivatives have been studied as a photoactive structure in polymer light-emitting devices and solar cells on account of their large band gap, high photoluminescence, electroluminescence efficiencies, good thermal/chemical stability, and good solubility in common organic solvents. Alternating polyfluorene copolymers with various band gaps have been synthesized, and solar cells based on some of these copolymers have demonstrated PCEs of ~1% [26,27]. A literature survey revealed that certain fluorene containing copolymers have been synthesized and used for BHJ solar cells very recently [28–32]. Finally, among the various types of reported polymer semiconductors, poly(*p*-phenylenevinylenes) (PPVs) [33–35] and their derivatives are widely used in solar cell applications as p-type donor materials. Poly[2-methoxy-5-(2-ethylhexyloxy)-1,4-phenlenevinylene] (MEH-PPV) is a PPV derivative which has been mainly used as electron donor for BHJ solar cells [36].

A series of low band gap SMs that contain cyanovinylene 4-nitrophenyl segments have been recently synthesized in our laboratory and used as donors with PCBM as acceptor for BHJ solar cells [37–41]. Additionally, we have very recently synthesized a modified PCBM derivative **F** (Scheme 1) carrying cyanovinylene 4-nitrophenyl segment [42]. Specifically, PCBM has been hydrolyzed to carboxylic acid and then converted to the corresponding carbonyl chloride. The latter was condensed with 4-nitro-4′-hydroxy-α-cyanostilbene to afford **F**. It showed higher solubility than PCBM in common organic solvents due to the increase of the organic moiety. Both solutions and thin films of **F** displayed stronger absorption than PCBM in the range of 250–900 nm. BHJ solar cells based on P3HT as electron donor with **F** as electron acceptor exhibited a PCE of 4.23%, while the device based on P3HT:PCBM exhibited PCE of 2.93% under the same conditions [42].

Herein, we report the synthesis of two low band gap SMs, **PH** and **FL**, based on phenylenevinylene and fluorenevinylene, respectively. They contain certain common structural characteristics, namely triphenylamine (TPA) and cyanovinylene 4-nitrophenyl segments. They are only

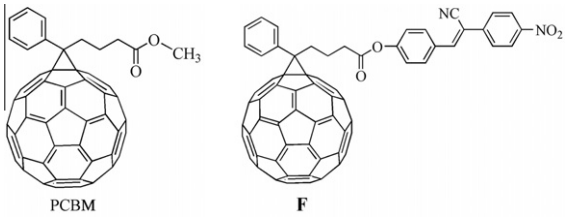

Scheme 1. Chemical structures of the electron acceptors (PCBM and **F**) used in this investigation.

differentiated by their central unit which is 2,5-dihexyloxy(phenylenevinylene) for **PH** and 9,9-dihexyl(fluorenevinylene) for **FL**. The aliphatic chains which are attached to the central unit enhanced the solubility of these SMs. They were successfully synthesized by a four-step reaction sequence. The last step of their synthesis included the condensation of a key-tetraaldehyde with 4-nitrobenzyl cyanide. Both SMs possess the D–A architecture. Specifically, they carry phenylenevinylene/fluorenevinylene and TPA as D units and cyanovinylene 4-nitrophenyl as A units which allow an intramolecular charge transfer (ICT), thus reducing the optical band gap (E_g^{opt}) of the SMs. Moreover, the presence of the TPA moieties is expected to increase the hole mobility of both SMs. We have used these SMs as electron donor along with PCBM or modified PCBM, i.e. **F** as electron acceptor for the fabrication of BHJ PV devices. The PCEs for the devices based on **PH**:PCBM and **FL**:PCBM cast from chloroform solvent are 1.02% and 1.46%, respectively. In addition, we investigated the effect of solvent used for the spin casting of the **FL**:PCBM blend on the PV response of the device and found that the solvent has a strong influence on the morphology of the blend films and on the PCE of the device. Finally, we have replaced the electron acceptor PCBM by the modified PCBM, i.e. **F**, which has strong absorption at lower wavelength region (below 500 nm) and fabricated BHJ devices using **FL** as electron donor. We have achieved PCE about 3.62% and 4.38% for **FL**:**F** BHJ active layer cast from o-dichlorobenzene (DCB) and 1-chloronaphthalene/o-dichlorobenzene (CN/DCB) solvent, respectively. The BHJ cast from the mixed solvents (CN/DCB) leads to an enhanced self organization and crystallinity of **FL** in active layer, which causes an increased charge transport, incident absorption and higher carrier mobility in the active layer thus contributing to the enhancement in the device performance.

2. Experimental

2.1. Reagents and solvents

4-Nitrobenzyl cyanide was synthesized from the nitration of benzyl cyanide with concentrated nitric and sulfuric acid [43]. It was recrystallized from ethanol. 1,4-Divinyl-2,5-bis(hexyloxy)-benzene was prepared by Stille coupling reaction [44] of 1,4-dibromo-2,5-bis(hexyloxy)-benzene with tributylvinyltin [45]. 9,9-Dihexyl-2,7-divinylfluorene was prepared by Stille coupling [44] of 2,7-dibromo-9,9-dihexylfluorene with tributylvinyltin [46]. *N*,*N*-dimethylformamide (DMF) and tetrahydrofuran (THF) were dried by distillation over CaH_2. Triethylamine was purified by distillation over KOH. All other reagents and solvents were commercially purchased and were used as supplied.

2.2. Preparation of small molecules

2.2.1. Compound ***3a***

A flask was charged with a mixture of **2** (0.2957 g, 0.778 mmol), 1,4-divinyl-2,5-bis(hexyloxy)-benzene (0.1285 g, 0.389 mmol), $Pd(OAc)_2$ (0.0017 g, 0.007 mmol), P(*o*-tolyl)$_3$ (0.0047 g, 0.015 mmol), DMF (10 mL), and triethylamine (3 mL). The flask was degassed and purged with N_2. The mixture was heated at 90 °C for 24 h under N_2. Then, it was filtered and the filtrate was poured into methanol. The precipitate was filtered and washed with methanol. The crude product was purified by dissolving in THF and precipitating into methanol (0.3072 g, yield 85%).

FT-IR (KBr, cm^{-1}): 2952, 2926 (C–H stretching of hexyloxy chains); 1676 (formyl); 3030, 1590, 1506 (aromatic); 1320 (C–N stretching of triphenylamine); 1286, 1272, 1214 (ether bond); 967 (*trans* vinylene bond).

^{1}H NMR ($CDCl_3$) ppm: 9.80 (s, 4H, formyl); 7.67 (m, 8H, TPA ortho to formyl); 7.30–7.2 (m, 16H, other TPA; 4H, vinylene); 6.75 (s, 2H, phenylene); 3.96 (m, 4H, $OCH_2(CH_2)_4CH_3$); 1.81 (m, 4H, $OCH_2CH_2(CH_2)_3CH_3$); 1.37 (m, 12H, $O(CH_2)_2(CH_2)_3CH_3$); 0.91 (t, 6H, $O(CH_2)_5CH_3$).

Anal. Calcd. for $C_{62}H_{60}N_2O_6$: C, 80.14; H, 6.51; N, 3.01. Found: C, 79.92; H, 6.43; N, 3.17.

2.2.2. Compound ***3b***

Compound **3b** was similarly prepared in 80% yield (0.22 g) from the reaction of **2** (0.2106 g, 0.554 mmol), with 9,9-dihexyl-2,7-divinylfluorene (0.1071 g, 0.277 mmol) in DMF (10 mL) in the presence of triethylamine (3 mL), $Pd(OAc)_2$ (0.0012 g, 0.005 mmol) and P(*o*-tolyl)$_3$ (0.0034 g, 0.011 mmol).

FT-IR (KBr, cm^{-1}): 2950, 2925 (C–H stretching of hexyl chains); 1675 (formyl); 3029, 1592, 1504 (aromatic); 1315 (C–N stretching of TPA); 965 (*trans* vinylene bond).

^{1}H NMR ($CDCl_3$) ppm: 9.80 (s, 4H, formyl); 7.72 (m, 2H, H4 of fluorene); 7.67–7.60 (m, 4H, H1 and H3 of fluorene; 8H, TPA ortho to formyl); 7.30–7.02 (m, 16H, other TPA; 4H, vinylene); 2.06 (m, 4H, $CH_2(CH_2)_4CH_3$); 1.11 (m, 16H, $CH_2(CH_2)_4CH_3$); 0.78 (t, 6H, $(CH_2)_5CH_3$).

Anal. Calcd. for $C_{69}H_{64}N_2O_4$: C, 84.11; H, 6.55; N, 2.84. Found: C, 83.85; H, 6.64; N, 2.68.

2.3. Small molecule ***PH***

A flask was charged with a solution of **3a** (0.3614 g, 0.389 mmol) and 4-nitrobenzyl cyanide (0.2523 g, 1.556 mmol) in DMF (15 mL). Sodium hydroxide (0.20 g, 5.00 mmol) dissolved in ethanol (5 mL) was added portionwise to the stirred solution. The mixture was stirred for 1 h at room temperature under N_2 and then was concentrated under reduced pressure. Water was added to the concentrate and the product precipitated as a dark green solid. It was filtered, washed thoroughly with water and dried to afford **PH**. It was purified by column chromatography, eluting with a mixture of dichloromethane and hexane (1:1) (0.46 g, 80%).

FT-IR (KBr, cm^{-1}): 2950, 2924 (C–H stretching of hexyloxy chains); 2158 (cyano); 1524, 1344 (nitro); 1316 (C–N stretching of TPA); 1284, 1248 (ether bond); 1584, 1504 (aromatic); 965 (*trans* vinylene bond); 1013 (cyanovinylene).

^{1}H NMR ($CDCl_3$) ppm: 8.19 (m, 8H, phenylene ortho to nitro); 7.83 (s, 4H, cyanovinylene); 7.52 (m, 8H, phenylene meta to nitro); 7.30–7.13 (m, 24H, TPA); 7.10 (m, 4H, vinylene); 6.75 (s, 2H, phenylene ortho to oxygen); 3.96 (m, 4H,

$OCH_2(CH_2)_4CH_3$); 1.81 (m, 4H, $OCH_2CH_2(CH_2)_3CH_3$); 1.37 (m, 12H, $O(CH_2)_2(CH_2)_3CH_3$); 0.91 (t, 6H, $O(CH_2)_5CH_3$).

Anal. Calcd. for $C_{94}H_{76}N_{10}O_6$: C, 74.98; H, 5.09; N, 9.30. Found: C, 74.37; H, 4.82; N, 9.13.

2.4. Small molecule *FL*

FL was similarly prepared in 83% yield (0.36 g) from the reaction of **3b** (0.2729 g, 0.277 mmol) with 4-nitrobenzyl cyanide (0.1797 g, 1.108 mmol) in DMF (15 mL) in the presence of sodium hydroxide (0.20 g, 5.00 mmol).

FT-IR (KBr, cm^{-1}): 2950, 2924 (C–H stretching of hexyl chains); 2160 (cyano); 1522, 1346 (nitro); 1314 (C–N stretching of TPA); 1584, 1506 (aromatic); 964 (*trans* vinylene bond); 1004 (cyanovinylene).

^1H NMR ($CDCl_3$) ppm: 8.19 (m, 8H, phenylene ortho to nitro); 7.83 (s, 4H, cyanovinylene); 7.72 (m, 2H, H4 of fluorene); 7.60 (m, 4H, H1 and H3 of fluorene); 7.52 (m, 8H, phenylene meta to nitro); 7.30–7.13 (m, 24H, TPA); 7.10 (m, 4H, vinylene); 2.06 (m, 4H, $CH_2(CH_2)_4CH_3$); 1.11 (m, 16H, $CH_2(CH_2)_4CH_3$); 0.78 (t, 6H, $(CH_2)_5CH_3$).

Anal. Calcd. for $C_{101}H_{80}N_{10}O_8$: C, 77.67; H, 5.16; N, 8.97. Found: C, 77.38; H, 5.21; N, 9.20.

2.5. Characterization methods

IR spectra were recorded on a Perkin–Elmer 16PC FT-IR spectrometer with KBr pellets. ^1H NMR (400 MHz) spectra were obtained using a Brucker spectrometer. Chemical shifts (δ values) are given in parts per million with tetramethylsilane as an internal standard. UV–Vis spectra were recorded on a Beckman DU-640 spectrometer. Elemental analyses were carried out with a Carlo Erba model EA1108 analyzer.

The electrochemical properties of both SMs, i.e. **PH** and **FL** were examined using cyclic voltammetry (CV) (EDCA electrochemistry system). A glassy carbon electrode was used as working electrode. The SMs were coated on glassy carbon electrode from tetrahydrofuran (THF) solution and immersed in 0.1 mol/L Bu_4NPF_6 acetonitrile solution used as supporting electrolyte. Cyclic voltammograms were recorded, using Ag/Ag+ as reference electrode at a scan rate of 100 mV/s.

The crystallinity of the films was studied using the X-ray diffraction (XRD) technique (panalytical make USA) having CuKα, as radiation source of wavelength λ = 1.5405 Å with the films coated on the quartz substrates. Atomic force microscopy (AFM) images were recorded using digital instrument nanoscope in trapping mode.

2.6. Device fabrication and characterization

All the devices were fabricated on indium tin oxide (ITO) coated glass substrates. The ITO coated glass substrates were cleaned with acetone in an ultrasonic bath. A thin layer of poly(3,4-ethylene-dioxythiophene): poly(styrene sulfonate) (PEDOT:PSS) (70 nm) was spin coated on it from PEDOT:PSS aqueous solution at 2000 rpm and dried subsequently at 80 °C for 20 min in air, and then transferred into a glove box. The active layer of the blend of **PH** or **FL** with PCBM was spin coated from different solvents (chloroform, chlorobenzene, o-dichlorobenzene, and 2% additive 1-chloronaphthalene (CN) in o-dichlorobenzene), onto the PEDOT:PSS layer, and then dried in ambient conditions. The concentration of **PH** or **FL**:PCBM blend solution used in this study for spin coating was 10 mg/mL in the solvent used. The thickness of the active layers is approximately 90–95 nm. The structure of the device is ITO/PEDOT:PSS/**PH** or **FL**:PCBM/Al. The effective active area of the devices is about 20 mm^2. Current–voltage (J–V) characteristics of the devices were measured using a computer controlled Keithley 238 source meter in dark and under illumination intensity of 100 mW/cm^2 in ambient conditions. A xenon light source was used to give simulated irradiance of 100 mW/cm^2 (equivalent to and AM1.5 irradiation) at the surface of the device.

We have also fabricated BHJ devices based on **FL**:**F** using the same method. To measure the hole and electron mobilities, the devices having structure ITO/PEDOT:PSS/**FL**:**F**/Au and Al/**FL**:**F**/Al were used, respectively and the J–V characteristics in dark have been recorded.

3. Results and discussion

3.1. Synthesis and characterization

Scheme 2 outlines the four-step reaction for the synthesis of SMs. Compounds **1** [47] and **2** [48] have been synthesized according to reported methods. Compound **2** reacted with 1,4-divinyl-2,5-bis(hexyloxy)-benzene and 9,9-dihexyl-2,7-divinylfluorene in a mol ratio 2:1 to afford **3a** and **3b**, respectively. This reaction took place in DMF using Et_3N as acid scavenger and $Pd(OAc)_2$ as catalyst. Finally, the condensation of **3a** and **3b** with 4-nitrobenzyl cyanide in the presence of sodium hydroxide gave **PH** and **FL**, respectively. These SMs were soluble in common organic solvents such as tetrahydrofuran, chloroform and dichloromethane owing to the aliphatic chains.

The SMs were characterized by FT-IR and ^1H NMR spectroscopy. The IR spectra showed common absorption bands approximately at 2952, 2926 (C–H stretching of aliphatic chains); 2128 (cyano); 1524, 1344 (nitro); 1316 (C–N stretching of TPA); 1584, 1504 (aromatic); 965 (vinylene), and 1013 cm^{-1} (cyanovinylene). On the other hand, the ^1H NMR spectra of SMs displayed common signals at 8.19 (phenylene ortho to nitro); 7.83 (cyanovinylene); 7.52 (phenylene meta to nitro); 7.30–7.13 (TPA) and 7.10 ppm (vinylene). Finally, the aliphatic chains resonated at the range of 3.96–0.91 ppm for **PH** and 2.06–0.78 ppm for **FL**.

3.2. Photophysical and electrochemical properties

Fig. 1 depicts the UV–Vis absorption spectra of SMs in both dilute (10^{-5} M) THF solution and thin film. All photophysical and electrochemical characteristics of SMs are summarized in Table 1. The solutions showed long-wavelength absorption maximum ($\lambda_{a,max}$) or shoulder around 605 and 643 nm, while the thin films showed $\lambda_{a,max}$ at 626–632 nm. The spectra were broad and extended approximately up to 750 nm in solutions and 800 nm in

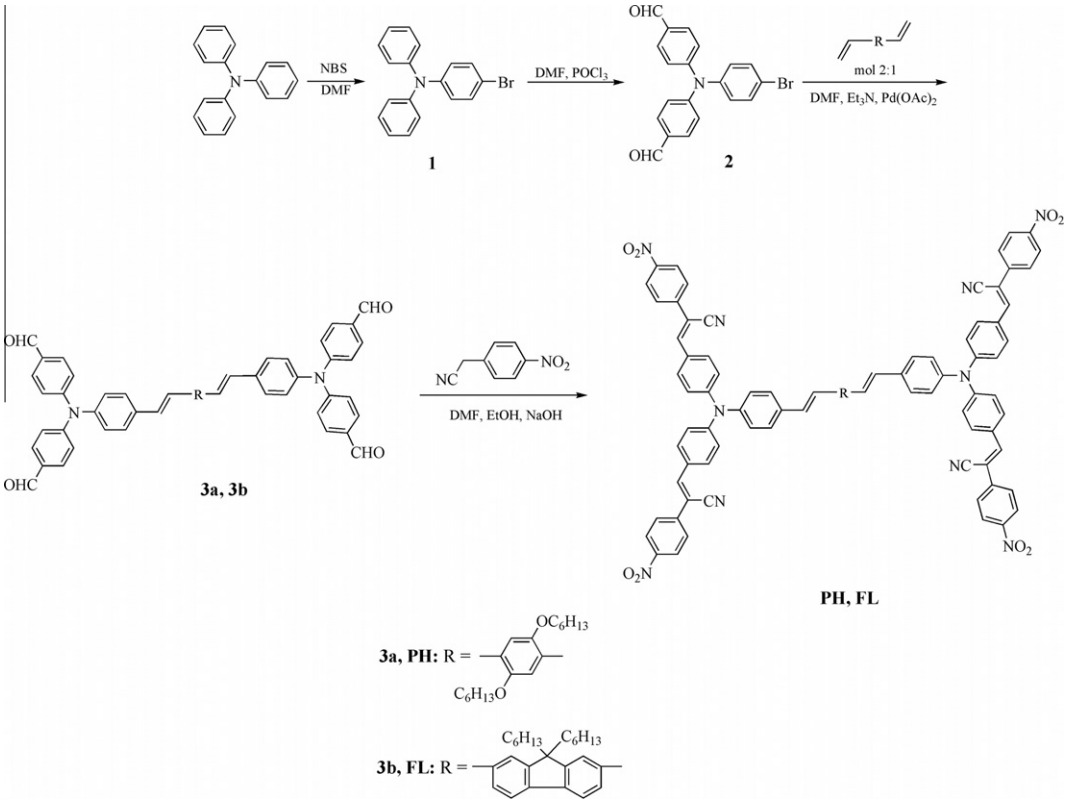

Scheme 2. Synthesis of SMs **PH** and **FL**.

thin films which is desirable for PV applications. This feature was attributed to an ICT between the electron-donating central unit (phenylenevinylene/fluorenevinylene and TPA) and the electron-accepting terminal units (cyanovinylene 4-nitrophenyl). The thin film absorption onset was located at 758 and 746 nm corresponding to an E_g^{opt} of 1.64 and 1.66 eV for **PH** and **FL**, respectively. The optical properties of SMs are similar thus supporting that their central unit did not influence significantly their photophysical characteristics.

The highest occupied molecular orbital (HOMO) and lowest unoccupied molecular orbital (LUMO) energy levels of the organic polymers and SMs are important parameters in the design of organic photovoltaic (OPV) devices, and they can be estimated from the onset oxidation (E_{onset}^{ox}) and reduction (E_{onset}^{red}) potentials [49]. Fig. 2 shows the cyclic voltammograms of **PH** and **FL**. Similar cyclic voltammograms have been reported for other small molecules in the literature [50]. The E_{onset}^{ox} and E_{onset}^{red} potentials vs. Ag/Ag+ (Table 1) were used for calculation of the HOMO and LUMO energy levels according to the following expressions [51].

$$\mathrm{HOMO} = -q(E_{onset}^{ox} + 4.7)\ \mathrm{eV}$$

$$\mathrm{LUMO} = -q(E_{onset}^{red} + 4.7)\ \mathrm{eV}$$

The values of the HOMO and LUMO levels of the **PH** and **FL** are given in Table 1. The LUMO level of both SMs is the same but the HOMO level is −5.35 and −5.30 eV for **PH** and **FL**, respectively. This implies that the HOMO levels are mainly affected by the D unit in SM, while the LUMO levels (−3.55 eV) are primarily controlled by the acceptor moieties. Since the LUMO level of PCBM is −3.95 eV, the energy difference between the LUMOs of these SMs and PCBM is about 0.3–0.4 eV, which should be sufficient for the exciton splitting and charge dissociation [52]. In addition, the deeper HOMO level of these SMs is desirable for higher open circuit voltage (V_{oc}) of the OPVs with organic semiconductors as D materials because the V_{oc} is usually proportional to the difference between the LUMO level of the acceptor and the HOMO level of the D. The electrochemical band gaps have been estimated from the energy difference between the HOMO and LUMO levels and they are 1.80 and 1.75 eV for **PH** and **FL**, respectively.

3.3. Photovoltaic properties

Fig. 3(a) shows the *J–V* characteristics of the OPVs based on SMs (**PH** or **FL**):PCBM cast from the chloroform solvent. The PV parameters of the OPVs, including V_{oc}, short circuit current (J_{sc}), fill factor (FF) and power conversion efficiency (PCE) are summarized in Table 2. The higher value of V_{oc} for the device based on **PH**:PCBM is attributed to the lower HOMO level of **PH** as compared to **FL**. The OPV based on the **FL**:PCBM blend showed higher J_{sc} and FF than the **PH**:PCBM based device, leading to PCE of 1.46% vs. 1.02%, respectively. However, the current density is still much

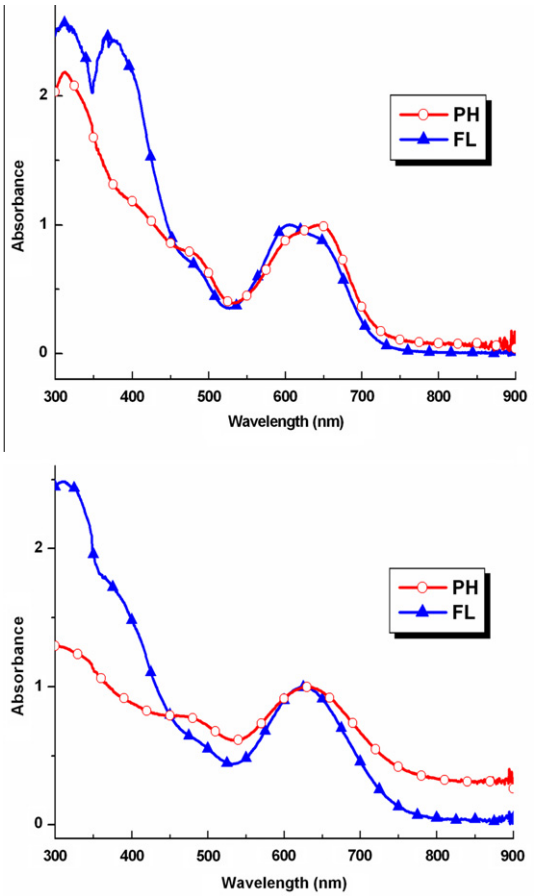

Fig. 1. UV–Vis absorption spectra of SMs in THF solution (top) and thin film (bottom).

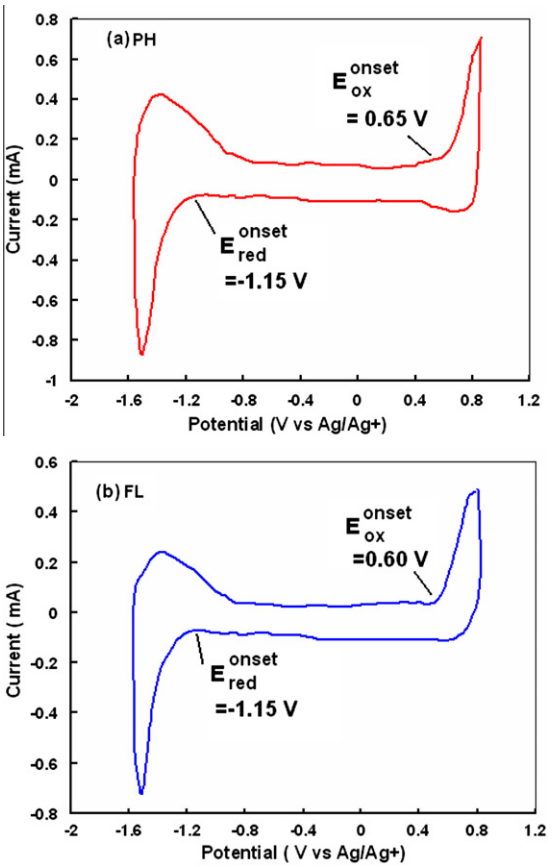

Fig. 2. Cyclic voltammograms of (a) **PH** and (b) **FL**.

lower than that for the state-of-the-art polymer/fullerene systems [13]. In order to understand the origins of the low current, we carried out the incident photon to current efficiency (IPCE) measurements. The IPCE spectra of the PV devices, as shown in Fig. 3(b), are consistent with the absorption spectra of the blend films of the active layers. The absorptions at shorter wavelength region, below 420 nm, are mainly contributed to PCBM, while those at longer wavelength region are contributed to SMs. The higher J_{sc} of the **FL**:PCBM based device compared to the **PH**:PCBM device is reflected on the higher IPCE values in the wavelength region corresponding to absorption of SMs. The higher value of the J_{sc} and PCE may also be attributed to the higher value of hole mobility for the device based on the **FL** film.

The relatively lower PCE of SM BHJ OSCs becomes the biggest hindrance to commercial application. In the case of OSCs based on polymers, some approaches have been used to improve the device efficiency including thermal annealing or utilizing additive to control the formation of interpenetrating D/A networks at nanometer scale for efficient exciton dissociation and charge transport within the BHJ devices [53]. The solvents used for the preparation of the active layer have shown a strong impact on the morphology of the blend films, which influence the performance of the devices. However, these methods are

Table 1
Optical and electrochemical properties of SMs.

SM	$\lambda_{a,max}$[a] in solution (nm)	$\lambda_{a,max}$[a] in thin film (nm)	Thin film absorption onset (nm)	E_g^{opt}[b] (eV)	E_{onset}^{ox} (V)	E_{onset}^{red} (V)	HOMO (eV)	LUMO (eV)	E_g^{el}[c] (eV)
PH	(604) 643	632	758	1.64	0.65	−1.15	−5.35	−3.55	1.80
FL	605 (648)	626	746	1.66	0.60	−1.15	−5.30	−3.55	1.75

Numbers in parentheses indicate a shoulder in the UV–Vis spectrum.
[a] $\lambda_{a,max}$: The absorption maxima from the UV–Vis spectra in THF solution or in thin film.
[b] E_g^{opt}: Optical band gap determined from the absorption onset in thin film.
[c] E_g^{el}: Electrochemical band gap determined from cyclic voltammetry.

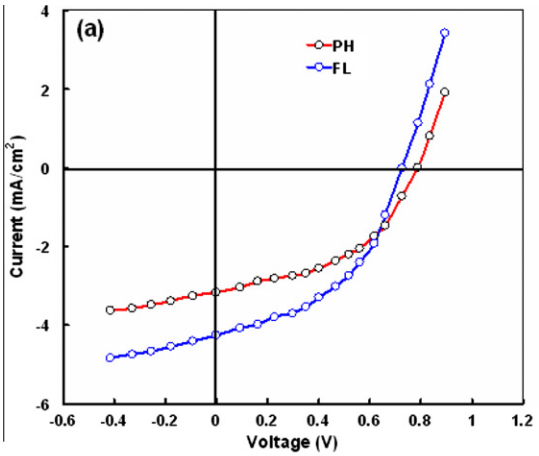

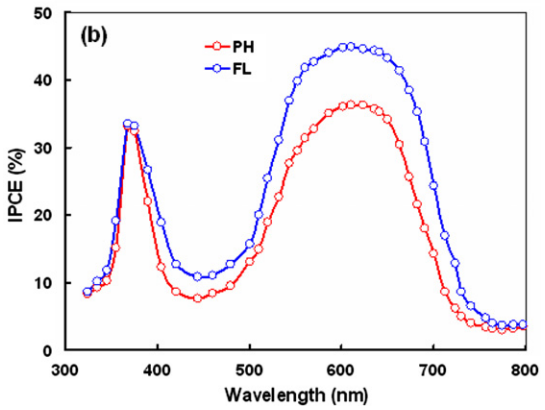

Fig. 3. (a) Current–voltage (J–V) characteristics and (b) IPCE spectra of the OSCs based on **PH**:PCBM and **FL**:PCBM cast from CF solvent under illumination of 100 mW/cm^2.

Table 2
Photovoltaic parameters of the devices based on **PH**:PCBM and **FL**:PCBM cast from chloroform (CF).

Blend	Short circuit current (J_{sc}) (mA/cm^2)	Open circuit voltage (V_{oc}) (V)	Fill factor (FF)	Power conversion efficiency (PCE) (%)
PH:PCBM	3.7	0.78	0.41	1.02
FL:PCBM	4.3	0.74	0.46	1.46

generally not applied for SM BHJ solar cells. We have studied the effect of different solvents on the performance of OPVs using the **FL**:PCBM blend.

Fig. 4 shows the UV–Vis absorption spectra of **FL**:PCBM thin films for different casting solvents. By changing the casting solvent certain differentiations appeared in the absorption spectra. For chloroform (CF) cast film the absorption spectra show two absorption bands around 360 and 626 nm. The absorption band having peak around 360 nm stems from PCBM [54], while the absorption band with peak around 626 nm represents the contribution from **FL**. For chlorobenzene (CB) cast film the peak absorption

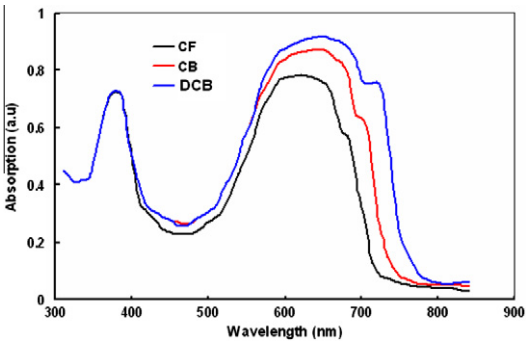

Fig. 4. Absorption spectra of **FL**:PCBM films (1:1 w:w) prepared by spin casting from different solvents.

wavelength is at 635 nm showing a 10 nm red-shift, with one shoulder peak around 670 nm. Compared to the former two films absorption spectra cast from CF and CB, the absorption spectrum of o-dichlorobenzene (DCB) cast film becomes more distinguishable and much stronger. The vibronic absorption is much more pronounced indicating strong interchain–interlayer interaction in **FL**, as well as a good ordering of blends films. Both significant red shift and pronounced shoulder appear in a more ordered film as high crystallinity order involves an enhanced conjugation length and hence a shift of the absorption spectra to lower energies.

Fig. 5 shows the XRD results from active layer **FL**:PCBM prepared by spin coating from various solvents. The XRD intensities values were obtained from peaks at $2\theta = 8.26°$ are 6.3, 10.5, 14.8, and 19.4 for the films cast from CF, CB, DCB, and CN/DCB solvents, respectively. These values correspond to the interchain spacing in **FL** associated with the degree of crystallinity. When high boiling point solvents (DCB and CB) instead of low boiling point (CF) were used for the active layer, the increased intensities were observed in the peak at $2\theta = 8.26°$. This indicates the active layers prepared from DCB and CB have higher ordered structure and more improved crystallinity than CF. In the high boiling point solvents, **FL** in the active layer may have longer time to solidify due to the slow evaporation rate of the solvents and the slow film growth rate may assist to form the high degree of self organized structure. The crystalline nature of the blend has been further improved as can be seen for the XRD pattern.

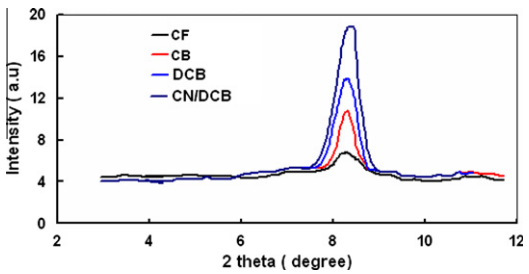

Fig. 5. X-ray diffraction spectra for **FL**:PCBM (1:1 w/w) blend thin films prepared from different solvents.

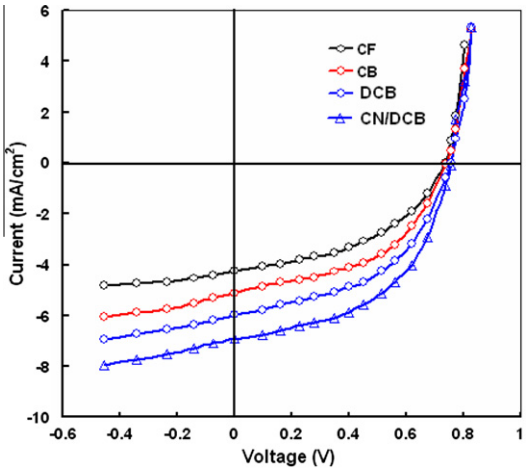

Fig. 6. Current–voltage (*J–V*) characteristics of the OSCs for **FL**:PCBM cast from different solvents under illumination intensity of 100 mW/cm^2.

Table 3
Summary of the photovoltaic parameters of the ITO/PEDOT:PSS/**FL**:PCBM/Al devices prepared from different solvents.

Solvent type	J_{sc} (mA/cm^2)	V_{oc} (V)	FF	PCE (%)
CF	4.3	0.74	0.46	1.46
CB	5.1	0.74	0.48	1.81
DCB	6.0	0.76	0.53	2.42
CN/DCB	7.15	0.76	0.57	3.0

The *J–V* characteristics under illumination intensity AM 1.5 (100 mW/cm^2) for the OSCs fabricated from various solvents employing **FL**:PCBM blend are shown in Fig. 6. The PV parameters of the devices are summarized in Table 3. It is seen from this table that the V_{oc} does not change under various solvent conditions but the J_{sc} and FF show a differentiation. Compared to the device made from CF solvent, the device based on CB solvent leads to an increase of PCE from 1.42% to 1.81%. Moreover, a PCE of 2.42% is observed from the device fabricated from DCB solvent, and the device fabricated from mixed CN/DCB solvents possesses PCE of 3.0%. The improvement of PCE for the devices is mainly due to the enhancement in both J_{sc} and FF values. This indicates an improved charge transport due to the expansion of the crystalline domains. The reason for this improved crystallinity in the coated films can be the different solvent evaporation speed during spin coating, since CF has a low boiling point of 60 °C, while the boiling points of CB and DCB are 130 and 180 °C, respectively. The film cast from DCB solvent is frozen very slowly owing to the high boiling point of DCB. This slow freezing of **FL** may cause a longer time for the **FL** self organization, leading to a higher degree of ordering in the material. The broadening of the absorption band and red shift in the absorption peak leads to an increase of the light harvesting by the active layer. The higher PCE for the device fabricated from mixed solvents (CN/DCB) is attributed to the increased ordering of the blend, which provides a more increased D–A interfacial area. The combined effects of the above leads to an increase in the overall PCE of the device.

3.4. Photovoltaic properties with F as electron acceptor

For the acceptor materials in OSCs, PCBM offers the advantage of good solubility in organic solvents, high electron mobility and high electron affinity. However, weak absorption in the visible region and a low LUMO energy level are the weak points of PCBM. Weak absorption in the visible region limits its contribution to light harvesting in the PV conversion. We attempted to increase the breadth of the IPCE spectrum and the overall PCE, by fabricating OSCs with a more light absorbing modified PCBM, i.e. **F** [42]. Fig. 7(a) shows the *J–V* curves of the devices based on **FL**:**F** (1:1 w/w) spin coated from DCB and CN/DCB solvents. The V_{oc}, J_{sc}, FF, and PCE of the devices are listed in Table 4. The devices based on **F** as electron acceptor show higher value of V_{oc} as compared to that for PCBM. This is attributed to the difference between the LUMO energy levels in PCBM (−3.95 eV) and **F** (−3.75 eV) [42], because the value of V_{oc} in BHJ photovoltaic device is related to the difference between the HOMO level of the donor and the LUMO level of the acceptor. The device fabricated with **FL**:**F** blend shows higher PCE (3.62%) as compared to **FL**:PCBM (2.42%) based device, cast from DCB. The overall PCE of the device based on **FL**:**F** has been further improved up to 4.38% when the blend is cast from

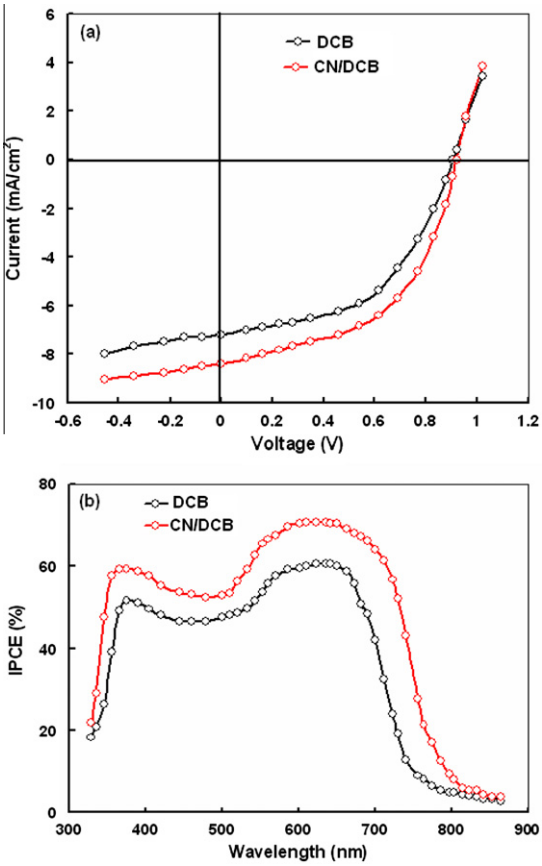

Fig. 7. (a) Current–voltage (*J–V*) characteristics and (b) of the OSCs for **FL**:**F** based on **FL**:PCBM cast from DCB and CN/DCB solvents.

Table 4
Summary of the photovoltaic parameters of the ITO/PEDOT:PSS/**FL**:**F**/Al devices prepared from different solvents.

Solvent	J_{sc} (mA/cm^2)	V_{oc} (V)	FF	PCE (%)
DCB	7.4	0.90	0.56	3.62
CN/DCB	8.3	0.88	0.60	4.38

mixed CN/DCB solvents. Fig. 7(b) shows the IPCE spectra of the devices fabricated from blends of **FL**:**F** cast from OCB and CN/DCB solvents. The IPCE spectra are similar with the absorption spectra of the blend. With the addition of CN in the solvent, the IPCE maximum at 630–680 nm increased from 55% to 71%, which is consistent with J_{sc} and PCE. The J_{sc} value calculated from the integration of the IPCE spectrum is 7.1 and 8.6 mA/cm^2 for the devices based on DCB and CN/DCB cast blends, respectively, which closely matches the J_{sc} values obtained from the J–V measurements under white light illumination.

The increase of J_{sc} is mainly related to more exciton and charge generation and more effective charge transport. It was found that the film cast from CN/DCB exhibits stronger absorption than that cast from DCB. The stronger absorption partially contributed to higher J_{sc} and IPCE of the device cast from CN/DCB as compared to the device cast from CB. A similar phenomenon has been observed by Yang et al. for P3HT:PCBM system [55].

Another important factor being responsible for increased J_{sc} is the charge transport in active layers. The space charge limited current (SCLC) method [56] was adopted to determine the electron and hole mobilities in blend films. Fig. 8(a) shows the dark J–V characteristics of the hole only devices having structure of ITO/PEDOT:PSS/**FL**:**F**/Au with the DCB and CN/DCB solvents casting layer films. In order to suppress the electron injection into the blend, a high work function metal gold (Au) was used as cathode. The applied voltage was corrected for the built-in voltage (V_{bi}). Compared to the device based on DCB solvent cast film, the device with CN/OCB solvent cast film shows an enhanced current density at the same driving voltage in Fig. 8(a). This indicates that the hole mobility is enhanced due to the self organization of **FL**. The J–V characteristics for the electron only devices with structure of Al/**FL**:**F**/Al are shown in Fig. 8(b). In order to suppress the hole injection into the blend, a low work function metal (Al) was used as anode. The electron and hole mobilities have been measured by fitting the dark J–V characteristics for electron and hole only devices, respectively to SCLC model at low voltages, in which the current density is given by

$$J = (9\varepsilon_o\varepsilon_r\mu V^2/8d^3)\exp[0.891\gamma(V/d)^{0.5}]$$

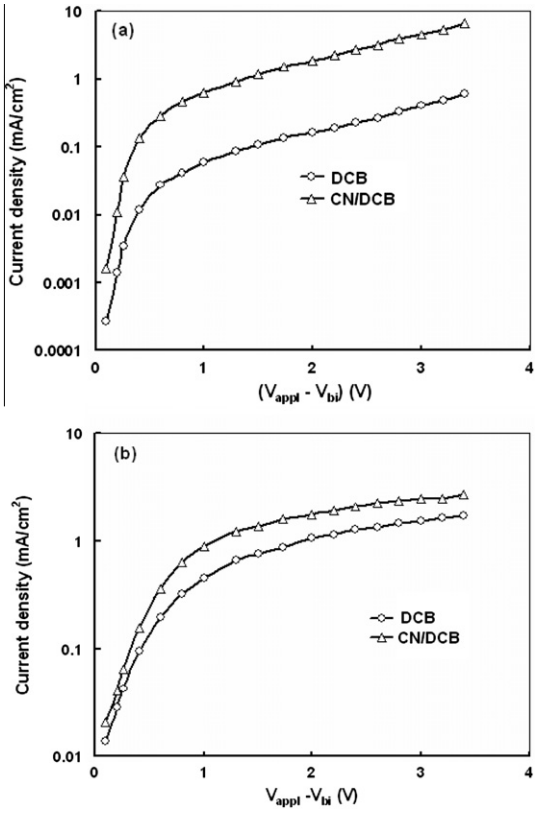

Fig. 8. Current–voltage characteristics for (a) hole only and (b) electron only devices based on **FL**:**F** blend films with DCB and CN/DCB solvents.

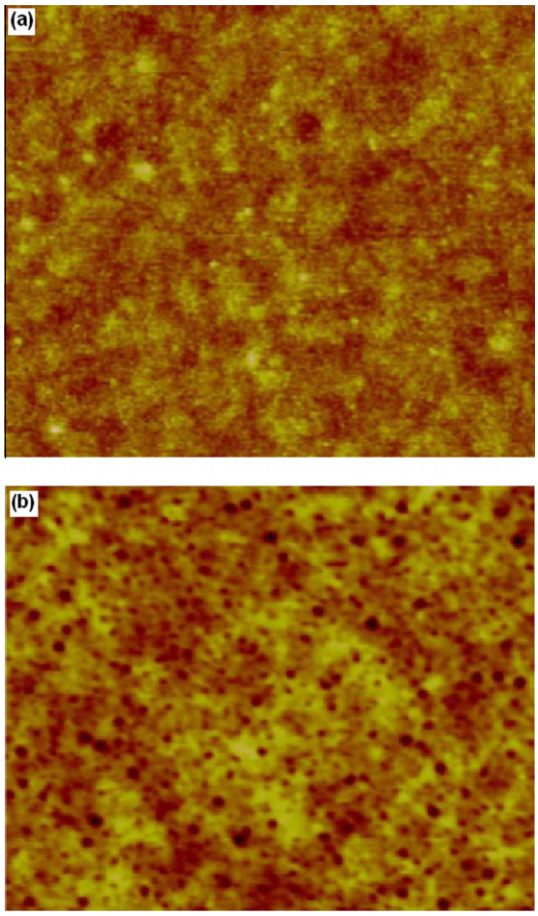

Fig. 9. AFM images of **FL**:**F** blends cast from (a) DCB and (b) CN/DCB solvents (scale 3 × 3 μm).

where $\varepsilon_o\varepsilon_r$ represent the permittivity of the material, μ is the mobility, γ is the field activation factor, and d is the thickness of the active layer and voltage $V = V_{appl} - V_{bi}$. The hole (μ_h) and electron (μ_e) mobilities of the film cast from DCB are 5.6×10^{-6} and 3.4×10^{-4} cm^2/Vs, respectively. The μ_h and μ_e for the film cast from the CN/DCB are about 1.8×10^{-5} and 2.2×10^{-4} cm^2/Vs, respectively. The smaller value of μ_e/μ_h (60.7 and 12.2 for CB and CN/DCB solvent cast film, respectively) indicates a more balanced charge transport. The more balanced charge transport contributes to the higher J_{sc} and higher PCE.

The difference in PV performance for the devices cast from DCB and CN/DCB solvents is most likely due to the change in the morphology. The effect of the solvents on the active layer morphology was also examined by the AFM technique. Fig. 9 compares the AFM images of the blend films of **FL**:**F** cast from the DCB and CN/DCB solvents. For the **FL**:**F** blend films cast from DCB solvent, its root mean square (rms) roughness is about 0.45 nm. However, when the film is cast from the CN/DCB solvent, the rms roughness is about 0.78 nm. Higher roughness of the film will give higher device efficiency. The rough surface is probably a signature of self organization of organic semiconductor, which in turn enhances ordered structure formation in thin films and increases the carrier mobility [57]. The increased roughness of the active layer enhances the D–A interfacial area leading to efficient dissociation of the excitons into free charge carriers.

4. Conclusions

Two soluble and low band gap SMs, **PH** and **FL**, were synthesized. They contained the D–A structure permitting an ICT. The absorption spectra were broad with long-wavelength absorption maximum at 605–643 nm and optical band gap of 1.64–1.66 eV, which is lower than that of P3HT. The HOMO and LUMO levels of both SMs estimated from cyclic voltammetry, suggest that they can be used as donor materials for organic BHJ PV devices. The solution processed organic BHJ PV devices using **PH**:PCBM and **FL**:PCBM cast from chloroform solvent show PCE about 1.02% and 1.42%, respectively. We have fabricated BHJ organic PV devices based on the **FL**:PCBM using various solvents such as chloroform, chlorobenzene, o-dichlorobenzene and mixed CN/DCB and investigated the influence of these solvents on the performance of the solar cells. The device with mixed CN/DCB solvents shows improved performance of PCE of 3.0%. The improved PCE is mainly attributed to the increased value of J_{sc}, which is due to the enhancement in the crystalline nature of the blend.

We have also fabricated BHJ PV devices based on **FL**:**F** blend to improve the light harvesting efficiency in the lower wavelength region and achieved PCE of about 3.62% and 4.38% with DCB and CN/DCB cast blend, respectively. The improved PCE of the device with **F** as electron acceptor is mainly attributed to both increase in J_{sc} and V_{oc}. The further improvement in the PCE, when the blend is cast from mixed CN/DCB, could be ascribed to efficient exciton dissociation at the D–A interface and a better morphological structure of the active layer.

Acknowledgment

We are thankful to Prof. Y.K. Vijay of Thin film and Membrane Science Laboratory, University of Rajasthan Jaipur (Raj.) for allowing us to undertake the device fabrication and characterization in his laboratory.

References

[1] J. Peet, J.Y. Kim, N.E. Coates, W.L. Ma, D. Moses, A.J. Heeger, G.C. Bazan, Nat. Mater. 6 (2007) 497.
[2] J.Y. Kim, K. Lee, N.E. Coates, D. Moses, T.Q. Nguyen, M. Dante, A.J. Heeger, Science 317 (2007) 222.
[3] S.H. Park, A. Roy, S. Beaupre, S. Cho, N. Coates, J.S. Moon, D. Moses, M. Leclerc, K. Lee, A.J. Heeger, Nat. Photonics 3 (2009) 297.
[4] (a) M.C. Scharber, D. Muhlbacher, M. Koppe, P. Denk, C. Waldauf, A.J. Heeger, C.J. Brabec, Adv. Mater. 18 (2006) 789;
(b) G. Dennler, M.C. Scharber, T. Ameri, P. Denk, K. Forberich, C. Waldauf, C.J. Brabec, Adv. Mater. 20 (2008) 579.
[5] Y. Li, Y. Zou, Adv. Mater. 20 (2007) 2952.
[6] W. Ma, C. Yang, X. Gong, K. Lee, A.J. Heeger, Adv. Funct. Mater. 15 (2005) 1617.
[7] M. Reyes, K. Kim, D.L. Carroll, Appl. Phys. Lett. 87 (2005) 083506.
[8] Y. Kim, S. Cook, S.M. Tuladhar, S.A. Choulis, J. Nelson, J.R. Durrant, D.D.C. Bradley, M. Giles, I. McCulloch, C.S. Ha, M. Ree, Nat. Mater. 5 (2006) 197.
[9] Q. Wei, T. Nishizawa, K. Tajima, K. Hashimoto, Adv. Mater. 20 (2008) 2211.
[10] G. Li, V. Shrotriya, J. Huang, Y. Yao, T. Moriarty, K. Emery, Y. Yang, Nat. Mater. 4 (2004) 864.
[11] M. Campoy-Quilles, T. Ferenczil, T. Agostinelli, P.G. Etchegoin, Y. Kim, T.D. Anthopoulos, P.N. Stavrinou, D.D.C. Bradley, J. Nelson, Nat. Mater. 7 (2008) 158.
[12] (a) J. Chen, Y. Cao, Acc. Chem. Res. 42 (2009) 1709;
(b) Y.J. Cheng, S.H. Yang, C.S. Hsu, Chem. Rev. 109 (2009) 5868.
[13] S. Gunes, H. Neugebauer, N.S. Sariciftci, Chem. Rev. 104 (2007) 1324.
[14] M.T. Lloyd, J.E. Anthony, G.G. Malliaras, Mater. Today 11 (2007) 34.
[15] B.P. Rand, J. Genoe, P. Heremans, J. Poortmans, Prog. Photovoltaics: Res. Appl. 15 (2007) 659.
[16] J. Roncali, P. Frere, P. Blanchard, R. de Bettignies, M. Turbiez, S. Roquet, P. Leriche, Y. Nicolas, Thin Solid Films 567 (2006) 511.
[17] X.B. Sun, Y. Zhou, W. Wu, Y. Liu, W. Tian, G. Yu, W. Qiu, S. Chen, D.J. Zhu, J. Phys. Chem. B 110 (2006) 7702.
[18] N. Kopidakis, W.J. Mitchell, J. van de Lagemaat, D.S. Ginley, G. Rumbles, S.E. Shaheen, Appl. Phys. Lett. 89 (2008) 103524.
[19] M.T. Lloyd, A.C. Mayer, S. Subramanian, D.A. Mourey, D.J. Herman, A. Bapat, V.J.E. Anthony, G.G. Malliaras, J. Am. Chem. Soc. 129 (2007) 9144.
[20] P.F. Xia, X.J. Feng, J. Lu, S.W. Tsang, R. Movileanu, Y. Tao, M.S. Wong, Adv. Mater. 20 (2008) 4810.
[21] S. Roquet, A. Cravino, P. Leriche, O. Alévêque, P. Frére, J. Roncali, J. Am. Chem. Soc. 128 (2006) 3459.
[22] F. Silvestri, M.D. Irwin, L. Beverina, A. Facchetti, G.A. Pagani, T.J. Marks, J. Am. Chem. Soc. 130 (2008) 17640.
[23] N.M. Kronenberg, M. Deppisch, F. Wurthner, H.W.A. Lademann, K. Deing, K. Meerholz, Chem. Commun. (2008) 6489.
[24] T. Rousseau, A. Cravino, T. Bura, G. Ulrich, R. Ziessel, J. Roncali, Chem. Commun. (2009) 1673.
[25] (a) A. Tamayo, T. Kent, M. Tantitiwat, M.A. Dante, J. Rogers, T.Q. Nguyen, Energy Environ. Sci. 2 (2009) 1180;
(b) Y. Li, Q. Guo, Z. Li, L. Pei, W. Tian, Energy Environ. Sci. doi:10.1039/Coo3946B.;
(c) J.A. Mikroyannidis, D.V. Tsagkournos, S.S. Sharma, A. Kumar, Y.K. Vijay, G.D. Sharma, Sol. Energy Mater. Sol. Cells 94 (2010) 2318;
(d) A.B. Tamayo, B. Walker, T.Q. Nguyen, J. Phys. Chem. C 112 (2008) 11545;
(e) B. Walker, A.B. Tamayo, X.D. Dang, P. Zalar, J.M. Seo, A. Garcia, M. Tantiwiwat, T.Q. Nguyan, Adv. Funct. Mater. 19 (2009) 3063;
(f) X. Zhao, C. Piliego, B. Kim, D.A. Poulsen, B. Ma, D.A. Unruh, J.M.J. Frechet, Chem. Mater. doi:10.1021/cm903329a.;
(g) B. Yin, L. Yang, Y. Liu, Y. Chen, Q. Qi, F. Zhang, S. Yin, Appl. Phys. Lett. 97 (2010) 023303;
(h) A.B. Tamayo, X.D. Dang, B. Walker, J. Seo, T. Kent, T.Q. Nguyen, Appl. Phys. Lett. 94 (2009) 103301.
[26] J. Roncali, Chem. Rev. 97 (1997) 173.
[27] C. Winder, N.S. Sariciftci, J. Mater. Chem. 14 (2004) 1077.

[28] J. Kim, S.H. Kim, I.H. Jung, E. Jeong, Y. Xia, S.N. Cho, I.W. Hwang, K. Lee, H. Suh, H.K. Shim, H.Y. Woo, J. Mater. Chem. 20 (2010) 1577.
[29] Z.G. Zhang, K.L. Zhang, G. Liu, C.X. Zhu, K.G. Neoh, E.T. Kang, Macromolecules 42 (2009) 3104.
[30] J.S. Park, T.I. Ryu, M. Song, K.J. Yoon, M.J. Lee, I.A. Shin, G.D. Lee, J.W. Lee, Y.S. Gal, S.H. Jin, J. Polym. Sci. Part A: Polym. Chem. 46 (2008) 6175.
[31] R.S. Ashraf, H. Hoppe, M. Shahid, G. Gobsch, S. Sensfuss, E. Klemm, J. Polym. Sci. Part A: Polym. Chem. 44 (2006) 6952.
[32] F. Wang, J. Luo, K.X. Yang, J.W. Chen, F. Huang, Y. Cao, Macromolecules 38 (2005) 2253.
[33] H. Becker, H. Spreitzer, E. Kruge, H. Schenk, I. Parker, Y. Cao, Adv. Mater. 12 (2000) 42.
[34] Q. Chu, P. Pang, L. Ding, F.E. Karasz, Macromolecules 35 (2002) 7569.
[35] S.H. Lee, B.B. Jang, T. Tsutsui, Macromolecules 35 (2002) 1356.
[36] Y.-G. Kim, B.C. Thompson, N. Ananthakrishnan, G. Padmanaban, S. Ramakrishnan, J.R. Reynolds, J. Mater. Res. 20 (2005) 3188.
[37] J.A. Mikroyannidis, S.S. Sharma, Y.K. Vijay, G.D. Sharma, ACS Appl. Mater. Interfaces 2 (2010) 270.
[38] J.A. Mikroyannidis, M.M. Stylianakis, P. Balraju, P. Suresh, G.D. Sharma, ACS Appl. Mater. Interfaces 1 (2009) 1711.
[39] J.A. Mikroyannidis, M.M. Stylianakis, P. Suresh, P. Balraju, G.D. Sharma, Org. Electron. 10 (2009) 1320.
[40] J.A. Mikroyannidis, A.N. Kabanakis, A. Kumar, S.S. Sharma, Y.K. Vijay, G.D. Sharma, Langmuir 26 (2010) 12909.
[41] J.A. Mikroyannidis, P. Suresh, G.D. Sharma, Org. Electron. 11 (2010) 311.
[42] J.A. Mikroyannidis, A.N. Kabanakis, S.S. Sharma, G.D. Sharma, Adv. Funct. Mater. 21 (2011) 746.
[43] G.R. Robertson, Org. Synth. Coll. 1 (1941) 396;
G.R. Robertson, Org. Synth. Coll. 2 (1922) 57.
[44] D.R. McKean, G. Parrinello, A.F. Renaldo, J.K. Stille, J. Org. Chem. 52 (1987) 422.
[45] Q. Peng, M. Li, X. Tang, S. Lu, J. Peng, Y. Cao, J. Polym. Sci. Part A: Polym. Chem. 45 (2007) 1632.
[46] J.A. Mikroyannidis, Y.J. Yu, S.H. Lee, J.I. Jin, J. Polym. Sci. Part A: Polym. Chem. 44 (2006) 4494.
[47] V. Promarak, M. Ichikawa, T. Sudyoadsuk, S. Saengsuwan, T. Keawin, Opt. Mater. 30 (2007) 364.
[48] G.K. Paul, J. Mwaura, A.A. Argun, P. Taranekar, J.R. Reynolds, Macromolecules 39 (2006) 7789.
[49] (a) Y. Li, Y. Cao, J. Gao, D. Wang, G. Yu, A.J. Heeger, Synth. Met. 99 (1999) 243;
(b) J. Bredas, J.E. Norton, J. Cornil, V. Coropceanu, Acc. Chem. Res. 42 (2009) 1691.
[50] (a) G. Zhao, G. Wu, C. He, F.Q. Bai, H. Xi, H.X. Zhang, Y. Li, J. Phys. Chem. C 113 (2009) 2636;
(b) J.J. Chen, T.L. Chen, B.S. Kim, D.A. Poulsen, J.L. Mynar, J.M.J. Frechet, B. Ma, ACS Appl. Mater. Interfaces 2 (2010) 2679.
[51] Q. Sun, H. Wang, C. Yang, Y. Li, J. Mater. Chem. 13 (2003) 800.
[52] B.C. Thompson, J.M.J. Frechet, Angew. Chem. Int. Ed. 47 (2008) 58.
[53] (a) C.V. Hoven, X.D. Dang, R.C. Coffin, J. Peet, T.Q. Nguyen, G.C. Bazan, Adv. Mater. 22 (2010) E63;
(b) S.H. Chan, Y.S. Hsiao, L.I. Hung, G.W. Hwang, H.L. Chen, C. Ting, C.P. Chen, Macromolecules 43 (2010) 3399;
(c) J.G. Liu, S.Y. Shao, H.F. Wang, K. Zhao, L.J. Xue, X. Gao, Z.Y. Xie, Y.C. Han, Org. Electron. 11 (2010) 775;
(d) J.K. Lee, N.E. Coates, S. Cho, N.S. Cho, D. Moses, G.C. Bazan, K. Lee, A.J. Heeger, Appl. Phys. Lett. 92 (2008) 243308;
(e) I.W. Hwang, S. Cho, J.Y. Kim, K. Lee, N.E. Coates, D. Moses, A.J. Heeger, J. Appl. Phys. 104 (2008) 033706.
[54] V. Shrotriya, J. Ouyang, R.J. Tseng, G. Li, Y. Yang, Chem. Phys. Lett. 138 (2005) 411.
[55] H.Y. Chen, H.C. Yang, G.W. Yang, S. Sista, R.B. Zadoyan, G. Li, Y. Yang, J. Phys. Chem. C 113 (2009) 7946.
[56] (a) P.N. Murgatroyd, J. Phys. D: Appl. Phys. 3 (1970) 151;
(b) Y. Yao, J.H. Hou, Z. Xu, G. Li, Y. Ynag, Adv. Funct. Mater. 18 (2008) 1783;
(c) V.D. Mihailetchi, H.X. Xie, B. de Boer, L.J.A. Koster, P.W.M. Blom, Adv. Funct. Mater. 16 (2006) 699.
[57] (a) H.Z. Yu, J.B. Peng, Chin. Phys. B 17 (2008) 3143;
(b) A.J. Moule, K. Meerholz, Adv. Funct. Mater. 19 (2009) 3028.

excitons to the guest molecules) [11–15]. The host materials for electrophosphorescence reported thus far are limited to a few functionalities, including carbazoles and phenylsilanes [13–16]. The carbazole derivatives, which possess sufficiently large triplet energies and carrier transport properties, are widely used as host materials in PHOLEDs [17–19]. Examples of these materials include 4,4′-bis(9-carbazolyl)-2,2′-biphenyl (CBP), 1,3-bis(9-carbazolyl)benzene (mCP) and 3,5-bis(9-carbazolyl)tetraphenylsilane (SimCP). The most commonly used host material CBP has been shown useful for green- and red-light-emitting PHOLEDs [20–26]. However, CBP has several problems such as low T_g and low triplet energy state which deteriorate efficiency and longevity of the device. It has been reported that fluorene derivatives have been important materials for OLEDs because of their high quantum yield of photoluminescence (PL), electroluminescence (EL) efficiencies and high thermal stability [27–29]. However, it has been reported that the extension of the carbazole conjugation, which decreases the triplet energy of the carbazole as in the case of CBP, can be minimized by altering the linkage group to carbazole unit, while also maximizing the thermal stability of the material [18,30]. Thus, the research directed towards the design and synthesis of new carbazole derivatives with high triplet energy and thermal stability has not been limited [31,32].

Thus, we designed highly twisted *N*-fluorenyl carbazole as a new host material. The introduction of fluorene unit, possessing high photoluminescence and electroluminescence efficiencies, to carbazole unit is to inhibit the extension of conjugation and improve the thermal stability of the material, which is suitable for host in the efficient electroluminescent devices. Moreover, the highly twisted structure due to coupling of *N*-fluorenylated carbazole would increase its glass transition temperature and molecular rigidity as well as inhibited intermolecular interaction. In the present study, we report on the synthesis and characterization of a new carbazole derivative BDFC in which fluorene-coupled at 3-position of carbazole unit. A new *N*-fluorenyl carbazole material BDFC shows the higher thermal stability ($\Delta T_{5\%}$) of 494.7 °C (CBP: 447 °C) with high glass transition temperature (T_g) of 177.8 °C (CBP: 62 °C) and a band energy gap of 3.01 eV with high triplet energy of 2.72 eV (CBP: 2.56 eV) for use as host material in the efficient organic light emitting diodes. We fabricate green-emitting phosphorescent organic light emitting diodes using the new BDFC as host and Ir(ppy) as guest emitter and report its higher device performances compared with that of the device based on widely used CBP host.

2. Experimental

2.1. Materials

All reagents and solvents were purchased from Aldrich Chemical Co. and Fluka. All the solvents were freshly distilled over appropriate drying reagents before use. The spectroscopic grade $CHCl_3$ (Aldrich) was used to measure UV–visible absorption and photoluminescence spectra of the samples. All other compounds were used as received. All the materials used in the phosphorescent organic light emitting diodes were purchased from Lumtec corp., Taiwan.

2.2. Synthesis

2.2.1. Synthesis of 9-(9′,9′-dimethyl-9H-fluoren-2-yl)-9H-carbazole (**1**)

A mixture of activated copper powder (11.4 g, 0.120 mol), K_2CO_3 (16.53 g, 0.120 mol), 9H-carbazole (20 g, 0.120 mol), 2-bromo-9′,9′-dimethyl-9H-fluorene (35.94 g, 0.132 mol) and 18-crown-6 (4.74 g, 0.0179 mol) in dichlorobenzene (200 mL) was heated to 200 °C for 30 h. After that, the reaction mixture was filtered with methylene chloride (MC). After dichlorobenzene was removed by vacuum distillation, the crude product was purified by column chromatography (using MC/hexane: 1/5 as eluent) and recrystallization with ethanol. Yield: 38.33 g (89.15%). ^{1}H NMR (300 MHz, $CDCl_3$) δ: 8.21–8.18 (d, 2H), 7.96–7.93 (d, 1H), 7.84–7.81 (t, 1H), 7.65–7.64 (d, 1H), 7.58–7.54 (dd, 1H), 7.51–7.39 (m, 7H), 7.35–7.30 (m, 2H), 1.58–1.55 (d, 6H). ^{13}C NMR (300 MHz, $CDCl_3$) δ: 155.16, 153.85, 141.03, 138.49, 138.45, 136.62, 127.60, 127.25, 125.96, 125.87, 123.38, 122.77, 121.46, 121.09, 120.36, 120.20, 119.89, 109.87, 47.16, 27.16. M^+: 359.

2.2.2. Synthesis of 3-bromo-9-(9′,9′-dimethyl-9H-fluoren-2-yl)-9H-carbazole (**2**)

N-Bromosuccinimide (13.37 g, 0.097 mol) was added to the solution of 9-(9′,9′-dimethyl-9H-fluoren-2-yl)-9H-carbazole (**1**) (35 g, 0.097 mol) and silica-gel (18 g) in methylene chloride (400 mL). The reaction mixture was stirred at room temperature. Before extraction with water and Methylene chloride, the reaction mixture was filtered with Methylene chloride. The mixture of reaction was purified by column chromatography (using MC/hexane: 1/5 as eluent) and recrystallization with ethanol. Yield: 40.59 g (95.10%). ^{1}H NMR (300 MHz, $CDCl_3$), δ: 8.29–8.28 (d, 1H), 8.14–8.12 (d, 1H), 7.96–7.93 (d, 1H), 7.60–7.59 (d, 1H), 7.53–7.52 (d, 1H), 7.51–7.50 (t, 3H), 7.47–7.33 (m, 6H), 1.57–1.56 (d, 6H). ^{13}C NMR (300 MHz, $CDCl_3$) δ: 155.56, 153.82, 141.36, 139.71, 138.83, 138.27, 136.08, 128.63, 127.72, 127.27, 126.68, 125.79, 125.08, 123.06, 122.77, 122.27, 121.35, 121.18, 120.52, 120.29, 120.24, 112.61, 111.37, 110.09, 47.18, 27.13. M^+: 439.

2.2.3. Synthesis of 9,9′-bis-(9,9-dimethyl-9H-fluoren-2-yl)-9H,9′H-[3,3′]bicarbazolyl (BDFC)

A mixture of bis(cyclooctadiene)nickel(0) (2.85 g, 10.37 mmol) and 2,2-bipyridyl (1.86 g, 11.92 mmol) in dimethylformamide (40 mL) and toluene (160 mL) was heated to 80 °C. After 30 min, cyclooctadiene (0.93 g, 8.64 mmol) and 3-bromo-9-(9′,9′-dimethyl-9H-fluoren-2-yl)-9H-carbazole (**2**) (4 g, 9.12 mmol) in toluene (40 mL) were added to the reaction mixture and stirred for 144 h. The reaction mixture in HCl and Dioxane was stirred for 15 min and washed with HCl. The reaction mixture was purified by column chromatography (using CH_2Cl_2/hexane: 1/10 as eluent) and recrystallization with methylene chloride and ethanol. Yield: 2.53 g (77.35%). FT-IR (KBr): 3043,

2954. ^{1}H NMR (300 MHz, $CDCl_3$) δ: 8.53–8.52 (s, 1H), 8.28–8.27 (d, 1H), 8.00–7.97 (d, 1H), 7.86–7.83 (m, 2H), 7.71 (s, 1H), 7.64–7.59 (m, 2H), 7.53–7.43 (m, 6H), 1.61–1.60 (d, 6H). ^{13}C NMR (300 MHz, $CDCl_3$) δ: 155.50, 153.86, 141.50, 140.17, 138.50, 138.46, 136.70, 134.37, 127.61, 127.26, 126.10, 125.87, 125.81, 124.02, 123.62, 122.78, 121.39, 121.14, 120.48, 120.21, 120.00, 118.94, 110.15, 110.01, 47.19, 27.18. HRMS: calcd. for $C_{54}H_{40}N_2$: 716.3191, found: 716.3192.

2.3. Measurements

^{1}H nuclear magnetic resonance (NMR) spectra were recorded using DRX 300 MHz Bruker spectrometer and chemical shifts in spectra were reported in parts per million (ppm) units with tetramethylsilane as internal standard. Infrared (IR) studies of the samples were carried out using a Genesis II FT-IR spectrometer. A Jeol JMS-700 high-resolution mass spectrometer (HRMS) was used to obtain the mass spectra of the samples. Thermogravimetric analysis (TGA) was performed under nitrogen using a TA instrument 2025 thermogravimetric analyzer. The sample was heated from 50 °C to 800 °C with a heating rate of 10 °C/min. Differential scanning calorimeter (DSC) studies were carried out under nitrogen using a TA instrument 2100 differential scanning calorimeter. The sample was heated from 30 °C to 300 °C with a heating rate of 10 °C/min. UV–visible absorption and photoluminescence (PL) studies at room temperature were carried out using Perkin Elmer LAMBDA-900 UV/VIS/NIR spectrometer and LS-50B luminescence spectrophotometer, respectively and the phosphorescence spectrum was recorded from the delayed emission of BDFC at 77 K. Cyclic voltammogram (CV) of the sample was recorded using a Epsilon E3

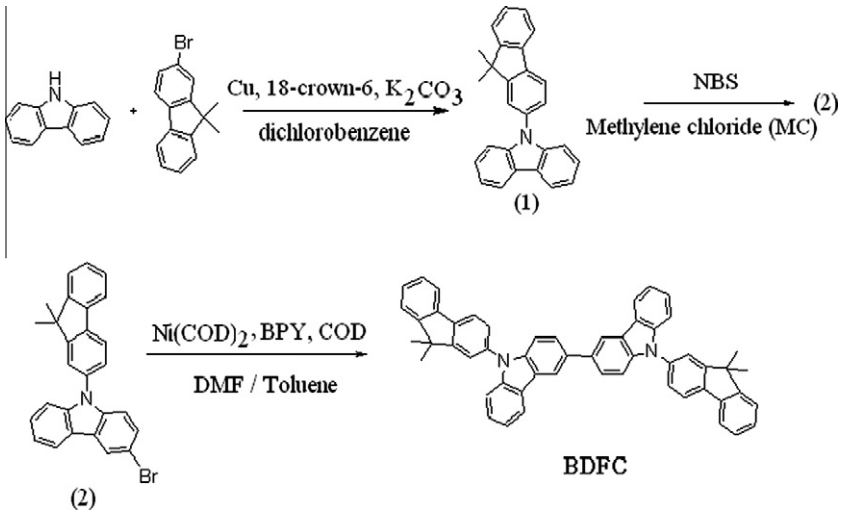

Fig. 1. The synthetic scheme of BDFC.

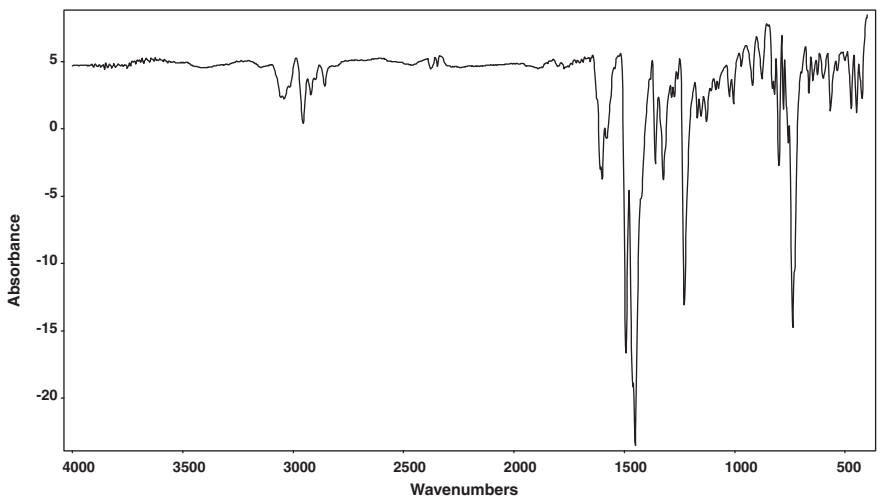

Fig. 2. FT-IR spectrum of BDFC.

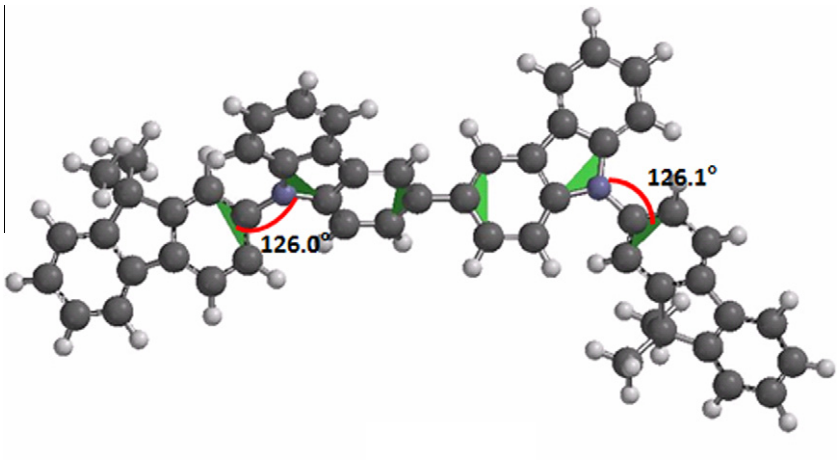

Fig. 3. The molecular structure (determined by Spartan08 software) of BDFC.

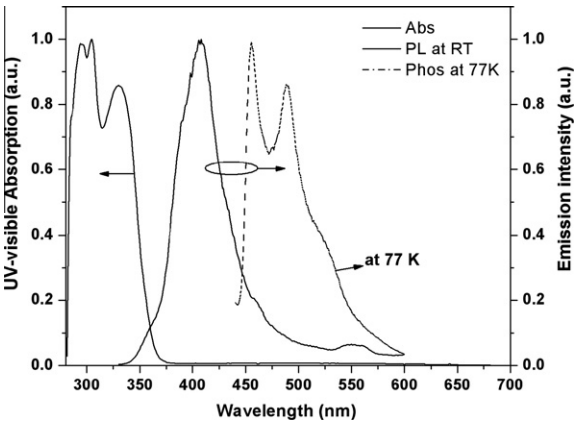

Fig. 4. The UV–visible absorption, photoluminescence (at room temperature) and phosphorescence (at 77 K) spectra of BDFC in toluene (1×10^{-5} M).

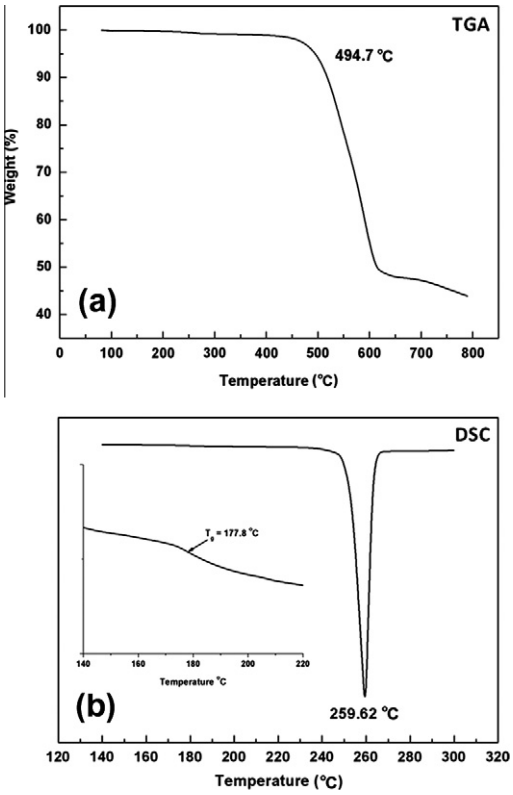

Fig. 5. (a) Thermogravimetric analysis (TGA) and (b) differential scanning calorimetry (DSC) studies of BDFC. Inset shows the glass transition temperature (T_g) of BDFC.

at room temperature in a 0.1 M solution of tetrabutylammonium perchlorate (Bu_4NClO_4) in acetonitrile under nitrogen environment at a scan rate of 50 mV/s. The platinum rod was used as working and the counter electrode, and a $Ag/AgNO_3$ electrode was used as the reference electrode. The mobility of BDFC molecule was determined from the Time-of-Flight (ToF) experiment. For ToF experiment, a semitransparent aluminum (Al) layer of 20 nm thickness was deposited on the glass substrate as bottom electrode by thermal evaporation process. A thick BDFC film of 1 μm thickness was drop-casted on the bottom electrode using the BDFC solution (3 wt.% in toluene) by vacuum drying at 60 °C for 24 h. The thickness and flatness of drop-cast BDFC film were measured using an alpha-stepper (Alpha step 500, Tencor). The device for ToF experiment was completed by depositing a thin Al film of 20 nm thickness on the above prepared BDFC film for the top electrode. The ToF experiment was performed in a vacuum cryogenic chamber by illuminating the sample with N_2 laser (337 nm) pulses of duration 6 ns under a dc bias for the ToF photocurrent transients [33].

2.4. Device fabrication

The phosphorescent organic light emitting diodes were fabricated as shown in Fig. 6. The device structure was as follows: indium-tin-oxide (ITO)/1,1-bis[di-4-tolylamino]phenyl]cyclohexane (TAPC) as the hole transport layer (HTL) (30 nm)/emissive layer (EML) (30 nm)/1,3,5-tris (m-pyrid-3-yl-phenyl)benzene (TmPyPB) as the electron

transport layer (ETL) (30 nm)/LiF (1 nm)/Al (120 nm). The (4,4′-*N*, *N*′-dicarbazole)biphenyl (CBP) host for device A or 9,9′-Bis-(9,9-dimethyl-9H-fluoren-2-yl)-9H,9′H-[3,3′]bicarbazolyl (BDFC) host for the device B doped with 5% green-emitting phosphorescent dopant, fac-tris(2-phenylpyridine)iridium [Ir(ppy)$_3$] was used as emissive layer (EML). The CBP host based device was fabricated for the comparison of the device performances with that of BDFC host based device. The patterned ITO (anode) coated glass substrates were ultrasonically cleaned in acetone for 10 min followed by isopropyl alcohol, dried in each step at 90 °C for 10 min and UV treated for 10 min before loading into the deposition chamber for the device fabrication. All organic layers were deposited by thermal evaporation process under a vacuum of $\sim 5 \times 10^{-6}$ Torr and LiF as electron injection layer and Al cathode were deposited without breaking the chamber vacuum. The fabricated devices were transferred into the glove-box for the encapsulation of the devices with moisture getter using UV curable epoxy. The current density–voltage (*J*–*V*) characteristics of all devices were measured using Keithley 236 source meter. The electroluminescence and luminescence characteristics of the devices were recorded using Spectrascan PR655 spectroradiometer under ambient condition.

3. Results and discussion

The new *N*-fluorenyl carbazole material, 9,9′-bis-(9,9-dimethyl-9H-fluoren-2-yl)-9H,9′H-[3,3′]bicarbazolyl (BDFC), was prepared as depicted in Fig. 1. The BDFC was synthesized via manifold chemical reactions such as bromination, Ullmann and Yamamoto coupling reactions as described below. The compound **1** was obtained by Ullmann coupling reaction of 9H-carbazole and 2-bromo-9′,9′-dimethyl-9H-fluorene using activated copper powder, K_2CO_3 and 18-crown-6. BDFC was prepared by Yamamoto coupling reaction of compound **2** obtained from mono-bromination of compound **1**. The structure of BDFC was confirmed by ^{1}H NMR, IR and HRMS. In the IR spectrum, we confirmed the structure from disappearing of aromatic C–Br stretching at 1060 cm^{-1} (Fig. 2). The angle of 126° between carbazole and fluorene units in the highly twisted structure of BDFC molecule was determined by Spartan08 software as shown in Fig. 3.

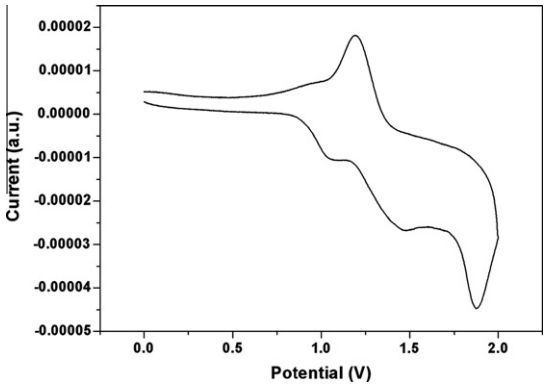

Fig. 6. Cyclic voltammogram of BDFC.

The UV–visible absorption, photoluminescence and phosphorescence (at 77 K) spectra of BDFC in toluene (1×10^{-5} M) are shown in Fig. 4. From the UV–visible absorption spectrum of BDFC, the absorption bands between 294 nm and 330 nm are assigned for S_0 to S_2 and S_0 to S_1 electronic transitions of the BDFC molecule [30]. BDFC showed the photoluminescence (PL) at 408 nm in toluene, indicating the emission from its lowest exited state. The phosphorescence spectrum of BDFC was obtained from the delayed emission of BDFC in toluene (1×10^{-5} M) at 77 K. From the phosphorescence spectrum of BDFC molecule, the triplet energy (T_1) was estimated from the highest energy peak (455 nm) to be 2.72 eV, which is higher than that (T_1: 2.56 eV) of CBP host [19,34]. The mobility of BDFC was determined from the Time-of-Flight (ToF) experiment. It was calculated using the equation $\mu = \frac{d^2}{Vt}$, where d is the thickness of the film, V is the applied dc bias voltage and t is the measured transit time [33]. The ToF mobility of BDFC host was found to be 3.4×10^{-4} cm^2/Vs at bias voltage of 28.26 mV and transit time of 10.45 μs. The thermal properties of BDFC sample were determined by differential scanning calorimeter (DSC) and thermogravimetric analysis (TGA) measurements. From the DSC data (Fig. 5b), the glass transition temperature (T_g) was observed at 177.8 °C, which is much higher than that (62 °C) of CBP, and the melting temperature (T_m) was observed at 259.62 °C as a sharp endothermic peak [19]. In TGA curve of BDFC (Fig. 5a), 5% weight loss was observed at 494.7 °C, showing the higher thermal stability compared with that (447 °C) of CBP. The higher

Table 1
The physical properties of BDFC.

Absorption[a]	Emission						
λ_{abs} (nm)	λ_{PL}[b] (nm)	λ_{Phos}[c] (nm) (at 77 K)	T_d[d]/T_g[e]/T_m[f] (°C)	HOMO (eV)	LUMO (eV)	E_g[g] (eV)	T_1[h] (eV)
294,305,330	408	455	494.7/177.8/259.6	5.38	2.37	3.01	2.72

[a] The major UV–visible absorption band peaks are listed.
[b] Photoluminescence (PL) maximum measured in tolune at room temperature.
[c] The highest energy peak of the phosphorescence spectrum in tolune at 77 K.
[d] T_d – Temperature corresponding to a 5% weight loss in thermogravimetric analysis.
[e] T_g – Glass transition temperature from differential scanning calorimetry (DSC) studies.
[f] T_m – Melting temperature from DSC studies.
[g] E_g – Band gap energy calculated from the equation $E_g = hc/\lambda = 1241/\lambda$, where λ is the edge wavelength (nm) of UV–visible absorption spectrum.
[h] T_1 – Triplet energy is estimated from the higher energy peak of the phosphorescence spectrum.

triplet energy and thermal stability of BDFC compared with CBP reveal the decreased conjugation of carbazole unit by fluorene unit coupled to it [18,30]. The electrochemical properties of BDFC sample was investigated by cyclic voltammetric (CV) studies. The CV curve of BDFC is shown in Fig. 6. It shows the reversible oxidation potential characterized by E_{onset} value at 0.88 V. The estimated ionization potential (IP = E_{onset} + 4.54 = HOMO level) was 5.38 eV. The higher HOMO energy level of BDFC can be useful for the efficient hole-injection and transport. The LUMO energy level of BDFC was calculated to be 2.37 eV from the edge wavelength of UV–visible absorption spectrum. BDFC having the band gap of 3.01 eV with high triplet energy of 2.72 eV could be suitable for use as host material for the efficient organic light emitting diodes. The thermal, photophysical and electrochemical properties of BDFC are listed in Table 1.

To investigate the new *N*-fluorenyl-carbazole material (BDFC) as host in organic light emitting diodes (OLEDs), the phosphorescent organic light emitting diodes (PHOLEDs) based on BDFC as host and green phosphorescent dopant, fac-tris(2-phenylpyridine)iridium [Ir(ppy)$_3$], as guest emitter were fabricated as shown in Fig. 7 and characterized. PHOLED based on widely used CBP was fabricated for the comparison. The energy level diagram and the structure of materials used in the devices are shown in Fig. 8 [19,34–38]. The PHOLEDs were fabricated using the following device structure: ITO/1,1-bis[di-4-tolylamino]phenyl]cyclohexane (TAPC) (30 nm)/host: Ir(ppy)$_3$ with optimized concentration of 5% (30 nm)/1,3,5-tris(m-pyrid-3-yl-phenyl)benzene (TmPyPB) (30 nm)/LiF/Al. The CBP was used as host in the device A and BDFC host was used in device B. TAPC with LUMO energy level of 2.0 eV (LUMO: 2.6 eV for CBP; 2.37 eV for BDFC) and higher triplet energy (T_1) of 2.9 eV (T_1: 2.56 eV for CBP; 2.72 eV for BDFC; 2.46 eV for Ir(ppy)$_3$) was used as hole transport layer (HTL), while TmPyPB with HOMO energy level of 6.68 eV (HOMO: 5.9 eV for CBP; 5.38 eV for BDFC) and higher triplet energy of 2.78 eV compared with that of host and dopants was used as electron transport layer (ETL) in the devices for the effective confinement of charge carriers and/or excitons within the emissive layer (EML). Fig. 9 shows the current density–voltage–luminescence (*J*–*V*–*L*) characteristics of devices A and B. From the *J*–*V*–*L* characteristics of device A, the drive voltages of 5 V for 100 cd/m^2 and 8 V for 1000 cd/m^2 were observed and it showed a maximum luminescence of 23,250 cd/m^2 at 16 V. Device A showed the turn-on voltage (defined as an applied voltage required for the luminescence of 1 cd/m^2) of 3 V. Fig. 10 shows the current- and external quantum-efficiency characteristics of devices A and B. Device A based on CBP host showed the maximum current efficiency of 48.0 cd/A, external quantum efficiency of 15.3% and power efficiency of 16.3 lm/W. The electroluminescence spectra of devices A and B at 10.5 V are shown in Fig. 11. The device A showed the electroluminescence (EL) emission

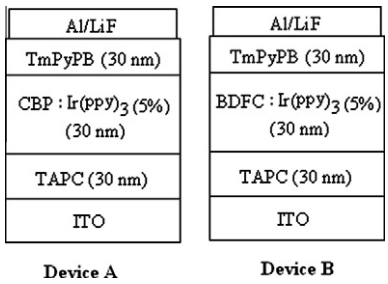

Fig. 7. The device structures of the devices A and B.

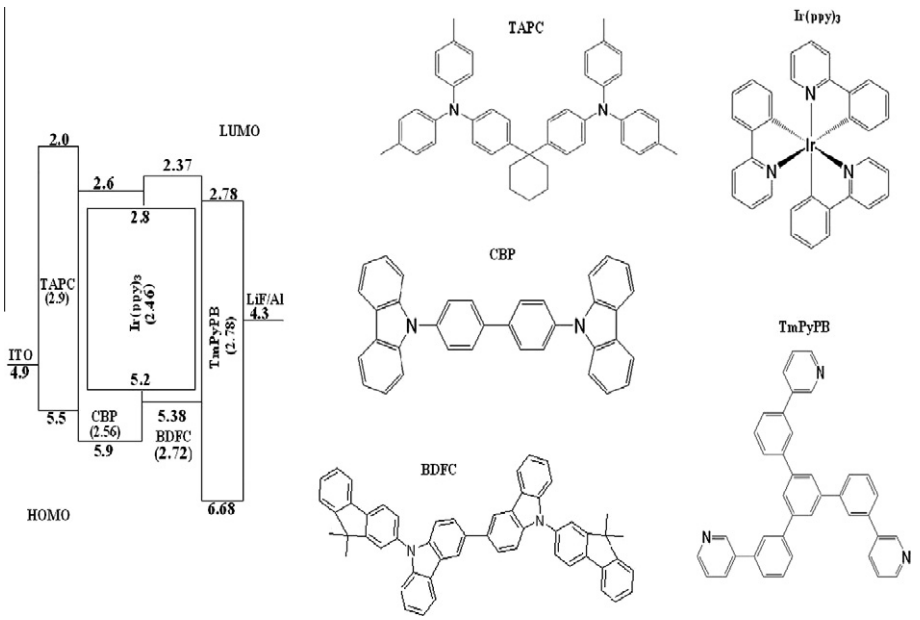

Fig. 8. The energy level diagram and molecular structures of the materials used in the devices.

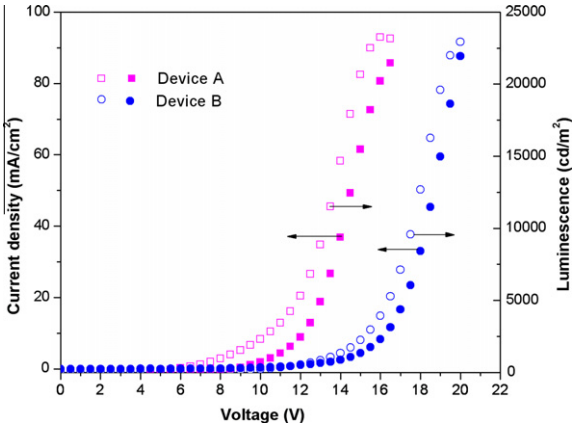

Fig. 9. The current density–voltage–luminescence (J–V–L) characteristics of devices A and B.

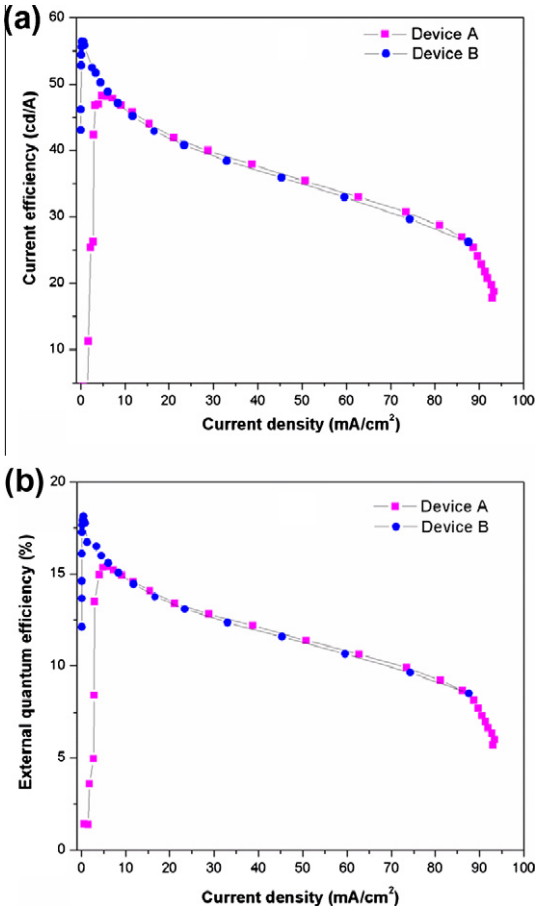

Fig. 10. (a) The current efficiency-current density- and (b) external quantum efficiency–current density-characteristics of the devices A and B.

peak at 512 nm with shoulder peak at 539 nm with CIE color coordinates of (0.31, 0.61), originating from $Ir(ppy)_3$ dopant [36,39–41]. No emissions from the host and/or

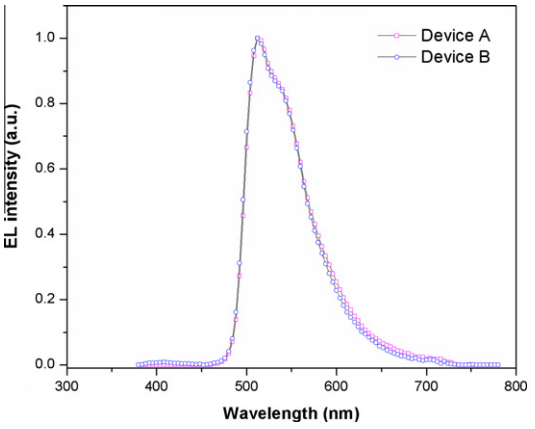

Fig. 11. The electroluminescence spectra of the devices A and B at 10.5 V.

adjacent charge transporting layers were observed, indicating the effective confinement of charge carriers and/or excitons and complete energy transfer to guest emitter in the EML of the device A.

Device B based on BDFC host showed the drive voltages of 8.5 V for 100 cd/m^2 and 13.5 V for 1000 cd/m^2, and a maximum luminescence of 22,930 cd/m^2 at 20 V as shown in Fig. 9. The turn-on voltage is increased to 3.5 V compared with that (3 V) of device A. The increased energy barrier of 0.41 eV for electron injection at BDFC/TmPyPB interface of the device B than that (0.18 eV) of device A using CBP host resulted in the higher operating voltage than that of device A. The device B using BDFC host exhibited the higher current efficiency of 56.8 cd/A, external quantum efficiency of 18.1% and power efficiency of 21.3 lm/W compared with that (48.1 cd/A, 15.3% and 16.3 lm/W) of device A using CBP host, resulting from the efficient energy transfer and the higher triplet energy (T_1: 2.72 eV) of BDFC host (T_1: 2.56 eV for CBP). The device B showed the higher quantum efficiency roll-off (17% at 8.3 mA/cm^2) for the increasing current densities compared with that (2% at 8.3 mA/cm^2) of the device A using CBP

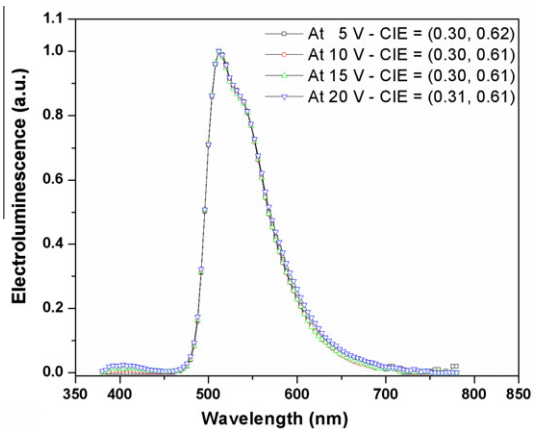

Fig. 12. The electroluminescence spectra of the device B at different voltages.

Table 2
The electroluminescence characteristics of the devices.[a]

Device[b]	Turn-on voltage (V)	L (cd/m^2, V)	η_c (cd/A, V)	η_{ext} (%, V)	η_p (lm/W, V)	EL[c] (nm)	CIE (x, y)
A	3	23,250, 16.0	48.0, 10.5	15.3, 10.5	16.3, 9.0	512	(0.31, 0.61)
B	3.5	22,930, 20.0	56.8, 10.5	18.1, 10.5	21.3, 8.0	512	(0.30, 0.61)

[a] The data for brightness (L), current efficiency (η_c), external quantum efficiency (η_{ext}) and power efficiency (η_p) are the maximum values of the corresponding device. The turn-on voltage for all the devices was defined as voltage required for luminescence of 1 cd/m^2.
[b] The device structure is ITO/TAPC (30 nm)/Host: Ir(ppy)$_3$ (5%) (30 nm)/TmPyPB (30 nm)/LiF/Al with CBP host for device A and BDFC host for device B.
[c] The peak emission wavelength of the EL spectrum of corresponding device.

host. The higher efficiency roll-off of the device B can be explained by the imbalance of charge carriers in the EML due to the higher HOMO (5.38 eV) and LUMO (2.37 eV) energy levels of BDFC host than that (HOMO: 5.9 eV; LUMO: 2.6 eV) of CBP host. In other words, the higher HOMO energy level of BDFC host in the device reduces the hole injection barrier, which is much favorable for hole injection, while the higher LUMO level increases the electron injection barrier, less favor for election injection, compared with that of CBP host in device and which in turn makes the charge imbalance in the EML of the device B based on BDFC, leading to the increased efficiency roll-off compared with that of device A based on CBP. The device B showed the characteristic dopant emission at 512 nm with shoulder peak at 539 nm with CIE color coordinates of (0.30, 0.61) at 10.5 V (Fig. 11). The device B based on BDFC host exhibits the EL emission at 512 nm with CIE color coordinates of (0.30, 0.62), (0.30, 0.61), (0.30, 0.61) and (0.31, 0.61) at 5 V, 10 V, 15 V and 20 V, respectively as shown in Fig. 12. The small residual emission of device B around 408 nm at higher operating voltage is attributed to the BDFC host emission. The device based on BDFC host showed the effective confinement of triplet excitons and efficient energy transfer to the guest emitter in the EML of the device, resulted in the higher device efficiencies compared with that of CBP based device. The characteristics of the devices A and B are summarized in Table 2. The higher thermal stability (BDFC; $\Delta T_{5\%}$: 494.7 °C and T_g: 177.8 °C, CBP; $\Delta T_{5\%}$: 447 °C and T_g: 62 °C), higher triplet energy (T_1: 2.72 eV for BDFC and 2.56 eV for CBP) for the effective confinement of triplet excitons to the emitter, and the higher device performances of BDFC host could make the new *N*-fluorenyl carbazole (BDFC) host superior than widely used CBP host for the efficient organic light emitting diodes.

4. Conclusion

A new *N*-fluorenyl carbazole (BDFC) host material was synthesized and characterized. The thermal stability ($\Delta T_{5\%}$) of 494.7 °C with the high glass transition temperature (T_g) of 177.8 °C was observed from TGA and DSC studies. The physical studies of BDFC showed the emission at 408 nm and a band energy gap of 3.01 eV with high triplet energy of 2.72 eV. The highly efficient PHOLEDs employing BDFC as host have been fabricated using the structure: ITO/Di-[4-(*N*,*N*-ditolyl-amino)-phenyl]cyclohexane (TAPC)/BDFC (host): fac-tris(2-phenylpyridine)iridium [Ir(ppy)$_3$] (5%)/1,3,5-tris(m-pyrid-3-yl-phenyl)benzene (TmPyPB)/LiF/Al. The device showed the effective confinement of triplet excitons and efficient energy transfer to the guest emitter in the EML, resulted in the higher current efficiency of 56.3 cd/A, external quantum efficiency of 18.1% and power efficiency of 21.3 lm/W compared with that (48.1 cd/A, 15.3% and 16.3 lm/W) of the device based on CBP host. The results show that the new host material BDFC could be useful for the efficient organic light emitting diodes.

Acknowledgements

This research was financially supported by MKE and KIAT through the Workforce Development Program in Strategic Technology, by Strategic Technology under Ministry of Knowledge Economy of Korea and by Basic Science Research Program through the National Research Foundation of Korea (NRF) funded by the Ministry of Education, Science and Technology (2011-0000310).

References

[1] C.W. Tang, S.A. VanSlyke, Appl. Phys. Lett. 51 (1987) 913.
[2] .J.H. Burroughes, D.D.C. Bradley, A.R. Broun, R.N. Marks, K. Mackay, R.H. Friend, P.L. Burn, A.B. Holms, Nature 347 (1990) 539.
[3] M.A. Baldo, D.F. O Brien, Y. You, A. Shoustikov, S. Silbey, M.E. Thampson, S.R. Forrest, Nature 395 (1998) 151.
[4] C. Adachi, M.A. Baldo, M.E. Thampson, Appl. Phys. Lett. 77 (2000) 904.
[5] S.O. Jung, Q. Zhao, J.-W. Park, S.O. Kim, H.-Y. Oh, S.-K. Kwon, Y.J. Kang, Org. Electron. 10 (2009) 1066.
[6] Y.-S. Park, J.-W. Kang, D.M. Kang, J.-W. Park, Y.-H. Kim, S.-K. Kwon, J.-J. Kim, Adv. Mater. 20 (2008) 1957.
[7] S.O. Jung, Y.J. Kang, H.-S. Kim, Y.-H. Kim, C.-L. Lee, J.-J. Kim, S.-K. Lee, S.-K. Kwon, Eur. J. Inorg. Chem. 2004 (2004) 3415.
[8] D.M. Kang, H.-D. Park, Y.-H. Kim, S.C. Shin, J.-J. Kim, S.-K. Kwon, J.-W. Kang, J.W. Park, S.O. Jung, S.-H. Lee, Adv. Mater. 20 (2008) 2003.
[9] S.O. Jung, Y.-H. Kim, S.-K. Kwon, H.-Y. Oh, J.-H. Yang, Org. Electron. 8 (2007) 349.
[10] S.-O. Jung, Y.-H. Kim, H.-S. Kim, S.-K. Kwon, H.-Y. Oh, Mol. Cryst. Liq. Cryst. 444 (2006) 95.
[11] D.-S. Leem, S.O. Jung, S.-O. Kim, J.-W. Park, J.W. Kim, Y.-S. Park, Y.-H. Kim, S.-K. Kwon, J.-J. Kim, J. Mater. Chem. 19 (2009) 8824.
[12] C. Adachi, M.A. Baldo, M.E. Thampson, S.R. Forrest, J. Appl. Phys. 90 (2001) 5048.
[13] J. Holmes, S.R. Forrest, Y.-J. Tung, R.C. Kwong, J.J. Brown, S. Garon, M.E. Thampson, Appl. Phys. Lett. 82 (2003) 2422.
[14] S.-J. Yeh, M.-F. Wu, C.-T. Chen, Y.-H. Song, Y. Chi, M.-H. Ho, S.-F. Hsu, C.-H. Chen, Adv. Mater. 17 (2005) 285.
[15] X. Ren, J. Li, R.J. Holmes, P.I. Djurovich, S.R. Forrest, M.E. Thampson, Chem. Mater. 16 (2004) 4743.
[16] M. Ikai, S. Tokito, Y. Sakamoto, T. Suzuki, Y. Taga, Appl. Phys. Lett. 79 (2001) 156.
[17] K. Brunner, A. Van Dijken, H. Borner, J.J.A.M. Bastiaansen, N.M.M. Kiggen, B.M.W. Langeveld, J. Am. Chem. Soc. 126 (2004) 6035.
[18] M.-H. Tsai, H.-W. Lin, H.-C. Su, T.-H. Ke, C.-C. Wu, F.-C. Fang, Y.-L. Liao, K.-T. Wong, C.-I. Wu, Adv. Mater. 18 (2006) 1216.

[19] M.-H. Tsai, Y.-H. Hong, C.-H. Chang, H.-C. Su, C.-H. Wu, A. Matoliukstyte, J. Simokaitiene, S. Grigalevicius, J.V. Grazulevicius, C.-P. Hsu, Adv. Mater. 19 (2007) 862.
[20] S. Lamansky, P. Djurovich, D. Murphy, F. Abdel-Razzaq, H.-E. Lee, C. Adachi, P.E. Burrows, S.R. Forrest, M.E. Thompson, J. Am. Chem. Soc. 123 (2001) 4304.
[21] W.Y. Wong, C.L. Ho, Z.Q. Gao, B.X. Mi, C.H. Chen, K.W. Cheah, Z.Y. Lin, Angew. Chem. Int. Ed. 45 (2007) 7800.
[22] A. Tsuboyama, H. Iwawaki, M. Furugori, T. Mukaide, J. Kamatani, S. Igawa, T. Moriyama, S. Miura, T. Takiguchi, S. Okada, M. Hoshino, K. Ueno, J. Am. Chem. Soc. 125 (2003) 12971.
[23] Y.-J. Su, H.-L. Huang, C.-L. Li, C.-H. Chien, Y.-T. Tao, P.-T. Chou, S. Datta, R.-S. Liu, Adv. Mater. 15 (2003) 884.
[24] W.S. Huang, J.T. Lin, C.H. Chien, Y.T. Tao, S.S. Sun, Y.S. Wen, Chem. Mater. 16 (2004) 2480.
[25] C.L. Li, Y.J. Su, Y.T. Tao, P.T. Chou, C.H. Chien, C.C. Cheng, R.S. Liu, Adv. Funct. Mater. 15 (2005) 384.
[26] S.G. Jung, Y.J. Kang, H.S. Kim, Y.H. Kim, C.L. Lee, J.J. Kim, S.K. Lee, S.K. Kwon, Eur. J. Inorg. Chem. 16 (2004) 3415.
[27] K.S. Kim, Y.M. Jeon, J.W. Kim, C.W. Lee, M.S. Gong, Org. Electron. 9 (2008) 797.
[28] A. Farcas, N. Jarroux, V. Harabagiu, P. Guégan, Eur. Polym. J. 45 (2009) 795.
[29] Y.-H. Kim, S.-J. Park, J.-W. Park, J.H. Kim, S.-K. Kwon, Macromol. Res. 15 (2007) 216.
[30] J. He, H. Liu, Y. Dai, X. Ou, J. Wang, S. Tao, X. Zhang, P. Wang, D. Ma, J. Phys. Chem. C 113 (2009) 6761.
[31] T. Tsuzuki, S. Tokito, Adv. Mater. 19 (2007) 276.
[32] Z.Q. Gao, M. Luo, X.H. Sun, H.L. Tam, M.S. Wong, B.X. Mi, P.F. Xia, K.W. Cheah, C.H. Chen, Adv. Mater. 21 (2009) 688.
[33] D.S. Chung, S.J. Lee, J.W. Park, D.B. Choi, D.H. Lee, J.W. Park, S.C. Shin, Y.-H. Kim, S.-K. Kwon, C.E. Park, Chem. Mater. 20 (2008) 3450.
[34] J. Lee, J.-I. Lee, K.-I. Song, S.J. Lee, H.Y. Chu, Appl. Phys. Lett. 92 (2008) 203305.
[35] B.D. Chin, C. Lee, Adv. Mater. 19 (2007) 2061.
[36] S.H. Kim, J. Jang, J.Y. Lee, Appl. Phys. Lett. 90 (2007) 223505.
[37] .J.Y. Lee, Appl. Phys. Lett. 89 (2006) 153503.
[38] N. Chopra, J. Lee, Y. Zheng, S.-H. Eom, J. Xue, F. So, Appl. Mater. Interface 1 (2009) 1169.
[39] Y. Zhang, G. Cheng, Y. Zhao, J. Hou, S. Liu, Appl. Phys. Lett. 86 (2005) 011112.
[40] G. Cheng, F. Li, Y. Duan, J. Feng, S. Liu, S. Qiu, D. Lin, Y. Ma, S.T. Lee, Appl. Phys. Lett. 82 (2003) 4224.
[41] Y. Wang, Appl. Phys. Lett. 85 (2004) 4848.

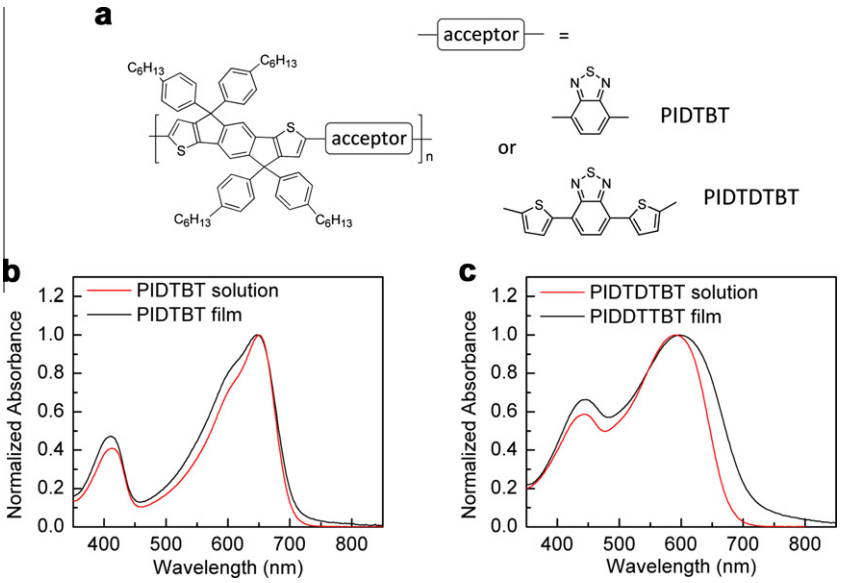

Fig. 1. (a) Structures of PIDTBT and PIDTDTBT. (b and c) Normalized absorption spectra of the PIDTBT and PIDTDTBT in dilute chloroform solution and in film state.

(J_{sc}) as high as 15 mA/cm^2, and high PCEs of greater than 5%. However, their relatively high-lying highest occupied molecular orbital (HOMO) levels limit their V_{oc} to be only around 0.6 V. Another class of poly[(9,9-dialkylfluorene)-2,7-diyl-*alt*-(4,7-bis(2-thienyl)-2,1,3-benzothiadiazole)-5,5′-diyl] (PFDTBT)-based polymers is noted for their deep HOMO levels which give high V_{oc} of ~1.0 V with corresponding PCE of 2–4% [24,25]. When the fluorene units in PFDTBT are replaced with either a carbazole [18] or a silafluorene [19] derivative, a significant enhancement of PCE (up to 6.1% PCE) could be achieved due to improved charge-transporting properties. However, these polymers have limited light harvesting capability due to their relatively large band gap (1.9 eV), which is similar to that of poly(3-hexylthiophene) (P3HT).

Indacenodithiophene (IDT)-based polymers [20,26], which show intermediate band gaps and V_{oc}s compared to the above-mentioned polymers, possess a ladder-type pentacyclic IDT moiety. It allows these polymers to function as good electron donors due to improved π electron delocalization. When this donor is copolymerized with BT, it gives a band-gap of 1.76 eV and a low-lying HOMO of ~5.23 eV. The multiple alkylphenyl side chains on IDT render polymers with better solubility and also prevent severe aggregation of the polymer chains.

Recently, a high PCE of 6.1% has been demonstrated for PSCs made from PIDTBT (Fig. 1a) containing alternating IDT and BT moieties [20]. Here, we report the photovoltaic characterizations of PIDTBT and a new polymer derivative, PIDTDTBT (Fig. 1a) in both conventional and inverted PSC device configurations. Under the AM 1.5G simulated solar illumination (100 mW/cm^2), PSCs based on PIDTBT and PIDTDTBT in a conventional architecture can reach PCE as high as 6.3% and 4.4%, respectively. Moreover, high PCEs of 4.9% and 4.2% could also be achieved for inverted architecture devices based on PIDTBT and PIDTDTBT, respectively.

2. Results and discussion

2.1. Analysis and thermal properties

PIDTBT and PIDTDTBT were synthesized using the Stille coupling reaction between the IDT monomer and 4,7-dibromo-2,1,3-benzothiadiazole or 4,7-bis(2-bromo-5-thienyl)-2,1,3-benzothiadiazole, using $Pd_2(dba)_3$ as catalyst in toluene/DMF (See Section 4.2). The number average molecular weight (M_n) of PIDTBT was 14.7 kDa with a polydispersity index (PDI) of 2.39. The M_n of PIDTDTBT was 21.4 kDa with a PDI of 1.53. Differential scanning calorimetry (DSC) thermogram with the second heating curves of the two polymers is presented in Fig. 2. No apparent thermal transitions between 30 and 350 °C were observed for PIDTBT; on the other hand, a transition around 220 °C

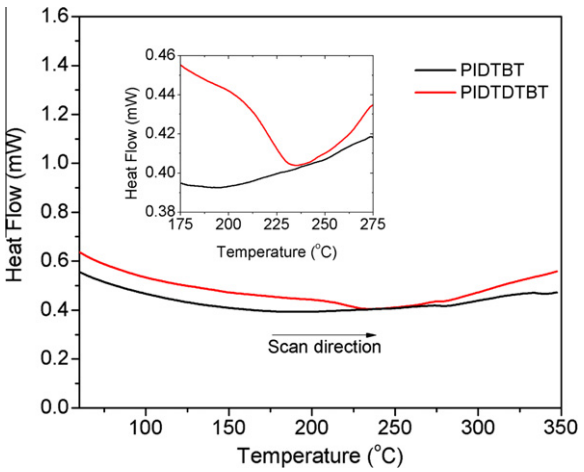

Fig. 2. DSC thermogram of PIDTBT and PIDTDTBT. Inset: enlarged image between 175 and 275 °C.

was given for PIDTDTBT, which was attributed to a glass transition.

2.2. Photophysical and electrochemical properties

The thin film absorption characteristics and the cyclic voltammogram of PIDTBT have been previously reported in Ref. [20]. The UV–Vis absorption spectra of PIDTBT and PIDTDTBT in dilute chloroform solution and in film state are shown in Fig. 1b and c, respectively. Similar to PIDTBT, PIDTDTBT shows two absorption bands due to the π–π^* transition and the intramolecular charge transfer with the absorption maxima at 445 and 590 nm, respectively. Negligible changes in the position of the peak maxima and only slight broadening of the absorption bands were observed in the cases of the cast films. From the low-energy onset of the thin film absorption, the optical bandgap of PIDTDTBT is estimated to be 1.74 eV, which is slightly smaller than 1.75 eV for PIDTBT. From the cyclic voltammograms (Fig. 3), the HOMO and LUMO levels of the PIDTDTBT were estimated to be −5.19 and −3.49 eV, respectively, using ferrocene (−4.8 eV) as the internal standard. The $E_0^{1/2}$ value of the ferrocene/ferrocinium couple vs. Ag/AgCl was 329 mV. PIDTBT has also been tested for comparison, and the HOMO and LUMO of PIDTBT were calculated to be −5.23 and −3.52 eV, respectively, giving a bandgap of 1.71 eV.

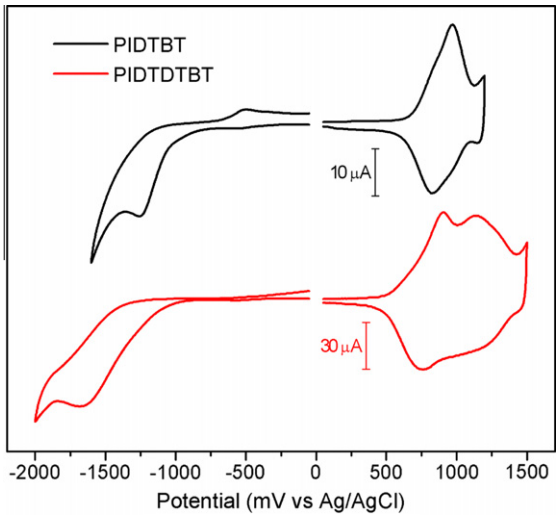

Fig. 3. Cyclic voltammograms of PIDTBT and PIDTDTBT.

2.3. Quantum mechanical calculations

The molecular geometry and the electron density of states distribution of these two polymers were calculated using density functional theory (DFT). All DFT [27,28] calculations were performed using Gaussian 09(A.02) employing the hybrid B3LYP [29,30] exchange–correlation functional with a split valence 6-31G* [31] basis set. Oligomers containing two repeating D–A pairs as illustrated in Table 1 were used for computational simplicity. The hexylphenyl side chains were also truncated to ethylphenyl groups as their replacement with shorter chains does not affect the optimized geometries of the polymers. This computational method is found to be an accurate

Table 1
Molecular geometries and the HOMO and LUMO surfaces of PIDTBT and PIDTDTBT.

	PIDTBT	PIDTDTBT
Side view	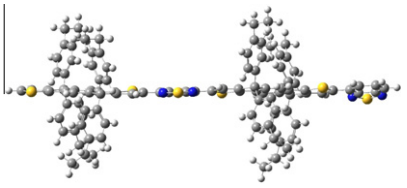	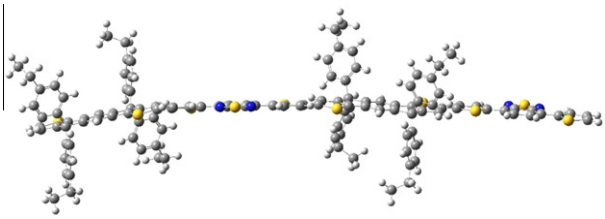
LUMO	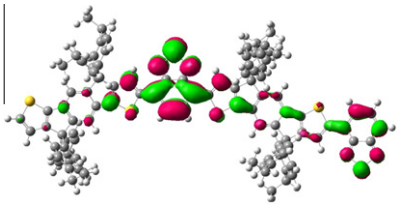	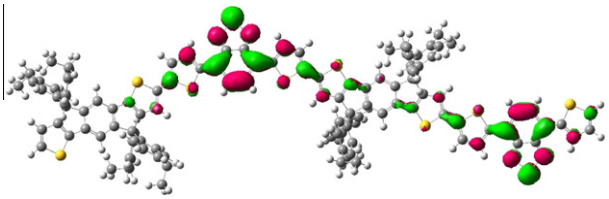
HOMO	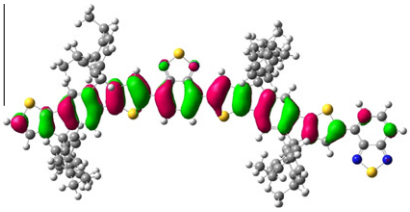	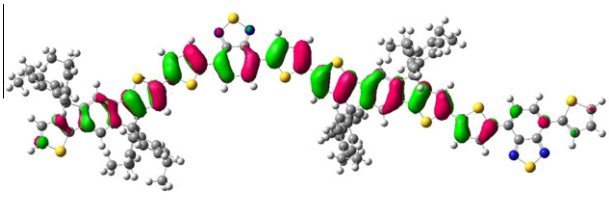

Table 2
Energy levels of PIDTBT and PIDTDTBT derived from cyclic voltammetry (CV) and DFT calculations.

	HOMO from CV (eV)	LUMO from CV (eV)	E_g from CV (eV)	E_g from absorption (eV)	HOMO from DFT (eV)	LUMO from DFT (eV)	E_g from DFT (eV)
PIDTBT	−5.23	−3.52	1.71	1.75	−4.68	−2.62	2.05
PIDTDTBT	−5.19	−3.49	1.70	1.74	−4.61	−2.69	1.92

All DFT calculations were performed using Gaussian 09.

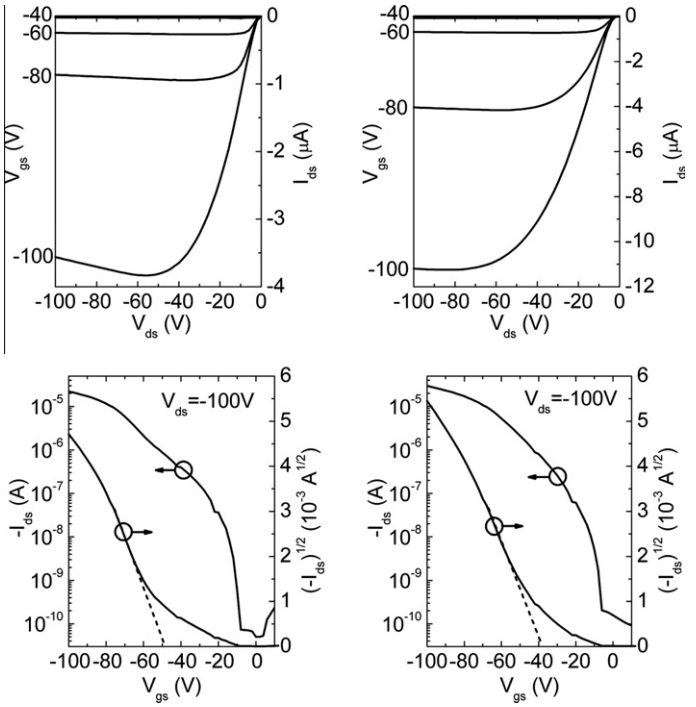

Fig. 4. Output (top) and transfer (bottom) characteristics of the FET devices of PIDTBT (left) and PIDTDTBT (right).

formalism for predicting the geometric and electronic properties of many conjugated polymers [32]. Frequency calculations were also performed on the optimized geometries of both polymers, and minima were verified through normal mode analyses which both resulted in zero imaginary modes. The ab initio simulations reveal that the conformations of the oligomer backbones of both PIDTBT and PIDTDTBT are highly coplanar (Table 1). The HOMO wave function is delocalized over the polymer backbones, and the LUMO wave function is localized on the BT acceptor group in both cases, proposing effective intramolecular charge-transfer transitions. The energy levels of the IDT-based polymers estimated from CV and DFT calculations are summarized in Table 2.

2.4. OFET characteristics

The hole-transporting properties of PIDTBT or PIDTDTBT were investigated by fabricating them into field effect transistors using a bottom-gate, top-contact configuration. The transfer and output characteristics are shown in Fig. 4. The hole mobilities extracted in the saturation regime from the linear fit of $(I_{ds})^{1/2}$ vs. V_{gs} are 0.020 and 0.013 $cm^2 V^{-1} s^{-1}$ for PIDTBT and PIDTDTBT, respectively. The more planar structure of the IDT moieties possibly reduces the degree of rotational disorder on the backbones of the polymers, leading to better charge transport. Another alternating IDTBT-based polymer with long alkyl solubilizing side chains has recently been reported to demonstrate an extraordinarily high FET mobility of 1.0 $cm^2 V^{-1} s^{-1}$ in a top-gate bottom-contact device [33], which is a further

Table 3
Performance of PSCs under the AM 1.5G Simulated Illumination (100 mW/cm^2).

	V_{oc} (V)	J_{sc} (mA/cm^2)	FF	PCE (%)
PIDTBT:$PC_{71}BM$[a]	0.84	11.3	0.62	5.9 (6.3)[c]
PIDTBT:$PC_{71}BM$[b]	0.84	10.4	0.54	4.7 (4.9)[c]
PIDTDTBT:$PC_{71}BM$[a]	0.78	10.0	0.55	4.3 (4.4)[c]
PIDTDTBT:$PC_{71}BM$[b]	0.83	9.3	0.53	4.1 (4.2)[c]

[a] Conventionl configuration.
[b] Inverted configuration.
[c] Numbers in parentheses represent the efficiency of the champion devices.

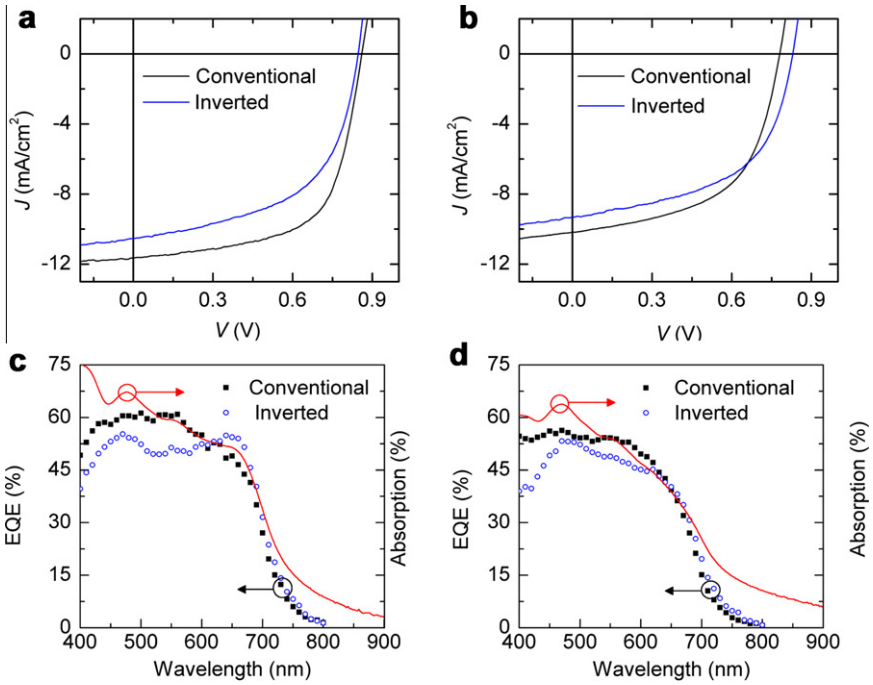

Fig. 5. *J–V* characteristics (a and b) and EQE (c and d) of PSCs based on PIDTBT and PIDTDTBT, respectively. The absorption spectra of the polymer:$PC_{71}BM$ composites are also shown in 2c and 2d.

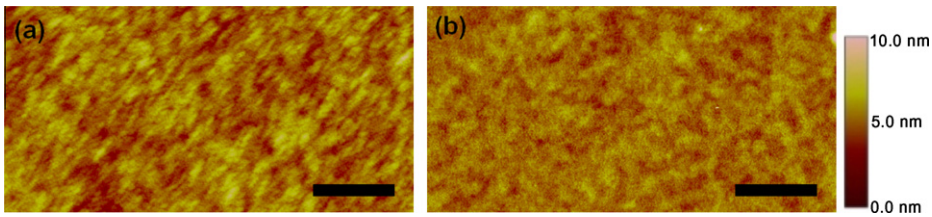

Fig. 6. AFM images of the active layers of (a) PIDTBT:$PC_{71}BM$ and (b) PIDTDTBT:$PC_{71}BM$. The black bar represents 1 μm.

evidence of the good charge transporting properties for the IDTBT backbone. Similarly, as we reported very recently, when the bridging carbons of PIDTBT and PIDTDTBT are substituted with silicon atoms, high mobilities could also be obtained [34].

2.5. Photovoltaic characteristics

The photovoltaic properties of PIDTBT and PIDTDTBT were investigated in both the conventional and inverted device configurations. [6,6]-Phenyl-C_{71}-butyric acid methyl ester ($PC_{71}BM$) is chosen as the n-type active material because of its stronger absorption in the visible region compared to its C_{60} counterpart. The device architectures of the conventional and the inverted devices are ITO/PEDOT:PSS/polymer:$PC_{71}BM$(1:3)/Ca/Al and ITO/ZnO/polymer:$PC_{71}BM$(1:3)/PEDOT:PSS/Ag, respectively. The photovoltaic parameters of the PSCs tested under simulated AM1.5G conditions (100 mW/cm^2) are summarized in Table 3. The *J–V* curves and the external quantum efficiency (EQE) of the best devices are shown in Fig. 5. The conventional configuration devices of PIDTBT showed a high PCE of 5.9% (6.3% for the best device), which is similar to the previously reported number for PIDTBT-based devices [20]. The PSCs based on PIDTDTBT also showed a very decent performance of 4.3%. The surface morphology of the uncovered area of the BHJ layer in the conventional structure devices was characterized by atomic force microscopy (AFM) and is shown in Fig. 6. The root-mean-square roughness of the PIDTBT:$PC_{71}BM$ and PIDTDTBT:$PC_{71}BM$ are 0.078 and 1.274 nm, respectively.

Inverted architecture PSCs feature the capability of using high work function and printable metal electrodes on top of the devices that provides better stability to the ambient atmosphere [35–37]. In addition, the unstable ITO/PEDOT:PSS interface, which is commonly observed for the conventional devices, could also be eliminated if the inverted configuration is used. Despite the advantages of inverted cells, the majority studies on inverted cells were based on polythiophene as active materials [38,39], while only few new low bandgap polymers had been tested in such configuration [15,40–42]. Therefore,

comparison of the photovoltaic properties of new materials in both conventional and inverted cells is very important to fully evaluate the performance of new polymers. For the inverted devices fabricated in this study, lower fill factor (FF) and current density (J_{sc}) were observed for PIDTBT may be due to un-optimized morphology in the BHJ layer. This leads to a slightly lower PCE of 4.7% (4.9% for the best device). The devices based on PIDTDTBT also showed a reasonable performance of 4.1%. EQEs of up to 61% and 56% were demonstrated from the conventional devices of PIDTBT and PIDTDTBT, respectively. Slightly lower EQE was observed for the inverted devices in most parts of the spectrum, resulting in lower photocurrent for the inverted devices. The EQE curves of the conventional devices deviate from the corresponding absorption curves of the active layers at wavelengths shorter than 530 nm, and in the inverted cases even greater deviations are observed between 400 and 630 nm. Since the majority of the short wavelength absorption of the active layer is mainly coming from $PC_{71}BM$, the deviations of the EQE from the absorption spectra suggest lower exciton harvesting efficiencies from $PC_{71}BM$. A similar result was also found by Burkhard et al. in the case of P3HT:$PC_{61}BM$-based BHJ cell [43].

3. Conclusions

We report the synthesis of two indacenodithiophene-containing low bandgap polymers and the characterization of highly efficient PSCs based on these polymers in their conventional and inverted device configurations. The conventional configuration device of PIDTBT shows a high PCE of around 6.3%. Its inverted device also shows a quite high efficiency (as high as 4.9%), which is among the highest reported for the inverted devices. The performance of the PSCs containing the new polymer PIDTDTBT reach PCEs of 4.4% and 4.2% for conventional and inverted structure devices, respectively. The high performance of these devices can be attributed to several of their desirable properties including low band gaps, low-lying HOMO levels, and high hole mobilities.

4. Experimental

4.1. Instruments and characterizations

^1H and ^{13}C NMR spectra were measured on a Bruker AV-500 spectrometer operating at 125 and 500 MHz for ^{13}C and ^1H, respectively, in deuterated chloroform solution with TMS reference. Molecular weights of the polymers were determined by a waters 1515 gel permeation chromatograph (GPC) with a refractive index detector in tetrahydrofuran (THF) using a calibration curve of polystyrene standards. UV–Vis spectra were obtained on a Perkin–Elmer Lambda-9 spectrophotometer. With 2 and 2.5 mg of PIDTBT and PIDTDTBT, respectively, loaded in aluminum cups, DSC analysis was performed using DSC2010 (TA instrument) under a scanning rate of 10 °C min^{-1} and a nitrogen flow of 50 mL min^{-1}. Cyclic voltammetric data were measured on a BAS CV-50W voltammetric analyzer using tetrabutylammonium hexafluorophosphate in acetonitrile (0.1 M) (electrochemical grade, Fisher Scientific) as electrolyte and indium tin oxide (ITO) and Ag/AgCl as the working and reference electrode, respectively, at a scanning rate of 100 mV/s at room temperature under nitrogen flow. The surface morphology of the active layers was characterized under tapping mode using the Veeco multimode AFM with a Nanoscope III controller.

4.2. Materials and syntheses

[6,6]-Phenyl-C_{71}-butyric methyl ester ($PC_{71}BM$, 98%) was purchased from American Dye Source or Nano-C. Poly(3,4-ethylenedioxythiophene):poly(styrene sulfonate) (PEDOT:PSS, Baytron P VP AI 4083) was purchase from H.C. Stark. Materials were used as received. The ZnO nanoparticles were prepared in our group using the procedure described by Beek et al. [44].

4.2.1. Synthesis of PIDTBT and PIDTDTBT

The synthetic procedure for PIDTBT can be found in Ref. [20]. Scheme 1 shows the synthetic procedures of PIDTDTBT. The donor and acceptor segments (compound

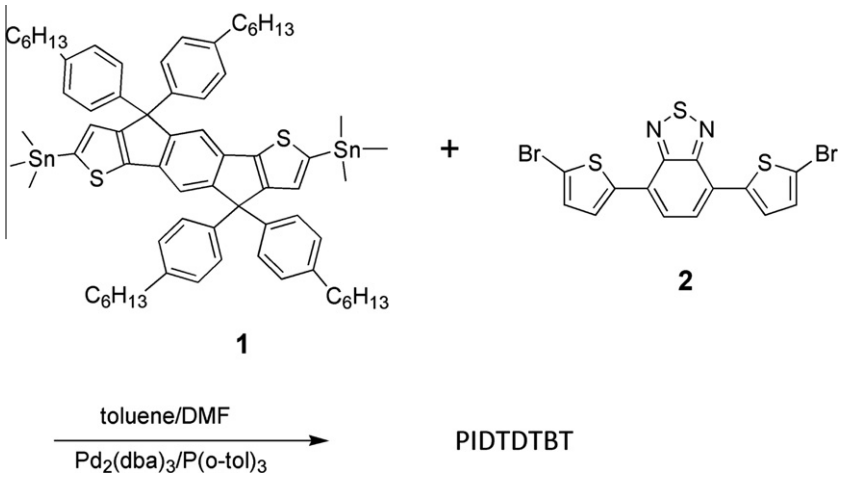

Scheme 1. Synthetic procedure of PIDTDTBT.

1–2) were synthesized according to the reported procedures [20,45]. The IDT-di-tin monomer (compound 1, 337 mg, 0.27 mmol) was charged with 4,7-bis(2-bromo-5-thienyl)-2,1,3-benzothiadiazole (compound 2, 114 mg, 0.25 mmol) in a 25 mL flask under N_2 protection. After the addition of toluene (3 mL) and DMF (0.5 mL), the mixture was degassed then $Pd_2(dba)_3$ (7 mg) and $P(o\text{-}tol)_3$ (6 mg) were added as catalyst. The mixture was heated to 120 °C and maintained at the same temperature for 24 h. After cooling to room temperature, the mixture was poured into methanol. The precipitate was collected and washed by Soxhlet extraction with methanol and acetone for 12 h, respectively. The resulting dark solid was dissolved into a small amount of chloroform and then poured into methanol again. The solid was collected and dried overnight under vacuum with the yields of 61% for PIDTDTBT. ^{1}H NMR (PIDTDTBT, $CDCl_3$, ppm): 7.85–8.02 (br, 4H), 7.11–7.44 (br, 22), 2.59 (m, 8H), 1.62 (m, 4H), 1.32 (s, 28H), 0.89 (m, 12H).

4.3. Device fabrication and characterization

4.3.1. Organic field-effect transistors

Heavily doped silicon substrates with a 300 nm thick thermally grown SiO_2 dielectric (Montco Silicon Technologies, Inc.) were cleaned sequentially by sonication in acetone and isopropyl alcohol, followed by a 5 min exposure to air plasma. The surface of the silicon substrates was treated with hexamethyldisilazane (HMDS) by vapor phase deposition in a vacuum oven (200 mTorr, 100 °C, 3 h). The water contact angle of the HMDS treated silicon substrates was around 70°. The polymer film was spin-coated from its 5 mg/ml chloroform solution at 2000 rpm under a dry nitrogen environment. No thermal treatment was performed on the polymer. Interdigitated source and drain electrodes (L = 9600 μm, W = 80 μm, W/L = 120) were defined by thermally evaporating 50 nm thick gold through a shadow mask. The transfer and output characteristics of the thin film transistors were obtained on an Agilent 4155B semiconductor parameter analyzer under nitrogen atmosphere.

4.3.2. Organic BHJ solar cells

1,2-Dichlorobenzene (DCB) solution of the polymer:$PC_{71}BM$ blends was stirred at 80 °C overnight before use. The concentration of the polymer and the $PC_{71}BM$ in DCB was 10 and 30 mg/ml, respectively. Indium tin oxide coated glass substrates (ITO, 15 Ω per square) were cleaned sequentially by sonicating in detergent, de-ionized water, acetone, and isopropyl alcohol, followed by blow-drying under nitrogen stream and exposing under oxygen plasma for 5 min. In the conventional architecture solar cells, a thin layer (ca. 40 nm) of PEDOT:PSS (filtered at 0.45 μm, Nylon) was first spin-coated onto the ITO surface and baked at 140 °C for 10 min in ambient. Subsequently, the substrates were transferred into a nitrogen-filled glovebox for further processing. The polymer:$PC_{71}BM$ BHJ layer (ca. 100 nm) was spin-coated at 1300 rpm from filtered (0.2 μm PTFE) DCB solution and the substrates were transferred into a glass petri-dish with excess DCB for 30 min of solvent vapor annealing. Ca (30 nm)/Al (100 nm) electrode was then thermally evaporated through the openings of the shadow masks with the size of 3.14 mm^2 under high vacuum (<2×10^{-6} Torr) to define the active area of the solar cells. In the case of inverted architecture devices, ZnO nanoparticles were first spin-coated onto ITO to form a 50 nm thick buffer layer. The active layer of the polymer:$PC_{71}BM$ blend was then spin-coated and vapor annealed using the same process as in the conventional architecture devices. Subsequently, a PEDOT:PSS layer (50 nm) was spin-coated on top of the active layer and again annealed for 10 min at 120 °C. Finally, Ag electrode (100 nm) was deposited under high vacuum to complete the fabrication of inverted devices. The active area of each device is also 3.14 mm^2. The current–voltage (I–V) characteristics were measured by using the Keithley 2400 source-measurement unit. An Oriel xenon lamp (450 W) coupled with an AM1.5G filter was used as the solar simulator. The light intensity was set to 1 sun (100 mW/cm^2) using a calibrated Hamamatsu silicon diode with a KG5 color filter, which can be traced to the National Renewable Energy Laboratory (NREL). The EQE system uses a lock-in amplifier (Stanford Research Systems SR830) to record the short-circuit current under chopped monochromatic light.

Acknowledgements

The authors thank the support from the National Science Foundation (DMR-0120967), the Department of Energy (DE-FC3608GO18024/A000), the AFOSR (FA9550-09-1-0426), the Office of Naval Research (N00014-08-1-1129), and the World Class University (WCU) program through the National Research Foundation of Korea under the Ministry of Education, Science and Technology (R31-21410035). A.K.-Y.J. thanks the Boeing Foundation for supports.

References

[1] G. Yu, J. Gao, J.C. Hummelen, F. Wudl, A.J. Heeger, Science 270 (1995) 1789.
[2] S. Günes, H. Neugebauer, N.S. Sariciftci, Chem. Rev. 107 (2007) 1324.
[3] G. Dennler, M.C. Scharber, C.J. Brabec, Adv. Mater. 21 (2009) 1.
[4] B.C. Thompson, J.M.J. Fréchet, Angew. Chem. Int. Ed. 47 (2008) 58.
[5] H.-Y. Chen, J. Hou, S. Zhang, Y. Liang, G. Yang, Y. Yang, L. Yu, Y. Wu, G. Li, Nat. Photon. 3 (2009) 649.
[6] Y. Liang, Z. Xu, J. Xia, S.-T. Tsai, Y. Wu, G. Li, C. Ray, L. Yu, Adv. Mater. 22 (2010) E135.
[7] F. Wudl, Acc. Chem. Res. 25 (1992) 157.
[8] M. Lenes, G.A.H. Wetzelaer, F.B. Kooistra, S.C. Veenstra, J.C. Hummelen, P.W.M. Blom, Adv. Mater. 20 (2008) 2116.
[9] R.B. Ross, C.M. Cardona, D.M. Guldi, S.G. Sankaranarayanan, M.O. Reese, N. Kopidakis, J. Peet, B. Walker, G.C. Bazan, E. Van Keuren, B.C. Holloway, M. Drees, Nat. Mater. 8 (2009) 208.
[10] Y. Zhang, H.-L. Yip, O. Acton, S.K. Hau, F. Huang, A.K.-Y. Jen, Chem. Mater. 21 (2009) 2598.
[11] Y. He, H.-Y. Chen, J. Hou, Y. Li, J. Am. Chem. Soc. 132 (2010) 1377.
[12] Y. Liang, Z. Xu, J. Xia, S. Tsai, Y. Wu, G. Li, C. Ray, L. Yu, Adv. Mater. 22 (2010) 1.
[13] C. Piliego, T.W. Holcombe, J.D. Douglas, C.H. Woo, P.M. Beaujuge, J.M.J. Fréchet, J. Am. Chem. Soc. 132 (2010) 7595.
[14] J.C. Bijleveld, A.P. Zoombelt, S.G. Mathijssen, M.M. Wienk, M. Turbiez, D.M. de Leeuw, R.A. Janssen, J. Am. Chem. Soc. 131 (2009) 11735.
[15] Y. Zhang, S.K. Hau, H.-L. Yip, Y. Sun, O. Acton, A.K.-Y. Jen, Chem. Mater. 22 (2010) 2696.

[16] J. Peet, J.Y. Kim, N.E. Coates, W.L. Ma, D. Moses, A.J. Heeger, G.C. Bazan, Nat. Mater. 6 (2007) 497.
[17] R.C. Coffin, J. Peet, J. Rogers, G.C. Bazan, Nat. Chem. 1 (2009) 657.
[18] S.H. Park, A. Roy, S. Beaupré, S. Cho, N. Coates, J.S. Moon, D. Moses, M. Leclerc, K. Lee, A.J. Heeger, Nat. Photon. 3 (2009) 297.
[19] E. Wang, L. Wang, L. Lan, C. Luo, W. Zhuang, J. Peng, Y. Cao, Appl. Phys. Lett. 92 (2008) 033307.
[20] Y.-C. Chen, C.-Y. Yu, Y.-L. Fan, L.-I. Hung, C.-P. Chen, C. Ting, Chem. Commun. 46 (2010) 6503.
[21] J. Hou, H. Chen, S. Zhang, G. Li, Y. Yang, J. Am. Chem. Soc. 130 (2008) 16144.
[22] H.-Y. Chen, J. Hou, A.E. Hayden, H. Yang, K.N. Houk, Y. Yang, Adv. Mater. 22 (2010) 371.
[23] M.C. Scharber, M. Koppe, J. Gao, F. Cordella, M.A. Loi, P. Denk, M. Morana, H.J. Egelhaaf, K. Forberich, G. Dennler, R. Gaudiana, D. Waller, Z.G. Zhu, X.B. Shi, C.J. Brabec, Adv. Mater. 22 (2010) 367.
[24] F. Zhang, K. Jespersen, C. Björström, M. Svensson, M. Andersson, V. Sundström, K. Magnusson, E. Moons, A. Yartsev, O. Inganäs, Adv. Funct. Mater. 16 (2006) 667.
[25] M.-H. Chen, J. Hou, Z. Hong, G. Yang, S. Sista, L.-M. Chen, Y. Yang, Adv. Mater. 21 (2009) 4238.
[26] C.-Y. Yu, C.-P. Chen, S.-H. Chan, G.-W. Hwang, C. Ting, Chem. Mater. 21 (2009) 3262.
[27] P. Hohenberg, W. Kohn, Phys. Rev. 136 (1964) B864.
[28] W. Kohn, L.J. Sham, Phys. Rev. 140 (1965) A1133.
[29] C. Lee, W. Yang, R.G. Parr, Phys. Rev. B: Condens. Mater. 37 (1988) 785.
[30] A.D. Becke, J. Chem. Phys. 98 (1993) 5648.
[31] R. Ditchfield, W.J. Hehre, J.A. Pople, J. Chem. Phys. 54 (1971) 724.
[32] N. Blouin, A. Michaud, D. Gendron, S. Wakim, E. Blair, R. Neagu-Plesu, M. Belletête, G. Durocher, Y. Tao, M. Leclerc, J. Am. Chem. Soc. 130 (2008) 732.
[33] W. Zhang, J. Smith, S.E. Watkin, R. Gysel, M.D. McGehee, A. Salleo, J. Kirkpatrick, S. Ashraf, T. Anthopoulos, M. Heeney, I. McCulloh, J. Am. Chem. Soc. 132 (2010) 11437.
[34] J.-Y. Wang, S.K. Hau, H.-L. Yip, J.A. Davies, K.-S. Chen, Y. Zhang, Y. Sun, A. K.-Y. Jen, Chem. Mater. 23 (2011) 765.
[35] S.K. Hau, H.-L. Yip, N. Baek, J. Zou, K. O'Malley, A.K.-Y. Jen, Appl. Phys. Lett. 92 (2008) 253301.
[36] S.K. Hau, H.-L. Yip, K. Leong, A.K.-Y. Jen, Org. Electron. 10 (2009) 719.
[37] F.C. Krebs, S.A. Gevorgyan, J. Alstrup, J. Mater. Chem. 19 (2009) 5442.
[38] L.-M. Chen, Z. Hong, G. Li, Y. Yang, Adv. Mater. 21 (2009) 1434.
[39] H. Ma, H.-L. Yip, F. Huang, A.K.-Y. Jen, Adv. Funct. Mater. 20 (2010) 1371.
[40] C.-H. Hsieh, Y.-J. Cheng, P.-J. Li, C.-H. Chen, M. Dubosc, R.-M. Liang, C.-S. Hsu, J. Am. Chem. Soc. 132 (2010) 4887.
[41] T. Yang, W. Cai, D. Qin, E. Wang, L. Lan, X. Gong, J. Peng, Y. Cao, J. Phys. Chem. C 114 (2010) 6849.
[42] C.-H. Chou, W.L. Kwan, Z. Hong, L.-M. Chen, Y. Yang, Adv. Mater., doi:10.1002/adma.201001033.
[43] G.F. Burkhard, E.T. Hoke, S.R. Scully, M.D. McGehee, Nano Lett. 9 (2009) 4037.
[44] W.J.E. Beek, M.M. Wienk, M. Kemerink, X. Yang, R.A.J. Janssen, J. Phys. Chem. B 109 (2005) 9505.
[45] Q. Hou, Y.S. Xu, W. Yang, M. Yuan, J.B. Peng, Y. Cao, J. Mater. Chem. 12 (2002) 2887.

light-emitting materials are rare. For example, a blue light emitter with four substituents at the 2,6,9,10-positions of anthracene (2,6-bis(9,9-diethyl-9H-fluoren-2-yl)-9,10-diphenylanthracene) has been proven to exhibit an EL efficiency of 5.8 cd/A and an external quantum efficiency of 2.11% [16]. Chen et al. synthesized 9,10-diphenylanthracene (DPA)-derived copolymers emitting blue light. The OLEDs fabricated using these DPA-derived copolymers exhibited sky-blue EL (at CIE coordinates of (0.19, 0.30)) with a peak luminous efficiency of 1.26 cd/A. Still, the development of OLEDs using anthracene-derived moieties remains a challenge [17].

Herein, we report the use of an anthracene-based blue host, 9-(phenanthryl)-10-(3-(9-phenylcarbazole-9-yl)anthracene (PPCA), and a dopant 9,10-bis-biphenyl-4-yl-2,6-diphenylanthracene (BDA) which contains PAHs without amino substituents (Schemes 1 and 2). Specifically, PPCA was synthesized from 9-phenyl-9H-carbazole, which possesses good hole-transporting properties, and phenanthrene, which has good electron-transporting properties [18]. We believe that the introduction of carbazole and phenanthrene elements in the 9,10-anthracene core of PPCA is an effective method for avoiding molecular aggregation and enhancing the efficiency of transporting electrons and holes (carriers). We examined the light-emitting performance in devices fabricated using aluminum tris(8-hydroxyquinoline) (Alq_3) and 1,6-di(pyridin-3-yl)-3,8-di(naphthalene-1-yl)pyrene (N1PP) [19] as electron-transport materials. In particular, with the use of N1PP, which shows high carrier mobility, the EL efficiency of the blue OLED devices based on PAHs without amino substituents was significantly improved.

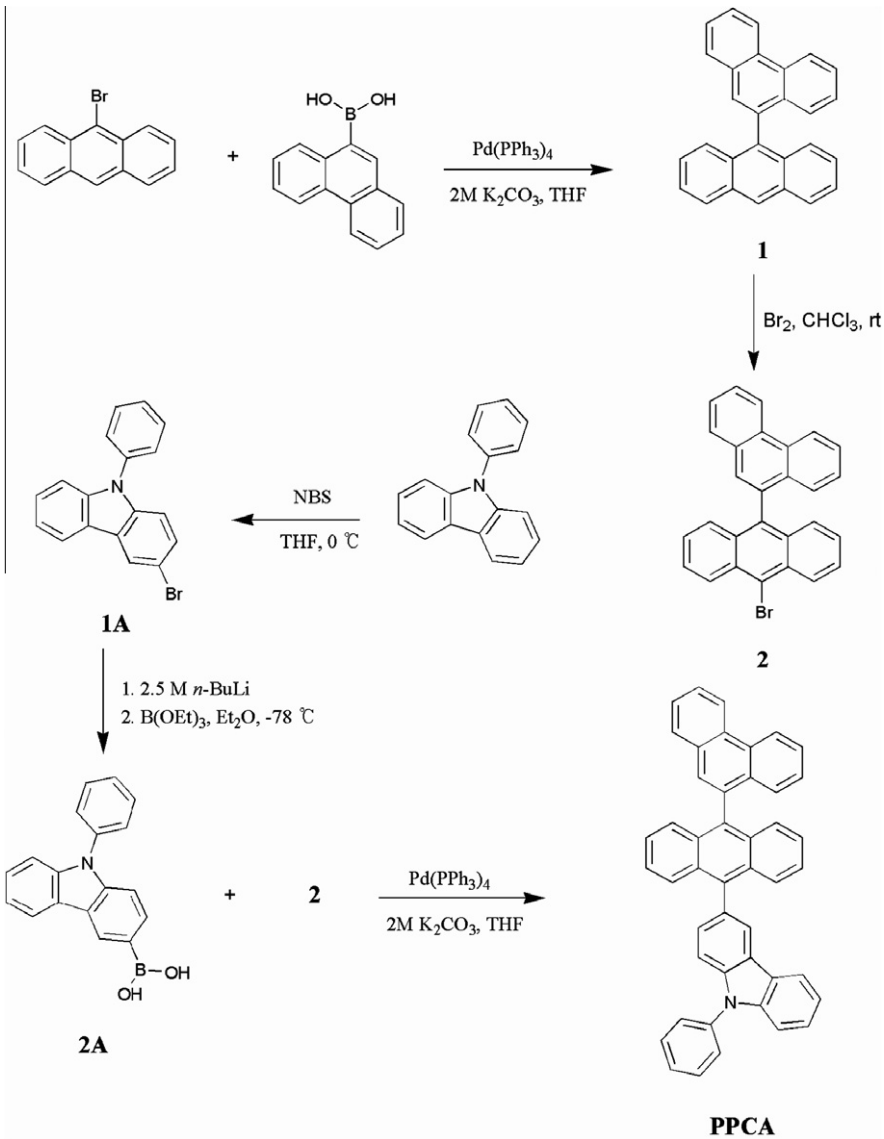

Scheme 1. Synthesis of PPCA.

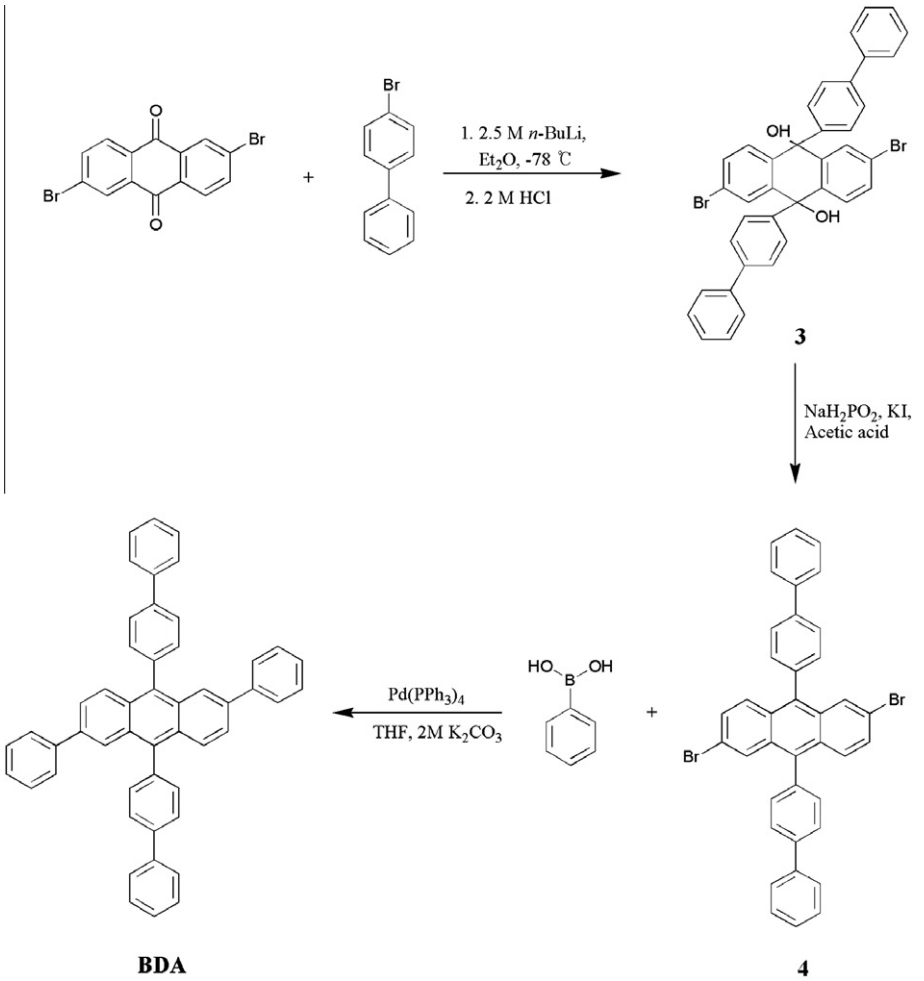

Scheme 2. Synthesis of BDA.

2. Experimental

2.1. Materials and instrument

9-Bromoanthracene, 9-phenanthreneboronic acid, 9-phenylcarbazole, and 4-bromobiphenyl were purchased from Tokyo Chemical Industry Co., Ltd., (TCI, Japan) and Aldrich Chemical Co., (USA). Compounds **1A**, **2A**, **3**, and **4** (Schemes 1 and 2) were synthesized according to literature methods as well as modified procedures [16,20]. Analytical thin-layer chromatography was performed using Kieselgel 60F-254 plates provided from Merck KGaA (Germany). Column chromatography was carried out on Merck silica gel 60 (70–230 mesh). All the solvents and reagents are commercially available and were used without further purification, unless otherwise noted. ^{1}H and ^{13}C nuclear magnetic resonance (NMR) spectra were recorded in $CDCl_3$ using a Bruker Advance 300 MHz spectrometer. Proton (^{1}H) NMR chemical shifts in $CDCl_3$ were referenced to $CHCl_3$ (7.27 ppm). Mass spectra were obtained by means of gas chromatography/high-resolution mass spectrometry. Ultraviolet and visible (UV–vis) absorption spectra were recorded with the use of a Beckman DU 650 spectrophotometer.

2.1.1. 9-Phenanthren-9-yl-anthracene (1)

A solution of 9-bromoanthracene (2 g, 7.78 mmol), 9-phenanthreneboronic acid (1.90 g, 8.56 mmol), $Pd(PPh_3)_4$ (3 mol%), and aqueous K_2CO_3 (10.8 g, 78 mmol, water 50 mL) in a toluene (10 mL)–tetrahydrofuran (THF, 50 mL) mixture was heated at a temperature of 100 °C for 10 h in a N_2 atmosphere. After the solvent was evaporated, the residue was treated with water and extracted with dichloromethane. The crude product was purified by silica gel column chromatography (10% dichloromethane (DCM) in *n*-hexane used as eluent) and further purified by recrystallization (yield: 87%). ^{1}H NMR (300 MHz, $CDCl_3$): δ (ppm) 7.18 (d, ^{1}H, J = 8.07 Hz), 7.24–7.35 (m, 3H), 7.49 (t, 2H, J = 7.4 Hz), 7.59 (d, 2H, J = 8.60 Hz), 7.75 (m, 2H), 7.80 (t, ^{1}H, J = 7.14 Hz), 7.86 (s, ^{1}H), 7.94 (d, ^{1}H, J = 7.73 Hz), 8.14 (d, 2H, 8.49 Hz), 8.78 (s, ^{1}H), 8.90 (d, 2H, J = 8.28 Hz).

2.1.2. 9-Bromo-10-phenanthren-9-yl-anthracene (2)

A solution of bromine (0.91 g, 5.70 mmol) in chloroform (20 mL) was slowly added to a solution of **1** (2 g, 5.64 mmol) in chloroform (50 mL) at room temperature. After stirring for 5 h, the mixture was poured into EtOH. The residue obtained after filtration was purified by flash chromatography using dichloromethane (yield: 89%). ^{1}H NMR (300 MHz, $CDCl_3$): δ (ppm) 7.13 (d, ^{1}H, J = 8.10 Hz), 7.26–7.34 (m, 3H), 7.56–7.73 (m, 6H), 7.68–7.81 (m, ^{1}H), 7.83 (s, ^{1}H), 7.93 (d, ^{1}H, J = 6.38 Hz), 8.70 (d, 2H, J = 8.82 Hz), 8.89 (d, 2H, J = 8.22 Hz).

2.1.3. 9-(Phenanthryl)-10-(3-(9-phenylcarbazole-9-yl)-anthracene (PPCA)

2A was allowed to react with **2** under Suzuki reaction conditions, as described in the synthesis of **1,** to afford PPCA (yield: 82%). ^{1}H NMR (300 MHz, $CDCl_3$): δ (ppm) 7.31–7.36 (m, 5H), 7.49–7.77 (m, 16H), 7.88–7.97 (m, 4H), 8.14–8.18 (m, ^{1}H), 8.39–8.32 (m, ^{1}H), 8.91 (d, 2H, J = 8.2 Hz); ^{13}C NMR (75 MHz, $CDCl_3$) δ 109.74, 109.77, 100.06, 120.21, 120.51, 122.78, 122.90, 123.19, 123.30, 12.55, 125.08, 125.30, 126.29, 126.74, 126.93, 127.0, 129.09, 127.23, 127.54, 127.65, 128.83, 129.37, 130.04, 130.45, 130.53, 130.69, 130.80, 131.82, 132.84, 134.65, 135.58, 137.78, 138.41, 140.41, 141.40; HRMS (FT MS) m/z: calcd. for $[C_{46}H_{29}N + H]^+$ 596.23, found $[M + H]^+$ 596.24; Anal. calcd. for $C_{46}H_{29}N$: C, 92.74; H, 4.91; N, 2.35. Found: C, 92.7033; H, 4.9502; N, 2.2309.

2.1.4. 9,10-Bis-biphenyl-4-yl-2,6-diphenylanthracene (BDA)

4 (2 g, 3.12 mmol) was allowed to react with phenylboronic acid (0.84 g, 6.87 mmol) under Suzuki reaction conditions, as described in the synthesis of PPCA, to afford BDA (yield: 72%); ^{1}H NMR (300 MHz, $CDCl_3$): δ (ppm) 7.33–7.42 (m, 8H), 7.53–7.73 (m, 14H), 7.81–7.91 (m, 10H), 8.01 (s, 2H); HRMS (FT MS) m/z: calcd. for $[C_{46}H_{29}N + H]^+$ 635.27, found $[M + H]^+$ 635.28. Anal. calcd. for $C_{50}H_{34}$: C, 94.60; H, 5.40. Found: C, 94.6206; H, 5.4299.

2.2. Electrochemical characterization

The electrochemical properties of PPCA and BDA were characterized by means of cyclic voltammetry. The oxidation scans were carried out in a 0.1 M solution of tetraethylammonium tetrafluoroborate in anhydrous CH_2Cl_2. A platinum and Ag/AgCl disk were used as the working and reference electrodes, respectively. Specifically, the platinum disk was used as the counter electrode. Based on the highest occupied molecular orbital (HOMO) energy of the ferrocene/ferrocenium redox system (-4.8 eV), we were able to calculate the HOMO energy values of PPCA and BDA which were both equal to 5.6 eV. The band-gap energies were measured from the absorption spectra, and the lowest unoccupied molecular orbital (LUMO) energies were estimated to be equal to 2.6 eV for PPCA and 2.8 eV for BDA. The energy levels of PPCA and BDA indicate that Förster resonance energy transfer (FRET) takes place between the host (PPCA) and the dopant (BDA), because as shown in Fig. 4 the band-gap energy of PPCA is greater than that of BDA (see Supporting Information) [21,22].

2.3. OLED fabrication

OLEDs were fabricated by means of vacuum deposition onto patterned ITO glasses that had been thoroughly cleaned and subsequently, treated with oxygen plasma. Blue OLEDs were sequentially fabricated onto the ITO substrates through thermal evaporation of organic layers (evaporation rate: 2 Å/s; base pressure: 3×10^{-6} Torr). The EL spectra and CIE color coordinates were obtained using a Spectrascan PR650 photometer, while the current–voltage–luminescence (J–V–L) characteristics were measured using a Keithley 2400 source unit.

3. Results and discussion

3.1. Synthesis

Scheme 1 shows the synthetic route to PPCA. Specifically, the Pd-catalyzed Suzuki coupling reaction of 9-bromoanthracene with 9-phenanthreneboronic acid afforded **1** in 87% yield. Bromination of **1** with 1.01 equiv. of bromine in chloroform solution led to the formation of **2** in 89% yield. **2A** was synthesized through the reaction of 3-bromo-9-phenylcarbazole with 1.1 equiv. of *n*-BuLi at −78 °C and subsequent quenching of the lithiated complex with triethylborate. PPCA was synthesized through a Pd-catalyzed Suzuki coupling reaction, similarly to the case of **1**.

Scheme 2 shows the synthetic route to BDA. Specifically, **4** was synthesized according to a previously described procedure [16]. A suspension of 2,6-dibromoanthraquinone in Et_2O was slowly added to lithium-substituted biphenyl in order to obtain **3**. The latter was aromatized using NaH_2PO_2 and KI to obtain **4** in 84% yield. The next step was to obtain BDA through the Pd-catalyzed Suzuki-coupling reaction of **4** with phenylboronic acid in 2 M aqueous K_2CO_3 solution. The molecular structures of PPCA and BDA were characterized by means of ^{1}H NMR, mass spectrometry, and elemental analysis (EA).

3.2. Thermal properties and quantum yields

The thermal behavior of BDA and PPCA was evaluated by means of (a) differential scanning calorimetry (DSC) and (b) thermogravimetric analysis (TGA) under a nitrogen atmosphere. A 5% weight loss was observed at 398 and 367 °C. The melting point (T_m) of BDA and PPCA was 396 and 326 °C and the decomposition temperature (T_d) was 445 and 440 °C, respectively. These data indicate that both these materials are stable enough to endure the high temperature at which the vacuum vapor deposition is carried out (see Supporting Information).

Additionally, the fluorescence quantum yield (Φ) was measured using the standard optically diluted method in CH_2Cl_2 solution and 9,10-diphenylanthracene (Φ = 0.90, in CH_2Cl_2) as the reference standard. The fluorescence quantum yield of BDA and PPCA were 0.74 and 0.83, respectively [23,24].

3.3. Optical properties of PPCA and BDA

Fig. 1 shows the UV absorption and PL spectra of PPCA and BDA dissolved in dichloromethane as well as in the

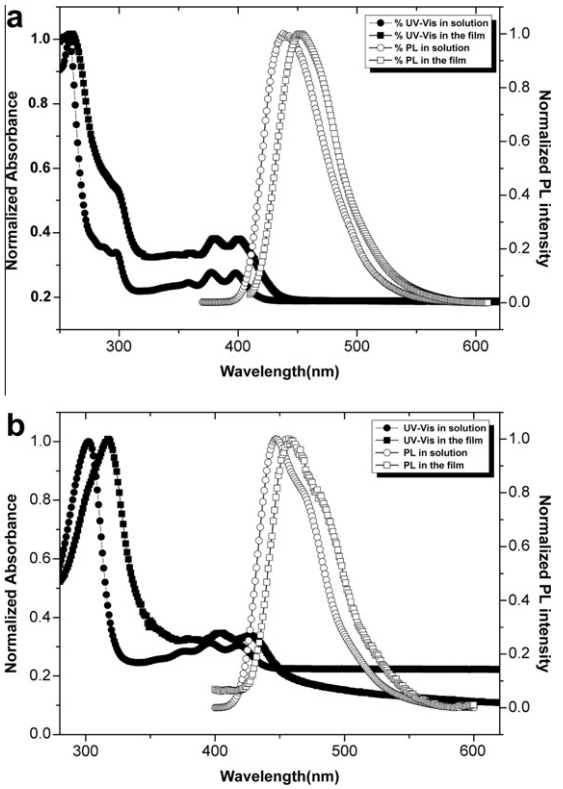

Fig. 1. UV absorption and PL spectra of PPCA and BDA dissolved in dichloromethane (CH_2Cl_2) and in the case of solid thin films deposited on a quartz substrate. (a) Normalized UV absorption and PL spectrum of PPCA. (b) Normalized absorption and PL spectrum of BDA.

form of solid thin films. Specifically, two major bands are observed in the UV absorption spectra of the material dissolved in dichloromethane and in the form of solid thin films (Fig. 1a). The first strong absorption, which is observed at a wavelength of 258 nm with a shoulder peak at 300 nm, can be attributed to the 9-phenyl-9H-carbazole moiety. The absorption peaks observed at a wavelength of 358 nm, 378 nm, and 398 nm are associated with the vibronic features of the anthracenyl core [25]. Upon photoexcitation, the PL emission of PPCA dissolved in the dichloromethane peaked at a wavelength of approximately 438 nm and at 452 nm in the case of the solid thin film. The spectral shift in solid state is due to the different dielectric constant of the surrounding medium [26].

In Fig. 1b, the absorption peaks of BDA dissolved in dichloromethane show vibrational patterns at a wavelength of 373 nm, 396 nm, and 419 nm, which are typical to aryl-substituted anthracene [16,20]. The maximum PL of BDA dissolved in dichloromethane was observed at a wavelength of 448 nm and at 456 nm in the case of the solid thin film. Additionally, in the host-dopant system, the probability of energy transfer from the excited energy donor to the energy acceptor depends on the overlap of the emission spectrum of the donor with the absorption spectrum of the acceptor. This is evident from the spectral overlap between the PL of PPCA and the UV absorption of BDA (see Supporting Information) [27–32].

3.4. EL properties and OLED characteristics

Fig. 2 shows the structures of Alq_3 and N1PP acting as electron-transporting materials and the EL spectra of the 5% doped devices driven at 10 mA/cm^2. To elucidate the energy transfer from PPCA to BDA, we fabricated two kinds of multilayer structures: ITO/DNTPD (600 Å)/α-NPB (300 Å)/

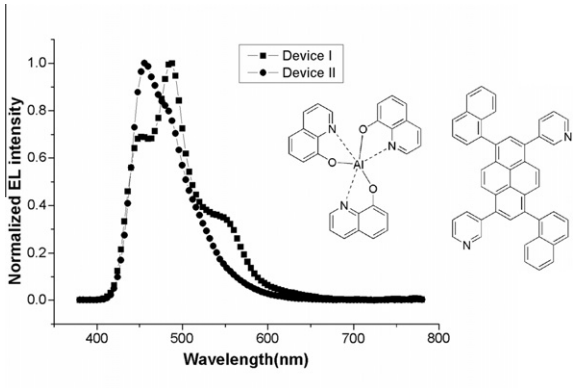

Fig. 2. EL spectra of Device I and II along with the structures of Alq_3 and N1PP.

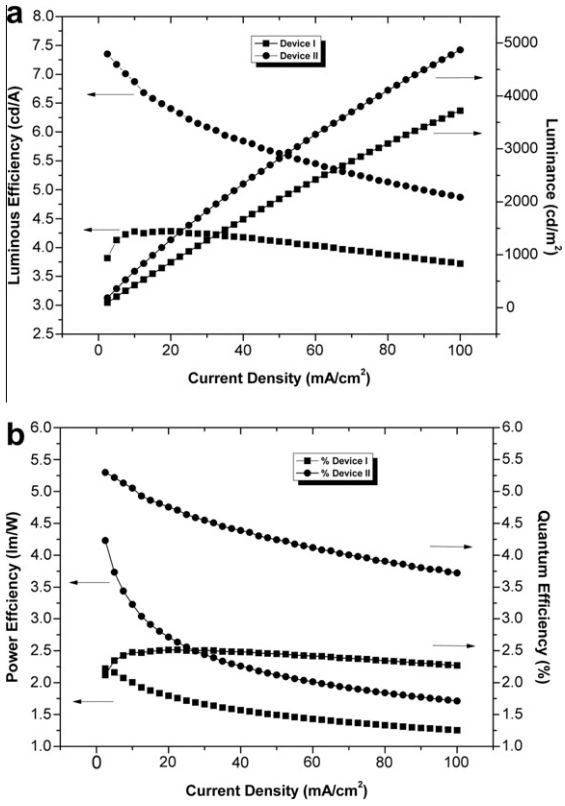

Fig. 3. EL performance of Device I and II. (a) The current–efficiency and density–luminance characteristics of Device I and II. (b) The power efficiency–current density–external quantum efficiency characteristics of Device I and II.

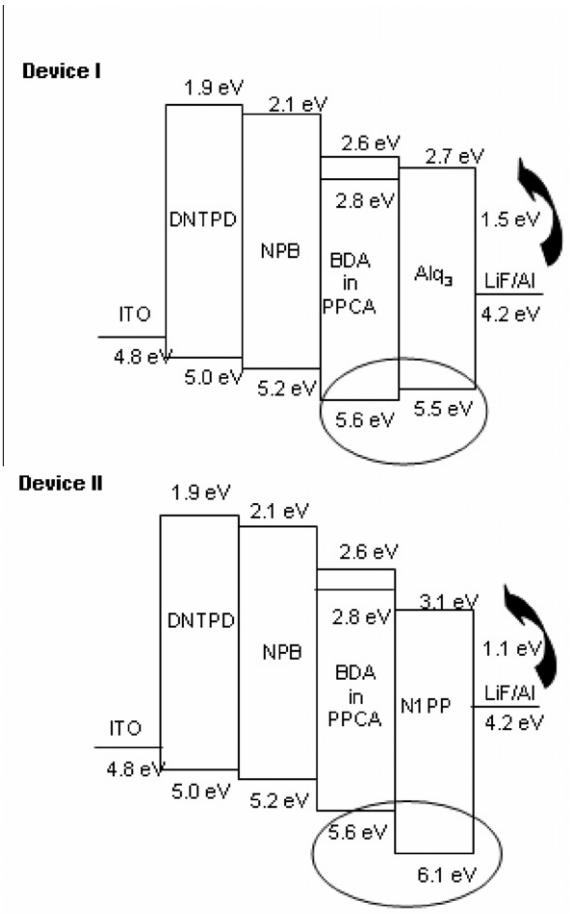

Fig. 4. HOMO and LUMO energy levels of the materials used for the fabrication of Device I and II.

PPCA:BDA 5 wt.% (250 Å)/Alq_3 (300 Å)/LiF (5 Å)/Al (1000 Å) (Device I) and ITO/DNTPD (600 Å)/α-NPB (300 Å)/PPCA:BDA 5 wt.% (250 Å)/N1PP (300 Å)/LiF (5 Å)/Al (1000 Å) (Device II). We used *N,N′*-di(4-*N,N′*-diphenylamino)phenyl)-*N,N′*-diphenylbenzidine (DNTPD) as the hole-injection layer (HIL), 4,4′-bis[*N*-(1-napthyl)-*N*-phenylamino]biphenyl (α-NPB) as the hole-transport layer (HTL), PPCA as the fluorescent blue host, BDA as the fluorescent blue dopant, N1PP and Alq_3 as the electron-transport layers (ETL) [19], and LiF as the electron-injection layer (EIL) at the LiF/Al cathode interface. The EL spectrum of Device I, in which Alq_3 was used as an ETL, was found to be different from that of Device II, which used N1PP as an ETL. In Device I, three major peaks were observed at a wavelength of 454 nm, 487 nm, and 525 nm. We believe that the two higher energy emissions are due to BDA, while the lower energy emission is due to Alq_3 [33–35].

The experimental results suggest that energy transfer takes place between the light-emitting and the electron-transporting layer. Specifically, a peak in the blue-light emission of Device II was observed at a wavelength of 456 nm, which is almost identical to that of the PL spectrum of BDA in the form of a solid thin film (Fig. 1b). This coincidence indicates that while the light emission of PPCA (host) is essentially quenched in the light emitting layer of the 5% doped device, FRET takes place between the host (PPCA) and the dopant (BDA) [35,36].

Fig. 3 shows the EL performance of Devices I and II, while their EL efficiencies are summarized in Table 1. Specifically, Device I showed a current efficiency of 4.30 cd/A, power efficiency of 2.00 lm/W, and an external quantum efficiency of 2.50% at 10 mA/cm^2 (at CIE coordinates of (0.15, 0.28)). Device II, on the other hand, delivered a better performance with a current efficiency of 6.90 cd/A, power efficiency of 3.23 lm/W, and external quantum efficiency of 5.10% at 10 mA/cm^2 (at CIE coordinates of (0.15, 0.18)).

To further verify the difference between the EL performances of Device I and II, we examined their band-gap energies. Fig. 4 show the HOMO and LUMO energy levels of the organic material, along with the work functions of their metal layers. This energy diagram reveals that the energy barrier (1.5 eV) between the EIL (4.2 eV) and ETL (Alq_3) (2.7 eV) in Device I is larger than the difference (1.1 eV) between the electrode and N1PP (3.1 eV) in Device II [19] Since Alq_3 is characterized by a higher LUMO level than N1PP, electron injection from the LiF/Al cathode into the 5% doped emission layer is rather difficult to be achieved in Device I. Furthermore, the difference between the HOMO values of the emitting layer (EML) and the ETL will cause leakage of holes from the 5% doped emitting zone into the ETL (Alq_3). In Device I, the HOMO level (5.5 eV) of Alq_3 is higher than that of PPCA (5.6 eV). This difference can explain why the electron–hole recombination may be unbalanced in the emitting zone of Device I. This unbalanced charge recombination also shifts the blue light-emitting zone to a region close to the ETL (Alq3) (Fig. 4) and therefore, Device I delivers a poor performance. On the other hand, the HOMO level of N1PP (6.1 eV) is lower than that of PPCA (5.6 eV). Because of the energy barrier (0.5 eV) between the HOMO level of PPCA (5.6 eV) and that of N1PP (6.1 eV), N1PP can act as a hole blocker preventing holes from leaking into the ETL. This behavior suggests that since N1PP has better carrier-transporting and hole-blocking characteristics, it facilitates electron–hole recombination in the 5% doped emitting zone. Consequently, the EL performance of Device II is superior to that of Device I.

Table 1
Summary of the characteristics of Devices I and II with Alq_3 and N1PP as an ETL.

Device	EL peak [nm]	Current efficiency @10 mA/cm^2 [cd/A]	Luminance @10 mA/cm^2 [cd/m^2]	Power efficiency @10 mA/cm^2 [lm/W]	External quantum efficiency [%]	CIE coordinates [*x,y*]
Device I	487	4.30	428/3720[a]	2.00	2.50	0.15, 0.28
Device II	456	6.90	687/4869[a]	3.23	5.10	0.15, 0.18

[a] Measured at 100 mA/cm^2.

4. Conclusions

In summary, we have synthesized new anthracene-based host (PPCA) and dopant (BDA) materials and used them to fabricate efficient blue OLEDs. PPCA carries an electron-transporting 9-phenanthrene moiety as well as a hole-transporting 9-phenyl-9H-carbazole moiety in the anthracene core. On the other hand, BDA consists of PAHs without amino substituents in the anthracene core. Charge balance could be achieved by using N1PP as the electron-transporting material. The device with the optimized structure, ITO/DNTPD (600 Å)/α-NPB (300 Å)/PPCA:BDA 5 wt.% (250 Å)/N1PP (300 Å)/LiF (5 Å)/Al (1000 Å) (Device II), is characterized by high blue EL performance with a current efficiency of 6.9 cd/A, a power efficiency of 3.23 lm/W, and an external quantum efficiency of 5.1% at 10 mA/cm^2 at CIE coordinates of (0.15, 0.18). This study shows that π-conjugated anthracene-functionalized PAHs without amino substituents can be used as efficient dopants for blue OLEDs.

Acknowledgments

This study was supported by the Basic Science Research Program through a National Research Foundation of Korea (NRF) grant funded by the Ministry of Education, Science and Technology (MEST) of Korea for the Center for Next-Generation Dye-sensitized Solar Cells (No. 2010-0001842).

Appendix A. Supplementary data

Supplementary data associated with this article can be found, in the online version, at doi:10.1016/j.orgel.2011.02.011.

References

[1] J. Shi, C.W. Tang, Appl. Phys. Lett. 80 (2002) 3201.
[2] P.-I. Shih, C.-Y. Chuang, C.-H. Chien, Diau, W-G. Eric, C-F. Shu, Adv. Funct. Mater. 17 (2007) 3141.
[3] C.-H. Chien, C.-K. Chen, F.-M. Hsu, C.-F. Shu, P.-T. Chou, C.-H. Lai, Adv. Funct. Mater. 19 (2009) 560.
[4] J.-H. Jou, Y.-P. Lin, M.-F. Hsu, M.-H. Wu, P. Lu, Appl. Phys. Lett. 92 (2008) 193313.
[5] K.-R. Wee, H.-C. Ahn, H.-J. Son, W.-S. Han, J.-E. Kim, D.-W. Cho, S.-O. Kang, J. Org. Chem. 74 (2009) 8472.
[6] B.M. Krasovitskii, B.M. Bolotin, Organic Luminescent Materials translated by V.G. Vopian, VCH, Weinheim, 1988.
[7] V.V. Jarikov, J. Appl. Phys. 100 (2006) 014901.
[8] R.J. Tseng, R.C. Chiechi, F. Wudl, Y. Yang, Appl. Phys. Lett. 88 (2006) 093512.
[9] B.K. Shah, D.C. Neckers, J. Shi, E.W. Forsythe, D. Morton, Chem. Mater. 18 (2006) 603.
[10] V.V. Jarikov, D.Y. Kondakov, C.T. Brown, J. Appl. Phys. 102 (2007) 104908.
[11] M.-T. Lee, C.-H. Liao, C.-H. Tsai, C.-H. Chen, Adv. Mater. 17 (2005) 2493.
[12] K. Danel, T.-H. Huang, J.-T Lin, Y.-T. Tao, C.-H. Chuen, Chem. Mater. 14 (2002) 3860.
[13] M.–H. Ho, Y.-S. Wu, S.-W. Wen, T.-M. Chen, C.-H. Chen, Appl. Phys. Lett. 91 (2007) 083515.
[14] P.-I. Shih, C.-Y. Chuang, C.-H. Chien, E.W.G. Diau, C.-F. Shu, Adv. Funct. Mater. 17 (2007) 3141.
[15] M.X. Yu, J.P. Duan, C.H. Lin, C.H. cheng, Y.T. Tao, Chem. Mater. 14 (2002) 3958.
[16] W.-J. Jo, K.-H. Kim, H.-C. No, D.-Y. Sim, S.-J. Oh, J.-H. Son, Y.-H. Kim, S.-K. Kwon, Synth. Met. 159 (2009) 1359.
[17] H.-Y. Chen, C.-Ti. Chen, C-Tsen. Chen, Macromolecules 43 (2010) 3613.
[18] H.W. Hung, N. Yokoyama, M. Yahiro, C. Adachi, Thin Solid Films 516 (2008) 8717.
[19] H.Y. Oh, C. Lee, S. Lee, Org. Electron. 10 (2009) 163.
[20] Li Li, J.-H. Zou, J. Huang, C. Li, Y. Zhang, C. Sun, X-H. Zhu, J. Peng, Y. Cao, J. Ronchali, Org. Electron. 9 (2008) 649.
[21] J. Wang, Y.D. Jiang, J.S. Yu, Appl. Phys. Lett. 91 (2007) 131105.
[22] K. Okumoto, Y. Shirota, Chem. Mater. 15 (2003) 699.
[23] S. Tao, S. Xu, X. Zhang, Chem. Phys. Lett. 429 (2006) 622.
[24] Z. Yang, Z. Chi, L. Zhou, X. Zhang, M. Chen, B. Xu, C. Wang, Y. Zhang, J. Xu, Opt. Mater. 32 (2009) 398.
[25] J.B. Lagowski, THEOCHEM 589–590 (2002) 125–137.
[26] J. Salbeck, F. Weissörtel, N. Yu, J. Bauer, H. Bestgen, Synth. Met. 91 (1997) 209.
[27] C. Adachi, M.A. Baldo, M.E. Thopmson, S.R. Forrest, J. Appl. Phys. 90 (2001) 5048.
[28] M.-S. Kim, B.-K. Choi, T.-W. Lee, D.S. Shin, S.K. Kang, J.M. Kim, S. Tamura, Appl. Phys. Lett. 91 (2007) 251111.
[29] Y. Zhang, G. Cheng, S. Chen, Y. Li, Y. Zhao, S. Liu, F. He, L. Tian, Y. Ma, Appl. Phys. Lett. 88 (2006) 223508.
[30] F. Li, M. Zhang, G. Cheng, J. Feng, Y. Zhao, Y. Ma, S. Liu, J. Shen, Appl. Phys. Lett. 84 (2004) 148.
[31] K.H. Lee, Y.S. Kwon, L.K. Kang, G.Y. Kim, J.H. Seo, Y.K. Kim, S.S. Yoon, Synth. Met. 159 (2009) 2603.
[32] J.K. Park, K.H. Lee, S. Kang, J.Y. Lee, J.S. Park, J.H. Seo, Y.K. Kim, S.S. Yoon, Org. Electron. 11 (2010) 905.
[33] E.-M. Han, L.-M. Do, N. Yamamoto, M. Fujihira, Thin Solid Films 273 (1996) 202.
[34] M.A. Baldo, D.F. O'Brien, M.E. Thompson, S.R. Forrest, Phys. Rev. B 60 (1999) 14422.
[35] M.-T. Lee, H.-H. Chen, C.-H. Liao, C.-H. Tsai, C.H. Chen, Appl. Phys. Lett. 85 (2004) 3301.
[36] S.O. Jeon, K.S. Yook, C.W. Joo, J.Y. Lee, Adv. Funct. Mater. 19 (2009) 3644.

By using phosphorescent materials that harvest both singlet and triplet excitons, the factor η_{ST} can be raised to 100% [11,12].

The factors γ, η_{ST} and q together yield the internal quantum efficiency η_{int}. By the employment of phosphorescent emitters with high radiative quantum efficiency, η_{int} can approach values close to one [13,14]. However, the most important factor still strongly limiting η_{EQE} is the outcoupling efficiency η_{out}. Due to the large difference in refractive index between air ($n = 1.0$), glass ($n \approx 1.5$) and the organic layers ($n \approx 1.7$–2.0), a large fraction of the emitted light can not leave the device due to total internal reflection and is trapped in the substrate or as waveguide modes in the thin film structure. In addition, the excitation of surface plasmons at the interface to the metallic cathode further reduces the light extraction efficiency to values typically around 20% [15]. By applying outcoupling enhancement structures like prisms, microlense arrays or microstructured substrates it is possible to extract a large fraction of substrate modes [3,16–18] and bring η_{out} up to some 30–40% at most, still representing a major limitation for high quantum efficiency.

At present, SM-OLEDs incorporating dye-doped emitting layers are superior to their polymeric counterparts concerning efficiency and lifetime, e.g. due to the straightforward implementation of doped transport layers as well as additional blocking and injection layers leading to better charge balance factor and a well-defined recombination zone. Nevertheless, polymer OLEDs often have the advantage of emitters being oriented parallel to the substrate plane [19–22]. Thus, the transition dipole moment that is usually oriented along the π-conjugated polymer chain is oriented in-plane. This considerably reduces coupling to unfavourable loss channels and can increase η_{out} by a factor of approximately 1.5 compared to a random orientation of the transition dipole moments [20]. For more than 20 years, however, it has generally been believed that evaporated amorphous films in SM-OLEDs have no preferential orientation of the molecules [19]. Though there have been reports about horizontally oriented molecules in evaporated neat films [23–25], only recently a non-isotropic dipole orientation in dye-doped films has been reported [25], opening up new possibilities for improvement of light outcoupling efficiency of OLEDs.

In this article we first explain the fundamental dependence of η_{out} on the dipole orientation by studying detailed optical simulations. Next, we investigate the orientation of the transition dipole moments in two blue fluorescent dyes, 4,4′-bis[4-(diphenylamino)styryl]biphenyl (BDASBi) [26] and 4-(2,2-diphenylethenyl)-*N*,*N*-bis(4-methylphenyl)benzenamine (PEBA) [27], doped into a 4,4′-bis(*N*-carbazole)-biphenyl (CBP) matrix. Angular dependent photoluminescence measurements yield strong evidence for a preferentially horizontal orientation for BDASBi and a random orientation for PEBA. Using BDASBi doped into CBP, horizontally oriented emitters are intentionally employed in dye-doped SM-OLEDs for the first time. By comparing to the PEBA reference device with random dipole orientation, strong evidence is found that the employment of oriented emitters can induce a substantial efficiency boost of almost 50% which is necessary for a widespread application of OLEDs in general lighting.

2. Materials, device structure and experimental methods

Organic semiconductor films generally show optical anisotropy only if the molecular shape is anisotropic as well [24,25]. Because organic solids are bound only by weak intermolecular van der Waals interaction, orientation effects can occur on any underlying substrate and even in a host matrix [25]. Fig. 1a shows the molecular structures of BDASBi and PEBA which are used as exemplary materials in this study. BDASBi is known to show a strong horizontal orientation when doped into CBP [28]. In contrast to BDASBi, which has an elongated shape, PEBA is a rather small and compact molecule. Thus, it is expected that PEBA will show much less pronounced orientation effects than BDASBi. The photoluminescence spectra of BDASBi and PEBA doped at a content of 6 wt.% into CBP are presented in Fig. 1b. Both spectra are very similar and have the same peak wavelength at around 470 nm. In addition, a comparable radiative quantum efficiency q of 0.65 and 0.55 was determined for 6 wt.%-BDASBi:CBP and PEBA:CBP films, respectively. Thus, both materials will

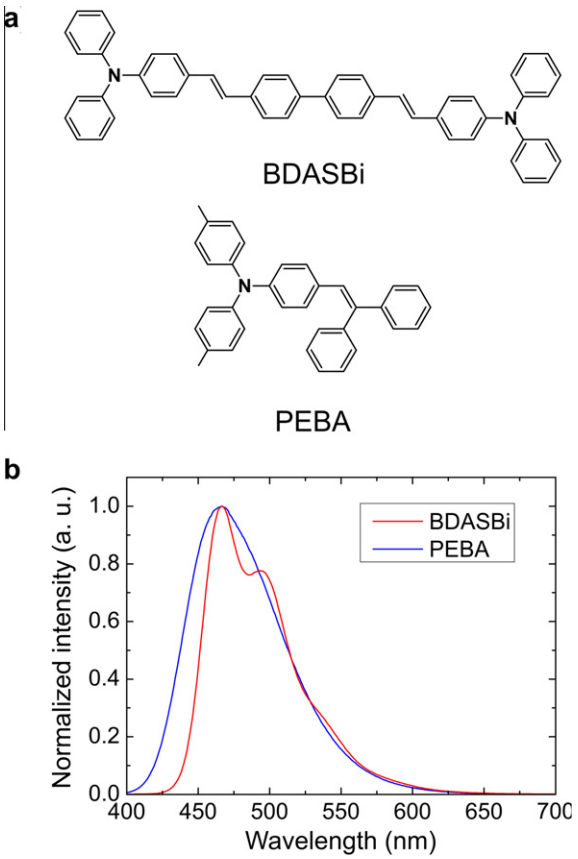

Fig. 1. (a) Molecular structures of BDASBi and PEBA. (b) Photoluminescence emission spectra of 50 nm films of BDASBi and PEBA doped into CBP (6 wt.%) measured perpendicular to the silica glass substrate.

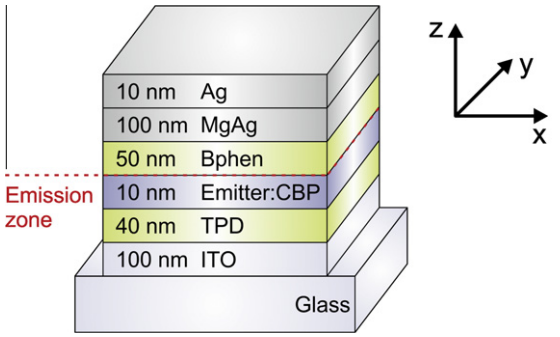

Fig. 2. Schematic diagram of the OLED structure and definition of the coordinate system and dipole orientations used in the simulation.

experience comparable cavity effects inside an OLED device.

Fig. 2 shows the basic OLED structure that is investigated in this work. The devices consist of a glass substrate covered with a patterned indium tin oxide (ITO) layer with 100 nm thickness, then 40 nm of the hole transport material *N*,*N*′-diphenyl-*N*,*N*′-bis(3-methylphenyl)-1,1′-biphenyl-4,4′-diamine (TPD), 10 nm of either BDASBi or PEBA doped into CBP (6 wt.%), 50 nm of the electron transport material 4,7-diphenyl-1,10-phenanthroline (Bphen) and a cathode consisting of 100 nm Mg:Ag (10:1) and a 10 nm thick Ag capping layer.

All organic layers were deposited in a vacuum of $<3 \times 10^{-3}$ Pa at an evaporation rate of ~0.2 nm/s except for the cathode, which was fabricated at a rate of ~0.1 nm/s. All layers of the BDASBi and PEBA OLEDs except for the doped emission layer were deposited simultaneously in order to rule out differences in layer thicknesses. In addition, the substrates were rotated at equivalent positions from the axis during deposition. The active area of the OLEDs was circularly shaped with a diameter of 1 mm.

The current density–voltage–luminance characteristics of the OLEDs were measured using a semiconductor parameter analyzer (E5273A, Agilent Co.) with an optical power meter (1930C, Newport Co.). The zero-degree spectra of the OLEDs were measured using a multichannel spectrometer (SD2000, Ocean Optics Co.) through an optical fibre whose end was located vertically towards the substrate of the working OLEDs. The silicon photodiode of the optical power meter was calibrated at a wavelength of 485 nm, corresponding to the emission peak wavelength of the OLEDs. The emission spectra of the OLEDs are sufficiently narrow to neglect the spectral dependence of the response of the silicon photodiode. The photodiode captures light within a cone of approximately 56°. For the calculation of EQE values from the measurement, a Lambertian emission was assumed which compares reasonably well with measured and simulated angular dependent spectra.

Samples for photoluminescence (PL) and quantum efficiency measurements comprised 50 nm thick doped films of 6 wt.% BDASBi or PEBA in CBP deposited on cleaned fused silica substrates. PL emission spectra were measured using a fluorescence spectrometer (FP-6500, Jasco Co.). The chosen thickness of the samples ensures that the spectra are not changed too much by waveguiding effects and that they match the emission spectra in free space. PL quantum efficiencies were determined using an absolute PL quantum yield measurement system (C9920-02, Hamamatsu Photonics K.K.).

Samples for angular dependent PL measurements consisted of 12 nm thick doped films of 6 wt.% BDASBi or PEBA in CBP deposited on cleaned glass substrates and capped with a 70 nm thick neat CBP layer. For the measurement, a fused silica half cylinder prism was attached to the substrate side of the samples by index matching fluid and the samples were mounted on a computer controlled rotation stage. A 375 nm cw laser diode incident under 45° through the encapsulated side was used as excitation source. Since CBP has only a small absorption at this wavelength, emission from the matrix is suppressed. The angular dependent PL spectrum from 0° to 90° was measured with a fibre optical spectrometer and a polarizer to distinguish between *s*- and *p*-polarized emission (for details see Ref. [28]).

3. Optical simulation of OLEDs

The effect of differently oriented transition dipole moments is most obvious by studying the results of an optical simulation which is based on a dipole model [15,29–31]. In this model, the dipoles are treated as damped forced harmonic oscillators embedded in a multilayer OLED. Without loss of generality, the substrate plane is assumed to be in the x–y-plane and the emission into the x–z-plane is considered, cf. Fig. 2. The simulation distinguishes three discrete dipole orientations p_x, p_y and p_z. According to the chosen coordinate system, the p_x- and p_y-dipoles are oriented horizontally whereas the p_z-dipoles have a vertical orientation. The p_y-dipoles emit only *s*-polarized light whereas the p_x- and p_z-dipoles are accounting for the *p*-polarized emission.

Fig. 3a shows the total dissipated optical power in a device with isotropic emitter orientation, where the emission spectrum is assumed to resemble the one of BDASBi:CBP (6 wt.%) and the radiative quantum efficiency is set to 1. Since CBP has higher hole than electron mobility [32] the emitter position is assumed to be at the interface to Bphen. Obviously, a large fraction of the dissipated power is coupled to two sharp waveguide modes (region 3) and to surface plasmons (region 4).

The contribution of each dipole orientation to the total power dissipation can be seen in Fig. 3b, which shows a cross section of Fig. 3a at 470 nm. The horizontally oriented p_x- and p_y-dipoles have their major contributions in regions (1) and (2) and couple to a *p*-polarized and an *s*-polarized waveguide mode (region 3), respectively. By contrast, the vertically oriented p_z-dipoles show almost no emission into air or substrate but couple most of their power to surface plasmons (region 4) [33]. This behaviour can be explained by taking into account that linear dipoles radiate strongest perpendicular to their direction of oscillation [31]. Thus the vertically oriented p_z-dipoles emit mainly at large angles, i.e. high in-plane wave vectors,

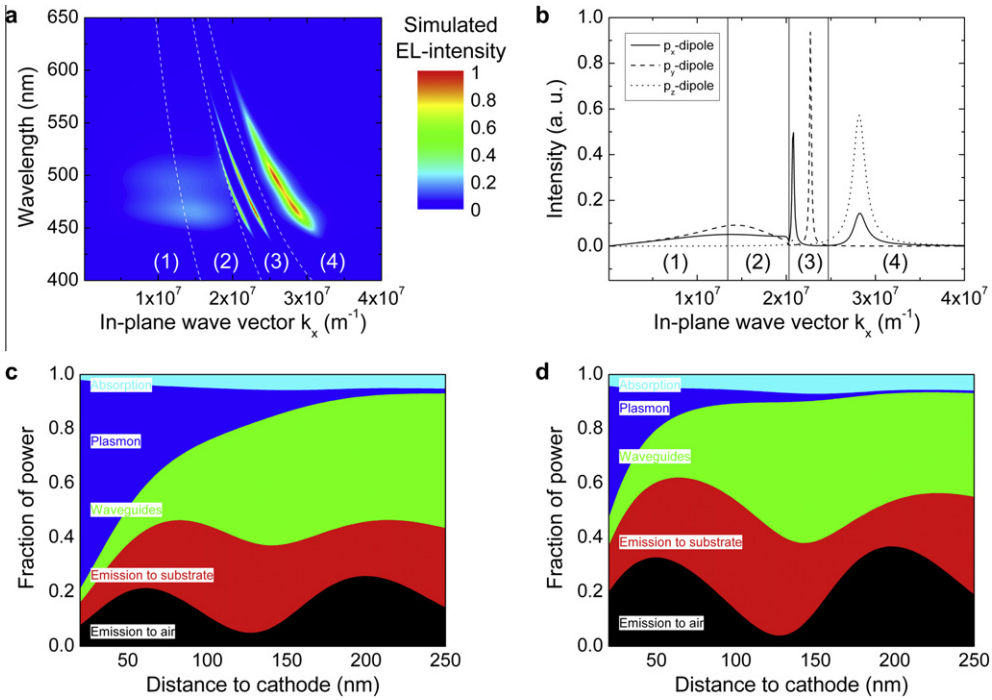

Fig. 3. (a) Simulation of the total optical power dissipation in an organic light-emitting diode as shown in Fig. 2 assuming isotropic emitter orientation with an emission spectrum resembling that of BDASBi:CBP (6 wt.%) and a radiative quantum efficiency $q = 1$. Red areas indicate high amount of dissipated power. The lines divide the graph into four regions: emission into air (1), emission into the glass substrate (2), waveguide modes (3) and coupling to surface plasmons (4). (b) Cross section of (a) at a wavelength of 470 nm. The dissipated power is split into the corresponding fractions of each dipole. The vertical lines divide the graph into four regions similar to (a). (c and d) Dissipated power in dependence of the distance to the cathode for (c) random dipole orientation and (d) horizontal dipole orientation. (For interpretation of the references to colour in this figure legend, the reader is referred to the web version of this article.)

Table 1
Dissipated power coupled into different optical channels depending on the orientation of the transition dipole moment. Simulations are based on an OLED as shown in Fig. 2 with BDASBi:CBP (6 wt.%) as an emitting layer. The residual percentage to 100% is lost due to absorption in ITO and the organic layers and at the cathode. For the last two columns it should be noted that these numbers are not simply the average of the corresponding values of each dipole. Instead of that, a weighting according to cavity effects has to be considered.

	p_x-dipole (%)	p_y-dipole (%)	p_z-dipole (%)	Random ($p_x/p_y/p_z$) (%)	Horizontal (p_x/p_y) (%)
Direct emission to air	28.7	36.5	0.1	20.0	32.6
Substrate emission	25.1	30.2	0.9	17.3	27.6
Waveguides	11.5	27.3	3.4	13.3	19.4
Plasmons	29.8	0.7	94.3	45.7	15.3

hence dissipating their power to an unfavourable loss channel.

The fraction of power dissipated by each dipole orientation to different optical channels is displayed in Table 1. Again, the values for the p_z-dipoles clearly show that this dipole orientation does hardly contribute at all to the desired emission into air or substrate. Consequently, the outcoupling efficiency can be significantly enhanced, if only horizontally oriented dipoles are present. This is apparent from the last two columns in Table 1 which show a comparison of OLEDs consisting of a completely random and a purely horizontal dipole orientation, respectively. Both the direct emission and the substrate emission are enhanced by more than 50%, demonstrating the enormous potential of using horizontally oriented emitters in SM-OLEDs.

The main reason for the increased efficiency is a reduced coupling to surface plasmons. This is even more obvious by investigating the distance dependence of the emitter to the metallic mirror. Fig. 3(c and d) show a variation of the electron transport layer thickness for random and horizontal dipole orientation, respectively. The oscillatory behaviour results from interference effects of the emitter with its image dipole [31,34,35]. The graphs clearly display the increased outcoupling efficiency for a horizontal dipole orientation. In addition, in this case the emitter may be positioned much closer to the cathode before the coupling to surface plasmons becomes the dominant loss channel. Apparently, this is an important aspect considering stack design and OLED optimization as will be discussed later.

4. Experimental results and discussion

4.1. Determination of dipole orientation by photoluminescence measurements

For a conclusive study of orientation effects in dye-doped SM-OLEDs it is necessary to use appropriate materials that differ primarily in the orientation of their transition dipole moments. The investigation of neat films by variable angle spectroscopic ellipsometry (VASE) often yields a first indication about molecular anisotropy. In this case, the optical constants determined by VASE for neat films of BDASBi indicate a strong optical anisotropy while the result for PEBA shows almost no anisotropy; however, VASE cannot yield reliable information about dye orientation in guest–host systems.

The horizontal orientation of emitting molecules as in the neat film of BDASBi can also be observed in doped films. A first demonstration of orientation in doped films was performed by edge emission measurements [25]. A more profound conclusion about the orientation in doped films can be achieved quantitatively from an angular dependent *p*-polarized photoluminescence measurement of a thin film and comparison with optical simulations [28]. In this experiment a stack without metallic layers is used so that the emission from vertically oriented p_z-dipoles is directly measurable and information about their existence and even the exact ratio between horizontal and vertical dipoles can be obtained.

The stack under investigation comprises a 12 nm thick layer of CBP containing 6 wt.% BDASBi or PEBA, respectively, capped with a 70 nm thick neat CBP layer. Fig. 4 (a and b) display the *p*-polarized simulation results of the BDASBi sample for a completely random and a purely horizontal dipole orientation, respectively. By comparing the measured spectra shown in Fig. 4c with the simulations, it is apparent that the transition dipoles in a BDASBi:CBP layer are primarily horizontally oriented.

A precise analysis of the dipole orientation is performed by comparing the cross sections of measurement and simulations, which is displayed in Fig. 5. In addition, the cross section of a stack containing PEBA instead of BDASBi with otherwise identical structure is shown. Comparison of the measured cross section for PEBA with the simulated curves yields excellent agreement assuming a random dipole orientation. Thus, PEBA doped into CBP shows no preferred molecular orientation and the dipole orientation is completely random, i.e. on average 2/3 of the dipoles are horizontally and 1/3 vertically oriented. On the contrary, the cross section of the sample containing BDASBi shows a clear tendency towards horizontal orientation. By weighting the simulations for random and horizontal dipole orientations with 0.27 and 0.73, respectively, very good agreement between the simulated and measured curve can be obtained. These values are in excellent agreement with Ref. [28]. Consequently, it follows that the total ratio between p_z and p_x is 0.27:1. Since the horizontal p_x- and p_y-dipoles are uniformly distributed in the substrate plane, the overall fraction of vertical (p_z) dipoles is 0.27/2.27 = 12% and the fraction of horizontal (p_x, p_y) dipoles is 2/2.27 = 88%.

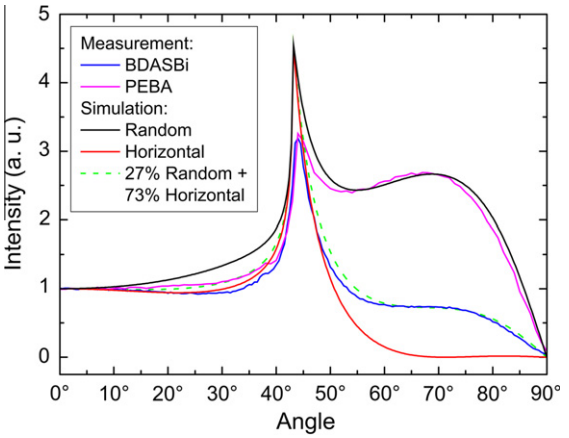

Fig. 5. Angular dependent cross section at 470 nm of the simulated and measured emission spectra shown in Fig. 4 and of a measurement with a sample containing PEBA instead of BDASBi. All cross sections are normalized to the emission at small angles because the emission in this range occurs exclusively from the horizontal p_x-dipoles. On the other hand, the emission at angles around 70° is dominated by the p_z-dipoles. The dashed line represents an average of random and horizontal dipole orientation with a relative weight of 0.27 and 0.73, respectively.

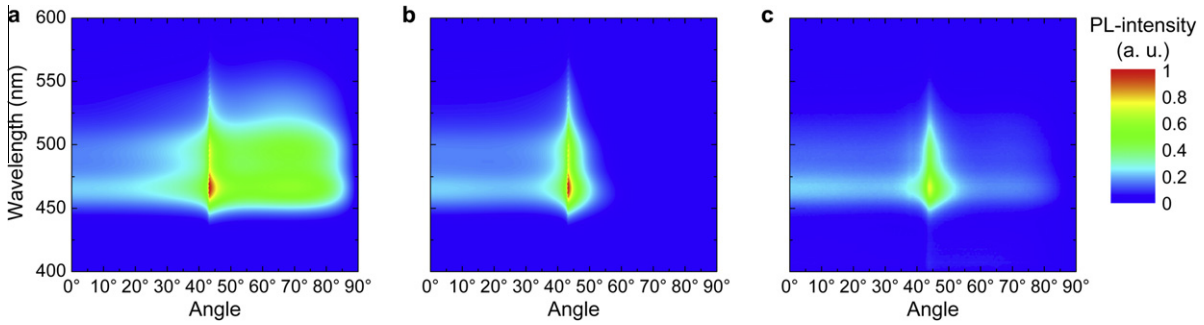

Fig. 4. Simulation and measurement of the angular dependent *p*-polarized emission spectrum of a 12 nm film of BDASBi:CBP (6 wt.%) on a glass substrate capped with 70 nm of neat CBP. Simulation assuming (a) a random dipole orientation, (b) a purely horizontal dipole orientation and (c) measured emission spectrum. The measured emission intensity is scaled so that the emission at small angles corresponds to the simulations.

We note that quantitative information about emitter orientation can also be obtained by fluorescence lifetime measurements, as reported in Ref. [31]. This requires the preparation of a series of samples with systematically varying distance between the emission zone and a metal layer. Though being more elaborate, this method has the benefit of independently yielding the value of the radiative quantum efficiency of the emitter, too, as will be published separately for a red phosphorescent OLED [36].

4.2. Quantum efficiency of dye-doped OLEDs

As a result of the previous analysis, BDASBi and PEBA are ideal candidates for studying the effect of molecular orientation in actual OLED devices. Both materials were incorporated in a rather simple stack in order to rule out differences in device fabrication. The same stack layout as already discussed in the simulations is employed, cf. Fig. 2. Neglecting any effects of orientation, it is expected that the OLED based on BDASBi has a 1.16 times larger external quantum efficiency than the OLED with PEBA because of the difference in radiative quantum efficiency q. The simulations can also be used to predict the influence of orientation which should additionally boost the efficiency of the OLED with BDASBi. Assuming 88% horizontal orientation from the analysis above, it is expected that the OLED based on BDASBi gains an extra enhancement of outcoupling efficiency and therewith external quantum efficiency of 37%. If BDASBi were perfectly oriented horizontally, this enhancement would even amount to 59%.

For a conclusive determination of η_{out} from a measurement of η_{EQE} it is critical that all other factors in Eq. (1) are comparable. First, the spin-allowed exciton fraction η_{ST} is generally accepted to have a value of 25% in SM-OLEDs based on fluorescent emitters [6,7]. Second, the radiative quantum efficiency q was determined to be 0.65 for the 6 wt.%-BDASBi:CBP and 0.55 for PEBA:CBP layers. This difference must be included in optical simulations due to different cavity enhancement [15,37,38]. Finally, the charge balance factor γ is mainly governed by the transport layers TPD and Bphen. Since both OLEDs comprise the same structure it can be assumed that γ is rather similar in both devices. Although charge trapping effects in the doped CBP matrix can not be fully ruled out due to slightly different energy of the lowest unoccupied molecular orbitals (LUMO) of BDASBi and PEBA [39], the almost identical current–voltage characteristics (see below) give strong evidence that minor differences in charge carrier transport and recombination in both devices do not play a dominant role. In addition, it is necessary to have information concerning the emitter position and therewith the distance to the cathode as this has an important influence for the simulated outcoupling efficiency as was demonstrated in Fig. 3(c and d). Since both BDASBi and PEBA contain triphenylamine substituents it is expected that they have a higher hole than electron mobility. CBP also shows a slightly larger hole than electron mobility, therefore it is reasonable to assume that the emission takes place close to the interface between the emitting layer and Bphen. However, the assumptions concerning charge balance and emitter position are further verified by investigating the current–voltage characteristics and the spectrum at different current densities (Fig. 6).

Fig. 6a shows the current–voltage characteristics for two OLEDs based on BDASBi and PEBA as emitters, respectively. Since the OLEDs only differ in their dopant,

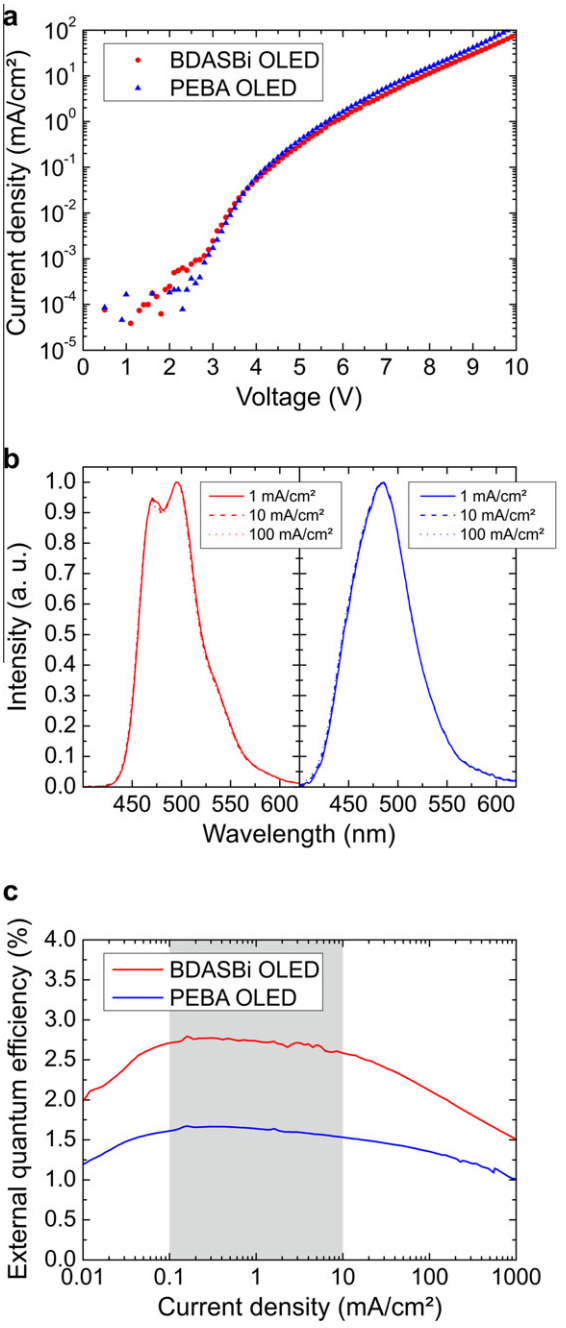

Fig. 6. (a) Measured current–voltage characteristics for OLEDs comprising either BDASBi:CBP or PEBA:CBP as an emitting layer. (b) Measured zero-degree emission spectra at different current densities. (c) Experimentally determined external EL quantum efficiencies depending on current density. The EQE values are averaged in the range between 0.1 and 10 mA/cm^2 because the measured curves show a plateau in this region. For smaller current densities there is probably no stable charge balance, while quenching processes occur for higher current densities.

the measured current density is nearly the same for both devices. This strengthens the assumption of comparable charge balance. The zero-degree spectra of both OLEDs are plotted in Fig. 6b for different current densities. The spectra are almost independent of current density, confirming that the emitter position does not depend significantly on current density as otherwise the spectra would shift due to changing cavity effects [34]. In addition, Fig. 6b illustrates again that the spectra of OLEDs fabricated with both materials are well comparable.

The external quantum efficiency is shown in Fig. 6c. Apparently, η_{EQE} of the OLED based on BDASBi is significantly larger than only a factor of 1.16 which would be expected from the difference in radiative quantum efficiency. An average in the range between 0.1 and 10 mA/cm^2 yields an η_{EQE} of 2.7% for the BDASBi-stack and 1.6% for the device based on PEBA. It should be noted that the absolute values of η_{EQE} for both devices are smaller than expected from simulations of the outcoupling efficiency yielding 3.9% for random orientation and 5.9% for perfectly parallel orientation of BDASBi molecules and 3.3% for randomly orientated PEBA molecules, respectively (see Supplementary Information S5). This is probably due to imperfect charge balance owing to the fact that no doped transport layers and selective carrier blocking layers were used in our simple OLED stack. However, since both types of OLEDs utilize identical HTL and ETL (fabricated in the same evaporation run) as well as the same matrix for the EML, we believe that both devices have quite comparable factor γ in Eq. (1). In addition we want to emphasize that we are mainly interested in the *relative* increase of outcoupling efficiency. Thus, any effects that reduce the efficiency and occur in both types of OLEDs cancel out.

Taking the difference in radiative quantum efficiency into account, it follows that the OLED based on BDASBi exhibits an increase of outcoupling efficiency by 45% due to the strongly horizontally oriented dipoles. This is even slightly higher than the value expected from the analysis of dipole orientation in both materials, but it validates the basic result of mainly horizontally oriented dipoles in BDASBi obtained by ellipsometry and the angular dependent photoluminescence measurement. Even allowing for different emitter positions in the simulation of both devices, the outcoupling and external quantum efficiency of the OLED based on BDASBi is significantly larger. Considering that the orientation of BDASBi is not yet perfectly horizontal, this manifests the enormous efficiency enhancement that can be obtained by incorporating oriented emitters into SM-OLED devices.

4.3. Discussion

The well-known concept of non-isotropic emitter orientation, presented here for the first time in dye-doped SM-OLEDs, to achieve enhanced light outcoupling, is of course not limited to fluorescent materials only, but can also be applied to phosphorescent dyes [36]. Since the latter are usually rather bulky metal–organic complexes, achieving horizontally oriented emitter molecules will be more challenging than with rod-like linear molecules used here. Nevertheless, tailoring phosphorescent materials with respect to this feature, e.g. by asymmetric organic ligands, might allow for a substantial increase in external quantum efficiency from about 20% with random emitter orientation to more than 30% in the case of flat lying dipoles – without any additional outcoupling structure.

Besides the enormous boost in outcoupling and external EL quantum efficiency, the use of oriented emitters in SM-OLEDs offers a series of additional benefits. First, the emitter position may move closer to the cathode without loosing too much energy to surface plasmons. Thus, the emitter can be placed at a position where it receives optimal interference and cavity enhancement. Additionally, with horizontally oriented emitters both the first and second cavity maxima are comparable in outcoupling efficiency, which offers more freedom in stack design. The freedom to place the emitter close to the cathode is especially important in white OLEDs and stacked OLEDs that comprise several emitting layers [40–42]. It should be noted that the advantage of horizontally oriented dipoles disappears, when high index glass substrates ($n \approx 1.8$) and thick electron transport layers are used in order to suppress coupling to waveguide modes and surface plasmons [3,4,43]. However, using substrates with such a high refractive index probably is too expensive for an application in large area OLED light sources.

Furthermore, it is essential to know the correct dipole orientation in any analysis of measured η_{EQE} values, since the outcoupling efficiency can change by more than a factor of 1.5. If the emitter orientation is not taken into account properly, this implies equivalently large errors in the determination of the internal quantum efficiency [36] and, e.g., the spin-allowed exciton fraction [21,38].

Considering material choice it must be taken into account that the effect of horizontally oriented emitter molecules can to some extend compensate for a lower radiative quantum efficiency as compared to an unoriented material. For example, the search for the longed-for stable deep-blue phosphorescent emitter could take a turn: The general difference of a factor of 4 in the external quantum efficiency between phosphorescent and fluorescent emitters reduces to only about 2.5 if the fluorescent emitter is horizontally oriented. Thus, present stability problems with blue phosphorescent emitters may be avoided without sacrificing too much in efficiency.

It is further noteworthy that oriented molecules in neat and doped films also play an important role in related disciplines. Because alignment enlarges the overlap of molecular orbitals between adjacent molecules, non-isotropic orientation can contribute to an improvement of the charge transport characteristics not only in OLEDs [44,45] but also in organic photovoltaic cells (OPVCs) and organic field-effect transistors (OFETs). Recently, small molecule OPVCs using an amorphous material with a high carrier mobility were reported [46], where the molecule has an anisotropic planar shape. We anticipate that horizontally oriented molecules with an anisotropic shape strongly improve device performance of OPVCs due to both increased absorption and enhanced charge transport. Similarly, it is well known that OFETs profit from an enhanced charge transport resulting from oriented molecules. Especially the development of electrically pumped organic lasers

based on light-emitting OFETs could benefit from oriented molecules with improved transport and light outcoupling [47].

5. Conclusions and outlook

In conclusion, an SM-OLED employing intentionally horizontally oriented emitter molecules was presented and compared to a reference device with random emitter orientation. The SM-OLED incorporating oriented emitters exhibits an increase in light-outcoupling and external quantum efficiency of about 45%. Certainly, horizontally oriented phosphorescent emitters would represent the ultimate material of choice for SM-OLEDs. Our presented technique of determining the orientation in dye-doped films by a simple angular dependent photoluminescence measurement offers a straightforward method to investigate numerous guest–host combinations and newly developed materials as well as fabrication procedures that influence molecular orientation. It should be emphasized that using horizontally oriented emitters fabricated in a common evaporation process does not change production costs at all. On the contrary, comparably efficient outcoupling enhancement techniques like scattering at Bragg gratings [48] or photonic crystal structures [49] significantly complicate the fabrication process and raise the costs accordingly.

Acknowledgements

We acknowledge financial support by the Elite Network of Bavaria through the international graduate school "Materials Science of Complex Interfaces" and by the Japan Society for the Promotion of Science (JSPS). This work was partly supported by Promotion of Environmental Improvement for Independence of Young Researchers Program of Ministry of Education, Culture, Sports, Science and Technology, Japan. We thank Prof. Junji Kido for using the ultraviolet photoelectron spectroscopy setup in his lab at Yamagata University, Japan. We also thank the Research Center for Computational Science (RCCS), Okazaki National Research Institutes, for the use of a SGI Altix4700 computer.

Appendix A. Supplementary data

Supplementary data associated with this article can be found, in the online version, at doi:10.1016/j.orgel.2011.02.005.

References

[1] C.W. Tang, S.A. VanSlyke, Organic electroluminescent diodes, Appl. Phys. Lett. 51 (1987) 913–915.
[2] J.H. Burroughes, D.D.C. Bradley, A.R. Brown, R.N. Marks, K. Mackay, R.H. Friend, P.L. Burns, A.B. Holmes, Light-emitting diodes based on conjugated polymers, Nature 347 (1990) 539–541.
[3] S. Reineke, F. Lindner, G. Schwartz, N. Seidler, K. Walzer, B. Lüssem, K. Leo, White organic light-emitting diodes with fluorescent tube efficiency, Nature 459 (2009) 234–239.
[4] S. Mladenovski, K. Neyts, D. Pavicic, A. Werner, C. Rothe, Exceptionally efficient organic light emitting devices using high refractive index substrates, Opt. Express 17 (2009) 7562–7570.
[5] T. Tsutsui, E. Aminaka, C.P. Lin, D.-U. Kim, Extended molecular design concept of molecular materials for electroluminescence: sublimed-dye films, molecularly doped polymers and polymers with chromophores, Philos. Trans. R. Soc. London. A 355 (1997) 801–814.
[6] M.A. Baldo, D.F. O'Brien, M.E. Thompson, S.R. Forrest, Excitonic singlet–triplet ratio in a semiconducting organic thin film, Phys. Rev. B 60 (1999) 14422–14428.
[7] M. Segal, M.A. Baldo, R.J. Holmes, S.R. Forrest, Z.G. Soos, Excitonic singlet–triplet ratios in molecular and polymeric organic materials, Phys. Rev. B 68 (2003) 075211.
[8] M. Pope, C.E. Swenberg, Electronic Processes in Organic Crystals and Polymers, second ed., Oxford Univ. Press, 1999.
[9] D.Y. Kondakov, T.D. Pawlik, T.K. Hatwar, J.P. Spindler, Triplet annihilation exceeding spin statistical limit in highly efficient fluorescent organic light-emitting diodes, J. Appl. Phys. 106 (2009) 124510.
[10] Y. Luo, H. Aziz, Correlation between triplet–triplet annihilation and electroluminescence efficiency in doped fluorescent organic light-emitting devices, Adv. Funct. Mater. 20 (2010) 1285.
[11] M.A. Baldo, D.F. O'Brien, Y. You, A. Shoustikov, S. Sibley, M.E. Thompson, S.R. Forrest, Highly efficient phosphorescent emission from organic electroluminescent devices, Nature 395 (1998) 151–154.
[12] J.S. Wilson, A.S. Dhoot, A.J.A.B. Seeley, M.S. Khan, A. Köhler, R.H. Friend, Spin-dependent exciton formation in π-conjugated compounds, Nature 413 (2001) 828–831.
[13] C. Adachi, M.A. Baldo, M.E. Thompson, S.R. Forrest, Nearly 100% internal phosphorescence efficiency in an organic light emitting device, J. Appl. Phys. 90 (2001) 5048–5051.
[14] E.L. Williams, K. Haavisto, J. Li, G.E. Jabbour, Excimer-based white phosphorescent organic light emitting diodes with nearly 100% internal quantum efficiency, Adv. Mater. 19 (2007) 197–202.
[15] S. Nowy, B.C. Krummacher, J. Frischeisen, N.A. Reinke, W. Brütting, Light extraction and optical loss mechanisms in organic light-emitting diodes: influence of the emitter quantum efficiency, J. Appl. Phys. 104 (2008) 123109.
[16] W.H. Koo, S.M. Jeong, F. Araoka, K. Ishikawa, S. Nishimura, T. Toyooka, H. Takezoe, Light extraction from organic light-emitting diodes enhanced by spontaneously formed buckles, Nat. Photonics 4 (2010) 222–226.
[17] Y. Sun, S.R. Forrest, Enhanced light out-coupling of organic light-emitting devices using embedded low-index grids, Nat. Photonics 2 (2008) 483.
[18] H.-Y. Lin, J.-H. Lee, M.-K. Wei, C.-L. Dai, C.-F. Wu, Y.-H. Ho, H.-Y. Lin, T.-C. Wu, Improvement of the outcoupling efficiency of an organic light-emitting device by attaching microstructured films, Opt. Commun. 275 (2007) 464–469.
[19] J.M. Ziebarth, M.D. McGehee, A theoretical and experimental investigation of light extraction from polymer light-emitting diodes, J. Appl. Phys. 97 (2005) 064502.
[20] J.-S. Kim, P.K.H. Ho, N.C. Greenham, R.H. Friend, Electroluminescence emission pattern of organic light-emitting diodes: implications for device efficiency calculations, J. Appl. Phys. 88 (2000) 1073–1081.
[21] A. Köhler, J. Wilson, Phosphorescence and spin-dependent exciton formation in conjugated polymers, Org. Electron. 4 (2003) 179–189.
[22] S.L.M. van Mensfoort, M. Carvelli, M. Megens, D. Wehenkel, M. Bartyzel, H. Greiner, R.A.J. Janssen, R. Coehoorn, Measuring the light emission profile in organic light-emitting diodes with nanometre spatial resolution, Nat. Photonics 4 (2010) 329–335.
[23] H.-W. Lin, C.-L. Lin, H.-H. Chang, Y.-T. Lin, C.-C. Wu, Y.-M. Chen, R.-T. Chen, Y.-Y. Chien, K.-T. Wong, Anisotropic optical properties and molecular orientation in vacuum-deposited ter(9,9-diarylfluorene)s thin films using spectroscopic ellipsometry, J. Appl. Phys. 95 (2004) 881–886.
[24] D. Yokoyama, A. Sakaguchi, M. Suzuki, C. Adachi, Horizontal molecular orientation in vacuum-deposited organic amorphous films of hole and electron transport materials, Appl. Phys. Lett. 93 (2008) 173302.
[25] D. Yokoyama, A. Sakaguchi, M. Suzuki, C. Adachi, Horizontal orientation of linear-shaped organic molecules having bulky substituents in neat and doped vacuum-deposited amorphous films, Org. Electron. 10 (2009) 127–137.
[26] H.S. Bang, S.Y. Seo, D.C. Choo, T.W. Kim, S.J. Lee, J.H. Seo, Y.K. Kim, C. Chu, J. Ha, Effect of doped emitting layer on electrical and optical properties in blue organic light-emitting devices, Thin Solid Films 517 (2009) 5314–5317.
[27] T. Niimi, M. Umeda, Electron transfer between a photoexcited azo pigment particle and an electron donor molecule in a solid system, J. Phys. Chem. B 106 (2002) 3657–3661.

[28] J. Frischeisen, D. Yokoyama, C. Adachi, W. Brütting, Determination of molecular dipole orientation in doped fluorescent organic thin films by photoluminescence measurements, Appl. Phys. Lett. 96 (2010) 073302.
[29] R.R. Chance, A. Prock, R. Silbey, Lifetime of an emitting molecule near a partially reflecting surface, J. Chem. Phys. 60 (1974) 2744–2748.
[30] W.L. Barnes, Topical review Fluorescence near interfaces: the role of photonic mode density, J. Mod. Opt. 45 (1998) 661–699.
[31] S.H. Garrett, J.A.E. Wasey, W.L. Barnes, Determining the orientation of the emissive dipole moment associated with dye molecules in microcavity structures, J. Mod. Opt. 51 (2004) 2287–2295.
[32] H. Matsushima, S. Naka, H. Okada, H. Onnagawa, Organic electrophosphorescent devices with mixed hole transport material as emission layer, Curr. Appl Phys. 5 (2005) 305–308.
[33] W.H. Weber, C.F. Eagen, Energy transfer from an excited dye molecule to the surface plasmons of an adjacent metal, Opt. Lett. 4 (1979) 236–238.
[34] H. Becker, S.E. Burns, R.H. Friend, Effect of metal films on the photoluminescence and electroluminescence of conjugated polymers, Phys. Rev. B 56 (1997) 1893–1905.
[35] Y. Cao, I.D. Parker, G. Yu, C. Zhang, A.J. Heeger, Improved quantum efficiency for electroluminescence in semiconducting polymers, Nature 397 (1999) 414–417.
[36] M. Flämmich, J. Frischeisen, D.S. Setz, D. Michaelis, B.C. Krummacher, T.D. Schmidt, W. Brütting, N. Danz, submitted for publication.
[37] B.C. Krummacher, S. Nowy, J. Frischeisen, M. Klein, W. Brütting, Efficiency analysis of organic light-emitting diodes based on optical simulation, Org. Electron. 10 (2009) 478–485.
[38] J.A.E. Wasey, A. Safonov, I.D. W Samuel, W.L. Barnes, Efficiency of radiative emission from thin films of a light-emitting conjugated polymer, Phys. Rev. B 64 (2001) 205201.
[39] HOMO levels of BDASBi and PEBA were determined by atmospheric ultraviolet photoelectron spectroscopy (Riken Keiki, AC-3) using vacuum-deposited films. Both materials have a HOMO of 5.6 eV. In addition, a HOMO level of 6.0 eV is reported for CBP [N. Matsumoto, et al., J. Phys. Chem. C 112 (2008) 7735–7741]. LUMO levels were calculated from the HOMO levels and the low energy edges of the absorption spectra of neat BDASBi, PEBA and CBP films on fused silica. The values are 2.9 eV for BDASBi, 2.7 eV for PEBA and 2.6 eV for CBP. Hence, it cannot be ruled out completely that electron trapping plays a slightly more important role in the BDASBi devices. However, strong trapping effects would probably cause significant differences between BDASBi and PEBA OLEDs in the current–voltage characteristics, which is not observed in the measurement, cf. Fig. 6a. We therefore conclude that an increase of outcoupling efficiency due to molecular orientation is the key factor for the higher EQE of BDASBi OLEDs.
[40] T. Tsutsui, M. Terai, Electric field-assisted bipolar charge spouting in organic thin-film diodes, Appl. Phys. Lett. 84 (2004) 440–442.
[41] L.S. Liao, K.P. Klubek, C.W. Tang, High-efficiency tandem organic light-emitting diodes, Appl. Phys. Lett. 84 (2004) 167–169.
[42] F. Guo, D. Ma, White organic light-emitting diodes based on tandem structures, Appl. Phys. Lett. 87 (2005) 173510.
[43] G. Gaertner, H. Greiner, Light extraction from OLEDs with (high) index matched glass substrates, Proc. SPIE 6999 (2008). 69992T-1-12.
[44] D. Yokoyama, A. Sakaguchi, M. Suzuki, C. Adachi, Enhancement of electron transport by horizontal molecular orientation of oxadiazole planar molecules in organic amorphous films, Appl. Phys. Lett. 95 (2009) 243303.
[45] D. Yokoyama, Y. Setoguchi, A. Sakaguchi, M. Suzuki, C. Adachi, Orientation control of linear-shaped molecules in vacuum-deposited organic amorphous films and its effect on carrier mobilities, Adv. Funct. Mater. 20 (2010) 386–391.
[46] H. Kageyama, H. Ohishi, M. Tanaka, Y. Ohmori, Y. Shirota, High performance organic photovoltaic devices using amorphous molecular materials with high charge-carrier drift mobilities, Appl. Phys. Lett. 94 (2009) 063304.
[47] H.-W. Lin, C.-L. Lin, C.-C. Wu, T.-C. Chao, K.-T. Wong, Influences of molecular orientations on stimulated emission characteristics of oligofluorene films, Org. Electron. 8 (2007) 189–197.
[48] J.M. Ziebarth, A.K. Saafir, S. Fan, M.D. McGehee, Extracting light from polymer light-emitting diodes using stamped bragg gratings, Adv. Funct. Mater. 14 (2004) 451–456.
[49] Y.R. Do, Y.-C. Kim, Y.-W. Song, Y.-H. Lee, Enhanced light extraction efficiency from organic light emitting diodes by insertion of a two-dimensional photonic crystal structure, J. Appl. Phys. 96 (2004) 7629–7636.

very good contestant for such applications is Cu, being a very inexpensive material with excellent electrical and optical properties already widely used in microelectronics [8]. However ultrathin (i.e. $\leqslant$10 nm) Cu films are strongly subjected to oxidation and corrosion, which alter significantly their electrical and optical properties.

In a parallel publication [9], we have shown that one can use a newly developed bilayered ultrathin-metal-film (UTMF) structure consisting of an ultrathin and continuous Cu film covered by a protective ultrathin Ni film as front electrode in organic photovoltaic (OPV) cells. The multilayer Cu–Ni UTMF exhibits significantly higher stability than single layer Cu films against temperature in ambient atmosphere. The obtained Cu–Ni bilayer UTMFs show transparency of 56% at wavelengths around 630 nm and sheet resistance of 16 Ω/sq. The Ni capping layer reduces slightly the transmission of the Cu layer while not influencing the sheet resistance. In this paper we efficiently use these multilayer transparent electrodes in OLEDs. In particular, with respect to the OPV work of Ref. [9], PEDOT:PSS instead of NiO is in contact with the transparent electrode. In terms of devices, the Cu–Ni bilayer-based OLED device shows comparable efficiency to the ITO-based OLED, which demonstrates that UTMF contacts are an effective alternative electrode to ITO because of their simple fabrication processing, mechanical flexibility [10,11] due to low thickness and ductability of metal and low cost.

2. Experimental

UTMFs were deposited by magnetron sputtering on double-side optically polished UV grade silica substrates. We prepared the following layers: Cu, Ni, and Cu with a constant 1 nm Ni capping layer, of total thickness 8 nm each. We deposited Cu and Ni by employing the same deposition conditions as mentioned in Ref. [9]. Surface roughness has to be kept below the thickness of the layer; otherwise films could be discontinuous and thus non-conductive. A Perkin–Elmer lambda 950 spectrometer was used for optical transmission measurements while Cascade Microtech 44/7 S 2749 four-point probe system with a Keithley 2001 multimeter for electrical sheet resistance measurements. The as-deposited Ni, Cu and Cu–Ni UTMFs were next used to fabricate PLED according to the following structure: Anode/PEDOT-PSS/SY/CaAg. Poly(phenylenevinylene) copolymer (SY), commercially available from Merck, was dissolved in toluene, stirred over night and filtered before being spin-coated onto the PEDOT-PSS layer for a thickness of around 80 nm. Ca and Ag were sequentially thermally evaporated ($<5 \times 10^{-6}$ mbar) onto the emitting layer using shadow mask. Additional details on the fabrication steps and corresponding characterization can be found elsewhere [6].

3. Results and discussion

Fig. 1 shows the optical transmittance spectra of as-grown Cu (8 nm), Ni (8 nm), bilayer Cu–Ni (Cu = 7 nm, Ni = 1 nm) and ITO (100 nm) commercial films. The ITO shows the highest transmittance value at 86% while the

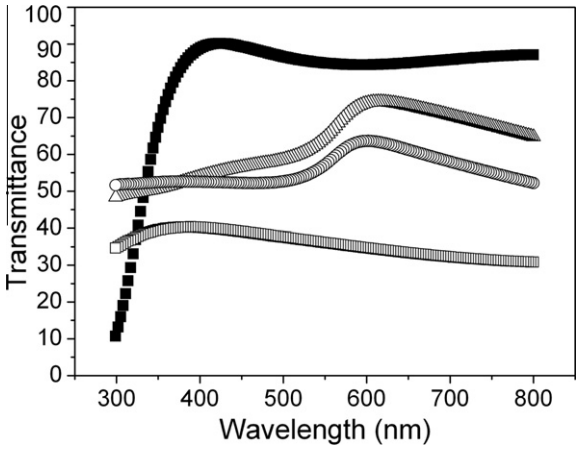

Fig. 1. Transmittance spectra over the full visible wavelength range, for all the different layers studied: ITO (■), Ni (□), Cu (△) or Cu–Ni (○).

Cu layer shows 65% and the Ni layer shows 36% (values given in Table 1). The capping of Cu by 1 nm Ni slightly suppressed the transmittance of the layer, but it is still higher than for Ni. For the sheet resistance, both ITO and Cu layers show a low value around 15–17 Ω/sq while Ni is slightly higher, around 30 Ω/sq. It is also observed that the conductivity behavior of the bilayer UTMF is mainly dominated by the underlying ultrathin Cu layer [12]. Therefore, it can be seen that the Ni capping layer slightly decreases the transparency while not affecting the sheet resistance of the Cu layer. As the sheet resistance is far more critical for device application than the transmittance (it will cause non uniformities in the emission for large area devices), such bilayer UTMF is highly promising as an electrode for optoelectronic devices. It is also well known that the reflectivity of the metallic layer, provided it to be sufficiently high, can be used to enhance the device performance via optical microcavity effect [13,14]. Furthermore, the Cu–Ni bilayer UTMF shows an improvement compared to the Ni UTMF previously studied [6].

The effect of the ozone treatment on the properties of the layer was also investigated and the details are shown in Table 1. Such treatment is a crucial step in the PLEDs fabrication process as it makes the anode material more hydrophilic, allowing for easy spin-coating of the PEDOT-PSS hole transporting layer. The 10 min ozone

Table 1
Values of transmittance, Rs and work function for the four anodes studied, before and after ozone treatment.

	ITO	Ni_8 nm	Cu_8 nm	CuNi_8 nm
Transmittance (%)				
Before ozone treatment	86	36.5	64.1	56.8
After ozone treatment	86	36.8	61.5	58.6
Rs (_/sq)				
Before ozone treatment	16.7	29.6	15.5	15.3
After ozone treatment	16.8	32.4	25.7	16.6
Work function (eV)	5.0	5.1	4.7[a]	5.1
Roughness (nm)	0.46	0.60	0.65	0.55

[a] From literature.

treatment results in an increase of the sheet resistance of 9% for Ni, 65% for Cu, 8.5% for Cu–Ni and has almost no influence at all on the ITO layer. The effect of the ozone treatment on the transmittance is more or less negligible for all the layers studied. Cu layer shows a better transmittance and lower resistivity than Ni but as it can be seen, the effect (by ozone treatment) is quite strong on the layer. While its transmittance is only 2% decreased, its sheet resistance is increased by about 65% after 10 min treatment in ozone. Capping the Cu layer with Ni offers a better stability of the resistivity with ozone exposure, with this time only an increase of 8%. The stability improvement of the Cu layer with a Ni capping is also observed upon thermal treatment of the layers as shown in Fig. 2. The variation of the sheet resistance with thermal treatment reaches high values for temperatures as low as 100 °C for the Cu layer, while for the Cu–Ni bilayer, even up to 220 °C the variation in the sheet resistance is small. Ni also provides a larger work-function, which is beneficial for the anodic injection. Another critical factor for the use of UTMFs as electrodes in devices is the roughness of the layer deposited. It has been shown that the hole injection in PLEDs depends not only on the barrier height of the junction but also on the surface morphology and interfacial chemistry of the anode [15,16], influencing therefore the PLEDs stability and performance [17]. As-deposited UTMFs layers are all very uniform and smooth, with a low root-mean-square (RMS) roughness by contact mode AFM of less than 0.65 nm over a 1 μm^2 area, similar to the RMS roughness of ITO (see Table 1). In one word, the main drawback of the Cu layer for device application, which is its low stability to oxidation and temperature, has been solved by simply using a 1 nm Ni capping layer. Therefore, the Ni capping makes Cu–Ni UTMF very interesting for the OLEDs application as it overcomes the stability issue of the Cu layer and increases the work function, still maintaining good optical and electrical properties.

Fig. 3 compares the current–voltage (I–V) and luminance characteristics of OLEDs with a thin metal anode with respect to those of a typical ITO anode. It can be seen that the lowest performance is obtained for the Ni-based device. Slightly higher voltage threshold, lower current density and lower luminance reflect the poor transmittance and high resistivity that the 8 nm Ni layer

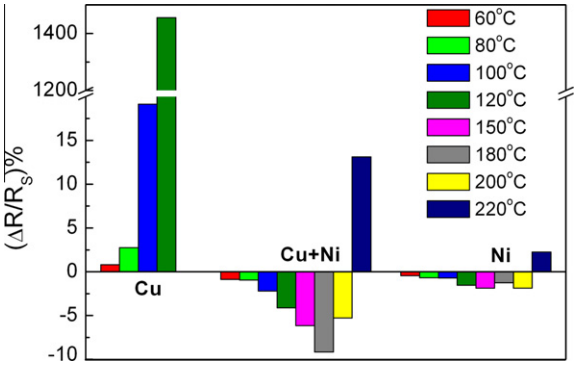

Fig. 2. Stability of the metallic layers upon temperature treatments.

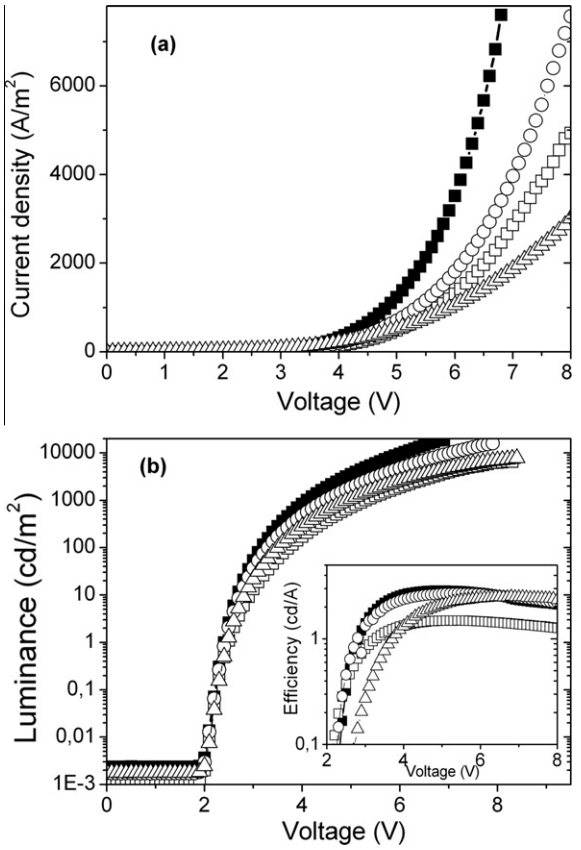

Fig. 3. I/V (a) and L/V (b) curves of SY-based OLEDs with the anode being ITO (■), Ni (□), Cu (△) or Cu–Ni (○).

exhibits. Although the work function of Ni is similar to that of ITO, the current of the Ni-based device is limited by the relatively high electrode's sheet resistance. As a consequence not enough charges enter the device to generate high efficiency as it is the case of the ITO-based device, which, on the contrary, shows a transport-limited behavior (the properties of the SY is the limiting factor here). The Cu-based device behaves very similarly to the Ni-based device, as the driving voltage at a given current density is found to be higher than that of ITO. This difference is due to the sheet resistance of Cu and Ni, which after the ozone treatment stands around 30 Ω/sq compared to 17 Ω/sq for ITO. In the case of Cu, this is evidenced for example by the difference in driving voltage increasing linearly with sheet resistance (i.e., following Ohm's law). The advantage of the Cu-based device lies in the higher transmittance of the Cu layer compared to the Ni layer and therefore it shows a higher luminance level than the Ni-based device. As a result, when looking at the device efficiency, while the Ni-based device shows a lower efficiency compared to the ITO-based device, the Cu-based device shows a similar efficiency as ITO but only at high driving voltages. Finally, the Cu–Ni-based device offers the best performance of the three UTMF anodes studied here. The current density is slightly higher than that of the ITO-based device although the sheet resistance is similar to that of ITO (around 17 Ω/

sq). The luminance level reached is similar to the ITO-based device. All in all, the efficiency of the Cu–Ni-based device is as good as the ITO-based device, as it can be seen in the inset of Fig. 3b.

An important aspect of metal based OLED is the possible presence of cavity effect, which leads to an angular dependence that is different from that of ITO-based devices. Hence, the fact that luminous efficacy is comparable in the normal direction does not necessarily guarantee that it is also in an off-normal direction. Indeed, microcavity OLED can exhibit significantly enhanced emission in the forward direction as well as a much narrower emission spectrum [18,19], making evident that possible microcavity effects of our metal-based devices have to be considered. To this end, we consider the equation of the cavity effect in OLEDs as cited in Ref. [19] to establish that a weak microcavity effect occurs associated to the low reflectivity of the Cu, Cu–Ni and ITO layers, which is about 10% at the wavelength of the emission peak (for Ni, it is about 25%). Using the same equation [19], Helander et al. [7] have shown that weak microcavity effect occurs in their OLEDs when using a thin 15 nm AuOx electrode, due to the low reflectivity of the AuOx layer (around 25%). In our case, our layers have an even lower reflectivity than for the AuOx layer of Helander et al. [7]. Furthermore, the electroluminescence (EL) spectra for all devices have been measured and are shown in Fig. 4. The full width half maximum (FWHM) of the spectrum is the same for ITO-based devices. Only the Ni-based device shows a thinner FWHM, which agrees with the value of its reflectivity – the highest among the three metal electrodes. We can thus conclude that, as in the paper by Helander et al. [7], the microcavity effect and angular dependence of our devices are quite weak.

Finally, it is important to point out again the role of the capping Ni layer which has enabled the Cu–Ni layer to retain good electrical and optical properties after the ozone treatment. This is even more visible when one studies the luminance decay as a function of operating time of the devices (shown in Fig. 5). The lifetime experiments were performed in inert atmosphere and dark condition without encapsulation, at constant voltage. For glass/ITO device, the luminance decay of the device is very slow, not reaching the half value for the 800 min of measurements. Although the luminance of the Cu–Ni anode/glass substrate device dropped initially, its decay is very smooth and reaches 50% for 800 min, at higher current as compared with the driving current for ITO anode/glass substrate. Cu anode/glass substrate devices decayed by about 50% of initial luminance after driving 20 and 25 min, respectively, whereas the glass/Cu–Ni device decayed by about 10% of initial luminance after driving the same amount of time. Actually, the ITO and Cu–Ni-based device show the same flat decay of the luminance (same slope) which really indicates the even performance of the Cu–Ni bilayer and ITO as anodes for OLEDs (Fig. 5).

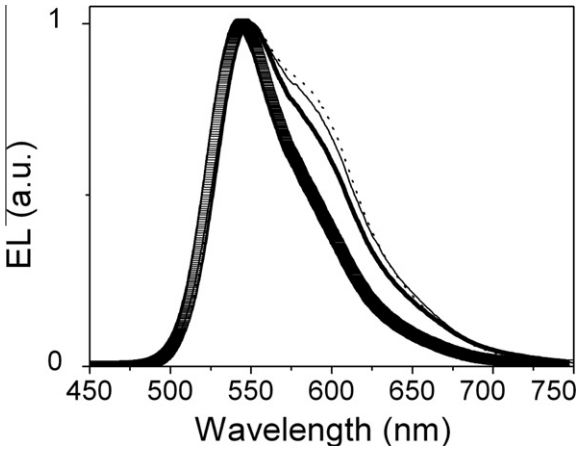

Fig. 4. Electroluminescence spectra of SY-based OLEDs with the anode being ITO (▬), Ni (□), Cu (•••) or Cu–Ni (—).

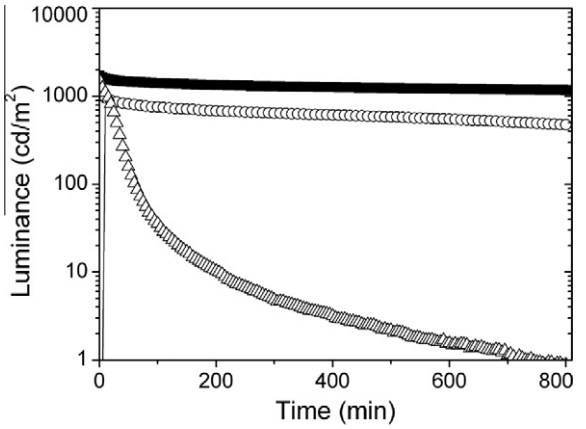

Fig. 5. Lifetime of the SY-based OLEDs with the anode being ITO (■), Cu (△) or Cu–Ni (○).

4. Conclusion

In summary, we have demonstrated the use of Cu–Ni UTMF as anode in high-performance OLEDs. Previous studies have shown the potential of Ni UTMF to replace ITO for OLED applications, due to their ease of fabrication and good optical and electrical qualities. In this work, we focused on Cu UTMF which has better optical and electrical properties than Ni, although showing poor stability. In fact, we showed that a good trade-off between the Ni stability and the Cu excellent optical and electrical properties for UTMF is an ultrathin Cu layer stabilized using a capping Ni layer. Its average visible transparency is as high as 64% and its sheet resistance as low as 15 Ω/sq. The bilayer Cu–Ni UTMFs show excellent stability against temperature and oxidation. When applied to OLEDs, the devices showed high efficiency, as good as ITO-based devices with good operation stability over time. In addition, the benefits of thin films metal electrodes such as easy fabrication, mechanical flexibility [10,11], and the affordability of metal make the proposed multilayer UTMF an attractive alternative to ITO electrodes.

Acknowledgement

This work was carried out with the financial support of the Generalitat de Catalunya ACC1Ó program and the Spanish Ministry of Education and Science through grant TEC 2010-14832 and the Consolider-Ingenio CSD2007-00007.

References

[1] K. Tamano, D.-C. Cho, T. Mori, T. Mizutani, M. Sugiyama, Thin Solid Fims 438 (2003) 182.
[2] C.-W. Chen, P.-Y. Hsieh, H.-H. Chiang, C.-L. Lin, H.-M. Wu, C.-C. Wu, Appl. Phys. Lett. 83 (2003) 5127.
[3] Y.Y. Yuan, S. Han, D. Grozea, Z.H. Lu, Appl. Phys. Lett. 88 (2006) 093503.
[4] S. Han, Y. Yuan, Z.H. Lu, J. Appl. Phys. 100 (2006) 074504.
[5] H. Peng, X. Zhu, J. Sun, Z. Xie, S. Xie, M. Wong, H.-S. Kwok, Appl. Phys. Lett. 87 (2005) 173505.
[6] D. Krautz, S. Cheylan, D.S. Ghosh, V. Pruneri, Nanotechnology 20 (2009) 275204.
[7] M.G. Helander, Z.-B. Wang, M.T. Greiner, Z.-W. Liu, J. Qiu, Z.-H. Lu, Adv. Mater. 21 (2009) 1.
[8] M.-G. Kang, L. Jay Guo, Adv. Mater. 19 (2007) 1391.
[9] D.S. Ghosh, R. Betancur, T.L. Chen, V. Pruneri, J. Martorell, Sol. Energy Mater. Sol. Cells. 95 (2011) 122895.
[10] J. Lewis, S. Grego, B. Chalamala, E. Vick, D. Temple, Appl. Phys. Lett. 85 (2004) 3450.
[11] C.W. Yang, J.W. Park, Surf. Coat. Technol. 204 (2010) 2761.
[12] D.S. Ghosh, T.L. Chen, V. Pruneri, Appl. Phys. Lett. 96 (2010) 091106.
[13] I. Hisao, S. Kiyoshi, I. Eisuke, S. Kazuhiko, Adv. Mater. 11 (1999) 605.
[14] R. Meerheim, R. Nitsche, K. Leo, Appl. Phys. Lett. 93 (2008) 043310.
[15] A. Andersson, N. Johansson, P. Bröms, N. Yu, D. Lupo, W.R. Salaneck, Adv. Mater. 10 (1998) 859.
[16] C.C. Wu, C.I. Wu, J.C. Sturm, A. Kahn, Appl. Phys. Lett. 70 (1997) 1348.
[17] J.S. Kim, M. Granström, R.H. Friend, N. Johansson, W.R. Salaneck, R. Daik, W.J. Feast, F. Cacialli, J. Appl. Phys. 84 (1998) 6859.
[18] R.H. Jordan, A. Dodabalapur, R.E. Slusher, Appl. Phys. Lett. 69 (1996) 1997.
[19] E.F. Shubert, N.E.J. Hunt, M. Micovic, R.J. Malik, D.L. Sivco, A.Y. Cho, G.J. Zydzik, Science 265 (1994) 943.

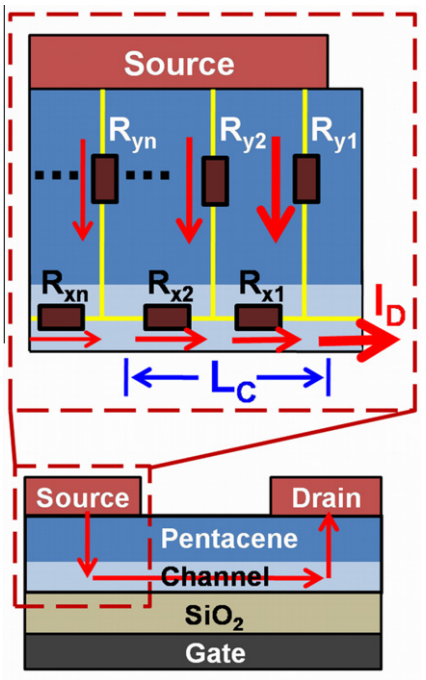

Fig. 1. Schematics of an equivalent circuit at source contact in a staggered OTFT, where charge accumulation layer is shown at vicinity above dielectric layer. Current crowding behavior and effective contact length are illustrated.

distribution in the contact region of OTFTs is not spatially uniform, and thus R_C is the total resistance of an equivalent circuit which can simulate the current flow through the contact region. Fig. 1 shows the equivalent circuit for the crowding current model in a staggered OTFT (top contact with bottom gate), where R_x and R_y are the local accumulation layer resistance in the horizontal direction and local bulk resistance in the vertical direction, respectively. The deduced expression of R_C has the same form as R_{ch}, i.e. [10,12]

$$R_C = \frac{L_C}{W\mu_{FE}C_i(V_{GS} - V_T)} \tag{2}$$

where L_C is the effective contact length referring to the equivalent extended L due to the existence of R_C. We measured ΔR_C under bias stress condition, and observed a continuous increase of both V_T and L_C with t. The observations indicate that the bias stress induced R_C instability stems from the time-dependent charge trapping, which occurs both in the charge accumulation layer and in the organic bulk in the contact region. The systematical comparison between the gold (Au) and copper (Cu) contacts suggests the charge trap distribution in the contact region having a great influence on the R_C instability.

2. Experimental

The pentacene-based OTFTs were fabricated on the heavily doped silicon (Si) substrates with 200-nm-thick thermal oxide (SiO_2) layers (University Wafer). After

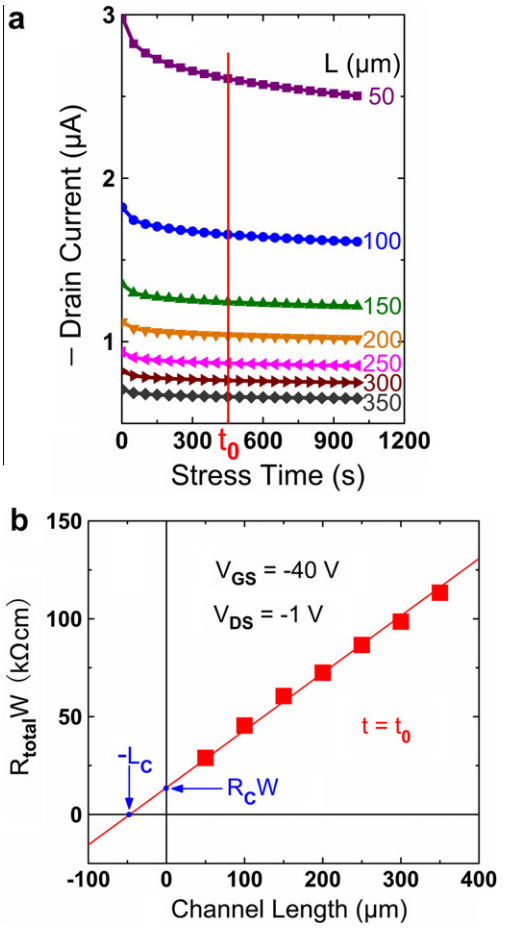

Fig. 2. (a) Drain current vs stress time in a set of pentacene-based OTFTs (Au contact) with varied channel lengths. (b) Transfer line method plot (normalized device total resistance vs channel length) of a set of pentacene-based OTFTs (Au contact) at a particular time point marked in (a), by which contact resistance and effective contact length can be precisely extracted. All TLM plots at different time points show good linearity, indicating that there is no channel length dependence of the threshold voltage shift.

standard cleaning, the substrates were precoated with a self-assembling monolayer of β-phenethyltrichlorosilane (TCI, immersed in β-phenethyltrichlorosilane solution for 6 h in a glove box). The pentacene (TCI, purified with temperature gradient sublimation) films with 40 nm thickness were subsequently deposited in high vacuum about 5×10^{-5} Pa, where the deposition rate and substrate temperature were kept at about 0.1 Å/s and 70 °C, respectively. Eventually, a set of OTFTs, having an identical W = 750 μm and varied L = 50–350 μm with 50 μm interval [8], were defined by depositing Au or Cu top electrodes (electrode length 100 μm, thermal evaporation through a shadow mask).

The bias stress measurements were carried out at room temperature in a high vacuum (about 1×10^{-4} Pa) probe station. After a quick transfer characteristics scan at t = 0 s, I_D at ON state (V_{DS} = −1 V, V_{GS} = −40 V) was continuously measured for 1000 s, followed by another quick transfer characteristics scan at t = 1000 s. As an example, the initial

and final transfer characteristics of OTFTs with Au or Cu contacts are shown in the inset in Fig. 4. The set of OTFTs with different L were measured one by one, taking a recovery time of 2 h at $V_{GS} = V_{DS} = 0$ V after each bias stress measurement. Fig. 2a shows the I_D change in the OTFTs with different L, where the transfer line method (TLM) [8] can be utilized to extract R_C and L_C at each t. For example, a plot of W-normalized total resistance (R_{total}) vs L obtained from Fig. 2a at any time point t_0 is illustrated in Fig. 2b, where W-normalized R_C and minus L_C are the y-intercept [8] and x-intercept [10] of the linear fit, respectively. Accordingly, ΔR_C with t can be experimentally recorded and analyzed. In addition, the slope of the linear fit in Fig. 2b is determined by μ_{FE} and V_T, and thus ΔV_T with t can be derived using constant μ_{FE}.

3. Results and discussion

Fig. 3 demonstrates that R_C of the Au/pentacene contact is larger than that of the Cu/pentacene contact, and in both the cases R_C is continuously increasing with t. These device behaviors are in good agreement with the reported ones [8,13], indicating R_C is not a constant parameter under bias stress condition as expressed in Eq. (1). As μ_{FE} is approximately unchanged (about 0.6 cm^2/Vs, estimated from the initial and final transfer characteristics of the long-channel OTFTs) after the bias stress measurements, the R_C increase with t may arise from an increase of V_T, L_C, or both based on Eq. (2). The t dependence of V_T and L_C can be separately measured by the TLM discussed above, and the results are discussed in the following.

In staggered OTFTs at ON state, as illustrated in Fig. 1, the charge accumulation layer is formed close to the organic/dielectric interface not only in the channel region but also in the contact region. Therefore, ΔV_T can lead to both the R_{ch} and R_C changes. Fig. 4 shows that V_T (calculated from R_{ch} using constant μ_{FE}, note that the apparent V_T extraction directly from the extrapolation of the transfer characteristics may have significant error in the case of large R_C [14]) is increasing with t as commonly observed in OTFTs [4–8], and from Eq. (2) this V_T increase contributes to the R_C increase in Fig. 3. There are two major understandings of bias stress induced ΔV_T in OTFTs (excluding the OTFTs using polarizable dielectrics): (1) Increasing charge trap sites resulting from defect generation in the channel, analogous to that in hydrogenated amorphous-Si TFTs [15]; (2) time-dependent charge trapping into a distribution of trap states in the channel [7,8]. Both the cases involve a decrease of mobile carriers with t, and the latter is more reasonable as the bias stress effect in OTFTs is to a large extent reversible corresponding to the charge trapping and release processes.

On the other hand, L_C (obtained directly from the TLM plot) is increasing with t as demonstrated in Fig. 5, and from Eq. (2) the L_C increase also contributes to the R_C increase in Fig. 3. As schematically depicted in Fig. 1, the magnitude of L_C is set by the balance of the vertical space charge limited current through the pentacene bulk (R_y) and the horizontal current through the charge accumulation layer (R_x) in the contact region [10,12]. In fact, the local current density is larger at the position closer to the contact edge next to the conducting channel, and L_C can

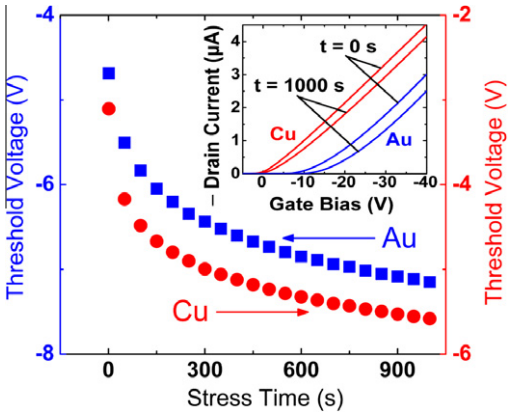

Fig. 4. Threshold voltage vs stress time of pentacene-based OTFTs with Au or Cu contacts, data calculated from experimentally derived channel resistance at different stress time. The inset shows initial and final transfer characteristics at $V_{DS} = -1$ V of OTFTs with 50 μm channel length.

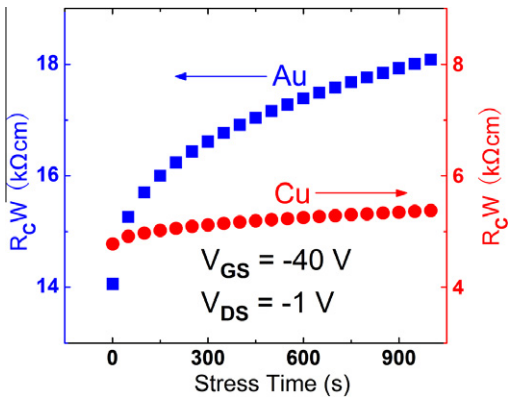

Fig. 3. Normalized contact resistance vs stress time of pentacene-based OTFTs with Au or Cu contacts, data obtained from transfer line method plots at different stress time.

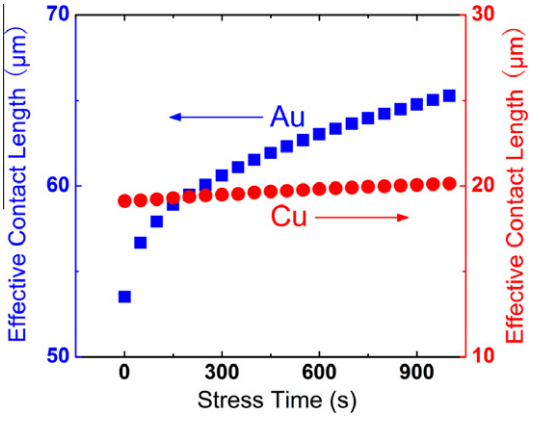

Fig. 5. Effective contact length vs stress time of pentacene-based OTFTs with Au or Cu contacts, data obtained from transfer line method plots at different stress time.

be regarded as an effective length over which the local current density is too small to contribute to the carrier injection. L_C is long when the conductivity of the charge accumulation layer is high and the bulk conductivity is relatively low, and vice versa. In the present case, the conductivity of the charge accumulation layer is decreasing with t as a result of the V_T increase demonstrated in Fig. 4, and thus L_C should be decreasing if the bulk conductivity is either increasing or unchanging with t. However, the experimental results in Fig. 5 show an opposite feature of L_C, indicating that the bulk conductivity is decreasing at the same time. Our previous works suggest that the contact region in OTFTs is a trap-rich low-mobility region, possibly arising from the metal atom diffusion and/or from the pentacene grain boundaries [13,14]. We therefore attribute the bulk conductivity decrease with t to the time-dependent charge trapping in the pentacene bulk, and the effect of this bulk trapping is stronger than that of the charge trapping in the accumulation layer. As a consequence, larger contact area is involved in the carrier injection and L_C is increasing with t. It should be noted that practically maximum L_C is the electrode length, thus Eq. (2) is no longer applicable and L_C has no more effect on ΔR_C when TLM-derived L_C exceeds the electrode length. In the present case, L_C is in the order of several tens μm as shown in Fig. 5, which is shorter than typical electrode length in OTFTs. For miniaturized devices, however, it may become an issue.

In order to further understand the R_C instability, Figs. 3–5 illustrate a comparison between the Au and Cu contacts. It is clear that the Au contact is much more unstable mainly owing to its larger L_C increase shown in Fig. 5, while ΔV_T for the both contacts are similar shown in Fig. 4. The Meyer–Neldel analysis on R_C reveals the Au contact having a wide distribution of trap states [13], described by a high characteristic temperature T_C which reflects the energy width of the trap distribution. In other words, the Au contact contains a high density of deep trap states, which is expected to enhance the charge trapping in the pentacene bulk and consequently result in a large L_C increase. In contrast, the Cu contact has a relatively narrow trap distribution [13] corresponding to a low density of deep trap states, so that the Cu contact appears more stable. Therefore, the lower R_C stability of the Au contact compared with the Cu one can be ascribed to the stronger charge trapping effect in the pentacene bulk. This consideration is consistent with the current crowding model [10], which predicts $R_C \sim T_C/T$.

The above findings indicate that both the R_{ch} and R_C instability in OTFTs may originate from a same microscopic mechanism, i.e. the time-dependent deep charge trapping. It is reasonable to consider that the deep trap states in organic thin films are spatially concentrated around particular sites, such as the grain boundaries and chemical impurities. The filling of these deep trap states can take time, e.g., the Coulomb repulsion of the pre-trapped charges build an energy barrier which impedes the further charge trapping [8]. Thus, reducing the density of the deep trap states by optimized film growth and effective interface modification is the approach to improve the operation stability of OTFTs.

4. Conclusion

The bias stress measurements combined with TLM are utilized to probe the R_C instability in pentacene-based OTFTs. R_C was observed to be increasing with t, resulting from (1) the V_T increase in the charge accumulation layer, and from (2) the L_C increase. The origin of this bias stress induced R_C instability is attributed to the charge trapping not only in the charge accumulation layer but also in the pentacene bulk. The R_C instability is strongly dependent on the extrinsic factors such as the type of electrode materials, and thus it can be suppressed by the optimization of device fabrication techniques. This work provides the hints to understand the underlying mechanism of the bias stress effect, which is considered to be correlated with the time-dependent charge trapping in OTFTs.

Acknowledgments

This work has been partially supported by the National Natural Science Foundation of China (Grant Nos. 61006015, 51033007), the National Basic Research Development Program of China (973 Program, Grant Nos. 2010CB934500, 2011CB808400), and the Natural Science Foundation of Jiangsu Province (Grant No. BK2010220).

References

[1] D. Braga, G. Horowitz, Adv. Mater. 21 (2009) 1473.
[2] H. Klauk, U. Zschieschang, J. Pflaum, M. Halik, Nature 445 (2007) 745.
[3] M.E. Roberts, A.N. Sokolov, Z.N. Bao, J. Mater. Chem. 19 (2009) 3351.
[4] H. Sirringhaus, Adv. Mater. 21 (2009) 3859.
[5] D. Knipp, R.A. Street, A.R. Völkel, J. Ho, J. Appl. Phys. 93 (2003) 347.
[6] H.L. Gomes, P. Stallinga, F. Dinelli, M. Murgia, F. Biscarini, D.M. de Leeuw, T. Muck, J. Geurts, L.W. Molenkamp, V. Wagner, Appl. Phys. Lett. 84 (2004) 3184.
[7] S.G.J. Mathijssen, M. Cölle, H. Gomes, E.C.P. Smits, B. de Boer, I. McCulloch, P.A. Bobbert, D.M. de Leeuw, Adv. Mater. 19 (2007) 2785.
[8] S.D. Wang, T. Minari, T. Miyadera, Y. Aoyagi, K. Tsukagoshi, Appl. Phys. Lett. 92 (2008) 063305.
[9] T. Richards, H. Sirringhaus, Appl. Phys. Lett. 92 (2008) 023512.
[10] S.D. Wang, Y. Yan, K. Tsukagoshi, Appl. Phys. Lett. 97 (2010) 063307.
[11] S.D. Wang, Y. Yan, K. Tsukagoshi, IEEE Electron Device Lett. 31 (2010) 509.
[12] T.J. Richards, H. Sirringhaus, J. Appl. Phys. 102 (2007) 094510.
[13] S.D. Wang, T. Minari, T. Miyadera, K. Tsukagoshi, Y. Aoyagi, Appl. Phys. Lett. 91 (2007) 203508.
[14] S.D. Wang, T. Miyadera, T. Minari, Y. Aoyagi, K. Tsukagoshi, Appl. Phys. Lett. 93 (2008) 043311.
[15] M.J. Powell, S.C. Deane, R.B. Wehrpohn, Phys. Rev. B 66 (2002) 155212.

plasma treatment [22,23] is required to tune the surface of the active layer from hydrophobic to hydrophilic before an aqueous PEDOT:PSS can be deposited. In the literature, an amphiphilic film [18], a layer of BPhen:Li [19] deposited in vacuum, and low-conductivity PEDOT:PSS formulations [20,21] have been proposed as an interlayer. Recently, we reported on a formulation of PEDOT:PSS CPP 105D (H.C. Starck CLEVIOS) (hereafter referred to as CPP-PEDOT) as the interlayer for depositing subsequently PEDOT:PSS PH-1000 (H.C. Starck CLEVIOS) (hereafter referred to as PH-1000) as the top electrode in semitransparent solar cells [24]. The CPP-PEDOT formulation contains surfactants and additives that result in good wetting properties on top of P3HT:$PC_{60}BM$ layers [25]. However, the conductivity of CPP-PEDOT is significantly lower than that of PH-1000, which explains the need for CPP-PEDOT/PH-1000 b*i*-layers. The need for such interlayers or bi-layers of different formulations of PEDOT:PSS increases the complexity of the device fabrication.

In this work, we report on semitransparent inverted solar cells with a top electrode that is comprised of a single layer of PEDOT:PSS that combines good wetting properties and high conductivity. The single PEDOT:PSS layer is a blend consisting of a mixture of PH-1000 and CPP-PEDOT. The new PEDOT:PSS blend (hereafter referred to as CPP-PEDOT:PH-1000) showed a conductivity as high as 420 S cm^{-1} and simultaneously good wetting on the P3HT:$PC_{60}BM$ layer. The semitransparent solar cells with an inverted geometry of glass/ITO/ZnO/P3HT:$PC_{60}BM$/CPP-PEDOT:PH-1000 (1:3, volume ratio) exhibited a short-circuit current (J_{SC}) of 7.2 mA cm^{-2}, an open-circuit voltage (V_{OC}) of 0.55 V, a fill factor (FF) of 0.58, leading to a power conversion efficiency (PCE) of 2.4% estimated for 100 mW cm^{-2} AM 1.5G illumination. The devices showed transmittance of 10–70% in the wavelength range from 400 to 800 nm (Fig. 1).

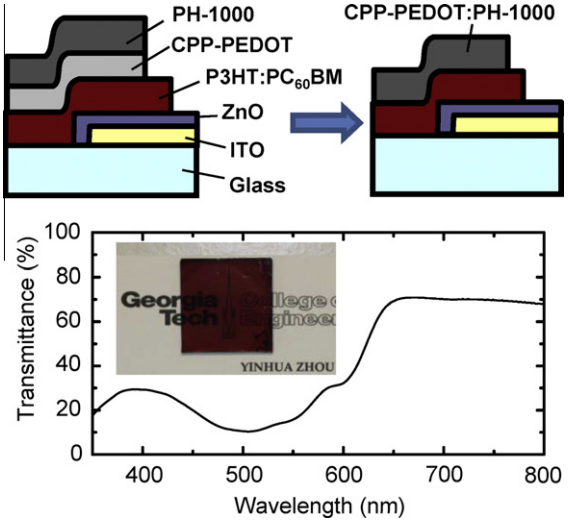

Fig. 1. (Top) Structure of a device using a bi-layer CPP-PEDOT/PH-1000 as the top electrode (left) and a simplified device using a CPP-PEDOT:PH-1000 blend as the top electrode (right). (Bottom) Transmittance spectrum of a semitransparent device using a CPP-PEDOT:PH-1000 (1:3, volume ratio) as the top electrode. The inset is a photograph of a semitransparent device with a CPP-PEDOT:PH-1000 (1:3, volume ratio) as the top electrode on a card to illustrate its level of transparency.

2. Experimental

ITO-coated glass (Colorado Concept Coatings LLC, Loveland, CO) with a sheet resistance of 15 Ω/sq was used as the substrates for the solar cells. The substrates were patterned using a kapton tape and etched by acid vapor (HNO_3: HCl, 1:3 by volume) at 60 °C for 5 min. The substrates were cleaned in an ultrasonic bath of detergent and water, rinsed with deionized water, and then cleaned in sequential ultrasonic baths of deionized water, acetone, and isopropanol. Each ultrasonic bath lasted for 20 min. Nitrogen was used to dry the substrates after each of the last three baths.

The patterned ITO substrates were transferred to an ALD system (Savannah 100, Cambridge NanoTech, Cambridge, MA) for ZnO deposition. ZnO films (200 cycles) were deposited on cleaned ITO substrates with pulses of H_2O for 15 ms and diethylzinc for 15 ms at 200 °C. The thickness of ZnO was 25 nm, measured using a profilometer (Dektak 6 M Stylus, Veeco, Plainview, NY). ZnO was patterned with a kapton tape around the ITO area and dipped into the afore mentioned dilute acid solution for 2 s at room temperature. The ITO/ZnO substrates were cleaned in sequential ultrasonic baths of acetone and isopropanol. Each ultrasonic bath lasted for 10 min and was followed by nitrogen drying. The active layer of P3HT (4002-E, Rieke Metals, Lincoln, NE): $PC_{60}BM$ (Nano-C, Westwood, MA) (1:0.7, by weight) was spin-coated on each substrate from a 34 mg/ml chlorobenzene solution and annealed at 160 °C for 10 min on a hot plate in a N_2-filled glove box. The thickness of the active layer was 200 nm.

5% dimethyl sulfoxide (DMSO) was added into PH-1000 solution and stirred overnight at 300 rpm at room temperature to increase its conductivity. Then, the PH-1000 was mixed with CPP-PEDOT in the volume ratios of 2:1, 1:1, 1:2, and 1:3 (CPP-PEDOT:PH-1000). Contact angle of these blend solutions on annealed P3HT:$PC_{60}BM$ films, was measured using a contact angle analyzer (SEO Phoenix 300, LA, CA). To evaluate the conductivity, the CPP-PEDOT:PH-1000 solutions were spin-coated onto cleaned glass substrates at a speed of 1000 rpm for 30 s and then annealed at 120 °C for 30 min in ambient air. Thicknesses of the films varied from 140 to 200 nm. The conductivities of the PH-1000 film, CPP-PEDOT film, and the CPP-PEDOT:PH-1000 films were measured using the transmission line method (TLM) with 200 nm thick Cu electrodes thermally deposited on the films.

Fig. 1, illustrates the geometries of the two different types of semitransparent solar cells considered in this study. For the devices having a bi-layer of CPP-PEDOT/PH-1000 as the top electrode (left panel in Fig. 1), a 90 nm thick layer of CPP-PEDOT was first spin-coated on the active layer at a speed of 5000 rpm for 60 s. The CPP-PEDOT layer was then patterned by contacting a polydimethylsiloxane (PDMS) layer to the unwanted area and peeling off the PDMS and CPP-PEDOT together. The samples were next annealed at 105 °C for 10 min in the N_2-filled glove box.

Then, PH-1000 (160 nm) was spin-coated on the patterned CPP-PEDOT area in ambient air. Samples were annealed at 105 °C for 10 min in the N_2-filled glove box.

For the devices with a single-layer of a CPP-PEDOT:PH-1000 blend (right panel in Fig. 1), mixtures of CPP-PEDOT:PH-1000 (1:1 and 1:3, volume ratio) were spin-coated on the active layer at a speed of 1000 rpm for 30 s in ambient air. The CPP-PEDOT:PH-1000 layers were patterned with PDMS as described above. Next, the samples were annealed at 105 °C for 10 min in the glove box. The lower panel in Fig. 1 shows the transmittance and the inset is a picture of an un-patterned solar cell with a CPP-PEDOT:PH-1000 (1:3, volume ratio) layer as the top electrode.

Before testing the device performance, Ag paste was used, outside the active area, to improve the electrical contact to the CPP-PEDOT:PH-1000 layer and to the ITO/ZnO electrodes. In order to have an accurate device area during illumination, an aperture with a well defined area of 6 mm^2 was used as a shadow mask in-front of each device. Light went through the ITO/ZnO side during the testing. Current–voltage (I–V) characteristics were measured inside a N_2-filled glove box by using a source meter (Keithley Instruments 2400, Cleveland, OH) controlled by a LabVIEW program. To test the solar cell properties under illumination, an Oriel lamp with an intensity of 100 mW cm^{-2} was used as the light source. A monochromator coupled to a 175 W Xenon lamp (ASB-XE-175EX, CVI Spectral Products, Putnam, CT) and a calibrated photodiode (S2386-44 K, Hamamatsu) were used to measure the external quantum efficiency (EQE).

3. Results and discussion

As shown in Fig. 2, PH-1000 films have a high conductivity of 560 ± 50 S cm^{-1}, but PH-1000 solutions show a high contact angle of 93 ± 4° on the P3HT:PC_{60}BM active layer. The high contact angle makes it difficult to form a uniform PH-1000 film on top of the active layer. In contrast, CPP-PEDOT solutions have a low contact angle of 31 ± 2° but films show a significantly lower conductivity of 32 ± 5 S cm^{-1} compared with PH-1000. To combine the advantages of the two PEDOT:PSS formulations, we prepared blend solutions with different volume ratios. Fig. 2 shows that the conductivity of the blend films is linearly dependent on the concentration of PH-1000, while the contact angle of the blend solutions on P3HT:PC_{60}BM remains almost unchanged for all the blend solutions, with a value that is similar to that of CPP-PEDOT solution. The combination of a high conductivity and a low contact angle allowed these blends to be used as the top electrode by solution-processing techniques, such as spin-coating.

Fig. 3 shows the I–V characteristics of devices with different top electrodes: bi-layers of CPP-PEDOT/PH-1000, CPP-PEDOT:PH1000 blends (1:1, volume ratio), and CPP-PEDOT:PH-1000 blends (1:3, volume ratio). Here, we use the current and not the current density because the photocurrent is generated only in the area defined by the aperture used during testing of the device under illumination. In contrast, the dark current flows through the whole device area which is defined by the intersection of ITO/ZnO and the top PEDOT:PSS electrode. To correct for the spectral mismatch between the lamp and AM 1.5G illumination, the values of J_{SC} under 100 mW cm^{-2} AM 1.5G illumination were estimated by convoluting the EQE with the AM 1.5G spectra [26]. Device performances with corrected values of J_{SC} and PCE are summarized in Table 1.

The devices with the bi-layer CPP-PEDOT/PH-1000 as the top electrode show a V_{OC} of 0.54 ± 0.01 V, a J_{SC} of 7.3 ± 0.4 mA cm^{-2}, a FF of 0.59 ± 0.02, and a PCE of 2.3 ± 0.1%, averaged over four devices, estimated for 100 mW cm^{-2} AM 1.5G illumination. In comparison, devices with a single layer of the CPP-PEDOT:PH-1000 (1:1, volume ratio) blend show a V_{OC} of 0.54 ± 0.01 V, a J_{SC} of 7.4 ± 0.6 mA cm^{-2}, a FF of 0.52 ± 0.01, and a PCE of 2.0 ± 0.2% averaged over four devices (Table 1). Comparing to the devices with the bi-layer CPP-PEDOT/PH1000 top electrode, the devices with CPP-PEDOT:PH1000 (1:1,

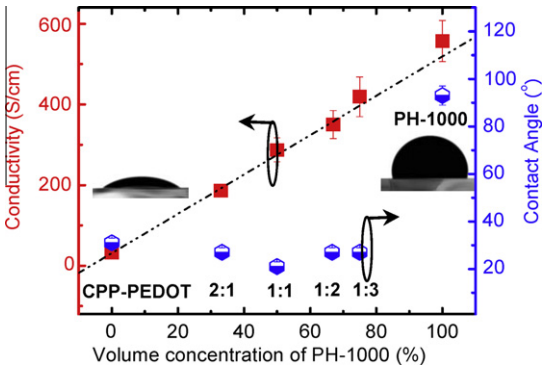

Fig. 2. Conductivity of CPP-PEDOT:PH-1000 blend films and contact angle of CPP-PEDOT:PH-1000 blend solutions on top of P3HT:PCBM layer as a function of the concentration of PH-1000 by volume. The dash-dot line is linear fit of the conductivity as a function of the concentration of PH-1000 by volume. The insets are pictures of the drops of a CPP-PEDOT solution and a PH-1000 solution on top of P3HT:PC_{60}BM layers.

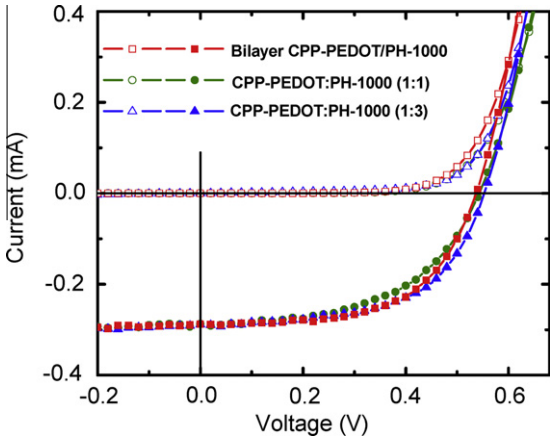

Fig. 3. I–V characteristics of devices with bi-layer CPP-PEDOT/PH-1000 (square), CPP-PEDOT:PH-1000 blend (1:1, volume ratio) (circle) and PEDOT:PH-1000 blend (1:3, volume ratio) (triangle) in the dark (open symbol) and under illumination of 100 mW cm^{-2} (filled symbol) before spectral mismatch correction. Aperture with an area of 6 mm^2 was used during the measurement.

Table 1
Photovoltaic performance of devices with different top electrodes. The data represent average values and standard deviations calculated over four devices. The values of J_{SC} were estimated by convoluting the EQE with the AM 1.5G spectra.

Device with top electrode	V_{OC} (V)	J_{SC} (mA cm^{-2})	FF	PCE (%)
CPP-PEDOT/PH-1000	0.54 ± 0.01	7.3 ± 0.4	0.59 ± 0.02	2.3 ± 0.1
CPP-PEDOT:PH-1000 (1:1)	0.54 ± 0.01	7.4 ± 0.6	0.52 ± 0.01	2.0 ± 0.2
CPP-PEDOT:PH-1000 (1:3)	0.55 ± 0.01	7.4 ± 0.3	0.58 ± 0.01	2.4 ± 0.2

volume ratio) have a lower FF. The lower FF is attributed to the higher series resistance, mainly due to the lower conductivity of CPP-PEDOT:PH-1000 (1:1, volume ratio) (186 ± 9 S cm^{-1}) than that of PH-1000 (560 ± 50 S cm^{-1}). With a blend of CPP-PEDOT:PH-1000 with a larger PH-1000 volume ratio (1:3), the higher conductivity (420 ± 5 S cm^{-1}) yielded devices with a FF of 0.58 ± 0.01, similar to that of devices with the bi-layer CPP-PEDOT/PH-1000. The PCE of the devices reached an average value of 2.4 ± 0.2%, comparable to that of devices with the bi-layer CPP-PEDOT/PH-1000 as the top electrode. For comparison, devices with a conventional structure of ITO/PEDOT:PSS AI 4083/P3HT:PC_{60}BM/Al were also fabricated [24]. These reference devices with a conventional architecture show a V_{OC} of 0.62 ± 0.01 V, a J_{SC} of 8.5 ± 0.4 mA cm^{-2}, a FF of 0.59 ± 0.01, and a PCE of 3.1 ± 0.2% (averaged over five devices). The PCE of the semitransparent solar cells with either a bi-layer CPP-PEDOT/PH-1000 top electrode, or a single layer of the blend CPP-PEDOT:PH-1000 (1:3, volume ratio) is lower than devices with a conventional structure because of the lower absorption in the active layer because of the absence of Al reflector [24]. We also note that from the CPP-PEDOT:PH-1000 blends studied, a volume ratio of 1:3 yields solar cells that are statistically almost identical to the solar cells using a bi-layer CPP-PEDOT/PH-1000. Hence, while it may be possible that blends with a higher ratio of PH-1000 could have marginally higher conductivity than the 1:3 blend, no major differences in terms of their performance in solar cell devices are expected.

We investigated the effect of changing the illuminated area through apertures, A, on the V_{OC}, FF, J_{SC} and PCE of a device using a CPP-PEDOT:PH1000 blend (1:3, by volume) as the top electrode. Fig. 4 shows the dependence of these parameters on the area illuminated through the apertures. Apertures with areas of 9.2, 4.6, 2.3, and 1.2 mm^2 were used. The maximum area considered was 22 mm^2, which corresponds to the device area, defined by the intersection of ITO/ZnO and the top PEDOT:PSS electrode. As shown in Fig. 4 the main effect of reducing A is to increase FF, because of the reduced series resistance $R_S A$, and to decrease the V_{OC}, which is a logarithmic function of area A. The logarithmic dependence of the V_{OC} on A, can be explained by considering that,

$$V_{OC} = n\frac{KT}{e}\ln\left\{1+\frac{I_{SC}}{I_0}\right\} \quad (1)$$

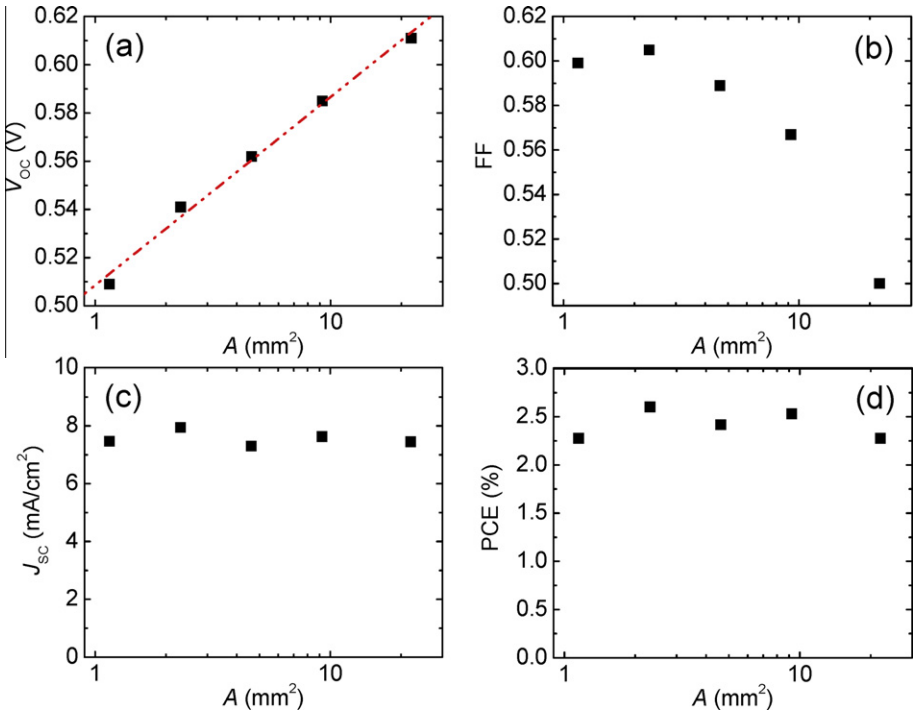

Fig. 4. The effect of the area illuminated through the apertures, A, on (a) V_{OC}, (b) FF, (c) J_{SC} and (d) PCE of a device using a CPP-PEDOT:PH1000 blend (1:3, by volume) as the top electrode. The dash-dot line in (a) is a fit of V_{OC} showing a logarithmic dependence on area A.

where n is the diode ideality factor, k is Boltzmann's constant, T is the temperature, I_0 is reverse saturation current and I_{SC} is the short circuit current, equal to $J_{SC}A$. Since $I_{SC}/I_0 \gg 1$, $V_{OC} \propto \ln(J_{SC}A)$, where J_{SC} remains constant, V_{OC} would be expected to vary logarithmically with A. However, this drop of V_{OC} is compensated with the increased FF to yield a PCE which, within the experimental error, is constant with respect to the illuminated area.

4. Conclusions

In summary, we demonstrated semitransparent organic solar cells using a single-layer of a PEDOT:PSS blend as the top electrode. Semitransparent metal-free solar cells showed an average power conversion efficiency of 2.4% estimated for 100 mW cm^{-2} AM 1.5G illumination. The single-layer PEDOT:PSS blend was prepared on top of P3HT:$PC_{60}BM$ by a one-step spin-coating process without any interlayers, which alleviates the need of vacuum deposition of a top electrode. The one-step solution-processed top electrode could be potentially applied to the fabrication of large-area devices using low-cost solution-based fabrication techniques such as by inkjet-printing or roll-to-roll processing. The higher sheet resistance of PEDOT:PSS electrodes compared with metal electrodes can be compensated by integrating these device geometries with metal grid electrodes [27,28]. These semitransparent solar cells are promising candidates for low-cost and large-area see-through power-generating windows applications.

Acknowledgements

This material is based upon work supported in part by the Center for Interface Science: Solar Electric Materials, an Energy Frontier Research Center funded by the U.S. Department of Energy, Office of Science, Office of Basic Energy Sciences under Award Number DE-SC0001084 (Y.Z., H.C, B.K.), by AFOSR (BIONIC Center grant No. FA9550-09-1-0162) (Y.Z., H.C., C.F.-H.), by the Office of Naval Research (H.C., B.K.), by the STC Program of the National Science Foundation under Agreement Number DMR-0120967 (S.C., C.F.-H., B.K.), and in part by AFOSR (grant No. FA9550-09-1-0418) (C.F.-H., H.C.).

References

[1] H.Y. Chen, J.H. Hou, S.Q. Zhang, Y.Y. Liang, G.W. Yang, Y. Yang, L.P. Yu, Y. Wu, G. Li, Nat. Photonics 3 (2009) 649.
[2] C. Piliego, T.W. Holcombe, J.D. Douglas, C.H. Woo, P.M. Beaujuge, J.M.J. Frechet, J. Am. Chem. Soc. 132 (2010) 7959.
[3] S.H. Park, A. Roy, S. Beaupre, S. Cho, N. Coates, J.S. Moon, D. Moses, M. Leclerc, K. Lee, A.J. Heeger, Nat. Photonics 3 (2009) 297.
[4] G.J. Zhao, Y.J. He, Y.F. Li, Adv. Mater. 22 (2010) 4355.
[5] Y.-J. Cheng, C.-H. Hsieh, Y. He, C.-S. Hsu, Y. Li, J. Am. Chem. Soc. 132 (2010) 17381.
[6] B. Kippelen, J.L. Bredas, Energy Environ. Sci. 2 (2009) 251.
[7] C.J. Brabec, S. Gowrisanker, J.J.M. Halls, D. Laird, S. Jia, S.P. Williams, Adv. Mater. 22 (2010) 3839.
[8] M. Helgesen, R. Sondergaard, F.C. Krebs, J. Mater. Chem. 20 (2010) 36.
[9] F.C. Krebs, T. Tromholt, M. Jorgensen, Nanoscale 2 (2010) 873.
[10] J. Meiss, K. Leo, M.K. Riede, C. Uhrich, W.M. Gnehr, S. Sonntag, M. Pfeiffer, Appl. Phys. Lett. 95 (2009) 213306.
[11] G.M. Ng, E.L. Kietzke, T. Kietzke, L.W. Tan, P.K. Liew, F.R. Zhu, Appl. Phys. Lett. 90 (2007) 103505.
[12] R. Koeppe, D. Hoeglinger, P.A. Troshin, R.N. Lyubovskaya, V.F. Razumov, N.S. Sariciftci, Chemsuschem 2 (2009) 309.
[13] R.F. Bailey-Salzman, B.P. Rand, S.R. Forrest, Appl. Phys. Lett. 88 (2006) 233502.
[14] H. Schmidt, H. Flugge, T. Winkler, T. Bulow, T. Riedl, W. Kowalsky, Appl. Phys. Lett. 94 (2009) 243302.
[15] J. Hanisch, E. Ahlswede, M. Powalla, Eur. Phys. J. Appl. Phys 37 (2007) 261.
[16] J.Y. Lee, S.T. Connor, Y. Cui, P. Peumans, Nano Lett. 10 (2010) 1276.
[17] J.S. Huang, G. Li, Y. Yang, Adv. Mater. 20 (2008) 415.
[18] Q.F. Dong, Y.H. Zhou, J.N. Pei, Z.Y. Liu, L.Y. W, S.Y. Yao, J.B. Zhang, W.J. Tian, Org. Electron. 11 (2010) 1327.
[19] F. Nickel, A. Puetz, M. Reinhard, H. Do, C. Kayser, A. Colsmann, U. Lemmer, Org. Electron. 11 (2010) 535.
[20] S.K. Hau, H.L. Yip, J.Y. Zou, A.K.Y. Jen, Org. Electron. 10 (2009) 1401.
[21] Y.H. Zhou, F.H. Li, S. Barrau, W.J. Tian, O. Inganas, F.L. Zhang, Sol. Energy Mater. Sol. Cells 93 (2009) 497.
[22] D. Baierl, B. Fabel, P. Gabos, L. Pancheri, P. Lugli, G. Scarpa, Org. Electron. 11 (2010) 1199.
[23] C. Girotto, B.P. Rand, S. Steudel, J. Genoe, P. Heremans, Org. Electron. 10 (2009) 735.
[24] Y.H. Zhou, H. Cheun, S. Choi, W.J. Potscavage Jr., C. Fuentes-Hernandez, B. Kippelen, Appl. Phys. Lett. 97 (2010) 153304.
[25] http://www.clevios.com/pages/985/coating_guide_clevios_p_formulations.pdf.
[26] Y.H. Zhou, H. Cheun, W.J. Potscavage Jr., C. Fuentes-Hernandez, S.J. Kim, B. Kippelen, J. Mater. Chem. 20 (2010) 6189.
[27] S. Choi, W.J. Potscavage, B. Kippelen, Opt. Express 18 (2010) A458.
[28] S. Choi, W.J. Potscavage Jr., B. Kippelen, J. Appl. Phys. 106 (2009) 054507.

characteristics I_D–V_{DS} of a transistor, (b) a proper model for the current–voltage characteristic in the region close to the contact, I_D–V_C, and its incorporation in the output characteristics model, and (c) an extraction method of the I_D–V_C curves at the contact and the rest of the model parameters out of the resulting combined model.

In this work, we analyze tetrasubstituted zinc phthalocyanine (ZnPc) based organic thin film transistors in which contact effects are present. Based on experimental data measured on these transistors and from other authors' measurements, we critically evaluate some of the most important previous efforts in modeling OTFTs. The results of extracting the voltage drop at the contacts from these models are compared. Some of them are mainly useful when transistors with different channel lengths are available [4–6]. Others are strictly valid for linear current–voltage (I_D–V_C) responses in the contact [7]. Others, although valid to interpret nonlinear contact effect, offer an exclusive circuit vision of the problem [8].

We incorporate a model for the I_D–V_C curves at the contact [9,10] in a recently proposed generic FET model [3]. We propose a method to extract the voltage drop at the contact (I_D–V_C curves) for single length transistors showing both linear and non-linear responses in the low drain-voltage regime of their output characteristics. From the analysis of the voltage drop at the contacts with the gate voltage, a relation of the ratio of free charge density to the total charge density with the gate voltage is deduced.

2. Material

The active semiconducting material in the OTFTs under test is as-deposited spun film of 2,9(10),16(17),23(24)-(13,17-dioxanonacosane-15-oxy)phthalocyaninato zinc(II) derivatives (ZnPc) (see Fig. 1). The compound is liquid crystalline at a relatively low temperature of 11.5 °C. The synthesis and characterization of this compound were reported in a previous publication [11]. The source and drain electrodes are gold (50 nm thick)/Ti (10 nm thick) films. The transistor configuration is bottom gated. The substrate is n-silicon (100) wafer. The gate dielectric is thermally grown SiO_2 with thickness t_{ox} = 250 nm. Transistors of 10 μm-channel-length, L, 1 mm width, W, and 150 nm organic-film thickness, t_{ox}, have been analyzed. The relative dielectric constant is assumed $\varepsilon_r = 3$ in the semiconductor film [12]; similar values are also reported for other organic materials [9,13]. The electrode work function is considered around 5.14 eV, and the HOMO and LUMO levels for the organic film are 3.34 and 5.28 eV, respectively [12].

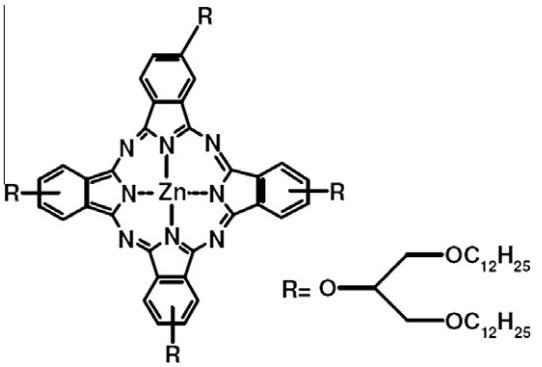

Fig. 1. Active semiconducting material analyzed in the work: as-deposited spun film of 2,9(10),16(17),23(24)-(13,17-dioxanonacosane-15-oxy)phthalocyaninato zinc(II) derivatives.

3. DC models

Fig. 2 shows experimental output characteristics measured in an Au–ZnPc bottom gated transistor at V_{GS} = 0, −10, −20, −30, and −40 V (symbols). Lines represent the fitting with the simple crystalline field-effect-transistor model (c-FET):

$$I_D = -k\left[(V_{GS} - V_T)V_{DS} - V_{DS}^2/2\right]; \quad k \equiv (\mu C_{ox} W)/L; \quad C_{ox} = \varepsilon_{ox}/t_{ox} \tag{1}$$

where εox is the dielectric constant of the gate insulator, Cox is the gate capacitance per unit area, L is the channel length and μ is the mobility. The drain current is defined as positive when entering the drain terminal (Fig. 3a). The similarity of the output characteristics of OTFTs with the I–V curves in c-FETs and amorphous thin-film transistors (a-TFTs) has been observed and explained in the past [14,15]. The fitting of experimental and theoretical curves in the saturation region produces the following parameters: k = 1.8 × 10−13 A/V2 and VT = −1.7 V. It is clear that the fitting is not good in the linear region of the curves. We can see that the experimental data are displaced around 2 V from the theoretical ones. A voltage drop at the contacts can explain this. Apart from the contact effects, there are other significant differences between organic and c-FETs, although a similarity in the current–voltage and other characteristics in these transistors exists [15]. The extraction of the mobility from the linear region produces

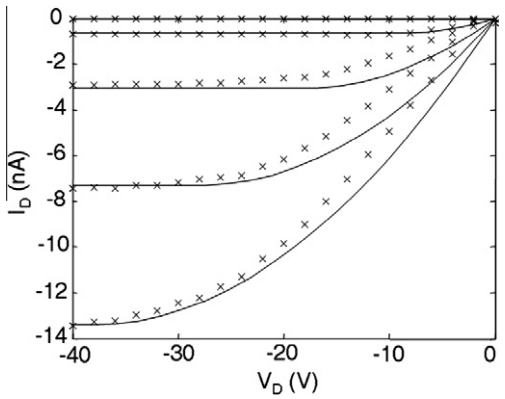

Fig. 2. Output characteristics of an Au–ZnPc bottom gated transistor at V_{GS} = 0, −10, −20, −30, and −40 V (from top to bottom). Symbols represent the experimental data. Lines represent the fitting with the simple c-FET model without contact effects ($k = 1.8 \times 10^{-13}$ A/V^2 and V_T = −1.73 V).

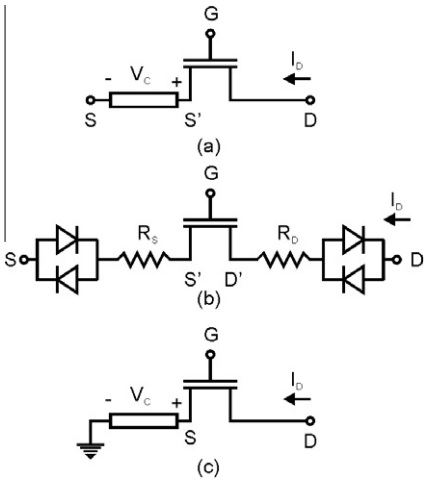

Fig. 3. (a) Equivalent circuit of a BC TFT including a voltage drop at the source contact V_C. V_{DS} is the extrinsic drain voltage. (b) Equivalent circuit of the BC TFT including nonlinear source and drain contact resistances [8]. (c) Equivalent circuit of a BC TFT including a voltage drop at the source contact V_C.

lower values than in the saturation region ($k = 1.4 \times 10-13$ A/V2). Clearly, contact effects are reducing the apparent mobility extracted in the linear region.

We can find in the literature different models that incorporate the voltage drop at the contacts, and associated methods to extract this voltage drop from the output characteristics of a transistor. This is not a trivial task because the contact effects interfere with other dependences in OTFTs [15]. The total source–drain voltage, V_{DS}, can be assumed split into a channel component, $V_{DS'}$, and a voltage drop at the contact, $V_C = V_{S'S}$ (Fig. 3a). This model takes into account that part of the external drain–source voltage is lost at the low conductivity regions near the contacts. However, this voltage drop V_C is located in the injecting contact (source). No voltage drop is considered at the extracting contact (drain). The reason is that the voltage lost at the extracting contact is much less important than the voltage lost at the injecting one, as supported by scanning potentiometry [1] and is therefore ignored.

By using the gradual channel approximation in the intrinsic channel and after integration of the potential along the channel, the current of OTFTs is obtained as [4,16]:

$$I_D = -[kL/(L-x_C)]\left[(V_{GS}-V_T)(V_{DS}-V_C) - \left(V_{DS}^2/2 - V_C^2/2\right)\right];$$
$$V_{DS} = V_{DS'} + V_C \text{ and } V_C \equiv \alpha V_{DS}, \tag{2}$$

where x_C is the width of the low conductivity region at the contact. This model is especially useful in identically processed transistors with different channel lengths (but the same channel width) [4–6]. This characterization technique, however, has two limitations. One is that a series of devices with different channel lengths, but otherwise identical, has to be available. Another is the channel transport properties in different devices might not be exactly the same. In such cases, alternative characterization techniques with variable gate biasing can be found in the literature [7,17,18]. Some of these techniques assume α as gate voltage dependant $\alpha = \alpha(V_{GS})$ but independent on V_{DS} [17–19]. That means that I_D is proportional to V_{DS}. For low values of V_{DS} the I_D–V_{DS} relation in Eq. (2) reduces to a linear one.

$$I_D = -k(V_{GS} - V_T)V_{DS}[1 - \alpha(V_{GS})]. \tag{3}$$

Other techniques model the contact effect by a series contact resistance, R_S, at source and drain [7]. The voltage drop across this series resistance modifies the I_D–V_{DS} relation. At low drain voltages this relation reduces to:

$$I_D = -k(V_{GS} - V_T)(V_{DS} - I_D R_S), \quad = -\frac{k(V_{GS}-V_T)V_{DS}}{1-kR_S(V_{GS}-V_T)}. \tag{4}$$

Non-linear I_D–V_{DS} relations such as the ones seen for low V_{DS} voltages in Fig. 2 are thus no reproducible by such linear expressions in Eqs. (3) and (4). Other approaches should be used instead [8]. These authors [8] proposed a model in which the carrier mobility depends on the gate voltage according to,

$$\mu = \mu_o[(V_G - V_T)/V_{AA}]^\gamma,\ \gamma > 0, \tag{5}$$

and highly non-linear drain and source contact series resistances are taken into account. In order to simulate non-linear I_D–V_{DS} output characteristics for organic BC TFTs, they proposed an equivalent BC TFT circuit that consists of the TFT with linear source and drain access resistances R_D and R_S, respectively, and a pair of anti-parallel leaky Schottky diodes connected to each access resistor in series, see Fig. 3b. Two diodes in parallel are needed to obtain a symmetric current–voltage characteristic. The diode non-ideality factor η, which is responsible for the steepness of the current–voltage characteristic, and the access resistances are the fitting parameters. There, $V_{DS} = (V_{D'S'} + R_S I_D + R_D I_D + 2V_{diode})$.

The idea of a gate voltage dependent mobility ($\mu \propto \{V_G - V_T\}^\gamma$, $\gamma > 0$) is based in theories such as the charge drift in the presence of tail-distributed traps (TDTs) [20] or variable range hopping (VRH) [21]. Another approach where this gate voltage dependent mobility was incorporated can be seen in [3]. In that work, the authors propose a generic analytical model for the current–voltage characteristics of organic thin-film transistors (OTFTs) [3] (Fig. 3c),

$$I_D = -k_0\left[(V_G - V_T - V_S)^{\gamma+2} - (V_G - V_T - V_D)^{\gamma+2}\right]/(\gamma+2)$$
$$k_0 = (\mu_0 C_{ox} W)/L, \tag{6}$$

where V_G and V_T are the gate bias voltage and the threshold voltage, respectively. The result is equivalent to the well-known and widely used generic FET model with a constant mobility. It is derived considering a voltage drop between the external source terminal and the internal source ($V_S \equiv V_C$) and the mobility μ is written according to the aforementioned common theoretical result [20], [21] or [22], $\mu = \mu_0(V_G - V_T - V_x)^\gamma$, where V_x is the potential in the semiconducting film of the TFT.

Assuming the values of k_0, γ, and V_T known, then a value for V_C can be found from an experimental drain current

characteristic. Thus, the complete I_D–V_C curves can be extracted from the experimental output characteristics $I_D = I_D(V_G, V_D)$. The extraction of the I_D–V_C curves requires the previous determination of k_0, γ, and V_T. The authors in [3] who proposed this generic drift model, also proposed an extraction method to determine these parameters [23]. It consists of a several step process [23] developed on identically processed transistors with different channel lengths (but the same channel width). It is similar to the model with a constant mobility in (2). By choosing the correct value for k_0, it makes all the I_D–V_C curves extracted from the different transistors to coincide. Thus, the usefulness of this extraction method is reduced to situations where several devices with different channel lengths, but otherwise identical, are available. In any case, prior to the determination of k_0, proper parameter extraction techniques are required to determine V_T and γ in (6) [23].

As mentioned in the introduction, the voltage drop at the contact region seriously affects the extraction of these (γ and V_T) and other parameters. Unless there is a method that eliminates these effects, an iterative procedure should be more convenient. Moreover, it would be very useful to find a simple and physically based model for the I_D–V_C relation at the contact in order to introduce this model in a previous generic FET model. It should employ as few parameters as possible, in order to maintain the compactness of the receiver generic FET model. In this paper, we have chosen (6) to incorporate the contact effects in, as it allows for an easy implementation and modification. Other details of the versatility of this model can be found in [3]. Our purpose is that the resulting model, after the incorporation of the contact effects, has parameters that can be characterized relatively easily, or even guessed, preventing unnecessary phenomenological fitting parameters. This is done in the following sections.

4. Contact model

For the contact region a functional model of the carrier injection $V_C = V_C(I_D)$, developed in [9,10] is initially used:

$$V_C = V_{injection}(I_D) + V_{redox}(I_D) + V_{drift}(I_D). \tag{7}$$

The model takes into account different physio-chemical mechanisms that take place at the contact: carrier injection through the barrier, $V_{injection}$, ion formation at the interface (redox reactions), V_{redox}, and charge drift in the low conductivity region of the organic material at the contact, V_{drift}. The expressions for the different components in (7) are detailed in [10]. For low values of the energy-barrier height (cases expected in well designed transistors), (7) is reduced to $V_C \approx V_{drift}(I_D)$. It is shown in [18] that the voltage drop associated with the charge drift depends on the free charge density at the interface, $p(0)$:

$$V_C = (2/3)[2J/(\varepsilon\mu\theta)]^{1/2}\left[(x_C + x_p)^{3/2} - (x_p)^{3/2}\right],$$
$$x_p \equiv J\varepsilon\theta\left[2e^2\mu(\theta p(0))^2\right], \tag{8}$$

where $J = I_D/S$ is the current density, ε is the permittivity of the organic material, μ is the mobility of the carriers, θ is the ratio of free to total charge density, x_C is the length of the contact region in the organic material, $(L–x_C)$ is the length of the intrinsic channel of the transistor, and x_p is a characteristic length defined as the point from the contact interface towards the organic film, at which the charge density $p(x_p)$ decays to $p(0)/\sqrt{2}$.

[*Note:* Please, be aware that the notations x_p and x_C have the meaning similar to those defined in [18]. In Ref. [9], L and x_C were used instead of x_C and x_p, respectively.]

Eq. (8) shows two asymptotical trends [18]. If the characteristic length x_p is a few times larger than the contact length x_C, Eq. (8) tends to Ohm's law:

$$I_D \approx eSp(0)\mu\theta V_C/x_C \equiv V_C/R. \tag{9}$$

A nonlinear relation between the current and voltage in the drift term occurs when the characteristic length x_p is much smaller than the contact length x_C and Eq. (8) reduces to the Mott–Gurney law [24,25]:

$$I_D \approx \frac{9}{8}\varepsilon\mu\theta S\frac{(V_C)^2}{(x_C)^3} \equiv M \times V_C^2. \tag{10}$$

These linear and quadratic behaviors are present in the experimental data. An example of this can be seen in poly(3-hexylthiophene) OTFTs with different source and drain electrodes, Cr and Au, (see Fig. 2 in [26]). The existence of different metallic electrodes produces different contact-voltage curves, showing these linear or non-linear responses. Transitions from linear to quadratic regimes can be seen not only by changing the electrodes, but also with the same electrode and varying the injection regime. This transition can be seen in Fig. 3 in [27], where current–voltage curves for hole injection into P3HT through Au are presented.

The inclusion of the I_D–V_C relations (9) or (10) in the generic model (6) adds a new parameter to the model. Drawing current curves $I_D = I_D(V_D, V_G)$ knowing the set of parameters (V_T, γ, k_0, M, or R) is an easy task. However, extracting these parameters from the experimental output characteristics is a major problem. There are well established parameter extraction techniques for FETs that can be used to extract the parameters in (6). An appropriate technique is proposed in [23], by the so-called H_{VG} function, which extracts the values of γ and threshold voltage V_T from the linear operation regime of the OTFT. The H_{VG} function is the ratio of the integral of the drain current over the gate bias divided by the drain current. The corresponding equation for the H_{VG} function derived from the TFT generic model (6) is:

$$H_{VG}(V_G) = \frac{\int_{<V_T}^{V_G} I_D(V_G)dV_G}{I_D(V_G)} = \frac{1}{\gamma+3} \times \frac{(V_G - V_T - V_S)^{(\gamma+3)} - (V_G - V_T - V_D)^{(\gamma+3)}}{(V_G - V_T - V_S)^{(\gamma+2)} - (V_G - V_T - V_D)^{(\gamma+2)}} \tag{11}$$

$$H_{VG}(V_G) = \begin{cases} = (V_G - V_T)/(\gamma+3), & V_D > V_G - V_T \\ \approx [(V_G - V_T)/(\gamma+2)]\{1 - R_2[V_D/(V_G - V_T)]\}, & V_D << V_G - V_T \end{cases} \tag{12}$$

where $R_2[V_D/(V_G - V_T)]$ is the remainder term, that represents the error in approximating $H_{VG}(V_G)$ by the above first order power series. In these equations, H_{VG} becomes a linear function of gate overdrive $(V_G - V_T)$ by setting $V_S = 0$, while k_0 is canceled, which is the advantage of the method. However, (12) explicitly neglects the effect of the contacts, as V_S is assumed null. That means that the values of V_T and γ may not be correct. To check this fact a hypothetical p-type transistor with the following parameters is considered: $V_T = 4.5$ V, $\gamma = 1$, $V_S = V_C = I_D R$, R varying in the range $[10^2–10^8\ \Omega]$ and k_0 in the range $[10^{-6}–10^{-12}\ A/V^2]$. The H_{VG} function, as defined in (12), is built, and parameters V_T and γ are determined in the saturation region as recommended in [23].

Fig. 4 shows the results of this method. There are ranges of R in which the extracted values for V_T and γ differ significantly from the original ones. A direct and easy-to-implement method like this one, in the absence of contact effects, is clearly altered under the presence of contact effects. Contact effects can really be a bottleneck in the extraction of the main parameter of the transistor. Despite these difficulties, we propose an extraction method in which the advantages of these methods are considered. In the next section, we propose a procedure to extract from experimental $I_D–V_{DS}$ curves, not only the values of V_T and γ,

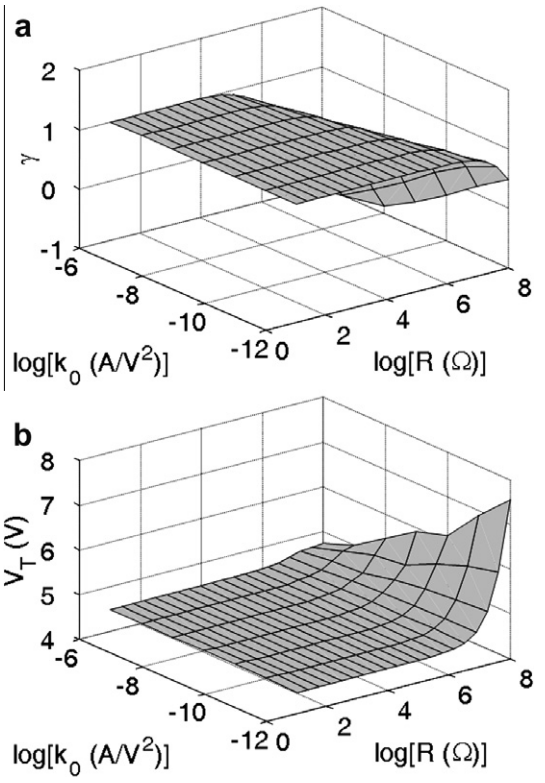

Fig. 4. (a) Extracted γ, and (b) extracted V_T from the generic drift model (6) using the H_{VG} method [22] for a transistor with initial parameters $V_T = 4.5$ V, $\gamma = 1$ and contact effects showing a linear behavior $V_S = V_C = I_D R$. The extracted γ and V_T are represented for transistors with different k_0 and R. Neglecting the voltage drop at the contact in the H_{VG} function makes the extracted values to differ from the original ones.

but also the contact voltage V_S, characterized by parameters M or R (Eqs. (9) and (10)), and the value of k_0.

5. Parameter extraction method

Upgrading a model by the introduction of new physical effects means the incorporation of additional fitting parameters that may not be possible to adjust consistently, or interfere with previous parameters of the model. The interference among parameters can be eliminated by a good initial estimation of some of them. In the case of contact effects, we provide a procedure that initially estimates the parameters associated to the contacts by slightly modifying the ideal c-MOS model. Although the ideal c-MOS model cannot accurately reproduce the complete output characteristics of an OTFT, it does provide a good initial estimation of the transistor parameters to be subsequently determined in (6), in particular those associated to the contacts. In this section, we define the steps followed to determine the complete set of parameters in (6), including the parameter associated to the contact region.

(1) Estimation of V_T and k from the ideal c-MOS model in saturation from (1).

(2) Estimation of the electric field degradation of mobility by analyzing the saturation region of the transistor. Eq. (5) is introduced in (1) and parameters defining the gate voltage dependent mobility are determined from the saturation region.

(3) Estimation of contact parameters (curves $I_D - V_C : I_D = M(V_{GS}) \times V_C^2$ or $I_D = V_C/R(V_{GS})$). The drain–source voltage is modified in (1) by the inclusion of the voltage drop at the source contact. The model is represented in Fig. 3a. For the TFT the usual analytic expression for the MOS transistor can be used:

$$I_D = -k\left((V_{GS'} - V_{T'})V_{DS'} - V_{DS'}^2/2\right), \tag{13}$$

where $V_{DS} = V_{DS'} + V_C$ and $V_{T'}$ is an internal threshold voltage defined for the intrinsic transistor in Fig. 3a. $V_{T'}$ can be evaluated as $V_{T'} = V_T - \overline{V_C(I_{Dsat})}$, where V_T is the threshold voltage extracted from the saturation region of the experimental data and $\overline{V_C(I_{Dsat})}$ is the average value of the contact voltage evaluated in saturation, $I_D = I_{Dsat}$, and different gate voltages. Note that $V_{T'}$ is not known as yet, as the contact voltage is not known at this step. In a first estimation, the modification of the gate voltage by the contact effects is neglected. It can be checked that this simplified model can reproduce the data in the linear region, where the contact effects are clearly dominant, by assuming $(V_{GS'}–V_{T'}) \sim (V_{GS}–V_T)$ in Eqs. (13), (7) and (9) (or (10)). The effect of the contact voltage on the gate voltage $V_{GS'} = V_{GS} - V_C(I_D)$ is compensated by a modification of the threshold voltage for the intrinsic TFT. The idea of the internal threshold voltage is formally introduced and physically derived in (2) (or in (6) if the gate voltage dependent mobility is considered). In this work, (13) is preferred for an initial estimation of the parameter M (or R). It avoids the mutual interference between the contact parameter M (or R) and the rest. It avoids the need of introducing an intrinsic threshold voltage, $V_{T'}$, in the OTFT model by the existence of contact effects.

(4) Estimation of an average value for the contact voltage V_S in the saturation region. Once the M (or R) parameter is extracted from the experimental data ($M = M(V_{GS})$ or $R = R(V_{GS})$), the average value of the contact voltages, evaluated at $I_D = I_{Dsat}$ for different gate voltages, can be determined, $V_S = \overline{V_C(I_{Dsat})}$.

(5) Determination of V_T and γ from the H_{VG} function. The H_{VG} function can be evaluated by introducing this average value for V_S in the saturation region: $H_{VG}(V_G) = (V_G - V_T - V_S)/(\gamma + 3)$. Once the effects of the contacts are introduced in this function, V_T and γ can be determined more accurately. The problems associated to the contact effects make the linear region no valid for the determination of such parameters. The saturation region has previously been suggested as the most appropriate region to carry on this characterization [23].

(6a) Final determination of k_0 and $M(V_{GS})$ (or $R(V_{GS})$). At this step, values for all the variables appearing in the drift generic model (6) have been derived. V_T and γ have been determined by considering the contact voltage and using a technique that eliminates the dependence with k_0 (see (11)). Thus, k_0 and M (or R) are the only parameters that require a final adjustment. In this case, Eq. (6) is used to find these values by comparing this equation with the experimental data. The parameter k_0 mainly affects the saturation region and M (or R) affects the linear region. Thus, these parameters are modified in order to fit the current voltage curves in these respective regions. Slight modifications of these two parameters found this way may be necessary to reproduce the complete set of experimental $I_D(V_D, V_G)$ curves.

(6b) Direct extraction of the I_D–V_C curves from (6). The objective of this step is twofold: (*i*) as a test to check the values of the parameters obtained in step 6a or (*ii*) as an alternative step for 6a when non reasonable values for γ are obtained in step 5.

(i) An inspection of Eq. (6) shows that with the values of the parameters k_0, V_T, γ, and M (or R) and the experimental $I_D(V_D, V_G)$ curves, one can derive I_D–V_C curves at different V_G. These I_D–V_C curves must match the ones obtained in step 6a (controlled by Eqs. (9) and (10)). Step 6b alone can be used to determine a unique I_D–V_C curve for several devices with different channel lengths, but otherwise identical [4–6], as mentioned in the previous section. All the extracted curves must converge into one. However, step 6b alone cannot be employed for the case of a set of single length transistors, as convergence is not guaranteed. Steps 1–5 provide such a procedure towards a convergence, for the physical trend given by Eqs. (9) and (10). In any case, the extraction of different I_D–V_C curves for different values of k_0, and its comparison with the value of k_0 and the curves extracted in step 6a are suggested.

(ii) The other situation where this step is necessary is when abnormal values of γ and/or V_T are obtained in previous steps, despite introducing an estimated value for the contact voltage V_S. A negative value of γ clearly indicates that the characterization needs further processing (see Fig. 4a)). In these situations, convergence between experimental data and Eq. (6) in step 6a is not achieved. An iterative procedure is suggested in this step 6b. The initial values used for γ, V_T, and k_0 in this procedure depend on the value of γ estimated in previous steps. The value of the threshold voltage is assumed initially correct. In case the value of γ extracted from step 2 is positive, this should be assumed as an initial estimation. On the contrary, the initial value for γ is assumed zero. For the selected value of γ, k_0 is varied until a physical result for the I_D–V_C curves is obtained. If it does not exist, then the value of γ is increased and k_0 is again modified. The values of γ and k_0 are alternatively modified until the I_D–V_C curves behave like (9) or (10). An arbitrary set of values for V_T, γ, and k_0, different from the actual solution, produces current voltage curves at the contact with no physical meaning (such as a change of the sign of the contact voltage or strange trends in the I_D–V_C curves).

In case, the extracted I_D–V_D curves provide a value of $V_S = \overline{V_C(I_{Dsat})}$ different from the one initially estimated in step 5, a new iteration is necessary. A new value for the threshold voltage would be determined in step 5 and 6b would be repeated.

6. Results

To check the validity of the extraction method for the contact voltage drop and the rest of the basic parameters appearing in the TFT generic model (6), we analyze data showing both linear and non-linear effects. We analyze measured I_D–V_D curves in ZnPc-based organic thin film transistors and data taken from other authors' experiments.

6.1. Non-linear contact current–voltage curves

In first place, we analyze the experimental data depicted in symbols in Fig. 2. They show a clear non-linear behavior at low drain voltages pointing out the existence of contact effects. Considering the values of the HOMO and LUMO levels for the organic film and the electrode work function given above, the energy barrier of the Au–ZnPc contact can be considered small enough to prevent current to flow through it. The current is thus dominated by the drift term. Due to the high non-linearity of the I_D–V_{DS} curves, the current–voltage relation at the contact is modeled by (10).

The extraction procedure detailed in the previous section can be followed in Fig. 5. We initially consider that the values of the mobility (assumed gate voltage dependent) and threshold voltage are extracted by fitting the experimental data in the saturation region with the ideal c-MOS model: $V_T = -1.7$ V, $\gamma = -0.03$, $V_{AA} = 24.4$ V and $\mu_{00} = 4.4 \times 10^{-6}$ cm^2/Vs. The result of this fitting (steps 1 and 2) can be seen in Fig. 2. If the contact effects are introduced in the ideal MOS model (step 3) a good agreement between the experimental data (symbols) and the combined expression resulting from (10) and (13) (solid lines) is seen in Fig. 5a. The values of M introduced in (10) to

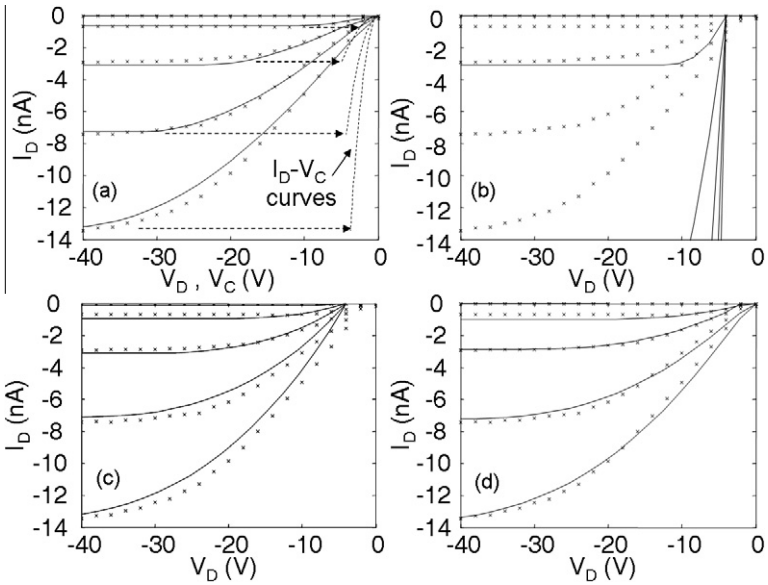

Fig. 5. Comparison of output characteristics of an Au–ZnPc bottom gated transistor measured at $V_{GS} = 0$, -10, -20, -30, and -40 V (from top to bottom in symbols) with the theoretical results obtained at different steps of our fitting procedure. (a) Fitting with the ideal MOS model corrected with the contact effects (Eq. (13)). The values of the mobility and threshold voltage are extracted from the saturation region. The mobility is considered gate voltage dependent, following expression (5). ($V_T = -1.7$ V, $\gamma = -0.03$, $V_{AA} = 24.4$ V and $\mu_{00} = 4.4 \times 10^{-6}$ cm^2/Vs). The current–voltage curves at the contact are modeled with the parameter $M(V_{GS})$. The parameter M is extracted by fitting the experimental data in the linear region ($M = 1.0 \times 10^{-10}$, 1.2×10^{-10}, 1.2×10^{-10}, 4.0×10^{-10}, and 9.5×10^{-10} A/V^2 for $V_{GS} = 0$, -10, -20, -30, and -40 V, respectively). The dashed curves on the right represent the current–voltage curves at the contact evaluated with the previous M parameter. The tips of the dashed arrows point out the value of the contact voltage evaluated in the saturation region for each gate voltage. An average value of $V_{S(average)} \approx -4$ V is obtained. (b) Fitting with the generic drift model (6). This equation is evaluated with the following parameters. Parameters V_T and γ are determined with the H_{VG} function (11) including the contact effects $V_S = V_{S(average)}$ ($\gamma = 0.8$, $V_T = 13$ V); the value of μ_0 is the one calculated from the saturation region with the ideal MOS model ($\mu_0 = 4.4 \times 10^{-6}$ cm^2/Vs); and $V_S = 0$. The last two parameters make the theoretical result to disagree with the experimental curves. (c) Fitting with the generic drift model (6) changing the parameter μ_0 to 1.7×10^{-7} cm^2/Vs; V_S is maintained null. (d) Fitting with the generic drift model (6) introducing the contact effects. μ_0 does not change. The extracted M parameter is $M = 0.3 \times 10^{-10}$, 0.7×10^{-10}, 1.2×10^{-10}, 5.0×10^{-10}, and 9.5×10^{-10} A/V^2 for $V_{GS} = 0$, -10, -20, -30, and -40 V, respectively. Despite the large modification of the values of V_T and μ_0 along the different steps of this procedure, the values of the parameter M associated to the contact voltage suffer almost no variation. That means that the use of single models, like the one propose in (13), helps finding a proper estimation of the contact I_D–V_C curves.

achieve such an agreement are $M = 1.0 \times 10^{-10}$, 1.2×10^{-10}, 1.2×10^{-10}, 4.0×10^{-10}, and 9.5×10^{-10} A/V^2 for $V_{GS} = 0$, -10, -20, -30, and -40 V, respectively. The contact I_D–V_C curves resulting from these parameters are depicted in dashed lines on the right region of Fig. 5a. Once we know these curves, the contact voltage can be evaluated in the saturation region for each gate voltage. These points are marked with the tips of the dashed arrows in Fig. 5a. An average value $V_{S(average)} \approx -4$ V is obtained from these points (step 4).

The fifth step corresponds to the determination of V_T and γ from the H_{VG} function, once a value for the contact voltage in the saturation region has been estimated. The analysis of the H_{VG} function provides the following values: $\gamma = 0.8$ and $V_T = -13$ V. A very different value for the threshold voltage is obtained in comparison to the one extracted in step 1. Fig. 5b illustrates the comparison of the experimental data with the generic drift model (6) using the values of these last two parameters, the value of μ_0 determined from the saturation region with the ideal c-MOS model ($\mu_0 = 4.4 \times 10^{-6}$ cm^2/Vs), and $V_S = 0$. It is apparent that the mixture of values of parameters extracted from different models and ignoring the contact effects produce such a disagreement. A change of the value of the mobility to 1.7×10^{-7} cm^2/Vs is necessary in order to fit the experiments in the saturation region (Fig. 5c). In this figure, V_S is maintained null in order to highlight this fact. Finally, the contact effects, by means of the parameter M in (10), are introduced in the generic drift model (6). The combined model fits the experimental data for the following set of values: $M = 0.3 \times 10^{-10}$, 0.7×10^{-10}, 1.2×10^{-10}, 5.0×10^{-10}, and 9.5×10^{-10} A/V^2 for $V_{GS} = 0$, -10, -20, -30, and -40 V, respectively (Fig. 5d). A unique value for M should be expected for a compact model. However, the compactness of this parameter is justified below by its relation with the charge density in the intrinsic channel.

The analysis of the values of the different parameters extracted in the six steps shows that the variations in V_T and γ (from the initial estimations to the final results) are very significant, while the parameter M is practically unaffected by when using either the ideal c-MOS model or the generic drift model, both in combination with our contact model. On the one hand, the generic drift model is physically well based. However, the inclusion of new parameters in it makes their extraction more difficult. On the other hand, the use of simple models like the one propose in (13), although based on approximations, are really helpful in finding a proper initial estimation of the contact

I_D–V_C curves. This is necessary to proceed with the determination of the exact values of the parameters appearing in (6).

The current–voltage curves at the contact can be directly extracted from (6) once the parameters μ_0, γ and V_T are known [23]. These curves can be seen with symbols in Fig. 6. The values of these parameters correspond to the ones extracted with our procedure in the previous paragraphs. The inset of Fig. 6 shows the comparison of the experimental data with (6) including these current voltage curves. The agreement is clearly better than the one shown in Fig. 5d. However, the current voltages curves extracted with our procedure (shown as solid lines in Fig. 6) provide a physical trend and a way to interpret the ones shown as symbols.

Experimental data measured in an Au-pentacene BC-TFT by other authors [8] are also reproduced by our model. Fig. 7 shows a comparison of the experimental data (symbols) with the generic drift model (6) in which the contact current–voltage relation (10) has been incorporated (solid lines). The transistor has the following characteristics: the SiO_2 gate-dielectric thickness is $t_{ox} = 290$ nm, the gate length is $L = 20$ μm and the gate width $W = 220$ μm.

The model parameters have been extracted using the procedure detailed in the previous section. This is a case where the value of γ extracted in step 5 shows an abnormal value despite including the contact effects, $\gamma = -0.4$. In this situation, step 6b was followed instead of step 6a. The value of γ extracted by analyzing the saturation region with the ideal c-MOS model (1) in combination with the electric field degradation of the mobility (5) was used instead, $\gamma = 0.118$. The value of the threshold voltage was determined in step 5 by means of the H_{VG} function applied to the generic drift model (6). The parameter obtained after the fitting procedure are: $k_0 = 7.78 \times 10^{-8}$ A/V^2, $\mu_0 = 0.19$ cm^2/Vs, $V_T = 17.3$ V, $\gamma = 0.118$, $M = 0.5 \times 10^{-6}$, 0.8×10^{-6}, 1.0×10^{-6}, 1.5×10^{-6}, 2.0×10^{-6}, 2.4×10^{-6}, and 2.5×10^{-6} A/V^2 for $V_{GS} = 0$, -10, -20, -30, -40, -50, and -60 V, respectively. Situations analyzed in Fig. 5 and Fig. 7 show the need to employ the advantages of simple models (although not exact ones) and to combine them in a precise sequence. The objective is to determine correct values for the transistor parameters that appear in a more compact and precise model, such as the one in (6).

Another feature of our model and its associated extraction procedure is that they allow us to determine the parameter M defined in (10). From this parameter, we can determine the evolution of the free to total charge-density ratio θ, with the gate voltage. Assuming the same value for the mobility in the transistor channel and in the low conductivity region at the contact, this ratio varies

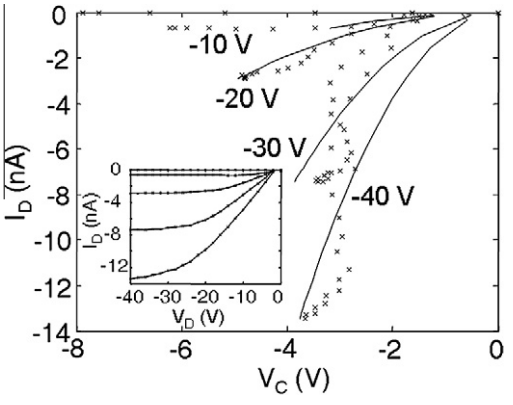

Fig. 6. Current voltage curves at the contact extracted from experimental output characteristics at different gate voltages with our procedure (solid lines) and directly from the generic drift model (6) (symbols). The parameters employed in the calculation correspond to the final ones obtained in Fig. 5. Inset: Comparison of output characteristics of an Au-ZnPc bottom gated transistor measured at $V_{GS} = 0$, -10, -20, -30, and -40 V (from top to bottom in symbols) with the theoretical results from (6) using the I_D–V_C curves shown in symbols in the main figure.

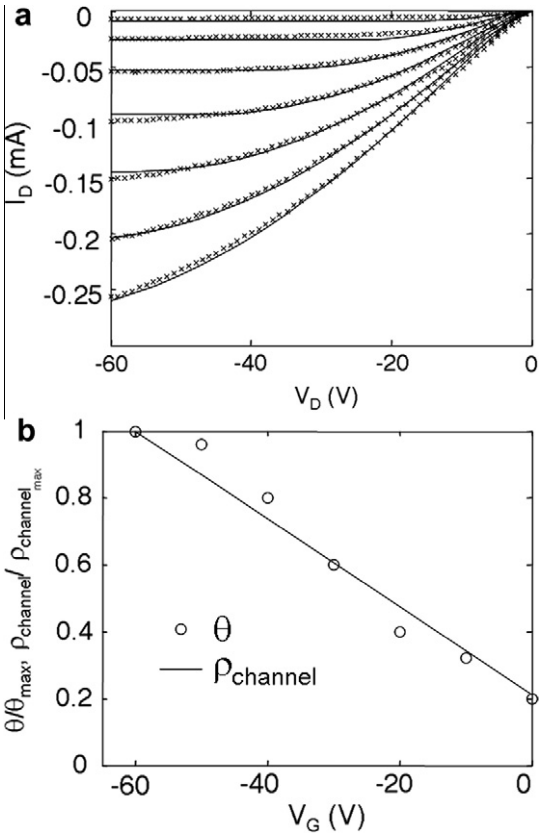

Fig. 7. (a) Comparison of output characteristics of an Au-Pentacene bottom gated transistor at $V_{GS} = 0$, -10, -20, -30, -40 V, -50 V, and -60 V from top to bottom (symbols) with the generic drift model (6) including non-linear contact effects (10) (solid lines). The dimensions of the transistor are $t_{ox} = 290 \times 10^{-7}$ cm, $W = 220 \times 10^{-4}$ cm, $L = 20 \times 10^{-4}$ cm. The parameters used in the model, determined according to the method detailed in this work, are $k_0 = 7.78 \times 10^{-8}$ A/V^2, $\mu_0 = 0.19$ cm^2/Vs, $V_T = 17.3$ V, $\gamma = 0.118$, $M = 0.5 \times 10^{-6}$, 0.8×10^{-6}, 1.0×10^{-6}, 1.5×10^{-6}, 2.0×10^{-6}, 2.4×10^{-6}, and 2.5×10^{-6} A/V^2 for $V_{GS} = 0$, -10, -20, -30, -40, -50, and -60 V, respectively. (b) Normalized values of the charge density in the channel, ρ, and free to total charge-density ratio θ in the low conductivity region near the contact. The values of θ are extracted from the previous values of M and its definition in (10). The normalization values are: $\rho_{max} = 3.4 \times 10^{18}$ cm^{-3} and $\theta_{max} = 0.06$. The charge densities in the channel and in the contact region are correlated meaning that the values of M extracted by our procedure are acceptable.

from 0.012 at $V_{GS} = 0$ V to 0.060 at $V_{GS} = -60$ V. The values of θ, necessary to fit the experimental data with our model (Fig. 7a), are represented as a function of the gate voltage in Fig. 7b (circles). In this figure, we also represent the values of the charge density in the intrinsic channel, estimated according to the equation (solid line) [28],

$$\rho_{channel} = C_{ox}\frac{1}{t_o}(V_{GS} - V_T). \quad (14)$$

The evolution of the ratio of free to total charge density with the gate voltage is in excellent agreement with the evolution of the charge density in the channel. This agreement validates the physical model we propose for the dc characteristics of organic TFTs affected by contact effects.

The non-linear behavior shown at low drain voltages in the experiments of Figs. 5 and 7 can also be reproduced by diodes in series with a resistance connected at the source and drain terminals (Fig. 3b). Good agreements between the experimental data and this model are obtained. For the experimental data in Fig. 5, the values of the model parameters in Fig. 3b that achieve the best fit are $\gamma = -0.032$, $\mu_0 = 2.65 \times 10^{-4}$ cm^2/Vs, $V_{AA} = 25.0$ V, $R_{D,S} = 10^4\ \Omega$, energy barrier at the interface $\varphi_B = 0.65$ eV and non-ideality factor of the diode $\eta = 5$. For the experimental data in Fig. 7, the values of the model parameters that achieve the best fit are $\gamma = 0.118$, $\mu_0 = 0.2$ cm^2/Vs, mobility evaluated at $V_{GS} = -60$ V, $\mu = 0.27$ cm^2/Vs, $V_{AA} = 5.70$ V, $R_{D,S} = 5$ kΩ, energy barrier at the interface $\varphi_B = 0.65$ eV and non-ideality factor of the diode $\eta = 2.5$. Although the model in Fig. 3b can reproduce the experimental data, the values of the resulting parameters should be analyzed with care, especially when high values of the non-ideality factor of the diodes and/or negative values of γ are extracted. The advantage of our model (Fig. 3c) is its physical approach to the real mechanisms affecting the low conductivity region near the contacts, [1,9].

6.2. Linear contact current–voltage curves

Current–voltage I_D–V_D curves showing linear responses at low drain voltages have also been studied in this work. Here, we apply the procedure from the previous section to extract the mobility, threshold voltage and the contact voltage drop from the output characteristics of poly(3-hexadecylthiophene)(P3HDT) transistors [17] (symbols in Fig. 8a). The solid lines correspond to the evaluation of the generic drift model (6) in which the linear contact voltage-current model in (9) has been incorporated. The values of the contact resistances $R = R(V_G)$ and the rest of the model parameters are detailed in the same figure. A good agreement is observed between the experiments and the theoretical results. The extraction procedure followed with these data does not end in step 6a, but goes through step 6b. This is another example where the parameter γ is clearly affected by the contact effects (see Fig. 4). In step 5, $\gamma = -0.3$ and $V_T = -4.5$ V are obtained assuming an average value for the contact voltage in the saturation region $V_S = \overline{V_C(I_{Dsat})} = -1.5V$. The value of γ is gradually increased and the value of k_0 is modified until the extracted I_D–V_D curves show a perfectly linear behavior, as expected by the trend of the experimental data at low drain voltages.

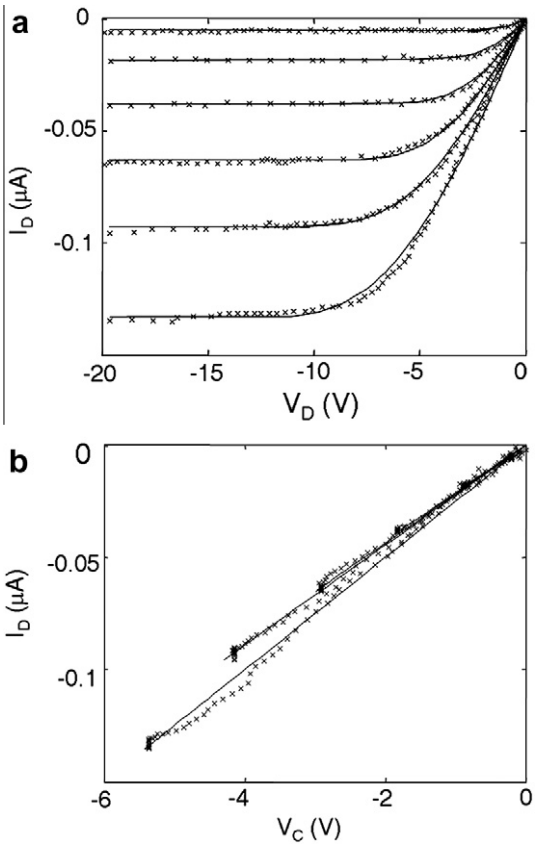

Fig. 8. (a) Output characteristics of an Au–P3HDT BC transistor at $V_G = -8$, -10, -12, -14, -16, and -18 V from the top to the bottom. Symbols represent the experimental data [17] based on material described in [29,30]. Lines represent the fitting with the generic drift model (6) including non-linear contact effects (10). The details of the samples are: thermally grown SiO_2 ($\backsim$ 200 nm), channel width $W = 0.5$ cm (multifinger configuration), and channel length $L = 10$ μm. The polymer film is 7 nm thick and was deposited by spin coating. The parameters used in the model, determined according to the method detailed in this work, are $k_0 = 3 \times 10^{-8}$ A/V^2, $\mu_0 = 1.2 \times 10^{-5}$ cm^2/Vs, $V_T = -4.5$ V, $\gamma = 1.5$, $R = 4.9 \times 10^7$, 4.8×10^7, 4.7×10^7, 4.6×10^7, 4.5×10^7, $4.0 \times 10^7\ \Omega$ for $V_G = -8$, -10, -12, -14, -16, and -18 V, respectively. (b) Current voltage curves at the contact extracted from the experimental output characteristics at different gate voltages with our procedure (solid lines). The parameters employed in the calculation correspond to the final ones obtained in Fig. 8a. The current voltage curves at the contact extracted directly from the generic drift model (6) are shown in symbols.

This occurs for $\gamma = 1.5$ (Fig. 8b). The value of the threshold voltage needs no modification.

In order to check, that this solution is unique, other pairs of values for γ and k_0 are tested. As an example, Fig. 9 shows I_D–V_D curves extracted from (6) for a lower γ, $\gamma = 0.15$, $V_T = -4.5$ V and different values of k_0, after equating I_D, V_G, and V_D to the experimental data (symbols). They are compared to the solution obtained in Fig. 8b. The set of figures shows that there is no acceptable I_D–V_D curve in any case. Fig. 9a shows positive values for V_C when negative ones are expected. Fig. 9b–d show linear responses at low values of V_C. However, the curves tend to saturate, reflecting the saturation response of the intrinsic channel,

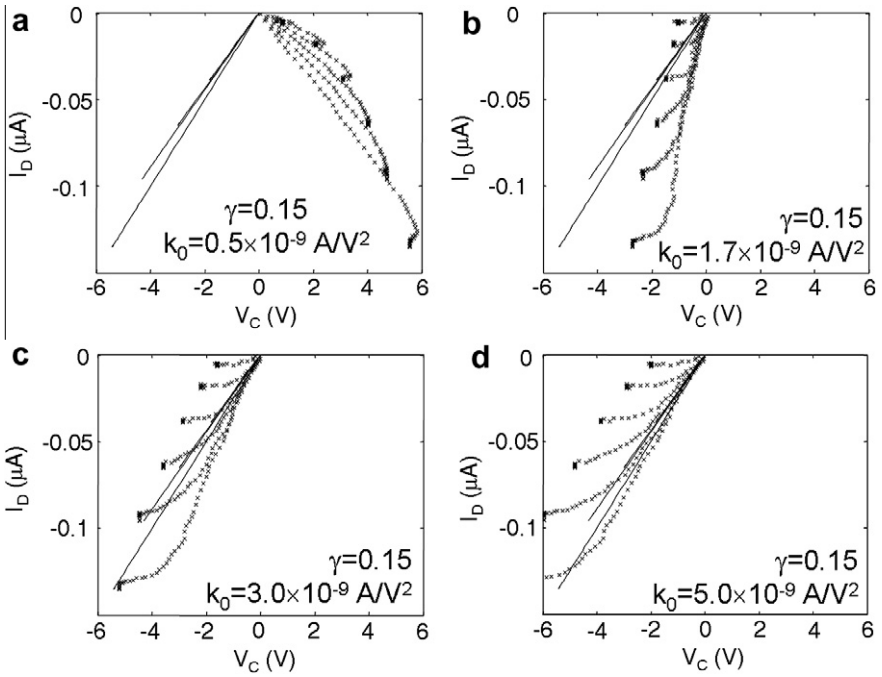

Fig. 9. Contact current–voltage curves extracted from the experimental data of Fig. 8, directly from Eq. (6) (symbols) providing this model with the parameter values $V_T = -4.5$ V and γ and k_0 given in the figures. The solid lines are used as a reference. They correspond to the final results obtained with our procedure for the I_D–V_C curves (Fig. 8). No convergence to a physical acceptable solution is seen when varying the parameter k_0 for $\gamma = 0.15$: figures (a) to (d). A similar lack of convergence towards a physical acceptable trend for the I_D–V_C curves is seen for other values of γ, except for the actual solution depicted in Fig. 8.

not the actual response of the contact region. A similar study was made with different values of γ, showing that the solution depicted in Fig. 8 is unique.

As seen in these two sub-sections, the model is able to distinguish between linear and quadratic responses for the current voltage relation at the contact region. Both responses are included under the assumption that the energy barrier at the contact imposes no restriction to the current, i.e. under the assumption of space charge limited transport $V_C \approx V_{drift}(I_D)$. Therefore, the model is limited to these situations. Outside these limits, when the energy barrier at the interface imposes a restriction to the current, non-linear I–V responses are also obtained, however not necessarily quadratic ones (thermionic emission or tunnel injection should be considered (7)). An example of this can be seen in Fig. 1 in [10], where the voltage drop at the contact of an OTFT is the sum of the voltage drop at the space charge region and the voltage necessary to surpass the barrier at the contact (a combination of injection through the barrier and space charge transport). For these cases, the quadratic model can still be used by taking into account that we are working under a second order approximation, and no connection with the physical parameters appearing in (10) is possible. In any case, properly designed transistors are expected to use contacts with low energy barriers at the interface in order to reduce the injection-voltage term. Therefore, from this practical point of view, the procedure can be considered of full applicability.

7. Conclusions

We have made use of a physical model to interpret contact effects in organic/polymeric thin film transistors, and we have incorporated it in a generic compact model that describes the output characteristics of OTFTs. The resulting model reproduces experimental data of output characteristics showing linear and highly nonlinear responses at low drain voltages. Our model is compared with previous circuit models proposed to explain these behaviors. Our model provides a way to gain physical insight about the charge density in the low conductivity region near at the contact region and mirrors the changes of charge density in the rest of the device. Actually, the evolution with the gate voltage of the free to total charge density ratio in the low conductivity region at the contact is in agreement with the estimated charge density in the channel.

In parallel to this model, a parameter extraction procedure has been proposed in order to determine the model parameters, including the additional ones associated to the contact effects. The advantages of previous procedures (although less precise) are combined in our method. Although more physically advanced model are necessary in order to take into account all the effects that appear in the OTFT, previous simple models cannot be completely disregarded. We have demonstrated their usefulness in the characterization process. The different steps of our procedure are monitored with experimental

measurements from organic thin film transistors based on zinc phthalocyanine and data from other authors' experiments.

Acknowledgments

This work was carried out within the framework of research Project No. TEC2007-66812/MIC supported by the Ministerio de Educación y Ciencia and FEDER. The authors are grateful to Professor Vefa Ahsen of Department of Chemistry, Gebze Institute of Technology, P.O. Box 141, 41400 Gebze-Kocaeli, Turkey for providing zinc phthalocyanine compounds.

References

[1] L. Bürgi, T.J. Richards, R.H. Friend, H. Sirringhaus, Close Look at Charge Carrier Injection in Polymer Field-Effect Transistors, J. Appl. Phys. 94 (2003) 6129–6137.
[2] D. Gupta, N. Jeon, S. Yoo, Modeling the electrical characteristics of TIPS-pentacene thin film transistors: effect of contact barrier, field-dependent mobility, and traps, Org. Electron. 9 (2008) 1026–1031.
[3] O. Marinov, M.J. Deen, U. Zschieschang, H. Klauk, Organic Thin-Film Transistors. Part I – Compact DC modeling, IEEE Trans. Electron Dev. 56 (2009) 2952–2961.
[4] B.H. Hamadani, D. Natelson, Extracting contact effects in organic FETs, Proc. IEEE 93 (2005) 1306–1311.
[5] B.H. Hamadani, D. Natelson, Gated nonlinear transport in organic polymer field effect transistors, J. Appl. Phys. 95 (2004) 1227–1232.
[6] E.J. Meijer, G.H. Gelinck, E. van Veenendaal, B.H. Huisman, D.M. De Leeuw, T.M. Klapwijk, Scaling behavior and parasitic series resistance in disordered organic field-effect transistors, Appl. Phys. Lett. 82 (2003) 4576–4578.
[7] G. Horowitz, R. Hajlaoui, D. Fichou, A. Edl Kassmi, Gate voltage dependent mobility of oligothiophene field-effect-transistors, J. Appl. Phys. 85 (1999) 3202–3206.
[8] P.V. Necliudov, M.S. Shur, D.J. Gundlach, T.N. Jackson, Modeling of organic thin film transistors of different designs, J. Appl. Phys. 88 (2000) 6594–6597.
[9] P. Lara Bullejos, J.A. Jiménez Tejada, M.J. Deen, O. Marinov, W.R. Datars, Unified Model for the Injection and Transport of Charge in Organic Diodes, J. Appl. Phys. 103 (2008) 064504.
[10] P. Lara Bullejos, J.A. Jiménez Tejada, F.M. Gómez-Campos, M.J. Deen, O. Marinov, Evaluation of the charge density in the contact region of organic thin film transistors, J. Appl. Phys. 106 (2009) 094503.
[11] M. Durmuş, C. Lebrun, V. Ahsen, Synthesis and characterization of novel liquid and liquid crystalline phthalocyanine, J. Porphyrins Phthalocyanine 8 (2004) 1175–1186.
[12] W. Gao, A. Kahn, Controlled p-doping of zinc phthalocyanine by coevaporation with tetrafluorotetracyanoquinodimethane: A direct and inverse photoemission study, Appl. Phys. Lett. 79 (2001) 4040–4042.
[13] G. Horowitz, M.E. Hajlaoui, R. Hajlaoui, Temperature and gate voltage dependence of hole mobility in polycrystalline oligothiophene thin film transistors, J. Appl. Phys. 87 (2000) 4456–4463.
[14] Z. Xie, M. Abdou, A. Lu, M.J. Deen, S. Holdcroft, Electrical characteristics of poly(3-hexylthiophene) thin film MISFETs, Can. J. Phys. 70 (1992) 1171–1177.
[15] O. Marinov, M.J. Deen, B. Iniguez, Charge Transport in Organic and Polymer Thin-Film Transistors: Recent Issues, IEE Proc. Circuits Dev. Syst. 152 (2005) 189–209.
[16] R.A. Street, A. Salleo, Contact effects in polymer transistors, Appl. Phys. Lett. 81 (2002) 2887–2889.
[17] M.J. Deen, M.H. Kazemeini, S. Holdcroft, Contact effects and extraction of intrinsic parameters in poly(3-alkylthiophene) thin film field-effect transistors, J. Appl. Phys. 103 (2008) 124509.
[18] P. Lara Bullejos, J.A. Jiménez Tejada, S. Rodríguez-Bolívar, M.J. Deen, O. Marinov, Model for the injection of charge through the contacts of organic transistors, J. Appl. Phys. 105 (2009) 084516.
[19] M.J. Deen, M.H. Kazemeini, Y.M. Haddara, J. Yu, G. Vamvounis, S. Holdcroft, W. Woods, Electrical Characterization of Polymer-Based Field-Effect Transistors Fabricated by Spin-Coating Poly(3-alkylthiophene)s, IEEE Trans. Electron Dev. 50 (2004) 1892–1901.
[20] M. Shur, M. Hack, Physics of amorphous silicon based alloy field-effect transistors, J. Appl. Phys. 55 (1984) 3831–3842.
[21] M. Vissenberg, M. Matters, Theory of the field-effect mobility in amorphous organic transistors, Phys. Rev. B: Condens. Matter 57 (1998) 12964–12967.
[22] O. Marinov, M.J. Deen, W.R. Datars, Compact Modeling of Charge Carrier Mobility in Organic Thin-Film Transistors, J. Appl. Phys. 106 (2009) 064501.
[23] M.J. Deen, O. Marinov, U. Zschieschang, H. Klauk, Organic Thin-Film Transistors. Part II-Parameter extraction, IEEE Trans. Electron Dev. 56 (2009) 2962–2968.
[24] K. Tsukagoshi, F. Fujimori, T. Minari, T. Miyadera, T. Hamano, Y. Aoyagi, Suppression of short channel effect in organic thin film transistors, Appl. Phys. Lett. 91 (2007) 113508.
[25] P.N. Murgatroyd, Theory of space-charge-limited current enhanced by Frenkel effect, J. Phys. D 3 (1970) 151–156.
[26] B.H. Hamadani, D. Natelson, Nonlinear charge injection in organic field-effect transistors, J. Appl. Phys. 97 (2005) 064508.
[27] D. Chirvase, Z. Chiguvare, M. Knipper, J. Parisi, V. Dyakonov, J.C. Hummelen, Temperature dependent characteristics of poly(3 hexylthiophene)-fullerene based heterojunction organic solar cells, J. Appl. Phys. 93 (2003) 3376–3383.
[28] B.G. Streetman, Solid State Electronic Devices, Prentice-Hall, Englewood Cliffs, NJ, 1980.
[29] M.S.A. Abdou, X. Lu, Z.W. Xie, F. Orfino, M.J. Deen, S. Holdcroft, Nature of impurities in π-conjugated polymers prepared by ferric chloride and their effect on the electrical properties of metal-insulator-semiconductor structures, Chem. Mater. 7 (1995) 631–641.
[30] M.S.A. Abdou, F. Orfino, Z.W. Xie, M.J. Deen, S. Holdcroft, Reversible charge transfer complexes between molecular oxygen and poly(3-alkylthiophene)s, Adv. Mater. 6 (1994) 838–841.

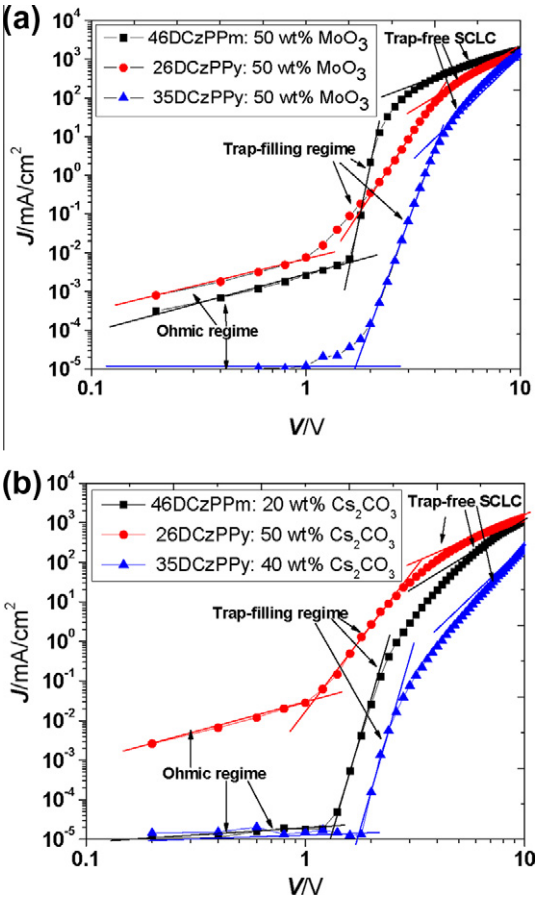

Fig. 1. Current density versus voltage characteristics of the hole- (a) and electron- (b) only devices consisting of *p*/*n*-doped 46DCzPPm, 35DCzPPy and 26DCzPPy layers.

voltage of the device so as to obtain high power efficiency [10]. However, there are few reports focused on homojunction OLEDs, which are only centered on fluorescent and red phosphorescent devices with quite high driving voltages [11]. In the present paper, we systematically demonstrate efficient red, green and blue homojunction phosphorescent OLEDs with various emitting dopants of tris(1-phenylisoquinolinolato-C^2,*N*)iridium(III) (Ir(piq)$_3$), *fac*-tris(2-phenylpyridine) iridium (Ir(ppy)$_3$) and iridium(III) bis(4,6-(di-fluorophenyl)pyridinato-*N*,C2′) picolinate (FIrpic) by using a series of bipolar host materials, including 2,6-bis(3-(carbazol-9-yl)phenyl) pyridine (26DCzPPy), 3,5-bis(3-(carbazol-9-yl)phenyl) pyridine (35DCzPPy) and 4,6-bis(3-(carbazol-9-yl)phenyl) pyrimidine (46DCzPPm).

2. Results and discussion

2.1. Mobility of 46DCzPPm, 26DCzPPy, 35DCzPPy and hole and electron-only devices with p/n-doped layers

In order to demonstrate the effect of *p*/*n*-doped layers, hole/electron-only devices were fabricated. Hole-only devices of indium tin oxide (ITO)/host:MoO_3 (30 nm)/host (10 nm)/*N*,*N*′-bis(naphthalen-1-yl)-*N*,*N*′-bis(phenyl)-2,2′-dimethylbenzidine (NPD) (10 nm)/Al (80 nm) and electron-only devices of ITO/2,9-dimethyl-4,7-diphenyl-1,10-phenanthroline (BCP) (10 nm)/host (30 nm)/host:Cs_2CO_3 (20 nm)/Al (80 nm) were fabricated to compare the injection and transport property of various doped host materials. Fig. 1 shows current density versus voltage characteristics of the devices, indicating that *p*/*n*-doped layers could get quite efficient charge carrier injection and transport in the devices. In order to obtain the best charge carrier injection and transport, here we fabricated a series of hole-only and electron-only devices with different *p*/*n*-doping concentrations to decide the optimum ones. For *p*-doped layers, 50 wt.% MoO_3 is the best one to enhance the hole injection and transport, which is shown in Fig. 1(a). For *n*-doped layers, the optimum concentrations of Cs_2CO_3 are 20 wt.% for 46DCzPPm, 50 wt.% for 26DCzPPy and 40 wt.% for 35DCzPPy, respectively, which are shown in Fig. 1(b). Here, the 46DCzPPm-based hole-only device shows the most efficient hole injection and transport. Current density versus voltage curves of hole/electron-only device show the typical shape of space charge limited current. For the electron-only device, the slopes, whose values are 1.5 for 26DCzPPy-, 0.36 for 46DCzPPm- and 0.02 for 35DCzPPy-based devices, refers to the Ohmic regime, described by $J_\Omega = q\mu nV/L$ (noted by solid lines). The regions with steep slope, trap-filling regime, correspond to the rapid change undergone by the current. The slopes, referring to the trap-free space-charge-limited-current region are 1.8 for 26DCzPPy-, 2.9 for 46DCzPPm- and 6.4 for 35DCzPPy-based devices, respectively, obeying the Mott-Gurney law $J_{SCLC} = 9\varepsilon\varepsilon_0\mu\Theta V^2/8L^3$ [13]. Three regions for hole-only devices were also marked in Fig. 1(a).

Table 1 shows hole and electron mobilities of 46DCzPPm, 35DCzPPy and 26DCzPPy neat films. Mobilities reveal that 26DCzPPy and 35DCzPPy are quite well-balanced bipolar host materials, because electron and hole mobilities are similar within one material on the order of about 10^{-5}. For 46DCzPPm, it is also a bipolar host, although its hole mobility is slightly higher than its electron mobility.

2.2. Performance of RGB homojunction devices by using 46DCzPPm, 26DCzPPy and 35DCzPPy

To evaluate 46DCzPPm, 26DCzPPy and 35DCzPPy as host materials applied in *p*–*i*–*n* homojunction devices, phosphorescent OLEDs were fabricated with commercially available phosphorescent emitters of FIrpic, Ir(ppy)$_3$ and

Table 1
Hole and electron mobilities of 46DCzPPm, 26DCzPPy and 35DCzPPy neat films prepared by vacuum vapor deposition.

Hosts	Hole mobility ($cm^2\,V^{-1}\,S^{-1}$)	Electron mobility ($cm^2\,V^{-1}\,S^{-1}$)	Electric field ($V\,cm^{-1}$)
46DCzPPm	1.3×10^{-5}	4.2×10^{-6}	8.1×10^5
26DCzPPy	2.0×10^{-5}	2.0×10^{-5}	5.6×10^5
35DCzPPy	3.7×10^{-5}	3.2×10^{-5}	5.6×10^5

Table 2
HOMO, LUMO and triplet energy levels of materials used in this study.

Material	HOMO (eV)	LUMO (eV)	T_1 (eV)
26DCzPPy	6.05	2.65	2.71
35DCzPPy	6.18	2.75	2.71
46DCzPPm	6.19	3.06	2.64
FIrpic	6.15	3.47	2.65
$Ir(ppy)_3$	5.40	2.40	2.41
$Ir(piq)_3$	5.10	3.10	2.00

$Ir(piq)_3$. Triplet energy levels (T_1) of all materials used in this study were shown in Table 2. As well known, T_1 is of great importance on the confinement of triplet exciton in a host/guest system, which is relevant with the device performance. For 26DCzPPy and 35DCzPPy, they possess a similar T_1 level of 2.71 eV, which is high enough for all triplet emitters used in this study to prevent reverse energy transfer from the guest to the host. For 46DCzPPm, its T_1 level of 2.64 eV is high enough for $Ir(ppy)_3$ (T_1 = 2.4 eV) and $Ir(piq)_3$ (T_1 = 2.0 eV) but not for FIrpic (2.65 eV), probably leading to a efficiency loss in FIrpic-based device [12].

The device with a *p–i–n* homojunction structure used in this study as shown in Fig. 2 is the following: ITO (130 nm)/host:MoO_3 (30 nm)/host (10 nm)/host:12 wt.% FIrpic or 10 wt.% $Ir(ppy)_3$ or 4 wt.% $Ir(piq)_3$ (30 nm)/host (10 nm)/host:Cs_2CO_3 (20 nm)/Al (80 nm). Fig. 3(a) and (b) shows the current density and luminance versus applied voltage characteristics and the external quantum efficiency (EQE) and power efficiency (PE) of the blue homojunction devices with various host materials. Fig. 3(a) shows that the current densities of the 46DCzPPm- and 26DCzPPy-based blue devices are almost identical, but the 46DCzPPm-based device exhibits a rather low turn-on voltage of 2.6 V (luminance of 1 cd m^{-2} was detected) and a low driving voltage of 3.1 V at 100 cd m^{-2} and 3.9 V at 1000 cd m^{-2}. Although the 35DCzPPy-based device shows a poor current density versus voltage characteristic, which could be due to inefficient charge carrier injection, a EQE of 12.9%, corresponding to a current efficiency (CE) of 27.2 cd A^{-1} with a PE of 19.6 lm W^{-1} was obtained at 100 cd m^{-2}, which is much higher than the EQE (9.1%) for the 46DCzPPm-based device with a current efficiency of 20.5 cd A^{-1} and a PE of 20.9 lm W^{-1}. High efficiencies of 10.0%, 11.6 lm W^{-1}, and 7.0%, 12.8 lm W^{-1} were realized at 1000 cd m^{-2} for the 35DCzPPy- and 46DCzPPm-based devices, respectively. Although it has been reported that 26DCzPPy is a well-known host material for FIrpic-based blue OLEDs with a heterojunction structure, efficiencies of 8.0%, 13.5 lm W^{-1} at 100 cd m^{-2} and 7.2%, 9.5 lm W^{-1} at 1000 cd m^{-2} did not show an excellent performance in a homojunction structure made during this study [14,15].

Encouraged by the results of blue *p–i–n* homojunction devices, 46DCzPPm, 26DCzPPy and 35DCzPPy were also used as host materials for fabricating $Ir(ppy)_3$-based green and $Ir(piq)_3$-based red homojunction OLEDs. Fig. 3(c) and (d) shows the current density and luminance versus applied voltage characteristics, EQE and PE of the $Ir(ppy)_3$-based green devices. Here we found out that there is an obvious difference between the *J–V* performances of the 46DCzPPm- and 26DCzPPy-based green devices. This result is quite different from the 46DCzPPm/26DCzPPy-based blue devices with almost identical *J–V* characteristic. Taking the difference in the *J–V* performance caused by using different emitting dopant into account, we could make a conclusion that the emitting dopants could have a strong influence on the charge carrier transport of the emission layer. The 46DCzPPm-based device shows high

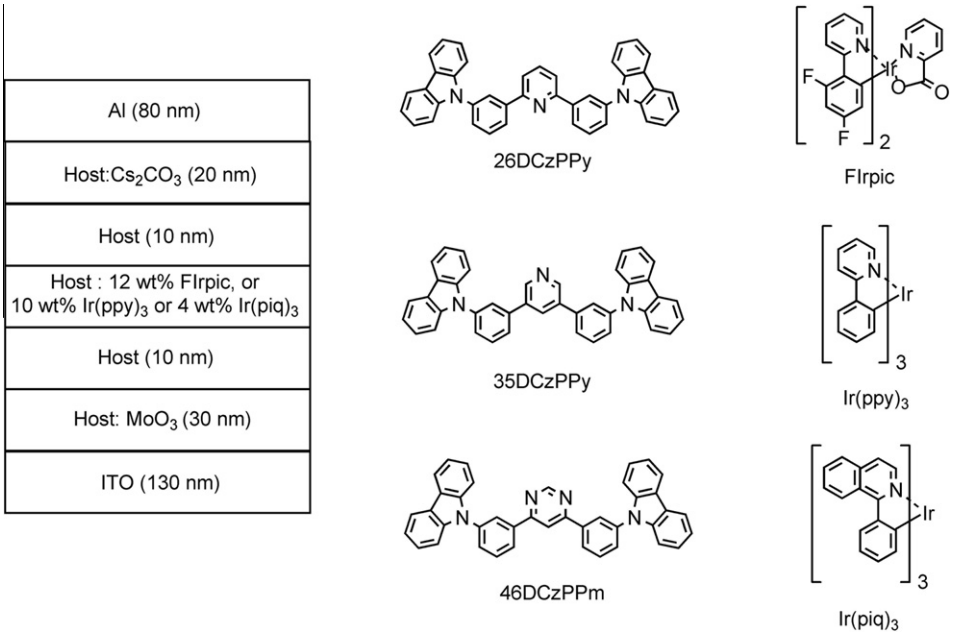

Fig. 2. Device structure of the *p–i–n* homojunction phosphorescent OLEDs. Also shown the structures for host materials 26DCzPPy, 35DCzPPy, 46DCzPPm and emitting dopants FIrpic, $Ir(ppy)_3$ and $Ir(piq)_3$.

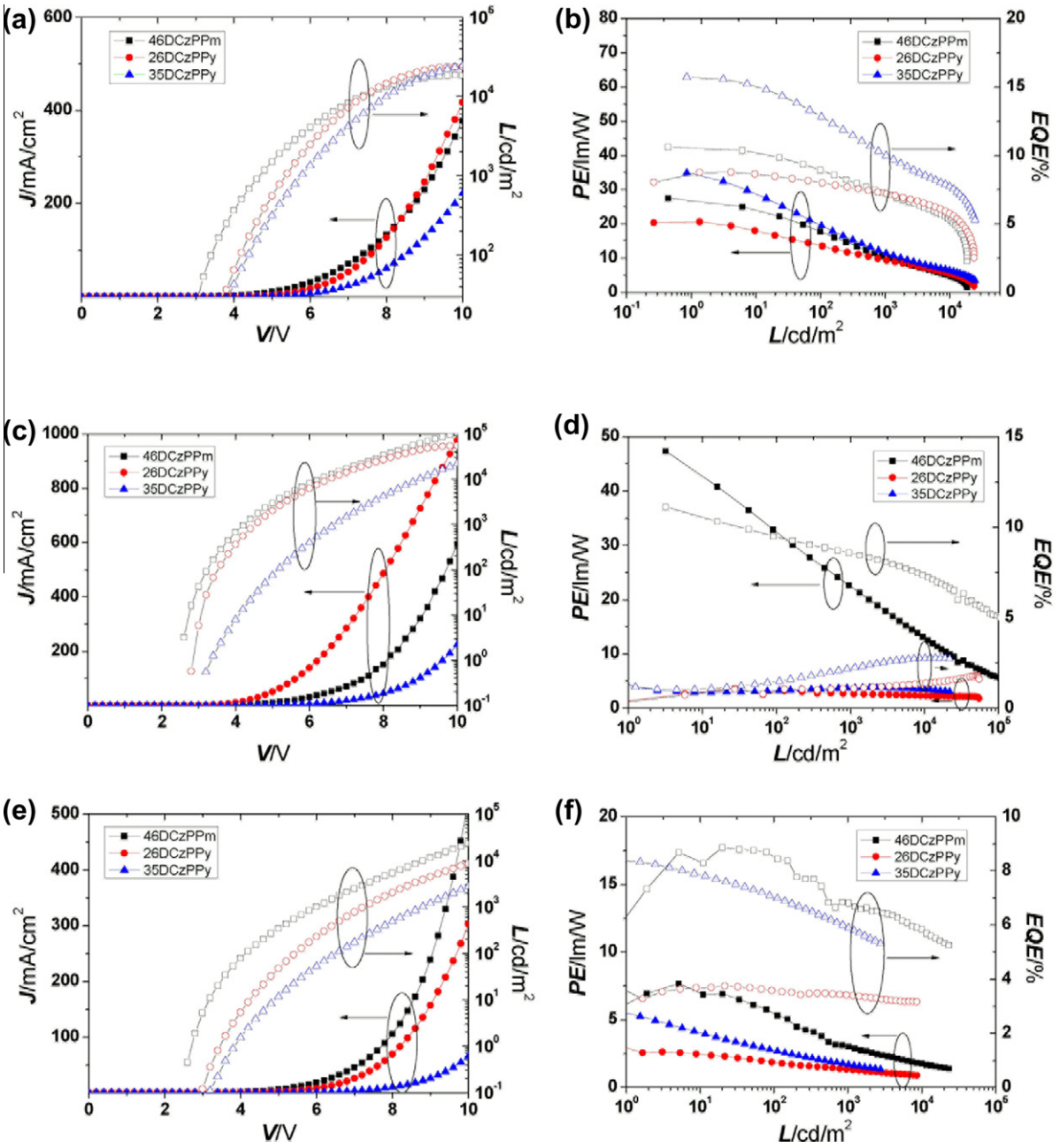

Fig. 3. *J–V–L* and power- and current efficiency characteristics of phosphorescent *p–i–n* homojunction OLEDs: ITO/host:MoO_3 (30 nm)/host (10 nm)/host:dopant (30 nm)/host (10 nm)/host:Cs_2CO_3 (20 nm)/Al by using 46DCzPPm (■□), 26DCzPPy (●○) and 35DCzPPy (▲△). (a) and (b): blue devices by using 12 wt.% FIrpic as a dopant; (c) and (d): green devices by using 8 wt.% $Ir(ppy)_3$ as a dopant; (e) and (f): red devices by using 4 wt.% $Ir(piq)_3$ as a dopant. (For interpretation of the references to colour in this figure legend, the reader is referred to the web version of this article.)

efficiencies of 9.5%, 32.5 lm W^{-1} and 8.6%, 22.4 lm W^{-1} at 100 and 1000 cd m^{-2}, respectively. However, to our surprise, the 26DCzPPy- and 35DCzPPy-based devices show quite low EQE of less than 5% which is far below the typical phosphorescent efficiency.

For the $Ir(piq)_3$-based red phosphorescent homojunction devices, whose performances were shown in Fig. 3(e) and (f), the 46DCzPPm-based device shows high efficiencies of 8.5%, 5.5 lm W^{-1}, and 6.8%, 3.0 lm W^{-1} at 100 and 1000 cd m^{-2}, respectively. Although the 35DCzPPy-based device also shows high EQE of 7.0% at 100 cd m^{-2} and 5.9% at 1000 cd m^{-2}, its quite high driving voltage, which could probably be attributed to inefficient charge carrier injection from electrodes into the emission layer, leads to low power efficiency of only 2.7 and 1.7 lm W^{-1} at 100 and 1000 cd m^{-2}, respectively. For the 26DCzPPy-based device, EQE of 3.6% at 100 cd m^{-2} and 3.4% at 1000 cd m^{-2} were realized. These results are more

Table 3
Performance data of red, green and blue *p–i–n* homojunction devices by using 46DCzPPm, 26DCzPPy and 35DCzPPy.

Dopant material	Host material	Turn on voltage	Performance at 100 cd m^{-2}			Performance at 1000 cd m^{-2}		
		(V)	V (V)	EQE (%)	PE (lm W^{-1})	V (V)	EQE (%)	PE (lm W^{-1})
Flrpic	46DCzPPm	2.6	3.1	9.1	21.0	3.9	7.0	12.8
	26DCzPPy	2.9	4.2	8.0	13.5	5.4	7.2	9.5
	35DCzPPy	3.3	4.4	12.9	19.6	5.8	10.0	11.6
lr(ppy)3	46DCzPPm	2.5	3.2	9.5	32.5	4.2	8.6	22.4
	26DCzPPy	2.8	3.5	0.9	2.9	4.5	1.1	2.6
	35DCzPPy	3.3	5.1	1.5	3.2	6.7	2.2	3.7
$lr(piq)_3$	46DCzPPm	2.7	4.1	8.5	5.5	6.0	6.8	3.0
	26DCzPPy	3.4	5.4	3.6	1.8	7.2	3.4	1.3
	35DCzPPy	3.8	6.5	7.0	2.7	8.8	5.9	1.7

efficient than the previously reported $Ir(piq)_3$-based homojunction devices [11]. Regarding the *J–V* characteristics, which are shown in Fig. 3(e), the 46DCzPPm-based device showed a better performance than the 26DCzPPy-based device, proving that there is a strong relationship between the charge carrier transport and the emitting dopant. All device performance data are summarized in Table 3.

2.3. Influence of carrier balance and position of recombination zone of holes and electrons on performances of homojunction devices

Charge carrier balance is a quite important factor for the performance of an OLED, and EQE is directly related to the balance of holes and electrons in the devices [6]. For maximizing the efficiency of an OLED, we need to confine the recombination zone in the bulk of emission layer. However, for homojunction devices, partially due to the lack of hole/electron-blocking layers, the main recombination zone of holes and electrons could not be effectively confined. Instead, the recombination zone resembles to be smeared out in the 30-nm-thick emission layer. Thus, generated excitons that have long diffusion length could be quenched by *p*-type dopant MoO_3 or *n*-type dopant Cs_2CO_3. The generated excitons could also be harvested by the 10-nm-thick intrinsic bipolar host, which leads to an efficiency loss, resulting in a visible fluorescent emission of the intrinsic bipolar host [16]. This can be observed in the EL spectrum of the 26DCzPPy:$Ir(ppy)_3$-based green homojunction device (shown in Supporting Information). Thus, there exists a strong relation between the position of the recombination zone of charge carriers and the EQE of the device.

Firstly, in order to find out the main factor for the quite low efficiency in the 26DCzPPy:$Ir(ppy)_3$-based *p–i–n* homojunction device and investigate the carrier balance so as to probe the position of the recombination zone, the following control device comprising a 5-nm-thick 26DCzPPy doped with 1 wt.% 4-(dicyanomethylene)-2-tert-butyl-6-(1,1,7,7-tetramethyljulolidin-4-yl-vinyl)-4H-pyran (DCJTB) layer, which is close to the cathode side, was fabricated with the structure: ITO/26DCzPPy:MoO_3 (30 nm)/26DCzPPy (10 nm)/26DCzPPy:$Ir(ppy)_3$ (10 wt.%, 30 nm)/26DCzPPy (2.5 nm)/26DCzPPy:DCJTB (1 wt.%, 5 nm)/26DCzPPy (2.5 nm)/26DCzPPy:Cs_2CO_3 (20 nm)/Al (80 nm). In this device, red fluorescent material DCJTB was doped at 1 wt.% into the device to act as a sensor that aims to probe the density of charge carrier via EL spectrum of the device. The influence of DCJTB on the transport characteristic of the device could be negligible due to the quite low doping concentration of only 1 wt.%. In Fig. 4(a), for the device containing a 26DCzPPy: DCJTB layer close to the cathode side, a typical phosphorescent emission from $Ir(ppy)_3$ peaking around 520 nm was found. There also exists an obvious fluorescent emission resulted from the host near 430 nm. The EL spectrum of another control device containing a 26DCzPPy: DCJTB layer close to the anode side with the structure ITO/26DCzPPy:MoO_3 (30 nm)/26DCzPPy (2.5 nm)/26DCzPPy:DCJTB (1 wt.%, 5 nm)/26DCzPPy (2.5 nm)/26DCzPPy:$Ir(ppy)_3$ (10 wt.%, 30 nm)/26DCzPPy (10 nm)/26DCzPPy:Cs_2CO_3 (20 nm)/Al (80 nm) was shown in Fig. 4(b). As expected, this device also shows a vivid emission from $Ir(ppy)_3$, however, a clear visible emission from DCJTB around 600 nm replaces the fluorescent emission of 26DCzPPy around 430 nm that appeared in the control device containing a 26DCzPPy: DCJTB layer close to the cathode side. The possible reason for these two different EL spectra is that in the 26DCzPPy: $Ir(ppy)_3$-based device containing a 26DCzPPy:DCJTB layer close to cathode side, few holes are able to go across the 30-nm-thick 26DCzPPy:$Ir(ppy)_3$ layer and reach the 26DCzPPy:DCJTB layer so as to generate a fluorescent emission, whereas for the 26DCzPPy:$Ir(ppy)_3$-based device containing a 26DCzPPy: DCJTB layer close to the anode side, the EL spectrum including a vivid emission from DCJTB indicates that significant amount of electrons could transport through the 26DCzPPy:$Ir(ppy)_3$ layer. Thus a large number of holes are recombined in the 5-nm-thick 26DCzPPy:DCJTB layer, generating a clear visible fluorescent emission from DCJTB, indicating that the 26DCzPPy-based green *p–i–n* homojunction device is hole deficient and the recombination zone should be quite close to the anode side. The EL spectrum of the device containing a DCJTB-doped layer close to anode side varies significantly depending on the current density of the device, which increases from 0.25 to 25 mA cm^{-2}. The increasing intensity of $Ir(ppy)_3$ and decreasing intensity of DCJTB with increasing current

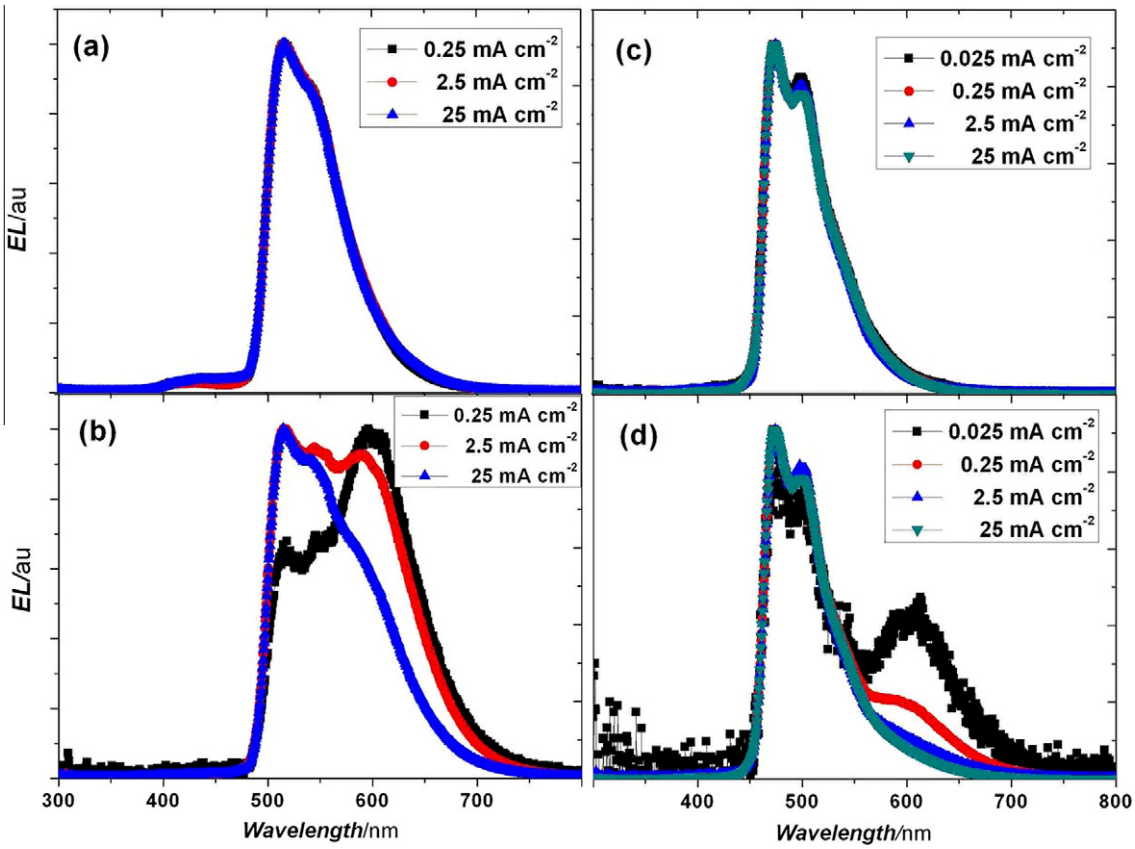

Fig. 4. EL spectra for the devices containing DCJTB. (a) ITO/26DCzPPy:MoO_3 (30 nm)/26DCzPPy (10 nm)/26DCzPPy:Ir(ppy)$_3$ (10 wt.%, 30 nm)/26DCzPPy (2.5 nm)/26DCzPPy:DCJTB (1 wt.%, 5 nm)/26DCzPPy (2.5 nm)/26DCzPPy:Cs_2CO_3 (20 nm)/Al (80 nm). (b) ITO/26DCzPPy:MoO_3 (30 nm)/26DCzPPy (2.5 nm)/26DCzPPy:DCJTB (1 wt.%, 5 nm)/26DCzPPy (2.5 nm)/26DCzPPy:Ir(ppy)$_3$ (10 wt.%, 30 nm)/26DCzPPy (10 nm)/26DCzPPy:Cs_2CO_3 (20 nm)/Al (80 nm). (c) ITO/26DCzPPy:MoO_3 (30 nm)/26DCzPPy (10 nm)/26DCzPPy:FIrpic (12 wt.%, 30 nm)/26DCzPPy (2.5 nm)/26DCzPPy:DCJTB (1 wt.%, 5 nm)/26DCzPPy (2.5 nm)/26DCzPPy:Cs_2CO_3 (20 nm)/Al (80 nm). (d) ITO/26DCzPPy:MoO_3 (30 nm)/26DCzPPy (2.5 nm)/26DCzPPy:DCJTB (1 wt.%, 5 nm)/26DCzPPy (2.5 nm)/26DCzPPy:FIrpic (12 wt.%, 30 nm)/26DCzPPy (10 nm)/26DCzPPy:Cs_2CO_3 (20 nm)/Al (80 nm).

density indicates the shift of the recombination zone from the anode side to the 30-nm-thick 26DCzPPy:Ir(ppy)$_3$ layer. An improved charge carrier balance attributed to the stronger hole injection when the device is under a higher external biased voltage is beneficial for the efficiency.

Considering that 26DCzPPy should be an excellent bipolar host material with well-balanced hole and electron mobilities that is shown in Table 1, the poor carrier balance is not believed to be due to low mobility of the host material, but probably due to the deficient hole injection from the anode into the emission layer. Although a 26DCzPPy:Ir(ppy)$_3$-based homojunction device was found to be hole deficient, when the blue phosphorescent material FIrpic was used as the emitting dopant, an EQE of 8.0% of the FIrpic-based blue device at 100 cd m^{-2} was obtained, which is even higher than that of the 26DCzPPy:Ir(ppy)$_3$-based device. The EL spectrum of the 26DCzPPy:FIrpic-based device (shown in Supporting Information) shows a pure emission from FIrpic without any fluorescent emission from 26DCzPPy. DCJTB was also doped at 1 wt.% into 26DCzPPy:FIrpic-based homojunction device in order to investigate its carrier balance. For the 26DCzPPy:FIrpic-based device comprising a 26DCzPPy:DCJTB layer close to cathode side, its EL spectrum shown in Fig. 4(c) does not include any emission from DCJTB. For the device comprising a 26DCzPPy:DCJTB layer close to anode side, there still exists an obvious fluorescent emission from DCJTB in the EL spectrum shown in Fig. 4(d), it can be observed that the intensity of DCJTB is far weaker than that of FIrpic, indicating a sharply decreased density of electrons in 5-nm-thick 26DCzPPy:DCJTB layer that is close to anode side. Thereby, compared with the 26DCzPPy:Ir(ppy)$_3$-based device, the improved EQE in the 26DCzPPy:FIrpic-based device should be probably due to the electron-trapping function of FIrpic that could decrease the electron current in the device and effectively improve the position of the charge carrier recombination zone throughout the device.

Carrier balances of other green and blue homojunction devices by using 46DCzPPm or 35DCzPPy as host material were also examined by observing EL spectra of DCJTB-doped devices (shown in Supporting Information). These EL spectra reveal that the 46DCzPPm/35DCzPPy-based devices are hole deficient and FIrpic functions as an electron trap, which could benefit EQE. We noticed that these devices are also hole deficient which may be attributed to

inefficient hole injection from anode to *p*-doped host layer since there should be no problem for hole transport in these hosts as they are balanced bipolar host materials.

There are obvious differences in device performances by using 26DCzPPy, 35DCzPPy, and 46DCzPPm, for example, which are the driving voltage and EQE. For the 46DCzPPm-based devices, the turn-on voltage of 2.6 V for blue, 2.5 V for green and 2.7 V for red devices are lower than that of other RGB devices by using 26DCzPPy or 35DCzPPy as a bipolar host. It seems that 46DCzPPm is the most suitable one for fabricating homojunction devices, because only it gives high efficiencies of 10.2% for blue, 11.1% for green and 8.9% for red devices under maximum EQE. This could be attributed to the fact that the poor hole supply in these homojunction devices causes the recombination zone to be close to anode side, therefore, the host with best hole injection/transport will give the best performance. From performance of hole-only devices that is shown in Fig. 1(a), we know that the 46DCzPPm-based device has the best hole injection/transport, which benefits a well-balanced system [18–20].

2.4. Electron transport characteristics of emission layers doped with FIrpic, Ir(ppy)$_3$ and Ir(piq)$_3$

From the discussion above, the 46DCzPPm-, 26DCzPPy- and 35DCzPPy-based homojunction devices were found out to be hole deficient and the recombination zones in these devices are close to ITO side. In this case, the charge trapping effect of emitting dopant will play an important role in these devices. If the emitting dopant can trap electrons, further decreasing the electron transport and improving the recombination zone of charge carriers, then the device could show a better performance.

Usually, when a guest with narrow band gap was doped into a host with a wide band gap, the energy difference of HOMO/LUMO levels between the guest and the host will be quite significant, and then the guest could become a deep trap due to this difference [17]. Energy levels HOMO (the highest occupied molecular orbital), LUMO (the lowest unoccupied molecular orbital), and triplet energy levels (T_1) of the materials used in this work were summarized in Table 2 [12]. The HOMO levels of Ir(ppy)$_3$ (5.4 eV) and Ir(piq)$_3$ (5.1 eV) are much shallower than those of the bipolar host materials (6.05 eV for 26DCzPPy, 6.18 eV for 35DCzPPy and 6.19 eV for 46DCzPPm), and the LUMO levels of Ir(piq) (3.1 eV) and FIrpic (3.47 eV) are deeper than those of the bipolar host materials (2.65 eV for 26DCzPPy, 2.75 eV for 35DCzPPy and 3.06 eV for 46DCzPPm). Thus in this host/guest system, Ir(ppy)$_3$ and Ir(piq)$_3$ could trap holes while FIrpic and Ir(piq)$_3$ could effectively trap electrons. Ir(ppy)$_3$ seems not to function as a electron-trap state probably due to its high LUMO level (2.4 eV).

To further demonstrate the influence of the emitting dopants FIrpic, Ir(ppy)$_3$ and Ir(piq)$_3$ on hole/electron transport of a 30-nm-thick emission layer, hole-only devices with a structure of ITO/NPD (20 nm)/26DCzPPy (10 nm)/26DCzPPy:12 wt.% FIrpic or 10 wt.% Ir(ppy)$_3$ or 4 wt.% Ir(piq)$_3$/26DCzPPy (10 nm)/NPD (20 nm)/Al (80 nm) and electron-only devices with a structure of ITO/1,3,5-tri (p-pyrid-3-yl-phenyl)benzene (TpPyPB) (10 nm)/26DCzPPy (10 nm)/26DCzPPy:12 wt.% FIrpic or 10 wt.% Ir(ppy)$_3$ or 4 wt.% Ir(piq)$_3$/26DCzPPy (10 nm)/TpPyPB (20 nm)/LiF (0.5 nm)/Al (80 nm) were fabricated. Fig. 5 shows the current density versus applied voltage characteristics of these devices. For the hole-only devices doped with 4 wt.% Ir(piq)$_3$ or 10 wt.% Ir(ppy)$_3$ those are shown in Fig. 5(a), they show a clearly decreased current density than that of the device with an intrinsic 30-nm-thick 26DCzPPy layer due to the hole trapping functions of Ir(ppy)$_3$ and Ir(piq)$_3$. Besides, FIrpic does not show any hole trapping effect just due to its deep HOMO level of 6.15 eV. In Fig. 5(b), compared with the electron-only device with an intrinsic 30-nm-thick 26DCzPPy layer, devices doped with 4 wt.% Ir(piq)$_3$ show a notably decreased current density which could be due to the electron-trapping function of Ir(piq)$_3$. FIrpic also shows electron-trapping function because after the turn-on voltage the current density increasing of the 26DCzPPy:FIrpic-based device is slower

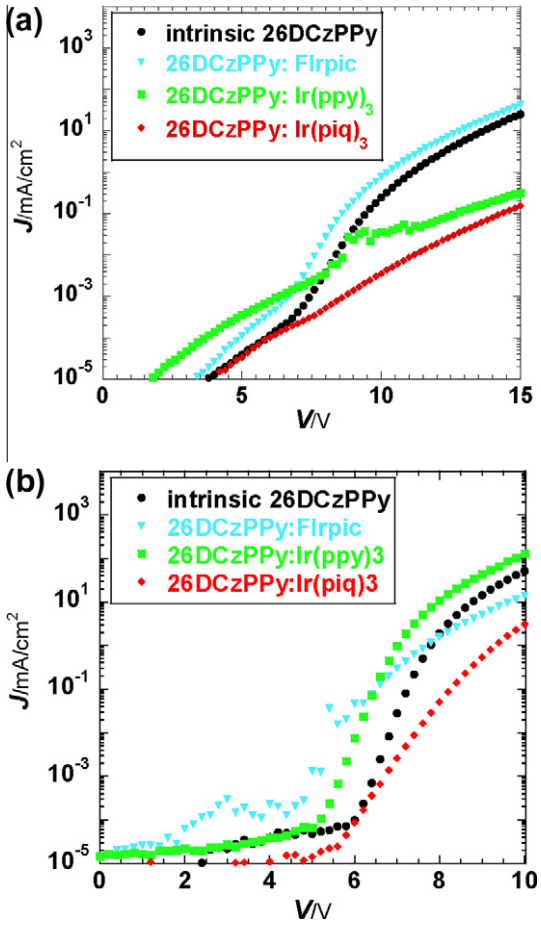

Fig. 5. Current density-driving voltage characteristics of the hole/electron-only devices for evaluating hole/electron transport of 26DCzPPy-based emission layers doped with FIrpic, Ir(ppy)$_3$ or Ir(piq)$_3$. (a) hole-only devices with a structure of ITO/NPD (20 nm)/26DCzPPy (10 nm)/26DCzPPy:12 wt.% FIrpic, or 10 wt.% Ir(ppy)$_3$ or 4 wt.% Ir(piq)$_3$ (30 nm)/26DCzPPy (10 nm)/NPD (20 nm)/Al. (b) electron-only devices with a structure of ITO/TpPyPB (10 nm)/26DCzPPy (10 nm)/26DCzPPy:12 wt.% FIrpic, or 10 wt.% Ir(ppy)$_3$ or 4 wt.% Ir(piq)$_3$ (30 nm)/26DCzPPy (10 nm)/TpPyPB (20 nm)/LiF (0.5 nm)/Al.

than that of the intrinsic 26DCzPPy-based device. Hence, the position of recombination zone in the 26DCzPPy:FIrpic/Ir(piq)$_3$-based homojunction devices could be sufficiently far away from the anode side, thereby confining charge carriers in the 30-nm-thick emission layer and eliminating the fluorescent emission from the 10-nm-thick intrinsic 26DCzPPy close to the anode. This also leads to the knowledge that most of triplet excitons are confined in the 30-nm-thick emitting layer. Current density versus voltage characteristic of the electron-only devices comprising 26DCzPPy:Ir(ppy)$_3$ layer reveals that Ir(ppy)$_3$ could keep, or slightly enhance the electron transport performance of the emission layer, making a worse carrier balance, which leads to an efficiency loss. The influence of emitting dopants doped into 35DCzPPy and 46DCzPPm on hole/electron transport were also examined (shown in Supporting Information). The results imply that Ir(ppy)$_3$ and Ir(piq)$_3$ efficiently function as hole traps and FIrpic as well as Ir(piq)$_3$ are electron traps due to their HOMO/LUMO energy level alignments when they are doped into 35DCzPPy/46DCzPPm. Ir(ppy)$_3$ can also function as an electron trap only when it is doped into 46DCzPPm, resulting in a high EQE of 9.5% at 100 cd m^{-2} in the 46DCzPPm:Ir(ppy)$_3$-based homojunction device.

3. Conclusion

In conclusion, efficient *p–i–n* homojunction OLEDs were reported that emit across the full visible color range by using a series of bipolar host materials. Several record efficiencies of 12.9% for blue, 9.5% for green, and 8.5% for red homojunction devices (at 100 cd m^{-2}) were achieved. Performance of these homojunction OLEDs is strongly dependent on the well-balanced charge carrier injection and transport of injected holes and electrons. With suitable chemical adjustment in the material structure, it is possible to obtain a more well-balanced bipolar host material. Hereby the performance of homojunction devices can be enhanced. However, for the present homojunction devices shown in this study, we did not do any further optimization and there still remains room for improvement. For example, with carefully varying the concentration of emitting dopant, we can adjust the transport performance of the organic layer. In this way, carriers can be confined in the emission layer, and a better efficiency can be expected.

4. Experimental

All devices were grown on glass substrates pre-coated with a ~130 nm thick of ITO. The substrates were cleaned with ultra purified water and organic solvents, and then dry-cleaned for 30 min by exposure to an UV-ozone ambient. All the organic layers were deposited by vacuum evaporation. The fabrication procedure of the hole-only device is described as follows: first, a bipolar host was codeposited with MoO_3 for a thickness of 30 nm, followed by an intrinsic 10-nm-thick host material. After that another 10-nm-thick NPD layer was deposited successively. Cathodes consisting of a 80-nm-thick layer Al were patterned using a shadow mask with an array of 2×2 mm^2 openings. For the electron-only devices, firstly a 10-nm-thick BCP layer was deposited, followed by an intrinsic 30-nm-thick host material. Then an *n*-doped transport layer was deposited by co-evaporation of host material and Cs_2CO_3, following a 80-nm-thick Al layer of cathode.

The fabrication procedure of homojunction devices is described as follows: first, the bipolar host with MoO_3 was deposited with a thickness of 30 nm, followed by a 10-nm-thick intrinsic host material. Subsequently, the emitting layer consisting of the host material doped with 12 wt.% FIrpic for blue, 10 wt.% Ir(ppy)$_3$ for green or 4 wt.% Ir(piq)$_3$ for red devices was deposited with a thickness of 30 nm, followed by another 10-nm-thick intrinsic host material. After that an *n*-doped transport layer was deposited by co-evaporation of host material and Cs_2CO_3. Then, a 80 nm-thick Al layer was vacuum deposited and the active area of the devices was defined as 2×2 mm^2 by using a shadow-mask. All devices were encapsulated by a glass lid with a getter attached under nitrogen atmosphere.

Appendix A. Supplementary data

Supplementary data associated with this article can be found, in the online version, at doi:10.1016/j.orgel.2011.01.021.

References

[1] B.W. D'Andrade, S.R. Forrest, Adv. Mater. 16 (2004) 1585.
[2] M.A. Baldo, D.F. O'Brien, Y. You, A. Shoustikov, S. Sibley, M.E. Thompson, S.R. Forrest, Nature 395 (1998) 151.
[3] C.W. Tang, S.A. VanSlyke, Appl. Phys. Lett. 51 (1987) 913.
[4] L.S. Hung, C.H. Chen, Mater. Sci. Eng. R 39 (2002) 143.
[5] K. Goushi, R. Kwong, J.J. Brown, H. Sasabe, C. Adachi, J. Appl. Phys. 95 (2004) 7798.
[6] N. Chopra, J. Lee, J.-G. Xue, F. So, IEEE Trans. Electron. Devices 57 (2010) 101.
[7] S.Y. Kim, W.S. Jeon, T.J. Park, R. Pode, J. Jang, J.H. Kwon, Appl. Phys. Lett. 94 (2009) 133303.
[8] Z.W. Liu, M.G. Helander, Z.B. Wang, Z.H. Lu, Org. Electron. 10 (2009) 1146.
[9] S.M. Sze, Physics of Semiconductor Devices, second ed., Wiley, New York, 1981.
[10] (a) J. Endo, T. Matsumoto, J. Kido, Jpn. J. Appl. Phys. 41 (2002) 358;
(b) K. Walzer, B. Maennig, M. Pfeiffer, K. Leo, Chem. Rev. 107 (2007) 1233;
(c) S. Watanabe, Y. Agata, D. Tanaka, J. Kido, J. Photopolym. Sci. Technol. 18 (2005) 83;
(d) J. Kido, T. Matsumoto, Appl. Phys. Lett. 73 (1998) 2866;
(e) K. Harada, A.G. Werner, M. Pfeiffer, C.J. Bloom, C.M. Elliott, K. Leo, Phys. Rev. Lett. 94 (2005) 036601;
(f) K. Harada, M. Riede, K. Leo, Phys. Rev. B 77 (2008) 195212.
[11] (a) T. Mori, A. Oda, J. Kido, Proceedings of The Japan Society of Applied Physics and Related Societies 53 (2006) 1395;
(b) H. Tsuji, C. Mitsui, Y. Sato, E. Nakamura, Adv. Mater. 21 (2009) 3776.
[12] S.-J. Su, C. Cai, J. Kido, Chem. Mater. 23 (2011) 274.
[13] A. Carbone, B.K. Kotowska, D. Kotowski, Phys. Rev. Lett. 95 (2005) 236601.
[14] S.-J. Su, H. Sasabe, T. Takeda, J. Kido, Chem. Mater. 20 (2008) 1691.
[15] S.-J. Su, Y. Takahashi, T. Chiba, T. Takeda, J. Kido, Adv. Funct. Mater. 19 (2009) 1260.
[16] M.A. Baldo, S.R. Forrest, Phys. Rev. B. 62 (2000) 10958.
[17] T. Tsuzuki, S. Tokito, Adv. Mater. 19 (2007) 276.
[18] M. Pfeiffer, S.R. Forrest, K. Leo, M.E. Thompson, Adv. Mater. 14 (2002) 1633.
[19] J. Huang, M. Pfeiffer, A. Werner, J. Blochwitz, S. Liu, K. Leo, Appl. Phys. Lett. 80 (2002) 139.
[20] G.F. He, M. Pfeiffer, K. Leo, M. Hofmann, J. Birnstock, R. Pudzich, J. Salbeck, Appl. Phys. Lett. 85 (2004) 3911.

methods and comparing in some cases the two different contributions [3]. No direct correlation between the contributions in-dark and in-light to the electrical properties has been reported as measured on the same device.

It is known that the electrical conduction in liquid crystals and in particular in phthalocyanine-based materials is greatly affected by contaminants and environmental conditions [11,28–32]. Although a controlled doping produces a strengthening of the sensing capability, it becomes a major limitation in organic electronics applications. The amount of contaminants is less controllable when the films are deposited or cast starting from solutions, where the solvent itself or the process can provide dopants, determining unstable electrical response.

2. Experiments, results and discussion

In our work we simultaneously measured the photocurrent and the current in-dark vs. time and temperature. These measurements allow us to assess the instability of the electrical measurements and the influence of contaminants on the electrical device response.

Here we used a metal-free mesogenic phthalocyanine 2(3),9(10),16(17),23(24)-tetra(2-decyltetradecyloxy)-phthalocyanine (H_2Pc) (Fig. 1), containing very low level of ionic impurities (see Supporting information of Ref. [20]). H_2Pc is a prototype DLC compound exhibiting a columnar rectangular (Col_r) ↔ columnar hexagonal (Col_h) phase transition at T_{rh} = 333 K [33].

When a H_2Pc thin film is deposited onto a surface, in general the planar alignment of columns is spontaneously achieved regardless of the nature of the surface [33]. We performed the experiment on a thin film of H_2Pc deposited in-between two interdigitated electrodes on a test pattern with a bottom-contact layout (Fig. 2) using a sourcemeter–femtoammeter to bias the device and measure the DC current flow. Details of set-up is described in Ref. [34]. We biased the device with a voltage V = 5 V and acquired current measurements repeating thermal cycles between 303 K and 363 K at a controlled rate of 1.0 K/min. We chose this range because it is the most common condition of working temperatures without relevant effects on reorganization or on electrically induced dewetting [27];

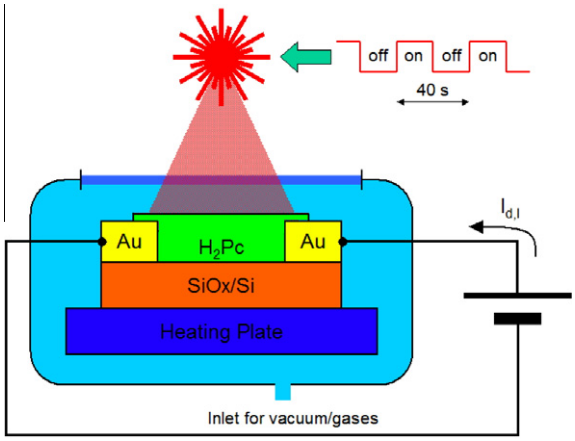

Fig. 2. Experimental setup, including the heating stage and the laser, which illuminates the sample with intermittent light during the thermal cycles.

furthermore within this range the Col_r–Col_h phase transition is expected [20]. All the measurements were performed in vacuum (P = 0.01 mbar) by illuminating the film during the thermal cycles with an intermittent light (frequency = 1/40 s) whose 680 nm wavelength is near to the maximum absorption of H_2Pc [20]. The experiment output is a set of alternating dark and light (indicated as I_d and I_l, respectively) DC current measurements.

Fig. 3a shows the I_d measurement. The triangular shape of the projection in the (t, T) plane represents the temperature sweep performed by the heating stage, assuming t_0 = 0 at 303 K as starting point and using a heating/cooling rate of 1 K/min (thus arriving to the temperature of 363 K after 1 h); the temperature is then returned to 303 K and the cycle is repeated 10.5 times. In Fig. 3b the corresponding I_l values are shown. With an interpolation routine (see methods) we generated the I_d (t, T) and the I_l (t, T) surfaces presented in Fig. 3a and b. By subtracting I_d from the corresponding I_l values we extracted the photocurrent contribution (I_p), which is due to excited H_2Pc states generated by light absorption (Fig. 3c) [35]. The noise level in the I_l and I_d measurements was less than 6pA rms, making the calculated values of I_p at least 11 times bigger than its

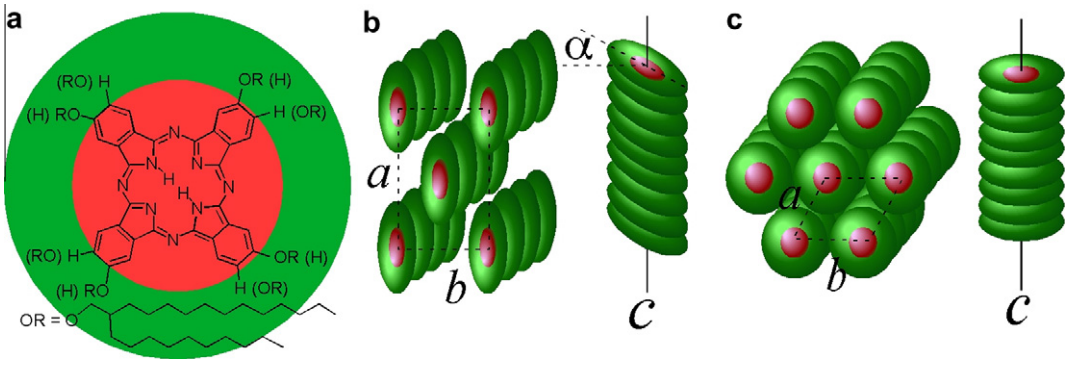

Fig. 1. (a) Chemical structure of 2(3),9(10),16(17),23(24)-tetra(2-decyltetradecyloxy)-phthalocyanine (H_2Pc). (b) Columnar rectangular and (c) columnar hexagonal organization. a, b, c are the cell parameters [17,30] and α is the tilt angle with respect to the column axis.

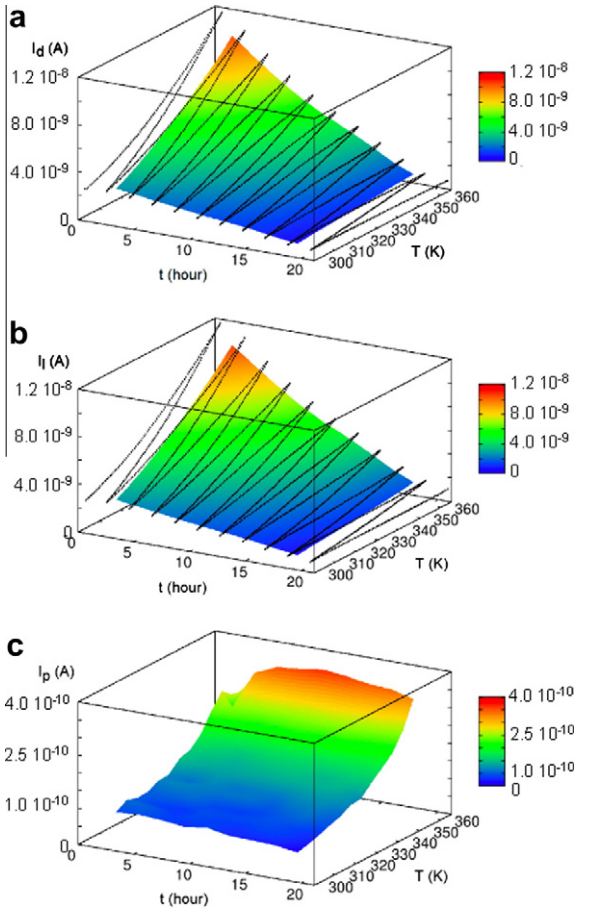

Fig. 3. Surfaces of current in-dark (I_d) (a), during laser irradiation (I_l) (b) and photocurrent contribution (I_p) (c) vs. time and temperature measured in vacuum.

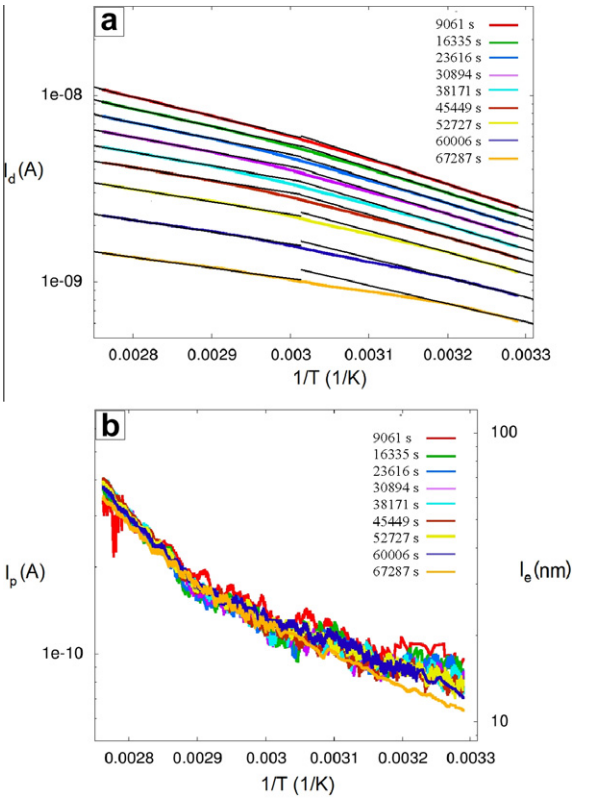

Fig. 4. Dependence of current in-dark (I_d) (a), photocurrent contribution (I_p) (b, left axis) and photogenerated charge carriers diffusion length (l_e) (b, right axis) from the absolute temperature for fixed times (A = 9061 s, B = 16,335 s, C = 23,616 s, D = 30,894 s, E = 38,171 s, F = 45,449 s, G = 52,727 s, H = 60,006 s, I = 67,287 s).

indetermination $\sigma_{Ip} = \sqrt{2} \cdot \sigma_{Id}$ (see details of error analysis in Section 4.5).

We find that I_p is almost independent on time, in contrast with I_d (t, T) and I_l (t, T).

Fig. 4a shows sections of the surface I_d (t, T) performed at intervals of 2 h in an Arrhenius plot.

We identified two different activated regimes corresponding to each liquid crystalline phase:

$$I_d = \begin{cases} A_r \cdot \exp(-\frac{E_r}{k_B T}) & T < T_{rh}; \\ A_h \cdot \exp(-\frac{E_h}{k_B T}) & T > T_{rh}. \end{cases} \quad (1)$$

The prefactor A_r and the activation energy E_r belong to the Col_r phase, while A_h and E_h to the Col_h phase. T_{rh} is the temperature of the Col_r–Col_h phase transition. We identified the two regimes and we extracted the prefactors and the activation energies without fixing a priori T_{rh}. Then we calculated the temperature where the two lines in the Arrhenius plot corresponding to the two regimes of Eq. (1) intersect each other. This temperature (328.40 ± 5.07) K is in good agreement with the DSC results (331.45 K) [36].

Both A_r and A_h decrease in time with a decay constant of respectively 6420 (±590) s and 5451 (±146) s. From the fit according to Eq. (1) we extracted E_r = (0.245 ± 0.024) eV and E_h = (0.153 ± 0.030) eV. Assuming the Drude model, the in-dark current is given by:

$$I_d = q \cdot p(t, T) \cdot \mu_p \cdot V \cdot d \cdot W \cdot L^{-1} \quad (2)$$

where q is the elementary charge, $p(t, T)$ the number density of holes, μ_p their mobility, V is the electrical potential and d, W, L, the channel height, width and length, respectively.

By performing experiments in different atmospheric conditions (air, N_2, H_2O_2 vapours), thus in very different doping conditions, we obtained similar value of E_r and E_h.

Since in our range of T, μ_p is almost constant or weakly dependent on temperature [5] and time [20,21], the change of I_d with time and temperature can be ascribed to the change (decrease) of doping levels and possibly to the reorganization of ionic impurities inside the H_2Pc thin film [32].

The holes responsible for the electrical p-conduction are induced in the HOMO level by the presence an acceptor level introduced by doping [37]. This acceptor level is distant from the HOMO by E_r and E_h, depending on temperature. The change of activation energy at the Col_r–Col_h transition can be assigned to the stacking of H_2Pc molecules. In the Col_r mesophase, the normal to the disk-like molecules is

tilted by $\alpha = 15–18°$ vs. the column axis, whereas in Col_h mesophase is parallel [20]. The two supramolecular arrangements impose different overlaps between stacked molecules that finally impact on the energy of the HOMO level and consequently on its distance in energy with respect to the acceptor level.

The prefactors A_r and A_c are proportional to the doping level (number of acceptor states) in the film [38,39]. The fact that they decay in time can be interpreted as after the fabrication process relatively a high level of doping remains in the film. This is consistent with oxygen doping from air. By keeping the film in vacuum during the thermal cycles, the contaminants are progressively removed (evaporated).

By exciting the H_2Pc molecules in the film with the laser electron–holes pairs are generated [20,35] and their contribution to the current is independent from the doping level introduced during the film growth. The following equation for the photocurrent flowing between the electrodes in the case of intrinsic semiconductors applies [40]:

$$I_p = q \cdot \eta \cdot \frac{P_{opt}}{h\nu} \cdot \frac{(\mu_n + \mu_p) \cdot \tau \cdot V}{L^2} \tag{3}$$

where η is the quantum efficiency (i.e.; number of carriers generated per photon absorbed), P_{opt} the optical power, h the Planck constant, ν the frequency of the incident photons, τ the carriers lifetime, μ_{n-p}, respectively the electrons and holes mobility and L the channel length, viz. the distance between the electrodes. $q \cdot \eta \cdot P_{opt} \cdot (h \cdot \nu)^{-1}$ is the primary photocurrent.

Considering that the photogenerated charge carriers diffusion length l_e is the distance travelled by the carriers with a drift velocity $\langle v_n \rangle + \langle v_p \rangle = (\mu_n + \mu_p) \cdot V \cdot L^{-1}$ during their lifetime τ, the relationship between the diffusion length and the channel length is equal to the ratio between the measured photocurrent and the primary photocurrent:

$$\frac{\langle l_e \rangle}{L} = \frac{I_p}{q \cdot \eta \cdot \frac{P_{opt}}{h\nu}} \tag{4}$$

Fig. 4b shows the plot of I_p and l_e vs. temperature. l_e is obtained upon re-scaling the time-sections of the surface $I_p(t, T)$ by the constant factor $L \cdot q^{-1} \cdot \eta^{-1} \cdot P_{opt}^{-1} \cdot h\nu$, assuming a quantum efficiency $\eta = 0.5\%$, which is the value reported in Ref. [16] for phthalocyanines. The diffusion length increases with temperature, varying from 10 to 70 nm. This value, of the order of few hundreds molecular cores, is consistent with the reported excitons migration length [41] and intra column coherence length (150 nm) obtained by XRD [42] on DLCs.

We systematically observed two activated regimes in the I_p vs. temperature plot, but we did not find a significant correlation with the temperature of the Col_r–Col_h phase transition. Applying the same analysis as the one reported for I_d, we extracted a temperature of 344 ± 3 K for the example of Fig. 4b, and a mean value of 339 ± 10 K among different experiments performed in vacuum. Noticeably, in contrast with the measurements in-dark, we systematically observed that the average activation energy at low temperatures $E_{LT}^{p} = 0.125 \pm 0.047$ eV is smaller than the activation energy at high temperatures $E_{HT}^{p} = 0.509 \pm 0.067$ eV.

Furthermore, also in the case of the I_p curves, tiny fluctuations in the transport properties are present that seem to be correlated with the elapsed time. In Fig. 4b a small change in the local slope at the lowest temperatures is observed, suggesting slow reorganization dynamics affecting the photocurrent at these temperatures. From the linear fits in the range 0.0031–0.0033 K^{-1} the slopes increase of about three times, from −737.4 K at 9061 s to −2387.1 K at 67,287 s. This behaviour is not systematic, either for the direction of the slope change or for the temperature range in which it occurs; it is still under investigation.

3. Conclusions

In conclusion we observed that the two measurements of DC current in-dark and photocurrent exhibit a very different behaviour with respect to the functional form and the stability over time and temperature.

The measurement in-dark is characterized by two activation energies that depend on the liquid crystalline phase, indicating a different relative position between the HOMO and the acceptor levels for each phase. The acceptor level can be introduced by doping during the fabrication process. Doping levels are mainly responsible for the conductivity of the film in-dark conditions, causing instabilities in the electrical measurements because during the experiment the contaminants are partially removed by evaporation or they reorganize [32]. This instability is particularly influent when the timescale for reorganization of dopants is comparable with the time scale of the temperature sweep. For this reason it is crucial to perform a procedure of interpolation, which leads to a time correction of the current vs. temperature curves in order to extract instantaneous $I_d(T)$ curves, as indicated here.

On the other hand, the functional form of the measurements at light reflects the photogenerated charge carriers diffusion length, which seems to be not much correlated with the film phase [20]. The amount of carriers in the photocurrent measurements is generated with the laser and is constant with temperature, in contrast to the measure in-dark, where the carriers are promoted by thermal excitation from acceptor states. The electric field separates the photo-generated carriers and the behaviour of I_p vs. temperature reflects the variation in the distance that carriers travel unperturbed until they find a structural defect or a trap. This distance can be indeed considered as the coherence (correlation) length of a column; we did not find any significant change of regime in the diffusion length of the photogenerated charge carriers that could be correlated with the phase transition. The observation that the current in-dark decreases in time (Fig. 3a), while the photocurrent contribution remains stable (Fig. 3c), suggests that the decay of I_d in time is not due to degradation of the material during the experiment. Here we used H_2Pc as representative material; however our approach is general and can be extended to other liquid crystals and more in general to other classes of organic materials such as molecular [43,44] or polymeric [45,46] semiconductors.

4. Experimental details

4.1. Substrate cleaning and film preparation

The test pattern is made up of a highly doped Si layer of 0.5 mm, with a 1 μm thick layer of thermal SiO*x*. The Au interdigitated electrodes are fabricated by photolithography and have a thickness of 150 nm. This test pattern was provided by Philips Research Laboratory, Eindhoven, The Netherlands. It features four devices with channel length equal to 10 μm and channel width equal to 10 mm.

We washed the test pattern with Heptane (HPLC grade) and we dry it with pure Nitrogen; then we washed it with Acetone (HPLC grade), drying with pure Nitrogen. We finally dip the test pattern in HF 4% for 20 s, washed it with electronic grade water and then dried it with pure Nitrogen. We put the substrate in an air plasma chamber (PELCO easiGlow 91000) for 10 min, setting $I = 30$ mA and $P = 0.4$ mbar.

After the cleaning procedure we deposited the H_2Pc film by spin coating from a 20 mg/mL solution in heptane (HPLC grade), setting the angular velocity to 2000 rpm. With these conditions we obtained a film 130 nm thick. We attached the film to the sample holder of the heating stage and made the electrical connections with silver paint. We baked the film at 313 K in vacuum ($P = 0.01$ mbar) for 30 min, then we heated it up to 456 K in order to induce the columnar organization, that we verified by optical microscopy using cross polarizers filters. We performed the same experiment described in the text on H_2Pc films in different ambient conditions, verifying the film stability during the experiment by using an optical microscope.

4.2. Determination of optical power transferred to the film (P_{opt}) and sample overheating by laser irradiation

To excite the sample we used a standard 680 nm laser diode with a nominal optical power of 1 mW coupled to a variable focus optic system. We determined the power deposited in the film P_{opt} using the formula:

$$P_{opt} = P_{laser} \cdot Ads \cdot L \cdot W \cdot s_{spot}^{-1} = 2.1 \cdot 10^{-5} W \quad (5)$$

where P_{laser} is the total power emitted by the laser in a spot of surface s_{spot}, $L{\cdot}W$ is the sensitive area of the device and Ads is the relation between the power transferred to the film and the power that arrives to the surface, i.e. excludes the power that is transferred to the substrate or reflected out of the sample. We measured the actual $P_{laser} = 0.4$ mW using a photodiode Thorlabs, Inc. model DET36A. We regulated the area of the spot to cover all the sensitive area of the device; then we measure $s_{spot} = 0.7 \times 10^{-6}$ m^2 from an image taken using the optical microscope. Also we took periodically images with the microscope to verify that the position of the laser remains unchanged during the experiment. To determine Ads we made a Monte Carlo simulation of the photons trajectory. It considers 10^7 photons arriving to a system which is made up of four layers: (1) air with an absorption coefficient $\alpha = 0$ and refractive index $n = 1$; (2) a 130 nm thick H_2Pc layer with $\alpha = 4.2 \cdot \times 10^4$ cm^{-1} and $n = 2.66$ [47]; (3) a 1 μm thick SiO*x* layer with $\alpha = 10$ cm^{-1} and $n = 1.46$; and (4) a 0.5 mm thick Si layer with $\alpha = 3 \times 10^3$ cm^{-1} and $n = 3.5$.

This simulation considers reflections at the interfaces and light attenuation in the different layers. The percentage of the laser power is distributed as follows: 37.1(6)% remains in the H_2Pc film, 0.0476(2)% in the SiO*x* layer, and 38.7(3)% in the Si layer. The remaining 24.1(5)% is reflected out of the sample.

Using these results we estimated that the increase of temperature between the bottom of the Si substrate and the H_2Pc top interface is less than 1 mK using a 1-D heat transmission model.

4.3. Experimental setup

The measurement system is based on a heating stage (Linkham TMHS600). We replaced one of the gas inlets of the heating stage with a feed through that allows the electrical connections from the sample to the sourcemeter. We used the stage input for vacuum/gases to control the atmosphere in the chamber. The stage is connected to a TP94 controller, a Keithley 6430 sourcemeter–femtammeter and a laser connected to a Keithley 3930A function generator. We substituted the optics of the laser diode with a 3.3 Macro Zoom lens (Edmund Optics) to regulate the focal distance between the laser and the sample, illuminating completely the active area of the device.

The TP94 controller is connected to the computer through a RS232 interface. The Keithley 6430 and the Keithley 3930A are connected to the computer through an IEEE-488 Bus. In this configuration we are able to set from the computer a temperature ramp, to set the voltage, to take at pre-set intervals an electrical measurement of current and to control the laser intensity on the sample, alternating dark–light cycles.

4.4. Generation of I_d, I_l and I_p surfaces

The measurement cycles give alternating I_d and I_l data at intervals of 0.3 K. Performing a 2D interpolation of the data points in Fig. 3a and b in the heating part of the cycles we obtained the three surfaces shown in Fig. 3a–c.

We first performed the interpolation of I_d and I_l in T with a linear function because the variation on I_d (T) and I_l (T) is very smooth. At this point we subtracted the I_p curve from the I_l to obtain I_p. The use of a linear interpolation avoids artefacts in the subtraction. We then performed exponential interpolation in time (a linear interpolation on the logarithm of the current) to obtain the three surfaces.

4.5. Error analysis

The error propagation of I_l and I_d into I_p was calculated by the equation:

$$\sigma_{I_p}^2 = \sigma_{I_l}^2 + \sigma_{I_d}^2 - 2 \cdot \mathrm{cov}[I_l, I_d] \quad (6)$$

As the sourcemeter measures consecutive I_d and I_l values, which are in the same range, we consider $\sigma_{I_l} = \sigma_{I_d}$. For uncorrelated noise (i.e. thermal/shot noise) $\mathrm{cov}[I_l, I_d] = 0$, thus the error in I_p calculation is: $\sigma_{I_p} = \sqrt{2} \cdot \sigma_{I_d}$ (Table 1).

Table 1
Summarizes the relevant values for the calculation of the signal to noise ratio (SNR).

Time→	9061 (s)	67287 (s)	Note
Range I_d	2–12 nA	0.6–1.4 nA	Data of Fig. 4
Range I_p	0.1–0.4 nA	0.06–0.35 nA	Data of Fig. 4
$(I_l - I_d)/I_d$	5–3.3%	10–25%	
σ_{I_d}	<6pA rms	<2pA rms	Measured current noise in the same range and same conditions than the I_d
SNR (I_p)	>11	>21	Calculated as $\frac{I_p}{\sqrt{2}\cdot\sigma_{I_d}}$

Acknowledgements

The research leading to these results has received funding from the European Community Seventh Framework Programme (FP7/2007-2013) under grant agreement No: 212311 of the ONE-P project. MC and PS are supported by ESF-EURYI DYMOT. The authors gratefully thank A. Brillante for useful discussions.

References

[1] S. Chandrasekhar, G.S. Ranganath, Rep. Prog. Phys. 53 (1990) 57.
[2] Z. An, J. Yu, S.C. Jones, S. Barlow, S. Yoo, B. Domercq, P. Prins, L.D.A. Siebbeles, B. Kippelen, S.R. Marder, Adv. Mater. 17 (2005) 2580.
[3] A.M. van de Craats, J.M. Warman, M.P. de Haas, D. Adam, J. Simmerer, D. Haarer, P. Schuhmacher, Adv. Mater. 8 (1996) 823.
[4] J.M. Warman, M.P. de Haas, G. Dicker, F.C. Grozema, J. Piris, M.G. Debjie, Chem. Mater. 16 (2004) 4600.
[5] M.G. Debije, J. Piris, M.P. de Haas, J.M. Warman, Ž. Tomović, C.D. Simpson, M.D. Watson, K. Müllen, J. Am. Chem. Soc. 126 (2004) 4641.
[6] W. Pisula, A. Menon, M. Stepputat, I. Lieberwirth, U. Kolb, A. Tracz, H. Sirringhaus, T. Pakula, K. Müllen, Adv. Mater. 17 (2005) 684.
[7] A.M. van de Craats, N. Stutzmann, O. Bunk, M.M. Nielsen, M. Watson, K. Müllen, H.D. Chanzy, H. Sirringhaus, R.H. Friend, Adv. Mater. 15 (2003) 495.
[8] D. Adam, P. Schuhmacher, J. Simmerer, L. Haussling, K. Siemensmeyer, K.H. Etzbach, H. Ringsdorf, D. Haarer, Nature 371 (1994) 141.
[9] H. Iino, J. Hanna, R.J. Bushby, B. Movaghar, B.J. Whitaker, M.J. Cook, Appl. Phys. Lett. 87 (2005) 132102.
[10] C.F. van Nostrum, R.J.M. Nolte, Chem. Commun. 21 (1996) 2385.
[11] F.I. Bohrer, A. Sharoni, C. Colesniuc, J. Park, I.K. Schuller, A.C. Kummel, W.C. Trogler, J. Am. Chem. Soc. 129 (2007) 5640.
[12] M. Cavallini, A. Calò, P. Stoliar, J.C. Kengne, S. Martins, F.C. Matacotta, F. Quist, G. Gbabode, N. Dumont, Y.H. Geerts, F. Biscarini, Adv. Mater. 46 (2009) 4688.
[13] A. Fechtenkötter, N. Tchebotareva, M. Watson, K. Müllen, Tetrahedron 57 (2001) 3769.
[14] R.I. Gearba, A.I. Bondar, B. Goderis, W. Bras, D.A. Ivanov, Chem. Mater. 17 (2005) 2825.
[15] X. Crispin, J. Cornil, R. Friedlein, K.K. Okudaira, V. Lemaur, A. Crispin, G. Kestemont, M. Lehmann, M. Fahlman, R. Lazzaroni, Y. Geerts, G. Wendin, N. Ueno, J.-L. Brédas, W.R. Salaneck, J. Am. Chem. Soc. 126 (2004) 11889.
[16] S. Sergeyev, W. Pisula, Y.H. Geerts, Chem. Soc. Rev. 36 (2007) 1902.
[17] V. Lemaur, D.A. Da Silva Filho, V. Coropceanu, M. Lehmann, Y. Geerts, J. Piris, M.G. Debjie, A.M. van de Craats, K. Senthilkumar, L.D.A. Siebbeles, J.M. Warman, J.-L. Brédas, J. Cornil, J. Am. Chem. Soc. 126 (2004) 3271.
[18] J. Cornil, V. Lemaur, J.P. Calbert, J.L. Brédas, Adv. Mater. 14 (2002) 726.
[19] J.L. Brédas, D. Beljonne, V. Coropceanu, J. Cornil, Chem. Rev. 104 (2004) 4971.
[20] J. Tant, Y.H. Geerts, M. Lehmann, V. de Cupere, G. Zucchi, B.W. Laursen, T. Bjørnholm, V. Lemaur, V. Marcq, A. Burquel, E. Hennebicq, F. Gardebien, P. Viville, P. Beljonne, R. Lazzaroni, J. Cornil, J. Phys. Chem. B 109 (2005) 20315.
[21] X. Feng, V. Marcon, W. Pisula, M.R. Hansen, J. Kirkpatrick, F. Grozema, D. Andrienko, K. Kremer, K. Müllen, Nat. Mater. 8 (2009) 421.
[22] Y. Olivier, L. Muccioli, V. Lemaur, Y.H. Geerts, C. Zannoni, J. Cornil, J. Phys. Chem. B 13 (2009) 14102.
[23] A.M. van de Craats, J.M. Warman, Adv. Mater. 13 (2001) 130.
[24] I.O. Shklyarevskiy, P. Jonkheijm, N. Stutzmann, D. Wasserberg, H.J. Wondergem, P.C.M. Christianen, A.P.H.J. Schenning, D.M. de Leeuw, Ž. Tomović, J. Wu, K. Müllen, J.C. Maan, J. Am. Chem. Soc. 127 (2005) 16233.
[25] C. Deibel, D. Janssen, P. Heremans, V. de Cupere, Y. Geerts, M.L. Benkhedir, G.J. Adriaenssens, Org. Electron. 7 (2006) 495.
[26] L. Schmidt-Mende, A. Fechtenkötter, K. Müllen, E. Moons, R.H. Friend, J.D. MacKenzie, Science 293 (2001) 1119.
[27] A. Calò, P. Stoliar, M. Cavallini, S. Sergeyev, Y.H. Geerts, F. Biscarini, J. Am. Chem. Soc. 130 (2008) 11953.
[28] J.D. Wright, Prog. Surf. Sci. 31 (1989) 1.
[29] J. Yuan, J. Zhang, J. Wang, D. Yan, W. Xu, Thin Solid Films 450 (2004) 316.
[30] Q. Zhou, R.H. Gould, Thin Solid Films 317 (1998) 432.
[31] M. Funahashi, J. Hanna, Chem. Phys. Lett. 397 (2004) 319.
[32] R. James, G. Stojmenovik, C. Desimpel, F.A. Fernández, S.E. Day, K. Neyts, J. Display Technol. 2 (2006) 237.
[33] V. De Cupere, J. Tant, P. Viville, R. Lazzaroni, W. Osikowicz, W.R. Salaneck, Y.H. Geerts, Langmuir 22 (2006) 7798.
[34] A. Calò, P. Stoliar, M. Cavallini, Y.H. Geerts, F. Biscarini, Rev. Sci. Instrum. 81 (2010) 033907.
[35] G.L. Pakhomov, D.M. Gaponova, A.Yu. Luk'yanov, E.S. Leonov, Proceedings of the Conference "Nanophotonics 2004" Nizhni Novgorod, Russia 2 (2004) 6.
[36] G. Schweicher, G. Gbabode, F. Quist, O. Debever, N. Dumont, S. Sergeyev, Y.H. Geerts, Chem. Mater. 21 (2009) 5867.
[37] N.W. Ashcroft, N.D. Mermin, Solid State Physics, Harcourt, Orlando, 1976.
[38] T.S. Shafai, R.D. Gould, Thin Solid Films 515 (2006) 1138.
[39] D.F. Barbe, C.R. Westgate, J. Chem. Phys. 52 (1970) 4046.
[40] S.M. Sze, K.K. Ng, Physics of Semiconductor Devices, John Wiley & Sons, 1981.
[41] D. Markovitsi, S. Marguet, J. Bondkowski, S. Kumar, J. Phys. Chem. B 105 (2001) 1299.
[42] S.B. Lei, J. Wang, Y.H. Dong, C. Wang, L.J. Wan, C.L. Bai, Surf. Interface Anal. 34 (2002) 767.
[43] V. Corradini, C. Menozzi, M. Cavallini, F. Biscarini, M.G. Betti, C. Mariani, Surf. Sci. 532 (2003) 249.
[44] C. Menozzi, V. Corradini, M. Cavallini, F. Biscarini, M.G. Betti, C. Mariani, Thin Solid Films 428 (2003) 227.
[45] D.A. Serban, P. Greco, S. Melinte, S. Vlad, C.A. Dutu, S. Zacchini, M.C. Iapalucci, F. Biscarini, M. Cavallini, Small 5 (2009) 1117.
[46] P. Leclere, M. Surin, R. Lazzaroni, A.F.M. Kilbinger, O. Henze, P. Jonkheijm, F. Biscarini, M. Cavallini, W.J. Feast, E.W. Meijer, A. Schenning, J. Mater. Chem. 14 (2004) 1959.
[47] F. Yakuphanoglu, M. Durmuş, M. Okutan, O. Köysal, V. Ashen, Physica B 373 (2006) 262.

The electrical transport through SAMs of alkanemonothiols with a methyl end group (–CH_3), and alkanedithiols with a thiol end group (–SH), has been reported previously [4,6]. Alkanedithiols with a length of *N* carbon atoms (HS–C_NH_{2N}–SH) are abbreviated as *CN*DT and alkanemonothiols (C_NH_{2N+1}–SH) as *CN*MT. The transport mechanism is nonresonant tunneling. The transmission of a junction can be modeled with a multi-barrier tunnel [7] model yielding for the resistance of a single molecule, *R*, at low bias:

$$R = \frac{h}{2e^2}T^{-1} = 12.9\ k\Omega T_{\mathrm{Au-S}}^{-1}T_{mol}^{-1}T_{SAM\ PEDOT}^{-1} \quad (1)$$

where *h* is Planck constant, *e* is the elementary charge, *T* is the overall transmission probability and where $T_{\mathrm{Au-S}}$, T_{mol} and $T_{SAM\ PEDOT}$ are the transmission probabilities for the gold–sulfur bottom contact, the molecule itself and the SAM/PEDOT:PSS top contact, respectively. Rewriting in practical terms yields:

$$R = 12.9\ k\Omega r_{\mathrm{Au-S}}r_{mol}r_{SAM\ PEDOT} \quad (2)$$

where $r_{\mathrm{Au-S}}$, r_{mol} and $r_{SAM\ PEDOT}$ are dimensionless resistance contribution factors accounting for the resistance contribution of the bottom contact, the molecule and the top contact, respectively. The molecule contribution is given by $r_{mol} \sim exp(\beta n)$, where β is the decay coefficient and *n* the number of carbon atoms in the backbone. Note that the resistance behavior of the PEDOT:PSS layer itself in a junction is nontrivial [8], and this can hold for the $r_{SAM\ PEDOT}$ contribution. Nevertheless, for a *monocomponent* SAM junction the $r_{SAM\ PEDOT}$ factor is constant and the dependence of the resistance on molecular length is found exponential [4,6,9]. This dependence derives from the r_{mol} *single-molecule* term, as long as the overall resistance is dominated by the molecule. The SAM junction resistance is then given by the single molecule resistance divided by the grafting density, under the plausible assumption that cooperative effects can be disregarded.

What about *mixed* SAMs? To investigate the contribution of both the length of the molecule and the nature of the end group we systematically studied the electric resistance of binary mixed monolayers of alkanemonothiols and alkanedithiols. First we kept the end group constant in the series of mixed monothiols and mixed dithiols, varying only the length of the molecule. Subsequently we investigated mixed SAMs of an alkanemonothiol and an alkanedithiol. In this case, both the length of the molecule as well as the interfacial composition are varied.

2. Results and discussion

2.1. "Walking along the lines"

The simplest binary SAM in terms of molecular interactions is a mixture of alkanemonothiols, in which the chemical composition of the end group is similar to that of the main chain. Let us focus on the mixed monolayers of C12MT and C18MT. In Fig. 1 the normalized resistance, *RS*, is presented on a semi-logarithmic scale as a function of the mole fraction of C18MT in the SAM solution. Each data point represents the average value of about 40 junctions. The data can be fitted with a straight line in semi-logarithmic coordinates that might indicate an exponential dependence of the normalized resistance on the composition in the SAM solution. Note that the segregation coefficient was verified to be unity, meaning that the composition of the SAM is the same as that of the solution (see Section 4). The chemical structures of the end points are schematically depicted in Fig. 1. A variation in composition translates as a linear variation in average layer thickness. Fig. 1 shows that the resistance increases with layer thickness exponentially.

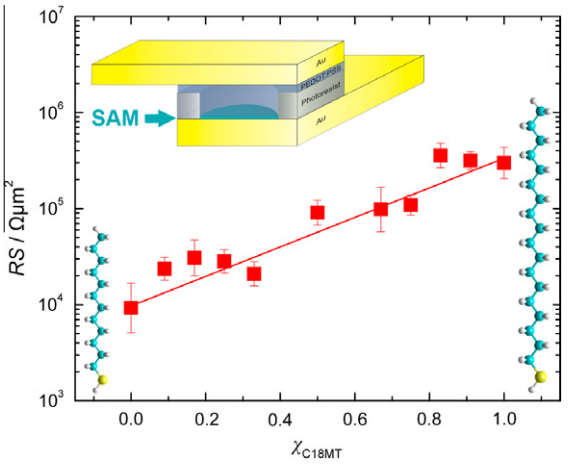

Fig. 1. Normalized resistance, *RS*, of binary mixed SAMs of C12 and C18 monothiols (C12MT and C18MT), as a function of mole fraction of C18MT in solution, χ_{C18MT}. The solid red line represents an exponential fit to the data. The inset shows a schematic cross section of the junction. The chemical structures of the end points are included to illustrate that the resistance increases with increasing layer thickness. (For interpretation of the references to colour in this figure legend, the reader is referred to the web version of this article.)

Next we turn to the resistance of a series of mixed monothiol–dithiol monolayers, namely C17MT with the dithiol C12DT. In this series both the average thickness and the interfacial composition are varied simultaneously. The normalized resistance is presented in Fig. 2 on a semi-logarithmic scale as a function of the mole fraction of C17MT in solution. Each data point represents the average value over about 20 junctions. As in the case of the mixed monothiols we observe that the normalized resistance appears to depend exponentially on composition. However, the dithiol, which is the shortest of the two molecules, has a higher resistance in monocomponent SAM than the monothiol, which is longer (their chemical structures are schematically depicted in Fig. 2). Therefore, Fig. 2 unambiguously shows that the resistance of the mixed C12DT–C17MT SAM decreases with increasing average layer thickness.

To complete this study, we fabricated all the binary monolayers of four components, *viz.* two alkanemonothiols C17MT and C20MT and two alkanedithiols C12DT and C16DT, except for the C12DT–C20MT mixed SAM. In this latter system, the big difference in the number of carbons is expected to lead to a non-unity segregation factor due to preferential adsorption [10,11]. The normalized resistances are presented in Fig. 3 on a semi-logarithmic scale

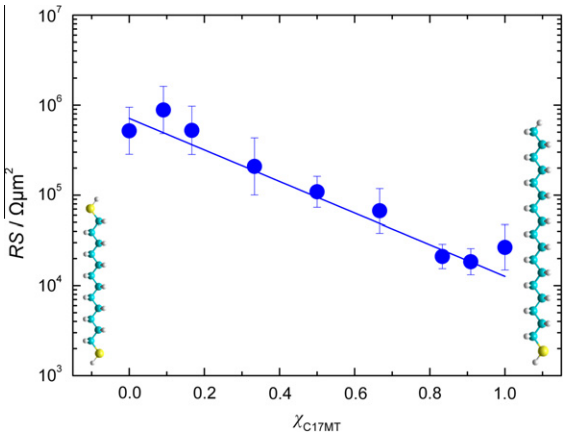

Fig. 2. Normalized resistance, *RS*, of binary mixed SAMs of C12 dithiol and C17 monothiol (C12DT and C17MT), as a function of mole fraction of C17MT in solution, χ_{C17MT}. The solid blue line represents an exponential fit to the data. The chemical structures of the end points are included to illustrate that the resistance *decreases* with *increasing* layer thickness. (For interpretation of the references to color in this figure legend, the reader is referred to the web version of this article.)

as a function of average number of atoms, as calculated from the mole fraction in solution assuming a segregation coefficient of unity. The resistances of all binary SAMs can be fitted with straight lines that might indicate an exponential dependence on the average number of atoms.

The constructed resistance diagram of Fig. 3 shows a trapezoidal correlation. The mixed monothiol C17MT–C20MT SAM and the mixed dithiol C12DT–C16DT SAM exhibit the same slope, yielding parallel lines. Throughout each of these two series, the contributions to the resistance from the top and bottom contacts are constant. The resistance changes only due to a different number of carbon atoms. The contribution of the top contact is reflected in

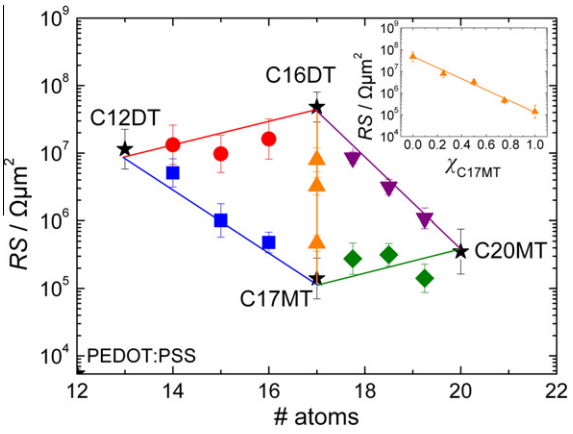

Fig. 3. Geometric resistance diagram showing a trapezoidal correlation. Normalized resistance, *RS*, of all binary mixed SAMs based on the end points C12DT, C16DT, C17MT and C20MT, as a function of average number of atoms. The fully drawn curves are a guide to the eye. The inset shows the normalized resistance of the C16DT–C17MT mixed SAMs as a function of the mole fraction of C17MT in solution. The vertical axis starts at $5 \times 10^3\ \Omega\,\mu m^2$, the value for the corresponding PEDOT:PSS only junction.

the series C16DT–C17MT. The average number of atoms in the mixed SAM is constant, while the interfacial composition is varied. The resistance systematically varies with composition over more than two orders of magnitude. The simultaneous effect of molecular length and nature of the end group is observed along the C12DT–C17MT and C16DT–C20MT lines. For both these series an apparently exponential dependence on the average number of atoms is found. The slope, however, is different because the change in the number of atoms at the end points is different; hence the corresponding lines in the trapezoid are not parallel.

2.2. Discussion

As a matter of fact, the experimental results leading to the diagram in Fig. 3 are quite puzzling. The first hypothesis to consider is that in a mixed SAM the overall resistance is given by the resistance of all its constituent individual molecules connected in parallel, i.e. as in a monocomponent SAM. It is easy to show that the behavior this hypothesis predicts contradicts experiment. Indeed, addition of significantly more conductive molecules would quickly reduce the resistance of a mixed SAM already when their fraction is low, because they would act as "shorts". On the other hand, a low share of less conductive molecules has no spectacular effect. The dependence of resistance on composition simulated in Figs. 4 and 5 is far from both the experimental points and from the straight line in semilogarithmic coordinates. We are forced to conclude that not every molecule in the mixed SAM carries current fully and independently.

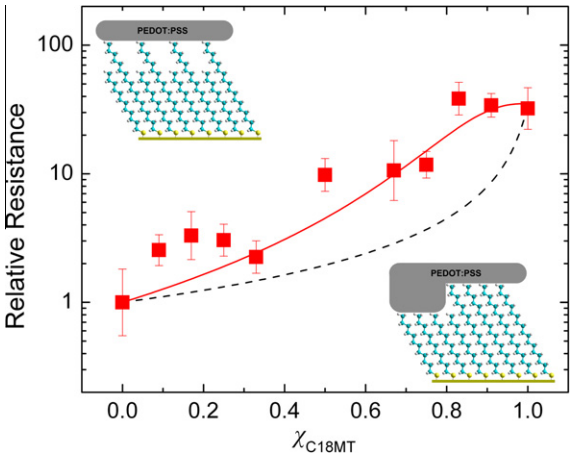

Fig. 4. Relative resistance of binary mixed SAMs of C12 and C18 monothiols (C12MT and C18MT), as a function of mole fraction of C18MT in solution, χ_{C18MT}, taken from Fig. 1 and normalized to the end point C12MT. The insets show the two cases of the mixed SAM microstructure. The top left depicts intermixing and the bottom right inset depicts phase separation. The dashed black line is calculated assuming that all the molecules of each component have the same resistance equal to their resistance in their respective monocomponent SAMs and are connected in parallel in the mixed SAMs. The solid red line is calculated by parameterization of the microstructure using Eq. (3). (For interpretation of the references to colour in this figure legend, the reader is referred to the web version of this article.)

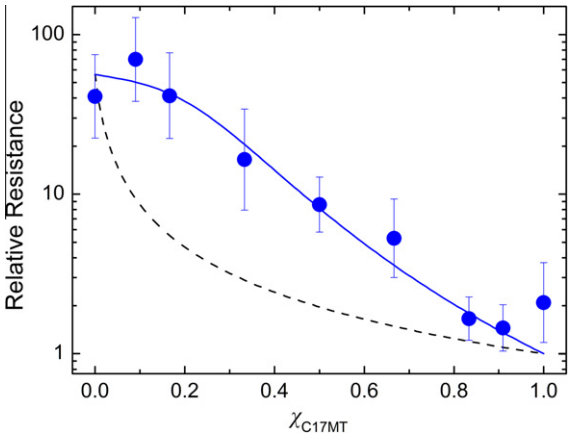

Fig. 5. Relative resistance of binary mixed SAMs of C12 dithiol and C17 monothiol (C12DT and C17MT), as a function of mole fraction of C17MT in solution, χ_{C17MT}, as taken from Fig. 2 and normalized to the end point C17MT. The dashed black line is calculated assuming that all the molecules of each component have the same resistance equal to their resistance in their respective monocomponent SAMs and are connected in parallel in the mixed SAMs. The blue line is calculated by parameterization of the microstructure using Eq. (3). (For interpretation of the references to color in this figure legend, the reader is referred to the web version of this article.)

Another extreme hypothesis would be that molecular composition of the SAM is irrelevant, it just serves as an effective medium (spacer) that only modifies the average width of the tunneling barrier between the contacts. Such a model seems compatible with the exponential dependence on average thickness found. We note that for MT–MT and DT–DT mixed SAMs the slope obtained amounts to 3.54 per fraction. The difference between the end points is six carbon atoms, yielding a slope of 0.6 per carbon atom. Apparently, both systems exhibit the same length dependence with a decay coefficient of about 0.6 per carbon atom. This value corresponds to the one derived in Fig. 1 and to published decay constants for alkane based molecules of 0.5–1.2 [4,6,9]. The resistance changes only due to a different number of carbon atoms, according to Eq. (2), where molecular contribution is given by $r_{mol} \sim exp(\beta n)$, where β is the constant decay coefficient and n in this case is the *average* number of carbon atoms.

Whatever the possible physical justification of this model, not all the observed facts are compatible with it. Note that the absolute value for the resistances of the mixed monothiols is different from that of the mixed dithiols. According to Eq. (2), this offset originates from the different end groups, $-CH_3$ versus –SH, yielding a different top contact contribution, $r_{SAM\ PEDOT}$ [5,6,9,12–14]. The numbers imply a more transparent contact barrier, i.e. a higher transmission coefficient, for the methyl/PEDOT:PSS interface as for the thiol/PEDOT:PSS interface. We note that this behavior is counterintuitive: the water-based suspension PEDOT:PSS is expected to be repelled by the hydrophobic methyl end group of the alkanemonothiols, yielding a less intimate physical contact. Therefore the absolute resistance of a dithiol SAM is expected to be lower than that of a monothiol SAM, contrary to what is experimentally observed; at the moment, we have no explanation for this fact. This difference is significant enough to make certain monocomponent SAMs of longer MT less resistive than those of DT with shorter molecules. Consequently, a systematic resistance *decrease* with *increasing* average layer thickness for certain monothiol–dithiol mixed SAMs (Fig. 3) was observed, which contradicts the effective medium model and stresses the importance of microscopic structure of the junction.

2.3. A phenomenological model for the mixed SAM resistance

The consideration in the previous section demonstrates that a viable model for mixed SAMs should take into account their microstructure in a realistic way, assuming that the resistance can be calculated as for an equivalent circuit of a parallel resistor network. With this in mind, we propose a microdomain model that by parameterization of the microstructure explains the resistance data.

A mixed monolayer is a dynamic system formed at room temperature at relatively low concentrations. Though full phase segregation is thermodynamically favorable, the SAM will nevertheless contain phases with kinetically-formed compositions [15] where domains of different sizes coexist probably even with single molecules. For the purpose of an equivalent circuit of a mixed SAM composed of molecules A and B, we limit the model to four parallel resistances, per molecule: (i) A-domain, (ii) A-single, (iii) B-domain and (iv) B-single. The difference in effective resistance of the same molecule as single or a domain member is supposed to reflect contact and conformational issues, rather than mutual influence of the molecules that we consider irrelevant. Indeed, the longer molecules likely act as pillars and only they are fully contacted by PEDOT:PSS, preventing all short molecules from being equally well contacted and fully contribute to the current. On the other hand, the longer molecules trapped into the shorter molecule domains can hardly stand straight but rather adopt bent conformations. Consequently, "domain" in this context signifies an ensemble of molecules vast enough to be fully contacted (i.e. the fraction of molecules at its boundaries being relatively small), while "singles" might as well apply to groups of a few molecules. Therefore, the resistance of the A and B in domains corresponds to that of the monocomponent SAMs of A and B, respectively, while the resistances of A and B singles have to be parameterized.

We need now a model for the composition of a mixed SAM in terms of domains and singles for both components. It has been known that alkanethiol SAM formation is a two-stage process, the initial fast step being diffusion-limited adsorption and the second slow step reorganization of the primary monolayer described as surface crystallization [16]. For a *mixed* monolayer, we suppose that only a part of the molecules of each type will assemble into domains, while the rest will be in the form of singles. It is reasonable to assume that the shares of the domains and singles depends on the composition of the SAM. Let the molecular composition of the monolayer be characterized by the mole fraction of A denoted by χ; the fraction of B is then $1 - \chi$, $\chi = 0$ corresponds to pure B and $\chi = 1$ corresponds to pure A. When $\chi \to 0$, all molecules B are expected to be organized in domains, while for $\chi \to 1$ practically all

molecules B are single: a view supported by previously reported STM data [17]. We suppose further that a certain number of molecules, n, must meet to form a critical nucleus leading to the formation of a domain, which is more likely to occur when there are more molecules of a given component in the mixed monolayer, hence at a higher mole fraction of this component. Within such a probabilistic approach, the population, of A and B arranged in domains is, χ^n and $(1-\chi)^n$, respectively. The population of singles is then $\chi-\chi^n$ for A and $(1-\chi)$–$(1-\chi)^n$ for B. The resistance of the mixed SAM as a function of composition is then given by:

$$\frac{1}{R}=\frac{\chi^n}{R_{\text{A-domain}}}+\frac{(1-\chi^{n-1})\chi}{R_{\text{A-single}}}+\frac{(1-\chi)^n}{R_{\text{B-domain}}}+\frac{(1-\chi)\left[1-(1-\chi)^{n-1}\right]}{R_{\text{B-single}}} \quad (3)$$

For the mixed SAMs of Fig. 4, the molecule A is C18 monothiol and the molecule B is C12 monothiol. The resistances of the domains, $R_{\text{A-domain}}$ and $R_{\text{B-domain}}$, are taken equal to that of the corresponding end points, *viz.* the pure single component SAMs. As in the case of a perfectly mixed monolayer, the top inset of Fig. 4, we assume that the single molecules C12 monothiol embedded in domains of C18 monothiols, are not contacted by the PEDOT:PSS top contact. Therefore they do not contribute to the overall resistance. Only when organized in sufficiently large domains the short molecules contribute to the overall resistance, as schematically depicted in the lower inset of Fig. 4. The only parameters left are the exponent n and the resistance of a single molecule C18 monothiol in domains of C12 monothiol, $R_{\text{A-single}}$. Fitting the experimental data with Eq. (3) (fully drawn red curve in Fig. 4) yields $n = 2.3$ and $R_{\text{A-single}} = 43$. The resistance of single C18MT molecules in domains of C12MT, $R_{\text{A-single}}$, is in the same order of magnitude as the C18MT domains.

Parameterization of the microstructure can also explain the observed resistance behavior of the mixed C12DT–C17MT system of Fig. 2, where the resistance actually *decreases* with *increasing* average layer thickness. The resistances are replotted in Fig. 5 where the values are normalized to the pure C17MT SAM. Similarly as above, we take the resistances of the domains equal to that of the corresponding end points, the pure monocomponent SAMs. The contribution of the short single molecules is again disregarded. The only parameters left in Eq. (3) are the exponent n and the resistance of a single molecule C17 monothiol in domains of C12 dithiol, $R_{\text{A-single}}$. The dashed black curve in Fig. 4 is calculated assuming that the resistance for single C17MT molecules is the same as that in domains. Contrary to Fig. 4, this assumption does not lead to a fit to the data. This is because C17MT molecules are highly conductive in comparison with C12DT molecules and constitute electric shorts in a C12DT domain. A fitting of both n and $R_{\text{A-single}}$ yields a good agreement, however, with $n = 3.3$ and the relative resistance of the single C17MT molecule equal to 27, an order of magnitude higher than when organized in domains.

This approximately 20-fold increase in the resistance of single long monothiols can be related to their molecular conformation. It has been shown that the resistance of an alkane molecule increases an order of magnitude when gauche defects are introduced [18]. The emergence of defects can be due to conformational disorder, whose origin in a mixed SAM has been described previously [11,15]. Close to the gold surface, the mixed SAM is ordered. The free volume introduced into the outer part of the longer molecules in the monolayer by the presence of the shorter chains makes it disordered and liquid-like. The loss of lateral and orientational order implies the existence of gauche defects.

We note that the degree of conformational disorder in the longer molecules depends on their share in the mixed SAM. At low fraction the gauche densities per molecule are higher [15], meaning that most of the longer molecules exist as singles, in agreement with the assumption that the domain fraction depends on the monolayer composition.

Conformational changes, or gauche defects, affect the charge transport through a molecule directly [18,19], by reducing the periodicity. Indirectly, the resistance can be affected by the presence of bent molecules via altered interface energy of a methyl- to a methylene terminated interface [15,20], as well as by diminishing the electronic coupling of the shorter SAM domains to the top contact [21].

For the monothiol-dithiol SAMs, the presence of gauche defects can be inferred from analysis. On the other hand, conformational disorder in mixed monothiols does not manifest in our electric measurements as the single long molecules already have a higher resistance.

Relatively small values for n support the hypothesis that the dependence of the normalized resistance on the fraction is non-exponential, but follows a power law. Moreover, as simple as our model might be, it embodies some tracts of nucleation and growth phenomena. The assumption of a critical nucleus size of 1–2 molecules might be reasonable [22], although weaker intermolecular interactions can lead to critical nucleus sizes larger than two [23]. The different interactions between the components in the two systems, owing to their different chemical structures, could explain the variation in the value of n. A more rigorous treatment, which would account for the dynamics of the binary SAM in order to relate the trend to the critical nucleus size is beyond the scope of the present work.

3. Synopsis

We have investigated the electrical transport through mixed self-assembled monolayers in large-area molecular junctions. The SAM is formed on a gold bottom electrode inside a photolithographically defined interconnect in photoresist. The conducting polymer PEDOT:PSS is used as top contact. To investigate the contribution of both the length of the molecule and the nature of the end group on the resistance, we systematically studied the charge transport through mixed monolayers of alkanemonothiols and alkanedithiols. We verified by ellipsometry measurements that the segregation coefficient is unity for all investigated binary SAMs. To disentangle the role of the length of the molecule and the interfacial composition we prepared mixed monolayers of all different binary combinations of

two monothiols and two dithiols. The end group is fixed in a series of mixed monothiols and in a series of mixed dithiols.

A trapezoidal correlation in semi-logarithmic resistance-composition coordinates has been obtained (Fig. 3). The straight lines seem to indicate an exponential dependence on composition, or on the average molecular length, also in the case of mono- and dithiol mixed SAMs where resistance can decrease with increasing layer thickness, as the longer component is more conductive in monocomponent SAM. However mathematically simple, exponential dependence is difficult to justify physically for mixed monolayers, unlike the case of monocomponent SAMs where this dependence has a single-molecule tunneling origin.

We search for the origin of the resistance-composition dependence in mixed SAMs in an equivalent circuit model based on their microdomain structure for which we suggest a simple model. In essence, we suppose that the effective resistance of a molecule can differ depending on whether it is isolated (that is, trapped within an alien molecular domain) or belongs to a domain of the same molecules, due to contact and conformational issues. The simulated dependence is non-exponential and leads to a good agreement between calculated and measured resistances with only two fit parameters.

4. Experimental section

A 4-in. silicon wafer with a 500 nm thermally grown oxide was passivated using hexamethyldisilazane (HMDS). A 1 nm layer of chromium was thermally evaporated through a shadow mask, followed by 60 nm of gold. The rms roughness of the bottom contact is about 0.7 nm over an area of 0.25 μm^2.

The two terminal junctions were photolithographically defined in an insulating matrix of photoresist, ma-N 1410 (Micro Resist Technology GmbH). The negative photoresist was spincoated on the wafer resulting in a layer of 570 nm. After a pre-bake step to remove any remaining solvents, the layer was exposed to UV light with a Karl Süss MA1006 mask aligner, to define the vertical interconnects, ranging from 5 to 100 μm in diameter. After development, the film was hard baked at 200 °C for at least 1 h to render the photoresist insoluble in ethanol, the solvent used in the SAM formation. The wafer was subsequently cut in several pieces using a diamond tip pen. This allowed the simultaneous processing of different mixed SAMs on a single wafer, thereby eliminating processing variations that can affect device performance. A last step before self-assembly was cleaning of the bottom gold contacts with a PDC plasma cleaner (Harrick plasma) to remove any photoresist residuals.

The self-assembled monolayers were formed from molecules dissolved in ethanol. The series of molecules used in this work include 1-dodecanethiol (C12MT), 1-heptadecanethiol (C17MT), 1-octadecanethiol (C18MT), 1-eicosanethiol (C20MT), 1,12-dodecanedithiol (C12DT) and 1,16-hexadecanedithiol (C16DT). All solvents and molecules except C17MT, C20MT, C12DT and C16DT were purchased from Sigma–Aldrich. The synthesis of the other molecules was performed starting from the carboxylic acid, hydroxyl or bromide precursor, depending on the commercially available compounds.

Mixed solutions of various molar ratios between the two components were prepared by mixing stock solutions of each component at the appropriate volume ratio. The wafer pieces were immersed in the solutions for at least 36 h, under nitrogen. The concentration in ethanol was 3×10^{-3} M for the C12DT–C17MT system, 6×10^{-3} M for the C12MT–C18MT systems and 1×10^{-2} M for the mixed SAMs of Fig. 3. The higher concentration is required to prevent formation of a looped phase when using longer alkanedithiols (C16DT) [24]. After the self-assembly, the wafer pieces were thoroughly rinsed with ethanol, toluene and *iso*-propanol to remove any remaining alkanethiol molecules.

Subsequently, the interlayer of PEDOT:PSS, a water-based suspension of poly(3,4-ethylenedioxythiophene) and poly(4-styrenesulphonic acid), was spin coated. PEDOT:PSS acts as a highly conductive buffer layer that protects the SAM during subsequent evaporation of the top gold contact. Two blends were used. (a) Baytron® PH500, H.C. Starck GmbH & Co., filtered over a 1 μm Whatman® glass filter. Dimethylsulfoxide (5% v/v) was added to increase the conductivity [25] and (b) AGFA® ICP new type filtered over a 5 μm Whatman® glass filter. Blend (a) was used for the C12MT–C18MT system, while blend (b) was used for all other experiments. The PEDOT:PSS solution was spincoated, resulting in a layer thickness of about 90 nm. The wafer was then immediately transferred to a vacuum oven for at least 1 h to dry the film.

To facilitate contacting the top electrode, 100 nm of gold was evaporated through a shadow mask. This gold layer, apart from ensuring a better contact with the measurement probes, also serves as a self aligned mask for the removal of redundant PEDOT:PSS by reactive ion etching (O_2 plasma). This step eliminates any parasitic currents from top to bottom electrode.

Current–voltage (*I–V*) measurements were performed in two home-built probe stations using a Keithley 4200 Semiconductor Analyzer Characterization System. The probe stations were pressurized at 10^{-6}–10^{-7} mbar for at least 6 h before the measurements, to remove any water absorbed in the PEDOT:PSS layer. Devices were swept in the voltage range of 0 to 1 to −1 V and back to 0 V and the recorded current densities were averaged for all devices with different diameter. The normalized resistance (*RS*, resistance × area, $\Omega\,\mu m^2$) was then calculated at 0.1 V bias. The resistance scales linearly with device area for junctions of 5–100 μm in diameter, resulting in identical *RS* values.

Ellipsometric measurements, to verify that the segregation coefficient is unity and that the layer thickness linearly increases with composition, were performed using a V-VASE® ellipsometer (J.A. Woolam Co., Inc.) equipped with an HS-190 high speed monochromatic system and controlled with a VB-400 module. All measurements were performed at the reflection geometry in the spectral range from 350 to 500 nm with a step of 3 nm, at an angle of incidence of 65–75° with a step of 5° and 10 revisions/measurement. Acquired data were analyzed using WVASE32® software. The index of refraction for monothiols and

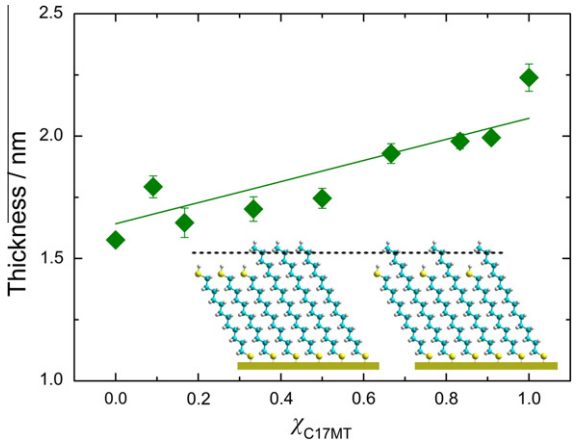

Fig. 6. The thickness obtained from ellipsometry measurements on binary mixed SAMs of C12 dithiol and C17 monothiol (C12DT and C17MT), as a function of the fraction C17MT in solution, χ_{C17MT}. The fully drawn curve is a linear extrapolation between the end points, which have been calculated using Hyperchem 7.5.

dithiols was taken equal as 1.45. The layer thickness derived as a function of composition in solution for the C12DT–C17MT mixed SAMs is presented in Fig. 6. A linear dependence is found indicating that within experimental error the segregation coefficient is unity, as has been reported previously [26]. This conclusion is substantiated by the calculated layer thicknesses indicated by the fully drawn curve. The end points follow from the length of the molecule, calculated with Hyperchem 7.5, adding 2.3 Å for the S–Au bonds and taking an off-normal tilt angle of 30°. The fully drawn curve is obtained by a linear extrapolation between the end points and fits the data well. This analysis applies for all binary SAMs here investigated.

For the sample preparation, a silicon wafer with 500 nm thermally grown oxide was rinsed with *iso*-propanol, dried in a dry spinner and coated with 1 nm Cr adhesion layer and 60 nm of Au, according to the procedure described above. The wafer was cut to pieces, which were transferred in nitrogen filled bottles for the ellipsometry measurements (one reference point per piece). Subsequently, the pieces were treated in a plasma cleaner and immersed in the respective solutions to self-assemble the monolayers. Ellipsometry samples and molecular junctions were prepared simultaneously from the same solutions. The thickness of the SAMs was determined by averaging at least three different measurements on each piece.

Acknowledgements

The authors thank P.A. van Hal and E.H. Huisman for stimulating discussions, and J. Harkema and F. van der Horst for technical support. We are grateful to an anonymous referee for his/her valuable comments and suggestions. We acknowledge financial support from the Zernike Institute for Advanced Materials, the European Community's Seventh Framework Programme (FP7/2007–2013) under the Grant agreements ONE-P No. 212311, the Interuniversity Attraction Pole IAP 6/27 Program of the Belgian Federal Government, and NanoNed, a national nanotechnology program coordinated by the Dutch Ministry of Economic Affairs.

References

[1] (a) J.C. Love, L.A. Estroff, J.K. Kriebel, R.G. Nuzzo, G.M. Whitesides, Chem. Rev. 105 (2005) 1103–1170 (and references therein);
(b) M.D. Porter, T.B. Bright, D.L. Allara, C.E.D. Chidsey, J. Am. Chem. Soc. 109 (1987) 3559–3568;
(c) C. Vericat, M.E. Vela, G.A. Benitez, J.A.M. Gago, X. Torrelles, R.C. Salvarezza, J. Phys.: Condens. Matter 18 (2006) R867–R900.
[2] (a) P.E. Laibinis, G.M. Whitesides, J. Am. Chem. Soc. 114 (1992) 1990–1995;
(b) A. Ulman, S.D. Evans, Y. Shnidman, R. Sharma, J.E. Eilers, J.C. Chang, J. Am. Chem. Soc. 113 (1991) 1499–1506;
(c) C. Pale-Grosdemange, E.S. Simon, K.L. Prime, G.M. Whitesides, J. Am. Chem. Soc. 113 (1991) 12–20;
(d) D.L. Allara, A.F. Heburd, F.J. Padden, R.G. Nuzzo, D.R. Falcon, J. Vac. Sci. Technol. A 1 (1983) 376–382;
(e) V. DePalma, N. Tillman, Langmuir 5 (1989) 868–872;
(f) C.E.D. Chidsey, Science 251 (1991) 919–922;
(g) G.K. Rowe, S.E. Creager, Langmuir 7 (1991) 2307–2312;
(h) B. de Boer, A. Hadipour, M.M. Mandoc, T. van Woudenbergh, P.W.M. Blom, Adv. Mater. 17 (2005) 621–625.
[3] (a) G.K. Ramachandran, T.J. Hopson, A.M. Rawlett, L.A. Nagahara, A. Primak, S.M. Lindsay, Science 300 (2003) 1413–1416;
(b) A.S. Blum, J.G. Kushmerick, D.P. Long, C.H. Patterson, J.C. Yang, J.C. Henderson, Y. Yao, J.M. Tour, R. Shashidhar, B.R. Ratna, Nat. Mater. 4 (2005) 167–172;
(c) Z.J. Donhauser, B.A. Mantooth, T.P. Pearl, K.F. Kelly, S.U. Nanayakkara, P.S. Weiss, Jpn. J. Appl. Phys. 41 (2002) 4871–4877.
[4] H.B. Akkerman, P.W.M. Blom, D.M. de Leeuw, B. de Boer, Nature 441 (2006) 69–72.
[5] T.W. Kim, G. Wang, H. Lee, T. Lee, Nanotechnology 18 (2007) 315204. p. 8.
[6] P.A. van Hal, E.C.P. Smits, T.C.T. Geuns, H.B. Akkerman, B.C. de Brito, S. Perissinotto, G. Lanzani, A.J. Kronemeijer, V. Geskin, J. Cornil, P.W.M. Blom, B. de Boer, D.M. de Leeuw, Nat. Nanotechnol. 3 (2008) 749–754 (including supporting info).
[7] G. Wang, T.-W. Kim, H. Lee, T. Lee, Phys. Rev. B 76 (2007) 205320. p. 7.
[8] A.J. Kronemeijer, E.H. Huisman, I. Katsouras, P.A. van Hal, T.C.T. Geuns, P.W.M. Blom, S.J. van der Molen, D.M. de Leeuw, Phys. Rev. Lett. 105 (2010) 156604. p. 4.
[9] H.B. Akkerman, B. de Boer, J. Phys.: Condens. Matter 20 (2008) 013001 (p. 20, and references therein).
[10] (a) S. Chen, L. Li, C.L. Boozer, S. Jiang, Langmuir 16 (2000) 9287–9293;
(b) K. Heister, D.L. Allara, K. Bahnck, S. Frey, M. Zharnikov, M. Grunze, Langmuir 15 (1999) 5440–5443.
[11] C.D. Bain, G.M. Whitesides, J. Am. Chem. Soc. 111 (1989) 7164–7175.
[12] J.M. Seminario, L. Yan, Int. J. Quantum Chem. 102 (2005) 711–723.
[13] (a) H. Haick, O. Niitsoo, J. Ghabboun, D. Cahen, J. Phys. Chem. C 111 (2007) 2318–2329;
(b) F. Chen, X. Li, J. Hihath, Z. Huang, N. Tao, J. Am. Chem. Soc. 128 (2006) 15874–15881;
(c) B. Kim, J.M. Beebe, Y. Jun, X.Y. Zhu, C.D. Frisbie, J. Am. Chem. Soc. 128 (2006) 4970–4971.
[14] (a) F. Tao, S.L. Bernasek, Chem. Rev. 107 (2007) 1408–1453 (and references therein);
(b) P.E. Laibinis, G.M. Whitesides, D.L. Allara, Y.-T. Tao, A.N. Parikh, R.G. Nuzzo, J. Am. Chem. Soc. 113 (1991) 7152–7167;
(c) H. Basch, R. Cohen, M.A. Ratner, Nano Lett. 5 (2005) 1668–1675;
(d) X. Li, J. He, J. Hihath, B. Xu, S.M. Lindsay, N. Tao, J. Am. Chem. Soc. 128 (2006) 2135–2141.
[15] P.E. Laibinis, R.G. Nuzzo, G.M. Whitesides, J. Phys. Chem. 96 (1992) 5097–5105.
[16] A. Ulman, Chem. Rev. 96 (1996) 1533–1554.
[17] G.E. Poirier, Chem. Rev. 97 (1997) 1117–1127.
[18] (a) C. Li, I. Pobelov, T. Wandlowski, A. Bagrets, A. Arnold, F. Evers, J. Am. Chem. Soc. 130 (2008) 318–326;
(b) M. Fujihira, M. Suzuki, S. Fujii, A. Nishikawa, Phys. Chem. Chem. Phys. 8 (2006) 3876–3884.
[19] (a) M. Paulsson, C. Krag, T. Frederiksen, M. Brandbyge, Nano Lett. 9 (2009) 117–121;
(b) K. Tagami, M. Tsukada, e-J. Surf. Sci. Nanotechnol. 2 (2004) 186–190.

[20] A. Ulman, An Introduction to Ultrathin Organic Films: From Langmuir-Blodgett to Self-Assembly, Academic Press, Inc., San Diego, 1991. pp. 48–58.
[21] R.L. York, K. Slowinski, J. Electroanal. Chem. 327 (2003) 550–551.
[22] I. Doudevski, D.K. Schwartz, Phys. Rev. B 60 (1999) 14–17.
[23] (a) M. Brinkmann, S. Graff, F. Biscarini, Phys. Rev. B 66 (2002) 165430. p. 11;
(b) S. Verlaak, S. Steudel, P. Heremans, D. Janssen, M.S. Deleuze, Phys. Rev. B 68 (2003) 195409. p. 8.
[24] H.B. Akkerman, A.J. Kronemeijer, P.A. van Hal, D.M. de Leeuw, P.W.M. Blom, B. de Boer, Small 4 (2008) 100–104.
[25] J.Y. Kim, J.H. Jung, D.E. Lee, J. Joo, Synth. Met. 126 (2002) 311–316.
[26] J.P. Folkers, P.E. Laibinis, G.M. Whitesides, Langmuir 8 (1992) 1330–1341.

The phosphorescent white EML is fabricated with solution-process. The fluorescent white EML is prepared with solution-premixed method and deposited with thermal deposition method [13]. The hole-modulation layer (TPBi), electron transporting layer (TPBi), electron injection layer (LiF), and aluminum cathode were also deposited with thermal deposition method.

2.2. Device characterization

The luminance of the resultant white OLEDs were measured by using a Minolta CS-100 luminance-meter. The CIE chromatic coordinates and EL spectrum were measured by using a Photo Research PR-655 spectrascan spectroradiometer. A Keithley 2400 electrometer was used to measure the current–voltage (I–V) characteristics. The emission area of all the resultant devices was 25 mm^2 and only the luminance in the forward direction was measured.

3. Results and discussion

Fig. 1 compares the CRI and power-efficiency results of the studied white OLED device, against previously reported ones [4–6,8–12,14–23]. The most efficient white OLED, showed power-efficiency of 44 lm/W, while exhibiting a medium CRI of 68. The high-CRI white OLEDs showed an efficiency ranging between 5 and 36 lm/W. The highest reported CRI was 97, but the device showed a relatively low efficiency of 0.6 lm/W. By employing five emitters, in two white EMLs separated by an HML, we achieved a record-breaking CRI of 98 was with a comparatively high power-efficiency, 8.3 lm/W, at 100 cd/m^2, or 96 with 5.2 lm/W at 1000 cd/m^2.

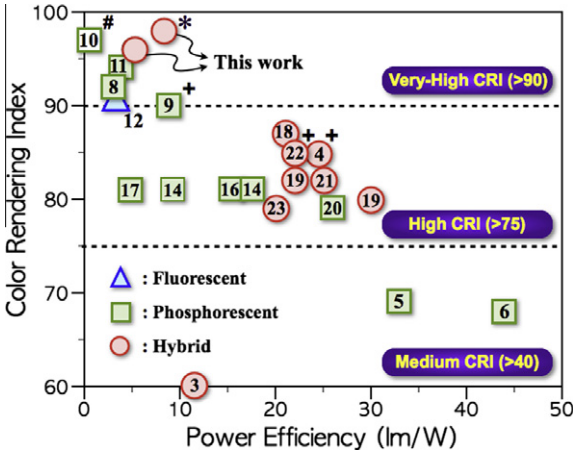

Fig. 1. Color rendering index (CRI) results with respect to efficacy of the studied OLED with double white emissive layers, compared with those reported previously. All the data, unless otherwise specified, are compared at 1000 cd/m^2 on devices without the use of light outcoupling methods (∗: 100 cd/m^2, +: 500 cd/m^2, #: maximum brightness), The OLEDs with fluorescent, phosphorescent, and hybrid material systems are presented with symbols of blue triangle (△), green square (□) and red circle (○), respectively. Except the device in Ref. [10], all the others are composed of multiple emissive layers. (For interpretation of the references to color in this figure legend, the reader is referred to the web version of this article.)

Fig. 2 shows the energy diagrams of Devices I–V. Devices I and II consisted of only one EML, while Devices III–V had two EMLs. Device III did not contain an HML, and Devices IV and V were comprised of an HML with 4 and 2.5 nm, respectively. All these devices used 125 nm indium tin oxide as the anode, a 25 nm poly(3,4-ethylene-dioxythiophene)-poly-(styrenesulfonate) (PEDOT:PSS) the HTL, a 32 nm 1,3,5-trisN-phenylbenzimidazol-2-ylbenzene (TPBi) the ETL, a 0.7 nm lithium fluoride the EIL and 150 nm aluminum for the cathode.

In Device I, three phosphorescent emitters were employed in the white EML with a host of 4,4′-Tris(carbazol-9-yl)triphenylamine (TCTA). The respective doping concentrations were 14, 0.5, and 1.0 wt.% for the blue dye of bis(3,5-difluoro-2-(2-pyridyl)-phenyl-(2-carboxypyridyl)) iridium (III) (FIrpic), green dye tris(2-phenylpyridine)iridium (III) [Ir(ppy)$_3$] and red dye bis(1-phenylisoquinoline)(acetylacetonate) iridium (III) [Ir(piq)$_2$(acac)].

The white EML in Device II comprised a fluorescent deep-blue light emitting host 2,7-bis{2[phenyl(m-tolyl)amino]-9,9-dimethyl-fluorene-7-yl}-9,9-dimethyl-fluorene (MDP3FL) doped with 1% fluorescent yellow dye 5,6,11,12-tetra-phenylnaphthacene (Rubrene). Devices III–V comprised both the aforementioned phosphorescent white and fluorescent white EMLs, with respective thicknesses of 20 and 8 nm.

Fig. 3 shows the EL spectra and CRI values of the studied devices. Device I exhibited a three-wavelength white emission with 78 CRI at 1000 cd/m^2. Device II exhibited a white emission composed of two complementary colors, but had only 72 CRI. To improve the CRI, we attempted to stack the two white EMLs to integrate their EL spectra and fabricated

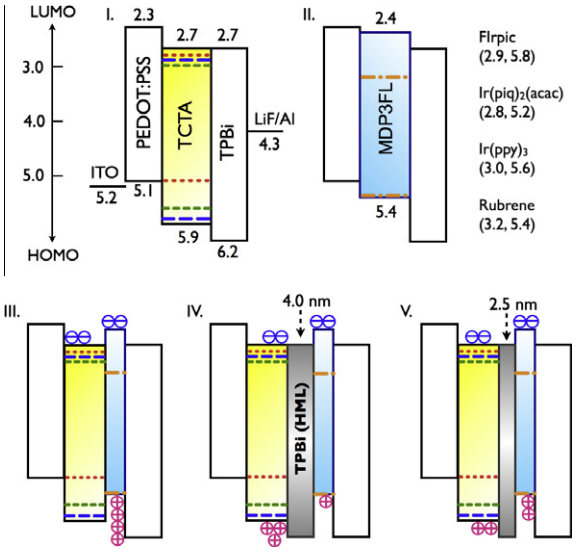

Fig. 2. Schematic illustrations of the three-wavelength phosphorescent white OLED (Device I) and the two-wavelength fluorescent white OLED (Device II). Devices III–V are five-wavelength white OLEDs with the three-wavelength phosphorescent and two-wavelength fluorescent white emissive layers, where Device III contains no hole modulation layer (HML), Device IV 4 nm HML, and Device V 2.5 nm HML. With the use of an HML with a proper thickness (Device V), the entering holes and electrons can be well distributed into the two white emissive zones.

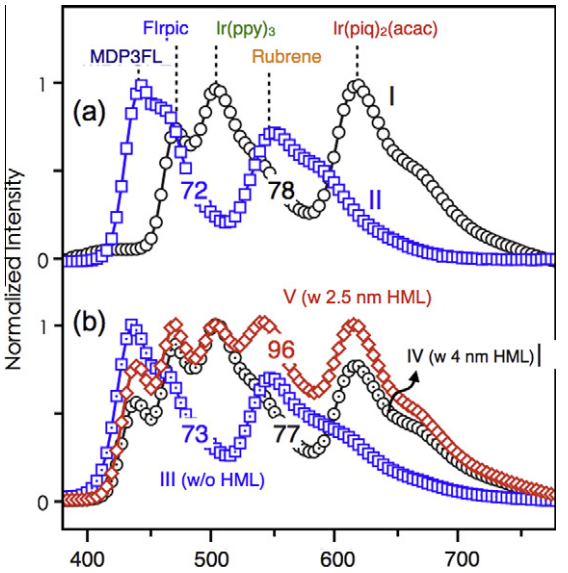

Fig. 3. The resultant EL-spectra of (a) the single white emissive layer containing OLEDs, Devices I and II, and (b) the double white emissive layers containing OLEDs, Devices III–V. A five-wavelength emission with 96 CRI at 1000 nits is observed as a 2.5 nm HML is employed, or 77 CRI if the HML is 4 nm. Whilst, only two-wavelength emission with 73 CRI is observed in the absence of the HML.

a five-wavelength very-high CRI OLED. However, the resulting device (Device III) showed an EL spectrum similar to that of Device II, with a CRI of only 73. This could be attributed to the fact that the transport of the holes was faster than that of electrons in Device III, leading to holes and electrons recombining in the MDP3FL-composing EML. This was the same in Device II, which emitted a two-wavelength spectrum [24,25].

In order to achieve a five-wavelength spectrum OLED, we had to increase the emitting strength of TCTA-composed EML. Therefore, we incorporated a 4 nm hole-modulation layer TPBi between the two EMLs to block some holes in the TCTA-composed EML. However, the resulting primary emission of Device IV was contributed by the Blue FIiric, green Ir(ppy)$_3$, and red Ir(piq)$_2$(acac), with relatively weaker intensities of deep-blue MDP3FL and yellow Rubrene, exhibiting a 77 CRI. This implied that TPBi layer had provided a 0.3 eV hole-injection barrier at the interface of TCTA and TPBi, blocking most of the holes in the TCTA-composed EML, leading to the major recombination zone formed within it.

Surprisingly, as we decreased the thickness of the TPBi layer to 2.5 nm, the CRI markedly improved to 96 (Device V). This was attributed to the fact that an appropriate layer thickness of TPBi could distribute the holes into two white EMLs and control the recombination zones, resulting in a balance intensity of all emitters, thereby producing a full-wavelength spectrum with a very-high CRI.

Fig. 4 showed the hole-modulation layer effects on the resultant current densities. For the double EMLs devices, the current density deceased as the thickness of TPBi hole-modulation layer increased. This effect could be attributed to the 0.3 eV hole-injection barrier at the interface of TCTA and TPBi as well as that the thicker

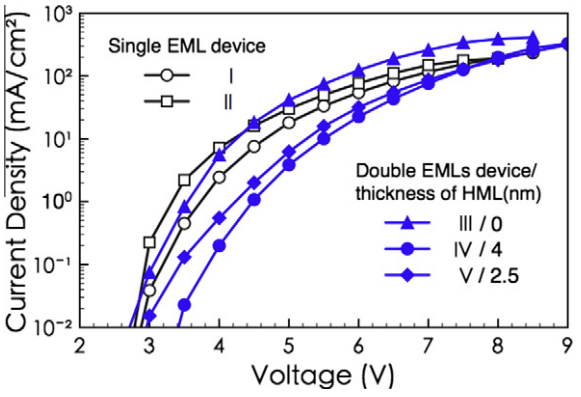

Fig. 4. The resultant current density of the five devices studied. The addition of the HML (TPBi) indeed effectively decreases the current density of the device, proving TPBi to be an effective hole modulating layer in these devices.

HML would form stronger barrier and block more holes, resulting in lower current density.

Fig. 5 shows the electroluminescence (EL) spectra with corresponding Commission International de l'Eclairage (CIE) 1931 coordinates of Device V at different luminance. The increased intensity of the blue- and green-emissions (relative to the red emission), with respect to the luminance explains why the CIE coordinates were blue shifted. This shift showed that a greater degree of recombination had to have been taking place in the blue- and green-emission dyes under high luminance. This was due to fact that the hole-injection barriers from PEDOT to dyes were 0.1 eV to Ir(piq)$_2$(acac), 0.5 eV to Ir(ppy)$_3$ and 0.7 eV to FIrpic, as shown in Fig. 2. Therefore, the holes preferred to inject red Ir(piq)$_2$(acac) at low applied voltage, due to the comparatively low hole-injection barrier. The holes would

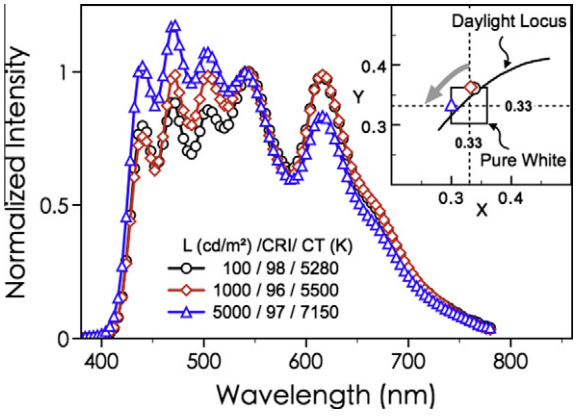

Fig. 5. The EL spectra of the double white emissive layers containing OLED (Device V) at varying luminance. The corresponding CRI varies slightly between 96 and 98 and color temperature increases from 5280 to 7150 K for brightness changing from 100 to 5000 cd/m^2. The inset shows the corresponding 1931 CIE coordinates that fall within the pure-white region and are very close to the daylight (Planckian) locus, indicating Device V to be an ideal candidate for high-quality illumination.

Table 1
Effects of the absence and presence of a hole-modulation layer on the resultant color rendering index, efficacy, and color-temperature of the five-wavelength white OLEDs with double white emissive layers.

Device	HML thickness (nm)	CRI	Power efficiency (lm/W)	Color temperature (K)	1931 CIE coordinates
		At 100/1000 cd/m^2			
I	–	71/78	7.8/4.1	4000/4380	(0.39, 0.42)/(0.37, 0.40)
II	–	67/72	11.3/8.4	7530/8840	(0.30, 0.31)/(0.29, 0.30)
III	–	69/73	6.4/3.6	7350/9570	(0.30, 0.32)/(0.29, 0.29)
IV	4	78/77	8.2/4.9	5580/6600	(0.33, 0.36)/(0.31, 0.34)
V	2.5	98/96	8.3/5.2	5280/5500	(0.34, 0.36)/(0.33, 0.36)

have enough energy to overcome higher barriers and inject green Ir(ppy)$_3$ and blue FIrpic at high applied voltage, leading to an increase in the generation of exciton and observable blue- and green-emissions. It is worth mentioning that the CRI remained around 96–98 throughout the brightness range over which we investigated. As seen in the inset (Fig. 5), the CIE coordinates of Device V indeed fall within the pure-white region and are very close to daylight (Planckian) locus, indicating Device V to possess the characteristics required for high-quality illumination [26].

Table 1 summarizes the electroluminescence (EL) characteristics of the studied devices. As shown, the single white EML devices (Devices I and II) exhibited 78 and 72 CRI at 1000 cd/m^2. By combining two white EMLs, Device III exhibited only 73 CRI and the lowest power efficiency of 3.6 lm/W. With the use of 4 nm HML, the CRI and power efficiency of the device (Device IV) were slightly improved to 77 and 4.9 lm/W. After decreasing the thickness of HTL to 2.5 nm, the resulting device (Device V) showed a very-high CRI of 96 and a comparatively high power efficiency of 5.2 lm/W at 1000 cd/m^2. Device V also yielded a pure-white emission and a color temperature of approximately 5500 K, which would be a suitable source of daylight equivalent illumination, enabling people to remain awake and active.

In conclusion, we demonstrate a very-high CRI white OLED by using double white emitting layers and incorporating a 2.5 nm hole-modulation layer to regulate the intensities of the emitters. The resultant device showed a very-high CRI of 98 with a power efficiency of 8.3 lm/W at 100 cd/m^2.

Acknowledgements

Partial financial support was granted by the National Science Council (Grant No. NSC-96-2628-E-007-019-MY3 and NSC-100-3113-E-007-002), National Tsing Hua University, and Taiwan Semiconductor Manufacturing Company.

References

[1] T.F. So, J. Kido, P. Burrows, MRS Bull. 33 (2008) 663.
[2] C.H. Chang, Y.H. Lin, C.C. Chen, C.K. Chang, C.C. Wu, L.S. Chen, W.W. Wu, Y. Chi, Org. Electron. 10 (2009) 1235–1240.
[3] C.H. Chang, Y.J. Lu, C.C. Liu, Y.H. Yeh, C.C. Wu, J. Disp. Technol. 3 (2007) 193–199.
[4] Y. Sun, N.C. Giebink, H. Kanno, B. Ma, M.E. Thompson, S.R. Forrest, Nature 440 (2006) 908–912.
[5] S. Reineke, F. Lindner, G. Schwartz, N. Seidler, K. Walzer, B. Lüssem1, K. leo, Nature 459 (2009) 234–239.
[6] S.J. Su, E. Gonmori, H. Sasabe, J. Kido, Adv. Mater. 20 (2008) 4189–4194.
[7] J.H. Jou, C.C. Chen, Y.C. Chung, M.F. Hsu, C.H. Wu, S.M. Shen, M.H. Wu, W.B. Wang, Y.C. Tsai, C.P. Wang, J.J. Shyue, Adv. Funct. Mater. 18 (2008) 121–126.
[8] X. Niu, L. Ma, B. Yao, J. Ding, G. Tu, Z. Xie, L. Wang, Appl. Phys. Lett. 89 (2006) 213508.
[9] J. Kalinowski, M. Cocchi, D. Virgili, V. Fattori, J.A.G. Williams, Adv. Mater. 19 (2007) 4000–4005.
[10] G. Zhou, Q. Wang, C.L. Ho, W.Y. Wong, D. Ma, L. Wang, Chem. Commun. 24 (2009) 3574–3576.
[11] C.H. Chang, K.C. Tien, C.C. Chen, M.S. Lin, H.C. Cheng, S.H. Liu, C.C. Wu, J.Y. Hung, Y.C. Chiu, Y. Chi, Org. Electron. 11 (2010) 412–418.
[12] H. Yang, Y. Shi, Y. Zhao, Y. Meng, W. Hu, J. Hou, S. Liu, Displays 29 (2008) 327–332.
[13] J.H. Jou, Y.S. Chiu, C.P. Wang, R.Y. Wang, H.C. Hu, Appl. Phys. Lett. 88 (2006) 193501.
[14] X. Yang, Z. Wang, S. Madakuni, J. Li, G.E. Jabbour, Appl. Phys. Lett. 93 (2008) 193305.
[15] M. Cocchi, J. Kalinowski, L. Murphy, J.A.G. Williams, V. Fattori, Org. Electron. 11 (2010) 388–396.
[16] S. Seidel, R. Krause, A. Hunze, G. Schmid, F. Kozlowski, T. Dobbertin, A. Winnacker, J. Appl. Phys. 104 (2008) 064505.
[17] C.H. Chang, C.C. Chen, C.C. Wu, S.Y. Chang, J.Y. Hung, Y. Chi, Org. Electron. 11 (2010) 266–272.
[18] Y. Sun, S.R. Forrest, J. Appl. Phys. 100 (2006) 073106.
[19] H. Kanno, N.C. Giebink, Y. Sun, S.R. Forrest, Appl. Phys. Lett. 89 (2006) 023503.
[20] S.H. Eom, Y. Zheng, E. Wrzesniewski, J. Lee, N. Chopra, F. So, J. Xue, Appl. Phys. Lett. 94 (2009) 153303.
[21] G. Schwartz, S. Reineke, K. Walzer, K. Leo, Appl. Phys. Lett. 92 (2008) 053311.
[22] G. Schwartz, S. Reineke, T.C. Rosenow, K. Walzer, K. Leo, Adv. Funct. Mater. 19 (2009) 1319–1333.
[23] H. Kannoa, Y. Sun, S.R. Forrest, Appl. Phys. Lett. 89 (2006) 143516.
[24] J.H. Jou, M.H. Wu, S.M. Shen, H.C. Wang, S.Z. Chen, S.H. Chen, C.R. Lin, Y.L. Hsieh, Appl. Phys. Lett. 95 (2009) 013307.
[25] J.H. Jou, S.M. Shen, S.H. Chen, M.H. Wu, W.B. Wang, H.C. Wang, C.R. Lin, Y.C. Chou, P.H. Wu, J.J. Shyue, Appl. Phys. Lett. 96 (2010) 143306.
[26] B.W. D'Andrade, S.R. Forrest, Adv. Mater. 16 (2004) 1585–1595.

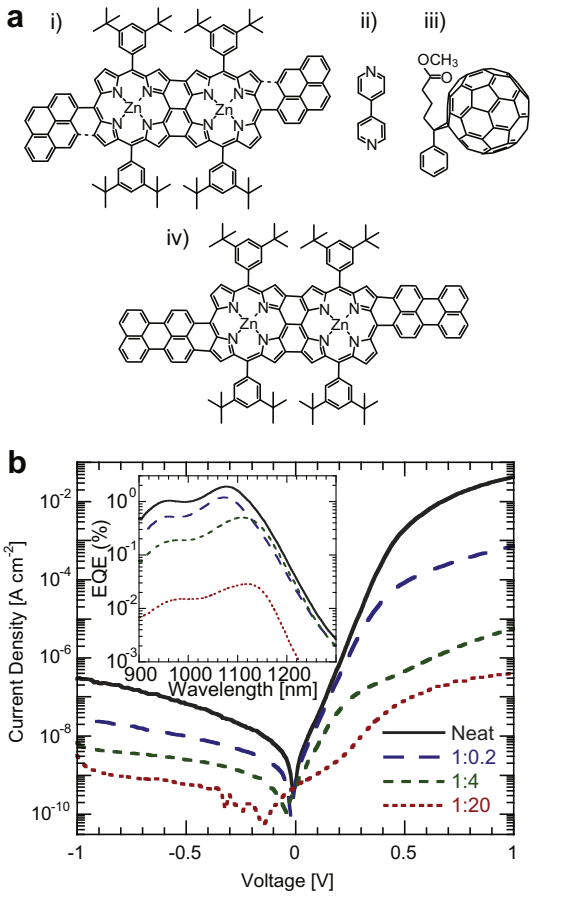

Fig. 1. (a) (i) Molecular structure of zinc pophyrin tape dimer with pyrene end groups where the dashed lines represent hydrogen positions for Psub and a carbon–carbon bond for Pfused, (ii) 4,4'-Bipyridyl, (iii) phenyl-C_{61}-butyric acid methyl ester (PCBM), and (iv) perylene-fused Zn porphyrin dimer. (b) Current density–voltage characteristics and spectrally resolved *EQE* (inset) for varying molar ratios of Psub in PCBM.

and, hence, modify their energetics, exciton diffusion lengths, and electrical conductivities [6]. Specifically, fullerenes, such as PCBM, interact strongly with porphyrin molecules because of strong π–π interactions between the porphyrin center and the curved fullerene surface [6a]. Thus, PCBM tends to evenly disperse among porphyrin molecules to form supramolecular complexes rather than phase-separate into a bulk heterojunction, as observed in polymer–PCBM photovoltaic cells [7].

We have examined other additives based on pyridine compounds. Here, the lone electron pair on the nitrogen atom forms a coordination bond with the Zn atom in the porphyrin core. In fact, small quantities (1–5 vol%) of pyridine are commonly added to organic solvents to increase porphyrin solubility by disrupting intermolecular π-stacking. In particular, complexes involving Bipy coordination to Zn porphyrins are well documented [6d–f], and may form 2:1 or 3:2 complexes, depending on the constituent concentrations [6d]. Here, Bipy stabalizes the porphyrins in a co-facial configuration, increasing short-range ordering and electronic coupling between the π-systems, red shifts the Zn–porphyrin absorption spectrum, and may modify the excited state relaxation dynamics [6d,6f].

In this work, we use Bipy and other pyridines to understand the effects of coordination complexation on device performance. We show that addition of both PCBM and Bipy to the donor layer can increase the zero-bias specific detectivity of porphyrin dimer photodetectors to $D^* = 8.8 \pm 0.2 \times 10^{11}$ Jones ($EQE = 3.6 \pm 0.1\%$) at $\lambda = 1150$ nm, and $D^* = 8.2 \pm 0.2 \times 10^{10}$ Jones ($EQE = 10.5 \pm 0.2\%$) at $\lambda = 1400$ nm. When only Bipy is added, an $EQE = 13.5 \pm 0.3\%$ is achieved. These efficiencies are roughly double and specific detectivities roughly 4-fold higher than previous reports of detectors employing porphyrin tapes [4b], and the specific detectivities are similar to those of commercially available, room temperature Ge photodetectors ($\sim 2 \times 10^{11}$ Jones).

The fabrication and measurement procedures follow previous work [4b], except that the porphyrin–dimer solutions (10 mg/ml in chlorobenzene with 5 vol% pyridine) were first passed through activated alumina to remove oxidized impurities. Additives, dissolved in chlorobenzene, were introduced and the solutions were further diluted to 5 mg/ml of porphyrin in chlorobenzene with 5 vol% pyridine. Devices were fabricated on detergent- and solvent-cleaned indium tin oxide (150 nm thick, ~5 Ω/square) on glass, coated with a 45 nm-thick planarizing layer of poly(3,4-ethlenedioxythiophene)-poly(styrenesulfonate). Donor materials were deposited on a heated substrate ($T = 100$ °C) with a film-casting knife, resulting in film thicknesses of 60 ± 12 nm. The 125 nm-thick C_{60} electron acceptor layer, 10 nm-thick bathocuproine exciton blocking layer, and 150 nm-thick 1 mm-diameter Ag cathodes were sequentially deposited by vacuum thermal evaporation at a base pressure of $\sim 10^{-7}$ torr. The neat C_{60} acceptor layer was required to dissociate excitons generated in the porphyrin layer, prevent shorts, and maximize NIR absorption [4b].

Current–voltage characteristics were measured using a semiconductor parameter analyzer, and the *EQE* was measured using a lock-in amplifier with devices illuminated with monochromatic, chopped light at ~200 Hz. The effect that additives have on the energies of the porphyrin dimer films was studied by ultraviolet photoelectron spectroscopy (UPS).

Donor layers with molar ratios of Psub:PCBM ranging from 1:0 to 1:20 were used to investigate the effects of fullerene incorporation. As the PCBM concentration was increased, the *EQE* decreased from $1.9 \pm 0.1\%$ for neat Psub to below 0.1% for a Psub:PCBM ratio of 1:20 (Fig. 1). This behavior is distinctly different than when PCBM is used as an electron acceptor for polymers [7] or some small molecules [8], in which case the donor and PCBM phases separate into an interpenetrating network with an increased exciton dissociation efficiency, and thus *EQE* [7] Although the *EQE* of the porphyrin detectors decreases upon addition of PCBM, the dark current decreases, and thus the diode differential resistance increases from $1.4 \pm 0.1 \times 10^9\ \Omega\,cm^2$ for a neat film to $2.9 \pm 0.4 \times 10^{10}\ \Omega\,cm^2$ at a 1:20 M ratio of Psub:PCBM. At that same time, the Q-band absorption peak undergoes a bathochromic shift from $\lambda = 1090$ nm to $\lambda = 1120$ nm with increasing

PCBM concentration, consistent with previous observations [4c,6b].

In this series, the highest specific detectivity ($D^* = 4.0 \pm 0.3 \times 10^{11}$ Jones) was obtained for a Psub:PCBM ratio of 1:0.2. Here, $D^* = \mathscr{R}A^{1/2}S_N^{-1}$, where $\mathscr{R}$ is the responsivity, A is the detector active area, and S_N is the spectral noise density. At zero bias where our detectors are characterized, S_N is dominated by thermal noise with $S_N = (4k_BT/R_D)^{1/2}$, where k_B is the Boltzmann constant, T is the temperature, and R_D is the zero-bias differential resistance [9]. The decrease in *EQE* and increase in R_D have opposite effects on specific detectivity; however, at low PCBM concentrations the increase in differential resistance significantly outweighs the reduction in *EQE*, thereby increasing D^*.

We also investigated a variety of modified pyridines and found that donor-like pyridines (e.g. pyridine, pyrazine, isoquinoline, 4-dimethylaminopyridine) red shift the Psub absorption peak from $\lambda = 1090$ nm to $\lambda = 1100$–1120 nm, disrupt molecular packing and decrease *EQE*, while acceptor-like compounds (e.g. 4-trifluoromethylpyridine or 4-pyridinecarbonitrile) decrease the *EQE* without affecting wavelength response. However, Bipy, a bidentate pyridine molecule, both red shifts the Psub absorption to $\lambda = 1150$ nm, as commonly observed [10] and doubles the NIR *EQE*.

The effects of Bipy additives were explored by varying Pfused:Bipy molar ratios from 1:0.5 to 1:4. Current density (J)-voltage (V) characteristics and spectrally resolved *EQE* are shown in Fig. 2. The specific detectivity is the highest for a neat film (*EQE* = 10.2 ± 0.2% and $D^* = 3.4 \pm 0.2 \times 10^{10}$ Jones at $\lambda = 1330$ nm), although the photoresponse was highest at a ratio of Pfused:Bipy = 1:3 (where *EQE* = 13.5 ± 0.3% and $D^* = 2.1 \pm 0.1 \times 10^{10}$ Jones at $\lambda = 1385$ nm). For the Psub:Bipy = 1:1 device, similar improvements were observed; the *EQE* increased from 1.9 ± 0.1% to 4.0 ± 0.1% accompanied by a decrease in differential resistance from $1.4 \pm 0.1 \times 10^9\ \Omega\,cm^2$ to $7.7 \pm 0.1 \times 10^8\ \Omega\,cm^2$, leading to an increase in detectivity from $D^* = 4.2 \pm 0.2 \times 10^{11}$ Jones to $7.1 \pm 0.2 \times 10^{11}$ Jones. The increase in *EQE* with Bipy additives suggests an increase in the exciton diffusion length in the porphyrin film due to the increased molecular coupling associated with the Bipy linkage.

To maximize D^*, varying amounts of PCBM were added to films with a dimer:Bipy ratio of 1:1. For Psub:PCBM:Bipy = 1:0.1:1, a maximum detectivity of $D^* = 8.8 \pm 0.2 \times 10^{11}$ Jones and *EQE* = 3.6 ± 0.1% at $\lambda = 1150$ nm was observed, and a Pfused:PCBM:Bipy ratio of 1:0.75:1 was found to have a maximum detectivity of $D^* = 8.2 \pm 0.2 \times 10^{10}$ Jones and *EQE* = 10.5 ± 0.2% at $\lambda = 1400$ nm. The J–V characteristics, spectrally resolved *EQEs*, and specific detectivities for Psub:PCBM:Bipy and Pfused:PCBM:Bipy devices are shown in Fig. 3.

Ultraviolet photoelectron spectroscopy was used to investigate the source of the changes in the J–V characteristics. From the measurements, we infer a highest occupied molecular orbital (HOMO) energy of −4.6 ± 0.1 eV for the neat Psub film, −4.7 ± 0.1 eV for a Psub:PCBM ratio of 1:0.2, and −4.5 ± 0.1 eV for a Psub:Bipy ratio of 1:1. For organic heterojunction devices, the saturation dark current density due to generation and recombination at the donor–acceptor heterointerface is: $J_s = J_{S0}exp(-\Delta E_{DA}/k_BT)$, where ΔE_{DA} is the difference between the HOMO energy of the donor and the lowest unoccupied molecular orbital energy of the acceptor, and $J_{S0} = J_S(T = \infty)$ [11]. Using the saturation current for neat Psub ($J_S = 1.1 \pm 0.1 \times 10^{-9}$ A cm^{-2}), Psub:PCBM = 1:0.2 ($J_S = 5.0 \pm 2.0 \times 10^{-10}$ A cm^{-2}) and Psub:Bipy = 1:1 ($J_S = 5.8 \pm 0.2 \times 10^{-9}$ A cm^{-2}), the change in ΔE_{DA} and thus changes in the HOMO energy

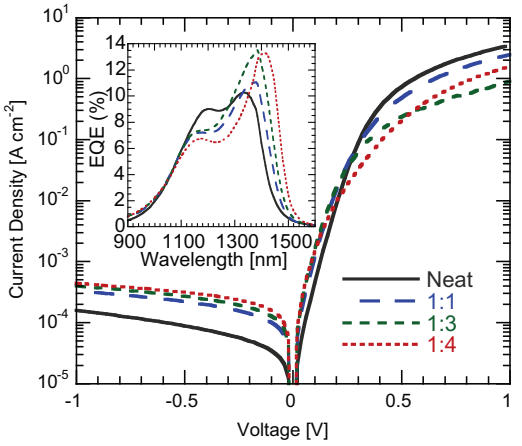

Fig. 2. Current density–voltage characteristics and spectrally resolved EQE (inset) for varying molar ratios of Pfused in Bipy.

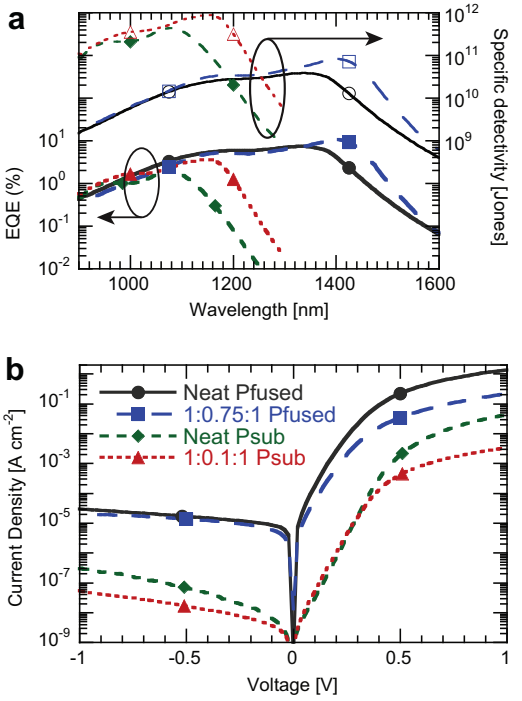

Fig. 3. (a) Spectrally resolved external quantum efficiency (*EQE*-closed symbols) and specific detectivity (solid symbols), and (b) current density–voltage characteristics and for neat Psub (diamonds) and 1:0.1:1 ratio of Psub:PCBM:Bipy (triangles) and for neat Pfused (circles) and 1:0.75:1 ratio of Pfused:PCBM:Bipy (squares).

can be calculated. Relative to neat Psub (HOMO = −4.6 ± 0.1 eV), it was found that PCBM reduced the calculated HOMO energy by 0.02 ± 0.01 eV and Bipy increased the calculated HOMO energy by 0.06 ± 0.01 eV. The agreement between the measured saturation current and the HOMO energy for Psub is within the error of the UPS measurements.

The addition of PCBM to the Psub films optimized for D^* results in insignificant changes to the root-mean square (RMS) roughness of 0.7 ± 0.1 nm (as determined by atomic force microscopy) and the intensity of the (0 0 1) X-ray diffraction peak. The addition of Bipy to Psub (1:1) reduced the intensity of the (0 0 1) diffraction peak by ~90% indicating a reduced crystallinity, and also had an insignificant effect on the film RMS roughness (0.7 ± 0.1 nm and 0.8 ± 0.1 nm for a neat film, and one containing Bipy, respectively), while the addition of Bipy to the less soluble Pfused increases the RMS roughness from 1.3 ± 0.1 nm to 2.3 ± 0.1 nm. The addition of Bipy to the porphyrin solution reduces the solubility of the dimers, resulting in eventual precipitation of the Pfused. The decreased solubility limited the use of Bipy to a dimer similar to Pfused, but having the meso- and beta-positions bonded to the 3- and 4-positions of perylene, as shown in Fig. 1a. Devices using films of neat perylene-fused porphyrin dimers achieved an $EQE = 9.1 \pm 0.2\%$ at $\lambda = 1485$ nm while devices with molar ratios ranging from pyrene-fused:Bipy = 1:0.5 to 1:3 resulted in devices with reduced efficiency.

As noted above, the PCBM and Bipy additives resulted in a red shift in the porphyrin Q-band absorption with increasing concentration. The spacing between Zn-cores in adjacent molecules of our porphyrin tapes is characterized by large distances of 9.5–10 Å [4b], while complexes of fullerenes and metalloporphyrins are characterized by distances of only 2.6–3 Å [4b,6b]. For porphyrin fullerene complexes, an absorption red shift is commonly observed and attributed to favorable van der Waals attraction with a contribution of weak charge transfer between the porphyrin and the fullerene, decreasing the energy of the porphyrin π–π^* transition and the HOMO and LUMO energies [4c,6b]. For the axial metaloprophyrin–imine complexes, the red shift is a well documented phenomenon and typically interpreted as combination of several factors [12]. The first is a decrease in the energy of the π–π^* transition in the metalloporphyrin-additive complex, resulting from the metal becoming more electropositive on coordination of the π-acidic imine ligand, leading to an increase in HOMO energy and stabilization of the LUMO [12a,b]. Metal to pyridine charge transfer on imine coordination to the metalloporphyrin as well as geometry changes in the complex as a result of imine coordination also contribute to the red shift [6f,12c]. Lastly, coordination of two porphyrins through the bidentate Bipy molecule in related systems is thought to provide enhanced coupling between the π-orbitals of linked porphyrin molecules, significantly increasing mobility of positive charges along olygoporphyrin wires [19b]. The substantial increase in exciton diffusion length with the addition of Bipy additives observed here can also be explained by the increased coupling between π-orbitals of diporphyrin cores mediated by the Bipy ligands.

In conclusion, we have demonstrated that adding PCBM to both Psub and Pfused donors reduces *EQE* and increases differential resistance, while adding Bipy increases *EQE* and decreases differential resistance. Both additives cause the NIR photoresponse to red shift with increasing concentration. Psub:PCBM:Bipy = 1:0.1:1 devices have $EQE = 3.6\%$ and $D^* = 8.8 \pm 0.2 \times 10^{11}$ Jones at $\lambda = 1150$ nm, whereas Pfused:PCBM:Bipy = 1:0.75:1 detectors have $EQE = 10.5\%$ and $D^* = 8.2 \pm 0.2 \times 10^{10}$ Jones at $\lambda = 1400$ nm. An $EQE = 13.5\%$ and $D^* = 2.1 \pm 0.1 \times 10^{10}$ Jones at $\lambda = 1385$ nm, was achieved for Pfused:Bipy = 1:3. The decrease in dark current with the addition of PCBM, the increase in *EQE* with addition of Bipy, and the absorption red shift with the addition of Bipy or PCBM are direct consequences of the resulting changes in the frontier orbital energies, and may apply to other porphyrin-based detectors or photovoltaics.

Acknowledgements

The authors thank the National Science Foundation SOLAR program, the Defense Advanced Research Projects Agency HARDI program, and Universal Display Corp. for partial support of this work.

References

[1] X. Xu, X.F. Qi, M. Davanco, S.R. Forrest, Organic photodetector focal plane arrays fabricated on hemispherical substrates by three dimensional stamping, IEEE LEOS Ann. Meet. Conf. Proc. 1 and 2 (2007) 578–579.

[2] Y.J. Xia, L. Wang, X.Y. Deng, D.Y. Li, X.H. Zhu, Y. Cao, Photocurrent response wavelength up to 1.1 μm from photovoltaic cells based on narrow-band-gap conjugated polymer and fullerene derivative, Appl. Phys. Lett. 89 (8) (2006) 081106;
L. Wen, B.C. Duck, P.C. Dastoor, S.C. Rasmussen, Poly(2,3-dihexylthieno 3,4-b pyrazine) via GRIM polymerization: Simple preparation of a solution processable, low-band-gap conjugated polymer, Macromolecules 41 (13) (2008) 4576–4578;
E. Perzon, F.L. Zhang, M. Andersson, W. Mammo, O. Inganas, M.R. Andersson, A conjugated polymer for near infrared optoelectronic applications, Adv. Mater. 19 (20) (2007) 3308.

[3] X. Gong, M.H. Tong, Y.J. Xia, W.Z. Cai, J.S. Moon, Y. Cao, G. Yu, C.L. Shieh, B. Nilsson, A.J. Heeger, High-detectivity polymer photodetectors with spectral response from 300 nm to 1450 nm, Science 325 (5948) (2009) 1665–1667.

[4] (a) A. Tsuda, A. Osuka, Fully conjugated porphyrin tapes with electronic absorption bands that reach into infrared, Science 293 (5527) (2001) 79–82;
(b) J.D. Zimmerman, V.V. Diev, K. Hanson, R.R. Lunt, E.K. Yu, M.E. Thompson, S.R. Forrest, Porphyrin-tape/C_{60} organic photodetectors with 6.5% external quantum efficiency in the near infrared, Adv. Mater. 22 (25) (2010) 2780–2783;
(c) V.V. Diev, K. Hanson, J.D. Zimmerman, S.R. Forrest, M.E. Thompson, Fused pyrene–diporphyrins: shifting near-infrared absorption to 1.5 μm and beyond, Angew. Chem. Int. Ed. 49 (32) (2010) 5523–5526.

[5] J. Peet, J.Y. Kim, N.E. Coates, W.L. Ma, D. Moses, A.J. Heeger, G.C. Bazan, Efficiency enhancement in low-band gap polymer solar cells by processing with alkane dithiols, Nat. Mater. 6 (7) (2007) 497–500.

[6] (a) P.D.W. Boyd, M.C. Hodgson, C.E.F. Rickard, A.G. Oliver, L. Chaker, P.J. Brothers, R.D. Bolskar, F.S. Tham, C.A. Reed, Selective supramolecular porphyrin/fullerene interactions, J. Am. Chem. Soc. 121 (45) (1999) 10487–10495;
(b) P.D.W. Boyd, C.A. Reed, Fullerene–porphyrin constructs, Acc. Chem. Res. 38 (4) (2005) 235–242;
(c) C.M. Drain, A. Varotto, I. Radivojevic, Self-organized porphyrinic materials, Chem. Rev. 109 (5) (2009) 1630–1658;
(d) A.D. Shukla, P.C. Dave, E. Suresh, A. Das, P. Dastidar, Multicomponent Zn-tetraphenylporphyrins: syntheses, characterization and their self assembly in the solid state, J. Chem. Soc., Dalton Trans. 23 (2000) 4459–4463;

(e) I. Beletskaya, V.S. Tyurin, A.Y. Tsivadze, R. Guilard, C. Stern, Supramolecular chemistry of metalloporphyrins, Chem. Rev. 109 (5) (2009) 1659–1713;
(f) K.M. Kadish, K.M. Smith, R. Guilard, The Porphyrin Handbook, Academic Press, San Diego, 2000.

[7] G. Yu, J. Gao, J.C. Hummelen, F. Wudl, A.J. Heeger, Polymer photovoltaic cells: enhanced efficiencies via a network of internal donor-acceptor heterojunctions, Science 270 (5243) (1995) 1789–1791.

[8] G.D. Wei, S.Y. Wang, K. Renshaw, M.E. Thompson, S.R. Forrest, Solution-processed squaraine bulk heterojunction photovoltaic cells, ACS Nano 4 (4) (2010) 1927–1934.

[9] S.M. Sze, Physics of Semiconductor Devices, 2nd ed., Wiley, New York, 1981.

[10] B.R. Danger, K. Bedient, M. Maiti, I.J. Burgess, R.P. Steer, Photophysics of self-assembled zinc porphyrin–bidentate diamine ligand complexes, J. Phys. Chem. A 114 (41) (2010) 10960–10968.

[11] N.C. Giebink, G.P. Wiederrecht, M.R. Wasielewski, S.R. Forrest, Ideal diode equation for organic heterojunctions. I. Derivation and application, Phys. Rev. B 82 (15) (2010) 155305.

[12] (a) M. Gouterman, J. Mol. Spectr. 6 (1961) 138–163;
(b) M. Gouterman, J. Chem. Phys. 30 (1959) 1139–1161;
(c) D. Gust, T.A. Moore, A.L. Moore, H.K. Kang, J.M. Degraziano, P.A. Liddell, G.R. Seely, Effect of coordinated ligands on interporphyrin photoinduced-electron-transfer rates, J. Phys. Chem. Us 97 (51) (1993) 13637–13642.

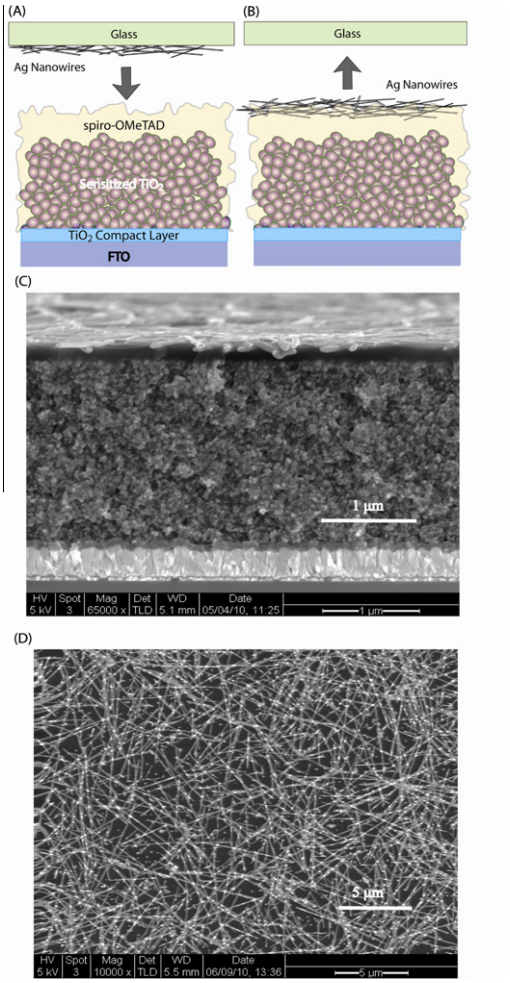

Fig. 1. Device schematic of dye sensitized solar cell (A) before and (B) after Ag NW lamination. (C) SEM side view image (65,000× magnification, 1 μm scale bar) and (D) SEM top view image (10,000× magnification, 5 μm scale bar) of solid-state DSC after Ag NW lamination.

Ag NWs show high transparency in the solar spectrum, have low sheet resistance, and can be processed with high throughput. As the nanowire concentration of the film increases, the transmission decreases and the films become more reflective. In this letter, we show that thick Ag NW meshes can be deposited on top of ss-DSCs as the reflective counter electrode without an annealing step producing comparable power conversion efficiencies versus the evaporated Ag control devices.

ss-DSCs have an empirically optimized titania film thickness of ~2.2 μm (versus >10 μm for liquid DSCs); which is likely due to higher rates of recombination [12,13]. Despite the thinner device architecture, which lowers overall light absorption, ss-DSCs have recently achieved maximum power conversion efficiencies of 6.1% [14]. ss-DSCs have the potential to match or exceed liquid based DSC performance by developing higher molar extinction coefficient dyes for increased light absorption [15–17], hole conductors with lower HOMO levels, new architectures to increase light harvesting [18–23], and tandem devices.

2. Experimental

2.1. Solid-state dye-sensitized solar cell device fabrication

Solid-state DSCs are shown schematically in Fig. 1A. ss-DSCs consist of Flourine doped SnO_2 conducting glass (Hartford Glass TEC 15) which was partially etched using zinc powder and HCl (12%) then cleaned by sonication sequentially in 10% extran, acetone, isopropanol, and water. A 50 nm compact TiO_2 layer was deposited via aerosol spray pyrolysis using air as the carrier gas [24]. Mesoporous titania films were deposited via doctor blading of commercially available paste (Dyesol 18NR-T) and slowly heated to 500 °C for 30 min in air. It should be noted, that TiO_2 paste deposition was performed in a laminar flow hood to minimize dust contamination that can affect the Ag NW transfer. Films were subsequently treated in 0.02 M $TiCl_4$ aqueous solution overnight at room temperature [25]. Samples were then heated to 450 °C for 10 min cooled to approximately 80 °C and immersed in 0.3 mM of Z907 (Solaronix SA) in a 1:1 mixture of acetonitrile and tert-butyl alcohol for 12–18 h. The organic hole conductor solution was made by dissolving 72 mg of 2,2′,7,7′tetrakis-(*N*,*N*-di-*p*-methoxyphenylamine)-9,9′-spirobifluorene (spiro-OMeTAD) in 400 μl of chlorobenzene and then adding 7 μl of tert-butylpyridine and 15 μl of 0.6 M bis(trifluoromethane)sulfonamide lithium salt (Fluka) in acetonitrile. The doped spiro-OMeTAD solution was deposited on the substrate and allowed to infiltrate the TiO_2 for 30 s prior to spin coating (2000 RPM for 40 s) and dried in a dessicator for several hours. Ag counter electrodes (200 nm) for the control devices were evaporated at 2×10^{-6} torr on half of the substrate.

2.2. Silver nanowire synthesis and lamination onto DSC

Silver nanowires were synthesized by reducing Ag nitrate in the presence of poly(vinyl pyrrolidione) in ethylene glycol which resulted in Ag NWs that were on average 8.7 μm long and have 103 nm diameters [11,26]. To create films on the host substrate, Ag NWs were deposited from methanol onto coverslip glass and annealed at 180 °C to fuse the junctions between the wires and enhance conductivity [10,11,27]. The Ag NW films were then pressed onto the spiro-OMeTAD at a pressure of 1.6×10^4 psi for approximately 30 s, as illustrated in Fig. 1A and B. Care should be taken during lamination to remove any debris on the press and align the press to consistently apply pressure across the glass surface; inconsistent pressure can cause substrate cracking. Laminated Ag NW films were roughly 2–4 nanowires thick (100–200 nm) as shown in the SEM image in Fig. 1C. During lamination >95% of the Ag NWs are transferred to the ss-DSC substrate. The overall surface coverage is relatively sparse as shown in Fig. 1D. ImageJ software was used to analyze the SEM image and determined that approximately 59% of the spiro-OMeTAD surface is covered by AgNWs. A four-point probe measurement was used to determine a sheet resistance of 4.5 Ω/□ for AgNWs counter electrode versus 1.3 Ω/□ for 200 nm of evaporated silver on inert

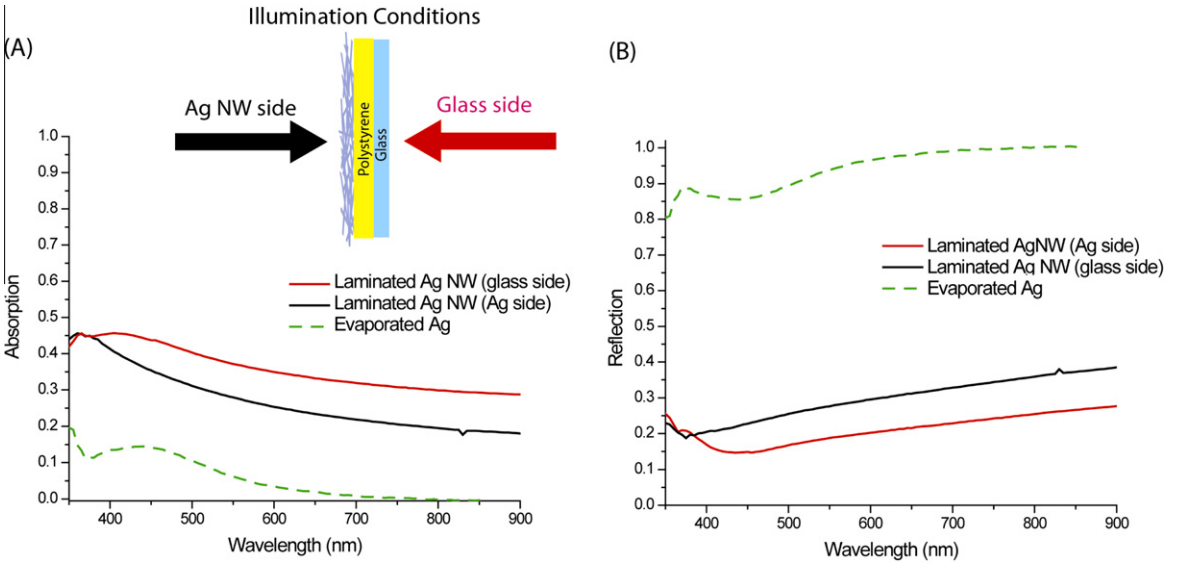

Fig. 2. Specular and diffuse (A) Absorption and (B) reflection of evaporated Ag versus laminated Ag NW electrodes on polystyrene/glass substrate under various illumination conditions described in the inset.

polystyrene films. The counter electrode makes a relatively small contribution to the series resistance which is dominated by the FTO (15 Ω/□) and the internal resistance of the doped spiro-OMeTAD. It should be noted, that Ag NWs were laminated on the same substrate as evaporated Ag to ensure the most accurate comparison.

3. Results and discussion

For measurements to determine the optical properties of the counter electrodes, Ag was evaporated and Ag NWs were pressed into a thin layer (<100 nm) of polystyrene on a glass slide as shown in the inset of Fig. 2. Polystyrene is a wide band gap polymer with negligible absorption in the visible and near-infrared portion of the spectrum. Absolute (i.e. specular and diffuse) light absorption (Fig. 2A) and transmission were measured with an integrating sphere (Labsphere) with methods previously described [28]. The absolute reflection (Fig. 2B) was calculated from the absorption and transmission values (i.e. $R = 1 - T - A$). The absorption of Ag NWs is dependent upon the illumination condition; Ag NWs absorb more light when illuminated from the glass/polystyrene side (red solid)[1] versus the Ag NW side (black solid) as shown in Fig. 2A. The increase in absorption may be caused by increased light scattering due to changes in the Ag NW morphology during lamination and via total internal reflections inside the polystyrene/glass. During lamination, the cylindrically shaped silver nanowires penetrate into the soft polymer surface creating a rough, scattering interface on the polystyrene side. However, the portion of the Ag NW touching the host substrate is flattened and becomes relatively smooth (Fig. 1C) reducing light scattering. Secondly, light scattered in the polystyrene, which has an index of refraction of approximately 1.55, can undergo total internal reflection increasing the optical path length and increasing overall light absorption by Ag NWs. Evaporated Ag (green dash) is only slightly absorptive and is highly reflective throughout the spectrum for both illumination directions. The variation in reflection between Ag NWs and evaporated Ag films is primarily related to higher light absorption by the Ag NWs and the low surface density of Ag NWs compared to the unity surface coverage of evaporated Ag.

Fig. 3A displays the total light absorption of all layers in ss-DSC devices using Ag NWs and evaporated Ag contacts illuminated through the FTO side. Spiro-OMeTAD dominates light absorption inside the ss-DSC from 350 to 425 nm. Both the evaporated Ag and Ag NW ss-DSCs have similar absorption profiles in the region where the sensitizing dye absorbs most strongly (425–550 nm). At the peak absorption of the Z907 (525 nm), roughly 80% of the light is absorbed by the control versus 71% for the Ag NW ss-DSCs. Most of the loss in absorption is due to transmission through the device; specular transmission measurements (not shown) reveal that 15% of the light at 525 nm is transmitted through the Ag NW ss-DSC. In the red/near-infrared portion of the spectrum, the Ag NW ss-DSCs have overall higher absorption due to Ag NW absorption that does not contribute to the photocurrent. It should be noted that the Ag NW ss-DSC absorption profile is smoother and does not contain the interference effects typically seen with evaporated electrodes. Because these measurements were taken on the same substrate, the smooth profile further strengthens our hypothesis that pressing nanowires into the spiro-OMeTAD overlayer roughens the rear interface, increasing scattering off of the back contact and reducing interference effects.

External quantum efficiency (EQE) measurements were performed at a chopping frequency of 45 Hz using a Stanford Research System lock-in amplifier (Model SR830) under white light bias equivalent to 10% sun. The

[1] For interpretation of the references to colour in Figs. 1 and 2, the reader is referred to the web version of this article.

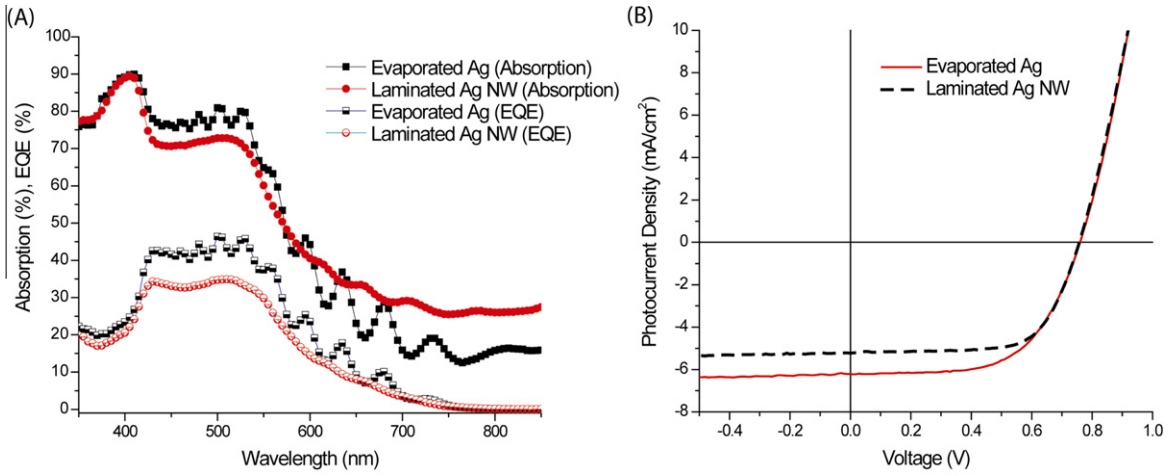

Electrode	Device Area	Jsc [mA/cm^2]	Voc [mV]	FF	PCE (%)
Evaporated Ag	0.09 cm^2	6.2	765	0.60	2.8
Laminated Ag NW	0.07 cm^2	5.2	755	0.69	2.7

Fig. 3. (A) Total light absorption and external quantum efficiency plots of solid-state dye-sensitized solar cells made with evaporated Ag and laminated Ag NW counter electrodes. (B) Photocurrent density versus voltage (JV) plot of ss-DSCs with Ag NW counter electrode (red line) versus evaporated Ag control (dashed black line). PV device characteristics are shown in the figure inset.

EQE, shown in Fig. 3A, scales with light absorption and explains the correspondingly lower photocurrent of Ag NW ss-DSCs versus the control shown in Fig. 3B. Ag NW devices have comparable power conversion efficiency (2.7%) versus the control ss-DSC (2.8%). Ag NW devices have lower short-circuit current density (Jsc), due to a lower reflectivity, but consistently displayed higher fill factors (FF) and behaved differently during light soaking. Evaporated Ag devices initially had very low fill factors (0.4–0.45) and required >15 min of light soaking (100% sun) under +1 V bias to dramatically increase the fill factor (0.55–0.60). Ag NW based devices had significantly higher initial fill factors (0.57–0.65) that increased slightly over <5 min of light soaking to (0.62–0.69). It should be noted that FF ranges were based on five devices that contained an equal number of evaporated Ag and Ag NW electrodes. Despite the slightly higher sheet resistance of Ag NW electrodes, the overall series resistance, which can be approximated as the slope of the JV curves at far forward bias, is nominally the same for both devices. The spiro-OMeTAD overlayer is known to increase the series resistance and decrease the fill factor of ss-DSCs [29]. Pressed Ag NWs penetrate into the 150–200 nm spiro-OMeTAD overlayer, which we believe helps lower the effective series resistance within the spiro-OMeTAD layer, compensating for the higher sheet resistance of the Ag NWs. In addition, Ag NWs films are fabricated and stored in air, which creates a thin silver oxide layer on the surface that increases the work function and may improve charge collection. The work function of Ag, at 4.4 eV, is significantly higher than the HOMO level of spiro-OMeTAD (5.2 eV), which requires large band bending or Fermi-level pinning [30] at the spiro-OMeTAD/Ag interface for good electrical contact. However, silver oxide (Ag_2O) has a work function of 5.1 eV and often exhibits p-type conductivity [31], which would act as an ideal charge collector with minimal recombination losses at this interface [5]. Evaporated Ag electrodes, however, are deposited in vacuum and may require time to allow for oxygen to diffuse and oxidize Ag at the metal/spiro-OMeTAD interface, possibly explaining the requirement of longer light soaking times to achieve a higher FF. A complete explanation of the effects of light soaking on solid-state DSCs is beyond the scope of this work and will be discussed in a future study.

4. Discussion and conclusion

Reflectivity, and thus overall power conversion efficiency of metal nanowire based electrodes, can be improved by developing new procedures to deposit more nanowires on the ss-DSC. Laminated Ag NWs are limited due to the pressing procedure, as each wire must come into contact with the soft hole conductor to be transferred. Wire meshes that are too thick cannot be completely transferred to another substrate. Directly spray coating or doctor blading NWs onto the cell could increase the overall surface concentration. These techniques would require solvents that do not dissolve the spiro-OMeTAD and a low temperature sintering step to prevent degradation of the ss-DSC. Laminating Ag nanoparticle films, which can be made into more densely packed films, may also result in more reflective films [9,32].

To the best of our knowledge, reflective silver nanowire meshes represent the first replacement of evaporated metal counter electrodes used in solid-state DSCs. This work demonstrates the general feasibility of laminating Ag NWs on ss-DSCs and achieves comparable device performance with standard thermally deposited Ag electrodes but with the potential for high throughput processing and unity material usage. This work may be extended to

semi-transparent Ag NW electrodes for ss-DSCs. Semi-transparent Ag NW meshes could be used as the front contact on glass-free, flexible ss-DSCs which use titania nanoparticles on metal foil [33] and also as an intermediary electrode in a tandem ss-DSC architecture. Finally, it should be noted that Ag NWs are dissolved by iodide based electrolytes, but may be implemented in liquid DSCs that use organic electrolytes [34,35].

Acknowledgements

M. McGehee and P. Peumans acknowledge support from the Center for Advanced Molecular Photovoltaics through a Grant from King Abdullah University of Science and Technology.

References

[1] B. O'Regan, M. Grätzel, A low-cost, high-efficiency solar cell based on dye-sensitized colloidal TiO_2 films, Nature 353 (1991) 737–740.
[2] L.M. Peter, Dye-sensitized nanocrystalline solar cells, Physical Chemistry Chemical Physics 9 (2007) 2630–2642.
[3] A. Hagfeldt, M. Grätzel, Molecular photovoltaics, Accounts of Chemical Research 33 (2000) 269–277.
[4] Y. Cao, Y. Bai, Q. Yu, Y. Cheng, S. Liu, D. Shi, F. Gao, P. Wang, Dye-sensitized solar cells with a high absorptivity ruthenium sensitizer featuring a 2-(hexylthio)thiophene conjugated bipyridine, The Journal of Physical Chemistry C 113 (2009) 6290–6297.
[5] H.J. Snaith, A.J. Moule, C. Klein, K. Meerholz, R.H. Friend, M. Grätzel, Efficiency enhancements in solid-state hybrid solar cells via reduced charge recombination and increased light capture, Nano Letters 7 (2007) 3372–3376.
[6] R.A. Street, W.S. Wong, S.E. Ready, M.L. Chabinyc, A.C. Arias, S. Limb, A. Salleo, R. Lujan, Jet printing flexible displays, Materials Today 9 (2006) 32–37.
[7] C. Girotto, B.P. Rand, S. Steudel, J. Genoe, P. Heremans, Nanoparticle-based, spray-coated silver top contacts for efficient polymer solar cells, Organic Electronics 10 (2009) 735–740.
[8] S.K. Hau, H.-L. Yip, K. Leong, A.K.Y. Jen, Spraycoating of silver nanoparticle electrodes for inverted polymer solar cells, Organic Electronics 10 (2009) 719–723.
[9] J.R. Greer, R.A. Street, Thermal cure effects on electrical performance of nanoparticle silver inks, Acta Materialia 55 (2007) 6345–6349.
[10] W. Gaynor, J.-Y. Lee, P. Peumans, Fully solution-processed inverted polymer solar cells with laminated nanowire electrodes, ACS Nano 4 (2009) 30–34.
[11] J.-Y. Lee, S.T. Connor, Y. Cui, P. Peumans, Solution-processed metal nanowire mesh transparent electrodes, Nano Letters 8 (2008) 689–692.
[12] L. Schmidt-Mende, S.M. Zakeeruddin, M. Gratzel, Efficiency improvement in solid-state-dye-sensitized photovoltaics with an amphiphilic ruthenium-dye, Applied Physics Letters 86 (2005) 13504.
[13] L. Schmidt-Mende, H.J. Snaith, Advances in liquid-electrolyte and solid-state dye-sensitized solar cells, Advanced Materials 19 (2007) 3187–3200.
[14] X. Liu, W. Zhang, S. Uchida, L. Cai, B. Liu, S. Ramakrishna, An efficient organic-dye-sensitized solar cell with in situ polymerized poly(3,4-ethylenedioxythiophene) as a hole-transporting material, Advanced Materials 22 (2010) E1–E6.
[15] R. Li, J. Liu, N. Cai, M. Zhang, P. Wang, Synchronously reduced surface states, charge recombination, and light absorption length for high-performance organic dye-sensitized solar cells, The Journal of Physical Chemistry B 114 (2010) 4461–4464.
[16] A. Mishra, M.K.R. Fischer, P. Bäuerle, Metal-free organic dyes for dye-sensitized solar cells: from structure: property relationships to design rules, Angewandte Chemie International Edition 48 (2009) 2474–2499.
[17] S. Ardo, G.J. Meyer, Photodriven heterogeneous charge transfer with transition-metal compounds anchored to TiO_2 semiconductor surfaces, Chemical Society Reviews 38 (2009) 115–164.
[18] B.E. Hardin, E.T. Hoke, P.B. Armstrong, J.-H. Yum, P. Comte, T. Torres, J.M.J. Frechet, M.K. Nazeeruddin, M. Gratzel, M.D. McGehee, Increased light harvesting in dye-sensitized solar cells with energy relay dyes, Natural Photon 3 (2009) 406–411.
[19] J.H. Yum, B.E. Hardin, S.J. Moon, E. Baranoff, F. Nüesch, M.D. McGehee, M. Grätzel, M.K. Nazeeruddin, Panchromatic response in solid-state dye-sensitized solar cells containing phosphorescent, Angewandte Chemie International Edition 48 (2009) 9277–9280.
[20] G.K. Mor, J. Basham, M. Paulose, S. Kim, O.K. Varghese, A. Vaish, S. Yoriya, C.A. Grimes, High-efficiency forster resonance energy transfer in solid-state dye sensitized solar cells, Nano Letters 10 (2010) 2387–2394.
[21] J.A. Chang, J.H. Rhee, S.H. Im, Y.H. Lee, H.-j. Kim, S.I. Seok, M.K. Nazeeruddin, M. Grätzel, High-performance nanostructured inorganic-organic heterojunction solar cells, Nano Letters 10 (2010) 2609–2612.
[22] M. Shalom, J. Albero, Z. Tachan, E. Martinez-Ferrero, A. Zaban, E. Palomares, Quantum dot-dye bilayer-sensitized solar cells: breaking the limits imposed by the low absorbance of dye monolayers, The Journal of Physical Chemistry Letters 1 (2010) 1134–1138.
[23] S. Buhbut, S. Itzhakov, E. Tauber, M. Shalom, I. Hod, T. Geiger, Y. Garini, D. Oron, A. Zaban, Built-in quantum dot antennas in dye-sensitized solar cells, ACS Nano 4 (2010) 1293–1298.
[24] L. Kavan, M. Grätzel, Highly Efficient semiconducting TiO_2 photoelectrodes prepared by aerosol pyrolysis, Electrochimica Acta 40 (1995) 643–652.
[25] P.M. Sommeling, B.C. O'Regan, R.R. Haswell, H.J.P. Smit, N.J. Bakker, J.J.T. Smits, J.M. Kroon, J.A.M. van Roosmalen, Influence of a $TiCl_4$ post-treatment on nanocrystalline TiO_2 films in dye-sensitized solar cells, Journal of Physical Chemistry B 110 (2006) 19191–19197.
[26] A. Tao, F. Kim, C. Hess, J. Goldberger, R. He, Y. Sun, Y. Xia, P. Yang, Langmuir-blodgett silver nanowire monolayers for molecular sensing using surface-enhanced raman spectroscopy, Nano Letters 3 (2003) 1229–1233.
[27] J.-Y. Lee, S.T. Connor, Y. Cui, P. Peumans, Semitransparent organic photovoltaic cells with laminated top electrode, Nano Letters 10 (2010) 1276–1279.
[28] J. Zhu, Z. Yu, G.F. Burkhard, C.-M. Hsu, S.T. Connor, Y. Xu, Q. Wang, M. McGehee, S. Fan, Y. Cui, Optical absorption enhancement in amorphous silicon nanowire and nanocone arrays, Nano Letters 9 (2008) 279–282.
[29] I.K. Ding, N. Tétreault, J. Brillet, B.E. Hardin, E.H. Smith, S. Rosenthal, F. Sauvage, M. Grätzel, M.D. McGehee, Pore-filling of spiro-OMeTAD in solid-state dye sensitized solar cells: quantification, mechanism, and consequences for device performance, Advanced Functional Materials 19 (2009) 2431–2436.
[30] C. Tengstedt, W. Osikowicz, W.R. Salaneck, I.D. Parker, C.-H. Hsu, M. Fahlman, Fermi-level pinning at conjugated polymer interfaces, Applied Physics Letters 88 (2006) 053502–053503.
[31] U. Kumar Barik, S. Srinivasan, C.L. Nagendra, A. Subrahmanyam, Electrical and optical properties of reactive DC magnetron sputtered silver oxide thin films: role of oxygen, Thin Solid Films 429 (2003) 129–134.
[32] V. Sholin, S.A. Carter, R.A. Street, A.C. Arias, High work function materials for source/drain contacts in printed polymer thin film transistors, Applied Physics Letters 92 (2008) 063307.
[33] S. Ito, N.-L.C. Ha, G. Rothenberger, P. Liska, P. Comte, S.M. Zakeeruddin, P. Pechy, M.K. Nazeeruddin, M. Grätzel, High-efficiency (7.2%) flexible dye-sensitized solar cells with Ti-metal substrate for nanocrystalline–TiO_2 photoanode, Chemical Communications (2006) 4004–4006.
[34] M. Wang, N. Chamberland, L. Breau, J.-E. Moser, R. Humphry-Baker, B. Marsan, S.M. Zakeeruddin, M. Grätzel, An organic redox electrolyte to rival triiodide/iodide in dye-sensitized solar cells, Natural Chemistry 2 (2010) 385–389.
[35] Z. Zhang, P. Chen, T.N. Murakami, S.M. Zakeeruddin, M. Grätzel, The 2,2,6,6-tetramethyl-1-piperidinyloxy radical: an efficient, iodine-free redox mediator for dye-sensitized solar cells, Advanced Functional Materials 18 (2008) 341–346.

In the current work, we focus on investigating the S-shape effect in bilayer heterojunction photovoltaic devices induced by the exciton blocking layer (EBL) which has shown to be an essential layer for high performance bilayer OPV devices [8]. Previously, the effect of different kinds of materials working as EBL on the performance of OPV have been researched by Yu et al. [19] and demonstrated the J_{SC} of the device would decrease exponentially with the thicknesses of the buffer layer thicknesses and they attributed this effect to the decrease of conductivity. Particularly for the bathocuproine (BCP), Peumans et al. have shown that favorable hopping states were induced by the thermalization of the hot metal atoms on the BCP layer and they found the optimum BCP thickness is around 15 nm. Here, instead of just comparing the *J–V* curves of the devices with various BCP thicknesses, we tried to understand the physics origin of the EBL thickness effect by using *C–V* measurements to study the charge accumulation effect due to the presence of thick exciton blocking layer in the bilayer heterojunction photovoltaic devices. We demonstrated the occurrence of the S-shape effect in the *J–V* curves and charge accumulation in the device can be controlled by modulating the BCP layer thickness from 5 to 20 nm. We also applied a numerical model to simulate the *J–V* curve of the devices and the model suggests that the interfacial recombination near the C_{60}/BCP interface and BCP layer cause S-shape effect in *J–V* curves. Our finding indicates the importance of the charge accumulation effect and a careful control of the exciton blocking layer in bilayer heterojunction OPV devices.

2. Experimental

In our bilayer heterojunction OPV devices, MoO_3 (99.5%, Aldrich), CuPc (99%, Aldrich), C_{60} (99.5%, Aldrich), BCP (98%, Aldrich), were used as received. Indium-tin-oxide (ITO) coated glass substrates with sheet resistance of 13 Ω/□ were cleaned using DI water and chemical solvents [8,20]. After cleaning, the substrates were dried by 99.995% pure nitrogen and treated by O_2 plasma for 15 min prior to loading into vacuum chamber. All the materials were deposited using thermal evaporation under a pressure of $<1 \times 10^{-6}$ Torr at a deposition rate of 0.1 nm/s for organic layers and Ag cathode. Fig. 1 shows the schematic structure of bilayer heterojunction small molecule organic solar cells, ITO/MoO_3(10 nm)/CuPc(20 nm)/C_{60}(45 nm)/BCP(5–20 nm)/Ag(100 nm). In the work, all the processing factors were kept identical except the thicknesses of the BCP layers and a quartz crystal monitor was used to determine film thickness and deposition rate. The Ag cathodes were evaporated through a metal shadow mask with 2 mm diameter openings. The *J–V* characteristics were measured by a Keithley 2400 under illumination of AM1.5G 95 mW/cm^2 simulated solar spectrum from a solar simulator (Newport 69911). The power density of the solar simulator was calibrated by a silicon reference cell (NIST) and monitored by a power meter throughout the measurement. The *C–V* curve was measured by Agilent B1500A Semiconductor Device Analyzer.

3. Numerical model

Although the S-shape effect in the bilayer heterojunction photovoltaic has not been intensively investigated, the S-shape effect in bulk heterojunction OPV has been recently studied by numerical simulation and it has been observed that surface recombination rate as a boundary condition governs the S-shape properties in the *J–V* curves of the bulk heterojunction OPV [21]. Similar to the numerical model in Ref. [21], the one-dimensional carrier transport model for the device is based on the Poisson equation and continuity equation under steady state,

$$\frac{\partial^2 \psi}{\partial x^2} = \frac{q}{\varepsilon_0 \varepsilon_r}(p - n) \tag{1}$$

$$\nabla \cdot J - R + G = 0 \tag{2}$$

The current density can be further substituted by the charge transport equations,

$$J_p = -KT\mu_p \partial p/\partial x + qp\mu_p F \tag{3}$$

$$J_n = KT\mu_n \partial n/\partial x + qn\mu_n F \tag{4}$$

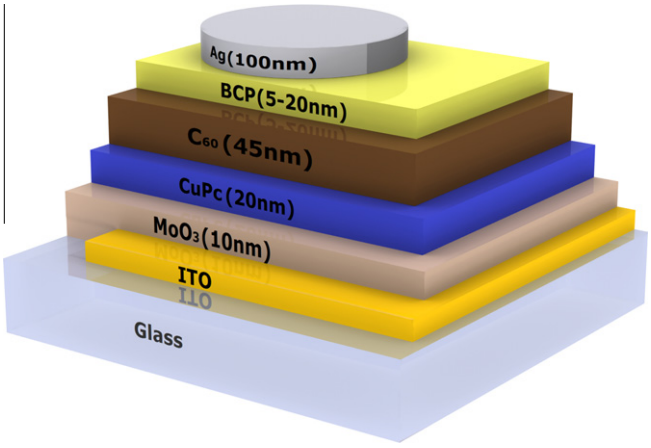

Fig. 1. The schematic of bilayer heterojunction small molecule organic solar cell.

In the above equations, μ_n and μ_p are the charge carrier mobility for electrons and holes, q is the elementary charge, T is the temperature, n and p are the electron and hole density and ε_r is the material effective dielectric permeability, F denotes the electrical field, R and G describe the recombination and generation rate of the charge carriers. According to the thermionic emission theory [22], the boundary conditions can be written as,

$$n(0) = N_c \exp\left[-\frac{(E_{g1} - \phi_1)}{KT}\right] \quad (5)$$

$$p(0) = N_v \exp\left(-\frac{\phi_1}{KT}\right) \quad (6)$$

$$n(L) = N_c \exp\left(-\frac{\phi_2}{KT}\right) \quad (7)$$

$$p(L) = N_v \exp\left[-\frac{(E_{g2} - \phi_2)}{KT}\right] \quad (8)$$

Eqs. (5)–(8) state the hole and electron concentrations at the interfaces between anode/donor and cathode/acceptor, respectively, and the band diagram of the simulation model is shown in Fig. 2. N_c and N_v are the corresponding effective charge carrier density. The electron and hole concentrations at the anode/donor interface are calculated by the energy difference between the anode work function and hole conducting highest occupied molecular orbital (HOMO), i.e. ϕ_1 in Fig. 2. In analogy, ϕ_2 is used to evaluate the carrier concentration at the buffer layer and cathode interface. The set of equations are solved by numerical approach AMPS-1D [23].

In bilayer heterojunction OPV devices, excitons are generated by the irradiated photon and diffuse to the interface of donor/acceptor where the excitons will then be split up. Due to the favor in energy, the holes remain on donor's HOMO whereas the electrons are transferred to acceptor's LUMO [20,24]. In the current model, the generation process is represented by inserting a 5 nm generation layer with a bandgap (E_g) between the donor and acceptor layers (as shown in Fig. 2) and the free carriers are generated from this layer [25]. Furthermore, we considered BCP layer effect by introducing the buffer layer with thickness varying from 5 to 20 nm as shown in Fig. 2. It is important to noticed that using the buffer layer with a smaller bandgap to replace BCP layer is due to (i) preventing the numerical instability in the simulation model which is based on inorganic semiconductor theories; (ii) the buffer layer consists of two opposite effects; one is the charge hopping states induced by silver deposition for carrier transfer and the other is the gap states for recombination. When the buffer layer is thin, the hopping states would be dominant and when the buffer layer is thick, as the generated charges cannot hop to the electrode effectively, they will recombine near the C_{60}/BCP interface hence the gap states for recombination would be dominant. For simplicity, we adapted the buffer layer for qualitatively study of the S-shape effect in the J–V curves. The parameters used in the simulation are given in Table 1.

Table 1
The parameters used in simulation.

Parameter	Symbol	Numerical value
Bandgap [9,23]	E_{gA}, E_{gD}	1.7 eV, 1.7 eV
	E_g	1.4 eV
Electron mobility	μ_n	10^{-1} cm^2/Vs
Hole mobility	μ_p	10^{-2} cm^2/Vs
Eff. density of states	N_c, N_v	1.7×10^{21} cm^{-3}
Dielectric constant[a] CuPc, C_{60}	ε_r	3, 4
Injection barrier	ϕ_1, ϕ_2	0 eV, 0.1 eV
Temperature	T	300 K
Thickness of organic semiconductor	L_1, L_2, L_3	20, 5 and 45 nm
Contact recombination rate	S_{NO}, S_{PO}	10^{10} cm/s, 10^{10} cm/s
	S_{NL}, S_{PL}	10^{10} cm/s, 10^{10} cm/s
Discrete donor-like gap state concentration	ND[b]	10^{18} cm^{-3}
Capture cross section	σ[c]	10^{-10} cm^2

[a] From SES research Corp.
[b,c] From Ref. [26].

4. Results and discussion

The J–V curves of the experimental and simulated devices are shown in Fig. 3(a) and (b), respectively. In Fig. 3(a), it can be noticed that when the thickness of BCP is below 15 nm, normal exponential J–V curves are

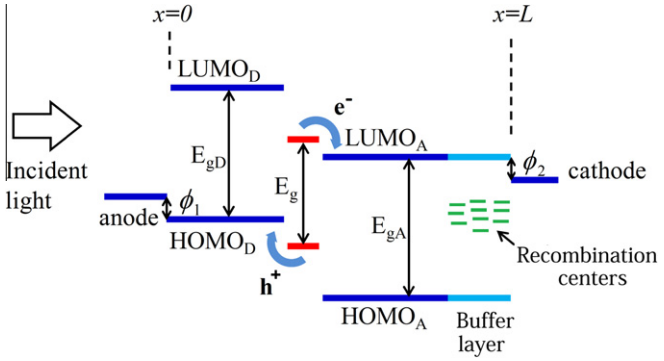

Fig. 2. Band diagram used in simulation with insert of a thin generation layer.

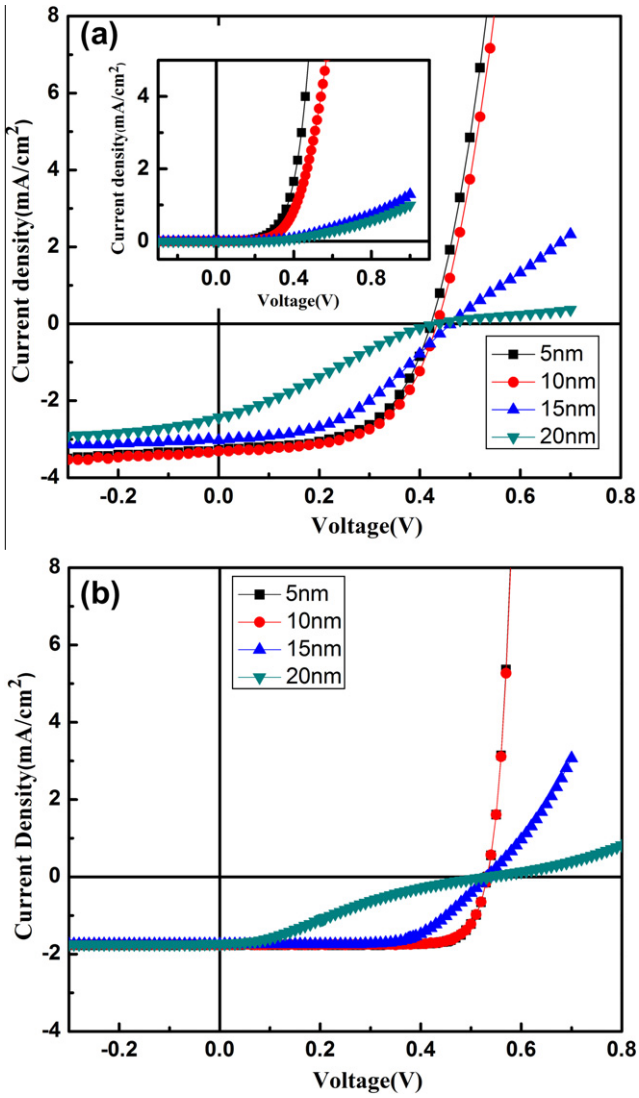

Fig. 3. The *J–V* characteristic varies with the thickness of BCP layer; (a) ITO/MoO_3(10 nm)/CuPc(20 nm)/nmC_{60}(45 nm)/BCP(x)/Ag, inset shows the *J–V* curves of the devices under dark. (b) The numerically simulated *J–V* curves with different buffer layer thicknesses.

observed. When the thickness of the BCP equals to 15 nm, an S-shape characteristic appears and the exponential diode curve degrades remarkably, leading to a significant drop in the FF. When increasing the BCP thickness up to 20 nm, the S-shape is further reinforced. It is worthy to mention that the *J–V* curves of the device under dark does not show the kinks (inset of Fig. 3(a)) which implies the kink observed in the *J–V* curves under illumination is related to the photo-generated carriers. The current observation about the critical thickness of the BCP layer agrees with the previous work [8], where the permeated depth of the hot metal atoms in BCP layer during evaporating of electrode is around 15 nm. We argue the BCP layer consists of two regions (sub-layers): an unaffected BCP layer and the metal permeated BCP layer. The unaffected region is a barrier for electron transport, and cause charge accumulation at the contact with C_{60} layer, while the metal permeated region has favorable hopping site for the electrons to hop through. If the BCP layer thickness is thin and the metal permeated layer is dominant, the S-shape effect would be vanished. On the other hand, when the BCP layer is 15 nm or thicker, the unaffected BCP region will dominate the electron transport process in the device and S-shape *J–V* curves would be observed. The simulation results shown in Fig. 3(b) agree with the experimental results when the buffer layer is thin, the charge carriers will be extracted by cathode effectively and resulting an exponential *J–V* curve. While the buffer layer is thick, the charge extraction will be hindered; the photo-generated charges would be recombined in the buffer layer and induce the S-shape *J–V* curve.

The thickness effect of the BCP exciton blocking layer is further illustrated by the band diagram as shown in Fig. 4(a) and (b). The extracted current density (J_E) presents at *J–V* curve is related to the recombination current (J_R) and the photo-generated current (J_G) by

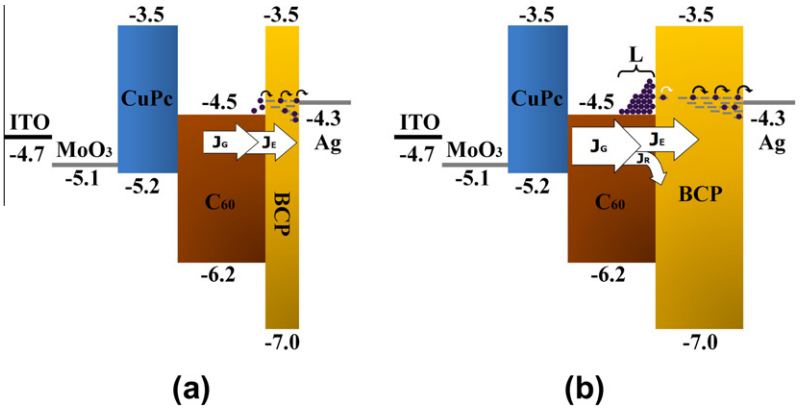

Fig. 4. The energy diagram of the bilayer heterojunction solar cell, including a distribution of trap density in BCP layer. The units are in eV and the inserted arrows show the interfacial electrical process before extracted by cathode, (a) device with 5nmBCP, (b) device with 20nmBCP. The curved arrows represent the hopping mechanism across the BCP layer.

$$J_E = J_G - J_R \tag{9}$$

Similar to the surface recombination boundary condition in the bulk heterojunction OPV [21], the space charge recombination current density at the charge accumulation region can be written as [26],

$$J_R = q \cdot R \cdot L = q \cdot \frac{\Delta n}{\tau} \cdot L \tag{10}$$

where Δn refers to the accumulated charge density at the interface between acceptor and cathode, τ is the lifetime for electron in acceptor, L is the charge accumulation layer thickness and R is recombination rate. According to the experimental results, when the BCP thickness is equal to 5 or 10 nm (Fig. 4(a)), the charge accumulation carrier density (Δn) is small and the charge accumulation layer region L cannot be formed hence the recombination current can be neglected. When the thickness of BCP layer increases (Fig. 4(b)), the blocking effect induces the charge accumulation and the gap states recombination current (J_R) makes a significant influence on the J_E and induces the shape change in the J–V curves as shown in both experimental and simulation results.

To further confirm the charge accumulation effect in the devices with thick BCP layer, we performed C–V measurements (Fig. 5) in the 5 and 20 nm BCP devices both under dark and illumination with AM 1.5 filter [27]. One can deviate the C–V bias range into two different regions, smaller than the V_{oc} (around 0.43 V) and larger than V_{oc}. In the dark environment, the capacitances of both devices remain nearly constant until the applied bias is close to V_{oc}. The constant capacitances of both devices under dark are considered as the geometric capacitance of the device and it is around 3 nF. When the applied bias is larger than V_{oc}, the capacitances begin to be uptrend, where charges are injected from the electrode and the 5 nm BCP device has larger capacitance than that with the 20 nm BCP which implies more effective charge injection in the former. While under illumination, the 5 nm BCP devices does not show a significant increase in the capacitance at the voltage range between negative bias to V_{oc}, it indicates that the photo-generated charges can be effectively collected

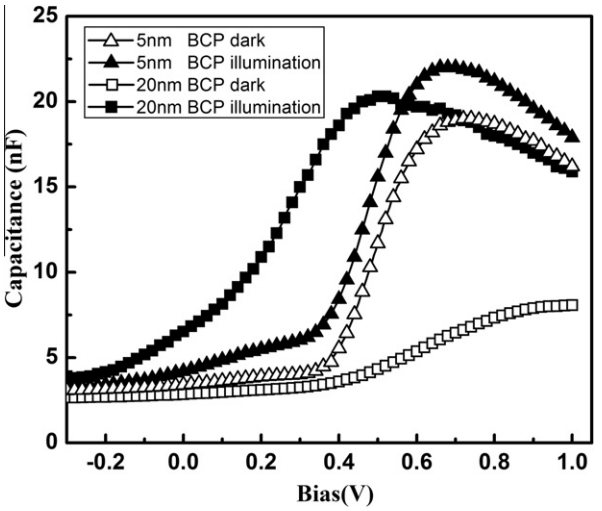

Fig. 5. Capacitance–voltage curve of devices with 5 and 20 nm BCP under dark and AM1.5 filer, the frequency used is 1 kHz, OSC is 20 meV.

by the electrode and no charge accumulation occurs; however, for the 20 nm BCP device, a significant increase is observed in the same bias range, which implies the photo-generated carriers are accumulated within the device and cannot be collected by the electrode effectively. The charge accumulation effect can also be used to explain the S-shape effect in the J–V curves; by considering the case of zero applied electric field ($V = 0$), the 20 nm BCP device has the larger capacitance value than the 5 nm BCP device which implies not all photo-generated charges are collected and measured externally at the electrode hence the short circuit current (J_{SC}) of the 20 nm device is smaller as shown in Fig. 3(a). By comparing the J–V and C–V measurement results, we attribute the increases of BCP thickness would cause charge accumulation within the device and resulting in the S-shape effect in the J–V curves. Accompany with the S-shape effect in the J–V curves of the device, the fill factors and the power conversion efficiencies would also decrease when the BCP layer increases as shown in Table 2. It can be

Table 2
The parameters of device performance.

BCP	S-shape	FF	J_{SC} (mA/cm^2)	V_{oc} (V)	η (%)	R_s (Ω cm^2)	R_p (Ω cm^2)
5 nm	–	0.57	3.28	0.43	0.84	4.397	1212
10 nm	–	0.58	3.31	0.43	0.87	4.700	1329
15 nm	√	0.44	3.03	0.47	0.66	–	–
20 nm	√	0.26	2.44	0.44	0.29	–	–

seen that there is an undesirable drop on the FF of the devices caused by increasing the thickness of BCP from 10 to 20 nm. The more than 2-fold degradation of FF from 0.58 to 0.26 is induced by the S-shape *J–V* curves. It is also worthy to mention that the open circuit voltage V_{oc} of the bilayer heterojunction devices does not show a general variation trend when the BCP thickness increases. It may be due to the band bending at the interfaces between the organic layers could partly compensate for band bending at the metal–organic interface hence no significant change in V_{oc} is observed as in the bilayer heterojunction devices where V_{oc} drops when S-shape *J–V* curves occur [28].

5. Conclusion

In conclude, we study the thickness effect of exciton blocking layer in bilayer heterojunction organic solar cells. We demonstrated charge accumulation would occur in thick BCP layer which causes S-shape effect in the *J–V* curves and significantly degrades the device performance. A numerical method is developed to reproduce the *J–V* curves by inserting a buffer layer with a gap state recombination site. The simulation results indicate when the BCP layer is thicker than 15 nm, the interfacial recombination will modulate the extracted current and induce an S-shape characteristic in the *J–V* curves. The charge accumulation hypothesis is further confirmed experimentally by the *C–V* measurement of the devices under dark and under solar simulator illumination. Our work demonstrated the thickness of exciton blocking layer plays an important role in the performance and provides insights into the origin of the S-shape phenomenon in planar bilayer heterojunction organic photovoltaics.

Acknowledgements

This work is supported by research grants (Grant Nos. A-PJ28 and A-PJ73) from Hong Kong Polytechnic University. Funding from HKSAR through UGC grant (Grant No. PolyU 5112/08E) is also acknowledged.

References

[1] D. Cheyns, H. Gommans, J. Poortmans, J. Genoe, P. Heremans, Sol. Energy Mater. Sol. Cells (2007) 399–404.
[2] A. Colsmann, J. Junge, C. Kayser, U. Lemmer, Appl. Phys. Lett. 89 (2006) 203506.
[3] S. Srinivas, Mi-Hyae Park, Z.R. Hong, Y. Wu, J.H. Hou, W.L. Kwan, G. Li, Y. Yang, Adv. Mater. 22 (2010) 380–383.
[4] C. Alexander, J.J. Junge, K. Christian, Appl. Phys. Lett. 89 (2006) 203506.
[5] Q.K. Shu, J.Q. Wei, K.L. Wang, H.W. Zhu, Z. Li, Y. Jia, X. Chun, G.N. Guo, X.M. Li, C.R. Ma, D.H. Wu, Nano Lett. 9 (2009) 12.
[6] A. Opitz, J. Wagner, W. Brutting, A. Hinderhofer, F. Schreiber, Phys. Status Solidi A 206 (2009) 2683.
[7] I.A. Levitsky, W.B. Euler, J. Castracane, N. Tokranova, B. Xu, J. Castracane, Appl. Phys. Lett. 85 (2004).
[8] P. Peumans, A. Yakimov, S.R. Forrest, Appl. Phys. Lett. 79 (2001) 126.
[9] K. Schulze, C. Uhrich, R. Schüppel, K. Leo, M. Pfeiffer, E. Brier, E. Reinold, P. Bäuerle, Adv. Mater. 18 (2006) 2872.
[10] K. Takahashi, N. Kuraya, T. Yamaguchi, T. Komura, K. Murata, Sol. Energy Mater. Sol. Cells 61 (2000) 403.
[11] P. Ravirajan, S.A. Haque, J.R. Durrant, D. Poplavskyy, D.D.C. Bradley, J. Nelson, J. Appl. Phys. 95 (2004) 1473.
[12] D. Gupta, M. Bag, K.S. Narayan, Appl. Phys. Lett. 92 (2008) 093301.
[13] B. Tremolet de Villers, Christopher J. Tassone, H. Sarah Tolbert, Benjamin J. Schwartz, J. Phys. Chem. C 113 (2009) 18978–18982.
[14] P. Sullivan, S. Heutz, S.M. Schultes, T.S. Jones, Org. Electron 9 (2008) 656–660.
[15] H. Jin, M. Tuomikoski, J. Hiltunen, P. Kopola, A. Maaninen, F. Pino, J. Phys. Chem. C 113 (2009) 16807–16810.
[16] T.A.M. Ferenczi, J. Nelson, C. Belton, A.M. Ballantyne, M. Campoy-Quiles, F.M. Braun, D.D.C. Bradley, J. Phys. Condens. Matter 20 (2008) 475203.
[17] K. Ankit, S. Srinivas, Y. Yang, J. Appl. Phys. 105 (2009) 094512.
[18] C. Uhrich, R. Schueppel, A. Petrich, M. Pfeiffer, K. Leo, E. Brier, P. Kilickiran, P. Baeuerle, Adv. Funct. Mater. 17 (2007) 2991.
[19] N.N. Wang, J.S. Yu, Y. Zhang, J. Huang, Y.D. Jiang, Sol. Energy Mater. Sol. Cells 94 (2007) 263.
[20] P. Peumans, A. Yakimov, S.R. Forrest, J. Appl. Phys. 93 (2003).
[21] A. Wagenpfahl, D. Rauh, M. Binder, C. Deibel, Phys. Rev. B 82 (2010) 115306.
[22] J.C. Scott, G.G. Malliaras, Chem. Phys. Lett. 299 (1999) 115.
[23] AMPS-1D approach is developed by prof. S.J. Fonash and his students at The Pennsylvania State University. It utilized a numerical method to solve the very general equations which describe the basic phenomena present in photovoltaic devices: Diffusion, drift, generation, recombination, space charge, electronstatic fields, and effective field.
[24] B.P. Rand, D.P. Burk, S.R. Forrest, Phys. Rev. B 75 (2007) 115327.
[25] J. Cuiffi, T. Benanti, W.J. Nam, S. Fonash, Appl. Phys. Lett. 96 (2010) 143307.
[26] P. Bhattacharya, Semiconductor Optoelectronic Device, second ed., Prentice-Hall, 1997.
[27] G. Friesen, E.D. Dunlop, R. Wendt, Thin Solid Films 387 (2001) 239–242.
[28] D. Cheyns, J. Poortmans, P. Heremans, C. Deibel, S. Verlaak, B.P. Rand, J. Genoe, Phys. Rev. B 77 (2008) 165332.

the absorption enhancement due to scattering [16–20]. Moreover, the backside structures do not increase the optical transmission at oblique angles of incidence (AOIs).

Herein, we present a quasi-periodic structure (QPS) on the indium tin oxide (ITO) anode, fabricated by scalable colloidal lithography. The ITO-QPS effectively couples the incident light to the photo-active layer via antireflection and light trapping mechanisms to boost the conversion efficiency of organic solar cells. Moreover, angle-resolved absorption spectroscopy reveals outstanding light coupling via ITO-QPS at large AOIs, promising omnidirectional and broadband light harvesting.

2. Experimental

The schematic illustration of the fabrication process is shown in Fig. 1. The ITO-QPS was fabricated with scalable colloidal lithography utilizing polystyrene (PS) nanospheres with a diameter of 600 nm as sacrificial masks. First, the PS spheres were spun-coated onto 260 nm thick ITO glass which self-assembled into a monolayer of closely-packed beads. A metal etcher (ILD-4100) was then employed to fabricate the ITO nanorod structure with BCl_3 = 100 sccm injection, pressure of 5 mtorr and an etching time of 170 s, which resulted in an ITO nanorod with a height of 100 nm. Removal of leftover PS was performed by dipping the ITO glass into acetone with sonification for 5 min. The scanning electron images (SEM) of the ITO-QPS before depositing the active layers are shown in Fig. 2a and b.

The glass substrate with ITO-QPS was then cleaned by ultrasonic treatment in detergents, including methanol, acetone and isopropyl alcohol, and finally dried overnight in an oven. Then, 12 nm PEDOT:PSS (Baytron P VP A1 4083) was spun-cast on the ultraviolet ozone-treated ITO. After annealing the PEDOT:PSS film at 120 °C for 30 min in the air, the sample was transferred to a glove box. The active material consisted of 2 wt.% RR-P3HT (Mw 3.7×10^4 g mol^{-1}) and 2 wt.% PCBM in a dichlorobenzene solution, obtained from Rieke Metals and Nano-C Inc., respectively.

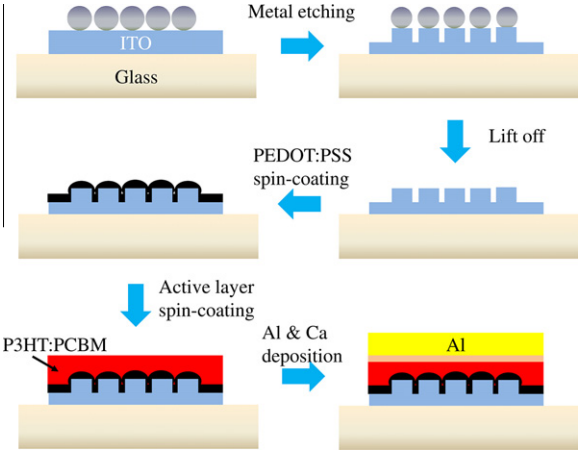

Fig. 1. The fabrication process of an organic solar cell with a patterned frontal electrode using colloidal lithography.

The solution blend was then spun-cast onto the PEDOT:PSS layer at a speed of 600 rpm for 60 s and then dried in covered Petri glass dishes for 30 min at room temperature. The thickness of P3HT:PCBM is 170 nm. Next, the semi-finished samples were baked on a hotplate for 30 min at 120 °C. Finally, 30 nm thick calcium followed by 60 nm thick aluminum was thermally coated onto the active material at a pressure of 6×10^{-6} torr through a 0.1 cm^2 shadow mask. The samples are prepared with a size of 20 × 50 mm and the results shown here are the averages of three samples.

Efficiency measurements were performed under simulated AM1.5G irradiation (100 mW/cm^2) using a Xenon lamp-based Thermal Oriel 1000 W solar simulator. The spectrum of the solar simulator was calibrated by a PV-measurement (PVM-154) mono-Si solar cell (NREL calibrated), and a Si photo diode with KG-5 color filter (Hamamatsu, Inc.) was used to check the irradiation of the exposed area (100 mW/cm^2). The PVM-154 combined with a KG-5 filter (350–700 nm passed, Newport) was used to simulate a reference solar cell with a spectral response from 350 to 700 nm, where the calibration was based on the IEC-69094-1 spectrum. *I–V* curves were measured with a semiconductor source measure unit (Keithley 2400) using a four wire connection and the measurements were corrected for the external series resistance. Stability in time is continuously monitored by routinely repeating the measurements on c-Si solar cells. The temperature of the cells was actively controlled during the measurements at 25 ± 1 °C.

The external quantum efficiency (EQE) system is equipped with a 450 W Xenon lamp (Oriel Instrument, model 6266) light source, a water-based IR filter (Oriel Instrument, model 6123 NS) and a monochromator (Oriel Instrument, model 74,100). The beam spot on the sample is rectangular, measuring roughly 1 × 3 mm. A calibrated silicon photodetector (Newport 818-UV) was used to calibrate the EQE system before measurements. A lock-in amplifier (Standard Research System, SR830) and an optical chopper controller (SR540), set in the voltage mode, were also equipped to lock the output signal and the photocurrent was converted to the voltage using a 1 ohm resistor, which was parallel to the sample. The temperature of cells was again actively controlled during the measurements at 25 ± 1 °C.

3. Results and discussion

Fig. 3 depicts the measured absorption and external quantum efficiency (EQE) spectra of organic solar cells with the ITO-QPS and with a flat ITO layer at normal incidence. The absorption measurement was carried out using an integrating sphere system to collect the scattered reflected photons. The superior absorption in the entire spectrum for the ITO-QPS cell is shown, especially in the wavelength range between 520 and 670 nm. The enhanced absorption results from the light coupling by the ITO-QPS, which serves both functions as the antireflection and forward scattering for light trapping. Inspection of the absorption and EQE spectra confirms that the enhanced carrier generation is contributed from the superior photon absorption.

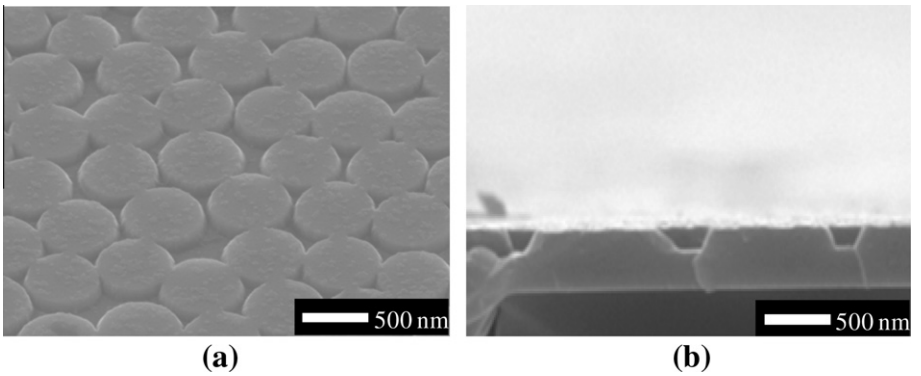

Fig. 2. The (a) top view and (b) cross-section SEM images of the ITO-QPS before the deposition of organic materials.

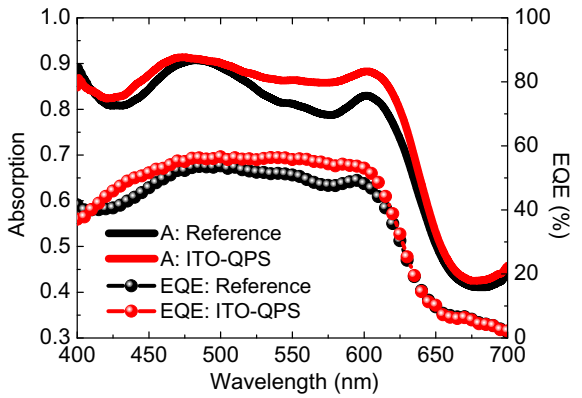

Fig. 3. Measured absorption and external quantum efficiency (EQE) spectra for the flat cell and the cell with an ITO-QPS.

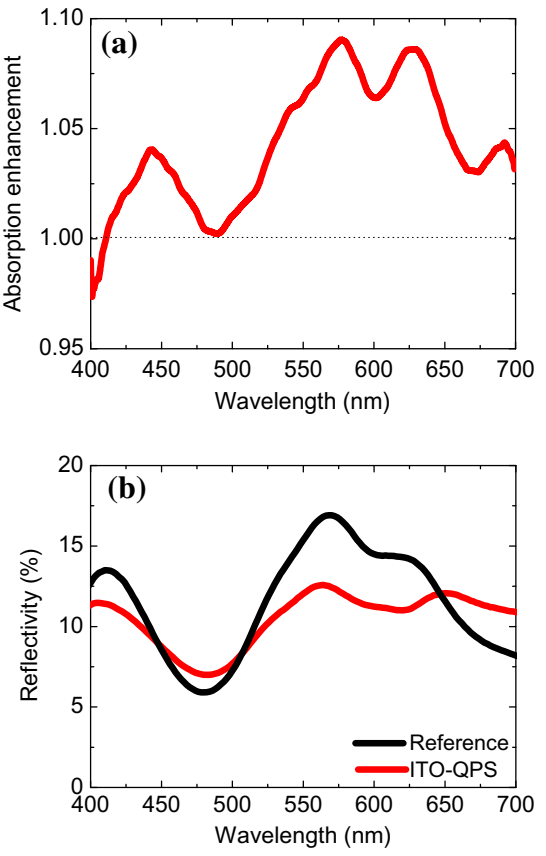

Fig. 4. (a) Absorption enhancement of the ITO-QPS cell to the reference. (b) Measured reflectivity of the devices without an Al back reflector.

The absorption enhancement by taking the ratio of absorption in Fig. 3 is plotted in Fig. 4a, which demonstrates a broadband improvement from 500 to 700 nm due to sufficient photon coupling by the frontal pattern. A required absorption length for different wavelengths can be calculated by $L = 1/\alpha$, where α is the measured absorption coefficient of P3HT:PCBM. The round-trip light propagation length is twice the thickness of P3HT:PCBM, approximately 340 nm, which corresponds to the absorption length for the 620 nm wavelength. The absorption enhancement in the spectrum region below $\lambda = 620$ nm, where the incident photons can be completely absorbed within a round-trip path length in the P3HT:PCBM layer, shows the antireflective property of the frontal ITO nanostructure. Forward scattering by the frontal ITO-QPS contributes to the absorption enhancement in P3HT:PCBM layer after $\lambda = 620$ nm. The measured reflectivity of the devices without Al back reflector is shown in Fig. 4b. In the wavelength range of $640 < \lambda < 700$ nm, the ITO-QPS device has higher reflection than the reference device before the Al back reflector deposition. However, after the deposition of Al back reflector, the absorption for the ITO-QPS cell was enhanced, which indicates the absorption enhancement (see in Fig. 4a) was contributed by light trapping. The enhanced absorption of the ITO-QPS cell reflects the boosting of the power conversion efficiency. The current density–voltage (J–V) characteristics for the reference and ITO-QPS cells under AM 1.5 conditions are shown in Fig. 5. The conversion efficiencies for the reference and ITO-QPS cells are measured at 2.91% and 3.26%, respectively. Compared to the reference cell, the ITO-QPS cell shows a 12% enhancement. This efficiency enhancement is contributed from the optical absorption, which results in an increase in the short-circuit current density,

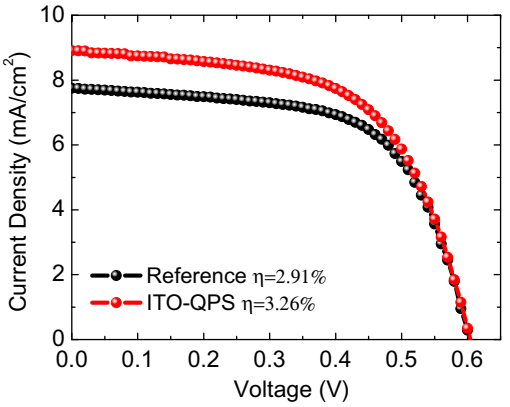

Fig. 5. Measured current–voltage curve of cells.

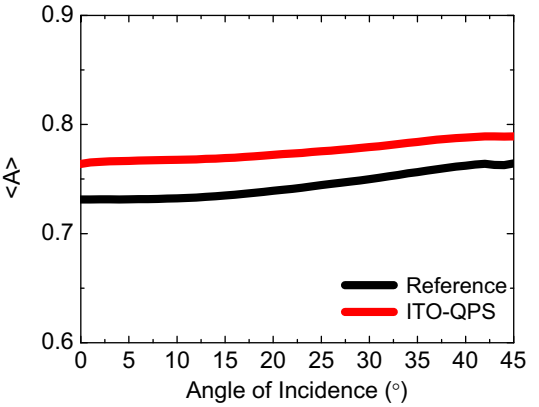

Fig. 7. Averaged absorption of the reference film and the ITO-QPS cell.

J_{sc} = 8.91 mA/cm^2 compared to the reference cell with J_{sc} = 7.75 mA/cm^2. The open circuit voltage V_{oc} of the ITO-QPS cell remains the same (0.6 V) and the deterioration of fill factors (from 63.6% to 61%) could result from the damaged ITO after metal etching.

The light harvesting at large angles of incidence is another key issue for thin film solar cells. The large-angle light harvesting of the cell benefits sufficient power generation in the daytime. Fig. 6a and b show the measured angle-resolved absorption spectroscopy of the reference cell and the ITO-QPS cell, respectively. Angle-resolved absorption spectroscopy is performed within the wavelength of 400 and 700 nm. However, only the wavelength range between 400 and 650 nm is shown, to reveal a clear contrast in the color maps. The measuring systems utilize a custom-built 15 cm radius integrating sphere with a motor-controlled rotational sample stage in the center and a randomly polarized broadband Xenon lamp to simulate the polarization state of sun light. The collection of reflected photons is then analyzed by a spectrometer (QE65000, Ocean Optics) to obtain the absorption spectrum with respect to different angles of incidence, of up to 45°. The system is calibrated by the reflective spectrum of a NIST-standard, intrinsic Si at normal incidence. Evidently, the angular absorption is enhanced by the ITO-QPS, especially in the range of $540 < \lambda < 620$ nm. The optical coupling at oblique AOI is tailed by the ITO-QPS, which modified the guiding conditions of the thin film layers. The coupling only takes place when the optical momentum of incident photons satisfies the guided modes of the ITO-QPS patterned films. We define a parameter, averaged absorption <A>, to express the capability of solar power harvesting by each cell:

$$< A >= \frac{\int_{400\,nm}^{700\,nm} A(\lambda,\theta) I_{AM1.5G}(\lambda) d\lambda}{\int_{400\,nm}^{700\,nm} I_{AM1.5G}(\lambda) d\lambda} \quad (1)$$

Where A(λ, θ) is the measured angular absorption spectrum, θ is the incident angle with respect to the normal surface, and $I_{AM1.5G}$ is the photon flux density of the solar spectrum [21]. We neglect taking the normal component of incident solar photon flux (i.e. $I_{AM1.5G}\cos\theta$) as varying the incident angle, to have a better understanding of the angular absorption of the patterned cells. Fig. 7 shows <A> with respect to the AOIs up to 45° for the reference cell and the ITO-QPS cell. The results illustrate that the ITO-QPS cell sufficiently absorbs the incident solar power at large AOIs. As seen in Fig. 7, the averaged absorption of the ITO-QPS cell does not rise as fast as the reference, indicating the insensitivity to the angles of incidence.

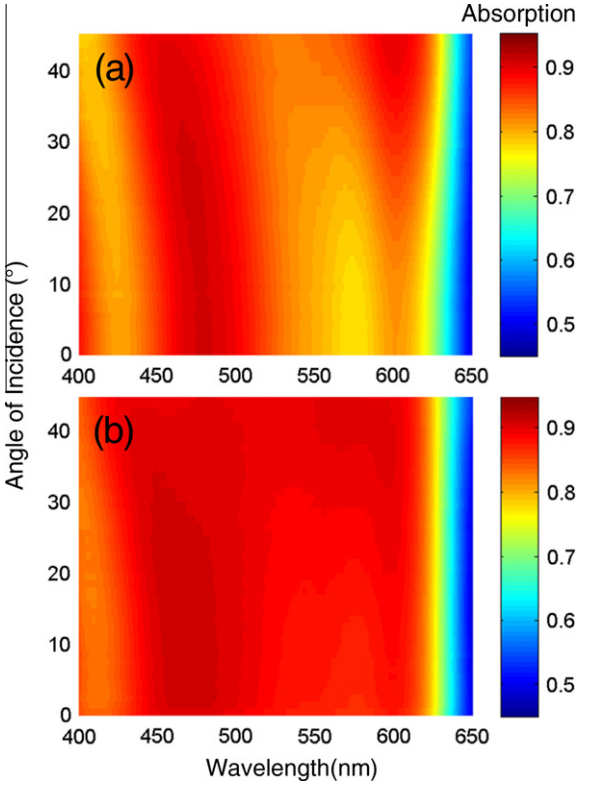

Fig. 6. Angular absorption spectra of (a) the reference cell, and (b) the ITO-QPS cell.

4. Conclusion

In conclusion, we have demonstrated thin-film organic solar cells with a frontal ITO quasi-periodic structure. The

ITO-QPS is fabricated by colloidal lithography, which is applicable for large scale production. The measured cell absorption spectra closely matches the external quantum efficiencies and results in power conversion efficiencies of 3.26% for the ITO-QPS cell, compared to a conversion efficiency of 2.91% for the reference cell. Angle-resolved absorption spectroscopy measurements also show enhanced light coupling at the cells at an oblique angle of incidence. This new design is not strictly relevant to organic based devices, but may be broadly applicable to other common thin-film solar cell materials systems such as a-Si:H, CdTe, and CIGS. This result can directly impact the attainment of the scalable green energy from thin-film solar cells.

Acknowledgment

The authors would like to thank Dr. Chung-Hsiang Lin for his technical support and helpful suggestions.

References

[1] J.M. Nunzi, C. R. Phys. 3 (2002) 523.
[2] L.A.A. Pettersson, L.S. Roman, O. Inganäs, J. Appl. Phys. 86 (1999) 487.
[3] T. Stübinger, W. Brütting, J. Appl. Phys. 90 (2001) 3632.
[4] A.P. Smith, R.R. Smith, B.E. Taylor, M.F. Durstock, Chem. Mater. 16 (2004) 4687.
[5] T. Aernouts, W. Geens, J. Poortmans, P. Heremans, S. Borghs, R. Mertens, Thin Solid Films 403 (2002) 297.
[6] P. Lalanne, G.M. Morris, Proc. SPIE 2776 (1996) 300.
[7] M. Niggemann, B. Zimmermann, J. Haschke, M. Glatthaar, A. Gombert, Thin Solid Films 511 (2006) 628–633.
[8] M. Niggemann, M. Riede, A. Gombert, K. Leo, Phys. Stat. Sol. A 205 (No. 12) (2008) 2862.
[9] S.B. Rim, S. Zhao, S.R. Scully, M.D. McGehee, Appl. Phys. Lett. 91 (2007) 243501-1–243501-3.
[10] K. Tvingstedt, S.D. Zilio, O. Inganas, M. Tormen, Optics Express 16 (No. 26) (2008) 21608.
[11] D.H. Ko, J.R. Tumbleston, L. Zhang, S. Williams, J.M. DeSimone, R. Lopez, E.T. Samulski, Nano Lett. 9 (No. 7) (2009).
[12] D. Zhou, R. Biswas, J. Appl. Phys. 103 (2008) 093102.
[13] L. Zeng, P. Bermel, Y. Yi, B.A. Alamariu, K.A. Broderick, J. Liu, C. Hong, X. Duan, J. Joannopoulos, L.C. Kimerling, Appl. Phys. Lett. 93 (2008) 221105.
[14] P. Bermel, C. Luo, L. Zeng, L.C. Kimerling, J.D. Joannopoulos, Opt. Express 15 (2007) 16986.
[15] N.N. Feng, J. Michel, L. Zeng, J. Liu, C.Y. Hong, L.C. Kimerling, X. Duan, IEEE T. Electron. Dev. 54 (2007) 1926.
[16] W. Wang, S. Wu, K. Reinhardt, Y. Lu, S. Chen, Nano Lett. 10 (2010) 2012.
[17] K. Tvingstedt, N. Persson, O. Inganäs, A. Rahachou, I.V. Zozoulenko, Appl. Phys. Lett. 91 (2007) 113514.
[18] R.H. Franken, R.L. Stolk, H. Li, C.H.M. van der Werf, J.K. Rath, R.E.I. Schropp, J. Appl. Phys. 102 (2007) 014503.
[19] F.J. Haug, T. Söderström, O. Cubero, V. Terrazzoni-Daudrix, C. Ballif, J. Appl. Phys. 104 (2008) 064509.
[20] J. Springer, A. Poruba, L. Müllerova, M. Vanecek, O. Kluth, B. Rech, J. Appl. Phys. 95 (2004) 1427.
[21] ASTMG173-03, Standard Tables for Reference Solar Spectral Irradiances, ASTM International, Conshohocken, Pennsylvania, 2005.

strategies have been proposed, including the confinement of the emissive zone [9] and the synthesis of white light polymers for voltage-independency [10] or the utilization of a phosphorescent moiety in the polymer chain [11] for high efficiency. However, the simplest and most effective way to solve these problems would be to make a miscible polymer blend. Recently, some researches that improved miscibility by blending the copolymer with the compound, both of which have the same moiety, have been reported [12,13].

In this work, we fabricated voltage-independent white-light-emitting diodes thanks to the homogeneity of the blue and green miscible polymers, due to their having the same moiety. Fluorene-based polymers including copolymers are well blended with each other without phase separation and the polymer chains, which contribute to the blue and green emissions, are mixed with each other at the molecular level. Moreover, these polymers have good chemical compatibility with $Ir(PIQ)_3$ which is the red phosphorescent dye that is used. Therefore, each component interacts with the others in a single active layer without phase separation. The energy transfer from the conjugated polymers to the Ir complex can be controlled by means of the homogeneous blend film. The phosphorescent dye ($Ir(PIQ)_3$) enhances the luminous efficiency by enabling both the singlet and triplet excitons to contribute to the electrophosphorescent emission through radiative decay, and is miscible with the polymer blends, which leads to a highly efficient Förster energy transfer from these fluorene-based polymers to $Ir(PIQ)_3$. This results in voltage-independent and highly efficient white light-emitting diodes.

2. Experimental

Herein, we fabricated a miscible polymer blend for use as the emissive layer by using copolymer to improve the chemical miscibility. The emissive layer consists of three components, polyfluorene-type blue LEP (Lumation BlueJ light-emitting polymers, Trademark of Dow Chemical Company, BlueJ) [blue emitter], Lumation Green 1304 (Dow Chemical Company) [green emitter], and Tris(1-phenylisoquinoline) iridium (III) ($Ir(PIQ)_3$) [red emitter] for color tuning as well as for enhancing the efficiency. Unlike the other polymer blend, BlueJ and Green 1304 form a homogeneous film, because Green 1304 has the same fluorene moiety as the one in BlueJ [14–17]. The structures of these components are shown in Scheme 1. Due to this homogeneity, we were able to obtain highly efficient voltage-independent white-light emitting devices.

Poly(3,4-ethylenedioxithiophene)/poly(styrene sulfonate) (PEDOT:PSS) was purchased from Baytron PH, H. C. Starck (Germany) and 2,9-dimethyl-4,7-diphenyl-1,10-phenanthroline (Bathocuproine BCP) was purchased from American Dye Sources, Inc. The heavy metal phosphorescent material for the red emission, tris(1-phenylisoquinoline) iridium (III) ($Ir(PIQ)_3$), was purchased from Sigma–Aldrich Co. The polymers were used as received. Indium tin oxide (ITO)-coated glass substrates were cleaned by sonication in chloroform for 30 min and then in acetone/isopropyl alcohol (1:1) solution for 30 min and treated with an oxygen plasma before use. A layer of PSS:PEDOT with a thickness of 20 nm was first spin-coated on the treated substrate, and annealed at 120 °C for 1 h in a vacuum. Then, blends of BlueJ, Green 1304, and $Ir(PIQ)_3$ in chlorobenzene (10 mg/mL) were spin coated on top of the substrate precoated with the PSS:PEDOT layer. For device fabrication, we employed a single-active-layer architecture (ITO/PEDOT/BlueJ:Green 1304:$Ir(PIQ)_3$ blend/BCP/Li:Al with a 2,9-dimethyl-4,7-diphenyl-1,10-phenanthroline (BCP) layer as the hole blocking layer. The BCP layer (10 nm) was thermally evaporated onto the blend layer at a pressure below 1×10^{-6} Torr before the deposition of the electrodes and, then, a cathode layer consisting of 150-nm-thick Li:Al alloy was vacuum deposited at a pressure of 1×10^{-6} Torr.

All measurements of the EL properties were performed on the devices encapsulated with a cover glass using epoxy adhesive. The emission light of the devices was measured by a luminance meter (Minolta, LS-100). The electrical and luminescent characteristics of the devices were analyzed by means of a current and voltage source measurement unit (Keithley 236) and a luminance meter (LS-100), respectively. The photoluminescent (PL) and electroluminescent (EL) spectra were measured using fluorospectroscopy (ISS PC1 Photon Counter Meter). The CIE coordinate was quantitatively evaluated from the EL spectra (using the previously reported numerical formulas) [18,19]. Lastly, the morphology of the top surface of the polymer blend was investigated by scanning probe microscopy (SPM, DI NanoScope IIIa). SPM measurements were performed in air with an etched silicon probe with a length of 125 μm and spring constants ranging from 20 to 100 N/m. Scanning was carried out in Tapping™ mode and the frequency was about 0.5 Hz.

3. Results and discussion

Fig. 1a shows the absorption (Abs) and photoluminescence (PL) spectra of the BlueJ and Green 1304 polymers and of $Ir(PIQ)_3$. The emission of BlueJ ($\lambda_{max} = 457$) is broadly overlapped with the absorption of Green 1304 ($\lambda_{max} = 390$), and the absorptions of $Ir(PIQ)_3$ at 430 and 475 nm, which correspond to the transitions from the ground state to the singlet MLCT and triplet MLCT excited

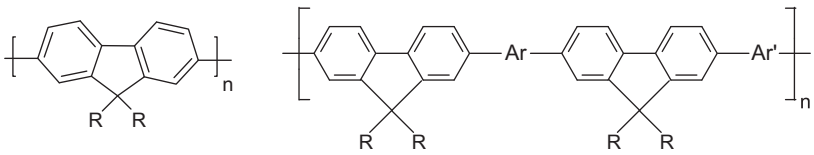

BlueJ Green 1304

Scheme 1. Chemical structures of fluorene-based polymer(BlueJ) and alternating fluorene-based copolymer (Green 1304). Ar, Ar′: aromatic groups.

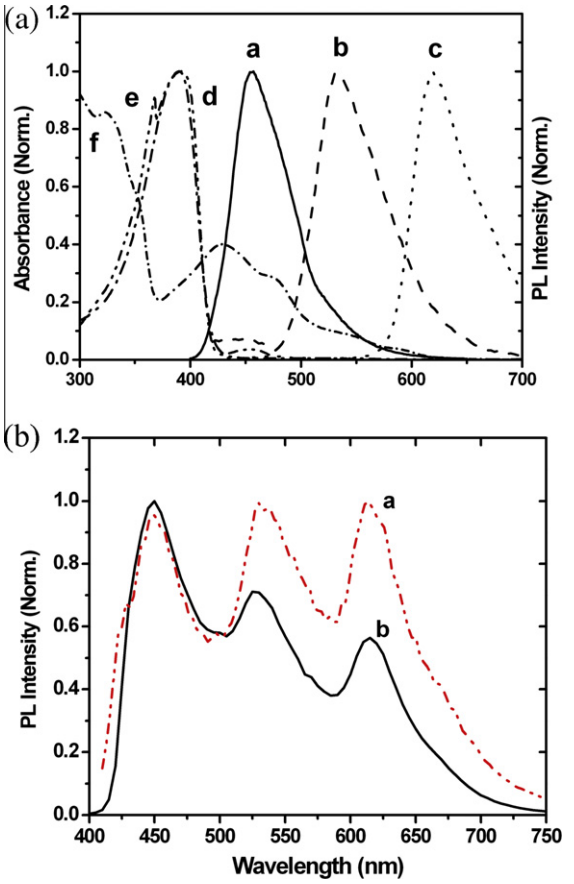

Fig. 1. (a) Normalized absorption (Abs) and photoluminescence (PL) spectra of BlueJ, Green, and Ir(PIQ)$_3$ (a): PL of BlueJ, (b): PL of Green, (c): PL of to Ir(PIQ)$_3$, (d): Abs of BlueJ, (e): Abs of Green, (f): Abs of Ir(PIQ)$_3$). (b) Normalized photoluminescence spectra of thin blend films of BlueJ:-Green: Ir(PIQ)$_3$ (a): blend film at a ratio of 87.9:10.9:1.2, (b): blend film at a ratio of 91.8:7.6:0.6).

states, respectively, are well overlapped with the emissions of BlueJ and Green 1304 (λ_{max} = 530) [20]. These spectra overlapping meet the necessary condition of Förster-type dipole–dipole energy transfer. Based on this, we would expect energy transfer to occur not only from BlueJ to Green 1304 and Ir(PIQ)$_3$, but also from Green 1304 to Ir(PIQ)$_3$. The energy of the singlet excitons from the host conjugated polymers is transferred to Ir(PIQ)$_3$, in spite of the absence of a medium for energy transfer, because the triplet energy state of the red-emissive Ir complex is relatively lower than that of the blue or green phosphorescent materials, which results in a partial energy transfer from the polymers to Ir(PIQ)$_3$.

Fig. 1b shows the normalized PL spectra of the blended films of the three materials. A pure white emission was observed at a blending ratio of 87.9(BlueJ): 10.9(Green 1304): 1.2(Ir(PIQ)$_3$). However, the optimal ratio required to obtain pure white electroluminescence was slightly different from that of the white photoluminescent spectrum, because direct charge injection and charge trapping occur in Ir(PIQ)$_3$, due to the relatively small bandgap, and partial energy transfer from the conjugated polymers to Ir(PIQ)$_3$ also contributes to the charge trapping mechanism. Therefore, we gradually decreased the intensity of the PL spectrum from blue to red by controlling the composition of the emissive layer, as can be seen in Fig. 1b. We varied the blending ratios of BlueJ and Green 1304, while fixing the ratio of Ir(PIQ)$_3$ at 0.6 wt.%. We found that the optimal blending ratio for the pure white electroluminescent emission is 91.8(BlueJ): 7.6(Green 1304): 0.6(Ir(PIQ)$_3$). At this ratio, most of the singlet excitons generated from BlueJ can contribute to the blue EL emission, due to the small amount of green and red guests, resulting in its having a similar EL intensity to those from Green 1304 and Ir(PIQ)$_3$. Each component emits three individual colors simultaneously due to the partial energy transfer from these conjugated polymers to the phosphorescent dye. Therefore, a pure white emission is obtained.

The atomic force microscopic (AFM) images of the blended film with the optimal ratio (BlueJ: Green: Ir(PIQ)$_3$ = 91.8:7.6:0.6) are shown in Fig. 2. In these images, the film does not show any significant phase-separated morphology (root mean square value is 2.1 nm) even at the nano scale. Based on this, we could confirm that a miscible blend was obtained for the light-emitting layer by employing polymers having the same moiety. Due to this homogeneous morphology, the blue, green and red emitters cannot emit individually, resulting in a stable white light emission without any variation of the color with increasing voltage.

The EL spectra of the ITO/PEDOT/BlueJ: Green 1304: Ir(PIQ)$_3$ blend/BCP/Li:Al device measured at various voltages are shown in Fig. 3. The spectra contain three main peaks at 457, 530 and 618 nm, respectively, which are generated by BlueJ, Green 1304, Ir(PIQ)$_3$, respectively. The EL spectra covered the whole visible range from 400 to 800 nm and, thus, the device emits white light. In previously reported WLEDs based on immiscible polymer blends, the composition is not so homogeneous normal to the surface, due to the different wettability of each component to the surface. This can induce changes of the emissive zone as a function of the bias voltage, resulting in a non-pure white emission [21,22]. However in this study, the compositional change in the miscible polymer blend is negligible and, hence, our WLED is insensitive to the applied voltage. The Commission Internationale de L'Eclariage (CIE) coordinates of the WLEDs are shown in Fig. 4 and their performances are summarized in Table 1. The CIE coordinate is near to "pure" white light (0.33, 0.33) at a wide range of voltages from 10 to 16 V.

It is very interesting to observe the difference between the EL and PL spectra. In the EL spectra, the intensity of BlueJ is smaller and that of Ir(PIQ)$_3$ is larger, as compared to the PL spectra. The first difference is caused by the similar absorption spectra of BlueJ and Green 1304. When the blended film is excited at 380 nm, which corresponds to the maximum absorption peak of the host BlueJ, to obtain its PL spectra, the emission of Green 1304 is triggered simultaneously, because it has the same maximum absorption peak as BlueJ. Thus, the intensity of Green 1304 in the PL spectra includes the absorption at 380 nm as well as the excitation energy transfer from BlueJ. In

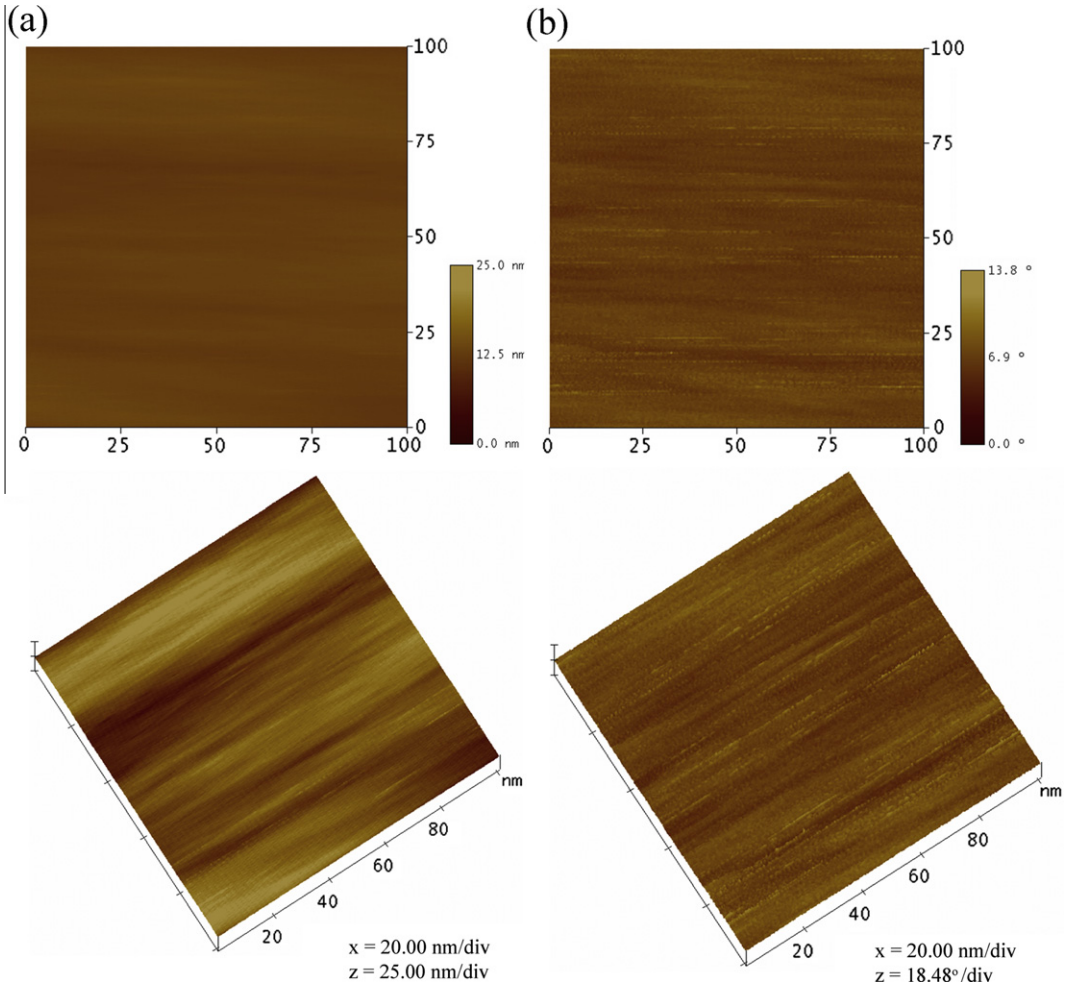

Fig. 2. AFM images of the surfaces of the blend film of BlueJ:Green:Ir(PIQ)$_3$ at a ratio of 91.8:7.6:0.6. The size of each image is 0.1 μm × 0.1 μm. (a) height and (b) phase.

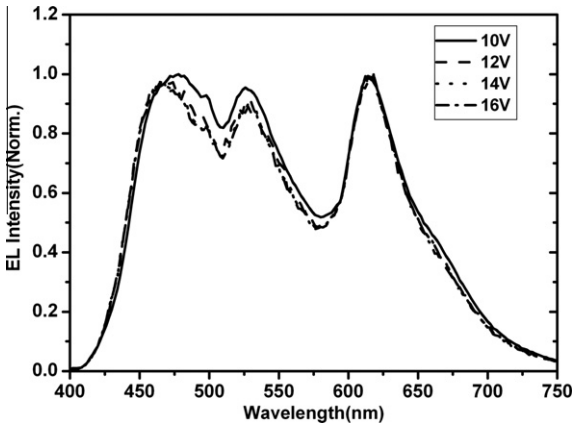

Fig. 3. Nomalized EL spectra of the ITO/PEDOT/BlueJ:Green:Ir(PIQ)$_3$ blend/BCP/Li:Al device measured at various voltages.

the PL spectra, the energy transfer from the host molecules to the dopants is dominant for the white light emission. However, in the EL spectra, a charge-trapping mechanism, in which the dopant serves as a charge trap and provides a recombination site, can occur. In the PL studies, the red and green emissions are mostly generated by energy transfer from the host material. In the EL studies, however, the charge-trapping mechanism can contribute to the green and red emissions.

The current–density vs. voltage and brightness vs. voltage characteristics of the ITO/PEDOT/BlueJ 91.8: Green 1304 7.6: Ir(PIQ)$_3$ 0.6 (wt.%) blend/BCP/Li:Al device are shown in Fig. 5a and b, respectively. The device achieved a maximum brightness of 10295 cd/m^2 at 16.4 V and a current density of 174 mA/m^2. The luminous efficiencies (LE) of the various light-emitting devices are shown as a function of the current density in Fig. 6. The maximum LE values of the reference devices, B: ITO/PEDOT/BlueJ/BCP/Li:Al and G: ITO/PEDOT/Green 1304/BCP/Li:A are 2.61 cd/A at 38.1 mA/cm^2 and 14.4 cd/A at 63.4 mA/cm^2, respectively. Green 1304 is a copolymer which contains an energy donor and electron transport material in its

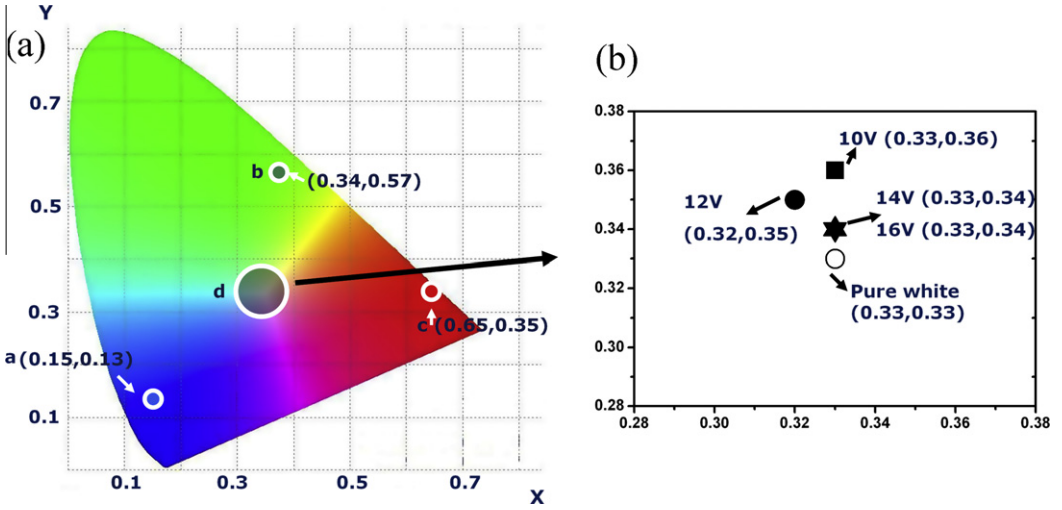

Fig. 4. The CIE coordinate of the devices. (a) a: BlueJ, b: Green c: $Ir(PIQ)_3$ d: ITO/PEDOT/BlueJ:Green:$Ir(PIQ)_3$ blend/BCP/Li:Al device measured at various voltages (10–16 V) and (b) the CIE coordinate of d is enlarged and indicated.

Table 1
The performance of the white light-emitting device is summarized. The luminance, current density, external quantum efficiency (EQE), luminance efficiency, and CIE coordinates are the results corresponding to each voltage.

Voltage (V)	Current density (mA/cm^2)	Efficiency		Luminance	CIE
		EQE (%)	(cd/A)		
10	2.6	2.6	7.77	208	(0.33, 0.36)
12	10.8	2.8	8.22	918	(0.32, 0.35)
14	39.9	2.7	7.89	3248	(0.33, 0.34)
16	145	2.4	6.57	9885	(0.33, 0.34)

structure, so it shows a much better LE than BlueJ. When we blend these two materials at the optimized ratio, the maximum LE of B + G: ITO/PEDOT/BlueJ: Green 1304 blend/BCP/Li:Al is slightly higher than that of BlueJ, 3.59 cd/A at 25.6 mA/cm^2. However, after we doped this blend with the phosphorescent dye, $Ir(PIQ)_3$, the maximum LE was enormously increased from 3.59 to 8.34 cd/A at 5.99 mA/cm^2 (a voltage of 11.2 V and a brightness of 516 cd/m^2). Even at a luminance of 3500 cd/m^2, the luminance efficiency remained high (around 8 cd/A) due to the efficient energy transfer and charge trapping. These efficiencies are very high compared to the reported values for other white light-emitting devices, in spite of the poor balance of the charge carriers. It is known that excitons are separated into electrons and holes at the interfaces of phase-separated morphologies and this lowers the efficiency of WLEDs based on immiscible polymer blends. However, in this work, this effect was diminished by preparing miscible blends. A gradual decrease of the luminance efficiency was observed as the current density increased, which is probably due to triplet–triplet annihilation [23].

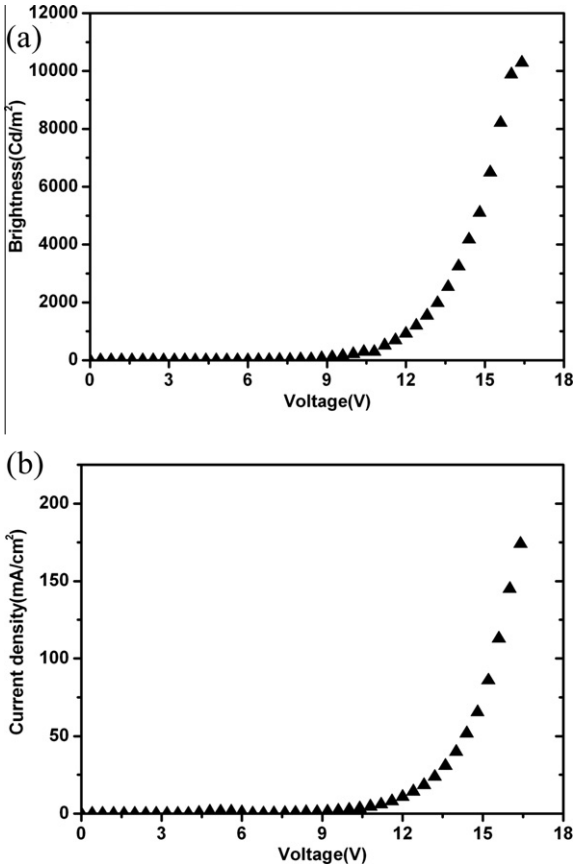

Fig. 5. (a) The current density vs. voltage characteristics of the ITO/PEDOT/BlueJ:Green:$Ir(PIQ)_3$ blend/BCP/Li:Al device and (b) The luminance vs. voltage characteristics of the ITO/PEDOT/BlueJ:Green:$Ir(PIQ)_3$ blend/BCP/Li:Al device.

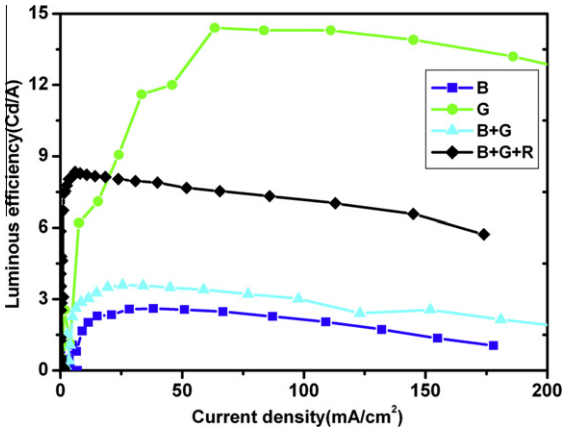

Fig. 6. The luminance efficiency vs. current density characteristics of the devices. (■) B: ITO/PEDOT/BlueJ/BCP/Li:Al device. (●) G: ITO/PEDOT/Green/BCP /Li:Al device. (▲) B + G: ITO/PEDOT/BlueJ:Green blend/BCP/Li:Al device. (♦) B + G + R: ITO ITO/PEDOT/BlueJ:Green:$Ir(PIQ)_3$ blend/BCP/Li:Al device.

4. Conclusions

We demonstrated color-invariant and highly efficient white light-emitting diodes with a homogeneous single emissive layer. By utilizing a miscible polymer blend system which uses the polymers with same fluorene moiety, typical problems of immiscible polymer systems such as their voltage-dependence and low efficiency were solved. High luminous efficiency was also obtained via efficient energy transfer from these polymers to the phosphorescent dye. A near pure white-light emission was observed over a wide range of voltage from 10 to 16 V, with a maximum brightness of 10295 cd/m^2, luminous efficiency of 8.34 cd/A and external quantum efficiency of 2.86%. These white-light emitting diodes were single-active-layer devices fabricated by spin-casting from a solution. The simple device structure and the promise of low-cost manufacturing make this approach attractive for large-area solid-state-lighting applications.

Acknowledgements

This work was supported by ERC grant of National Research Foundation (NRF) funded by the Korea Ministry of Education, Science and Technology (MEST) (No. R11-2007-045-01002-0(2009)). It was also partially supported by a Grant (code #: 2010k000345) from 'Center for Nanostructured Materials Technology' under '21st Century Frontier R&D Programs' of the Ministry of Education, Science and Technology, South Korea.

References

[1] J. Kido, M. Kimura, K. Nagai, Science 267 (1995) 1332.
[2] R.H. Jordan, A. Dodabalapur, M. Strukelj, T.M. Miller, Appl. Phys. Lett. 68 (1996) 1192.
[3] Y.Z. Wang, R.G. Sun, F. Meghdadi, G. Leising, A.J. Estein, Appl. Phys. Lett. 74 (1999) 3613.
[4] J. Kido, H. Shionoya, K. Nagai, Appl. Phys. Lett. 67 (1995) 2281.
[5] D.H. Hwang, M.J. Park, S.K. Kim, N.H. Lee, C.H. Lee, Y.B. Kim, J.K. Shi, J. Mater. Res. 19 (2004) 2081.
[6] J.J. Su, F.I. Wu, C.F. Shu, Macromolecules 37 (2004) 7197.
[7] A.G. Cambell, in: Z.H. Kafafi (Ed.), Proceedings of SPIE 2002 4464, PIE, Washington, 2002, pp. 211–222.
[8] M. Geoghegan, G. Krausch, Prog. Polym. Sci. 28 (2003) 261.
[9] J.H. Park, T.W. Lee, Y.C. Kim, O.O. Park, J.K. Kim, Chem. Phys. Lett. 403 (2005) 293.
[10] S.K. Lee, D.H. Hwang, B.J. Jung, N.S. Cho, J. Lee, J.D. Lee, H.K. Shim, Adv. Funct. Mater. 15 (2005) 1647.
[11] S. Tokido, M. Suzuki, F. Sato, M. Kamachi, K. Shirane, Org. Elect. 4 (2003) 105.
[12] J.-C. Kuhlmann, P. Bruyn, R.K.M. Bouwer, A. Meetsma, P.W.M. Blom, J.C. Hummelen, Chem. Commun. 46 (2010) 7232.
[13] L.M. Popescu, P. Hof, A.B. Sieval, H.T. Jonkman, J.C. Hummelen, Appl. Phys. Lett. 89 (2006) 213507.
[14] F. So, B. Krummacher, M.K. Mathai, D. Poplavskyy, S.A. Choulis, V.-E. Choong, J. Appl. Phys. 102 (2007) 091101.
[15] M.C. Suh, H.K. Chung, S.-Y. Kim, J.H. Kwon, B.D. Chin, Chem. Phys. Lett. 413 (2005) 205.
[16] B.D. Chin, N.S. Kang, J.-W. Yu, S.M. Jo, J.Y. Lee, J. Appl. Phys. 102 (2007) 024506.
[17] T.-H. Kim, H.K. Lee, O.O. Park, B.D. Chin, S.-H. Lee, J.K. Kim, Adv. Funct. Mater. 16 (2006) 611.
[18] G. Wyszecki, W.S. Stiles, Color Science, second ed., Wiley, New York, 1982.
[19] D.B. Judd, G. Wyszecki, Color in Business Science and Industry, third ed., Wiley, New York, 1975.
[20] X. Gong, J.C. Ostrowski, D. Moses, G.C. Bazan, A.J. Heeger, Adv. Funct. Mater. 13 (2003) 439.
[21] J. Chappell, D.G. Lidzey, P.C. Jukes, A.M. Higgnis, R.L. Thompson, S. O'Connor, I. Grizzi, R. Fletcher, J. O'brien, M. Geoghegan, R.A.L. Jones, Nat. Mater. 2 (2003) 616.
[22] F. P. Schafer, Dye Lasers, vol. 1, Springer, New York, 1973.
[23] M.A. Baldo, C. Adachi, S.R. Forrest, Phys. Rev. B 62 (2000) 10967.

current crowding [3,7,8] and charge accumulation [7] effects, in the framework of a physically based analytical theory.

2.1. Current crowding mechanism

As shown in Fig. 1, the current crowding mechanism approximates the total access resistance by a simplified network of distributed resistances [3,8,9]. In this approach, the total contact resistance can be expressed as:

$$R_c = \sqrt{\rho_B r_{ch}}\coth\left(d\sqrt{\frac{r_{ch}}{\rho_B}}\right) \quad (1)$$

where d represents the electrode length. r_{ch} ($\Omega\,m^{-1}$) is equal to $R_{ch}/\Delta y$ where R_{ch} (Ω) is the infinitesimal channel resistance (see Fig. 1), supposed to be uniform [3], and Δy (m) is an infinitesimal length. ρ_B (Ω m) is equal to $R_b.\Delta y$ where R_b is the bulk infinitesimal resistance (Ω) between the source and the channel as illustrated in Fig. 1. In strong accumulation, i.e. well above threshold voltage V_T, one has:

$$r_{ch} = \frac{1}{W\mu C_i(V_G - V_T)} \quad (2)$$

where μ is the channel mobility, C_i is the gate dielectric capacitance per unit area ($F\,m^{-2}$), V_g is the gate voltage and W (m) is the transistor width. In order to calculate the total contact resistance given by Eq. (1), the resistivity ρ_B need also to be evaluated.

2.2. Equation of ρ_B

The calculation of the vertical bulk resistivity needs to include the impact of accumulation layers created by the action of both the gate voltage (at the top) and the ohmic metal contact (at the back). In the following, to derive ρ_B, the 1D Metal Insulator Semiconductor Metal (MISM) stack has been considered (inset of Fig. 2). This architecture represents the stack above the source (or drain) electrode

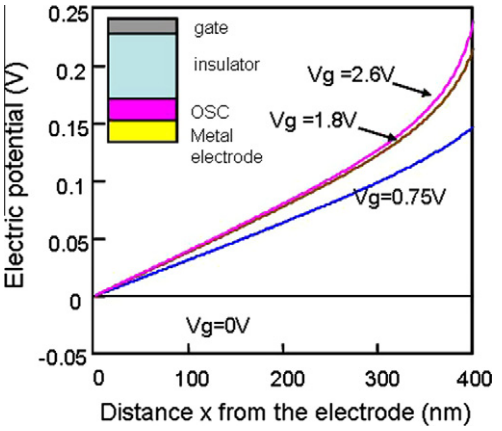

Fig. 2. Numerical simulation of the electric potential in the organic semiconductor of a Metal Insulator Semiconductor Metal capacitance, shown in the inset ($n_0 = 10^{13}$ cm^{-3}, $V_m = 0$ V, $th_{ins} = 1$ μm).

contact in OTFT's. In the drift diffusion model, the current density j in the vertical direction x is given by:

$$j = -e\frac{kT}{e}\mu_{vt}\frac{dn}{dx} - en\mu_{vt}\frac{dV}{dx} \quad (3)$$

where μ_{vt} represents the vertical mobility, n the electron concentration, V is the electric potential, e the elementary charge, T the temperature and k the Boltzmann constant. The current density can be expressed as a function of the applied voltages, integrating Eq. (3), as follow:

$$j\cdot\int_0^{th}\frac{dx}{en\mu_{vt}} = (V_m - V_i - \Delta V) + \frac{kT}{e}[\ln(n(x = th)) - \ln(n(x = 0))] \quad (4)$$

where V_m is the potential at the metal/OSC back interface (which corresponds to an "effective" work function difference between the OSC and the metal electrode [15]), V_i is

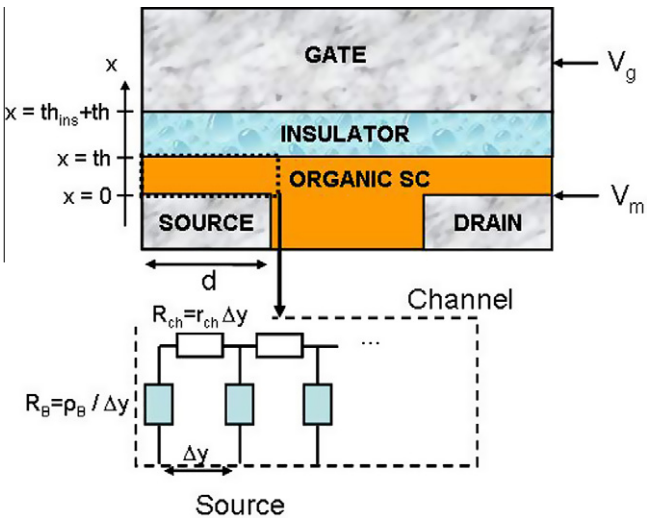

Fig. 1. Schematic device architecture, illustrating the current crowding mechanism between source and channel, and the resistance network used to model it.

the potential at the insulator OSC interface, ΔV the potential drop between the back electrode and the channel, *th* represents the OSC thickness.

Assuming that the current flow is low enough such that it does not alter the carrier distribution from its equilibrium ($j = 0$) value, the carrier concentration n may be approximated by:

$$n(x) \approx n_0 \exp\left(\frac{eV(x)}{kT}\right) \tag{5}$$

where n_0 represents the free thermal charge carriers. Inserting Eq. (5) into Eq. (4) leads to:

$$j \cdot \int_0^{th} \frac{dx}{en\mu_{tr}} \approx (V_m - V_i - \Delta V) + \frac{kT}{e}\left[\ln\left(n_0 \exp\left(\frac{eV_i}{kT}\right)\right) - \ln\left(n_0 \exp\left(\frac{eV_m}{kT}\right)\right)\right] = -\Delta V \tag{6}$$

As a consequence, the vertical bulk resistivity may be expressed as:

$$\rho_B = \frac{-\Delta V}{jW} = \frac{1}{W}\int_0^{th} \frac{dx}{e\mu_{vt} n(x)} \tag{7}$$

2.3. Calculation of the electric potential V(x) and carrier profile n(x)

From Eq. (7), it appears that the calculation of ρ_B requires to derive the carrier concentration profile $n(x)$, and thus, according to Eq. (5), the electric potential $V(x)$. To this aim, the potential is calculated solving Poisson equation in the 1D MISM capacitance at different gate voltages:

$$\frac{d^2V}{dx^2} = -\frac{\rho(V)}{\varepsilon_{OSC}} \tag{8}$$

$$\text{where } \rho(V) = -e\left[n_0 \exp\left[\frac{eV}{kT}\right] - n_0\right] \tag{9}$$

The boundary conditions are given by the following equations:

$$V(0) = V_m \text{ and } -\varepsilon_{OSC}\frac{dV}{dx}(x = th) = \varepsilon_{ins}E_{ins} \tag{10}$$

where V_m represents the effective work function difference between the OSC and the metal electrode, E_{ins} the electric field in the insulator. $\varepsilon_{ins/OSC}$ represents respectively the dielectric constant of the insulator and the organic semiconductor OSC. In all calculations, in agreement with the materials used in experiments, ε_{ins} has been taken equal to $2 \cdot \varepsilon_0$ [16] and ε_{OSC} to $3 \cdot \varepsilon_0$ (value often used for organic semiconductors [17]).

Numerical solutions of Eq. (8) have been plotted in Fig. 2. These results reveal that the electric potential in the volume of the OSC varies almost linearly. Indeed, for gate voltage higher than the threshold voltage, due to the channel screening, the potential does not depend anymore on the applied gate bias (except, of course, at the insulator/OSC interface) (Fig. 2). This maximum surface potential is called V_i and corresponds to the surface potential at threshold conditions. As a result, the potential profile in the OSC volume can be approximated by:

$$V(x) \approx (V_i - V_m)\frac{x}{th} + V_m \tag{11}$$

Here we assume that the source to drain bias is very low (which is the case in the regime of extraction of the contact resistances in [10] and [11]: $V_d = 1$ V). Thus the potential $V(x)$ is assumed independent of the position along the source electrode. This would be exact if the source to drain bias was equal to zero.

Noticing that the surface potential at threshold V_i corresponds to the value of the surface potential where the bending due to electron charge concentration ($-e\,n(x)$) can no longer be neglected, this potential can be numerically deduced solving the following equation (see Appendix):

$$V_i = \frac{2en_0}{\varepsilon_{OSC}}\left(\frac{kTth}{e(V_i - V_m)}\right)^2\left(\exp\left(\frac{eV_i}{kT}\right) - \exp\left(\frac{eV_m}{kT}\right)\right) \tag{12}$$

Finally, the surface potential at threshold V_i corresponds to a particular value of the gate voltage, which is in fact the MIS capacitor threshold voltage, and is given by:

$$V_T = V_i\left(1 + \frac{\varepsilon_{OSC}}{\varepsilon_{ins}}\frac{th_{ins}}{th}\right) - V_m\left(\frac{\varepsilon_{OSC}}{\varepsilon_{ins}}\frac{th_{ins}}{th}\right) \tag{13}$$

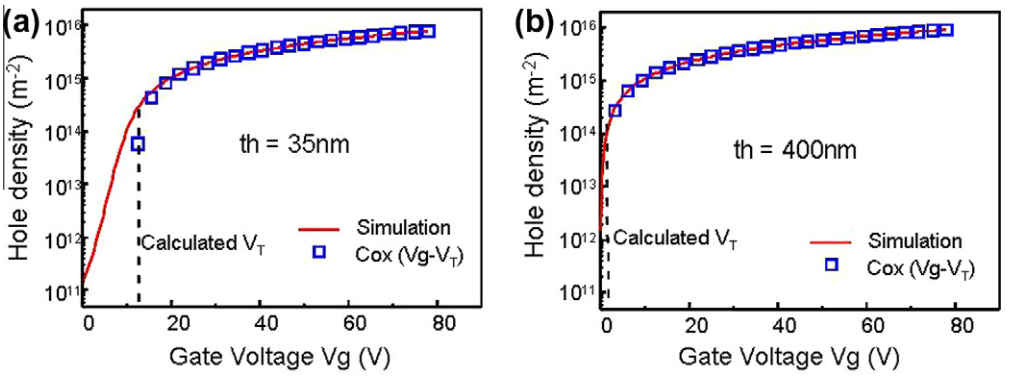

Fig. 3. Hole density calculated by numerical (line) and analytical (symbol) calculations for an organic semiconductor thickness of (a) 35 nm and (b) 400 nm ($n_0 = 3.6\ 10^{12}$ cm^{-3}, $V_m = 0$ V, $th_{ins} = 1$ μm).

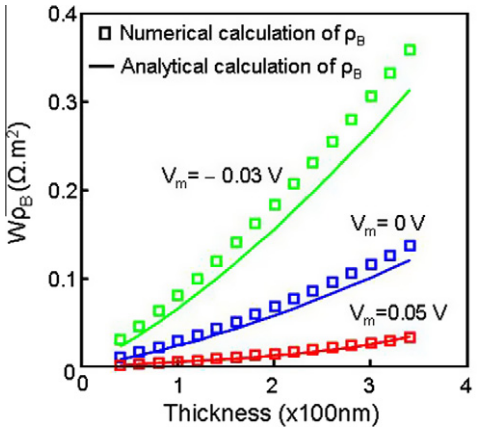

Fig. 4. Vertical bulk resistivity versus organic semiconductor thickness calculated using the analytical model Eq. (14) (lines) and a numerical integration of Eqs. (7) and (8) (symbols), for several effective work function differences at the back electrode ($n_0 = 5.5\ 10^{12}$ cm^{-3}, $\mu_{vt} = 0.0045$ cm^2 V^{-1} s^{-1}, $th_{ins} = 1.2$ μm).

This expression of V_T has been found in good agreement with the threshold voltage extracted from numerical calculations of the charge, as shown in Fig. 3. Using Eq. (11), the vertical bulk resistivity (ρ_B) can be derived as follows:

$$W\rho_B = \int_0^{th} \frac{1}{e\mu_{vt}n_0 \exp(eV(x)/kT)}\,dx = \frac{th}{e\mu_{vt}n_0}\frac{kT}{e(V_i - V_m)}\left[\exp\left(\frac{-eV_m}{kT}\right) - \exp\left(\frac{-eV_i}{kT}\right)\right] \quad (14)$$

Combining Eqs. (1), (2), (12), and (14), the series resistance can thus be analytically calculated.

Comparison between Eq. (14) and numerical calculations of Eq. (7) are shown in Fig. 4. It appears that simulations and model are in good agreement. In particular, as shown in Fig. 4, the back electrode effective work function difference dependency of the vertical resistivity is well captured by the analytical model. In the next section, models for threshold voltage (Eq. (13)) and series resistance (Eq. (14)) are compared with experiments.

3. Device fabrication and discussion

The model presented in the last section has been compared with experiments, first performed in Metal Insulator Semiconductor Metal (MISM) capacitors, to validate the $n(x)$ calculation, and then carried out on transistor, to validate the overall contact resistance model.

3.1. MISM fabrication

The 1D model can be partly validated by comparing threshold voltages calculated using (Eq. (13)) with measurements extracted from MISM capacitance measurements. MISM capacitance was fabricated using the following process. Polyethylene naphthalate (PEN) films were used as flexible substrates. Thirty nanometers of thick Au bottom electrode was deposited by plasma vapor deposition. A *N*,*N*-dialkylsubstituted-(1,7&1,6)-dicyanoperylene-3,4:9, 10-bis(dicarboximide) derivative (Polyera ActivInk™ N1400) bought from Polyera Corporation was diluted in 1,2-dichloro-benzene at a concentration of 4 mg mL^{-1} and spin-coated at 4 different rotation speed to get different thickness. Then the semiconductor films were cured at a temperature of 115 °C for 5 min to eliminate the solvent. For all the spin-coating steps of the process, the plastic substrates were mounted on a silicon wafer using a drop of ethanol. The thickness of the OSC layer was measured with a profilometer. Samples with thicknesses varying from 50 to 140 nm have been processed. Cytop™ dielectric was then spin-coated on top of the semiconductor and cured at 100 °C for 20 min. The thickness of the layer was measured with a profilometer around 1 μm. To promote adhesion of the gate electrode on the highly hydrophobic insulating layer, solution of Nafion diluted at 30 mg mL^{-1} in isopropanol was spin-coated at 1000 rpm. Finally an Ag ink gate electrode was printed by ink-jet using a Dimatix set up.

3.2. Threshold voltage dependency versus OSC thickness

Capacitance measurements of MISM device were performed on a Agilent 4980A at low frequencies i.e. below 10 kHz. Threshold voltages were then extracted using the maximum of the first derivative of *C*–*V* curves (a similar procedure to the one used in transistors [18]). Experimental values and modeling results obtained using Eq. (13) are both represented in Fig 5. As can be seen, the same trend was found between simulations and experiments, showing the consistency of our model.

3.3. Contact resistance simulations

Modeling results have been compared with experimental contact resistances taken from [11] featuring different OSC thicknesses and gate voltages (Fig 6). Again, using the same set of parameters, the model can satisfactory capture both thickness and bias dependencies.

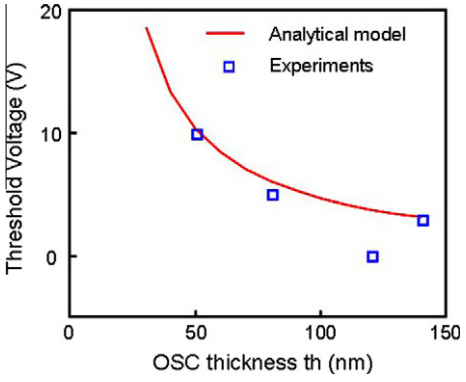

Fig. 5. Experimental (square) and theoretical (line, Eq. (3)) threshold voltage (V_T) of a capacitor versus organic semiconductor thickness *th*. Experimental V_T have been extracted on CV measurements performed on capacitor featuring different thicknesses ($n_0 = 10^{13}$ cm^{-3}, $V_m = -0.02$ V, $th_{ins} = 1$ μm).

Finally, the impact of the back electrode work function difference has been investigated both in modeling and experiments taken from [10] (Fig. 7), where the gold work function was modified by treatment with self assembled monolayers (SAM) on its surface before semiconductor deposition. From simulation, the work function difference between gold treated with 4-(methylsulfanyl)-thiophenol (MeSTP) and with 4-nitrothiophenol (NOTP) was found equal to 0.065–0.01 = 0.055 eV. This value is much lower than the 0.7 eV that can be found in [10] from UPS measurements performed on metal only treated with SAMs (before semiconductor deposition). This difference can be explained by the modification of the surface's work function of the system metal including SAMs, once organic semiconductors are deposited. This might originate from the formation of a dipole at the interface metal/semiconductor [19].

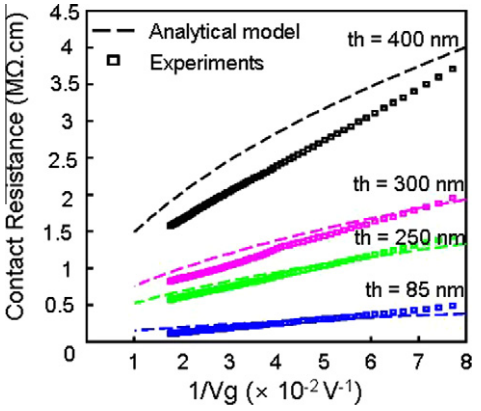

Fig. 6. Comparison of the analytical and experimental contact resistance versus $1/V_g$, featuring different OSC thicknesses ($n_0 = 5.5\ 10^{12}$ cm^{-3}, $\mu_{vt} = 0.007$ cm^2 V^{-1} s^{-1}, channel mobility μ from experiments [9], $V_m = 0$ V, $d = 20$ μm, $th_{ins} = 1.2$ μm).

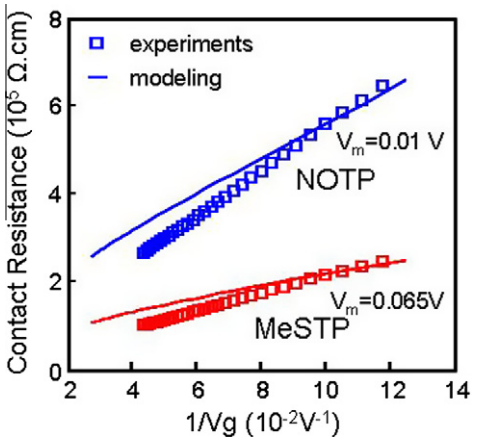

Fig. 7. Comparison between the theoretical and experimental contact resistance versus $1/V_g$, for two different effective work functions V_m (obtained using two different Self Assembled Monolayer – MST and NT) ($th = 130$ nm, $n_0 = 5.5\ 10^{12}$ cm^{-3}, $\mu_{vt} = 0.007$ cm^2 V^{-1} s^{-1}, channel mobility μ from experiments $\mu = 0.05$ cm^2 V^{-1} s^{-1} [8], $d = 20$ μm, $th_{ins} = 1.2$ μm).

4. Conclusion

In this work, an analytical model of the contact resistance in top gate/bottom contacts organic thin film transistors has been proposed. It combines both the current crowding mechanism and an original modelling of the vertical accumulation of charges between channel and back electrode.

The modelling of the charge versus gate voltage in vertical stacks has been validated by comparing theoretical and experimental threshold voltages in simple capacitance structure.

In addition, the gate voltage dependency of the contact resistance has been found to be nicely reproduced by this model, much better than in a pure current crowding approach, without requiring any numerical simulations or empirical vertical resistivity formulas. Finally, this model well captures the semiconductor thickness and metal work function dependencies of the contact resistance, in agreement with previously reported experimental data. It should be noted that it has not been necessary to invoke any traps or specific injection/transport mechanisms.

Appendix A

In the following appendix, the derivation of (Eq. (12)), i.e. the determination of the surface potential at threshold condition, is detailed. The solution of the Poisson equation in 1D is simply:

$$V(x) = \int_0^x \left(\int_0^y -\frac{\rho(z)}{\varepsilon_{OSC}} dz \right) dy + bx + c$$

where b and c represent two constants to determine. Given that:

$$\rho(x) = -e\left[n_0 \exp\left[\frac{eV(x)}{kT}\right] - n_0 \right] \approx -en_0 \exp\left[\frac{eV(x)}{kT}\right]$$

and considering that the potential varies linearly with position (which is the case before the channel formation), we get:

$$\int_0^x \left(\int_0^y -\frac{\rho(z)}{\varepsilon_{OSC}} dz \right) dy = \frac{en_0}{\varepsilon_{OSC}} \left[\left(\frac{kTth}{e(V_i - V_m)} \right)^2 \exp\left(\frac{eV_m}{kT}\right) \times \left(\exp\left(\frac{e(V - V_m)}{kT} \frac{x}{th} \right) - 1 \right) - x \left(\frac{kTth}{e(V_i - V_m)} \right) \exp\left(\frac{eV_m}{kT}\right) \right.$$

Using the first boundary condition $V(0) = V_m$,

$$V(x) = \frac{en_0}{\varepsilon_{OSC}} \left(\frac{kTth}{e(V_i - V_m)} \right)^2 \times \exp\left(\frac{eV_m}{kT}\right) \left(\exp\left(\frac{e(V - V_m)}{kT} \frac{x}{th} \right) - 1 \right) + cx + V_m$$

And applying the second boundary condition $V(th) = V_i$ leads to:

$$c \cdot th + V_m = V_i - e \times \frac{n_0}{\varepsilon_{OSC}} \left(\frac{kTth}{e(V_i - V_m)} \right)^2 \left(\exp\left(\frac{eV_i}{kT}\right) - \exp\left(\frac{eV_m}{kT}\right) \right)$$

The electron charge starts to significantly impact the potential shape (moving away from its linear dependency at the interface), when,

$$c \cdot x + V_m < \int_0^x \left(\int_0^y -\frac{\rho(z)}{\varepsilon_{OSC}} dz \right) dy$$

which means when,

$$V_i = \frac{2en_0}{\varepsilon_{OSC}} \left(\frac{kTth}{e(V_i - V_m)} \right)^2 \left(\exp\left(\frac{eV_i}{kT} \right) - \exp\left(\frac{eV_m}{kT} \right) \right)$$

This equation can be used to find the surface potential V_i at threshold condition. Above threshold, the potential increases mostly inside the channel, while the rest of the $V(x)$ curve remains unchanged.

References

[1] A. Hoppe, D. Knipp, B. Gburek, A. Benor, M. Marinkovic, V. Wagner, Organic Electronics 11 (2010) 626.
[2] G. Horowitz, Journal of Materials Research 19 (2004) 1946.
[3] K.D. Jung, Y.C. Kim, B.J. Kim, B.G. Park, H. Shin, J.D. Lee, Japanese Journal of Applied Physics 47 (2008) 3174.
[4] R. Street, A. Salleo, Applied Physics Letters 81 (2002) 2887–2889.
[5] P.V. Necliudov, M.S. Shur, D.J. Gundlach, T.N. Jackson, Solid-State Electronics 47 (2003) 259.
[6] P.V. Pesavento, K.P. Puntambekar, C.D. Frisbie, J.C. McKeen, P.P. Ruden, Journal of Applied Physics 99 (2006) 094504.
[7] T.J. Richards, H. Sirringhaus, Journal of Applied Physics 102 (2007) 094510.
[8] C.S. Chiang, S. Martin, J. Kanicki, Y. Ugai, T. Yukawa, S. Takeuchi, *Japanese Journal of Applied Physics* **Part 1** 37 (1998) 5914.
[9] A. Bajolet, R. Clerc, G. Pananakakis, E. Picollet, N. Segura, S. Boret, S. Bruyère, J.P. Manceau, J.C. Giraudin, P. Delpech, L. Montès, G. Ghibaudo, Solid State Electronics 50 (2006) 1244.
[10] D. Boudinet, M. Benwadih, Y.B. Qi, S. Altazin, J.M. Verilhac, M. Kroger, C. Serbutoviez, R. Gwoziecki, R. Coppard, G. Le Blevennec, A. Kahn, G. Horowitz, Organic Electronics 11 (2010) 227.
[11] D. Boudinet, M. Benwadih, S. Altazin, R. Gwoziecki, J.M. Verilhac, R. Coppard, G. Le Blevennec, I. Chartier, G. Horowitz, Organic Electronics 11 (2010) 291.
[12] T. Li, J.W. Balk, P.P. Ruden, I.H. Campbell, D.L. Smith, Journal of Applied Physics 91 (2002) 4312.
[13] V. Vinciguerra, M. La Rosa, D. Nicolosi, G. Sicurella, L. Occhipinti, Organic Electronics 10 (2009) 1074.
[14] S.D. Wang, T. Minari, T. Miyadera, K. Tsukagoshi, Y. Aoyagi, Applied Physics Letters 91 (2007) 203508.
[15] S.M. Sze, Physics of Semiconductors, 2nd Edition., John Wiley&Sons, New York, 1981.
[16] J. Veres, S. Ogier, G. Lloyd, Chemistry of Materials 16 (2004) 4543.
[17] P.W.M. Blom, M.C.J.M. Vissenberg, Materials Science and Engineering 27 (2000) 53.
[18] D. Boudinet, G. Le Blevennec, C. Serbutoviez, J.M. Verilhac, G. Horowitz, Journal of Applied Physics 105 (2009) 084510.
[19] M. Knupfer, H. Peisert, Physica Status Solidi (a) 201 (2004) 1055.

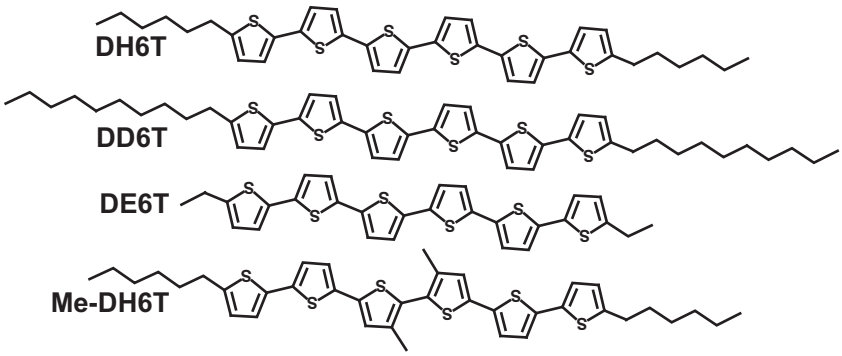

Fig. 1. Chemical structure of the alkylated sexithiophene derivatives.

increases not only solubility and thus processability of 6T, but also device performance by changing the microstructure of the thin films. In such a way, vacuum-sublimed COMs like 6T on metal substrates often grow in a flat lying orientation in ultra-thin films (a few molecular layers), which gradually changes to a vertically inclined or even standing orientation for thicker (several ten nm) films [12,30,31]. Hexylated sexithiophene (α,ω-dihexylsexithiophene, DH6T) on metal substrates, however, undergoes a defined orientational transition from flat lying molecules in monolayers to nearly upright standing molecules starting from the second molecular layer onwards [3,32,33]. The IE/EA of a layer of standing DH6T are lower than those of flat lying DH6T, and a highest occupied molecular orbital (HOMO)-level offset of 0.6 eV was reported for this organic/organic homointerface [3,32,33]. For DH6T on Ag(1 1 1) pre-covered with a monolayer of the molecular acceptor tetrafluoro-tetracyanoquinodimethane (F4-TCNQ), which undergoes a charge transfer reaction with metals and therewith significantly increases the substrate work function [34–36], the HOMO-level of the lying monolayer is just below the Fermi-level (E_F) of the substrate [37]. The HOMO-level of the standing second layer with reduced IE is, however, not found above the Fermi-level, instead the HOMO is pinned below the substrate E_F, accompanied by an interface dipole [37]. Thus, hexyl chains are not long enough to form a layer that is capable to electronically decouple the layers of standing and lying DH6T, and the question arises whether longer alkyl chains are able to do so. Furthermore, the mechanism of *Fermi-level pinning* [38–41] attracts interest, since the proposed integer or fractional "charge transfer" across the nominally insulating hexyl layers of standing DH6T in the DH6T/F4-TCNQ/Ag(1 1 1) system [37] seems implausible. A slight shift of the center-of-mass of the electron density of the conjugated moieties of the molecules with respect to the atomic nuclei might be an alternative scenario, which was recently suggested to explain Fermi-level pinning at metal/self-assembled monolayers (SAMs)/COM interfaces [42]. Such a charge rearrangement, or polarization, might be related to induced density of states at the interface caused by either charge neutrality levels [43–45] or disorder of the adsorbate [46,47]. Even though polarization is widely discussed as origin for vacuum-level shifts at organic/metal and organic/organic interfaces [2,48] it is not commonly used to describe Fermi-level pinning at such interfaces [37–40].

To elucidate the impact of alkyl chains on the growth mode and electronic structure of COMs on metal substrates, we performed thickness dependent ultraviolet photoelectron spectroscopy (UPS) experiments on the 6T-derivatives α,ω-didecylsexithiophene (DD6T) [49], α,ω-diethylsexithiophene (DE6T) and 3′,4′-dimethyl-α,ω-dihexylsexithiophene (Me-DH6T) (chemical structures shown in Fig. 1) on Ag(1 1 1) substrates. Furthermore, to freeze out thermal motion and to thus increase the impact of a possible molecular fastener effect of long alkyl chains [19–21], we also investigated the samples' electronic structure at low temperatures (∼35 K). The charge rearrangement in the context of Fermi-level pinning was examined using DD6T on the high work function substrate Ag(1 1 1) pre-covered with F4-TCNQ.

2. Experimental details

Organic molecular thin films (6T derivatives from Heraeus Clevios GmbH, F4-TCNQ from Sigma–Aldrich) were prepared by vacuum sublimation on clean Ag(1 1 1) surfaces (repeated Ar-ion sputtering and annealing cycles (up to 550 °C)) using resistively heated quartz crucibles with deposition rates of about 0.25 Å/min. The film mass thickness was monitored with a quartz crystal microbalance. Hence, the values for the coverage correspond to values of nominal film thickness. UPS experiments were performed using a custom built apparatus [50] equipped with a HeI UV-light-source and a hemispherical electron energy analyzer (Scienta R3000). The interconnected sample preparation chambers (base pressure 2×10^{-10} mbar) and analysis chamber (base pressure 4×10^{-10} mbar) allowed sample transfer without breaking ultrahigh vacuum conditions. The angle between the incident beam and the sample was fixed to 65°. The spectra were measured at photoelectron emission angles (θ_e) of 0° (normal emission) and 45° (off-normal emission) with an acceptance angle of ±10°. The energy resolution at room temperature was set to 80 meV. The error of UPS binding energy (BE) values is estimated to be ± 0.05 eV. For the measurement of the secondary electron cutoff (SECO) the sample was biased at −3.00 V. All preparation steps were performed at room

temperature. UPS measurements were carried out at room temperature and additionally at low temperatures (~35 K) for multilayer films.

3. Impact of alkyl chains at sexithiophene thin film growth

Deposition of 2 Å DD6T on a clean Ag(1 1 1) substrate attenuated the Ag(1 1 1) photoemission features (d-bands around 4–7 eV BE, Shockley surface state and Fermi-edge) and several new features appeared, most notable a peak centered at 1.60 eV BE, which is assigned to emission from the HOMO of DD6T (Fig. 2). The HOMO peak showed enhanced intensity measured at a photoelectron emission angle of 45 ° compared to normal emission, which is commonly observed for flat lying COMs [51–53]. The vacuum level decreased by 0.49 eV (as derived from the shift of the SECO), which is mainly ascribed to the push-back effect [2,54,55] due to the weak interaction between 6T moieties and Ag. Increasing the coverage up to 6 Å decreased the vacuum level further, resulting in a total vacuum-level shift of 0.80 eV. In the valence electron region the molecular derived features gained intensity without a notable change of binding energy. Our nominal coverage of ~6 Å may thus correspond to an essentially flat lying monolayer of DD6T on Ag(1 1 1) because further increase of the coverage up to the final value of 30 Å did not change the vacuum level significantly. Starting from a nominal coverage of 10 Å a new peak (centered at 0.98 eV BE) arose at the low BE side of the monolayer HOMO (Fig. 2, best visible in the normal emission spectra). In addition, a peak centered around 11 eV BE, which is assigned to stem mainly from nonbonding S-orbitals [56], lost intensity with increasing coverage and got masked by emission dominated by the alkyl chains [33,56] in the energy range from 4 to 12 eV BE.

The spectra of DD6T/Ag(1 1 1) are virtually identical with the UPS spectra of DH6T/Ag(1 1 1) [3,32,33], where the emission at the low BE side of the monolayer HOMO was ascribed to emission from the multilayer HOMO of standing molecules. In both cases, the IE (defined as difference from the low BE HOMO onset to the vacuum level) is decreased from monolayer to multilayer coverage (for DH6T from 4.85 eV to 4.35 eV [32] and for DD6T from 4.95 eV to 4.48 eV). For DH6T/Ag(1 1 1) the lying monolayer/standing multilayer growth mode was confirmed by X-ray diffraction, metastable atom electron spectroscopy [33] and atomic force microscopy [32], thus it is straightforward to conclude on the same growth mode prevailing also for DD6T. This growth model (Fig. 3a) is further supported by the decrease of the S-derived peak around 11 eV BE (Fig. 2), which is hardly accessible (due to the limited photoelectron mean free path) by UPS through a layer of standing decyl chains. Note that the terms "lying" and "standing" are used to describe the basic orientation of the conjugated backbone of the 6T derivatives and the actual orientation might differ slightly from being totally parallel (perpendicular) to the substrate surface. Moreover, alkylated oligothiophenes are well known to exhibit rich conformational freedom in thin films [14,15,25,29], e.g., the hexyl chains of the standing layers of DH6T on Ag(1 1 1) are twisted by 28° with respect to the conjugated backbone [33].

Nominal 30 Å DD6T might be somewhat less than one closed layer of standing molecules on an almost closed layer of lying molecules. However, the 30 Å DD6T spectra already exhibited signs of slight charging during photoemission, which led to a rigid shift of all photoemission features of 0.08 eV to lower kinetic energy after ~1 h of

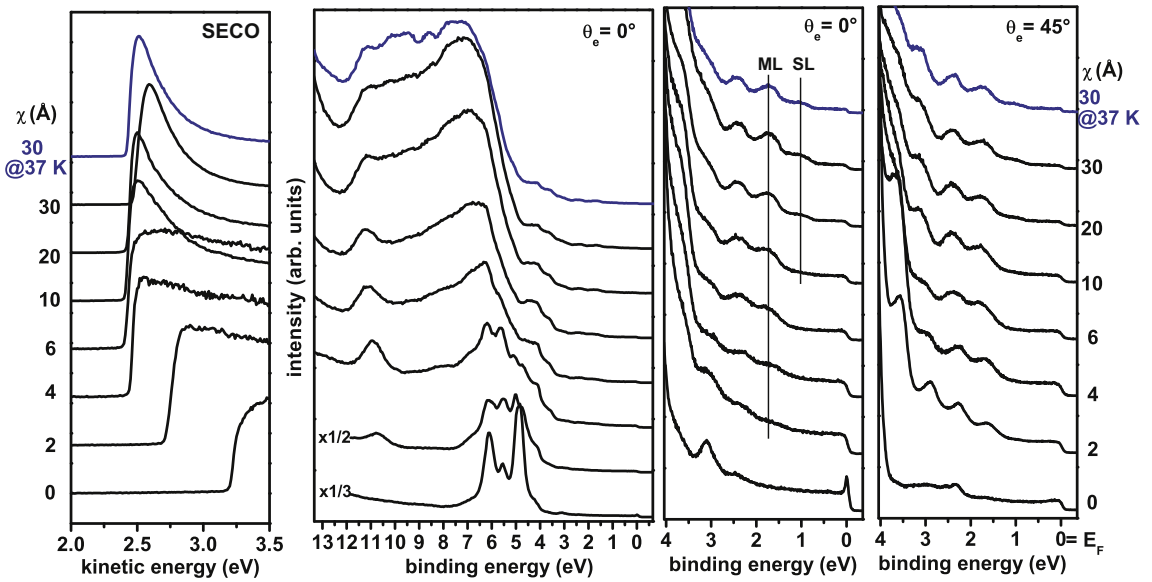

Fig. 2. Thickness dependent UPS spectra of DD6T on Ag(1 1 1). From left to right the secondary cut-off (SECO) region, a wide range spectra in normal emission and a close up of the region near to the Fermi-level (E_F) for photoelectron emission angles (θ_e) of 0° and 45° are displayed. χ denotes the nominal film thickness. The emission from the monolayer HOMO (ML) and second layer HOMO (SL) is marked by lines.

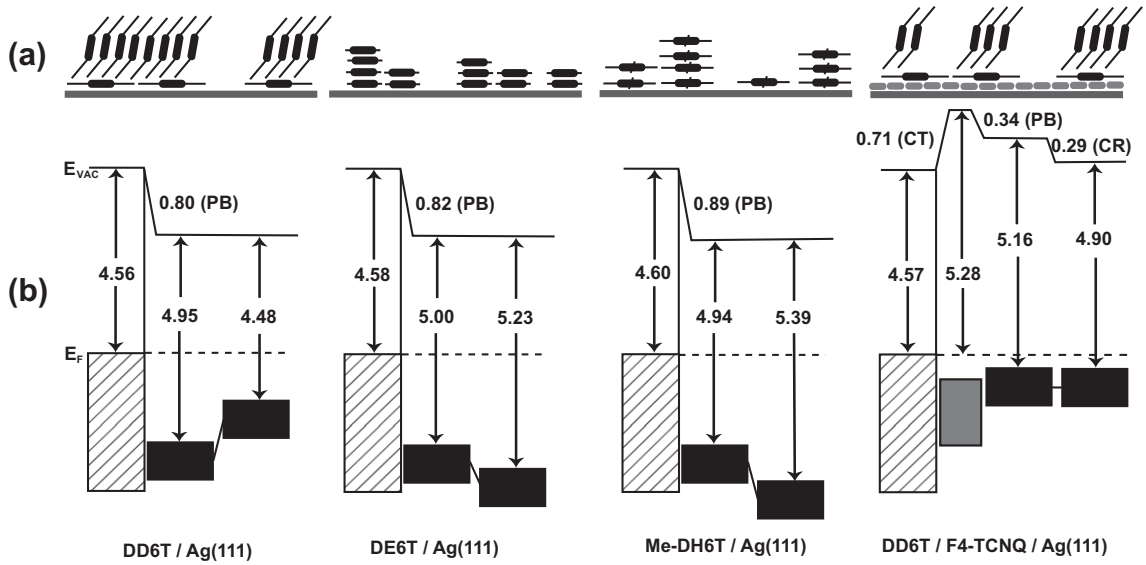

Fig. 3. (a) Schematic growth modes of the 6T-derivatives on Ag(1 1 1) as deduced from UPS measurements. The conformation of standing DD6T layers is adopted from the DH6T/Ag(1 1 1) system [33], however, the actual tilt angle between decyl chains and 6T-backbone might be different. (b) Schematic energy-level diagrams of substrate, monolayer and multilayer of the respective molecule. For the substrates the work functions and for the 6T-derivative thin films the ionization energies (defined as difference from the HOMO onset to the vacuum level (E_{VAC})) are given in eV. The main origin of vacuum-level shifts is indicated by PB (push-back effect), CT (charge transfer between metal substrate and F4-TCNQ) and CR (charge rearrangement), respectively. E_F corresponds to the Fermi-level of the substrate.

exposure to the UV-light and thus prohibited reliable UPS measurements on samples with higher nominal coverage. The multilayer spectra measured at low temperature (Fig. 2) were essentially the same as room temperature spectra (slight shifts in BE position are probably due to enhanced charging at this low temperature), however the alkyl emission part of the spectra changed, most notably a new clear peak centered at 8.57 eV BE appeared, which is probably because thermal excitations of the alkyl chains are frozen.

In contrast to DD6T, for DE6T *no* new emission features at the low BE side of the monolayer HOMO could be observed (Fig. 4a, full set of spectra in the Supporting Information) for coverages beyond the nominal monolayer. The DE6T multilayer IE (5.23 eV) is larger than the monolayer IE (5.00 eV), resembling the experimental findings for 6T on Ag(1 1 1) [57]. The shift of COM energy levels to higher BE in the second layer of organic thin films at metal surfaces is commonly observed and can be mainly attributed to a final-state effect, i.e., a decreased photohole screening efficiency of the molecular monolayer compared to the metal substrate [55,57,58]. Thus, the growth mode of DE6T on Ag(1 1 1) is similar to 6T on Ag(1 1 1) [57] with flat lying molecules also in the multilayer (Fig. 3a).

For DE6T multilayers (20 Å and 100 Å), the maxima of a peak that is derived from six nearly degenerate localized S-orbitals [33,56,59] have different BE for θ_e of 0° (4.59 eV) and of 45° (4.23 eV). For crystalline 6T on p(2 × 1) oxygen reconstructed Cu(1 1 0) a similar behavior was observed and ascribed to an intermolecular band dispersion [59]. As the 6T bandwidth (~0.5 eV) is similar to the shift of the DE6T peak center (0.37 eV) also for DE6T a reasonable crystalline quality can thus be expected. Note that the actual bandwidth of this feature for DE6T/Ag(1 1 1) was not determined in detail as only spectra at θ_e of 0° and of 45° were acquired. Moreover, also other factors like different angular dependent photoemission cross sections [9] of the six orbitals giving rise to the peak might contribute to the peak shift. Another S-derived peak (~11.50 eV) and the peaks derived from the delocalized HOMO, HOMO-1 and HOMO-2 (centered at 1.99, 2.63 and 3.25 eV BE, respectively) did not show any dispersion, which is consistent with the absence of intramolecular band dispersion of crystalline 6T [59]. Cooling the sample to 32 K increased the assumed dispersion width of the localized peak to 0.46 eV.

The spectra of Me-DH6T (Fig. 4b and Supporting Information) resemble the DE6T spectra, with an increase of the IE from 4.94 eV (4 Å coverage) to 5.39 eV (80 Å coverage). This increase in IE and the absence of charging during photoemission of multilayer films (in contrast to DD6T multilayers but in accordance with DE6T multilayers) points to essentially flat lying molecules also in the multilayer. The growth mode of Me-DH6T (Fig. 3a) is thus similar to DE6T and 6T with no orientational transition and in contrast to the unmethylated parent molecule DH6T on Ag(1 1 1) [3,32,33]. However, the unusually large BE shift of the valence electron region between mono- and multilayer of 0.45 eV may not be explained by screening alone, also the microstructure of the different layers might be different and thus impacting the electronic structure by intermolecular interactions [60] and/or slightly different – but still essentially lying – orientations [7,10,61]. In addition, the steric effect of the methyl groups at the third and fourth thiophene unit in Me-DH6T may cause a non-planar molecular conformation in the bulk, while the molecule

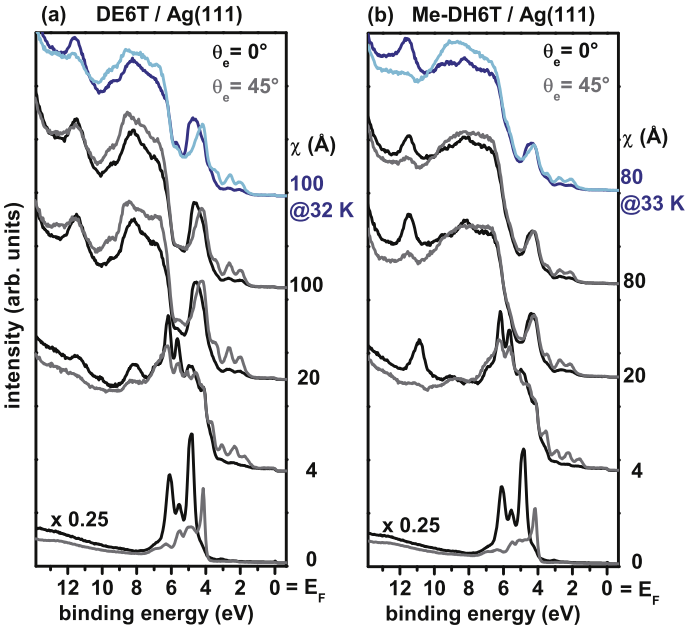

Fig. 4. UPS spectra of (a) DE6T and (b) Me-DH6T on Ag(1 1 1) for increasing nominal film thickness (χ). Wide range spectra for photoelectron emission angles (θ_e) of 0° (black, dark blue) and 45° (gray, light blue) are displayed. The 45°-emission spectra are slightly scaled in order to match the intensity of the S-derived peak around 4.50 eV BE of the 0°-spectra. (For interpretation of the references to colour in this figure legend, the reader is referred to the web version of this article.)

may be forced in a more planar conformation in the monolayer, which increases conjugation along the backbone and consequently lowers the IE [57]. In contrast to DE6T, the θ_e-dependence of the S-derived peak at ~4.40 eV BE is smaller for Me-DH6T (0.09 eV), which points to more disorder and/or a slightly different average orientation of Me-DH6T/Ag(1 1 1) compared to DE6T/Ag(1 1 1). Upon cooling the BE shift increased to 0.15 eV.

The growth models and associated interface energy level diagrams (Fig. 3) allow a discussion of the rules of molecular self-assembly at metal surfaces (without strong molecule–metal interactions) with particular attention on the influence of the saturated alkyl-chain length and position on the conjugated backbone. In the case of the straight molecules DE6T, DH6T [3,32,33] and DD6T, it is obvious that the critical length of alkyl side chains, which leads to sufficient hydrophobic interaction between themselves and triggers the lying/standing orientation–transition is between three and six repeat units. Increasing the alkyl length further, e.g., to ten units in the present case for DD6T, does not change the growth mode significantly. An interesting case is Me-DH6T, where the addition of two methyl groups (compared to DH6T) at the two central thiophene units leads to a completely different growth mode. The structure of standing DH6T on lying DH6T on Ag(1 1 1) [33] is similar to the known bulk crystal phase [24,28,62,63]. For Me-DH6T this structure is suppressed by the methylation of DH6T and Me-DH6T assembles in a markedly different way. In comparison, also β,β'-DH6T vacuum sublimed at Au substrates did not adopt a standing orientation already in the second layer, but exhibited a 6T-like growth mode [64]. Furthermore, DH6T deposited on Ag(1 1 1) pre-covered with a monolayer of tetratetracontane – a simple long alkyl chain – did not adopt an almost standing orientation [33]. Thus, the balanced interplay of favored mutual alkyl interaction (molecular fastener effect) and attractive π-system–substrate interaction leads to the specific orientation and structure of the organic thin film.

Notably, the valence spectra measured at low temperature did not exhibit significant changes compared to the room temperature spectra, with exception of DD6T/Ag(1 1 1). Here, the emission from the alkyl chains gained features by cooling the sample, most pronounced a new peak emerging at 8.57 eV BE (Fig. 2). This may be a hint for increased ordering of the alkyl chains by the molecular fastener effect, which is prevented at room temperature by thermal motion. However, the denser packing of the alkyl chains does not affect the conjugated backbone of the molecule significantly, as no unusual sharpening of the HOMO-peak could be observed at low temperature compared to room temperature. For the other 6T-derivatives the packing structure and/or the smaller alkyl chains hinder a pronounced alkyl–alkyl interaction. DE6T, with the shortest alkyl chains within the investigated molecule series, shows the largest bandwidth of the S-derived localized peak, which might be interpreted as the system with the best intermolecular order of the conjugated molecular moieties.

4. Charge rearrangement across alkyl layers

To realize a high work function substrate for deposition of DD6T, F4-TCNQ was deposited stepwise onto Ag(1 1 1) until the increase of the vacuum level (in total 0.71 eV) (Fig. 5) saturated, resulting in an effective substrate work

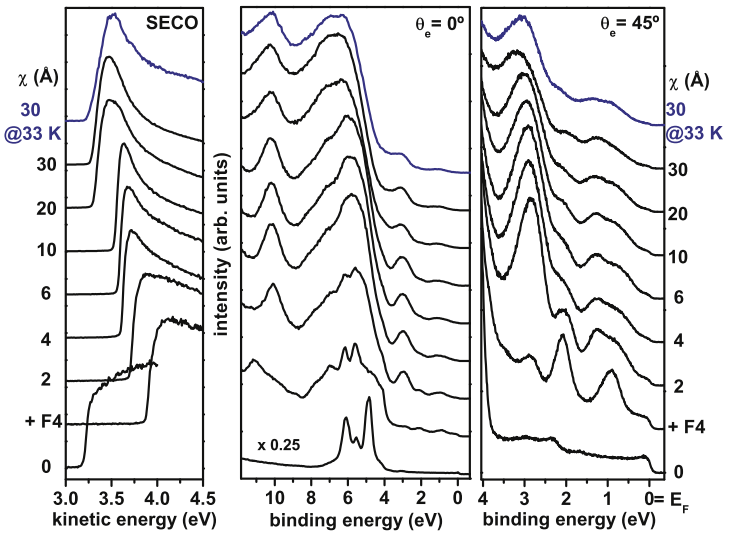

Fig. 5. UPS spectra of DD6T on F4-TCNQ (F4) pre-covered Ag(1 1 1). The secondary electron cut-off (SECO) region, a wide range spectra in normal emission and a close up of the region near to the Fermi-level (E_F) for a photoelectron emission angle (θ_e) of 45° are displayed.

function of 5.28 eV. Depositing up to 6 Å DD6T on the F4-TCNQ/Ag(1 1 1) substrate attenuated the F4-TCNQ features [36,37] and led to a dominant photoemission peak centered at 2.90 eV BE, which is assigned to the localized S-derived states of DD6T. The features at lower BE were comparably smeared out, the low BE onset of photoemission was at 0.22 eV. The vacuum level decreased by 0.34 eV. Deposition of DD6T up to the final coverage of 30 Å decreased the vacuum-level further by 0.29 eV and did not change the valence electron spectral signature. Thus, also in this case the IE of the multilayer is reduced compared to the monolayer, i.e., the orientation is changing from lying to standing (Fig. 3). The absolute IE values for monolayer (5.16 eV) and multilayer (4.90 eV) DD6T on F4-TCNQ/Ag(1 1 1) do not correspond exactly to the values of DD6T on pristine Ag(1 1 1). However, the IE is difficult to interpret for organic heterostructures without exact knowledge of thin film morphology [65]. Also for molecules that form amorphous films, where collective electrostatic orientation effects can be excluded, a change in the IE on F4-TCNQ pre-covered metals has been observed [66]. Moreover, standing DD6T exhibits pronounced island growth, because the two peaks due to localized S-derived states (~2.90 eV BE and ~10.20 eV BE) were not attenuated sufficiently even for a nominal coverage of 30 Å as for DD6T on pristine Ag(1 1 1). The IE change from lying to standing DD6T is only 0.26 eV for DD6T on F4-TCNQ pre-covered Ag(1 1 1) compared to 0.47 eV for DD6T on pristine Ag(1 1 1). For (on a molecular level) inhomogeneously covered surfaces the SECO quantifies the area averaged arithmetic mean of the vacuum levels of covered and uncovered substrate patches, whereas the valence electron photoemission spectrum is the superposition of the spectral features of the respective sample patches [67,68]. This makes the correct assignment of ionization energies at such interfaces very difficult if a shift of the vacuum-level occurs at the interface. Thus, the 0.47 eV IE difference at the organic homointerface of DD6T on pristine Ag(1 1 1) might reflect the more realistic difference in the IE of lying and standing DD6T. Consequently, most probably half of the lying DD6T on F4-TCNQ/Ag(1 1 1) was covered with standing DD6T for nominal 30 Å coverage. However, also this 30 Å DD6T/F4-TCNQ/Ag(1 1 1) film showed charging during UPS measurements which is expected for photoemission across standing alkyl layers [32].

Without the vacuum-level shift between lying and standing DD6T the HOMO onset of standing DD6T would be *above* the substrate Fermi-level (Fig. 3). Thus, the situation at this organic/organic homointerface is reminiscent to Fermi-level pinning [38–41]. The results reveal that decyl chains are *not* long enough to electronically decouple two semiconducting layers (lying DD6T and the 6T core of standing DD6T). Fermi-level alignment at the DH6T/F4-TCNQ/Ag(1 1 1) system, which shows an analogous behavior to DD6T/F4-TCNQ/Ag(1 1 1), was explained to be facilitated by a charge transfer from standing DH6T to the substrate [37]. However, in this case the calculated average charge transfer per molecule was only ~0.03 q, which could also be interpreted in terms of one transferred charge per 33 molecules. Recently, it was shown by means of two photon photoemission that the alkyl layers at the DH6T/Ag(1 1 1) interface lead to charge localization in standing DH6T layers [69]. In the case of integer charge transfer the small fraction of charged molecules would thus lead to laterally isolated dipoles at the organic/metal interface (Fig. 6a). Since the electron potential energy around such a dipole rapidly converges to a common value [7], the energy-level alignment of neighboring molecules is not (or only negligible) affected by an isolated dipole [70]. Consequently, an integer charge transfer would not lead to thermodynamic equilibrium at this interface. Thus, a static charge transfer from standing DD6T to the metal substrate is quite improbable. In addition, the charging of the 30 Å DD6T layers (on both, pristine Ag(1 1 1) as F4-TCNQ pre-covered substrate) demonstrates that even the charge density gradient originating from the photoholes cannot

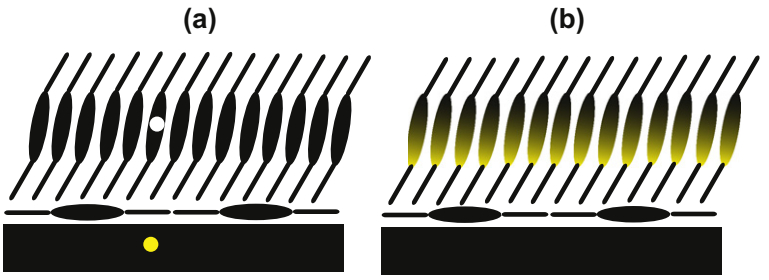

Fig. 6. Sketch of two different mechanisms for explaining the interface dipole between lying and standing DD6T: (a) integer charge transfer, (b) polarization of the conjugated parts of DD6T.

trigger sufficient dynamic charge transfer across the decyl layers.

In a recent density functional theory study [42] on interfaces between metal/SAM and COM a directly related issue was addressed. It was found that in the case of Fermi-level pinning no charge transfer from the COM to the metal substrate occurs but a charge rearrangement at the COM/SAM interface. Thus, the interface dipole has its origin in a slight shift of the adsorbate's electron density center-of-mass with respect to the atomic nuclei, corresponding to a localized polarization. For DD6T and DH6T thin films such a screening would make the unlikely static charge transfer across the alkyl chains obsolete and thus offers a new view on the insulating properties of alkyl chains. The basic mechanism is sketched in Fig. 6b. As the polarizability of the saturated alkyl chains is much smaller compared to the conjugated backbone, the polarization of the 6T backbone could be dominating. Furthermore, the polarization might yield structural changes of standing DD6T and thus lead to a density of disorder induced gap-states [46,47], which might additionally impact the energy-level alignment. The basic principle of polarization instead of charge transfer may not be restricted to the special case of alkylated COMs but may also prevail for other cases of Fermi-level pinning of organic thin films.

5. Conclusions

We could demonstrate that both, the substitution-position and the length of alkyl chains of 6T derivatives play an important role in the self-assembly of these molecules on Ag(1 1 1) surfaces. If the alkyl chains are long enough and attached only at the α,ω position of 6T, the molecules exhibit a growth mode with flat lying monolayer and standing second layer. This orientational transition can be prevented by adding additional methyl groups at the 6T backbone. Since the orientation to a substrate is crucial for energy-level alignment and thus the charge transport efficiency in an organic film, these findings offer an approach for engineering organic thin film structures for enhanced performance of organic devices. Moreover, decyl chains are not long enough to electronically decouple two semiconducting layers. A previously proposed charge transfer across long alkyl chains is, however, unlikely and thermodynamic equilibrium in the context of Fermi-level pinning might also be achieved by a small shift of the center-of-mass of the molecule's electron density.

Acknowledgments

The authors thank Shunsuke Hosoumi for assistance during UPS measurements, Ingo Salzmann for fruitful discussions and Heraeus Clevios GmbH for providing the 6T derivatives. SD gratefully acknowledges a JSPS fellowship for foreign researchers. SK acknowledges financial support by a Grant-in-Aid for Young Scientists (A) and NU by a Grant-in-Aid for Scientific Research (A). This work was financially supported partly by the Global-COE Program of MEXT (Advanced School for Organic Electronics, Chiba University).

Appendix A. Supplementary data

Supplementary data associated with this article can be found, in the online version, at doi:10.1016/j.orgel.2011.03.009.

References

[1] N. Koch, ChemPhysChem 8 (2007) 1438.
[2] H. Ishii, K. Sugiyama, E. Ito, K. Seki, Adv. Mater. 11 (1999) 605.
[3] S. Duhm, G. Heimel, I. Salzmann, H. Glowatzki, R.L. Johnson, A. Vollmer, J.P. Rabe, N. Koch, Nat. Mater. 7 (2008) 326.
[4] W. Chen, H. Huang, S. Chen, Y.L. Huang, X.Y. Gao, A.T.S. Wee, Chem. Mater. 20 (2008) 7017.
[5] I. Salzmann, S. Duhm, G. Heimel, M. Oehzelt, R. Kniprath, R.L. Johnson, J.P. Rabe, N. Koch, J. Am. Chem. Soc. 130 (2008) 12870.
[6] S. Duhm, S. Hosoumi, I. Salzmann, A. Gerlach, M. Oehzelt, B. Wedl, T.-L. Lee, F. Schreiber, N. Koch, N. Ueno, et al., Phys. Rev. B 81 (2010) 045418.
[7] G. Heimel, I. Salzmann, S. Duhm, N. Koch, Chem. Mater. 23 (2011) 359.
[8] H.N. Tsao, D. Cho, J.W. Andreasen, A. Rouhanipour, D.W. Breiby, W. Pisula, K. Müllen, Adv. Mater. 21 (2009) 209.
[9] S. Kera, H. Yamane, N. Ueno, Prog. Surf. Sci. 84 (2009) 135.
[10] G. Heimel, I. Salzmann, S. Duhm, J.P. Rabe, N. Koch, Adv. Funct. Mater. 19 (2009) 3874.
[11] J. Fraxedas, Adv. Mater. 14 (2002) 1603.
[12] G. Witte, C. Wöll, J. Mater. Res. 19 (2004) 1889.
[13] S. Liu, W.M. Wang, A.L. Briseno, S.C.B. Mannsfeld, Z. Bao, Adv. Mater. 21 (2009) 1217.
[14] J.-O. Vogel, I. Salzmann, S. Duhm, M. Oehzelt, J.P. Rabe, N. Koch, J. Mater. Chem. 20 (2010) 4055.
[15] F. Garnier, A. Yassar, R. Hajlaoui, G. Horowitz, F. Deloffre, B. Servet, S. Ries, P. Alnot, J. Am. Chem. Soc. 115 (1993) 8716.
[16] R. Azumi, G. Götz, T. Debaerdemaeker, P. Bäuerle, Chem.-Eur. J. 6 (2000) 735.

[17] H. Glowatzki, S. Duhm, K.-F. Braun, J.P. Rabe, N. Koch, Phys. Rev. B 76 (2007) 125425.
[18] W. Pisula, X. Feng, K. Müllen, Adv. Mater. 22 (2010) 3634.
[19] G. Saito, Y. Yoshida, Bull. Chem. Soc. Jpn. 80 (2007) 1.
[20] N. Ueno, H. Kurosu, K. Seki, G. Saito, K. Sugita, H. Inokuchi, Mol. Cryst. Liq. Cryst. 218 (1992) 171.
[21] H. Inokuchi, G. Saito, P. Wu, K. Seki, T.B. Tang, T. Mori, K. Imaeda, T. Enoki, Y. Higuchi, K. Inaka, et al., Chem. Lett. 15 (1986) 1263.
[22] T. Vondrak, H. Wang, P. Winget, C.J. Cramer, X.-Y. Zhu, J. Am. Chem. Soc. 122 (2000) 4700.
[23] D. Aswal, S. Lenfant, D. Guerin, J. Yakhmi, D. Vuillaume, Anal. Chim. Acta 568 (2006) 84.
[24] G. Horowitz, B. Bachet, A. Yassar, P. Lang, F. Demanze, J.-L. Fave, F. Garnier, Chem. Mater. 7 (1995) 1337.
[25] M. Halik, H. Klauk, U. Zschieschang, G. Schmid, S. Ponomarenko, S. Kirchmeyer, W. Weber, Adv. Mater. 15 (2003) 917.
[26] Q. Xia, M. Burkhardt, M. Halik, Org. Electron. 9 (2008) 1061.
[27] Y. Ishii, R. Ye, M. Baba, K. Ohta, Jpn. J. Appl. Phys. 47 (2008) 1256.
[28] B. Servet, S. Ries, M. Trotel, P. Alnot, G. Horowitz, F. Garnier, Adv. Mater. 5 (1993) 461.
[29] M. Lu, S. Nagamatsu, Y. Yoshida, M. Chikamatsu, R. Azumi, K. Yase, Chem. Lett. 39 (2010) 60.
[30] C.E. Heiner, J. Dreyer, I.V. Hertel, N. Koch, H.-H. Ritze, W. Widdra, B. Winter, Appl. Phys. Lett. 87 (2005) 093501.
[31] G. Beernink, T. Strunskus, G. Witte, C. Wöll, Appl. Phys. Lett. 85 (2004) 398.
[32] S. Duhm, H. Glowatzki, J.P. Rabe, N. Koch, R.L. Johnson, Appl. Phys. Lett. 88 (2006) 203109.
[33] S. Duhm, I. Salzmann, N. Koch, H. Fukagawa, T. Kataoka, S. Hosoumi, K. Nebashi, S. Kera, N. Ueno, J. Appl. Phys. 104 (2008) 033717.
[34] L. Romaner, G. Heimel, J.-L. Brédas, A. Gerlach, F. Schreiber, R.L. Johnson, J. Zegenhagen, S. Duhm, N. Koch, E. Zojer, Phys. Rev. Lett. 99 (2007) 256801.
[35] N. Koch, S. Duhm, J.P. Rabe, A. Vollmer, R.L. Johnson, Phys. Rev. Lett. 95 (2005) 237601.
[36] G.M. Rangger, O.T. Hofmann, L. Romaner, G. Heimel, B. Bröker, R.-P. Blum, R.L. Johnson, N. Koch, E. Zojer, Phys. Rev. B 79 (2009) 165306.
[37] S. Duhm, H. Glowatzki, J.P. Rabe, N. Koch, R.L. Johnson, Appl. Phys. Lett. 90 (2007) 122113.
[38] H. Fukagawa, S. Kera, T. Kataoka, S. Hosoumi, Y. Watanabe, K. Kudo, N. Ueno, Adv. Mater. 19 (2007) 665.
[39] N. Koch, A. Vollmer, Appl. Phys. Lett. 89 (2006) 162107.
[40] S. Braun, W.R. Salaneck, M. Fahlman, Adv. Mater. 21 (2009) 1450.
[41] H.Y. Mao, F. Bussolotti, D.-C. Qi, R. Wang, S. Kera, N. Ueno, A.T.S. Wee, W. Chen, Org. Electron. 12 (2011) 534.
[42] F. Rissner, G.M. Rangger, O.T. Hofmann, A.M. Track, G. Heimel, E. Zojer, ACS Nano 3 (2009) 3513.
[43] H. Vázquez, R. Oszwaldowski, P. Pou, J. Ortega, R. Pérez, F. Flores, A. Kahn, Europhys. Lett. 65 (2004) 802.
[44] F. Flores, J. Ortega, H. Vázquez, Phys. Chem. Chem. Phys. 11 (2009) 8658.
[45] H. Vázquez, F. Flores, A. Kahn, Org. Electron. 8 (2007) 241.
[46] T. Sueyoshi, H. Fukagawa, M. Ono, S. Kera, N. Ueno, Appl. Phys. Lett. 95 (2009) 183303.
[47] T. Sueyoshi, H. Kakuta, M. Ono, K. Sakamoto, S. Kera, N. Ueno, Appl. Phys. Lett. 96 (2010) 093303.
[48] M. Häming, M. Greif, C. Sauer, A. Schöll, F. Reinert, Phys. Rev. B 82 (2010) 235432.
[49] S. Ponomarenko, S. Kirchmeyer, J. Mater. Chem. 13 (2003) 197.
[50] S. Machida, Y. Nakayama, S. Duhm, Q. Xin, A. Funakoshi, N. Ogawa, S. Kera, N. Ueno, H. Ishii, Phys. Rev. Lett. 104 (2010) 156401.
[51] O. McDonald, A.A. Cafolla, Z. Li, G. Hughes, Surf. Sci. 600 (2006) 1909.
[52] N. Koch, A. Vollmer, S. Duhm, Y. Sakamoto, T. Suzuki, Adv. Mater. 19 (2007) 112.
[53] S. Kera, H. Yamane, H. Fukagawa, T. Hanatani, K. Okudaira, K. Seki, N. Ueno, J. Electron Spectrosc. Relat. Phenom. 156–158 (2007) 135.
[54] A. Kahn, N. Koch, W.Y. Gao, J. Poly. Sci. B 41 (2003) 2529.
[55] N. Koch, J. Phys.: Condens. Matter 20 (2008) 184008.
[56] H. Fujimoto, U. Nagashima, H. Inokuchi, K. Seki, Y. Cao, H. Nakahara, J. Nakayama, M. Hoshino, K. Fukuda, J. Chem. Phys. 92 (1990) 4077.
[57] N. Koch, G. Heimel, J. Wu, E. Zojer, R.L. Johnson, J.-L. Brédas, K. Müllen, J.P. Rabe, Chem. Phys. Lett. 413 (2005) 390.
[58] I.G. Hill, A.J. Mäkinen, Z.H. Kafafi, J. Appl. Phys. 88 (2000) 889.
[59] S. Berkebile, G. Koller, P. Puschnig, C. Ambrosch-Draxl, F. Netzer, M. Ramsey, Appl. Phys. A-Mater. Sci. Process. 95 (2009) 101.
[60] N. Ueno, S. Kera, Prog. Surf. Sci. 83 (2008) 490.
[61] W. Chen, D.C. Qi, Y.L. Huang, H. Huang, Y.Z. Wang, S. Chen, X.Y. Gao, A.T.S. Wee, J. Phys. Chem. C 113 (2009) 12832.
[62] J. Bernstein, J.A.R.P. Sarma, A. Gavezzotti, Chem. Phys. Lett. 174 (1990) 361.
[63] T. Siegrist, R.M. Fleming, R.C. Haddon, R.A. Laudise, A.J. Lovinger, H.E. Katz, P. Bridenbaugh, D.D. Davis, J. Mater. Res. 10 (1995) 2170.
[64] T. Schwieger, X. Liu, H. Peisert, B. Adolphi, N. Kiriy, M. Knupfer, J. Appl. Phys. 97 (2005) 123712.
[65] S. Duhm, I. Salzmann, R.L. Johnson, N. Koch, J. Electron Spectrosc. Relat. Phenom. 174 (2009) 40.
[66] S. Duhm, I. Salzmann, B. Bröker, H. Glowatzki, R.L. Johnson, N. Koch, Appl. Phys. Lett. 95 (2009) 093305.
[67] R. Fischer, S. Schuppler, N. Fischer, T. Fauster, W. Steinmann, Phys. Rev. Lett. 70 (1993) 654.
[68] G. Koller, B. Winter, M. Oehzelt, J. Ivanco, F.P. Netzer, M.G. Ramsey, Org. Electron. 8 (2007) 63.
[69] J.E. Johns, E.A. Muller, J.M.J. Frechet, C.B. Harris, J. Am. Chem. Soc. 132 (2010) 15720.
[70] H. Fukagawa, H. Yamane, S. Kera, K.K. Okudaira, N. Ueno, Phys. Rev. B 73 (2006) 04130(R).

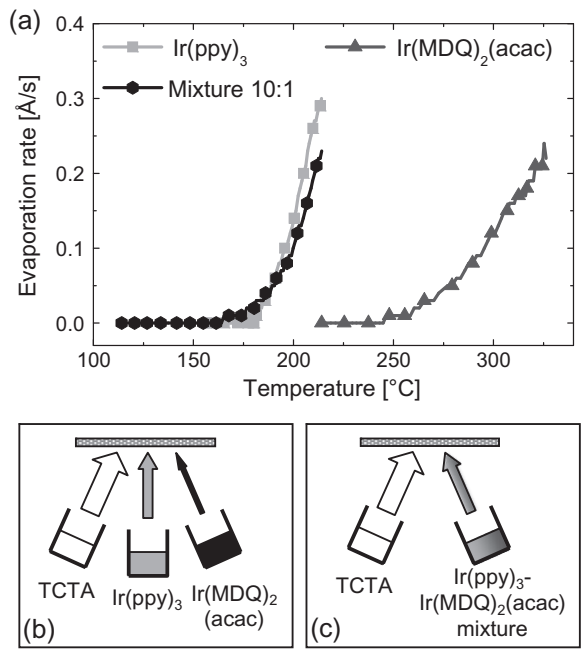

Fig. 1. (a) Evaporation rate vs. the crucible temperatures for $Ir(ppy)_3$, $Ir(MDQ)_2(acac)$, and an (10:1) $Ir(ppy)_3$ to $Ir(MDQ)_2(acac)$ mixture; geometry of (b) a co-evaporation from three individual sources and (c) a co-evaporation from only two sources using premixed dyes. In (b) and (c), thickness of arrows indicates evaporation rate.

from the same crucible. Obviously, the combined rate is mainly influenced by the one of the higher concentrated $Ir(ppy)_3$. This makes co-doped EMLs possible with this kind of approach.

To fabricate OLEDs with mixed EMLs and a balanced emission spectrum, the dye with the lower triplet level has to have a very low doping concentration [9]. The other emitter can have typical concentrations between 1% and 15%. At a certain temperature (e.g. 210 °C) the two dyes $Ir(ppy)_3$ and $Ir(MDQ)_2(acac)$ evaporate at a rate of roughly 0.25 Å/s and less than 0.01 Å/s, respectively. Since the sublimation curve for $Ir(MDQ)_2(acac)$ in Fig. 1 always lies below the one of $Ir(ppy)_3$, we assume that the evaporation rate of $Ir(MDQ)_2(acac)$ in the mixture is also lower than the one of $Ir(ppy)_3$. Therefore, a co-evaporation of a premix of $Ir(ppy)_3$ and $Ir(MDQ)_2(acac)$ results in a strongly different rate for green and red which can lead to mixed EMLs with very low red concentrations and a nearly balanced emission. The two different evaporation curves are the key to generate this doping difference. For example, for a weight ratio of (10:1) in the crucible, the ratio of $Ir(ppy)_3$ to $Ir(MDQ)_2(acac)$ in the final layer should be even larger as the ratio of the evaporation rates is >25:1. But the difference in the evaporation curves of the materials will have consequences on the long term stability of the mixture's molecular composition. A detailed discussion on this will be shown in the next section.

To prepare the dye mixture, appropriate amounts of both materials are weighed and stirred in Argon atmosphere. Special care has to be taken to reach a homogeneous blend as the $Ir(ppy)_3$ molecules tend to stick together easily. Thus, the mixture is pestled in an agate mortar to guarantee a proper intermixing of the dyes before it is filled into the evaporation crucible.

2. PL pretests

In order to characterize co-doped EMLs fabricated by co-evaporation of premixed dyes from one crucible, we prepare layers on float glass substrates for Photoluminescence (PL) characterization. These consist of the matrix 4,4′,4″-tris(carbazol-9-yl)triphenylamine (TCTA) and the two dyes $Ir(ppy)_3$ and $Ir(MDQ)_2(acac)$ from the same evaporation source. The geometry of the evaporation can be seen in Fig. 1(c). All layers are thermally evaporated at a background pressure of 5×10^{-6} Pa, are 40 nm thick and encapsulated afterwards in Argon atmosphere. For PL measurements they are excited at a wavelength of λ_{exc} = 385 nm so that excitons are only formed on the dyes, not on the matrix TCTA. Since all PL samples have identical thickness and are excited with the same wavelength and optical power, PL spectra show the relative changes caused by different film compositions.

Fig. 2 shows the PL signal of these layers with the dyes evaporated from the same source. The different PL spectra belong to samples with an increasing number of evaporations from the mixed crucible. The ratio of $Ir(ppy)_3$ to $Ir(MDQ)_2(acac)$ in the crucible was set to (10:1), the doping ratio between TCTA and the dyes is [89:11]. After several evaporation cycles a substantial change in the emission color of the layers is detected. The more evaporations from the crucible the stronger is the color shift towards a purely red emission. Having in mind the high sensitivity of the color of mixed EMLs on the concentration of the dye with the lowest triplet level ($Ir(MDQ)_2(acac)$) [3,9], the spectral shift over several processed samples indicates that the change in the molecular ratio is of the order of 3 (cf. classical evaporation in Fig. 4). Even the last evaporation (14th sample), just before the crucible was empty, still shows a green emission from $Ir(ppy)_3$. As the change of the dye ratio probably takes place at the surface of the

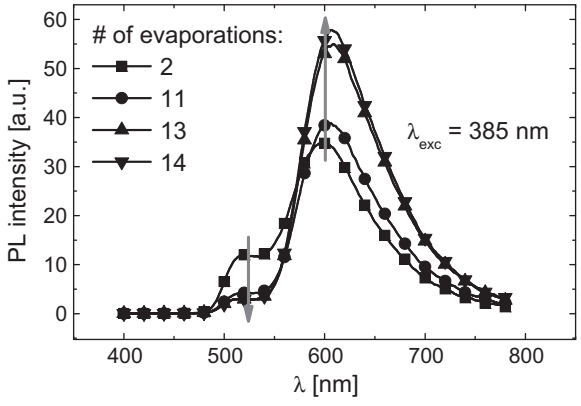

Fig. 2. PL spectra of layers of TCTA doped with $Ir(ppy)_3$ and $Ir(MDQ)_2(acac)$ (TCTA:dyes [89:11]). The emitters were evaporated from the same source with a mixing ratio of (10:1). After several evaporations the spectral composition has changed significantly.

mixture, the color change could possibly be reduced by continuously stirring the mixture during the evaporation.

The depletion of Ir(ppy)$_3$ molecules over time can also be used from the start to reach different emission spectra. As various crucible compositions can lead to different molecular ratios in the layers they also affect the relative strength of green and red emission. Fig. 3 shows PL signals of layers which used different mixtures of Ir(ppy)$_3$ and Ir(MDQ)$_2$(acac) with a doping ratio of [89:11] for TCTA:-dyes. The higher the percentage of Ir(ppy)$_3$ is in the crucible, the lower is the emission of Ir(MDQ)$_2$(acac) in the layer. The rate detection during evaporation only monitors the rate of the entire mixed crucible. If the green to red ratio in the source is high, the overall rate is mainly given by Ir(ppy)$_3$ molecules. If it is decreased, more Ir(MDQ)$_2$(acac) needs to be evaporated to reach the same combined rate. This results in different molecular ratios in the final layer which lead to shifts in the emission spectra.

How do these results compare to PL spectra of layers realized by classical co-evaporation from individual sources (Fig. 1(b))? For this, three different layers were fabricated using the same materials by co-doping from single sources. The concentration of Ir(ppy)$_3$ was kept constant at 10% while the one of Ir(MDQ)$_2$(acac) was varied from 0.3% to 1%. The remaining percentage up to 100% is given by the matrix TCTA. Fig. 4 shows the PL spectra of these three layers as well as the one of the first mixture with the (10:1) composition in the crucible. They all show the typical behavior of mixed EMLs containing two dyes with different emissive levels.

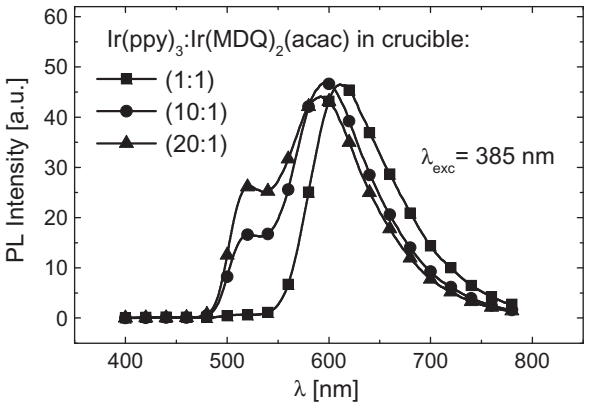

Fig. 3. PL spectra of layers of TCTA doped with Ir(ppy)$_3$ and Ir(MDQ)$_2$(acac) (TCTA:dyes [89:11]). The emitters were evaporated from the same source with different mixing ratios leading to different spectra.

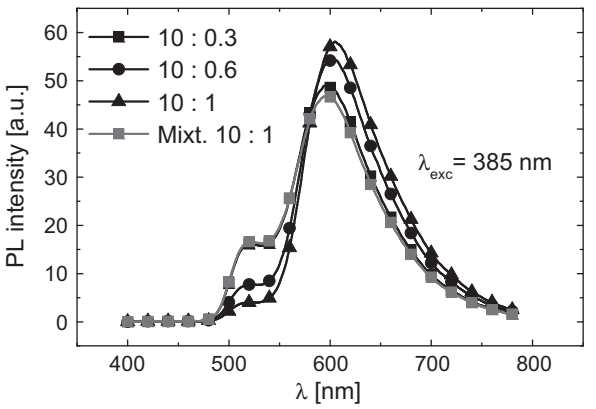

Fig. 4. PL spectra of layers of TCTA doped with Ir(ppy)$_3$ and Ir(MDQ)$_2$(acac). Black curves represent classically evaporated layers from three individual sources with 10% Ir(ppy)$_3$ and 0.3% to 1% Ir(MDQ)$_2$(acac). Gray curve represents a co-evaporated layer using a premixed crucible of (10:1) Ir(ppy)$_3$ to Ir(MDQ)$_2$(acac).

Already a small addition of Ir(MDQ)$_2$(acac), co-doped into the same layer as the Ir(ppy)$_3$, causes a significant change in the emission color of the otherwise green OLED. The strong orange-red peak ($\lambda_{Ir(MDQ)_2(acac)} \approx 600$ nm) generated by relatively few molecules is due to an exciton transfer from the lowest triplet level $T_1 = 2.4$ eV of Ir(ppy)$_3$ to the one of Ir(MDQ)$_2$(acac) with $T_1 = 2.1$ eV which reduces green emission ($\lambda_{Ir(ppy)_3} \approx 515$ nm) [3]. Even at red concentrations much smaller than the 10% of Ir(ppy)$_3$, the majority of excitons decays on Ir(MDQ)$_2$(acac) molecules. These characteristic spectra can also be achieved with a co-evaporation using a premix of dyes which confirms the purpose of this technique. The sensitivity of the spectrum with respect to the exact concentration of Ir(MDQ)$_2$(acac) allows us to detect even small changes in the red concentration with simple PL measurements. Additionally, there is no decrease in the PL efficiency of the layers by the co-evaporation from the same crucible.

The classical sample with [89.7:10:0.3] contains the lowest red doping concentration which can be reproducibly fabricated with our evaporation tool, therefore, representing the most greenish classical spectrum possible. Fig. 3 shows that even greener spectra are possible using the co-evaporation from the same crucible which means that it allows us to cross this procedural barrier.

3. Yellow OLEDs

Yellow OLEDs with mixed EMLs from classical evaporation and co-evaporation of a premix are prepared to show the feasability of this process. For this, we choose a yellow test device which can be easily combined with a blue fluorescent or phosphorescent emitter, e.g. 2,2′,7,7′-tetrakis(2,2-diphenylvinyl)spiro-9,9′-bifluorene (Spiro-DPVBi) or iridium(III)bis(4,6-difluorophenylpyridinato-N,C20)picolinate (FIrpic) to create a warm white light-emitting diode [6,7].

The device structure of the OLED which can be seen in Fig. 5 is the following: 120 nm indium tin oxide (ITO) anode/40 nm di-[4-(*N*,*N*-ditolyl-amino)-phenyl]cyclohexane (TAPC)/7 nm TCTA co-doped with Ir(ppy)$_3$ and Ir(MDQ)$_2$(acac)/10 nm 4,7-diphenyl-1,10-phenanthroline (BPhen)/40 nm tris(8-hydroxy-quinolinato)aluminum (Alq$_3$)/0.7 nm lithium fluoride (LiF)/200 nm aluminum cathode. The EML consisting of the matrix material TCTA and the two dyes is either classically co-doped from two separate evaporation sources for Ir(ppy)$_3$ and Ir(MDQ)$_2$(acac) or the one source containing the dye mixture. The classically co-doped devices are the references to assess the performance of the OLEDs realized by the dye mixture.

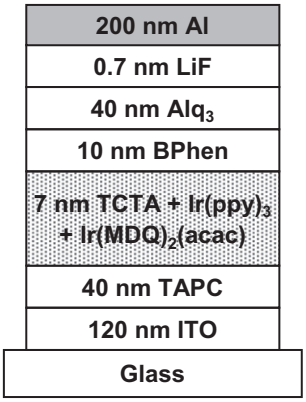

Fig. 5. Stack layout of yellow OLED with mixed EML.

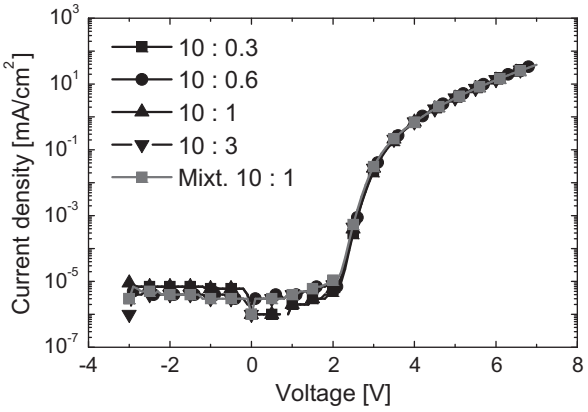

Fig. 6. IV characteristics of the different OLEDs.

The first four curves in Fig. 6 show the IV characteristics of the reference diodes with concentrations of 10% $Ir(ppy)_3$ and a variation of 0.3%, 0.6%, 1%, and 3% $Ir(MDQ)_2(acac)$ in 89.7%, 89.4%, 89%, and 87% TCTA, respectively. The $Ir(ppy)_3$ concentration was chosen to be 10% since devices with $Ir(ppy)_3$ concentrations around this value have shown high external quantum efficiencies (EQE) [10]. The gray curve is the one of the OLED which used the premix during fabrication. As can be seen, the evaporation from the same crucible has no effects on the IV characteristics of the devices. All samples seem to have the same injection barriers as well as identical charge carrier mobilities.

Fig. 7 shows the corresponding spectra of the five diodes. These results are similar to the ones for the PL pretests and other publications which show how sensitive co-doped EMLs are to the concentration of the dye with the lowest triplet level [3,9,11]. Again, the nearly balanced spectrum of the classically evaporated reference of [89.7:10:0.3] is closely met by the one of the premix co-evaporation given by the gray curve. It is confirmed that the red concentration within the layer is significantly lower than the nominal value of (10:1). In fact, it would be very close to a device with 10% $Ir(ppy)_3$ and 0.4% $Ir(MDQ)_2(acac)$. The external quantum efficiency of the diode

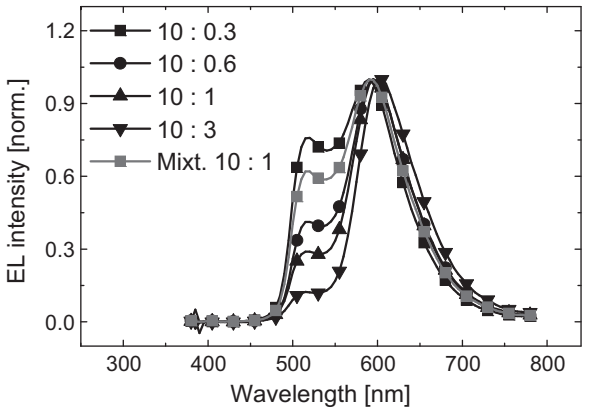

Fig. 7. Normalized electroluminescence spectra of OLEDs with classically co-evaporated EML with TCTA:$Ir(ppy)_3$:$Ir(MDQ)_2(acac)$ doping ratios of [89.7:10:0.3], [89.4:10:0.6], [89:10:1], [87:10:3], and the one with the EML from the (10:1) mixture and a matrix to mixture ratio of [89:11]. Only the emitter ratios are shown to describe the curves in the graph.

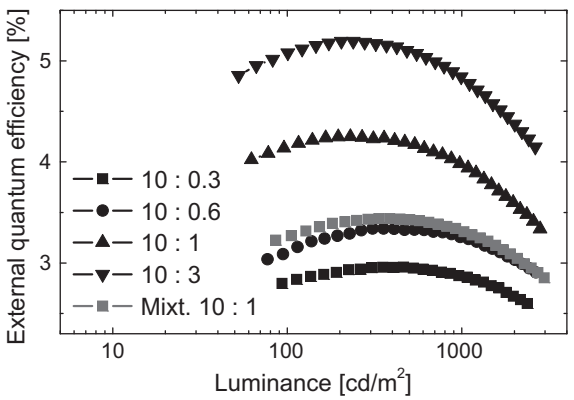

Fig. 8. External quantum efficiency of OLEDs with classically co-evaporated EML with TCTA:$Ir(ppy)_3$:$Ir(MDQ)_2(acac)$ doping ratios of [89.7:10:0.3], [89.4:10:0.6], [89:10:1], [87:10:3], and the one with the EML from the (10:1) mixture and a matrix to mixture ratio of [89:11]. Only the emitter ratios are shown to describe the curves in the graph.

from the mixture is even better than expected for a device with 10% $Ir(ppy)_3$ and 0.4% $Ir(MDQ)_2(acac)$ (cf. Fig. 8).

Nevertheless, the efficiency increases if more red molecules are added to the co-doped layer. Possible reasons for this effect can be: (i) $Ir(MDQ)_2(acac)$ is a more efficient emitter than $Ir(ppy)_3$; (ii) exciton transfer to $Ir(MDQ)_2(acac)$ reduces quenching effects in the device; (iii) $Ir(MDQ)_2(acac)$ molecules act as traps for charge carriers which improves the charge balance; (iv) the microcavity of the device allows for better extraction of red light. The IV characteristics do not indicate a trap behavior of the $Ir(MDQ)_2(acac)$ molecules and optical simulations show that the microcavity is even better for green light, ruling out the last two reasons. Also, $Ir(ppy)_3$ is a very efficient emitter so that device efficiencies cannot be increased that strongly by a higher internal quantum efficiency of $Ir(MDQ)_2(acac)$ [12]. Therefore, the reduction of triplet–triplet annihilation (TTA) in the EML is the most reasonable explanation. Excitons which have been transferred to the few

Table 1
Characteristics of the five fabricated OLEDs at a luminance of 1000 cd/m^2.

OLED	V (V)	EQE (%)	Lum. eff. (lm/W)	CIE x/y
10:0.3	5.9	2.87	4.2	0.46/0.51
10:0.6	5.9	2.93	4.2	0.51/0.47
10:1	5.8	3.97	5.0	0.53/0.45
10:3	5.8	4.84	5.0	0.58/0.41
Mixt. 10:1	5.9	3.32	4.7	0.47/0.50

$Ir(MDQ)_2(acac)$ molecules are located on the lowest triplet level in the EML. Since the red concentration is so low, the diffusion of these excitons is hindered compared to the ones still remaining on $Ir(ppy)_3$. The more excitons are transferred to $Ir(MDQ)_2(acac)$ the less they diffuse and encounter each other thus, reducing TTA. Table 1 gives an overview of the OLEDs' characteristics at a luminance of 1000 cd/m^2.

However, the biggest advantage of this combined evaporation of both dyes is the rate control. In the case of classical co-evaporation the rate of the dye with the lowest triplet level has to be very small compared to the second emitter and especially the matrix material. Only then a spectrum can be reached in which both dye peaks are nearly balanced. This can be seen in Fig. 7 where already a concentration of 1% $Ir(MDQ)_2(acac)$ results in a dominating orange-red emission. This asymmetry in the detection of evaporation rates and the subsequent temperature control of the evaporation sources can be difficult, expensive and potentially lowering the overall yield. A doping concentration of 0.3% is already close to the limit of reliable processability in an evaporation machine with a rate detection by oscillating crystals and a simple geometry. In case of the mixed evaporation, the rate of the dye source is significantly higher since the difference in the dyes' concentrations does not need to be monitored but is determined by the weight ratio within the crucible. This allows for simpler machine layouts and an easier process control for the production of organic light-emitting diodes which would result in higher yield and lower cost.

4. Conclusion

In summary, we have compared two different production techniques leading to co-doped emission layers on glass as well as in OLEDs. The alternative approach of evaporating a mixture of two dyes from one source gives results similar to the classical one which uses an individual source for each dye. Using this technique, the ratio between the two emitters in the layer is determined by the relative concentration within the evaporation crucible which makes it easier to control a high mixing ratio. The resulting spectra show that both dye moieties are present and work efficiently in an emission layer, even though the evaporation temperatures of the dyes are very different. This holds several advantages for production as the evaporation can be simpler and cheaper compared to the classical method. On the other hand, the composition of the mixture in the crucible changes constantly due to the different evaporation temperatures of the two dyes. This results in the reproducibility of the layers still being an issue.

Acknowledgment

The work leading to these results has received funding from the European Community's Seventh Framework Program under Grant Agreement No. FP7-224122 (OLED 100.eu-project).

References

[1] Y. Sun, N.C. Giebink, H. Kanno, B. Ma, M.E. Thompson, S.R. Forrest, Nature 440 (2006) 908.
[2] J. Kido, H. Shionoya, K. Nagai, Appl. Phys. Lett. 67 (1995) 2281.
[3] B.W. D'Andrade, R.J. Holmes, S.R. Forrest, Adv. Mater. 16 (2004) 624.
[4] T. Nakayama, K. Hiyama, K. Furukawa, H. Ohtani, SID Symposium Digest of Technical Papers, Long Beach, 2007, p. 101.
[5] A. Werner, M. Burghart, S. Murano, O. Schneider, T. Stübinger, M. Limmert, J. Blochwitz-Nimoth, SID Symposium Digest of Technical Papers, San Francisco, 2006, p. 1099.
[6] G. Schwartz, K. Fehse, M. Pfeiffer, K. Walzer, K. Leo, Appl. Phys. Lett. 89 (2006) 083509.
[7] S. Reineke, F. Lindner, G. Schwartz, N. Seidler, K. Walzer, B. Lüssem, K. Leo, Nature 459 (2009) 234.
[8] B. Ma, P.I. Djurovich, S. Garon, B. Alleyne, M.E. Thompson, Adv. Funct. Mater. 16 (2006) 2438.
[9] T.-W. Lee, J.H. Park, O.O. Park, J. Lee, Y.C. Kim, Opt. Mater. 30 (2007) 486.
[10] G. He, M. Pfeiffer, K. Leo, M. Hofmann, J. Birnstock, R. Pudzich, J. Salbeck, Appl. Phys. Lett. 85 (2004) 3911.
[11] G. Schwartz, S. Reineke, T.C. Rosenow, K. Walzer, K. Leo, Adv. Funct. Mater. 19 (2009) 1319.
[12] Y. Kawamura, K. Goushi, J. Brooks, J.J. Brown, H. Sasabe, C. Adachi, Appl. Phys. Lett. 86 (2005) 071104.

single more flexible polymers such as polystyrenesulfonate, nanostructured surfaces were applied [10], since flexible polymers, including alkylated polythiophenes, tend to collapse or aggregate [11], causing significant heterogeneities in sub-monolayer films. Due to the notorious difficulty to fabricate ultrathin (sub-monolayer range) semiconducting polymer films, detailed investigations on the coverage dependent evolution of electrode Φ and valence electronic energy levels for such polymers are rare [12]. On the other hand, spin coating is a well suited method for preparing polymer films of 10 nm thickness and beyond. In principle, one could use thicker conjugated polymer films for evaluating the energy level alignment under the assumption that the energy levels throughout the semiconductor layer are constant as function film thickness, i.e., no band bending occurs. Nonetheless, clearly discriminating between these two competing effects is complicated if actual polymer film thickness and homogeneity are not well established [13]. It is thus still uncertain to what extent an interface dipole determines polymer/electrode energetics and whether it can clearly be delineated from band bending.

In the present study, we investigate the energy level alignment at a prototypical semiconductor polymer/polymer electrode interface of direct relevance for organic photovoltaics with the polymeric donor poly(3-hexylthiophene) (P3HT) and the intrinsically conductive polymer poly(ethylenedioxythiophene):poly(styrenesulfonate) (PEDT:PSS) as electrode. We focus on the initial stage of interface formation by measuring Φ and the valence electronic structure with ultraviolet photoelectron spectroscopy for defined P3HT coverage from the submonolayer regime to thick films. Clear evidence for the formation of an abrupt interface dipole between the P3HT monolayer and PEDT:PSS is found.

2. Experimental details

Indium-tin-oxide (ITO) coated glass (sheet resistance 15–30 Ω) was used as substrate. ITO coupons were cleaned by sonication in acetone and isopropanol, followed by 20 min UV/ozone exposure in ambient. PEDT:PSS (Al4083, H.C. Stark GmbH & Co. KG) was spin coated from aqueous dispersion at 1500 rpm and dried at 200 °C for 5 min in ambient atmosphere. P3HT (Aldrich, M_n ~64,000 g/mol) was spin coated (3000 and 1500 rpm) in inert atmosphere from chloroform solution with concentrations of 0.5, 1 and 2 mg/ml to vary film thickness. The chemical structures of the polymers are shown in Fig. 1. Ultraviolet photoelectron spectroscopy (UPS) and X-ray photoelectron spectroscopy (XPS) measurements were performed at the end station SurICat (beamline PM4) at the synchrotron light source BESSY II (Berlin, Germany). Spectra were collected with a hemispherical electron energy analyzer (Scienta SES 100) using an excitation photon energy of 30 eV for UPS and 620 eV for XPS. The secondary electron cutoff (SECO) spectra were recorded with a sample bias of −10 V to clear the analyzer work function. The error of binding energy and work function values reported below is estimated to be smaller than ±0.05 eV. After UPS

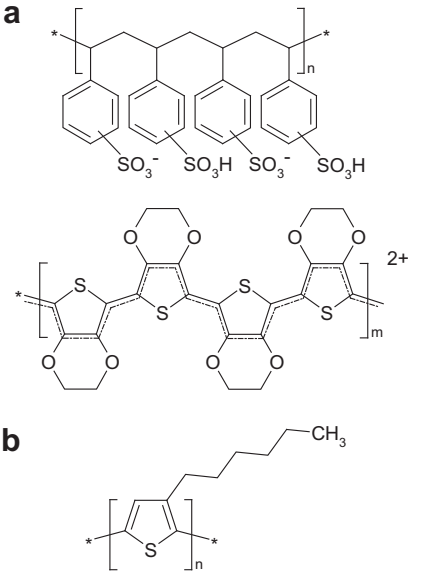

Fig. 1. Chemical structure of (a) PEDT:PSS and (b) P3HT.

and XPS measurements samples were washed in 25 ml chloroform for 10 s at ambient atmosphere to reduce the thickness of the P3HT layer to the monolayer regime. A second series of samples were annealed *in situ* at ~120 °C for 30 min. Annealed samples were also washed subsequently in order to reduce the film thickness.

To determine the thickness of P3HT films the optical absorption at 550 nm wavelength was used in conjunction with atomic force microscopy (AFM) thickness measurements. For this purpose, P3HT films were spin coated on fused silica with various thicknesses and the absorbance was measured using standard UV–vis spectroscopy (Perkin Elmer, Lambda 650). The film thickness was determined by measuring the step height across a mechanical scratch within the film with an AFM (Veeco Multimode). The slope of a linear fit of absorbance *versus* film thickness yielded a P3HT absorption coefficient at 550 nm of 0.009(4) nm^{-1}. The thickness of P3HT films used for UPS was estimated measuring the absorbance at 550 nm of control samples prepared under identical preparation conditions. The absorbance of control the samples was measured right after preparation to avoid bleaching in ambient conditions. The absorbance of the ITO/PEDT:PSS substrates was measured before spin coating P3HT for every individual sample to establish reliable background spectra for each P3HT film. The thickness of washed ultrathin films was additionally confirmed by evaluating the intensity of the S2p core level signal of the PEDT:PSS substrate in XPS. The P3HT film thickness was calculated assuming an exponential decrease of the substrate signal with increasing P3HT coverage and an elastic mean free path for photoelectrons of 2 nm [14]. The results on P3HT thickness were in good agreement with the values obtained from the absorbance measurements within a maximum error of 25% for ultrathin P3HT films. The main error cause is most likely an inhomogeneous P3HT coverage on top of PEDT:PSS in the

ultrathin (ca. monolayer) regime. Overall, P3HT films were homogeneous, with surface roughness values below 1.4 nm at all thicknesses as determined by AFM (see Supplementary information). Comparable surface roughness was measured for pristine PEDT:PSS films.

3. Results and discussion

The presentation of data and their discussion is organized as follows. First, we discuss the pristine PEDT:PSS surface properties and revisit the overall electronic structure of a thick (20 nm) P3HT film. Subsequently, we turn towards thinner and ultrathin P3HT films and their electronic structure on PEDT:PSS.

The work function (Φ) of pristine PEDT:PSS was 4.70 eV (Fig. 2a). To quantify the influence of the P3HT solvent alone on the conductive polymer Φ a pristine PEDT:PSS film was exposed to chloroform by mimicking a spin-coating process. This yielded an increase of Φ to 4.90 eV (Fig. 2b), which is most likely the result of changes in the surface morphology of PEDT and PSS, which is known to strongly affect Φ [15]. In addition, chloroform treatment may aid the removal of residual water from PEDT:PSS, which also increases Φ [15]. In the following, we thus refer all Φ changes due to P3HT deposition to this higher value of 4.90 eV because it includes the effect of the P3HT solvent on the results.

Representative UPS SECO and valence spectra of a 20 nm P3HT film on PEDT:PSS are shown in Fig. 2c and d. The intense peak centered at ca. 3 eV binding energy in the valence region is dominated by emission from a localized π-band. The comparably flat feature between 0.25 and 2.5 eV is due to emission from the delocalized frontier π-band of P3HT [16]. The low binding energy onset of this band at 0.25 eV below the Fermi-level (E_F) defines the valence band maximum. The sample Φ is reduced to 4.35 eV upon P3HT film deposition, and the P3HT ionization energy (IE) is 4.60 eV, obtained by adding the energy difference between the valence band onset and E_F (i.e., the hole injection barrier) to Φ. Because the IE of P3HT is smaller than Φ of the substrate, hypothetical vacuum level alignment at the interface would position part of the filled valence band states above E_F, corresponding to a non-equilibrium situation. Consequently, electrons from P3HT are transferred to PEDT:PSS and an "interface dipole" (ID; equivalent to a change of sample Φ) develops. This interfacial charge transfer induces an electric field that moves the electronic states of P3HT below E_F, thus limiting further charge transfer and pinning of the P3HT levels relative to E_F. In a simple approximation, the ID might be estimated as the difference between Φ of PEDT:PSS (4.9 eV) and IE of P3HT (4.6 eV), yielding 0.3 eV in the present case. In contrast, the measured ID for the 20 nm thick P3HT film is 0.55 eV (*cf.* Fig. 2b and c). The discrepancy of 0.25 eV can be explained by the model that suggests that pinning does not occur directly at the valence band onset of the semiconducting polymer but at the positive polaron levels that result on P3HT due to electron transfer to PEDT:PSS [17,18]. Thus pinning should occur at the positive polaron level, which was proposed to be in the gap of the organic semiconductor due to relaxation of the conjugated system upon charging, typically a few 100 meV above the valence band onset of the neutral polymer [19–22]. The interfacial charge transfer between P3HT and PEDT:PSS might be written, in analogy to the ID mechanism proposed for pentacene and PEDT:PSS [13]:

$$PEDT^+ + PSS^- + P3HT^0 \rightarrow PEDT^0 + PSS^- + P3HT^+ \qquad (1)$$

where the PSS^- moieties counterbalance the charge of the PEDT and P3HT positive polarons. An alternative model to pinning at defined polaron levels takes into account that real polymer films contain conformational and structural defects, which lead to a broadening of the effective density of states compared to an idealized defect-free single crystal. This gives rise to intra-gap states between the valence band maximum and E_F, whose density may be well below the sensitivity of the present experimental setup [23,24]. Consequently, pinning may occur at these states and will as well involve electron transfer from P3HT to PEDT:PSS.

However, the above discussion is only relevant if all energy levels in P3HT are flat across the entire film thickness and the valence band binding energy and vacuum level position measured at the surface of the 20 nm thick film represent those at the interface. For instance, any effects due to band bending cannot be captured in such an experiment. The above assumption is not readily justified as numerous reports suggest that band bending in organic semiconductor films exits [7,25–29]. Because UPS measurements are very surface sensitive (~1 nm information depth) no information about the position of the energy levels neither in the bulk nor at the interface of the P3HT film with PEDT:PSS are available without decreasing the film thickness significantly below 20 nm. While preparing defined thin films with small molecular materials *via* sublimation is straight forward, the controlled formation of ultrathin polymer films *via* spin coating is highly challenging. For our further investigations of the intimate

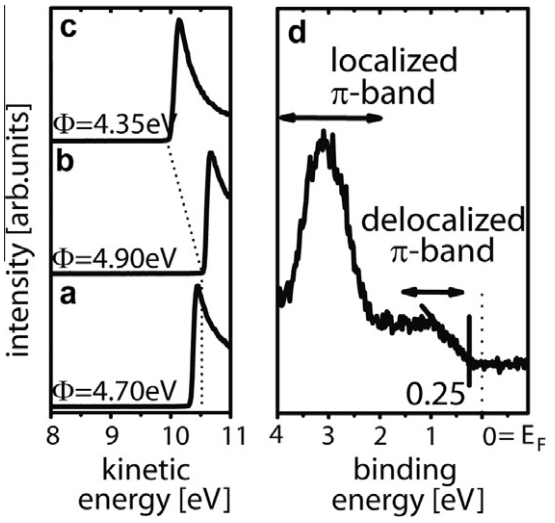

Fig. 2. Secondary electron cutoff of (a) pristine PEDT:PSS, (b) PEDT:PSS washed with chloroform, and (c) 20 nm P3HT on PEDT:PSS. (d) Valence band UPS spectrum of 20 nm P3HT on PEDT:PSS.

P3HT/PEDT:PSS interface with UPS we prepared samples by spin coating highly diluted solutions and also by employing additional solvent-washing for realizing ultrathin P3HT films with ca. 1 nm thickness, i.e., in the monolayer range. We investigated such samples with and without annealing in UHV at 120 °C for 30 min to (i) eliminate residual solvents and (ii) to investigate possible influences of annealing-induced polymer conformation changes. Fig. 3 shows UPS spectra of annealed P3HT films on PEDT:PSS with various thickness, and apparently the energy level positions vary as a function of film thickness. This observation already justifies the critical assessment of the reliability to derive interface energetic from just measuring rather thick polymer films from above. For instance, the vacuum level (and therefore Φ) and the position of the valence band onset remained constant for P3HT films in the thickness range 20–3.6 nm, but a significant decrease of Φ by ~0.20 eV and a shift of the valence band onset by ~0.15 eV to lower binding energy were observed for ultrathin films. Note that the peak maximum of the localized π-band shifted to lower binding energy by almost the same amount as the valence band onset (Fig. 3b). To check whether the annealing step impacted the crystallinity and/or morphology in our P3HT films, possibly influencing the electronic properties [30], we measured analogous samples without annealing. These spectra exhibited fully analogous shifts of the vacuum level and of the valence band, with marginally different absolute values (typically within 0.05 eV) for the individual samples (Fig. 4). Therefore, significant morphological changes that would compromise our results can be ruled out.

Fig. 5 summarizes the evolution of sample Φ and the valence band onset position of P3HT films as function of film thickness. As can be seen in Fig. 5a the qualitative trend of Φ and the valence band onset are different. While Φ exhibits a gradual decrease for increasing P3HT thickness (up to 2 nm where saturation sets in), the valence band onset position exhibits an abrupt shift by 0.15 eV above film thicknesses of 2 nm. Considering that the distance between two P3HT chains perpendicular to the π–π stacking direction is ~1.6 nm [16], our ultrathin films (<2 nm) are in the monolayer or even sub-monolayer regime. Therefore, pinholes in the P3HT layers or even extended uncovered PEDT:PSS areas may exist. Because UPS measures Φ area-averaged as long as the inhomogeneous surface patches are not extending over several 100 nm, the measured Φ is an average of that of pristine PEDT:PSS and that of P3HT covered areas, leading in the present case to a gradual decrease of Φ with increasing coverage. Once full monolayer coverage is reached, sample Φ should remain constant for higher film thickness in this scenario, which we indeed observe beyond 2 nm P3HT thickness (Fig. 5a). This kind of behavior was observed so far only for small molecules evaporated on PEDT:PSS or clean metal surfaces [3,15,23,31], whereas band bending was evoked for polymers when vacuum level shifts were observed after deposition on electrode materials [7,29]. Note that the concept of band bending within a monolayer of a polymer cannot be applied meaningfully. The absence of band bending in the thickness region below 2 nm can be ruled out formally because of the abrupt shift of the valence band onset position while Φ decreases continuously. If band bending were occurring, all energy levels, thus also the valence band and Φ should shift in parallel.

The charge transfer area-density at the interface, needed to create typically occurring vacuum level shifts, is in general relatively low. For this reason the positive polaron pinning level that is created in P3HT because of the predicted charge transfer contributes only very little to the UPS spectra and could not be directly detected yet. To estimate the transferred charge at the interface per area for our work function change $\Delta\Phi$ of 0.55 eV between pristine PEDT:PSS and at least a full P3HT monolayer, we calculate the dipole density using the Helmholtz equation:

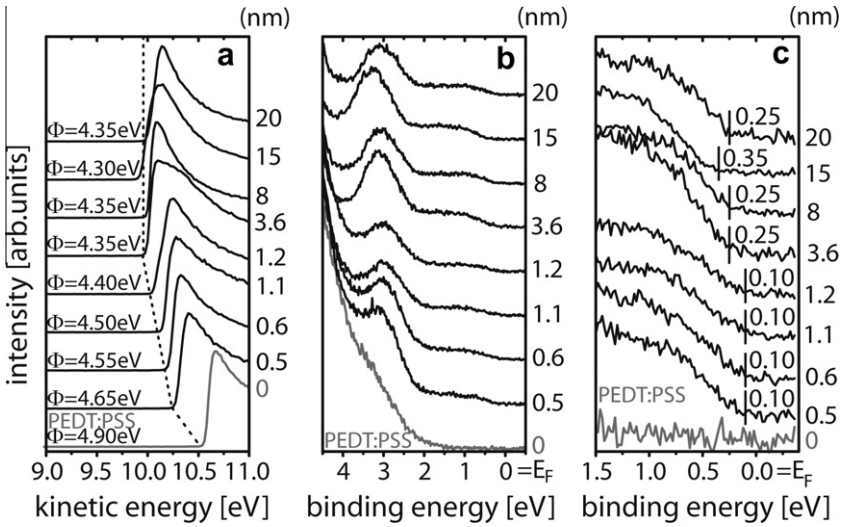

Fig. 3. UPS spectra of P3HT films with varying thickness (given at the right side of axes) on PEDT:PSS after *in situ* annealing at 120 °C for 30 min: (a) SECO, (b) valence region and (c) zoom on the valence band onset.

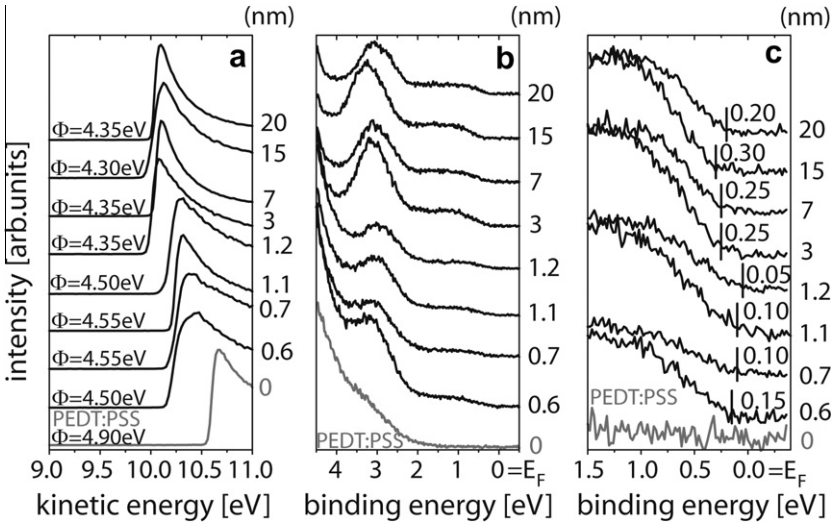

Fig. 4. UPS spectra of not-annealed P3HT films with varying thickness (given at the right side of axes) on PEDT:PSS: (a) SECO, (b) valence region and (c) zoom on the valence band onset.

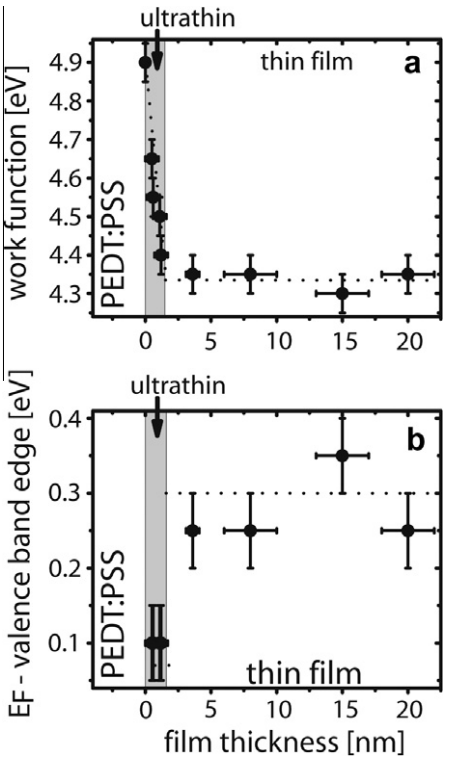

Fig. 5. Work function (a) and position of the low binding energy valence band onset (b) as a function of P3HT thickness on PEDT:PSS (data for annealed samples from Fig. 3).

$$\Delta\Phi = \frac{e \cdot n \cdot |\vec{\mu}|}{\varepsilon_0 \varepsilon_r} \tag{2}$$

with e the elementary charge, n the surface dipole density, $|\vec{\mu}|$ the dipole moment perpendicular to the surface, ε_0 the vacuum permittivity, and ε_r the relative dielectric constant. With $|\vec{\mu}| = 1.6 \times 10^{-28}$ Cm (charge separation of one electron over a distance of 1 nm) and setting ε_r at 3, which is a commonly accepted value for P3HT, one obtains $n = 0.1\ \mathrm{nm}^{-2}$. If we assume a crystalline P3HT film with the π–π stacking direction parallel to the substrate surface the density of thiophene units amounts to $n_{th} = 11\ \mathrm{nm}^{-2}$ [16,31,32]. Taking additionally into account that the polaron state is approximately delocalized over 4–10 thiophene units [33,34], roughly 3–10% of the thiophene units are involved in polaron state formation, which should be detectable with UPS if they indeed form intra-gap states. In fact, UPS spectra of ultrathin films in the sub-monolayer regime exhibit spectral changes of the valence band that might correspond to such additional intensity in the nominally empty energy gap. Fig. 6 compares the valence spectra of 20 and 0.5 nm thick P3HT films. In this plot, the valence band onsets are aligned to 0 eV binding energy and the intensity at 1.5 eV binding energy is normalized to 1. In direct

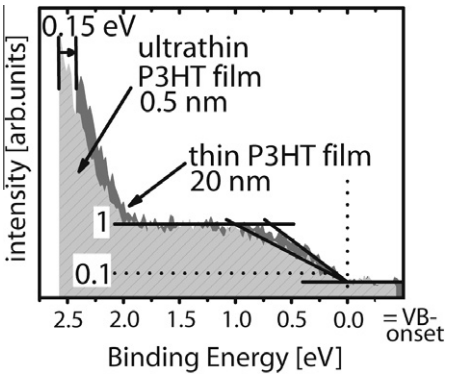

Fig. 6. Comparison of valence band UPS spectra of P3HT films on PEDT:PSS with 20 nm and ca. 0.5 nm film thickness. The intensity at 1.5 eV was normalized to one and the low binding energy valence band onset was set to 0 eV binding energy.

comparison, the 0.5 nm film appears to have a wider delocalized π-band and a smaller slope at its low binding energy onset. This observation, together with the smaller absolute binding energy of ultrathin film valence bands with respect to E_F (by ca. 0.15 eV, *cf*. Fig. 5b) might indicate the existence of polarons formed by the charge transfer reaction between the PEDT:PSS substrate and P3HT.

4. Conclusions

Ultraviolet photoelectron spectroscopy was used to investigate the energy level alignment at the P3HT/PEDT:PSS interface from sub-monolayer to multilayer coverage, using solution processing. Sample Φ decreased monotonically from 4.90 (pristine PEDT:PSS) to 4.35 eV for a monolayer-equivalent of P3HT (ca. 2 nm) and remained constant for larger semiconducting polymer thickness. In contrast, a sudden binding energy increase by ca. 0.15 eV of the valence band onset at the monolayer-multilayer transition was observed. This is interpreted by a P3HT/PEDT:PSS charge exchange reaction that lowers Φ as a function of P3HT coverage up to a full monolayer. This is in accordance with the changes of the valence spectral signatures that occur upon monolayer completion. Consequently, these observations are in full analogy to the established behavior of evaporated small organic molecule/electrode interfaces with an interface dipole, where the first molecular layer determines Φ while the valence level position is determined by interfacial chemistry. The thorough use of ultrathin polymer films allow us to rule out that effects in relation to band bending play a role upon intimate interface formation between a conductive polymer electrode and semiconducting polymers. Band bending may occur at polymer thicknesses well beyond the monolayer, but the initial Φ change of electrodes upon polymer monolayer formation should not be evaluated as classical doping-related space charge effects.

Acknowledgements

This work was supported by the SPP1355 (DFG). The authors thank G. Heimel and B. Bröker for helpful discussions and support, and A. Elschner (H.C. Starck) for kindly providing PEDT:PSS.

Appendix A. Supplementary data

Supplementary data associated with this article can be found, in the online version, at doi:10.1016/j.orgel.2011.03.005.

References

[1] S. Braun, W.R. Salaneck, M. Fahlman, Energy-level alignment at organic/metal and organic/organic interfaces, Adv. Mater. 21 (2009) 1450–1472.
[2] W.R. Salaneck, S. Stafstrom, J.L. Brèdas, Conjugated Polymer Surfaces and Interfaces: Electronic and Chemical Structure of Interfaces for Polymer Light Emitting Devices, Cambridge University Press, 1996.
[3] H. Ishii, K. Sugiyama, E. Ito, K. Seki, Energy level alignment and interfacial electronic structures at organic/metal and organic/organic interfaces, Adv. Mater. 11 (1999) 605–625.
[4] I.G. Hill, A.J. Makinen, Z.H. Kafaf, Distinguishing between interface dipoles and band bending at metal/tris-(8-hydroxyquinoline) aluminium interfaces, Appl. Phys. Lett. 77 (2000) 1825–1827.
[5] A. Kahn, N. Koch, W. Gao, Electronic structure and electrical properties of interfaces between and π-conjugated molecular films, J. Polym. Sci. Part B: Polym. Phys. 41 (2003) 2529–2548.
[6] G.M. Ranger, O.T. Hoffmann, L. Romaner, G. Heimel, B. Bröker, R.-P. Blum, R.L. Johnson, N. Koch, E. Zojer, F4TCNQ on Cu, Ag, and Au as prototypical example for a strong organic acceptor on coinage metals, Phys. Rev. B 79 (2009) 165306.
[7] A.J. Cascio, J.E. Lyon, M.M. Beerbom, R. Schlaf, Y. Zhu, S.A. Jenekhe, Investigation of a polythiophene interface using photoemission spectroscopy in combination with electrospray thin-film deposition, Appl. Phys. Lett. 88 (2006) 062104.
[8] A.D. Schlüter, J.P. Rabe, Dendronized polymers: synthesis, characterization, assembly at interfaces, and manipulation, Angew. Chem. Int. Ed. 39 (2000) 864.
[9] S.S. Sheiko, M. Möller, Visualization of macromolecules – A first step to manipulation and controlled response, Chem. Rev. 101 (2001) 4099.
[10] N. Severin, I.M. Okhapkin, A.R. Khokhlov, J.P. Rabe, Adsorption of polyelectrolyte molecules to a nanostructured monolayer of amphiphiles, Nano Lett. 6 (2006) 1018.
[11] N. Kiriy, E. Jähne, H.-J. Adler, M. Schneider, A. Kiriy, G. Gorodyska, S. Minko, D. Jehnichen, P. Simon, A.A. Fokin, M. Stamm, One-dimensional aggregation of regioregular polyalkylthiophenes, Nano Lett. 3 (2003) 707.
[12] J. Hwang, E.-G. Kim, J. Liu, J.-L. Bredas, A. Duggal, A. Kahn, Photoelectron spectroscopic study of the electronic band structure of polyfluorene and fluorene–arylamine copolymers at interfaces, J. Phys. Chem. C 111 (2007) 1378–1384.
[13] H. Ishii, N. Hayashi, E. Ito, Y. Washizu, K. Sugi, Y. Kimura, M. Niwano, Y. Ouchi, K. Seki, Kelvin probe study of band bending at organic semiconductor/metal interfaces: examination of Fermi level alignment, Phys. Stat. Sol. (a) 201 (2004) 1075–1094.
[14] P.J. Cumpson, Estimation of inelastic mean free paths for polymers and other organic materials: use of quantitative structure–property relationships, Surf. Interface Anal. 31 (2001) 23–34.
[15] N. Koch, A. Vollmer, Electrode-molecular semiconductor contacts: work-function-dependent hole injection barriers versus Fermi-level pinning, Appl. Phys. Lett. 89 (2006) 162107.
[16] W.R. Salaneck, O. Inganäs, B. Thémans, J.O. Nilsson, B. Sjögren, J.-E. Österholm, J.L. Brèdas, S. Svensson, Thermochromism in poly(3-hexylthiophene) in the solid state: a spectroscopic study of temperature-dependent conformational defects, J. Chem. Phys. 89 (1988) 4613–4619.
[17] A. Crispin, X. Crispin, M. Fahlman, M. Berggren, W.R. Salaneck, Transition between energy level alignment regimes at a low band gap polymer–electrode interfaces, Appl. Phys. Lett. 89 (2006) 213503.
[18] N. Koch, Organic electronic devices and their functional interfaces, ChemPhysChem 8 (2007) 1438–1455.
[19] J.-L. Brèdas, D. Beljonne, V. Coropceanu, J. Cornil, Charge-transfer and energy-transfer processes in π-conjugated oligomers and polymers: a molecular picture, Chem. Rev. 104 (2004) 4971–5004.
[20] C. Tengstedt, W. Osikowicz, W.R. Salaneck, I.D. Parker, C.-H. Hsu, M. Fahlman, Fermi-level pinning at conjugated polymer interfaces, Appl. Phys. Lett. 88 (2006) 053502.
[21] S. Rentenberger, A. Vollmer, E. Zojer, R. Schennach, N. Koch, UV/ozone treated Au for air-stable, low hole injection barrier electrodes in organic electronics, J. Appl. Phys. 100 (2006) 053701.
[22] S. Braun, W.R. Salaneck, M. Fahlman, Energy-level alignment at organic/metal and organic/organic interfaces, Adv. Mater. 21 (2009) 1450–1472.
[23] N. Koch, A. Elschner, J. Rabe, R. Johnson, Work function independent hole-injection barriers between pentacene and conducting polymers, Adv. Mater. 17 (2005) 330–335.
[24] T. Sueyoshi, H. Fukagawa, M. Ono, S. Kera, N. Ueno, Low-density band-gap states in pentacene thin films probed with ultrahigh-sensitivity ultraviolet photoelectron spectroscopy, Appl. Phys. Lett. 95 (2009) 183303.
[25] T. Shimada, K. Hamaguchi, A. Koma, F.S. Ohuchi, Electronic structures at the interfaces between copper phthalocyanine and layered materials, Appl. Phys. Lett. 72 (1998) 1869.
[26] R. Schlaf, C.D. Merritt, L.A. Crisafulli, Z.H. Kafafi, Organic semiconductor interfaces: discrimination between charging and band bending related shifts in frontier orbital line-up measurements with photoemission spectroscopy, J. Appl. Phys. 86 (1999) 5678.
[27] J.X. Tang, K.M. Lau, C.S. Lee, S.T. Lee, Substrate effects on the electronic properties of an organic/organic heterojunction, Appl. Phys. Lett. 88 (2006) 232103.

[28] Y. Gao, H. Ding, H. Wang, D. Yan, Electronic structure of interfaces between copper-hexadecafluoro-phthalocyanine and 2,5-bis(4-biphenylyl) bithiophene, Appl. Phys. Lett. 91 (2007) 142112.
[29] J. Hwang, A. Wan, A. Kahn, Energetics of metal–organic interfaces: new experiments and assessment of the field, Mater. Sci. Eng. R 64 (2009) 1–31.
[30] G. Heimel, I. Salzmann, S. Duhm, J.P. Rabe, N. Koch, Intrinsic surface dipoles control the energy levels of conjugated polymers, Adv. Funct. Mater. 19 (2009) 3874–3879.
[31] C.Y. Yang, C. Soci, D. Moses, A.J. Heeger, Aligned rrP3HT film: structural order and transport properties, Synth. Met. 155 (2005) 639–642.
[32] H. Sirringhaus, P.J. Brown, R.H. Friend, M.M. Nielsen, K. Bechgaard, B.M.W. Langeveld-Voss, A.J.H. Spiering, R.A.J. Janssen, E.W. Meijer, P. Herwig, D.M. de Leeuw, Two-dimensional charge transport in self-organized, high-mobility conjugated polymers, Nature 401 (1999) 685–688.
[33] H.A. Mizes, E.M. Conwell, Polarons and their stability in poly(phenylenevinylene), Synth. Met. 68 (1995) 145–151.
[34] V.M. Geskin, A. Dkhissi, J.L. Brèdas, Oligothiophene radical cations: polaron structure in hybrid DFT and MP2 calculations, Int. J. Quantum Chem. 91 (2003) 350–354.

systemically. We discuss two types of TEWOLEDs according to the anode: (1) metal and (2) 1D metallic–dielectric photonic crystal. Our results indicated that TEWOLEDs could be used as lighting devices with high CRI and stable angular color uniformity or displays with wide color gamut by carefully designing the structure of the devices.

2. Review of current developments in TEWOLEDs

Extensive efforts have focused on eliminating the microcavity effects in TEWOLEDs. Transparent conductive oxide like ITO and semitransparent metals with or without light outcoupling layer are commonly used in TEWOLEDs. In 2005, Kanno et al. [23] fabricated a TEWOLED with Ni anode and ITO cathode. The power efficiency and the CIE coordinates of the device are 9.8 lm/W ± 1.0 lm/W and (0.42, 0.39), respectively. There is only weak angular dependence in the spectra, and the CIE coordinates shifted by (0.02, −0.01) from 0° to 60°.

However, the ITO sputtering technology is hard to control and more researchers would like to use metal films as cathodes. In 2005, Hsu et al. [17] reported a TEWOLED employing a SnO_2 index-matching layer on the Ca (5 nm)/Ag (15 nm) cathode. A near-white light emission (0.31, 0.47) with an efficiency of 22.2 cd/A is obtained and the emission shows less angular dependence. In 2007, Zhu et al. [18] reported a TEWOLED with Ca (6 nm)/Au (15 nm)/Alq_3 (50 nm) cathode. The device shows a maximum power efficiency of 12.8 lm/W. There is less angular dependence in the spectra, and the CIE shifted by (0.01, −0.03) from 0° to 60°. In 2008, Lee and Tseng [24] reported a nearly Lambertian TEWOLED with low-reflectivity molybdenum (Mo) anode and Al (1.5 nm)/Ag (17.5 nm)/N,N′-bis-(1-naphthyl)-N, N′diphenyl-1,1-biphenyl-4,4′diamine (NPB, 30 nm) as cathode. A white emission with efficiency of 3.7 cd/A and CIE coordinates of (0.33, 0.39) is obtained, and the emission shows less angular dependence. In 2010, Freitag et al. [12] demonstrated a TEWOLED with Al (60 nm) as anode and Al (1 nm)/Ag (15 nm)/NPB (50 nm) as cathode. The emission shows CIE coordinates of (0.420, 0.407) at approximately 1000 cd/m^2, the power efficiency and color rendering indices (CRI) are 8.0 lm/W and 75.6, respectively. However, the light emission from the device exhibits a rather strong directionality, rather than a Lambertian behavior. Currently, Xie et al. [11] reported a TEWOLED with Cu anode and Al (2 nm)/Ag (18 nm)/4,4′,4″-tris-(3-methylphenyl-phenylamino)-tripheny-lamine (m-MTDATA, 50 nm) cathode. The device reaches high efficiencies of 17.6 lm/W at a current density of 10 mA/cm^2, and low voltage of 4.4 V at 1000 cd/m^2. And the emission shows less angular dependence.

TEWOLEDs utilizing microcavity effect also have been reported. In 2008, Kim et al. [25] reported the TEWOLED with Ag/ITO anode and Al (2.0 nm)/Ag (20 nm)/ITO (63 nm)/SiO_2 (42 nm) cathode. By varying the microcavity length of TEOLEDs through the variation of the anode ITO thickness and, by optimizing the dopant DCJTB concentration and the thickness of the emissive 4,4′-bis(2,2′-diphenylvinyl)-1,1′-biphenyl (DPVBi) layer, an EL spectrum composed of two complementary wavelengths close to white light could be obtained. But the light-emitting efficiency was merely about 1.4 lm/W and there is no report on the angular dependence characteristics in the EL spectra.

In 2009 and 2010, we reported the microcavity TEWOLED with 1D metallic–dielectric photonic crystal anode and Al (1 nm)/Ag (20 nm)/MoO_x (35 nm) cathode [13,26]. By simply adjusting the thickness of the dielectric layer, multiple-peak TEWOLEDs with EL peaks at desired wavelengths were achieved. However, the emission is obvious angular dependence, for example, the CIE coordinates shifted by (0.06, 0.01) from 0° to 60° in a two-peak TEWOLED.

In 2010, Wang et al. [27] reported a microcavity inverted TEWOLED with Al (100 nm) anode and Ag (24 nm)/NPB (80 nm) cathode. The device showed an efficiency of 5.6 cd/A and the CRI is 68. However, the emission is severe angular dependence, and the CIE coordinates shifted by (0.06, 0.1) from 0° to 60°.

3. Results and discussion

The approximate theoretical spectrum for emission in the microcavity device can be calculated following the approach of Deppe et al. [28]. The emission properties of TEWOLEDs are investigated using the optical module of the OLED simulation software SimOLED [29].

In our simulation, two kinds of devices with the following configurations were prepared: Blue–yellow (BY) device: anode/MoO_x (1.5 nm)/m-MTDATA (28 nm)/NPB (10 nm)/DPVBi (15 nm)/4,4-N,N-dicarbazole-biphenyl (CBP, 5 nm)/CBP:bis(2-(2-fluorphenyl)-1,3-benzothiozolato-N,C2′) iridium (acetylacetonate) [$(F–BT)_2Ir(acac)$] (7 nm)/4,7-diphenyl-1,10-phenanthroline (Bphen, 30 nm)/cathode; Red–green–blue (RGB) device: anode/MoO_x (1.5 nm)/m-MTDATA (25 nm)/NPB (10 nm)/DPVBi (15 nm)/CBP (2 nm)/CBP:$Ir(ppy)_3$ (5 nm)/CBP:$Ir(piq)_2(acac)$ (5 nm)/4,7-diphenyl-1,10-phenanthroline (Bphen, 35 nm)/cathode. According to the energy levels of the materials, we assume that the excitons will form at the interfaces of NPB/DPVBi and CBP:$(F–BT)_2Ir(acac)$/Bphen in BY device, and at the interfaces of NPB/DPVBi, CBP/CBP:$Ir(ppy)_3$, and CBP:CBP:$Ir(piq)_2(acac)$/Bphen in RGB device. The refractive index data for metals were taken from the literature [30]. The optical constants of the organic materials and light outcoupling layers were measured using a variable angle spectroscopic ellipsometer [31].

3.1. Metal–metal microcavity TEWOLED

3.1.1. Influence of different metals on the performance of TEWOLED

The calculations have been performed for six metals (Ag, Au, Al, Mo, Cu and Sm) in BY devices. Ag, Au, Al, Mo and Cu were considered for the bottom anode, and LiF/Al (1 nm)/Ag (15 nm), LiF/Al (1 nm)/Au (15 nm) and Sm (30 nm) were considered for the top cathode. Fig. 1 shows the calculated spectra of the BY devices with different anodes and LiF/Al/Ag cathode in a forward direction.

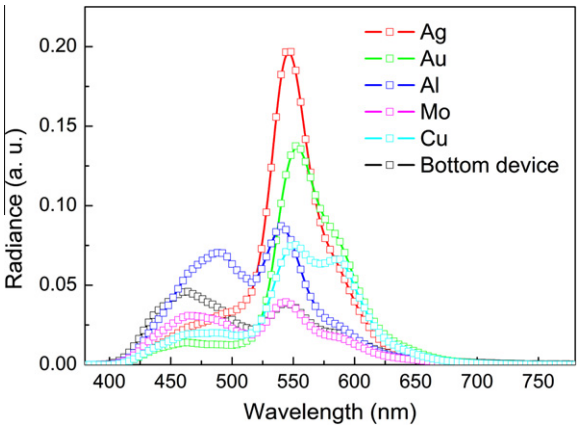

Fig. 1. The calculated spectra of the BY devices with different anodes and LiF/Al/Ag cathode in forward direction.

The spectra of the TEWOLEDs reveal dependence on the anode metals. Only the Mo device shows similar EL spectra with the bottom one. The Ag and Au devices present strongly enhanced yellow emission and suppressed blue emission, while Al device presents enhanced green emission and Cu device presents enhanced red emission. It can be explained by the forward directed cavity emission and the reflection of their anode as shown in Fig. 2. The cavity emission was obtained by considering wavelength-independent intrinsic luminescence spectra of the emitters [12]. The calculated resonant wavelength of Ag, Au, Al, Mo, and Cu devices are 548, 560, 504, 504 and 584 nm, respectively. And Ag, Au, Al, and Cu devices showed strong cavity emission intensity due to the high reflection in the resonant wavelength. The different resonant wavelengths of the devices could be attributed to the different phase changes on the reflection of the metal anodes. Thus, the Ag and Au devices show enhanced yellow emission, Cu device shows enhanced red emission and Al device shows enhanced green emission. Although the resonant wavelength of Mo device is 504 nm, the relatively low reflection of Mo makes a relatively weak cavity emission in this device, thus, the Mo device shows similar EL spectra with the bottom one in the forward direction.

The angular emission characteristics of the TEWOLED with LiF/Al/Ag cathode and Ag anode are shown in Fig. 3. The device shows a strong change in EL spectra with a varying observation angle. The enhanced blue emission and suppressed yellow emission were observed with the increase of the observation angle. And the CIE coordinates shifted by $(0.036, 0.017)$ from 0° to 30° and shifted by $(0.157, 0.366)$ from 0° to 80°. The devices with Au, Al, Mo and Cu anodes also present severe angular dependence. Although the Mo device shows relatively weak microcavity effect, the CIE coordinates also shifted by $(0.017, 0.039)$ from 0° to 30° and shifted by $(0.047, 0.170)$ from 0° to 80°. Besides, the performance of the LiF/Al/Au-cathode TEWOLEDs with different metal anodes is similar to that of the LiF/Al/Au-cathode devices.

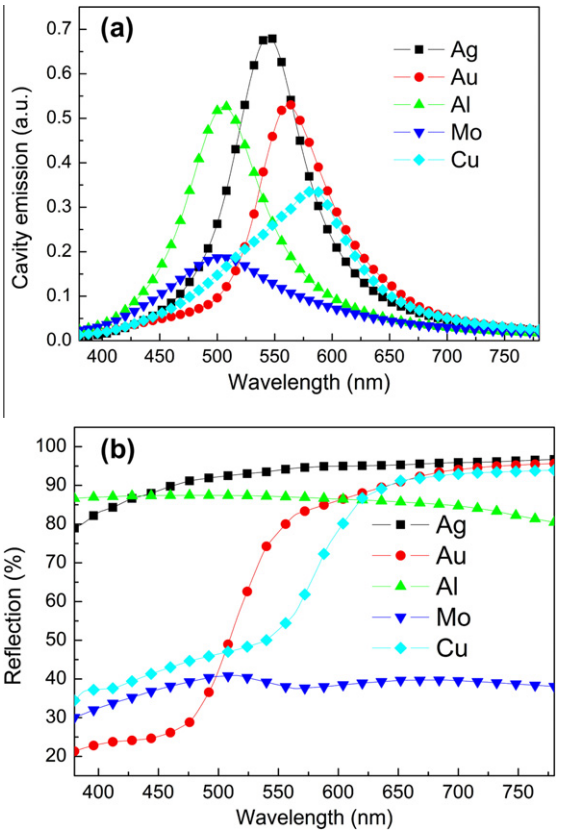

Fig. 2. (a) Forward directed cavity emission of the device, and (b) reflection of the anode materials.

The severe angular dependence characteristics of the above device can be attributed to the high reflection of the cathode as shown in Fig. 4. If using a low reflection metal such as Sm, the angular dependence characteristics of the devices could be meliorated. Fig. 5 shows the calculated EL spectra of the device with Ag anode and Sm cathode. There is no obvious changing on the spectra with a varying observation angle. And the CIE coordinates only shifted by $(0.008, 0.009)$ from 0° to 30° and shifted by $(0.044, 0.024)$ from 0° to 80°. The improvement of the angular dependence characteristics of the device can be attributed to the low reflection and high transmission of the Sm cathode (about 5% and 45% in the visible region).

3.1.2. Influence of light outcoupling layer on the performance of TEWOLED

The angular color uniformity of the TEWOLEDs could be improved by introducing a light outcoupling layer on the top of the cathode. Thomschke et al. [19] had described a numerical simulation of the effect of the light outcoupling layer on the angular emission characteristics of the TEWOLEDs. Here, we present a detailed optical simulation of the light outcoupling layer on the performance of the TEWOLEDs.

Firstly, the influence of different light outcoupling layers according to their reflective index (n) on the performance of the TEWOLEDs was discussed. Low-n material

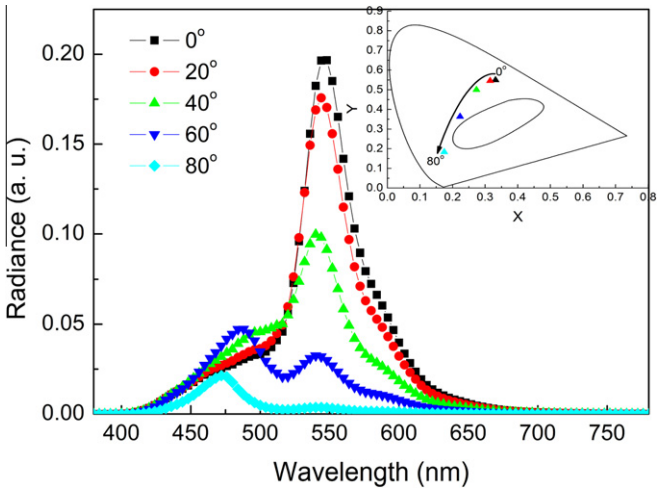

Fig. 3. The angular characteristics of the TEWOLED with LiF/Al/Ag cathode and Ag anode.

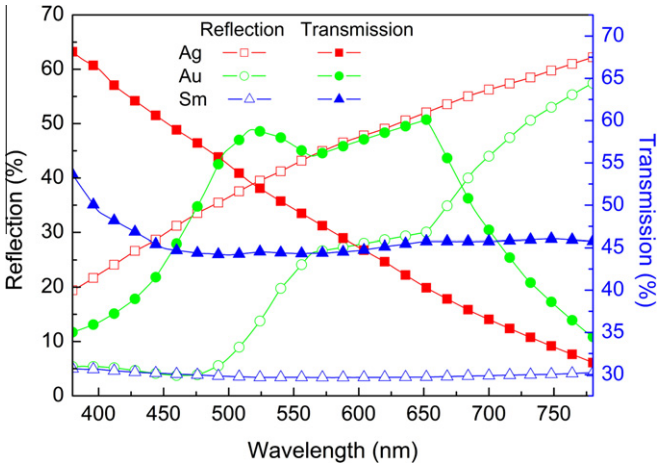

Fig. 4. Reflection and transmission of the cathode materials.

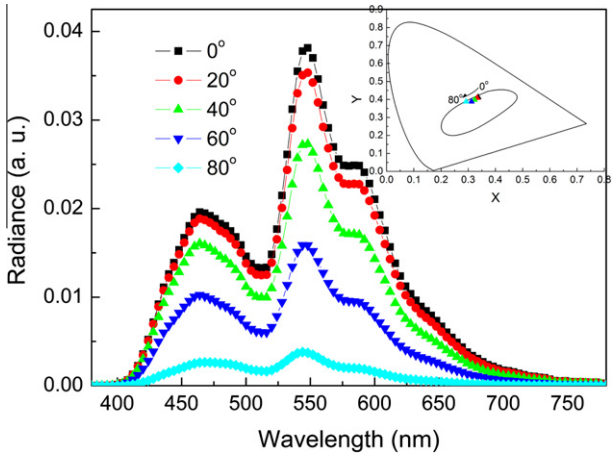

Fig. 5. The calculated EL spectra of the device with Ag anode and Sm cathode.

MgF_2 (~1.37), moderate-*n* material Alq_3 (~1.7–1.85) and high-*n* material MoO_x (~2–2.4) are used as the light outcoupling layers. As an example, the BY device using Ag as cathode and anode is presented. And the thickness of the light outcoupling layer has been optimized. Fig. 6 shows the calculated EL spectra of the BY devices with different light outcoupling layers. The introduction of the light outcoupling layers improved the angular color uniformity, but the improvement level is dependent on the reflective index of the layer. A low-*n* light outcoupling layer shows slight improvement in the angular color uniformity. The color shifted by (0.065, 0.086) for MgF_2 light outcoupling layer, by (0.03, 0.05) for Alq_3 light outcoupling layer, and only by (0.014, 0.018) for MoO_x light outcoupling layer

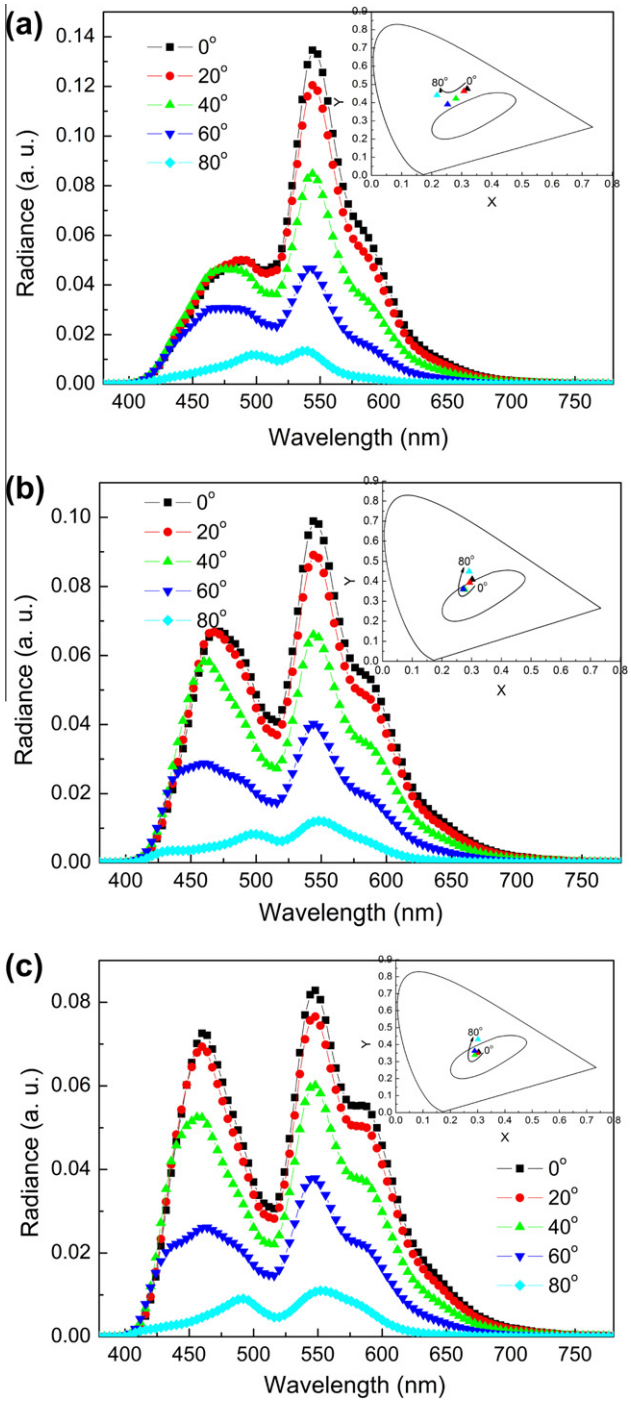

Fig. 6. Calculated EL spectra of the BY devices with (a) MgF_2, (b) Alq_3, and (c) MoO_x light outcoupling layer.

from 0° to 60°. It can be explained by the cavity emission of the devices as a function of the viewing angle as shown in Fig. 7. We can see that the higher the reflective index, the wider the cavity emission spectra are. The wide and flat cavity emission spectra indicated that the microcavity effect in the devices is similar at any wavelength, especially at the peak wavelengths of the device. Beside, the normalized cavity emission spectra of the high-n light outcoupling layer device are relatively angle independent at the viewing angle less than 60°. However, for devices without or with low-n light outcoupling layer, the cavity emission spectra are narrow and a blue shift in resonance wavelength λ_R of 52 nm and 20 nm can be observed. Hence, a high-n light outcoupling layer shows obvious

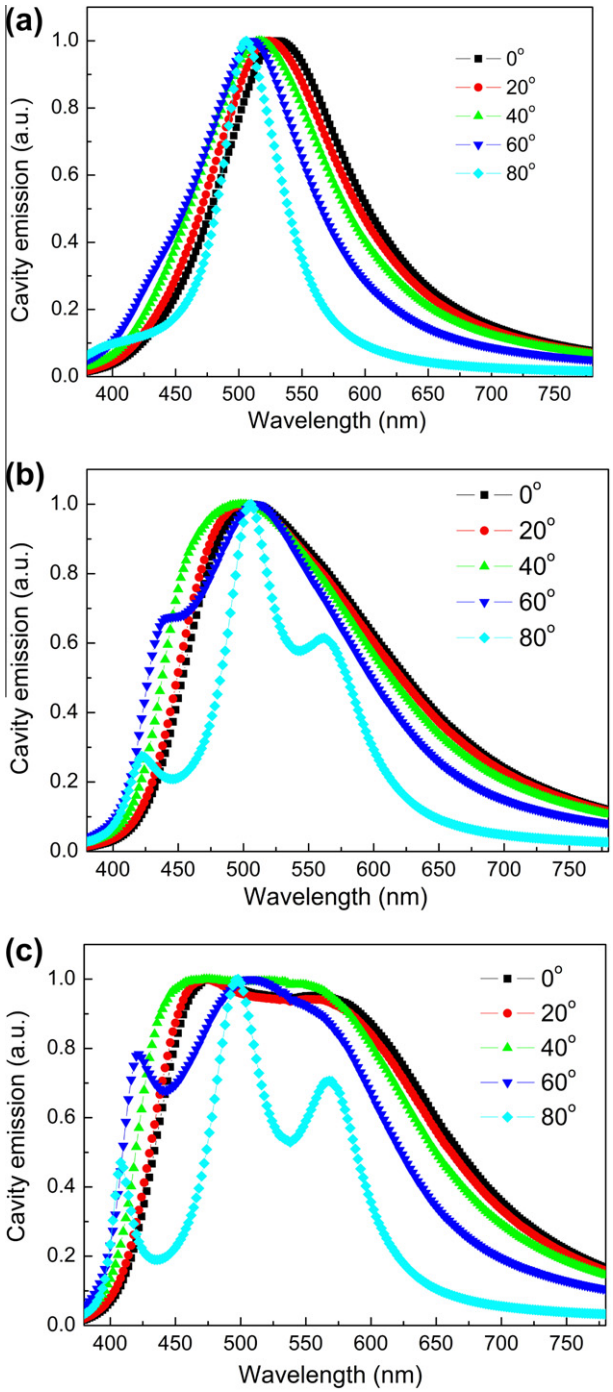

Fig. 7. Cavity emission of the devices as a function of the viewing angle with (a) MgF_2, (b) Alq_3, and (c) MoO_x light outcoupling layer.

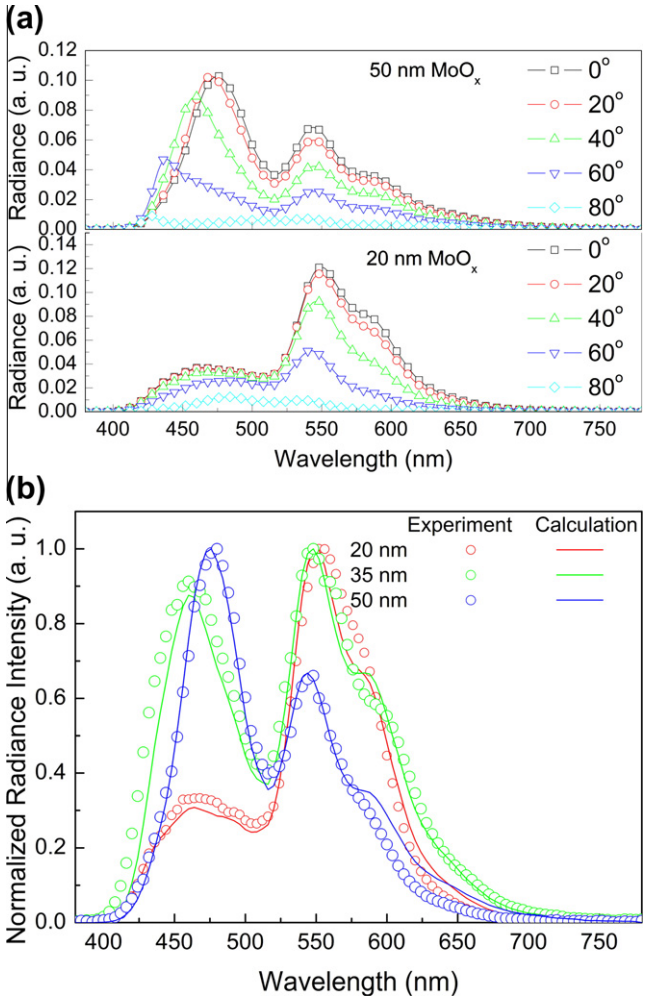

Fig. 8. (a) Calculated EL spectra of the devices with 20- or 50-nm MoO_x light outcoupling layer, and (b) calculated and experimental results of the normalized radiance intensity in forward direction of the TEWOLED.

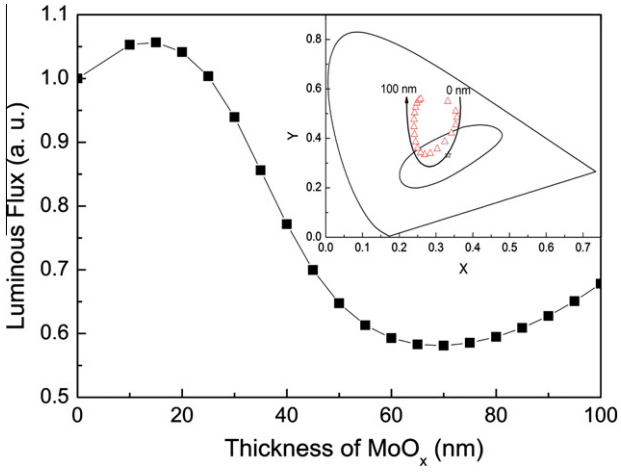

Fig. 9. Normalized luminous flux of the TEWOLED as a function of the thickness of MoO_x layer.

improvement in the angular color uniformity and the corresponding color coordinates of the device are stable with increasing viewing angle.

The thickness of the light outcoupling layer also plays an important role in the angular color uniformity. Fig. 8(a) shows the calculated EL spectra of the BY devices with 20- and 50-nm MoO_x light outcoupling layers at different viewing angle. The blue shift of blue emission in device with 50 nm MoO_x light outcoupling layer and blue shift of yellow emission in device with 20 nm MoO_x light outcoupling layer are observed with increasing viewing angles. The CIE coordinates shift by (0.06, 0.08) for 20-nm MoO_x light outcoupling layer and by (0.09, 0.03) for 50-nm MoO_x light outcoupling layer from 0° to 60°. It also can be explained by the cavity emission of the devices. The cavity emission spectra of the devices with 20 and 50 nm MoO_x light outcoupling layers are narrow. For a device with 20 nm MoO_x light outcoupling layers, λ_R is 564 nm in forward direction and with increasing viewing angle, a blue shift in λ_R of 34 nm from 0° to 60° is observed. In comparison, for a device with 50 nm MoO_x light outcoupling layers, λ_R is 484 nm in the forward direction and with an increasing viewing angle, a blue shift in λ_R of 48 nm from 0° to 60° is observed. Fig. 8(b) shows the calculated and experimental results of the normalized radiance intensity in the forward direction of the TEWOLED. We can see that the calculated results agree well with the experimental results.

The light outcoupling layer also plays an important role in the luminance of the TEWOLED. Fig. 9 shows the normalized luminous flux (obtained from luminous intensity by integration with respect to the solid angle θ in the forward hemisphere) of the TEWOLED as a function of the thickness of MoO_x layer. The luminous flux of the device is dependent on the thickness of the light outcoupling layer. Generally speaking, the light outcoupling layer will not affect the electrical characteristic of the device. Then, the change of luminous flux could respond to the changing of efficiency of the device. Although the efficiency of the device with a 15-nm-thick MoO_x is the highest, the emission of the device is not a white light emission. Thus, the optical optimization of the TEWOLED must depend on the synthetic consideration of angular color uniformity, CIE coordinates and efficiency (luminous flux).

3.1.3. Optimization of the TEWOLED for lighting

Based on the above analysis, the BY TEWOLED with a 35-nm MoO_x light outcoupling layer has stable angular color uniformity and relatively strong radiated power. However, a high CRI is important for a lighting device. The CRI of this device is 64. The CRI in the greyish red and reddish purple regions is not good because of the relatively low intensity of the red emission. If a red emission is enhanced in the device, the CRI of the device can be improved. Thus, we optimized the RGB TEWOLED using Ag anode and LiF/Al/Ag (15 nm) cathode considering the angular color uniformity and the radiated power. A 35-nm MoO_x was used as the light outcoupling layer. Fig. 10 shows the calculated EL spectra of the device. The device had relatively stable angular color uniformity and the CIE coordinates shifted by (0.027, 0.019) from 0° to 60°. The CRI and the correlated color temperature (CCT) in the forward direction of the device are 90 and 6750 K, respectively. And the CRI of this device is also less angular dependent. The CRI can reach 83 at a viewing angle of 60°. The results indicated that a color-stable and high-CRI TEWOLED could be obtained by carefully designing the structure, and such a device could be used as a white lighting device.

We passed emission of this device through the color filters whose transmission spectra are shown in Fig. 11 and we assume the transmission of the color filters is unchanged with the increasing of the incident angle. The CIE coordinates of the filtered R, G, B emission are (0.668, 0.327), (0.208, 0.637), and (0.131, 0.118) in the forward direction, which change to (0.659, 0.333), (0.201, 0.649), (0.133, 0.119) at 60°. The R, G, and B colors shifted by (0.009, −0.006), (0.007, −0.008), and (−0.002, −0.001) from 0° to 60° and the device gives a color gamut [relative to the NTSC (National Television Standards Committee) standard] of 82.9% at 0°, to 83.5% at 30° and to

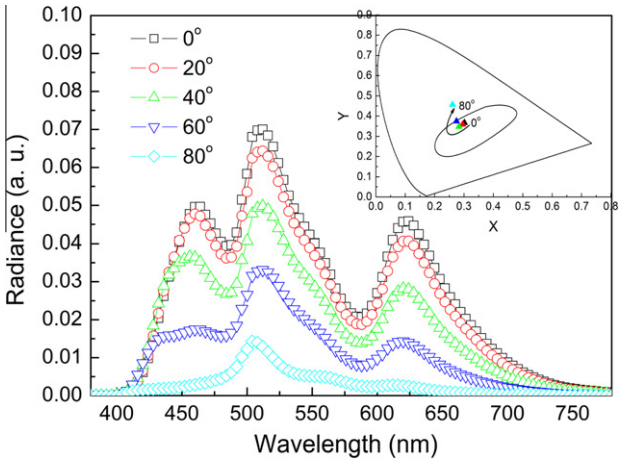

Fig. 10. Calculated EL spectra of RGB device with optimized structure.

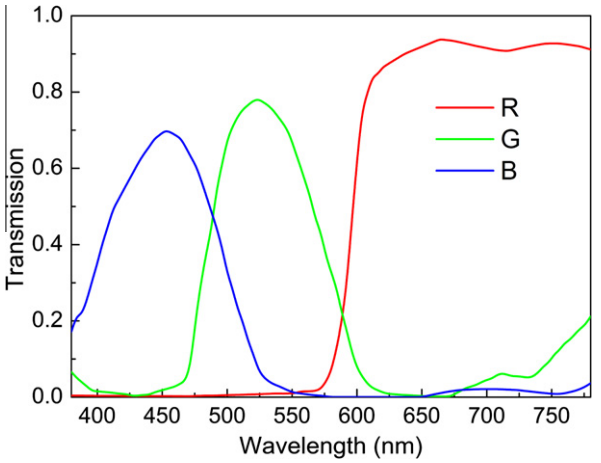

Fig. 11. Transmission spectra of the R, G, and B color filters. (For interpretation of the references to color in this figure legend, the reader is referred to the web version of this article.)

84% at 60°, which is same as 84% of the corresponding bottom device.

3.2. Microcavity TEWOLED Based on MDPC anode

We have reported the microcavity TEWOLED with MDPC anode in our previous work. In principle, a multiple-peak TEWOLED with EL peaks at desired wavelengths can be achieved by adjusting the thickness of the dielectric layer or the period of the MDPC. If we carefully design the structure of this device, the emission spectra of the device could well match the transmission spectra of RGB color filters to achieve a wide color gamut display.

3.2.1. Influence of dielectric layer thickness on the performance of TEWOLED

Firstly, the influence of the dielectric layer thickness on the performance of the TEWOLED is demonstrated. The LiF/Al (1 nm)/Ag (20 nm)/MoO_x (35 nm) was used as the cathode, and the MDPC has a structure of Ag (150 nm)/Alq_3 (x nm)/Ag(20 nm)/Alq_3 (y nm)/Ag (20 nm).

Fig. 12 shows the EL spectra of the TEWOLED with the MDPC anode (x = 50 nm and y change from 20 to 100 nm) in the forward direction. The spectra of the device are sensitive to the y. With the increasing of y, the red shift in cavity emission was observed. Besides, a new resonance peak appeared in the blue region and the resonance intensity increased with the increasing of y. Therefore, the EL spectra of the device are red shifted and present enhanced short-wavelength emission and suppressed long-wavelength emission. If y is increased further, no more resonance peak could be occurred except that we changed the value of x.

Fig. 13 shows the EL spectra of the TEWOLED with the MDPC anode (y = 80 nm and x change from 50 to 130 nm) in the forward direction. The spectra of the TEWOLEDs also reveal a dependence on x. With the increasing of x, the red shift in cavity emission was also observed. And when x > 90 nm, the cavity emission shows a three-peak resonance. Hence, the three-peak resonance TEWOLED was obtained.

In order to validate the accuracy of the simulation, the calculated results are compared to the experimental results. A two-peak TEWOLED with LiF/Al (1 nm)/Ag (20 nm)/MoO_x (35 nm) as the cathode and Ag (150 nm)/Alq_3 (75 nm)/Ag (20 nm)/Alq_3 (45 nm)/Ag (20 nm) as anode were performed. From Fig. 14, we can see that the calculated EL spectra and CIE coordinates agree very well with the experimental results. In the calculation, the layer thicknesses were adjusted on the order of a few percent, which is well within the experimental uncertainties.

3.2.2. Influence of metal in the MDPC on the performance of TEWOLED

A two-peak or three-peak TEWOLED could be obtained by simply adjusting the thickness of the dielectric layers in the MDPC based on the above simulation and our experiment. However, the emission is obvious angular dependence in the above device. It could be slightly improved

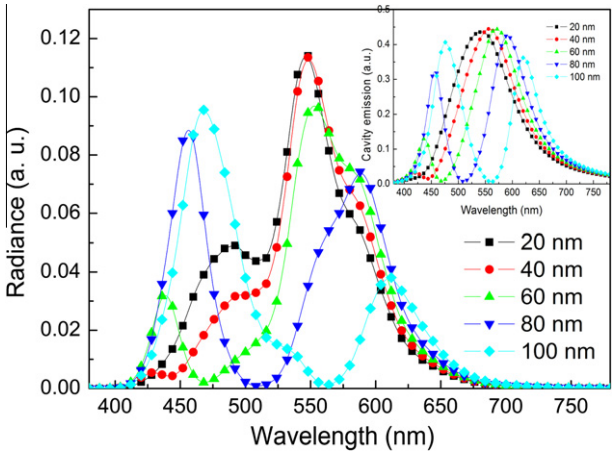

Fig. 12. The EL spectra of the TEWOLED with Ag (150 nm)/Alq_3 (50 nm)/Ag (20 nm)/Alq_3 (y nm)/Ag (20 nm) anode (y change from 20 to 100 nm, inset is the cavity emission of the devices).

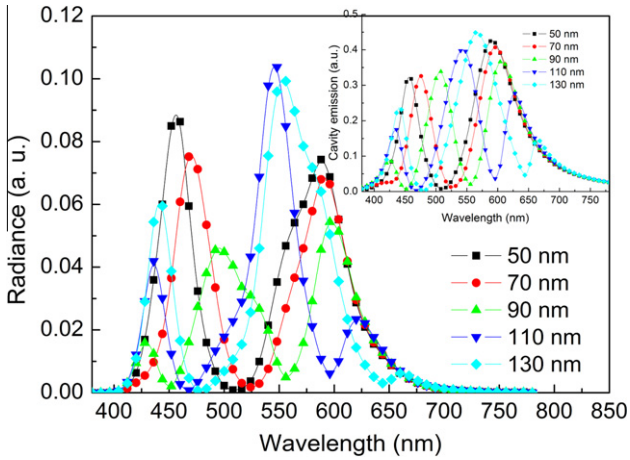

Fig. 13. The EL spectra of the TEWOLED with Ag (150 nm)/Alq_3 (x nm)/Ag(20 nm)/Alq_3 (80 nm)/Ag (20 nm) anode (x change from 50 to 130 nm, inset is the cavity emission of the devices).

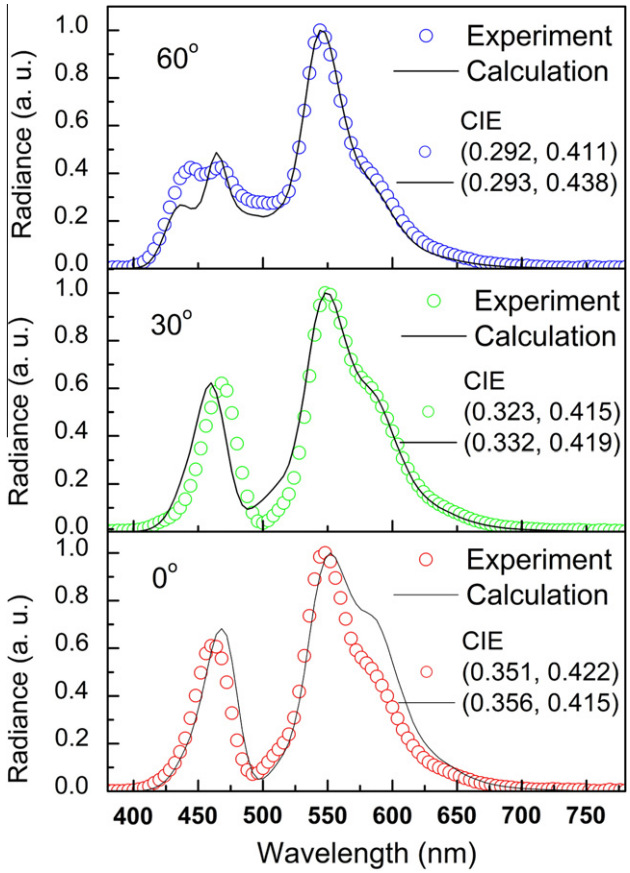

Fig. 14. Calculated and experimental EL spectra of the two-peak TEWOLEDs.

by optimized light outcoupling layer on the top of the cathode. The color shifted by $(0.035, -0.029)$ and $(-0.026, 0.042)$ from 0° to 60° for the two-peak and three-peak TEWOLEDs with the optimized light outcoupling layer.

The angular dependence characteristics of such devices could be improved by using a low reflective metal in the MDPC. For example, the device with Au (150 nm)/Alq_3 (75 nm)/Au (20 nm)/Alq_3 (65 nm)/Au (20 nm) anode and LiF/Al (1 nm)/Ag (20 nm)/MoO_x (55 nm) cathode shows

angular dependence in the EL spectra [Fig. 15(a)]. However, as we all know, two different light spectra that have the same effect on the three color receptors in the human eye will be perceived as the same color. Thus, the CIE coordinates of this device only shift by (±0.013, 0.013) from 0° to 80°. But, the CRI of device [Fig. 15(b)] depended on the viewing angle which is undesirable for lighting applications.

3.2.3. Optimization of the TEWOLED for display

Based on the above analysis, we can find that there is a strong microcavity effect in the TEWOLED based on MDPC anode. Although the CIE of the device can keep stable, the CRI and the CCT of the device are angular dependent which is undesirable for lighting applications. However, a wide color gamut display could be obtained by using TEWOLED based on MDPC anode.

Fig. 16 shows the EL spectra of the RGB device with Au (150 nm)/Alq_3 (100 nm)/Ag (20 nm)/Alq_3 (105 nm)/Ag (20 nm) anode and LiF/Al (1 nm)/Ag (20 nm)/MoO_x (65 nm) cathode. A narrow-three-peak TEWOLED was obtained. And we can see that the blue shifts were observed in the EL spectra of the device with the increasing of the viewing angle. However, the CIE coordinates of this device only shift by (−0.018, 0.009) from 0° to 30°. And the spectra of the TEWOLED well match the transmission spectra of RGB color filters as shown in Fig. 17. If we passed emission

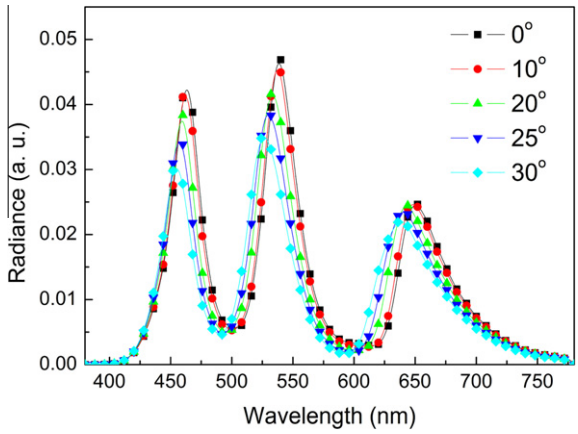

Fig. 16. EL spectra of the RGB device with a Au/Alq_3/Ag/Alq_3/Ag anode and LiF/Al (1 nm)/Ag (20 nm)/MoO_x (65 nm) cathode.

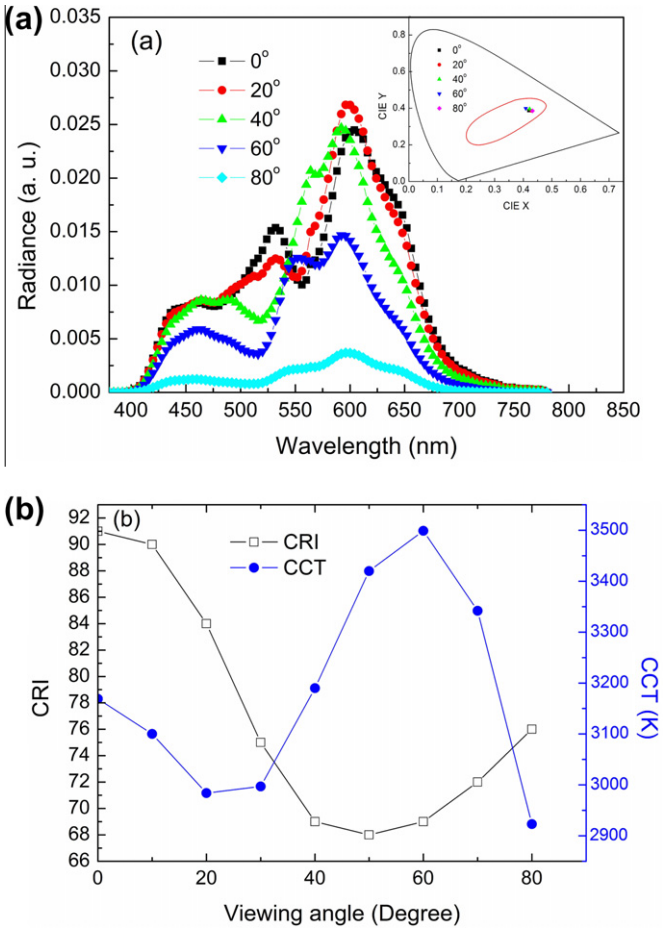

Fig. 15. (a) The angular characteristics, and (b) CRI and CCT of the TEWOLED with a Au/Alq_3/Au/Alq_3/Au anode and LiF/Al (1 nm)/Ag (20 nm)/MoO_x (55 nm) cathode.

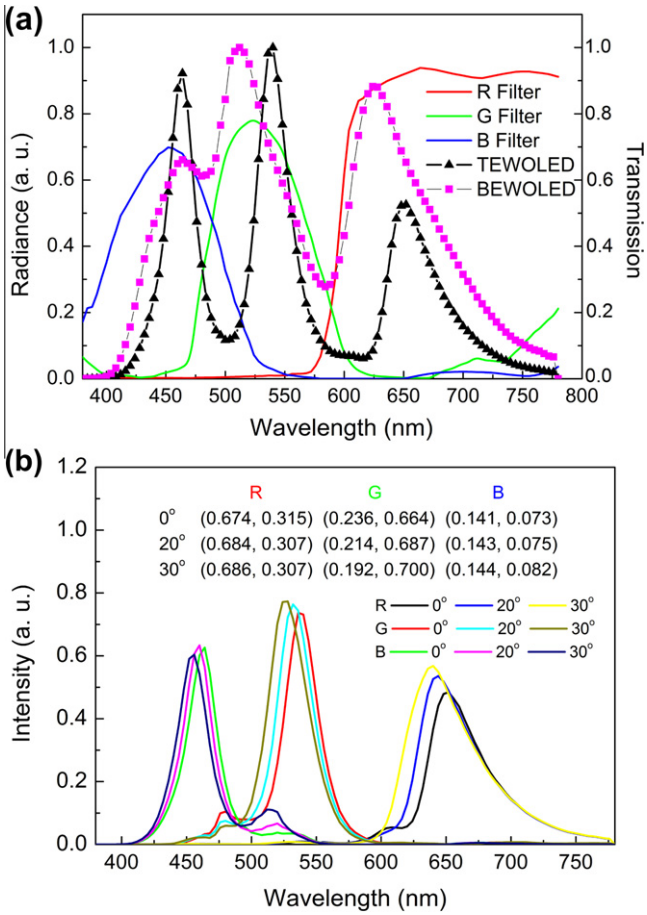

Fig. 17. (a) White OLED and color filter spectra, and (b) filtered R, G, and B spectra obtained by passing emission of TEWOLEDs through the RGB color filters. (For interpretation of the references to color in this figure legend, the reader is referred to the web version of this article.)

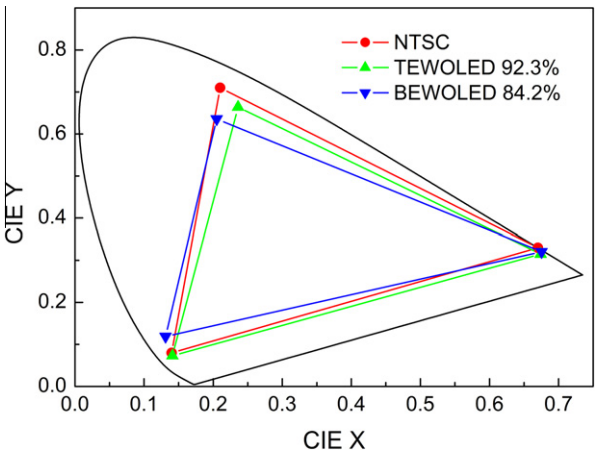

Fig. 18. CIE coordinates of filtered RGB colors for TEWOLED and BEWOLED in comparison with the NTSC standard.

of this device through the color filters, the CIE coordinates of the filtered R, G, B emissions are (0.674, 0.315), (0.236, 0.664), (0.141, 0.073) in the forward direction, which change to (0.684, 0.307), (0.214, 0.687), (0.143, 0.075) at 20° and (0.686, 0.307), (0.192, 0.700), (0.144, 0.082) at 30° [Fig. 17(b)]. The R, G, and B colors shifted by (−0.010, 0.008), (0.022, −0.023), and (−0.002, −0.002) from 0° to 20°. And the device gives a color gamut of 92.3% at 0° and to 99.4% at 20°. CIE coordinates of filtered RGB colors for TEWOLED and BEWOLED in the forward direction are shown in Fig. 18 for comparison. TEWOLED gives a greatly enhanced color gamut of 92.3% versus 84.2% of BEWOLED. The results indicated that the TEWOLED with an MDPC anode could be a selective light source for a near-to-eye display, such as headset microdisplay.

4. Conclusion

Optical properties of ITO-free top-emitting white organic light-emitting devices are simulated and optimized. The main conclusions supported by simulation are as follows.

- Metal–metal microcavity TEWOLED could be used as lighting with high CRI by a carefully designed structure of the devices. The angular characteristics of such devices can be improved by using low reflective electrodes or by introducing a light outcoupling layer with a high reflective index.

- Microcavity TEWOLED based on MDPC anode could realize a near-to-eye display with a wide color gamut. An over 90% NTSC color gamut and viewing angle of 20° could be obtained by a carefully designed structure of the device. And a white device with relative stable CIE coordinates also can be obtained by a carefully designed structure of the MDPC.
- Recent advances in conductive doping of organic semiconductors gave us more choices in electrodes and in structure of the device. The efficiency of the TEWOLED could be compared with that of the bottom one. For example, the top-emitting OLEDs reported by Xie et al. [11] and Freitag et al. [12] exhibit a performance superior to similar devices in the bottom-emission configuration.

Acknowledgments

This work was supported by the National Nature Science Foundation of China (Grant Nos. 60937001, 60707016, 60723002, 11074096, 61077045) and Ministry of Science & Technology of China (Grant No. 2010CB327701).

References

[1] L.S. Hung, C.W. Tang, M.G. Mason, P. Raychaudhuri, J. Madathil, Appl. Phys. Lett. 78 (2001) 544.
[2] Z.Y. Xie, L.S. Hung, F.R. Zhu, Chem. Phys. Lett. 381 (2003) 691.
[3] C.C. Wu, C.W. Chen, C.L. Lin, C.J. Yang, J. Display Technol. 1 (2005) 248.
[4] C.J. Yang, C.L. Lin, C.C. Wu, Y.H. Yeh, C.C. Cheng, Y.H. Kuo, T.H. Chen, Appl. Phys. Lett. 87 (2005) 143507.
[5] C.L. Lin, H.C. Chang, K.C. Tien, C.C. Wu, Appl. Phys. Lett. 90 (2007) 071111.
[6] S. Reineke, F. Lindner, G. Schwartz, N. Seidler, K. Walzer, B. Lüssem, K. Leo, Nature 459 (2009) 234.
[7] Y.R. Sun, N.C. Giebink, H. Kanno, B. Ma, M.E. Thompson, S.R. Forrest, Nature 440 (2006) 908.
[8] B.W. D'Andrade, Nat. Photon. 1 (2007) 33.
[9] S. Kim, S. Lee, M. Kim, J. Song, E. Hwang, S. Tamura, S. Kang, H. Kim, C. Kim, J. Lee, J. Kim, S. Cho, J. Cho, M.C. Suh, H. Kim, J. Soc. Inf. Display 17 (2009) 145.
[10] C.W. Han, H.K. Kim, H.S. Pang, S.H. Pieh, C.J. Sung, H.S. Choi, W.C. Kim, M.S. Kim, Y.H. Tak, J. Display Technol. 5 (2009) 541.
[11] G.H. Xie, Z.S. Zhang, Q. Xue, S.M. Zhang, L. Zhao, Y. Luo, P. Chen, B.F. Quan, Y. Zhao, S.Y. Liu, Org. Electron. 11 (2010) 2055.
[12] P. Freitag, S. Reineke, S. Olthof, M. Furno, B. Lüssem, K. Leo, Org. Electron. 11 (2010) 1676.
[13] W.Y. Ji, L.T. Zhang, T.Y. Zhang, G.Q. Liu, W.F. Xie, S.Y. Liu, H.Z. Zhang, L.Y. Zhang, B. Li, Opt. Lett. 34 (2009) 2703.
[14] C.L. Lin, H.W. Lin, C.C. Wu, Appl. Phys. Lett. 87 (2005) 021101.
[15] A.B. Djurišić, A.D. Rakić, Appl. Opt. 41 (2002) 7650.
[16] A. Dodabalapur, L.J. Rothberg, T.M. Miller, E.W. Kwock, Appl. Phys. Lett. 64 (1994) 2486.
[17] S.F. Hsu, C.C. Lee, S.W. Hwang, C.H. Chen, Appl. Phys. Lett. 86 (2005) 253508.
[18] X.L. Zhu, J.X. Sun, X.M. Yu, M. Wong, H.S. Kwok, Jpn. J. Appl. Phys. 46 (2007) 4054.
[19] M. Thomschke, R. Nitsche, M. Furno, K. Leo, Appl. Phys. Lett. 94 (2009) 083303.
[20] C.H. Chang, H.C. Cheng, Y.J. Lu, K.C. Tien, H.W. Lin, C.L. Lin, C.J. Yang, C.C. Wu, Org. Electron. 11 (2010) 247.
[21] Y.J. Lu, C.H. Chang, C.L. Lin, C.C. Wu, H.L. Hsu, L.J. Chen, Y.T. Lin, R. Nishikawa, Appl. Phys. Lett. 92 (2008) 123303.
[22] R.S. Cok, J.D. Shore, J. Soc. Info. Display. 17 (2009) 617.
[23] H. Kanno, Y.R. Sun, S.R. Forrest, Appl. Phys. Lett. 86 (2005) 263502.
[24] M.T. Lee, M.R. Tseng, Curr. Appl. Phys. 8 (2008) 616.
[25] M.S. Kim, C.H. Jeong, J.T. Lim, G.Y. Yeom, Thin Solid Films 11 (2008) 3590.
[26] W.Y. Ji, L.T. Zhang, T.Y. Zhang, W.F. Xie, H.Z. Zhang, Org. Electron. 11 (2010) 202.
[27] Q. Wang, Z.Q. Deng, J.S. Chen, D.G. Ma, Opt. Lett. 35 (2010) 462.
[28] D.G. Deppe, C. Lei, C.C. Lin, D.L. Huffaker, J. Mod. Opt. 41 (1994) 325.
[29] Sim4tec GmbH, <www.sim4tec.com>.
[30] E.D. Palik, Handbook of Optical Constants of Solids (I, II, III), Academic, Orlando, 1985, 1991, 1998.
[31] W.F. Xie, Y. Zhao, J.Y. Hou, S.Y. Liu, Jpn. J. Appl. Phys. 42 (2003) 1466.

2. Unit-area fringing capacitance at the "back" of the thin film

The TFT is a planar structure with semiconducting thin film for the transistor's channel, and conducting (metal) thin films for the drain and source contacts, as depicted in the bottom of Fig. 1. The films are stacked together with thin films for a gate insulator and a gate terminal conductor. There are several possible arrangements for the stack, but we will assume that the aspect ratio of film thicknesses to planar sizes is very small, and the semiconducting film and the metal electrodes are in the same plane, as shown at the top of Fig. 1. With this assumption, there are formulas for the fringing capacitance C_W per unit width of planar capacitors. We utilize these formulas to obtain the fringing capacitance C_B per unit area of channel, because the unit-area capacitances are significant quantities in the expressions for field-effect transistors. For example, one uses the gate insulator (oxide) capacitance per unit area, C_{ox}, to write the equation for the channel current $I_D = (W/L)\mu C_{ox}(V_G - V_T)^2/2$ in the saturation regime of an ideal field-effect transistor. The notations will be introduced later, along with the derivations.

It is shown in [3,4] by conformal mapping, that the capacitance C_W (per unit width) of a planar capacitor with infinite width (W), and a separation (s) between the neighbouring edges of the capacitor plates is given as ratio of the complete elliptic integrals of first kind $K(m)$

$$C_W = \varepsilon_0 \frac{K(m')}{K(m)},$$
$$\text{with } m = k^2 \text{ and } m' = 1 - m = 1 - k^2 = (k')^2, \tag{1}$$

where $\varepsilon_0 = 8.85 \times 10^{-14}$ F/cm is the permittivity of free space taken as an approximation for the actual permittivity of the air or other media in the "back" of the TFT semiconducting film. The complete elliptic integral of first kind $K(m)$ is

$$K(m) = \int_0^1 \frac{dt}{\sqrt{1-t^2}\sqrt{1-mt^2}}, \tag{2}$$

where (m) is called "parameter", $k = m^{1/2}$ is called "elliptic modulus", and the corresponding complementary quantities m', k' and $K'(m) = K(m')$ are in relations as indicated in Eq. (1).

The elliptic integrals do not have closed-form analytical solutions, but there are power series expansions for the complete elliptic integral of first kind, and numerical calculations are implemented in many computer programs such as MatLab, Mathematica or Maple. In addition, there is a very useful analytical approximation for the ratio $K(m')/K(m)$, given by [3]

$$\frac{C_W}{\varepsilon_0} = \frac{K(m')}{K(m)} \approx \begin{cases} \frac{1}{\pi}\ln\left(2\frac{1+(1-m)^{1/4}}{1-(1-m)^{1/4}}\right), \text{if } m \leqslant 1/2 \\ \pi/\ln\left(2\frac{1+m^{1/4}}{1-m^{1/4}}\right), \text{if } m \geqslant 1/2 \end{cases}, \tag{3}$$

which we have verified to be accurate at least for 5 significant digits, as compared with the numerical calculation using MatLab. As per the first derivative, the approximation is also reasonably accurate, with a small spurious glitch at $m = 1/2$, and except for the first and last 2–3 points when $0 \leftarrow m \rightarrow 1$, but this is easily avoidable by choosing sufficiently small step for m.

It is shown in [3,4] that Eq. (1) is general. It is based on conformal Christoffel–Schwarz transformation of a complex half-plane to a polygon, and is applicable for many geometries of capacitor plates and dielectric layers. The different geometries cause differences in the functions used in the conformal mapping toward parallel-plate capacitor, from which different expressions follow for the "parameter" m, or equivalently for the elliptic modulus k. As follows from Eq. (41) in [4], for the geometry shown at the top in Fig. 1, the "parameter" m is

$$m = \frac{(L + 2L_1)s}{(L + L_1)(s + L_1)}. \tag{4}$$

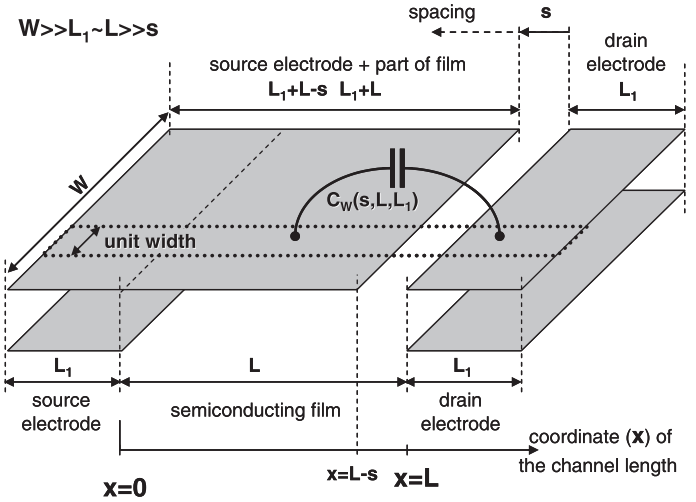

Fig. 1. TFT planar layout (in the bottom) and idealized zero-thickness geometry (on the top) with artificial separation (s) used to obtain fringing capacitance $C_W(s)$ per unit width between drain and semiconducting film. The derivative $C_{BD} = \partial C_W/\partial s$ will represent the geometrical fringing capacitance per unit area of the channel between the "back" of the semiconducting film and drain electrode at position $x = (L - s)$ along the channel axis (x).

Two details are worth mentioning. First, Eq. (1) is after half-plane conformal mapping, and therefore, it is for the fringing capacitance C_W only on one side of the planar capacitor, as depicted in Fig. 1. If the planar capacitor was with free-standing plates, then the actual capacitance would be $2C_W$. However, via the large gate capacitance at the "front" of the TFT semiconducting film, the conductive gate electrode screens the electric field on one side of the TFT film, so, the fringing capacitance between the semiconducting film and drain or source electrode is only in the "back" of the semiconducting film, and is given with C_W by Eq. (1) without the need to double it.

The second detail is that C_W is per unit width W of the TFT channel, as indicated in Fig. 1, whereas one desires an expression for fringing capacitance C_{BD} per unit area of the TFT channel in order to derive equations for the current in the TFT. The channel-drain unit-area fringing capacitance C_{BD} can be obtained as a derivative of C_W in respect with the coordinate (x) along the TFT channel length

$$C_{BD} = \frac{\partial C_W}{\partial x} = -\frac{\partial C_W}{\partial s} \approx \frac{\varepsilon_0}{\pi s} = \frac{\varepsilon_0}{\pi(L-x)} \tag{5}$$

Eq. (5) is a "1/distance" approximation. This equation is valid for a TFT with a wide and not very short channel. Also, the sizes of the drain and source film electrodes are assumed to be similar to the channel sizes, and the layers are sufficiently thin, that is, $W \gg L_1 \sim L \gg s > t_s \sim t_{ox}$, where t_{ox} is the thickness of the gate insulator and t_s is the thickness of semiconducting film. The analytical validation of Eq. (5) at these conditions is given in Appendix A.

The accuracy of the "1/distance" approximation for C_{BD} is illustrated in Fig. 2 for two cases: narrow drain electrode (L_1 = 3 μm) and normal length of the drain electrode (L_1 = 30 μm). One may observe some deviation from the "1/distance" approximation in the left-hand figure only when both of the following conditions are encountered: $L > 10L_1$ and $s > L_1$. These conditions are rarely occurring in practical devices, since one uses normally wide contact electrodes for drain and source with $L_1 \geqslant L$. Also, even if $L > 10L_1$, the loss of accuracy is for large distances $s > L_1$, at which the fringing capacitance is several orders of magnitude smaller as compared with the values corresponding to the proximity of electrode. Thus, the "1/distance" approximation of Eq. (5) for C_{BD} can be used to analyze the effects related to "back" of the semiconducting film.

3. "Extra" biasing through the fringing capacitance at the "back" of the film

Consider the cross-section of the TFT depicted in Fig. 3a on left and take the approximation from Eq. (5) for the fringing capacitance C_{BD} (per unit area of the channel) between the drain terminal and the "back" of the TFT film at position (x) along the channel length. The approximation is given by

$$C_{BD} \approx \frac{\varepsilon_0 \varepsilon_B}{\pi(L-x)}, \text{capacitance from film's "}back\text{" to drain,}$$
$$\text{with source} = 0 \leqslant x \leqslant L = \text{drain,} \tag{6}$$

where ε_B is the relative permittivity of the media at the "back" of the semiconducting film in the TFT, C_{BD} is biased by the drain bias voltage $V = V_D$, and the insulator "thickness" of C_{BD} is $\pi(L-x)$ and varies with the position (x) along the channel length. Similarly, the fringing capacitance C_{BS} (per the same unit area of the channel) between the source terminal and the "back" of the TFT film at position (x) along the channel length is

$$C_{BS} \approx \frac{\varepsilon_0 \varepsilon_B}{\pi x}, \text{capacitance from film's "}back\text{" to source,}$$
$$\text{with source} = 0 \leqslant x \leqslant L = \text{drain,} \tag{7}$$

the insulator "thickness" of C_{BS} is πx, and C_{BS} is shown in Fig. 3 in a gray color, since the source bias voltage is V_S = 0.

Consider the equivalent circuit of the TFT depicted in Fig. 3b. The mobile charge Q_s induced in the thin film provides the conduction (current) in the TFT. Normally, at gate bias V_G above the threshold voltage V_T of the TFT, Q_s is

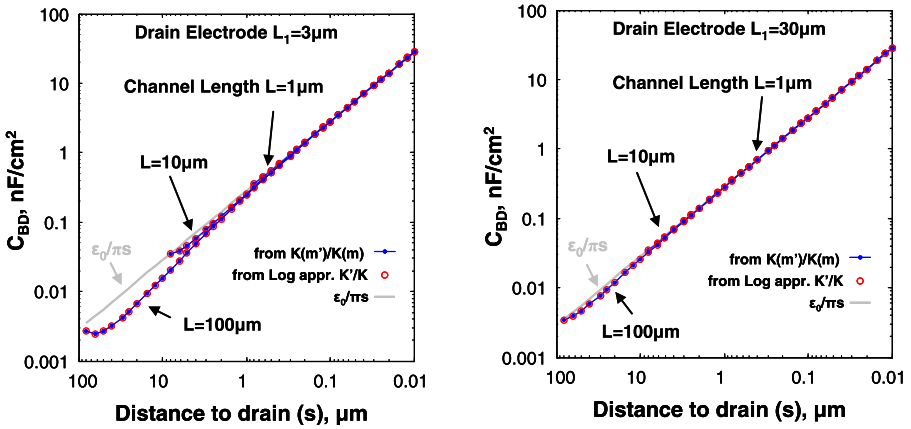

Fig. 2. Accuracy of the "1/distance" approximation (gray lines without symbols) of Eq. (5) for the unit-area fringing capacitance C_{BD} between the "back" of the thin film and drain electrode in TFTs of different channel lengths (L = 1, 10 and 100 μm) with narrow (left-hand figure, L_1 = 3 μm) and normal (right-hand figure, L_1 = 30 μm) drain electrodes. The thin lines with dots are when the ratio $K(m')/K(m)$ in Eq. (1) is obtained from numerically evaluated elliptic integrals, and the larger open circles are when $K(m')/K(m)$ is obtained from the analytical approximation of Eq. (3), showing very accurate approximation. The horizontal axes are reversed to correspond to other figures, in which the drain electrode is drawn on the right-hand side.

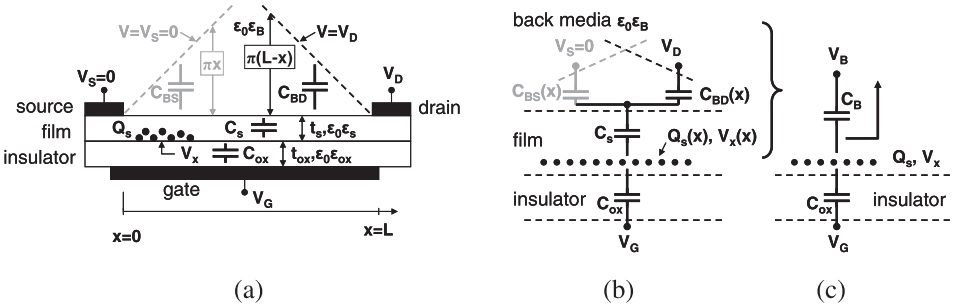

Fig. 3. Schematic representation of the TFT cross-section (a) and equivalent circuits (b) and (c) with capacitances, voltages and other notations.

induced mainly by the bias V_G through the gate insulator (oxide) capacitance C_{ox} and additionally by the drain bias voltage V_D via the capacitive divider C_{BD}–C_{BS}–C_s, where C_s is the unit-area capacitance of the thin film. The expressions for the unit-area oxide and semiconducting film capacitances are

$$C_{ox} \equiv C_I = \frac{\varepsilon_0 \varepsilon_{ox}}{t_{ox}}, \text{gate insulator capacitance at the "}\textit{front}\text{" of semiconducting film,} \quad (8)$$

$$C_s = \frac{\varepsilon_0 \varepsilon_s}{t_s}, \text{semiconducting film capacitance toward the "}\textit{back}\text{" of the film,} \quad (9)$$

with relative permittivity ε_{ox} and ε_s, respectively, usually $\varepsilon_{ox} \approx \varepsilon_s \sim 3$–4 for OTFTs, and corresponding thicknesses t_{ox} and t_s.

The charge due the gate bias voltage V_G is a linear function of the potential V_x (x) of the film along the channel coordinate (x), since C_{ox} is a constant in the TFT. In contrast, C_{BD} and C_{BS} depend reciprocally on the channel coordinate, and one needs to rationalize the capacitive divider C_{BD}–C_{BS}–C_s associated with the "back" of the semiconducting film, in order to obtain an expression for the "extra" bias through the fringing capacitances. An equivalent capacitance C_B and an equivalent voltage V_B that describe the "extra" bias, which the TFT encounters from the "back" of the semiconducting film, seen at point in Fig. 3c, can be obtained by means of Thevenin's theorem. Considering that $V_S = 0$, then only V_D contributes to the "extra" bias, and the expressions are

$$C_B = \frac{1}{\frac{1}{C_s} + \frac{1}{C_{BD}+C_{BS}}} = \frac{C_L}{\frac{C_L}{C_s} + \frac{x}{L}\left(1 - \frac{x}{L}\right)} > 0, \text{ film's "}\textit{back}\text{" capacitance per unit area,} \quad (10)$$

$$V_B = \frac{V_D C_{BD}}{C_{BD} + C_{BS}} = V_D \frac{x}{L}, \text{ equivalent bias voltage at the "}\textit{back}\text{" of the TFT,} \quad (11)$$

where C_L is the characteristic fringing capacitance (per unit area) of the TFT with channel length L, and for the planar arrangement discussed in the previous section, C_L is

$$C_L = \frac{\varepsilon_0 \varepsilon_B}{\pi L}. \quad (12)$$

Note that the channel coordinate ($0 \leqslant x \leqslant L$) is between zero and the channel length L, but this does not cause division by zero in Eq. (10), since $C_L/C_s \approx (\varepsilon_B/\varepsilon_s)(t_s/L)/\pi > 0$ is a positive and non-zero number, although it can be very small. Thus, a multiplication of equalities and non-equalities by the expression in the denominator of Eq. (10) is allowable in the following derivations.

4. "Extra" current due to the fringing capacitance at the "back" of the film in TFT

As shown in Fig. 3, the drain bias voltage V_D will cause an "extra" charge ΔQ_s and consequently an "extra" current ΔI_D in the TFT. This is in comparison to the ideal case when the charge Q_{so} and the corresponding current I_o are determined only by the gate bias voltage V_G, since the DC current I_D in the TFT is proportional to the induced charge $Q_s = Q_{so} + \Delta Q_s$ (per unit channel area). At a given position (x) along the TFT channel, the current is

$$\frac{I_D}{\mu W} = Q_s \frac{\partial V_x}{\partial x} = (Q_{so} + \Delta Q_s)\frac{\partial V_x}{\partial x} = \frac{I_o + \Delta I_D}{\mu W}, \quad (13)$$

where W is the width of the TFT channel, μ is the carrier mobility, and V_x is the potential in the semiconductor film ($0 = V_S \leqslant V_x(x) \leqslant V_D$). Here, the potential V_S of the TFT's source terminal is taken as a zero reference potential and the effective value of the gate bias dependent mobility μ is assumed approximately independent of the channel position, considering a much lower impact of V_D on μ. Note also that the electric field and electric potential have opposite polarities by the sign convention in principle, but we omit the minus sign since we give explicitly the direction of the current from the drain terminal to the source terminal, and we use the equation only to determine the magnitudes.

The general solution of Eq. (13) is not a trivial explicit analytical expression, because the potential V_x and the lateral electric field $\partial V_x/\partial x$ in the semiconducting film are not known *a priori*. Furthermore, Q_{so} and ΔQ_s are functions of V_x, and, ΔQ_s also depends on the position (x) along the channel length L, owing to the product of the position-dependent capacitance C_B, Eq. (10), and the equivalent voltage V_B, Eq. (11). Nevertheless, it is possible to obtain partial solutions of Eq. (13) for several distinct cases, namely, at gate bias V_G above the TFT threshold voltage V_T, and for off-state of the TFT when $V_G \ll V_T$. The two cases, respectively assume either dominant or negligible

contribution of the gate-induced charge Q_{so} in the total charge Q_s.

In this section, we address the case of the TFT operating at the above threshold condition, $V_G \gg V_T$. For this bias condition, the drain bias voltage V_D causes an "extra" current that is observable as an increase of the drain current in the saturation regime, when $V_D > (V_G - V_T)$. In the next section, we will discuss the other distinct case, $V_G \ll V_T$, which is usually termed as operation deep in sub-threshold regime, or off-state of the TFT. In this case, the high drain bias voltage independently induces the charge ΔQ_s in the semiconducting film via the fringing capacitance at the "back" of the semiconducting film in the TFT.

For the operation of the TFT at above-threshold conditions, the total induced charge Q_s is taken as $Q_s \approx Q_{so}$, assuming that the charge Q_{so} due to the gate bias voltage V_G is dominant and the charge ΔQ_s due to the fringing capacitance and drain bias is small. Therefore, the gate-induced charge is

$$Q_{so} = (V_G - V_T - V_x)C_{ox}, \tag{14}$$

and Q_{so} is proportional to the product of the gate insulator capacitance C_{ox} and the gate overdrive voltage $V_{GT} = (V_G - V_T)$ reduced with the potential V_x in the semiconducting film. In addition to Q_{so}, and with the condition that the potential in the film is weakly or not affected by V_D via C_B and V_B, that is $\Delta Q_s \ll Q_{so}$, then the drain bias will induce a charge

$$\Delta Q_s = V_B \times C_B = V_D \frac{x}{L} \times \frac{C_L}{\frac{C_L}{C_s} + \frac{x}{L}\left(1 - \frac{x}{L}\right)}. \tag{15}$$

The threshold voltage and gate bias voltage are not present in Eq. (15) for the additional minor charge ΔQ_s. This is because V_T is already overcome by V_G in the voltage term for the dominant charge Q_{so}, as given with Eq. (14). Also, the relatively large-magnitude of Q_s screens the film's "front" (gate) and "back" biases from each other. Since the gate-induced charge Q_{so} is dominant, then the pinch-off condition $(V_{GT} - V_{xo}) = 0$ for zero induced charge at $V_x > V_{xo}$ is determined from $Q_{so}(V_{xo}) = 0$. Thus, the two components I_o and ΔI_D in Eq. (13) for the DC current I_D are

$$\frac{I_o}{\mu W} = Q_{so}\frac{\partial V_x}{\partial x} = C_{ox}(V_G - V_T - V_x)\frac{\partial V_x}{\partial x}, \text{and} \tag{16}$$

$$\frac{\Delta I_D}{\mu W} = \Delta Q_s \frac{\partial V_x}{\partial x} = \frac{V_D C_L \frac{x}{L}}{\frac{C_L}{C_s} + \frac{x}{L}\left(1 - \frac{x}{L}\right)}\frac{\partial V_x}{\partial x} \leqslant \frac{V_D C_L}{\frac{C_L}{C_s} + \frac{x}{L}\left(1 - \frac{x}{L}\right)}\frac{\partial V_x}{\partial x} \tag{17}$$

with $0 = V_S \leqslant V_x \leqslant V_m = \min(V_D, V_G - V_T)$, where one has to take V_x spanning from the zero potential of the source terminal $V_S = 0$ to a maximum value V_m in the calculations of the induced unipolar charge Q_s, with V_m being the lesser of the drain bias voltage V_D and gate overdrive voltage $V_{GT} = (V_G - V_T)$. As noted after Eq. (12), the factor in the denominator of Eq. (17) is finite and positive, and therefore, one can multiply the equation by this factor to arrange it as

$$\frac{\Delta I_D}{\mu W}\left[\frac{C_L}{C_s} + \frac{x}{L}\left(1 - \frac{x}{L}\right)\right] = V_D C_L \frac{x}{L}\frac{\partial V_x}{\partial x} \leqslant V_D C_L \frac{\partial V_x}{\partial x}. \tag{18}$$

It can be shown that the area under $V_D V_L (x/L)\partial V_x/\partial x$ and $V_D V_L \partial V_x/\partial x$ disagree with a maximum error of 50% for the linear regime, for which $\partial V_x/\partial x \approx$ constant. However, the error is much lower for the saturation regime, since the magnitude $\partial V_x/\partial x$ of the lateral electric field is a peaking function at $x \to L$, so $x/L \to 1$. Thus, the approximation $x/L \approx 1$ in the numerators of Eqs. (17) and (18) capture the order of magnitude of the effects associated with the fringing capacitances at the "back" of the semiconducting film in the TFT with reasonable accuracy, when the TFT operates in the above-threshold regimes.

Performing the integrations in Appendix B, the current I_o driven by the gate bias V_G–C_{ox} in TFT is

$$\frac{I_o L}{\mu W} = C_{ox}\frac{(V_G - V_T)^2 - (V_G - V_T - V_m)^2}{2} = C_{ox} \times \begin{cases} (V_G - V_T - 0.5V_D)V_D, & \text{when } V_m = V_D \\ & \text{in the linear regime,} \\ 0.5(V_G - V_T)^2, & \text{when } V_m = (V_G - V_T) \\ & \text{in the saturation regime,} \end{cases} \tag{19}$$

as expected for an ideal TFT without effects from fringing capacitances. The "extra" current ΔI_D driven by the drain bias V_D through the fringing capacitances at the "back" of the semiconducting film in the TFT at gate bias above threshold, $V_G > V_T$, is

$$\frac{\Delta I_D L}{\mu W} \approx \frac{C_L V_D V_m}{\frac{1}{6} + \frac{C_L}{C_s}} \approx 6 C_L V_D V_m \approx 6\frac{\varepsilon_0 \varepsilon_B}{L} \times \begin{cases} V_D^2, & \text{in the linear regime,} \\ V_D(V_G - V_T), & \text{in the saturation regime,} \end{cases} \tag{20}$$

considering that the ratio $C_L/C_s \ll 1$, as mentioned earlier by Eq. (l2). Thus, combining Eqs. (19) and (20), the impact of the fringing capacitance at biasing of TFT above threshold $(V_G > V_T)$ can be summarised by the ratio $\delta = \Delta I_D/I_o$, as

$$\delta = \frac{\Delta I_D}{I_o}\bigg|_{V_G > V_T} \approx \frac{\frac{6 C_L V_D V_m}{1 + 6C_L/C_s}}{C_{ox}\frac{(V_G - V_T)^2 - (V_G - V_T - V_m)^2}{2}} \approx 12\frac{C_L}{C_{ox}} \times \begin{cases} \frac{V_D}{2(V_G - V_T) - V_D}, & \text{when } V_m = V_D \leqslant (V_G - V_T) \text{ in the linear regime,} \\ \frac{V_D}{V_G - V_T}, & \text{when } V_m = (V_G - V_T) \leqslant V_D \text{ in the saturation regime.} \end{cases} \tag{21}$$

Note that this result is approximate since we have used an inequality to derive it and have made assumptions for a dominant Q_{so}, so that the integration limits for V_x are set by $V_{xo} = (V_G - V_T)$, as stated after Eq. (15). Furthermore, for simplicity of the derived equations, we have not included the bias dependence of the mobility, which is a typical effect in amorphous and organic TFTs that can be included as explained in details in [6–8]. As estimated in Appendix B, the exclusion of the mobility enhancement factor is not critical, both for the behaviours and magnitudes related to C_L. We have also omitted other charge transport phenomena, such as contact effects [6,7,9,10] and space-charge limited conduction (SCLC) [5,11], which are not negligible in the TFTs, since the charge carrier mobility in

these transistors is low compared to the crystalline transistors. Nevertheless, we will demonstrate below that Eq. (21) captures the order of magnitude for effects that are usually attributed to the so-called channel length modulation by an empirical analogy with crystalline field-effect transistors.

4.1. Channel length modulation and fringing capacitance effects

One can make several qualitative observations from Eq. (21) for the dependences that are typical for the channel length modulation caused by an increased drain bias $V_D > V_{Dsat} \approx (V_G - V_T)$ in crystalline field-effect transistors, e.g., MOS transistors operating in the saturation regime [1]. The origin of the channel length modulation is the small depleted region ΔL near the drain of the MOS transistor with potential $V_x > V_{Dsat}$, which reduces the integration limit for the current from L to $(L-\Delta L)$ by the integration on the left-hand side of Eq. (16), c.f., Eq. (34) in Appendix B. Consequently, as detailed in Appendix C, the actual current I_{MOS} becomes larger than the saturation current I_{SAT} of the ideal MOS transistor, and as a first-order of approximation, the relative increase of the channel current due to channel modulation is

$$\delta_{MOS} = \frac{I_{MOS} - I_{SAT}}{I_{SAT}} \approx \frac{\Delta L}{L} \approx \lambda[V_D - (V_G - V_T)], \text{ when } V_D > (V_G - V_T) \quad (22)$$

implying that δ_{MOS} and λ are reciprocal functions of the channel length L. The channel length modulation parameter λ has a dimension $1/V$, its reciprocal value $1/\lambda = V_A \propto L$ is known as the Early voltage, and it does not vary much with the bias of the MOS transistor. Several other expressions can be found in [1], but the comparison of the above expression for δ_{MOS} with Eq. (21) for the corresponding δ in TFT clearly demonstrates the analogy that can be made for similar impacts from channel length modulation and fringing capacitances in TFTs. Namely, by Eqs. (21) and (22), the "extra" drain current ΔI_D in the TFT operating in the saturation regime at above-threshold gate biasing is proportional to the drain bias voltage V_D, and it is a reciprocal function of the channel length, since $C_L \propto L^{-1}$, as previously given in Eq. (12). The difference between the models is in the place for the expression of the gate overdrive voltage $V_{GT} = (V_G - V_T)$. V_{GT} is subtracted from V_D in the first-order equations for channel length modulation, whereas V_{GT} is in the denominator of the equation derived from fringing capacitance in TFT. Nevertheless, both models suggest reduction of the ratio $\delta = \Delta I/I$ when the gate bias increases. Perhaps is worth mentioning that the correspondence between channel length modulation parameter λ, the Early voltage V_A and the ratio C_L/C_{ox} of fringing to gate dielectric capacitances in the TFT is given generally by the following chain of relations

$$\lambda \sim \frac{1}{V_A} \sim 12\frac{C_L}{C_{ox}}\frac{1}{(V_G - V_T)} \approx \frac{12\varepsilon_0\varepsilon_B}{C_{ox}\pi L(V_G - V_T)}. \quad (23)$$

The terms in this chain are inversely proportional to the gate length L of field-effect transistors, but the values vary, since the models differ in physical origin and arrangement of equations, while the behaviour and the prediction of these models are similar.

4.2. Characterization of TFT by means of fringing capacitance at the "back" of the film

From the above discussion, the impact of channel length modulation and effects from fringing capacitance might be not distinguished qualitatively in practice. Instead, we propose a quantitative analysis of experimental data for TFTs based on the model in Eqs. (19) and (21). In this analysis, we consider ε_B as a fitting parameter. Its value will distinguish the fringing capacitance from other effects, such as channel length modulation or space charge limited conduction and contact effects. One expects $\varepsilon_B \sim 1$, if the fringing capacitance is in the origin of the "extra" current, and higher values for ε_B, when the other effects contribute to the "extra" current. The quantitative analysis uses the characterization procedure detailed in Appendix D. The procedure has two main steps. In the first step, we evaluate the ratio C_L/C_{ox} from the saturation I_D–V_D characteristic at given gate bias voltage $V_G > V_T$. In the second step, the mobility corresponding to the same V_G and from the same I_D–V_D characteristic is evaluated, assuming that the mobility variation is weak as function of the drain bias in the saturation regime, following the arguments given after Eq. (21) earlier. An intermediate averaging between the steps is helpful to remedy unavoidable scattering of data for C_L. Such averaging is usually possible, since one normally measures a family of I_D–V_D characteristic at several gate bias voltages.

To obtain the ratio C_L/C_{ox} in the first step, one uses data only for the saturation region in the output characteristics ($I_D = f(V_D > V_G - V_T)$ at constant V_G) of the TFT at a given gate bias voltage $V_G > V_T$. Thus, Eqs. (24) and (25) are only for the saturation regime of operation of the TFT. One data point in the saturation region is chosen as a reference current $I_{Dref} = I_D(V_{Dref} > V_G - V_T)$ at a reference drain bias voltage V_{Dref}. If the TFT is a normally-off field-effect transistor (the threshold voltage V_T has the same polarity as the gate V_G and drain V_D bias voltages), then a convenient choice for I_{Dref} and V_{Dref} is the biasing condition that corresponds to the diode connection of the TFT. In this case, the drain and gate bias voltages are equal, $V_{Dref} = V_G$, thus, I_{Dref} is easily measured during experiments, and therefore, we provide the expressions for the case of I_{Dref} chosen at the diode connection, $V_{Dref} = V_G > V_{GT} = (V_G - V_T)$. This case is denoted by "for normally-off TFT" in Eq. (24). One uses the larger general expression for normally-on TFTs, or if data for diode connection is not available.

Since I_D and I_{Dref} are measured in the saturation regime at predetermined bias voltages V_G, V_D, V_{Dref}, and also knowing the threshold voltage V_T of the TFT, then one experimentally characterizes the ratio C_L/C_{ox} from

$$\frac{C_L}{C_{ox}} = \frac{(V_G - V_T)\delta_{ref}}{12[V_D - V_{Dref}(1+\delta_{ref})]} = \frac{\varepsilon_0\varepsilon_B}{C_{ox}\pi L} = \frac{t_{ox}}{\varepsilon_{ox}}\frac{\varepsilon_B}{\pi L}, = \frac{(V_G - V_T)\delta_{ref}}{12[V_D - V_G(1+\delta_{ref})]} \text{ for normally-off TFT}, \quad (24)$$

where the supplementary relative difference between I_{Dref} and $I_D(V_D \neq V_{Dref})$ is $\delta_{ref} = (I_D - I_{Dref})/I_{Dref}$. Knowing the values of V_T, L and C_{ox}, one calculates the characteristic fringing capacitance C_L by using Eq. (24). The effective values for the relative permittivity ε_B of the media at the "back" of the film can also be obtained. It is expected that the calculated effective values for ε_B will be larger than the actual relative permittivity of the media in the "back" of the TFT. This is because Eq. (12) is for an ideal planar structure, while in the real TFT, there are edges, corners and other geometric features, e.g., encapsulation and protection layers. Also, the characterization technique attributes the "extra" current ΔI_D solely to the fringing capacitance, which is not the only transport phenomenon that contributes to ΔI_D. Therefore, one should be careful by the interpretation of the values, especially for ε_B. We have observed, in the application of this characterization procedure to experimental data, that there is some scattering in the values for the ratio C_L/C_{ox} and ε_B. This scattering is a result of the neglected space-charge limited conduction in amorphous films, contact effects and variation of mobility with bias, or other uncertainties in the information for layout sizes, V_T and C_{ox}. Therefore, one should implement data post-processing, such as averaging, and optimization of values by fitting to the measured data. It is recommended, in the post-processing step, to consider several gate bias conditions and to estimate a single value for C_L/C_{ox} or ε_B, before proceeding to the second step for characterization of the mobility.

The second step for evaluation the mobility uses the ratio C_L/C_{ox} obtained from the first step in the following equation

$$\mu(V_G, V_D) = \frac{2L}{WC_{ox}} \frac{I_o}{(V_G - V_T)^2}, \text{ at } V_D > (V_G - V_T), \\ = \frac{2L}{WC_{ox}(V_G - V_T)} \frac{I_D}{(V_G - V_T + V_D 12C_L/C_{ox})}. \quad (25)$$

The values for the ratio C_L/C_{ox} in this formula can be adopted point-by-point, as calculated by Eq. (24) for the various biasing voltages V_D and V_G in the saturation regime. However, the better choice is to use a single representative value, in order to avoid unnecessary scattering, and also, to obtain a value for a model parameter, e.g., the effective value for relative permittivity ε_B of the media at the "back" of the film. Despite these precautions, there is still scattering in the values for the effective mobility, as calculated from the formula. This scattering is for the same reasons described above for the values of the ratio C_L/C_{ox}. Nevertheless, one obtains data for the mobility, which can be used further for compact modeling of the mobility [8], and then modeling of the characteristics of the TFT with generic and more sophisticated compact models such as described in [6,7,12].

4.3. Verification with pentacene thin film transistors

By performing all the steps in the above characterization techniques, we present in Fig. 4 the results from the quantitative study of experimental data for organic TFTs against the hypothesis for impact from fringing capacitance. The black lines in the figure are the experimentally gathered data, as reported in the literature. The gray lines represent the "ideal" current I_o of the TFT, which is driven by the gate bias voltage V_G via the gate insulator capacitance C_{ox} and I_o is according to Eq. (19). Obviously, I_o saturates to constant values at $V_D > (V_G - V_T)$. We show only several curves for I_o in the figure, since the plots became too crowded when drawing all lines.

The symbols in Fig. 4 represent the recalculated total current $I_D = I_o + \Delta I_D = I_o(1 + \delta)$, where $\delta = \Delta I_D/I_o$ is according to Eq. (21), with $C_L = \varepsilon_0\varepsilon_B/\pi L$ given by Eq. (12). The drain current I_D is the sum of I_o and the "extra" current ΔI_D, the latter driven by the drain bias voltage V_D through the fringing capacitance. Since $\varepsilon_B \sim 1$ is expected for the fringing capacitance, then the value of ε_B becomes an indicator whether the deviation from the flat I_o–V_D characteristic in the saturation regime is consistent with the hypothesis for an impact from fringing at the "back" of the film in the TFT. Each sub-figure shows the data in linear and logarithmic plots to provide better perspective on problems encountered during the analysis. When problems were encountered, then the affected data points are shown in Fig. 4 with symbols in gray color. Thus, the black symbols in the figure are representing the results from the reliable fitting to the experimental data.

Fig. 4a shows the data reported in [13] for a TFT with pentacene semiconducting film and channel length $L = 10$ μm. The "extra" current ΔI_D is relatively small. Fig. 4b shows the data reported in the same publication for another pentacene TFT with a short channel of length $L = 1$ μm, but otherwise identical and simultaneously fabricated with the 10 μm long-channel TFT in Fig 4a. The saturation of I_D is weak in the 1 μm short-channel TFT, and the "extra" current ΔI_D becomes large in this TFT, as depicted with several arrows in Fig 4b. Importantly, the single value of $\varepsilon_B = 1.12$ used to fit the experimental data in Fig. 4a and b confirms the derived model for the impact of the fringing capacitance at the "back" of the semiconducting film in the TFT, because the value of ε_B is very close to the expected value of unity. This result builds a confidence that the fringing takes place in TFTs, and also verifies the characterization technique, although several data points in Fig. 4b do not match the experimental data, owing to the increased contribution of contact effects at low drain bias and higher currents [6,7,11].

4.4. Verification with rubrene single crystal organic transistors

The result from the second quantitative study for the impact of fringing capacitance in TFTs is shown in Fig. 4c for data reported in [14] for a rubrene single-crystal organic transistor. This transistor is fabricated by a very different approach, as compared to the typical fabrication approaches for TFTs. The semiconductor is a small freestanding faceted plate of rubrene with planar sizes 2–3 mm and thickness of about 0.5 mm. The rubrene plate is mechanically contacted by laminating to an elastomeric stamp with drain, source and gate embedded in the stamp. Rubrene has a relatively high mobility, effective value of about 3 cm^2/Vs in this transistor, and the transistor conducts

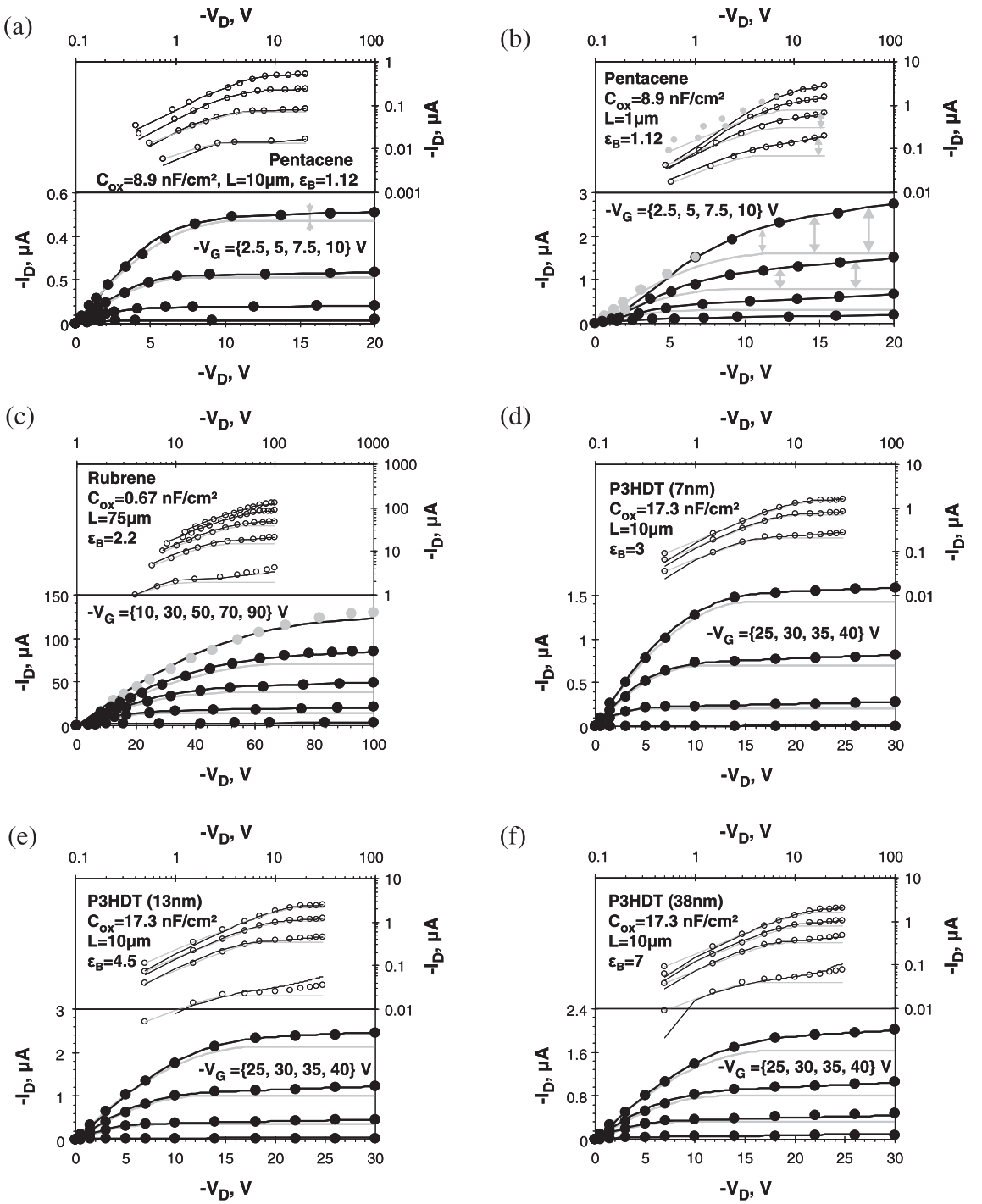

Fig. 4. Quantitative study of the "extra" current due to fringing capacitance in organic TFTs in terms of the effective relative permittivity ε_B of the media in the film's "back" (a) and (b) are pentacene TFTs with different channel lengths [13] (c) is a rubrene single-crystal TFT, mechanically contacted to elastomeric stamp with drain, source and gate embedded in the stamp [14] (d), (e) and (f) are poly(3-hexadecylthiophene), P3HDT, bottom-contact TFTs with different thicknesses of the semiconducting film [15]. Each data set is shown in linear and logarithmic plots. Black lines are measured data. Gray lines represent the ideal current I_o, driven by V_G. The symbols represent the sum of Io and the "extra" current ΔI_D driven by V_D. Gray symbols denote questionable fitting, owing to other effects in TFTs.

currents in the range of 0.1 mA at high gate and drain bias voltages, which caused problem to fit the data when neglecting the weak electrical contact between the stamp and the crystal, as indicated with the gray-color symbols in the figure. Nevertheless, at lower $V_G < 80$ V, the fitting was good and the symbols in Fig. 4c are obtained by

calculation with $\varepsilon_B = 2.2$. The value of ε_B is slightly higher than unity, and we attribute this to the arrangement of the transistor. The transistor is not exactly a thin-film transistor, because the thickness of the rubrene crystal is larger than the transistor's channel length, and the fringing fields in the "back" are actually inside the relatively thick plate of rubrene. Since rubrene has a relative permittivity in the range of 4, then one expects a value larger than unity for the effective relative permittivity ε_B of the planar fringing capacitance in this sample. Thus, $\varepsilon_B = 2.2$ is justified to be reasonable and the good fit to experimental data verifies the applicability of the derived equations for the "extra" current from fringing capacitance even for not-very thin-film transistors.

4.5. Verification with thin film transistors with varying semiconducting polymer thicknesses

Looking back at the derivations, we have made the assumption by Eq. (20) that the thickness t_s of the semiconducting film has a negligible effect in the TFTs, since the corresponding capacitance $C_s = \varepsilon_0\varepsilon_s/t_s \gg C_L$. In an attempt to evaluate the effect of the film thickness, we have analyzed the data reported in [15] for TFTs with different thicknesses t_s of the poly(3-hexadecylthiophene), P3HDT, semiconducting films. The results shown in Fig. 4d for $t_s = 7$ nm, in Fig. 4e for $t_s = 13$ nm and in Fig. 4f for $t_s = 38$ nm indicate a very good fit between the fringing capacitance model and the experimental data, both at low and high drain voltages and currents. This observation implies that the model is sustainable, and the place of the gate overdrive voltage (V_G–V_T) in a product with V_D in Eq. (20) and in a ratio in Eq. (21) is correct, although different from the format of the equations usually used to model the "extra" current in the saturation regime of operation of the TFT in terms of channel length modulation, compare again to Eq. (22).

For the data in Fig. 4d–f, the effective values of the relative permittivity ε_B gradually increase from 3 to 7, when increasing the film thickness from $t_s = 7$ nm to 38 nm. These TFTs have planar bottom-contact structure with comb-shaped drain and source electrodes (10 μm finger width) separated by the channel meander at distance $L = 10$ μm, the latter being the channel length of the TFT. One may expect some increase of ε_B, either owing to corners or cross-capacitance between fingers and meander, but the values $\varepsilon_B = 3$–7 for relative permittivity are too large to be realistic consequence from the TFT layout, since only the room atmosphere was on the top of the semiconducting film, and the room air has relative permittivity close to unity. Thus, while the derived model is suitable for compact modeling, one should be careful with the physical interpretation of the values of the model parameters, especially, with the value for ε_B. Values of ε_B above 2.5 indicate that the fringing effects, although existing, are only a portion of the many charge transport phenomena in the TFTs [10]. Indeed, the analyses of the experimental data in [15] were in terms of space charge limited conduction (SCLC); the analyses in this publication clearly distinguished SCLC in the leakage currents of these TFTs at low gate biasing and off-state.

In the next section, we examine the contribution of fringing capacitance at the condition of low gate bias, which is the other distinct case, when the charge ΔQ_s induced by the drain bias voltage V_D in the semiconducting film can dominate over the charge Q_{so} weakly induced by the gate bias voltage V_G, or generated by other means, e.g., thermally or optically.

5. "Extra" FET due to the fringing capacitance at the "back" of the film in TFT

Consider the cross-section of the TFT schematically depicted in Fig. 5 for the semi-insulating "off" state with some small amount of induced charges $Q_s = Q_{so} + \Delta Q_s$ (per unit channel area, as defined by Eq. (13) earlier). In this case, the gate bias voltage V_G is low, and the charge Q_{so}, induced by V_G, cannot be taken as the dominant charge in the semiconducting film. Apart from this detail, the cross-section in Fig. 5 is identical to Fig. 3. The detail, however, leads to several consequences. First, since Q_s is low, then the structure is semi-insulating. Second, the low Q_s cannot screen the "back" and the "front" interfaces of the semiconducting film each from other, and Gauss' law has to be applied from the top to the bottom of the structure, as depicted in the equivalent circuit in Fig. 5. Third, the induced charges Q_{so} and ΔQ_s are separated, while they are induced in the same manner in the capacitive divider C_{ox}–C_B by the "front" bias voltage V_G and "back" bias voltage V_B, with the later given by Eq. (11). The expressions for

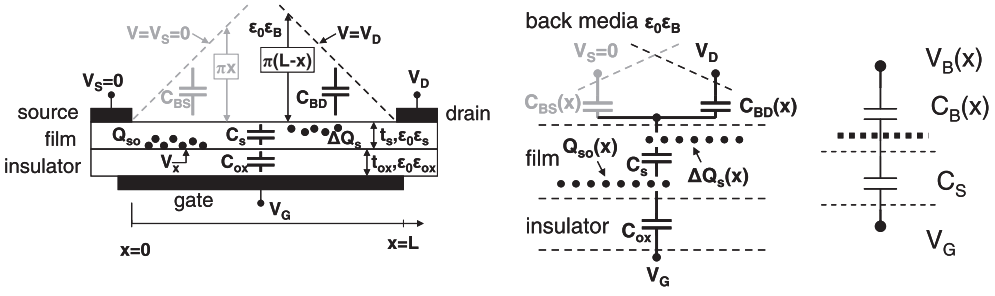

Fig. 5. Schematic representation of the cross-section and equivalent circuit of the TFT in semi-insulating state.

C_{ox} and C_B are the same as in Eqs. (8) and (10), respectively, and C_B includes C_{BD}, C_{BS} and C_s shown in the equivalent circuit of Fig. 5.

So, without the screening due to Q_s, one can place the threshold voltage V_T in series with the capacitive divider for the calculation of the induced charge Q_s, or equivalently, V_T can be added to the potential V_x in the semiconducting film. Consequently, from Gauss' law in the C_{ox}–C_B divider, one gets

$$\frac{V_G C_{ox} + V_B C_B}{C_{ox} + C_B} - V_x - V_T = V_{EODR} = \frac{Q_s}{C_{ox} + C_B}. \quad (26)$$

The left-hand side of this equation is an equivalent overdrive voltage V_{EODR}, caused by the simultaneously applied "front" V_G and "back" V_B bias voltages. Substituting the "back" bias voltage V_B with the expression given by Eq. (11), and after multiplication with the non-zero quantity $(C_{ox} + C_B)$, one easily obtains that

$$Q_s = C_{ox}(V_G - V_T - V_x) + C_B(V_D - V_T - V_x). \quad (27)$$

This result indicates the superposition of the "front" and "back" biases due to V_G and V_D, respectively. Similar to Eqs. (14) and (15), Q_s can be separated into two parts:

$$Q_{so} = (V_G - V_T - V_x)C_{ox}, \text{ for } V_x \leqslant (V_G - V_T), \text{ and } Q_{so} = 0 \text{ otherwise; and} \quad (28)$$

$$\Delta Q_s = (V_D - V_T - V_x)C_B, \text{ for } V_x \leqslant (V_D - V_T), \text{ and } \Delta Q_s = 0 \text{ otherwise}, \quad (29)$$

which indicate independence of the gate and drain bias voltages biases, as expected for the semi-insulating case of the TFT, and different integration limits when considering that Q_{so} and ΔQ_s are unipolar charges.

Since Eq. (28) is identical to Eq. (14), including the limits for V_x, then the current I_o driven by V_G is given by Eq. (19). In contrast, the expression for the "extra" current ΔI_L driven by V_D will be different from Eq. (20), because the expressions in Eqs. (15) and (29) are different, along with the different integration limits. Consequently, one performs the integrations of Eq. (29), as shown in Appendix E, and obtains the "extra" current ΔI_L driven by V_D in the semi-insulating "off" state of the TFT as

$$\frac{\Delta I_L L}{\mu W} \approx \frac{C_L}{\frac{1}{6}+\frac{C_L}{C_s}} \frac{[\max(0, V_D - V_T)]^2 - [\max(0, -V_T)]^2}{2} \approx 6\frac{\varepsilon_0 \varepsilon_B}{\pi L} \times \begin{cases} 0, \text{ if } V_D < V_T, \text{ possible only for normally-off TFT} \\ \frac{(V_D - V_T)^2}{2}, \text{ if } V_D \geqslant V_T \text{ for normally-off TFT} \\ \frac{(V_D - V_T)^2 - V_T^2}{2} = \frac{V_D(V_D - 2V_T)}{2}, \text{ if } V_T < 0 \text{ for normally-on TFT} \end{cases} \quad (30)$$

Observe that the gate bias voltage V_G does not participate in the expressions for ΔI_L, thus, ΔI_L is a leakage-like current in the off-state of the TFT, driven only by V_D. Therefore, the "extra" current ΔI_L driven by V_D in the semi-insulating "off" state of the TFT can be viewed as a current from an "extra" transistor in parallel to the main transistor with the ideal current I_o, the latter driven by the gate bias voltage V_G. A close examination of Eq. (30) indicates that V_D substitutes V_G in the expressions for ΔI_L, that is a virtual $V_G = V_D$, and corresponds to a diode connection of the "extra" FET with a virtual "back"-gate capacitance $6C_L = 6\varepsilon_0\varepsilon_B/\pi L$. This "extra" FET is shown with gray color in Fig. 6, because it affects normally only the leakage of the TFT (see the log–log plots at the lowest V_G in Fig. 4e and Fig. 4f), which is not of significant concern for a good quality TFT. While the "back"-gate capacitance of the "extra" FET is different, the remaining parameters, e.g., channel sizes W and L, threshold voltage V_T, mobility μ, etc., are identical to the corresponding parameters of the main gate-controlled FET, driven by V_G via C_{ox}. Note that if the TFT is a normally-off device (V_T and V_D are of the same polarity), then the "extra" FET operates in the saturation regime. On the other hand, it operates in the linear regime, if the TFT is normally-on device (V_T and V_D are of different polarities). The current source in Fig. 6 corresponds to the "extra" current ΔI_D given by Eq. (20), and its significance was discussed in the previous section. The multiplying term $\mu W/L$ for ΔI_D is omitted in the figure for clarity, and to observe that the effects of fringing capacitance at the "back" of the TFT film result in a capacitance $6C_L$ for both "extra" currents ΔI_L and ΔI_D.

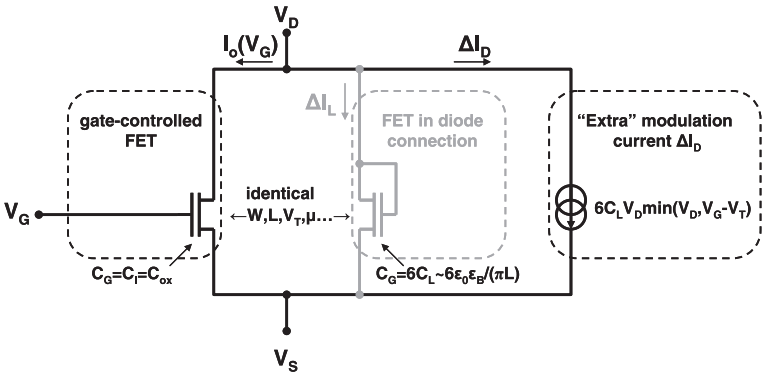

Fig. 6. Equivalent circuit suitable for TFT compact modeling with the impact of the fringing film-"back" capacitance included as "gate" capacitance C_L in an "extra" FET in diode connection (in gray color) according to Eq. (30), and the "extra" current ΔI_D, the latter according to Eq. (20) with $\mu W/L$ omitted in the figure for clarity. Normally, $C_L \ll C_{ox}$.

6. Discussions

The analysis of results from the conformal mapping of the TFT planar structure implies that the unit-area capacitances at the "back" of the semiconducting film have reciprocal dependences on the distances between the electrodes and the position along the channel (see Eqs. (5)–(7)). Consequently, the drain terminal bias voltage is forwarded to the channel by the "back"-film fringing capacitance with a characteristic value C_L, as given by Eq. (12). Therefore, the TFT is additionally driven by the drain bias voltage V_D, causing "extra" currents ΔI_D (Eq. (20)), and ΔI_L (Eq. (30)), in addition to the "ideal" current I_o (Eq. (19)), driven by the gate bias voltage V_G.

The "extra" current ΔI_D corresponds to the case of high gate bias voltage $V_G \gg V_T$, when the gate bias induces large areal density of charge carriers Q_s. The effect of ΔI_D is similar in behaviour to channel length modulation in field-effect transistors operating in the saturation regime. We provide a characterization technique that evaluates the characteristic value C_L of the "back"-film fringing capacitance from this regime and, consequently, the effective value of the relative permittivity ε_B of the media in the "back" of the TFT film. One should be careful in the interpretation of the values for ε_B, since $\varepsilon_B \sim 1\ldots2$ are reasonable, considering the assumptions by the derivation of the relations, while values $\varepsilon_B > 2$ indicate that the fringing capacitance is contributing, but might be not the dominant cause for modulation of the output I_D–V_D characteristics in the saturation regime of the operation of the TFT. Nevertheless, the derived Eq. (21) provides the format in which the modulation can be implemented in compact models for TFT, having also the correspondence to other empirical models for channel length modulation, as indicated by Eq. (23).

The "extra" current ΔI_L corresponds to the case of low gate bias voltage $V_G \sim V_T$, when the areal density Q_s of charge carriers is negligible, and ΔI_L depends only on the drain bias voltage V_D. The dependence is equivalent to consider an "extra" TFT in a diode connection with a "back"-gate capacitance $6C_L$, instead of C_{ox}, but otherwise identical and in parallel to the main TFT. Consequently, ΔI_L has a quadratic dependence on the ratio V_D/L, which is qualitatively similar to a leakage from space-charge limited conduction (SCLC) in the semiconducting film of the TFT, since SCLC current in thin films is given by [5]

$$\frac{I_{SCLC}L}{\mu W} = 2\frac{\varepsilon_0\varepsilon_s}{\pi L}V_D^2. \tag{31}$$

A simple comparison between Eqs. (30) and (31) implies that SCLC uses the doubled permittivity of the semiconducting film, $2\varepsilon_s$, whereas ΔI_L uses the tripled permittivity of the media in the "back" of the film, $3\varepsilon_B$. Since $\varepsilon_B \sim 1$ and $\varepsilon_s \sim 3$ for organic materials, then I_{SCLC} and ΔI_L have very similar magnitudes; and the two effects might be difficult to distinguish even quantitatively in the leakage current of the organic TFT.

Several other observations can be made in the results from the above derivations. The "extra" currents ΔI_D and ΔI_L caused by the drain bias via the film-"back" fringing capacitance are reciprocal functions of the channel length $\Delta I_D \propto L^{-2}$, Eq. (20), and $\Delta I_L \propto L^{-2}$, Eq. (30), which is normally observed as inverse proportionality $\Delta L/L \propto 1/L$ for the channel length modulation $\Delta L/L$, see Eqs. (22) and (23). Second, $\Delta L/L$ is proportional to the ratio t_{ox}/L of the gate insulator thickness t_{ox} and channel length L. Third, the "leakage" ΔI_L is a quadratic function of the drain bias voltage V_D in short-channel organic transistors [15,16], whereas the modulating current ΔI_D is a nearly linear function of V_D, when the TFT is operating at high gate and drain biases in the saturation regime.

7. Conclusions

The analysis of the fringing capacitance at the "back" surface of the film of TFT indicates that this capacitance contributes to the enhancement of the channel current, which at present is usually attributed to channel length modulation in the TFT operating in the saturation regime at high drain bias voltages V_D, and space-charge limited conduction in the leakage current of the TFT at low gate bias. A method to derive the capacitance models and simple analytical expressions are provided for the impact of the fringing capacitance at the "back" of the film of the TFT. These expressions are in agreement with dependences routinely observed in experiments, which, however, implies that the impact from the fringing capacitance behaviourally is very similar to effects due to channel length modulation and leakage effects, and these effects can be distinguished only quantitatively. It should be mentioned that the simple expressions presented here may need to be refined, since they are derived from non-equalities and with approximations. Therefore, they can be considered as a step towards a more elaborate study of the effects related to fringing capacitances in TFTs. From a detailed literature search up to 2010, we did not find any publication describing the effects related to the fringing capacitance at the "back" of the semiconducting film, to perform a comparison. Therefore, we state that the effects described in this work are possible, and that they need to be verified in detail with specific experiments.

Acknowledgements

This work was supported in part by the Canada Research Chair program. The work of M.J. Deen was supported in part by the South Korean Ministry of Education, Science, and Technology Program under Project R31-2008-000-10100-0 while he was a Distinguished Visiting Professor.

Appendix A

Eq. (5) can be validated by considering $L \approx L_1 \gg s$ in Eq. (4) and substituting the small values of the "parameter" $m \sim 1.5\ s/L_1 \ll 1/2$ in the upper line of Eq. (3). The substitutions yield

$$\frac{C_W}{\varepsilon_0} = \frac{K(m')}{K(m)} \approx \frac{1}{\pi}\ln\left(2\frac{1+(1-m)^{1/4}}{1-(1-m)^{1/4}}\right) \approx \frac{1}{\pi}\ln\left(2\frac{1+1-m/4}{1-1+m/4}\right) \approx \frac{1}{\pi}\ln\left(\frac{16}{m}\right) \approx \frac{\ln(10L_1)-\ln(s)}{\pi}, \tag{32}$$

taking also a binomial expansion $(1-m)^{1/4} \approx 1 - m/4$ for $m \ll 1$. Consequently, the derivative is

$$\frac{\partial C_W/\partial s}{\varepsilon_0} = \frac{\partial}{\partial s}\left[\frac{K(m')}{K(m)}\right] \approx \frac{\partial}{\partial s}\left[\frac{\ln(10L_1) - \ln(s)}{\pi}\right] = -\frac{1}{\pi}\frac{\partial \ln(s)}{\partial s} = -\frac{1}{\pi s}, \quad (33)$$

from which the "1/distance" approximate result in Eq. (5) follows.

Appendix B

Rewriting Eqs. (16) and (18) in integral form with separated variables, we get

$$\int_0^L \frac{I_o}{\mu W} dx = \int_{V_s=0}^{\min(V_D,V_{GT})} C_{ox}(V_G - V_T - V_x) dV_x, \text{ and} \quad (34)$$

$$\int_0^L \frac{\Delta I_D}{\mu W}\left[\frac{C_L}{C_s} + \frac{x}{L}\left(1 - \frac{x}{L}\right)\right] dx \leqslant \int_{V_{S=0}}^{\min(V_D,V_{GT})} V_D C_L dV_x. \quad (35)$$

These integrals are easily solved, taking into account that the currents I_o and ΔI_D have unchanged magnitudes along the channel length coordinate (x). The remaining parameters are constants set either by the materials and the layout of the TFT, or by the biasing conditions. The integrations in Eqs. (34) and (35) yield the results given in Eqs. (19) and (20).

Including the bias enhancement of the mobility, $\mu = \mu_o(V_G - V_T - V_x)^\gamma$, where μ_o is constant mobility prefactor at gate overdrive $(V_G - V_T) = 1$ V and γ is mobility enhancement factor, Eqs. (34) and (35) are rewritten as

$$\int_0^L \frac{I_o}{\mu_{oW}} dx = \int_{V_s=0}^{\min(V_D,V_{GT})} C_{ox}(V_G - V_T - V_x)^{1+\gamma} dV_x, \text{ and} \quad (36)$$

$$\int_0^L \frac{\Delta I_D}{\mu_{oW}}\left[\frac{C_L}{C_s} + \frac{x}{L}\left(1 - \frac{x}{L}\right)\right] dx \leqslant \int_{V_{S=0}}^{\min(V_D,V_{GT})} V_D C_L (V_G - V_T - V_x)^\gamma dV_x. \quad (37)$$

The integration of Eq. (36) yields the TFT generic DC model [6]

$$\frac{I_o L}{\mu_o W} = C_{ox}\frac{(V_G - V_T)^{2+\gamma} - [\max(0, V_G - V_T - V_D)]^{2+\gamma}}{2+\gamma} \approx C_{ox} \times \begin{cases} (V_G - V_T))^{1+\gamma} V_D (1 - \text{err}_o), \text{ when} \\ \quad V_D \ll (V_G - V_T) \text{in the linear regime,} \\ \frac{(V_G - V_T))^{2+\gamma}}{2+\gamma}, \text{ when } (V_G - V_T) \leqslant V_D \\ \quad \text{in the saturation regime} \end{cases} \quad (38)$$

The error term for the linear regime is in the order of $\text{err}_o = O[1/2(1+\gamma)(V_D/V_{GT})^2]$, where $V_{GT} = (V_G - V_T)$ is the gate overdrive.

The integration of Eq. (37) yields the "extra" current due to fringing capacitance

$$\frac{\Delta I_D L}{\mu_o W} \leqslant \frac{C_L V_D}{\frac{1}{6} + \frac{C_L}{C_s}} \frac{(V_G - V_T)^{1+\gamma} - [\max(0, (V_G - V_T - V_D))]^{1+\gamma}}{1+\gamma} \approx 6\frac{\varepsilon_0 \varepsilon_B}{\pi L} \times \begin{cases} V_D^2 (V_G - V_T)^\gamma (1 - err_\Delta), \text{ when} \\ \quad V_D \ll (V_G - V_T) \text{ in the linear regime,} \\ V_D \frac{(V_G - V_T))^{1+\gamma}}{1+\gamma}, \text{ when } (V_G - V_T) \leqslant V_D \\ \quad \text{in the saturation regime,} \end{cases} \quad (39)$$

which is similar to Eq. (20) for the case without bias enhancement of mobility. The error term for the linear regime is in the order of $\text{err}_\Delta = O[1/2\gamma(V_D/V_{GT})^2]$.

Consequently, the bias enhancement term $(V_G - V_T)^\gamma$ is cancelled in the ratio $\delta = \Delta I_D/I_o$, as

$$\delta = \frac{\Delta I_D}{I_o}\Big|_{V_G > V_T, \gamma > 0} \approx 12\frac{C_L}{C_{ox}} \times \begin{cases} \frac{V_D}{2(V_G - V_T) - V_D(1 - err)}, \text{ when } V_D \ll (V_G - V_T) \\ \quad \text{in the linear regime,} \\ \frac{V_D}{V_G - V_T}\frac{1+\gamma/2}{1+\gamma}, \text{ when } (V_G - V_T) \leqslant V_D \\ \quad \text{in the saturation regime,} \end{cases} \quad (40)$$

The comparison between Eqs. (21) and (40) indicates identical bias dependences. The error term for the linear regime is in the order of $\text{err} = O[\gamma/(2+\gamma)]$, and is in the denominator, because $\text{err}_\Delta < \text{err}_o$. When the mobility enhancement factor γ is included, then the full expression for δ is tedious and inappropriate for manual analyses. Provided that $\gamma < 1$ in TFTs with good electrical performance, then $\text{err} < 50\%$ and the omission of γ will not cause deviations larger than 25% between the values of δ calculated by Eqs. (21) and (40). These deviations are lower than the uncertainty for the values of the fringing capacitance C_L. Therefore, we pursued the analyses with the simpler equations without including the mobility enhancement factor γ.

Appendix C

The shortening of the channel with the small depleted region Δ L near the drain of the MOS transistor with potential $V_x > V_{Dast}$ reduces the integration limit for the current from L to $(L - \Delta L)$ by the integration on the left-hand side of Eq. (34). Consequently,

$$\int_0^{L-\Delta L} \frac{I_{MOS}}{\mu W} d = \int_{V_S=0}^{V_G - V_T} C_{ox}(V_G - V_T - V_x) dV_x \Rightarrow \frac{I_{MOS} L}{\mu W}\left(1 - \frac{\Delta L}{L}\right) = C_{ox}\frac{(V_G - V_T)^2}{2} = \frac{I_{SAT} L}{\mu W} \quad (41)$$

Comparing the relative increase of the current with the free of channel modulation current I_{SAT}, then

$$\delta_{MOS} = \frac{I_{MOS} - I_{SAT}}{I_{SAT}} = \frac{1}{1 - \Delta L/L} - 1 \approx \frac{\Delta L}{L} \propto \frac{V_D - (V_G - V_T)}{L}, \quad (42)$$

Since $\Delta L/L \ll 1$, then one usually takes the first order approximation $\Delta L/L = \lambda(V_D - V_{Dsat})$, as follows from above, and given by Eq. (22).

Appendix D

By analogy with MOS transistors, one usually takes the drain current at biasing condition $V_D = V_{GT} = (V_G - V_T)$ as the saturation current I_{SAT} in the TFT and uses Eq. (19) to evaluate mobility from the equality $I_{SAT}L = W\mu C_{ox}(V_G - V_T)^2/2$. However, we see in Eq. (20) that the "extra" current ΔI_D is not zero at this condition, and also $\delta = \Delta I_D/I_o > 0$ in Eq. (21). Therefore, at a given gate bias voltage V_G, we choose a reference current $I_{Dref} = I_D(V_{Dref} > V_G - V_T)$ in the saturation region of the output characteristic ($I_D = f(V_D)$ at constant V_G) of the TFT. If the TFT is normally-off field-effect transistor (the threshold voltage V_T has the same polarity as the gate V_G and drain V_D bias voltages), then a convenient choice is the biasing condition $V_{Dref} = V_G$ that corresponds to the diode connection of the TFT, because I_{Dref} is easily measured during experiments. In this case, the equations are simpler, therefore, when possible, we provide the corresponding expressions, labelled with "for normally-off TFT". The equations in this appendix are only for the saturation regime of operation of the TFT above threshold $V_G > V_T$, so these expressions should not be applied to data from other regions of operation.

From eq. (21) we have

$$I_{Dref} = I_o(1+\delta) = I_o\left(1 + \frac{V_{Dref}}{V_G - V_T}12\frac{C_L}{C_{ox}}\right), \\ = I_o\left(1 + \frac{V_G}{V_G - V_T}12\frac{C_L}{C_{ox}}\right) \text{ for normally-off TFT.} \tag{43}$$

For the same V_G, and at any other $V_D > (V_G - V_T)$ in the saturation regime

$$I_D = I_o\left(1 + \frac{V_D}{V_G - V_T}12\frac{C_L}{C_{ox}}\right), \text{ with } V_D \neq V_{Dref}. \tag{44}$$

Therefore, the ratio I_D/I_{Dref} and the relative difference δ_{ref} between I_D and I_{Dref} are

$$\frac{I_D}{I_{Dref}} = \frac{V_G - V_T + V_D 12C_L/C_{ox}}{V_G - V_T + V_{Dref}12C_L/C_{ox}} = \delta_{ref} + 1, \\ = \frac{V_G - V_T + V_D 12C_L/C_{ox}}{V_G(1 + 12C_L/C_{ox}) - V_T} \text{ for normally-off TFT,} \tag{45}$$

and

$$\delta_{ref} = \frac{I_D}{I_{Dref}} - 1 = \frac{(V_D - V_{Dref})12C_L/C_{ox}}{V_G - V_T + V_{Dref}12C_L/C_{ox}}, \\ = \frac{(V_D - V_G)12C_L/C_{ox}}{V_G(1 + 12C_L/C_{ox}) - V_T} \text{ for normally-off TFT.} \tag{46}$$

Since I_D and I_{Dref} are measured at predetermined bias voltages V_G, V_D, V_{Dref}, and also knowing the threshold voltage V_T of the TFT, then one rearranges the terms, and experimentally characterizes the ratio C_L/C_{ox} from

$$\frac{C_L}{C_{ox}} = \frac{(V_G - V_T)\delta_{ref}}{12[V_D - V_{Dref}(1+\delta_{ref})]} = \frac{\varepsilon_0\varepsilon_B}{C_{ox}\pi L} = \frac{t_{ox}}{\varepsilon_{ox}}\frac{\varepsilon_B}{\pi L}, \\ = \frac{(V_G - V_T)\delta_{ref}}{12[V_D - V_G(1+\delta_{ref})]} \text{ for normally-off TFT.} \tag{47}$$

The calculation of $\delta_{ref} = I_D/I_{Dref} - 1$ by Eq. (46) from measured data and the consequent substitution of the values of δ_{ref} in Eq. (47) comprise the experimental characterization of the characteristic fringing capacitance C_L (see Eq. (12)) at the "back" of the film in the TFT from operation of the TFT in the saturation regime, because knowing the value of C_{ox}, one calculates C_L and can also obtain the effective value for the relative permittivity ε_B of the media at the "back" of the film, since the channel length L is also known. Therefore, Eqs. (46) and (47) are given also in the text by Eq. (24), and their use is discussed there. From the discussion, one should consider in practice data post-processing for determination of a single value for C_L/C_{ox} or ε_B.

Once the ratio C_L/C_{ox} is obtained, then one can reduce the measured current I_D with the "extra" current ΔI_D due to fringing capacitance at the "back" of the semiconducting film in the TFT, and can also obtain the ideal current I_o due to the gate bias and C_{ox} at the "front" of the film. The ideal current I_o is given by Eq. (19) and the reduction is based on Eq. (21) for the ratio $\delta = \Delta I_D/I_o$ of currents driven by the drain bias V_D through the fringing capacitances and by the gate bias V_G through C_{ox}. Consider as in Eq. (43) that $I_D = (1+\delta)I_o$. Then, $I_o = I_D/(1+\delta)$, and in the saturation regime

$$I_o = \frac{W}{L}\mu C_{ox}\frac{(V_G - V_T)^2}{2} = \frac{I_D}{1 + \frac{V_D}{V_G - V_T}12\frac{C_L}{C_{ox}}}, \text{ at } V_D > (V_G - V_T). \tag{48}$$

Generally, the channel width W, channel length L, the threshold voltage V_T and gate insulator capacitance C_{ox} (per unit area) of the TFT are known. Also, V_G, V_D and I_D are known from the measured I–V curves of the TFT in the saturation regime. Therefore, the last equation above is rearranged as a formula for calculation of the charge carrier mobility at various biasing conditions, as given by Eq. (25) in the text.

Appendix E

One obtains the "extra" current ΔI_L in the semi-insulating state of the TFT, from a derivation that is similar with the derivation of the "extra" current ΔI_D for the above-threshold regime, but using a different equation for the charge ΔQ_s. Using Eq. (29) for ΔQ_s, we write the transport equation for ΔI_L as

$$\frac{\Delta I_L}{\mu W} = \Delta Q_s\frac{\partial V_x}{\partial x} = \frac{(V_D - V_T - V_x)C_L\frac{x}{L}}{\frac{C_L}{C_s} + \frac{x}{L}\left(1 - \frac{x}{L}\right)}\frac{\partial V_x}{\partial x} \\ \leqslant \frac{(V_D - V_T - V_x)C_L}{\frac{C_L}{C_s} + \frac{x}{L}\left(1 - \frac{x}{L}\right)}\frac{\partial V_x}{\partial x}, \tag{49}$$

with $0 = V_s \leqslant V_x \leqslant V_{mD} = \min(V_D, V_D - V_T)$. Observe that $V_{mD} \neq V_m = \min(V_D, V_G - V_T)$, since V_D induces charge independently of V_G. As noted after Eq. (12), the factor in the denominator of Eq. (49) is finite and positive. Therefore, one can multiply the equation by this factor, in order to obtain an integral with separated variables

$$\int_0^L \frac{\Delta I_L}{\mu W}\left[\frac{C_L}{C_s} + \frac{x}{L}\left(1 - \frac{x}{L}\right)\right]dx \\ \leqslant \int_{\min(V_S=0,\ V_D - V_T)}^{\min(V_D,\ V_D - V_T)} (V_D - V_T - V_x)C_L dV_x. \tag{50}$$

The lower boundary of the last integral is modified so that spurious negative currents are avoided when writing the solution of the integrals, given by

$$\frac{\Delta I_L}{\mu W}\left(\frac{C_L}{C_s}+\frac{L}{2L}-\frac{L^2}{3L^2}\right) \leqslant C_L\frac{[\max(0,V_D-V_T)]^2-[\max(0,V_D-V_T-V_D)]^2}{2}. \quad (51)$$

Cancelling the channel length L in the left-hand brackets, followed by division of the equation on the resulting positive term $(C_L/C_s + 1/6)$, one obtains the final expression, given by Eq. (30) in the text. The three possible cases stated there explain the purpose of the function max(0,x), which generates expressions for TFT with virtual "back"-gate capacitance $6C_L$ in the diode connection.

References

[1] Y. Tsividis, Operation and Modeling of the MOS Transistor, second ed., McGraw-Hill, USA, 1999.

[2] C. Wann, K. Noda, T. Tanaka, M. Yoshida, C. Hu, A comparative study of advanced MOSFET concepts, IEEE Transactions on Electron Devices 43 (10) (1996) 1742–1753.

[3] O. Vendik, S. Zubko, M. Nikolskii, Modeling and calculation of the capacitance of a planar capacitor containing a ferroelectric thin film, Technical Physics 44 (4) (1999) 349–355.

[4] Y. Xiang, The electrostatic capacitance of an inclined plate capacitor, Journal of Electrostatics 64 (1) (2006) 29–34.

[5] J.A. Geurst, Theory of space-charge-limited currents in thin semiconductor layers, Physica Status Solidi (b) 15 (1) (1966) 107–118.

[6] O. Marinov, M.J. Deen, U. Zschieschang, H. Klauk, Organic thin-film transistors. Part I: compact DC modeling, IEEE Transactions on Electron Devices 56 (12) (2009) 2952–2961.

[7] M.J. Deen, O. Marinov, U. Zschieschang, H. Klauk, Organic thin-film transistors. Part II: parameter extraction, IEEE Transactions on Electron Devices 56 (12) (2009) 2962–2968.

[8] O. Marinov, M.J. Deen, R. Datars, Compact modeling of charge carrier mobility in organic thin-film transistors, Journal of Applied Physics 106 (6) (2009) 064501. 13 pages.

[9] P. Bullejos, J. Tejada, S. Rodriguez-Bolivar, M.J. Deen, O. Marinov, Model for the injection of charge through the contacts of organic transistors, Journal of Applied Physics 105 (8) (2009) 084516. 8 pages.

[10] O. Marinov, M.J. Deen, B. Iniguez, Charge transport in organic and polymer thin-film transistors: recent issues, IEE Proceedings-Circuits Devices Systems 152 (3) (2005) 189–209.

[11] M.J. Deen, M. Kazemeini, S. Holdcroft, Contact effects and extraction of intrinsic parameters in poly(3-alkylthiophene) thin-film field-effect transistors, Journal of Applied Physics 103 (12) (2008) 124509. 7 pages.

[12] E. Calvetti, L. Colalongo, Zs.M. Kovacs-Vajna, Organic thin film transistors: a DC/dynamic analytical model, Solid-State Electronics 49 (4) (2005) 567–577.

[13] G. Gelinck, T. Geuns, D. de Leeuw, High-performance all-polymer integrated circuits, Applied Physics Letters 77 (10) (2000) 1487–1489.

[14] V. Sundar, J. Zaumseil, V. Podzorov, E. Menard, R. Willett, T. Someya, M. Gershenson, J. Rogers, Elastomeric transistor stamps: reversible probing of charge transport in organic crystals, Science 303 (5664) (2004) 1644–1646.

[15] M.J. Deen, M. Kazemeini, Y. Haddara, J. Yu, G. Vamvounis, S. Holdcroft, W. Woods, Electrical characterization of polymer-based FETs fabricated by spin-coating poly(3-alkylthiophene)s, IEEE Transactions on Electron Devices 51 (11) (2004) 1892–1901.

[16] M. Austin, S. Chou, Fabrication of 70 nm channel length polymer organic thin-film transistors using nanoimprint lithography, Applied Physics Letters 81 (23) (2002) 4431–4433.

that charge generation efficiencies of metal oxide dopants are predominantly controlled by the dispersion characteristics of the dopant in an organic semiconductor. This finding opens a way toward the development of efficient dopants for organic semiconductors by improving the dispersion characteristics.

2. Experimental

The films were deposited on a copper TEM grid covered with formvar and carbon films for the TEM analysis. TEM (Jeol, JEM-3000F) with an accelerating voltage of 300 kV was used for the imaging of a doped sample, respectively. Doped organic layers were formed by coevaporation of each dopant and host by thermal evaporation in a high vacuum. The doping concentration was controlled by the evaporation rates of the dopant and host in the range 0.02–2 Å/s. "Image J" was used for the image treatment and the particle analysis of the TEM image.

The hole-only devices are consisting of indium tin oxide (ITO)/MoO_3- or ReO_3-doped 1,4-bis[*N*-(1-naphthyl)-*N*′-phenylamino]-4,4′ diamine (NPB) (50 nm)/Ag (50 nm). Glass substrates with patterned ITO (150 nm thick) were used to fabricate hole-only devices after they were cleaned with acetone and isopropyl alcohol. The fabricated devices were encapsulated with a getter in a dry nitrogen glove box prior to testing. *J*–*V* characteristics were measured with a Keithley 2400 semiconductor parameter analyzer.

3. Results and discussion

Fig. 1 shows bright-field TEM images of (a) undoped NPB, (b) ReO_3- and (c) MoO_3-doped NPB films containing 25 mol% dopant. MoO_3 and ReO_3, which both possess a larger work function than 6 eV, were selected as dopants because of their efficient charge transfer from various organic hosts. The undoped NPB film shows a featureless image and broad ring diffraction patterns (Fig. 1a and d), indicating the amorphous structure of the organic thin film. On the other hand, the NPB films doped with the metal oxides (MO) shows dark spots in the TEM images (Fig. 1b and c) that arise from nanoclusters. The dopant clusters have an amorphous structure in the doped films, as confirmed by their diffuse halos without sharp peaks in the diffraction pattern (Fig. 1e) [15]. Moreover, the dark spots do not exhibit the periodic lattice of the crystalline structure of ReO_3 in the high-resolution TEM (HR-TEM) image in Fig. 1f, in contrast to the evaporated intrinsic metal oxide, which displayed a nanocrystallite structure [16]. The TEM image of the MoO_3-doped film (Fig. 1c) appeared similar to those of the ReO_3-doped film (Fig. 1b), apart from the size distribution of the dopant clusters.

Statistical analyses of the nanoclusters were conducted using high angle annular dark field (HAADF) images instead of bright-field images because the HAADF images possessed definite contrast due to the different masses of the host and dopant molecules. To define the clusters in the image, the full gray-colored image was changed to a binary image with only black and white using the image analyzing software "Image J" [17]. The size and the number of the clusters were measured and counted from the binary images. Uncertainty coming from the small difference in contrast by the different exposure times and foci of the TEM images was removed by adjusting the contrast of the images to have the same total volume fraction of the clusters in the binary image as the theoretical volume fraction calculated through the density, molecular weight and

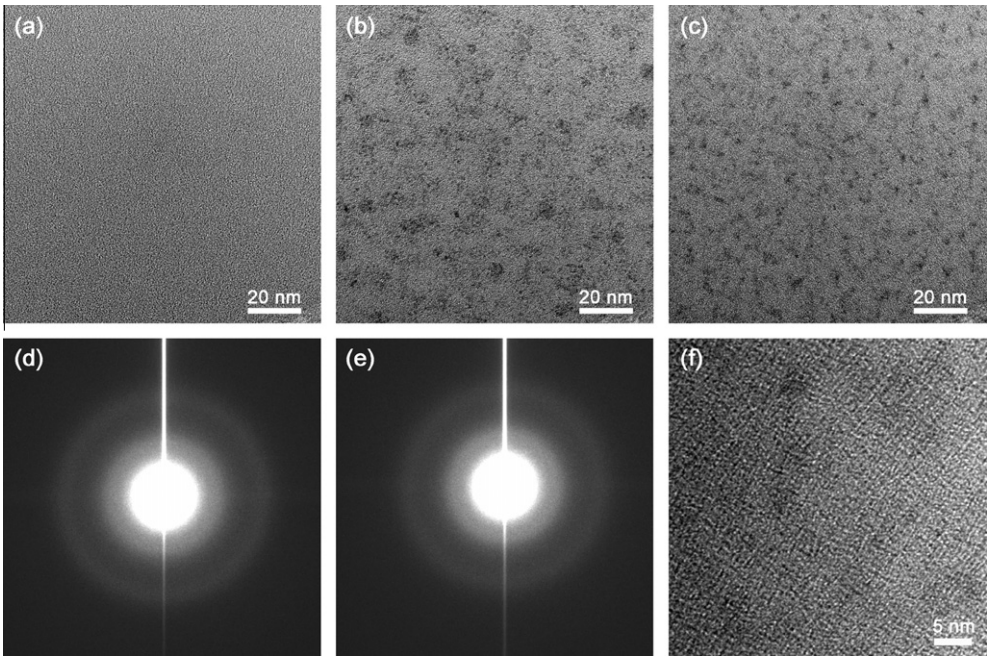

Fig. 1. Bright-field TEM image of (a) undoped NPB, (b) ReO_3- and (c) MoO_3-doped NPB (25 mol%). (d) and (e) Diffraction patterns of (a) and (b), respectively. (f) High-resolution TEM image of (b). The NPB film doped with MO shows dark spots in the image coming from the MO nanoclusters.

doping concentration. In the process, we assumed that every cluster has a spherical shape and is composed of dopant molecules. The cluster size of the two dopants was compared at two different doping concentrations. Fig. 2a and b display binary-treated, inverted HAADF TEM images of 10 mol% ReO_3- and MoO_3-doped NPB films (50 nm), respectively. The MoO_3-doped NPB film has a larger number of small clusters than the ReO_3-doped NPB film. In contrast, the ReO_3-doped NPB film has a larger number of clusters that exceed 2 nm in radius. Radius of nanoclusters was calculated under assumption that the shape of nanoclusters is a sphere. The cluster size distributions of the two different dopants are well described by the log-normal distribution (Fig. 2c). The log-normal distribution can be expressed as

$$f(r) = \frac{A}{r\sqrt{2\pi}\ln\ \sigma}\exp\left(-\frac{(\ln\ r - \ln\ r_c)^2}{2\ln^2\ \sigma}\right) \quad (1)$$

and is defined by the radius of the dopant cluster r, the area of curve A and the mean cluster radius and its standard deviation, r_c and σ, respectively [18].

The log-normal distribution characteristics indicate that the dopant clusters predominantly aggregate on the substrate by diffusion [19]. The formation of clusters during the growth of the thin film on a substrate can in general be described by two stages: an initial stage where newly arrived seed monomers agglomerate, namely the nucleation stage, and then a second stage involving diffusion of molecules that increases the size of the agglomerate, i.e., the growth stage [20]. Therefore, the size distribution of the clusters is influenced by the amount of initial clusters supplied by the evaporated gas and the diffusion processes that are affected by the substrate temperature and phase equilibrium properties between the dopant and host [20–22]. Generally, inverse power law dependence of the cluster size is observed in the initial stage, when seed generation is dominant. In contrast, when the diffusion process is dominant, the size distribution follows a Gaussian distribution or log-normal distribution with a certain average size that depends on the substrate temperature [19]. Therefore, the log-normal distribution of cluster size observed in these systems indicates that the formation of the clusters is dominated by diffusion of the dopants instead of nucleation.

Although all of the dispersion characteristics of the dopants can be described by the log-normal distribution, the details of the distribution vary for different dopants and doping concentrations. The average radius and standard deviation of MoO_3 nanoclusters in a 2 mol% MoO_3-doped NPB film are 0.7 and 1.5 nm, which are much smaller than those of the ReO_3 nanoclusters in the 2 mol% ReO_3-doped NPB film at 1.2 and 2.4 nm, respectively. The small standard deviation and average size of the MoO_3 aggregates indicate that these clusters have a much narrower size distribution in small size. When the doping concentration ratio increases to 10 mol%, the average radius and standard deviation increase to 1.1 and 1.7 nm for the MoO_3-doped and 1.4 and 2.6 nm for the ReO_3-doped NPB films, respectively. These different dispersion characteristics may stem from the intrinsic physical properties of the dopants, including the size of the monomers, evaporation temperature or the structure of molecules, and requires further investigation.

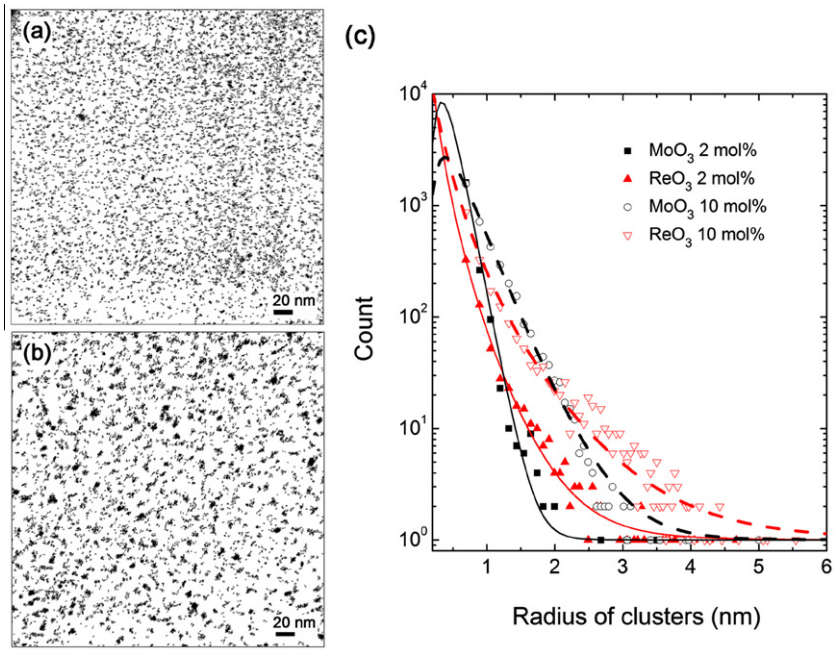

Fig. 2. Binary-treated, inverted HAADF image of NPB films (50 nm) doped with 10 mol% (a) MoO_3 and (b) ReO_3. HAADF images were processed prior to statistical analyses using the image analyzing software "Image J". (c) Histogram of the cluster size and fitting curve for a log-normal distribution of NPB doped with 2 (solid squares, solid line) and 10 mol% (open circles, dashed line) MoO_3 and 2 (solid triangles, dotted line) and 10 mol% (open triangles, dashed-dotted line) ReO_3.

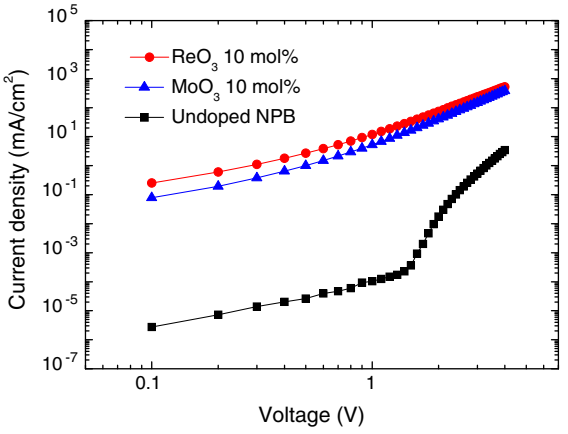

Fig. 3. *J–V* characteristics of hole-only devices containing undoped (squares) or 10 mol% ReO_3- (circles) or MoO_3-doped (triangles) NPB films. The hole-only devices consisting of ITO/MoO_3- or ReO_3-doped NPB (50)/Ag (50) show that ReO_3 has better charge generation efficiency than MoO_3.

Dispersion efficiency of the dopants defined by the number ratio of the nanoclusters to dopant molecules was calculated as follows. Firstly, the number of the clusters was counted from the binary images shown in Fig. 2. The number of nanoclusters under 1 nm^2 (530 $pixel^2$) was included by the extrapolation of fitted log-normal distribution curves instead of the counting process, because these spots are confused with the contrast fluctuation in the TEM images. In the case of 10 mol% ReO_3-doped NPB, the total number of nanoclusters in Fig. 2b was 4500 from the fitted log-normal distribution curve. The number of the clusters was proportional to the thickness of the films, eliminating the possibility of underestimation due to the overlapping of dopant clusters in the TEM images. Secondly, the number of dopants molecules in the doped films was calculated from the known doping concentration, molecular weight (588 g/mol) and the density (1.2 g/cm^3) of the doped films. The number of ReO_3 molecules (10 mol%) in Fig. 2b ($320 \times 320 \times 50\ nm^3$) is 7.2×10^5 based on the calculation. Comparison of the number of the clusters and the number of the dopant molecules results in the dispersion efficiency of 0.62% for the 10 mol% ReO_3 doped NPB films. The low dispersion efficiency of metal oxide dopants limits their charge generation efficiency in doped organic semiconductors. The charge generation efficiency of 10 mol% ReO_3-doped NPB was calculated to be 0.7% from the carrier density of $9.5 \times 10^{17}\ cm^{-3}$ which was measured for a MIS device containing the doped film [7] if each nanocluster can accept one electron from a host molecule due to the charging effect of nanoclusters. For 2 mol% ReO_3-doped NPB, the dispersion and charge generation efficiencies increased slightly to 1.3% and 1.1%, respectively. The similarity between the dispersion efficiency and charge generation efficiency leads to the conclusion that the formation of nanoclusters by metal complex dopants is an origin of the low charge generation efficiency in doped organic semiconductors. Even though the different surface characteristics between ITO and TEM grid substrate might adjust the diffusion and nucleation formation of dopant molecules in host molecules on the surface of substrate, we consider that the dispersion characteristics of dopants in the films could be similar on the different substrate, based on the results of AFM analysis (data are not shown).

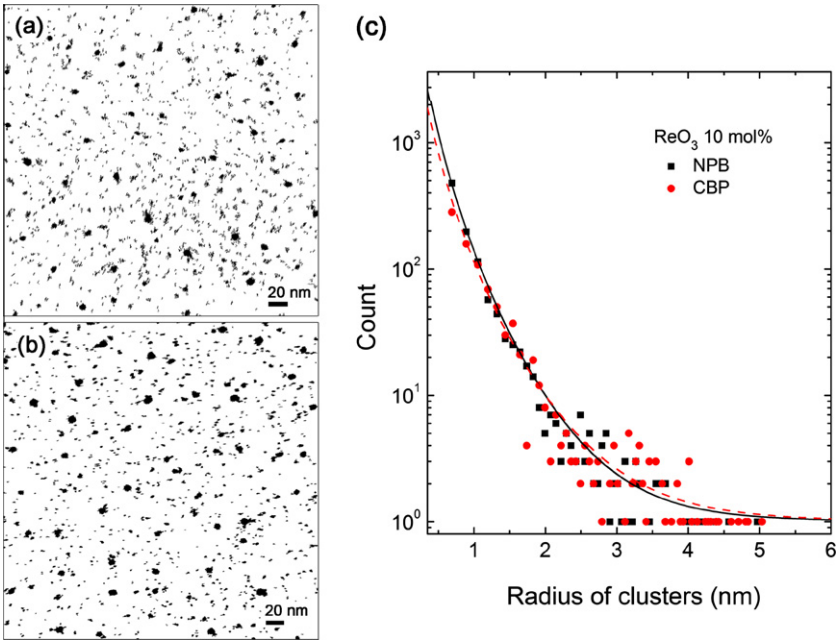

Fig. 4. Binary-treated, inverted HAADF images of 10 mol% ReO_3-doped (a) NPB and (b) CBP films (20 nm). (c) Histogram of the cluster size and fitted log-normal distribution curve for 10 mol% ReO_3-doped NPB (squares, solid line) and CBP (circles, dashed line).

The relationship between the dispersion characteristics and charge generation efficiency for different dopants was investigated using the current density–voltage (J–V) characteristics of hole-only devices consisting of indium tin oxide (ITO)/MoO_3- or ReO_3-doped NPB (50 nm)/Ag (50 nm), as shown in Fig. 3. When a forward bias was applied to each device, hole injection through the interface between ITO and doped NPB dominates over electron injection from the Ag electrode due to the large difference in charge injection barriers. The ReO_3-doped NPB layer possessed a higher current density and electrical conductivity due to higher carrier concentration than the MoO_3-doped NPB layer, even though MoO_3 has larger dispersion efficiency (0.77%) than ReO_3 (0.62%) at a doping concentration of 10 mol%. This fact suggests that the charge generation efficiency can be affected by other factors such as the energy difference (ΔE) between the acceptor level of the dopant and the donor level of the host, as we noted previously [7,9]. The ReO_3-NPB system has larger ΔE values than the MoO_3-NPB system. Further evidence of the ΔE dependence can be obtained by doping the same dopant in two hosts with different highest occupied molecular orbital (HOMO) levels.

Fig. 4a and b shows binary-treated, inverted HAADF TEM images of 10 mol% ReO_3-doped NPB and *N*,*N*′-dicarbazolyl-4,4′-biphenyl (CBP) films with a thickness of 20 nm. To fabricate devices with the same doping concentration in different hosts, the evaporation speed of the dopant was fixed and the evaporation speed of the host was varied to avoid monomer flux dependence such as that shown in Fig. 2c. As shown in Fig. 4c, ReO_3 shows nearly identical dispersion characteristics in the two hosts, because these hosts have similar molecular structures based on triphenylamine groups [23]. However, the ReO_3 doped NPB film had the 2.5 times higher carrier density than ReO_3 doped CBP film [7]. This behavior can be interpreted based on the respective ΔE of the films. NPB has a higher HOMO level than CBP (−5.4 versus −6.0 eV), resulting in a larger ΔE value in the ReO_3-doped NPB system than in ReO_3-doped CBP. The larger ΔE value facilitates charge generation from NPB to ReO_3 [7].

4. Conclusion

In summary, TEM analysis revealed that the formation of dopant nanoclusters is an origin of the low charge generation efficiencies of metal oxides in organic semiconductors. Dopant nanoclusters of ReO_3 and MoO_3 possess cluster sizes with a log-normal distribution and average size of 0.7–1.4 nm, depending on the dopant and their concentration. The low dispersion efficiency of ReO_3 of 0.62% dictates its charge generation efficiency in the organic host of 0.7% in 10 mol% ReO_3-doped NPB. This work demonstrates that the charge generation efficiencies of dopants are predominantly controlled by the dispersion characteristics of the dopant in the host organic semiconductor and also the energy differences (ΔE) between acceptor levels of the dopant and donor levels of organic hosts. It is expected that our findings will be valuable for indentifying efficient dopants for various organic semiconductors.

Acknowledgments

This work was supported by the Industrial Strategic Technology Development Program (10035225, Development of core technology for high performance AMOLED on plastic) funded by MKE/KEIT. J.-H. Lee and Prof. J.-J. Kim thank Prof. Stephen R. Forrest from the University of Michigan for valuable discussion.

References

[1] D.-S. Leem, H.-D. Park, J.-W. Kang, J.-H. Lee, J. Kim, J.-J. Kim, Appl. Phys. Lett. 91 (2007) 011113.
[2] H. Ikeda, J. Sakata, M. Hayakawa, T. Aoyama, T. Kawakami, K. Kamata, Y. Iwaki, S. Seo, Y. Noda, R. Nomura, S. Yamazaki, SID Int. Symp. Digest Tech. Pap. 37 (2006) 923.
[3] K. Walzer, B. Maennig, M. Pfeiffer, K. Leo, Chem. Rev. 107 (2007) 1233.
[4] Y. Qi, T. Sajoto, S. Barlow, E.-G. Kim, J.-L. Brédas, S.R. Marder, A. Kahn, J. Am. Chem. Soc. 131 (2009) 12530.
[5] D.-S. Leem, S.-Y. Kim, J.-H. Lee, J.-J. Kim, J. Appl. Phys. 106 (2009) 063114.
[6] J.-H. Lee, D.-S. Leem, J.-J. Kim, Org. Electron. 9 (2008) 805.
[7] J.-H. Lee, D.-S. Leem, J.-J. Kim, Org. Electron. 11 (2010) 486.
[8] S. Hamwi, J. Meyer, T. Winkler, T. Riedl, W. Kowalsky, Appl. Phys. Lett. 94 (2009) 253307.
[9] J.-H. Lee, D.-S. Leem, H.-J. Kim, J.-J. Kim, Appl. Phys. Lett. 94 (2009) 123306.
[10] S. Olthof, W. Tress, R. Meerheim, B. Lüssem, K. Leo, J. Appl. Phys. 106 (2009) 103711.
[11] M.-T. Hsieh, M.-H. Ho, K.-H. Lin, J.-F. Chen, T.-M. Chen, C.H. Chen, Appl. Phys. Lett. 96 (2010) 133310.
[12] G. He, C. Rothe, S. Murano, A. Werner, O. Zeika, J. Birnstock, J. SID 17 (2009) 159.
[13] J. Xue, S.R. Forrest, Phys. Rev. B 69 (2004) 245322.
[14] T. Matsushima, C. Adachi, Thin Solid Films 517 (2008) 874.
[15] L. Duan, J. Xie, D. Zhang, L. Wang, G. Dong, J. Qiao, Y. Qiu, J. Phys. Chem. C 112 (2008) 11985.
[16] K. Nina, Y. Kimura, K. Yokoyama, O. Kido, G. Binyo, C. Kaito, Physica E 40 (2008) 2995.
[17] P. Svoboda, D. Svobodova, P. Slobodian, T. Ougizawa, T. Inoue, Eur. Polym. J. 45 (2009) 1485.
[18] R.E. Lamaëstre, H. Bernas, Phys. Rev. B 73 (2006) 125317.
[19] V. Agarwal, I. Aruna, V. Banerjee, B.R. Mehta, Phys. Rev. B 74 (2006) 035412.
[20] C. Binns, Surf. Sci. Rep. 44 (2001) 1.
[21] B. Satpati, J. Ghatak, P.V. Satyam, B.N. Dev, J. Appl. Phys. 98 (2005) 064904.
[22] S.B. Simonsen, I. Chorkendorff, S. Dahl, M. Skoglundh, J. Sehested, S. Helveg, J. Am. Chem. Soc. 132 (2010) 7968.
[23] M. Kröger, S. Hamwi, J. Meyer, T. Riedl, W. Kowalsky, A. Kahn, Org. Electron. 10 (2009) 932.

inorganic layer, with the constraint that it has to be processed at low temperature to remain compatible with a flexible plastic foil. Many methods have been investigated to process high quality oxide at low temperatures [9–11]. However, few of them can be process at room temperature at low cost. In this paper, we show that anodization is able to generate high-quality, dense and thin oxide layer at room temperature. In addition to other studies that show anodized metal oxide as the dielectric in OTFTs [12,13], we also present a method for patterning gate and anodized gate dielectric compatible with bottom-contact transistor geometries. Moreover, it should be noted that anodization is compatible with flexible substrate and has potential for roll-to-roll processing.

2. Material and methods

Bottom gate, bottom contact pentacene transistors with a thin dielectric layer consisting of aluminum oxide were prepared as follows. First, a continuous (non-patterned) aluminum layer was thermally evaporated on a glass or foil substrate. This layer was partly anodized into (50 nm thickness) aluminum oxide which forms the gate dielectric. The electrochemical anodization of aluminum was realized in a mixture of citrates containing potassium phosphate dibasic trihydrate and potassium citrate tribasic monohydrate, using a two electrode cell configuration consisting of the aluminum working electrode and a platinum mesh counter electrode. Aluminum was anodized at the anode into Al_2O_3 according to Eq. 2 [14]:

$$2Al + 3H_2O \rightarrow Al_2O_3 + 6H^+ + 6e^- \quad (2)$$

In order to form a high quality barrier-type oxide layer [15], the oxidation was carried out by a two stages process, consisting of a galvanostatic step determining the thickness of the anodized layer, and a potentiostatic step improving the quality of the oxide layer. In the first stage, a constant current density ($+0.07$ mA/cm^2) was applied to the aluminum working electrode until the voltage difference between this electrode and the Pt mesh reached +30 V, corresponding in our case to 50 nm oxide formation. In the second (potentiostatic) stage remaining defects (pinholes) were repaired by maintaining the applied voltage (+30 V) until the current density dropped to 0.006 mA/cm^2.

The roughness of the dielectric layer has been proven very important to the organic semiconductor growth and therefore carrier mobility in the materials [16,17]. We found that anodized Al_2O_3 is conformal to the underlying Al, and that therefore the smoothness and surface quality of the original Al layer is the key factor for obtaining a high-quality Al_2O_3 surface. Fig. 1 shows atomic force microscopy (AFM) images of evaporated aluminum before anodization (on the left of each picture) and the anodized aluminum oxide (on the right of each picture). Nine different aluminum layers were thermally evaporated at various

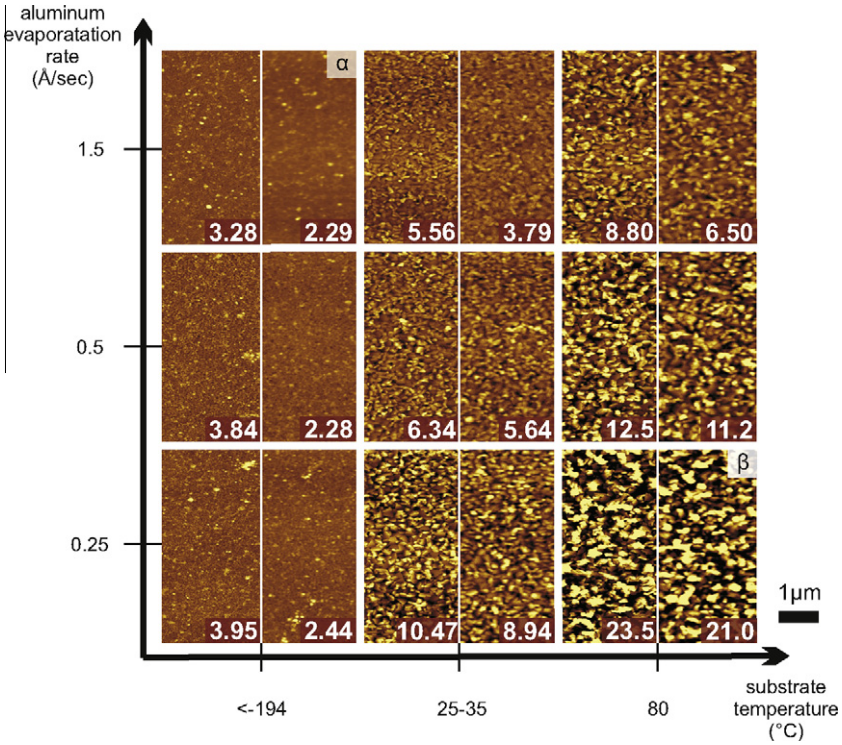

Fig. 1. Atomic force microscopy (AFM) images of thermally evaporated aluminum on glass (on the left of each picture) and after anodization (on the right of each picture). Nine samples were prepared at different evaporation rates and substrate temperatures. The roughness of each surface (nm) is indicated in the corner of each picture. The similarity between before and after anodization illustrates anodized aluminum oxide is conformal to the original surface. The smoothest sample after anodization (α) and the roughest sample (β) were characterized by XRD (Fig. 2).

evaporation rates and substrate temperatures, giving rise to large variation in surface roughness. Smooth layers with roughness as small as 3 nm can be achieved at high rate and low substrate temperature. After anodization (under identical conditions for all samples), the surfaces of the anodized film have almost identical morphology as the original metal layer. In short, the anodized aluminum oxide is conformal to the aluminum layer, and anodization does not generate extra roughness compare to the original aluminum.

The smoothest sample (α) and the roughest sample (β) in Fig. 1 are examined by X-ray diffraction measurement (XRD), and the results are shown in Fig. 2. XRD spectra presents only an Al (111) signal, and no signal from aluminium oxide, indicating that the aluminium oxide is amorphous. We have verified the uniformity of the growth of Al_2O_3 using cross-sectional transmission electron microscopy (TEM) (Fig. 3), confirming that there are no obvious defects or pinholes. From the electric measurement shown in Fig. 4, we infer that a 50 nm thick film of anodized aluminium oxide withstands an electric field as high as 6 MV/cm. This is comparable with 100 nm sputtered aluminium oxide. In addition, the capacitance is around 160 nF/cm^2 and the correspondence dielectric constant is around 9.

We conclude that smooth and dense films of Al_2O_3 with excellent electrical leakage and breakdown characteristics can be prepared at room temperature, and this should have a potential for application in thin-film electronics [18]. In particular, the underlying Al layer can be envisioned as the gate metal, and the anodized Al_2O_3 as the gate dielectric. There remains, however, the problem of patterning the gate/dielectric stack. Indeed, the oxide cannot be formed by anodization of isolated Al islands on a substrate, since electrical current has to be applied to the area to be anodized. Because of the small size of the individual gate electrodes and the large number of gates in electronic circuits, it is impractical to contact each individual gate electrode to anodize it. The only option is to anodize a uniformly deposited layer of Al over the complete area of the substrate, and pattern islands of gate (Al) and gate dielectric (Al_2O_3) afterwards. However, the lateral isolation of the patterned Al gate is now problematic, as the exposed

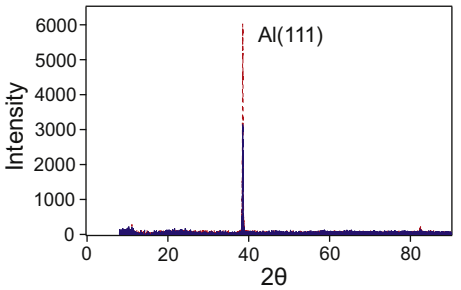

Fig. 2. X-ray diffraction (XRD) spectra of the smoothest (α) (dashed line in red) and roughest (β) (solid line in blue) anodized aluminum layer of Fig. 1. It shows only an Al (111) signal, and no signal from aluminium oxide, indicating that the aluminium oxide is amorphous. (For interpretation of the references in colour in this figure legend, the reader is referred to the web version of this article.)

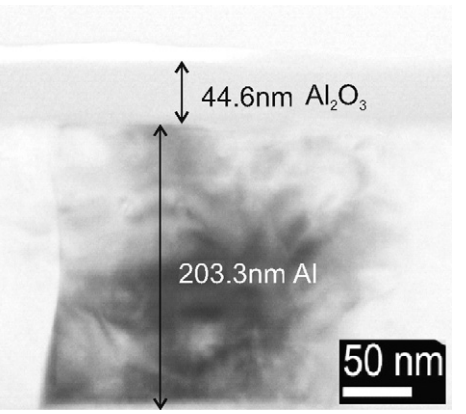

Fig. 3. Cross section transmission electron microscopy (TEM) picture of (α) in Fig. 1 reveals the presence of an amorphous aluminum oxide conformal to the crystalline aluminum surface without obvious defects or pinholes.

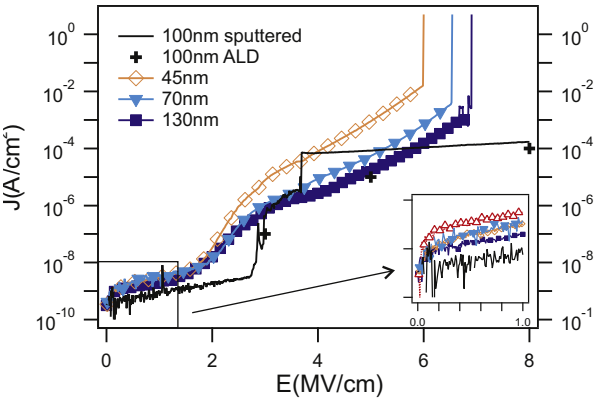

Fig. 4. Leakage current measurement at different fields for different thickness of anodized aluminum oxide compared to sputtered and atomic layer deposit (ALD) aluminum oxide. The anodization voltages are 30 V, 50 V and 100 V, corresponding to 45 nm, 70 nm and 130 nm. The result from 70 nm anodized aluminum oxide is comparable with 100 nm ALD aluminum oxide and sputtered aluminum oxide.

edges of the patterned Al cannot be covered with dielectric during anodization. This problem is the main reason why anodization has not been applied to circuits with large numbers of transistors so far.

We provide a solution that relies on overetching the Al layer in the above process. Our experiments were carried out as shown in Fig. 5. First, a continuous (non-patterned) aluminium layer is deposited by thermal evaporation and anodized to a thickness of 50 nm. Next, a photoresist layer is provided on the metal-insulator stack, and patterned by photolithography, followed by a wet etching step. The wet etchant comprises a mixture of phosphoric acid, nitric acid and acetic acid. The etch rate of Al is higher than that of Al_2O_3, such that the Al layer at the edges is overetched.

Fig. 6 presents an optical micrograph of a top view of this structure, comprising a patterned Al layer with an anodized Al_2O_3 layer and source-drain contacts above. The overetch of the metal oxide layer is in the range be-

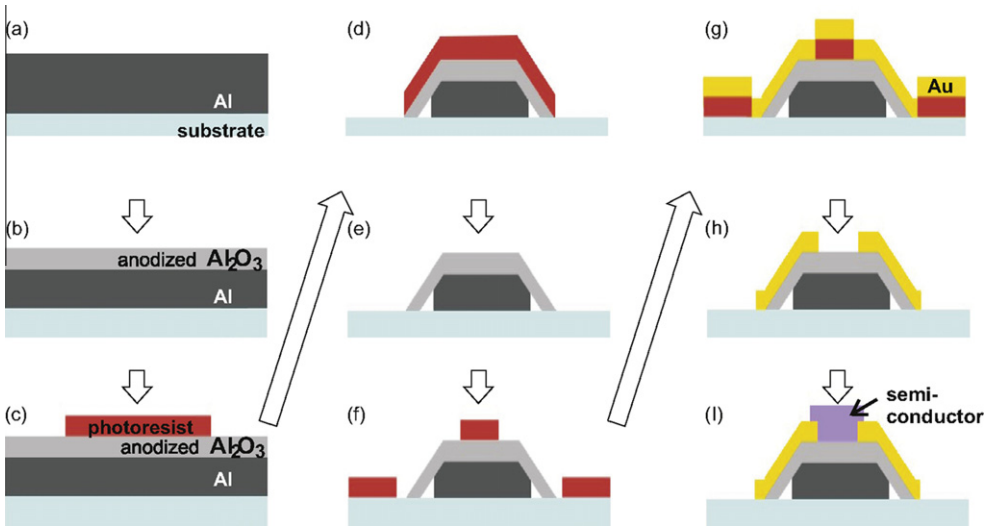

Fig. 5. Process flow of a bottom-gate bottom-contact transistor proposed in this work: (a) thermal evaporation of a continuous (non-patterned) aluminium layer, (b) partial anodization of aluminum layer, (c) photolithographic patterning of a photoresist on the metal-insulator stack, (d) wet etching of Al and Al_2O_3, with overetch Al layer at the edges, (e) removal of photoresist, and (f)–(h) patterning of Au source/drain contacts by lift-off. (i) deposition of semiconductor in the channel.

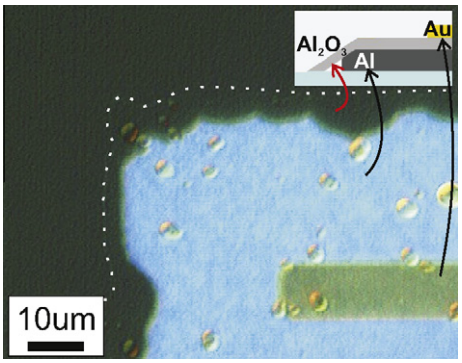

Fig. 6. Optical micrograph (polarized light) showing a top view of a patterned Al layer covered with an anodized Al_2O_3 layer. The white dotted line points out the edge of the collapsing aluminum oxide. Inset: schematic drawing of the corresponding area in cross-view.

tween 2.3 μm and 4.7 μm, much larger than the thickness of the oxide layer, giving a modest bending of the oxide layer without cracks as shown in the cross-section TEM picture in Fig. 7. It indicates the perfect collapse of the Al_2O_3 to cover the edge of the Al pattern. The collapse of the Al_2O_3 can be seen running over the gate edge in Fig. 6, and it ensures complete lateral insulation of the gate

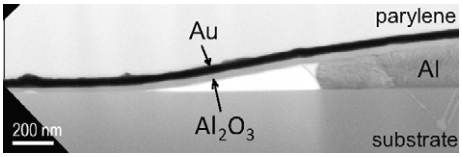

Fig. 7. Cross section TEM picture of overetch aluminum layer demonstrates perfect coverage of the Al edge by the collapsed Al_2O_3, leading to complete lateral insulation of the gate island and preventing short circuits between the gate and the source/drain contacts.

island and prevents short circuits between gate and the drain finger (or source finger). One could argue that the edge line of Fig. 6 is not straight enough for a reliable technology, but this edge is not relevant for the application. The source-drain distance is crucial for correct operation and this is not influenced by this gate patterning technique.

Fig. 8 shows the transfer characteristic of the transistors shown in Fig. 6. Both pentacene and Ga–In–Zn–O are used as a semiconductor layer. After applying self assembled monolayers (pentafluorobenzenethiol and phenethylchlorosilane), pentacene is thermally evaporated at the rate 0.25 Å/sec with substrate temperature 68 °C. Ga–In–Zn–O is sputtered at room temperature and patterned by oxalic acid in room temperature. Both transistors present excellent electrical characteristics with low voltage operation, fairly high charge carrier mobility and close to 0 V onset and threshold voltages: the mobilities for the pentacene transistor on glass, on plastic foil and the Ga–In–Zn–O transistor are 0.47 cm^2/Vs, 0.26 cm^2/Vs, and 0.91 cm^2/Vs; the threshold voltages are 0.51 V, 0.97 V and 0.04 V; the subthreshold swings for these devices are 0.23 V/decade, 0.53 V/decade and 0.21 V/decade. The difference of the off current for these two materials comes from the patterning of the active material. Even though pentacene is unpatterened here, the off current and threshold voltage is low enough for circuit application, and further improvement can be achieved by several methods [19,20]. More importantly, the dashed line in Fig. 8 is the gate to source current showing no current going through between gate and source-drain fingers, confirming that (i) the metal oxide formed by anodization presents an excellent dielectric quality, (ii) the gate electrode is effectively laterally isolated from the source and drain contacts, thanks to the collapsed metal oxide.

In this process, a zero V_{GS} inverter with channel length of 5 μm, channel width of 140 μm for the drive transistors

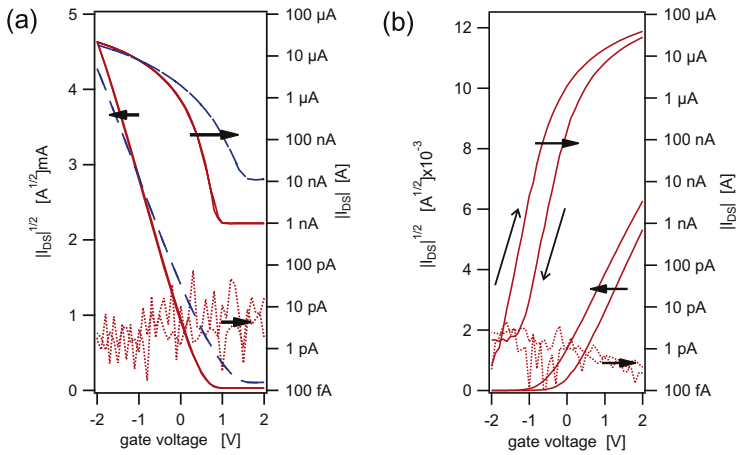

Fig. 8. Transfer characteristics of (a) pentacene (dashed line in blue: on plastic foil substrate, 0.27 cm^2/Vs; solid line in red: on glass substrate, $\mu = 0.47$ cm^2/Vs), (b) Ga–In–Zn–O (on plastic foil substrate, $\mu = 0.91$ cm^2/Vs) transistors (W/L = 1000 µm/10 µm and $V_{DS} = -2V$) prepared according to the process flow of Fig. 5. The low gate to source current (dotted line) confirms an excellent dielectric quality and an effective lateral insulation between gate and source or drain fingers. (For interpretation of the references in colour in this figure legend, the reader is referred to the web version of this article.)

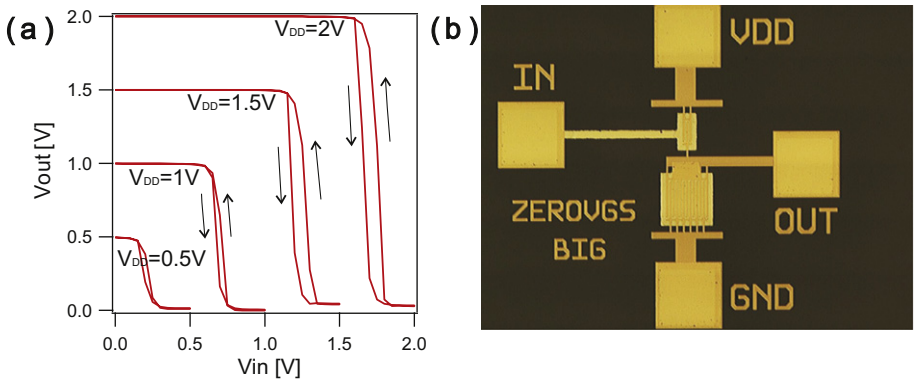

Fig. 9. (a) Voltage transfer curve of a zeroVgs-load inverter, with pentacene as semiconductor, (b) the optical microscopy picture of the inverter. The channel length is 5 µm and the channel width is 140 µm for the drive transistors, 1400 µm for the load transistors.

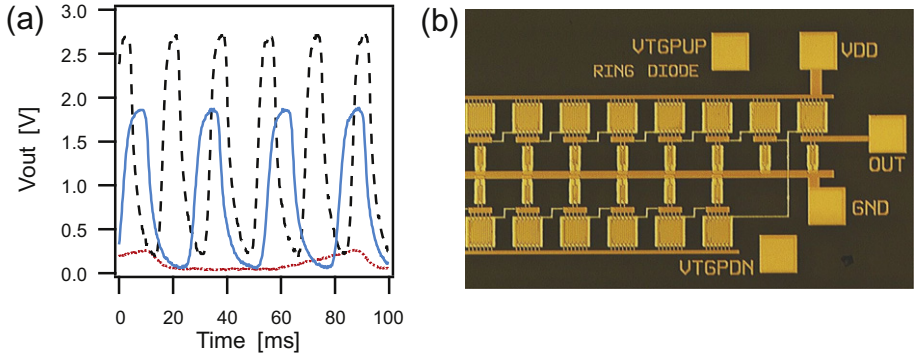

Fig. 10. Ring oscillator consisting of 40 pentacene transistors with channel length 5 µm prepared according the process flow of Fig. 5. Input voltages for dashed line (black), solid line (blue) and dotted line (red) are 3.5V(60Hz), 2.5V(40Hz) and 1V(12Hz). Correct functioning of such ring oscillator made with the above process is shown. It demonstrates the feasibility of the proposed process flow for larger integration. (For interpretation of the references in colour in this figure legend, the reader is referred to the web version of this article.)

and 1400 µm for the load transistors is realized as shown in Fig. 9. In addition, a 19 stage ring oscillator combining 40 transistors (including output buffer transistor) with channel length of 5 µm are also realized and shown in Fig. 10. It demonstrates the feasibility of the proposed process flow for larger integration.

3. Conclusion

We demonstrate a method to make a room-temperature high-k dielectric film, for high-performance organic transistors by anodization of Al to Al_2O_3. An innovative patterning technique circumvents the problem that reliable anodizaton needs to be performed on blank (unpatterned) Al film. It is based on overetching of the Al gate film and collapse of the overlying Al_2O_3 dielectric over the edges to provide efficient and reliable gate edge isolation. Finally, we demonstrate the technique by making and characterising a 19-stage ring oscillator using pentacene.

Acknowledgements

We thank M. Nag (IMEC) for Ga–In–Zn–O deposition and patterning, K. Vasseur (IMEC) for XRD measurement and A.K. Tripathi from Holst Center (Eindhoven, The Netherlands) for leakage current measurement of ALD Al_2O_3. This work was performed in a collaboration between IMEC and TNO in the frame of the HOLST Centre. This work was partly supported by the European funded project COSMIC (FP7-ICT No. 247681) and ORICLA (FP7-ICT No. 247798).

References

[1] Y.L. Guo, G. Yu, Y.Q. Liu, Functional organic field-effect transistors, Advanced Materials 22 (40) (2010) 4427–4447, doi:10.1002/adma.201000740.

[2] G.H. Gelinck, H.E.A. Huitema, E. Van Veenendaal, E. Cantatore, L. Schrijnemakers, J.B.P.H. Van der Putten, T.C.T. Geuns, M. Beenhakkers, J.B. Giesbers, B.H. Huisman, E.J. Meijer, E.M. Benito, F.J. Touwslager, A.W. Marsman, B.J.E. Van Rens, D.M. De Leeuw, Flexible active-matrix displays and shift registers based on solution-processed organic transistors, Nature Materials 3 (2) (2004) 106–110, doi:10.1038/nmat1061.

[3] J.A. Rogers, Z. Bao, K. Baldwin, A. Dodabalapur, B. Crone, V.R. Raju, V. Kuck, H. Katz, K. Amundson, J. Ewing, P. Drzaic, Paper-like electronic displays: large-area rubber-stamped plastic sheets of electronics and microencapsulated electrophoretic inks, Proceedings of the National Academy of Sciences of the United States of America 98 (9) (2001) 4835–4840.

[4] C.D. Sheraw, L. Zhou, J.R. Huang, D.J. Gundlach, T.N. Jackson, M.G. Kane, I.G. Hill, M.S. Hammond, J. Campi, B.K. Greening, J. Francl, J. West, Organic thin-film transistor-driven polymer-dispersed liquid crystal displays on flexible polymeric substrates, Applied Physics Letters 80 (6) (2002) 1088–1090.

[5] T. Sekitani, T. Yokota, U. Zschieschang, H. Klauk, S. Bauer, K. Takeuchi, M. Takamiya, T. Sakurai, T. Someya, Organic nonvolatile memory transistors for flexible sensor arrays, Science 326 (5959) (2009) 1516–1519, doi:10.1126/science.1179963.

[6] K. Myny, S. Steudel, P. Vicca, M.J. Beenhakkers, N.A.J.M. van Aerle, G.H. Gelinck, J. Genoe, W. Dehaene, P. Heremans, Plastic circuits and tags for 13.56 MHz radio-frequency communication, Solid-State Electronics 53 (12) (2009) 1220–1226, doi:10.1016/j.sse.2009.10.010.

[7] A. Facchetti, M.H. Yoon, T.J. Marks, Gate dielectrics for organic field-effect transistors: new opportunities for organic electronics, Advanced Materials 17 (14) (2005) 1705–1725, doi:10.1002/adma.200500517.

[8] H. Klauk, Organic thin-film transistors, Chemical Society Reviews 39 (7) (2010) 2643–2666, doi:10.1039/b909902f.

[9] X.H. Zhang, B. Domercq, X.D. Wang, S. Yoo, T. Kondo, Z.L. Wang, B. Kippelen, High-performance pentacene field-effect transistors using Al_2O_3 gate dielectrics prepared by atomic layer deposition (ald), Organic Electronics 8 (6) (2007) 718–726, doi:10.1016/j.orgel.2007.06.009.

[10] A.L. Deman, M. Erouel, D. Lallemand, M. Phaner-Goutorbe, P. Lang, J. Tardy, Growth related properties of pentacene thin film transistors with different gate dielectrics, Journal of Non-crystalline Solids 354 (15-16) (2008) 1598–1607, doi:10.1016/j.jnoncrysol.2007.10.027.

[11] R.P. Ortiz, A. Facchetti, T.J. Marks, High-k organic, inorganic, and hybrid dielectrics for low-voltage organic field-effect transistors, Chemical Reviews 110 (1) (2010) 205–239, doi:10.1021/cr9001275.

[12] Y. Fujisaki, Y. Inoue, T. Kurita, S. Tokito, H. Fujikake, H. Kikuchi, Improvement of characteristics of organic thin-film transistor with anodized gate insulator by an electrolyte solution and low-voltage driving of liquid crystal by organic thin-film transistors, Japanese Journal of Applied Physics Part 1-regular Papers Short Notes and Review Papers 43 (1) (2004) 372–377, doi:10.1143/JJAP.43.372.

[13] L.A. Majewski, R. Schroeder, M. Grell, One volt organic transistor, Advanced Materials 17 (2) (2005) 192–196, doi:10.1002/adma.200400809.

[14] C.F. Yeh, J.Y. Cheng, J.H. Lu, The characterization of Al_2O_3 prepared by anodic-oxidation, Japanese Journal of Applied Physics Part 1-regular Papers Short Notes and Review Papers 32 (6A) (1993) 2803–2808.

[15] J.W. Diggle, T.C. Downie, C.W. Goulding, Anodic oxide films on aluminum, Chemical Reviews 69 (3) (1969) 365–405, doi:10.1021/cr60259a005.

[16] S. Steudel, S. De Vusser, S. De Jonge, D. Janssen, S. Verlaak, J. Genoe, P. Heremans, Influence of the dielectric roughness on the performance of pentacene transistors, Applied Physics Letters 85 (19) (2004) 4400–4402, doi:10.1063/1.1815042.

[17] A.A. Virkar, S. Mannsfeld, Z.A. Bao, N. Stingelin, Organic semiconductor growth and morphology considerations for organic thin-film transistors, Advanced Materials 22 (34) (2010) 3857–3875, doi:10.1002/adma.200903193.

[18] S. Goettling, B. Diehm, N. Fruehauf, Active matrix otft display with anodized gate dielectric, Journal of Display Technology 4 (3) (2008) 300–303, doi:10.1109/JDT.2008.921903.

[19] S. De Vusser, S. Steudel, K. Myny, J. Genoe, P. Heremans, Integrated shadow mask method for patterning small molecule organic semiconductors, Applied Physics Letters 88 (10) (2006) 103501–103503.

[20] S. Steudel, K. Myny, S. De Vusser, J. Genoe, P. Heremans, Patterning of organic thin film transistors by oxygen plasma etch, Applied Physics Letters 89 (18) (2006). 183503-3.

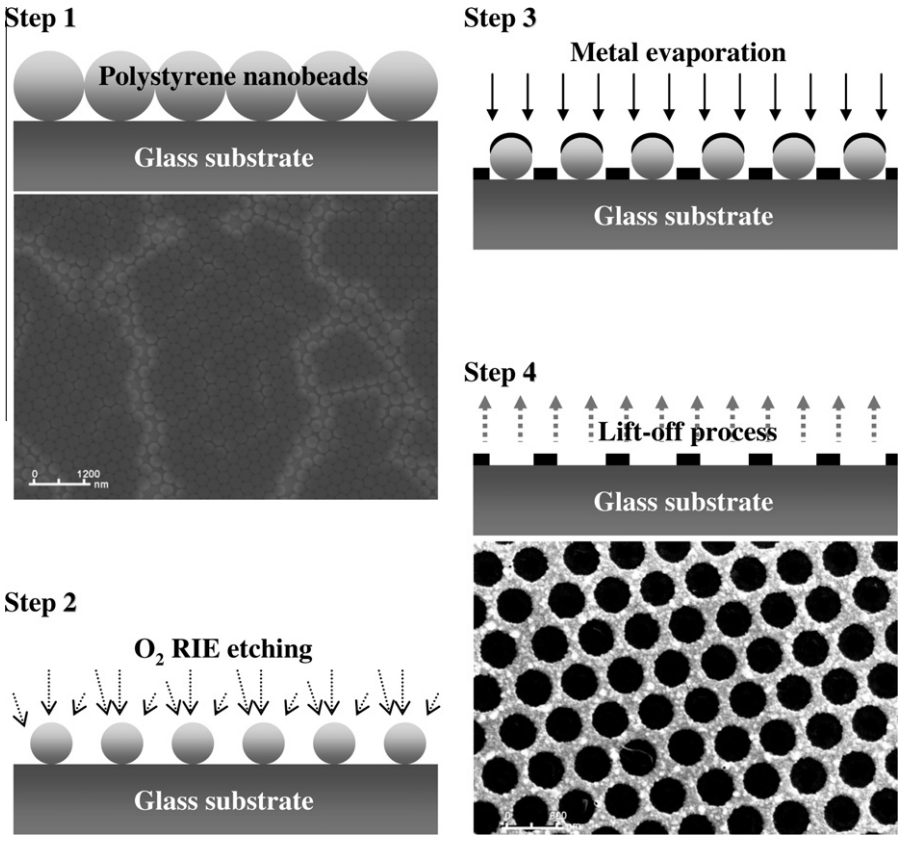

Fig. 1. The diagrams for making metallic nanohole arrays for the anodes of OLED devices.

(H_2SO_4) mixed with hydrogen peroxide (H_2O_2) and then rinsed with deionized water. By controlling the concentration of nanosphere solution and the rotation speed of the spin coater, a single layer of nanospheres was coated on the substrate. After minutes of settling down, the hexagonal close-packed nanostructures were formed. The period of the hexagonal array was determined by the original diameter of the polystyrene spheres. We further reduced the diameter of these spheres by a RIE etcher. In the RIE process, argon ions etched the polystyrene balls isotropically. The periphery of the ball was etched away. It thus reduced the diameter of the polystyrene ball. Subsequently, we used electron-gun evaporation to fill the gap with silver thin film. The sample was then put into dichloromethane (CH_2Cl_2) solution in an ultrasonic cleaner to remove the polystyrene balls. The remained silver film on the substrate formed a periodic nanohole array as shown in Fig. 1 (step 4). For different RIE etching time, the diameter of the polystyrene ball was different. It resulted in different size of holes in the silver film. We defined a parameter, fill-factor, to describe the difference. The fill-factor is defined by the ratio of the area of nanohole array divided by the total area.

The patterned thin film was further treated with an annealing process at 200 °C for 3 h under ultra-high vacuum conditions (<10^{-7} torr) in order to form more compact metal grains. The annealing treatment is crucial to the reduction of the background defects and decrease the grain boundary scattering resistivity [15]. Fig. 2 shows the measured sheet resistance as a function of the fill-factor for different deposition rates of silver film. When the deposition rate changed from 0.2 to 0.6 nm/s, the sheet resistance was greatly reduced, especially for high fill-factors. This implies that the evaporated silver grains construct a more compact structure when the deposition rate is high. After annealing at 250 °C for 3 h, the sheet

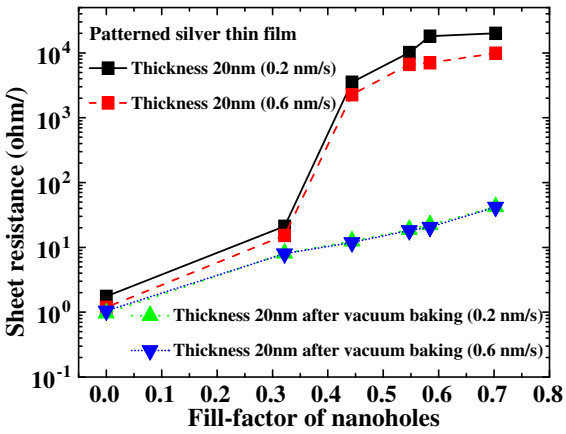

Fig. 2. Sheet resistances of 20-nm-thick silver thin film with different deposition rate and annealing process as a function of the fill-factor. The vacuum baking indicates that the annealing process was done in a high vacuum (<10^{-7} torr) chamber.

resistance decreased greatly. It is noted that the sheet resistances after the annealing process were identical, no matter what the deposition rate was. This was evidence that thermal annealing can reconstruct the silver grains and improve conductance of the nanoscale electrodes.

The averaged visible transmissions for different thicknesses of patterned silver films with different fill-factors were shown in Fig. 3(a). The period of the nanohole array was 590 nm. The flat silver thin film (fill-factor = 0) has a low transmittance. With the nanohole array, it resulted in a great improvement of transparency. For 10 nm thick silver film, the transparency was increased with an increase in fill-factor. However, there was extraordinary increase in transmission for the 20 nm thick Ag film. Fig. 3(b) shows the transmission spectra of 20 nm thick Ag film with different fill-factors. It can be seen that the transmission is increased near the 600 nm wavelength. The wavelength is close to the period. We attribute such transmission enhancement due to the surface plasmon resonant effect in the silver nanohole arrays [16]. The small fill-factor indicates small holes in the silver film. It is known that surface plasmons are generated in these metallic nanoholes. For periodic metallic nanostructures, the surface plasmon resonance can enhance the transmission at wavelengths near the period (590 nm) [17]. This patterned thin film with 0.321 fill-factor had an average transparency of 0.65 for green light. The transparency was smaller than the transparent ITO. Its sheet resistance was only 6.17 Ω/□, lower than the 15 Ω/□ of ITO. A small fill-factor also avoids the problems of the vertical current spreading in optoelectronic devices. Therefore it is more suitable for making light emitting devices.

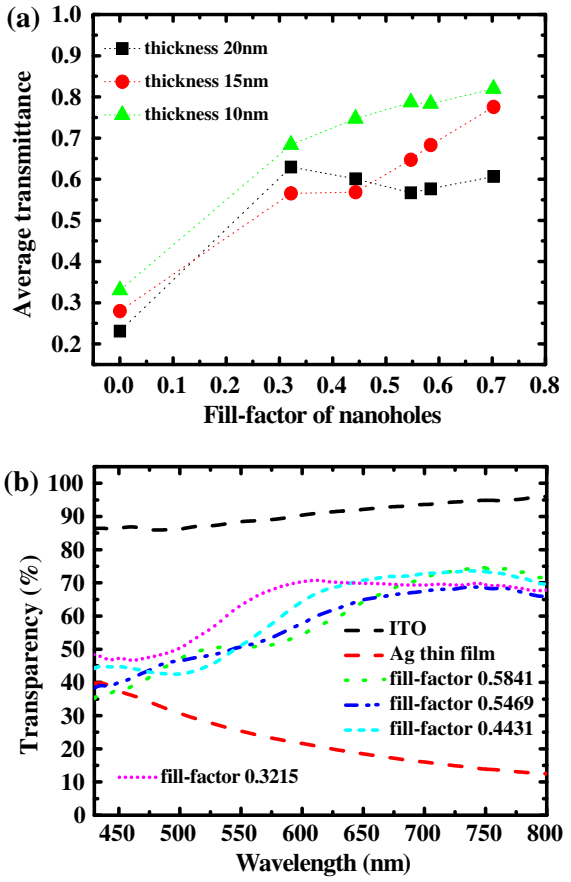

Fig. 3. (a) Transmittance of the patterned Ag films with different fill-factors and film thickness. (b) Transmission spectra of 590-nm-period patterned Ag thin film with 20 nm thickness.

3. OLED with patterned silver thin film

Our OLED fabrication process can be divided into two major parts, including patterned anode smoothing and conventional organic layers evaporation. Because the strong electric field at the sharp point of the patterned anode could result in the penetration of organic layers, the way to smooth the roughness of the patterned anode is a crucial issue to building patterned anode OLEDs. Polymer material spun onto the patterned anode can form a protection layer to smooth its surface and help hole-injection. The PEDOT: RSS (Poly(3,4-ethylenedioxythiophene) poly(styrenesulfonate)) and SAM (self-assemble monolayer) are both suitable polymer materials to be the protection layer. However, the SAM layer also helps increasing the work function of the silver thin film (from 4.68 to 5.6 eV). It provides a better energy level alignment between the work function of the anode and the HOMO level of the NPB [18]. Hence, we used SAM as the protection layer. The PEDOT: RSS was not used in this study. After smoothing the patterned anode, organic layers were deposited in an ultra high vacuum (around 5×10^{-6} torr) thermal evaporator. Hole-transport layer (NPB, *N*, *N*'-di-[(1-naphthalenyl)-*N*, *N*'-diphenyl]-(1,1'-biphenyl)-4,4'-diamine) and electron-transport layer (Alq_3, Tris-(8-quinolinolato) aluminum) were evaporated sequentially on the patterned anode. LiF and Al were set as the opaque cathode of the device. After evaporation, the devices were encapsulated with glass in a glove box chamber. We fabricated OLEDs with conventional ITO anodes, unpatterned and patterned silver thin films with SAM coatings. The fabrication parameters for OLEDs with different kinds of anodes are listed in Table 1.

Fig. 4(a) shows the *I*–*V* curves and the picture of the bottom emission for those devices. The turn-on voltages at the current density of 100 mA/cm^2 were 7.54 V (control device), 5.81 V (unpatterned device) and 6.72 V (patterned device). It is noted that the sheet resistances of the patterned film and the ITO anode are similar (patterned film with SAM modification: 6.17 Ω/□, ITO: 15 Ω/□). However, the hole injection efficiency for the patterned film is much better than the ITO ones due to a better energy alignment for SAM modified silver anodes. Therefore, the patterned silver anode has a turn-on voltage lower than the ITO one. Fig. 4(b) shows the efficiency versus the current density. The saturated current efficiencies were 3.2 cd/A (control device), 4.6 cd/A (unpatterned device), and 5.4 cd/A (patterned device). Even though the current efficiency of the patterned film was depressed by the confinement of the vertical current spreading, it still showed an 84.6% improvement compared to the ITO devices. Such

Table 1
Device structures with different transparent anodes.

Device	Anode	Surface treatment	NPB	Alq_3	LiF	Al
Control	ITO	O_2 plasma	60 nm	60 nm	1 nm	100 nm
Unpatterned	Ag (20 nm)	SAM				
Patterned nanohole array (*FF*: 0.32)	Ag (20 nm)	SAM				

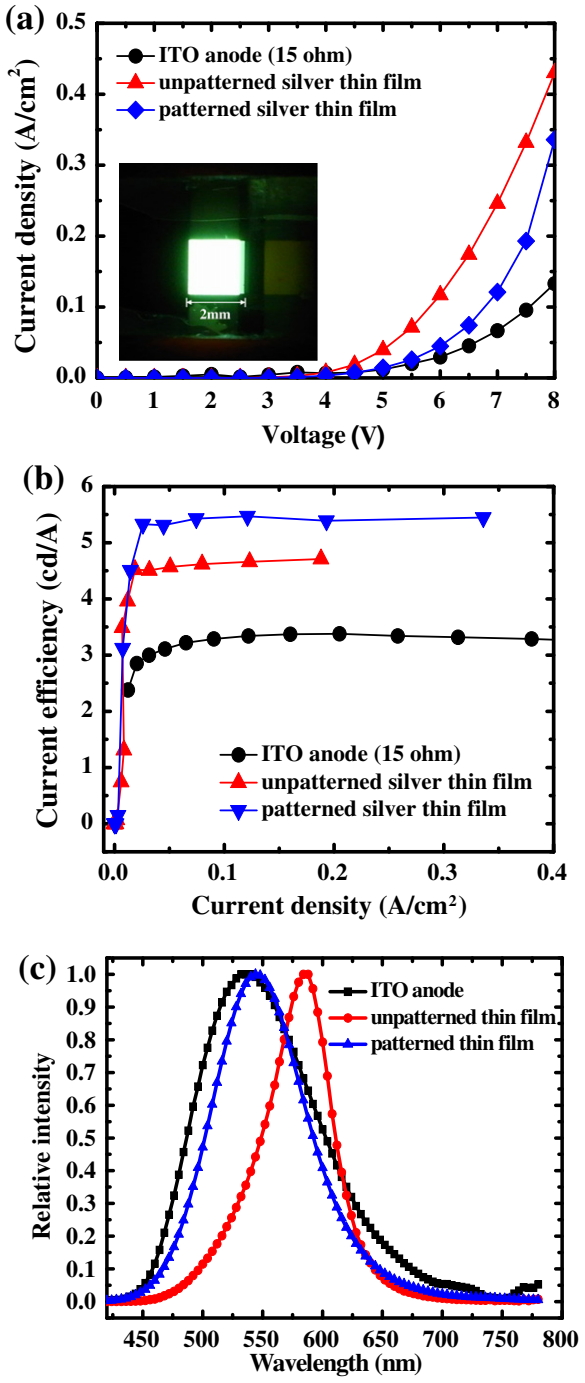

Fig. 4. (a) *I–V* curves, (b) current efficiency versus current density, and (c) normalized EL spectra of OLED devices with different types of anodes.

efficiency enhancement is attributed to the light extraction by the metallic nanostructures. In a typical OLED, less than one third of the generated photons can escape from the emitting devices. One third of these photons are guided in the glass substrate and the others are trapped in the organic layers. The patterned anode was composed of periodic metallic nanostructure. It helps in scattering light out of the organic layer and substrate simultaneously. Therefore, a large improvement of the total quantum efficiency is achieved. Fig. 4(c) shows the diagram of the emission spectra. There is a strong Fabry–Perot effect in the non-patterned silver film device [19]. Such cavity effects narrowed the emission spectrum. For the patterned device, the cavity effect is weaker and the scattering by the silver nanostructures makes the emission spectrum broader and more similar to the ITO ones. If we took the EL (electroluminescence) spectra and calculated the CIE (International Commission on Illumination) coordinate, the resultant emission spectra of the patterned films provided the best color purity (CIE 1931: control device: (0.3529, 0.5337), unpatterned device: (0.4773, 0.502), and patterned device: (0.3484, 0.5953)).

4. Conclusion

We have fabricated an ITO comparable transparent anode using nanosphere lithography. About an 85% transparency and 35 Ω/□ silver anodes were created. The electricity of the anode is better than the ITO anode. The optical transmittance is lower but can be enhanced by the surface plasmon resonance effect. Compared to the traditional ITO based device, the SAM modified patterned silver anode leads to a 0.82 V reduction in turn-on voltage and a 68.8% improvement in current efficiency.

Acknowledgements

This research is supported by the National Science Council, Taiwan (Grant No. NSC-99-2120-M-007-009) and the Nano Program of Academia Sinica, Taiwan.

References

[1] E. Fortunato, D. Ginley, H. Hosono, D. Paine, MRS Bull. 32 (3) (2007) 242–247.
[2] B. O'Connor, C. Haughn, K. An, K. Pipe, M. Shtein, Appl. Phys. Lett. 93 (2008) 223304.
[3] M. Izaki, T. Omi, Appl. Phys. Lett. 68 (1996) 2439.
[4] R. Hoffman, B. Norris, J. Wager, Appl. Phys. Lett. 82 (2003) 733.
[5] X. Jiang, F. Wong, M. Fung, S. Lee, Appl. Phys. Lett. 83 (2003) 1875.
[6] G. Jain, R. Kumar, Opt. Mater. 26 (1) (2004) 27–31.
[7] F. Yang, S. Forrest, Adv. Mater. 18 (15) (2006) 2018–2022.
[8] S. Iijima, Nature 354 (6348) (1991) 56–58.
[9] P. Britto, K. Santhanam, A. Rubio, J. Alonso, P. Ajayan, Adv. Mater. 11 (2) (1999) 154–157.

[10] S. Carter, M. Angelopoulos, S. Karg, P. Brock, J. Scott, Appl. Phys. Lett. 70 (1997) 2067.
[11] Y.Q. Li, J.X. Tang, Z.Y. Xie, L.S. Hung, S.S. Lau, Chem. Phys. Lett. 368 (2004) 128.
[12] Y.R. Do, Y.-C. Kim, Y.-W. Song, Y.-H. Lee, J. Appl. Phys. 96 (12) (2004) 7629–7636.
[13] S. Hsu, M. Lee, K. Lee, P. Wei, Appl. Phys. Lett. 92 (2008) 013303.
[14] M. Winzer, M. Kleiber, N. Dix, R. Wiesendanger, Appl. Phys. A: Mater. Sci. Process. 63 (6) (1996) 617–619.
[15] C. Durkan, M. Welland, Phys. Rev. B 61 (20) (2000) 14215–14218.
[16] T. Ebbesen, H. Lezec, H. Ghaemi, T. Thio, P. Wolff, Nature 391 (1998) 667.
[17] S. Chang, S. Gray, G. Schatz, Opt. Express 13 (2005) 3150.
[18] K.Y. Wu, S.Y. Yu, Y.T. Tao, Langmuir 25 (11) (2009) 6232.
[19] E.F. Schubert, N.E.J. Hunt, M. Micovic, R.J. Malik, D.L. Sivco, A.Y. Cho, G.J. Zydzik, Science 265 (1994) 943.

layers. PbPc is a shuttlecock-shaped molecule (Fig. 1a) and a promising material for solar energy conversion at a wavelength that covers the near-infrared region [20]. The mechanism of the structural variation of the PbPc layer with the change of the organic buffer layer was investigated by X-ray diffraction (XRD), synchrotron X-ray diffraction (SR-XRD), and atomic force microscopy (AFM). A clear relationship between the structural, optical, and electrical properties of PbPc-based OSCs with inserted buffer layers was reported.

2. Experimental

PbPc layers and buffer layers were deposited on a polished ITO substrate by organic molecular-beam deposition (OMBD) under a base pressure of 1×10^{-7} Pa. The ITO substrates were chemically treated with a 1:1:4 $NH_4OH/H_2O_2/H_2O$ mixture at 350 K and then dried under a nitrogen flow. We initially deposited poly(3,4-ethylene dioxythiophene):poly(styrene sulfonate) (PEDOT:PSS) (Bytron 4083, Bayer) on the substrate by spin coating at 4000 rpm to obtain reproducible results on structural and electrical properties of organic layers. The substrate surface was then smoothed by drying it at 100 °C for 10 min. Next, the PbPc layers were deposited onto the PEDOT:PSS layer. Pristine phthalocyanine (H_2Pc), oxovanadium phthalocyanine (VOPc), sexithiophene (6T), and para-sexiphenylene (p-6P), all of which had almost constant hole mobilities ($\sim 10^{-2}$ cm^2/Vs) [13,21–23] were adopted as buffer layers that were inserted between the PEDOT:PSS and PbPc layers. The chemical structure, ionized potential, and electron affinity of PbPc, H_2Pc, VOPc, 6T, and p-6P are shown in Fig. 1a–e, respectively [24–27]. The film thickness was controlled using a crystal oscillator monitor, and the buffer layer and PbPc layer were grown at 0.02 and 0.05 nm/s, respectively. Deposition temperature for all organic materials was kept constant at room temperature (RT).

XRD and SR-XRD analyses were performed using a thin-film X-ray diffractometer (Rigaku RINT2100) with a Cu Kα source ($\lambda = 0.154$ nm) and a Huber six-axis diffractometer at beam line 4C in the KEK photon factory, respectively. The wavelength of the incident synchrotron X-ray for SR-XRD was fixed at $\lambda = 0.1907$ nm, which corresponds to the photon energy of 6.5 keV. Since the intensity of the synchrotron X-rays is much higher than that of the Cu Kα source used in the laboratory system, SR-XRD was used for the structural characterization of the buffer layers, the thicknesses of which were relatively thin. In the out-of-plane XRD analyses, we used the Bragg–Brentano configuration (θ–2θ mode) and the Seemann-Bohlin geometry (incident angle = $\sim 0.15°$) to examine the lattice periodicity perpendicular to the substrate surface [8,28]. The in-plane XRD analysis, on the other hand, is used to examine the lattice periodicity parallel to the substrate surface. Therefore, the three-dimensional crystalline structure can be observed in these measurements. Tapping-mode AFM was performed using a probe system (Seiko Instruments SPI3800) at RT in air. The optical absorption spectra of the films were obtained using a Jasco Ubest V-570 system.

The solar cells (device area: 4 mm^2) were fabricated using a combination of PbPc and C_{60}; the characteristics of these cells were determined using simulated solar light with an air mass of 1.5 (AM 1.5) under 100 mW/cm^2 irradiation in air. The spectrum sensitivity was investigated at RT using a xenon lamp with a 25-cm focal-length single monochromator (Bunko Keiki SM-1700A).

3. Results and discussion

3.1. Structural and electrical properties of PbPc layers

Fig. 2 shows the XRD profiles of 100-nm-thick PbPc layers formed on PEDOT:PSS (a) without a buffer layer and with (b) H_2Pc, (c) VOPc, (d) p-6P, and (e) 6T buffer layers measured in θ–2θ mode. The thickness of the buffer layers was fixed at 5 nm. The structural variation of the PbPc crystal from a monoclinic phase (Fig. 2f; lattice parameter: $a = 2.55$ nm, $b = 2.55$ nm, $c = 0.373$ nm; $\gamma \sim 90°$) [29] to a

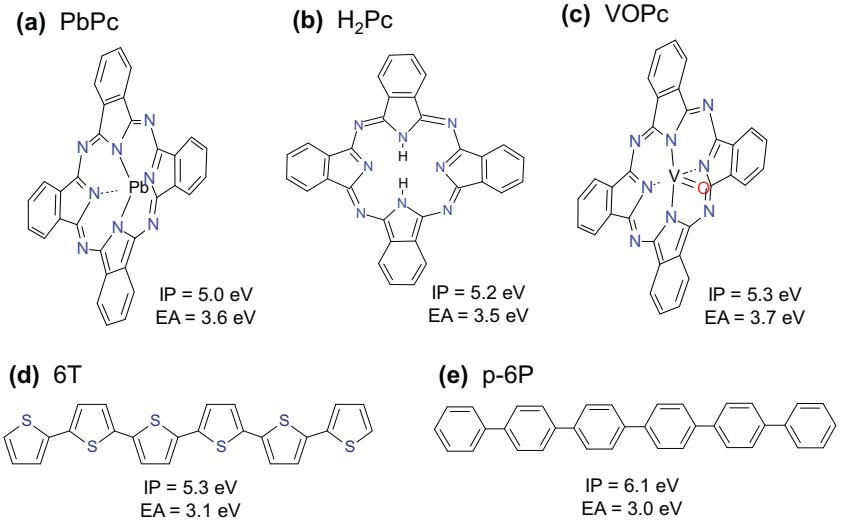

Fig. 1. Chemical structure, ionized potential (IP), and electron affinity (EA) of (a) PbPc, (b) H_2Pc, (c) VOPc, (d) 6T, and (e) p-6P.

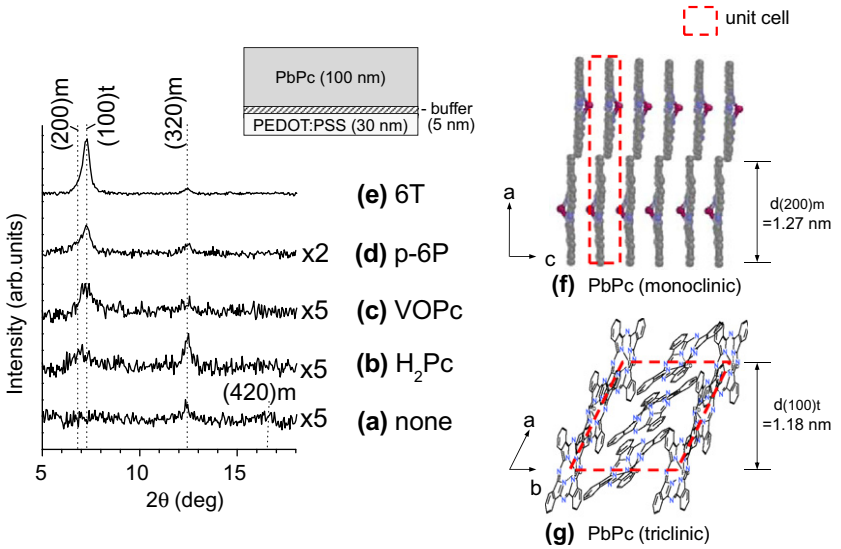

Fig. 2. XRD profiles of 100-nm-thick PbPc layers formed on PEDOT:PSS (a) without a buffer layer and with (b) H_2Pc, (c) VOPc, (d) p-6P, and (e) 6T buffer layers measured in θ–2θ mode. The thickness of buffer layers was fixed at 5 nm. Schematic crystal structures of (f) monoclinic PbPc and (g) triclinic PbPc are also shown in the figure.

triclinic phase (Fig. 2g; $a = 1.31$ nm, $b = 1.61$ nm, and $c = 1.29$ nm; $\alpha = 94.2°$, $\beta = 96.2°$, and $\gamma = 114.2°$) [30] was observed by changing the buffer layers. In the case of the specimen without a buffer layer, diffraction peaks corresponding to monoclinic PbPc (3 2 0), expressed as (3 2 0)m, and (4 2 0)m and were observed at $2\theta = 12.7°$ and 16.5°, respectively [31,32]. The diffraction peaks corresponding to monoclinic PbPc were also observed for the PbPc layer with the H_2Pc buffer layer, whereas a new peak was observed for PbPc (2 0 0)m at $2\theta = 6.9°$. This result indicates that the molecular orientation of PbPc was modified due to the variation in the molecule–substrate interaction resulting from the insertion of the H_2Pc buffer layer, while the weak diffraction peaks suggest that PbPc has a disordered crystalline structure. On the other hand, in the case of the specimens containing VOPc, 6P, and 6T buffer layers, the diffraction peak corresponding to triclinic PbPc (1 0 0), expressed as (1 0 0)t, was newly identified at $2\theta = 7.35°$. In the case of the PbPc/6T and PbPc/p-6P heterostructures, the PbPc (1 0 0)t diffraction peak was observed to have a high intensity and a narrow width, indicating the well-ordered crystalline structure of the PbPc layers. It is known that the crystalline structure of PbPc can be controlled by the variation of the deposition condition (e.g., deposition rate and substrate temperature) [31,32]. The influence of the organic buffer layer on the phase variation of PbPc has not been systematically studied yet.

In order to discuss the variations in the structural properties of PbPc layers grown on buffer layers, we investigated the crystalline structure of the buffer layers using SR-XRD. Fig. 3 shows the out-of-plane and in-plane SR-XRD profiles for (a) VOPc (100 nm), (b) p-6P (50 nm), and (c) 6T (10 nm) layers formed on PEDOT:PSS. The out-of-plane SR-XRD profile was measured using Seemann-Bohlin geometry. The thicknesses of these layers were several times larger than 5 nm, which was applied for the PbPc/buffer layer heterostructures shown in Fig. 2, due to the weak diffraction intensities. The in-plane diffraction profile for the VOPc layer shows no peak probably because of a weak diffraction intensity, while the out-of-plane diffraction peaks were observed at $q = 5.3$, 9.1, 15.5, 17.1, and 19.9 nm^{-1}, where q is the diffraction vector. These peaks correspond to lattice spacings of 1.18, 0.692, 0.405, 0.367, 0.343, and 0.315 nm, respectively, and are in good agreement with the results reported by Pan and co-workers [33]. The monoclinic ($a = 1.35$ nm, $b = 1.33$ nm, and $c = 1.39$ nm; $\beta = 105°$) [34] and triclinic ($a = 1.20$ nm, $b = 1.25$ nm, and $c = 0.869$ nm; $\alpha = 96.0°$, $\beta = 94.8°$, and $\gamma = 68.2°$) [35] phases were observed to coexist in the VOPc layer, as assigned by Miller indices of the planes for each diffraction peak shown in Fig. 3a-i. The crystal structure of triclinic VOPc is shown in Fig. 3a-ii; the out-of-plane diffraction peak related to VOPc (0 1 0)t suggests that the molecular plane of VOPc is perpendicular to the substrate surface, while the VOPc $(2\,1\,\bar{2})$t peak indicates that the stacking direction of the molecular planes of VOPc is parallel to the surface normal [13,36]. Thus, the molecular orientation and crystalline phase in the VOPc layer were disturbed. On the other hand, in the case of the p-6P layer, the out-of-plane diffraction profile shows p-6P (0 0 l) ($l = 2$, 3, 6) diffraction peaks representing the interplanar distance of 2.60 nm at $q = 4.8$, 7.3, and 14.3 nm^{-1}, respectively, and the in-plane diffraction profile shows p-6P $(1\,1\,\bar{1})$ and $(2\,0\,\bar{3})$ related diffraction peaks at $q = 13.7$ and 16.2 nm^{-1}, corresponding to the lattice spacings of 0.458 and 0.388 nm, respectively [37,38]. Considering the crystal structure of p-6P ($a = 0.809$, $b = 0.557$, and $c = 2.62$ nm; $\beta = 98.2°$ (monoclinic)) [37] shown in Fig. 3b-ii, it can be assumed that the molecular plane of p-6P is approximately perpendicular to the substrate surface. A similar trend was observed in the structural properties of the 6T film, the schematic crystal structure of which ($a = 4.47$, $b = 0.785$,

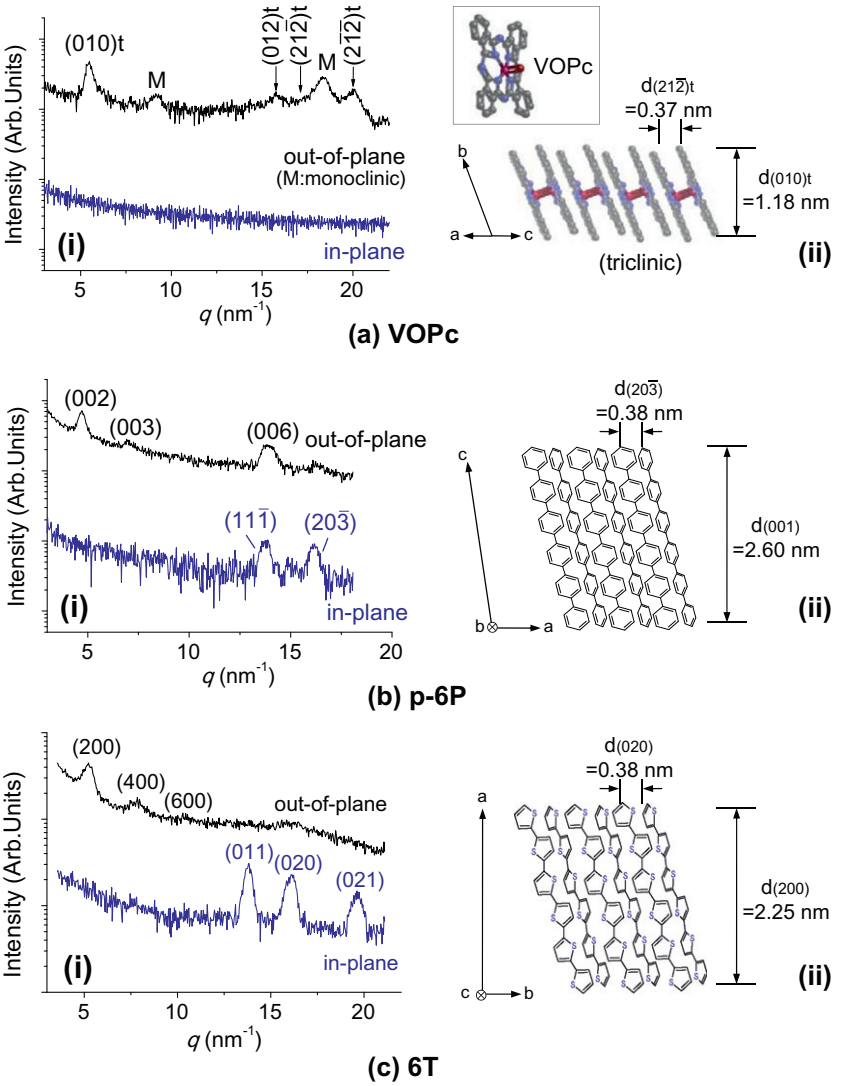

Fig. 3. SR-XRD profiles for (a) VOPc (100 nm), (b) p-6P (50 nm), and (c) 6T (10 nm) layers formed on PEDOT:PSS; (i) out-of-plane and in-plane diffraction profiles, (ii) schematic crystalline structure.

and c = 0.603 nm; β = 90.8° (monoclinic)) [39] is illustrated in Fig. 3c-ii. The out-of-plane diffraction profile for the 6T layer showed 6T (l 0 0) (l = 2, 4, 6) peaks indicating the interplanar distance of 4.48 nm, while the in-plane diffraction profile showed 6T (0 1 1), (0 2 0), and (0 2 1) peaks at q = 13.8, 16.2, and 19.6 nm^{-1}, corresponding to the lattice spacings of 0.455, 0.388, and 0.321 nm, respectively [40]. These results suggest that the molecular plane of 6T is almost perpendicular to the substrate surface since a-axis of 6T observed in the out-of-plane diffraction pattern is perpendicular to both b- and c-axes observed in the in-plane diffraction profiles [39]. Fig. 4 shows an AFM image of the 6T (10 nm) layer formed on PEDOT:PSS. Clear step and terrace structures were observed, and the step height was 2.2 nm, corresponding well with the lattice spacing of 6T (2 0 0). The atomically flat terrace represents the in-plane ordering of 6T in accordance with the in-plane diffraction peaks shown in Fig. 3c-i [40–42]. Our results correspond to the previous reports that suggest that the 6T and p-6P layers tend to grow in a layer-by-layer fashion on inert substrate surfaces such as glass and ITO, while maintaining their standing molecular orientation [12,40–42]. On the basis of these considerations, we assume that the structural properties of the buffer layer are important for the crystal growth of the PbPc layers.

The crystal growth of organic semiconductor layers is dominated by the delicate balance between molecule–molecule and molecule–substrate interactions. The anisotropic van der Waals intermolecular interactions, which arise from the π-orbital in organic semiconductors, stimulate the formation of the specific configuration between two molecules at organic hetero-interfaces [4,8,9,11]. As for the PbPc layer with the VOPc buffer layer, the random orientation of VOPc results in the deterioration of the structural properties of the PbPc layer. In contrast, upright oriented p-6P and 6T molecules appear to promote the

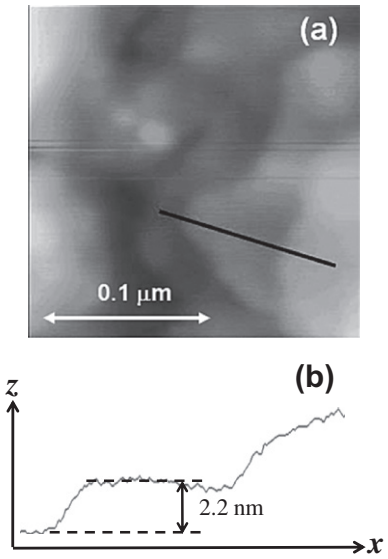

Fig. 4. (a) 0.2 × 0.2 μm^2 AFM images of 10-nm-thick 6T layer grown at room temperature on a PEDOT:PSS/ITO structure. (b) Height profile of black line in (a).

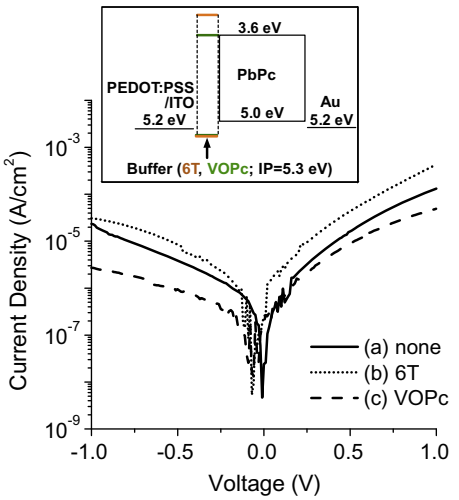

Fig. 5. Current density and bias voltage (*J–V*) characteristics of ITO/PEDOT:PSS/buffer layer (5 nm)/PbPc (200 nm)/Au structures (a) without a buffer layer (solid line) and with (b) 6T (dotted line) and (c) VOPc (dashed line) buffer layers. The inset shows the schematic energy level diagram for ITO/PEDOT:PSS/buffer layer/PbPc/Au structure.

growth of a well-ordered structure of PbPc. Recently, several reports have suggested that atomically flat p-6P and 6T buffer layers with well-ordered in-plane crystalline structures, as in the case of our specimens, promote the heteroepitaxial growth of organic semiconductor layers [12,13,43]. Thus, the control of structural properties of buffer layers is indispensable for obtaining a highly ordered organic heterostructure.

Fig. 5 shows the current density and bias voltage (*J–V*) characteristics of ITO/PEDOT:PSS/buffer layer/PbPc (200 nm)/Au structures (a) without a buffer layer and with (b) 6T and (c) VOPc buffer layers. The thickness of the buffer layers was fixed at 5 nm. The work functions of the electrodes (ITO, PEDOT:PSS, and Au) approximately correspond to the ionized potentials of the organic layers (PbPc, VOPc, and 6T), as illustrated in the energy level diagram shown in the inset of Fig. 5; therefore, these structures can be considered as hole-only single-carrier devices. Since the electrical properties of VOPc (ionized potential and hole mobility) are almost same as those of 6T, the variations in the *J–V* characteristics of these devices suggest the change in the structural properties of the PbPc layers. The electric conductivity of the device with the 6T buffer layer is several times greater than that of the device without a buffer layer. Previous researches have demonstrated that the conductivity of monoclinic PbPc, which corresponds to the device without a buffer layer, is several times higher than that of triclinic PbPc [44–46], which corresponds to the devices with a 6T buffer layer. Considering the analytical result on the structural properties of PbPc layers (Fig. 2), it can be assumed that control of both crystal quality and phase is indispensable for enhancing the electric conductivity of the PbPc film. It was also observed that the degradation of the crystal quality of triclinic PbPc formed on a VOPc buffer layer affected the reduction in the electric conductivity, as shown in Fig. 5c; this was in agreement with the former assumption. Thus, the appropriate buffer layer promotes the crystal growth of the PbPc and improves its electrical properties.

3.2. Performance of PbPc based organic solar cells

Solar cells composed of PbPc and C_{60} were fabricated with and without organic buffer layers. The structure of the cell is given as ITO/PEDOT:PSS/buffer layer(5 nm)/PbPc (30 nm)/C_{60}(30 nm)/bathocuproine(BCP; 6 nm)/Ag. H_2Pc, VOPc, 6T, and p-6P, all of which had almost the same hole mobilities [13,21–23], were used as buffer layers. All the layers were sequentially deposited in an OMBD chamber. The device parameters of the cells are listed in Table 1. The *J–V* characteristics of the cells under light irradiation are shown in Fig. 6a. The cell performance was remarkably enhanced by the insertion of 6T and VOPc buffer layers. The optimum efficiency of 2.1% was obtained for the cell with a 6T buffer layer; this efficiency was 1.6 times higher than that of the cell without a buffer layer. On the other hand, device parameters deteriorated in case of the introduction of H_2Pc and p-6P buffer layers. The degradation of the performance of the cell with a p-6P buffer layer was caused by a large energy level offset for holes of

Table 1
Parameters of PbPc-based solar cells under AM 1.5 illumination at room temperature (~25 °C) for different buffer layers; J_{SC} is a short-circuit current, V_{OC} is an open-circuit voltage, FF is the fill factor, η is the conversion efficiency, and R_S is the series resistance.

Buffer	J_{SC} (mA/cm^2)	V_{OC} (V)	FF	η (%)	R_S (Ω cm^2)
None	6.5	0.51	0.41	1.3	18
H_2Pc	6.6	0.50	0.31	1.0	33
VOPc	7.9	0.46	0.43	1.6	16
6T	9.3	0.49	0.46	2.1	6.8
p-6P	5.0	0.43	0.15	0.3	–

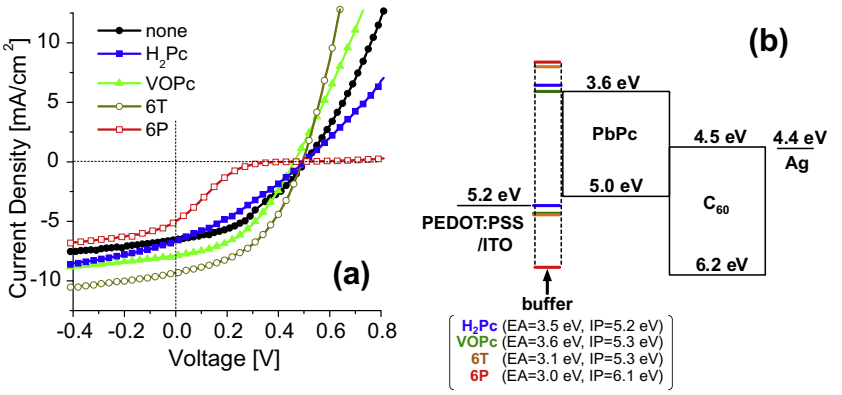

Fig. 6. (a) *J–V* characteristics of the OSCs without a buffer layer (solid circle) and with H_2Pc (solid square), VOPc (solid triangle), 6T (open circle), and p-6P (open square) buffer layers under light irradiation. The structure of OSCs is given as ITO/PEDOT:PSS (30 nm)/buffer layer (5 nm)/PbPc (30 nm)/C_{60} (30 nm)/BCP (6 nm)/Ag. (b) Schematic energy level diagram for OSCs shown in (a).

~1 eV; this offset was present at the p-6P/PbPc (PEDOT:PSS/p-6P) interface, as illustrated in the energy level diagram shown in Fig. 6b. The ionized potentials of H_2Pc, VOPc, and 6T were ~5.3 eV; this value is almost the same as that of PbPc (5.0 eV) and PEDOT:PSS (5.2 eV), indicating the presence of a small energy barrier for holes around the buffer layer. Therefore, in order to understand the variation of the cell performance, other factors apart from the energy level offset should be considered.

Fig. 7 shows the spectral sensitivity of OSCs (a) without a buffer layer and with (b) 6T and (c) VOPc buffer layers. Integration of the external quantum efficiency (EQE) data multiplied by the AM 1.5 solar emission spectrum approximately corresponded with the value of the observed short-circuit current (J_{sc}) shown in Table 1. The OSC without a buffer layer shows a single absorption band at around 750 nm, which corresponds to the Q-band (π–π^* transition) spectrum for monoclinic PbPc [29]. On the other hand, in the case of OSCs with 6T and VOPc buffer layers, both spectra exhibited an absorption shoulder at around 890 nm except for the band at 750 nm, corresponding to the Q-band spectrum for triclinic PbPc [29]. Since the sensitivity data at around 750 nm were not significantly affected by the sort of buffer layers, it can be assumed that absorption at 890 nm enhanced J_{sc}. Consequently, the spectral sensitivity was influenced by the phase of the PbPc layers. The sensitivity data suggests a higher overall efficiency in the case of the OSC with the 6T buffer layer, while the optical absorption spectrum of the 30-nm-thick PbPc layers formed on 6T buffer layer (Fig. 8a), of which spectral profile corresponds to that of the sensitivity data shown in Fig. 7, does not indicate the enhancement of the absorption intensity as compared with the spectrum of PbPc/VOPc heterostructure (Fig. 8b). As can be observed from the structural and electrical properties of the PbPc/6T heterostructure shown in Figs. 2–5, the well-ordered crystalline structure of PbPc formed on 6T enhances the electric conductivity of the PbPc films and reduces the series resistance of the OSC. Such enhancements in the electrical properties of PbPc enhance the spectrum sensitivity of OSC, although further studies, e.g., influence of the PbPc/C_{60} interfaces and the residual monoclinic PbPc domains on EQE, are indispensable to clarify the underlying physics in more detail. Thus, control of both crystal quality and phase of PbPc layers using a proper buffer layer is effective in enhancing the device performance of OSCs.

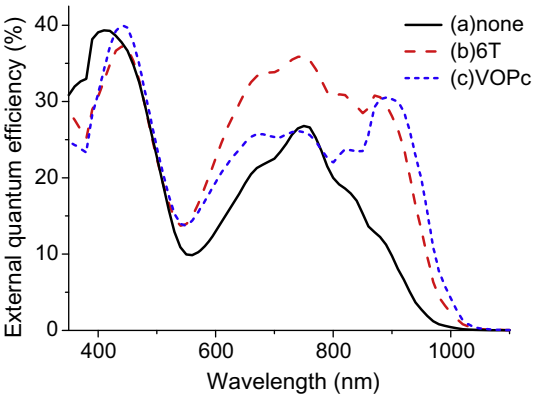

Fig. 7. Spectral sensitivity of OSCs (a) without a buffer layer (solid line) and with (b) 6T (dashed line) and (c) VOPc (dotted line) buffer layers.

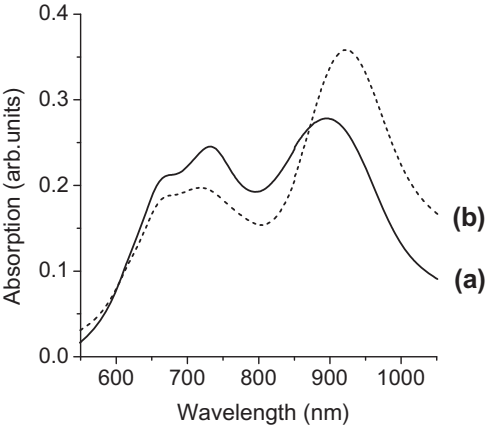

Fig. 8. Optical absorption spectra for 30-nm-thick PbPc layers formed on (a) 6T (solid line) and (b) VOPc (dotted line) buffer layers. The thickness of buffer layers was fixed at 5 nm.

4. Conclusions

We have investigated the influence of an organic buffer layer on structural properties and performances of PbPc-based solar cells. H_2Pc, VOPc, and 6T, all of which had almost the same ionized potential as PbPc, were used as buffer layers. The device performance of the cells with VOPc and 6T buffer layers was enhanced by about 1.6 times as compared to that of the cells without a buffer layer. On the other hand, no enhancement was observed in the case of the cell with the H_2Pc buffer layer. The crystal structure of the PbPc layer formed on VOPc and 6T buffer layers was different from that of the PbPc layer formed on the H_2Pc layer or that without a buffer layer. The electrical conductivity and spectrum sensitivity of OSCs are directly correlated with their structural parameters determined by X-ray diffraction. From these results, we conclude that structural variation in PbPc layers directly affects the performance of OSCs containing these layers.

Acknowledgments

We are grateful to the Japanese Ministry of Education, Culture, Sports, Science and Technology for providing us with a Grant-in-Aid for Young Scientists (B) (No. 21760229) and Nissan Science Foundation.

References

[1] B.P. Rand, J. Genoe, P. Heremans, J. Poortmans, Solar cells utilizing small molecular weight organic semiconductors, Prog. Photovoltaics 15 (2007) 659–676.
[2] M. Riede, T. Mueller, W. Tress, R. Schueppel, K. Leo, Small-molecule solar cells-status and perspectives, Nanotechnology 19 (2008) 424001.
[3] J. Xue, S. Uchida, B.P. Rand, S.R. Forrest, Asymmetric tandem organic photovoltaic cells with hybrid planar-mixed molecular heterojunctions, Appl. Phys. Lett. 85 (2004) 5757–5759.
[4] T. Sakurai, R. Naito, S. Toyoshima, T. Ohashi, K. Akimoto, Orientation-controlled phthalocyanine-based photovoltaic cell formed on pentacene buffer layer, Nanosci. Nanotechnol. Lett. 1 (2009) 23–27.
[5] T. Sakurai, R. Fukasawa, K. Saito, K. Akimoto, Control of molecular orientation of organic p–i–n structures by using molecular templating effect at heterointerfaces, Org. Electron. 8 (2007) 702–708.
[6] B. Yu, L. Huang, H. Wang, D. Yan, Efficient organic solar cells using a high-quality crystalline thin film as a donor layer, Adv. Mater. 22 (2010) 1017–1020.
[7] D. Placencia, W. Wang, R.F. Shallcross, K.W. Nebesny, M. Brumbach, N.R. Armstrong, Organic photovoltaic cells based on solvent-annealed, textured titanyl phthalocyanine/C_{60} heterojunctions, Adv. Funct. Mater. 19 (2009) 1913–1921.
[8] S. Yim, S. Heutz, T.S. Jones, Influence of intermolecular interactions on the structure of phthalocyanine layers in molecular thin film heterostructures, Phys. Rev. B 67 (2003) 165308.
[9] T. Sakurai, S. Kawai, J. Shibata, R. Fukasawa, K. Akimoto, Influence of 3,4,9,10-perylene tetracarboxylic dianhydride intermediate layer on molecular orientation of phthalocyanine, Jpn. J. Appl. Phys. 44 (2005) 1982–1986.
[10] S. Liu, W.M. Wang, A.L. Briseno, S.C.B. Mannsfeld, Z. Bao, Controlled deposition of crystalline organic semiconductors for field-effect transistor applications, Adv. Mater. 21 (2009) 1217–1232.
[11] S. Heutz, R. Cloots, T.S. Jones, Structural templating effects in molecular heterostructures grown by organic molecular-beam deposition, Appl. Phys. Lett. 77 (2000) 3938–3940.
[12] J. Yang, D. Yan, Weak epitaxy growth of organic semiconductor thin films, Chem. Soc. Rev. 38 (2009) 2634–2645.
[13] H. Wang, D. Song, J. Yang, B. Yu, Y. Geng, D. Yan, High mobility vanadyl-phthalocyanine polycrystalline films for organic field-effect transistors, Appl. Phys. Lett. 90 (2007) 253510.
[14] C.D. Sheraw, T.N. Jackson, D.L. Eaton, J.E. Anthony, Functionalized pentacene active layer organic thin-film transistors, Adv. Mater. 25 (2003) 2009–2011.
[15] A.S. Killampalli, J.R. Engstrom, Nucleation of pentacene thin films on silicon dioxide modified with hexamethyldisilazane, Appl. Phys. Lett. 88 (2006) 143125.
[16] H. Yang, T.J. Shin, M.-M. Ling, K. Cho, C.Y. Ryu, Z. Bao, Conducting AFM and 2D GIXD studies on pentacene thin films, J. Am. Chem. Soc. 127 (2005) 11542–11543.
[17] N. Li, B.E. Lassiter, R.R. Lunt, G. Wei, S.R. Forrest, Open circuit voltage enhancement due to reduced dark current in small molecule photovoltaic cells, Appl. Phys. Lett. 94 (2009) 023307.
[18] O.D. Gordan, T. Sakurai, M. Friedrich, K. Akimoto, D.R.T. Zhan, Ellipsometric study of an organic template effect: H_2Pc/PTCDA, Org. Electron. 7 (2006) 521–527.
[19] R. Naito, S. Toyoshima, T. Ohashi, T. Sakurai, K. Akimoto, Molecular orientation control of phthalocyanine thin film by inserting pentacene buffer layer, Jpn. J. Appl. Phys. 47 (2008) 1416–1418.
[20] J. Dai, X. Jiang, H. Wang, D. Yan, Organic photovoltaic cells with near infrared absorption spectrum, Appl. Phys. Lett. 91 (2007) 253503.
[21] F. Dinelli, M. Murgia, P. Levy, M. Cavallini, F. Biscarini, D.M. de Leeuw, Spatially correlated charge transport in organic thin film transistors, Phys. Rev. Lett. 92 (2004) 116802.
[22] J. Kjelstrup-Hansen, H. Henrichsen, P. Bøgild, H.-G. Rubahn, Electrical properties of a single p-hexaphenylene nanofiber, Thin Solid Films 515 (2006) 827–830.
[23] M.M. El-Nahass, A.M. Farid, A.A. Attia, H.A.M. Ali, Electrical transport properties of thermally evaporated phthalocyanine (H_2Pc) thin films, Appl. Surf. Sci. 252 (2006) 7553–7561.
[24] R.O. Loutfy, Y.C. Cheng, Investigation of energy levels due to transition metal impurities in metal-free phthalocyanine, J. Chem. Phys. 73 (1980) 2902–2910.
[25] A.J. Ikushima, T. Kanno, S. Yoshida, A. Maeda, Valence and conduction band edges of metal-phthalocyanines and carrier behavior, Thin Solid Films 273 (1996) 35–38.
[26] H. Fujimoto, U. Nagashima, H. Inokuchi, K. Seki, Y. Cao, H. Nakahara, J. Nakayama, M. Hoshino, K. Fukuda, Ultraviolet photoemission study of oligothiophenes: π-band evolution and geometries, J. Chem. Phys. 92 (1990) 4077–4092.
[27] N. Koch, L.M. Yu, V. Parenté, R. Lazzaroni, R.L. Johnson, G. Leising, J.J. Pireaux, J.L. Brédas, Evidence for physisorption of aluminum on the surface of electroluminescent sexiphenyl, Adv. Mater. 10 (1998) 1038–1043.
[28] T. Sakurai, T. Yamanari, M. Kubota, S. Toyoshima, T. Taima, Y. Yoshida, K. Akimoto, Comparative study on structural properties of poly(3-hexylthiophene) and poly(3-hexylthiophene):6,6-phenyl-C_{61} butyric acid methyl ester thin films using synchrotron X-ray diffraction, Jpn. J. Appl. Phys. 49 (2010) 01AC01.
[29] K. Ukei, Lead phthalocyanine, Acta Cryst. B 29 (1973) 2290–2292.
[30] Y. Iyechika, K. Yakushi, I. Ikemoto, H. Kuroda, Structure of lead phthalocyanine (triclinic form), Acta Cryst. B 38 (1982) 766–770.
[31] L. Ottaviano, L. Lozzi, A.R. Phani, A. Ciattoni, S. Santucci, S. Di Nardo, Thermally induced phase transition in crystalline lead phthalocyanine films investigated by XRD and atomic force microscopy, Appl. Surf. Sci. 136 (1998) 81–86.
[32] A. Miyamoto, K. Nichogi, A. Taomoto, T. Nambu, M. Murakami, Structural control of evaporated lead-phthalocyanine films, Thin Solid Films 256 (1995) 64–67.
[33] Y.L. Pan, Y.J. Wu, L.B. Chen, Y.Y. Zhao, Y.H. Shen, F.M. Li, S.Y. Shen, D.H. Huang, Structure and spectroscopic characterization of polycrystalline vanadyl phthalocyanine (VOPc) films fabricated by vacuum deposition, Appl. Phys. A 66 (1998) 569–573.
[34] S. Hashimoto, T. Ogawa, S. Isoda, T. Kobayashi, Electron diffraction analysis of polymorph structures in ultra thin film of vanadyl-phthalocyanine on KBr (0 0 1), J. Electron Microsc. 48 (1999) 731–738.
[35] C.H. Griffiths, M.S. Walker, P. Goldstein, Polymorphism in vanadyl phthalocyanine, Mol. Cryst. Liq. Cryst. 33 (1976) 149–170.
[36] H. Ohta, T. Kambayashi, M. Hirano, H. Hoshi, K. Ishikawa, H. Takezoe, H. Hosono, Application of a transparent conductive substrate with an atomically flat and stepped surface to lateral growth of an organic molecule: vanadyl phthalocyanine, Adv. Mater. 15 (2003) 1258–1262.
[37] K.N. Baker, A.V. Fratini, T. Resch, H.C. Knachel, W.W. Adams, E.P. Socci, B.L. Farmer, Crystal structures, phase transitions and energy calculations of poly(p-phenylene) oligomers, Polymer 34 (1993) 1571–1587.
[38] Y. Yoshida, H. Takiguchi, T. Hanada, N. Tanigaki, E.M. Han, K. Yase, In situ X-ray characterization of oligophenylene thin films prepared by

organic molecular beam deposition, Appl. Surf. Sci. 130–132 (1998) 651–657.
[39] G. Horowitz, B. Bachet, A. Yassar, P. Lang, F. Demanze, J.-L. Fave, F. Garnier, Growth and characterization of sexithiophene single crystals, Chem. Mater. 7 (1995) 1337–1341.
[40] J.-F. Moulin, F. Dinelli, M. Massi, C. Albonetti, R. Kshirsagar, F. Biscarini, In situ X-ray synchrotron study of organic semiconductor ultra-thin films growth, Nucl. Instrum. Methods Phys. Res. Sect. B 246 (2006) 122–126.
[41] C. Aruta, P. D'Angelo, M. Barra, G. Ausanio, A. Cassinese, Improved structural ordering in sexithiophene thick films grown on single crystal oxide substrates, Appl. Phys. A 97 (2009) 387–394.
[42] J. Ivanco, J. Krenn, M.G. Ramsey, F.P. Netzer, T. Haber, R. Resel, A. Haase, B. Stadlober, G. Jakobic, Sexithiophene films on clean and oxidized Si(1 1 1) surfaces: growth and electronic structure, J. Appl. Phys. 96 (2004) 2716–2724.
[43] M. Oehzelt, G. Koller, J. Ivanco, S. Berkebile, T. Haber, R. Resel, F.P. Netzer, M.G. Ramsey, Organic heteroepitaxy: p-sexiphenyl on uniaxially oriented alpha-sexithiophene, Adv. Mater. 18 (2006) 2466–2470.
[44] K. Ukei, K. Takamoto, E. Kanda, Lead phthalocyanine: a one-dimensional conductor, Phys. Lett. 45 (1973) 345–346.
[45] H. Yasunaga, K. Kojima, H. Yohda, K. Takeya, Effect of oxygen on electrical properties of lead phthalocyanine, J. Phys. Soc. Jpn. 37 (1974) 1024–1030.
[46] A.K. Ray, S.M. Tracey, A.K. Hassan, Conduction in partially monoclinic films of lead phthalocyanine, IEE Proc. Sci. Meas. Technol. 146 (1999) 205–209.

studies, the mobilities were determined by the time-of-flight (TOF) technique which generally requires several micron thick films and is highly out of equilibrium, thus it gives different values from other steady techniques [14]. Alternatively, admittance spectroscopy (AS) appears to be a powerful tool for the investigation of mobility in organic materials with the advantage of no specific requirements for the sample thickness [7,15–18]. Moreover, the space-charge-limited current (SCLC) model with exponentially distributed traps is commonly used to describe the current–voltage (*I–V*) characteristics in organic amorphous semiconductors [19]. It yields information on the energy and density of traps. Nevertheless, how the total density of traps will be changed by doping has rarely been reported.

In this paper, we study the effects of trapping and scattering on the hole transport properties of NPB by *I–V* and capacitance–frequency (*C–f*) characteristics. The variations in the mobility and the total density of traps by doping are well determined. Two different charge transport mechanisms caused by trapping and scattering are clearly shown. It can be seen that this also directly affects the performance of the fabricated organic light-emitting devices.

2. Experimental

2.1. Materials

In order to address how dopants affect hole transport in NPB, three molecules were chosen, i.e., 4,4′,4″-tris (*N*-3-methylphenyl-*N*-phenylamine) triphenylamine (*m*-MTDATA), tris-(8-hydroxyquinolinato) aluminum (Alq_3), and 4,4′,4″-tri(*N*-carbazolyl)-triphenylamine (TCTA). The molecular structures and the corresponding HOMO levels are depicted in Fig. 1. The *m*-MTDATA has a higher-lying HOMO level relative to that of NPB. So it is expected to introduce hole traps when doping it into NPB. In contrast, the Alq_3 and TCTA have lower-lying HOMO levels therefore they would act as scattering centers when doping them into NPB [12,13]. All organic materials were purchased from Nichem and used as delivered.

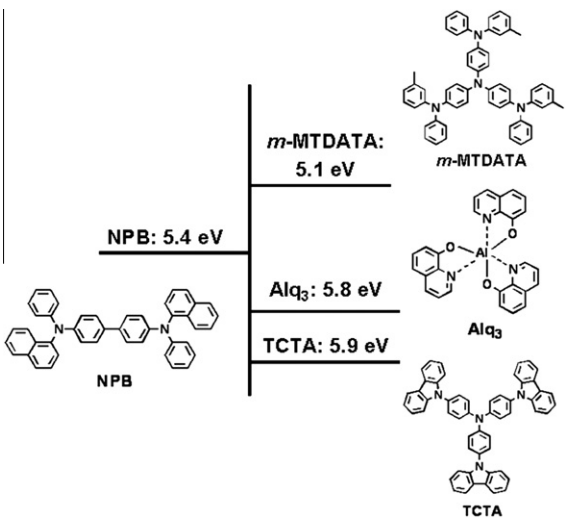

Fig. 1. HOMO energy levels of host material (NPB) and dopants used in this study as well as the corresponding chemical structures.

2.2. Device fabrication

The devices were fabricated by thermal evaporation of the organic materials on indium–tin-oxide (ITO)-coated glass substrates. Prior to deposition, the substrate was thoroughly cleaned in an ultrasonic bath using subsequently detergents and de-ionized water. The surface of ITO substrate was treated with oxygen plasma for 2 min to enhance its work function. Pure and doped NPB films were deposited under a high vacuum (pressure < 10^{-4} Pa). The doped films were deposited by coevaporation process with doping concentration of 4% by weight. In such a low concentration, there are no continuous charge transport channels on the dopant molecules [20]. The thickness was controlled *in situ* by a quarter crystal monitor, and calibrated by Dektak 6M Profiler (Veeco). The aluminum (Al) electrodes were deposited on the organic films through shadow masks. The active area of each device is 16 mm^2.

For the measurements of the temperature dependent *I–V* characteristics, the device had a structure of ITO/molybdenum oxide (MoO_3) (5 nm)/pristine or doped NPB (120 nm)/MoO_3 (5 nm)/Al, where MoO_3 was used to facilitate hole injection from ITO and suppress electron injection from Al [7]. For the AS measurements, the samples had the same structure as mentioned above but the thicknesses were between 120 and 1400 nm for efficiently deriving mobilities in different samples due to the limitation of the maximum frequency in the impedance analyzer [15].

2.3. Measurements

The *I–V* characteristics were carried out using a Keithley 2400 sourcemeter integrated with a vacuum cryostat (Optistat DN-V, Oxford Instruments). The admittance was measured at room temperature by using an Agilent E4980A precision LCR meter in the frequency range of 20 Hz–2 MHz with the oscillation amplitude of the ac voltage kept at 100 mV. The luminance–voltage (*L–V*) characteristics were recorded using a Keithley 2400 sourcemeter and a Keithley 2000 multimeter with a calibrated silicon photodiode.

3. Results and discussion

3.1. I–V and C–f characteristics

Fig. 2a shows the *I–V* characteristics of the hole-only devices based on pristine NPB and doped NPB at room temperature. At a constant current density, the driving voltage increases when dopants are introduced in NPB. In particular, the device based on NPB:*m*-MTDATA shows a pronounced increase in the driving voltage compared with that of NPB: Alq_3 and NPB:TCTA. For example, the high driving voltage is as high as 18.8 V at the current density of 5 mA/cm^2. However, the driving voltages for devices

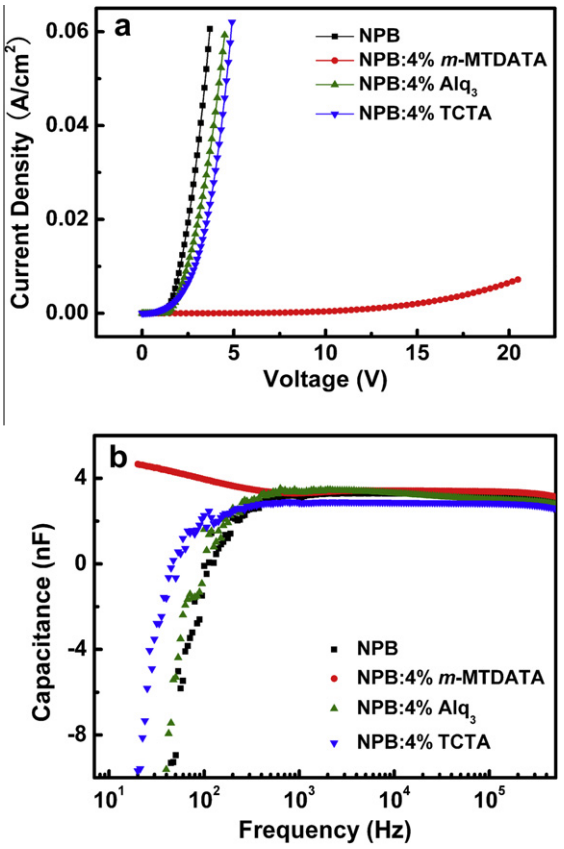

Fig. 2. (a) Current density–voltage characteristics and (b) capacitance–voltage characteristics of undoped and doped devices.

based on NPB, NPB:Alq_3 and NPB:TCTA at 5 mA/cm^2 are 1.6 V, 2.0 V and 2.3 V, respectively. As we know, the mobility and the total trap density play important roles in determining the *I–V* characteristics of organic semiconductor-based devices, which usually obey the SCLC model with exponentially distributed traps [19]. The large differences in *I–V* characteristics in the cases of different dopants should indicate the different roles of traps and scatters in hole transport properties, thus leading to the different changes of the hole mobility and the total trap density in the doping systems.

In order to clearly demonstrate the differences, the capacitance properties of devices based on different doping cases are studied. The frequency dependence of capacitance for different devices at a constant voltage of 3 V is plotted in Fig. 2b. A negative capacitance is observed at lower frequencies for pristine NPB, NPB:Alq_3 and NPB:TCTA, while a positive contribution to capacitance can be seen for NPB:*m*-MTDATA. The negative capacitance stems from the space-charge relaxation transit time [17,21]. When a bias voltage is applied to a device in which SCLC mechanism is dominant, the injected carriers that move into the device will relax to a new equilibrium space-charge distribution, leading to a redistribution of the net charges within a certain transit time. Owing to the finite transit time τ_t for relaxation, the corresponding current lags behind the ac voltage, thus an inductive contribution adds onto the capacitance. For times shorter than τ_t, or frequencies greater than τ_t^{-1}, the injected carriers cannot respond to the frequency within this short duration. Therefore, the negative capacitance disappears. Since the τ_t is directly related with the charge carrier mobility at a constant thickness, it can be concluded that the negative capacitance is prone to appear in a material with high mobility. This fact directly explains the reason why the current densities of NPB:Alq_3- and NPB:TCTA-based devices are higher than that of NPB:*m*-MTDATA-based device, and also implies that the scatterer-doped organic films will show higher mobilities than the trap-doped organic films.

3.2. Mobility determination

In order to gain a deep insight into different effects of trapping and scattering on hole transport properties, admittance spectroscopy (AS) was used to derive the mobilities of different doping cases. In this method, the current response i_{ac} to a small oscillating voltage $v_{ac} = v_o \cdot \cos(\omega t)$ is monitored. The complex admittance Y_{ac} is related to i_{ac} and v_{ac} as follows:

$$Y_{ac} = \frac{i_{ac}}{v_{ac}} = G(\omega) + iB(\omega) = G(\omega) + i\omega C(\omega) \tag{1}$$

where G is the conductance, B is the susceptance, C is the capacitance, and $i^2 = -1$. In addition, the complex admittance Y can be deduced analytically and written by [15]:

$$Y(\Omega) = \frac{\varepsilon\varepsilon_o A}{\tau_{dc} d}\left\{\frac{\Omega^3}{2i[0.75\tilde{\mu}(\Omega)]^2[1-\exp(-\frac{i4\Omega}{3\tilde{\mu}(\Omega)})]+1.5\tilde{\mu}(\Omega)\Omega - i\Omega^2}\right\} \tag{2}$$

where d and A are the thickness and the area of the sample, respectively, ε is the dielectric constant of material, and ε_o is the permittivity of the free space. In the above equation, τ_{dc} is the average hole transit time in the absence of the ac signal, and $\Omega = \omega\tau_{dc}$. The normalized mobility is defined as $\tilde{u}(\Omega) = \mu(\Omega)/\mu_{dc}$, where $\mu_{dc} = d^2/(V\tau_{dc})$ is the *dc* hole mobility in the absence of the *ac* field. To derive the carrier mobility, the imaginary part of *Y*, i.e., the susceptance in frequency domain can be analyzed. Particularly, the negative differential susceptance of the device can be defined as $-\Delta B = -2\pi f(C - C_{geo})$. By plotting $-\Delta B$ as a function of frequency, a characteristic frequency f_{max} at which a maximum of $-\Delta B$ occurs is correlated with the average hole transit time via $f_{max} = 0.56/\tau_{dc}$ [15]. Consequently the carrier mobility can be extracted by the following equation:

$$\mu_{dc} = \frac{f_{max} d^2}{0.56(V - V_{bi})} \tag{3}$$

Fig. 3 presents a series of representative *C–f* and $-\Delta B$–*f* plots for four devices at the given electric field strength. It can be observed that each case shows a minimum capacitance in the intermediate frequency region and then the capacitances tend to their respective geometrical capacitances with increasing frequencies. As shown in insets of Fig. 3, a clear maximum in $-\Delta B$ occurs at a well defined frequency f_{max} for each device. Using Eq. (3), the hole

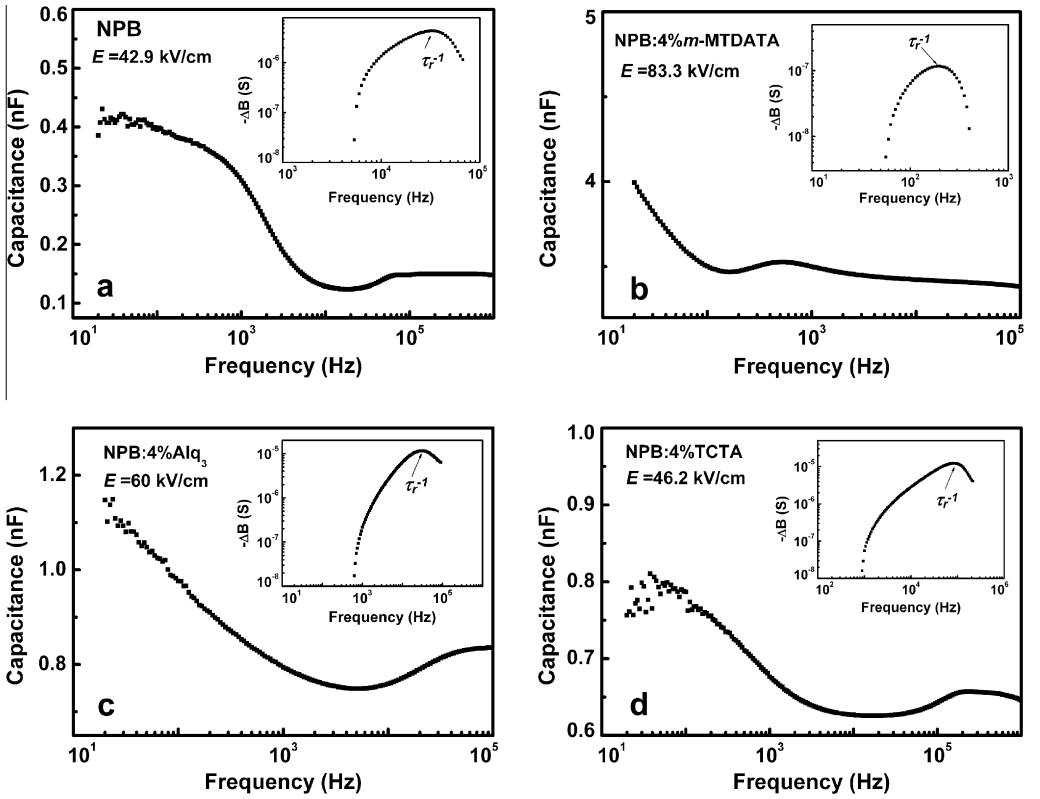

Fig. 3. Capacitances of NPB, NPB:*m*-MTDATA, NPB:Alq_3, NPB:TCTA at room temperature. The insets are the negative differential susceptance $-\Delta B$ versus frequency plots.

mobilities can be evaluated, which are summarized in Fig. 4.

From Fig. 4, it can be clearly seen that the hole mobilities follow the empirical field dependent expression [22]. The hole mobility for the pristine NPB film is in the range of $(2–4) \times 10^{-4}$ $cm^2V^{-1}s^{-1}$ and agrees well with the values reported earlier [16]. In the case of *m*-MTDATA-doped NPB, the hole mobility shows a dramatic decrease of four orders of magnitude. Whereas for NPB doped with Alq_3 and TCTA, the reduction of mobilities is less than one order of magnitude. This phenomenon suggests that trap and scatterer have different effects on hole transport mechanisms [12,13]. In the case of trapping, the mobile holes may be trapped in the generated trap level and detrapped by thermal energy. The processes will lead to the reduction of the mobility due to the additional trap residing times. In the case of scattering, the mobile holes may be hindered by the dopant with a lower-lying HOMO level due to colliding. Although the mobility will lower to a certain degree depending on the difference between the HOMO of NPB and the dopant, holes may transport nearly freely in the film.

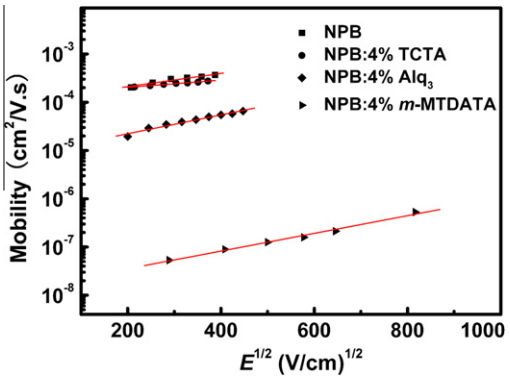

Fig. 4. Hole mobilities of NPB and doped NPB against the square root of the electric field strength. The solid lines are the best linear fits to the data.

3.3. The total density of traps

To further distinguish the different effects of trapping and scattering on the hole transport in NPB, we investigate the temperature dependent *I–V* characteristics of different doping devices. As shown in Fig. 5, the slopes of the *I–V* curves in double logarithmic for each device are greater than 2 at room temperature and increase rapidly with decreasing temperature. This relation leads to the following SCLC model with exponentially distributed traps [19],

$$J = q^{1-l}\mu N_v \left(\frac{2l+1}{l+1}\right)^{l+1} \left(\frac{l}{l+1}\frac{\varepsilon\varepsilon_0}{N_t}\right)^{l} \frac{V^{l+1}}{d^{2l+1}}, \quad (4)$$

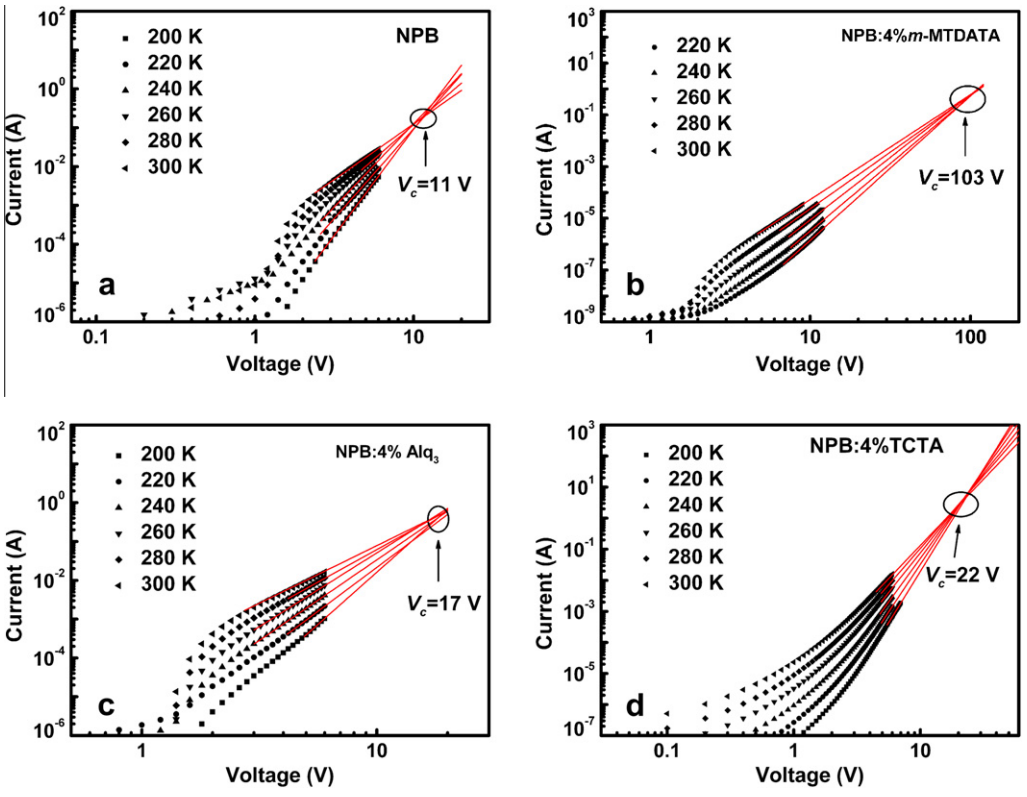

Fig. 5. Extrapolation of the *I*–*V* curves at different temperatures in log–log scale for NPB and doped NPB devices.

where q is the elementary charge, μ is the hole mobility, N_v is the density of states in the valence band, l is an energy parameter given by T_c/T (T_c is characteristic temperature of traps), and N_t is the total density of hole traps. As an analytical method introduced by Kumar et al. [23] to determine N_t, Eq. (4) can be rearranged as follows:

$$J = \frac{q\mu N_v V}{d} f(l) \exp\left[-\frac{T_c}{T} \ln\left(\frac{qd^2 N_t}{2\varepsilon\varepsilon_o V}\right)\right], \tag{5}$$

with

$$f(l) = \left(\frac{2l+1}{l+1}\right)^{l+1} \left(\frac{l}{l+1}\right)^{l} \frac{1}{2^l} \tag{6}$$

For $l > 2$, the value of $f(l)$ is about 0.5, so it can be considered as a constant of 0.5. With this approximation, Eq. (5) becomes a typical Arrhenius form,

$$J = J_o \exp\left(-\frac{E_a}{kT}\right) \tag{7}$$

where

$$E_a = \frac{T_c}{T} \ln\left(\frac{qN_t d^2}{2\varepsilon\varepsilon_o V}\right) \tag{8}$$

For $E_a = 0$, $J = J_o$ and current becomes independent of temperature. The *I*–*V* curves for different temperatures should then converge at a critical voltage,

$$V_c = \frac{qN_t d^2}{2\varepsilon\varepsilon_o} \tag{9}$$

By extrapolating log *I*–log *V* characteristics at various temperatures to higher voltages, V_c can be determined, as shown in Fig. 5. With the obtained V_c and assuming $\varepsilon = 3$, the total density of traps can be calculated as listed in Table 1.

It appears that when *m*-MTDATA is introduced into NPB, the total density of traps increases about one order of magnitude. On the contrary, the total densities of traps for NPB:Alq$_3$ and NPB:TCTA changes a little. This result convinces that the *m*-MTDATA indeed acts as traps in NPB. As a result, the total density of traps is increased and the hole mobility is greatly reduced.

3.4. Electroluminescent device performance

Based on the undoped and doped NPB as the hole-transporting layers (HTL), we also fabricate organic light-emit-

Table 1
The total densities of traps in NPB and doped NPB.

	V_c (V)	N_{total} (cm^{-3})
NPB	11	2.5×10^{17}
NPB:4%Alq$_3$	17	3.8×10^{17}
NPB:4%TCTA	22	5.0×10^{17}
NPB:4%*m*-MTDATA	103	2.4×10^{18}

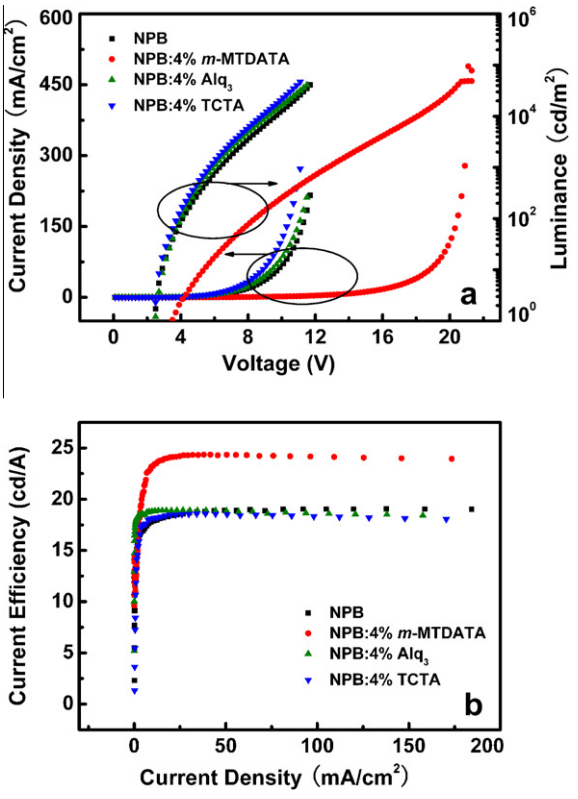

Fig. 6. Performances of OLEDs with NPB or doped NPB as hole transport layer. (a) *J*–*V*–*L* characteristics. (b) Current efficient versus current density characteristics.

ting diodes with a general configuration of ITO/MoO_3 (5 nm)/NPB or doped NPB layer (60 nm)/NPB (20 nm)/Alq_3: 10-(2-benzothiazolyl)-2,3,6,7-tetrahydro-1,1,7,7-tetramethyl-1H,5H,11H-benzo[*l*]-pyrano-[6,7,8-*ij*]quinolizin-11-one (C545T) (1%, 30 nm)/Alq_3 (30 nm)/LiF (1 nm)/Al. The purpose of inserting a layer of pure NPB between HTL and emitting layer is to block electrons from reaching HTL and make the interfaces between different HTLs and emitting layers the same. It can be observed from Fig. 6a that the current density–voltage (*J*–*V*) and luminance–voltage (*L*–*V*) characteristics differ strongly for OLEDs with trap doped HTL from scatterer doped HTL. The lowest current density in *m*-MTDATA-doped HTL device is obviously consistent with the lowest mobility of *m*-MTDATA-doped NPB film which is in the same order of magnitude as the electron mobility of Alq_3 [24]. Consequently, the *m*-MTDATA-doped HTL device shows the best electroluminescent efficiency due to the balanced electron and hole transport, as shown in Fig. 6b.

4. Conclusions

The effects of trapping and scattering on the hole transport properties of NPB has been well investigated by doping *m*-MTDATA, Alq_3 and TCTA. Temperature dependent current–voltage characteristics, admittance spectroscopy, and luminance–voltage characteristics were used to interpret the roles of trap and scatter played in NPB. It can be seen that doping molecules as trapping increases the density of traps and decreases the hole mobility whereas doping molecules as scattering then does not obviously affect the hole transport, which are attributed to their different roles in hole transporting. This also supplies a method of adjusting charge carrier transport behavior by doping molecules as trapping or scattering, thus optimizing device performance.

Acknowledgements

The authors gratefully acknowledge the Science Fund for Creative Research Groups of NSFC (20921061), the National Natural Science Foundation of China (50973104, 60906020), Ministry of Science and Technology of China (973 program No. 2009CB623604, 2009CB930603), and the Foundation of Jilin Research Council (20080337, 20090127) for the support of this research.

References

[1] C.W. Tang, S.A. Vanslyke, Appl. Phys. Lett. 51 (1987) 913–915.
[2] C.W. Tang, Appl. Phys. Lett. 48 (1986) 183–185.
[3] A. Tsumura, H. Koezuka, T. Ando, Appl. Phys. Lett. 49 (1986) 1210–1212.
[4] H. Aziz, Z.D. Popovic, Appl. Phys. Lett. 80 (2002) 2180–2182.
[5] Y. Kim, E. Oh, H. Lim, C.-S. Ha, Appl. Phys. Lett. 88 (2006) 043504.
[6] H. Aziz, Z.D. Popovic, N.X. Hu, A.M. Hor, G. Xu, Science 283 (1999) 1900–1902.
[7] M. Hoping, C. Schildknecht, H. Gargouri, T. Riedl, M. Tilgner, H.H. Johannes, W. Kowalsky, Appl. Phys. Lett. 92 (2008) 213306.
[8] Z. Chiguvare, V. Dyakonov, Phys. Rev. B 70 (2004) 235207.
[9] D. Poplavskyy, F. So, J. Appl. Phys. 99 (2006) 033707.
[10] N. von Malm, J. Steiger, R. Schmechel, H. von Seggern, J. Appl. Phys. 89 (2001) 5559–5563.
[11] R. Schmechel, H. von Seggern, Phys. Status Solidi A 201 (2004) 1215–1235.
[12] K.K. Tsung, S.K. So, Appl. Phys. Lett. 92 (2008) 103315.
[13] K.L. Tong, S.W. Tsang, K.K. Tsung, S.C. Tse, S.K. So, J. Appl. Phys. 102 (2007) 093705.
[14] P.M. Borsenberger, D.S. Weiss, Organic Photoreceptors for Imaging Systems, Dekker, New York, 1993.
[15] S.W. Tsang, S.K. So, J.B. Xu, J. Appl. Phys. 99 (2006) 013706.
[16] S.W. Tsang, S.C. Tse, K.L. Tong, S.K. So, Org. Electron. 7 (2006) 474–479.
[17] H.C.F. Martens, H.B. Brom, P.W.M. Blom, Phys. Rev. B 60 (1999) R8489–R8492.
[18] K.K. Tsung, S.K. So, J. Appl. Phys. 106 (2009) 083710.
[19] M.A. Lampert, P. Mark, Current Injection in Solids, Academic Press, New York, 1970.
[20] S.-W. Liu, J.-H. Lee, C.-C. Lee, C.-T. Chen, J.-K. Wang, Appl. Phys. Lett. 91 (2007) 142106.
[21] H.C.F. Martens, J.N. Huiberts, P.W.M. Blom, Appl. Phys. Lett. 77 (2000) 1852–1854.
[22] P.N. Murgatroyd, J. Phys. D Appl. Phys. 3 (1970) 151–156.
[23] V. Kumar, S.C. Jain, A.K. Kapoor, J. Poortmans, R. Mertens, J. Appl. Phys. 94 (2003) 1283–1285.
[24] S. Barth, P. Müller, H. Riel, P.F. Seidler, W. Rieß, H. Vestweber, H. Bässler, J. Appl. Phys. 89 (2001) 3711–3719.

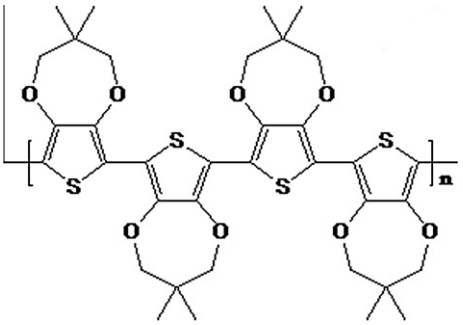

Fig. 1. Structure of PProDOT-Me_2.

decreases, causing the polymer film to become transparent. Slight reduction of the oxidized PProDOT-Me_2 causes the polymer back to its neutral state, resulting in increased the energy band gap and absorption. Further reduction leads the polymer to its deeply colored state. Thus, we can reversibly switch the material's optical properties. We chose this material because of its low oxidation potential, high color-changing and electrochemical stability, ultra fast color-changing speed, and large light transmittance contrast ratio. Furthermore, when exposed to oxygen, moisture, and varying temperatures, it is significantly more stable than other EC polymer candidates [13]. The monomers were electropolymerized in an organic solvent. They underwent oxidation to form radical cations and reacted with other monomers or radical cations to become insoluble polymer chains precipitating on the electrode surface. This easy, inexpensive method can form very thin films (tens of nanometers) [14].

The ECD has a multilayer structural configuration. The EC layer, PProDOT-Me_2 thin film, is electrochemically deposited on indium tin oxide (ITO)-coated polyethylene terephthalate (PET) plastic. The ECD's counter layer, V_2O_5/TiO_2 composite thin film, is also deposited on ITO/PET substrate. The V_2O_5/TiO_2 thin film acts as an ion storage layer that, when paired with the PProDOT-Me_2 thin film, works to maintain the electrical charge balance inside the ECD during color changes. A solution-type electrolyte is sandwiched between the EC and counter layers. This transparent electrolyte layer is a good conductor for small ions, such as ClO_4^- and Li^+, but is an insulator for electrons; inside this layer, ions move quickly during switching.

Our laboratory has developed high-performance ECDs of different sizes and substrates [9–11]. This paper will use both model simulation and experimentation to explore aspects of PProDOT-Me_2: the thin film deposition, its electrochemical and EC properties, its color-changing kinetics, microstructure of the thin film, and charge transport at the polymer/electrolyte interface.

2. Materials and methods

2.1. Materials and reagents

Our lab synthesized ProDOT-Me_2 monomers via an improved method previously reported [2,15]. All starting materials were purchased from Aldrich, except lithium perchlorate ($LiClO_4$, 99% anhydrous, packed under argon), which was purchased from Alfa Aesar. We dried all materials before use and stored them in a glove box filled with argon.

An electrolyte solution was prepared by dissolving 0.1 M of $LiClO_4$ in propylene carbonate (PC). This solution electrolyte was injected into the EC device later using vacuum filling. Special attention must be paid to avoid any contamination from moisture and oxygen. The solution of electrolyte needs to be bubbled by argon gas before use, and all containers should be dried in an oven.

2.2. EC and counter electrodes

PProDOT-Me_2 polymer films were deposited from a 0.01 M monomer in a 0.1 M $LiClO_4$/acetonitrile (ACN) solution. Electrochemical polymerization was carried out on an electrochemical analyzer (CHI 604C, CH Instruments, TX, USA), utilizing the chronoamperometry method [9,16]. We used a three-electrode cell with a silver (Ag) wire as a reference, ITO/PET (purchased from CPFilm, CA, USA, 50 Ω/square surface resistance) as a working electrode and a stainless steel plate as a counter electrode to electrochemically polymerize the film.

In this device design, we adopted vanadium pentoxide and titanium oxide (V_2O_5/TiO_2) composite films. As the ECD's counter film, this composite film exhibits improved performance over the V_2O_5 films used previously. The V_2O_5/TiO_2 composite films were deposited on ITO/PET substrates with the chronoamperometry method [17].

Both of the PProDOT-Me_2 and V_2O_5/TiO_2 composite thin films must be placed into a 0.1 M $LiClO_4$/PC electrolyte solution after deposition. We used the chronocoulometry method to electrochemically condition the films in order to change the inorganic ions in the films, to make them compatible with a $LiClO_4$/PC environment.

2.3. ECD assembly

We placed the V_2O_5/TiO_2-coated ITO/PET on the top of the PProDOT-Me_2-coated ITO/PET so that the active materials faced each other. The electrolyte solution was injected into the space between the two sheets using a vacuum filling system [18]. A UV-curable film sealant (IS 90453, Adhesives Research, Inc., PA, USA) was used as a hermetic barrier to seal the device.

2.4. Characterization methods

We used a surface *profiler* (Dektak 3030, Veeco, NY, USA) and scanning electron microscopy (SEM, FEI Sirion, OR, USA) to study the microstructure of the polymer thin film. We conducted a cyclic voltammetry (CV) study, measured the alternating current (AC) impedance, and conducted an equivalent circuit model simulation using a three-electrode cell on the electrochemical analyzer (CHI 604C) with analysis software (CHI Version 8.13, TX, USA). Optical characterization of the thin film and devices was carried out using a UV–vis–IR spectrophotometer (V-570, JASCO, Tokyo, Japan). The digital photos were recorded

by a high-definition camera (HDR-SR11, Sony, Tokyo, Japan).

3. Results and discussion

3.1. PProDOT-Me_2 film deposition

Generally, ITO substrates must be highly uniform, conductive, and transparent for high-quality optical devices. As the ITO/plastic substrate has greater surface resistance than the ITO/glass substrate, the electric potential drop across the substrate surface is more obvious, resulting in less uniform polymer film. To overcome this disadvantage of the ITO/plastic substrate, we placed an adhesive copper tape electrode (3M, St. Paul, MN, USA) along the edge of the substrate to enhance its electrical conductivity and uniformity. Additionally, we covered the copper tape surface with Teflon tape (Chukoh Chemical Industries, Ltd., Tokyo, Japan) to prevent the polymerization on the copper surface.

Because of the fragility and sensitivity of the PProDOT-Me_2 thin film to experimental conditions, we paid extra attention to electrochemical deposition. We conducted the experiment in inert gas conditions. We achieved a uniform film for the plastic goggle lens that we designed by optimizing the voltage at 1.6 V and using a deposition time of 20 s (Fig. 2). The defect-free deposited film had a vivid blue color. Experimentation demonstrated that films with an approximate thickness of 90–100 nm had the largest light transmittance contrast ratios.

3.2. PProDOT-Me_2 film microstructure and the kinetics of color switching

We performed a color-changing test for the PProDOT-Me_2 film by applying potentials between −1.2 and +1.2 V. The electrochemical process consists of an ion intercalation/deintercalation among the polymer film. In this particular case, anions ClO_4^- in the electrolyte participated in the ion doping/dedoping process [19], as shown in Scheme 1.

We used the cyclic voltammetry (CV) measurement to study the reduction/oxidation of PProDOT-Me_2 thin film. The measurement was recorded at scan rates of 10, 20, 50, and 100 mV/s (see Fig. 3a). The EC polymer film changed from light blue to deep blue, corresponding to a further reduction reaction. When oxidized, the film switched to the transparent state. We found a linear relationship between the square root of the scan rate (X axis) and the cathodic peak current (Y axis), as shown in Fig. 3b. This relationship indicated the color-changing kinetics: the diffusion of ions from the electrolyte into the polymer thin film was the limiting factor for the color-switching speed [20–22].

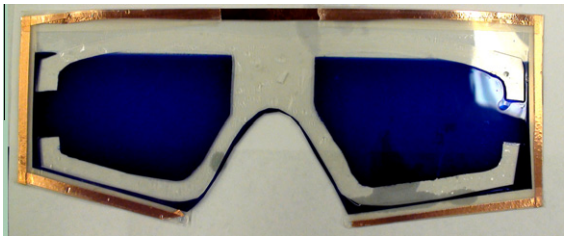

Fig. 2. Electrochemically deposited PProDOT-Me_2 film on prepatterned ITO/PET substrate.

$$\text{PProDOT-Me}_2 + n\text{ClO}_4^- \leftrightarrow (\text{PProDOT-Me}_2)^{n+}\, n\text{ClO}_4^- + ne^-$$
(blue, neutral) (transparent, oxidized)

Scheme 1. The redox process of PProDOT-Me_2.

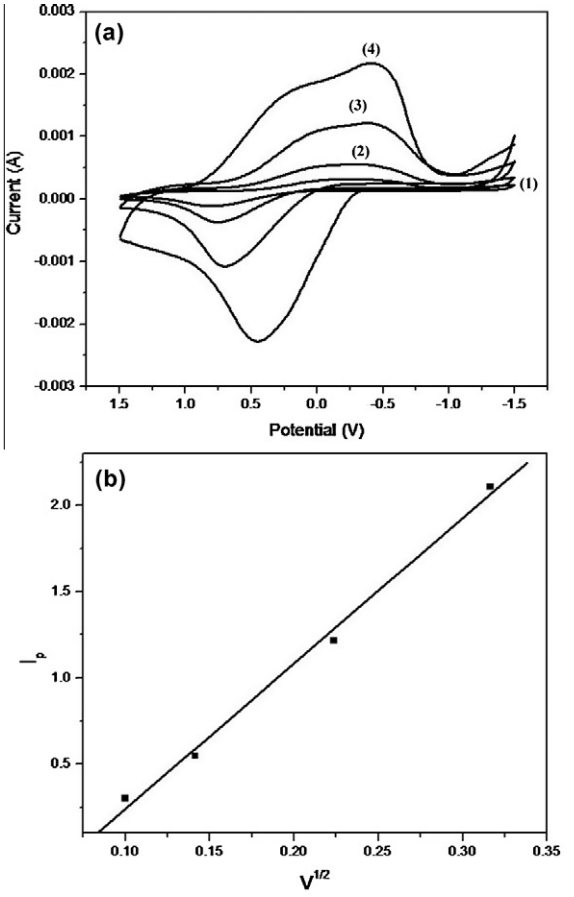

Fig. 3. (a) CV of the PProDOT-Me_2 film at different scan rates (1) 10, (2) 20, (3) 50, (4) 100 mV/s. (b) The linear relationship between the square root of the scan rate (X axis) and the cathodic peak current (Y axis).

The deposited PProDOT-Me_2 thin film had an ultra fast color-changing speed. In a 0.1 M $LiClO_4$/PC electrolyte solution, the film took less than one second to change between its transparent and fully colored states. The EC property of PProDOT-Me_2 arises principally from its redox reaction. During oxidation and reduction of the polymer film, its energy band gap E_g changes, which determines the intrinsic optical/color properties and light transmittance of the material. In order to maintain the charge balance of the polymer film during oxidization (electron removal), counter anions ClO_4^- intercalation is involved. This anion transport through the electrolyte/solid interface to the solid EC polymer film limits the color-changing speed. The

color-changing time is determined by the ion diffusion coefficient [23], as the following equation:

$$T \propto x^2/D \tag{1}$$

where T is the color-changing time, x is the length of ion diffusion path, and D is the ion diffusion coefficient of the polymer film. In this research, the diffusion coefficient D can be calculated using the CV measurement of the polymer film and the Randles–Sevick equation [12]:

$$Ip = (2.6 \times 10^5) n^{3/2} A D^{1/2} C v^{1/2} \tag{2}$$

where Ip is the cathodic peak current from the CV measurement, n is the electron number involved in redox reaction, A is the film area, C is the concentration of electrolyte, v is the scan rate of the CV measurement, and D is the ion diffusion coefficient.

We calculated the ion diffusion coefficient of the PProDOT-Me_2 thin film to be 4.1×10^{-8} cm^2/s, which is comparable to the value of 2.82×10^{-8} cm^2/s obtained from a fast-switching ECD with a color-changing time of 6 ms [24]. This high diffusion coefficient suggests that the film has the potential to change color in milliseconds, an essential advantage for color changeable devices used in intensively light-changing conditions.

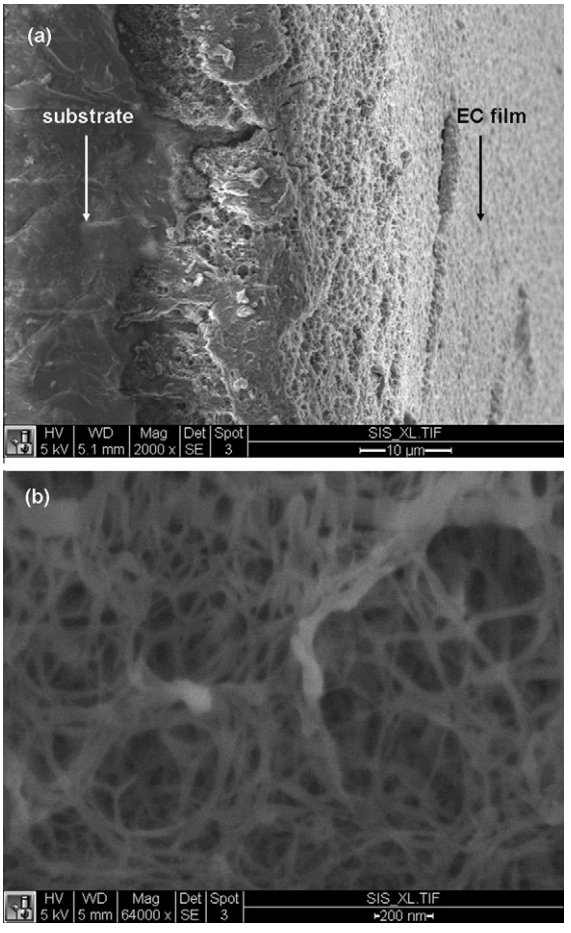

Fig. 4. SEM photos of the PProDOT-Me_2 film (a) cross-section view 2000× and (b) front view 64000×.

We characterized the microstructure of electrochemically deposited PProDOT-Me_2 thin film. Fig. 4 shows the SEM photo of the deposited polymer thin film on ITO/plastic substrate, where (a) is the cross-section view at low magnification and (b) is the front view at high magnification. The rough, porous surface of PProDOT-Me_2 thin film was clearly shown on the substrate. Fig. 4b shows the polymer-wired 3-D network. The polymer wires have diameters of about 30–50 nm, and the holes have diameters of about a hundred nanometers. The porous nanostructure indicates two advantageous EC properties. First, the polymer film has a rich surface area to contact the electrolyte, thus enhancing such EC properties as the light transmittance contrast ratio and coloration efficiency. Second, the nanoscale holes of the film, which fully fill the polymer network, provide good ion diffusion paths that allow ions to migrate easily and smoothly through the "solid" polymer film. Thus, the ions in the EC films are highly mobile.

3.3. Electrochemical AC impedance studies

AC impedance measurements provide important information for charge transfer kinetics [25–30]. Our experiment recorded the electrochemical impedance data using a three-electrode cell setup. To set the redox states of the polymer thin film, we applied a constant base potential, initial E. Negative E signifies the EC film at reduction state, and vice versa. We superimposed a sine waveform onto the base potential. The frequency was scanned from high to low (100 K to 0.01 Hz). The waveform had an amplitude of 5 mV, and we set the initial E to +1.0, +0.1, −0.1, −0.5, and −1.0 V. Fig. 5 shows the measured Nyquist plots : (a) shows the impedance data obtained at +1.0, +0.1, and −0.1 V; (b) shows the enlarged high-frequency region of Fig. 5a; (c) shows the data obtained at −0.5 and −1.0 V with an insert figure showing the enlarged high frequency; (d) shows the simplified and idealized Nyquist plot generalized from the measured AC impedance data of this research. The typical plots can be divided into three regions: the first unfinished semicircle in the high-frequency range, the second semicircle in the middle-frequency range, and a 45° slope Warburg region in the low-frequency range. The tail of the plots curved up, becoming vertical to the real (X) axis at Z'_{low}, because of the pure capacitance response of the polymer thin film. Applying a different initial E set the PProDOT-Me_2 thin film to different redox states, resulting in significant changes to the Nyquist plots. When the applied E changed from positive to negative, the PProDOT-Me_2 thin film transformed from a conductive (transparent) state to an insulative (blue) state. The width of the second semicircle in the Nyquist plots increased with the decreased E. As shown in Fig. 5d, when E became more negative, Z'_{high} stayed constant but Z'_{middle} increased dramatically. This result indicated increased charge transfer impedance at the polymer thin film/electrolyte interface, when the film was reduced. We also noticed that the Warburg region deviated from the ideal 45° angle, which indicated the roughness and non-uniformity of the film surface [31,32]. Meanwhile, the

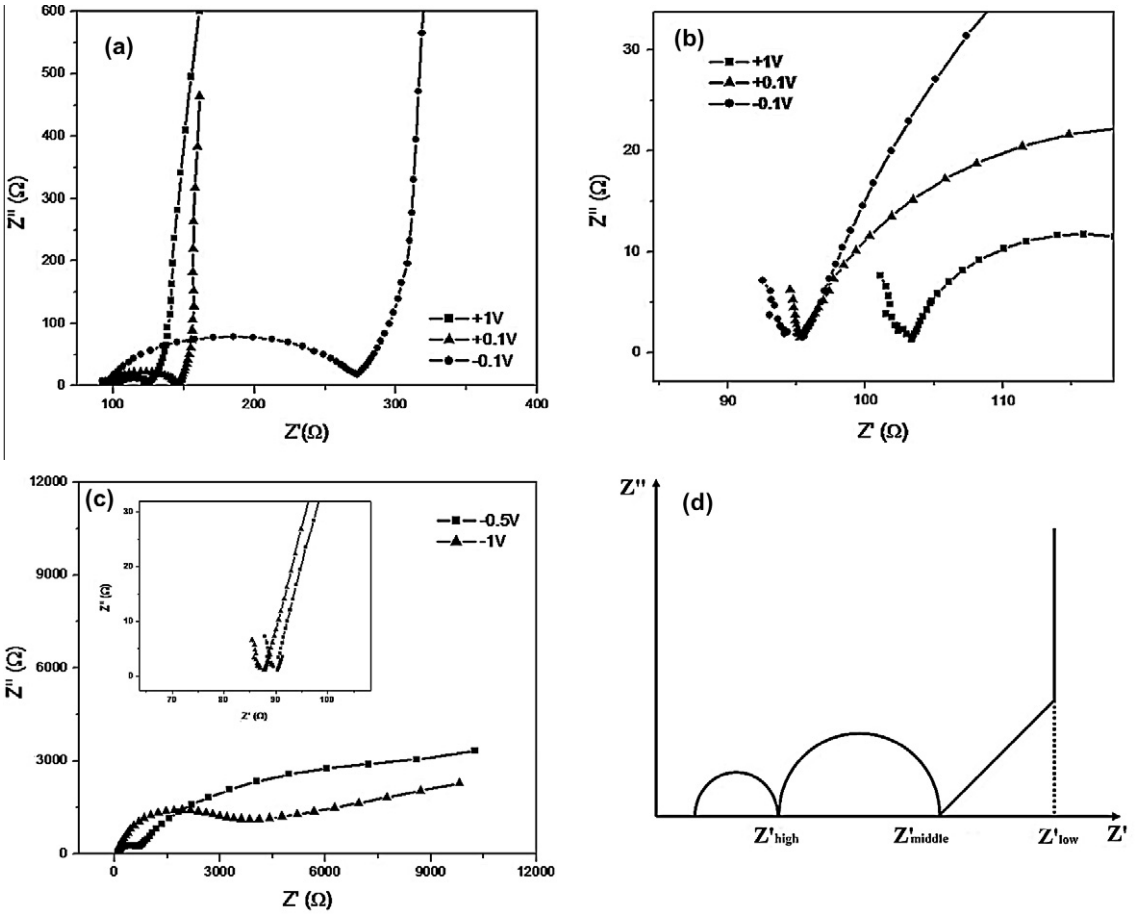

Fig. 5. (a) Nyquist plots of the PProDOT-Me_2 film measured at +1.0, +0.1, and −0.1 V; (b) enlarged high-frequency region of (a); (c) Nyquist plots of the PProDOT-Me_2 film measured at −0.5 and −1.0 V with an insert figure showing the enlarged high-frequency region and (d) simplified and idealized Nyquist plot generalized from the measured AC impedance data.

Warburg region was broadened with the decreased potential, which suggested that the diffusion-controlled impedance was more obvious at negative potentials.

To better understand the charge transfer and color-changing kinetics of the PProDOT-Me_2 thin film, we built an equivalent circuit to describe the behavior of the system at the different redox states, as shown in Fig. 6. In this circuit model, R_0 is the uncompensated resistance related to the solution electrolyte and the polymer thin film/ITO contact; C_g is the geometric capacitance of the electrodes; R_f and C_f are the polymer thin film resistance and capacitance, describing the impedance behavior through the film; R_{ct} is the charge transfer resistance and C_{dl} is the double-layered capacitance at the thin film/electrolyte interface; and W is the Warburg impedance due to the diffusion. The fitting process and estimation of the circuit components were carried out on the electrochemical analyzer (CHI 604C) with preinstalled software. Fig. 7 shows the fitting results; the hollow icons are experimental data, and the solid lines are simulation data. This equivalent circuit provides an accurate fit to the experimental data, especially when the PProDOT-Me_2 thin film is conductive or slightly insulative. As shown in Fig. 7a, the good agreement between experimental data and calculated data continues through the entire measured frequency (insert figure shows the high-frequency range). However, when the polymer thin film was fully reduced at negative potentials, we could observe a deviation from the experimental data at the lower frequency range, as shown in Fig. 7b. The reduction process may be more sensitive to the non-uniform microstructure of the PProDOT-Me_2 thin film, so that the measured Warburg impedance deviated more significantly from the theoretical 45° angle, which was difficult to calculate using the software, resulting in an inaccurate fitting.

3.4. Light transmittance, color-switching speed and repeatability

We monitored the light transmittance of the PProDOT-Me_2 thin film deposited on ITO/PET substrate (shown in Fig. 2) in colored and transparent states in the visible light region (wavelengths from 380 to 800 nm). Fig. 8 shows typical light transmittance data when we applied electric potential of −1.2 and +1.2 V. The flat dashed line shows the light transmittance of the polymer thin film in its

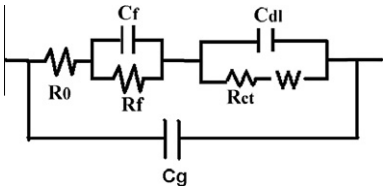

Fig. 6. Equivalent circuit model to describe the impedance behavior of the PProDOT-Me_2 film at different redox states.

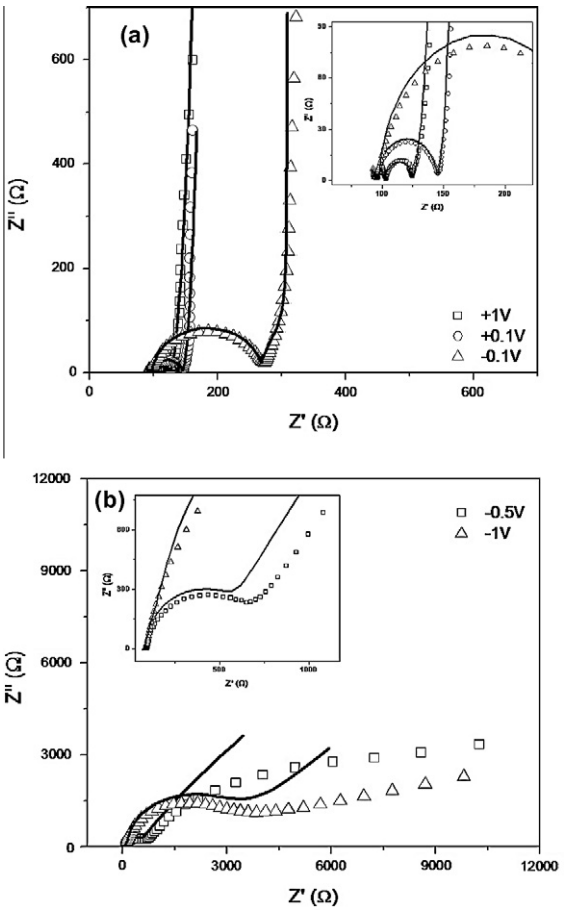

Fig. 7. Fitting of the experimental data at (a) +1.0 V (R_0 = 102.9 Ω, R_f = 1.047e + 10 Ω, C_f = 0.01345F, R_{ct} = 21.5 Ω, C_{dl} = 2.761e-5F, W = 0.05885 Ω $s^{-1/2}$, C_g = 1.269e-9F); +0.1 V (R_0 = 95.97 Ω, R_f = 1.188e + 13 Ω, C_f = 0.03058F, R_{ct} = 48.36 Ω, C_{dl} = 2.79e-5F, W = 0.1151 Ω $s^{-1/2}$, C_g = 1.192e-9F); and −0.1 V (R_0 = 96.85 Ω, R_f = 5.291e + 14 Ω, C_f = 0.02399F, R_{ct} = 156.3 Ω, C_{dl} = 3.274e-5F, W = 0.02538 Ω $s^{-1/2}$, C_g = 1.459e-9F); (b) −0.5 V (R_0 = 92.19 Ω, R_f = 517.8 Ω, C_f = 0.00006605F, R_{ct} = 876.7 Ω, C_{dl} = 0.0007619F, W = 0.0007645 Ω $s^{-1/2}$, C_g = 1.589e-9F) and −1.0 V (R_0 = 89.1 Ω, R_f = 64.34 Ω, C_f = 0.0001377F, R_{ct} = 2890 Ω, C_{dl} = 6.765e-5F, W = 0.0008447 Ω $s^{-1/2}$, C_g = 1.55e-9F).

transparent state, while the "U" shape solid line shows the light transmittance in the colored state. The light transmittance contrast ratio ($\Delta T\%$) is defined in the equation:

$$\Delta T\% = T_t(\lambda) - T_c(\lambda) \quad (3)$$

where $T_t(\lambda)$ and $T_c(\lambda)$ are the light transmittance of certain wave length λ in the transparent state (t) and the colored state (c). Because the absorption peak of the polymer in color state occurred at the 580 nm wavelength, we also calculated the largest contrast ratio at this wavelength. As a result, the transmittance contrast ratio reached 66% (13–79%, shown in Fig. 8). Such a large contrast ratio yields extremely sensitive and effective color changes, as human eyes are most sensitive to light in the 550–600 nm wavelength.

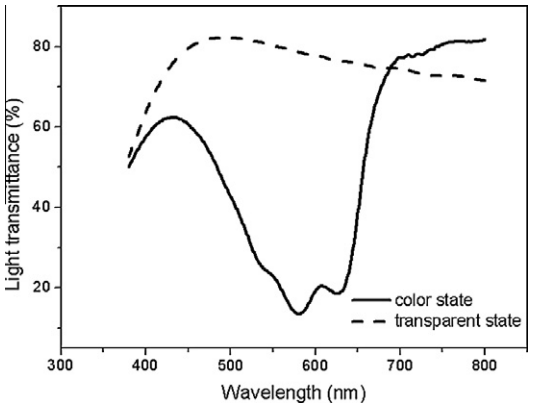

Fig. 8. Light transmittance of the PProDOT-Me_2 film at wavelengths from 380 to 800 nm.

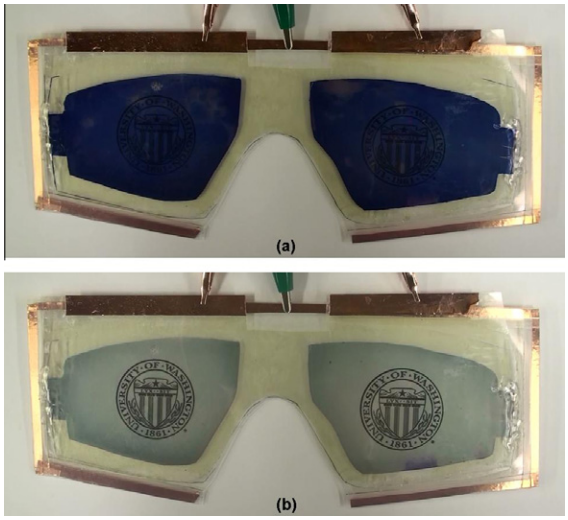

Fig. 9. Assembled goggles lens in (a) colored and (b) transparent states.

The electrolyte was injected into the device by vacuum filling. We describe details of the ECD configuration and assembly elsewhere [10,18]. Fig. 9 shows photos of the assembled goggles lens in the colored and transparent states. We observed fast and vivid color changing of the flexible goggles. We could change the device's color completely using driving electric potentials below 1.2 V. When we subjected the device repeated cyclic changes in the electric potential, the color changed continuously. Fig. 10a shows the repeated cyclic light transmittance data recorded at the 580 nm wavelength. Our apparatus changed the driving electric potential every 2 s to set the every

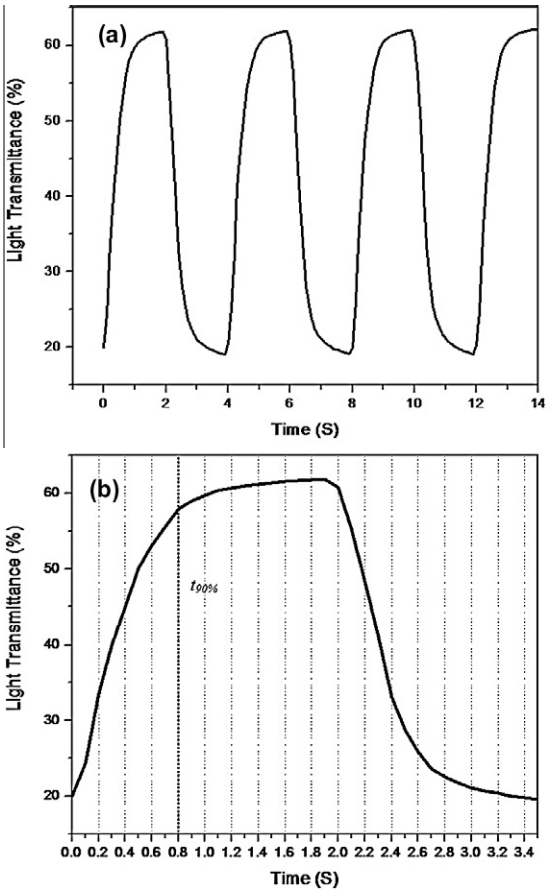

Fig. 10. (a) Cyclic light transmittance data for color switchable goggle lens at 580 nm wavelength. (b) Enlarged 1st cycle.

color-switching period. As the goggles must respond to various lights conditions and perform rapidly during outdoor activities, the color-changing speed of the lens is critical. To determine the switching time, we used the parameter $t_{90\%}$; here, we define $t_{90\%}$ as the time needed for the ECD to reach 90% of a complete color change at the 580 nm wavelength. Fig. 10b shows that $t_{90\%}$ takes about 0.8 s for both bleaching and coloring the lens, as one marked by the thicker dotted line in the bleaching process. This speed, extremely fast for an all-plastic EC device of that size, will suffice for hiking, skiing, motorcycling, and daily driving. The lens also displayed good repeatability and stability. As it continuously changed between the colored and transparent states, the optical spectra curves of different cycles were stable and almost identical to each other. We saw no obvious decay or aging over the 60,000 cycles tested.

4. Conclusions

The calculated high ion diffusion coefficient (4.1×10^{-8} cm^2/s) of the nanoporous PProDOT-Me$_2$ film is consistent with the fast color-changing speed ($t_{90\%}$ 0.8 s) we observed in the device we designed. Our CV study revealed that ion diffusion controls the redox process during color switching. The impedance model, based on the equivalent circuit, fits conductive polymer thin films well but only fits partially for completely reduced films. The goggles we designed and assembled using the film had good dynamic properties and showed promise for military and outdoor activity applications.

Acknowledgements

Financial support, partially from Revision Eyewear Ltd., USA, partially from National Natural Science Foundation, China, and partially from Solar Energy Initiative program of Chinese Academy of Sciences, are gratefully acknowledged.

References

[1] Y. Dong, C. Xu, Conducting polymer-based patterned electrochromic window for vehicle sun strips, International Journal of Nonlinear Sciences and Numerical Simulation 11 (1) (2010) 63–70.
[2] C. Xu, H. Tamagawa, M. Uchida, M. Taya, Enhanced contrast ratios and rapid switching color changeable devices based on poly(3,4-propylenedioxythiophene) derivative and counterelectrode, Smart Structures and Materials 2002, Proceeding of SPIE 4695 (2002) 442–450.
[3] C.M. Lampert, Large-area smart glass and integrated photovoltaics, Solar Energy Materials and Solar Cells 76 (2003) 489–499.
[4] C. Kaneko, C. Xu, L. Liu, D. Ning, M. Taya, Electro-deposited vanadium oxide as a counter-electrode for PProDOT-Me$_2$ based electrochromic devices (ECDs), Proceedings of SPIE 5759 (2005) 518–525.
[5] S.K. Deb, A novel electrophotographic system, Applied Optics Supplements 3 (1969) 192.
[6] T.A. Skotheim, R.L. Elsenbaumer, J.R. Reynolds, Handbook of conducting polymers, second ed., Marcel Dekker, Inc., New York, US, 1998.
[7] Q. Pei, G. Zuccarello, M. Ahlskog, O. Inganas, Electrochromic and highly stable poly(3,4-ethylenedioxythiophene) switches between opaque blue-black and transparent sky blue, Polymer 35 (7) (1994) 1347–1351.
[8] O. Turkarslan, A.K. Metin, C. Tanyeli, I. Akhmedov, L. Toppare, Enhancing electrochromic properties of conducting polymers via copolymerization: copolymer of 1-(4-fluorophenyl)-2,5-di(thiophen-2-yl)-1H-pyrrole with 3,4-ethylene dioxythiophene, Journal of Polymer Science: Part A: Polymer Chemistry 45 (2007) 4496–4503.
[9] C. Xu, L. Liu, S.E. Legenski, D. Ning, M. Taya, Switchable window based on electrochromic polymers, Journal of Materials Research 19 (7) (2004) 2072.
[10] C. Ma, M. Taya, C. Xu, Flexible electrochromic device based on poly (3,4-(2,2-dimethylpropylenedioxy)thiophene), Electrochimica Acta 54 (2008) 598–605.
[11] C. Ma, M. Taya, C. Xu, Smart sunglasses based on electrochromic polymers, Polymer Engineering and Science 48 (11) (2008) 2224–2228.
[12] P. Monk, R. Mortimer, D. Rosseinsky, Electrochromism: Fundamentals and Applicatoins, VCH, Weinheim, New York, 1995.
[13] K.N. Guimard, N. Gomez, C.E. Schmidt, Conducting polymers in biomedical engineering, Progress in Polymer Science 32 (2007) 876–921.
[14] C. Xu, X. Kong, L. Liu, F. Su, S. Kim, M. Taya, Smart glass based on elelctrochromic polymers, Proceedings of SPIE (2006). 6168, 61681N.
[15] D.M. Welsh, A. Kumar, E.W. Meijer, J.R. Reynolds, Fast electrochromic polymers based on new poly(3,4-alkylenedioxythiophene) derivatives, Advanced Materials 11 (16) (1999) 1379.
[16] P.T. Kissinger, W.R. Heineman, Laboratory Techniques in Electroanalytical Chemistry, second ed., Marcel Dekker Inc., New York, US, 1996.
[17] S. Kim, M. Taya, C. Xu, The contrast, switching speed and durability of V_2/O_5–TiO_2 film based electrochromic windows, Journal of the Electrochemistry Society 156 (2) (2009) E40–E45.
[18] C. Xu, C. Ma, X. Kong, M. Taya, Vacuum filling process for electrolyte in enhancing electrochromic polymer window assembly, Polymers for Advanced Technology 20 (2009) 178–182.

[19] J. Hwang et al., Optical properties of nondegenerate ground-state polymers: three dioxythiophene-based conjugated polymers, Physical Review B 67 (2003) 115205.
[20] S. Bhandari, M. Deepa, S. Singh, G. Gupta, R. Kant, Redox behavior and optical response of nanostructured poly(3,4-ethylenedioxythiophene) films grown in a camphorsulfonic acid based micellar solution, Electrochimica Acta 53 (2008) 3189–3199.
[21] S. Higgins, K. Lovell, R. Rajapakse, N. Walsby, Grafting and electrochemical characterisation of poly-(3,4-ethylenedioxythiophene) films, on Nafion and on radiation-grafted polystyrenesulfonate–polyvinylidene fluoride composite surfaces, Journal of Materials Chemistry 13 (2003) 2485–2489.
[22] F. Tran-Van, L. Beouch, F. Vidal, P. Yammine, D. Yeyssie, C. Chevrot, Self-supported semi-interpenetrating polymer networks for new design of electrochromic devices, Electrochimica Acta 53 (2008) 4336–4343.
[23] S. Cho, W. Kwon, S. Choi, et al., Nanotube-based ultrafast electrochromic display, Advanced Materials 17 (2) (2005) 171–175.
[24] V. Jain, H.M. Yochum, R. Montazami, J.R. Heflin, Millisecond switching in solid state electrochromic polymer devices fabricated from ionic self-assembled multilayers, Applied Physics Letters 92 (2008) 033304.
[25] S. Refaey, Electrochemical impedance studies on the electrochemical properties of poly(3-methylthiophene) in aqueous solutions, Synthetic Metals 140 (2004) 87–94.
[26] R. Vergaz, J. Pena, D. Barrios, C. Vazquez, Electrical analysis of new all-plastic devices, Optical Engineering 45 (11) (2006) 110501.
[27] X. Ren, P. Pickup, An impedance study of electron transport and electron transfer in composite polypyrrole + polystyrenesulphonate films, Journal of Electroanalytical Chemistry 420 (1997) 251–257.
[28] G. Casalbore-Miceli, M. Yang, N. Camaioni, et al., Investigations on the ion transport mechanism in conducting polymer films, Solid State Ionices 131 (2000) 311–321.
[29] A. Riul Jr., A. Gallardo Soto, S.V. Mello, et al., An electronic tongue using polypyrrole and polyaniline, Synthetic Metals 132 (2003) 109–116.
[30] J. Bell, J. Matthews, I. Skryabin, Modelling switching of electrochromic devices—a route to successful large area device design, Solid State Ionics 152-153 (2002) 853–860.
[31] M. Deepa, S. Bhandari, R. Kant, A comparison of charge transport behavior in functionalized and non-functionalized poly 3,4-(ethylenedioxythiophene) films, Electrochimica Acta 54 (2008) 1291–1303.
[32] H. Ding, Z.Pan.L. Pigani, R. Seeber, p- and n-doping processes in polythiophene with reduced bandgap. An electrochemical impedance spectroscopy study, Journal of New Materials for Electrochemical Systems 4 (2001) 61–67.

we herein report the novel concept of an organic bistable device with thickness control of the insulating layer (LiF) that consists of a new charge trap system (CTS, LiF/Al/LiF) embedded in the organic layer (Alq_3), yielding a device structure of Al/Alq_3/LiF/Al/LiF/Alq_3/Al. The CTS was designed to trap electron carriers, because the insulating layer, LiF, serves as a potential barrier while the Alq_3/LiF structure is a good electron transporting layer (ETL) in an organic light emitting diode (OLED). We reasoned that if the LiF layer was very thin, no electron carriers would accumulate due to easy transport of electron carriers. As the thickness of the LiF layer increases, however, the electrical current would decrease and simultaneously, electron carriers would be trapped. If the LiF layer was sufficiently thick, the electrical current would be expected to decrease sharply with little charge-trapping due to a too high a potential barrier for the charge carriers. Novel devices with thickness control of the insulating layer could potentially be used to exclude subtle filamentary effects in crossbar-type organic memory devices, and guide the development of new prototypes of non-volatile organic memory devices.

2. Experimental

The simple crossbar memory device used for this work was fabricated as follows. All layers were evaporated by thermal evaporation under vacuum (below 2×10^{-6} torr:1 torr $\sim$ 133 Pa). The Al (50 nm) electrode, used as a bottom electrode, was coated on the precleaned glass substrates, followed by Alq3 (50 nm) used as the electron-transporting layer (ETL) in OLED. Then, an LiF layer (2.0, 4.0, or 6.0 nm), a potential barrier of charge carriers, was deposited on the Alq3 to effectively trap electrons from the ETL. The Al layer (3.0 nm), second LiF layer (2.0, 4.0, or 6.0 nm), and second Alq3 (50.0 nm) were sequentially deposited. Finally, the Al (50.0 nm) electrode, as the top electrode, was deposited through a shadow mask defined with an active area of $700 \times 700\ \mu m^2$, resulting in the Al/organic/NT layer/organic/Al structure of memory cells. Current–voltage (I–V) characteristics of the devices were measured using a Keithley 4200 semiconductor characterization system. The I–V curves of the cycle, write–read–erase–read, and stress test were characterized by two Keithley 2400 Series sourcemeters controlled by computer. All electrical measurements were done under ambient conditions.

3. Results and discussion

We fabricated an organic memory device, Al/Alq_3/LiF/Al/LiF/Alq_3/Al, with a CTS consisting of LiF/Al/LiF, located at the center of the Alq_3/Al layer. All layers were evaporated by thermal evaporation under a vacuum. The film thickness of the LiF layer of the CTS was optimimized. The optimized film thickness of the CTS was LiF (4 nm)/Al (3 nm)/LiF (4 nm) and that of the organic-metal layer was Alq_3 (50 nm)/Al (50 nm). Without both Alq3 layers (50.0 nm) served as a buffer layer as well as transporting layer, we used to observe an electrical short problem due to possible diffusion of Al particles even with 6 nm of LiF. Both the top and bottom Al electrodes had a width of 700 μm, giving the device an active area of $700 \times 700\ \mu m^2$. The organic layer consisted of a typical light-emitting material with known organic semiconductor properties (Alq_3) that is commonly used as the ETL in OLEDs. Insertion of a very thin ($\sim$0.5 nm) layer of LiF between the organic layer and the metal cathode has previously resulted in reduced driving voltage of OLEDs [17]. In another report [18], photoelectron emission measurements showed energy-banding and subsequent enhancement of electron carrier injection at the Alq_3/LiF interface. However, thick LiF film ($\sim$ > 4 nm) is a very good insulator with a conductivity of 10^{-10} Scm^{-1} [19], making decomposition of LiF during the evaporation process unlikely. This is consistent with reported photoelectron spectroscopy results [20]. Moreover, even in organic [21] and polymer [22] materials, this buffer layer may isolate the metal impurities in the active medium formed due to diffusion of the metal electrode, which may cause filamentary conduction. Thus, we hypothesized that the use of an adequately thick LiF layer would not only prevent a filamentary conduction mechanism caused by the diffusion of nanoparticles from the metal electrodes, but also provide the advantage of charge trapping in the CTS within the thin-Al layer, yielding a non-volatile organic memory effect.

Typical current–voltage (I–V) characteristics of the device are shown in Fig. 1(a). The device exhibits two states of different electrical conductivity at the same voltage. During the voltage-bias scan, a low current was observed in the bias range from 0 to 4.1 V. A sharp increase in the current took place near 4.1 V, showing the transition of the device from a high-resistance state (OFF state) to a low-resistance state (ON state). As a voltage scan arte increased starting from 100μs, 1, 10 and 100 ms/V, our device showed negligible hysteresis changes [23]. This curve reveals the nonvolatile nature of the memory effect and also indicates that "erasing" is possible; the OFF state can be recovered simply through a reverse voltage scan. To develop a bipolar memory device, we designed the device with structurally and electrically symmetrical structures. Accordingly, regardless of voltage scan direction, the electrical bistable property should be nearly the same, with the exception of the turn-on voltage. A similar phenomenon was observed with Al/Alq_3/Al/Alq_3/Al with a lower turn-on voltage (2.6–3.0 V) [11]. It should be noted that the LiF layer acts as an insulating layer and that this layer is a potential barrier to electron carriers. Because of the LiF insulating layer, the conductivity of the device in the ON state was more than three orders of magnitude larger than that in the OFF state. Electrical switching between the two different states is shown in Fig. 1(b). The voltages for writing, reading, and erasing were 7.0, 2.0, and −0.2 V, respectively. The ON state could be read by a 2.0 V pulse at a current of $\sim 10^{-5}$ A. A negative bias of −0.2 V erased the ON state, producing the OFF state. The OFF state could be detected by a 2.0 V pulse with a current of $\sim 10^{-8}$ A. In addition, the use of a thicker LiF layer to maintain charge trapping resulted in a high write/erase voltage and a slow switching speed. Thus, the device could be controlled by applying an appropriate voltage pulse, resulting in good rewritable characteristics. In addition, we measured the stability of the device under stress using continuous-bias

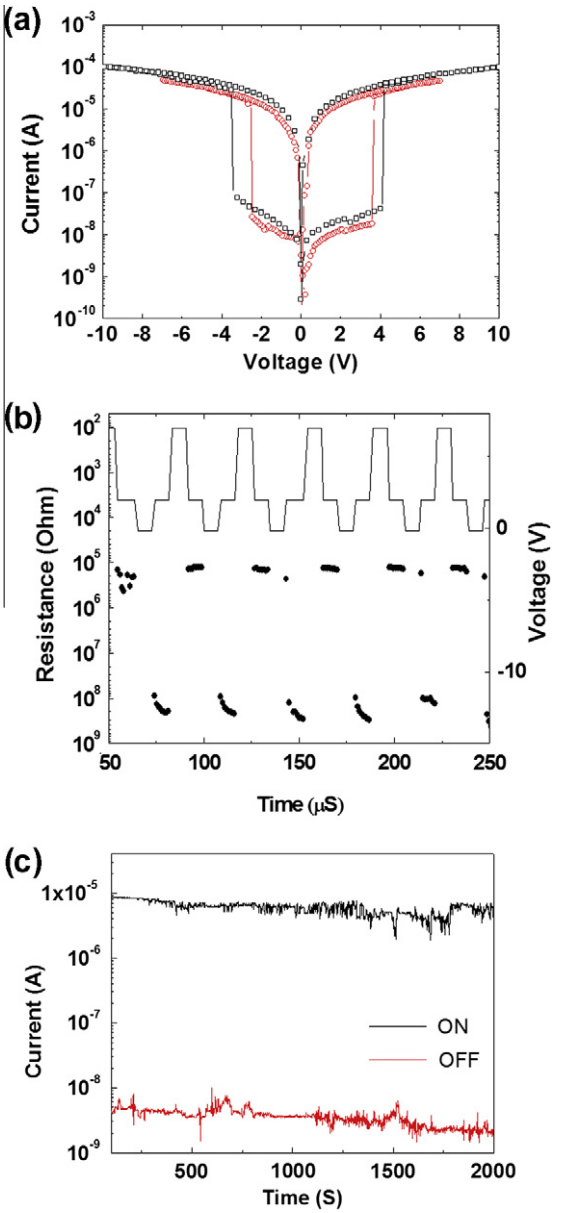

Fig. 1. (a) Current–Voltage characteristics of the Al/Alq3/LiF/Al/LiF/Alq3/Al organic memory device at ±10 V (black rectangle) and ±7 V (red circle). (b) Write–multiple read–erase–multiple read cycles. The top and bottom curves are the applied voltage and the corresponding current response, respectively. (c) Stress tests in both the ON and OFF states. A constant voltage (2.0 V) bias was applied to the device.

conditions; the reuslts are shown in Fig. 1(c). Once the device switched to the other state, it remained in that state for a period of time. Performance under stress is important for practical applications such as binary-information storage. Therefore, we tested the memory retention ability under ambient conditions and evaluated the device under continuous bias conditions. A constant voltage (2.0 V) was applied to the device in the OFF and ON states and each current was recorded at different times. As can be seen from Fig. 1(c), there was little significant degradation of the device in either the ON or OFF state after a continuous stress test. It should be noted that the time scale could not be controlled due to the inherent limitations of the testing equipment and program.

To elucidate the electron transport mechanism of the organic heterostructure device, an energy diagram was used to understand the hysteretic effects shown in Fig. 2(a). When a positive voltage was applied, electrons were injected (1) from the top of the Al (−4.3 eV) electrode into Alq_3 (−3.9 eV). The electrons were further transported through a thick LiF (∼−2.6 eV) [18] layer and then fell into the CTS due to the lower energy levels of Al between the LiF isolating layers. The electrons were trapped in this layer and either accumulated in the thin Al layer or the hetero-interface between the Al and LiF layers beause of the relatively high-energy barrier at a lower bias voltage, until the electrons were filled. However, at the higher bias volt-

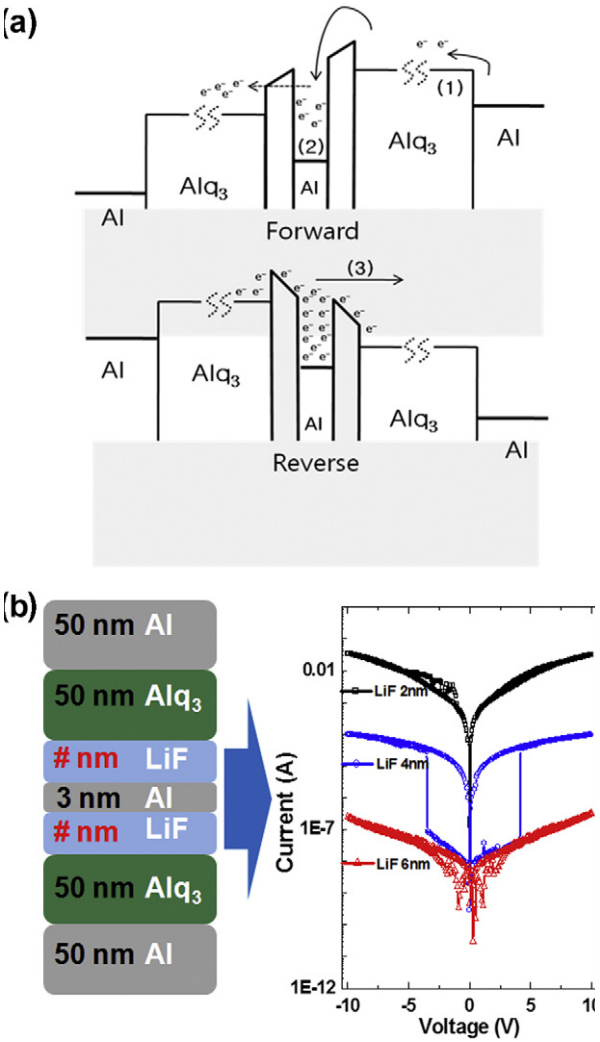

Fig. 2. (a) Schematic diagram of the energy levels of the heterostructure device obtained by applying a bias. (b) Divce structure and current–voltage characteristics of the devices as a function of LiF film thickness (2, 4, and 6 nm).

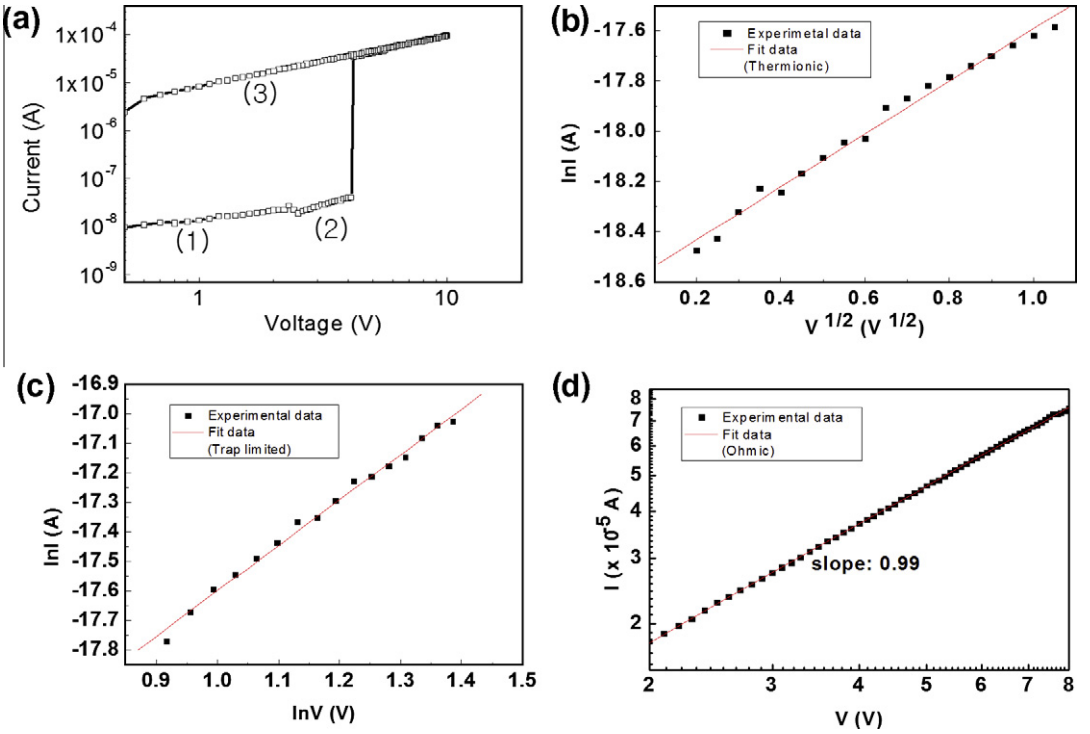

Fig. 3. (a) Current–Voltage characteristics of a heterostructured memory device in a log–log scale. The turn-on voltage is 4.1 with 44 nA and ON current starts from 35 mA at 4.2 V. (b) Thermionic emission fitting on the OFF current (1). (c) Space charge limited current in the CTS layer (2). (d) Ohmic conduction of the turned-on device under high bias conditions.

age, the electrons were able to tunnel (2) through the second LiF blocking layer into the second ETL, causing the device to switch from a high-resistance state to a low-resistance state. At the highest applied voltage, the traps in the CTS are likely to be completely filled, and the electrons kinetically activated by the electrical field could easily run (3) over the potential barrier with preservation of the ON state. As a control experiment, a device with only a thick LiF layer (6.0–11.0 nm) without Al layers between the two LiF layers was evaluated; this device showed no hysteresis.

We suggest that the optimum film thickness for the CTS is 11 nm (LiF (4 nm)/Al (3 nm)/LiF (4 nm)) to observe the hysteresis shown in the middle curve of Fig. 2(b). Due to the chemical reactivity of LiF and Al [24], ultrathin LiF layers have been used to enhance the injection of electrons from metal cathodes. For films with a thickness of 2.0 nm LiF and a fixed Al thickness (3.0 nm), no hysteresis was observed and the electrical current was highest among the three lines depicted in Fig. 2(b). As the thickness of the LiF layer increased to 6.0 nm, however, insulating properties were observed, as shown by the bottom line of Fig. 2(b). Thus, we assumed that a thin LiF layer (<2.0 nm) is not able to trap electrons due to the low potential barrier of the LiF layer, resulting in no hysteresis, while a thick LiF layer (>6.0 nm) does not allow electron transport because of too high a potential barrier, resulting in much less current with little hysteresis. A high built-in field was formed in the CTS under an optimum LiF thickness [25] despite the large dielectric constant of this material ($\varepsilon \sim 9.1$). In summary, control of the thickness of LiF in the CTS enables electron capture across the potential energy barriers of the LiF layers. A combination of potential energy barriers and variations in the thickness of interfacial metal halides in a film could guide the design of nano-scaled, organic hybrid, hetero-structured non-volatile memory devices.

The current–voltage curves have been analyzed to study the mechanism underlying the bistable switching in the memory devices, Fig. 3(a). For the as-fabricated devices under the lower positive bias (step 1 of Fig. 3(a)), the thermionic emission is dominant in the current mechanism as shown in Fig. 3(b). At higher voltages in the intermediate bias region (step 2 of Fig. 3(a)), the dominant current became a space-charged limited current (SCLC) as depicted in Fig. 3(c), indicating that the current was controlled by the trap in the thin Al layer via thermally activated hopping conduction [26,27]. In this regime, the current obeys the Mott-Gurney law as:

$$J = \frac{9\varepsilon\varepsilon_0\mu\Theta V^2}{d^3} \quad (1)$$

where Θ is the trapping fraction, ε is the dielectric constant, and ε_0 is the permittivity of free space. When the voltage was increased further (step 3 of Fig. 3(a)), the traps in the Al metal layer were nearly filled. The current flowed via thermionic emissions and a Fowler–Nordheim conduc-

tion mechanism so that the injected current increased sharply and the electrical state of the device changed simultaneously. After transition from the OFF state to the ON state, most of the traps in the CTS layer were filled and the current flow was free from the influence of traps in the organic heterostructure. When the electrical bias was removed, Fig. 3(d), the current was linearly proportional to the voltage (line slope: 0.99) under the turn-on voltage (4.1 V) as a result of the nonvolatile memory effect. In this regime, the current density J can be described [26,27] as:

$$J = \frac{qn_0\mu V}{d} \quad (2)$$

where n_0 is the density of free carrier, d is the thickness of organic heterostructure, and μ is the carrier mobility. Based on the analysis of the log–log plot of the *I–V* curve, the reversible switching behavior of the organic heterostructure device is due to a release of the stored charge at the middle Al metal layer between the LiF layers. Accordingly, with respect to the above experimental results and discussion, it can be concluded that the electronic transition was attributed to an electrical-field-induced charge transfer between two LiF layers and an Al layer located at the center of the CTS layer through the Alq3 layers.

4. Conclusions

In conclusion, an organic, electrically bistable device with a novel charge trap system (LiF/Al/LiF) was fabricated to develop a vertically oriented crossbar array memory device. Non-volatile memory behavior with a large on/off ratio (more than three orders of magnitude) and writing–reading–erasing–reading cycles were demonstrated. By controlling the thickness of the LiF layer, we were able to determine that the origin of hysteresis was electron charging at the CTS, thereb excluding the possibility of filamentary and metal particle effects. Although the retention time of the devicde still needs to be improved, we anticipate that organic–inorganic heterostructures, such as the one developed in this study, may potentially be applied in nano-scaled organic non-volatile memory devices.

Acknowledgements

The authors thanks the Creative Research Initiatives (project title: Smart Molecular Memory) of MEST/NRF of Korea for the finantial support.

References

[1] A.R. Elsharkawi, K.C. Kao, J. Phys. Chem. Solids 38 (1977) 95.
[2] D. Tondelier, K. Lmimouni, D. Vuillaume, C. Fery, G. Haas, Appl. Phys. Lett. 85 (2004) 5763.
[3] A.K. Mahapatro, R. Agrawal, S. Ghosh, J. Appl. Phys. 96 (2004) 3583.
[4] C.H. Tu, Y.S. Lai, D.L. Kwong, IEEE Electron Device Lett 27 (2006) 354.
[5] W. Tang, H. Shi, G. Xu, B.S. Ong, Z.D. Popovic, J. Deng, J. Zhao, G. Rao, Adv. Mater. 17 (2005) 2307.
[6] A. Bandyopadhyay, A.J. Pal, Appl. Phys. Lett. 82 (2003) 1215.
[7] L.D. Bozano, B.W. Kean, V.R. Deline, J.R. Salem, J.C. Scott, Appl. Phys. Lett. 84 (2004) 607.
[8] Y.-S. Lai, C.-H. Tu, D.-L. Kwong, J.S. Chen, Appl. Phys. Lett. 87 (2005) 122101.
[9] H.S. Majumdar, A. Bandyopadhyay, A. Bolognesi, A.J. Pal, J. Appl. Phys. 91 (2002) 2433.
[10] H.S. Majumdar, A. Bolognesi, A.J. Pal, Synth. Met. 140 (2004) 203.
[11] L.D. Bozano, B.W. Kean, M. Beinhoff, K.R. Carter, J.C. Scott, Adv. Funct. Mater. 15 (2005) 1933.
[12] M. Cölle, M. Büchel, D.M. de Leeuw, Org. Electron. 7 (2006) 305.
[13] M. Lauters, B. McCarthy, D. Sarid, G.E. Jabbour, Appl. Phys. Lett. 89 (2006) 013507.
[14] L.P. Ma, J. Liu, Y. Yang, Appl. Phys. Lett. 80 (2002) 2997.
[15] L. Ma, S. Pyo, J. Quyang, Q. Xu, Y. Yang, Appl. Phys. Lett. 82 (2003) 1419.
[16] R.E. Thurstans, D.P. Oxley, J. Phys. D 35 (2002) 802.
[17] L.S. Hung, C.W. Tang, M.G. Mason, Appl. Phys. Lett. 70 (1997) 152.
[18] T. Mori, H. Fujikawa, S. Tokito, T. Taga, Appl. Phys. Lett. 73 (1998) 2763.
[19] K.R. Choudhury, J.H. Yoon, F. So, Adv. Mater. 20 (2008) 1456.
[20] M.G. Mason, C.W. Tang, L.S. Hung, P. Raychaudhuri, J. Madathil, D.J. Giesen, L. Yan, T. Le, Y. Gao, S.T. Lee, L.S. Liao, L.F. Cheng, W.R. Salaneck, D.A. dos santos, J.-L. Bredas, J. Appl. Phys. 89 (2001) 2756.
[21] J. Chen, D. Ma, Appl. Phys. Lett. 87 (2005) 023505.
[22] Z. Liu, F. Xue, Y. Su, K. Varahramyan, IEEE Electron Device Lett. 27 (2006) 151.
[23] S. Paul, A. Kanwal, M. Chhowalla, Nanotechnology 17 (2006) 145–151.
[24] L.S. Hung, C.W. Tang, M.G. Mason, P. Raychaudhuri, J. Madathil, Appl. Phys. Lett. 78 (2001) 544.
[25] T. Yokoyama, D. Yoshimura, E. Ito, H. Ishii, Y. Ouchi, K. Seki, Jpn. J. Appl. Phys. Part I 42 (2003) 3666.
[26] H. T. Lin, Z. Pei, and Y. J. Chan, IEEE Electron Device Lett. 28 (2007) 569. M.A. Lampert, P. Mark, Current injection in Solid (Academic, New York), 1970.
[27] M. Arif, M. Yun, S. Gangopadlhyay, K. Ghosh, L. Fadiga, F. Galbrecht, U. Scherf, S. Guha, Phys. Rev. B. 75 (2007) 195202.

Besides the Suzuki and Stille couplings, Sonogashira coupling is another important way to synthesize conjugated copolymers, which can result into the conjugated polymers with C≡C bonds in the polymer backbone. The C≡C bonds can increase the rigidity and planarity of the conjugated polymers, giving rise to higher charge carrier mobility [25–33]. However, polymerization *via* Sonogashira coupling proceeds quite slowly under a normal heating like oil bath. The molecular weight of the produced polymers is usually low even after polymerization of several days, and the PVs using these polymers as the donor usually exhibit low power conversion efficiency (PCE) [33]. Here, we report the syntheses of copolymers of electron-donating ethynylfluorene and electron-withdrawing 3,6-dithiophen-2-yl-2,5-dihydropyrrolo[3,4-*c*]pyyrole-1,4-dione (DPP) *via* Sonogashira coupling. DPP is used as a unit in the copolymer because it is a very important electron-withdrawing unit in low-band gap copolymers [34–43]. The molecular weight of the copolymers and the photovoltaic performance of the corresponding polymer PVs were significantly improved when the polymers were synthesized under the microwave irradiation.

2. Experimental

2.1. Materials

All reagents were purchased from Sigma–Aldrich and used without further purification unless otherwise noted. All reactions were performed in N_2 unless otherwise noted. 1-Iodo-3,7,11-trimethyldodecane and 3,6-di(thiophen-2-yl)-2,5-dihydropyrrolo[3,4-*c*]pyrrole-1,4-dione were prepared in terms of the literature [38,44].

2.2. Characterization of materials

^{1}H and ^{13}C NMR spectra were measured with a Bruker AC300 spectrometer at 300 and 75 MHz, respectively. Elemental analyses were carried out using a Vario EL elemental analysis instrument (Elementar Co.). Mass spectra were recorded with an EI ionization source and an FAB ionization source using 3-nitrobenzyl alcohol (3-NBA) as the matrix. Absorption spectra were taken with a Varian Cary 5000 ultraviolet–visible spectrometer. Thermogravimetric analyses (TGA) were measured with a Perkin-Elmer TGA-7 at a heating rate of 10 °C min^{-1}. Cyclic voltammetry (CV) was conducted using an Autolab Electrochemical Station. A Pt disk, Pt plate, and Ag/Ag$^+$ electrode were used as working electrode, counter electrode, and reference electrode, respectively. The electrolyte was 0.1 M tetrabutylammonium hexafluorophosphate (Bu_4NPF_6) in anhydrous acetonitrile, and the scan rate was 50 mV s^{-1}. Number-average (M_n) and weight-average (M_w) molecular weights were determined by the gel permeation chromatography (GPC) with a Polymer Laboratories PL220 Chromatograph. 1,2,4-Trichlorobenzene and mono-dispersed polystyrenes were used as the solvent and references, respectively. The temperature of the columns was 135 °C during the tests.

2.3. Synthetic procedures

Two copolymers, poly(9,9-bis(2-ethylhexyl)-2,7-diethynylfluorene-*alt*-3,6-dithiophen-2-yl-2,5-dihydropyrrolo[3,4-*c*]pyyrole-1,4-dione) (PFEEDPP) and poly(9,9-dioctyl-2,7-diethynylfluorene-*alt*-3,6-dithiophen-2-yl-2,5-dihydropyrrolo[3,4-*c*]pyyrole-1,4-dione (PFEODPP), were synthesized. The synthetic routes are shown in Scheme 1. The last step, the copolymerization of the two units, was through the Sonogashira coupling, which was carried out in an oil bath or a CEM SP microwave synthesizer.

2.3.1. Synthesis of 9,9-dialkyl-2,7-bis(3-hydroxy-3-methylbutynyl)fluorene (**2a**–**2b**) [45]

2-Methyl-3-butyn-2-ol (1.23 g, 14.6 mmol) was added into a solution of 9,9-dialkyl-2,7-dibromofluorene (**1a** or **1b**) (2 g, 3.65 mmol) in 20 mL of dry THF/diisopropylamine (1:1, v/v). After the solution was degassed with nitrogen for 15 min, $PdCl_2(PPh_3)_2$ (52 mg, 0.07 mmol), PPh_3 (58 mg, 0.22 mmol) and CuI (14 mg, 0.07 mmol) were added. The mixture was then refluxed for 20 h. Then, the reaction mixture was dried by the reduced-pressure evaporation. The title compounds were obtained by purifying the residue with the column chromatography using silica gel (eluent: *n*-hexane/ethyl acetate = 5:1, v/v). **2a**: Pale-yellow powder (1.72 g, 85%). ^{1}H NMR ($CDCl_3$, 300 MHz) δ: 7.59 (d, 2H, J = 7.4 Hz), 7.37–7.41 (m, 4H), 2.02–2.04 (m, 2H), 1.94 (d, 4H, J = 5.4 Hz), 1.65 (s, 12H), 0.70–0.98 (m, 22H), 0.52 (t, 6H, J = 7.2 Hz). ^{13}C NMR ($CDCl_3$, 75 MHz) δ: 150.82, 150.76, 140.65, 130.66, 127.21, 119.72, 93.64, 82.99, 65.74, 54.81, 44.51, 34.67, 33.37, 33.34, 31.56, 27.94, 27.02, 22.72, 14.07, 10.33. **2b**: Pale-yellow powder (1.78 g, 88%). ^{1}H NMR ($CDCl_3$, 300 MHz) δ: 7.59 (dd, 2H, J = 0.5, 7.8 Hz), 7.37–7.41 (m, 4H), 1.87–1.95 (m, 6H), 1.03–1.24 (m, 22H), 0.82 (t, 6H, J = 6.9 Hz), 0.55 (br, 4H). ^{13}C NMR ($CDCl_3$, 75 MHz) δ 150.93, 140.61, 130.74, 126.02, 121.38, 119.79, 93.88, 83.02, 65.75, 55.17, 40.30, 31.77, 31.56, 29.97, 29.21, 23.63, 22.57, 14.05.

2.3.2. Synthesis of 9,9-dialkyl-2,7-diethynylfluorene (**3a**–**3b**) [45]

Compound **2a** or **2b** (1.2 g, 2.16 mmol) was mixed with KOH (0.9 g, 16 mmol) in 2-propanol (20 mL). The solution was refluxed with vigorous stirring for 8 h. Then, the solution was poured into water (50 mL). The organic layer was extracted with diethyl ether, dried over $MgSO_4$, and dried by the evaporation. The title compounds were obtained by purifying the residue with the column chromatography using silica gel (eluent: *n*-hexane). **3a**: Pale-yellow oil (0.88 g, 93%). ^{1}H NMR ($CDCl_3$, 300 MHz) δ: 7.63 (dd, 2H, J = 0.7, 7.7 Hz), 7.46–7.52 (m, 4H), 3.12 (s, 2H), 1.96 (d, 4H, J = 5.6 Hz), 0.69–0.90 (m, 22H), 0.44–0.55(m, 6H). ^{13}C NMR ($CDCl_3$, 75 MHz) δ: 150.79, 140.98, 131.12, 127.76, 120.35, 119.78, 84.44, 76.98, 54.82, 44.35, 34.57, 33.49, 27.94, 26.92, 22.59, 13.87, 10.18. EI-MS: m/z = 438.4 [M]$^+$ (Calcd. 438.3). **3b**: White solid (0.85 g, 90%). ^{1}H NMR ($CDCl_3$, 300 MHz) δ: 7.63 (dd, 2H, J = 0.5, 7.8 Hz), 7.46–7.50 (m, 4H), 3.14 (s, 2H), 1.91–1.96 (m, 4H), 0.98–1.26 (m, 20H), 0.80–0.88 (m, 6H), 0.57 (m, 4H). ^{13}C NMR ($CDCl_3$, 75 MHz) δ: 151.05, 140.98, 131.24, 126.55, 120.85, 119.96,

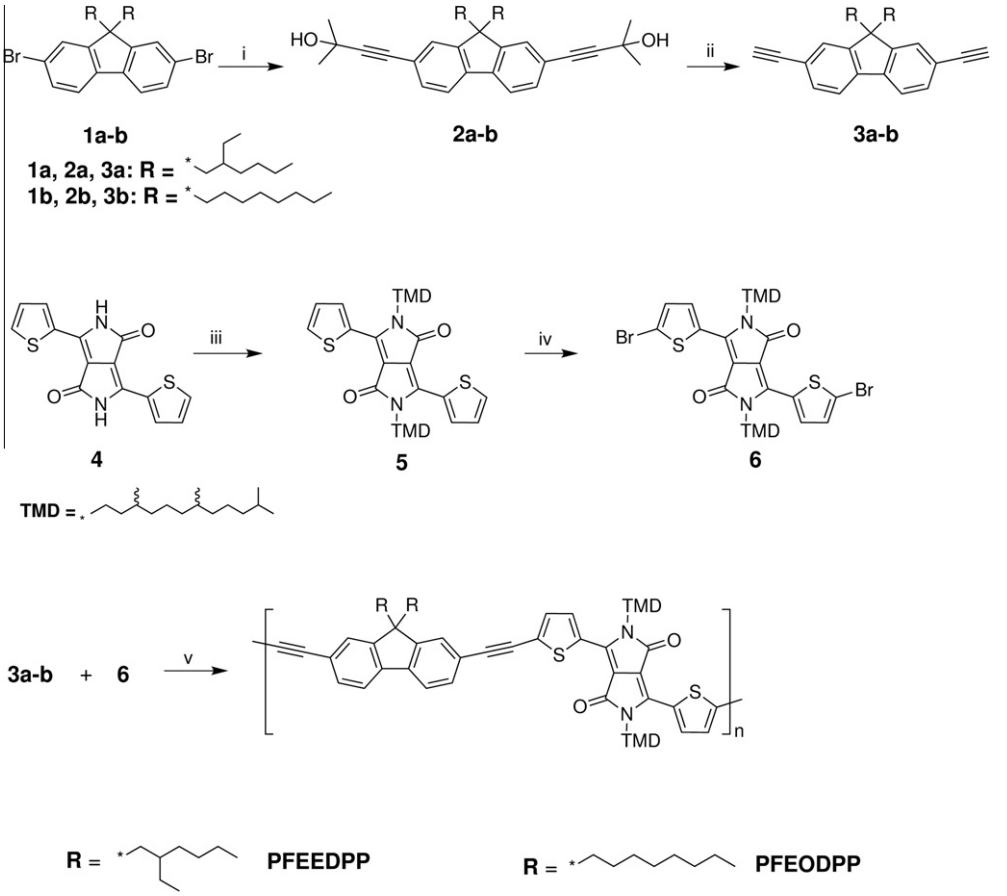

Scheme 1. Synthetic routes of PFEEDPP and PFEODPP. Reagent and conditions: (i) $PdCl_2(PPh_3)_2$, PPh_3, CuI, diisopropylamine; (ii) KOH, isopropanol; (iii) 1-iodo-3,7,11-trimethyldodecane, DMF, K_2CO_3; (iv) NBS, $CHCl_3$; (v) $Pd(PPh_3)_4$, CuI, toluene, diisopropylamine, oil bath or microwave synthesizer.

84.52, 77.30, 55.21, 40.19, 31.75, 29.92, 29.18, 23.64, 22.57, 14.04. EI-MS: m/z = 438.4 $[M]^+$ (Calcd. 438.3).

2.3.3. Synthesis of 3,6-di(thiophen-2-yl)-2,5-bis(3,7,11-trimethyldodecyl) pyrrolo[3,4-c]pyrrole-1,4-dione (**5**)

Compound **4** (1.0 g, 3.3 mmol) was mixed with K_2CO_3 (1.84 g, 13.3 mmol) in DMF (60 mL). The solution was refluxed at 120 °C for 1 h. Then, 1-iodo-3,7,11-trimethyldodecane (3.94 g, 11.7 mmol) was dropwisely added. The solution was refluxed at 130 °C for 24 h. After cooled down to room temperature, it was poured into water (100 mL). After stirred for 30 min, the water layer was extracted with $CHCl_3$. The $CHCl_3$ phase was combined with the DMF phase. The combined organic phase was dried over $MgSO_4$, and the solvents were removed by the rotary evaporation. The title compound was obtained by purifying the residue with the column chromatography using silica gel (eluent: $CHCl_3$/hexane = 1/1 (v/v) → $CHCl_3$). It was a purple-brown solid (1.6 g, 67%). ^{1}H NMR ($CDCl_3$, 300 MHz) δ: 8.90 (dd, 2H, J = 1.1 Hz, 4.0 Hz), 7.63 (dd, 2H, J = 1.1, 5.1 Hz), 7.28 (dd, 2H, J = 4.0, 5.1 Hz), 4.03–4.19 (m, 4H), 0.99–1.77 (m, 40H), 0.82–0.87 (m, 18H). ^{13}C NMR ($CDCl_3$, 75 MHz) δ: 161.29, 140.01, 135.17, 130.56, 129.72, 128.56, 107.78, 40.83, 39.35, 37.35, 37.26, 37.21, 36.79, 36.71, 32.77, 31.26, 27.95, 24.80, 24.78, 24.33, 22.70, 22.61, 19.71, 19.65, 19.54, 19.47. FAB-MS: m/z = 720.4 $[M]^+$ (Calcd. 720.4).

2.3.4. Synthesis of 3,6-bis(5-bromothiophen-2-yl)-2,5-bis(3,7,11-trimethyldodecyl)pyrrolo[3,4-c]pyrrole-1,4-dione (**6**)

Compound **5** (1.2 g, 1.66 mmol) was dissolved in chloroform in a two-necked round bottom flask covered with aluminum foil. The solution was stirred for 15 min. It was then put in an ice-water bath, and *N*-bromosuccinimide (NBS, 0.622 g, 3.49 mmol) was portionwisely added. The solution was refluxed for 36 h. After the reaction, it was rinsed with water and brine. The organic phase was collected and dried over $MgSO_4$. After the solvent was removed, a dark purple solid was obtained by purifying the residue with the column chromatography using silica gel (eluent: $CHCl_3$) to afford (0.92 g, 63%). ^{1}H NMR ($CDCl_3$, 300 MHz) δ: 8.65 (d, 2H, J = 4.1 Hz), 7.22 (d, 2H, J = 4.1 Hz), 3.92–4.09 (m, 4H), 0.99–1.73 (m, 40H), 0.82–0.87 (m, 18H). ^{13}C NMR ($CDCl_3$, 75 MHz) δ: 160.93, 138.96, 135.26, 131.60, 131.08, 119.08, 107.87, 40.89, 39.36, 37.34, 37.28, 37.18, 37.16, 36.81, 36.73, 32.78,

31.19, 27.97, 24.79, 24.33, 22.71, 22.62, 19.71, 19.65, 19.55, 19.48. FAB-MS: m/z = 878.3 $[M]^+$ (Calcd. 878.3).

2.3.5. Polymerzation

The two copolymers, poly(9,9-bis(2-ethylhexyl)-2,7-diethynylfluorene-*alt*-3,6-dithiophen-2-yl-2,5-dihydropyrrolo[3,4-*c*]pyyrole-1,4-dione) (PFEEDPP) and poly(9,9-dioctyl-2,7-diethynylfluorene-*alt*-3,6-dithiophen-2-yl-2,5-dihydropyrrolo[3,4-*c*]pyyrole-1,4-dione (PFEODPP), were synthesized by the Sonogashira coupling. PFEEDPP-*o* and PFEODPP-*o* were used to denote the two polymers synthesized in a conventional oil bath, respectively. The Sonogashira coupling was performaned by the following procedure. Compound **6** (176 mg, 0.2 mmol), compound **3a** or **3b** (87 mg, 0.2 mmol), $Pd(PPh_3)_4$ (6 mg, 5.2 μmol), and CuI (2 mg, 10.5 μmol) were mixed with anhydrous diisopropylamine (DIPA, 1.4 mL) and anhydrous toluene (4.2 mL) in a 50 mL three-neck flask. The solution was stirred for 30 min at room temperature and then refluxed at 100 °C for 48 h. After the reaction, polymer was precipitated from the solution by adding methanol (250 mL). The precipitate was filtered through a Soxhlet thimble and subsequently purified *via* the Soxhlet extraction for 12 h with methanol, 12 h with *n*-hexane and finally was collected with chloroform. The chloroform solution was concentrated under a reduced pressure. Then, polymer was precipitated by adding methanol again. Solvents were removed by filtration. PFEEDPP-*o*: A blue purple solid (210 mg, 82%). ^{1}H NMR (300 MHz, $CDCl_3$) δ: 8.92 (br, 2H), 7.42–7.69 (br, 8H), 4.12 (br, 4H), 0.55–2.01 (m, 92H). Found: C, 79.20; H, 9.73; N, 2.31; S, 5.59%. Calcd. for $(C_{77}H_{106}N_2O_2S_2)_n$: C, 80.02; H, 9.24; N, 2.42; S, 5.55%. PFEODPP-*o*: A blue purple solid (200 mg, 78%). ^{1}H NMR (300 MHz, $CDCl_3$) δ: 8.94 (br, 2H), 7.39–7.75 (m, 8H), 4.12 (br, 4H), 0.81–2.03 (m, 92H). Found: C, 80.15; H, 9.35; N, 2.44; S, 5.78%. Calcd. for $(C_{77}H_{106}N_2O_2S_2)_n$: C, 80.02; H, 9.24; N, 2.42; S, 5.55%.

The Sonogashira couplings for PFEEDPP and PFEODPP were also carried out in a microwave synthesizer. The polymers obtained with the microwave synthesizer were called PFEEDPP-*m* and PFEODPP-*m*, respectively. Compound **3a** or **3b** (87 mg, 0.2 mmol), compound **6** (176 mg, 0.2 mmol), $Pd(PPh_3)_4$ (6 mg, 5.2 μmol), and CuI (2 mg, 10.5 μmol) were mixed in a 10 mL microwave tube. The tube was subjected to the following reaction conditions in the microwave synthesizer: close vessel, 100 °C for 15 min (hold time), 200 W for power. Then, the polymers were collected and purified through the similar procedure to that for PFEEDPP-*o* and PFEODPP-*o*. PFEEDPP-*m*: A blue purple solid (238 mg, 93%). ^{1}H NMR (300 MHz, $CDCl_3$) δ: 8.93 (br, 2H), 7.43–7.70 (m, 8H), 4.11 (br, 4H), 0.57–2.02 (m, 92H). Found: C, 80.09; H, 9.51; N, 2.21; S, 5.66%. Calcd. for $(C_{77}H_{106}N_2O_2S_2)_n$: C, 80.02; H, 9.24; N, 2.42; S, 5.55%. PFEODPP-*m*: A blue purple solid (246 mg, 96%). ^{1}H NMR (300 MHz, $CDCl_3$) δ: 8.95 (br, 2H), 7.39–7.73 (m, 8H), 4.12 (br, 4H), 0.80–2.01 (m, 92H). Found: C, 80.10; H, 9.45; N, 2.31; S, 5.76%. Calcd. for $(C_{77}H_{106}N_2O_2S_2)_n$: C, 80.02; H, 9.24; N, 2.42; S, 5.55%.

2.4. Fabrication and characterization of polymer PVs

Polymer PVs were fabricated through the conventional process. Patterned indium tin oxide (ITO) glass substrates were sequentially cleaned with detergent, de-ionized (DI) water, acetone, and isopropanol. They were then treated with UV ozone for 15 min. A layer of poly(3,4-ethylenedioxythiophene):poly(styrenesulfonate) (PEDOT:PSS) with a thickness of 30 nm was formed on each ITO glass by spin-coating a PEDOT:PSS aqueous solution (Baytron 4083 from H.C. Starck) and dried at 150 °C for 30 min. The active layer was prepared on the PEDOT:PSS film by spin coating a solution consisting of a polymer synthesized in this research work and [6,6]-phenyl-C61-butyric acid methyl ester (PCBM) in a glove box filled with N_2. The film thickness of the active layer was controlled at about 80 nm, which was measured with a profilometer (Alfa-Step 500, Tencor Instruments). The PVs were completed by thermally depositing a 5 Å-thick LiF layer and subsequently a 100 nm-thick Al layer in a vacuum of 10^{-6} Pa. Each device had an area of 0.11 cm^{-2}.

The polymer PVs were encapsulated with a UV-curable epoxy and glass sheets in the glove box. Then, they were taken out for the electrical tests in air. The photovoltaic performance was measured with a computer-programmed Keithley 2400 source/meter and PVs under the illumination of a Newport's Oriel class A solar simulator, which simulated the AM 1.5G sunlight (100 mW cm^{-2}) and was certified to the JIS C 8912 standard.

Incident photon-to-current conversion efficiencies (IPCE) of the PVs were measured with a 300 W Xenon Lamp (Oriel 6258) as the light source and a Cornerstone 260 Oriel 74125 monochromator that had a resolution of 10 nm. The light intensity was calibrated with a NREL-recommended Si detector (Oriel 71030NS), and the short circuit currents of the PVs were determined with an Oriel 70310 optical power meter.

3. Results and discussion

3.1. Material synthesis and characterization

Two copolymers, PFEEDPP and PFEODPP, were synthesized by Pd-catalyzed Sonogashira coupling. The electron-donating fluorene is connected with the electron-withdrawing DPP unit through the rigid C≡C. Alkyl chains are attached to fluorene and DPP units in order to improve the polymer solubility in organic solvents. The differences in the chemical structure of the two polymers are the side chains connected to the fluorene moiety.

Two heating methods, oil bath and microwave synthesizer, were applied during the Sonogashira coupling of two monomers for PFEEDPP and PFEODPP. Suffices "-*o*" and "-*m*" are attached to PFEEDPP and PFEODPP to indicate the polymerization in the oil bath and the microwave synthesizer, respectively. Applying the microwave synthesizer remarkably lowered the Sonogashira coupling time. The polymerization took 2 days by refluxing in the oil bath at 100 °C, while it was shortened to 15 min in the microwave synthesizer at 100 °C.

Table 1
Number-average molecular weight (M_n), polydispersity index (PDI), and optical parameters of PFEEDPP-*o*, PFEODPP-*o*, PFEEDPP-*m*, and PFEODPP-*m*.

Polymer	M_n (kDa)	PDI	Absorption maxima (nm)		E_g^{opt} [b] (eV)
			Film	Solution[a]	
PFEEDPP-*o*	24	2.2	378, 650	378, 633	1.85
PFEODPP-*o*	20	2.5	391, 648	374, 635	1.86
PFEEDPP-*m*	63	4.4	379, 652	373, 635	1.85
PFEODPP-*m*	89	5.3	372, 668	374, 635	1.85

[a] Chloroform solution.
[b] Optical band gap values obtained from solution spectra.

Besides the polymerization rate, applying the microwave irradiation during the polymerization significantly improved the quality of the polymers as well. The solutions of PFEEDPP-*m* and PFEODPP-*m* were more viscous than that of PFEEDPP-*o* and PFEODPP-*o* at the same weight concentration. This is due to the different molecular weights of the polymers (Table 1). As determined by GPC, PFEEDPP-*m* and PFEODPP-*m* had the number-average molecular weights of 63,000 and 89,000 Da. They were significantly higher than that (24,000 and 20,000 Da) of PFEEDPP-*o* and PFEODPP-*o* (Table 1). All the polymers had good solubility in chloroform and chlorobenzene but a poor solubility in 1,2-dichlorobenzene (DCB) at room temperature. Their solubility in DCB became good at 90 °C.

3.2. Optical properties

The chloroform solutions of these polymers were investigated by UV–vis absorption spectroscopy (Fig. 1a). The optical data are summarized in Table 1. The solution spectra of the four polymers are quite similar. Two absorption bands appear in the range from 480 to 700 nm, which include a shoulder band peaked at *ca.* 590 nm and another peak at *ca.* 635 nm. Both of them can be assigned to intramolecular charge transfer (ICT) of donor–acceptor structures of the polymers [38,42]. In addition, we did not observe any difference in the absorption of these polymers

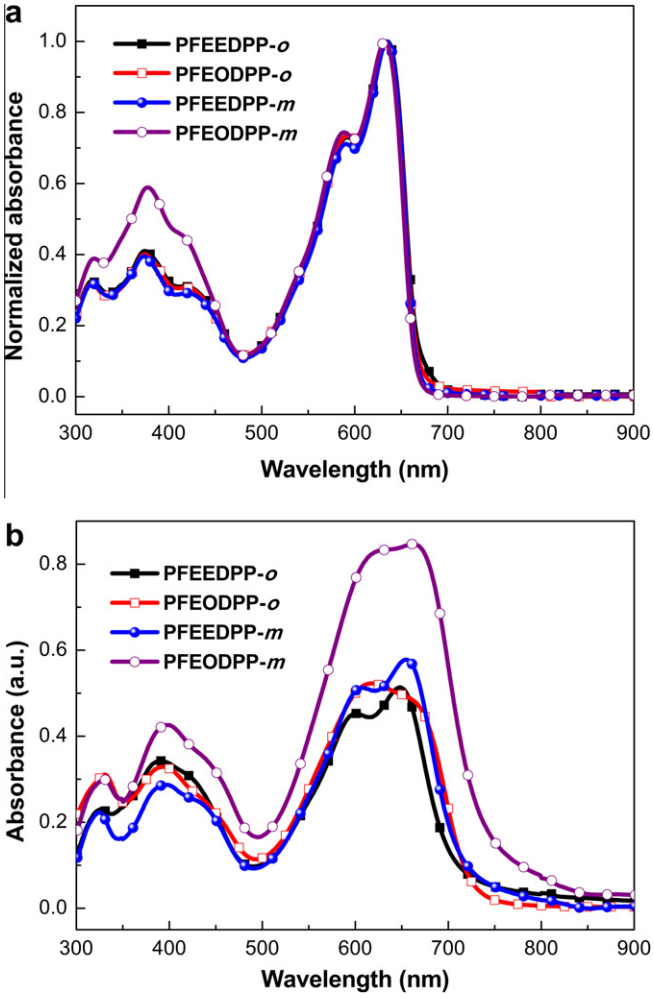

Fig. 1. UV–vis absorption spectra of PFEEDPP and PFEODPP (a) solutions in chloroform and (b) films on quartz. All the polymer films in (b) have the same thickness of 80 nm.

in $CHCl_3$ and DCB. This is different from some DPP copolymers, which exhibits absorption sensitive to the solvent [35,43].

Polymer films formed on quartz by spin coating their chloroform solutions were studied by UV–vis absorption spectroscopy as well (Fig. 1b). Though the PFEEDPP-*m* with PFEEDPP-*o* and PFEODPP-*m* with PFEODPP-*o* films have the same normalized absorption spectrum, PFEEDPP-*m* and PFEODPP-*m* have higher absorption coefficient in the visible range. This may be due to higher interchain interactions in the latter two polymer films [46,47]. The absorptions of PFEEDPP-*o* and PFEEDPP-*m* films shift to red by 17 nm compared with their solution absorptions. More significant change was observed in the absorption of PFEODPP-*o* and PFEODPP-*m* from solution to film. The absorption shifts to red by 33 nm. The red shifts in the absorption from solution to film of the polymers can be attributed to the interchain interactions in the polymer films. It is inferred that the interactions among the PFEODPP chains are stronger than among the PFEEDPP chains. This arises from the different side chains of these two polymers, as a linear side chain can usually cause the polymer chains more compact [13,48]. This may also be the reason for the higher absorption coefficient of the PFEODPP-*m* film than the PFEEDPP-*m* film in the visible range.

3.3. Electrochemical behavior and thermal stability

The highest occupied molecular orbital (HOMO) and lowest unoccupied molecular orbital (LUMO) energy levels of the donor materials determine the open-circuit voltage (V_{oc}) and the charge separation of PVs. The HOMO and LUMO levels of PFEEDPP and PFEODPP were studied by CV and calculated in terms of the oxidation (E_{ox}) and reduction (E_{red}) potentials versus Ag/AgCl [49],

$$E_{HOMO} = -e(E_{ox} + 4.71)\ (eV) \quad \text{and}$$
$$E_{LUMO} = -e(E_{ox} + 4.71)\ (eV).$$

Fig. 2 presents the CVs of the four polymers in acetonitrile solutions. E_{ox}, E_{red}, and the calculated HOMO/LUMO levels are listed in Table 2. The band gaps of the polymers by the electrochemical study agree well with the optical absorption spectroscopy.

Thermal stability of these polymers was investigated by TGA (Fig. 3). The TGAs of PFEEDPP-*o* and PFEODPP-*o* coincide with that of PFEEDPP-*m* and PFEODPP-*m*, respectively, so they are not shown. The temperature corresponding to the weight loss of 5% (T_d) is defined as the decomposition temperature. They are higher than 380 °C for these polymers.

3.4. Polymer PVs

The HOMO/LUMO levels, the band gap and the thermal stability of these polymers suggest that they can be used as the donor materials in polymer PVs. Polymer PVs were fabricated using these polymers as donors and PCBM as acceptor. The *J*–*V* curves of the polymer:PCBM PVs with the active layers processed from the DCB solution are presented in Fig. 4. All the polymer PVs exhibited relatively high V_{oc} values, due to the lower HOMO levels of the polymers. These V_{oc} values are comparable to polymer PVs using other fluorene-DPP copolymers [37,38,41].

The device fabrication conditions were optimized, including the donor-to-acceptor ratio, annealing temperature and time, and solvent. The optimal polymer-to-PCBM weight ratio was 1:3, and the optimal thickness of the active layers was 80 nm. These optimal conditions are similar for the PVs with other DPP-based polymer donors

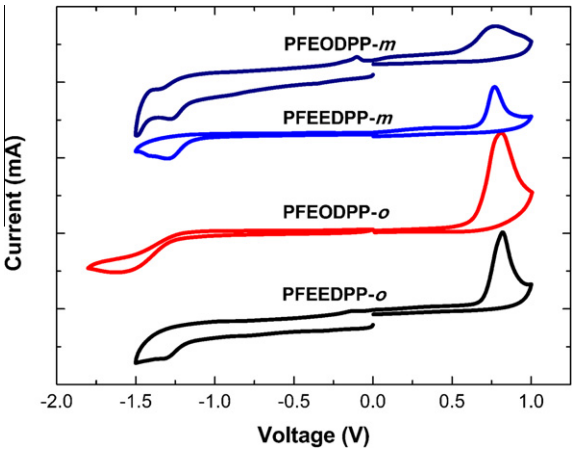

Fig. 2. Cyclic voltammograms of PFEEDPP-*o*, PFEODPP-*o*, PFEEDPP-*m* and PFEEDPP-*m* films.

Table 2
Electrochemical potentials and decomposition temperatures of PFEEDPP-*o*, PFEODPP-*o*, PFEEDPP-*m* and PFEODPP-*m*.

Polymer	E_{ox} (V)	E_{red} (V)	E_{HOMO} (eV)	E_{LUMO} (eV)	T_d (°C)
PFEEDPP-*o*	0.70	−1.17	−5.41	−3.54	388
PFEODPP-*o*	0.63	−1.23	−5.34	−3.48	394
PFEEDPP-*m*	0.68	−1.15	−5.39	−3.56	388
PFEODPP-*m*	0.56	−1.16	−5.27	−3.55	395

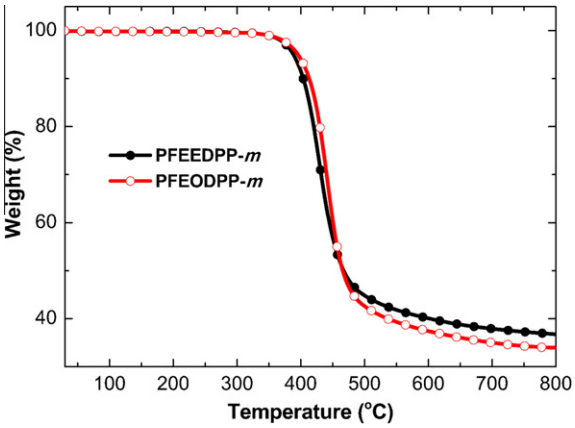

Fig. 3. TGA of PFEEDPP-*m* and PFEODPP-*m*.

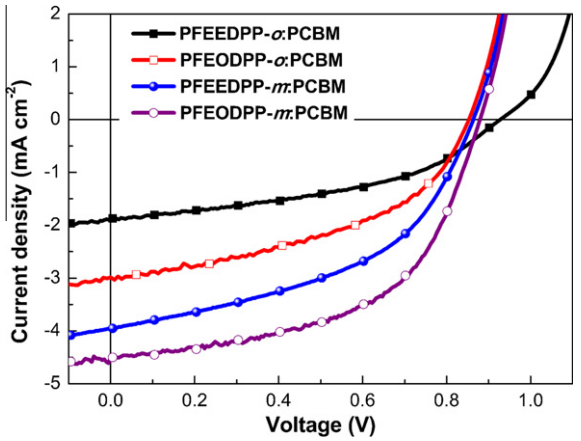

Fig. 4. *J–V* curves of PVs glass/ITO/PEDOT:PSS/polymer:PCBM/LiF/Al with PFEEDPP-*o*, PFEODPP-*o*, PFEEDPP-*m* and PFEODPP-*m* as the donor materials under AM 1.5G illumination. The active films with the polymer-to-PCBM weight ratio of 1:3 were fabricated by spin coating DCB solutions of polymers and DCB. The polymers are indicated in the figure.

Table 3
Short-circuit current (J_{sc}), open-circuit voltage (V_{oc}), fill factor (FF) and PCE of PVs ITO/PEDOT:PSS/polymer:PCBM/LiF/Al under AM 1.5G illumination. Different solvents were used for the fabrication of the polymer:PCBM films.

Polymer	Solvent	J_{sc} (mA cm^{-2})	V_{oc} (V)	FF	PCE (%)
PFEEDPP-*o*	Chloroform	1.76	0.89	0.42	0.66
PFEEDPP-*o*	Cosolvent[a]	2.01	0.92	0.43	0.80
PFEEDPP-*o*	DCB[b]	1.90	0.93	0.44	0.78
PFEODPP-*o*	Chloroform	1.54	0.87	0.48	0.64
PFEODPP-*o*	Cosolvent[a]	2.99	0.85	0.46	1.16
PFEODPP-*o*	DCB[b]	3.28	0.88	0.47	1.34
PFEEDPP-*m*	Chloroform	2.45	0.82	0.48	0.96
PFEEDPP-*m*	Cosolvent[a]	3.41	0.85	0.43	1.25
PFEEDPP-*m*	DCB[b]	3.95	0.86	0.48	1.63
PFEODPP-*m*	Cosolvent[a]	4.24	0.90	0.59	2.25
PFEODPP-*m*	DCB[b]	4.52	0.88	0.55	2.19

[a] Cosolvent of chloroform and 1,2-dichlorobenzene (DCB) with volume ratio of 4:1.
[b] The active layer was spin coated from DCB solution at 90 °C.

[34,38,42]. We studied the effect of annealing the polymer:PCBM films on the photovoltaic performance of the devices. But no remarkable effect was observed.

Chloroform, DCB and their cosolvents were used as the solvent for the polymers and PCBM since polymer PVs using DDP-based polymers usually have photovoltaic performance sensitive to the solvent [34,38]. The PVs fabricated from chloroform solutions exhibited low photovoltaic performance (Table 3). The photovoltaic efficiency was significantly improved when cosolvent of chloroform and DCB was used. In addition, we found that the PVs fabricated from DCB solutions at 90 °C had a photovoltaic efficiency comparable to that from the cosolvent solution. The PFEEDPP-*m*:PCBM PVs fabricated from the DCB solution exhibited the photovoltaic efficiency even higher than from the solution of cosolvent.

Compare the photovoltaic performances of the polymer PVs with the four polymers, we can conclude that the heating method during the Sonogashira coupling

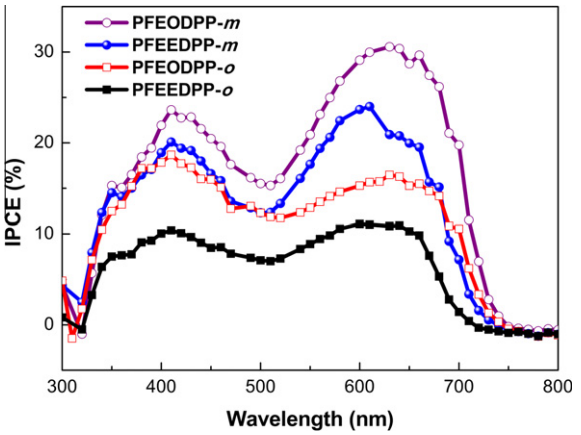

Fig. 5. IPCEs of polymer:PCBM (1:3 w/w) PVs. The active layers were fabricated from DCB solutions.

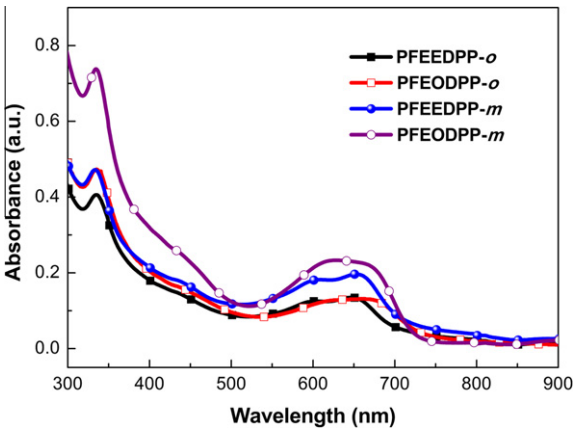

Fig. 6. UV–vis absorption spectra of polymer:PCBM films. All the films had a same thickness of 80 nm.

strongly affects the performance of the polymer PVs. The PFEEDPP-*m*:PCBM and PFEODPP-*m*:PCBM PVs always exhibited higher photovoltaic efficiencies than the PFEEDPP-*o*:PCBM and PFEODPP-*o*:PCBM PVs. The optimal PCE of the PFEEDPP-*m*:PCBM PV was 1.63%, which was twice of that of the PFEEDPP-*o*:PCBM PV. The PFEODPP-*m*:PCBM PV exhibited the highest PCE of 2.25% among the PVs.

In order to understand the different photovoltaic performances of these PVs with the four polymers, we studied the IPCE, absorption, surface morphology and mobility of the active films. Fig. 5 presents the IPCEs of the four PVs in Fig. 4. They are consistent with the UV–vis absorption spectra of the four active films as shown in Fig. 6. The differences can be attributed to the different absorption coefficients of the polymer films.

Besides the optical absorption of the active films, the film morphology can affect the photovoltaic performance of the devices as well [50–52]. The AFM images of the four polymer:PCBM films are presented in Fig. 7. Salient difference in the film morphology was observed. The PFEEDPP-*o*:PCBM and PFEODPP-*o*:PCBM films have remarkably

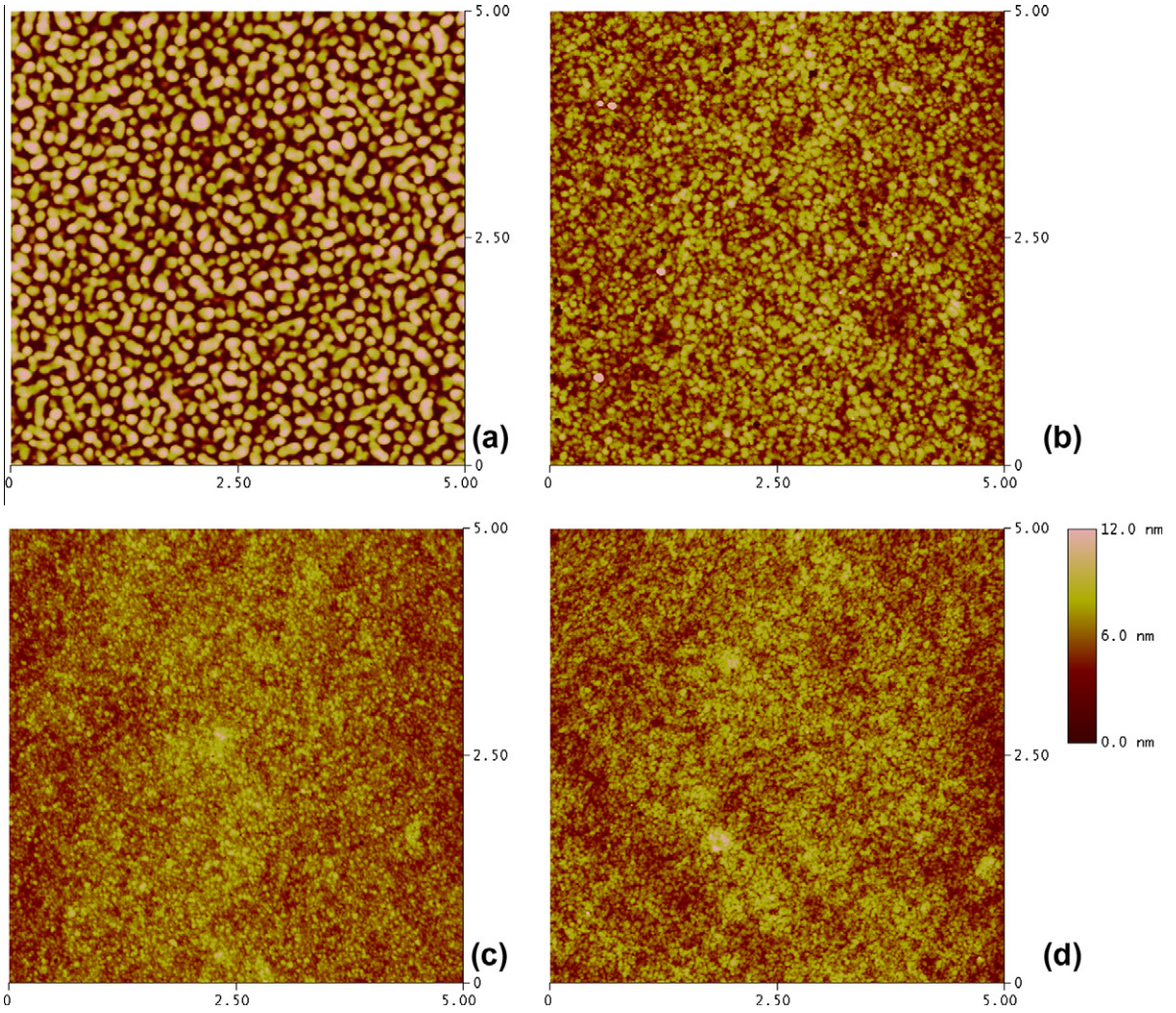

Fig. 7. AFM images of (a) PFEEDPP-*o*:PCBM, (b) PFEODPP-*o*:PCBM, (c) PFEEDPP-*m*:PCBM, and (d) PFEODPP-*m*:PCBM film. The films were prepared by spin coating DCB solutions with the polymer-to-PCBM weight ratio of 1:3. The unit of the AFM images is μm.

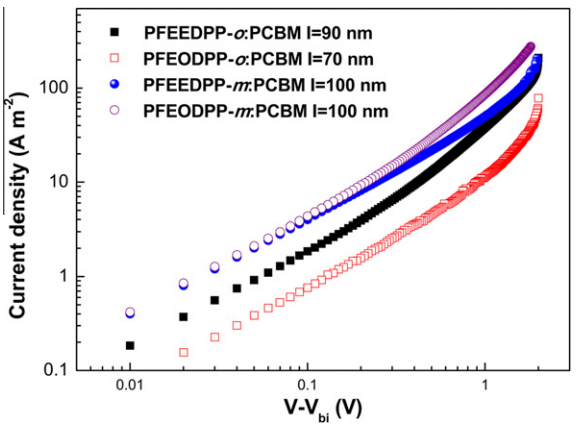

Fig. 8. Current density versus V–V_{bi} curves of polymer:PCBM (1:3, w/w) film. The thicknesses (l) of the films are indicated in the plot.

bigger domains than the PFEEDPP-*m*:PCBM and PFEODPP-*m*:PCBM films. The bigger domains indicate the reduced interface between donor and acceptor, leading to lower photovoltaic performance.

The hole mobilities of the polymer films were estimated in terms of the space charge limited current (SCLC) model,

$$J = \frac{9}{8}\varepsilon_r\varepsilon_0\mu_h\frac{V^2}{L^3},$$

where J is the current density, ε_0 is the permittivity of free space, ε_r is the dielectric constant of the polymer, μ_h is the hole mobility, V is the applied voltage ($V_{applied}$) corrected from the built-in voltage (V_{bi}) arising from difference in the work function of the contacts, and L is the thickness of the organic film [53–55]. The hole mobilities of the polymers:PCBM films (1:3, w/w) were studied by measuring the current through hole-only devices of ITO/PEDOT:PSS/the blend films/Au (Fig. 8). ε_r of 3 was adopted for the estimation of the hole mobilities of all the polymer films [56].

The hole mobilities, estimated by fitting the curves with the SCLC model, were 1.03×10^{-5}, 0.96×10^{-5}, 1.86×10^{-5}, 3.05×10^{-5}, and for the blend films of

PFEEDPP-*o*:PCBM, PFEODPP-*o*:PCBM, PFEEDPP-*m*:PCBM, and PFEODPP-*m*:PCBM, respectively. These hole mobility values are consistent with the PCEs of corresponding PVs.

4. Conclusion

Copolymers of electron-donating ethynylfluorene and electron-withdrawing DPP were synthesized *via* the Pd-catalyzed Sonogashira coupling in an oil bath and a microwave synthesizer. They have low-band gaps and can be used as the donor materials for polymer PVs. Applying the microwave irradiation during the Sonogashira coupling can significantly shorten the polymerization time from several days to a couple of minutes, improve the molecular weight of the copolymers and photovoltaic performances of the polymer PVs using the polymers as the donor material.

Acknowledgements

This research work was financially supported by a grant from the National University of Singapore (Project number: RG-284-001-136).

References

[1] G. Zhao, Y. He, Y. Li, 6.5% efficiency of polymer solar cells based on poly(3-hexylthiophene) and indene-C_{60} bisadduct by device optimization, Adv. Mater. 22 (2010) 4355–4358.
[2] W. Ma, C. Yang, X. Gong, K. Lee, A.J. Heeger, Thermally stable, efficient polymer solar cells with nanoscale control of the interpenetrating network morphology, Adv. Funct. Mater. 15 (2005) 1617–1622.
[3] Y. Li, Y. Zou, Conjugated polymer photovoltaic materials with broad absorption band and high charge carrier mobility, Adv. Mater. 20 (2008) 2952–2958.
[4] B.C. Thompson, J.M.J. Fréchet, Polymer–fullerene composite solar cells, Angew. Chem. Int. Ed. 47 (2008) 58–77.
[5] M. Siddiki, J. Li, D. Galipeau, Q. Qiao, A review of polymer multijunction solar cells, Energy Environ. Sci. 3 (2010) 867–883.
[6] H.M. Zhang, J.Y. Ouyang, High-efficiency inverted heterojunction polymer solar cells with UV ozone-treated ultrathin aluminum interlayer, Appl. Phys. Lett. 97 (2010) 063509.
[7] J. Chen, Y. Cao, Development of novel conjugated donor polymers for high-efficiency bulk-heterojunction photovoltaic devices, Acc. Chem. Res. 42 (2009) 1709–1718.
[8] Y.J. Cheng, S.H. Yang, C.S. Hsu, Synthesis of conjugated polymers for organic solar cell applications, Chem. Rev. 109 (2009) 5868–5923.
[9] R. Kroon, M. Lenes, J.C. Hummelen, P.M.W. Blom, B. De Boer, Small bandgap polymers for organic solar cells, Polym. Rev. 48 (2008) 531–582.
[10] E. Wang, L. Wang, L. Lan, W. Zhuang, J. Peng, Y. Cao, High-performance polymer heterojunction solar cells of a polysilafluorene derivative, Appl. Phys. Lett. 92 (2008) 033307.
[11] J. Hou, M.H. Park, S. Zhang, Y. Yao, L.M. Chen, J.H. Li, Y. Yang, Bandgap and molecular energy level control of conjugated polymer photovoltaic materials based on benzo[1,2-b:4,5-b′]dithiophene, Macromolecules 41 (2008) 6012–6018.
[12] Y. Zou, A. Najari, P. Berrouard, S. Beaupré, B.R. Aïch, Y. Tao, M. Leclerc, A thieno[3,4-c]pyrrole-4,6-dione-based copolymer for efficient solar cells, J. Am. Chem. Soc. 132 (2010) 5330–5331.
[13] C. Piliego, T.W. Holcombe, J.D. Douglas, C.H. Woo, P.M. Beaujuge, J.M.J. Fréchet, Synthetic control of structural order in N-alkylthieno[3,4-c]pyrrole-4,6-dione-based polymers for efficient solar cells, J. Am. Chem. Soc. 132 (2010) 7595–7597.
[14] Y. Liang, Z. Xu, J. Xia, S.T. Tsai, Y. Wu, G. Li, C. Ray, L. Yu, For the bright future-bulk heterojunction polymer solar cells with power conversion efficiency of 7.4%, Adv. Mater. 22 (2010) E135–E138.
[15] E. Wang, M. Wang, L. Wang, C. Duan, J. Zhang, W. Cai, C. He, H. Wu, Y. Cao, Donor polymers containing benzothiadiazole and four thiophene rings in their repeating units with improved photovoltaic performance, Macromolecules 42 (2009) 4410–4415.
[16] P.F. Xia, J. Lu, C.H. Kwok, H. Fukutani, M.S. Wong, Y. Tao, Synthesis and properties of monodisperse multi-triarylamine-substituted oligothiophenes and 4,7-bis(2′-oligothienyl)-2,1,3-benzothiadiazoles for organic solar cell applications, J. Polym. Sci. Part A Polym. Chem. 47 (2009) 137–148.
[17] C.H. Chen, C.H. Hsieh, M. Dubosc, Y.J. Cheng, C.S. Hsu, Synthesis and characterization of bridged bithiophene-based conjugated polymers for photovoltaic applications: acceptor strength and ternary blends, Macromolecules 43 (2010) 697–708.
[18] C.O. Kappe, Controlled microwave heating in modern organic synthesis, Angew. Chem. Int. Ed. 43 (2004) 6250–6284.
[19] A. Khan, S. Hecht, Microwave-accelerated synthesis of lengthy and defect-free poly(m-phenyleneethynylene)s via AB′ and A(2) + BB′ polycondensation routes, Chem. Commun. (2004) 300–301.
[20] S. Tierney, M. Heeney, I. McCulloch, Microwave-assisted synthesis of polythiophenes via the Stille coupling, Synth. Met. 148 (2005) 195–198.
[21] I. McCulloch, M. Heeney, C. Bailey, K. Genevicius, I. MacDonald, M. Shkunov, D. Sparrowe, S. Tierney, R. Wagner, W. Zhang, M.L. Chabinyc, R.J. Kline, M.D. McGehee, M.F. Toney, Liquid-crystalline semiconducting polymers with high charge-carrier mobility, Nat. Mater. 5 (2006) 328–333.
[22] F. Galbrecht, T.W. Bünnagel, U. Scherf, T. Farrell, Microwave-assisted preparation of semiconducting polymers, Macromol. Rapid. Commun. 28 (2007) 387–394.
[23] A. Tsami, X.-H. Yang, T. Farrell, D. Neher, E. Holder, Alternating fluorene-di(thiophene)quinoxaline copolymers via microwave-supported Suzuki cross-coupling reactions, J. Polym. Sci. Part A Polym. Chem. 46 (2008) 7794–7808.
[24] R.C. Coffin, J. Peet, J. Rogers, G.C. Bazan, Streamlined microwave-assisted preparation of narrow-bandgap conjugated polymers for high-performance bulk heterojunction solar cells, Nat. Chem. 1 (2009) 657–661.
[25] F. Silvestri, A. Marrocchi, Acetylene-based materials in organic photovoltaics, Int. J. Mol. Sci. 11 (2010) 1471–1508.
[26] R.S. Ashraf, M. Shahid, E. Klemm, M. Al-Ibrahim, S. Sensfuss, Thienopyrazine-based low-bandgap poly(heteroaryleneethynylene)s for photovoltaic devices, Macromol. Rapid. Commun. 27 (2006) 1454–1459.
[27] D.A.M. Edge, L.H. Nguyen, K. Schmidtke, A. Wild, C. Sieber, S. Guenes, N.S. Sariciftci, Combined effects of conjugation pattern and alkoxy side chains on the photovoltaic properties of thiophene-containing PPE-PPVs, J. Polym. Sci. Part A Polym. Chem. 45 (2007) 1619–1631.
[28] D.A.M. Egbe, S. Türk, S. Rathgeber, F. Kühnlenz, R. Jadhav, A. Wild, E. Birckner, G. Adam, A. Pivrikas, V. Cimrova, G. Knör, N.S. Sariciftci, H. Hoppe, Anthracene based conjugated polymers: correlation between pi–pi-stacking ability, photophysical properties, charge carrier mobility, and photovoltaic performance, Macromolecules 43 (2010) 1261–1269.
[29] Z. Wu, B. Fan, F. Xue, C. Adachi, J. Ouyang, Organic molecules based on dithienyl-2,1,3-benzothiadiazole as new donor materials for solution-processed organic photovoltaic cells, Sol. Energy Mater. Sol. Cells 94 (2010) 2230–2237.
[30] F. Silvestri, A. Marrocchi, M. Seri, C. Kim, T.J. Marks, A. Facchetti, A. Taticchi, Solution-processable low-molecular weight extended arylacetylenes: versatile p-type semiconductors for field-effect transistors and bulk heterojunction solar cells, J. Am. Chem. Soc. 132 (2010) 6108–6123.
[31] W.Y. Wong, X.Z. Wang, Z. He, A.B. Djurii, C.T. Yip, K.Y. Cheung, H. Wang, C.S.K. Mak, W.K. Chan, Metallated conjugated polymers as a new avenue towards high-efficiency polymer solar cells, Nat. Mater. 6 (2007) 521–527.
[32] R.S. Ashraf, J. Gilot, R.A.J. Janssen, Fused ring thiophene-based poly(heteroarylene ethynylene)s for organic solar cells, Sol. Energy Mater. Sol. Cells 94 (2010) 1759–1766.
[33] Y. Hou, Y. Chen, Q. Liu, M. Yang, X. Wan, S. Yin, A. Yu, A novel tetrathiafulvalene-(TTF-) fused poly(aryleneethynylene) with an acceptor main chain and donor side chains: intramolecular charge transfer (CT), stacking structure, and photovoltaic property, Macromolecules 41 (2008) 3114–3119.
[34] M.M. Wienk, M. Turbiez, J. Gilot, R.A.J. Janssen, Narrow-bandgap diketo-pyrrolo-pyrrole polymer solar cells: the effect of processing on the performance, Adv. Mater. 20 (2008) 2556–2560.
[35] Y. Zou, D. Gendron, R. Badrou-Aïch, A. Najari, Y. Tao, M. Leclerc, A High-mobility low-bandgap poly(2,7-carbazole) derivative for photovoltaic applications, Macromolecules 42 (2009) 2891–2894.

[36] Y. Zou, D. Gendron, R. Neagu-Plesu, M. Leclerc, Synthesis and characterization of new low-bandgap diketopyrrolopyrrole-based copolymers, Macromolecules 42 (2009) 6361–6365.
[37] J.C. Bijleveld, A.P. Zoombelt, S.G.J. Mathijssen, M.M. Wienk, M. Turbiez, D.M. de Leeuw, R.A.J. Janssen, Poly(diketopyrrolopyrrole-terthiophene) for ambipolar logic and photovoltaics, J. Am. Chem. Soc. 131 (2009) 16616–16617.
[38] L. Huo, J. Hou, H.-Y. Chen, S. Zhang, Y. Jiang, T.L. Chen, Y. Yang, Bandgap and molecular level control of the low-bandgap polymers based on 3,6-dithiophen-2-yl-2,5-dihydropyrrolo[3,4-c]pyrrole-1,4-dione toward highly efficient polymer solar cells, Macromolecules 42 (2009) 6564–6571.
[39] E. Zhou, S. Yamakawa, K. Tajima, C. Yang, K. Hashimoto, Synthesis and photovoltaic properties of diketopyrrolopyrrole-based donor-acceptor copolymers, Chem. Mater. 21 (2009) 4055–4061.
[40] E. Zhou, Q. Wei, S. Yamakawa, Y. Zhang, K. Tajima, C. Yang, K. Hashimoto, Diketopyrrolopyrrole-based semiconducting polymer for photovoltaic device with photocurrent response wavelengths up to 1.1 μm, Macromolecules 43 (2010) 821–826.
[41] G.-Y. Chen, C.-M. Chiang, D. Kekuda, S.-C. Lan, C.-W. Chu, K.-H. Wei, Synthesis and characterization of a narrow-bandgap polymer containing alternating cyclopentadithiophene and diketo-pyrrolopyrrole units for polar pell applications, J. Polym. Sci. Part A Polym. Chem. 48 (2010) 1669–1675.
[42] A.P. Zoombelt, S.G.J. Mathijssen, M.G.R. Turbiez, M.M. Wienk, R.A.J. Janssen, Small band gap polymers based on diketopyrrolopyrrole, J. Mater. Chem. 20 (2010) 2240–2246.
[43] N. Allard, R.B. Aïch, D. Gendron, P.-L.T. Boudreault, C. Tessier, S. Alem, S.-C. Tse, Y. Tao, M. Leclerc, Germafluorenes: new heterocycles for plastic electronics, Macromolecules 43 (2010) 2328–2333.
[44] G. Hernández-Torres, A. Urbano, M.C. Carreño, F. Colobert, Stereocontrolled generation of the (2R) chroman core of vitamin E: total synthesis of (2R,4′RS,8′RS)-alpha-tocopherol, Org. Lett. 11 (2009) 4930–4933.
[45] X. Zhan, Y. Liu, D. Zhu, W. Huang, Q. Gong, Large femtosecond third-order nonlinear optical response in a novel donor-acceptor copolymer consisting of ethynylfluorene and tetraphenyldiaminobiphenyl units, Chem. Mater. 13 (2001) 1540–1544.
[46] J.-F. Chang, J. Clark, N. Zhao, H. Sirringhaus, D.W. Breiby, J.W. Andreasen, M.M. Nielsen, M. Giles, M. Heeney, I. McCulloch, Molecular-weight dependence of interchain polaron delocalization and exciton bandwidth in high-mobility conjugated polymers, Phys. Rev. B 74 (2006) 115318.
[47] D.J.D. Moet, M. Lenes, J.D. Kotlarski, S.C. Veenstra, J. Sweelssen, M.M. Koetse, B. de Boer, P.W.M. Blom, Impact of molecular weight on charge carrier dissociation in solar cells from a polyfluorene derivative, Org. Electron. 10 (2009) 1275–1281.
[48] G. Koeckelberghs, L.D. Cremer, A. Persoons, T. Verbiest, Influence of the substituent and polymerization methodology on the properties of chiral poly(dithieno[3,2-b:2′,3′-d]pyrrole)s, Macromolecules 40 (2007) 4173–4181.
[49] Y. Li, Y. Cao, J. Gao, D. Wang, G. Yu, A.J. Heeger, Electrochemical properties of luminescent polymers and polymer light-emitting electrochemical cells, Synth. Met. 99 (1999) 243–248.
[50] H. Hoppe, M. Niggemann, C. Winder, J. Kraut, R. Hiesgen, A. Hinsch, D. Meissner, N.S. Sariciftci, Nanoscale morphology of conjugated polymer/fullerene-based bulk-heterojunction solar cells, Adv. Funct. Mater. 14 (2004) 1005–1011.
[51] J. Peet, J.Y. Kim, N.E. Coates, W.L. Ma, D. Moses, A.J. Heeger, G.C. Bazan, Efficiency enhancement in low-bandgap polymer solar cells by processing with alkane dithiols, Nat. Mater. 6 (2007) 497–500.
[52] J. Ouyang, Y. Xia, High-performance polymer photovoltaic cells with thick P3HT:PCBM films prepared by a quick drying process, Sol. Energy Mater. Sol. Cells 93 (2009) 1592–1597.
[53] V. Shrotriya, Y. Yao, G. Li, Y. Yang, Effect of self-organization in polymer/fullerene bulk heterojunctions on solar cell performance, Appl. Phys. Lett. 89 (2006) 063505.
[54] C. Melzer, E.J. Koop, V.D. Mihailetchi, P.W.M. Blom, Hole transport in poly(phenylene vinylene)/methanofullerene bulk-heterojunction solar cells, Adv. Funct. Mater. 14 (2004) 865–870.
[55] V.D. Mihailetchi, H. Xie, C. Melzer, B. de Boer, J.A. Koster, P.W.M. Blom, Charge transport and photocurrent generation in poly(3-hexylthiophene):methanofullerene bulk-heterojunction solar cells, Adv. Funct. Mater. 16 (2006) 699–708.
[56] P.W.M. Blom, V.D. Mihailetchi, L.J.A. Koster, D.E. Markov, Device physics of polymer:fullerene bulk heterojunction solar cells, Adv. Mater. 19 (2007) 1551–1566.

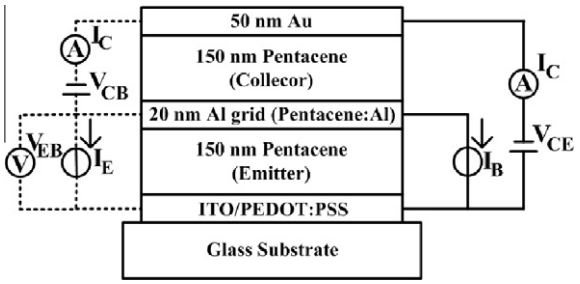

Fig. 1. The schematic diagram of the studied device structure, and the circuits used for transistor characterization in common-base mode (dash line) and common-emitter mode (solid line).

2. Experimental

Fig. 1 shows the schematic diagram of the studied device structure. The patterned ITO/glass substrate is first cleaned and dried. A 40 nm PEDOT:PSS is then deposited on the ITO/glass substrate from its aqueous solution by spin-coating, and the substrate is heated to 120 °C for 30 min in a vacuum oven. In the sequence, a 150 nm pentacene (emitter), 20 nm pentacene:Al (base), 150 nm pentacene (collector) and 50 nm Au are sequentially deposited on the substrate via thermal evaporation under a pressure of 3×10^{-4} Pa in situ. The pentacene:Al base is formed by co-evaporating pentacene and Al, where the deposition rate of pentacene is 0.05, 0.1 and 0.2 nm/s while maintaining 1 nm/s for Al. In

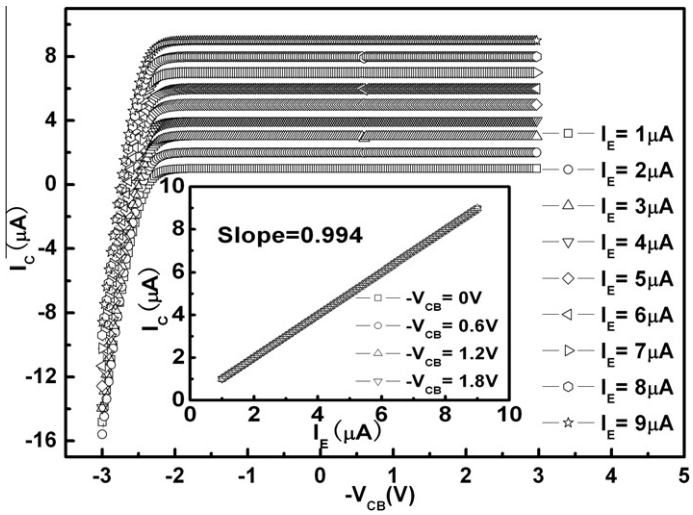

Fig. 2. Common-base characteristics of the ITO/PEDOT:PSS/Pentacene/Pentacene:Al/Pentacene/Au device, where the evaporation rate of pentacene in the pentacene:Al co-evaporation is 0.1 nm/s. The inset shows I_C dependence on I_E at different values of $-V_{CB}$ = 0, 0.6, 1.2 and 1.8 V.

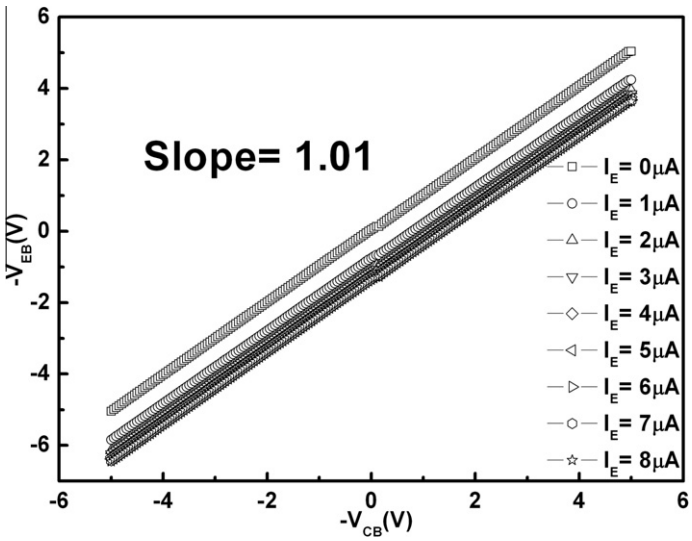

Fig. 3. Dependence of $-V_{EB}$ on $-V_{CB}$ for constant I_E of the ITO/PEDOT:PSS/Pentacene/Pentacene:Al/Pentacene/Au device, where the evaporation rate of pentacene in the pentacene:Al co-evaporation is 0.1 nm/s.

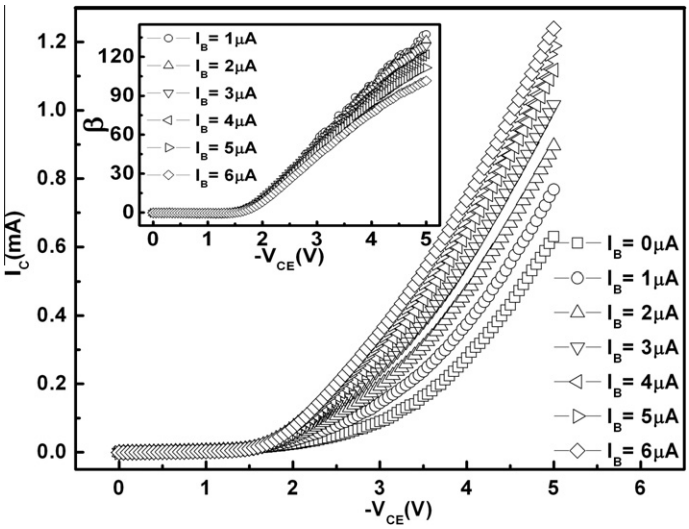

Fig. 4. Common-emitter characteristics of the ITO/PEDOT:PSS/Pentacene/Pentacene:Al/Pentacene/Au device, where the evaporation rate of pentacene in the pentacene:Al co-evaporation is 0.1 nm/s. The inset shows β dependence on $-V_{CE}$ at different values of I_B ranging from 1 to 6 μA at steps of 1 μA.

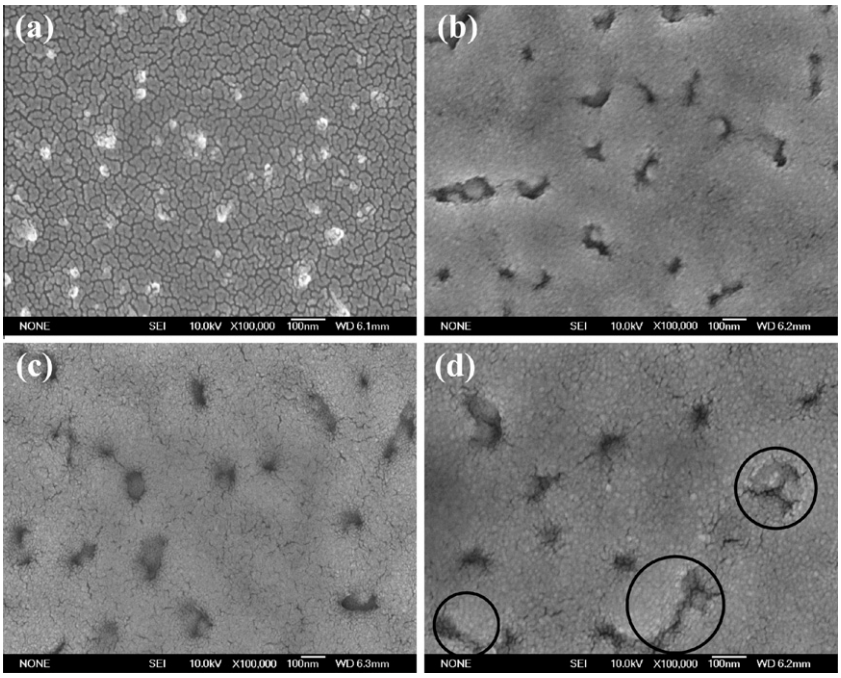

Fig. 5. SEM image of the bare Al metal base (a) and co-evaporated pentacene:Al base with different pentacene evaporation rates of 0.05 nm/s (b), 0.1 nm/s (c) and 0.2 nm/s (d). The circles in (d) indicate the obvious unequal pinhole regions.

addition, the deposition rate of pentacene emitter and collector are 0.05 and 0.1 nm/s for Au electrode. The device area defined as the overlap of three electrodes is 1 mm^2.

Electrical measurements are performed in the dark under argon condition, using three Keithley 2400 Sourcemeters for common-base mode and two for common-emitter mode. The circuits for common-base (dash line) and common-emitter (solid line) characterization are illustrated in Fig. 1.

3. Results and discussion

Fig. 2 shows the common-base characteristics of a ITO/PEDOT:PSS/Pentacene/Pentacene:Al/Pentacene/Au device, where the evaporation rate of pentacene in the pentacene:Al co-evaporation is 0.1 nm/s. For increasingly negative $-V_{CB}$, large negative I_C can be observed due to the significant hole injection in forward-biased base–collector junction. When $-V_{CB}$ increases to positive values,

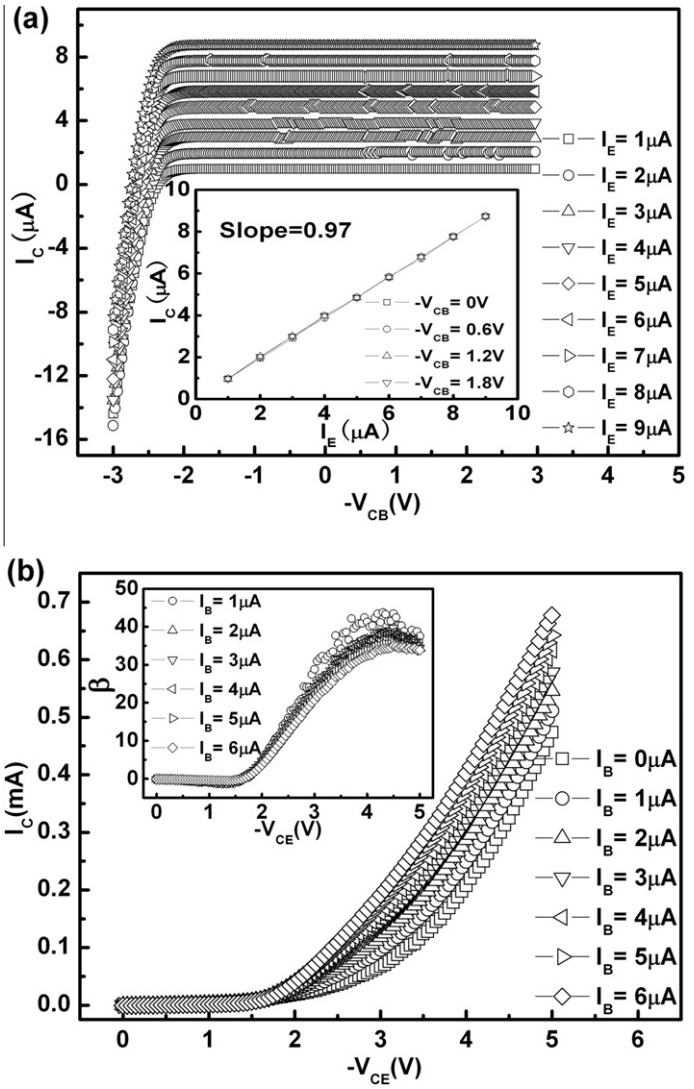

Fig. 6. (a) Common-base characteristics and; (b) common-emitter characteristics of the ITO/PEDOT:PSS/Pentacene/Pentacene:Al/Pentacene/Au device, where the evaporation rate of pentacene in the pentacene:Al co-evaporation is 0.05 nm/s. Inset: (a) I_C dependence on I_E at different values of $-V_{CB}$ = 0 V, 0.6 V, 1.2 V and 1.8 V; (b) β dependence on $-V_{CE}$ at different values of I_B ranging from 1 to 6 μA at steps of 1 μA.

a saturation current I_C can be observed for each given constant I_E. The saturation value of I_C can be controlled by I_E, i.e., I_C increases with I_E, which should be the expected common-base characteristics of permeable-base transistor [22]. As shown in the inset of Fig. 2, I_C depends on I_E linearly at a given $-V_{CB}$. For all the four selected $-V_{CB}$, the slopes of the I_C–I_E curves are ~0.994, corresponding to the common-base current gain $\alpha \equiv \partial I_c/\partial I_E$ of the device [22,23]. This high α value, near to ideal value of one, indicates that almost all holes injected from the emitter are able to cross the base area, being collected by the collector, promising well transistor operation. Additionally, the leakage current is negligible, indicating there is no significant minority carrier injection in the Pentacene/Au interface.

The transistor device shows permeable-base characteristics, since at constant I_E, $\partial(-V_{EB})/\partial(-V_{CB}) \cong 1$ [22], as can be seen in Fig. 3. As a result, it is supposed that the observed high α should be attributed to the pinholes existing within the pentacene:Al base area, which results in the emitter not being effectively shielded electrically from the collector.

Fig. 4 presents the common-emitter characteristics of the ITO/PEDOT:PSS/Pentacene/Pentacene:Al/Pentacene/Au device, where the evaporation rate of pentacene in the pentacene:Al co-evaporation is 0.1 nm/s. There is a significant high I_C can be observed at I_B = 0, defined as leakage current I_L. On the other hand, I_C increases remarkably after applying a small input I_B. At V_C = 5 V, I_C is increased from 0.63 to 1.24 mA when I_B is changed from 0 to 6 μA. This indicates that the transistor device is capable of current amplification in common-emitter mode. The calculated common-emitter current gain $\beta \equiv (I_C - I_L)/I_B$ [24] reaches ~137 at I_B = 1 μA and $-V_{CE}$ = 5 V.

In order to further investigate the device performance of the proposed permeable-base transistor, device based on bare thermally evaporated Al metal base, and devices

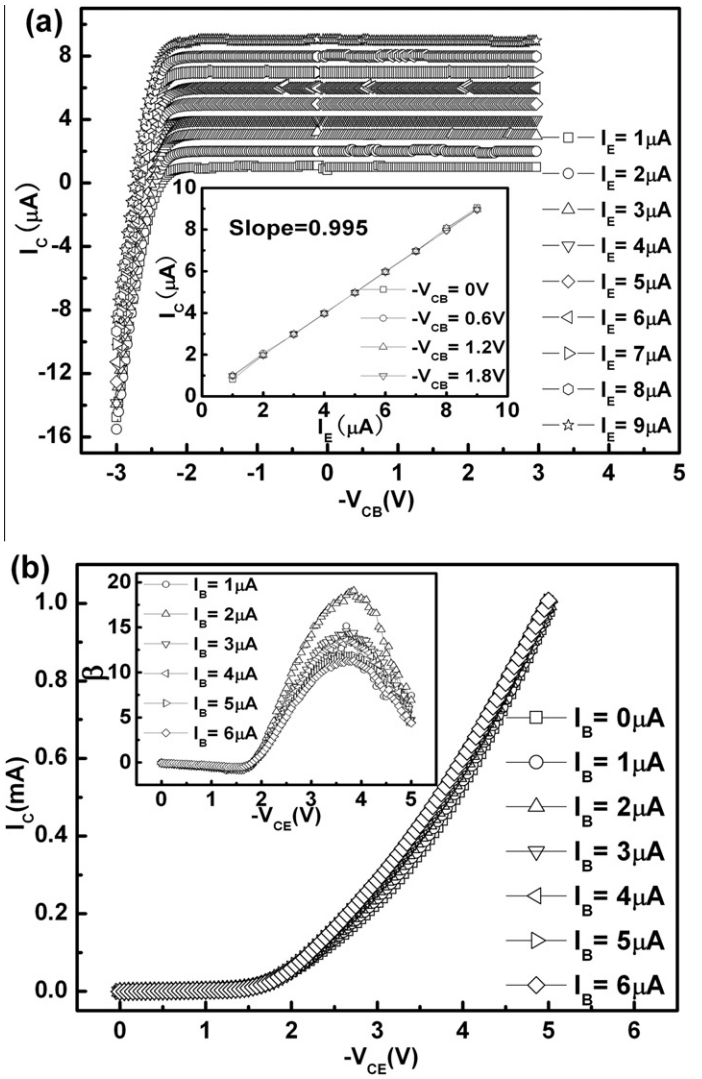

Fig. 7. (a) Common-base characteristics and; (b) common-emitter characteristics of the ITO/PEDOT:PSS/Pentacene/Pentacene:Al/Pentacene/Au device, where the evaporation rate of pentacene in the pentacene:Al co-evaporation is 0.2 nm/s. Inset: (a) I_C dependence on I_E at different values of $-V_{CB}$ = 0 V, 0.6 V, 1.2 V and 1.8 V; (b) β dependence on $-V_{CE}$ at different values of I_B ranging from 1 to 6 μA at steps of 1 μA.

based on co-evaporated pentacene:Al base with different evaporation rates for pentacene (0.05, 0.1 and 0.2 nm/s) are prepared. Firstly, it is found that the device based on Al metal base does not demonstrate any common-base and common-emitter characteristics expected for permeable-base transistors. This indicates that doping pentacene in Al deposition plays a relevant role. Fig. 5 shows the SEM image of 20 nm thick bare Al (a), pentacene (0.05 nm/s):Al (b), pentacene (0.1 nm/s):Al (c), pentacene (0.2 nm/s):Al (d) base. It can be clearly seen that adequate pentacene-doping in Al deposition ((b), (c) and (d)) is supposed to cause dispersive pinholes with diameters of several tens to a hundred nanometers, instead of a planar and continuous Al metal base (a). These pinholes promise direct connection between the emitter and collector, resulting in permeable-base operation mode, in accordance with the results shown in Fig. 3. Furthermore, it is found that the evaporation rate of pentacene in the pentacene:Al co-evaporation, i.e., the pentacene doping level are crucial to the base construction and device performance. Figs. 6 and 7 show the common-base and common-emitter characteristics of the devices with 0.05 and 0.1 nm/s evaporated pentacene, respectively. The α (at $-V_{CB}$ = 0 V) and β (at $-V_{CE}$ = 5 V, I_B = 1μA) values of the devices based on co-evaporated pentacene:Al base with different evaporation rates for pentacene (0.05, 0.1 and 0.2 nm/s) are compared in Fig. 8. It can be clearly seen that higher evaporation rate of pentacene causes bigger pinhole diameter [comparing the SEM images b, c and d in Fig. 5], which results in higher α value, indicating that the α value increases with increasing pinhole size [24]. The α value tends to ideal one as the evaporation rate of pentacene increases. On the other hand, β reaches the maximum value of ~137 by controlling the evaporation rate of pentacene at 0.1 nm/s. As a result,

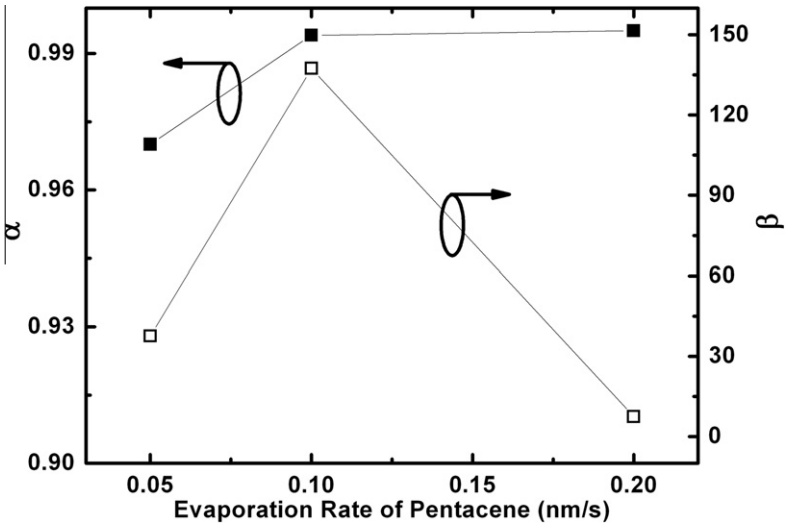

Fig. 8. Comparing the α (at $-V_{CB} = 0$ V) and β (at $-V_{CE} = 5$ V, $I_B = 1$ μA) values of the devices based on co-evaporated pentacene:Al base with different pentacene evaporation rates of 0.05, 0.1 and 0.2 nm/s.

the evaporation rate ratio in the pentacene:Al co-evaporation and the base construction are the key factors for well device operation. The optimal evaporation rate of pentacene in the pentacene:Al co-evaporation falls around 0.1 nm/s, where the transistors operate well in both common-base and common-emitter configurations. It should be noted that the values of α and β, in the case of 0.05 and 0.1 nm/s evaporated pentacene, follow exactly the expected relation $\beta = \alpha/1 - \alpha$ [25], not valid for the case of 0.2 nm/s evaporated pentacene. As shown in the inset of Figs. 4 and 6b, the β values in the case of 0.05 and 0.1 nm/s evaporated pentacene are almost independent on I_B and tend to saturate as $-V_{CE}$ increases, leading to β values that obey $\beta = \alpha/1 - \alpha$ [25]. On the contrary, the strong dependence of β on $-V_{CE}$ and I_B between ~2.5 V and the upper measurements limit, 5 V; and the degradation of β observed above $-V_{CE} = \sim 3.7$ V in the case of 0.05 nm/s evaporated pentacene [inset of Fig. 7b] result in β values that disobey $\beta = \alpha/1 - \alpha$ [25]. Here, we believe that excessive high evaporation rate of pentacene (0.2 nm/s) should bring very unequal pinhole regions [assigned by circles in Fig. 5d] within the base area. In the case, the current flow through the pinholes is difficult to be modulated by potential barrier because the central region of the pinhole is too far from the pinhole edges [14,22], resulting in very low β value (smaller than 20). Moreover, the electrostatic potential of the emitter electrode and the collector electrode with regard to the base electrode are strongly affected by each other via such a base area of large permeability, which results in variable β value. However, the concerning mechanism attributes to this phenomenon is still under investigation. Finally, the methods to quantify the pinhole size and distribution, and the way to achieve equably dispersed pinholes of homogeneous diameter will be the key issues for further study. In addition, developments that lead to suppress the leakage current observed in common-emitter measurements are required.

4. Conclusion

In summary, pentacene-based p-type permeable-base organic transistor ITO/PEDOT:PSS/Pentacene/Pentacene:Al/Pentacene/Au is demonstrated. The permeable pentacene:Al base is formed by co-evaporating pentacene and Al in vacuum. The permeability of the base, consequently the device performance, can be intentionally modulated by controlling the evaporation rate of pentacene in the pentacene:Al co-evaporation. In the case of 0.1 nm/s, the permeable-base transistor operates well in common-base and common-emitter mode, presenting high α value near to ideal 1 and ~137 for β at $I_B = 1$ μA and $-V_{CE} = 5$ V. This opens an effective method to fabricate permeable-base organic transistors.

Acknowledgements

The authors gratefully acknowledge the financial support from NSFC (60676051 and 61076065), Tianjin Natural Science Foundation (07JCYBJC12700), Key Project of Chinese Ministry of Education (209007), and the Tianjin Key Discipline of Material Physics and Chemistry.

References

[1] H. Koezuka, A. Tsumura, T. Ando, Synth. Met. 18 (1987) 699.
[2] K. Ziemelis, Nature 393 (1998) 619.
[3] B. Crone, A. Dodabalapur, Y.Y. Lin, R.W. Filas, Z. Bao, A. LaDuca, R. Sarpeshkar, H.E. Katz, W. Li, Nature 403 (2000) 521.
[4] Florian Eder, Hagen Klauk, Marcus Halik, Ute Zschieschang, Günter Schmid, Christine Dehm, Appl. Phys. Lett. 84 (2004) 2673.
[5] L.P. Ma, Y. Yang, Appl. Phys. Lett. 85 (2004) 5084.
[6] S. Zorba, Y. Gao, Appl. Phys. Lett. 86 (2005) 193508.
[7] Natalie Stutzmann, Richard H. Friend, Henning Sirringhaus, Science 299 (2003) 1881.
[8] Sheng-Han Li, Zheng Xu, Guanmen Yang, Liping Ma, Yang Yang, Appl. Phys. Lett. 93 (2008) 213301.
[9] Ken-ichi Nakayama, Shin-ya Fujimoto, Masaaki Yokoyama, Appl. Phys. Lett. 88 (2006) 153512.

[10] Yu-Chiang Chao, Ming-Hong Xie, Ming-Zhi Dai, Hsin-Fei Meng, Sheng-Fu Horng, Chain-Shu Hsu, Appl. Phys. Lett. 92 (2008) 093310.
[11] Wilson J. da Silva, Ivo A. Hümmelgen, Regina M.Q. Mello, Dongge Ma, Appl. Phys. Lett. 93 (2008) 053301.
[12] Y. Yang, A.J. Heeger, Nature 372 (1994) 344.
[13] Michelle S. Meruvia, Adriano R.V. Benvenho, Ivo A. Hümmelgen, André A. Pasa, Walther Schwarzacher, Appl. Phys. Lett. 86 (2005) 263504.
[14] Yu-Chiang Chao, Hsin-Fei Meng, Sheng-Fu Horng, Appl. Phys. Lett. 88 (2006) 223510.
[15] Mingdong Yi, Shunyan Yu, Chengang Feng, Tong Zhang, Dongge Ma, M.S. Meruvia, Ivo A. Hümmelgen, Org. Electron. 8 (2007) 311.
[16] Jinying Huang, Mingdong Yi, Dongge Ma, Ivo A. Hümmelgen, Appl. Phys. Lett. 92 (2008) 232111.
[17] Mingdong Yi, Jinying Huang, Dongge Ma, Ivo A. Hümmelgen, Appl. Phys. Lett. 92 (2008) 243312.
[18] Yu-Chiang Chao, Hsin-Fei Meng, Sheng-Fu Horng, Chain-Shu Hsu, Org. Electron. 9 (2008) 310.
[19] Mingdong Yi, Jinying Huang, Dongge Ma, Ivo A. Hümmelgen, Org. Electron. 9 (2008) 539.
[20] J.P. M Serbena, J.Y. Huang, D. Ma, Z.Y. Wang, I.A. Hümmelgen, Org. Electron. 10 (2009) 357.
[21] J. McElvain, M. Keshavarz, H. Wang, F. Wudl, A.J. Heeger, J. Appl. Phys. 81 (1997) 6468.
[22] Michelle S. Meruvia, Ivo A. Hümmelgen, Adv. Funct. Mater. 16 (2006) 459.
[23] K.K. Ng, Complete Guide to Semiconductor Devices, first ed., Wiley, New York, 2002.
[24] Shiau-Shin Cheng, Chuan-Yi Yang, You-Che Chuang, Chun-Wei Ou, Meng-Chyi Wu, Shih-Yen Lin, Yi-Jen Chan, Appl. Phys. Lett. 90 (2007) 153509.
[25] S.M. Sze, Physics of Semiconductor Devices, first ed., Wiley, New York, 1981.

emission [23]. Of course, a direct transition from the CT state to the ground state has also been confirmed by the experimentally reported near infrared emission from CT states in organic heterojunction devices [24,25]. In the past few years, an unusual phenomenon of "organic spintronics", called as organic magnetoresistance (OMAR), has attracted great attention for both basic research and applications. One of the focused questions is its underlying mechanism. Recently, Wang [26] and Majumdar [27] sequentially investigated such an effect in organic heterojunctions. It is interesting that both of them attributed it to the formation of the CT states.

Thus, the formation of CT states, especially the competition between their dissociation and various types of recombination, determines the different optoelectronic and magnetic applications for the D–A polymer heterojunctions. A crucial parameter affecting the above physical process is the energy offset. For example, for the application of D–A polymer heterojunctions in organic photovoltaic cells, one would like to improve the dissociation probability of a CT state, or suppress its various types of recombination, and in this case, a large energy offset should be expected. However, the energy offset is not as larger as expected, which will reduce the available open-circuit voltage and limit the photovoltaic efficiency [28,29]. So, how to choose the optimalizing energy offset becomes to be a key challenge for the different applications of D–A heterojunctions. Theoretically, Bittner et al. investigated the dependence of the charge transfer (or exciton dissociation) on the energy offset. They speculated that the exciton dissociation requires the energy offset to be greater than the exciton binding energy [6,7]. That is, there exists a critical energy offset for the charge transfer, which numerically equals to the exciton binding energy. However, we have known that this charge transfer does not directly generate free charge carriers, but a CT state. In view of this, we should further modify the critical energy offset by considering the formation of a CT state.

In this paper, a D–A polymer heterojunction consisting of two parallel molecules is modeled, in which we firstly consider the formation of a CT state following a direct transition between the two molecules [16,30,31]. Creation and binding energy of the CT state is sequentially calculated, by which we analyze its stability in a static picture. After that, the dynamic process of the charge transfer and recombination will be focused. Through the discussions, we aim to give a light to choose the optimalizing energy offset in different applications of D–A polymer heterojunctions. The paper is organized as follows. The model and method are presented in Section 2. The results and discussions are shown in Section 3. Finally in Section 4, a summary is given.

2. Model and method

As early as the 1930s, Onsager proposed a phenomenological theory (i.e., Onsager theory) to describe a CT state [32]. Although it has proven to be an effective theory in predicting the experimentally observed variations of charge photogeneration, there remain some restrictions in its application at D–A interfaces [33,34]. In particular, the current modified Onsager theory still can not take into account the effect of the dynamic lattice distortions or relaxations, which have been proven to be crucial for an organic polymer with strong electron-lattice interactions [35]. In this paper, we employ the tight-binding electron-lattice interacting model, i.e., the well-known Su–Schrieffer–Heeger (SSH) model [36]. To constitute an organic heterojunction with a D–A-type characteristic, we consider two coupled parallel poly(*p*-phenylene vinylene) (PPV) molecules with different on-site energy. By a renormalization treatment for the benzene rings, a PPV molecule can be modeled as a one-dimensional chain [11,13]. Thus, the Hamiltonian of the two PPV chains is written as:

$$H = H_1 + H_2 + H_{1-2}, \tag{1}$$

where H_j (j shows the chain index) describes an isolated PPV chain, consisting of two parts

$$H_j = H_{j,e} + H_{j,\text{lattice}}. \tag{2}$$

$H_{j,e}$ is the electronic part,

$$H_{j,e} = \sum_{n,s} \Delta_{j,n} C^+_{j,n,s} C_{j,n,s} - \sum_{n,s} t_{j,n,n+1} \left(C^+_{j,n+1,s} C_{j,n,s} + C^+_{j,n,s} C_{j,n+1,s} \right) + U \sum_n C^+_{j,n,\uparrow} C_{j,n,\uparrow} C^+_{j,n,\downarrow} C_{j,n,\downarrow} + V \sum_{n,s,s'} C^+_{j,n,s} C_{j,n,s} C^+_{j,n+1,s'} C_{j,n+1,s'}. \tag{3}$$

$\Delta_{j,n}$ denotes the on-site energy of electrons on site n, and $C^+_{j,n,s}$ ($C_{j,n,s}$) the creation (annihilation) operator of an electron at site n with spin s ($s = \uparrow, \downarrow$). The second term shows the electron hopping between the nearest neighboring sites, where the transfer integral $t_{j,n,n+1}$ between site n and $n + 1$ is written as:

$$t_{j,n,n+1} = t_0 - \alpha(u_{j,n+1} - u_{j,n}) - t_1 \cos n\pi + t_2 \cos\left(\frac{n+1}{3}\pi\right) \cdot \delta\left(\frac{n+1}{3}, \text{int}\right). \tag{4}$$

Here $\delta(\frac{n+1}{3}, \text{int}) = 1$, if $\frac{n+1}{3} = \text{int}$; and $\delta(\frac{n+1}{3}, \text{int}) = 0$, if $\frac{n+1}{3} \neq \text{int}$. "int" means an integer. t_0 represents the nearest-neighbor transfer integral for a uniform bond structure, α the electron-lattice interaction constant and $u_{j,n}$ the displacement of a unit at site n. t_1 and t_2 are the symmetry-breaking parameters introduced to reflect the lattice feature of a PPV monomer. The last two terms show the e–e interaction, which is treated with the Hartree–Fock approximation for simplicity. U presents the strength of the on-site Coulomb interactions and V the nearest-neighbor interactions:

$$H_{j,\text{lattice}} = \frac{1}{2} K \sum_n (u_{j,n+1} - u_{j,n})^2 + \frac{1}{2} M \sum_n \dot{u}^2_{j,n} \tag{5}$$

describes the classical treatment of the elastic potential and kinetic energy of the sites. K denotes the elastic constant and M the mass of a site.$H_{1,2}$ describes the interactions between the two chains, which consists of two parts,

$$H_{1,2} = -\sum_{n,s} t_\perp (C^+_{1,n,s} C_{2,n,s} + C^+_{2,n,s} C_{1,n,s}) + \sum_{n,s,s'} V_\perp (C^+_{1,n,s} C_{1,n,s} C^+_{2,n,s'} C_{2,n,s'}) \tag{6}$$

$t_\perp$ and $V_\perp$ separately presents the interchain transfer integral and e–e interaction between sites labeled by the same index n on the two chains.

Due to the strong electron-lattice interactions of the organic system, the lattice displacement $u_{j,n}$ is not fixed, and it will change with the electron–hole excitation. The temporal evolution is classically described by the Newtonian equation of motion:

$$M\ddot{u}_{j,n} = -K(2u_{j,n} - u_{j,n+1} - u_{j,n-1}) + 2\alpha(\rho_{j,n,n+1} - \rho_{j,n,n-1}) - \lambda M\dot{u}_{j,n}, \quad (7)$$

where the density matrix ρ is defined as

$$\rho_{j,n,n'} = \sum_s \rho_{j,n,n',s} = \sum_{\mu,s} \Psi_{j,\mu,s}(n,t) f_\mu \Psi^*_{j,\mu,s}(n',t). \quad (8)$$

f_μ is the time-independent distribution function determined by the initial electron occupation. In Eq. (7), a damping term is introduced to describe the energy dissipation into the surrounding medium by a tuning parameter λ [37].

The evolutions of electronic states $\Psi_{j,\mu,s}(n, t)$ are the solutions of the time-dependent Schrödinger equation:

$$i\hbar\frac{\partial}{\partial t}\Psi_{j,\mu,s}(n,t) = -t_{j,n,n+1}\Psi_{j,\mu,s}(n+1,t) - t_{j,n-1,n}\Psi_{j,\mu,s}(n-1,t) + [U\rho_{j,n,n,-s} + V(\rho_{j,n-1,n-1} + \rho_{j,n+1,n+1}) + V_\perp\rho_{j',n,n} + \Delta_{j,n}]\Psi_{j,\mu,s}(n,t) - t_\perp\Psi_{j',\mu,s}(n,t), \quad (9)$$

where j and j' mean different chain.

At beginning or for the static picture, we set $\Psi_{j,\mu,s}(n, t = 0) = Z_{j,\mu,s}|n\rangle$, which is obtained by solving the Schrödinger equation of Hamiltonian H with $u_n = 0$. When the system is photoexcited, electrons will gain energy and $\Psi_{j,\mu,s}(n, t)$ consequently experience an evolution determined by the coupled differential Eqs. (7) and (9), which can be solved by the Runge–Kutta method of order eight with step-size control.

3. Results and discussion

Referring to Refs. [11] and [13], the values of parameters in the Hamiltonian are separately set as $\alpha = 102.9$ eV/nm, $t_0 = 2.66$ eV, $t_1 = 0.02$ eV, $t_2 = -0.2$ eV, $K = 9900$ eV/nm^2, and $M = 1.35 \times 10^5$eV · fs^2/nm^2. For the e–e interactions, the values are fixed to be $U = 2.0$ eV, $V = 1.0$ eV, and $V_\perp = 0.1$ eV. To constitute a D–A-type electronic structure, we set different values to the on-site energy of the two chains: $\Delta_{1,n} = \Delta E$, $\Delta_{2,n} = 0$, where $\Delta E > 0$ is chosen in connection with the results discussed as follows. Then the first chain is a D-type molecule and the second chain an A-type one. Consequently, an energy offset ΔE between LUMO of the D-chain (LUMO^D) and that of the A-chain (LUMO^A) [or HOMO of the D-chain (HOMO^D) and that of the A-chain (HOMO^A)] is obtained, as sketched in Fig. 1.

For such a system, if the photoexcitation takes place only in a single chain, such as in the D-chain, an electron will be excited from HOMO^D to LUMO^D [11], as shown in Fig. 1, which corresponds to the intramolecular transition P_{intra}. After that, we give the net charge distribution $q_n = e(\rho_{n,n} - 1)$ of the two chains with $t_\perp = 0.1$ eV and $\Delta E = 0.2$ eV, as shown by the dashed line in Fig. 2. We can see that it does not appear any charge transfer between the D–A chains. In such a case, an exciton forms and is localized in the D-chain. In addition, the photoexcitation can also take place near the D–A interface, as reported by recent experiments [16,30,31]. It will result in the charge transfer between the chains. To realize such a process, the intermolecular transition P_{inter} is especially considered, as also shown in Fig. 1. After the transition, the net charge distribution of the two chains is presented by the solid line in Fig. 2. Apparently, it is no longer an exciton as there appears a charge transfer. As we know, if an electron transfer between the two chains, a negative polaron and a positive polaron will be formed, separately residing in the D-chain and A-chain. However, as the chains are coupled together, the initial transferred electron and the left hole still exhibit a significant attraction due to the overlapping of the corresponding electronic states. A direct result is that the transferred charges are not the initial one electronic charge (e), but usually fractional electric charges. For example, in present parameters the transferred charges are about 0.5e, which are bound together with the left 0.5h on the D-chain as a CT state.

To compare the two states, we calculate their creation energies. The solid line and the dashed line in Fig. 3 show

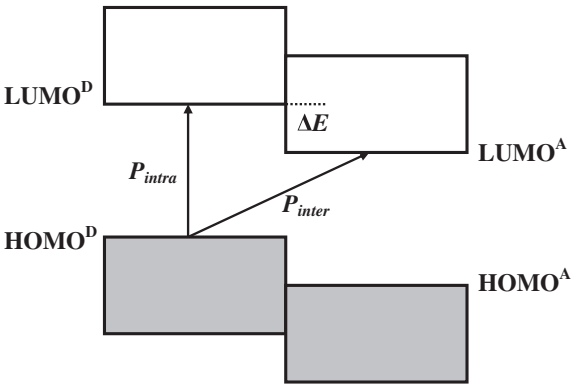

Fig. 1. Schematic diagram of the energy levels of a D–A polymer heterojunction, where ΔE is the energy offset. P_{intra} indicates the intramolecular transition, and P_{inter} the intermolecular one.

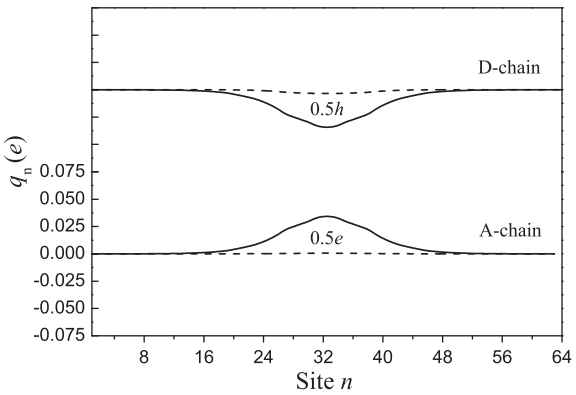

Fig. 2. Two possible states photogenerated in the D–A polymer heterojunction with $t_\perp = 0.1$ eV and $\Delta E = 0.2$ eV, where the dashed line and the solid line separately indicates the result after P_{intra} and P_{inter}.

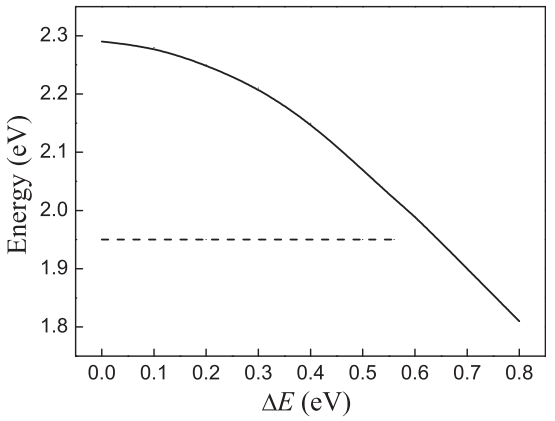

Fig. 3. Dependences of the creation energy of a CT state (solid line) and an exciton (dashed line) on the energy offset.

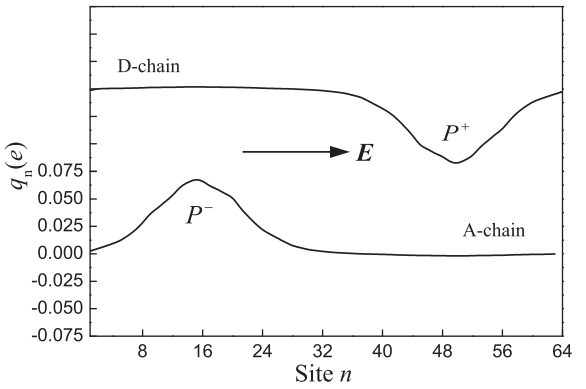

Fig. 4. Dissociation of a CT state in the D–A polymer heterojunction by an external electric field E with the direction from left to right along the chain.

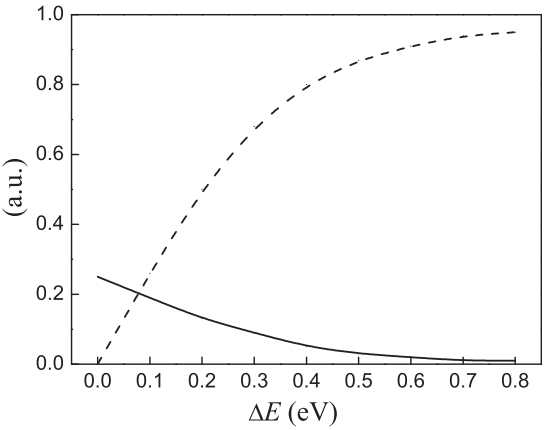

Fig. 5. Dependences of the binding energy (solid line) and the transferred charges (dashed line) of a CT state on the energy offset ΔE in a D–A polymer heterojunction with $t_\perp = 0.1$ eV .

the dependence of the creation energy for a CT state (ΔE_{CT}) and an exciton (ΔE_{exc}) on the energy offset (ΔE), respectively. It is found that there exists a turnover value ΔE_C ($\Delta E_C = 0.56$ eV in present parameters) of the energy offset. When $\Delta E \leqslant \Delta E_C$, not only a CT state but also an exciton can be obtained, and the latter is always energetically favorable to the former. When $\Delta E > \Delta E_C$, we can not obtain an exciton any more. It implies that an exciton is energetically unstable at the D–A interface with $\Delta E > \Delta E_C$. From the speculation of Bittner et al., we know that the critical energy offset ΔE_C is determined by the exciton binding energy E_B^{exc}, and $\Delta E_C = E_B^{exc}$ [6]. Here, we calculate the exciton binding energy referring to [38], and get the value $E_B^{exc} = 0.55$eV in present parameters. The result is approximately consistent with that obtained by Bittner et al., which will be further discussed in the following.

As stated above, the excited electron and hole in a CT state still remain bound across the D–A interface. To dissociate these generated CT states and get the desired free charge carriers, we should consider some external effects, e.g., thermal fluctuation or electric field. Here, we consider the dissociation of a CT state by applying an external electric field E with the form referring to [13]. Compared with the result without considering E, we find that an electric field should help to facilitate the charge transfer. Especially, there exists a critical value of E_C, beyond which the CT state shown in Fig. 2 will be dissociated into a positive polaron (P^+) and a negative polaron (P^-) (see Fig. 4). It indicates that the "energetic barrier" between the CT state and the free charge carriers can be reduced, even eliminated, by an electric field. Of course, such an "energetic barrier" can be quantitatively reflected by the binding energy of a CT state E_B^{CT}, which is defined as the energy difference between the creation energy of free charge carriers shown in Fig. 4 and that of a CT state shown in Fig. 2 ($E_B^{CT} = \Delta E_{P^+P^-} - \Delta E_{CT}$). In present parameters ($t_\perp = 0.1$eV and $\Delta E = 0.2$ eV), we get $E_B^{CT} = 0.13$eV, which is greatly smaller than the exciton binding energy ($E_B^{exc} = 0.55$eV). As we know, the energetics of the dissociation of either a CT state or an exciton is determined by its binding energy. Usually, a larger binding energy means that the state is more stable, and the dissociation is much harder. Therefore, the dissociation of a CT state is much easier than that of an exciton. For example, in present parameters the critical electric field dissociating a CT state is $E_C = 1.9 \times 10^5$ V/cm, while that dissociating an exciton needs a field as high as $E_C = 1.6 \times 10^6$ V/cm.

However, the dissociation of a CT state is found to be dependent upon the energy offset. The solid line in Fig. 5 shows the calculated binding energy of a CT state in different energy offset. It is obtained that the binding energy decreases apparently with the increase of the energy offset. It indicates that a CT state is more easily dissociated in a D–A heterojunction with a large energy offset. Especially, when the energy offset is large enough, the binding energy will fall below the room temperature thermal energy (0.025 eV), which means that the thermal fluctuation at room temperature is sufficient to dissociate a CT state into free charge carriers contributing to the photocurrent. In addition, we check the dependence of the transferred charges between the chains on the energy offset, as shown by the dashed line in Fig. 5. As can be seen, the transferred

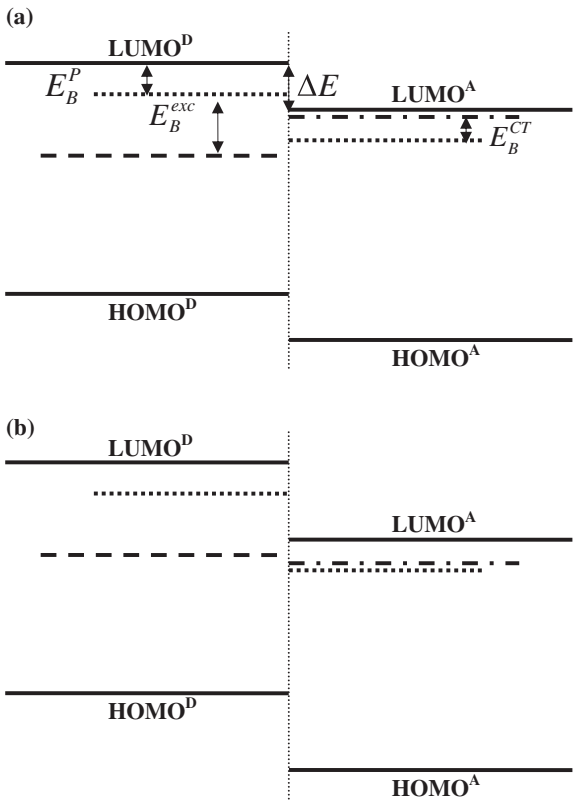

Fig. 6. Energy level diagram of a D–A interface showing a simplified viewpoint of electron transfer and subsequent recombination between the two molecules. The dashed line indicates the energy level of an exciton, the dotted line the energy level of a polaron, and the dash dotted line the energy level of a CT state. E_B^{exc} and E_B^{CT} indicate the binding energy of an exciton and a CT state, respectively, which are both shown relative to the polaron level. E_B^P indicates the binding energy of a polaron.

charges increase with the increase of the energy offset, and finally saturate to one electronic charge (e). It further indicates that, with the increase of the energy offset, the charge separation extent in a CT state will be more complete and approaches the free charge carriers.

On the contrary, if there does not exist any external effects, the weakly bound electron and hole in a CT state are not allowed to separate or drift away from each other, and various types of recombination events may occur [22,23,25]. It has been found to be a major limitation for the efficiency of organic heterojunction solar cells [28]. Here, we consider the recombination of a CT state into an exciton, which can be simply understood by considering the energetics of the D–A interface, as illustrated in Fig. 6. The dashed and dash dotted line present the upper localized energy levels for an exciton and a CT state, respectively. In addition, to obtain their binding energies we give the localized energy level of a polaron (see the dotted line). Thus, the binding energy of an exciton E_B^{exc} and a CT state E_B^{CT} can be simply obtained relative to the polaron level, since we have found that both of them are dissociated into oppositely charged polarons. E_B^P shows the binding energy of a polaron, which is obtained relative to the LUMO [39]. As stated above, with the formation of a CT state, there appears charge transfer from the D-polymer to the A-one, which occupy the CT state level. For the case of a small energy offset ΔE, as shown in Fig. 6a, the energy level of a CT state lies higher in energy than that of an exciton. The initial transferred charges will surely transit from the CT state level to the exciton level due to the energetic downhill, and the CT state consequently recombine into an exciton. With the increase of the energy offset, the exciton binding energy E_B^{exc} and the polaron one E_B^P keep unchanged, while the CT state binding energy E_B^{CT} presents an apparent reduction (see Fig. 5), as shown in Fig. 6b. As a result, the CT state level may lie lower in energy than the exciton level, and the recombination of a CT state into an exciton is energetically unfavorable.

To give a quantitative relation between the recombination and the energy offset, a driving potential P resulting from the energy difference between the exciton energy level and the CT energy level is introduced, which is written as:

$$\begin{aligned} P &= -(\Delta E + E_B^p - E_B^{CT}) - \left[-(E_B^{exc} + E_B^p)\right] \\ &= \left(E_B^{exc} + E_B^p\right) - \left(\Delta E + E_B^p - E_B^{CT}\right). \end{aligned} \tag{10}$$

Fig. 7 shows the dependence of the driving potential P upon the energy offset ΔE. It is apparent that there exists a turnover value ΔE_C (ΔE_C = 0.56 eV in present parameters) of the energy offset. When $\Delta E < \Delta E_C$, the driving potential is positive ($P > 0$). It means that the initially generated CT state at the D–A interface, whether by a photoexcitation here or by electrical injection where else [24,25], should be inclined to recombine into an exciton. Such a situation is desirable for the light emission, and so, the D–A heterojunction is suitable to be used as the functional layer in a light-emitting device. When $\Delta E > \Delta E_C$, the driving potential is negative ($P < 0$). It implies that the initially generated CT state can not recombine into an exciton, however, the reverse process, that is, the dissociation of an exciton into a CT state will surely take place. Therefore, at the D–A interface with $\Delta E > \Delta E_C$, we can only get a CT state, which

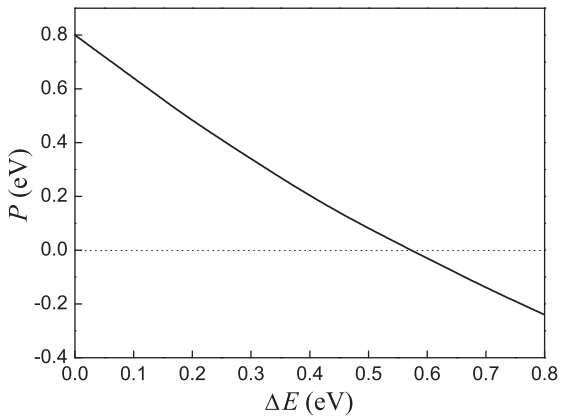

Fig. 7. Dependence of the driving potential P on the energy offset ΔE.

is consistent with the result shown in Fig. 3. Such a situation is desirable for photovoltaic devices, since a CT state is more easily dissociated than an exciton.

In addition, from Fig. 7 we can see that, in the case of $\Delta E < \Delta E_C$, the driving potential P tends to weaken with the increase of the energy offset. It shows that the recombination of a CT state into an exciton will be harder and harder with the energy offset. To give a further confirmation, the dynamic process for the charge transfer and recombination in the D–A polymer heterojunction is addressed. As shown in Fig. 8, at beginning (i.e., $t = 0$), both of the two chains are in their ground state with $q(n) = 0$. When $t > 0$, an electron is excited from $HOMO^D$ to $LUMO^A$, or the case corresponding to transition P_{inter} shown in Fig. 1. We find that there appears net charges in each of the two chains, and $0 < q(n < 64) = -q(n > 64)$. It shows that electrons are transferred from the D-chain to the A-one. Initially, the transferred charges behave in a spread state in respective chain. However, due to the strong electron-lattice interactions in the organic molecules, the spread charges quickly (~10 fs) assemble together to form a localized state. As stated above, the two localized states are not completely separated from each other, but coupled together as a CT state due to the interchain coupling included.

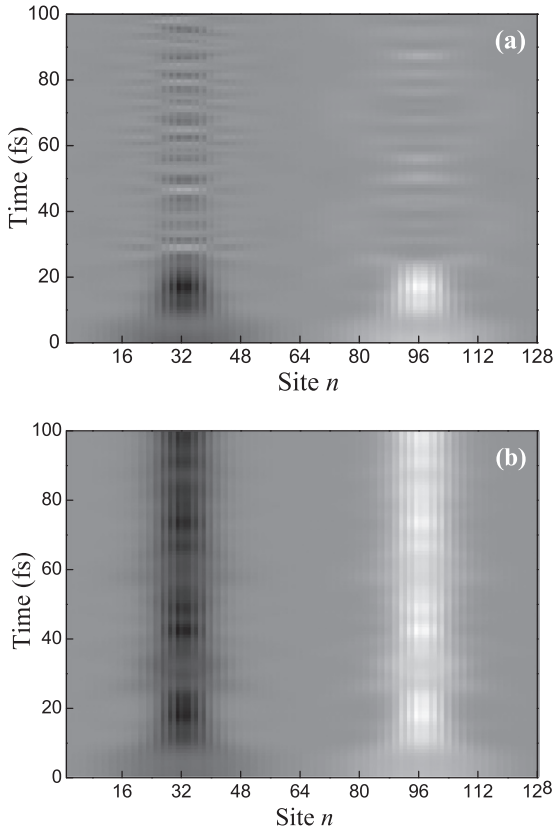

Fig. 8. Time dependence of q_n for the D–A polymer heterojunction with the same interchain coupling $t_\perp = 0.1$ eV and different energy offset $\Delta E = 0.2$ eV (a), $\Delta E = 0.6$ eV (b).

However, after the formation of the CT state, the dynamic evolution of the system is different for different energy offset. Fig. 8a shows the result with $\Delta E = 0.2$ eV. It is found that the initially transferred charges into the A-chain quickly return back to the D-chain, which finally behaves in an exciton, while the A-chain eventually reverts to its ground state. It means that the generated CT state at the D–A interface rapidly recombines into an exciton. For the case of $\Delta E = 0.6$ eV, as shown in Fig. 8b, the transferred charges nearly keep unchanged, and the generated CT state does not recombine into an exciton. Fig. 9 further presents the dependence of the recombination time of the CT state on the energy offset. With the increase of the energy offset, the recombination of the CT state needs a long time. Once the energy offset exceeds the critical value ($\Delta E > \Delta E_C$), the CT state can not recombine any more. The results are consistent with those obtained by the static picture.

Finally, it should be stressed that the critical energy offset ΔE_C for the charge transfer and recombination in the D–A polymer heterojunction is determined not only by the exciton binding energy, but also by the CT state one. By setting $P = 0$ in Eq. (10), we can get the critical energy offset ΔE_C written as:

$$\Delta E_C = E_B^{exc} + E_B^{CT}. \tag{11}$$

However, we note that the CT state binding energy E_B^{CT} is very weak (see Fig. 5) at $\Delta E_C = 0.56$ eV. So, when we consider the exciton dissociation or charge transfer, the critical energy offset is approximately only determined by the exciton binding energy. While in some conditions, e.g., in PPV crystal with strong interchain couplings, the exciton binding energy will be apparently reduced [40]. Consequently, the critical energy offset may also present a reduction. In such a case, the CT state binding energy can not be neglected for the contribution to ΔE_C. In addition, although a large energy offset favors the photogeneration of free charges in a D–A heterojunction. In actual applications of the D–A heterojunctions in photovoltaic devices, a large energy offset will reduce the available open-circuit voltage and fundamentally limit the photovoltaic efficiency [28,29]. Therefore, how to efficiently reduce the critical en-

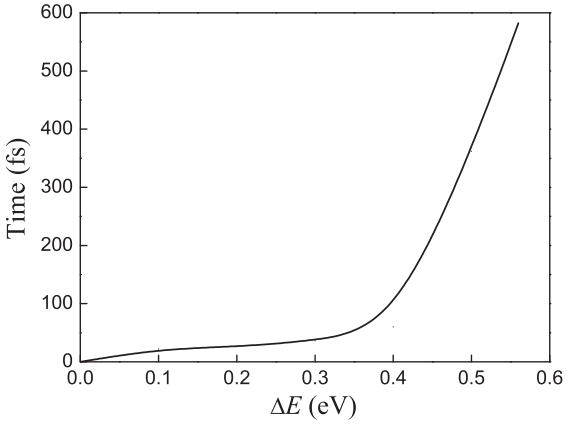

Fig. 9. Dependence of the recombination time of the CT state into an exciton on the energy offset ΔE with the interchain coupling $t_\perp = 0.1$ eV .

ergy offset ΔE_C should be one of the keys to improve the photovoltaic efficiency. So, further investigations should be done in the future that include some physical factors, which can reduce the exciton binding energy or the CT state one, such as the control of the distance between the molecules by applying a hydrostatic pressure [41].

4. Summary

In view of the significant influence of the CT states on the optoelectronic and magnetic applications of D–A polymer heterojunctions, we theoretically investigated the formation and stability of a CT state, and especially the dynamic mechanism of the charge transfer and recombination. It was found that the critical energy offset, which determines the formation and recombination of a CT state, depends on not only the exciton binding energy but also the CT state one. A quantitative relation for them is obtained. When the energy offset is less than the critical value, the electrons in the A-polymer, whether by the intermolecular electron transition or by the electrical injection, will quickly return back to the D-one, and the generated CT state consequently recombine into an exciton. With the increase of the energy offset, the recombination needs a long time. Once the energy offset exceeds the critical value, the generated CT state can not recombine any more.

Acknowledgments

The authors would like to acknowledge the financial support from The National Key Basic Research Program (No. 2009CB929204), The National Natural Science Key Foundation (Nos. 10804062, 10874100, and 10904082), The Research Fund for the Doctoral Program of Higher Education (No. 200804221005), and The Excellent Youth and Middle Age Scientists Fund of Shandong Province (No. BS2009NJ006).

Reference

[1] G. Yu, J. Gao, J.C. Hummelen, F. Wudl, A.J. Heeger, Science 270 (1995) 1789.
[2] J.Y. Kim, K. Lee, N.E. Coates, D. Moses, T.-Q. Nguyen, M. Dante, A.J. Heeger, Science 317 (2007) 222.
[3] Y. Liang, Z. Xu, J. Xia, S.–T. Tsai, Y. Wu, G. Li, C. Ray, L. Yu, Adv. Mater. 22 (2010) E135.
[4] J.D. Anderson, E.M. McDonald, P.A. Lee, M.L. Anderson, E.L. Ritchie, et al., J. Am. Chem. Soc. 120 (1998) 9646.
[5] N.R. Armstrong, R.M. Wightman, E.M. Gross, Annu. Rev. Phys. Chem. 52 (2001) 391.
[6] E.R. Bittner, J.G.S. Ramon, S. Karabunarliev, J. Chem. Phys. 122 (2005) 214719.
[7] H. Tamura, E.R. Bittner, I. Burghardt, J. Chem. Phys. 126 (2007) 021103.
[8] T.M. Clarke, J.R. Durrant, Chem. Rev. (2010). doi:10.1021/cr900271s.
[9] J.L. Brédas, J.E. Norton, J. Cornil, V. Coropceanu, Acc. Chem. Res. 42 (2009) 1691.
[10] E. Hendry, J.M. Schins, L.P. Candeias, L.D.A. Siebbeles, M. Bonn, Phys. Rev. Lett. 92 (2004) 196601.
[11] K. Gao, S.J. Xie, S. Yin, Y. Li, D.S. Liu, X. Zhao, Org. Electron. 10 (2009) 1601.
[12] V.I. Arkhipov, H. Bässler, Phys. Status Solidi A 201 (2004) 1152.
[13] K. Gao, X.J. Liu, D.S. Liu, S.J. Xie, Phys. Rev. B 75 (2007) 205412.
[14] C. Deibel, T. Strobel, V. Dyakonov, Adv. Mater. 22 (2010) 4097.
[15] M. Muntwiler, Q.X. Yang, W.A. Tisdale, X.–Y. Zhu, Phys. Rev. Lett. 101 (2008) 196403.
[16] M. Hallermann, S. Haneder, E.D. Como, Appl. Phys. Lett. 93 (2008) 053307.
[17] X.–Y. Zhu, Q. Yang, M. Muntwiler, Acc. Chem. Res. 42 (2009) 1779.
[18] T. Drori, J. Holt, Z.V. Vardeny, Phys. Rev. B 82 (2010) 075207.
[19] Y.–S. Huang, S. Westenhoff, I. Avilov, P. Sreearunothai, J.M. Hodgkiss, C. Deleener, R.H. Friend, D. Beljonne, Nat. Mater. 7 (2008) 483.
[20] Z.D. Wang, S. Mazumdar, A. Shukla, Phys. Rev. B 78 (2008) 235109.
[21] K. Aryanpour, D. Psiachos, S. Mazumdar, Phys. Rev. B 81 (2010) 085407.
[22] A.C. Morteani, P. Sreearunothai, L.M. Herz, R.H. Friend, C. Silva, Phys. Rev. Lett. 92 (2004) 247402.
[23] J.J. Benson-Smith, J. Wilson, C. Dyer-Smith, K. Mouri, S. Yamaguchi, H. Murata, J. Nelson, J. Phys. Chem. B 113 (2009) 7794.
[24] K. Tvingstedt, K. Vandewal, A. Gadisa, F.L. Zhang, J. Manca, O. Inganäs, J. Am. Chem. Soc. 131 (2009) 11819.
[25] A.M.C. Ng, A.B. Djurišić, W.-K. Chan, J.-M. Nunzi, Chem. Phys. Lett. 474 (2009) 141.
[26] F.J. Wang, H. Bässler, Z.V. Vardeny, Phys. Rev. Lett. 101 (2008) 236805.
[27] S. Majumdar, H.S. Majumdar, H. Aarnio, D. Vanderzande, R. Laiho, R. Österbacka, Phys. Rev. B 79 (2009) 201202(R).
[28] S. Westenhoff, I.A. Howard, J.M. Hodgkiss, K.R. Kirov, H.A. Bronstein, C.K. Williams, N.C. Greenham, R.H. Friend, J. Am. Chem. Soc. 130 (2008) 13653.
[29] L.J.A. Koster, V.D. Mihailetchi, P.W.M. Blom, Appl. Phys. Lett. 88 (2006) 093511.
[30] P. Parkinson, J. Lloyd-Hughes, M.B. Johnston, L.M. Herz, Phys. Rev. B 78 (2008) 115321.
[31] T. Drori, C.–X. Sheng, A. Ndobe, S. Singh, J. Holt, Z.V. Vardeny, Phys. Rev. Lett. 101 (2008) 037401.
[32] L. Onsager, Phys. Rev. 54 (1938) 554.
[33] V.I. Arkhipov, P. Heremans, H. Bässler, Appl. Phys. Lett. 82 (2003) 4605.
[34] P. Peumans, S.R. Forrest, Chem. Phys. Lett. 398 (2004) 27.
[35] A.J. Heeger, S. Kivelson, J.R. Schrieffer, W.P. Su, Rev. Mod. Phys. 60 (1988) 781.
[37] A.A. Johansson, S. Stafström, Phys. Rev. B 69 (2004) 235205.
[38] K. Gao, X.J. Liu, D.S. Liu, S.J. Xie, Phys. Lett. A 372 (2008) 2490.
[39] Y. Li, K. Gao, Z. Sun, S. Yin, D.S. Liu, S.J. Xie, Phys. Rev. B 78 (2008) 014304.
[40] A. Ruini, M.J. Caldas, G. Bussi, E. Molinari, Phys. Rev. Lett. 88 (2002) 206403.
[41] J.P. Schmidtke, R.H. Friend, C. Silva, Phys. Rev. Lett. 100 (2008) 157401.

difficult to do even for a molecular conductor comprising a moderate number of atoms. Another way out was proposed by Büttiker over two decades ago [12,13]. He came up with an elegant idea of incorporating the effect of phase breaking due to inelastic scattering phenomenologically by introducing some fictitious voltage probes into the coherent system. While moving from source to drain electrons get scattered into the fictitious floating voltage probes and then re-emitted into the device by loosing the phase memory. To implement this idea each inelastic scatterer is modeled in terms of electron reservoir (or infinite impedance voltage probe) and coupled to the device. Since the net current flowing through the fictitious probes has to be zero to satisfy the conservation of total number of particles, electro-chemical potentials (μ) of each lead has to be adjusted accordingly. Due to its appealing simplicity Büttiker probe model has been extensively used in studying quantum transport in low-dimensional systems.

The idea of using molecules as active components of a device was suggested by Aviram and Ratner over three decades ago [14]. Since then several ab-initio and model calculations have been performed to investigate molecular transport theoretically [15–23]. But experimental realizations took a little longer time to get feasible. In 1997, Reed et al. studied the current-voltage (I–V) characteristics of a single benzene molecule attached to electrodes via thiol groups [24]. Various other experiments have been reported in literature exploring many interesting features, e.g., ballistic transport, quantized conductance, negative differential resistance (NDR), gate controlled transistor operation to name a few. Effect of dephasing in molecular systems has been studied in few literatures both theoretically [25,26] as well as experimentally. In 1989, D'Amato and Pastawski investigated the effect of inelastic scattering processes on a tight-binding linear disordered chain using Büttiker probe model [6]. In 2007, Datta and co-worker proposed a different phenomenological model which provides the flexibility of adjusting degree of phase and momentum relaxation independently [27]. In 2008, Nozaki et al. obtained transport properties through various molecular junctions by Büttiker model using Extended Hückel theory [28]. In 2009, Guo et al. have reported an ab-initio calculation [29] including the effect of phase breaking in 1,4-benzenedithiol molecule attached to two Al electrodes, gold QPC and a very thin Al(001) nanowire. They have also done a comparative analysis between Büttiker probe model and Datta dephasing model [27]. Though various efforts have already been made to explain the basic features of electron dephasing on molecular transport, but to the best of our knowledge, no rigorous effort has been made so far to unravel the combined effect of quantum interference and electron dephasing on molecular transport. This is the main motivation behind this work.

In our present article we study two terminal electron transport through a single benzene molecule including the effect of dephasing by a discrete tight-binding model. We obtain the transmission probability using Green's function technique within the framework of Landauer–Büttiker formulation. Transmittance–energy and current–voltage characteristics are obtained for three different configurations (*para*, *ortho* and *meta*) of benzene molecule depending on three different positions of the drain with respect to the source. The presence of dephasing provides a significant change in the spectral properties of the molecule and here we essentially focus our results in this aspect. Our model calculation can be extended further for any complicated molecular structure.

In what follows, we present the results. In Section 2, the model and the theoretical formulation are presented. Section 3 describes the results, and finally, we make our conclusions in Section 4.

2. Molecular model and theoretical formulation

We start by describing our model, illustrated in Fig. 1, where a single benzene molecule is connected symmetrically to two one-dimensional, semi-infinite leads, commonly known as source and drain. The leads are characterized by the electrochemical potentials μ_S and μ_D), respectively, under the non-equilibrium condition when an external bias voltage is applied. Both the two leads and the molecule are simulated by a simple tight-binding Hamiltonian within nearest-neighbor hopping approximation. Following Büttiker's idea, the effect of dephasing due to inelastic scattering is incorporated in the model phenomenologically by coupling each spatial sites to a different fictitious electron reservoir or in other words an infinite impedance voltage probe (shown by the pink shaded area in Fig. 1) via perfect leads. The key idea is that *the fictitious floating probes extract electrons from the device to the reservoir, but as the net current flowing through these probes is zero, so they re-inject the electrons into the conductor after phase randomization and thus effectively play the role of phase breaking scatterers.*

The Hamiltonian for the entire system is given by the sum of four terms:

$$H = H_{mol} + H_{leads} + H_{tun} + H_{dephase}. \quad (1)$$

The first term represents the Hamiltonian for the single benzene molecule consisting of six sites ($N = 6$) which is coupled to two electron reservoirs through conducting

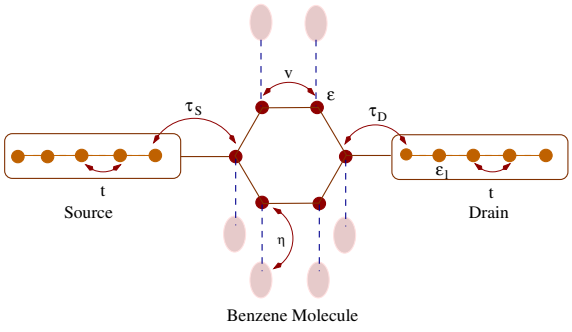

Fig. 1. Schematic diagram of a single benzene molecule attached to two leads, namely, source and drain. Each molecular site is assumed to be coupled to a fictitious electron reservoir, shown by the pink shaded area, which takes into account the effect of phase breaking processes. (For interpretation of the references to color in this figure legend, the reader is referred to the web version of this article.)

leads, namely, source and drain. The molecule is modeled by the nearest-neighbor tight-binding Hamiltonian which in Wannier basis can be written as,

$$H_{mol} = \sum_i \epsilon d_i^\dagger d_i + \sum_i v[d_{i+1}^\dagger d_i + h.c.], \tag{2}$$

where ϵ refers to the site energy of an electron at the ith site of the molecular system and v represents the isotropic nearest-neighbor coupling strength between the molecular sites. $d_i^\dagger$ and d_i correspond to the creation and annihilation operators, respectively, of an electron at the ith site of the molecule.

Similarly the second and third terms of Eq. (1) denote the Hamiltonians for the one-dimensional semi-infinite leads (source and drain) and molecule-to-lead coupling. In Wannier basis representation they can be written as follows:

$$\begin{aligned} H_{leads} &= H_S + H_D \\ &= \sum_{\alpha=S,D} \left\{ \sum_n \epsilon_l c_n^\dagger c_n + \sum_n t[c_{n+1}^\dagger c_n + h.c.] \right\}, \end{aligned} \tag{3}$$

and,

$$\begin{aligned} H_{tun} &= H_{S,mol} + H_{D,mol} \\ &= \tau_S[d_1^\dagger c_0 + h.c.] + \tau_D[d_p^\dagger c_{N+1} + h.c.]. \end{aligned} \tag{4}$$

Here, ϵ_l and v stand for the site energy and nearest-neighbor hopping between the sites of the two leads. $c_n^\dagger$ and c_n are the creation and annihilation operators, respectively, of an electron at the site n of the leads. The hopping integral between the source and the molecule is τ_S, while it is τ_D between the molecule and the drain. Usually benzene molecules are attached to gold leads via thiol groups (–SH bond) in the chemisorption technique. Here, the effect of such substituent (e.g., thiol group) is included in the parameters τ_S and τ_D. The source is assumed to be connected at the site number 1, while the drain is coupled to the pth site, which is variable, of the molecular system. The integer p becomes 2, 3 and 4 for the *ortho*, *meta* and *para* configurations, respectively.

In order to incorporate the effect of dephasing, external electron reservoirs are phenomenologically introduced and they are connected to all the molecular sites (six) through fictitious probes. The phase breaking probes are identically represented within tight-binding framework like source and drain as given below:

$$H_{dephase} = \sum_{i=1}^{N} \left[H_i^{d,probes} + H_i^{d,tun} \right], \tag{5}$$

where,

$$H_i^{d,probes} = \sum_m \epsilon_d c_m^{Di\dagger} c_m^{Di} + \sum_m t_d[c_{m+1}^{Di\dagger} c_m^{Di} + h.c.], \tag{6}$$

and,

$$H_i^{d,tun} = \eta \left[c_0^{Di\dagger} d_i + h.c. \right]. \tag{7}$$

Here, ϵ_d and t_d being the site energy and the hopping strength between the nearest-neighbor sites of the dephasing probes, respectively. $c_m^{Di\dagger}(c_m^{Di})$ is the creation (annihilation) operator of an electron at the mth site of the ith lead. The dephasing strength is characterized by the coupling parameter η.

To obtain the transmission probability of an electron through such a molecular bridge system, we use Green's function formalism. Within the regime of coherent transport and in the absence of Coulomb interaction this technique is well applied.

The single particle Green's function operator representing the entire system for an electron with energy E is defined as,

$$G = (E - H + i\eta)^{-1} \tag{8}$$

where $\eta \to 0^+$.

Following the matrix form of $\boldsymbol{H}$ and $\boldsymbol{G}$ the problem of finding $\boldsymbol{G}$ in the full Hilbert space $\boldsymbol{H}$ can be mapped exactly to a Green's function $\boldsymbol{G}_{\boldsymbol{mol}}^{\boldsymbol{eff}}$ corresponding to an effective Hamiltonian in the reduced Hilbert space of the molecule itself and we have,

$$\mathscr{G} = \boldsymbol{G}_{\boldsymbol{mol}}^{\boldsymbol{eff}} = \left(\boldsymbol{E} - \boldsymbol{H}_{\boldsymbol{mol}} - \boldsymbol{\Sigma}_{\boldsymbol{S}} - \boldsymbol{\Sigma}_{\boldsymbol{D}} - \sum_{\boldsymbol{k}=1}^{\boldsymbol{N}} \boldsymbol{\Sigma}_{\boldsymbol{k}} \right)^{-1}, \tag{9}$$

where,

$$\begin{aligned} \boldsymbol{\Sigma}_{\boldsymbol{S(D)}} &= \boldsymbol{H}_{\boldsymbol{S,mol(mol,R)}}^{\dagger} \boldsymbol{G}_{\boldsymbol{S(D)}} \boldsymbol{H}_{\boldsymbol{S,mol(mol,R)}}, \\ \boldsymbol{\Sigma}_{\boldsymbol{k}} &= \boldsymbol{H}_{\boldsymbol{k}}^{\boldsymbol{d,tun}\dagger} \boldsymbol{G}_{\boldsymbol{k}} \boldsymbol{H}_{\boldsymbol{k}}^{\boldsymbol{d,tun}}. \end{aligned} \tag{10}$$

These $\boldsymbol{\Sigma}_{\boldsymbol{S(D)}}$ and $\boldsymbol{\Sigma}_{\boldsymbol{k}}$ are the contact self-energies introduced to incorporate the effect of coupling of the molecule to the source (drain) and the fictitious electron reservoirs. It is evident from Eq. (10) that the form of the self-energies are independent of the molecule itself through which transmission is studied. Using Dyson equation the analytic form of the self energies can be evaluated as follows:

$$\Sigma_v = \frac{\tau_v^2}{E - \epsilon_v - \sigma_v}. \tag{11}$$

Here, $\sigma_v = (E - \epsilon_v)/2 - i\sqrt{t_v^2 - (E - \epsilon_v)^2/4}$; and $v = S,\ D,\ 1,\ 2,\ \ldots,\ N$. For source and drain, $v = S(D),\ \tau_v = \tau_{S(D)},\ \epsilon_v = \epsilon$, and $t_v = t$; while considering the dephasing probes, $v = k\ (k = 1,\ 2,\ \ldots,\ N),\ \tau_v = \eta,\ \epsilon_v = \epsilon_l$, and $t_v = t_d$.

Following D'Amato–Pastawski model [6] the effective transmission probability of an electron from source to drain including the partially phase breaking process is given by the following expression:

$$T_{eff} = T_{S,D} + \sum_{i,j=1}^{N} \boldsymbol{T}_{D,i} \boldsymbol{W}_{i,j}^{-1} \boldsymbol{T}_{j,S}. \tag{12}$$

The above expression has a significant physical implication. The first term is the coherent contribution to electron transmission, whereas the second term refers to the incoherent component of tunneling due to electrons suffering phase randomizing scattering at the fictitious dephasing reservoirs. $T_{i,j}$ is the transmission probability between any pair of reservoirs $i,\ j\ (i,\ j = S,\ D,\ 1,\ 2,\ \ldots,\ N)$ and it is expressed as follows:

$$T_{i,j} = \mathrm{Tr}[\boldsymbol{\Gamma}_{\boldsymbol{i}} \mathscr{G}^{\boldsymbol{r}} \boldsymbol{\Gamma}_{\boldsymbol{j}} \mathscr{G}^{\boldsymbol{a}}]. \tag{13}$$

Γ_is are the coupling matrices representing the coupling between the molecule and the leads and they are mathematically defined by the relation:

$$\boldsymbol{\Gamma_i} = i\left[\boldsymbol{\Sigma_i^r} - \boldsymbol{\Sigma_i^a}\right] \tag{14}$$

Here, $\boldsymbol{\Sigma_k^r}$ and $\boldsymbol{\Sigma_k^a}$ are the retarded and advanced self-energies associated with the kth lead, respectively.

In the second term of Eq. (12), $\boldsymbol{W}$ matrix is defined by the following relation:

$$W_{i,j} = [(1 - R_{i,i})\delta_{ij} - T_{i,j}(1 - \delta_{ij})], \tag{15}$$

where,

$$R_{i,i} = 1 - \sum_{j \neq i} T_{i,j}. \tag{16}$$

$R_{i,i}$ is the reflection probability of an electron from ith lead.

It is shown in literature by Datta [3,4] that the self-energy can be expressed as a linear combination of a real and an imaginary part in the form,

$$\boldsymbol{\Sigma_j^r} = \boldsymbol{\Lambda_j} - i\boldsymbol{\Delta_j}. \tag{17}$$

The real part of self-energy describes the shift of the energy levels and the imaginary part corresponds to the broadening of the levels. The finite imaginary part appears due to incorporation of the semi-infinite leads having continuous energy spectrum. Therefore, the coupling matrices can easily be obtained from the self-energy expression and is expressed as,

$$\boldsymbol{\Gamma_i} = -2\,\mathrm{Im}(\boldsymbol{\Sigma_i}). \tag{18}$$

Considering linear transport regime, at absolute zero temperature the linear conductance (g_{eff}) is obtained using two-terminal Landauer conductance formula,

$$g_{eff} = \frac{2e^2}{h} T_{eff}(E_F). \tag{19}$$

With the knowledge of the effective transmission probability we compute the current–voltage (I–V) characteristics by the standard formalism based on quantum scattering theory:

$$I(V) = \frac{2e}{h} \int_{-\infty}^{\infty} T_{eff}[f_S(E) - f_D(E)]dE. \tag{20}$$

Here, $f_{S(D)}(E) = \left[1 + e^{\frac{E-\mu_{S(D)}}{k_B T}}\right]^{-1}$ is the Fermi function corresponding to the source and drain. At absolute zero temperature the above equation boils down to the following expression:

$$I(V) = \frac{2e}{h} \int_{E_F - \frac{eV}{2}}^{E_F + \frac{eV}{2}} T_{eff} dE. \tag{21}$$

In our present work we use the above expression assuming that the potential drop takes place only at the boundary of the molecular system. This assumption is good enough for molecules of smaller size. Throughout our study we choose $c = e = h = 1$ for the sake of simplicity.

3. Numerical results and discussion

In this section we present the results obtained by numerical simulation considering a single benzene molecule sandwiched between source and drain. The orbital energies (ϵ) of the molecule are set to zero and the nearest-neighbor hopping matrix element (t) is fixed at 2.4 eV [17] for an aromatic ring structure of the benzene molecule. The other hopping parameters in the leads (t) and the dephasing probes (t_d) are fixed at 4 eV, while the site energies are chosen to be zero, i.e., $\epsilon_l = \epsilon_d = 0$. The dephasing strength, characterized by the parameter η, is fixed at 1 eV. Throughout our analysis the coupling strengths of the molecule to the source and drain, characterized by the parameters τ_S and τ_D, are set at 1 eV. The molecular coupling to the contacting leads is one of the most important factors which regulates the electronic transmission through a molecular wire and this phenomenon has been extensively studied in our previous works [22,23]. Accordingly, here we describe all the essential features of electron transport for a particular molecular coupling strength. The molecular transport properties are also highly sensitive on the molecule-to-lead interface geometry, and, in the present work we illustrate how they are influenced in the presence of electron dephasing. To reveal these facts first we discuss the behavior of transmittance–energy characteristics and then we describe the nature of current–voltage spectra for three different configurations (*ortho*, *meta* and *para*) of the benzene molecule.

Here, we establish all the results at absolute zero temperature and restrict ourselves within elastic dephasing so that no energy is exchanged between the transported electrons and the external fictitious reservoirs, only the phase informations get lost. This condition allows the incoherent electrons to generate a steady-state current through the sample.

3.1. Transmittance–energy characteristics

3.1.1. Molecule coupled symmetrically

In Fig. 2 we show the variation of transmission probability as a function of injecting electron energy for a benzene molecule, where the molecule is coupled symmetrically to the source and drain, i.e., the upper and

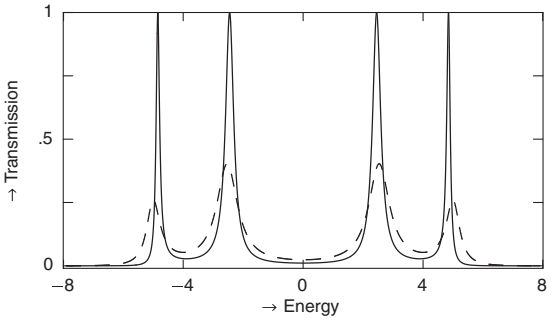

Fig. 2. Variation of transmission probability as a function of energy for a benzene molecule where the drain is connected at the *para* position with respect to the source. The solid and dashed curves correspond to the results in the absence and presence of dephasing, respectively.

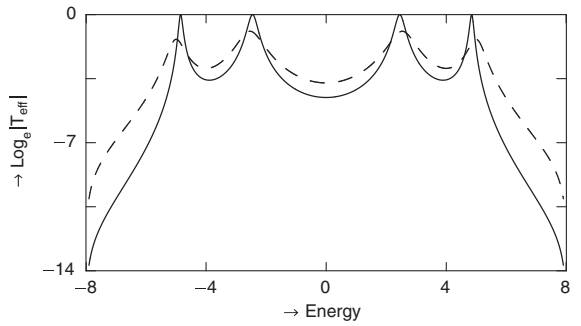

Fig. 3. The results of Fig. 2 are re-plotted in a logarithmic scale to clarify the effect of dephasing more clearly.

lower arms of the molecular ring have identical length. This is the so-called *para* configuration. The solid curve represents the variation of coherent transmission probability, while the dashed curve depicts the result in the presence of electron dephasing. It is observed that, in the absence of dephasing the transmission probability exhibits sharp resonant peaks (see solid line) for some specific energies, whereas it almost vanishes for all other energy values. At these resonances, the transmission probability T_{eff} goes to unity. All the resonant peaks are associated with the energy eigenvalues of the benzene molecule, and therefore, we can say the transmittance spectrum is a fingerprint of the electronic structure of the molecule. The situation becomes much interesting when the effect of dephasing is introduced. It shows that the magnitude of the resonant peaks gets suppressed enormously (dashed line) compared to the coherent transmission (solid line). This is due to the increased rate of scattering in the additional fictitious electron reservoirs. Additionally, we also notice that the widths of the resonant peaks become broadened. This broadening is caused by the dominance of phase randomizing effect over backscattering due to loss of phase coherence of interfering electrons in the presence of dephasing reservoirs. To judge the effect of dephasing more transparently, in Fig. 3 we re-plot the results of Fig. 2 in a logarithmic scale, where the solid and dashed lines represent the identical meaning as above. Since the transmission probability lies within the range 0–1, it

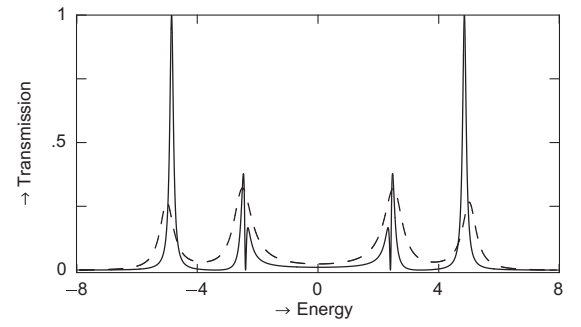

Fig. 4. Transmission probability vs. energy characteristics of a benzene molecule where the drain is connected at the *ortho* position with respect to the source. The solid and dashed lines represent the results in the absence and presence of dephasing, respectively.

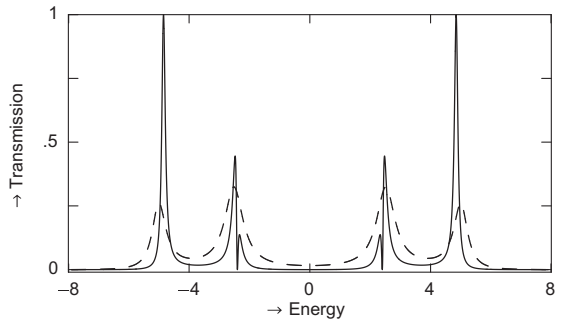

Fig. 5. Transmission probability vs. energy characteristics of a benzene molecule where the drain is coupled to the *meta* position with respect to the source. The solid and dashed curves correspond to the results in the absence and presence of dephasing, respectively.

becomes zero or negative in the logarithmic scale as shown in Fig. 3. It is observed that the variations in the transmission peaks between the two curves (solid and dashed) get suppressed, but the broadening effect in the presence of dephasing can be much clearly observed from the 'log' scale.

3.1.2. Molecule coupled asymmetrically

A significant change in the transmission spectrum is observed when the benzene molecule is coupled asymmetrically to the source and drain, i.e., the upper and lower arms of the molecular ring have unequal lengths. For the *ortho* configuration the results are given in Fig. 4, while in Fig. 5 the results are shown for the *meta* configuration. From the spectra (Figs. 4 and 5) we notice that in the absence of dephasing some resonant peaks do not reach to unity and their amplitudes are significantly reduced compared to the other resonant peaks. This is solely due to the effect of quantum interference between the electronic waves passing through the upper and lower arms of the molecular ring. Quite interestingly we observe that in these asymmetric molecular wires (*ortho* and *meta*) two anti-resonant states appear in the transmittance spectrum where transmission probability drops exactly to zero. These anti-resonant states are specific to the interferometric nature of the molecular system and their positions in the energy scale are independent of the molecule-to-lead coupling strength. A careful observation reveals that a

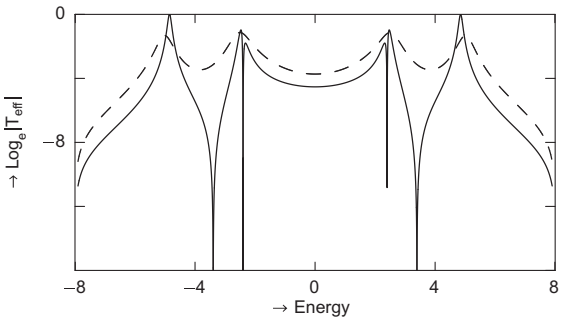

Fig. 6. The results of Fig. 4 are re-plotted in a 'log' scale.

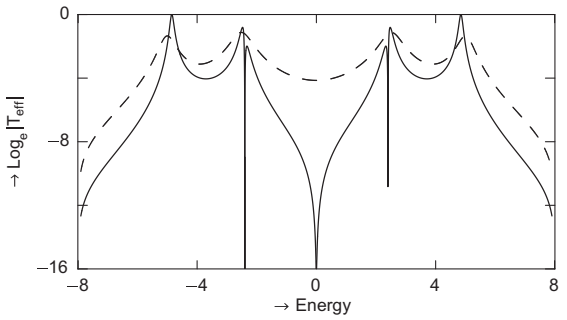

Fig. 7. The results of Fig. 5 are re-plotted in a 'log' scale.

sharp peak is followed by a sharp dip and vice versa across the anti-resonant energy which is quite analogous to a Fano-like line shape. All these anti-resonant states disappear as long as dephasing of electrons is taken into account those are clearly observed from the dashed lines of Figs. 4 and 5. Here also the magnitudes of the resonant peaks get decreased and they become broadened as we describe earlier in the *para* configuration.The results of Figs. 4 and 5 are re-drawn in Figs. 6 and 7, respectively, where the transmission probabilities are determined in the 'log' scale. From these spectra (Figs. 6 and 7) the characteristic features of anti-resonant states in the case of coherent transmission and the broadening of resonant peaks in the presence of electron dephasing are clearly noticed. Our results also predict that in the asymmetric molecular ring the positions of the anti-resonant states are strongly sensitive on the location of measuring electrodes. Broadening of transmission peaks in presence of dephasing is much pronounced in the case where the drain is connected at the *meta* position of the benzene molecule rather than the *ortho* position, and, it can be clearly observed from the Log_eT_{eff} vs. E plot instead of the transmittance–energy spectra.

3.2. Current–voltage characteristics

All the above features of electron transmission become much clear from our study of current-voltage (I–V) characteristics. The current through the molecular system is obtained by integrating the transmission function following Eq. (21). Here we fix the Fermi energy E_F at zero.

3.2.1. Molecule coupled symmetrically

In Fig. 8 we plot the variation of current as a function of applied bias voltage for a benzene molecule where the leads are connected symmetrically. The orange and green lines represent the currents in the absence and presence of electron dephasing. The current varies quite continuously with the applied bias voltage V. Depending on the molecular coupling to the side attached leads, the current shows continuous-like or step-like behavior [22]. Tuning the molecular coupling strength the current amplitude through the molecular wire can be regulated nicely for a fixed bias voltage. This provides an interesting behavior in designing molecular electronic devices. Both in the absence and presence of electron dephasing current shows almost identical variation though a significant change is observed in their conductance spectra. This is due to the fact that the dephasing broadens the transmission peaks, while it also suppresses the magnitude. These two effects nullify each other showing almost identical spectrum in the I–V characteristics.

3.2.2. Molecule coupled asymmetrically

The effect of dephasing becomes much prominent in the current–voltage characteristics when the molecule is coupled asymmetrically to the source and drain. For the *ortho* configuration, the currents are shown in Fig. 9, while in Fig. 10 the results are shown when the molecule is coupled to the leads in the *meta* configuration. Quite similar to the *para* configuration (Fig. 8), in these two cases (*ortho* and *meta* configurations) also the current varies almost continuously with the applied bias voltage V. In these asymmetric configurations, the current amplitude gets enhanced significantly when the phase breaking effect is considered (deep blue curve in Fig. 9 and light blue curve in Fig. 10) compared to the case where the molecule is free from any phase randomizing process (pink line in Fig. 9 and red line in Fig. 10). Such an enhancement in current amplitude takes place because of notable broadening of the transmission peaks due to reduced destructive interfer-

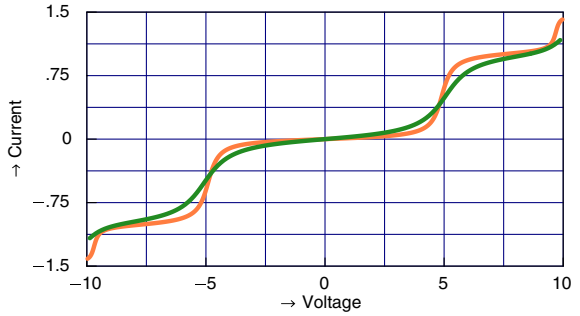

Fig. 8. I–V characteristics of a benzene molecule where the drain is connected at the *para* position with respect to the source. The orange and green curves correspond to the currents in the absence and presence of dephasing, respectively. (For interpretation of the references to color in this figure legend, the reader is referred to the web version of this article.)

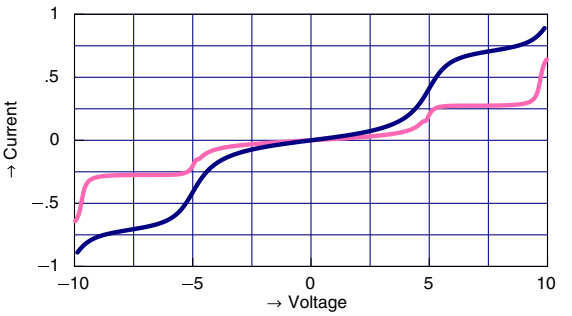

Fig. 9. I–V characteristics of a benzene molecule where the drain is connected at the *ortho* position with respect to the source. The pink and deep blue lines represent the currents in the absence and presence of dephasing, respectively. (For interpretation of the references to color in this figure legend, the reader is referred to the web version of this article.)

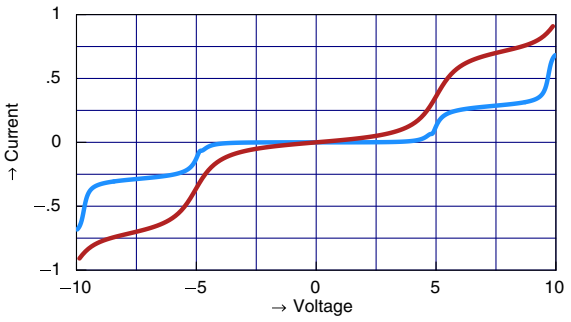

Fig. 10. *I–V* characteristics of a benzene molecule where the drain is connected at the *meta* position with respect to the source. The light blue and red lines correspond to the currents in the absence and presence of dephasing, respectively. (For interpretation of the references to color in this figure legend, the reader is referred to the web version of this article.)

ence for dominance of phase decoherence over the back-scattering effect.

4. Closing remarks

To summarize, in the present work we have examined electron transport phenomena through a single benzene molecule including the effect of phase breaking using a phenomenological model introduced by Büttiker. Experimentally the benzene molecule is usually coupled to noble metal electrodes (e.g., gold leads) through thiol linking groups. In our theoretical work, we present the entire system (source-molecule-drain) by a discrete lattice model within a simple one-electron, tight-binding framework. We have studied transmission–energy spectrum and current–voltage characteristics considering three different configurations of the system depending on the position of the drain contact (*ortho*, *meta* and *para* positions). We have observed that the sharp transmission peaks are broadened and their magnitude is also suppressed in the presence of dephasing due to loss of phase coherence and thus it provides an enhancement in the current amplitude. But the broadening effect and so as the increase in current amplitude is much pronounced in the case where the drain is connected asymmetrically to the molecule with respect to the source. Another significant feature is that the two anti-resonant states, observed in the transmittance spectrum of an asymmetrically connected benzene molecule, completely disappear in the presence of strong dephasing due to reduced destructive interference. Thus the effect of dephasing can provide a significant change in the current–voltage relation.

In the Büttiker probe model fictitious voltage probes are introduced into the coherent system. These virtual probes introduce additional resistance in the system by relaxing the momentum of the electrons by partially reflecting them, i.e., back-scattering. This model is appropriate for those molecular systems where the dominant scattering source does not conserve electron momentum, for example, electron–phonon scattering which is very important in molecular conductor in finite temperature. However, Büttiker model does not consider the effect of momentum relaxation. In experimental situations dephasing may also arise from electron–electron scattering which destroy phase but not momentum [27,29]. Datta model presents the flexibility of tuning phase and momentum independently of each other and we intend to study this phenomenological model in near future.

Recent experimental progresses have significantly inspired in model calculations and numerical simulations to study vibronic effects on electron transport in molecular junctions [30–33]. Most of the studies of vibronic effects in the resonant tunneling regime (for higher voltages) have illustrated that vibrational motion may affect the current–voltage spectra quite significantly. But, the point is that in the resonant tunneling region vibronic effect becomes significant only when the molecule is coupled to the measuring leads *weakly*. In a very recent work Benesch et al. [34] have studied vibronic effects on conductance in molecular junctions where a benzene ring is coupled *weakly* to two gold electrodes and shown that the vibronic motion affects current–voltage spectra. On the other hand, when the molecule is coupled *strongly* to the electrodes, the vibrational effects in resonant transport are almost negligible. This phenomenon has been clearly justified in the reference [35]. In the present work we have investigated all the essential features of electron transport in the limit of strong molecule-to-electrode coupling, and accordingly, we neglect the vibronic effect.

Throughout our work we have neglected the intra- and inter-site Coulomb interactions as well as the effect of the leads, which we wish to consider in our future studies. Another important assumption is the zero temperature approximation. Although the electron–phonon interaction becomes significant at non-zero temperature, but in our case, we have already considered the dephasing effect phenomenologically at every molecular sites, which takes into account the effect of dephasing of electrons without any exchange of energy between the electron and the external leads. Accordingly, we compute the current–voltage relation at absolute zero temperature. At finite non-zero temperature, the transmission peaks will broaden due to thermal broadening effect, but the basic features will not change significantly as long as the thermal energy (k_BT) is less than the average level spacing of the benzene molecule. Now-a-days various organic compounds and polymers (for example, Tris(8-hydroxyquinolino) aluminum (Alq_3) and 1,2,3,4,5-pentaphenylcyclopentadiene (PPCP)) are used as electroluminescent devices. Knowledge of electronic structure and current–voltage relation is important to elucidate the light emitting mechanism [36]. It may be interesting to see the effect of electron dephasing on this mechanism. Our presented results may be useful in understanding the effect of phase breaking processes on the basic two-terminal molecular transport phenomena.

References

[1] A. Nitzan, M.A. Ratner, Science 300 (2003) 1384.
[2] F. Chen, N.J. Tao, Acc. Chem. Res. 42 (2009) 429.
[3] S. Datta, Electronic Transport in Mesoscopic Systems, Cambridge University Press, Cambridge, 1995.
[4] S. Datta, Quantum Transport: Atom to Transistor, Cambridge University Press, Cambridge, 2005.
[5] R. Landauer, IBM J. Res. Dev. 1 (1957) 223.

[6] J.L. D'Amato, H.M. Pastawski, Phys. Rev. B 41 (1990) 7411.
[7] B.C. Stipe, M.A. Rezaei, W. Ho, Science 280 (1998) 1732.
[8] W. Wang, T. Lee, I. Kretzschmar, M.A. Reed, Nano Lett. 4 (2004) 643.
[9] M. Galperin, M.A. Ratner, A. Nitzan, J. Phys.: Condens. Matter 19 (2007) 103201.
[10] N. Sergueev, D. Roubtsov, H. Guo, Phys. Rev. Lett. 95 (2005) 146803.
[11] N. Sergueev, A.A. Demkov, H. Guo, Phys. Rev. B 75 (2007) 233418.
[12] M. Büttiker, Phys. Rev. B 33 (1986) 3020.
[13] M. Büttiker, IBM J. Res. Dev. 32 (1988) 63.
[14] A. Aviram, M. Ratner, Chem. Phys. Lett. 29 (1974) 277.
[15] M.D. Ventra, S.T. Pentelides, N.D. Lang, Appl. Phys. Lett. 76 (2000) 3448.
[16] M.D. Ventra, N.D. Lang, S.T. Pentelides, Chem. Phys. 281 (2002) 189.
[17] D.M. Cardamone, C.A. Stafford, S. Mazumdar, Nano Lett. 6 (2006) 2422.
[18] K. Tagami, L. Wang, M. Tsukada, Nano Lett. 4 (2004) 209.
[19] P. Orellana, F. Claro, Phys. Rev. Lett. 90 (2003) 178302.
[20] J.H. Ojeda, R.P.A. Lima, F. Domnguez-Adame, P.A. Orellana, J. Phys.: Condens. Matter 21 (2009) 285105.
[21] M. Araidai, M. Tsukada, Phys. Rev. B 81 (2010) 235114.
[22] S.K. Maiti, Phys. Lett. A 366 (2007) 114.
[23] P. Dutta, S.K. Maiti, S.N. Karmakar, Org. Electron. 11 (2010) 1120.
[24] M.A. Reed, C. Zhou, C.J. Muller, T.P. Burgin, J.M. Tour, Science 278 (1997) 252.
[25] X.-Q. Li, Y.J. Yan, Appl. Phys. Lett. 79 (2001) 2190.
[26] X.-Q. Li, Y.J. Yan, J. Chem. Phys. 115 (2001) 4169.
[27] R. Golizadeh-Mojarad, S. Datta, Phys. Rev. B 75 (2007) 081301(R).
[28] D. Nozaki, Y. Girard, K. Yoshizawa, J. Phys. Chem. C 112 (2008) 17408.
[29] J. Maassen, F. Zahid, H. Guo, Phys. Rev. B 80 (2009) 125423.
[30] A. Pecchia, A.D. Carlo, Nano Lett. 4 (2004) 2109.
[31] Y. Chen, M. Zwolak, M.D. Ventra, Nano Lett. 5 (2005) 813.
[32] J. Bonca, S.A. Trugman, Phys. Rev. Lett. 75 (1995) 2566.
[33] J. Koch, F. von Oppen, Phys. Rev. Lett. 94 (2005) 206804.
[34] C. Benesch, M. Cizek, J. Klimes, I. Kondov, M. Thoss, W. Domcke, J. Phys. Chem. C 112 (2008) 9880.
[35] C. Benesch, M. Cizek, M. Thoss, W. Domcke, Chem. Phys. Lett. 430 (2006) 355.
[36] K. Sugiyama, D. Yoshimura, T. Miyamae, T. Miyazaki, H. Ishii, Y. Ouchi, K. Seki, J. Appl. Phys. 83 (1998) 4928.

charge injection from the charge transport layer to the emitting layer. However, more systematic study about the relationship between the chemical structure of the phenylcarbazole based phosphine oxide host material and physical properties of the host material is required to develop better high triplet host materials for deep blue PHOLEDs.

In this work, the effect of the substitution position of the phosphine oxide on the physical properties of the host material and device performances of the deep blue PHOLED were investigated. The diphenylphosphine oxide was attached to the ortho, meta and para position of the phenyl group in the phenylcarbazole unit. It was demonstrated that the para substitution is better than ortho or meta substitution in terms of quantum efficiency. A high quantum efficiency of 20.4% was demonstrated from the deep blue PHOLED with the phenylcarbazole based host substituted at para position of the phenyl group.

2. Experimental

2.1. Materials and measurements

9H-carbazole, *n*-butyllithium, chlorodiphenylphosphine, *N*-bromosuccinimide, and 4-bromobenzene (Aldrich Chem. Co.) and hydrogen peroxide (Duksan Sci. Co.) were used without further purification. Tetrahydrofuran (THF) was distilled over sodium and calcium hydride. Detailed.

The ^{1}H and ^{13}C nuclear magnetic resonance (NMR) spectra were obtained using a Varian 200 (200 MHz) spectrometer. The photoluminescence (PL) spectra were recorded on a fluorescence spectrophotometer (HITACHI, F-7000) and the ultraviolet–visible (UV–vis) spectra were obtained using UV–vis spectrophotometer (Shimadzu, UV-2501PC). Samples were dissolved in THF at a concentration of 1.0×10^{-4} M. Hexane and methanol were also used as the solvents for the PL measurement to confirm solvatochromic effect. Low temperature PL spectra were obtained at 77 K under liquid nitrogen. The differential scanning calorimetry (DSC) measurements were carried out using a Mettler DSC 822 at a heating rate of 10 °C/min under nitrogen atmosphere. The mass spectrometry (MS) was performed using a JEOL, JMS-AX505WA spectrometer in FAB (fast atom bombardment) mode. Cyclic voltametry (CV) measurement was carried out in acetonitrile solution with tetrabutylammonium perchlorate at 0.1 M concentration. Organic materials were coated on indium tin oxide substrate and were immersed in electrolyte for analysis. Scan rate was 0.1 mV/s. Ferrocene was used as the reference material for the CV analysis. Elemental analysis of the materials was carried out using EA1110 (CE instrument). High performance liquid chromatography (HPLC) analysis of the synthesized materials was carried out using HPLC from Youngrin Instrument. A mixed eluent of acetonitrile:methanol (90:10) was used for the analysis.

2.2. Synthesis

Detailed synthesis of the 3-(diphenylphosphoryl)-9-(4-(diphenylphosphoryl)phenyl)-9-carbazole (PPO21) was described in previous work [10].

2.3. Synthesis of 9-(3-bromophenyl)-9H-carbazole (**3**)

A mixture of 9H-carbazole (4.0 g, 23.92 mmol), 1-bromo-3-iodobenzene (8.08 g, 28.70 mmol), Cu-powder (3.04 g, 47.84 mmol), potassium carbonate (13.20 g, 95.68 mmol) and dibenzo-18-crown-6 (0.63 g, 2.39 mmol) in dimethylformamide (DMF, 40 ml) was purged with argon and heated at reflux for 7 h. The mixture was quenched with H_2O and extracted with dichloromethane. The organic fractions were dried with magnesium sulfate, filtered, and the solvent was removed under reduced pressure. The residue was purified by column chromatography on silica gel using hexane to provided 5.67 g of title compound as white solid (m.p. 69–70 °C; 71% yield).

^{1}H NMR (200 MHz, $CDCl_3$): (ppm) 8.15–8.12 (d, J = 6.0 Hz, 1H), 7.74–7.68 (m, 2H), 7.58–7.41 (m, 7H), 7.34–7.30 (m, 2H).

2.4. Synthesis of 9-(2-bromophenyl)-9H-carbazole (**5**)

A mixture of 9H-carbazole (3.0 g, 17.94 mmol), 1-bromo-2-iodobenzene (10.15 g, 35.88 mmol), copper iodide (2.39 g, 12.55 mmol) and potassium carbonate (4.95 g, 35.88 mmol) in xylene (40 ml) was purged with argon and heated at reflux for 48 h. The mixture was quenched with H_2O and extracted with dichloromethane. The organic fractions were dried with magnesium sulfate, filtered, and the solvent was removed under reduced pressure. The residue was purified by column chromatography on silica gel using hexane to provide 2.5 g of title compound as white solid (m.p. 93–94 °C; 56% yield).

^{1}H NMR (200 MHz, $CDCl_3$): (ppm) 8.17–8.13 (d, J = 8.0 Hz, 1H), 7.90–7.68 (m, 1H), 7.57–7.29 (m, 8H), 7.08–7.02 (t, J = 6.0 Hz, 1H).

2.5. Synthesis of 3-bromo-9-(3-bromophenyl)-9H-carbazole

Compound **3** (2.0 g, 6.20 mmol) was dissolved in dimethylformamide (DMF, 20 ml) under argon atmosphere. The reaction vessel was immersed in a ice bath until the temperature was about −20 °C and then *n*-bromosuccinimide (NBS, 1.32 g, 7.44 mmol) in DMF (5 ml) was added dropwise slowly into and stirred for 12 h. The mixture was allowed to gradually warm to room temperature overnight and then quenched with H_2O followed by extraction with dichloromethane. The organic fractions were dried with magnesium sulfate, filtered, and the solvent was removed under reduced pressure. The residue was purified by column chromatography on silica gel using hexane to provided 1.8 g of title compound as white solid (m.p. 187 °C; 80% yield).

^{1}H NMR (200 MHz, $CDCl_3$): (ppm) 8.45 (s, 1H), 8.25–8.08 (t, J = 17.0 Hz, 3H), 7.86–7.66 (m, 3H), 7.55–7.31 (m, 5H).

2.6. Synthesis of 3-(diphenylphosphoryl)-9-(3-(diphenylphosphoryl)phenyl)-9H-carbazole (PPO25)

3-Bromo-9-(3-bromophenyl)-9H-carbazole (4.73 g, 11.79 mmol) was dissolved in tetrahydrofuran (THF, 50 ml) under argon atmosphere. The reaction vessel was immersed in a dry ice/acetone bath until the temperature

was about −78 °C. To this solution 11.32 ml (28.30 mmol) of 2.5 M *n*-BuLi solution in hexane was added dropwise slowly and stirred for 3 h. Chlorodiphenylphosphine (5.22 ml, 28.30 mmol) was then added to the solution and stirred for 3 h in a dry ice/acetone bath. The mixture was allowed to gradually warm to room temperature overnight and then quenched with methanol, extracted with dichloromethane. The organic fractions were dried with magnesium sulfate, filtered, and the solvent was removed under reduced pressure. The residue was purified by column chromatography on silica gel using hexane/dichloromethane (10:1) to provided 2.2 g of title compound as white solid (32% yield).

The white solid was dissolved in dichloromethane (40 ml) and hydrogen peroxide (8 ml) was stirred overnight at room temperature. The organic layer was separated and washed with dichloromethane and water. The extract was evaporated to dryness affording a white solid, which was further purified by column chromatography to yield 2.2 g of chemically pure PPO25 (purity 99.0% by HPLC).

Tg: 110 °C, ^{1}H NMR (200 MHz, $CDCl_3$): (ppm) 8.55–8.49 (d, J = 12.0 Hz, 1H), 8.08–8.05 (d, J = 6.0 Hz, 1H), 7.88–7.69 (m, 12H), 7.61–7.50 (m, 14H), 7.37–7.30 (t, J = 7.0 Hz, 3H) ^{13}C NMR (200 MHz, $CDCl_3$): (ppm) 142.2, 140.8, 137.5, 137.1, 136.3, 134.3, 134.0, 132.6, 132.0, 131.4, 130.8, 130.9, 129.2, 129.0, 128.9, 128.2, 128.0, 127.9, 127.4, 126.1, 124.9, 123.9, 123.6, 123.0, 121.9, 121.4, 120.8, 120.2, 110.3, 109.2 MS (FAB) m/z 644 [$(M + H)^+$] Anal. Calcd. for $C_{42}H_{31}NO_2P_2$: C, 78.37; H, 4.85; N, 2.18; O, 4.97. Found: C, 78.12; H, 4.81; N, 2.00; O, 5.04.

2.7. Synthesis of 3-bromo-9-(2-bromophenyl)-9H-carbazole

Compound **5** (5.0 g, 15.51 mmol) was dissolved in dimethylformamide (DMF, 30 ml) under argon atmosphere. The reaction vessel was immersed in a ice bath until the temperature was about −20 °C and then *n*-bromosuccinimide (NBS, 3.0 g, 17.07 mmol) in DMF (15 ml) was added dropwise slowly into and stirred for 12 h. The mixture was allowed to gradually warm to room temperature overnight and then quenched with H_2O followed by extraction with dichloromethane. The organic fractions were dried with magnesium sulfate, filtered, and the solvent was removed under reduced pressure. The residue was purified by column chromatography on silica gel using hexane to provided 5.54 g of title compound as white solid (m.p. 190–194 °C; 89% yield).

^{1}H NMR (200 MHz, $CDCl_3$): (ppm) 8.26–8.22 (d, J = 8.0 Hz, 1H), 8.12–8.08 (d, J = 8.0 Hz, 1H), 7.88–7.68 (m, 2H), 7.55–7.30 (m, 5H), 7.07–7.01 (t, J = 6.0 Hz, 1H), 6.96–6.99 (t, J = 3 Hz, 1H).

2.8. Synthesis of 3-(diphenylphosphoryl)-9-(2-(diphenylphosphoryl)phenyl)-9H-carbazole (PPO26)

3-Bromo-9-(2-bromophenyl)-9H-carbazole (5.20 g, 12.96 mmol) was dissolved in tetrahydrofuran (THF, 50 ml) under argon atmosphere. The reaction vessel was immersed in a dry ice/acetone bath until the temperature was about −78 °C. To this solution 15.55 ml (38.89 mmol) of 2.5 M *n*-BuLi solution in hexane was added dropwise slowly and stirred for 3 h. Chlorodiphenylphosphine (7.18 ml, 38.89 mmol) was then added to the solution and stirred for 3 h in a dry ice/acetone bath. The mixture was allowed to gradually warm to room temperature overnight and then quenched with methanol followed by extraction with dichloromethane. The organic fractions were dried with magnesium sulfate, filtered, and the solvent was removed under reduced pressure. The residue was purified by column chromatography on silica gel using hexane/dichloromethane (10:1) to provided 2.6 g of title compound as white solid (33% yield).

The white solid was dissolved in dichloromethane (40 ml) and hydrogen peroxide (8 ml) was stirred overnight at room temperature. The organic layer was separated and washed with dichloromethane and water. The extract was evaporated to dryness affording a white solid, which was further purified by column chromatography to yield 2.8 g of chemically pure PPO26 (purity 99.1% by HPLC).

Tg: 110 °C, ^{1}H NMR (200 MHz, $CDCl_3$): (ppm) 8.33–8.27 (d, J = 12.0 Hz, 1H), 7.96–7.64 (m, 7H), 7.58–7.43 (m, 6H), 7.39–7.29 (m, 8H), 7.18–7.09 (t, J = 9.0 Hz, 3H), 7.01–6.94 (m, 6H) ^{13}C NMR (200 MHz, $CDCl_3$): (ppm) 143.7, 142.6, 139.6, 136.4, 135.6, 134.6, 133.6, 132.9, 132.5, 132.1, 131.8, 130.4, 129.9, 129.2, 128.9, 128.1, 127.9, 127.5, 126.8, 123.0, 122.7, 121.2, 120.8, 120.5, 120.2, 119.6, 111.8, 110.8 MS (FAB) m/z 644 [$(M + H)^+$] Anal. Calcd. for $C_{42}H_{31}NO_2P_2$: C, 78.37; H, 4.85; N, 2.18; O, 4.97. Found: C, 78.21: H, 4.84; N, 2.18; O, 4.99.

2.9. Device fabrication

A basic device configuration of indium tin oxide(ITO, 150 nm)/*N*,*N*′-diphenyl-*N*,*N*′-bis-[4-(phenyl-m-tolyl-amino)-phenyl]-biphenyl-4,4′-diamine (DNTPD, 60 nm)/*N*,*N*′-di(1-naphthyl)-*N*,*N*′-diphenylbenzidine (NPB, 5 nm)/*N*,*N*′-dicarbazolyl-3,5-benzene (mCP, 10 nm)/PPO21 or PPO25 or PPO26: tris((3,5-difluoro-4-cyanophenyl)pyridine) iridium (FCNIr) (30 nm, 15%)/diphenylphosphine oxide-4-(triphenylsilyl)phenyl (TSPO1, 15 nm)/LiF (1 nm)/Al (200 nm) was used for the device fabrication. Hole only and electron only devices had device configurations of ITO/DNTPD (60 nm)/NPB (5 nm)/mCP (10 nm)/host (30 nm)/Au and ITO/TSPO1 (10 nm)/host (30 nm)/TSPO1 (25 nm)/LiF (1 nm)/Al (100 nm), respectively. The evaporation rate of the organic materials was 0.1 nm/s and the deposition rate of the dopant was controlled according to the doping concentration of the dopant. Al was deposited at a deposition rate of 0.5 nm/s, while LiF deposition rate was 0.01 nm/s. The devices were encapsulated with a CaO getter and a glass rid after the device fabrication. The device performances of the blue PHOLEDs were measured with Keithley 2400 source measurement unit and CS1000 spectroradiometer.

3. Results and discussion

Three host materials based on a phenylcarbazole core and a diphenylphosphine oxide substituent were synthesized. Three host materials had two diphenylphosphine

oxide groups. One diphenylphosphine oxide group was attached to the phenyl unit of the phenylcarbazole, while the other diphenylphosphine oxide group was attached to the 3 position of the carbazole unit. The position of the diphenylphosphine oxide group attached to the phenyl unit was changed to study the effect of substitution position on the physical properties of the host material. All materials were synthesized by the reaction of the chlorodiphenylphosphine with brominated *N*-phenylcarbazole moiety followed by oxidation with hydrogen peroxide. Synthetic scheme of all materials is shown in Scheme 1. All materials were purified by column chromatography and a high purity level over 99% was obtained in all materials.

The energy level of the host material is critical to device performances of the PHOLED and is closely related with the molecular orbital distribution. Therefore, density functional theory (DFT) calculation of the host materials was carried out using a suite of Gaussian 03 program. The nonlocal density functional of Becke's 3-parameters employing Lee–Yang-Parr functional (B3LYP) with 6–31G* basis sets was used for the calculation [25]. Fig. 1 shows the HOMO and the lowest unoccupied molecular orbital (LUMO) orbital distribution of host materials synthesized in this work. The HOMO was mostly distributed over the carbazole unit of the phenylcarbazole core, while the LUMO was dispersed over the phenyl unit of the phenylcarbazole core and diphenylphosphine oxide in all host materials [15]. The carbazole unit is an electron donating group and the HOMO was localized in the carbazole group. The diphenylphosphine oxide is a strong electron withdrawing group and the LUMO was dispersed over the phenyl and diphenylphosphine oxide groups. There was little difference of the molecular orbital distribution between the three materials. The calculated HOMO levels of the PPO21, PPO25 and PPO26 were 5.56, 5.66 and 5.74 eV, while the LUMO levels were 1.12, 1.17 and 1.07 eV. Although the molecular orbital distribution of the three host materials was similar, the HOMO level was increased in the PPO26 with the diphenylphosphine oxide at ortho position. This indicates the

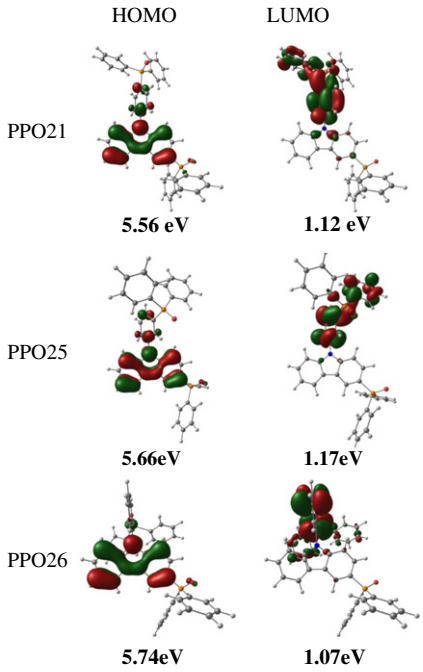

Fig. 1. Molecular simulation results of PPO21, PPO25 and PPO26. HOMO and LUMO orbital distribution is shown in this figure.

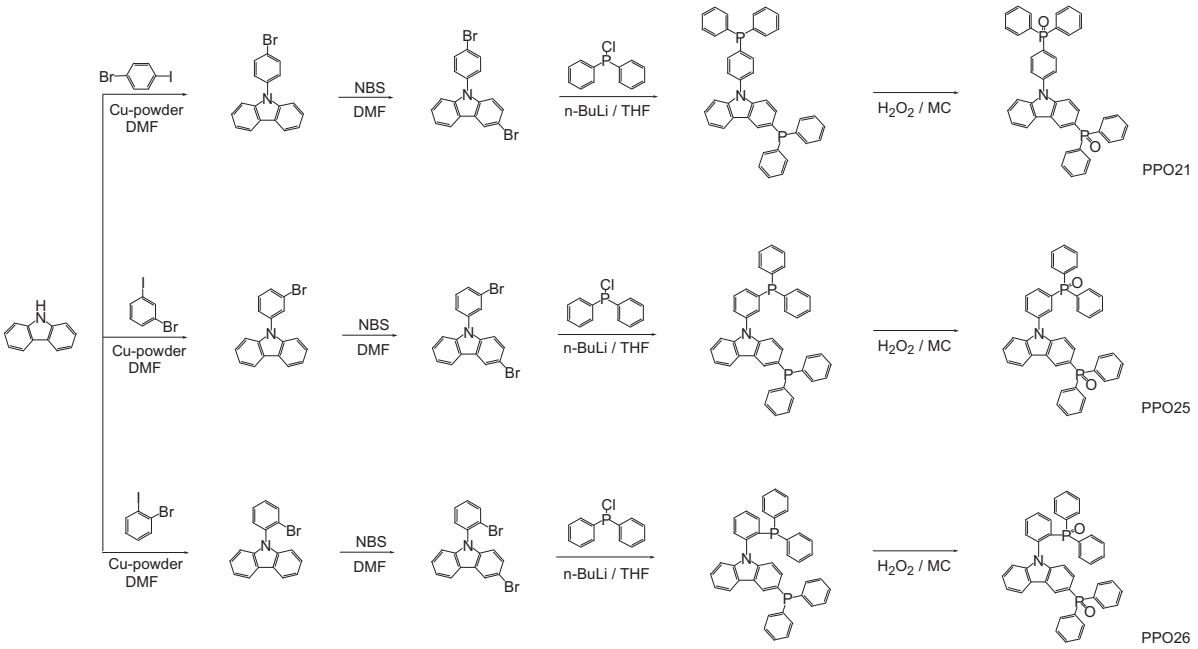

Scheme 1. Synthetic scheme of PPO21, PPO25 and PPO26.

reduction of the electron density in the carbazole group of the PPO26.

Photophysical properties of the host materials were analyzed with ultraviolet–visible (UV–vis) and photoluminescence (PL) measurements. UV–vis and PL spectra of the host materials are shown in Fig. 2. UV–vis absorption of the three host materials was similar and there was little shift of the UV–vis absorption peak. The main absorption of the three host materials is $\pi-\pi$ transition of the phenylcarbazole core at 338 nm, resulting in similar absorption spectra. However, the PL spectra were different depending on the substitution position of the diphenylphosphine oxide. In particular, the PL spectrum of the PPO26 with the diphenylphosphine oxide at ortho position of the phenyl group was red-shifted and broadened compared with that of other host materials. The peak maximum of the PPO26 was 375 nm compared with 361 nm of the PPO25. The electron is partially transferred from the carbazole unit to the phosphine oxide unit, resulting in intramolecular charge transfer complex formation. The bandgap is reduced by the charge transfer complex formation, and the PL emission is red-shifted and broadened.

Solid PL spectra of the evaporated host materials are shown in Fig. 3. The solid PL spectra of the host materials were red-shifted and the full width at half maximum was also increased due to intermolecular interaction in solid state. In particular, the PPO26 with a phosphine oxide at ortho position showed two PL emission peaks at 367 and 450 nm. The PL emission peak at 367 nm is assigned to the PL emission of the phenylcarbazole core, while the PL emission at 450 nm is assigned to the emission of the intramolecular charge transfer complex. The intramolecular charge transfer emission was strong in the solid state by the solvent effect of polar PPO26 molecules. The UV–vis absorption spectrum of the dopant material is also shown in Fig. 3. The PL emission of host materials was well overlapped with the UV–vis absorption of the FCNIr dopant, indicating efficient energy transfer from the host to dopant in solid state.

The intramolecular charge complex formation was confirmed from solution PL of host material using various solvents with different polarity. It is well known that strong solvatochromic effect is observed in the organic material

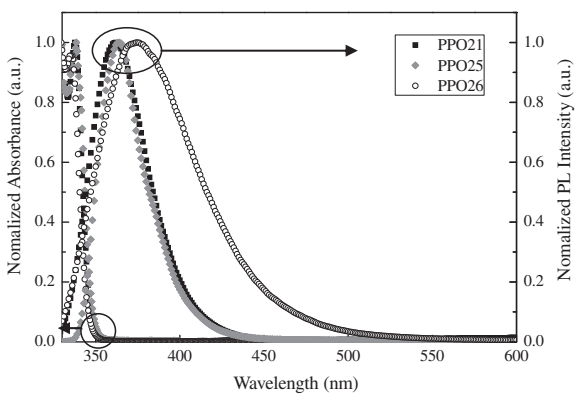

Fig. 2. UV–vis and solution PL spectra of PPO21, PPO25 and PPO26.

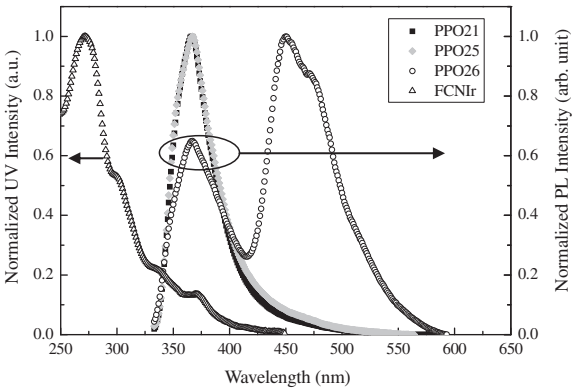

Fig. 3. Solid PL spectra of PPO21, PPO25 and PPO26. UV–vis spectrum of the FCNIr dopant was also added.

with charge transfer complex formation [26]. Fig. 4 shows the solution PL spectra of PPO25 and PPO26 at different solvents. Hexane, THF and methanol (MeOH) were used as the solvents. In the case of PPO25 with little intramolecular charge transfer complex formation, the PL emission was shifted only by 3–5 nm in highly polar MeOH solvent. However, the PL emission of PPO26 was red-shifted by more than 40 nm in highly polar solvent, proving the intramolecular charge transfer complex formation. Therefore, the solid PL emission of the PPO26 at long wavelength is originated from intramolecular charge transfer complex formation. The PPO26 is surrounded by higly polar PPO26 molecule and red-shifted PL emission of PPO26 by intramolecular charge transfer complex formation is observed.

The HOMO levels of three host materials were measured from the oxidation potential of the cyclic voltametry and the bandgap from UV–vis spectra. Energy levels of the host materials are summarized in Table 1. There was little difference of the HOMO and LUMO levels between the host materials. The HOMO was dispersed over the phenylcarbazole core in all host materials and similar HOMO levels were obtained. The LUMO was also distributed over the phenyl group substituted with diphenylphosphine oxide in all materials, resulting in similar LUMO levels. This can be further understood by analyzing the HOMO and LUMO distribution of 3-(diphenylphosphoryl)-9-phenyl-9H-carbazole (PPO1) without the diphenylphosphine oxide unit attached to the phenyl unit of the 9-phenylcarbazole [11]. The HOMO (6.16 eV) and LUMO (2.60 eV) of the PPO1 were localized in the carbazole unit with little dispersion over the phenyl unit. This indicates that the HOMO and LUMO of PPO1 are not greatly affected by substitution of electron withdrawing or donating moiety to the phenyl unit (less than 0.1 eV). Therefore, the substitution of the diphenylphosphine oxide group to the phenyl unit did not significantly change the HOMO and LUMO levels of host materials. In our previous work, the substitution of the diphenylphosphine oxide at the carbazole unit change the energy level by about 0.3 eV [11]. Therefore, the substitution of the diphenylphosphine oxide at the phenyl unit showed less significant effect on the energy level than the substitution of the diphenylphosphine oxide at the carbazole unit. Although the calculated HOMO level from

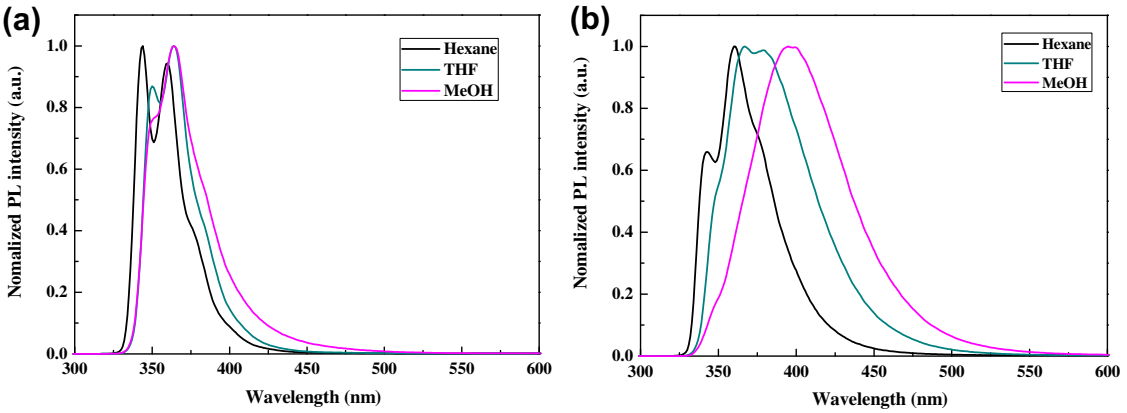

Fig. 4. Solution PL spectra of PPO25 (a) and PPO26 and (b) according to the polarity of solvent.

Table 1
Physical properties of PPO21, PPO25 and PPO26.

	Optical analysis				Electrical analysis		
	UV absorption (nm)	PL solution (nm)	PL solid (nm)	HOMO (eV)	LUMO (eV)	Bandgap (eV)	E_T (eV)
PPO21	337	362	366	6.25	2.68	3.57	3.01
PPO25	338	364	367	6.25	2.70	3.55	2.99
PPO26	335	375	367 450	6.25	2.67	3.58	3.01

molecular simulation was shifted in the three host materials, experimental HOMO levels were the same in the three organic materials.

The triplet energy of the host materials was measured from low temperature PL emission peak and the triplet energy was 2.99–3.01 eV. All host materials showed a high triplet energy about 3.00 eV irrespective of the substitution position of the diphenylphosphine oxide. The triplet energy of the phenylcarbazole core was 3.01 eV and the diphenylphosphine oxide did not change the triplet energy of the phenylcarbazole core. As reported earlier, the diphenylphosphine oxide unit does not extend the conjugation of the core structure and did not reduce the triplet energy of the core [8]. Therefore, all host materials synthesized in this work can be effective as host materials for deep blue phosphorescent device.

Deep blue PHOLEDs were fabricated using three host materials doped with deep blue emitting FCNIr dopant. Fig. 5 shows the current density–voltage–luminance curves of the deep blue PHOLEDs doped with FCNIr at a doping concentration of 20%. The current density was high in the PPO26 with the diphenylphosphine oxide at ortho position, while it was low in the PPO21 with the diphenylphosphine oxide at para position. The current density generally depends on the hole and electron density in the device. Therefore, hole and electron current density of three host materials was compared.

Current density–voltage curves of hole only and electron only devices of three host materials are shown in Fig. 6. The PPO26 showed the highest hole current density and lowest electron current density. The hole and electron current density depends on the energy barrier for charge

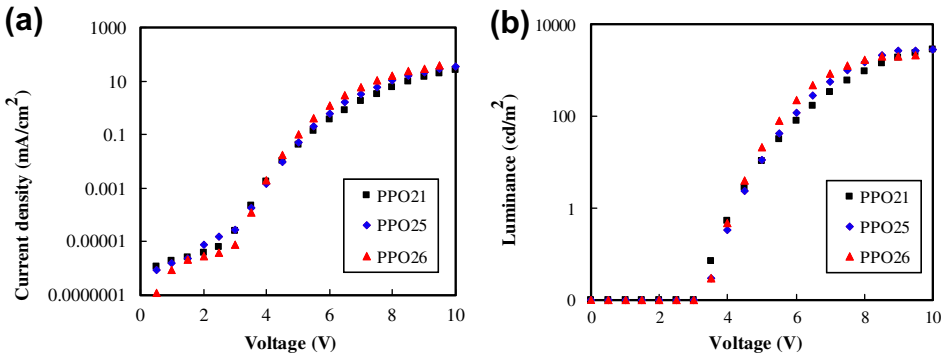

Fig. 5. Current density–voltage (a) and luminance–voltage and (b) curves of the deep blue PHOLEDs with the PPO21, PPO25 and PPO26.

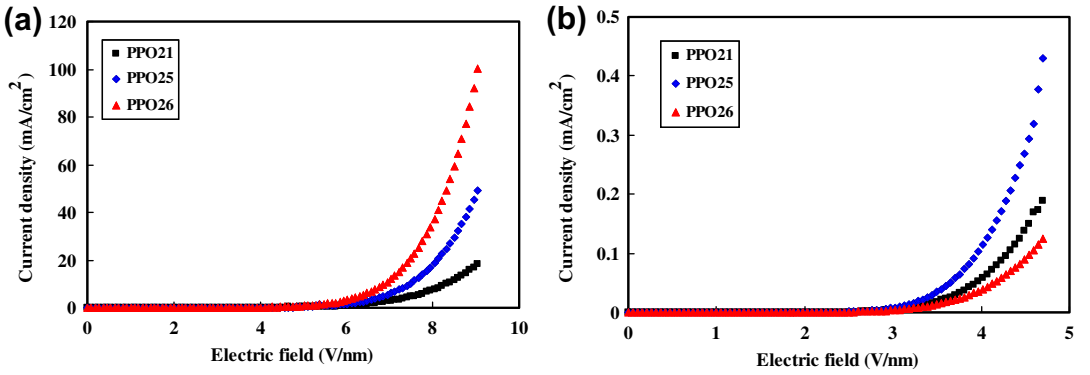

Fig. 6. Current density–electric field curves of the hole only (a) and electron only and (b) devices with PPO21, PPO25 and PPO26.

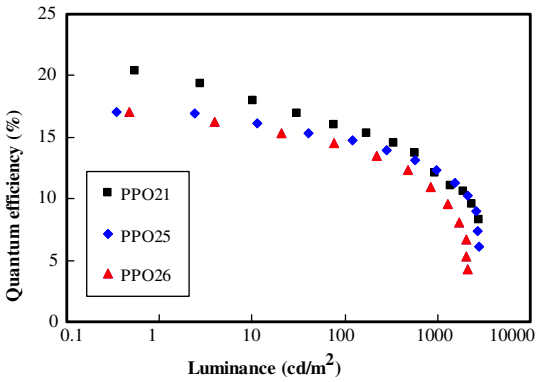

Fig. 7. Quantum efficiency–luminance curves of the deep blue PHOLEDs with PPO21, PPO25 and PPO26 hosts.

injection and charge transport properties. Considering the HOMO level for hole injection, there should be no difference of the hole current density. Therefore, the increased hole current density of the PPO26 is due to improved hole transport properties of the PPO26. The origin for the improved hole transport properties of the PPO26 can be found in the intramolecular charge transfer complex formation in the PPO26. The carbazole unit donates electrons to the partially positive P atom in the phosphine oxide unit. This can give rise to weak p type doping effect in the carbazole unit, enhancing the hole transport properties of the PPO26. Similar increase of the hole current density by the weak p-type doping effect was reported in other work [27]. On the contrary, the electron donating effect of the carbazole to the P atom in the phosphine oxide has negative effect on the electron transport properties, leading to the low electron current density. The high hole and electron current density of the PPO25 compared with PPO21 may be due to small molecular size of the PPO25 for good hole and electron hopping. The HOMO and LUMO of the host materials were localized in the molecular structure and large molecule size hinders the charge transport through hopping.

Considering the hole and electron current density of the device, the high current density of the PPO26 device is due to high hole current density [28]. Both hole and electron current density of the PPO21 was lower than that of the PPO25, leading to low current density in the PPO21 device. The luminance followed the same relationship as the current density.

The quantum efficiency–luminance curves of the deep blue PHOLEDs are shown in Fig. 7. The PPO21 showed the highest maximum quantum efficiency of 20.4%, while the PPO25 and PPO26 showed the same maximum quantum efficiency of 17.1%. The maximum quantum efficiency of the PPO21 device is one of the best quantum efficiency value reported in the literature. Comparing the quantum efficiency at 1000 cd/m^2, the PPO21 and PPO25 showed better quantum efficiency than PPO26. The quantum efficiency is generally affected by the charge balance in the emitting layer. As shown in the hole only and electron only device data, the PPO26 showed the highest hole current density and lowest electron current density. Therefore, the charge balance is worse than other host materials, which decreased the quantum efficiency of the PPO26 device. PPO25 was better than PPO21 in terms of efficiency roll-off. Balanced charge injection and balanced hole/electron density at low and high voltage improved the quantum efficiency at high luminance. Device data of the host materials are summarized in Table 2.

Table 2
Device performances of PPO21, PPO25 and PPO26 blue devices.

	Turn on voltage (V)	Driving voltage (V)[a]	Maximum quantum efficiency (%)	Quantum efficiency (%)[a]	Maximum power efficiency (lm/W)	Power efficiency (lm/W)[a]	Color coordinate[a]
PPO21	3.5	8.2	20.4 ± 1.7	11.9 ± 1.1	26.1 ± 2.4	6.6 ± 0.9	(0.14, 0.19)
PPO25	3.5	7.6	17.1 ± 1.3	12.3 ± 1.4	21.2 ± 1.9	7.3 ± 1.0	(0.15, 0.19)
PPO26	3.5	7.2	17.1 ± 1.2	10.4 ± 1.3	20.6 ± 2.1	6.4 ± 0.8	(0.15, 0.18)

[a] Data were measured at 1000 cd/m^2.

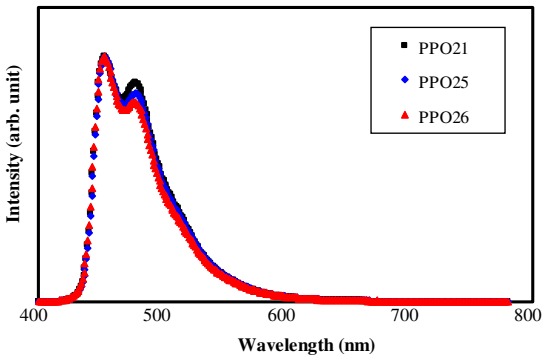

Fig. 8. Electroluminescence spectra of the deep blue PHOLEDs with the PPO21, PPO25 and PPO26 hosts.

Electroluminescence (EL) spectra of the deep blue PHOLEDs are shown in Fig. 8. Three blue PHOLEDs showed similar EL spectra with a peak maximum at 454 nm. The color coordinate of the deep blue PHOLEDs was (0.14, 0.18) in all host materials. Therefore, high efficiency deep blue PHOLEDs with a *y* color coordinate less than 0.20 could be developed using the phenylcarbazole based phosphine oxide compounds.

4. Conclusions

The photophysical properties and device performances of phenylcarbazole based phosphine oxide host materials were correlated with the substitution position of the phosphine oxide. The substitution at ortho position of the phenyl group induced an intramolecular charge transfer complex formation, while meta or para substitution did not significantly change the physical properties of the core structure. The ortho substitution enhanced the current density through intramolecular charge transfer, while the meta and para substitution enhanced the quantum efficiency of the deep blue PHOLEDs. A high quantum efficiency of 20.4% could be achieved using the high triplet energy host materials in deep blue PHOLEDs.

References

[1] M.A. Baldo, D.F. O'Brien, T. You, A. Shoustikov, S. Sibley, M.E. Thompson, S.R. Forrest, Nature 395 (1998) 151.
[2] R.J. Holmes, S.R. Forrest, Y.-J. Tung, R.C. Kwong, J.J. Brown, S. Garon, M.E. Thompson, Appl. Phys. Lett. 82 (2003) 2422.
[3] K.S. Yook, S.O. Jeon, C.W. Joo, J.Y. Lee, Org. Electron. 10 (2009) 170.
[4] .R.J. Holmes, B.W. D'Andrade, S.R. Forrest, X. Ren, J. Li, M.E. Thompson, Appl. Phys. Lett. 83 (2003) 3818.
[5] X. Ren, J. Li, R.J. Holmes, P.I. Djurovich, S.R. Forrest, M.E. Thompson, Chem. Mater. 16 (2004) 4743.
[6] M.H. Tsai, H.W. Lin, H.C. Su, T.H. Ke, C.C. Wu, F.C. Fang, Y.L. Liao, K.T. Wong, C.I. Wu, Adv. Mater. 18 (2006) 1216.
[7] M.F. Wu, S.J. Yeh, C.T. Chen, H. Murayama, T. Tsuboi, W. Li, I. Chao, S. Liu, J.K. Wang, Adv. Funct. Mater. 17 (2007) 1887.
[8] A.B. Padmaperuma, L.S. Sapochak, P.E. Burrows, Chem. Mater. 18 (2006) 2389.
[9] S.O. Jeon, K.S. Yook, C.W. Joo, J.Y. Lee, Appl. Phys. Lett. 94 (2009) 013301.
[10] S.O. Jeon, K.S. Yook, C.W. Joo, J.Y. Lee, Adv. Mater. 22 (2010) 1872.
[11] S.O. Jeon, K.S. Yook, C.W. Joo, J.Y. Lee, Adv. Funct. Mater. 19 (2009) 3644.
[12] P.A. Vecchi, A.B. Padmaperuma, H. Qiao, L.S. Sapochak, P.E. Burrows, Org. Lett. 8 (2006) 4211.
[13] N. Chopra, J.S. Swensen, E. Polikarpov, L. Cosimbescu, F. So, A.B. Padmaperuma, Appl. Phys. Lett. 97 (2010) 033304.
[14] F.-M. Hsu, C.-H. Chien, P.-I. Shih, C.-F. Shu, Chem. Mater. 21 (2009) 1017.
[15] L.S. Sapochak, A.B. Padmaperuma, X. Cai, J.L. Male, P.E. Burrows, J. Phys. Chem. C 112 (2008) 7989.
[16] X. Cai, A.B. Padmaperuma, L.S. Sapochak, P.A. Vecchi, P.E. Burrows, Appl. Phys. Lett. 92 (2008) 083308.
[17] L.S. Sapochak, A.B. Padmaperuma, P.A. Vecchi, X. Cai, P.E. Burrows, Proc. SPIE 6655 (2007) 665506.
[18] D. Yu, Y. Zhao, H. Xu, C. Han, D. Ma, Z. Peng, S. Gao, P. Yan, Chem. Eur. J. 17 (2011) 2592.
[19] C. Han, G. Xie, H. Xu, Z. Zhang, D. Yu, Y. Zhao, P. Yan, Z. Deng, Q. Li, S. Liu, Chem. Eur. J. 17 (2011) 445.
[20] J. Ding, Q. Wang, L. Zhao, D. Ma, L. Wang, X. Jing, F. Wang, J. Mater. Chem. 20 (2010) 8126.
[21] S. Tokito, T. Iijima, Y. Suzuki, H. Kita, T. Tsuzuki, F. Sato, Appl. Phys. Lett. 83 (2003) 569.
[22] . S.-J. Su, H. Sasabe, T. Takeda, J. Kido, Chem. Mater. 20 (2008) 1691.
[23] H. Fukagawa, K. Watanabe, T. Tsuzuki, S. Tokito, Appl. Phys. Lett. 93 (2008) 133312.
[24] W. Li, J. Qiao, L. Duan, L. Wang, Y. Qiu, Tetrahedron 63 (2007) 10161.
[25] M.J. Frisch, G.W. Trucks, H.B. Schlegel, G.E. Scuseria, M.A. Robb, J.R. Cheeseman, J.A. Montgomery, T. Vreven, Jr., K.N. Kudin, J.C. Burant, J.M. Millam, S.S. Iyengar, J. Tomasi, V. Barone, B. Mennucci, M. Cossi, G. Scalmani, N. Rega, G.A. Petersson, H. Nakatsuji, M. Hada, M. Ehara, K. Toyota, R. Fukuda, J. Hasegawa, M. Ishida, T. Nakajima, Y. Honda, O. Kitao, H. Nakai, M. Klene, X. Li, J.E. Knox, H.P. Hratchian, J.B. Cross, C. Adamo, J. Jaramillo, R. Gomperts, R.E. Stratmann, O. Yazyev, A.J. Austin, R. Cammi, C. Pomelli, J.W. Ochterski, P.Y. Ayala, K. Morokuma, G.A. Voth, P. Salvador, J.J. Dannenberg, V.G. Zakrzewski, S. Dapprich, A.D. Daniels, M.C. Strain, O. Farkas, D.K. Malick, A.D. Rabuck, K. Raghavachari, J.B. Foresman, J.V. Ortiz, Q. Cui, A.G. Baboul, S. Clifford, J. Cioslowski, B.B. Stefanov, G. Liu, A. Liashenko, P. Piskorz, I. Komaromi, R.L. Martin, D.J. Fox, T. Keith, M.A. Al-Laham, C.Y. Peng, A. Nanayakkara, M. Challacombe, P.M.W. Gill, B. Johnson, W. Chen, M.W. Wong, C. Gonzalez, J.A. Pople, Gaussian 03, Revision B05, Gaussian, Inc., Pittsburgh, PA 2003.
[26] A. Weller, Pure Appl. Chem. 16 (1968) 115.
[27] J.Y. Lee, J.H. Kwon, Appl. Phys. Lett. 86 (2005) 063514.
[28] K.S. Yook, S.O. Jeon, C.W. Joo, J.Y. Lee, J. Ind. Eng. Chem. 15 (2009) 907.

tens of volts and poor subthreshold slopes on the order of several volts/decade, both of which depend on the dielectric capacitance. Such characteristics would render these devices unusable in practical O-CMOS circuits.

Gundlach et al. [6] discuss the large threshold voltage of PTCDI devices. They note that although a relatively small threshold voltage hysteresis of only a few volts occurs between successive off–on and on–off sweeps, which they refer to as the reversible threshold voltage shift (TVS), a very large, irreversible (on the timescale of the measurement) threshold voltage shift of several 10 s of volts occurs when the devices are first biased in the on state (positive V_{gs}). The large initial shift most likely indicates a large density of deep electron traps in either the bulk or at the semiconductor/dielectric interface that are populated when the device is initially operated. As will be discussed later, great care must be taken when calculating carrier mobilities from such initial sweeps, as the threshold voltage continues to shift to more positive values throughout the duration of the measurement, leading to large errors in the extracted mobility.

Recently, Walser et al. [8] have reported that PTCDI-C_{13} devices fabricated using a Cytop® CTL-809M fluoropolymer single-layer dielectric show negligible threshold voltage shift (including the initial, irreversible component), and have near-zero, slightly positive threshold voltages and excellent subthreshold swings. Even with a lower-capacitance, bilayer SiO_2 (260 nm)/Cytop® (7–9 nm) dielectric, these devices exhibit excellent subthreshold swings of 0.6 V/decade and relatively small threshold voltages of 7 V [10]. We note, however, that the low dielectric constant ($\varepsilon_r = 2.1$) and dielectric strength (900 kV/cm) [11] reported by the manufacturer of Cytop® are disadvantageous properties for a transistor gate dielectric, although there are reports of significantly higher dielectric strengths in the literature [8]. In addition, the non-wetting nature of the fluoropolymer surface makes subsequent processing, such as patterning using photoresists or solution deposition of organic semiconductor materials, problematic.

To investigate these effects, and to try to find more suitable, stable and hysteresis-free dielectrics, we have performed a systematic study of PTCDI-C_{13} transistors fabricated using several dielectrics: Cytop®, bare SiO_2, alkyl-phosphonic acid self-assembled monolayer (SAM) terminated SiO_2, and poly(chloro-*p*-xylylene), or parylene-c, which has a dielectric strength three times that of Cytop® and a relative permittivity of 3.1. Although parylene-c has previously been demonstrated as a suitable gate dielectric material for p-channel devices [12], we believe this is the first investigation of its use in n-channel OTFTs.

2. Experimental

PTCDI-C_{13} transistors were fabricated on heavily doped Si wafers (p-type; boron; <0.005 Ω cm) with 100 nm thermal SiO_2. The Si wafer served as a common gate electrode for all transistors, and the thermal oxide plus various overlayers (SAMs, Cytop®, parylene) as the gate dielectric. Si coupons were sonicated in methanol, immediately blown dry with dry compressed air, followed by oxygen plasma cleaning in a parallel plate reactive ion etcher (Trion Technologies Phantom) at 250 W rf power, 200 mTorr, 20 sccm O_2 for 1 min. After removal from the plasma, each coupon underwent further processing, depending on the dielectric to be studied.

For phosphonic acid SAMs, the coupons were immediately immersed in 0.5 mmol solutions of n-alkyl phosphonic acids (Strem Chemical) in 2-propanol, where the alkyl chain length was one of C_6–C_{18}, in steps of 2 carbon atoms. After immersion for 24 h, the coupons were removed from the solution, annealed under rough vacuum at 145 °C for 10 min, rinsed in clean 2-propanol and immediately blown dry with compressed air.

Cytop® dielectrics were prepared by spin coating 3 parts Cytop® CTL-809 M dissolved in 14 parts CTSolv-180 at 500 rpm for 30 s, resulting in a Cytop® film 110 nm thick on top of the 100 nm SiO_2 film. Capacitors of 0.5, 1 and 2 mm diameters were fabricated by deposition of metal electrodes through a stencil mask. The specific capacitance was determined at frequencies from 100 Hz to 100 kHz, and was found to be 11 nF/cm^2, independent of frequency within experimental uncertainty. This corresponds to a relative permittivity of 2.1 for Cytop®, in close agreement with the values given by the manufacturer [11].

Parylene dielectrics were prepared in a Specialty Coating Systems Labcoater 2 parylene deposition system. Film thickness is determined by the amount of di-(chloro-*p*-xylylene) dimer processed, and measured post-deposition using a Dektak 150 Surface Profiler. Specific capacitance was determined as above, and was found to be 15 nF/cm^2, independent of frequency, for the compound dielectric with a 101 nm-thick film. This corresponds to a relative permittivity of 3.1 for parylene-c, in close agreement with accepted values.

Following dielectric preparation, the samples were transferred to a vacuum deposition system (base pressure 1×10^{-6} Torr; pressure during deposition $<8 \times 10^{-6}$ Torr). 50 nm of PTCDI-C_{13} (Sigma Aldrich PN 3837783; as-received) was deposited through a stencil mask at 0.05–0.1 nm/s onto the coupons held at 90 °C. The samples were allowed to cool to <40 °C before vacuum was broken (briefly exposing the samples to air), and a source-drain stencil mask was aligned with the active semiconductor. Aluminum source-drain contacts were deposited at a rate of 0.1 nm/s to a thickness of between 50 and 60 nm with the samples nominally held at room temperature. Each coupon contained an array of 24 transistors with channel lengths ranging from 25 μm to 250 μm and widths between 0.5 mm and 1.5 mm. After metal deposition, the samples were again exposed to air for a few minutes before transferring to a N_2 glove box for testing (MBraun Unilab; <1 ppm H_2O, O_2). All testing, unless otherwise noted, was performed under N_2.

Electrical characteristics of the PTCDI-C_{13} OTFTs were measured using two Keithley 236 source-measure units – one to control the source-drain voltage and measure the drain current, and one to control the source-gate voltage and measure the gate leakage current. The saturation and linear transfer curves were measured by applying +50 V and +1 V, respectively, to the drain and sweeping the gate from −5 V to +50 V and back for the off-to-on and on-to-off

scans, respectively. In all cases, an initial off-to-on scan is performed prior to an on-to-off scan to determine threshold voltage shifts/hysteresis due to electron trapping. The sweep rate is dependent on the integration time of the Keithley 236 SMUs, which is dynamically adjusted, depending on the magnitude of the current being measured. For most of the sweep, an effective rate of 2 V/s was used, although it was as low as 0.5 V/s in the "off" region, where the currents are very small. Device parameters were not studied as functions of sweep rate. The saturation and linear threshold voltages and electron mobilities were extracted from the transfer curves from the intercept and slope, respectively, of the linear portion of the square root of the drain current (for saturation) or drain current (for linear) as a function of gate voltage, assuming the ideal n-channel FET equations to hold:

$$I_{\mathrm{Dsat}} = \mu_n C_{\mathrm{ox}} \frac{W}{2L}(V_{\mathrm{gs}} - V_{\mathrm{t}})^2, \quad V_{\mathrm{ds}} \geqslant V_{\mathrm{gs}} - V_{\mathrm{t}} \tag{1}$$

$$\sqrt{I_{\mathrm{Dsat}}} = \sqrt{\mu C_{\mathrm{ox}} \frac{W}{2L}}(V_{\mathrm{gs}} - V_{\mathrm{t}}) \tag{2}$$

$$I_{\mathrm{Dlin}} = \mu_n C_{\mathrm{ox}} \frac{W}{L}\left[(V_{\mathrm{gs}} - V_{\mathrm{t}})V_{\mathrm{ds}} - \frac{V_{\mathrm{ds}}^2}{2}\right], \quad V_{\mathrm{ds}} \leqslant V_{\mathrm{gs}} - V_{\mathrm{t}} \tag{3}$$

Device stability was investigated by repeating the above off–on–off cycle one hundred times, and device parameters were extracted as functions of cycle number. One hundred such cycles corresponds to a total stress time of approximately two and a half hours.

3. Results

3.1. SiO_2 control

A typical first cycle of a control PTCDI-C_{13} transistor on bare SiO_2 is shown in Fig. 1a. We note the large degree of hysteresis between the off–on and on–off scans. Such shifts are typical of PTCDI/SiO_2 devices, and have been noted before [6]. Gundlach et al. refer to these large initial shifts as the irreversible threshold voltage shift, as the threshold voltage does not recover to its initial value on the timescale of the experiment. Indeed, they note that while some devices do seem to recover after several days, others never return to the initial, near-zero threshold voltage seen in the first off–on scan. We have made the same observation. We will refer to this effect simply as the threshold voltage shift. A much smaller shift, seen between subsequent off–on and on–off sweeps, that recovers on the timescale of a single cycle, will be referred to as the threshold voltage hysteresis.

It is important to be aware of these large initial threshold voltage shifts when extracting parameters from the device transfer curves. For instance, referring to Eq. (2), the saturation mobility is typically extracted from the slope of the square root of the drain current plotted against the gate-source voltage, V_{gs}. In such analysis, it is implicitly assumed that the threshold voltage, V_{t} is a constant. In the case of the devices described here, however, V_{t} is not a constant, and further more, it is not simply dependent on the value of V_{gs}. It is dependent of the past history of V_{gs}. Considering the first sweep, as performed above from the off state to the on state, the threshold voltage is shifting to more positive voltages during the measurement. This causes the drain current to increase more slowly that it would if V_{t} were constant, and the electron mobility extracted assuming constant V_{t} greatly underestimates the true mobility (which we define as the value that would be extracted in the absence of dynamic filling/emptying of traps during a gate voltage sweep). For the data shown in Fig. 1a, the true electron mobility is approximately 0.23 cm^2/Vs, while the mobility extracted from the initial off–on sweep, assuming constant V_{t}, is only 0.05 cm^2/Vs. The converse is also true. If we had chosen our initial sweep to be from the on state to the off state, the threshold voltage would still have shifted to more positive values as the sweep progressed, and the current would have decreased more sharply than it would if V_{t} were constant, resulting in an overestimate of the electron mobility. By using initial sweeps from on to off (not shown) we have extracted erroneous electron mobilities as high as 2 cm^2/Vs. Obviously, great care must be taken when analyzing data from devices exhibiting such threshold voltage shifts.

By repeated cycling of these devices between the off, on and off states, we have studied the evolution of the threshold voltage as a function of cycle number. A selection of saturation transfer curves from one such experiment is presented in Fig. 1b. We note that both the threshold voltage shift and hysteresis appear to asymptotically approach steady-state values. The overall threshold voltage shift is approximately 35 V and the steady-state threshold voltage hysteresis between off–on and on–off sweeps is approximately 1.5 V. We also note that the mobility appears to approach a steady-state value of 0.23 cm^2/Vs for the off–on sweep, and 0.26 cm^2/Vs for the on–off sweep. A summary of the evolution of device parameters with cycle number is presented in Fig. 2.

3.2. Alkyl phosphonic acid SAMs

Devices were fabricated and tested using alkyl phosphonic acid modified SiO_2 dielectrics with chain lengths of 6–18 carbon atom in steps of two. Our previous work found that pentacene devices had superior performance when chain lengths of 8 and 10 carbon atoms were used [13]. In the case of PTCDI-C_{13} devices, however, the performance was found to improve monotonically with increasing chain length. The results that follow will therefore focus on PTCDI-C_{13} films deposited on octadecyl phosphonic acid modified SiO_2.

The first cycle (off–on–off) of a device fabricated using octadecyl phosphonic acid is presented in Fig. 3a. The appearance of the hysteresis loop is similar to that of the SiO_2 control devices with two important differences. First, the threshold voltage shift, while still large, appears to be significantly smaller than that of the control devices, and second, there appears to be an inflection point in the on–off sweep, well below threshold, at a V_{gs} of approximately 12–14 V. Gundlach et al. noted a similar feature in the second sweep of similar devices fabricated on untreated SiO_2, and attributed it to a discrete trap level [6]. Here, while we have found evidence of such a state on some untreated

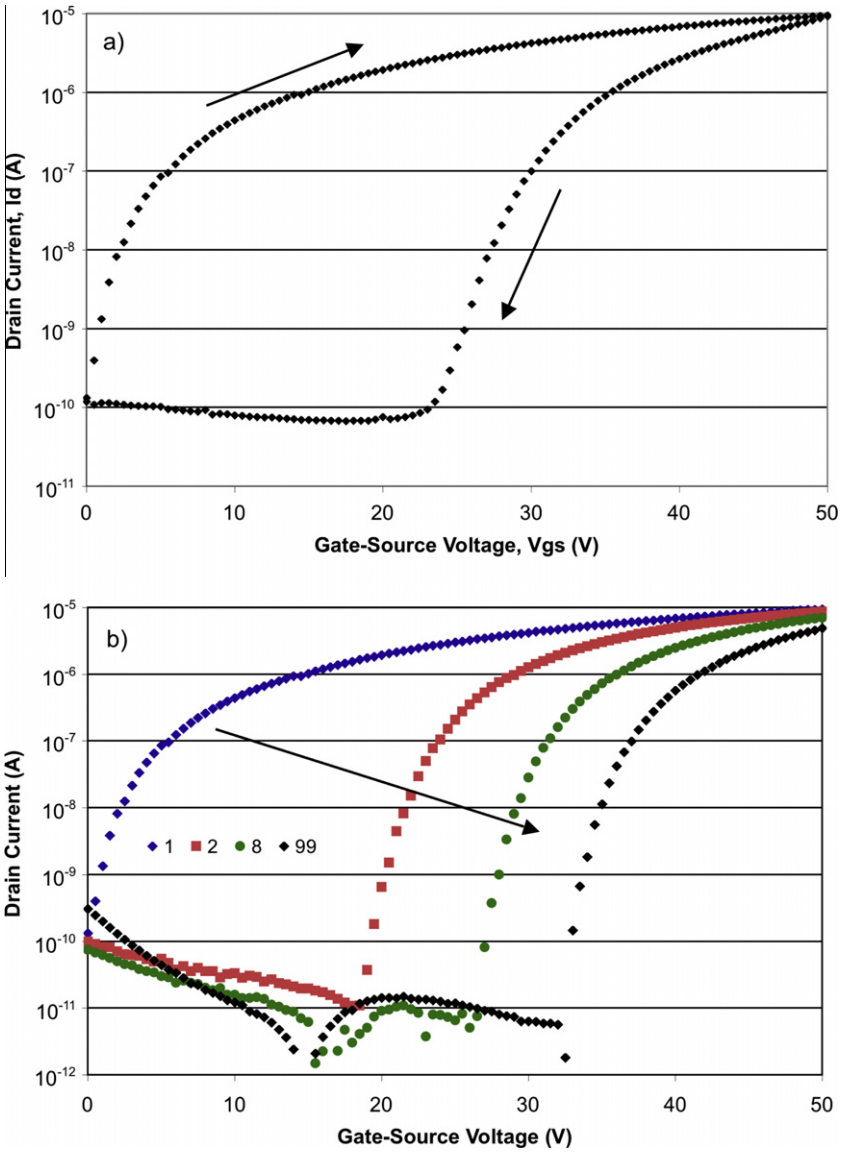

Fig. 1. PTCDI-C_{13}/SiO_2 (a) first off–on–off sweep indicating the large initial, irreversible threshold voltage shift (b) off–on sweeps from repeated cycling tests. Cycle numbers indicated.

SiO_2 devices, we have found much more pronounced and consistent evidence of a significant density of trap states induced by the presence of the alkyl-PA monolayer at all chain lengths. When the devices are cycled (Fig. 3b), we find the threshold voltage continues to shift to more positive values, approaching a steady state value. The evolution of device parameters versus scan number is presented in Fig. 2. Note the erroneously high electron mobility of almost 0.9 cm^2/Vs extracted from the first on–off sweep caused by the positive shift of the threshold voltage during the sweep as discussed above.

3.3. Cytop®

In Fig. 4a we present the first off–on–off cycle of the saturation transfer curve for a typical PTCDI-C_{13} device fabricated on a Cytop® dielectric. We note that virtually no hysteresis between the initial off–on and on–off scans is evident, as previously reported [8,10]. Additionally, the trap state evident in the alkyl-PA devices that resulted in the inflection point below threshold is completely absent in the Cytop® devices, clearly indicating that the origin of this feature is related to the dielectric or the semiconductor/dielectric interface, and not to the bulk semiconductor material. Off–on scans for a selection of cycle numbers are presented in Fig. 4b, with an inset on an expanded *x*-scale to illustrate the small degree of shift observed. The evolution of device metrics is presented in Fig. 5. We note an initial threshold voltage shift of *negative* 0.1–0.15 V during the first few sweeps, after which the threshold voltage begins to increase slowly with increasing cycle number. A small hysteresis of −50 mV is observed between initial

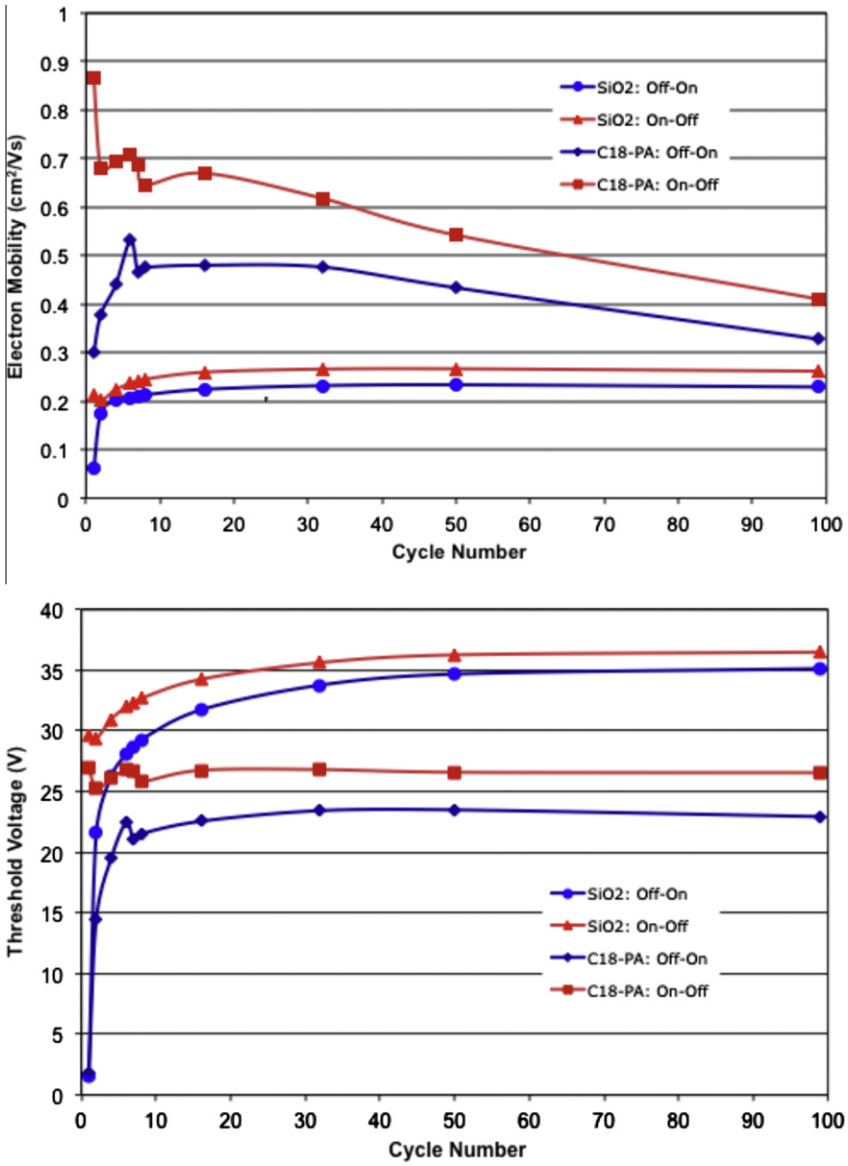

Fig. 2. Parameters extracted from repeated cycling of PTCDI-C_{13}/SiO_2 and PTCDI-C_{13}/octadecyl phosphonic acid/SiO_2 devices.

off–on and on–off sweeps, and is almost completely absent in later cycles. Negative (counter clockwise) hysteresis in n-channel devices can be attributed to the slow drift of ions or the reorientation of dipolar species within the polymer dielectric. Similar effects have been seen in p-channel pentacene transistors that exhibit positive (clockwise) hysteresis [14,15]. We also note a slight but consistent decrease in the electron mobility over time.

3.4. Parylene-C

The initial off–on–off cycle and a subset of the repeated sweep data for PTCDI-C_{13} devices fabricated with a parylene-c dielectric are presented in Fig. 6a and b, respectively. As in the case of Cytop® dielectrics, we find almost no visible hysteresis between off–on and off–on sweeps. Upon closer inspection (Fig. 6a, inset) we find an off–on/on–off hysteresis of −50 mV, similar to that of the Cytop® devices. Also, in contrast to all other devices reported here, the threshold voltage tends to shift to more negative values with repeated cycling (Figs. 6b and 5). After 100 cycles, the threshold voltage has shifted by ∼−1 V, significantly larger than the shift observed for Cytop® devices, but much smaller than the shift observed for SiO_2 or alkyl-PA devices. As in the case of Cytop®, we attribute the counter clockwise hysteresis and negative threshold voltage shift to the drift of ions and slow reorientation of dipoles within the polymeric dielectric [14,15]. Furthermore, we note that the shift has a much longer time constant, continuing to shift throughout the 100-cycle experiment. In contrast with Cytop® devices, we find that the measured mobility tends to *increase* slightly with increased cycling. Note the

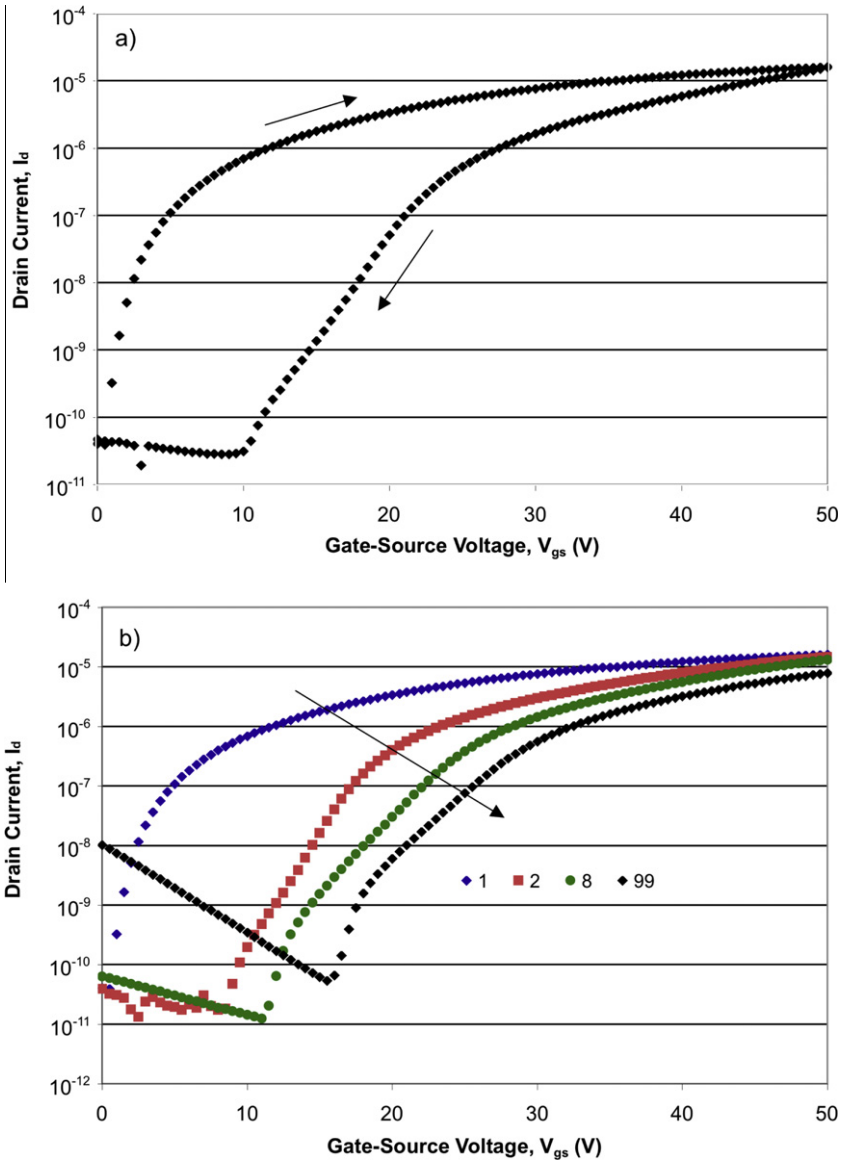

Fig. 3. PTCDI-C_{13}/octadecyl phosphonic acid/SiO_2 devices (a) initial off–on–off cycle, (b) repeated cycling (cycle numbers indicated).

apparent contradiction between the voltage hysteresis of 50 mV from Fig. 6a, and the almost 0.4 V threshold voltage hysteresis reported in Fig. 5. The mobility measured from the on–off sweep is consistently lower than that of the off–on sweep. Thus, the slope of the $\sqrt{I_d}$ plots will be lower for the on–off sweep than the off–on sweep. The horizontal distance (voltage) between points of equal current must therefore decreases as we approach the common point at V_{gs} = 50 V.

4. Discussion

The large degree of hysteresis, irreversible threshold voltage instability, and high operating voltages of PTCDI-C_{13} devices fabricated on SiO_2 dielectrics and alkyl-PA treated SiO_2 render these OTFTs unsuitable for use in electronic devices, including O-CMOS digital logic circuits. We attribute these undesirable characteristics to a large density of electron trapping sites at the semiconductor/dielectric interface, most likely due to hydroxyl groups present on the SiO_2 interface [16]. While the phosphonic acid monolayer does displace a large number of these groups, they are not completely eliminated. We therefore observe improved transistor characteristics when the monolayers are introduced, including smaller irreversible threshold voltage shifts, lower threshold voltages and less hysteresis between off–on and off–on sweeps, but the influence of the remaining traps is still too large for a feasible technology. Furthermore, we stress again the care that must be taken when extracting mobilities from the transfer curves of such devices during the first few sweeps, while the

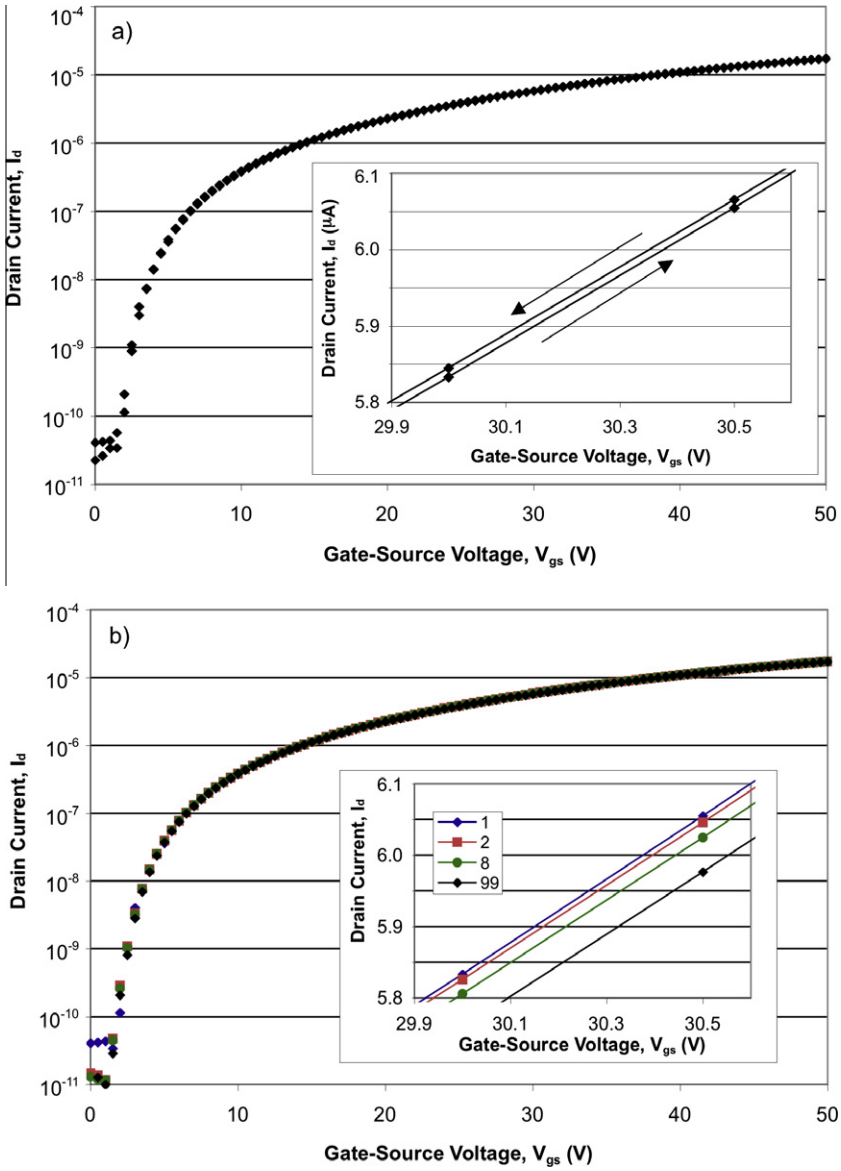

Fig. 4. PTCDI-C_{13}/Cytop devices (a) initial off–on–off cycle, (b) repeated cycling (cycle numbers indicated). Insets are included so that the small hysteresis (a) and threshold shift (b) are visible.

threshold voltage is continually shifting to larger positive voltage. If extracted from the initial off–on sweeps, the resulting mobility will be lower than the true value and if extracted from the initial on–off sweep (especially if this is the first sweep of a fresh device), the reported mobility can be nearly an order of magnitude larger than the true value. Surprisingly, we note almost no difference between the mobility extracted from the steady-state sweeps on devices with large densities of electron trapping states, and those measured on Cytop® and parylene-c devices, which appear to have much lower trap densities. This would seem to indicate that the dominant trap states associated with the semiconductor/dielectric interface are energetically deep, with detrapping times that are long compared to the length of the experiment. We would expect the elimination of shallow traps (such as those described in a multiple trap and release model) to increase the macroscopically observed electron mobility, while populating deep, long-lived traps will result in electrostatic shifting of the threshold voltage, as observed here. It is most likely that a continuum of electron trap states exists below the conduction band edge, with a corresponding distribution of detrapping times, as evidenced by the very long-lived irreversible threshold voltage shift, and the smaller off–on/on–off hysteresis observed between subsequent sweeps. We cannot rule out the existence of shallow electron traps in the bulk of the PTCDI-C_{13} film, or traps at the semiconductor/dielectric interface that are insensitive to the choice of dielectrics we have presented here (although this seems unlikely, given the very different physical and

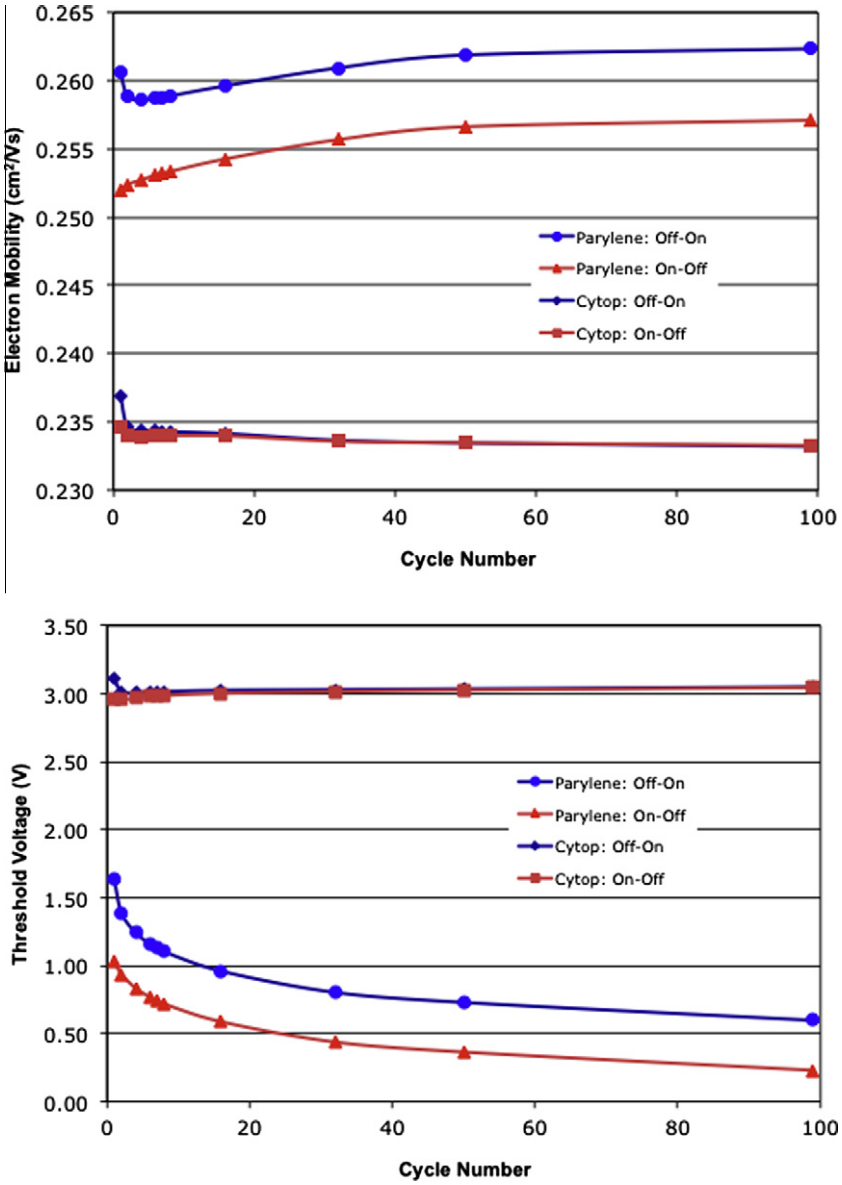

Fig. 5. Evolution of parameters extracted from repeated cycles of PTCDI-C_{13}/Cytop and PTCDI-C_{13}/parylene-c devices. Note vertical scales.

chemical properties of the materials studied). The results clearly show, however, that the electron traps associated with the SiO_2 surface that are attributed to hydroxyl groups are energetically very deep, as their elimination does not strongly influence the macroscopically observed electron mobility.

Both Cytop® and parylene-c are suitable dielectrics for PTCDI-C_{13}. Both result in devices with stable, positive, near-zero threshold voltages. Both have vanishingly small off–on/on–off hysteresis. These properties indicate that the deep electron trapping states, present on SiO_2 and SAM-treated SiO_2 are largely absent on these dielectrics, consistent with the absence of hydroxyl groups. We also note advantages and disadvantages of each material. Many of the device metrics for Cytop®-based devices are superior to those constructed using parylene-c. Threshold voltage shifts and hysteresis are smaller, stability appears to be better, and drain currents at $V_{gs} = 0$ are 1–2 orders of magnitude smaller than parylene-c devices. On the other hand, parylene-c has a higher relative permittivity, easily forms uniform, conformal pinhole-free coatings, and has a dielectric breakdown strength three times that of Cytop® – all desirable qualities for a gate dielectric.

It should be noted that although we have chosen to use thick, bilayer dielectrics for ease of fabrication and to ensure high yields, extremely thin films of both Cytop® and parylene can be formed. Walser et al. [8] have demonstrated that Cytop® films <20 nm thick can be successfully used as gate dielectrics. Increases in specific capacitance on the order of 10 times can therefore be realized. By increasing the specific capacitance of the gate dielectric, many of the stability metrics, including threshold voltage shift and

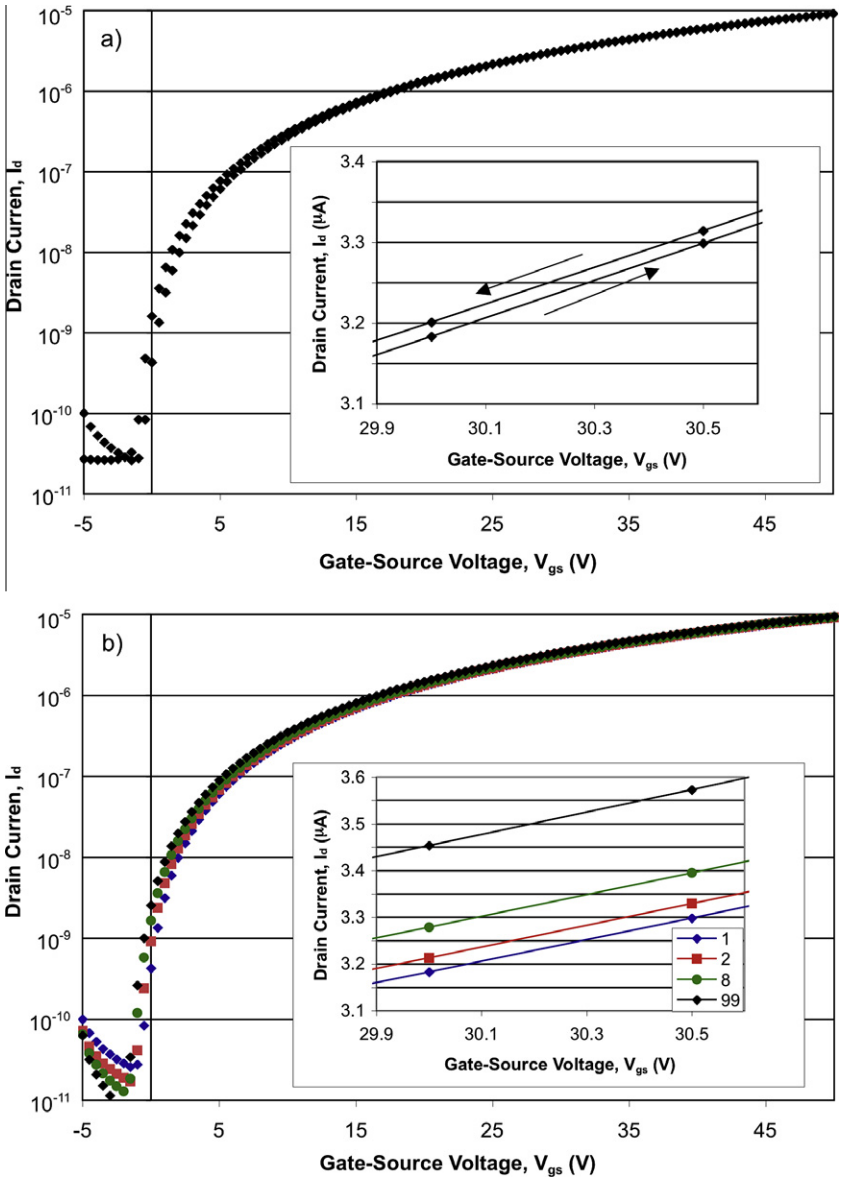

Fig. 6. PTCDI-C_{13}/parylene-c devices (a) initial off–on–off cycle, (b) repeated cycling (cycle numbers indicated). Insets are included so that the small hysteresis (a) and threshold shift (b) are visible.

hysteresis, as well as the operating voltages, will decrease by the same factor.

5. Conclusion

N-channel PTCDI-C_{13} OTFTs fabricated using Cytop® and parylene-c have excellent device performance and stability. Both exhibit high, stable, electron mobilities, very small threshold voltage shifts and hysteresis under repeated cycling. While the performance of Cytop® devices is slightly better than those fabricated using parylene-c, parylene-c possesses better dielectric properties, is inexpensive, and can more easily form uniform, pinhole-free films. Furthermore, parylene-c is easily wet by organic solvents, such as those used in solution deposition of organic semiconductor materials and those used in photoresists, making it an attractive gate dielectric material for organic thin-film transistors.

In contrast, both phosphonic acid SAM-modified SiO_2 and bare SiO_2 gate dielectrics have been shown to be unacceptable for use in n-channel PTCDI-C_{13} OTFTs. Large densities of electron trapping states result in large positive threshold voltage shifts, on–off hysteresis, and threshold voltage instability with repeated cycling.

Acknowledgements

This work was supported by the Natural Sciences and Engineering Research Council of Canada and the Canada

Foundation for Innovation. Ahmad G. Ismail thanks University Science Malaysia fellowship award.

References

[1] T.N. Jackson, Organic thin film transistors – electronics anywhere, Proceedings of 2001 International Semiconductor Device Research Symposium 340 (2001).
[2] L.S. Zhou, A. Wanga, S.C. Wu, J. Sun, S. Park, T.N. Jackson, All-organic active matrix flexible display, Appl. Phys. Lett. 88 (2006) 083502.
[3] C.D. Sheraw, L. Zhou, J.R. Huang, D.J. Gundlach, T.N. Jackson, M.G. Kane, I.G. Hill, M.S. Hammond, J. Campi, B.K. Greening, J. Francl, J. West, Organic thin-film transistor-driven polymer-dispersed liquid crystal displays on flexible polymeric substrates, Appl. Phys. Lett. 80 (2002) 1088.
[4] Kung-Ching Liao, Ahmad G. Ismail, Laurent Kreplak, Jeffrey Schwartz, Ian G. Hill, Designed Organophosphonate Self-Assembled Monolayers Enhance Device Performance of Pentacene-Based Organic Thin-Film Transistors, Adv. Mater. 22 (2010) 3081.
[5] M. McDowell, I.G. Hill, J.E. McDermott, S.L. Bernasek, J. Schwartz, Improved organic thin-film transistor performance using self-assembled monolayers, Appl. Phys. Lett. 88 (2006) 073505.
[6] D.J. Gundlach, K.P. Pernstich, G. Wilckens, M. Gruter, S. Haas, B. Batlogg, High mobility n-channel organic thin-film transistors and complementary inverters, J. Appl. Phys. 98 (2005) 064502.
[7] Patrick R.L. Malenfant, Christos D. Dimitrakopoulos, Jeffrey D. Gelorme, Laura L. Kosbar, Teresita O. Graham, Alessandro Curioni, Wanda Andreoni, N-type organic thin-film transistor with high field-effect mobility based on a *N,N'*-dialkyl- 3, 4, 9, 10-perylene tetracarboxylic diimide derivative, Appl. Phys. Lett. 80 (2002) 2517.
[8] M.P. Walser, W.L. Kalb, T. Mathis, B. Batlogg, Low-voltage organic transistors and inverters with ultrathin fluoropolymer gate dielectric, Appl. Phys. Lett. 95 (2009) 233301.
[9] Reid J. Chesterfield, John C. Mckeen, Christopher R. Newman, Paul C. Ewbank, Demétrio A. da Silva Filho, Jean-Luc Bredas, Larry L. Miller, Kent R. Mann, C. Daniel Frisbie, Organic thin film transistors based on *N*-alkyl perylene diimides: charge transport kinetics as a function of gate voltage and temperature, J. Phys. Chem. B 108 (2004) 19281.
[10] M.P. Walser, W.L. Kalb, T. Mathis, T.J. Brenner, B. Batlogg, Stable complementary inverters with organic field-effect transistors on Cytop fluoropolymer gate dielectric, Appl. Phys. Lett. 94 (2009) 053303.
[11] Cytop Amorphous Fluoropolymer Catalog, AGC Chemicals, Asahi Glass Company Limited, Tokyo, January 2009.
[12] C.D. Dimitrakopoulos, B. Furman, T. Graham, S. Hegde, S. Purushothaman, Field effect transistors comprising molecular beam deposited α,ω-dihexyl-hexathienylene and polymeric insulator, Synthetic Metals 92 (1998) 47.
[13] I.G. Hill, C.M. Weinert, L. Kreplak, B.P. van Zyl, Influence of self-assembled monolayer chain length on modified gate dielectric pentacene thin-film transistors, Appl. Phys. A: Mater. Sci. Process. 95 (2009) 81.
[14] S.J. Zilker, C. Detcheverry, E. Cantatore, D.M. de Leeuw, Bias stress in organic thin-film transistors and logic gates, Appl. Phys. Lett. 79 (2001) 1124.
[15] D.K. Hwang, Min Suk Oh, Jung Min Hwang, Jae Hoon Kim, Seongil Im, Hysteresis mechanisms of pentacene thin-film transistors with polymer/oxide bilayer gate dielectrics, Appl. Phys. Lett. 92 (2008) 013304.
[16] Lay-Lay Chua, Jana Zaumsell, Jui-Fen Chang, Eric C.-W. Ou, Peter K.-H. Ho, Henning Sirringhaus, Richard H. Friend, General observation of n-type field-effect behaviour in organic semiconductors, Nature 434 (2005) 194.

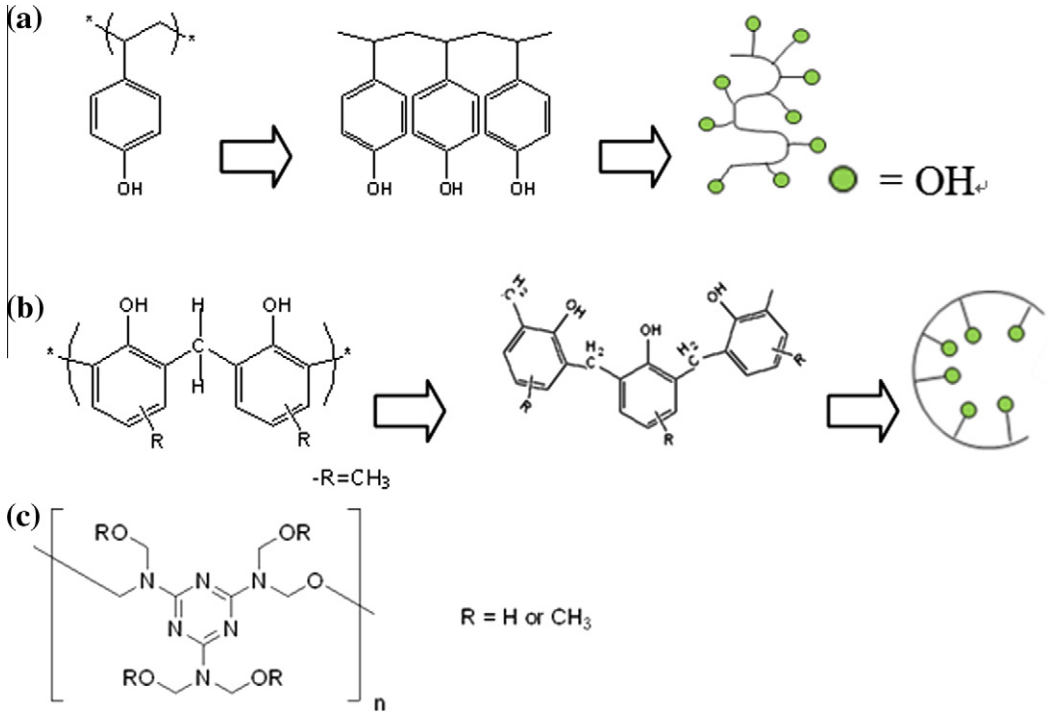

Fig. 1. Chemical structures of polymeric dielectric as (a) conventional PVP resin and (b) phenolic resin as alternative PVP and (c) low molecule melamine as cross-linker.

outside from the backbone chain. However, the alternative PVP resin has a backbone with hydroxyl phenol, which takes the shape of the micellar structure with 6–12 pieces of hydroxyl phenol after cross-linking as shown in Fig. 1b; the phenolic resin has identical structure with Bismethylol Para-Substituted Phenol that has calixarene like structure [14,15]. All of PVP resins were prepared from solution with low molecule melamine as a cross-linker in propylene glycol monomethyl ether acetate (PGMEA) as a solvent.

Initially, to evaluate the functions of the PVP films as dielectric materials, electrical properties were analyzed: the *I–V* characteristic by making an element-OTFT and *C–V* and *C–F* by applying elements MIM and MISM, respectively. Furthermore, the film properties of the chemical bonding structures were analyzed through FTIR.

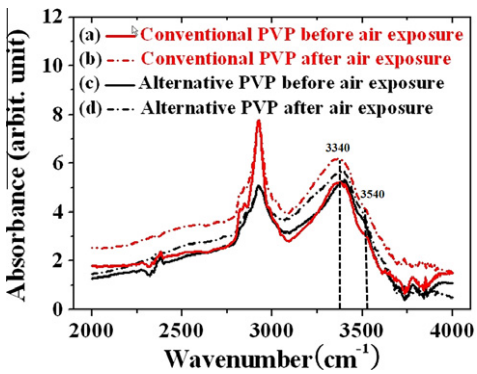

Fig. 2. FT-IR spectra of the polymer dielectrics absorption spectra of conventional PVP and alternative PVP films, used to examine the existence of hydroxyl (O–H) bonds.

For fabrication of the OTFT test devices, after the PVP–OGI solution was prepared, chrome gate electrode was patterned on the glass substrate by the conventional photo-lithography process. PVP–OGI solution was spun on the patterned Cr gate electrode and subsequently, cross-linked at 200 °C for 1 h in the vacuum oven. The PVP–OGI layer was approximately 400 nm thick after cross-linking as measured by the surface profiler (Alpha-step). The gold source–drain electrodes were patterned by the conventional photolithography and wet etching method; nominal channel width (*W*) and length (*L*) of OTFTs were 200 and 10 μm, respectively. Pentacene were deposited by thermal evaporation with the base pressure of 10^{-7} Torr and the deposition rate of 0.02 nm/s at room-temperature, and the final thickness was 40 nm.

3. Results and discussion

Fig. 2 presents the FTIR analysis data of the conventional and the alternative PVP films. Both resins have the O–H stretching bonds, which are affected by polar molecule showing peaks at 3340 cm^{-1} and 3540 cm^{-1} as the non-hydrogen bonded O–H group and the hydrogen bonded O–H group, respectively; the non-hydrogen bonded O–H group are easily responded with the polar molecule and induce slow polarization by attracting charge carriers [16,17]. Both the conventional and the alternative PVP films show 3340 cm^{-1} peak and non-hydrogen bonded hydroxyl group, for the same content volume under 5%.

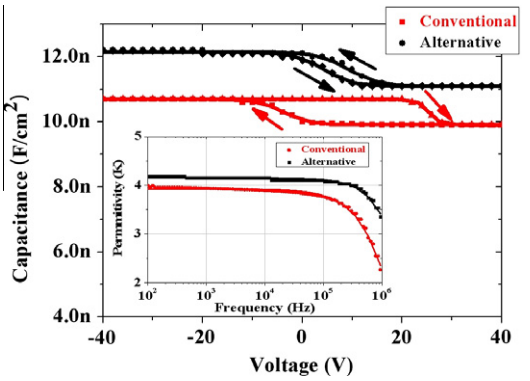

Fig. 3. Voltage dependent capacitance plot for conventional and alternative PVP films with MISM structures; (inset) frequency dependent permittivity plot with MIM structure.

With equal thickness of conventional and alternative PVP films, FTIR analysis was started after exposing them in the air for 200 h. Both films confirmed that the content proportion of the non-hydrogen bonded OH group (3340 cm^{-1}) had been increased.

If slow polarization was induced by the polar molecules, where absorption of moisture is the primary factor as an example, the dielectric material applied by two resins might be seen to have equal or similar form of hysteresis phenomenon by the slow polarization. In order to confirm this result, the dielectric constant and hysteresis of a thin film were analyzed with metal–insulator–metal (MIM) and metal–insulator–semiconductor–metal (MISM) test devices.

Fig. 3 shows the voltage dependent capacitance plot for conventional and alternative PVP films with MISM structure which shows conflicting hysteresis phenomenon each other, while Fig. 3 inset shows the frequency dependent permittivity plot for conventional PVP (k_{con} = 3.89) and alternative PVP (k_{alt} = 4.16) films with MIM structure. The permittivities of both resins were not much different from each other. The conventional PVP film shows a typical hysteresis, which is fundamentally caused by the slow

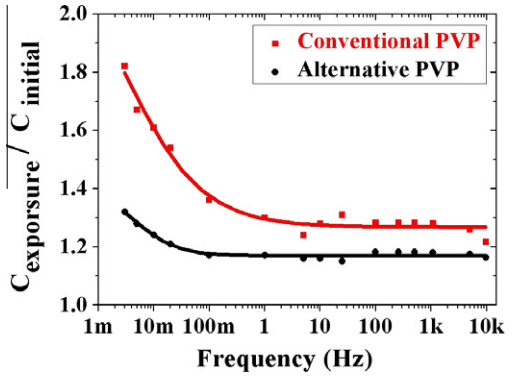

Fig. 4. Frequency dependent capacitance scans using MIM devices with various dielectrics. (In the axis of C_{expo}/C_{ini}, indicating a numerical value of the ratio of capacitance of thin film after exposure in the ambient air and the capacitance of thin film in the initial state.)

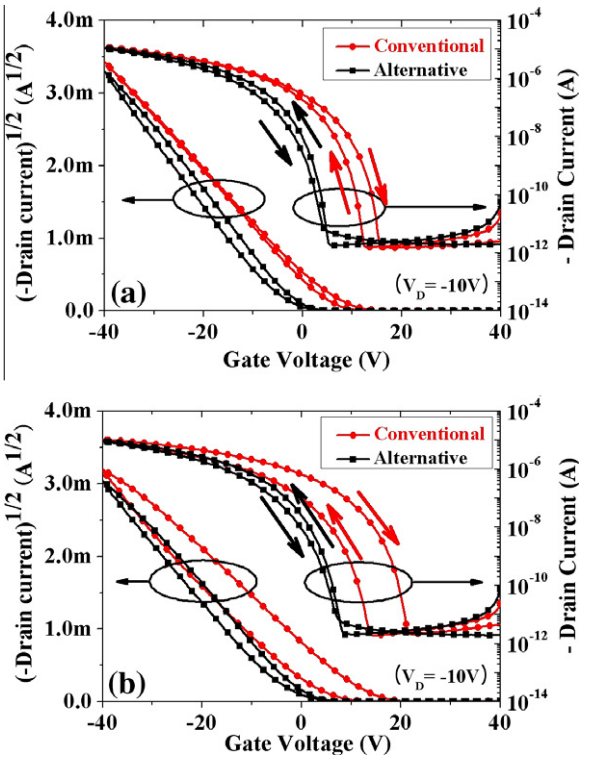

Fig. 5. Transfer (I_D–V_G) characteristics of pentacene based OTFTs with V_{DS} = −10 V, swept in both directions, of device with length (L = 10 μm) and width (W = 200 μm). (a) Without air exposure, (b) air exposure (60 h).

polarization in the PVP–OGI [18,20]. However, the alternative PVP film shows the opposite direction of the hysteresis loop, which means that the alternative PVP film was nearly free of hysteresis mainly caused by PVP–OGI itself. The slow polarization induced hysteresis should be dependent on the amount of dipolar groups in the dielectric [21]. In other words, dielectric films containing a small number of OH groups, may show reduced hysteresis [22]. However, two species of PVP–OGI films showed a similar proportion of non-bonded OH-group peak formation in the FTIR as shown in Fig. 2. That is contradicting result.

To clarify this phenomenon, we investigated the frequency dependent capacitance measurement including very low frequency range (below 100 milli Hz) with the MIM device.

Slow polarization can be analyzed by capacitance variation of MIM device through C–F measurement in the section at low frequency [26]. Provided that a polymer dielectric absorbs the water molecule, capacitance at low frequency is rapidly increased. As a result, it caused surface screening on interface between semiconductor and polymer dielectric as memory effect and obtained voltage is not permitted to respond rapidly so that induces hysteresis. Simply, an increase in capacitance at low frequency causes the dielectric material to show a large hysteresis effect.

In Fig. 4, instead of capacitance value in the initial state, the ratio of capacitance of thin film after exposure in the air is inscribed. In the result of Fig. 4, it is confirmed that

Table 1
Electrical characteristics of the pentacene OTFTs.

Performance parameter	Device configurations [W/L = 200/10]			
	Without air exposure		Ail exposure (60 h)	
	Conventional	Alternatives	Conventional	Alternative
*V*th (V)	5.3	−1.4	3.6	0.5
Hysteresis (V)	0.79	−2.5	8.87	−3.3
Mobility (cm^2/V s)	0.179	0.17	0.14	0.12
S-slope (V/Dec)	1.86	1.67	2.5	1.99

the ratio of capacitance for conventional PVP was 1.82 times higher (40% increasing), while that of alternative PVP was just 1.3 times higher (10% increasing) in the rate of increasing at low frequency (3 milli Hz); so to figure it out that the capacitance of conventional PVP in the rate of increasing was relatively higher than the other one. According to the result from Figs. 2 and 3, both PVP thin films showed no large difference of the content volume of the non-hydrogen bonded OH group and the absorption volume of water molecule; this means that the capacitance of the conventional PVP is relatively much higher in the rate of increasing, which is not only due to the effect of water absorption but also due to other factors that affect slow polarization as one of root cause of hysteresis in OTFT.

We assumed that the backbone structure of PVP is effective suppressing hysteresis, and planned an experiment. The result above was in agreement with the result from our hypothesis. In order to confirm the hysteresis of the OTFT based on the result, the changes of hysteresis before and after OTFT exposure to air were measured with pentacene based OTFT using two dielectric materials as mentioned in previous section.

Fig. 5a shows the comparative current dependent voltage (*I*–*V*) curves obtained from our pentacene OTFTs with initial state dielectrics, conventional and alternative PVP films, and Table 1 summarizes the transistor parameters extracted from the measurement. Conventional PVP based OTFT shows typical hysteresis with clockwise direction of the hysteresis loop, which is caused by slow polarization in OGI, however, the alternative PVP based OTFT shows totally different hysteresis with a counter-clockwise loop direction which is caused by mainly electronic traps in semiconductor [18–27]. Fig. 5b shows the *I*–*V* characteristic of the OTFT after exposure in the air. Although hysteresis does not change with the element that uses the alternative PVP, large hysteresis was observed with the element that uses the conventional PVP.

According to our modeling, the conventional PVP–OGI is shown to be the effect of slow polarization by the ambient air, but there was not any change of hysteresis after exposure in the air though alternative PVP–OGI contained OH-phenol with the same way of the conventional PVP. This result that all of OH group and water molecule cannot be revealed to slow polarization even though they can be combined in dielectric bulk by analogy. It can be found the reason to distinguish differences of hysteresis between both dielectric materials from the backbone structure which resin has.

With this kind of difference of fusion, the absorption and the arrangement between the dielectric material and water molecule make a difference. Therefore, the approach, in which the fusion structure such as phenolic alternative PVP film with the shape of partially micelle structure induces the localization of the dipoles by O–H group, can be suggested as one method to suppress hysteresis.

4. Summary

We suggested that the amelioration of PVP backbone structure as a method to constrain hysteresis is caused by O–H group which OGIs consisting of OH-phenol has in the nature of the case and analyzed a difference between two kinds of OGIs, the conventional PVP and the phenolic alternative PVP through various analysis methods. Both of the two PVP–OGIs seem to have a similar chemical behavior of what caused by the absorption of water molecules from O–H group but show totally different hysteresis characteristics, and OTFT, which we had designed and ameliorated by applying resin was shown to have stable characteristic in the side hysteresis. The result of hysteresis is the conclusion induced by the amelioration of backbone structure of PVP as OGI to be localization of O–H group and hysteresis caused by the dipole which was formed by combining with the O–H group and the water molecule is possible to be eliminated.

Acknowledgements

We gratefully acknowledge helpful technical support of low frequency *C*–*F* measurement by Prof. J.G. Song at DongA University, and this research was supported by a Grant (F0004012-2010-33) from information display R&D Center, one of the 21st Century Frontier R&D Program funded by the Ministry of Knowledge Economy of Korean Government.

References

[1] M. Fadlallah, G. Billiot, W. Eccleston, D. Barclay, Solid-State Electron. 51 (2007) 1047.
[2] L. Torsi, A. Dodabalapur, L. Sabbatini, P.G. Zambonin, Sens. Actuators B 67 (2000) 312.
[3] S.H. Lee, D.J. Choo, S.H. Han, J.H. Kim, Y.R. Son, J. Jang, Appl. Phys. Lett. 90 (2007) 033502.
[4] T. Ahn, J.W. Kim, Y.J. Choi, M.H. Yi, Org. Electron. 9 (2008) 711.
[5] T. Ahn, Y.J. Choi, H.M. Jung, M.H. Yi, Org. Electron. 10 (2009) 12.
[6] G.H. Kim, S.M. Yoon, C.A. Kim, K.S. Suh, Jpn. J. Appl. Phys. 44 (2005) L416.
[7] M. Yoshida, S. Uemura, T. Kodzasa, T. Kamata, M. Matsuzawa, T. Kawai, Synth. Met. 137 (2003) 967.
[8] J.A. Cheng, C.S. Chuang, M.N. Chang, Y.C. Tsai, H.P. Shieh, Org. Electron. 9 (2008) 1069.

[9] H. Klauk, M. Halik, U. Zschieschang, G. Schmid, W. Radlik, W. Weber, J. Appl. Phys. 92 (2002) 5259.
[10] S.C. Lim, S.H. Kim, J.B. Koo, J.H. Lee, C.H. Ku, Y.S. Yang, T.H. Zyung, Appl. Phys. Lett. 90 (2007) 173512.
[11] C. Drury, C. Mutsaers, C. Hart, M. Matters, D. de Leuw, Appl. Phys. Lett. 73 (1998) 108.
[12] C. Sheraw, L. Zhou, J.R. Huang, D.J. Gundlach, T.N. Jacson, M.G. Kane, I.G. Hill, M.S. Hammond, J. Campi, B.K. Greening, J. Francl, J. West, Appl. Phys. Lett. 80 (2002) 1088.
[13] R. Rotzoll, S. Mohapatra, V. Olariu, R. Wenz, M. Grigas, K. Dimmer, O. Shchekin, A. Dodabalapur, Appl. Phys. Lett. 88 (2006) 123502.
[14] R. Dammel, in: Diazonaphthoquinone-based Resists 5th Printing, The Society of Photo-Optical Instrumentation Engineers, 1993, pp. 29–80.
[15] A. Gardziella, L.A. Pilato, A. Knop, in: Phenolic Resins, Springer-Verlag, Berlin, Heideberg, 2000, pp. 46–48.
[16] S.H. Kim, J. Jang, H. Jeon, W.M. Yun, S. Nam, C.E. Park, Appl. Phys. Lett. 92 (2008) 183306.
[17] L.F. Scantena, M.G. Brown, G.L. Richmond, Science 292 (2001) 908.
[18] T. Jung, A. Dodabalarpur, R. Wenz, S. Mohapatra, Appl. Phys. Lett. 87 (2005) 182109.
[19] H. Klauk, Organic Electronics, Wiley, Weinheim, 2006 (Chapter 6).
[20] D.K. Whang, J.H. Park, J. Lee, J.-M. Choi, J.H. Kim, E. Kim, S. Im, J. Electrochem. Soc. 153 (2006) G23.
[21] J.H. Schön, B. Batlogg, J. Appl. Phys. 89 (2001) 336.
[22] D.K. Hwang, K. Lee, J.H. Kim, S. Im, J.H. Park, E. Kim, Appl. Phys. Lett. 89 (2006) 093507.
[23] A. Völkel, R.A. Street, D. Knipp, Phys. Rev. B 66 (2002) 195336.
[24] C.A. Lee, D.W. Park, K.D. Jung, B.J. Kim, Y.C. Kim, J.D. Lee, B.G. Park, Appl. Phys. Lett. 89 (2006) 262120.
[25] G. Gu, M.G. Kane, J.E. Doty, A.H. Firester, Appl. Phys. Lett. 87 (2005) 243512.
[26] Zhenan Bao, Organic Field Effect Transistors, Jason Locklin, CRC Press, Taylor & Francis Group, Boca Raton, London, New York, 2007 (Chapters 3 and 6).
[27] S. Lee, B. Koo, J. Shin, E. Lee, H. Park, H. Kim, Appl. Phys. Lett. 88 (2006) 162109.

electron-deficient moieties into the polymer backbone [4,25,26].

Aromatic 1,2,4-triazole shows good electron affinity and hole-blocking properties. However, its high rigidity may lead to low solubility in common organic solvents [4,20,27,28]. On the other hand, triphenylamine exhibits good hole affinity and solubility properties [25,26,29–31]. These complementary properties make 1,2,4-triazole and triphenylamine couple well, and they have been incorporated as electron- and hole-transporting moieties in organic- and polymeric-emitting materials. The incorporation of electron-rich and electron-deficient components into a single polymer is expected to enhance the hole-transporting and electron-transporting properties of that polymer. Barriers to charge injection from both electrodes into the polymer matrix would therefore be reduced. Moreover, the bulky pendant side chain substituent triphenylamine is also expected to prevent the polymer from aggregating. Self-quenching would therefore be reduced, and the light-emitting efficiency would be enhanced.

Some studies [26,29,30] had reported that polymers containing donor–acceptor main chains show a reduction in the band gap of the polymers due to the backbone charge transfer from the donor to the acceptor. Based on the aforementioned considerations, our research group previously reported the synthesis and electroluminescent properties of donor–acceptor conjugated polymers **TPAF** and **TPABTF** with triphenylamine main chains and 1,2,4-triazole side chains [4]. The presence of the bipolar moiety significantly improves charge injection and charge transport in the polymer matrix.

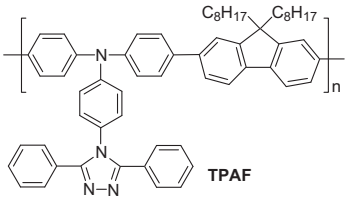

TPAF

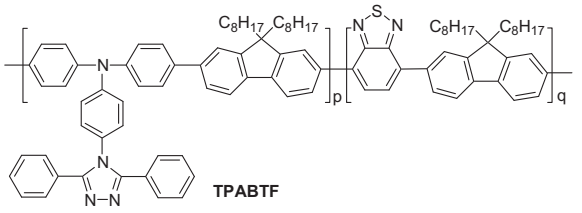

TPABTF

It is well-known that the molecular architectures importantly affect physical properties of polymers, such as molecular skeleton, side chains, functional groups, bond connections and stereo structures. Therefore, it is interesting to study the relationship between the physical properties and chemical structure of polymers as shown below. The LUMO and HOMO of the polymers will be significantly different due to the different moiety connection; and the physical properties such as solubility, thermal, photophysical properties and emitting properties as an emitting material will be different.

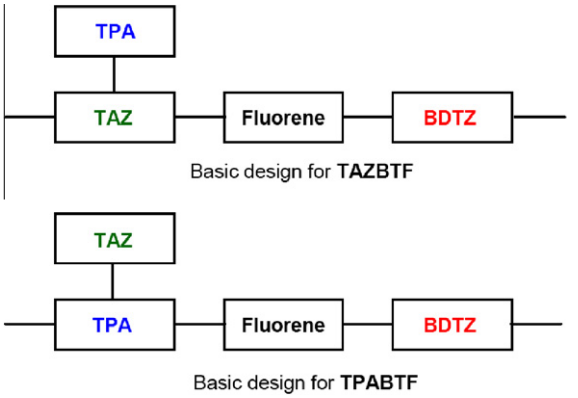

In this paper, contrary to the previous donor–acceptor main chain-pendant design, we report the synthesis and light-emitting properties of a series of copolymers containing electron-deficient main chains with electron-rich pendant groups. The electron-deficient main chains contain 1,2,4-triazole and 2,1,3-benzothiadiazole as their major components. The electron-rich side chains are mainly composed of triphenylamine groups. The thermal, PL, and EL properties of the polymers are discussed.

2. Experimental

2.1. Materials

N-Bromosuccinimide (Acros), 4-bromobenzoyl chloride (Fluka), phosphorus pentachloride (Riedel-de Haën), 4-nitrofluorobenzene (Acros), tin (II) chloride anhydrous (Showa), hydrazine monohydrate (Alfa Aesar), heptanoyl chloride (Acros), tetrakis(triphenylphosphine)palladium (0) (Acros), aluminum chloride (Acros), and 9,9-dioctylfluorene-2,7-diboronic acid bis(1,3-propanediol) ester (Aldrich) were used as received. *N*-Methyl-2-pyrrolidinone (NMP), *N,N*-dimethylacetamide (DMAc) and dimethyl sulfoxide (DMSO) were purchased from TEDIA, and tetrahydrofuran (THF), *N,N*-dimethylformamide (DMF) were purchased from ECHO. These solvents were distilled after drying with appropriate agents and stored over 4 Å molecular sieves. The surfactant trioctylmethylammonium chloride (Aliquat336®) was purchased from TCI and used as received.

2.2. Measurements

Infrared (IR) spectra were recorded on a PerkinElmer GX FT-IR spectrometer. NMR spectra were recorded using a BRUKER DRX-500 NMR (^{1}H at 500 MHz and ^{13}C at 125 MHz). Elemental analyses were made using a Perkin-Elmer 2400 instrument. Weight-average (M_w) and number-average (M_n) molecular weight were determined by gel permeation chromatography (GPC). Five Waters (Ultrastyragel) columns 300 × 7.7 mm (guard, 500, 10^3, 10^4, 10^5 in a series) were chained with a refractive index detector (RI 2000), using tetrahydrofuran (THF) (1 mL min^{-1}) as the eluent and polystyrene as the standard for GPC analysis. Thermogravimetric data were obtained

with a PerkinElmer Pyris 6 TGA under nitrogen flow at a rate of 20 cm^3 min^{-1} and a heating rate of 20 °C min^{-1}. Differential scanning calorimetric analysis was performed using a PerkinElmer Pyris DSC 6 under nitrogen flow at a rate of 20 cm^3 min^{-1} and a heating rate of 10 °C min^{-1}. Absorption spectra were recorded with a UV–Visible spectrometer (UV 500) at room temperature in air. Photoluminescence (PL) spectra were performed using a PerkinElmer LS 55 Luminescence spectrometer. Cyclic voltammetry (CHI model 619A) was conducted with the use of a three-electrode cell in which ITO was used as the working electrode, a platinum wire was used as the auxiliary electrode, and an Ag/AgCl couple was used as the reference electrode. Ferrocene was used as the internal standard for potential calibration.

2.3. EL device fabrication and characterization

PLEDs were fabricated into an ITO glass/PEDOT:PSS/polymer/LiF/Al structure. ITO-coated glass, with a sheet resistance of 15 Ω/sq, was purchased from Applied Film Corp. Glass substrates with patterned ITO electrodes were washed well and cleaned by an oxygen plasma treatment. A thin film (850 Å) of hole-transporting material poly(3,4-ethylenedioxythiophene):poly(styrene sulfonate) (PEDOT:PSS; Bayton PVPAI 8000) was spin-cast on the ITO glass, followed by spin-coating of the polymer film from the filtered (0.45-μm filter) dioxane solution (20 mg/mL). The films were dried at 80 °C for 1 h in a glove box. Subsequently, the metallic cathode was thermally deposited in a high-vacuum chamber (5×10^{-6} torr). Then, the PLED was transferred from the evaporation chamber to a glove box under nitrogen atmosphere (oxygen and moisture <1 ppm), inside which the device was then encapsulated with glass covers using UV-cured epoxy glue. Current–voltage characteristics were measured on a programmable source-meter (Keithley 2400). Luminance was recorded with a BM-8 luminance meter (Topcon).

2.4. Synthesis of monomers

The synthetic pathways are summarized in Scheme 1. Compounds **2**, **3**, **4**, and **8** were prepared and characterized as described in the literatures [3,4,32]. The syntheses of **5**, **6**, and the polymers **TAZF1**, **TAZF2**, and **TAZBTF** are summarized as follows.

2.4.1. 3,5-Bis-(4-bromophenyl)4-([4-(N,N-di(phenyl)amino)]phen-1-yl)-1,2,4-triazole (**5**)

Compounds **3** (2.70 g, 6.2 mmol) and **4** (3.40 g, 13 mmol) and xylene (80 mL) were added to a three-necked flask fitted with a stirrer. The mixture was refluxed with stirring at 160 °C for 72 h. After cooling, the solvent was evaporated to collect the crude product, which was further washed with hot ethanol and recrystallized from a cosolvent of ethanol and tetrahydrofuran (1:1) to yield **5** as gray–white crystals (65%): mp 294 °C (by DSC); FT-IR (KBr, cm^{-1}): 1072 (C–Br); 1509 (C=N). ^{1}H NMR ($CDCl_3$, ppm): δ 6.94–6.96 (d, 2H, Ar–H, *J* = 9.04 Hz), 7.00–7.02 (d, 2H, Ar–H, *J* = 8.82 Hz), 7.11–7.14 (m, 6H, Ar–H), 7.31–7.34 (t, 4H, Ar–H, *J* = 7.84 Hz), 7.38–7.40 (d, 2H, Ar–H, *J* = 8.41 Hz), 7.48–7.50 (d, 2H, Ar–H, *J* = 8.49 Hz). ^{13}C NMR ($CDCl_3$, ppm): δ 121.5, 124.6, 124.7, 125.2, 125.6, 126.2, 128.2, 129.7, 130.2, 131.7, 146.3, 149.4, 154.0. Anal. Calcd.

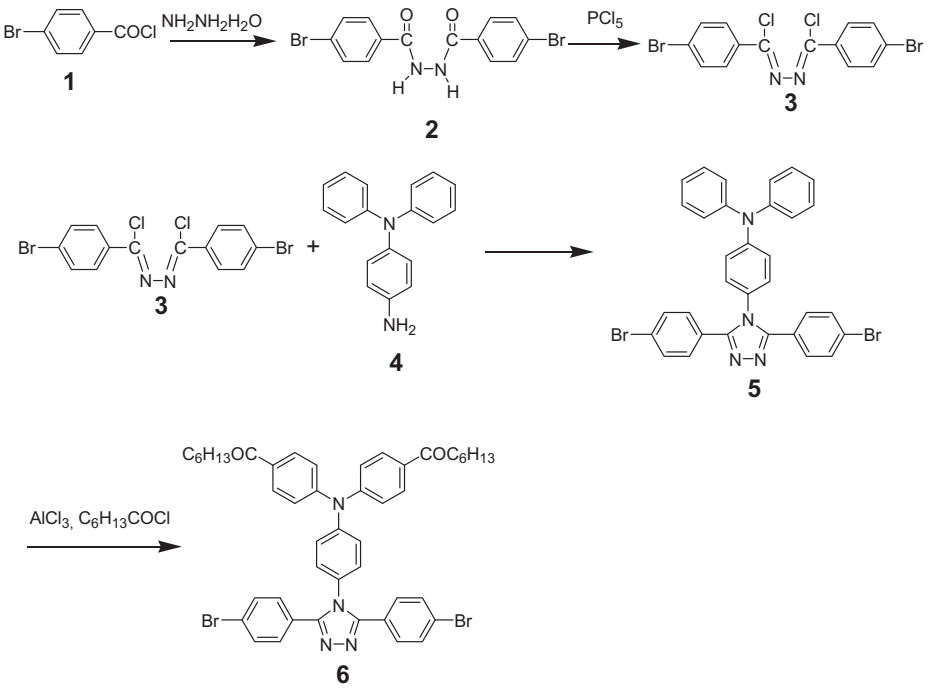

Scheme 1. Synthetic route for dipolar dibromo monomers.

for $C_{32}H_{22}Br_2N_4$: C, 61.76; N, 9.00; H, 3.56; found: C, 61.59; N, 8.90; H, 3.61.

*2.4.2. 3,5-Bis-(4-bromophenyl)4-([4-(N,N-di(4-heptanoylphen-1-yl)amino)]phen-1-yl)-1,2,4-triazole (**6**)*

$AlCl_3$ (1.41 g, 11 mmol), **5** (1.00 g, 1.6 mmol), and CH_2Cl_2 (50 mL) were added to a three-necked flask fitted with a stirrer. The mixture was stirred in an ice bath for 5 min under nitrogen atmosphere. A solution of heptanoyl chloride (1.8 mL, 12 mmol) in CH_2Cl_2 was added drop-wise into the mixture. The mixture was then allowed to further react for 4 h. The resulting mixture was quenched by pouring into water. The product was extracted into CH_2Cl_2 and washed with water several times. The extracts were then dried over anhydrous $MgSO_4$, concentrated, and purified with liquid column chromatography (silica gel, ethyl acetate/hexane (1/1) as eluent) to yield **6** (0.80 g, 59%) as a yellowish solid: mp 167 °C (by DSC); FT-IR (KBr, cm^{-1}): 1074 (C–Br); 1506 (C=N); 1685 (C=O); 2852, 2930 (alkyl group). ^1H NMR ($CDCl_3$, ppm): δ 0.84–0.89 (m, 6H, aliphatic H), 1.22–1.36 (m, 12H, aliphatic H), 1.67–1.73 (m, 4H, aliphatic H), 2.88–2.91 (t, 4H, aliphatic H, J = 7.38 Hz), 7.09–7.17 (m, 8H, Ar–H), δ 7.31–7.32 (d, 4H, Ar–H, J = 8.34 Hz), 7.45–7.46 (d, 4H, Ar–H, J = 8.24 Hz), 7.90–7.91 (d, 4H, Ar–H, J = 8.55 Hz). ^{13}C NMR ($CDCl_3$, ppm): δ 13.9, 22.4, 24.2, 28.9, 31.5, 38.3, 123.5, 124.5, 125.3, 125.4, 128.9, 129.7, 129.8, 130.0, 131.6, 132.7, 147.5, 149.8, 153.9, 198.8. Anal. Calcd. for $C_{46}H_{46}Br_2N_4O_2$: C, 65.25; N, 6.62; H, 5.48; found: C, 65.49; N, 6.52; H, 5.56.

*2.4.3. Preparation of **TAZF1**, **TAZF2** and **TAZBTF***

The polymers were prepared *via* the facile Suzuki coupling reaction (Scheme 2). The standard procedure for **TAZF2** is described below.

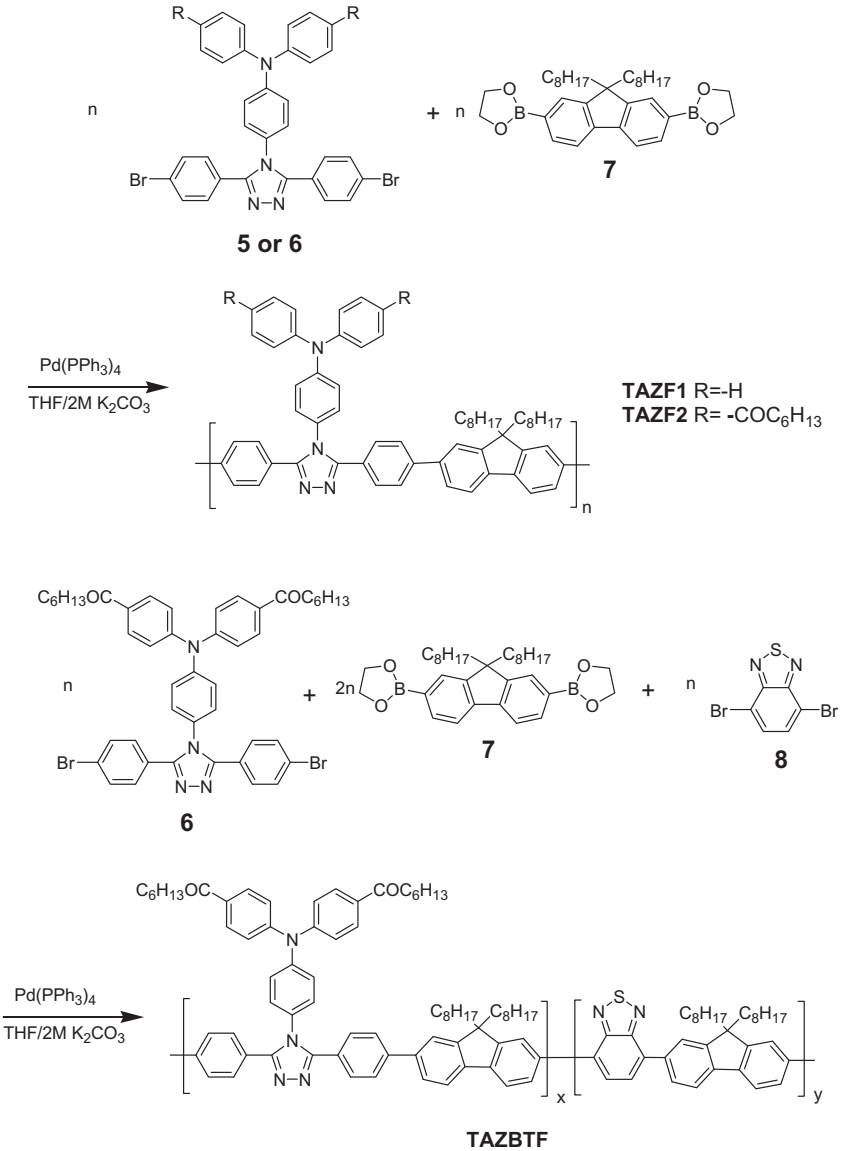

Scheme 2. Preparation of conjugated polymers.

To a mixture of **6** (1 g, 1.61 mmol) and 2,7-bis(4,4,5,5-tetramethyl-1,3,2-dioxaborolan-2-yl)-9,9-dioctylfluorene (**7**) (0.68 g, 1.22 mmol), several drops of Aliquat336® and $Pd(PPh_3)_4$ (0.027 g, 23 mmol) and aqueous K_2CO_3 (2 M, 6.7 mL) and toluene (20 mL) were added under argon. The mixture was heated to 110 °C and stirred for 96 h and then quenched by pouring into a mixture of deionized water and methanol (1:10). The precipitate was collected by filtration and dried. The precipitate was further purified by dissolving in $CHCl_3$ and re-precipitated into a mixture of deionized water and methanol several times. The polymer was further washed by Soxhlet extraction with methanol for 24 h. The polymer (**TAZF2**) was obtained after drying under vacuum at 60 °C overnight (0.708 g, 56%). FT-IR (KBr, cm^{-1}): 1507 (C=N); 1677 (C=O); 2852, 2924 (alkyl group). ^1H NMR ($CDCl_3$, ppm): δ 0.76–0.80 (m, 10H), 0.87–0.89 (t, 6H), 1.08–1.17 (m, 20H), 1.25–1.37 (m, 12H), 1.71–1.74 (t, 4H), 2.08 (s, 4H), 2.89–2.92 (m, 4H), 7.05–7.25 (m, 8H), 7.59–7.85 (m, 14H), 7.85–7.95 (m, 4H). Anal. Calcd. for $C_{75}H_{88}N_4O_2$: C, 83.60; N, 5.20; H, 8.23; found: C, 83.53; N, 5.06; H, 8.14.

The yield of **TAZF1** was 53%. Because **TAZF1** is highly insoluble in organic solvents, a good quality NMR is difficult to obtain. Therefore, **TAZF1** was characterized by FT-IR and elemental analysis. FT-IR (KBr, cm^{-1}): 1508 (C=N); 1676 (C=O); 2852, 2925 (alkyl group). Anal. Calcd. for $C_{61}H_{62}N_4$: C, 86.08; N, 6.58; H, 7.34; found: C, 86.56; N, 6.44; H, 7.16.

TAZBTF copolymer (98% yield) was prepared by reacting equal moles of **6** and **8**. FT-IR (KBr, cm^{-1}): 1507 (C=N); 1678 (C=O); 2853, 2925 (alkyl group). $^{1H\ NMR}$ ($CDCl_3$, ppm): δ 0.75–0.88 (m, 25H), 1.12–1.16 (m, 41H), 1.25–1.38 (m, 14H), 1.73 (t, 5H), 2.10 (d, 5H), 2.92 (s, 4H), 7.19–7.25 (m, 10H), 7.63–8.09 (m, 24H). Anal. Calcd. for $C_{110}H_{130}N_6O_2S$: C, 82.56; N, 5.25; H, 8.19; found: C, 81.56; N, 5.44; H, 8.16.

3. Results and discussion

Monomers **5** and **6** containing the electron-donating triphenylamine and the electron-accepting 1,2,4-triazole moieties were prepared as shown in Scheme 1. Bromobenzoyl chloride (**1**) was reacted with hydrazine hydrate to give hydrazide **2**, which was further chlorinated in the presence of PCl_5 to give chlorinated azine **3**. Cyclocondensation of compounds **3** and **4** gave compound **5**, which was further acetylated through Friedel–Crafts acylation to give **6**. Formation of the 1,2,4-triazole ring on **5** could be monitored by the change of a characteristic band in the FT-IR spectra; the characteristic band of the chlorinated azine **3** at 1571 cm^{-1} gradually disappeared as a new characteristic band of the 1,2,4-triazole ring appeared at 1509 cm^{-1}. Formation of **6** was evidenced by the appearance of a band at 1685 cm^{-1} for the carbonyl group in the IR spectrum. The NMR spectra and 2D C–H COSY of **5** are shown in the supplementary material (Fig. S1). Fig. 1 shows the ^1H NMR and ^{13}C NMR spectra of **6** in $CDCl_3$. In the ^1H NMR spectrum of **6**, the H_g shifted to δ 7.90 ppm due to incorporation of the electron-withdrawing carbonyl groups at the *para*-positions. The peaks appearing at δ 0.8–2.9 ppm with correct integral ratios for the aliphatic protons indicated that the acylation was completely carried out as proposed. In the ^{13}C NMR spectrum, observation of 6 peaks of the aliphatic carbons, 13 peaks of the aromatic carbons, and 1 peak of carbonyl carbon at 198.8 ppm again supported the proposed structure.

Fluorene-based conjugated polymers were readily prepared by facile Suzuki cross-coupling of **7** with **5/6** and **8** as shown in Scheme 2. The polymerization was carried out in a mixture of aqueous $NaHCO_3$ and THF with freshly prepared $Pd(PPh_3)_4$ as the catalyst. Unfortunately, the solubility of **TAZF1** obtained by this approach was so poor that **TAZF1** could only be identified by FT-IR and elemental analysis, which supported the proposed structure. In contrast, **TAZF2** and **TAZBTF** are soluble in several different organic solvents and, therefore, could be further identified by NMR. In the FT-IR spectra, the observation of the characteristic bands of 1,2,4-triazole at 1507 cm^{-1} and of the alkyl chains at 2852 and 2925 cm^{-1} strongly suggested polymeric structures. Moreover, disappearance of the characteristic stretching C–Br band of the dibromo monomers at 1074 cm^{-1} is consistent with the assumption of condensation polymerization. The ^1H NMR spectra of **TAZF2** and **TAZBTF** are illustrated in Fig. 2. The spectra are assigned by matching the chemical-shift data with those of the corresponding dibromo and fluorene monomers. For **TAZBTF**, the copolymerized segment ratio (x/y) of 5/6 was determined (Fig. 2B) on the basis of the peak integrals of H_e (α-protons adjacent to the C=O groups) against the total aliphatic protons attached to triphenylamine and fluorene moieties.

The molecular weights and thermal properties of the conjugated polymers are summarized in Table 1. The weight-average molecular weights (M_w) of the polymers were 1.28×10^4 and 2.56×10^4 for **TAZF2** and **TAZBTF**, respectively, as measured by gel permeation chromatography (GPC) relative to the polystyrene standards. The thermal properties of the conjugated polymers were evaluated by differential scanning calorimetry (DSC) and thermogravimetric analysis (TGA). The glass transition temperatures (T_g) of the polymers were found to be 153–185 °C, which are much higher than that of poly(9,9-dioctylfluorene) (**POF**; T_g = 75 °C) [28]. The thermal properties reported in the literature [4] for polymers **TPAF** and **TPABTF** containing triphenylamine main chains and 1,2,4-triazole pendant groups were collected in the table for comparison. It is evident that incorporation of the rigid 1,2,4-triazole and triphenylamine subunits into the polymer enhances the rigidity of the chain and increases T_g. Obviously, **TAZF1** and **TAZF2**, with their 1,2,4-triazole main chains, show much higher T_g than previously reported for **TPAF** (135 °C) [4], in which the triphenylamine is in the main chain. However, **TPABTF** and **TAZBTF** containing 2,1,3-benzothiadiazole (**BTDZ**) moiety have similar T_gs. In contrast, the thermal properties of these polymers with 1,2,4-triazole main chains exhibit slightly lower degradation temperatures than the reported polymers with triphenylamine main chains due to the lower molecular weight and higher content of aliphatic segments.

The results of the qualitative solubility test (1 mg/10 mL) of the polymers are summarized in Table 2. The

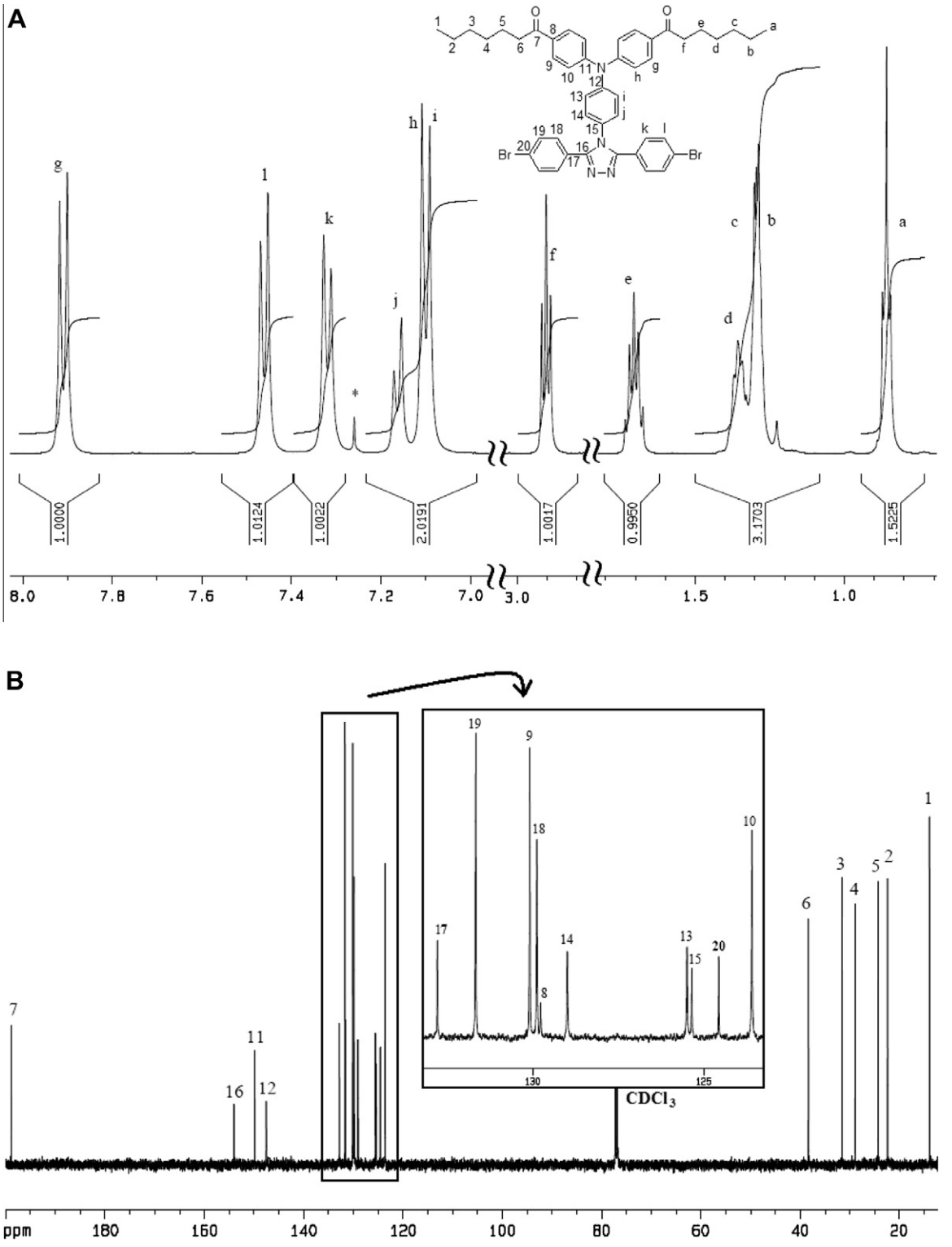

Fig. 1. (A) ^{1}H NMR, (B) ^{13}C NMR spectra of the dibromo monomer **6.**

previously reported **TPAF** exhibited good solubility due to the propeller triphenylamine structure in the main chain [4]. However, **TAZF1** has much lower solubility in comparison to **TPAF** due to its relatively rigid 1,2,4-triazole main chain structure. However, **TAZF2** was reasonably soluble or partially soluble in some organic solvents; the aliphatic

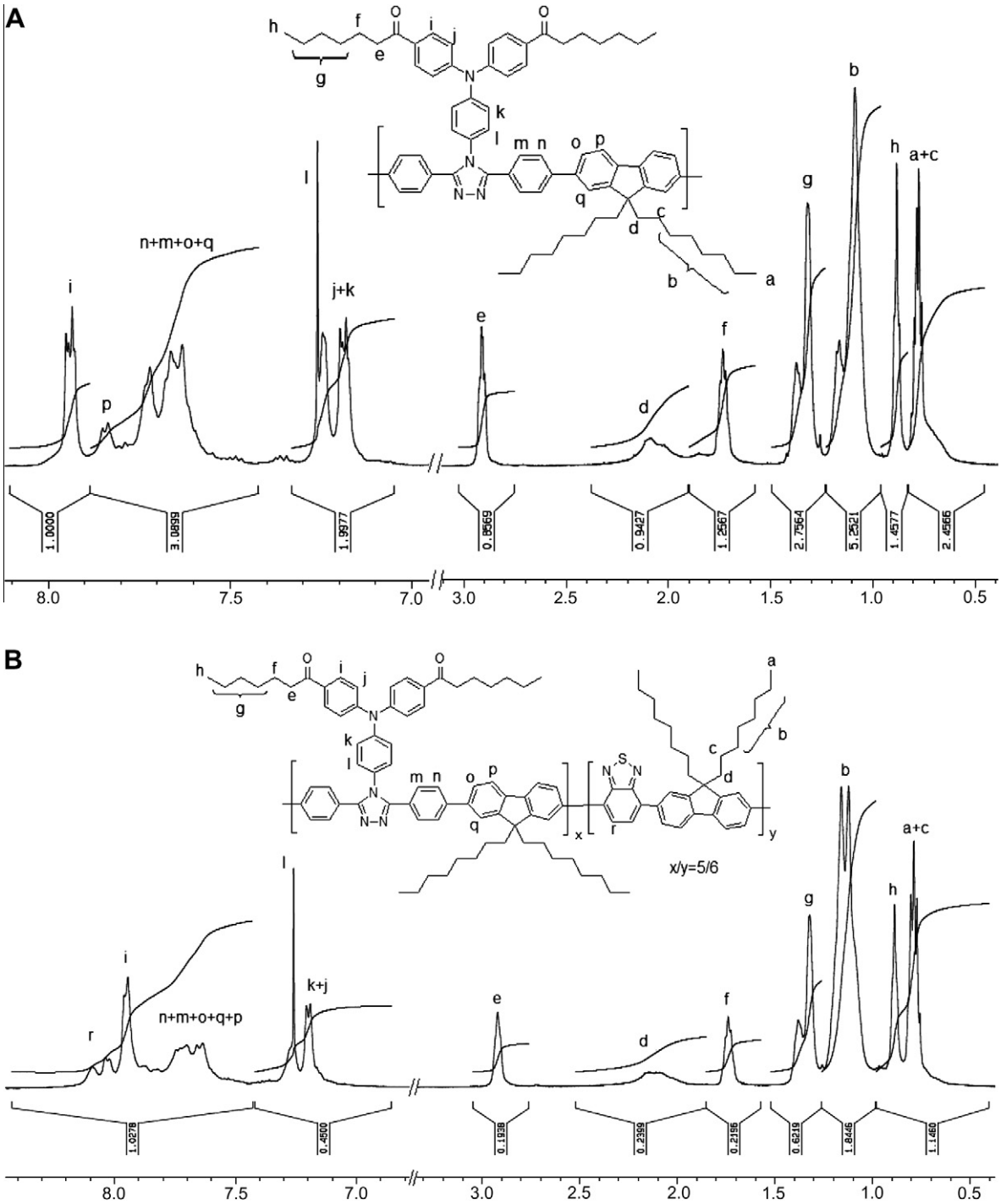

Fig. 2. ^{1}H NMR spectrum of conjugated polymers: (A) **TAZF2** and (B) **TAZBTF**.

side chains attached on the triphenylamine help **TAZF2** to increase the solubility. The **TAZBTF** shows much better solubility due to the higher flexible aliphatic contents.

The optical properties of the conjugated polymers are summarized in Table 3. The optical properties of the polymers were investigated by UV–Vis and photoluminescence spectroscopy in the solid state and in chloroform (1 mg/10 mL). The UV–Vis and photoluminescence spectroscopy of the polymers are shown in Fig. 3. In chloroform, **TAZF2** exhibits absorption with λ_{max}^{UV} at 355 nm (Fig. 3A). By comparing this spectrum with the absorption spectra of poly(9,9-dioctylfluorene) (**POF**), one might ascribe the

Table 1
Molecular weights and thermal properties of the conjugated polymers.

Polymer	GPC data[a]			Thermal properties[b]		
	M_w	M_n	PDI	T_g	Td_5	Td_{10}
TAZF1	–[c]	–[c]	–[c]	178	383	427
TAZF2	12,800	8500	1.49	185	411	436
TAZBTF	25,600	13,000	1.95	153	406	434
TPAF [4]	32,500	20,500	1.58	135	428	455
TPABTF [4]	38,000	24,000	1.60	155	433	456

[a] The molecular weights are relative to polystyrene standard.
[b] By DSC and TGA measurements, respectively. Td_5 and Td_{10} are 5% and 10% degradation temperature, respectively.
[c] The polymer is insoluble in THF.

absorption at 355 nm to a π–π* transition derived from the conjugated polymer backbone. However, a blue shift by 36 nm relative to that observed for **POF** (at 391 nm) [33] is due to the twist (31–35°) between 1,2,4-triazole and adjacent phenyl in the main chain (see below), which shortens the conjugated length of the polymer. Thin-film **TAZF2** shows an absorption peak at 356 nm, which is close to that in solution. The cut-off for absorption was 404 nm for the film state, and the optical energy band gap (E_g) was calculated to be 3.1 eV. **TAZF2** emits blue fluorescence with λ_{max}^{PL} at 425 nm in chloroform, while in solid film the emission is slightly blue-shifted and exhibits λ_{max}^{PL} at 413 nm (Fig. 3A). The charge-transfer properties in the excited-state emission in chloroform are apparently significant so that a broad and red-shifted emission band was observed. Low PL quantum yield (Φ_f) of 0.29 in chloroform and 0.08 in the film state for **TAZF2**, as excited at 355 nm, were recorded by comparing against the fluorescence standard 9,10-diphenylanthrancene (Φ_f = 0.9).

For **TAZBTF**, two major bands are observed at 435 and 345 nm in chloroform (Fig. 3B). The first absorption band at 435 nm is attributed to the π–π* transitions of the benzothiadiazole–fluorene component of the main chain. The second absorption band at 345 nm might arise from the π–π* transition of the conjugated polymer backbone. However, a red shift by 10 nm relative to that was observed for **TAZF2**. **TAZBTF** fluoresces at λ_{max}^{PL} of 538 nm in chloroform. Because the emission from the **TAZ** subunit at 425 nm has a good overlap with the spectral absorption of the **BTDZ** subunit at 435 nm, Förster energy transfer [34] from **TAZ** to **BTDZ** is expected so that light emission at 425 nm is quenched and transferred to the emission at 538 nm. Similarly, emission with λ_{max}^{PL} at 541 nm was found in solid film. The emission is red-shifted by 113 and 128 nm in comparison to the spectra observed for **TAZF2** in solution and in the film state, respectively (Table 3). The high quantum yield of **TAZBTF** is over 0.9 in solution [35] indicating that the Förster energy transfer from the **TAZ** to **BTDZ** unit is efficient. Although the quantum yield of 0.4 in the film state is higher than that of 0.08 for **TAZF2** in solid film, this value is relatively low in comparison to that in solution as well as to other **BTDZ**-based polymers reported in the literature [35], indicating that fluorescence quenching would occur in solid films.

Careful study of the PL spectra of **TAZBTF** in $CHCl_3$ revealed that some residue emission from the **TAZ** component exists at 425 nm. Although this detectable emission was concentration-dependent, the corresponding PL intensity was very weak even under high dilution (<2%) (Fig. 4). Because the ratio of the integrated intensities of 550 nm peaks to 425 nm peaks can be considered a measure of internal energy transfer efficiency from **TAZ** subunits to **BTDZ** subunits [35], this result indicates that the internal Föster energy transfer is efficient and may play a major role in the energy transfer process. However, the energy transfer might still operate intermolecularly at high concentration or in the condensed phase and cannot be simply

Table 2
Solubilities of the conjugated polymers.[a]

Polymer	CH_2Cl_2	$CHCl_3$	THF	Toluene	Dichlorobenzene	1,4-Dioxane
TAZF1	–	–	–	–	–	–
TAZF2	+–	++	+–	+–	+–	+–
TAZBTF	++	++	++	+–	++	+–
TPAF [4]	++	++	++	+–	++	++
TPABTF [4]	++	++	++	+–	++	+–

[a] The solubility was measured in the concentration of 1 mg/mL. ++: soluble at room temperature; +–: partially soluble at room temperature; –: insoluble on heating.

Table 3
Optical properties of the conjugated polymers.

Polymer	λ_{max}^{UV} (nm)		λ_{max}^{PL} (nm)[a]		Φ_f (%)[b]		
	Chloroform	Film	Chloroform	Toluene	Film	Chloroform	Film
TAZF2	355	356	425	–	413	28.5	8.3
TAZBTF	345, 435	347, 450	538	522	541	>90	39.9
TPAF [4]	275, 371	280, 364	421, 442	–	435	>90	18.4
TPABTF [4]	346, 438	346, 453	543	526	546	>90	33.1

[a] The maximum wavelength (nm) of photoluminescence was excited by the maximum wavelength (nm) of absorption.
[b] The PL quantum yields (Φ_f) were measured relative to a 9,10-diphenylanthrancene (Φ_f = 0.9) standard.

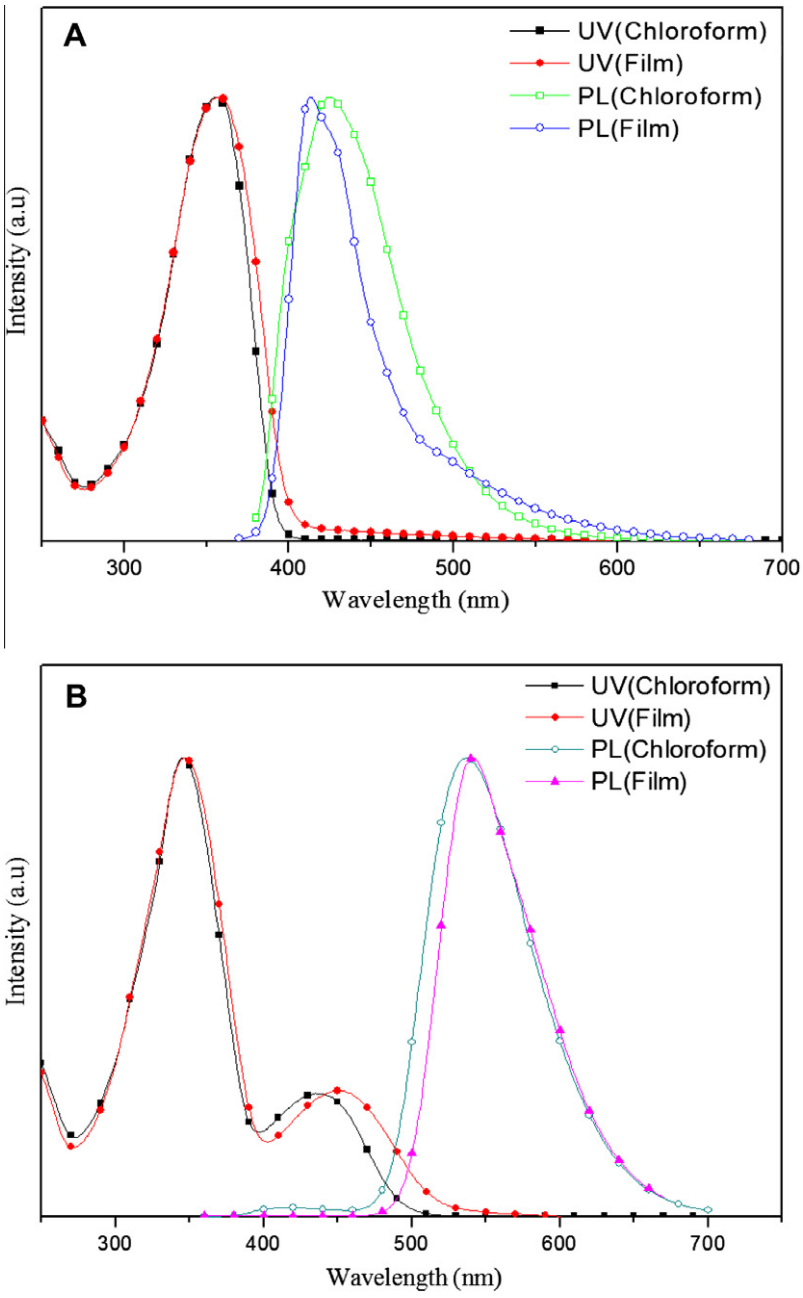

Fig. 3. Absorption and PL spectra of the conjugated polymers: (A) **TAZF2** and (B) **TAZBTF**.

excluded [36,37]. The Stokes shifts for polymer films are greater than 57 nm (Table 3), indicating that the spectral overlap between PL and UV spectra is not significant. Therefore, the interference in the emissive spectral properties of **TAZF2** and **TAZBTF** in the solid phase through self-absorption in luminescence should be insignificant.

Theoretical studies provide insights into polymers and have been making a great contribution to support experimental results [38–40]. To better understand the absorption behavior of the polymers, we used density functional theory (DFT) and semiempirical ZINDO calculation to study the electronic and optical properties of the polymers. All theoretical calculations in this study are carried out using quantum mechanical package Gaussian 03. The electronic states for the polymers are determined using DFT calculation with the B3LYP functional and the 6-31G* basis set. The calculated excitation energies with the largest oscillator strength (f) are compared to the maximum absorption in UV–Vis spectrum. The simulated results with two repeating units ($n = 2$) are shown in Fig. 5. Fig. 5A shows that the $S_0 \rightarrow S_5$ electronic transition has the largest oscillator strength for **TAZF2** with maximum absorption at

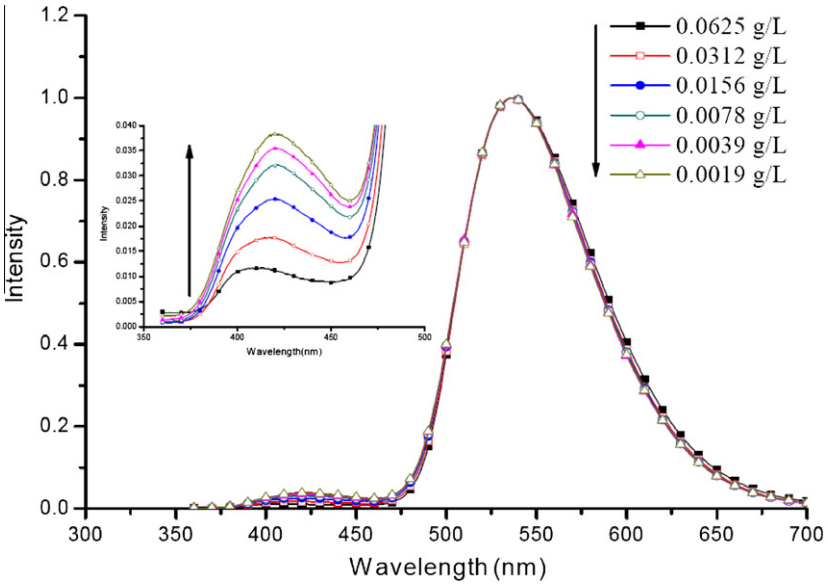

Fig. 4. Emission spectra of the polymer **TAZBTF** in chloroform solution at different concentrations.

357 nm, which corresponds to the maximum absorption at 355 nm in the UV–Vis spectrum. The HOMO → LUMO+2 transition mainly dominates the $S_0 \rightarrow S_1$ transition, and the absorption is mainly distributed by the charge transfer from the conjugated main chain to the triphenylamine side chain. For **TAZBTF** polymer (Fig. 5B), the $S_0 \rightarrow S_1$, $S_0 \rightarrow S_7$ and $S_0 \rightarrow S_9$ electronic transitions have the larger oscillator strengths with maximum absorption at 499, 360 and 352 nm, respectively. The HOMO−1 → LUMO transition mainly dominates the $S_0 \rightarrow S_1$ transition, and the absorption is mainly distributed by the charge transfer from the conjugated main chain to the 2,1,3-benzothiadiazole (**BTDZ**) moiety. The HOMO → LUMO+6 and HOMO-3 → LUMO+1 transitions mainly dominate, respectively, the $S_0 \rightarrow S_7$ and $S_0 \rightarrow S_9$ transitions, and the absorptions are mainly distributed by the combination of π–π^* transitions in the main chain. The UV–Vis spectra for the polymers are also calculated based on the electronic states as shown in Fig. 6. The calculated results are comparative to the experimental results in Fig. 3, especially for **TAZF2**. For **TAZBTF**, the $S_0 \rightarrow S_7$ and $S_0 \rightarrow S_9$ electronic transitions with maximum absorption at 360 and 352 nm, respectively, are converse to an absorption peak corresponding to the actual absorption at 345 nm. The $S_0 \rightarrow S_1$ electronic transition with maximum absorption at 499 nm corresponds to the actual absorption at 435 nm.

The electrochemical behavior of the polymers was investigated by cyclic voltammetry (CV) (Fig. 7). From the oxidation potential relative to ferrocene/ferrocenenium, which refers to an energy level of −4.8 eV below the vacuum level, we can estimate the HOMO energy level of the conjugated polymers, although the LUMO level of the polymers could, in principle, be estimated according to the equation: LUMO = HOMO + E_g, where E_g is the value of the optical band gap. The HOMO and LUMO values of the polymers are summarized in Table 4. The HOMO and LUMO values of **TAZF2** and **TAZBTF** were found to be −5.72 and −2.62 eV, and −5.78 and −3.40 eV, respectively. According to the above results, we first conclude that the HOMO and LUMO levels of **TAZF2** and **TAZBTF**, with 1,2,4-triazole main chains and triphenylamine pendant groups, are much lower than those of **TPAF** and **TPABTF** with triphenylamine main chains and 1,2,4-triazole pendant groups. However, the energy gaps for the similar polymer pairs (**TAZF2** *vs* **TPAF** and **TAZBTF** *vs* **TPABTF**) are almost the same. As simulated results shown in Fig. 5, the HOMOs and LUMOs were controlled by the conjugated backbone. Therefore, the polymers with triazole acceptor moieties in the main chain will lower the HOMOs and LUMOs comparing to those polymers with triphenylamine donor moieties in the main chain. Because the similar polymers have the same functional moieties in the polymer structure, the HOMOs and LUMOs decrease in the similar values that makes the band gaps are almost the same for the polymer pairs. The polymers with **BTDZ** in the main chain (**TAZBTF** and **TPABTF**) have lower HOMOs and LUMOs than those (**TAZF2** and **TPAF**) without **BTDZ** due to the same reason. The second conclusion from the experimental results is that the polymers with **BTDZ** in the main chain (**TAZBTF** and **TPABTF**) have lower energy gaps than those (**TAZF2** and **TPAF**) without **BTDZ** moieties. As sown in the simulation, the **BTDZ** involves in the main chain conjugation. Therefore, the **BTDZ** increases the conjugation lengths and results in smaller energy gaps of the polymers (**TAZBTF** and **TPABTF**).

To further understand the optoelectronic properties of the polymers, electroluminescence (EL) devices were fabricated with the configuration ITO/HTL/polymer/cathode, in which poly(3,4-ethylenedioxythiophene):poly(styrene sulfonic acid) (PEDOT:PSS) or poly(vinyl carbazole) (**PVK**) was used as the hole-injection layer. The hole-transporting **PVK** was blended with the emissive polymer due to good solu-

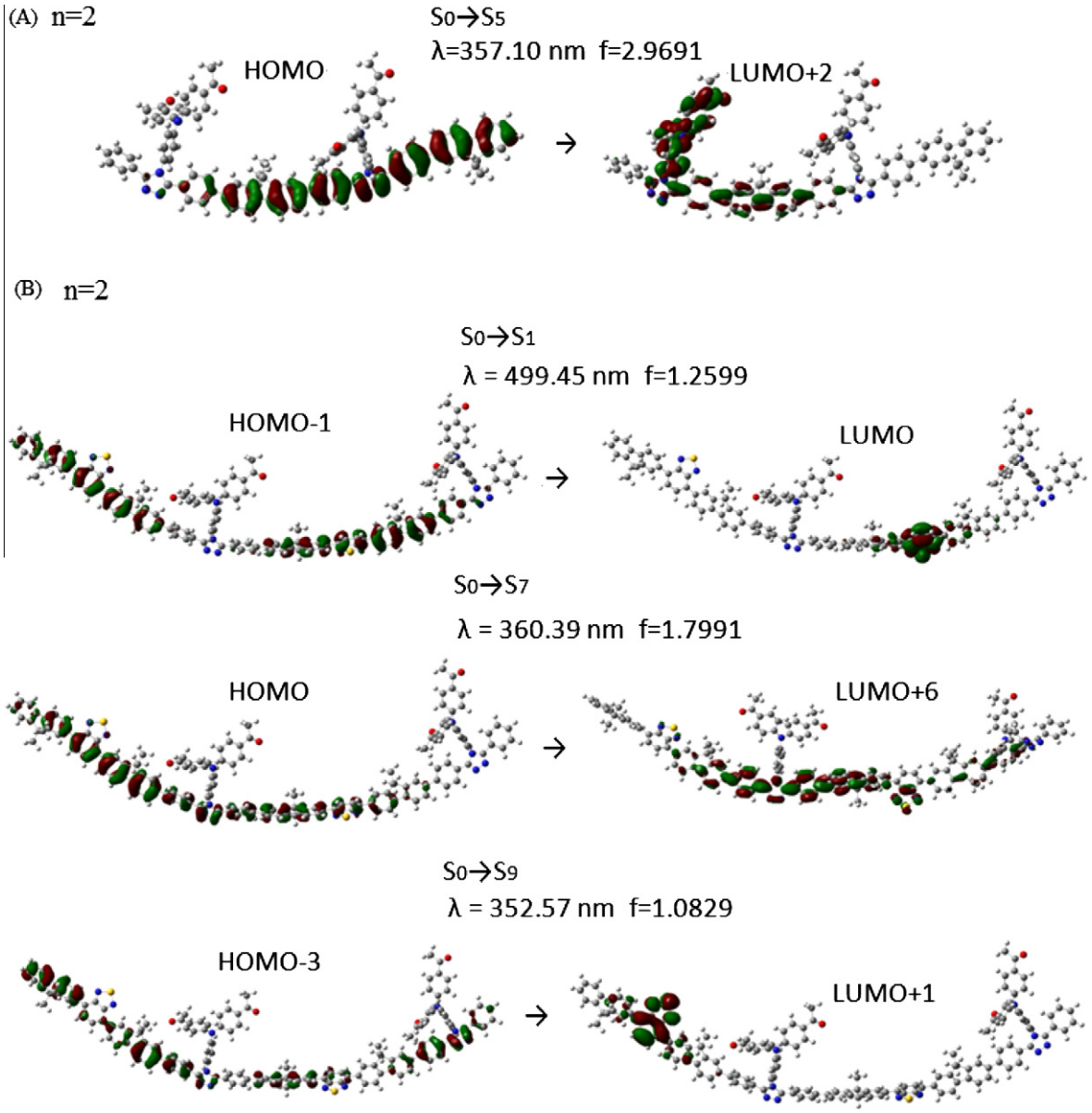

Fig. 5. Electron distribution in Frontier molecular orbitals for (A) **TAZF2** and (B) **TAZBTF** with two repeating units ($n = 2$).

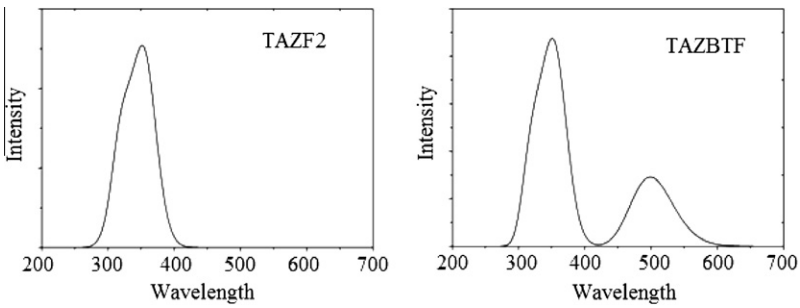

Fig. 6. Calculated UV–Vis spectra for **TAZF2** and **TAZBTF.**

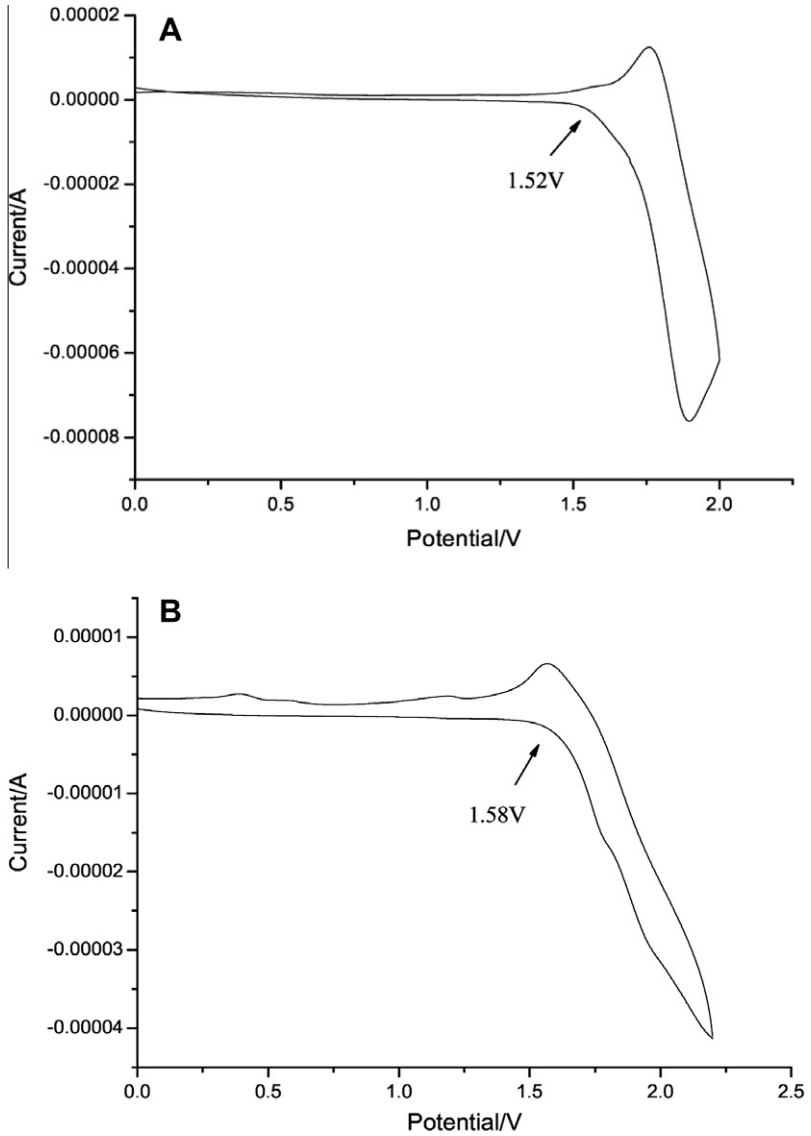

Fig. 7. CV diagrams of (A) **TAZF2** and (B) **TAZBTF**.

Table 4
Electrochemical properties of the conjugated polymers.

Polymer	E_g (eV)[a]	E_{onset} (V)[b]	HOMO (eV)[c]	LUMO (eV)[c]
TAZF2	3.10	1.52	−5.72	−2.62
TAZBTF	2.38	1.58	−5.78	−3.40
POF [33]	2.95	1.40	−5.80	−2.85
TPAF [4]	2.91	1.11	−5.31	−2.39
TPABTF [4]	2.36	1.18	−5.38	−3.02

[a] Energy gap (E_g) = 1240/λ_{onset} (nm).
[b] Initial oxidation potential in film state.
[c] HOMO = $-(E_{ox,onset} - E^{Fc}_{ox,onset}) - 4.8$; LUMO = E_g − HOMO.

bility in chloroform; it is likely that the interface between the **PVK** and polymer layer is diffused rather than being flat and well defined. Two layers of Mg or Ca followed by Ag (150 nm) were used as the cathode. The EL performance of all devices obtained from the current density (J)–voltage (V)–luminance (L) characteristics is summarized in Table 5. The relative energy level diagrams for the devices are sketched in Fig. 8.

Among the devices we fabricated, the EL devices of **TAZF2** are non-emissive. However, devices I and II, using **TAZBTF** as the emissive layer, exhibit green–yellow emission with λ_{max} (EL) at 534–542 nm, similar to the PL emission. This result suggests that the **BTDZ** subunit functions as the major core of light emission; all excitons formed within the polymer matrix will have their energy transferred to the **BTDZ** subunit to emit. It should be noted that the devices using the same PEDOT:PSS as the hole-injection layer but using different metallic cathodes of Mg and Ca show the same switch-on voltage at 8 V. This result implies that the electron-injection could not be improved even using a metal with a lower work function. This phe-

Table 5
EL performance of devices with configuration of ITO/HTL/polymer/metal.

Device	HTL[a]	Polymer	Cathode	V_{on} (V)[b]	L_{max} (cd/m^2)[c]	E_{max} (cd/A)[d]	λ_{max}^{EL} (nm)	CIE (x, y)
I	PEDOT	**TAZBTF**	Mg:Ag	8	147	2.07	538	0.340, 0.615
II	PEDOT	**TAZBTF**	Ca:Ag	8	172	2.60	542	0.339, 0.624
III	–	**TAZBTF** **PVK** (10%)	Ca:Ag	15	392	0.208	534	0.328, 0.628
I′ [4]	PEDOT	**TPABTF**	Mg:Ag	7	516	1.24	544	0.355, 0.618
II′ [4]	PEDOT	**TPABTF**	Ca:Ag	5	696	2.02	542	0.345, 0.625
III′ [4]	–	**TPABTF** **PVK** (5%)	Ca:Ag	14	629	0.06	538	0.306, 0.628

[a] Hole transporting layer.
[b] Turn-on voltage observed at 1 cd/m^2.
[c] Maximum luminance.
[d] Maximum luminance efficiency.

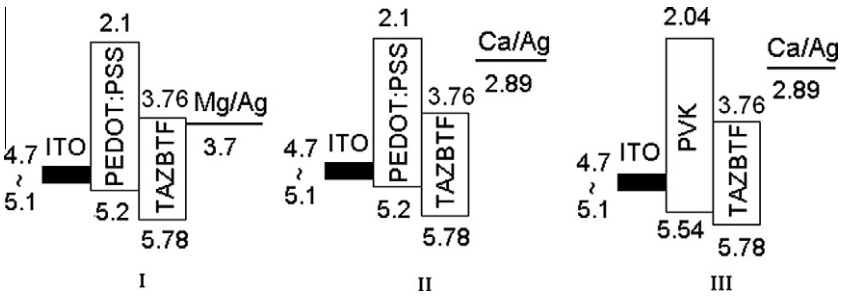

Fig. 8. Relative energy level diagrams for the devices.

nomenon can be rationalized by the low-lying LUMO level of −3.40 eV for **TPABTF**; electron injection either from Mg or Ca cathode into the LUMO of the polymer matrix should be energetically favorable (Fig. 8C). Nevertheless, the switch-on voltage of 8 V is relatively high in comparison to the devices of **TPABTF**. We attribute this to the lower-lying HOMO level of the triphenylamine units on **TAZBTF**. The large energy gap of 0.58 eV between the PEDOT:PSS and **TAZBTF** (Fig. 8D) might become a major factor in causing a high Fowler–Nordheim barrier for tunneling injection. Furthermore, the presence of the barrier may also prevent high current injection into the device, limiting the value of the highest brightness. Nevertheless, the luminance efficiencies of the EL devices are as high as 2.07 and 2.60 cd/A, indicating a good balance of charge carriers within the device.

Jen has recently found that conjugated polymers having electron-deficient benzothiadiazole main chains show very poor electron-injection ability compared to polymers with electron-rich polyfluorene main chains [41]. This phenomenon is quite different from that obtained from conventional designs of electron-injection materials. Similar to Jen's observations, the low brightness with high efficiency strongly indicates in our EL devices the difficulty of charge injection through both electrodes, which limits the carrier density inside the polymer matrix.

The reasons for the failure of the EL devices using **TAZF2** are still unclear. In our device, the triphenylamine group is also the major hole-transport component, which is oxidized to form a radical cation under applied electrical potentials. Luminescence quenching can be by two basic mechanisms: (1) normal diffusional or dynamic quenching of Stern–Volmer type and (2) associational or static quenching where the donor and quencher form a nonluminescent association pair which reduces the amount of excitation energy absorbed by potentially luminescent donors [42]. Brudvig et al. reported that oxidized chlorophyll (a redox-active site) is a potent quencher of chlorophyll fluorescence with 15% of oxidized chlorophyll sufficient to quench 70% of the fluorescence intensity, which involves electron donation to the electron donor [43]. The situation is not the same but similar to this system. Therefore, we suppose that formation of the triphenylaminyl radical cation during hole-injection may lead to a quenching effect that prohibits its electroluminescence in the **TAZ** group.

Blending 10% hole-transporting **PVK** with a **TAZBTF** emissive layer, device III exhibits electroluminescence with higher brightness but much lower efficiency. Because the introduction of **PVK** in the blending approach plays a role in reducing the hole-injection barrier (Fig. 8E), higher current density is allowed, which leads to higher brightness. Because **PVK** is unable to function effectively as an electron block, charge recombination within the **PVK** matrix may cause the low efficiency.

Comparing the structural designs of **TPABTF** and **TAZBTF**, the electron-deficient **TAZ** group was incorporated into the main chain while the electron-rich **TPA** group was grafted as the pendant group in **TAZBTF**. The re-

ported EL performance of devices fabricated from **TPABTF** is also shown in Table 5 for comparison. Under this configuration, the HOMO and LUMO of the polymers were significantly altered by exchanging the structures in main chain and pendant group. These changes are reflected in the HOMO–LUMO values of **TAZBTF**, which are approximately 0.4 eV lower than those of **TPABTF** (Table 4). However, similar photophysical properties are maintained. These provide us an opportunity to tune the HOMO–LUMO levels of the polymers.

4. Conclusion

Conjugated polymers containing electron-deficient 1,2,4-triazole-fluorene main chains and electron-rich triphenylamine pendant groups were successfully synthesized *via* the Suzuki coupling reaction. The thermal stability of the conjugated polymers was enhanced due to introduction of the rigid bipolar component. The incorporation of 2,1,3-benzothiadiazole structure further reduced the coplanarity of the conjugated polymer. Intramolecular and intermolecular energy transfers were clearly evidenced, leading to a shift of PL and EL to the yellow–green region. The connection of functional moiety in the polymer strongly is an approach to tune the HOMO and LUMO energy levels of the polymers.

Acknowledgements

Financial support by National Science Council of Taiwan (NSC98-2221-E-027-002; NSC98-2119-M-002-006-MY3) and Thematic Project, Academia Sinica is gratefully acknowledged. The authors would also like to thank Ms. S.-H. Wang (Taipei Medical University) for NMR technical support.

Appendix A. Supplementary data

Supplementary data associated with this article can be found, in the online version, at doi:10.1016/j.orgel.2011.03.020.

References

[1] G. Zhang, W. Li, B. Chu, Z. Su, D. Yang, F. Yan, Y. Chen, D. Zhang, L. Han, J. Wang, H. Liu, G. Che, Z. Zhang, Z. Hu, Highly efficient photovoltaic diode based organic ultraviolet photodetector and the strong electroluminescence resulting from pure exciplex emission, Org. Electron. 10 (2009) 352–356.
[2] B. Ma, B.J. Kim, L. Deng, D.A. Poulsen, M.E. Thompson, J.M.J. Fréchet, Bipolar copolymers as host for electroluminescent devices: effects of molecular structure on film morphology and device performance, Macromolecules 40 (2007) 8156–8161.
[3] S.H. Chen, Y. Chen, Poly(p-phenylenevinylene) derivatives containing electron-transporting aromatic triazole or oxadiazole segments, Macromolecules 38 (2005) 53–60.
[4] S.T. Huang, D.J. Liaw, L.G. Hsieh, C.C. Chang, M.K. Leung, K.L. Wang, W.T. Chen, K.R. Lee, J.Y. Lai, L.H. Chan, C.T. Chen, Synthesis and electroluminescent properties of polyfluorene-based conjugated polymers containing bipolar groups, J. Polym. Sci. A Polym. Chem. 47 (2009) 6231–6245.
[5] C.C. Chi, C.L. Chiang, S.W. Liu, H. Yueh, C.T. Chen, Achieving high-efficiency non-doped blue organic light-emitting diodes: charge-balance control of bipolar blue fluorescent materials with reduced hole-mobility, J. Mater. Chem. 19 (2009) 5561–5571.
[6] H. Wu, J. Zou, F. Liu, L. Wang, A. Mikhailovsky, G.C. Bazan, W. Yang, Y. Cao, Efficient single active layer electrophosphorescent white polymer light-emitting diodes, Adv. Mater. 20 (2008) 696–702.
[7] M.H. Kim, M.J. Cho, K.H. Kim, M.H. Hoang, T.W. Lee, J.I. Jin, N.S. Kang, J.W. Yu, D.H. Choi, Organic donor-σ-acceptor molecules based on 1,2,4,5-tetrakis((E)-2-(5′-hexyl-2,2′-bithiophen-5-yl)vinyl)benzene and perylene diimide derivative and their application to photovoltaic devices, Org. Electron. 10 (2009) 1429–1441.
[8] S. Karak, V.S. Reddy, S.K. Ray, A. Dhar, Organic photovoltaic devices based on pentacene/N,N′-dioctyl-3,4,9,10-perylenedicarboximide heterojunctions, Org. Electron. 10 (2009) 1006–1010.
[9] J.D. Myers, T.K. Tseng, J. Xue, Photocarrier behavior in organic heterojunction photovoltaic cells, Org. Electron. 10 (2009) 1182–1186.
[10] E. Zhou, S. Yamakawa, K. Tajima, C. Yang, K. Hashimoto, Synthesis and photovoltaic properties of diketopyrrolopyrrole-based donor–acceptor copolymers, Chem. Mater. 21 (2009) 4055–4061.
[11] S. Celebi, A. Balan, B. Epik, D. Baran, L. Toppare, Donor acceptor type neutral state green polymer bearing pyrrole as the donor unit, Org. Electron. 10 (2009) 631–636.
[12] M. Içli, M. Pamuk, F. Algi, A.M. Önal, A. Cihaner, A new soluble neutral state black electrochromic copolymer via a donor–acceptor approach, Org. Electron. 11 (2010) 1255–1260.
[13] A. Benor, A. Hoppe, V. Wagner, D. Knipp, Electrical stability of pentacene thin film transistors, Org. Electron. 8 (2007) 749–758.
[14] D.H. Kim, B.L. Lee, H. Moon, H.M. Kang, E.J. Jeong, J.I. Park, K.M. Han, S. Lee, B.W. Yoo, B.W. Koo, J.Y. Kim, W.H. Lee, K. Cho, H.A. Becerril, Z. Bao, Liquid-crystalline semiconducting copolymers with intramolecular donor–acceptor building blocks for high-stability polymer transistors, J. Am. Chem. Soc. 131 (2009) 6124–6132.
[15] W. Wu, Y. Liu, Y. Wang, H. Xi, X. Gao, C. Di, G. Yu, W. Xu, D. Zhu, High-performance, low-operating-voltage organic field-effect transistors with low pinch-off voltages, Adv. Funct. Mater. 18 (2008) 810–815.
[16] K.L. Wang, Y.L. Liu, J.W. Lee, K.G. Neoh, E.T. Kang, Nonvolatile electrical switching and write-once read-many-times memory effects in functional polyimides containing triphenylamine and 1,3,4-oxadiazole moieties, Macromolecules 43 (2010) 7159–7164.
[17] G. Liu, Q.D. Ling, E.T. Kang, K.G. Neoh, D.J. Liaw, F.C. Chang, C.X. Zhu, D.S.H. Chan, Bistable electrical switching and write-once read-many-times memory effect in a donor–acceptor containing polyfluorene derivative and its carbon nanotube composites, J. Appl. Phys. 102 (2007), Art No. 024502.
[18] Y.L. Liu, K.L. Wang, G.S. Huang, C.X. Zhu, E.S. Tok, K.G. Neoh, E.T. Kang, Volatile electrical switching and static random access memory effect in a functional polyimide containing oxadiazole moieties, Chem. Mater. 21 (2009) 3391–3399.
[19] Y.L. Liu, Q.D. Ling, E.T. Kang, K.G. Neoh, D.J. Liaw, K.L. Wang, W.T. Liou, C.X. Zhu, D.S.H. Chan, Volatile electrical switching in a functional polyimide containing electron-donor and -acceptor moieties, J. Appl. Phys. 105 (2009), Art No. 044501.
[20] K.L. Wang, T.Y. Tseng, H.L. Tsai, S.C. Wu, Resistive switching polymer materials based on poly(aryl ether)s containing triphenylamine and 1,2,4-triazole moieties, J. Polym. Sci. A Polym. Chem. 46 (2008) 6861–6871.
[21] K.L. Wang, Y.L. Liu, I.H. Shih, K.G. Neoh, E.T. Kang, Synthesis of polyimides containing triphenylamine-substituted triazole moieties for polymer memory applications, J. Polym. Sci. A Polym. Chem. 48 (2010) 5790–5800.
[22] Q.D. Ling, D.J. Liaw, E.Y.H. Teo, C. Zhu, D.S.H. Chan, E.T. Kang, K.G. Neoh, Polymer memories: bistable electrical switching and device performance, Polymer 48 (2007) 5182–5201.
[23] M. Pamuk, S. Tirkeş, A. Cihaner, F. Algi, A new low-voltage-driven polymeric electrochromic, Polymer 51 (2010) 62–68.
[24] S. Tarkuc, Y.A. Udum, L. Toppare, Tuning of the neutral state color of the π-conjugated donor–acceptor–donor type polymer from blue to green via changing the donor strength on the polymer, Polymer 50 (2009) 3458–3464.
[25] P. Karastatiris, J.A. Mikroyannidis, I.K. Spiliopoulos, Bipolar poly(p-phenylene vinylene)s bearing electron-donating triphenylamine or carbazole and electron-accepting quinoxaline moieties, J. Polym. Sci. A Polym. Chem. 46 (2008) 2367–2378.
[26] S. Xun, Q. Zhou, H. Li, D. Ma, L. Wang, X. Jing, F. Wang, Synthesis, characterization, and electroluminescence of PPV copolymers containing electron and hole-transporting units, J. Polym. Sci. A Polym. Chem. 46 (2008) 1566–1576.
[27] C. Nagamani, C. Versek, M. Thorn, M.T. Tuominen, S. Thayumanavan, Proton conduction in 1H-1,2,3-triazole polymers: imidazole-like or pyrazole-like?, J Polym. Sci. A Polym. Chem. 48 (2010) 1851–1858.

[28] R.A. Potrekar, M.P. Kulkarni, R.A. Kulkarni, S.P. Vernekar, Polybenzimidazoles tethered with N-phenyl 1,2,4-triazole units as polymer electrolytes for fuel cells, J. Polym. Sci. A Polym. Chem. 47 (2009) 2289–2303.
[29] L. Huo, Z. Tan, X. Wang, Y. Zhou, M. Han, Y. Li, Novel two-dimensional donor–acceptor conjugated polymers containing quinoxaline units: synthesis, characterization, and photovoltaic properties, J. Polym. Sci. A Polym. Chem. 46 (2008) 4038–4049.
[30] L. Huo, C. He, M. Han, E. Zhou, Y. Li, Alternating copolymers of electron-rich arylamine and electron-deficient 2,1,3-benzothiadiazole: synthesis, characterization and photovoltaic properties, J. Polym. Sci. A Polym. Chem. 45 (2007) 3861–3871.
[31] K.L. Wang, S.T. Huang, L.G. Hsieh, G.S. Huang, Synthesis, optical and electrochemical properties of new hyperbranched poly(triphenylamine amide)s, Polymer 49 (2008) 4087–4093.
[32] F.S. Mancilha, B.A. DaSilveira Neto, A.S. Lopes, P.F. Moreira Jr, F.H. Quina, R.S. Gonçalves, J. Dupont, Are molecular 5,8-π-extended quinoxaline derivatives good chromophores for photoluminescence applications?, Eur J. Org. Chem. (2006) 4924–4933.
[33] M. Grell, D.D.C. Bradley, M. Inbasekaran, E.P. Woo, A glass-forming conjugated main-chain liquid crystal polymer for polarized electroluminescence applications, Adv. Mater. 9 (1997) 798–802.
[34] T. Förster, 10th Spiers Memorial Lecture. Transfer mechanisms of electronic excitation, Discuss. Faraday Soc. 27 (1959) 7–17.
[35] F. Huang, L. Hou, H. Wu, X. Wang, H. Shen, W. Cao, W. Yang, Y. Cao, High-efficiency, environment-friendly electroluminescent polymers with stable high work function metal as a cathode: green- and yellow-emitting conjugated polyfluorene polyelectrolytes and their neutral precursors, J. Am. Chem. Soc. 126 (2004) 9845–9853.
[36] M. Yan, L.J. Rothberg, F. Papadimitrakopoulos, M.E. Galvin, T.M. Miller, Defect quenching of conjugated polymer luminescence, Phys. Rev. Lett. 73 (1994) 744–747.
[37] D. Oelkrug, A. Tompert, J. Gierschner, H.J. Egelhaaf, M. Hanack, M. Hohloch, E. Steinhuber, Tuning of fluorescence in films and nanoparticles of oligophenylenevinylenes, J. Phys. Chem. B 102 (1998) 1902–1907.
[38] Y.Y. Li, A.M. Ren, J.K. Feng, L. Yang, C.C. Sun, A theoretical investigation on the absorption and emission properties of isomeric benzofuran trimers, Opt. Mater. 29 (2007) 1571–1578.
[39] L. Yang, J.K. Feng, Y. Liao, A.M. Ren, Theoretical studies on the electronic and optical properties of two blue-emitting fluorene–pyridine-based copolymers, Opt. Mater. 29 (2007) 642–650.
[40] L. Yang, J.K. Feng, W.Y. Wong, S.Y. Poon, Electronic structure and optical properties of germanium-bridged platinum(II)-containing diethynylfluorene monomer and oligomers: a theoretical investigation, Polymer 48 (2007) 6457–6463.
[41] F. Huang, Y. Zhang, M.S. Liu, A.K.Y. Jen, Electron-rich alcohol-soluble neutral conjugated polymers as highly efficient electron-injecting materials for polymer light-emitting diodes, Adv. Funct. Mater. 19 (2009) 2457–2466.
[42] J. Demas, J. Addington, Luminescence quenching of the tris (2,2′-bipyridine) ruthenium (II) and tris (1,10-phenanthroline) ruthenium (II) cations, J. Am. Chem. Soc. 98 (1976) 5800–5806.
[43] R.H. Schweitzer, G.W. Brudvig, Fluorescence quenching by chlorophyll cations in photosystem II, Biochemistry 36 (1997) 11351–11359.

the hole transporting layer (HTL). In addition, TCTA has a high triplet energy level (2.7 eV), which can play the role of an exciton blocking layer (ExBL) in phosphorescent OLEDs [13]. In addition, TCTA has good solubility and film forming properties, as well as good adhesion to the next organic layer. In order to study the effect of the printing process on the device performance, an emitting layer (EML) was processed by contact printing and spin-coating onto a small molecule layer. Although thermal evaporation was used after formation of an EML, this is needed as an assured method for measurement and analysis of a completed device utilizing the printing process. These results would be a possibility of the layer transfer process for high-performance OLED in low-cost process, and next step is working in progress for all-printing process. Finally, the enhanced performance of OLEDs fabricated without intermixing problems by using contact printing was studied, which demonstrates a suitable process that can fabricate high-performance OLEDs based on solution-processes with a low-cost method.

This contact printing technique utilizes a planar poly(dimethylsiloxane) (PDMS) elastomer. The PDMS stamps are suitable for a repeatable process since they are characterized by their low adhesion, durability, and elasticity. When the next layer is printed onto the preceding layers mounted on a substrate, the intermixing problem between the layers does not occur since the organic solvents are completely dried before the transfer.

2. Experiment

In order to fabricate the stamps, PDMS (Sylgard 184, Dow Corning Co.) was poured onto a plain silicon wafer substrate. The PDMS was then cured in an oven at 70 °C for over 3 h. The PDMS stamp can then be easily peeled-off from the master since the PDMS has a good elasticity and a low surface energy.

In order to fabricate the OLED devices, indium-tin-oxide (ITO) coated glass was sonicated in acetone, methanol and deionized water; and then cleaned in an oxygen plasma. Poly(ethylenedioxythiophene):poly(stylenesulfonate) (PEDOT:PSS) as a hole injection layer (HIL) was then spin-coated onto the ITO substrates to a thickness of 30 nm and annealed at 115 °C for 10 min on a hot plate in order to remove the solvent. Subsequently, TCTA as a HTL with a 0.5 wt.% in toluene was spin-coated at 2500 rpm to obtain a thickness of 25 nm, then annealed at 150 °C for 30 min on a hot plate. Next, the prepared plain PDMS stamps were treated using oxygen plasma in order to enhance their surface energy for a better wetting of the EML on the PDMS. Poly(N-vinylcarbazole) (PVK) based green emitting material was used for the EML (Fig. 1d). After a few drops of the EML solution suspended in chlorobenzene were applied to the surface of the PDMS stamps, the stamps were spin-coated at 3000 rpm in order to obtain a thickness of 30 nm, and then dried. Fig. 1 shows the schematic illustration of the contact printing process. The EML coated PDMS stamp was then brought into contact with the TCTA coated substrate at 80 °C for 20 s. The PDMS stamp was then carefully peeled-off, leaving the EML on the substrate. After releasing the layer, the substrate was annealed at 150 °C for 30 min on a hot plate.

We compared our device to spin-coated EMLs on TCTA coated devices in order to define the effect of the EML printing process has on the device.

Reference device 1: ITO/PEDOT:PSS (25 nm)/EML (30 nm, spin-coated).
Reference device 2: ITO/PEDOT:PSS (25 nm)/TCTA (25 nm)/EML (30 nm, spin-coated).
Reference device 3: ITO/PEDOT:PSS (25 nm)/TCTA (50 nm)/EML (30 nm, spin-coated).
Contact printing: ITO/PEDOT:PSS (25 nm)/TCTA (25 nm)/EML (30 nm, contact-printed).

In order to examine the dissolution problems of the EML solvent on the TCTA layer, the TCTA was spin-coated at 2500 and 800 rpm to obtain thicknesses of 25 and 50 nm, respectively, and then annealed. Subsequently, the EML was spin-coated to a thickness of 30 nm on the TCTA layer. Finally, in order to study the effect on the electroluminescence (EL) efficiencies of the spin-coated and contact-printed devices, we deposited layers of 10 nm 4,4′-di(triphenylsilyl)-biphenyl (BSB) as a hole blocking layer (HBL), 45 nm 4,7-diphenyl-1,10-phenanthroline (Bphen) as an electron transport layer (ETL), 0.8 nm lithium-fluoride (LiF) as an electron injection layer (EIL), and 100 nm aluminum as a cathode using thermal evaporation. The emission area of the devices was 5 mm × 5 mm. The current–voltage characteristics were measured using a Keithley 237 High-Voltage Source-Measure Unit (Keithley Instruments, Inc.), the EL efficiency was measured using a PR-670 SpectraScan Spectroradiometer (Photo Research, Inc.) in a dark box.

3. Results and discussion

Fig. 2 shows the current density and the luminance as a function of the applied voltage. The multilayered OLEDs using spin-coating were fabricated as reference devices with the same organic layers and metal layers under the same conditions. The turn-on voltage of the contact-printed device was lower than the spin-coated devices: 5.1 and 6.2 V, respectively. The luminance of the contact-printed device was also enhanced compared to the spin-coated devices at the same voltage, since the contact-printed device has a higher current density than the spin-coated devices. The spin-coated devices have the interlayer dissolution issue when the EML solvent chlorobenzene is spin-coated onto the top of the TCTA interlayer. The dissolution test was examined by measuring the thickness of the remaining TCTA layer after the spin-coating of the chlorobenzene on the 25 and 50 nm TCTA layers. As a result, only the thickness of the PEDOT:PSS layer was measured without the TCTA layer. Fig. 2 shows that the *I–V* curves of Refs. [2,3] are almost the same as Ref. [1]'s without TCTA layer. This interlayer dissolution by the organic solvent affects the current–voltage characteristics, since the thickness of the TCTA is insufficient to play the role of the HTL. However,

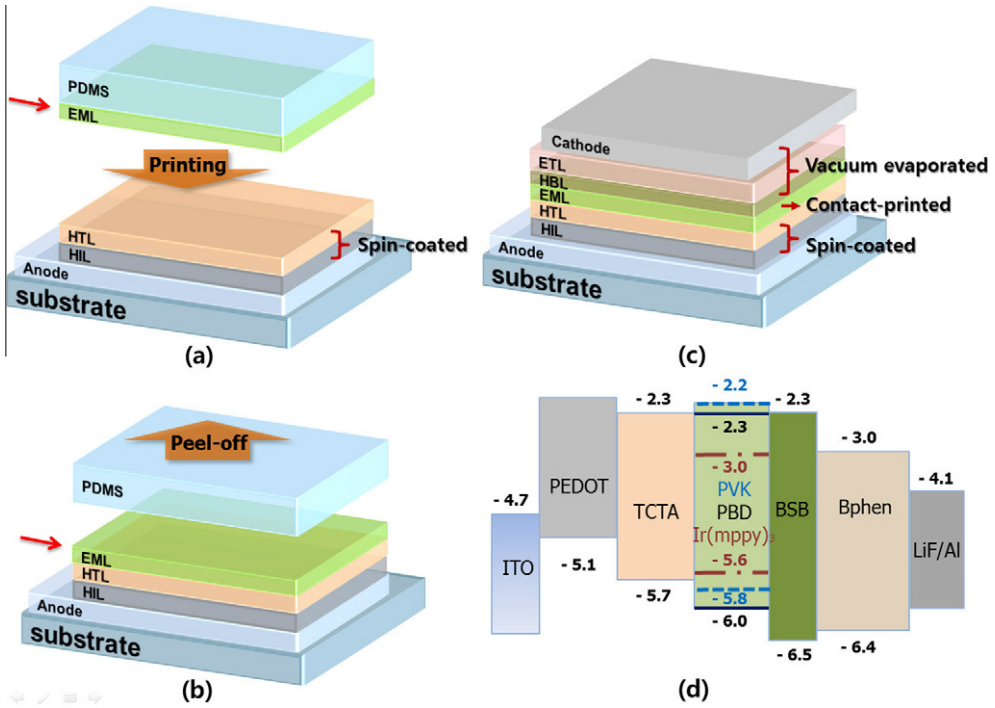

Fig. 1. The schematic illustration for the contact printing technique and the structure of the multilayered OLED. The EML spin-coated PDMS stamp is applied to the HIL and HTL coated substrate (a). The PDMS stamp is then carefully peeled-off leaving the EML on the substrate (b). The HBL, ETL, and cathode are thermal evaporated, sequentially (c). The energy band diagram of the OLEDs (The energy levels LUMO and HOMO are taken from literature) (d).

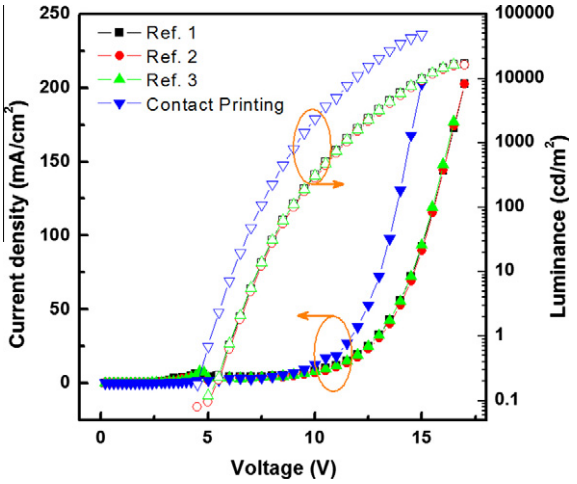

Fig. 2. The current density and the luminance characteristics as a function of the applied voltage.

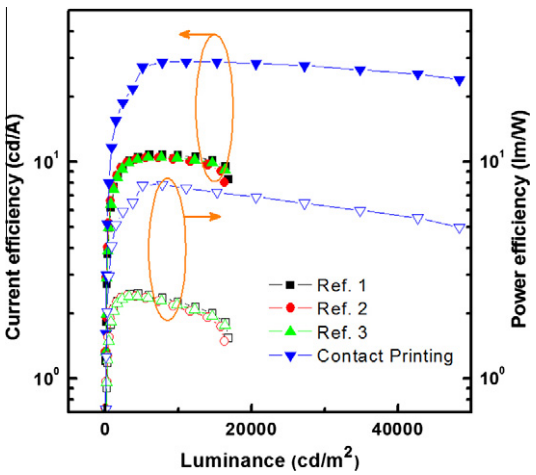

Fig. 3. The current efficiency and power efficiency characteristics as a function of the luminance.

the device using contact printing with the dried EML allows a well formed TCTA interlayer on the PEDOT:PSS; it is a good HTL. Therefore, the hole injection efficiency of the contact-printed device is higher than the spin-coated device. In addition, Joo et al. demonstrated that the transfer printing process was better than the spin-coating process in terms of current density, because the interfacial contact was improved by the pressure and heat applied during the transfer printing process [14].

Fig. 3 shows the current efficiency and power efficiency characteristics as a function of the luminance. The contact-printed device shows an enhanced performance compared to the spin-coated devices in terms of both the current efficiency and the power efficiency. In this multilayered OLED, the TCTA interlayer plays desirable roles in hole transportation, electron blocking, and in preventing exciton quenching caused by the PEDOT:PSS [15]. Refs. [1–3] also show a significant tendency for a short device life time,

due to the exciton quenching between the PEDOT:PSS and the EML. The contact printing process improves the maximum device current efficiency on the multilayered OLEDs from 10.82 to 28.93 cd/A; it also improves the power efficiency from 2.45 to 7.88 lm/W.

The contact printing technique improves not only the availability of multilayered structures without any damage but also lends itself to the compatibility of the organic materials, since it is solvent-free when the layer is printed onto the substrate. This enables the organic materials to be free from the limitations of having to be selected for compatibility and crosslinkability in a multilayered OLED. The solution based multilayered OLEDs employing contact printing allow the use of any suitable material in order to enhance the OLED performance. Fig. 4 shows the images of the stacked layers and the patterned layers using contact printing on various substrates. Fig. 4a and b show capability of stacking organic multi-layers on glasses. Fig. 4c and d show that the contact printing process is suitable for the formation of organic layers and patterns on the flexible substrate. Also, Fig. 4e and f show uniformity of fabricated OLEDs utilizing the contact printing process. The light-emission images of the OLEDs were taken at 6 and 8 V, respectively, at the same exposure time. Only one cell was contact-printed for visual emphasis. In addition, Fig. 5 shows the voltage dependence of electroluminescence spectra for the contact-printed device and the spin-coated device to demonstrate the color stability. The contact-printed device revealed that the peak wavelength is same as the spin-coated device under continuous operation which means the contact printing process does not affect the color stability.

Even though OLEDs have advantages in display devices compared to LCDs, they are still limited by the expensive processes necessary to create commercial displays. Solution based processes, such as ink-jet, spin-coating, and microcontact printing have been developed in order to achieve a low cost process, however, these are restricted to the deposition of only a couple of layers because of the intermixing problem. The contact printing technique outlined in this paper is a good method to solve this problem in solution-based small molecule multilayered OLEDs since this process allows the next layer not to damage the preceding layer due to the organic solution. In addition, contact printing is available for patterning on large sized substrates using the roll-to-roll process with a low cost and a high processing speed, and does not need expensive

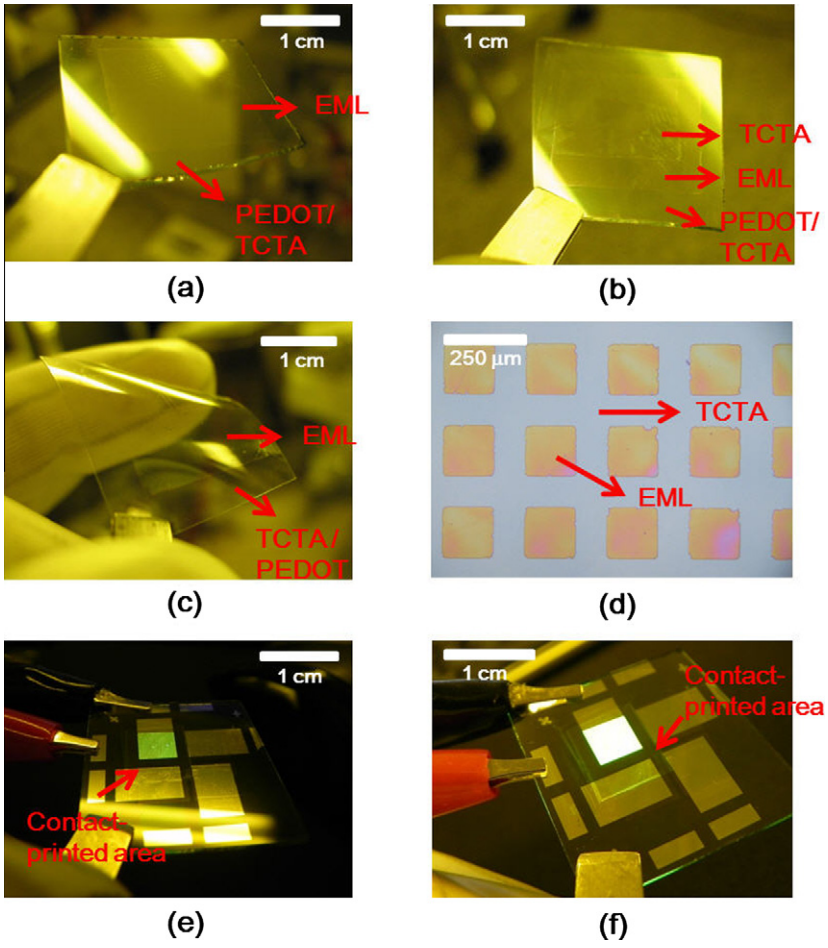

Fig. 4. Images of the stacked layers and patterned layers using contact printing. (a) Three layers on a glass. (b) Four layers on a glass. (c) Three layers on a plastic. (d) One hundred and fifty micrometer pattern size. (e) An emission photo at 6 V. (f) An emission photo at 8 V.

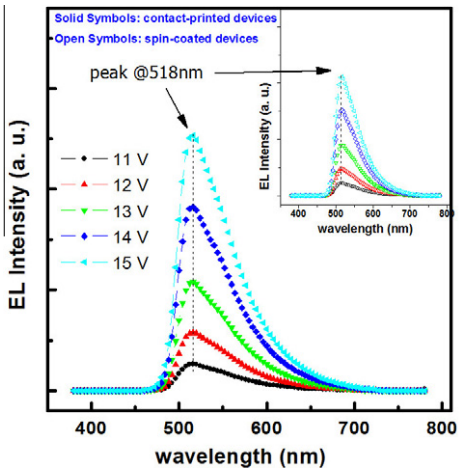

Fig. 5. The normalized electroluminescence (EL) spectra of the contact-printed device and the spin-coated device (inset) operated at different biased voltages.

vacuum equipment, high temperature processes, or UV exposure for the patterning. Therefore, our contact printing is a very simple and low cost process that needs to be considered as a candidate for the next generation printing processes.

4. Conclusions

In summary, efficient multilayered OLEDs have been demonstrated using the contact printing process with PDMS stamps. Unlike the conventional solution processes, this contact printing process does not damage the preceding layer. Therefore, this technique is suitable for solution-based small molecule multilayered OLEDs, which allow a high performance and a low cost process. In this study, the performance of the multilayered OLEDs made by contact printing significantly outperforms devices using spin-coating. As a result, efficient multilayered OLEDs have been developed by contact printing, which allows for the replacement of the thermal evaporation needed for the deposition of the organic layers and metal electrodes for future display devices.

Acknowledgments

This research was supported by Basic Science Research Program through the National Research Foundation of Korea (NRF) funded by the Ministry of Education, Science and Technology (MEST) (CAFDC-20100009869), World Class University (WCU, R32-2008-000-10082-0) Project of the MEST (KOSEF), and the IT R&D Program of MKE/KEIT (No. 2009-F-016-01, Development of Eco-Emotional OLED Flat-Panel Lighting). We thank the staff of KBSI for technical assistance. T.H. Park was financially supported by Hi Seoul Science (Humanities) Fellowship funded by Seoul Scholarship Foundation.

References

[1] C.W. Tang, S.A. VanSlyke, Appl. Phys. Lett. 51 (1987) 913.
[2] R.H. Friend, R.W. Gymer, A.B. Holmes, J.H. Burroughes, R.N. Marks, C. Taliani, D.D.C. Bradley, D.A. Dos Santos, J.L. Bredas, M. Logdlund, W.R. Salaneck, Nature (London) 397 (1999) 121.
[3] J. Bharathan, Y. Yang, Appl. Phys. Lett. 72 (1998) 2660.
[4] S.A. Choulis, V. Choong, M.K. Mathai, F. So, Appl. Phys. Lett. 87 (2005) 113503.
[5] X. Gong, S. Wang, D. Moses, G.C. Bazan, A.J. Heegeer, Adv. Mater. (Weinheim, Ger.) 17 (2005) 2053.
[6] S. Sivaramakrishnan, M. Zhou, A.C. Kumar, Z. Chen, R. Png, L. Chua, P.H. Ho, Appl. Phys. Lett. 95 (2009) 213303.
[7] Z. Zhou, X. Sheng, K. Nauka, L. Zhao, G. Gibson, S. Lam, C.C. Yang, J. Brug, R. Elder, Appl. Phys. Lett. 96 (2010) 013504.
[8] K. Meerholz, Nature (London) 437 (2005) 327.
[9] N. Rehmann, D. Hertel, K. Meerholz, H. Becker, S. Heun, Appl. Phys. Lett. 91 (2007) 103507.
[10] Q. Sun, D.W. Chang, L. Dai, J. Grote, R. Naik, Appl. Phys. Lett. 92 (2008) 251108.
[11] D. An, J. Zou, H. Wu, J. Peng, W. Yang, Y. Cao, Org. Lett. 10 (2009) 299.
[12] K.-H. Yim, Z. Zheng, Z. Liang, R.H. Friend, W.T.S. Huck, J.S. Kim, Adv. Funct. Mater. 18 (2008) 1012.
[13] J.J. Park, T.J. Park, W.S. Jeon, R. Pode, J. Jang, J.H. Kwon, E. Yu, M. Chae, Org. Lett. 10 (2009) 189.
[14] C.W. Joo, S.O. Jeon, K.S. Yook, J.Y. Lee, Org. Lett. 10 (2009) 372.
[15] J. Kim, R.H. Friend, I. Grizzi, J.H. Burroughes, Appl. Phys. Lett. 87 (2005) 023506.

In previously studies, we have demonstrated that a carbazole-substituted aromatic enyne derivative (*E*)-CPEY [5], which are easily prepared by catalytic dimerization of a terminal alkyne [6] and shows wonderful blue fluorescence in dilute solution, can act as an excellent single-emitting-component for WOLEDs, as a result of combination of the blue emission from an isolated molecule with the longer-wavelength emissions (green and orange-red) from eximers. Herein, we report series of blue fluorescent OLEDs based on the emitting layer of (*E*)-CPEY doped in the CBP (4, 4′-*N*, *N*′-dicarbazolylbiphenyl) host with the easily controlled doping concentrations, where the host matrix widens the intermolecular distance between the dopant molecules and eliminates the possibility of forming excimer in the emitting layer. The resulting EL devices based on (*E*)-CPEY with the pure and stable blue light (0.15, 0.10 ± 0.01) not only show relatively insensitive EL performances to the doping concentration changing in a high and wide range of 10–20 wt%, but also exhibit the highest EL efficiency ever reported for the saturated deep-blue OLEDs up to now.

2. Experimental section

2.1. Instrumentation

Photoluminescence spectra were recorded on a Perkin–Elmer LS 55 spectrophotometer, whereas UV–visible spectra were recorded on a Shimadzu UV-2550 PC spectrometer. The PL quantum yields were measured by use of quinine sulfate in 1 M sulfuric acid as a standard ($\Phi = 0.546$) [7]. Electrochemical measurements were performed in anhydrous CH_2Cl_2 with a BAS 100 W bioanalytical electrochemical work station, using Pt as the working electrode, platinum wire as the auxiliary electrode, and a porous glass wick Ag/Ag^+ as the reference electrode. It was standardized against a ferrocene/ferrocenium couple with a scan rate of 100 mV s^{-1}. Elemental analyses were performed on a Flash EA 1112 spectrometer. The EL spectra, brightness, CIE coordinates, and current–luminance–voltage characteristics of the devices were measured with a rapid scan system using a Photo Research PR650 spectrophotometer combined with a computer-controlled, programmable direct-current (DC) source (Keithley 2400).

2.2. Materials and OLED fabrication

The chemical structures and proposed energy diagram of the materials used in OLEDs are shown in Fig. 1. Prior to deposition, all organic materials were purified by sublimation. The devices were grown on a glass substrate precoated with an indium tin oxide (ITO) anode having a sheet resistance of 20 Ω^{-2}. The ITO substrate was routinely cleaned via ultrasonic treatment in detergent solutions, followed by rinsing with acetone, boiling in isopropanol, rinsing in methanol, and finally rinsing in de-ionized water. The substrate was dried in a vacuum oven between each cleaning step. The devices were fabricated by successive vacuum deposition of organic materials onto the substrate. A very thin layer of LiF can enhance electron injection from the aluminum cathode. A shadow mask with 2×3 mm^2 openings was used to define the cathodes.

3. Results and discussion

3.1. Absorption and photoluminescent (PL) properties

To investigate the PL emission properties of (*E*)-CPEY, a series of evaporated-film samples based on CBP and (*E*)-CPEY were prepared on quartz substrates, and their PL spectra are shown in Fig. 2. The PL spectra of the neat (*E*)-CPEY film and the thin film of (*E*)-CPEY doped in CBP with the high concentration of 30 wt% show extra broad emissions at 510–520 nm and tailed to 600 nm in addition to the strong emission at about 460 nm, because of formation of excimers based on (*E*)-CPEY molecules [5]. However, the PL curves of the doped film with the low concentration of 20 wt% and 10 wt% are similar to that of the solution except the dominant emission with a peak at 455 nm is slight blue-shifted by about 5 nm, which reveals that the excimer emission has been eliminated in such doped-concentration level and the emission of 455 nm band comes from the isolated (*E*)-CPEY molecules. It is consistent with the quantum yield alignment of the doping films (0.33 for 10 wt%, 0.29 for 20 wt% and 0.18 for 30 wt%). In addition, the similarly secondary PL emission band located at 390–420 nm in 10, 20 and 30 wt% doped solid films are observed, which should be the PL contribution from the host CBP. The fluorescence of CBP not being quenched effectively in spite of the doping concentration up to 30 wt% indicates that no or incomplete energy transfer from the host to the dopant. This result is supported by the characteristics of almost no overlap between the UV absorption spectrum of (*E*)-CPEY and PL spectrum of CBP in their solid films.

3.2. EL properties

To check the EL properties of (*E*)-CPEY as a blue emitter, a series of OLEDs (device I–III) with the device configuration of [ITO/NPB (50 nm)/emitting layer (40 nm)/TPBI (20 nm)/LiF (1 nm)/Al] were fabricated, where NPB (4,4′-bis(*N*-(1-naphthyl)-*N*-phenylamino)biphenyl) was hole-transporting layer (HTL) and TPBI (1,3,5-tris(*N*-phenylbenzimidazol-2-yl)benzene) was employed as electron-transporting layer (ETL) and hole-blocking layer (HBL) [8]. The films of (*E*)-CPEY doped in CBP were adopted as the emitting layers (EML) with the doping concentrations of 5 wt% (device I), 10 wt% (device II) and 20 wt% (device III).

Fig. 3 shows the normalized EL spectra of device I, II and III and all of them have similar emission peak at around 450 nm. Device II and III show narrow spectral shape with the half-maximum width ranging from 60 to 70 nm, which present very saturated blue light with CIE (Commission Internationale de l'É clairage) coordinates of (0.15, 0.09) and (0.15, 0.11) detected at the brightness of 5000 cd m^{-2}, respectively. The CIE and EL spectral curves of device II and III remain almost unchanged in the driving voltage range of 4–9 V. When the brightness of device II with the doping

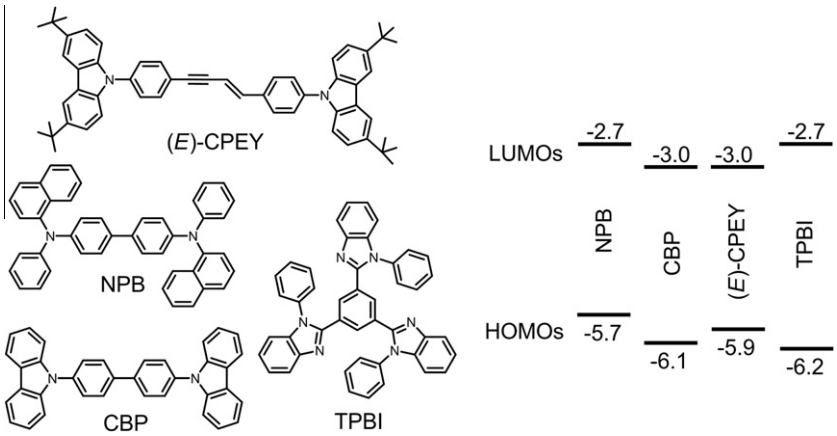

Fig. 1. Chemical structures (left) and proposed energy diagram (right) of the materials used in OLEDs.

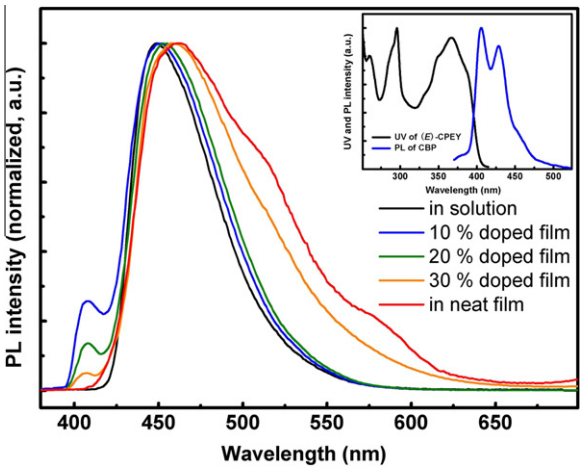

Fig. 2. PL spectra of (*E*)-CPEY in the dilute CH_2Cl_2 solution and in the neat evaporated film. PL spectra of (*E*)-CPEY doped in CBP with different concentrations in the evaporated films. Inset: UV absorption spectrum of (*E*)-CPEY and PL spectrum of CBP in the evaporated films.

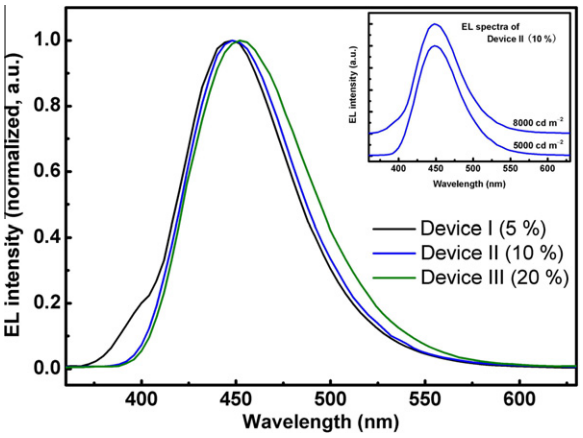

Fig. 3. Normalized EL spectra of device I, II and III at the brightness of 5000 cd m^{-2}. Inset: EL spectra of device II at the brightness of 5000 and 8000 cd m^{-2}, respectively.

concentration of 10 wt% increases above 8000 cd m^{-2}, a slight shoulder emission in the wavelength region of about 400 nm from CBP is observed (Fig. 3, inset), which appears more obviously in the EL spectrum of device I with the low doping concentration (5 wt%) during its whole driving process.

The current density–brightness–voltage characteristics of device II and III are plotted in Fig. 4. Device II and device III exhibited similar turn-on voltage of 2.9 V and 2.8 V (recorded at 1 cd m^{-2}) and the maximum brightness of 11,020 and 9120 cd m^{-2} are reached at 10 V, respectively. In both devices, brightness increased linearly with current density, indicating that they are highly efficient blue OLEDs. Compared with device II, device III shows faster rise of the EL intensity and the current density after the onset voltages and up to about the brightness of 1000 cd m^{-2}. For this case in particular, the reduction in driving voltage of device III should result from the higher HOMO (The highest occupied molecular orbital) of (*E*)-CPEY than that of CBP [9], which leads to that more holes can easily and directly inject from the HTL into the EML in device III with relatively high doping concentration (20 wt%) and it can be understood in terms of the proposed energy diagram

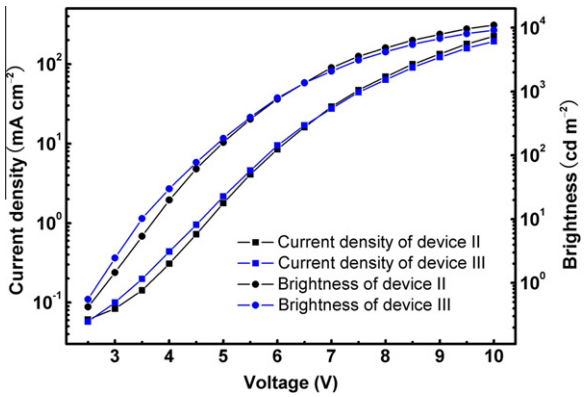

Fig. 4. Current density–brightness–voltage characteristics of device II and III.

(Fig. 1). In contrast, when the brightness is over 1000 cd m^{-2}, the slightly rapid increase of the EL intensity and the current density showed in device II, which should partly due to the better charge-transporting ability of CBP than that of (*E*)-CPEY and indicates also that the concentration quenching of (*E*)-CPEY molecules might still occur in device III, specially at the high current density.

Fig. 5 plots the LE (luminous efficiency), PE (power efficiency) and EQE (external quantum efficiency) of the devices as functions of the current density and the corresponding values of the EL efficiencies based on different brightness level are listed in Table 1. Device II and III exhibit the exciting peak EL efficiencies of 9.1 cd A^{-1} (7.1%) and 5.9 lm W^{-1}, 8.6 cd A^{-1} (6.0%) and 5.6 lm W^{-1} at the reliable brightness of 370 and 60 cd m^{-2}, 395 and 75 cd m^{-2}, respectively. Notably, the EL efficiencies of both devices at the brightness of 100 cd m^{-2} and 1000 cd m^{-2}, which are the practical level used in the fields of display and lighting, remain as high as 8 cd A^{-1}, 4 lm W^{-1} and 5%. The values mentioned above are the highest EL efficiencies ever reported for a saturated deep-blue OLED to the best of our knowledge, even including the devices utilizing doped [4] and non-doped emitting systems [10]. In addition, both devices keep the EL efficiency over 6 cd A^{-1}, 2 lm W^{-1} and 4% in very wide current density range (0.2–100 mA cm^{-2}) and brightness range (20–5000 cd m^{-2}), indicating the good operational stability of the devices.

Clearly, the observed EL efficiencies in the blue OLEDs are remarkably high, and the measured high EQE value is larger than the apparent limit of ca. 5% EQE for fluorescence-based OLEDs [11]. The 5% theoretical limit is based on the two assumptions of a statistical singlet/triplet formation ratio of 1:3 and a light outcoupling efficiency η_c of ca. 20% ($\eta_c < 0.5/n^2$, n being the refractive index of the emitter, typically about 1.6–1.8). However, the validity of both these assumptions is currently debatable [10a]. High η_c values of 30–50% have been estimated depending on the choice and optimization of device parameters such as the refractive index and the thickness of ITO glass and organic thin films, position of the emission zone in the device, and a combination of other factors [11,12].

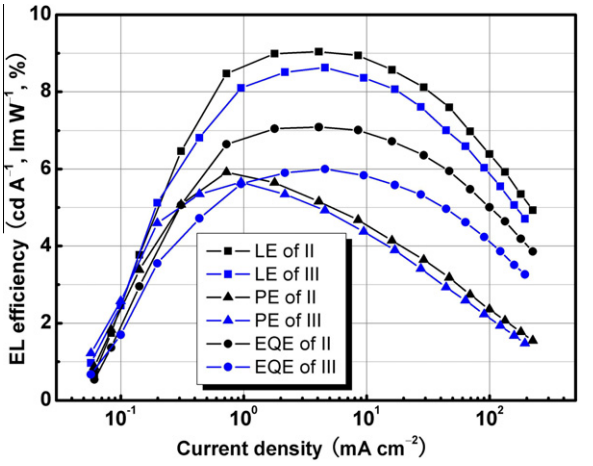

Fig. 5. EL efficiency of the device II and III as functions of the current density.

Table 1
Corresponding values of driving voltage, LE, PE and EQE based on different brightness level of device II and III.

Device		Max. efficiency	10 cd m^{-2}	100 cd m^{-2}	1000 cd m^{-2}	5000 cd m^{-2}
II	V (V)		3.7	4.7	6.2	8.1
	LE (cd A^{-1})	9.1 (5.5, 370)[a]	5.2	8.6	8.7	6.8
	PE (lm W^{-1})	5.9 (4.5, 60)[a]	4.3	5.8	4.4	2.6
	EQE (%)	7.1 (5.5, 370)[a]	4.1	6.6	6.7	5.2
III	V (V)		3.5	4.6	6.2	8.3
	LE (cd A^{-1})	8.6 (5.5, 395)[a]	5.1	8.2	8.2	6.1
	PE (lm W^{-1})	5.6 (4.5, 75)[a]	4.6	5.5	4.1	2.3
	EQE (%)	6.0 (5.5, 395)[a]	3.6	5.7	5.7	4.4

[a] Numbers in parentheses are the corresponding voltages (*V*) and brightness (cd m^{-2}), respectively.

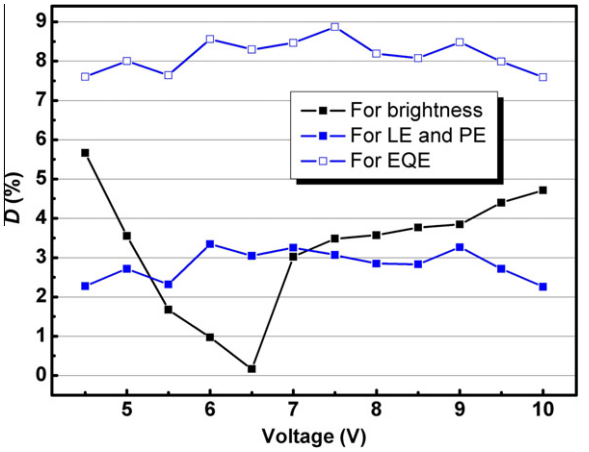

Fig. 6. Deviation (*D*,%) for the brightness and the EL efficiency between device II and III with respect to the driving voltages.

Additionally, EQE values greater than the apparent limit have been previously reported for fluorescence-based OLEDs, including the EQE of 5–7% for a blue OLED [4b,10,13] and 7–10% for green OLEDs [14]. Thus, there is evidence in the literature that the apparent 5% limit on EQE and the underlying assumptions are questionable.

More importantly, it is clear that device II and III present very similar EL performance such as the similar values of the EL efficiency and brightness upon the same current density and driving voltage level, as shown in Figs. 4 and 5, respectively. Fig. 6 shows intuitively the deviation (*D*,%) for the brightness (*B*) and the EL efficiency (*E*) between device II and III with respect to the driving voltages. The corresponding deviation is defined by the formula of D_B (for brightness) = ½Δ*B* (II and III)/½Σ*B* (II and III) and D_E (for EL efficiency) = ½Δ*E* (II and III)/½Σ*E* (II and III), respectively, and the values of brightness or efficiency using in one formula should base on same driving voltage. Obviously, although the doping concentration changes such large span as between device II (10 wt%) and device III (20 wt%), the deviation for both the brightness and the EL efficiency always keep within a small range of 9%, especially, the deviations for LE and PE even remain as low as 4%. This result reveals the high EL performance of the blue devices based on (*E*)-CPEY are relatively insensitive to the doping concentration changing in such high and wide

range as 10–20 wt%, which is one gratifying property suggesting the easy and reproducible fabrication process of mass production and not provided by all the blue guest emitters previously reported up to now [4]. The excellent EL performance (*E*)-CPEY-based devices should be attributed to the pronounced photoelectric properties of (*E*)-CPEY, which is demonstrated by being acted successfully as a single-emitting-component for highly efficient white OLED [5]. On the other hand, the morphological likeness and the well-matched energy levels between CBP and (*E*)-CPEY lead to that CBP is a favorable host for this blue dopant, is another possible reason.

4. Conclusions

In summary, highly efficient deep-blue OLEDs employing the emitting layer based on an aromatic enyne derivative (*E*)-CPEY doped in the CBP with the easily controlled doping concentrations have been developed. The series of OLEDs show high peak EL efficiencies (>8.5 cd A^{-1}, >5.5 lm W^{-1} and $\geqslant$6.0%) with pure and stable blue emission (0.15, 0.10 ± 0.01), which are the highest EL efficiencies ever reported up to now for the saturated deep-blue OLEDs. More importantly, both the EL efficiency and the brightness of these blue OLEDs just present very small deviation within such a high and wide range of doping concentration (10–20 wt%), which should lead to the easy and reproducible fabrication process of high performance EL devices. The easily controlled doping concentrations together with high EL efficiency and pure blue emission, are the unique gratifying properties provided by the OLEDs based on (*E*)-CPEY, which suggest that the blue OLEDs have high potential for the applications in large flat panel displays and solid-state lighting in future.

Acknowledgements

This work was partly supported by National Basic Research Program of China (973 Program, 2009CB623600), Natural Science Foundation of China (50733002 and 50903036), Provincial Science and Technology Bureau of Jilin Province (201105010), Special Project from MOST of China (10409A111463).

References

[1] C.W. Tang, S.A. Vanslyke, Appl. Phys. Lett. 51 (1987) 913.
[2] (a) R.J. Holmes, S.R. Forrest, Y.-J. Tung, R.C. Kwong, J.J. Brown, S. Garon, M.E. Thompson, Appl. Phys. Lett. 82 (2003) 2422;
(b) R.J. Holmes, B.W. D'Andrade, S.R. Forrest, X. Ren, J. Li, M.E. Thompson, Appl. Phys. Lett. 83 (2003) 3818;
(c) S.-C. Lo, G.J. Richards, J.P.J. Markham, E.B. Namdas, S. Sharma, P.L. Burn, I.D.W. Samuel, Adv. Funct. Mater. 15 (2005) 1451;
(d) J.-J. Lin, W.-S. Liao, H.-J. Huang, F.-I. Wu, C.-H. Cheng, Adv. Funct. Mater. 18 (2008) 485;
(e) K.S. Yook, S.O. Jeon, C.W. Joo, J.Y. Lee, Org. Electron. 10 (2009) 170;
(f) C.-H. Chang, C.-C. Chen, C.-C. Wu, C.-H. Yang, Y. Chi, Org. Electron. 10 (2009) 1364.
[3] (a) Y. Liu, J.H. Guo, J. Feng, H.D. Zhang, Y.Q. Li, Y. Wang, Appl. Phys. Lett. 78 (2001) 2300;
H.-T. Shih, C.-H. Lin, H.-Hsin Shih, C.-H. Cheng, Adv. Mater. 14 (2002) 1409;
(c) F.S. Liang, J.S. Chen, L.X. Wang, D.G. Ma, X.B. Jing, F.S. Wang, J. Mater. Chem. 13 (2003) 2922;
(d) W.L. Jia, X.D. Feng, D.R. Bai, Z.H. Lu, S. Wang, G. Vamvounis, Chem. Mater. 17 (2005) 164;
(e) Y. Liu, X.T. Tao, F.Z. Wang, X.N. Dang, D.C. Zou, Y. Ren, M.H. Jiang, Org. Electron. 09 (2008) 609.
[4] (a) Y.Z. Wu, X.Y. Zheng, W.Q. Zhu, R.G. Sun, X.Y. Jiang, Z.L. Zhang, S.H. Xu, Appl. Phys. Lett. 83 (2003) 5077;
(b) M.-T. Lee, C.-H. Liao, C.-H. Tsai, C.H. Chen, Adv. Mater. 17 (2005) 2493;
(c) R.C. Chiechi, R.J. Tseng, F. Marchioni, Y. Yang, F. Wudl, Adv. Mater. 18 (2006) 325;
(d) Z.Q. Gao, Z.H. Li, P.F. Xia, M.S. Wong, K.W. Cheah, C.H. Chen, Adv. Funct. Mater. 17 (2007) 3194;
(e) S.-L. Jeon, Y.-M. Jeon, J.-W. Kim, C.-W. Lee, M.-S. Gong, Org. Electron. 19 (2008) 522;
T.Z. Yu, P. Zhang, Y.L. Zhao, H. Zhang, J. Meng, D.W. Fan, Org. Electron. 10 (2009) 653;
G.S. Samal, K.N. Narayanan Unni, S. Bharat, S. Gupta, Deepak, Org. Electron. 10 (2009) 1201;
(h) Q.J. Qi, X.M. Wu, Y.L. Hua, Q.C. Hou, M.S. Dong, Z.Y. Mao, B. Yin, S.G. Yin, Org. Electron. 11 (2010) 503.
[5] Y. Liu, M. Nishiura, Y. Wang, Z.M. Hou, J. Am. Chem. Soc. 128 (2006) 5592.
[6] (a) M. Nishiura, Z.M. Hou, J. Mol. Catal. A: Chem. 213 (2004) 101;
(b) M. Nishiura, Z.M. Hou, Y. Wakatsuki, T. Yamaki, T. Miyamoto, J. Am. Chem. Soc. 125 (2003) 1184;
H.J. Heeres, J.H. Teuben, Organometallics 10 (1991) 1980.
[7] J.N. Demas, G.A. Crosby, J. Phys. Chem. 75 (1971) 991.
[8] (a) K.R.J. Thomas, J.T. Lin, Y.-T. Tao, C.-W. Ko, J. Am. Chem. Soc. 123 (2001) 9404;
(b) B.W. D'Andrade, S.R. Forrest, Adv. Mater. 16 (2004) 1585.
[9] (a) H. Bi, K. Ye, Y. Zhao, Y. Yang, Y. Liu, Y. Wang, Org. Electron. 11 (2010) 1180;
(b) Y. Yang, T. Peng, K. Ye, Y. Wu, Y. Liu, Y. Wang, Org. Electron. 12 (2011) 29.
[10] (a) C.J. Tonzola, A.P. Kulkarni, A.P. Gifford, W. Kaminsky, S.A. Jenekhe, Adv. Funct. Mater. 17 (2007) 863;
(b) P.-I. Shih, C.-Y. Chuang, C.-H. Chien, E. W.-Guang Diau, C.-F. Shu, Adv. Funct. Mater. 17 (2007) 3141.
[11] N.K. Patel, S. Cinà, J.H. Burroughes, IEEE J. Sel. Top. Quantum Electron. 8 (2002) 346.
[12] M.-H. Lu, J.C. Sturm, Appl. Phys. Lett. 78 (2001) 1927.
[13] C.-C. Wu, Y.-T. Lin, K.-T. Wong, R.-T. Chen, Y.-Y. Chien, Adv. Mater. 16 (2004) 61.
[14] (a) J. Kido, Y. Iizumi, Appl. Phys. Lett. 73 (1998) 2721;
(b) H.Y. Chen, W.Y. Lam, J.D. Luo, Y.L. Ho, B.Z. Tang, D.B. Zhu, M. Wong, H.S. Kwok, Appl. Phys. Lett. 81 (2002) 574;
(c) K. Okumoto, H. Kanno, Y. Hamaa, H. Takahashi, K. Shibata, Appl. Phys. Lett. 89 (2006) 063504.

[12,13]. Such high temperatures are not compatible with the use of plastic substrates and prohibit the full integration of inorganic materials with organic electronics. To this end, low temperature atomic layer deposition (ALD) has also been used to make TiO_2 films [14,15]. However, a room temperature solution process would be the ultimate solution from the point of view of large-scale, cost-effective manufacture of electronic devices.

In this letter, we report the synthesis of TiO_2 nanoparticles via a sol–gel process, and the deposition of transparent TiO_2 thin films by spin-coating from an aqueous dispersion at room temperature, without any further heat treatment. We show that these films are suitable for applications in polymer optoelectronic devices (photovoltaic cells and light emitting diodes). The developed process yields TiO_2 thin films that are suitable for large-area deposition on practically any substrate, and thus it makes low cost, large-scale manufacturing of organic electronics possible in the not-so-distant future.

2. Experimental

2.1. Nanoparticle synthesis

TiO_2 was synthesized by hydrolysis of $TiCl_4$ (Fluka, 99.0%) at 40 °C in an aqueous solution containing hydrochloric acid (HCl, Fishersci.) and 2-propanol (Mallinckrodt) [16]. $TiCl_4$ (1 mol/L) aqueous solution was prepared by dissolving $TiCl_4$ in a mixture of deionized (DI) water (18.2 MΩ Barnstead EASYpure® RoDI) and HCl (volume ratio of 19:1, H_2O:36–38% HCl). Because the reaction was highly exothermic and produced high quantities of fumes, $TiCl_4$ was added dropwise into the ice cooled HCl solution with vigorous stirring, and the reaction had to be carried out inside a fume hood. The $TiCl_4$ solution (4 mL) was filtered (syringe filter; 0.2 μm, Nylon, Millipore) and then added into a 2-propanol solution (32 mL of 2-propanol mixed with 4 mL of DI water). The obtained reaction mixtures were incubated at 40 °C in a water bath (Fishersci.) for 12 h, which led to the formation of white TiO_2 particles. The particles were separated by centrifugation, washed with ethanol, and then dried at 40 °C overnight.

Particle size and morphology were investigated by transmission electron microscopy (TEM, FEI Tecnai G2 T12, field emission gun, 120 kV), and thin film sections were examined by field emission scanning electron microscopy (FESEM, Hitachi S4500, 10 kV) after being sputter-coated with Au/Pd. The crystal phase of the particles was determined by powder X-ray diffraction (XRD) in θ–2θ scan mode from 15° to 80° (Scintag Inc., Theta–Theta Diffractometer; Radiation: Cu Kα1; Scan rate: 0.012°/min; Step: 0.02°). The surface morphology of the films was examined with an atomic force microscope (AFM, DI 3100 Dimension microscope) using tapping mode. UV/Vis absorption spectra were obtained using a Shimadzu UV-3101PC UV/Vis/Near-IR Spectrophotometer; thin films to be measured were spin-coated on quartz slides to obtain accurate UV/Vis absorption spectra. The chemical states of titanium and oxygen were analyzed by X-ray photoelectron spectroscopy (XPS, Surface Science Instruments SSX-100, monochromatic Al Kα; 1486.6 eV) at a take-off angle of 90°.

2.2. Device fabrication

Devices were fabricated on pre-patterned indium tin oxide (ITO)-coated soda lime glass substrates (<20 Ω/sq, Kintec, Hong Kong). Before thin film deposition, these substrates were cleaned by sonication in non-ionic detergent and DI water, and then treated with a 10-min UV-ozone (Jelight) exposure.

The photovoltaic cells had a structure of glass/ITO/TiO_2 (15 nm)/P3HT (40 nm)/Au (50 nm). Before the TiO_2 thin film deposition, the TiO_2 nanoparticles were dissolved in DI water (5–10 mg/mL) to form a clear dispersion. TiO_2 thin films were deposited on top of cleaned ITO glass substrates by spin-coating. Prior to the deposition of P3HT (poly-3-hexylthiophene), the as-deposited TiO_2 thin films were treated in UV-ozone for 10 min. P3HT (American Dye Source) was dissolved in chlorobenzene to a concentration of 10 mg/mL before it was spin-coated at 1500 rpm in air on top of the TiO_2 layer. After P3HT deposition, the films were annealed on a hot-plate at 230 °C in N_2 atmosphere for 15 s and then cooled down slowly (~40 min) to improve the crystallinity of P3HT. Finally, 50 nm of Au was thermally evaporated at 0.05 nm/s under high vacuum (~10^{-6} Torr) to form the anode of the devices.

The light emitting diodes had an inverted structure of glass/ITO/TiO_2 (10 nm)/Al_2O_3 (5 nm)/F8BT copolymer (75 nm)/WO_3 (20 nm)/Au (40 nm). Similar to photovoltaic cell fabrication, TiO_2 dispersed in DI water was spin-coated onto cleaned ITO glass substrates in air to yield films with thickness of about 10 nm. A 10-min UV-ozone treatment of these films was followed by the deposition of 5 nm of Al, which was then oxidized under UV-ozone for 15 min. Subsequently, the F8BT light-emitting copolymer, namely poly[(9,9-dioctylfluorenyl-2,7-diyl)-co-(1,4-benzo-{2,1′,3}-thiadiazole)], with 10% benzothiadiazole was spin coated. The F8BT copolymer had a molecular weight of 15,000 and a polydispersity of 3.0. It was dissolved in p-xylene to yield a solution of 15 mg/mL and was spin-coated at 1000 rpm in a N_2 environment. Finally a top contact of WO_3 (20 nm)/Au (40 nm) was thermally evaporated at 0.1 and 0.05 nm/s, respectively.

3. Results and discussion

TiO_2 nanoparticles were prepared by hydrolysis of $TiCl_4$ at 40 °C in an isopropanol based sol–gel environment. TEM images show that nanoparticles, which did not aggregate, were obtained with an average particle size of 2 ± 0.4 nm (Fig. 1a). Fig. 1d shows the XRD pattern of as-prepared TiO_2 nanoparticles. From the XRD analysis, it is evident that both anatase and rutile structures exist in the sample, with anatase as the major phase. The XRD pattern of the formed phases is consistent with the data recorded in JCPDS file no. 21-1272 (anatase) and 21-1276 (rutile). The broad width of the diffraction peaks is attributed to the small crystallite size of the TiO_2 nanoparticles. The

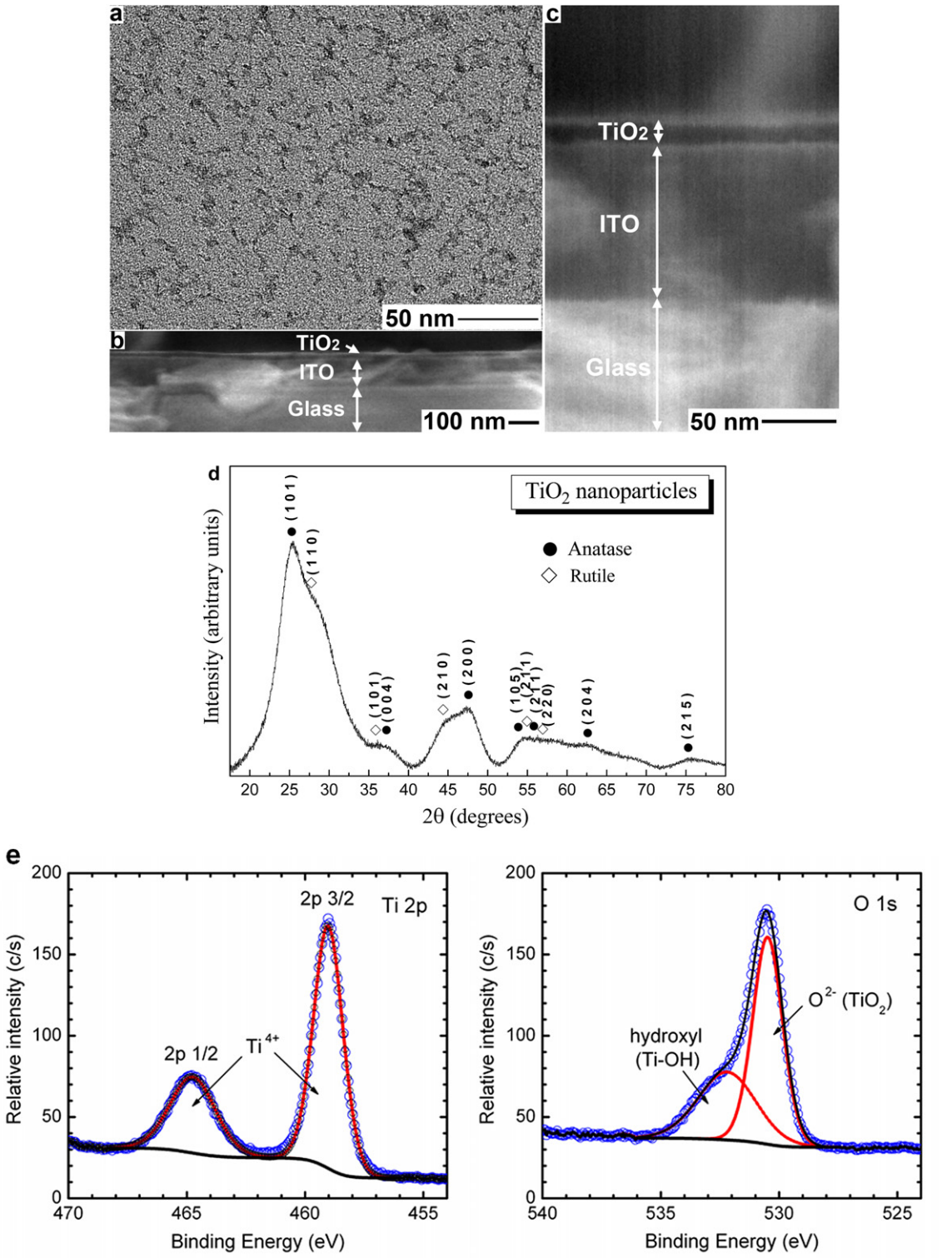

Fig. 1. (a) TEM image of the TiO_2 nanoparticles. (b and c) FESEM image of a TiO_2 thin film deposited on ITO-coated glass substrate. (d) XRD pattern of the TiO_2 nanoparticles. (e) XPS spectra (Ti 2p and O1s) of the deposited TiO_2 thin film after treated with UV-ozone exposure.

crystallite size of as-prepared TiO_2 nanoparticles could be calculated from the full width at half maximum of the (1 0 1) peak for anatase and (1 1 0) peak for rutile by the Debye–Scherrer formula (the distribution of these two partially overlapping peaks was analyzed with Pearson 7 waveform). It was found to be about 2 nm, which

is consistent with the particle-size measured from TEM images. Fig. 1e shows the high-resolution XPS spectra of the Ti 2p and the O1s peaks taken on the surface of deposited TiO_2 thin film after UV-ozone exposure. The shape of the Ti 2p 3/2 peak at 459.0 eV is symmetric, which proves Ti^{4+} to be the only oxidation state in our TiO_2 material. This reinforces the distinction between our TiO_2 thin films and amorphous TiO_x films, which contain a substantial amount of coordinatively unsaturated Ti species (e.g. Ti^{3+}) in the films [3,17]. The O1s peak is deconvoluted into two individual subpeaks: metal oxide (O^{2-}) and hydroxyl group (OH^-). The resulting peak positions for the O^{2-} and OH^- peaks are in good agreement with values reported by other studies [18,19]. The observed O^{2-} is assigned to the Ti–O bonding in bulk TiO_2 while the hydroxyl group is ascribed to the Ti–OH bonding on the surface of TiO_2 nanoparticles. The hydroxyl content of our TiO_2 materials is greater than other TiO_2 nanoparticles (e.g. P25 [20]) owing to the much larger surface area of the characteristically small nanoparticles (~2 nm).

One advantage of these nanoparticles is that they are easily dispersed in water and form a clear dispersion [21], which enables low-cost and environmental-friendly thin-film processing by means of spin-coating. No further annealing was needed to make our process more amenable to the fabrication of TiO_2/polymer hybrid devices, as compared to previously reported high-temperature processes [22–24]. A section of a typical TiO_2 thin film spin-coated on ITO coated soda-lime-glass substrate was examined by FESEM. The FESEM images show that the TiO_2 thin film is uniform in thickness along the section (Fig. 1b) which was measured to be around 15 nm in the high-magnification image (Fig. 1c). By adjusting the conditions of spin-coating, the thickness of TiO_2 films could be varied from several nanometers to the sub-micrometer scale.

The morphology of the as-prepared TiO_2 thin films on ITO glass substrate was investigated by AFM and it was found that it can be adjusted by changing the concentration of dispersion and the deposition conditions. Under specific conditions (high TiO_2 concentration and low spin speed, e.g. 10 mg/mL and 1000 rpm), rougher films with an RMS roughness (over a scan area of 10 μm × 10 μm) of 1.33 nm were obtained (Fig. 2a and b). These TiO_2 films with a typical thickness around 15 nm were used for photovoltaics. In the case of TiO_2 thin films for use in LED fabrication (typical thickness around 6 nm), the surface roughness could be significantly reduced by coating lower concentration dispersions with higher spin speeds (e.g. 5 mg/mL, 9000 rpm). The RMS roughness of these smoother films (over a scan area of 10 μm × 10 μm) was only 0.6 nm (Fig. 2c and d), similar to the surface roughness of the ITO coated glass substrate.

Photovoltaic cells were designed using room temperature deposited TiO_2 thin films as the electron extraction layer, while P3HT was spin-coated on top as the hole transporting layer. Annealing was applied after the deposition of P3HT on TiO_2 to improve the crystallinity of P3HT. In order to test the light absorption behavior of TiO_2 and P3HT, UV/

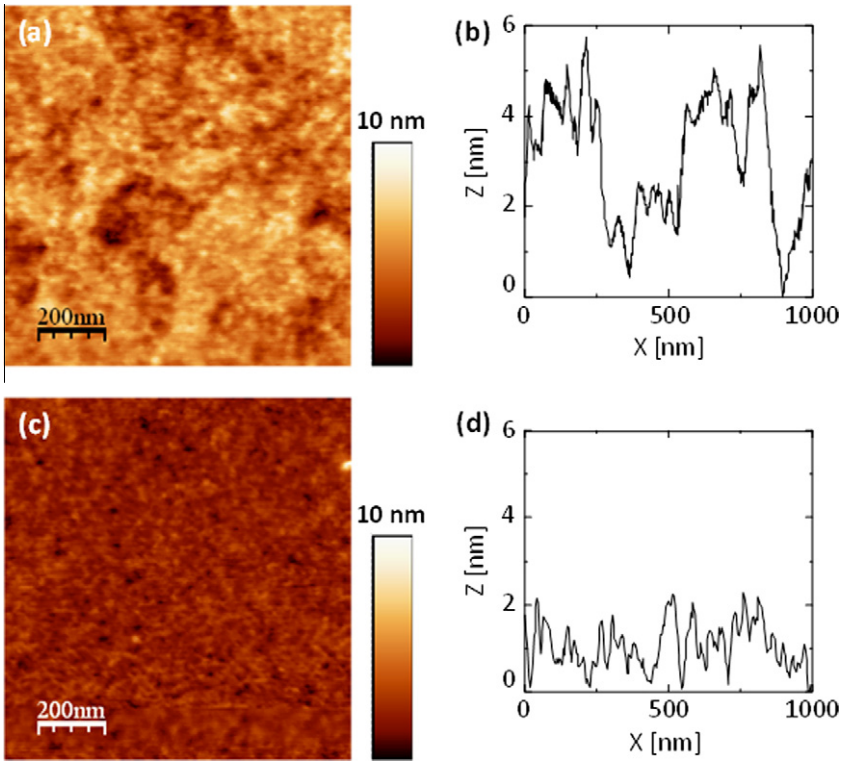

Fig. 2. (a and b) AFM images (left) and 1D profiles (right) for TiO_2 coated on ITO-coated glass for applications in photovoltaics. (c and d) AFM images (left) and 1D profiles (right) for TiO_2 coated on ITO-coated glass for applications in polymer LEDs.

Vis absorption spectra of these films were measured (Fig. 3a). The UV/Vis absorption spectrum of the TiO_2 thin film exhibits an absorption peak at 257 nm with the band-gap of about 3.5 eV estimated from the absorption onset (350 nm). The absorption onset is found to be blue-shifted as compared both to bulk rutile (~413 nm) and anatase (~387 nm) TiO_2, and this phenomenon is attributed to the quantum-size effects since the size of nanocrystals

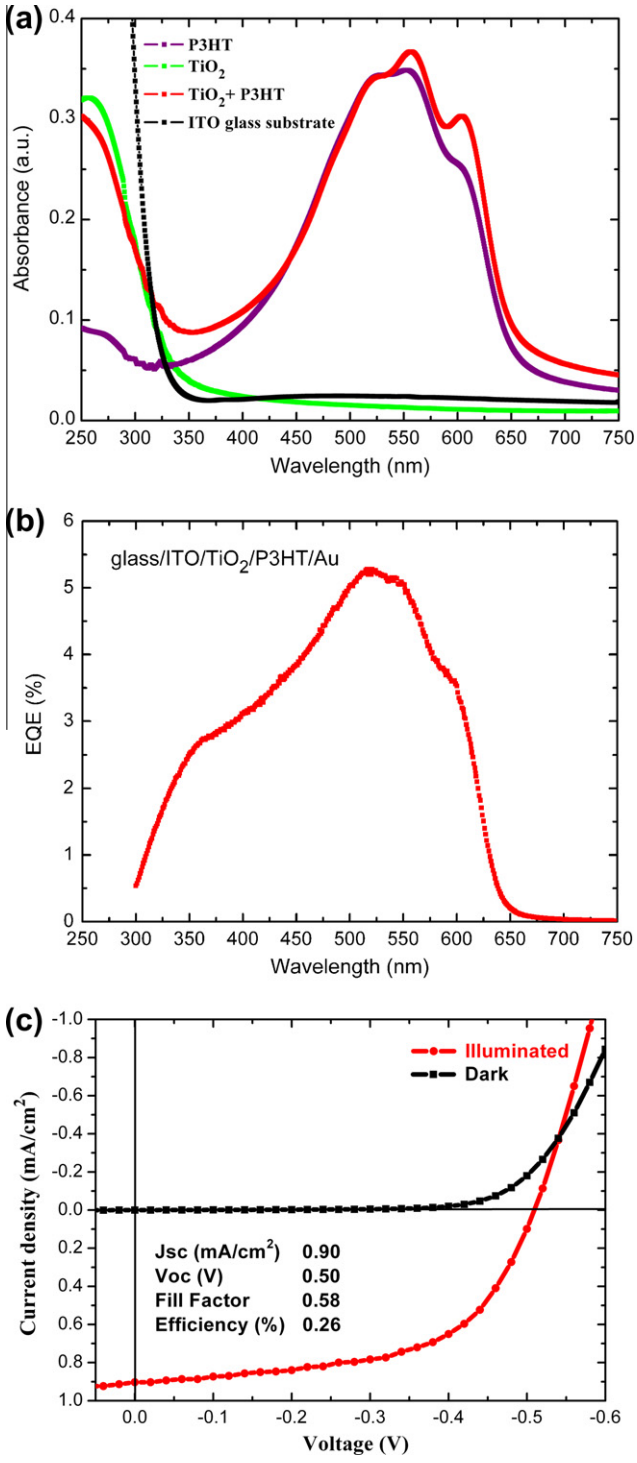

Fig. 3. (a) UV/Vis absorption for thin films of TiO_2, P3HT, a bilayer of the two (all on quartz), and the glass substrate used for device fabrication. (b) External quantum efficiency scan from an ITO/TiO_2/P3HT/Au device. (c) *I–V* curves of the photovoltaic cell.

comprising the TiO_2 thin films is only 2 nm on average (Fig. 1a) [21,25,26]. TiO_2 absorbs in the UV range, while P3HT absorbs from about 350 to 650 nm, thus the TiO_2 layer has the potential to extend the spectral response of P3HT-based solar cells. Moreover, the TiO_2 layer can protect the polymer overlayer from photo-bleaching by absorbing UV light. Fig. 3a also shows the enhanced vibronic transitions in the UV/Vis spectrum of TiO_2/P3HT films. P3HT on TiO_2 thin film displays two discernible intrachain π–π^* absorption peaks at 560 and 610 nm, which is associated with stronger interchain interactions in more ordered polymers. This phenomenon was due to the slow cooling process after annealing, which increased the degree of order in P3HT on TiO_2. Similar behavior was also observed as P3HT deposited on ZnO layer with similar annealing/cooling treatment after [7].

The relationship between light absorption and photocurrent was examined by external quantum efficiency (EQE) measurements. Gold was chosen as top electrode of the device due to its appropriate work function (~5.1 eV). Fig. 3b shows the EQE values for the hybrid photovoltaic device. The glass/ITO/TiO_2 (15 nm)/P3HT (40 nm)/Au (50 nm) device achieved an EQE of 5% in the 500–550 nm spectral region. A shoulder in the 300–350 nm spectral region shows that the device also generates current in the UV region, which could be attributed to the contribution of the TiO_2 layer. The open circuit voltage (V_{oc}), short circuit current (J_{sc}), fill factor (FF) and power conversion efficiency (PCE) of the hybrid photovoltaic cell under AM 1.5 100 mW/cm^2 illumination were calculated from the *I*–*V* curves. As shown in Fig. 3c, the hybrid photovoltaic cell achieved a V_{oc} of 0.50 V, a J_{sc} of 0.90 mA/cm^2, a FF of 0.58 and a PCE of 0.26%. The efficiency of our photovoltaic cell is comparable to the efficiency (0.28% PCE) reported by Shen et al. of a photovoltaic cell with similar combination of materials (ITO/TiO_2/P3HT/Au) [27]. However, in that report, the TiO_2 thin films were deposited from a sol–gel precursor and required post annealing at 450 °C, which is significantly higher than the process temperature reported here. In comparison to inverted devices based on ZnO layer, the performance of TiO_2/P3HT photovoltaic cell reported here is better than the performance of bi-layer ZnO/P3HT devices [5], and is comparable to the ZnO nanorod/P3HT composite devices (0.20–0.28% PCE) [5,7]. However, the performance of ZnO/P3HT photovoltaic devices reported by Olson et al. shows an improved efficiency (0.53% PCE)

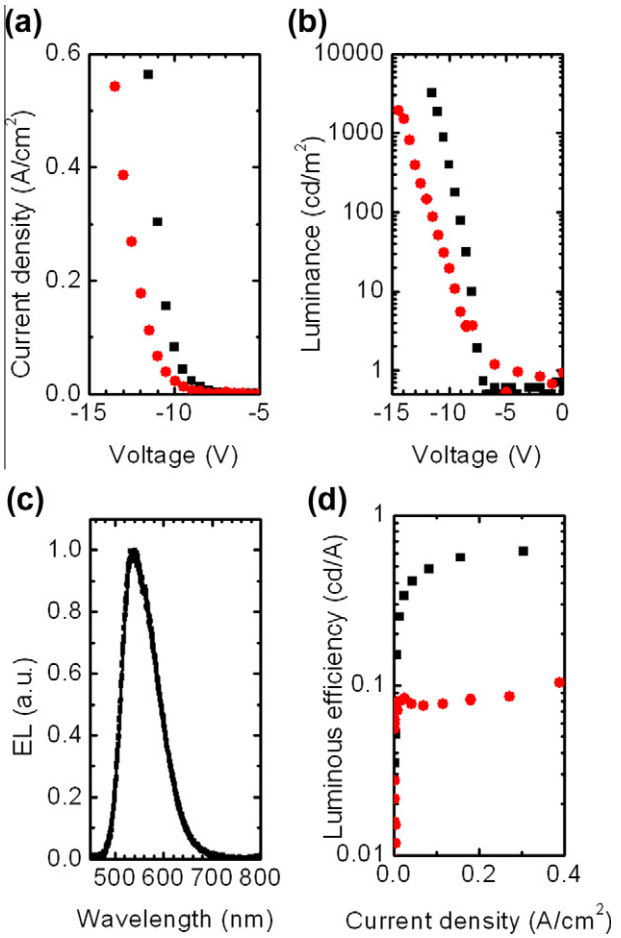

Fig. 4. (a) Current vs. voltage (*J*–*V*), (b) luminance vs. voltage (*L*–*V*) characteristics, (c) EL spectrum, and (d) luminous efficiency of a TiO_2/polymer hybrid LED. Data from two devices are shown: ITO/TiO_2/Al_2O_3/F8BT copolymer/WO_3/Au (squares ■) and one with a similar structure but utilizing only ITO as the cathode (circles ●).

due to a mesoporous structure of ZnO nanofibers that were grown via a hydrothermal process [6].

We found that if we spin-coat TiO_2 thin films with suspensions dispersing larger size TiO_2 nanoparticles (e.g. P25 with the average particle size of about 21 nm, a generous gift from Degussa Corporation), the photovoltaic devices fabricated with the similar process as this study often suffer from large current leakage and poor photovoltaic response. This result is due to the rough surface of as-deposited TiO_2 layer with large nanoparticle clusters (~100 nm) "sprinkled" on the surface. A strong point of the process described in this letter is that smooth and homogeneous TiO_2 thin films with very small roughness can be prepared readily at room-temperature via a liquid phase process. The good dispersibility and the good film forming properties can be attributed to the small and uniform size of the TiO_2 nanoparticles.

Fig. 4a and b show the current vs. voltage and luminance vs. voltage characteristics of the TiO_2/polymer hybrid light emitting diode with a structure of ITO/TiO_2 (10 nm)/Al_2O_3 (5 nm)/F8BT copolymer (75 nm)/WO_3 (20 nm)/Au (40 nm). The electroluminescence spectrum shows an emission peak at 536 nm (Fig. 4c). This hybrid LED turns on at ~7 V and reaches 100 cd/m^2 at ~8.5 V. The maximum brightness approaches ~4000 cd/m^2 at 12 V. The corresponding luminous efficiency at 100 mA/cm^2 is ~0.6 cd/A (Fig. 4d). This value is six times higher than that of a reference inverted device (~0.1 cd/A) utilizing only ITO as the cathode (Fig. 4a, b, and d, circle symbols), and comparable to that of a reference typical bottom anode device (ITO/PEDOT:PSS (AI4083) (60 nm)/F8BT copolymer (75 nm)/CsF (1 nm)/Al (40 nm)), in which the turn-on voltage was ~4.5 V, and the maximum brightness was ~4500 cd/m^2 at 9 V.

Previous reports attempted to incorporate either dense or porous TiO_2 into inverted polymer LEDs by following different schemes. For example, by means of spray-pyrolysis using a titanium organic precursor on heated substrates and then annealing at 520 °C, to obtain dense TiO_2 films [13]. The corresponding hybrid light emitting diodes showed an efficiency of about 0.6 cd/A. In a second example, spin-coating of a TiO_2 colloidal suspension of nanoparticles, followed with sintering at 450 °C, yielded a mesoporous film structure [28]. This method was used to prepare a TiO_2 layer for hybrid light emitting diodes, which showed a substantially lower current efficiency [28,29] than the one we report here. Therefore, the devices reported here show comparable or better performance than light emitting diodes employing TiO_2 films prepared and sintered at higher temperatures. To the best of our knowledge, the data described here constitute the first demonstration of a room-temperature processed TiO_2 film for hybrid light emitting diodes.

4. Conclusions

In conclusion, we show that TiO_2 thin films suitable for polymer optoelectronic device fabrication can be prepared at room temperature via a properly designed liquid phase deposition process. TiO_2/P3HT photovoltaic cells show comparable performance to devices utilizing TiO_2 layers sintered at high temperatures. TiO_2/F8BT hybrid light emitting diodes show an efficiency of 0.65 cd/A. These results show that it is now possible to apply TiO_2 films to the fabrication of low cost organic devices.

Acknowledgments

Funding for this work was provided by Grants from the NSF, DOE and ONR. C.H. Wu acknowledges support from the Taiwan Merit Scholarship (TMS-94-1-A-007). L.A. Estroff and H.Y. Li acknowledges partial support from the NSF (DMR 0845212), J.D. Watson Investigator Program (NYSTAR Contract #C050017), and the Cornell Center for Materials Research (CCMR), a Materials Research Science and Engineering Center of the National Science Foundation (DMR 0520404).

References

[1] G. Malliaras, R. Friend, Phys. Today 58 (2005) 53.
[2] H.H. Liao, L.M. Chen, Z. Xu, G. Li, Y. Yang, Appl. Phys. Lett. 92 (2008) 173303.
[3] K. Lee, J.Y. Kim, S.H. Park, S.H. Kim, S. Cho, A.J. Heeger, Adv. Mater. 19 (2007) 2445.
[4] T. Kuwabara, H. Sugiyama, M. Kuzuba, T. Yamaguchi, K. Takahashi, Org. Electron. 11 (2010) 1136.
[5] A.M. Peiro, P. Ravirajan, K. Govender, D.S. Boyle, P. O'Brien, D.D.C. Bradley, J. Nelson, J.R. Durrant, J. Mater. Chem. 16 (2006) 2088.
[6] D.C. Olson, J. Piris, R.T. Collins, S.E. Shaheen, D.S. Ginley, Thin Solid Films 496 (2006) 26.
[7] D.C. Olson, Y.-J. Lee, M.S. White, N. Kopidakis, S.E. Shaheen, D.S. Ginley, J.A. Voigt, J.W.P. Hsu, J. Phys. Chem. C 111 (2007) 16640.
[8] S.K. Hau, H.L. Yip, N.S. Baek, J. Zou, K. O'Malley, A.K.-Y. Jen, Appl. Phys. Lett. 92 (2008) 253301.
[9] B. O'Regan, J. Moser, M. Anderson, M. Grätzel, J. Phys. Chem. 94 (1990) 8720.
[10] B. O'Regan, M. Grätzel, Nature 353 (1991) 737.
[11] K. Morii, M. Ishida, T. Takashima, T. Shimoda, Q. Wang, Md.K. Nazeeruddin, M. Grätzel, Appl. Phys. Lett. 89 (2006) 183510.
[12] L. Kavan, M. Grätzel, Electrochim. Acta. 40 (1995) 643.
[13] H.J. Bolink, E. Coronado, D. Repetto, M. Sessolo, E.M. Barea, J. Bisquert, G. Garcia-Belmonte, J. Prochazka, L. Kavan, Adv. Funct. Mater. 18 (2008) 145.
[14] H. Kim, S. Sohn, D. Jung, W.J. Maeng, H. Kim, T.S. Kim, J. Hahn, S. Lee, Y. Yi, M.-H. Cho, Org. Electron. 9 (2008) 1140.
[15] B.W. Kang, W.S. Kim, C.M. Hwang, D.Y. Moon, J.J. Kim, J.G. Park, J.W. Park, Jpn. J. Appl. Phys. 49 (2010) 08JG05.
[16] W. Wang, B.H. Gu, L.Y. Liang, W.A. Hamilton, D.J. Wesolowski, J. Phys. Chem. B 108 (2004) 14789.
[17] D. Luca, D. Macovei, C.-M. Teodorescu, Surf. Sci. 600 (2006) 4342.
[18] E. McCafferty, J.P. Wightman, T.F. Cromer, J. Electrochem. Soc. 146 (1999) 2849.
[19] S. Hofman, J.M. Sanz, J. Trace Microprobe Tech. 1 (1982/1983) 213.
[20] B. Erdem, R.A. Hunsicker, G.W. Simmons, E.D. Sudol, V.L. Dimonie, M.S. El-Aasser, Langmuir 17 (2001) 2664.
[21] P. Wang, D.J. Wang, H.Y. Li, T.F. Xie, H.Z. Wang, Z.L. Do, J. Colloid Interface Sci. 314 (2007) 337.
[22] L.B. Roberson, M.A. Poggi, J. Kowalik, G.P. Smestad, L.A. Bottomley, L.M. Tolbert, Coord. Chem. Rev. 248 (2004) 1491.
[23] K. Takahashi, Y. Takano, T. Yamaguchi, J. Nakamura, C. Yokoe, K. Murata, Synth. Met. 155 (2005) 51.
[24] A. Sergawie, T. Yohannes, T. Solomon, Synth. Met. 157 (2007) 75.
[25] C. Kormann, D.W. Bahnemann, M.R. Hoffmann, J. Phys. Chem. 92 (1988) 5196.
[26] A.L. Linsebigler, G. Lu, J.T. Yates Jr., Chem. Rev. 95 (1995) 735.
[27] L. Shen, G. Zhu, W. Guo, C. Tao, X. Zhang, C. Liu, W. Chen, S. Ruan, Z. Zhong, Appl. Phys. Lett. 92 (2008) 073307.
[28] S.A. Haque, S. Koops, N. Tokmoldin, J.R. Durrant, J. Huang, D.D.C. Bradley, E. Palomares, Adv. Mater. 19 (2007) 683.
[29] D. Kabra, M.H. Song, B. Wenger, R.H. Friend, H.J. Snaith, Adv. Mater. 20 (2008) 3447.

experimental and theoretical investigations in order to understand the factors affecting its molecular rectification. Some theoretical studies examined the rectification properties of diblock diode, [16,18–22] but very little addressed the issue of the effect of structural factors [16,20]. A good reported example of single diblock molecular diode is the dipyrimidinyl-diphenyl dithiol (**DPDPh1**), Fig. 1. Experiment demonstrated that the electronic structure of this molecule allows the current to pass preferably in one direction [11]. Consequently, recent theoretical studies were interested in studying the effect of some structural factors on the electrical behavior of the **DPDPh1** molecule [16,20,22]. These studies indicated that the anchoring group [16] and molecular length [20] have obvious effects on the molecular rectification. It was also found that the asymmetric feature in the calculated current–voltage curve increases with increasing the molecular length [20]. On the experimental side, the rectification of current by diblock diode is enhanced by increasing the dipole moment of the molecule [11,14].

In this work, the authors investigated the effect of two new structural factors on the rectification properties of the **DPDPh1** molecule within a range of applied voltages: the constitutional and conformational isomery. It is worth mentioning that the isomery effect on the electron transport through two different molecular wires has been studied [23,24]. It was apparent that the relative position of nitrogen atoms in the molecular rings can significantly affect the transport characteristics due to changes in the electronic structures. The effect of constitutional isomery on the electrical properties of molecular diode was studied through four isomers: **DPDPh1**, **DPDPh2**, **DPDPh3** and **DPDPh4**. Fig. 1 illustrates these isomers in sandwiched form between two equatorial triangles of Au atoms. On the other hand, the conformational isomery effect was examined by varying the mid torsion angle between the donor and acceptor subunits of the **DPDPh1** molecule. To achieve these objectives, geometrical and electronic structures of all isomers were investigated using density functional theory (DFT) for the calculations of the intrinsic properties of all isomers. Moreover, the effect of electric field on the electronic properties of constitutional isomers was considered. The current–voltage (I–V) curves for the promising isomers were calculated to support our interpretations.

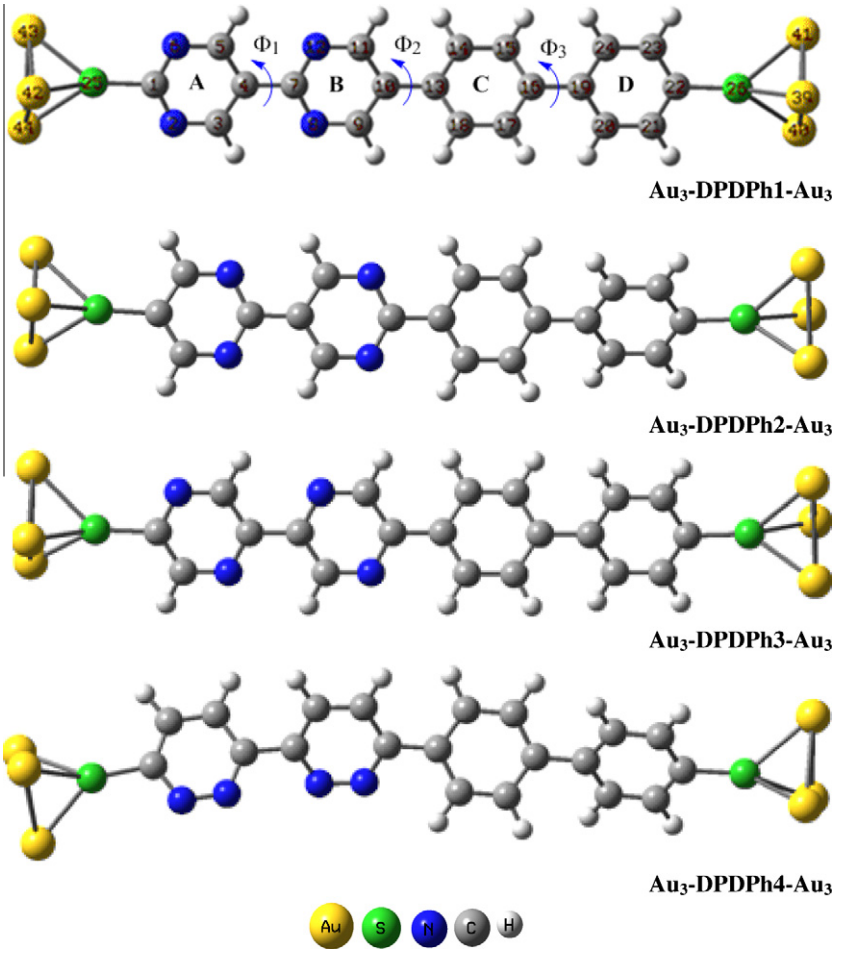

Fig. 1. B3LYP-optimized structures of the studied diblock molecular systems. The numbering and label scheme is presented on the structure of **Au_3–DPDPh1–Au_3** as a representative for all isomers. Φ_1, Φ_2 and Φ_3 are the torsion angles between each two adjacent rings.

In general, the electrical properties of molecules could be calculated by quantum chemical method, electron transport method, or both of them. The former deals with studying of molecular electronic structures in the absence [1–3] or presence of electric field [22,25–31]. Many authors prefer to use the electric field on isolated molecules without taking into account the effect of electrodes because they consider electrical properties of a given molecular device is an intrinsic character of the molecule itself [22,25–24,31] Others simulate the effect of electrodes by connecting the molecule with two small clusters representing the metal as semi-infinite electrodes [18,9,32]. On the other hand, the electron transport method uses two-probe configuration to calculate experimentally observable quantities like current or conductivity [20,33–35], see Fig. 2. This configuration is divided into three regions, two electrodes and the central region. The latter involves the molecule and the surface atoms of electrodes on each side. Some recent studies tried to combine them to validate their interpretations [18,23,35].

2. Background and methodology

In order to link the chemical properties of the molecular diode with its physics, we try to examine the response of some chemical parameters to the effect of electric field. When a single molecular diode is placed between two electrodes, electrons flow from the source to the drain through the molecule [3,18]. Thus, we can consider the molecule as an electrophile with respect to the source electrode. Accordingly, some electronic parameters such the global electrophilicity index "ω" were calculated in the framework of DFT approach [36]. The electrophilicity index measures the electrophilic power of a given system and is defined as follows:

$$\omega = \frac{\mu^2}{2\eta} \tag{1}$$

where μ and η are the chemical potential and global hardness, respectively. They could be calculated using the following mathematical expressions:

$$\eta = I - A \text{ and } \mu = -(I + A)/2 \tag{2}$$

where I and A represent the vertical ionization potential and electron affinity of a chemical species. Another related quantity, ΔN_{max}, [36] is the maximum amount of electronic charge that an electrophile may accept from its environment (i.e., the source electrode in this case),

$$\Delta N_{max} = -\mu/\eta \tag{3}$$

We preformed the calculations as follows:

2.1. The isolated molecules

Geometry optimization of all isomers were performed using the hybrid B3LYP functional [37–39] with the 6-31+G(d,p) basis set as implemented in the Gaussian 03 suite [40]. Single point energy calculations of the cationic and anionic species at B3LYP/6-31+G(d,p) using the optimized geometries of the neutrals. Then the vertical I and A were calculated from subtracting the energies of the cations and anions, respectively, from that of the neutral systems.

2.2. Effect of electric field

To simulate the connection of a molecular device to electrodes, the two anchoring sulfur atoms of the fully optimized structure of the isolated molecules were fixed in the space and then allowed to be optimized again under the effect of a uniform electric field [22] ranges from 0 to 5.00×10^{-3} a.u. in its strength. This corresponds to a range of bias voltage from 0 to 4.90 volt (V). The field was aligned along and against the z-molecular axis (dihetrocyclic-diphenyl direction).

2.3. Au_3–molecule–Au_3

It is well known that the thiol group losses its hydrogen atom when attached to the metal surface, thus forming a strong covalent bond that provides a good electrical contact between the molecule and the electrodes [41–44]. Each optimized molecular fragment is sandwiched between two equatorial triangles of Au atoms, with an Au–Au bond length of 2.88 Å as shown in Fig. 1 [41,42]. Each sulfur atom is attached at the hallow site on Au clusters with vertical distance 1.90 Å, where the attachment by this way give local energy minimum [41–44]. In such configuration, the small Au clusters were used to simulate the attachment of the Au(1 1 1) surfaces. The relative positions of the Au atoms were frozen in each triangle, but the distance between the clusters were relaxed during the

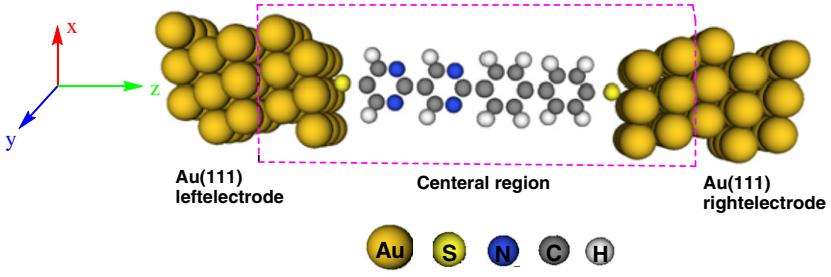

Fig. 2. Schematic illustration of the two-probe configuration for computing the I–V curve of the molecule coupled to pair of (3×3) gold electrodes. The central region includes the molecule between two surface layers.

geometric optimization. Geometry optimizations have been conducted using B3LYP/mixed basis sets: Los Alamos National Laboratory Double Zeta basis set (LANL2DZ) [45] for the gold atoms and 6-31+G(d,p) basis sets for the rest of atoms.

2.4. Calculation of I–V curve

The current (I) is calculated through two-probe system as a function of steadily increasing bias in both directions. The applied bias ranges from −2.0 to 2.0 V similar to the range of the experimental measurement [11]. The two-probe system is built by sandwiching the optimized isolated molecules from step (i), without the two terminal hydrogen atoms, between two gold electrodes through sulfur atoms. The non-equilibrium Green's function (NEGF) combined with exchange correlation DFT functional (LDA/PZ, the local density approximation with the Perdew–Zunger parameterization) [46] to compute the current using Atomistix ToolKit computer code (ATK 2.0) [47–48]. Double-zeta plus polarization (DZP) basis set was chosen for all atoms except gold for which single-zeta plus polarization (SZP) was used. Fig. 2 shows a representative example for the two-probe systems which divides into three regions: left electrode (L), central region, and the right electrode (R). Each electrode Au(1 1 1) surface is simulated by a (3×3) cell with the periodic boundary conditions. The central region includes the molecular fragment between couple of two surface layers.

3. Results and discussion

3.1. Diblock diode versus AR diode

It has been demonstrated that the diblock and AR diodes are able to rectify the alternating current [1–22]. The diblock diode (***A–D***) consists of donor (***D***) and acceptor (***A***) parts covalently connected, while the AR-diode (***A–S–D***) includes a spacer group (***S***) such as CH_2 between ***A*** and ***D***. Experiment proved that the **DPDPh1** junction has an ability to rectify alternating current [11]. However, what is the effect of turning this diblock molecule into AR-like model by inserting a spacer group between the diphenyl and dipyrimidinyl moieties? Both models were fully optimized to investigate the effect of spacer on the geometrical and electronic structures of the **DPDPh1** molecule. The results are given in Table 1. It is clear that the insertion of a CH_2 group induces bending ($<C_A–C–C_D = 114°$). The HOMO and LUMO are delocalized over the **DPDPh1** molecule with high weight on ***D*** and ***A*** subunits, respectively. Apparently, inserting CH_2-spacer produces AR-diode character [1–3]; where HOMO and LUMO are entirely localized at D and A subunits. Moreover, the inserted CH_2 group raises the dipole moment and increases the HOMO–LUMO energy gap due to interruption of conjugation, introduced by bending, and impedes electron-flow through the molecule.

3.2. Constitutional isomery

The diblock diode consists of donor and acceptor parts, where the donor part is the same in all isomers while the type of acceptor part depends on the relative positions of nitrogen atoms, see Fig. 1. To clearly understand the effect of constitutional isomery, the acceptor and donor units which constitute the ***A–D*** molecules were optimized separately. The HOMO and LUMO energies and HOMO–LUMO energy gaps for ***A*** and ***D*** are collected in Table 2. Evidently, the LUMO energy of the acceptor molecules decreases dramatically upon insertion of the nitrogen atoms, which can be ascribed to reducing electron density on the aromatic rings. Therefore, the diphenyl block can act as n-type molecular device, while insertion of nitrogen atoms gives it a p-type character. The potential drop was estimated to examine the effect of relative positions of nitrogen atoms on the accepting ability of p-type device and then the extent of coupling between it and the other individual n-type when they are chemically connected. As an approximation, the potential drop is defined as the energy difference between the LUMO energies of individual n-type and p-type [1]. According to the results given in Table 2, the accepting ability of 2,2′-dipyrazinyl molecule is higher than that of

Table 1
The energies of HOMO, LUMO and E_g (eV) and the dipole moment (Debye) as well as spatial orientations of HOMO and LUMO of **DPDPh1** molecule (***A–D***) and its acceptor–spacer–donor analogue (***A–S–D***) calculated at B3LYP/6-31+G(d,p) level.

Parameter	***A–D*** (**DPDPh1**)	***A–S–D***
ε_{LUMO}	−2.35	−2.12
ε_{HOMO}	−6.13	−6.08
E_g	3.78	3.97
Dipole moment	5.62	6.01
LUMO	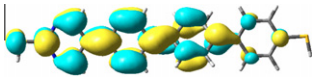	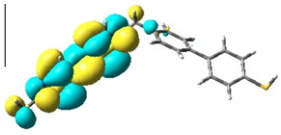
HOMO	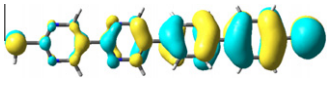	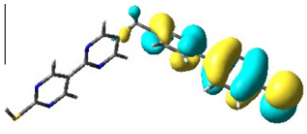

Table 2
The energies of HOMO, LUMO, E_g and the potential drop (ΔE_{LUMO}) (eV) of the diphenyl and its isoelectronic constitutional isomers calculated at B3LYP/6-31+G(d,p) level.

Constituent	ε_{HOMO}	ε_{LUMO}	E_g	ΔE_{LUMO}
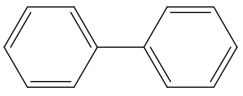 diphenyl	−6.93	−0.72	6.21	–
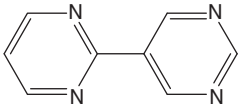 [2,5′]dipyrimidinyl	−7.09	−2.26	4.82	1.54
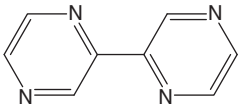 [2,2′]dipyrazinyl	−6.97	−2.43	4.54	1.71
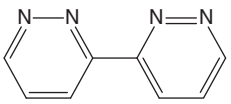 [3,3′]dipyridazinyl	−6.75	−2.24	4.51	1.52

2,5′-dipyrimidinyl or 3,3′-dipyridazinyl molecule. This would affect the HOMO–LUMO energy gap of the combined ***A–D*** molecules.

Fig. 3 displays the molecular orbital energy levels of the donor and acceptor molecules compared to their combination in the **DPDPh1** molecule. It is apparent that the insertion of nitrogen atoms in biphenyl block has a similar effect as the electron-withdrawing substituent in AR-model, where both HOMO and LUMO energies are decreased [1]. It is also clear that the LUMO level of ***A–D*** is close to that of the acceptor molecule. This may be attributed to the relatively high-weight localization of LUMO on the acceptor moiety of ***A–D***. On contrary, the HOMO of the donor molecule is far away from the HOMO of ***A–D***, but the degeneracy of HOMO and HOMO-1 of the donor may cause relatively high-weight localization of HOMO on the donor moiety of ***A–D*** species.

The optimized geometries of all isomers in between two equatorial triangles of gold atoms are shown in Fig. 1. The calculations shows that the effect of connecting gold clusters on the geometry of the molecules is little where average deviation of bond lengths and bond angles for the common fragment between the isolated and **Au3–molecule–Au3** species hovers around 0.001 Å and 0.03°, respectively. Thus it suffices here to discuss the geometrical parameters of the isolated molecules. Further details about the geometries of the isomers and the comparison between some selected geometrical parameters of the isolated molecules and **Au3–molecule–Au3** species are given in the supporting information, Tables S1 and S2. The torsion angles Φ_1, Φ_2 and Φ_3 between each two adjacent rings and the bond lengths located on the molecular axis are given in Table 3. All isomers adopt twisted structures. The extent of twisting depends on the relative positions of nitrogen atoms. For example, rings ***A***, ***B***, and ***C*** of the **DPDPh2** isomer are almost coplanar. The shift of two nitrogen atoms from positions 9 and 11 to 8 and 12, increases Φ_1 and Φ_2 to 1.5 and 37°, respectively, leading to a high twist between ***B*** and ***C*** rings. Also, the **DPDPh4** molecule is the most twisted isomer giving a simple concave shape where all adjacent rings are twisted with respect to each other. However, the angle between the two phenyl rings, Φ_3, and most of bond lengths of all isomers are independent on the position of the nitrogen atoms. The angle Φ_2 between the donor and acceptor parts of the molecule is correlated to a great extent with the dipole moment; larger Φ_2 the higher the dipole moment. Furthermore, the constitutional isomery has a remarkable effect on the anchor atoms, especially S25, and the binding properties with metallic electrodes, Table 3. For example, the Mulliken atomic charge on S25 is dramatically reduced (from 0.258 to 0.004 e). The effect of isomery on the charge on S25 atom follows the order: **DPDPh1** > **DPDPh4** > **DPDPh3** > **DPDPh2**, while that of S26 atom shows the order: **DPDPh3** ≈ **DPDPh2** > **DPDPh1** ≈ **DPDPh4**.

Conjugated systems provide channels for electrons to transfer from a part to another part within the molecule, where π-electron cloud extends over the fully delocalized molecular orbitals [15,49,50].Table 4 shows the surfaces of four molecular orbitals of the **Au3–molecule–Au3** systems. These systems are considered extended molecules, where the molecule is attached to the nearest three gold atoms in each side. The depicted orbitals of the **Au3–molecule–Au3** species correspond to LUMO, HOMO, HOMO-1 and HOMO-2 of the isolated molecule. Although we used a different DFT methodology compared to that used by Gasyna et al. [18], we got very similar results for the spatial distribution of frontier molecular orbitals (FMOs) of the **Au3–DPDPh1–Au3** molecule. An inspection of Table 4 also indicates that the LUMO surface is almost delocalized over

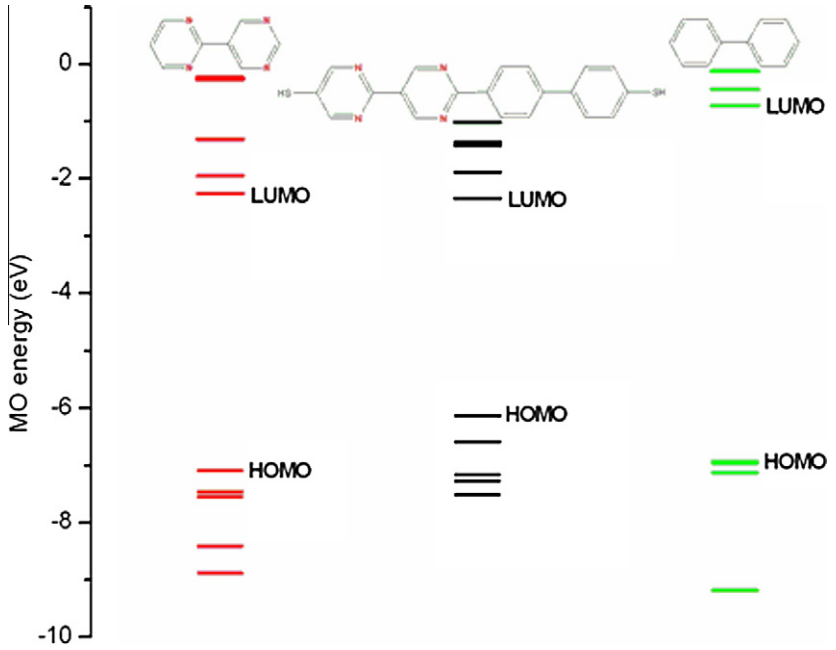

Fig. 3. the molecular orbital diagram of the five highest occupied and five lowest unoccupied orbital energy levels for 2,5′-dipyrimidinyl, **DPDPh1**, and diphenyl molecules calculated at B3LYP/6-31+G(d,p) level.

Table 3
The torsion angles (°) between adjacent rings, atomic charges (e) on S25 and S26 atoms, and bond lengths (Å) of the bonds located on the molecular axis in the molecular systems calculated at B3LYP/6-31+G(d,p) level. The angles and bonds are assigned in Fig. 1.

	Φ_1	Φ_2	Φ_3	Q_{S25}	Q_{S26}	C1–S25	C4–C7	C10–C13	C16–C19	C22–S26
DPDPh1	−2.05	−38.27	37.84	0.258	−0.076	1.775	1.475	1.476	1.482	1.782
DPDPh2	0.59	0.25	37.77	0.004	−0.140	1.776	1.474	1.479	1.482	1.783
DPDPh3	−1.09	−18.33	37.69	0.168	−0.138	1.779	1.477	1.479	1.482	1.783
DPDPh4	43.38	−20.37	37.58	0.209	−0.075	1.776	1.485	1.481	1.482	1.783

the molecular skeleton and does not change by isomerisation. The HOMO state tends to be mainly localized at biphenyl subunit while HOMO-1 and HOMO-2 states are localized on the pyrimidinyl ring. The orbital overlap between the π-electrons of the subunits looks weak which resembles *p–n* semiconductor junction [18]. Accordingly, applying electric field in the direction of the molecular axis (from acceptor to donor) will direct the free π-electrons to move from the source-side to the drain-side. This process creates a potential barrier in the inter-subunit region. Upon reversing the direction of electric field, the potential barrier becomes higher than in the case of forward one [18].

Upon applying positive bias voltages, electrons move from source to drain overcoming tunneling potential barrier between the donor and acceptor subunits. With reversing the bias, the potential barrier becomes higher and thus electrons are difficult to flow. It is known that the transport property depends mainly on the alignment of molecular orbital to the Fermi level, i.e. the molecular orbital whose energy lies closer to the Fermi level [18,51,52]. If a gold metal is used as an electrode, the equilibrium Fermi level is assumed to be −5.31 eV for single crystal Au (1 1 1) electrode [11]. Therefore; one can expect that HOMO would be used in the electron tunneling process due to the closeness of HOMO of the molecule to the Fermi level compared to LUMO. This agrees with other previous studies [14,16,18,22].

Some electronic structure parameters from quantum chemical calculations are collected in Table 5. Most of these parameters are comparable for all isomers reflecting the similarity in their electronic structures, which may rectify the alternating current like **DPDPh1**. For example, the tunnelling process of rectification of **DPDPh1** depends on the alignment of the HOMO with the Fermi energy level of the gold electrode (−5.31 eV). Compared to that of the **DPDPh1** molecule, the HOMO energy levels of the other three isomers are slightly closer to the Fermi level. The effect of electric field on the FMOs of the **DPDPh1** molecule has been reported in previous studies [18,22]. They found that the energy of HOMO is closer to Fermi level than does the LUMO which implies that the electron tunnelling occurs mainly through HOMO. On contrary, LUMO of substituted oligophenylene ethynylenes is the closest orbital to Fermi level [10]. Here we try to extend these studies by correlating some chemical properties with the physics of

Table 4
The spatial orientations of the FMOs of the **Au3–molecule–Au3** molecular systems calculated at B3LYP/mixed basis set level.

	Au3–DPDPh1–Au3	**Au3–DPDPh2–Au3**	**Au3–DPDPh3–Au3**	**Au3–DPDPh4–Au3**
LUMO	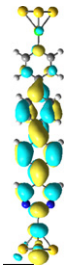	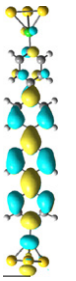	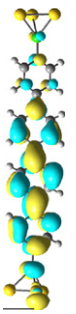	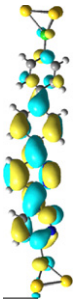
HOMO		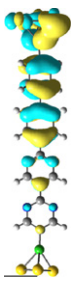	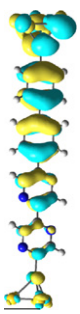	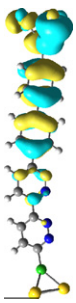
HOMO-1	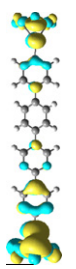	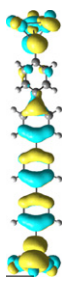	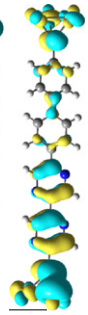	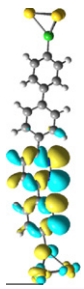
HOMO-2	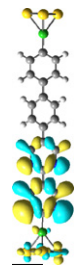	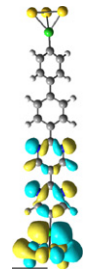	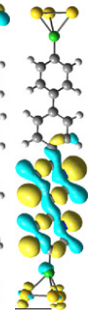	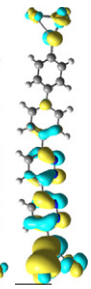

the device. These chemical properties include the global electrophilicity and the maximum propensity of the systems to acquire electronic charges from the source electrode as described in Section 2. These parameters follow the order: **DPDPh3** > **DPDPh2** > **DPDPh1** > **DPDPh4** in the absence of electric field.

However, we could follow the maximum propensity of the system to acquire electronic charge from the circuit under application of electric field. This was performed by plotting ΔN_{max} against bias voltage as displayed in Fig. 4a. The plots for all isomers have nearly *I–V*-like shape. By sweeping negative bias, ΔN_{max} shows a limited increase, if any. On the other hand, raising of positive indicated a slight increase in the ΔN_{max} until 0.98 V and then a rapid increase by further moving toward more positive bias. This result agrees with the observed rectifying character of the **DPDPh1** junction, where the current flows easily under positive voltage and is impeded under negative voltage [11]. Therefore, one could expect that junctions of **DPDPh2**, **DPDPh3** and **DPDPh4** may able to rectify alternating current. This promising rectification ability of the new isomers can also be confirmed from the plot of global electrophilicity index ω against bias voltage which shows an *I–V*-like shape as given in Fig. 4b. These plots can be utilized to examine the response of the intrinsic electrical properties of the isolated molecule under the effect of applied bias.

The asymmetrical response of the ΔN_{max} and ω parameters of the promising isomers to the applied voltage bias in the positive direction relative to the negative one can be proved by computing the electrical current using NFEG-DFT as described in Section 2. The prediction of the rectification efficiency of a given molecular junction can be judged by computing the *I–V* curve. Fortunately, the *I–V* curve of **DPDPh1** molecular junction has been measured experimentally using a.c.-assisted STM break-junction method [11]. Therefore, calculations of the *I–V* curve of the **DPDPh1** junction and its isomers will help in giving clear evidence about the unknown rectification ability of the new isomers. The current was computed for the experimentally measured voltage (from −2 to +2 V) [11] and the results are depicted in Fig. 5. At first glance, it is apparent that the transport ability is dependent on the constitutional isomery of the molecular junctions. For example, the current at 2 V is about 6.0, 6.3, 8.9 and 1.9 μA for the **DPDPh1**, **DPDPh2**, **DPDPh3** and **DPDPh4** junctions, respectively. Another important observation is that the **DPDPh1**, **DPDPh2** and **DPDPh3** junctions show clear asymmetric features in the computed *I–V* curves. This means that the transport ability under positive bias is significantly stronger than that at the negative bias. On contrary, the **DPDPh4** junction almost shows slightly asymmetric feature. By inspection Fig. 4 again in the bias windows from −2 to 2 V, we find the order of ΔN_{max} is **DPDPh3** > **DPDPh2** > **DPDPh1** > **DPDPh4** (or for ω **DPDPh3** > **DPDPh2** ≈ **DPDPh1** > **DPDPh4**) which agrees qualitatively to a great extent with that of *I–V* curves. Therefore, we could link the chemistry of the molecules with the physics of the molecular junctions.

To quantify the asymmetric response of the molecular junctions under positive and negative biases, we have

determined the rectification ratio, $R(V)$, which is defined as $R(V) = |I(V)/I(-V)|$. If $R(V)$ approaches 1, the molecular junction does not rectify the alternating current. The obtained rectification ratio of the molecular junctions as a function of the applied voltage is shown in Fig. 6. In general, the **DPDPh3** junction exhibits relatively significant rectification within the whole applied voltage especially at higher voltage, while the **DPDPh4** junction exhibits relatively weak rectification especially at high voltages. However, the effect of isomery on the rectification depends on the applied voltage. For instance, at voltage less than 1 V, the $R(V)$ values of the investigated molecular diodes are very close to each other (ca. 1.5). After 1 V, the isomers behave differently with respect to the rectification where the **DPDPh3** junction exhibits an enhancement, while the **DPDPh4** junction shows a weakness. At 2 V, the order of $R(V)$ is **DPDPh3** > **DPDPh2** > **DPDPh1** > **DPDPh4**. Therefore, we propose the **DPDPh3** junction as a better rectifier than the **DPDPh1** isomer especially at relatively higher voltages and it is worthy to be tested experimentally. However, the **DPDPh4** junction has a relatively slight rectification character. The difference between the **DPDPh2** and **DPDPh1** junctions depends on the applied voltage.

As the investigated diblock molecules and substituted oligophenylene ethylenes [10] represent two models for current rectification from the molecular wire, comparing

Table 5
The HOMO and LUMO energies, energy gap (E_g), global electrophilicity index (ω) and ΔN_{max} (eV) and the dipole moment (Debye) of the molecular systems calculated at B3LYP/6-31+G(d,p) level.

Species	ε_{HOMO}	ε_{LUMO}	E_g	Dipole moment	Global electrophilicity index (ω)	ΔN_{max}
DPDPh1	−6.13	−2.35	3.78	5.62	2.38	1.12
DPDPh2	−5.86	−2.39	3.48	4.02	2.45	1.19
DPDPh3	−5.97	−2.50	3.47	2.13	2.59	1.22
DPDPh4	−6.01	−2.23	3.78	5.26	2.25	1.09

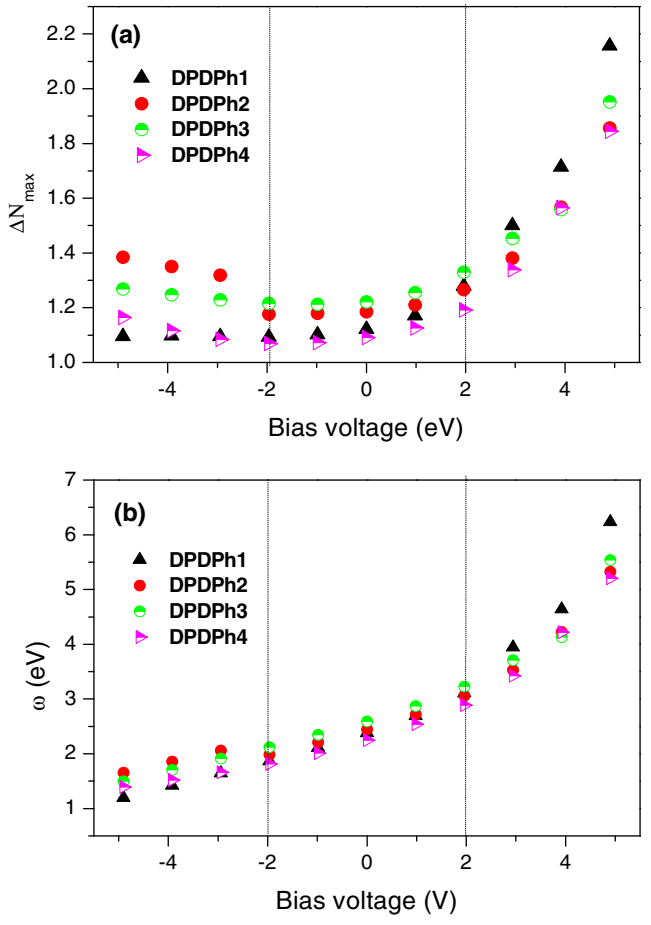

Fig. 4. (a) The maximum amount of electronic charge that the constitutional isomer molecules would acquire from the source (ΔN_{max}), and (b) the global electrophilicity index (ω) as a function of bias voltage calculated at B3LYP/6-31+G(d,p) level.

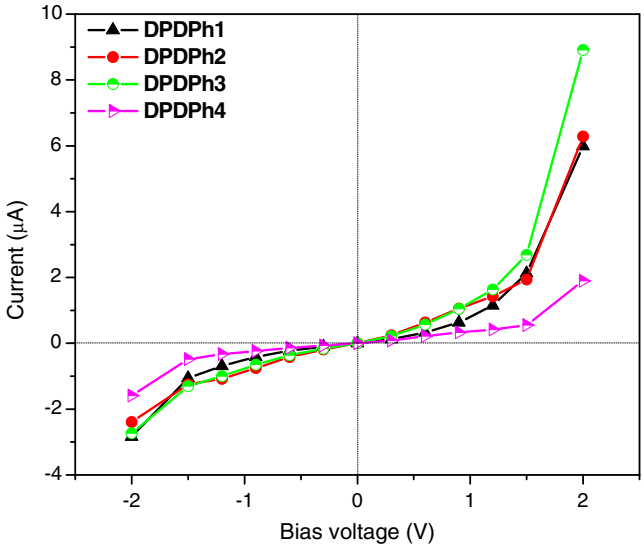

Fig. 5. The current–voltage curves of the studied molecular junctions.

the calculated molecular rectification between them is worthy. There are three differences between rectification plots of both classes. NEGF calculation indicated that the diblock oligomers exhibit higher $R(V)$ than the other class. The average values of $R(V)$ of the diblock oligomers equal about 1.5 compared to less than 0.2 for phenylene ethylene oligomers. However, the plots of rectification ratio of phenylene ethylene oligomers have a curvature while those of the diblock oligomers show a quasi-linear feature. Other difference between them appears at higher bias voltages, the $R(V)$ of diblock junction has high values while that of oligophenylene ethylenes.drops down to negative values [10].

3.3. Conformational isomery

To study the effect of conformational isomery on the electrical properties of molecular diode **DPDPh1**, the torsion angle between the donor and the acceptor segments was fixed at a given value while optimizing other geometrical parameters. Fig. 7 displays the relaxed potential energy surface and the corresponding HOMO energies. The graph shows that the potential energy is symmetrical around 90° with two minima at low twist angle of ca. 45 and 135°. This rotation is similar to the rotation of the phenyl ring in the biphenyl molecule which shows a double well energy diagram [53] with a twist angle of 44.4° from electron diffraction studies [54]. These preferred configurations results from a competition between the repulsion between ortho hydrogens and π-electron delocalization [55]. The latter factor favors fully planar structures while the former prefers the perpendicular position. The energy barrier of rotation for the **DPDPh1** molecule is small (∼2 kcal/mol). The energy of the HOMO decreases with twisting. This means it becomes far from the Fermi energy

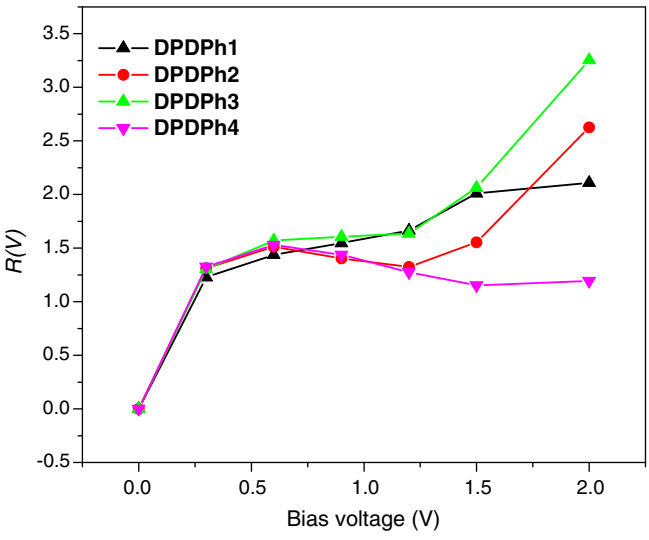

Fig. 6. The rectification ratio, $R(V)$ as a function of the applied voltage.

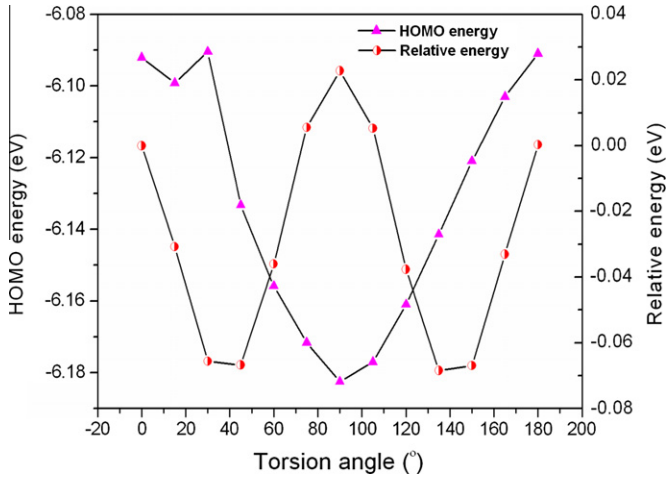

Fig. 7. The relative energy and the corresponding HOMO energy of **DPDPh1** molecule as a function of torsion angle between the donor and acceptor subunits calculated at B3LYP/6-31+G(d,p) level.

Table 6
The HOMO and LUMO surfaces of **DPDPh1** molecule with $\Phi_2 = 0$ and 90° calculated at B3LYP/6-31+G(d,p) level.

	0°	90°
LUMO	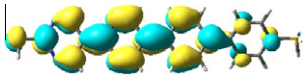	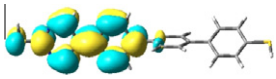
HOMO	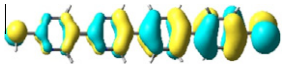	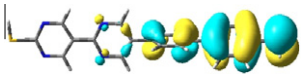

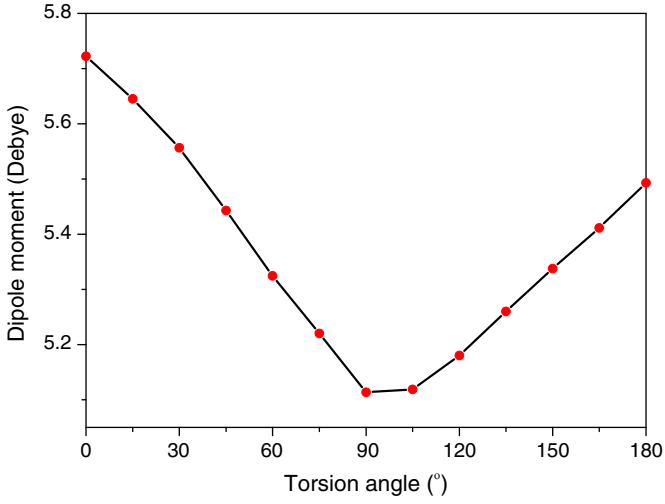

Fig. 8. The dipole moment of **DPDPh1** molecule as a function of torsion angle (Φ_2) calculated at B3LYP/6-31+G(d,p).

level and then the tunneling process through the HOMO, decreases. However, the HOMO–LUMO energy gap increases due to the interruption of the π-electron delocalization upon twisting.

Table 6 displays spatial orientations of FMOs of the **DPDPh1** molecule with planar and perpendicular conformations. The HOMO and LUMO are entirely delocalized over the whole molecule in the planar configuration, while they totally shrink towards the donor and acceptor parts, respectively in the case of perpendicular configuration, reflecting an AR-diode behavior [1–3].

It has been reported that the rectification of diblock diode depends, to somewhat extent, on its dipole moment [14,15]. For example, it was observed that rectification ra-

tio of the **DPDPh1** diblock diode is larger than that of dithiophene–dithiazole one because the former has a stronger intrinsic polarization [11,19]. In this context, one could expect that varying the torsion angle between the donor and acceptor units of the **DPDPh1** molecule will have a direct impact on its dipole moment, see Fig. 8. Indeed, the dipole moment decreases with increasing the twist angle; the maximum value of dipole moment of the **DPDPh1** molecule was reached when both subunits are coplanar. This result could be taken into account as a guide for designing new diblock diodes.

Because the electric current corresponds to an experimentally observable quantity, it has been calculated to support our interpretations. The two-probe configuration is built by sandwiching a B3LYP-optimized fragment at each angle between two electrodes, Fig. 2. The current passed through **DPDPh1** junction as a function of the mid torsion angle was calculated under selected applied voltages of 1 and −1 V, Fig. 9. The asymmetric feature of the **DPDPh1** junction remains prominent whatever the change in Φ_2, where the electric current under 1 V is nearly twice than that under −1 V. Under the effect of voltage 1 V, increasing the torsion angle, decreases the forward current until the torsion angle reaches 90°, hence the current becomes at its minimum limit, just with very small leakage current (0.0055 μA). Further increase of the torsion angle leads to gradual increase in the current. The opposite behaviour is observed under −1 V. The rectification ratio

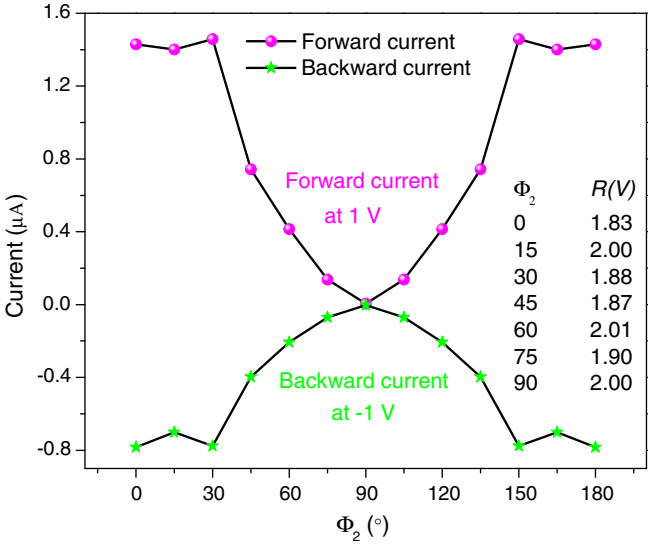

Fig. 9. The calculated current through **DPDPh1** junction as function of mid torsion angle (Φ_2) under voltages 1 and −1 V. The rectification ratio, $R(V)$ versus Φ_2 is inset in the figure. Notice the forward current (0.0055 μA) at angle 90° is not coincided with the backward current (0.0028 μA) in the figure giving rectification ratio of 2.

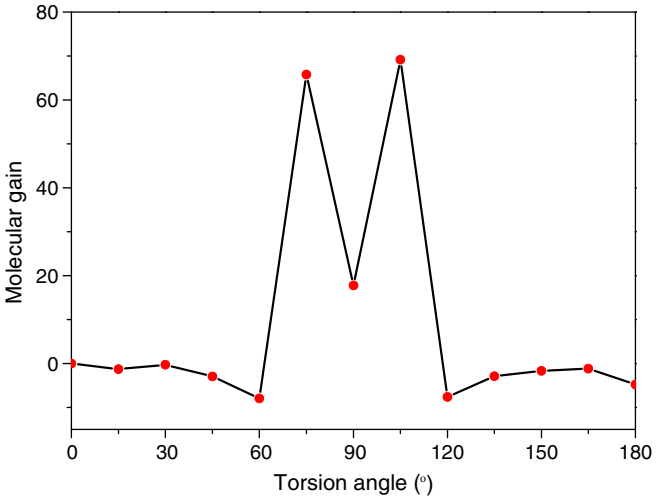

Fig. 10. The gain of molecular diode, **DPDPh1**, as a function of torsion angle (Φ_2) between the donor and acceptor subunits calculated at B3LYP/6-31+G(d,p).

as a function of Φ_2 is inset in Fig. 9. It is clear that the value of $R(V)$ hovers around 2. This may be ascribed to the size of molecular polarization which does not affected greatly by changing the mid torsion angle where the dipole moment ranges between 5.12 and 5.72 D (Fig. 8). The synthetic tailorability can be used to increase the molecular polarization and enhance the rectifying property.

The molecular gain is defined as the quotient of the differences between the HOMO–LUMO energy gaps of two isomers and the difference in their corresponding total energies [56,57]. The molecular gain of the **DPDPh1** molecule was plotted against twist angle in Fig. 10. It is apparent that the gain reaches its maximum value close to perpendicular conformations (75°, 90° and 105°). It is expected that, if **DPDPh1** molecule is subjected to electric field the output voltage signals would be larger than the input ones which requires twisting the mid angle by 75°, 90° and 105°. The relation between the molecular gain of diblock molecular diode and the torsion angle between the donor and acceptor moieties could be used to guide organic chemists to synthesize a specific molecular system with low or high molecular gain through controlling torsion angle *via* chemical substituents.

4. Conclusions

Density Functional Theory (DFT) and Green's function approach combined with DFT (NEGF-DFT)) have been used to study the effect of constitutional and conformational isomery on the electrical properties of **DPDPh1** molecular diode. The results obtained can be summarized as follows:

1. The qualitative agreement between the effect of electric field on the maximum propensity of the molecular system to acquire electronic charge from the circuit, ΔN_{max} or index ω (electrophilicity), and I–V curve could link the chemistry of molecules with the physics of molecular junctions. The plot of ΔN_{max} or ω *vs* voltage may be beneficial for examining the rectifying property of other systems.
2. The effect of variation of the twist angle between the donor and acceptor subunits of the **DPDPh1** molecular diode on its electrical properties such as dipole moment, HOMO energy, relative energy, electrical current, rectification ratio and molecular gain has been studied. The results indicated that the increase in the twist slightly decreases the dipole moment while the HOMO energy becomes gradually far away from the Fermi level of electrode leading to a decrease in the passing current. However, the net rectification ratio does not greatly affected because the change in the value of molecular polarization is limited. For this reason, the asymmetric feature of the current remains prominent whatever the change in the mid torsion angle.
3. Introducing a spacer or twisting the mid torsion angle by 90° produces AR-like diode.
4. The constitutional and conformational isomery could be a guide for modifying the electrical properties of molecular diodes through the synthetic tailorability.
5. Based on the calculations, we propose the **DPDPh3** molecule as a better rectifier than the **DPDPh1** isomer particularly at higher voltages and it is worthy to be tested experimentally. The **DPDPh2** junction does not show a big advantage over the **DPDPh1** one. However, the **DPDPh4** junction has relatively a slight rectification character.
6. This study could provide basic knowledge for the design of new molecular devices.

Acknowledgements

The authors are thankful for Dr. Z.L. Gasyna for his advice in the calculations.

Appendix A. Supplementary data

Supplementary data associated with this article can be found, in the online version, at doi:10.1016/j.orgel.2011.03.022.

References

[1] C. Majumder, H. Mizuseki, Y. Kawazoe, J. Phys. Chem. A 105 (2001) 9454.
[2] J.L. Rao, Acta Chim. Slov. 56 (2009) 826.
[3] H. Mizuseki, K. Niimura, C. Majumder, R.V. Belosludov, A.A. Farajian, Y. Kawazoe, Mol. Cryst. Liq. Cryst. 406 (2003) 11.
[4] J.M. Tour, M. Kozaki, J.M. Seminario, J. Am. Chem. Soc. 120 (2001) 8486.
[5] Z.J. Donhauser, B.A. Mantooth, K.F. Kelly, L.A. Bumm, J.D. Monnell, J.J. Stapleton, D.W. Price, A.M. Rawlett, D.L. Allara, J.M. Tour, P.S. Weiss, Science 292 (2001) 2303.
[6] J. Chen, M.A. Reed, A.M. Rawlett, J.M. Tour, Science 286 (1999) 1550.
[7] A. Staykov, D. Nozaki, K. Yoshizawa, J. Phys. Chem. C 111 (2007) 11699.
[8] J. Taylor, M. Brandbyge, K. Stokbro, Phys. Rev. Lett. 89 (2002) 138301.
[9] J.G. Kushmerick, C.M. Whitaker, S.K. Pollack, T.L. Schull, R. Shashidhar, Nanotechnology 15 (2004) S489.
[10] X. Yin, H. Liu, J. Zhao, J. Chem. Phys. 125 (2006) 094711.
[11] I. Díez-Pérez, J. Hihath, Y. Lee, L.P. Yu, L. Adamska, M.A. Kozhushner, I.I. Oleynik, N.J. Tao, Nat. Chem. 1 (2009) 635.
[12] M.K. Ng, L.P. Yu, Angew. Chem. Int. Ed. Engl. 41 (2002) 3598.
[13] M.K. Ng, D.C. Lee, L.P. Yu, J. Am. Chem. Soc. 124 (2002) 11862.
[14] G.M. Morales, P. Jiang, S. Yuan, Y. Lee, A. Sanchez, W. You, L. Yu, J. Am. Chem. Soc. 127 (2005) 10456.
[15] P. Jiang, G.M. Morales, W. You, L. Yu, Angew. Chem., Int. Ed. Engl. 43 (2004) 4471.
[16] Y. Lee, B. Carsten, L. Yu, Langmuir 25 (2009) 1495.
[17] Y. Liang, H. Wang, S. Yuan, Y. Lee, L. Gan, L. Yu, J. Mater. Chem. 17 (2007) 2183.
[18] Z.L. Gasyna, G.M. Morales, A. Sanchez, L. Yu, Chem. Phys. Lett. 417 (2006) 401.
[19] I.I. Oleynik, M.A. Kozhushner, V.S. Posvyanskii, L. Yu, Phys. Rev. Lett. 96 (2006) 096803.
[20] J. Huang, Q. Li, Z. Li, J. Yang, J. Nanosci. Nanotechnol. 9 (2009) 774.
[21] Y.W. Li, J.H. Yao, C.L. Yang, S.K. Zhong, G.P. Yin, Mol. Simul. 35 (2009) 301.
[22] M.M. El-Hendawy, A.M. El-Nahas, M.K. Awad, J. Phys. Chem. C 114 (2010) 21728.
[23] W.W. Cheng, H. Chen, R. Note, H. Mizuseki, Y. Kawazoe, Physica E 25 (2005) 643.
[24] P.A. Priya, C.P. Kala, D.J. Thiruvadigal, J. Comput. Theor. Nano. 6 (2009) 1697.
[25] Y. Li, J. Zhao, G. Yin, Comput. Mater Sci. 93 (2007) 775.
[26] Y. Li, J. Zhao, X. Yin, G. Yin, J. Phys. Chem. A 110 (2006) 11130.
[27] A. Saraiva-Souza, B.G. Sumpter, V. Meunier, A.G. Souza, J. Del Nero, J. Phys. Chem. C 112 (2008) 12008.
[28] Y. Zhang, Y. Ye, Y. Li, X. Yin, H. Liu, J. Zhao, J. Mol. Struct. (theochem) 802 (2007) 53.
[29] S. Dutta, S.K. Pati, Resonance 14 (2009) 80.

[30] Y.F. Ye, M.L. Zhang, H.M. Liu, X.W. Liu, J.W. Zhao, J. Phys. Chem. Solids 69 (2008) 2615.
[31] H. Sabzyan, D. Farmanzadeh, J. Comput. Chem. 28 (2007) 922.
[32] S. Hou, J. Zhang, R. Li, J. Ning, R. Han, Z. Shen, X. Zhao, Z. Xue, Q. Wu, Nanotechnology 16 (2005) 239.
[33] J. Zhao, C. Yu, N. Wang, H. Liu, J. Phys. Chem. C 114 (2010) 4135.
[34] H. Liu, P. Li, J. Zhao, X. Yin, H. Zhang, J. Chem. Phys. 129 (2008) 224704.
[35] R. Stadler, V. Geskin, J. Cornil, J. Phys.: Condens. Matter 20 (2008) 374105.
[36] R.G. Parr, L.V. Szentpaly, S. Liu, J. Am. Chem. Soc. 121 (1999) 1922.
[37] A.D. Becke, J. Chem. Phys. 98 (1993) 5648.
[38] C. Lee, W. Yang, R.G. Parr, Phys. Rev. B 37 (1988) 785.
[39] P.J. Stephens, F.J. Devlin, C.F. Chabalowski, M.J. Frisch, J. Phys. Chem. 98 (1994) 11623.
[40] M.J. Frisch, G.W. Trucks, H.B. Schlegel, G.E. Scuseria, M.A. Robb, J.R. Cheeseman, J.A. Montgomery, Jr., T. Vreven, K.N. Kudin, J.C. Burant, J.M. Millam, S.S. Iyengar, J. Tomasi, V. Barone, B. Mennucci, M. Cossi, G. Scalmani, N. Rega, G.A. Petersson, H. Nakatsuji, M. Hada, M. Ehara, K. Toyota, R. Fukuda, J. Hasegawa, M. Ishida, T. Nakajima, Y. Honda, O. Kitao, H. Nakai, M. Klene, X. Li, J. E. Knox, H.P. Hratchian, J.B. Cross, C. Adamo, J. Jaramillo, R. Gomperts, R.E. Stratmann, O. Yazyev, A.J. Austin, R. Cammi, C. Pomelli, J.W. Ochterski, P.Y. Ayala, K. Morokuma, G.A. Voth, P. Salvador, J.J. Dannenberg, V.G. Zakrzewski, S. Dapprich, A.D. Daniels, M.C. Strain, O. Farkas, D.K. Malick, A.D. Rabuck, K. Raghavachari, J.B. Foresman, J.V. Ortiz, Q. Cui, A.G. Baboul, S. Clifford, J. Cioslowski, B.B. Stefanov, G. Liu, A. Liashenko, P. Piskorz, I. Komaromi, R.L. Martin, D.J. Fox, T. Keith, M.A. Al-Laham, C.Y. Peng, A. Nanayakkara, M. Challacombe, P.M.W. Gill, B. Johnson, W. Chen, M.W. Wong, C. Gonzalez, and J.A. Pople, Gaussian 03, Revision D.01; Gaussian, Inc., Wallingford, CT, 2004.
[41] X. Yin, Y. Li, Y. Zhang, P. Li, J. Zhao, Chem. Phys. Lett. 422 (2006) 111.
[42] X. Yin, H. Liu, J. Zhao, J. Chem. Phys. 125 (2006) 094711.
[43] M. Kondo, T. Tada, K. Yoshizawa, J. Phys. Chem. A 108 (2004) 9143.
[44] H. Grcnbeck, A. Curioni, W. Andreoni, J. Am. Chem. Soc. 122 (2000) 3839.
[45] P.J. Hay, W.R. Wadt, J. Chem. Phys. 82 (1985) 288.
[46] J.P. Perdew, A. Zunger, Phys. Rev. B 23 (1981) 5048.
[47] ATK version 2.0, Atomistix A/S (www.atomistix.com).
[48] M. Brandbyge, J.-L. Mozos, P. Ordejón, J. Taylor, K. Stokbro, Phys. Rev. B 65 (2002) 165401.
[49] C. Majumder, H. Mizuseki, Y. Kawazoe, Jpn. J. Appl. Phys. 41 (2002) 2770.
[50] J.C. Ellenbogen, J.C. Love, Proc. IEEE 88 (2000) 386.
[51] R. Stadler, J. Phys: Conf. Ser. 61 (2007) 1097.
[52] G. Peng, M. Strange, K.S. Thygesen, M.J. Mavrikakis, Phys. Chem. C 113 (2009) 20967.
[53] G.-P. Charbonneau, Y. Delugeard, Acta Crystallogr. B 32 (1976) 1420.
[54] A. Almenningen, O. Bastiansen, L. Fernholt, B.N. Cyvin, S.J. Cyvin, S.J. Samdal, Mol. Struct. (theochem) 128 (1985) 59.
[55] F. Grein, J. Phys. Chem. A 106 (2002) 3823.
[56] C. Majumder, T. Briere, H. Mizuseki, Y. Kawazoe, J. Phys. Chem. A 106 (2002) 7911.
[57] J.M. Seminario, P.A. Derosa, J. Am. Chem. Soc. 123 (2001) 12418.

their 4-(dialkylamino) aryl analogues [8]. Moreover, the incorporating diarylamino–heteroaryl donors were able to achieve an improvement of almost one order of magnitude in r_{33} over alkylamino chromophores [9]. Despite the advantages of increasing β by using these donors, very little experimental research is known due to the synthetic difficulty of diarylamino aromatic units using unstable starting materials.

In this study, we developed a novel donor modification approach by attaching a benzyloxy group as an additional electron-donating part on 2-dicyanomethylen-3-cyano-4-{2-[E-(4-N,N-di(2-acetoxyethyl)-amino)-phenylene-(3,4-dibutyl)thien-5]-E-vinyl}-5,5-dimethyl-2,5-dihydrofuran (denoted as FTC) type donor-π-acceptor molecules. The motivation of this study is to improve the EO response by a simple donor-strengthening method for mature FTC chromophores. If this strategy takes effect on NLO activities of FTC series micro- and macro-scopically, it may also be utilized for other known chromophore systems to further enhance the r_{33} for the EO device application.

The structures of new chromophores are depicted as A1–A3 in Fig. 1, along with the FTC series (B1–B3) references are included for comparison. The synthesis of given chromophores is carried out by the modified procedures according to the literature [4] and [10]. As an example, a typical preparation route for chromphore A3 is depicted as Scheme 1, and the details of these are discussed elsewhere. The new synthesized chromphores contain the same key thiophene bridge and TCF acceptor as the FTC. Acceptor TCF, stronger CF_3–TCF, and CF_3–Ph–TCF are used to investigate the impact of the new donor on different acceptors. As the synthesis run differs only in the step of donor moiety, there is almost no extra synthesis cost associated with the new chromophores, and the total yields of A1, A2, and A3 are 33.8%, 53.2%, and 53.6%, respectively, which are comparable to those of the FTC series. Thermal properties of A1–A3 explored by differential scanning calorimetry and thermal gravity analysis revealed that the additional donor had no negative impact for actual applications, having a range of decomposition temperature of 253 °C, 194 °C, and 220 °C, respectively (Table 1).

All of the chromophores are well dissolved in either chloroform ($\varepsilon = 4.81$) or 1,4-dioxane ($\varepsilon = 2.21$) and the absorption spectra in both solvents are recorded to determine the wavelength of the maximum absorption (λ_{max}) of the charge-transfer band as depicted in Fig. 2. For the FTC benchmark (B1), the λ_{max} shows up at 685 nm in $CHCl_3$ (Table 1). With an additional benzyloxy group attached on the dialkyamino aryl group, the λ_{max} of A1 red-shifted to 714 nm, implying that the benzyloxy group effectively provides an extra electron-donating strength to the π-conjugated bridge. Such a trend becomes more evident for chromophore A2 and A3 with stronger acceptors, rendering a larger red-shift of 40 nm relative to their counterparts B2 and B3. The comparison of UV–visible absorption spectra in $CHCl_3$ with those in less polar 1,4-dioxane enable us to examine the solvatochromic behavior of the chromophores, and the results are also listed in Table 1. Based on the following two facts: (1) the solvatochromic effects are indicative of the product ($\mu\beta$) of dipole moment (μ) and first hyperpolarizability (β) of a NLO chromophore [11] and (2) the difference of series A and B lies only in the auxiliary benzyloxy group, it can be asserted that the donor strengthening route is favorable to improve the nonlinear optical property of chromophores.

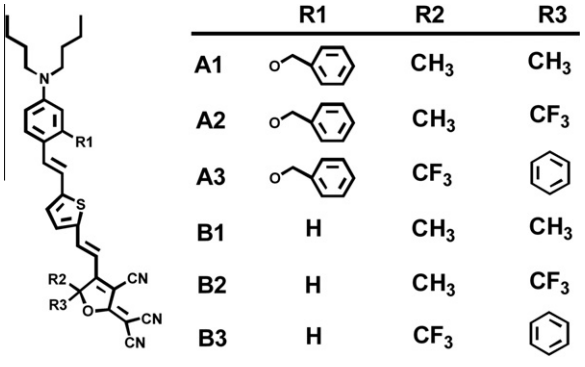

	R1	R2	R3
A1		CH_3	CH_3
A2		CH_3	CF_3
A3		CF_3	
B1	H	CH_3	CH_3
B2	H	CH_3	CF_3
B3	H	CF_3	

Fig. 1. Structure of the NLO chromophores A1–3 and B1–3 investigated in this study.

The β values of chromophore series are measured in diluted $CHCl_3$ solution (5 μmol/L) by the hyper-Rayleigh scattering (HRS) technique at the wavelength of 1.9 μm and the results are tabulated (Table 1). Series A show a systematic improvement of β values over B analogous: A1 (3161×10^{-30} esu), A2 (9491×10^{-30} esu), and A3 (10,203 $\times 10^{-30}$ esu). As the strong solvatochromic effect discussed above, the resonance contribution for series A is reasonably more significant. The intrinsic β_0 is roughly estimated according to the two-level model [12], and the results reveal that the β_0 of the series A are still significantly enhanced over the B analogues, which confirms the effective strengthening effect of the additional donor. In addition, a semiempirical quantum simulation for gaseous model is performed by the software package MOPAC 09 [13] and the results are also included in Table 1 for comparison. The discrepancy of absolute magnitudes of calculated and measured β values is owing to resonant effect in the diluted $CHCl_3$ solution [2], whereas the quantum calculation is carried out for the gaseous model. Although some deviation exists, the increasing trend that experimentally observed on β by the auxiliary donor is consistent with the prediction made on the basis of semiempirical calculations.

To investigate the influence of an extra donor on the macroscopic nonlinearity, the r_{33} is measured in poly (methyl methacrylate) (PMMA) host, and the number density of all chromophores are fixed as 2.1×10^{20} molecules/cm^3 which results in weight percentage in chromphore/PMMA composite ranging from 17% to 26%. The real time r_{33} measurement is performed (Teng-Mann reflection method [14,15]) under an electric filed: $V(t) = V_{dc} + V_{ac} \sin \omega t$ in order to observe the EO activity during the poling process, where V_{dc} is the applied voltage and $V_{ac} \sin \omega t$ is modulating voltage. According to the given calculation equation in Ref. [16], the r_{33} is in proportion to I_m/I_c, where I_m is the amplitude of EO modulation and I_c is the intensity of incident light when phase retardation is 90° between the TE and TM mode. Fig. 3a–d shows a typical poling

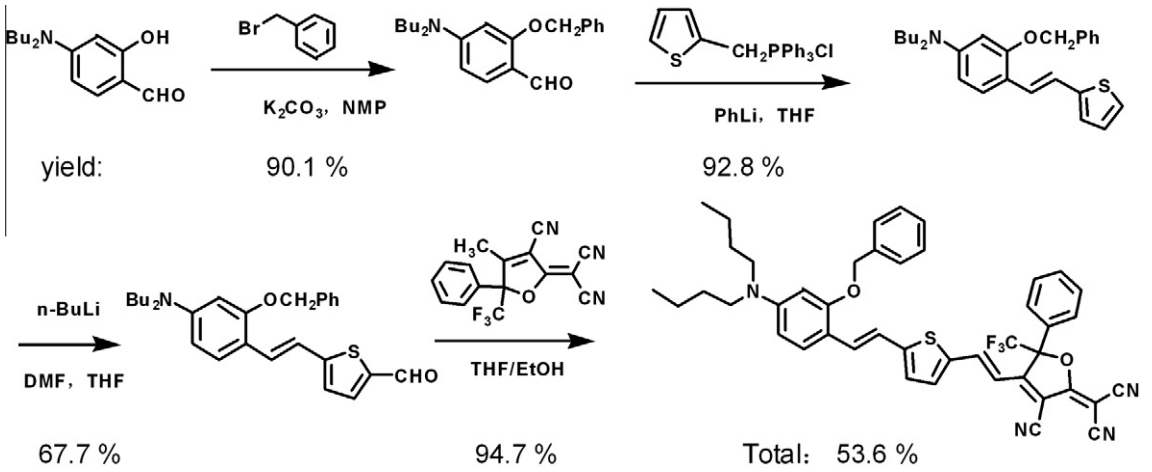

Scheme 1. Synthesis of chromophore A3.

Table 1
Glass transition temperature (T_g), absorption maximum, β, and r_{33} of chromophores/PMMA.

	A1	A2	A3	B1	B2	B3
T_d (°C)[a]	253	194	220	220	175	209
λ_{max} (nm)/$CHCl_3$ (5 μmol/L)	714	814	821	685	774	781
λ_{max} (nm)/dioxane	644	711	725	624	686	699
Δ Shift (eV)	0.19	0.22	0.20	0.17	0.20	0.18
β_{HRS} @ 1.9 μm (10^{-30} esu)	3161	9491	10,203	1498	5932	6762
β_0[b]	1166	2061	2111	627	1662	1828
μ[c]	22.21	21.11	21.34	19.92	18.83	18.05
β[c]	394.9	428.21	392.95	241.65	261.53	256.11
r_{33} at 1.31 μm (pm/V)	61	101	75	43	57	59
E_{poling} (V/μm)	70	55	45	130	80	82
Poling efficiency $(nm/V)^2$	0.87	1.84	1.67	0.33	0.71	0.72

[a] The T_g is recorded by a DSC with a scanning rate of 5 °C/min.
[b] Corrected for resonance enhancement using a two-level model: $\beta_0 = \beta\,[1-(\lambda_{max}/1900)^2]/[1-4(\lambda_{max}/1900)^2]$.
[c] Dipole moment (μ) and β calculated by software package MOPAC 2009.

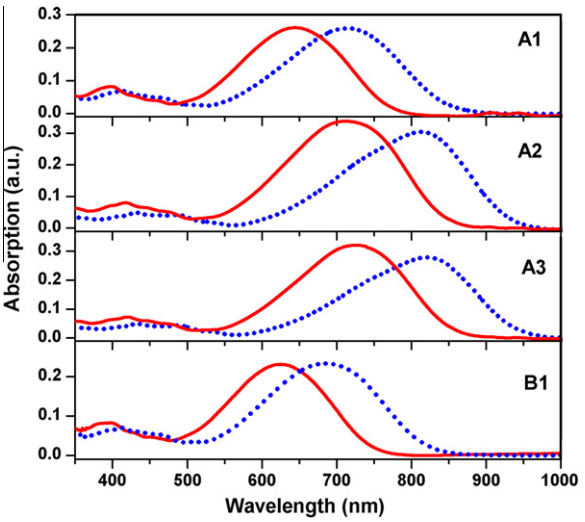

Fig. 2. Absorption spectra of chromophores A1–A3 and B1 in $CHCl_3$ (dashed line) and 1,4-dioxane solutions (solid line).

process recording r_{33} and flowing current against temperature and applied voltage of A2/PMMA composite.

Apparently, the additional donor on the chromophore results in not only a great strengthening effect on microscopic molecular hyperpolarizabiliy, but also some remarkable characteristics during the poling process. The first of these characteristics is the large r_{33} with the applying electric field. With the increase of temperature and poling voltage, the r_{33} maximizes at about 250 pm/V, a level that has rarely been reported previously in conventional guest/host systems. Whereas only 70 pm/V is detected for B2/PMMA even at a poling field of 130 V/μm. The high r_{33} of A2/PMMA reflects the significant enhancement of $\mu\beta$ value on macroscopic scale. At an external field of 50 V/μm, the r_{33} stabilized and saturated at a certain level, even the electrical field is raised up to 55 V/μm (Fig. 3b). Actually, the electrode area is very close to the threshold of dielectric breakdown though the poling is processed under such a moderate external field.

Second, the flowing current reaches its maximum simultaneously with the r_{33} and sustains its intensity until

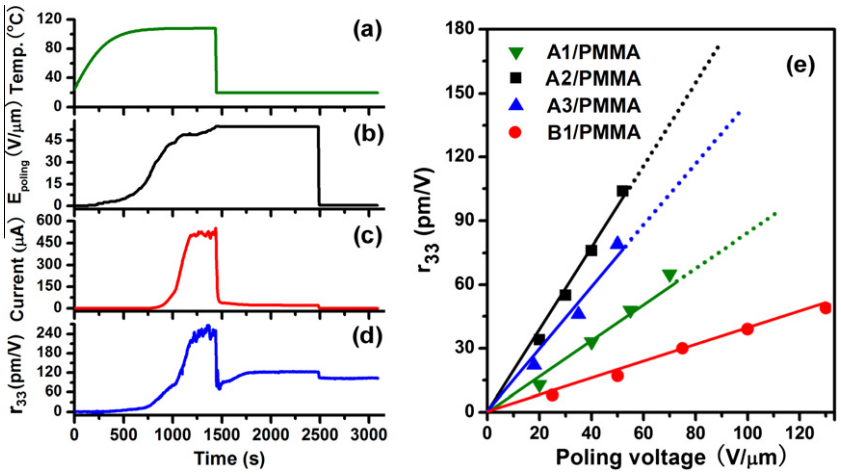

Fig. 3. Time-dependent temperature (a), flowing current (b), applied voltage (c), and r_{33} (d) of A2/PMMA, together with the poling efficiencies (e) of A1, A2, A3, and B1 in PMMA.

the cooling process begins. In this case, the flowing current reaches 550 μA (Fig. 3c) and it is more than 10 times of that in the B2/PMMA counterpart. The origin of flow current is temporarily ascribed to the charge hopping mechanism which increases the conductivity of molecularly doped polymer [16]. Generally, the hopping occurs in a distribution of states, the width of which is determined by the variation in spacing between the individual dopant molecules [17]. The additional benzyloxy donor on the chromophore A2, in effect, increases the effective volume and shortens the intermolecular distance between two A2 chromophores in PMMA host, which undoubtedly facilitates charge hopping from one chromophore to another. Considering the uniform number density (2.1×10^{20} molecules/cm^3) of A2 and B2 in PMMA, it is the shortening of intermolecular distance that leads to a ten times higher current flow. More importantly, such a hopping procedure in the disordered system is thermally activated [18]. Higher temperature improves the charge transport by providing the energy required to overcome the barriers created by the energetic disorder. The relationship has been often fitted to an Arrhenius-like law [18]: $M \propto \exp(-\Delta/k_B T)$, where M is the mobility, Δ, k_B, and T are activation energy, Boltzmann constant, and temperature, respectively. Conversely, it is also responsible for the decrement of current from 550 μA to 30 μA during the rapid cooling process, which accompanying with a significant drop of r_{33} as shown in Fig. 3d. Currently, we have not come to an exact ascertainment for the reason of this large decay and it is still under investigation. There are, however, two factors that should be taken into account which potentially have contributions: (1) Reversion of host to the rigid state. Though the initial orientation of chromophore is much high ($r_{33} \sim 250$ pm/V) at the temperature around T_g of the composite, the rubber-like composite will return to the rigid state in a rapid cooling process. This process may eventually leads to enhance the degree of disorder and decrease the r_{33}. The additional electron-donating group also brings unfortunately a considerable trade-off electrostatic effect. This large decay is quite related to the strong molecular electrostatic interaction between the chromphores with a low activation energy for dipolar relaxation [19]. The sum of above two contributions eventually accounts for the dramatic reduction of final macroscopic nonlinearity. Even so, the r_{33} above 100 pm/V maintains eventually with the electrical field removed.

Eventually, it is worth noting the increased poling efficiency (PE) of the new chromophores, which is plotted as the slope of r_{33} *vs.* poling voltage in Fig. 3e. For A1/PMMA, the PE is about 0.87 (nm/V)^2, which is more than twice of that for B1/PMMA [0.33 (nm/V)^2], and further gains are realized for A2 and A3 analogues. These results are consistent with the stronger electron-withdrawing ability of the CF_3–TCF and CF_3–Ph–TCF moieties. Though a higher intrinsic β_0 is observed for the chromophore B3 bearing stronger electro-drawing group CF_3–Ph–TCF, the large volume of phenyl group somewhat hinders the electrical alignment. Thus, A2/PMMA achieves the highest PE of 1.84 (nm/V)^2, and this value is comparable to that of the phenyltertraene-type (CLD) analogue [3].

As the molecular dipole–dipole interaction plays an important role for the alignment of the NLO chromophore under the external field and it increase the flow current which influence the poling efficiency, the dependence of r_{33} and current on the dopant concentration for A2/PMMA is investigated as Fig. 4. With increasing of chromophore introducing concentration, the r_{33} experiences firstly a linear climb up to the maximum of about 100 pm/V, then a considerable drop is followed ascribing to the strong electrostatic effect at high concentration region. For the flow current observed during the poling process, it ascends steeply with increasing concentration and the value exceeds 1 mA at the concentration of 35 wt.%. Such a high flow current limits the poling by the occurrence of dielectric breakdown. This obstacle is expected to be overcome by exploiting other three-dimensional network polymers with sterical hindering or by using a TiO_2 buffer layer on ITO substrate [5,20]. Thus, an r_{33} of about 200 pm/V is

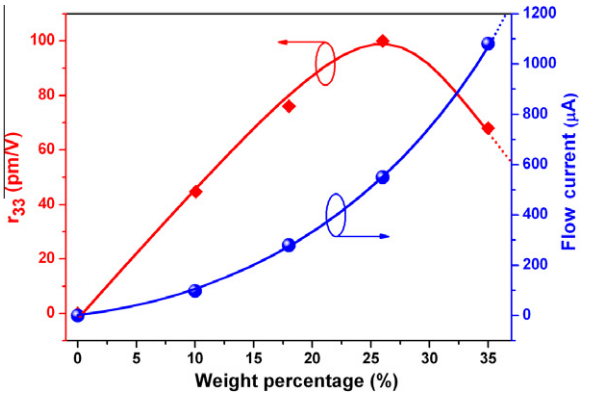

Fig. 4. Dependence of r_{33} and flow current on the chromophore concentration for A2/PMMA.

achievable for this NLO chromophore if an electrical field of 100 V/μm is exerted. Additionally, due to the distinct drawbacks of guest–host system, more suitable strategies, such as side-chain, cross-linking or dendrimer methods are urgently required to delay the intermolecular interaction to higher dopant concentration scale. Currently, we adopted the side-chain route to enhance the doping concentration of B3 up to 40 wt.% at which the r_{33} about 150 pm/V was obtained without causing severe aggregation. Furthermore, the T_g of such side-chain polymer is also much enhanced up to 140 °C to meet the device applications. These subsequent works will be reported in detail elsewhere [21].

In summary, we synthesized and characterized the NLO chromophores by using a donor modified strategy. The electro-optic coefficient (r_{33}) was remarkably enhanced by simply introducing a benzyloxy group as an additional donor part. Comparing with the traditional FTC benchmark, the first hyperpolarizability was improved by increasing the electron donating strength, which was confirmed by the absorption spectral analysis and HRS measurement. An in situ poling was performed by controlling the temperature and external field, and an r_{33} above 100 pm/V was eventually achieved for the A2/PMMA with a poling efficiency of 1.84 (nm/V). A simple and effective donor strengthening route was proposed for further electro-optic materials and applications.

The authors acknowledge partial financial support from a Grant-in-Aid for Young Scientists (S) and the Global Centers of Excellence (GCOE) Program of the Ministry of Education, Culture, Sports, Science and Technology, Japan. This work was partially performed under the Cooperative Research Program of "Network Joint Research Center for Materials and Devices".

References

[1] R.W. Boyd, Nonlinear Optics, third ed., Academic Press, 2008.
[2] S.H. Jang, J. Luo, N.M. Tucker, A. Leclercq, E. Zojer, M.A. Haller, T.D. Kim, J.W. Kang, K. Firestone, D. Bale, D. Lao, J.B. Benedict, D. Cohen, W. Kaminsky, B. Kahr, J.L. Bredas, P. Reid, L.R. Dalton, A.K.Y. Jen, Chem. Mater. 18 (2006) 2982.
[3] J. Luo, S. Liu, M.A. Haller, J.-W. Kang, T.-D. Kim, S.-H. Jang, B. Chen, N. Tucker, H. Li, H.-Z. Tang, L.R. Dalton, Y. Liao, B.H. Robinson, A.K.Y. Jen, Proc. SPIE 5351 (2004) 36.
[4] (a) Y. Shi, C. Zhang, H. Zhang, J.H. Bechtel, L.R. Dalton, B.H. Robinson, W.H. Steier, Science 288 (2000) 119;
(b) M.-Q. He, T.M. Leslie, J.A. Sinicropi, Chem. Mater. 14 (2002) 4662.
[5] L.R. Dalton, D. Lao, B.C. Olbricht, S. Benight, D.H. Bale, J.A. Davies, T. Ewy, S.R. Hammond, P.A. Sullivan, Opt. Mater. 32 (2010) 658.
[6] S.H.Z. Shi, J.-D. Luo, T.-D. Kim, N.M. Tucker, J.-W. Ka, H.-S. Sun, L.D. Anna Pyajt, A.-T. Chen, A.K.-Y. Jen, Adv. Funct. Mater. 17 (2007) 2557.
[7] P.A. Sullivan, H. Rommel, Y. Liao, B.C. Olbricht, A.J.P. Akelaitis, K.A. Firestone, J.-W. Kang, J. Luo, J.A. Davies, D.H. Choi, B.E. Eichinger, P.J. Reid, A. Chen, A.K.Y. Jen, B.H. Robinson, L.R. Dalton, J. Am. Chem. Soc. 129 (2007) 7523.
[8] Y.J. Cheng, J. Luo, S. Hau, D.H. Bale, T.D. Kim, Z. Shi, D.B. Lao, N.M. Tucker, Y. Tian, L.R. Dalton, P.J. Reid, A.K.Y. Jen, Chem. Mater. 19 (2007) 1154.
[9] J.A. Davies, A. Elangovan, P.A. Sullivan, B.C. Olbricht, D.H. Bale, T.R. Ewy, C.M. Isborn, B.E. Eichinger, B.H. Robinson, P.J. Reid, X. Li, L.R. Dalton, J. Am. Chem. Soc. 130 (2008) 10565.
[10] B.H. Robinson, L.R. Dalton, A.W. Harper, A. Ren, F. Wang, C. Zhang, G. Todorova, M. Lee, R. Aniszfeld, S. Garner, A. Chen, W.H. Steier, S. Houbrecht, A. Persoons, I. Ledoux, J. Zyss, A.K.Y. Jen, Chem. Phys. 245 (1999) 35.
[11] M.S. Paley, J.M. Harris, J. Org. Chem. 54 (1989) 3774.
[12] S.J. Singer, M.G. Kuzyk, J.E. Sohn, J. Opt. Soc. Am. B 4 (1987) 968.
[13] J.J.P. Stewart, MOPAC2009 (2008). Available from: <http://www.openMOPAC.net>.
[14] C.C. Teng, H.T. Man, Appl. Phys. Lett. 56 (1990) 1734.
[15] Y. Shuto, M. Amano, J. Appl. Phys. 77 (1995) 4632.
[16] M.A. Pauley, C.H. Wang, A.K.Y. Jen, Macromolecules 29 (1996) 7064.
[17] L.B. Schein, A. Rosenberg, S.L. Rice, J. Appl. Phys. 60 (1986) 4287.
[18] V. Coropceanu, J. Cornil, D.A. da Silva Filho, Y. Olivier, R. Silbey, J.L. Bredas, Chem. Rev. 107 (2007) 926.
[19] M.J. Cho, S.K. Lee, J. Jin, D.H. Choi, L.R. Dalton, Thin Solid Films 505 (2006) 2303.
[20] S. Huang, T.D. Kim, J.D. Luo, S.K. Hau, Z.W. Shi, X.H. Zhou, H.L. Yip, A.K.Y. Jen, Appl. Phys. Lett. 96 (2010) 243311.
[21] X. Piao, X. Zhang, M. Koishi, A. Nakaya, K. Koyama, S. Inoue, I. Aoki, A. Otomo, S. Yokoyama, J. Polym. Sci. Part A 49 (2011) 47.

purchased from Sigma–Aldrich Company and used as received. The light-emitting conjugated polymer polyfluorene (PFO, purchased from H.W. Sand Company) and Super-Yellow (purchased from Merck Company) were used as received. The electrophosphorescent material Iridium (III) tris(2-(4-totyl)pyridinato-N,C^2) [Ir(mppy)$_3$] was purchased from American Dye Source Inc. In order to investigate the role of SWNTs on the performance of the OLEDs, three types of device architecture were fabricated. The first type of devices have the structure of ITO/PEDOT:SWNT (*x* wt.%, 40 nm)/PFO (80 nm)/Ca (20 nm)/Al (80 nm), where *x* is 0, 0.001, 0.01, and 0.02, relative to solid PEDOT content. The second one is ITO/PEDOT:SWNT (0.01 wt.% relative to solid PEDOT content, 40 nm)/PVK:PBD:Ir(mppy)$_3$ (69 wt.%:30 wt.%:1 wt.%, 60 nm)/Ca (20 nm)/Al (80 nm), which use Ir(mppy)$_3$ as a phosphorescent emissive material. The third one has a structure of ITO/PEDOT (40 nm)/Super-Yellow:SWNTs (*x* wt.%, 80 nm)/Ca (20 nm)/Al (80 nm), where *x* is 0 and 0.005.

To get the uniform dispersion of SWNTs in PEDOT, we suspended the SWNTs functionalized by with crown ether, making them dispersible in deionized water [11]. They were then ultrasonicated the SWNTs solution 30 min, and then we mixed the SWNT solution with PEDOT solution and deionized water to form the composites at designed doping concentration. For the Super-Yellow:SWNTs composite preparation, SWNTs dispersed in chloroform were added into Super-Yellow chloroform solution to give the desired doping concentrations. The PEDOT:SWNTs composites were spin-coated onto ITO-coated glass substrate and the thickness of the film was 40 nm. The light-emitting layers for the three types of devices were all formed by spin coating from their chloroform solutions. Finally, the calcium (Ca) and aluminum (Al) electrode were deposited sequentially by thermal evaporation under the vacuum of 2×10^{-6} Torr, and the deposition rate was typically about 1 Å/s. The thicknesses and the morphology of the films and were measured by a Veeco atomic force microscopy (AFM) using a tapping mode. The resistivity and conductivity of PEDOT:SWNTs composite films on glass substrates were measured by a four-probe method with a Keithley source meter. The current and voltage characteristics of the OLEDs were measured with Keithley 2400 source meter. The EL spectra of OLEDs were recorded by a HORIBA Jobin Yvon spectrometer. The luminance and efficiency of OLEDs were measured by an OLED testing system calibrated by the National Institute of Standards and Technology.

3. Results and discussion

We investigated the roles of SWNTs in a hole conducting layer on the performance of OLEDs at first. Fig. 1a shows the current density–voltage (*J*–*V*) characteristics of OLEDs employing PEDOT:SWNTs composites with various doping concentrations under a forward bias. With increasing the SWNTs concentration in PEDOT, the current density of devices becomes higher under the same voltage, which means the hole injection and/or transport are improved by introducing SWNTs in the PEDOT layer of devices. However, the EL intensity did not show a monotonous increase when increasing the SWNTs concentration in PEDOT under the same current density. From Fig. 1b we can see that when the SWNTs concentration in PEDOT is no higher than 0.01 wt.%, then the higher the doping concentration, the stronger the EL intensity. But when the doping concentration of SWNTs reaches 0.02 wt.%, the EL performance of the devices deteriorates, and the EL intensity becomes lower than that of the device without SWNTs doping. Our results have some differences compared to those reported by Woo et al. [8]. In their case, the doping concentration of SWNTs in PEDOT is no less than 0.05 wt.%. Although they also observed the enhancement of current density when increasing the SWNTs doping concentration in PEDOT, they only found that EL brightness in devices employing PEDOT:SWNTs composites was reduced relative to the device without using SWNTs. As a result, their explanation of SWNTs as hole traps in PEDOT film should be reconsidered, since there would be no EL intensity enhancement in our case if the injected holes were initially trapped by SWNTs in PEDOT film.

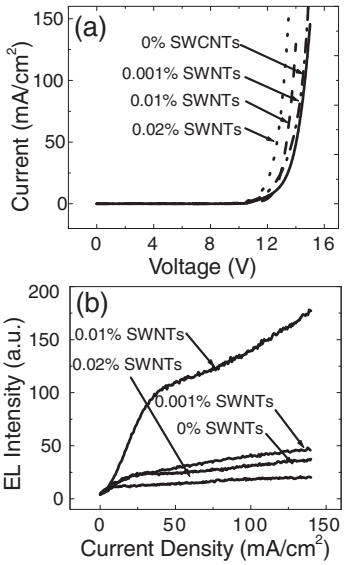

Fig. 1. The *J*–*V* curves (a) and the EL intensity–current density curves (b) of devices with the structure of ITO/PEDOT:SWNTs (*x* wt.%, 40 nm)/PFO (80 nm)/Ca (20 nm)/Al (80 nm).

We investigated the conductivity of PEDOT:SWNTs composite films with different doping concentration of SWNTs. It is shown in Table 1 that when the SWNTs

Table 1
The resistivity (ρ) and conductivity (C) of PEDOT:SWNT composite films with various SWNT concentration.

SWNT concentration (%)	ρ (Ω cm)	C (S/cm)
0	44,902	2.23×10^{-5}
0.0004	40,778	2.45×10^{-5}
0.0042	31,709	3.15×10^{-5}
0.0010	29,775	3.36×10^{-5}
0.6622	23,666	4.23×10^{-5}

concentration changed from 0 wt.% to a high value of 0.66 wt.%, the conductivity of the composite film increased monotonously. This can be ascribed to the increase in partial conductive paths when introducing SWNTs into the polymer film [12], since the metallic components in SWNTs have a better conductivity than PEDOT. As a result, the enhancement of EL intensity shown in Fig. 1b when increasing the SWNTs concentration in PEDOT from 0.001 to 0.01 wt.% can be ascribed to the increase of the conductivity in PEDOT film with SWNTs doping, and thus leading to the improvement of hole transport in devices. It should be noted that although SWNTs can be beneficial in improving the carrier transport, they also can act as trap sites for quenching the excitons [13,14]. It is well known that when excitons are formed in the emissive layer, they can migrate during their lifetime and the singlet excitons usually have a migration distance of ~20 nm [15]. Thus if the excitons are formed near the interface of PEDOT:SWNTs/PFO interface, they can easily migrate to the SWNTs trapping sites and thus be quenched provided that the SWNTs concentration is high enough near the interface.

We notice that PEDOT has a highest occupied molecular orbital (HOMO) energy level of −5.2 eV while PFO has a HOMO energy level of −5.8 eV [16], so there is an energy barrier of 0.6 eV for holes to overcome. In our devices with the structure of ITO/PEDOT:SWNTs/PFO/Ca/Al, the lowest unoccupied molecular orbital (LUMO) energy level of the light-emitting material PFO aligns with the Fermi level of the Ca cathode. Consequently, the electron transport from the cathode into the light-emitting layer is not hindered. However, since an energy barrier between the HOMO levels prevents holes from entering the light emitting layer, the exciton recombination zone in the PFO layer must be close to the interface of PEDOT:SWNTs/PFO interface. As a result, the excitons formed in the PFO layer can migrate to the PEDOT:SWNTs layer and be quenched by the SWNTs if the SWNTs concentration is high enough in the PEDOT:SWNTs film. That is the reason why we see reduced EL intensity in OLEDs when the SWNTs concentration is as high as 0.02 wt.% in the PEDOT:SWNTs film compared with pure PEDOT film.

Fig. 2a shows the luminance–voltage curves of OLEDs using pure PEDOT and PEDOT:SWNTs (0.01 wt.%) composite. The maximum luminance of the device with SWNTs in PEDOT is 2150 cd/m^2, which is as 1.4 times high as the one without SWNTs. Fig. 2b and c illustrate the EL efficiency vs. current density curves of device with and without SWNTs doping. We can see the maximum luminous efficiency and

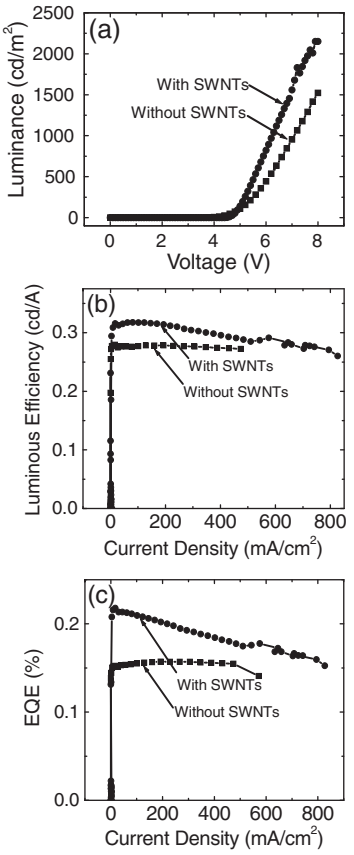

Fig. 2. The *L–V* curves (a), the luminous efficiency (b), and the external quantum efficiency (c) characteristics of devices without and with SWNTs doping. The device structure is ITO/PEDOT (40 nm)/PFO (80 nm)/Ca (20 nm)/Al (80 nm) and ITO/PEDOT:SWNTs (0.01 wt.%, 40 nm)/PFO (80 nm)/Ca (20 nm)/Al (80 nm), respectively.

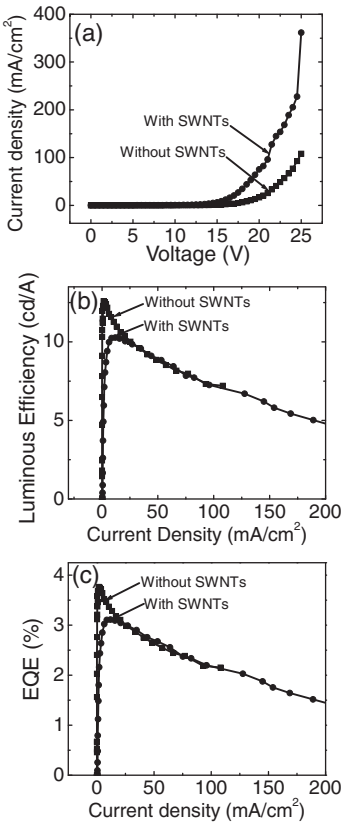

Fig. 3. The *J–V* curves (a), the luminous efficiency (b), and the external quantum efficiency (c) characteristics of the electrophosphorescent devices without and with SWNT doping. The device structure is ITO/PEDOT (40 nm)/PVK:PBD:Ir(mppy)$_3$ (69 wt.%:30 wt.%:1 wt.%, 60 nm)/Ca (20 nm)/Al (80 nm) and ITO/PEDOT:SWNTs (0.01 wt.%, 40 nm)/PVK:PBD:Ir(mppy)$_3$ (69 wt.%:30 wt.%:1 wt.%, 60 nm)/Ca (20 nm)/Al (80 nm), respectively.

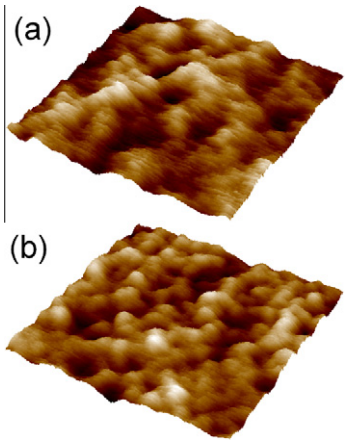

Fig. 4. The AFM images of the pure PEDOT film (a) and the PEDOT:SWNTs (0.01 wt.%) composite film (b), measured by tapping mode.

the maximum external quantum efficiency (EQE) of the device with SWNTs in PEDOT are 0.32 cd/A (1.2 times than that without SWNTs) and 0.22% (1.4 times than that without SWNTs), respectively. The enhancement of EL efficiency in devices employing SWNTs in PEDOT can be ascribed to the improvement of hole transport, thus leading to more balanced holes and electrons in the light-emitting layer.

As we mentioned above, the improvement of EL performance in devices with the SWNTs concentration no higher than 0.01 wt.% lies in their role of increasing hole transport in the conducting PEDOT film. Consequently, for OLEDs with holes as the minor carriers in the light-emitting layer (such as our PFO case), the EL performance can be improved by doping a very low amount of SWNTs into the hole conducting polymer. To investigate the impact of the mixture of the hole conducting polymer and SWNTs on the EL performance of OLEDs with balanced electrons and holes in the light-emitting layer, we have fabricated devices with the structure of ITO/PEDOT:SWNT (0.01 wt.%)/PVK:PBD:Ir(mppy)$_3$/Ca/Al. It has been reported that when the mixture of PVK, PBD and Ir(mppy)$_3$ is used as a light-emitting layer in OLEDs, highly efficient electrophosphorescence is achieved due to balanced electrons and holes in the light-emitting layer [17].

Fig. 3a shows the *J–V* curves of the electrophosphorescent devices with and without SWNTs doped in the PEDOT films. As can be seen from the figure, the *J–V* curve of the device with PEDOT:SWNTs composite shifts to a lower voltage compared with the one without SWNTs, which is similar with the PFO case. However, the maximum EL efficiency in the device with SWNTs is reduced relative to the one without SWNTs (shown in Fig. 3a and b). As we

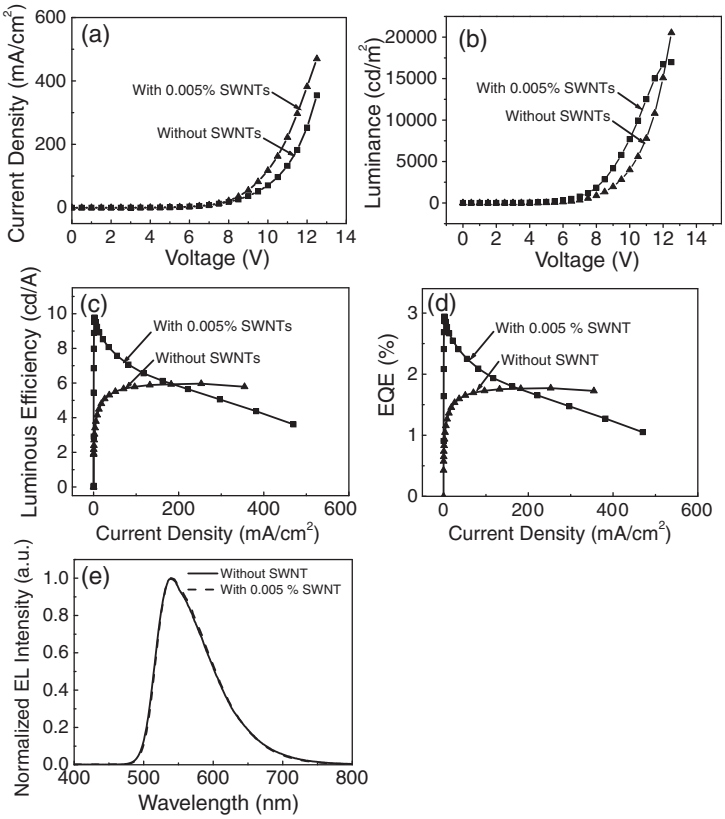

Fig. 5. The *J–V* curves (a), the *L–V* curves (b), the luminous efficiency (c), the external quantum efficiency (d), and EL spectra (e) of devices without and with SWNT doping. The device structure is ITO/PEDOT (40 nm)/Super-Yellow (80 nm)/Ca (20 nm)/Al (80 nm) and ITO/PEDOT (40 nm)/Super-Yellow:SWNTs (0.005 wt.%, 80 nm)/Ca (20 nm)/Al (80 nm), respectively.

expected, a low concentration of SWNTs in PEDOT film will enhance the hole transport in devices and shift the *J–V* curve to a lower voltage. Nevertheless, in OLEDs with balanced holes and electrons, introducing more holes to the light-emitting layer will upset the balance thus reducing the EL efficiency. Fig. 4 shows AFM images of the PEDOT film with and without SWNT dopants. In the case of pure PEDOT film, the islands have big sizes. But in the PEDOT:SWNTs (0.01 wt.%) composite film, the islands have small sizes, which means the contact at the interface between the PEDOT:SWNTs and the light-emitting layers will be improved. This morphological result suggests that using SWNTs in PEDOT layer can enhance hole injection into the light-emitting layer in the ITO/PEDOT:SWNTs/PFO/Ca OLED.

Besides acting as dopants in a hole conducting polymer in OLEDs, SWNTs can also be used in the light-emitting polymer layer. To investigate the SWNT's effect on the EL performance when it is in the light-emitting layer, we have fabricated devices with the structure of ITO/PEDOT/Super-Yellow:SWNTs/Ca/Al. Fig. 5a shows the *J–V* characters of devices with and without SWNTs in the light-emitting layer. Introducing SWNTs into the Super-Yellow layer shifts the *J–V* curve to the lower voltage compared with the pure Super-Yellow layer. Since Super-Yellow is a poly(*p*-phenylene vinylene) (PPV) derivate and it can transport holes more easily than electrons [18], OLEDs based on Super-Yellow are hole-dominated devices and electrons are minority carriers. It is well known that SWNTs have an electron-withdrawing ability [19,20], so they can act as an n-type material to improve the electron transport when doped into a polymer host, and can improve charge injection at interfaces [21]. Consequently, the *J–V* curve of the device with the Super-Yellow:SWNTs composite shifts to a lower voltage due to improved electron transport in the Super-Yellow layer. It can also be seen in Fig. 5b that the Super-Yellow:SWNTs OLED exhibits a lower threshold voltage in electroluminescence as compared to Super-Yellow only OLED. This result further suggests that the minority charge carrier (electron) transport is enhanced in Super-Yellow:SWNTs OLED. As can be seen from Fig. 5c and d, the EL efficiency has also been improved in devices with the Super-Yellow:SWNTs composite. The maximum luminous efficiency and maximum EQE reaches 9.8 cd/A and 2.9%, which is 1.6 times and 1.7 times than the one with pure Super-Yellow layer, respectively. Such enhancement in EL efficiency is also the result of the improvement of electron transport in the Super-Yellow layer due to the SWNTs acting as n-type dopants, thus leading to more balanced electrons and holes in the light-emitting layer. Fig. 5e shows the EL spectra of devices with and without SWNTs in the light-emitting layer and we can see that mixing the Super-Yellow with SWNTs does not change the EL emission spectra.

4. Conclusion

Here we elucidate that SWNTs play different roles when used as polymer:SWNTs composites in OLEDs. When SWNTs are mixed in a hole-conducting layer, they can have a helpful or a hurtful influence on the EL performance of OLEDs, which depends on the SWNTs concentration. If the SWNTs concentration is low enough (in our case $\leqslant$0.01 wt.%), they can play a role in improving the conductivity thus enhancing the hole transport in the hole-conducting layer. Also, they improve contact at interfaces by inducing much smaller surface islands than the ones on the surface of purely hole-conducting layers. But if the SWNTs concentration is too high (in our case higher than 0.02 wt.%), they can act as centers to quench the excitons that have migrated to the interface between the hole-conducting layer and the light-emitting layer. When SWNTs are incorporated into an emitting polymer layer, they improve the electron transport since SWNTs can act as n-type dopants in the light-emitting layer, which profits from the electron-withdrawing nature of SWNTs.

Acknowledgements

This research was supported by Center for Materials Processing at the University of Tennessee, Solid State Lighting Program of the Energy Efficiency and Renewable Energy, US Department of Energy. A portion of this research was conducted at the Center for Nanophase Materials Sciences through a user project (CNMS2009-055), which is sponsored at Oak Ridge National Laboratory by the Basic Energy Sciences, US Department of Energy. Authors express gratitude to Prof. Stanislaus S. Wong (Department of Chemistry, SUNY) for providing water-soluble SWNTs.

References

[1] F. Massuyeau, J.L. Duvail, H. Athalin, J.M. Lorcy, S. Lefrant, J. Ẃery, E. Faulques, Nanotechnology 20 (2009) 155701.
[2] L. Qian, T. Feng, X. Zheng, S.Y. Quan, D.A. Liu, Y.M. Wang, Y.S. Wang, X.R. Xu, Spectrosc. Spect. Anal. 26 (2006) 601.
[3] B. Hu, Y. Wu, Z.T. Zhang, S. Dai, J. Shen, Appl. Phys. Lett. 88 (2006) 022114.
[4] Z. Tan, F. Zhang, T. Zhu, J. Xu, A.Y. Wang, J.D. Dixon, L. Li, Q. Zhang, S.E. Mohney, J. Ruzyllo, Nano Lett. 7 (2007) 3803.
[5] Y.G. Ha, E.A. You, B.J. Kim, J.H. Choi, Synth. Met. 153 (2005) 205.
[6] S.A. Curran, P.M. Ajayan, W.J. Blau, D.L. Carroll, J.N. Coleman, A.B. Dalton, A.P. Davey, A. Drury, B. McCarthy, S. Maier, A. Strevens, Adv. Mater. 10 (1998) 1091.
[7] H.S. Woo, R. Czerw, S. Webster, D.L. Carroll, J. Ballato, A.E. Strevens, D. O'Brien, W.J. Blau, Appl. Phys. Lett. 77 (2000) 1393.
[8] H.S. Woo, R. Czerw, S. Webster, D.L. Carroll, J.W. Park, J.H. Lee, Synth. Met. 116 (2001) 369.
[9] J.Y. Kim, E.S. Kim, J.H. Choi, J. Appl. Phys. 91 (2002) 1944.
[10] T.W. Odem, J.L. Huang, P. Kim, C.M. Liber, Nature 391 (1998) 62.
[11] M.G.C. Kahn, S. Banerjee, S.S. Wong, Nano Lett. 2 (2002) 1215.
[12] J.Y. Kim, M. Kim, J.-H. Choi, Synth. Met. 139 (2003) 565.
[13] C. Yang, M. Wohlgenannt, Z.V. Vardeny, W.J. Blau, A.B. Dalton, R. Baughman, A.A. Zakhidov, Physica B 338 (2003) 366.
[14] E. Kymakis, G.A.J. Amaratung, Appl. Phys. Lett. 80 (2002) 112.
[15] A.L. Burin, M.A. Ratner, J. Phys. Chem. A 104 (2000) 4704.
[16] A.J. Campell, D.D.C. Bradley, H. Antoniadis, J. Appl. Phys. 89 (2000) 3343.
[17] X. Yang, D. Neher, D. Hertel, T.K. Daubler, Adv. Mater. 16 (2004) 161.
[18] H. Spreitzer, H. Becker, E. Kluge, W. Kreuder, H. Schenk, R. Demandt, H. Schoo, Adv. Mater. 10 (1998) 1340.
[19] A. Kongkanand, P.V. Kamat, ACS Nano 1 (2007) 13.
[20] J.M. Holt, A.J. Ferguson, N. Kopidakis, B.A. Larsen, J. Bult, G. Rumbles, J.L. Blackburn, Nano Lett. 10 (2010) 4627.
[21] D. Liu, M. Fina, J. Guo, X. Chen, G. Liu, S.G. Johnson, S.S. Mao, App. Phys. Lett. 94 (2009) 013110.

p–n diode and the gate electrodes of TFTs were patterned with ITO etchant solution (LCE-12K) through conventional photolithography method. Then, 40 nm-thick ZnO n-type layer for p–n diode was deposited at room temperature (RT) by 100 W rf magnetron sputtering of a ZnO target (99.999%) in the 10 mtorr Ar/O_2 (6:1) gas mixture, through the first shadow mask for patterning. Then, 100 nm-thick AlO_x layer was deposited by rf magnetron sputtering of an Al_2O_3 target (99.99%) in a 20 mtorr Ar gas, through the 2nd shadow mask. A 150 nm-thick pentacene (Aldrich Chem. Co., 99% purity, with no other purification) was deposited as the p-type layer on n-ZnO through the 3rd shadow mask by thermal evaporation at RT and then, 50 nm-thin pentacene was also deposited as p-channels of TFTs on AlO_x through 4th mask. Pentacene deposition rate was fixed to 1 Å/s. For a semi-transparent anode of p–n diode and source/drain electrode of pentacene TFTs (W/L = ~500/90 μm), 100 nm-thick NiO_x ($E_g \sim 4.0$ eV, transmittance ~30%, sheet resistance ~100 Ω/□, anode pattern area ≃1.4 × 1.4 (= 1.96) mm^2) was deposited on the pentacene layer by the thermal evaporation of NiO powder (99.97% purity), [11] through the last shadow mask. As the final process for our semitransparent photo-detector, the NiO_x drain electrode of pentacene TFT was serially connected to the ITO cathode of p–n diode by the same thermally-evaporated NiO_x. In order to improve the transparency of our p–n diodes and pentacene TFTs, we also attempted sequential double deposition of 30 nm-thin NiO_x buffer (by thermal evaporation on pentacene) and 70 nm-thick indium zinc oxide (IZO) layer (by sputter deposition on NiO_x). The first two photographs in Fig. 1(a) display optical microscope images of photo-detector cells (photodiode and TFT) with semitransparent NiO_x and transparency-improved NiO_x/IZO top electrodes, respectively; Arabic numbers typed on a paper were seen through our p–n diodes. All current–voltage (I–V) properties of our p–n diodes were measured with a semiconductor parameter analyzer (HP 4155C, Agilent Technologies) in an air ambient (relative humidity ~40%) at RT. Photoresponse measurements were performed with a light source unit consisting of a 500 W Hg–Xe arc lamp and a monochromator covering the range of 250–1000 nm (Oriel optical system). The optical power was measured by a Si-based optical power meter (TQ8210, ADVANTEST) and the photons were delivered through an optical fiber that plays as an optical probe. All transmittance measurements of p–n diode structures were carried out with a spectrophotometer (Varian Cary 5G).

3. Results and discussion

Fig. 1(b) displays the transmittance spectra of our thin-film p–n diodes (inset) fabricated on ITO glass with two different kinds of top electrode: 100 nm-thick NiO_x (black line) and 67 nm IZO/30 nm NiO_x (red line). In both cases, the pentacene layer-induced optical absorption was clearly shown in the visible range of 710–410 nm (1.75–3.0 eV) while ZnO-induced absorption was observed at over 3.2 eV, although the diode with the double layer electrode appeared slightly more transparent as expected. It is

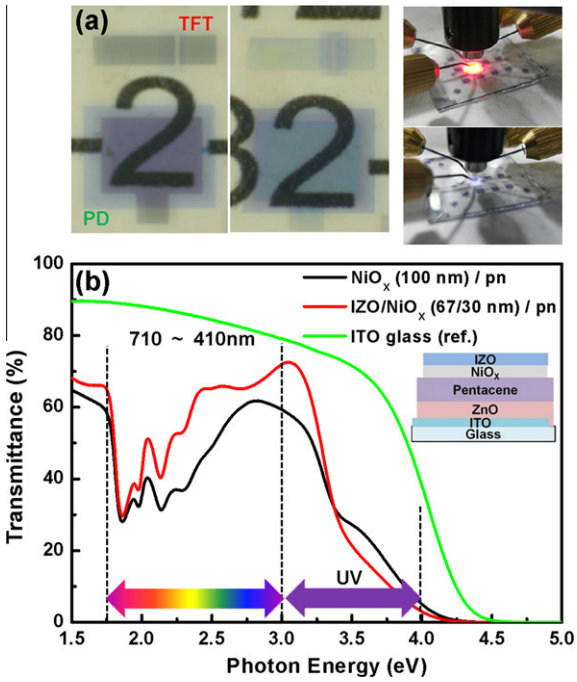

Fig. 1. (a) Photographs of our semitransparent photo-detector cells (composed of pentacene-TFT and pentacene/ZnO p–n diode) with NiO_x (1st left) and IZO/NiO_x (2nd left) top electrodes. Right-side photos show photoresponse measurement under red (640 nm: up)) and UV (364 nm: down) light. (b) Transmittance spectra of our p–n diodes with the two types of top electrodes. The inset is a schematic device structure of p–n diode with IZO/NiO_x top electrode. Reference ITO glass shows a high transmittance of more than 80% in visible range. (For interpretation of the references to colour in this figure legend, the reader is referred to the web version of this article.)

known that thermally-evaporated Ni-rich conducting NiO_x has a limited transmittance but is well matched with pentacene for a good ohmic contact (having a large work function of more than 5.1 eV) [12]. In the present study, we could divide the photo-detection ranges of our photo-detector into two by photon energy as indicated in Fig. 1(b): 1.75–3.0 eV (visible) and 3.0–4.0 eV (UV). These detection ranges were determined by considering the respective energy gaps of pentacene and ZnO materials; the up and down photos located in the right-side of Fig. 1(a) demonstrate our photo-detection measurements by visible and UV photons.

The photoresponse of our p–n diodes with the two types of top electrodes was measured as shown in the dark/photo I–V curves of Fig. 2(a and b), where the dark curves displayed rectifying behavior (the ideality factor of our hybrid diode was as high as ~7.9 and its schematic band diagram is shown in the inset of Fig. 2(c)). Dark leakage current appears to be ~1 nA at −3 V reverse bias while it increases to 20 nA under blue light with 440 nm wavelength. According to the figures, the current minimum is not observed at zero volt but at a negative bias side near −0.6 V in the dark. It is because our pentacene/ZnO is a heterojunction diode containing interface trap charges; under a large reverse bias those trap charges are released and transported to play as the source of junction leakage but the leakage current would be minimized at a certain

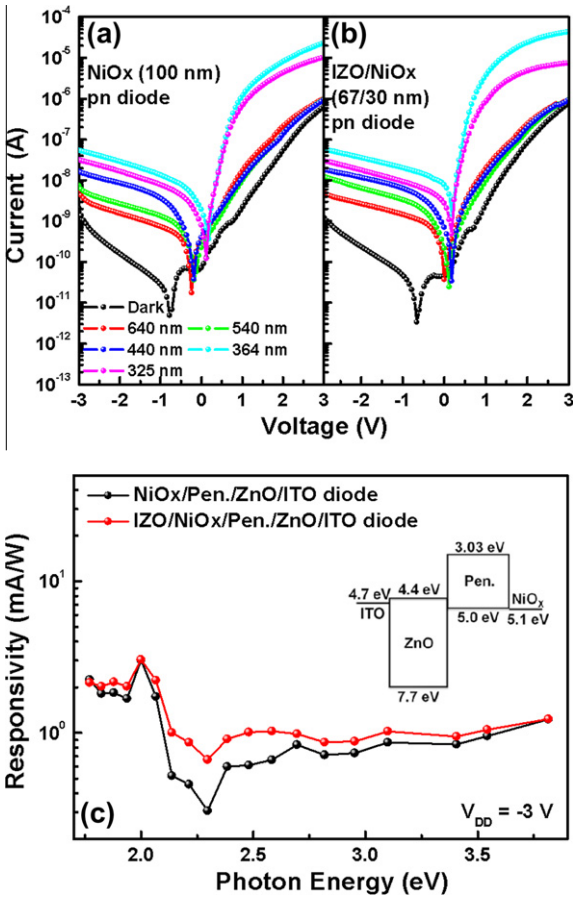

Fig. 2. Dark and photo *I–V* curves of our p–n diodes with two semitransparent electrodes of (a) NiO_x (100 nm) and (b) IZO (67 nm)/NiO_x (30 nm). (c) Spectral responsivity curves of our pentacene/ZnO photodiode with the two electrodes. The inset is the band diagram of the hybrid p–n diode with NiO_x and ITO electrodes.

small reverse bias which may make a flat p–n band condition. Such photoresponse was spectrally analyzed in the visible photon energy range of 1.75–3 eV, as shown in Fig. 2(c). Main mechanism of the photo-current generation under a reverse bias might be involved with the following serial events: photo-absorption and exciton generation in pentacene, exciton diffusion and dissociation into electron–hole carrier, and carrier transport to ZnO or ITO electrode under electric field. The responsivity spectra in the range between 1.75 and 2.5 eV almost follow that of the pentacene Schottky photodiode which was previously shown by our group, [10] now showing its peak responsivity of ~2 mA/W at 1.97 eV at −3 V (the respective optical power of all monochromatic lights could not be normalized for the spectral responsivity measurements: 640 nm–0.11 mW/cm^2, 540 nm–0.92 mW/cm^2, 440 nm–1.08 mW/cm^2, 364 nm–3.28 mW/cm^2, 325 nm–1.29 mW/cm^2). However, from 2.5 to 3 eV the responsivity does not vary much, unlike the behavior of the Schottky diode, where the responsivity monotonically decreases after 2.5 eV. It is likely that the present p–n diode with n-ZnO layer displays additional responses due to the deep level defects of transparent ZnO in the high photon energy regime [13,14]. Another point to note is that somewhat higher photoresponse is achieved from the diode with IZO/NiO_x double electrode than the other one with thick NiO_x single electrode (Fig. 2(c)). It is because slightly higher density of photons was received by the pentacene/ZnO diode through the IZO/NiO_x double electrode than through the 100 nm-thick NiO_x (see the transmittance data in Fig. 1(b)).

Fig. 3(a) displays the transfer curves of the pentacene TFT as obtained through several times of repeated gate voltage (V_G) sweeps while green illumination was applied only on the photodiode by an optical probe. At the both applied drain voltages (V_D) of −5 V and −0.5 V, the original dark transfer curve was hardly changed regardless of any scattered illumination and sweep number. (Our pentacene TFT with thin channel is known to be quite photo-stable unlike the photodiode with thick pentacene layer) [4]. The saturation mobility of our pentacene TFT was

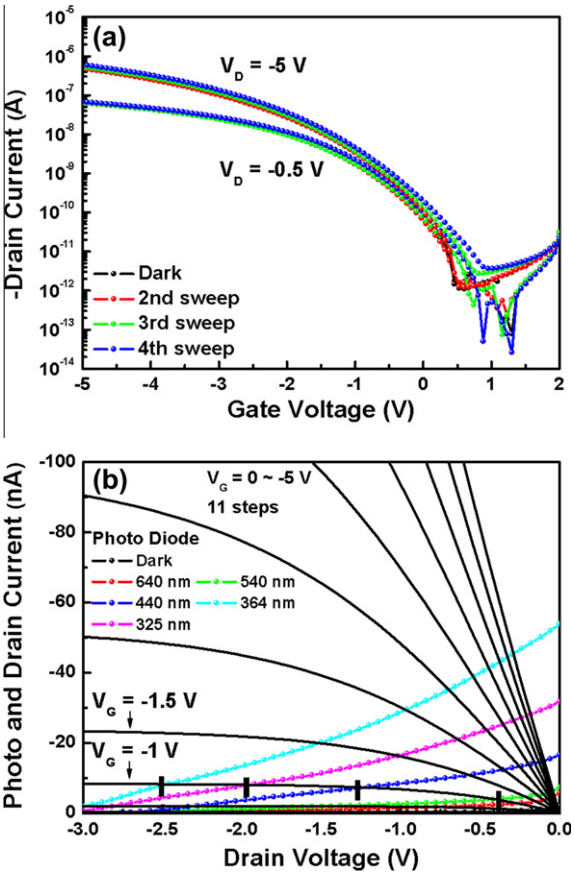

Fig. 3. (a) Transfer curves of our pentacene TFT at $V_D = -0.5$ V (linear regime) and −5 V (saturation regime). Green illumination was collimated only on the photodiode, and any scattered light could hardly change the dark original transfer characteristics during several sweeps. (b) A load-line analysis for our photo-detector cell. The cross points between the output curves of pentacene TFT and photo *I–V* curves of reverse-biased p–n diode were obtained as photo-induced V_{out}. $V_G = -1$ V appears an optimum condition for the photo V_{out} signals. (For interpretation of the references to colour in this figure legend, the reader is referred to the web version of this article.)

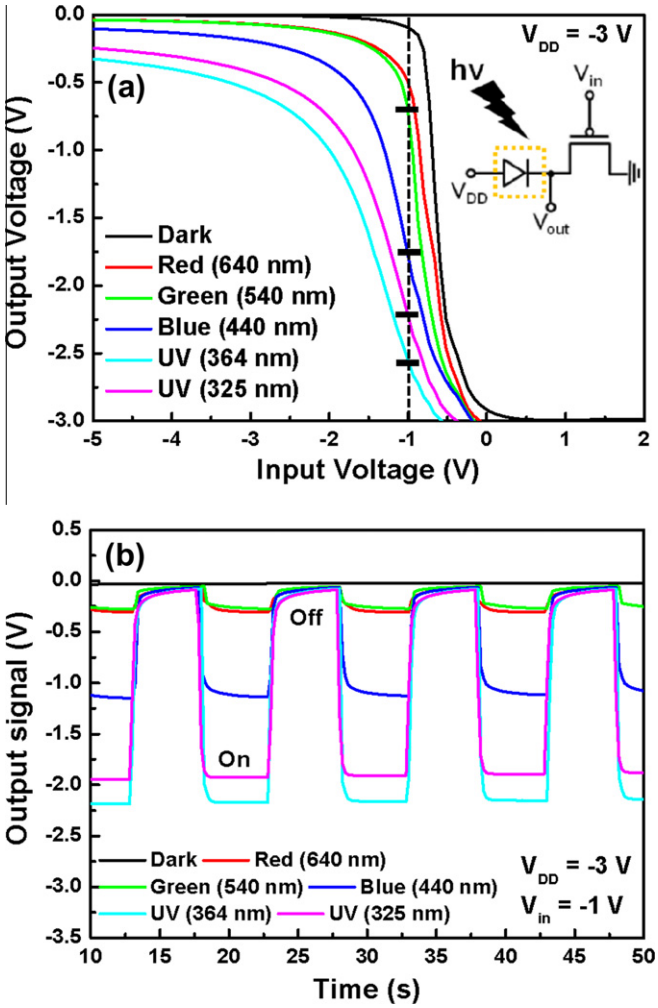

Fig. 4. (a) Photo-induced VTC curves of our detector cell (TFT + illuminated photodiode). The inset illustrates the photo-detection measurement. The dashed line indicates an optimum V_{in} (−1 V) and the cross points indicate the photo-induced V_{out} as signals. (b) Dynamic response of our photo-detector cell under the illuminations, that were repetitively turned on and off for the measurements. (For interpretation of the references to colour in this figure legend, the reader is referred to the web version of this article.)

0.21 cm^2/Vs (at $V_D = -5$ V) while the linear mobility was 0.11 cm^2/Vs (at $V_D = -0.5$ V) as estimated from the transfer curves. As a load-line analysis of Fig. 3(b) was implemented between the output curves (drain current I_D vs. V_D) of the TFT and photo I–V curves of our reverse-biased p–n diode, an optimum V_G was turned out to be −1 V. Clear V_D values were obtained at $V_G = -1$ V as indicated by cross points between two types of curves: TFT output and photodiode I–V curves. This analysis is, however, more efficiently expressed by voltage transfer characteristics (VTC) as shown in Fig. 4(a), where V_G is now input voltage (V_{in}) for sweep, V_{DD} is supply voltage, and V_{out} is output voltage to be obtained at the node between TFT and serially connected p–n diode. (Note that V_{out} signals are now about the same as the cross points V_D values of Fig. 3(b)). Inset circuit illustrates our photo-detection measurements, and according to our VTC curves the most effective photo-induced V_{out} signals may come from the V_{in} of −1 V under V_{DD} of −3 V as expected from the load-line analysis of Fig. 3(b).

Dynamic photo-induced V_{out} response was also measured under the optimum voltage condition: $V_{in} = -1$ V at $V_{DD} = -3$ V. According to Fig. 4(b), less than 1 s (minimum ~300 ms) was nicely observed as response time when visible and UV illuminations were turned on and off. The V_{out} for dynamic turn-on was not exactly the same as that of VTC in Fig. 3(b), but very much approaches to: for 364 nm UV, 2.6 V in VTC and 2.2 V in dynamics. (Reason for such slight deviations is not clearly understood, yet). A slight delay was observed in our detector particularly under UV-off situations. It is primarily because our photodetector cell has relatively a large diode area to receive more light, but then the diode may possess more junction traps where photo-induced trapped charges can not be easily transported. However, despite such delays we regard our detector still worthy and promising since its spectral

response in static VTC characteristics quite well matches with the response in voltage dynamics.

4. Conclusion

In summary, we have fabricated semi-transparent organic–inorganic hybrid photo-detector cells, composed of pentacene/ZnO photodiodes and serially connected pentacene TFTs. Our photodiode well demonstrated the detection of visible and UV photons utilizing pentacene and ZnO, respectively, although its responsivity was not high. Our photo-detector cell thus exhibited good photo-induced V_{out} in VTC and in dynamic response behavior as well at -1 V input and -3 V supply voltage. We thus conclude that our semitransparent pentacene/ZnO hybrid cell is quite promising as a visible/UV detector fabricated on glass for a host of applications.

Acknowledgements

The authors acknowledge the financial support from NRF (NRL program: Grant No. 2011-0000375), the MKE (IT R&D program: No. 2006-S-079-5), Seoul R&BD Program (ST090839) and Brain Korea 21 program. K.H. Lee would like to thank for the Seoam and Agency of Defense Development (ADD) Fellowships.

References

[1] K. Nomura, H. Ohta, A. Takagi, T. Kamiya, M. Hirano, H. Hosono, Nature 432 (2004) 488.
[2] D.K. Hwang, C.S. Kim, J.M. Choi, K. Lee, J.H. Park, E. Kim, H.K. Baik, J.H. Kim, S. Im, Advanced Materials 18 (2006) 2299.
[3] E.M.C. Fortunato, P.M.C. Barquinha, A.C.M.B.G. Pimentel, A.M.F. Gonçalves, A.J.S. Marques, L.M.N. Pereira, R.F.P. Martins, Advanced Materials 17 (2005) 590.
[4] M.S. Oh, K. Lee, K.H. Lee, S.H. Cha, J.M. Choi, B.H. Lee, M.M. Sung, S. Im, Advanced Functional Materials 19 (2009) 726.
[5] C.H. Park, S. Im, J. Yun, G.H. Lee, B.H. Lee, M.M. Sung, Applied Physics Letters 95 (2009) 223506.
[6] S.-H.K. Park, C.-S. Hwang, M. Ryu, S. Yang, C. Byun, J. Shin, J.-I. Lee, K. Lee, M.S. Oh, S. Im, Advanced Materials 21 (2009) 678.
[7] J.-M. Choi, J. Lee, D.K. Hwang, J.H. Kim, S. Im, E. Kim, Applied Physics Letters 88 (2006) 043508.
[8] T. Someya, Y. Kato, S. Iba, Y. Noguchi, T. Sekitani, H. Kawaguchi, T. Sakurai, IEEE Transactions on Electron Devices 52 (2005) 2501.
[9] S. Aihara, H. Seo, M. Namba, T. Watabe, H. Ohtake, M. Kubota, N. Egami, T. Hiramatsu, T. Matsuda, M. Furuta, H. Nitta, T. Hirao, IEEE Transactions on Electron Devices 56 (2009) 2570.
[10] J. Lee, S.S. Kim, K. Kim, J.H. Kim, S. Im, Applied Physics Letters 84 (2004) 1701.
[11] J.-M. Choi, D.K. Hwang, J.H. Kim, S. Im, Applied Physics Letters 86 (2005) 123505.
[12] K. Lee, J.H. Kim, S. Im, Applied Physics Letters 88 (2006) 023504.
[13] H.S. Bae, S. Im, J.H. Song, Journal of the Electrochemical Society 153 (2006) G791.
[14] S. Bethke, H. Pan, B.W. Wessels, Applied Physics Letters 52 (1988) 138.

current under constant bias stress [10–13]. On the other hand, dipolar groups such as hydroxyl groups (OH) in the bulk of the gate dielectric, and/or gate charge injection cause clockwise hysteresis in *p*-channel (anticlockwise for *n*-channel) transistors and increase the drain current under prolonged bias stress [10,11,13–16]. The stability of FETs can in general be rationalized by one, or a combination of these mechanisms. In a recent study, we proposed the concept of compensation of some of these degradation effects and demonstrated OFETs on rigid substrates, with excellent operational stability. Such transistors were comprised of a bi-layer top-gate insulator of CYTOP followed by a high-*k* Al_2O_3 layer grown by atomic layer deposition (ALD), and a hole-transporting semiconductor composed of a 6,13-bis(triisopropylsilylethynyl) pentacene (TIPS-pentacene) and poly(triarylamine) (PTAA) blend fabricated on rigid glass substrates [17].

Here, we report on solution-processed TIPS-pentacene and PTAA blend OFETs fabricated on a flexible polyethersulfone (PES) substrate. Changing from a glass substrate to a flexible one can be a challenging task as differences in surface energy and roughness of the substrate are likely to affect the properties of the semiconductor layer and consequently the performance of the transistor and its stability. Furthermore, the temperature of all processing steps during the device fabrication must be compatible with the temperature load that the flexible polymeric substrate can sustain. These flexible OFETs exhibit degradation compensation mechanisms due to the use of a CYTOP/Al_2O_3 top gate dielectric bi-layer that are similar to those observed previously in devices on glass substrates. Good electrical stability under constant dc bias stress for 2 h could be achieved without significant changes of mobility (μ) or threshold voltage (V_{th}). Furthermore, we verify the potential of these OFETs to form circuit components by connecting them to external load resistors (R_L), thereby creating a resistive-load inverter. We demonstrate that in such inverters the switching threshold voltage (V_M) remained almost unchanged after a constant dc bias stress for 2 h due to the excellent electrical stability of the transistor. Besides the operational stability, environmental and mechanical stabilities are also challenging issues to achieve when OFETs are transition from glass to flexible substrates. These OFETs and inverters showed negligible changes on μ, V_{th}, and V_M after 4 months of air exposure and mechanical bending tests for 30 min.

2. Device fabrication and electrical characterization

OFETs with a bottom-contact and top-gate structure were fabricated on a flexible PES substrate. Poly-4-vinylphenol (PVP) buffer layers were prepared from 2 wt.% solutions of PVP ($M_w \sim 20{,}000$) and poly (melamine-co-formaldehyde), as a cross-linking agent, in propylene glycol monomethyl ether acetate (PGMEA), which were deposited by spin coating at 3000 rpm for 40 s and subsequently cross-linked at 175 °C on a hot plate for 1 h in a N_2-filled glove box. Au (50 nm) bottom contact source/drain electrodes were deposited by thermal evaporation through a shadow mask. To improve contact at the metal and organic semiconductor interface, a self-assembled monolayer of pentafluorobenzenethiol (PFBT) was formed on the Au electrodes by immersion in a 10 mM PFBT solution in ethanol for 15 min in a N_2-filled dry box, rinsed with pure ethanol, and dried. The TIPS-pentacene and PTAA blend solution was prepared as follows: TIPS-pentacene and PTAA were individually dissolved in 1,2,3,4-tetrahydronaphthalene anhydrous, 99%, (Sigma–Aldrich) for a concentration of 30 mg/mL and the two individual solutions were mixed to yield a weight ratio of 1:1. Blends of TIPS-pentacene and PTAA were deposited by spin coating at 500 rpm for 10 s and at 2000 rpm for 20 s. Then, samples were annealed at 100 °C for 15 min in a N_2-filled dry box. A CYTOP (40 nm)/Al_2O_3 (50 nm) bi-layer was used as the top-gate dielectric. A CYTOP solution (CTL-809 M) was purchased from Asahi Glass with a concentration of 9 wt.%. To deposit the 40 nm-thick CYTOP layers, the original solution was diluted with a solvent (CT-solv.180) to have a 2 wt.% of CYTOP. The 40 nm-thick CYTOP layers were deposited by spin coating at 3000 rpm for 60 s. The CYTOP (40 nm) films were annealed at 100 °C for 20 min. All spin coating and annealing processes were carried out in a N_2-filled dry box. Then, the Al_2O_3 dielectric films were deposited on top of the CYTOP layer using a Savannah 100 ALD system from Cambridge Nanotech Inc. Films were grown at 110 °C using alternating exposures of trimethyl aluminum [$Al(CH_3)_3$] and H_2O vapor at a deposition rate of approximately 0.1 nm per cycle. Details about the Al_2O_3 films grown by ALD are described elsewhere [18]. Finally, Al (150 nm) gate electrodes were deposited by thermal evaporation through a shadow mask. Fig. 1(a) and (b) shows a schematic cross-sectional view of the OFET and a photograph of an OFET array on a flexible PES substrate.

The electrical characterization of the OFETs was carried out in a N_2-filled glove box (O_2, $H_2O < 0.1$ ppm). Current–voltage (*I–V*) characteristics of OFETs and voltage transfer characteristics (*VTC*) of resistive-load inverter were measured with an Agilent E5272A source/monitor unit. Field-effect mobility in the saturation regime was calculated from the slope of the |drain current (I_{DS})|$^{1/2}$ versus V_{GS} plot by the standard thin-film transistor equation:

$$\sqrt{I_{DS}} = \sqrt{\frac{W}{2L} C_{in} \mu_{sat}}\ (V_{GS} - V_{th}) \quad (1)$$

where C_{in} is the capacitance per unit area of the gate dielectric [F/cm^2], and W (width) and L (length) are the dimensions of the semiconductor channel defined by the source/drain electrodes of the transistor. Resistive-load inverters consisted of an OFET and an external R_L of 5, 10, and 20 MΩ.

3. Results and discussion

Fig. 2(a) and (b) show hysteresis-free transfer and output characteristics of OFETs (W/L = 2550 μm/180 μm) with the CYTOP (40 nm)/Al_2O_3 (50 nm) bi-layer dielectric. OFETs operated below 8 V due to the high capacitance density of the bi-layer dielectric (34.8 nF/cm^2) and showed an average (over 4 devices) saturation μ of 0.24 ± 0.08 cm^2/Vs and an averaged V_{th} of −1.3 ± 0.1. In comparison with previous OFETs on a glass substrate (μ = 0.46 ± 0.08 cm^2/Vs), the average μ value slightly degrades but is still reasonably

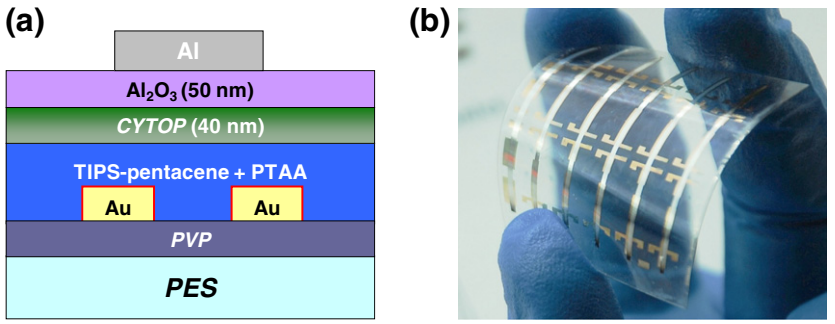

Fig. 1. (a) Schematic cross-sectional view and (b) a photograph of the OFET array fabricated on a flexible PES substrate.

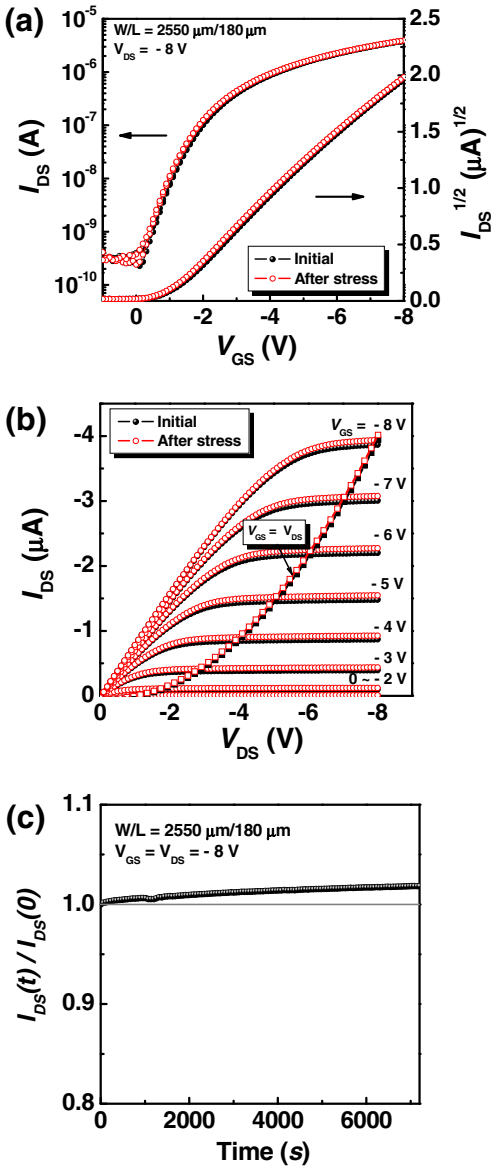

Fig. 2. Representative hysteresis-free (a) transfer and (b) output characteristics of OFETs (W/L = 2550 μm/180 μm) before and after bias stress test. (c) Temporal evolution of the normalized drain current for the stress condition of $V_{GS} = V_{DS} = -8$ V.

high. The operational stability of these OFETs was evaluated through a constant direct current (dc) bias stress test. Fig. 2(c) shows the temporal evolution of the I_{DS} measured in all OFETs normalized to the initial value for the bias stress condition of $V_{GS} = V_{DS} = -8$ V. It is noted that the I_{DS} slightly increases, reaching a value of 1.02 after 2 h, similar to results we have previously obtained in similar OFETs on rigid glass substrates [17]. This behavior is different from the conventional decay of I_{DS} during bias stress. As mentioned above, the high stability of these OFETs can be explained by compensating effects arising from filling of deep traps at the semiconductor/gate dielectric interface and, simultaneously, field-induced dipolar orientation at the CYTOP/Al_2O_3 interface and/or charge injection from the gate electrode [17]. After the bias stress tests, we re-measured the transfer and output characteristics to confirm that neither μ nor V_{th} underwent significant changes, which is clearly shown by the open symbols in Fig. 2(a) and (b).

To evaluate the real potential of these OFETs, towards their application as circuit components in electronic applications, we implemented a resistive-load inverter by connecting an external R_L to an OFET. An important parameter in the static performance of an inverter is V_M which is defined as the voltage when the input voltage (V_{IN}) equals the output voltage (V_{OUT}). This parameter can be directly extracted from the inverter voltage transfer characteristics (*VTCs*). High and balanced noise margins are found when the ideal condition $V_M = 0.5V_D$ is met, hence when $V_M = V_{IN} = 0.5V_D = V_{OUT}$. For reliable circuit operations, V_M should be constant during operation. In a previous study, we developed a technique to calculate V_M which does not require any fitting parameters such as μ and V_{th} [19]. The transistor can be modeled as a voltage dependent variable resistor (*p*-channel resistance, $R_P = -V_{IN}/-I_{DS}$ at $V_{GS} = V_{DS}$), which can be directly interpolated from the measured output characteristics, as shown in Fig. 2(b). The voltage distribution simply follows the difference between two series resistances. Hence, the value of V_M is determined at $R_P = R_L$. Fig. 3(a) shows R_P and R_L before and after bias stress. At $R_P = R_L$, the calculated V_M values were 5.48 V for R_L = 20 MΩ, 4.85 V for R_L = 10 MΩ, and 4.08 V for R_L = 5 MΩ, respectively, before bias stress. After bias stress, those values were 5.58 V for R_L = 20 MΩ, 4.95 V for R_L = 10 MΩ, and 4.16 V for R_L = 5 MΩ, respectively. Fig. 3(b) and (c) show the *VTCs* and static circuit gain

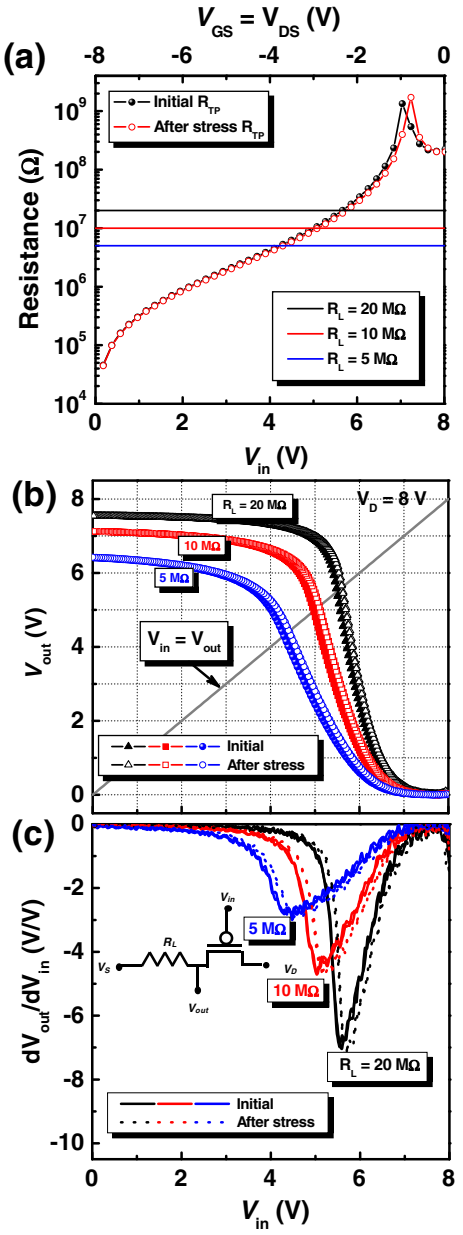

Fig. 3. (a) Resistance of *p*-channel TIPS-pentacene and PTAA blend OFET at $V_{GS} = V_{DS}$ by sweeping V_{GS} from 0 V to −8 V. (b) Voltage transfer characteristics and (c) static gain of the resistive-load inverter.

of these resistive-load inverters. As expected from the hysteresis-free transistor current–voltage characteristics, the resistive-load inverters showed negligible hysteresis. After a constant bias stress for 2 h, negligible changes in *VTCs* were observed. Hysteresis-free *VTCs* and negligible changes of V_M before and after bias stress are attributed to the excellent operational stability of the individual transistor, which allows reliable circuit operations. As shown in Fig. 3(b), the measured V_M values from *VTCs* were 5.50 V for R_L = 20 MΩ, 4.98 V for R_L = 10 MΩ, and 4.31 V for R_L = 5 MΩ, respectively, before bias stress. After bias stress, those values were 5.62 V for R_L = 20 MΩ, 5.10 V for R_L = 10 MΩ, and 4.42 V for R_L = 5 MΩ, respectively. Measured and calculated values of V_M are comparable with negligible variations of circuit gains before and after bias stress, as shown in Fig. 3(c). The maximum static gain value of 7 was obtained from R_L = 20 MΩ. The static gain value of the resistive-load inverter is low but it can be improved by fabricating complementary inverters combining *p*-channel FET with *n*-channel FET.

After the operational stability tests, the environmental and mechanical properties were also studied. These OFETs were exposed to normal ambient conditions with a relative humidity between 30 and 50% for 4 months. Fig. 4(a) and (b) show hysteresis-free transfer and output characteristics of OFETs before and after air exposure. While no significant degradation was observed in μ and V_{th} before and after air exposure, the on/off current ratio slightly decreased due to an increase in the off current. This can be explained by the diffusion of oxygen, and probably water, into the semiconductor layer. A similar behavior was observed on OFETs fabricated on glass substrates [17]. On the other hand, Fig. 4(a) and (b) also shows the hysteresis-free transfer and output characteristics of these OFETs after they were subjected to bending for 30 min under tensile stress. As shown in Fig. 4(c), for the bending test, the sample (with the OFETs located on the top surface) was bent at a radius of curvature (R_c) of 13.5 ± 0.5 mm. Considering that the substrate thickness (D) was measured to be 0.2 mm, a strain (ε) of 0.74% can be calculated from the equation, $\varepsilon = D/2R_c$ [6]. Even after this bending test, the electrical characteristics of the OFETs remained practically unchanged. Hence, as expected, the resistive-load inverter also showed hysteresis-free *VTCs* and negligible changes of V_M after undergoing air exposure and mechanical deformation as shown in Fig. 4(d). The electrical performance parameters of the inverter after bias stress, air exposure, and mechanical bending tests are summarized in Table 1.

4. Conclusion

In summary, we demonstrated electrically stable TIPS-pentacene and PTAA blend OFETs with a top-gate geometry on a flexible PES substrate. A CYTOP/Al_2O_3 bi-layer was employed as a top gate dielectric with a high capacitance density to realize OFETs with excellent electrical stability. TIPs-pentacene and PTAA blend OFETs with the CYTOP/Al_2O_3 bi-layer gate dielectric showed an average saturation mobility value of 0.24 ± 0.08 cm^2/Vs without hysteresis at operation voltages below 8 V. Under a dc bias stress at $V_{GS} = V_{DS} = -8$ V for 2 h, the change in I_{DS} was less than 2%. Neither serious μ degradation nor significant V_{th} shift was observed. As expected from the excellent electrical stability of this transistors, resistive-load inverters showed hysteresis-free voltage transfer characteristics as well as negligible changes of switching threshold voltage after a dc bias stress test. In addition, after exposure to air for 4 months and mechanical deformation for 30 min, no significant changes in performance were observed in either a single transistor device or in a resistive-load inverter. Therefore, OFETs comprised of a CYTOP/Al_2O_3 bi-layer gate dielectric can be a promising building block to realize stable electronic circuits.

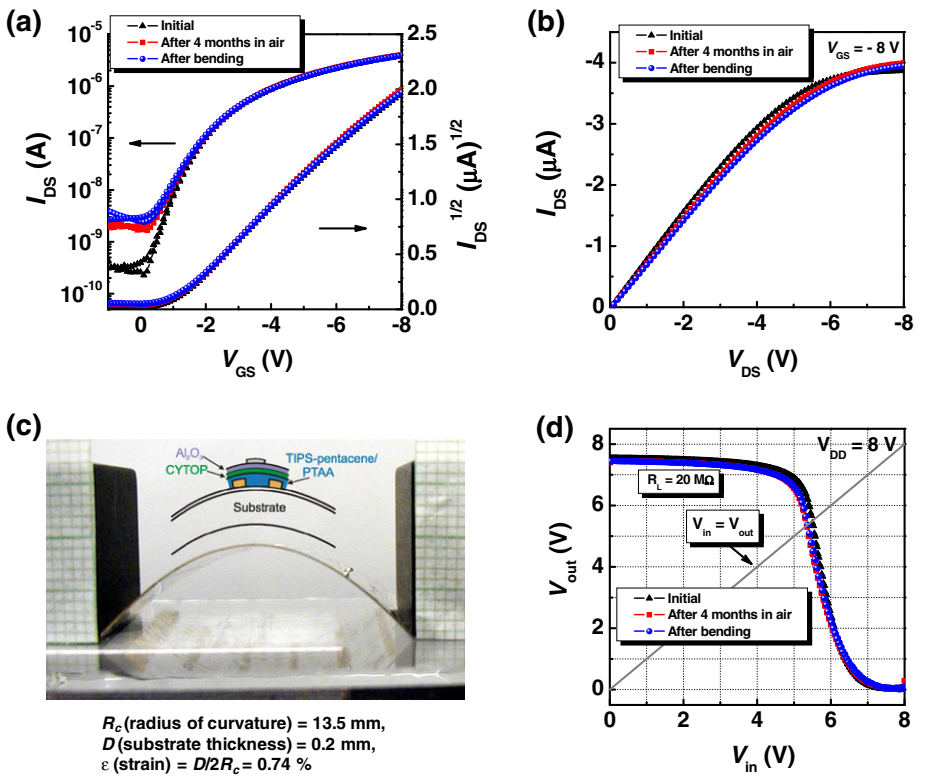

Fig. 4. Hysteresis-free (a) transfer and (b) output characteristics of OFETs (W/L = 2550 μm/180 μm); (c) photograph of the mechanical bending experiment; and (d) voltage transfer characteristics of the resistive-load inverter before and after air exposure and mechanical deformation.

Table 1
Performance of resistive-load inverters after undergoing different tests.

Condition	V_D (V)	R_L (MΩ)	dV_{out}/dV_{in} (V/V)	V_M (calculated) (V)	V_M (measured) (V)
Initial	8	20	−7	5.48	5.50
		10	−5	4.85	4.98
		5	−3	4.08	4.31
After bias stress for 2 h	8	20	−7	5.58	5.62
		10	−5	4.95	5.10
		5	−3	4.16	4.42
After air exposure for 4 months	8	20	−7	5.31	5.35
		10	−5	4.78	4.77
		5	−3	4.09	4.07
After bending test for 30 min (tensile stress)	8	20	−7	5.33	5.39
		10	−5	4.78	4.82
		5	−3	4.09	4.11

Acknowledgements

This material is based upon work supported in part by Solvay S.A., by the Office of Naval Research through Contract Award Number N00014-04-1-0120 and by the STC Program of the National Science Foundation under Agreement Number DMR-0120967.

References

[1] L.S. Zhou, A. Wanga, S.C. Wu, J. Sun, S. Park, T.N. Jackson, All-organic active matrix flexible display, Appl. Phys. Lett. 88 (2006) 083502.
[2] T. Sekitani, T. Someya, Stretchable, large-area organic electronics, Adv. Mater. 22 (2010) 2228.
[3] G. Gelinck, P. Heremans, K. Nomoto, T.D. Anthopoulos, Organic transistors in optical displays and microelectronic applications, Adv. Mater. 22 (2010) 3778.
[4] T. Sekitani, H. Nakajima, H. Maeda, T. Fukushima, T. Aida, K. Hata, T. Someya, Stretchable active-matrix organic light-emitting diode display using printable elastic conductors, Nat. Mater. 8 (2009) 494.
[5] H. Klauk, U. Zschieschang, J. Pflaum, M. Halik, Ultralow-power organic complementary circuits, Nature 445 (2007) 745.
[6] X.H. Zhang, W.J. Potscavage, S. Choi, B. Kippelen, Low-voltage flexible organic complementary inverters with high noise margin and high dc gain, Appl. Phys. Lett. 94 (2009) 043312.
[7] T. Someya, A. Dodabalapur, J. Huang, K.C. See, H.E. Katz, Chemical and physical sensing by organic field-effect transistors and related devices, Adv. Mater. 22 (2010) 3799.
[8] T. Sekitani, T. Yokota, U. Zschieschang, H. Klauk, S. Bauer, K. Takeuchi, M. Takamiya, T. Sakurai, T. Someya, Organic nonvolatile memory transistors for flexible sensor arrays, Science 326 (2009) 1516.

[9] H. Sirringhaus, Reliability of organic field-effect transistors, Adv. Mater. 21 (2009) 3859.
[10] D.K. Hwang, K. Lee, J.H. Kim, S. Im, J.H. Park, E. Kim, Comparative studies on the stability of polymer versus SiO_2 gate dielectrics for pentacene thin-film transistors, Appl. Phys. Lett. 89 (2006) 093507.
[11] D.K. Hwang, M.S. Oh, J.M. Hwang, J.H. Kim, S. Im, Hysteresis mechanisms of pentacene thin-film transistors with polymer/oxide bilayer gate dielectrics, Appl. Phys. Lett. 92 (2008) 013304.
[12] X.H. Zhang, S.P. Tiwari, B. Kippelen, Pentacene organic field-effect transistors with polymeric dielectric interfaces: performance and stability, Org. Electron. 10 (2009) 1133.
[13] S.H. Kim, S. Nam, J. Jang, K. Hong, C. Yang, D.S. Chung, C.E. Park, W.S. Choi, Effect of the hydrophobicity and thickness of polymer gate dielectrics on the hysteresis behavior of pentacene-based field-effect transistors, J. Appl. Phys. 105 (2009) 104509.
[14] S.J. Mun, K. Lee, K.H. Lee, M.S. Oh, S. Im, Organic inverter using two transistors with different channel thicknesses, Org. Electron. 11 (2010) 169.
[15] K.H. Lee, K. Lee, M.S. Oh, J.M. Choi, S. Im, S. Jang, E. Kim, Flexible high mobility pentacene transistor with high-*k*/low-*k* double polymer dielectric layer operating at −5 V, Org. Electron. 10 (2009) 194.
[16] K. Lee, G. Ko, G.H. Lee, G.B. Han, M.M. Sung, T.W. Ha, J.H. Kim, S. Im, Density of trap states measured by photon probe into ZnO based thin-film transistors, Appl. Phys. Lett. 97 (2010) 082110.
[17] D.K. Hwang, C. Fuentes-Hernandez, J. Kim, W.J. Potscavage, S.-J. Kim, B. Kippelen, Top-gate organic field-effect transistors with high environmental and operational stability, Adv. Mater. 23 (2011) 1293.
[18] J.B. Kim, C. Fuentes-Hernandez, W.J. Potscavage, X.H. Zhang, B. Kippelen, Low-voltage InGaZnO thin-film transistors with Al_2O_3 gate insulator grown by atomic layer deposition, Appl. Phys. Lett. 94 (2009) 142107.
[19] J.B. Kim, C. Fuentes-Hernandez, S.J. Kim, S. Choi, B. Kippelen, Flexible hybrid complementary inverters with high gain and balanced noise margins using pentacene and amorphous InGaZnO thin-film transistors, Org. Electron. 11 (2010) 1074.

molecules in order to maintain a high E_T results in a reduction of the carrier transporting properties [6]. Particularly, most of the host materials with high E_T, i.e. carbazole-containing compounds or aromatic phosphine oxides, are unipolar in nature. As charge balance plays an important role in determining the device efficiency, this ultimately limits the device efficiency and leads to a detrimental efficiency roll-off at high current densities owing to triplet–triplet annihilation [10].

Until very recently, Lee et al. reported an effective approach to increase the charge transporting property in EML [11,12]. Through the incorporation of hole-transporting host material into the electron-transporting EML to form a mixed triplet host system, the EQE of blue PHOLEDs can be dramatically increased up to 20.5%, doubling that of single host device (8.96%) [12]. The enhanced EQE is mainly due to the improvement on charge carrier transport balance as well as a broader recombination zone within the EML. This finding opens up the possibility to further improve the performance of PHOLEDs where the doping approach might be applicable for other commonly used host materials.

In this letter, we present the utilization of mixed triplet host systems to improve device performance and reduce the power consumption of blue PHOLEDs; particularly, either an electron-transporting or a hole-transporting triplet host material was intentionally doped into the commonly used *N*,*N*′-dicarbazolyl-3,5-benzene (mCP) host to form mixed triplet host system. We found that the device efficiency is very sensitive to the energy levels and the relative composition of the host materials in the EML, in which a superior device performance with high current and power efficiencies of 47.4 cd/A and 37.3 lm/W, respectively, can be obtained for an optimized device. Particularly, device efficiencies are strongly dependent on the choice of triplet host materials, as suggested by time-resolved phosphorescence decay studies for different mixed host thin films.

2. Experimental

Patterned indium-tin-oxide (ITO)-coated glass substrates (30 Ω/square) were cleaned with Decon 90, rinsed in deionized water, then dried in an oven, and finally treated in an ultraviolet-ozone chamber. PHOLEDs were fabricated with a hole-transporting α-naphthylphenylbiphenyl diamine (NPB) layer, a carrier confinement 4,4′,4″-tris(*N*-carbazolyl)triphenylamine (TCTA) layer, and an electron-transporting bis(2-methyl-8-quinolinato)-4-phenylphenolate aluminum(III) (BAlq) layer. Devices with the configuration of ITO/NPB (70 nm)/TCTA (5 nm) (30 nm)/EML (30 nm)/BAlq (30 nm)/LiF (0.8 nm)/Al (200 nm) were fabricated, in which either TCTA or 3-(4-biphenyl)-4-phenyl-5-(4-*tert*-butylphenyl)-1,2,4-triazole (TAZ) was doped into mCP to form mixed host system as EML. Six percent of bis [2-(4′,6′-difluorophenyl)pyridinato-*N*,$C^{2'}$]iridium(III) (FIrpic) was doped into EML as phosphorescent guest. In particular, TCTA and TAZ are well-known hole-transporting and electron-transporting materials, respectively; while mCP is hole-transporting triplet host material. For comparison, a standard device with 6% FIrpic:mCP as EML was also made as reference. Fig. 1 shows the proposed energy level diagram for the devices, in which HOMO, LUMO levels, and E_T of the organic materials are taken from the literature [1,13,14]. All organic materials were used as purchased and the films are sequentially deposited by thermal evaporation in high vacuum chamber without vacuum break. A shadow mask was used to define the cathode and to make four 0.1 cm^2 devices on each substrate. The deposition rates were controlled by a quartz oscillating thickness monitor to be 1–2 Å/s for the organic materials and metals. The current density–voltage–luminance (*J*–*V*–*L*) characteristics and electroluminescence (EL) spectra were measured simultaneously with a programmable Keithley model 2420 power source and a Photoresearch PR655 colorimeter. All measurements were carried out in air at room temperature.

Time-resolved photoluminescence decay measurements were performed using a conventional laser system. The excitation source used was a 355-nm output (third harmonic) of a Spectra-Physics Quanta-Ray Q-switched GCR-150-10 pulsed Nd-YAG laser. Luminescence decay signals were detected by a Hamamatsu R928 PMT and recorded on a Tektronix Model TDS-620A (500 MHz, 2 GS/s) digital oscilloscope and analyzed using a program for exponential fits.

3. Results and discussion

Fig. 2(a) depicts the EL spectra for devices doped with various TAZ concentrations to form mixed hosts. Apparently, for the reference device (i.e. 0% TAZ), it exhibits a characteristic FIrpic emission peaking at 472 and 496 nm in the absence of any undesirable emission from adjacent hole- or electron-transporting layers. This confirms that

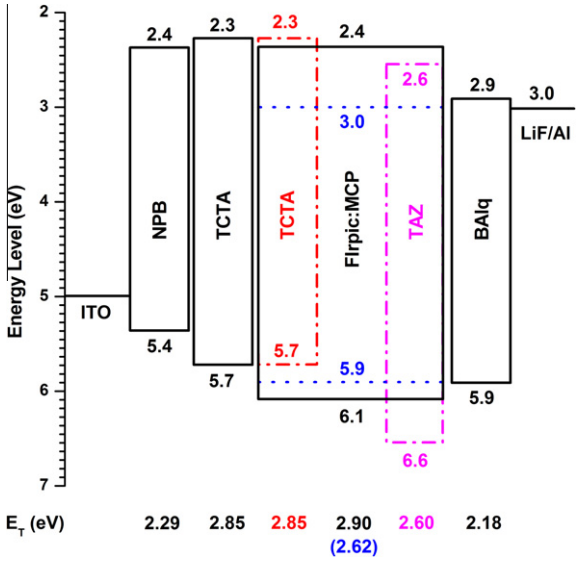

Fig. 1. Proposed energy level diagram for the devices. Note that numbers indicate the respective HOMO and LUMO energies relative to the vacuum as well as the E_T in eV. HOMO and LUMO energies of FIrpic are also indicated with dotted lines; while E_T of FIrpic is shown in parentheses.

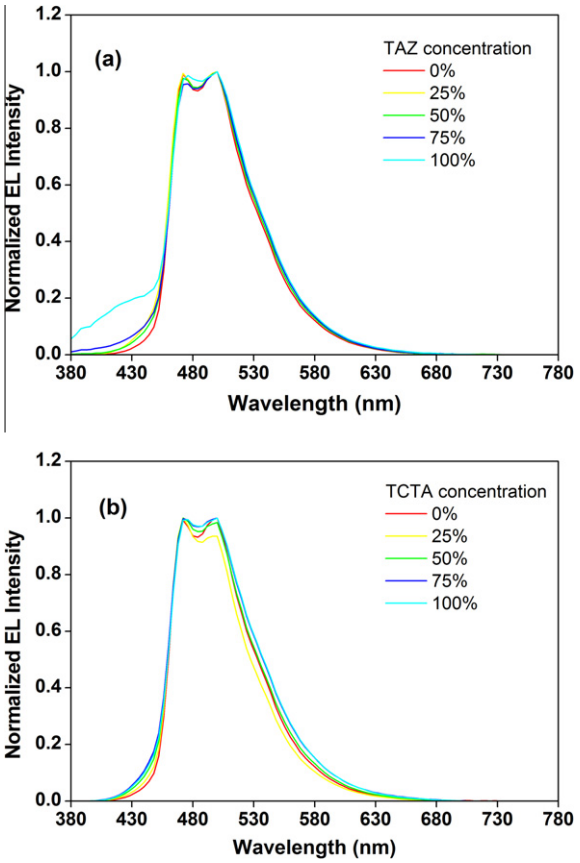

Fig. 2. EL spectra for devices doped with various concentrations of (a) TAZ and (b) TCTA to form mixed hosts.

efficient energy transfer between mCP and FIrpic takes place due to effective confinements of both charge carriers and triplet excitons. On the other hand, as TAZ concentration increases up to 100%, a new EL peak at ~400 nm is also noticed, which is tentatively assigned to the fluorescence of the carrier confinement layer of TCTA. This observation suggests that a portion of excitons may be formed within the TCTA charge confinement layer, perhaps due to the mismatch of HOMO levels between TCTA and TAZ. As shown in Fig. 1, we infer a large hole injection barrier at TCTA/TAZ interface of 0.9 eV, much larger than that at the TCTA/mCP contact (0.4 eV), impeding hole injection from TCTA into the EML. Thus, holes are expected to be accumulated at the TCTA/TAZ interface, leading to the formation of excitons within TCTA layer. On the other hand, it is not the case for the TCTA-doped devices (see Fig. 2(b)).

Fig. 3 shows the *J–V–L* characteristics and efficiencies of the TAZ-doped devices with different TAZ concentrations. With increasing TAZ concentration, both *J–V* and *L–V* curves shift to a higher driving voltage. For instance, to generate a luminance of 1000 cd/m^2, the driving voltage increases from 7.1 V (for 0% TAZ device) to 13.0 V (for 100% TAZ device). In addition, the incorporation of TAZ would result in poor device performance with device efficiencies dropped by an order of magnitude. For the reference device, high current, power efficiencies, and EQE of 21.9 cd/A, 14.8 lm/W, and 9.7%, respectively, can be obtained at current density of 0.1 mA/cm^2, which are in good agreement with other previous studies for the 6% FIrpic-doped mCP devices [1,6,15]. As TAZ concentration increases, the efficiencies drop sharply to 3.2 cd/A, 1.8 lm/W, and 1.4% for 100% TAZ-doped device. The poor performance can be explained in terms of the mismatch of both

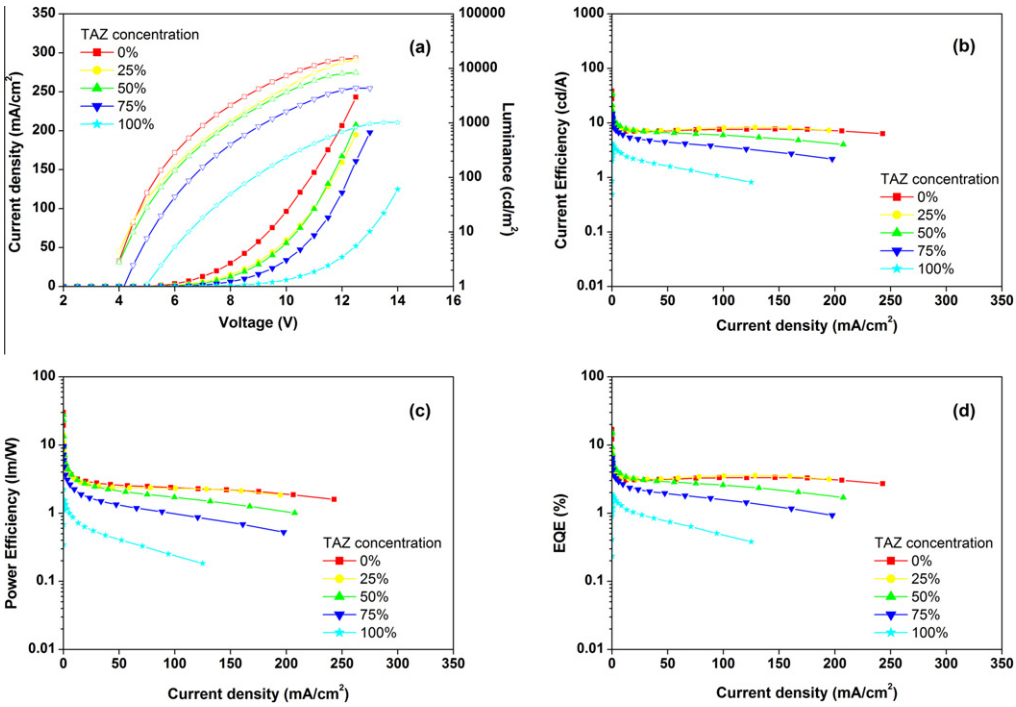

Fig. 3. *J–V–L* characteristics and efficiencies of the TAZ-doped devices with different TAZ concentrations.

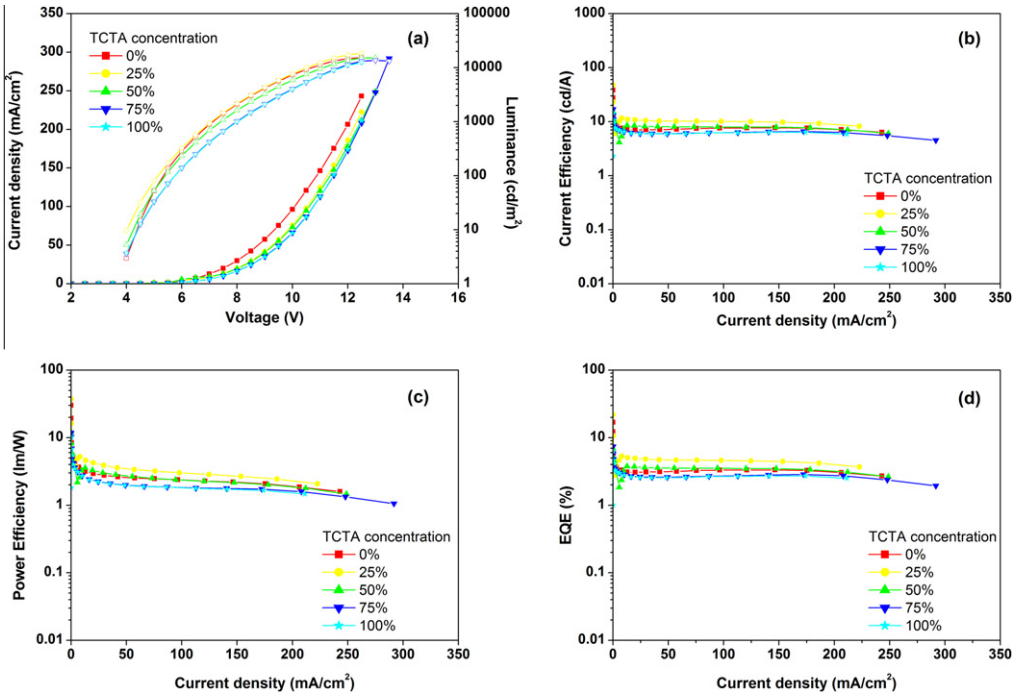

Fig. 4. *J–V–L* characteristics and efficiencies of the TCTA-doped devices with different TCTA concentrations.

Table 1
Characteristics of the TAZ-doped and TCTA-doped devices. η_c, η_P, η_{EQE} are the maximum current, power, and external quantum efficiencies.

	η_L (cd/A)	η_P (lm/W)	η_{EQE} (%)
TAZ concentration (%)			
0	32.2	24.1	14.2
25	19.4	15.0	8.4
50	34.4	24.1	14.2
75	13.9	9.8	6.5
100	4.3	2.3	2.0
TCTA concentration (%)			
0	32.2	24.1	14.2
25	47.4	37.3	21.9
50	15.4	12.1	6.9
75	16.9	11.8	7.4
100	14.6	10.2	6.3

HOMO levels and E_T of TAZ and mCP. As aforementioned, the relatively large HOMO level of TAZ restricts the hole injection into the EML, leading to a higher driving voltage and a lower EL efficiency. Meanwhile, the endothermic energy transfer from the excited state of the TAZ host to the phosphor FIrpic with higher E_T of 2.62 eV results in a further reduction in device efficiency. Similar to the case of FIrpic:CBP system [15,16], the relatively low E_T of TAZ (2.60 eV) will provide a non-radiative path for exciton quenching and thus reduces the phosphorescent light emission from FIrpic. Particularly, a pronounced efficiency roll-off is observed for all the TAZ-doped devices. Notably, the EQE for 25% TAZ-doped device dramatically drops from 6.1% at a current density of 0.1 mA/cm^2 to 3.1% at current density of 200 mA/cm^2. This detrimental efficiency roll-off is indicative of the sensitivity of backward energy transfer to the presence of energy dissipative pathways via triplet–triplet annihilation (see discussion below).

On the contrary, it is not the case for the TCTA-doped devices. Fig. 4 depicts the *J–V–L* characteristics and efficiencies of the TCTA-doped devices with different TCTA concentrations. As TCTA concentration increases, both *J–V* and *L–V* curves slightly shift to a higher driving voltage. For example, the driving voltage for generating a luminance of 1000 cd/m^2 slightly increases from 7.1 V (for 0% TCTA) to 8.1 V (for 100% TCTA). Meanwhile, both current and power efficiencies increase with increasing TCTA concentrations. At an optimal TCTA concentration of 25%, the device achieves excellent performance with current efficiency of 26.2 cd/A and power efficiency of 18.5 lm/W at a current density of 0.1 mA/cm^2, about 25% higher than those of the reference device. It is worth noting that, at a current density of 0.02 mA/cm^2, peak current and power efficiencies of 47.4 cd/A and 37.3 lm/W can be obtained. This corresponds to an extremely high EQE of 21.9%, reaching the theoretical limit of phosphorescent OLEDs. Table 1 summarizes the characteristics of the TAZ-doped and the TCTA-doped devices. The reason for the performance improvement may be attributed to a relatively lower hole mobility in TCTA. In particular, under an electric field of 6.4×10^3 V/cm, hole mobility in TCTA is $\sim 4.0 \times 10^{-4}$ cm^2 V^{-1} s^{-1} [17]; while that in mCP is $\sim 9.0 \times 10^{-4}$ cm^2 V^{-1} s^{-1} [18]. The doping of TCTA with a relatively lower hole mobility would definitely decrease the hole transporting ability in EML, leading to a better carrier balance and thus an improved device efficiency. On the other hand, with a further increase in the TCTA concentrations, the device efficiencies are found to show a slight drop due to an inefficient Förster energy transfer. In order to

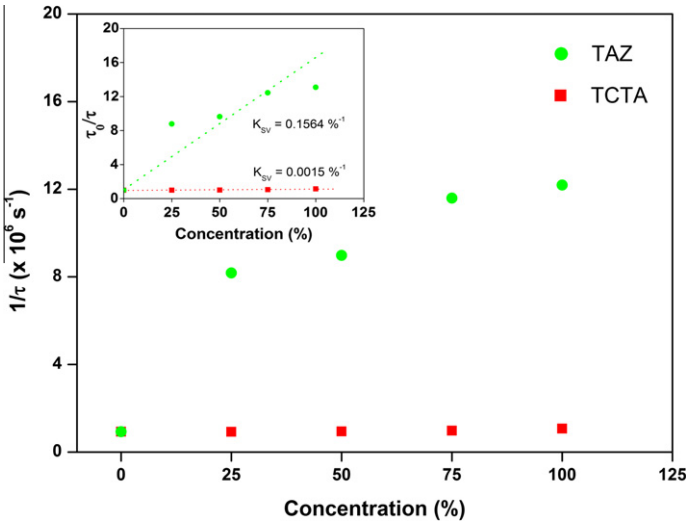

Fig. 5. A plot of the reciprocal of the lifetimes of FIrpic obtained as a function of TAZ or TCTA concentration. Inset: the Stern–Volmer plot of the TAZ- and TCTA-doped FIrpic:mCP films.

achieve 100% internal quantum efficiency, harvesting of both singlet and triplet excitons are important. Taking into the account the fact that the HOMO level of FIrpic is 0.2 eV lower-lying than that of TCTA, the mismatching of spectral overlap between the absorption spectrum of the FIrpic and the fluorescence spectrum of TCTA would definitely inhibit the energy transfer from singlet excitons of TCTA to those of FIrpic via long-range Förster transfer, reducing the EL efficiency. Nevertheless, the present results suggest that, in addition to the well-known effect of charge balance within the EML, both energy levels and E_T of mixed host materials play crucial roles in determining the device performance of PHOLEDs.

In order to confirm the mechanism for energy loss, time-resolved photoluminescence decay properties were measured by means of a direct excitation of thermally evaporated thin films, in which either TAZ or TCTA was doped into 6% FIrpic:mCP layer to form mixed host systems. Fig. 5 plots the reciprocal of the phosphorescence lifetimes (τ) of FIrpic obtained as a function of TAZ or TCTA concentration. For the reference film (i.e. 100% mCP), the phosphorescence decay of FIrpic consists of a single component with a time constant of ~1.06 μs, consistent with other previous studies (~1 μs at room temperature in neat film) [15,16,19]. No longer-lived phosphorescence was observed, which indicates that the triplet excitons are efficiently trapped within FIrpic. As TCTA concentration increases, the phosphorescent behavior of FIrpic is almost identical to that in mCP host. On the other hand, the lifetime is found to decrease steadily with increasing concentration of TAZ. It is interesting to note that the phosphorescence lifetime of FIrpic obeys the Stern–Volmer quenching equation, i.e. $\tau_0/\tau = 1 + K_{SV}[Q]$, where τ_0 is the lifetime of FIrpic in the absence of either TAZ or TCTA, K_{SV} is the Stern–Volmer constant, and Q is the concentration of TAZ or TCTA. As shown in the inset of Fig. 5, the Stern–Volmer constants of the TCTA- and TAZ-doped films derived from the slope of linear fits are estimated to be $0.0015\%^{-1}$ and $0.1564\%^{-1}$ (corresponding to the quenching constants of $\sim 1415\%^{-1}\,s^{-1}$ and $\sim 147{,}545\%^{-1}\,s^{-1}$). The higher K_{SV} for the TAZ-doped films confirms that the FIrpic blue dopant is quenched by the presence of TAZ [20]. Both shorter lifetime and higher K_{SV} values are further indications of endothermic energy transfer from TAZ to FIrpic and the presence of significant dissipative non-radiative transitions. As the phosphorescence efficiency is approximately proportional to the lifetime of triplet excitons [21,22], the shorter lifetime in TAZ is consistent with the lower EL efficiencies of the TAZ-doped devices.

4. Conclusion

In conclusion, the influences of different host materials on the performance of FIrpic-based blue phosphorescent OLEDs have been systematically studied. In addition to the well-known effect of charge balance, both energy levels and E_T of mixed host materials play crucial roles in determining the device performance. Particularly, a theoretical limit on EQE of 21.9% can be achieved by using hole-transporting TCTA to form mixed host. It is found that the lifetime of FIrpic is strongly dependent on the composition of triplet host materials, in which a shorter lifetime with a higher K_{SV} of $0.1564\%^{-1}$ (corresponding to the quenching constant of $\sim 147{,}545\%^{-1}\,s^{-1}$) is observed for all the FIrpic:TAZ systems. This observation clearly explains the poor performance of all TAZ-doped devices.

Acknowledgments

The work described in this paper was fully supported by a grant from the Research Grants Council of the Hong Kong Special Administrative Region, China (Project No. HKU 700409P). Infrastructural and facility support from the Strategic Research Theme on Molecular Materials, the University Development Fund of The University of Hong Kong,

and the UGC Areas of Excellence Scheme (AoE/P-03/08), are also gratefully acknowledged. D.P.K. Tsang acknowledges the receipt of a postgraduate studentship and A.Y.Y. Tam a University Postdoctoral Fellowship, both from The University of Hong Kong.

References

[1] J. Lee, N. Chopra, S.H. Eom, Y. Zheng, J. Xue, F. So, J. Shi, Appl. Phys. Lett. 93 (2008) 123306.
[2] S.H. Eom, Y. Zheng, N. Chopra, J. Lee, F. So, J. Xue, Appl. Phys. Lett. 93 (2008) 133309.
[3] C. Adachi, M.A. Baldo, M.E. Thompson, S.R. Forrest, J. Appl. Phys. 90 (2001) 5048.
[4] R.J. Holmes, B.W. D'Andrade, S.R. Forrest, X. Ren, J. Li, M.E. Thompson, Appl. Phys. Lett. 83 (2003) 3818.
[5] N. Seidler, S. Reineke, K. Walzer, B. Lüssem, A. Tomkeviciene, J.V. Grazulevicius, K. Leo, Appl. Phys. Lett. 96 (2010) 093304.
[6] F.M. Hsu, C.H. Chien, C.F. Shu, C.H. Lai, C.C. Hsieh, K.W. Wang, P.T. Chou, Adv. Funct. Mater. 19 (2009) 2834.
[7] Y. Tao, Q. Wang, L. Ao, C. Zhong, J. Qin, C. Yang, D. Ma, J. Mater. Chem. 20 (2010) 1759.
[8] Y. Tao, Q. Wang, C. Yang, J. Qin, D. Ma, Appl. Mater. Interfaces 2 (2010) 2813.
[9] M.T. Chu, M.T. Lee, C.H. Chen, M.R. Tseng, Org. Electron. 10 (2009) 1158.
[10] M.A. Baldo, C. Adachi, S.R. Forrest, Phys. Rev. B 62 (2000) 10967.
[11] S.H. Kim, J. Jang, K.S. Yook, J.Y. Lee, M.S. Gong, S. Ryu, G.K. Chang, H.J. Chang, J. Appl. Phys. 103 (2008) 054502.
[12] J. Lee, J.I. Lee, J.Y. Lee, H.Y. Chu, Appl. Phys. Lett. (2009) 253304.
[13] S.H. Kim, J. Jang, J.Y. Lee, Appl. Phys. Lett. 90 (2007) 223505.
[14] Y. Kawamura, K. Goushi, J. Brooks, J.J. Brown, H. Sasabe, C. Adachi, Appl. Phys. Lett. 86 (2005) 071104.
[15] R.J. Holmes, S.R. Forrest, Y.J. Tung, R.C. Kwong, J.J. Brown, S. Garon, M.E. Thompson, Appl. Phys. Lett. 82 (2003) 2422.
[16] S. Tokito, T. Iijima, Y. Suzuri, H. Kita, T. Tsuzuki, F. Sato, Appl. Phys. Lett. 83 (2003) 569.
[17] S. Noh, C.K. Suman, Y. Hong, C. Lee, J. Appl. Phys. 105 (2009) 033709.
[18] T. Tsuboi, S.W. Liu, M.F. Wu, C.T. Chen, Org. Electron. 10 (2009) 1372.
[19] C. Adachi, R.C. Kwong, P. Djurovich, V. Adamovich, M.A. Baldo, M.E. Thompson, S.R. Forrest, Appl. Phys. Lett. 79 (2001) 2082.
[20] M. Sudhakar, P.I. Durovich, T.E. Hogen-Esch, M.E. Thompson, J. Am. Chem. Soc. 125 (2003) 7796.
[21] J. Sun, Z. Zhu, X. Yu, M. Wong, H.S. Kwok, SID 07 Digest, p. 168.
[22] C. Adachi, M.A. Baldo, S.R. Forrest, M.E. Thompson, Appl. Phys. Lett. 77 (2000) 904.

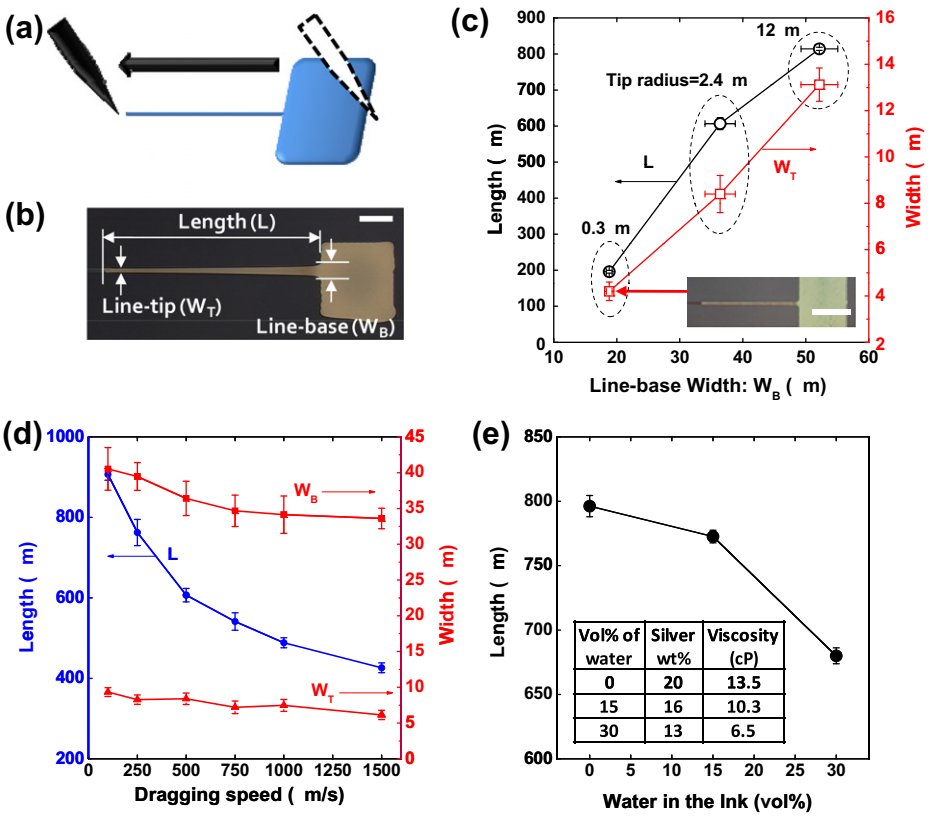

Fig. 1. (a) Schematic diagram showing the PND process flow. (b) A typical dragged line with length, line-tip and line-base defined. (c) Length and line-tip width as a function of line-base width. Three data sets correspond to three probe tip radius respectively. Inset: the dragged line with a 5 μm linewidth. The dragging speed is 1000 μm/s. (d) Dragged length and line-tip and line-base width as a function of dragging speed. (e) Dragged length as a function of water vol.% in the ink. The ink concentration and the corresponding viscosity are listed in the inset table. All the scale bars represent 100 μm.

surface tension. While there have been demonstrations of femtoliter and attoliter inkjet heads using electrohydrodynamic techniques, scaling of the complex patterns necessary to realize circuits has remained elusive due to the difficulty in controlling the landing and positioning of such small drops [7,8]. Thus, to achieve highly scaled and high performance printed transistors using a low-cost approach has remained tremendously challenging. Therefore, in this work, we have demonstrated a novel hybrid-printing technique to realize printed features as narrow as 5 μm using a state-of-the-art printer. Using this technique, we have demonstrated all printed highly scaled transistors and inverters. Due to the substantially reduced capacitance and reduced linewidth, the fully printed inverter has a propagation delay as low as 15 μs, in contrast to the typical value of ~0.01 s obtained by previously reported all-printed processes [9–11]. We thus demonstrate orders of magnitude improvement in performance relative to other reported fully printed circuits.

2. PND technique

The novel hybrid-printing technique used in this work was inspired by dip-pen nanolithography, in which molecules are delivered from an atomic force microscope tip to a solid substrate of interest via capillary transport [12]. Here, we implemented the technique in a low-cost manner by merging a multi-nozzle inkjet head with a mechanical probe system to provide both the high throughput of inkjet and the feature scalability of a mechanical pen. The process consists of two steps – print-and-drag (PND) as illustrated in Fig. 1a. First, large pads and other large features were printed on a conventional Dimatix DMP-2800 inkjet printer equipped with a 10 pL piezoelectric head, using silver nanoparticle ink (Suntronic U5603). The silver ink solvent evaporated slowly and thus allowed the pads to act as ink reservoirs for the subsequent process. Next, a micron-scale mechanically controlled tungsten probe was used as a pen to drag through the pad to create a highly scaled feature. Note that the ink flow is facilitated by the meniscus formed between the tip and the pad; therefore actual contact of the probe tip to the surface is not necessary. Thus the PND technique is also expected to be applicable to surfaces such as soft plastic substrates. The technique combines high-throughput low resolution printing (via inkjet) with high-resolution critical feature patterning (via pen printing), and since the pen can address multi-nozzle inkjetted patterns, high throughput is achievable. The printed lines become conductive with a resistance of ~100 Ω for a 195 μm long line with a cross-section of 9 μm by 73 nm after a 150 °C and 20 min sintering.

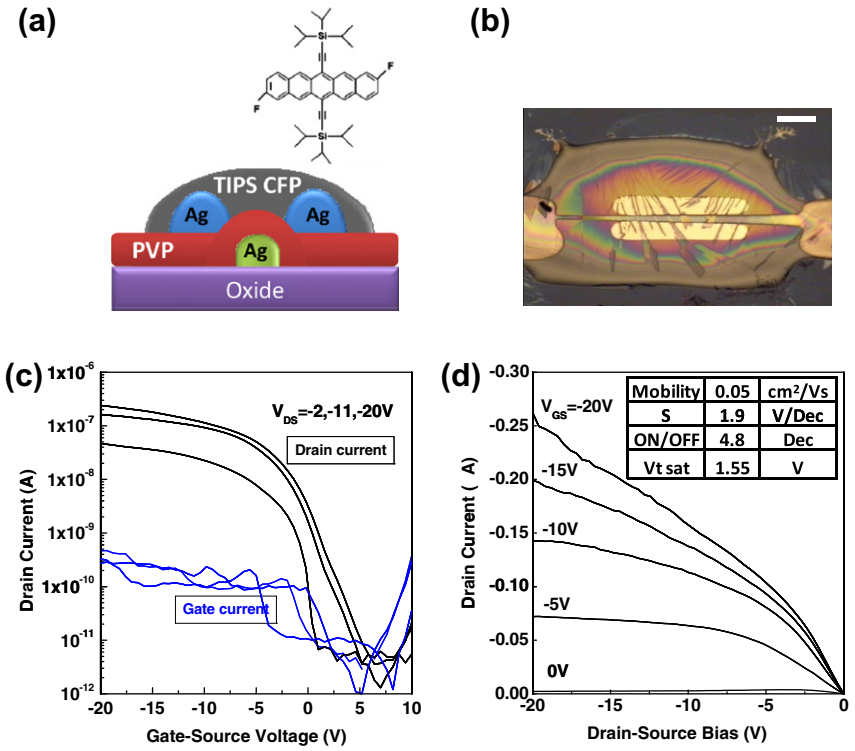

Fig. 2. (a) Cross-sectional view of a fully printed transistor. Chemical structure of TIPS CFP is also shown. The transistors and inverters were fabricated on 1 μm oxide wafers. (b) The optical micrograph of the fully printed transistor. The scale bar represents 100 μm. (c) Transfer characteristics with the gate current. (d) Output characteristics of the transistor. The channel length of the transistor is 14 μm.

Fig. 1b shows the optical micrograph of a typical dragged line. The length (L), line-tip width (W_T) and line-base width (W_B) defined in Fig. 1b were measured using an optical microscope, and the average and standard deviation from 20 measured lines were used for the following discussions. It is noted that W_B was measured right at the junction of the line and the pad. The line geometry as a function of dragging speed, probe tip radius and ink concentration was then studied. Since the PND performed in this work involved a direct physical contact, the printed lines are expected to strongly correlate with the probing method and the probe tip radius. The probe tip was probed on the surface with a constant tilt angle and probing depth by controlling a vertical stepping motor with one micron resolution. In our initial system used here, feedback control was not implemented into the system to adjust the probing depth and angle in a real-time basis; hence W_B was checked afterward to confirm the consistency of the probing because W_B is expected to be directly proportional to the probing depth and angle. Probe tips with three different point radii were used in the study (see Section 5.1). Fig. 1c shows the L and W_T as a function of W_B and the corresponding probe tip radius at a fixed dragging speed of 1000 μm/s. It is clear that the linewidth can be scaled down by using a smaller tip radius. Dragged lines as narrow as 5 μm can be consistently formed using a probe tip of 0.3 μm radius as shown in the inset of Fig. 1c.

The dragging speed was controlled by setting up the probe tip on a stage with programmable moving velocity. As shown in Fig. 1d, increasing dragging speed reduces the length of the feature, as well as both W_B and W_L (Fig. 1d). From the previous discussion, the reduction of W_B indicated a change in the probing depth and angle. However, those changes were not clearly observed under a microscope with a 45× magnification. Therefore it is possible that when dragging at a higher speed, the ink from the pads does not have sufficient time to form the meniscus on the tip, resulting in a relatively smaller amount of ink being transferred and thus a smaller L, W_B and W_L. Note the fact that line-base being wider and thicker than the line-tip is not ideal for gate electrode applications. Fortunately, the difference in thickness should not affect the insulator thickness atop if a conformal layer such as PVP is used. The difference in linewidth, however, could result in a non-uniform channel length if a self-aligned S/D is applied [6]. This can be mitigated by producing a longer line, where the transition from W_B to W_T takes place over a longer distance, resulting in a more uniform linewidth. Moreover, the gate lines can be dragged from two ink pads and merged in the middle. Using this method, the PND lines become more uniform and symmetric in the middle for gate electrode applications.

The ink concentration also affects the dragged line feature. The ink concentration was diluted by adding water to the aqueous silver ink, which is a common method to adjust the viscosity of this ink. Three different concentrations and the corresponding viscosities were then obtained as listed in the inset table of Fig. 1e. Square pads were printed

with three different inks and the lines were then produced using the PND technique. The dragging speed was fixed at 500 μm/s and the probing conditions were kept constant. The W_B and W_T were then verified to be independent of ink concentration, indicating the probing condition was consistent. Higher ink concentration results in longer dragged lines as shown in Fig. 1e. Note that the measured viscosities do not account for changes in ink concentration occurring prior to and during the PND process due to evaporation. More studies on the feature formation will be done in the future to completely understand the PND process. It is important to note that no limitation on further scaling of linewidth using this technique has been observed to date; further scaling should be possible by using a smaller probe tip.

3. Fully printed transistors and inverters

Fully printed, highly-scaled, p-type bottom-gate bottom-contact transistors were then demonstrated using the PND gate electrodes. The printing process flow (See Section 5.2) is similar to our previous work [13] except that the downscaled gate lines are now produced by the PND technique. Poly(4-vinylphenol) (PVP) was printed as the insulator and the silver S/D were then printed to align the gate. The S/D electrodes were then treated with PFBT (pentafluorobenzenethiol) to form good contacts with the semiconductor; TIPS CFP (triisoprophylsilylethynyl catafluoro-pentacene) with two Fluorine atoms added in the regular TIPS molecule to improve its chemical interaction with PFBT was used in this work [14]. The semiconductor was inkjet printed using an ink consisting of TIPS CFP dissolved in a cosolvent of dichlorobenzene:dodecane (3:1 vol. ratio) to cover the S/D. The cosolvent has been reported to suppress the coffee ring effect and thus allow the deposition of a more uniform film [15]. The printing of TIPS CFP was done at a substrate temperature of 60 °C to facilitate drop pinning and the simultaneous crystallization. The cross-sectional structure of a single printed transistor is shown in Fig. 2a and the optical micrograph of the transistor is shown in Fig. 2b. The transistor shown has a mobility of 0.05 $cm^2 V^{-1} s^{-1}$ and an on/off ratio of almost 10^5 as outlined in the inset table of Fig. 2d (see Supplementary information Fig. S1 for statistical data). The mobility obtained in this work is similar to previous work using TIPS CFP [14]. This indicates that TIPS CFP also forms good contacts with PFBT treated silver electrodes. The on/off ratio is not as high as devices fabricated using thermal oxide gate insulators due to increased gate leakage current through the printed PVP film; however, in general, the obtained electrical characteristics are consistent with other reported results using PVP. The threshold voltage of 1.55 V and the average sub-threshold swing of 1.1 V/Dec are also similar to previous work using a full solution process [16], indicating the combination of TIPS-based pentacene and PVP can yield a good channel interface. The channel length and width are 14 μm and 243 μm respectively. Note that the channel width was measured from the effective coverage of the printed TIPS CFP on the channel. Fig. 2c and d shows the transfer and output characteristics of the printed transistor, attesting to the well-behaved nature of this highly-scaled device produced by the novel PND technique.

Fully printed inverters consisting of one drive transistor and one diode-connected load transistor were then demonstrated. The gate electrodes were produced by the PND technique with a dragging speed of 100 μm/s. PVP (Poly-4-vinylphenol) dielectric was printed to cover both gate lines and cross-linked as the insulator. Dewetting of the printed PVP film was observed between the PND electrodes as shown in Fig. 3a, due to some point defects on the oxide surface and the preferential wetting of PVP on

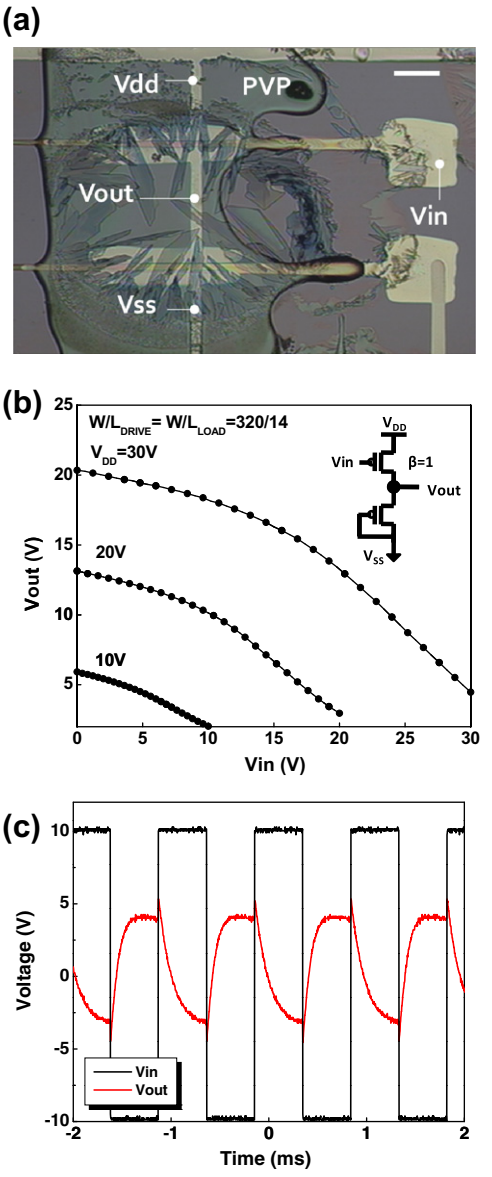

Fig. 3. (a) Optical micrograph of a fully printed inverter. TIPS CFP was printed in the form of a big drop to cover both transistor channels. The scale bar represents 100 μm. (b) Voltage transfer characteristics of the printed inverter. Inset shows the equivalent circuit of the inverter. (c) Transient characteristics of the printed inverter showing a 1 kHz and 20 V_{P-P} square wave input. The inverted output waveform was measured at a fan-out of 6.

silver lines. Nevertheless, the overall printed PVP film is smooth and conformal (See Supplementary information Fig. S2 for measured profile of the PVP). The S/D electrode and the interconnection were then printed to align to the gate, followed by a sintering step. The S/D was then treated with PFBT to form a good contact to TIPS CFP. Finally, TIPS CFP was inkjet printed with the drop size controlled to cover the two transistors. As shown in Fig. 3a, higher evaporation at the drop edge causes the TIPS CFP to crystallize from the perimeter towards the center, resulting in symmetric coverage of both transistors. The printed TIPS film showed a large crystallize size, which is beneficial for obtaining high mobility, but also resulted in device-to-device variation. Fortunately, the uniformity can be improved in the future by using a polymer-small molecule blend while also maintaining high performance [17]. Fig. 3b shows the voltage transfer characteristics and the equivalent circuit of the inverter with a W_{DRIVE}/W_{LOAD} ratio of one. Fig. 3c shows the transient characteristics of the inverter (See Section 5.3). Due to the extra parasitic capacitance from the bottom silicon wafer, the inverter has a fan-out of six ($C_{OUT}/C_{IN} = 6$). The average propagation delay from Fig. 3c is 90 μs, indicating that the inverter at a fan-out of one will has a propagation delay as low as 15 μs. The propagation delay corresponds to an operation frequency of 66 kHz, which is in good agreement with the calculated value (see Supplementary information Fig. S3 for statistical data and details of the calculations). This high speed operation is achieving despite the relatively low mobility of the semiconductor used here, attesting to the beneficial impact of PND-based scaling. The benefits of the scaling in terms of the speed enhancement are clear across all devices.

4. Conclusions

We have developed and demonstrated a new technique that provides an alternative low-cost solution to create highly-scaled printed features. Using a combination of inkjet printing and mechanical pen dragging, we demonstrate features as small as 5 μm while exploiting the benefits of multi-nozzle inkjet printing. Using this technique, we have successfully demonstrated highly scaled transistors and inverters with sufficient performance for the realization of the low-cost electronics.

5. Experimental

5.1. Probe tips

Probe Tips with three different point radii were used in this study. (1) Cascade PTT-120-25, point radius 12 μm (2) Cascade PTT-24-25, point radius 2.4 μm (3) Micromanipulator model 7s, point radius 0.35 μm, Tungsten tip, Nickel shank.

5.2. Transistor printing process

An N-type silicon wafer with thermally grown oxide of 1 μm was used as underlying mechanical substrate. Silver nanoparticle ink (Suntronic U5603) was used to print the large pads for PND process. The silver pads were then dragged by a tungsten tip with 2.4 μm point radius at 100 μm/s to create a long gate line. The gate electrode was then sintered at 150 °C for 20 min. 7.6 wt.% of Poly(4-vinylphenol) (PVP) dissolved in hexanol with 0.6 vol.% of cross linker poly(melamine-co-formaldehyde) was printed atop the gate and cross-linked at 200 °C for 10 min. Five nozzles were used simultaneously to print the PVP layer with a drop spacing of 30 μm, resulting in a dielectric thickness of 110 nm. Silver ink was then printed to form source and drain electrodes with a drop spacing of 20 μm. This was followed by a sintering step identical to that used for the gate electrode. The S/D electrodes were then treated with PFBT (pentafluorobenzenethiol) to form good contacts with the TIPS CFP (triisoprophylsilylethynyl cata-fluoro-pentacene). PFBT was deposited in an ethanol solution with 10 mM concentration, followed by an ethanol wash step. The transistor was then completed by inkjet printed TIPS CFP dissolved in a cosolvent of dichlorobenzene:dodecane (3:1 vol. ratio) to cover the S/D. All inkjetting was performed using a Dimatix DMP-2800 printer with a jetting frequency of 2 kHz except the TIPS CFP, which was inkjet printed using a custom-built printer with a Microfab nozzle (60 μm orifice).

5.3. Transient behavior of the inverter

To measure the inverter transient output, an Agilent 4156C was used to provide Vdd at 20 V and ground. The input square wave of 1 k Hz was provided by an Interstate Electronics Corporation F34 function generator. The output was buffered by an operational amplifier Burr Brown OPA602BP and the waveform was measured using an Acute DS-1202 Oscilloscope.

Acknowledgments

We gratefully acknowledge Dimatix Fujifilm for printer-related support and the Semiconductor Research Corporation and the World Class University Program at Sunchon National University for funding support.

Appendix A. Supplementary material

Supplementary data associated with this article can be found, in the online version, at doi:10.1016/j.orgel.2011.04.004.

References

[1] T. Sekitani, H. Nakajima, H. Maeda, T. Fukushima, T. Aida, K. Hata, T. Someya, Nature Materials 8 (2009) 494–499.
[2] T. Someya, Y. Kato, T. Sekitani, S. Iba, Y. Noguchi, Y. Murase, H. Kawaguchi, T. Sakurai, Proceedings of the National Academy of Sciences of the United States of America 102 (2005) 12321–12325.
[3] P.F. Baude, D.A. Ender, M.A. Haase, T.W. Kelley, D.V. Muyres, S.D. Theiss, Applied Physics Letters 82 (2003) 3964.
[4] N. Zhao, M. Chiesa, H. Sirringhaus, Y. Li, Y. Wu, B. Ong, Journal of Applied Physics 101 (2007) 064513.
[5] J.Z. Wang, Z.H. Zheng, H.W. Li, W.T.S. Huck, H. Sirringhaus, Nature Materials 3 (2004) 171–176.
[6] Huai-Yuan Tseng, V. Subramanian, Electron Devices Meeting (IEDM), IEEE International, 2009, pp. 15.6.1–15.6.4.
[7] T. Sekitani, Y. Noguchi, U. Zschieschang, H. Klauk, T. Someya, Proceedings of the National Academy of Sciences 105 (2008) 4976–4980.

[8] J. Park, M. Hardy, S.J. Kang, K. Barton, K. Adair, D.K. Mukhopadhyay, C.Y. Lee, M.S. Strano, A.G. Alleyne, J.G. Georgiadis, P.M. Ferreira, J.A. Rogers, Nature Materials 6 (2007) 782–789.
[9] A. Knobloch, A. Manuelli, A. Bernds, W. Clemens, Journal of Applied Physics 96 (2004) 2286.
[10] A. Huebler, F. Doetz, H. Kempa, H. Katz, M. Bartzsch, N. Brandt, I. Hennig, U. Fuegmann, S. Vaidyanathan, J. Granstrom, S. Liu, A. Sydorenko, T. Zillger, G. Schmidt, K. Preissler, E. Reichmanis, P. Eckerle, F. Richter, T. Fischer, U. Hahn, Organic Electronics 8 (2007) 480–486.
[11] M. Hambsch, K. Reuter, M. Stanel, G. Schmidt, H. Kempa, U. Fügmann, U. Hahn, A. Hübler, Materials Science and Engineering: B 170 (2010) 93–98.
[12] R.D. Piner, J. Zhu, F. Xu, S. Hong, C.A. Mirkin, Science 283 (1999) 661–663.
[13] H. Tseng, V. Subramanian, Organic Electronics 12 (2011) 249–256.
[14] O.D. Jurchescu, M. Feric, B. Hamadani, D. Mourey, S. Subramanian, B. Purushothaman, J. Anthony, T. Jackson, D. Gundlach, in:, ECS Transactions, Honolulu, HI, 2008, pp. 283–289.
[15] J. Lim, W. Lee, H. Lee, J. Lee, Y. Park, K. Cho, Advanced Functional Materials 18 (2008) 229–234.
[16] J. Kim, J. Jeong, HD Cho, C. Lee, SO Kim, S-K Kwon, Y. Hong, Journal of Physics D: Applied Physics 42 (2009) 115107.
[17] R. Hamilton, J. Smith, S. Ogier, M. Heeney, J.E. Anthony, I. McCulloch, J. Veres, D.D.C. Bradley, T.D. Anthopoulos, Advanced Materials 21 (2009) 1166–1171.

Herein, we present the use of a soluble QA precursor for the fabrication of organic solar cells via solution processing. As one of the most important low-cost industrial pigments with exceptional color and weather fastness, QA has been used extensively in a variety of applications, e.g., automobile coatings, artist's paints, and ink for printers [16]. Recently, the application of QA in electronic devices, i.e., organic light emitting diodes, solar transistors and solar cells, has gained a great deal of attention [17–24]. Most of these QA based devices have been fabricated via high vacuum vapor deposition due to its low solubility. More recently, a few soluble QA derivatives have been developed, affording solution processed QA based devices with high performance [5,24]. For instance, the organic field effect transistors (OFETs) fabricated by *t*-BOC QA have been found to exhibit nearly equivalent device characteristics to vacuum deposited devices. The objective of our present investigation is to evaluate the performance of QA based organic solar cells prepared via solution processing and thermal treatment of *t*-BOC QA.

2. Experimental

2.1. Materials and equipments

Pre-patterned ITO-coated glass substrates ($R = 20\ \Omega/sq$) were purchased from Thin Film Devices, Inc. Phenyl-C61-butyric acid methyl ester ($PC_{60}BM$) was purchased from Nano-C Inc. Poly(3,4-ethylenedioxythiophene) poly (styrenesulfonate) (PEDOT:PSS) (Baytron PH) was purchased from H.C. Starck. Pristine QA was purchased from Aldrich. *t*-BOC QA was prepared according to the procedures described in literature, i.e., stirring the pigment in tetrahydrofuran (THF) at room temperature with two equivalents of di-(*t*-butyl)-dicarbonate and *N,N′*-dimethylaminopyridine as a catalyst for 24 h, producing *t*-BOC QA at a yield of ~65%.

TGA was carried out on Thermogravimetric Analyzer (TGA) Q5000 IR (TA instruments). UV–Vis data were obtained using CARY 5000 UV–Vis-NIR spectrophotometer with film samples spin-coated on glass substrates. Film thickness was measured with a Veeco Dektak 150 surface profilometer. Tapping-mode atomic force microscopy (AFM) was carried out on a Veeco Nanoscope V scanning probe microscope. SEM was performed on Zeiss Gemini Ultra-55 Analytical Scanning Electron Microscope.

2.2. Device fabrication and testing

Organic solar cells with three device architectures, bilayer, bulk heterojunction, and p-i-n structure, were fabricated. The pre-patterned ITO-coated glass substrates were cleaned using the following procedure: sonication in soap solution, rinsing in deionized water, sonication in acetone and isopropanol, respectively, for 15 min, and UV ozone cleaning for 10 min. A thin-layer (~30 nm) of PEDOT:PSS (Baytron PH) was spin-coated onto the ITO glass substrate at 4000 RPM for 40 s and then baked at 140 °C for 15 min in air.

For p-n devices, *t*-BOC QA solutions with concentrations varying from 2 to 14 mg/mL (thickness 15–70 nm) and $PC_{60}BM$ with concentrations of 8–14 mg/mL (thickness 30–70 nm) were used. The optimal condition was found to be 10 mg/mL of *t*-BOC QA (57 nm) and 12 mg/mL of $PC_{60}BM$ (60 nm) both in chloroform. The *t*-BOC QA film was baked at 170 °C for 15 min on the hot plate prior to spin casting of the $PC_{60}BM$ layer.

For i devices, the photoactive layers were prepared by spin casting a blend *t*-BOC QA and $PC_{60}BM$ chloroform solution with varying weight ratios and concentrations of 6–20 mg/mL (40–110 nm thick). The optimal *t*-BOC QA:$PC_{60}BM$ weight ratio was found to be 1:1.5 with a concentration of 16 mg/mL (87 nm). The blend film was then baked at 170 °C for 15 min on the hot plate.

For p-i-n devices, *t*-BOC QA (p), *t*-BOC QA:$PC_{60}BM$ (i), and $PC_{60}BM$ (n) were varied from 2 to 4 mg/mL (17–32 nm), 10 to 20 mg/mL (55–117 nm), and 6 to 20 mg/mL (22–41 nm), respectively, to find the optimal conditions. The optimal condition was found to be 2 mg/mL (18 nm) in chloroform for *t*-BOC QA, 15 mg/mL (80 nm) in chloroform for *t*-BOC QA:$PC_{60}BM$, and 16 mg/mL (33 nm) in chlorobenzene for $PC_{60}BM$. The p and i layer were each baked at 170 °C for 15 min on the hot plate prior to deposition of the subsequent layer. All active layers were cast at 2000 rpm and passed through a 0.2 μm polytetrafluoroethylene filter prior to spin casting.

After the depositions of organic layers, an Al cathode (100 nm) was thermally evaporated under high vacuum (~10^{-7} Torr) through a shadow mask defining an active device area of ~0.03 cm^2. The current density–voltage (*J–V*) curves were measured using a Keithley 236 source-measure unit under AM 1.5 G solar illumination at 100 mW cm^{-2} (1 sun) using a Thermal-Oriel 300 W solar simulator. External Quantum Efficiencies (EQEs) were obtained with a monochromator and calibrated with a silicon photodiode.

3. Results and discussion

Soluble *t*-BOC QA precursor is prepared by replacing the H atom of the NH group of QA with a *t*-butoxycarbonyl (*t*-BOC) group in high yield. The soluble precursor can be converted into insoluble parent pigment QA in high purity and quantitative yield by thermal treatment, as shown in Fig. 1a. This process has been well characterized by UV–Vis spectroscopy, TGA and SEM. (See Supplementary data) Spin casting of *t*-BOC QA solutions in chloroform allowed for the formation of uniform thin yellow colored films. Thermal treatment of those films at 170 °C for 15 min resulted in the generation of polycrystalline red colored films of QA pigment, as evidenced by absorption spectra (Fig. 1b) and SEM (Fig. 1c and d). The change of photophysical and morphological properties is attributed to the NH···O hydrogen-bonding effect of QA. The field effect mobility of the regenerated QA film was previously reported to be p-type with a value of ~8×10^{-6} $cm^2\ V^{-1}\ s^{-1}$ [24]. The optical and electronic properties of QA suggest that it can act as an electron donor for organic solar cells.

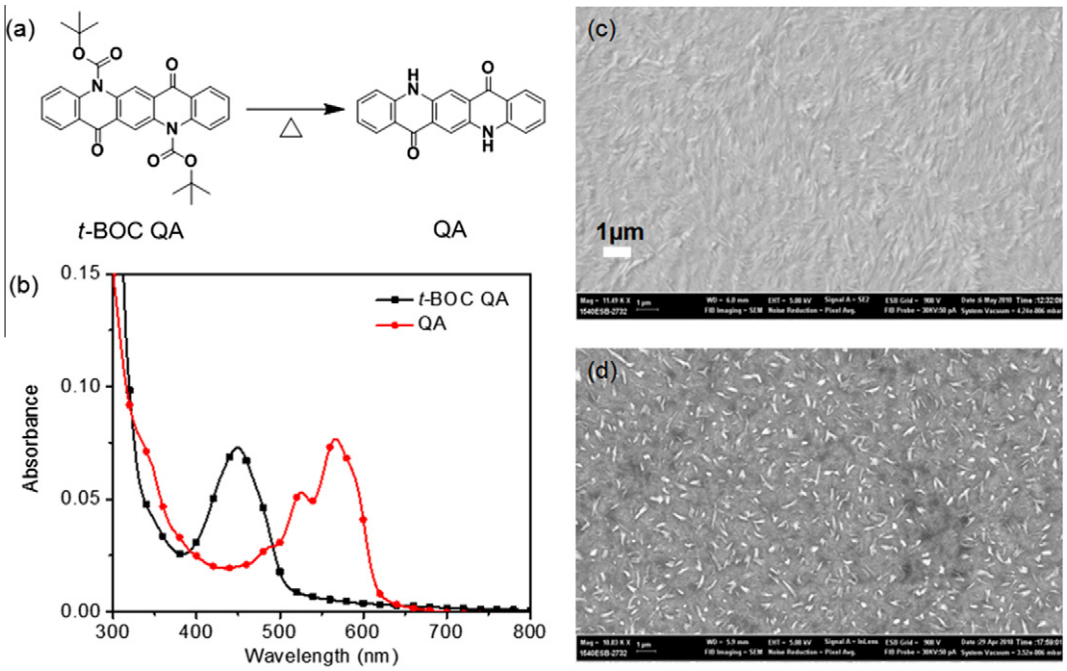

Fig. 1. (a) Molecular structures of soluble *t*-BOC QA and insoluble QA, (b) UV–Vis absorption spectra of 32 nm thick neat films of *t*-BOC QA spin-coated and after baking at 15 min at 170 °C (QA), (c) SEM image of spin-coated neat film of *t*-BOC QA, (d) SEM image of regenerated film of QA.

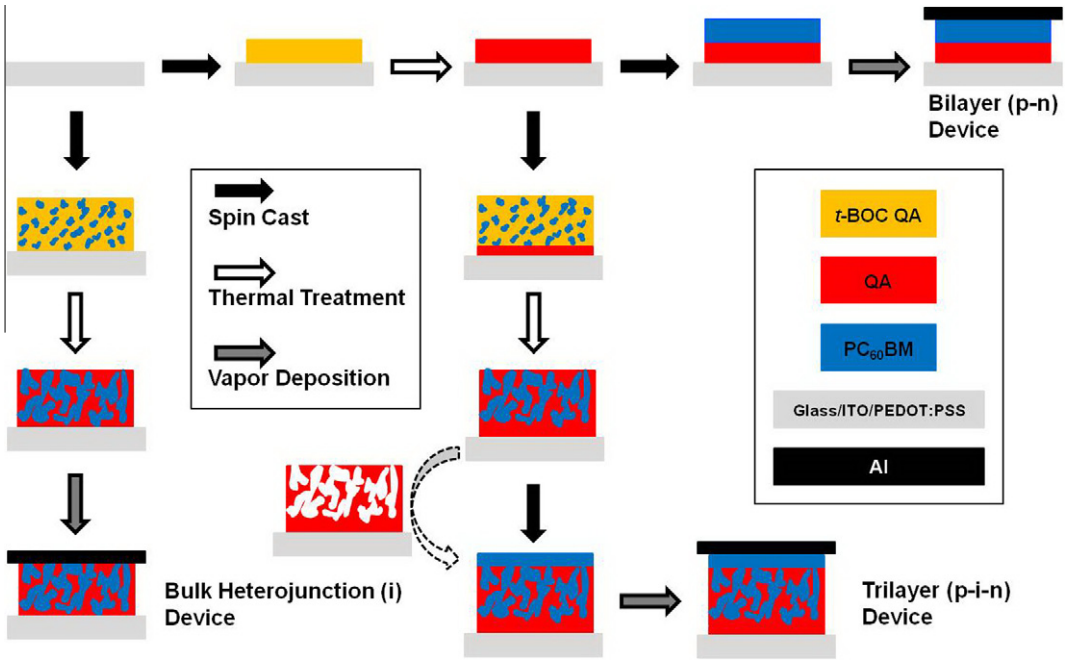

Fig. 2. Solution processing of organic solar cells with three different device architectures: bilayer (p-n) device, bulk heterojunction (i) device, and trilayer (p-i-n) device. The fabrication processes involve spin coating, thermal treatment and vapor deposition of Al cathode.

The thermal transformation of solution processed thin films into insoluble ones allows for solution processing of multilayer structures. As illustrated in Fig. 2, bilayer organic solar cells were fabricated by depositing the acceptor layer of $PC_{60}BM$ from solution on the top of the regenerated QA layer. Fig. 3a shows the current density–voltage (*J*–*V*) characteristics of the optimized p-n device with a structure of ITO/PEDOT:PSS(30 nm)/QA(57 nm)/$PC_{60}BM$

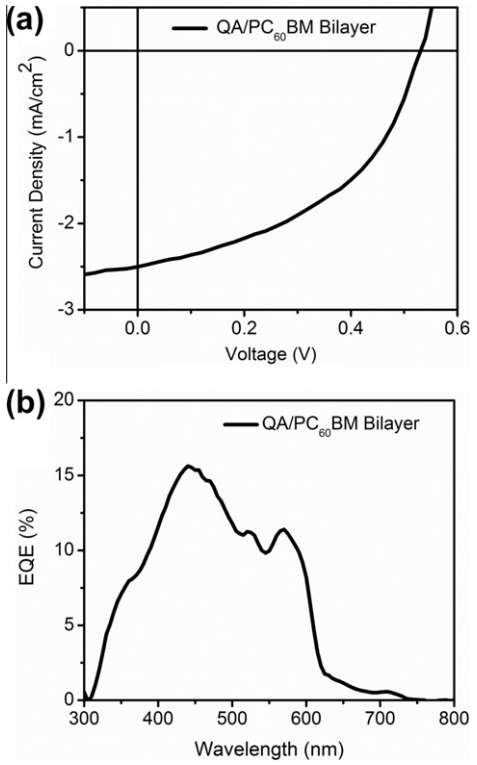

Fig. 3. (a) The *J–V* curve under 1 sun illumination for the optimized p-n device that shows a PCE of 0.61%; (b) The EQE curve of the p-n device.

(60 nm)/Al. The device showed a modest PCE of 0.61% with V_{oc} = 0.53 V, J_{sc} = 2.50 mA/cm^2, and FF = 0.46 (Table 1). Fig. 3b shows the external quantum efficiency of this device, with photocurrent generation in a broad range from 300 nm to 750 nm. An EQE of 10–15% is very typical for planar heterojunction devices. The photocurrent at short wavelengths (300–500 nm) and long wavelengths beyond 610 nm is mainly contributed by $PC_{60}BM$. The contribution from QA is mainly in the region of 500–600 nm, where QA exhibits high absorption intensity as shown in Fig. 1b.

To further improve the device performance, we have adapted a more advanced device architecture, i.e., trilayer p-i-n structure, which contains an additional mixing layer (i) sandwiched between the pure donor (p) and acceptor (n) layers. The fabrication process for p-i-n device is shown in Fig. 2. As control, a single layer (i) device was also fabricated. The i layer was prepared by spin casting of blends of *t*-BOC QA and $PC_{60}BM$ followed by thermal treatment to convert soluble *t*-BOC QA into insoluble QA. We have investigated various ratios of *t*-BOC QA to $PC_{60}BM$ and different thicknesses of i layer to obtain optimized device performance. Spin casting of pure $PC_{60}BM$ solution on the top of the regenerated QA:$PC_{60}BM$ mixing layer might dissolve the existing $PC_{60}BM$ component, creating porous structures while filling the pores at the same time. Nevertheless, a neat film of $PC_{60}BM$ can be generated with careful control of the concentration of the $PC_{60}BM$ solution.

The device characteristics of i and p-i-n devices are shown in Fig. 4. A PCE of 0.83% has been achieved for the p-i-n device with V_{oc} = 0.79 V, J_{sc} = 2.34 mA/cm^2, and FF = 0.44 (Table 1). In contract, the i device exhibited a much lower PCE of 0.57%. The improvements in open circuit voltage and fill factor account for the enhanced device performance of p-i-n over i device. As demonstrated in a number of systems, high open circuit voltage can be achieved by reducing the electron leakage current though the introduction of carrier blocking layers between the organic layers and the electrodes [25–29]. As shown in Fig. 4b, reduced dark current was observed for the p-i-n device, indicating the blocking effects induced by the neat film layers of QA and $PC_{60}BM$. Moreover, the improved organic/electrode interface properties is likely to lower the series resistance affording a higher fill factor, as evidence by the higher current density under forward bias of >1 V.

Interestingly, the EQEs for both i and p-i-n devices showed little-to-no change as compared to the p-n device, which are significantly lower than typical values of 40–60% for typical bulk heterojunction devices with nanophase separations [30]. This is likely due to the morphology of the blends of QA and $PC_{60}BM$, i.e., micron sized phase separation is formed in the i layer, similar to what has been observed in the blends of diethylhexyl functionalized QA and $PC_{70}BM$ [5]. This suggests that further improvement of device performance can be realized with better control of the phase separation between QA and acceptor materials. In addition, the p-i-n device has a slightly lower EQE than the i device. Provided that both devices have very similar absorption spectra (See Supplementary data), this can be explained by that a portion of light was harvested by the neat films to generate excitons, which were not able to reach the donor/acceptor interfaces to produce the photocurrent. Another interesting finding is that both i and p-i-n devices exhibited much higher V_{oc} than the p-n device (See Supplementary data for the dark current curves as well). This might be attributed to the different nature of the donor/acceptor interfaces for the devices. For the p-n device, the interfaces consist of QA that was regenerated from the neat film of *t*-BOC QA and solution processed $PC_{60}BM$. While for the devices with an i layer, the interfaces consist of QA regenerated from the blends of *t*-BOC QA and $PC_{60}BM$, and solution processed and/or leftover thermally annealed $PC_{60}BM$. Thermal treatment of the blends likely produces QA domains with less crystallinity and encourages the phase separation between QA and

Table 1
Device parameters for OSCs in three device structures.

Devices	Structures	V_{oc} (V)	J_{sc} (mA/cm^2)	FF	PCE (%)
Bilayer (p-n)	QA (57 nm)/$PC_{60}BM$(60 nm)	0.53	2.50	0.46	0.61
BHJ (i)	QA:$PC_{60}BM$ (1:1.5, 87 nm)	0.70	2.54	0.32	0.57
Trilayer (p-i-n)	QA(18 nm)/QA:$PC_{60}BM$ (1:1.5, 80 nm)/$PC_{60}BM$(33 nm)	0.79	2.34	0.44	0.83

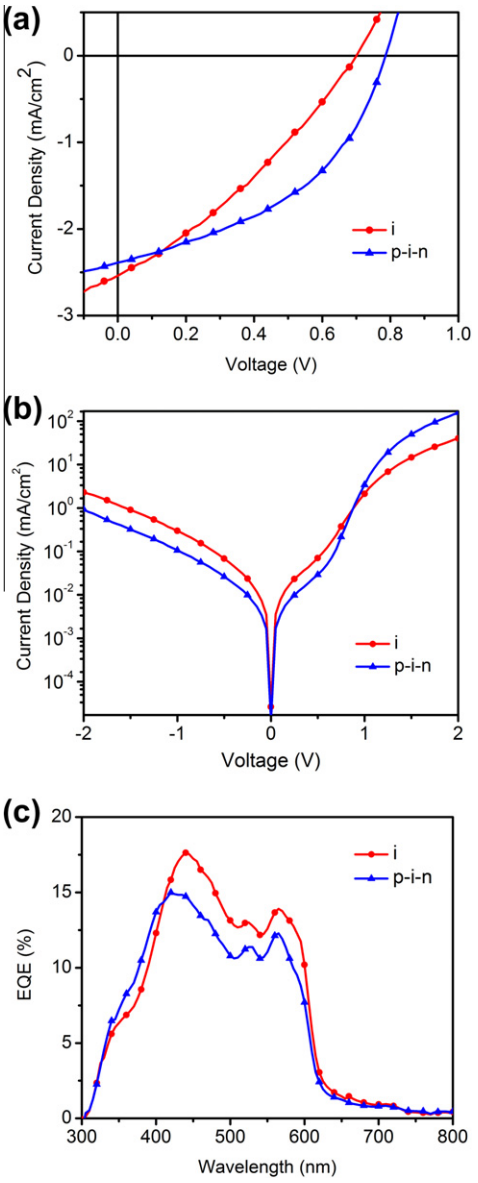

Fig. 4. (a) The *J–V* curves under 1 Sun illumination for the optimized p-i-n and i devices that exhibit PCE of 0.83% and 0.57% respectively; (b) The dark current characteristics of the optimized p-i-n and i devices; (c) The EQE curves of the i and p-i-n device.

$PC_{60}BM$, which would lead to weaker donor/acceptor interactions and subsequently higher open circuit voltages [31].

4. Conclusions

In summary, we have demonstrated a simple device fabrication approach for p-i-n junction organic solar cells based on an "old" industrial pigment, quinacridone. The pristine insoluble quincridone molecule was easily functionalized with solubilizing *t*-BOC groups, yielding a solution processable material with suitable properties for photovoltaic application. Although the overall power conversion efficiencies of these cells of up to 0.83% are still below those of state-of-the-art, our work is a proof-of-concept for the great potential of solution processing of highly stable industrial pigments for solar cells. On-going research is to develop effective approaches to realizing controlled nanophase separation within the blends of pigment donors and fullerene acceptors.

Acknowledgements

This work was performed at the Molecular Foundry, Lawrence Berkeley National Laboratory, and was supported by the Office of Science, Office of Basic Energy Sciences, Scientific User Facilities Division, of the US Department of Energy under Contract No. DE-AC02—05CH11231.

Appendix A. Supplementary data

Supplementary data associated with this article can be found, in the online version, at doi:10.1016/j.orgel.2011.03.039.

References

[1] J. Kalowekamo, E. Baker, Estimating the manufacturing cost of purely organic solar cells, Solar Energy 83 (2009) 1224–1231.
[2] C.W. Tang, 2-Layer organic photovoltaic cell, Appl. Phys. Lett. 48 (1986) 183–185.
[3] G. Yu, J. Gao, J.C. Hummelen, F. Wudl, A.J. Heeger, Polymer photovoltaic cells – enhanced efficiencies via a network of internal donor–acceptor heterojunctions, Science 270 (1995) 1789–1791.
[4] A.B. Tamayo, B. Walker, T.Q. Nguyen, A low band gap, solution processable oligothiophene with a diketopyrrolopyrrole core for use in organic solar cells, J. Phys. Chem. C 112 (2008) 11545–11551.
[5] J.J.A. Chen, T.L. Chen, B. Kim, D.A. Poulsen, J.L. Mynar, J.M.J. Frechet, B.W. Ma, Quinacridone-based molecular donors for solution processed bulk-heterojunction organic solar cells, ACS Appl. Mater. Interfaces 2 (2010) 2679–2686.
[6] M.T. Lloyd, J.E. Anthony, G.G. Malliaras, Photovoltaics from soluble small molecules, Mater. Today 10 (2007) 34–41.
[7] F. Silvestri, M.D. Irwin, L. Beverina, A. Facchetti, G.A. Pagani, T.J. Marks, Efficient squaraine-based solution processable bulk-heterojunction solar cells, J. Am. Chem. Soc. 130 (2008) 17640-+.
[8] P. Heremans, D. Cheyns, B.P. Rand, Strategies for increasing the efficiency of heterojunction organic solar cells: material selection and device architecture, Acc. Chem. Res. 42 (2009) 1740–1747.
[9] B.W. Ma, C.H. Woo, Y. Miyamoto, J.M.J. Frechet, Solution processing of a small molecule, subnaphthalocyanine, for efficient organic photovoltaic cells, Chem. Mater. 21 (2009) 1413–1417.
[10] B. Walker, A.B. Tomayo, X.D. Dang, P. Zalar, J.H. Seo, A. Garcia, M. Tantiwiwat, T.Q. Nguyen, Nanoscale phase separation and high photovoltaic efficiency in solution-processed, small-molecule bulk heterojunction solar cells, Adv. Funct. Mater. 19 (2009) 3063–3069.
[11] Y. Matsuo, Y. Sato, T. Niinomi, I. Soga, H. Tanaka, E. Nakamura, Columnar structure in bulk heterojunction in solution-processable three-layered p-i-n organic photovoltaic devices using tetrabenzoporphyrin precursor and silylmethyl[60]fullerene, J. Am. Chem. Soc 131 (2009) 16048-+.
[12] M. Hiramoto, H. Fujiwara, M. Yokoyama, P-I-N like behavior in 3-layered organic solar-cells having a co-deposited interlayer of pigments, J. Appl. Phys. 72 (1992) 3781–3787.
[13] P. Peumans, S. Uchida, S.R. Forrest, Efficient bulk heterojunction photovoltaic cells using small-molecular-weight organic thin films, Nature 425 (2003) 158–162.
[14] P. Peumans, A. Yakimov, S.R. Forrest, Small molecular weight organic thin-film photodetectors and solar cells, J. Appl. Phys. 93 (2003) 3693–3723.
[15] J.S. Zambounis, Z. Hao, A. Iqbal, Latent pigments activated by heat, Nature 388 (1997) 131–132.
[16] G. Lincke, A review of thirty years of research on quinacridones, X-ray crystallography and crystal engineering, Dyes Pigments 44 (2000) 101–122.

[17] D. Berg, C. Nielinger, W. Mader, M. Sokolowski, Quinacridone organic field effect transistors with significant stability by vacuum sublimation, Synthetic Metals 159 (2009) 2599–2602.
[18] H.G. Jeon, T. Sugiyama, H. Masuhara, T. Asahi, Preparation and photoconductive property of electrophoretically deposited film of quinacridone nanoparticles prepared by laser ablation in water, Jpn. J. Appl. Phys. Part 2-Lett. Exp. Lett. 46 (2007) L733–L735.
[19] K. Manabe, S. Kusabayashi, M. Yokoyama, Long-life organic solar-cell fabrication using quinacridone pigment, Chem. Lett. (1987) 609–612.
[20] T.V. Pho, P. Zalar, A. Garcia, T.Q. Nguyen, F. Wudl, Electron injection barrier reduction for organic light-emitting devices by quinacridone derivatives, Chem. Commun. 46 (2010) 8210–8212.
[21] M. Tomida, S. Kusabayashi, M. Yokoyama, Organic solar-cell fabrication using quinacridone pigments, Chem. Lett. (1984) 1305–1308.
[22] T. Wakimoto, Y. Yonemoto, J. Funaki, M. Tsuchida, R. Murayama, H. Nakada, H. Matsumoto, S. Yamamura, M. Nomura, Stability characteristics of quinacridone and coumarin molecules as guest dopants in the organic LEDs, Synthetic Metals 91 (1997) 15–19.
[23] Z.X. Xu, H.F. Xiang, V.A.L. Roy, S.S.Y. Chui, Y. Wang, P.T. Lai, C.M. Che, Organic field-effect transistors fabricated with N, N′-substituted dialkyl-1, 3, 8, 10-tetramethylquinacridone compounds, Appl. Phys. Lett. 95 (2009).
[24] H. Yanagisawa, J. Mizuguchi, S. Aramaki, Y. Sakai, Organic field-effect transistor devices based on latent pigments of unsubstituted diketopyrrolopyrrole or quinacridone, Jpn. J. Appl. Phys. 47 (2008) 4728–4731.
[25] N. Li, B.E. Lassiter, R.R. Lunt, G. Wei, S.R. Forrest, Open circuit voltage enhancement due to reduced dark current in small molecule photovoltaic cells, Appl. Phys. Lett. 94 (2009).
[26] L.J. Pegg, S. Schumann, R.A. Hatton, Enhancing the open-circuit voltage of molecular photovoltaics using oxidized Au nanocrystals, ACS Nano 4 (2010) 5671–5678.
[27] A. Hayakawa, O. Yoshikawa, T. Fujieda, K. Uehara, S. Yoshikawaa, High performance polythiophene/fullerene bulk-heterojunction solar cell with a TiOx hole blocking layer, Appl. Phys. Lett. 90 (2007).
[28] M.D. Irwin, B. Buchholz, A.W. Hains, R.P.H. Chang, T.J. Marks, P-Type semiconducting nickel oxide as an efficiency-enhancing anode interfacial layer in polymer bulk-heterojunction solar cells, Proc. Natl. Acad. Sci. USA 105 (2008) 2783–2787.
[29] A.W. Hains, J. Liu, A.B.F. Martinson, M.D. Irwin, T.J. Marks, Anode interfacial tuning via electron-blocking/hole-transport layers and indium tin oxide surface treatment in bulk-heterojunction organic photovoltaic cells, Adv. Funct. Mater. 20 (2010) 595–606.
[30] K. Suemori, T. Miyata, M. Yokoyama, M. Hiramoto, Three-layered organic solar cells incorporating a nanostructure-optimized phthalocyanine: fullerene codeposited interlayer, Appl. Phys. Lett. 86 (2005).
[31] M.D. Perez, C. Borek, S.R. Forrest, M.E. Thompson, Molecular and morphological influences on the open circuit voltages of organic photovoltaic devices, J. Am. Chem. Soc 131 (2009) 9281–9286.

amorphous InGaZnO (*a*-IGZO) and a vacuum deposited pentacene TFTs as channel semiconductors, respectively. The inverters yielded high DC gain values of 61 V/V with high and balanced noise margins at a low supply voltage of 5 V [9]. However, to reduce the cost of such inverters, it would be desirable to demonstrate that such structures can also be implemented using solution-processed semiconductors.

A challenge to implement vertically stacked TFTs and consequently inverters with vertical geometries and solution-processed semiconductors, is to find gate dielectric materials and processing methods that do not damage the organic semiconductor layers during deposition. An amorphous fluoropolymer, CYTOP, has recently provided a particularly attractive way to realize TFTs with a top-gate geometry. This is because CYTOP dissolves in fluorinated solvents that are orthogonal to most organic semiconductor materials, has an excellent chemical stability and is highly hydrophobic [10,11]. Furthermore, we recently demonstrated 6,13-bis(triisopropylsilylethynyl) pentacene (TIPS-pentacene) and poly(triarylamine) (PTAA) blended *p*-channel TFTs using a top-gate bi-layer gate insulator which operated at low voltages with remarkable long-term environmental and operational stabilities [12]. The bi-layer was comprised of a spin-coated CYTOP layer and a high-*k* metal-oxide layer, fabricated by atomic layer deposition (ALD).

Here, we combine this *p*-channel TFTs with a solution-processed [6,6]-phenyl c_{61} butyric acid methyl ester (PCBM) *n*-channel TFT in a vertically stacked complementary inverter geometry. In this geometry, a bottom-gate *n*-channel TFT is fabricated on top of a top-gate *p*-channel TFTs with a shared common gate electrode positioned between two dielectric layers. The *p*- and *n*-channel TFTs showed saturation mobility values of 0.25 and 0.004 cm^2/V s, respectively. We demonstrate a complementary inverter that shows a DC gain value of −24 V/V with a switching threshold voltage value of 3.3 V, close to half of the supply voltage, and NM_L and NM_H values of 2.5 and 2.1 V, respectively.

2. Device fabrication and electrical characterization

Fig. 1(a) shows the geometry of the complementary inverter in which a bottom-gate top-contact *n*-channel TFT was fabricated on top of a top-gate bottom-contact *p*-channel TFT with a shared gate electrode. The inverter was fabricated on a glass substrate by first depositing at room temperature 60 nm-thick Au source and drain electrodes through a shadow mask using a thermal evaporator. A self-assembled layer of pentafluorobenzenethiol (PFBT) was deposited on the Au electrodes to improve the contact between the metal and the organic semiconductor interface and to increase the work function of Au. The PFBT layer was deposited by immersing the substrates in a 10 mM PFBT solution in ethanol for 15 min inside a N_2-filled dry box, were the substrates were also rinsed with pure ethanol, and dried. The TIPS-pentacene and PTAA blend solution was prepared as follows: TIPS-pentacene and PTAA were individually dissolved in 1,2,3,4-tetrahydronaphthalene anhydrous, 99%, (Sigma Aldrich) with a concentration of 30 mg/mL, then, the two individual solutions were mixed to yield a weight ratio of 1:1. Blends of TIPS-pentacene and PTAA were deposited by following a two-step spin coating process comprising of a first cycle at 500 rpm for 10 s and followed by a second cycle at 2000 rpm for 20 s. Then, the samples were annealed at 100 °C for 15 min in a N_2-filled dry box. A CYTOP/Al_2O_3 bi-layer was then fabricated as top-gate dielectric for the *p*-channel TFTs. A CYTOP solution (CTL-809M) was purchased from Asahi Glass with a concentration of 9 wt.% and diluted with a solvent (CT-solv.180) to reduce the concentration to 2 wt.%. This diluted solution was used to deposit 40 nm-thick CYTOP layers by spin casting at 3000 rpm for 60 s. The CYTOP film was then annealed at 100 °C for 20 min. All spin-coating and annealing processes were carried out in a N_2-filled dry box. After that, a Savannah100 ALD system from Cambridge Nanotech Inc. was used to deposit 50 nm-thick Al_2O_3 layers at 110 °C by using alternating exposures of tri-methyl-aluminum ($Al(CH_3)_3$) and H_2O vapor at a deposition rate of approximately

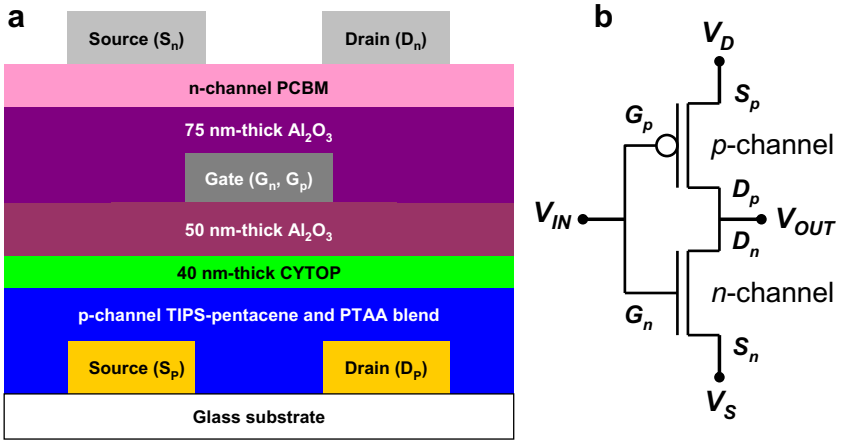

Fig. 1. (a) Schematics of vertically stacked *n*-channel (PCBM) transistor on the top of an *p*-channel (TIPS-pentacene and PTAA blend) transistor on a glass substrate. (b) Complementary inverter circuit diagram.

0.1 nm per cycle. A 50 nm-thick Al electrode was then deposited by thermal evaporation through a shadow mask to serve as a common gate electrode. Then, a 75 nm-thick Al_2O_3 was deposited by ALD as previously described. A thin layer of PCBM (Solenne B.V., 99.5%) was then deposited by spin-coating from a 10 mg/mL chlorobenzene solution at 1000 rpm for 60 s in a N_2-filled dry box. Hence, PCBM was never exposed to normal ambient during the fabrication process. Finally, Au (100 nm) source/drain electrodes were deposited through a shadow mask over the PCBM channel. After fabrication, the electrical properties of the samples were measured in a N_2-filled glove box (O_2, $H_2O < 0.1$ ppm).

The dielectric properties of the gate dielectrics used in both transistors were measured in parallel plate capacitors fabricated using the same procedures previously described but on independent substrates with the following geometries, glass/Au/CYTOP (40 nm)/Al_2O_3 (50 nm)/Al and glass/Au/Al_2O_3 (75 nm)/Al, with areas ranging from 1 to 5 mm^2. Capacitance densities of 35 ± 1 and 114 ± 2 nF/cm^2 were measured for the CYTOP/Al_2O_3 bi-layer and the Al_2O_3 single layer, respectively. The properties of these Al_2O_3 and CYTOP/Al_2O_3 layers are consistent with our previous reports [9,12,13]. The current–voltage characteristics of the vertically stacked, bottom-gate *p*-channel and top-gate *n*-channel TFTs with channel widths of $W_P = W_N = 2550$ μm and lengths of $L_P = L_N = 180$ μm are shown in Fig. 2(a) and (d). The output characteristics (drain current I_{DS} vs. drain–source voltage V_{DS} at multiple constant gate–source voltages V_{GS}) and transfer characteristics (I_{DS} vs. V_{GS} at fixed V_{DS}) of the TFTs were measured using an Agilent E5272A medium-power source/monitor unit connected to a probe station. Transfer and output curves are shown in Fig. 2(a) and (b) (*p*-channel) and Fig. 2(c) and (d) (*n*-channel). Saturation mobility values of 0.25 and 0.004 $cm^2/V\,s$ and threshold voltage values of −3.9, and 0.3 V were obtained for the *p*-channel and *n*-channel TFTs, respectively. The relatively high contact resistance and threshold voltage observed in the *p*-channel TFTs could be attributed to an incomplete Au surface

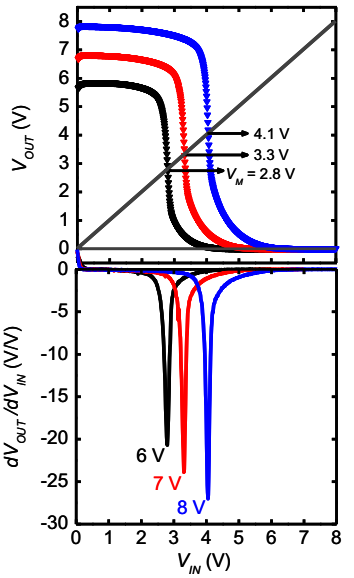

Fig. 3. Voltage transfer characteristics and static gains of the vertically stacked complementary inverters at different supply voltages of 6, 7, and 8 V.

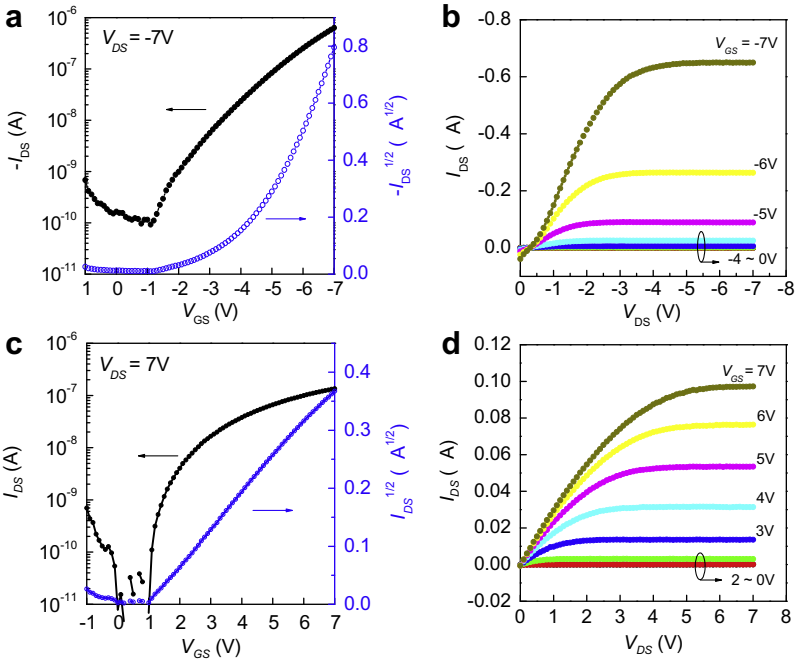

Fig. 2. Representative (a) transfer and (b) output characteristics of TIPS-pentacene and PTAA blend *p*-channel TFTs with $L_P = 180$ μm and $W_P = 2550$ μm. Representative (c) transfer and (d) output characteristics of PCBM *n*-channel TFTs with $L_N = 180$ μm and $W_N = 2550$ μm.

Table 1
Performance of a complementary inverter using vertically stacked *n*-channel ([60] PCBM) TFT on top of a *p*-channel (TIPS-pentacene and PTAA blend) TFT.

$W_P = W_N$ [μm]	$L_P = L_N$ [μm]	V_{IN} [V]	V_D [V]	*Maximum* dV_{OUT}/dV_{IN}	V_M [V]	NM_L [V]	NM_H [V]	ΔV_{IN} [V]
2550	180	0 to +6	+6	−22	2.8	2.10	1.99	0.98
		0 to +7	+7	−24	3.3	2.51	2.09	1.16
		0 to +8	+8	−26	4.1	3.10	2.17	1.27

modification by the PFBT and the negative shifts of threshold voltage introduced by the unintended vacuum annealing during the second ALD deposition [12]. Further optimization of the processing conditions of TFTs with this geometry could reduce these effects. For instance exposing this *p*-channel TFT to air has been found to cause positive shifts of the threshold voltage, bringing it closer to zero. Hence, a longer air exposure prior to the second ALD deposition could reduce the threshold voltage of the *p*-channel TFT. The low mobility values obtained in the PCBM TFTs compared with previous reports [14,15] is attributed to the unpassivated gate dielectric interface.

3. Vertically stacked complementary inverters with solution-processed organic semiconductors

The static performance of an inverter is evaluated by its static gain and noise margin values, both extracted from the measured voltage transfer characteristics (*VTC*s) [16,17]. Achieving high and balanced noise margin values is necessary for reliable circuit operation in complex logic circuits such as ring oscillators. Noise margin values are defined by the noise margin low ($N_{ML} = V_{IL} - V_{OL}$) and noise margin high ($N_{MH} = V_{OH} - V_{IH}$), where V_{IH}, V_{IL}, V_{OH}, and V_{OL} are input (V_{IN}) and output (V_{OUT}) voltages at high and low levels of a given inverter *VTC*s. The noise margin is limited by the steepness ($\Delta V_{IN} = V_{IH} - V_{IL}$) of the transition and by the position of the switching threshold voltage ($V_M = V_{IN} = -V_{OUT}$). High and balanced noise margins are found when the ideal condition $V_M = 0.5V_D$ is met, hence when $V_M = V_{IN} = 0.5V_D = V_{OUT}$. However, the value of V_{IN} at which this transition occurs is generally not $0.5V_D$. In complementary inverters with a vertically stacked geometry the control of thicknesses of the top- and bottom-gate transistors with the use of different dielectric materials is used to compensate for: (1) differences in hole (μ_h) and electron mobility (μ_e) in the TIPS-pentacene and PTAA blend and PCBM transistors; and (2) differences in the threshold voltages of the two transistors. To test the inverter characteristics of these vertically stacked TFTs, the drain electrodes of the top and bottom TFTs were connected by using a single probe at the region of electrode overlap. The common gate electrode for both *n*- and *p*-channel TFTs served as the input voltage (V_{IN}) of the inverter circuit. Fig. 3 shows the corresponding hysteresis *VTC*s and static gain (dV_{OUT}/dV_{IN}) values of the inverters for V_D = 6, 7, and 8 V. The maximum static gain value at V_D = 7 V was −24 V/V with V_M = 3.3 V. The corresponding value of NM_L and NM_H are 2.51 and 2.09 V with the steepness of ΔV_{IN} = 1.27 V (18% of max. V_{IN}). The performance of this complementary inverter at different V_D is summarized in Table 1. We note that further optimization of the inverter performance could be achieved by passivating the *n*-channel dielectric interface, and by selecting *n*-channel materials with better air stability than PCBM, which here has been selected for its ease of processing and reproducible behavior. The geometry demonstrated in this study shows many degrees of freedom that allow for the optimization of inverters as illustrated by the use of two un-patterned solution-processed materials with very different charge mobilities. Hence, the proposed geometry allows the use of solution-processed semiconductors in vertically stacked complementary inverter geometries, which is a step forward towards the development of low-cost complementary electronics.

4. Conclusion

In summary, we have demonstrated a vertically stacked complementary inverter geometry using solution-processed PCBM *n*-channel and TIPS-pentacene/PTAA blend *p*-channel TFTs. The *p*- and *n*-channel TFTs showed saturation mobility values of 0.25 and 0.004 $cm^2/V\,s$ and threshold voltages of −3.9 and 0.3 V, respectively. The complementary inverters yielded a maximum gain value of −24 V/V with high and balanced noise margins at a low voltage of 7 V. The use of vertically stacked *p*- and *n*-channel TFTs in complementary circuits is a promising way to realize higher packing density and higher interconnectivity with low power by the reduction of the interconnection lengths and parasitic resistances. Balanced "*on*-currents" during inverter operation were achieved because this geometry allows for the independent control of the channel widths, the *n*- to *p*-channel ratios, as well as separate control of the thickness of the gate dielectric layers. Furthermore, the low processing temperature (<110 °C) used in this work would make possible the implementation of the complementary circuits on flexible substrates.

Acknowledgements

This material is based upon work supported in part by the STC Program of the National Science Foundation under Agreement No. DMR-0120967 and by the Office of Naval Research (Grant No. N00014-04-1-0120). This work was performed in part at the Microelectronics Research Center at Georgia Institute of Technology, a member of the National Nanotechnology Infrastructure Network, which is supported by NSF (Grant No. ECS-03-35765).

References

[1] S. Lee, B. Koo, J. Shin, E. Lee, H. Park, H. Kim, Effects of hydroxyl groups in polymeric dielectrics on organic transistor performance, Appl. Phys. Lett. 88 (2006) 162109.

[2] X.H. Zhang, B. Domercq, B. Kippelen, High-performance and electrically stable C-60 organic field-effect transistors, Appl. Phys. Lett. 91 (2007) 092114.
[3] H. Klauk, U. Zschieschang, J. Pflaum, M. Halik, Ultralow-power organic complementary circuits, Nature 445 (2007) 745.
[4] H. Yan, Z.H. Chen, Y. Zheng, C. Newman, J.R. Quinn, F. Dotz, M. Kastler, A. Facchetti, A high-mobility electron-transporting polymer for printed transistors, Nature 457 (2009) 679.
[5] X.H. Zhang, W.J. Potscavage, S. Choi, B. Kippelen, Low-voltage flexible organic complementary inverters with high noise margin and high dc gain, Appl. Phys. Lett. 94 (2009) 043312.
[6] J.B. Kim, C. Fuentes-Hernandez, S.J. Kim, S. Choi, B. Kippelen, Flexible hybrid complementary inverters with high gain and balanced noise margins using pentacene and amorphous InGaZnO thin-film transistors, Org. Electron. 11 (2010) 1074.
[7] M.S. Oh, W. Choi, K. Lee, D.K. Hwang, S. Im, Flexible high gain complementary inverter using *n*-ZnO and *p*-pentacene channels on polyethersulfone substrate, Appl. Phys. Lett. 93 (2008) 033510.
[8] C. Baek, S.M. Seo, Vertical organic inverter with stacked pentacene thin film transistors, Appl. Phys. Lett. 94 (2009) 153305.
[9] J.B. Kim, C. Fuentes-Hernandez, D.K. Hwang, W.J. Potscavage, H. Cheun, B. Kippelen, Vertically stacked hybrid organic–inorganic complementary inverters with low operating voltage on flexible substrates, Org. Electron. 12 (2011) 45.
[10] R. Hamilton, J. Smith, S. Ogier, M. Heeney, J.E. Anthony, I. Mcculloch, J. Veres, D.D.C. Bradley, T.D. Anthopoulos, High-performance polymer-small molecule blend organic transistors, Adv. Mater. 21 (2009) 1166.
[11] S.H. Kim, S. Nam, J. Jang, K. Hong, C. Yang, D.S. Chung, C.E. Park, W.S. Choi, Effect of the hydrophobicity and thickness of polymer gate dielectrics on the hysteresis behavior of pentacene-based field-effect transistors, J. Appl. Phys. 105 (2009) 104509.
[12] D.K. Hwang, C. Fuentes-Hernandez, J.B. Kim, W.J. Potscavage, S.-J. Kim, B. Kippelen, Top-gate organic field-effect transistors with high environmental and operational stability, Adv. Mater. 23 (2011) 1293.
[13] J.B. Kim, C. Fuentes-Hernandez, W.J. Potscavage, X.H. Zhang, B. Kippelen, Low-voltage InGaZnO thin-film transistors with Al_2O_3 gate insulator grown by atomic layer deposition, Appl. Phys. Lett. 94 (2009) 142107.
[14] S.P. Tiwari, X.H. Zhang, W.J. Potscavage, B. Kippelen, Low-voltage solution-processed n-channel organic field-effect transistors with high-k HfO_2 gate dielectrics grown by atomic layer deposition, Appl. Phys. Lett. 95 (2009) 223303.
[15] S.P. Tiwari, X.H. Zhang, W.J. Potscavage, B. Kippelen, Study of electrical performance and stability of solution-processed *n*-channel organic field-effect transistors, J. Appl. Phys. 106 (2009) 054504.
[16] S.-M. Kang, Y. Leblebici, CMOS Digital Integrated Circuits Analysis & Design, McGraw-Hill, New York, 2003.
[17] J.M. Rabaey, Digital Integrated Circuits: A Design Perspective, Prentice Hall, New Jersey, 1995.

ITO/Ag/ITO (IMI) structure with higher conductivity [24]. Recently, Lewis et al. reported flexible OLEDs based on IMI stacks which fabricated onto polyethylene terephthalate (PET) by sputtering deposition process [22]. In addition, multilayer InZnSnOx/Ag/InZnSnOx, ZnS/Ag/ZnS, WO_3/Ag/WO_3, and ITO/Ag/WO_3 were also reported as electrodes for OLEDs [25–28]. But all the reported multilayer electrodes above were almost used in monochrome OLEDs, having no white light emission devices reported.

In this article, we reported a warm and high color-rendering TEWOLED with MoO_3/Ag/MoO_3 (MAM) multilayer used as a cathode. We prepared conductive transparent MAM coating on PET substrates by vacuum thermal evaporation and measured the optical transmittance. The TEWOLED we fabricated had a comparable efficiency but superior CRI relative to bottom-emitting OLED.

2. Experimental details

The device A consisted of PET substrate/Al (100 nm)/MoO_3 (1.5 nm)/4, 4′, 4″-tris(3-methylphenyl–phenylamino)-tripheny-lamine (m-MTDATA, 30 nm)/N, N′-bis-(1-naphthyl)-N, N'diphenyl-1, 1-biphenyl-4, 4′diamine (NPB, 10 nm)/4, 4′-bis(2, 2′-diphenylvinyl)-1, 1′-biphenyl (DPVBi, 15 nm)/4, 4-N, N- dicarbazole-biphenyl (CBP, 3 nm)/CBP: bis(2-(2-fluorphenyl)-1, 3-benzothiozolato-N, C2′)iridium(acetylacetonate) [(F–BT)2Ir(acac)] (7 nm)/4, 7-diphenyl -1, 10-phenanthroline (Bphen, 30 nm)/LiF (1 nm)/Al (1 nm)/Ag (1 nm)/MoO_3 (40 nm)/Ag (17 nm)/MoO_3 (40 nm). In this device, Al/MoO_3, m-MTDATA, NPB, DPVBi, CBP: $(F–BT)_2Ir(acac)$, Bphen, and LiF/Al/Ag/M/A/M were used as the anode, hole injection layer, hole transporting layer, blue emitting layer, orange emitting layer, electron transporting layer and cathode, respectively. Here, we use metal Al as the anode replacing the common metal Ag because Al film has larger phase shift on reflection than that of metal Ag. The neat CBP is introduced to separate blue and orange emitting layers to avoid the Dexter energy transfer between the two emitters. For comparison, the bottom-emitting device (ITO glass substrate) with the same organic layers (device B) was fabricated, which consisted of glass coated with ITO /m-MTDATA (30 nm)/NPB (10 nm)/DPVBi (15 nm)/CBP (3 nm)/CBP: $(F–BT)_2Ir(acac)$ (7 nm)/Bphen (30 nm)/LiF (1 nm)/Al (200 nm). All films were deposited at pressure below 4×10^{-6} Torr. The deposition of each layer and the measure of devices characteristics were described before [20].

3. Results and discussion

Ryu et al. reported that the Ag thin film was the dominant factor of the sheet resistance in a dielectric/Ag/dielectric multilayer [28]. Consequently, a low resistance of multilayer cathode will be obtained by adjusting the thickness of Ag layer in MAM electrode. We measured the sheet resistance of the prepared MAM multilayer by four-point probe and a low resistance of 11 Ω/□ was obtained. If the film boundary effects are negligible, the sheet resistance of the multilayer is the sheet resistance of MoO_3, Ag, MoO_3 layer coupled in parallel: [28].

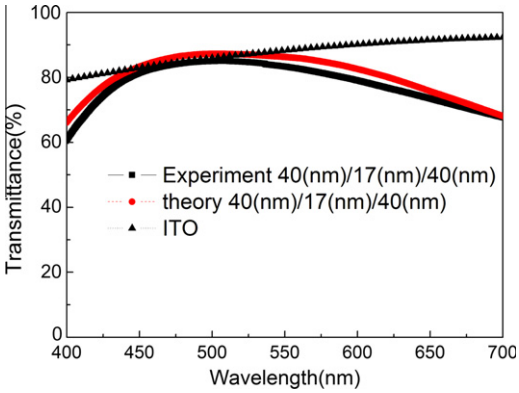

Fig. 1. The measured optical transmittance curves of MAM and ITO, the calculated optical transmittance of MAM is also plotted.

$$\frac{1}{R_{total}} = \frac{1}{R_{MoO3}} + \frac{1}{R_{Ag}} + \frac{1}{R_{MoO3}}.$$

R_{total}, R_{Ag}, R_{MoO3} is the sheet resistance of MAM, Ag, MoO_3 layer, respectively. Fig. 1 shows the measured and calculated optical transmittance curves of multilayer MAM as a function of the wavelength. The optical transmittance is calculated by the transfer-matrix method [29]. The measured optical transmittance curve of ITO was also plotted in Fig. 1. It can be seen that a high average transmittance of over 84% is obtained for the MAM-based transparent multilayer, which is comparable with the conventional ITO. Here, we also calculated the transmittance of MoO_3 (y nm)/Ag (17 nm)/MoO_3 (y nm) for different y value (the data was not shown) and found that the MAM multilayer had the highest transmittance when $y = 40$. Considering the electric and optical properties, we choose a 17 nm Ag layer for MAM coating. One should note that the MAM multilayer with superior features is obtained by simple thermal evaporation without subjecting to substrate heating and post-annealing, which is especially favorable for flexible OLEDs and top-emitting OLEDs.

Fig. 2a shows the normalized EL spectra of device A and B at operating voltage of 6, 8, and 10 V. It can be seen that the narrowness of the full width at half maximum (FWHM) of the DPVBi and $(F\text{-}BT)_2Ir(acac)$ emission in device A is not observed at all. Insert is the normal spectra normalized to blue emission. We can see that the devices have the same blue emission spectral profile. However, the spectra have large difference in long wavelength region. In order to explain this, we calculated the phase shift characteristics of the TEWOLED by the transfer-matrix method [29], as shown in Fig. 2b, the calculated round-trip phase changes for organic layers sandwiched between two reflection electrodes [i.e., $\varphi_1(\lambda) = \sum_i \frac{4\pi d_i n_i(\lambda)}{\lambda}$], and the phase changes at two reflective electrodes [i.e., $\varphi_2(\lambda) = \varphi_{cathode} + \varphi_{anode}$]. In our calculation, the multilayer MoO_3 (40 nm)/Ag (17 nm)/MoO_3 (40 nm) was considered the cathode. The point of intersection is the resonant wavelength (RW). It can be seen that a RW at 635 nm is observed. Insert is the absorptance and reflectance of multilayer MAM. The absorptance is almost the same over the visible range, which will not affect the distribution of the spectrum intensity. High reflectance (>25%) at longer wavelength (>600 nm) will benefit

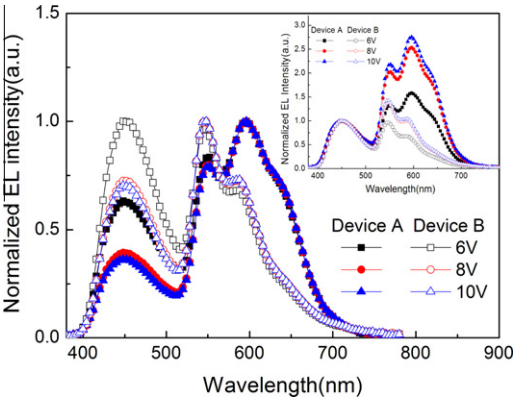

Fig. 2a. The normalized EL spectra of devices A and B at different voltage of 6, 8, and 10 V; Insert is the EL spectra of devices A and B normalized to blue emission.

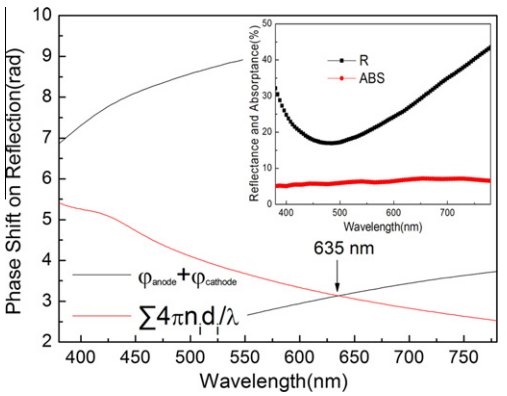

Fig. 2b. The calculated round-trip phase changes for 95 nm organic layers between two electrodes and the phase changes on two electrodes for normal incidence; Insert is the calculated optical reflectance and absorptance curves of MAM coating.

to the light emission near 635 nm due to constructive interference. High reflectance at shorter wavelength would attenuate the blue emission intensity near 439 nm where the destructive interference arises. In order to clarify the microcavity effect in the device, we calculated the cavity emission by considering wavelength-independment instrsinc luminescence spectra of the emitters [30], as shown in Fig. 2c. The calculated resonant wavelength of the device is 638 nm, which is agreement with the calculated result for the phase shift. We can see that the cavity emission is varied with wavelength, which will result in a different enhanced emission st different wavelength for device A. Thus, device A shows a more enhanced orange emission and less enhanced blue emission. The spectrum of device B is also shown in Fig. 2c. As can be seen from the power distribution of the spectrum of device B and the trend of the cavity emission, we can deduce the spectrum of device A. In Fig. 2c, we also calculated the normal emisson of the device, which is excellent agreement with the experiment results. All of the descriptions above result in the difference of the spectra between devices A and B.

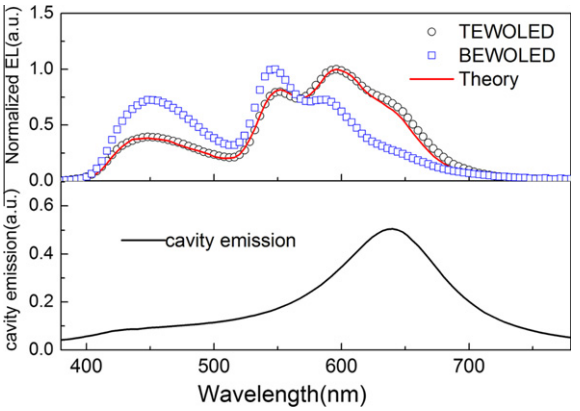

Fig. 2c. The normalized EL spectra by calculating and measuring of the devices (top) and the calculated forward directed cavity emission of device A (down).

Fig. 3 shows the CIE coordinates of devices A and B operated from 5 to 10 V. The CIE coordinates of device A change from (0.3532, 0.3270) to (0.4277, 0.3894) and that of device B change from (0.2562, 0.2689) to (0.323, 0.3533) over all the range of operation voltages. We can see that the CIE coordinates are fairly stable at high operation voltages for the two devices. Besides, the device A has a higher color rendering index (CRI) of 84 at correlated color temperature (CCT) of T_c = 3736 K (Ideal CCT values for warm white is 2500–4500 K [2]) than that of device B (CRI = 75 at T_c = 8224 K), which is an important parameter for lighting sources. This TEWOLED satisfies the CRI need for future solid-state lighting applications (with a CRI > 80) [31].

Fig. 4a shows the current density–voltage–luminance characteristics of the devices, revealing a luminance of 6398 and 6435 cd/m^2 at 9 V for devices A, and B, respectively. When the operating voltage is below 8 V, device A has a lower current density than that of device B. Fig. 4b shows the voltage-efficiency characteristics of the devices. The maximum current efficiency can reach 8.66 and 9.10 cd/A for devices A and B, respectively. We can also see that the MAM-based device has a lower roll-off of efficiency than that of ITO-based one due to the microcavity effect. The microcavity effect increases the optical mode density and consequently increases the radiation rate,

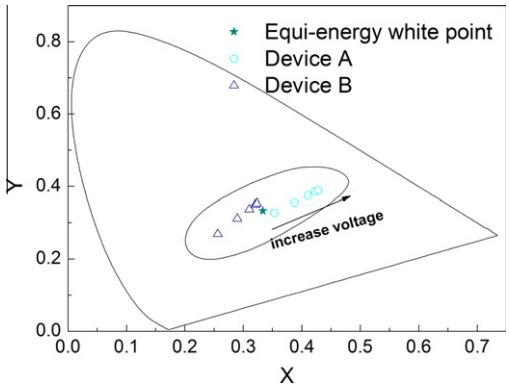

Fig. 3. The CIE coordinates of devices A and B at different operation voltage.

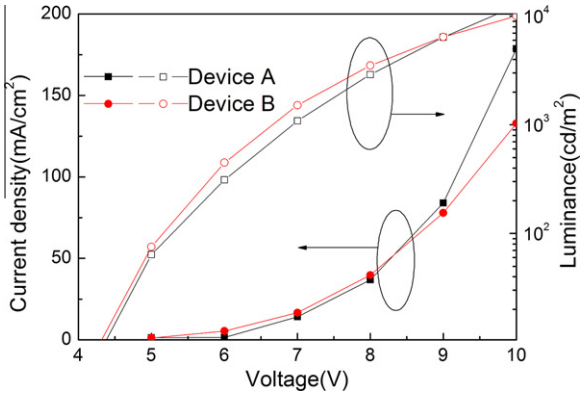

Fig. 4a. The voltage-luminance-current characteristics of the devices.

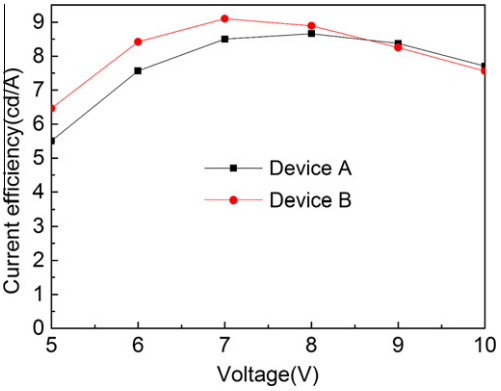

Fig. 4b. The voltage-efficiency characteristics of the devices.

which reduces the possibility of triplet–triplet annihilation [32,33]. However, the TEWOLED exhibits a lower efficiency than that of the ITO-based device. The poor contact and high energy barrier at MAM/organic interface may be two important factors which influenced the performance of MAM-based device. In addition, the thick MoO_3 layer will increase the operating voltage of the devices, as described in Ref. [34], in which thick (>10 nm) MoO_3-doped NPD hole injection layer increased the operating voltage of the device.

4. Conclusions

In summary, we have successfully obtained a warm-white top-emitting organic light-emitting device with MAM multilayer transparent cathode. A high average transmittance of 84% and low resistance of 11 Ω/□ for MAM coatings was obtained. Therefore, the MAM-based electrode structure can be used as a low resistance transparent cathode and anode for transparent or top-emitting OLEDs, especially for flexible devices, in practical applications. Comparing to ITO-based device, MAM-based TEWOLED exhibits some superior performance, such as high CRI and low CCT, which are the key factors to estimating the performance of lighting sources. Most important, the MAM multilayer can be prepared by vacuum thermal evaporation, which is compatible with OLEDs fabrication process.

Acknowledgments

This work was supported by The National Natural Science Foundation of China (Grant Nos. 60937001, 11074096, 61077045, 60723002) and The Ministry of Science and Technology of China (Grant No. 2010CB327701).

References

[1] M.A. Baldo, M.E. Thompson, S.R. Forrest, High-efficiency fluorescent organic light-emitting devices using a phosphorescent sensitizer, Nature (London) 403 (2000) 750.
[2] B.W. D'Andrade, S.R. Forrest, White Organic Light-Emitting Devices for Solid-State Lighting, Adv. Mater. 16 (2004) 1585.
[3] Y.R. Sun, N.C. Giebink, H. Kanno, B. Ma, M.E. Thompson, S.R. Forrest, High-efficiency and color-stable white organic light-emitting devices based on sky blue electrofluorescence and orange electrophosphorescence, Nature (London) 440 (2006) 908.
[4] C.L. Ho, M.F. Lin, W.Y. Wong, W.K. Wong, C.H. Chen, High-efficiency and color-stable white organic light-emitting devices based on sky blue electrofluorescence and orange electrophosphorescence, Appl. Phys. Lett. 92 (2008) 083301.
[5] C.L. Ho, W.Y. Wong, Q. Wang, D.G. Ma, L.X. Wang, Z.Y. Lin, A multifunctional iridium-carbazolyl orange phosphor for high-performance two-element WOLED exploiting exciton-Managed fluorescence/phosphorescence, Adv. Funct. Mater. 18 (2008) 928.
[6] S.J. Su, E. Gonmori, H. Sasabe, J. Kido, Highly efficient organic blue- and white-light-emitting devices having a carrier- and exciton-confining structure for reduced efficiency roll-off, Adv. Mater. 20 (2008) 4189.
[7] S. Reineke, F. Lindner, G. Schwartz, N. Seidler, K. Walzer, B. Lüssem, K. Leo, White organic light-emitting diodes with fluorescent tube efficiency, Nature (London) 459 (2009) 234.
[8] N.T. Salim, K.C. Aw, W. Gao, Z.W. Li, B. Wright, ZnO as a dielectric for organic thin film transistor-based non-volatile memory, Microelectron. Eng. 86 (2009) 2127.
[9] C.H. Li, F. Pan, F. Zhu, D. Song, H. Wang, D.H. Yan, Very low hysteresis organic thin-film transistors, Semicond. Sci. Technol. 24 (2009) 085009.
[10] D.J. Yun, S.H. Lim, T.W. Lee, S.W. Rhee, Fabrication of the flexible pentacene thin-film transistors on 304 and 430 stainless steel (SS) substrate, Org. Electron. 10 (2009) 970.
[11] M. Fischer, M. Nägele, D. Eichner, C. Schö11horn, R. Strobel, Integration of surface-micromachined polysilicon mirrors and a standard CMOS process, Sensor Actuat A: Phys. 52 (1996) 140.
[12] K.A. Honer, G.T.A. Kovacs, Integration of sputtered silicon microstructures with pre-fabricated CMOS circuitry, Sensor. Actuat. A: Phys. 91 (2001) 386.
[13] L.S. Pakula, H. Yang, H.T.M. Pham, P. French, P.M. Sarro, Fabrication of a CMOS compatible pressure sensor for harsh environments, J. Micromech. Microeng. 14 (2004) 1478.
[14] H. Kanno, Y.R. Sun, S.R. Forrest, High-efficiency top-emissive white-light-emitting organic electrophosphorescent devices, Appl. Phys. Lett. 86 (2005) 263502.
[15] S.F. Hsu, C.C. Lee, S.W. Hwang, C.H. Chen, Highly efficient top-emitting white organic electroluminescent devices, Appl. Phys. Lett. 86 (2005) 253508.
[16] M.T. Lee, M.R. Tseng, Efficient, long-life and Lambertian source of top-emitting white OLEDs using low-reflectivity molybdenum anode and co-doping technology, Curr. Appl. Phys. 8 (2008) 616.
[17] M.S. Kim, C.H. Jeong, J.T. Lim, G.Y. Yeom, White top-emitting organic light-emitting diodes using one-emissive layer of the DCJTB doped DPVBi layer, Thin Solid Films 516 (2008) 3590.
[18] W.Y. Ji, L.T. Zhang, T.Y. Zhang, G.Q. Liu, W.F. Xie, S.Y. Liu, H.Z. Zhang, L.Y. Zhang, B. Li, Top-emitting white organic light-emitting devices with a one-dimensional metallic-dielectric photonic crystal anode, Opt. Lett. 34 (2009) 2703.
[19] W.Y. Ji, L.T. Zhang, T.Y. Zhang, W.F. Xie, H.Z. Zhang, High-contrast and high-efficiency microcavity top-emitting white organic light-emitting devices, Org. electron. 11 (2009) 202.
[20] W.Y. Ji, L.T. Zhang, R.X. Gao, L.M. Zhang, W.F. Xie, H.Z. Zhang, B. Li, Top-emitting white organic light-emitting devices with down-

conversion phosphors: Theory and experiment, Opt. Express 16 (2008) 15489.
[21] D.R. Cairns, R.P. Witte, D.K. Sparacin, S.M. Sachsman, D.C. Paine, G.P. Crawford, Strain-dependent electrical resistance of tin-doped indium oxide on polymer substrates, Appl. Phys. Lett. 76 (2000) 1425.
[22] J. Lewis, S. Grego, B. Chalamala, E. Vick, D. Temple, Highly flexible transparent electrodes for organic light-emitting diode-based displays, Appl. Phys. Lett. 85 (2004) 3450.
[23] J.C.C. Fan, F.J. Bachner, H. Foley, P.M. Zavracky, Transparent heat-mirror films of TiO_2/Ag/TiO_2 for solar energy collection and radiation insulation, Appl. Phys. Lett. 25 (1974) 693.
[24] M. Bender, W. Seelig, C. Daube, H. Frankenberger, B. Ocker, J. Stollenwerk, Dependence of film composition and thicknesses on optical and electrical properties of ITO-metal-ITO multilayers, Thin Solid Films 326 (1998) 67.
[25] K.H. Choi, H.J. Nam, J.A. Jeong, S.W. Cho, H.K. Kim, J.W. Kang, D.G. Kim, W.J. Cho, Highly flexible and transparent InZnSnOx/Ag/InZnSnOx multilayer electrode for flexible organic light emitting diodes, Appl. Phys. Lett. 92 (2008) 223302.
[26] H.Q. Pang, Y.B. Yuan, Y.F. Zhou, J.R. Lian, L.F. Cao, J. Zhang, X. Zhou, ZnS/Ag/ZnS coating as transparent anode for organic light emitting diodes, J. Lumin. 122–123 (2007) 587.
[27] K.S. Yook, S.O. Jeon, C.W. Joo, J.Y. Lee, Transparent organic light emitting diodes using a multilayer oxide as a low resistance transparent cathode, Appl. Phys. Lett. 93 (2008) 013301.
[28] S.Y. Ryu, J.H. Noh, B.H. Hwang, C.S. Kim, S.J. Jo, J.T. Kim, H.S. Hwang, H.K. Baik, H.S. Jeong, C.H. Lee, S.Y. Song, S.H. Choi, S.Y. Park, Transparent organic light-emitting diodes consisting of a metal oxide multilayer cathode, Appl. Phys. Lett. 92 (2008) 023306.
[29] C.L. Mitsas, D.I. Siapkas, Generalized matrix method for analysis of coherent and incoherent reflectance and transmittance of multilayer structures with rough surfaces, interfaces, and finite substrates, Appl. Opt. 34 (1995) 1678.
[30] P. Freitag, S. Reineke, S. Olthof, M. Furno, B. Lüssem, K. Leo, White top-emitting organic light-emitting diodes with forward directed emission and high color quality, Org. Electron. 11 (2010) 1676.
[31] S. Nizamoglu, G. Zengin, H.V. Demir, Color-converting combinations of nanocrystal emitters for warm-white light generation with high color rendering index, Appl. Phys. Lett. 92 (2008) 031102.
[32] M.A. Baldo, C. Adachi, S.R. Forrest, Transient analysis of organic electrophosphorescence. II. Transient analysis of triplet-triplet annihilation, Phys. Rev. B 62 (2000) 10967.
[33] S. Reineke, K. Walzer, K. Leo, Triplet-exciton quenching in organic phosphorescent light-emitting diodes with Ir-based emitters, Phys. Rev. B 75 (2007) 125328.
[34] S.W. Cho, L.F.J. Piper, A. DeMasi, A.R.H. Preston, K.E. Smith, K.V. Chauhan, R.A. Hatton, T.S. Jones, Soft X-ray spectroscopy of C60/copper phthalocyanine/MoO_3 interfaces: role of Reduced MoO_3 on energetic band alignment and improved performance, J. Phys. Chem. C 114 (2010) 18252.

adjustable slit with the right side of the stripe always maintained in the edge of the sample. The photoluminescence (PL) emission was collected from the edge and focused into an Ocean Optics USB4000 Miniature Spectrometer. The pump intensity I is measured very near the sample, after the laser beam had been shaped into a stripe. In our experimental procedure the edge emission spectra were obtained for constant lengths L of the excitation laser stripe. At each L the laser intensity was varied from a relatively small value up to the well established ASE peak.

3. Results and discussions

In order to fit the experimental results we followed the method developed in Ref. [20], where the ASE output integrated PL intensity I_{out} from the sample edge is given by,

$$I_{out}(I,L) = \left[\frac{\alpha I_{max}}{(1+Ce^{-I/I_0})}\right]\left\{\int_0^L e^{-Ibwz^2}dz\right\}e^{IbwL^2}, \quad (1)$$

where α is a constant related to the cross section for spontaneous emission, I_0 is a threshold pump intensity, establishing the crossing from spontaneous emission (SE) to ASE regime. The value of the parameter C corresponds to how fast the system reaches an intensity higher than the threshold pump intensity. I_{max} is the maximum value of the pump intensity when $I \gg I_0$, in the saturation region of the Arrhenius expression inside brackets in Eq. (1). The integrand expression $Ibwz^2$, comes as a result of the intermediary integration process [20] where the expression $g(z) = 2Ibzw$ was assumed for the net gain. The dependence of the b parameter on the excitation length is obtained experimentally from the fits of each different $I_{out} \times I$ curve.

The experimental curves $I_{out} \times I$ (symbols) and the corresponding fits (full lines) are shown in Fig. 1 for 5 representative excitation lengths, considering the complete integration of the emitted spectra. The parameters αI_{max}, I_0, C and b used in the fitting process are displayed in Table 1. The experimental threshold intensities were determined by the method shown in Ref. [10]. The theoretical threshold intensities in Fig. 2 are found to be underestimated in comparison to the experimental ones for $L \leqslant 0.06$ cm. Although the $I_{out}(I,L)$ expression (Eq. (1)) presents this limitation it enabled us to fit quantitatively well the experimental $I_{out} \times I$ data (Fig. 1) and provided the same trend for both experimental and theoretical I_0 behavior (Fig. 2). The qualitative agreement shown in Fig. 2 also gives a further support that the interpretation of the ASE effect should take into account the excitation length dependence.

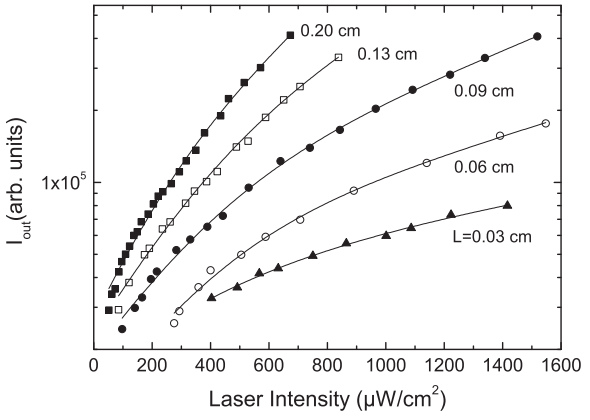

Fig. 1. Integrated I_{out} intensity as a function of pump intensity I for the excitation lengths $L = 0.03$, 0.06, 0.09, 0.13 and 0.20 cm at room temperature. The full lines are the fits obtained from Eq. (1).

The same increase of the threshold intensity with decreasing excitation length has been observed in $In_xGa_{1-x}N$ inorganic multiple quantum well waveguides [1] at room and low temperatures. In Ref. [1] it was observed that two modes competed for the gain. The mode at higher energy, even though suffering a higher self-absorption effect, possessed a higher gain in order to overcome the total losses and attain the minimum threshold intensity more easily for a relatively lower excitation length. The threshold intensity would then vary little for a further increase of the excitation length. In our case, the decrease of the threshold intensity reaching a more stable behavior at longer excitation length, has been observed experimentally. The lower the losses the smaller the variation of the threshold intensity with the excitation length.

The net gain as a function of the excitation length has been shown and discussed in the literature for different materials [2,12,14,20]. In inorganic materials it initially increases rapidly, reaching a maximum and then decreases up to a stabilized value [2,12]. For erbium-doped fiber amplifiers [14] the gain increases monotonically to a saturation regime. In this work the net gain, for excitation lengths longer than 0.03 cm, decreases slowly to a broad minimum at around 0.15 cm and then increases slightly for higher excitation lengths (Fig. 3). For excitation lengths shorter than 0.03 cm, the net gain curve (dashed line in Fig. 3) was estimated by considering the extrapolation of the b parameter, which was based on its growing trend with decreasing excitation length, as derived from the experimental data (see Table 1). We have also considered that $g(0) = 0$ (i.e. for the zero excitation length the gain should be zero). In comparison with the net gain curve in Ref. [20], the maximum in our case (Fig. 3) occurs at a shorter length around $L = 0.03$ cm, which would be expected due to the relatively higher PL quantum yield of PFO. Thus, the model used here points out that the smaller the L required for maximum gain, the better the material gain characteristic of the polymer.

In a general way the net gain curve as a function of the excitation length follows some common trends for these different materials, which does not agree with a constant g assumed to analyse the ASE intensity [3,6,10]. The gL function considering the net gain g as obtained here and a constant net gain $g = 420\ \text{cm}^{-1}$ (inset of Fig. 3) shows a match between the curves only at smaller excitation lengths. In addition, by assuming a net gain independent of the excitation length, only dependent on the laser intensity($g \propto I$), we find a final ASE intensity expression given by a simple exponential function $I_{out} \propto (e^{\sigma IL} - 1)$ (σ being a

Table 1
Fit parameters for the $I_{out} \times I$ curves at different lengths of the excitation laser stripe L. The error of the excitation length L corresponds to a maximum 0.005 cm. The errors of the other parameters are given by the standard deviation coming from the fitting method. The column I_{0exp} depicts the values of the experimental threshold intensities.

L (cm)	αI_{max} ($\times 10^6$)	C	I_0 (μW/cm^2)	I_{0exp} (μW/cm^2)	b (μW/cm^{-1})
0.03	1.4 ± 0.5	1.7 ± 0.5	361 ± 212	644 ± 220	108 ± 49
0.04	1.1 ± 0.2	1.7 ± 0.2	301 ± 84	626 ± 220	75 ± 12
0.06	0.9 ± 0.1	3.6 ± 0.5	269 ± 51	319 ± 38	43 ± 5
0.07	0.8 ± 0.1	2.5 ± 0.4	272 ± 63	327 ± 50	39 ± 3
0.09	0.9 ± 0.1	3.5 ± 0.2	279 ± 21	270 ± 65	25 ± 1
0.11	0.8 ± 0.1	3.3 ± 0.5	256 ± 25	238 ± 38	23 ± 2
0.13	0.9 ± 0.3	4.0 ± 1.6	257 ± 30	237 ± 35	17 ± 3
0.15	0.6 ± 0.2	2.6 ± 0.9	239 ± 39	168 ± 38	16 ± 2
0.17	0.8 ± 0.3	4.0 ± 1.6	226 ± 22	173 ± 20	11 ± 2
0.20	0.5 ± 0.2	2.7 ± 1.2	199 ± 38	176 ± 24	11 ± 2

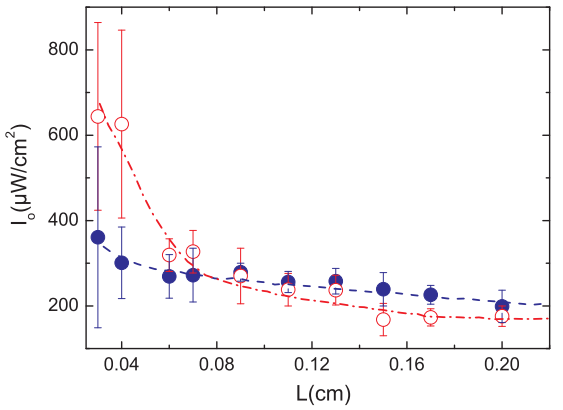

Fig. 2. The theoretical (full circles) and experimental (open circles) threshold intensity I_0 as a function of the excitation length L. The dashed and dot-dashed lines in the respective curves are guides for the eyes.

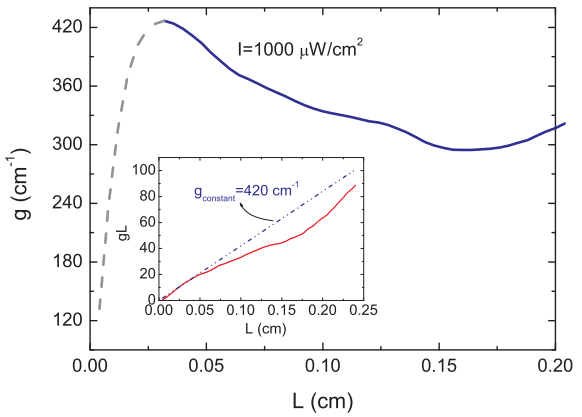

Fig. 3. The net gain curve as a function of the excitation length L with $I = 1000$ μW/cm^2. The net gain curve was obtained from the expression $g(z) = 2Ib(z)zw$ given in Ref. [20]. The dashed part of the gain curve is an estimate of the net gain in the range $0 < L < 0.03$ cm obtained by extrapolation (see text). The full line part is obtained by interpolation of the b data from Table 1. In the inset we compare the gL expression as a function of L for the net gain considered in this work (full line) and for a constant net gain $g = 420$ cm^{-1} (dashed dot dot line), which corresponds to the maximum value of the gain curve.

constant), which does not allow us to perform the fitting of all $I_{out} \times I$ experimental curves.

4. Conclusions

In summary, the theoretical method whereby the net gain depends on the excitation length L [20], was successfully employed to fit the experimental ASE intensity behavior of PFO thin film waveguides, as well as to provide the same qualitative behavior for the threshold intensity as a function of L. The experimental threshold intensity was observed to increase about 3-fold with decreasing excitation length in comparison to the work of Silvestre et al. [22], where an increase of about 6 times has been observed. This is a direct consequence of the higher PL quantum yield [PLQY = (21 ± 2) %] of the PFO film used here [23], which also presented a threshold intensity three orders of magnitude lower. The variation of the threshold intensity with the excitation length depends on the quantum efficiency characteristic of the luminescent material and gives further support to the gain dependence on the excitation length. The enhancement of the ASE intensity at different excitation lengths, however, represents a more general characteristic of the conjugated polymer waveguided systems, being independent if it is a low or high gain material, and can only be explained assuming the gain dependence on the excitation length.

Acknowledgments

We kindly acknowledge K.T. Kamtekar and M.R. Bryce from the Department of Chemistry, University of Durham, UK, to provide us the PFO polymer. L.A.C. thanks FAPEMIG, CAPES for financial support, and also CNPq from Brazil for the visitor fellowship during his sabbatical period at the Physics Department, University of Durham, United Kingdom.

References

[1] T.J. Schmidt, S. Bidnyk, Y.-H. Cho, A.J. Fischer, J.J. Song, S. Keller, U.K. Mishra, S.P. DenBaars, Amplification path length dependence studies of stimulated emission from optically pumped InGaN/GaN multiple quantum wells, MRS Internet J. Nitride Semicond. Res. 4S1 (1999) G6.54.

[2] K. Kihm, R.A. Taylor, J.F. Ryan, T. Someya, Y. Arakawa, Analysis of gain saturation in $In_{0.02}Ga_{0.98}N/In_{0.16}Ga_{0.84}N$ multiple quantum wells, Appl. Phys. Lett. 79 (2001) 3434–3436.
[3] Y. Sorek, R. Reisfeld, I. Finkelstein, S. Ruschin, Light amplification in a dye-doped glass planar waveguide, Appl. Phys. Lett. 66 (1995) 1169–1171.
[4] F. Hide, M.A. Díaz-García, B.J. Schwartz, M.R. Andersson, Q. Pei, A.J. Heeger, Semiconducting polymers: a new class of solid-state laser materials, Science 273 (1996) 1833–1836.
[5] C. Zens, W. Graupner, S. Tasch, G. Leising, K. Müllen, U. Scherf, Blue green stimulated emission from a high gain conjugated polymer, Appl. Phys. Lett. 71 (1997) 2566–2568.
[6] M.D. McGehee, R. Gupta, S. Veenstra, E. Kirk Miller, María A. Díaz-García, A.J. Heeger, Amplified spontaneous emission from photopumped films of a conjugated polymer, Phys. Rev. B 58 (1998) 7035–7039.
[7] S.V. Frolov, W. Gellemann, M. Osaki, K. Yoshino, Z.V. Vaderny, Cooperative emission in π-conjugated polymer thin films, Phys. Rev. Lett. 78 (1997) 729–732.
[8] T. Kobayashi, M. Flämmich, G. Jordan, R. D'Arcy, M. Rüther, W.J. Blau, Y. Suzuki, T. Kaino, Blue-green small-signal gain and saturation in a luminescent polymer gain medium, Appl. Phys. Lett. 89 (2006) 131119.
[9] M. Reufer, J. Feldmann, P. Rudati, A. Ruhl, D. Mller, K. Meerholz, C. Karnutsch, M. Gerken, U. Lemmer, Amplified spontaneous emission in an organic semiconductor multilayer waveguide structure including a highly conductive transparent electrode, Appl. Phys. Lett. 86 (2005) 221102.
[10] J.Y. li, F. Laquai, G. Wegner, Amplified spontaneous emission in optically pumped neat films of a polyfluorene derivative, Chem. Phys. Lett. 478 (2009) 37–41.
[11] J. Mysliwiec, L. Sznitko, S. Bartkiewicz, A. Miniewicz, Z. Essaidi, F. Kajzar, B. Sahraoui, Amplified spontaneous emission in the spiropyran-biopolymer based system, Appl. Phys. Lett. 94 (2009) 241106.
[12] C. Lange, M. Schwalm, S. Chatterjee, W.W. Rühle, N.C. Gerhardt, S.R. Johnson, J.-B. Wang, Y.-H. Zhang, The variable stripe-length method revisited: improved analysis, Appl. Phys. Lett. 91 (2007) 191107.
[13] M. Anni, The role of the β-phase content on the stimulated emission of poly(9,9-dioctylfluorene) thin films, Appl. Phys. Lett. 93 (2008) 023308.
[14] K. Bertilsson, P.A. Andrekson, T. Carlnãs, A method to predict the large signal gain dependence on length of erbium-doped fiber amplifiers, Opt. Fiber Tech. 1 (1995) 158–161.
[15] S. Kim, R. Sharma, B. Kim, H.-S. Yang, K. Kyhm, Modal gain enhancement by cylindrical waveguide and gain saturation in CdSe nanocrystal quantum dots, J. Phys. D Appl. Phys. 42 (2009) 095403.
[16] M.D. McGehee, M.A. Díaz-García, F. Hide, R. Gupta, E.K. Miller, D. Moses, A.J. Heeger, Semiconducting polymer distributed feedback lasers, Appl. Phys. Lett. 72 (1998) 1536–1538.
[17] C. Karnutsch, C. Gärtner, V. Haug, U. Lemmer, T. Farrell, B.S. Nehls, U. Scherf, J. Wang, T. Weimann, G. Heliotis, C. Pflumm, J.C. deMello, D.D.C. Bradley, Low threshold blue conjugated polymer lasers with first- and second-order distributed feedback, Appl. Phys. Lett. 89 (2006) 201108.
[18] C. Karnutsch, C. Pflumm, G. Heliotis, J.C. deMello, D.D.C. Bradley, J. Wang, T. Weimann, V. Haug, C. Gärtner, U. Lemmer, Improved organic semiconductor lasers based on a mixed-order distributed feedback resonator design, Appl. Phys. Lett. 90 (2007) 131104.
[19] K. Yamashita, A. Arimatsu, N. Takeuchi, M. Takayama, K. Oe, H. Yanagi, Multilayered solid-state organic laser for simultaneous multiwavelength oscillations, Appl. Phys. Lett. 93 (2008) 233303.
[20] I. Silvestre, P.W.B. Marques, M. Valadares, L.A. Cury, Gain coefficient method for amplified spontaneous emission in thin waveguided film of a conjugated polymer, Appl. Phys. Lett. 93 (2008) 163307.
[21] M. Ariu, M. Sims, M.D. Rahn, J. Hill, A.M. Fox, G.D. Lidzey, M. Oda, J. Cabanillas-Gonzalez, D.D.C. Bradley, Exciton migration in β-phase poly(9,9-dioctylfluorene), Phys. Rev. B 67 (2003) 195333.
[22] I. Silvestre, P.W.B. Marques, M. Valadares, L.A. Cury, Response to comment on 'Gain coefficient method for amplified spontaneous emission in thin waveguided film of a conjugated polymer' [Appl. Phys. Lett. 94, 106101 (2009)], Appl. Phys. Lett. 94 (2009) 106102.
[23] The PLQY of the PFO material was measured following the method developed by L.-O. Palsson, A.P. Monkman, Measurements of solid-state photoluminescence quantum yields of films using a fluorimeter, Adv. Mater. 14 (2002) 757–758.

(p-type) semiconductor film by using PVA as the dielectric layer and PLGA as the substrate of a biodegradable p-type thin-film transistor [27]. These previous accomplishments point to the importance of combining organic electronics and synthetic organic biodegradable materials to take a first step towards biodegradable and environmentally sustainable electronic devices.

Very recently silk fibroin was used as dielectric in a p-type pentacene transistor with a high mobility value [28], which confirms the feasibility of using silk as gate dielectrics in OFETs. Here, we show that silk-fibroin can be integrated as an efficient dielectric also in n-type and light-emitting field-effect organic transistors. These results open the way towards the development of multifunctional optoelectronic devices, which in perspective can be made fully biocompatible, and eventually bioresorbable, if used in combination with biocompatible substrates and active materials.

2. Experimental

Fig. 1 shows the schematic of the fabricated n- and p-type silk organic thin film transistors. A 400 nm thick film of silk fibroin is spin coated from aqueous solution onto an optically transparent glass/ITO substrate, patterned 150 nm-thick ITO acting as a gate contact. The silk film is rendered water insoluble by inducing beta sheet formation (i.e. crosslinking) as previously described [18]. A 15 nm thick film of N,N′-ditridecylperylene-3,4,9,10-tetracarboxylic diimide (P13) is vacuum deposited at a sublimation rate of 0.1 Å/s as a n-type organic semiconductor for electron conduction on top of the silk film. A 50 nm thick source and drain gold contacts are vacuum thermo-deposited through a metal mask thus completing a 70 μm and 15 mm channel length and width top-contact organic field-

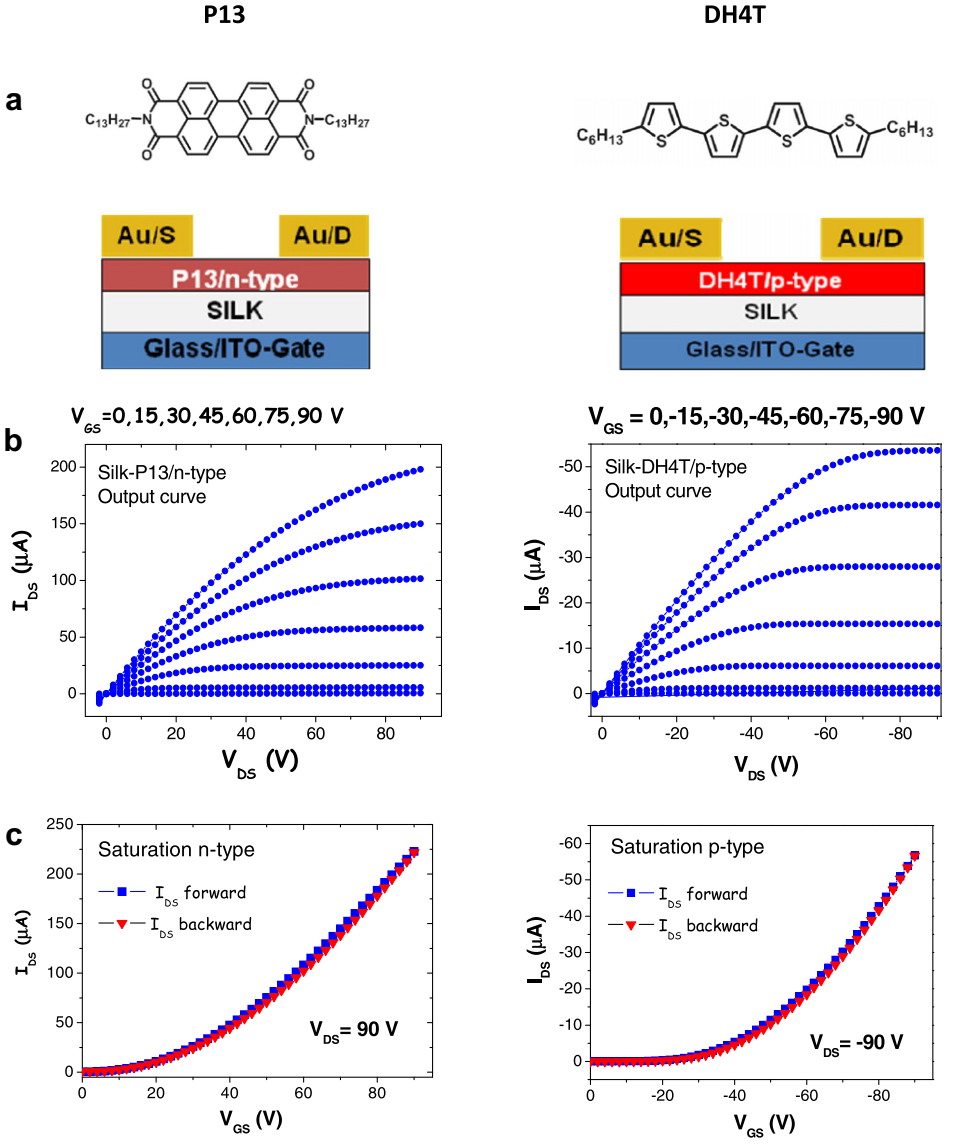

Fig. 1. Molecular structures and device architecture (a) electrical characterization of n- and p-type silk-OFET (b) *I–V* output curves and (c) saturation curves. The double experimental points are for forward and backward cycle.

effect transistor (OFET) configuration. With the same protocol and parameters, a p-type semiconductor, namely the α,ω-dihexyl-quaterthiophene (DH4T) has been grown for hole conduction. It is worth nothing that the semiconductor compounds were not modified or manipulated from their commercially available from namely, P13 by Sigma–Aldrich, and DH4T (ActivInk P0400) by Polyera Corporation. The molecular structure of the grown moieties and the output curves of the respective n- and p-type silk organic FET are shown as well in Fig. 1. Both P13 and DH4T are well known and extensively researched materials for electron (n-type) and hole (p-type) transport organic thin film transistors [6,29,30]. As such, they provide an ideal system to benchmark the silk-based OFETs and OLETs. Indeed, reference P13 and DH4T based devices were fabricated implementing different dielectric and gate electrode materials. In particular, the substrates consisted of heavily doped n^{+2} silicon with a 300 nm thick-layer of thermal oxide (SiO_2) and of glass/ITO with 450 nm-thick polymethylmethacrylate (PMMA). The electrical characterization of the fabricated silk-organic transistors has been performed by probe station equipped with a parametric analyzer both in atmosphere controlled dry-box systems and in air-room temperature. Is worth noting how the *I–V* characteristics of OFETs can be adequately described by standard models [31,32] and the mobility of the n- and p-type silk based transistors were derived from the saturation curves. For electroluminescence measurements the probe station was equipped with a planar S1337 Hamamatsu photodiode for collecting light through the ITO/PMMA/substrate. The elec-

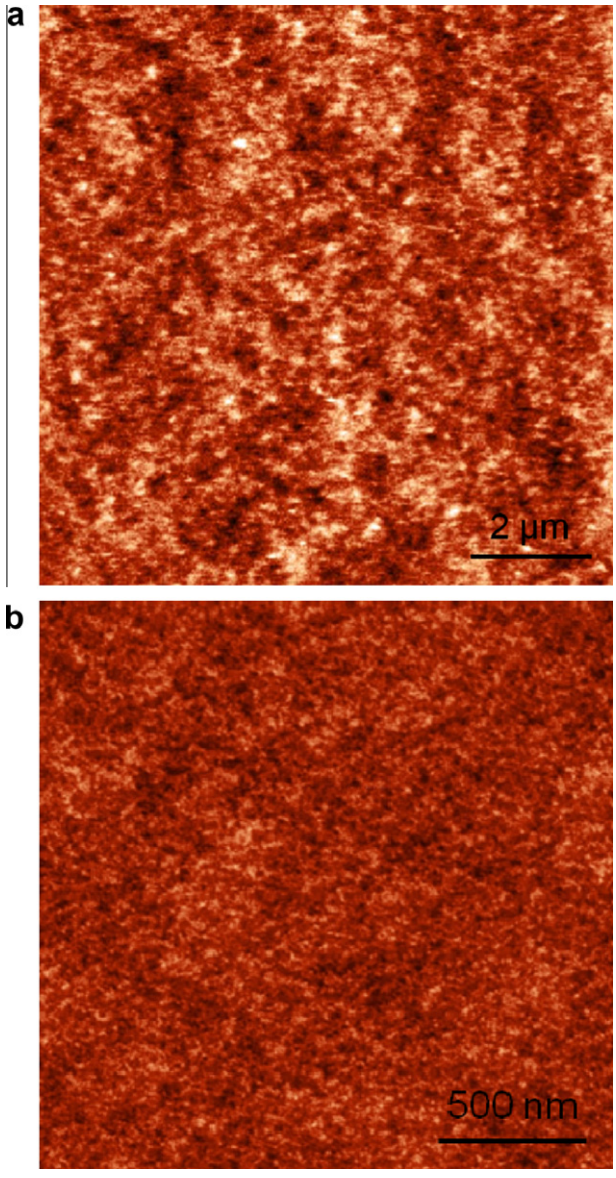

Fig. 2. Topographic AFM image of (a) the silk dielectric layer deposited onto glass/ITO and (b) of the PMMA layer deposited onto glass/ITO.

troluminescent signal was corrected for the photosensitivity of the photodiode considering the P13 photoluminescence spectrum.

Atomic Force Microscope (AFM) topographical images were collected using an NT-MDT Solver Scanning Probe Microscope in tapping mode with the samples kept in air.

3. Results and discussion

The saturation curves measured at $V_{d-s} = \pm 90$ V, where V_{d-s} is the voltage between drain–source contacts depending on the n- or p-type semiconducting material, are reported in Fig. 1. The two nearly overlapping lines are for forward and backward scanning of the gate–source voltage while V_{d-s} is kept constant. This indicates the near absence of hysteresis and consequently low charge trapping in the silk dielectric layer in particular for electron transport, i.e. the silk–P13 device.

Indeed, as it can be seen from Fig. 2a the AFM investigation on silk dielectric layer reveals a smooth and homogeneous morphology with a root-mean-square roughness value similar to that of PMMA (Fig. 2b) which is around 0.5 nm. This feature can explain the almost complete absence of hysteresis in the electrical characteristics of silk based OFETs and OLETs.

Table 1
Comparison of the mobility, threshold values and on/off ratio for silk p and n-type OFETs and respective standard PMMA and SiO_2 devices. The measured silk dielectric constant in the device configuration $\varepsilon_s = 6$. The channel length and width are 70 μm and 15 mm, respectively for both silk and PMMA devices. For SiO_2 the channel length is 300 μm and width 10 mm.

	DH4T p-type			P13 n-type		
	Mobility (μm)	Threshold (V_T)	On/off ratio	Mobility (μm)	Threshold (V_T)	On/off ratio
SiO_2	4×10^{-2} cm^2/V s	−3 V	10^3	0.13 cm^2/V s	21 V	10^3
PMMA	9×10^{-2} cm^2/V s	−20 V	10^2	0.3 cm^2/V s	18 V	10^4
Silk	1.3×10^{-2} cm^2/V s	−17 V	10^4	4×10^{-2} cm^2/V s	2 V	10^4

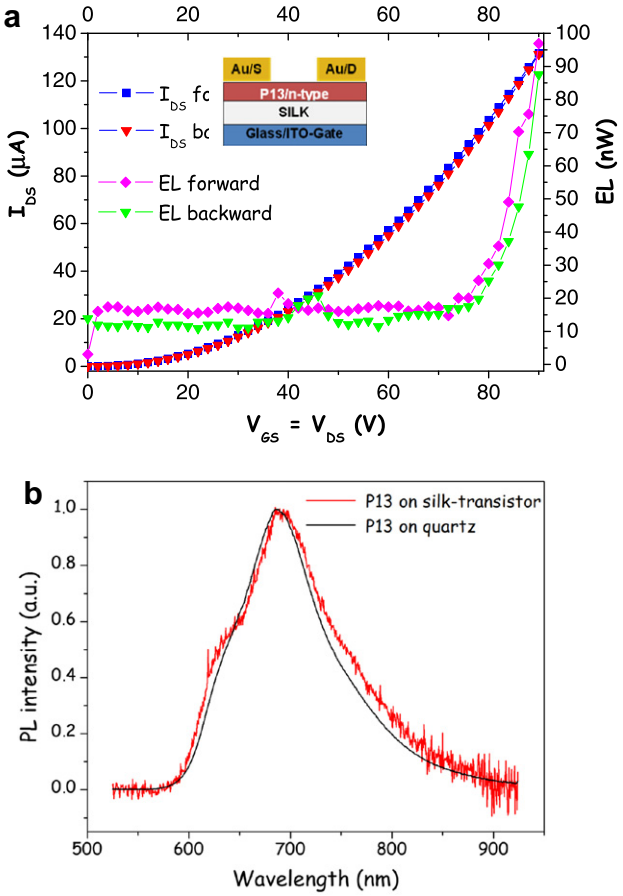

Fig. 3. (a) Electroluminescence collected from a glass/ITO/silk/P13/Au top contact unipolar silk-OLET device. The device is biased in the locus mode. The double experimental points are for forward and backward cycle. (b) Comparison of the photoluminescence spectra from P13 deposited on quartz and from P13 in silk-based OLET.

The charge mobility values associated to the measurement are $\mu_n = 4 \times 10^{-2}$ cm^2/V s for the silk–P13 and $\mu_p = 1.3 \times 10^{-2}$ cm^2/V s for the silk–DH4T. A comparison of the parameters of the silk-based devices and PMMA and SiO_2-based devices are reported in Table 1. We note that the measurements are comparable to efficient charge mobility values (n- and p-type) of thin film OFET reported in the literature [29–31] and with our results from standard SiO_2–PMMA gated OFETs [29]. Moreover, we should underline how the measured voltage threshold for the silk–P13 transistor is one order of magnitude lower, namely 2.0 V at 20 V, than the respective standard OFET. The other defining parameter to assess the performance of an OFET is the on/off switch ratio. Which we also include in the comparisons of Table 1. In this case, the switching rate of 10^4 matches the highest values reported for thin film organic transistor based on P13 and DHFT organic semiconductors.

To explore optical utility in these devices, organic light emitting transistors have been also studied, These recently designed structures [6–11] have the ability to combine in a single device the advantages and functions of a transistor and of electroemission. Moreover, electroemission efficiency and nanoscale localization of the light emission make OLETs a breakthrough multifunctional device concept. The first evidence of OLETs emission has been demonstrated for a unipolar emitting device [6,7].

To study these results in silk, we have leveraged the best-performing silk-transistor, (the silk–P13), and operated the device in the locus mode. The emission was collected by using a calibrated photodiode. The obtained results are shown in Fig. 3. When $V_{g-s} = V_{d-s}$ of 75 V, a nonlinear intensity of the emitted light is observed. The measured relevant operation parameters assessing the performance of the unipolar silk-OLET device are: V_{th} = 1.4 V; n-mobility = 0.013 cm^2/V s; light emission intensity = 100 nW at $V_{g-s} = V_{d-s}$ = 90 V. This clearly demonstrates the first observation of electroluminescence emission from OFET devices employing silk as gate dielectric. In order to check possible effects on the optical properties of P13 due to the interaction with the silk layer, we compared the photoluminescence spectrum of P13 layer measured directly in the OLET device with the photoluminescence spectrum of an optically inert quartz substrate (Fig. 3b). It is shown that silk does not affect the optical properties of the P13 layer and that P13 is the only emitting species in the OLET device.

A systematic and quantitative comparison of the optoelectronic characteristics of the silk-based OLET with those of the conventional ones [8] is beyond the scope of present paper.

4. Conclusions

The present results demonstrate how natural silk fibroin can be successfully used as a dielectric material for fabrication of advanced n- type silk-based organic transistors and light emitting transistors. The combined use of silk in electronics as presented here in combination with previous work on silk-based photonics, thin-film and conformal electronics sets the stage for a powerful approach towards the fabrication of eco-sustainable and multifunctional bioactive devices. The favorable substrate properties of this all natural biopolymeric substrate [33,34] can be also exploited in the future as an alternative to the rigid substrates used here enabling fully degradable devices and opening a path for sustainable high-tech manufacturing.

Acknowledgments

Financial support from EU projects PF6 035859-2 (BIMORE) and FP7-ICT-248052 (PHOTO-FET), Italian MIUR projects FIRB-RBIP06YWBH (NODIS), FIRB-RBIP0642YL (LUCI), FIRB-RBPR05JH2 (ITALNANONET) and Italian MSE project Industria2015 (ALADIN) is acknowledged.

This material is based upon work supported in part by the US Army Research Laboratory and the US Army Research Office under Contract No. W911 NF-07-1-0618 and by the DARPA-DSO the AFOSR and the NIH P41 Tissue Engineering Resource Center.

References

[1] John A. Rogers, Yonggang Huang, PNAS 27 (2009) 10875–10876.
[2] Dae-Hyeong Kim, John A. Rogers, Adv. Mater. 20 (2008) 4887–4892.
[3] S.R. Forrest, Nature 428 (2004) 911.
[4] Th. Birendra Singh, Niyazi Serdar Sariciftci, Ann. Rev. Mater. Res. 36 (2006) 199–230.
[5] Ananth Dodabalapur, Mater. Today 9 (2006) 24–30.
[6] Michele Muccini, Nat. Mater. 5 (2006) 605–613.
[7] A. Hepp et al., Phys. Rev. Lett. 91 (2003) 157406.
[8] C. Rost et al., Appl. Phys Lett. 85 (2004) 1613–1615.
[9] J. Zaumseil, R.H. Friend, H. Sirringhaus, Nat. Mater. 5 (2006) 69–74.
[10] R. Capelli et al., Nat. Mater. 9 (2010) 496–503.
[11] C. Santato et al., Appl. Phys. Lett. 86 (2005) 141106.
[12] P. Melpignano, V. Biondo, S. Sinesi, Michael T. Gale, Susanne Westenhöfer, M. Murgia, S. Caria, R. Zamboni, Appl. Phys. Lett. 88 (2006) 153514.
[13] J.A. Hagen, W. Li, A.J. Steckl, J.G. Grote, Appl. Phys. Lett. 88 (2006) 171109.
[14] Fiorenzo G. Omenetto, David L. Kaplan, Nat. Photonics 2 (2008) 641–643.
[15] X. Wang, J.A. Kluge, G.G. Leisk, D.L. Kaplan, Biomaterials 29 (2008) 1054–1064.
[16] U.-J. Kim et al., Biomacromolecules 5 (2004) 786–792.
[17] H.-J. Jin, S.V. Fridrikh, G.C. Rutledge, D.L. Kaplan, Biomacromolecules 3 (2002) 1233–1239.
[18] H.-J. Jin et al., Adv. Funct. Mater. 15 (2005) 1241–1247.
[19] X. Wang, H.J. Kim, P. Xu, A. Matsumoto, D.L. Kaplan, Langmuir 21 (2005) 11335–11341.
[20] C. Jiang et al., Adv. Funct. Mater. 17 (2007) 2229–2237.
[21] H. Perry, A. Gopinath, D.L. Kaplan, L. Dal Negro, F.G. Omenetto, Adv. Mater. 20 (2008) 3070–3072.
[22] B.D. Lawrence, M. Cronin-Golomb, I. Georgakoudi, D.L. Kaplan, F.G. Omenetto, Biomacromolecules 9 (2008) 1214–1220.
[23] Andrew Wiltz, Eleanor M. Pritchard, Tianfu Li, Jin-Quan Lan, David L. Kaplan, Detlev Boison, Biomaterials 29 (2008) 3609–3616.
[24] Valentina Benfenati, Stefano Toffanin, Raffaella Capelli, Laura M.A. Camassa, Stefano Ferroni, David L. Kaplan, Fiorenzo G. Omenetto, Michele Muccini, Roberto Zamboni, Biomaterials 31 (2010) 7883–7891.
[25] Peter Domachuk, Hannah Perry, Jason J. Amsden, David L. Kaplan, Fiorenzo G. Omenetto, Appl. Phys. Lett. 95 (2009) 253702.
[26] Dae-Hyeong Kim, Yun-Soung Kim, Jason Amsden, Bruce Panilaitis, David L. Kaplan, Fiorenzo G. Omenetto, Mitchell R. Zakin, John A. Rogers, Appl. Phys. Lett. 95 (2009) 133701.
[27] Christopher J. Bettinger, Zhenan Bao, Adv. Mater. 21 (2009) 1–5.
[28] C.-H. Wang, C.-Y. Hsieh, J.-C. Hwang, Adv. Mater. 23 (2011), doi:10.1002/adma.201004071.
[29] F. Dinelli, R. Capelli, M.A. Loi, M. Murgia, M. Muccini, A. Facchetti, T.J. Marks, Adv. Mater. 18 (2006) 1416–1420.

[30] P.R.L. Malenfant, C.D. Dimitrakopoulos, J.D. Gelorme, L.L. Kosbar, T.O. Graham, A. Curioni, W. Andreoni, Appl. Phys. Lett. 80 (2002) 2517–2519.
[31] S.M. Sze, Physics of Semiconductor Devices, second ed., Wiley-InterScience, New York, 1981.
[32] G. Horowitz, R. Hajlaoui, R. Bourgouga, M. Hajlaoui, Synth. Met. 101 (1999) 401–404.
[33] Dae-Hyeong Kim et al., Nat. Mater. 9 (2010) 511–517, doi:10.1038.
[34] Hu. Tao et al., Adv. Mater. 22 (2010) 3527–3531.

the need for masks used in vapor deposition and is often chosen over nozzle based methods when higher viscosity inks are required or the unreliable characteristic of nozzle clogging must be avoided. In addition, the entire LIFT process is conducted in ambient conditions making it a cost effective and convenient technique for the rapid prototyping of novel devices.

When dealing with organic molecules, LIFT presents a number of challenges. For instance, special care must be taken when the material of interest is particularly susceptible to thermal, optical, or mechanical damage [11]. Conversely, when the ink material does not strongly absorb incident laser energy, transmitted radiation inevitably interacts with the receiver substrate and can cause undesired vaporization of the transparent conducting oxide. The addition of foreign materials in the ink to absorb the laser can enable transfer in these cases but can also quench electroluminescence and hinder device operation.

To avoid these drawbacks we incorporate a polymer film absorbing layer (thickness = 2–8 μm) between the glass substrate and ink material on the donor [11,18,19]. Upon laser irradiation, a small volume of polymer nearest the polymer/glass interface absorbs the energy, forming an enclosed high pressure vapor that deforms the remaining polymer film into the adjacent ink and induces its transfer. This modified LIFT technique is termed blister-actuated laser-induced forward transfer (BA-LIFT) because the ink transfer is a consequence of laser-generated blister motion (Fig. 1a). BA-LIFT eliminates possible contamination issues associated with laser-absorbing additives or thinner laser absorbing layers by tuning the process for the absorption of laser energy solely in the polymer film and by selecting a thick enough polymer layer that will not fully decompose. In addition, BA-LIFT has been shown to successfully deposit weak laser-absorbing organic and biological materials, including systems that are optically and thermally sensitive [11,19].

In this work we use ambient laser direct-write techniques for fabricating patterned $[Ru(dtb\text{-}bpy)_3]^{2+}(PF_6^-)_2$ (Complex **1**) electroluminescent devices. To confirm the viability of the BA-LIFT process for printing damage-free luminophore molecules, nuclear magnetic resonance (NMR) spectroscopy is employed. Our devices are characterized by acquiring emission spectra and measuring luminous efficiencies and lifetimes, which are similar to literature values of devices fabricated in nitrogen environments. Finally we demonstrate the versatility of BA-LIFT, by printing multi-color luminophore patterns for future use in high-resolution device fabrication.

2. Experimental

The two employed iTMC examples are tris(4,4′-di-tert-butyl-2,2′-bipyridyl)ruthenium, $[Ru(dtb\text{-}bpy)_3](PF_6)$ [20] (Complex **1**), and bis(5-trifluoromethyl,2-(2′,4′-difluorophenyl)pyridyl), (4,4′-di-tert-butyl-2,2′-bipyridyl)iridium, $[Ir(F_5\text{-}mppy)_2(dtb\text{-}bpy)](PF_6)$ [21] (Complex **2**), both of which are prepared as previously described [20,21]. In the absence of a blue-emitting iTMC, 9-anthracenemethanol (Aldrich, 97%, Complex **3**) is selected as a surrogate, and used without further purification.

Donor substrates are produced by soaking glass slides in a solution of NOCHROMIX and sulfuric acid to remove oils and loosen debris. Slides are subsequently washed in deionized water, rinsed with acetone and ethanol, and blow dried with nitrogen. Slides are then spin coated with commercially available polyimide (HD Microsystems PI2525) at different spin speeds (3000 and 6000 RPM), and cured as in previous work to produce final film thicknesses of approximately 7 μm and 4 μm, respectively [19]. Luminophore solution is subsequently spread onto donor substrates with a wirecoater, or an aliquot of solution is drop cast onto donor substrates and spun at 1000 rpm

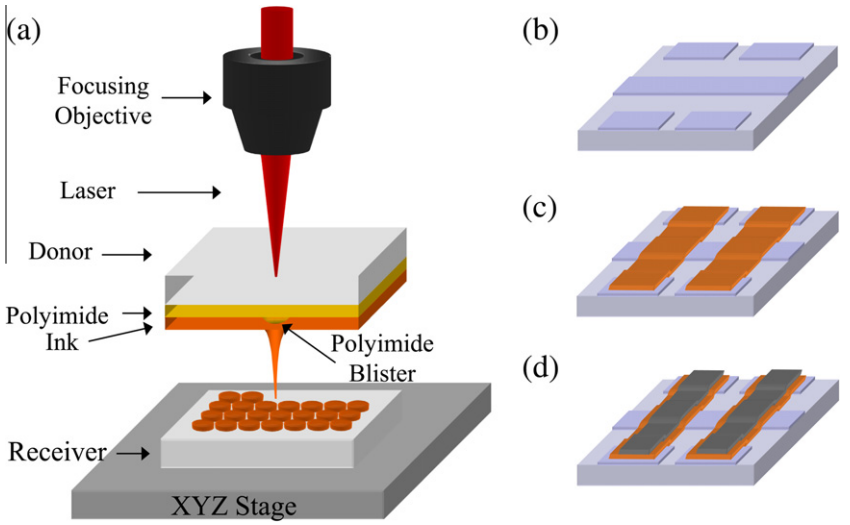

Fig. 1. (a) Illustration of the BA-LIFT process depicting ink transfer in the form of a coherent jet. Device fabrication begins with (b) laser micromachined indium tin oxide coated glass followed by (c) BA-LIFT printing of the organic ink in ambient conditions defining two $3.5 \times 12.5\ mm^2$ pads. (d) Vapor deposition of the aluminum bottom electrode completes the fabrication process.

for 20 s. Wirecoating produces a donor film thickness of 10 μm and is used to print luminophore material for the device and for the NMR measurements. Spin coating decreases the donor film thickness (1 μm) and is used to print multi-color luminophore patterns. For NMR spectroscopy and multi-color patterning experiments, solutions are created for each complex by adding 38 mg of the complex into a solution of acetonitrile/*N*-methyl-2-pyrrolidone (NMP, 1/1 v/v, 1 mL). This is heated to 50 °C for 5 min to dissolve the solute. For electroluminescent device fabrication Complex **1** (38 mg) is added to the same solvent (1 mL) with an addition of poly(methyl methacrylate) (PMMA, 6 mg).

Device fabrication begins by laser micromachining the electrically isolated Indium Tin Oxide (ITO) patterns in Fig. 1b. This is accomplished with a Nd:YVO_4 laser (λ = 355 nm, τ = 20 ns) at a laser fluence of 0.5 J/cm^2. Polyimide donor substrates and ITO receiver substrates are cleaned in acetonitrile prior to the deposition of the organo-metallic layer. Complex **1** luminophore solution is subsequently wirecoated onto a donor substrate and held at a 100 μm distance from the ITO receiver. Transfer is with the same laser focused to a 10 μm diameter at the glass/polyimide interface (fluence = 2.5 J/cm^2). The BA-LIFT process produces arrays of overlapping voxels that form two uniform pads as shown in Fig. 1c. The receiver is then dried in vacuum for 1 h to evaporate the remaining solvent. The aluminum bottom electrode is vapor deposited through a shadow mask to a final thickness of 50 nm at a rate of 1–2 Å/s. This produces two pixels located at the intersection of the top and bottom electrode (2.5 × 2.5 mm^2 each, Fig. 1d).

Photoluminescence measurements are carried out using an Hg lamp equipped with an optical filter centered at 370 nm. The devices are pre-biased to 4 V for 3 min to assist the drift of PF_6^- counterions to the ITO electrode, followed by a quick ramp to a higher voltage (~6 V) to ensure the device turns on. All emission spectra are recorded with a colorimeter and are later normalized by peak intensity. Time-dependent electroluminescent measurements are conducted from pristine devices without a pre-bias. For NMR measurements ½ mL of deuterated acetone is used to rinse the luminophore material off the ITO acceptor slides. For droplet characterization printed arrays are illuminated and images are captured with a fluorescent microscope equipped with a standard CCD camera.

3. Results and discussion

An image of the working device is shown in Fig. 2a. Under room light illumination, two bands of printed luminophore (orange–red hue) are visibly wider than the aluminum electrode, eliminating the possibility of shorting between the top and bottom electrodes. Under forward bias (ITO+, Al−), bright electroluminescence is visible from the pixels (Fig. 2b). The uniformity of the electroluminescence suggests that the ITO electrode remains undamaged during the BA-LIFT process, since damage would impede uniform charge transfer across the electrode and into the active material.

Charge injection in this organo-metallic molecule differs from typical small molecule organics due to the presence of mobile counterions. In forward bias, PF_6^- counterions migrate towards the ITO electrode [5], creating high electric fields in its vicinity, aiding the injection of holes to the highest occupied molecular orbital of the $[Ru(dtb\text{-}bpy)_3]^{2+}$ metal center [6,7]. This depletes the region near the aluminum electrode of PF_6^- ions, enhancing the injection of electrons to the lowest unoccupied molecular orbit of the $[Ru(dtb\text{-}bpy)_3]^{2+}$ ligand. This implies that for a given voltage, device current and light emission are time dependent quantities that depend on the extent of counterion migration. To mitigate this behavior, turn-on time can either be reduced by the addition of an ionic solvent containing PF_6^- counterions [5,21] or through prebiasing the device [22], the later of which is done in this work according to the prior literature [5,23].

We characterize the emission spectrum of the printed Complex **1** film via photoluminescence (PL) as shown in Fig. 2c. The PL spectrum of the printed luminophore matches the non-printed control solution, with a peak wavelength (630 nm) analogous to literature values [20,22,24]. This ensures that the photoluminescent properties of the molecule are not altered during the BA-LIFT process. Similarly, a direct match in peak wavelength (630 nm) and shape is present between the electroluminescence (EL) and PL spectra in Fig. 2c, indicating undamaged electroluminescent properties. Similar results are available for devices fabricated in nitrogen environments from a spin coated solution of Complex **1** [20,22]. This implies that the presence of air and moisture during the fabrication and testing of our device does not alter its

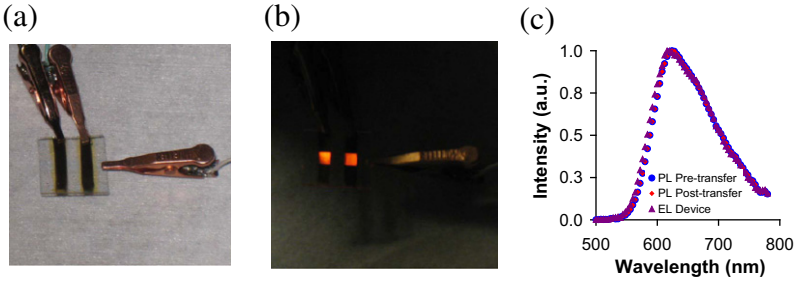

Fig. 2. (a) Image of the device (12.5 × 12.5 mm^2) under room light illumination. (b) Device operation under ambient conditions depicting two 2.5 × 2.5 mm^2 orange–red pixels. (c) Post-transfer PL and device EL match the pre-transfer solution PL. (For interpretation of the references to colour in this figure legend, the reader is referred to the web version of this article.)

emission spectrum and verifies the air tolerance of this complex.

Molecular damage, which can limit device performance, cannot always be properly detected via PL and EL spectroscopy. To ensure the printing of non-damage molecules, NMR spectra are acquired using a procedure described in our earlier work [11]. Fig. 3 depicts the NMR results for the green and red molecules featured in this manuscript. The NMR spectra for the blue molecule are given in earlier work [11] and reproduced here for comparison. Spectra of samples printed via BA-LIFT are depicted in (d–f), and corresponding control samples are in (a–c). As seen, samples printed via BA-LIFT produce identical NMR spectra to control samples, indicating the absence of molecular damage during the printing process. This ensures that device performance, as in the case of the $[Ru(dtb\text{-}bpy)_3](PF_6)_2$ molecule depicted in (c and f), will not be hindered by molecular damage created during device processing.

To verify that a continuous luminophore pad is printed using BA-LIFT and not a pinhole structure often characteristic of drop-on-demand techniques, we further examine the electrical performance of the device. Current density (J) versus applied voltage (V) (Fig. 4a) is seen to exhibit the expected trend of a proper light-emitting diode. The smooth nature of the curve and absence of spikes is indicative of a device that is free of short circuits. Likewise, the linearity of luminance (EL) versus current density (Fig. 4b) is also indicative of a properly functioning device. A luminance

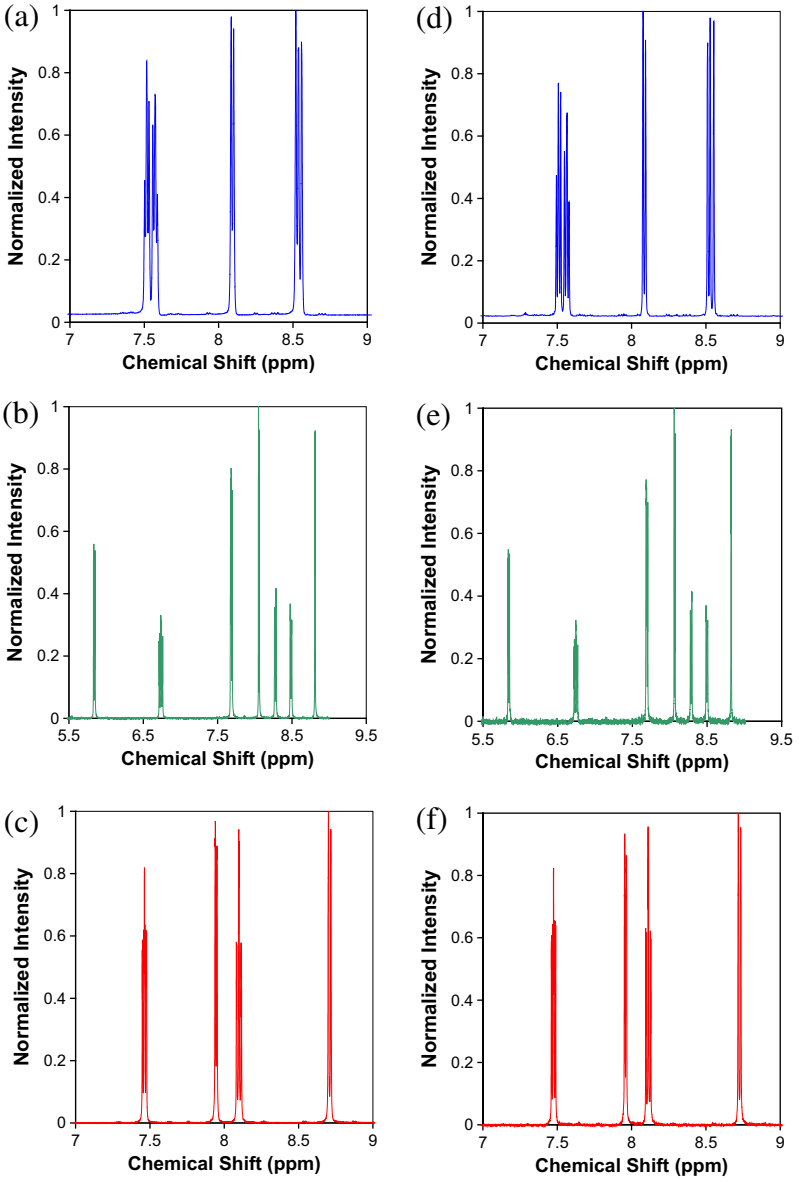

Fig. 3. Control sample NMR spectra for the (a) blue, (b) green, and (c) red molecule. BA-LIFT printed samples for the (d) blue, (e) green, and (f) red molecule display identical spectra to the control samples. The spectra from the blue molecule are reproduced from [11] for comparison. (For interpretation of the references to colour in this figure legend, the reader is referred to the web version of this article.)

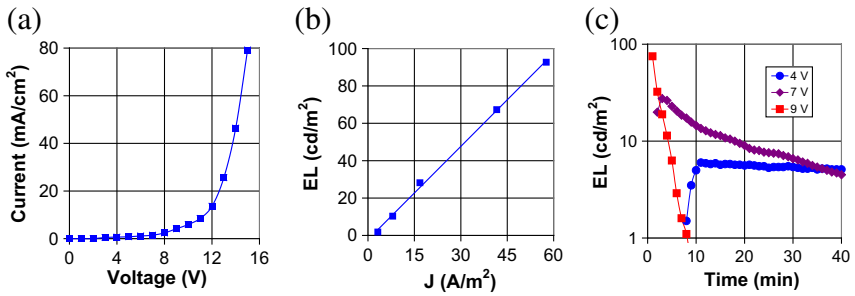

Fig. 4. (a) *I–V* and (b) EL-J measurements, and (c) time dependent EL of pristine devices for 3 bias voltages under ambient conditions.

of 93 cd/m^2 is measured at 11 V (Fig. 4b) with a device luminous efficiencies of roughly 0.39 ± 0.03 Lm/W at 3 V. This is comparable to literature values of 0.3 Lm/W given for devices fabricated by spin coating $[Ru(bpy)_3]^{2+}(PF_6^-)_2$, a molecule similar to ours, and vapor depositing a gold bottom electrode [25].

To probe the air stability of Complex **1** devices, time-dependent EL at different voltages is acquired from pristine, non-packaged and non-pre-biased devices (Fig. 4c). As expected, a reduction in turn on time and an increase in luminance is evident at higher voltages. However in accordance with literature observations, the benefits of higher voltage are outweighed by a reduction in device lifetime [5,22]. For example, at 9 V, (75 cd/m^2) peak luminance rapidly decays to its half life within two minutes of operation. The expected decrease in radiant flux is attributed to irreversible degradation of the molecule [20,22]. In contrast, a balance can be struck between peak luminance and device lifetime, through the application of a lower bias (7 V). Although device degradation rate is lower, it is still too high for practical purposes. A further decrease in applied voltage to 4 V can stabilize the device to a constant 6 cd/m^2 over 40 min. This measured lifetime increase is comparable to that reported in the literature [20] and is attributed to a combination of added poly(methyl methacrylate) and applied voltage close to the redox potential (2.5–3.0 V) [23]. We attribute the lower intensity relative to the literature to a thicker than optimal luminophore film. However, device intensity can be improved through optimized luminophore concentration, better solvent selection, or through deliberate ligand modification [26].

While our results demonstrate the ability to print millimeter sized electroluminescent devices, higher-resolution patterning is desirable in many applications. In order to demonstrate the applicability of BA-LIFT as a technique capable of creating novel architectures, micron-sized arrays of ink voxels are printed from spin coated donor substrates. The ability to handle arbitrary inks is demonstrated by laser transferring an additional green fluorescing $[Ir(F_5\text{-mppy})_2(dtb\text{-bpy})]^+(PF_6^-)$ (Complex **2**) molecule from a second donor substrate. Fig. 5a shows a phosphor array printed (fluence = 1.8 J/cm^2) from 7 μm polymer-film-coated donor substrates with an average voxel diameter of 80 μm. The irregularity in green versus red voxels is explained by a change in the overall solvent/solute surface tension which alters the voxels interaction with the receiver substrate and modifies the solute transport mechanism during solvent evaporation. More uniform voxels may be achieved by independently fine tuning each solvent for the particular molecule at hand, either through the selection of a different solvent or through the judicious combination of many. Nevertheless, the direct-write nature of BA-LIFT enables high-resolution luminophore patterning, through independent motion control of the receiver substrate, without the need for additional patterning steps. High throughput for large area coverage can be readily accomplished by high-speed laser scanning, splitting single beams into multiple beams, using patterned masks [27] or

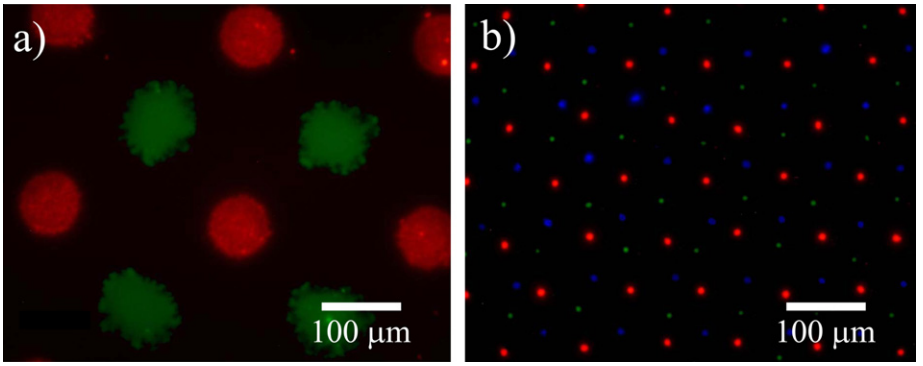

Fig. 5. (a) Fluorescent microscopy images of a typical luminophore array depicting voxel dimensions of approximately 80 μm. Ink/receiver surface tension sets the circumferential geometry. (b) Red, green, and blue voxel size is reduced to approximately 10 μm through BA-LIFT processing parameter optimization. (For interpretation of the references to colour in this figure legend, the reader is referred to the web version of this article.)

using arrays of glass microspheres [28,29] to generate high-resolution patterns.

Another attractive capability of BA-LIFT is the easy miniaturization of voxel size through processing parameter optimization. As a demonstration, a thinner polymer film thickness (4 μm) and lower fluence (0.7 J/cm^2) is selected based on previous knowledge that both quantities affect voxel size [18]. These processing parameters enable us to print multi-color voxel diameters of approximately 10 μm (Fig. 5b). Here an additional blue emitting 9-anthracenemethanol molecule (Complex **3**) is laser transferred to further demonstrate the technique's ability at printing the three colors found in standard organic light-emitting diode (OLED) display technologies. Transfers are conducted in a sequential manner from three luminophore-coated donor substrates to obtain multi-color printed arrays. Since all transfers are conducted at the same fluence, the small scatter in diameter size between colors is attributed to the variation in each of the inks fluid/substrate surface tension [30]. This can be easily controlled by altering the ink properties through small additions of different solvents to the host solution or by modulating the laser energy. Deviation in voxel diameter and position for a given color is primarily affected by statistical variations in the transferred droplet size due to the detailed fluid mechanics of the transfer process [18]. Size effects can be mitigated in a number of ways, for instance, by creating isolated wells in the donor substrate prior to transfer to pre-define the volume of transferred liquid [31], whereas positioning accuracy can be improved by reducing the spacing between the donor and receiving substrates. Nevertheless, resting voxel diameters of 10 μm are an appropriate size for future organic electronic technologies, and serve as a staring point to begin the study of structure–function relationships in these iTMCs.

4. Conclusion

This work presents a novel approach to printing light-emitting diodes from organo-metallic luminophore compounds. By employing air and moisture tolerant molecules, devices are fabricated in ambient conditions using a laser-based process termed BA-LIFT. The direct-write nature of this approach enables printing of the active organo-metallic luminophore with resolution down to 10 μm, without damage and without the need for masks, molds, etching, or vacuum processes. Devices are tested and shown to exhibit electroluminescence emission, diode behavior, and lifetimes in agreement with literature results for spin-coated devices fabricated in nitrogen environments. Our laser-based approach is compatible with rapid-prototyping and large-area electronics yet at the same time, the high printing resolution opens the door to novel experiments characterizing the structure–property relations for this important class of materials.

Acknowledgements

This work was supported by the National Science Foundation (MRSEC Program) through the Princeton Center for Complex Materials (DMR 0819860) and the Air Force Office of Scientific Research. The authors would like to thank Jim Sturm and Sigurd Wagner for time on their equipment.

References

[1] S.E. Shaheen, D.S. Ginley, G.E. Jabbour, Organic-based photovoltaics: toward low-cost power generation, MRS Bull. 30 (2005) 10.
[2] F. So, J. Kido, P. Burrows, Organic light-emitting devices for solid-state lighting, MRS Bull. 33 (2008) 663.
[3] C.J. Brabec, J.R. Durrant, Solution-processed organic solar cells, MRS Bull. 33 (2008) 670.
[4] C.J. Brabec, J.A. Hauch, P. Schilinsky, C. Waldauf, Production aspects of organic photovoltaics and their impact on the commercialization of devices, MRS Bull. 30 (2005) 50.
[5] J.D. Slinker, J. Rivnay, J.A. Defranco, D.A. Bernards, A.A. Gorodetsky, S.T. Parker, M.P. Cox, R. Rohl, G.G. Malliaras, S. Flores-Torres, H.D. Abruña, Direct 120 V, 60 Hz operation of an organic light emitting device, J. Appl. Phys. 99 (2006) 074502.
[6] A.A. Gorodetsky, S. Parker, J.D. Slinker, D.A. Bernards, M.H. Wong, G.G. Malliaras, S. Flores-Torres, H.D. Abruña, Contact issues in electroluminescent devices from ruthenium complexes, Appl. Phys. Lett. 84 (2004) 807.
[7] J.D. Slinker, J. Rivnay, J.S. Moskowitz, J.B. Parker, S. Bernhard, H.D. Abruña, G.G. Malliaras, Electroluminescent devices from ionic transition metal complexes, J. Mater. Chem. 17 (2007) 2976.
[8] C.B. Arnold, P. Serra, A. Piqué, Laser direct-write techniques for printing of complex materials, MRS Bull. 32 (2007) 23.
[9] E. Menard, M.A. Meitl, Y. Sun, J.U. Park, D.J. Shir, Y.S. Nam, S. Jeon, J.A. Rogers, Micro- and nanopatterning techniques for organic electronic and optoelectronic systems, Chem. Rev. 107 (2007) 1117.
[10] S.H. Ko, H. Pan, S.G. Ryu, N. Misra, C.P. Grigoropoulos, H.K. Park, Nanomaterial enabled laser transfer for organic light emitting material direct writing, Appl. Phys. Lett. 93 (2008) 151110.
[11] N.T. Kattamis, N.D. McDaniel, S. Bernhard, C.B. Arnold, Laser direct write printing of sensitive and robust light emitting organic molecules, Appl. Phys. Lett. 94 (2009) 103306.
[12] L. Rapp, A.K. Diallo, A.P. Alloncle, C. Videlot-Ackermann, F. Fages, P. Delaporte, Pulsed-laser printing of organic thin-film transistors, Appl. Phys. Lett. 95 (2009) 171109.
[13] M. Kandyla, S. Chatzandroulis, I. Zergioti, Laser induced forward transfer of conducting polymers, Optoelectron. Rev. 18 (2010) 345.
[14] R. Fardel, M. Nagel, F. Nüesch, T. Lippert, A. Wokaun, Fabrication of organic light-emitting diode pixels by laser-assisted forward transfer, Appl. Phys. Lett. 91 (2007) 061103.
[15] R. Fardel, M. Nagel, F. Nüesch, T. Lippert, A. Wokaun, Laser-induced forward transfer of organic LED building blocks studied by time-resolved shadowgraphy, J. Phys. Chem. C 114 (2010) 5617.
[16] A.J. Birnbaum, H. Kim, N.A. Charipar, A. Pique, Laser printing of multi-layered polymer/metal heterostructures for electronic and MEMS devices, Appl. Phys. A 99 (2010) 711.
[17] M. Colina, M. Duocastella, J.M. Fernandez-Pradas, P. Serra, J.L. Morenza, Laser induced forward transfer of liquids: study of the droplet ejection process, J. Appl. Phys. 99 (2006) 84909.
[18] M.S. Brown, N.T. Kattamis, C.B. Arnold, Time-resolved study of polyimide absorption layers for blister-actuated laser-induced forward transfer, J. Appl. Phys. 107 (2010) 083103.
[19] N.T. Kattamis, P.E. Purnick, R. Weiss, C.B. Arnold, Thick film laser induced forward transfer for deposition of thermally and mechanically sensitive materials, Appl. Phys. Lett. 91 (2007) 171120.
[20] S. Bernhard, J.A. Barron, P.L. Houston, H.D. Abruña, J.L. Ruglovksy, X. Gao, G.G. Malliaras, Electroluminescence in ruthenium(II) complexes, J. Am. Chem. Soc. 124 (2002) 13624.
[21] J.D. Slinker, C.Y. Koh, G.G. Malliaras, M.S. Lowry, S. Bernhard, Green electroluminescence from an ionic iridium complex, Appl. Phys. Lett. 86 (2005) 173506.
[22] E.S. Handy, A.J. Pal, M.F. Rubner, Solid-state light-emitting devices based on the tris-chelated ruthenium(II) complex. 2. Tris(bipyridyl)ruthenium(II) as a high-brightness emitter, J. Am. Chem. Soc. 121 (1999) 3525.
[23] H. Rudmann, M.F. Rubner, Single layer light-emitting devices with high efficiency and long lifetime based on tris(2,2′bipyridyl) ruthenium(II) hexafluorophosphate, J. Appl. Phys. 90 (2001) 4338.
[24] V. Balzani, F. Barigelletti, L. Decola, Metal-complexes as light-absorption and light-emission sensitizers, Top. Curr. Chem. 158 (1990) 31.

[25] J.D. Slinker, A.A. Gorodetsky, M.S. Lowry, J. Wang, S. Parker, R. Rohl, S. Bernhard, G.G. Malliaras, Efficient yellow electroluminescence from a single layer of a cyclometalated iridium complex, J. Am. Chem. Soc. 126 (2004) 2763.
[26] R.D. Costa, E. Ortí, H.J. Bolink, S. Graber, C.E. Housecroft, M. Neuburger, S. Schaffner, E.C. Constable, Two are not always better than one: ligand optimisation for long-living light-emitting electrochemical cells, Chem. Commun. (2009) 2029.
[27] A. Narazaki, T. Sato, R. Kurosaki, Y. Kawaguchi, H. Niino, Nano- and microdot array formation of FeSi2 by nanosecond excimer laser-induced forward transfer, Appl. Phys. Express 1 (2008) 057001.
[28] C.M. Othon, A. Laracuente, H.D. Ladouceur, B.R. Ringeisen, Sub-micron parallel laser direct-write, Appl. Surf. Sci. 255 (2008) 3407.
[29] L. Landstrom, J. Klimstein, G. Schrems, K. Piglmayer, D. Bauerle, Single-step patterning and the fabrication of contact masks by laser-induced forward transfer, Appl. Phys. A-Mater. 78 (2004) 537.
[30] M.S. Brown, N.T. Kattamis, C.B. Arnold, Time-resolved dynamics of laser induced micro jets from thin liquid films, Microfluid. Nanofluid. (2011), doi:10.1007/s10404-011-0787-4.
[31] J.A. Barron, D.B. Krizman, B.R. Ringeisen, Laser printing of single cells: statistical analysis, cell viability, and stress, Anal. Biomed. Eng. 33 (2005) 121.

areas and to prevent the formation of shorts during the top electrode contact soldering, the ITO layers were patterned by a photolithographical process. Four kinds of ITO/PEDOT/PF6/Al OLEDs – denoted as *A*, *B*, *C* and *D* – were manufactured employing four commercial PEDOT dispersions: Clevios™ P CH 8000 (previously known as Baytron® P 8000), a dispersion with PEDOT:PSS ratio 1:20 (w/w) for the *A* device; Clevios™ P AI 4083 (previously known as Baytron® P 4083), a dispersion with PEDOT:PSS ratio 1:6 (w/w) for the *B* device; a poly(3,4-ethylenedioxythiophene)-*block*-poly(ethylene glycol) – PEDOT–PEG – dispersion with *p*-toluenesulfonate (PTS) as dopant for the *C* device; a PEDOT–PEG dispersion with perchlorate (PC) as dopant for the *D* device. The dispersions characteristics and the deposition parameters are summarised in Table 1. For all the devices the PEDOT layer is 70 nm thick. After the PEDOT coating, the devices were completed with the same following steps: the obtained films were backed under nitrogen flow at 120 °C for 15 min and then PF6 was spun over the PEDOT layer at 1500 rpm from a 1.0% (w/w) chlorobenzene solution obtaining a thickness of 90 nm. After the deposition the samples were backed in vacuum at 50 °C for 3 h. Finally, the OLED structure was completed with a 200 nm thick Al layer deposited by thermal evaporation with a base pressure of 10^{-7} mbar. The active device area is 12.6 mm^2 and the final realized structure is shown into the inset of Fig. 1. Electrical analysis was performed by the means of a HP 4192A impedance analyzer and a Keithley 4200 semiconductor parameter analyzer under ambient condition.

3. Results and discussion

In Fig. 1 typical current density–voltage characteristics are shown; both the devices realized using PEDOT–PEG (C and D) are more conductive than those realized using PEDOT:PSS, and the most conductive one is that realized with a layer doped with perchlorate (D device). Comparing the results shown in Fig. 1 and Table 2 an anomalous behaviour can be observed: the device current increases with the anode potential barrier. In fact, as shown into the inset of Fig. 1, since the ITO work function is 4.8 eV and the PF6 HOMO level is 5.8 eV, reducing the PEDOT work function from 5.2 to 4.2 eV an increase of the PEDOT/PF6 hole barrier is awaited, with the effect of a reduction of the number of injected holes and therefore a reduction of the device current. Instead, the experimental results show an opposite behaviour suggesting the presence of other dominant phenomena into the device about the charge injection and transport. Capacitance-frequency and conductance-frequency measurements have been performed at various biases for all the devices and, as shown in Fig. 2 (for simplicity only for device A), these spectra don't vary with the applied voltage below the optical threshold. The bias independent capacitance is a known result tuned by charge phenomena, and it is well analyzed in literature [23]. In order to analyze the device in the under-threshold regime, we have performed all the admittance spectra at 0 V bias.

The spectra reported in Fig. 3 show capacitances having decreasing monotonic behaviour with low frequency unitary value of about 21 nF/cm^2 for the first three kinds of device and 48 nF/cm^2 for the D one. The Fig. 4 show the loss (L) spectra defined as

$$L = \frac{G}{\omega} \tag{1}$$

where G is the electrical conductance and ω the angular frequency of the applied signal: the devices A, B and C have one loss-peak while the D device shows two peaks. The loss-peak specifies the relaxation time constant (τ): 220 ns, 290 ns and 2.31 μs for A, B, C, respectively, while the device D has a low frequency peak with a time constant of 160 μs and a high frequency one of 140 ns. In literature [24] it is reported an experiment similar to ours where the authors study OLED devices with a similar structure, ITO/PEDOT:PSS/PF8/cathode, but with different PF8 layer thicknesses. The results of their measurements show an unexplained thickness dependence of the relaxation time. Our spectral results can be interpreted by a physical key shown in literature [25–31]: it is known that a semiconductor junction shows peaks in Loss vs. Frequency diagram when a trap distribution is at the semiconductor interface. In the case of a single energy level, Nicollian and Brews [32] proved that the device conductance and capacitance are described by the following equations

$$\frac{G}{\omega} = \frac{qD_S\omega\tau}{1+(\omega\tau)^2} \tag{2}$$

$$C_S = \frac{qD_S}{1+(\omega\tau)^2} \tag{3}$$

where C_S is the capacitance, q is the electron charge, D_S is the interface state density and τ is the time constant. For a distribution of more close energy trap levels [32], the device admittance is described by

$$\frac{G}{\omega} = \frac{qD_S}{2\omega\tau}\ln\left[1+(\omega\tau)^2\right] \tag{4}$$

$$C_S = \frac{qD_S}{\omega\tau}tan^{-1}(\omega\tau) \tag{5}$$

Table 1
Technological parameters of the PEDOT layers.

	PEDOT dispersion	Constituent ratio	Solution	Dopant	Deposition rate and time
A	PEDOT:PSS	1:20	3 wt.% in water	None	2000 rpm for 30 s
B	PEDOT:PSS	1:6	1.7 wt.% in water	None	2000 rpm for 20 s
C	PEDOT–PEG	1:1	1 wt.% in nitromethane	p-toluenesulfonate (PTS)	1000 rpm for 30 s
D	PEDOT–PEG	1:1	1 wt.% in perchlorate	Perchlorate (PC)	1000 rpm for 30 s

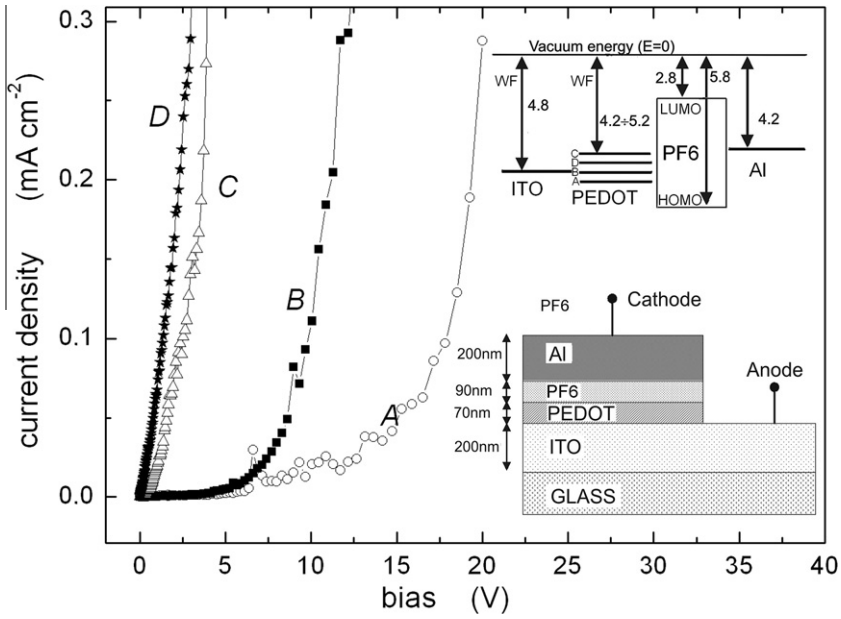

Fig. 1. Current–voltage characteristics of the polymeric OLEDs realized at different PEDOT dispersions. In the upper inset the energetic diagram of the realized samples where the PF6 HOMO and LUMO, and the ITO, PEDOT and Al work functions are drawn: the devices differ only for the kind of PEDOT dispersion with a variation in work function between 4.2 and 5.2 eV. In the lower inset the devices structure (the figure is not in scale).

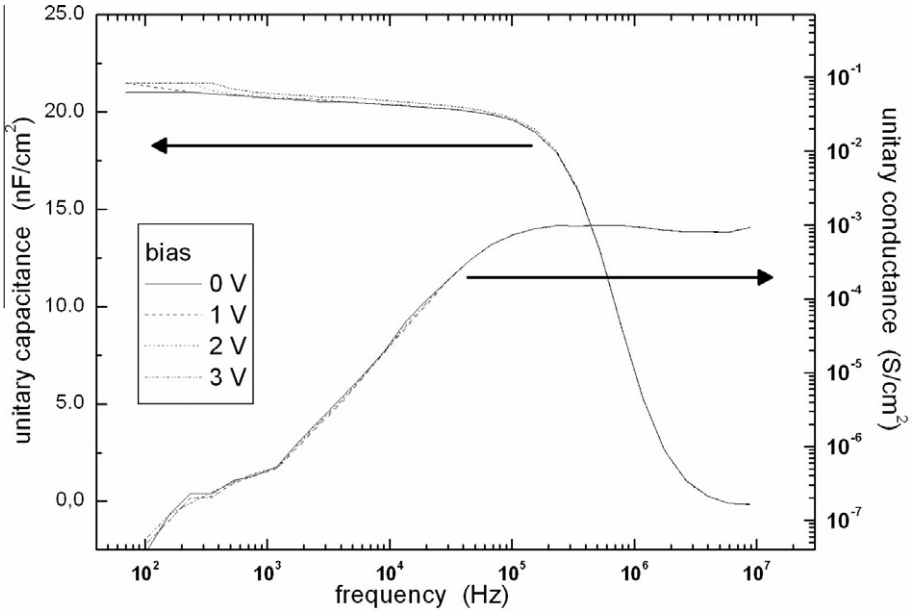

Fig. 2. Typical unitary capacitance and conductance spectra at different biases (for simplicity only the A device measurements are shown). For all A, B, C, D devices the spectra do not change with bias.

The Nicollian and Brews model was developed to study the trap effect in MOS Field Effect Transistor, but it has also been used in the analysis of the interface state distribution in MIS structure (Metal/Insulator/Semiconductor) and in particular for organic and inorganic diodes [33–36].

For each device, besides the time constant τ, we have extracted the interface state density D_S from the peaks in Fig. 4, as reported in Table 2. In Figs. 3 and 4 the continuous lines represent the Eqs. 2,3,4,5, drawn using the experimental estimation of D_S and τ. As it can be seen, a good agreement between the experimental data and the single energy level model (Eqs. 2 and 3) is obtained for the devices A, B, C and the high frequency peak of D (denoted with *c* in Figs. 3 and 4). The low frequency peak of device

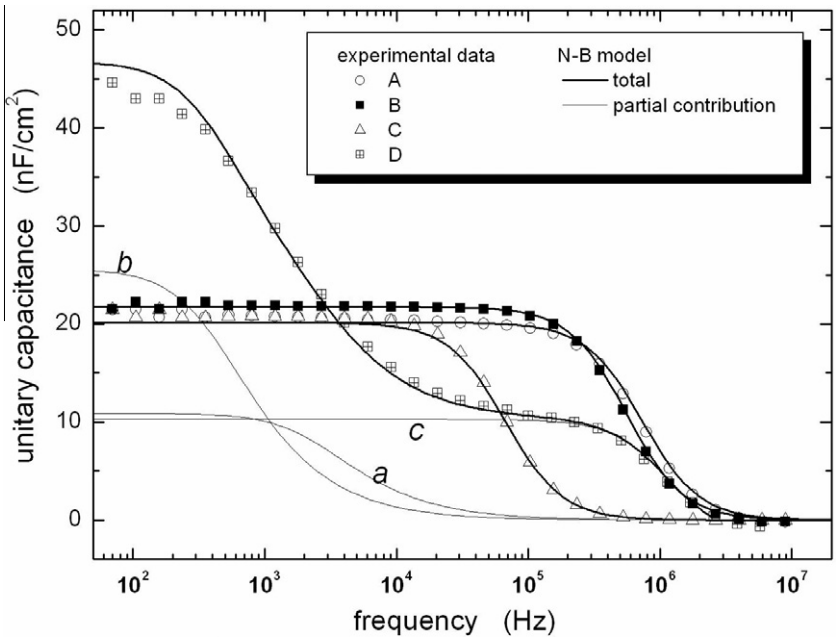

Fig. 3. Unitary capacitance spectra of the polymeric OLEDs. Decays with single time constant are visible in the figure for the A, B, C devices while a decay with a double time constant is evident for the D device.

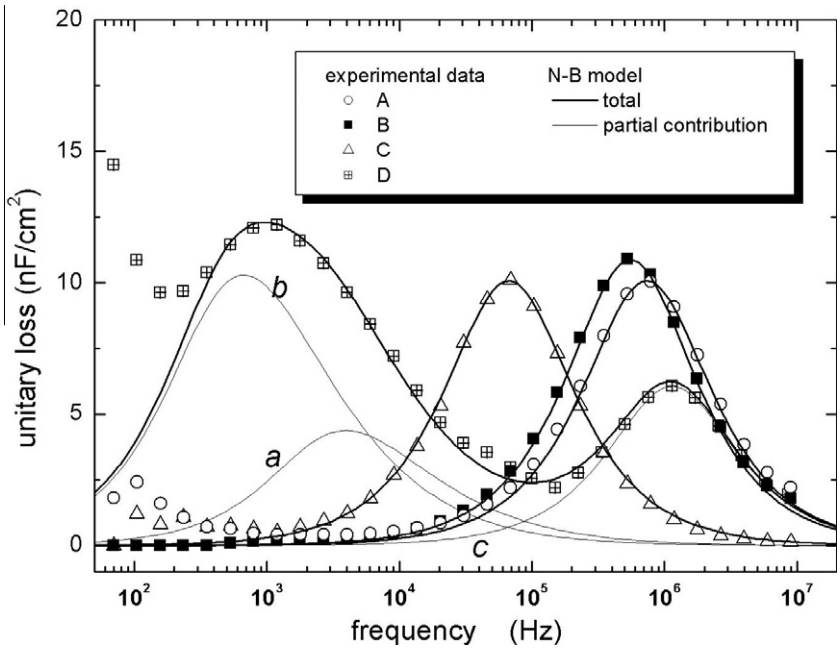

Fig. 4. Unitary loss spectra (G/ω) of the devices. A single peak spectra are visible in the figure for A, B, C devices while a double peak spectrum is evident for the D device.

D results to be the sum of two multiple-level distributions (denoted with *a* and *b* in Figs. 3 and 4) modelled by Eqs. 4, 5. The results confirm the model applicability in our case. Because the devices vary exclusively for the kind of PEDOT, the differences in admittance measurements are only imputable to this layer: in other words, the found variability between the four interface trap distributions is only ascribable to the four different PEDOT dispersions. As proposed in [41], the curves shown in Fig. 4 can be interpreted also as the effect of both interface and bulk trap distributions: in fact the low frequency peak can be ascribed to interface phenomena while the high frequency one is

usually due to bulk traps. Considering the Brunson interpretation [41] only in *D* device the bulk traps have a prominent effect. However, as pointed out by Lang [42], the capacitance measurements experience mainly the interface states, being their spatial sensitivity higher at the interface and decreasing towards bulk material [25].

As indicated above, A and B devices differ only for the PEDOT:PSS ratio determining two similar interface state distributions. The C device differs from the D only for the dopant (both are PEDOT–PEG block-copolymers), resulting in different defect state distribution; the time constant of the C device is similar to those of the A and B ones, while, for the D device, the higher frequency time constant is lower than those of the A and B devices, the two lower frequency time constants cannot be compared the other ones. As described in [25,26] the relaxation time τ can be described by the following energetic law (Arrhenius)

$$\omega_R = \frac{1}{\tau} = A_t e^{-\Delta E/k_B T} \tag{6}$$

where A_t is a material constant, ΔE is the energy deep of the state respect the band edge, k_B is the Boltzmann constant and T the absolute temperature. The hole anode barrier φ_i (for the *i*-device) can be indicated respect to one of the four kinds of device. Choosing A device as reference, we can write

$$\varphi_i = \varphi_A + \Delta\varphi_i \tag{7}$$

The total current density in every point of the device is constant. The current density at the PEDOT/PF6 junction, neglecting the electron current, can be written as the product between the holes concentration (p) and the probability of the barrier crossing (Boltzmann law), obtaining

$$J(V_{app}) = Kqp\mu_{PEDOT_i} e^{\gamma V_{app}} e^{\beta\varphi_i} = K\sigma_{PEDOT_i} e^{\gamma V_{app}} e^{\beta\varphi_i} \tag{8}$$

similar to the classical p–n junction equation. The constant K collects all the effects not ascribable to the PEDOT, μ_{PEDOT_i} is the hole mobility of the PEDOT layer, V_{app} is the applied bias, γ and β are the exponential factors related to the anode hole barrier, considered independent from the particular kind of device and finally, σ_{PEDOT_i} is the bulk conductivity of the *i* PEDOT layer.

In order to remove the effect of the PEDOT conductivity, we can divide Eq. 8 for σ_{PEDOTi}

$$\frac{J(V_{app})}{\sigma_{PEDOT_i}} = Ke^{\gamma V_{app}} e^{\beta\varphi_i} \tag{9}$$

obtaining the curves J/σ shown in Fig. 5 as function of the hole anode barrier variation $\Delta\varphi_i$ (respect to the A device) at various biases. This values follow linear behaviours for many bias voltages in a semi-log plot (except for C device which values are out of liner trend): this result suggests that the exponential dependence (at fixed temperature) on φ_i described in Eq. 8 is verified. Moreover, the slopes in Fig. 5 are different for each bias value: this result suggests that the β factor is bias dependent, but the purpose of this work is only to point out that the experimental points of Fig. 5 follows linear trends. In order to explain why the values extracted from the current–voltage characteristic of the C device do not follow the behaviour predict by Eq. 8 or Eq. 9, other phenomena have to be taken into account. The exception of the *C* device can be justified considering the different trap time constants and in particular the lower τ of the device (dominant τ). As described in [25,26] the time constant is related to the carrier capture rate c_c

$$\tau = \frac{2\pi}{c_c} \tag{10}$$

When the applied signal frequency ω is less than $1/\tau$, the traps can follow the voltage variations by the means of the emission and capture processes. Instead, for $\omega > 1/\tau$, only the untrapped charge can respond to the voltage variations giving rise to a decrement of the device capacitance and the slope of the conductance. This implies that the maximum of the normalized conductance (loss) is at $\omega = 1/\tau$, in other words at the resonance pulsation of the trapping phenomenon. From Eqs. 6 and 10 the increment of τ gives rise to a decrement of the capture rate resulting in a higher fraction of untrapped carriers available for the conduction. From Table 2, the devices A, B and D show a similar dominant τ ($140 \div 290$ ns) and so they have trap distributions with similar energetic depth. Instead the C device shows a greater dominant τ (2.31 μs), then a deeper trap distribution (a higher energy gap), that allows an higher fraction of carriers available for the conduction, for this reason the J/σ values for the device C are higher then for the other devices. The plot of Fig. 5 help us to understand also the previous reported anomaly about the current increment with the hole anode barrier (see Fig. 1 and Table 2): in fact, in Fig. 5 we can see how the current density normalized through the conductivity decreases increasing the anode hole barrier, as expected. Considering Fig. 1, where the current–voltage characterises are reported, we have to take account of the effects of the different PEDOT conductivities that have a fundamental role in the device electrical behaviour.

Table 2
Electrical and energetical properties of the PEDOT layers and interfaces.

Device/ distribution	Energy distribution	PEDOT work function (eV)	PEDOT conductivity σ $(\Omega\,\mathrm{cm})^{-1}$	State density D_S $(\mathrm{eV}^{-1}\,\mathrm{cm}^2) \times 10^{11}$	Time constant τ $(\mathrm{s}) \times 10^{-6}$
A	Single level	5.15 [20]	5×10^{-6} [40]	1.26	0.22
B	Single level	4.85 [20]	2×10^{-4} [37]	1.36	0.29
C	Single level	4.19 [38]	1×10^{-3} [39]	1.26	2.31
D (a)	Multiple levels	4.33 [38]	0.4 [39]	0.68	80.4
D (b)	Multiple levels			1.62	4.71
D (c)	Single level			0.76	0.14

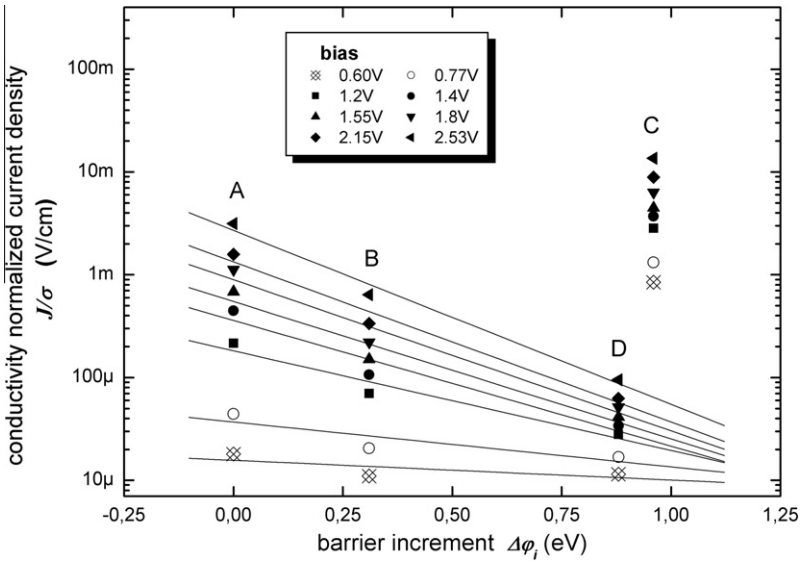

Fig. 5. Normalized current densities (J/ω) as function of the anode hole barrier increment (respect to the PEDOT work function of the A device) at different voltage biases. Only the C device does not follow the linear trend in the semi-log plot.

4. Conclusions

The analysis of polymeric OLEDs varying only for the kind of PEDOT dispersion has allowed to ascribe the variations of the admittance spectra to the effects of interface trap distribution: a good agreement between the experimental data and the Nicollian–Brews model has been found. The exponential dependence of the current on the hole barrier height has been verified only for three kinds of devices; the exception of the fourth has been explained in terms of trapping rate that tunes the increment of the number of carriers available for the conduction. The study of the normalized current has allow to evidence the importance of the PEDOT conductivity of the layer, often forgotten to advantage of consideration about the energetic levels of the layers work functions.

Acknowledgments

Support by the PHONEMA project financed by the *Ministero dell'Università e della Ricerca (MIUR)* in the ambit of the *Futuro in Ricerca* program is gratefully acknowledged.

The authors thank the precious and fundamental aid of Dr. Paolo Vacca (at the time with Portici ENEA Research Centre) in the fulfilment of the experimental part of this work.

References

[1] P.A. Lane, P.J. Brewer, J. Huang, D.D.C. Bradley, J.C. deMello, Phys. Rew. B 74 (2006) 125320.
[2] P.J. Brewer, J. Huang, P.A. Lane, A.J. deMello, D.D. Bradley, J.C. deMello, Phys. Rew. B 74 (2006) 115202.
[3] A. van Dijken, A. Perro, E.A. Meulenkamp, K. Brunner, Org. Electr. 4 (2003) 131.
[4] H.S. Woo, R. Czerw, S. Webster, D.L. Carroll, J.W. Park, J.H. Lee, Synth. Met. 116 (2001) 369.
[5] A.C. Arias, M. Granstrom, K. Petrisch, R.H. Friend, Synth. Met. 102 (1999) 953.
[6] S.W. Tsang, S.C. Tse, K.L. Tong, S.K. So, Org. Electr. 7 (2006) 474.
[7] C. Carlberg, X. Chen, O. Inganas, Solid State Ionics 85 (1996) 73.
[8] H.S. Kang, J.W. Lee, M.K. Kim, J. Joo, J.M. Ko, J.Y. Lee, J. Appl. Phys. 100 (2006) 064508.
[9] J. Yang, D.C. Martin, Sens. Actuators, A 113 (2004) 204.
[10] K.Z. Xing, M. Fahlman, X.W. Chen, O. Inganas, W.R. Salanek, Synth. Met. 89 (1997) 161.
[11] K. Lota, V. Khomenko, E. Frackowiak, J. Phys. Chem. Solids 65 (2004) 295.
[12] D. Wakizaka, T. Fushimi, H. Ohkita, S. Ito, Polymer 45 (2004) 8561.
[13] H.S. Kang, H.-S. Kang, J.K. Lee, J.W. Lee, J. Joo, J.M. Ko, M.S. Kim, J.Y. Lee, Synth. Met. 155 (2005) 176.
[14] G. Sonmez, P. Schottland, J.R. Reynolds, Synth. Met. 155 (2005) 130.
[15] P. Vacca, M. Petrosino, R. Miscioscia, G. Nenna, C. Minarini, D. Della Sala, A. Rubino, Thin Solid Films 516 (2008) 4232.
[16] H.J. Snaith, H. Kenrick, M. Chiesa, R.H. Friend, Polymer 46 (2005) 2573.
[17] Liqiang Li, M. Hirtz, W. Wang, Chuan Du, H. Fuchs, Lifeng Chi, Adv. Mater. 22 (2010) 1374.
[18] H. Okuzaki, Y. Harashina, H. Yan, Eur. Polym. J. 45/1 (2009) 256.
[19] E. Vitoratos, S. Sakkopoulos, E. Dalas, N. Paliatsas, D. Karageorgopoulos, F. Petraki, S. Kennou, S.A. Choulis, Org. Electr. 10/1 (2009) 61.
[20] N. Koch, A. Elschener, J.P. Rabe, R.L. Johnson, Adv. Mater. 17 (2005) 330.
[21] P. Vacca, M. Petrosino, A. Guerra, R. Chierchia, C. Minarini, D. Della Sala, A. Rubino, J. Phys. Chem. C 111 (2007) 17404.
[22] P. Vacca, M. Petrosino, R. Chierchia, A. Guerra, C. Minarini, A. Rubino, Macromol. Symp. 247 (2007) 333.
[23] Vishal Shrotriya, Yang Yang, J. Appl. Phys. 97 (2005) 054504.
[24] T. Okachi, T. Nagase, T. Kobayashi, H. Naito, Thin Solid Films 517 (2008) 1327.
[25] D.V. Lang, J.D. Cohen, J.P. Harbison, Phys. Rev. B 25 (8) (1982) 5285.
[26] J.D. Cohen, D.V. Lang, Phys. Rev. B 25 (8) (1982) 5321.
[27] S.S. Hegedus, E.A. Fagen, IEEE Trans. Electr. Dev. 39 (10) (1992) 2368.
[28] S.S. Hegedus, E.A. Fagen, J. Appl. Phys. 71 (12) (1992) 5941.
[29] I. Balberg, E. Gal, J. Appl. Phys. 58 (7) (1985) 2617.
[30] D. Jousse, S. Deleonibus, J. Appl. Phys. 54 (7) (1983) 4001.
[31] A. Khan, J. Woollam, Y. Chung, B. Banks, Electr. Dev. Lett. 4 (5) (1983) 146.
[32] E.H. Nicollian, J.R. Brews, MOS Physics and Technology, J. Wiley & Sons, 2003.
[33] M. Yun, R. Ravindran, M. Hossain, S. Gangopadhyay, U. Scherf, T. Bünnagel, F. Galbrecht, M. Arif, S. Guhaa, Appl. Phys. Lett. 89 (2006) 013506.
[34] R. Sahingoz, H. Kanbur, M. Voigt, C. Soykan, Synth. Met. 158 (2008) 727–731.
[35] A. Azim Khan, J.A. Woollam, Y. Chung, B. Banks, IEEE Electr. Dev. Lett. 4 (5) (1983) 146–149.

[36] D.T. Simon, M.S. Griffo, R.A. DiPietro, S.A. Swanson, S.A. Carter, Appl. Phys. Lett. 89 (2006) 133510.
[37] T. Sakurai, M. Nishiyama, Y. Nishioka, H. Kobayashi, Appl. Phys. Lett. 81 (2) (2002) 271.
[38] Y. Mochizuki, M. Mizuta, Appl. Phys. Lett. 69 (20) (1996) 3051.
[39] S. Sapp, S. Luebben, Y.B. Losovyj, P. Jeppeson, D.L. Schulz, A.N. Caruso, Appl. Phys. Lett. 88 (2006) 152107.
[40] M. Petrosino, P. Vacca, R. Miscioscia, G. Nenna, C. Minarini, A. Rubino, Proc. SPIE 6593 (2007) 659310–659311.
[41] K.M. Brunson, D. Sands, C.B. Thomas, H.S. Reehal, J. Appl. Phys. 62 (1) (1987) 185–189.
[42] D.V. Lang, in: P. Bräunlich (Ed.), Space Charge Spectroscopy in Semiconductors in Thermally Stimulated Relaxation In Solids, Springer-Verlag, USA, 1979.

an independent colour conversion layer on top of the transistor. The colour conversion is achieved by the mixture of the transmitted light from the transistor channel and the reemitted light after photoexcitation from the conversion layer at longer wavelength due to a material specific Stokes shift. Since the colour conversion layer is deposited subsequently onto the completed transistor, the electrical properties of the transistor are not altered. The semiconductor and the conversion layer do not need to match electronically and thus, an optimized ambipolar transistor setup with an efficient bipolar and light emitting material can be chosen without risking a destructive interaction with the colour conversion layer.

2. Experimental section

We used a bottom-contact top-gate ambipolar transistor with F8BT (poly(9,9-di-*n*-octyl-fluorene-alt-benzothiadiazole)) as bipolar semiconductor, PMMA (poly (methylmethacrylate)) as gate insulator and Au as source and drain metal. This OLET was first introduced by Zaumseil et al. [4] and emits efficiently in the green region of the visible spectrum with an external quantum efficiency of up to 0.85% [9]. On float glass 50 nm thick Au source and drain contacts were deposited via physical vapour deposition (PVD) at a base pressure of 2×10^{-7} mbar. Subsequently, F8BT and PMMA were spin cast from toluene and butyl acetate solution, respectively. The semiconductor and PMMA layers were dried for 15 min at 280 and 110 °C, respectively, resulting in 50 and 430 nm thick layers. Finally, a semitransparent 15 nm thick Au gate was deposited on the PMMA layer. An approximately 350 nm thick rubrene colour conversion layer was evaporated on the gate. Utilizing a parallax technique [10], a conversion layer that covered the transistor channel only partially was obtained. Rubrene was deposited at a base pressure of $<10^{-6}$ mbar and a deposition rate of about 1 Å s^{-1} at room temperature. Fig. 1d points out the evaporation process using the displacement between substrate and material source.

The transistors were electrically characterised by a HP4155A semiconductor parameter analyzer in nitrogen atmosphere, the emitted light was measured by a calibrated photodiode S1227-1010BR from Hamamatsu. The electroluminescence spectra were recorded in parallel with a PI-MAX ICCD camera from Roper Scientific and an Acton 2300i monochromator. The absorption and photoluminescence measurements were carried out with a Lambda 900 spectrometer (Perkin Elmar) and a Cary Eclipse spectrometer (Varian), respectively. The layer topographies were measured with a Profilometer Dektak IIA from VECCO.

3. Results and discussion

In Fig. 1a the drain current I_{Drain} and the corresponding electroluminescence (EL) intensity versus gate bias V_{Gate} demonstrate the ambipolar character of the F8BT transistor, whereby the electron and hole mobility were measured to be 1.2×10^{-4} and 4.8×10^{-4} $cm^2 V^{-1} s^{-1}$,

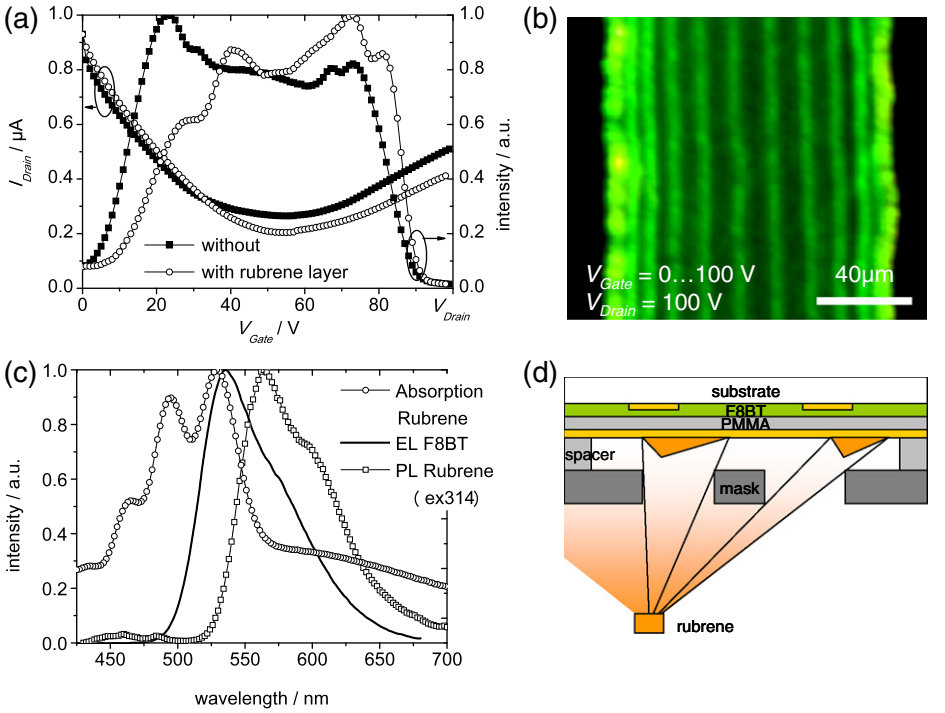

Fig. 1. (a) I_{Drain} and electroluminescence intensity versus V_{Gate} of a F8BT transistor without and with rubrene layer covering half of the channel. (b) Micrograph of the channel of a pure F8BT transistor at gate voltage increased from 0 to 100 V in 5 V steps and at V_{Drain} = 100 V. The micrograph is taken with long exposure time. (c) Normalized absorption and photoluminescence spectrum (excitation wavelength 314 nm) of rubrene and the electroluminescence spectrum of F8BT and (d) principle of rubrene deposition utilizing parallactic displacement.

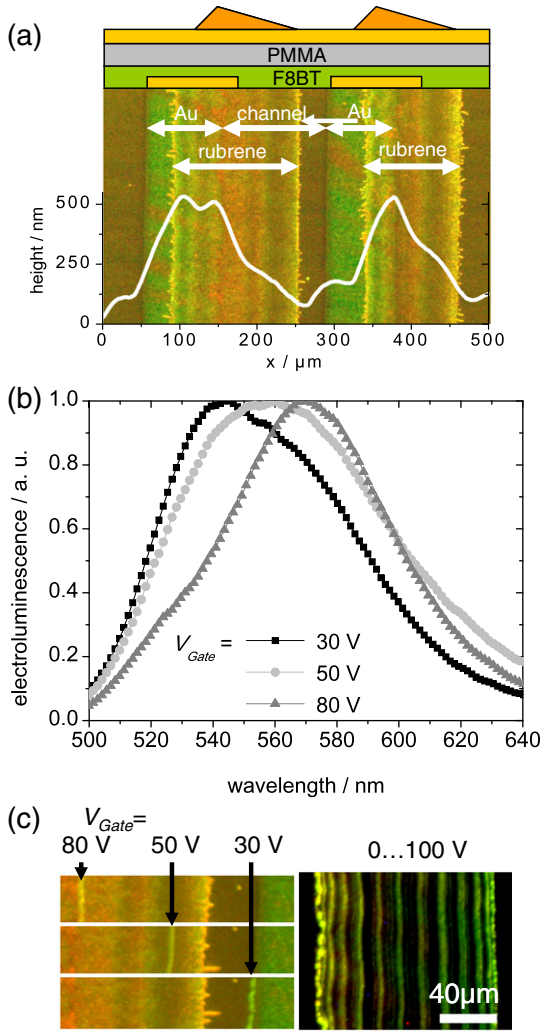

Fig. 2. (a) Setup of the F8BT/rubrene transistor and micrograph of the transistor with profile. (b) Electroluminescence spectra of a F8BT/rubrene transistor at different gate voltages at V_{Drain} = 100 V. (c) Respective micrographs of the transistor channel at different gate voltages V_{Drain} = 100 V. The position of the emission region appears as bright but narrow vertical strip in the transistor channel highlighted by the arrows. Micrograph of the channel at gate voltage increased from 0 to 100 V in 5 V steps and at V_{Drain} = 100 V. The micrograph is taken with long exposure time.

respectively. The photograph in Fig. 1b displays an EL map at increasing V_{Gate} in 5 V steps at constant source-drain voltage V_{Drain} of 100 V. The position of charge carrier recombination x_R within the transistor channel can be changed by V_{Gate} in the ambipolar regime [3,4,11]. The green emitted light has a maximum at 535 nm as shown by the EL spectrum in Fig. 1c and exhibits CIE coordinates (calculated for a 2° standard observer) of x = 0.394 and y = 0.565. The external electroluminescence quantum efficiency (EQE) was estimated to 0.56% being in the same range as reported by Zaumseil et al. [4]. To estimate the EQE we did not introduce any corrections related to the device geometry, but calculated the efficiency directly as the ratio between the emitted photons per time and the flowing charge per time given by the drain current. The emitted photons per time are proportional to the current of the calibrated photo diode and the proportionality factor is determined by the emission spectrum and the wavelength dependent sensitivity of the calibrated photodiode. To achieve a colour shift of the emitted light, rubrene often used as single-crystalline semiconductor in organic transistors [12] was evaporated on the semitransparent top-gate contact of the F8BT transistor. Fig. 1c shows that the absorption spectrum of an amorphous rubrene layer prepared by PVD matches the emission spectrum of F8BT. Thus the emitted light from F8BT can be used to excite the rubrene layer. The photoluminescence spectrum of rubrene, excited at 314 nm, is also displayed in Fig. 1c. The photoluminescence maximum is located at 565 nm in the yellow range of the visible spectrum and hence, a colour change can be expected once the rubrene layer is excited via the F8BT emission.

To realize a voltage dependent colour change the rubrene layer is supposed to cover only a part of the channel region of the F8BT transistor. Fig. 2a shows a micrograph of the transistor channel comprising the confined rubrene layer covering only half of the channel. Thus depending on the position of charge carrier recombination, emission occurs either underneath the rubrene layer or at regions of undisturbed light extraction path.

Fig. 1a proves that the transfer characteristic and the EL intensity versus V_{Gate} dependence of the F8BT/rubrene transistor compares to a transistor without rubrene layer. This demonstrates the advantage of the selected colour conversion concept leaving electrical properties of the transistor unchanged.

To investigate the impact of x_R on the emission colour, V_{Gate} was set to 30, 50 and 80 V at V_{Drain} of 100 V and the EL spectra were recorded. The normalized spectra are displayed in Fig. 2b and the respective micrographs of the channel region are depicted in Fig. 2c. At V_{Gate} = 30 V a green light emission with a peak emission at 540 nm is observed from a narrow recombination zone positioned in a channel region where no rubrene layer exists. In the contrary, the micrograph at V_{Gate} = 50 V shows the charge carrier recombination under the additional rubrene layer. The respective spectrum in Fig. 2b has a maximum at about 560 nm, 20 nm shifted to the red range compared to the pure F8BT spectrum. This shift is based on a partial wavelength conversion by rubrene. In Fig. 2a the transistor cross section along the transistor channel shows that the rubrene strip does not have a constant thickness but a decreased thickness towards the centre of the transistor channel. At V_{Gate} = 50 V the position of charge carrier recombination is located at the edge of the rubrene strip and therefore, the colour change is weak. At V_{Gate} = 80 V the emission zone reaches the region where the rubrene layer has its full thickness of 350 nm being thick enough for a full colour conversion as the yellow emission colour of the recombination zone in the micrographs of Fig. 2c already indicates. The maximum of the respective spectra in Fig. 2b is with 570 nm indeed close to the maximum of the photoluminescence spectra of pure rubrene films leading to a change of the emission wavelength maximum of about 30 nm. The bias controlled colour switch changes the CIE

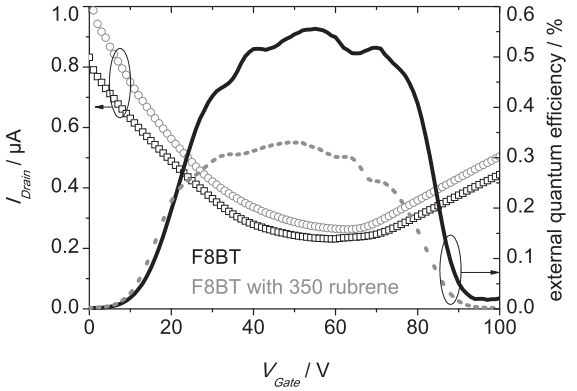

Fig. 3. Transfer characteristic and efficiency of a pure F8BT transistor and a F8BT transistor with 350 nm rubrene deposited across the entire channel.

coordinates from $x = 0.384$, $y = 0.590$ at $V_{Gate} = 30$ V to $x = 0.450$, $y = 0.537$ at $V_{Gate} = 80$ V. This colour shift is summarized in Fig. 2c where a micrograph is depicted which was taken at long exposure times while at constant $V_{Drain} = 100$ V V_{Gate} was increased stepwise. The EQE of a transistor including a rubrene layer over the entire channel reached 0.33%. Fig. 3 shows the transfer characteristic and the respective EQE for a pure F8BT transistor and a F8BT transistor with an additional rubrene layer covering the whole channel, whereby the EQE shows constant values in the ambipolar window. Even though the EQE was reduced by losses during the absorption-reemission process in rubrene 59% of the EQE of the pure F8BT transistor was obtained after all which demonstrates that the spatial separation of the colour conversion layer from the transistor conserves the good device performance of the employed OLET.

4. Summary

In summary, we demonstrated an ambipolar OLET with colour-tuneable light emission. The emission colour is controlled by the position of the recombination zone within the transistor channel and achieved by colour conversion in a layer on top of the transistor covering partially the transistor channel. The advantage of the employed concept can be seen in the decoupling of electronic processes of the OLET from the colour conversion in the optical active organic layer. This appears to be crucial, since the fragile balance of complementary charge carrier injection and transport should not be disturbed by the conversion process in order to retain full control over the emission position along the transistor channel.

Acknowledgements

The authors thank the German Research Foundation for financial support through Graduiertenkolleg 1037 (TICMO) and Prof. Dr. H. von Seggern for the scientific and financial support as well as for the supply of the essential infrastructure. F8BT was kindly provided by S. Janietz of the Fraunhofer-Institut für Angewandte Polymerforschung, Potsdam.

References

[1] A. Hepp, H. Heil, W. Weise, M. Ahles, R. Schmechel, H. von Seggern, Phys. Rev. Lett. 91 (2003) 57406.
[2] S. Seo, B.-N. Park, P.G. Evansa, Appl. Phys. Lett. 88 (2006) 232114.
[3] M. Schidleja, C. Melzer, H. von Seggern, Adv. Mater. 21 (2009) 1–5.
[4] J. Zaumseil, C.L. Donley, J.-S. Kim, R.H. Friend, H. Sirringhaus, Adv. Mater. 18 (2006) 2708–2712.
[5] M. Schidleja, C. Melzer, M. Roth, T. Schwalm, C. Gawrisch, M. Rehahn, H. von Seggern, Appl. Phys. Lett. 95 (2009) 113303.
[6] H. Nakanotani, M. Saito, H. Nakamura, C. Adachi, Adv. Funct. Mater. 20 (2010) 1610–1615.
[7] R. Capelli, S. Toffanin, G. Generali, H. Usta, A. Facchetti, M. Mucchini, Nat. Mater. 9 (2010) 496.
[8] E.J. Feldmeier, M. Schidleja, C. Melzer, H. von Seggern, Adv. Mater. 22 (2010) 3568–3572.
[9] M.C. Gwinner, S.KhodabakshsH. Giessen, H. Sirringhaus, Chem. Mater. 21 (2009) 425.
[10] R. Schmechel, M. Ahles, H. von Seggern, J. Appl. Phys. 98 (2005) 084511.
[11] J. Zaumseil, R.J. Kline, H. Sirringhaus, Appl. Phys. Lett. 92 (2008) 073304.
[12] A.R. Murphy, J.M.J. Fréchet, Chem. Rev. 107 (2007) 1066.

it is important to analyze the movement of the molecules inside a droplet during drying. We set up a system to collect images of the movement of the particles inside a droplet using a CCD camera and laser beam [15]. A droplet containing fluorescence particles with 1 μm diameter was dropped onto a glass substrate, and then images of the flow of the particles were taken at 10 shots per second to analyze the velocity vector of the movement of the particles. The measurement was carried out on a droplet dried in air and also under the influence of Ar gas which was injected toward the droplet in order to change the movement of the particles. The velocity vectors within the droplet subjected to Ar gas injection were compared with those within the droplet dried in air in order to analyze the effects of Ar gas on particle movement. The solution comprising the droplet was pure water with a volume of 1.8 μl and the diameter of the droplet was 1.98 mm.

The OTFTS employed a bottom contact structure whose source and drain electrodes were located below the semiconductor layer as shown in Fig. 1. The fabrication process was as follows. An aluminum layer with 1000 Å thickness was evaporated on a glass substrate and patterned by photolithography for gate electrodes. Polyvinylphenol (PVP) was spin coated on the gate electrode to deposit a gate dielectric layer. The detailed process for the PVP layer can be found in the literature [16,17]. Subsequently, for the source and drain (S/D) electrodes, Au was evaporated on the PVP layer and patterned by a lift-off process. Finally, the TIPS-pentacene solution was jetted onto the S/D electrodes by an ink jet. Three types of OTFTs were fabricated and were dried in different environments. The first group of OTFTs was dried in air (air-OTFT), and the other OTFTs were dried in a quartz tube under the influence of Ar gas injection as described below. The second group of OTFTs was dried under Ar gas whose injection direction was parallel to the current flow between the S/D electrodes (par-OTFT). The third group of OTFTs was subjected to Ar gas injection perpendicular to the current (per-OTFT). The effects of Ar gas injection were analyzed by comparing the morphology of the grains and the performance of the OTFTs.

The OTFTs with ink-jetted TIPS-pentacene droplets were placed in a quartz tube with a diameter of 10 cm as shown in Fig. 1. Ar gas was then injected into the quartz tube in order to alter the movement of the molecules and also to push back the front contact line, which directly faces the Ar gas, of the droplet, and thus obtain grains with

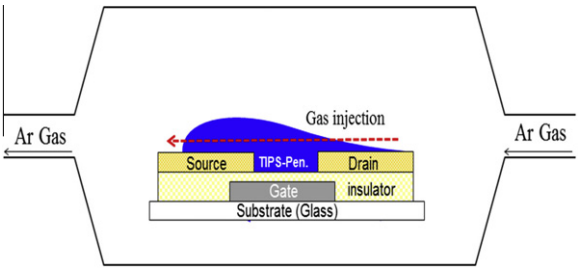

Fig. 1. The structure of OTFTs using TIPS-pentacene semiconductor droplet which was dried under Ar gas injection in a quartz tube.

uniform thickness and morphology. The droplet of TIPS-pentacene was comprised of 2 wt.% of TIPS-pentacene mixed with anisole solvent. The flow rate of the Ar gas was adjusted to be laminar. However, turbulence reflected from the quartz wall could not be avoided near the wall, and consequently some devices near the wall did not reflect the influence of the Ar gas injection. The flow rate was varied from 300 to 1000 sccm to examine the effects of the flow rate on the morphology of TIPS-pentacene grains.

The morphology of the grains was analyzed via a microscope, 3D profiler, AFM, and XRD. The electrical characteristics of the OTFTs were measured by a Kithley 4200.

3. Results and discussion

The movement of particles in a droplet on a glass substrate heated at 30 °C was analyzed during drying in air. Since the contact point P is pinned on the hydrophilic substrate, a convective flow of solvent from the center surface to the contact point was generated as shown in Fig. 2 in order to provide a certain volume of solvent to the contact point, which was necessary to keep the contact point pinned. Thus, the molecules in the droplet also moved together with the solvent convective flow and accumulated at the contact point resulting in a so-called "coffee stain". Therefore, the final crystal of the TIPS-pentacene droplet, which was dried in air, typically had a thick coffee stain at the contact point and thin grains in the middle area with a random size and shape and location as shown in the inset of Fig. 2.

When Ar gas was injected into the droplet as shown in Figs. 1 and 3, the solvent flow changed to move from the contact point to the center surface inversely as shown in Fig. 3. Furthermore, the contact point itself also moved back along the gas direction instead of being pinned while it dried because the solvent near the front contact point was compulsorily dried by the Ar gas injection.

The velocity vectors of the solvent flow were obtained by taking the images of the particle movement at 10 shots per second and then calculating the particle velocity with the PIV (Particle Image Velocimetry) method. As the gas flow rate was varied from 300 to 500 to 1000 sccm, the velocity increased from 0.41 to 0.68 to 1.41 mm/s, respectively. It was clearly seen that the particles on the droplet surface moved backward from the front contact line to the back contact line as shown in Fig. 3.

Depending on the Ar gas flow rate, the shape and the morphology of the crystal grains changed. At 1000 sccm it was clearly seen that the crystal grains grew along the direction of the gas injection as shown in Fig. 4c. Meanwhile, at 300 sccm there was no clear correlation between the grain morphology and the gas flow direction as shown in Fig. 4a. The correlation started to appear at 500 sccm as shown in Fig. 4b. The correlation was maximized at 1000 sccm where slender and longish grains started to grow at the front contact line and elongated up to the back contact line of the droplet. As the flow rate was increased, the length of the grain increased while the width decreased.

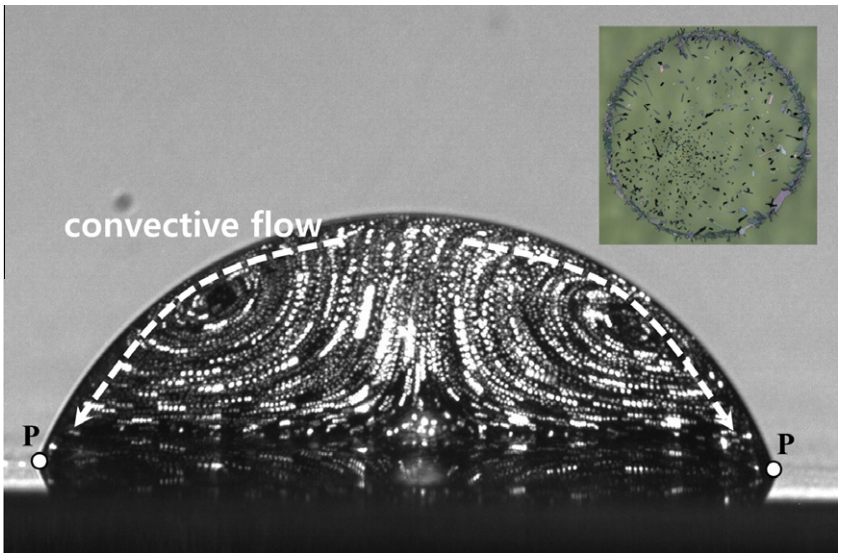

Fig. 2. Convective movement of fluorescent particles inside a water droplet during drying in air; P represents the contact point of the droplet with the substrate, and this point was pinned during drying; the inset show crystals of TIPS-pentacene dried in air where a large coffee stain is formed on the contact line and the small crystals are randomly distributed in the middle region.

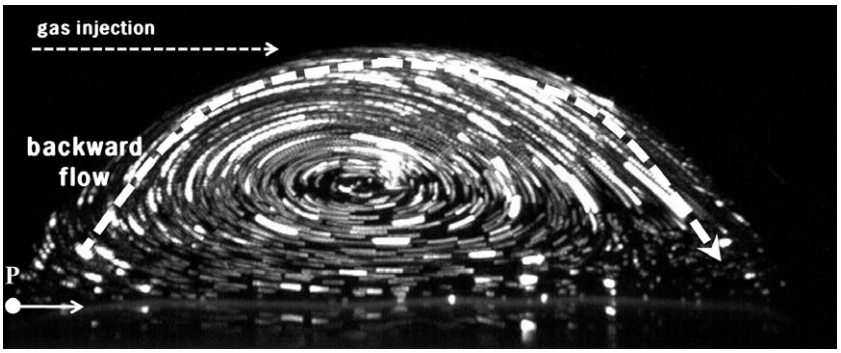

Fig. 3. Due to Ar gas injection the convective flow was perturbed and thus the particles moved backward from the front contact point to the back contact point. Additionally, at an appropriate Ar gas injection rate the contact point P itself moved along the direction of gas injection during drying.

At a small flow rate the backward flow created by the gas was not sufficient to perturb the ordinary convective flow, and the final grains were consequently similar to those without the gas flow. A large flow, such as 1000 sccm, generated a strong backward flow, causing the grains to grow along the direction of the backward flow. Additionally, the front contact line also moved backward toward the back contact line, and the grains grew along the movement of the front contact line. Above 1000 sccm, crystals did not form because of the very strong perturbation.

This gas effect was also found in the uniformity of grain thickness. The thickness was relatively uniform all over the crystal in a range of 90–110 nm at 1000 sccm as shown in Fig. 5c. The surface roughness was also very small, at 1.2 nm. However, at 300 sccm and at 500 sccm the thickness varied extensively in the range of 120–190 nm and 110–150 nm, respectively, and the surface roughness was 6.3 nm at 300 sccm and 7.5 nm at 500 sccm as shown in Fig. 5a and b.

A coffee stain was created for all gas flow rates because the droplets were dropped before being placed into the quartz tube, and thus the grains started to grow before the Ar gas was injected. Due to the backward flow the coffee stain at the back contact line was larger than that at the front. If we can develop a way to apply Ar gas simultaneously to dropping the droplet, crystal grains without coffee stain could be obtained.

In the XRD data the signature peak of the pentacene crystal at $2\theta = 5.7^\circ$ was also stronger for 1000 sccm than for 300 sccm or 500 sccm as shown in insets of Fig. 5, reflecting a strong crystallinity for 1000 sccm.

By comparing the enlarged crystal grains produced at 1000 sccm in the inset of Fig. 4c with the schematic of TIPS-pentacene crystal planes of the referenced article [9] the crystal grains appear to grow in the direction of (1 2 0). Several 1000 μm long grains with a few 100 μm narrow width grains were found oriented toward (1 2 0).

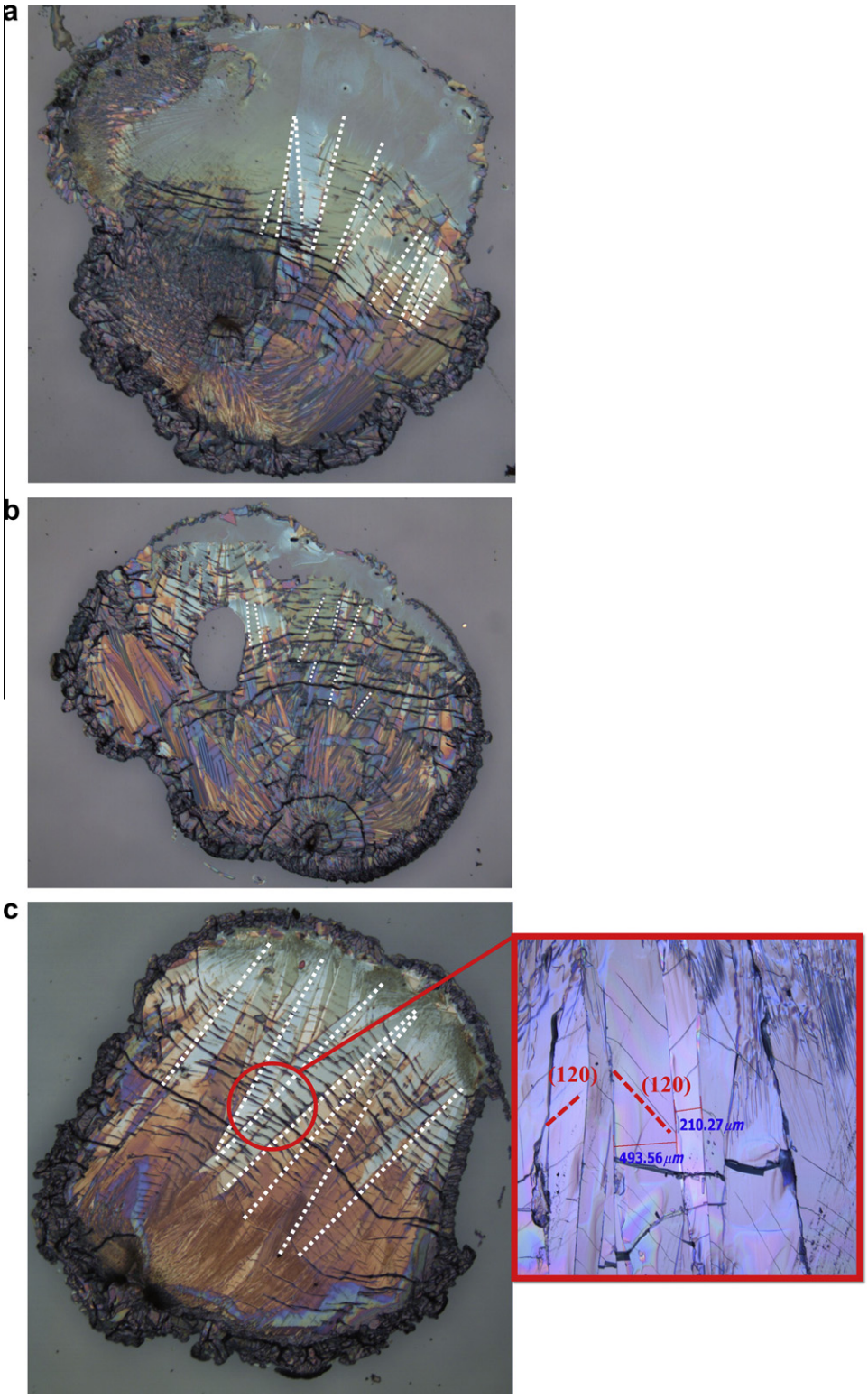

Fig. 4. Depending on the Ar gas flow rate the shape of TIPS-pentacene grains on the PVP dielectric layer was changed, (a) at 300 sccm the shape did not show a clear correlation with the flow rate, (b) at 500 sccm the correlation started to appear, (c) at 1000 sccm the grains became slender and longish along the direction of Ar gas injection.

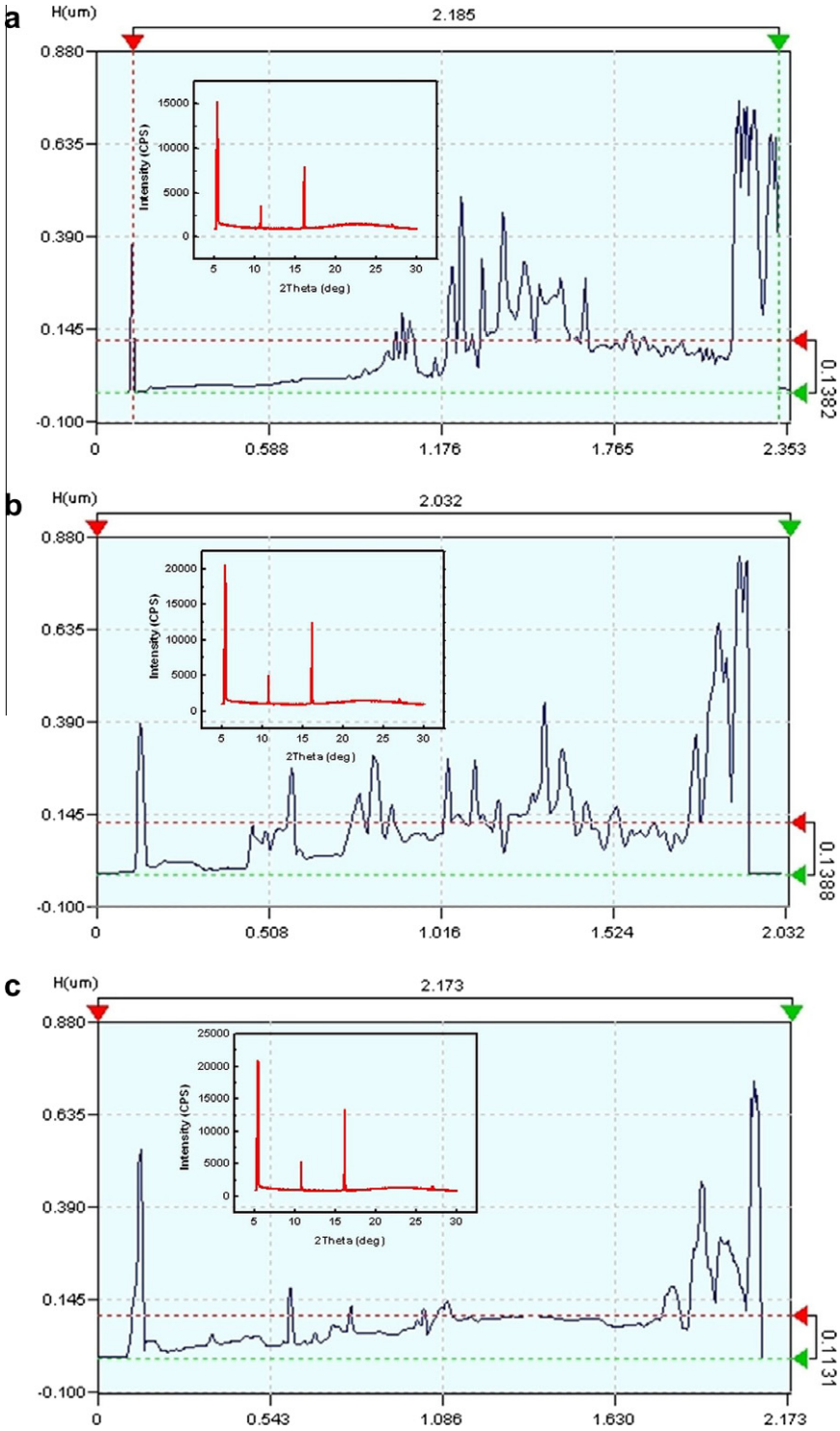

Fig. 5. Depending on the Ar gas flow rate the thickness of the TIPS-pentacene grains changed, (a) at 300 sccm the thickness was not uniform and the surface roughness was also quite large, (b) at 500 sccm the thickness became relatively uniform but the surface was still rough, (c) at 1000 sccm the best results were exhibited in terms of thickness uniformity and surface roughness; the enlarged grain of TIPS-pentacene clearly exhibited crystal direction of (1 2 0).

To investigate the effects of the direction of Ar gas injection on electrical performance, three types of OTFTs were prepared. Microscope pictures of the channel area of the OTFTs are presented in Fig. 6. In the air-OTFTs the grains have random size and shape. The par-OTFTs display grain boundaries parallel to the Ar gas direction and thus parallel

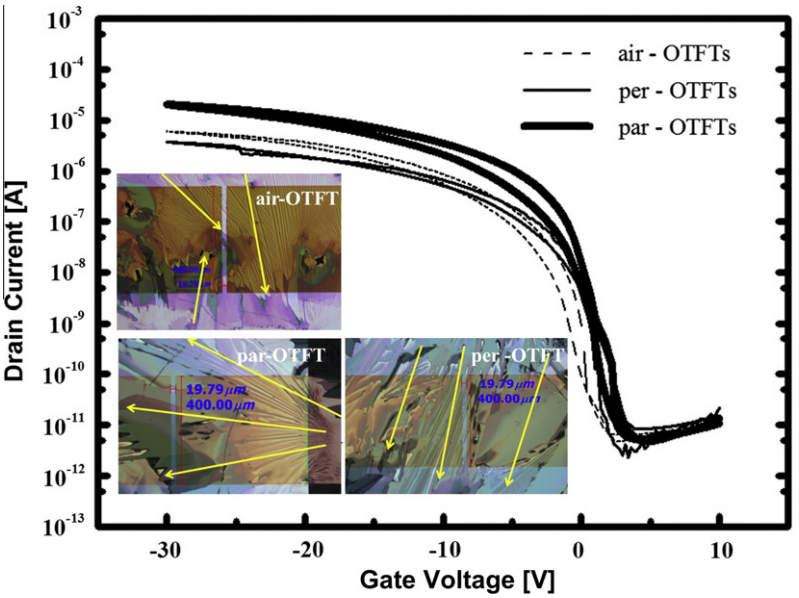

Fig. 6. The transfer characteristics of three type of OTFTs, air-OTFTs, per-OTFTs, and per-OTFTs; the insets show microscope images of the channel area of the OTFTs.

Table 1
The performance parameters of three types of OTFTs using TIPS-pentacene as a semiconductor dried under different environments.

Device type	Channel (W/L)	Mobility (cm^2/V s)	I_{on}/I_{off}	V_{th} (V)	SS (V/dec)	Off state current (pA/μm)
Air-OTFTs	400/20	0.12 ± 0.05	2.23×10^5	−0.8	0.5	0.016
Par OTFTs	400/20	0.53 ± 0.02	4.45×10^6	0.97	0.6	0.011
Per-OTFTs	400/20	0.06 ± 0.02	1.34×10^6	1.03	1.0	0.007

to the current direction. The per-OTFTs produced grain boundaries perpendicular to the gas direction as well as to the current flow.

The electrical characteristics strongly depended on the direction of the grain boundaries as shown in Fig. 6. The performance parameters were averaged from 36 devices of each type of OTFT, and are presented in Table 1. The par-OTFTs produced the largest mobility among the devices; 0.53 ± 0.02 cm^2/V s with the smallest standard deviation less than 10%, while the per-OTFTs exhibited the smallest mobility at 0.06 ± 0.02 cm^2/V s, and the air-OTFTs lied between them with 0.12 ± 0.05 cm^2/V s and a large deviation of 42%. These results clearly present the relationship of performance with the grain boundary direction. The parallel grains of par-OTFTs easily directed the current along the grain direction because the grain boundaries were located parallel to the current and thus rarely interrupted the current flow. However, in the per-OTFTs, the grain boundaries vertically directed to the current appeared to severely block the current flow. In the air-OTFTs, the above two effects appeared together and thus produced the intermediate performance. The off-state current also exhibited similar results: the smallest was obtained for the per-OTFTs, with a value of 0.007 pA/μm, while a value of 0.016 pA/μm was derived for the air-OTFTs, and the largest value, 0.011 pA/μm, was obtained for the par-OTFTs. Meanwhile the on-state current at $V_{GS} = -30$ V was the largest for the par-OTFTs, with a value of 20.5 μA, and the smallest for the per-OTFTs, with a value of 3.7 μA, thus reflecting the same gas direction effect as described above.

4. Conclusion

In this study Ar gas was injected to the droplets of TIPS-pentacene of OTFTs while drying the droplets in a quartz tube in order to change the flow of the molecules inside the droplet and also move backward the front contact line which faced the Ar gas during drying. As a result, we could control the morphology and the growth direction of the grain boundaries and thus improve the performance of the TIP-pentacene OTFTs. The OTFTs with the growth direction of grain boundaries parallel to the current flow between the source and drain electrodes displayed the best results with mobility of 0.53 ± 0.02 cm^2/V s, as compared to 0.06 ± 0.02 cm^2/V s for the OTFTs where the grain boundaries were perpendicular to the current flow.

Acknowledgements

This research was supported by a Grant (F0004020) from Information Display R&D Center, one of the Knowl-

edge Economy Frontier R&D Program funded by the Ministry of Knowledge Economy of Korea government.

References

[1] M.W. Lee, M.Y. Lee, J.C. Choi, J.S. Park, C.K. Song, Org. Electron. 11 (2010) 854.
[2] R.L. Headrick, S. Wo, F. Sansoz, J.E. Anthony, Appl. Phys. Lett. 92 (2008) 063302.
[3] K. Nomoto, N. Hirai, N. Yoneya, N. Kawashima, M. Noda, M. Wada, J. Kasahara, IEEE Trans. Electron Dev. 52 (2005) 1519.
[4] D.M. deLeeuw, G.H. Gelinck, T.C.T. Geuns, van Veenendaal, E. Cantore, E. Huisman, in: Tech. Dig. Int. Electron Dev. Meet. 2002, 2002, p. 293.
[5] M.Y. Lee, M.W. Lee, J.E. Park, J.S. Park, C.K. Song, Microelectron. Eng. 87 (2010) 1922.
[6] K.H. Shin, in: 1st International Conference on R2R Printed Electronics, 2008.
[7] S.K. Park, C.C. Kuo, J.E. Anthony, T.N. Jackson, in: Tech. Dig. Int. Electron. Devices Meet., 2006, p. 113.
[8] S.H. Lee, M.H. Choi, S.H. Han, D.J. Choo, J. Jang, S.K. Kwon, Org. Electron. 9 (2008) 721.
[9] J. Chen, C.K. Tee, M. Shtein, D. Martin, J. Anthony, Org. Electron. 10 (2009) 696.
[10] J.A. Lim, W.H. Lee, H.S. Lee, J.H. Lee, Y.D. Park, K.W. Cho, Adv. Funct. Mater. 18 (2008) 229.
[11] W.H. Lee, D.H. Kim, Y.S. Jang, J.H. Cho, Appl. Phys. Lett. 90 (2007) 132106.
[12] J. Chen, C.K. Tee, M. Shtein, J. Anthony, D.C. Martin, Appl. Phys. 103 (2008) 114513.
[13] J. Chen, D.C. Martin, J. Mater. Res. 22 (2007) 1701.
[14] J. Chen, C.K. Tee, J. Yang, C. Shaw, M. Shtein, J. Anthony, D.C. Martin, Polymer Sci. 10 (2006) 3631.
[15] Y.G. Heo, Y.H. Jeon, Y.K. Suh, J. Korean Soc. Visual. 7 (2) (2010) 42.
[16] H.S. Byun, Y.X. Xu, C.K. Song, Thin solid Films 493 (2005) 278.
[17] Y.X. Xu, H.S. Byun, C.K. Song, IMID'04 August 23–27, 2004, p. 1027.

2. Experimental

2.1. Buckling fabrication

The fabrication process of buckling and OLED devices was almost the same as in our previous studies [12,13]. Standard commercial PDMS materials (Wacker ELASTOSIL RT 601) were spincoated and cured at 100 °C for 1 h on glass substrates. 5-, 10-, 15- and 20-nm-thick Al layers were deposited on PDMS by thermal evaporation without external heating. After cooling to ambient temperature, the difference in thermal expansion coefficients between the Al film and PDMS generates a buckling structure [9–11]. For shorter periodicity of buckles, the UVO treatment was conducted on the cured PDMS before a 10-nm-thick Al layer. Finally, the buckled PDMS templates with the peak wavelengths (periodicities) ranging from 300 to 800 nm were fabricated. PDMS replicas were replicated by pouring and curing the PDMS materials at 60 °C for 2 h.

2.2. Device fabrication and measurement

For the fabrication of devices with gratings of different periodicities, glass substrates were coated with UV curable resin (Norland Optical Adhesive 81) by spincoating. After curing by UV irradiation for 10 min, a drop of resin was placed on the resin-coated substrates. Then the buckling patterns of the PDMS replicas with various periodicities were transferred to UV-curable resin layers by imprinting technique. After UV curing of the resin layers for 10 min, each buckled resin layer was produced on the glass substrates. After UV/ozone treatment on the cured resin layers for 5 min, a 120-nm-thick ITO anode layer was formed by DC sputtering at room temperature. The following layers were then thermally evaporated on the ITO-coated substrate: 40-nm-thick TPD (*N*,*N*′-bis(3-methylphenyl)-*N*,*N*′-diphenylbenzidine) layer for hole transport, 30-nm-thick Alq_3 (tris-(8-hydroxyquinoline) aluminium) layer for light emission and electron transport, 1.5-nm-thick LiF layer for electron injection, and 100-nm-thick Al cathode layer. The devices with the emitting area of 3 mm × 3 mm were encapsulated with glass and UV curable resin in a glove box under Ar atmosphere.

Electroluminescence (EL) spectra were recorded with a source meter (Keithley 2400) and a spectrometer (Ocean Optics USB 2000). The angular emission patterns were measured by integrating the EL spectra of devices according to emission angles.

2.3. Attenuated total reflection Fourier transform infrared (ATR-FTIR)

The PDMS was spincoated on bare silicon wafer and cured at 100 °C for 1 h, and the UVO treatment was conducted on the cured PDMS for 5 min. In order to eliminate an effect of a corrugated structure in measurements, 5-nm-thick Al layer that shows no buckling structure was deposited on PDMS. FTIR spectra were recorded by the attenuated total reflection (ATR) technique, using a Jeol-SPX 200 spectrometer. For each sample, 1837 scans were collected using a Ge-crystal detector with a resolution of 4 cm^{-1}.

3. Results and discussion

AFM images of buckles formed on PDMS under different conditions are shown in Fig. 1(a–d). All the AFM images with inserted fast Fourier transform (FFT) patterns with symmetric rings clearly indicate that these buckles have characteristic wavelengths with wide distributions and without preferred orientation. Fig. 1(e) presents the power spectra of various buckles, plotted against wavelength (periodicity). It is known that the wavelength of the buckles λ depends on the film thickness t and the elastic modulus of the film and the substrate E_f and E_s by the equation $\lambda \sim t(E_f/E_s)^{1/3}$ [14]. Buckles produced by depositing 20- and 10-nm-thick Al layers are shown in Fig. 1(a) and (b), where controllability due to the above equation is qualitatively shown. This is more quantitatively shown in Fig. 1(e); i.e., the characteristic wavelengths for 10-, 15- and 20-nm-thick Al layers are ~460, 650 and 800 nm, respectively. In order to have shorter periodicity, we tried a 5-nm-thick Al layer. However, no buckles were formed on the surface, indicating that it is difficult to decrease the periodicity of buckles anymore by the Al layer thickness. Since the pitch of periodic grating applied to OLED should be below 400 nm for efficient outcoupling of waveguide mode into normal direction, we introduced ultraviolet/ozone (UVO) treatment on PDMS to control the periodicity of the buckles.

Fig. 1(c and d) shows the buckled structure by 10-nm-thick Al layer on the PDMS treated by UVO for 1 and 2 min. As the exposure time increases, the periodicity decreases and the diffuse FFT ring pattern becomes larger, indicating a shorter characteristic wavelength. The power spectra in Fig. 1(e) represent that the peak wavelength are ~400, ~315, and ~300 nm for 1, 2, and 3 min UVO treatment. It is well known that UVO treatment of PDMS converts its surface into silica-like structure, and particularly at short treatment time of a few minutes the modification extends to 10–20 nm below the surface, converting the density of the top surface to below ~10% of that of silica [15]. These modified layers by UV or UVO are considered as a composite layer with metal films deposited on them. The increased thickness $t_{composite}$ and elastic modulus $E_{composite}$ of the composite layer have been believed to increase the characteristic wavelength of buckles λ due to the relation $\lambda \sim t_{composite}(E_{composite}/E_s)^{1/3}$. Actually this relation was confirmed using buckles formed by a noble gold film of 50 nm; i.e., λ increases with a UV exposure time because of increasing $t_{composite}$ and $E_{composite}$ [11]. However, the situation was completely opposite, as shown in Fig. 1(c–e), if a reactive metal film such as Al was deposited on UVO-treated PDMS with very thin thickness of 10 nm; the periodicity of buckles decreases with increasing UV exposure time. We will describe why such opposite situation resulted in the following.

Kovacs and Vincett have shown that a metal subsurface is formed beneath a polymer surface when a metal is thermally evaporated onto a polymer substrate above its glass transition temperature [16–18]. The formation of

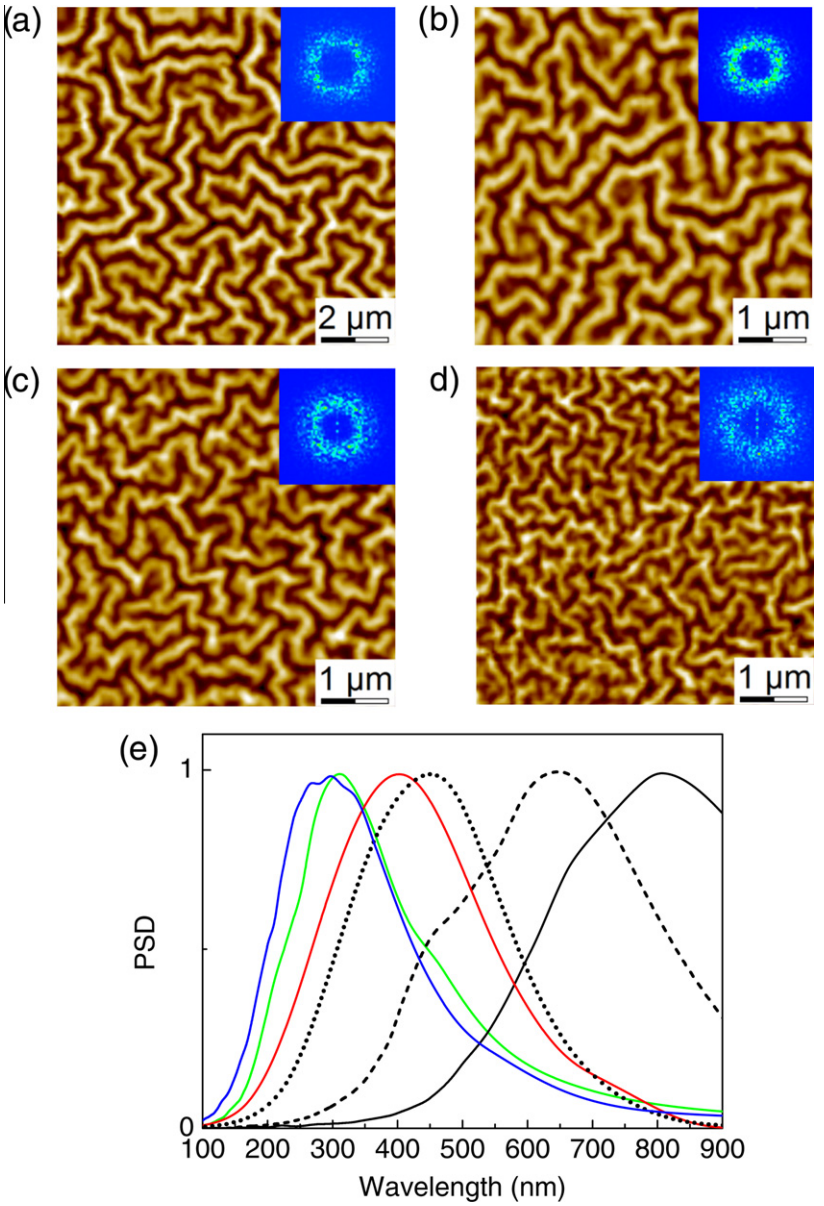

Fig. 1. AFM analysis of buckling patterns on UV curable resin, transferred from the buckled PDMS by imprinting technique. (a) Buckle by 20-nm-thick Al layer without the UVO treatment (Dimensions, 10 × 10 μm). (b) Buckle by 10-nm-thick Al layer with 0 min, (c) 1 min, and (d) 2 min UVO treatment (Dimensions, 5 × 5 μm). Inset: The FFT pattern of each image. (e) The power spectra from FFTs as a function of wavelength for the buckling patterns by 20-nm-thick (–), 15-nm-thick (- - -) and 10-nm-thick (.....) Al layer without the UVO treatment, and by 10-nm-thick Al layer with UVO treatment for 1 min (▬), 2 min (▬) and 3 min (▬).

sub-surface structures is thermodynamically favorable because the surface energies of inorganic evaporants γ_1, organic polymer γ_2, and interface γ_{12} generally satisfy $\gamma_1 > \gamma_2 + \gamma_{12}$. The deposited sub-surface consists of spherical clusters, embedded with a deeper distribution of several tens of nanometers below the surface, instead of the nominal film thickness. Considering the low surface energy (15–20 mJ/m^2) and the low glass transition temperature (∼−125 °C) of PDMS, it is expected that evaporated Al adatoms sink and coalesce beneath the PDMS surface, being oxidized by chemical reaction with PDMS, rather than showing the surface nucleation and growth on PDMS, when thermally evaporated. However, the stiffer and activated silica-like surface formed by UVO treatment on PDMS may prevent the Al adatoms from being sank beneath surface and induce three- or two-dimensional growth mode above the surface [19]. We found that this is actually the case, as will be shown in the following.

The magnified AFM images (500 nm × 500 nm) of an Al layer on silica glass, bare PDMS and 30-min-UVO-treated PDMS are shown in Fig. 2. Although an Al-deposited layer emerged as a typical granular surface morphology on silica glass (Fig. 2(a)), a smooth and buckled (large bump) surface morphology was obtained on bare PDMS

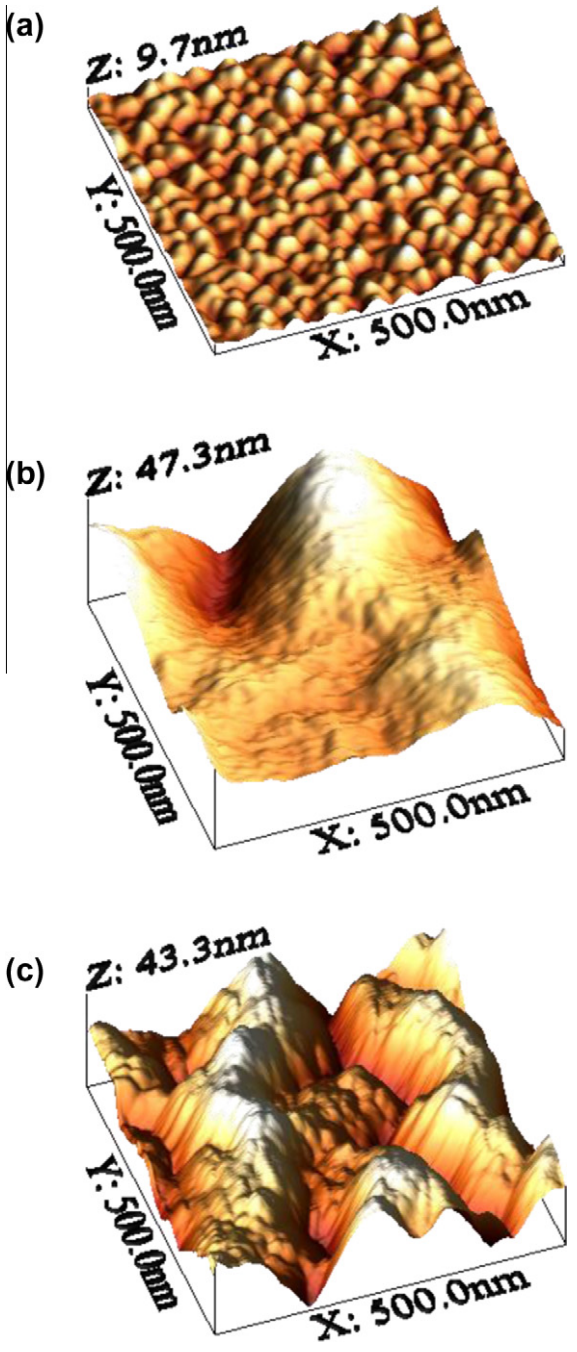

Fig. 2. Magnified three-dimensional AFM analysis of 10-nm-thick Al layer (Dimensions, 500 nm × 500 nm). (a) Granular surface morphology of Al layer on glass substrate. (b) Smooth morphology in the buckled structure of Al layer on bare PDMS (a–c). (c) Granular-like surface morphology in the buckled structure of Al layer on 30-min-UVO-treated PDMS.

(Fig. 2(b)), indicating the sub-surface nucleation and growth. In a 30-min-UVO-treated PDMS (Fig. 2(c)), in which the surface is converted to a more dense material (~50% density of pure silica) [15], the granular-like surface morphology, similar to the granular structure of Fig 2(a), is formed in the buckles.

To examine the oxidation condition of these films, Fourier transform infrared spectroscopy was conducted in the attenuated total reflection mode (FTIR–ATR). Fig. 3 shows the spectra of pristine PDMS (a), Al-deposited PDMS without (b) and with (c) UVO pretreatment. Characteristic peaks showing oxidation of the Al layer were observed over a broad range of 650–1000 cm^{-1} [20–22], in addition to the peaks of pristine PDMS [15]; the O–Al–O bending mode (650–700 cm^{-1}), the Al–O stretching mode (750–1000 cm^{-1}), and the Al–OH bending mode (850–1000 cm^{-1}). The absorption intensities of these characteristic IR bands particularly of O–Al–O bending peak are stronger for the Al layer on the bare PDMS (b) than on the UVO-treated PDMS (c), indicating that the silica-like surface of the PDMS treated by UVO restrains the Al adatoms from being sank and oxidized. Another difference can be also seen in their appearance; i.e., the 50-nm-thick Al layer on the PDMS without UVO treatment is optically transparent by naked eye, whereas that on the 10-min-UVO-treated PDMS is opaque (Supporting Figure). Therefore, the Al layer on the UVO-treated PDMS forms a thinner composite layer with less oxidized conditions. Considering the elastic modulus of bulk alumina (~370 GPa) and Al (~69 GPa) [23], the elastic modulus in UVO-treated case becomes smaller than that without UVO treatment. Because the characteristic wavelength of the buckles is strongly dependent on the thickness and the elastic modulus of the composite layer, the reduced thickness and elastic modulus by the UVO treatment are responsible for the decreased characteristic wavelength of the buckles, as experimentally obtained (Fig. 1(c–e)).

The depth of a buckling structure D generally depends on the buckling periodicity λ and the imposed compressive strain (stress) Δ; $D \sim \lambda \bullet \Delta^{1/2}$ [24]. The decreased periodicity of the buckles by the UVO treatment reduces the depth of buckle to 55–65, 50–60, 40–50, and 35–45 nm for the treatment of 0, 1, 2, and 3 min, respectively. The buckle by 3 min treatment in Fig. 1(e) has a large fraction in the periodicity

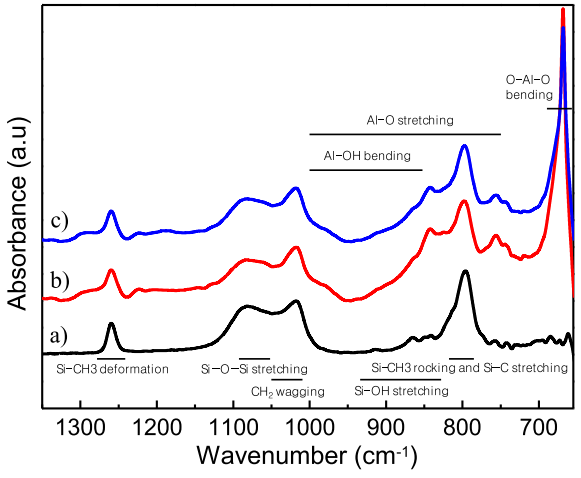

Fig. 3. FTIR–ATR spectra of (a) pristine PDMS (–), (b) PDMS deposited by 5-nm-thick Al layer without (▬), and (c) with the UVO pretreatment for 5 min (▬). The PDMS shows no buckling structure by 5-nm-thick Al layer, so the effect of the corrugated structure on the measurement was excluded. The bars represent the characteristic IR bands corresponding to various chemical functionalities.

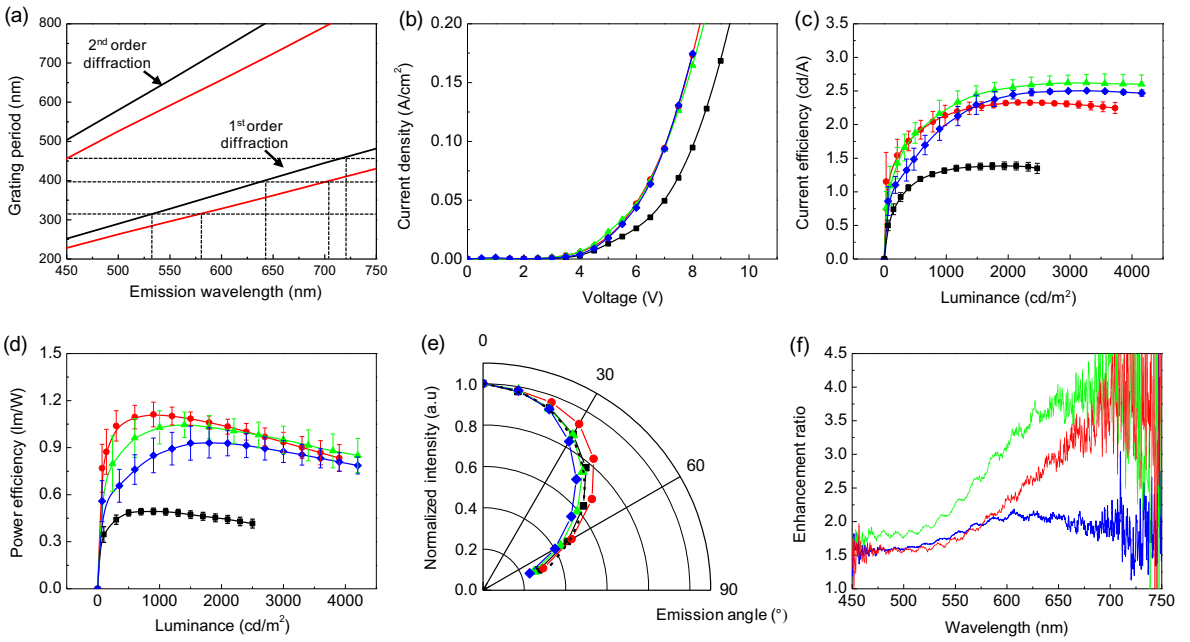

Fig. 4. (a) Relation between the outcoupled emission wavelength in the normal direction and the grating period for the TE_0 (–), and TM_0 (▬) modes. The first- and second-order diffractions were considered. The dotted horizontal lines correspond to the peak wavelengths of the buckles by 0 (λ_{peak} = 460 nm), 1 (λ_{peak} = 400 nm), and 2 min (λ_{peak} = 315 nm) UVO treatment. (b) Current density of the devices without (■) and with the buckles by 0 (●), 1 (—●—), and 2 min (—●—) UVO treatment. (c) Current efficiency, (d) Power efficiency, and (e) Angular depedence of normalized light intensity for the devices with the same information as (b). The dashed line (- - -) represents the Lambertian emission pattern. (f) Light enhancement ratio of the devices as a function of wavelength for the devices with the buckles by 0 (▬), 1 (▬), and 2 min (▬) UVO treatment. The data were obtained by dividing the EL spectra of each device with buckles by that without buckles.

below ~250 nm, which is too short to diffract the waveguiding light of ~520 nm into normal direction. Moreover, the higher depth of the buckle by 2 min treatment than that by 3 min treatment is more suitable for effective diffraction. Therefore, we fabricated the OLED devices with the buckle by 2 min treatment, in addition to those by 0 and 1 min treatment for comparison. The pattern of the buckled PDMS mold was transferred to UV-curable resin by an imprinting technique [12], on which we fabricated OLED devices.

To characterize the waveguide modes existing in this structure, we calculated their in-plain propagation vector, k_{wg}, for the emission wavelength by using a transfer matrix method [12,25–27]. One transverse-electric (TE_0) and one transverse-magnetic (TM_0, surface plasmon) modes were calculated. Based on the Bragg grating equation of $k_{||} = k_0 \sin\theta = k_{wg} \pm mk_g$ (k_0, the absolute values (wavenumbers) of the wave vectors in free space; $k_{||}$, its in-plain component; k_G, grating (buckling); θ, polar angle of emitted light with respect to the surface normal; and m, an integer), the grating period satisfying the Bragg equation for the first- and second-order diffractions in the normal direction (m = 1 and 2, θ = 0) is plotted in Fig. 4(a) as a function of wavelength of the outcoupled light. The buckles by 0, 1, and 2 min UVO treatment with the peak wavelength of ~460, 400, and 315 nm are expected to mainly outcouple the TE_0 mode at ~720, 640, and 530 nm and the TM_0 mode at ~800, 705, and 580 nm, respectively. However, the broad distribution of the buckles in periodicity allows the waveguide modes to be extracted over the broad emission wavelength ranges through even the second-order diffraction as well as the first-order diffraction. Moreover, the diffractions toward off-normal directions occur in all azimuthal directions because of random orientation of buckles.

The current densities for the devices with and without buckles are plotted as a function of applied voltage in Fig. 4(b). The devices with buckles show higher current density than the reference device, irrespective of the UVO treatment time. This larger current density in the corrugated device due to a partial reduction of the organic layer thickness is a well-known phenomenon [6,12][28]. The current efficiencies at a luminance of 2000 cd/m^2 were 1.38 cd/A for the reference device and 2.32, 2.55, and 2.43 cd/A for the devices with the buckles by 0, 1, and 2 min UVO treatment, respectively (Fig. 4(c)). Although the periodicity of the buckle by 2 min treatment is most suitable to outcouple the waveguide modes at the main emission peak of ~520 nm into normal direction, its relatively low depth may limit the effective diffraction. For the devices with buckles on non-treated PDMS, in contrast, the peak wavelength of the periodicity distribution is too long (~460 nm) to effectively outcouple the main emission peak (Fig. 4(a)) despite of its highest depth of the buckles. Therefore, the device with the buckle by 1 min treatment shows the highest current efficiency of the enhancement ratio 1.85.

The power efficiencies at a luminance of 2000 cd/m^2 were 0.45 lm/W for the reference device, and 1.04, 1.02, and 0.93 lm/W for the devices with the buckles by 0, 1,

and 2 min treatment, respectively, as shown in Fig. 4(d). The device with the non-UVO-treated buckle shows the highest power efficiency, being enhanced by a factor of 2.3. This result is related to the angular distribution of emitted light from the devices in Fig. 4(e). While the reference device shows a nearly Lambertian emission pattern, the device with the buckle by 0 min treatment shows a broader distribution and that by 1 and 2 min treatment a narrower distribution compared with the Lambertian emission pattern. According to the Bragg grating equation, the TE_0 and TM_0 modes at 520 nm are diffracted to the polar angle of 35–50°, 25–35°, and 0–13° by grating with the periodicity of 460, 400, and 315 nm, respectively. However, because of wide distribution of grating vectors and periodicities of buckles, the outcoupled light concentrates into normal direction, resulting in the Lambertian-like emission pattern without any particular angle dependence [12], although the tendency of the stronger diffraction toward off-normal directions by the longer periodicity is maintained.

In order to examine the relationship between the buckling periodicity and the wavelength with highest enhancement, we evaluate the enhancement ratio as a function of wavelength in Fig. 4(f), where electroluminescence (EL) spectra of 0, 1 and 2 min UVO-treated devices normalized by that of the reference device for normal direction are displayed. With increasing the treatment time, the peak wavelength showing the highest enhancement shifts toward shorter wavelength according to the shortened periodicity, as expected. For instance, the expected peak wavelengths of the outcoupled TE_0 and TM_0 modes by the buckles without UVO treatment (0 min) with the periodicity of 460 nm are about 790 and 740 nm, respectively (Fig. 4(a)). Actually, the observed highest enhancement ratio is located above 700 nm, although exact peak cannot be estimated because of weak EL intensity. Good agreement was obtained for the buckles by 1 min UVO treatment, i.e., highest enhancement ratio at 680 nm (experiment) is quite close to the expected wavelength 710 (TE_0) and 640 nm (TM_0) for 400 nm periodicity. Thus, although the main outcoupled peak wavelengths through the buckles by 0 and 1 min treatment are far from the main emission wavelength of ~520 nm, overall enhancement for entire emission wavelength ranges was observed because of the broad periodicity and the second-order diffraction as well as the first-order diffraction. The agreement is not so good for the buckle with the periodicity of 315 nm by 2 min treatment compared with previous two examples (buckles by 0 and 1 min treatments). This device is expected to show the highest enhancement ratio at the emission wavelength of 530 and 580 nm for the TE_0 and TM_0 modes, but the highest intensity shown in Fig. 4(f) is located at around 600 nm. The disagreement can be attributed to the asymmetric power spectrum shown in Fig. 1(e) (green line). Namely the power spectrum has wider distribution and longer tail in longer wavelength side, which make the enhancement ratio at longer wavelengths high. Thus, we succeeded in getting high enhancement ratio in a visible wavelength region, although the low depth of the buckles limits the effective diffraction. If a multiple deposition process of Al layer, as demonstrated in our previous study [12], is applied to the buckles by 2 min treatment, a better outcoupling efficiency through the higher depth of the buckle is expected.

4. Conclusions

The spontaneously formed buckling patterns were able to be controlled by the UVO treatment time. Both the periodicity and depth of the buckle decreased with increasing UVO treatment time. The controllability for the periodicity from 300 to 400 nm is particularly important, since the periodicity in those ranges determines the wavelength of enhanced outcoupling for visible EL light. Actually we succeeded in obtaining the device with buckles of 315 nm periodicity by 2 min UVO treatment, and in shifting the wavelength showing the highest enhancement ratio toward the shorter wavelengths with this device. With the simple controllability of the periodicity by the UVO treatment, the advantages of buckles such as broad distribution in periodicity and directional randomness supply a practical solution for all kind of display and lighting applications suffering from power loss by waveguide modes.

Appendix A

Photographs of the buckled PDMS layers on glass substrates by depositing a 50-nm-thick-Al layer on the PDMS layer without (Left) and with 10-min-UVO-treatment (Right). The Al layer on the buckled PDMS without UVO treatment looks optically transparent but white by diffuse scattering, indicating the Al layer is fully oxidized by a chemical reaction with the PDMS layer during deposition.

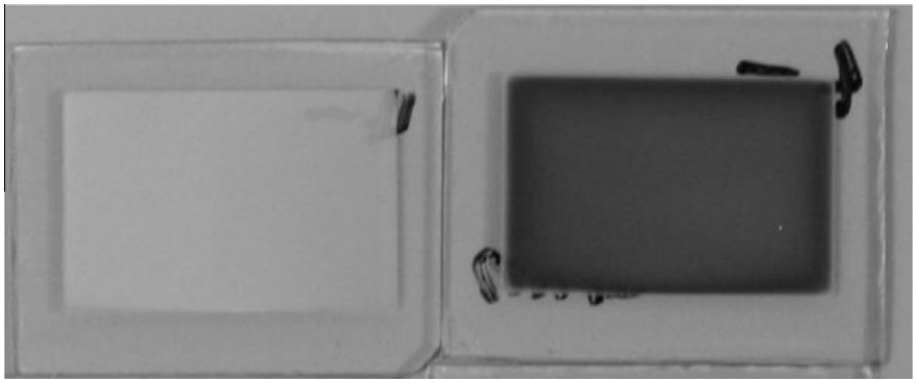

However, the Al layer on the buckled PDMS with 10-min-UVO-treatment looks opaque, indicating that the silica-like surface of the PDMS by the UVO treatment restrains the Al adatoms from being sank and oxidized.

References

[1] M. Fujita, K. Ishihara, T. Ueno, T. Asano, S. Noda, H. Ohata, T. Tsuji, H. Nakada, N. Shimoji, Jpn. J. Appl. Phys., Part 1 1 (44) (2005) 3669–3677.
[2] J.M. Ziebarth, A.K. Saafir, S. Fan, M.D. Mcgehee, Adv. Funct. Mater. 14 (2004) 451–456.
[3] B.J. Matterson, J.M. Lupton, A.E. Safonov, M.G. Salt, W.L. Barnes, I.D. Samuel, Adv. Mater. 13 (2001) 123–127.
[4] P.A. Hobson, J.A.E. Wasey, I. Sage, W.L. Barnes, IEEE J. Sel. Top. Quantum Electron. 8 (2002) 378–386.
[5] S.M. Jeong, F. Araoka, Y. Machida, Y. Takanishi, K. Ishikawa, H. Takezoe, S. Nishimura, G. Suzaki, Appl. Phys. Lett. 92 (2008) 083307.
[6] S.M. Jeong, F. Araoka, Y. Machida, Y. Takanishi, K. Ishikawa, H. Takezoe, S. Nishimura, G. Suzaki, Jpn. J. Appl. Phys. 47 (2008) 4566–4571.
[7] K. Ishihara, M. Fujita, I. Matsubara, T. Asano, S. Noda, H. Ohata, A. Hirasawa, H. Nakada, N. Shimoji, Appl. Phys. Lett. 90 (2007) 111114.
[8] T.K. Shih, J.R. Ho, H.Y. Liao, C.F. Chen, C.Y. Liu, Thin Solid Films 516 (2008) 5339–5343.
[9] N. Bowden, S. Brittain, A.G. Evans, J.W. Hutchinson, G.M. Whitesides, Nature 393 (1998) 146–149.
[10] T. Okayasu, H.L. Zhang, D.G. Bucknall, G.A. Briggs, Adv. Funct. Mater. 14 (2004) 1081–1088.
[11] W.T.S. Huck, N. Bowden, P. Onck, T. Pardoen, J.W. Hutchinson, G.M. Whitesides, Langmuir 16 (2000) 3497–3501.
[12] K.W.H. Koo, S.M. Jeong, F. Araoka, K. Ishikawa, S. Nishimura, T. Toyooka, H. Takezoe, Nat. Photonics 4 (2010) 222–226.
[13] K.W.H. Koo, H.J. Yun, F. Araoka, K. Ishikawa, S.M. Jeong, S. Nishimura, T. Toyooka, H. Takezoe, Appl. Phys. Express 3 (2010) 082501.
[14] H.G. Allen, Analysis and Design of Structural Sandwich Panels, Pergamon, New York, 1969.
[15] K. Efimenko, W.E. Wallace, J. Genzer, J. Colloid Interface Sci. 254 (2002) 306–315.
[16] G.J. Kovacs, P.S. Vincett, J. Vac. Sci. Technol. 20 (1982) 419–420.
[17] G.J. Kovacs, P.S. Vincett, J. Vac. Sci. Technol., A 1 (1983) 369–370.
[18] G.J. Kovacs, P.S. Vincett, C. Tremblay, A.L. Pundsak, Thin Solid Films 101 (1983) 21–40.
[19] R.S. Payne, A. Swann, P.J. Mills, J. Mater. Sci. 25 (1990) 3133–3138.
[20] A.R. Chowdhuri, C.G. Takoudis, R.F. Klie, N.D. Browning, Appl. Phys. Lett. 80 (2002) 4241–4243.
[21] Z. Katz-Tsameret, A. Raveh, J. Vac. Sci. Technol., A 13 (1995) 1121–1127.
[22] M. Ohman, D. Persson, C. Leygraf, Prog. Org. Coat. 57 (2006) 78–88.
[23] W.D. Callister, Materials Science and Engineering – An Introduction, third ed., New York, John Wiley and Sons, 1994.
[24] E. Cerda, L. Mahadevan, Phys. Rev. Lett. 90 (2003) 074302.
[25] J. Chilwell, I. Hodgkinson, J. Opt. Soc. Am. A 7 (1984) 742–753.
[26] P. Yeh, Optical Waves in Layered Media, Wiley, New Jersey, 1988.
[27] T. Fuhrmann, K. Samse, J. Salbeck, A. Perschke, H. Franke, Org. Electron. 4 (2003) 219–226.
[28] M. Fujita, T. Ueno, K. Ishihara, T. Asano, S. Noda, H. Ohata, T. Tsuji, H. Nakada, N. Shimoji, Appl. Phys. Lett. 85 (2004) 5769–5771.

polymers with structural units containing in the side-chains both photoconductive and electro-optic functionalities, such as poly{(4-nitrophenyl)-[3-[*N*-[2-(methacryloyloxy)ethyl]-carbazolyl]]diazene} [poly(CARBA)], it is possible to observe photorefractive and non-linear optical (NLO) properties as well as photoinduced molecular reorientation and the formation of surface relief gratings [38,39].

In this context, we have recently shown [40] how the photorefractive properties of non-poled azo-polymers containing carbazole moieties in the side-chain can be observed at more than 100 °C below their glass transition temperatures. The chemical structures of the four materials (**1–4**) used in that study are shown in Fig. 1. In these particular materials, although light activated conformational mobility is a necessary requirement at such temperatures, a photogenerated electric field is also necessary in order to encode a phase-shifted hologram, via the reorientation of polar chromophores. Such photogenerated field is directly dependent on the photoconductive properties of the polymers, which have not yet been studied in detail.

In the present work, in order to fully investigate the charge photogeneration and transport mechanisms of this class of multifunctional polymers, we have considered compounds **1**–**9**, including five homopolymers without azochromophores (**5–9**). The chemical structures of all the materials used in this study are shown in Fig. 1. The reason for studying also polymers not containing azochromophores relates to the necessity of simplifying structures, reducing the possibility of interferences of the azo-groups over the measured properties. In addition, this allows a comparison between the properties of similar polymers, with and without azochromophores.

2. Experimental

2.1. Polymers

Structures, molecular weight distributions, glass transition (T_g) and decomposition (T_d) temperatures of the studied polymers, obtained by AIBN initiated radical polymerization, are shown in Fig. 1 and Table 1. Poly[(*S*)-(4-cyanophenyl)-[3-[9-[2-(2-methacryloyloxypropanoyloxy) ethyl]carbazolyl]]diazene] {poly[(*S*)-MLECA]} (**1**) was synthesized as previously described [41]. It bears three distinct functional groups (i.e., the azoaromatic, carbazole, and chiral groups of one single configuration) directly linked to a single side chain. Poly[(*S*)-(−)-3-methacryloyloxy-*N*-[3-(9-ethylcarbazolyl)]pyrrolidine-*co*-(*S*)-3-methacryloyloxy-1-(4′-nitro-4-azobenzene)pyrrolidine] 50/50 {poly[(*S*)-(−)-MECP-co-(*S*)-MAP-N] 50/50} (**2**) was synthesized as previously described [40]. Copolymers poly [(*S*)-(+)-2-methacryloyloxy-*N*-[3-(9-ethylcarbazolyl)]succinimide-*co*-(*S*)-(+)-2-methacryloyloxy-*N*-(4-azobenzene)-succinimide] 24/76 {poly[(*S*)-(+)-MECSI-co-(*S*)-(+)-MOSI] 24/76} (**3**) and poly[(*S*)-(+)-2-methacryloyloxy-N-[3-(9-ethylcarbazolyl)]succinimide-*co*-(*S*)-(+)-2-methacryloyloxy-N-(4-azobenzene)succinimide] 76/24 {poly [(*S*)-(+)-MECSI-co-(*S*)-(+)-MOSI] 76/24} (**4**) were synthesized as previously described [42]. Copolymeric compounds **2–4** have two different side-chains: one comonomer with either a (*S*)-3-hydroxy pyrrolidinyl (**2**) or a (*S*)-2-hydroxy succinimide (**3**,**4**) ring as a chiral moiety, covalently linked to a photochromic azoaromatic group, substituted (**2**) or not (**3**,**4**) in the 4-position with a nitro (electron withdrawing) residue. In the side-chain of the second kind of comonomer, the same chiral rings are linked to photoconductive carbazole chromophores. In **2–4**, the conformationally rigid pyrrolidine or succinimide rings increase the stiffness of the macromolecules and induce high T_g values (see Table 1). The presence of a strong electron-withdrawing or donating group such as the five membered cyclic succinimide moiety or the pyrrolidine residue, respectively, within a highly conjugated carbazolyl systems, can potentially modify the charge photogeneration and transport properties. In addition, strongly electron-withdrawing cyano or nitro groups are present in **1** and **2**, respectively, inducing considerable permanent dipole moments. Poly[(*S*)-(+)-2-methacryloyloxy-*N*-[3-(9-ethylcarbazolyl)]succinimide] {poly[(*S*)-(+)-MECSI]} (**5**) and poly[(*S*)-(−)-3-methacryloyloxy-*N*-[3-(9-ethylcarbazolyl)]-pyrrolidine] {poly[(*S*)-(−)-MECP]} (**6**) were synthesized as previously described [43]. The three homopolymers containing 9-phenylcarbazolyl moieties, poly[(*S*)-(+)-3-methacryloyloxy-*N*-[4-(9-carbazolyl) phenyl]-pyrrolidine] {poly[(*S*)-(+)-MCPP]} (**7**), poly[*N*-(2-methacryloyloxyethyl)-*N*-[4-(9-carbazolyl)phenyl]ethylamine] {poly-[MCPE]} (**8**) and poly[(*S*)-(+)-2-methacryloyl oxy-*N*-[4-(9-carbazolyl)phenyl]succinimide] {poly[(*S*)-(+)-MCPS]} (**9**), were synthesized as previously described [44]. The macromolecular compounds **5** and **6** are the corresponding homopolymers of **3/4** and **2**, respectively. Homopolymeric derivatives **7** and **9** contain instead in the side chain a 9-phenylcarbazole moiety linked either to the (*S*)-3-hydroxy pyrrolidinyl (**7**) or to the (*S*)-2-hydroxy succinimide (**9**) ring. The replacement of the alkyl substituent usually bound to the N atom of carbazole by a phenyl group, is expected to expand the electronic conjugation in the chromophores, while at the same time increasing their rigidity. In this respect, polyacrylates and polymethacrylates with pendant 9-phenylcarbazolyl moiety have been largely studied in order to correlate the architecture of the chromophores to the photochemical and photophysical properties [45].

The glass transition temperatures of the investigated polymers are listed in Table 1. All the polymeric derivatives exhibit by differential scanning calorimetry (DSC) measurements only a second order thermal transition attributed to the glass transition (T_g). No endothermic melting peaks, attributable to crystalline domains, were detected. This is in accordance with a substantially amorphous character of the macromolecules in the solid state, expected when, as in this case, side-chain polymers are obtained via free radical polymerization.

2.2. Electrochemistry

HOMO (Highest Occupied Molecular Orbital) and LUMO (Lowest Unoccupied Molecular Orbital) energy levels of the polymers were estimated by cyclic voltammetry, in some cases through a correlation with UV–Vis absorption spectroscopy. Cyclic voltammetry data were performed in dry

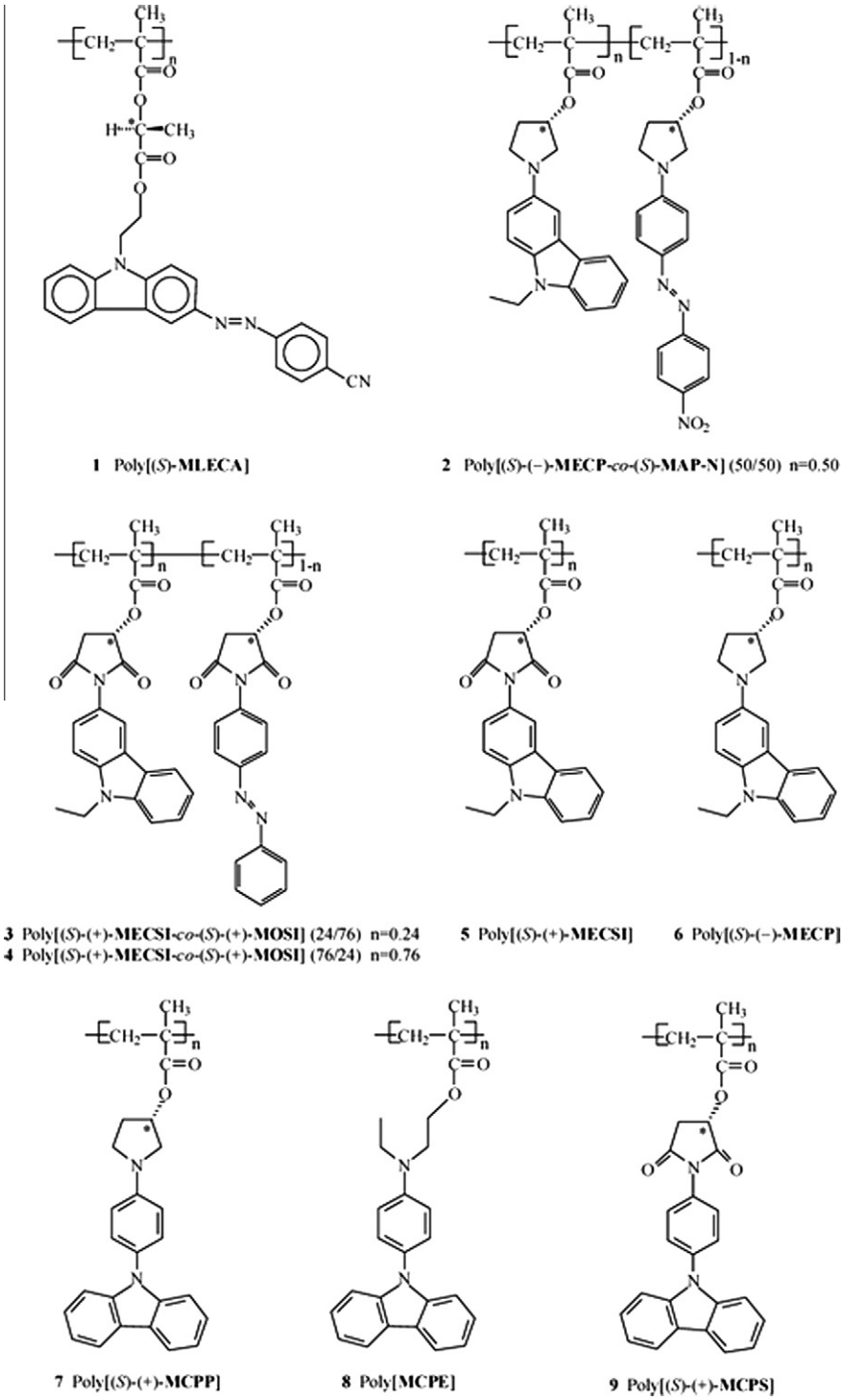

Fig. 1. Chemical structures of the investigated polymers.

dichloromethane solutions using tetrabutylammonium hexafluorophosphate (0.1 M) as an electrolyte, a Pt disk working electrode, a Pt wire counter electrode and an Ag/AgCl reference electrode at a scan rate of 100 mV s^{-1}. An equimolar amount of ferrocene was added to the solution for internal reference. For irreversible (Irr) oxidation or reduction waves, values of the irreversible peak were considered, while for Quasi Reversible (QR) redox waves, the average value (Epc + Epa)/2 was taken into account. Energy values were calculated by comparing the polymer

Table 1
Relevant characterization data of the investigated polymeric derivatives.

Polymer	$\bar{M}_n$[a] (g mol^{-1})	$\bar{M}_w/\bar{M}_n$	T_g[b] (°C)	T_d[c] (°C)
1 Poly[(*S*)-**MLECA**]	13,400	1.8	147	363
2 Poly[(*S*)-(−)-**MECP**-*co*-(*S*)-**MAP-N**] 50/50	6700	1.5	214	328
3 Poly[(*S*)-(+)-**MECSI**-*co*-(*S*)-(+)-**MOSI**] 24/76	9400	1.9	227	297
4 Poly[(*S*)-(+)-**MECSI**-*co*-(*S*)-(+)-**MOSI**] 76/24	10,200	2.0	228	298
5 Poly[(*S*)-(+)-**MECSI**]	12,700	1.7	202	330
6 Poly[(*S*)-(−)-**MECP**]	6600	1.6	210	349
7 Poly[(*S*)-(+)-**MCPP**]	7000	1.9	194	343
8 Poly[**MCPE**]	10,100	1.9	129	320
9 Poly[(*S*)-(+)-**MCPS**]	11,400	1.9	244	336

[a] Determined by SEC in THF solution at 25 °C.
[b] Glass transition temperature of pure compounds determined by DSC at a 10 °C/min heating rate under nitrogen flow (between brackets the values for the mixtures containing 20% of the DPP plasticizer).
[c] Initial decomposition temperature as determined by TGA at a 20 °C/min heating rate under air flow.

oxidation/reduction potentials to the ferrocene/ferrocenium oxidation potential, taking the value of −4.8 eV for the HOMO of ferrocene [46]. With the exception of **1**, all analyzed polymers have shown two oxidative waves, as shown in Fig. 2 in the case of **6** and **7**. HOMO levels were evaluated considering the first oxidation potential. Polymers **1** and **2** showed irreversible oxidation waves and irreversible (**1**) and quasi-reversible (**2**) reductions waves. For all other compounds no reduction was detected within the solvent potential window, while a quasi-reversible behaviour was observed for oxidation. When reduction waves were not observed, the highest wavelength band observed in the absorption spectrum was considered in order to estimate the HOMO/LUMO band gap.

2.3. Photoconductivity

Samples were prepared by sandwiching materials between two glass slides, each one covered with five 1 mm wide strips of conducting Indium Tin Oxide (ITO). Substrates were obtained by acid etching of conducting glass slides uniformly covered with ITO (110 nm, from Unaxis). Sample preparation starts by placing a proper amount of polymer on one substrate and heating above its glass transition temperature (T_g) on a hot plate. When the material is soft enough, it is covered and pressed with another hot glass and finally the sample is quickly cooled to room temperature. The thickness of the polymeric film was controlled by glass spacers and measured by interferometry.

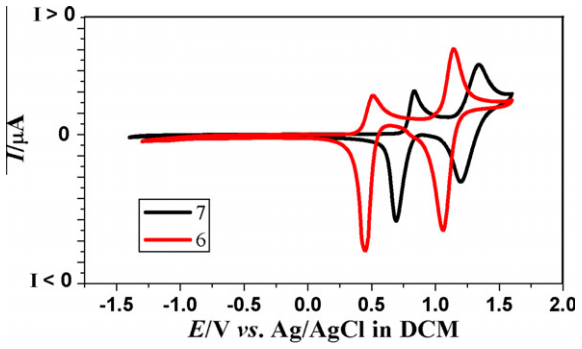

Fig. 2. Cyclic voltammograms of 6 and 7 in dry dichloromethane, using a Pt working electrode, a Pt wire as counter electrode, an Ag/AgCl reference electrode and tetrabutylammonium hexafluorophosphate as an electrolyte (0.1 M). Scan rate: 100 mV s^{-1}.

Photoconductivity measurements were performed by applying an electric field $E = 18$ V/m to the sample and measuring the electric current through the sample, both in the dark and under illumination. The current was measured by a 6517A Keithley electrometer, while the light was provided by a DPSS laser at $\lambda = 532$ nm. For polymers **1**, **2** and **4**, where absorption at such wavelength is too high, measurements were carried out using a He–Ne laser at $\lambda = 633$ nm. In order to take into account the different absorption properties of the investigated compounds, photoconductivity was always normalized with respect to the absorption coefficient.

2.4. Hole mobility

A layer of the material was deposited on an ITO covered glass by spin coating tetrahydrofuran solutions (30 mg/ml) at 800 rpm. The thickness of the resulting films (between 0.4 and 1.4 m) was measured using a Veeco Dektak 8 stylus profilometer. A gold electrode was then deposited on the films by high vacuum thermal evaporation. Considering their HOMO energy levels, polymers **1** and **9** cannot have ohmic contacts with gold and therefore they were not considered for hole mobility measurements via the Space-Charge Limited Current (SCLC) technique described below. In addition, the quality of films obtained from **2**, **4** and **7** was poor, so that measurements was restricted to **3**, **5, 6** and **8**. Measurements were performed by recording I-V curves using a 6517A Keithley electrometer. At low applied voltages, the current is a linear function of voltage and the resistive behaviour is ohmic:

$$J = ne\mu\frac{V}{d} \quad (1)$$

where J is the current density, n is the charge carrier density, e is the elementary charge, μ is the charge carrier drift mobility, V is the applied voltage and d is the sample thickness. At higher voltages and charge densities, the electric field in the material is determined not only by the applied voltage but also by the space-charges. In such case, the

voltage dependence of the current can be approximated by the Mott-Gurney equation [47]:

$$J = \frac{9}{8}\varepsilon\varepsilon_0\mu\frac{V^2}{d^3} \quad (2)$$

where ε_0 is the free space permittivity and ε is the relative dielectric constant of the material. Therefore, from a measurement of cell thickness and dielectric constant, it is possible to obtain the mobility from the *I–V* curves, assuming an ohmic contact from the injecting electrode. The dielectric constants of the materials were obtained via capacitance measurements by using an Agilent B905A precision bridge.

A reliability check of the mobility measurement can be carried out considering that, according to Eqs. (1), (2), the voltage V_T at which the slope of the *I–V* curves change from linear to quadratic is:

$$V_T = \frac{8}{9}en\frac{d^2}{\varepsilon\varepsilon_0} \quad (3)$$

The measured value of the mobility can be used in Eq. (1) to obtain n which, in turn, can be used in Eq. (3) to obtain V_T. A good matching between such calculated value of V_T and the experimental value extracted from *I–V* curves is an indicator of reliable measurements.

3. Results and discussion

3.1. Frontier orbitals

Table 2 shows the values of the HOMO and LUMO energy levels of the investigated polymers, as determined by Cyclic Voltammetry. A clear trend can be highlighted when the energy of the HOMO's, which are directly involved in hole transport, are considered in relation with molecular structure. Not surprisingly, the highest energy HOMO's are found for **2** and **6**, where an electron-donating pyrrolidine–nitrogen is directly linked to the 3-position of carbazole. Note that the HOMO levels of the homopolymer **6** and of the copolymer **2** are the same, a result pointing out the importance of the carbazolyl moiety in determining HOMO's, with the azo side-chain being irrelevant in this respect. The same can be said comparing the HOMO's of **3**/**4** and **5**. However, in these last compounds the presence of an electron-withdrawing succinimide-nitrogen in the 3-position of the carbazolyl group lowers their HOMO's, if they are compared with **2** and **6**. A similar, although less marked, effect was found when the amino or succinimide groups were linked to the nitrogen atom of carbazole through a phenyl bridge (compare **7**/**8** with **9**). Comparing instead the effect of a given substituent on different positions, results show relevant differences for amino substituents (compare **2**/**6** with **7**/**8**) but not for succinimide (compare **3**/**4**/**5** with **9**). Polymer **1** is the only compound of the series with an azo-group directly linked to the carbazolyl moiety. Its HOMO is by far the most stable, probably as a consequence of the presence of a strongly electron-withdrawing cyano moiety directly connected with the conjugated carbazole.

Table 2
HOMO and LUMO energies of polymers **1–9.** All the LUMO energies (except those for **1** and **2**, obtained by CV) were estimated by using UV–Vis data.

Polymer	LUMO (eV)	HOMO (eV)
1	−3.1	−5.7
2	−3.4	−4.8
3	−2.5	−5.3
4	−2.5	−5.3
5	−1.9	−5.3
6	−1.8	−4.8
7	−1.5	−5.1
8	−1.55	−5.1
9	−1.8	−5.4

3.2. Hole mobility

Being the HOMO levels of all polymers (with the exception of **1** and possibly of **9**) within 0.3 eV from the work function of gold, the Space Charge Limited Current method in samples with one Au electrode could be used in order to measure hole mobility. As explained in the experimental section, samples suitable for hole mobility (μ) measurements could be obtained only for **3**, **5**, **6** and **8**. A typical current voltage plot is illustrated in Fig. 3.

The resulting mobilities for the four compounds are listed in Table 3. The striking result is that in **5** and **6** the mobility is several orders of magnitude lower than in **3** and **8**. Mobility thus depends neither on the chemical nature of the linking group nor on the HOMO energy level. The only trend that can be found is that homopolymers in which the carbazolyl group is linked to the main-chain through a conformationally stiff linker (**5** and **6**) have a much lower mobility than copolymers (**3**) or homopolymers with a more mobile linker (**8**). Although the number of investigated polymers is not high enough to allow the drawing of a final conclusion, our data indicate that a higher degree of conformational freedom of the carbazole-containing side-chains favours charge mobility, probably via a more favourable arrangement in space of the carbazolyl

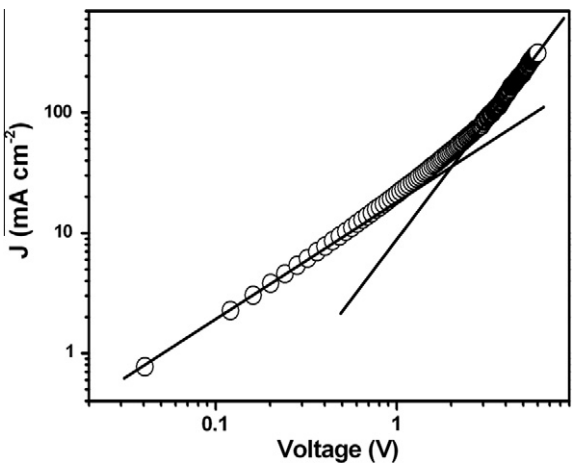

Fig. 3. Voltage dependence of the current in a sample of polymer **8**. The thickness of the spin-coated polymer layer was $d = 400$ nm. The two straight lines have slopes 1 and 2.

Table 3
Absorption coefficient (α), hole mobility (μ), photogenerated charge carrier density (n_D), number of carriers per watt of absorbed power (η) and photogeneration efficiency (ϕ) for polymers 3, 5, 6 and 8.

Polymer	α (λ = 532 nm) (cm−1)	μ ($cm^2\ V^{-1}\ s^{-1}$)	n_D (cm^{-3})	η (W^{-1})	ϕ
3	358	2.2×10^{-3}	$<8.5 \times 10^{+5}$	$<1.0 \times 10^{+4}$	$<3.3 \times 10^{-9}$
5	987	2.6×10^{-7}	$2.6 \times 10^{+10}$	$1.3 \times 10^{+8}$	1.5×10^{-9}
6	1267	1.3×10^{-8}	$5.1 \times 10^{+15}$	$2.8 \times 10^{+13}$	1.6×10^{-5}
8	78	2.1×10^{-3}	$1.9 \times 10^{+10}$	$5.6 \times 10^{+8}$	5.0×10^{-5}

moieties. This result is in agreement with previous observations [1] on carbazole side-chain polymers, in which a higher charge mobility was tied to a lower density of charge traps: in our case, the conformational freedom of the side-chains should contribute to a decrease of trap-forming structural defects.

Considering the absolute values of the measured hole mobilities, the low values obtained for both **5** and **6** are in line with what measured in most carbazole polymers. But while the high mobility in **8** can be accounted for by the higher conformational freedom, the equally high mobility measured in **3** is surprising. In fact, for **3** one would expect a mobility even lower than for **5**, on account of the fact that the density of carbazole charge carriers is decreased. The only possible explanation of such experimental evidence is an involvement of the azo-containing side-chain in charge transport. Studies are in progress to verify such hypothesis.

It should be underlined that, as usual in side-chain polymers obtained via radical polymerization, the polymers under investigation are amorphous, as confirmed by the absence of melting peaks in DSC curves. As a consequence, in contrast to what observed in many main-chain polymers, the differences in molecular weight (see Table 1) do not affect the degree of crystallization and the morphology of the polymeric films. In other words, the effect of molecular weight on charge mobility can safely be neglected.

3.3. Photoconductivity

Charge photogeneration in carbazole-containing polymers is often studied in blends with electron acceptors, because such composites find application in photovoltaic devices [48,49]. In this work instead, charge photogeneration and photoconductivity is studied in pure, undoped samples. The photoresponsivity (photoconductivity per watt of incident power I) of the investigated polymers is listed in Table 4. In order to better compare the different materials, data were normalized with respect to the absorption coefficient α. Photoresponsivities span a range of more than 5 orders of magnitude. In the best performing compounds, **2** and **8**, photoconductivity measured at an applied field E = 18 V/μm is two orders of magnitude lower than in poly(vinylcarbazole) photorefractive composites [50], where however it was measured at E = 80 V/m and in samples doped in order to increase absorption.

Hole photoconductivity in organics is often found to decrease with increasing stability of the HOMO's, and this is usually attributed to a decrease in photogeneration efficiency due to the lower tendency of the donor (in our case the carbazolyl moiety) to ionize [51]. The photoresponsivity dependence on the HOMO energy level for the investigated polymers is shown in Fig. 4. The correlation is good, with the notable exceptions of **3**, **5** and **8**. Note that in the case of **3** (E_{HOMO} = 5.3 eV), photoconductivity was below the detection limit of the instrumentation used, so that its photoresponsivity would be found in Fig. 4 somewhere below the point corresponding to compound **5**.

An attempt towards the rationalization of such a behaviour is instructive and, to some extent, even enlightening. Photoconductivity (σ) depends on two factors: the density of photogenerated charge carriers and their mobility:

Table 4
Photoresponsivity of polymers **1**–**9** measured at an applied electric filed E = 18 V/m.

Polymer (% DPP)	$\sigma/\alpha I$ ($cm^2\ \Omega^{-1}\ W^{-1}$) λ = 532 nm	$\sigma/\alpha I$ ($cm^2\ \Omega^{-1}\ W^{-1}$) λ = 633 nm
1		1.7×10^{-16}
2 (20%)		1.7×10^{-13}
3	$<10^{-15}$	
4		4.9×10^{-15}
5 (20%)	2.3×10^{-18}	
6 (20%)	2.0×10^{-14}	
7	5.3×10^{-15}	
8 (15%)	1.6×10^{-13}	
9 (15%)	3.0×10^{-15}	

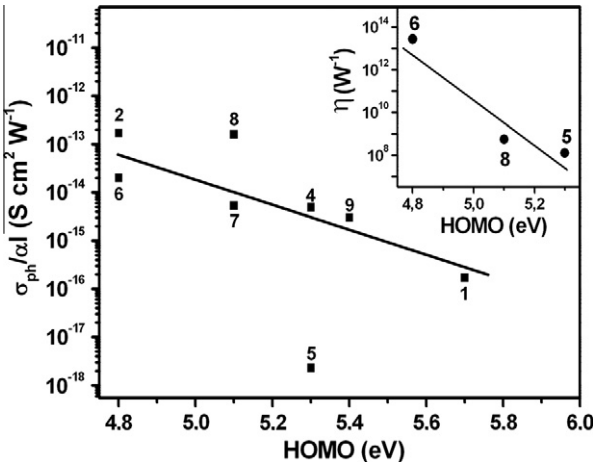

Fig. 4. Photoresponsivity as a function of the HOMO energy level measured at an applied electric filed E = 18 V/m for **1**–**9**. The inset shows the estimated number of carriers per watt of absorbed power for the three polymers for which this parameter could be obtained. Lines are guides to the eye.

$$J_{Ph} = en_D\mu E = \sigma E \quad (4)$$

where J_{Ph} is the photocurrent density, e is the electron charge, n_D is the photogenerated charge carrier density and E is the applied electric field. Mobility was independently measured for four of the polymers. The density of photogenerated charges is instead a direct consequence of the photogeneration efficiency ϕ, defined as the ratio between the number of photogenerated carriers and the number of absorbed photons. If we write the intensity of light absorbed through the volume of a sample of thickness d as

$$I_{abs} = I(1 - e^{-\alpha d}) \quad (5)$$

where I is the incident power per unit surface, the photogeneration efficiency can be written as:

$$\phi = \frac{\sigma E \hbar\omega}{eI_{abs}} \quad (6)$$

where ħ is the energy of a single photon of the incident light. However, Eq. (6) neglects trapping and recombination and it does not allow a discrimination between the contributions of the density of carriers and of their mobility. Since mobility data are available, even if not for the whole series of polymers, it seems more appropriate to discuss the results in terms of the density of carriers n_D, that can be obtained from Eq. (4), and to compare the properties of the different polymers by taking, as an indicator of photogeneration efficiency, the following ratio:

$$\eta = \frac{dn_D}{I_{abs}} \quad (7)$$

i.e. the number of carriers per watt of absorbed power. Such parameter is listed in Table 3 for the four polymers for which mobility was measured. Polymer **3** shows the lowest η, with less than 10^4 carriers per Watt, while for polymers **5** and **8** this figure increases by at least four orders of magnitude. In polymer **6**, we see a further increase by five orders of magnitude. These data clearly indicate how the succinimide linker depresses photogeneration efficiency when compared to an amino linker (**5** vs. **6**). In addition, when the amino linker is in position 3 of the carbazole (**6**), it enhances photogeneration much more than when it is further removed (**8**). Note that when the "real" photogeneration efficiency is calculated by using Eq. (6), a completely different scale of relative efficiency among the different polymers is obtained. Values of are also listed in Table 3. This discrepancy is due to the fact that in Eq. (6), charge mobility (included in σ) is seen as a factor directly influencing photogeneration efficiency. We believe instead that, if charge mobility values are available, the η ratio obtained using Eqs. (4,7) is a better indicator of charge photogeneration efficiency. The inset of Fig. 4 shows the dependence of on the HOMO energy, in the case of the three materials for which n_D could be obtained. Although it consists of only three points, such dependence follows the expected trend, in contrast with the results illustrated in the main Figure for the photoconductivity of the same three polymers. This shows that if mobility and photogeneration efficiency of a series of compounds are not independently determined, the simple consideration of the photoconductivity (which depends on both properties) may be misleading when attempting the rationalization of structure/property relationships.

This is also evident, for example, if we compare the results for polymers **3**, **4** and **5,** with a gradually increasing content of the carbazole-containing side-chain. One would expect a regularly varying trend of photoconductivity in the series, but instead **4**, the compound with an intermediate composition, shows the highest σ. This result is understandable only by considering the mobility and η figures of Table 3. Charge mobility in **3** is four orders of magnitude higher than in **5**. However, its photoconductivity is lower, due to a much lower density of carbazole-containing side-chains, which is reflected in a lower efficiency of photogeneration. However, both **3** and **5** show a photoconductivity which is orders of magnitude lower than in **4**. Although mobility data for **4** are not available, these results suggest that compound **4** shares the high mobility of **3** and the higher carrier density of **5**. As it was already mentioned, the higher mobility of **3** and **4** can be attributed to the higher conformational freedom present in a co-polymer. Notice that the lower content of carbazole bearing side-chains of **3** does not seem to affect mobility, but it greatly reduces the carrier density. A possible explanation of this observation is an involvement of the azo-group in the hole transport process but not in the photogeneration. Further studies are needed in order to clarify this point.

It is also interesting to compare in Fig. 4 the photoresponsivities of **7**–**9**, three compounds with a very similar structure. Polymer **8** shows the highest value, which is more than one order of magnitude higher than what measured for **7** and **9**. This could again be tied with the higher conformational freedom of the side-chains in **8**, inducing a higher charge mobility, while the effects of the different groups on photogeneration efficiency should be leveled by the interposition of a phenyl ring between the carbazole and the amino/succinimide bridging group. The observation that the carrier density in **8** is much lower than in **6** (see Table 3) confirms this lower influence on charge photogeneration of a group far removed from the carbazole unit.

4. Conclusions

The described experimental studies of the charge photogeneration and transport properties of a series of carbazole side-chain polymers underline several structure-related properties. The comparison between homo- and co-polymers clearly points out that in carbazole/azo copolymers the HOMO energy level is only determined by the carbazole containing side-chain, a relevant result when considering the charge transport and other HOMO related properties in multifunctional polymers. In addition, different electron-withdrawing or donating substituents on the 3-position of carbazole have a large influence on the HOMO energy, while their effect is much reduced if they are further removed from the carbazole moiety. In turn, the HOMO energy level is one of the important factors determining photoconductivity, via the control of photogeneration efficiency: in general, a lower photogeneration

efficiency is found for compounds with a more stable HOMO. This is an extremely relevant effect, as we found that the density of charge carriers per Watt of absorbed power can span a 10 orders of magnitude range, with more carriers being generated when (a) the density of carbazole moieties is higher and (b) the HOMO is less stable due to the presence of electron-donating groups linked to the 3-positions of carbazole. Charge mobility seems instead not to depend on the HOMO energy but rather on the conformational freedom of the side chains. The very high value of hole mobility, of the order of 10^{-3} cm^2 V^{-1} s^{-1}, obtained for two of the investigated polymers, should be highlighted. In addition, a possible contribution of the azo-moieties to charge transport was observed.

This study shows how it is necessary to separately measure and consider the different contributions of charge photogeneration and charge transport in order to rationalize the relationship between photoconductivity and chemical structure. The picture that emerges is that photoconductivity in azo/carbazole co-polymers depends on the contribution of several factors affecting charge photogeneration and transport, that can be controlled by carefully selecting the nature of the linker between the carbazole unit and the main chain and the position on the carbazole where this linker is attached.

Acknowledgments

This work has been supported by INSTM (PRISMA 2007 Grant) and by MiUR through the PRIN 2007 (2007WJMF2W) project.

References

[1] J.V. Grazulevicius, P. Strohriegl, J. Pielichowskic, K. Pielichowski, Prog. Polym. Sci. 28 (2003) 1297.
[2] N. Blouin, M. Leclerc, Acc. Chem. Res. 41 (2008) 1110.
[3] W.E. Moerner, A. Grunnet-Jepsen, C.L. Thompson, Ann. Rev. Mater. Sci. 27 (1997) 583.
[4] P.N. Prasad, M.E. Orczyk, J. Zieba, J. Phys. Chem. 98 (1994) 8699.
[5] K. Meerholz, B.Volodin, Sandalphon, B. Kippelen, N. Peyghambarian, Nature 497 (1994) 371.
[6] P.-L.T. Boudreault, S. Beaupré, M. Leclerc, Polym. Chem. 1 (2010) 127.
[7] A.D. Schlüter, J. Polym. Sci. Part A: Polym. Chem. 39 (2001) 1533.
[8] Z. Bao, W.K. Chan, L. Yu, J. Am. Chem. Soc. 117 (2002) 12426.
[9] J.Q. Qu, Y. Suzuki, M. Shiotsuki, F. Sanda, T. Masuda, Polymer 48 (2007) 4628.
[10] F. Sanda, T. Kawaguchi, T. Masuda, N. Kobayashi, Macromolecules 36 (2003) 2224.
[11] F. Sanda, T. Nakai, N. Kobayashi, T. Masuda, Macromolecules 37 (2004) 2703.
[12] Y. Takihana, M. Shiotsuki, F. Sanda, T. Masuda, Macromolecules 37 (2004) 7578.
[13] K. Tamura, T. Fujii, M. Shiotsuki, F. Sanda, T. Masuda, Polymer 49 (2008) 4494.
[14] T. Fulghum, S.M.A. Karim, A. Baba, P. Taranekar, T. Nakai, T. Masuda, R.C. Advincula, Macromolecules 39 (2006) 1467.
[15] T. Fujii, M. Shiotsuki, Y. Inai, F. Sanda, T. Masuda, Macromolecules 40 (2007) 7079.
[16] J. Qu, R. Kawasaki, M. Shiotsuki, F. Sanda, T. Masuda, Polymer 48 (2007) 467.
[17] X. Gong, S. Wang, D. Moses, G.C. Bazan, A.J. Heeger, Adv. Mater. 17 (2005) 2053.
[18] Y. Kawamura, S. Yanagida, S.R. Forrest, J. Appl. Phys. 92 (2002) 87.
[19] L.Angiolini, T. Benelli, L. Giorgini, F. Mauriello, E. Salatelli, Macromol. Chem. Phys. 207 (2006) 1805.
[20] D.Bogdal, V. Yashchuk, J. Pielichowski, T. Ogul'Chansky, M. Warzala, V.J. Kudrya, Appl. Polym. Sci. 84 (2002) 1650.
[21] C. Engels, D. Van Steenwinckel, E. Hendrickx, M. Schaerlaekens, A. Persoons, C.J. Samyn, Mater. Chem. 12 (2002) 951.
[22] C.Y. Huang, G.Q. Jiang, R. Advincula, Macromolecules 41 (2008) 4661.
[23] K. Kim, Y.R. Hong, S.W. Lee, J.I. Jin, Y. Park, B.H. Sohn, W.H. Kim, J.K. Park, J. Mater. Chem. 11 (2001) 3023.
[24] P.D. Vellis, J.A. Mikroyannidis, J. Cho, H. Choi, J. Polym. Sci. Part A: Polym. Chem. 46 (2008) 5592.
[25] R. Ravindranath, P.K. Ajikumar, S. Bahulayan, N.B.M. Hanafiah, A. Baba, R.C. Advincula, W. Knoll, S. Valiyaveettil, J. Phys. Chem. B 111 (2007) 6336.
[26] E. Schwartz, E. Lim, C.M. Gowda, A. Liscio, O. Fenwick, G. Tu, V. Palermo, R. de Gelder, J.J.L.M. Cornelissen, E.R.H. Van Eck, A.P.M. Kentgens, F. Cacialli, R.J.M. Nolte, P. Samori, W.T.S. Huck, A.E. Rowan, Chem. Mater. 22 (2010) 2597.
[27] G.S. Liou, H.W. Chen, H.J. Yen, J, Polym. Sci. Part A: Polym. Chem. 44 (2006) 4108.
[28] G.S. Liou, S. Hsiao, H.N.K. Huang, Y.L. Yang, Macromolecules 39 (2006) 5337.
[29] Proceedings of the Symposium on Azobenzene-Containing Materials, Boston MA (USA) 1998, A. Natansohn (Ed.), Macromolecular Symposia 137, Wiley, New York, 1999, pp. 1–165.
[30] A. Natansohn, P. Rochon, M.S. Ho, C. Barrett, Macromolecules 28 (1995) 4179.
[31] Y. Wu, Q. Zhang, A. Kanazawa, T. Shiono, T. Ikeda, Y. Nagase, Macromolecules 32 (1999) 3951.
[32] C. Maertens, P. Dubois, R. Jerome, P.A. Blanche, J. Polym. Sci. Part B: Polym. Phys. 38 (2000) 205.
[33] C.R. Mendonca, A. Dhanabalan, D.T. Balogh, L. Misoguti, S. Dos Santos Jr., M.A. Pereira-da-Silva, J.A. Giacometti, S.C. Zilio, O.N. Oliveira Jr., Macromolecules 32 (1999) 1493.
[34] J.H. Kim, S. Kumar, S.D. Lee, Phys. Rev. E 57 (1998) 5644.
[35] K. Ichimura, Chem. Rev. 100 (2000) 1847.
[36] J. Gao, Y. He, F. Liu, X. Zhang, Z. Wang, X. Wang, Chem. Mater. 19 (2007) 14.
[37] O. Kulikovska, L.M. Goldenberg, L. Kulikovsky, J. Stumpe, Chem. Mater. 20 (2008) 3528.
[38] M. Ho, C. Barrett, J. Paterson, M. Esteghamatian, A. Natansohn, P. Rochon, Macromolecules 29 (1996) 4613.
[39] C. Barrett, B. Choudhury, A. Natansohn, P. Rochon, Macromolecules 31 (1998) 4845.
[40] H. Li, R. Termine, L. Angiolini, L. Giorgini, F. Mauriello, A. Golemme, Chem. Mater. 21 (2009) 2403.
[41] L. Angiolini, T. Benelli, L. Giorgini, F. Mauriello, E. Salatelli, Macromol. Chem. Phys. 207 (2006) 1805.
[42] L. Angiolini, T. Benelli, L. Giorgini, F. Mauriello, E. Salatelli, Proc. SPIE 66531 (2007) C/1.
[43] L. Angiolini, T. Benelli, L. Giorgini, A. Golemme, F. Mauriello, E. Salatelli, R. Termine, Macromol. Chem. Phys. 209 (2008) 944.
[44] L. Angiolini, L. Giorgini, H. Li, A. Golemme, F. Mauriello, R. Termine, Polymer 51 (2010) 368.
[45] X. Zhang, L. Zi-Chen, L. Kai-Bo, L. Song, D. Fu-Sheng, L. Fu-Mian, Prog. Polym. Sci. 31 (2006) 893.
[46] Y. Liu, M.S. Liu, X.-C. Li, A.K.-Y. Jen, Chem. Mater. 10 (1998) 3301.
[47] M.A. Lampert, P. Mark, Current Injection in Solids, Academic Press, New York, 1970.
[48] C. Dridi, V. Barlier, H. Chaabane, J. Davenas, H. Ben Ouada, Nanotechnology 19 (2008) 375201.
[49] M. Tong, N.E. Coates, D. Moses, A.J. Heeger, S. Beaupré, M. Leclerc, Phys. Rev. B 81 (2010) 125210.
[50] E. Hendrickx, Y. Zhang, K.B. Ferrio, J.A. Herlocker, J. Anderson, N.R. Armstrong, E.A. Mash, A.P. Persoons, N. Peyghambarian, B. Kippelen, J. Mater. Chem. 9 (1999) 2251.
[51] E. Hendrickx, B. Kippelen, S. Thayumanavan, S.R. Marder, A. Persoons, N.J. Peyghambarian, Chem. Phys. 112 (2000) 9557.

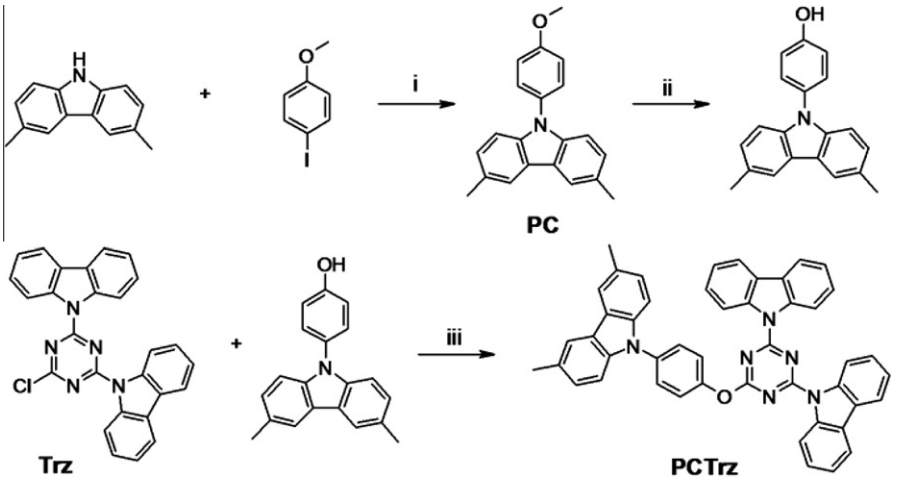

Scheme 1. Synthesis of 2-(4-(3,6-dimethylcarbazol-9-yl)-phenoxy)-bis-4,6-biscarbazolyl-1,3,5-triazine PCTrz: (i) CuI, K_3PO_4, trans-1,2-diamino-cyclohexane, dioxane, 120 °C, 18 h, 68%; (ii) BBr_3, CH_2Cl_2, −78 °C, 12 h, 92%; (iii) NaOH, H_2O, dioxane, 100 °C, 6 h, 80%.

of those triazines were limited and yielded a recombination zone close to the HTL/EML interface. Thus enhanced hole injection properties are desirable and supposed to improve the charge carrier balance and the OLED performance.

In this work we present 2-(4-(3,6-dimethylcarbazol-9-yl)-phenoxy)-bis-4,6-biscarbazolyl-1,3,5-triazine PCTrz as a new bipolar host material for blue phosphorescent OLEDs. PCTrz comprises one hole conducting phenoxy-carbazole and one electron deficient biscarbazolyl-triazine moiety, which are connected by an ether bond, that breaks the conjugation between the two parts of the molecule. This was proved by cyclic voltammetry and density functional theory calculations. The separation of the oxidation- and reduction-site results in a "monodisperse molecular mixed host" which combines good transport properties for both types of charges. PCTrz has a triplet energy of 2.91eV, which makes it suitable as host material for blue phosphorescent emitters. The material exhibits high thermal stability and good sublimation properties. The glass transition temperature of 148 °C ensures morphological stability of the host–guest emission layer during the operation of the device. An organic light emitting diode with PCTrz as host for FIrpic were fabricated. They exhibited a high current efficiency of 13.5 cd/A at a luminance of 1000 cd/m^2 combined with a maximum luminance of 29,000 cd/m^2.

2. Experimental

2.1. Synthesis of the host material

The synthesis of PCTrz is outlined in Scheme 1. The donor part is prepared by a modified *Goldberg* reaction [13] of 3,6-dimethylcarbazole and 4-iodoanisole followed by methyl ether cleavage with boron tribromide to yield 9-(4-hydroxyphenyl)-3,6-dimethylcarbazole in 62% yield. The synthesis of 2-chloro-4,6-biscarbazolyl-1,3,5-triazine (Trz) is described elsewhere [12]. Finally, PCTrz is prepared by a nucleophilic substitution at the triazine core in 80% yield.

2.1.1. Materials

All commercially available reagents were purchased from Aldrich and used without further purification. The synthesis of 2,4-biscarbazolyl-6-chloro-1,3,5-triazine [12], tris[(3-phenyl-1H-benzimidazol-1-yl-2(3H)-ylidene)-1,2-phenylene]-Iridium (DPBIC) [14] and 2,8-bis(triphenylsilyl)-dibenzofuran (DBFSi) [15] is described in the literature.

2.1.2. 9-(4-Methoxyphenyl)-3,6-dimethylcarbazole (PC)

3,6-Dimethylcarbazole (3.90 g, 20 mmol), 4-iodanisole (5.15 g, 22 mmol), copper(I)-iodide (0.38 g, 2 mmol), potassium phosphate (4.24 g, 20 mmol) and (trans)-1,2-diaminocyclohexane (0.23 g, 2 mmol) were dissolved in 80 ml dry dioxane before the reaction mixture was refluxed for 14 h in an argon atmosphere. After cooling to room temperature the mixture was filtered to remove all inorganic salts and the solvent was removed under reduced pressure. The crude product was purified with column chromatography using a hexane/THF (10/1; V/V) eluent to yield 9-(4-methoxyphenyl)-3,6-dimethylcarbazol (4.01 g, 13.6 mmol) as white solid. (Yield: 68%). ^{1}H NMR (300 MHz, $CDCl_3$, δ): 7.90.(s, 2H), 7.44 (d, 2H), 7.21 (m, 4H), 7.10 (d, 2H), 3.91 (s, 3H), 2.54 (s, 6H); ^{13}C NMR (75 MHz, $CDCl_3$, δ): 158.6, 139.8, 130.8, 128.7, 128.3, 126.9, 123.1, 120.1, 114.9, 109.3, 55.6, 21.4; EI-MS (m/z (%)): 301 (100) [M$^+$], 286 (25).

2.1.3. 9-(4-Hydroxyphenyl)-3,6-dimethylcarbazole

9-(4-Methoxyphenyl)-3,6-dimethyl-carbazole (3.45 g, 11.5 mmol) was dissolved in dry dichloromethane (60 ml) under argon and cooled to −78 °C before boron tribromide (8.80 ml of a 1 M solution in dichloromethane, 12.6 mmol) was added dropwise. The mixture was allowed to warm to room temperature under stirring. After the addition of water (20 ml) the organic phase was collected and the solvent was

removed under reduced pressure. The crude product was purified with column chromatography using a hexane/THF (7/1; V/V) eluent to yield 9-(4-hydroxyphenyl)-3,6-dimethylcarbazol (3.03 g, 10.6 mmol) as white solid. (Yield: 92%) ^{1}H NMR (300 MHz, $CDCl_3$, δ): 7.89 (s, 2H), 7.39–7.37 (d, 2H), 7.20 (m, 4H), 7.03–7.00 (d, 2H), 5.03 (s, 1H), 2.54 (s, 6H); ^{13}C NMR (75 MHz, $CDCl_3$, δ): 154.6, 139.8, 130.9, 128.8, 128.6, 127.0, 123.1, 120.1, 116.4, 109.3, 21.4;EI-MS (m/z (%)): 286 (100) [M^+].

2.1.4. 2,4-Biscarbazolyl-6-(4-(3,6-dimethylcarbazol-9-yl)phenoxy)-1,3,5-triazine (PCTrz)

4-Hydroxyphenyl-3,6-dimethylcarbazole (0.77 g, 2.67 mmol) and sodium hydroxide (0.10 g, 2.5 mmol) were dissolved in a water/dioxane mixture (20 ml, 1/1 (V/V)) at room temperature and stirred for 10 min until the solution was added to a solution of 2,4-biscarbazolyl-6-chloro-1,3,5-triazine (0.99 g, 2.23 mmol) in dioxane (40 ml). The mixture is stirred for 8 h at 70 °C. After cooling to room temperature and addition of water (20 ml) the solid is filtered and washed with water and ethanol. The crude product is further purified by recrystallisation from a hexane/THF mixture and sublimation to yield 2,4-biscarbazolyl-6-(4-(3,6-dimethylcarbazol-9-yl)phenoxy)-1,3,5-triazine (PCTrz) (1.24 g, 80%) as white crystalline solid. ^{1}H NMR (300 MHz, $CDCl_3{}^-F_3CCOOD$, δ): 8.73–8.70 (m, 4H), 8.08–8.05 (m, 4H), 7.96 (s, 2H), 7.78 (d, 2H), 7.64 (d, 2H), 7.44–7.40 (m, 10H), 7.28–7.25 (m, 2H), 2.59 (s, 6H); ^{13}C NMR (75 MHz, $CDCl_3{}^-F_3CCOOD$, δ): 171.5, 164.9, 150.4, 139.2, 138.5, 136.6, 129.6, 128.2, 127.3, 127.2, 126.8, 124.0, 123.7, 123.6, 120.3, 119.8, 117.4, 109.4, 21.3; EI-MS (m/z (%)): 696 (100) [M^+], 530 (30) [$M^+-C_{12}H_8N$], 348 (30) [M^{2+}], 166 (30) [$C_{12}H_8N$ (carbazole)]; T_m: 301 °C; T_g: 148 °C; T_d^1: 425 °C.

2.2. Characterization of the host material

2.2.1. Characterization

1H NMR spectra were recorded on a Bruker AC-300 at 300 MHz. All NMR-data given are given as chemical shifts δ (ppm) downfield from $Si(CH_3)_4$. MS spectra were obtained on a Finnigan Mat 8500, MAT 112 S Varian machine using EI-ionization. Melting points and glass transition temperature determination was carried out on a Perkin Elmer Diamond DSC at a heating/cooling rate of 10 K/min under nitrogen atmosphere. Thermogravimetric analysis (TGA) was performed on a Mettler Toledo TGA/SDTA851e machine at a heating rate of 10 K/min under nitrogen atmosphere. UV–vis absorption spectra were recorded on a Hitachi U-3000 instrument. Photoluminescence spectra were obtained using a Shimadzu Spectrofluorophotometer RF-5301PC. UVASOL solvents purchased from Merck were used to prepare solutions and films for optical characterization. Cyclic voltammetry measurements were carried out in absolute solvents measuring at a platinum working electrode vs. a $Ag/AgNO_3$ reference electrode. Each measurement was calibrated against an internal standard (ferrocene/ferrocenium redox system).

2.2.2. Single carrier device and OLED fabrication

The organic layers were deposited by thermal evaporation in high vacuum (<10^{-6} mbar) onto indium-tin-oxide (ITO, 10 ohm/square) precoated glass substrates. Prior to use the ITO glass was degreased using organic solvents and cleaned using an UV-ozon treatment for 30 min. The organic layers and the metal cathode were evaporated without breaking the vacuum.

2.2.3. Computational calculations

The transport levels of the materials used were determined via density functional calculations. For the ionization potential and the electron affinity first the geometry of the neutral as well as the charged states were optimized using the BP86-functional [16,17] in combination with a split-valence basis set (SV(P)) including polarization functions on all heavy atoms [18]. For the energetics single point calculations at the optimized geometries using the same functional in combination with a valence triple zeta basis set (TZVP) [19] were conducted. To account for dielectric solid state effects a UPS/IEPS-calibrated version of the conductor like screening model (COSMO) [20] was used in conjunction with the single point calculations. All calculations were carried out with the turbomole program package [21].

3. Results and discussion

3.1. Thermal properties of the host material

The thermal properties of PCTrz were investigated using thermogravimetric analysis (TGA) and differential scanning calorimetry (DSC). The TGA curve in Fig. 1 (left) illustrates thermal stability up to 400 °C. A weight loss of 1% (T_D^1) is observed at 425 °C while T_D^5 is reached at a temperature of 453 °C. This value is more than 150 °C above the sublimation temperature of PCTrz and therefore substantiates its very high thermal stability. The morphological stability of an amorphous film strongly depends on the glass transition temperature (T_g) of the material. The T_g should exceed the operational temperature by 50 °C to guarantee morphological stability [22,23]. Regarding the temperature requirements of potential technological applications for OLEDs [24] a T_g of more than 110 °C should be high enough to prevent the crystallization of an amorphous film during operation. In the inset in Fig. 1 (left) the second DSC heating scan of PCTrz is shown. The T_g is observed at 148 °C followed by an exothermic peak at 201 °C which is assigned to the crystallization of the material. The endothermic peak at 301 °C corresponds to the melting of the sample. These thermal properties, especially the high T_g, fit very well into the profile of requirements for a host material.

3.2. Optical properties of the host material

The absorption and fluorescence spectra measured in cyclohexane solution are given in Fig. 1 (right). The absorption spectrum of PCTrz is an almost perfect addition of the absorption of its two parts 2-chloro-4,6-biscarbazolyl-1,3,5-triazine (Trz) and 9-(4-methoxyphenyl)-carbazole (PC) (gray line and gray dotted line in Fig. 1 (right)). Therefore the low energy maximum at 349 nm is attributed to the phenoxy-carbazole moiety. The maximum at 327 nm

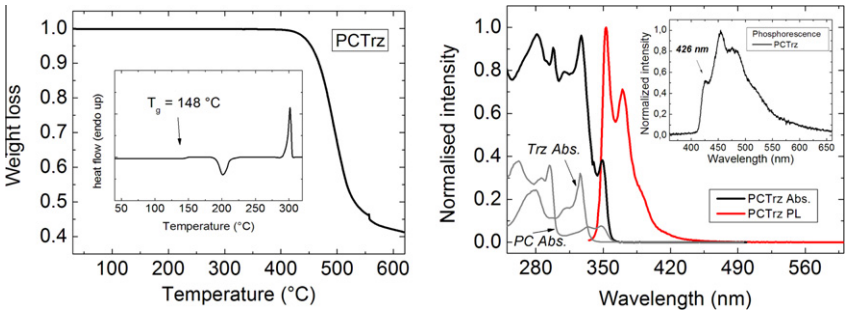

Fig. 1. Left: Thermal characterization of PCTrz:TGA curve (10 K/min; N_2); inset: second DSC scan (10 K/min; N_2; after; fast cooling of the melt at 40 K/min); right: absorption of PCTrz (black line), PC (gray line) and Trz (gray line) as well as fluorescence (red line) in cyclohexane solution at room temperature. Inset: phosphorescence of PCTrz at 10 K. (For interpretation of the references to color in this figure legend, the reader is referred to the web version of this article.)

is attributed to the π–π^* transition of the carbazole moiety of the carbazolyl-triazine. The optical bandgap of 3.45 eV was estimated from the absorption edge at 359 nm. On excitation the fluorescence of PCTrz is detected. It consists of two maxima at 353 and 370 nm as well as a shoulder at 390 nm. This fluorescence behavior is identical to phenylcarbazole with a small hypsochromic shift due to the strong electron accepting character of the triazine which is located para to the carbazole. However, the influence of the triazine is only weak due to the non-conjugated ether bond.

In contrast to that the two carbazoles which are directly bound to the triazine are strongly influenced and possess a more electron deficient character. It can be supposed that the energy which is absorbed by the carbazolyltriazine part undergoes intramolecular transfer to the phenoxy-carbazole part. Therefore, only the fluorescence of this moiety is detected. To determine the triplet energy of PCTrz a phosphorescence spectrum (see inset in Fig. 1 (right)) of a film (120 nm) consisting of 10% PCTrz and 90% PMMA was measured at a temperature of 10 K. The triplet energy is obtained from the first vibronic transition of the phosphorescence spectrum. PCTrz shows a 0–0 phosphorescence transition at 426 nm (2.91 eV) and a maximum centered at 472 nm which correspond to the 0–1 transition. From this high triplet energy value it can be assumed that exothermic energy transfer to most blue phosphorescent emitters is possible.

3.3. Electrochemical properties and single carrier devices of the host material

In order to demonstrate the improved hole injection properties of PCTrz compared to other carbazole substituted triazines [12], cyclic voltammetry (CV) and single carrier device (SCD) measurements were carried out. The electrochemical behavior upon oxidation and reduction was studied in CH_2Cl_2 and THF solution, respectively (see Fig. 2 (middle)). Both oxidation and reduction processes of PCTrz exhibit reversible behavior in multi-scan experiments. The oxidation is observed at a half-wave potential of 0.68 V (vs. Fc/Fc^+). This result is in contrast to the irreversible oxidation of donor-substituted triazines without phenoxy-carbazole moiety like TRZ2 (see Fig. 2). Furthermore, the oxidation of TRZ2 was observed at distinctly higher potential (1.16 V vs. Fc/Fc^+). Therefore the oxidation wave of PCTrz at 0.68 V is attributed to the oxidation of the phenoxy-carbazole moiety. This is supported by the similar oxidation behavior of 9-(4-methoxyphenyl)-3,6-dimethylcarbazole (PC; E_{ox} = 0.69 V). The perfectly reversible oxidation behavior can be explained by the blocking of the reactive 3- and 6-position of the phenoxy-carbazole, since it is known that unprotected carbazoles undergo side-reactions upon oxidation [25]. The reduction of PCTrz is observed at a half wave potential of −2.61 V (vs. Fc/Fc^+). Due to the similarity to the reduction of TRZ2 it is attributed to the reduction of the triazine moiety. Furthermore these results are invigorated by computational calculations of the electron density distribution of the HOMO and LUMO (see Fig. 2). It was found that the electron density is centered on the HOMO of the phenoxy-carbazole moiety, while the LUMO is mainly confined on the triazine ring. These results substantiate the successful separation of electron accepting and donating counterparts. The oxidation and reduction potentials of PCTrz can be translated to an ionization potential (IP) of 5.48 eV and an electron affinity (EA) of 2.20 eV, respectively. The decreased HOMO of PCTrz compared to TRZ2 should yield improved hole injection properties. The *I*–*V*-characteristics of hole- and electron-only devices are presented in Fig. 2 (left).

The charge transport properties of PCTrz were investigated with single carrier devices with the following configuration: hole-only-device: ITO/HIL (80 nm)/NPD (p-doped, 35 nm)/NPD (10 nm)/PCTrz (30 nm)/NPD (10 nm)/NPD (p-doped, 35 nm)/Al; electron-only-device: ITO/BCP (n-doped, 70 nm)/BCP (10 nm)/PCTrz (30 nm)/BCP (10 nm)/BCP (n-doped, 30 nm)/Al. For the electron-only devices the n-doped BCP (HOMO = 6.5 eV) effectively prevented the injection of holes from the ITO anode (4.8 eV) and enhances the electron injection and transport. In a similar way the p-doped NPD prevents the injection of electrons from the cathode in case of the hole-only devices and enhances the hole injection and transport. In Fig. 2 (left) the current density–voltage (*I*–*V*)-characteristics of hole- and electron-only-devices of PCTrz and TRZ2 are compared. From the hole-only-device characteristics it can be seen that the turn on voltage of the PCTrz device is about 2.5 V lower compared to that of TRZ2. Also at current-densities of 100 mA cm^{-2} the

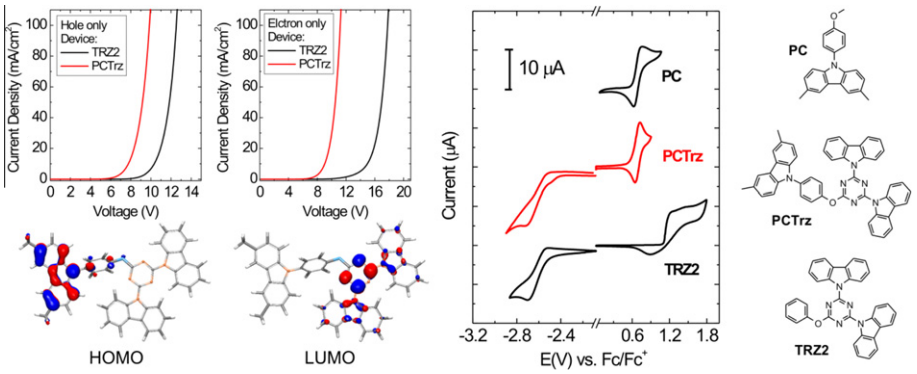

Fig. 2. Left: Single carrier devices of PCTrz and TRZ2 (left: hole only devices; right: electron only devices) and DFT-calculated electron density of the HOMO and LUMO state of PCTrz; middle: cyclic voltammetry: reduction (in THF) and oxidation (in CH_2Cl_2) waves of PC (upper black line), PCTrz (middle red line) and TRZ2 (lower black line); right: chemical structures of PC, PCTrz and TRZ2. (For interpretation of the references to color in this figure legend, the reader is referred to the web version of this article.)

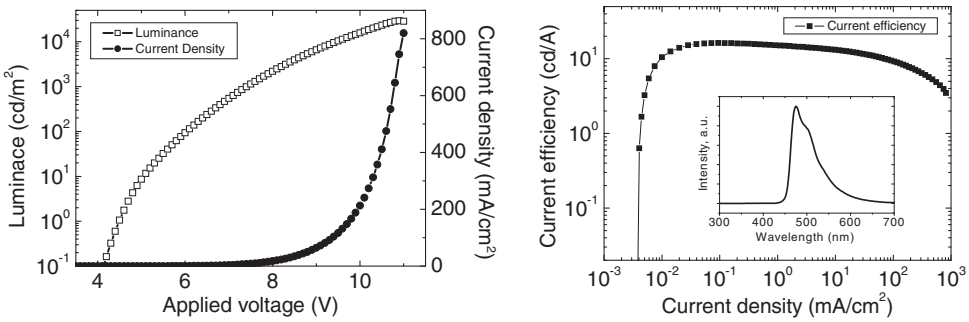

Fig. 3. Left: Luminance–voltage–current density characteristics and right: current efficiency–voltage characteristics of the blue phosphorescent OLED (for details see text) inset: electroluminescence spectrum of the device.

difference in driving voltage is about 2.5 V. This behavior can be understood with respect to the higher IP of PCTrz which facilitates the hole injection from the hole transporting NPD layer. From the *I–V* curves of the electron-only devices it can be seen that the device with PCTrz exhibits a much lower threshold voltage. At current densities of 100 mA cm^{-2} the difference in voltage is as high as 7 V. This behavior cannot be explained by a restrained injection as the LUMO levels are very similar for both materials. Therefore we speculate that a different packing behavior (morphology) might favor electron transport in PCTrz.

3.4. Phosphorescent organic light emitting diodes

In order to demonstrate the potential of PCTrz as host material for blue phosphorescent emitters an OLED with the following configuration was fabricated. On top of indium-tin-oxide (ITO) poly(thiophene-3-[2-(2-methoxyethoxy)ethoxy]-2,5-diyl) was used as hole-injection layer followed by 35 nm of DPBIC p-doped with molybdenum(VI) oxide as hole-transporting layer. An additional 10 nm thick layer of DPBIC followed as exciton and electron blocker. The 20 nm thick emission layer consisted of PCTrz doped with 16% FIrpic. The hole-blocking and electron-conduction layers consisted of 5 nm DBFSi and 40 nm BCP. The devices were finalized by deposition of a LiF (0.7 nm)/Al (100 nm) cathode.

Fig. 3 displays the current density–voltage–luminance (left) and current efficiency–voltage characteristics (right) of the device. The inset in Fig. 3 (right) shows the electroluminescence spectrum of the devices at a current density of 10 mA cm^2. The spectrum shows the pure emission of FIrpic with a maximum at 473 nm and CIE coordinates of $x = 0.17$ and $y = 0.33$. The device exhibits a maximum current efficiency of 16.2 cd/A at a luminance of 20 cd/m^2. The maximum values of external quantum efficiency and power efficiency are 7.8% and 10.1 lm/W, respectively. The maximum luminance of 29,000 cd/m^2 is reached at 10.9 V. At a luminance of 1000 cd/m^2 the current efficiency of 13.5 cd/A was measured. These results demonstrate the potential of PCTrz as host material for blue phosphorescent OLEDs.

In summary we have designed a new bipolar host material, which contains a phenoxy-carbazole that is separated from the biscarbazolyl-triazine by a non-conjugated ether bond. PCTrz exhibits a very high thermal stability and its glass forming properties are excellent. The T_g of 148 °C is high enough to ensure morphological stability in OLED applications. Results from cyclic voltammetry and computational calculations proved the separation of the oxidation- and reduction-site. The charge carrier injection and

transport properties were significantly improved compared to donor-substituted triazines like TRZ2. A phosphorescent OLED with PCTrz as host and FIrpic as blue emitter yielded high current efficiencies of up to 16.2 cd/A.

Acknowledgments

We thank C. Bonsignore for his support during the preparation and characterization of the single carrier devices and organic light emitting diodes. We also like to thank S. Hoffmann for recording the phosphorescence spectrum. We are grateful to the BMBF for financial support through the project OPAL 2008 (Grant No. 13N8992).

References

[1] C.W. Tang, S.A. van Slyke, Appl. Phys. Lett. 51 (1987) 913.
[2] H. Yersin (Ed.), Highly Efficient OLED's with Phosphorescent Materials, Wiley-VCH, Weinheim, Germany, 2008.
[3] S. Reineke, F. Lindner, G. Schwartz, N. Seidler, K. Walzer, B. Luessem, K. Leo, Nature 459 (2009) 234.
[4] M.A. Baldo, D.F. O'Brian, Y. You, A. Shoustikov, S. Sibley, M.E. Thompson, S.R. Forrest, Nature 395 (1998) 151.
[5] R. Fink, Y. Heischkel, M. Thelakkat, H.-W. Schmidt, C. Jonda, M. Hüppauff, Chem. Mater. 10 (1998) 3620.
[6] R. Klenker, H. Aziz, A. Tran, Z.D. Popovic, G. Xu, Org. Electron. 9 (2008) 285.
[7] H. Inomata, K. Goushi, T. Masuko, T. Konno, T. Imai, H. Sasabe, J.J. Brown, C. Adachi, Chem. Mater. 16 (2004) 1285.
[8] Z. Ge, T. Hayakawa, S. Ando, M. Ueda, T. Akiike, H. Miyamoto, T. Kajita, M. Kakimoto, Adv. Funct. Mater. 18 (2008) 584.
[9] S. Takizawa, V.A. Montes, P. Anzenbacher, Chem. Mater. 21 (2009) 2452.
[10] K.S. Son, M. Yahiro, T. Imai, H. Yoshizaki, C. Adachi, Chem. Mater. 20 (2008) 4439.
[11] S.O. Jeon, K.S. Yook, C.W. Joo, J.Y. Lee, Adv. Funct. Mater. 19 (2009) 3644.
[12] M.M. Rothmann, S. Haneder, E. Da Como, C. Schildknecht, C. Lennartz, P. Strohriegl, Chem. Mater. 22 (2010) 2403.
[13] A. Klapars, J.C. Antilla, X. Huang, S.L. Buchwald, J. Am. Chem. Soc. 123 (2001) 7727.
[14] M. Bolt, C. Lennartz, M. Prinz, H.-W. Schmidt, M. Thelakkat, M. Baete, C. Neuber, W. Kowalsky, C. Schildknecht, H.-H. Johannes, WO Patent, 2005, 019373.
[15] N. Langer, K. Kahle, C. Lennartz, O. Molt, E. Fuchs, J. Rudolph, C. Schildknecht, S. Watanabe, G. Wagenblast, WO Patent, 2009, 003898.
[16] J.P. Perdew, Phys. Rev. B 3319 (1986) 8822.
[17] A.D. Becke, Phys. Rev. A 36 (1988) 3098.
[18] A. Schäfer, H. Horn, R. Ahlrichs, J. Chem. Phys. 9 (1992) 2571.
[19] A. Schäfer, C. Huber, R. Ahlrichs, J. Chem. Phys. 100 (1994) 5829.
[20] A. Klamt, J. Phys. Chem. 99 (1995) 2224.
[21] R. Ahlrichs, M. Bär, M. Häser, H. Horn, C. Cölmel, Chem. Phys. Lett. 162 (1989) 165.
[22] G. Adam, J.H. Gibbs, J. Chem. Phys. 43 (1965) 139.
[23] K. Naito, A. Miura, J. Phys. Chem. 97 (1993) 6240.
[24] H. Aziz, Z.D. Popovic, N.-X. Hu, Appl. Phys. Lett. 81 (2002) 370.
[25] J.F. Ambrose, L.L. Carpenter, R.F. Nelson, J. Electrochem. Soc. 122 (1975) 876.

a variety of intermolecular interactions such as van der waals (vdw) interactions, weak hydrogen bondings, π...π stacking, and sulfur...sulfur interactions [14,15]. In contrast to linear oligomer, a new family of oligothiophenes, namely, the macrocyclic oligothiophenes, has been synthesized by Bäuerle and co-workers [16–18]. Several papers which characterize these novel molecules and investigate their physical properties by X-ray and scanning tunneling microscopy (STM) coupled with semiempirical theoretical calculations have been reported by the same group [19–21]. Due to the novel structures of these macrocycles, some groups investigated their ring strain, the geometry of cyclic oligomers, optical spectra, Raman spectra, ionization energy, and the factors influencing the band gap, etc. and showed that these materials probably possessed excellent electronic properties [22–24], but so far, their carrier mobility have not been quantitatively obtained by neither experimental nor theoretical investigation. Many groups systemically investigated charge transport properties of linear oligothiophenes and the factors influencing these properties, such as the relative orientations, intermolecular separations, solid-state packing of these molecules, reorganization energies, and substituent effects, etc. [25–32]. But the investigation of these properties of cyclic oligothiophenes is only at the initial stage. So this work mainly predicted theoretically their carrier mobility, and investigated the factors influencing the mobility and some intrinsic reasons that gave rise to the differences in charge transport properties between linear and cyclic oligothiophenes studied (Fig. 1). The theoretical investigations may be useful to find new leading materials and likely to provide important information for improving transport efficiency (enhancing device response), reducing power, and finding new applications of the promising materials.

2. Theoretical and computational methodology

There are mainly two types of carrier transport mechanisms in organic electronic materials: (1) the coherent

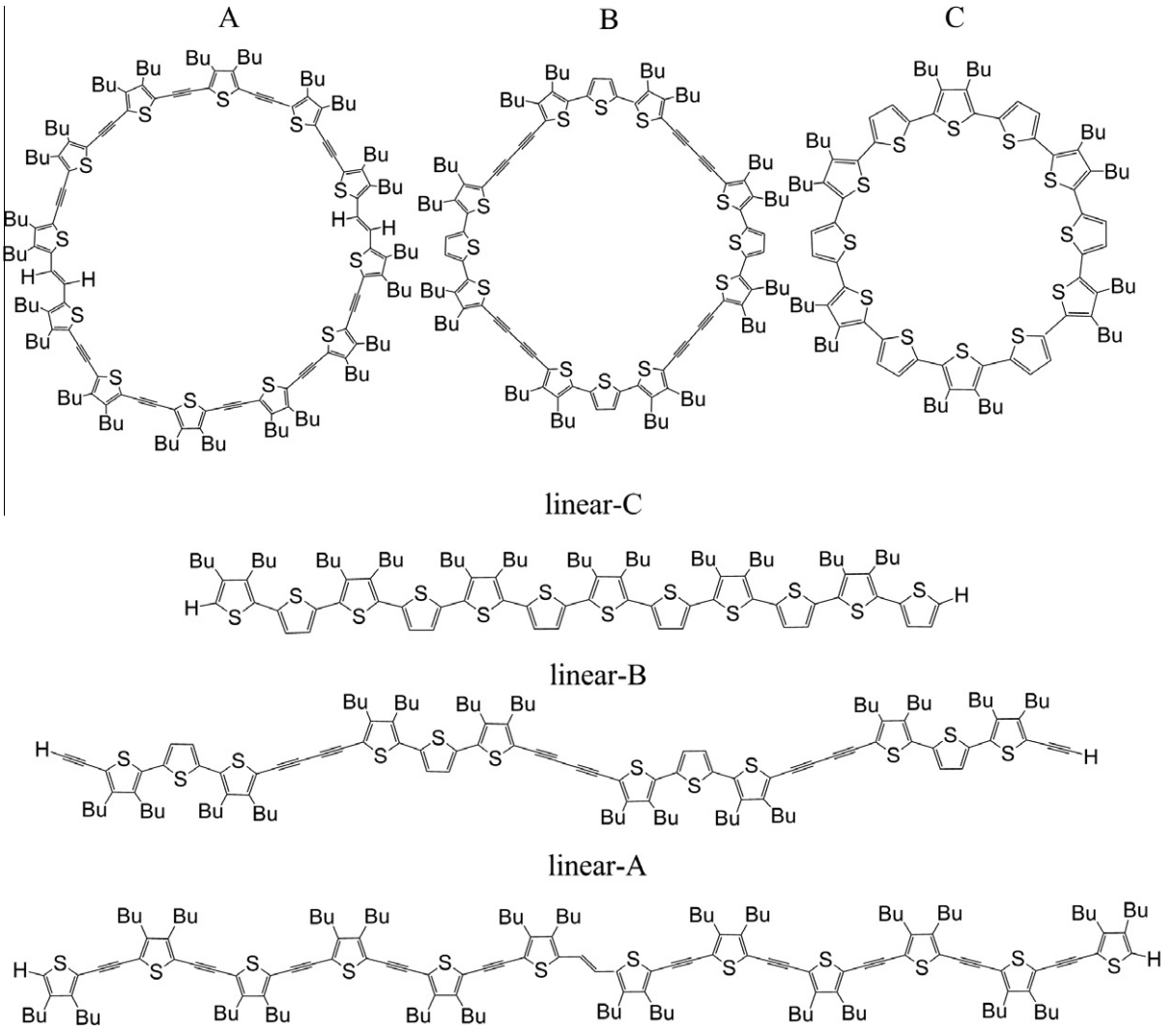

Fig. 1. Chemical structures of the compounds studied.

band mechanism and (2) the incoherent hopping mechanism. In low temperature, the band mechanism dominates for organic materials. The carrier moves as a highly delocalized plane wave in an energy band. The interaction between the nearest-neighbor sites is large compared with dynamic structural disorder, for instance, the reorganization energies resulting from charge transfer process from one molecule to another. At high temperature (are probably at room temperature), the band mechanism may be invalid, because charge carriers are expected to be localized over a single molecule (due to the strong electron–phonon coupling, which is a major nature of π-conjugated materials). The motion of the carrier can be described as the sequential jumps of the relaxed charges between adjacent molecules, that is, the mechanism can be referred to as hopping mechanism. Extensive experimental evidences, particularly the observed thermal signatures and optical spectra are consistent with this assumption [33–36].

Here, each hopping event is viewed as a nonadiabatic charge transfer reaction: $M+M^{+/-} = M^{+/-}+M$, which is a self-exchange reaction. Charge transfer rate between neighboring molecules can be expressed by standard Marcus theory by the following equation: [37–40]

$$k_{ct} = \frac{4\pi^2}{h}\frac{V^2}{\sqrt{4\pi\lambda k_B T}}\exp\left\{-\frac{(\Delta G^0+\lambda)^2}{4\lambda k_B T}\right\} \quad (1)$$

where ΔG^0 is the free energy difference between the initial and final states, λ is the reorganization energy, and V is the electronic coupling matrix element between the two species M and $M^{+/-}$. For our case, where charge transfer reaction is the self-exchange reaction, ΔG^0 is zero. Thus the rate is mainly determined by two important parameters: the intermolecular electronic coupling matrix element (V) and reorganization energy (λ) (see Fig. 2(a)). For the hopping approximation to be valid, the system needs to be strongly localized in one of the two states in Fig. 2(a), that is, the coupling between neighboring molecules are small. The reaction coordinate Q in Fig. 2(a) is an ensemble of geometric modifications of the dimer system. The reorganization energy (λ) contains the internal reorganization energy (λ_{int}) and external reorganization energy (λ_{ext}). λ_{int} reflects the geometric relaxation associated with going from the neutral to the ionized state, and vice versa. λ_{ext} describes the relaxation of the surrounding medium. λ_{ext} is commonly neglected. The internal reorganization energies (λ_{int}) are evaluated directly from the adiabatic potential-energy surfaces of neutral/cation or neutral/anion species (see Fig. 2(b)). λ for hole can be defined as follows

$$\lambda_h = \lambda_+ + \lambda_1 = [E^+(M) - E^+(M^+)] + [E(M^+) - E(M)] = IP(v) - HEP \quad (2)$$

As illustrated in Fig. 2(b), $E^+(M^+)$ and $E(M)$ represent the energies of the cation and neutral species in their lowest energy geometries, respectively, while $E^+(M)$ and $E(M^+)$ represent the energies of cation and neutral species with the geometries of neutral and cation respectively. In this way, λ for electron can be expressed as follow

$$\lambda_e = \lambda_- + \lambda_2 = [E^-(M) - E^-(M^-)] + [E(M^-) - E(M)] = EEP - EA(v) \quad (3)$$

The obove quantities were calculated at density functional theory (DFT) level, using the B3LYP functional and 6-31g(d) basis set. All calculations on open shell (ionized) states used the unstricted formalism (UB3LYP).

To calculate the electronic coupling matrix element, V, all the possible nearest-neighbor intermolecular hopping pathways are shown in Fig. 3. Within the framework of the Marcus–Hush two-state model, we calculated the coupling matrix element between adjacent molecules using the "energy splitting in dimer" (ESD) method [41,42], as sketched in Fig. 4. V for hole/electron in this scheme can be obtained by the following equation [43,44].

$$V = \frac{1}{2}\sqrt{(E_{HOMO/LUMO+1} - E_{HOMO-1/LUMO})^2 - (e_2 - e_1)^2} \quad (4)$$

where $E_{HOMO/LUMO+1}$ and $E_{HOMO-1/LUMO}$ are the energies of the HOMO and HOMO − 1(LUMO and LUMO + 1) levels

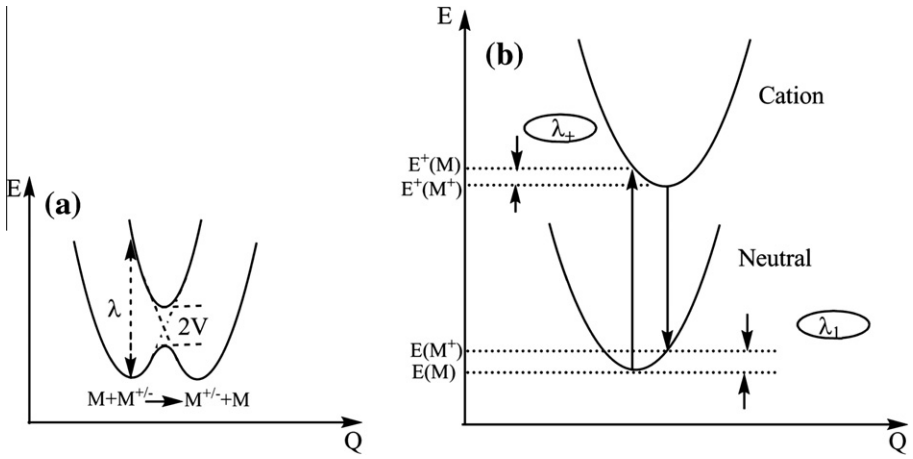

Fig. 2. (a) Schematic representation of a charge exchange reaction pathway for hole transfer through a transition state by weak (nonadiabatic) coupling. The solid curves are the adiabatic surfaces, while the dashed lines refer to diabatic surfaces. (b) Schematic description of internal reorganization energy for hole transfer.

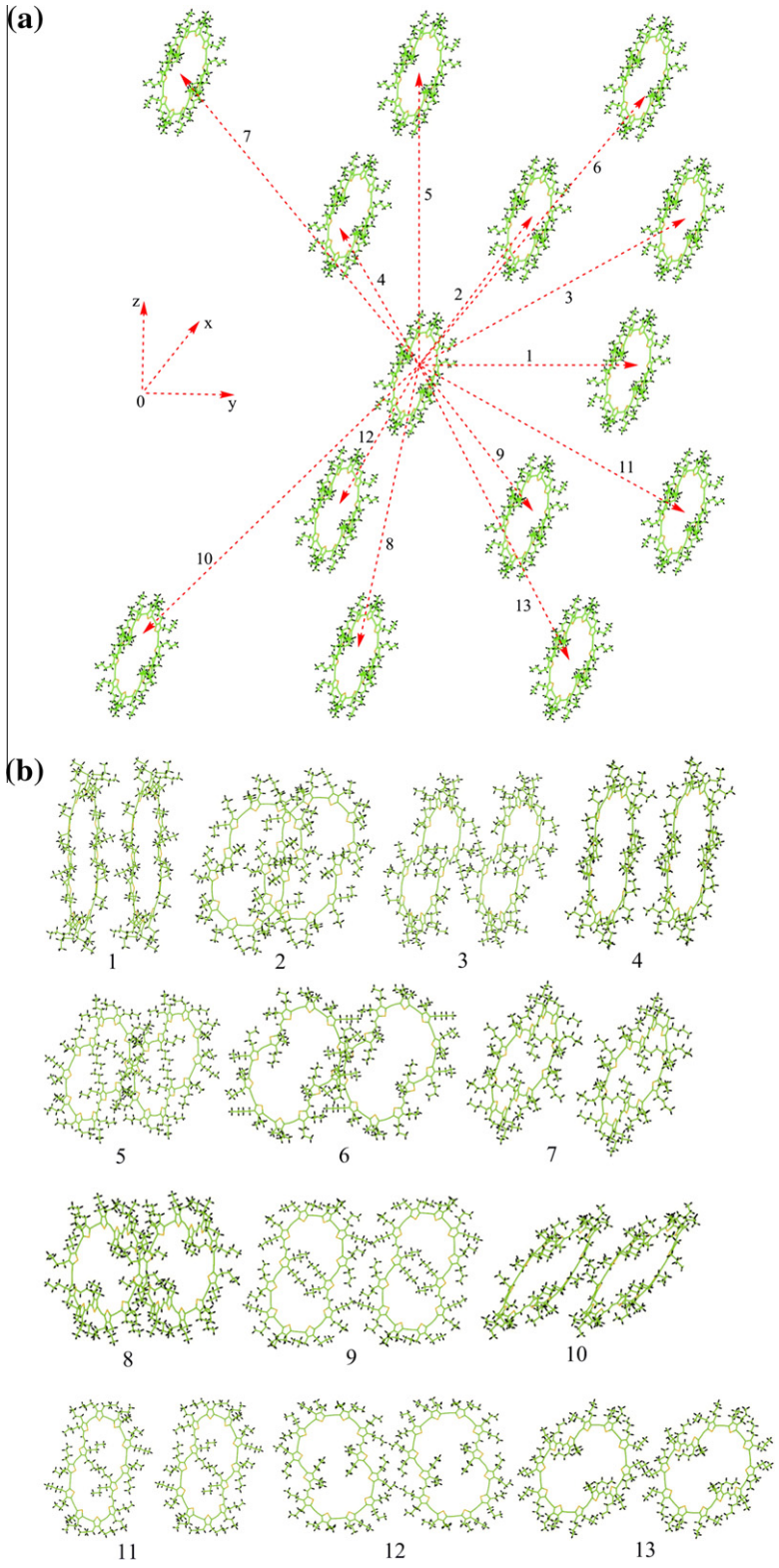

Fig. 3. (a) Charge hopping pathways schemes of molecule A from the crystal structure (and that of molecule B is the same as molecule A). (b) Schematic representation of the dimer in each specific pathway of charge transfer for molecule A.

taken from the closed-shell configuration of the neutral dimer, respectively; e_1 and e_2 is the site energy of the isolated molecule in the dimer, respectively. As sketched in Eq. (4), the electronic coupling matrix element can be

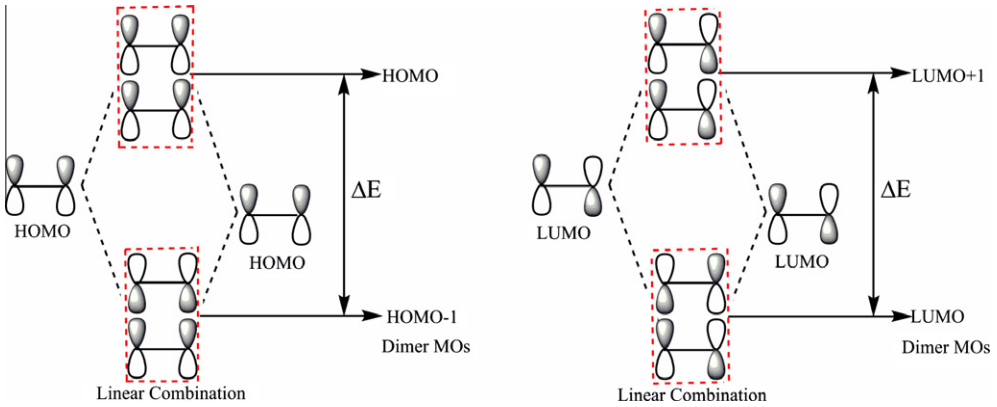

Fig. 4. Diagram for the estimate of coupling matrix element in the neutral dimer.

strongly affected by the site energies. In our case, the molecules stack symmetrically (see Fig. 3), that is, the isolated molecules are in equivalent sites in the crystal, so the site energy difference Δe_{12} ($= e_2 - e_1$) is zero, so Eq. 4 can be written as

$$V = \frac{E_{\mathrm{HOMO/LUMO+1}} - E_{\mathrm{HOMO-1/LUMO}}}{2} \tag{5}$$

The electronic coupling matrix elements for all the hopping pathways were calculated by employing the pw91pw91/6-31g(d) method. The study of Huang et al. showed that the functional gave the best description for the bandwidth of organic solid [45] and Shuai et al. also investigated many conjugated molecules and obtained very good results using the pw91pw91 functional [28,46,47]. Many groups investigated the effects of the basis sets on the *V* values, such as 6-31g, 6-31g(d) and 6-311g(d,p). The results indicated that the *V* values were largely independent of the above base sets [26,48]. To clarify the effects of the diffuse function on electronic coupling matrix elements for our systems studied, these V values for molecule B were calculated and compared by using the two basis sets: 6-31g(d) and 6-31+g(d). (the results calculated by using 6-31+g(d) are listed in Table S2 of Supporting Information). We found that for most of the hopping pathways, these values and their variation trend possess small change, in result that the lack of the diffuse function can not largely affect the *V* values for the dominant transfer pathways and hence the final mobility. In addition, many investigations have obtained the reliable results for the different systems by employing 6-31 g(d) basis set [26,42,46–50]. So for our systems studied, it should be reliable that these electronic coupling matrix elements for all the hopping pathways were predicted by using 6-31 g(d) basis set.

In this context, the charge transport is modeled as a Brownian motion process, as described by a particular diffusion process. The mobility can be obtained by the Einstein equation [51]

$$\mu = \frac{e}{k_B T} D \tag{6}$$

where μ is the carrier mobility, D is the isotropic charge diffusion coefficient, T is the temperature, K_B is the Boltzmann constant and e is the electronic charge. Given the hopping rate between the nearest-neighbor molecules, the diffusion coefficient can be evaluated from the hopping rates as

$$D = \frac{1}{2n} \sum_i r_i^2 k_i P_i \tag{7}$$

where n is the dimensionality (when n is equal to 3, the average mobility of all the hopping pathways can be evaluated), k_i is the hopping rate due to charge carrier to the ith neighbor, r_i is the distance to neighbor i, P is the relative probability for charge carrier to a particular ith neighbor,

$$P_i = k_i \Big/ \sum_i k_i \tag{8}$$

Summing over all possible hops leads to the diffusion coefficient in Eq. (7). All the calculations were performed with the GAUSSIAN 03 package [52].

3. Results and discussions

The geometrical structures for the neutral and ionized states of compounds studied were optimized by employing the B3LYP/6-31g(d) method, presenting their geometrical parameters in Table S1 (Supporting Information), and then calculated the ionization potentials (*IP*s), electron affinities (*EA*s) and reorganization energies (λs) on the base of their equilibrium geometries for comprehensive understanding the charge injection and transport properties of organic electronic materials. The ionization potential (*IP*) and electron affinity (*EA*) are well-defined properties that can be calculated by DFT to estimate the charge injection barrier. And for improving the ability of electron and hole injection of electronic devices, the achievement of high *EA* and low *IP* is crucial. According to Eq. 1, lower λ value leads to bigger charge transport rate according to Eq. 1, so one of the aims of material design is the obtainment of low λ value. Table 1 contains the ionization potentials (*IP*s), electron affinities (*EA*s), both vertical (*v*; at the geometry of the neutral molecule) and adiabatic (*a*; optimized structures for both the neutral and charged molecules), and the extraction potentials (*HEP* and *EEP* for the hole and electron,

Table 1
*IP*s, *EA*s, extraction potentials, reorganization energies and the HOMO and LUMO energies for each molecule (eV).

Species	$IP(v)$	HEP	λ_h	$IP(a)$	$EA(v)$	EEP	λ_e	$EA(a)$	HOMO	LUMO	ΔE_{H-L}
A	5.06	4.93	0.13	4.99	1.71	1.85	0.14	1.79	−4.54	−2.24	2.30
B	5.29	5.18	0.11	5.22	1.62	1.78	0.16	1.69	−4.74	−2.18	2.56
C	5.43	5.15	0.28	5.30	1.00	1.33	0.33	1.16	−4.73	−1.71	3.02
Linear-A	5.02	4.87	0.15	4.94	1.85	2.01	0.16	1.93	−4.48	−2.40	2.08
Linear-B	5.38	5.08	0.30	5.09	1.67	1.95	0.28	1.93	−4.84	−2.22	2.62
Linear-C	5.46	4.98	0.48	5.18	1.13	1.58	0.45	1.39	−4.76	−1.84	2.92

respectively) that refer to the geometries of the ions, the reorganization energies for both hole and electron transport.

The charge injection and transport properties of these materials studied are discussed from the following several points.

3.1. Charge injection properties

Good charge injection and transport properties of organic semiconductors as electron/hole transport layer (ETL/HTL) are crucial to improve the performance of OLED. In terms of the energy difference between the Fermi level (E_F) of electrodes and the highest occupied molecular orbital (HOMO)/lowest unoccupied molecular orbital (LUMO) of organic semiconductor materials, the hole/electron injection barrier can be understood to measure the ability of the charge injection. IP and EA values of organic materials are the most important parameters that characterize the reduction and oxidation performance of the materials, respectively. So the decrease of the charge injection barrier, the achievement of high EA for ETL materials and low IP for HTL materials playing an important in improving the electroluminescence (EL) efficiency of OLED. For the comparison of the ability of charge injection for these organic materials studied, Fig. 5 shows their energy levels alignment.

From Table 1, cyclic oligomers mostly possess lower $IP(v)$ and $EA(v)$ values compared with their corresponding linear molecules. For molecules linear-A, better planarity decreases its energy gap (ΔE_{H-L}), which leads to higher

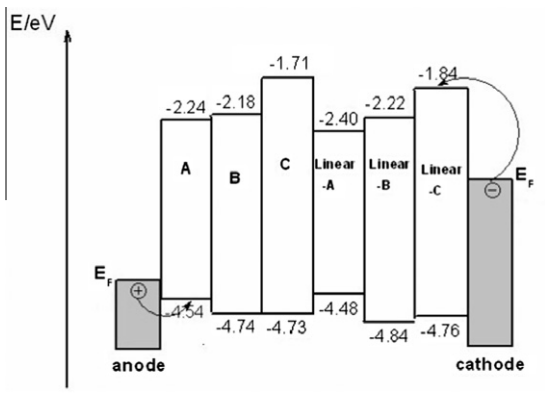

Fig. 5. Schematic drawing of the energy levels alignment of the molecules studied.

HOMO level and thus lower $IP(v)$ value. The fact can be found that cyclic oligomers mostly possess stronger reduction ability, whereas the linear ones show better oxidation performance. From Fig. 5, hole injection barriers of cyclic oligothiophenes are almost lower than those of the corresponding linear ones, while the electron injection from cathode into linear molecules is easier.

Due to their low charge injection barriers and small λ values for molecules A, B and linear-A, they can be excellent charge transport layer materials. From the investigation of the following section, high carrier mobility of molecular materials A and B also demonstrates their fine charge transport properties.

3.2. Charge transport properties

3.2.1. Reorganization energy: A. Molecular geometrical structures

From Table S1, it can be found that the bond lengths and bond angles have little change between the neutral and corresponding ions geometries for all the compounds and these changes are very close among different compounds, while the changes of the torsion angles of two adjacent thiophene rings have greatly difference among different compounds. For compound A, the maximal change value of the torsion angles between the neutral one and cation(anion) is 14.1° (13.5°). The changes of the torsion angles for molecule B are similar to that for molecule A. But for molecule C, the changes of the torsion angles resulting from hole (electron) transfer are within a wide range from 7.1° (3.3°) to 13.1° (32.1°), and most of torsion angle changes for the molecule C are larger than those for both molecules A and B. These facts are the indication of the intrinsic difference of the relaxation processes occurring in these systems: small differences between the neutral and ion geometries lead to low reorganization energy, and vice versa. Due to larger torsion angle changes for molecule C compared with both molecules A and B, it possesses larger internal reorganization energies for both the hole and electron. The introduction of the alkynyl relieves the strain of the macrocycles composed of twelve thiophene rings for molecules A and B, which make their structures more stable. But for molecule A, C–C double bond improves the flexibility of the whole macrocycle, so their introduction gives rise to a "ring flip" of the thiophene adjacent to double bond and large changes of the torsion angles between the thiophene rings adjacent to double bonds in charge transfer process.

To reveal the effects of the closed ring structure on transport properties of these molecules, cyclic oligothioph-

enes are compared with their corresponding linear ones. Through the comparisons, we find that the geometric deformations in charge transfer process are no greatly different between compounds A and linear-A. But for molecule linear-B, the changes of the torsion angles accompanying with hole (electron) transfer are within a wide range from 18.6° (11.5°) to 60.6° (63.8°), while for cyclic molecule B, these changes are within a narrow range from 4.7° (3.2°) to 9.8° (9.8°). For molecules C and linear-C, the changes of the torsion angles have a similar situation (see Table S1). These facts show that the closed ring structure effectively suppresses the rotation of the thiophene rings and reduce the geometrical deformation accompanying with charge transfer, so it leads to low reorganization energy and consequently improves charge transport properties of these macrocycles.

B. Frontier molecular orbitals, ionization potentials and electron affinities. From the perspective of electronic structure, charge injection and transport properties of these compounds can be fundamentally understood. It is useful to examine HOMOs and LUMOs of these compounds because their relative ordering can provide a reasonable qualitative indication of the ability of charge injection and transport. We have plotted the contour plots of HOMO and LUMO of the linear oligothiophenes and cyclic oligothiophenes in Figs. 6 and 7, respectively.

As sketched in Figs. 6 and 7, the electronic cloud of the frontier orbitals of all compounds spread over the whole π-conjugated backbone, although dense electronic cloud distributes on the different parts of chromophores. For molecule C, the HOMO shows antibonding character between two adjacent thiophene rings, while the LUMO shows a bonding character. So the variation of torsion angles between the adjacent thiophene rings should have larger effects on the LUMO. Indeed, for molecule C, the torsion angles are mostly larger than those for both molecules A and B. Large torsion angles decrease the bonding character between two adjacent thiophene units for LUMO level and thus destabilize it, so it weakens the abilities of electron injection and transport, and hence leads to low EA and large electronic reorganization energy. It may be the reason that two neighboring thiophene rings show the cis-conformation, namely, two sulfur atoms in the two rings are in the same side, and the sulfur atom in every thiophene ring possesses a lone electron pair which gives rise to very strong coulomb repulsion between sulfur atoms in adjacent thiophene rings. But for molecules A and B, the introduction of the alkynyl and double bond increases the separation between the thiophene rings, which are beneficial to weakening this repulsion and steric effects. To present the frontier orbitals more quantitatively, the sum of the square of the LCAO coefficients for HOMOs and LUMOs of all the molecules studied was analyzed in Fig. S1 (Supporting Information); a large value on a atom reflects large electronic density on the atom, and the results are presented in Fig. S1 (Supporting Information). For cyclic oligothiophenes, as the introduction of the alkynyl and double bonds increases their conjugation extent, this gives rise to lower electronic density of π-conjugated backbone of both molecules A and B compared with that of molecule C. So the geometric deformation in charge transfer process for molecules A and B is less remarkable, which leads to smaller reorganization energies.

The fashion of the introduction of the alkynyl largely influences the torsion angle between two neighboring thiophene rings. Each alkynyl is located in the middle of neighboring thiophene rings for molecule A, which weakens efficiently the repulsion and the steric effects, and hence leads to small torsion angles. But for molecule B, it can not largely lower those interactions, because of its molecular fragments similar to that of molecule C and larger torsion angles between adjacent thiophene rings. Compared with molecules B and C, the increase of the conjugation extent and smaller torsion angles for molecule A give rise to higher HOMO and lower LUMO levels, in result to lead to lower IP, higher EA values and smaller

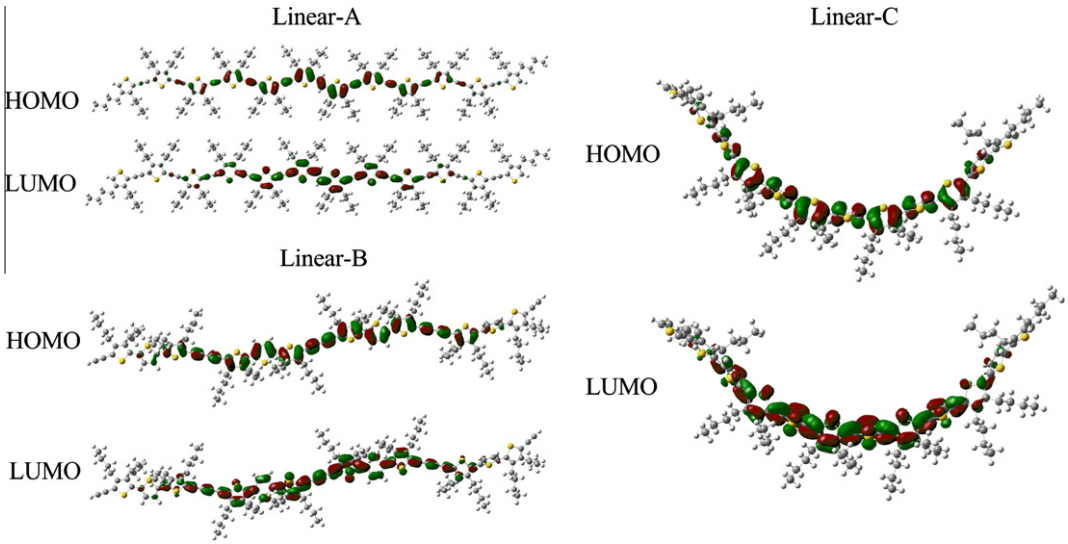

Fig. 6. The contour plots of the frontier orbitals for molecules linear-A, linear-B and linear-C.

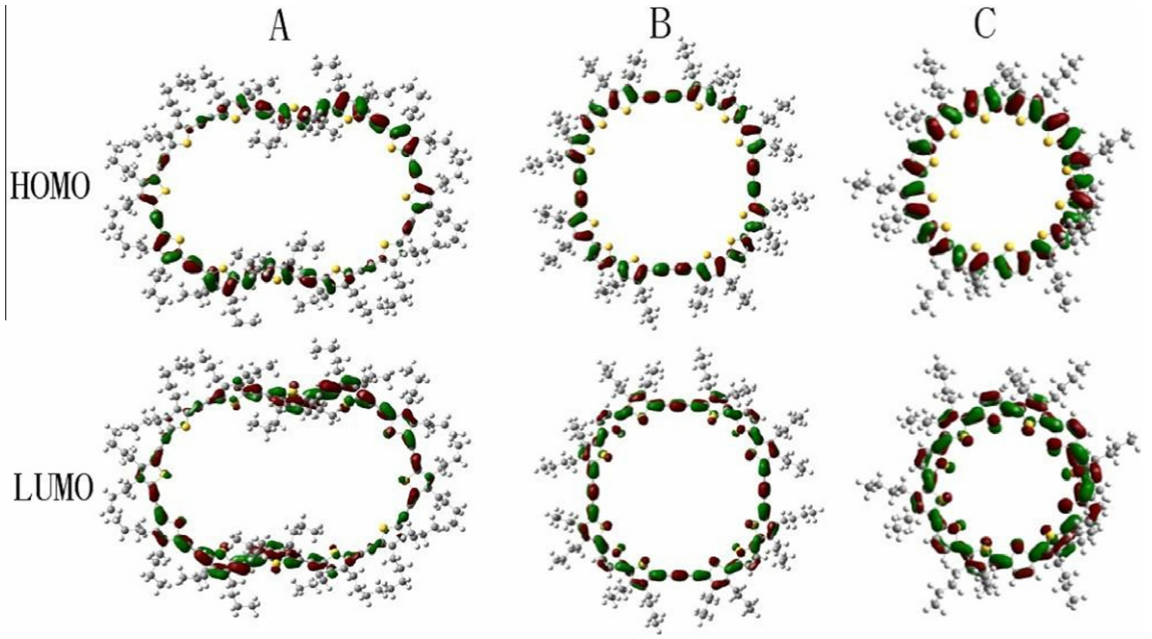

Fig. 7. The contour plots of the frontier orbitals for cyclic oligthiophenes A, B and C.

reorganization energies, and hence improve its charge injection and transport properties. Compared with the macrocycles, except for molecule linear-A, the torsion angles of other corresponding linear molecules do not possess large change in charge transfer progress. This is fully understandable: the fashion of the introduction of the alkynyl does not change and the steric effects resulting from the butyls still are obvious. For molecule linear-A, the breakage of one of double bonds and favorable position of the alkynyl give rise to the best planarity comparing with other molecules. It leads to high HOMO level and low LUMO level, so it possesses good properties of hole/electron injection ($IP(v) = 5.02$ eV, $EA(v) = 1.85$ eV) and transport. ($\lambda_h = 0.15$ eV, $\lambda_e = 0.16$ eV).

3.2.2. Electronic coupling matrix element

According to Eq. 1, it is obvious that for the achievement of high charge transport rate, the materials not only possess λ value, but also large V value. To calculate V, we identified 13 distinct nearest-neighbor hopping pathways (see Fig. 3) based on the crystal structures of molecules A and B, and hence calculated the corresponding V values for all the pathways using Eq. (5) (these results were presented in Table 2, (a) for A, while, (b) for B). The crystal structures of the two molecules belong to the triclinic system with space group $P\bar{1}$ and lattice constants: $a = 12.69$ Å, $b = 16.13$ Å, $c = 20.02$ Å, $\alpha = 93.98°$, $\beta = 96.60°$, $\gamma = 107.50°$ (for A) and $a = 11.91$ Å, $b = 16.44$ Å, $c = 17.75$ Å, $\alpha = 113.17°$, $\beta = 98.40°$, $\gamma = 104.63°$ (for B) [16,53]. From Table 2, it is interesting to note following points:

(i) For molecule A, most coupling matrix elements for the electron are close to those for the hole. The dominant transfer pathways are pathways 2 ($V_h = 62.586 \times 10^{-4}$ eV, $V_e = 176.874 \times 10^{-4}$ eV), 6 ($V_h = 142.862 \times 10^{-4}$ eV, $V_e = 58.504 \times 10^{-4}$ eV), and 8 ($V_h = 168.711 \times 10^{-4}$ eV) (Fig. 8(a)). According to Eq. 1, the maximal k_{ct}s for the hole and electron should occur in pathway 8 and pathway 2, respectively and should be very close, because the reorganization energy for the hole is only 0.01 eV smaller than that for the electron. In Table 2, The mass center distance (D_1) of two adjacent molecules in pathway 1 is close to that in pathway 2, but their V values for both the hole and electron make notably difference. The phenomena can be rationalized by examining the crystal structure and major interactions taking place between two adjacent molecules. For the crystal structure of molecule A, although the D_1 of the dimer in pathway 1 is 3.44 Å smaller than that in pathway 2, the perpendicular distance (D_2) of the dimer in pathway 1 is 9.65 Å larger than that in pathway 2. Large perpendicular distance leads to a poor overlap of HOMOs and LUMOs of two interacting molecules and consequently small V_h and V_e values, such as pathways 3, 4, 5, 7, 9, 11, 13. Small perpendicular distance leads to good overlap of orbitals of two interacting molecules, because of much intermolecular interaction in these systems, such as sulfur...sulfur and π...π interaction. For pathways 2, 6 and 8, the nearest sulfur...sulfur distances are within 4.15, 4.37, and 3.88 Å and the nearest π...π distances are within 3.74, 4.08, and 4.05 Å, respectively, which is promising to lead to significant intermolecular electronic coupling. From the HOMO and LUMO plots of molecule A in Fig. 7, the HOMO and LUMO wave functions are mainly localized on around the flipping thiophene ring and C–C double bonds. The major interactions of the dimers in the three dominant pathways occur in

Table 2
The mass center distance (D_1) (Å), the perpendicular distance (D_2) (Å), electronic coupling matrix elements V_h and V_e (eV) for all pathways, and the carrier mobility μ_h and μ_e ($cm^2\ V^{-1}\ s^{-1}$) at room temperature (298 K), (a) and (b) for molecules A and B, respectively.

Pathway	1	2	3	4	5	6	7	8	9	10	11	12	13
(a)													
D_1	12.69	16.13	17.27	23.33	20.02	22.44	24.91	24.82	26.57	24.41	28.32	30.52	30.96
D_2	11.49	1.84	13.25	9.34	7.31	4.04	18.51	5.43	9.04	5.87	20.35	0.00	16.60
$V_h/10^{-4}$	0.671	62.586	0.216	0.559	1.033	142.862	0.487	168.711	0.108	0.422	0.393	5.734	0.872
$V_e/10^{-4}$	0.449	176.874	0.253	0.410	3.607	58.504	0.237	5.442	0.095	0.368	0.056	6.546	0.026
	$\mu_h = 4.720 \times 10^{-2}$							$\mu_e = 1.227 \times 10^{-3}$					
(b)													
D_1	11.91	16.44	17.70	22.61	17.75	19.88	22.78	18.86	28.55	18.36	30.33	25.66	31.53
D_2	11.88	5.88	5.76	17.71	7.81	3.39	17.76	8.23	10.42	2.24	22.76	14.85	0.00
$V_h/10^{-4}$	35.375	14.966	27.211	4.082	48.981	357.830	1.361	110.206	1.361	35.375	2.721	39.457	29.933
$V_e/10^{-4}$	28.572	110.200	27.211	17.687	61.226	47.620	2.721	38.096	5.442	53.062	4.082	40.817	38.096
	$\mu_h = 1.164 \times 10^{-2}$							$\mu_e = 5.814 \times 10^{-3}$					

the region, so a good overlap of orbitals of two interacting molecules gives rise to large V_h and V_e values. It is interesting to note the pathways 10 and 12. The D_1 and D_2 values of the dimer in pathway 10 are close to those in pathway 8, but the V values make a great difference between them. From the crystal structures of molecule A in Fig. 8(b), the region of the major interactions of the two molecules in pathway 10 occurs in the two thiophene rings. Due to little electronic density on one of the two thiophene rings (see Figs. 7 and S1), this gives rise to a poor overlap of HOMOs and LUMOs of two interacting molecules and consequently small the coupling matrix elements. For pathway 12, although the perpendicular distance of the dimer is zero, the mass center distance is very large (30.52 Å), and the reduced contact in the colinear dimer induces interaction only between the p_z atomic orbitals located on the terminal atoms. This largely reduces the overlap of orbitals and consequently leads to small V_h and V_e values.

(ii) It is well known that most unsubstituted π-conjugated organic semiconductors are *p*-type. Shuai et al. systemically studied the hole transport properties of unsubstituted linear oligothiophene [28]. Our study indicates that not only hole mobility of molecule A is largely similar to unsubstituted linear oligothiophene, but also the electronic mobility is large, which makes it probably become the promising charge transport layer materials in application to OLED. Large electronic mobility of the annular molecule firstly is due to smaller electronic reorganization energy. Secondly, the good overlap between LUMOs of the interacting molecules occurs in transport pathways, such as pathway 2. There, V_e is much larger than V_h. This can be explained by different degree of bonding versus antibonding interactions in the overlapping region and the charge distributions of the corresponding frontier orbital. It can be seen that its interring interactions give rises to fully constructive or destructive interring overlap of LUMOs from the overlapping region of the two interacting molecules in Fig. 8(b) and the charge distributions of the region in Figs. 7 and S1. In contrast, the mixing of bonding and antibonding interring overlap of HOMOs leads to a cancelation of the interring interaction, and from the HOMO and LUMO plots of molecule A and Fig. S1, the electronic density on all the sulfur atoms is very small in the HOMO level, while it is larger in the LUMO level. These facts give rise to more significant energetic splitting between LUMO and LUMO + 1 of the dimer in pathway 2 and hence larger coupling matrix element for the electron than that for the hole. For the hole, the maximal k_{ct} should occur in pathway 8 (Fig. 8(b)) and the splitting energy between HOMO and HOMO−1 of the dimer in pathway 8 is much larger than that between LUMO and LUMO+1. The overlap of LUMOs is very large mixing of bonding and antibonding interring overlap, which leads to cancelation of interring interaction. This fact results in a better overlap of HOMOs and consequently much larger V_h value. In a word, the coupling matrix element is increased if both are bonding or antibonding π-orbital interactions and decreased when there occurs a cancelation between bonding and antibonding overlaps.

For molecule B, its transport properties including transfer pathways, electronic coupling matrix elements and charge transfer rate are similar to those for molecule A and these properties are rationalized with the similar reasons. It is particularly pointed out that although the mass center distance of the dimer in the pathway 10 is very close to those in these dominant transfer pathways such as pathways 2, 6 and 8 and the perpendicular distance is even smaller than those in dominant pathways, the V values in pathway 10 are great different from them. We find that the nearest sulfur...sulfur and π...π distances are within 7.06 and 7.58 Å in pathway 10, respectively, while for the pathways 2, 6 and 8, the nearest sulfur...sulfur distances are within 3.81, 3.67 and 3.51 Å and π...π distances are within 4.03, 3.75 and 5.21 Å, respectively. So such large s...s and π...π distances weaken the intermolecular interaction of the dimer in pathway 10 and hence lead to a poor overlap of orbitals.

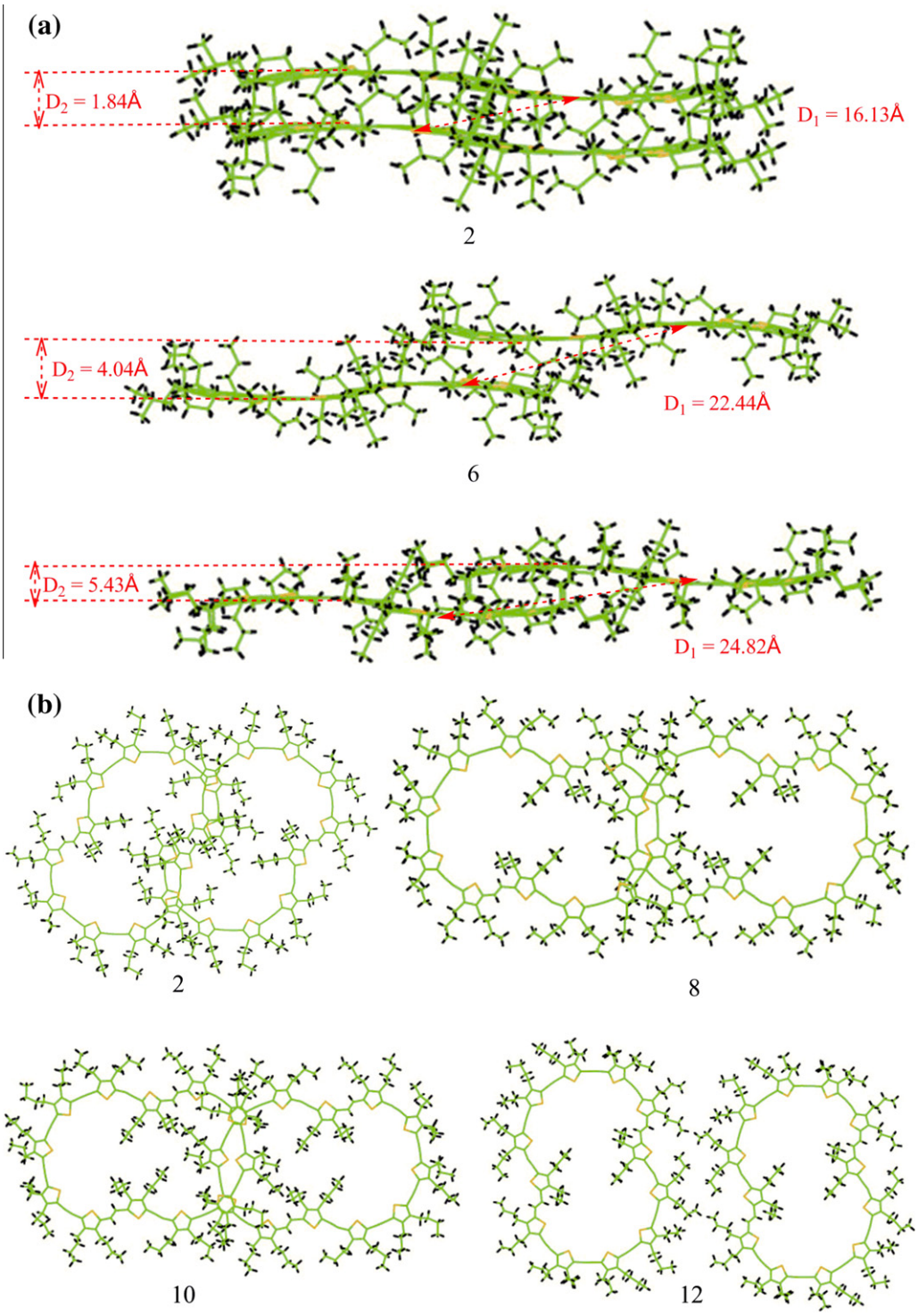

Fig. 8. (a) Schematic representation (side-view) of dominant charge transfer pathways (2, 6 and 8). (b) Schematic representation (top-view) of pathways (2, 8, 10 and 12) of charge transfer for molecule A.

3.2.3. Carrier mobility and temperature dependences of carrier mobility

On the basis of the above discussions, we estimated the carrier mobility of molecules A and B according to the Eqs. (1), (6), (7), and (8), because X-ray structures of other molecules have not been reported. To have a rough estimate on the intermolecular charge transfer rate and the carrier mobility, it is assumed that the external reorganization

energy (λ_{ext}) is within the range 0.2–0.6 eV [54]. λ_{ext} is chose as 0.4 eV to estimate the carrier mobility at T = 298 K, listing the results in Table 2. It can be seen that large carrier mobility of both molecules A and B makes them become the promising bipolar charge transport materials, $\mu_h = 1.164 \times 10^{-2}$ cm^2 V^{-1} s^{-1}and $\mu_e = 5.814 \times 10^{-3}$ cm^2 V^{-1} s^{-1} for molecule A, while, $\mu_h = 4.720 \times 10^{-2}$ cm^2 V^{-1} s^{-1} and $\mu_e = 1.227 \times 10^{-3}$ cm^2 V^{-1} s^{-1} for molecule B. It should be noticed that the relative ordering of the carrier mobility is consistent with that of their reorganization energies for the two cyclic molecules. It should be ascribed to the dominating role of λ in the exponential term of Eq. (1) in the charge transfer rate. The fact indicates that for these studied macrocycles possessing similar crystal structures, the magnitude of the reorganization energy can qualitatively predict that of the mobility. So the relative ordering of hole carrier mobility should be B > A > C; that of electron carrier mobility should be A > B > C.

The hole carrier mobility of molecules A and B is close to those of the traditional unsubstituted linear oligthiophenes [28], while they also possess very good electron transport properties. It maybe the major reason that the closed ring structure suppresses the rotation of the thiophene units in charge transfer process, and the introduction of the alkynyl and double bonds weakens the repulsion and steric effects between two adjacent thiophene rings to stabilize the LUMO level, in result to decrease the electronic reorganization energy (λ_e) and thus improve their electron transport ability. For the studied linear and cyclic oligothiophenes with the butyl, so large substituent should lead to loose molecular packing, in result to weaken the intermolecular interaction and largely decrease the electronic coupling matrix element. So their charge transfer rate should be dominated by the corresponding reorganization energies in the exponential term of Eq. (1). For our case, the small difference of λ values between cyclic and linear oligothiophenes probably gives rise to the difference of one order of magnitude for the calculated mobility, which is similar to that case reported in the literature [47]. So smaller λ values for these macrocycles probably give rise to better charge transport properties than their corresponding linear molecules. To further enhance these macrocycles' ability of charge transport, ones can tune their crystal structures to decrease the separation between the neighboring molecules in the charge transfer pathways by varying their substituents.

As we mentioned in Section 2, the charge transfer mechanism and carrier mobility are closely related to temperature (T), so the temperature dependence of the carrier mobility was examined. Huang–Rhys factor, S_j characters the electron–phonon coupling strength. In the case of weak local electron–phonon coupling, the mobility is dominated by tunneling and displays band-like temperature dependence in the whole range of temperature. For strong local coupling ($\sum_j S_j \gg 1$), (i) at low temperature, the mobility is band-like, that is, it is decreased with the increase of

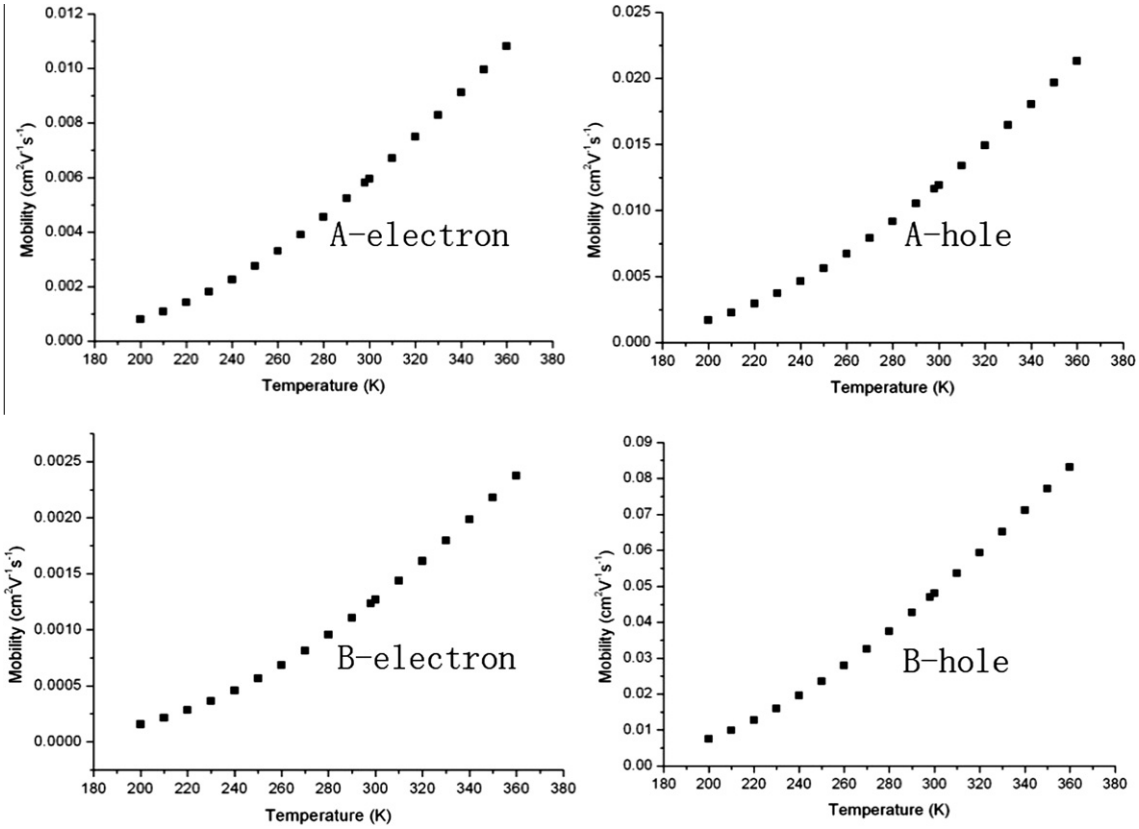

Fig. 9. The predicted temperature dependences of hole and electron carrier mobility for molecular materials A and B.

temperature; (ii) as the temperature increases, the hopping mechanism starts to dominate for organic electronic materials from coherent transport to an incoherent temperature-activated transport; (iii) at very high temperature, at which the thermal energy becomes large enough to dissociate the polaron, the residual charge is scattered by thermal phonons, and as a result the mobility decreases again with increasing the temperature [41]. Because of large separation between the neighboring molecules in the pathways of charge transfer for our case, the magnitudes of Vs are about one to several orders of magnitude less than the λ values. So the hopping mechanism and standard Marcus theory are applicable for our systems. It is firstly assumed that the reorganization energies and the electronic coupling matrix elements are temperature independent. The hopping mechanism predicts the mobility to follow a temperature dependence of $T^{-3/2}\exp(-\lambda/4k_BT)$ according to the Eqs. (1), (6), (7), and (8). Many groups also successfully obtained some reliable results in terms of the hopping mechanism and the above temperature dependence of the mobility [41,47,55]. Due to the decomposition temperature of the two molecules (about 370 K) [56]. We only plot the curves of the temperature dependences of the mobility within a temperature range from 200 to 360 K (Fig. 9). The exponential law dominates within the temperature range, so one can enhance their carrier mobility by increasing the temperature.

4. Conclusion

The work shows that the closed ring structure and the introduction of the alkynyl and double bond are beneficial to decreasing the internal reorganization energy for thiophene-based materials. A rationale based on molecular geometric structure and molecule-orbital arguments is provided: the closed ring structure restricts the rotation of the thiophene units in charge transfer reaction and the introduction of the alkynyl and double bonds weakens the coulomb repulsion between lone electron pairs of sulfur atoms and the steric effects resulting from the butyls, in result to decrease the reorganization energy (λ_e) and hence improve their ability of charge transport. In two-state model, by employing the "energy splitting in dimer" (ESD) method, we estimate the electronic coupling matrix element (V) values for all pathways for molecules A and B. The results indicate that the amplitude of the coupling matrix element is highly sensitive to various aspects of molecular packing. By assuming localized charge hopping described be the Marcus electron transfer model and the Brownian diffusion process, we theoretically predicted the carrier mobility at room temperature for molecules A and B, and investigated the temperature dependence of the mobility. The hole carrier mobility for the two molecular materials is large and close to unsubstituted linear oligthiophenes, more importantly, their ability of electron transport is very outstanding, which mainly results from small reorganization energy for the electron. According to the temperature dependence of the mobility, we predicted that their carrier mobility should be enhanced by increasing the temperature within a temperature range from 200 to 360 K. As the internal reorganization energy and electronic coupling matrix element are the important properties of these molecules, the insights gained from this study will benefit to the design of other organic electronic devices such as OLED.

Acknowledgements

This work is supported by the Natural Science Foundation of China (Nos. 20973078 and 20673045) Graduate Innovation Fund of Jilin University (NO. 2011103), Special Funding to Basic Scientific Research Projects for Central Collages as well as the Open Project of the State Key Laboratory for Supramolecular Structure and Material of Jilin University (SKLSSM200716).

Appendix A. Supplementary data

Supplementary data associated with this article can be found, in the online version, at doi:10.1016/j.orgel.2011.03.029.

References

[1] C.W. Tang, S.A. VanSlyke, Appl. Phys. Lett. 51 (1987) 913.
[2] P.K.H. Ho, J.-S. Kim, J.H. Burroughes, H. Becker, S.F.Y. Li, T.M. Brown, F. Cacialli, R.H. Friend, Nature (Lond.) 404 (2000) 481.
[3] H.E. Katz, J. Mater. Chem. 7 (1997) 369.
[4] G. Horowitz, M.E. Hajlaoui, Adv. Mater. 12 (2000) 1046.
[5] C.R. Newman, C.D. Frisbie, D.A. da Silva Filho, J.L. Brédas, P.C. Ewbank, K.R. Mann, Chem. Mater. 16 (2004) 4436.
[6] F. Padinger, R.S. Rittberger, N.S. Sariciftci, Adv. Funct. Mater. 13 (2003) 85.
[7] C.J. Brabec, N.S. Sariciftci, J.C. Hummelen, Adv. Funct. Mater. 11 (2001) 15.
[8] W.F. Beadle, J.C.C. Tsai, R.D. Plummer, Quick Reference Manual of Semiconductor Engineers, Wiley, New York, 1985.
[9] V.C. Sundar, J. Zaumseil, V. Podzorov, E. Menard, R.L. Willett, T. Someya, M.E. Gershenson, J.A. Rogers, Science (Washington, D.C.) 303 (2004) 1644.
[10] V. Podzorov, E. Menard, A. Borissov, V. Kiryukhin, J.A. Rogers, M.E. Gershenson, Phys. Rev. Lett. 93 (2004) 86602.
[11] P.F.H. Schwab, J.R. Smith, J. Michl, Chem. Rev. 105 (2005) 1197.
[12] P. Frere, P.J. Skabara, Chem. Soc. Rev. 34 (2005) 69.
[13] T. Otsubo, Y. Aso, K. Takimiya, J. Mater. Chem. 12 (2002) 2565.
[14] E.A. Marseglia, F. Grepioni, E. Tedesco, D. Braga, Mol. Cryst. Liq. Cryst. 348 (2000) 137.
[15] H.D. Nalwa (Ed.), Handbook of Organic Conductive Molecules and Polymers. Conductive Polymers: Synthesis and Electrical Properties, vol. 2, Wiley, Chichester, 1997.
[16] L. Krömer, I. Rios-Carreras, G. Fuhrmann, C. Musch, M. Wunderlin, T. Debaerdemaeker, E. Mena-Osteritz, P. Bäuerle, Angew. Chem. Int. Ed. 39 (2000) 3481.
[17] G. Fuhrmann, L. Krömer, P. Bäuerle, Synth. Met. 119 (2001) 125.
[18] G. Fuhrmann, T. Debaerdemaeker, P. Bäuerle, Chem. Commun. 8 (2003) 948.
[19] E. Mena-Osteritz, P. Bäuerle, Adv. Mater. 13 (2001) 243.
[20] E. Mena-Osteritz, Adv. Mater. 14 (2002) 609.
[21] M. Bednarz, P. Rwineker, E. Mena-Osteritz, P. Bäuerle, J. Lumin. 110 (2004) 225.
[22] S.S. Zade, M. Bendikov, J. Org. Chem. 71 (2006) 2972.
[23] J. Fabian, H. Hartmann, J. Phys. Org. Chem. 20 (2007) 554.
[24] J. Casado, M.Z. Zgierski, G. Fuhrmann, P. Bäuerle, J.T.L. Navarrete, J. Chem. Phys. 125 (2005) 044518.
[25] J. Cornil, D. Beljonne, P.J. Calbert, J.L. Brédas, Adv. Mater. 13 (2001) 1053.
[26] G.A. Hutchison, M.A. Ratner, T.J. Marks, J. Am. Chem. Soc. 127 (2005) 16866.
[27] G.A. Hutchison, M.A. Ratner, T.J. Marks, J. Am. Chem. Soc. 127 (2005) 2339.
[28] X.D. Yang, L.J. Wang, C.L. Wang, W. Long, Z.G. Shuai, Chem. Mater. 20 (2008) 3205.

[29] D. Fichou, Handbook of Oligo- and Polythiophenes, Wiley-VCH, New York, 1999.
[30] D. Fichou, J. Mater. Chem. 10 (2000) 571.
[31] W.A. Schoonveld, J. Wildeman, D. Fichou, P.A. Bobbert, B.J. van Wees, T.M. Klapwijk, Nature (Lond.) 404 (2000) 977.
[32] M. Melucci, M. Gazzano, G. Barbarella, M. Cavallini, F. Biscarini, P. Maccagnani, P. Ostoja, J. Am. Chem. Soc. 125 (2003) 10266.
[33] M.S. Nam, A. Ardavan, R.J. Cava, P.M. Chaikin, Appl. Phys. Lett. 83 (2003) 4782.
[34] R.W.I. de Boer, M. Jochemsen, T.M. Klapwijk, A.F. Morpurgo, J. Niemax, A.K. Tripathi, J. Pflaum, J. Appl. Phys. 95 (2004) 1196.
[35] N.F. Mott, E.A. Davis, Electronic Process Non-crystalline Materials, second ed., Oxford University Press, Oxford, 1979.
[36] A.J. Epstein, W.P. Lee, V.N. Prigodin, Synth. Met. 117 (2001) 9.
[37] R.A. Marcus, Rev. Mod. Phys. 65 (1993) 599.
[38] R.A. Marcus, Annu. Rev. Phys. Chem. 15 (1964) 155.
[39] N.S. Hush, J. Chem. Phys. 28 (1958) 962.
[40] R.A. Marcus, J. Chem. Phys. 24 (1956) 966.
[41] V. Coropceanu, J. Cornil, D.A. da Silva Filho, Y. Olivier, R. Silbey, J.L. Brédas, Chem. Rev. 107 (2007) 926.
[42] W.Q. Deng, W.A. Goddard III, J. Phys. Chem. B 108 (2004) 8614.
[43] J.L. Brédas, P.J. Calbert, D.A. da Silva Filho, J. Cornil, Proc. Natl. Acad. Sci. USA 99 (2002) 5804.
[44] V. Lemaur, D.A. da Silva Filho, V. Coropceanu, M. Lehmann, Y. Geerts, J. Piris, M.G. Debije, A.M. van de Craats, K. Senthilkumar, L.D. A Siebbeles, J.M. Warman, J.L. Brédas, J. Cornil, J. Am. Chem. Soc. 126 (2004) 3271.
[45] J.S. Huang, M. Kertesz, Chem. Phys. Lett. 390 (2004) 110.
[46] Y.B. Song, C.A. Di, X.D. Yang, S.P. Li, W. Xu, Y.O. Liu, L.M. Yang, Z.G. Shuai, D. Zhang, D.B. Zhu, J. Am. Chem. Soc. 128 (2006) 15940.
[47] X.D. Yang, Q.K. Li, Z.G. Shuai, Nanotechnology 18 (2007) 424029.
[48] S. Chen, J. Ma, J. Comput. Chem. 30 (2009) 1959.
[49] B.C. Lin, C.P. Cheng, Z.-Q. You, C.-P. Hsu, J. Am. Chem. Soc. 127 (2005) 66.
[50] W. Zhang, W. Zhu, W. Liang, Y. Zhao, S.F. Nelsen, J. Phys. Chem. B 112 (2008) 11079.
[51] L.B. Schein, A.R. McGhie, Phys. Rev. B: Condens. Matter Mater. Phys. 20 (1979) 1631.
[52] M.J. Frisch, G.W. Trucks, H.B. Schlegel, G.E. Scuseria, M.A. Robb, J.R. Cheeseman, J.A. Montgomery Jr., T. Vreven, K.N. Kudin, J.C. Burant, J.M. Millam, S.S. Iyengar, J. Tomasi, V. Barone, B. Mennucci, M. Cossi, G. Scalmani, N. Rega, G.A. Petersson, H. Nakatsuji, M. Hada, M. Ehara, K. Toyota, R. Fukuda, J. Hasegawa, M. Ishida, T. Nakajima, Y. Honda, O. Kitao, H. Nakai, M. Klene, X. Li, J.E. Knox, H.P. Hratchian, J.B. Cross, C. Adamo, J. Jaramillo, R. Gomperts, R.E. Stratmann, O. Yazyev, A.J. Austin, R. Cammi, C. Pomelli, J.W. Ochterski, P.Y. Ayala, K. Morokuma, G.A. Voth, P. Salvador, J.J. Dannenberg, V.G. Zakrzewski, S. Dapprich, A.D. Daniels, M.C. Strain, O. Farkas, D.K. Malick, A.D. Rabuck, K. Raghavachari, J.B. Foresman, J.V. Ortiz, Q. Cui, A.G. Baboul, S. Clifford, J. Cioslowski, B.B. Stefanov, G. Liu, A. Liashenko, P. Piskorz, I. Komaromi, R.L. Martin, D.J. Fox, T. Keith, M.A. Al-Laham, C.Y. Peng, A. Nanayakkara, M. Challacombe, P.M.W. Gill, B. Johnson, W. Chen, M.W. Wong, C. Gonzalez, J.A. Pople, Computer Code GAUSSIAN 03, Revision A.I, Gaussian Inc., Pittsburgh, PA, 2003.
[53] M. Harry-Williams, A. Bhaskar, G. Ramakrishna, T. Goodson III, M. Imamura, A. Mawatari, K. Nakao, H. Enozawa, T. Nishinaga, M. Iyoda, J. Am. Chem. Soc. 130 (2008) 3252.
[54] V. Lemeur, M. Steel, D. Beljonne, J.L. Brédas, J. Cornil, J. Am. Chem. Soc. 127 (2005) 6077.
[55] G. Nan, X. Yang, L. Wang, Z. Shuai, Y. Zhao, Phys. Rev. B 79 (2009) 115203.
[56] G. Fuhrmann, Synthesis and Characterization of Oligothiophene-based Fully π-Conjugated Macrocycles [D], University of Ulm, Germany, 2006.

that the optimal band gap of a donor polymer is in the range of 1.2–1.7 eV [3].

Recent research efforts on developing low-band-gap polymers and device processing techniques are fruitful, and some BHJ solar cells based on new low-band-gap polymers have demonstrated efficiencies well above 5% [14–18]. In many of these works, processing additives have been used to tune the nano-scale morphology [16–18]. A selective solubility to fullerene and a higher boiling point than the host solvent have been identified as two criteria for effective processing additives [17]. One of the most commonly used additives is 1,8-diiodooctane (DIO) that has been reported to improve both the short-circuit current density (J_{sc}) and fill factor (*FF*) in several types of polymer: fullerene BHJ systems [17,18].

More recently, a new class of low-bandgap polymers have shown a PCE above 7% when blended with $PC_{71}BM$ [19,20]. The backbones of these polymers consist of alternating ester or ketone substituted thieno[3,4-*b*]thiophene and dialkyloxy substituted benzodithiophene units. In this design, the thieno[3,4-*b*]thiophene in each repeating unit is used to stabilize the quinoidal structure that not only narrows the energy gap but also enhances the planarity of the backbone. In addition, the planarity as well as the rigidity of the backbone offered by the benzodithiophene units ensures a high hole mobility in this type of polymers. In this paper, we report a new low-band-gap polymer based on ketone substituted thieno[3,4-*b*]thiophene and dioctylbenzodithiophene units, PTTBDT-C8, for high-performance polymer solar cells (Fig. 1a). As compared with the materials reported in literature, PTTBDT-C8 contains two linear octyl groups on the benzodithiophene unit instead of two 2-ethylhexyloxy side chains, with an attempt to enhance the interchain interaction. The resulting polymer is soluble in a wide range of organic solvents, such as chlororform, chlorobenzene, and dichlorobenzene. By introducing the processing additive, DIO, to the host solvent of chloroform, the efficiency of the BHJ solar cells based on PTTBDT-C8 and $PC_{71}BM$ (1:2 by weight) has been dramatically improved from 1.45% to 4.83%. The correlation between the film morphology, charge mobility, and overall device performance has been investigated in detail.

2. Experimental

The BHJ solar cells prepared in this study have a structure of ITO/PEDOT:PSS (30 nm)/PTTBDT-C8:$PC_{71}BM$ (110–115 nm)/BCP (bathocuproine) (3 nm)/LiF (1 nm)/Al (100 nm). The indium tin oxide (ITO) coated glass substrate was cleaned stepwise by ultrasonic bath in acetone and isopropanol before UV-ozone treatment. The PEDOT:PSS and the active layers were successively deposited by solution spin casting, and the BCP, LiF, and Al layers were deposited by thermal evaporation. Chloroform or a mixture of chloroform with DIO was used as the solvent for the active layer. The BCP layer sandwiched between active layer and LiF/Al cathode was used to block pinholes and suppress micro short-circuits. The resulting devices have an active area of 0.49 cm^2. The current density–voltage (*J–V*) characteristics were measured under simulated air mass 1.5 global (AM 1.5G) irradiation of 100 mW/cm^2. The charge mobility data were obtained from field effect transistor (FET) measurements with a bottom contact structure and calculated from the saturation regime.

The new polymer, PTTBDT-C8, was synthesized via Stille coupling reaction of 1-(4,6-dibromothieno[3,4-*b*]thiophen-2-yl)-2-ethylhexan-1-one with 2,6-bis(trimethylstannyl)-4,8-dioctylbenzo[1,2-*b*:4,5-*b*′]dithiophene in refluxing toluene under Ar using $Pd(PPh_3)_4$ as the catalyst. After purification by Soxhlet extraction, the obtained polymer has a number averaged molecular weight of 37.6 kDa and weight averaged molecular weight of 100.9 kDa with a polydispersity of 2.68. The branched ketone substituent on the thieno[3,4-b]thiophene unit renders the resulting polymer good solubility in organic solvents, while the linear octyl groups on the benzodithiophenethe unit allow intimate Π–Π stacking and thus offer high hole mobility. DSC measurement showed that this polymer is an amorphous material with a glass transition temperature around 122 °C. The hole mobility is 2×10^{-4} cm^2/Vs as measured from the OFETs. The LUMO and HOMO energy levels are at −3.41 eV and −5.10 eV respectively, as determined by cyclic voltammetry (CV), corresponding to an electrochemical band gap of 1.69 eV.

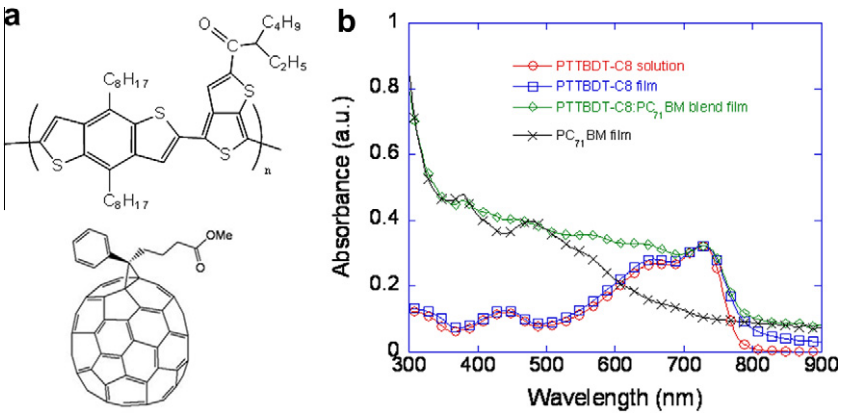

Fig. 1. (a) Structure of PTTBDT-C8 (top) and $PC_{71}BM$ (bottom). (b) Absorption spectra of PTTBDT-C8 solution in chloroform, PTTBDT-C8 film, $PC_{71}BM$ film, and PTTBDT-C8:$PC_{71}BM$ blend film. The absorption spectra of PTTBDT-C8 solution and PTTBDT-C8 film are normalized at 730 nm with reference to that of the blend film. The ratio of the blend film is PTTBDT-C8:$PC_{71}BM$ = 1:2 by weight.

3. Results and discussion

The UV–vis absorption spectra of PTTBDT-C8 solution and solid films overlap quite well and both show a double peak at 650 nm and 730 nm. The absorption onset of the solid film at 800 nm translates into an optical band gap of 1.55 eV which agrees well with CV results. The strong absorption in the wavelength region between 550 and 760 nm coincides with the maximum photon flux region of the solar spectrum (~700 nm), which ensures an efficient harvest to long-wavelength photons. $PC_{71}BM$ was used as the electron acceptor to harvest short-wavelength (300–500 nm) photons (Fig. 1b).

Fig. 2a shows the *J–V* curves of BHJ solar cells prepared using chloroform with various amounts of DIO under 1 sun of simulated air mass 1.5 global (AM 1.5G) irradiation. We chose chloroform as the processing solvent because it readily dissolves PTTBDT-C8 even at room temperature. Upon heating, this polymer is also soluble in toluene and chlorobenzene, but it will precipitate out when cooling down. The photovoltaic parameters, including open circuit voltage (V_{oc}), J_{sc}, *FF*, PCE, series resistance (R_s), and shunt resistance (R_{sh}), are extracted from these *J–V* curves and summarized in Table 1. The solar cell made without DIO additive exhibited a high V_{oc} of 0.75 V and *FF* of 0.57. But the J_{sc} of this cell was surprisingly low, only about 3.20 mA/cm^2, resulting in a low PCE of 1.39%. After adding 1% (by volume) DIO to the host solvent of chloroform, the resulting J_{sc} increased more than 3 folds reaching 12.74 mA/cm^2, with a slight drop in V_{oc} and *FF*. The PCE was thus improved by more than three times, reaching 4.79%. But the device performance remained nearly unchanged at this level when further increasing the amount of DIO to 3% and 6%. As DIO content increased from 1% to 3%, and to 6%, the V_{oc} showed no change, being about 0.71 V all the time. The *FF* showed a tiny drop from 0.53 to 0.52, and the J_{sc} decreased less than 3%. As a result, the overall change in PCE was less than 4%. The short-circuit current densities measured from the *J–V* curves were compared with the J_{sc} calculated from the integration of the corresponding external quantum efficiency (EQE) curve and solar spectrum. These two values were found in excellent agreement with an error less than 2%. Fig. 2b and c show the EQE and reflectance spectra of the same solar cells referred to in Fig. 2a. Both EQE and reflectance spectra of all these four devices show a similar broad response covering a spectral range from 300 to 800 nm. Without DIO additive, the resulting EQE is averaged at about 10–15%. With a few volume percentages (1–6%) of DIO additive, the EQE spectra are lifted up to an average of 40–50%.

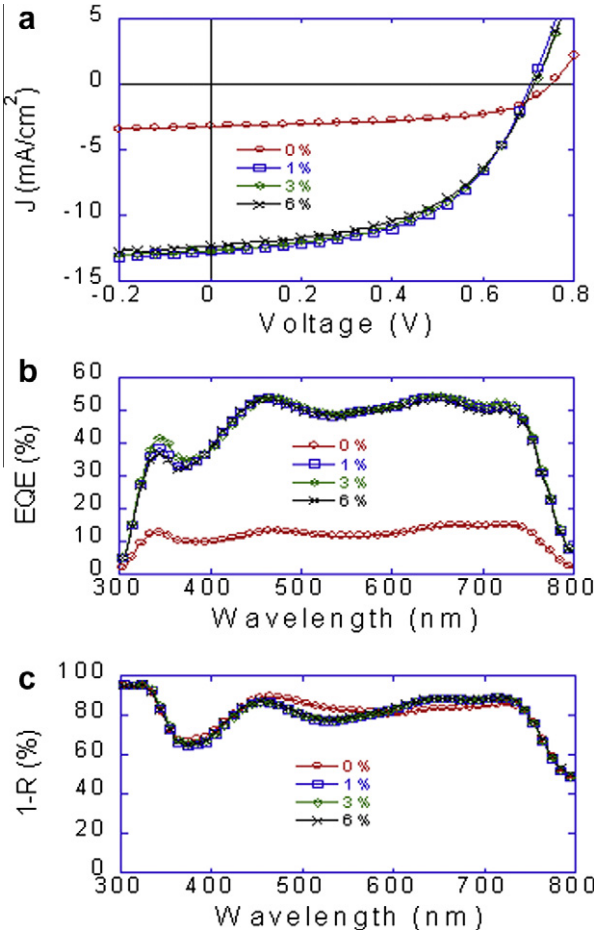

Fig. 2. (a) Current density–voltage (*J–V*) characteristics, (b) External Quantum Efficiency (EQE) spectrum, and (c) Reflectance spectrum of the PTTBDT-C8-$PC_{71}BM$ BHJ solar cells prepared with various volume percents of DIO additive in the host solvent of chloroform. The DIO percentages are 0% (no DIO additive), 1%, 3%, and 6%.

Table 1
Photovoltaic performance of the BHJ solar cells prepared with various amounts of DIO additive. The data were extracted from the *J–V* curves shown in Fig. 2a. Values in parentheses are the J_{sc} calculated from EQE spectra and PCE calibrated from the calculated J_{sc}.

DIO content (%)	V_{oc}	J_{sc} (mA/cm^2)	*FF*	PCE (%)	R_s (Ωcm^2)	R_{sh} (Ωcm^2)
0	0.75	3.20 (3.35)	0.58	1.39 (1.45)	14	1070
1	0.71	12.74 (12.87)	0.53	4.79 (4.83)	6	441
3	0.71	12.72 (12.74)	0.52	4.68 (4.69)	7	425
6	0.71	12.32 (12.60)	0.52	4.56 (4.66)	7	388

The dramatic improvement in J_{sc} must be related to the changes in nano-scale morphology since DIO does not react with the polymer or fullerene and there is no DIO present in the completely dried films. Fig. 3 shows the surface topography of BHJ films as directly measured from the same solar cell devices referred to in Fig. 2 by atomic force microscopy (AFM) and two Auger electron spectroscopy (AES) sulfur mapping images. The BHJ film prepared with no DIO additive has a separated-islands like structure (Fig. 3a); the brown phase forms round islands (about 200 nm in diameter), and the yellow phase fills the gaps between islands. The yellow phase in the gaps consists of well interconnected bulky domains (about 40 nm in diameter) and obviously shows good continuity. AES sulfur mapping experiment unambiguously shows that the separated islands are composed primarily of $PC_{71}BM$ since this phase has a very low S content (Fig. 3b, shown as dark area), and the yellow phase mainly consists of the polymer because PTTBDT-C8 contains rich S element in the polymer

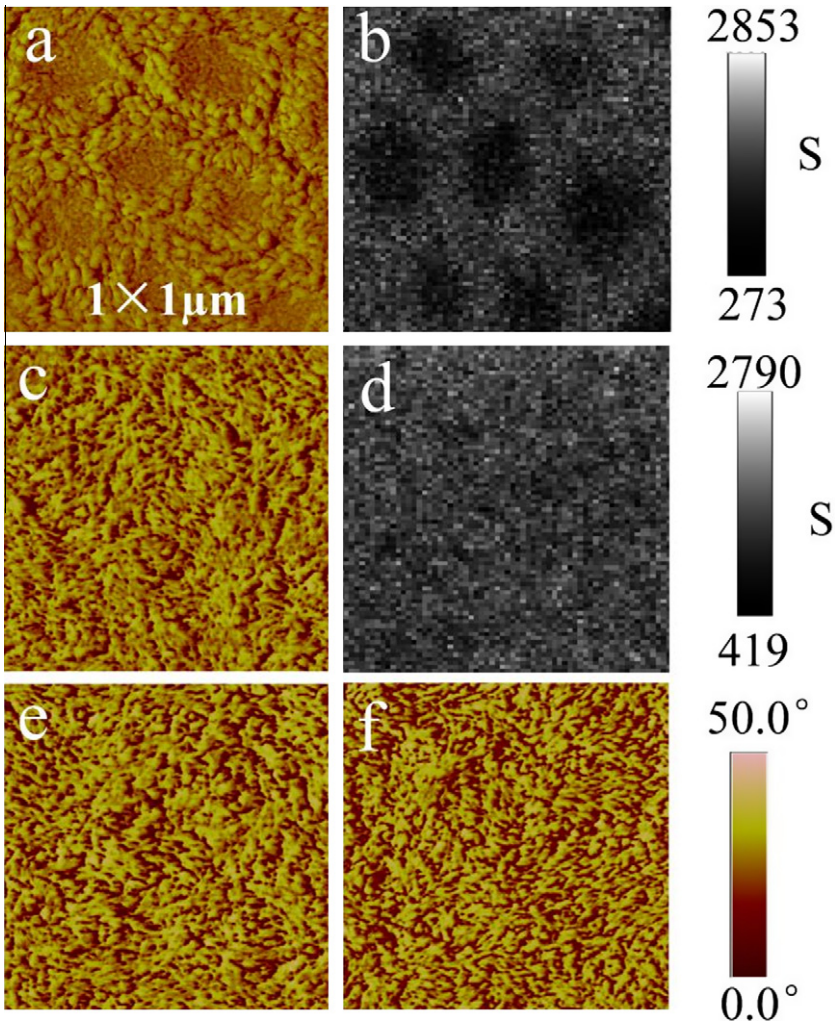

Fig. 3. AFM phase images and AES sulfur mapping images of films with various amounts of DIO additive as directly measured from the same solar cells referred in Fig. 2. The DIO percentages corresponding to AFM images (a, c, e) and (f) are 0%, 1%, 3%, and 6%, respectively. The AES sulfur mapping image (b) was measured on the same sample as (a), and (d) was measured on the same sample as (c). All images have a scan range of 1×1 μm2.

Table 2
FET mobility of films with various amounts of DIO additive.

DIO content (%)	μ_h (10^{-7} cm^2/Vs)	μ_e (10^{-7} cm^2/Vs)
0	1122	0.55
1	30	35497
3	16	19017
6	14	14713

backbone. The assignment of the polymer to the yellow phase is also well consistent with the FET mobility data. The continuous polymer network contributes to a high hole mobility of 1.12×10^{-4} cm^2/Vs while the separated fullerene islands only give an electron mobility on the order of 5.50×10^{-8} cm^2/Vs (Table 2). Note that the hole mobility of this film is very close to that of neat polymer film (2.09×10^{-4}), confirming a good continuity of polymer phase in the mixture. The morphology of large separated fullerene islands embedded in polymer matrix not only hampers exciton diffusion to the donor/acceptor interface and is highly unfavorable for exciton dissociation, but also significantly impedes electron transport in the BHJ film, leading to an extremely low electron mobility. As a result, although the device absorbs about 80% of the incident photons as indicated by the device reflectance spectrum (Fig. 2c), the J_{sc} of this device is rather low.

The use of DIO additive when preparing BHJ films eliminated the island pattern and changed the bulky polymer domains into branched ones, resulting in greatly increased donor–acceptor interface. As seen in films prepared with 1%, 3%, and 6% of DIO (Fig. 3c,e, and f), the two phases are well interpenetrating and the films look much more uniform. AES sulfur mapping experiment also demonstrates the disappearance of the large isolated $PC_{71}BM$ islands (Fig. 3d). As a result of the enhanced continuity in fullerene phase, the electron mobility was improved by more than four orders of magnitude, with the highest value of 3.55×10^{-3} cm^2/Vs achieved from the BHJ film processed with 1% DIO. On the other hand, the continuity of the polymer phase was affected by the addition of DIO,

and thus the hole mobility decreased to the order of 10^{-6} cm^2/vs. The drop in hole mobility might be caused by the vertical phase separation during the film forming process, it would leave a very thin, slightly $PC_{71}BM$ rich region on the substrate, and will inevitably affect the hole mobility data; by the same token, the measured electron mobility could also be slightly higher due to this $PC_{71}BM$ rich region on the FET substrate. Nevertheless, the overall device performance was greatly improved by the use of DIO, regardless of the drop in hole mobility. It is safe to say that both the electron mobility and the exciton dissociation efficiency were greatly improved by this processing technique.

The difference in the morphology of the polymer-$PC_{71}BM$ BHJ films prepared with and without DIO additive is very pronounced. However, when the DIO content was increased from 1% to 6%, the change in morphology is quite small, so are the changes in the hole and electron mobilities as well as the device performance. The observed DIO effects on morphology may be related to the selective solubility of DIO to fullerene. The host solvent of chloroform is a good solvent for polymers but a poor one for fullerene. In the case of chloroform-only solvent (0% DIO), fullerene precipitates out first from the solution during a spin casting process and crystallizes to form big islands, and polymer comes out after, filling the gaps between islands. If the solvent is a mixture of DIO and chloroform (1–6% DIO), chloroform vaporizes first due to its high vapor pressure relative to that of DIO. Some portion of fullerene is pushed to DIO phase in the film-forming process so that chloroform phase has less fullerene left. In other words, DIO additive is tuning the relative content of polymer and fullerene in chloroform phase towards an ideal case in which the two materials come out at the same time during a spin casting process. Of course, the tuning ability of DIO and thus the morphology of the resulting film depend on the DIO percentage. With an optimal DIO content, a simultaneous precipitation may be realized giving rise to an interpenetrating network of polymer and fullerene.

4. Conclusions

In conclusion, we have investigated the morphology and device performance relation of BHJ solar cells based on a new low-bandgap polymer with a backbone of alternating thieno[3,4-*b*]thiophene and benzodithiophene. By adding a suitable amount of DIO additive to the host solvent (chlorofoorm in this study), the PCE was improved by a factor of more than 3 from 1.45% to 4.83%. The enhancement in PCE is attributed to the improvement in the nano-scale morphology of the BHJ film. A dynamic picture of film-forming process has been proposed.

Acknowledgements

The authors thank Mr. Terry Quance, Ms. R. Movileanu, Mr. H. Fukutani, and Mr. E. Estwick for their technical support. The authors would also like to acknowledge the financial support from the Nano Initiative sponsored by National Research Council of Canada, Natural Science and Engineering Council of Canada and the Business Development Bank of Canada.

References

[1] G. Yu, J. Gao, J.C. Hummelen, F. Wudl, A.J. Heeger, Science 270 (1995) 1789.
[2] P.W.M. Blom, V.D. Mihailetchi, L.J.A. Koster, D.E. Markov, Adv. Mater. 19 (2007) 1551.
[3] G. Dennler, M.C. Scharber, C.J. Brabec, Adv. Mater. 21 (2009) 1323.
[4] K.M. Coakley, M.D. McGehee, Chem. Mater. 16 (2004).
[5] C.J. Brabec, Sol. Energy Mater. Sol. Cells. 83 (2004) 273.
[6] Y. Kim, S.A. Choulis, J. Nelson, D.D.C. Bradley, S. Cook, J.R. Durrant, Appl. Phys. Lett. 86 (2005) 063502.
[7] M. Reyes-Reyes, K. Kim, D.L. Carroll, Appl. Phys. Lett. 87 (2005) 083506.
[8] W. Ma, C. Yang, X. Gong, K. Lee, A.J. Heeger, Adv. Funt. Mater. 15 (2005) 1617.
[9] J.Y. Kim, S.H. Kim, H. Ho. Lee, K. Lee, W. Ma, X. Gong, A.J. Heeger, Adv. Mater. 18 (2006) 572.
[10] M.D. Irwin, D.B. Buchholz, A.W. Hains, R.P.H. Chang, T.J. Marks, PNAS 105 (2008) 2783.
[11] T.A. Chen, X. Wu, R.D. Rieke, J. Am. Chem. Soc. 117 (1995) 233.
[12] R. Joseph Kline, Michael D. McGehee, Ekaterina N. Kadnikova, Jinsong Liu, Jean.M.J. Frechet, Adv. Mater. 15 (2003) 1519.
[13] R. Joseph Kline, Michael D. McGehee, Ekaterina N. Kadnikova, Jinsong Liu, Jean.M.J. Frechet, Michael.F. Toney, Macromolecules 38 (2005) 3312.
[14] S.H. Park, A. Roy, S. Beaupre, S. Cho, N. Coates, J.S. Moon, D. Moses, M. Leclerc, K. Lee, A.J. Heeger, Nat. Photonics 3 (2009) 297.
[15] Y. Liang, Y. Wu, D. Feng, S. Tsai, H. Son, G. Li, L. Yu, J. Am. Chem. Soc. 131 (2009) 56.
[16] J. Peet, J.Y. Kim, N.E. Coates, W.L. Ma, D. Moses, A.J. Heeger, G.C. Bazan, Nat. Mater. 6 (2007) 497.
[17] J. Lee, W. Ma, C.J. Brabec, J. Yuen, J. Moon, J. Kim, K. Lee, G.C. Bazan, A.J. Heeger, J. Am. Chem. Soc. 130 (2008) 3619.
[18] Y. Liang, D. Feng, Y. Wu, S. Tsai, G. Li, C. Ray, L. Yu, J. Am. Chem. Soc. 131 (2009) 7792.
[19] Y. Liang, Z. Xu, J. Xia, S. Tsai, Y. Wu, G. Li, C. Ray, L. Yu, Adv. Mater. 22 (2010) 1.
[20] H. Chen, J. Hou, S. Zhang, Y. Liang, G. Yang, Y. Yang, L. Yu, Y. Wu, G. Li, Nat. Photonics 3 (2009) 649.

2. Experimental details

2.1. General

All chemicals and reagents used in this paper, unless otherwise specified, were purchased from Aldrich, Aladdin, Alfa Aesar and TCI Chemical Co. and used as received. All the solvents were further purified before use. All important compounds synthesized were characterized by ^{1}H NMR, ^{13}C NMR. ^{1}H NMR spectra were measured on a Bruker AV 300 (300 MHz) spectrometer at the ambient temperature with tetramethylsilane (TMS) as an internal standard. ^{13}C NMR spectra were recorded on Bruker AV 300 (75 MHz) spectrometer at the ambient temperature and chemical shifts were recorded in ppm from the solvent resonance employed as the internal standard. Atmospheric pressure chemical ionization mass spectra were obtained on a Bruker HCT Mass Spectrometer. Melting points were determined by differential scanning calorimetry (TAQ 100) at a heating rate of 10 °C/min under Ar atmosphere. Infrared spectroscopic measurements were performed in the range of 4000–400 cm^{-1} on a Bruker Tensor 27 FTIR Spectrometer. UV spectra were performed on a Unico UV-4802H UV–visible spectrophotometer connected to a computer. Cyclic

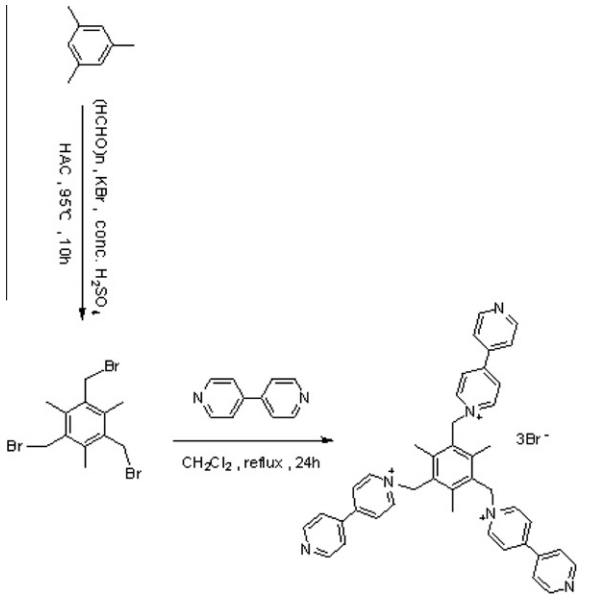

Scheme 1. Synthesis of 1,3,5-tri(1-methyl-4,4′-bipyridinium bromide)-2,4,6-trimethyl benzene.

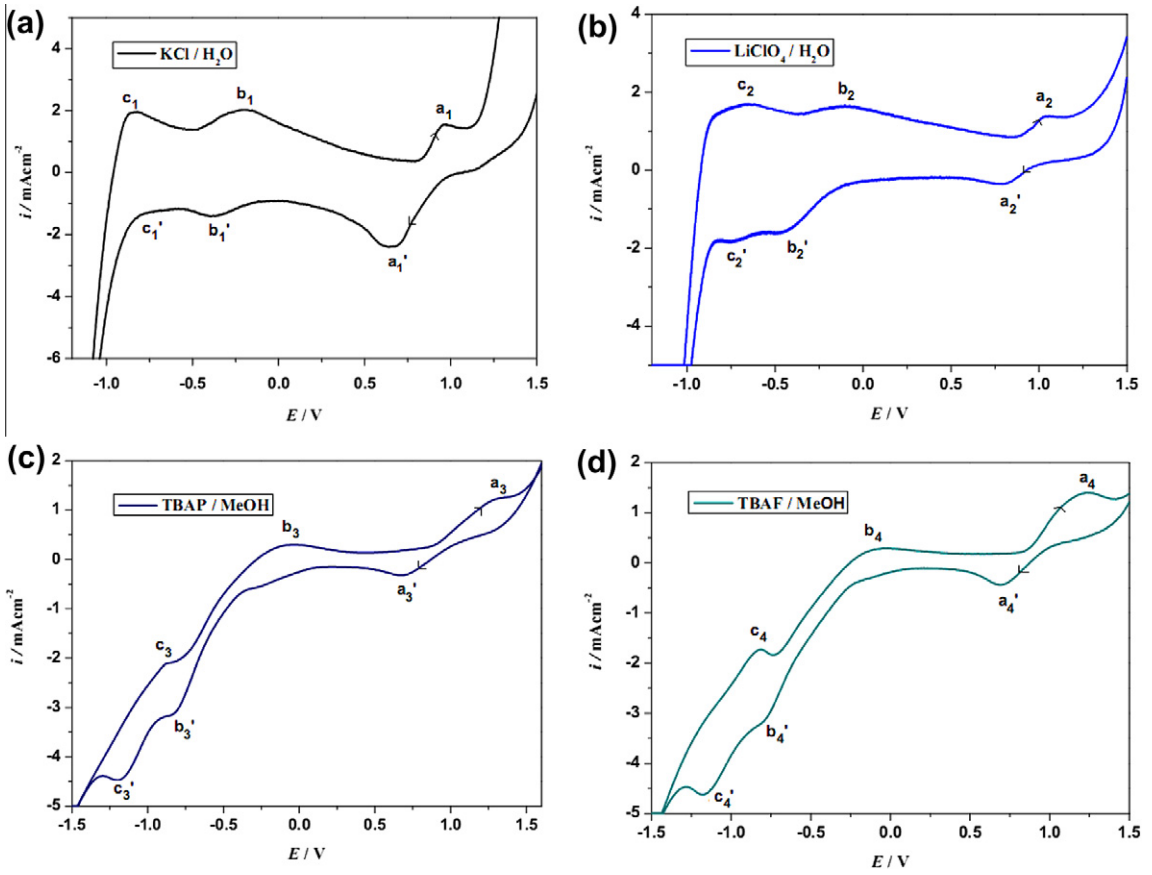

Fig. 1. Redox behavior of TBTB in 0.1 M different electrolyte solution: (a) KCl/H_2O; (b) $LiClO_4/H_2O$; (c) TBAP/MeOH; (d)TBAF/MeOH vs. Ag/AgCl at 100 mV $s^{-}1$.

voltammetry was carried out on CHI 650B electrochemical workstation using three-electrode system. All solid ECD were fabricated, sealed and tested at room temperature.

2.2. Synthesis of (1,3,5-tri(1-methyl-4,4′-bipyridinium bromide)-2,4,6-trimethyl- benzene) (TBTB)

1,3,5-Tri(bromomethyl)-2,4,6-triethylbenzene [23] (0.8 g, 2.0 mmol) in CH_2Cl_2 (300 mL) was added dropwise to a stirred solution containing a 1.5 times excess of 4,4′-bipyridine in CH_2Cl_2 (500 mL) over a period of 24 h. The desired product was isolated as a pale yellow solid by filtration of the resulting mixture. Then the crude product was further purified by washing with diethyl ether and then recrystallising from methanol (Scheme 1). Yield: 1.5 g, 1.73 mmol, 87%. m.p. – decomposed by about 250 °C. ^{1}H NMR (D_2O, 300 M, δ/ppm): 8.85 (m, 6H, bipy), 8.73 (m, 6H, bipy), 8.41 (m, 6H, bipy), 7.87 (m, 6H, bipy), 6.16 (s, 6H, CH_2N^+), 2.36 (s, 9H, Me). ^{13}C NMR (D_2O, 300M, δ/ppm): 153.9, 149.7, 144.5, 142.7, 128.6, 127.6, 126.4, 122.7, 59.0, 16.4. APCI-MS (m/z): 785 $[M{\cdot}Br_2]^+$. FT-IR (KBr, cm^{-1}): 3145 (m, Ar C—H)$_s$, 3108 (m, Ar C-H)$_s$, 2991 (m, CH_2/CH_3)$_s$, 2919 (m, CH_2/CH_3)$_s$, 1634 (s, Ar C═C)$_s$, 1562 (s, Ar C═C)$_s$, 1508 (m, Ar C═C)$_s$, 1442 (m, CH_2/CH_3)$_\delta$, 1375 (m, CH_2/CH_3)$_\delta$, 1203, 1110, 1007, 786, 570.

3. Results and discussion

3.1. Electrochemical properties

Electrochemical measurements were performed by using cyclic voltammetry at room temperature in a conventional three-electrode system using platinum disk (0.02 cm^2) as working electrodes, platinum wire as counter electrodes and Ag/AgCl in 3 M NaCl (aq) solution as a reference. In order to investigate the electrochemical properties exactly, TBTB was tested in different electrolyte solution ((a) KCl/H_2O; (b) $LiClO_4/H_2O$; (c) TBAP (tetrabutylammonium perchlorate)/MeOH; (d) TBAF (tetrabutylammonium hexafluorophosphate)/MeOH) at a scan rate of 100 mV s^{-1}. As shown in Fig. 1, the redox behavior of TBTB in the electrolyte solution above was quite similar, which showed three reversible redox couples at similar potentials. Based on this fact, the possible redox mechanism and states of TBTB were proposed. As shown in Scheme 2, four redox states and accepting–donating e^- process of TBTB were presented.

Taking Fig. 1c for example, there were three coupled redox peaks ($a_3 - a_3'$, $b_3 - b_3'$, $c_3 - c_3'$) in electrolyte solution of TBAP/MeOH for TBTB. The first redox couple at ca. 1.31 V (a_3) and ca. 0.67 V (a_3') was correlated with the redox reaction between the colorless tri-cationic species,

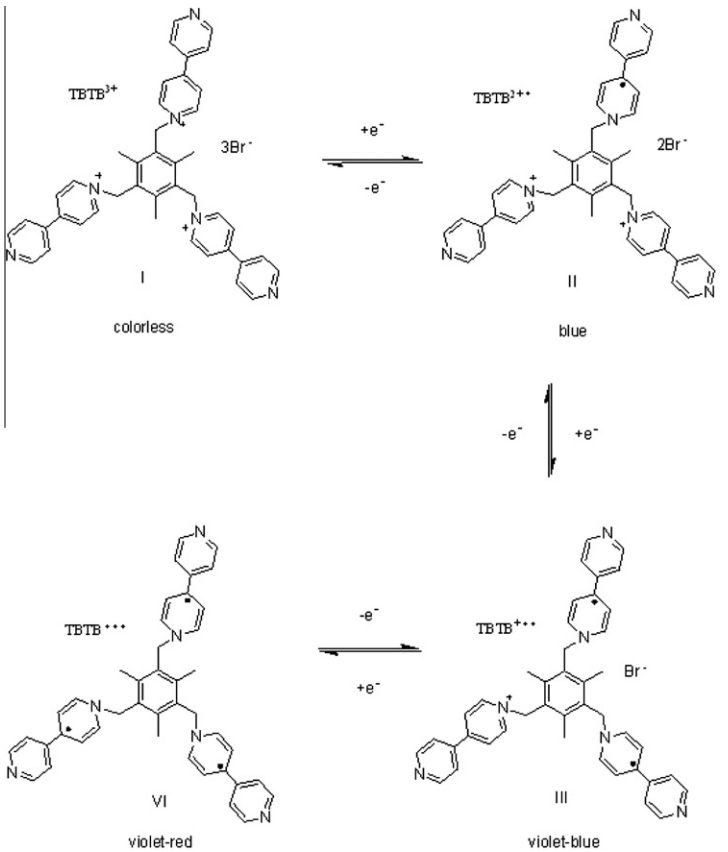

Scheme 2. Different redox states of TBTB in electrolyte solution and the corresponding color in ECD.

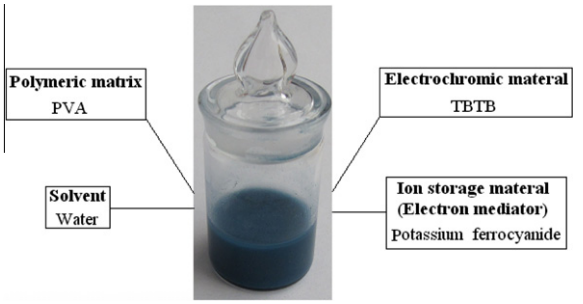

Scheme 3. Electrochromic material and additional materials of electrochromic layer.

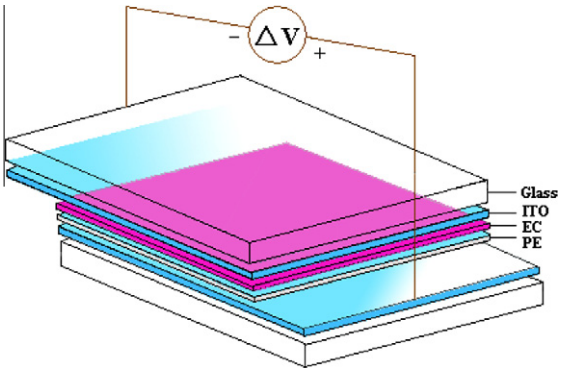

Fig. 2. Sandwich configuration of ECD (EC: electrochromic layer; PE: polymer gel electrolyte ionic conductive layer).

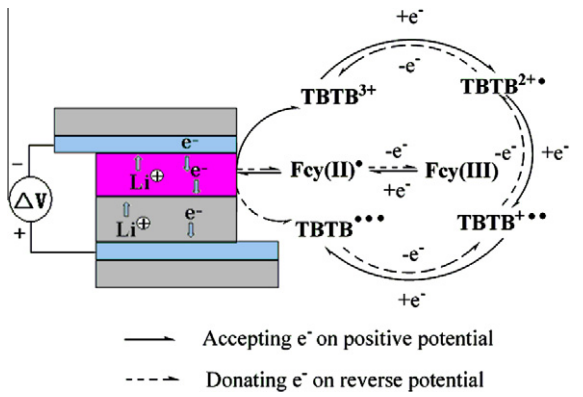

Fig. 3. The accepting–donating electron mechanism of TBTB monocation-Fcy(II) complex in ECD.

$TBTB^{3+}$, and blue di-radical-cation, $TBTB^{2+}$, respectively. The second redox couple at ca. 0.09 V (b_3) and −0.82 V ca. (b_3') was assigned to the blue di-radical-cation, $TBTB^{+\cdot}$·and the violet–blue radical-cation, $TBTB^{+\cdot\cdot}$, respectively. The third redox couple at ca. −0.87 V (c_3) and ca.−1.20 V (c_3') was related to the violet–blue radical–cation, $TBTB^{+\cdot\cdot}$ and the violet–red tri-reduced species, $TBTB^{\cdot\cdot\cdot}$, respectively.

3.2. Electrochromic devices construction

Electrochromic devices were assembled in sandwich configuration with electrochromic materials (TBTB) deposited on ITO glass electrodes and a polymer gel electrolyte. TBTB, potassium ferrocyanide (abbreviated as Fcy(II)) and polyvinyl acetate (PVA) were dissolved in water and thinly spread onto the ITO glass (50 Ω/sq, 3 cm × 5 cm) and then dried to form thin films as electrochromic layer (Scheme 3). P(MMA-VAc)/$LiClO_4$ polymer gel electrolyte [28] and propylene carbonate (PC) were dissolved in THF and thinly spread onto the ITO glass and then dried to form thin films as ionic conductive layer. All the edges of the ECD were sealed with an insulating epoxy resin. The structure of the ECD is shown in Fig. 2, including conductive ITO glass||TBTB + potassium Fcy(II)||polymer gel electrolyte||conductive ITO glass.

3.3. Electrochromic mechanism and behavior study

In order to further investigate their electrochromic behavior, a serial of environmentally friendly (no organic solvents) solid ECD (3 cm × 4 cm) were assembled and the accepting–donating electron mechanism of electrochromic materials contained in the ECD was proposed (Fig. 2 and Fig. 3) and discussed. The migration movement of the cations and anions between the polymer gel electrolyte layer and electrochromic layer during electrochemical redox process had already been studied. The rate of mobility of the cations and anions, their respective sizes, and their interaction would determine the extent of ion exchange in electrochromic layer [29]. When the positive potential was charged (the reduction process of TBTB), counter ions, usually lithium ions (Li^+) with small size and fast mobility, intercalated into the electrochromic layer because the system wanted to be electrically neutral [14]. Then the electrostatic interaction between Li^+ and Fcy(II) anions would be an obstacle for Li^+ to move further. So Fcy(II) anions in the electrochromic layer played a role of counter electrode layer which were helpful for the

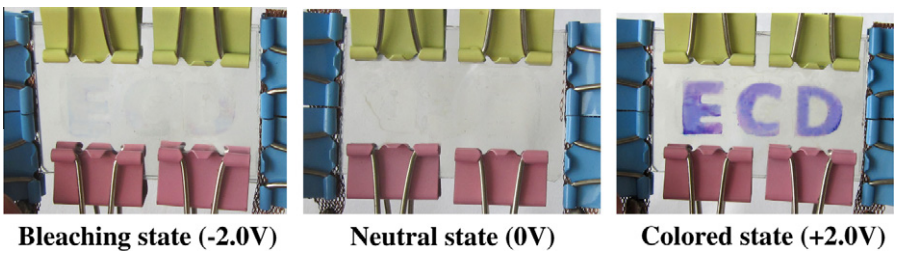

Fig. 4. The electrochromic behavior of characters in ECD (3 cm × 4 cm).

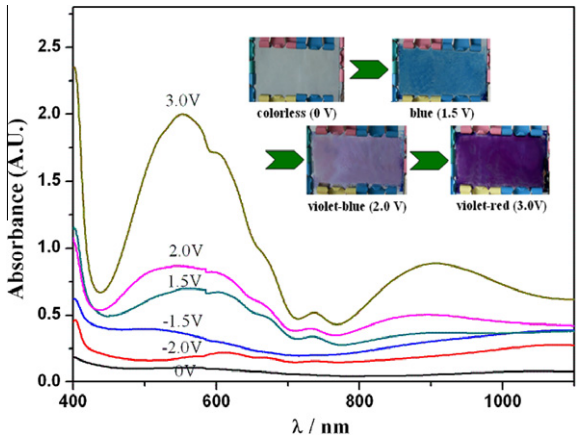

Fig. 5A. UV absorption spectra from −2.0 V to +3.0 V of ECD based on TBTB. Inset: Multichromic behavior of ECD at (a) 0 V (colorless); (b) +1.5 V (blue); (c) +2.0 V (violet–blue); (d) +3.0 V (violet–red).

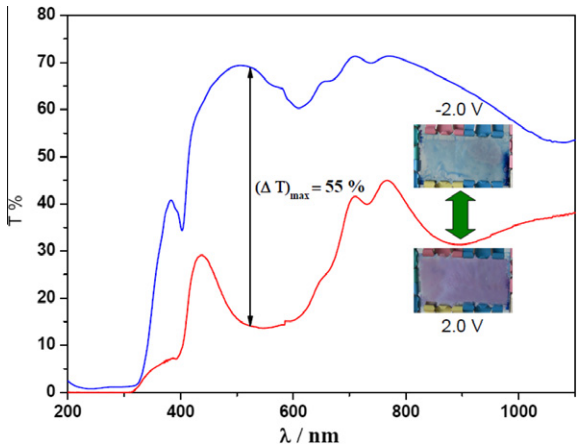

Fig. 5B. Transmission spectra of ECD based on TBTB at −2.0 V (transparent light blue) and +2.0 V (violet–blue).

storage of Li^+. While the reverse potential (the oxidation process of TBTB) was charged, Li^+ were ejected from the electrochromic layer and injected into the polymer gel electrolyte layer again.

It was reported that viologen dication and Fcy(II) could form viologen dication-Fcy(II) complex. And complex formation was an important aspect of viologen electrochemistry [13]. The viologen dication-Fcy(II) complex, as a popular choice of electron mediators [13,30–33] could improve the write–erase (coloring–bleaching) efficiency of the ECD. In this paper, TBTB monocation-Fcy(II) complex formation promoted the conversion among the four redox states (Scheme 2 and Fig. 3).

Because of the multi-electrochromic feature of the electrochromic material TBTB, it was necessary to choose an appropriate operating range of potential for the ECD from the viewpoint of complementary color-matching considerations. Furthermore, to avoid unnecessary formation of peroxide and other byproducts (which could decrease and even destroy the performance of the ECD) in the devices, two proper potential points (between −2.0 V and 2.0 V) were chosen to monitor and investigated the electrochromic behavior of characters in ECD. As shown in Fig. 4, when the potential of +2.0 V was charged to the ECD, the color of characters shifted from colorless to violet–blue. While the reverse potential (−2.0 V) was charged, the color of characters changed from violet–blue to almost transparent (light blue). The corresponding electrochromic mechanism (from violet to blue to light blue) was also discussed and given. In addition to the conversion

$$TBTB^{2+\cdot} \underset{-e}{\overset{+e^-}{\rightleftharpoons}} TBTB^{+\cdot} \quad (1)$$

when the potential was charged, the other possible process for the conversion of $TBTB^{2+\cdot}$ to $TBTB^{+\cdot}$ between −2.0 V and 2.0 V in ECD was given by the reaction with the oxidized or reduced form of the anodic compound [34].

$$TBTB^{2+\cdot} + Fcy(II)^{\cdot} \rightleftharpoons TBTB^{+\cdot} + Fcy(III) \quad (2)$$

Herein, in TBTB monocation-Fcy complex, as counter ions of TBTB monocation, the anodic compounds Fcy(II) and Fcy(III) promoted the conversion between $TBTB^{2+\cdot}$ and $TBTB^{+\cdot}$, which further improved the performance of color change between light blue and violet–blue.

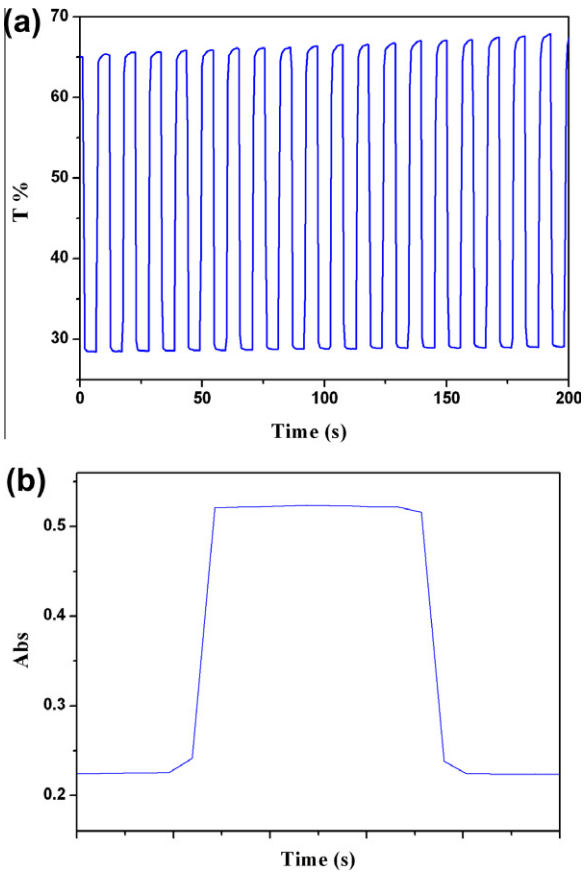

Fig. 6A. (a) Optical transmittance changes and (b) optical switching studies for ECD based on TBTB was monitored at 530 nm while the ECD was switched between −2.0 V and +2.0 V with a switch time of 5 s.

3.4. Spectroelectrochemistry study

Spectroelectrochemical study on ECD (3 cm × 4 cm) based on TBTB was carried out by varying the voltage between +3.0 V and −2.0 V. For monitoring the electrochromic process of the ECD, four potential points were chosen and corresponding electrochromic photos were taken and recorded. The ECD revealed multicolor electrochromism exhibiting several colored states between 0 V (colorless), +1.5 V (blue), +2.0 V (violet–blue) and +3.0 V (violet–red) (Fig. 5A). The optical contrast is given as the transmittance difference between the reduced and oxidized states and is reported as ΔT% which is monitored as a function of time at the specified wavelength. The ECD exhibited high contrast between +2.0 V and −2.0 V at 530 nm and the ΔT% was observed up to 55% (Fig. 5B).

3.5. Switching and stability

Switching and stability are two important properties of an electrochromic material and its corresponding ECD. In order to exactly investigate these properties, the ECD (3 cm × 4 cm) based on TBTB, fabricated as shown in Fig. 2, were switched under ambient conditions by repeated potential steps (500 electrochromic cycles) between the oxidized (−2.0 V) and reduction states (+2.0 V) with a residence time of 5 s. Quantification of switching time is performed by defining a change in 95% of the total absorbance span, since the naked eye can not distinguish the color change after this point.

In order to further testify the mechanism proposed in Section 3.3, as a reference, the ECD in which Fcy(II) was not contained were also assembled and monitored. As shown in Fig. 6A(a) and (b), the ECD which contained Fcy(II) had a switching time of ~0.3 s for coloring and a bleaching time of ~0.5 s at switching voltages of +2.0 V to −2.0 V and the optical switching was for the color change from violet to blue to transparent light blue. The difference in coloring and bleaching time of the devices is due to the different time constants for ejection/insertion of ions from/to electrochromic layer [35–36].

However, the reference ones (Fcy(II) was not added) showed an obvious degradation on ΔT% and longer switching time (Fig. 6B(c) and (d)). This result showed that TBTB monocation-Fcy(II) complex formation could remarkably improve the write–erase (coloring–bleaching) efficiency and stability of the ECD.

Furthermore, the optical contrast of the ECD, measured as ΔT%, ranged from 25% (after the 500th cycle) to 40% (the 1st cycle) at 530 nm between −2.0 V and 2.0 V (Fig. 7(a)). To compare with this result, cyclic voltammetry was employed to monitor the stability of the devices. Non-stop

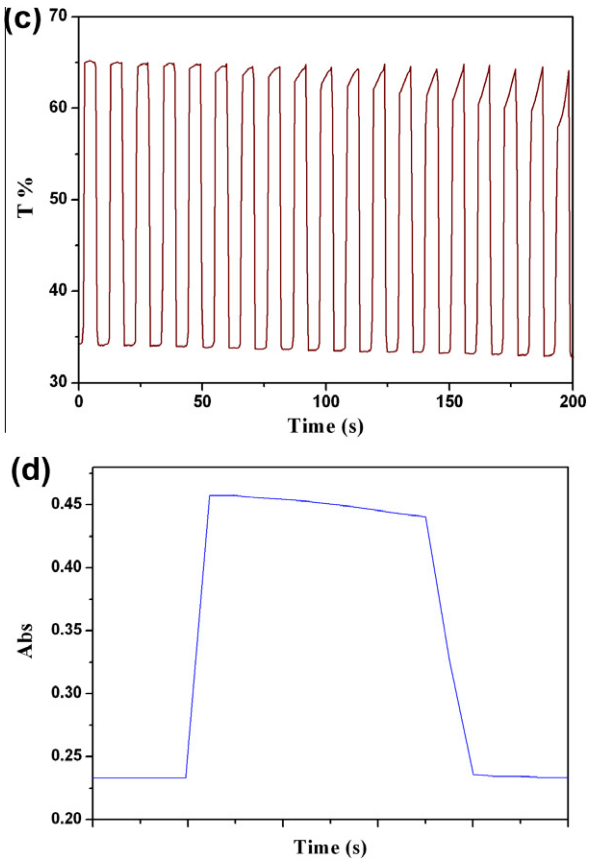

Fig. 6B. (c) Optical transmittance changes and (d) optical switching studies for the reference ECD (Fcy(II) was not added) based on TBTB was monitored at 530 nm while the ECD was switched between −2.0 V and +2.0 V with a switch time of 5 s.

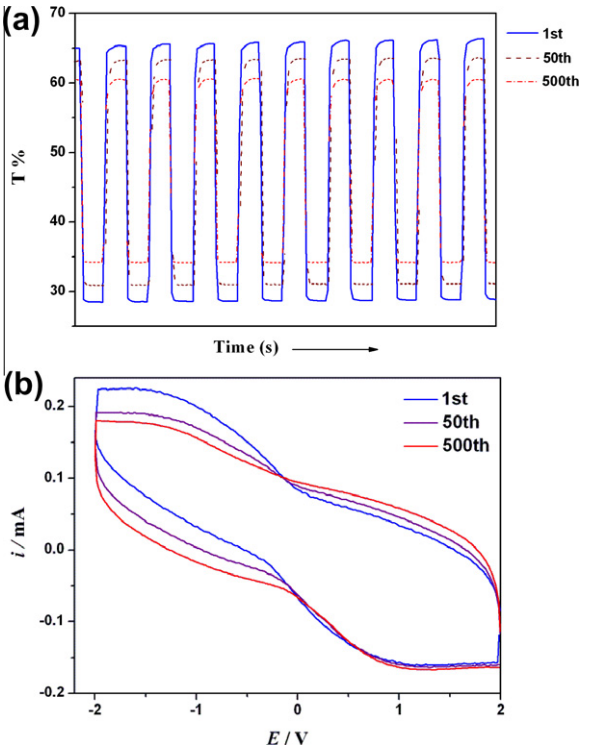

Fig. 7. (a) Optical switching changes for ECD at 530 nm between −2.0 V and +2.0 V with a switch time of 5 s and (b) Cyclic voltammogram of ECD as a function of repeated scans at 500 mV s^{-1}; 1st, the 50th and after the 500th cycle.

cycling between −2.0 V and +2.0 V for the ECD with 500 mV s^{-1} was performed to analyze the stability of devices. Fig. 7(b) presented the change in the anodic and cathodic peak currents as a function of the potential. The ECD showed only a slight decrease in electroactivity after 500 cycles. This result, which was consistent with the previous one, revealed that the ECD had reasonable environmental and redox stability. Therefore, the devices could be operated with applied potentials between −2.0 V and +2.0 V for future applications. Furthermore, the optical density (ΔOD) and coloration efficiency (CE) are two key parameters in order to compare electrochromic materials and devices. The ΔOD and CE between −2.0 V and +2.0 V at 530 nm of the ECD can be calculated using the following equations [37],

$$\Delta OD = \log \frac{T_{bleached}}{T_{colored}} \text{ and } CE \frac{\Delta OD}{Q_d}$$

where Q_d is the injected/ejected charge during a redox step of the ECD; $T_{colored}$ and $T_{bleached}$ are the transmittance in the colored and bleached states of the ECD, respectively. On the basis of these equations, the ΔOD and CE were calculated to be 0.39 cm^2 C^{-1} and 279 cm^2 C^{-1}, respectively.

4. Conclusions

In conclusion, a new kind of star-shaped monosubstitute 4,4′-bipyridine derivative TBTB was successfully synthesized and characterized. The environmentally friendly solid ECD based on TBTB were assembled and their corresponding electrochromic mechanism was investigated. As a popular choice of electron mediators, TBTB monocation-Fcy(II) complex played an important role in improving the electrochromic performance of the ECD. The solid ECD presented a stable as well as multicolor electrochromic change from blue to violet–blue and then to violet–red. Their environmental friendliness, easy preparation, abundant color, fairly fast electrochromic switching at low voltages, along with their stability under atmospheric conditions, made the ECD good candidates for electrochromic display.

Acknowledgements

All authors herein are grateful to the support from National Ministry of Science and Technology Innovation Fund for High-tech Small and Medium Enterprise Technology (No. 09C26215112399). And National Ministry of Human Resources and Social Security Start-up Support Projects for Students Returned to Business, Office of Human Resources and Social Security Issued 2009 (143).

References

[1] C.G. Granqvist, Nat. Mater 5 (2006) 89.
[2] I. Kaya, M. Yıldırım, A. Aydın, Org. Electron. 12 (2011) 210.
[3] R.J. Mortimer, A.L. Dyer, J.R. Reynolds, Displays 27 (2006) 2.
[4] D.R. Rosseinsky, R.J. Mortimer, Adv. Mater. 13 (2001) 783.
[5] R. Baetens, B.P. Jelle, A. Gustavsend, Sol. Energy Mater. Sol. Cells 94 (2010) 87.
[6] F.G.K. Baucke, Electrochromic mirrors with variable reflectance, Sol. Energy Mater. Sol. Cells 16 (1987) 67.
[7] G. Sonmez, Chem. Commun. 42 (2005) 5251.
[8] I.D. Brotherson, D.S.K. Mudigonda, J.M. Ocborn, J. Belk, et al., Electrochim. Acta 44 (1999) 2993.
[9] L. Michaelis, E.S. Hill, J. Gen. Physiol. 16 (1933) 859.
[10] C.J. Schoot, J.J. Ponjee, H.T. van Dam, R.A. van Doorn, P.J. Bolwijn, Appl. Phys. Lett. 23 (1973) 64.
[11] R.J. Jasinski, Soc 125 (1978) 1619.
[12] F. Campus, P. Bonhote, M. Gratzel, S. Heinen, L. Walder, Sol. Cells 56 (1999) 281.
[13] P.M.S. Monk, N.M. Hodgkinson, R.D. Partridge, Dyes Pigments 43 (1999) 241.
[14] M. Gratzel, Ultrafast color displays, Nature 409 (2001) 575.
[15] Y.C. Sung, M. Mamak, N. Coombs, N. Chopra, A.O. Geoffrey, Nano Lett. 4 (2004) 1231.
[16] W.S. David, R. Tseng, A.J. Peters, A.H. Flood, et al., Angew. Chem. Int. Ed. 43 (2004) 6486.
[17] J.H. Ryu, J.H. Lee, S.J. Han, K.D. Suh, Adv. Funct. Mater. 27 (2006) 1156.
[18] A. Michaelis, H. Berneth, D. Haarer, S. Kostromine, R. Neigl, R. Schmidt, Adv. Mater. 13 (2001) 1825.
[19] V. Jain, H. Yochum, H. Wang, R. Montazami, et al., Macromol. Chem. Phys. 209 (2008) 150.
[20] R.J. Mortimer, J.R. Reynolds, Displays 29 (2008) 424.
[21] V. Jain, M. Khiterer, R. Montazami, H.M. Yochum, K.J. Shea, J.R. Hefiin, Appl. Mater. Interfaces 1 (2009) 83.
[22] P.G. Cristina, M. Salsamendi, A. Vinuales, J.A. Pomposo, H.J. Grande, Sol. Energy Mater. Sol. Cells 93 (2009) 2093.
[23] W.J. Belcher, M. Fabre, T. Farhana, J.W. Steed, Org. Biomol. Chem. 4 (2006) 781.
[24] M. Felderhoff, S. Heinen, N. Molisho, S. Webersinn, L. Walder, Helv. Chim. Acta 83 (2000) 181.
[25] S.J. Dickson, E.V.B. Wallace, A.N. Swinburne, et al., New J. Chem. 32 (2008) 786.
[26] D.R. Rosseinsky, P.M.S. Monk, J. Appl. Electrochem. 24 (1994) 1213.
[27] A.N. Swinburne, M.J. Paterson, K.H. Fischer, et al., Chem. Eur. J. 16 (2010) 1480.
[28] D.J. Yang, X.K. Fu, Y.F. Gong, Acta Chim. Sinica 8 (2008) 975.
[29] H.W. Heuer, R. Wehrmann, S. Kirchmeyer, Macromol. Rapid. Commun. 12 (2002) 89.
[30] P.M.S. Monk, J. Electroanal. Chem. 432 (1997) 175.
[31] A. Yasuda, H. Mori, Y. Takehana, A. Ohkoshi, J. Appl. Electrochem. 14 (1984) 323.
[32] A. Nakahara, J.H. Wang, J. Phys. Chem. 67 (1963) 496.
[33] A.S.N. Murthy, A.P. Bhardwaj, Spectrochim. Acta 38 (1982) 207.
[34] G. Chidichimo, M.D. Benedittis, et al., Chem. Mater. 19 (2007) 353.
[35] A.P. Baioni, M. Vidotti, P.A. Fiorito, E.A. Ponzio, S.I.C. Torresi, Langmuir 23 (2007) 6796.
[36] V. Jain, H. Yochum, et al., Chem. Phys. 209 (2008) 150.
[37] G. Wang, X.K. Fu, J. Huang, L. Wu, Q.L. Du, Electrochim. Acta 55 (2010) 6933.

2. Experimental

The photovoltaic device has a structure of ITO/nc-TiO_2/RR-P3HT: PCBM/V_2O_5/Ag/V_2O_5, as shown schematically in Fig. 1. The ITO-conducting glass substrate (a sheet resistance of 15Ω/□ was precleaned by acetone, ethanol, and de-ionized water, respectively, for 15 min. Anatase TiO_2 thin films were prepared as described in our previous papers [18,19]. The thickness of TiO_2 is 25 nm. P3HT (Lumtec Corp., used as received) was dissolved in 1,2-dichlorobenzene to produce 18 mg/ml solution, followed by blending with PCBM (Lumtec Corp, used as received) in 1:1 weight ratio [20]. The blend was stirred for 72 h in the air before spin coating on top of TiO_2 film surface. Then the samples were baked in low vacuum (vacuum oven) at ~160°C or 20 min. The typical film thickness of P3HT: PCBM is about 200 nm. Finally 10 nm V_2O_5, 13 nm Ag, and x (x = 20, 40, 60, 80 nm) V_2O_5 were thermally evaporated in sequence under a high vacuum (5×10^{-4} Pa) without disrupting the vacuum. The deposition rate was about 0.02 nm/s, which was monitored with a quartz-oscillating thickness monitor (ULVAC, CRTM-9000). The active area of the device was about 6.4 mm^2.

Current density–voltage (J–V) characteristics were measured with a computer-programmed Keithley 2400 source/meter under AM1.5G solar illuminations with an Oriel 300 W solar simulator. The intensity of the solar simulator was 100 mW/cm^2. The light intensity was measured with a photometer (International light, IL1400) which was corrected by a standard silicon solar cell. The transmission spectra and the reflection spectra were measured by means of ultraviolet/visible spectrometer (UV 1700, Shimadzu).

3. Results and discussion

Fig. 2a shows the J–V characteristics of semitransparent inverted polymer solar cells with outer 40 nm (device II) and without V_2O_5 (device I) under AM1.5G illumination of 100 mW/cm^2. The incidence light irradiate from the ITO side (Bottom). The detailed results are given in Table 1. Device I shows short circuit current density (J_{sc}) of

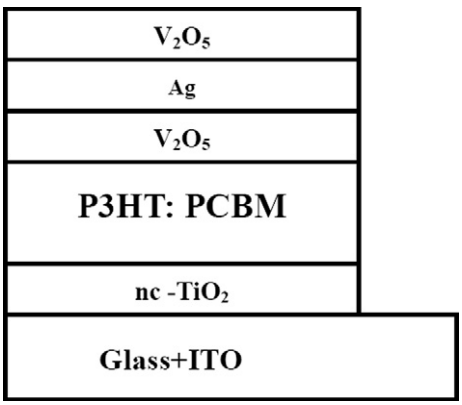

Fig. 1. The schematic structure drawing of the semitransparent inverted polymer solar cells.

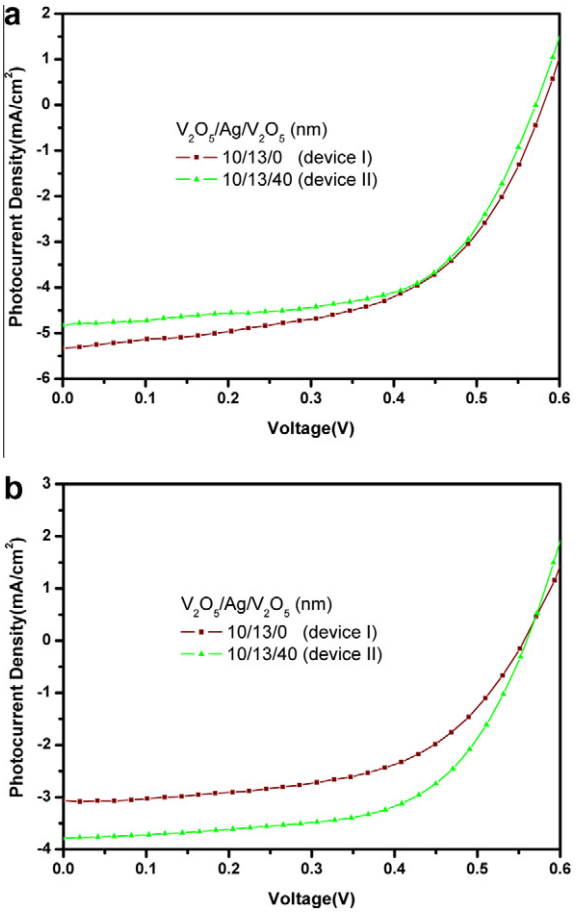

Fig. 2. The J–V characteristics of device ITO/nc-TiO_2/P3HT: PCBM/V_2O_5 (10 nm)/Ag (13 nm)/V_2O_5 (x = 0, 40 nm) when illuminated from (a) ITO side and (b) V_2O_5/Ag/V_2O_5 side.

Table 1
Characteristic data of semitransparent inverted polymer solar cells with different thickness of the V_2O_5 capping layer illuminated from ITO (bottom) and V_2O_5/Ag/V_2O_5 (top) side.

Device (nm)	Illumination	J_{sc} (mA/cm^2)	V_{oc} (V)	*FF* (%)	*PCE* (%)
20	Bottom	5.09	0.585	60.3	1.79
20	Top	3.44	0.561	60.2	1.16
40	Bottom	4.83	0.581	60.6	1.70
40	Top	3.79	0.565	60.6	1.30
60	Bottom	5.36	0.592	59.9	1.91
60	Top	2.99	0.553	59.8	0.99
80	Bottom	5.96	0.594	59.8	2.12
80	Top	2.67	0.551	59.8	0.88

5.31 mA/cm^2, open circuit voltage (V_{oc}) of 0.590 V, fill factor (*FF*) of 0.540, and power conversion efficiency (*PCE*) of 1.69. Device Π shows J_{sc} of 4.83 mA/cm^2, V_{oc} of 0.581 V, *FF* of 0.606, *PCE* of 1.70. It can be seen that the *PCE* of device I is almost same as that of device II. The J_{sc} of device Π decreases, but *FF* increases dramatically compared to that of device I. We attribute the decrease of J_{sc} to lower reflectance of V_2O_5/Ag/V_2O_5 from 400 to 650 nm, which is shown in Fig. 3b. It is evident that the resistivity of the thin

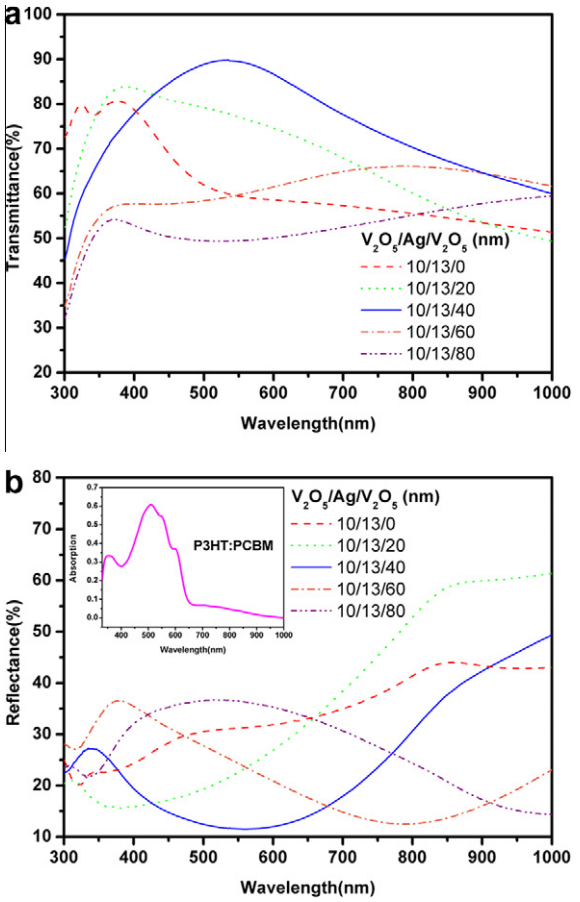

Fig. 3. (a) The transmittance spectra of the transparent electrode V_2O_5 (10 nm)/Ag (13 nm)/V_2O_5 (x = 0, 20, 40, 60, 80 nm) (b) the reflectance spectra of the transparent electrode V_2O_5 (10 nm)/Ag (13 nm)/V_2O_5 (x = 0, 20, 40, 60, 80 nm).

metal film (13 nm Ag here) is higher than that of the bulk metal due to the scattering of the electrons from the surface of the discontinuous film. The outer V_2O_5 decreases the series resistance (R_{sc}), which is defined by the slope of the J–V curve at J = 0 mA/cm^2. The series resistance is estimated to be 33.6Ω for device I and 23.3Ω for device Π. The decrease of R_{sc} results in the increase of *FF* from 0.540 to 0.606. Fig. 2b shows the J–V characteristics of semitransparent inverted polymer solar cells (device I and Π) under AM1.5G illumination of 100 mW/cm^2 when illuminated from V_2O_5/Ag/V_2O_5 side (Bottom). Here, the mixture of P3HT and PCBM, which has main absorption spectrum from 400 to 650 nm, is chosen as active layers. The photocurrent density is in direct proportion to light absorption of the active layer. Since device Π has higher transmittance from 400 to 650 nm, as shown in Fig. 3a, it has bigger J_{sc} than device I.

Fig. 3a shows the transmittance spectra of the V_2O_5/Ag/V_2O_5 from 300 to 1000 nm. It can be seen that the transmittance becomes week with the increase of wavelength, and high transmittance of 80% appears in short wavelength range when the thickness of V_2O_5 is zero. When introducing outer V_2O_5 (capping layer), the transmittance is changed dramatically. With the increase of the thickness of V_2O_5 capping layer, the transmittance peaks are redshifted. The maximum transmittance of 90%, which appears from 400 to 700 nm, is obtained when the thickness of V_2O_5 is 40 nm. To continue increasing the thickness of V_2O_5, the transmittance gradually descends. It is evident that transmission can vary with the thickness of the V_2O_5 capping layer.

Fig. 3b shows the reflectance spectra of the V_2O_5/Ag/V_2O_5 from 300 to 1000 nm. Since the absorption is little, the reflectance spectrum is nearly one to one complement with the transmittance spectrum. It can be seen that reflectance peaks are redshifted gradually and would match better to the absorption spectra of the active layer (400–650 nm) when the thickness of the V_2O_5 capping layer increases.

Fig. 4a shows the the J–V characteristics of semitransparent inverted polymer solar cells under AM1.5G illumination of 100 mW/cm^2 when illuminated from ITO side (Bottom). The detailed results are given in Table 1. When the thickness of V_2O_5 is 40 nm, the J_{sc} is 4.83 mA/cm^2, the V_{oc} is 0.581 V, the *FF* is 60.6%, and the PCE is 1.70%. When

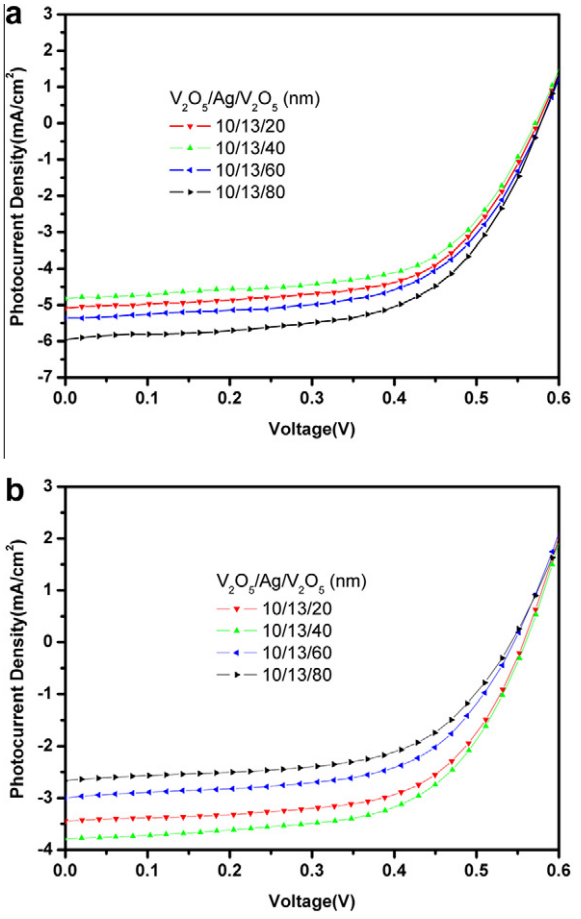

Fig. 4. The J–V characteristics of device ITO/nc-TiO_2/P3HT: PCBM/V_2O_5 (10 nm)/Ag (13 nm)/V_2O_5 (x = 20, 40, 60, 80 nm) dependent on the thickness of the V_2O_5 capping layer when illuminated from (a) ITO side and (b) from V_2O_5/Ag/V_2O_5 side.

the thickness of V_2O_5 is 80 nm, the photovoltaic device has a J_{sc} of 5.96 mA/cm^2, V_{oc} of 0.594 V, *FF* of 59.8%, and *PCE* of 2.12%. The J_{sc} of the device with 40 nm V_2O_5 is the smallest; and the J_{sc} of the device with 80 nm V_2O_5 is the biggest. It is known that the reflectance of the top electrode plays an important role in trapping light for the active layer to reabsorb. The reflectance of V_2O_5/Ag/V_2O_5 (80 nm) from 400 to 650 nm is the strongest, but the reflectance of V_2O_5/Ag/V_2O_5 (40 nm) is poorest in Fig. 3b.

Fig. 4b shows the the *J–V* characteristics of semitransparent inverted polymer solar cells under AM1.5G illumination of 100 mW/cm^2 when illuminated from V_2O_5/Ag/V_2O_5 side (Top). The detailed results are given in Table 1. When the thickness of V_2O_5 is 40 nm, the J_{sc} is 3.79 mA/cm^2, the V_{oc} is 0.565 V, the *FF* is 60.6%, and the PCE is 1.30%. When the thickness of V_2O_5 is 80 nm, the photovoltaic device has a J_{sc} of 2.67 mA/cm^2, V_{oc} of 0.551 V, *FF* of 59.8%, and *PCE* of 0.88%. The J_{sc} of the device with 40 nm V_2O_5 is the biggest, and that for the device with 80 nm V_2O_5 is the smallest. This is because the transmittance of V_2O_5/Ag/V_2O_5 (40 nm) is the highest, and the absorption of active layer material is directly proportional to the transmittance of the incidence electrode. When illuminated from V_2O_5/Ag/V_2O_5 side, the V_{oc} becomes smaller compared with that illuminated from the ITO side. The dependence of the V_{oc} and the photocurrent (I_{ph}) can be generally expressed as follows [21]:

$$V_{oc} = \frac{kT}{q} Log\left(\frac{I_{ph}}{I_s} + 1\right) \quad (1)$$

Where I_s is reverse saturation current, k is Boltzman constant, T is the temperature, and q is charge. Under Eq. (1), the V_{oc} is directly proportional to I_{ph}. The I_{ph} from ITO side is much bigger than that from V_2O_5/Ag/V_2O_5 side, which is shown in Table 1.

4. Conclusion

In summary, we present efficient semi-transparent inverted polymer solar cells with highly transparent V_2O_5/Ag/V_2O_5 anodes. The inner V_2O_5 layer was introduced as a buffer layer to improve holes collection, while the outer V_2O_5 served as a light coupling layer to enhance optical transmittance. The incident light transmittance changed with the thickness of V_2O_5.When the thickness of V_2O_5 is 40 nm, the highest transmittance is obtained. The reflectance peaks are redshifted gradually and would match better to the absorption spectra of the P3HT: PCBM layer when the thickness of the V_2O_5 capping layer increases.

Acknowledgements

The authors are grateful to Major Project of Science and Technology Development Plan of Jilin Provincial Science and Technology Department (Grant Nos. 20070402, 20080330, 20100103), the China 863 Program (Grant No. 2007AA03Z406, 2009AA032402), Scientific Frontier and Interdiscipline Innovative Projects of Jilin University (Grant Nos. 200903087), National Natural Science Foundation of China (Grant Nos. 60977031, 50977038, 61007022, 61077046, 61006013) and Doctoral Found of Ministry of Education of China Grant Nos. 20090061110040, 20100061120045 for the support to the work.

References

[1] M. Helgesen, R. Søndergaard, F.C. Krebs, J. Mater. Chem. 20 (2010) 36.
[2] F.C. Krebs, Sol. Energy Mater. Sol. Cells 93 (2009) 394.
[3] C. Deibel, V. Dyakonov, Rep. Prog. Phys. 73 (2010) 096401.
[4] R. Po, M. Maggini, N. Camaioni, J. Phys. Chem. C. 114 (2010) 695.
[5] F.C. Krebs, T.D. Nielsen, J. Fyenbo, M. Wadstrøm, M.S. Pedersen, Energy Environ. Sci. 3 (2010) 512.
[6] F.C. Krebs, J. Fyenbo, M. Jørgensen, J. Mater. Chem. 20 (2010) 8994.
[7] F.C. Krebs, T. Tromholt, M. Jørgensen, Nanoscale 2 (2010) 873.
[8] S.H. Park, A. Roy, S. Beaupré, S. Cho, N. Coates, J.S. Moon, D. Moses, M. Leclerc, K. Lee, A.J. Heeger, Nat. Photonics 3 (2009) 297.
[9] H.Y. Chen, J. Hou, S. Zhang, Y. Liang, G. Yang, Y. Yang, L. Yu, Y. Wu, G. Li, Nat. Photonics 3 (2009) 649.
[10] P. Peumans, A. Yakimov, S.R. Forrest, J. Appl. Phys. 93 (2003) 3693.
[11] G. Dennler, M. C. Scharber, C. J. Brabec, Adv. Mater. 21 (2009) 1323.
[12] T. Ameri, G. Dennler, C. Lungenschmied, C. J. Brabec, Energy Environ. Sci. 2 (2009) 347.
[13] J. Gilot, M.M. Wienk, R.A.J. Janssen, Appl. Phys. Lett. 90 (2007) 143512.
[14] F.C. Chen, J.L. Wu, K.H. Hsieh, W.C. Chen, S.W. Lee, Org. Electron. 9 (2008) 1132.
[15] G.M. Ng, E.L. Kietzke, T. Kietzke, L.W. Tan, P.K. Liew, F.R. Zhu, Appl. Phys. Lett. 90 (2007) 103505.
[16] V. Shrotriya, G. Li, Y. Yao, C. Chu, Y. Yang, Appl. Phys. Lett. 88 (2006) 073508.
[17] K. Norrman, M.V. Madsen, S.A. Gevorgyan, F.C. Krebs, J. Am. Chem. Soc. 132 (2010) 16883.
[18] C. Tao, S.P. Ruan, X.D. Zhang, G.H. Xie, L. Shen, X.Z. Kong, W. Dong, C.X. Liu, W.Y. Chen, Appl. Phys. Lett. 93 (2008) 193307.
[19] L. Shen, G.H. Zhu, W.B. Guo, C. Tao, X.D. Zhang, C.X. Liu, W.Y. Chen, S.P. Ruan, Z.C. Zhong, Appl. Phys. Lett. 92 (2008) 073307.
[20] V. Shrotriya, G. Li, Y. Yao, T. Moriarty, K. Emery, Y. Yang, Adv. Funct. Mater. 16 (2006) 2016.
[21] A. Moliton, J.M. Nunzi, Polym. Int. 55 (2006) 583.

"any design or process improvements specifically directed at a reduction of the contact resistance in organic TFTs should be regarded as equally important to improving the performance of organic electronic devices as improvements directed at increasing the intrinsic carrier mobility of the organic semiconductor material" [16].

So far, gold has proven to be the most successful material for the fabrication of source and drain (S/D) electrodes of bottom gate (BG) bottom contact (BC) transistors (Fig. 1a) used as building blocks of high speed organic circuits. This can be attributed to its manifold benefits such as: (i) high chemical inertness (no spontaneous oxidation in air) allowing easy cleaning after photolithographic patterning (for example by solvents, strong chemical oxidizers or ultraviolet–ozone (UV/O_3)), (ii) simple deposition by evaporation or sputtering, (iii) good electrical conductivity, and (iv) the ability to fix self-assembled monolayers (SAMs) that improves charge injection into the organic semiconductor, enabling ohmic contacts, an asset for successful transistor downscaling. All these properties together lead to well-behaved pentacene transistors based on gold S/D BC exhibiting low contact resistance and high extrinsic hole saturation mobilities (μ_{sat}) of up to 0.5–1 $cm^2/(V\,s)$ even for short channel lengths ($L \leqslant 10\,\mu m$) [17]. Further on, gold has proven to be the material of choice to successfully scale-down transistor dimensions, thus boosting circuit speeds. Current high-speed state-of-the art organic circuits such as full-wave rectifier circuits operating at 13.56 MHz [18] and 64-bit and 128-bit plastic transponder chips for RFID-tags [6] are based on pentacene transistors with gold S/D BCs. On the other hand, the high cost of the gold layer (typical thickness of around 30 nm [8]) precludes commercialization in low-cost applications such as RFID-tags. Indeed, for a 1 cm^2 area RFID-tag [6] the cost of such a gold layer (based on the current gold price of 44 USD per gram) would already reach 25% of the target price of 0.01 USD, to which additional costs of the antenna, the substrate, the dielectric, the organic semiconductor, solvents and chemicals, yields below 100%, and the processing have to be added.

During the past years a huge number of alternative BC materials for pentacene transistors have been investigated, such as metals [19–24], metal oxides [22,24], ionic salts [25–27], carbon (including carbon nanotubes and graphene [28–35]) and conductive polymers [36–39]. For some of the non metallic materials, pentacene BG BC transistors with mobilities in the range of 0.1–1 $cm^2/(V\,s)$ could be achieved with *large* channel lengths [24–26,28,29,32,37,39]. However, this does not imply that such high carrier mobility could be reached for similar transistors with short channel lengths, a requirement for high speed organic circuits. Academic research has proven that mobilities within the 10^{-2} $cm^2/(V\,s)$ range can be reached with organic semiconductors and metallic or conductive polymer based BCs of sub-micrometer channel length [36,40–42], where the channels were defined by innovative processes such as nanoscratching and self-aligned printing. Although such developments are highly valuable for future generations of organic electronic circuits, additional research will likely be required for reaching sufficient high yield of operational transistors and low spread of their electrical parameters required for circuits involving several hundred organic transistors [6], which can currently be obtained with photolithography based patterning of S/D BCs.

In this paper, we propose a different approach towards cost-effective while high performing S/D electrodes. These consist of metallic bilayers: a thick layer of an inexpensive first metal, Ti or Al, directly deposited onto the substrate, assuring good adhesion and high electrical conductivity, and a second, thin layer – deposited above the first one – of a noble metal, Au or Pd, providing good charge injection into pentacene. Using these metallic bilayer structures, we demonstrate the feasibility of low cost, short channel ($L \leqslant 5\,\mu m$) BG BC pentacene transistors, yielding performances that favorably compare to equivalent reference transistors based on 30 nm thick Au-only S/D electrodes, and this for metal costs down to 5% of those of the traditional route.

2. Experimental

Transistors were processed on a highly doped Si wafer (200 mm diameter, IMEC production line) with aluminum backside, acting respectively as the substrate and the gate electrode. A uniform, about 140 nm thick thermally grown SiO_2 provides the gate dielectric; the exact thickness of which is evaluated by ellipsometry. Source and drain electrodes made with various metallizations (see below) were patterned by double layer photoresist (AZ6612 and LOR™ 1A (MicroChem)) lithography and lift-off. The use of a double layer resist permits a negative slope that ensures the absence of spikes after resist lift-off. Subsequently, the substrates were thoroughly cleaned by ultrasonication in acetone (10 min.) and isopropylalcohol (10 min), blown dry with nitrogen, and cleaned by a UV/O_3 step (15 min). A self-assembled monolayer of pentafluorobenzenethiol (PFBT) was then deposited from a 5 mM solution in ethanol

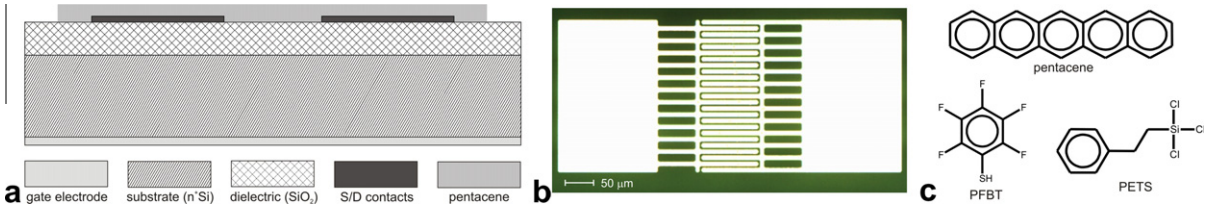

Fig. 1. (a) Schematic view of a BG BC pentacene transistor (optional surface modification layer on the dielectric and the S/D bottom contacts are omitted for clarity); (b) Optical micrograph of a bottom S/D contacts (W/L = 2500/5 µm/µm) on SiO_2; and (c) Chemical structure of pentacene, PFBT and PETS.

(30 min) onto the Au containing S/D contacts; this step was omitted for Pd metallizations. Then a silane based self-assembled monolayer was deposited onto the SiO_2 dielectric by exposure of the substrates to vapors of phenylethyltrichlorosilane (PETS, 60 °C, reduced pressure) during 30 min. Pentacene, purified by gradient sublimation, was evaporated onto the substrates in an ultrahigh vacuum chamber (10^{-8} Torr) at 0.25 Å/s, while the substrate was kept at 68 °C. After pentacene evaporation, the samples were directly transferred from the vacuum chamber into a nitrogen filled glovebox ($[O_2] < 1$ ppm, $[H_2O] < 1$ ppm), where transistors were measured using an Agilent 4156C parameter analyzer. All indicated mobilities were evaluated in saturation mode. Transistor structures had nominal channel width/length (W/L) of 2500 μm/5 μm. Exact channel lengths (typically around 3.7–4.5 μm), measured by optical microscopy (Olympus AX70) were used for the computation of the saturation mobility and are reported in the corresponding figures. BC substrates were characterized by scanning electron microscopy (SEM, Philips XL30) and the morphology of the organic polycrystalline film by atomic force microscopy (AFM, Agilent 5100), operated in tapping mode.

3. Results and discussion

In order to replace the 30 nm thick (sputtered) Au layer used in our standard process BCs, we investigated alternative BC metallizations consisting of thin (5 nm) Au and Pd layers formed on a thicker (25 nm) evaporated Al layer. Although preliminary experiments revealed that Ti (25 nm) is also suitable for this lower layer, the entire study reported within this paper is performed with Al. Indeed, this metal – in addition to lower cost – has a significant lower electrical resistivity as compared to that of Ti (Table 1) [43].

A simple calculation, based on resistivity values indicated in Table 1 and the formula of two resistors connected in parallel, reveals that the resistance of the BC consisting of 5 nm Au on 25 nm Al, and 5 nm Pd on 25 nm Al, are respectively only 15% and 35% higher to that of a 30 nm thick pure Au layer. This slight increase in resistivity is fully acceptable for the envisaged circuit applications.

Since Al adheres very well to SiO_2 it was also possible to investigate a thin *evaporated* Au layer on top of Al, in addition to the thin *sputtered* Au layer on Al. As will be shown later, this processing detail leads to a significant difference in electrical performance of the corresponding pentacene transistors.

Table 1
Electrical resistivity of metals at 20 °C. The value for Cu is given for comparison.

Metal (Symbol)	Electrical resistivity μΩ cm at 20 °C [43]
Gold (Au)	2.24
Palladium (Pd)	10.54
Aluminum (Al)	2.6548
Titanium (Ti)	42.0
Copper (Cu)	1.678

3.1. Characterization of bottom contacts with different metallizations schemes

After the patterning of the BCs, it is important to ascertain that transistors BCs and channels are free of contaminants (as for example remaining photoresist). Indeed, the presence of insulating particles could hinder current flow into the channel and/or act as injection barrier at the BC/semiconductor interface. For this reason substrates were investigated by SEM directly after the UV/O_3 cleaning step that follows the BC layer patterning. Corresponding micrographs, depicted in Fig. 2, confirm the absence of photoresist for all different BC metallizations. In addition, we observe a difference between 5 nm thick sputtered Au and 5 nm thick evaporated Au, both on 25 nm thick evaporated Al (Fig. 2b and c). In the case of evaporated Au (Fig. 2c) the border between the metal and the dielectric is sharp – similar to the case of evaporated Pd (Fig. 2d) – whereas in the case of sputtered Au on Al, an additional intermediate zone is present, as depicted in the inset of Fig. 2b. This discrepancy is related to differences in mass transport in the two considered metallization methods: lower pressures in evaporation ensure a straight ballistic transport (Fig. 3a), whereas sputtering occurs at higher pressure, resulting in a more random angled delivery of the metal (Fig. 3b). As a consequence, when using a negative resist for lift-off, sputtered Au provides a good step coverage on the thick evaporated Al, resulting in a slightly larger finger width of the S/D contacts (Fig. 3c).

3.2. Pentacene growth on bottom contact transistor substrates with different metallization schemes

Morphology of the polycrystalline pentacene layer (30 nm thickness) on BC structures after PFBT (only Au based substrates) and PETS treatment (all substrates) is investigated by AFM. Being interested in injection properties of the BCs, this investigation focuses on the contact/channel region. The left column on Fig. 4 shows AFM topographical images of transistors with a 5 μm long channel (nominal length). The right column displays a closer view of the contact/channel area (right). As expected, on the dielectric (PETS treated SiO_2) in the channel, pentacene growth is independent of the BC metallization scheme (Fig. 4a–d). In this region, pentacene forms large dendritic and terraced grains, with here and there, higher 3-dimensionnal grains, a growth that is typical for this type of substrate and processing conditions. When growing pentacene on thiol-treated sputtered Au, no morphological difference can be observed between the thick 30 nm Au (Fig. 4a) and the bilayer 25 nm Al/5 nm Au substrates (Fig. 4b). On the other hand, pentacene growth on top of S/D contacts appears to be influenced by the upper metallization layer. Firstly, pentacene on thiol treated Au reveals larger grains and rougher layers on the sputtered (Fig. 4b) than on the evaporated metal (Fig. 4c). This is related to a smoothness difference between evaporated and sputtered Au. Secondly, pentacene on evaporated Pd (Fig. 4d) surprisingly shows small dendritic grains, a growth that is similar to that of pentacene in the channel, and this *without* any thiol treatment of the Pd.

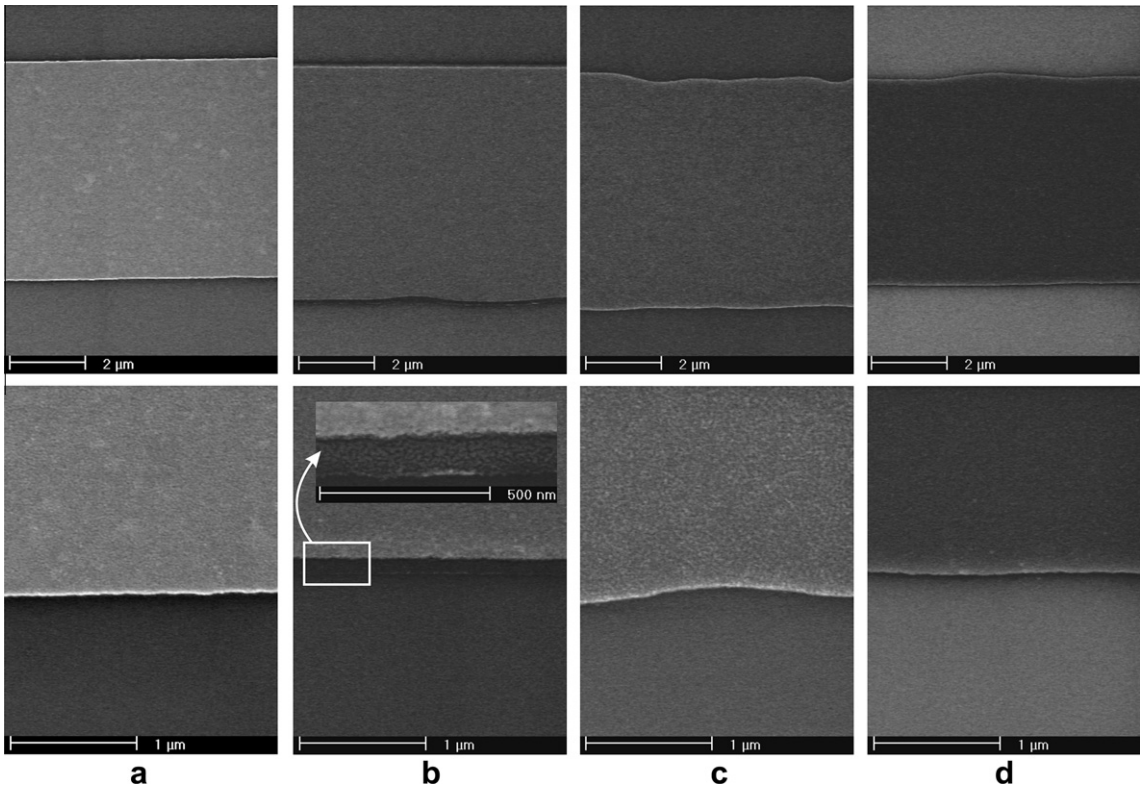

Fig. 2. Scanning electron micrographs (top view) of BC metallizations on SiO_2: (a) 30 nm sputtered Au, (b) 5 nm sputtered Au on 25 nm evaporated Al, (c) 5 nm evaporated Au on 25 nm evaporated Al, and (d) 5 nm evaporated Pd on 25 nm evaporated Al.

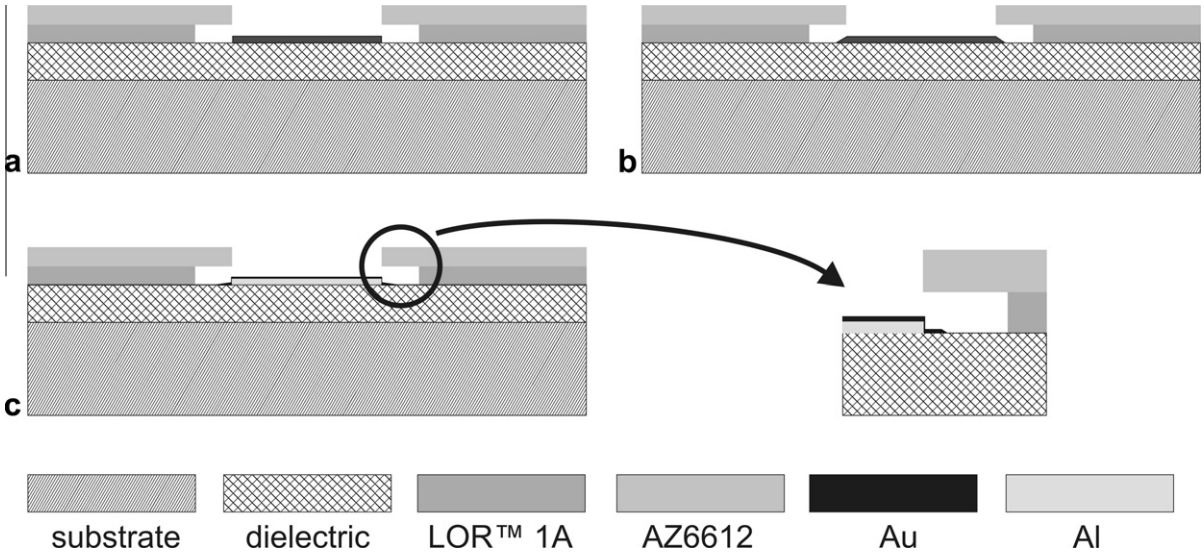

Fig. 3. Schematic representation of the BC metallization process: (a) evaporated metal (Au), (b) sputtered metal (Au), (c) thin layer of sputtered metal (Au) on top of a thicker layer evaporated metal (Al).

In the closer view of the contact/channel interface (right column of Fig. 4), it appears that, in all cases, pentacene two dimensional grains nucleate along the metal wall and subsequently grow inside the channel by step flow. This leaves a pattern of superimposed terraces all stemming from the same nucleation point and propagating inside the channel. In the case of the thin sputtered Au layer on Al, the small grained morphology that is typical of pentacene growth on top of thiol treated Au slightly extends to the right of the thick contact region (Fig. 4b,

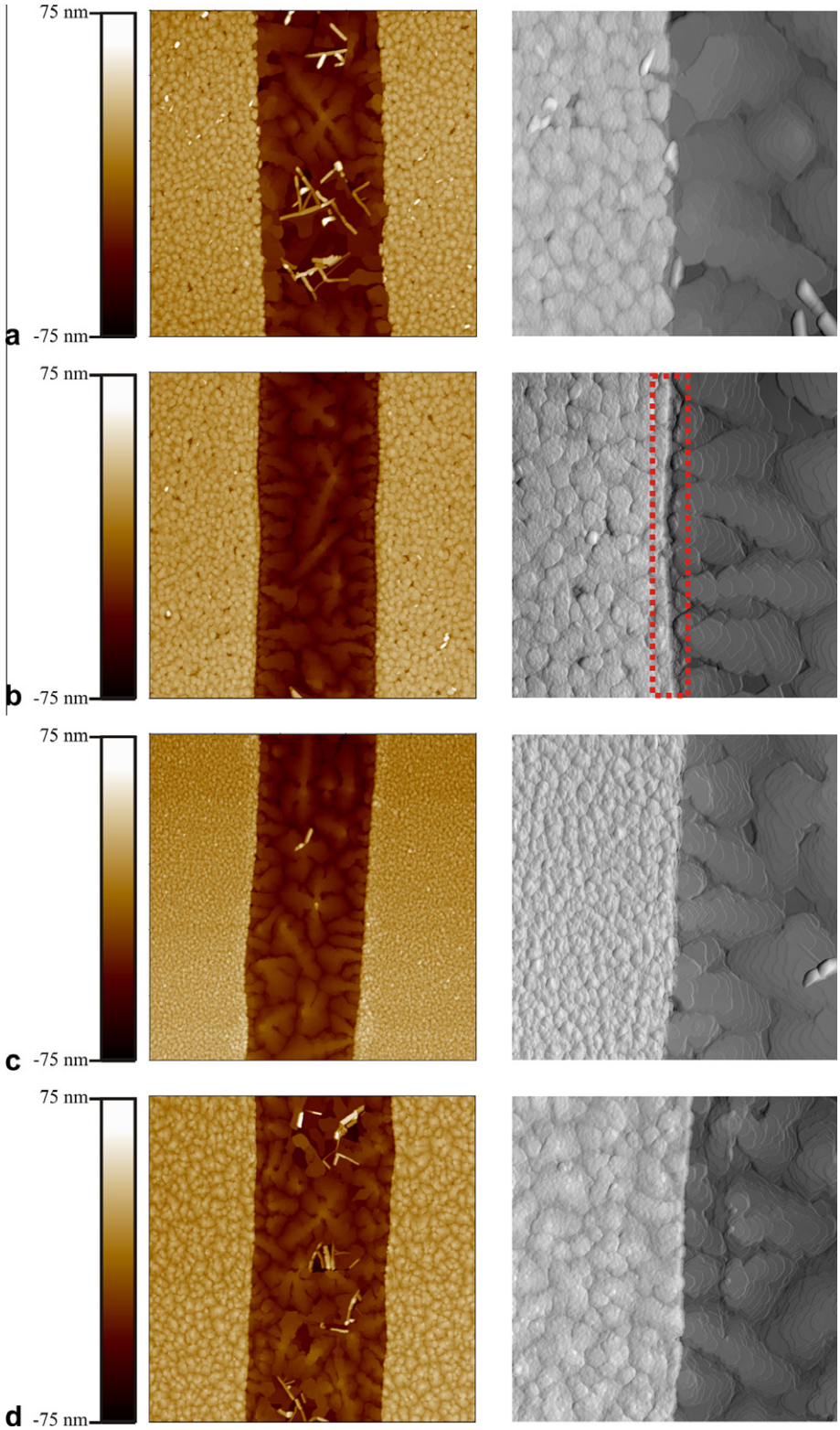

Fig. 4. AFM pictures of the source/drain BCs and the channel region for (a) 30 nm Au (sputtered) BC, (b) 5 nm Au sputtered onto 25 nm Al, (c) 5 nm Au evaporated onto 25 nm Al, (d) 5 nm Pd evaporated onto 25 nm Al. SiO_2 dielectric was treated with a silane (PETS) and Au containing substrates with a thiol (PFBT). Left pictures: 10 μm by 10 μm scan of the channel between source and drain contacts; right pictures with shaded contrast enhancement: 3 μm by 3 μm scan of the contact/channel interface.

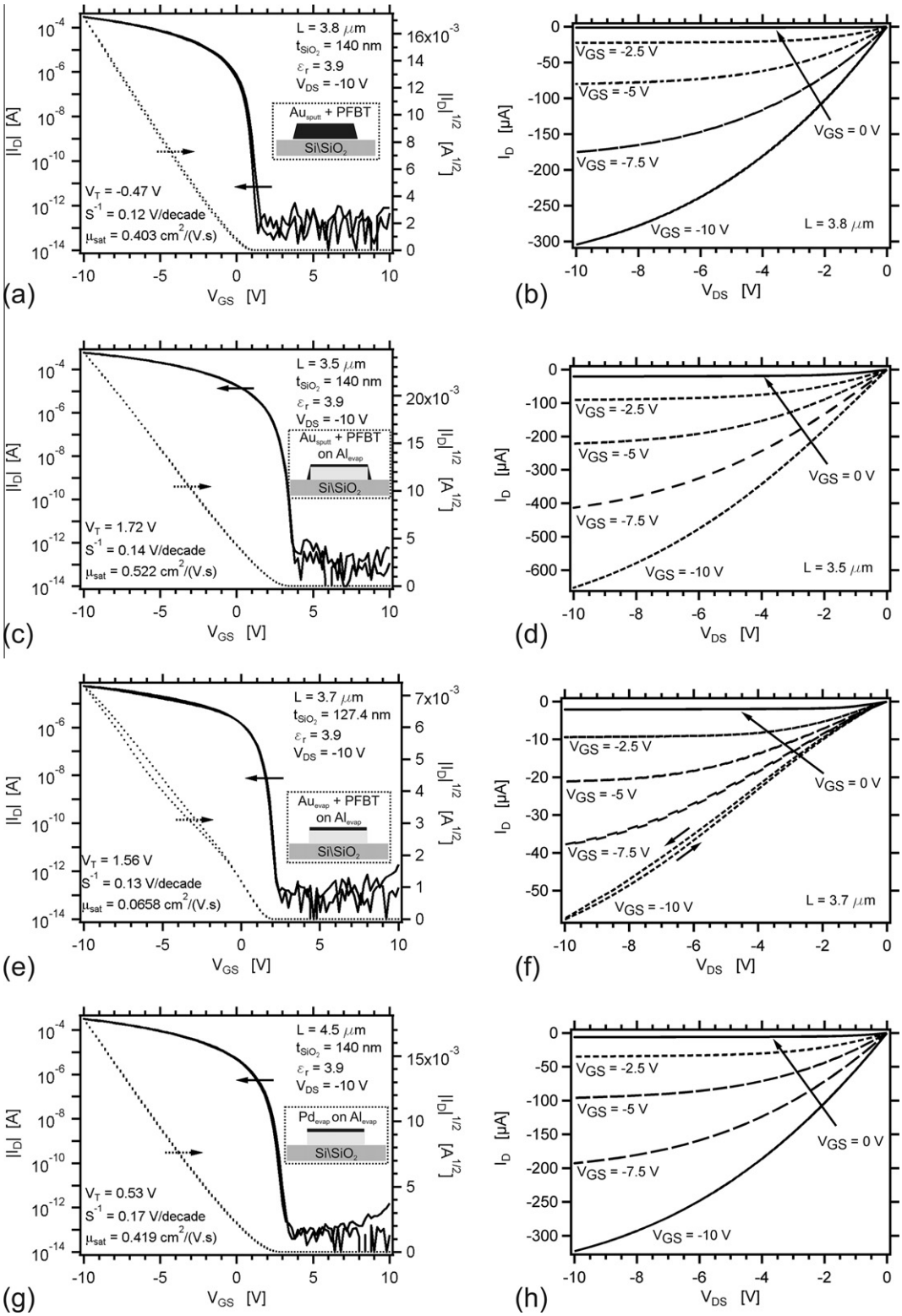

Fig. 5. Electrical transfer (a,c,e, and g) and output (b,d,f, and h) characteristics of pentacene transistors (nominal W/L = 2500/5 μm/μm) with various BC metallization schemes: (a,b) 30 nm sputtered Au, (c and d) 5 nm sputtered Au on 25 nm evaporated Al, (e and f) 5 nm evaporated Au on 25 nm evaporated Al, and (g and h) 5 nm evaporated Pd on 25 nm evaporated Al (L: measured channel length, t_{SiO2}: thickness of SiO_2 dielectric, ε_R: dielectric constant of the gate dielectric, V_T: threshold voltage, S^{-1}: subthreshold slope). SiO_2 dielectric was treated with a silane (PETS) and Au containing substrates with a thiol (PFBT).

dashed rectangle). This confirms the earlier observation that the thin sputtered Au layer extends beyond the width of the evaporated Al (inset in Fig. 2b).

Previously reported SEM micrographs published by Bock et al. [20] for pentacene growth on 25 nm thick Pd and Au bottom contacts (both on 1 nm thick Ti adhesion layer and without thiol treatment) showed a film morphology similar in the channel and on the Pd electrode, but not on the Au electrode. Our results indicate that the metallic bilayer structure is not detrimental for pentacene growth. In all studied cases, homogeneous pentacene films can be obtained.

3.3. Effect of bottom contact metallization on transistor characteristics

Electrical performances of the investigated S/D metallization schemes for pentacene BG BC transistors with nominal W/L = 2500 μm/5 μm are shown in Fig. 5, with transfer and output curves respectively in the left and in the right column. The reference transistor with 30 nm thick Au BC displays well-behaved characteristics. From the transfer curve, a saturation mobility μ of 0.4 $cm^2/(V\,s)$ and a threshold voltage V_T close to 0 V are extracted (Fig. 5a). The output curve displays a good saturation behavior with no evidence of injection problem at the contacts. Such characteristics are fully representative of a stable and optimized pentacene BG BC transistor technology. We observe comparable characteristics for pentacene transistors with 5 nm sputtered Au on 25 nm evaporated Al (Fig. 5c and d) and with 5 nm evaporated Pd on 25 nm evaporated Al (Fig. 5g and h). Both metallic bilayer BC architectures deliver excellent transistors, with μ in the range of 0.4–0.5 $cm^2/(V\,s)$, low V_T and no evidence of injection problems at the contacts. On the other hand, in the case of the 5 nm evaporated Au on 25 evaporated Al BC architecture, the S-shaped output curves in Fig. 5f clearly exhibit signs of non-ohmic contacts [44]. This adversely affects the source/drain current flowing through the device whose μ decreases by almost one order of magnitude (Fig. 5e).This unexpected difference between a thin sputtered (Fig. 5c and d) and evaporated (Fig. 5e and f) Au film on Al finds its explanation in the earlier evidences from the SEM and AFM device characterizations that sputtered Au extends beyond the width of the evaporated Al film whereas the evaporated Au has the same width as the Al film underneath. Indeed, experiments reported for BG BC pentacene transistors with 50 nm thick Au layers on 0.5–10 nm thick Ti adhesion layers revealed that good charge injection into the pentacene could only be achieved for Ti layer thicknesses *below* 3 nm, which is about the thickness of the accumulation layer in a pentacene channel [12]. The requirement to have a direct contact between the noble metal and the pentacene in the transistor channel region explains why the BC metallization with evaporated Au on Al led to poor charge injection (Fig. 5e and f) whereas injection from the sides of the sputtered Au on Al led to excellent transistor properties (Fig. 5c and d).

Considering this advantage of sputtering over evaporation for the thin Au layer, it is surprising that we obtain such good transistors for the 5 nm evaporated Pd on 25 nm Al BC architecture (Fig. 5g and h) who favorably compare to those reported in the pioneering work by Klauk et al. on pentacene transistors based on ion-beam sputtered Pd BC [10]. Moreover the absence of any specific contact treatment besides the UV/O_3 exposure constitutes an advantage of Pd over the for Au obligatory thiol treatment, leading to potentially air sensitive Au-thiolates [45]. The reason for not encountering similar injection problems with the thin evaporated Pd as with the thin evaporated Au is not clear. It could find its origin in the improved continuity of the pentacene film formed on top of the Pd contact and on top of the dielectric in the channel, as hinted by the similar dendritic morphologies in Fig. 4d.

3.4. Metal cost reduction for S/D bottom contacts

Since noble metals like gold and palladium are significantly more expensive than aluminum, simple calculations – neglecting the cost of the aluminum layer – have been made in order to estimate the material cost reduction by using a 5 nm thin Au or Pd layer as metallization for BC instead of a 30 nm thick pure Au layer. In this way, metallization cost of the thin Au layer was only 1/6th of the standard Au metallization, and this with similar performance of the short-channel pentacene transistors (Fig. 5a–d).

The relative metallization cost of a 5 nm thick Pd layer with respect to 30 nm thick Au layer was calculated using the following formula, in which C_M, d_M, A_M, ρ_M and P_M respectively represent the metallization cost, the layer thickness, the metallization area, the density, and the prize/weight of the metal M:

$$C_M = d_M \times A_M \times \rho_M \times P_M$$

From this formula, the ratio of C_{Au}/C_{Pd} was computed as follows:

$$\frac{C_{Au}}{C_{Pd}} = \frac{d_{Au}}{d_{Pd}} \times \frac{A_{Au}}{A_{Pd}} \times \frac{\rho_{Au}}{\rho_{Pd}} \times \frac{P_{Au}}{P_{Pd}}$$

Knowing (i) that the metallization areas are identical for Au and Pd, (ii) d_{Au} = 30 nm and d_{Pd} = 5 nm, (iii) ρ_{Au} = 19.30 and ρ_{Pd} = 12.0 g/cm^3 at 20 °C [46] and (iii) the current ratio of the gold prize with respect to the palladium prize $P_{Au}/P_{Pd} \approx 2.1$, the metallization cost ratio is $C_{Au}/C_{Pd} \sim 19.8$.

This indicates that the material cost of a 5 nm thin Pd layer (on 25 nm thick Al) is only about 5% of the cost of the traditional metallization consisting of 30 nm Au.

4. Conclusions

The issue addressed in this paper can be wrapped up in the three following facts: (i) organic circuits require high mobility short channel pentacene transistors to reach sufficient speeds, (ii) up to now, such high mobilities in short channel devices could only be achieved with Au S/D contacts, (iii) in mass production, the gold cost amounts for a significant fraction of the final device price. In this work, we prove the concept of using metallic bilayers (5 nm thin sputtered Au or evaporated Pd on 25 nm thick evaporated Al) as replacement of traditional plain Au (30 nm thick) S/D

contacts in short channel ($L \leqslant 5$ μm) pentacene BG BC transistors. Using this new BC architecture, transistors achieve similar saturation hole mobilities to those of reference transistors with pure Au contacts, and this with at metal costs of respectively 17% and 5% of the reference transistor. With its equivalent performance at a significantly lower cost, the bilayer approach presented here represents the only credible alternative to plain Au electrodes and can be considered as significant step towards the commercialization of low-cost high quality organic electronic circuits. The achievement of good electrical performance with bilayers consisting of evaporated metals is furthermore promising for future cost reductions since the metal bilayer profile can be expected to be similar to the one obtained by etching processes, which typically gives higher yields than lift-off processes and are therefore used in industrial processes of the display industry.

Acknowledgments

Erwin Vandenplas (IMEC) is acknowledged for metal deposition on the substrates. This work was performed in a collaboration between IMEC and TNO in the frame of the HOLST Centre. The authors acknowledge financial support of EC-funded project Polaric (FP7-247978).

References

[1] D.M. de Leeuw, G.H. Gelinck, T.C.T. Geuns, E. van Veenendaal, E. Cantatore, B.H. Huisman, Polymeric integrated circuits: fabrication and first characterisation, IEDM Tech. Digest. (2002) 293–296.
[2] P.F. Baude, D.A. Ender, M.A. Haase, T.W. Kelley, D.V. Muyres, S.D. Theiss, Pentacene-based radio-frequency identification circuitry, Appl. Phys. Lett. 82 (2003) 3964–3966.
[3] G. Gelinck, P. Heremans, K. Nomoto, T.D. Anthopoulos, Organic transistors in optical displays and microelectronic applications, Adv. Mat. 22 (2010) 3778–3798.
[4] T. Sekitani, U. Zschieschang, H. Klauk, T. Someya, Flexible organic transistors and circuits with extreme bending stability, Nat. Mat. 9 (2010) 1015–1022.
[5] K. Myny, S. Steudel, S. Smout, P. Vicca, F. Furthner, B. van der Putten, A.K. Tripathi, G.H. Gelinck, J. Genoe, W. Dehaene, P. Heremans, Organic RFID transponder chip with data rate compatible with electronic product coding, Org. Electron. 11 (2010) 1176–1179.
[6] K. Myny, S. Steudel, P. Vicca, M.J. Beenhakkers, N.A.J.M. van Aerle, G.H. Gelinck, J. Genoe, W. Dehaene, P. Heremans, Plastic circuits and tags for 13.56 MHz radio-frequency communication, Solid-State Electron. 53 (2009) 1220–1226.
[7] T.W. Kelley, P.F. Baude, C. Gerlach, D.E. Ender, D. Muryres, M.A. Haase, D.E. Vogel, S.D. Theiss, Recent progress in organic electronics: materials, devices, and processes, Chem. Mater. 16 (2004) 4413–4422.
[8] H. Klauk, M. Halik, U. Zschieschang, F. Eder, G. Schmid, C. Dehm, Pentacene organic transistors and ring oscillators on glass and on flexible polymeric substrates 82 (2003) 4175–4177.
[9] B.C. Shekar, J. Lee, S.-W. Rhee, Organic thin film transistors: materials processes and devices, Korean J. Chem. Eng. 21 (2004) 267–285.
[10] H. Klauk, G. Schmid, W. Radlik, W. Weber, L. Zhou, C.D. Sheraw, J.A. Nichols, T.N. Jackson, Contact resistance in organic thin film transistors, Solid-State Electron. 47 (2003) 297–301.
[11] J. Zaumseil, K.W. Baldwin, J.A. Rogers, J. Appl. Phys. 93 (2003) 6117–6124.
[12] N. Yoneya, M. Noda, H. Hirai, K. Nomoto, M. Wada, J. Kasahara, Reduction of contact resistance in pentacene thin-film transistors by direct carrier injection into a-few-molecular-layer channel, Appl. Phys. Lett. 85 (2004) 4663–4665.
[13] D.J. Gundlach, L. Zhou, J.A. Nichols, T.N. Jackson, P.V. Necliudov, M.S. Shur, An experimental study of contact effects in organic thin film transistors, J. Appl. Phys. 100 (2006) 024509.
[14] H. Kim, R.C.Y. Auyeung, S.H. Lee, A.L. Huston, A. Piqué, Laser forward transfer of silver electrodes for organic thin-film transistors, Appl. Phys. A 69 (2009) 441–445.
[15] M.J. Panzer, C.D. Frisbie, Contact effects in organic field-effect transistors, in: Z. Bao, J. Locklin (Eds.), Organic field-effect transistors Vol. 128, Optical Science and Engineering Series, CRC Press, 2007, pp. 139–157.
[16] J.-A. Chu, J.-J. Zeng, K.-C. Wu, Y.-J. Lin, Pentacene ohmic contact on the transparent conductive oxide films, Thin Solid Films 519 (2010) 868–871.
[17] S. De Vusser, S. Steudel, K. Myny, J. Genoe, P. Heremans, Integrated shadow mask method for patterning small molecule organic semiconductors, Appl. Phys. Lett. 88 (2006) 103501.
[18] R. Rotzoll, S. Mohapatra, V. Olariu, R. Wenz, M. Grigas, K. Dimmler, O. Shchekin, A. Dodabalapur, Radio frequency rectifiers based on organic thin-film transistors, Appl. Phys. Lett. 88 (2006) 123502.
[19] C.-L. Fan, T.-H. Yang, C.-Y. Chiang, Performance degradation of pentacene-based organic thin-film transistors under positive drain bias stress in the atmosphere, IEEE Electr. Dev. Lett. 31 (2010) 887–889.
[20] C. Bock, D.V. Pham, U. Kunze, D. Käfer, G. Witte, Ch. Wöll, Influence of contact metals on the performance and morphology of pentacene bottom-contact field-effect transistors, Phys. E 40 (2008) 2107–2109.
[21] D.J. Gundlach, L.L. Jia, T.N. Jackson, Pentacene TFT with improved linear region characteristics using chemically modified source and drain electrodes, IEEE Electr. Dev. Lett. 22 (2001) 571–573.
[22] S.-W. Rhee, D.-J. Yun, Metal-semiconductor contact in organic thin film transistors, J. Mat. Chem. 18 (2008) 5437–5444.
[23] H. Kim, R.C.Y. Auyeung, S.H. Lee, A.L. Huston, A. Piqué, Laser forward transfer of silver electrodes for organic thin-film transistors, Appl. Phys. A 96 (2009) 441–445.
[24] D.-J. Yun, S. Lee, K. Yong, S.-W. Rhee, In situ ultraviolet photoemission spectroscopy measurement of the pentacene-RuO_2/Ti contact energy structure, Appl. Phys. Lett. 97 (2010) 073303.
[25] C.-a. Di, G. Yu, Y. Liu, X. Xu, D. Wei, Y. Song, Y. Sun, Y. Wang, D. Zhu, J. Liu, X. Liu, D. Wu, High-performance low-cost organic field-effect transistors with chemically modified bottom electrodes, J. Am. Chem. Soc. 128 (2006) 16418–16419.
[26] K. Shibata, H. Wada, K. Ishikawa, H. Takezoe, T. Mori, (Tetrathiafulvalene)(tetracyanoquinodimethane) as a low-contact-resistance electrode for organic transistors, Appl. Phys. Lett. 90 (2007) 193509.
[27] Y. Yu, M. Kanno, H. Wada, Y. Bando, M. Ashizawa, A. Tanioka, T. Mori, Enhanced performance of bottom-contact organic field-effect transistors with M(DMDCNQI)2 buffer layers, Physica B 405 (2010) S378–S380.
[28] H. Wada, T. Mori, Solution-processed carbon electrodes for organic field-effect transistors, Appl. Phys. Lett. 93 (2008) 213303.
[29] H. Wada, T. Mori, High-resolution transparent carbon electrodes for organic field-effect transistors patterned by laser sintering, Appl. Phys. Lett. 95 (2009) 253307.
[30] J.-I. Inoue, H. Wada, T. Mori, Self contact organic transistors, Jap. J. Appl. Phys. 49 (2010) 071605.
[31] C.-a. Di, D. Wei, G. Yu, Y. Liu, Y. Guo, D. Zhu, Patterned graphene as source/drain electrodes for bottom-contact organic field-effect transistors, Adv. Mater. 20 (2008) 3289–3293.
[32] C.-H. Chang, C.-H. Chien, J.-Y. Yang, Pentacene-based thin-film transistors with multiwalled carbon nanotube source and drain electrodes, Appl. Phys. Lett. 91 (2007) 083502.
[33] Y. Chen, Y. Xu, K. Zhao, X. Wan, J. Deng, W. Yan, Towards flexible all-carbon electronics: flexible organic field- effect transistors and inverter circuits using solution-processed all-graphene source/drain/gate electrodes, Nano Res. 3 (2010) 714–721.
[34] H.A. Becerril, R.M. Stoltenberg, M.L. Tang, M.E. Roberts, Z. Liu, Y. Chen, D.H. Kim, B.-L. Lee, S. Lee, Z. Bao, Fabrication and evaluation of solution-processed reduced graphene oxide electrodes for p- and n-channel bottom-contact organic thin-film transistors, ACS Nano 4 (2010) 6343–6352.
[35] S. Lee, G. Jo, S.-J. Kang, G. Wang, M. Choe, W. Park, D.-Y. Kim, Y.H. Kahng, T. Lee, Enhanced charge injection in pentacene field-effect transistors with graphene electrodes, Adv. Mater. 23 (2011) 100–105.
[36] L. Li, M. Hirtz, W. Wang, C. Du, H. Fuchs, L. Chi, Patterning of polymer electrodes by nanoscratching, Adv. Mater. 22 (2010) 1374–1378.
[37] M.A. Ali, H.H. Kim, K.H. Jeong, H.S. Soh, H.S. Nam, J.G. Lee, E.G. Lee, Application of poly(3 tosylate-doped 4ethylenedioxythiophene) (PEDOT) films into bottom contact pentacene organic thin film transistors (OTFTs), Thin Solid Films 518 (2010) 6315–6319.

[38] P. Cosseddu, A. Bonfiglio, Soft lithography fabrication of all-organic bottom-contact and top-contact field effect transistors, Appl. Phys. Lett. 88 (2006) 023506.
[39] S.L. Hellstrom, R.Z. Jin, R.M. Stoltenberg, Z. Bao, Driving high-performance n- and p-type organic transistors with carbon nanotube/conjugated polymer composite electrodes patterned directly from solution, Adv. Mater. 22 (2010) 4204–4208.
[40] J.Z. Wang, Z.H. Zheng, H.W. Li, W.T.S. Huck, H. Sirringhaus, Polymer field effect transistors fabricated by dewetting, Synth. Met. 146 (2004) 287–290.
[41] M. Leufgen, U. Bass, T. Muck, T. Borzenko, G. Schmidt, J. Geurts, V. Wagner, L.W. Molenkamp, Optimized sub-micron organic thin-film transistors: the influence of contacts and oxide thickness, Synth. Met. 146 (2004) 341–345.
[42] C.W. Sele, T. von Werne, R.H. Friend, H. Sirringhaus, Lithography-free self-aligned inkjet printing with sub-hundred-nanometer resolution, Adv. Mater. 17 (2005) 997–1001.
[43] CRC Handbook of Chemistry and Physics, 64th edition, 1983-1984, CRC Press, Boca Raton (Fl), p. F–125.
[44] G. Horowitz, Interfaces in organic field-effect transistors, Adv. Polym. Sci. 223 (2010) 113–153.
[45] M.-T. Lee, C.-C. Hsueh, M.S. Freund, G.S. Ferguson, Air oxidation of self-assembled monolayers on polycrystalline gold: the role of the gold substrate, Langmuir 14 (1998) 6419–6423.
[46] CRC Handbook of Chemistry and Physics, 64th edition, 1983-1984, CRC Press, Boca Raton (Fl), pp. B-94 and B-118.

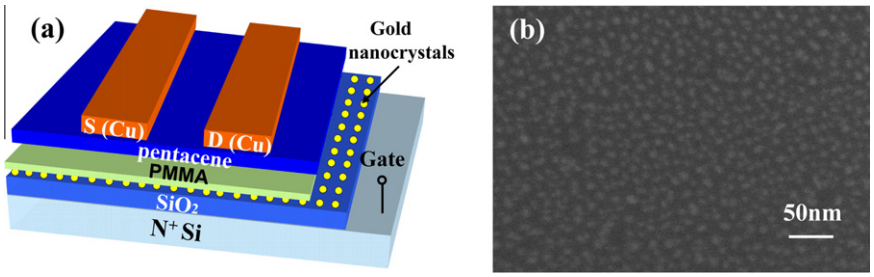

Fig. 1. (a) Schematic illustration of the fabricated organic memory devices. (b) SEM image of the Au nanocrystals used as the charge trapping elements.

memory devices were fabricated on heavily doped n-type Si wafers with a 300 nm thermal oxides SiO_2 as the gate electrode and the blocking layer. Au nanocrystals were obtained by e-beam evaporating a 1.5 nm thick Au layer at a deposition rate of 0.3 Å/s. The polymethylmethacrylate (PMMA) tunneling layer was then prepared from a PMMA solution in *O*-xylene by spin-coating on the surface of Au nanocrystals and then baked in the oven at 180 °C for 30 min to remove the solvent. The thickness of the PMMA film was 60 nm. The pentacene film with a thickness of 50 nm was deposited by vacuum thermally evaporated at a deposition rate of 0.3 Å/s with a typical background pressure of 4×10^{-4} Pa and the substrates were kept at 60 °C. Finally, 50-nm-thick copper (Cu) top source/drain electrodes were deposited by e-beam evaporation through a shadow mask, the defined channel lengths (L) and channel widths (W) were 500 μm and 60 μm, respectively. Cu top contacts were employed because of their smaller contact resistance compared with conventional gold contacts [19]. The electrical characteristics of the transistors were measured with a Keithley 4200 semiconductor characterization system at room temperature in air. No illumination was applied during all the measurements of output and transfer characteristics. The morphologies of the Au nanocrystals were observed by scanning electron microscope (SEM).

3. Results and discussion

Fig. 1(b) shows the SEM image of uniform Au nanocrystals on SiO_2 dielectric layer. The average diameter of the Au nanocrystals is 10 ± 2 nm and the density was 6.9×10^{11} cm^{-2}. Devices with this configuration exhibit excellent transistor performance, which is comparable to those reported elsewhere. Shown in Fig. 2 are the typical output and bidirectional transfer characteristics of the OFET memory device. A hysteresis window of 5 V was observed in the transfer curve and the calculated saturation mobility, V_T, and on/off current ratio (I_{on}/I_{off}) from the forward curve were 0.5 cm^2 V^{-1} s^{-1}, 1 V, and 10^7, respectively.

To study programmable characteristics of fabricated memory devices, the transfer curves under programming/erasing bias pulses of ±80 V both in dark and with light-assisted program were measured. As shown in Fig. 3(a), the shift in the transfer characteristics of the fabricated memory devices at $V_{DS} = -60$ V, under programming and erasing operations were observed where bias pulses of 80 and −80 V were applied to the gate for 1 ms in dark. Hysteresis was observed in transfer curves for both states and the hysteresis window for the programmed state was slightly larger than that of erased state. However, comparing with the memory window, the hysteresis under both states was negligible. The programmed and erased V_T extracted from forward transfer curves were found to be −1 V and −19 V, respectively. The memory window was defined as the change of V_T with respect to the applied program/erase bias pulses. The memory window of our device was 18 V with program/erase operation in dark. In addition, the on/off memory ratio with a reading voltage of $V_{DS} = -60$ V, $V_{GS} = 0$ V was 10^2. Fig. 3(b) shows the programmable memory characteristics of the memory devices with light assisted program. When using a program with top light irradiation (white light with a power density of 1.33 mW/cm^2 from a lighting emitting diode lamp) and gate bias pulses of 80 V for 1 ms, the programmed V_T was found to be 43 V. Meanwhile, erased state with V_T of

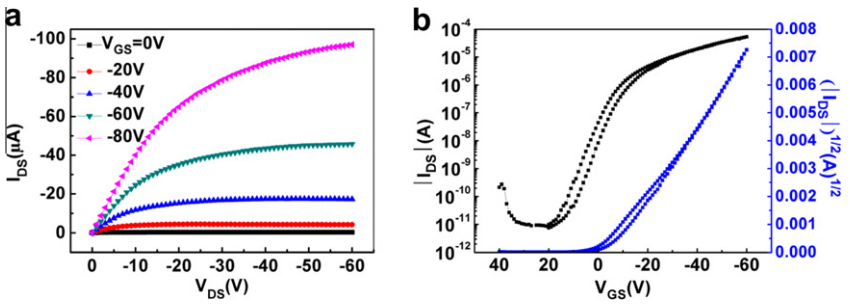

Fig. 2. (a) The output characteristic of the organic transistor devices. The device had the following structure: n + Si/SiO_2/Au nanocrystals/PMMA/pentacene/Cu source/drain. (b) The initial bidirectional transfer characteristics of organic transistors.

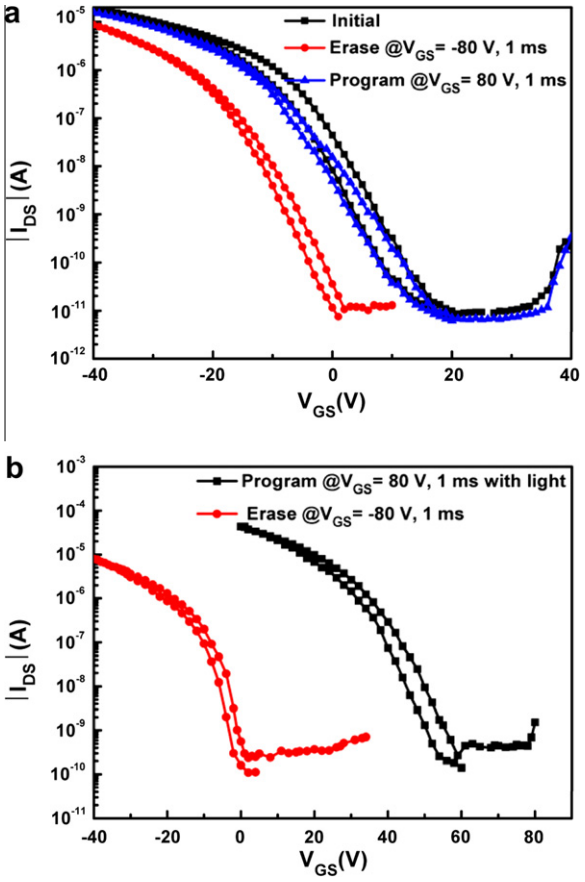

Fig. 3. (a) Bidirectional transfer curves of the organic memory devices according to the programming/erasing bias pulses of ±80 V for 1 ms in dark. (b) Bidirectional transfer curves of the organic memory devices under V_{GS} = 80 V, 1 ms with light assisted program and V_{GS} = −80 V, 1 ms erase conditions.

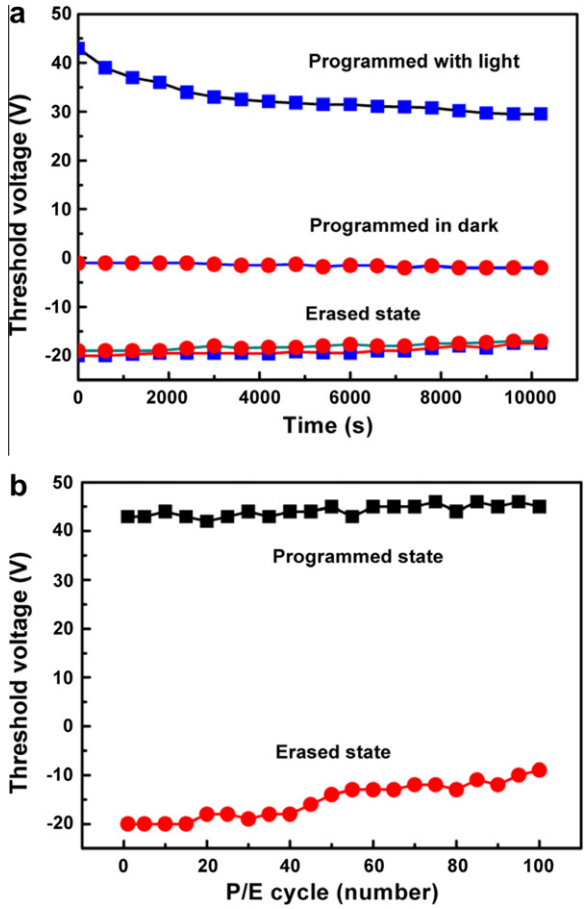

Fig. 4. (a) Data retention characteristics in terms of the threshold voltage for the memory device in the programmed/erased states. (b) Endurance characteristics of the memory device with light assisted program.

−20 V could be obtained when a bias pulse of −80 V applied to gate for 1 ms in dark. It should be indicated that the hysteresis characteristics were similar to that of programmed in dark and V_T were also extracted from forward transfer curves. Therefore, the memory window of 63 V and on/off memory ratio of 10^5 with a reading voltage of V_{DS} = −60 V, V_{GS} = 0 V were obtained. It is noted that the memory window and on/off memory ratio can be significantly increased through light assisted program.

The reliable operations of the memory devices are very important in nonvolatile memory devices. Fig. 4(a) shows the data retention properties that were measured as a function of time using the memory devices in the programmed/erased states at room temperature. The same bias pulses were applied to set the programmed/erased states as shown in Fig. 3. The initial memory windows were approximately 63 V and 18 V for light assisted program and conventional program, respectively. The memory window of the devices under the two kinds of states showed little degradation and memory windows of 47 V and 15 V can be preserved after 10^4 s. The retention time was estimated from the measured data to be more than 10^7 s for the devices with light assisted program. Also, endurance properties were measured by consecutive applications of program/erase bias pulses to the memory devices. After certain endurance cycles the reading operations were done to verify the change of the V_T, as shown in Fig. 4(b). The programmed states have no obvious change of V_T over 100 program/erase cycles. For erased state, there is some fluctuation of V_T and V_T has a slight shift to the positive direction over 100 program/erase cycles. But overall, the V_T did not change much as the number of endurance cycles varied.

The OFETs without Au nanocrystals were also proposed to determine the charging effects of Au nanocrystals in the transistor devices. Comparing with the memory devices, the only difference was the absence of the Au nanocrystals in the gate dielectric layer. All of the devices used in our experiment were fabricated under the same processing conditions. The device exhibited almost no hysteresis in the transfer curves, as shown in Fig. 5(a). We further investigated the charging effect by the application of programming/erasing bias pulses to the gate which were the same as used for memory device operations. There was no obvious V_T shift after application of programming/erasing bias pulses in dark. However, a memory window of 35 V was observed with light assisted program, and

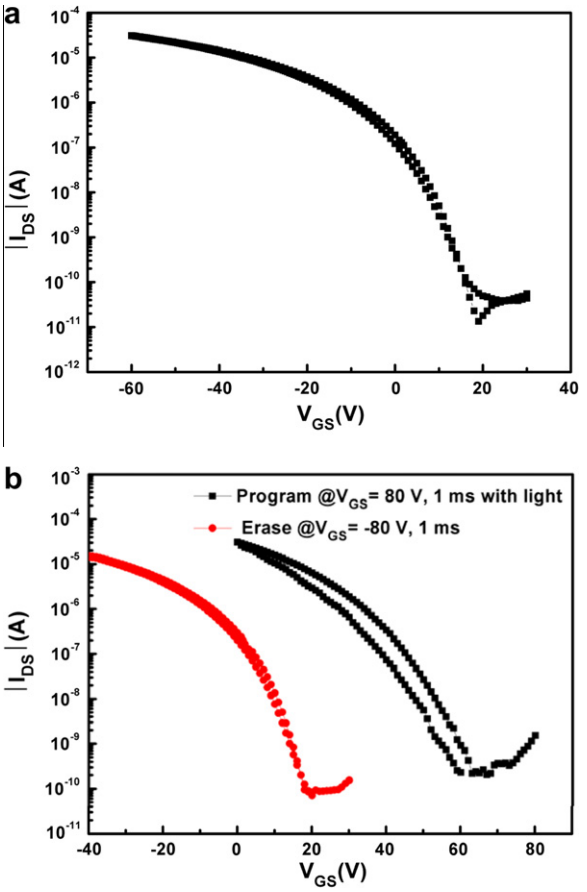

Fig. 5. (a) Bidirectional transfer characteristics of the devices without Au nanocrystals. (b) Bidirectional transfer curves of the devices without Au nanocrystals under V_{GS} = 80 V, 1 ms with light assisted program and V_{GS} = −80 V, 1 ms erase conditions.

a hysteresis window of 9 V for the programmed state was observed (Fig. 5(b)). In addition, the retention time was only 10^3 s for the devices. The results indicated that the memory performances of the device are strongly depending on the existence of Au nanocrystals.

The memory performances of the device with light assisted program are much better than that of with conventional program. To clarify the reason for this improvement, the charge storage mechanism of memory device was studied. Due to the low carrier mobility of the organic semiconductor, Fowler–Nordheim (FN) tunnelling should dominate the transfer mechanism for the organic memory devices [20]. Under dark conditions, holes charging/discharging from the pentacene to the Au nanocrystals and vice versa play a dominant role in the programming/erasing processes because pentacene is a p-type semiconductor. When a large negative voltage is applied to the gate electrode, holes are injected from the channel into the Au nanocrystals through the FN tunnelling process and of being captured in the Au nanocrystals. The trapped holes in Au nanocrystals perturbed and modulated a subsequently applied gate field, resulting in substantial shifts in V_T by the amount of Eq. (1) [6].

$$\Delta V_T = -\frac{Q}{C_i} \tag{1}$$

Where C_i is the dielectric capacitance of total dielectrics and ΔV_T is the memory window. From Eq. (1), we calculated the total number of trapped holes at Au nanocrystals to be 1.1×10^{12} cm^{-2} at a bias pulse of −80 V applied to gate for 1 ms. When a relatively large positive voltage is applied to the gate electrode, the holes stored in the Au nanocrystals are ejected back into the pentacene channel through FN tunnelling. Thus, the programmed state is thought to be an empty state and the erased state is regarded as a state that holes are trapped in the Au nanocrystals. When the OFET is illuminated by light, excitons are photogenerated in the bulk of pentacene film through absorption of photons with higher energy than the band gap energy of pentacene [17]. When a positive gate bias is applied, excitons are separated into electrons and holes, and the separated electrons are injected and stored into the Au nanocrystals. From Eq. (1) we can conclude that the stored electrons in the Au nanocrystals resulting in a positive directional V_T shift. In addition, the calculated total number of trapped electrons in the Au nanocrystals is 2.3×10^{12} cm^{-2} at a program with top light irradiation and gate bias pulses of 80 V for 1 ms. It should be noted when the program process is finished, there is no illumination applied. When a negative gate bias is applied, the electrons stored in the Au nanocrystals will be released back to the pentacene film and recombined with those photogenerated holes in the channel; with the increase of the negative bias, holes are injected into the Au nanocrystals and of being captured in the Au nanocrystals, the same as described above. The number of trapped holes is 1.16×10^{12} cm^{-2}. Thus, the programmed state is regarded as a state that electrons are trapped in the Au nanocrystals with number of 2.3×10^{12} cm^{-2} and the erased state is regarded as a state that holes are trapped in the Au nanocrystals with number of 1.16×10^{12} cm^{-2}. So the memory performances were significantly improved with light assisted program.

4. Conclusions

In summary, OFETs based nonvolatile nano-crystal floating gate memory devices with light assisted program were studied. The memory performances could be significantly enhanced with light assisted program compared with conventional program. The memory window of 63 V and on/off memory ratio of 10^5 were obtained. In addition, the data retention and programming/erasing operation cycles measurements suggested that the memory devices have good reliability. Therefore, this method has a great potential for OFETs nano-crystal floating gate memory devices in the near future.

Acknowledgements

This work was partially supported by the National 973 Program (2011CB808404, 2009CB939703), and the National Science Foundation of China under Grant Nos. 60825403, 90607022, and 61001043.

References

[1] H. Yan, Y. Zheng, R. Blache, C. Newman, S.F. Lu, J. Woerle, A. Facchetti, Adv. Mater. 20 (2008) 3393.
[2] S.H. Kim, S.H. Lee, J. Jang, IEEE Electron Device Lett. 31 (2010) 1044.
[3] S. Ju, J. Li, J. Liu, P.C. Chen, Y.G. Ha, F. Ishikawa, H. Chang, C. Zhou, A. Facchetti, D.B. Janes, T.J. Marks, Nano Lett. 8 (2008) 997.
[4] C.S. Kim, S.S. Lee, E.D. Gomez, J.B. Kim, Y.L. Loo, Appl. Phys. Lett. 94 (2009) 113302.
[5] J.C. Scott, L.D. Bozano, Adv. Mater. 19 (2007) 1452.
[6] K.J. Baeg, Y.Y. Noh, H. Sirringhaus, D.Y. Kim, Adv. Funct. Mater. 20 (2010) 224.
[7] Z. Liu, F. Xue, Y. Su, Y.M. Lvov, K. Varahramyan, IEEE Trans. Nanotechnol. 5 (2006) 379.
[8] M.F. Chang, P.T. Lee, S.P. Mcalister, A. Chin, Appl. Phys. Lett. 93 (2008) 233302.
[9] T. Sekitani, T. Yokota, U. Zschieschang, H. Klauk, S. Bauer, K. Takeuchi, M. Takamiya, T. Sakurai, T. Someya, Science 326 (2009) 1516.
[10] W. Wang, J. Shi, D. Ma, IEEE Trans. Electron Devices 56 (2009) 1036.
[11] J.S. Lee, J. Cho, C. Lee, I. Kim, J. Park, Y.M. Kim, H. Shin, J. Lee, F. Caruso, Nat. Nanotechnol. 2 (2007) 790.
[12] C. Lee, J.H. Kwon, J.S. Lee, Y.M. Kim, Y. Choi, H. Shin, J. Lee, B.H. Sohn, Appl. Phys. Lett. 91 (2007) 153506.
[13] Y.M. Kim, S.J. Kim, J.S. Lee, IEEE Electron Device Lett. 31 (2010) 503.
[14] Y.S. Park, S. Chung, S.J. Kim, S.H. Lyu, J.W. Jang, S.K. Kwon, Y. Hong, J.S. Lee, Appl. Phys. Lett. 96 (2010) 213107.
[15] S.J. Kim, Y.S. Park, S.H. Lyu, J.S. Lee, Appl. Phys. Lett. 96 (2010) 033302.
[16] S.J. Kim, J.S. Lee, Nano Lett. 10 (2010) 2884.
[17] Y. Guo, C. Di, S. Ye, X. Sun, J. Zheng, Y. Wen, W. Wu, G. Yu, Y. Liu, Adv. Mater. 21 (2009) 1954.
[18] C. Feng, T. Mei, X. Hu, N. Pavel, Org. Electron. 11 (2010) 1713.
[19] C. Di, G. Yu, Y. Liu, Y. Guo, Y. Wang, W. Wu, D. Zhu, Adv. Mater. 20 (2008) 1286.
[20] L. Zhen, W. Guan, L. Shang, M. Liu, G. Liu, J. Phys. D Appl. Phys. 41 (2008) 135111.

process the stamp has to be a commodity and it has to be on the centimeter scale. However, stamps are typically fabricated using e-beam lithography which makes these two requirements contradicting.

The goal of this paper is to show that it is possible to use NIL as part of an optimization procedure and specifically to explore the dependency between features depth/height and the power conversion efficiency of imprinted bi-layer organic solar cells. To this end, we first report a robust and parallel method to produce master stamps with nanometer resolution and centimeter scale area which is based on solution casting of block co-polymers. This is then followed by a report of systematic enhancement of the power conversion efficiency of double layer organic solar cells demonstrating that a twofold enhancement can already be reached using relatively low resolution (~80 nm) patterns and not very deep (~35 nm) features.

2. Results and discussion

2.1. Stamp fabrication and nanoimprinting

The fabrication process allowing the production of multiple centimeter scale master stamps in parallel (see also Supplementary Information) is shown schematically in Fig. 1.

Master stamps were prepared on at least ~1 cm × 1 cm highly hydrophilic silicon samples onto which a solution of the diblock copolymer poly(styrene-*block*-methyl methacrylate) (PS-*b*-PMMA) was spin coated resulting in ~90 nm thick film.

Spin coated samples were transferred to a solvent annealing chamber [21] where they were exposed to chloroform vapor under controlled conditions. We have found that controlling the solvent annealing conditions, such as temperature and vapor pressure, is crucial to obtain uniform patterns over the entire sample with negligible number of defects resulting from incipient dewetting. The resulting BCP film (Fig. 2A) exhibits 80–100 nm wide phase separated domains in a "worm" like morphology over the entire sample. Replicating the pattern into the silicon substrate begins with exposing the films to 254 nm light, exploiting the different response of the two blocks to UV light exposure: [22,23] the PMMA degrades while the PS is cross-linked and becomes insoluble. The relatively thick film used dictated morphology of PS cylinders lying parallel to the surface with a thin PMMA layer separating them from the substrate (see inset in Fig. 2A). In this case, rinsing out the PMMA would result in deformation of the PS and to defects which are noticeable on cm scale samples. To ensure defect free master stamps, we did not remove the PMMA but relied on differences in the resistance to etching between the degraded PMMA blocks and the cross-linked PS blocks. This naturally had a penalty in the maximum achievable feature depth which could be ~50% deeper. Alternatively, one could use the morphology of vertically oriented PS cylinders and remove the PMMA without inducing defects [24]. However, such morphology is achieved only for thinner films thus making no difference

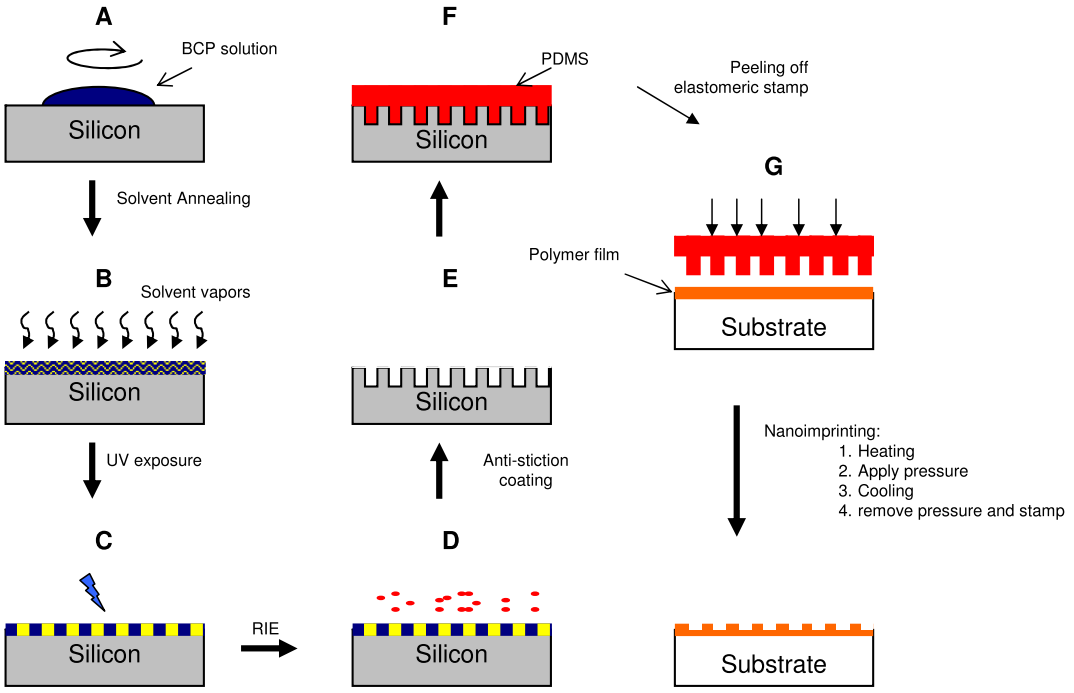

Fig. 1. Schematic illustration of centimeter scale NIL process that was developed. (A) Spin coating BCP solution on top of silicon substrate. (B) Solvent annealing. (C) Exposure of the now phase separated BCP film to UV light. (D) Reactive ion etching (RIE) to transfer the pattern into the silicon substrate. (E) Master stamp is completed with the deposition of anti-stiction layer. (F) Molding elastomeric stamp (PDMS) from the silicon template. (G) Imprinting semiconducting organic layer using the elastomeric stamp.

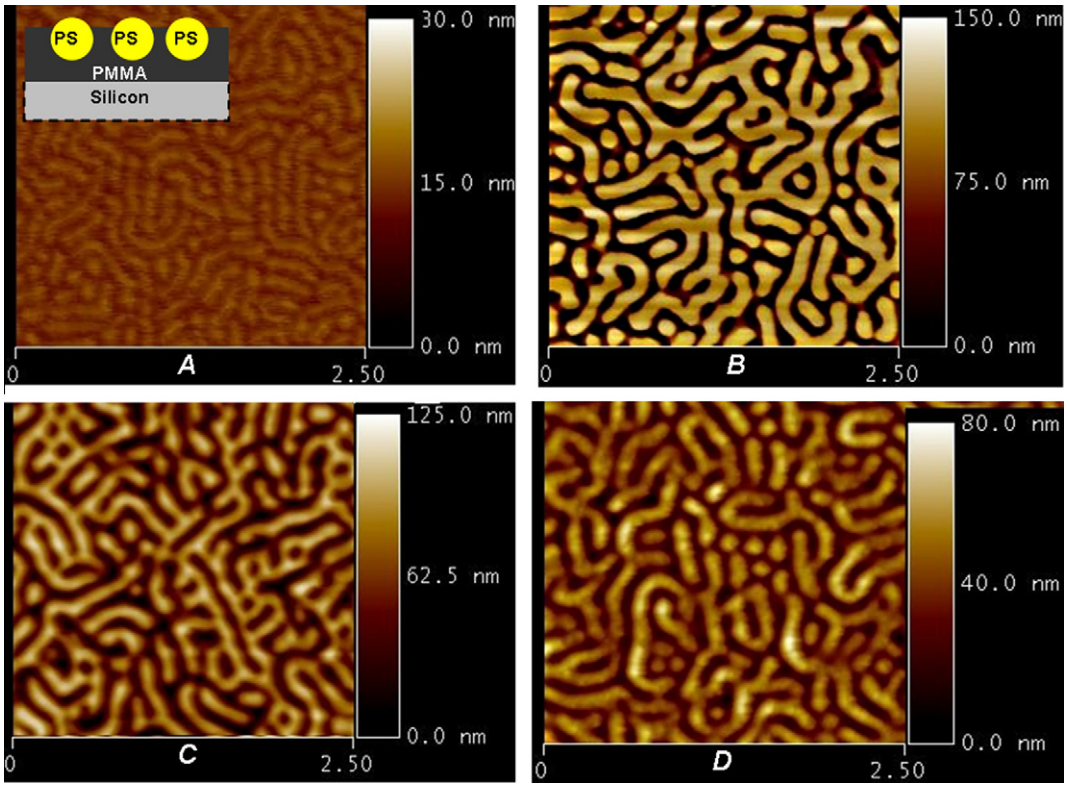

Fig. 2. AFM images (height contrast) of samples during the different process stages. (A) PS-*b*-PMMA film after solvent annealing. Left inset shows a schematic illustration of the suggested film morphology (see text). (B) Silicon samples after pattern was transferred using reactive ion etching. (C) Elastomeric stamp molded from the silicon master. (D) Nanoimprinted P3HT film.

in the final features depth. Etching of the silicon was carried out using SF_6 as the etchant gas. By optimizing the etching time it was possible to transfer the pattern into the silicon with aspect ratio (height:width) of 1.2:1 (Fig. 2B). Master stamps were completed with the deposition of a self assembled monolayer that serves as an anti-stiction layer. In all the above steps we would typically produce in parallel about 10 stamps.

Although the fabricated master stamps can be used directly in a NIL process we chose to use elastomeric stamps as their flexibility permits their use even on non planar surfaces. Following a process adopted from Ref. [16], elastomeric stamps based on polydimethylsiloxane (PDMS) were molded from the master stamps. As can be seen in Fig. 2C, pattern resolution was maintained but feature height decreased by roughly 30%.

The NIL process was carried out in a home-built nanoimprinting setup. Imprinting was done using an elastomeric stamp and the feature height could be adjusted by controlling the imprinting pressure. Fig. 2D shows an AFM image of imprinted P3HT film. The depth of the features shown was 35–40 nm in an initially 80 nm thick film.

2.2. Device fabrication

The availability of multiple stamps through the above process enabled us to integrate the imprinting procedure with the fabrication and optimization of organic solar cells (see Supplementary Information). We found that in order to achieve reliable and reproducible imprinted features the stamp has to be of a relatively large size and that the nano-scale features should extend over the entire area. As this was enabled by the procedure described above we could test the effect due to enhancement of junction area by fabricating organic solar cells with controlled interpenetrating heterojunction and comparing these devices to simple bi-layer devices. For this comparison we chose the layers thicknesses through optimization of the efficiency measured for the non-imprinted bi-layer structure. We used P3HT as the donor and PCBM as the acceptor, a materials combination that was found to produce relatively high efficiency solar cells in both bi-layer [8] and BHJ [25] structures. Devices were fabricated with the following layered structure: patterned indium-doped tin oxide (ITO)/45 nm of poly(ethylenedioxythiophene):poly(styrenesulfonic acid) (PEDOT:PSS)/80 nm P3HT/60 nm PCBM/0.6 nm LiF/Aluminum. NIL was performed on some of the devices, prior to PCBM deposition, using PDMS elastomeric stamps prepared by the process described above. As stamps were much larger than the defined pixels area (2.7 mm^2) we could emboss all pixels simultaneously and avoid the need for any alignment. By varying the applied pressure we have fabricated imprinted devices with average features height of ~10, ~20, and ~35 nm. In order to avoid damage to

the patterned P3HT during PCBM deposition we have used dichloromethane (DCM) as the PCBM solvent. We have verified that DCM does not affect the P3HT layer or the pattern created in it using AFM and absorption measurements. The AFM features of an imprinted P3HT film before PCBM casting are as described in Fig. 2D. The films after PCBM removal were essentially similar but careful examination revealed that in small fraction of the sample there was a slight (~10%) decrease in features height. Absorption measurements (Fig. 3A) support this conclusion as almost no change is observed between the samples.

Recently it was shown that PCBM can substantially interdiffuse into P3HT even when the two materials are deposited from orthogonal solvents or even stamp transferred [26–28]. However, critical reading of the papers indicates that PCBM interdiffusion into P3HT requires that either the P3HT is not fully dry and/or that post heating is applied. Namely, interdiffusion of PCBM into P3HT is dependent on the processing conditions. In the current study we made sure the P3HT films are fully dry (110 °C for 3 h in a vacuum oven) before depositing PCBM and we did not apply any post-heating (post annealing). While we do not provide depth-profiling to indicate that PCBM did not penetrate into the films we do report that by simply spin coating pure DCM on the P3HT/PCBM stack the PCBM was removed to the point it had none to negligible effect on the photoluminescence (PL) efficiency Fig. 3B shows PL measurements confirming that almost no change is observable between samples before PCBM deposition and after it was removed. As the PL of P3HT is highly sensitive to minute amounts of the PCBM quencher and since a spin coating procedure would not suck the PCBM out from the bulk of the film, we are led to conclude that PCBM never penetrated the bulk of the P3HT film.

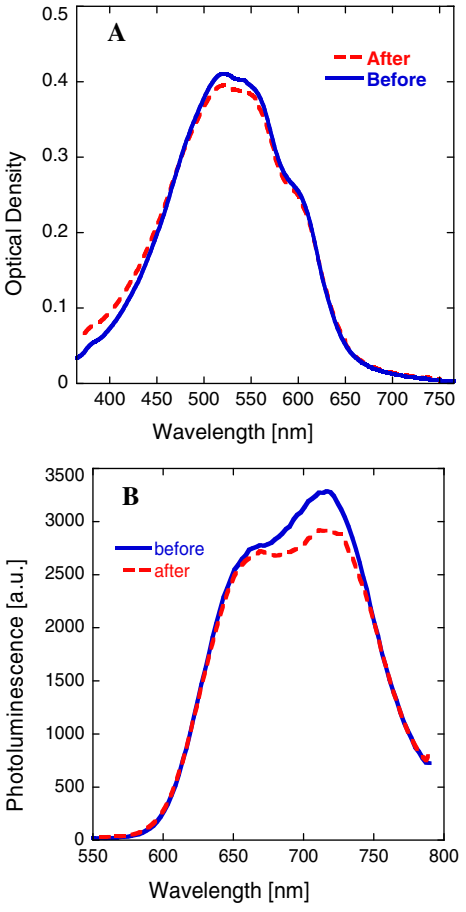

Fig. 3. The absorption (A) and photoluminescence (B) spectra of imprinted P3HT film before PCBM deposition (full line) and after PCBM removal (dashed line).

2.3. Device characterization

The photovoltaic response of our devices was examined by measuring their external quantum efficiency (EQE) as a function of incident photon wavelength and by measuring their current versus voltage (*I–V*) response under a 100 mW/cm^2, A.M 1.5 G illumination. All measurements were performed under nitrogen atmosphere. The EQE spectra of our devices, i.e. the ratio between the number of carriers collected and the number of photons arriving to the device at a given wavelength, is presented in Fig. 4. The EQE of the devices is clearly increased with imprinted feature height up to about 40–53% in the device with ~35 nm features height compared to the bi-layer, not imprinted, device. In the imprinted devices we expect to have an increased interface area due to the sidewalls of the imprinted features. Using image processing of the AFM images we were able to estimate the surface area in the imprinted devices. For the 35 nm deep imprint, the surface area is 1.75 times larger than that in the flat, non-imprinted device. But, accounting for up to 10 nm exciton diffusion length will reduce the ratio between the junction volumes to a factor of 1.55. Hence, while it may seem that the imprinted devices do not exploit the full potential-offered (55%) by the increased interface area/junction volume, the value is almost within experimental error

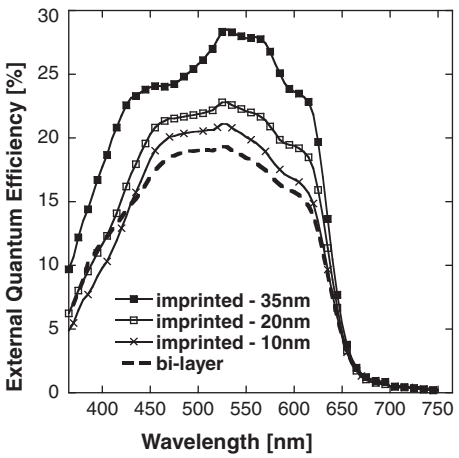

Fig. 4. External quantum efficiency (EQE) spectra of the fabricated devices. The bi-layer device is the non-imprinted control device (dashed line) and imprinted devices are with features height of approximately 10, 20, and 35 nm.

Table 1
Summary of average values obtained for the different type of devices. At least 3 separate devices from each type were measured and the values in brackets indicate the standard deviation between the different independent measurements. The bi-layer device is the non-imprinted control device and imprinted devices are with approximately 10, 20, and 35 nm features height. J_{sc} is the short circuit current, V_{oc} the open circuit voltage, FF the fill factor, r_s the serial resistance, EQE the external quantum efficiency (measured at 525 nm wavelength), and PCE is the power conversion efficiency under 100 mW/cm^2, A.M 1.5 G illumination.

Average values obtained for the different types of devices						
Device type	J_{sc} (mA/cm^2)	V_{oc} (V)	FF (%)	r_s (Ω)	EQE (%)	PCE (%)
Bi-layer (not imprinted)	−3.28 (±0.27)	0.51 (±0.01)	42 (±2)	55.3 (±6.3)	20 (±1)	0.69 (±0.05)
Imprinted (10 nm)	−2.47 (±0.72)	0.52 (±0.02)	44 (±2)	59.5 (±21.3)	18 (±2)	0.57 (±0.21)
Imprinted (20 nm)	−3.86 (±0.17)	0.55 (±0.01)	50 (±2)	29.2 (±3.0)	23 (±1)	1.07 (±0.06)
Imprinted (35 nm)	−4.58 (±0.10)	0.54 (±0.01)	57 (±2)	17.5 (±1.2)	28 (±1)	1.41 (±0.03)

mentioned above of 40–53% (see also Table 1). We note that accounting for the 10 nm diffusion length is also consistent with the observation that the differences between the 10 nm deep features device and the non embossed device are within experimental error (see also Table 1). It is also interesting to note that the above dependence of the EQE on the embossing depth provides another indirect evidence that the PCBM diffusion into P3HT is negligible under the processing conditions used here (i.e. fully dry P3HT film and no post heating). The argument regarding the junction area made using the exciton diffusion could be interchanged with PCBM diffusion into the P3HT film and hence indicates that PCBM did not diffuse more than 10 nm into the P3HT.

Typical *I–V* curves of the different devices measured under illumination are presented in Fig. 5. The statistical averages and standard deviations of the different figures of merit extracted from the measurements of all devices are presented in Table 1.

Two pronounced differences between imprinted and non-imprinted devices can be observed. First, with the exception of the shallowest imprinted device (imprinted – 10 nm), there is an increase in the short-circuit current (J_{sc}) with increased features height. The magnitude of this increase corresponds to the observed increase in the EQE measured at low (μW/cm^2) intensities, indicating that this

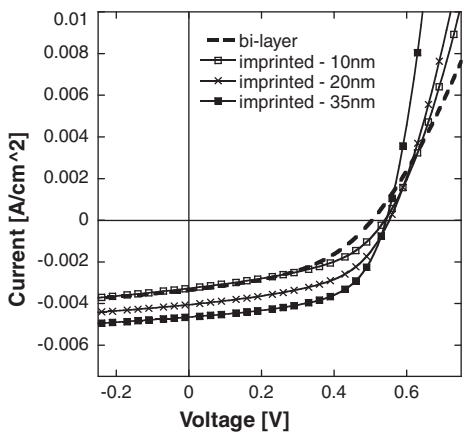

Fig. 5. Current–voltage (*I–V*) characteristics of the fabricated devices under 100 mW/cm^2, A.M 1.5 G illumination. The bi-layer device is the non-imprinted control device (dashed line) and imprinted devices are with features height of approximately 10, 20, and 35 nm.

is due to the larger junction volume. Secondly, the imprinted devices exhibit reduced serial resistance (r_s) combined with an improved open circuit voltage (V_{oc}). The origin of this second effect could be due to shorter minimal film thickness associated with the embossed features. An alternative explanation could be related to the potential contribution from pressure induced changes as was suggested by Shih et al. [29], yet, the fact that the 10 nm imprinted device do not exhibit improvement suggest that pressure does not play a significant role here.

The increased J_{sc} and FF in the imprinted devices manifested in improved power conversion efficiency (PCE) of those devices (Table 1). The device exhibiting the deepest features (imprinted – 35 nm), displays on average more than a twofold improvement in PCE compared to the simple bi-layer device.

3. Conclusion

We have demonstrated that it is possible to use nanoimprinting to systematically enhance the charge generation and extraction efficiency in bi-layer solar cells. This optimization was enabled by the development of large area and low cost process which is based on solution processed block copolymer. An added value of using block copolymer lithography is that it should be possible to scale down the lateral feature size even below 30 nm and approach the resolution dictated by excitons diffusion lengths. The linear relation found between the enhancement in charge generation efficiency (EQE) and the junction area together with the relatively low resolution of the current stamp, suggest that the efficiency enhancement could be made even higher.

Acknowledgements

We acknowledge the support of the Ollendorff Minerva Center, the NanoSci-ERA program, and the Russell Berrie Nanotechnology Institute at the Technion. E.A. acknowledges the support of the Israeli ministry of science.

Appendix A. Supplementary data

Supplementary data associated with this article can be found, in the online version, at doi:10.1016/j.orgel.2011.03.041.

References

[1] S.H. Park, A. Roy, S. Beaupre, S. Cho, N. Coates, J.S. Moon, D. Moses, M. Leclerc, K. Lee, A.J. Heeger, Bulk heterojunction solar cells with internal quantum efficiency approaching 100%, Nat. Photonics 3 (2009) U295–U297.

[2] G. Yu, J. Gao, J.C. Hummelen, F. Wudl, A.J. Heeger, Polymer photovoltaic cells – enhanced efficiencies via a network of internal donor–acceptor heterojunctions, Science 270 (1995) 1789–1791.

[3] J.J.M. Halls, C.A. Walsh, N.C. Greenham, E.A. Marseglia, R.H. Friend, S.C. Moratti, A.B. Holmes, Efficient photodiodes from interpenetrating polymer networks, Nature 376 (1995) 498–500.

[4] H. Jin, Y.B. Hou, F. Teng, P. Kopola, M. Tuomikoski, A. Maaninen, Effect of molecular aggregation by thermal treatment on photovoltaic properties of MEH-PPV: fullerene-based solar cells, Sol. Energy Mater. Sol. Cells 93 (2009) 289–294.

[5] L.M. Chen, Z.R. Hong, G. Li, Y. Yang, Recent progress in polymer solar cells: manipulation of polymer: fullerene morphology and the formation of efficient inverted polymer solar cells, Adv. Mater. 21 (2009) 1434–1449.

[6] J. Peet, M.L. Senatore, A.J. Heeger, G.C. Bazan, The role of processing in the fabrication and optimization of plastic solar cells, Adv. Mater. 21 (2009) 1521–1527.

[7] B.J. Kim, Y. Miyamoto, B.W. Ma, J.M.J. Frechet, Photocrosslinkable polythiophenes for efficient, thermally stable, organic photovoltaics, Adv. Funct. Mater. 19 (2009) 2273–2281.

[8] A.L. Ayzner, C.J. Tassone, S.H. Tolbert, B.J. Schwartz, Reappraising the need for bulk heterojunctions in polymer-fullerene photovoltaics: the role of carrier transport in all-solution-processed P3HT/PCBM bilayer solar cells, J. Phys. Chem. C 113 (2009) 20050–20060.

[9] C. Cocoyer, L. Rocha, C. Fiorini-Debuisschert, L. Sicot, D. Vaufrey, C. Sentein, B. Geffroy, P. Raimond, Implementation of a submicrometer patterning technique in azopolymer films towards optimization of photovoltaic solar cells efficiency, Thin Solid Films 511 (2006) 517–522.

[10] M. Hiramoto, Design of nanostructure for photoelectric conversion by vertical organic superlattice, Electron. Commun. Jpn. Pt. II-Electron. 89 (2006) 13–18.

[11] W.J. Zeng, K.S.L. Chong, H.Y. Low, E.L. Williams, T.L. Tam, A. Sellinger, The use of nanoimprint lithography to improve efficiencies of bilayer organic solar cells based on P3HT and a small molecule acceptor, Thin Solid Films 517 (2009) 6833–6836.

[12] X.M. He, F. Gao, G.L. Tu, D. Hasko, S. Huttner, U. Steiner, N.C. Greenham, R.H. Friend, W.T.S. Huck, Formation of nanopatterned polymer blends in photovoltaic devices, Nano Lett. 10 (2010) 1302–1307.

[13] L.S. Roman, O. Inganas, T. Granlund, T. Nyberg, M. Svensson, M.R. Andersson, J.C. Hummelen, Trapping light in polymer photodiodes with soft embossed gratings, Adv. Mater. 12 (2000) 189+.

[14] Y.N. Xia, G.M. Whitesides, Soft lithography, Ann. Rev. Mater. Sci. 28 (1998) 153–184.

[15] S.Y. Chou, P.R. Krauss, P.J. Renstrom, Nanoimprint lithography, J. Vac. Sci. Technol. B 14 (1996) 4129–4133.

[16] S.Y. Chou, P.R. Krauss, W. Zhang, L.J. Guo, L. Zhuang, Sub-10 nm imprint lithography and applications, J. Vac. Sci. Technol. B 15 (1997) 2897–2904.

[17] D.G. Choi, H.K. Yu, S.M. Yang, 2D nano/micro hybrid patterning using soft/block copolymer lithography, Mater. Sci. Eng. C – Biomimetic and Supramolecular Syst. 24 (2004) 213–216.

[18] J.Z. Wang, J. Gu, F. Zenhausern, H. Sirringhaus, Low-cost fabrication of submicron all polymer field effect transistors, Appl. Phys. Lett. 88 (2006) 133502.

[19] D. Cheyns, K. Vasseur, C. Rolin, J. Genoe, J. Poortmans, P. Heremans, Nanoimprinted semiconducting polymer films with 50 nm features and their application to organic heterojunction solar cells, Nanotechnology 19 (2008).

[20] M.S. Kim, J.S. Kim, J.C. Cho, M. Shtein, L.J. Guo, J. Kim, Flexible conjugated polymer photovoltaic cells with controlled heterojunctions fabricated using nanoimprint lithography, Appl. Phys. Lett. 90 (2007).

[21] K.A. Cavicchi, T.P. Russell, Solvent annealed thin films of asymmetric polyisoprene–polylactide diblock copolymers, Macromolecules 40 (2007) 1181–1186.

[22] T. Thurn-Albrecht, R. Steiner, J. DeRouchey, C.M. Stafford, E. Huang, M. Bal, M. Tuominen, C.J. Hawker, T.P. Russell, Nanoscopic templates from oriented block copolymer films, Adv. Mater. 12 (2000) 1138.

[23] J.F. Rabek, B. Ranby, Photodegradation, Photo-Oxidation and Photostabilization of Polymers, Wiley, New York, 1975.

[24] A.J. Ben-Sasson, E. Avnon, E. Ploshnik, O. Globerman, R. Shenhar, G.L. Frey, N. Tessler, Patterned electrode vertical field effect transistor fabricated using block copolymer nanotemplates, Appl. Phys. Lett. 95 (2009).

[25] W.L. Ma, C.Y. Yang, X. Gong, K. Lee, A.J. Heeger, Thermally stable, efficient polymer solar cells with nanoscale control of the interpenetrating network morphology, Adv. Funct. Mater. 15 (2005) 1617–1622.

[26] N.D. Treat, M.A. Brady, G. Smith, M.F. Toney, E.J. Kramer, C.J. Hawker, M.L. Chabinyc, Interdiffusion of PCBM and P3HT reveals miscibility in a photovoltaically active blend, Adv. Energy Mater. 1 (2011) 82–89.

[27] J.S. Moon, C.J. Takacs, Y. Sun, A.J. Heeger, Spontaneous formation of bulk heterojunction nanostructures: multiple routes to equivalent morphologies, Nano Lett. (2011).

[28] D.H. Wang, D.-G. Choi, K.-J. Lee, S.H. Im, O.O. Park, J.H. Park, Unexpected solid-solid intermixing in a bilayer of poly(3-hexylthiophene) and [6,6]-phenyl C61-butyric acidmethyl ester via stamping transfer, Org. Electron. 11 (2010) 1376–1380.

[29] C.F. Shih, K.T. Hung, J.W. Wu, C.Y. Hsiao, W.M. Li, Efficiency improvement of blended poly(3-hexylthiophene) and 1-(3-methoxycarbonyl)-propyl-1-phenyl-(6,6)C-61 solar cells by nanoimprinting, Appl. Phys. Lett. 94 (2009).

In the present study, counter electrode containing NCS groups were prepared, and connected with the NCS groups of the dye molecules by CuI. A highly efficient all solid state DSSC have been prepared by the specific interaction of CuI with the NCS groups of the dye molecules and those of the counter electrode. The specific interaction of CuI with NCS groups could facilitate the hole injection from the CuI into the NCS groups of the counter electrode. The PEG containing NCS groups/FTO heterojunction device was modified by inserting a PEDOT interlayer. PEDOT interlayer has been widely used to modify the electronic devices [31,32]. The resulting all solid state DSSC were stable (the decrease of the conversion efficiency were lower than 5% for 1000 h) and exhibited remarkably high conversion efficiency (4.2%). The solid state DSSC are manufactured with inexpensive and low quality materials. A lot of DSSC have been prepared for the past 20 years, however, most of them were not so stable, and the conversion efficiencies were relatively low. This is the first DSSC which can be applied for practical use.

2. Experimental

2.1. Preparation of the samples of XPS

The CuI film was prepared by coating the CuI–acetonitrile solution(0.15 M) onto nanostructured TiO_2 covered on the FTO (AGC type U TCO glass). The CuI film was soaked in 0.05 mM ethanol solution of Ru(dcbpyH$_2$)$_2$(NCS)$_2$ (N3 dye, kojima chemicals co.) for 10 min, followed by rinsing in ethanol. FTO covered with a TiO_2 was soaked for 30 min in 0.5 mM ethanol solution of N3 dye. The CuI film was soaked in the ethanol solution containing 0.5 mM lithium thiocyanate and equivalent amount of poly(ethylene glycol) (PEG20000) for 10 min, followed by rinses in ethanol. The ethanol solution of 0.5 M lithium thiocyanate and PEG20000 (1:1) was coated on the substrate layers of TiO_2 on FTO conducting glass.

2.2. Fabrication of DSSC

A compact TiO_2 layer was deposited onto FTO by spray pyrolysis. The TiO_2 paste was prepared [33] and coated onto the FTO using squeeze printing technique (film area = 0.5 cm^2), and then the electrode was heated at 450 °C for 30 min in air. The post-treatment with $TiCl_4$ aqueous solution was applied to the prepared films by soaking in 0.2 M aqueous $TiCl_4$ at 70 °C for 30 min, followed by a water rinse and fired at 450 °C for 30 min. The thickness of porous TiO_2 film was about 7 μm. The porous TiO_2 film was immersed into 0.5 mM ethanol solution of N3 dye for 12 h at room temperature. The coating of CuI onto dyed electrodes was performed in N_2-atmosphere in a glove box. The CuI–acetonitrile solution(0.15 M) was lightly coated over the dyed electrode. After coating, the electrode was heated to 80 °C to evaporate the solvent. This process was repeated several times. The amount of CuI solution is about 0.06 mL cm^{-2}. The counter electrode was prepared by coating the solution of PEG containing NCS groups onto the FTO modified by PEDOT. The PEDOT modified FTO was prepared by spin coating of PEDOT:PSS aqueous dispersion (Clevios PH) on FTO and dried at 100 °C for 30 min in vacuum. The PEG containing NCS groups was prepared by dissolving PEG20000 and lithium thiocyanate (or guanidium thiocyante) (1:1) in acetonitrile and heated to 80 °C to evaporate the solvent. The CuI/dye/TiO_2 glass plate was fixed together with the counter electrode. The resulting cells had an active area of 0.25 cm^2.

2.3. Characterization

X-ray photoelectron spectroscopy (XPS) measurement was performed using SSX-100 instrument using a monochromatized Al Kα X-rays at hν = 1487 eV. IR spectra of the samples were measured with the spectrometer Perkin Elmer BX-FT-IR for disks diluted with KBr. The photoelectrochemical properties of the DSSC were studied by recording the current–voltage (*I–V*) characteristics under illumination of AM 1.5 (1 Sun; 100 mW cm^{-2}) by using a solar simulator (Yamashita Denso). Stability tests on DSSC were conducted with Xe lamp at an intensity of 40 mW cm^{-2} at room temperature. The electrochemical impedance spectroscopy (EIS) of the DSSC was measured with an impedance analyzer (Solartron Analytical, 1260) connected with a potentiostat (Solartron Analytical, 1287) under illumination of AM1.5 by using a solar simulator. The EIS was recorded over frequency range of 0.1–10^6 Hz. The AC amplitude and the applied voltage were 10 mV and set at Voc of the cells, respectively.

3. Results and discussion

3.1. The specific interaction between the NCS groups of dye molecules with CuI

Possible interaction between the NCS groups of the dye molecules and the CuI was investigated by the N 1s and S 2p core level spectra. The N 1s core level spectra for the dye-sensitized CuI surface and for nonbonded dye molecules are shown in Fig. 1a. In the spectrum of the nonbonded dye molecules two clearly resolved peaks were observed representing the bipyridine nitrogen (the peak at higher binding energy) and the NCS nitrogen (the peak at lower binding energy). The structure of N 1s spectrum measured for the dye-sensitized CuI surface is similar expect for a clear shift of the peak originating from NCS. This peak shift about +0.6 eV, showing a strong interaction between the NCS groups with the surface. This presumption is further supported by the S 2p spectra in Fig. 1b. A shift of +0.9 eV is obtained for the position of the S 2p signal for the nonbonded dye molecules compared with that obtained from the dye-sensitized CuI.

3.2. Preparation of the counter electrode containing NCS groups

A mixture of lithium thiocyanate and PEG were dissolved in acetonitrile. The solution was coated on FTO glass modified by PEDOT. The IR spectra of PEG containing NCS groups were shown in Fig. 2.

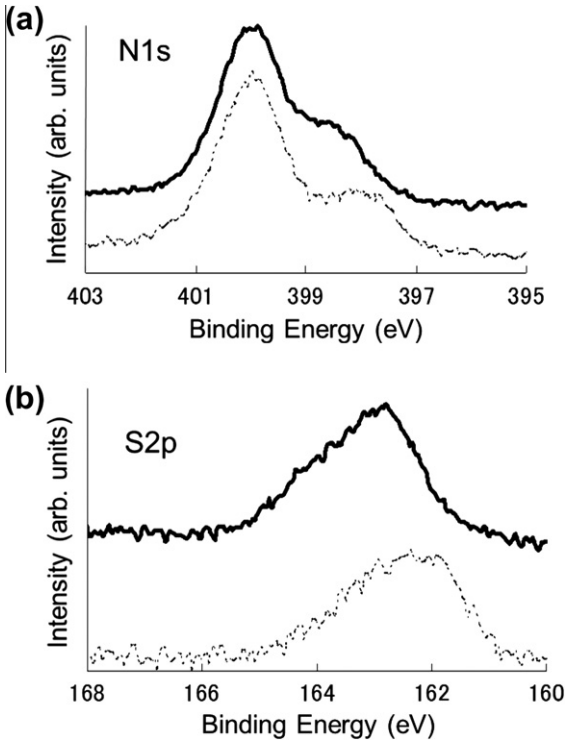

Fig. 1. (a) N 1s core level spectra of nonbonded dye molecules (dotted curve) and dye-sensitized CuI surface (solid curve). (b) S 2p core level spectra of nonbonded dye molecules (dotted curve) and dye-sensitized CuI surface (solid curve).

3.3. The interaction between the NCS groups of the counter electrode with CuI

The interaction of the NCS groups of the counter electrode with CuI was investigated by the N 1s core level spectrum, which is shown in Fig. 3a. The peak shift about +0.8 eV, showing a strong interaction with the CuI surface. This conclusion is also supported by the S 2p spectrum, a shift of +1.0 eV, as shown in Fig. 3b.

3.4. Fabrication of all solid state DSSC

A highly efficient all solid state DSSC were fabricated by the specific interaction of CuI with the NCS groups of the dye molecules and that of the counter electrode. The counter electrodes of DSSC A, DSSC B and DSSC C were prepared by coating the solution of PEG + guanidium thiocyanate, PEG + lithium thiocyanate and PEG on FTO glass modified by PEDOT, respectively. Fig. 4 shows the photocurrent–voltage characteristics of the series of all solid state DSSC.

DSSC A and DSSC B were fabricated by connecting the NCS groups of the dye molecules and that of the counter electrode by CuI. The DSSC A and DSSC B exhibited much higher performance compared with DSSC C. DSSC C is the conventional solid state DSSC.

The interaction was investigated by impedance spectroscopy. Fig. 5 shows the impedance spectra of the specific

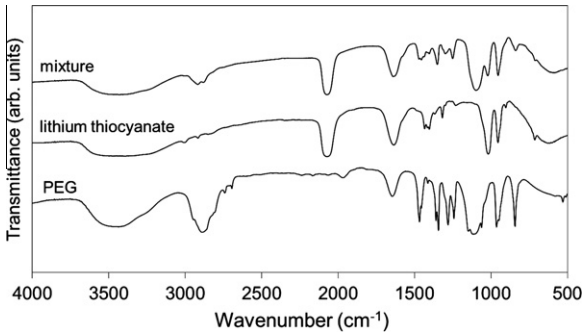

Fig. 2. IR spectra of PEG containing NCS groups.

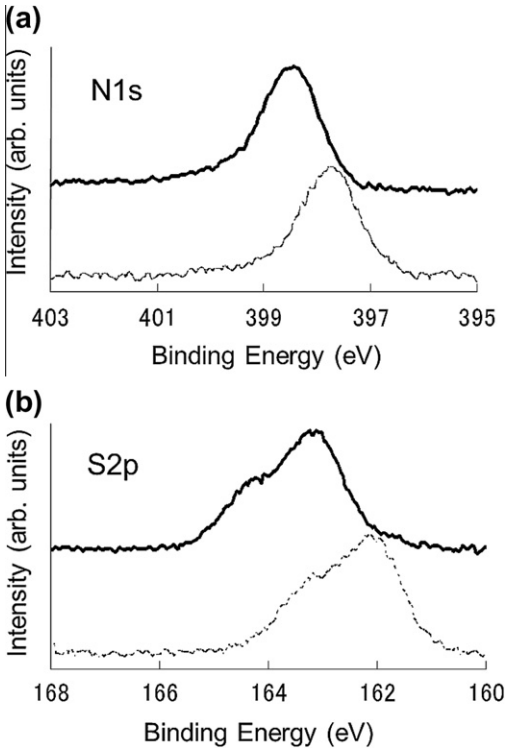

Fig. 3. (a) N 1s core level spectra of nonbonded PEG containing NCS groups (dotted curve) and PEG containing NCS groups coated CuI surface(solid curve). (b) S 2p core level spectra of nonbonded PEG containing NCS groups (dotted curve) and PEG containing NCS groups coated CuI surface (solid curve).

interaction of CuI with PEG and the PEG containing NCS groups. The interaction of CuI with PEG containing NCS groups gave small impedance, compared with the PEG not containing NCS groups. This is attributed to the specific interaction of CuI with NCS groups.

3.5. The impedance of the all solid state DSSC

Fig. 5 shows the electrochemical impedance spectra recorded over frequency range of 0.1–10^6 Hz of DSSC B and DSSC C (without NCS groups) under open circuit condi-

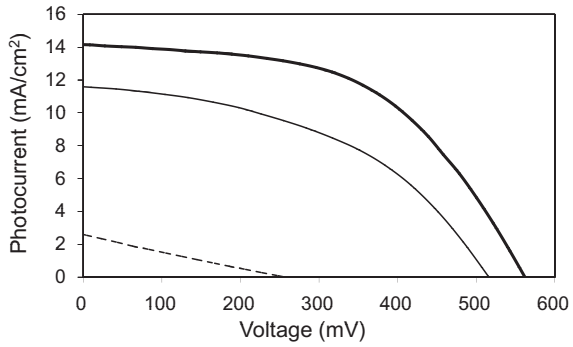

Fig. 4. Photocurrent–voltage curves of all solid state DSSC fabricated from different counter electrodes: PEG + guanidium thiocyanate (bold curve), PEG + lithium thiocyanate (solid curve), PEG (dash curve).

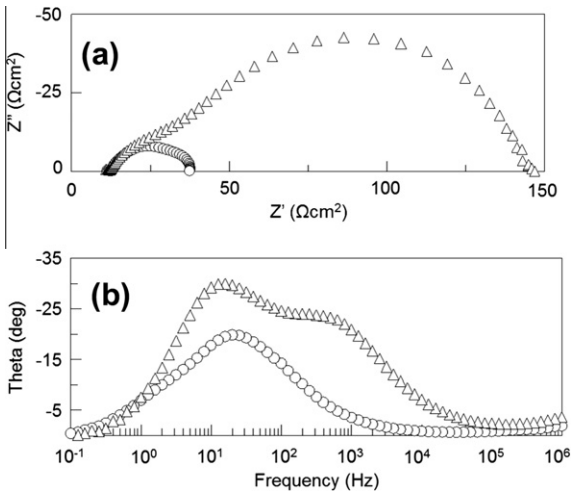

Fig. 5. Nyquist (a) and Bode (b) diagrams of impedance spectra obtained under illumination for the cell with the PEG containing NCS groups (DSSC B:○) and the cell with PEG without NCS group (DSSC C:△).

tions. The equivalent circuits of these DSSC which contain at least three RC parallel circuits can be proposed in the above frequency region as shown in Fig. 6. Based on previous studies [12,13,34–36], we assumed that R_1C_1, R_2C_2 and R_3C_3 correspond to a charge-transfer resistance and an electrochemical capacitance formed by TiO_2 dye/CuI, CuI/polymer and polymer/substrate interface, respectively. R_0 indicates the sheet resistance of DSSC [34–36]. Constant Phase Elements (CPE), with an electrical impedance written as $Z_{CPE} = 1/T(j\omega)^{\alpha}$, were used instead of pure capacitances for a better fit. Those values of R, C and α were obtained by fitting with Z-view software are shown in Table 1.

The counter electrode of DSSC B was prepared by coating the solution of PEG containing NCS groups on FTO glass modified by PEDOT, and that of DSSC C was prepared by coating the solution of PEG without the NCS group on the modified FTO glass. R_1 is attributed to the resistance of TiO_2 dye/CuI interface. DSSC B and C exhibited nearly same R_1 value. Concerning R_2, DSSC B exhibited much smaller value than DSSC C. That can be explained by the strong interaction between the NCS group of the polymer and CuI, which facilitate the hole injection from CuI into NCS groups of counter electrode.

3.6. Enhancement of photovoltaic characteristics using a PEDOT interlayer

PEDOT has been widely used to modify the anodes of electronic devices, including those of organic light emitting diodes [32] and thin-film transistors [37]. In the present study, the basic structure of FTO and the PEG containing NCS groups was modified by inserting a PEDOT interlayer between the FTO and the PEG containing NCS groups. The counter electrode of DSSC D was prepared by coating the solution of PEG containing NCS groups on FTO glass. Fig. 7 shows the electrochemical impedance spectra of DSSC B and DSSC D under open circuit conditions. DSSC B containing the interlayer exhibited much smaller value of R_3 compared with that of DSSC D.

The insertion of PEDOT interlayer between the FTO and PEG containing NCS groups enhanced photovoltaic properties.

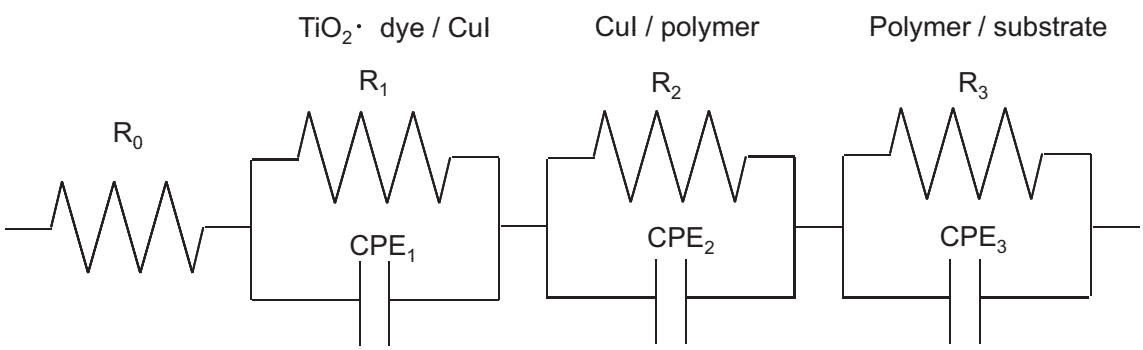

Fig. 6. Equivalent circuit of all solid state DSSC.

Table 1
Parameters obtained by fitting the impedance spectra of DSSC containing different counter electrode, using the equivalent circuit (Fig. 6).

	R_0 (Ω cm^2)	R_1(Ω cm^2)	C_1(F cm^{-2})	α	R_2(Ω cm^2)	C_2(F cm^{-2})	α	R_3(Ω cm^2)	C_3(F cm^{-2})	α
DSSC B	12.4	6.8	12.4×10^{-3}	1	9.3	2.0×10^{-3}	0.74	9.4	16.2×10^{-4}	0.98
DSSC C (without NCS)	12.0	6.7	11.6×10^{-3}	1	94.8	4.2×10^{-4}	0.89	30.5	2.4×10^{-4}	0.69
DSSC D (without PEDOT)	12.2	7.1	14.4×10^{-3}	1	9.7	2.6×10^{-3}	0.71	106.9	2.8×10^{-5}	0.93

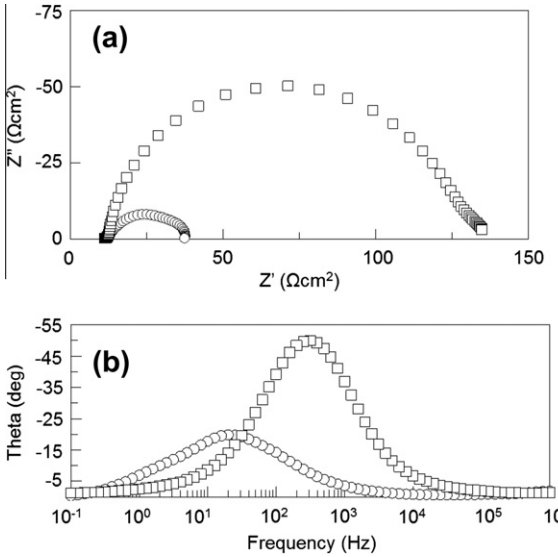

Fig. 7. Nyquist (a) and Bode (b) diagrams of impedance spectra obtained under illumination for cells with PEDOT interlayer (DSSC B: ○) and cell without PEDOT inter layer (DSSC D: □).

3.7. The properties of the all solid state DSSC

DSSC A and DSSC B were fabricated utilizing the specific interaction of CuI with the NCS groups of counter electrode modified by the insertion of PEDOT layer, while no NCS groups was contained in the counter electrode of DSSC C. The properties of the DSSC were summarized in Table 2. Fig. 8 shows the normalized efficiency of DSSC containing different counter electrode. DSSC A and DSSC B were stable and exhibited high efficiency but DSSC C was unstable and the performance was lost in short time. The DSSC A and DSSC B were stable in longer time, and the decrease of the conversion efficiency of DSSC A was smaller than 5% for 1000 h under filtering UV region quasi-sunlight (λ < 435 nm).

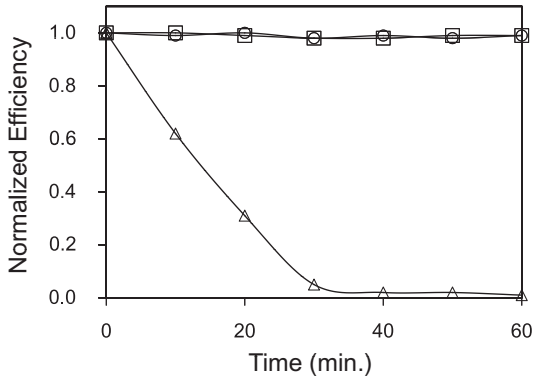

Fig. 8. Changes of the normalized energy conversion efficiency of DSSC A(□), DSSC B(○) and DSSC C(△) under one-sun condition(100 mW cm^{-2}), with the lapse of time after fabrication.

4. Conclusion

A highly efficient all solid state dye-sensitized solar cells (DSSC) have been prepared by the specific interaction of CuI with the NCS groups of the dye molecules and the NCS groups of the counter electrode. The resulting all solid state DSSC were stable, and exhibited high conversion efficiency.

The specific interaction of the CuI with the NCS groups of the working electrode and the counter electrode was investigated by X-ray photoelectron spectroscopy. The structure of the N 1s spectrum measured for the dye-sensitized CuI surface is similar except for a clear sift of the originating from NCS group. The peak shifts about +0.6 eV, showing a strong interaction between the NCS groups with the surface CuI.

In the present study, the counter electrodes containing NCS groups were prepared, and the NCS groups were connected with the NCS groups of the dye molecule by CuI. The specific interaction of CuI with the NCS groups of both electrodes could lower the impedances of the interfaces and facilitate the flow of the hole into the electrodes, which resulted in the high efficiency of the resulting DSSC. The performance was improved by introducing PEDOT

Table 2
Comparison of the performance parameters of the solid state DSSC.

	Jsc (mA cm^{-2})	Voc (mv)	FF	η (%)
DSSC A (guanidium thiocyanate)	14.2	562.0	0.52	4.19
DSSC B (lithium thiocyanate)	11.6	516.1	0.45	2.72
DSSC C (without NCS)	2.59	256.6	0.24	0.15

layer between the FTO and the PEG containing NCS groups. These improvements are due to the reduction of the junction resistance across the interface in the presence of PEDOT interlayer. The resulting all solid state DSSC were stable (the decrease of the conversion efficiency were lower than 5% for 1000 h) and exhibited high conversion efficiency (4.2%). The solid state DSSC could be manufactured with inexpensive and low quality materials, and the practical use is promising.

References

[1] B. O'Regan, M. Grätzel, A low-cost, high-efficiency solar cell based on dye-sensitized colloidal TiO_2 films, Nature (Lond) 353 (1991) 737–740.

[2] M.K. Nazeeruddin, A. Kay, I. Rodicio, R. Humohry-Baker, E. Müller, P. Liska, N. Vlachopoulos, M. Grätzel, Conversion of light to electricity by cis-X2Bis(2, 2′-bipyridyl-4, 4′-dicarboxylate)ruthenium(II) charge-transfer sensitizers (X=Cl-, Br-, I^-, CN^-, and SCN^-) on nanocrystalline TiO_2 electrodes, J. Am. Chem. Soc. 115 (1993) 6382–6390.

[3] A. Hagfeldt, M. Grätzel, Light-induced redox reactions in nanocrystalline systems, Chem. Rev. 95 (1995) 49–68.

[4] M. Matsumoto, Y. Wada, T. Kitamura, K. Shigaki, T. Inoue, M. Ikeda, S. Yanagida, Fabrication of solid-state dye-sensitized Tio_2 solar cell using polymer electrolyte, Bull. Chem. Soc. Jpn. 74 (2001) 387–393.

[5] T. Ueki, M. Watanabe, Macromolecules in ionic liquids: progress, challenges, and opportunities, Macromolecules 41 (2008) 3739–3749.

[6] J.N. Freitas, A.F. Nogueira, M.-A.D. Paoli, New insights into dye-sensitized solar cells with polymer electrolytes, J. Mater. Chem. 19 (2009) 5279–5294.

[7] M. Matsumoto, H. Miyazaki, K. Matsuhiro, Y. Kumashiro, Y. Takaoka, A dye sensitized TiO_2 photoelectrochemical cell constructed with polymer solid electrolyte, Solid State Ionics 89 (1996) 263–267.

[8] U. Bach, D. Lupo, P. Comte, J.E. Moser, F. Weissörtel, J. Salbeck, H. Speitzer, M. Grätzel, Solid-state dye-sensitized mesoporous TiO_2 solar cells with high photon-to-electron conversion efficiencies, Nature 395 (1998) 583–585.

[9] S. Spiekermann, G. Smestad, J. Kowalik, L.M. Tolbert, M. Grätzel, Poly(4-undecyl-2, 2′-bithiophene) as a hole conductor in solid state dye sensitized titanium dioxide solar cells, Synth. Met. 121 (2001) 1603–1604.

[10] J. Krüger, R. Plass, L. Cevey, M. Piccirelli, M. Grätzel, High efficiency solid-state photovoltaic device due to inhibition of interface charge recombination, Appl. Phys. Lett. 79 (2001) 2085–2087.

[11] K. Murakoshi, R. Kogure, Y. Wada, S. Yanagida, Solid state dye-sensitized tio_2 solar cell with polypyrrole as hole transport layer, Chem. Lett. 26 (1997) 471–472.

[12] N. Fukuri, N. Masaki, T. Kitamura, Y. Wada, S. Yanagida, Electron transport analysis for improvement of solid-state dye-sensitized solar cells using poly(3, 4-ethylenedioxythiophene) as hole conductors, J. Phys. Chem. B 110 (2006) 25251–25258.

[13] J. Xia, N. Masaki, M. Lira-Cantu, Y. Kim, K. Jiang, S. Yanagida, Influence of doped anions on poly(3, 4-ethylenedioxythiophene) as hole conductors for iodine-free solid-state dye-sensitized solar cells, J. Am. Chem. Soc. 130 (2008) 1258–1263.

[14] J. Bandara, H. Weerasinghe, Solid-state dye-sensitized solar cell with p-type NiO as a hole collector, Sol. Energy Mater. Sol. Cells 85 (2005) 385–390.

[15] B. O' Regan, D.T. Schwartz, Efficient dye-sensitized charge separation in a wide-band-gap p–n heterojunction, J. Appl. Phys. 80 (1996) 4749–4754.

[16] B. O'Regan, D.T. Schwartz, S.M. Zakeeruddin, M. Grätzel, Electrodeposited nanocomposite n–p heterojunctions for solid-state dye-sensitized photovoltaics, Adv. Mater. 12 (2000) 1263–1267.

[17] G.R.R.A. Kumara, A. Konno, G.K.R. Senadeera, P.V.V. Jayaweera, D.B.R.A. De Silva, K. Tennakone, Dye-sensitized solar cell with the hole collector p-CuSCN deposited from a solution in n-propyl sulphide, Sol. Energy Mater. Sol. Cells 69 (2001) 195–199.

[18] K. Tennakone, G.R.R.A. Kumara, A.R. Kumarasinghe, K.G.U. Wijayantha, P.M. Sirimanne, A dye-sensitized nano-porous solid-state photovoltaic cell, Semicond. Sci. Technol. 10 (1995) 1689–1693.

[19] K. Tennakone, G.R.R.A. Kumara, I.R.M. Kottegoda, K.G.U. Wijayantha, V.P.S. Perera, A solid-state photovoltaic cell sensitized with a ruthenium bipyridyl complex, J. Phys. D Appl. Phys. 31 (1998) 1492–1496.

[20] G.R.R.A. Kumara, A. Konno, K. Shiratychi, J. Tukahara, K. Tennakone, Dye-sensitized solid-state solar cells: use of crystal growth inhibitors for deposition of the hole collector, Chem. Mater. 14 (2002) 954–955.

[21] P.M. Sirimanne, T. Jeranko, P. Bogdanoff, S. Fiechter, H. Tributsch, On the photo-degradation of dye sensitized solid-state TiO_2|dye|CuI cells, Semicond. Sci. Technol. 18 (2003) 708–712.

[22] V.P.S. Perera, K. Tennakone, Recombination processes in dye-sensitized solid-state solar cells with CuI as the hole collector, Sol. Energy Mater. Sol. Cells 79 (2003) 249–255.

[23] K. Tennakone, V.P.S. Perera, I.R.M. Kottegota, L.A.A. De Silva, G.R.R.A. Kumara, A. Konno, Dye-sensitized solid-state photovoltaic cells: suppression of electron-hole recombination by deposition of the dye on a thin insulating film in contact with a semiconductor, J. Electron. Mater. 30 (2001) 992–996.

[24] X.-T. Zhang, H.-W. Liu, T. Taguchi, Q.-B. Meng, O. Sato, A. Fujishima, Slow interfacial charge recombination in solid-state dye-sensitized solar cell using Al_2O_3-coated nanoporous TiO_2 films, Sol. Energy Mater. Sol. Cells 81 (2004) 197–203.

[25] A. Fujishima, X.-T. Zhang, Solid-state dye-sensitized solar cells, Proc. Japan Acad. 81(B) (2005) 33–42.

[26] Q.-B. Meng, K. Takahashi, X.-T. Zhang, I. Sutanto, T.N. Rao, O. Sato, A. Fujishima, H. Watanabe, T. Nakamori, M. Uragami, Fabrication of an efficient solid-state dye-sensitized solar cell, Langmuir 19 (2003) 3572–3574.

[27] G.R.R.A. Kumara, S. Kaneko, M. Okuya, K. Tennakone, Fabrication of dye-sensitized solar cells using triethylamine hydrothiocyanate as a CuI crystal growth inhibitor, Langmuir 18 (2002) 10493–10495.

[28] A.J. Mozer, D.K. Panda, S. Gambhir, T.C. Romeo, B.W. Jensen, G.G. Wallace, Flexible and compressible Goretex–PEDOT membrane electrodes for solid-state dye-sensitized solar cells, Langmuir 26 (2010) 1452–1455.

[29] B. Mahrov, G. Boschloo, A. Hagfeldt, H. Sieqbahn, H. Rensmo, Photoelectron spectroscopy studies of $Ru(dcbpyH_2)_2(NCS)_2$/CuI and $Ru(dcbpyH_2)_2(NCS)_2$/CuSCN interfaces for solar cell applications, J. Phys. Chem. B 108 (2004) 11604–11610.

[30] P.G. Karlsson, S. Bolik, J.H. Richter, Interfacial properties of the nanostructured dye-sensitized solid heterojunction TiO_2/$RuL_2(NCS)_2$/CuI, J. Chem. Phys. 120 (2004) 11224–11232.

[31] M.Y. Song, K.-J. Kim, D.Y. Kim, Enhancement of photovoltaic characteristics using a PEDOT interlayer in TiO_2/MEHPPV heterojunction devices, Sol. Energy Mater. Sol. Cells 85 (2005) 31–39.

[32] W.H. Kim, A.J. Mäkinen, N. Nikolov, R. Shashidhar, H. Kim, Z.H. Kafafi, Molecular organic light-emitting diodes using highly conducting polymers as anodes, Appl. Phys. Lett. 80 (2002) 3844–3846.

[33] U.O. Krašovec, M. Bergic, M. Hočevar, M. Topič, Unique TiO_2 paste for high efficiency dye-sensitized solar cells, Sol. Energy Mater. Sol. Cells 93 (2009) 379–381.

[34] C. Longo, A.F. Nogueira, M.-A. Paoli, Solid-state and flexible dye-sensitized Tio_2 solar cells: a study by electrochemical impedance spectroscopy, J. Phys. Chem. B. 106 (2002) 5925–5930.

[35] T. Hoshikawa, R. Kikuchi, K. Eguchi, Ceram. Japan 39 (2004) 455–458.

[36] T. Hoshikawa, T. Ikebe, R. Kikuchi, K. Eguchi, Effects of electrolyte in dye-sensitized solar cells and evaluation by impedance spectroscopy, Electrochim. Acta 51 (2006) 5286–5294.

[37] M. Halik, H. Klauk, U. Zschieschang, G. Schmid, W. Radlik, W. Weber, Polymer gate dielectrics and conducting-polymer contactsfor high-performance organic thin-film transistors, Adv. Mater. 14 (2002) 1717–1722.

operation include cross-linked polymers [16], self-assembled monolayers [17,18] and the use of electrolytes [19,20]. The latter can achieve very low voltage ranges due to the very high electric field generated at the interface between the electrolyte and the organic semiconductor. Mobile ions inside the electrolyte move to form an electric double layer (EDL) at the interface, with a capacitance that can reach several hundreds of $\mu F/cm^2$ [19,21,22]. These devices typically operate below 1 V. Furthermore, increasing the capacitance leads to an increase of the charge carrier mobility for polymer semiconductors and the subsequent increase in the output current [23].

In a previous work [24], we successfully used pure water to isolate the gate from the semiconductor. We managed to show that within the water stability potential range, our devices run in the field-effect mode with negligible electrochemical reactions, which is usually the main issue for electrolyte-gated OFETs [25].

Here, we investigate the use of semiconductor/insulator blends as active layer in water-gated OFETs in order to improve the performance of the device.

2. Experimental

2.1. Materials

Poly(3-hexylthiophene) (P3HT) (MW = 37,000 g mol^{-1}, 98% regioregular) and poly(methyl methacrylate) (PMMA MW = 120,000 g mol^{-1}) were purchased to Sigma–Aldrich and used without further purification. Chlorobenzene was purified by distillation.

Solutions of P3HT/PMMA (1 wt.%) blends with different ratios were prepared as followed. First PMMA was dissolved in chlorobenzene by stirring overnight. Then P3HT was added to the PMMA solution and stirred until the P3HT is totally dissolved. Finally, solutions were filtered with a 200 nm polytetrafluoroethylene (PTFE) filter.

2.2. OFETs preparation

A general view of the device is sketched in Fig. 1 together with the chemical structure of P3HT and PMMA. The transistors were built in a bottom contacts and top gate configuration. The substrate consisted of a silicon wafer with 300 nm thermally grown oxide. Contacts were made of evaporated gold patterned by conventional micro-lithography. P3HT/PMMA solutions were spin-coated onto the substrates at 1500 rpm for 30 s in ambient conditions. The devices were then kept overnight in an oven at 110 °C under a pressure of 50 mbar to remove the residual solvent.

A water droplet was generated with a calibrated microsyringe and deposited onto the semiconductor. The water used was obtained from a Elgastat UHQ II purification system with a resistivity of 18 MΩ cm. In ambient conditions, the main contaminant of water is dissolved carbon dioxide, which forms carbonic acid that dissociates in turn into hydrogenocarbonate and hydronium ions with a concentration of about 10^{-6} mol/L. The concentrations of other species in solution are negligible. The gate electrode consisted of a platinum wire dipped into the droplet.

2.3. Electrical characterization and thin-films morphological study

Electrical measurements were realized using a semiconductor parameter analyzer (Keithley 4200-SCS) in a humid environment to prevent the water droplet from drying. Before measuring each blend, the platinum wire was cleaned in an ultrasonic bath for 10 min in deionized water and 10 min in acetone then put in a UV surface decontamination system (Novascan PSD-UV) for 15 min to get rid of any trace of organic contamination.

Three different channel lengths (3, 10 and 40 μm) were used and for each length, six transistors were tested. The reported data correspond to the mean of these six measurements.

Atomic force microscopy was realized on a multimode SPM with Nanoscope III controller (Digital Instruments) in tapping mode on thin-films deposited on silicon wafers with thermally grown oxide (300 nm).

3. Results and discussion

Fig. 2 shows AFM 10 × 10 μm^2 topographic images of the P3HT/PMMA films with various weight ratios. Blends with PMMA concentrations up to 30% (Fig. 2a and b) do not show any clear phase separation at this scale. However,

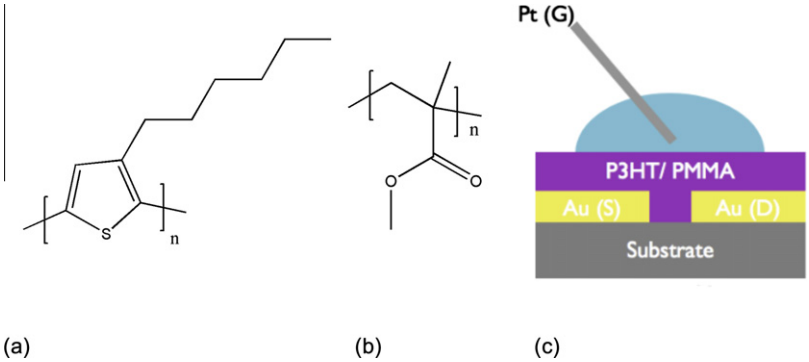

Fig. 1. Chemical structure of (a) P3HT and (b) PMMA. (c) Cross-section of the water-gated OFET.

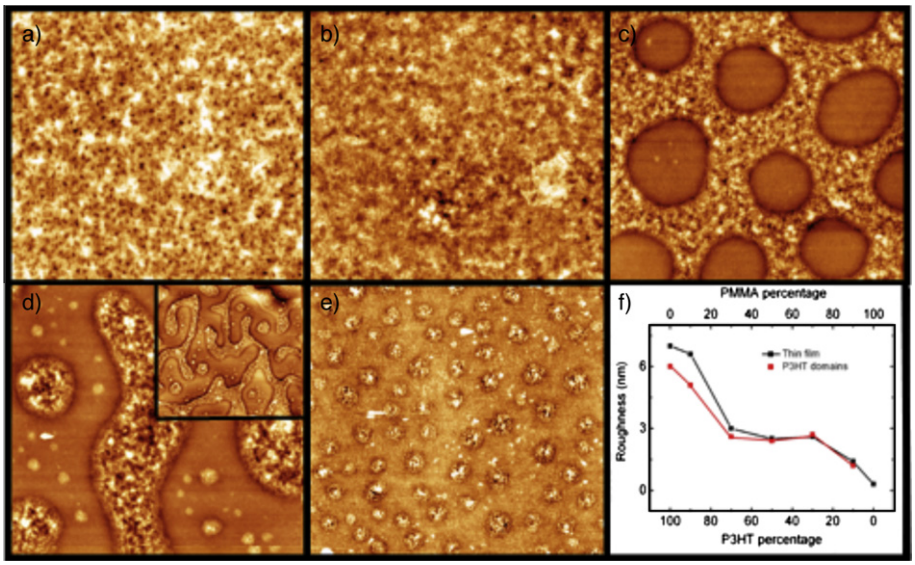

Fig. 2. AFM topographic images ($10 \times 10\ \mu m^2$) of (a) 100%, (b) 70%, (c) 50%, (d) 30% (the inset shows the topography of a $30 \times 30\ \mu m^2$ image) and (e) 10% of P3HT/PMMA blend thin films. (f) RMS roughness as a function of P3HT percentage. The RMS was estimated over the whole image or over the P3HT domains only.

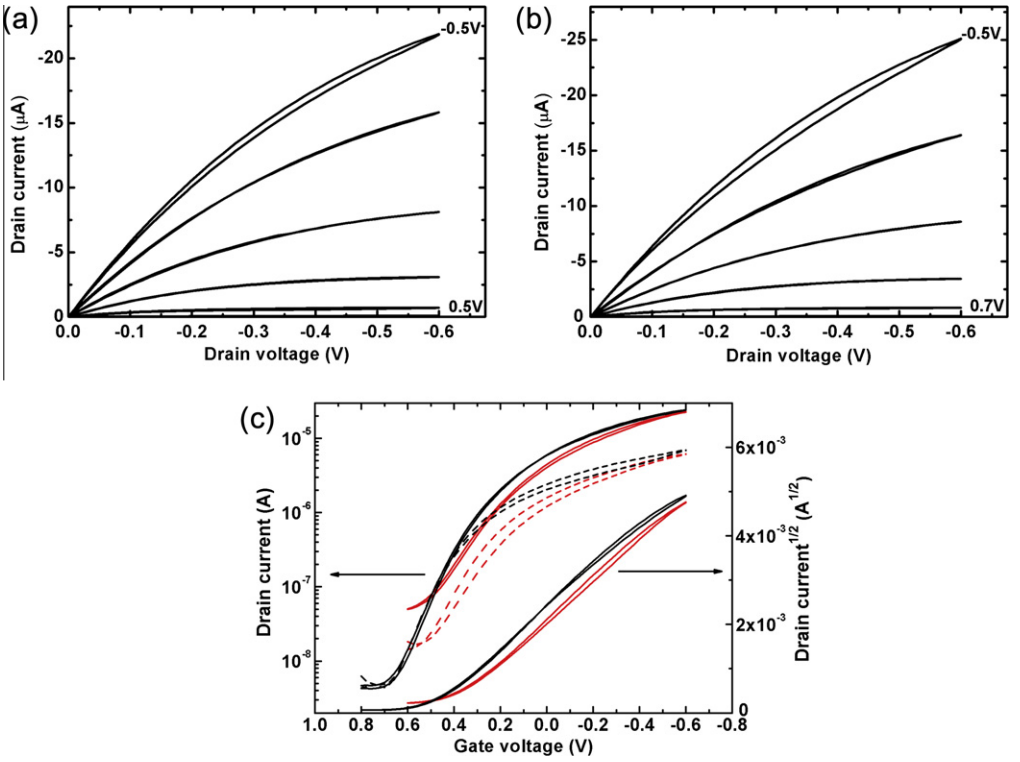

Fig. 3. Output curves of OFETs with (a) pure P3HT and (b) P3HT:PMMA 3:7 blend. (c) Transfer curves of homo-P3HT (red line) and P3HT:PMMA 3:7 blend (black line) plotted in a semi-log scale (left scale) for $V_d = -0.1$ V (dashed line) and $V_d = -0.5$ V (full line) and in a square root scale (right scale) for $V_d = -0.5$ V. (For interpretation of the references to color in this figure legend, the reader is referred to the web version of this article.)

an abrupt decrease of the RMS roughness (Fig. 2f) occurs, indicating an enhancement of the homogeneity due to the increase of PMMA content (RMS roughness of pure PMMA was found to be below 0.5 nm). For a ratio of P3HT/PMMA of 1:1 (Fig. 2c), lateral phase separation clearly occurs as indicated by the dark nanospheres of PMMA into a matrix of P3HT. With 70% of PMMA (Fig. 2d), the two phases tend to form two continuous net-

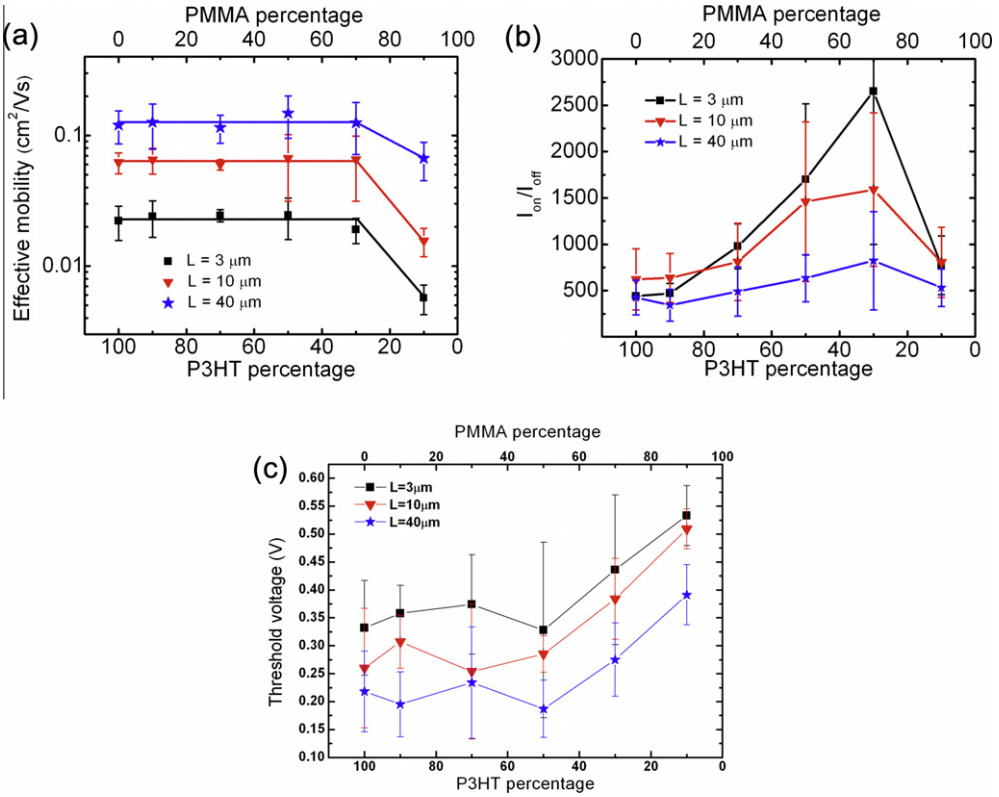

Fig. 4. Compositional dependence of the (a) effective hole mobility; (b) I_{on}/I_{off} ratio and (c) threshold voltage. The data and error bars are estimated from the measurements on six different devices.

works that extend all over the film, as indicated by the $30 \times 30\ \mu m^2$ image given in the inset. Increasing the PMMA weight ratio to 90% (Fig. 2e) results in isolated nanospheres of P3HT. Furthermore, above this amount of PMMA, the roughness decreases to reach a plateau that extends up to 70% of PMMA, resulting in a smoother film. A further decrease of the roughness occurs for PMMA concentrations above 70%. This trend is also observed when measuring the roughness of the domains composed of P3HT only. We note that a similar behavior has been recently reported on P3HT/PMMA blends [26].

All OFETs made of polymer blends show a typical p-channel behavior. Output characteristics of pure-P3HT and blend with 70% of PMMA are presented in Fig. 3.

The field-effect mobility of holes was extracted from the transfer characteristics in the saturation regime (Fig. 3c). The mobility is estimated from the slope of the $I_d^{1/2}$ vs. V_g curve and the capacitance used is that measured in a previous work [24]; data for various blend ratios are gathered in Fig. 4a. Three different channel lengths have been used. Increasing the channel length from 3 to 40 μm improves the effective mobility by almost one order of magnitude. This phenomenon is well documented and is a consequence of contact resistance [27,28]. For small channels, the contact resistance considerably reduces the effective mobility. This lowering is less pronounced as the channel length increases.

For pure-P3HT spin-coated from a chlorobenzene solution, the highest mobility with a 3 μm channel length is 0.03 $cm^2/V\,s$, which is higher than what reported in our previous work where the film was deposited from a chloroform solution [24]. We attribute this increase to the highest boiling point of chlorobenzene. Chloroform is widely used as solvent for P3HT. However, due to its low boiling point (62 °C) and fast evaporation rate, the corresponding films have a lesser degree of crystallinity. It has been shown that the use of a higher boiling point solvent such as chlorobenzene (132 °C) leads to an improvement of the mobility due to a higher crystallinity consecutive to a slower evaporation speed [29].

Of interest is that in blends, the mobility remains practically constant within a broad range of PMMA concentration (up to 70%). As the phase separation is lateral, one would expect a variation of the mobility due to a decrease of the P3HT area at the interface. Instead, it seems that the percolation paths observed on the AFM pictures suffices to warrant a good charge carrier transport through the blend. However, above 70% of PMMA, P3HT domains change into isolated islands, leading to discontinuous conducting paths and a subsequent lowering of the hole mobility.

Blends with 90% of PMMA show a clear (although substantially reduced) field-effect behavior. The presence of a thin P3HT film on top of the blend (vertical phase separation) is unlikely because it is at variance with the observed decrease of the RMS roughness. Instead, we attribute this reduced charge transport capability to a partial dilution of P3HT into the PMMA matrix; although this hypothesis

would deserve further investigations, evidence for it can already be found in the literature [26].

Fig. 3c shows the transfer curves, in the saturation regime, for pure-P3HT and P3HT:PMMA 3:7 blend. The on current is almost identical in both cases, while the off current is lowered by one order of magnitude for the blend, thus resulting in a significant increase of the on/off ratio. The dependence of the on/off ratio with the composition of the blend is shown in Fig. 4b; it increases up to 5000 when decreasing the P3HT concentration down to 30%. Below this value, the on/off ratio drops down to the value of pure-P3HT, because of the drop of the on current, while the off current still decreases. Several explanations can be put forward. One is the fact that the formation of insulating domains decreases the leakage current. An alternative explanation would be the decrease of the charge density at the semiconductor/water interface resulting of the lowering of the P3HT concentration in the film, because the off current is known to be inversely proportional to the charge density [30,31]. Of interest is the fact that for high PMMA concentrations (above 50%), the off current measured on the transfer curves does not depend on the drain voltage (Fig. 3c).

Finally, Fig. 4c shows the variation of the threshold voltage as a function of the concentration of PMMA. A threshold voltage close to 0 V is desired for low-voltage applications. In the blends, this voltage shifts towards more positive values for PMMA concentration above 50%, yet remaining at a low level (<1 V).

4. Conclusion

Used in a water-gated configuration, P3HT/PMMA blends can lead to transistors with reasonably high mobility (up to 0.15 $cm^2/V\,s$) working at very low voltage (below 1 V). The mobility is not affected when increasing the proportion of PMMA up to 70%, while the off current is significantly lowered, thus resulting in an enhancement in the on/off ratio. AFM images showed that up to 70% of PMMA, a percolation path exists, thus allowing an efficient charge transport through the channel, in good agreement with the electrical measurements.

Acknowledgments

One of the author (L.K.) thanks the French Ministry of Education and Research for a scholarship. We would like to thank Lars Herlogsson (Linköping University) for providing the photolithography patterned substrates.

References

[1] J. Takeya, J. Kato, K. Hara, R. Hirahara, K. Yamada, Y. Nakazawa, S. Ikehata, K. Tsukagoshi, Y. Aoyagi, T. Takenobu, Y. Iwasa, Phys. Rev. Lett. 98 (2007) 196804.
[2] S. Lee, B. Koo, J. Shin, E. Lee, H. Park, Appl. Phys. Lett. 88 (2006) 162109.
[3] C.D. Sheraw, T.N. Jackson, D.L. Eaton, J.E. Anthony, Adv. Mater. 15 (2003) 2009.
[4] K.H. Yim, Z. Zheng, R.H. Friend, W.T.S. Huck, J.S. Kim, Adv. Funct. Mater. 18 (2008) 2897.
[5] N. Ananthakrishnan, G. Padmanaban, S. Ramakrishnan, J.R. Reynolds, Macromolecules 38 (2005) 7660.
[6] H. Hoppe, N.S. Sariciftci, J. Mater. Chem. 16 (2006) 45.
[7] R. Schroeder, L.A. Majewski, M. Grell, Adv. Mater. 17 (2005) 1535.
[8] F.Y. Yang, M.Y. Hsu, G.W. Hwang, K.J. Chang, Org. Electron. 11 (2010) 81.
[9] J. Smith, R. Hamilton, I. McCulloch, N. Stingelin-Stutzmann, M. Heeney, D.D.C. Bradley, T.D. Anthopoulos, J. Mater. Chem. 20 (2010) 2562.
[10] A. Babel, S.A. Jenekhe, Macromolecules 37 (2004) 9835.
[11] A. Babel, S.A. Jenekhe, J. Phys. Chem. B 107 (2003) 1749.
[12] S. Goffri, C. Müller, N. Stingelin-Stutzmann, D.W. Breiby, C.P. Radano, J.W. Andreasen, R. Thompson, R.A.J. Janssen, M.M. Nielsen, P. Smith, H. Sirringhaus, Nat. Mater. 5 (2006) 950.
[13] A.C. Arias, F. Endicott, R.A. Street, Adv. Mater. 18 (2006) 2900.
[14] J. Sun, B.J. Jung, T. Lee, L. Berger, J. Huang, Y. Liu, D.H. Reich, H.E. Katz, Appl. Mater. Interfaces 2 (2009) 412.
[15] L. Qiu, J.A. Lim, X. Wang, W.H. Lee, M. Hwang, K. Cho, Adv. Mater. 20 (2008) 1141.
[16] M.H. Yoon, H. Yan, A. Facchetti, T.J. Marks, J. Am. Chem. Soc. 127 (2005) 10388.
[17] M. Halik, H. Klauk, U. Zschieschang, G. Schmid, C. Dehm, M. Schütz, S. Maisch, F. Effenberger, M. Brunnbauer, F. Stellacci, Nature 431 (2004) 963.
[18] H. Klauk, U. Zschieschang, M. Halik, J. Appl. Phys. 102 (2007) 074514.
[19] M.J. Panzer, C.D. Frisbie, Adv. Mater. 20 (2008) 3177.
[20] L. Herlogsson, X. Crispin, N.D. Robinson, M. Sandberg, O.J. Hagel, G. Gustafsson, M. Berggren, Adv. Mater. 19 (2007) 97.
[21] S. Mitra, A.K. Shukla, S. Sampath, J. Power Sources 101 (2001) 213.
[22] J.H. Cho, J. Lee, Y. Xia, B. Kim, Y. He, M.J. Renn, T.P. Lodge, C.D. Frisbie, Nat. Mater. 7 (2008) 900.
[23] Y. Xia, J.H. Cho, J. Lee, P.P. Ruden, C.D. Frisbie, Adv. Mater. 21 (2009) 1.
[24] L. Kergoat, L. Herlogsson, D. Braga, B. Piro, M.C. Pham, X. Crispin, M. Berggren, G. Horowitz, Adv. Mater. 22 (2010) 2565.
[25] M.J. Panzer, C.D. Frisbie, J. Am. Chem. Soc. 129 (2007) 6599.
[26] M.C. Wu, H.C. Liao, Y. Chou, C.P. Hsu, W.C. Yen, C.M. Chuang, Y.Y. Lin, C.W. Chen, Y.F. Chen, W.F. Su, J. Phys. Chem. B 114 (2010) 10277.
[27] E.J. Meijer, G.H. Gelinck, E. van Veenendaal, B.H. Huisman, D.M. de Leeuw, T.M. Klapwijk, Appl. Phys. Lett. 82 (2003) 4576.
[28] H. Klauk, G. Schmid, W. Radlik, W. Weber, L. Zhou, C.D. Sheraw, J.A. Nichols, T.N. Jackson, Solid-State Electron. 47 (2003) 297.
[29] J.F. Chang, B. Sun, D.W. Breiby, M.M. Nielsen, T.I. Sölling, M. Giles, I. McCulloch, H. Sirringhaus, Chem. Mater. 16 (2004) 4772.
[30] A.R. Brown, C.P. Jarrett, D.M. de Leeuw, M. Matters, Synth. Met. 88 (1997) 37.
[31] C. Tanase, E.J. Meijer, P.W.M. Blom, D.M. de Leeuw, Org. Electron. 4 (2003) 33.

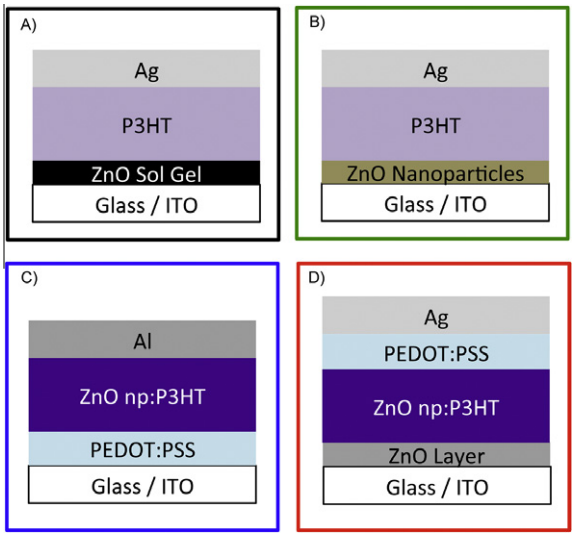

Fig. 1. Schematic representation of device architectures for (A) sol–gel bilayer, (B) nanoparticle bilayer, (C) conventional blend and (D) inverted blend devices.

Blended devices may be constructed in either a conventional or an inverted architecture. In a conventional architecture, holes are collected through the ITO by first applying poly(3,4-ethylenedioxythiophene):poly(styrene sulfonate) (PEDOT:PSS) to increase the ITO work function and using a low work function metal top contact, e.g. Ca or Al, to collect the electron (Fig. 1C). In the inverted architecture, electrons are collected through ITO by first applying ZnO to decrease its work function and using a hole transport layer, e.g. PEDOT:PSS, and a high work function metal to collect holes (Fig. 1D). One obstacle to viable ZnO np blended devices is a sharp decline in the solar cell performance with exposure to even low amounts of UV [18,19]. While blended all-organic P3HT:PCBM bulk heterojunction devices have been shown to benefit from an inverted architecture [20–22] in terms of device stability, [20–26] an inverted architecture has not been widely investigated in devices with other active layers. When ZnO is used as the acceptor, the deposition of commercial acid PEDOT:PSS layer on top of the active layer results in removal/damage of the active layer. Krebs et al. demonstrated the ZnO np hybrid cells blended with poly-(3-carboxydithiophene) [27] using commercial PEDOT:PSS as the hole transport layer, but the very poor performance of the device indicates that the ZnO in the active layer might have been damaged. Here, we report the first demonstration of inverted ZnO np:P3HT blended devices using a neutral pH PEDOT:PSS [28–30]. The device performance and UV stability of ZnO:P3HT bilayer and blend devices in conventional and inverted architectures are compared.

2. Experimental methods

ZnO np were synthesized in methanol (Fisher Chemical, ACS grade) following a published procedure [18]. The ZnO np were rinsed three times in methanol by settling under gravity to a final concentration of 350 mg/ml. The nanoparticles were diluted with a solution of chlorobenzene and 10% 1-propanol to a final concentration of 50 mg/ml, with approximately 10% methanol in the final solution, or diluted to 7 mg/ml in butanol (ACS certified, Fisher Chemical) with a trace amount of methanol in the final solution.

The devices are prepared on patterned ITO substrates ($R \leqslant 15\ \Omega\ cm^2$) (Thin Film Devices, Anaheim, CA), which are sonicated in soapy water and isopropyl alcohol (ACS grade, Fisher Chemical) for 10 min each and then dried under flowing nitrogen, followed by a 20 min UV ozone treatment. For the sol–gel bilayer device (Fig. 1A), a 35 nm ZnO film is prepared by spin coating a 0.75 M zinc acetate solution with 0.045 ml ethanolamine/ml in 2-methoxyethanol onto the ITO at 1000 rpm and annealing in air on a hotplate at 300 °C for 10 min. P3HT films of 100 nm are then spun from a 24 g/L solution of P3HT (electronics grade regioregular P3HT 4002-E, Rieke Metals) dissolved in chlorobenzene (Sigma Aldrich, 99.8%) at 1000 rpm for 1 min in air. In the ZnO np bilayer (Fig. 1B), the ZnO np layer is prepared by spinning four layers of the ZnO np in butanol solution at 1000 rpm to form a 50 nm thick film, and a P3HT layer spun on top as in sol–gel bilayer devices.

For conventional blend devices (Fig. 1C), a 50 nm PEDOT:PSS (H.C. Starck, Clevios) layer was deposited on the ITO by spinning at 2000 rpm for 1 min followed by heating at 120 °C for 10 min in air to remove water. In inverted blend devices (Fig. 1D), a ZnO sol–gel layer or ZnO np layer is spun on ITO as described above. The active layer in either architecture uses a ZnO np:P3HT blended suspension with 15 wt.% ZnO and 10 mg/ml P3HT prepared in a solution of 10% 1-propanol (certified normal, Fisher Chemical):90% chlorobenzene (99+%, ACROS). A 100 nm blended active layer is spun at 500 rpm for 1 min in air. For inverted blend devices, a PEDOT:PSS solution was spun at 2000 rpm for 1 min. The PEDOT:PSS has 1% by weight surfactant (Aldrich, Zonyl 100) added to aid wetting, and is adjusted to pH 7.5 with 1 M NaOH to prevent etching of the ZnO np in the active layer [31]. The PEDOT:PSS film was dried on a hotplate at 120 °C for 10 min. Conventional blend devices were likewise heated to 120 °C for 10 min in a nitrogen box after spinning to ensure the same heat treatment of the active layer in both blend architectures. The top aluminum (99.999%, Kurt J. Lesker Co.) (conventional) or silver (99.999%, Williams Advanced Materials) (inverted) contacts are prepared by thermal evaporation of 100 nm of metal on top of the devices in vacuum.

The device performance was then measured under simulated one-sun illumination, using a KG5 filtered tungsten–halogen lamp adjusted with an NREL calibrated Si photodiode to 100 mW/cm^2. Devices were stored and tested under ambient condition, and humidity was not controlled. No UV filter was used. Conventional devices were tested immediately after Al deposition while inverted devices were aged in the dark for three days before testing. Ag is used as the hole-collecting electrode for the inverted device. It has been documented that the work function of the Ag increases over time with air exposure, resulting in improved device performance [25,32]. In contrast, conventional devices degrades quickly with air exposure. Hence, the initial measurements of the two kinds of devices are offset by 3 days, and represent the best possible values

for each. Each of the six individual devices per sample was tested upon initial exposure to light, and the results averaged to get the initial current–voltage characteristics. Subsequently, the devices were tested at regular increments for 70 min under continuous white light illumination in the solar simulator. The device cross-section was prepared by focused ion beam (FIB), and was imaged using a Philips CM30 TEM at an operating voltage of 300 kV.

3. Results and discussion

Fig. 2A depicts the *I–V* response for the four types of photovoltaic devices shown in Fig. 1. The device parameters are summarized in Table 1. The average and standard deviation in the device parameters in Table 1 are determined from six devices measured from each substrate. Bilayer devices have an open circuit voltage (V_{oc}) of ~400 mV when the ZnO layer is made from sol–gel (Fig. 1A), while they have a V_{oc} of ~600 mV when using ZnO np (Fig. 1B). The increase in V_{oc} in the ZnO np bilayer solar cells originates from an increased ZnO bandgap, resulting in an larger band offset between the highest occupied molecular orbital of the P3HT and the conduction band of ZnO [31]. While there is an increased V_{oc} in the nanoparticle bilayer device, this device suffers from a decreased short circuit current (J_{sc}) and fill factor compared with the sol–gel bilayer, resulting in an efficiency of 0.08%, similar to the sol–gel based bilayer device which has $\eta = 0.10\%$ (Table 1).

Conventional blended ZnO np:P3HT devices (Fig. 1C) work when excitons are generated in the P3HT, and electrons collected by the ZnO np and transported up to the Al electrode, while holes are carried through the P3HT to the PEDOT:PSS and down to the ITO. Not only do conventional blend devices have an increased V_{oc} above sol–gel bilayer devices due to the larger bandgap in the ZnO np, as in the np bilayer device, they also have a greatly increased J_{sc}, resulting from a much larger interfacial surface area. These blended devices have an average resulting efficiency of 0.62%; 7.75 times the efficiency of the ZnO np bilayer (Table 1). Our best single conventional blend device achieved a η of 0.75% with $J_{sc} = 2.64$ mA/cm^2, $V_{oc} = 510$ mV, and FF = 55%. However, even this device has not achieved as high efficiency as previous published result by Beek et al., of 0.9% [1].

Optimizing blend morphology between the electron donor and acceptor is critical for achieving high efficiency [17]. By spin coating the blend from a single solution, control over this final morphology is a significant challenge. A representative TEM of the cross-section of a conventional blend device is shown in Fig. 2B, revealing large agglomerations of ZnO np in the blend layer. There are areas of P3HT devoid of ZnO np (light regions) and dark regions of ZnO np aggregates. In addition, pure P3HT regions are found preferentially near the bottom PEDOT:PSS hole transport layer while ZnO np are at the top electrode interface. A higher efficiency can be expected if less aggregation in the blend morphology can be produced with optimized processing conditions.

Inverted ZnO np:P3HT blend devices have not been previously reported in the literature due to the acidity of the commercially available PEDOT:PSS. However, an inverted device structure is made possible by adjusting PEDOT:PSS from being highly acidic to neutral pH to prevent ZnO np in the active layer from being etched out when PEDOT:PSS is deposited on top. Neutral PEDOT:PSS has been used in the literature to make tandem solar cells, [28–30] but has not been utilized in making inverted ZnO np blend solar cells. The inverted blend structure (Fig. 1D) using a sol–gel derived bottom ZnO electron transport layer demonstrates an $\eta = 0.47\%$; 5.9 times that of the bilayer analog, though not quite as high as the conventional architecture. The increases in efficiency come primarily from the increased J_{sc}; 2.9 mA/cm^2 for the conventional blend device, and 2.0 mA/cm^2 in the inverted blend, compared with 0.45 mA/cm^2 for the sol–gel bilayer device (Fig. 2A and Table 1). The TEM micrograph of an inverted device (Fig. 2C) reveals similar ZnO np aggregations as in the conventional device (Fig. 2B). In addition, pure P3HT regions are found near the bottom ZnO np electron transport layer and ZnO np aggregates are in contact with the PEDOT:PSS hole transport layer. Since both kinds of devices have been annealed at 120 °C for 10 min, it is not surprising that the distributions of ZnO and P3HT in the blend are similar in both. In conventional devices, the high concentration of ZnO np at the top surface of the active layer may act as an electron

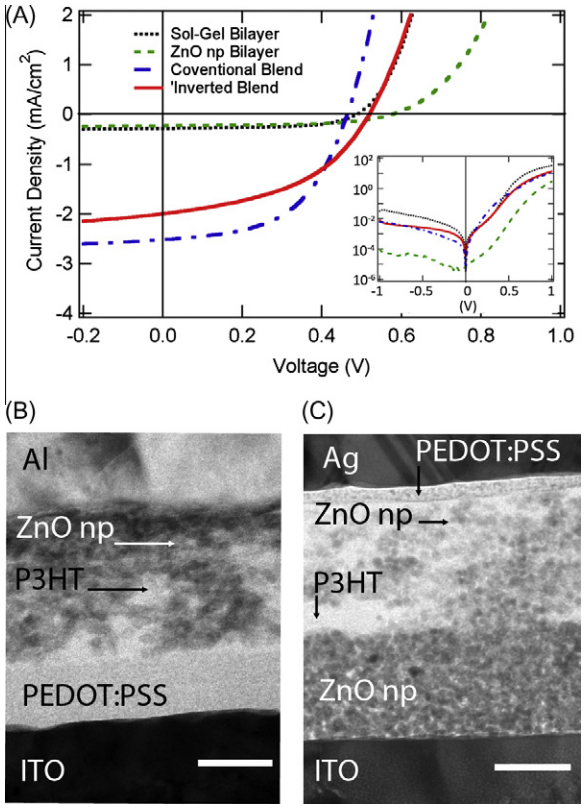

Fig. 2. (A) Current density–voltage response of each of the four device architectures measured under white light illumination at 100 mA/cm^2. Inset: current density–voltage dark response for each device. Cross-sectional TEM micrograph of (B) a conventional blend device and (C) an inverted device.

Table 1
Photovoltaic device characteristics for each hybrid device architecture are averaged over six devices with standard deviations. Characteristics include open circuit voltage (V_{oc}), current density (J_{sc}), fill factor (FF), efficiency (η), and series resistance (R_s).

Sample	V_{oc} (mV)	J_{sc} (mA/cm^2)	FF (%)	η (%)	R_s (Ω cm^2)
Sol–gel bilayer	394 ± 7	0.45 ± 0.01	58.1 ± 3.78	0.10 ± 0.00	14 ± 1.4
Nanoparticle bilayer	579 ± 11	0.23 ± 0.01	56.2 ± 0.05	0.08 ± 0.01	35 ± 2.8
Conventional blend	468 ± 48	2.52 ± 0.11	52.3 ± 0.02	0.62 ± 0.11	9 ± 0.23
Inverted blend	520 ± 24	2.00 ± 0.09	45.2 ± 2.58	0.47 ± 0.05	18 ± 0.5

transport layer, readily transporting the electrons accepted by the ZnO throughout the blend to the Al electrode. In contrast, having the donor material adjacent to the electron transport layer and acceptor material in contact with the hole transport layer in the inverted devices are not ideal. Therefore, the blend morphology could explain the difference in device performance for the two architectures, where a lower J_{sc} is observed in the inverted device as compared to the conventional device.

Under white light exposure, we observe degradation behavior, with decreases in current, voltage, as well as fill factor, for all nanoparticle based hybrid devices, albeit with different rates (Fig. 3). Each of the data plots in Fig. 3 are taken from one device, however, they are representative of the white-light-exposure degradation behavior for each architecture observed across numerous devices. While the sol–gel bilayer device has a relatively low $\eta = 0.1$, it has superior stability in light (Fig. 3). By contrast, the nanoparticle bilayer degrades moderately over the 70 min testing time to 60% of its original efficiency, primarily through a decline in the short circuit current density (Fig. 3A). Since both bilayer devices have the same architectures, this difference in light-exposure stability indicates the difference in the microstructure in the ZnO acceptor layer. The sol–gel derived ZnO layer consists of nanometer-sized crystallites that are sintered and connected during the thermal pyrolysis. The nanoparticle ZnO film is not further heated, leaving behind a close packed layer of individual nanoparticles, presumably with acetate groups on the surfaces. These differences in surface chemistry and structure of the ZnO nanocrystallites are most likely responsible for the differences in light-exposure stability. If the ZnO np film is annealed to 300 °C, i.e., the same heat treatment as the sol–gel ZnO film, the device performance would be similar to that of devices containing sol–gel ZnO.

In the conventional blend devices, as noted previously in the literature, [19] there is a significant loss of performance with white light exposure due to the UV components. We observe sharp drops in J_{sc} (Fig. 3A), V_{oc} (Fig. 3B) and fill factor (Fig. 3C), resulting in a loss of 60% of device efficiency in 70 min of white light exposure (Fig. 3D). Quist et al. explain the degradation in performance originating from electrons generated by the UV illumination, causing filled electron traps in the ZnO. Once electron traps are filled, free electrons are formed leading to the ZnO acting as a conductor, leading to loss of photovoltaic behavior [19]. Since the inverted device shown in Fig. 3 uses an unannealed ZnO np film as the electron transport layer, it exhibits similar J_{sc} and V_{oc} degradation behavior as the ZnO np bilayer device with white light exposure. Although the inverted blend devices have the

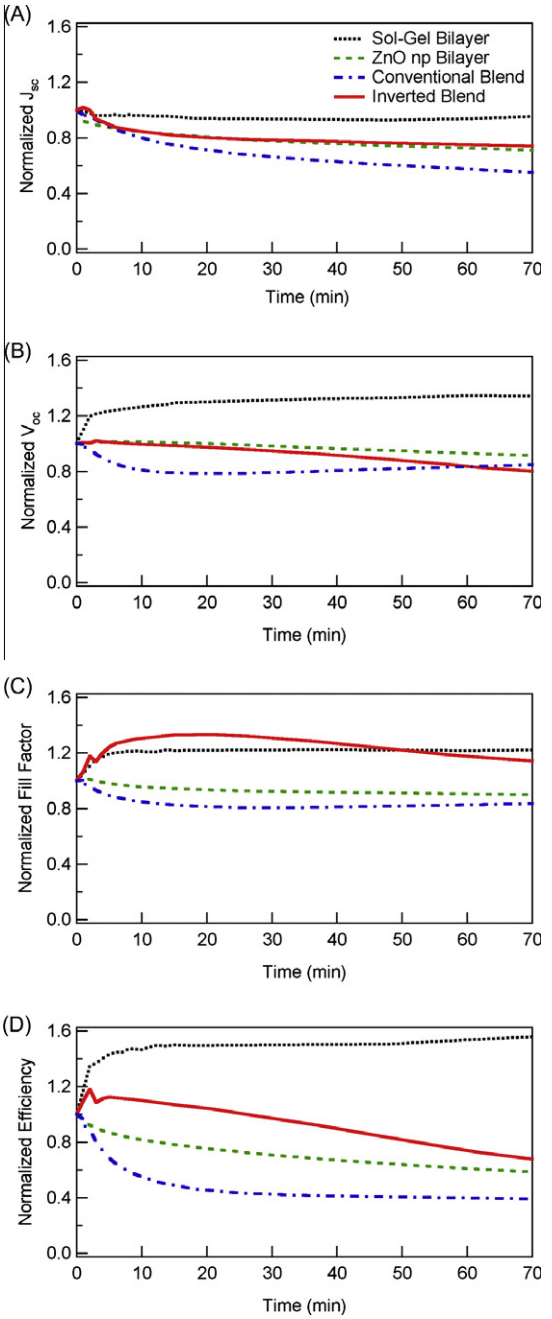

Fig. 3. Plots of normalized (A) current density (J_{sc}), (B) open circuit voltage (V_{oc}), (C) fill factor, and (D) efficiency for each hybrid device as a function of white light exposure time in minute. Dotted lines included to guide the eye.

same active layer as the conventional blend devices, they exhibit enhanced stability, dropping only to 60% of its initial efficiency compared to 40% of the initial efficiency in the conventional blend devices.

The improved stability observed in inverted architecture over conventional, similar to P3HT:PCBM devices, indicates that the relationship between device stability and architecture might be more broadly applicable. It points out that the change in the Al electrode, rather than changes in the active layer, might be the culprit for the degradation of conventional devices, as water and oxygen can transport through the Al grain boundaries [33,34]. A question arises about whether conventional devices using Ag, a more inert metal than Al, would exhibit better stability. As shown previously on P3HT:PCBM BHJ devices, conventional devices with Ag electrodes have lower efficiency [35] and actually degrade faster than ones with low work function electrodes [25,36]. The origin of the faster degradation using Ag as the cathode arises from a work function increase of Ag, which makes Ag ineffective in collecting electrons. We wanted to compare the degradation behavior for the highest efficiency cells of the two architectures. Thus, we chose Al as the electron-collecting electrode for the conventional cell and Ag as the hole-collecting electrode for the inverted cell.

4. Conclusions

We have shown that in bilayer hybrid devices, by using ZnO np in the acceptor layer, the V_{oc} is increased by 200 mV above sol–gel based ZnO devices due to the increase in the ZnO bandgap in the nanoparticles. For the first time, an inverted ZnO np:P3HT blend solar cell is demonstrated. Blend devices have a 6–8 times higher efficiency over bilayer devices due to the increased interfacial area between electron donor and acceptor when both are intimately mixed, leading to higher J_{sc}. However, we find that devices employing ZnO np are more susceptible to light-exposure degradation when compared to those employing ZnO sol–gel films. Similar to previous publications, we observe rapid device degradation as a result of white light exposure in conventional ZnO np:P3HT blended devices. We find that when the device architecture is changed from a conventional to an inverted blend structure, the response to light exposure is dramatically altered, and the devices show significant improvement in stability. If ZnO np hybrid devices can be designed with light-exposure stability, their performance is promising for future applications. Determining the origin of improved light-exposure stability in inverted and bilayer nanoparticle devices may benefit future work in these hybrid devices.

Acknowledgements

We thank Nelson Bell for discussions and assistance with the nanoparticle synthesis. This work was supported by Sandia LDRD program. Sandia is a multiprogram laboratory operated by Sandia Corporation, a Lockheed Martin Company, for the United States Department of Energy under Contract DE-AC04-94AL85000.

References

[1] W.J.E. Beek, M.M. Wienk, R.A.J. Janssen, Hybrid solar cells from regioregular polythiophene and ZnO nanoparticles, Adv. Funct. Mater. 16 (2006) 1112–1116.
[2] D.C. Olson, J. Piris, R.T. Collins, S.E. Shaheen, D.S. Ginley, Hybrid photovoltaic devices of polymer and ZnO nanofiber composites, Thin Solid Films 496 (2006) 26–29.
[3] P. Ravirajan, A.M. Peiro, M.K. Nazeeruddin, M. Graetzel, D.D.C. Bradley, J.R. Durrant, J. Nelson, Hybrid polymer/zinc oxide photovoltaic devices with vertically oriented ZnO nanorods and an amphiphilic molecular interface layer, J. Phys. Chem. B 110 (2006) 7635–7639.
[4] L.E. Greene, M. Law, B.D. Yuhas, P.D. Yang, ZnO–TiO_2 core-shell nanorod/P3HT solar cells, J. Phys. Chem. C 111 (2007) 18451–18456.
[5] D.C. Olson, Y.-J. Lee, M.S. White, N. Kopidakis, S.E. Shaheen, D.S. Ginley, J.A. Voigt, J.W.P. Hsu, Effect of ZnO processing on the photovoltage of ZnO/Poly(3-hexylthiophene) solar cells, J. Phys. Chem. C 112 (2008) 9544–9547.
[6] Y.J. Lee, M.T. Lloyd, D.C. Olson, R.K. Grubbs, P. Lu, R.J. Davis, J.A. Voigt, J.W.P. Hsu, Optimization of ZnO nanorod array morphology for hybrid photovoltaic devices, J. Phys. Chem. C 113 (2009) 15778–15782.
[7] D.C. Olson, S.E. Shaheen, M.S. White, W.J. Mitchell, M.F.A.M. van-Hest, R.T. Collins, D.S. Ginley, Band-offset engineering for enhanced open-circuit voltage in polymer-oxide hybrid solar cells, Adv. Funct. Mater. 17 (2007) 264–269.
[8] M.T. Lloyd, Y.J. Lee, R.J. Davis, E. Fang, R.M. Fleming, J.W.P. Hsu, R.J. Kline, M.F. Toney, Improved efficiency in poly(3-hexylthiophene)/zinc oxide solar cells via lithium incorporation, J. Phys. Chem. C 113 (2009) 17608–17612.
[9] P.E. Shaw, A. Ruseckas, I.D.W. Samuel, Exciton diffusion measurements in poly(3-hexylthiophene), Adv. Mater. 20 (2008) 3516.
[10] N. Sekine, C.H. Chou, W.L. Kwan, Y. Yang, ZnO nano-ridge structure and its application in inverted polymer solar cell, Org. Electron. 10 (2009) 1473–1477.
[11] D.C. Olson, Y.J. Lee, M.S. White, N. Kopidakis, S.E. Shaheen, D.S. Ginley, J.A. Voigt, J.W.P. Hsu, Effect of polymer processing on the performance of poly(3-hexylthiophene)/ZnO nanorod photovoltaic devices, J. Phys. Chem. C 111 (2007) 16640–16645.
[12] W.J.E. Beek, M.M. Wienk, R.A.J. Janssen, Hybrid polymer solar cells based on zinc oxide, J. Mater. Chem. 15 (2005) 2985–2988.
[13] J. Boucle, H.J. Snaith, N.C. Greenham, Simple approach to hybrid polymer/porous metal oxide solar cells from solution-processed ZnO nanocrystals, J. Phys. Chem. C 114 (2010) 3664–3674.
[14] S. Shao, F. Liu, Z. Xie, L. Wang, High-Efficiency hybrid polymer solar cells with inorganic P- and N-type semiconductor nanocrystals to collect photogenerated charges, J. Phys. Chem. C 114 (2010) 9161–9166.
[15] W.J.E. Beek, L.H. Slooff, M.M. Wienk, J.M. Kroon, R.A.J. Janssen, Hybrid solar cells using a zinc oxide precursor and a conjugated polymer, Adv. Funct. Mater. 15 (2005) 1703–1707.
[16] D.J.D. Moet, L.J.A. Koster, B. de Boer, P.W.M. Blom, Hybrid polymer solar cells from highly reactive diethylzinc: MDMO-PPV versus P3HT, Chem. Mater. 19 (2007) 5856–5861.
[17] S.D. Oosterhout, M.M. Wienk, S.S. van Bavel, R. Thiedmann, L.J.A. Koster, J. Gilot, J. Loos, V. Schmidt, R.A.J. Janssen, The effect of three-dimensional morphology on the efficiency of hybrid polymer solar cells, Nat. Mater. 8 (2009) 818–824.
[18] W.J.E. Beek, M.M. Wienk, M. Kemerink, X.N. Yang, R.A.J. Janssen, Hybrid zinc oxide conjugated polymer bulk heterojunction solar cells, J. Phys. Chem. B 109 (2005) 9505–9516.
[19] P.A.C. Quist, W.J.E. Beek, M.M. Wienk, R.A.J. Janssen, T.J. Savenije, L.D.A. Siebbeles, Photogeneration and decay of charge carriers in hybrid bulk heterojunctions of ZnO nanoparticles and conjugated polymers, J. Phys. Chem. B 110 (2006) 10315–10321.
[20] M.S. White, D.C. Olson, S.E. Shaheen, N. Kopidakis, D.S. Ginley, Inverted bulk-heterojunction organic photovoltaic device using a solution-derived ZnO underlayer, Appl. Phys. Lett. 89 (2006) 143517.
[21] G. Li, C.W. Chu, V. Shrotriya, J. Huang, Y. Yang, Efficient inverted polymer solar cells, Appl. Phys. Lett. 88 (2006) 253503.
[22] L.M. Chen, Z.R. Hong, G. Li, Y. Yang, Recent progress in polymer solar cells: manipulation of polymer: fullerene morphology and the formation of efficient inverted polymer solar cells, Adv. Mater. 21 (2009) 1434–1449.
[23] S.K. Hau, H.L. Yip, N.S. Baek, J.Y. Zou, K. O'Malley, A.K.Y. Jen, Air-stable inverted flexible polymer solar cells using zinc oxide nanoparticles as an electron selective layer, Appl. Phys. Lett. 92 (2008) 253301.

[24] F.C. Krebs, Air stable polymer photovoltaics based on a process free from vacuum steps and fullerenes, Sol. Energy Mater. Sol. Cells 92 (2008) 715–726.
[25] M.T. Lloyd, D.C. Olson, P. Lu, E. Fang, D.L. Moore, M.S. White, M.O. Reese, D.S. Ginley, J.W.P. Hsu, Impact of contact evolution on the shelf life of organic solar cells, J. Mater. Chem. 19 (2009) 7638–7642.
[26] C.Y. Li, T.C. Wen, T.H. Lee, T.F. Guo, J.C.A. Huang, Y.C. Lin, Y.J. Hsu, An inverted polymer photovoltaic cell with increased air stability obtained by employing novel hole/electron collecting layers, J. Mater. Chem. 19 (2009) 1643–1647.
[27] F.C. Krebs, Y. Thomann, R. Thomann, J.W. Andreasen, A simple nanostructured polymer/ZnO hybrid solar cell – Preparation and operation in air, Nanotechnology 19 (2008) 424013.
[28] J. Gilot, M.M. Wienk, R.A.J. Janssen, Double and triple junction polymer solar cells processed from solution, Appl. Phys. Lett. 90 (2007) 143512.
[29] J. Gilot, M.M. Wienk, R.A.J. Janssen, Optimizing polymer tandem solar cells, Adv. Mater. 22 (2010) E67–E71.
[30] D.J.D. Moet, P. de Bruyn, P.W.M. Blom, High work function transparent middle electrode for organic tandem solar cells, Appl. Phys. Lett. 96 (2010) 153504.
[31] Y.J. Lee, R.J. Davis, M.T. Lloyd, P.P. Provencio, R.P. Prasankumar, J.W.P. Hsu, Open-circuit voltage improvement in hybrid ZnO–polymer photovoltaic devices with oxide engineering, IEEE J. Sel. Top. Quantum. 16 (2010) 1587–1594.
[32] J.B. Kim, C.S. Kim, Y.S. Kim, Y.L. Loo, Oxidation of silver electrodes induces transition from conventional to inverted photovoltaic characteristics in polymer solar cells, Appl. Phys. Lett. 95 (2009) 183301.
[33] M. Jorgensen, K. Norrman, F.C. Krebs, Stability/degradation of polymer solar cells, Sol. Energy Mater. Sol. Cells 92 (2008) 686–714.
[34] F.C. Krebs, S.A. Gevorgyan, J. Alstrup, A roll-to-roll process to flexible polymer solar cells: model studies, manufacture and operational stability studies, J. Mater. Chem. 19 (2009) 5442–5451.
[35] H.L. Yip, S.K. Hau, N.S. Baek, H. Ma, A.K.Y. Jen, Polymer solar cells that use self-assembled-monolayer-modified ZnO/Metals as cathodes, Adv. Mater. 20 (2008) 2376–2382.
[36] M.O. Reese, A.K. Sigdel, J.J. Berry, D.S. Ginley, S.E. Shaheen, A simple miniature controlled-atmosphere chamber for optoelectronic characterizations, Sol. Energy Mater. Sol. Cells 94 (2010) 1254–1258.

In inorganic semiconductor devices, there is an extensive literature already dealing with the effects of spin–orbit interaction on transport and spin filtering. As early as 1990, Datta and Das predicted that the spin–orbit coupling in a semiconductor results in spin precession that can be used to tune a spin valve effect in spin transistor devices [23]. Since then, there have been many theoretical and experimental studies on that topic [24–28]. In recent years, some theoretical investigations were carried out on the effect of spin-flip scattering in organic devices [21,29,30]. For instance, when the spin-flip effect caused by Co penetration in the organic layer is considered in a Co/OSC/LSMO device, the magnetoresistance obtained theoretically is consistent with experimental data [21]. Also, in one study the effect of spin-flip on spin injection into a DNA chain led to some valuable conclusions [30]. Therefore, an improvement of the two-current model is necessary to include the spin-flip scattering during the transport in an organic spin device.

Recently, there have also been several studies on inorganic spin filters, such as Europium-based spin filters [4], mutiferroic spin filters [31], and graphene spin filters [32], however, the investigations of organic spin filters are relatively few. In this paper, we modify the two-current model to include the spin flip of carriers and then investigate the spin-polarized current in an organic spin filter. A schematic diagram of the device is shown in Fig. 1, the interlayer is an organic ferromagnet poly-BIPO [1,4-bis(2,2,6,6-tetramethyl-4-piperidyl-oxyl)] [33], which can be described using a simple quasi-one dimensional model. To demonstrate the effect of spin flip on the spin polarized current through the device, we compare our result to that of the two-current model. The paper is organized as follows: the model and formulation are presented in Section 2. In Section 3, we provide the numerical calculations and analyze the results. Finally in Section 4, we summarize our main results. In particular, the spin filter effect is found to exist even when spin-flip scattering is included; thus it is a robust effect.

2. Model and method

We have investigated a metal/organic ferromagnet/metal (M/OF/M) device with a two-current approach and predicted that such a device can serve as a spin filter, which means that only one kind of spin can tunnel through the device, that is, the current through the device will be fully spin polarized [13]. To confirm the spin filter effect when the spin-flip scattering is included, we adopt the device model used in Ref. [13]. The modeling scheme is shown in Fig. 1. An organic ferromagnetic polymer poly-BIPO [1,4-bis(2,2,6,6,-tetramethyl-4-piperidyl-1-oxyl)] is connected with two semi-infinite metallic electrodes. The Hamiltonian is written as,

$$H = H_{OF} + H_{sf} + H_{l(r)} + H_{coup}, \tag{1}$$

where the first term is the Hamiltonian of the organic ferromagnetic polymer without spin-flip. The polymer has a main chain composed of carbon atoms. The side radicals are connected with odd (or even) sites and each radical has an unpaired electron which can offer a residual spin. A theoretical model has been well established to obtain the ferromagnetic ground state of this molecule [34].

$$H_{OF} = -\sum_{n,s} t_{n,n+1}(c^{+}_{n,s}c_{n+1,s} + c^{+}_{n+1,s}c_{n,s}) + \frac{K}{2}\sum_{n}(u_{n+1} - u_n)^2 + J_f \sum_{n} \delta_{n,odd}\,\vec{S}_{nR}\cdot\vec{S}_n. \tag{2}$$

Here $t_{n,n+1} = t_0 - \alpha(u_{n+1} - u_n)$, t_0 is the hopping integral of π electrons along the main chain with a uniform lattice; α stands for the electron–lattice coupling parameter and u_n the lattice displacement at site$n$; K is the elastic constant between the two lattice atoms; $c^{+}_{n,s}(c_{n,s})$ denotes the creation (annihilation) operator of an electron at site n with spin s; J_f denotes the spin coupling strength between the conduction electron (π-electron) spins $\vec{S}_n$ and the side radical spins $\vec{S}_{nR}$. It is assumed that the radicals (R) connect with the odd sites in the chain which is written as $\delta_{n,odd}$. We take the mean-field approach for $\vec{S}_{nR}$ and set $\vec{S}_{nR}\cdot\vec{S}_n = -\frac{1}{4}\left(c^{+}_{n,\uparrow}c_{n,\uparrow} - c^{+}_{n,\downarrow}c_{n,\downarrow}\right)$.

H_{sf} describes the spin-flip effect in the organic magnetic polymer of the interlayer, which may be caused by spin–orbit coupling, magnetic environment, temperature, etc.,

$$H_{sf} = -\sum_{n} t_{sf}(c^{+}_{n,\uparrow}c_{n,\downarrow} + c^{+}_{n,\downarrow}c_{n,\uparrow}), \tag{3}$$

with t_{sf} denoting spin-flip transfer integral. It is not easy to give an exact value of the spin-flip parameter t_{sf}. In a recent work, Wohlgenannt et al. studied the spin–orbit interaction in a conjugated polymer based on a simple model. They obtained t_{sf} values of the magnitude of about 10 μeV and pointed out that the spin–orbit value is structure dependent [35]. Here we assume that the spin flip contribution arises from both the spin–orbit coupling and other factors, such as magnetic environment and temperature.

$H_{l(r)}$ is the Hamiltonian of the left (right) electrode, which is supposed to be a simple metal chain,

$$H_{l(r)} = \sum_{m,s} \varepsilon_{l(r)} a^{+}_{m,s}a_{m,s} - \sum_{m,s} t_{l(r)}(a^{+}_{m,s}a_{m+1,s} + h.c.), \tag{4}$$

where $\varepsilon_{l(r)}$ is the on-site energy of a metal atom compared to that of a carbon atom, $t_{l(r)}$ is the transfer integral of adja-

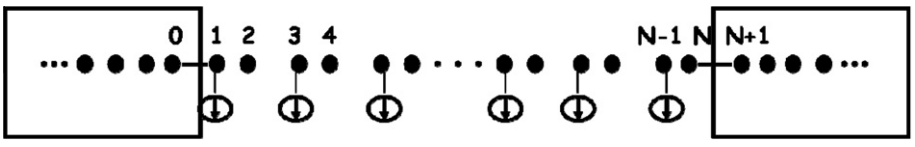

Fig. 1. One-dimensional scheme for a poly-BIPO based device, the arrows indicate the localized spin direction of side radicals.

cent sites, $a^+_{m,s}(a_{m,s})$ is the creation (annihilation) operator of an electron in the electrodes.

The coupling between the electrodes and the polymer is assumed to take place only at the nearest connecting atoms at the interfaces.

$$H_{coup} = -\sum_s t_{lM}(a^+_{0,s}c_{1,s} + h.c.) - \sum_s t_{rM}(c^+_{N,s}a_{N+1,s} + h.c.), \quad (5)$$

where $t_{l(r)M}$ is the interfacial coupling, which is simplified by neglecting the spin-dependent scattering at the interfaces. N is the total number of carbon sites in the organic ferromagnetic polymer.

For an M/OF/M device, the current is spin-dependent due to the ferromagnetic polymer interlayer. If there is no spin-flip process in the transport, we may consider the spin up and spin down current separately, i.e. the two-current model. If the spin-flip scattering is included during the transport, the spin up current measured at the acceptor electrode is contributed not only from the transmission of spin up electrons but also from the spin down electrons. Similar is the case for the current of spin down electrons. Therefore, to estimate the spin-dependent current measured at the acceptor side, we have to extend the Landauer–Büttiker formula [36] to include the possible spin flip transmission,

$$I_s(V) = \frac{e}{h}\int_{-\infty}^{+\infty}[T_{ss}(E,V) + T_{-ss}(E,V)][f(E-\mu_l) - f(E-\mu_r)]dE, \quad (6)$$

where $f(E-\mu_{l(r)}) = 1/\{1+\exp[(E-\mu_{l(r)})/k_BT]\}$ is the Fermi distribution function and $\mu_{l(r)} = E_F \pm eV/2$ is the chemical potential of the left (right) electrode with Fermi energy E_F. If the spin-flip transmission coefficient $T_{-ss} = 0$, then the two-current model is recovered. In order to discuss the spin-polarized transport in the M/OF/M device, the spin polarization of the current is defined as,

$$P(V) = \frac{I_\uparrow(V) - I_\downarrow(V)}{I_\uparrow(V) + I_\downarrow(V)}, \quad (7)$$

which is voltage (V) dependent. The zero-bias spin polarization of the device is given by $P_0 = \lim_{V\to 0} P(V)$.

The spin-dependent transmission coefficient is calculated using the transfer matrix method. The wavefunction on the μ th orbital with spin s is written as $\psi_{\mu,s} = \sum_n Z_{n,\mu,s}|n\rangle$, where $Z_{n,\mu,s}$ expresses the amplitude of the wavefunction on site n. From the relevant Schrödinger equation, we obtain the transfer relation,

$$\begin{pmatrix} Z_{N+2,\mu,\uparrow} \\ Z_{N+1,\mu,\uparrow} \\ Z_{N+2,\mu,\downarrow} \\ Z_{N+1,\mu,\downarrow} \end{pmatrix} = M_r \prod_{n=1}^{N} P^{(n)} M_l \begin{pmatrix} Z_{0,\mu,\uparrow} \\ Z_{-1,\mu,\uparrow} \\ Z_{0,\mu,\downarrow} \\ Z_{-1,\mu,\downarrow} \end{pmatrix}, \quad (8)$$

where M_l, M_r and $P^{(n)}$ are written as,

$$M_l = \begin{pmatrix} \frac{t_l}{t_{lM}}e^{ik_la} & 0 & 0 & 0 \\ 0 & e^{ik_la} & 0 & 0 \\ 0 & 0 & \frac{t_l}{t_{lM}}e^{ik_la} & 0 \\ 0 & 0 & 0 & e^{ik_la} \end{pmatrix} M_r = \begin{pmatrix} e^{ik_ra} & 0 & 0 & 0 \\ 0 & \frac{t_{rM}}{t_r}e^{ik_ra} & 0 & 0 \\ 0 & 0 & e^{ik_ra} & 0 \\ 0 & 0 & 0 & \frac{t_{rM}}{t_r}e^{ik_ra} \end{pmatrix}, \quad (9)$$

$$P^{(n)} = \begin{pmatrix} \frac{(E-\varepsilon^\uparrow_n+\frac{J_f}{4}\delta_{n,o})}{t^\uparrow_{n,n+1}} & -\frac{t^\uparrow_{n-1,n}}{t^\uparrow_{n,n+1}} & \frac{t_{sf}}{t^\uparrow_{n,n+1}} & 0 \\ 1 & 0 & 0 & 0 \\ \frac{t_{sf}}{t^\downarrow_{n,n+1}} & 0 & \frac{(E-\varepsilon^\downarrow_n-\frac{J_f}{4}\delta_{n,o})}{t^\downarrow_{n,n+1}} & -\frac{t^\downarrow_{n-1,n}}{t^\downarrow_{n,n+1}} \\ 0 & 0 & 1 & 0 \end{pmatrix}, \quad (10)$$

and $\cos(k_{l(r)}a) = \frac{E-\varepsilon_{l(r)}}{2t_{l(r)}}$.

Within the left electrode ($n \leqslant 0$) and the right electrode ($n \geqslant N+1$), we suppose that the electronic state is a simple plane wave. For a spin up electron, it is written as,

$$\begin{aligned} Z_{-1,\mu,\uparrow} &= e^{-ik_la} + \rho^{\uparrow\uparrow}e^{ik_la}, Z_{-1,\mu,\downarrow} = \rho^{\uparrow\downarrow}e^{ik_la}, \\ &\times Z_{0,\mu,\uparrow} = 1 + \rho^{\uparrow\uparrow}, Z_{0,\mu,\downarrow} = \rho^{\uparrow\downarrow}, Z_{N+1,\mu,\uparrow} = \tau^{\uparrow\uparrow}e^{i(N+1)k_ra}, \\ &\times Z_{N+1,\mu,\downarrow} = \tau^{\uparrow\downarrow}e^{i(N+1)k_ra}, Z_{N+2,\mu,\uparrow} = \tau^{\uparrow\uparrow}e^{i(N+2)k_ra}, \\ &\times Z_{N+2,\mu,\downarrow} = \tau^{\uparrow\downarrow}e^{i(N+2)k_ra}, \end{aligned} \quad (11)$$

where $\rho^{\uparrow\uparrow(\uparrow\downarrow)}$ and $\tau^{\uparrow\uparrow(\uparrow\downarrow)}$ are the amplitudes of the reflected and transmitted electron wavefunctions with spin up, which include spin-conserving parts $\rho^{\uparrow\uparrow}, \tau^{\uparrow\uparrow}$ as well as spin-flipping parts $\rho^{\uparrow\downarrow}, \tau^{\uparrow\downarrow}$. A similar form can be written down for the spin down state. Then, the spin-dependent transmission coefficients T_{ss} and T_{-ss}, which are defined as the ratio of the transmitted flux to the incident flux are obtained as,

$$T_{ss} = \frac{t_r\sin(k_ra)}{t_l\sin(k_la)}|\tau^{ss}|^2, \; T_{-ss} = \frac{t_r\sin(k_ra)}{t_l\sin(k_la)}|\tau^{-ss}|^2. \quad (12)$$

We carry out numerical calculations by taking the parameters as follows: for the organic ferromagnet [13,34], $t_0 = 2.5$ eV, $\alpha = 4.1$ eV/Å, $K = 21$ eV/Å^2, which appropriately describe the properties of poly-BIPO. For the electrodes, we take $\varepsilon_{l(r)} = 0$, $t_l = t_r = 2.5$ eV, $E_F = 0.5$ eV. The interfacial coupling is taken as $t_{lM} = t_{rM} = 0.5$ eV. We choose a low temperature of $T = 11$ K.

3. Results and discussion

First, we consider an isolated organic ferromagnetic polymer with half-filled occupation of electrons (one itinerant π-electron for each carbon site in the main chain). When the spin-flip scattering is absent, it is known that the polymer described with Hamiltonian (2) has a dimerization structure along the main chain. The polymer has a ferromagnetic ground state and exhibits a semiconducting behavior. There is an oscillatory variation of the spin amplitude from site to site along the main carbon chain, and the amplitude is mainly determined by the Heisenberg spin coupling between the side radical and the main carbon chain.

When the spin-flip scattering is included, we find that the polymer still has a ferromagnetic state. The amplitude of the spin oscillation is enhanced compared to that without the spin-flip. In this case, the electronic state is a spin mixed state, i.e. $\psi_\mu = a_\mu|\uparrow\rangle + b_\mu|\downarrow\rangle$, where $|a_\mu|^2$ and $|b_\mu|^2$ reflect the probability of electron spin direction (up or down). The spin-flip affects the electronic density of the ferromagnetic polymer and thus affects the lattice distortion due to the strong electron–lattice interaction of the or-

ganic polymer, which results in a redistribution of the Peierls distortion of the polymer chain. This effect is reflected in the energy level structure. As shown in Fig. 2, with increasing spin-flip parameter t_{sf}, the energy gap decreases gradually. It means that the Peierls gap in the organic molecule is reduced due to the spin-flip effect, which is a peculiar property of the organic ferromagnetic polymer.

To understand the conduction properties of the organic device, in the following, the electronic states near the Fermi level are checked. As shown in Fig. 3(a and b), where there is no spin-flip scattering, i.e. $t_{sf} = 0$, the orbitals are spin separated. The LUMO (lowest unoccupied molecular orbital) of the organic ferromagnetic polymer is the eigenstate of spin up Hamiltonian, while the LUMO + 1 is the spin down eigenstate. If a bias is applied, the spin up transport occurs first and the current is 100% spin polarized. With increasing bias, the LUMO + 1 goes into the conduction region. As LUMO + 1 has an opposite spin state to LUMO, the spin polarization decreases.

When the spin-flip scattering is included (i.e. nonzero t_{sf}), the electronic state of each orbital becomes a mixed state of different spins, as shown in Figs. 3(c and d). (To emphasize the effect of spin-flip scattering, for illustrative purposes hereafter a much larger value of t_{sf} is taken). In this case, the LUMO has a probability of $|a_{\mathrm{LUMO}}|^2$ for spin up electrons and $|b_{\mathrm{LUMO}}|^2$ for spin down electrons, as stated above. Therefore, even at low applied bias so that only one orbital (LUMO in the present case) enters the conduction region, a fully spin polarized current could not be realized. However, as $|a_\mu|^2 \neq |b_\mu|^2$, it is expected that the current is still spin polarized. The polarization of current will depend on the spin-flip scattering.

Next we study the effect of spin-flip scattering on the current spin polarization in an M/OF/M device at a fixed bias of $V = 0.8$ V (just above the turn-on voltage). The interlayer polymer has 20 carbon sites and each site provides one π-electron. The result is shown in Fig. 4, In the case of $t_{sf} = 0$, the current is fully polarized with $P = 100\%$. When the spin-flip scattering is considered, it is found that the spin polarization decreases gradually. But the current still keeps a good spin polarization even for a significant value of t_{sf}. For example, if we consider that the spin flip is caused only by the spin–orbit interaction in the organic semiconductor interlayer, which is of the order of tens of μeV [35], then from the calculation it is found that the current spin polarization remains nearly unchanged for these vaules of t_{sf}. Of course here we only consider a very short chain, $N = 20$ or the length of the 'interlayer' $L \approx 3$ nm, which is much shorter than the interlayer thickness of an actual device.

Further, if we include the spin flip contribution from all possible factors in addition to the spin–orbit interaction, such as the leakage field of the ferromagnet, the magnetic effect of the radical, temperature and doped ions the effective value of t_{sf} may be considerably large. We take $t_{sf} = 0.2$ eV, which is much larger than the room-temperature thermal energy ($k_BT \sim 0.026$ eV) and the Zeeman energy corresponding to one Tesla magnetic field ($g\mu_B\vec{S}\cdot\vec{B} \sim 10^{-5}$ eV). It is found that the current has a spin polarization of about 75%. We note that an organic semiconductor has a long spin relaxation time (much longer than that in an inorganic semiconductor), which means that the spin-flip scattering should be very weak in organic semiconductors (the real value of t_{sf} should be much smaller than 0.2 eV used here). Therefore, our calculation shows that even when a spin-flip scattering is included, such an organic device still keeps a high spin polarization. The device can still serve as a spin filter.

In the following, we study the effect of Heisenberg coupling J_f on the spin polarization by setting $t_{sf} = 0.25$ eV at a fixed bias of $V = 0.8$ V. As shown in Fig. 5, we find that the spin polarization of the current increases with J_f rapidly. Combined with the above result, we note that the spin-flip scattering and the side radical's Heisenberg coupling are

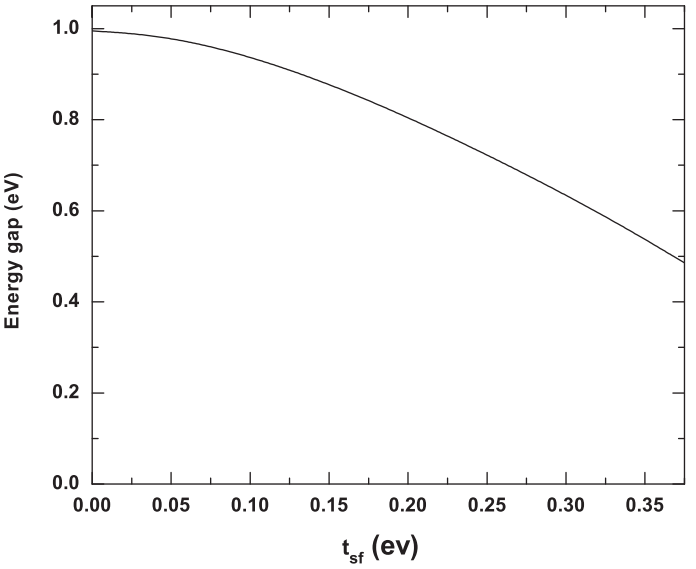

Fig. 2. Dependence of the energy gap on the spin-flip parameter t_{sf}.

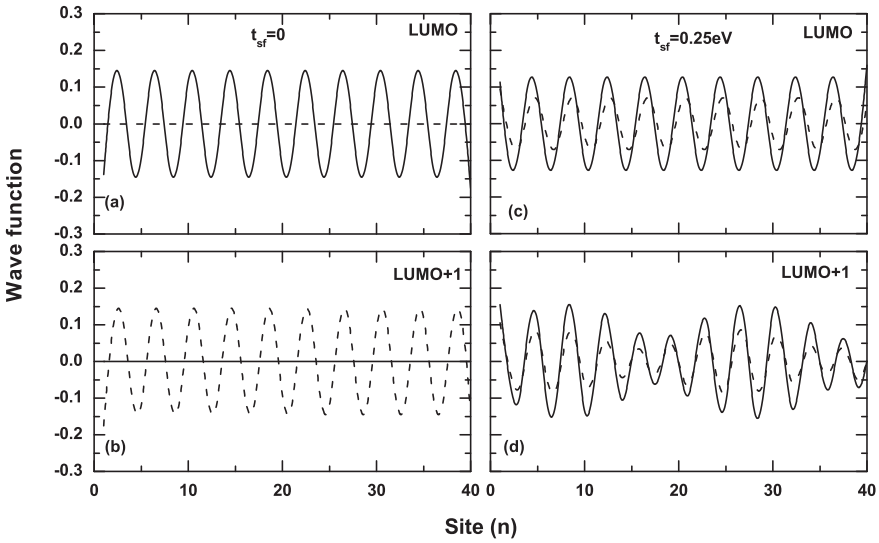

Fig. 3. Wave functions near the Fermi level: LUMO and LUMO + 1 states. (a) and (b) $t_{sf} = 0$; (c and d) $t_{sf} = 0.25$ eV. A large value of t_{sf} is chosen for illustrative purposes. (Spin up: solid line and spin down: dashed line).

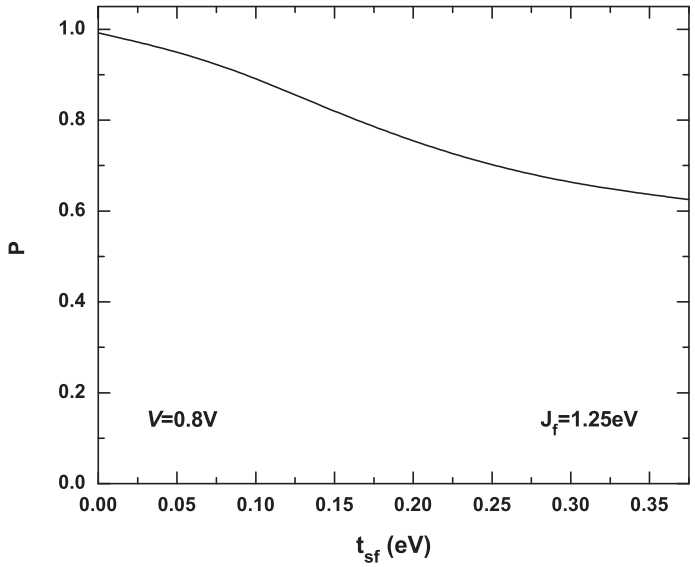

Fig. 4. Dependence of current polarization on the spin-flip scattering t_{sf} at $V = 0.8$ V.

competing effects for the spin polarization. To obtain a good spin filter, one hopes to adopt an organic ferromagnetic polymer with a strong side radical spin coupling and a weak spin-flip scattering. Comparatively, the effect of the side radical spin coupling on the spin filter is more sensitive than that of the spin-flip scattering. This conclusion is helpful in designing an organic spin filter.

To understand the current polarization mechanism with the spin-flip scattering included, we calculate the spin-dependent transmission coefficient at a fixed bias. When the spin-flip scattering is considered, the incident electrons from the left electrode have four channels to get to the right electrode. The transmission coefficients include spin-conserving parts $T_{\uparrow\uparrow}, T_{\downarrow\downarrow}$ and spin-flip ones $T_{\uparrow\downarrow}, T_{\downarrow\uparrow}$. The total transmission coefficient of spin up electrons is $T_{\uparrow} = T_{\uparrow\uparrow} + T_{\downarrow\uparrow}$, and that of spin down electrons is $T_{\downarrow} = T_{\downarrow\downarrow} + T_{\uparrow\downarrow}$. When spin-flip parameter $t_{sf} = 0$, the transmissions $T_{\uparrow\downarrow}$ and $T_{\downarrow\uparrow}$ are absent, i.e. the spin remains conserved during the transport process. As shown in Fig. 6(a), the peaks of $T_{\uparrow}$ and $T_{\downarrow}$ appear independently. In this case, we can treat the transport with the two-current model. Under a low bias, the peak of $T_{\uparrow} = T_{\uparrow\uparrow}$ appears first, which corresponds to the transport of only spin up LUMO state and a 100% spin polarized current can be obtained. When the spin-flip scattering is included during the transport process, as shown in Fig. 6(b), the transmissions $T_{\uparrow\downarrow}$

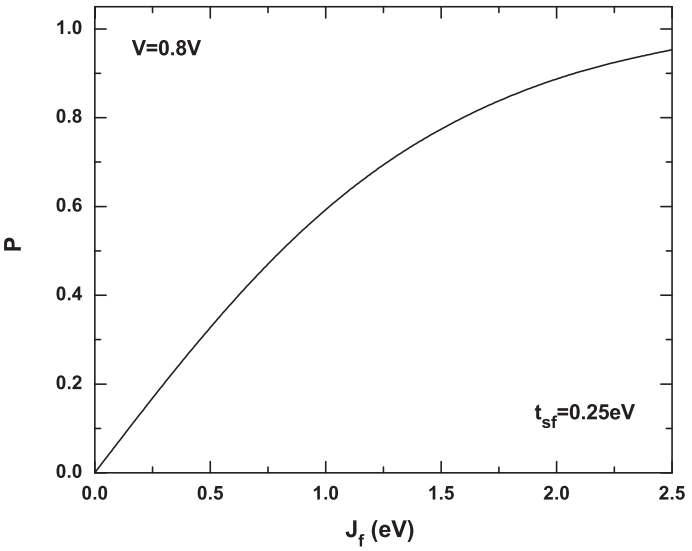

Fig. 5. Dependence of current polarization on the Heisenberg coupling J_f at $V = 0.8$ V.

and $T_{\downarrow\uparrow}$ will take place and the peaks of $T_\uparrow$ and $T_\downarrow$ appear simultaneously, which destroy the full polarization of the current. For example, the couple of peaks of $T_\uparrow$ and $T_\downarrow$ near $E - E_F \approx 0.1eV$ (as shown in Fig. 6) correspond to the LUMO. As this state contains both the component of spin up and spin down with a probability of $|a_{\mathrm{LUMO}}|^2$ and $|b_{\mathrm{LUMO}}|^2$, respectively, the current contributed from this state will become partly spin polarized. Since $|a_{\mathrm{LUMO}}|^2$ is much larger than $|b_{\mathrm{LUMO}}|^2$ in the present case, the spin polarization of the current still keeps a high value at a positive low bias when the LUMO enters the conducting window.

4. Summary

In conclusion, we considered the possible spin flip of an electron when it passes through an organic device and calculated the effect of spin-flip scattering on the current spin polarization. It is known that Datta and Das first indicated the spin precession of electrons through the Rashba spin orbit coupling effect in narrow-gap inorganic semiconductors [23]. The Rashba spin orbit coupling describes spin flip from one site to another due to the motion of electrons. Here in our model, the spin flip takes place at the same site, which may be contributed from the leakage field of the ferromagnet, the magnetic effect of the radical, temperature and doped ions. We did not study the details of spin precession here, instead we considered the measurable spin current polarization and investigated the effect of spin-flip coupling.

First, we studied the basic properties of an organic ferromagnetic polymer in the presence of spin-flip scattering. We found that the π-electronic orbital becomes a spin mixed state. Due to the strong electron–lattice interaction

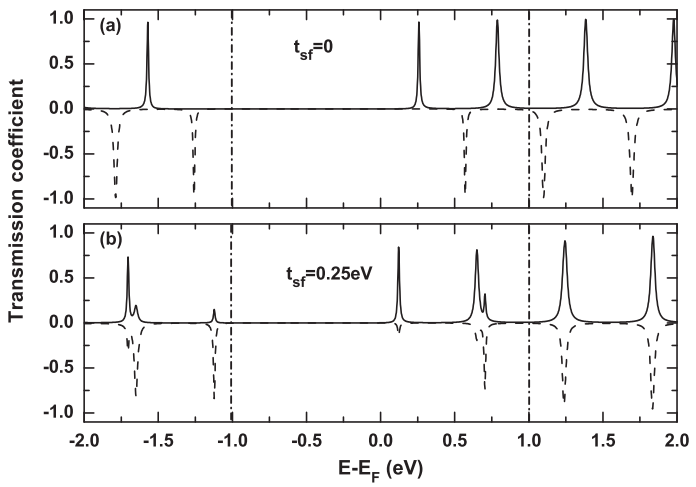

Fig. 6. Spin-dependent transmission coefficient at (a) $t_{sf} = 0$ and (b) $t_{sf} = 0.25$ eV. ($T_\uparrow$: solid line and $T_\downarrow$: dashed line).

in an organic polymer, the spin-mixing of the orbital results in a decrease of the LUMO–HOMO gap or the Peierls energy gap. This kind of spin-induced change in the Peierls gap is a peculiar property of an organic ferromagnetic polymer. Then, we extended the Landauer–Büttiker formula to include spin dependence and calculated the current spin polarization in an organic spin filter. We found that, although the spin polarization of the current through the device decreases due to the spin-flip scattering, the device still functions well as a spin filter even with a considerable spin-flip scattering. We also considered the competing effects of the spin-flip scattering and the ferromagnetism of the organic interlayer on the spin filter and found that it is more sensitive to the latter. These findings are important for designing an optimal organic spin filter.

Acknowledgments

The authors would like to acknowledge the financial support from the National Basic Research Program of China (Grant Nos. 2009CB929204 and 2010CB923402) and the National Natural Science Foundation of the People's Republic of China (Grant No. 10874100). This work was supported in part by the US Department of Energy.

References

[1] N.F. Mott, Proc. R. Soc. London, A 153 (1936) 699.
[2] E.Y. Tsymbal et al., J. Phys.: Condens. Matter 15 (2003) R109.
[3] J.S. Moodera et al., J. Phys.: Condens. Matter 19 (2007) 165202.
[4] T. Nagahama, T.S. Santos, J.S. Moodera, Phys. Rev. Lett. 99 (2007) 016602.
[5] T.S. Santos, J.S. Moodera, K.V. Raman, E. Negusse, J. Holroyd, J. Dvorak, M. Liberati, Y.U. Idzerda, E. Arenholz, Phys. Rev. Lett. 101 (2008) 147201.
[6] L. Zhu, K.L. Yao, Z.L. Liu, Appl. Phys. Lett. 96 (2010) 082115.
[7] C. Herrmann, G.C. Solomon, M.A. Ratner, J. Am. Chem. Soc. 132 (2010) 3682.
[8] J.H. Wei, S.J. Xie, L.M. Mei, J. Berakdar, Y. Yan, Org. Electron. 8 (2007) 487.
[9] C.D. Pemmaraju, I. Rungger, S. Sanvito, Phys. Rev. B 80 (2009) 104422.
[10] Nadjib Baadji, Manuel Piacenza, Tugba Tugzuz, Fabio Della Sela, Giuseppe Maruccio, Stefano Sanvito, Nat. Mater. 8 (2009) 813.
[11] J.D. Bergeson, V.N. Prigodin, D.M. Lincoln, A.J. Epstein, Phys. Rev. Lett. 100 (2008) 06720.
[12] S. Pramanik, C.G. Stefanita, S. Patibandla, S. Bandyopadhyay, K. Garre, N. Harth, M. Cahay, Nat. Nanotechnol. 2 (2007) 216.
[13] G. Hu, Y. Guo, J. Wei, S. Xie, Phys. Rev. B 75 (2007) 165321.
[14] Z.H. Xiong, D. Wu, Z. Valy Vardeny, J. Shi, Nature 427 (2004) 821.
[15] J.-W. Yoo, H.W. Jang, V.N. Prigodin, C. Kao, C.B. Eom, A.J. Epstein, Synth. Met. 160 (2010) 216.
[16] F. Wang, Z.V. Vardeny, Synth. Met. 160 (2010) 210.
[17] H. Dalgleish, G. Kirczenow, Phys. Rev. B 73 (2006) 235436.
[18] G. Hu, K. He, A. Saxena, S. Xie, J. Chem. Phys. 129 (2008) 234708.
[19] P.A. Bobbert, W. Wagemans, F.W.A. van Oost, B. Koopmans, M. Wohlgenannt, Phys. Rev. Lett. 102 (2009) 156604.
[20] S. Majumdar, H.S. Majumdar, R. Laiho, R. Osterbacka, New J. Phys. 11 (2009) 013022.
[21] Y. Zhang, J. Ren, J. Lei, S. Xie, Org. Electron. 10 (2009) 568.
[22] T. Sugawara, M. Minamoto, M.M. Matsushita, P. Nickels, S. Komiyama, Phys. Rev. B 77 (2008) 235316.
[23] S. Datta, B. Das, Appl. Phys. Lett. 56 (1990) 665.
[24] F. Mireles, G. Kirczenow, Phys. Rev. B 64 (2001) 024426.
[25] T. Koga, J. Nitta, H. Takaganagi, Phys. Rev. Lett. 88 (2002) 126601.
[26] T. Koga, J. Nitta, T. Akaziki, H. Takaganagi, Phys. Rev. Lett. 89 (2002) 046801.
[27] E.I. Rashba, A.L. Efros, Phys. Rev. Lett. 91 (2003) 126405.
[28] Q.-F. Sun, J. Wang, H. Guo, Phys. Rev. B 71 (2005) 165310.
[29] H. Zhao, Y.-G. Chen, Y. Yao, C.-Q. Wu, X.-M. Zhang, Z. An, J. Chem. Phys. 131 (2009) 154901.
[30] X.F. Wang, T. Chakraborty, Phys. Rev. B 74 (2006) 193103.
[31] S. Ju, T.Y. Cai, G.Y. Guo, Z.Y. Li, Phys. Rev. B 75 (2007) 064429.
[32] A. Rycrz, J. Tuorzydlo, C.W.J. Beenakker, Nat. Phys. 3 (2007) 172.
[33] Y.V. Korshak, T.V. Medvedeva, A.A. Ovchinnikov, V.N. Spector, Nature 326 (1987) 370.
[34] Z. Fang, Z.L. Liu, K.L. Yao, Z.G. Li, Phys. Rev. B 51 (1995) 1304.
[35] J. Rybicki, T.D. Nguyen, Y. Sheng, M. Wohlgenannt, Synth. Met. 160 (2010) 280.
[36] S. Datta, Electronic Transport in Mesoscopic Systems, Oxford University Press, New York, 1995.

of 5–6 nm, and are coated with *n*-butylamine ligands. The ZnO nanoparticle layer is prepared by spin-coating from chloroform solution, followed by annealing at 250 °C in air. Here the ZnO nanoparticle layer is a hole-blocking layer, which can dramatically reduce the switching current density [5]. Fig. 1 also shows *JV* curves of three different devices with different ZnO nanoparticle layer thickness, scanning from 0 V to 3 V to 0 V. The three curves are very similar, indicating that the current is determined largely by the properties of the PEDOT:PSS layer and its interfaces. Scanning towards +3 V (Al positive), the current density has a peak at ~1.3 V at a value of less than 1 mA cm^{-2}. The device current is about 2–3 orders of magnitude lower when the voltage is swept back to below 2 V. The device conductivity cannot be recovered, indicating a permanent change. There is no significant recovery observed after 6 months storage.

3. WORM device operation mechanism

To investigate the mechanism responsible for the conductance switching, Raman spectra (633 nm excitation) have been measured before and after switching (Fig. 2A). Before switching, the spectrum shows broad peaks in the region around 1420 cm^{-1}, whereas after switching the spectrum shows sharp peaks in this region, with clear peaks at 1422 and 1516 cm^{-1} corresponding to symmetric and antisymmetric C=C stretching modes respectively. This change in spectrum is consistent with a change from *p*-doped to undoped PEDOT [10,11]. Further evidence for the dedoping of PEDOT can be obtained from the UV–visible absorbance of the devices, obtained by measuring the change in intensity of light incident through the glass substrate, passing through the PEDOT:PSS layer, and reflected at the Al electrode. Fig. 2B shows the change in reflectance between 375 and 750 nm while sweeping the bias from 0 to 3.3 V. In the conducting, *p*-doped state the PEDOT is highly transparent, leading to high reflectivity across the spectral range. As the bias increases, the reflectance decreases, corresponding to the formation of undoped PEDOT, which is much more absorbing [10,12]. The change in reflectance peaks at 510 nm, and the observed behavior is consistent with the color change seen in electrochromic cells based on doping and dedoping of PEDOT [13]. Fig. 2C shows the reflectance change at 510 nm together with the current flowing in the device. It can clearly be seen that the reflectance change is associated with the reduction in current. The maximum reflectance change is over 80%, which, considering the other reflection losses present in the structure, corresponds to a very significant change in absorbance of the PEDOT. The combination of in situ Raman and reflectance measurements therefore provides unambiguous evidence that the change in conductivity is due to dedoping of the PEDOT.

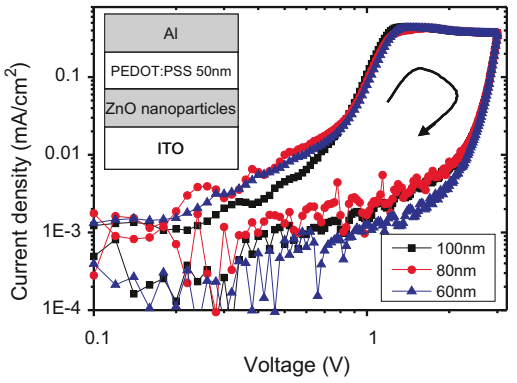

Fig. 1. Device structure and log–log current–voltage curves for ITO/ZnO/PEDOT:PSS/Al devices using different ZnO layer thickness (as indicated in the figure). The measurement was performed using the pulse mode of an Agilent 4155B Semiconductor Parameter Analyzer. The pulse period was 20 ms, and the pulse duration was 10 ms. The voltage step was 0.02 V.

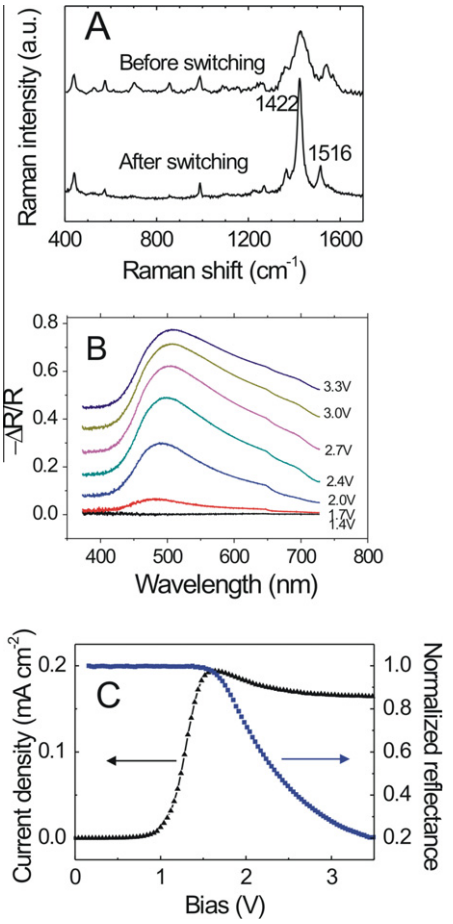

Fig. 2. (A) Raman spectra (633 nm excitation) before and after switching. (B) Reflectance spectrum (fractional reduction in reflectance relative to unswitched device) as a function of bias voltage. (C) Normalized reflectance at 510 nm and current density as a function of bias voltage. Voltage scan rate for (C) 0.2 V/s.

Dedoping of the PEDOT requires injected electrons to be captured by the PEDOT. We can estimate the amount of transient electrochemical current related to this dedoping process. Taking a rough estimate of the doping density in PEDOT:PSS as 10^{19} cm^{-3} [7], for a 50 nm film 5×10^{13} electrons/cm^2 are required to completely dedope the

PEDOT layer. From our previous work [5], we know that timescale of switching is typically about 20 ms. To completely dedope the PEDOT within this time requires a current of about 0.4 mA cm^2, which is close to our device switching current, indicating that the switching process in our device is very efficient. In reality, the electrochemical current could be less than this value because even a thin dedoped interfacial layer might be sufficient to reduce device conductivity dramatically, however the spectroscopic data presented above suggest that the bulk of the film is indeed dedoped.

We have confirmed that the change in device conductivity is caused by dedoping of the PEDOT. The electrochemical doping and dedoping of PEDOT usually is a reversible process [10–13]. However, when it is followed by electrolysis of water to form stable neutral PSSH, then the PEDOT doping level is irreversibly changed [2,8,9], which results in a permanent change of the device conductivity, as we suggested in our previous work [5].

We note that electrical switching behavior has also been observed in ZnO nanoparticles [14,15]. We believe that the switching mechanism in our device is not due to a change in conductivity of ZnO layer. Besides the spectroscopic investigations described above, we also found that the device performance is independent of the ZnO layer thickness (Fig. 1). In our device, the role of the ZnO layer is to block holes and inject electrons, which results in a dramatic reduction in device operation current.

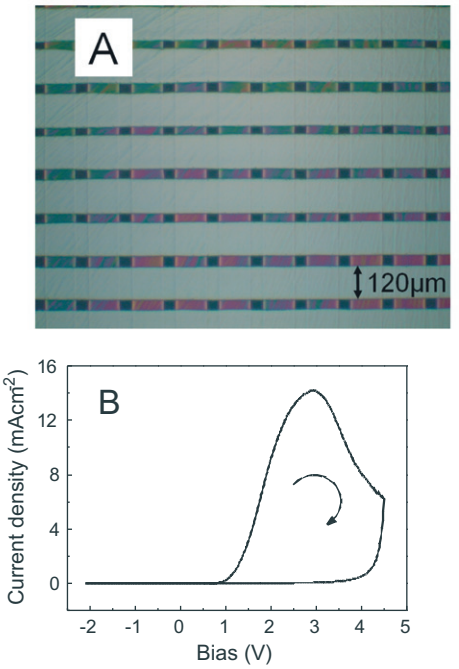

Fig. 3. (A) Optical micrograph of inkjet-printed memory array. (B) Current–voltage characteristic of an Au/ZnO/PEDOT:PSS/ZnO/Ag device. The measurements were performed using an Agilent 4155B Semiconductor Parameter Analyzer (SPA) in pulse mode, in air. The pulse period was 20 ms, and the duration was 10 ms. The voltage step is 0.015 V.

4. Towards entirely solution-processed WORM

In order to obtain low-cost PEDOT:PSS WORM memories, it is useful to fabricate arrays of devices without lithographic substrate patterning or high-vacuum processing. However, it is difficult to print metals directly on top of the PEDOT:PSS layer in the structure described above without forming short-circuits. To solve this problem, we use an additional ZnO nanoparticle layer on top of the PEDOT:PSS to prevent shorting, while still maintaining the electron-only device structure. This allows arrays to be fabricated entirely by solution processing. Bottom electrodes were formed by inkjet printing of 120 μm wide lines of gold nanoparticle ink (NPG-J, Harima Chemicals), followed by annealing at 250 °C for 1 h. ZnO nanoparticle and PEDOT:PSS films were deposited as before, followed by spin-coating of a further ZnO nanoparticle layer of 200 nm thickness. The device was then annealed at 200 °C for 30 min under nitrogen. Top electrodes were deposited by inkjet printing 120 μm wide lines of a silver complex ink (InkTec TEC-IJ-010 or InkTec TEC-IJ-050) perpendicular to the bottom electrode lines, followed by annealing at 130 °C for 5 min. The possibility to realize a highly conductive second level of printed metallization thanks to a low sintering temperature silver complex based ink was first demonstrated by Caironi et al. [16]. Fig. 3A shows an optical micrograph of the array, and Fig. 3B shows a typical current–voltage curve of a single device (gold electrode positive, −2 V to 4.5 V to −2 V). Rectifying behavior is again observed due to the difference in electrode properties. Switching occurs at 3–4 V, and the conductance in the range 1–3 V is reduced by a factor of approximately 500 after switching. We note that the current density of this printed structure WORM device is higher than the spin-coated structure device (Fig. 1). This is probably due to the different amount of water contained in the PEDOT:PSS layers of this two devices. The importance of water in the dedoping process has been discussed in our previous work [5]. In the printed structure device, the extra annealing process after deposition of the top ZnO nanoparticle layer can also dry the PEDOT:PSS layer, making it more difficult to permanently reduce the device conductivity. This 120 μm × 120 μm size printed WORM device can thus be programmed with powers of only 10 μW. Low programming power is essential for low-cost printed RFID tags where the total power is limited. We note the inkjet printed line width can be easily downscaled to 10–50 μm, so it is possible that the programming power of the WORM device can be further reduced to below 1 μW. Using simple pulses rather than voltage pulse ramps the required power can be higher, depending on the programming time required, as we found in Ref. [5].

5. Conclusions

In summary, by spectroscopic investigation, we have shown direct evidence that the switching in low-power WORM devices based on PEDOT:PSS is due to dedoping of the PEDOT. Based on this understanding, we have demonstrated an entirely solution-processed WORM

device, which is promising for application in low-cost RFID tags.

Acknowledgements

We are grateful to Dr. Ji-Seon Kim, Dr. Jeremy Burroughes, Dr. Thomas Kugler and Siong-Hee Khong for helpful discussions and to Cambridge Display Technology Ltd. for funding.

References

[1] S. Möller, C. Perlov, W. Jackson, C. Taussig, S.R. Forrest, Nature 426 (2003) 166.
[2] S. Möller, S.R. Forrest, C. Perlov, W. Jackson, C. Taussig, J. Appl. Phys. 94 (2003) 7811.
[3] S. Smith, S.R. Forrest, Appl. Phys. Lett. 84 (2004) 5019.
[4] B.C.d. Brito, E. Smiths, P. van Hal, T. Geuns, B. de Boer, C. Lasance, H. Gomes, D. de Leeuw, Adv. Mater. 20 (2008) 3750.
[5] J. Wang, F. Gao, N. Greenham, Appl. Phys. Lett. 97 (2010) 053301.
[6] X. Xu, R. Register, S. Forrest, Appl. Phys. Lett. 89 (2006) 142109.
[7] J.-S. Kim, P.K.H. Ho, C.E. Murphy, N. Baynes, R.H. Friend, Adv. Mater. 14 (2002) 206.
[8] G. Greczynski, T. Kugler, M. Keil, W. Osikowicz, M. Fahlman, W. Salaneck, J. Electron Spectrosc. Relat. Phenom. 121 (2001) 1.
[9] P.-J. Chia, L. Chua, S. Sivaramakrishnan, J. Zhuo, L. Zhao, W. Sim, Y. Yeo, P. Ho, Adv. Mater. 19 (2007) 4202.
[10] S. Garreau, G. Louarn, J.P. Buisson, G. Froyer, S. Lefrant, Macromolecules 32 (1999) 6807.
[11] S. Garreau, G. Louam, S. Lefrant, J.P. Buisson, G. Froyer, Synth. Met. 101 (1999) 312.
[12] Q. Pei, G. Zuccarello, M. Ahlskog, O. Inganäs, Polymer 35 (1994) 1347.
[13] H.W. Heuer, R. Wehrmann, S. Kirchmeyer, Adv. Funct. Mater. 12 (2002) 89.
[14] J. Wang, B. Sun, F. Gao, N. Greenham, Phys. Status Solidi A 207 (2010) 484.
[15] F. Verbakel, S.C.J. Meskers, R.A.J. Janssen, Appl. Phys. Lett. 89 (2006) 102103.
[16] M. Caironi, E. Gili, T. Sakanoue, X. Cheng, H. Sirringhaus, ACS Nano 4 (2010) 1451.

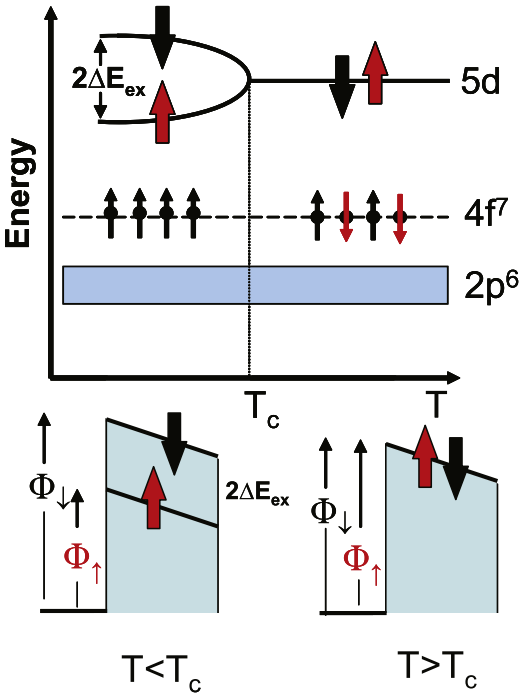

Fig. 1. Energy levels of EuS showing the splitting in the 5d conduction band below T_c (16.6 K) by the exchange energy, $2\Delta E_{ex}$ ($\sim$ 0.36 eV in bulk). When used as a tunnel barrier, it leads to lowering of the barrier height for spin-up electrons ($\Phi_\uparrow$) relative to the spin-down electrons ($\Phi_\downarrow$).

to serve as a good source for injecting spin-polarized electrons into an OS. There has been a recent report of utilizing a spin filter (EuO) for spin injection into rubrene [13]. However, in this preliminary study the interface and device stability was a significant issue. In the present work, we show that the use of SF barrier does not only provide spin injection, but also leads to enhanced spin injection at high applied voltage biases. Recently, chemically synthesized organic ferromagnetic semiconductor, $V(TCNE)_x$, has also been used to inject spins in OS. However, its stability especially in thin film form and high resistance as an electrode need to be addressed.

In the current study, the quasi-magnetic junction (QMJ) devices were fabricated using an *in situ* shadow mask technique in a vacuum chamber with a base pressure of 7×10^{-8} Torr. The geometry of the device (junction area: $200 \times 200\ \mu m^2$) is shown in Fig. 2. A thin film of EuS (2 nm) was grown at room temperature over Al, followed by the deposition of rubrene. Different thicknesses of the rubrene layer were grown ranging from 5 to 12 nm. A thin film of Fe (12 nm) was used as the top FM electrode and the whole structure was subsequently protected by 8 nm of Al_2O_3. The growth of rubrene, as seen in previous studies, has been shown to be influenced by the local surface electronic properties of the bottom seed layer [7,14]]. The insulating property of EuS can be expected to lead to azimuthal growth of rubrene at the interface, as in the case with alumina seed layer. Such interface ordering has been reported to improve the spin injection efficiency in rubrene [7].

MR measurements were performed at 1 K to achieve full exchange splitting of the conduction band in EuS, below its T_c, for higher spin filtering efficiency. MR was measured for different rubrene film thicknesses ranging from 5 to 12 nm. For 5 nm thick rubrene, the bulk of the junction resistance was coming from EuS and the anti-parallel state of the magnetization between EuS and Fe layer was not observed, whereas for 7 nm rubrene, although there was magnetic coupling between EuS and Fe, independent switching of EuS and Fe magnetizations could be seen (see Fig. 2a). Here, the large background non-saturating MR signal observed might be attributed to the magnetic field dependent resistance of the EuS barrier. With increasing rubrene thickness, the device showed a transition from a EuS dominated to a rubrene barrier dominated junction resistance. For 9 nm rubrene, higher MR was seen with a well-defined parallel and anti-parallel magnetization state of the EuS and Fe layer (see Fig. 2b). In these devices, the resistance was observed to increase at zero fields before reaching the anti-parallel state of the two FM electrodes. This could be caused by the dipolar coupling of EuS and Fe layer. The coercivity of bottom EuS layer was confirmed to be $\sim$90 Oe by SQUID measurements. A MR of 6% was

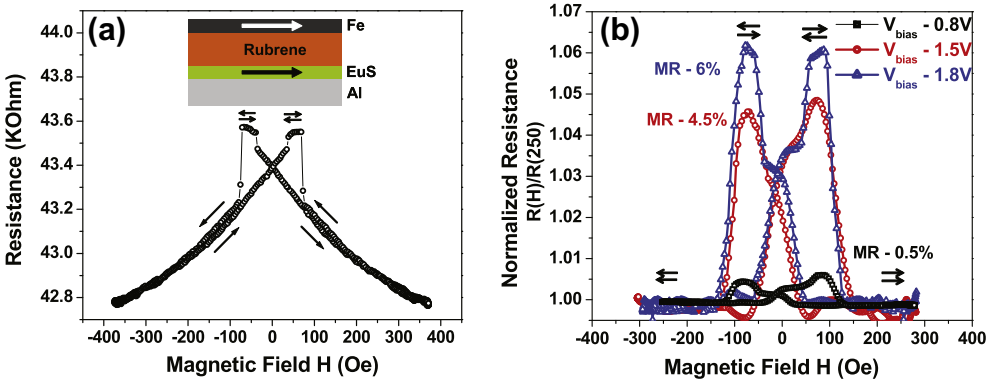

Fig. 2. (a) MR measured for rubrene barrier thickness of 7 nm at 1 K in a quasi-magnetic junction (schematically shown in the inset) having the layer structure: Al (8 nm)/EuS (2 nm)/Rub (x nm)/Fe (12 nm). (b) Increase in MR with applied voltage bias, for a junction with 9 nm rubrene barrier, measured at 1 K. The DC resistance of the device reduced from $\sim$12 MΩ at 0.8 V to $\sim$300 KΩ at 1.8 V.

observed in this device for an applied bias of 1.8 V. The increase in MR at high bias is interesting and will be discussed later.

The current–voltage (I–V) characteristics and the junction resistance of the 9 nm rubrene device as a function of temperature measured at different voltage bias are shown in Fig. 3a. Junctions, where the OS barrier dominated the resistance, showed stronger temperature dependence. The decrease in the junction resistance below ~12 K is attributed to the exchange splitting of EuS below its T_c and the accompanying decrease in the barrier height [11]. These results show good tunneling behavior as well as spin filtering to be occurring, as expected in these junctions. I–V plot shows non-linear behavior with some asymmetry: higher current in the negative bias implying lower injection barrier for electrons coming from the top Fe electrode. This is expected due to the large rubrene molecules that introduce roughness and defect states at the top interface. This can also create magnetic dipolar coupling between Fe and EuS, as observed in Fig. 2b, with magnetic switching starting even before zero field is reached. On increasing the thickness of rubrene to 11 nm, the dipolar coupling between EuS and the top Fe is considerably weakened (see Fig. 3b). As a result, magnetic switching of Fe was sharper and the device resistance only marginally increased near zero field (showing near independent switching of Fe and EuS), improving the device response. In this case, MR ~1.8% peaked at around 1.6 V.

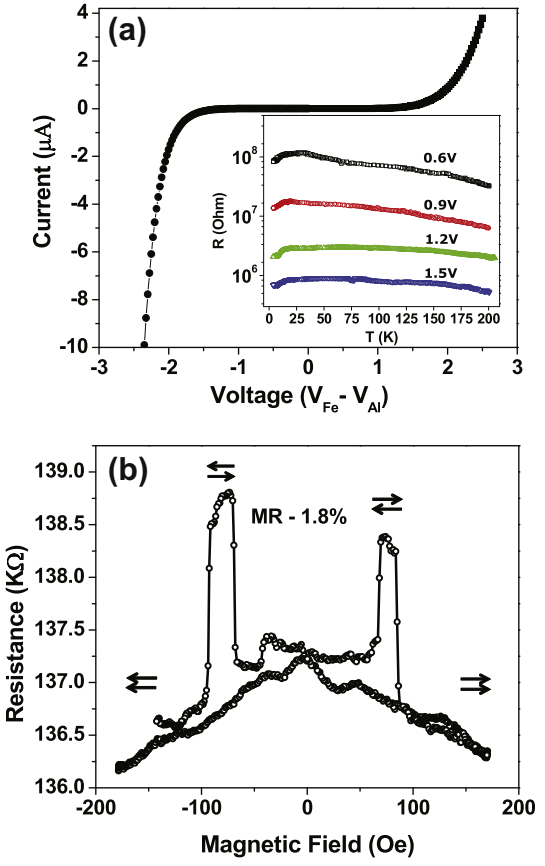

Fig. 3. (a) Non-linear I–V characteristics of the device Al/EuS/Rub (9 nm)/Fe measured at 1 K. Inset: temperature dependence of the junction resistance (semi-log scale) measured at different biases – the slight drop in the resistance at low temperatures shows EuS becoming ferromagnetic below ~12 K. (b) MR measured at 1 K with a bias voltage of 1.6 V for the device: Al/EuS/Rub (11 nm)/Fe.

These junctions showed unconventional dependence of MR with voltage bias (see Fig. 4). In contrast to MTJs having typical FM electrodes, QMJs showed a monotonic decrease in MR with increase in bias-voltage, which can be attributed to excitations of magnons, phonons and band effects [15]. However, in the present case, MR increased from 2% to 6% on increasing the voltage bias from 0.8 to 1.8 V and thereafter it decreased. The bias dependence of the MR was extracted from the I–V measurements in the parallel (300 Oe) and the anti-parallel (80 Oe) magnetization configurations of the junction, using the expression $\mathrm{MR}(V) = [(I_{\mathrm{parallel}}(V) - I_{\mathrm{anti\text{-}parallel}}(V))/I_{\mathrm{anti\text{-}parallel}}(V)] * 100$ and is shown in Fig. 4. The noise at low voltage bias resulted from very high impedances, where the measured currents were extremely small (~ tens of pA). Five sets of samples were measured and three of the devices showed similar bias dependence of MR. However, the peak value of MR varied from 3% to 6% and the position of the maximum MR changed between 1.3 and 1.8 V.

Earlier studies on a quasi-magnetic tunnel junction device without an OS barrier such as Al/EuS/Al_2O_3/Co/CoO have shown similar bias dependence of MR [16]. This MR vs bias behavior has been attributed to Fowler–Nordheim (FN) tunneling mechanism. However, the conduction process in these earlier devices is slightly different to the one reported in the present work. In the earlier study, a thin Al_2O_3 layer (1.2 nm) was used as an insulator spacer layer to magnetically decouple the two FM electrodes, with direct tunneling as the main conduction process. In the present study, a thicker OS (>7 nm) film served as the spacer layer. As a result, multi-step tunneling involving the energy levels in the OS barrier is the expected conduction process. The process of FN tunneling in these QMJs can be understood schematically from the energy diagram shown in Fig. 4. When bias is applied to the junction, voltage drops across rubrene as well as EuS barrier: the voltage drop across the EuS barrier causes its spin-split conduction band to bend. As the bias increases, the band bends sufficiently (with spin-up barrier of EuS falling below the electrode Fermi level) to cause the onset of FN tunneling, resulting in preferential tunneling of spin-up electrons into the organic electronic levels. This leads to enhanced spin-polarized tunneling injection into the organic barrier leading to higher MR signals. Occurrence of the MR peak at higher bias (~1.8 V) compared to the previous report of 1.2 V for the non-OS barrier junctions mentioned before confirm that considerable voltage drops across the rubrene barrier as well. As the applied bias increased further, the spin-down band bends sufficiently to contribute to tunneling and thus reducing the MR. At higher thicknesses of rubrene (>12 nm), the MR was reduced and the signal became weaker and noisier.

In conclusion, our study has shown an alternate method to inject spin-polarized carriers into rubrene, using SF materials. In addition to the observation of MR, it was interesting to find the increase in MR at higher voltage

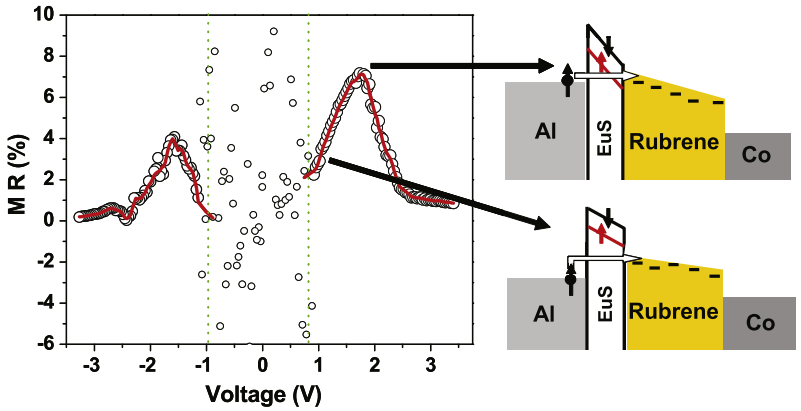

Fig. 4. Left: unconventional bias dependence of MR in a QMJ device with 9 nm rubrene barrier, measured at 1 K. Line through the data is guide to the eye. Data points in between the dotted lines have large fluctuations due to the difficulty in data extraction from *I–V* curves at these low bias regions (current ~100 pA). Tunneling mechanism at low and high bias regions are shown schematically on the right: direct Fowler–Nordheim tunneling at high bias (top) compared to the indirect tunneling at low bias (bottom) of the spin-up electrons into the organic layer.

bias. This could prove important for injecting spin-polarized carriers into organic light emitting diodes close to the device turn-on voltage and in-turn investigate spin-excitonic recombination processes by electroluminescence studies. At present, due to the low T_c of EuS, the observations are confined to low temperature studies. There have been studies on oxide-based ferrites where the possibility of spin filtering at room temperature is shown [17]. It might be worth extending the above investigation to these ferrite materials for achieving the room-temperature operation. Also, if organic molecules having SF properties close to room temperature could be synthesized, it could lead to major advance in organic spintronics.

Acknowledgements

This work was supported by the NSF grant DMR 0504158, ONR grant N00014-09-1-0177 and KIST-MIT program funds.

References

[1] V.A. Dediu, L.E. Hueso, I. Bergenti, C. Taliani, Nat. Mater. 8 (2009) 707.
[2] Zeev Valy Vardeny, Organic Spintronics, CRC Press, 2010.
[3] C.B. Harris, R.L. Schlupp, H. Schuch, Phys. Rev. Lett. 30 (1973) 1019–1022.
[4] T.S. Santos, J.S. Lee, P. Migdal, I.C. Lekshmi, B. Satpati, J.S. Moodera, Phys. Rev. Lett. 98 (2007) 016601.
[5] J.H. Shim, K.V. Raman, Y.J. Park, T.S. Santos, G.X. Miao, B. Satpati, J.S. Moodera, Phys. Rev. Lett. 100 (2008) 226603.
[6] Z.H. Xiong, Di Wu, Z. Valy Vardeny, Jing Shi, Nature 427 (2004) 821.
[7] K.V. Raman, S.M. Watson, J.H. Shim, J.A. Borchers, J. Chang, J.S. Moodera, Phys. Rev. B 80 (2009) 195212.
[8] Jung-Woo Yoo, H.W. Jang, V.N. Prigodin, C. Kao, C.B. Eom, A.J. Epstein, Phys. Rev. B 80 (2009) 205207.
[9] Tho D. Nguyen, Golda Hukic-Markosian, Fujian Wang, Leonard Wojcik, Xiao-Guang Li, Eitan Ehrenfreund, Z. Valy Vardeny, Nat. Mater. 9 (2010) 345.
[10] Jung-Woo Yoo, C.-Y. Chen, H.W. Jang, C.W. Bark, V.N. Prigodin, C.B. Eom, A.J. Epstein, Nat. Mater. 9 (2010) 638.
[11] J.S. Moodera, T.S. Santos, T. Nagahama, J. Phys. Condens. Matter 19 (2007) 165202.
[12] J.S. Moodera, X. Hao, G.A. Gibson, R. Meservey, Phys. Rev. Lett. 61 (1988) 637–640.
[13] D.J. Choi, N.J. Lee, T.H. Kim, J. Magn. 15 (4) (2010) 184.
[14] G.E. Thayer, J.T. Sadowski, F. Meyer zu Heringdorf, T. Sakurai, R.M. Tromp, Phys. Rev. Lett. 95 (2005) 256106.
[15] J.S. Moodera, J. Nowak, R.J.M. van de Veerdonk, Phys. Rev. Lett. 80 (1998) 2941.
[16] T. Nagahama, T.S. Santos, J.S. Moodera, Phys. Rev. Lett. 99 (2007) 016602.
[17] M. Gajek, M. Bibes, A. Barthélémy, K. Bouzehouane, S. Fusil, M. Varela, J. Fontcuberta, A. Fert, Phys. Rev. B 72 (2005) 020406(R).

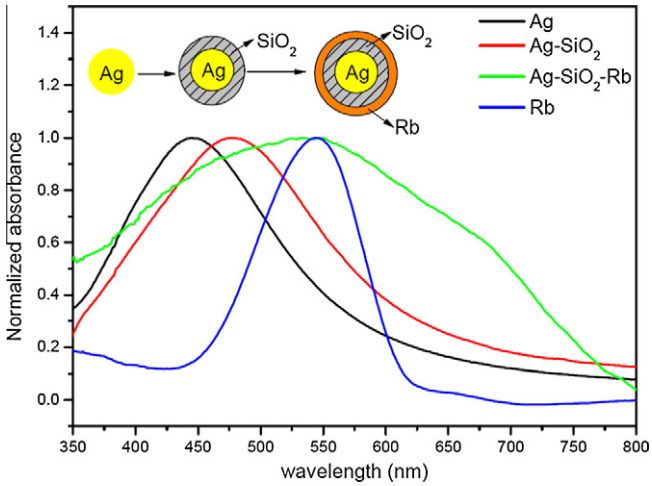

Fig. 1. Evolution of the absorption spectrum from Ag NPs, to Ag–SiO_2 core–shell NPs, till Ag–SiO_2–Rb hybrid NPs.

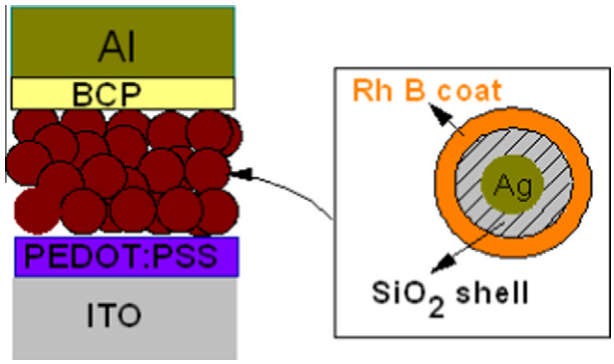

Fig. 2. OLED structure with hybrid NP as emitting centers.

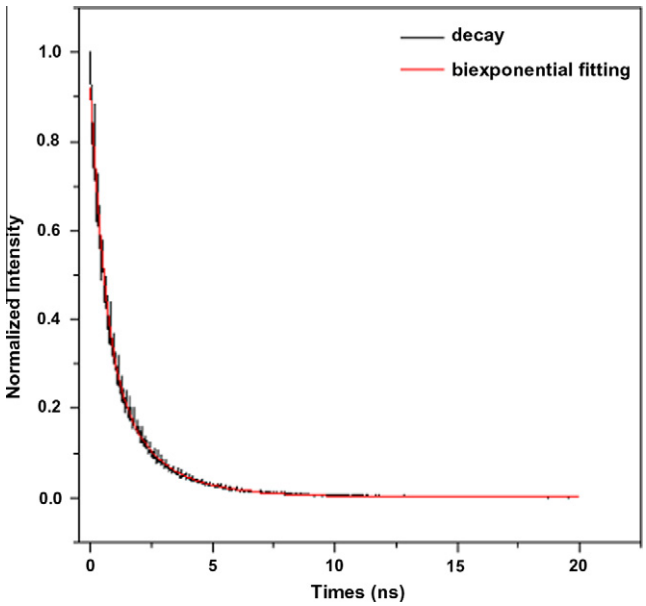

Fig. 3. Time resolved PL decay of Ag–SiO_2–Rb hybrid NPs.

Subsequently, 1.25 mL of 10 mM tetraethyl orthosilicate (TEOS) ethanol solution was added into silver NPs solution every half an hour, and totally 20 mL TEOS solution has been added within 8 h period. The mixture was kept for another 24 h before separation. Finally the silver–silica core–shell NPs were obtained by centrifugation at 3500 rpm for 30 min, washed with ethanol three times and dried in an oven (insert in Fig. 1). The silver–silica core–shell NPs were dispersed into 50 mL anhydrous toluene, 2 mmol silanized rhdoamine B, synthesized in the way reported by Nedelcev et al. [12] and 314 mL (1 mmol) triethoxy(octyl)silane were added into the NPs solution. The obtained mixture was refluxed at 110 °C for 12 h under dry nitrogen. The functionalized NPs were separated from solution by centrifugation, washed with toluene three times and dried in oven overnight. The dark red NPs powder indicates that rhodamine dye was successfully bound to the silver–silica core–shell nanostructure.

The OLED containing hybrid NPs was fabricated as follows (Fig. 2). PEDOT was spin coated on pre-cleaned ITO glass at the speed of 4000 rpm for 40 s. The spin coating method was attempted for hybrid NPs deposition, but only little amount of NPs could be deposited on the slice due to the low viscosity. Therefore a spray method was developed to deposit hybrid NPs. 6 nm bathocuproine (BCP) was sublimated on hybrid NPs by thermal vacuum deposition. Here BCP serves as a hole blocking layer. We did not employ Tris(8-hydroxyquinolinato)aluminium (Alq_3) as electron transport layer in our diodes because the EL of Alq_3 would overlap with the EL of hybrid NPs. Finally, 200 nm aluminum was deposited as cathode.

The absorption spectra were taken with a Lambda 20 UV/Vis spectrometer, and the PL spectra were measured by USB2000-Ocean Optics spectrometer. Atomic force microscope (AFM) image was captured with an Ambios multimode microscope. Current–voltage curves were measured on Keithley semiconductor characterization system. OLED luminance intensity was obtained by a calibrated silicon photodiode (S2281 series, Hamamatsu Photonics).

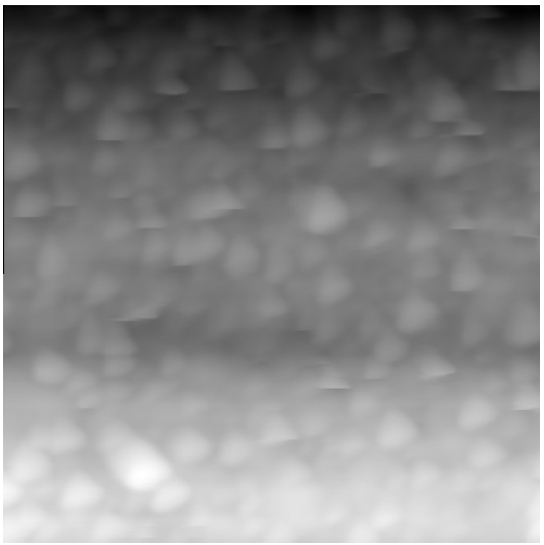

Fig. 5. AFM image ($1 \times 1\ \mu m^2$) of sprayed Ag–SiO_2–Rb hybrid NPs.

3. Results and discussion

Fig. 1 shows the UV–Vis spectra measured at each functionalization step, from the bare silver NPs to the final product. The pure silver NPs dispersed in ethanol shows an absorption peak at around 440 nm, which represents

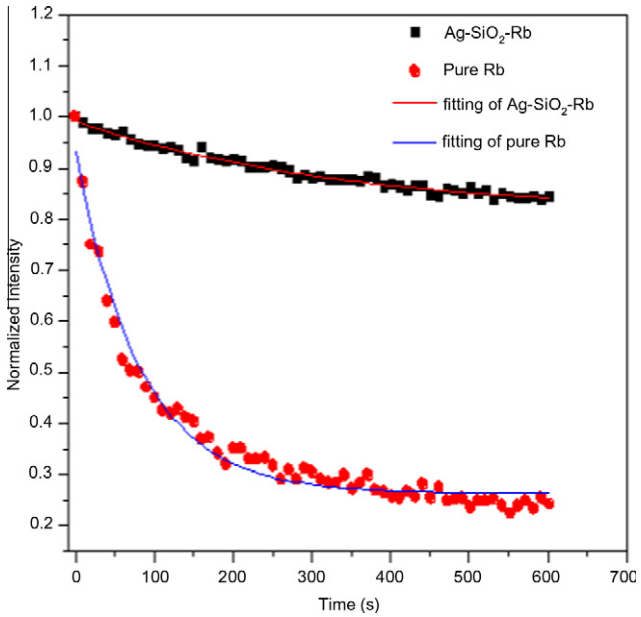

Fig. 4. Photobleaching dynamics of pure rhodamine B and hybrid NPs on glass substrate. Samples were irradiated under 200 mW/cm^2 Nd-YAG laser light at 532 nm.

the typical resonance peak of metallic silver. When the silver NPs are coated by silica, the absorption peak red shifts to 480 nm, this can be attributed to the refractive index change according to Mie theory [13]. With the binding of rhodamine onto silver–silica NPs, the absorption spectrum evolves into a broad hump with absorption maximum around 550 nm which is identical to that of pure rhodamine B. It may result from the superposition between silver NP plasmon and rhodamine B absorption.

We have measured the luminescence lifetime of hybrid NPs, The time-correlated single photon counting PL intensity decay curve shown in Fig. 3 can be fitted with a bi-exponential decay. Two lifetime components 0.58 and 1.96 ns are obtained, while the lifetime of rhodamine B in solution is around 7 ns [14]. The much shorter lifetime component from hybrid NPs can be attributed to metal enhanced fluorescence (MEF) [10]. As known to us the collective oscillation of electrons on the surface of metal results in a localized evanescent electric field (E-field) [15]. According to Fermi's golden rule, the transition probability from one state to another is proportional to the square of the E-field strength which molecule experiences. Thus the surface plasmon induced localized E-field increases the radiative decay rate of the exciton, it means that the electrons in the excited state have larger probability to relax back to ground state via the photoluminescence channel instead of phonon relaxation which is a nonradiative decay. As a result, the photoluminescence quantum efficiency is improved due to surface plasmon effect and consequently fluorescent lifetime is shortened. We attribute the longer lifetime component to the part of the rhodamine molecules which are away from the silver NPs, they thus experience lower E-field enhancement. The 1.07 ns average lifetime implies that hybrid NPs may have better photostability than pure rhodamine B molecules for which degradation channels have larger probability.

We have investigated the photostability of hybrid NPs by recording the PL intensity evolution under the irradia-

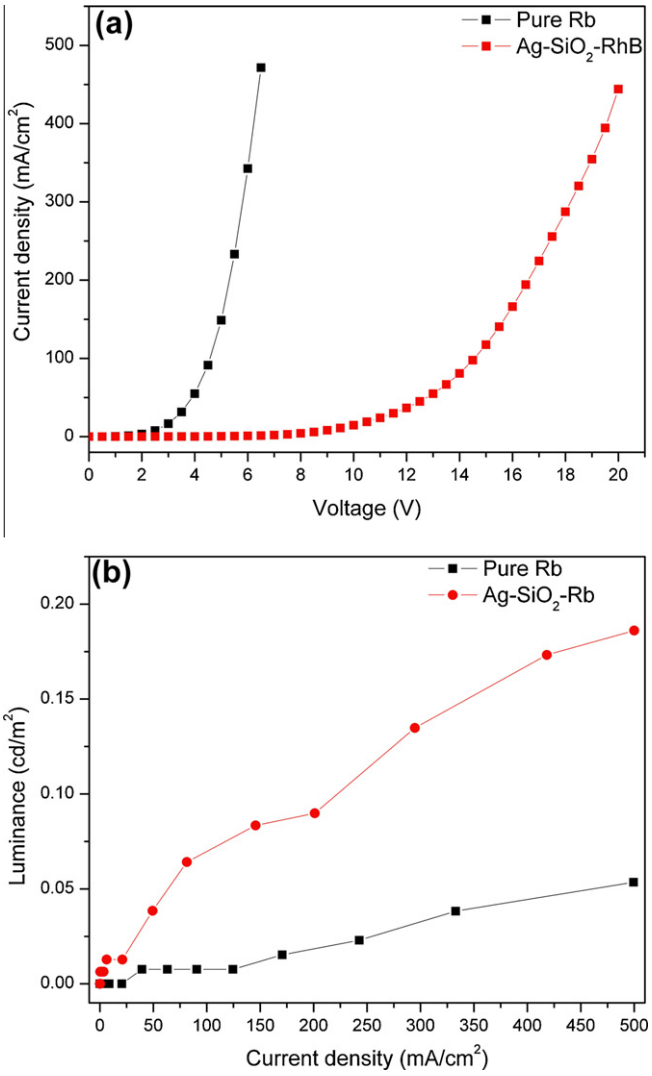

Fig. 6. (a) Current density–voltage curves of OLEDs with pure rhodamine B and hybrid nanoparticles as emitting layer respectively; (b) corresponding luminance–current density curves.

tion with 532 nm laser light (Nd-YAG, 200 mW/cm^2). As shown in Fig. 4 the PL intensity of hybrid NPs degrades to 85% of its original intensity after 600s exposure. While it only takes 10 s for rhodamine B to reach the same intensity decay. This remarkable improvement of photostability indicates that hybrid NPs are a much stable luminescence source which might find potential application in single photon emitting devices.

The AFM profile of spray deposited hybrid NPs on the substrate is shown in Fig. 5. The hybrid NPs have quite even distribution with diameter around 65 nm, and it is clearly observed that the emission layer consists of NPs multilayer, this stacked NPs structure ensures enough thickness for the emission layer and thus prevents the device from current leakage and short circuit.

We have investigated the performance of OLEDs with hybrid NPs and pure rhodamine B as emission layers. Fig. 6a shows the *J*–*V* curves of the diodes, and both of them present very good rectification characteristic. However, the hybrid NPs diode has higher turn-on voltage compared with the pure rhodamine B diode, which can be attributed to deep charge trapping in the hybrid NPs layer. The luminance–current density curves of both diodes are shown in Fig. 6b. We see that the hybrid NPs diode presents much higher luminance intensity compared to pure rhodamine B diode under the same current density, the maximum luminance efficiency of the hybrid NP diode is about 6.8 times larger than that of the rhodamine B diode. This benefits from the surface plasmon enhanced luminescence.

Fig. 7 presents the EL from the hybrid NP OLED. The EL spectrum shows remarkable broadening compared with its PL spectrum. Because the spectral broadening only occurs in the EL experiment, it rules out dimer formation induced spectral broadening that should also be observed in the PL. It is most likely that the spectral broadening originates from charge recombination at an interface. As commonly known, the excitation by an external light source on a bulk material will not induce charge accumulation at an interface since the exciton decay occurs on a nanosecond time scale. However, charge carriers tend to gather at an interface in the EL process due to massive charge injection from electrodes and low mobility in hybrid materials, which offers a considerable probability to form exciplexes [16]. It is also expected that owing to disorder, interface exciplexes will display broad emission spectra. In order to validate that hypothesis, we fabricated another OELD with the same structure except that the hybrid NPs were replaced by concentrated rhodamine B dye, but we failed to observe the spectral broadening. This indicates that the surface plasmon of silver NPs plays an important role in facilitating exciplex recombination at the interface. Indeed, surface plasmons induce an enhanced evanescent E-field which in turn favors exciplex recombination. Direct exciplex luminescence from the LUMO level of rhodamine at −3.5 eV to the depleted HOMO level of PEDOT at −5.1 eV is thus temptatively assigned to the broad emission spectrum in Fig. 7.

In order to investigate charge transport behavior in our OLED structure, we measured time resolved EL as shown in Fig. 8. Electric pulse width was 100 μs, the duty cycle 50%, and both rise and fall time were 1 μs. The bias voltage was set to 15 V and the EL signal was collected by an avalanche single photon detector (APD). There is no obvious delay time t_d observed in the present OLED, which usually corresponds to the charge carrier (holes or electrons) transport time in a diode with thicker organic film. In the present diode structure, holes should reach the NPs layer within a very short time interval since PEDOT is a conductor, meanwhile electrons are injected into the NPs by means of tunneling through the BCP, which is also a fast process. Thus it is understandable that we do not observe any delay time.

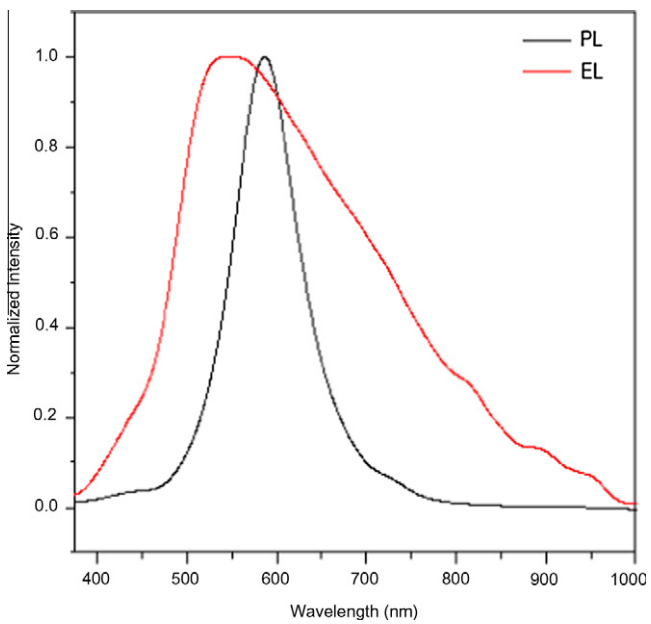

Fig. 7. The PL and EL spectra of OLED with Ag–SiO_2–Rb hybrid NPs.

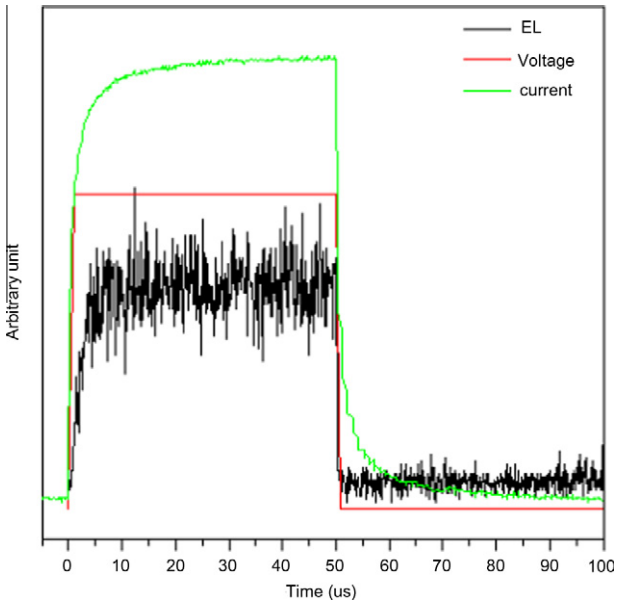

Fig. 8. Time resolved EL of OLED with hybrid NPs.

However, we clearly observe that EL signal takes about 5–6 μs to reach saturation, which is limited by charge carrier dynamics. With the increase of EL signal, the current density also increases. That cannot be explained by the classic capacitor model, in which the current density should decrease along with the accumulation of charge at the interface of organic layers. We interpret our charge transport process as follows: the holes can easily pass through the PEDOT layer and accumulate into the NPs layer due to the BCP hole blocking layer. A space charge induced electrical field builds up, expediting electron tunneling from the aluminum cathode into the NPs layer. As a result, both the current and EL intensity increase. When charge distribution comes to equilibrium, i.e. the minimum hole concentration is established in the hybrid NPs layer, both the current and EL intensity saturate. Finally when the bias voltage is turned off, we can still observe a current decay due to relaxation of the trapped charges inside the diode [17]. However, we do not observe a corresponding EL decay, because the bias voltage falls below the threshold (turn-on) voltage, and no EL can be generated although current flows through the diode.

4. Conclusion

A novel rhodamine dye functionalized Ag–SiO_2 core–shell NPs has been synthesized and applied into OLED as an emitting layer. The EL of hybrid NPs shows much broader spectrum than its PL spectrum. It is observed that the presence of surface plasmon enhanced E-field favors the spectral broadening. This will inspire us to tune OLED electroluminescence, to design and optimize white light OLED from a novel point of view. In addition, much more stable luminescence benefiting from surface plasmon also makes the hybrid NPs a good light source for the study of single photon emission.

Acknowledgements

Work was supported by the Natural Sciences and Engineering Research Council, the Canada Research Chair Program on Chiral Photonics and Queen's University.

References

[1] D.S. Wang, M. Kerker, Phys. Rev. B 24 (1981) 1777.
[2] J.M. Nunzi, D. Ricard, Appl. Phys. B 35 (1984) 209.
[3] S. Mackowski, S. Wormke, A.J. Maier, T.H.P. Brotosudarmo, H. Höarutyunyan, A. Hartschuh, A.O. Govorov, H. Scheer, C. Bräuchle, Nano. Lett. 8 (2008) 558.
[4] S. Pillai, K.R. Catchpole, T. Trupke, M.A. Green, J. Appl. Phys. 101 (2007) 093105.
[5] W. Li, S. Pan, L.J. Rothberg, Proc. SPIE 7032 (2008) 703224;
J.H. Park, Y.T. Lim, O.O. Park, J.K. Kim, J. Yu, Y.C. Kim, Chem. Mater. 16 (2004) 688.
[6] K.Y. Yang, K.C. Choi, C.W. Ahn, Appl. Phys. Lett. 94 (2009) 173301;
A. Fujiki, T. Umemura, N. Zettsu, M. Akai-Kasaya, A. Saito, Y. Kuwahara, Appl. Phys. Lett. 96 (2010) 043307.
[7] J. Shinar, Organic Light-Emitting Devices, Springer Press, New York, 2004.
[8] H. Aziz, Z.D. Popovic, N. Hu, A. Hor, G. Xu, Science 283 (1999) 1900;
E. Gautier-Thianche, C. Sentein, A. Lorin, C. Denis, P. Raimond, J.M. Nunzi, J. Appl. Phys. 83 (1998) 4236.
[9] S. Reineke, F. Lindner, G. Schwartz, N. Seidler, K. Walzer, B. Lüssem, K. Leo, Nature 459 (2009) 234;
C. Hubert, C. Fiorini-Debuisschert, I. Hassiaoui, L. Rocha, P. Raimond, J.M. Nunzi, Appl. Phys. Lett. 87 (2005) 191105.
[10] F. Liu, G. Aldea, J.M. Nunzi, J. Lumin. 130 (2010) 56.
[11] P.C. Lee, D. Meisel, J. Phys. Chem. 86 (1982) 3391.
[12] T. Nedelcev, D. Racko, I. Krupa, Dyes Pigments 76 (2008) 550.
[13] W.A. Murray, W.L. Barnes, Adv. Mater. 19 (2007) 3771.
[14] T.H. Nhung, M. Canva, F. Chaput, H. Goudket, G. Roger, A. Brun, D.D. Manh, N.D. Huang, J.-P. Boilot, Opt. Commun. 232 (2004) 343.
[15] J.R. Lakowicz, Y. Shen, S. D'Auria, J. Malicka, J. Fang, Z. Gryczynski, I. Gryczynski, Anal. Biochem. 301 (2002) 261.
[16] S.P. Singh, Y.N. Mohapatra, M. Qureshi, S.S. Manoharan, Appl. Phys. Lett. 86 (2005) 113505;
A.M.C. Ng, A.B. Djurisic, W.K. Chan, J.M. Nunzi, Chem. Phys. Lett. 474 (2009) 141–145.
[17] S. Barth, P. Müller, H. Riel, P.F. Seidler, W. Rieß, J. Appl. Phys. 89 (2001) 3711.

broadening and enable the electroluminescence (EL) even in the planar geometry of electrodes [23,24]. Recently we have demonstrated that the LE-OFET based on a polyfluorene (PFO)–ZnO nanoparticles film exhibits very high FET mobility values at high concentration of the ZnO nanoparticles in a unipolar regime [25]. However, the ambipolar regime of the PFO:ZnO LE-OFET was not demonstrated so far. We have focused our attention on the PFO, which is a most promising stable conjugated polymer semiconductor for OLEDs and OFETs active layers and ZnO nanoparticles which is a relatively nontoxic n-type, solution processible inorganic semiconductor. ZnO has extremely high electron mobility (up to ~20 cm^2/Vs [26]), excellent environmental stability, and high transparency [27]. Most recently, solution-processed ZnO FETs were presented with a high electron mobility up to ~5.25 cm^2/Vs [28] and ~7.2 cm^2/Vs [29] and with a high on/off ratio. To reach the ambipolar LE-OFET regime we have decided to use a hybrid structure of composite film consists of n-ZnO and p-PFO semiconductors. The main problem for ambipolar LE-OFETs is the injection of both: electron and holes from the electrodes [7], due to the mismatch in the energy levels of the electrodes and the semiconductors. Injection of holes into the HOMO level of p-type polymer semiconductors can be achieved by using gold electrodes because the HOMO level of many conjugated polymers (~4.8–5.3 eV) and the work function of gold (~5.1 eV) are very close. However, gold electrodes are not appropriate for electron injection into the LUMO level of conjugated polymers due to very high injection barrier of ~2–3 eV [18]. This problem was solved in our present work by using two different metal electrodes (gold and aluminum) with high and low work functions values.

In this article we report on a solution-processed PFO–ZnO nanoparticles composite ambipolar LE-OFET. We have analyzed the behavior of absorption, PL spectra and EL intensity of the PFO:ZnO hybrid films with different ZnO concentration. It was found that by changing the PFO/ZnO nanoparticles concentration ratio the PFO:ZnO LE-OFET shows either unipolar or ambipolar behavior of current–voltage characteristics (I–Vs) and operates in the hole/electron accumulation mode with current saturation behavior. The transistor shows transfer characteristics with a small reversible hysteresis. We have found that for the ambipolar PFO:ZnO LE-OFET with the modest PFO/ZnO nanoparticles ratio (1:0.2) well balanced electron and hole mobility values at 300 K are ~0021 and ~0029 cm^2/Vs respectively, whereas for films with high ZnO nanoparticles concentration (1:1) the mobility (~2 cm^2/Vs) is close to that of polycrystalline ZnO. It was observed that the ambipolar PFO:ZnO LE-OFET emits light at both positive and negative gate bias. The working mechanism of the PFO:ZnO LE-OFET is discussed.

2. Experimental

Fig. 1a and b provides chemical structure of the conjugated polymer poly[9,9-bis-(2-ethylhexyl)-9*H*-fluorene-2,7-diyl] (PFO), used in our experiments and schematic illustration of the polymer–inorganic nanoparticles hybrid FET, which comprise a n-Si/SiO_2/Au/PFO:ZnO/Al structure. An n+ silicon substrate was used with 200 nm thermally grown SiO_2 as gate dielectric with thermally evaporated gold and aluminum electrodes on top. The distance between the electrodes was ~7 μm and the width of the electrode ~1 mm. The conjugated polymer, PFO, and ZnO nanoparticles (diameter ~ 50–70 nm) used in our study were purchased from Sigma–Aldrich and used as received. PFO polymer and ZnO nanoparticles were dissolved and dispersed in chloroform respectively, and then they were mixed together and subjected to ultrasonic treatment for 10 min ($f \sim 22$ kHz). The mixtures with different concentration ratios of components were drop-cast or spin-coated onto a Si substrate. The thickness of the composite films was about ~0.6 μm according to Atomic Force Microscopy (AFM) results. The composite films were dried and heated at 80 °C in N_2 atmosphere for 15 min. The samples for absorption measurements were drop cast onto quartz substrates (the film thickness ~1 μm) and studied by using a Cary-50 (Varian) spectrometer. The detailed microstructure of these films was studied by AFM using P47-Solver NT-MDT. A LGI-21 pulse laser (λ = 337, 1 nm, E_i >10^{-4} J/cm^2, $\tau \sim 10^{-8}$ s) was used to excite the PL. The laser beam was focused onto the sample using the quartz lens (The diameter of the focused beam was ~2–3 mm). The PL spectra and the EL intensity at 300 K were analyzed using a SPM-2 spectrometer (spectral resolution ~2 nm) and a photomultiplier with a spectral sensitivity range 300–850 nm. The PL/EL light collection was about ~100% owing to the use of a special mirror. The I–V characteristics of OFETs were measured in vacuum (3×10^{-3} torr) in the dark at 300 K using a liquid N_2 cryostat holder and a dc electronic computer controlled measuring system with a Keithley 6487 picoammeter/voltage source and AKIP-1124 programmable voltage source. The source – drain and gate voltages were varied between – 40 and +40 V in variable steps. Field-effect hole/electron mobility, μ_{FET}, was calculated using the following equations for the saturation and low field regimes respectively [2]:

$$I_{DS} = (W/2L)\mu_{FET}C_I(V_G - V_{th})^2 \quad (1)$$

$$I_{DS} = (W/L)\mu_{FET}C_I(V_G - V_{th})V_{DS} \quad (2)$$

Here W is the channel width, L is the channel length, C_I is the capacitance per unit area of the SiO_2 layer (for SiO_2 layer thickness of about 200 nm, $C_I \sim 7$–10 nF/cm^2). V_G is the gate voltage, and V_{th} is the threshold voltage, which corresponds to the onset of the strong accumulation regime.

3. Results and discussion

Fig. 2 shows the absorption and PL spectra of the PFO pristine and the PFO:ZnO composite (ZnO concentration ~17 wt.%, 1:0.2) films. It is evident from Fig. 2, the absorption spectra of both: pristine PFO and PFO:ZnO films have maxima at ~380 nm, however in the case of hybrid film this maximum is lower that confirms the presence of weak interaction between the polymer molecules and inorganic nanoparticles. As regards the PL spectra, Fig. 2 shows that

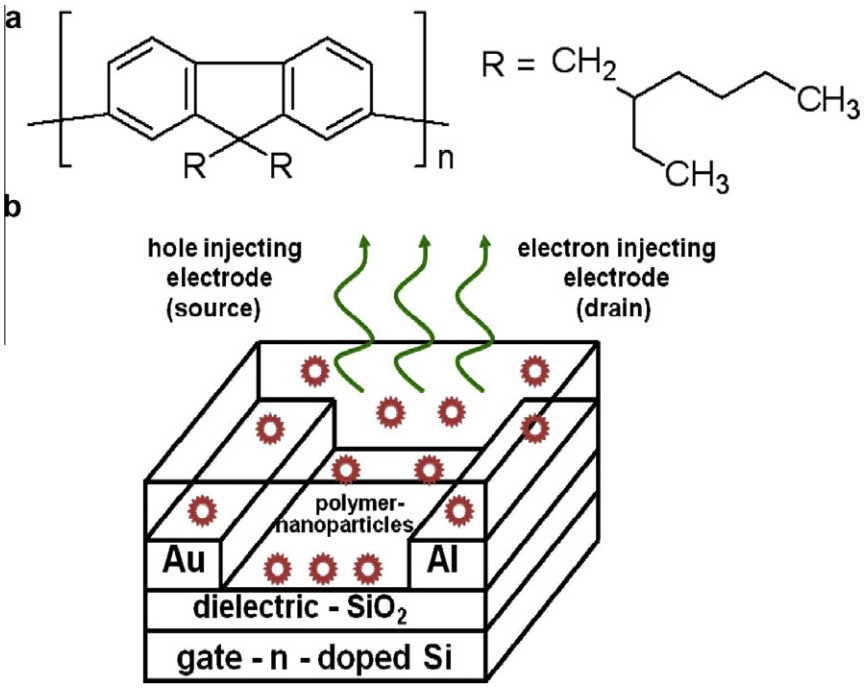

Fig. 1. Chemical structure of the PFO polymer (a) and schematic device structure of PFO:ZnO OFET (b).

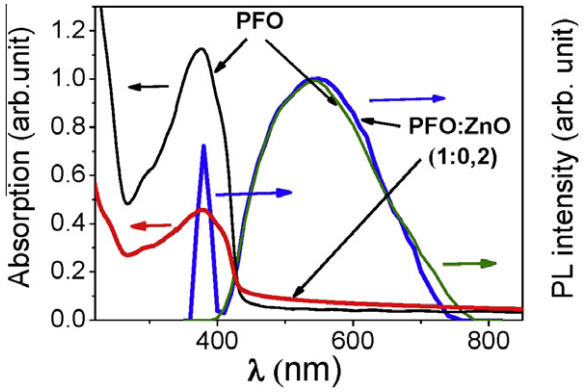

Fig. 2. Absorption and PL spectra of PFO (thin solid lines) and PFO:ZnO (thick solid lines) films. Concentration of the ZnO nanoparticles for PFO:ZnO ~17 wt.% (1:0.2). Film thickness ~0.6 μm.

an introduction of the ZnO nanoparticles results in shifting of the PL maximum from ~580 nm (pristine PFO) toward the ultraviolet (hybrid PFO:ZnO) spectral region. The increase of the ZnO nanoparticles concentration leads to an increase of intensity of the PL peak at 380 nm related to the emission of the ZnO nanoparticles. There are no distinct signs of complexes formation in visible spectral region that can be explained by high values of the ionization potential I_D of PFO (I_D >8.2 eV), which results in relatively weak interaction between the PFO molecules and ZnO nanoparticles.

Fig. 3a–c shows the AFM micrographs of pure PFO and PFO:ZnO (1:0.2) films between Au and Al electrodes on a n-Si/SiO_2 substrate. It is worth noting that the channel length of ~7 μm is much larger with respect to the diameter of the ZnO nanoparticles ~50–70 nm. As can be seen from Fig. 3a, detailed AFM surface examination indicates rather smooth pure PFO film structure. Introduction of the ZnO nanoparticles into the PFO matrix results in very rough composite film structure with few pinholes throughout the film between Au–Al electrodes (Fig. 3b and c). There are a number of the ZnO nanoparticles aggregates with a diameter of about several hundreds nm despite the PFO–ZnO solution was subjected to ultrasonic treatment before deposition. The presence of the ZnO nanoparticles aggregates can affect the I–Vs of OFETs and therefore they can influence the μ_{FET} (300 K) values as will be shown below.

Typical output I–V characteristics of the LE-OFET based on PFO:ZnO nanoparticles film (1:0.2) with a channel length of ~7 μm and a channel width of ~1 mm operated at different gate voltages in vacuum are displayed in Fig. 4a and b. It is evident from Fig. 4a, the PFO:ZnO OFET exhibits the output I–V characteristics for the hole-enhancement mode of a OFET with nearly saturation behavior. As can be seen from Fig. 4b, the output characteristics for the electron-enhancement mode at positive gate voltages are rather similar to those of the hole-enhancement mode. Fig. 4a and b, demonstrate that the saturated drain currents of I–Vs are not flat completely due to probably leakage currents between source and gate electrodes at high gate-to-source voltage (V_G). Moreover, there is a sharp increase of the source-drain current, I_{DS}, in the output characteristics at rather high V_{DS} >25 V at modest V_G for the PFO:ZnO LE-OFET structures (see inset to Fig. 4a) similar to that found for other LE-OFETs [13,18]. This indicates the onset of electron (negative V_G) or hole (positive

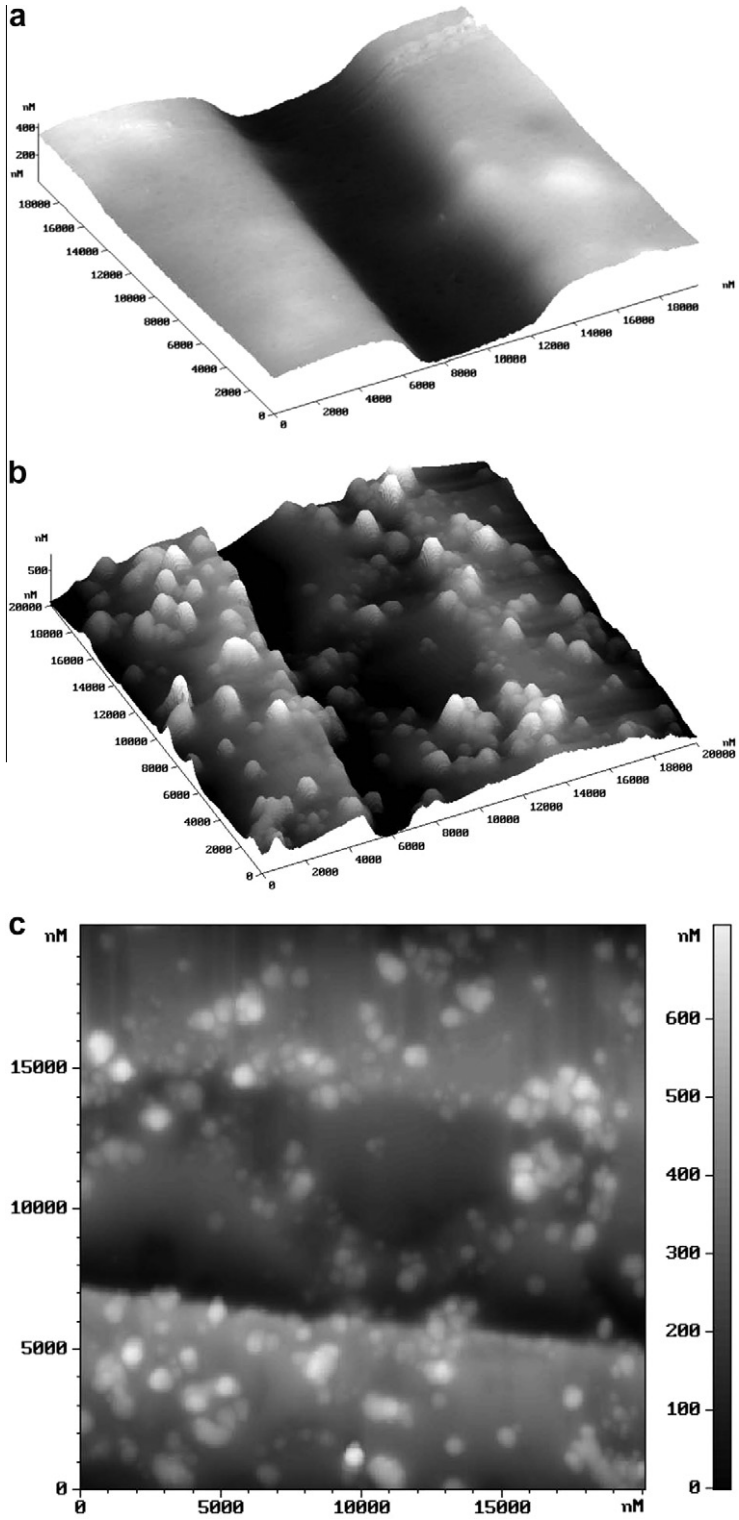

Fig. 3. AFM micrographs of PFO (a) and PFO:ZnO (b and c) films between Au–Al electrodes. Concentration of the ZnO nanoparticles ~17 wt.%.

V_G) transport. Such a behavior correlates well with numerical modeling results which predict an indication of the ambipolar regime by a superlinear current increase on top of a significant saturation current [30]. The transfer characteristic for the same device in the saturation regime for positive and negative gate voltage is shown in Fig. 4c.

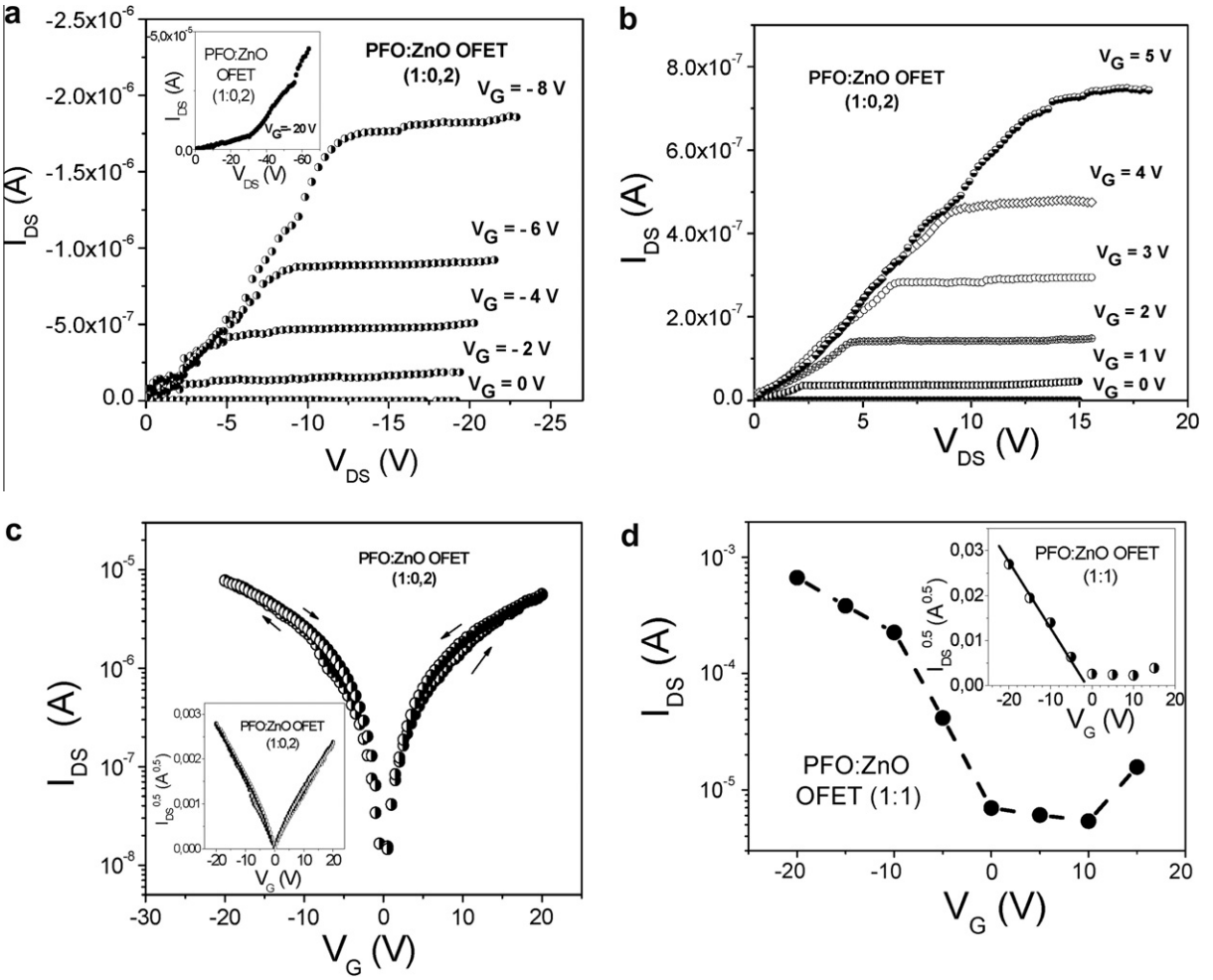

Fig. 4. (a) Output I–V characteristics of the PFO:ZnO OFET (1:0.2) at 300 K for different negative V_G; (inset) output I–V characteristics for the same sample at high V_{DS} >20 V and $V_G = -20$ V; (b) output I–V characteristics of the PFO:ZnO OFET (1:0.2) at 300 K for different positive V_G; (c) Transfer characteristic of the PFO:ZnO OFET (1:0.2) at 300 K for $V_{DS} = -10$ V; (inset) $I_{DS}^{0.5}$ versus V_G for the same sample; (d) transfer characteristic of the PFO:ZnO OFET (1:1) at 300 K for $V_{DS} = -10$ V; (inset) $I_{DS}^{0.5}$ versus V_G for the same sample.

The gate-to-source voltage was swept between +20 V to −20 V at 0.5 V step with a constant drain voltage $V_{DS} = -10$ V. Fig. 4c clearly shows both electron and hole accumulation regimes for the PFO:ZnO OFET with relatively low ZnO nanoparticles concentration (1:0.2). The PFO:ZnO OFET shows the transfer characteristics with a small reversible hysteresis. Electron and hole field-effect hole mobility, μ_{FET}, was calculated for the saturation and low field regimes according to Eqs. (1) and (2). For the PFO:ZnO OFET (1:0.2) shown in Fig. 4a and b, the threshold voltages V_{th} estimated from the slope of the $I_{DS}^{0.5}$ versus V_G plot at $V_{DS} = -10$ V were found to be about ∼−0.2 and ∼+0.2 V for negative and positive V_G, respectively (Fig. 4c). Therefore electron and hole mobility values at 300 K for this OFET estimated according to Eq. (1) were found to be ∼0021 and ∼0029 cm^2/Vs, respectively. The μ_{FET} (300 K) values estimated for the same sample using Eq. (2) are of the same order of magnitude. On/off ratio determined for this device from the transfer characteristics was found to be in the range of $\sim 10^3$ for $V_G \sim -20$ V, but it is obviously higher for higher V_G values. As the concentration of the ZnO nanoparticles increases the transfer plot of the PFO:ZnO OFET becomes asymmetric that indicates the transition to the unipolar regime (Fig. 4d). For such PFO:ZnO OFET (1:1), shown in Fig. 4d, we observed the $V_{th} \sim -1$ V and on/off ratio $\sim 10^2$ for $V_G = -20$ V. The μ_{FET} (300 K) values calculated for this PFO:ZnO OFET (1:1) using Eq. (1) at $V_G = -20$ V and $V_{DS} = -10$ V were found to be unusually high and reached the value of ∼2 cm^2/vs. These results demonstrate that on/off ratio decreases whereas the μ_{FET} (300 K) value increases significantly with increase of concentration of the ZnO nanoparticles. The observed rather low threshold voltages and on/off ratios indicate a low concentration of trap states as well as low injection barriers at the contacts. The obtained mobility values for PFO:ZnO OFET (1:0.2 and 1:1) are much higher than those observed in our experiments and reported in the literature for pure PFO OFETs (∼4×10^{-4} cm^2/Vs [12]). We have suggested that the μ_{FET} (300 K) values obtained in our experiments for PFO:ZnO OFET with modest ZnO nanoparticles

concentration (~17 wt.%) reflects the contribution to charge transport from both p- and n-components of the PFO:ZnO film. The μ_{FET} (300 K) at high ZnO nanoparticles concentration is mostly related to the mobility of ZnO nanoparticles, which may form some bridges or thin ZnO layers between Al–Au electrodes, according to our AFM data (Fig. 3b and c). This suggestion correlates well the μ_{FET} (300 K) values obtained by other authors for the polycrystalline ZnO (~20 cm^2/Vs [26]) and for the ZnO FETs (up to ~7.2 cm^2/Vs [29]).

The optical output characteristics (EL intensity versus V_{DS}) at different negative and positive gate voltages of the ambipolar PFO:ZnO LE-OFET (1:0.2) are shown in Fig. 5. We found that the EL intensity at 300 K is increasing with increasing of source – drain, V_{DS}, and both: negative and positive gate voltages, V_G, at nearly saturated drain currents. It is worth noting that the EL intensity measured at the same conditions of the PFO:ZnO LE-OFET with high ZnO nanoparticles concentration (1:1) is higher by factor of 3 with respect to that of the PFO:ZnO LE-OFET (1:0.2), but it has been observed at negative values of V_{DS} and V_G only. That correlates well with an increase of the ZnO nanoparticles concentration that affects strongly the EL intensity. There is the almost fixed onset of the light EL emission at $V_{DS} \sim -5$ V independent of the ZnO nanoparticles concentration and the gate voltage polarity. This onset have been observed even for gate voltages up to −60 V, where the only intensity of the emitted light changes after application of V_G (Fig. 5). This behavior is similar to that observed earlier for tetracene and pure PFO LE-OFETs [11,12], but in our case of the PFO:ZnO LE-OFET the onset of the V_{DS} values is lower significantly. Inset to Fig. 5 presents the EL intensity vs electric field for the PFO:ZnO LE-OFET (1:0.2) at different spectral regions: I_0 – integral; I_1 – 600–830 nm; I_2 – 450–620 nm; I_3 – 300–400 nm. It is evident from these data that the EL emission of the PFO:ZnO LE-OFET (1:0.2) takes place mainly in the green spectral region. In particular, for the PFO:ZnO LE-OFET (1:0.2) it reaches ~40% of the integral EL intensity, whereas the EL emission intensity in the blue region reaches ~20% of the integral EL that correlates with the PL spectra of such composite films (Fig. 2). The same result was obtained for the PFO:ZnO LE-OFET (1:1). The mechanism for the formation of the excited states in the PFO:ZnO composite films implies the presence of a LUMO–HOMO recombination channel in the PFO polymer as well as the contribution of UV excitonic emission (at ~380 nm) from radiative recombination in the ZnO nanoparticles. The latter channel can be suppressed by changing the concentration of ZnO nanoparticles [24]. The PL line observed at 550 nm (Fig. 2) corresponds to the excimer emission from the original polymer aromatic (fluorene) fragments.

Our results demonstrate that the light output of the PFO:ZnO LE-OFET is controlled by the ZnO nanoparticles concentration and the gate voltage. To determine the charge carrier injection mechanism one can consider the energy band diagram of the Au–PFO:ZnO–Al structure shown in Fig. 6. It is evident from this band diagram that the work functions for Au and Al are ~5.1 and ~4.3 eV, respectively, compared with the highest occupied molecular orbital (HOMO) and the lowest unoccupied molecular orbital (LUMO) energy levels of PFO of ~5.8 and ~2.1, respectively [31]. Therefore the injection barrier for holes in Au–PFO is ~0.7 eV and for electrons in Al–PFO is ~2.1 eV. From another side the conduction and valence bands energy levels of ZnO are ~7.5 and ~4.2 eV, respectively. That makes the injection barrier for electrons in Al–ZnO of about ~0.1 eV. It is clear evident from these values that the structure Au–PFO:ZnO–Al should work as ambipolar LE-OFET, that is in good agreement with our experimental results for PFO:ZnO LE-OFET with modest concentration of the ZnO nanoparticles (1:0.2). It is worth noting that some signs of ambipolar transport manifest themselves even for high mobility unipolar PFO:ZnO LE-OFETs (1:1) but at relatively high values of positive V_G only (see Fig. 4d). The reason why the hole accumulation mode still dominates in the unipolar regime of the PFO:ZnO LE-OFET with high concentration of ZnO nanoparticles is not clear completely. One may suggest that this behavior

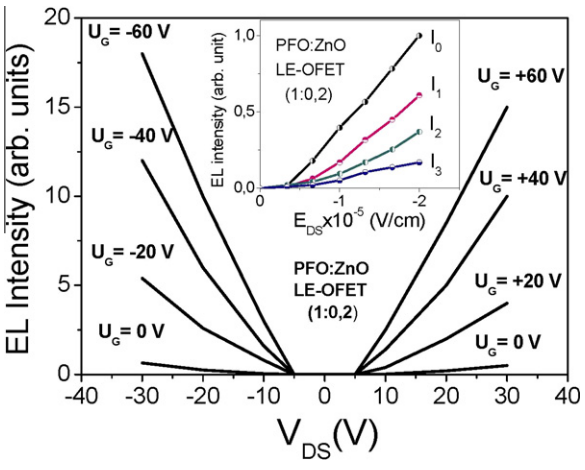

Fig. 5. Optical output characteristics of the PFO:ZnO LE-OFET (1:0.2): EL intensity versus V_{DS} at different V_G at 300 K. (Inset): EL intensity vs electric field for the PFO:ZnO LE-OFET (1:0.2) at different spectral regions: I_0 – integral; I_1 – 600–830 nm; I_2 – 450–620 nm; I_3 – 300–400 nm.

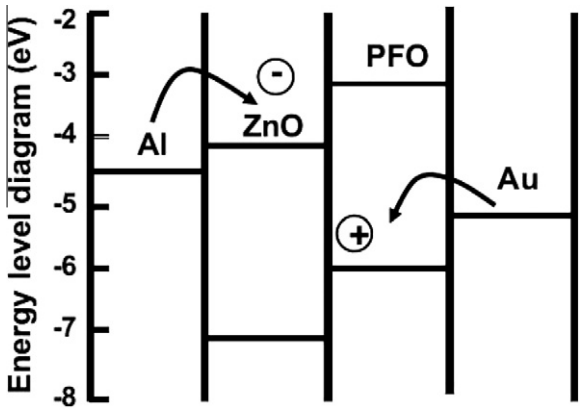

Fig. 6. Band diagram of the Au–PFO:ZnO–Al composite structure.

is due to absence of the robust electrical contact between ZnO nanoparticles and Al/Au electrodes.

As regards the model for the light emission mechanism for the composite active layer LE-OFET, it has been developed recently by Schidleja et al. [21,32]. Follow this model we suggest that for the PFO:ZnO LE-OFET the light emission in the unipolar p-type regime is due to a stable reservoir of electrons established in the PFO in the vicinity of the Al contact. Since the work function of Al and PFO differ, a charge transfer occurs after contact formation and a constant electrochemical potential across the contact is the consequence. The diffusion of electrons from the metal into the organic semiconductor is stopped by the self-induced electric field of the transferred charge. Thus, a reservoir of excess electrons establishes close to the Al contact. In the unipolar p-type regime accumulated holes flow from the Au electrode to the Al electrode. At the Al contact they can either be ejected in the metal or recombine with the electrons of the reservoir. Therefore light emission can be observed even in the unipolar p-type regime of the LE-OFET. Switching from the unipolar to the ambipolar transport regime the position of the charge carrier recombination zone can be moved through the channel from one contact to the other [16,18,21,32]. In the ambipolar regime the charge carrier recombination takes rather place at the polymer/dielectric and polymer/ZnO nanoparticle interfaces than at the contacts. Consequently, the position of the recombination zone is moved from the metal/polymer interface to the polymer/dielectric and polymer/ZnO nanoparticle interfaces by changing the transport regime from unipolar to ambipolar. One may suggest that the spatial heterogeneity of the PFO:ZnO LE-OFET channel affects strongly the EL emission and the electrons and holes injections from different electrodes (Al and Au) is not completely balanced especially at high concentration of the ZnO nanoparticles. The results demonstrate that LE-OFETs based on solution processible polymers such as PFO and semiconducting nanoparticles such as ZnO provide a good example of the multifunctional devices obtained by the deposition technique compatible with up-to-date printed organic electronic technology.

4. Conclusions

We have investigated the solution-processed PFO–ZnO nanoparticles composite light-emitting organic field-effect transistor. We have analyzed the behavior of absorption, PL spectra, EL intensity and I–Vs of the PFO:ZnO hybrid films with different ZnO nanoparticles concentration. The field effect mobility of charge carriers depends on ZnO concentration. It was found that by changing the PFO/ZnO nanoparticles concentration ratio the PFO:ZnO OFET shows either unipolar or ambipolar behavior of I–Vs (at high and low ZnO nanoparticles concentration, respectively) and operates in the hole/electron accumulation mode with nearly current saturation behavior. The FET mobility of charge carriers in PFO:ZnO films depends on ZnO concentration and at high concentration of the ZnO nanoparticles it is close to the mobility of polycrystalline ZnO. The observed ambipolar regime for the PFO:ZnO LE-OFET with relatively low ZnO nanoparticles concentration makes these devices useful for applications in complementary logic circuits.

Acknowledgements

Research funding from the Program No. 7 of Presidium of Russian academy of sciences; subprogram: "Polyfunctional materials for molecular electronics" and RFBR #11-02-00451a is gratefully acknowledged. We would like to thank I.N. Trapeznikova, F.N. Fedichkin and P.N. Gusakov for help with absorption and electrical measurements, respectively.

References

[1] H. Sirringhaus, Device physics of solution-processed organic field-effect transistors, Adv. Mater. 17 (2005) 2411–2425.
[2] C.D. Dimitrakopoulos, P.R.L. Malenfant, Organic thin film transistors for large area electronics, Adv. Mater. 14 (2002) 99–117.
[3] D.B. Mitzi, L.L. Kosbar, C.E. Murray, M. Copel, A. Afzali, High-mobility ultrathin semiconducting films prepared by spin coating, Nature 428 (2004) 299–303.
[4] H.E. Katz, A.J. Lovinger, J. Johnson, C. Kloc, T. Siegrist, W. Li, Y.Y. Lin, A. Dodabalapur, A soluble and air-stable organic semiconductor with high electron mobility, Nature 404 (2000) 478–481.
[5] H. Sirringhaus, N. Tesler, R.H. Friend, Integrated optoelectronic devices based on conjugated polymers, Science 280 (1998) 1741–1744.
[6] A. Dodabalapur, Z. Bao, A. Makhija, J.G. Laquindanum, V.R. Raju, Y. Feng, H.E. Katz, J. Rogers, Organic smart pixels, Appl. Phys. Lett. 73 (1998) 142 (3pp).
[7] J.W. Shi, H.B. Wang, D. Song, H.K. Tian, Y.H. Geng, D.H. Yan, n-Channel, ambipolar, and p-channel organic heterojunction transistors fabricated with various film morphologies, Adv. Funct. Mater. 17 (2007) 397–400.
[8] E.J. Meijer, D.M. de Leeuw, S. Setayesh, E. van Veenendaal, B.-H. Huisman, P.W.M. Blom, J.C. Hummelen, U. Scherf, T.M. Klapwijk, Solution-processed ambipolar organic field-effect transistors and inverters, Nat. Mater. 2 (2003) 678–682.
[9] D. Schlettwein, K. Hesse, N.E. Gruhn, P.A. Lee, K.W. Nebesny, N.R. Armstrong, Electronic energy levels in individual molecules, thin films, and organic heterojunctions of substituted phthalocyanines, J. Phys. Chem. B 105 (2001) 4791–4800.
[10] J. Wang, H.B. Wang, X.J. Yan, H.C. Huang, D.H. Yan, Organic heterojunction and its application for double channel field-effect transistors, Appl. Phys. Lett. 87 (2005) 093507 (3pp).
[11] A. Hepp, H. Heil, W. Weise, M. Ahles, R. Schmechel, H. von Seggern, Light-emitting field-effect transistor based on a tetracene thin films, Phys. Rev. Lett. 91 (2003) 157406 (4pp).
[12] M. Ahles, A. Hepp, R. Schmechel, H. von Seggern, Light emission from a polymer transistor, Appl. Phys. Lett. 84 (2004) 428–430.
[13] F. Cicoira, C. Santato, M. Melucci, L. Favaretto, M. Gazzano, M. Muccini, G. Barbarella, Organic light-emitting transistors based on solution-cast and vacuum-sublimed films of a rigid core thiophene oligomer, Adv. Mater. 18 (2006) 169–174.
[14] J. Reynaert, D. Cheyns, D. Janssen, R. Muller, V.I. Arkhipov, J. Genoe, G. Borghs, P. Heremans, Ambipolar injection in a submicron-channel light-emitting tetracene transistor with distinct source and drain contacts, J. Appl. Phys. 97 (2005) 114501 (5pp).
[15] J.S. Swensen, C. Soci, A.J. Heeger, Light emission from an ambipolar semiconducting polymer field-effect transistor, Appl. Phys. Lett. 87 (2005) 253511 (3pp).
[16] J. Zaumseil, C.L. Donley, J.-S. Kim, R.H. Friend, H. Sirringhaus, Efficient top-gate, ambipolar, light-emitting field-effect transistors based on a green-light-emitting polyfluorene, Adv. Mater. 18 (2006) 2708–2712.
[17] J. Cornil, J.-L. Bredas, J. Zaumseil, H. Sirringhaus, Ambipolar transport in organic conjugated materials, Adv. Mater. 19 (2007) 1791–1799.
[18] J. Zaumseil, H. Sirringhaus, Electron and ambipolar transport in organic field-effect transistors, Chem. Rev. 107 (2007) 1296–1323.
[19] M.A. Loi, K. Rost-Bietsch, M. Murgia, S. Karg, W. Riess, M. Muccini, Tuning optoelectronic properties of ambipolar organic light-emitting transistors using a bulk-heterojunction, Approach Adv. Func. Mater. 16 (2006) 41–47.

[20] F. Dinelli, R. Capelli, M.A. Loi, M. Murgia, M. Muccini, A. Facchetti, T.J. Marks, High mobility ambipolar transport in organic light-emitting transistors, Adv. Mater. 18 (2006) 1416–1420.
[21] E.J. Felmeier, M. Schidleja, C. Melzer, H. von Seggern, A color-tunable organic light-emitting transistor, Adv. Mater. 22 (2010) 3568–3572.
[22] R. Capelli, S. Toffanin, G. Generali, H. Usta, A. Facchetti, M. Muccini, Organic light-emitting transistors with an efficiency that outperforms the equivalent light-emitting diodes, Nat. Mater. 9 (2010) 496–503.
[23] A.N. Aleshin, I.P. Shcherbakov, E.L. Alexandrova, E.A. Lebedev, Effect of electric field on the photoluminescence of polymer-inorganic nanoparticles composites, Solid State Commun. 146 (2008) 161–165.
[24] A.N. Aleshin, E.L. Alexandrova, I.P. Shcherbakov, Hybrid active layers from a conjugated polymer and inorganic nanoparticles for organic light emitting devices with emission color tuned by electric field, J. Phys. D: Appl. Phys. 42 (2009) 105108 (7pp).
[25] A.N. Aleshin, I.P. Shcherbakov, Light-emitting field-effect transistor based on a polyfluorene–ZnO nanoparticles film, J. Phys. D: Appl. Phys. 43 (2010) 315104 (5pp).
[26] R. Wang, L.L.H. King, A.W. Sleight, Highly conducting transparent thin films based on zinc oxide, J. Mater. Res. 11 (1996) 1659–1664.
[27] U. Ozgur, Ya.I. Alivov, C. Liu, A. Teke, M.A. Reshchikov, S. Dogan, V. Avrutin, S.-J. Cho, H. Morkocd, A comprehensive review of ZnO materials and devices, J. Appl. Phys. 98 (2005) 041301 (103pp).
[28] B.S. Ong, C. Li, Y. Li, Y. Wu, R. Loutfy, Stable, solution-processed, high-mobility ZnO thin-film transistors, J. Am. Chem. Soc. 129 (2007) 2750–2751.
[29] B.N. Pal, P. Trottman, J. Sun, H.E. Katz, Solution-deposited zinc oxide and zinc oxide/pentacene bilayer transistors: high mobility n-channel, ambipolar, and nonvolatile devices, Adv. Funct. Mater. 18 (2008) 1832–1839.
[30] S. Verlaak, D. Cheyns, M. Debucquoy, V. Arkhipov, P. Heremans, Numerical simulation of tetracene light-emitting transistors: a detailed balance of exciton process, Appl. Phys. Lett. 85 (2004) 2405–2407.
[31] S. Janietz, D.D.C. Bradley, M. Grell, C. Giebeler, M. Inbasekaran, E.P. Woo, Electrochemical determination of the ionization potential and electron affinity of poly-9,9-dioctylfluorene, Appl. Phys. Lett. 73 (1998) 2453–2455.
[32] M. Schidleja, C. Melzer, M. Roth, T. Schwalm, C. Gawrisch, M. Rehahn, H. von Seggern, The impact of contact formation on the light emission from ambipolar transistors, Appl. Phys. Lett. 95 (2009) 113303 (3pp).

PHOLEDs. A previous report showed that high triplet energy electron transport material improves the quantum efficiency of vacuum-deposited blue PHOLEDs by exciton and charge confinement [16]. The high triplet energy material can also confine excitons and charges inside the emitting layer and enhance the quantum efficiency of soluble blue PHOLEDs.

In this study, a high triplet energy exciton blocking material, diphenylphosphine oxide-4-(triphenylsilyl)phenyl (TSPO1), was deposited on a PVK:FIrpic blue emitting layer and the device performance was investigated. A high quantum efficiency of 19.4% at 20 cd/m^2 was achieved in the soluble blue PHOLEDs using TSPO1 as the electron transport type exciton blocking material. In addition, solution processed three-color white PHOLEDs were also fabricated and a quantum efficiency of 12.3% at 119 cd/m^2 was demonstrated. This study revealed that the solution-processed blue PHOLEDs can show the same quantum efficiency as vacuum deposited blue PHOLEDs by confining the triplet excitons and blocking holes, which could not be realized in other studies. This is the first demonstration of ~20% external quantum efficiency in solution-processed blue PHOLEDs.

2. Experimental

The basic device configuration of indium thin oxide (ITO)/poly-3,4-ethylenedioxythiophene:polystyrenesulfonate (PEDOT:PSS, 60 nm)/PVK: iridium(III) bis(4,6-(di-fluorophenyl)-pyridinato-*N*,C′) picolinate (FIrpic) (66 nm, 15%)/TSPO1(x nm)/LiF (1 nm)/Al (100 nm) was used to evaluate the TSPO1 as the exciton blocking material for solution processed blue PHOLEDs. The thicknesses of the TSPO1 were 25, 30, 35 and 40 nm. The device structure of the white PHOLEDs was ITO/PEDOT:PSS (60 nm)/PVK:FIrpic: tris[2-(p-tolyl)pridine]iridium(III)(Ir(mppy)$_3$): iridium(III) bis(2-phenylquinoline) acetylacetonate (Ir(pq)$_2$acac) (70 nm, 15%, *x*%, 0.5%)/TSPO1 (30 nm)/LiF (1 nm)/Al (100 nm). The doping concentrations of the Ir(mppy)$_3$ in the white PHOLEDs were 1% and 0.3%. Fig. 1 shows the chemical structure of TSPO1 and the device structures of blue and white PHOLEDs. The PVK emitting layer was spin coated from toluene solution at a concentration of 1.5 wt%. The spin coated PVK layer was baked at 80 °C from 20 min to remove the residual solvent. TSPO1 was deposited by vacuum evaporation. The current density (*J*)–voltage (*V*)–luminance (*L*) characteristics and electroluminescence (EL) spectra of the devices were measured using a Keithley 2400 source measurement unit and a Minolta CS 1000 A spectroradiometer. The Lambertian distribution of light emission was observed in all devices and the quantum efficiency was calculated based on the Lambertian distribution of light emission.

3. Results and discussion

A high triplet energy and deep highest occupied molecular orbital (HOMO) level of the electron transport materials are important for confining the holes and triplet excitons inside the emitting layer. The TSPO1 has a high triplet energy of 3.36 eV and a HOMO level of 6.79 eV [16]. The triplet energy of the TSPO1 was much higher than

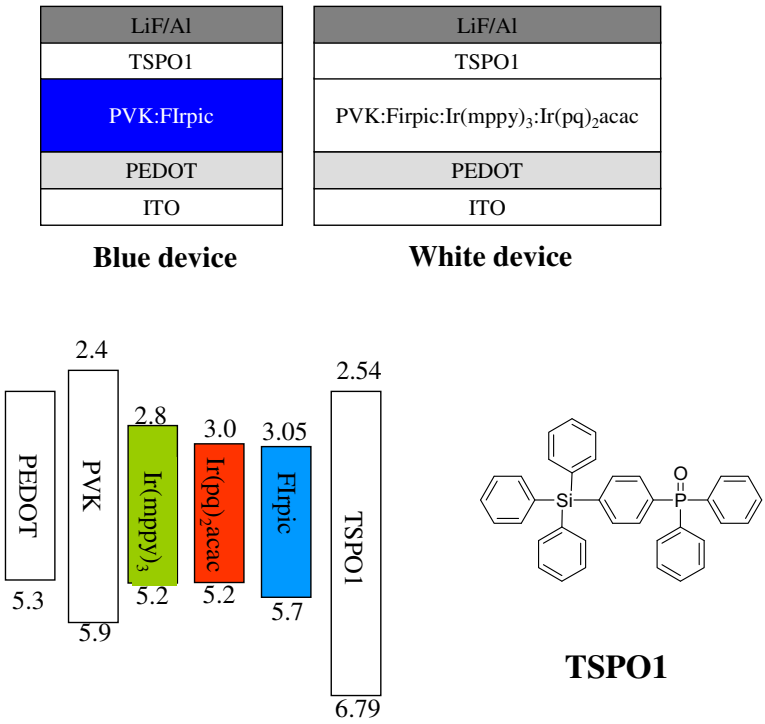

Fig. 1. Device structures of the blue and white PHOLEDs. Energy level diagram of the PHOLEDs is also shown in this figure.

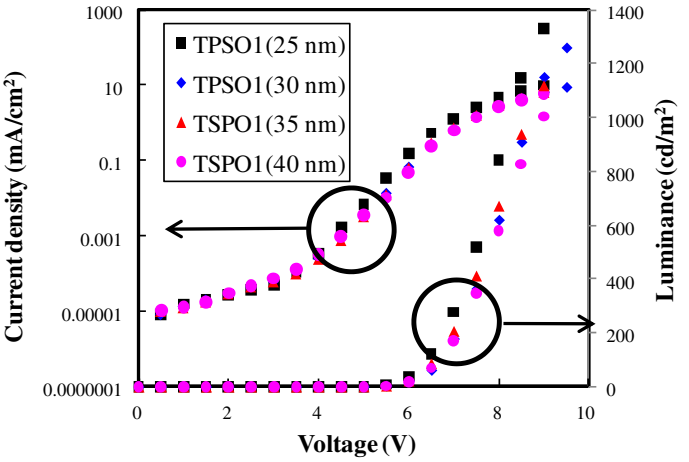

Fig. 2. Current density–voltage–luminance curves of the blue PHOLEDs with TSPO1 exciton blocking layer according to TSPO1 thickness.

that of the common blue phosphorescent dopant and the HOMO level was deep enough to block hole injection from the common host materials. Therefore, TSPO1 was efficient as an electron transport type exciton blocking material in blue PHOLEDs. As the TSPO1 was effective as an electron transport layer, it can also improve the quantum efficiency of the solution processed blue PHOLEDs by blocking the holes and confining the triplet excitons.

The TSPO1 was applied as the electron transport type exciton blocking material in PVK based blue PHOLEDs. Fig. 2 shows the current density–voltage–luminance curves of the PVK based blue PHOLEDs. The thickness of the TSPO1 exciton blocking layer was changed from 25 to 40 nm to optimize the device performance. The current density was high in the PVK blue PHOLEDs with 25 nm TSPO1 exciton blocking layer and decreased with increasing TSPO1 thickness. The luminance was also high in the PVK blue PHOLED with a 25 nm thick TSPO1 layer but the luminance of the blue PHOLED with a 30 nm thick TSPO1 layer was lower than that of the blue PHOLED with a 35 nm thick TSPO1 layer. This suggests that the recombination efficiency of the blue PHOLED with a 35 nm TSPO1 layer is better than that of the blue PHOLED with a 30 nm TSPO1 layer.

Fig. 3 shows the quantum efficiency–luminance curves of the blue PHOLEDs. The quantum efficiency of the PVK devices increased with increasing thickness of the TSPO1 layer. The maximum quantum efficiency of the blue PHOLEDs with 35 nm thick TSPO1 layer was 19.4% at 20 cd/m^2 and the quantum efficiency at 1000 cd/m^2 was 11.2%. This quantum efficiency is one of the best efficiency values reported in solution-processed blue PHOLEDs (15.5%) [11]. The high quantum efficiency of the blue PHOLEDs can be explained by the hole and triplet exciton blocking properties of TSPO1. TSPO1 has a high triplet energy of 3.36 eV for triplet exciton blocking and a HOMO level of 6.79 eV for hole blocking. The triplet energy of the FIrpic dopant in PVK layer is 2.65 eV and the triplet exciton quenching of the FIrpic by the TSPO1 layer is suppressed. Hole leakage from the PVK emitting layer to the TSPO1 layer is also blocked by the TSPO1 layer because of the high energy barrier for hole injection from the HOMO of PVK (5.9 eV) to the HOMO of TSPO1. Fig. 1 shows the energy level

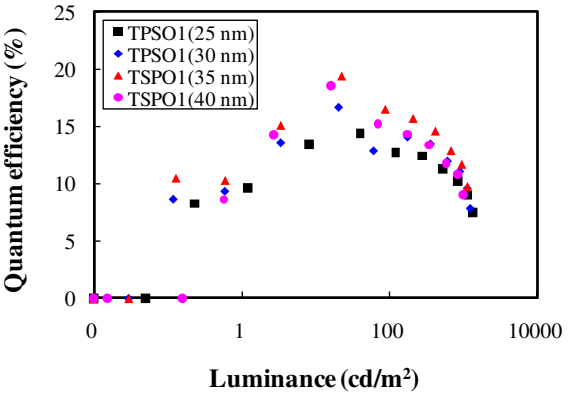

Fig. 3. Quantum efficiency–luminance curves of the blue PHOLEDs with TSPO1 exciton blocking layer according to TSPO1 thickness.

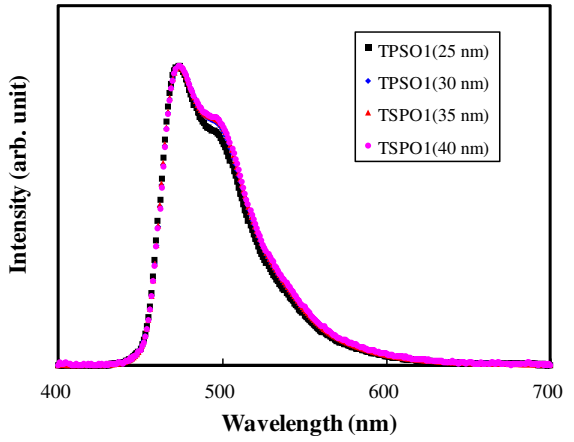

Fig. 4. Electroluminescence spectra of the blue PHOLEDs with TSPO1 exciton blocking layer according to TSPO1 thickness.

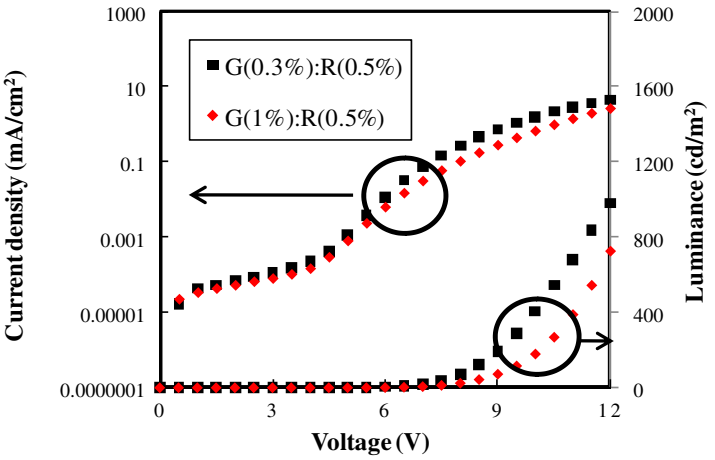

Fig. 5. Current density–voltage–luminance curves of the white PHOLEDs with TSPO1 exciton blocking layer.

diagram of the blue PHOLEDs. In addition to the hole and triplet exciton blocking effect, efficient electron injection from the TSPO1 layer to the PVK emitting layer contributes to the high quantum efficiency of the blue PHOLEDs. The LUMO level of PVK is 2.4 eV, whereas the LUMO level of TSPO1 is 2.54 eV. The energy barrier for electron injection is between PVK and TSPO1 only 0.14 eV, which facilitates electron injection from TSPO1 to PVK. The LUMO level of common electron transport materials is in the range, 2.8–3.2 eV, and the energy barrier for electron injection is 0.4–0.8 eV [13]. Therefore, the reduced energy barrier for electron injection improved the electron injection, enhancing the quantum efficiency of blue PHOLEDs. The maximum current efficiency of the blue PHOLEDs with a 35 nm thick TSPO1 layer was 35.9 cd/A at 20 cd/m^2 and the current efficiency at 1000 cd/m^2 was 20.4 cd/A. The color coordinates of the blue PHOLEDs were (0.15, 0.34). The efficiency of the solution processed PVK:FIrpic device was improved by more than 50% using the TSPO1 exciton blocking layer [14].

Fig. 4 shows the electroluminescence (EL) spectra of the blue PHOLEDs with TSPO1 exciton blocking layer. All devices showed similar EL spectra, even though the vibrational peak of the blue PHOLEDs with the 30, 35 and 40 nm thick TSPO1 layer was intensified slightly by the optical effect. The maximum emission wavelength of the blue PHOLEDs was 472 nm and no emission peak from the electron transport layer was observed. The color coordinates of the solution processed blue PHOLEDs were (0.15, 0.34).

As the TSPO1 was effective as an electron transport type exciton blocking layer in blue PHOLEDs, it was applied as an exciton blocking layer in PVK-based white PHOLEDs. Three color PHOLEDs with red, green and blue phosphorescent dopants were fabricated. The doping concentration of the blue dopant was fixed to 10% and the doping concentration of the red dopant was 0.5%. The doping concentrations of the green dopant were 0.3% and 1.0%. Fig. 5 shows the device performance of the white PHOLEDs. The current density and luminance of the white PHOLED with a 1% Ir(mppy)$_3$ doping concentration were lower than those of

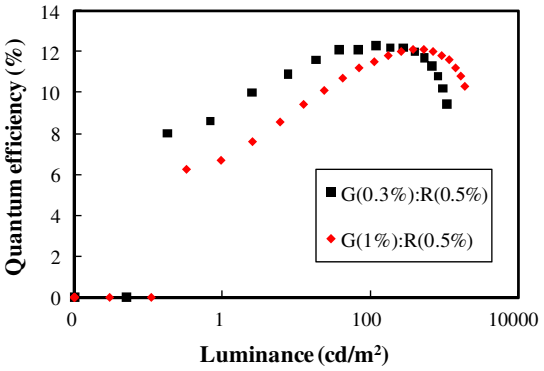

Fig. 6. Quantum efficiency–luminance curves of the white PHOLEDs with TSPO1 exciton blocking layer.

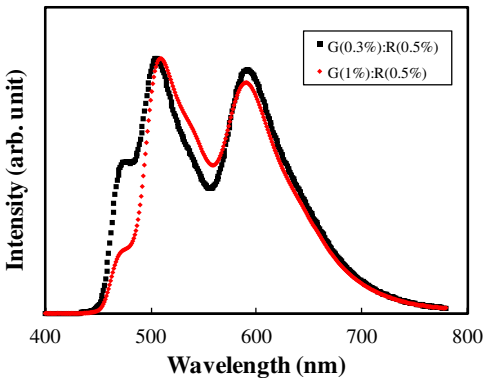

Fig. 7. Electroluminescence spectra of the white PHOLEDs with TSPO1 exciton blocking layer.

the white PHOLED with a 0.3% Ir(mppy)$_3$ doping concentration because of the charge trapping effect by the green dopant. The green dopant traps both holes and electrons, reducing the current density of the white PHOLED at a 1% doping concentration. The current density and

luminance of the white PHOLEDs were lower than those of the blue PHOLEDs due to charge trapping by the green and red dopants.

Fig. 6 presents the quantum efficiency–luminance curves. The maximum quantum efficiency of the white PHOLEDs with 0.3% Ir(mppy)$_3$ and 0.5% Ir(pq)$_2$acac was 12.3% at 119 cd/m^2 and the quantum efficiency at 1000 cd/m^2 was 10.0%. The color coordinates of the white PHOLED were (0.39, 0.45). Similar quantum efficiency was observed in the white PHOLEDs with 1.0% Ir(mppy)$_3$ and 0.5% Ir(pq)$_2$acac. The TSPO1 exciton blocking layer improved electron injection and enhanced the charge balance of the emitting layer, resulting in high efficiency white PHOLEDs. The current efficiency was slightly high in the white PHOLEDs with 1% Ir(mppy)$_3$ because of the stronger green emission, as shown in the electroluminescence spectra (Fig. 7). The maximum current efficiency of the white PHOLEDs was 28.2 cd/A at 544 cd/m^2 and a high current efficiency was kept at 1,000 cd/m^2. The current efficiency at 1000 cd/m^2 was 27.4 cd/A. The color coordinates of the white PHOLEDs with 1% and 0.3% Ir(mppy)$_3$ doping concentration were (0.40, 0.49) and (0.37, 0.44), respectively. The green and red emission was intensified at high Ir(mppy)$_3$ concentrations due to more energy transfer from the blue emitting FIrpic to the green dopant, resulting in a color shift at a 1% Ir(mppy)$_3$ doping concentration.

4. Conclusions

The TSPO1 exciton blocking layer was effective in improving the quantum efficiency of the solution processed blue and white PHOLEDs. A high quantum efficiency of 19.4% and a high current efficiency of 35.9 cd/A were achieved in the solution processed blue PHOLEDs with a PVK:FIrpic emitting layer. The efficiency was one of the best efficiencies reported in the solution-processed blue emitting layer. In addition, high efficiency solution-processed white PHOLEDs with a quantum efficiency of 12.3% were also fabricated using the TSPO1 exciton blocking layer. Therefore, TSPO1 is promising as an electron transport type exciton blocking layer in solution-processed PHOLEDs.

References

[1] H.B. Wu, J.H. Zou, F. Liu, L. Wang, A. Mikhailovsky, G.C. Bazan, W. Yang, Y. Cao, Adv. Mater. 20 (2008) 696.
[2] M.A. Baldo, D.F.O. Brian, Y. You, A. Shoustikov, S. Sibley, M.E. Thompson, S.R. Forrest, Nature 395 (1998) 151.
[3] Y. Kawamura, S. Yanagida, S.R. Forrest, J. Appl. Phys. 92 (2002) 87.
[4] M.J. Yang, T. Tsutsui, Jpn J. Appl. Phys. 39 (2000) 828.
[5] M.K. Mathai, V. Choong, S.A. Choulis, B. Krummacher, F. So, Appl. Phys. Lett. 88 (2006) 243512.
[6] S. Lamansky, P.I. Djurovich, F.A. Razzaq, S. Garon, D.L. Murphy, M.E. Thompson, J. Appl. Phys. 92 (2002) 1570.
[7] K.S. Yook, S.O. Jeon, O.Y. Kim, J.Y. Lee, Electrochem. Sol. Lett. 13 (2010) 71.
[8] X. Yang, D.C. Müller, D. Neher, K. Meerholz, Adv. Mater. 18 (2006) 948.
[9] S. Tokito, M. Suzuki, F. Sato, M. Kamachi, K. Shirane, Org. Electron. 4 (2003) 105.
[10] X.H. Yang, F. Jaiser, S. Klinger, D. Neher, Appl. Phys. Lett. 88 (2006) 021107.
[11] T. Earmme, E. Ahmed, S.A. Jenekhe, Adv. Mater. 22 (2010) 4744.
[12] K.S. Yook, S.E. Jang, S.O. Jeon, J.Y. Lee, Adv. Mater. 22 (2010) 4479.
[13] S. Ye, Y. Liu, K. Lu, W. Wu, C. Du, Y. Liu, H. Liu, T. Wu, G. Yu, Adv. Mater. 22 (2010) 4167.
[14] K.S. Yook, S.E. Jang, J.Y. Lee, Electrochem. Sol. Lett. 13 (2010) 122.
[15] V. Adamovich, S.R. Cordero, P.I. Djurovich, A. Tamayo, M.E. Thompson, B. Andrade, S.R. Forrest, Org. Electron. 4 (2003) 77.
[16] S.O. Jeon, S.E. Jang, H.S. Son, J.Y. Lee, Adv. Mater. 23 (2011) 1436.

fields were extracted using the nucleation-limited-switching (NLS) model [15]. We found that for the electric field range evaluated, the activation field increases faster for higher electrical field stress. Only a small frequency dependence on the activation field is observed. The suppression of switchable polarization after fatigue (1 million switching cycles) remains at approximately 10% of the total initial switching polarization. There is little dependence on the stress voltage or frequency of the electric field used for fatigue characterization.

2. Experimental

The films were prepared using P(VDF-TrFE) copolymer powder with a 70/30 M ratio (Hisense Electronics Co., China) without further purification. The copolymer powder was dissolved in 2-butanone at a concentration of 2.5 wt.%. The solution was then spin-coated on photo-lithographically patterned Cr/Au contacts. The films were dried and annealed at 120 °C for 2 h in vacuum (approximately 20 Torr). The resulting films showed an RMS roughness of 1.8 nm, as measured using atomic force microscopy (AFM, DM09 Veeco), and a thickness of approximately 100 nm (measured by a Dektak profilometer). Next, gold is thermally evaporated as the top contact. Both the copolymer film and top contact are patterned using photolithography. Details of the fabrication process can be found in [16].

The hysteresis loop of the MFM capacitor is measured using a 1 Hz triangular wave. The switching and nonswitching polarization (P_{sw} and P_{ns}), as well as the switching kinetics are measured using the Positive Up Negative Down (PUND) method [17,18]. The time delay between each pulse is set to 1 s. All measurements use a virtual ground circuit (RT66B, Radiant Technology).

3. Results and discussions

In an FeRAM memory circuit, the two states (“0” and “1”) are read and differentiated by using the switching and nonswitching polarization (P_{sw} and P_{ns}). Therefore, it is important to study the effects of repeated switching between P_{sw} and P_{ns}. MFM capacitors with a size of 5×10^{-4} cm^{-2} were first stressed by using square wave pulses with a frequency of 500 Hz at a voltage of 14 V. Fig. 1a shows the results using the PUND method to characterize the P_{sw} and P_{ns} in both positive and negative directions. Voltage pulses used for the PUND characterization were the same as those used for stressing the devices [19]. P_{sw} begins to decrease after 10^4 switching cycles. After 10^6 switching cycles, P_{sw} is at 87% of its initial value whereas P_{ns} remains unchanged. The symmetric results of P_{sw} and P_{ns} indicate that the devices evaluated show no preference in polarization direction. The hysteresis loop was also measured at 1 Hz and 14 V before and after fatigue (Fig. 1b). The switching polarization is approximately 88% of its initial value, in agreement with the PUND measurements shown in Fig. 1a. The coercive voltage increases from 5.3 to 8.9 V (corresponding to coercive fields of 0.53 MV/cm and 0.89 MV/cm, respectively).

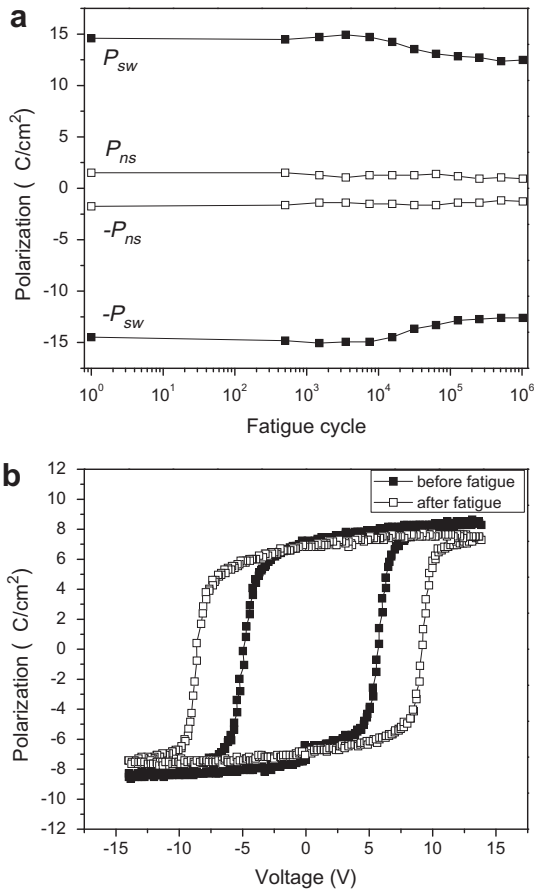

Fig. 1. The degradation of switching and nonswitching polarizations in positive and negative directions as a function of stress cycle at 14 V and 500 Hz (a), and the hysteresis loop measured at 14 V and 1 Hz before and after one million switching cycles (b). The P(VDF-TrFE) film thickness is 100 nm.

The effects of fatigue on the polarization switching kinetics are presented in Fig. 2. Fig. 2a corresponds to the study of P_{sw} and P_{ns} measured with pulse widths swept from 0.1 ms to 1 s. Plots A and B represent the measurements using 14 V pulses before and after fatigue, respectively. After fatigue, no switching is observed for films measured at pulse widths of 0.1 ms, and a decrease of approximately 10% of the initial maximum switching polarization is observed for all other pulse widths. Plot C in Fig. 2a shows that by increasing the PUND voltage pulse to 16 V for characterizing the P_{sw} and P_{ns} after fatigue, P_{sw} partially recovers. The observed increases in P_{sw} and P_{ns} at pulse widths >100 ms are likely due to the large D.C. conductance for high voltage and low frequency [20]. Fig. 2b shows the P_{sw} and P_{ns} measured by sweeping the pulse voltage from 4 to 14 V. Plots A and B were obtained using 500 Hz (1 ms pulse width) pulses before and after fatigue, respectively. After fatigue, the voltage needed to initialize the switching polarization increases from 8 to 12 V. Increasing the pulse width to 10 ms after fatigue results in a lower switching voltage, approximately 11 V (plot C).

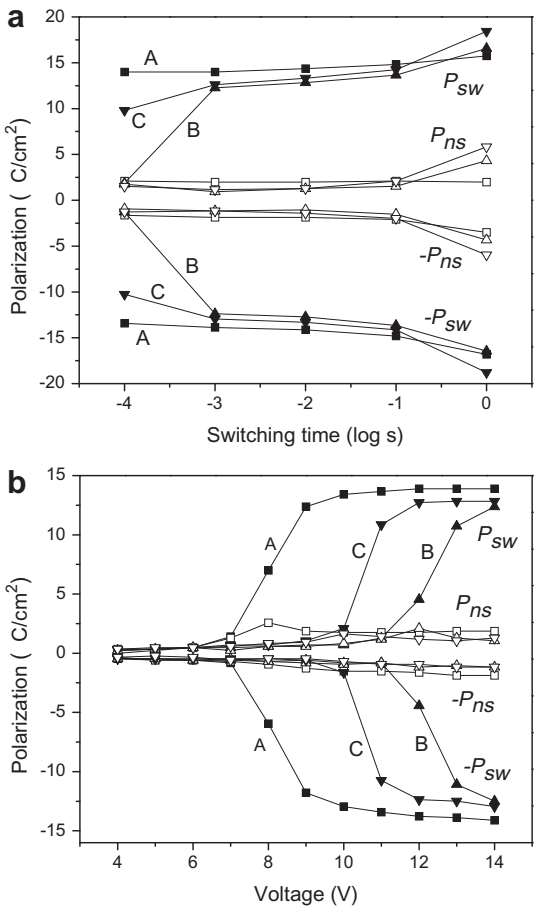

Fig. 2. The switching and nonswitching polarizations in positive and negative directions as a function of applied pulse width (a) and voltage (b) before and after fatigue. In (a), plot A and B are measured at 14 V before and after fatigue, and plot C is measured at 16 V after fatigue. In (b), plot A and B are measured at 1 ms pulse width before and after fatigue, and plot C is measured at 10 ms pulse width.

The results shown in Fig. 2a and b demonstrate that repeated switching of the MFM capacitors during stress induces an increase in both switching time and voltage. The activation fields were extracted by using the nucleation-limited-switching (NLS) model [15]. The activation field increases from 10.6 MV/cm for a new MFM capacitor to 15.6 MV/cm after 10^6 switching cycles at 14 V and 500 Hz. It is important to mention that the decrease in saturation polarization (10%) observed in both the hysteresis loop and PUND measurements does not recover with increasing voltage or pulse width. This is defined as the suppression of switchable polarization [21].

Fatigue properties as a function of stress voltage and frequency for P_{sw} and P_{ns} in both the positive and negative directions were also studied using identical MFM capacitors with a size of 3.0×10^{-4} cm^2. In Fig. 3, which shows the voltage dependence, all the plots correspond to MFM capacitors stressed and characterized at 1000 Hz with different voltages. Plots A and B represent the MFM capacitors stressed at 12 and 10 V pulses, respectively, with both characterized at 10 V. For $<10^4$ switching cycles, the P_{sw} for both conditions reach saturation. However, as the number of stress cycles increases, plot A decreases first, indicating a larger induced degradation compared to plot B. The recovery of the P_{sw} from plot A to D as the characterization voltage increases to 12 V indicates that this portion of the degradation of P_{sw} is due to an increase in the switching activation field leading to incomplete switching at lower voltage after fatigue. For devices characterized at 12 V, the one stressed at 14 V (plot C) shows faster degradation compared to the one stressed at 12 V (plot D). As the characterization voltage increases to 14 V, the results move from plot C to plot E. These results indicate that a higher stress voltage causes a larger increase in the activation field.

In order to determine the frequency dependence, all the devices were stressed and characterized at 12 V. The P_{sw} and P_{ns} of devices stressed at 1000 and 5000 Hz, with both characterized using 5000 Hz, are plotted in Fig. 4 as plot A and B, respectively. A larger induced P_{sw} degradation was observed for plot A, indicating a larger induced fatigue effect for lower frequency stressing. However, when the characterization frequency is decreased to 1000 Hz, P_{sw} increases from plot A to D, indicating that this loss of P_{sw} is also mainly due to the increase in the switching activation field. For plot C and D, MFM capacitors stressed at 200 Hz show a slightly larger degradation of P_{sw} compared to the one stressed at 1000 Hz, but the capacitors partially recover when they are measured at a lower frequency (200 Hz), as shown in plot E.

In order to study the increase of the activation field and the suppression of switchable polarization at different fatigue voltages and frequencies, the switching kinetics of the MFM devices before and after fatigue in each condition were characterized. P_{sw} was measured as a function of pulse width, and the activation field for each set of stress conditions was extracted from the data using the NLS model. The stress voltage and frequency dependence of the activation field are shown in Tables 1 and 2, respectively. It is found that as the stress voltage increased from 10 to 14 V for 1000 Hz pulses, after 1 million switching cycles, the activation field increased from the initial value of 10.6 to 13.6 MV/cm and 15.6 MV/cm, respectively. The activation field is less dependent on the stress frequency.

The suppression of switchable polarization was extracted using the PUND technique using 100 ms pulses with the same stress voltages as were used for each fatigue condition. The mean values of P_{sw} in both positive and negative directions as a ratio of the initial P_{sw} are plotted vs. fatigue voltage and frequency in Fig. 5. It is found that, after one million switching cycles, the suppression of switchable polarization for all characterized fatigue conditions reaches a constant value, which is approximately 10% of the initial switching polarization value.

Fang et al. reported that for 68/32 P(VDF-TrFE) copolymer film (not stretched) based MFM capacitors, electrical stress increases the degree of the film crystallinity [13]. This is because the electromechanical coupling from the repeated rotation of the H–F dipoles within the copolymer chain along the *c* axis in the A.C. electric field results in a higher oriented chain morphology, creating a longer range ordering of β phase. Therefore, the energy barrier required

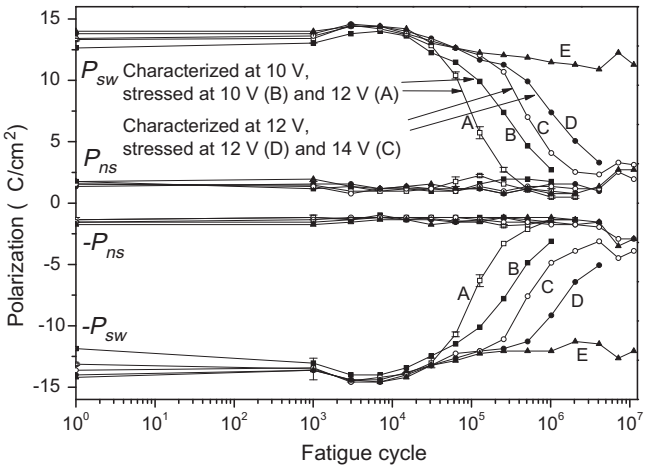

Fig. 3. The voltage dependence of the switching and nonswitching polarizations vs. electrical stress cycles at 1 kHz. Plot A and B are for the devices characterized at 10 V, and electrical stressed at 12 and 10 V, respectively. Plot C and D are for the devices characterized at 12 V, and electrical stressed at 14 and 12 V, respectively. Plot E represents the device characterized and stressed at 14 V.

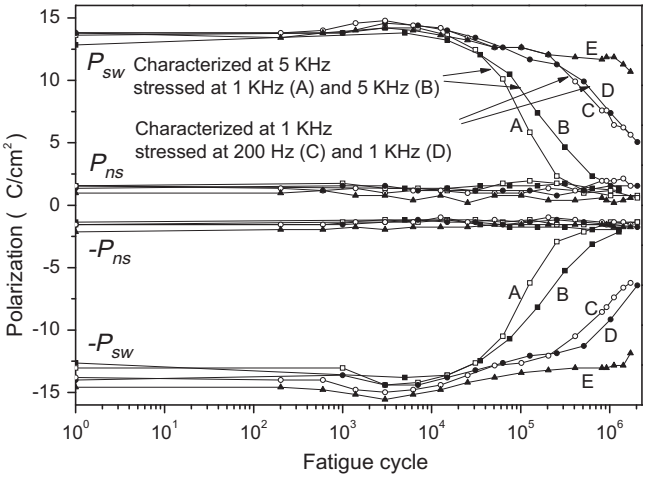

Fig. 4. The frequency dependence of the switching and nonswitching polarizations vs. electrical stress cycles at 12 V. Plot A and B are for the devices characterized at 5 kHz, and electric stressed at 1 and 5 kHz, respectively. Plot C and D are for the devices characterized at 1 kHz, and electrical stressed at 200 Hz and 1 kHz, respectively. Plot E represents the device characterized and stressed at 200 Hz.

Table 1
The increase of the activation field for fatigue at different voltages.

Fatigue voltage (V)	Fatigue frequency (Hz)	Activation field before fatigue (MV/cm)	Activation field after fatigue (MV/cm)	Number of fatigue cycle (Million)
10	1000	10.6	13.6	~1.0
12			14.8	
14			15.6	

Table 2
The increase of the activation field for fatigue at different frequencies.

Fatigue frequency (Hz)	Fatigue voltage (V)	Activation field before fatigue (MV/cm)	Activation field after fatigue (MV/cm)	Number of fatigue cycle (Million)
5000	12	10.6	14.6	~1.2
1000			14.8	~1.0
200			15.2	~1.7

for switching the dipole and the coercive field increase due to the stronger interchain coupling. The increased degree of crystallinity corresponds to a higher activation field [15]. This agrees with our data and explains the increased activation field after fatigue. In addition, a higher stress electric field induces a larger increase of the crystallinity [22], explaining the voltage dependence of the activation field in our data.

For the suppression of switchable polarization after fatigue, Warren et al. reported that in a PZT thin film system with Pt electrodes, it is due to electronic charge trapping or ionic defects. The relative roles of electronic or ionic charge

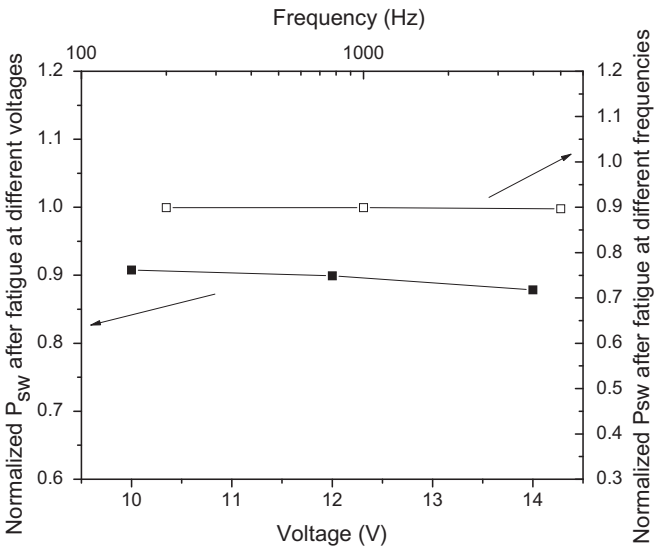

Fig. 5. The normalized switching polarization after approximately one million switching cycles at different stressed voltage and frequency conditions. The devices are characterized using 100 ms pulses in each fatigue condition. The loss of switching polarization represents the suppression of switchable polarization.

defects depend on the material [21]. As an external electric field is applied between the two contacts on the ferroelectric film, charges are injected into the film and localized on trap sites (impurities, vacancies, domain boundaries, etc.). In the repeated polarization switching process, due to the strong interaction between the dipoles and the trapped charges in the film, the trapped charges tend to redistribute through the ferroelectric film and lock the domain walls, and eventually prevent the domains from switching. The inhibition or locking of the opposite polarization at the electrode-ferroelectric interfaces also corresponds to a decrease of the switching dipoles [9,13]. Therefore, the number of switchable dipoles decreases during repeated switching, corresponding to a decrease of switchable P_{sw}. This charge injection could be one of the major contributions to the origin of the suppression of switchable polarization after fatigue in our data.

4. Conclusion

We have studied the electrical fatigue effects of P(VDF-TrFE) copolymer based MFM capacitors using different stress voltages and frequencies. The switching kinetics was studied before and after fatigue. The increase of the activation field of the switching polarization can be explained by an increase in the degree of film crystallinity. The suppression of switchable polarization is possibly caused by trapped charges. A higher stress electric field causes a larger increase of the activation field. The activation field is less dependent on the stress frequency. The nonswitching polarization stays low throughout the characterization range. The amount of suppression of switchable polarization after approximately 1 million stress cycles for the characterized voltage and frequency ranges is approximately 10% of the initial switching polarization. It is demonstrated that in certain working conditions, our optimized MFM capacitors can switch with limited polarization degradation, which is compatible with flexible electronics.

Acknowledgements

The authors would like to thank Dr. Scott R. Summerfelt of Texas Instruments for helpful discussions on FRAM characterization, and the Army Research Laboratory (ARL) for partial financial support of this project. We would also like to thank Dr. Eric Forsythe of ARL for helpful discussions regarding non-volatile memory integration.

References

[1] R.C.G. Naber, C. Tanase, P.W.M. Blom, G.H. Gelinck, A.W. Marsman, F.J. Touwslager, S. Setayesh, D.M. de leeuw, Nat. Mater. 4 (243) (2005) 19–25.
[2] G.H. Gelinck, A.W. Marsman, F.J. Touwslager, S. Setayesh, D.M. de Leeuw, R.C.G. Naber, P.W.M. Blom, Appl. Phys. Lett. 87 (092903) (2005).
[3] R.C.G. Naber, P.W.M. Blom, A.W. Marsman, D. M de Leeuw, Appl. Phys. Lett. 85 (2032) (2004).
[4] R.C.G. Naber, B. de Boer, P.W.M. Blom, D.M. de Leeuw, Appl. Phys. Lett. 87 (203509) (2005).
[5] S. Gowrisanker, M.A. Quevedo-Lopez, H.K. Alshareef, B.E. Gnade, S. Venugopal, R. Krishna, K. Kaftanoglu, D.R. Allee, Org. Electron. 10 (1217) (2009).
[6] X.J. Lou, J. Appl. Phys. 105 (024101) (2009).
[7] A.K. Tagantsev, I. Stolichnov, E.L. Colla, N. Setter, J. Appl. Phys. 90 (1387) (2001).
[8] J.F. Scott, Ferroelectric Memories, Springer, Germany, 2000.
[9] E.L. Colla, D.V. Taylor, A.K. Tagantsev, N. Setter, Appl. Phys. Lett. 72 (2478) (1998).
[10] E.L. Colla, S. Hong, D.V. Taylor, A.K. Tagantsev, N. Setter, K. No, Appl. Phys. Lett. 72 (2763) (1998).
[11] G.D. Zhu, Y. Cong, J.H. Zhang, X.Y. Luo, X.J. Yan, Electron Dev. Lett. 31 (359) (2010).
[12] G.D. Zhu, Z.G. Zeng, L. Zhang, X.J. Yan, Appl. Phys. Lett. 89 (102905) (2006).
[13] F. Fang, W. Yang, M.Z. Zhang, J. Appl. Phys. 101 (044902) (2007).

[14] D. Mao, I. Mejia, H. Stiegler, M.A. Quevedo-Lopez, B.E. Gnade, J. Appl. Phys. 108 (094102) (2010).
[15] A.K. Tagantsev, I. Stolichnov, N. Setter, Phys. Rev. B 66 (214109) (2002).
[16] D. Mao, M.A. Quevedo-Lopez, H. Stiegler, H.N. Alshareef, B.E. Gnade, Org. Electron. 11 (925) (2010).
[17] N. Kin, K. Takai, K. Honda, Jpn. J. Appl. Phys. 47 (4638) (2008).
[18] RT66B Vision ferroelectric memory characterization manual, Radiant Technologies
[19] M. Grossmann, D. Bolten, O. Lohse, U. Boettger, R. Waser, S. Tiedke, Appl. Phys. Lett. 77 (1894). 2000.
[20] T. Nakajima, R. Abe, Y. Takahashi, T. Furukawa, Jpn. J. Appl. Phys. Part 2 44 (L 1385) (2005).
[21] W.L. Warren, D. Dimos, B.A. Tuttle, R.D. Nasby, G.E. Pike, Appl. Phys. Lett. 65 (8) (1994). 1018.
[22] R.G. Kepler, R.A. Anderson, R.R. Lagasse, Phys. Rev. Lett. 48 (1274) (1982).

its many advantages, this approach is widely used to fabricate low voltage, high performance organic FETs [14,17].

To make useful devices, the electrical stability/reliability of organic FETs is another important parameter, which has not yet reached the stage of the practical use. After a much dedicated research, it has been found that employing a FET structure with dual dielectric is an efficient way to enhance the device stability, where they would compensate both dielectrics' drawbacks, for example, the buffer dielectric forms few defects at the interface but has a low electrical strength/dielectric constant, while high-k gate insulator uses low voltage but has poor interface [14]. A proper buffer dielectric also can depress the absorption of moisture at the dielectric interface and the penetration of oxygen into OSCs, thus further retarding device characteristics decay throughout its shelf-life and operating life. In order to characterize its significance, application of a gate bias is normally utilized. Zhang et al. [19] showed that FET devices of polycrystalline pentacene with polystyrene (PS) buffer dielectric and Al_2O_3 gate insulator exhibited a steady current output ($I_{ds}(t)/I_{ds0} > 95\%$) and little threshold voltage shift ($\Delta V_{th} < 0.1$ V) upon gate-bias stress at $V_{gs} = V_{ds} = -10$ V for 1 h in a N_2-filled glovebox (O_2, $H_2O <$ 1 ppm). It is comparable to or even better than that of a-Si FETs, ascribing to the excellent interface of PS and its lack of dipole moments. Good device stability now can be achieved, but not to the point of having no degradation for a more prolonged period of time, e.g. more than a year. Usually, the shift of the threshold voltage is one of manifestations of device degradation, which was proposed to arise from the following factors: (i) charging/polarization of gate dielectric and changes in dielectric constant over time; (ii) the presence of oxygen, moisture, chemical impurities and light irradiation etc.; and (iii) intrinsic structural and energetic disorder of organic semiconductors (OSCs) and/or specific structural defects [20–29]. Despite the wide range of possible dielectric-dielectric combinations, it should be pointed out that trapping states at the surface of gate insulator actually still exist but are simply shielded from carriers' access, when a polymeric buffer dielectric is used for surface passivation. Previously, Ng et al. [29] investigated the influence of different gate insulators by the charge injection from the gate electrode, and water ion movement on the stability of PQT-based FETs with pMSSQ buffer dielectric. However, the effect of buried trapping states on the device stability, especially under applied extrinsic stimulus, is still lack of in-depth study.

In this work, we studied the electrical stability of both p- and n-channel FET devices, in which the gate insulator SiO_2 is modified by poly(methyl methacrylate) (PMMA). The bottom layer of the bilayer dielectrics investigated in this study is thermally oxidized SiO_2 grown on n^{++}-Si due to the material's high chemical stability and excellent insulating properties with extremely low current leakage, which would minimize the effect of charge injection from the gate electrode. More importantly, a large amount of Si–OH silanol groups tend to be present on the SiO_2 surface, leading to electrochemical trapping of electrons, when thermal SiO_2 is grown at 800–1000 °C [15]. On the other hand, the selection of trap-free PMMA buffer dielectric is motivated by its hydrophobic methyl radical groups that can serve as moisture inhibitors and the absence of hydroxyl groups, providing a defect-free high-quality interface [14,17,30]. In the present study, both electrical and optical signals are utilized to trigger the response of these buried trapping states in ambient condition, which can be manifested by the shift of threshold voltage. It was reported that although moisture causes charge trapping, trap formation was only observed after negative bias stress in pentacene flip-crystal FETs [27], and thus had little impact on studying how these buried traps were approached by minority carriers in our devices shown below.

2. Experimental

Organic FET devices were fabricated with a top-contact configuration. A heavily doped n-type silicon wafer and 500 (or 200)-nm thermally oxidized SiO_2 were used as a gate electrode and gate dielectric layer, respectively. Before being processed, the substrates were cleaned by acetone and IPA in an ultrasonic bath and rinsed in deionized-water. The substrates were then dried using a nitrogen gun. The PMMA buffer dielectric was spin-coated from the solution in anisole and the thickness was evaluated by a Dektak surface profilometer. Pentacene and C_{60} were deposited onto the PMMA/SiO_2 surface by high-vacuum thermal evaporation at room temperature and deposition rates were controlled at 0.5 Å s^{-1} and 1 Å s^{-1}, respectively. The gold (Au) and aluminum (Al) used as the source–drain contacts for pentacene and C_{60} FETs, respectively, were thermally evaporated through a shadow mask. The channel length (L) and width (W) were 0.1 and 2 mm, respectively.

In the bilayer insulators, PMMA buffer dielectric acts as part of the dielectric layer during the device operation. The capacitance (C_i) of the devices can be calculated using the following equation:

$$\frac{1}{C_i} = \frac{1}{C_3} + \frac{1}{C_P} = \frac{t_3}{\varepsilon_0 \varepsilon_3} \frac{t_P}{\varepsilon_0 \varepsilon_P}, \quad (1)$$

where t_s and t_P are the thickness of SiO_2 dielectric layer and PMMA buffer dielectric, respectively; ε_s and ε_P are the dielectric constants of SiO_2 dielectric layer and PMMA buffer dielectric, respectively.

The electrical characterization of the devices was measured using a Keithley 4200 SCS semiconductor parameter analyzer under ambient condition at room temperature on a standard probe station with or without light illumination. The visible light illumination was used for the study of photo-induced charge transfer, shining at the top surface of the device from a halogen lamp and focused to a spot size approximately equal to the area of the device to cover the entire channel with an estimated light intensity of 1 mW cm^{-2}. AFM images were obtained using a Nanoscope IIIa AFM (digital instrument) in tapping mode.

3. Results and discussion

3.1. Electrical characteristics in dark condition

The pentacene FET with 10 nm PMMA buffer dielectric (see Fig. 1a) exhibits unipolar p-channel field-effect

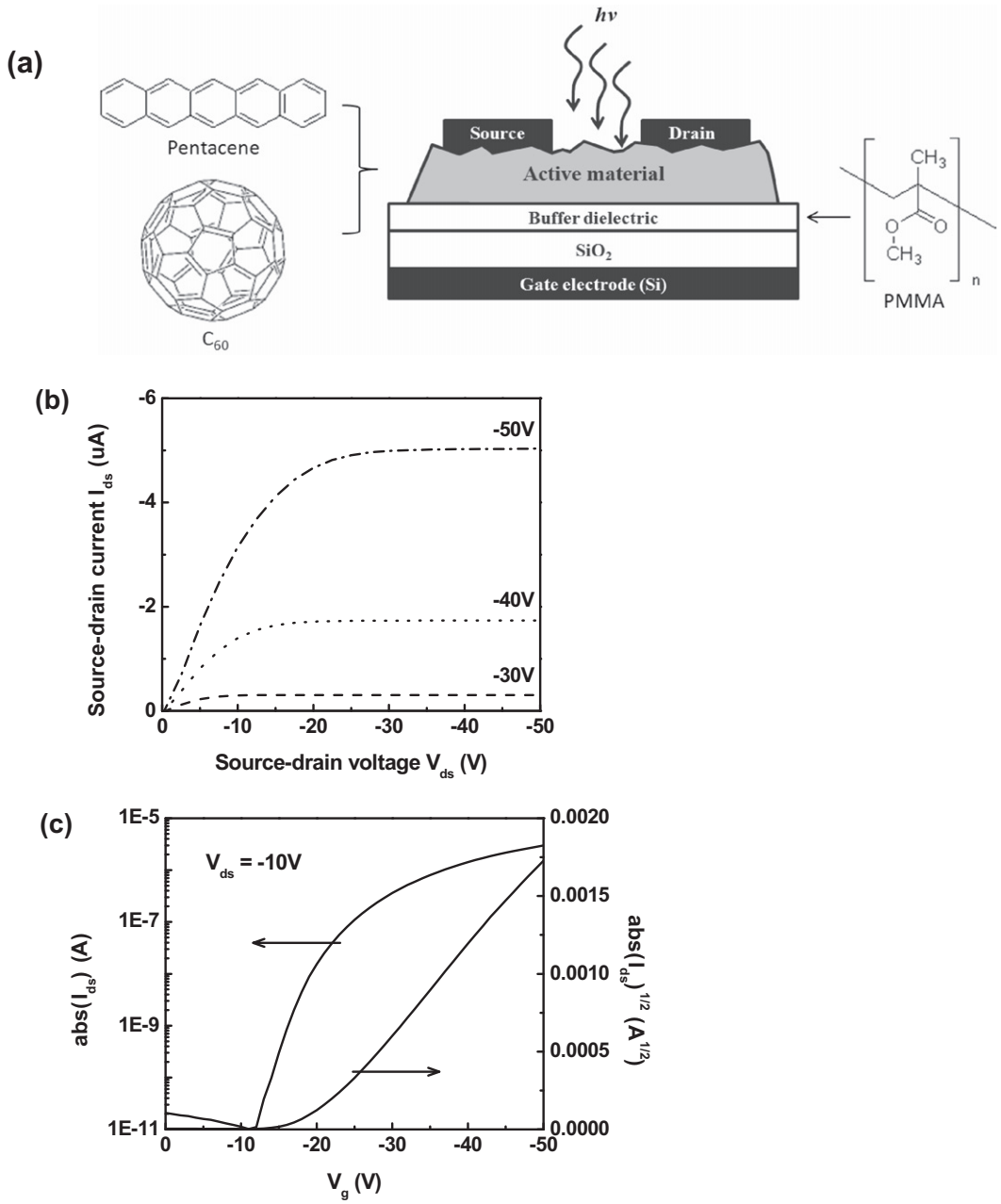

Fig. 1. (a) A schematic cross-section of the organic FET presented in this study, (b) the output and (c) transfer characteristics of pentacene FETs with PMMA buffer dielectric.

behavior, i.e. hole accumulation in the channel, as seen from the output characteristics in Fig. 1b. The output characteristics show two distinct regions of device operation: linear and saturation. In the linear region (also known as the ohmic mode), the FETs operate like a resistor, controlled by the gate voltage related to both the source and drain voltage. The source–drain current is modeled as:

$$I_{ds} = \frac{W}{L}\mu C_i\left[(V_g - V_{th})V_{ds} - \frac{V_{ds}^2}{2}\right], \tag{2}$$

where W and L are the channel width and length, μ is the charge carrier mobility, C_i is the gate dielectric capacitance per unit area, V_g is the applied gate-to-source bias, V_{ds} is the applied drain-to-source bias, and V_{th} is the threshold voltage described as follows [31]:

$$V_{th} = V_{fb} + 2\psi_b + \frac{\sqrt{2\epsilon_s q N_a(2\psi_b)}}{C_i}, \tag{3}$$

$$V_{fb} = \phi_{ms} - \frac{Q_f}{C_i}, \tag{4}$$

where ψ_b is the potential difference between the Fermi level E_f and the intrinsic Fermi level E_i of the semiconductor, ϵ_s is the permittivity of the semiconductor, q is the charge

of electron, N_a is the density of the acceptor, ϕ_{ms} is the potential difference the metal gate and semiconductor bulk at zero gate bias, and Q_f is the interface charge. When $V_g > V_{th}$ and $V_{ds} > (V_g - V_{th})$, the accumulated layer in the channel is pinched off, as indicated by the lack of channel region near the drain. The drain current is now weakly dependent on drain voltage and controlled primarily by V_g, and modeled approximately as:

$$I_{ds} = \frac{W}{2L}\mu C_i (V_g - V_{th})^2. \quad (5)$$

Using the above equations, several key parameters of FET devices can be extracted from transfer and output characteristics, as summarized in Table 1.

It is known that V_{th} can be shifted through the change in the density of charge at the interface. In order to investigate this effect, the device characteristics were measured after programing with a gate bias at $V_{ds} = 0$ V for various durations. When a negative bias was applied to the gate, the shift in transfer curves increased with increasing bias time, as shown in Fig. 2a. A shift in V_{th} as large as 8 V was obtained after programing with a gate bias of $V_g = -200$ V for 500 ms, indicating that a great number of field-induced holes were trapped. It suggested that device failure would occur when the device operates successively at "ON" state. This phenomenon is generally observed when SiO_2 is employed as the gate dielectric, which is proposed to result from structural defects present in polycrystalline pentacene film and/or hole trapping states due to absorbed water molecules on the SiO_2 surface [26,32]. When the device was programed with positive gate bias, the shift in transfer curves was hardly observed as shown in Fig. 2b and the inset of Fig. 4b. Compared with the devices with bare SiO_2 [15,33], our devices appeared to be more immune to V_{th} shift caused by positive bias, which actually is a preferred feature for practical application of organic integrated circuits (ICs). It can be proposed that such a feature results from: (i) the charge injection barrier provided by the 10 nm-thick PMMA layer, which hinders the field-induced minority carriers (electrons) from being captured by the surface silanol groups; (ii) the large electron injection barrier between Au and pentacene; (iii) the low electron carrier density in the p-type pentacene active layer. The above hypotheses were also applicable for the n-channel FETs with C_{60} as active layer, but these devices exhibited the opposite trend as compared to that of pentacene FETs, as shown in Fig. 3. The inset in Fig. 3b showed that the drain current I_{ds} began to decrease due to the oxygen molecules acting as electron traps [34], when V_{ds} swept to the saturation region. The trapping of electrons appeared even more significant at higher gate voltage, e.g. with threshold voltage shift $\Delta V_{th} = 18$ V for biasing at $V_g = 200$ V and $V_{ds} = 0$ V for 1 s. The I_{ds}–V_g curve would return to the initial state when the device was left unbiased for around 1 h due to the release of trapped electrons (data not shown here). The trapping of holes was hardly observed, i.e. almost no shift in the subsequent I_{ds}–V_g curves, although a gate bias of −200 V for 1 s was applied.

The above results indicated that the silanol group-related electron traps for p-channel devices and the water-related hole traps for n-channel devices at the interface of SiO_2 almost cannot be accessed, which was primarily attributed to the charge injection barriers, originating from the large mismatch between the work functions of source/drain contacts and LUMO/HOMO levels of used active layers, and from the additional buffer dielectric. Given that $\Phi_{Au} = -5.1$ eV and $LUMO_{Pen} = -3.2$ eV and $HOMO_{Pen} = -5$ eV, $\Phi_{Al} = -4.2$ eV and $LUMO_{Ful} = -3.8$ eV and $HOMO_{Ful} = -7.1$ eV, the charge injection barrier of electrons (holes) for pentacene (C_{60}) FETs is as large as 1.9 (2.9) eV, without taking PMMA into account, which is already too large to be surmounted [35,36]. This is slightly different from that of memory devices based on the FET structure employing floating gate (FG) and/or the metal–nitride-oxide-silicon (MNOS) transistor [31,37,38]. In the case of devices with FG, electrons are easily induced and injected through a thin insulator at high transverse electrical field, even though high work-function metal is used as the source–drain contact in p-channel FETs. The average electrical field during writing/erasing in flash memory is about 10 MV cm^{-1}, we might need to increase the applied voltage to verify our results. But due to the voltage limitation of our equipment, a thinner gate insulator shall be employed. The exact mechanism for preventing charge carriers from being captured in

Table 1
Extracted FET parameters for OSCs using pentacene and C_{60} grown on (10 nm) PMMA/(500 nm) SiO_2 bilayer gate dielectric.

	Pentacene	C_{60}
Morphology	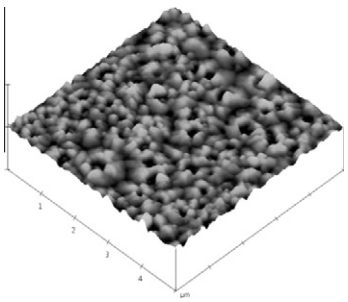	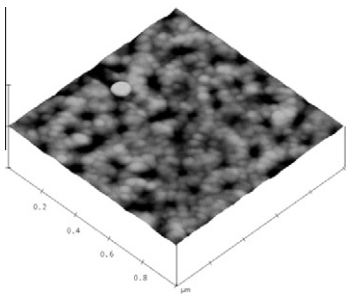
V_{th} (V)	−19.7	12.4
μ ($cm^2\ V^{-1}\ s^{-1}$)	0.16	0.14
On/off ratio	$\sim 10^5$	$\sim 10^4$

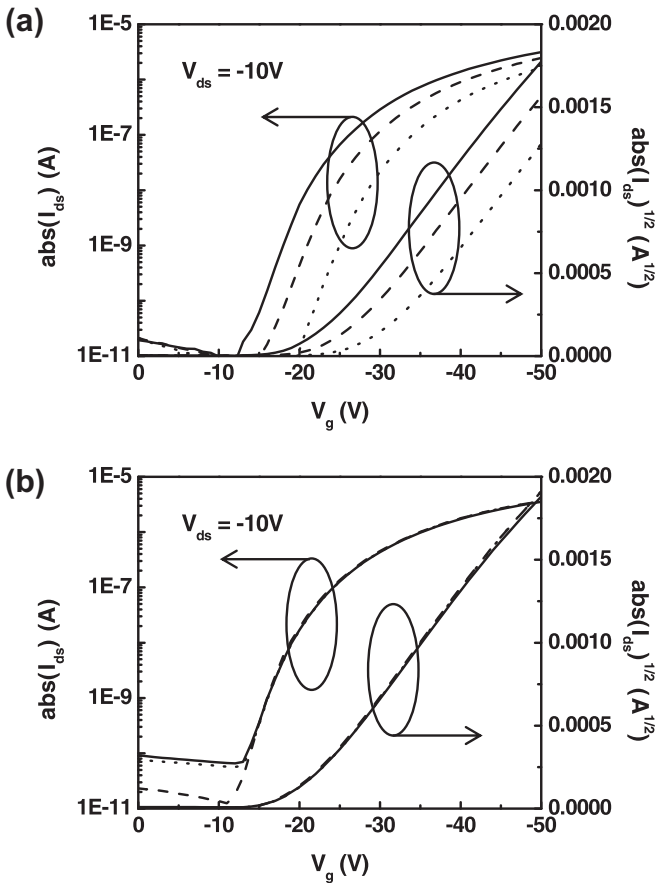

Fig. 2. Transfer curves of pentacene FETs with 10 nm PMMA buffer dielectric at $V_{ds} = -10$ V before (solid line) and after programing with a gate bias of (a) 200 V and (b) −200 V at $V_{ds} = 0$ V for 100 ms (dash line) and 500 ms (dot line).

pentacene (C_{60}) FETs would be investigated in future. On the other hands, the trapping of majority carriers occurred in pentacene (C_{60}) FETs when devices operated under working state. We assumed that the amount of trapped charge Q_{trap} at their initial state was zero. When negative (positive) gate bias was applied, the amount of trapped charges, Q_{trap}, can be evaluated through the following equation:

$$Q_{trap} = \pm C_i \Delta V_{th}. \quad (6)$$

By applying a gate bias of ±200 V with 1 (0.5) s bias time for C_{60} (pentacene) FETs, respectively, the calculated value of Q_{trap} was around ±1 (0.5) × 10^{-7} C cm^{-2}. Obviously, Q_{trap} increases when the bias time was extended and long time biasing would completely turn the device off leading to the failure of switching function. A similar phenomenon was also observed in the devices using SAMs as buffer dielectric when these devices were repeatedly stressed by measuring transfer characteristics in the saturation regime, because surface silanol groups cannot be fully passivated by SAMs [15,39].

3.2. Under illumination

It is important to understand light illumination effects on electrical performance of these devices, as well as the underlying physics of these effects in applications such as switches for flat panel displays (FPDs). Light absorption generates electrons and holes, and these electrons and holes may be paired in form of excitons that diffuse like neutral particles. The bound electron–hole pairs can be dissociated by applying an appropriate gate-to-source bias in the FET devices, and the separated electrons (holes) begin to move under the influence of the electrical field. It was expected that the shift of V_{th} toward the positive (negative) side in pentacene (C_{60}) FETs would be brought out due to the involvement of non-equilibrium charge carriers, when a positive (negative) gate bias was applied under illumination [40]. When investigating the effect of steady-state broadband illumination on the electrical performance of our devices, the illumination power was controlled at a low level to minimize the degradation of OSCs under light irradiation and the programing time was not more than 30 s to minimize the charge trapping in the grain boundaries of our polycrystalline films. Before programing by a gate bias, the incident light was stabilized for 5 s. This was done by shining the top of the entire channel region.

As expected, the entire transfer curve of pentacene FETs with 10 nm PMMA buffer dielectric was greatly shifted toward the positive direction by applying a gate bias of 200 V for 20 s under illumination, as shown in Fig. 4a. As a result,

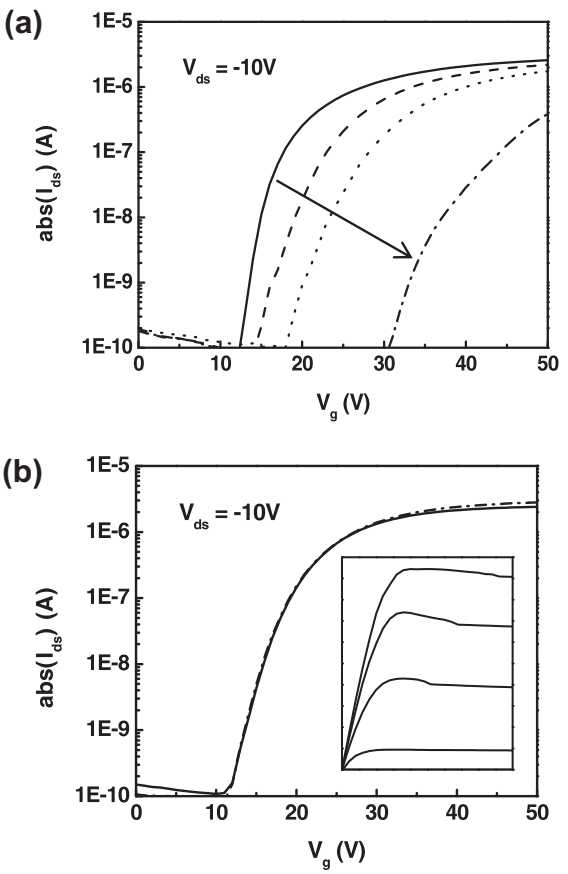

Fig. 3. Transfer curves of C_{60} FETs with 10 nm PMMA buffer dielectric with V_{ds} = 10 V before (solid line) and after programing with a gate bias of (a) 200 V and (b) −200 V at V_{ds} = 0 V for 10 ms (dash line), 100 ms (dot line) and 1 s (dash dot line). The inset shows its output characteristics.

the value of V_{th} was changed by more than 125 V, as seen from Fig. 4b. In contrast, there was little change in V_{th} when the device was merely illuminated for 20 s without gate bias, shown by the solid circle in Fig. 4b, or programed by a positive gate bias without illumination, shown in the inset of Fig. 4b. Usually, the drain current in the "OFF" state is slightly affected, which is attributed to the enhancement of carrier density in the channel of the device and thus the conductivity. The change in V_{th} was attributed to the generation of non-equilibrium charge carriers, which were transferred under the electrical field and trapped by buried trapping states at the PMMA–SiO_2 interface. It showed a good agreement with published results observed in p-channel FETs with 10 nm PS (or PMMA) buffer dielectric [41]. However, the time of positive gate bias needed for inducing the shift in V_{th} was much shorter than ours, which might result from the variation of conductivity of polymers because of different processing conditions, e.g. the effect of solvent [42]. The charge transport can either tunnel between localized states, depending on the density of defect states in polymers, or hop via extended electronic states, though clearly one mechanism would dominate. In the case of transport via extended states, carrier motion is repeatedly interrupted by trapping of carriers in localized states and then re-emission into the extended states. The drift mobility in such situations in greatly reduced from the free carrier mobility due to the time the carriers spend in traps. Although it is still far away from the well understanding of the exact mechanism in OFET memory devices, a potential mechanism was proposed, in which the charge transfer was greatly related with the applied electrical field [41,42]. An electrical field F of ca. 4.6 MV cm^{-1} (according to $F = \frac{V_g}{t_P + t_3(\varepsilon_P/\varepsilon_3)}$), much larger than the dielectric strength of PMMA (ca. 0.2 MV cm^{-1}), was applied to facilitate the charge injection. Fig. 4b shows the resulting shift in V_{th} of our pentacene FETs as a function of bias time. Clearly, there was a turning point. For $t < 1$ s, the change in threshold voltage ΔV_{th} was less than 4 V. For $1 \leqslant t \leqslant 20$ s, the value of ΔV_{th} increased sharply. This was ascribed to a response time τ, which the photogenerated electrons needed to be transferred through PMMA and trapped at the interface of SiO_2. It seemed that this was a slow process, as a long bias time was indispensable to achieve the considerable shift in V_{th} under a constant transverse electrical field F. Given that the mobility of PMMA at room temperature is ca. 1.0×10^{-11} cm^2 V^{-1} s^{-1} [43], it took nearly 0.02 s for electrons to transport through 10 nm PMMA), which was reasonable compared to the observed response time τ. It is believed that the observed photoinduced shift in V_{th} is caused by the charging of the bilayer gate dielectric with non-equilibrium carriers that are photogenerated in pentacene near the interface and transferred/trapped in these buried trapping states at the interface of SiO_2, schematically shown in Fig. 4d. The variation of the surface density of charges transferred/trapped at the PMMA–SiO_2 interface, $\Delta n = Q_{trap}/q$, is related to the observed shift of threshold voltage V_{th} according to Eq. (6). The charge transfer rate can be roughly estimated from the shift ΔV_{th} after applying a V_g at V_{ds} = 0 V for a (short) time interval Δt under illumination:

$$dn/dt = \frac{C_i \Delta V_{th}}{q \Delta t}. \tag{7}$$

Interestingly, the electron transfer rate decreased quickly ($t < 1$ s) and gradually reached a constant level ($1 \leqslant t \leqslant 20$ s), as shown in Fig. 4c. This indicated that the average charge transfer rate across 10 nm PMMA under illumination was ca. 1.6×10^{11} cm^{-2} s^{-1}. It was because a surface potential created by charge trapped in the buried states decelerated the injecting electrons and reduced the electron penetration range, resulting in a saturation of trapped charges. An electron transfer rate of ca. 5×10^9 cm^{-2} s^{-1} under short wavelength light illumination ($400 < \lambda < 500$ nm) was reported in the single crystal rubrene FETs with parylene as the gate dielectric, which was much smaller than our results [40]. This was mainly ascribed to (i) the different flux of photons, (ii) the injection barrier provided by the bulk material of parylene, and (iii) the transverse electrical field F, which determined the extent of the charge injection and transport.

When a charge is injected and trapped, the de-trapping also occurs simultaneously to restore the neutral state by transferring the excessive charges to the ground, which was characterized by the retention time in dark condition.

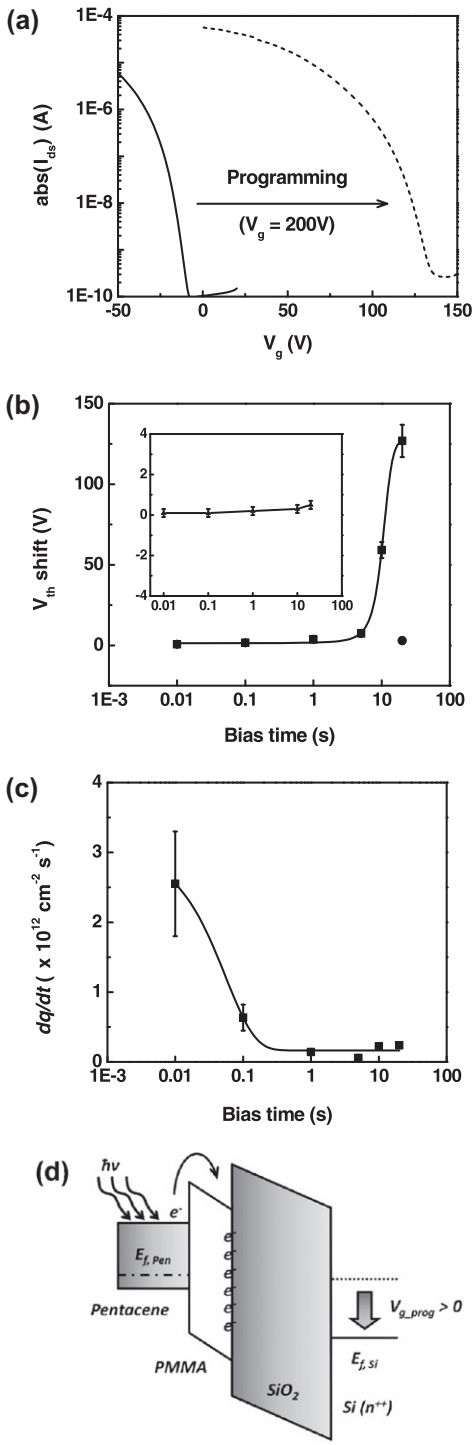

Fig. 4. (a) Transfer curves of pentacene FETs with 10 nm PMMA buffer dielectric at $V_{ds} = -50$ V before and after programing with a gate bias of 200 V for 20 s at $V_{ds} = 0$ V under illumination; (b) V_{th} shift versus programing duration under illumination (solid square) and in dark condition (solid triangle, shown in the inset), and solid circle represents the V_{th} shift was induced by the illumination for 20 s without application of gate bias; (c) the transfer rate of electrons versus programing time; (d) schematic illustration of electron generation under illumination, transfer across PMMA barrier, and trapping at the PMMA/SiO_2 interface, where $E_{f,Si}$ and $E_{f,Pen}$ are the Fermi energy of pentacene and silicon, respectively.

After programing, a decay process of I_{ds} (measured at $V_{ds} = -50$ V and $V_g = 0$ V) in the "ON" state in dark condition was recorded and plotted in Fig. 5b, where the time required for the "ON" state current to decrease to 10% of its initial value was estimated to be around 10^4 s. In Fig. 5a, it was more obvious that the shift in V_{th} toward

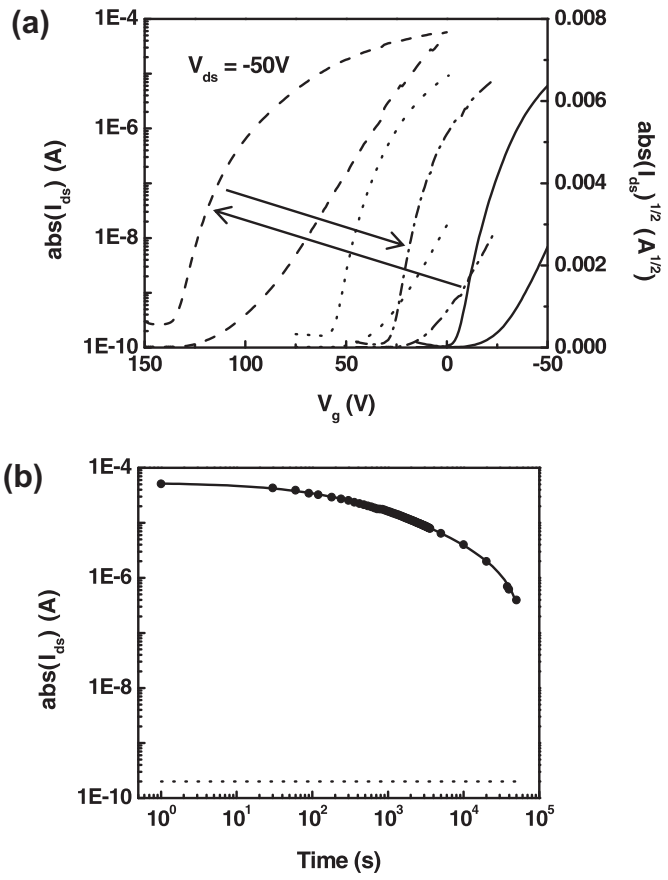

Fig. 5. (a) Transfer curves of pentacene FETs with 10 nm PMMA buffer dielectric at $V_{ds} = -50$ V: initial characteristics (solid line), measured in the dark after programing ($V_g = 200$ V, $V_{ds} = 0$ V for 20 s under illumination) immediately (dash line), 1 h later (dot line), and 10.5 h later (dash dot line); (b) Time evolution of I_d measured in the dark at $V_{ds} = -50$ V and $V_g = 0$ V after programing ($V_g = 200$ V, $V_{ds} = 0$ V, for 20 s under illumination). The off current (dot line) is shown for reference.

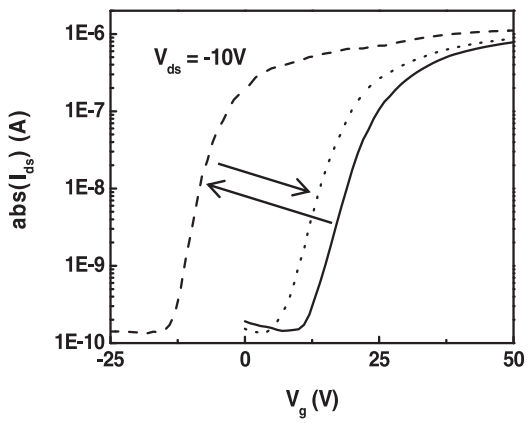

Fig. 6. Transfer curves of C_{60} FETs with 10 nm PMMA buffer dielectric at $V_{ds} = 10$ V: initial characteristics (solid line), measured in the dark after programing ($V_g = -200$ V, $V_{ds} = 0$ V for 1 s under illumination) immediately (dash line) and 1 min later (dot line).

negative side was very fast in the first hour and became very slow in the next 10 h, indicating that there were two distinguishable decay rates: (i) an initial rapid relaxation due to the recombination of closely packed holes and electrons and (ii) a subsequent slower relaxation that originated from deeply trapped carriers, depending on the quality and conductivity of the PMMA buffer dielectric. Our results indicated that a charge storage lifetime in the dark can be estimated to be several days long. On the other hand, based upon our discussion in section 3.1, the trapped electrons can also be swept out and/or recombined with field-induced holes by applying a negative gate bias in the dark. Consequently, the shifted transfer curve can restore to its initial state, completing a cycle of turning "ON" and "OFF".

The photo-induced charge transfer was also studied in the n-channel FETs. However, when programing the device, only a short time period of gate bias was used in order to minimize the degradation of C_{60} due to the exposure to the ambient air and light irradiation [34,44,45]. Two mechanisms of degradation had been described as following: (i) the absorbed oxygen molecule acts as electron traps within the lattice of C_{60} molecule and epoxidation reaction might take place on C_{60} [34], and (ii) the fragmentation of C_{60} caused by ultraviolet (UV) light [44–46]. When a gate bias of -200 V with a period of 1 s was applied, the transfer curve was greatly shifted toward the negative direction, as shown in Fig. 6a. However, it quickly went back to the

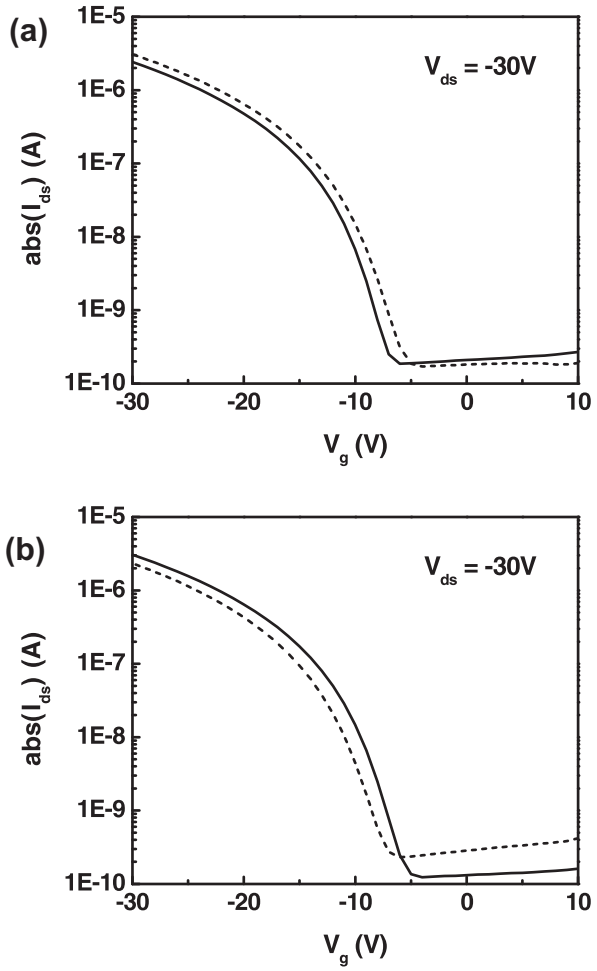

Fig. 7. Transfer curves of pentacene FETs with 45 nm PMMA buffer dielectric with $V_{ds} = -30$ V before (solid line) and after (dash line) programing, where a programing gate bias of (a) 100 V and (b) −100 V for 30 s at $V_{ds} = 0$ V was applied under illumination.

original state within a few minutes in the dark, attributing to the rapid release of trapped holes. This suggested that the trapping of electrons was much more supportive in this device due to the presence of oxygen dopants and accessible hydroxyl groups, as compared to that of holes.

To further verify our previous hypothesis that the charge trapping primarily took place at the dielectric–dielectric interface, 45 nm-thick PMMA was used as the buffer dielectric to minimize the pinhole defects and increase the barrier width, and 200 nm-thick SiO_2 was used as the gate insulator. To compare with the previous results, the effect of light illumination on inducing the shift in V_{th} was carried out by applying a gate bias of ±100 V in order to equalize the value of F (ca. 4.7 MV cm^{-1}) across the dual-dielectric. When programed by a gate bias of 100 V with a period of 30 s under illumination, the transfer curve only shifted slightly toward the positive direction (see Fig. 7a), giving rise to a ΔV_{th} of less than 2 V. This was ascribed to a small quantity of electrons trapped in the structural defects of polycrystalline pentacene thin films, i.e. grain boundaries, and at the interface between pentacene and PMMA. The transfer of electrons from the active layer into these buried trapping states at SiO_2 surface was greatly depressed as the thick PMMA film effectively shielded the underneath hydroxyl groups. At the same time, a gate bias of −100 V with a period of 30 s was also applied under illumination, the shifted transfer curves due to the application of the positive gate bias was almost restored to the initial state (see Fig. 7b), showing only a little shift (ca. 0.5 V) to the negative direction. This indicated that the trapping of holes was suppressed because the reduction of absorbed water molecules thanking to the hydrophobic surface of PMMA. By utilizing the thickness-optimized PMMA, our devices were very resistive to the high transverse electric field and light illumination, resulting in excellent device stability. This differed from that of devices with $\geqslant$60 nm styrenic polymers (or PMMA), who exhibited considerable shift in V_{th} after programing [22,41]. To further improve the device stability, the purification of active materials as well as the buffer dielectrics is needed to cut down the unintentional doping acting as the charge trapping centers.

4. Conclusions

In conclusion, the shift of threshold voltage due to the charge trapping (both electron and hole) in the buried states between PMMA and SiO_2 was evaluated in p- and n-channel OFETs, respectively. The trapping of electrons (compared to holes) in p-channel devices and the trapping of holes (compared to electrons) in n-channel devices are more difficult in the dark condition due to the large injection barrier between the contact and the active layer. Although the 10 nm-thick PMMA layer also provides an additional charge injection barrier, when the device is programed under illumination, the photo-generated non-equilibrium charge carriers in the active layer can be easily injected through 10 nm PMMA into these buried states and trapped under the high electrical field. The trapped electrons in p-channel FETs can retain for several days while the release of trapped holes in n-channel FETs is much faster. However, such photo-induced charge transfer can be effectively suppressed by an optimized thickness of buffer dielectric (45 nm) at the same characterization condition, and thus stabilize the threshold voltage. Besides the device encapsulation and the development of new OSC combining high mobility with excellent stability, data presented in this work brings out an alternative approach to enhance the stability and reliability of organic transistors using bi-layer gate dielectric. In order to selecting a proper buffer dielectric, attention must be paid to the following: (i) non-polar buffer dielectrics with excellent film-forming and low surface/bulk states are preferred, such as low-k polymeric dielectric BCB and Cytop [15,47], and (ii) its thickness should also be optimized when it is applied in FET structures (both bottom- and top-gate architectures). Our findings should also be relevant to other cases, for example, in an OFET-based memory device where the charge dissociation/trapping process under light irradiation is involved.

Acknowledgements

We would like to thank Dr. Q.L. Song for the fabrication of C_{60} thin film. This work is supported by the Ministry of Education, Singapore (Research Grant No. RG 13/06).

References

[1] A. Dodabalapur, L. Torsi, H.E. Katz, Science 268 (1995) 270.
[2] E.L. Granstrom, C.D. Frisbie, J. Phys. Chem. B 103 (1999) 8842.
[3] F. Dinelli, M. Murgia, P. Levy, M. Cavallini, F. Biscarini, D.M. de Leeuw, Phys. Rev. Lett. 92 (2004) 116802.
[4] T. Muck, V. Wagner, U. Bass, M. Leufgen, J. Geurts, L.W. Molenkamp, Synth. Met. 146 (2004) 317.
[5] R. Ruiz, A. Papadimitratos, A.C. Mayer, G.G. Malliaras, Adv. Mater. 17 (2005) 1795.
[6] A. Salleo, M.L. Chabinyc, M.S. Yang, R.A. Street, Appl. Phys. Lett. 81 (2002) 4383.
[7] T.W. Kelley, L.D. Boardman, T.D. Dunbar, D.V. Muyres, M.J. Pellerite, T.Y.P. Smith, J. Phys. Chem. B 107 (2003) 5877.
[8] K.P. Pernstich, C. Goldmann, C. Krellner, D. Oberhoff, D.J. Gundlach, B. Batlogg, Synth. Met. 146 (2004) 325.
[9] K.P. Pernstich, S. Haas, D. Oberhoff, C. Goldmann, D.J. Gundlach, B. Batlogg, A.N. Rashid, G. Schitter, J. Appl. Phys. 96 (2004) 6431.
[10] S. Kobayashi, T. Nishikawa, T. Takenobu, S. Mori, T. Shimoda, T. Mitani, H. Shimotani, N. Yoshimoto, S. Ogawa, Y. Iwasa, Nat. Mater. 3 (2004) 317.
[11] M. Yoshida, S. Uemura, T. Kodzasa, T. Kamata, M. Matsuzama, T. Kawai, Synth. Met. 137 (2003) 967.
[12] J. Veres, S.D. Ogier, S.W. Leeming, D.C. Cupertino, S.M. Khaffaf, Adv. Funct. Mater. 13 (2003) 199.
[13] L.A. Majewski, R. Schroeder, M. Grell, P.A. Glarvey, M.L. Turner, J. Appl. Phys. 96 (2004) 5781.
[14] A.L. Deman, J. Tardy, Org. Electron. 6 (2005) 78.
[15] L.-L. Chua, J. Zaumseil, J.-F. Chang, E.C.-W. Ou, P.K.-H. Ho, H. Sirringhaus, R.H. Friend, Nature 434 (2005) 194.
[16] M.-H. Yoon, C. Kim, A. Facchetti, T.J. Marks, J. Am. Chem. Soc. 128 (2006) 12851.
[17] A.L. Deman, J. Tardy, Mater. Sci. Eng. C 26 (2006) 421.
[18] C. Kim, A. Facchetti, T.J. Marks, Adv. Mater. 19 (2007) 2561.
[19] X.-H. Zhang, S.P. Tiwari, B. Kippelen, Org. Electron. 10 (2009) 1133.
[20] H.E. Katz, X.M. Hong, A. Dodabalapur, R. Sarpeshkar, J. Appl. Phys. 91 (2002) 1572.
[21] R. Schroeder, L.A. Majewski, M. Grell, Adv. Mater. 16 (2004) 633.
[22] K.-J. Baeg, Y.-Y. Noh, J. Ghim, S.-J. Kang, H. Lee, D.-Y. Kim, Adv. Mater. 18 (2006) 3179.
[23] K.S. Narayan, N. Kumar, Appl. Phys. Lett. 79 (2001) 1891.
[24] S. Hoshino, M. Yoshida, S. Uemura, T. Kodzasa, N. Takada, T. Kamata, K. Yase, J. Appl. Phys. 95 (2004) 5088.
[25] T. Jung, A. Dodabalapur, R. Wenz, S. Mohapatra, Appl. Phys. Lett. 87 (2005) 182109.
[26] C. Ucurum, H. Goebel, F.A. Yildirim, W. Bauhofer, W. Krautschneider, J. Appl. Phys. 104 (2008) 084501.
[27] C. Goldmann, D.J. Gundlach, B. Batlogg, Appl. Phys. Lett. 88 (2006) 063501.
[28] G. Gu, M.G. Kane, Appl. Phys. Lett. 92 (2008) 053305.
[29] T.N. Ng, J.H. Daniel, S. Sambandan, A.-C. Arias, M.L. Chabinyc, R.A. Street, J. Appl. Phys. 103 (2008) 044506.
[30] J. Puigdollers, C. Voz, I. Martin, M. Vetter, A. Orpella, R. Alcubilla, Synth. Met. 146 (2004) 355.
[31] S.M. Sze, Physics of Semiconductor Devices, second ed., Wiley, New York, 1981.
[32] S.G.J. Mathijssen, M. Cölle, H. Gomes, E.C.P. Smits, B. de Boer, I. McCulloch, P.A. Bobbert, D.M. de Leeuw, Adv. Mater. 19 (2007) 2785.
[33] C. Goldmann, C. Krellner, K.P. Pernstich, S. Haas, D.J. Gundlach, B. Batlogg, J. Appl. Phys. 99 (2006) 034507.
[34] R.C. Haddon, A.S. Perel, R.C. Morris, T.T.M. Palstra, A.F. Hebard, R.M. Fleming, Appl. Phys. Lett. 67 (1995) 121.
[35] T. Yasuda, T. Goto, K. Fujita, T. Tsutsui, Appl. Phys. Lett. 85 (2004) 2098.
[36] A. Dodabalapur, H.E. Katz, L. Torsi, R.C. Haddon, Science 269 (1995) 1560.
[37] M. Mushrush, A. Facchetti, M. Lefenfeld, H.E. Katz, T.J. Marks, J. Am. Chem. Soc. 125 (2003) 9414.
[38] Z. Liu, F. Xue, Y. Su, Y.M. Lvov, K. Varahramyan, IEEE Trans. Nanotechnol. 5 (2006) 379.
[39] X.-H. Zhang, B. Domercq, B. Kippelen, Appl. Phys. Lett. 91 (2007) 092114.
[40] V. Podzorov, M.E. Gershenson, Phys. Rev. Lett. 95 (2005) 016602.
[41] Y. Guo, C.-A. Di, S. Ye, X. Sun, J. Zheng, Y. Wen, W. Wu, G. Yu, Y. Liu, Adv. Mater. 21 (2009) 1954.
[42] K.-J. Baeg, Y.-Y. Noh, J. Ghim, B. Lim, D.-Y. Kim, Adv. Funct. Mater. 18 (2008) 3678.
[43] H. Chen, H. Gong, C.K. Ong, J. Phys. Condens. Matter 7 (1995) 1129.
[44] R. Taylor, J.P. Parsons, A.G. Avent, S.P. Rannard, T.J. Dennis, J.P. Hare, H.W. Kroto, D.R.M. Walton, Nature 351 (1991) 277.
[45] P. Sullivan, T.S. Jones, Org. Electron. 9 (2006) 656.
[46] W.J. Potscavage, S. Yoo, B. Domercq, B. Kippelen, Appl. Phys. Lett. 90 (2007) 253511.
[47] W.L. Kalb, T. Mathis, S. Haas, A.F. Stassen, B. Batlogg, Appl. Phys. Lett. 90 (2007) 092104.

PO1 and SO1. The computed electronic properties of PO1 and SO1 are consistent with the available experimental data (discussed below). The vertical triplet energies evaluated at the TDDFT level (Table 1) are identical, 3.14 eV; they are significantly higher than that of FIrpic (2.70 eV at the same level of theory) and only 0.17 eV lower than that of the unsubstituted biphenyl core. The adiabatic triplet energies computed at the ΔSCF level (computed as the difference in the SCF energies at the optimized S_0 and T_1 geometries) are nearly identical, being 2.87 and 2.88 eV for PO1 and SO1, respectively. The dominant excitation giving rise to the triplet state is localized on the biphenyl moiety and corresponds in both cases to a HOMO-to-LUMO transition. The very similar nature of the HOMO and LUMO orbitals of PO1 and SO1 is evident from the isosurface plots displayed in Fig. 1. The stronger, predominantly inductive, electron-withdrawing character of the sulfonyl moiety relative to that of the phosphoryl substituent can be seen from the trends in the computed HOMO/LUMO energies and electron affinities (EAs). In general, the values for PO1 are calculated to lie between those of SO1 and biphenyl. Thus, the computational results are consistent with a largely inductive effect for the sulfonyl substitution and predict that the high triplet energy of PO1 should be maintained in SO1.

Compound SO1 is reversibly reduced at −2.06 V vs. $FeCp_2^{+/0}$ in 0.1 Bu_4NPF_6/*N*,*N*-dimethylformamide, i.e. somewhat more readily than PO1 under the same conditions (−2.4 V) [12], consistent with the trend in computed EAs. Its absorption and fluorescence maxima in dichloromethane (277 and 331 nm, respectively) are very similar to those reported for PO1 in the same solvent [12]. The adiabatic triplet energy for SO1 is estimated to be 2.72 eV from the phosphorescence spectrum acquired in a 2-methyltetrahydrofuran glass at 77 K. As in the case of the TDDFT values, the value for SO1 is indistinguishable within experimental uncertainty from the value for PO1 (2.72 eV) [12] and is higher than the value of 2.65 eV reported for FIrpic [20], suggesting that SO1 might also be an effective host for this phosphor. As expected, the experimental adiabatic triplet energies (based on the highest energy emission at the relaxed triplet geometry) are smaller than the computed vertical triplet energies (calculated at the singlet geometry), while the computed adiabatic triplet energies (ΔSCF level) provide energies that are only slightly higher than those measured from the phosphorescence spectra.

Small-molecule derivatives of the 3,6-bis(carbazol-9-yl)carbazole ("tricarbazole") moiety have been used as hole-transport components for OLEDs [21,22]. In order to simplify the fabrication process of our OLEDs we were

Table 1
Computed HOMO and LUMO energies, adiabatic ionization potentials and electron affinities, vertical TDDFT transition energies from the ground state to the lowest singlet (S0-S1*) and triplet (S0-T1*) excited states, and the ΔSCF adiabatic triplet energies ($S_0 - T_1$).[a]

	HOMO	LUMO	IP	EA	$S_0 - S_1^*$	$S_0 - T_1^*$	$S_0 - T_1$
PO1	−6.42	−1.51	7.40	0.65	4.47	3.14	2.87
SO1	−6.85	−2.02	7.96	1.04	4.39	3.14	2.88
Biphenyl	−6.06	−0.69	7.61	−0.70	5.02	3.31	3.04

[a] All values are in eV and computed at the DFT B3LYP/6-31G** level. EAs are defined as the negative of the free-energy change for the process M + e → M^-.

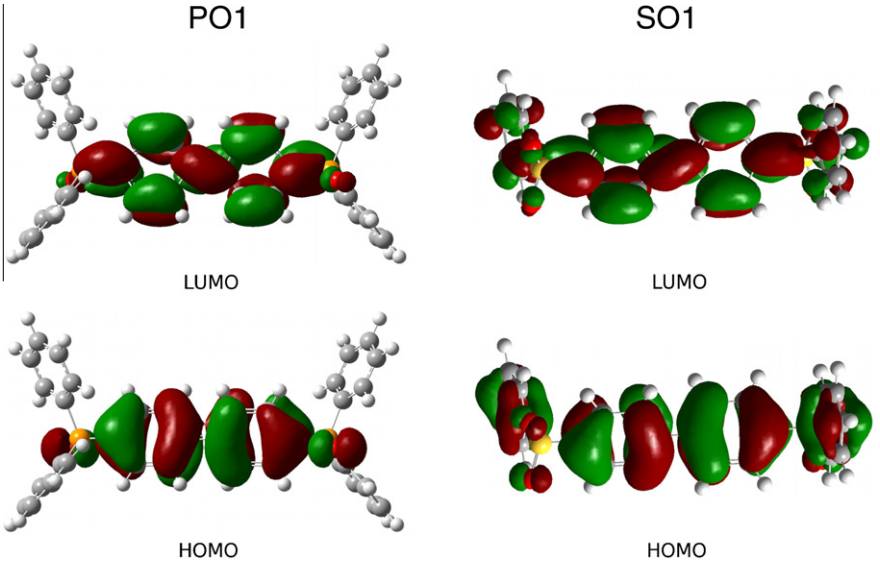

Fig. 1. Illustration of the HOMO and LUMO wave functions computed at the DFT B3LYP/6-31G** level for PO1 (left) and SO1 (right).

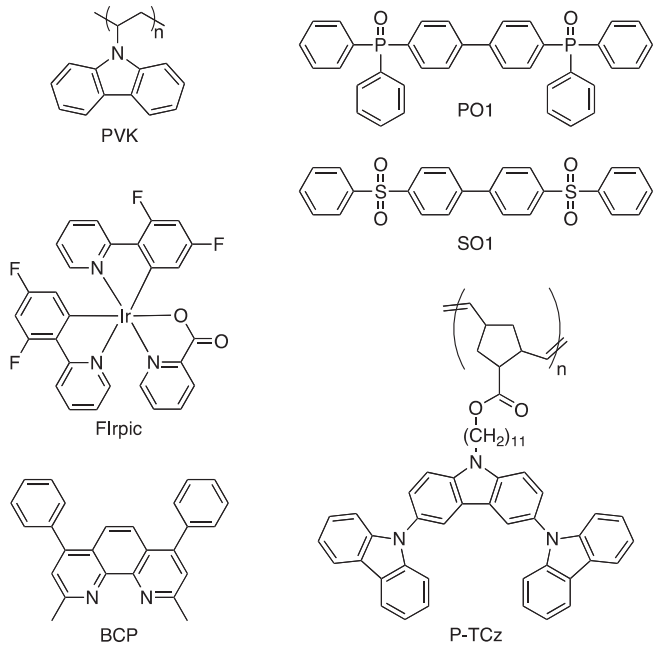

Fig. 2. Chemical structures of the materials used in this study.

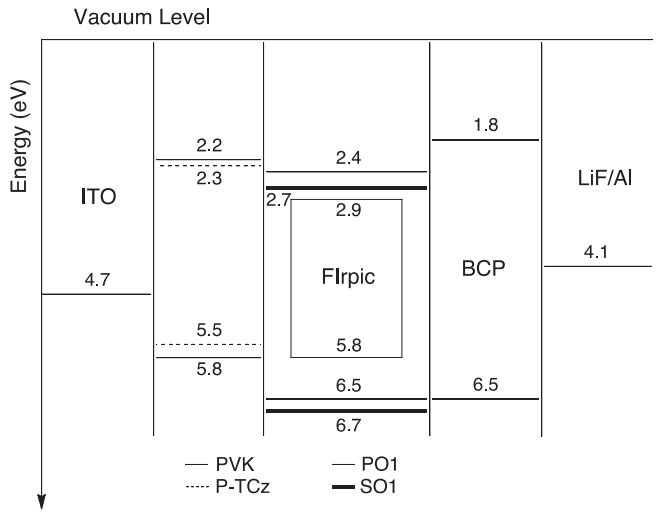

Fig. 3. Energy level diagram based on the estimated solid-state IPs and EAs of the materials discussed in this work.

interested in using a solution-processible tricarbazole-based material as a hole-transport layer (HTL), since this would reduce the number of layers requiring vacuum deposition. As earlier work on poly(norbornene) polymers functionalized with charge-transport side groups has shown that the backbone of the polymer does not adversely affect the energy levels of the moiety [23,24], polymer P-TCz, a poly(norbornene) with pendant tricarbazole moieties, was synthesized (M_w = 49,000; PDI = 1.9 according to GPC in chloroform vs. polystyrene standards) [25]. For comparison to devices incorporating P-TCz, analogous devices were also fabricated using the widely used hole-transport polymer, poly(*N*-vinylcarbazole) (PVK, M_w = 81,800; PDI = 1.68) as a solution-processible HTL with good hole-transport properties, as reported, for example, by Kido et al. [26].

Devices were fabricated on glass substrates precoated with indium tin oxide (ITO) with a sheet resistance of 20 Ω/□ (Colorado Concept Coatings, L.L.C.). The substrates were first cleaned in an ultrasonic bath using a dilute solution of Triton-X (Aldrich) in deionized (DI) water (20 min) followed by successive ultrasonication in DI water, acetone, and finally ethanol (20 min each). Washed ITO substrates were then dried in a vacuum oven at 70 °C under

vacuum (1×10^{-2} Torr) for 1 h. Films of PVK and polymer P-TCz with a thickness of 35 nm were spin-coated from toluene onto air-plasma treated ITO coated substrates in a nitrogen inert atmosphere. The substrates were then loaded into a Kurt J. Lesker Spectros vacuum system without being exposed to atmosphere. For all subsequent organic layers, materials were first purified using gradient zone sublimation, and were then thermally evaporated at a pressure below 1×10^{-7} Torr. The OLED devices have the following architecture: ITO/spin-coated carbazole-based polymer (35 nm) – either PVK (device **I**) or polymer P-TCz (device **II**) – as a HTL/compound SO1 layer doped with 6 or 10 wt% FIrpic (20 nm) as an emitting layer/2,9-dimethyl-4,7-diphenyl-1,10-phenanthroline (BCP) (40 nm) as a hole-blocking layer. The cathode consisted of a thin layer of lithium fluoride (LiF) (with an effective thickness of 2.4 nm based on the deposition rate and time) followed by a 200-nm thick layer of aluminum (Al). The thickness of the different layers was selected based on our experience with the optimization of electrophosphorescent devices with comparable geometry. The chemical structures of the materials used are shown in Fig. 2 and the estimated ionization potentials (IPs) and electron affinities (EAs) [27] of the materials used are shown in Fig. 3. Luminance–current density–voltage (*L*–*J*–*V*) characteristics of the devices were measured using a Keithley 2400 source meter for current–voltage measurements. The devices were tested inside a nitrogen-filled glovebox with O_2 and H_2O levels <20 and <1 ppm, respectively.

The current density–voltage (*J*–*V*) characteristics of the two device architectures, with PVK (device **I**) or polymer P-TCz (device **II**) as a HTL, are shown in Fig. 4. It is noted that the operation voltage of devices of type **I** are greater than that for devices of type **II**; for instance, the operation voltage at 2 mA/cm^2 is 9.3 V for device **I** with 6 wt% doping of the FIrpic phosphor and 9.7 V for device **I** with 10 wt% doping, whereas for device **II** the operation voltage is 7.1 V at 6 wt% doping and 6.4 V at 10 wt%. At a luminance of 100 cd/m^2, device **II** shows maximum external quantum efficiencies (EQE) of 6.9% and a current efficiency of 12.9 cd/A, while device **I** shows efficiencies of 6.4% and 11.3 cd/A, respectively. The luminance–voltage (*L*–*V*) and EQE curves of the OLED devices are compared in Fig. 5 and show that the luminances for SO1-based blue-green OLEDs incorporating polymer P-TCz are higher than for those incorporating PVK. Furthermore, the turn-on voltages (defined as the voltage required to obtain a brightness of 10 cd/m^2) of the P-TCz-based devices **II** (4.4 and 4.3 V for devices with 6 and 10 wt% FIrpic, respectively) are clearly lower than those of the PVK-based devices **I** (6.4 and 6.0 V for 6 and 10 wt%).

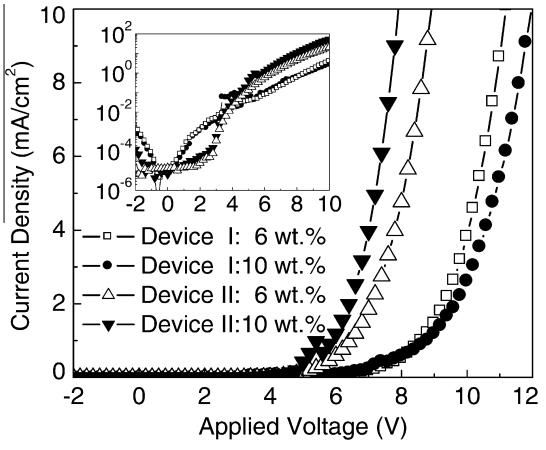

Fig. 4. *J*–*V* characteristics for devices using PVK (device **I**) and polymer P-TCz (device **II**) as a HTL. (Inset) Log scale *J*–*V* plot.

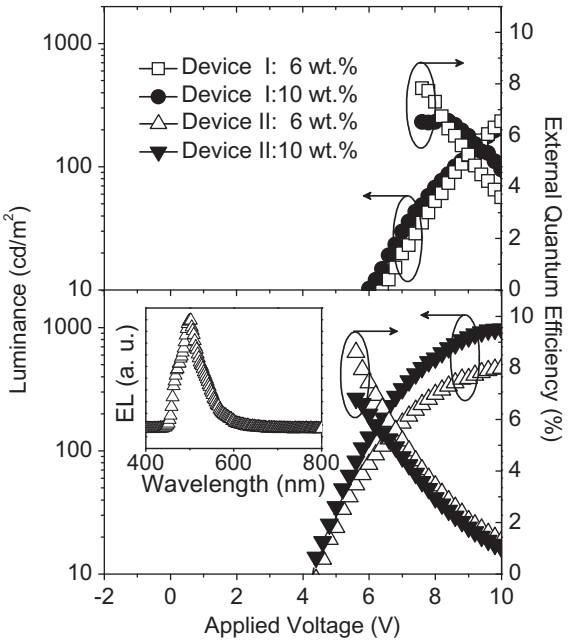

Fig. 5. Luminance and external quantum efficiency as a function of applied voltage for devices. (Inset) EL spectrum of device **II** (6 wt%).

The EQE, current efficiencies, and electroluminescence (EL) spectra demonstrate that compound SO1 is a good host material for FIrpic in electrophosphorescent OLEDs. Indeed, the performance of the current hybrid (mixed solution/vacuum-deposited) devices approaches that of fully vacuum-deposited devices in which its phosphine-oxide analog, PO1, was used as a host for FIrpic (EQE up to 7.8%) [28].

Carrier injection and transport efficiency may be crucial issues affecting the charge balance and quantum efficiency of OLEDs. The differences between devices of types **I** and **II** may be attributable either to different hole mobility values and/or injection efficiencies in the two polymers. Although the electrochemically estimated ionization potential of P-TCz is a little lower than that of PVK, this apparent difference should be treated with caution due to the irreversible oxidation of the latter material. Moreover, the increased chemical stability of charge carriers in P-TCz relative to PVK, which is reflected by the more reversible electrochemistry of the former, may play a role. The hole mobility of P-TCz will be investigated as part of our continuing study of this polymer.

In summary, we have demonstrated that a bis-sulfone host (SO1) can act as a high-triplet-energy host suitable for the fabrication of highly efficient blue-green phosphorescent OLEDs. We believe that the synthetic flexibility of sulfone chemistry opens the possibility for a range of useful organic electronic materials based upon bis-sulfones. Devices employing the new tricarbazole-functionalized polymer P-TCz as a HTL showed that the current density was increased by 20 times and that the operation voltage was also significantly lowered as compared to that of PVK devices.

Acknowledgments

This material is based upon work supported by Solvay SA and in part by the STC Program of the National Science Foundation under Agreement No. DMR-0120967. We are grateful to Jean-Pierre Catinat and Véronique Mathieu for measuring the adiabatic triplet energy of SO1.

References

[1] C. Adachi, M.A. Baldo, M.E. Thompson, S.R. Forrest, Nearly 100% internal phosphorescence efficiency in an organic light-emitting device, J. Appl. Phys. 90 (2001) 5048.
[2] V.V. Bulovic, B. Khalfin, G. Gu, P.E. Burrows, D.Z. Garbuzov, S.R. Forrest, Weak microcavity effects in organic light-emitting devices, Phys. Rev. B 58 (1998) 3730.
[3] J.H. Burroughes, D.D.C. Bradley, A.R. Brown, R.N. Marks, K. Macay, R.H. Friend, P.L. Burns, A.B. Holmes, Light-emitting-diodes based on conjugated polymers, Nature (London) 347 (1990) 539.
[4] J.R. Sheats, H. Antoniadis, M. Hueschen, W. Leonard, J. Miller, R. Moon, D. Roitman, A. Stocking, Organic electroluminescent devices, Science 273 (1996) 884.
[5] X. Zhou, M. Pfeiffer, J. Blochowitz, A. Werner, A. Nollau, T. Fritz, K. Leo, Very-low-operating-voltage organic light-emitting diodes using a p-doped amorphous hole injection layer, Appl. Phys. Lett. 78 (2001) 410.
[6] R.H. Friend, R.W. Gymer, A.B. Holmes, J.H. Burroughes, R.N. Marks, C. Taliani, D.D.C. Bradley, D.A.D. Santos, J.L. Bredas, M. Logdlund, W.R. Salaneck, Electroluminescence in conjugated polymers, Nature (London) 397 (1999) 121–128.
[7] C.W. Tang, S.A. VanSlyke, C.H. Chen, Electroluminescence of doped organic thin films, J. Appl. Phys. 65 (1989) 3610–3616.
[8] S.E. Shaheen, G.E. Jabbour, M.M. Morrell, Y. Kawabe, B. Kippelen, N. Peyghambarian, M.-F. Nabor, R. Schlaf, E.A. Mash, N.R. Armstrong, Bright blue organic light-emitting diode with improved color purity using a LiF/Al cathode, J. Appl. Phys. 84 (1998) 2324–2327.
[9] F. Li, W. Jia, S. Wang, Y. Zhao, Z.-H. Lu, Blue organic light-emitting diodes based on Mes2B [p-4,4′-biphenyl-NPh(1-naphthyl)], J. Appl. Phys. 103 (2008) 034509.
[10] M.-F. Lin, L. Wang, W.-K. Wong, K.-W. Cheah, H.-L. Tam, M.-T. Lee, C.H. Chen, Highly efficient and stable sky blue organic light-emitting devices, Appl. Phys. Lett. 89 (2006) 121913.
[11] H. Fukagawa, K. Watanabe, T. Tsuzuki, S. Tokito, Highly efficient, deep-blue phosphorescent organic light emitting diodes with a double-emitting layer structure, Appl. Phys. Lett. 93 (2008) 133312.
[12] L.S. Sapochak, A.B. Padmaperuma, P.A. Vecchi, H. Qiao, P.E. Burrows, Design strategies for achieving high triplet energy electron transporting host materials for blue electrophosphorescence, Proc. SPIE 6333 (2006) 63330F.
[13] E. Polikarpov, J.S. Swensen, N. Chopra, F. So, A.B. Padmaperuma, An ambipolar phosphine oxide-based host for high power efficiency blue phosphorescent organic light emitting devices, Appl. Phys. Lett. 94 (2009) 223304.
[14] F.-M. Hsu, C.-H. Chien, Y.-J. Hsieh, C.-H. Wu, C.-F. Shu, S.-W. Liub, C.-T. Chen, Highly efficient red electrophosphorescent device incorporating a bipolar triphenylamine/bisphenylsulfonyl-substituted fluorene hybrid as the host, J. Mater. Chem. 19 (2009) 8002.
[15] R. Adams, W. Reifschneider, M.D. Nair, The preparation of aryl thioethers by reaction of aromatic halogen compounds with cuprous thiophenolate or cuprous thiobutylate, Croat. Chem. Acta 29 (1957) 277.
[16] M.J. Frisch, G.W. Trucks, H.B. Schlegel, GAUSSIAN 09, Gaussian Inc., Pittsburgh, PA, 2009.
[17] W.J. Hehre, R. Ditchfie, J.A. Pople, Self-consistent molecular-orbital methods: 12. Further extensions of Gaussian-type basis sets for use in molecular-orbital studies of organic-molecules, J. Chem. Phys. 56 (1972) 2257–2261.
[18] C.T. Lee, W.T. Yang, R.G. Parr, Development of the Colle–Salvetti correlation-energy formula into a functional of the electron-density, Phys. Rev. B 37 (1988) 785–789.
[19] A.D. Becke, Density-functional thermochemistry: 3. The role of exact exchange, J. Chem. Phys. 98 (1993) 5648–5652.
[20] R.J. Holmes, S.R. Forrest, Y.-J. Tung, R.C. Kwong, J.J. Brown, S. Garon, M.E. Thompson, Blue organic electrophosphorescence using exothermic host–guest energy transfer, Appl. Phys. Lett. 82 (2003) 2422.
[21] Q. Zhang, Y.F. Hu, Y.X. Cheng, G.P. Su, D.G. Ma, L.X. Wang, X.B. Jing, F.S. Wang, Carbazole-based hole-transporting materials for electroluminescent devices, Synth. Met. 137 (2003) 1111.
[22] M.-H. Tsai, Y.-H. Hong, C.-H. Chang, H.-C. Su, C.-C. Wu, A. Matoliukstyte, J. Simokaitiene, S. Grigalevicius, J.V. Grazulevicius, C.-P. Hsu, 3-(9-Carbazolyl)carbazoles and 3,6-di(9-carbazolyl)carbazoles as effective host materials for efficient blue organic electrophosphorescence, Adv. Mater. 19 (2007) 862.
[23] J.-Y. Cho, B. Domercq, S. Barlow, K.Y. Suponitsky, J. Li, T.V. Timofeeva, S.C. Jones, L.E. Hayden, A. Kimyonok, C.R. South, M. Weck, B. Kippelen, S.R. Marder, Synthesis and characterization of polymerizable phosphorescent platinum(II) complexes for solution-processible organic light-emitting diodes, Organometallics 26 (2007) 4816.
[24] A. Kimyonok, B. Domercq, A. Haldi, J.-Y. Cho, J.R. Carlise, X.-Y. Wang, L.E. Hayden, S.C. Jones, S. Barlow, S.R. Marder, B. Kippelen, M. Weck, Norbornene-based copolymers with iridium complexes and bis(carbazolyl)fluorene groups in their side-chains and their use in light-emitting diodes, Chem. Mater. 19 (2007) 5602.
[25] Y. Zhang, S.R. Marder, C. Zuniga, S. Barlow, B. Kippelen, A. Haldi, B. Domercq, M. Weck, A. Kimyonok, Carbazole group-containing ROMP-prepared norbornene derivative polymer hole transport and/or electron blocking materials and/or host materials for luminescent layers, PCT Int., WO2009080799 (2009).
[26] J. Kido, K. Hongawa, K. Okuyama, K. Nagai, Bright blue electroluminescence from poly(N-vinylcarbazole), Appl. Phys. Lett. 63 (1993) 2627.
[27] The EA of SO1 was estimated from the electrochemical reduction potential vs. ferrocene according to $EA = eE^{red}_{1/2} + 4.8$ eV and the IP from the EA estimate and the absorption onset, as previously described for PO1 in Ref. [12]. The IP of P-TCz was estimated from the oxidation potential of the corresponding monomer vs. ferrocene according to $IP = eE^{ox}_{1/2} + 4.8$ eV and its EA from the IP estimate and the absorption onset. Accordingly the IP of SO1 and the EA of P-TCz are likely to be under- and overestimated, respectively, due to the neglect of exciton binding energy. The values for FIrpic and BCP were taken from V.I. Adamovich, S.R. Cordero, P.I. Djurovich, A. Tamayo, M.E. Thompson, B.W. D'Andrade, S.R. Forrest, New charge-carrier blocking materials for high efficiency OLEDs, Org. Electron. 4 (2003) 77 and A. Kahn, N. Koch, W. Gao, Electronic structure and electrical properties of interfaces between metals and π-conjugated molecular films, J. Polym. Sci. B 41 (2003) 2529, respectively.
[28] P.E. Burrows, A.B. Padmaperuma, L.S. Sapochak, P. Djurovich, M.E. Thompson, Ultraviolet electroluminescence and blue-green phosphorescence using an organic diphosphine oxide charge transporting layer, Appl. Phys. Lett. 88 (2006) 183503.

usage and a simpler process for device integration [15]. The challenge is to print well-defined structures from dilute inks. By blending the molecular semiconductor with a polymer, the viscosity of the printing solution can be varied. Blending, however, is also expected to impact the electrical performance of the final deposited transistor. This interplay is in fact the topic of this paper.

Two different approaches of ink-jet printing small-molecule semiconductors have been used: printing multiple droplets which coagulate into a film covering a relatively large area on the substrate, or single-droplet printing where each droplet forms an individual functional deposit. The former was adopted in a recent study by Madec et al. [16]. They ink-jet printed multiple droplets of inks containing TIPS-PEN and an amorphous and electrically insulating polymer, polystyrene (PS), at a blending ratio of 1/1 (w/w). By printing from a specific binary solvent mixture and/or using a multilayer printing method, a continuous layer with improved morphology was achieved, and they found an increased mobility of up to 10^{-2} cm^2/Vs (±71–80% variance) in bottom-gate/top-contact transistors. These mobilities are however much lower than the values of 0.12 cm^2/Vs reported by Lim et al. [17] for single-droplet printing of pure TIPS-PEN from a solvent mixture, making it thus far unclear if blending with an insulating polymer can result in a further improvement in high-performance ink-jet printed transistors.

In this paper, we investigate single-droplet ink-jet printing of TIPS-PEN/PS blends, with each printed single droplet being an individual transistor [6,18]. This eliminates the need for additional patterning steps. As in the previous work of Lim [17], we use a bottom-gate/bottom-contact device geometry. This device architecture offers a straightforward route for downscaling of the transistor channel length to a few micrometers. In contrast to Lim's work, we did not rely on the unusual concentric ring arrangement of source and drain electrodes, because that configuration does not allow simple device integration. Here, we use conventional interdigitated comb structure for the source and drain electrodes.

To gain insight into the charge-transport properties of our devices, we study the differences between the transistors based on pure TIPS-PEN and TIPS-PEN/PS blends with respect to macroscopic device operation and local charge-transport properties, by using channel scaling studies and surface potential profilometry, respectively, and relate them to the morphology of the devices. The fundamental understanding of device operation obtained for our blend transistors provides valuable guidelines to the development of next generation transistors based on small-molecule semiconductor and insulating polymer blends.

2. Experimental

6,13-Bis(triisopropyl-silylethynyl)pentacene (TIPS-PEN) was synthesized according to literature [19]. Polystyrene (PS), Mw = 9.58 kDa (Mn = 9.32 kDa, PDI = 1.03), was purchased from Fluka. 1,2,3,4-tetrahydronaphtalene (tetralin, purchased from Merck) was used as the solvent.

An ink-jet printing setup with a high-precision vertical translation stage and a Microfab glass nozzle (type MJ-ATP-01-50-DLC, 50 μm orifice diameter) was used to print inks with a constant TIPS-PEN concentration of 20 mg/ml and varied PS concentrations according to their blending weight ratios. Each droplet with a typical volume of 50 pL was jetted on demand and aligned to the transistor channel region to form an individual device, on substrates that were kept at 70 or 20 °C. All printing experiments were performed in ambient cleanroom conditions.

Bottom-contact/bottom-gate transistors were printed on Si (n++)/SiO_2 substrates with an oxide thickness of 140 nm and photolithographically patterned Au as source and drain electrodes. A pentafluorobenzenethiol monolayer was deposited on Au electrodes [20]. The SiO_2 was treated with trichlorophenylsilane. The transistor channel length was varied between 2 and 40 μm. Device characteristics were measured at room temperature in inert atmosphere using an Agilent 4155C semiconductor parameter analyser. The field-effect mobilities of our transistors in linear (μ_{lin}) and saturation (μ_{sat}) regime were calculated from the two equations as follows, with $V_{DS} = -1$ V and -10 V, respectively [21]:

$$\mu_{lin}(V_G) = \frac{L}{W \cdot C_i} \frac{1}{V_{DS}} \left(\frac{\partial I_{SD}}{\partial V_G} \right) \quad (1)$$

$$\mu_{sat}(V_G) = \frac{2L}{W \cdot C_i} \left(\frac{\partial \sqrt{I_{SD}(V_G)}}{\partial V_G} \right)^2 \quad (2)$$

where C_i is the capacitance per unit area of the gate dielectric layer, and L and W are channel length and width, respectively. The threshold voltage (V_{th}) of our devices is extracted by extrapolating the square root (SQRT) of $|I_{SD,sat}|$ vs. V_G plot to $I_{SD,sat} = 0$ (as depicted in the plots in Fig. 1a). The sub-threshold slope (SS) value was calculated from the measured I_{SD} values over more than two decades above noise level, using the following equation:

$$SS = \frac{V_{G_1} - V_{G_2}}{\log_{10}\left(\frac{I_{SD_1}}{I_{SD_2}}\right)} \quad (3)$$

Optical micrographs were taken on a Leica DM2500M Microscope with cross-polarizers. SKPM was performed using a Veeco Dimension 3100 with a NanoScope IVa controller operating in the lift mode. For the comparison of contact resistance in the pure and blend transistors, a maximized scan size of 80 × 80 μm^2 was used here to span over three active channels in the transistors to rule out any local effects. To avoid any effect of morphological anisotropy due to the direction of crystal growth from periphery towards centre of the droplets, the scanning regions of SKPM on two groups of devices (pure vs. blend) were chosen at the same location relative to the exact centre of the droplets, and with the same scanning direction with respect to the orientation of interdigitated electrodes of the devices. First, the height profile was recorded with tapping-mode atomic force microscopy (AFM). In the second pass the tip is lifted at a fixed height of 50 nm above the surface, and a voltage is applied to the tip, to record the local surface potentials. Several effects can influence the accuracy of SKPM measurements, e.g. the distance between SKPM tip and the sample surface, the geometry of the tip and cantilever, and the relative in-plane positioning of the cantilever with respect to the interdigitated electrodes of transistors

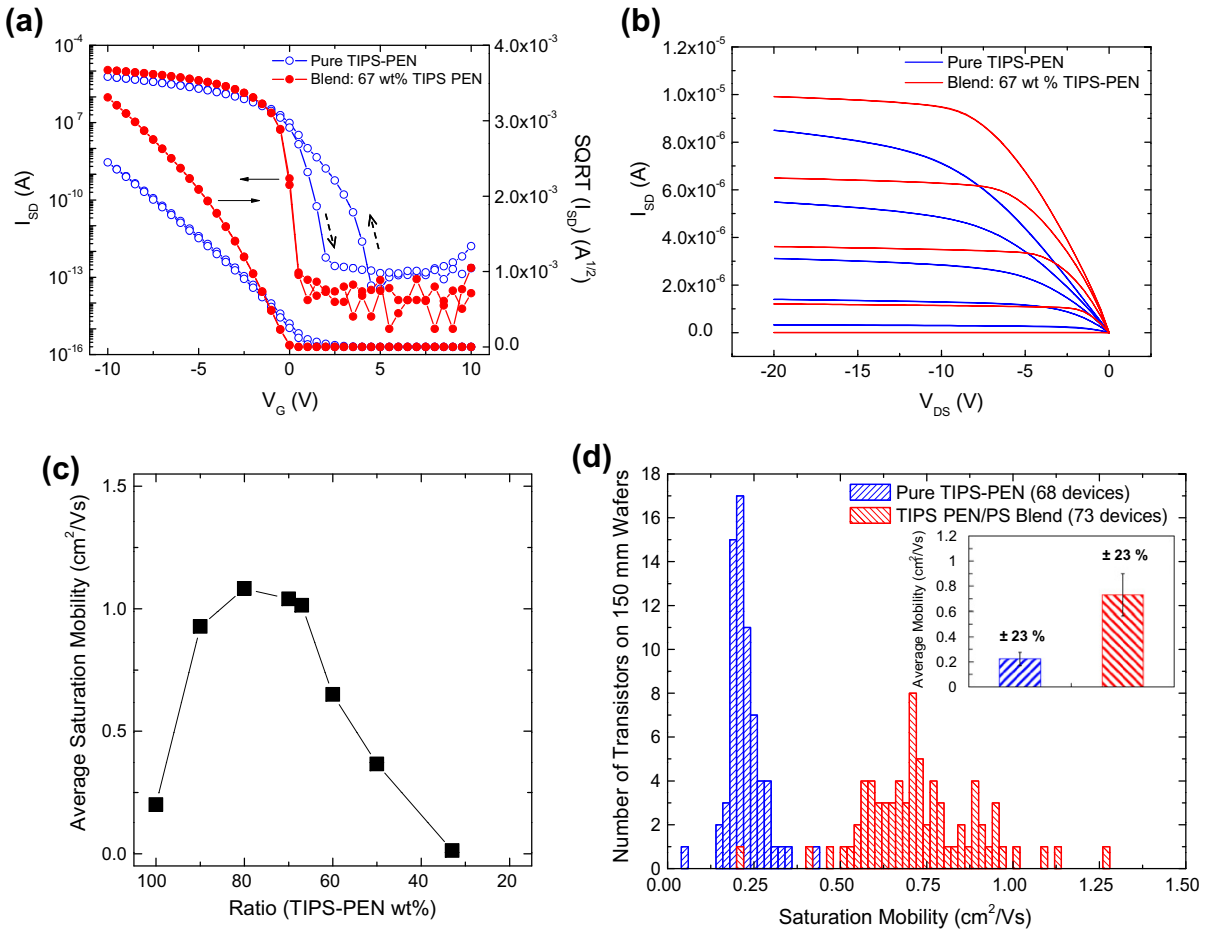

Fig. 1. (a) Transfer characteristics in saturation regime (V_{DS} = −10 V) for two representative transistors with pure TIPS-PEN channel (open circles in blue) and blend channel of 67 wt.% TIPS-PEN and 33 wt.% PS (solid circles in red). Channel length and width are 10 and 200 μm, respectively. The two dashed arrows indicate the counter-clockwise hysteresis for the pure device (gate swept from +10 V → −10 V → + 10 V). The plot of the square root (SQRT) of I_{SD} vs. V_G was used to extract mobility as well as the threshold voltage (V_{th}): the blend device shows a mobility of 1.04 cm^2/Vs and a near-zero V_{th}, while the pure one has a mobility of 0.29 cm^2/Vs and a V_{th} of 2.5 V. (b) Output characteristics of the same two transistors as shown in (a). V_G was varied between 0 and −10 V at a step of −2.5 V. (c) Average saturation mobilities as a function of TIPS-PEN weight ratios in TIPS-PEN/PS blend transistors (averaged from >10 devices for each ratio). All devices were printed on 15 mm × 15 mm square substrates at 70 °C. (d) Histograms of saturation mobilities for 68 pure TIPS-PEN transistors and 73 blend (67 wt.% TIPS-PEN) transistors printed on 150 mm wafers. The inset shows their average mobility values. The relative variance (standard deviation divided by the average value) is 23% for pure TIPS-PEN as well as the blend devices. Transistors were printed at 70 °C. Channel length and width are 5 and 1400 μm, respectively. (For interpretation of the references to color in this figure legend, the reader is referred to the web version of this article.)

[22–24]. The accuracy of our SKPM measurements is comparable to earlier reports on working organic transistors [22,25,26], with observed voltage drop from source to drain electrodes slightly lower than the actual bias applied (V_{DS}). Here we tend to attribute this smaller measured potential drops to the effect of non-local coupling between the entire cantilever/tip and the microscopic device surface, and/or a relatively high tip-sample distance of 50 nm in our measurements [23,24,27,28].

3. Results and discussion

3.1. Effect of insulating polymer (PS) on transistor device performance

Our transistors were independently processed over a period of 14 months on substrates that were prepared under identical conditions. Over time no significant drift in transistor parameters was observed. Representative transfer characteristics in saturation (V_{DS} = −10 V) for pure TIPS-PEN transistors printed at 70 °C are shown in Fig. 1a (open circles in blue). Non-ideal sub-threshold behavior was observed in the form of 'shoulder-like' I_{SD}, with an obvious hysteresis between the forward and backward sweeps. This phenomenon was also reported by Lee et al. [29]. The average saturation mobility of pure TIPS-PEN transistors is 0.20 cm^2/Vs, comparable with earlier reports of ink-jet printing pure TIPS-PEN [6,17]. Adding a polymer binder to the pure TIPS-PEN ink dramatically improves the device characteristics (solid circles in red, Fig. 1a): the transistors switch on sharply at ~0 V, the on-current and mobility are higher than the pure TIPS-PEN devices and no hysteresis is observed. The sharp turn-on is a desirable device property for a switching transistor as it allows

high-speed and low-power operation. Typical output characteristics for pure TIPS-PEN and blend (67% TIPS-PEN) transistors are compared in Fig. 1b. No notable non-linearity of I_{SD} is observed for the pure or blend transistor; not even when the output characteristics are plotted in the form of $\Delta I_{SD}/\Delta V_{DS}$ vs. V_{DS} (graphs not shown). Next, we found that the device mobility is a function of relative weight ratio of TIPS-PEN/PS (Fig. 1c). For blends with 90–67 wt.% of TIPS-PEN, the average mobility has increased up to ~1 cm^2/Vs, a factor of 5 higher than the pure TIPS-PEN (0.20 cm^2/Vs). At lower concentration of TIPS-PEN (e.g. 60 wt.%) the mobility decreases. The average value and standard deviation of mobility (μ) in linear and saturation regime, on-current (I_{on}), and on/off ratio (I_{on}/I_{off}) for transistors (channel length: 10 μm, on 15 mm × 15 mm square substrates) printed at 70 °C with different blending ratios are summarized in Table 1. At a processing temperature of 20 °C we obtain typically lower device performance (Table 2). To further study large area uniformity, we printed 68 pure TIPS-PEN and 73 blend (67 wt.% TIPS-PEN) transistors with a channel length of 5 μm on 150 mm diameter wafers at 70 °C. The histograms in Fig. 1d clearly demonstrate enhanced mobilities of our blend transistors over the entire wafer, with the relative variance (standard deviation divided by the average value) at the same level as the pure TIPS-PEN devices (±23% in the inset of Fig. 1d). This demonstrates the potential of our blend inks for applications in large-area and low-cost organic electronics.

The observation that the mobility is increased by the presence of an insulator up to a critical blending ratio demonstrates that introducing an insulating polymer does not negatively affect the charge transporting layer in the device. This implies that in particular the composition and morphology of the first few nanometers of our TIPS-PEN/PS blend are similar to that of pure TIPS-PEN, as charge transport takes place at this zone in the semiconductor layer [30]. Similar behavior was recently reported for spin-cast blends of TIPS-PEN with poly(α-methylstyrene) [8,9], and blends of TIPS-PEN or fluorinated 5,11-bis(triethylsilylethynyl) anthradithiophene (diF TES-ADT) with a semiconducting polymer, polytriarylamine [7,12]. The results were explained by the occurrence of vertical stratification upon casting and solvent evaporation. During solvent drying TIPS-PEN is predominantly expelled to both top and bottom interfaces of the deposited films [8,9,12]. As long as phase separation leads to almost pure phase of TIPS-PEN at the two interfaces, it should be possible to realize transistors with good performance. This hypothesis can explain why the mobility decreases at too high weight fraction of the polymer in our blends: phase separation is incomplete and no continuous film of TIPS-PEN is formed at the bottom interface of our devices. It can however not explain why the maximum mobility of the blends is higher than that of the pure TIPS-PEN transistors. At least two explanations have been proposed for the improved charge transport in the blend transistors. Ohe et al. suggested that the addition of polymer binder leads to slower drying and hence to a different morphology of the TIPS-PEN film [9]. Yoon et al. proposed that the polymer binder influences the film formation process of the small-molecule organic semiconductors and acts indirectly as a purification method [31].

Typical optical micrographs (cross-polarized reflection mode) in Fig. 2a present the morphology evolution of TIPS-PEN/PS blends printed at 70 °C, with TIPS-PEN weight ratios ranging from 100% to 50%. Pure TIPS-PEN devices have irregular shaped crystalline deposit attributed to the de-pinning of the contact line during solvent drying (image of 100 wt.%), leading to limited crystal coverage on transistor channels. The addition of PS up to ~40% gives circular deposits with large crystals of TIPS-PEN that cover the whole device area with an improved crystal morphology (images of 80 and 67 wt.% of TIPS-PEN). Devices with this type of morphology have high mobility. At further higher concentration of PS, small and isolated TIPS-PEN crystals in a matrix of amorphous materials are observed (images of 50 wt.%). The lack of crystalline TIPS-PEN in this deposit explains the lower transistor performance and large parameter spread (Table 1). Corresponding transfer characteristics for the four transistors of Fig. 2a are compared in

Table 2
Summary of transistor parameters for TIPS-PEN/PS transistors with different blending ratios printed on 15 mm × 15 mm square substrates at 20 °C, under the same processing conditions. Field-effect mobilities were extracted in linear (μ_{lin}) and saturation (μ_{sat}) regime, on-current (I_{on}) was measured at $V_G = -10$ V, with $V_{DS} = -10$ V. Data was obtained for >10 transistors of each ratio.

Ratio (TIPS-PEN wt.%)	μ_{lin} (cm^2/Vs)	μ_{sat} (cm^2/Vs)	I_{on} (μA)
100	0.17 ± 0.03	0.15 ± 0.05	4.4 ± 0.9
67	0.53 ± 0.13	0.55 ± 0.14	7.8 ± 1.7
50	0.58 ± 0.47	0.65 ± 0.51	8.3 ± 6.6
33	0.02 ± 0.02	0.04 ± 0.04	0.3 ± 0.3

Table 1
Summary of transistor parameters for TIPS-PEN/PS transistors with different blending ratios printed on 15 mm × 15 mm square substrates at 70 °C, under the same processing conditions. Field-effect mobilities were extracted in linear (μ_{lin}) and saturation (μ_{sat}) regime, on-current (I_{on}) and off-current were measured at $V_G = -10$ V and +10 V, respectively, with $V_{DS} = -10$ V. Data was obtained for >10 transistors of each ratio.

Ratio (TIPS-PEN wt.%)	μ_{lin} (cm^2/Vs)	μ_{sat} (cm^2/Vs)	I_{on} (μA)	On/off ratio
100	0.23 ± 0.06	0.20 ± 0.07	4.5 ± 1.1	$4.9 \times 10^6 \pm 3.0 \times 10^6$
90	0.72 ± 0.14	0.93 ± 0.23	8.6 ± 1.7	$1.2 \times 10^7 \pm 1.0 \times 10^7$
80	0.90 ± 0.14	1.08 ± 0.16	9.4 ± 1.7	$3.0 \times 10^7 \pm 1.8 \times 10^7$
70	0.83 ± 0.22	1.04 ± 0.26	9.7 ± 2.8	$2.9 \times 10^7 \pm 1.7 \times 10^7$
67	0.85 ± 0.09	1.01 ± 0.12	10.8 ± 1.3	$4.9 \times 10^7 \pm 2.3 \times 10^7$
60	0.53 ± 0.24	0.66 ± 0.30	5.7 ± 2.5	$3.8 \times 10^7 \pm 6.6 \times 10^7$
50	0.30 ± 0.27	0.37 ± 0.33	3.6 ± 3.4	$2.2 \times 10^7 \pm 3.1 \times 10^7$
33	0.005 ± 0.003	0.01 ± 0.009	0.06 ± 0.04	$2.1 \times 10^5 \pm 1.6 \times 10^5$

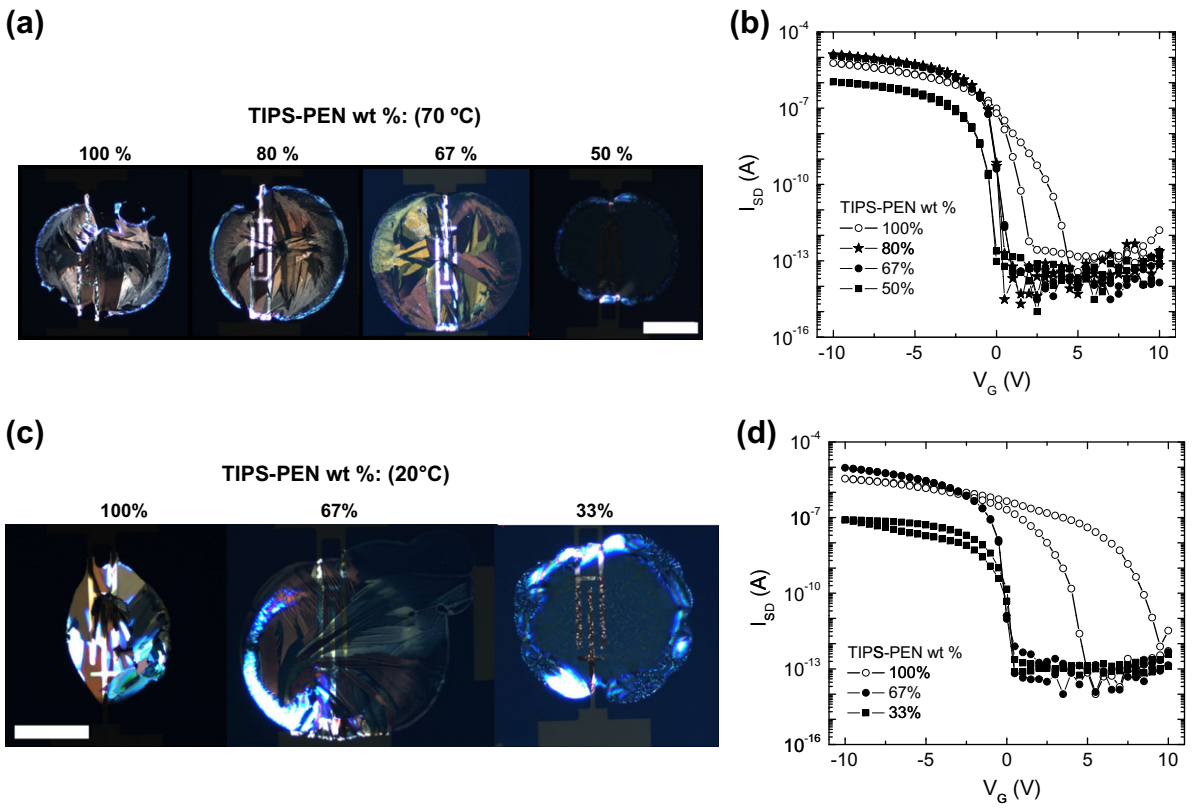

Fig. 2. (a) Representative cross-polarized optical micrographs showing the morphology transition of TIPS-PEN/PS blends with different TIPS-PEN concentrations printed at 70 °C. The scale bar indicates 100 μm. (b) Transfer characteristics in saturation regime ($V_{DS} = -10$ V) for transistors corresponding to the optical micrographs in (a). (c) Representative cross-polarized optical micrographs showing the morphology transition of TIPS-PEN/PS blends printed at 20 °C with decreased TIPS-PEN weight ratio from 100% to 33%. The scale bar indicates 100 μm. (d) Transfer characteristics in saturation regime ($V_{DS} = -10$ V) for the three transistors corresponding to the optical micrographs in (c).

Fig. 2b. Similar trends in contact-line pinning, transition of crystal morphology, and transistor performance as a function of polymer content were also observed when printing at a lower substrate temperature of 20 °C (Fig. 2c and d). The de-pinning effect, however, is more dominant for 20 °C: the lack of positioning control with ill-defined crystal coverage on transistor channels results in their lower device performance and larger spread (Table 2).

3.2. Channel scaling studies

In relation to the phase separation mentioned above, the steep on-switch of current (I_{SD}) of the blend devices is also informative. Steep sub-threshold slopes are observed for all blend transistors, i.e. independent of the TIPS-PEN/PS ratios and process temperatures. Steep sub-threshold slope and low threshold voltage (V_{th}) are usually taken as evidence of a high quality gate dielectric–semiconductor interface with few charge trapping centers [32,33]. This suggests that the polymer binder modifies the interface either directly, for instance, by forming a very thin wetting layer between the silane-treated dielectric and the molecular semiconductor, or indirectly, by influencing the molecular packing of the semiconductor leading to fewer grain boundaries. Meanwhile, reduced charging effects at the top surface of the semiconductor channel ('backchannel effect') by the passivation/encapsulation of phase-separated insulating polymer can also explain the improved characteristics [29]. Although these explanations can play a role also in our blend devices, we propose a third explanation below.

The sub-threshold slope in most blend transistors is very close to the theoretical minimum of 60 mV/decade ($= kT/q \times ln10$) for an Ohmic charge injection from a metal into a semiconductor at room temperature [34,35]. Fig. 3 shows a representative sub-threshold slope as steep as 67 mV/decade in saturation regime for a blend transistor, calculated over more than 2 decades of I_{SD}. This points towards the existence of a tunneling barrier at the metal contacts, which is characterized by a highly non-linear I–V behavior in transfer characteristics [35–38].

We measured the channel length (L) dependence of the total resistance ($R_t = V_{DS}/I_{SD}$) at different gate biases (V_G) in linear regime ($V_{DS} = -1$ V) for two groups of transistors: pure TIPS-PEN vs. blend (67 wt.% TIPS-PEN) (Fig. 4). For the sake of comparison we choose the device series to have similar extracted mobilities. This implies that this group of blend transistors has below-average mobilities. As compared in Fig. 4, R_t decreases linearly with L for the pure transistors, down to a channel length of 2 μm. In contrast,

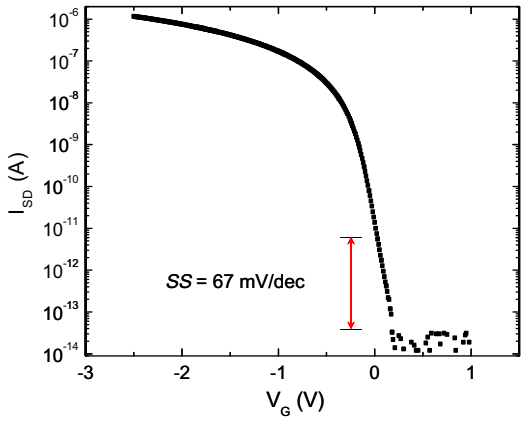

Fig. 3. A representative TIPS-PEN/PS blend (67 wt.% TIPS-PEN) transistor showing the extremely steep sub-threshold slope (*SS*) of 67 mV/decade in saturation regime ($V_{DS} = -10$ V). The *SS* value was calculated from the measured I_{SD} values over more than two decades above noise level, as indicated by the red arrows. The *I–V* curve was measured with 0.01 V increment per step of V_G. (For interpretation of the references to color in this figure legend, the reader is referred to the web version of this article.)

for the blend transistors, R_t does not decrease further if we decrease L below 10 μm, illustrating the importance of a parasitic contact resistance, R_{sd}, in series with the channel resistance. Apparently the influence of R_{sd} for the extraction of intrinsic channel mobility is substantial for the blend but relatively small for the pure TIPS-PEN transistors. From similar analysis for other blend device series, we know that in all cases the blend transistors are influenced by contact resistance (contact limited) and that the variation in R_{sd} is one of the major causes for the variation in mobility reported in Table 1. This makes it particularly relevant to study the origin of the parasitic contact resistance.

3.3. Contact resistance identified by SKPM

To study the origin of parasitic contact resistance in our devices and correlate it to local charge-transport properties, scanning Kelvin probe microscopy (SKPM) measurements were performed during device operation [39]. As shown in the potential image of Fig. 5a, the pure TIPS-PEN transistors show typical parabolic potential profiles from source to drain electrodes when devices were operated in saturation regime, with a small voltage drop at the source electrode, <15% relative to the voltage drop across the channel. Some negligible potential steps along the channel can be discerned and attributed to the grain boundary effects (see corresponding topography image in Fig. 5a), in line with previous studies [25]. In contrast, the potential profiles of the blend (67 wt.% TIPS-PEN) transistors show significant voltage drops at the electrodes (Fig. 5b). Because >80% of the voltage drastically drops at the source electrodes, the profile inside the channel is absent of details.

This high-Ohmic spatial zone close to the source electrodes of blend devices suggests a substantial barrier for charge injection from the contacts into the channels. Based on the potential profiles in Fig. 5, we can quantitatively compare the contact resistance (R_{sd}) for pure and blend devices operated at the 'on-state' (bias conditions: $V_{DS} = -10$ V and $V_G = -10$ V [22,40]) using [22,39]:

$$R_{sd} = \frac{\Delta V_S + \Delta V_D}{I_{on}} \tag{4}$$

where ΔV_S and ΔV_D are the voltages drops at the source and drain electrodes (in Fig. 5), respectively, and I_{on} is the measured 'on-state' source-drain current I_{SD}. With such calculations we found R_{sd} for pure (~0.13 MΩ) and blend (~0.51 MΩ) devices, respectively, much higher in the blend.

3.4. Charge-trapping at the edges of Au electrodes in blend transistors

Recently electric force microscopy (EFM) was adopted to study charge trapping in TIPS-PEN transistors by Jaquith et al. [41]. Clear evidence of long-lived charge trapping was observed. In their study the films were prepared using different processing conditions, leading to different mobilities (10^{-4}–10^{-3} cm^2/Vs). In that work frequency-shift EFM images were recorded to reflect the variations in local trap density. Here, we use SKPM to directly monitor the possi-

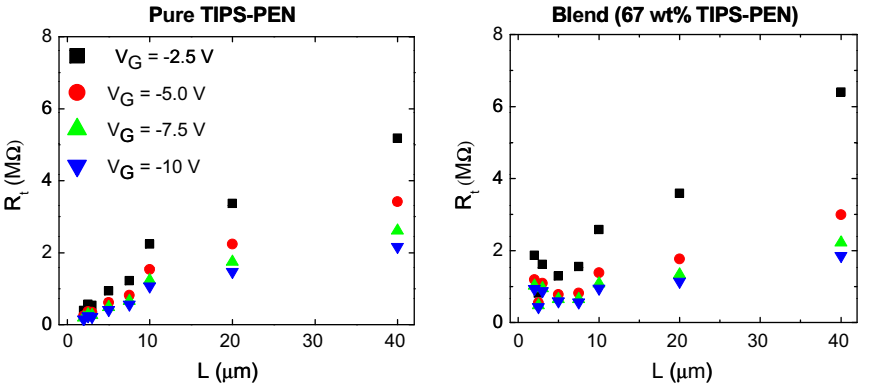

Fig. 4. Channel length dependence of total resistance (R_t) in linear regime ($V_{DS} = -1$ V) at different gate biases (V_G) for pure TIPS-PEN and blend (67 wt.% TIPS-PEN) transistors.

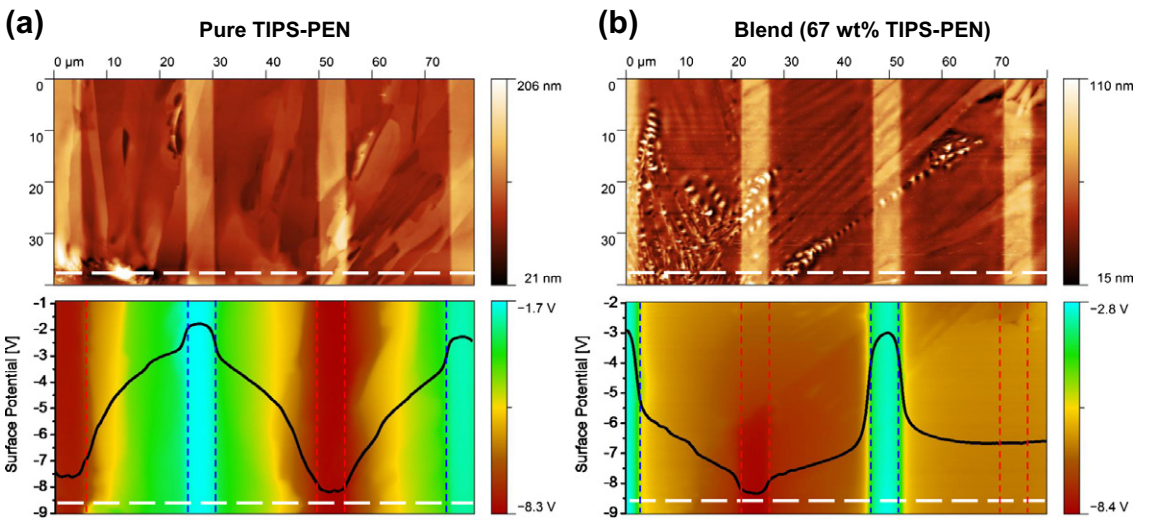

Fig. 5. 2D topography and corresponding surface potential images measured with SKPM of pure TIPS-PEN (a) and blend (67 wt.% TIPS-PEN) transistors (b), as shown in the upper and lower panels, respectively. White dashed lines indicate the positions where the potential cross-sections were taken. Solid black lines denote the cross-section potential profiles along the positions indicated by the dashed white lines. In the potential images, parallel dotted lines in the vertical direction indicate the positions of the edges of source (in blue) and drain (in red) electrodes. Channel length is 20 µm. The transistors were biased in saturation regime ($V_{DS} = -10$ V and $V_G = -10$ V). (For interpretation of the references to color in this figure legend, the reader is referred to the web version of this article.)

bly trapped charges by measuring their local surface potentials with time. To (possibly) create long-lived trapped charges in our samples, a gate bias of $V_G = -10$ V was applied for ~10 min. During this time, some of the mobile charges may become trapped. The biases were then set to zero in order to extract the mobile charges from the transistor channel, and the local electrostatic potential was measured immediately. Recorded potential images of a pure TIPS-PEN and a blend (67 wt.% TIPS-PEN) transistor are compared. As shown in Fig. 6a (middle image: $t = 0$), only few spots with slightly higher potentials are identified in pure TIPS-PEN channels. These can be correlated to grain boundaries or material voids from the corresponding topography image. The potential differences at these spots disappear on a time scale of ~1 h (bottom image in Fig. 6a: $t = 68$ min). In comparison, in the blend device we observed noticeable local surface potential variations (middle image in Fig. 6b: $t = 0$). If we attribute the contrast in these potential images to trapped positive charges (holes), then we observe substantial hole trapping at the edges of Au electrodes in the blend devices. These trapped holes in the blend films are very long-lived (bottom image in Fig. 6b: $t = 612$ min). For more than 10 h we observed no significant decrease of trapped charges as evidenced by the essentially unchanged potential image.

It has recently been shown that insulating polymer such as poly(α-methylstyrene) can trap charges (holes) in pentacene-based organic transistors [42], and these holes remain trapped in the insulating polymer until sufficient counter charges (electrons) can tunnel into the polymer from the channel [43]. Based on the clear differences of trapped charges in terms of locations, areal densities and life-times between our pure TIPS-PEN and blend devices, we argue that the hole trapping in our blend films is related to the local presence of insulating polymer (PS). The potential variations in the blend films (Fig. 6b) are explained by a lateral phase-separation between TIPS-PEN enriched crystal grains and PS enriched regions. In particular, our SKPM results reveal obvious hole trapping effects exactly at the edges of the source/drain Au electrodes with no apparent correlation with its local crystal morphology. This strongly suggests the presence of a thin film of PS (or PS enriched phase) at the Au electrodes. Such an insulating barrier can explain the differences in sub-threshold slope of the I–V characteristics, contact resistance observed in channel scaling measurements, potential drops and hole trapping at the electrodes observed by SKPM, between our pure TIPS-PEN and blend devices.

3.5. Discussion on the relation between charge-trapping, threshold voltage and channel conductivity

If charges are trapped (de-trapped), or fixed space charges are distributed in the transistor channel on a timescale comparable to the typical duration of the I–V measurement, it can be observed as a hysteresis during the forward and backward sweeps in transfer characteristics. We typically swept the voltages at a rate of 1 V/s, meaning a total measurement time of ~1 min.

In the case of pure TIPS-PEN transistors, non-ideal subthreshold behavior was observed in the form of 'shoulder-like' I_{SD}, with an obvious hysteresis during gate sweeps (Fig. 1a). The (counter-clockwise) hysteresis was independent of the sweep direction, i.e. it was the same when sweeping the gate biases (V_G) in the opposite direction (from -10 V → + 10 V → -10 V, graphs not shown). This hysteresis occurs in the depletion regime, i.e. when the bulk of the semiconductor is (partly) depleted of unintentional charges. We attribute it to charging effects at the top surface of the semiconductor channel (the so-called 'backchannel effect'),

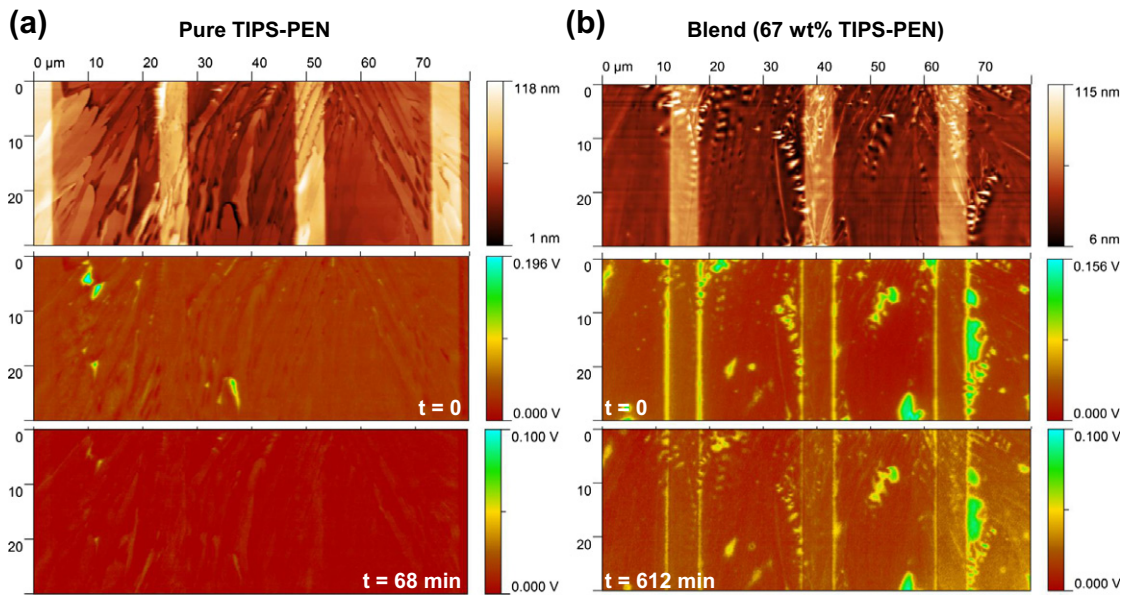

Fig. 6. Time-dependent surface potential images and corresponding 2D topographies recorded by SKPM, for pure TIPS-PEN (a) and blend (67 wt.% TIPS-PEN) transistors (b). The potential images in the middle row ($t = 0$) were measured by grounding all electrodes immediately after a gate bias of −10 V was applied for 10 min. The potential images at the bottom row were measured at $t = 68$ and 612 min after three electrodes were grounded for the pure and blend device, respectively.

as previously reported by Lee et al. [29]. The transfer characteristics of our blend transistors (with different TIPS-PEN/PS ratios) are essentially hysteresis-free, independent of the direction or range of the gate sweeps. Apparently, the 'back-channel effect' is absent in these blend devices. This points to an additional advantage of the insulating polymer binder. It passivates the charge transport layer.

Trapped channel charges can result in shifts of transistor threshold voltages. Furthermore, deep and shallow trapping can also influence the charge transport negatively. We found that in our blend devices that (1) the existence of insulating polymer causes long-term trapping of holes, and (2) the existence of insulating polymer increases the field-effect mobility and has only a marginal influence on the threshold voltage. We attribute this seeming contradiction to the fact that charge-trapping takes place almost exclusively at the contact edges and to a far lesser extent in the channel region of our blend transistors. Less than 1.6% [44] of the initially accumulated mobile charges induced by the gate bias can be trapped at only a few locations inside the channel (Fig. 6b). This explains why we do not observe threshold voltage shifts in our blend transistors. Whether and how much the trapped charges will mitigate charge transport in the channel cannot be determined or quantified. If any, it is expected to result in a decrease in channel conductivity, but in fact we observe the opposite. The net positive effect of polymer blending indicates that a complex interplay between different mechanisms is taking place here.

4. Conclusions

To conclude, we have presented a systematic study of the influence of material composition and ink-jet processing conditions on the charge transport in bottom-gate field-effect transistors based on single droplets of TIPS-PEN/PS blends. Under optimal conditions the field-effect mobility of the blends is significantly higher than that of the pure TIPS-PEN. In addition, blending results in much better sub-threshold characteristics. These results represent an important step towards the application of ink-jet printing for controlled deposition of high-performance transistors in large-area organic electronics. Using channel scaling measurements and SKPM measurements, we show that the sharp turn-on in current in the blends is the result of a contact resistance that originates from a thin insulating PS layer between the injecting contacts and the semiconductor channel. This insight suggests that reducing the contact resistance is the best way forward to improve the transistor characteristics even further.

Acknowledgements

We acknowledge Peter Graat (Philips Research) for helpful discussions. The research leading to these results has received funding from the European Community's Seventh Framework Programme (FP7/2007–2013) under grant agreement No. 212311 of the ONE-P project and No. 216546 of the FLAME project.

References

[1] G. Yu, J. Gao, J.C. Hummelen, F. Wudl, A.J. Heeger, Science 270 (1995) 1789–1791.
[2] G. Li, V. Shrotriya, J. Huang, Y. Yao, T. Moriarty, K. Emery, Y. Yang, Nat. Mater. 4 (2005) 864–868.
[3] S. Goffri, C. Muller, N. Stingelin-Stutzmann, D.W. Breiby, C.P. Radano, J.W. Andreasen, R. Thompson, R.A.J. Janssen, M.M. Nielsen, P. Smith, H. Sirringhaus, Nat. Mater. 5 (2006) 950–956.

[4] B.A. Brown, J. Veres, R.M. Anemian, R.T. Williams, S.D. Ogier, S.W. Leeming, WO Patent 2005055248, 2005.
[5] J. Smith, R. Hamilton, I. McCulloch, N. Stingelin-Stutzmann, M. Heeney, D. Bradley, T. Anthopoulos, J. Mater. Chem. 20 (2010) 2562–2574.
[6] B.K.C. Kjellander, W. Smaal, J.E. Anthony, G.H. Gelinck, Adv. Mater. 22 (2010) 4612–4616.
[7] R. Hamilton, J. Smith, S. Ogier, M. Heeney, J.E. Anthony, I. McCulloch, J. Veres, D.D.C. Bradley, T.D. Anthopoulos, Adv. Mater. 21 (2009) 1166–1171.
[8] J. Kang, N. Shin, D.Y. Jang, V.M. Prabhu, D.Y. Yoon, J. Am. Chem. Soc. 130 (2008) 12273–12275.
[9] T. Ohe, M. Kuribayashi, R. Yasuda, A. Tsuboi, K. Nomoto, K. Satori, M. Itabashi, J. Kasahara, Appl. Phys. Lett. 93 (2008) 053303-3.
[10] M. Madec, D. Crouch, G. Llorente, T. Whittle, M. Geoghegan, S. Yeates, J. Mater. Chem. 18 (2008) 3230–3236.
[11] J. Kwon, S. Shin, K. Kim, M.J. Cho, K.N. Kim, D.H. Choi, B. Ju, Appl. Phys. Lett. 94 (2009) 013506-3.
[12] J. Smith, R. Hamilton, Y. Qi, A. Kahn, D.D.C. Bradley, M. Heeney, I. McCulloch, T.D. Anthopoulos, Adv. Funct. Mater. 20 (2010) 2330–2337.
[13] S.D. Ogier, J. Veres, M. Zeidan, WO Patent 2007082584, 2007.
[14] J. Smith, M. Heeney, I. McCulloch, J.N. Malik, N. Stingelin, D.D. Bradley, T.D. Anthopoulos, Org. Electron. 12 (2011) 143–147.
[15] B. DeGans, P. Duineveld, U. Schubert, Adv. Mater. 16 (2004) 203–213.
[16] M. Madec, P. Smith, A. Malandraki, N. Wang, J. Korvink, S. Yeates, J. Mater. Chem. 20 (2010) 9155–9160.
[17] J.A. Lim, W.H. Lee, H.S. Lee, J.H. Lee, Y.D. Park, K. Cho, Adv. Funct. Mater. 18 (2008) 229–234.
[18] J.A. Lim, J. Kim, L. Qiu, W.H. Lee, H.S. Lee, D. Kwak, K. Cho, Adv. Funct. Mater. 20 (2010) 3292–3297.
[19] J.E. Anthony, J.S. Brooks, D.L. Eaton, S.R. Parkin, J. Am. Chem. Soc. 123 (2001) 9482–9483.
[20] M.M. Payne, S.R. Parkin, J.E. Anthony, C.C. Kuo, T.N. Jackson, J. Am. Chem. Soc. 127 (2005) 4986–4987.
[21] D. Braga, G. Horowitz, Adv. Mater. 21 (2009) 1473–1486.
[22] Y. Luo, F. Gustavo, J. Henry, F. Mathevet, F. Lefloch, M. Sanquer, P. Rannou, B. Grévin, Adv. Mater. 19 (2007) 2267–2273.
[23] D. Charrier, M. Kemerink, B. Smalbrugge, T. de Vries, R. Janssen, ACS Nano 2 (2008) 622–626.
[24] G. Koley, M.G. Spencer, H.R. Bhangale, Appl. Phys. Lett. 79 (2001) 545.
[25] L.C. Teague, B.H. Hamadani, O.D. Jurchescu, S. Subramanian, J.E. Anthony, T.N. Jackson, C.A. Richter, D.J. Gundlach, J.G. Kushmerick, Adv. Mater. 20 (2008) 4513–4516.
[26] L.C. Teague, O.D. Jurchescu, C.A. Richter, S. Subramanian, J.E. Anthony, T.N. Jackson, D.J. Gundlach, J.G. Kushmerick, Appl. Phys. Lett. 96 (2010) 203305-3.
[27] A. Liscio, V. Palermo, K. Mullen, P. Samori, J. Phys. Chem. C 112 (2008) 17368–17377.
[28] J. Brondijk, X. Li, H. Akkerman, P. Blom, B. de Boer, Appl. Phys. A Mater. Sci. Process. 95 (2009) 1–5.
[29] S.H. Lee, M.H. Choi, S.H. Han, D.J. Choo, J. Jang, S.K. Kwon, Org. Electron. 9 (2008) 721–726.
[30] G. Horowitz, P. Delannoy, J. Appl. Phys. 70 (1991) 469.
[31] D. Yoon, Y. Chung, N. Shin, Y. Jo, J. Kang, V. Prabhu, D. Delongchamp, J. Kline, L. Richter, D. Gundlach, J. Anthony, MRS Fall Meeting, 2010, Boston, USA.
[32] S.H. Kim, D. Choi, D.S. Chung, C. Yang, J. Jang, C.E. Park, S.K. Park, Appl. Phys. Lett. 93 (2008) 113306-3.
[33] K. Myny, S. De Vusser, S. Steudel, D. Janssen, R. Muller, S. De Jonge, S. Verlaak, J. Genoe, P. Heremans, Appl. Phys. Lett. 88 (2006) 222103-3.
[34] Z. Liu, J.H. Oh, M.E. Roberts, P. Wei, B.C. Paul, M. Okajima, Y. Nishi, Z. Bao, Appl. Phys. Lett. 94 (2009) 203301.
[35] W. Choi, B. Park, J. Lee, T. Liu, IEEE Electron Device Lett. 28 (2007) 743–745.
[36] K. Bhuwalka, J. Schulze, T. Eisele, Jpn. J. Appl. Phys. 43 (2004) 4073–4078.
[37] Q. Zhang, W. Zhao, A. Seabaugh, IEEE Electron Device Lett. 27 (2006) 297–300.
[38] Y. Khatami, K. Banerjee, IEEE Trans. Electron Devices 56 (2009) 2752–2761.
[39] K.P. Puntambekar, P.V. Pesavento, C.D. Frisbie, Appl. Phys. Lett. 83 (2003) 5539–5541.
[40] L. Bürgi, T. Richards, M. Chiesa, R.H. Friend, H. Sirringhaus, Synth. Met. 146 (2004) 297–309.
[41] M. Jaquith, J. Anthony, J. Marohn, J. Mater. Chem. 19 (2009) 6116–6123.
[42] K. Baeg, Y. Noh, J. Ghim, S. Kang, H. Lee, D. Kim, Adv. Mater. 18 (2006) 3179–3183.
[43] M. Debucquoy, M. Rockelé, J. Genoe, G. Gelinck, P. Heremans, Org. Electron. 10 (2009) 1252–1258.
[44] The ratio (Y) of trapped holes to the gate-induced charges by accumulation at this location is estimated by using the following equation (Ref. [41]): $Y = \Delta\varphi\ /|(V_G - V_{th})|$, where $\Delta\varphi$ is the surface potential difference within the transistor channel region, as determined from SKPM (Fig. 6b ($t = 0$)), a maximum of +0.156 V, under the charging gate bias of $V_G = -10$ V. Y is calculated to be a maximum of ~1.6% for the blend device.

This scalable, fully hierarchical library is well suited to simulate the accurate static and dynamic behavior of the functional blocks present in a RFID system based on organic processes. The SPICE CAD environment [5] has been chosen as the most suitable tool for time domain simulations, while the Agilent ADS suite has instead been adopted for its system-level environment, robust optimization, layouting, and routing capabilities. As a case study, the design of a complete organic RFID chip using the developed libraries is presented and discussed.

The paper is organized as follows: Section 2 presents the major organic technology issues, focusing on the OFET modeling strategy and implementation into commercial CAD tools. Section 3 describes the two basic architectures considered, a simplified memoriless RFID, and a full RFID with memory. The building blocks of the memoriless RFID are described in Section 4, where a full simulation of the RFID is also presented. Section 5 reports the analysis of the additional building blocks needed for the full RFID, in particular, the asynchronous counter. Finally, some conclusions are drawn in Section 6.

2. The OFET model

The core element of the library is the OFET active large-signal model, on which the design of all digital and analog circuits discussed is based. As a case study, the selected OFET refers to a specific public-domain process [6], based on pentacene organic semiconductors, although the proposed approach can be also applied in principle to other OFET technologies. The choice of a pentacene OFET is at present justified by the fact that, among organic semiconductors, this material allows for the development of OFETs with good performances and process stability, both being key issues in the development of organic integrated RF circuits [7]. In fact, among *p*-type materials that are today the most promising candidates for OFET implementation (see e.g. [8]) pentacene reaches comparatively high mobilities: the reported state-of-the-art mobility for the small-molecule pentacene, processed in different ways, are 1.8 cm^2/Vs for a solution processed pentacene, and 5.5 cm^2/Vs for an evaporated pentacene.

The use of a model expressly conceived for Organic Thin Film Transistors, instead of a general-purpose MOS model for digital applications [3], allows a more flexible (e.g. scalable) library to be implemented, also suitable for analog subsystems, such as for example the RF-receiver/harvesting block. The adopted OFET equivalent circuit, shown in Fig. 1, is generated by combining a literature nonlinear DC model with nonlinear, MOS-like capacitances. The DC model, taken from Marinov et al. [9], permits a systematic and accurate fitting [10] of *IV* experimental characteristic, in a wide range of values. Moreover, the model correctly works on all four quadrants of the output characteristics, i.e. for both negative and positive values of the drain-source voltage and drain current. This model feature, consistent with the OFET electrical and structural symmetry, is essential to simulate transistors operating in diode mode, as required in the energy harvesting section, see Section 4.1. A simulated example, showing the diode like

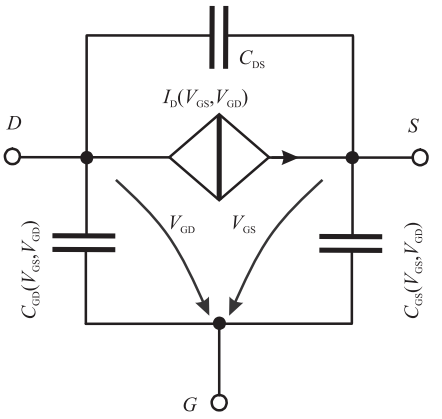

Fig. 1. SPICE and ADS equivalent circuit model of the OFET.

behavior of the direct and inverse output characteristics for zero gate-source voltage is reported in Fig. 2.

The model process (geometrical and physical) and fitting parameters are listed in Table 1 and Table 2 with their short description. The drain current generator I_D (see Fig. 1) is modeled as:

$$I_D = \frac{W\mu_0 C_{OX}}{L(1-\alpha_L)} \frac{V_{DEODR}^{2+\gamma} - V_{SEODR}^{2+\gamma}}{(2+\gamma)V_\gamma^\gamma}, \tag{1}$$

where the so-called source (V_{SEODR}) and drain (V_{DEODR}) effective overdrive voltages [9] are:

$$\begin{aligned} V_{SEODR} &= V_{SS} \ln\left\{1+\exp\left[\frac{V_T - V_{GSI}(1+\delta_{VT})}{V_{SS}}\right]\right\}, \\ V_{DEODR} &= V_{SS} \ln\left\{1+\exp\left[\frac{V_T - V_{GDI}(1+\delta_{VT})}{V_{SS}}\right]\right\}, \end{aligned} \tag{2}$$

where V_{GSI} and V_{GDI} are related to the gate-source V_{GS}, gate-drain V_{GD}, and drain to source current I_D by the following expressions:

$$\begin{aligned} V_{GSI} &= V_{GS} - \frac{R_T}{2}(I_D - |I_D|), \\ V_{GDI} &= V_{GD} + \frac{R_T}{2}(I_D + |I_D|). \end{aligned} \tag{3}$$

Second-order effects such as channel modulation, and bias sensitivity of the threshold voltage, have been included through:

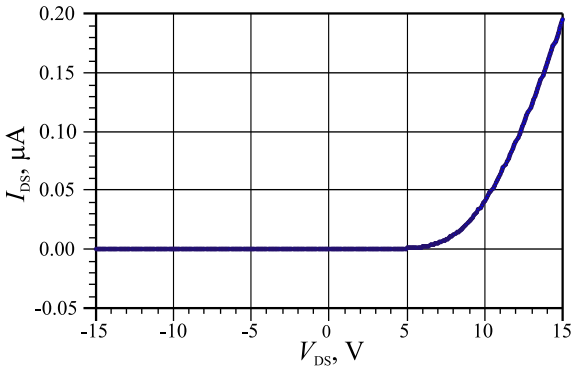

Fig. 2. Philips OFET direct and inverse output characteristic for V_{GS} = 0 V.

Table 1
Process (physical) parameters of the model.

Model parameter	Notation	Value
Channel width	W	300 μm
Channel length	L	4 μm
Gate capacitance per unit area	C_{OX}	345 μF/m^2
Threshold voltage	V_T	1.87 V
Fermi potential	ϕ_N	1 V
Low-field mobility	μ_0 (10^{-9})	54.4 m^2/Vs
Drain-source capacitance	C_{DS}	0.01 pF

Table 2
Fitted parameters of the model.

Model parameter	Notation	Value
Voltage overdrive	V_γ	5 V
Mobility enhancement	γ	1.58
Channel modulation	λ	0.067/V
Subthreshold voltage	V_{SS}	0.9078 V
Sensitivity of V_T to bias	δ_{VT}	−0.0084
Min. (contact) resistance	R_C	26 kΩ
Max. (contact) resistance	R_{Cmax}	88 kΩ
Max. current (R_{Cmax})	I_{Cmax}	1.62 nA
Reduction exp. (R_{Cmax})	N_{IC}	1.58

$$\alpha_L = \lambda|V_{GS}-V_{GD}|\frac{|V_{GS}-V_{GD}|+V_{GT\Delta L}}{2|V_{GS}-V_{GD}|+V_{GT\Delta L}} \qquad (4)$$
$$V_{GT\Delta L} = \max[(V_{GS}-V_T),\ 10\text{ mV}].$$

Eq. (3) shows that V_{GSI} and V_{GDI}, controlling I_D (see Eq. (1)), are the effective intrinsic gate-source and gate-drain voltages respectively, derived from the external ones (V_{GS} and V_{GD}) by deembedding the voltage drop on the contact resistance R_T. This resistance is fairly large in OFETs and has a non linear behavior approximated as a function of the drain current according to:

$$R_T = R_C + R_{Cmax}\left[\frac{I_{Cmax}}{I_{Cmax}+|I_D|}\right]^{N_{IC}}. \qquad (5)$$

The implementation of R_T, embedded in the non linear drain current generator of Fig. 1, preserves the symmetry of the OFET model with respect to an exchange of the drain and source terminals. This property can be verified from the previous reported model equations where, see Eq. (3), the R_T effects are moved from source to drain when the voltage $V_{DS} = V_{GS} - V_{GD}$, and thus the drain current I_D changes sign.

The static OFET model proposed by [9] has been coupled to a set of nonlinear capacitances, to account for dynamic effects that are essential in the design of some components, see for example the case of the oscillator of Section 4.3. We adopted the well-known Meyer's capacitance model, already successfully exploited for pentacene-based OFET [11]. The gate-source and gate-drain capacitances were implemented according to the piecewise analytical expressions in [12], that depend on the controlling voltages V_{GS} and V_{GD}, on the gate dielectric specific capacitance C_{OX}, and on the OFET gate width and length, W and L respectively. The Fermi potential ϕ_N, used within the subthreshold capacitance expressions, has a well defined meaning in p-channel MOS devices; however it can be considered here as a fitting parameter. For a p-channel MOS ϕ_N is of the order of one half of the semiconductor energy gap; taking into account that the pentacene gap is around 2.2 eV [13], this parameter has been set to 1 V. The expressions of C_{GS} and C_{GD} (the gate-source and gate-drain capacitances, respectively) used for $V_{GS} > V_{GD}$ ($V_{DS} > 0$), are:

$$V_{GS} < V_T - 2\phi_N \Rightarrow \begin{cases} C_{GS} = 0 \\ C_{GD} = 0 \end{cases},$$
$$V_T - 2\phi_N < V_{GS} < V_T \Rightarrow \begin{cases} C_{GS} = C_{OX}WL\frac{V_{GS}-V_T+2\phi_N}{3\phi_N} \\ C_{GD} = 0 \end{cases},$$
$$V_{GD} < V_T < V_{GS} \Rightarrow \begin{cases} C_{GS} = \frac{2}{3}C_{OX}WL \\ C_{GD} = 0 \end{cases}, \qquad (6)$$
$$V_{GD} > V_T \Rightarrow \begin{cases} C_{GS} = \frac{2C_{OX}WL}{3}\left[1-\frac{(V_{GD}-V_T)^2}{(V_{GS}+V_{GD}-2V_T)^2}\right] \\ C_{GD} = \frac{2C_{OX}WL}{3}\left[1-\frac{(V_{GS}-V_T)^2}{(V_{GS}+V_{GD}-2V_T)^2}\right] \end{cases},$$

where the last formula implies, since the previous relationships apply for $V_{DS} > 0$, that $V_{GS} > V_{GD} > V_T$. As already done for the drain current, the above relationships have been formulated so as to emphasize the electrical and topological OFET symmetry, thus making their derivation for $V_{GS} < V_{GD}$ ($V_{DS} < 0$) straightforward. In this case, the source and drain roles are exchanged, which is obtained by replacing in the previous expressions V_{GS} with V_{GD}, and viceversa. Although the effect of drain charge storage is negligible at the operating frequency considered, a drain-source constant capacitance C_{DS} has been added to the model, see Table 1.

The model includes 16 parameters that can be divided into two classes, 7 process (physical) parameters listed in Table 1, and 9 fitting parameters listed in Table 2. Process parameters were directly identified following [6], while the other parameters were fitted on the DC output and transimpedance characteristics of different devices of various periphery, using the Agilent ADS suite optimization tool. The model has been then tailored on the Philips process [6], and the fitted OFET model parameters are listed in Tables 1 and 2. As an example, Fig. 3 reports a comparison between the measured (data from [6]), and the simulated device transcharacteristic obtained using a simple MOS like model, already presented in [3], and the advanced OFET model before introduced. The results, relative to $V_{DS} = -1$ V, and -20 V, show the MOS loss of accuracy for higher V_{DS}, where instead the OFET model maintains its effectiveness to follow the measured behavior.

3. RFID architectures

To demonstrate the potential of the proposed library, we consider as a case study two RFID designs: a simplified, memoriless RFID (Fig. 4), and a more complex RFID system with an on-board memory (Fig. 5). From now on, the two schemes will be referred to as the memoriless and full RFID, respectively. In both schemes, the transponder link from and to the reader is represented by the antenna block, although, due to the low operating frequency (a few MHz), near-field coupling should be more correctly represented

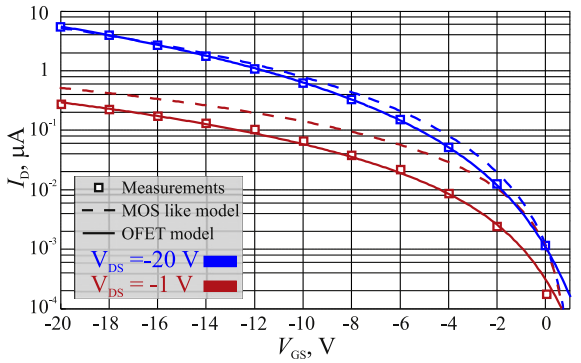

Fig. 3. Philips OFET DC transcharacteristic: comparison between experimental data (markers only) [6], and simulation with a MOS like model [3] (dashed traces), and with the OFET advanced model here described (continuous traces). Results are for $V_{DS} = -1$ V (red traces), and -20 V (blue traces). (For interpretation of the references to color in this figure legend, the reader is referred to the web version of this article.)

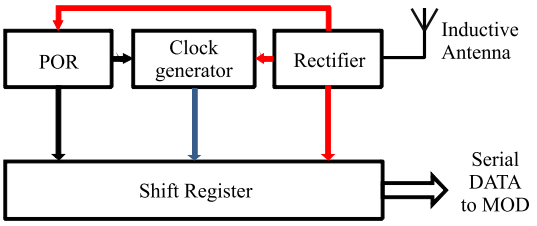

Fig. 4. Simplified RFID TAG system architecture (memoriless RFID).

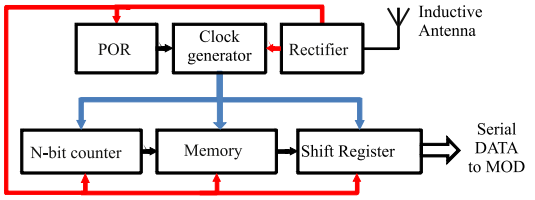

Fig. 5. General purpose RFID TAG system architecture with ROM memory (full RFID).

through in-air coupled coils, as sketched in Fig. 6. In the memoriless RFID (Fig. 4), the synchronous counter scans the data memory, and transfers the data read to the shift register for their serialization. A *n*-bit shift-register (8-bits in our case study), with preset/reset control, replaces the counter, memory and shift register blocks of the full RFID, see Fig. 5.

The memoriless RFID architecture is convenient when the number of bits written on the TAG is low (not exceeding a few tens), since it allows the circuit size and complexity to be reduced. This feature is particularly interesting if we consider the relative immaturity of presently available OFET processes, and the large device areas involved. All blocks of the simplified RFID will be analyzed in detail in Section 4, while some specific comments on the simulation of the full architecture will be presented in Section 5.

The data reading procedure, as exemplified in Fig. 6, is rather straightforward at the TAG side, and shall not be

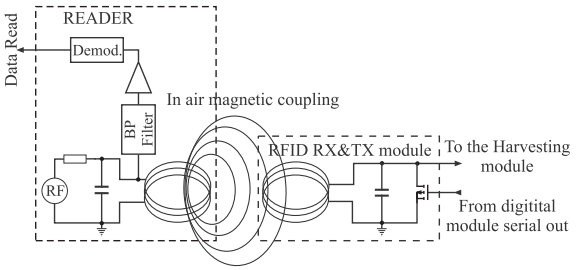

Fig. 6. Circuit exemplifying the implementation of the reader harvesting and data recovery functionalities.

dealt with in the paper: the RF CW signal generated and transmitted by the reader section (Fig. 6, left) energizes the RFID TAG (Fig. 6, right), and triggers the serialized binary data flow with a bit rate imposed by the TAG clock frequency. This data stream, that embeds the TAG code, drives the drain-source resistance of an OFET placed before the rectifier of the harvesting block, forcing an amplitude modulation of the RF inquiring carrier at the primary coil, that can be detected by the reader unit.[2]

4. Simplified architecture (memoriless RFID) analysis and simulation

In this section we will consider the simulation of the individual building blocks of the memoriless RFID (Fig. 4) and the simulation of the whole system.

4.1. Rectifier

The rectifier, i.e. the energy harvester unit, converts the RF CW input signal into DC power. Standard implementations are based on diodes (see e.g. [14]), but this strategy implies increased complexity in terms of process steps. As a more convenient alternative, the same OFET used for the logic gates was used, but in a diode configuration, exploiting the direct and inverse strongly different OFET channel resistance for $V_{GS} = 0$ (see Fig. 2). A limitation of the presently available OFET technology consists in the rather large drain bias voltages needed to properly drive the device (typically $|V_{DS}| \geqslant 10$ V in the process considered); therefore, a voltage booster is typically required within the harvesting unit. The architecture adopted is the classical three stage Cockcroft–Walton multiplier [15], whose circuit is reported in Fig. 7. This approach is modular and the number of stages can be tailored and optimized according to the required DC voltage. A SPICE simulation, assuming an input RF signal consistent with typical "on the field" conditions [16], is reported in Fig. 8, demonstrating the effectiveness of the proposed approach to generate voltage levels consistent with the required bias.

[2] More complex operations are required at the reader side where, before binary data recovery, filtering and amplification are needed. In fact, due to the low in-air coupling, the signal sidebands have small amplitude with respect to the carrier; therefore, analog or digital filtering is needed to separate them from the CW signal, before amplification and demodulation.

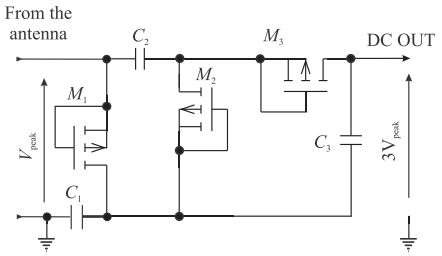

Fig. 7. Circuit of the rectifier/harvester module.

4.2. Digital logic blocks

Since *p*-type organic semiconductors only are practically available at present, the two choices considered in the literature (see e.g. [6]) for logical implementations are (1) logic gates with zero-V_{GS} load, and (2) logic gates with diode load and level shifters. Solution (1) is simpler but requires a larger aspect ratio between the drive and load device (M_1) and M_2 in Fig. 9, respectively) to optimize the inverter transfer curve (Fig. 9). Approach (2), instead, despite requiring a larger number of devices and higher routing complexity, ensures better performances in terms of the transfer characteristic. In our study, we focused on the technologically simpler solution (1). The aspect ratio between M_2, working with $V_{GS} = 0$, and acting as a non linear pull-down resistance, and M_1, has been optimized using SPICE and the Monte Carlo analysis available in the Agilent ADS suite to obtain the best trade-off between noise margins and port gain, thus maximizing the area of the square in Fig. 9 [6]. The final optimized aspect ratio of 25 between M_2 and M_1 ensures a noise margin of the order of 4 V, suitable for the digital blocks. The direct and inverse (mirrored) input–output inverter transfer characteristic with $V_{DD} = -15$ V are shown in Fig. 9.

Following a hierarchical approach, the NAND ports needed to implement logic functions were realized by direct connection of inverters [17], re-optimizing the device geometries in order to maximize the port performances. The values of the pull-down and pull-up device aspect ratio, optimized for the best noise margins, have been found to be 15 and 25, respectively, for the 2 and 3 input NAND.

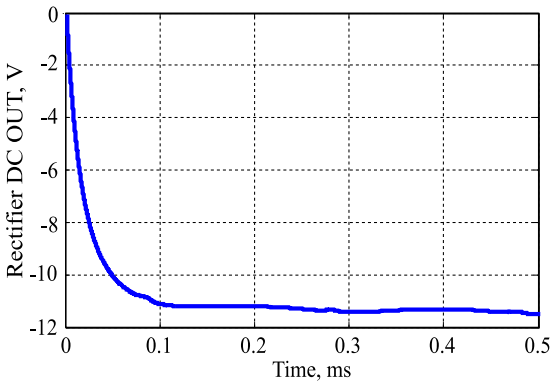

Fig. 8. Rectifier output voltage vs. time, with RF input frequency of 13.56 MHz.

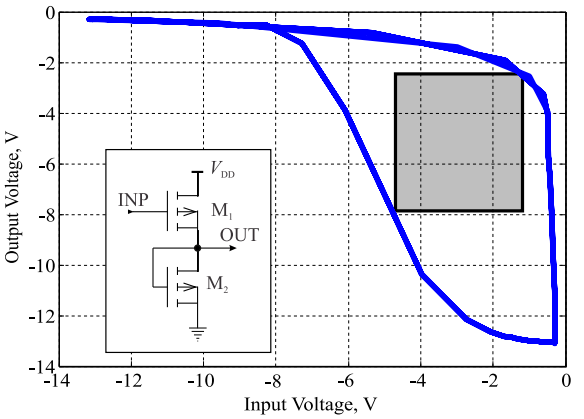

Fig. 9. Inverter (NOT) direct and inverse transfer curve. The inset reports the NOT schematic implementation.

To complete the analysis of the logical building blocks, the sequential basic cell structure, i.e. the elementary 1-bit memory unit, was considered. Among the several flip-flop NAND based architectures, the Delay (D) memory cell with preset and clear hardwiring, reported in Fig. 10, was adopted. The asynchronous preset and clear inputs are used to independently load each D flip-flop, accordingly to the preassigned values, when the POR (power on reset) block (see Section 4.4) generates the enable control signal. In Fig. 11 the correct master–slave D flip-flop simulated response in presence of a clock falling edge is shown; consistent with a master–slave behavior, the flip-flop inputs are sampled during the rising clock edges, then transferred at the outputs at the falling edges (Fig. 11).

4.3. Clock generator

The clock generator provides the timing and synchronization of all functional blocks. Oscillators realized on organic materials running up to 220 kHz have already been demonstrated, see [18]. However, increasing the operating frequency is not an issue, since, to be compatible with the logical gate time constraints in terms of setup and holding time, this has to be limited to a few kHz. The most stringent limitation is related instead to the small current driving capabilities of OFETs. To overcome this drawback, an output driver, made of a multistage (four stages in our case) progressive, exponential, buffer taper has been implemented and optimized. Agilent ADS has been exploited to find the best trade-off among output current level, time delay, power consumption [19], and reduce the oscillation

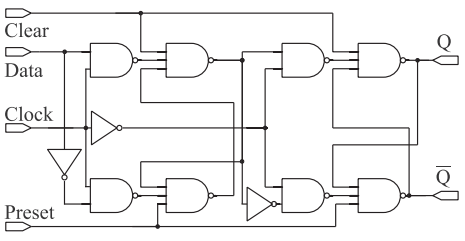

Fig. 10. D-flip flop NAND and NOT based implementation (from [3]).

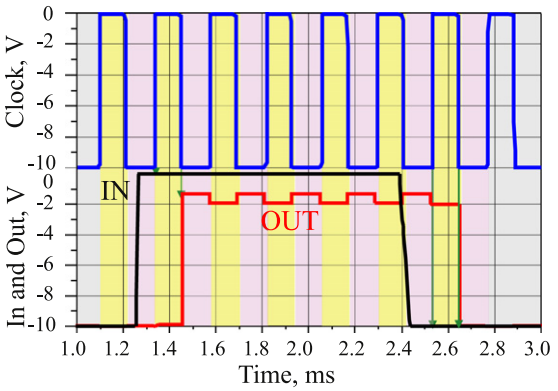

Fig. 11. Master–slave D flip-flop response. Clock at 4.2 kHz (blue curve, top plot), D input (black, bottom plot), output (red curve, bottom plot). (For interpretation of the references to color in this figure legend, the reader is referred to the web version of this article.)

frequency dependence on the load termination. The implemented topology relies on the classical *ring oscillator* odd stage cascade architecture, with enhanced oscillation frequency stability through interstage *RC* filter cells (see Fig. 12). The obtained results are summarized in Fig. 14, showing the simulation of the overall circuit: an oscillation frequency of 4.2 kHz, well compatible with the flip-flop timing requirements, has been obtained adjusting the capacitance *C* value. Further details can be found in [3].

4.4. Power-on-reset unit

The last block considered is the power-on-reset (POR). At the onset of the incoming RF signal, the system must be activated with proper timing, thus preventing flip-flop metastable behavior, and other spurious effects, such as shift register incorrect reading/loading due to preset activation while flip-flops are in non stable supply condition. The POR signal, generated when the voltage on a capacitor reaches a proper threshold (see Fig. 13), is initially used to drive the hardwired flip-flop preset and clear, and then, to initialize the system clock.

4.5. Complete system simulation

A complete system simulation of the 8-bit demonstrator of Fig. 4 is shown in Fig. 14. In the first ms in Fig. 14 the TAG identification data are loaded into the shift register then, when the POR signal (green curve, center plot of Fig. 14) becomes high, the serial transmission starts. The timing of the system (blue curve, top plot of Fig. 14) shows that the rising and falling edges of the signal were fast enough to avoid unwanted transitions and flip-flop metastates. The ripple exhibited by the serialized output data (red curve, bottom plot of Fig. 14) depends mainly on the voltage drop on the contact resistance R_T (not considered in [3]), that reduces the swing of the output voltage. It is worth noticing that, to test the system behavior in "low voltage" conditions, operation of all RFID components have been demonstrated with a supply voltage of 10 V, that is reduced with respect to the value used in [3]. This allows to significantly decrease the number of cascade stages needed to boost the RF signal in the energy harvesting block, thus reducing the circuit area.

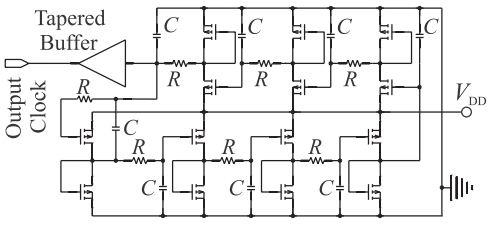

Fig. 12. Ring oscillator (from [3]).

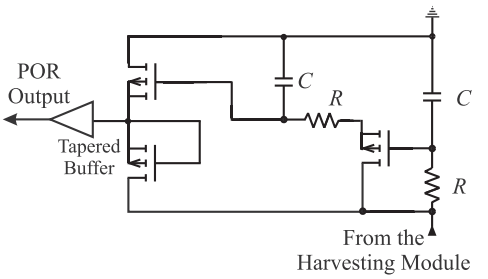

Fig. 13. Power-on-reset (POR) electrical scheme implementation.

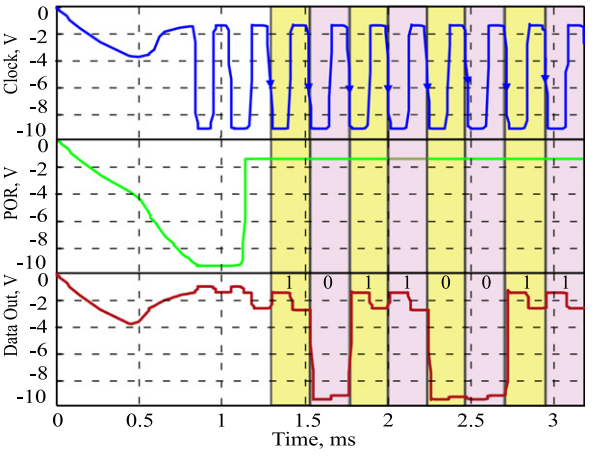

Fig. 14. Simulation result of the complete system. The stored bit code "10110011" is correctly serialized as the red trace shown by the red trace corresponding to the TAG data. The blue curve is the clock, at 4.2 kHz (valid falling edge are with arrows). The green trace is the POR enable signal. Sampling starts at the first clock falling edge after POR signal becomes high. (For interpretation of the references to color in this figure legend, the reader is referred to the web version of this article.)

5. Standard architecture (full RFID) analysis and simulation

To demonstrate the validity of the library in the design of high-capacity, full RFIDs (Fig. 5) including a memory block, we consider here additional building blocks; in particular, an asynchronous 4-bit counter has been also designed and tested. Larger counters can be derived from the 4-bit architecture by cascading more cells, thanks to the modular structure of asynchronous dividers [20].

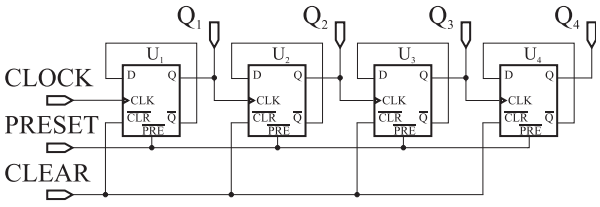

Fig. 15. Asynchronous counter implementation (from [17]).

Concerning the memory, this can be implemented through OFETs via a mask-programmed ROM approach [21], i.e. inserting transistors in a grid of row/column array of metallizations; despite the simplicity of the architecture, even a small-size memory requires a very large number of active devices, leading to computationally intensive circuit-level simulations. For this reason, the memory blocks, that can be more effectively handled through a system level approach, are not explicitly addressed here.

5.1. Asynchronous counter

An asynchronous 4-bit counter, able to completely scan a memory with 16-cells, was designed and simulated. To minimize the OFET number we exploited an asynchronous approach based on toggle T flip-flops. The basic cell of such "ripple counter" architecture (the T flip-flop) is obtained by connecting the input and negated output of a D flip-flop. The single-input, single-output T flip-flop divides by two the input signal and can be used to implement a n-bit counter, i.e. a 2^n binary divider, by simply chaining n T cells. The architecture is intrinsically modular, i.e. it can be tailored to scan memories of arbitrary size, even if there are limitations related to the propagation time along the chain. The implemented 4-bit asynchronous counter scheme is shown in Fig. 15, while simulation results, demonstrating the correct behavior of the block, are reported in Fig. 16.

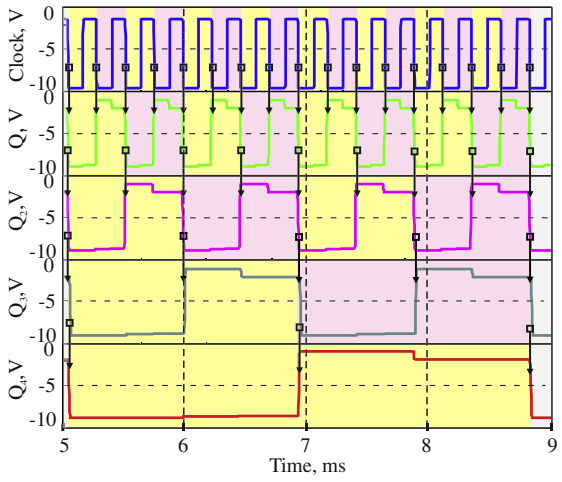

Fig. 16. Simulated behavior of the asynchronous counter. From top to bottom plot: clock at 4.2 kHz, Q_1 = clock/2, Q_2 = clock/4, Q_3 = clock/8, Q_4 = clock/16.

6. Conclusions

A SPICE and ADS analog/digital pentacene OFET library for the simulation and design of organic RFIDs has been presented. Starting from a nonlinear dynamic OFET model, the analog and digital functional blocks of a complete memoriless RFID demonstrator, including a rectifier, a 8-bit shift-register with preset/reset, a ring oscillator, a power on reset block have been discussed and tested. The simulation of the complete system has been shown, demonstrating the suitability of the developed CAD library for the design and optimization of a passive 8-bit RFID TAG operating at 10 V bias voltage. Further results concerning the asynchronous counter block of a full RFID were also presented.

Acknowledgment

The research was supported by the NAMATECH project of Regione Piemonte, Italy.

References

[1] V. Subramanian, J.M.J. Frechet, P.C. Chang, D.C. Huang, J.B. Lee, S.E. Molesa, A.R. Murphy, D.R. Redinger, S.K. Volkman, Progress toward development of all-printed RFID tags: materials, processes, and devices, Proc. IEEE 93 (7) (2005) 1330–1338.
[2] V. Vaidya, J. Kim, J.N. Haddock, B. Kippelen, D. Wilson, SPICE optimization of organic FET models using charge transport elements, IEEE Trans. Electron Devices 56 (1) (2009) 38–42.
[3] R. Tinivella, Shu Shen, M. Pirola, G. Ghione, V. Camarchia, A device-level analog and digital subsystem SPICE library for the design of low-cost pentacene OFET RFIDs, in: IMS Conference Proceedings, 2010, pp. 848–851.
[4] Agilent ADS, Version 2009, Agilent Technol., Palo Alto, CA, 2009.
[5] Spice Freeware. Available from: <http://www.spiceopus.si/>.
[6] E. Cantatore, T.C.T. Geuns, G.H. Gelinck, E. van Veenendaal, A.F.A. Gruijthuijsen, L. Schrijnemakers, S. Drews, D.M. de Leeuw, A 13.56-MHz RFID system based on organic transponders, IEEE J. Solid-State Circuits 42 (1) (2007) 84–92.
[7] V. Subramanian, F. Liao, H.-Y. Tseng, Printed RF tags and sensors: the confluence of printing and semiconductors, in: Proceedings of the European Microwave Integrated Circuits Conference 2010, Paris, France, 2010, pp. 258–261.
[8] H. Meng, F. Sun, M.B. Goldfinger, G.D. Jaycox, Z. Li, W.J. Marshall, High-performance, stable organic thin-film field-effect transistors based on bis-5′-alkylthiophen-2′-yl-2,6-anthracene semiconductors, J. Am. Chem. Soc. 127 (2005) 2406–2407.
[9] O. Marinov, M.J. Deen, U. Zschieschang, H. Klauk, Organic thin-film transistors: part I—compact DC modeling, IEEE Trans. Electron Devices 56 (12) (2009) 2952–2961.
[10] M.J. Deen, O. Marinov, U. Zschieschang, H. Klauk, Organic thin-film transistors: part II—parameter extraction, IEEE Trans. Electron Devices 56 (12) (2009) 2962–2968.
[11] Kangmin Kim, Youngmin Kim, Intrinsic capacitance characteristics of top-contact organic thin-film transistors, IEEE Trans. Electron Devices 57 (9) (2010) 2344–2347.
[12] P. Antognetti, G. Massobrio, Semiconductor device modeling with spice, second ed., McGraw-Hill Inc., 1993.
[13] D.V. Lang, X. Chi, T. Siegrist, A.M. Sergent, A.P. Ramirez, Amorphous like density of gap states in single-crystal pentacene, Phys. Rev. Lett. 93 (8) (2004) 086802.
[14] S. Steudel, K. Myny, V. Arkhipov, C. Deibel, S. De Vusser, J. Genoe, P. Heremans, 50 MHz rectifier based on an organic diode, Nat. Mater. 4 (2005) 597–600.
[15] F. Pang, T. Samaddar, Charge Pump Circuit Design, McGraw-Hill Inc., 2006.
[16] K. Finkenzeller, RFID Handbook, second ed., Wiley, Chichester, 2003.
[17] Shu Shen, R. Tinivella, M. Pirola, G. Ghione, V. Camarchia, SPICE library for low-cost RFID applications based on pentacene Organic FET, in: Proceedings of the 6th International Conference on Wireless Communications, Networking and Mobile Computing, 2010, pp. 1–4.

[18] W. Clemens, W. Fix, J. Ficker, A. Knobloch, A. Ullmann, From polymer transistors toward printed electronics, J. Mater. Res. 19 (7) (2004) 1963.
[19] N.C. Li, G.L. Haviland, A.A. Tuszynski, CMOS tapered buffer, IEEE J. Solid-State Circuits 25 (4) (1990) 1005–1008.
[20] B. Holdsworth, Digital Logic Design, fourth ed., Newnes, 2002.
[21] K. Myny, M.J. Beenhakkers, N.A.J.M. van Aerle, G.H. Gelinck, J. Genoe, W. Dehaene, P. Heremans, A 128b organic RFID transponder chip, including manchester encoding and ALOHA anti-collision protocol, operating with a data rate of 1529b/s, in: ISSCC Dig. Tech., 2009, pp. 206–207.

For this purpose, Capelli et al. have proposed adapting multilayered structures (MLS) as the channel layers of ambipolar FETs. A major advantage of multilayered structures is that various materials can be selected and combined as required to improve device performance, such as carrier injection, transport, and luminescent efficiency. For example, trilayer FETs, in which each layer acts independently for hole transport, light emission and electron transport, have been investigated as LE-FETs with the aim of enhancing luminous efficiency [2]. Even though their report demonstrates that multilayered structures are capable of high luminous efficiency, there is still room for progress in the interfacial morphology, molecular packing and orientation of the layer structures. A rough interface and random molecular packing cause a loss of carrier mobility. The field effect mobility observed in the multilayered FETs is, in fact, somewhat lower than that in single-component FETs. Well-defined film structures are therefore crucial for improving the device properties of multilayered FETs.

To overcome these problems, we have proposed a heteromolecular FET with well-ordered interfacial morphology and molecular orientation. A fine growth method based on an ultra-slow deposition technique has already been established that forms highly ordered molecular layers [6–9]. This method allows layer-by-layer growth and the precise preparation of a molecular superlattice combined with a very high degree of controllability of the monolayer (ML) level [10,11]. In this paper, we discuss a mechanism for ambipolar carrier transport in the thus prepared heteromolecular FET.

2. Experimental

PTCDI-C_8 and QT thin films were employed as channel layers of a heteromolecular FET. These molecules are expected to work as n-type and p-type semiconductors, respectively. Their chemical structures are shown in Fig. 1a and b. PTCDI-C_8/QT layers were formed on SiO_2 (200 nm)/Si substrates under a high vacuum of 10^{-8} Torr. The thicknesses of both the PTCDI-C_8 and QT layers were fixed at 2 MLs. Details of the growth conditions are reported in our previous studies [10,11]. The Al electrodes are deposited on the top of the PTCDI-C_8/QT heterolayers by electron beam deposition to form top-contact heteromolecular FETs. Channel length and width are 50 μm and 400 μm, respectively. The molecular orientation, roughness and density of the heteromolecular layers were confirmed by the X-ray reflection method (not described here) as illustrated in Fig. 2. Surface morphologies were examined by atomic force microscopy (AFM; Seiko Instruments Inc., SPI-4000 E-sweep) in dynamic force mode. FET characteristics were measured in a vacuum chamber ($\sim 10^{-4}$ Torr) using a semiconductor device analyzer (Agilent, B1500A). All experimental processes were carried out under vacuum, without exposure to air.

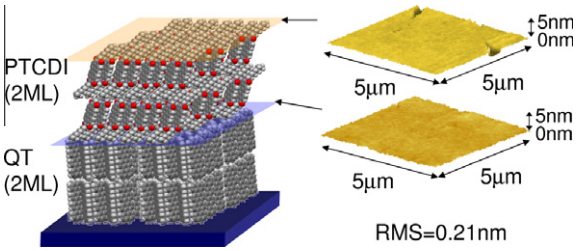

Fig. 2. Schematic illustration of PTCDI-C_8/QT heteromolecular layers and AFM images of surface morphologies of each layer.

3. Results and discussion

The AFM images in Fig. 2 show the surface morphologies of the first QT layer and overlying upper PTCDI-C_8 layer. The root mean square (RMS) roughness values of each layer were estimated to be 0.29 and 0.21 nm in 5×5 μm areas, almost identical to that of the SiO_2 surface (RMS = 0.19 nm): evidence of the perfect surface flatness of the PTCDI-C_8 and QT layers.

The transistor characteristics of the PTCDI-C_8/QT heteromolecular layer were examined under vacuum without exposure to air, since air exposure is known to cause deactivation of the n-type characteristics and debasement of field effect mobility [12]. Fig. 3a and b show the source-drain voltage (V_{DS})–source-drain current (I_{DS}) characteristics of PTCDI-C_8 (2 ML)/QT (2 ML) heteromolecular FETs. A typical p-channel operation was confirmed in the range of negative gate voltage as shown in Fig. 3a. In contrast, Fig. 3b exhibited a monotonic increase of I_{DS} with V_{SD}, even without gate bias voltage (V_G = 0 V), which decreased with increasing V_G up to 40 V. To switch the polarity of the FET operation from the p- to the n-channel, a V_G above 40 V was required, as can be seen in Fig. 3b. Ambipolar operation [13] was thus clearly demonstrated, in which the QT

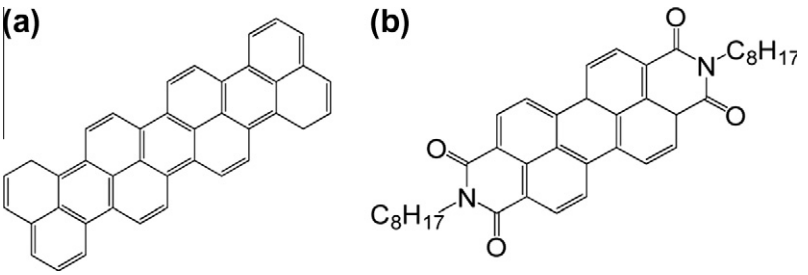

Fig. 1. Chemical structures of (a) QT and (b) PTCDI-C_8 molecules.

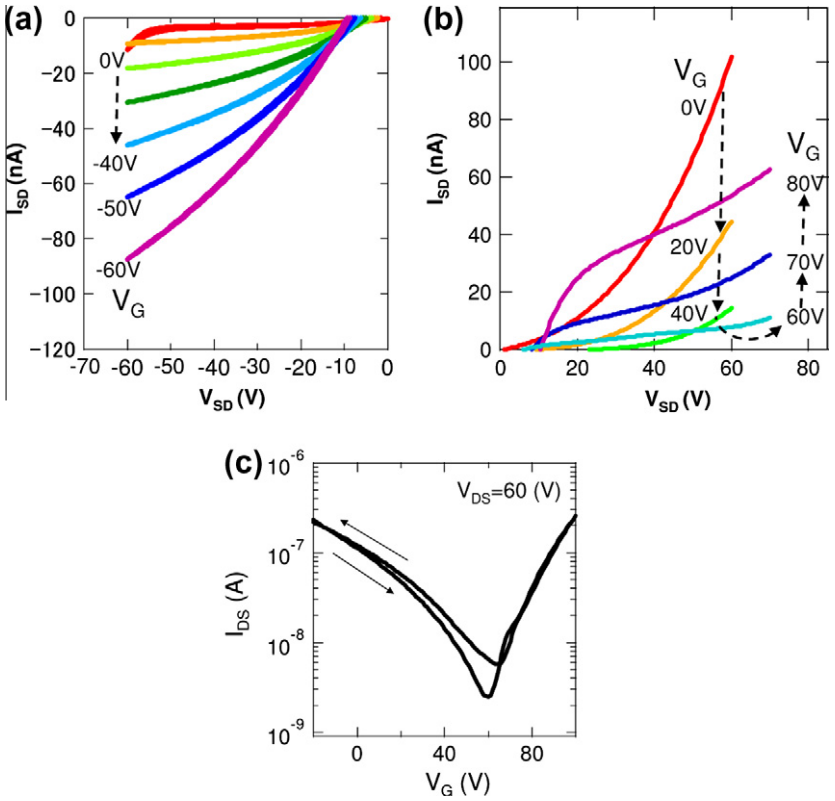

Fig. 3. I_{DS}–V_{DS} characteristics of (a) p- and (b) n-type operations in the PTCDI-C_8/QT heteromolecular FET. (c) Transfer characteristic of PTCDI-C_8/QT heteromolecular FET at source-drain voltage of 60 V.

and the PTCDI-C_8 layer worked as a p-channel and n-channel. Here, holes (electrons) were accumulated in the QT (PTCDI-C_8) layers, according to the polarity and magnitude of the applied V_G as shown in Fig. 3c.

The threshold voltage (Vth) was estimated using liner region data ($V_{SD} \sim 0$ V) by the following equation;

$$dI_{SD} = \mu \frac{CW}{L}(V_G - V\text{th})dV_{SD}$$

where L and W represent the channel length and width, C is the capacitance of the insulator per unit area, and I_{SD}, V_G are the drain current in the saturation region, gate voltage, and threshold voltage, respectively. The Vth values for holes and electrons were estimated to be 6.6 and 61.6 V, respectively. These values are reasonable for the ambipolar transport characteristics as mentioned above.

The carrier mobilities (μ) were calculated using the Eq. (1) to investigate the carrier transport in the FETs. The μ for holes and electrons was estimated to be 3.6×10^{-3} and 2.7×10^{-2} cm^2 V^{-1} s^{-1}, respectively. For comparison, the transistor characteristics of the respective neat layers of PTCDI (2 ML) and QT (2 ML) FETs are summarized in Table 1 [9,14]. It is noteworthy that the μ values for both carriers in the PTCDI-C_8/QT heterolayer FET were comparable to those of the individual FETs of PTCDI (2 ML) and QT (2 ML) neat layers. This fact indicates that the injected holes and electrons were transported independently through the QT and PTCDI-C_8 layers, and were not disturbed, even in the multilayered structure. We thus conclude that the formation of a perfect heteromolecular interface improves carrier transport. In the following section, our discussion is focused only on the electron transport in the PTCDI-C_8 layer. This is because the Vth values for the hole transport in the single-component and the heteromolecular QT FET cannot be compared due to the difference in the metal contacts (Au for QT single-component FET in Ref. [3] and Al for heteromolecular FET in this manuscript).

Another crucial finding is that the Vth for electron transport in PTCDI-C_8/QT heteromolecular FET shifted markedly compared with that of the PTCDI-C_8 single-component FET. The Vth for electron transport was estimated to be 61.6 V, whereas the value was calculated to be 5.0 V in the PTCDI (2 ML) FET [9]. Chemical treatments using self-assembling monolayers on the gate insulator surface have proved to be effective for fine control of Vth [15]. However, the drastic shifts in Vth observed in our study have not been reported elsewhere. Thus, elucidation of this mechanism should lead to control of the operation voltages in ambipolar FETs.

In many situations, this mechanism has been explained in terms of the interfacial dipole and/or charge transfer at the heteromolecular interface. Hence, the shift in the Vth needs to be considered in the context of energy-level alignment. We previously evaluated the energy levels of the PTCDI-C_8/QT heteromolecular layers by photoemission

Table 1
Transistor properties: field effect nobilities (μ) and threshold voltage (Vth) in single-component QT, PTCDI-C_8 and PTCDI-C_8/QT heteromolecular FETs. The mobility of QT 2 ML was estimated from the relation between thickness and mobility as described in Ref. [3], which were estimated from following equation;

$$\mu = \mu_{sat}\left[1 - \exp\left\{-\left(\frac{\theta}{\theta_c}\right)^{\alpha}\right\}\right]$$

where μ_{sat}, θc, and α are the saturated carrier mobility, crossover thickness, and exponent, respectively. The μ_{sat} = 0.015 cm ^{2}/V s, θc = 2.5 ML, and α = 5.0 were used for the mobility estimation of QT 2 ML. (*)Vth of QT FET with Au electrode.

	QT [3]	PTCDI [9]	(p) QT/PTCDI	(n) QT/PTCDI
μ (cm^2/V s)	4.3×10^{-3}	4.8×10^{-2}	3.6×10^{3}	2.7×10^{-2}
V_{th} (V)	58.5*	5.0	6.6	61.6

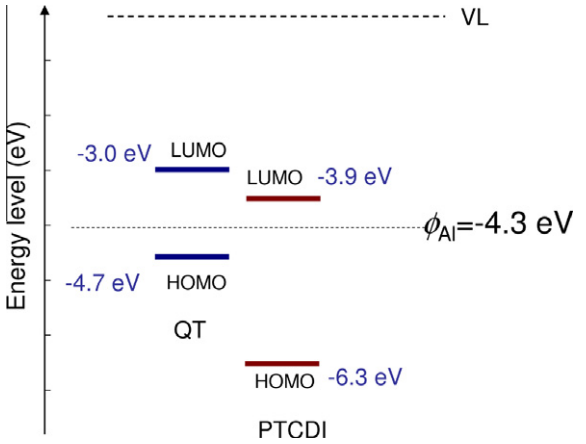

Fig. 4. The energy-level diagram of the PTCDI-C_8/QT heteromolecular layers.

spectroscopy and optical absorption measurements [11]. The energy-level diagram at the heterointerface, together with the work function of the Al electrode (Φ = –4.3 eV) is illustrated in Fig. 4. Here, the HOMO–LUMO levels were modified from those in our previous report by taking into account the effect of exciton binding energy [16–18]. The energy levels at the heteromolecular interface are known to be rearranged by certain effects: for instance, interfacial dipole and charge transfer between interlayers. These phenomena can be explained in terms of charge neutrality level [19,20]. However, no rearrangement of the energy levels was observed in our experiments, as can be seen in Fig. 4. We assume that rearrangement of the energy levels is not induced at well-established heteromolecular interfaces: this is consistent with recent observations by another group [21]. This is because the direct intermolecular interaction of π-electrons is restricted due to the upright orientations of the molecules at the heteromolecular interface, as illustrated in Fig. 2. We can thus rule out any causal link between the interfacial dipole and charge transfer at the heteromolecular interface and the observed shift in Vth.

Another possible reason is that charged carriers are intrinsically present in the films. Similar shifts in Vth have often been reported in other ambipolar FETs [22]. In fact, the heteromolecular FET exhibited a hole transport in

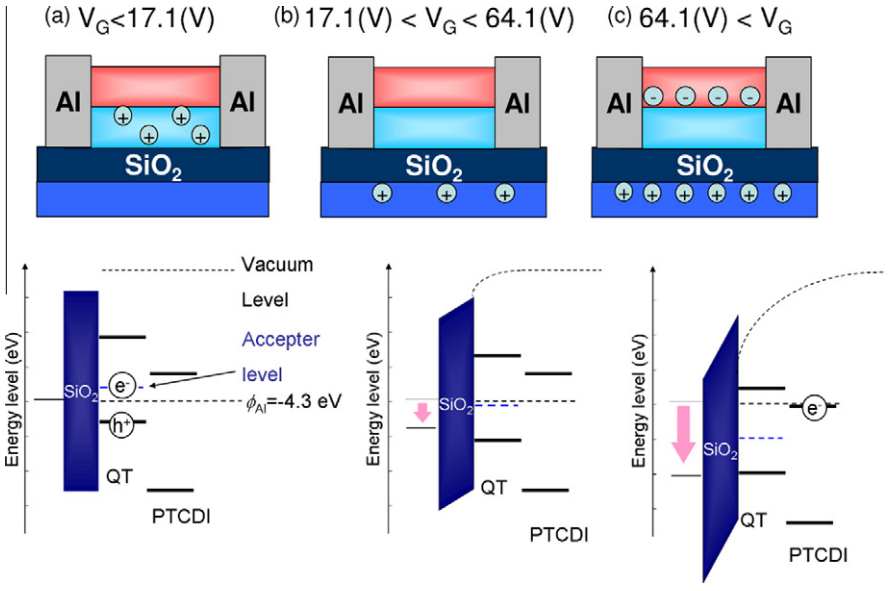

Fig. 5. Schematic illustration of hole and electron accumulation in the PTCDI-C_8/QT heteromolecular FET and respective energy-level diagrams in the range of (a) V_G < 6.6 V, (b) 6.6 V < V_G < 61.6 V, and (c) V_G > 61.6 V.

V_G = 0 V, as shown in Fig. 3, proving that hole carriers were intrinsically doped into the QT layer. Based on these results, we conclude that the observed shift in *V*th for n-channel operation was caused by the presence of hole carriers in the QT layer. The mechanism of this shift in *V*th is illustrated in Fig. 5. In the V_G range below 6.6 V, hole carriers remain in the QT layer (Fig. 5a, V_G < 6.6 V) that hinder the downward shift of the energy level of the PTCDI-C_8 layer. A gate voltage of more than 6.6 V is necessary to deplete the holes from the QT layer (Fig. 5b, 6.6 V < V_G < 61.6 V). A further increase in V_G above 64.1 V is needed to accumulate electrons in the PTCDI-C_8 layer (Fig. 5c, V_G > 61.6 V).

There are several possible reasons for the origin of the hole carriers being in the QT layers. One possibility is structural defects in the films, as proposed by Hayakawa et al. [14], which agree with the transport characteristics of QT FETs formed on SiO_2 substrate. Another is that the carriers are involuntarily doped into the QT layer. Maruyama et al. report that oxygen doping of the organic layer occurs even under high vacuum of below 10^{-4} Pa [23]. In this case, the doping level of oxygen is located at 4.1 eV to form acceptor levels (see the energy-level diagram in Fig. 5a), a picture which closely coincides with our model. By this mechanism, a certain amount of oxygen could be doped into the QT layer, although all experimental processes were carried out under vacuum to avoid air exposure. In either case, the electronic states of the QT layer contribute to the considerable shift of *V*th in PTCDI-C_8/QT heteromolecular FETs. This finding suggests there is potential to control *V*th by carrier doping into molecular layers in ambipolar transistors, without any loss of carrier transport.

In conclusion, this is the first report on the device performance of an ultra-thin heteromolecular FET consisting of well-defined PTCDI-C_8 and QT layers. Ambipolar behavior was clearly demonstrated in the PTCDI-C_8 (2 ML)/QT (2 ML) heterolayer FET. The carrier mobilities were comparable to those of the respective single-component FETs. We conclude that a well-defined multilayered structure is essential to exclude the influence of the hetero-layer interface and to sustain the device performance of the individual FETs. On the other hand, the heterolayer was observed to accumulate carriers in the PTCDI-C_8 layer with a considerable shift in *V*th. We attribute this phenomenon to the presence of hole carriers in the QT layer. Our findings suggest a potential method for radical control of *V*th according to the electronic state of the underlying layer in ambipolar transistors, without disturbing carrier transport.

References

[1] E. Kuwahara, Y. Kubozono, T. Hosokawa, T. Nagano, K. Masunari, A. Fujiwara, Appl. Phys. Lett. 85 (2004) 4765–4767.
[2] R. Capelli, S. Toffanin, G. Generali, H. Usta, A. Facchetti, M. Muccini, Nature Mater. 9 (2010) 496–503.
[3] T. Takenobu, S.Z. Bisri, T. Takahashi, M. Yahiro, C. Adachi, Y. Iwasa, Phys. Rev. Lett. 100 (2008) 066601.
[4] Y. Wang, R. Kumashiro, Z. Li, R. Nouchi, K. Tanigaki, Appl. Phys. Lett. 95 (2009) 103306.
[5] S.Z. Bisri, T. Takenobu, Y. Yomogida, H. Shimotani, T. Yamao, S. Hotta, Y. Iwasa, Adv. Funct. Mater. 19 (2009) 1728–1735.
[6] H. Sasaki, Y. Wakayama, T. Chikyow, E. Barrena, H. Dosch, K. Kobayashi, Appl. Phys. Lett. 88 (2006) 081907.
[7] R. Hayakawa, M. Petit, Y. Wakayama, T. Chikyow, Org. Electron. 8 (2007) 631–634.
[8] M. Petit, R. Hayakawa, Y. Wakayama, T. Chikyow, J. Phys. Chem. C. 111 (2007) 12747–12751.
[9] N. Hiroshiba, R. Hayakawa, M. Petit, T. Chikyow, K. Matsuishi, Y. Wakayama, Thin Solid Films 518 (2009) 441–443.
[10] N. Hiroshiba, R. Hayakawa, M. Petit, T. Chikyow, K. Matsuishi, Y. Wakayama, Org. Electron. 10 (2009) 1032–1036.
[11] N. Hiroshiba, R. Hayakawa, T. Chikyow, Y. Yamashita, H. Yoshikawa, K. Kobayashi, K. Morimoto, K. Matsuishi, Y. Wakayama, Phys. Chem. Chem. Phys. 13 (2011) 6280.
[12] Z. Bao, Adv. Mater. 12 (2000) 227.
[13] E.C.P. Smits, T.D. Anthopoulos, S. Setayesh, E. Veenendaal, R. Coehoorn, P.W.M. Blom, B. Boer, D.M. Leeuw, Phys. Rev. B 73 (2006) 205316.
[14] R. Hayakawa, M. Petit, T. Chikyow, Y. Wakayama, J. Appl. Phys. 104 (2008) 024506.
[15] S. Kobayashi, T. Nishikawa, T. Takenobu, S. Mori, T. Shimoda, T. Mitani, H. Shimotani, N. Yoshimoto, S. Ogawa, Y. Iwasa, Nature Mater. 3 (2004) 317–322.
[16] M. Knupfer, Appl. Phys. A. 77 (2003) 623–626.
[17] D.R.T. Zahn, T.U. Kampen, H. Méndez, Appl. Surf. Sci. 212–213 (2003) 423–427.
[18] Y. Harada, H. Inokuchi, Bull. Chem. Soc. Jpn. 39 (1966) 1443–1448.
[19] S. Braun, W.R. Salaneck, M. Fahlman, Adv. Mater. 21 (2009) 1450–1472.
[20] H. Vazquez, W. Gao, F. Flores, A. Kahn, Phys. Rev. B 71 (2005) 041306.
[21] S. Duhm, I. Salzmann, G. Heimel, M. Oehzelt, A. Haase, R.L. Johnson, J.P. Rabe1, N. Koch1, Appl. Phys. Lett. 94 (2009) 033304.
[22] F. Würthner, Chem. Commun. 12 (2004) 1564–1579.
[23] Y. Maruyama, H. Inokuchi, Bull. Chem. Soc. Jpn. 39 (1966) 1418–1422.

roughness of the [84]PCBM:PMMA composite layer. Current–voltage (*I–V*) and switching measurements were performed to investigate the memory performance of the fabricated devices. Retention measurements and current analyses of randomly selected cells were carried out to investigate the stability and the reproducibility of the devices. The memory mechanisms for the fabricated devices are described on the basis of the current density–voltage (*J–V*) results.

2. Experimental

The memory devices were fabricated on indium–tin-oxide (ITO)-coated glass substrates. The ITO-coated glass substrates were alternately cleaned ultrasonically in acetone and methanol at 27 °C for 10 min each and rinsed in de-ionized water thoroughly. The chemically-cleaned ITO-coated glass substrates were then dried by using N_2 gas with a purity of 99.99%. Then, 100 mg of PMMA (ALDRICH, M_W = 15000) was dissolved in 10 ml of chlorobenzene solvent, and 2 mg of [84]PCBM (ALDRICH, a mixture of isomers) was mixed with a PMMA/chlorobenzene solution. The chlorobenzene solution dissolved with the [84]PCBM and PMMA polymer was treated by using ultrasonics. The [84]PCBM:PMMA layer with a thickness of 50 nm was coated on the ITO-coated glass substrate at 300 rpm for 5 s, 3000 rpm for 25 s, and 300 rpm for 3 s at room temperature by using spin-coating method. The [84]PCBM:PMMA layers with thickness of 31 and 63 nm were also formed on the ITO-coated glass substrates. After the spin-coating of the mixed solution, the solvents existing on the samples were removed by putting the samples on a hot-plate at 135 °C for 30 min; then, the samples were cooled at room temperature for 1 h. Finally, the top Al electrodes with a thickness of 200 nm and a diameter of 500 μm were thermally deposited through a metal mask at a system pressure of 1×10^{-6} Torr. A schematic diagram of the OBDs fabricated with a [84]PCBM:PMMA composite is shown in Fig. 1. The *I–V*, retention, and reproducibility measurements were performed by using a HP 4140B pA meter and DC voltage source at 300 K.

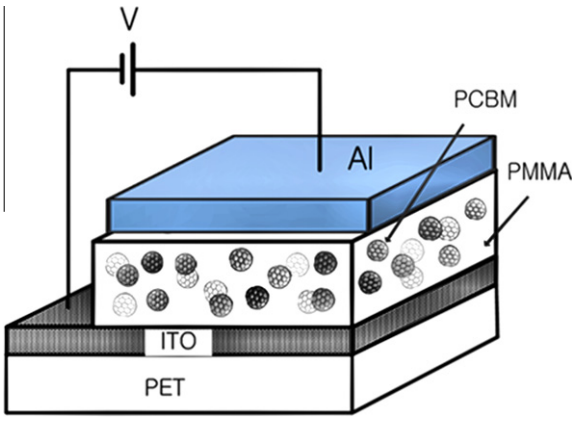

Fig. 1. Schematic diagram of the fabricated OBDs containing [84]PCBM:PMMA.

3. Results and discussion

Figure 2 shows an AFM image of the PMMA polymer layer containing [84]PCBM with a PCBM:PMMA layer thickness of 50 nm on an ITO-coated glass substrate. The AFM image shows that the surface of the PMMA layer containing the [84]PCBM is very uniform. The root-mean-square value of the surface roughness, approximately 0.5 nm, indicates a very good surface roughness, resulting in the fabrication of reliable and reproducible devices.

Figure 3(a) shows the *J–V* curves for the Al/[84]PCBM:PMMA/ITO/glass devices with a PCBM:PMMA layer thickness of 50 nm for voltage from −7 to 0, 0 to 7, 7 to 0, and 0 to −7 V. The *J–V* curves for the memory devices clearly show current hystereses, indicative of a memory effect in the nonvolatile memory device. The device currents abruptly increase at approximately −3.5 V, resulting in a conductivity transition from low to high values. The high conductivity state and the low conductivity state are defined as the ON state and the OFF state, respectively. The state variations from the OFF state to the ON state and from the ON state to the OFF state are equivalent to the writing and the erasing processes of a digital memory cell, respectively. The ON state of the device is achieved by applying a voltage above −3.5 V to the device. The ON state current at −7 V has a maximum value, and the ON state is maintained as the voltage is swept from −7 to 7 V. The state transition into the OFF state is achieved by applying an erase voltage of about 7 V. The *J–V* characteristics of the device did not change significantly, regardless of the number of voltage sweeps, as shown in Fig. 3(a), indicating good stability of the device fabricated with [84]PCBM. The maximum ON/OFF current ratio of the OBDs at 2 V was approximately 1×10^3.

Figure 3(b) shows the *J–V* curves for the OBDs with different PCBM:PMMA thicknesses of 31, 50, and 63 nm. The *J–V* curves for the OBDs are affected by the thickness of the PCBM:PMMA layer. While the *J–V* curves for the device with a thickness of 31 nm shows the largest ON and OFF current densities, the ON/OFF ratio of the device is smaller than that of the device with a thickness of 50 nm. The *J–V* curves for the device with a thickness of 63 nm exhibits the smallest ON/OFF ratio. The *J–V* curves for the device with a thickness of 50 nm shows the highest ON/OFF ratio among three devices. Because the electron injection probability at the electrodes decreases with increasing PCBM:PMMA layer thickness due to a lower interface electric field [20], the

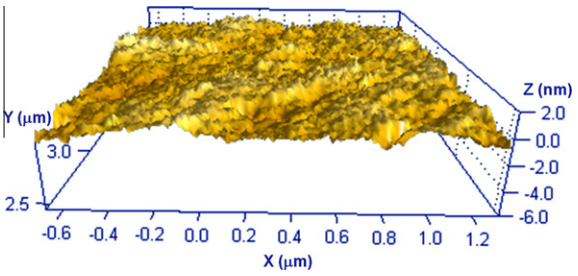

Fig. 2. AFM image of the PMMA polymer layer containing [84]PCBM with a PCBM:PMMA layer thickness of 50 nm on an ITO-coated glass substrate.

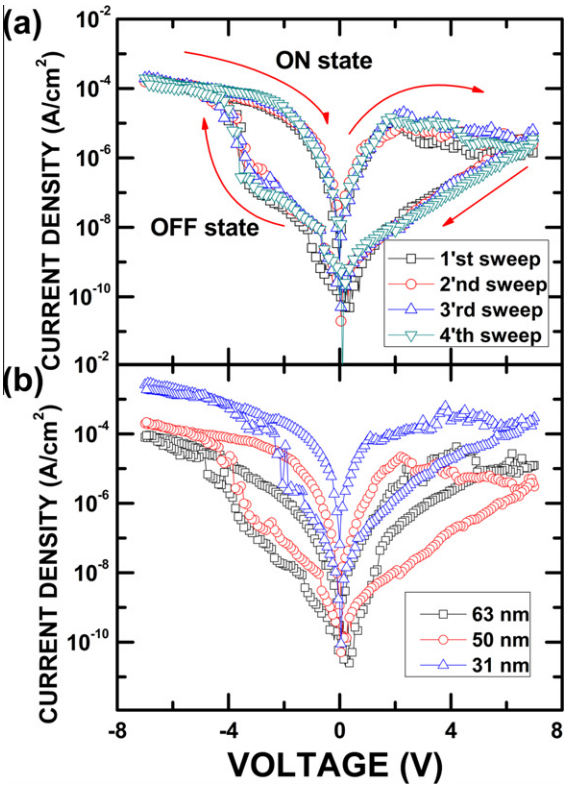

Fig. 3. (a) Current density–voltage (J–V) curves for the Al/[84]PCBM:PMMA/ITO/glass devices with a PCBM:PMMA layer thickness of 50 nm at different voltage sweeps, and (b) J–V curves for the devices with PCBM:PMMA layer thicknesses of 31, 50, and 63 nm.

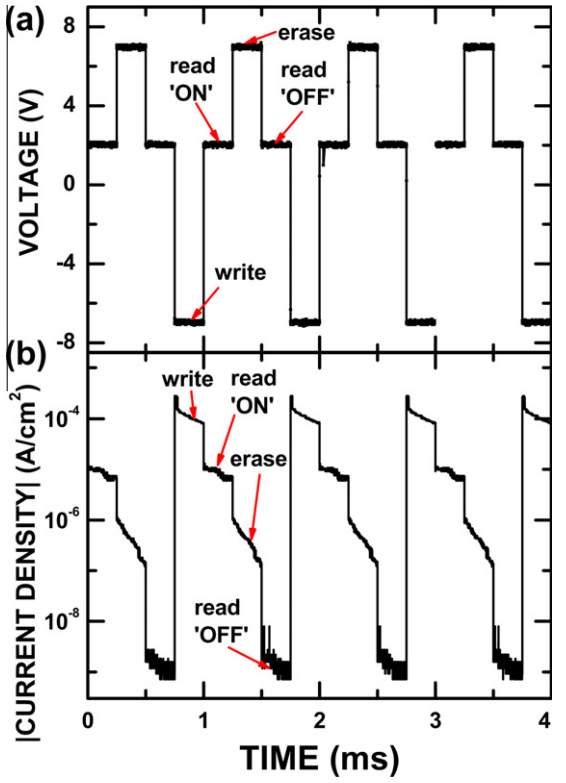

Fig. 4. Switching results for the (a) input voltage pulse and the (b) output current density for the OBDs with a PCBM:PMMA layer thickness of 50 nm in the atmosphere.

current density decreases with increasing layer thickness, as shown in Fig. 3(b). Because carrier trap sites increase with increasing layer thickness, the conductivity transition from the OFF to the ON states for the device with a thickness of 63 nm is not easily occurred due to a large number of trap sites. However, the traps of the PCBM:PMMA layer in the device with a layer thickness of 31 nm are not enough to occupy carriers for achieving the large ON/OFF ratio. Therefore, the OBDs with a thickness of 50 nm show the best electrical performance with the largest ON/OFF ratio.

Figure 4 shows the switching characteristics of the memory devices with a PCBM:PMMA layer thickness of 50 nm. The input voltage pulses of the write, read, and erase voltages for measuring the switching characteristics shown in Fig. 4(a) were set as −7, 2, and 7 V, respectively. A voltage pulse with a cycle of 0.001 s is applied to the memory device. The erase voltage pulse is applied to change the current state of the device to the OFF state. Then, the current densities at a read voltage pulse are approximately 8×10^{-9} A/cm^2, as shown in Fig. 4(b). Sequentially, the writing voltage pulse is applied to turn the device to the ON state. Then, the current densities at a read voltage pulse are approximately 1×10^{-5} A/cm^2, as shown in Fig. 4(b). The switching characteristics of the devices are sensitive to the electrodes due to the different work functions of the electrodes [21]. The J–V results of Fig. 3 and the switching results of Fig. 4(b) show excellent memory performance. These results offer opportunities for promising applications in next-generation nonvolatile memory devices.

Figure 5 shows the retention performances of the ON state and the OFF state current densities for the OBDs with a PCBM:PMMA layer thickness of 50 nm in the atmosphere. The ON state and the OFF state currents are monitored by applying the read voltage after applying the write

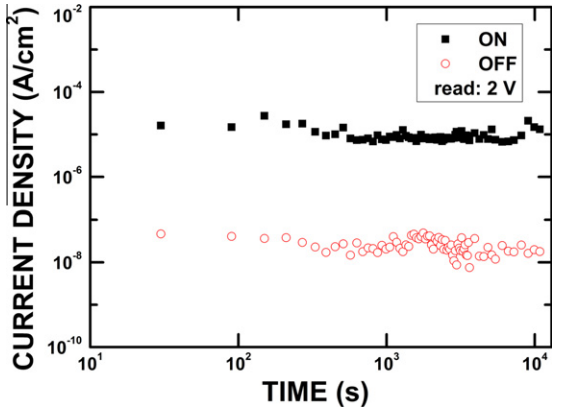

Fig. 5. Retention characteristics of the current densities of the ON state and the OFF state for the OBDs with a PCBM:PMMA layer thickness of 50 nm in the atmosphere.

voltage and the after applying the erase voltage, respectively. A read voltage of 2 V is applied to the ON state and the OFF state of the devices. A slight degradation of the ON state and the OFF state currents occurred, as shown in Fig. 5. No significant degradations of the devices were observed in the ON state and the OFF state until 10^4 s, indicative of the excellent memory retention performance of the memory devices.

Figure 6 shows the reproducibility results for the fabricated devices with a PCBM:PMMA layer thickness of 50 nm. The ON state and the OFF state currents are measured in 20 randomly selected cells. The ON/OFF ratios of the 20 cells for the memory devices are approximately 1×10^3, as shown in Fig. 6. The currents density of the ON state and the OFF state for the 20 cells were in the range of about 10^{-5} and 10^{-8} A/cm^2, respectively, indicative of the high reproducibility of the fabricated devices. The difference between the minimum current density of the ON state for the 17th cell and the maximum current density of the OFF state for the 2nd cell is above 10^2, indicative of a high memory margin. The high reproducibility of the OBDs originates from the stable material characteristics of [84]PCBM and from the uniform surface roughness of the [84]PCBM:PMMA composite. When the surface roughness of the [84]PCBM:PMMA composite layer is rough, the interface characteristics corresponding to carrier injection at the two electrodes are different from each other. The surface uniformity of the [84]PCBM:PMMA composite layer enhances the reproducibility of the memory devices.

The memory mechanism in the Al/[84]PCBM:PMMA/ITO/glass devices can be explained in terms of trapping and detrapping of electrons in defect sites in the organic layer [22]. *J–V* fittings were performed to investigate the carrier transport characteristics. The thermionic emission (TE) current of the OFF state at low voltages is dominant from 0 to −1 V. In the voltage range from −1 to −3.5 V, the TE current and the space-charge-limited current (SCLC) with a slope of 2 appear together, indicative of the existence of charge trapping sites. The current of the device abruptly increases at a threshold voltage of −3.5 V. When the traps in the organic materials are fully occupied by carriers, an abrupt increase in the current typically appears at a specific voltage [23]. After the abrupt increase in the current, the ON current of the device follows the trap-filled SCLC with a slope of 2. Because the device without [84]PCBM does not show any current hysteresis, the memory effect of the device with [84]PCBM originates from the [84]PCBM in the PMMA layer. The [84]PCBM in the device provides charge trapping sites; thus, the trap-filled SCLC in the ON state is attributed to the electrons trapped in the [84]PCBM, which is in reasonable agreement with another reported result [22]. A negative differential resistance (NDR) behavior of the ON current at positive voltages appears in the voltage range between 2 and 7 V. The electron tunneling between nearby [84]PCBM molecules can occur in a high electric field with the opposite polarity, resulting in a appearance of the NDR behavior [24]. When the [84]PCBM molecules are emptied by the electron tunneling, the device returns to the OFF state.

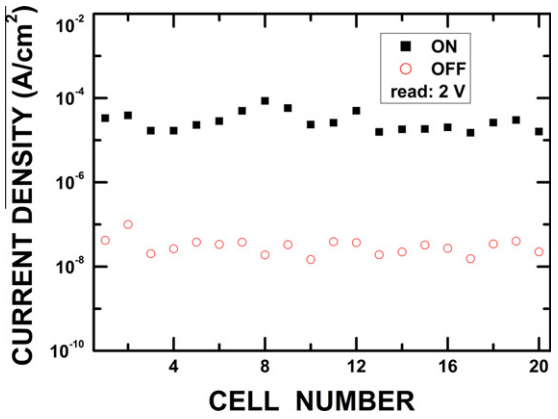

Fig. 6. Reproducibility results of 20 randomly selected cells for the OBDs with a PCBM:PMMA layer thickness of 50 nm.

4. Conclusions

AFM images of nonvolatile memory devices based on [84]PCBM embedded in a PMMA layer showed that the surface of the [84]PCBM:PMMA composite layer was uniform. The *J–V* curves for the OBDs clearly showed current hystereses, indicative of a memory effect in the nonvolatile memory device. The maximum ON/OFF ratio at 2 V for OBDs with a PCBM:PMMA layer thickness of 50 nm was approximately 1×10^3. The switching characteristics showed that the OBDs with a PCBM:PMMA layer thickness of 50 nm had a rewriteable characteristic and a retention time of about 10^4 s. The current densities of the ON state and the OFF state for 20 randomly-chosen cells with a PCBM:PMMA layer thickness of 50 nm were in the range of about 10^{-5} and 10^{-8} A/cm^2, respectively, indicative of the high reproducibility of the fabricated OBDs. The memory mechanisms for the fabricated device were described on the basis of the *J–V* results. The present results indicate that [84]PCBM:PMMA composites hold promise for potential applications in next-generation nonvolatile memory devices.

Acknowledgment

This work was supported by the National Research Foundation of Korea (NRF) grant funded by the Korea government (MEST) (No. 2010-0018877).

References

[1] W.L. Leong, P.S. Lee, S.G. Mhaisalkar, T.P. Chen, A. Dodabalapur, Charging phenomena in pentacene-gold nanoparticle memory device, Appl. Phys. Lett. 90 (2007) 0429061–0429063.
[2] T. Kimura, M. Hara, Nonvolatile multiple-valued memory device using lateral spin valve, Appl. Phys. Lett. 97 (2010) 1825011–1825013.
[3] C. Chen, Y.C. Yang, F. Zeng, F. Pana, Bipolar resistive switching in Cu/AlN/Pt nonvolatile memory device, Appl. Phys. Lett. 16 (2010) 0835021–0835023.
[4] A. Kanwal, M. Chhowalla, Stable, three layered organic memory devices from C_{60} molecules and insulating polymers, Appl. Phys. Lett. 89 (2006) 2031031–2031033.

[5] H.P. Wang, S. Pigeon, R. Lzquierdo, R. Martel, Electrical bistability by self-assembled gold nanoparticles in organic diodes, Appl. Phys. Lett. 89 (2006) 1835021–1835023.
[6] S.H. Kim, K.S. Yook, J.Y. Lee, J. Jang, Organic light emitting bistable memory device with high on/off ratio and low driving voltage, Appl. Phys. Lett. 93 (2008) 0533061–0533063.
[7] J. Ouyang, C-W. Chu, C.R. Szmanda, L. Ma, Y. Yang, Programmable polymer thin film and non-volatile memory device, Nat. Mater. 3 (2004) 918–922.
[8] J.C. Scott, L.D. Bozano, Nonvolatile memory elements based on organic materials, Adv. Mater. 19 (2007) 1452–1463.
[9] W.L. Leong, P.S. Lee, A. Lohani, Y.M. Lam, T. Chen, S. Zhang, A. Dodabalapur, S.G. Mhaisalkar, Non-volatile organic memory applications enabled by in situ synthesis of gold nanoparticles in a self-assembled block copolymer, Adv. Mater. 20 (2008) 2325–2331.
[10] S. Sahu, A.J. Pal, Non-interacting write and read processes in organic memory devices, Org. Electron. 9 (2008) 873–877.
[11] F. Lindner, K. Walzer, K. Leo, Organic heterostructure device with nonvolatile memory behavior using electrically doped layers, Appl. Phys. Lett. 93 (2008) 2333051–2333053.
[12] S. Song, B. Cho, T.W. Kim, Y. Ji, M. Jo, G. Wang, M. Choe, Y.H. Kahng, H. Hwang, T. Lee, Three-dimensional integration of organic resistive memory devices, Adv. Mater. 22 (2010) 5048–5052.
[13] J.N. Handdock, X. Zhang, B. Domercq, B. Kippelen, Fullerene based n-type organic thin-film transistors, Org. Electron. 6 (2005) 182–187.
[14] T.D. Anthopoulos, D.M. Leeuw, E. Cantatore, P.V. Hof, J. Alma, J.C. Hummelen, Solution processible organic transistors and circuits based on a C_{70} Methanofullerene, J. Appl. Phys. 98 (2005) 0545031–0545036.
[15] P.H. Wöbkenberg, D.D.C. Bradleya, D. Kronholmb, J.C. Hummelenc, D.M. de Leeuwd, M. Cölle, T.D. Anthopoulos, High mobility n-channel organic field-effect transistors based on soluble C_{60} and C_{70} fullerene derivatives, Synth. Met. 158 (2008) 468–472.
[16] L. Juha, B. Ehrenberg, S. Couris, E. Koudoumas, S. Leach, V. Hamplová, Z. Pokorná, A. Müllerová, P. Kubát, Single-photon photolysis of C_{60} C_{70} C_{76} and C_{84} in solutions Chem. Phys. Lett. 335 (2001) 539–544.
[17] T.D. Anthopoulous, F.B. Kooistra, H.J. Wondergem, D. Kronholm, J.C. Hummelen, D.M. de Leeuw, Air-stable n-channel organic transistors based on a soluble C_{84} fullerene derivative, Adv. Mater. 18 (2006) 1679–1684.
[18] M.A. Mamo, W.S. Machado, W.A.L. van Otterlo, N.J. Coville, I.A. Hümmelgen, Simple write-once-read-many-times memory device based on a carbon sphere-poly(vinylphenol) composite, Org. Electron. 11 (2010) 1858–1863.
[19] H. Hoppe, N.S. Sariciftci, Morphology of polymer/fullerene bulk heterojunction solar cells, J. Mater. Chem. 16 (2006) 45–61.
[20] J. K, Baral, H.S. Majumdar, A. Laiho, H. Jiang, E.I. Kauppinen, R.H.A. Ras, J. Ruokolainen, O. Ikkala, R. Österbacka, Organic memory using [6,6]-phenyl-C61 butyric acid methyl ester: morphology, thickness and concentration dependence studies, Nanotechnology 19 (2008) 0352031–0352037.
[21] H. Ha, O. Kim, Electrode-material-dependent switching characteristics of organic nonvolatile memory devices based on Poly(3,4-ethlyenedioxythiophene):poly(styrenesulfonate) film, IEEE Electron Device Lett. 31 (2010) 368–370.
[22] Z.S. Su, M.K. Fung, C.S. Lee, W.L. Li, S.T. Lee, Memory effect and negative differential resistance in tris-(8-hydroxy quinoline) aluminum/bathocuproine bilayer devices, Appl. Phys. Lett. 93 (2008) 0833011–0833013.
[23] K.C Kao, W. Hwang, Electrical transport in solids, international series in the science of solid state Vol. 14, in: B.R. Pamplin (Ed.), Pergamon Press, New York, 1981, pp. 64–144.
[24] A. Laiho, H.S. Majumdar, J.K. Baral, F. Jansson, R. Österbacka, O. Ikkala, Tuning the electrical switching of polymer/fullerene nanocomposite thin film devices by control of morphology, Appl. Phys. Lett. 93 (2008) 2033091–2033093.

and OSL based on the high performance host/guest system BN-PFO doped with the stilbene dye 1,4-bis(2-(4-(*N*,*N*-di(*p*-tolyl)amino)phenyl)vinylbenzene (DPAVB) [4]. First we studied the laser emission of second order distributed feedback (DFB) lasers under excitation with repetition rates up to 5 MHz. In the second experiment we pumped an BN-PFO/DPAVB based laser with a laser diode and studied the spectro-temporal behavior of the organic laser emission. By measuring the material gain and the triplet absorption spectra we could explain the substantially different behavior, of a quasi cw emission found for BN-PFO on the one hand and a termination of the laser emission in the doped system on the other hand. We attribute the latter phenomenon to the spectral overlap of the triplet induced absorption and the optical gain, leading to an increase of the laser threshold due to piled-up triplet excitons. For the pure BN-PFO we evidence spectrally separated material gain and triplet absorption spectra, which excludes absorption and quenching of the laser emission and leads to a quasi-cw operation.

2. Experimental

All organic layers were spin-cast from toluene solution with a layer thickness of 180–190 nm on silicon dioxide substrates. The layer thickness was controlled by a Veeco Dektak 8 surface profiler. As substrates for our second order DFB lasers we used structured silicon dioxide with a grating period of 270 nm for BN-PFO and 300–310 nm for BN-PFO/DPAVB. The gratings had a modulation depth of 50 nm and a duty cycle of 80:20 (hill:valley). The gain and triplet absorption measurements were carried out on silicon substrates covered with 2 μm silicon dioxide.

During all optical measurements the samples were mounted in a nitrogen purged sample chamber. The laser- and photoluminescence emission of the organic layers are detected with spectral and temporal resolution using a streak camera (Hamamatsu C4334).

The experiments with variable repetition rate (shown in Figs. 1 and 2) were carried out using a mode-locked, frequency-tripled, diode pumped solid state (DPSS) laser emitting at $\lambda = 355$ nm (Spectra-Physics, Vanguard) as a pumping source. The pulse width and repetition rate were 12 ps and 80 MHz, respectively. For the variation of repetition rate between 1 kHz and 5 MHz, an acousto–optical modulator was employed as pulse picker. Speed limitations of the modulator allowed only to pick a packet of approximately 8–10 of the mode-locked pulses at one time rather than individual pulses. The pump laser has additionally been chopped to deliver pulse trains of 400 μs duration which fits into the temporal window of the streak camera. The pump light was focused to a spot of $250 \times 250\ \mu m^2$ on the sample. Further details concerning the measurement setup have been published before [16].

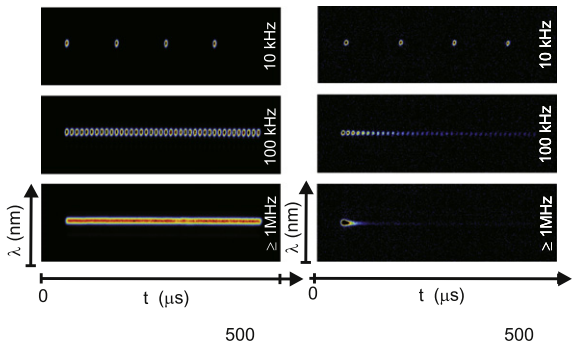

Fig. 1. Spectro-temporal images of the laser emission of pure BN-PFO excited at $1.4 \times E_{th}$ (left) and BN-PFO doped with 5 wt.% DPAVB excited at $1.9 \times E_{th}$ (right) for varied repetition rates. The displayed spectral windows are 440–451 nm for BN-PFO and 480–491 nm for BN-PFO/DPAVB, respectively.

To achieve diode pumped lasing in BN-PFO/DPAVB (Fig. 3) we used a GaN based laser diode emitting at $\lambda = 405$ nm, provided by Nichia Chemical (NDHV2200A-PAE1). The multimode output of the diode was focused to spot of approximately $200 \times 120\ \mu m^2$. By optimizing the grating period, the organic layer thickness and the doping concentration we were able to achieve a laser threshold of 0.75 $\mu J/cm^2$, which is sufficiently low to allow pumping with the limited output power of the inorganic laser diode. A grating period of 320 nm, a film thickness of 180 nm and a doping concentration of 4 wt.% was used. Further details can be found elsewhere [4].

As sources for optical pumping in the photo-induced absorption measurements (Figs. 5 and 7) the laser diode and a DPSS laser (AOT) emitting at $\lambda = 355$ nm were used as pump and probe excitation sources, respectively. The pulse width and the repetition rate of the DPSS laser were 700 ps and 2 kHz. The absorption was measured in a waveguide structure build up by the organic layer on top of the silicon dioxide substrate. A long laser diode pump pulse is used to generate triplet states via intersystem crossing in a defined area of the waveguide (pulse length 10 μs, spot size $0.77 \times 0.18\ mm^2$, pulse energy density 600 $\mu J/cm^2$). A probe pulse (DPSS) follows the pump pulse (laser diode) with a fixed time delay of 200 ns for the triplet absorption measurement and a variable time delay of 200 ns to 488 μs for triplet lifetime determination. The minimal delay of 200 ns between the pump and the probe pulse assures that all photoluminescence (PL) is decayed. The probe pulse is focused on a spatially separated area on the sample (spot size 27 μm × 0.5 mm). The waveguided emission generated by the probe pulse has to pass the region where the excitation by the pump pulse has led to the creation of triplet excitons. Therefore, the intensity of the edge emission, detected for different delay times between pump and probe pulse is directly related to the absorption due to triplet excitons in this region of the waveguide. Further details about the measurement technique have been reported previously [14,18].

The material gain was measured using the variable stripe length method (VSL) [19]. Here a Triax 320 monochromator (grating 300 lines/mm, Jobin Yvon) combined with an liquid nitrogen cooled charge couple device camera was used for signal detection. The DPSS laser (AOT) was used as optical pumping source. For further details see [20].

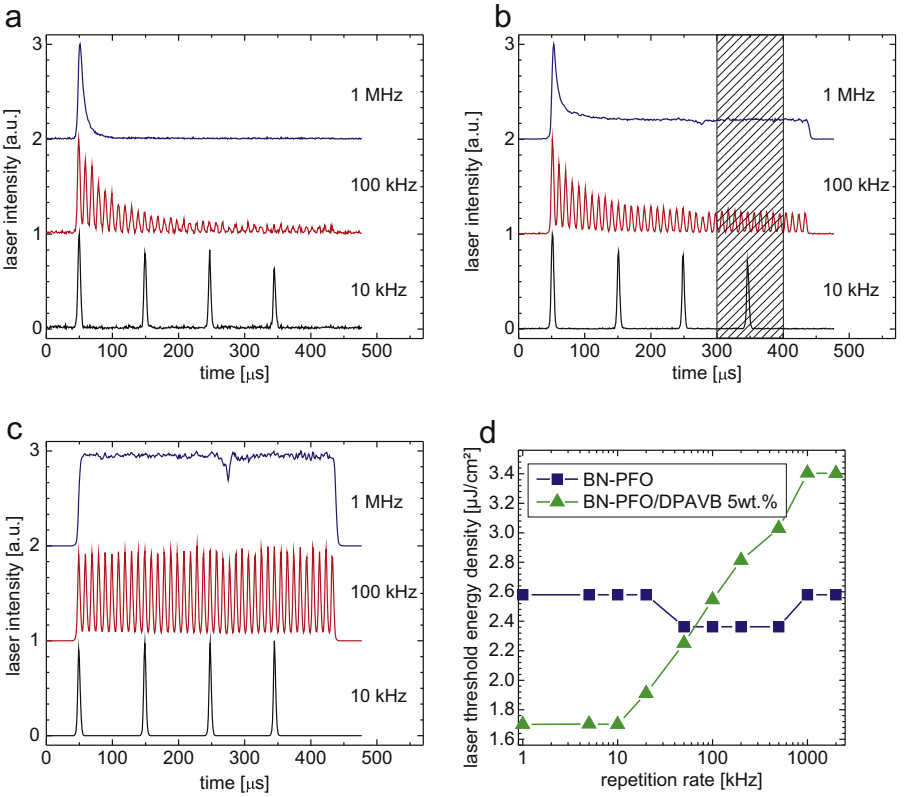

Fig. 2. Organic laser emission intensity of BN-PFO doped with 5 wt.% DPAVB, excited at $1.9 \times E_{th}$ (a) and $3.1 \times E_{th}$ (b). (c) Organic laser emission intensity of undoped BN-PFO, excited at $1.4 \times E_{th}$. (d) Evolution of E_{th} for doped and undoped BN-PFO for varied pump pulse repetition rates. E_{th} is measured in the shaded region shown in Fig. 2(b).

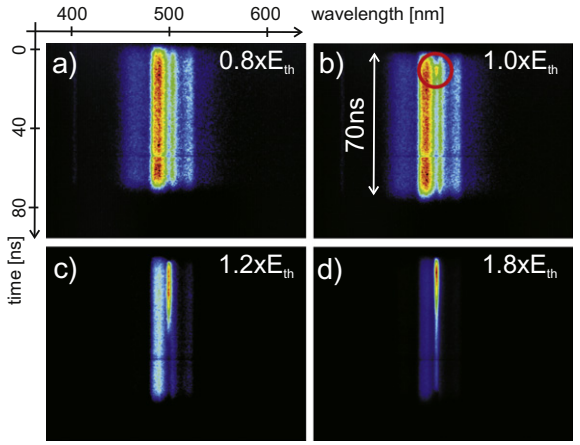

Fig. 3. Streak camera images of the emission of a laser diode pumped BN-PFO/DPAVB laser device excited with different excitation energies.

3. Results

3.1. High repetition rate excitation of BN-PFO and BN-PFO/DPAVB OSLs

Initially, we studied the output power of the OSL depending on the repetition rate of the pulsed optical excitation. We compared the laser emission of BN-PFO and BN-PFO/DPAVB based lasers at varied repetition rates between 1 kHz and 5 MHz. Fig. 1 shows streak camera images of the laser output for both laser devices at an excitation slightly above the laser threshold energy density (E_{th}). Here, the BN-PFO device is excited at $1.4 \times E_{th}$ which corresponds to 3.5 μJ/cm^2 and the doped device is excited with 3.2 μJ/cm^2 which equals to $1.9 \times E_{th}$. As reported before [16], the undoped device shows no influence of the repetition rate on the laser output. On contrary, in the doped system the laser emission terminates within the first μs from the beginning of the excitation at a repetition rate of 1 MHz. For lower repetition rates, the decrease of the laser emission becomes less severe. It is important to note, that the temporal decrease of the emission is not due to degradation of the organic material. For each individual pulse-train we repeatedly measured the same behavior on the same spot of the sample.

The OSL intensity, corresponding to the streak camera images shown in Fig. 1, is displayed in Fig. 2(a) and (c). At a high excitation energy density of $3.1 \times E_{th}$ the laser emission of the doped device persists during the excitation pulse even at 1 MHz (Fig. 2b). Nevertheless, also in this case a significant decrease of 80% of the emission (at 1 MHz) from the beginning of the excitation is observed. Subsequently, the OSL emission remains constant at a substantially lower level. Additionally, we determined the la-

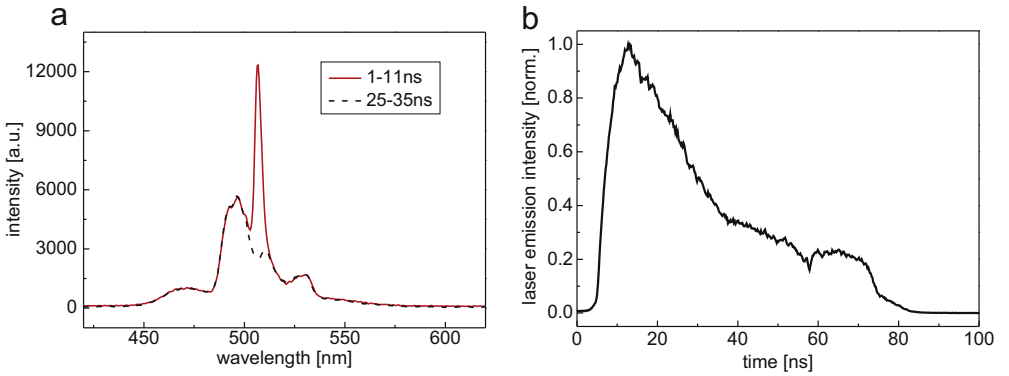

Fig. 4. (a) Emission spectra of a laser diode pumped BN-PFO/DPAVB laser excited at 1.2 × E_{th} (Fig. 3(c)). The average emission is displayed in a time region from 1 ns to 11 ns and 25 ns to 35 ns after the beginning of the excitation pulse. (b) Transient of the organic laser emission intensity shown in Fig. 3(d).

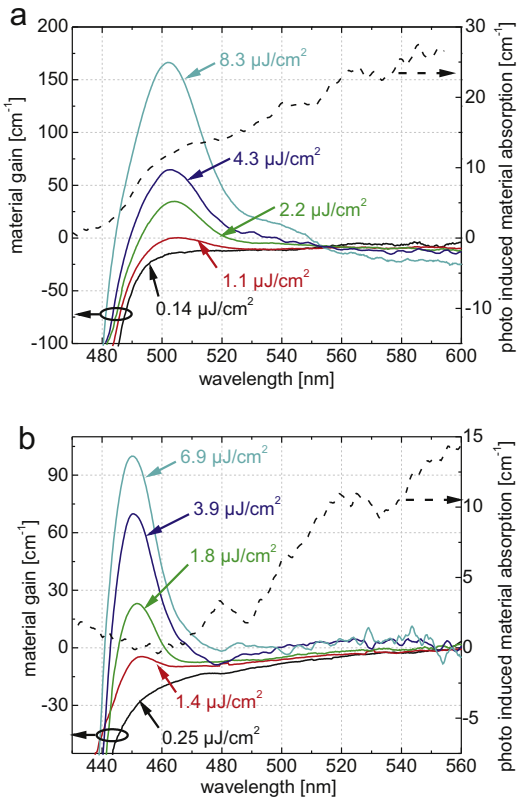

Fig. 5. Material gain and photo-induced absorption spectra of BN-PFO/DPABV 5 wt.% (a) and BN-PFO (b).

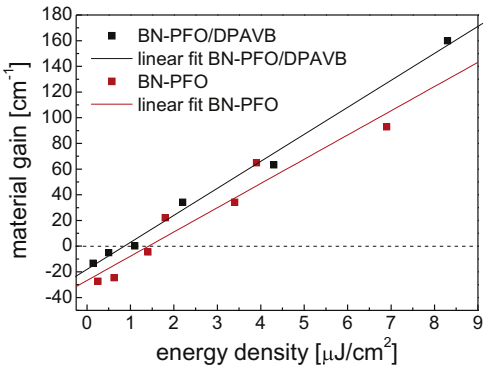

Fig. 6. Material gain slope at low excitation energy densities for BN-PFO and BN-PFO/DPAVB. The material gain is displayed at a wavelength of 453 nm for BN-PFO and 505 nm for BN-PFO/DPAVB, respectively.

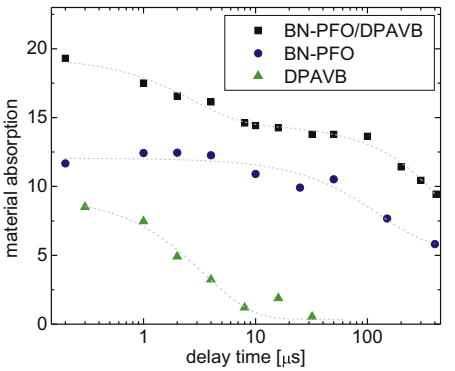

Fig. 7. Decay of photo-induced absorption in pristine BN-PFO, BN-PFO/DPAVB 5 wt.% and pristine DPAVB. The absorption is displayed for an average spectral range of 500–550 nm.

ser threshold E'_{th} in a steady region, 250 μs after the beginning of the excitation pulse (shaded region in Fig. 2(b)). The results are shown in Fig. 2(d). In case of pure BN-PFO we determined a constant laser threshold for all repetition rates. In the doped system E'_{th} is increasing with repetition rate by a factor of 2 at 1 MHz.

3.2. Laser diode pumping of BN-PFO/DPAVB

In the second experiment we studied the spectro-temporal behavior of an OSL based on BN-PFO/DPAVB pumped with an inorganic laser diode. Aside from the relevance of diode pumping for many applications, this allows to adjust the pump pulse length as desired. Specifically, a longer pump pulse duration as opposed to the DPSS laser is possible. Here, the inorganic laser diode was driven with a rectangular pulse of 70 ns length. As it can be seen from the photoluminescence in Fig. 3(a), the optical output of the la-

ser diode reproduces the rectangular electrical excitation pulse. Furthermore, the time resolved evolution of the organic laser emission is shown for different pump energy densities. Below lasing threshold (Fig. 3(a)), only photoluminescence is observed. At the lasing threshold a short laser emission peak appears immediately after the beginning of the excitation pulse (see Fig. 3(b) in the red circle[1]). With increasing pump power density, the laser emission becomes stronger but terminates after 25 ns at $1.2 \times E_{th}$ (Fig. 3(c)). Only at $1.8 \times E_{th}$ the laser emission persists during the all the excitation pulse (Fig. 3(d)). Even though, the output power decreases to 20% in comparison to the maximum laser emission at the beginning of the excitation pulse (Fig. 4(b)). Fig. 4(a) shows the average emission spectra for an excitation energy density of $1.2 \times E_{th,}$ in a time window of 1–11 ns following the start of the excitation pulse and in a time region of 25–35 ns, respectively. Obviously, the clearly visible laser line disappears after 25 ns.

Due to the higher laser threshold of undoped lasers and the very limited output power of inorganic laser diodes, similar experiments for pure BN-PFO lasers were not successful in our case. Nevertheless, the experiments, where we pump our laser with a variable repetition rate, presented in Section 3.1, offer an excellent alternative.

3.3. Gain and triplet absorption in BN-PFO and BN-PFO/DPAVB

In order to explain the temporal behavior of the laser emission at quasi-cw excitation, we studied the spectra of the optical gain and the triplet induced absorption in pure and doped BN-PFO. The material gain spectra of BN-PFO/DPAVB and BN-PFO are shown in Fig. 5(a) and (b). Compared to the undoped BN-PFO, the maximum gain is shifted from 450 nm to 505 nm in BN-PFO/DPAVB. As expected from the lower lasing threshold, the doped material system reaches a positive gain at lower energy densities than the pure BN-PFO. Furthermore, the doped system offers a broader gain spectrum. The material gain vs. energy density is shown in Fig. 5 for low excitation energy densities. Using a linear fit we can derive a gain slope of 24 $(cm^{-1})/(\mu J/cm^2)$ for BN-PFO/DPAVB and 21 $(cm^{-1})/(\mu J/cm^2)$ for BN-PFO.

In addition to the gain spectra the photo-induced absorption spectra are displayed in Fig. 5. The photo-induced absorption spectra of the doped and the undoped BN-PFO show similar spectral characteristics. We observed an increasing absorption for wavelengths longer than 480 nm in both cases. For a wavelength shorter than 480 nm the photo-induced absorption is less than 1 cm^{-1}. In case of BN-PFO/DPAVB the gain spectrum strongly overlaps with the photo-induced absorption spectrum, whereas both spectra are well separated in the undoped BN-PFO film.

By increasing the time delay between the pump and the probe pulse from 200 ns up to 488 μs we determined the lifetime of the photo-induced absorption. Our results for BN-PFO, BN-PFO/DPAVB and pristine DPAVB are displayed in Fig. 7. For the pristine materials a monoexponential fit is used. The doped system shows a biexponential behavior, which could be fitted well using the time constants of the pristine materials. The photo-induced absorption in BN-PFO and BN-PFO/DPAVB persists for several 100 μs, whereas in pristine DPAVB the absorption disappears after 10 μs.

4. Discussion

Our experimental results have shown very different dynamics of the OSL based on the neat- and the doped organic gain media pumped at high repetition rates. The organic laser emission of pure BN-PFO based lasers was unaffected by an increase of the repetition rate, whereas the DPAVB doped gain medium led to a dramatic decrease of laser emission at quasi-cw excitation (high repetition rates or long excitation pulses). In the doped system, Förster energy transfer [21] from the host to the guest molecules leads to a shift of the maximum gain by 55 nm. Our photo-induced absorption measurements evidenced a persisting absorption (several 100 μs) in both systems, which had a similar spectral behavior. Only in case of the doped system the measured photo-induced absorption overlaps with the material gain spectrum.

Previous reports have investigated the photophysical properties of PFO derivates. Particularly, triplet excitons with corresponding lifetimes on the order of 100 μs to 1 ms [22,23] would be a candidate to explain the above findings. The photo-induced absorption due to triplet states has a spectral maximum at around 750 nm in solution with a short wavelength tail extending well into the spectral region of the stimulated emission in our BN-PFO/DPAVB system [22–24]. Similar T_1-T_n absorption spectra have been reported in spin-cast PFO thin films [24].

Triplet formation occurs either by intersystem crossing from singlet state or through the recombination of polarons. Cadby et al. have reported that in glassy phase PFO intersystem crossing is the dominant mechanism for triplet generation [22]. They estimated a triplet quantum yield of 5%. Additionally to triplets, absorption due to polarons has been observed in PFO after optical excitation [22,24]. β-phase PFO has been shown to facilitate the formation of polaron pairs [22,24]. It is worth to note that polaron absorption observed in β-phase PFO peaks around 1.9 eV and could also contribute to our measured photo-induced absorption [22,24].

Our modified BN-PFO has been shown to suppress the formation of β-phase in spin coated films [16], which reduces the formation of polaron pairs [22,24]. In pure glassy phase PFO Hayer et al. did not observe any polaron absorption feature [24]. Therefore, we assume that the majority of the detected photo-induced absorption is attributed to triplets.

In the host/guest system triplet states can occur either on the guest or on the host. Regarding the triplet decay dynamics shown in Fig. 7 a similar decay is observed in BN-PFO and BN-PFO/DPAVB for delay times longer than 10 μs. For shorter delays, the decay in the host/guest sys-

[1] For interpretation of reference to color in this figure, the reader is referred to the web version of this article.

tem is alike to the decay in pristine DPAVB. Previous reports have reported on a stabilization of triplet excitons in host/guest systems on guest molecules for different material systems [18]. This effect is not observed in the host/guest system studied here. Due to the decay dynamics, we assume that triplets are located on the guest and on the host. An allocation of the triplets via the spectral characteristics of the triplet induced absorption is not possible due to the relatively small spectral window of our experiments (Fig. 5). Here, the doped and the undoped laser material show similar absorption spectra.

Regarding the laser threshold of the BN-PFO/DPAVB devices and the material gain slope shown in Fig. 6 we can derive a resonator loss in the order of 10 cm^{-1}. Here, the intrinsic absorption of the gain material and the scattering losses of the waveguide (DFB grating) contribute to the resonator losses. At an excitation pulse repetition rate of 1 MHz we measured a doubled laser threshold, comparing to the excitation at 1 kHz (Fig. 2(d)), where piled-up photo-induced absorption is negligible. In comparison, the measured photo-induced absorption of 10 cm^{-1} at the lasing wavelength (Fig. 4) is in the same order of magnitude. Here, an additional waveguide absorption around 10 cm^{-1} could favorably explain the doubled laser threshold. Nevertheless, an exact analysis of the quantitative influence of the absorption on the laser threshold is difficult, due to the different excitation sources used in the experiments described above. In Fig. 2(a) the laser emission stops within 30 μs at 1 MHz, whereas in Fig. 2(b) a constant emission is achieved after 20 μs. Summing up the energy of the excitation pulses within these time periods an energy density of 970 $\mu J/cm^2$ and 1050 $\mu J/cm^2$ was supplied to the samples. This is comparable to the energy density used in the experiments to determine the triplet absorption. Therefore we assume that a similar triplet density is generated in both experiments, leading to a comparable absorption. The constant laser emission shown in Fig. 2(b) suggests a saturation of the triplet density, preventing any further triplet absorption. This is in good accordance with the triplet absorption experiments, where we observed a saturation of the triplet absorption for excitation pulses longer than 10 μs (not shown here).

Aside from the additional waveguide absorption, the triplet states can also affect the laser emission by quenching. Carrying out photoluminescence (PL) quenching measurement in PFO (not shown here, for measurement details see [14]) under similar conditions to the photo-induced absorption measurement and to the laser devices presented above, we observed a PL decrease of about 12% at a wavelength of 505 nm and around 1–3% at 450 nm. This indicates that quenching is also taking place in our laser devices. However, due to the relatively small quenching effect we conclude that triplet absorption is mainly responsible for the increase of the laser threshold in the BN-PFO/DPAVB laser device under our experimental conditions.

5. Conclusion

In summary we studied the laser dynamics of organic thin film lasers at quasi-cw excitation conditions. We observed a constant laser output power in BN-PFO laser, whereas in devices based on BN-PFO/DPAVB the laser emission decreases dramatically towards longer pump pulses. We attributed this phenomenon to an accumulation of triplet excitons during the excitation pulse. By measuring the gain and the persistant photo-induced absorption we evidenced that gain and photo-induced absorption spectra are spectrally separated in BN-PFO. On the contrary, the gain spectrum is red shifted and overlaps with the photo-induced absorption spectrum in BN-PFO/DPAVB, which enables quenching and absorption at the lasing wavelength. The separation of gain and triplet absorption in BN-PFO seeds the prospect of simple organic thin film lasers operating under cw conditions. Furthermore, the high conversion efficiency at long pumping pulses greatly extends the number of appropriate pumping sources (e.g. laser diodes with a cheap driving unit). Regarding organic laser diodes triplet accumulation is supposed to be a major obstacle to prevent electrical driven lasing, which would be substantially relaxed in case of BN-PFO, due to the separated spectra.

References

[1] F. Hide, M. Diaz-Garcia, B. Schwartz, A. Andersson, Q. Pei, A. Heeger, Science 273 (1996) 1833.
[2] N. Tessler, G.J. Denton, R.H. Friend, Nature (London) 382 (1996) 695.
[3] D. Schneider, T. Rabe, T. Riedl, T. Dobbertin, M. Kröger, E. Becker, H. Johannes, W. Kowalsky, T. Weimann, J. Wang, P. Hinze, Appl. Phys. Lett. 85 (2004) 1886.
[4] T. Riedl, T. Rabe, H.H. Johannes, W. Kowalsky, J. Wang, T. Weimann, P. Hinze, B. Nehls, T. Farnell, U. Scherf, Appl. Phys. Lett. 88 (2006) 241116.
[5] J.M. Lupton, Nature (London) 453 (2008) 459.
[6] N. Tessler, Adv. Mater. 11 (1999) 363.
[7] C. Gärtner, C. Karnutsch, U. Lemmer, C. Pflumm, J. Appl. Phys. 101 (2007) 023107.
[8] N.C. Giebink, S.R. Forrest, Phys. Rev. B 79 (2009) 073302.
[9] C. Vannahme, S. Klinkammer, A. Kolew, P. Jacob, M. Guttmann, S. Dehm, U. Lemmer, T. Mappes, Microelectron. Eng. 87 (2010) 693.
[10] T. Mappes, C. Vannahme, M. Schelb, U. Lemmer, J. Mohr, Microelectron. Eng. 86 (2009) 1499.
[11] P.P. Sorokin, J.R. Lankard, IBM J. Res. Develop. 11 (1967) 148.
[12] P.P. Sorokin, J.R. Lankard, V.L. Moruzzi, E.C. Hammond, J. Chem. Phys. 48 (1968) 4726.
[13] O.G. Peterson, S.A. Tuccio, B.B. Snavely, Appl. Phys. Lett. 89 (1970) 245.
[14] M. Lehnhardt, T. Riedl, T. Weimann, W. Kowalsky, Phys. Rev. B 81 (2010) 165206.
[15] R. Bornemann, U. Lemmer, E. Thiel, Opt. Lett. 31 (2006) 1669.
[16] T. Rabe, K. Gerlach, T. Riedl, H.H. Johannes, W. Kowalsky, J. Niederhofer, W. Gries, J. Wang, T. Weimann, P. Hinze, F. Galbrecht, U. Scherf, Appl. Phys. Lett. 89 (2006) 081115.
[17] T. Rabe, M. Hoping, D. Schneider, E. Becker, H.H. Johannes, W. Kowalsky, T. Weimann, J. Wang, P. Hinze, B.S. Nehls, U. Scherf, T. Farnell, T. Riedl, Adv. Func. Mater. 15 (2005) 1188.
[18] M. Lehnhardt, T. Riedl, T. Rabe, W. Kowalsky, Org. Electron. 12 (2011) 486.
[19] K.L. Shaklee, R.F. Leheny, Appl. Phys. Lett. 18 (1971) 475.
[20] T. Rabe, S. Hamwi, J. Meyer, P. Görrn, T. Riedl, H.H. Johannes, Appl. Phys. Lett. 90 (2007) 151103.
[21] R. Gupta, M. Stevenson, A.J. Heeger, J. Appl. Phys. 92 (2002) 4874.
[22] A.J. Cadby, P.A. Lane, H. Mellor, S.J. Martin, M. Grell, C. Giebeler, D.D.C. Bradley, M. Wohlgenannt, C. An, Z.V. Vardeny, Phys. Rev. B 62 (2000) 15604.
[23] A.P. Monkman, H.D. Burrows, L.J. Hartwell, L.E. Horsburgh, I. Hamblett, S. Navaratnam, Phy. Rev. Lett. 86 (2001) 1358.
[24] A. Hayer, A.L.T. Khan, R.H. Friend, A. Köhler, Phys. Rev. B 71 (2005) 241302.

reported by Sen and Chakrabarti [24] in a fused thiophene trimer. In their quantum chemical study, the NDR feature was ascribed to the shift of the transmission resonance peak across the bias window as the bias voltage varied. Through the analysis of MPSH (Molecular projected self-consistent Hamiltonian) states contributing to the bias window at different bias voltages, they provided an explanation of the origin of the NDR character in this system.

It should be mentioned that in the above *ab initio* calculations, the molecular structure was first exactly described, and then the charge transportation process in the device was simulated using the NEGF method. However, the combination of the NEGF and the *ab initio* theory does not work well when electron–lattice (*e–l*) interactions are considered. The reason stems from the fact that the molecule was assumed to be rigid and lattice vibrations were ignored. Structural changes which are believed to contribute to NDR during the charge transport process can therefore not be accurately described [25]. Organic molecules, however, are characterized by strong *e–l* interactions, and the lattice structure is easily affected by additional charges and/or applied electric fields. Consequently, it could be expected that the origin of the NDR phenomenon in polythiophene goes beyond the redistribution of the conducting states or the shift of the transmission resonance peak under gate bias. Organic NDR involves strong *e–l* coupling that induces a structural change in the OSE. As a result, to get a comprehensive understanding of the above issues, it is necessary to capture the strong *e–l* coupling effect explicitly.

Based on these considerations, we have adopted the Su–Schrieffer–Heeger (SSH) model which well describes the *e–l* interactions in organic/molecular systems, combined with the NEGF (SSH + NEGF) to investigate the transport process in a metal/thiophene/metal structure and elucidate a possible mechanism for NDR in thiophene oligomers. The paper is organized as follows: in the following section, the model is described and the nonequilibrium quantum transport method is presented. The results are discussed in Section 3 where we show how a change in the structural conformation can induce NDR. Finally, a summary is given in Section 4.

2. Model and method

The Su–Schrieffer–Heeger (SSH) model [26], which captures the essential characteristics of the *e–l* coupling of organic materials, has been remarkably successful in the study of electronic conductivity and optical phenomena in π-conjugated molecules. Here we have extended the SSH model to describe the thiophene oligomer. The thiophene oligomer can be regarded as a quasi-one-dimensional chain of sp^2 hybridized carbon atoms analogous to that of *cis*-polyacetylene but also including the influence of a sulfur heteroatom on the π electrons [27]. As a consequence, the extended SSH Hamiltonian proposed to describe a molecule containing several thiophene units such as shown in Fig. 1 can be explicitly written as

$$H_{PTh} = \sum_{n,\sigma}\left[\varepsilon_0 c^{\dagger}_{n,\sigma}c_{n,\sigma} - \left(t_0 - \alpha y_n - t_e\cos\frac{n\pi}{2}\right)\left(c^{\dagger}_{n+1,\sigma}c_{n,\sigma} + h.c.\right)\right] - \sum_{n,\sigma}\left[t^{s}_{\triangle}\left(c^{\dagger}_{4n-3,\sigma}c_{4n,\sigma} + h.c.\right) + \varepsilon^{s}_{\triangle}\left(c^{\dagger}_{4n,\sigma}c_{4n,\sigma} + c^{\dagger}_{4n-3,\sigma}c_{4n-3,\sigma}\right)\right] + \frac{1}{2}K\sum_{n} y_n^2. \quad (1)$$

Here, the first term describes the electrons along a carbon chain, with a nondegeneracy parameter t_e to preserve the four-period structure [26]. The operator $c^{\dagger}_{n,\sigma}(c_{n,\sigma})$ denotes the creation (annihilation) operator of an electron at nth thiophene unit with spin σ, while ε_0 and t_0 are the electronic on-site energy and zero-displacement hopping integral between the nth and $n+1$th atoms, respectively. The lattice distortion is treated classically in terms of the bond distance $\{y_n = u_{n+1} - u_n\}$, where u_n is the displacement of the nth atom from its energy-minimum values determined via the Hellmann–Feynman theorem with the spring constant K and the *e–l* coupling constant α. The second term in Eq. (1) denotes the effects of the heteroatom sulfur, including the electron hopping integral $t^{s}_{\triangle}$ between lattice sites $4n-3$ and $4n$ via the sulfur atom and the effective confinement $\varepsilon^{s}_{\triangle}$ energy of π electrons from the sulfur atom (see Fig. 1). The last term represents the lattice elastic energy.

For the electrode, we chose two symmetric identical nonmagnetic metals, each of them described by a one-dimensional single band tight-binding Hamiltonian

$$H_M = \sum_{n,\sigma}\left[\varepsilon_f d^{\dagger}_{n,\sigma}d_{n,\sigma} + t_f\left(d^{\dagger}_{n+1,\sigma}d_{n,\sigma} + h.c.\right)\right]. \quad (2)$$

Here, $d^{\dagger}_{n,\sigma}(d_{n,\sigma})$ denotes the creation (annihilation) operator of an electron with spin σ at the nth site in the metal electrode, ε_f is the on-site energy of a metal atom, and t_f is the nearest neighbor transfer integral. The couplings between the thiophene and each of the metal electrodes were described by a tight-binding hopping integral

$$t_{ML} = t_{MR} = \beta(t_f + t_0), \quad (3)$$

where β denotes the OSE-metal binding parameter.

At the mean-field level for taking correlations into account, one can evaluate the current based on the NEGF formalism [28,29]

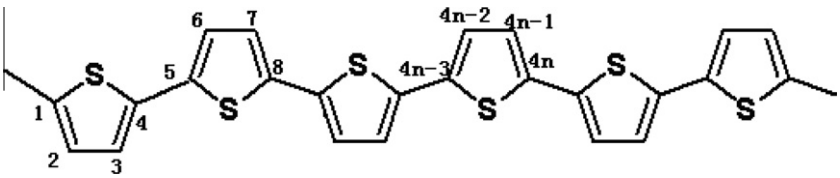

Fig. 1. Schematic structure of a polythiophene molecular.

$$I = \frac{2e}{h}\int_{-\infty}^{+\infty} T(E)[f(E,\mu_L) - f(E,\mu_R)]dE, \quad (4)$$

Here, $T(E)$ is the transmission coefficient function at a finite bias, which can be read as

$$T(E) = Tr\left(\Gamma_L G^r \Gamma_R G^\alpha\right). \quad (5)$$

The term involving $\Gamma_{L/R}$ denotes the lead reservoir-induced broadening matrix, while $G^r(E)$ and $G^\alpha = (G^r)^\dagger$ are the retarded and advanced single-particle Green's functions for the central scattering region (S region) which consists of the thiophene oligomer together with a number of metal atoms attached to each of its ends. $f(E,\mu_{L/R})$ is the Fermi distribution function with the lead chemical potential $\mu_{L/R}$. For an open quantum system, both the charging effect from the electrodes and the external potential from the bias voltage are contained in the nonequilibrium reduced density matrix of the coupled e–l system

$$\rho = \frac{1}{2\pi}\Sigma_{\alpha=L/R}\int_{-\infty}^{+\infty} G^r \Gamma_\alpha G^\alpha \Gamma_R f(E,\mu_\alpha)dE, \quad (6)$$

which should be evaluated self-consistently together with Poisson's equation and the Hellman–Feynman variation theorem for lattice distortion: $\partial[Tr(H_{s\rho})]/\partial u_n = 0$. The NEGF also determines the density of states, $D(E)$, through $D(E) = \frac{i}{2\pi}Tr[G^r(E) - G^\alpha(E)]$. The detailed self-consistent procedure can be found in Ref. [25].

In this study, the SSH parameters for the thiophene molecular were chosen as: $t_0 = 2.5$ eV, $t_e = 0.27$, $t_0 = 0.675$ eV, $\alpha = 4.4$ eV/Å, $K = 21.0$ eV/Å^2, $\varepsilon_0 = -4.9$ eV, and $t^s_\triangle = \varepsilon^s_\triangle = 0.05t_0 = 0.125$ eV. These parameters can reproduce the band gap (~2.0 eV) of polythiophene [30–32]. The tight binding parameters for fitting the Au band structure of the electrode metal in Eq. (2) are $t_f = 3.0$ eV and $\varepsilon_f = -4.9$ eV. The thiophene–Au metal binding parameter β represents the coupling strength, which affects the magnitude of current sensitively. In the calculations, one can adjust it, so the calculated I–V curve is the same amplitude as the measured one. We find that $\beta = 0.25$ for the molecular junction will produce the current in the magnitude of μA, which is comparable with the results for the same nanosize molecules reported in the Refs. [23,24]. These parameters can properly represent the bulk properties at the boundary and in the absence of applied bias, both the scattering region and the molecular segment are charge neutral.

3. Results and discussions

We are now in the position to calculate the I–V characteristics, especially the NDR behavior, of the model Au/PTh/Au structure at low temperature. For the sake of definiteness, we have chosen a temperature of $T = 11$ K. For a self-consistent evaluation of quantum transport based on the NEGF formalism, the central scattering region is chosen such that its Green's function can properly represent the bulk properties at the boundary. For the coupling parameters given above, we selected the S-region to consist of $20 + N + 20$ sites; i.e., 20-sites of Au atoms attached to each terminal of the polythiophene molecule which had N carbon sites. Due to the four-period structure of the thiophene, N is a multiple of 4. Numerical calculations show the NDR feature in the I–V curves of the device. At certain molecular lengths (3–5 thiophene units) the NDR effects are prominent. As an example, in Fig. 2, we show the I–V curve for a molecule with four thiophene units. For clarity, the inset also shows the differential resistance, dI/dV, as a function of V. From the figure, one can see that under the applied bias, the current increases markedly at $V \sim 1.05$ V (35 μA) (threshold voltage) and reaches a value of about 70 μA at $V \sim 1.5$ V. After the initial increase, the current drops abruptly from 70 to 1.2 μA at 1.55 V. The reduction in current with an increase in the external bias voltage indicates the presence of NDR. The NDR is prominent up to a bias voltage of 1.55 V. The peak-to-valley current ratio is as high as 70. The current then remains at a low level (about 1 μA) over the bias range from 1.55 to 1.75 V. Subsequently, the current again rapidly increases to about 70 μA as the voltage is raised above 1.75 V, and subsequently, the molecule remains in high conductance states.

To elaborate what happens across the NDR region, we also examined other nonequilibrium properties. Fig. 3a shows the representative results for the voltage-dependent transmission probabilities $T(E)$ at bias voltages of $0, 1.5, 1.55$ and 1.8 V. In this figure, E_f represents the energy of the Fermi level and the dashed lines indicate the bias window $\mu_R - \mu_L$. Consider first the case of the zero bias transmission spectra. We can see that no transmission resonance peaks exist near the Fermi energy. The current remains nearly zero until several transmission resonance peaks enter into the bias window at 1.05 V. As a consequence, current through the molecule increases and the molecule enters the conducting state. Subsequently, transmission spectra contributing to the bias window gradually increase with increasing external bias voltage (not represent in the figure). However, the existing resonance peaks disappear abruptly at 1.55 V, which induces an abrupt decline in the current. This is an indication of the appearance of the NDR feature, which is apparent in Fig. 2. In the bias range from 1.55 to 1.75 V, the structures of the

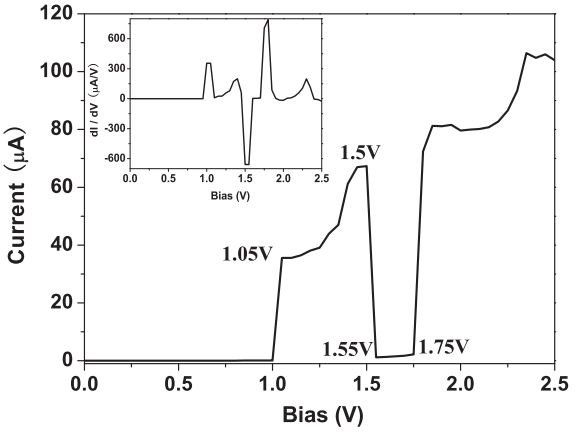

Fig. 2. The current–voltage characteristic of the Au–thiophene oligomer–Au system studied in the present paper. The inset shows the differential conductance (dI/dV) against the bias (V).

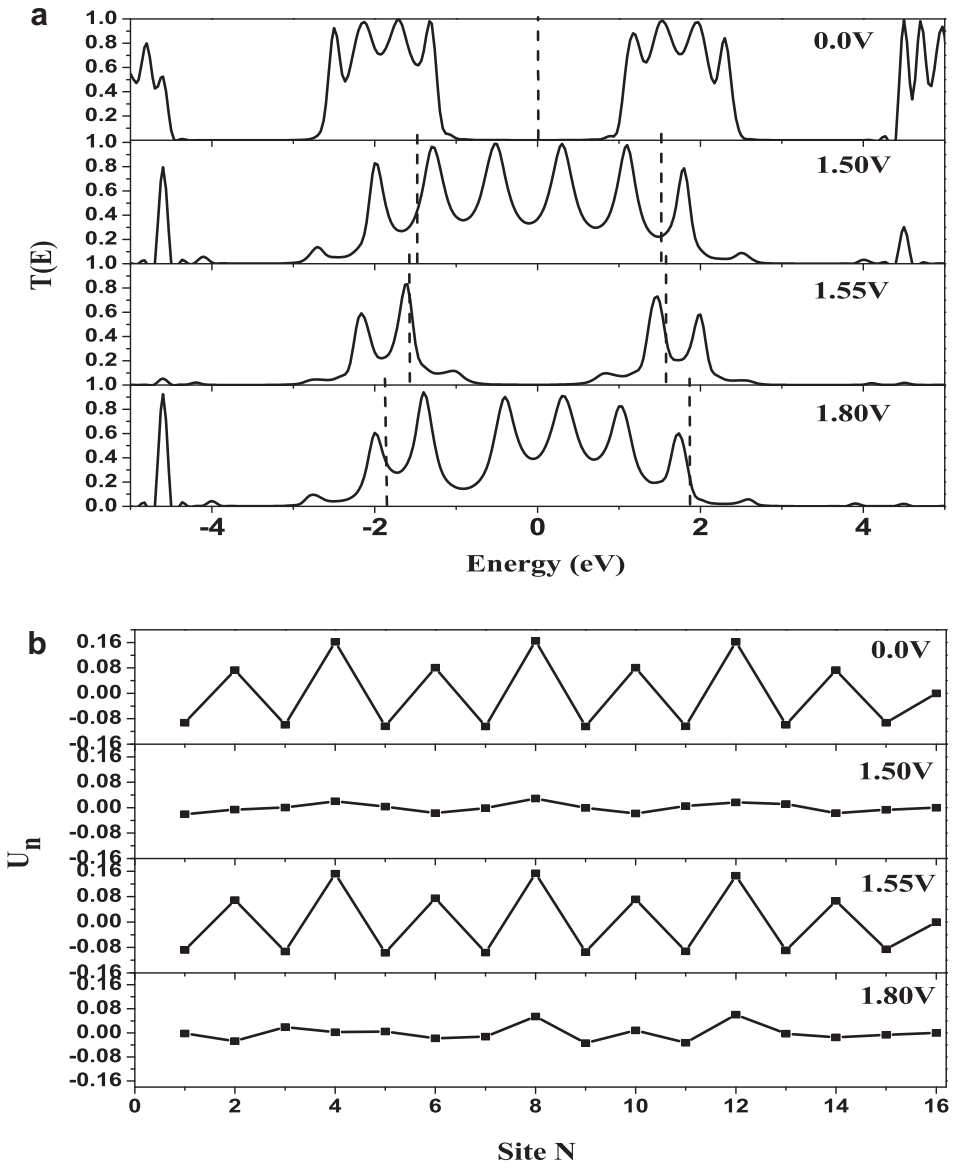

Fig. 3. (a) Energy-dependent transmission coefficient $T(E)$ near the Fermi energy at $V = 0, 1.5, 1.55$ and 1.8 V. The long dotted lines indicate the bias window, and the Fermi level is set to be the origin of energy. (b) Lattice distortion $\{y_n = u_{n+1} - u_n\}$ of the OSE substructure at $V = 0, 1.5, 1.55$ and 1.8 V.

transmission spectra are quite analogous and the currents of the system remain at a very low value, which corresponds to the insulating state. When the bias is greater than 1.75 V, some transmission resonance peaks enter into the bias window and the current through the molecular system again starts to increase.

In order to understand the conducting insulating states distinguished in the transmission spectrum, it is important to determine the underlying mechanism. This can be done by checking the lattice distortion of the molecule. Fig. 3b shows the changes of the lattice distortion at the representative biases $0, 1.5, 1.55$ and 1.8 V. Note that in Fig. 3b, the lattice distortions are reported in terms of the *e–l* coupling induced bond length variation $\{y_n = u_{n+1} - u_n\}$ between nearest neighbors. The zero bias curve has the dimerized lattice configuration in the Peierls phase. In contrast, the distinct reduction in the lattice distortion or single-double bond alteration at 1.5 V suggests a diminishing of the Peierls phase. In this condition, the atoms take on a uniform distribution and the molecule enters a conducting state. When the bias continues to increase, the lattice distortion re-appears and complete dimerization appears at 1.55 V. It is obvious that the lattice configuration is the same as in the equilibrium lattice distortion $(V = 0)$, which gives the largest contribution to the insulating state and results in a large band gap and small current. As a consequence, the NDR effect appears in Fig. 2. From 1.55 to 1.75 V, the lattice configuration is characterized by dimerization, so the conductance of the molecular remains at low values over this range. With increasing bias, the dimerization of

the lattice diminishes and when the voltage reaches 1.8 V the Peierls gap disappears. The molecule then starts to conduct again. The above analysis leads us to conclude that the external bias leads to important changes in the conformation of the molecule which in turn induces the NDR phenomenon.

In the following, we calculate the reduced eigenvalues of the bias-dependent Hamiltonian of the molecule to provide more information regarding the NDR phenomenon. The Hamiltonian is shown in Eq. (1), and the nonequilibrium lattice parameters are evaluated in a self-consistent manner. The Hamiltonian also contains the electric potential variation in the molecule, which was also determined self-consistently. The information contained in this Hamiltonian was shown in the discussion above to be able to reflect the bias-induced intrinsic changes of the organic molecule in the device. The resulting energy levels from the aforementioned self-consistent Hamiltonian, as they vary with the bias voltage, are shown in Fig. 4, where the dashed lines indicate the conducting window determined by the space between μ_L and μ_R. From the figure, we can see that at about 1.05 V, the LUMO enters the conducting window between μ_L and μ_R and induces a rapid increase in the current. However, at 1.55 V, the LUMO moves outside the conducting window. No available orbitals contributing to the conductance can then be found in the conducting window, so the current decreases abruptly, which constitutes the emergence of the NDR feature. Over the bias range 1.5—1.75 V, the molecular orbitals are always outside the bias window and the Peierls phase of the molecular substructure is recovered. The conductance of the molecule remains at a very low value. This is corresponds to the insulating state. Eventually, at 1.8 V, LUMO−1, a new orbital contributing to the conductance appears between the bias windows, and the current begins to increase again.

In most of the calculations based on the first principle combining with the NEGF method, the molecule is assumed rigid and its vibrations are ignored in the transport process. At last, we freeze the motion of the atoms when the bias is applied in order to compare the transport characteristics with that of the rigid molecule. Fig. 5 is the current–voltage characteristic of the Au–thiophene oligomer–Au system when the lattice is frozen. Due to the structure of the thiophene is dimerized throughout the transport process the current is weaker than that in Fig. 2. Furthermore, the NDR phenomenon is unobserved when the motion of the atoms is frozen, which manifests that the structural change in the organic molecule plays a key role in the NDR phenomenon.

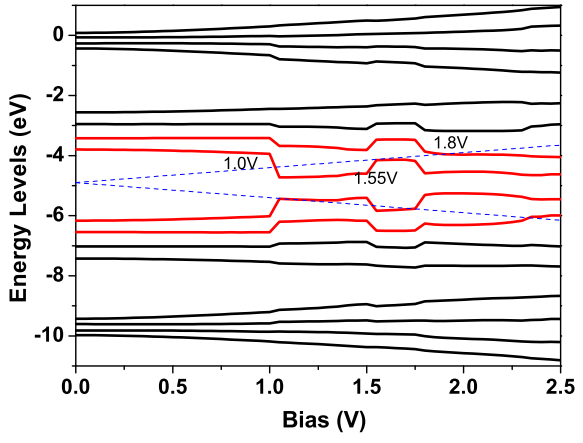

Fig. 4. Evolution with voltage of the energy levels of the thiophene molecule. The dashed lines indicate the conducting window determined by the space between μ_L and μ_R. The nearest four energy levels to the Fermi levels, LUMO, HOMO, LUMO+1, HOMO−1, are represented by red lines. (For interpretation of the references to color in this figure legend, the reader is referred to the web version of this article.)

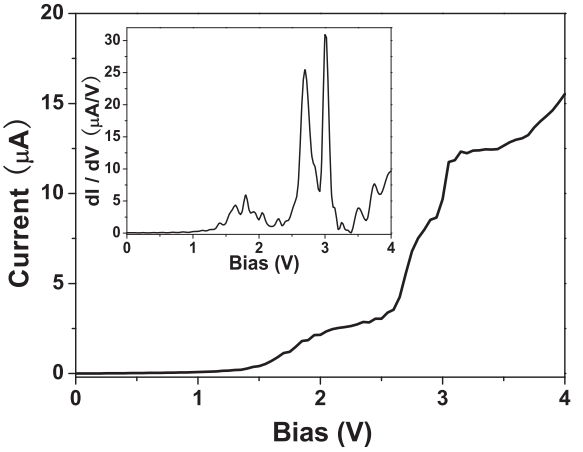

Fig. 5. The current–voltage characteristic of the Au–thiophene oligomer–Au system, the motion of the lattice is frozen when the bias applied. The inset shows the differential conductance (dI/dV) against the bias (V).

4. Summary

In summary, to study electron transport in an organic device, electron–lattice coupling effects in the organic material should be emphasized. In this article, by combining the SSH model and the Green's function method, we have calculated electron transport through thiophene oligomer molecular devices and have given an explanation of the negative differential resistance (NDR). The results of this model were found to capture the essential physics of the process. The NDR was found to be a result of conformation changes, induced by the external bias, between a dimerized state (low conductance) and a uniform (high conductance) state of the molecular structure of the lattice. These results provide further insight into the origin of NDR behavior in the I–V characteristic in organic molecular devices.

Acknowledgments

The authors like to acknowledge the financial support from the National Natural Science Foundation of China, Hebei Provincial Outstanding Youth Science Fund (No. A2009001512) and Hebei Education Department Natural Science Foundation (No. 2009142).

References

[1] J. Chen, M.A. Reed, A.M. Rawlett, J.M. Tour, Science 286 (1999) 1550.
[2] I. Kratochvilova, M. Kocirik, A. Zambova, J. Mbindyo, T.E. Mallouk, T.S. Mayer, J. Mater. Chem. 12 (2002) 2927.
[3] K. Walzer, E. Marx, N.C. Greenham, R.J. Less, P.R. Raithby, K. Stokbro, J. Am. Chem. Soc. 126 (2004) 1229.
[4] A.M. Rawlett, T.J. Hopson, I. Amlani, R. Zhang, J. Tresek, L.A. Nagahara, R.K. Tsui, H. Goronkin, Nanotechnology 14 (2003) 377.
[5] N.P. Guisinger, E.G. Mark, B. Rajiv, A.S. Baluch, C.H. Mark, Nanoletter 4 (2004) 55.
[6] X.N. Xie, X.Y. Gao, Y.Z. Wang, J.Z. Wang, K.P. Loh, A.T.S. Wee, Appl. Phys. Lett. 95 (2009) 063301.
[7] A.K. Rath, A.J. Pal, Org. Electron. 10 (2009) 1116.
[8] E.G. Emberly, G. Kirczenow, Phys. Rev. B 64 (2001) 125318.
[9] J.M. Seminario, A.G. Zacarias, J.M. Tour, J. Am. Chem. Soc. 122 (2000) 3015.
[10] Z.Q. Fan, K.Q. Chen, Q. Wan, B.S. Zou, W.H. Duan, Z. Shuai, Appl. Phys. Lett. 92 (2008) 263304.
[11] H. Ren, Q.X. Li, Y. Luo, J. Yang, Appl. Phys. Lett. 94 (2009) 173110.
[12] M. Wang, C.M. Li, Phys. Chem. Chem. Phys. 13 (2011) 5945.
[13] M.Q. Long, K.Q. Chen, L.L. Wang, W. Qing, B.S. Zou, Z. Shuai, Appl. Phys. Lett. 92 (2008) 243303.
[14] M. Galperin, M.A. Ratner, A. Nitzan, Nanoletter 5 (2005) 125.
[15] J.M. Seminario, A.G. Zacarias, P.A. Derosa, J. Chem. Phys. 116 (2002) 1671.
[16] C.W. Bauschlicher Jr., A. Ricca, Phys. Rev. B 71 (2005) 205406.
[17] B. Larade, A.M. Bratkovsky, Phys. Rev. B 72 (2005) 035440.
[18] K.J. Franke, G. Schulze, N. Henningsen, I. Fernndez-Torrente, J.I. Pascual, S. Zarwell, K. Rck-Braun, M. Cobian, N. Lorente, Phys. Rev. Lett. 100 (2008) 036807.
[19] L. Chen, Z. Hu, A. Zhao, B. Wang, Y. Luo, J. Yang, J.G. Hou, Phys. Rev. Lett. 99 (2007) 146803.
[20] M. Kobayashi, J. Chen, T.C. Chung, F. Moraes, A.J. Heeger, F. Wudl, Synth. Met. 9 (1984) 77.
[21] J.M. Lehn, G.M. Tsivgouli, Adv. Mater. 9 (1997) 39.
[22] J.A. Merlo, C.D. Frisbie, J. Phys. Chem. B 108 (2004) 19169.
[23] A.A. Farajian, R.V. Belosludov, H. Mizuseki, Y. Kawazoe, T. Hashizume, B.I. Yakobson, J. Chem. Phys. 127 (2007) 024901.
[24] S. Sen, S. Chakrabarti, Comp. Mater. Sci. 45 (2009) 889.
[25] J.H. Wei, S.J. Xie, L.M. Mei, J. Berakdar, Y.J. Yan, New J. Phys. 8 (2006) 82;
J.H. Wei, S.J. Xie, L.M. Mei, J. Berakdar, Y.J. Yan, Org. Electron. 8 (2007) 487;
J.H. Wei, S.J. Xie, X.J. Liu, Y.J. Yan, J. Chem. Phys. 131 (2009) 064906.
[26] W.P. Su, J.R. Schrieffer, A.J. Heeger, Phys. Rev. Lett. 42 (1979) 1698;
W.P. Su, J.R. Schrieffer, A.J. Heeger, Phys. Rev. B 22 (1980) 2099.
[27] S.J. Xie, L.M. Mei, Phys. Rev. B 50 (1994) 13364.
[28] M. Brandbyge, J.L. Mozos, P. Ordejn, J. Taylor, K. Stokbro, Phys. Rev. B 65 (2002) 165401.
[29] L.V. Keldysh, Zh. Eksp. Teor. Fiz. B 47 (1964) 1515;
L.V. Keldysh, J. Phys. II B 20 (1965) 1018.
[30] K. Kaneto, Y. Kohno, K. Yoshino, Solid State Commun. 51 (1984) 267.
[31] G. Harbeke, E. Meier, W. Kobel, M. Egli, H. Kiess, E. Tosatti, Solid State Commun. 55 (1985) 419.
[32] T.C. Chung, J.H. Kaufman, A.J. Heeger, F. Wuld, Phys. Rev. B 30 (1984) 702.

WEG films can approach the same magnitude of their single crystal film counterparts [21]. One of the promising candidate materials is vanadyl phthalocyanine (VOPc), which is a non-planar phthalocyanine with high mobility, as well as good air and electrical stability [27–29]. However, investigations on VOPc are less common than those on pentacene and rubrene. Wang et al. fabricated VOPc films consisting of lamellar crystals on a *p*-6P inducing layer and the mobility based on the VOPc/*p*-6P is up to 1.0 $cm^2 V^{-1} s^{-1}$ [30]. The lamellar crystals on the *p*-6P inducing layer are different from those of planar phthalocyanine films. They facilitate the in-plane transport of charge carriers by applying the WEG technique. However, at the contact surfaces between the VOPc and the *p*-6P, large lattice mismatching occurs, resulting in incommensurate epitaxy. The domain size of VOPc polycrystalline films is smaller than 1 μm, resulting in many domain boundaries that act as trap sites in VOPc films, thereby limiting the performance improvement of VOPc-based devices. Therefore, new inducing layer materials that have better lattice-matching relationship with VOPc and form smooth, continuous, large-size crystal domains are required to improve VOPc OTFT performance further.

In this paper, we report the inducing layer material 5,5‴-bis(4-fluorophenyl)-2,2′:5′,2″:5″,2‴-quaterthiophene (F2-P4T), which can form smooth, continuous bilayer films at an optimized substrate temperature, on which VOPc grows following a WEG pattern. A commensurate epitaxial relationship is formed between the F2-P4T and the VOPc films, leading to highly ordered VOPc films with grain size larger than 1 μm. Simultaneously, the crystal domains were extensively connected to each other, resulting in a decrease in the density of the grain boundary. This film morphology enhanced in-plane carrier transport; hence, a higher mobility was obtained. The organic field-effect transistors with VOPc/F2-P4T films active layers exhibited a high mobility of 2.6 $cm^2 V^{-1} s^{-1}$ with relatively good stability under ambient conditions.

2. Experimental

2.1. Materials and device fabrication

The VOPc samples were purchased from Aldrich Company (USA), and 5,5‴-bis(4-fluorophenyl)-2,2′:5′,2″:5″,2‴-quaterthiophene (F2-P4T) was synthesized according to Ref. [31] as a red solid with a yield of 60% after purified by vacuum sublimation twice, using 1-bromo-4-fluorobenzene instead of 4-bromotoluene. F2-P4T: Anal. Calcd for $C_{28}H_{16}F_2S_4$: C, 66.84; H, 3.11; Found: C, 66.65; H, 3.01. M.p. = 342 °C (from DSC measurement). T_d = 415 °C (corresponding to 5% weight loss). All the materials were purified twice by thermal sublimation prior to experiments. A heavily doped *n*-type silicon wafer with a 300 nm thermal oxidation SiO_2 layer (dielectric capacitance C = 10 nF/cm^2) was used as the substrate. The substrate was subjected to cleaning by acetone, alcohol, and deionized water. The cleaned substrates were dried at 100 °C for 30 min in the roast to eliminate the influence of the moisture. First, F2-P4T film with thickness of 6 nm was deposited on SiO_2, forming continuous bilayer films. Second, VOPc films with different thicknesses were deposited on the F2-P4T thin films. The organic thin films were deposited at 10^{-4}–10^{-5} Pa at a rate of about 1 nm/min, and the substrate temperatures were kept at 170 °C. Finally, the samples were rapidly transferred to another vacuum chamber to define the source and drain contacts by thermally evaporating Au with a mask shadow in vacuum at 10^{-4} Pa to complete the fabrication of organic field-effect transistors.

2.2. Characterization of organic film and OTFT measurements

Atomic force microscopy (AFM) measurements of film morphology were imaged by a SPI 3800/SPA 300HV (Seiko Instruments Inc., Japan) with tapping mode. The out-of-plane X-ray diffraction (XRD) patterns were taken from a D8 discovery thin-film diffractometer with Cu Kα radiation (λ = 1.54056 Å). The selected voltage and current were 40 kV and 40 mA, respectively. The selected area electron diffraction (SAED) was imaged with a JEOL JEM-1011 transmission electron microscope operated at 100 kV. The fabrication of samples was according to Ref. [32] Current–voltage measurements of OTFT were performed at room temperature in air with two Keithley 236 source-measurement units. Field-effect mobility (μ) was estimated from the saturation regime ($V_{GS} = V_{DS} = -50$ V) using the following equation:

$$I_{DS} = \frac{W}{2L}\mu C_i (V_{GS} - V_T)^2$$

in which L (180 μm) is the channel length, W (6000 μm) is the channel width, C_i (10 nF/cm^2) is the capacitance (per unit area) of the insulator, V_{GS} is the gate voltage, V_T is the threshold voltage, and I_{DS} is the drain-source current.

3. Results and discussion

3.1. Films morphology and properties

The molecular structures of F2-P4T and VOPc are shown in Fig. 1a. The morphology of the 6 nm (nearly two molecular layer) F2-P4T films deposited onto the SiO_2 substrate at 170 °C is shown in Fig. 1b. The first layer of F2-P4T has completely formed and the second layer has covered the surface of 98%, which indicated that the F2-P4T presents a layer-by-layer growth behavior in the first two layers. This growth behavior leads to large, continuous double-layer thin films with ultra-flat surfaces which show a root-mean-square (RMS) roughness of 0.5 nm. This is different from that of *p*-6P, which only shows layer-by-layer growth mode in the monolayer [33]. Furthermore the SAED pattern (Fig. 1c and d) of a single grain present a regular rectangular lattice, evidenced the highly crystalline of the F2-P4T layer and its similar packing to *p*-6P. The highly ordered smooth bilayer films of F2-P4T favored the nucleation and growth of VOPc. It is well known that carrier transport mainly in the several molecular layers of active layers at the interface between active layers and insulator [34]. So the morphology of initial several molecular layers of VOPc is essential for the organic thin film transistor. Fig. 1e shows the AFM morphology of the 6 nm VOPc

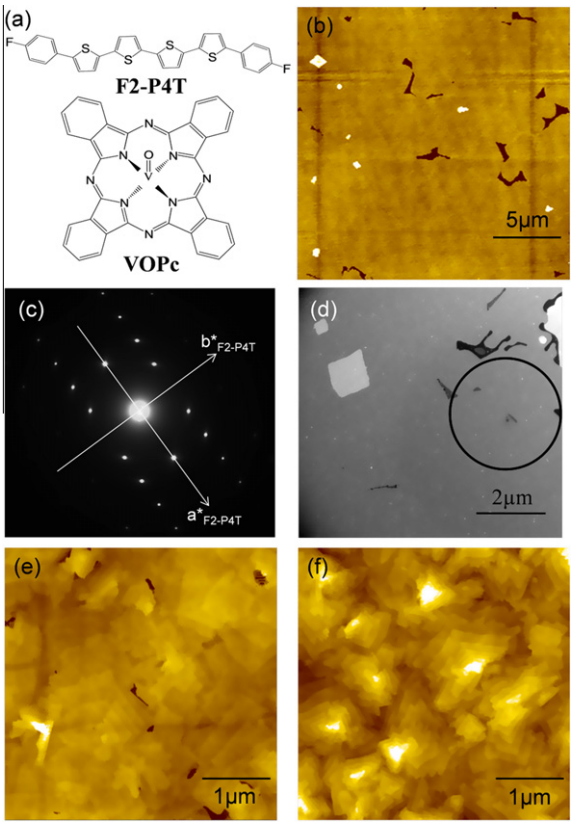

Fig. 1. (a) The molecular structures of 5,5‴-bis(4-fluorophenyl)-2,2′:5′,2″:5″,2‴-quaterthiophene (F2-P4T) and vanadyl phthalocyanine (VOPc), respectively. (b) 20 μm × 20 μm AFM image of the F2-P4T (6 nm) bilayer grown on SiO_2 at 170 °C, RMS = 0.5 nm. (c) and (d) The SAED pattern and corresponding electron micrograph of bilayer F2-P4T films. (e) 4 μm × 4 μm AFM image of the VOPc (6 nm) on the F2-P4T (6 nm) films at 170 °C. (f) 4 μm × 4 μm AFM image of the VOPc (30 nm) on the F2-P4T (6 nm) films at 170 °C.

deposited onto the F2-P4T bilayer. The VOPc films present layered crystal grains similar to that on *p*-6P films, however, the domain size of the VOPc is larger than 1 μm, which is larger than that on *p*-6P films [30]. In addition, although adjacent grains present different orientations, the crystal domains intimately coalesced with each other, resulting in a continuous film with less dense grain boundary which favors the in-plane charge carrier transport. Fig. 1f shows the AFM morphology of the 30 nm VOPc deposited onto the F2-P4T bilayer. With the increasing of the thickness of VOPc films, the lamellar shape of VOPc grains can be observed obviously, but the films still maintained good continuity and integrity. The quality of VOPc films on F2-P4T has been improved significantly compared with that on *p*-6P [30]. X-ray diffraction pattern of VOPc/F2-P4T films was shown in Fig. 2, which indicates the highly order of VOPc films. The intensity diffraction peak at 7.5° corresponds to the (0 1 0) lattice plane of VOPc films in phase II [35]. Simultaneously, the exclusive appearance of (0 *k* 0) peak indicated VOPc molecules preferentially stand on F2-P4T films. In other words, the π–π stacking direction is parallel to the substrate, which is favorable to carriers transporting in film plane.

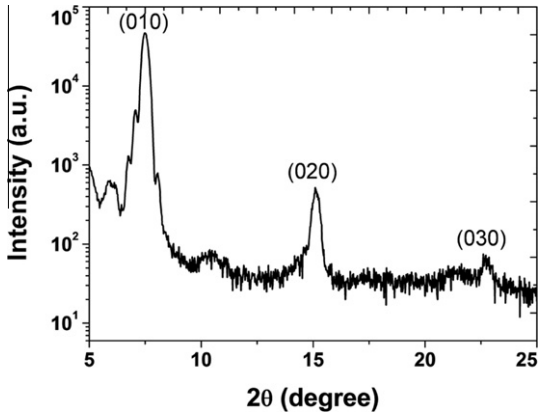

Fig. 2. Out of plane X-ray diffraction pattern of 30 nm VOPc film grown on F2-P4T (6 nm) at 170 °C.

Fig. 3a shows a typical SAED pattern of one typical orientation of VOPc films on the F2-P4T. For this orientation, the c* axis of the VOPc forms an angle of 37.5° with the a* axis of the F2-P4T similar to that of VOPc on *p*-6P [30]. It

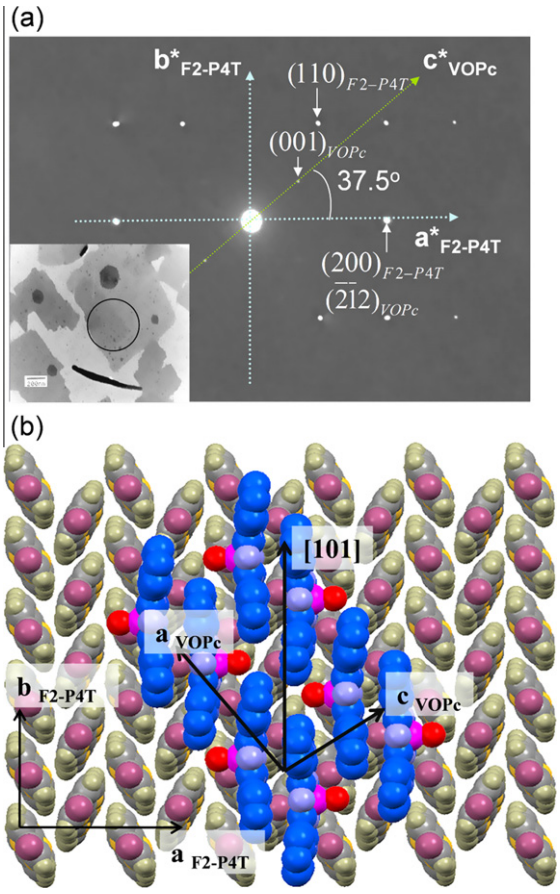

Fig. 3. (a) The selected area electron diffraction pattern of 2 nm thick VOPc grown on the F2-P4T bilayer, and its corresponding electron micrograph. (b) Schematic diagram of the VOPc epitaxial growth on the F2-P4T bilayer films.

Table 1
In-plane parameters of *p*-6P and F2-P4T bilayer films.

	p-6P	F2-P4T
$d_{(2\,0\,0)}$ (Å)	3.98 ± 0.08	3.85 ± 0.02
$d_{(0\,1\,0)}$ (Å)	5.58 ± 0.05	5.77 ± 0.02
γ (°)	90	90
	Ref. [30]	Extracted from SAED

also contains a symmetry orientation with an angle of −37.5°. As inferred from the diffraction pattern of VOPc, a coincidence of $(\bar{2}\,1\,2)$VOPc with the underlying $(2\,0\,0)_{F2\text{-}P4T}$ layer is observed which is indicative of commensurate epitaxy between the VOPc and the F2-P4T. This implies better lattice matching between the VOPc and the F2-P4T compared with that on *p*-6P wherein no coincidence was observed. Based on the lattice parameters of F2-P4T and *p*-6P (Table 1), the lattice spacing of $(2\,0\,0)_{F2\text{-}P4T}$ is much shorter than that of *p*-6P but close to the *d* spacing of $(\bar{2}\,1\,2)_{VOPc}$, thus leading to highly ordered VOPc films with continuous, large grain sizes. The epitaxial relationship of VOPc and F2-P4T are $(0\,1\,0)_{VOPc}$ || $(0\,0\,2)_{F2\text{-}P4T}$ and $[1\,0\,1]_{VOPc}$ || $[1\,0\,0]_{F2\text{-}P4T}$. Fig. 3b displays the corresponding packing diagram of this orientation, in which the molecular plane of VOPc is parallel to the lattice direction of [1 0 0] of F2-P4T. This packing diagram is favorable to the diffusion and growth of VOPc. The electron diffraction pattern and corresponding morphology, proved large-gain, low-defect, continuous VOPc epitaxial films on an F2-P4T inducing layer are formed by WEG. Such high quality organic thin films are desired for organic thin film transistors.

3.2. Device performance and air stability

The VOPc/F2-P4T transistor was fabricated on the SiO_2 insulator. The device configuration is shown in Fig. 4a. The output (I_{DS}–V_{DS}) characteristics at V_{GS} from 0 V to −50 V is shown in Fig. 4c. It can be seen that the device exhibits the p-channel accumulation operation mode. With the increasing of source-drain voltage (V_{DS}), the linear region and saturation region are observed obviously from output curve. Typical transfer (I_{DS}–V_{GS}) characteristics and plots of ($I_{DS}^{1/2}$) vs. V_{GS} at a fixed V_{DS} of −50 V are shown in Fig. 4d. The device exhibited high field-effect mobility (μ) of 2.4 $cm^2\,V^{-1}\,s^{-1}$ extracted from the saturation region of the transfer curve at a V_{DS} of −50 V, a low threshold voltage (V_T) of −2.7 V, and a high on–off current ratio (I_{on}/I_{off}) of 10^6. During device operation, F2-P4T served as the dielectric layer because of its low conductivity. OTFTs based on single 50 nm F2-P4T film active layers measured under both vacuum and ambient conditions at room temperature didn't present field effect property. Hence, carrier transport is mainly in the VOPc films. In addition, the F2-P4T layer is too thin to have a significant effect on capacitance. The curves of gate leak current vs. gate voltage were showed in Fig. 4b, the leak currents level were almost at 10^{-10} A. The performance of the F2-P4T/VOPc device under multiple optimized conditions is summarized in Table 2, which is much better than that of *p*-6P/VOPc. The improvement in the performance of the device is mainly due to the

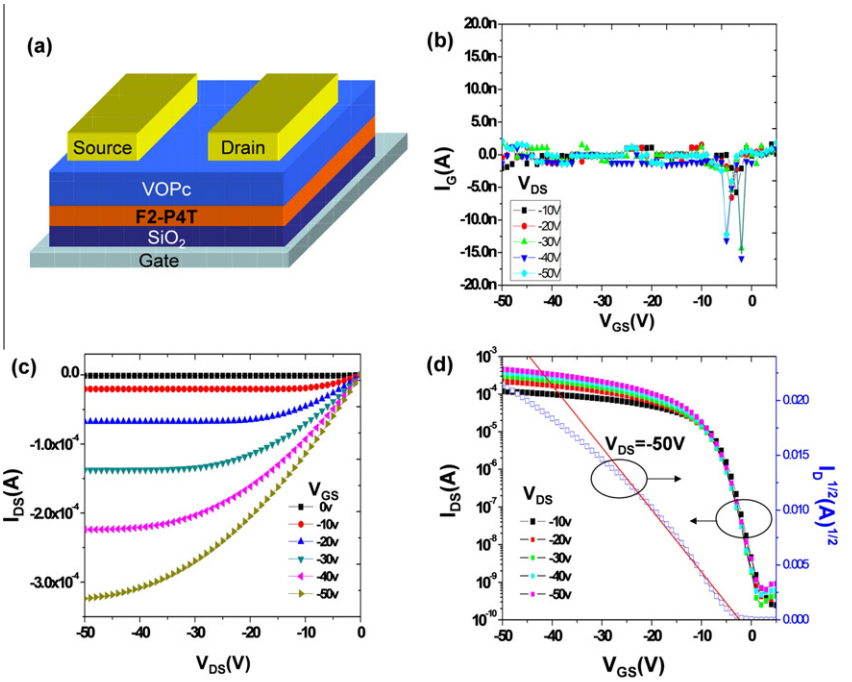

Fig. 4. (a) The device configuration of the VOPc (30 nm)/F2-P4T (6 nm). (b) The I_G–V_G curves of VOPc OTFT with F2-P4T/SiO_2 dielectrics at drain voltage (V_D) from −10 V to −50 V. (c) The output characteristics (I_{DS}–V_{DS}) of VOPc (30 nm)/F2-P4T (6 nm) OTFT at different V_{GS} from 0 V to −50 V. (d) The transfer characteristics (I_{DS}–V_{GS}) of VOPc (30 nm)/F2-P4T (6 nm) OTFT at different V_{DS} from −10 V to −50 V and the typical $I_{DS}^{1/2}$ vs. V_{GS} plot ($I_{DS}^{1/2}$–V_{GS}) at V_{DS} = −50 V.

Table 2
Summary of the performances for VOPc OTFTs based on the *p*-6P and the F2-P4T inducing layer.

Device structure	μ ($cm^2 V^{-1} s^{-1}$)	V_T (V)	I_{on}/I_{off}	
p-6P/VOPc	0.6–1.5	−9 to −15	10^6	Ref. [30]
F2-P4T/VOPc	1.2–2.6	−1 to −5	10^6–10^7	

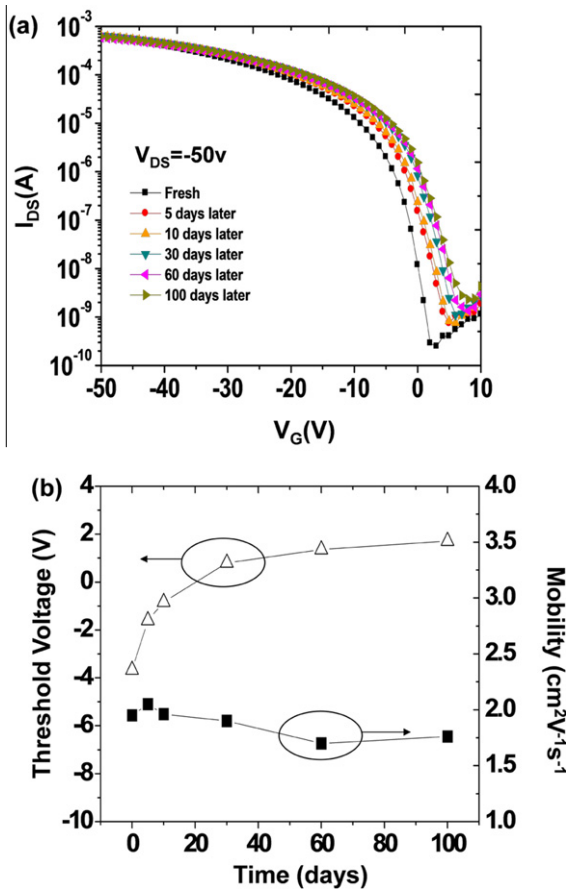

Fig. 5. (a) The air stability measurements of the VOPc (30 nm)/F2-P4T (6 nm) device: drain current (I_{DS}) vs. gate voltage (V_{GS}) at V_{DS} = −50 V as a function of time. (b) The field-effect mobility (μ) and the threshold voltage (V_T) of the VOPc (30 nm)/F2-P4T (6 nm) device as a function of time that exposed in air at room temperature.

improvement in the quality of the VOPc films. Larger grain size and fewer defects in the VOPc films led to a more continuous carrier transport channel formed near the interface between the F2-P4T and the VOPc layers, which facilitate higher mobility and lower threshold voltage. In addition, because the fluorine (F) groups introduced in the F2-P4T inducing layer formed F atomic arrangement surface, there might be a built-in electric field in the interface between the F2-P4T and the VOPc layers, leading to holes accumulating in the VOPc films. Thus, the threshold voltage is shifted to the positive side [36,37].

The F2-P4T/VOPc OTFTs also showed good air stability. The transfer curves obtained at different times are shown in Fig. 5a. After 100 days of storage under ambient conditions, the mobility of the F2-P4T/VOPc device slightly decreased from 1.99 to 1.76 $cm^2 V^{-1} s^{-1}$, the threshold voltage shifted from −3.6 V to 1.7 V, and on–off current ratio maintained a magnitude of 10^6. Fig. 5b shows the mobility (μ) and threshold voltage (V_T) as a function of exposure time to ambient conditions. The good stability of the F2-P4T/VOPc device is related to the large ionization potential of the VOPc (HOMO 5.5 eV) [38], which is against oxidation [39–41]. Furthermore, the closed packing of the F2-P4T/VOPc films with few defects prevents the physical absorption of the environmental gases that deteriorate the performance of device [42,43].

4. Conclusions

In summary, a new fluorinated inducing layer material called F2-P4T was introduced. It can form smooth and continuous bilayer films on which VOPc films exhibited weak epitaxial growth behavior. A commensurate epitaxial relationship was observed, which implied perfect lattice matching between the VOPc and the F2-P4T. The epitaxial VOPc films with highly oriented order, large domain size, and few defects were obtained on the F2-P4T inducing layer. The thin-film transistors based on such high quality films as active layers exhibited high performance. The field-effect mobility reached up to 2.6 $cm^2 V^{-1} s^{-1}$, the threshold voltage was lower than −5 V, the on–off current ratio was at a magnitude of 10^6, and it exhibited relatively good air stability. Such high performance OTFTs is a great impetus for realizing large-area, low-cost and flexible displays.

Acknowledgements

This work was supported by the National Natural Science Foundation of China (50803063) and The National Basic Research Program (2009CB939702).

References

[1] M. Katsuhara, I. Yagi, A. Yumoto, M. Noda, N. Hirai, R. Yasuda, T. Moriwaki, S. Ushikura, A. Imaoka, T. Urabe, K. Nomoto, A flexible OLED display with an OTFT backplane made by scalable manufacturing process, J. Soc. Inf. Disp. 18 (2010) 399–404.
[2] P.F. Baude, D.A. Ender, M.A. Haase, T.W. Kelley, D.V. Muyres, S.D. Theiss, Pentacene-based radio-frequency identification circuitry, Appl. Phys. Lett. 82 (2003) 3964–3966.
[3] R. Rotzoll, S. Mohapatra, V. Olariu, R. Wenz, M. Grigas, K. Dimmler, O. Shchekin, A. Dodabalapur, Radio frequency rectifiers based on organic thin-film transistors, Appl. Phys. Lett. 88 (2006) 123502.
[4] L. Torsi, G.M. Farinola, F. Marinelli, M.C. Tanese, O.H. Omar, L. Valli, F. Babudri, F. Palmisano, P.G. Zambonin, F. Naso, A sensitivity-enhanced field-effect chiral sensor, Nat. Mater. 7 (2008) 412–417.
[5] P. Gao, D. Beckmann, H.N. Tsao, X.L. Feng, V. Enkelmann, M. Baumgarten, W. Pisula, K. Mullen, Dithieno 2,3-d;2 '3 '-d' benzo 1,2-b;4,5-b' dithiophene (DTBDT) as semiconductor for high-performance, solution-processed organic field-effect transistors, Adv. Mater. 21 (2009) 213–216.
[6] T. Izawa, E. Miyazaki, K. Takimiya, Molecular ordering of high-performance soluble molecular semiconductors and re-evaluation of their field-effect transistor characteristics, Adv. Mater. 20 (2008) 3388–3392.
[7] K. Takimiya, H. Ebata, K. Sakamoto, T. Izawa, T. Otsubo, Y. Kunugi, 2,7-Diphenyl 1 benzothieno 3,2-b benzothiophene, a new organic semiconductor for air-stable organic field-effect transistors with mobilities up to 2.0 cm(2) V-1 s(-1), J. Am. Chem. Soc. 128 (2006) 12604–12605.

[8] L. Zhang, L. Tan, Z.H. Wang, W.P. Hu, D.B. Zhu, High-performance, stable organic field-effect transistors based on trans-1,2-(dithieno 2,3-b:3 ‘,2 ‘-d thiophene)ethene, Chem. Mater. 21 (2009) 1993–1999.
[9] Y. Ito, A.A. Virkar, S. Mannsfeld, J.H. Oh, M. Toney, J. Locklin, Z.A. Bao, Crystalline ultrasmooth self-assembled monolayers of alkylsilanes for organic field-effect transistors, J. Am. Chem. Soc. 131 (2009) 9396–9404.
[10] T.W. Kelley, L.D. Boardman, T.D. Dunbar, D.V. Muyres, M.J. Pellerite, T.Y.P. Smith, High-performance OTFTs using surface-modified alumina dielectrics, J. Phys. Chem. B 107 (2003) 5877–5881.
[11] T.W. Kelley, D.V. Muyres, P.F. Baude, T.P. Smith, T.D. Jones, High performance organic thin film transistors, Mater. Res. Soc. Symp. P 771 (2003) 169–179.
[12] H. Klauk, M. Halik, U. Zschieschang, G. Schmid, W. Radlik, W. Weber, High-mobility polymer gate dielectric pentacene thin film transistors, J. Appl. Phys. 92 (2002) 5259–5263.
[13] H.S. Tan, N. Mathews, T. Cahyadi, F.R. Zhu, S.G. Mhaisalkar, The effect of dielectric constant on device mobilities of high-performance, flexible organic field effect transistors, Appl. Phys. Lett. 94 (2009) 263303.
[14] H.C. Yang, T.J. Shin, M.M. Ling, K. Cho, C.Y. Ryu, Z.N. Bao, Conducting AFM and 2D GIXD studies on pentacene thin films, J. Am. Chem. Soc. 127 (2005) 11542–11543.
[15] A. Maliakal, K. Raghavachari, H. Katz, E. Chandross, T. Siegrist, Photochemical stability of pentacene and a substituted pentacene in solution and in thin films, Chem. Mater. 16 (2004) 4980–4986.
[16] F. De Angelis, S. Cipolloni, L. Mariucci, G. Fortunato, Aging effects in pentacene thin-film transistors: analysis of the density of states modification, Appl. Phys. Lett. 88 (2006) 193508.
[17] M.J. Kang, I. Doi, H. Mori, E. Miyazaki, K. Takimiya, M. Ikeda, H. Kuwabara, Alkylated dinaphtho[2,3-b:2′,3′-f]thieno[3,2-b]thiophenes (Cn-DNTTs): organic semiconductors for high-performance thin-film transistors, Adv. Mater. (2010), doi:10.1002/adma.201001283.
[18] T. Yamamoto, K. Takimiya, Facile synthesis of highly pi-extended heteroarenes, dinaphtho 2,3-b:2′,3′-f chalcogenopheno 3,2-b chalcogenophenes, and their application to field-effect transistors, J. Am. Chem. Soc. 129 (2007) 2224–2225.
[19] Z. Bao, A.J. Lovinger, A. Dodabalapur, Organic field-effect transistors with high mobility based on copper phthalocyanine, Appl. Phys. Lett. 69 (1996) 3066–3068.
[20] J. Zhang, J. Wang, H.B. Wang, D.H. Yan, Organic thin-film transistors in sandwich configuration, Appl. Phys. Lett. 84 (2004) 142–144.
[21] H.B. Wang, F. Zhu, J.L. Yang, Y.H. Geng, D.H. Yan, Weak epitaxy growth affording high-mobility thin films of disk-like organic semiconductors, Adv. Mater. 19 (2007) 2168–2171.
[22] N. Koch, Organic electronic devices and their functional interfaces, Chem. Phys. Chem. 8 (2007) 1438–1455.
[23] Y.D. Park, J.A. Lim, H.S. Lee, K. Cho, Interface engineering in organic transistors, Mater. Today 10 (2007) 46–54.
[24] M. Brinkmann, J.C. Wittmann, M. Barthel, M. Hanack, C. Chaumont, Highly ordered titanyl phthalocyanine films grown by directional crystallization on oriented poly(tetrafluoroethylene) substrate, Chem. Mater. 14 (2002) 904–914.
[25] K. Itaka, M. Yamashiro, J. Yamaguchi, M. Haemori, S. Yaginuma, Y. Matsumoto, M. Kondo, H. Koinuma, High-mobility C60 field-effect transistors fabricated on molecular-wetting controlled substrates, Adv. Mater. 18 (2006) 1713–1716.
[26] J.L. Yang, D.H. Yan, Weak epitaxy growth of organic semiconductor thin films, Chem. Soc. Rev. 38 (2009) 2634–2645.
[27] L.Q. Li, Q.X. Tang, H.X. Li, W.P. Hu, Molecular orientation and interface compatibility for high performance organic thin film transistor based on vanadyl phthalocyanine, J. Phys. Chem. B 112 (2008) 10405–10410.
[28] L.J. Wang, G.J. Liu, H.B. Wang, D. Song, B. Yu, D.H. Yan, Electrical properties in vanadyl-phthalocyanine-based metal-insulator-semiconductor devices, Appl. Phys. Lett. 91 (2007) 153508.
[29] L.J. Wang, G.J. Liu, F. Zhu, F. Pan, D.H. Yan, Electrical instability in vanadyl-phthalocyanine thin-film transistors, Appl. Phys. Lett. 93 (2008) 173303.
[30] H.B. Wang, D. Song, J.L. Yang, B. Yu, Y.H. Geng, D.H. Yan, High mobility vanadyl-phthalocyanine polycrystalline films for organic field-effect transistors, Appl. Phys. Lett. 90 (2007) 253510.
[31] S. Mohapatra, B.T. Holmes, C.R. Newman, C.F. Prendergast, C.D. Frisbie, A.D. Ward, Organic thin-film transistors based on tolyl-substituted oligothiopheneso, Adv. Funct. Mater. 14 (2004) 605–609.
[32] J.L. Yang, T. Wang, H.B. Wang, F. Zhu, G. Li, D.H. Yan, Weak epitaxy growth of metal-free phthalocyanine on p-sexiphenyl monolayer and double-layer films, J. Phys. Chem. B 112 (2008) 3132–3137.
[33] J.L. Yang, T. Wang, H.B. Wang, F. Zhu, G. Li, D.H. Yan, Ultrathin-film growth of para-sexiphenyl (II): formation of large-size domain and continuous thin film, J. Phys. Chem. B 112 (2008) 7821–7825.
[34] F. Dinelli, M. Murgia, P. Levy, M. Cavallini, F. Biscarini, D.M. de Leeuw, Spatially correlated charge transport in organic thin film transistors, Phys. Rev. Lett. 92 (2004) 116802.
[35] R.F. Ziolo, C.H. Griffiths, J.M. Troup, Crystal structure of vanadyl phthalocyanine, phase II, J. Chem. Soc. Dalton Trans. (1980) 2300–2302.
[36] S. Kobayashi, T. Nishikawa, T. Takenobu, S. Mori, T. Shimoda, T. Mitani, H. Shimotani, N. Yoshimoto, S. Ogawa, Y. Iwasa, Control of carrier density by self-assembled monolayers in organic field-effect transistors, Nat. Mater. 3 (2004) 317–322.
[37] K.P. Pernstich, S. Haas, D. Oberhoff, C. Goldmann, D.J. Gundlach, B. Batlogg, A.N. Rashid, G. Schitter, Threshold voltage shift in organic field effect transistors by dipole monolayers on the gate insulator, J. Appl. Phys. 96 (2004) 6431–6438.
[38] H.B. Wang, X.J. Wang, B. Yu, Y.H. Geng, D.H. Yan, p–p isotype organic heterojunction and ambipolar field-effect transistors, Appl. Phys. Lett. 93 (2008) 113303.
[39] H. Meng, Z.N. Bao, A.J. Lovinger, B.C. Wang, A.M. Mujsce, High field-effect mobility oligofluorene derivatives with high environmental stability, J. Am. Chem. Soc. 123 (2001) 9214–9215.
[40] J. Locklin, M.M. Ling, A. Sung, M.E. Roberts, Z.N. Bao, High-performance organic semiconductors based on fluorene-phenylene oligomers with high ionization potentials, Adv. Mater. 18 (2006) 2989–2992.
[41] H. Klauk, U. Zschieschang, R.T. Weitz, H. Meng, T. Sun, G. Nunes, D.E. Keys, C.R. Fincher, Z. Xiang, Organic transistors based on di(phenylvinyl)anthracene: performanace and stability, Adv. Mater. 19 (2007) 3882–3887.
[42] H.E. Katz, J. Johnson, A.J. Lovinger, W.J. Li, Naphthalenetetracarboxylic diimide-based n-channel transistor semiconductors: structural variation and thiol-enhanced gold contacts, J. Am. Chem. Soc. 122 (2000) 7787–7792.
[43] H. Meng, F.P. Sun, M.B. Goldfinger, F. Gao, D.J. Londono, W.J. Marshal, G.S. Blackman, K.D. Dobbs, D.E. Keys, 2,6-bis 2-(4-pentylphenyl)vinyl anthracene: a stable and high charge mobility organic semiconductor with densely packed crystal structure, J. Am. Chem. Soc. 128 (2006) 9304–9305.

[9]. Although the hole mobility in the $Ir(ppy)_3$-doped CBP thin films can be determined, the hole mobility of undoped CBP thin films was not evaluated because the hole injection barrier between ITO electrode and the undoped CBP thin film is 0.9 eV. The results indicate that holes are directly injected from the injecting electrode to $Ir(ppy)_3$ in $Ir(ppy)_3$-doped CBP thin films because the injection barrier between the injection electrode and the $Ir(ppy)_3$ is less than 0.2 eV.

The insertion of an injection layer between an injection electrode and an organic thin film reduces the injection barrier, and allows us to measure the charge carrier mobility of the organic thin film. Indeed, Hoping et al. have determined hole mobility of CBP thin films by inserting an injection layer of WO_3 between ITO and CBP [6].

Tris(8-hydroxy-quinolinato) aluminum (Alq_3) has shown to be one of the most promising material for an electron transport layer and/or a light emissive layer. Both electrons and holes are injected and transported in the Alq_3 layer and thus the Alq_3 layer is used as a light emissive layer. Notably, it is well known that the cationic Alq_3 is unstable [12] and understanding the hole transport of Alq_3 is useful for determining the degradation mechanism of OLEDs with the Alq_3 thin film as an emissive layer. The determination of the hole mobility in Alq_3 is therefore of fundamental importance.

Although the drift mobilities of the Alq_3 thin films obtained by means of TOF transient photocurrent measurements have been reported [13,14], the thickness of the Alq_3 thin film was between 0.4 and 13 μm and is much thicker than that of Alq_3 layer in OLEDs. Transient EL measurements are another method for determining a charge carrier mobility. However, it is difficult to determine the hole mobility in Alq_3 by them because the higher carrier mobility can be determined from the delay time of the EL signal; the electron mobility in the case of Alq_3. It is therefore important to measure the hole drift mobility in Alq_3 layer with thickness comparable to that in OLED application. However, IS measurements for hole mobility determination have not been carried out yet. To do this, an injection layer for hole injection is necessary because the hole injection barrier between ITO and Alq_3 is too high to measure hole drift mobility using IS. A candidate of the injection layer is 4,4′-bis[N-(1-naphthyl)-N-phenyl-amino]-biphenyl (NPB). A NPB/Alq_3 double layer is a prototypical OLED structure and hence IS measurements for the device structure is essential to understanding of drift-mobility measurements in double layer or multilayer OLEDs.

In this paper, we report on the IS measurement of Alq_3 hole-only devices (HODs) with NPB injection layers, and show that the hole mobility in Alq_3 thin films can be determined from IS measurements. The hole transit in Alq_3 thin films is also observed even in NPB/Alq_3 double layers where the thickness of NPB is comparable to that of Alq_3. The observation is a key information for the understanding of the charge carrier transit in double layer or multilayer OLEDs.

2. Experimental

Fig. 1 shows the device structure of the NPB/Alq_3 HODs, which consists of indium-tin oxide (ITO)/NPB/Alq_3/Au. A

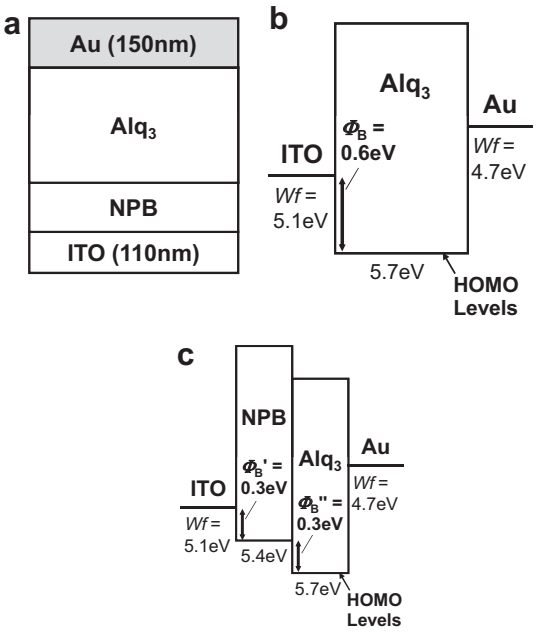

Fig. 1. (a) Cross-sectional view of a NPB/Alq_3 double layer hole-only device (HOD), which consists of ITO/NPB/Alq_3/Au. (b) Energy diagram of an Alq_3 HOD, which consists of ITO/Alq_3/Au. (c) Energy diagram of the NPB/Alq_3 HOD, which consists of ITO/NPB/Alq_3/Au. *Wf* is a work function, and Φ_B is the injection barrier between the *Wf* of ITO and the HOMO energy level of Alq_3. Φ'_B is the injection barrier between the *Wf* of ITO and the HOMO energy level of NPB and Φ''_B is the injection barrier between the HOMO energy level of NPB and the HOMO energy level of Alq_3.

vacuum deposition method was used to fabricate the NPB and Alq_3 thin films in series on a glass substrate with patterned ITO electrodes (pressure $\sim 5 \times 10^{-5}$ Pa). The glass substrate with the ITO electrodes was cleaned ultrasonically in deionized water and by an UV-ozone treatment before vacuum deposition of the organic thin films. The thickness of the NPB thin films were 0, 5, 125, and 310 nm. The film thickness of the Alq_3 was 110 and 180 nm. Au electrodes (150-nm-thick) were deposited on the organic thin films. The structures of samples 1–4 are ITO/NPB(5 nm)/Alq_3(180 nm)/Au, ITO/NPB(5 nm)/Alq_3(110 nm)/Au, ITO/NPB(310 nm)/Alq_3(180 nm)/Au, ITO/NPB(125 nm)/Alq_3(180 nm)/Au, respectively. The samples were then carried in a glove box (with less than 1 ppm water) without exposure to the laboratory atmosphere and sealed by a cap-glass with epoxy resin adhesives. The measurement area was 1×1 mm^2.

The IS was measured with a Solartron 1260 impedance analyser connected to a 1296 dielectric interface. The frequency range was from 10 mHz to 1 MHz, and the measurements were made at room temperature.

3. Results and discussion

3.1. Determination of hole mobility in Alq_3 with a thin NPB layer

The hole charge carrier mobility of Alq_3 thin films was determined from the transit-time, which was estimated

from the frequency dependence of the capacitance (C); the method for measuring charge carrier mobility has been known as $-\Delta B$ method, where $-\Delta B$ is a negative differential susceptance [1–9].

Fig. 2a shows the frequency dependence of capacitance in sample 1. The frequency response curves of capacitance at V = 3–7 V exhibit a minimum value, which is caused by the transit-time effect [1–8]. A transit-frequency which is proportional to the reciprocal of the transit-time is in the vicinity of the frequency at the minimum value of the C–f curve. In the frequency range higher than the transit-frequency, the capacitance reaches the geometrical capacitance C_0 because the period of the applied AC field is too short to redistribute the space charges in the device. Meanwhile, in the frequency range lower than the transit-frequency, the capacitance reaches $3/4C_0$ in the trap-free device because the space charges were redistributed in the device (the dashed line shown in the data at V = 7 V in Fig. 2a) [7,8]. In practice, the capacitance is increased with decreasing frequency in the low frequency range shown in Fig. 2a. The increase in capacitance is due to trapping of injected charge carriers in distributed localised states [8]. However, the increase in capacitance does not affect the determination of charge carrier mobility because the increase in the capacitance is observed below the transit-frequency [8]. The slight decrease in capacitance toward higher frequency is due to the series resistances of the device.

Fig. 2b shows the frequency dependence of $-\Delta B = -\omega\cdot(C-C_0)$ in sample 1. The frequency at the maximum value of $-\Delta B$, f_{max}, is indicated by arrows in Fig. 2b and is related to the transit-time, t_t, $f_{max} \approx 0.72 t_t^{-1}$ [7,8]. Charge carrier mobility μ is then determined by Eq. (1) from the transit-time, t_t [7,8]:

$$\mu = \frac{4}{3}\frac{L^2}{V_0}\frac{1}{t_t} \tag{1}$$

where L is the thickness of the organic thin film between the injecting electrode and the counter electrode, and V_0 is the applied voltage. In the Alq_3 HOD with the NPB injection layer, L is the thickness of the Alq_3 thin film because the thickness of the Alq_3 thin film is much thicker than that of the NPB injection layer. The hole mobility of the Alq_3

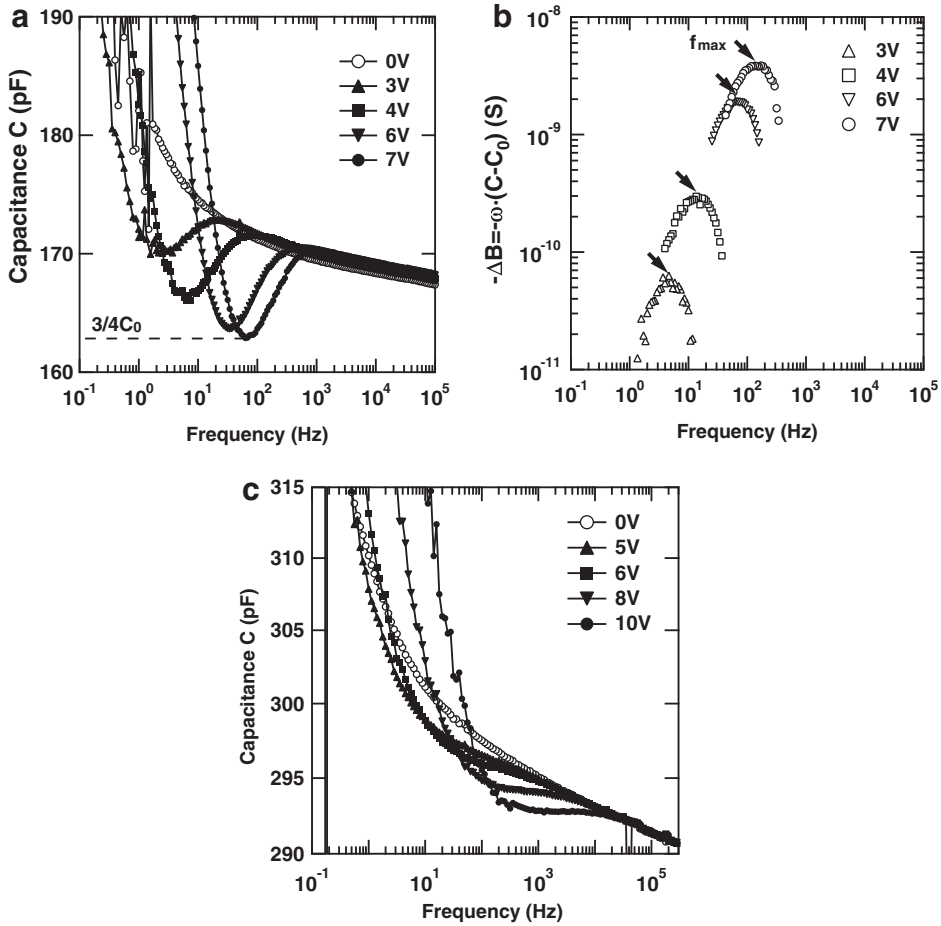

Fig. 2. (a) Frequency dependence of capacitance in sample 1 at DC bias voltages of 0, 3, 4, 6, and 7 V; sample 1 consists of ITO/NPB(5 nm)/Alq_3(180 nm)/Au. (b) Frequency dependence of $-\Delta B = -\omega\cdot(C-C_0)$ in sample 1 at DC bias voltages of 3, 4, 6, and 7 V. (c) Frequency dependence of capacitance in the Alq_3 HOD without the NPB injection layer at DC bias voltages of 0, 5, 6, 8, and 10 V. $-\Delta B$ is a negative differential susceptance, ω is an angular frequency, and C_0 is a geometrical capacitance. f_{max} is the frequency of the maximum value at the $-\Delta B$-frequency curves.

thin film is 9.3×10^{-10}–1.2×10^{-8} $cm^2 V^{-1} s^{-1}$ at $V = 3$–7 V (the data will be shown in Fig. 3).

Fig. 2c shows the frequency dependence of the capacitance in an Alq_3 HOD without a NPB injection layer. Since the minimum value of the C–f curves is not observed at $V = 5$–10 V, the transit-time is not estimated from the $-\Delta B$–f curves. We note that the hole mobility of the Alq_3 thin films is not determined in the Alq_3 HOD without the NPB injection layer.

Fig. 1b shows the energy diagram of the Alq_3 HOD without the NPB injection layer (ITO/Alq_3/Au). Holes are injected from the ITO electrode into the Alq_3 thin films; the hole injection barrier Φ_B is estimated to be 0.6 eV because the work function of ITO W_f is 5.1 eV and the energy level of the highest occupied molecular orbital (HOMO) of Alq_3 is 5.7 eV. As mentioned above, our simulation results show that the transit-time effect is observable using the $-\Delta B$ method when the injection barrier is less than 0.2 eV [7,8]. This explains why the transit-time effect was not observed in the Alq_3 HOD without the NPB injection layer. On the other hand, the transit-time effect can be observed in the Alq_3 HOD with the NPB injection layer (ITO/NPB/Alq_3/Au). Fig. 1c shows the energy diagram of the Alq_3 HOD with the NPB injection layer. The hole injection barrier Φ'_B between the Wf of ITO and the HOMO energy level of the NPB thin film and the hole injection barrier Φ''_B between the HOMO energy levels of the NPB thin film and of the Alq_3 thin film are estimated to be 0.3 eV and 0.3 eV, respectively because the HOMO energy level of NPB is 5.4 eV. The injection barriers, Φ'_B and Φ''_B are slightly higher than the threshold value of the injection barrier, 0.2 eV [7–8]: the criterion of the barrier heights, Φ'_B and Φ''_B, for the observation of the charge carrier mobility is that both barrier heights are less than 0.2 eV. The threshold value was estimated on the assumption that the HOMO energy level of an organic thin film is constant. However, the HOMO energy level in an amorphous organic thin film is, in practice, distributed in energy [13]. The increase in capacitance in the low frequency range shown in Fig. 2a supports the energy distribution of HOMO level in Alq_3 thin film. The transit-time is therefore observed at the injection barriers Φ'_B and Φ''_B, which are slightly larger than the threshold value.

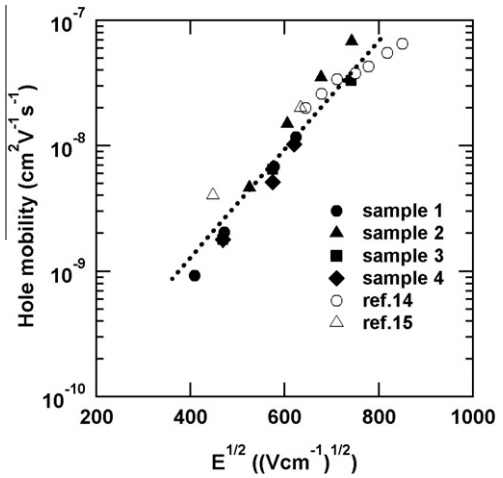

Fig. 3. Electric field dependence of hole mobility in the Alq_3 HODs using the 5-nm-thick NPB injection layer and the NPB/Alq_3 HODs; the structures of sample 1–4 are ITO/NPB(5 nm)/Alq_3(180 nm)/Au, ITO/NPB(5 nm)/Alq_3(110 nm)/Au, ITO/NPB(310 nm)/Alq_3(180 nm) /Au, and ITO/NPB(125 nm)/Alq_3(180 nm)/Au, respectively. As reference data, the hole mobility in Alq_3 films is shown [14–15]; these data were measured by the TOF method.

Fig. 3 shows the electric field dependence of hole mobilities in Alq_3 thin films estimated from the IS measurements of sample 1 and sample 2. For comparison, the hole mobilities of Alq_3 thin films measured using the TOF method are shown in Fig. 3 [14,15]. The hole mobility determined from the IS measurements of the Alq_3 HODs using the NPB injection layers is almost the same as the results of the TOF measurements. It is reasonable that both measurements give the same mobilities because drift mobilities can be measured by the IS and the TOF measurements [8] if the hole transport properties in the Alq_3 thin films are independent of film thickness; the thickness of the Alq_3 thin films measured by the TOF method was between 0.4 and 13 μm, whereas that measured by the IS method was 110 and 180 nm. We stress here that IS can determine the drift mobility of organic semiconductors with a thickness of about 100 nm (the TOF method is not applicable to such thin samples because we can not identify hole transit and electron transit separately). We have determined the hole mobility of Alq_3 thin films using the IS measurements with the 5-nm-thick NPB injection layer.

It was difficult to determine the carrier mobility of organic materials using IS measurements when the injection barrier between the injecting electrode and the organic thin films is high. We also stress that the injection layer, which reduces the injection barrier, allows us to determine the carrier mobility of the organic thin film.

3.2. Determination of hole mobility in NPB/Alq_3 double layers

We examine here IS of NPB/Alq_3 double layers. Fig. 4a shows the C–f curves of sample 3. In the frequency range higher than 10^4 Hz, the capacitance, approximately 60 pF, corresponds to the thickness of the sum of the NPB layer and the Alq_3 layer (the relative permittivity of both NPB and Alq_3 are assumed to be 3.5). The capacitance is increased with decreasing frequency below 10^4 Hz and then is constant in the frequency range between 10 and 10^3 Hz at $V = 0$ V. The capacitance in the frequency range between 10 and 10^3 Hz, approximately 160 pF, corresponds to that of Alq_3 layer. The minimum value of the capacitance, which is caused by a transit-time effect, is observed at $V = 4$, 6, and 7 V in the frequency range between 1 and 100 Hz in Fig. 4a. Fig. 4b shows the $-\Delta B$–f curves of sample 3 at $V = 4$, 6, and 7 V. The $-\Delta B$–f curves have the peaks and the frequency at the maximum value of $-\Delta B$, f_{max}, is indicated by arrows in Fig. 4b. The $-\Delta B$–f curves are similar to the $-\Delta B$–f curves for the Alq_3 HOD with the 5-nm-thick NPB layer shown in Fig. 2b and the transit-time effect was observed in sample 3. The hole mobility of the NPB/Alq_3 double layer is 1.8×10^{-9}–1.0×10^{-8} $cm^2 V^{-1} s^{-1}$ at $V = 4$–7 V, when we assume that L in Eq. (1) is equal to the thickness of the Alq_3 layer even in the double layer devices.

The transit-time can also be obtained from the $-\Delta B$–f curves of sample 4, and the hole drift mobilities calculated

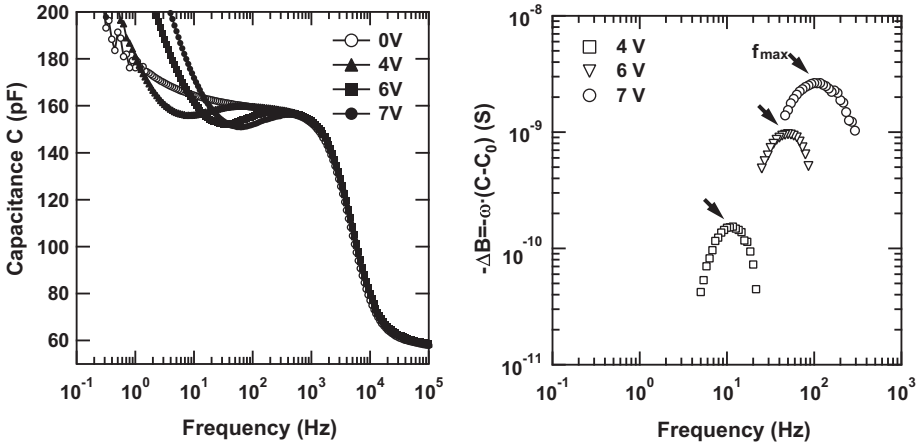

Fig. 4. (a) Frequency dependence of capacitance at DC bias voltages of 0, 4, 6, and 7 V in sample 3; sample 3 consists of ITO/NPB(310 nm)/Alq_3(180 nm)/Au. (b) Frequency dependence of $-\Delta B$ in sample 3 at DC bias voltages of 4, 6, and 7 V.

from the transit-time are shown in Fig. 3. It can be seen that the electric field dependence of the hole drift mobilities of sample 3 and sample 4 is in excellent agreement with those of Alq_3 layers with thin NPB injection layers and with those in literature measured by time-of-flight transient photocurrent technique [14,15]. Our assumption (L in Eq. (1) is equal to the thickness of the Alq_3 layer in sample 3 and sample 4) is reasonable.

We have performed device simulation based on the standard transport equations for HODs using a device simulator (ATLAS, Silvaco) to confirm that the observed transit-time effects results from the hole transit in the Alq_3 layers of sample 3 and sample 4. LUMO and HOMO levels, hole drift mobilities and dielectric constants of NPB and Alq_3 layers were the input parameters for the device simulation. The thicknesses of NPB and Alq_3 layers were set to be the same as those in sample 3 and sample 4.

At lower applied electric field, holes are injected into the NPB layer of the HOD, and injected holes are accumulated at the NPB/Alq_3 interface (Externally applied electric field is applied to the Alq_3 layer). The accumulated holes are injected into the Alq_3 layer at higher applied electric field whose strength is in the same range that we have observed the transit-time effects in Fig. 4. The energy band diagrams obtained from the simulation are consistent with those depicted in Fig. 4 in Ref [16]. The device simulation reproduced the transit-time effects in C–f curves and the values of hole drift mobility obtained from C–f curves using $-\Delta B$ method in sample 3 and sample 4 are in agreement with Alq_3 hole drift mobility. The simulation results are consistent with the experimental results.

The results presented here are the demonstration of the measurement of charge carrier mobilities in double layer OLEDs. Further device simulation and IS studies would be necessary for establishing the criteria for observing charge carrier transit in multilayer OLEDs.

4. Conclusions

The charge carrier mobility of Alq_3 thin films has been determined using IS measurements of the Alq_3 hole-only device with the NPB injection layer, which reduces the hole injection barrier between an injecting electrode and the Alq_3 thin film. The hole mobilities of Alq_3 thin films measured using IS are the same as those measured by TOF transient photocurrent technique. IS method can determine the drift mobility of organic semiconductors with a thickness of ~100 nm. An injection layer is useful for determining the charge carrier mobility of organic thin films when the injection barrier between an injecting electrode and the organic layer is high.

The charge carrier mobility of Alq_3 thin films has also been determined using IS measurements of NPB/Alq_3 double layer hole-only devices in which the thickness of NPB is comparable to that of Alq_3. This indicates that the external electric field is mostly applied to Alq_3 layer in the NPB/Alq_3 double layer hole-only devices. The information would be valuable for interpreting the transit-time effects in multilayer OLEDs.

Acknowledgements

We would like to thank Mr. Y. Sakaki, Mr. H. Kotaki and Mr. S. Oikawa for the fabrication of the devices studied here.

References

[1] H.C.F. Martens, H.B. Broom, P.W.M. Brom, Phys. Rev. B 60 (1999) R8489.
[2] S. Berleb, W. Brütting, Phys. Rev. Lett. 89 (2002) 286601.
[3] H.H.P. Gommans, M. Kemerink, G.G. Andersson, R.M.T. Pijper, Phys. Rev. B 69 (2004) 155216.
[4] S.W. Tsang, S.K. So, J.B. Xu, J. Appl. Phys. 99 (2006) 13706.
[5] N.D. Nguyen, M. Schmeits, H.P. Loebl, Phys. Rev. B 75 (2007) 75307.
[6] M. Hoping, C. Schildknecht, H. Gargouri, T. Riedl, M. Tilgner, H.-H. Johannes, Appl. Phys. Lett. 92 (2008) 213306.
[7] T. Okachi, T. Nagase, T. Kobayashi, H. Naito, Thin Solid Films 517 (2008) 1331.
[8] T. Okachi, T. Nagase, T. Kobayashi, H. Naito, Jpn. J. Appl. Phys. 47 (2008) 8965.
[9] S. Ishihara, T. Okachi, H. Naito, Thin Solid Films 518 (2009) 452.
[10] M.C.J.M. Vissenberg, P.W.M. Blom, Synth. Met. 102 (1999) 1053.
[11] H. Azuma, K. Asada, T. Kobayashi, H. Naito, Thin Solid Films 509 (2006) 182.

[12] H. Aziz, Z.D. Popovic, N.-X. Hu, A.-M. Hor, G. Xu, Science 283 (1999) 1900.
[13] H. Bässler, Phys. Status Solidi B 175 (1993) 15.
[14] S. Naka, H. Okada, H. Onnagawa, Y. Yamaguchi, T. Tsutsui, Synth. Met. 111–112 (2000) 331.
[15] R.G. Kepler, P.M. Beeson, S.J. Jacobs, R.A. Anderson, M.B. Sinclair, S.V. Valenica, P.A. Cahill, Appl. Phys. Lett. 66 (1995) 3618.
[16] Y. Noguchi, N. Sato, Y. Tanaka, Y. Nakayama, H. Ishii, Appl. Phys. Lett. 92 (2008) 203306.

with the mobilities previously reported for low-voltage DNTT TFTs [23]. Compared with the previous report [23] the thickness of the DNTT layer has been reduced from 30 to 25 nm, which is expected to reduce the parasitic potential drop associated with the vertical current path between the source/drain contacts (located on top of the semiconductor) and the carrier channel (located at the bottom of the semiconductor) and hence is expected to increase the transconductance and effective mobility of the TFTs [24].

The TFTs and circuits were fabricated on glass (Corning Eagle 2000) or flexible polyethylene naphthalate (Teonex® Q65 PEN; kindly provided by William A. MacDonald, DuPont Teijin Films, Wilton, UK). Aluminum with a thickness of 20 nm was evaporated directly onto the substrate through a polyimide shadow mask (CADiLAC Laser, Hilpoltstein, Germany) to define the gate electrodes. The aluminum was briefly exposed to an oxygen plasma to create a 3.6 nm thick AlO_x film, followed by immersion of the substrate in a 2-propanol solution of *n*-tetradecylphosphonic acid to form a 1.7 nm thick self-assembled monolayer (SAM) on the surface of the oxidized gates. This results in an AlO_x/SAM gate dielectric with a thickness of 5.3 nm and a capacitance of 800 nF/cm^2 [25–27]. A 25 nm thick DNTT layer was vacuum-deposited through a shadow mask, followed by the deposition of 30 nm thick gold through another shadow mask to define the source/drain contacts. The channel length is between 10 and 50 μm and the channel width is 100 μm or 200 μm. The maximum process temperature is 60 °C (the substrate temperature during the DNTT deposition). Fig. 1. shows the chemical structure of the semiconductor DNTT, a schematic cross-section of the TFTs, and photographs of a TFT with a channel length of 10 μm. All electrical measurements, including the shelf-life and bias–stress measurements, were performed in ambient air at room temperature.

The static performance of the flexible DNTT TFTs measured shortly after fabrication is summarized in Fig. 2. The TFTs have an on/off ratio of 10^8 and a subthreshold swing of 100 mV/decade. For the shortest channel length (L = 10 μm), the transconductance (normalized to the channel width) reaches 0.12 S/m. This is a factor of three larger than the transconductance of pentacene TFTs based on the same fabrication process and the same channel length fabricated on glass substrates [20] and similar to the transconductance of photolithographically patterned bottom-contact pentacene TFTs with a channel length of 5 μm on flexible polymeric substrates recently reported by the IMEC group [10]. The field-effect mobility extracted from the transfer characteristics of our DNTT TFTs in the saturation regime ranges from 1.2 cm^2/V s (L = 10 μm) to 2.1 cm^2/V s (L = 50 μm). The observation that the mobility extracted from the transfer characteristics decreases with decreasing channel length indicates that the relative contribution of the contact resistance to the total device resistance increases with decreasing channel length. This effect has been analyzed in detail for pentacene TFTs [28] and is expected to be even more pronounced for DNTT TFTs, since the larger ionization potential of DNTT (5.4 eV) compared with pentacene (5.0 eV) [18] is expected to produce a larger energy barrier at the interface between the semiconductor and the Au source and drain contacts (Fermi energy about 5 eV), and hence a larger contact resistance.

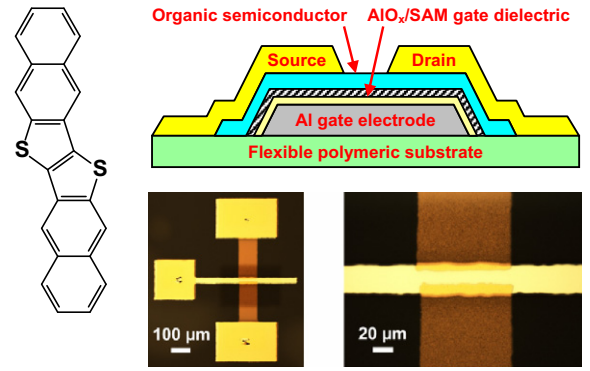

Fig. 1. Chemical structure of the conjugated organic semiconductor dinaphtho[2,3-b:2′,3′-f]thieno[3,2-b]thiophene (DNTT), schematic TFT cross-section, and photographs of a DNTT TFT with a channel length of 10 μm and a channel width of 100 μm patterned using polyimide shadow masks.

Fig. 3a. shows how the saturation mobility of a flexible DNTT TFT with a channel length of 50 μm evolves over time when the substrate is kept in ambient air with a humidity of 40–70% under weak yellow light (laboratory conditions). The mobility decreases from initially 2.1 to 2.0 cm^2/V s after three months and then to 1.5 cm^2/V s after a total of eight months in air. For comparison, Fig. 3a. also shows that the DNTT TFTs have substantially better air stability than pentacene TFTs fabricated with the same technology (i.e., same type of substrate, same gate dielectric, same contacts).

Although the air stability of the DNTT transistors is better than that of the pentacene devices, there is a slight drop in the mobility of the DNTT TFTs, from initially 2.1 to 1.5 cm^2/V s after eight months in air. The mechanism for this slow degradation is unknown. Although oxidation of the DNTT molecules cannot be completely ruled out, it is unlikely given the molecular structure of DNTT. An alternative explanation for the observed mobility degradation is that air-borne molecules (e.g., H_2O, O_2, O_3) penetrate into the grain boundaries of the polycrystalline DNTT film and then interact with the mobile charge carriers or with the DNTT molecules at or near the grain boundaries in a way that is detrimental for the field-effect mobility [29,30].

In addition to the shelf-life stability we have also investigated the bias–stress stability. Fig. 3b illustrates the time-dependent decrease in drain current and the associated shift in threshold voltage of DNTT TFTs fabricated on a glass substrate during prolonged gate–bias stress. As in the case of TFTs based on hydrogenated amorphous silicon [31,32] and pentacene [33] the drain current decays faster when the applied gate–source voltage is larger. The reason is that a larger gate–source voltage results in a larger carrier density in the channel and hence in a larger trapping rate. The carrier density accumulated in the transistor channel at a certain gate–source voltage can be estimated as follows:

$$n = \frac{1}{q} C_{\mathrm{diel}} |V_{\mathrm{GS}} - V_{\mathrm{th}}| \qquad (1)$$

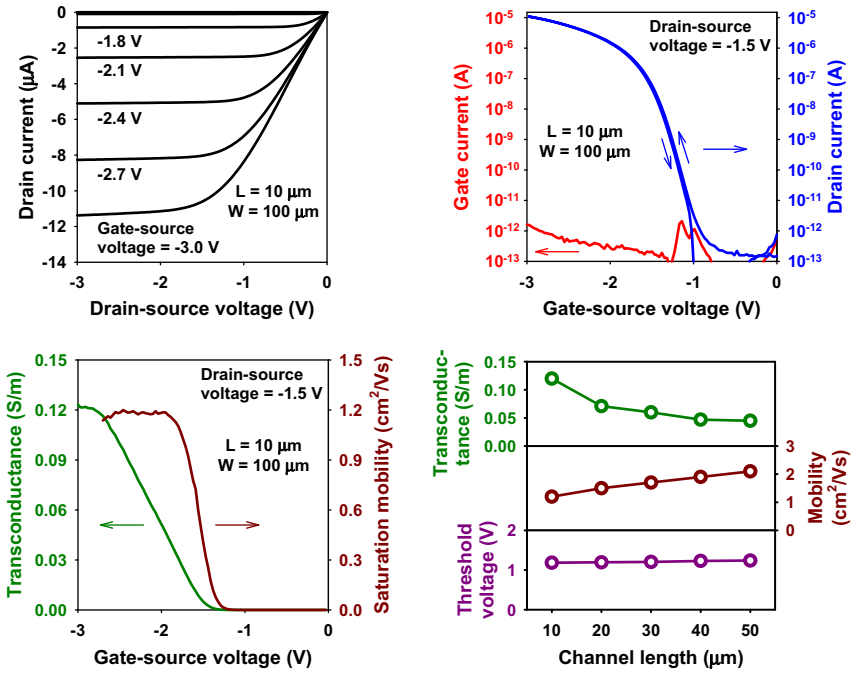

Fig. 2. Electrical characteristics of a DNTT TFT with a channel length of 10 μm. The transconductance has been normalized to the channel width (W = 100 μm). The influence of the channel length on the transconductance, the saturation mobility extracted from transfer characteristics and the threshold voltage is also shown.

where q is the elementary charge (1.6×10^{-19} C), C_{diel} is the capacitance of the gate dielectric per unit area, and V_{th} is the threshold voltage. According to Eq. (1), the carrier density in our DNTT TFTs (C_{diel} = 800 nF/cm^2, V_{th} = −1.4 V) is about 8×10^{12} cm^{-2} at a gate–source voltage of −3 V and 3×10^{12} cm^{-2} at a gate–source voltage of −2 V. In addition to the carrier density it is also useful to estimate the sheet resistance of the transistor channel, as suggested by the Princeton group [32]:

$$R_{sheet} = \frac{V_{DS}}{I_D}\frac{W}{L} \qquad (2)$$

where V_{DS} is the drain–source voltage, I_D is the drain current, W is the channel width, and L is the channel length. According to Eq. (2), the sheet resistance of the DNTT TFT in Fig. 3b. (W=100 μm, L = 30 μm) in the linear regime (V_{DS} = −0.1 V) is about 1 MΩ/sq at a gate-source voltage of −3 V and 2.5 MΩ/sq at a gate–source voltage of −2 V. When the DNTT TFTs are stressed with a gate-source voltage of −3 V it takes 10^4 s for the drain current to decay by 10%, whereas at a gate-source voltage of −2 V the lifetime for a 10% decay is 10^5 s. These lifetimes are similar to those reported by the Princeton group for a-Si:H TFTs fabricated at a temperature of 285 °C [31,32] despite the fact that the DNTT TFTs were fabricated at a more flexible-substrate-friendly temperature of 60 °C.

A direct comparison between the bias stress-induced drain-current decay of DNTT and pentacene TFTs is more difficult, since the drain current of pentacene TFTs decays in part simply due to the rapid oxidation of the pentacene molecules. In order to decouple the bias stress-induced threshold-voltage shift from the oxidation-induced degradation, the MIT group has performed bias–stress measurements on the pentacene TFTs in nitrogen [33]. However, since their pentacene TFTs utilized a different gate dielectric (parylene–N), a direct comparison with our DNTT TFTs is not possible.

To assess the dynamic performance of the TFTs we have fabricated unipolar ring oscillators based on inverters with saturated load [20,23]. The drive TFTs have a channel length of 10 μm and a gate overlap of 15 μm, from which a gate capacitance of 0.3 pF/μm (normalized to the channel width) can be estimated. Fig. 4 shows the signal delay per stage of a 5-stage ring oscillator on a glass substrate measured as a function of supply voltage. At a supply voltage of −5 V, the stage delay is 7 μsec. This is the shortest signal delay reported for an organic ring oscillator at this supply voltage (5 V), and it is within a factor of 20 of the fastest organic ring oscillators reported to date [10], despite the smaller supply voltage (5 V instead of 10 V) and the more relaxed channel length (10 μm instead of 2 μm).

Although functional active-matrix displays based on organic light-emitting diodes (LEDs) and organic TFTs have been demonstrated [1,3,4], there is some uncertainty about whether organic TFTs are capable of driving organic LEDs to the brightness required for practical display applications [34]. Fig. 5 shows photographs of a blue organic LED controlled by a DNTT TFT for five different gate–source voltages. The TFT has a channel width (W) of 200 μm and a channel length (L) of 10 μm (W/L = 20). The LED is a bottom-emitting fluorescent low-voltage device manufactured by Novaled [35,36] and has an active area of 0.067 cm^2. This area is about 1000 times larger than the pixel area in a notebook computer display (e.g., the area

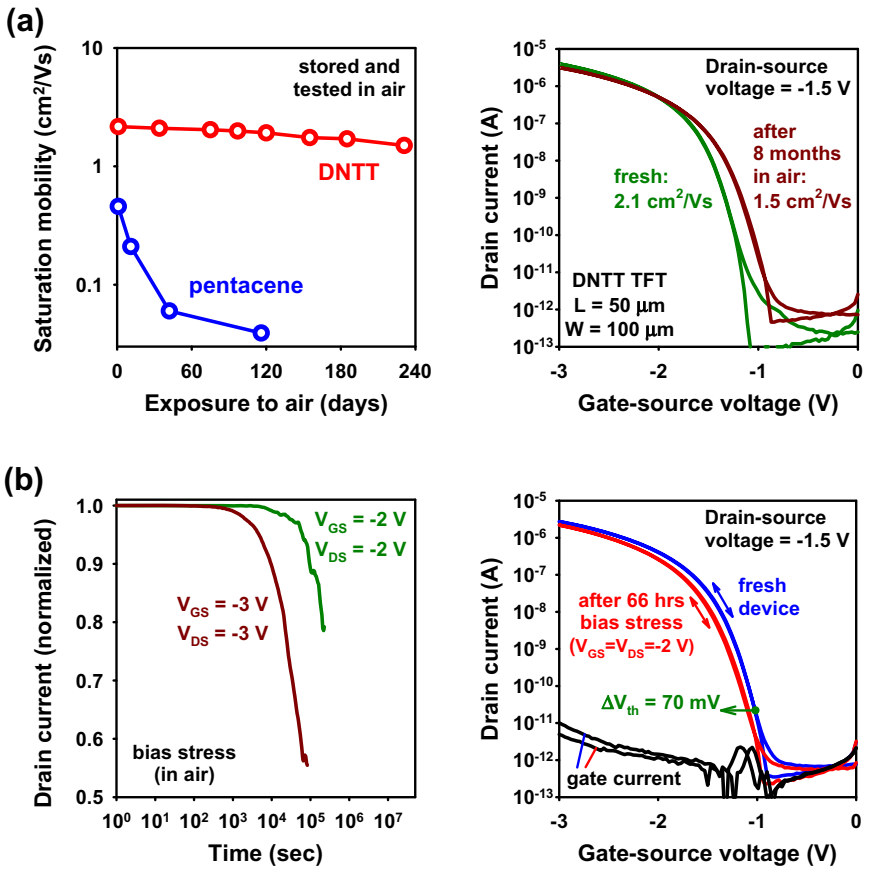

Fig. 3. (a) Shelf-life stability of a DNTT TFT (channel length 50 µm) in comparison to that of a pentacene TFT based on the same technology. (b) Bias–stress stability of DNTT TFTs (channel length 30 µm).

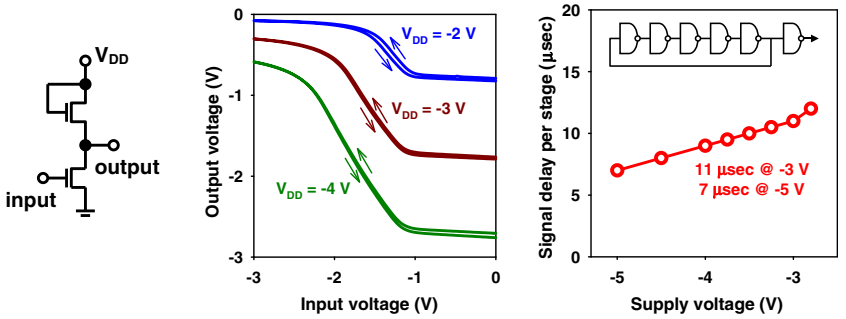

Fig. 4. Circuit schematic and transfer characteristics of a unipolar inverter with saturated load, and signal delay per stage as a function of supply voltage for a unipolar five-stage ring oscillator based on DNTT TFTs (channel length 10 µm, gate overlap 15 µm).

of an RGB subpixel in a display with a 17-inch diagonal and SXGA resolution is about 7×10^{-5} cm^2). The LED has a luminous efficiency of 7 cd/A and CIE color coordinates of 0.14/0.25. The LED and the TFT were connected using a BNC cable. When a gate–source voltage of −3.5 V is applied to the TFT and a potential of −5 V to the cathode of the LED, the TFT drives a current of 67 µA through the LED. At this current, the potential difference between source and drain of the TFT is 2.2 V and the potential difference between anode and cathode of the LED is 2.8 V. The current of 67 µA produces a luminance of 70 cd/m^2, which is within an order of magnitude of the maximum brightness of most commercially available computer monitors (typical display brightness: ~500 cd/m^2; typical subpixel brightness: 600–1500 cd/m^2). Assuming the luminance is approximately proportional to the current density, a TFT with $W/L = 1$ would be able to drive an LED with the same efficiency (7 cd/A), but with a typical display subpixel area of 10^{-4} cm^2 to a brightness of 2500 cd/m^2, which is well above the maximum brightness required for most display

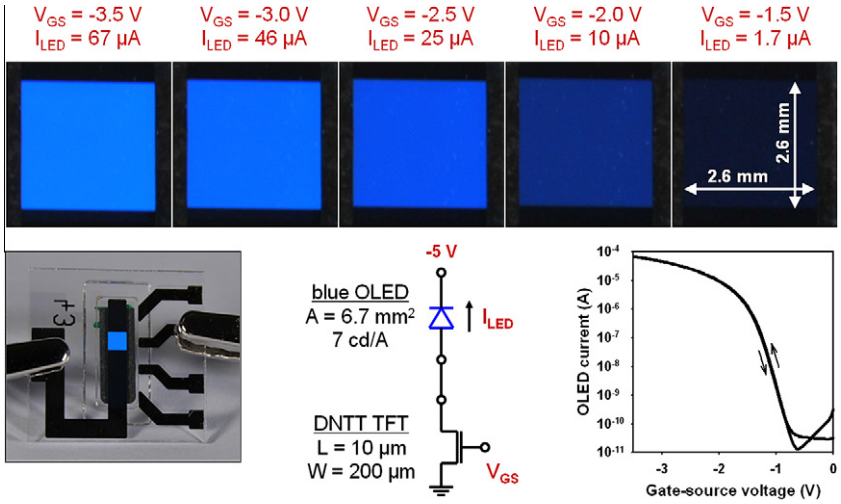

Fig. 5. Photographs of a blue organic light-emitting diode (LED) with an area of 6.7 mm^2 controlled by a DNTT TFT with a channel width of 200 µm and a channel length of 10 µm. At the maximum gate–source voltage (−3.5 V), the luminance of the organic LED reaches 70 cd/m^2. (For interpretation of the references to colour in this figure legend, the reader is referred to the web version of this article.)

applications. Organic LEDs based on phosphorescent emitter materials, which typically have luminous efficiencies between 30 and 70 cd/A, depending on color [35–37], would reach a brightness of 10,000–20,000 cd/m^2 when controlled by a DNTT TFT with $W/L = 1$. This clearly shows that organic TFTs even with the smallest possible footprint ($W/L = 1$) are fully capable of providing the electrical current required to drive organic LEDs in active-matrix displays.

In summary we have evaluated the current–voltage characteristics, the air stability, the bias–stress stability, the dynamic performance, and the OLED-drive capability of low-voltage TFTs based on the organic semiconductor dinaphtho-thieno-thiophene (DNTT), a fused heteroarene with large ionization potential. We have found that DNTT TFTs have larger mobility, better air stability, better bias–stress stability, and better dynamic performance than pentacene TFTs fabricated with the same technology, suggesting that DNTT has great potential for organic electronics, including flexible active-matrix OLED displays.

Acknowledgements

The authors thank Richard Rook at CADiLAC Laser for providing high-quality shadow masks and Carmen Müller at the Max Planck Institute for Solid State Research for professional photography. We gratefully acknowledge financial support provided by the New Energy and Industrial Technology Development Organization (NEDO) of Japan.

References

[1] C.D. Sheraw, L. Zhou, J.R. Huang, D.J. Gundlach, T.N. Jackson, M.G. Kane, I.G. Hill, M.S. Hammond, J. Campi, B.K. Greening, J. Francl, J. West, Appl. Phys. Lett. 80 (2002) 1088.
[2] H.E.A. Huitema, G.H. Gelinck, P.J.G. van Lieshout, E. van Veenendaal, F.J. Touwslager, J. Soc. Inf. Display 14 (2006) 729.
[3] I. Yagi, N. Hirai, Y. Miyamoto, M. Noda, A. Imaoka, N. Yoneya, K. Nomoto, J. Kasahara, A. Yumoto, T. Urabe, J. Soc. Inf. Display 16 (2008) 15.
[4] Y. Nakajima, T. Takei, T. Tsuzuki, M. Suzuki, H. Fukagawa, T. Yamamoto, S. Tokito, J. Soc. Inf. Display 17 (2009) 629.
[5] T. Someya, Y. Kato, S. Iba, Y. Noguchi, T. Sekitani, H. Kawaguchi, T. Sakurai, IEEE Trans. Electr. Dev. 52 (2005) 2502.
[6] Y. Kato, T. Sekitani, M. Takamiya, M. Doi, K. Asaka, T. Sakurai, T. Someya, IEEE Trans. Electr. Dev. 54 (2007) 202.
[7] T. Sekitani, M. Takamiya, Y. Noguchi, S. Nakano, Y. Kato, T. Sakurai, T. Someya, Nat. Mater. 6 (2007) 413.
[8] T. Sekitani, T. Yokota, U. Zschieschang, H. Klauk, S. Bauer, K. Takeuchi, M. Takamiya, T. Sakurai, T. Someya, Science 326 (2009) 1516.
[9] P. Baude, D.A. Ender, M.A. Haase, T.W. Kelley, D.V. Muyres, S.D. Theiss, Appl. Phys. Lett. 82 (2003) 3964.
[10] K. Myny, S. Steudel, S. Smout, P. Vicca, F. Furthner, B. van der Putten, A.K. Tripathi, G.H. Gelinck, J. Genoe, W. Dehaene, P. Heremans, Org. Electronics 11 (2010) 1176.
[11] F. De Angelis, M. Gaspari, A. Procopio, G. Cuda, E. Di Fabrizio, Chem. Phys. Lett. 468 (2009) 193.
[12] J.H. Lee, G.H. Kim, S.H. Kim, S.C. Lim, Y.S. Yang, J.H. Youk, J. Jang, T. Zyung, Synth. Metals 143 (2004) 21.
[13] W.J. Kim, W.H. Koo, S.J. Jo, C.S. Kim, H.K. Baik, J. Lee, S. Im, J. Vac. Sci. Technol. B 23 (2005) 2357.
[14] S.H. Han, J.H. Kim, J. Jang, S.M. Cho, M.H. Oh, S.H. Lee, D.J. Choo, Appl. Phys. Lett. 88 (2006) 073519.
[15] H. Jung, T. Lim, Y. Choi, M. Yi, J. Won, S. Pyo, Appl. Phys. Lett. 92 (2008) 163504.
[16] K. Takimiya, Y. Kunugi, T. Otsubo, Chem. Lett. 36 (2007) 578.
[17] T. Yamamoto, K. Takimiya, J. Photopolym. Sci. Technol. 20 (2007) 57.
[18] T. Yamamoto, K. Takimiya, J. Am. Chem. Soc. 129 (2007) 2224.
[19] S. Haas, Y. Takahashi, K. Takimiya, T. Hasegawa, Appl. Phys. Lett. 95 (2009) 022111.
[20] H. Klauk, U. Zschieschang, M. Halik, J. Appl. Phys. 102 (2007) 074514.
[21] U. Zschieschang, M. Halik, H. Klauk, Langmuir 24 (2008) 1665.
[22] H. Ma, O. Acton, G. Ting, J.W. Ka, H.L. Yip, N. Tucker, R. Schofield, A.K.Y. Jen, Appl. Phys. Lett. 92 (2008) 113303.
[23] U. Zschieschang, F. Ante, T. Yamamoto, K. Takimiya, H. Kuwabara, M. Ikeda, T. Sekitani, T. Someya, K. Kern, H. Klauk, Adv. Mater 22 (2010) 982.
[24] P.V. Pesavento, K.P. Puntambekar, C.D. Frisbie, J.C. McKeen, P.P. Ruden, J. Appl. Phys. 99 (2006) 094504.
[25] A. Jedaa, M. Burkhardt, U. Zschieschang, H. Klauk, D. Habich, G. Schmid, M. Halik, Org. Electron. 10 (2009) 1442.
[26] K. Fukuda, T. Hamamoto, T. Yokota, T. Sekitani, U. Zschieschang, H. Klauk, T. Someya, Appl. Phys. Lett. 95 (2009) 203301.
[27] O. Acton, G.G. Ting, P.J. Shamberger, F.S. Ohuchi, H. Ma, A.K.Y. Jen, ACS Appl. Mater. Interface. 2 (2010) 511.
[28] D.J. Gundlach, L. Zhou, J.A. Nichols, T.N. Jackson, P.V. Necliudov, M.S. Shur, J. Appl. Phys. 100 (2006) 024509.
[29] D. Li, E.J. Borkent, R. Nortrup, H. Moon, H.E. Katz, Z. Bao, Appl. Phys. Lett. 86 (2005) 042105.

[30] R.T. Weitz, K. Amsharov, U. Zschieschang, M. Burghard, M. Jansen, M. Kelsch, B. Rhamati, P.A. van Aken, K. Kern, H. Klauk, Chem. Mater. 21 (2009) 4949.
[31] B. Hekmatshoar, K.H. Cherenack, A.Z. Kattamis, K. Long, S. Wagner, J.C. Sturm, Appl. Phys. Lett. 93 (2008) 032103.
[32] B. Hekmatshoar, S. Wagner, J.C. Sturm, Appl. Phys. Lett. 95 (2009) 143504.
[33] K.K. Ryu, I. Nausieda, D.D. He, A.I. Akinwande, V. Bulovic, C.G. Sodini, IEEE Trans. Electr. Dev. 57 (2010) 1003.
[34] B. Liu, M.A. McCarthy, Y. Yoon, D.Y. Kim, Z. Wu, F. So, P.H. Holloway, J.R. Reynolds, J. Guo, A.G. Rinzler, Adv. Mater. 20 (2008) 3605.
[35] J. Birnstock, T. Canzler, M. Hofmann, A. Lux, S. Murano, P. Wellmann, A. Werner, "PIN OLEDs – Improved structures and materials to enhance device lifetime, " J. Soc. Inf. Display 16 (2008) 221.
[36] R. Meerheim, R. Nitsche, K. Leo, Appl. Phys. Lett. 93 (2008) 043310.
[37] N. Chopra, J.S. Swensen, E. Polikarpov, L. Cosimbescu, F. So, A.B. Padmaperuma, Appl. Phys. Lett. 97 (2010) 033304.

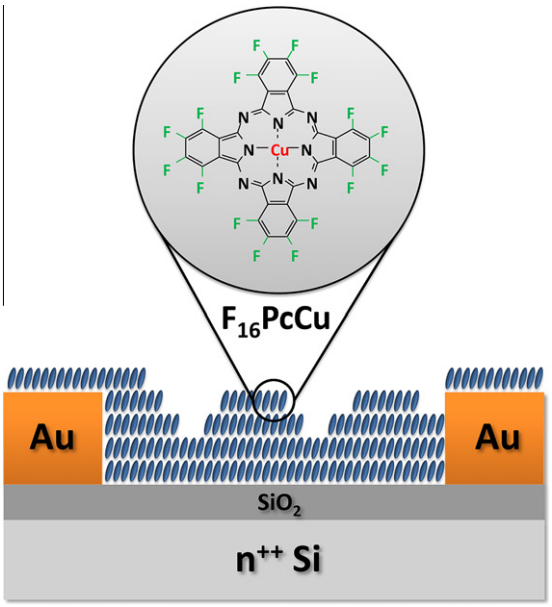

Scheme 1. Schematic drawing of the OFET device structure with F_{16}PcCu as organic semiconductor thin film.

particular of ultrathin films [14,20] it is hard to study the thickness-dependence of a quantity which is as sensitive as μ_{FET} in a comparison of different films prepared in parallel with different thickness because of large scatter in the results.

The general electrical characteristics of OFET are well described within the model of MOSFET theory [21] since the electrical properties of the semiconductor layer in OFET depend on the interface between the gate dielectric and the organic layer. However, the characteristics of OFET often deviate substantially from the expected linear increase of the drain-source current (I_{SD}) on the drain-source voltage in the output characteristics and develop a sigmoidal ("*S*-") shape [22]. Such characteristics were argued to arise from the field-effect mobility of charge carriers to depend on the applied bias [23], the density of charge carriers in the conductive channel [24] or injection barriers to/from the contact metals [23,25–27]. Such complications in modeling hampered the safe identification of μ_{FET} of a given material. The mobility μ_{FET}, however, plays a crucial role in the understanding of charge carrier transport and its control is critical for the success of many applications using OFET.

Charge transport at the interface with the gate dielectric of an OFET involves an accumulation layer thickness on the order of only several times the spacing between molecule layers. Estimates based on classic continuum electrostatics give thicknesses of only a few nanometers [28]. F_{16}Pc showed the formation of ultrathin conductive films already in the regime of one or few monolayers [14,29]. The structure of such ultrathin F_{16}Pc films has been analyzed *in situ* during growth by electron diffraction [30], optical spectroscopy [31,32], and very detailed *in situ* X-ray diffraction analysis [33–35]. A detailed control of the films in the ultrathin regime in the very interface with the gate dielectric as explicitly accessible for F_{16}PcCu is the key to optimize devices.

In the present work we studied films of F_{16}PcCu from the monolayer regime to films of about 40 nm thickness. Further, full transfer characteristics for varied gate voltages were measured as needed to safely determine the threshold gate voltage and the on/off ratio as technically relevant parameters and as quantities that clearly indicate the degree of interfacial charge transfer to the conductive channel. We determined the output characteristics for gate voltages between 1 and 50 V during deposition of F_{16}PcCu (*in situ*) at subsequently growing film thickness. Thickness-dependent changes were therefore safely determined and scattering of results among samples was thereby avoided. Applied electric fields above 1000–2500 kV m^{-1} during deposition can have an influence on the growth of organic semiconductor films [36,37]. Our experiments were therefore performed at significantly lower electric field strength. The formation of an active channel of F_{16}PcCu was studied in bottom gate, bottom contact field-effect transistors in a setup that allowed electrical characterization in real time, fast compared to typical growth rates of vapor-deposited organic semiconductor thin films. Since metal adhesion layers beneath the desired contact metal had led to difficulties in the interpretation of contact formation in particular for organic films in the monolayer range [19] we used pure metal contacts of either silver or gold without any adhesion layer in the present study. The evolution of the apparent charge carrier mobility and the development of the threshold voltage as well as the on/off ratio were studied in dependence on the formation of conductive layers in real time as opposed to preceding and subsequent island formation and an optimum accumulation layer crucial for device operation is explicitly discussed.

2. Experimental details

Highly n-doped silicon [1 1 1] wafers with a 300 nm thermally grown oxide layer were used as substrate. The wafers were cleaned with acetone (Roth, 99.8%) and ethanol (Roth, 99.8%) in an ultrasonic bath and dried with nitrogen (Air Liquide, 99.999%). Optical UV lithography has been used to structure inter digital source drain contacts with channel length of 40 and 20 μm, respectively. Therefore, positive resist ma-P1215 (MicroResist) was spun onto the wafer, exposed to UV-light through a shadow mask and resist removed from the illuminated areas by rinsing in a ma-D331 (MicroResist) developer solution. A 50 nm thick film of Ag or Au was deposited in a Leybold-Heraeus Z400 sputter machine (10^{-4} mbar Ar, Air Liquide, 99.999%). The interdigitated electrode arrays were achieved by lift-off in acetone within an ultrasonic bath. Such structures with the silicon wafer as gate electrode were mounted onto a ceramic sample holder and contacted with spring loaded pins.

Perfluoro copper phthalocyanine (F_{16}PcCu) was obtained from D. Wöhrle's group at the University of Bremen, purified by 3-zone sublimation (Lindbergh) in vacuum (5×10^{6} mbar) and then used as organic semiconductor and thermally evaporated under high vacuum conditions

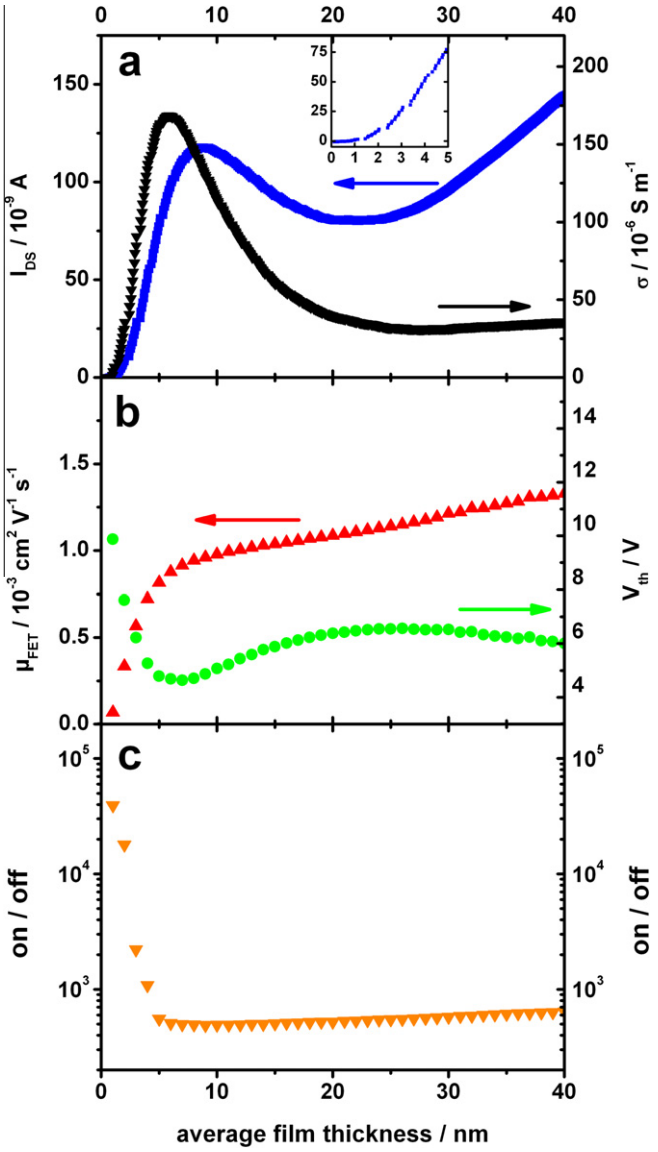

Fig. 1. Development of current I_{DS} (■) and the specific conductivity σ (▼) across a channel length of L = 40 μm between the source and drain gold electrodes at a constant source-drain-voltage of 10 V (a), charge carrier mobility μ_{FET} (▲) and threshold voltage V_{th} (●) calculated from the output and transfer characteristics determined by voltage sweeps (b) and the maximum on/off-ratio of the transistor (c) during deposition of F_{16}PcCu. The inset in (a) depicts initial percolation towards a conductive channel.

(10^{-7} mbar) from resistively heated BN crucibles (Lesker) leading to a deposition rate of 0.5 nm per minute as monitored by a calibrated quartz crystal microbalance. The substrate temperature increased from 22 to 43 °C during deposition and subsequently decreased again to 22 °C as monitored by a Pt100. For electrical measurements a Keithley 6430 digital multimeter and a Keithley 487 Picoamperemeter were used.

These structures with bottom gate and bottom contact enabled us to investigate electrical properties during film growth from the earliest stage of material deposition in the range of mono layer formation up to the final film thickness of typically 40 nm. Every 10 s the formation of conductive pathways within the transistor structure was monitored by measurements of the source-drain current at a constant voltage of 10 V. At each nm of deposited material (about every 2 min) during the organic layer deposition full output and transfer characteristics were measured to determine the charge carrier mobility μ_{FET} in the saturation regime of the output characteristics and the threshold voltage V_{th} from the linear fit to the square root of the drain current as a function of gate voltage according to MOSFET theory [21] for the transistor in a range of typically 1–30 V of applied voltages which took about 20 s. The corresponding electric field strength in our experiments of less than 250 kV m^{-1} was therefore chosen to avoid a significant influence on film growth. Further, the very same preparation procedure was used for the discussed films.

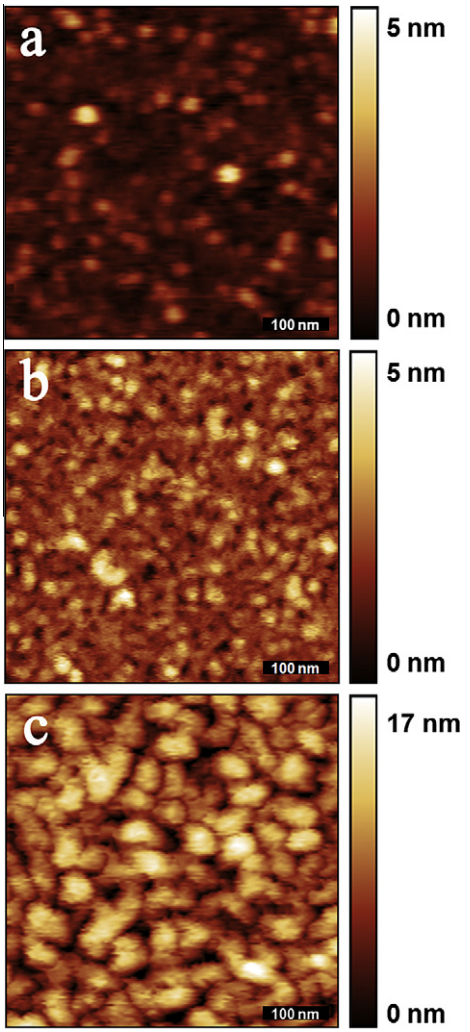

Fig. 2. Atomic force microscopy (AFM) images and calculated root means square roughness (rms) of the SiO_2 gate dielectric substrate (a, rms = 0.49 nm), a $F_{16}PcCu$ film of 3 nm average film thickness deposited on SiO_2 (b, rms = 0.62 nm) and a 40 nm $F_{16}PcCu$ film on SiO_2 (c, rms = 3.16 nm) showing 0.5 × 0.5 μm sections with a height range as indicated in the figure (black to white).

Stabilization of the transistor characteristics was studied following these experiments in vacuum without any thermal annealing procedures and by venting with synthetic air (20.5% O_2 in N_2, Air Liquide, 99.999% each). In order to provide optimum consistency of the different methods we discuss in this work the properties of only two separate films in different growth states although similar characteristics were reproduced for other films also. Subsequent to the electrical studies, atomic force microscopy (AFM) was performed with a smart SPM 1000 by AIST-NT in the resonant mode using N1A cantilevers.

3. Results and discussion

$F_{16}PcCu$ was deposited onto silicon oxide with bottom contact electrodes at room temperature. The conductivity

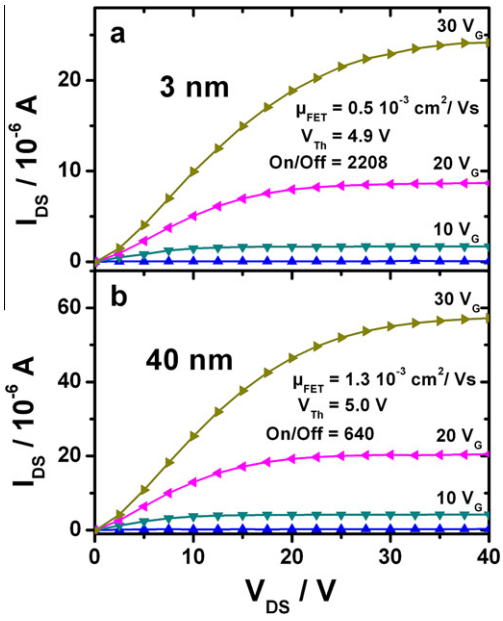

Fig. 3. Output characteristics of a thin film $F_{16}PcCu$ transistor at 3 nm (a) and 40 nm (b) average film thickness measured subsequently during one deposition.

during the film growth was measured every 10 s corresponding to 0.1 Å average film thickness during deposition. In Fig. 1a the current distribution over increasing film thickness is shown for a structure with Au interdigitated source and drain electrodes. The background current of about 10^{-11} A increased with the deposited amount of $F_{16}PcCu$ from the very beginning showing the geometric percolation of the semiconductor material on the gate insulator. From earlier experiments it is known that $F_{16}PcCu$ grows in layers of upright standing molecules (~1.5 nm height) with the molecular plane almost parallel to the surface normal on oxide surfaces after treatments similar to the present one [38,39]. Such layered growth continues up to an average film thickness of about 8 nm. This increase in current is also reflected in an increase of the specific conductivity as also shown in Fig. 1a. A maximum conductivity of 1.7×10^{-4} Sm^{-1} was reached at about 6 nm average film thickness. Deposition beyond a monolayer (~1.5 nm) obviously led to the formation of additional conductive layers of up to about four monolayers contributing efficiently to the electrical charge transport by adding parallel conduction paths. This growth mode changed for deposition beyond an average film thickness of four monolayers. Additional $F_{16}PcCu$ contributed less efficiently to the conduction presumably by growth on top of islands for which the layers were not completed shown by a decreasing conductivity and an only slightly increasing current before the current also even decreased beyond about 8 nm. Such decrease in both, conductivity and current could either be caused by a decrease of μ_{FET} at widely constant diameter of the conductive path or by a decrease of the diameter of the conductive path by a rearrangement of molecules from already formed layers toward presumably more stable

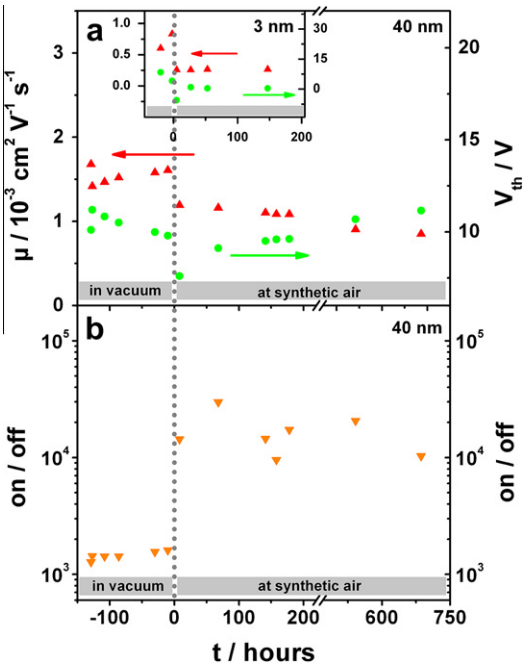

Fig. 4. Charge carrier mobility μ_{FET} and threshold voltage V_{th} over elapsed time t after deposition of a 40 nm $F_{16}PcCu$ film with the dotted line indicating the ventilation with synthetic air and an ultra thin film transistor with 3 nm $F_{16}PcCu$ shown as inset in the same units (a) and the maximum on/off-ratio of the 40 nm transistor (b).

three-dimensional isolated islands on top of it. These characteristics continued up to an average film thickness of 20–30 nm. Upon further deposition these islands started to percolate forming additional conductive pathways. The current increased at almost constant conductivity as shown in Fig. 1a. The AFM image of such $F_{16}PcCu$ film with 40 nm average film thickness was measured (Fig. 2c) and was compared to the SiO_2 surface of an uncovered substrate (Fig. 2a). The film growth had led to a significant increase of the roughness from rms = 0.49 nm for the uncovered SiO_2 to rms = 3.16 nm indicating the island characteristics of film growth. Compared with the film thickness of 40 nm, however, such little roughness showed a widely percolated structure of the islands.

The electronic properties of transistors in such structures with Au electrodes were measured for every nm of average film thickness (Fig. 1b). The field-effect-mobility μ_{FET} determined from the saturation of the output characteristics sharply rose from the formation of the first pathways to the maximum in current and conductivity. Such characteristics were explained by the presence of only a few conductive pathways, a large number of grain boundaries or defects in monolayer islands and hence a large influence of hopping barriers and a low value of μ_{FET} in the beginning. In this regime the threshold voltage V_{th} determined from the transfer characteristics started out with a rather high value of 10 V and decreased to 5 V. An initially high positive threshold in the gate voltage arose from a large density of electron traps in grain boundaries or defects in the monolayers that had to be filled before additional electrons could participate in charge transport [21]. At increased average film thickness beyond about 8 nm the increase of μ_{FET} leveled off and V_{th} reached a minimum indicating a minimum trap density. The growing films showed a lower number of grain boundaries leading to less trap density. The increasing film thickness obviously led to a stabilization of the first mono layers where the active transistor channel was formed [38]. V_{th} increased beyond 8 nm speaking for a less efficient utilization of electrons in the conductive channel of $F_{16}PcCu$. At a simultaneously increasing μ_{FET} such characteristics indicate charge diffusion from the interface region into additional islands on top of the conductive channel as also detected in the decreasing current and conductivity in Fig. 1a. Percolation of these islands on top of the conductive channel was observed by an increasing current and a constant conductivity at about 22 nm film thickness. Beyond this range percolation of the islands and healing of grain boundaries that led to increasing current and conductivity, also led to more efficient participation of injected electrons in the conduction and hence a decrease in V_{th}. Very similar development of the electrical characteristics during film growth of $F_{16}PcCu$ speaking for similar percolation and growth characteristics were observed also for the growth between Ag contacts (Supplemental Information). Almost identical values of μ_{FET} were observed at, however, an increased electron injection from the Ag contacts as reflected in an increased conductivity and decreased V_{th}.

As expected, all transistors prepared in this study showed accumulation mode n-channel field-effect transistor characteristics. In Fig. 3b typical output characteristics of a 40 nm thin film between Au electrodes on SiO_2 are shown with an increasing drain current for positive gate voltages. A charge carrier mobility $\mu_{FET} = 1.3 \times 10^{-3}$ cm^2/Vs and a threshold voltage of $V_{th} = 5.0$ V was determined. These compare favorably with known values from the literature for thin films of $F_{16}PcCu$ on untreated SiO_2 where $\mu_{FET} = 2.0 \times 10^{-3}$ cm^2/Vs for bottom contacts [18] and $\mu_{FET} = 5.6 \times 10^{-3}$ cm^2/Vs for top contacts were typically determined for films deposited at room temperature as in the present case [13]. A maximum on/off = 640 ratio of the drain current was reached in this structure within the present range of gate voltages from 0 to 30 V and drain voltages from 0 to 50 V. In Fig. 1, however, it was seen that thinner films already showed similar characteristics. The output characteristics of such transistor with an ultra-thin semiconductor layer of only 3 nm was analyzed and plotted in Fig. 3a. At slightly smaller $\mu_{FET} = 0.5 \times 10^{-3}$ cm^2/Vs, a comparable $V_{th} = 4.9$ V and an even increased on/off = 2208 was determined. Such clear competitiveness of the device constructed with the thinner film was confirmed by a plot of the on/off ratio determined during the growth of the film (Fig. 1c). The maximum values above 10.000 were reached for the initial stage of monolayer percolation for which all electrons in the interface of $F_{16}PcCu$ with the dielectric efficiently participated in the drain current. As expected from the discussion of the development of the electrical characteristics with film thickness (Fig. 1) the surface roughness of a (separately prepared) 3 nm thin $F_{16}PcCu$ semiconductor layer of rms = 0.62 nm (Fig. 2b) was found just slightly increased relative to rms = 0.49 nm for the uncovered SiO_2 (Fig. 2a) confirming

the layered growth in the percolation range leading to such smooth films.

Since structural studies at $F_{16}PcCu$ films on SiO_2 reported a detailed dependence of the film structure on film thickness [33] widely independent of the preparation conditions, the present results serve to discuss the mobility within these different structures. Since a $\beta_{bilayer}$ structure of $F_{16}PcCu$ was found within the first two monolayers of $F_{16}PcCu$ on SiO_2 which carried almost completely the drain current in the present study a rather high charge carrier mobility typically used in devices can be assigned to $F_{16}PcCu$ in the $\beta_{bilayer}$ structure. The β structure found for further increased film thickness proved to be of almost negligible mobility in the present study.

The storage of transistors in vacuum led to an increased μ_{FET} and decreased V_{th} as shown in Fig. 4 a for the 40 nm thin film ($t < 0$ s). The field effect mobility increased from $\mu_{FET} = 1.4- \times 10^{-3}$ cm^2/Vs. to $\mu_{FET} = 1.6 \times 10^{-3}$ cm^2/Vs. Since this was studied for the very same film, this could be explained by some healing of structural defects in the organic semiconductor, specifically within the first layers at the semiconductor–insulator interface. Simultaneously the threshold voltage therefore decreased from $V_{th} = 11.2$ to $V_{th} = 9.8$ V because of a smaller number of trapped electrons at a given total concentration in the interface of $F_{16}PcCu$ with SiO_2.

The stability of $F_{16}PcCu$ field-effect transistors at air was reported in various earlier reports [13,18,40] and was also confirmed in the present study. Of particular interest, however, is the change of decisive parameters and differences between ultrathin films and films of the usual thickness. In Fig. 4a, a small decrease was observed for the 40 nm thick film as discussed above from $\mu_{FET} = 1.6 \times 10^{-3}$ cm^2/Vs in vacuum to $\mu_{FET} = 1.2 \times 10^{-3}$ cm^2/Vs following exposure to synthetic air. Oxygen diffused into the organic layer and led to an increased concentration of deep traps and structural defects which resulted in further decreasing electron mobility towards $\mu_{FET} = 0.9 \times 10^{-3}$ cm^2/Vs within 5 weeks and an increase of the threshold voltage from $V_{th} = 7.6$ V to $V_{th} = 11.2$ V. After such elongated period of exposure almost constant characteristics were observed. Stability of the organic field-effect transistor over more than 4 weeks at air was proven. The performance of the device even improved under air as seen in an increased on/off-ratio by an order of magnitude (Fig. 4b). For optimized devices with an ultrathin conductive channel of some monolayers of $F_{16}PcCu$ (3 nm) only, the time-dependent analysis in vacuum and air showed clearly shorter response times (inset of Fig. 4a). Upon storage in vacuum the mobility increased from $\mu_{FET} = 0.7 \times 10^{-3}$ cm^2/Vs to $\mu_{FET} = 0.8 \times 10^{-3}$ cm^2/Vs within one day. Upon exposure to air this organic field-effect transistor showed a fast stabilization of the charge carrier mobility at $\mu_{FET} = 0.3 \times 10^{-3}$ cm^2/Vs and a stable value of the threshold voltage at $V_{th} = 0.4$ V after less than a day compared to weeks for the thicker films.

4. Conclusions

It was reproducibly confirmed that a thin conductive channel of $F_{16}PcCu$ was formed already in the beginning of deposition within a few monolayers. The formation started in the interface region at about 2 nm average film thickness. Once the threshold thickness of about 8 nm was reached for this conductive channel, $F_{16}PcCu$ showed a constant charge carrier mobility and threshold voltage independent of further increasing the film thickness. The threshold voltage increased with the metal work function. A decreased electron density in the conductive channel of $F_{16}PcCu$ is thereby indicated, well in line with decreased electron injection into the organic semiconductor. Upon ventilation with air the threshold voltage also increased also speaking for a decreased electron concentration in the conductive channel in this case caused by electron transfer from $F_{16}PcCu$ (or the electrode metal) to oxygen.

Additional islands of $F_{16}PcCu$ deposited on top of the initially formed conductive channel showed only minor increase of μ_{FET}, presumably only caused by healing of defects within the underlying channel. No separate contribution to charge transport from the source to the drain electrodes was found, in good agreement with earlier reports of conductivity measurements in similar structures for (per)fluorinated zinc phthalocyanines [14]. The threshold voltage, however, reacted quite sensibly on the formation of such additional islands on top of the conductive channel by a positive shift indicating a decreased electron concentration within the channel caused by charge diffusion from the interface region into the additional islands and by a subsequent negative shift upon percolation of these additional islands.

It was confirmed that field effect transistors of $F_{16}PcCu$ showed a mobility widely stable in air. However, the detailed present investigation showed a decrease of the mobility by about 50%, reproducibly observed for thin as well as 40 nm thick films. The stabilization was considerably faster for thinner films and reached a stable value proving long time stability of $F_{16}PcCu$ conductive channels at air. An increased on/off-ratio at air showed an overcompensation of the decreased mobility by a strongly decreased charge carrier concentration and off-current following interaction with air.

We conclude that a film limited in thickness to the fully developed conductive channel in the interface with SiO_2 of about 8 nm average film thickness without additional parasitic island formation represents the optimum film thickness for device applications in OFET. Further increase of the film thickness did not improve the mobility, but decreased the device performance by an increased threshold voltage up to about 22 nm and by an increased off-current caused by an increased bulk transport beyond about 22 nm. This led to a decreased on/off ratio.

Field-effect measurements for different film thicknesses of the organic semiconductor layer can serve to discuss in detail the development of a conductive channel. It was shown before for spin-coated polymeric semiconductors that the charge carrier mobility changed with the thickness of the organic film thickness which was explained by poor ordering in thin films and improved ordering at about 50 nm [19]. The present *in situ* measurements performed during film preparation by PVD and starting at considerably smaller channel thickness showed the most significant changes already far below such reordering threshold

and showed the strong influence of direct interaction in the interface of gate dielectric as substrate and a growing organic film. To clearly assign such influence it is mandatory to study the channel formation in real time during growth to exclude any subsequent influence of external parameters. Such measurements led us to a clear optimization of the organic semiconductor film thickness for device performance and we assume that such approach can serve to efficiently optimize OFET structures beyond the present films of F_{16}PcCu.

Acknowledgments

The authors are grateful to T. Henning and the crew of the Clean Room Facilities (MiNa) within the Laboratory of Materials Science (LaMa) of JLU Gießen for help and support and to the group of D. Wöhrle at the University of Bremen (Germany) for providing the F_{16}PcCu material and for helpful discussions.

Appendix A. Supplementary data

Supplementary data associated with this article can be found, in the online version, at doi:10.1016/j.orgel.2011.04.016.

References

[1] H.E. Katz, J. Huang, Thin-film organic electronic devices, Ann. Rev. Mater. Res. 39 (2009) 71–92.
[2] C.D. Dimitrakopoulos, D.J. Mascaro, Organic thin-film transistors: a review of recent advances, IBM J. Res. Soc. 45 (2001) 11–27.
[3] G. Horowitz, Organic thin film transistors: from theory to real devices, J. Mater. Res. 19 (2004) 1946–1962.
[4] J.L. Brédas, J.E. Norton, J. Cornil, V. Coropceanu, Molecular understanding of organic solar cells: the challenges, Accounts. Chem. Res. 42 (2009) 1691–1699.
[5] M. Helgesen, R. Søndergaard, F.C. Krebs, Advanced materials and processes for polymer solar cell devices, J. Mater. Chem. 20 (2010) 36–60.
[6] H. Klauk, Organic thin-film transistors, Chem. Soc. Rev. 39 (2010) 2643–2666.
[7] C. Reese, M. Roberts, M. Ling, Z. Bao, Organic thin film transistors, Mater. Today 7 (2004) 20–27.
[8] Z. Bao, A.J. Lovinger, A. Dodabalapur, Organic field-effect transistors with high mobility based on copper phthalocyanine, Appl. Phys. Lett. 69 (1996) 3066–3068.
[9] S. Hoshino, T. Kamata, K. Yase, Effect of active layer thickness on device properties of organic thin-film transistors based on Cu(II) phthalocyanine, J. Appl. Phys. 92 (2002) 6028.
[10] J. Lee, K. Kim, J.H. Kim, S. Im, D.-Y. Jung, Optimum channel thickness in pentacene-based thin-film transistors, Appl. Phys. Lett. 82 (2003) 4169.
[11] G. Horowitz, X. Peng, D. Fichou, F. Garnier, The oligothiophene-based field-effect transistor: how it works and how to improve it, J. Appl. Phys. 67 (1990) 528–532.
[12] G. Horowitz, D. Fichou, X. Peng, Z. Xu, A field-effect transistor based on conjugated alpha-sexithienyl, Solid State Commun. 72 (1989) 381–384.
[13] Z. Bao, A.J. Lovinger, J. Brown, New air-stable n-channel organic thin film transistors, J. Am. Chem. Soc. 120 (1998) 207–208.
[14] H. Brinkmann, C. Kelting, S. Makarov, O. Tsaryova, G. Schnurpfeil, D. Wöhrle, D. Schlettwein, Fluorinated phthalocyanines as molecular semiconductor thin films, Phys. Status Solidi A 205 (2008) 409–420.
[15] A. Facchetti, J. Letizia, M.-han Yoon, M. Mushrush, H.E. Katz, T.J. Marks, Synthesis and characterization of diperfluorooctyl-substituted phenylene-thiophene oligomers as n-type semiconductors. Molecular structure-film microstructure-mobility relationships, organic field-effect transistors, and transistor nonvolatile memory elements, Chem. Mater. 16 (2004) 4715–4727.
[16] A. Facchetti, M. Mushrush, H.E. Katz, T.J. Marks, n-type building blocks for organic electronics: a homologous family of fluorocarbon-substituted thiophene oligomers with high carrier mobility, Adv. Mater. 15 (2003) 33–38.
[17] S. Ando, J.-I. Nishida, H. Tada, Y. Inoue, S. Tokito, Y. Yamashita, High performance n-type organic field-effect transistors based on pi-electronic systems with trifluoromethylphenyl groups, J. Am. Chem. Soc. 127 (2005) 5336–5337.
[18] H. Tada, H. Touda, M. Takada, K. Matsushige, Field effect mobility of F_{16}PcCu films in various gas atmospheres, J. Porphyr. Phthalocya. (1999) 667–671.
[19] B. Gburek, V. Wagner, Influence of the semiconductor thickness on the charge carrier mobility in P3HT organic field-effect transistors in top-gate architecture on flexible substrates., Org. Electron. 11 (2010) 814–819.
[20] T. Muck, J. Fritz, V. Wagner, Better bottom contact properties in organic field-effect transistors with ultrathin layers, Appl. Phys. Lett. 86 (2005) 232101.
[21] S.M. Sze, Physics of Semiconductor Devices, Wiley, New York, 1981.
[22] S. Scheinert, G. Paasch, Interdependence of contact properties and field- and density-dependent mobility in organic field-effect transistors, J. Appl. Phys. 105 (2009) 1–9.
[23] C. Reese, Z. Bao, Detailed characterization of contact resistance, gate-bias-dependent field-effect mobility, and short-channel effects with microscale elastomeric single-crystal field-effect transistors, Adv. Funct. Mater. 19 (2009) 763–771.
[24] A. Herasimovich, S. Scheinert, I. Hörselmann, Influence of traps on top and bottom contact field-effect transistors based on modified poly(phenylene-vinylene), J. Appl. Phys. 102 (2007) 054509.
[25] E.J. Meijer, D.M. de Leeuw, S. Setayesh, E. van Veenendaal, B.H. Huisman, P.W.M. Blom, J.C. Hummelen, U. Scherf, J. Kadam, T.M. Klapwijk, Solution-processed ambipolar organic field-effect transistors and inverters, Nat. Mater. 2 (2003) 678–682.
[26] S. Scheinert, G. Paasch, I. Hörselmann, A. Herasimovich, Influence of source/drain contacts on sub-micrometer organic field-effect transistors, Phys. Status Solidi A 202 (2005) R82–R84.
[27] M. Weis, M. Nakao, J. Lin, T. Manaka, M. Iwamoto, Thermionic emission model for contact resistance in organic field-effect transistor, Thin Solid Films 518 (2009) 795–798.
[28] G. Horowitz, Organic field-effect transistors, Adv. Mater. 10 (1998) 365–377.
[29] D. Schlettwein, K. Hesse, H. Tada, S. Mashiko, U. Storm, J. Binder, Ordered growth of substituted phthalocyanine thin films: hexadecafluorophthalocyaninatozinc on alkali halide (100) and microstructured Si surfaces, Chem. Mater. 12 (2000) 989–995.
[30] D. Schlettwein, H. Tada, S. Mashiko, Substrate-induced order and multilayer epitaxial growth of substituted phthalocyanine thin films, Langmuir 16 (2000) 2872–2881.
[31] W. Michaelis, D. Wöhrle, D. Schlettwein, Organic n-channels of substituted phthalocyanine thin films grown on smooth insulator surfaces for organic field effect transistors applications, J. Mater. Res. 19 (2004) 2040–2048.
[32] C.C. Mattheus, W. Michaelis, C. Kelting, W. Durfee, D. Wöhrle, D. Schlettwein, Influence of the molecular shape on the film growth of a substituted phthalocyanine, Synthetic Met. 146 (2004) 335–339.
[33] D.G. de Oteyza, E. Barrena, J.O. Ossó, S. Sellner, H. Dosch, Thickness-dependent structural transitions in fluorinated copper-phthalocyanine (F_{16}CuPc) films, J. Am. Chem. Soc. 128 (2006) 15052–15053.
[34] D.G. de Oteyza, E. Barrena, S. Sellner, J.O. Ossó, H. Dosch, Structural rearrangements during the initial growth stages of organic thin films of F_{16}CuPc on SiO_2, J. Phys. Chem. B 110 (2006) 16618–16623.
[35] J. Ossó, F. Schreiber, M. Alonso, M. Garriga, E. Barrena, H. Dosch, Structure, morphology, and optical properties of thin films of F_{16}CuPc grown on silicon dioxide, Org. Electron. 5 (2004) 135–140.
[36] K. Hayashi, S. Kawato, Y. Fujii, T. Horiuchi, K. Matsushige, Effect of applied electric field on the molecular orientation of epitaxially grown organic films, Appl. Phys. Lett. 70 (1997) 1384.
[37] B.-E. Schuster, T.V. Basova, H. Peisert, T. Chassé, Electric field assisted effects on molecular orientation and surface morphology of thin titanyl-(IV)phthalocyanine films, Chem. phys. chem. 10 (2009) 1874–1881.
[38] B.N. Park, S. Seo, P.G. Evans, Channel formation in single-monolayer pentacene thin film transistors, J. Phys. D: Appl. Phys. 40 (2007) 3506–3511.
[39] I. Biswas, H. Peisert, M.B. Casu, B.-E. Schuster, P. Nagel, M. Merz, S. Schuppler, T. Chasse, Initial molecular orientation of phthalocyanines on oxide substrates, Phys. Status Solidi A 206 (2009) 2524–2528.
[40] M.M. Ling, Z. Bao, Copper hexafluorophthalocyanine field-effect transistors with enhanced mobility by soft contact lamination, Org. Electron. 7 (2006) 568–575.

electrode. We find that the light-emitting efficiency of top or bottom side emissions as well as bottom/top emitting ratio is greatly influenced by the top metal cathode thickness. We also investigate the radiation distribution pattern of the transparent OLEDs with increasing top metal cathode thickness by a separate examination of the top and bottom side emissions with spectrogoniometer measurements. We find significant deviations from the Lambertian characteristics on emission direction. Moreover, we analyze our transparent OLEDs with an OLED numerical optical model software calculating the flux of outcoupled photons [18–21], and then compare theoretical predictions with our experimental results.

2. Experimental

A series of seven different red emitting phosphorescent semi-transparent OLEDs based on *p–i–n* doped structures [18–23] are fabricated as shown in Fig. 1. The organic layers are sandwiched between a 90 nm thick indium tin oxide (ITO) anode and a thin Ag metal cathode. The effect of varying the thickness of the Ag cathode layer from 15 to 45 nm on the device performance of the TOLEDs is investigated. All samples are deposited by thermal evaporation onto ITO-coated structured glass substrates in an ultra-high vacuum (UHV) chamber (Kurt J. Lesker Co.) in ultrahigh vacuum at a base pressure around 10^{-8} mbar. The devices are encapsulated immediately after preparation under nitrogen atmosphere using epoxy glue and glass lids.

As *p*-type hole injection and transport layer, we use 60 nm thick films of N,N,N,N′-tetrakis(4-methoxyphenyl)-benzidine (Meo-TPD) which is doped with 4 wt% of the Novaled dopant *p*-type 2 (NDP-2, Novaled AG, Dresden).

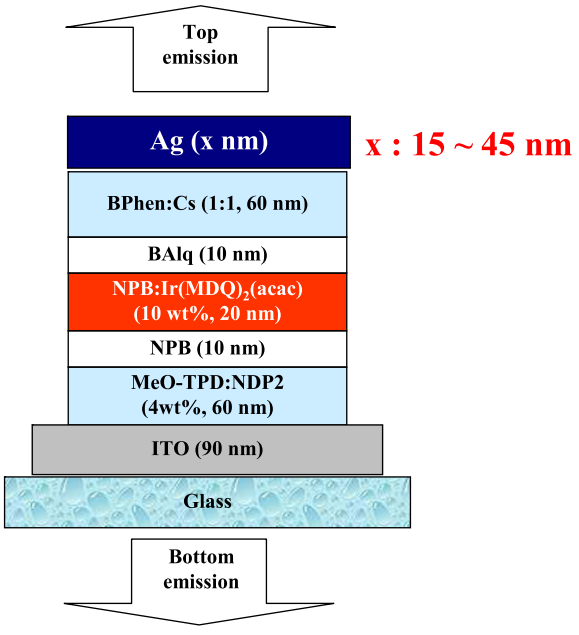

Fig. 1. Device structures of the transparent OLEDs tested in this study.

This *p*-type dopant has similar electric properties to 2,3,5,6-tetrafluoro-7,7,8,8-tetracyanoquinodimethane (F4-TCNQ) and exhibits a conductivity of around 10^{-5} S cm^{-1} [18–23]. As *n*-type electron injection and transport layer, we use 60 nm of cesium (Cs) doped 4,7-diphenyl-1,10-phenanthroline (BPhen) with a conductivity comparable to the *p*-side. The *p* and *n* layer thicknesses of these structures have been optimized in terms of constructive interference for maximal outcoupled photon flux using optical simulations based on classical electrodynamics [21]. Optimization of OLED transport layer will not alter the electrical properties of the OLED since the electrical conductivity of the *p* and *n* sides is almost independent of the thickness due to electrical doping [18–23]. N,N′-di (naphthalene-1-yl)N,N′-diphenyl-benzidine (NPB, 10 nm) and bis(2-methyl-8-quinolinolato)-4-(phenyl-phenolato) aluminum-(III) (Balq2, 10 nm) are used as electron and hole blocking layers, respectively, to confine not only holes but also electrons in the emitting layer (EML). The 20 nm thick red EML consists of NPB doped with 10% of the triplet red emitter iridium (III)bis [2-methyldibenzo-(f,h) quinoxaline](acetylacetonate) (Ir(MDQ)2(acac)). The overall active area of a single OLED device is 6.7 mm^2.

The devices emit bright red light from both sides when a positive voltage is applied to the ITO anode; no light is observed in reverse bias. For OLED characterization we utilize a Keithley Source Measure Unit 2400 to obtain the current–voltage data, while an INSTRUMENT SYSTEMS GmbH CAS140 spectrometer is used to measure luminance and spectral radiant intensity in the forward direction at the same time. Afterward, the spatial emission of the OLED is evaluated with a spectrogoniometer setup to estimate external quantum efficiency and luminous efficacy [18–21,24]. These data can be directly determined from the integration of the azimuthal angle θ resolved radiant intensity over the solid angle, assuming the emission to the invariant with respect to the polar angle φ because of the planar geometry of the samples.

3. Results and discussion

The current density–voltage–luminance (*J–V–L*) curves of the semi transparent OLEDs are shown in Fig. 2((a) bottom side, (b) top side) according to the thickness of the top Ag cathode. Both Fig. 2(a) and (b) clearly show that the *J–V* curves as well as the EL onset voltages of the OLEDs at the luminance region are almost identical, i.e. the thickness variation of the top Ag electrode does not alter the electrical characteristics of our transparent OLEDs. However, significant differences in *L–V* curves depending on the thickness variation of the top Ag electrode can be observed. The luminance of the bottom direction increases gradually with increasing Ag thickness in the transparent OLEDs, while in the top direction it gradually decreases. For example, luminance values of 2143, 3112, 3950, and 4084 cd/m^2, respectively, are measured in the bottom direction at a driving voltage of 3.5 V with an Ag thickness of 15, 25, 35 and 45 nm, respectively (whereas luminance of 444, 216, 128, 47 cd/m^2 were observed in the top direction). This luminance behavior can be easily understood

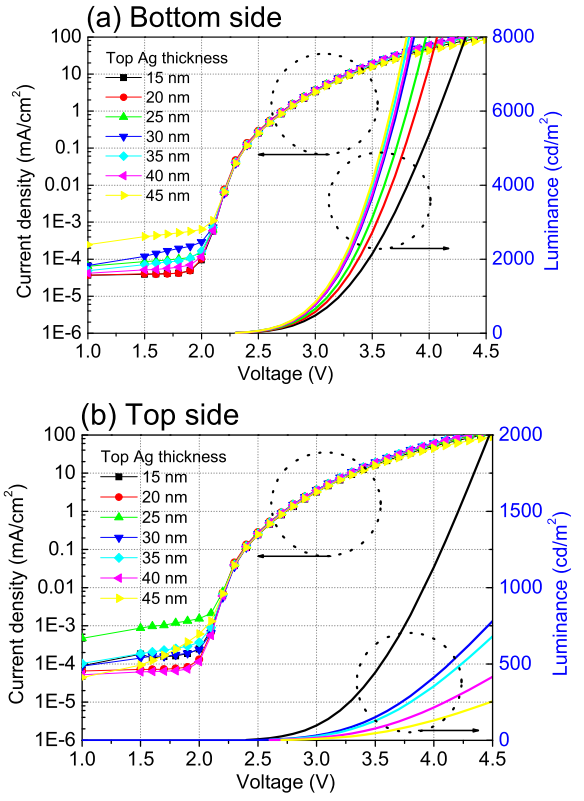

Fig. 2. Current density versus voltage (I–V) and voltage versus luminance (V–L) characteristics of (a) bottom side emission and (b) top side emission.

by transmittance and reflectance changes of the top Ag electrode with increasing thickness. With increasing the thickness of the top Ag electrode, the reflectance also increased while the transmittance decreased. Therefore, light emission toward the bottom side was highly enhanced, but that toward the top side was gradually reduced.

To examine the transmittance change depending on the top Ag electrode thickness, we measure the transmittance of all TOLEDs in this study with air reference. As shown in Fig. 3, the overall transmittance of devices is reduced gradually by increasing the thickness of the top Ag layer. For a

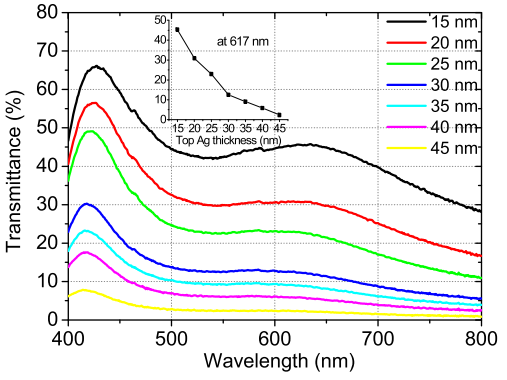

Fig. 3. Transmittance characteristics of the transparent OLEDs tested in this study with air reference (inset: transmittance at 617 nm).

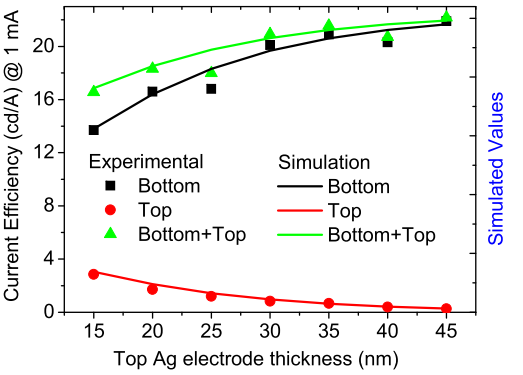

Fig. 4. Current efficiency and bottom to top ratio characteristics of the transparent OLED at a driving current density of 1 mA/cm^2.

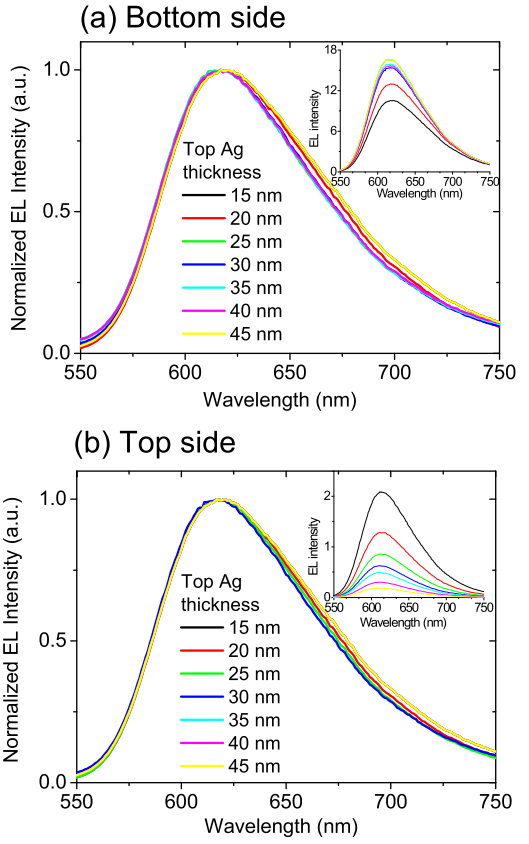

Fig. 5. Normalized electroluminescence (EL) intensity of (a) bottom side and (b) top side (inset: EL intensity at a driving current density of 15 mA/cm^2).

15 nm thick Ag layer the transmittance is over 45% at 617 nm which is the maximum wavelength of devices in this study. However, the transmittance of devices with over 35 nm thick Ag is less than 10%. From these results, we can easily confirm that the luminance behavior which shows a gradual increase in the bottom direction while a decrease in the top direction with increasing top Ag thickness is originated by the thickness dependent optical property change of the Ag layer.

As shown in Fig. 4, the dependence of the luminance behaviors with the top Ag electrode thickness is also reflected in the behavior of the current efficiency. With the 15 nm thick top Ag electrode a current efficiency of 13.7 cd/A is obtained in the bottom side at a driving current of 1 mA/cm^2. These values at a driving current density of 1 mA/cm^2 are chosen to compare to simulation results because the simulation does not consider an additional *roll-off* effect at a higher current density caused by triplet quenching processes such as triplet–triplet annihilation or triplet–polaron annihilation. With increasing Ag thickness the current efficiency is enhanced 1.6 times, up to 21.9 cd/A. On the other hand, the current efficiency of the top side decreases from 2.85 to 0.26 cd/A with increasing Ag thickness. Interestingly, the overall current efficiency by gathering both the bottom and top side emissions is also enhanced by 34%, from 16.55 to 22.16 cd/A at a driving current density of 1 mA/cm^2. The current efficiency for both the bottom and top sides also is compared with simulation results [18–21]. Quantum physical effects such as the Purcell effect are not taken into account in this study and we assume that the recombination zone is positioned at the EML/ETL interface because the host material (NPB) of EML is a strong *p*-type material. As described in Fig. 4, the trend of the current efficiency agrees well with that from simulation even though there are slight variations between them.

One of the interesting aspects of transparent OLEDs is the bottom to top ratio. As the luminance behavior of the bottom and top sides changes, the bottom to top ratio of our transparent OLEDs is also dramatically changed. With a 15 nm thick Ag electrode, the bottom side emission is 4.8 times higher than that of the top side. In case of a 45 nm thick Ag contact, the bottom to top ratio is larger than 84. Therefore, the variation in the thickness of the top Ag electrode can be considered as a powerful method to control the bottom to top ratio.

Fig. 5 shows normalized electroluminescence (EL) spectra of our transparent OLEDs for the (a) bottom and (b) top sides. All devices exhibit similar EL spectra with maximum luminescence wavelength near 617 nm originated from the triplet emission of Ir(MDQ)2(acac) emitter. However, we observe that the light emission for both the bottom and top sides is slightly broadened in the region from 650 to 700 nm. This slight EL spectra change depending on the top Ag thickness might be understood by optical property changes such as reflectance as well as transmittance of the Ag layer.

To examine the optical effect of a variation of the top Ag thickness in detail, and also to obtain accurate power and quantum efficiencies, we characterize the fabricated devices with a spectrogoniometer again. Generally, BEOLEDs can be described well by the Lambertian emitters, while TEOLEDs are assumed to be a non-Lambertian emitter

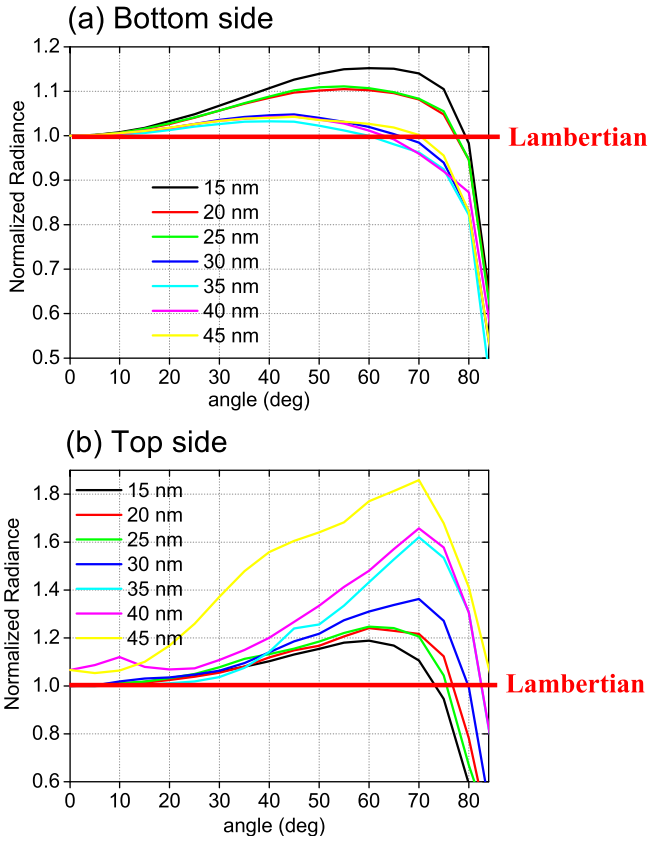

Fig. 6. Normalized radiance versus viewing angle characteristics of (a) bottom side and (b) top side at a driving current density of 15 mA/cm^2.

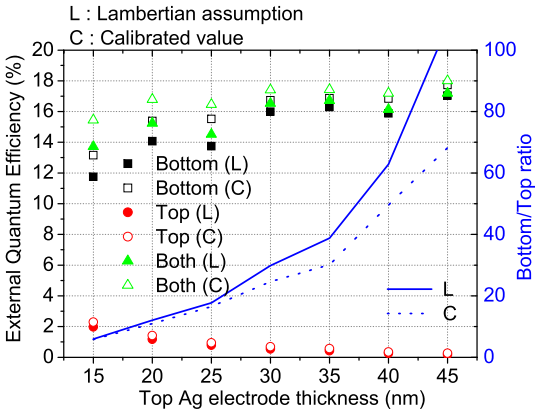

Fig. 7. External quantum efficiency and bottom to top ratio characteristics with calibration (open symbol, line) and with a Lambertian assumption (closed symbol, dot) at a driving current density of 15 mA/cm^2.

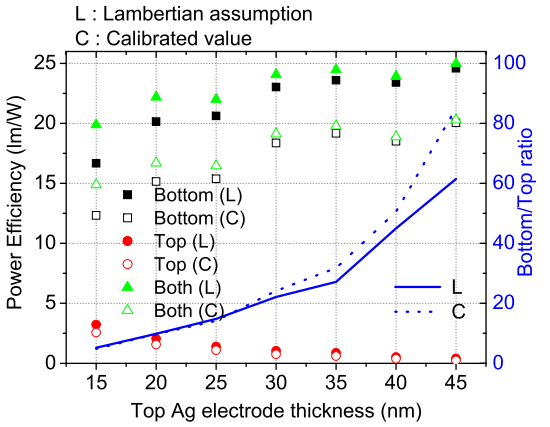

Fig. 8. Power efficiency and bottom to top ratio characteristics with calibration (open symbol, line) and with a Lambertian assumption (closed symbol, dot) at a driving current density of 15 mA/cm^2.

due to the microcavity effect. In case of transparent OLEDs with both bottom and top emissions, therefore, it is difficult to tell a priori whether the device is a Lambertian emitter or not, and there has been no report which relates to these aspects up to date. Here, we evaluate the distribution patterns of transparent OLEDs for both the bottom and top sides, and we further compare them to a Lambertian assumption.

Fig. 6 shows the normalized radiance versus viewing angle of the transparent OLEDs. Even with a 15 nm thick top Ag electrode, both bottom and top side emission patterns are far different from a Lambertian distribution. This might be attributed to the weak microcavity effect caused by a thin Ag layer as similar to TEOLED. Note that the normalized radiance trends as increasing the top Ag thickness are different depending on the bottom or top side. In case of bottom emission, the emission distribution is getting closer to Lambertian distribution with increasing top Ag thickness, i.e. the overall emission pattern is approaching common BEOLEDs. On the other hand, the emission distribution for the top side deviates from a Lambertian distribution with increasing top Ag thickness.

Based on these results from spectrogoniometer measurements, we evaluate the power (PE) and external quantum efficiencies (EQE) by considering the angular and spectrally resolved emissions over the whole forward emission hemisphere [18–21,24,25]. The calibrated (open symbols) EQE and PE at a driving current density of 15 mA/cm^2 are plotted together with those for a Lambertian (closed symbols) in Figs. 7 and 8. The EQE and PE characteristics show similar trends with the current efficiency, i.e. they are enhanced in the bottom side but reduced in the top side with increasing Ag thickness. The overall EQE and PE obtained by summing both the bottom and top emissions are enhanced to 17%, and 26%, respectively, at a driving current density of 15 mA/cm^2 (EQE: from 15.45% to 18.0%, PE: from 19.89 to 24.99 lm/W).

Note that the calibrated values for both the bottom and top sides do not agree with those from a Lambertian assumption as we expect from the angular dependent radiance results in Fig. 6. For example, the device with a 15 nm thick Ag electrode shows a calibrated external quantum efficiency of 13.16% (bottom side) and 2.29% (top side), respectively, however, the Lambertian assumption leads to slightly lower values (11.75% for the bottom side and 1.97% for the top side). We also find that the discrepancy between the values from calibration and a Lambertian assumption is much larger for PE than for EQE as shown in Fig. 8.

Finally, we compared the scale of difference between calibration and a Lambertian assumption as plotting Fig. 9. Interestingly, we found that the discrepancy of

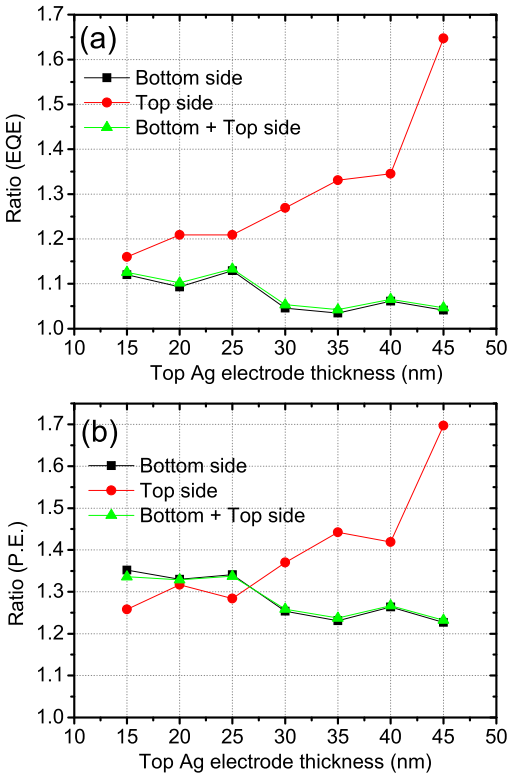

Fig. 9. Discrepancy ratio of values between a calibration and a Lambertian assumption. (a) External quantum efficiency, (b) power efficiency.

values between calibration and a Lambertian assumption decreases for the bottom side while it increases for the top side with increasing top Ag thickness. For a 15 nm thick Ag electrode, the EQE ratio between calibration and a Lambertian assumption is almost 1.12, and is gradually reduced for increasing top Ag thickness, resulting in only 1.04 with the 45 nm thick Ag electrode. On the contrary, the ratio increases from 1.16 to 1.63 for the top side with increasing top Ag thickness. These results show that the assumption of a Lambertian emitter is not valid for transparent OLEDs. Therefore, more careful measurement systems such as a spectrogoniometer or an integrating sphere are required to provide meaningful values for the EQE and PE of TOLEDs. Additionally, we find that there is an efficiency/transmittance trade-off depending on the thickness of the transparent top electrode and devices with a thicker top Ag electrode show enhanced overall efficiency.

4. Conclusion

We have studied the dependence of phosphorescent red emitting transparent OLEDs on the thickness of the top metal electrode. We find that the bottom or top emission shows different optical characteristics depending on the top Ag electrode thickness. The overall efficiency can be enhanced by varying the thickness of the top electrode, with an efficiency/transmittance trade-off. Moreover, we investigate the light-emitting distribution of transparent OLEDs for bottom and top side emissions separately, and find that the emission pattern does not agree with a Lambertian assumption.

Acknowledgments

The authors thank Novaled AG, Dresden for cooperation and J.L. acknowledges funding of the Alexander von Humboldt Foundation.

References

[1] M.A. Baldo, D.F. O'Brien, I. You, A. Shoustikov, S. Sibley, M.E. Thompson, S.R. Forrest, Nature 395 (1998) 151.
[2] S. Reineke, F. Lindner, G. Schwartz, N. Seidler, K. Walzer, B. Lussem, K. Leo, Nature 459 (2009) 234.
[3] J.Y. Lee, J.H. Kwon, H.K. Chung, Org. Electron. 4 (2003) 143.
[4] G. He, M. Pfeiffer, K. Leo, M. Hofmann, J. Birnstock, R. Pudzich, J. Salbeck, Appl. Phys. Lett. 85 (2004) 3911.
[5] B.W. D'Andrade, S.R. Forrest, Adv. Mater. 16 (2004) 1595.
[6] S. Chen, L. Deng, J. Xie, L. Peng, L. Xie, Q. Fan, W. Huang, Adv. Mater. 22 (2010) 5227.
[7] G. Gu, V. Bulovic, P.E. Burrows, S.R. Forrest, Appl. Phys. Lett. 68 (1996) 2606.
[8] X. Zhou, M. Pfeiffer, J.S. Huang, J. Blochwitz-Nimoth, D.S. Qin, A. Werner, J. Dreshsel, B. Maennig, K. Leo, Appl. Phys. Lett. 81 (2002) 922.
[9] X. Zhou, J. Blochwitz-Nimoth, M. Pfeiffer, B. Maennig, J. Dreshsel, A. Werner, K. Leo, Synth. Metals 138 (2003) 193.
[10] K.S. Yook, S.Ok. Jeon, C.W. Joo, J.Y. Lee, Appl. Phys. Lett. 93 (2008) 013301.
[11] S. Ju, J. Li, J. Liu, P.-C. Chen, Y. Ha, F. Ishikawa, H. Chang, C. Zhou, A. Facchetti, D.B. Janes, T.J. Marks, Nano Letters 8 (2008) 997.
[12] T.H. Gil, C. May, S. Scholz, S. Franke, M. Toerker, H. Lakner, K. Leo, S. Keller, Org. Electron. 11 (2010) 322.
[13] Q. Huang, K. Walzer, M. Pfeiffer, V. Lyssenko, G. He, K. Leo, Appl. Phys. Lett. 88 (2006) 113515.
[14] Q. Huang, K. Walzer, M. Pfeiffer, M. Hofmann, T. Stuebinger, K. Leo, J. Appl. Phys. 100 (2006) 064507.
[15] J.H. Lee, D.S. Leem, J.J. Kim, Org. Electron. 9 (2008) 1112.
[16] L. Smith, J.A.E. Wasey, W.L. Barnes, Appl. Phys. Lett. 84 (2004) 2986.
[17] S. Wedge, A. Giannattasio, W.L. Barnes, Org. Electron. 8 (2007) 136.
[18] R. Meerheim, R. Nitsche, K. Leo, Appl. Phys. Lett. 93 (2008) 043310.
[19] M. Thomschke, R. Nitsche, M. Furno, K. Leo, Appl. Phys. Lett. 94 (2009) 083303.
[20] S. Hofmann, M. Thomschke, P. Freitag, M. Furno, B. Lüssem, K. Leo, Appl. Phys. Lett. 97 (2010) 253308.
[21] M. Furno, R. Meerhein, M. Thomschke, S. Hofmann, B. Lüssem, K. Leo, Proc. SPIE 7617 (2010) 761716.
[22] M. Pfeiffer, K. Leo, X. Zhou, J.S. Huang, M. Hofmann, A. Werner, J. Blochwitz-Nimoth, Org. Electron. 4 (2003) 89.
[23] P. Wellmann, M. Hofmann, O. Zeika, A. Werner, J. Birnstock, R. Meerheim, G. He, K. Walzer, M. Pfeiffer, K. Leo, in: SID Int. Symp. Digest Tech. Papers, vol. 13, 2005, p. 393.
[24] The angular-dependent spectra are recorded with a spectrogoniometer, where the device is adjusted on a rotary table (DMT 65-DM4-HSM, OWIS GmbH) in a distance of 15 cm from an Ocean Optics USB4000 miniature fiber optic spectrometer.
[25] J. Lee, S. Hofmann, M. Furno, M. Thomschke, Y.H. Kim, B. Lüssem, K. Leo, Opt. Lett. 36 (2011) 1443.

degradation of the basic materials used within the device [18–20]. Those new works describe in detail the action of ozone attack as well as of direct photo-oxidation occurring in conjugated polymers.

The correlation of nanostructure and (macroscale) device performance is still far from being fully understood, even though this issue is of outstanding relevance: while the basic physical processes determining photoelectric energy conversion occur at the nanoscale, technologically relevant devices – in particular solar cells – are macroscopic in size. We note that increased lifetime is at the present stage a goal as important as the efficiency improvement [12]. In this article we report a study on P3OT thin films with special focus on the effect of UV irradiation – and therefore ozone exposure – on nanoscale morphology and electronic behavior, as well as on optical properties of the material. We will present correlations between these properties and point out interesting effects that should improve the understanding of the degradation mechanisms of the poly-alkyl-thiophenes, one of the most promising families of conjugated polymers for the fabrication of organic solar cells.

2. Experimental

Regioregular P3OT was purchased from Sigma–Aldrich, with 98.5% head to tail couplings, molecular weight $M_n = 54000$, polydispersity index $D = 2.6$ and density $\rho = 1.05\ g/cm^3$ [21]. We recall that a monomer of the P3OT chain has a molecular weight of $m_{Mol} = 194$ g/Mol (P3OT linear formula $C_{12}H_{18}S$), therefore a number density $n_{P3OT} = \rho \cdot N_A / m_{Mol} \approx 3.26 \times 10^{27}$ monomers/m^3 is obtained, corresponding to a volume of $(0.67\ nm)^3$ per monomer. Glass cover slips have been used in this study as substrates. P3OT thin films of approximately 110 nm thickness were prepared by spin-coating a 10 mg/ml solution in toluene at 2500 rpm for 90 s in air and at room temperature.

UV/O_3 exposure was performed using a commercial 50 W UV/ozone cleaning system from Novascan Technologies (Ames, IA, USA). According to manufacturer specifications this system delivers most of its energy (about 50%) into the 254 nm peak and about 5% into the more energetic 185 nm peak. The lamp has a tube diameter of approximately 0.5 cm and a total length of 100 cm. The tube is bent and folded so that the light is emitted from 10 parallel segments that are about 10 cm long and separated 1 cm. A simple calculation shows that this geometry illuminates the sample homogeneously when the distance between the light and the sample is larger than the tube separation, which was the case in our experimental set-up (distance light-sample: 2 cm, tube separation: 1 cm). We therefore estimate an irradiance of $G_0 \approx 25\ W/(0.1\ m)^2 = 2.5\ kW/m^2$ for the main wavelength of $\lambda_0 = 254$ nm, which is about 3 orders of magnitude more UV energy than that delivered by sunlight at AM 1.5G standard conditions. We note that at this high UV irradiation the expected ozone generation in the cleaning system is quite high. The ozone concentration was higher than the standard measurement range of commercial ozone instrumentation (of the order of 1 ppm); we estimate the ozone concentration in our experiments to be of the order of 100 ppm. The corresponding photon flux is $j_{ph} = I_0/(h\nu_0) = I_0\,\lambda/(hc) \approx 3.2 \times 10^{21}$ photons/(m^2 s). In the experiments to be discussed an important quantity will be the photon flux per conjugated electronic bond. Since each P3OT monomer has two conjugated electronic bonds, the corresponding number density is $2\ n_{P3OT.}$ In a $d = 110$ nm thick film, each bond is therefore illuminated by $j_{ph}/(2\ n_{P3OT}\ d) = 4.5$ photons per second.

A Nanotec Electronica SFM system with a phase locked loop (PLL)/dynamic measurement board [22] was used with Olympus OMCL-AC-type cantilevers (nominal force constant: 2 N/m; resonance frequency: 70 kHz). This SFM system uses red laser light ($\lambda = 665$ nm) focused on the free end of the cantilever to detect the bending of the cantilever using the optical beam deflection technique. We have confirmed that neither the red light, nor the laboratory illumination degrades the sample or modifies its electrostatic properties. Topographic imaging was performed in non-contact dynamic SFM (NC-DSFM) using the oscillation amplitude as feedback channel to maintain a constant tip-sample interaction, and thus a constant tip-sample distance. A small reduction of oscillation amplitude ($A_{set} \approx 0.95\ A_{free}$) was chosen for feedback in order to maintain the tip-sample system in the "attractive" part of the interaction and avoid tip-sample contact. In addition to topography images, also the electrostatic interaction – so called Electrostatic Force Microscopy (ESFM) [23,24] – was measured in order to determine the electronic properties of the sample. In particular, Kelvin Probe Microscopy (KPM) and capacitance images were acquired working in non-contact dynamic mode with Platinum coated silicon tips ($\nu_0 = 70$ kHz). An external lock-in board was employed for the ESFM and KPM measurements using modulation V_{ac} voltages as low as 500 mV at a (electrical) modulation frequency $\nu_{elec} = 7$ kHz. The ESFM technique and the details of how it is implemented in our group are described elsewhere [25,26]. Essentially, we use the frequency shift induced by the modulation voltage V_{ac} in order to determine the local contact potential as well as the tip sample capacitance [27].

We have developed a new micron-precision sample holder integrated in the Nanotec SFM system for these investigations [28]. This experimental set-up allows ex-situ manipulation of the sample and SFM imaging of the same region with a very accurate re-positioning of about 5 μm. We can therefore attribute changes of morphology or other properties to a particular effect of UV radiation and/or ozone, which are monitored for the same exact location on the sample. Without this precise re-allocation, that is, if only the approximate position of the sample is recovered as in most SFM experiments, only statistical variations of surface properties can be determined. The SFM experiments were performed in air and with the standard illumination conditions of a laboratory.

In order to characterize the variations of optical properties, an inverted optical microscope was used (Nikon Eclipse TE2000-E). In this case large scale optical transmission images were acquired in order to observe variations of the absorption of the thin films as they were exposed to UV radiation. Images were digitally acquired with a Cannon

EOS 400D camera and analyzed with standard image processing software.

3. Results and discussion

3.1. Evolution of surface morphology

We will first discuss the large scale morphological variations of the sample as it is irradiated with UV-light. Fig. 1 shows a series of images ($60 \times 60\ \mu m^2$) taken for the pristine sample and for 3, 7, 10, 15 and 30 min of irradiation. As discussed above, our SFM system allows removal of the sample, external manipulation (here UV-irradiation) and precise re-allocation at the same position. Therefore the evolution of the same individual features can be studied in detail. During the first 7 min of irradiation no significant changes of surface morphology are observed on this large scale. The surface is covered by round structures with a diameter of either about 0.5 μm, or 1–2 μm. We think that these round features are polymer aggregates which have not been well dissolved or air bubbles inside the film formed during the preparation method. The smaller structures tend to have a ring (donut-) like shape and are about 50 nm high, while the larger structures are mostly disk-like, some seem to have a protrusion in the center and are about 200 nm high. The largest structure, however, is also donut-shaped, as the smaller ones. After 7 and 10 min of irradiation, the disk-like larger structures start to develop a center hole. In addition, the hole of the smaller structures becomes more pronounced. In the case of the largest structure, this hole reaches all the way down to the glass substrate (depth about 100 nm, see below). After 15 min, a characteristic ring of small spherical particles – satellites – develops around the circular structures that were present from the beginning. These rings have a diameter of 5–10 μm while the satellites have a diameter of 0.5–1 μm. Interestingly, the region between the initial center particle and the satellites has a lower roughness than the rest of the surface. The rings are also seen after 30 min of irradiation, even though then the surface looks more blurred and the surface roughness has significantly increased.

In addition to the large scale images, a series of small scale images ($5 \times 5\ \mu m^2$) were acquired on the flat areas seen in the large scale images; that is, between the disk and the donut-shaped structures. As for the large scale images, during the first 5 min the surface morphology does not vary significantly, see Fig. 2. We recall that the images show always the same region of the sample, in particular, the arrow points to the same feature in all images. After 7 min of irradiation, small granular structures (50 nm diameter) grow over the whole surface. These grains become denser after 10 min of irradiation. After 15 min, the surface morphology has completely changed: the grains have merged into clusters containing several grains, separated by rather smooth areas in-between. And, finally, after 30 min the surface morphology has changed again: the grains are larger (100–200 nm) and the overall RMS roughness has increased significantly (14 nm), as it is observed in Fig. 3, where within the experimental error the roughness is constant in first 10 min of UV/ozone exposure and increases after 15 min.

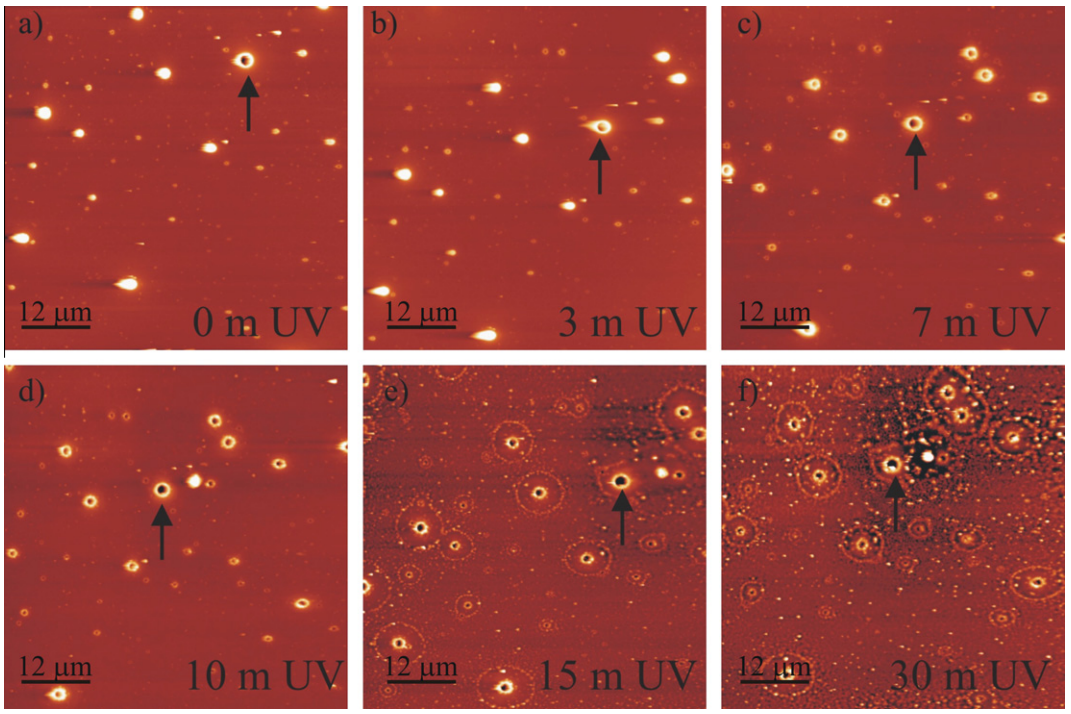

Fig. 1. A series of large area ($60 \times 60\ \mu m^2$) SFM topographic images showing the morphology of the P3OT thin film (a) pristine sample, (b) after 3 min, (c) 7 min, (d) 10 min, (e) 15 min and (f) 30 min of UV/ozone exposure. In all images $\Delta z = 200$ nm. An arrow indicates the same feature in all images.

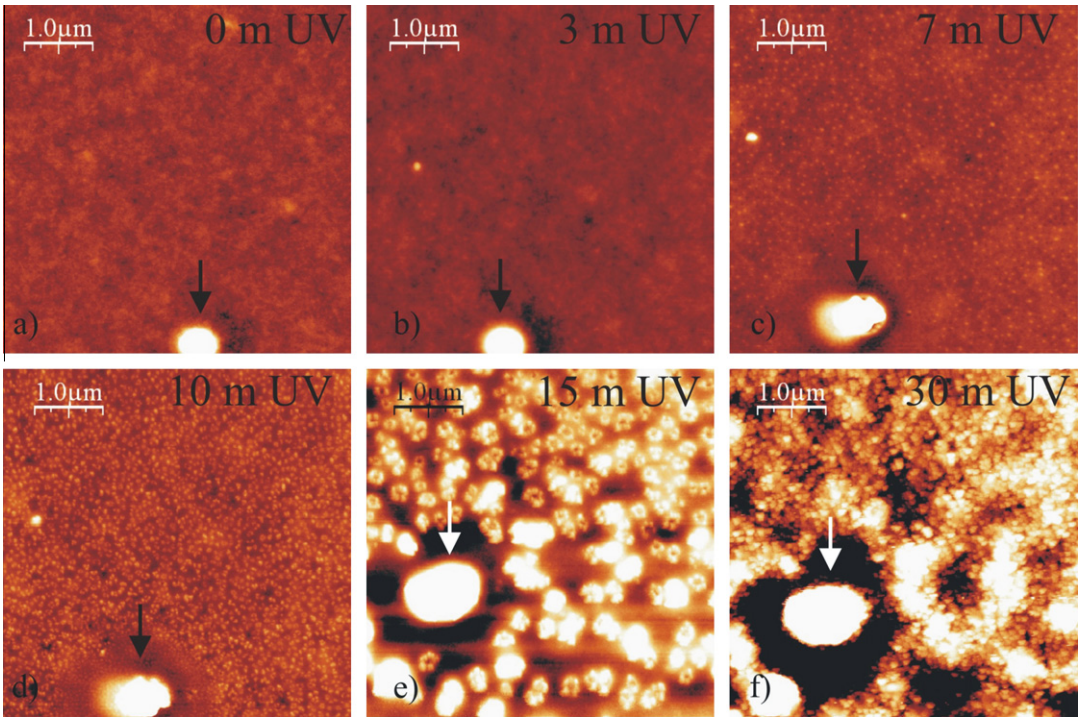

Fig. 2. A series of SFM topographic images showing the morphology of the P3OT thin film (a) pristine sample, (b) after 3 min, (c) 7 min, (d) 10 min, (e) 15 min and (f) 30 min of UV/ozone exposure. In all images $\Delta z = 100$ nm. An arrow indicates the same feature in all images.

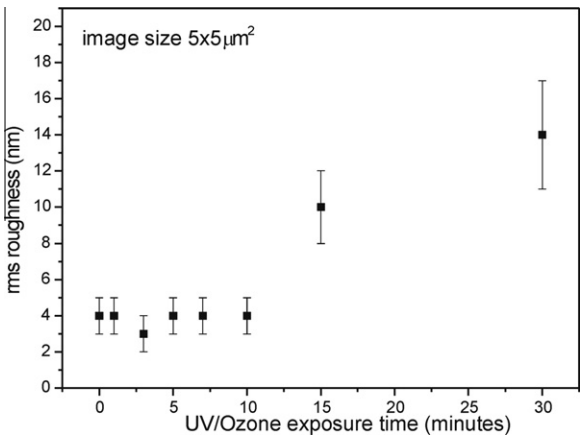

Fig. 3. RMS roughness, from the images of Fig. 2, as function of the UV irradiation.

In order to analyze more quantitatively the effect of irradiation on the surface morphology of the samples, the power spectral density of surface roughness (PSD) has been computed (see Fig. 4a) for each of the images shown in Fig. 1. The PSD-curves corresponding to the early stages of irradiation show that the morphology does not vary significantly: all curves can be described by an approximately linear decrease of surface roughness with an excess roughness at about $\log(1/\lambda) = -3.5 \pm 0.4$ corresponding to a wavelength of about 3 μm, which is in good agreement with the 0.5–2 μm size of the disk and donut shaped structures discussed above. For larger irradiation times (7 and 10 min), however, this peak becomes much less pronounced and finally for large irradiation times a new peak appears around $\log(1/\lambda) = -3$, which corresponds to the size of the satellites around the larger donut-shaped structures. The PSD curves calculated for the small scale images in Fig. 2 (see Fig. 4b) show a similar behavior in the sense that at the beginning of the irradiation (0–5 min) the curves are similar and approximately linear in the region $-3 \leqslant \log 1/\lambda \leqslant -2$. Note that the peak at $\log 1/\lambda = -3.5$ observed in PSD-curves corresponding to the large scale images is not observed in these PSD-curves since it would be at the very left of the graph, where data is filtered by the FFT-algorithm used to compute the PSD curves. The PSD-curves obtained from the images after 7 and 10 min of irradiation show a peak around $\log 1/\lambda = -2$, which corresponds to the small granular structure in the 50–100 nm range observed in the small scale images. For the final stages of irradiation process the PSD curves show a significant increase of surface roughness for $\log 1/\lambda = -3$, which hides the initial peak at $\log 1/\lambda = -2$. We note that while the increased surface roughness at $\log 1/\lambda = -3$ is also observed in the large scale images, the small peak at $\log 1/\lambda = -2$ is not detected in these images, since it is at the limit of their resolution.

Figs. 1 and 2 show how the surface morphology of the films varies as they are irradiated. From this data, however, we cannot deduce information on how the film thickness varies and in particular on possible removal of material. In order to solve this issue, SFM has been used to measure the film thickness as the films are irradiated. Since the

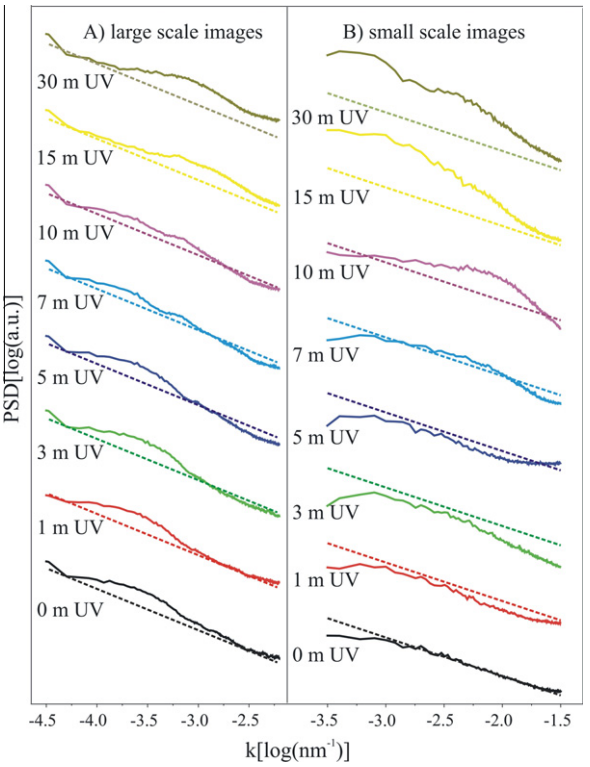

Fig. 4. Power spectral density of surface roughness (PSD) from (a) large scale images of Fig. 1 and (b) small scale images of Fig. 2. The dotted straight lines correspond to lines which approximate the PDS curves at the beginning of the irradiation process (lowest curves). For each irradiation time this line is then shifted with respect to the initial line by the same amount as the corresponding PSD curve, therefore these lines serve as reference in order to visualize the variation of the PSD curves as the sample is irradiated.

P3OT films are mechanically much softer than glass these films can be carefully scratched in order to expose the glass substrate. The depth of the corresponding trenches has been measured by SFM and gives a faithful average value for the film thickness at different stages of the irradiation process. Figs. 5 and 6 shows images of the trenches, as well as a graph of the film thickness as a function of UV-exposure. Data are shown for different films, and the results

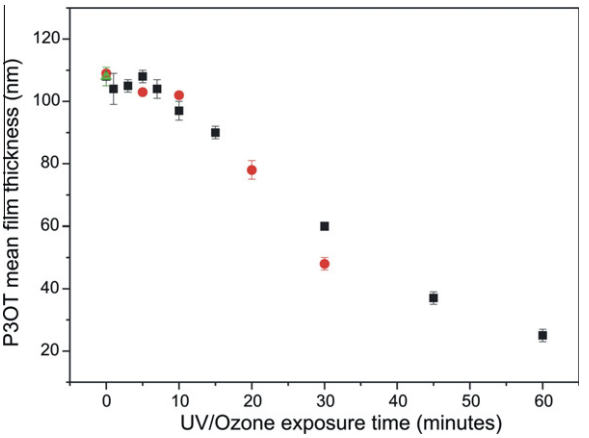

Fig. 6. Mean P3OT film thickness as function of the UV/ozone exposure. Squares, circles and triangle correspond to different P3OT samples.

of these experiments agree quite well. During the first 5 min, the film thickness stays essentially constant. Then, between 5 and about 30 min, the thickness decreases at a constant rate of about 2 nm/min. Finally, after 30 min the film still decreases, but at a slower rate. The evolution of surface morphology and film thickness are clearly related: during the first 5 min, neither thickness nor the morphology vary appreciably. Then, the film thickness starts to decrease at a constant rate while the surface roughness increases. In this regime the film thickness is considerably larger than the surface roughness and the film predominantly covers the glass substrate. After about 30 min of irradiation, the film is so thin and so rough that the mean film thickness and the surface roughness are of the same order of magnitude. At this stage, significant portions of the glass substrate will start to be uncovered by the thinning P3OT-film (see, in particular, the surface after 30 min in Fig. 1) and after 60 min most of the glass substrate has been exposed (see Fig. 5c). When this occurs, it is reasonable that the rate of thinning decreases: now the UV light does not shine only on the P3OT film, but also on the exposed glass substrate; therefore the UV-light is less effective in the film removal process, which is precisely the behavior observed in our experiment. The loss of material in thin films of poly(3-hexythiophene) P3HT,

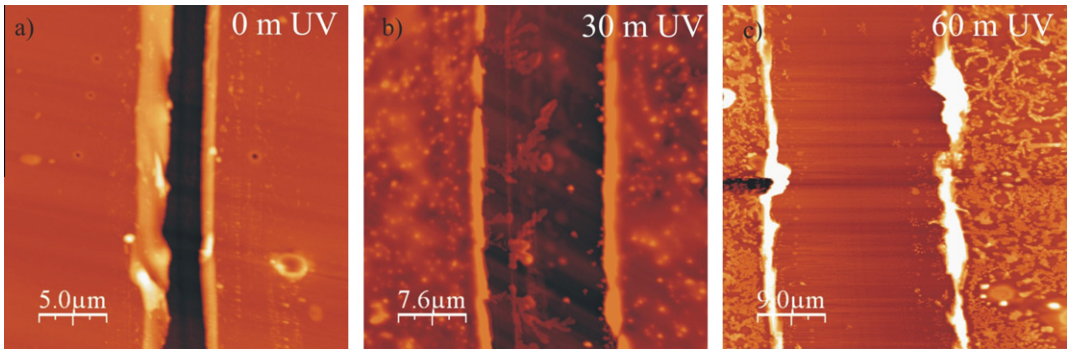

Fig. 5. SFM images of different trenches in P3OT thin films (a) pristine sample, (b) after 30 min and (c) after 60 min of UV/ozone exposure. In all images $\Delta z = 400$ nm.

which is a very similar chemical compound to the polymer P3OT used in the present study during the illumination under oxygen has been also observed by Hintz et al. [18]. They report the appearance of the X-ray photoelectron spectroscopy signal of Indium, which is part of the substrate material ITO, at later stages of degradation.

3.2. Nanoscale electronic properties

In addition to the topography, also the electrostatic properties of the sample have been measured. Using ESFM techniques the nanoscale contact potential and capacitance (more precisely, the second derivative of the tip-sample capacitance, see [27]) have been determined. Fig. 7 shows high resolution images of the topography, the contact potential and the capacitance signal measured on (approximately) the same location. Images are shown for a pristine sample, and for 3 and 5 min of UV irradiation. In agreement with the topographic results discussed above, during the first 5 min of irradiation the morphology of the sample does not change significantly. The electrostatic properties, however, do show important variations. On the one hand, although no nanoscale structure is observed, the overall contact potential difference between tip and sample decreases already after 3 min of irradiation. On the other hand, after about 5 min of irradiation the capacitance signal shows a marked contrast (darker spots in Fig. 7c) with rounded structures of 20–40 nm. We associate these regions of lower tip-sample capacitance with a locally lower electrical conductivity of the sample. These regions of lower conductivity are correlated with grains in the topography image. Similar grains were observed in the previous experiment (Fig. 2), where after 7 min of irradiation a grain like structure started to become visible,

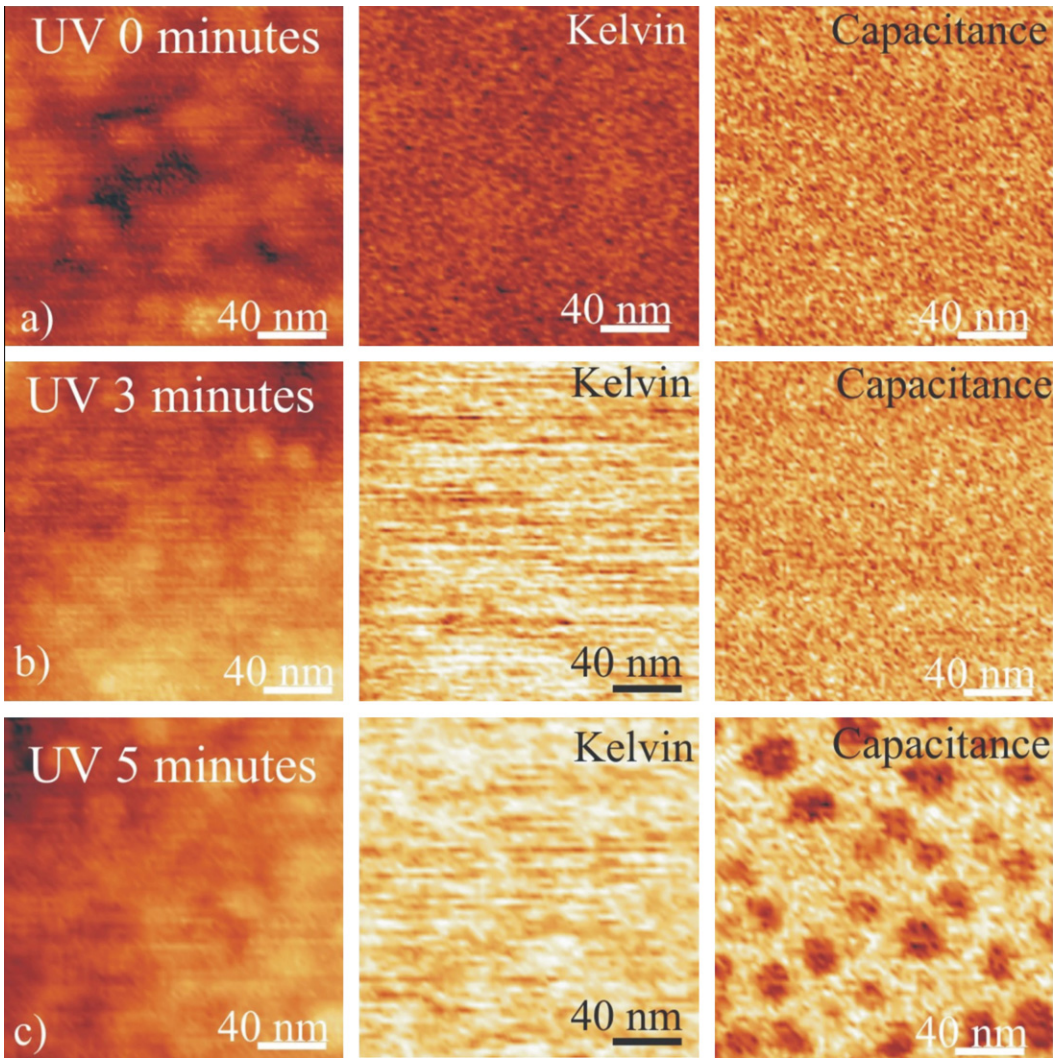

Fig. 7. Topography (left column), contact potential (central column) and capacitance images (right column) acquired on similar topographic regions of a thin film P3OT sample. Top row (a) was measured on the pristine sample, the middle row (b) after 3 min and the lower row after (c) 5 min of UV irradiation. For all topographic images the gray scale corresponds to $\Delta z = 5$ nm, for the contact potential the gray scale is $\Delta CP = 600$ mV, while the capacitance images are shown in arbitrary units, corresponding to a signal output of $\Delta U = 200$ mV of our lock-in amplifier.

increasing in density and size as the sample was further irradiated. From a series of topographic and contact potential images acquired for the first 15 min of UV irradiation, the evolution of the contact potential difference between tip and sample was monitored. As shown in Fig. 8, this contact potential difference is largest for the pristine sample and rapidly varies from about 0.5 V to about 0.1 V during the first 5 min of irradiation. After this initial variation, the contact potential remains constant. From the evolution of surface morphology and electronic data we conclude that the first variation of surface properties is observed for the contact potential, which starts to change as soon as the sample is irradiated. Then, after 3–5 min of irradiation the local conductivity of the sample changes and becomes inhomogeneous with regions of lower conductivity (lower tip-sample capacitance) corresponding to small grains (20–40 nm) in the topography. During this initial stage of irradiation, neither the surface morphology nor the film thickness varies appreciably. Only after 5–7 min small grains appear that are correlated with regions of lower conductivity, and after about 10 min the roughness increases and the film thickness starts to decrease.

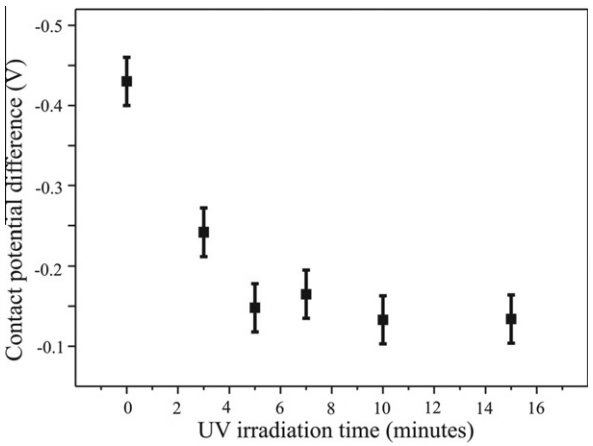

Fig. 8. Evolution of the tip-sample contact potential difference as function of the UV/ozone irradiation time.

3.3. Optical Measurements

In addition to the nanoscale SFM measurements we have performed simple optical experiments in order to study how the optical absorption of the P3OT films varies with UV irradiation. Fig. 9 shows a set of optical images taken with an inverted microscope in white light transmission mode. These images show a scratch in the P3OT film in addition to some much smaller circular inhomogeneities which we associate to the round structures observed in the previous SFM images. All images were taken with the same illumination intensity and the same acquisition parameters (in particular speed) of the camera. Clearly, the P3OT film becomes brighter as the film is irradiated by UV-light, therefore the absorption of the film decreases. Since the scratch observed in the images is free of P3OT, it allows

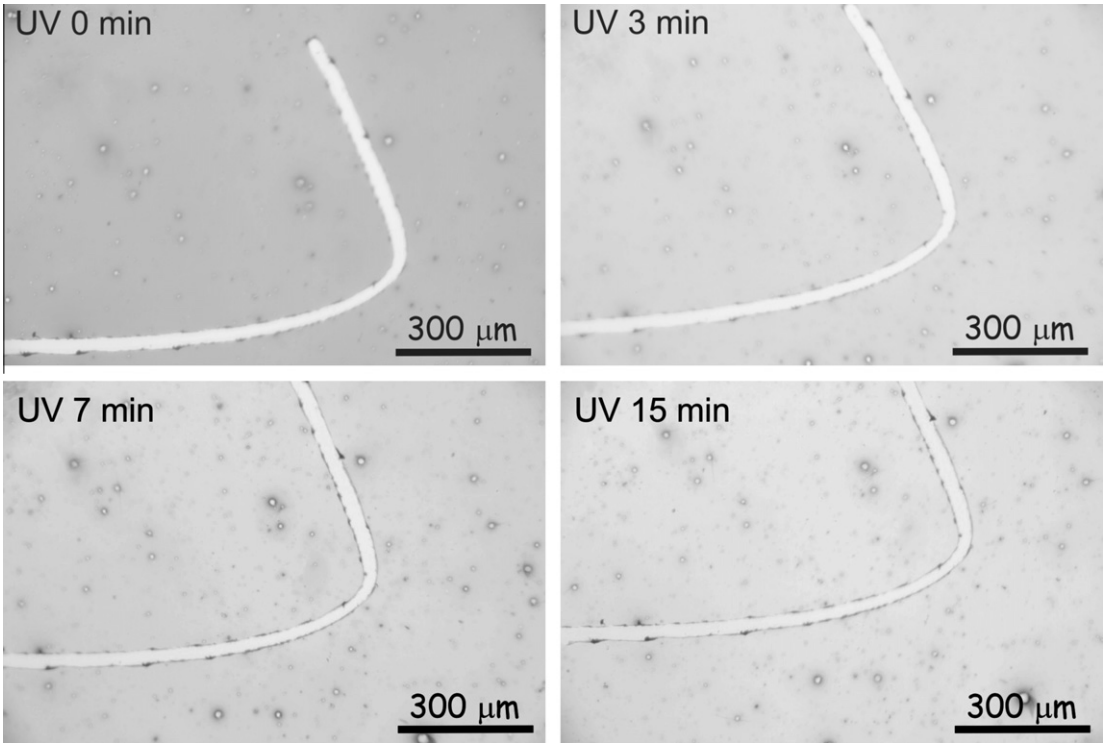

Fig. 9. A series of optical images showing a scratched P3OT thin film (a) pristine sample, (b) after 3 min, (c) 7 min, and (d) 15 min of UV/ozone exposure. The streak has been performed to compare the color contrast between the polymer film and the substrate.

calibrating the light passing through the bare glass substrate which is used as a reference for the calculation of the absorption of the P3OT film. The main differences found between the images are the loss of contrast between the polymer film and the glass substrate. After 15 min of UV/ozone exposure the contrast is almost lost and the polymer thin film turns colorless. The evolution of light absorption as a function of UV-irradiation is shown in Fig. 10. During the first 5 min, we observe a very fast decrease of absorption, followed by a transition regime between 5–15 min and a much slower reduction after 30 min. These results are in agreement with those obtained by Hintz et al. [18] and Rivaton et al. [20] for P3HT films, where the illumination under oxygen leads to the loss of the optical absorption in the range between 330 and 650 nm. In order to quantitatively discuss the measured light absorption, we will first assume that the material properties of the film stay constant during the experiments. Then the transmitted light intensity $T(d)$ should follow the well known relation:

$$T(d) = I_0 e^{-d/\kappa} \quad (1)$$

where I_0 is the light intensity without film (measured in the scratch), d is the film thickness and κ the absorption length (often, the absorption coefficient $\alpha = 1\kappa$ is used instead of κ). Since the light attenuation A and transmittance T are related through $A(d) + T(d) = I_0$, we may rewrite (1) as

$$A(d(t)) = I_0 - T(d(t)) = I_0(1 - e^{-d(t)/\kappa}) \quad (2)$$

where we have explicitly taken into account that in our experiments the film thickness $d(t)$ varies with time. As will be discussed in more detail below, our data does not follow this behavior, but we will nevertheless use it at starting point for our analysis. From Eq. (2) we define the (relative) light attenuation $a(d(t))$ as $1-(T(d(t))/I_0)$. In the inset of Fig. 10 this relative light attenuation across the polymer film is plotted as a function of the UV/ozone exposure time. It shows a very pronounced decrease during the first few minutes of exposure, a slower decrease between about 5 and 15 min. After 30 min the absorbance is essentially zero, since the color of the film is very similar to that of the scratch used as reference for I_0 (image not shown, but see for example Fig. 9 after 15 min, were the contrast between the scratch and the film is already quite low).

Since not only the optical absorption, but also the film thickness has been measured as a function of irradiation time, the absorption can be plotted as a function of the film thickness (Fig. 10). As a function of film thickness the decrease of adsorption is even more pronounced than when plotted as a function of time. Comparing the data of light absorption with the SFM data we directly find an apparent contradiction: the strong variation of light absorption during the first minutes of UV exposure corresponds to the time period were essentially no variation of surface morphology or film thickness is observed. In order to explore this issue further, in Fig. 11a), the logarithm of the transmitted light is plotted as a function of film thickness. If relation (1) was applicable in our experiment, the measured data should lay on a straight line, which is clearly not the case. We therefore conclude that in our experiments the absorption length κ is not constant, but varies with time: $\kappa = \kappa(t)$. Since the film thickness $d(t)$, the

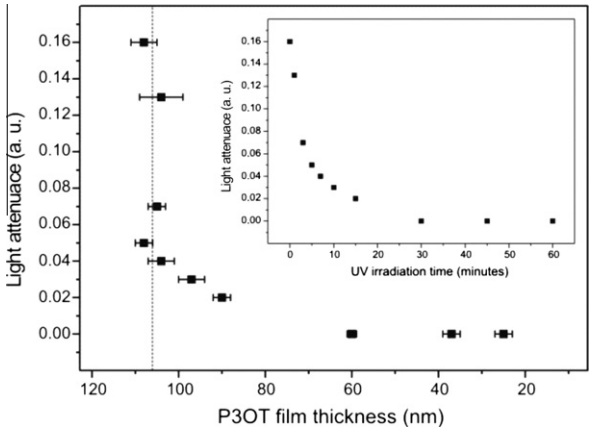

Fig. 10. Light attenuation of the polymer film as function of film thickness obtained from Fig. 5. Inset: light attenuation of the polymer film as function of UV/ozone irradiation time.

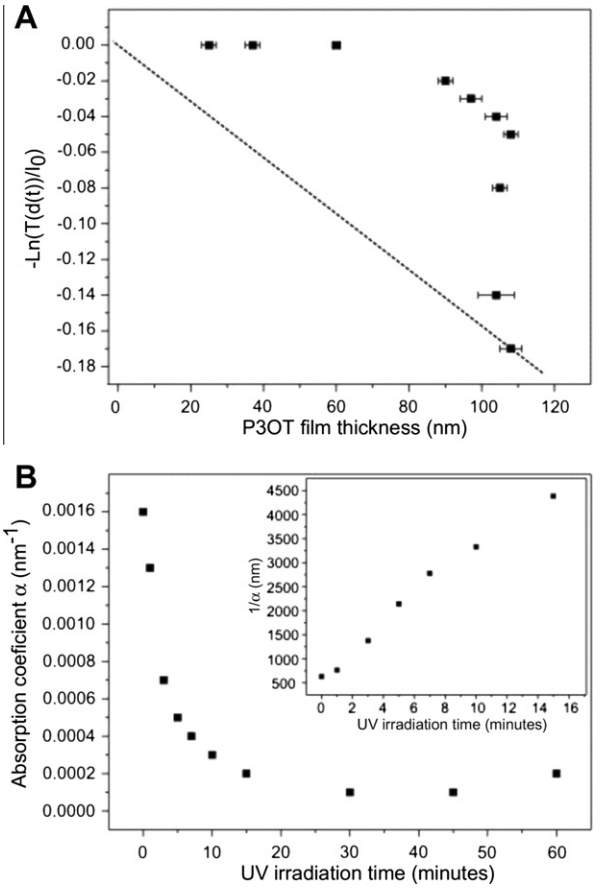

Fig. 11. (a) $-\mathrm{Ln}[T(d(t))/I_0]$ as function of film thickness. (b) Evolution of the absorption coefficient (α) as function of the UV/ozone irradiation time. Inset: evolution of the absorption length $\lambda = 1/\alpha$ as a function of the UV irradiation time.

transmission $I(d(t))$ as well as the transmission without film are known, the absorption coefficient αt and absorption length the can be computed for each time. The corresponding data is shown in Fig. 11b). Interestingly the absorption length increases approximately linearly during the first 15 min. During this period, the absorption length increases by almost an order of magnitude; from about 600 nm to 4500 nm. After the first 15 min, the errors in the measurement of the absorption coefficient increase drastically, since the film has become almost transparent. In addition, for long irradiation time the surface roughness becomes comparable to the film thickness, therefore light transmission may not only be affected only by absorption, but also by light scattering of the rough surface and the simple assumption $A(d) + T(d) = I_0$ may not be applicable because it does not take into account scattering effects.

In order to determine the main degradation mechanism (UV or ozone) an additional experiment has been carried out. Three equivalent samples were prepared as described in detail in the experimental section by deposition of polymer films onto a glass substrate. The three samples were put inside our UV/ozone cleaning system at the same time, the first one without protection (that is, as exposed in the experiments described above), the second one shaded from the UV radiation but exposed to the ozone produced by the UV lamp and the third one protected from the ozone but exposed to the UV radiation from the lamp. This experiment is summarized in Fig. 12, where the light attenuation coefficient is shown as a function of UV/ozone exposure time for the three samples. In addition, an exponential fit is plotted for the two data sets that show a clear non-linear behavior (unprotected and UV-protected sample) and a linear fit is plotted for the ozone-protected sample. Clearly, the unprotected and UV-protected samples degrade very similarly with a typical time scale of a few minutes, as observed in the experiments discussed above, while the sample that is exposed only to UV irradiation is degraded (at least) an order of magnitude slower. Therefore, for our experiments, the bleaching of the samples is clearly attributed to the degradation by ozone exposure.

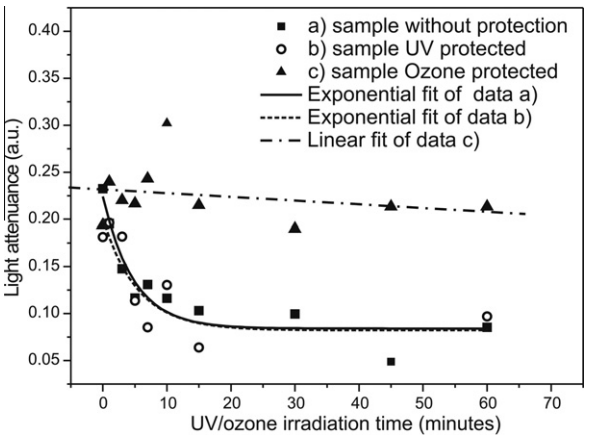

Fig. 12. Light attenuation coefficient as function of UV/ozone exposure time for the samples: (a) sample without any protection (squares), (b) sample protected against UV radiation (circles) and (c) sample protected against ozone exposure (triangles). In addition to the experimental data a linear fit is shown for the data corresponding to the ozone protected sample, and exponential fits are shown for the two other samples (unprotected and UV-protected).

4. Conclusions

The UV/ozone degradation on P3OT thin films was investigated by means of SFM and classical optical microscopy. Our experimental set-up allows to perform a nanoscale study of the same area of the sample, therefore we can attribute individual changes of the film morphology to the effect of UV irradiation. We find that during the first 10 min of exposure neither the overall film morphology nor its thickness change. The nanoscale electrical properties, however, do change significantly in this initial stage of irradiation: on the one hand the overall contact potential varies by about 0.4 V, and on the other hand the conductivity becomes inhomogeneous and decreases locally on a nanometer scale. The variation of contact potential is in good agreement with results reported in the literature [18] where a shift of the Fermi level of 0.4 V of P3HT is observed. During the initial stage of UV irradiation also the macroscopic optical properties change. In fact, already a simple visual inspection of the samples shows that the color of the sample is lost, that is, the light attenuation significantly decreases and after 10–15 min the film is essentially colorless.

We clearly find that electro-optical and morphological processes are decoupled, indicating that the degradation process occurs in two distinct stages: during the first stage (first 5–10 min) a degradation occurs which varies the electro-optical properties (light absorption, contact potential and local conductivity) of the material and only after this process the film morphology varies and its thickness decreases. Based on the results of the literature, in particular in reference [18], and taking into account the results of Fig. 12, we propose that both effects, the electro-optical, as well as the morphological degradation are due to the reaction of P3OT with ozone generated by the UV-radiation. In Ref. [18] the degradation of P3HT is studied using UV/VIS and photoelectron spectroscopy. There it is shown that in a typical laboratory environment at AM 1.5 the degradation of P3OT films by chemical reaction with ozone is two orders of magnitude lower than the rate of direct photo oxidation. In addition, it was shown that the two mechanisms of degradation have different paths: while ozone reacts with the double bonds in the thiophene ring, photo-oxidation is initiated at the ends of the polymer chain and at the alkyl chain of the corresponding monomer [19] leading to reactive peroxides which subsequently cause the oxidation of sulfur and the destruction of the thiophene ring [18].

In our case, even though (direct) photochemical degradation as well as ozone generation (see Fig. 2 in [18]) should increase linearly with UV irradiation, we propose that chemical reaction with ozone is the predominant degradation mechanism (note that our UV irradiation system is closed, and ozone generated is thus accumulated in the system, which does not happen with the photons). This is confirmed by the reaction kinetics observed in the corresponding experiments: the decay of absorption occurs

exponentially in our case (inset of Figs. 11 and 12) as well as in the experiments reported in [18] for ozonisation, while direct photo-oxidation leads to a linear decay of absorption (Fig. 1 in [18]).

A similar degradation behavior as that discussed here for P3OT thin films has been reported in the literature for the UV/ozone degradation of polypropylene films [29,30]. These works show that after 1 min of UV/ozone treatment the chemistry of the surface is modified, while the morphology remains unchanged. However, after 4 min of UV/ozone treatment the morphology changes completely, as the result of the polymer surface oxidation, resulting in the formation of low molecular weight oxidized material.

In conclusion, from the experiments reported in this work as well as from previous experiments reported in the literature, we conclude that degradation of P3OT thin films when irradiated by UV light occurs in two steps: in a first initial process a chemical reaction with ozone generated by the UV irradiation varies the optical absorption and the contact potential (Fermi level) of the films. We attribute these changes to the breaking of the conjugated bonds of the polymer chain. In addition, the local conductivity is reduced. In a second step, the films are etched away by further chemical reaction with ozone. With respect to the implications for the operation of Organic Solar Cells, already the first process will degrade device performance, since it will on the one hand reduce optical absorption, and on the other – probably even more important – change the band structure within the cell, in particular change the open circuit voltage, which is a fundamental parameter for device operation.

Acknowledgements

The work was supported by the Comunidad Autonoma de la Región de Murcia under the project "Organic Solar Cells: From molecular and nanoscale structure to macroscale operational devices" as well as through the project "Propiedades Nanométricas de Células Solares Orgánicas" (MAT2010-21267-C02) from the MICINN. AU acknowledges financial support from MICINN through project HOPE CSD2007-00007 (Consolider-Ingenio 2010). The authors acknowledge stimulating discussions with E. Palacios-Lidón and R. García Valverde.

References

[1] C.J. Brabec, N.S. Sariciftci, J.C. Hummelen, Adv. Funct. Mater. 11 (2001) 15.
[2] H. Sirringhaus, P.J. Brown, R.H. Friend, M.M. Nielsen, K. Bech-gaard, B.M.W. Langeveldvoss, A.J.H. Spiering, R.A.J. Janssen, E.W. Meijer, P. Herwig, D.M. de Leeuw, Nature 401 (1999) 685.
[3] F. Hide, M.A. Diaz-Garcia, B.J. Schwartz, M.R. Andersson, Q.B. Pei, A.J. Heeger, Science 273 (1996) 1833.
[4] R.H. Friend, R.W. Gymer, A.B. Holmes, J.H. Burroughes, R.N. Marks, C. Taliani, D.D.C. Bradley, D.A. dos Santos, J.-L. Brédas, M. Logdlund, W.R. Salaneck, Nature 397 (1999) 121.
[5] N. Camaioni, M. Catellani, S. Luzzati, A. Magliori, Thin Solid Films 403 (2002) 489.
[6] T.J. Prosa, M.J. Winokur, J. Moulton, P. Smith, A.J. Heeger, Phys. Rev. B 51 (1995) 159.
[7] B.S. Ong, Y. Wu, P. Liu, S. Gardner, Adv. Mater. 17 (2005) 1141.
[8] T. Kaniowski, S. Niziol, J. Sanetra, M. Trznadel, A. Pron, Synth. Met. 94 (1998) 111.
[9] R. Singh, J. Kumar, R.K. Singh, A. Kaur, K.N. Sood, R.C. Rastogi, Polymer 46 (2005) 9126.
[10] S. Chambon, A. Rivaton, J. Gardette, M. Firon, Sol. Energy Mater. Sol. Cells 91 (2007) 394.
[11] F.C. Krebs, K. Norrman, Prog. Photovoltaics Res. Appl. 15 (2007) 697.
[12] M. Jørgensen, K. Norrman, F.C. Krebs, Sol. Energy Mater. Sol. Cells 92 (2008) 686.
[13] D.R. Lide (Ed.), CRC Handbook of Chemistry and Physics, 74th ed., CRC Press, 1994, pp. 8–24.
[14] F. Cataldo, Polym. Degrad. Stab. 60 (1998) 223.
[15] W. Czerwiñski, J. Nowaczykand, K. Kania, Polym. Degrad. Stab. 72 (2001) 287.
[16] G. Yu, C. Zhang, A.J. Heeger, Appl. Phys. Lett. 64 (1994) 1540.
[17] B.H. Cumpston, K.F. Jensen, J. Appl. Polym. Sci. 69 (1998) 2451.
[18] H. Hintz, H.-J. Egelhaaf, H. Peisert, T. Chassé, Polym. Degrad. Stab. 95 (2010) 818.
[19] M. Manceau, A. Rivaton, J.-L. Gardette, S. Gutierrez, N. Lemaitre, Polym. Degrad. Stab. 94 (2009) 898.
[20] A. Rivaton, S. Chambon, M. Manceau, J.-L. Gardette, N. Lemaître, S. Guillerez, Polym. Degrad. Stab. 95 (2010) 278.
[21] J. Mardalen, H.J. Fell, E.J. Samuelsen, E. Bakken, P.H.J. Carlsen, M.R. Andersson, Macromol. Chem. Phys. 196 (1995) 553.
[22] I. Horcas, R. Fernandez, J.M. Gomez-Rodriguez, J. Colchero, J. Gomez-Herrero, A.M. Baro, Rev. Sci. Instrum. 78 (2007) 013705.
[23] J.M.R. Weaver, D.W. Abraham, J. Vac. Sci. Technol., B 9 (1991) 1559.
[24] M. Nonnenmacher, M.P. ÓBoyle, H.K. Wickramasinghe, Appl. Phys. Lett. 58 (1991) 2921.
[25] E. Palacios-Lidon, B. Perez-Garcia, J. Colchero, Nanotechnology 20 (2009) 085707.
[26] B. Perez-Garcia, J. Abad, A. Urbina, J. Colchero, E. Palacios-Lidon, Nanotechnology 19 (2008) 065709.
[27] J. Colchero, A. Gil, A.M. Baro, Phys. Rev. B 64 (2001) 245403.
[28] J. Abad, J. Colchero, in press.
[29] H.-Y. Nie, M.J. Walzak, B. Berno, N.S. McIntyre, Appl. Surf. Sci. 144/145 (1999) 627.
[30] M.J. Walzak, S. Flynn, R. Foerch, J.M. Hill, E. Karbashewski, A. Lin, M. Strobel, J. Adhes. Sci. Technol. 9 (1995) 1229.

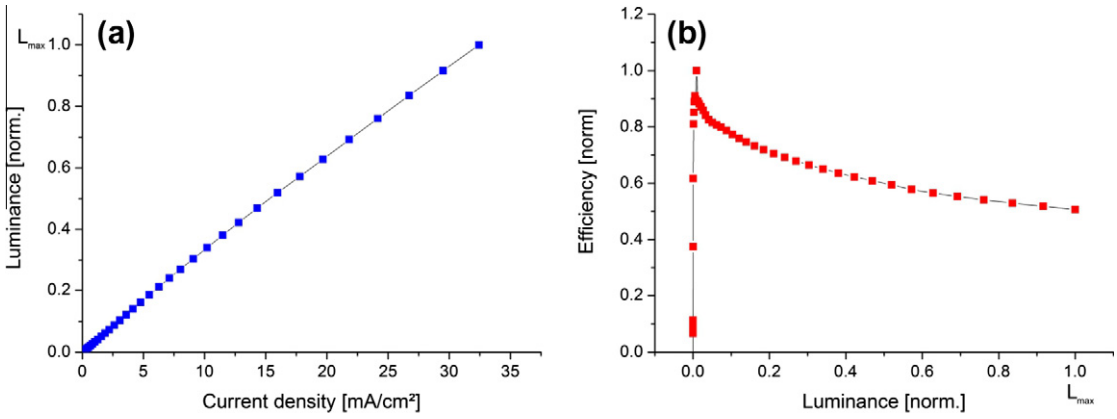

Fig. 1. Current density–luminance plot (a) and device efficiency (b).

2. Explanation of the coupled electrothermal model

2.1. Electrical model

The electrical model considers an OLED as a system of three conducting thin layers (anode, stack of organic films and cathode) (Fig. 2). The thickness of these conducting layers is much smaller (100–250 nm) than the lateral dimensions (>1 cm), which leads to high aspects ratios. Anode and cathode are connected at the edges. As a consequence, the following approximations are acceptable:

(1) Lateral (x- and y-direction) current densities are much higher than vertical (z-direction) currents along anode and cathode layers.
(2) Current flow through organic films between anode and cathode has only a vertical component (negative z-direction).

Combining these approximations with Ohm's law [12], the potential distribution along anode and cathode can be described by continuity equations [7]

$$\frac{1}{R_{sh,A}} div(grad\ \Phi_A) = -J_Z \tag{1}$$

for the anode potential and

$$\frac{1}{R_{sh,K}} div(grad\ \Phi_C) = J_Z \tag{2}$$

for the cathode potential, with R_{sh} as sheet resistance of the contact, Φ_A and Φ_C as contact potentials and J_Z as vertical current density through the organic stack.

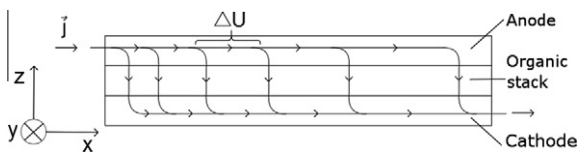

Fig. 2. Schematic delineation of current flow in an OLED. The organic films are summarized to one conducting layer in the model. ΔU is the horizontal voltage drop.

The charge transport through the organic layers is described by a lumped-element model (Fig. 3a). $G(V,T)$ describes the conductivity of the organic layers, C the geometric OLED capacitance. The conductivity is a voltage (V)- and temperature (T)-dependent element. Under the assumption of a homogenous current distribution, which is approximately correct for devices smaller than 1 cm^2, the current density J_Z can be described by

$$J_Z = \frac{V \cdot G(V,T) + C\frac{dV}{dt}}{A} \tag{3}$$

with A as device area. The voltage is defined by the potential difference between anode and cathode ($V = \Phi_A - \Phi_C$). The term $C\frac{dV}{dt}$ describes currents caused by time dependent change of voltage and allows transient simulation.

The model calculates the potential distribution as a result of current density in the organic layers. Current density itself is a function of voltage resulting from the potential distribution in the anode and cathode layer. Consequentially, the electrical model is an iterative one.

We use a small 5×5 mm^2 device to extract $G(V,T)$ from I–V–T measurements and assuming a homogeneous current distribution for such a small geometry. From the I–V–T curve, the G–V–T behavior can be derived with

$$G(V,T) = \frac{I(V,T)}{V} \tag{4}$$

Fig. 3b shows the measured G–V curves at different temperatures. A strong increase of conductivity with temperature, which is typical for organic semiconductors [13], can be recognized. During the measurement the OLED was immersed into a temperature controlled oil bath.

The sheet resistance of anode and cathode contacts was determined by four-point-probe measurements [14]. Voltage dependency for OLED capacitance has been investigated by impedance spectroscopy [15]. There is only a negligible voltage dependency of this capacitance, which allows a simple calculation of C. The geometric capacitance is described by

$$C = \varepsilon_r \varepsilon_0 \frac{A}{d} \tag{5}$$

with ε_r as dielectric function, ε_0 electrical permeability, A as electrode area and d as electrode distance. We

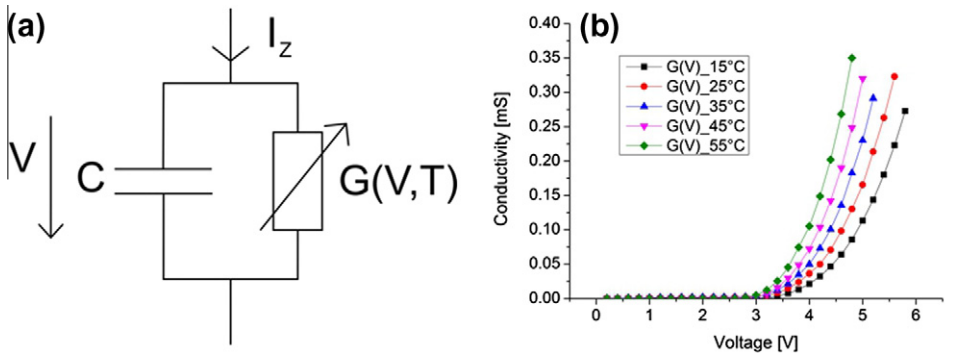

Fig. 3. Lumped-element model for current density J_Z [$I_Z = J_Z \cdot A$] (a) and G–V–T measurement results for characterizing thermal behavior of OLED (b).

calculated values for C with given geometric properties of our devices and assume a temperature- and voltage-independent dielectric function ($\varepsilon_r = 3$) [16].

The extracted parameters are summarized in Table 1.

2.2. Thermal model

The thermally modeled device is an encapsulated OLED processed on a glass substrate. The encapsulation is performed via a lid with a thin getter material layer which protects the device from residual air and humidity.

The device geometry was implemented into a CAD drawing, which provides as a basis for the thermal model. The single elements of this geometry are divided into different subdomains representing different materials.

Following assumptions for the thermal model are being made:

(1) Heat transport inside the device is carried by thermal conduction.
(2) Thermal exchange with the ambient is based on convection and thermal radiation.

The heat equation is described by [17]

$$\rho c_p \frac{dT}{dt} + div(-\lambda\, grad\, T) = Q \tag{6}$$

with ρ as material density, c_p as specific heat capacitance, λ as specific heat conductivity and Q as heat source. For the interfaces between the device and ambient, boundary conditions for exchange by convection and radiation are calculated with [16]

$$\vec{n}(-\lambda\, grad\, T) = h(T - T_{amb}) + \epsilon\sigma(T^4 - T_{amb}^4) \tag{7}$$

with $\vec{n}$ as normal vector to the boundary, h as heat transfer coefficient, ϵ as emissivity, σ as Stefan–Boltzmann constant [18] and T_{amb} as ambient temperature (we assume that the convective air flow has the same temperature as the ambient).

Table 1
Parameters used in the electrical OLED model.

C (nF) (5×5 mm^2)	$R_{sh,A}$ ($\Omega/\square$)	$R_{sh,C}$ ($\Omega/\square$)
5	20	0.3

We have solved this problem by the finite-element method using *Comsol 3.5* [19]. Material parameters (Table 2) have been taken from literature [20,21].

We consider an ambient temperature of 298 K with calm-air conditions (h = 5) [22].

The active OLED (anode, organics and cathode) is modeled as a thin layer with $Q \neq 0$. The connection of the thermal and electrical model by this layer is part of the following chapter. All the other subdomains of the model are solenoidal ($Q \neq 0$).

2.3. Coupling to the electrothermal model

Heat generation in an operating OLED is caused by joule-heating. The heating power density is equal to the scalar product of electric field and current density ($Q = p = \vec{E} \cdot \vec{J}$). We consider the total power density of the device as the sum of electrical losses in the three conducting layers

$$p = p_{Anode} + p_{Org} + p_{Cathode} \tag{8}$$

The power densities are calculated in the electrical model

$$p_{Anode,Cathode} = \frac{1}{d\,R_{sh\,A,C}} |\, grad\, \Phi_{A,C}|^2; \quad p_{Org} = \frac{|J_Z|^2}{\sigma_{Org}(V,T)} \tag{9}$$

with d as contact thickness and $\sigma_{Org}(V,T) = G(V,T) \cdot d_{Org}/A$ as organic specific conductivity.

The coupled electrothermal model is iterative, too. The values for p are calculated in the electrical model which contains the temperature dependence of the organic films. Fig. 4 demonstrates the complete iterative system.

The following chapters compare and analyze the thermoelectrical behavior of an OLED. All measurements and simulations were performed with an applied voltage of 5.4 V and a total current flow of 300 mA.

Table 2
Parameters used in the thermal OLED model.

	ρ (kg/m^3)	c_p (kJ/K kg)	λ (W/K m)	ϵ
Glass	2500	0.80	1.0	0.86
Air	1.24	0.712	0.024	–
Getter	2500	0.80	1.8	–
OLED	2000	0.90	100	–
Aluminum	2700	0.912	250	–

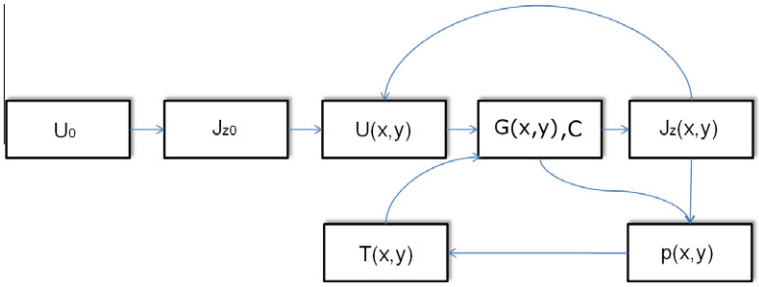

Fig. 4. Iterative system of the coupled electrothermal model. U_0 and J_{z0} represent initial voltage and current values.

3. Validation

There are many ways to measure the surface temperature of an OLED [23]. We have used infrared spectroscopy results to compare measured with simulated stationary results. The measurements were taken from a free-standing (surrounded by calm air) $5 \times 5\,cm^2$ OLED. Fig. 5 shows both results for temperature distribution at the OLED bottom side (light emitting side). We recognize a qualitatively good agreement between measured and simulated temperature distribution. There is a U-shaped hot area in the devices center and decreasing temperatures at the edges.

The quantitative validation of the model is performed by a comparison along two defined lines which are marked in Fig. 5 (green lines). We denote the horizontal line as *x*- and the vertical line as y-axis. Fig. 6 presents the comparison.

The horizontal temperature profiles show two local maxima at about 55 °C. Simulation shows a symmetric profile while measured results weakly differ from symmetry. The measurement shows a stronger temperature decrease to the edges. These differences are probably affected by the measurement setup holders (dark areas in Fig. 5a). These work as additional heat drains, which are not accounted for the simulation.

There is a second decrease of temperature to the center of the device. In this case, the measured decrease is lower than the simulated one. Differences of sheet resistance or layer thickness between measured and simulated device are possible explanations for this deviation.

The vertical profiles show decreasing temperatures from top to bottom edge. A good agreement of measured and simulated result can be achieved. The measured decrease of temperature to the edges is stronger again.

Despite some differences, there is a good qualitative and quantitative agreement of the temperature distribution across the OLED. Deviations can be explained by experimental conditions not covered by the simulation.

4. Thermal OLED analysis

4.1. Stationary

As a first analysis, we discuss the development and consequences of temperature distribution for a $5 \times 5\,cm^2$ OLED. Fig. 7 shows the simulated distribution of power density *p*.

We have recognized a strong correlation between temperature und power distributions. The maximum values of power density are found at the edges while maximum temperature values are located more central to the device area. The simulation predicts higher heat currents at the device edges caused by a large temperature gradient between the actively heated OLED and its encapsulation (heat current $\vec{q} \sim -grad\,T$). As a result, there is a stronger cooling at the edges.

Most publications assume a direct correlation between potential distribution along the TCO, current distribution and distribution of power density. Fig. 8 shows the distribution of anode potential and the distribution of vertical current J_Z.

Obviously, the correlation between current distribution and power distribution is much stronger than the correlation between potential distribution and power distribution (Fig. 7). From Eqs. (8) and (9) we can also deduce that the power density is dominated by the contribution of the organic layer ($p_{Org}/p \geqslant 0.9$). It has a quadratic relation to J_Z. That causes the strong correlation between J_Z and *p*. In contrast to the potential distribution, the current density in the organic layers shows strong temperature dependence, which is neglected in published models [7,8]. This results in a significant difference between merely electrical and coupled electrothermal analysis of large-area OLED. An example profile of current density J_Z along the *x*-axis is shown in Fig. 9a.

Note the two local maxima anticipated by the electrothermal model simulation. They are based upon a rise of temperature overcompensating the drop of voltage along this axis.

As a second example, an investigation of the vertical temperature profile (across the air gap) will be presented. Fig. 9b demonstrates the simulated profile through the OLED center.

There is a strong decrease of temperature along the air gap between the glass lid and OLED, which corresponds to the low thermal conductivity of air. The temperature difference between OLED and substrate surface is very small (<1 K), caused by the low thermal resistance of the thin glass substrate. That is the reason why knowledge about substrate temperature seems to be a good indicator to estimate OLED temperature.

We demonstrate the benefits of our stationary electrothermal model for characterization of large-area OLED. Especially the results for current distribution give useful

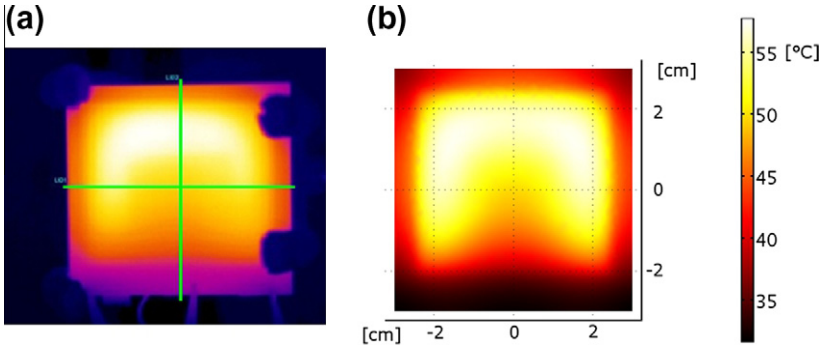

Fig. 5. Comparison of measured (a) and simulated (b) temperature distribution at the bottom side of an OLED. Hot areas are signed by brighter colors. (For interpretation of the references to color in this figure legend, the reader is referred to the web version of this article.)

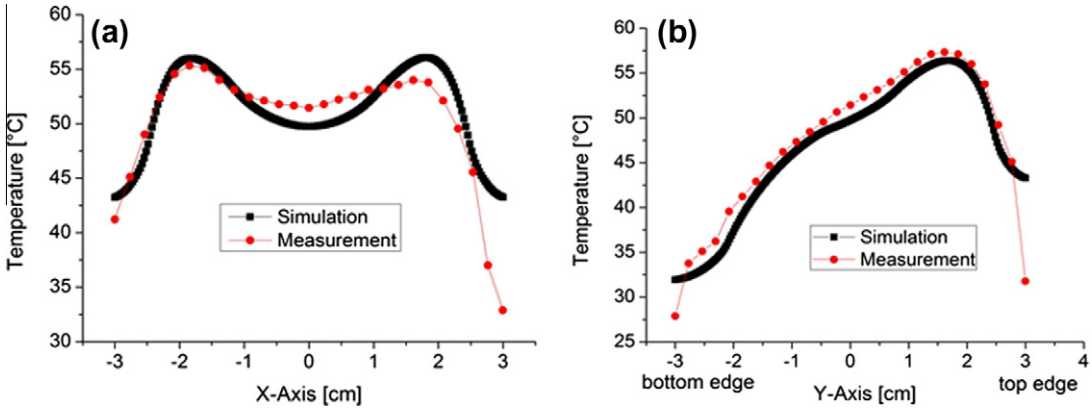

Fig. 6. Temperature profile along *x*- (a) and *y*-axis (b).

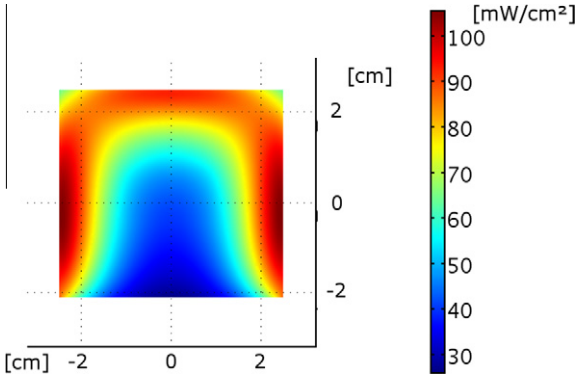

Fig. 7. Distribution of power density over the OLED area.

information for the development of large-area devices with homogeneous luminance distribution.

4.2. Transient

Beside stationary analysis to characterize the homogeneity of an OLED, transient characteristic have to be investigated to analyze switching behavior. Although the electrical relaxation time of an OLED is in the order of ms [24], stationary luminance characterization of a large-area OLED need some minutes under constant electrical operating conditions [19]. This is the result of the long thermal relaxation time and the temperature dependence of organic semiconductors. We simulate the transient behavior of T and J_Z in the center of the 5×5 cm^2 OLED (Fig. 10).

The OLED with an applied voltage of 5.4 V has been simulated (Fig. 10a). The transient behavior of temperature and current density is almost equal. It can be described by an exponential function, which corresponds to a time-dependent solution of the thermal equivalent circuit

$$y = y_0 + a\left(1 - e^{\frac{-t}{\tau}}\right) \tag{10}$$

Following values fit this function for the values of Fig. 10a:

$$y_{0_T} = 25.23; \quad y_{0_J} = 49.65; \quad a_T = 22.13; \quad ; a_J = 32.24; \quad \tau_T = \tau_J = 215.4$$

y_{0_T} and y_{0_J} are temperature and current values at room temperature (25 °C), respectively, α_T and α_J represent the temperature and current hub at steady-state conditions. τ_T and τ_T are the temperature and current relaxation times.

The simulation predicts the same relaxation time for current density and temperature of 215.4 s. It is possible to accelerate current relaxation by voltage regulation. An

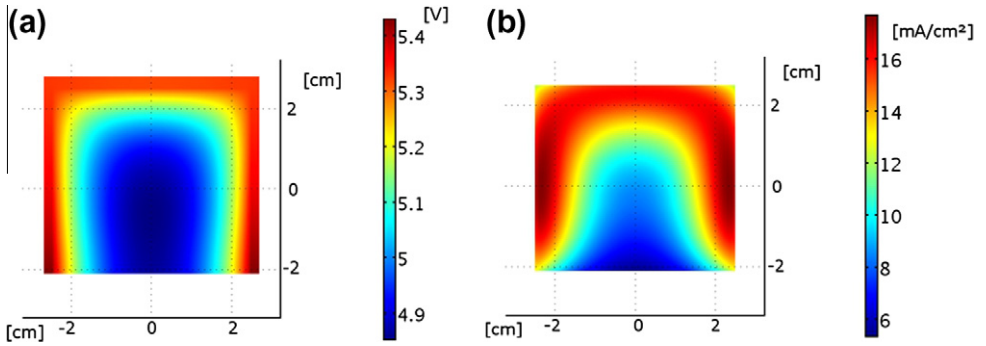

Fig. 8. Anode potential (a) and current distribution (b) of the 5×5 cm^2 OLED.

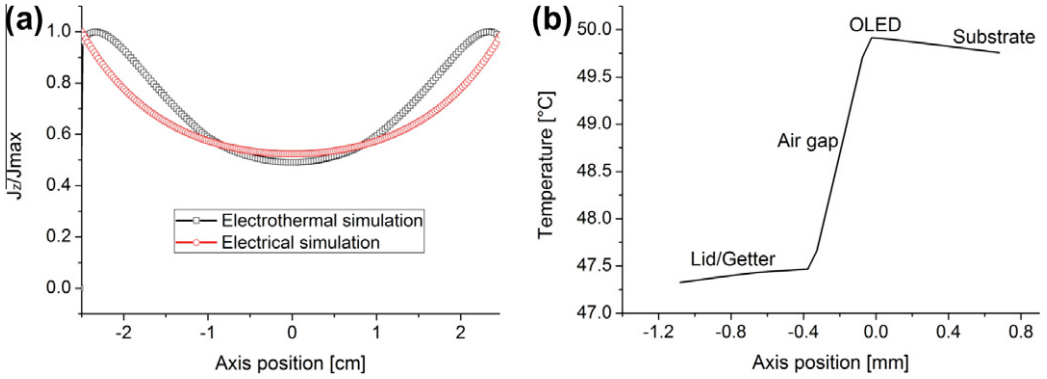

Fig. 9. Normalized current profile along the *x*-axis for the merely electrical and the coupled electrothermal model (a) and vertical temperature profile of the glass encapsulated 5×5 cm^2 OLED (b).

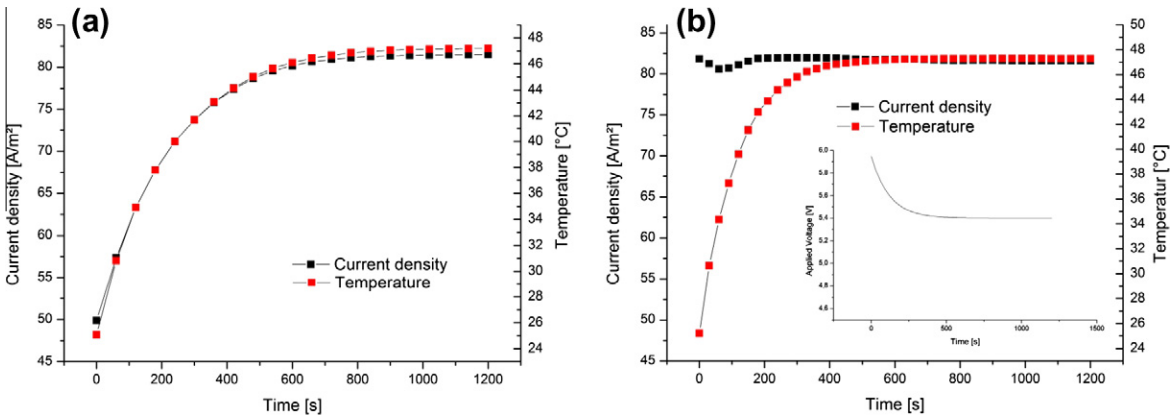

Fig. 10. Time-dependent simulation of temperature and current density in the center of the 5×5 cm^2 OLED at constant driving voltage (a) and with an exponentially decaying driving voltage (b).

exponentially decaying voltage as regulation has been simulated:

$$u_0 = 5.4V + 0.55Ve^{\frac{-t}{120}}$$

Fig. 10b demonstrates the reduction of current and temperature relaxation time for this case.

This result underlines the importance of transient electrothermal characterization for an optimized regulation of OLED switching. Our model serves as a helpful tool to analyze the reasons for the dynamic behavior of a large-area OLED.

5. Summary and outlook

We demonstrate the advantages of electrothermal OLED characterization for analysis and development of

large-area devices. The validation by comparison of simulated and measured temperature profiles was successful. Significant differences between the results of an electrical and a coupled electrothermal model were shown. Results for current distribution have been demonstrated caused by its strong correlation to luminance distribution [25]. Another result documented the informative value of substrate temperature for estimations of OLED (i.e. organic layer) temperature. The impact of the thermal relaxation process on current relaxation has been shown. A possible acceleration of current relaxation by voltage modulation has been demonstrated.

Further steps to increase the informative value of our simulation have to be performed. Temperature-dependent voltage–luminance measurements promise direct information about luminance distribution including the drop of OLED efficiency with rising temperatures [10]. Temperature-dependent lifetime measurement will allow simulation of local aging under continuous operation. The integration of metal grid or shunt lines into our model could clarify many questions and actively support device development.

References

[1] F. So, J. Kido, P. Burrows, MRS Bull. 33 (2008) 663–669.
[2] J.-H. Lee, D.N. Liu, S.-T. Wu, Introduction to Flat Panel Displays, Wiley, 2008. pp. 177–231.
[3] L. Duan, S. Liu, D. Zhang, J. Qiao, G. Dong, L. Wang, Y. Qiu, J. Appl. Phys. D 42 (2009) 075103.
[4] S. Reineke, F. Lindner, G. Schwartz, N. Seidler, K. Walzer, B. Lüssem, K. Leo, Nature 459 (2009) 234–238.
[5] R. Meerheim, K. Walzer, M. Pfeiffer, K. Leo, Appl. Phys. Lett. 89 (2006) 061111.
[6] C. Piliego, M. Mazzeo, M. Salerno, R. Cingolani, G. Gigli, A. Moro, Appl. Phys. Lett. 89 (2006) 103514.
[7] K. Neyts, M. Marescaux, A.U. Nieto, A. Elschner, W. Lovenich, K. Fehse, Q. Huang, K. Walzer, K. Leo, J. Appl. Phys. 100 (2006) 114513.
[8] K. Neyts, A. Real, M. Marescaux, S. Mladenovski, J. Beeckman, J. Appl. Phys. 103 (2008) 093113.
[9] C. Gärditz, A. Winnacker, F. Schindler, R. Paetzold, Appl. Phys. Lett. 90 (2007) 103506.
[10] A. Poppe, L. Pohl, E. Kollar, Zs. Kohari, H. Lifke, C. Tanase, CIE, PWDAS-38 Book of Abstracts, 2009.
[11] J.C. Sturm, W. Wilson, M. Iodice, IEEE JSTQE 4 (1998) 75.
[12] K. Simonyi, Theoretische Elektrotechnik, Wissenschaften Edition Deutscher Verlag, New York, 1993.
[13] H. Bässler, Phys. Status Solidi B 175 (1993) 15.
[14] D.K. Schroder, Semiconductor Material and Device Characterization, Wiley, 2005.
[15] J. Kowal, D. Hente, U. Sauer, IEEE Trans. Instrum. Meas. 58 (2009) 2343–2350.
[16] V. Bulovic, A. Shoustikov, M.A. Baldo, E. Bose, V.G. Kozlov, M.E. Thomson, S.R. Forrest, Chem. Phys. Lett. 287 (1998) 455–460.
[17] F. Incropera, D.P. deWitt, Fundamentals of Heat and Mass Transfer, Wiley, 2001.
[18] R.L. Webber, College Physics, fourth ed., Englewood, 1959, p. 156.
[19] Available from: <http://www.comsol.com/>.
[20] S. Chung, J.-H. Lee, J. Jeong, J.-J. Kim, Y. Hong, Appl. Phys. Lett. 94 (2009) 253302.
[21] Available from: <http://www.jahm.com/>.
[22] Available from: <http://www.schweizer-fn.de/stoff/wuebergang_gase/v2_wuebergang_gase.htm>.
[23] F.A. Boroumand, M. Voigt, D.G. Lidzey, Appl. Phys. Lett. 84 (2004) 4890–4892.
[24] J. Kowal, Ph.D. Thesis, ISEA RWTH, Aachen, 2010.
[25] G.E. Jabbour, Y. Kawabe, S.E. Shaheen, J.F. Wang, M.M. Morrell, B. Kippelen, N. Peyghambarian, Appl. Phys. Lett. 71 (1997) 1762.

have a greater effect on this transition, compared to the electron-deficient building units. In other words, the position of the high-energy absorption band will be strongly influenced by the number of electron-rich moieties in the polymer backbone [11]. For TQ1, having only one thiophene donor between the electron deficient units, the high-energy peak is almost completely pushed into the UV-region, giving the polymer an intense blue color in its reduced state. Having two absorption bands in the visible or close to the visible region makes it possible to obtain cathodically coloring electrochromic polymers with a variety of colors, even green where both the red and blue light have to be absorbed simultaneously [12].

Besides PEDOT [13–15], several blue cathodically coloring electrochromic polymers have been reported [3,16–22]. However, only a few are solution processable [3,20–22]. Herein, we report on the electrochemical and electrochromic properties of TQ1. To gain understanding about the structure–property relationships of cathodically coloring electrochromic polymers, two additional polymers were synthesized (Scheme 1). TQ2, having oligoethylene oxide side chains, was designed with the intention of improved counter ion transport and adhesion to the substrate. TQ3 was designed having ethylhexyloxy sidechains on the pendent phenyl rings of the acceptor moiety.

2. Experimental

2.1. Synthesis

The synthetic routes to the polymers are presented in Scheme 1. The synthesis of TQ1 has previously been described [5]. Compound **I** was prepared following a previously published method [23]. All synthetic work was performed under nitrogen atmosphere. ^{1}HNMR spectra were recorded at ambient temperature on a Bruker Avance 500 MHz spectrometer, using chloroform-d as solvent. The peak values were calibrated relative to tetramethyl silane (δ_H = 0 ppm).

2.1.1. 5,8-Dibromo-2,3-bis(3-(2-(2-methoxyethoxy) ethoxy) phenyl)quinoxaline (*II*:*2*)

A solution of **I** (0.60 g, 2.26 mmol) in ethanol (40 mL) was stirred at 60 °C for 30 min. 1,2-Bis(3-(2-(2-methoxyethoxy)ethoxy)phenyl)ethane-1,2-dione (0.99 g, 2.26 mmol) was added and the reaction was continued for 24 h. After addition of *p*-toluenesulfonic acid monohydrate (50 mg, 0.27 mmol) the reaction was allowed to continue for an additional 24 h. The ethanol was evaporated and column chromatography on silica gel (dichloromethane/ethyl acetate, 7:1 as eluent) yielded **II:2** (0.99 g, 1.46 mmol, 65%) as a yellow oil. δ_H(500 MHz, $CDCl_3$, Me_4Si) 7.92 (2 H, d, ArH), 7.31 (2 H, s, ArH), 7.22 (2 H, t, ArH), 7.13 (2 H, d, ArH), 6.97 (2 H, d, ArH), 4.08 (4 H, t, OCH_2), 3.71 (4 H, t, OCH_2), 3.58 (4 H, t, OCH_2), 3.39 (6 H, s, OCH_3). δ_C(400 MHz, $CDCl_3$, Me_4Si) 158.8, 153.8, 139.3, 139.1, 133.1, 129.3, 123.7, 122.9, 116.5, 115.8, 71.9, 70.7, 69.6, 67.5, 59.1.

2.1.2. Poly(2,3-bis(3-(2-(2-methoxyethoxy)ethoxy)phenyl)-5-(thiophen-2-yl)quinoxaline)(TQ2) (general procedure for polymerization)

To a mixture of **II:2** (0.46 g, 0.69 mmol), 2,5-bis(trimethylstannyl)thiophene (0.28 g, 0.69 mmol), tris(dibenzylideneacetone)dipalladium(0) (25 mg, 0.027 mmol) and tri(*o*-tolyl)phosphine (67 mg, 0.22 mmol) was added degassed toluene (15 mL) and the reaction was stirred at 89 °C for 48 h. The reaction mixture was precipitated from methanol and filtered. The solid material was redissolved in chloroform (300 mL) and stirred with sodium diethyldithiocarbamate trihydrate solution (10 wt.% in water, 150 mL) at 60 °C for 1 h. The organic phase was concentrated and reprecipitated from methanol. Soxhlet extraction was performed using methanol, acetone, hexane, and chloroform. The chloroform solution was concentrated

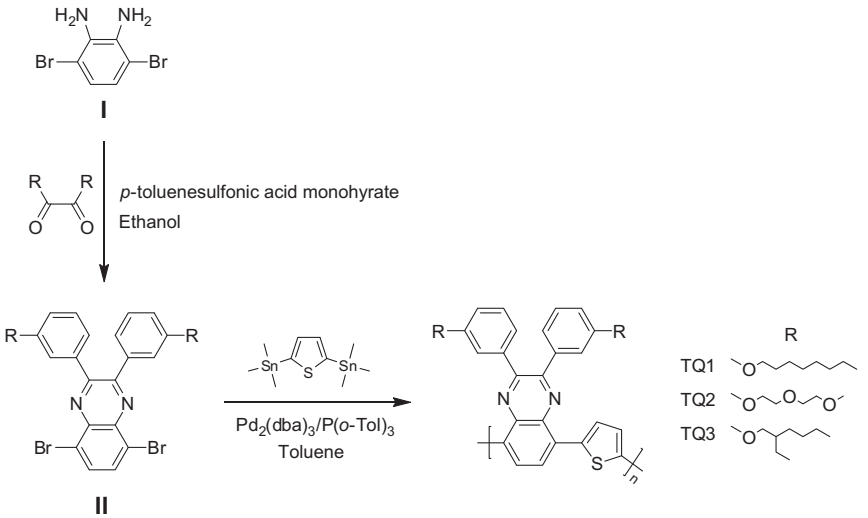

Scheme 1. Synthetic route to TQ1, TQ2, and TQ3.

and precipitated from methanol yielding TQ2 (0.35 g, 84%) as a dark blue solid.

2.1.3. 5,8-Dibromo-2,3-bis(3-(2′-ethylhexyloxy) phenyl) quinoxaline (II:3)

To a mixture of **I** (0.18 g, 0.68 mmol), 1,2-bis(3-(2′-ethylhexyloxyphenyl)ethane-1,2-dione (350 mg, 0.75 mmol) and *p*-toluenesulfonic acid monohydrate (14 mg, 0.075 mmol) was added ethanol (20 mL) and the reaction continued at reflux overnight. The ethanol was evaporated and column chromatography on silica gel (dichloromethane/hexane, 1:1 as eluent) yielded **II:3** (0.44 mg, 0.57 mmol, 84%) as a yellow oil. δ_H(500 MHz, $CDCl_3$, Me_4Si) 7.93 (s, 2 H, ArH), 7.20–7.30 (m, 6 H, ArH), 6.97 (d, 2 H, ArH), 3.71 (d, 4 H, O–CH_2), 1.75–1.60 (m, 2 H), 1.55–1.2 (m, 16 H), 1.00–0.80 (t, 12 H). δ_C(500 MHz, $CDCl_3$, Me_4Si) 183.0, 161.9, 156.8, 142.0, 135.7, 132.0, 126.4, 125.1, 119.3, 114.7, 66.3, 41.8, 33.1, 31.7, 26.7, 26.4, 16.8, 13.7.

2.1.4. Poly(2,3-bis(3-((2-ethylhexyl)oxy)phenyl)-5-methyl-8-(5-methylthiophen-2-yl)quinoxaline) (TQ3)

Synthesized following the general procedure with **II:3** (0.47 g, 0.67 mmol) and 2,5-bis(trimethylstannyl)thiophene (0.28 g, 0.67 mmol) giving TQ3 (0.80 g, 90%) as a dark blue/purple material.

2.2. Size-exclusion chromatography

Size-exclusion chromatography on TQ1 and TQ3 was performed on a Waters Alliance 2000 with a refractive index detector. The working temperature was 135 °C and 1,2,4-trichlorobenzene was used as eluent with a flow rate of 1 mL min^{-1}. Size-exclusion chromatography on TQ2 was performed at ambient temperature on a Waters 486 with a UV detector. Tetrahydrofuran was used as eluent with a flow rate of 0.5 mL min^{-1}. Molecular weights and polydispersity indices were obtained by calibration relative to polystyrene standards.

2.3. Electrochemistry

All electrochemical measurements were performed on a CH Instruments 650D potentiostat with platinum wire or ITO-covered glass substrate as working electrode, platinum wire as counter electrode, and a Ag/Ag^+ reference electrode. The polymers were solution-casted onto Pt-wire or spray-coated onto ITO from chloroform solution. A solution of 0.1 M tetrabutyl ammonium hexafluorophosphate (Bu_4NPF_6) in anhydrous acetonitrile was used as supporting electrolyte. The electrochemical cell was purged with nitrogen gas prior to the measurements in order to remove electroactive impurities. During the scans the nitrogen inlet was moved above the electrolyte surface.

2.4. Spectroelectrochemistry

Polymers were dissolved in chloroform (5 mg/mL), filtered, and spray-coated onto cleaned ITO-covered glass slides. Spectroelectrochemical measurements were performed in a similar fashion to the above described electrochemical spectroscopy but in series with a Perkin Elmer Lambda 900 UV–vis–NIR spectrophotometer. Spectra were recorded, after obtaining a converging CV between 0 V and +1.0 V (vs. Ag/Ag^+) at 100 mV/s, by optical absorption measurements at 1500 nm/min under an external applied fixed potential.

3. Results and discussion

3.1. Polymer molecular weights

The molecular weight of polymers is an important property for non-emissive display applications. Besides guaranteeing an adequate conjugation length, a high molecular weight also improves the adhesion to the substrate. In non-emissive displays, the active material has to be resistant to not slowly dissolving in the supporting electrolyte. A high molecular weight will generally help maintaining a high optical contrast after repeatedly electrochromic switching.

Molecular weights of all polymers are presented in Table 1. Due to the easy synthetic procedure and the excellent photovoltaic properties, several batches of TQ1 have been prepared. The electrochromic properties presented herein are based on a batch of TQ1 with molecular weight averages according to Table 1. The octyloxy side chains in *meta*-position facilitate good solubility, yielding a satisfactory molecular weight by preventing precipitation of oligomer chains during the polymerization step. Furthermore, TQ2 and TQ3 also show satisfactory molecular weights. Molecular weight averages of TQ2 were analyzed using THF as eluent during the SEC-measurements as we experienced problems using 1,2,4-trichlorobenzene. To guarantee data reliability, we also analyzed molecular weight averages of TQ3 in THF, which showed similar values as the 1,2,4-trichlorobenzene measurements.

3.2. Electrochemistry

Electrochemical measurements are of great importance for evaluation of a conjugated polymer to work as electrochromic material. First, the distance between the potentials required to oxidize and reduce the polymer film can give an estimation of the electrochemical bandgap. Second, it can give information about the position of the individual energy levels, *i.e.* the highest occupied molecular orbital (HOMO) and the lowest unoccupied molecular orbital (LUMO) of the polymer. The oxidation potential is an important parameter for electrochromic polymers. There is a trade-off between a low oxidation potential, increasing the possibility of the conjugated polymer to switch reversibly without degradation from electrolyte-containing

Table 1
Molecular weights obtained by SEC using 1,2,4-trichlorobenzene at 135 °C (TQ1, TQ3) and THF at ambient temperature (TQ2).

Polymer	M_n	M_w	PDI
TQ1	56,000	170,000	3.0
TQ2	30,000	118,000	4.0
TQ3	15,000	26,000	2.2

species, *e.g.* oxygen and water [24], and a higher oxidation potential which will reduce the time-induced degradation processes. We employed square-wave voltammetry [25,26] to estimate the electrochemical bandgap and oxidation potential of the polymers. Results from square-wave voltammetry are presented in Fig. 1. The electrochemical bandgap of TQ1 was estimated to 2.4 eV from oxidation and reduction peak potentials. Although the oxidation potential of TQ1 is somewhat high, the sharpness of the oxidation peak allows high optical contrast changes within a small potential window for electrochromic switching. TQ2 and TQ3 both showed similar positions of oxidation and reduction peaks compared to TQ1, as is expected from the similarity in polymer structure.

The scan-rate dependence of spray-coated polymer films on ITO was investigated. The films were cycled between 0 and +1.0 V vs. Ag/Ag^+, varying the scan rate from 50 to 300 mV/s. The scan-rate dependence of TQ1 is depicted in Fig. 2. A linear relationship between the scan rate and the maximum current density was noticed for all three polymers, indicating that the polymer films are well adhered to the substrate and that the oxidation processes are non-diffusion limited [27].

3.3. Spectroelectrochemistry

To investigate the optical switching properties of the polymers, spectroelectrochemical measurements were performed (Fig. 3). All three polymers display similar absorption in the reduced state, with two distinct absorption bands. The high-energy peaks of TQ1–TQ3 are mainly absorbing in the UV-region, with minor tailing into the visible region, limiting the contribution of the high-energy peak to the color perceived by the human eye. On the other hand, the low-energy peaks, originating from the D–A interaction, have pronounced absorption in the red part of the visible region, making the polymers appear blue in the reduced state. The low-energy peak of TQ1 is sharp with a significant difference in absorption between the absorption maximum and the valley at 440 nm, yielding

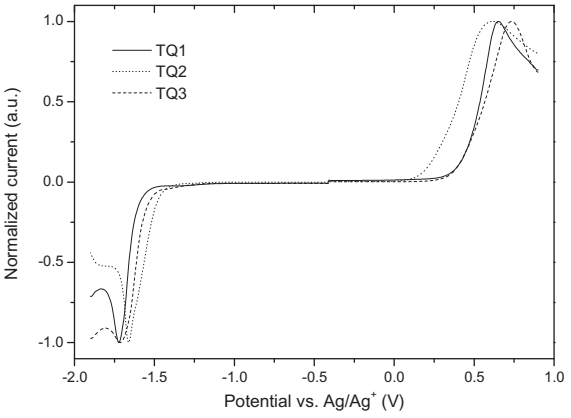

Fig. 1. Square-wave voltammetry of the polymers. 0.1 M Bu_4NPF_6/acetonitrile was used as supporting electrolyte. The plots were obtained by combining the oxidation and reduction scans.

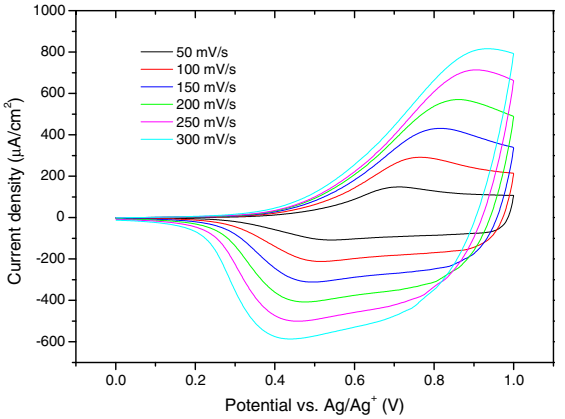

Fig. 2. Scan-rate dependence of TQ1 on ITO. 0.1 M Bu_4NPF_6/acetonitrile was used as supporting electrolyte.

an intense blue color as a result of good reflection of the shorter wavelength photons in the visible region. A broader peak, partly absorbing the blue light, will imply a blue-gray color.

The optical contrast ($\Delta T\%$), monitored at local low-energy absorption maxima, were 50%, 45%, and 37% for TQ1, TQ2, and TQ3, respectively. The excellent optical contrast of TQ1, switching from an intense blue color to a yellow-brown transmissive state, makes TQ1 an interesting polymer for electrochromic applications. The relatively low optical contrast of TQ3 has a couple of explanations. First, the ethylhexyloxy side chains to some extent induce more separated chains and a more ordered morphology of polymer films, giving vibronic features, as indicated by the broad absorption maximum of the low-energy absorption peak and the small absorption bump above 700 nm. The optical contrast of TQ3 is monitored at 645 nm, and because of the vibronic features, the optical contrast is increased to 41% at 600 nm (Fig. 4). Second, the charge-carrier peak at 800–900 nm is not as well depleted as for TQ1 and TQ2. Third, the discussed charge-carrier peak is somewhat blue shifted for TQ3, increasing the tailing into the visible region of the oxidized polymer, and hence a lower optical contrast.

3.4. Influence of film thickness on optical contrast

Evaluation of electrochromic polymers, based on their optical contrast, must be done with careful consideration of the film thickness. Obviously, the optical contrast, monitored at a fixed wavelength, will reach a maximum value at a certain film thickness. Using film thicknesses corresponding to maximum optical contrast will facilitate proper comparison of electrochromic polymers. The relationship between absorption in the reduced state and optical contrast was investigated for TQ1 (Fig. 5). The black and white squares represent experimental values from spectroelectrochemical measurements on spray-coated films with different thicknesses. The lines are based on calculations with the prerequisite that absorption values of the reduced state and the oxidized state can be normalized with

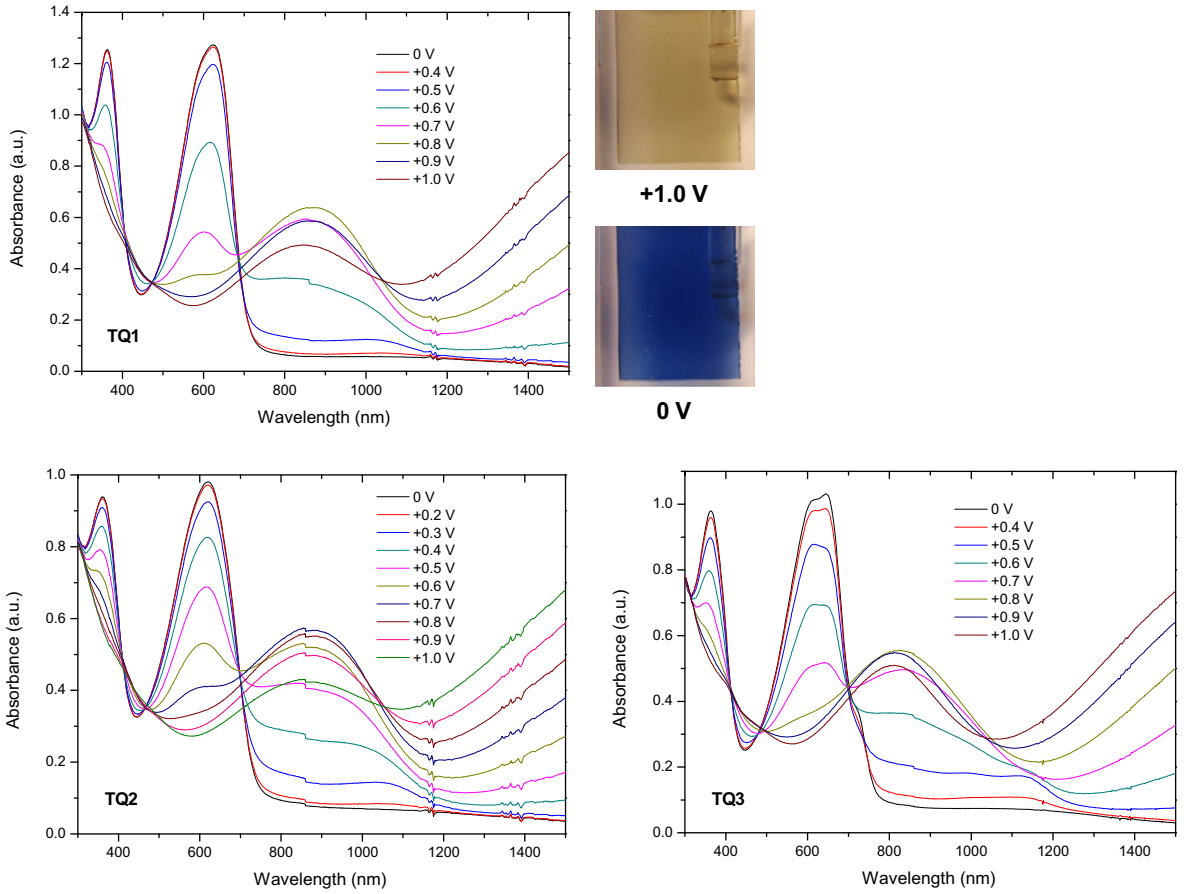

Fig. 3. Spectroelectrochemical measurements on TQ1–TQ3 films on ITO, using 0.1 M NBu_4PF_6 in anhydrous acetonitrile as supporting electrolyte. Potentials are vs. Ag/Ag^+. Photos show electrochromic switching of TQ1.

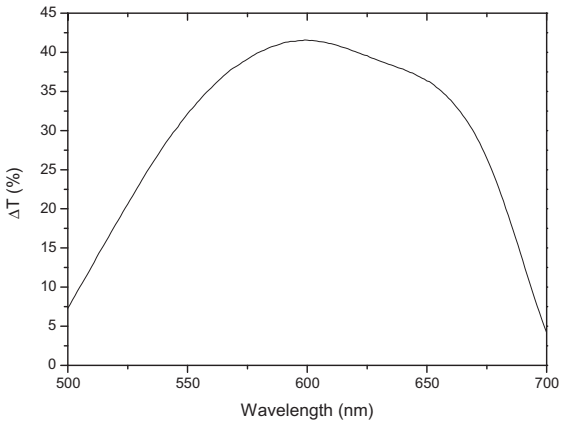

Fig. 4. Difference in optical contrast of TQ3 vs. wavelength.

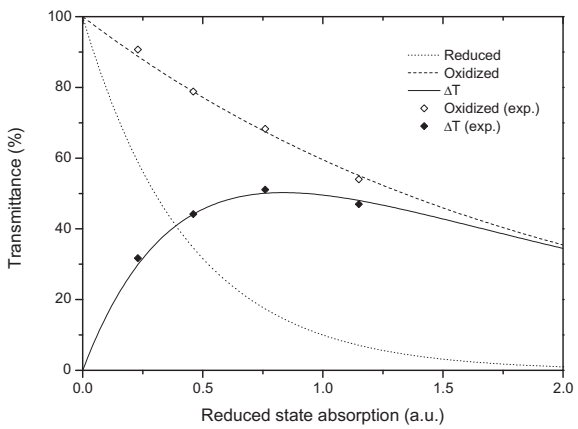

Fig. 5. Dependence of absorption in the reduced state on optical contrast for TQ1. Absorption/transmission data was monitored at the low-energy peak (623 nm).

respect to a single pair of data. The strong correlation between the experimental values and the calculated lines strengthens the hypothesis that the spectroelectrochemical data can be normalized. Looking at Fig. 5, it is clear that maximum optical contrast for TQ1 at 623 nm (50.2%) is reached at a film thickness giving an absorption of 0.84 a.u. for the reduced polymer. However, the shape of the curve allows for a small deviation from optimal film thickness, when comparing polymers, as it only will have a minor influence on the optical contrast. This is gratefully

acknowledged as spray-coating polymer films with a predetermined absorption of the reduced state is a challenging and patient task.

3.5. Kinetic studies

Switching properties and response times were analyzed monitoring the transmittance change at low-energy absorption maxima while applying a square-wave potential to spray-coated polymer films on ITO. The time of the applied potential pulse was successively decreased from 10 to 0.5 s. The results from the kinetic measurements are presented in Fig. 6. TQ3 shows the fastest response times where 92% of the transmittance modulation was maintained at switching times of 0.5 s. A reasonable explanation is that the branched side chains of TQ3 create an open morphology of the polymer film with less closely packed polymer chains, facilitating fast transport of charge balancing ions during the redox processes. TQ1 and TQ2 also display fast response times with 72% and 76% of the transmittance modulation maintained at switching times of 0.5 s. The polar oligoethylene oxide side chains of TQ2 to some extent improve the response times, compared to TQ1, *via* improved ion conductivity.

3.6. Stability measurements

As an initial test of the polymers resistance to electrochemical degradation, polymer films were repeatedly switched between the reduced and oxidized state. All three polymers show a decent stability after 200 full switches (Fig. 7). The observed loss in optical contrast is most probably due to the relatively high oxidation potential of the polymers. The oligoethylene oxide side chains did not result in improved stability for TQ2. A reasonable explanation for this is that the high molecular weight of the polymers already facilitates good film-forming properties and adhesion to the substrate.

4. Conclusions

Blue-to-transmissive electrochromic switching has been demonstrated for three donor–acceptor based polymers. The polymer TQ1 showed an impressive transmittance change of 50%, recorded at the low-energy absorption maximum (623 nm). The high optical contrast and fast response times makes the polymers interesting for non-emissive display applications. Moreover, the high correlation between experimental data and calculations

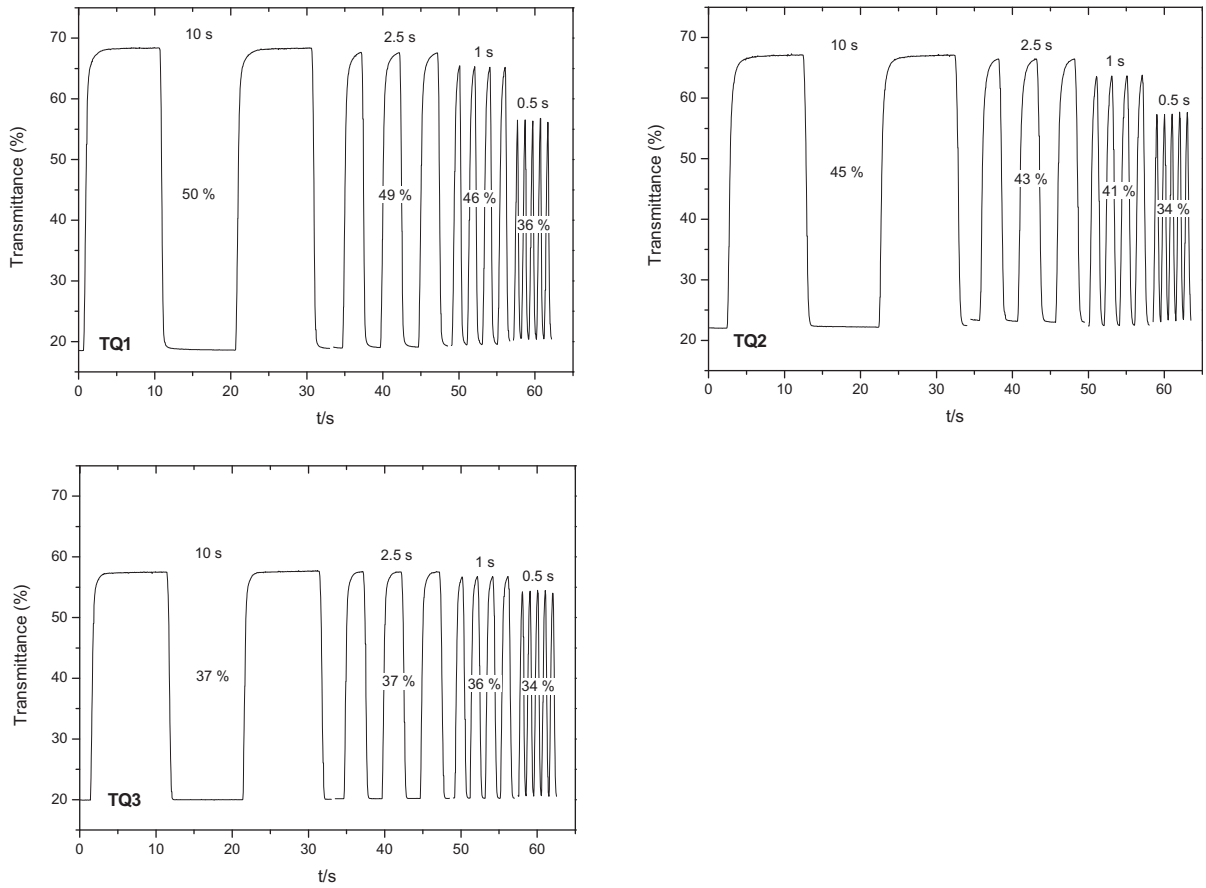

Fig. 6. Kinetic measurements on TQ1–TQ3 films on ITO, using 0.1 M NBu_4PF_6 in anhydrous acetonitrile as supporting electrolyte. Films were switched between 0 and +1.0 V.

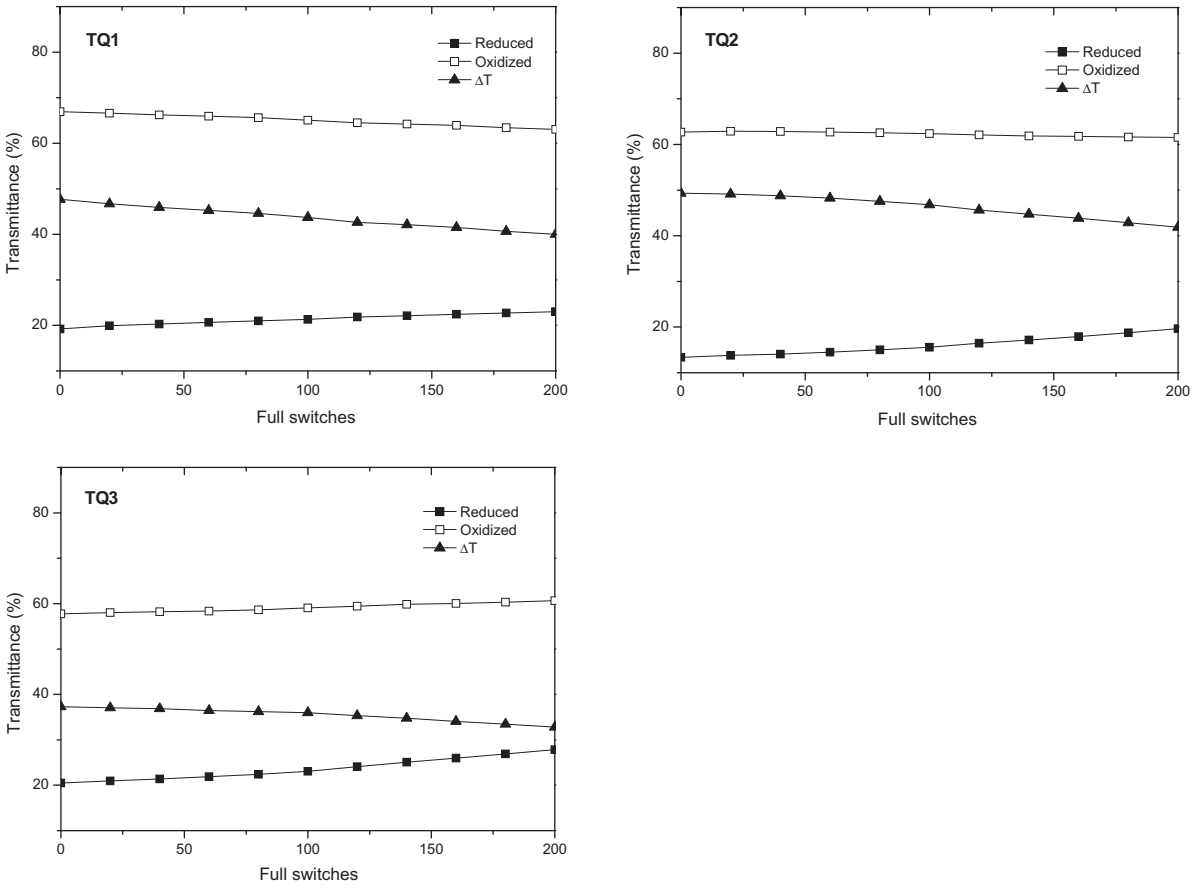

Fig. 7. Stability measurements of TQ1, TQ2, and TQ3. A square-wave potential, switching between 0 V and +1.0 V, was applied to polymer films on ITO in 0.1 M NBu_4PF_6/anhydrous acetonitrile. Switching times are 2 s. Total cycle is 4 s. Transmittance was recorded at low-energy absorption maxima.

strengthens the hypothesis that maximum optical contrast of electrochromic polymers, with respect to film thickness, can be estimated by normalizing absorption/transmission values of the reduced and oxidized state.

Acknowledgements

We thank the National Graduate School in Materials Science, the Swedish Research Council, the Swedish Energy Agency, and EC FP7 ONE-P Project No. 212311 for financial support.

References

[1] P.M. Beaujuge, S. Ellinger, J.R. Reynolds, The donor–acceptor approach allows a black-to-transmissive switching polymeric electrochrome, Nature Materials 7 (2008) 795–799.
[2] A.L. Dyer, M.R. Craig, J.E. Babiarz, K. Kiyak, J.R. Reynolds, Orange and red to transmissive electrochromic polymers based on electron-rich dioxythiophenes, Macromolecules 43 (2010) 4460–4467.
[3] M. Icli, M. Pamuk, F. Algi, A.M. Onal, A. Cihaner, Donor–acceptor polymer electrochromes with tunable colors and performance, Chemistry of Materials 22 (2010) 4034–4044.
[4] F.C. Krebs, Electrochromic displays: the new black, Nature Materials 7 (2008) 766–767.
[5] E. Wang, L. Hou, Z. Wang, S. Hellström, F. Zhang, O. Inganäs, M.R. Andersson, An easily synthesized blue polymer for high-performance polymer solar cells, Advanced Materials 22 (2010) 5240–5244.
[6] T. Yamamoto, B.-L. Lee, H. Kokubo, H. Kishida, K. Hirota, T. Wakabayashi, H. Okamoto, Synthesis of a new thiophene/quinoxaline ct-type copolymer with high solubility and its basic optical properties, Macromolecular Rapid Communications 24 (2003) 440–443.
[7] E.E. Havinga, W. ten Hoeve, H. Wynberg, Alternate donor–acceptor small-band-gap semiconducting polymers, polysquaraines and polycroconaines, Synthetic Metals 55 (1993) 299–306.
[8] C. Kitamura, S. Tanaka, Y. Yamashita, Design of narrow-bandgap polymers. Syntheses and properties of monomers and polymers containing aromatic-donor and o-quinoid-acceptor units, Chemistry of Materials 8 (1996) 570–578.
[9] T. Yamamoto, Z.-H. Zhou, T. Kanbara, M. Shimura, K. Kizu, T. Maruyama, Y. Nakamura, T. Fukuda, B.-L. Lee, N. Ooba, S. Tomaru, T. Kurihara, T. Kaino, K. Kubota, S. Sasaki, π-Conjugated donor–acceptor copolymers constituted of π-excessive and π-deficient arylene units. Optical and electrochemical properties in relation to CT structure of the polymer, Journal of the American Chemical Society 118 (1996) 10389–10399.
[10] H.A.M. van Mullekom, J.A.J.M. Vekemans, E.E. Havinga, E.W. Meijer, Developments in the chemistry and band gap engineering of donor–acceptor substituted conjugated polymers, Materials Science and Engineering, R: Reports 32 (2001) 1–40.
[11] P.M. Beaujuge, C.M. Amb, J.R. Reynolds, Spectral engineering in π-conjugated polymers with intramolecular donor–acceptor interactions, Accounts of Chemical Research 43 (2010) 1396–1407.
[12] Hellström S., Cai T., Inganäs O., Andersson M. R., Influence of side chains on electrochromic properties of green donor–acceptor–donor polymers, Electrochimica Acta, in press doi:10.1016/j.electacta.2010.11.018.

[13] F. Jonas, L. Schrader, Conductive modifications of polymers with polypyrroles and polythiophenes, Synthetic Metals 41 (1991) 831–836.
[14] M. Dietrich, J. Heinze, G. Heywang, F. Jonas, Electrochemical and spectroscopic characterization of polyalkylenedioxythiophenes, Journal of Electroanalytical Chemistry 369 (1994) 87–92.
[15] Q. Pei, G. Zuccarello, M. Ahlskog, O. Inganäs, Electrochromic and highly stable poly(3,4-ethylenedioxythiophene) switches between opaque blue-black and transparent sky blue, Polymer 35 (1994) 1347–1351.
[16] A. Balan, G. Gunbas, A. Durmus, L. Toppare, Donor–acceptor polymer with benzotriazole moiety: enhancing the electrochromic properties of the "Donor Unit", Chemistry of Materials 20 (2008) 7510–7513.
[17] M.A. Invernale, V. Seshadri, D.M.D. Mamangun, Y. Ding, J. Filloramo, G.A. Sotzing, Polythieno[3,4-b]thiophene as an optically transparent ion-storage layer, Chemistry of Materials 21 (2009) 3332–3336.
[18] M. Li, Y. Sheynin, A. Patra, M. Bendikov, Tuning the electrochromic properties of poly(alkyl-3,4-ethylenedioxyselenophenes) having high contrast ratio and coloration efficiency, Chemistry of Materials 21 (2009) 2482–2488.
[19] M. Li, A. Patra, Y. Sheynin, M. Bendikov, Hexyl-derivatized poly(3,4-ethylenedioxyselenophene): novel highly stable organic electrochromic material with high contrast ratio, high coloration efficiency, and low-switching voltage, Advanced Materials 21 (2009) 1707–1711.
[20] B.C. Thompson, Y.-G. Kim, T.D. McCarley, J.R. Reynolds, Soluble narrow band gap and blue propylenedioxythiophene-cyanovinylene polymers as multifunctional materials for photovoltaic and electrochromic applications, Journal of the American Chemical Society 128 (2006) 12714–12725.
[21] C.G. Wu, M.I. Lu, S.J. Chang, C.S. Wei, A solution-processable high-coloration-efficiency low-switching-voltage electrochromic polymer based on polycyclopentadithiophene, Advanced Functional Materials 17 (2007) 1063–1070.
[22] C.M. Amb, P.M. Beaujuge, J.R. Reynolds, Spray-processable blue-to-highly transmissive switching polymer electrochromes via the donor–acceptor approach, Advanced Materials 22 (2010) 724–728.
[23] J.C. Bijleveld, M. Shahid, J. Gilot, M.M. Wienk, R.A.J. Janssen, Copolymers of cyclopentadithiophene and electron-deficient aromatic units designed for photovoltaic applications, Advanced Functional Materials 19 (2009) 3262–3270.
[24] D.M. de Leeuw, M.M.J. Simenon, A.R. Brown, R.E.F. Einerhand, Stability of ntype doped conducting polymers and consequences for polymeric microelectronic devices, Synthetic Metals 87 (1997) 53–59.
[25] J.G. Osteryoung, R.A. Osteryoung, Square wave voltammetry, Analytical Chemistry 57 (1985) 101–110.
[26] S. Hellström, F. Zhang, O. Inganäs, M.R. Andersson, Structure–property relationships of small bandgap conjugated polymers for solar cells, Dalton Transactions (2009) 10032–10039.
[27] A. Kumar, D.M. Welsh, M.C. Morvant, F. Piroux, K.A. Abboud, J.R. Reynolds, Conducting poly(3,4-alkylenedioxythiophene) derivatives as fast electrochromics with high-contrast ratios, Chemistry of Materials 10 (1998) 896–902.

regioregular poly(3-hexylthiophene) (P3HT) has been extensively studied in organic field-effect transistors (OFETs) due to its comparatively high hole carrier mobility, simple solution processability, and commercial availability [4]. However, P3HT-based OFETs typically face the problem of relatively poor ambient stability and unfull flexibility, which has strongly limited its practical application for industry. The bending stability in relation to above device reliability is also one of the most challenging issues for choosing the suitable device structures towards fully flexible electronic device application.

In present study, we attempt to use the Si_3N_4 as passivation layer on the plasma treated HfO_2 film enable one to obtain reliable OTFT on a fully flexible PI substrate, as regards their mechanical flexibility and environmental stability. The device's electrical properties with respect to saturation mobility, on/off current ratio, and bending conditions (i.e., the numbers of bending times and the bending radii) are also carefully investigated.

2. Experimental section

2.1. Materials synthesis and device fabrication

Plastic 30 μm-thick DuPont Kapton® PI films were used as flexible substrates for device fabrication process. They were cleaned ultrasonically with ethanol (Fluka; water content <0.1%) for 30 min and deionized water for 10 min, and then high-pressure N_2 gas was used to remove the water and any remaining surface particles from the PI. PI films were annealed at 200 °C for 2 h in vacuum to achieve relatively thermal stable, and enhance the adhesion strength. Next, Cr (thickness: 50 nm; adhesion layer) and Au (thickness: 100 nm) films were sequentially deposited for the gate electrode over the PI substrate by using a thermal evaporation system under patterning with designed mask. To deposit the HfO_2 dielectric layer, a sol–gel solution was prepared by dissolving $HfCl_4$ (98%, Aldrich, USA) in ethanol (95%) at a suitable concentration. Ethanol (10 mL) as the solvent was prepared to yield a molar ratio of $HfCl_4$ to C_2H_5OH of 1:1000. Under a magnetic stirring condition, the solution was heated under reflux while stirring for 30 min. The dielectric film was grown by spin-coating the sol–gel solution over PI at 1000 rpm for 10 s and then 3000 rpm for 30 s at room temperature by using a spin coater. The as-prepared samples were treated with O_2 plasma for 2 min in an oxygen plasma reactor (Harrick Scientific Corp.), which supplied a plasma power of 30 W. The silicon–nitride (Si_3N_4) layer was deposited as a passivation layer onto the high-*k* film by plasma-enhanced chemical vapor deposition (Oxford-PECVD).

To deposit the channel layer, the commercially available poly-(3-hexylthiophene) i.e., P3HT (obtained from Merck) was used as an organic semiconductor layer. The desired solution was prepared when 1.2 mg P3HT were obtained and placed in a sealable clean glass container. Then, 10 mL of $CHCl_3$ was added to a flask containing the P3HT. The solution was then gently heated at 50 °C using a hot plate to further break down the polymer chains in solution. After stirring the solution with reflux for 1 h, and then placed in an oven to be cooled. The light intensity was shielded under a standard aluminum foil to minimize the oxidation. The organic semiconductor layer of mixed solution was fabricated by spin-coating a P3HT chloroform solution at 1000 rpm for 20 s. After the deposition, the film was dried at 80 °C for 2 min and then dried gel film was annealed in nitrogen atmosphere using different thermal treatment techniques for 1 h. Au electrodes (100 nm) for TFT devices on the PI sheet with a device structure as shown in Fig. 1(A) were formed through a shadow mask by using a thermal coater. The molecular structure of the P3HT was shown on right-side of Fig. 1(A). The channel width (W) and length (L) for our flexible device were 200 and 60 μm, respectively. Fig. 1(B) illustrated the semi-transparent images of 30 μm-thick DuPont Kapton PI film, demonstrating the text on the layer behind the PI substrate was clearly visible. Our P3HT-TFT device on plastic PI film under a large surface strain was displayed in Fig. 1(C), and the surface appeared no cracks.

2.2. Device characterization and measurements

The surface morphology of the flexible devices was evaluated by atomic force microscopy (AFM, Digital Instruments Nanoscope, D-5000). The surface morphology of the P3HT film as channel area on Si_3N_4–HfO_2/Au/Cr/PI substrate was obtained from AFM measurement under the tapping mode at 2 μm scan size and scan rate of 0.5 Hz. We used ellipsometry technique to measure the thickness of the HfO_2 and P3HT layers. The current density–electric field (*J*–*E*) measurements were performed by using an Agilent-4156 probe station. A customized bending machine (depicted and described elsewhere in this text) was used to perform the bending test in tension or compression modes where the bending radious ranged from 2 to 4 cm for both convex and concave types of bending.

3. Results and discussion

3.1. Effect of passivation layer on leakage-current density

Prior to achieve the flexible organic–inorganic hybrid TFT devices based on P3HT material, we firstly fabricated the metal–insulator–metal (MIM) device with 10 nm high-*k* HfO_2 as dielectric layer over fully flexible polyimide (PI) substrate. Under high electric field stress, the carriers of leakage current will impact the weak bonding and result in the high leakage current. We measured the quantitative leakage current to evaluate the electrical performance of the HfO_2 film which was fabricated by very simple and cost-effective sol–gel spin-coating technique in MIM configuration. Fig. 2(A) displayed the leakage current density and electric field (*J*–*E*) characteristics for the fully flexible MIM capacitors prepared by HfO_2 film with O_2 plasma treatment. The O_2 plasma treated sample did not have sufficiently high thermal budgets and many trap states still existed over film surface. Inset of Fig. 2(A) showed AFM image of HfO_2 film with existence of various trap states over film surface. The RMS roughness was about 1.52 nm.

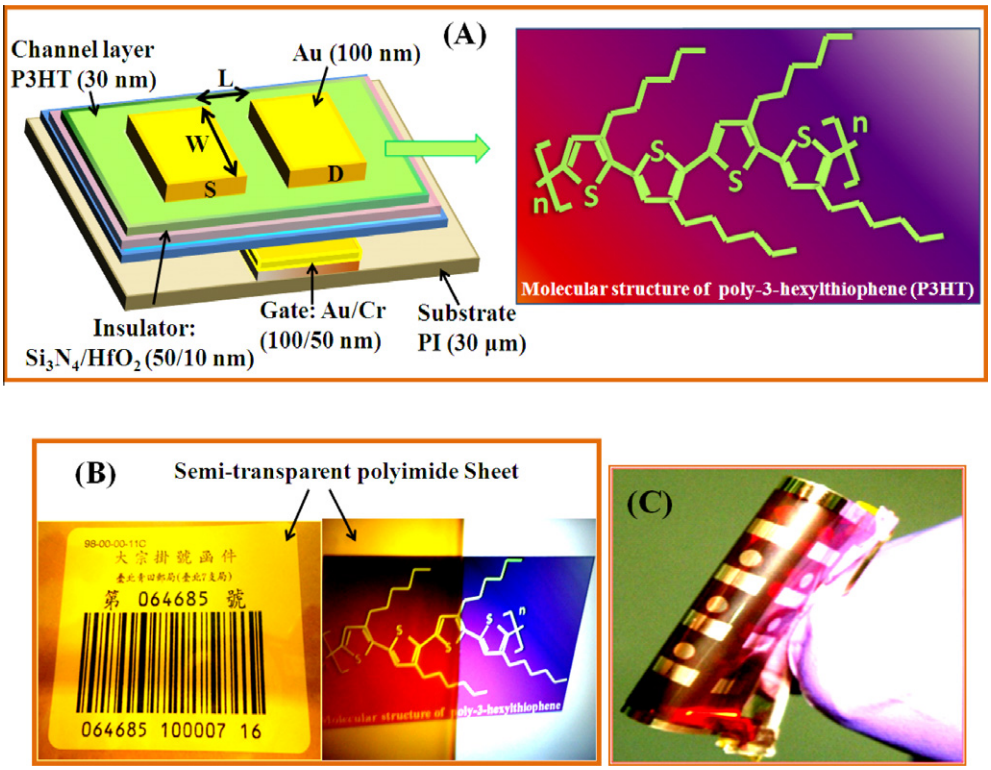

Fig. 1. (A) Schematic structure of P3HT-based OTFT with HfO_2–Si_3N_4 as a dielectric layer on PI substrate; (B) the photograph of semi-transparent polyimide sheet; (C) photograph of proposed TFT device on a 30 μm-thick flexible PI substrate and under a large surface strain.

Hence, their breakdown electric field was relatively low and their leakage current density was very high (i.e. 4.6×10^{-6} A cm^{-2}) at the applied voltage. This observation was attributed to the availability of the traps over film surface. In order to achieve the better device, the Si_3N_4 passivation layer was proposed to deposit onto the HfO_2 film in Fig. 2(B). Interestingly, the surface roughness was minimized by the passivation layer. AFM image in inset of Fig. 2(B) revealed that the surface of Si_3N_4 film was smooth, and rms roughness decreased almost 5 times from 1.52 to 0.34 nm. In addition, the superior low leakage current density for the corresponding films subjected to 50-nm Si_3N_4 as the efficient passivation layer on top of 10-nm HfO_2 film was found as low as 10^{-11} A cm^{-2} in Fig. 2(B) during voltage stressing. The proposed MIM device structure, including of Si_3N_4 layer on O_2 plasma-treated HfO_2 film, exhibited the superior low leakage current than that only O_2 plasma treated HfO_2 film. The high leakage current density from the sample adopted O_2 plasma treated HfO_2 film could be attributed to the existence of numerous traps over the film surface and hence poor dielectric characteristics. Similarly, the traps over the film surface could also affect the performance of the following TFT device. In a simple-minded classical approach, it might appear that electrons tunneled easily as moved through the trap states of HfO_2 surface. However, the trap induced breakdown effect was effectively suppressed by HfO_2–Si_3N_4 film structure.

In addition, the schematic energy band diagrams in Fig. 2(C) were proposed to explain the trap-dependent leakage and the passivation of traps over HfO_2 film surface. The traps in HfO_2 film had occurred and affected the energy band, indicating that the electrons can easily move through the HfO_2 film due to trap-assisted tunneling effect. This observation was responsible for high leakage current in the MIM device [9]. These trap centers created intermediate energy levels due to the presence of impurities in the material [10]. After surface Si_3N_4 film passivation, the reliability related current transport mechanism was improved from reduction of trap-assisted tunneling. Under passivation treatment with Si_3N_4 film, the potential barrier became thick enough not to allow electrons from gate to tunnel through the barrier. Thus, the leakage current densities apparently decreased as strong energy band-pass for electrons can shift toward a higher energy level. The O_2 plasma treated-HfO_2 film after Si_3N_4 passivation exhibited better reliability even under high electric field in Fig. 2(B). This observation suggested that HfO_2 film was extremely suitable as a gate dielectric in future flexible devices. From the formation of a passivated Si_3N_4 layer, the reduction of parasitic resistance could suppress the surface trap density effect and improve the performance of flexible devices.

3.2. Surface morphology of P3HT film

The surface morphology of the P3HT film by AFM measurement in tapping mode at 2 μm scan size was demonstrated in Fig. 3; the sample was deposited by sol–gel spin-coating process on Si_3N_4–HfO_2/Au/Cr-coated flexible PI film. It could be seen from the figure that the surface

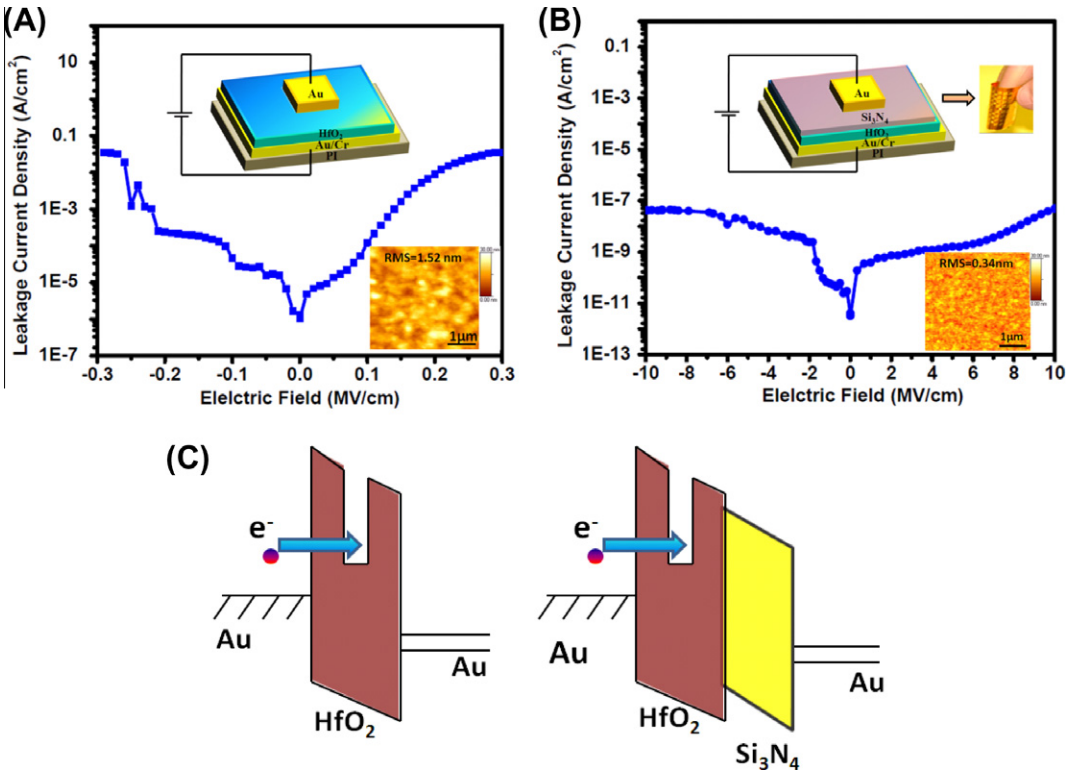

Fig. 2. (A) *J–E* Plot of leakage current density versus electric field for MIM-structural sample prepared by using sol–gel HfO_2 film and inset of AFM image (surface roughness: 1.52 nm) from HfO_2 film; (B) *J–E* plot for MIM-structural sample prepared by using Si_3N_4–HfO_2 stacked film and inset of AFM image (surface roughness: 0.34 nm) from Si_3N_4–HfO_2 stacked film; (C) schematic energy band diagrams to explain trap-dependent leakage and the passivation of traps.

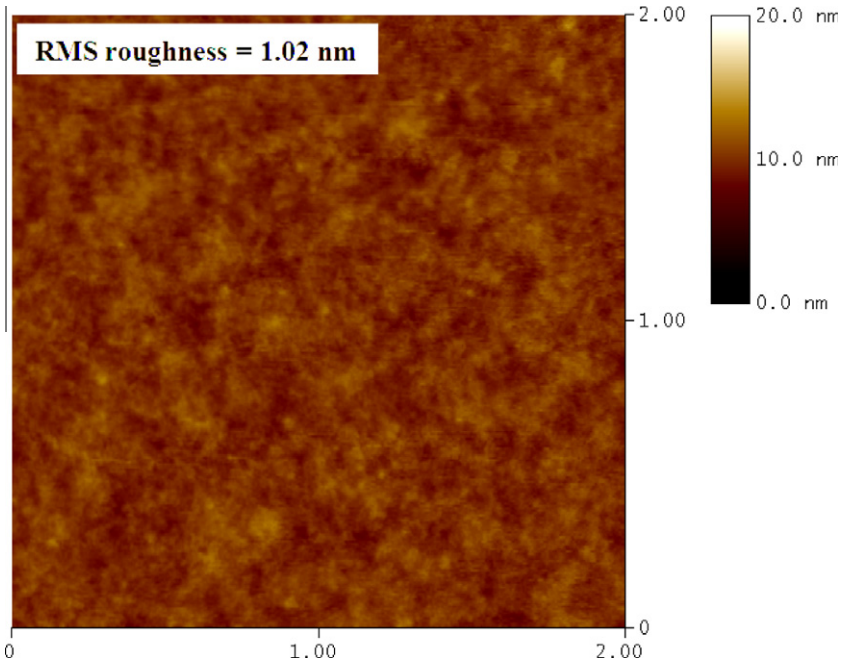

Fig. 3. AFM image from P3HT thin film as channel area on Si_3N_4–HfO_2/Au/Cr/PI substrate at a length scale of 2 μm (surface roughness: 1.02 nm).

morphology of the spin-coated P3HT film was dense and crack-free. Thin films of P3HT with regioregularity and order structure were obtained with the thermal treatment at 80 °C of curing, and the performance of the device would be enhanced. The average P3HT thickness was about to 30 nm measured by ellipsometery technique. The root-mean-square (RMS) surface roughness of the P3HT film grown on Si_3N_4–HfO_2/Au/Cr/PI surface was 1.02 nm. We observed that the fabrication process with chloroform solvent yields higher mobility over a wide variety of tested devices mentioned in the following. Goetz et al., revealed that P3HT films from chloroform solution behaved a higher tendency to form ordered fibrillar networks without sharp boundaries [11]. By the utilization of AFM for the analysis of the surface morphology of the P3HT film, we suggested that the sol–gel deposited P3HT film was crack-free, uniform, and well adhered on Si_3N_4–HfO_2/Au/Cr-coated PI for the fabrication of high performance flexible devices.

3.3. Transfer and output characteristics

The TFT devices were fabricated after the beneficial effect of HfO_2–Si_3N_4 film structure in MIM device was understood. To indicate the influence of the gate leakage current, we measured the transfer characteristic of P3HT-OTFT for HfO_2 as gate dielecric layer on flexible PI substrate where V_{DS} was set at −5 V. Fig. 4(A) and (B) showed the transfer and output characteristic curves of the P3HT-TFT on the flexible PI substrate with O_2 plasma treated HfO_2 film as dielectric layer. The output characteristics of the applied drain voltage (V_{DS}) ranged from 0 to −5 V with gate biases (V_{GS}) varying from 0 to −5 V in steps of 1 V. The trap state problem in the HfO_2 film of this TFT device might also contribute to leakage property. The transfer characteristic curve was abnormal and the output characteristics were only observed at a higher gate voltage. Even under −5 V of gate and drain voltage, reasonable device properties were not observed with an on/off current ratio of about 10^2, which would not afford to minimum requirement of TFT devices. Moreover, as Fig. 4(B) illustrated, the output characteristics were not stable and drain currents were not satisfactory.

The OTFT device achieved a much better performance while using Si_3N_4 as a passivation layer onto O_2 plasma treated HfO_2 film. As shown in Fig. 4(C), P3HT-OTFT exhibited typical p-type output characteristics [source-drain current (I_{DS}) versus drain voltage (V_{DS}) at different gate voltages (V_{GS})], when operated in the accumulation mode. The OTFTs operated in the accumulation mode when a negative gate voltage was applied, since positive carriers

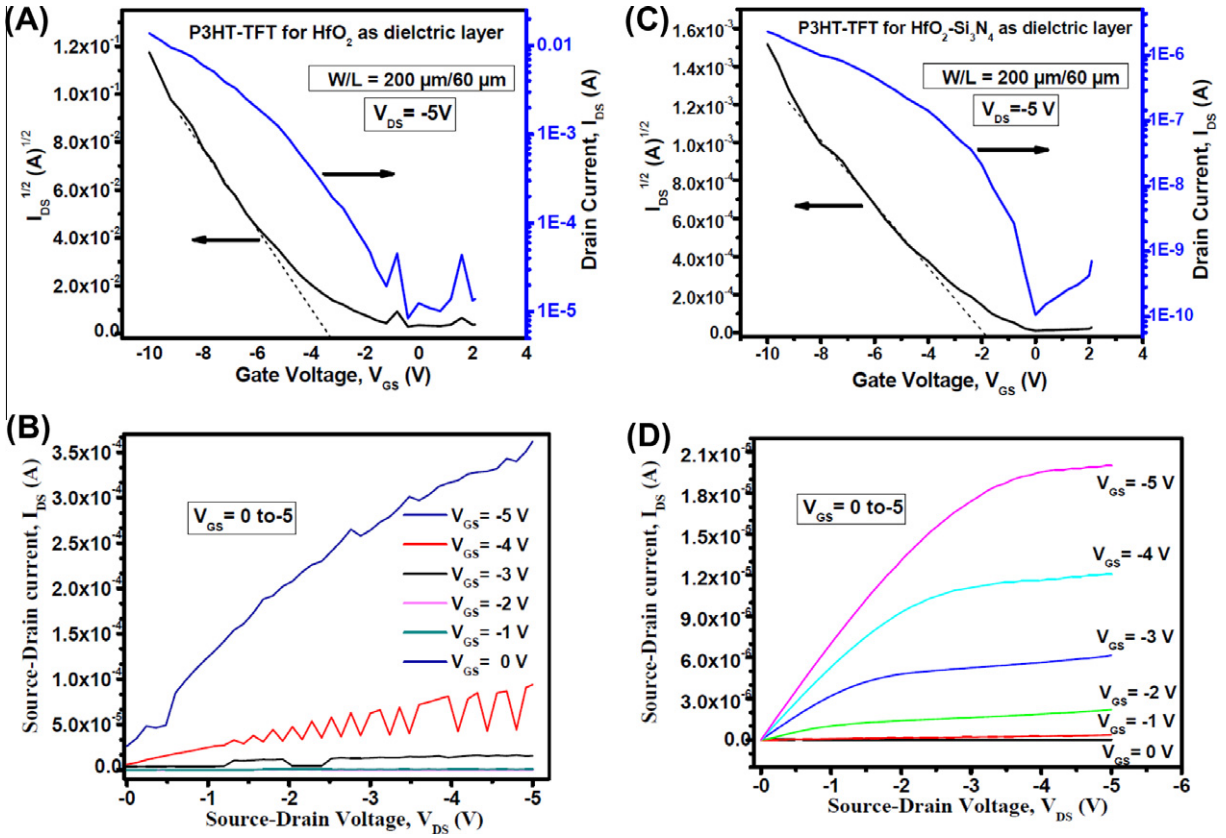

Fig. 4. (A) Plot of drain current and square root of drain current with respective to gate voltage (I_{DS}–V_{GS}) for P3HT-OTFT on flexible PI substrate by using HfO_2 as gate dielectric under V_{DS} = −5 V, and (B) output characteristic (I_{DS}–V_{DS}) as V_{GS} ranging from 0 to −5.0 V at 1 V step for above device. (C) Plot of drain current and square root of drain current with respective to gate voltage (I_{DS}–V_{GS}) for P3HT-OTFT on flexible PI substrate by using Si_3N_4–HfO_2 stacked film as gate dielectric under V_{DS} = −5 V, and (D) output characteristic (I_{DS}–V_{DS}) as V_{GS} ranging from 0 to −5.0 V at 1 V step for above device.

were generated in the P3HT organic semiconductor layer. In order to get a reasonable estimation for the possible dependence of the mobility along the TFT device channel, we have plotted the linear and saturated field-effect mobilities extracted from the transfer characteristics of the TFT according to Eq. (1) and (2). In the linear regime, the field-effect mobility (μ_{lin}) can be calculated from transconductance [12].

$$(g)m = \frac{\partial I_{DS}}{\partial V_{GS}}|V_{DS} = \text{const} = \frac{WC_i}{L}\mu_{lin}V_{DS} \quad (1)$$

where, C_i was the gate capacitance and W/L was the ratio of the channel width to channel length. In the saturation region ($V_{DS} > V_{GS}-V_{Th}$), I_{DS} can be described by following equation [12,13] and then the saturated field-effect mobility (μ_{sat}) can be calculated as

$$I_{DS} = W\mu_{sat}\frac{C_i}{2L}(V_{GS} - V_{TH}), \quad (2)$$

where, μ_{sat} was the field-effect mobility, C_i (=1.02 nF cm^{-2}) was the capacitance of the Si_3N_4–HfO_2 dielectric layer, W = 200 μm, L = 60 μm, and V_{Th} was the threshold voltage. As Eq. (2) implied, a plot of V_{GS} versus square root of I_{DS} gave a straight line, and V_{Th} was obtained. The threshold voltage and the field-effect mobility were to be −1.9 V and 0.041 cm^2 V^{-1}s^{-1}. The on/off current ratio was 2.0×10^4 when V_{GS} was scanned from +2 to −10 V. In addition, the output characteristic illustrated in Fig. 4(D) indicated that the device had good saturation behavior. The drain current increased linearly with an increase in drain voltage in the low drain–voltage regime, whereas it tent to saturate in the higher drain–voltage regime because of the pinch-off of the accumulation layer. Furthermore, a large increase of the electrical conductivity was expected due to an enhancement of the hole mobility in these crystalline P3HT domains. A thermal treatment had intense effects on the charge carrier for P3HT blending from chloroform. Annealing at 80 °C for this channel layer resulted in the formation of crystalline P3HT and thus enhanced the hole mobility in these regions by an order of magnitude. It was also likely to happen that the use of high-k materials as the gate insulator had reduced the device operating voltage for flexible devices. The field-effect mobility, on/off current ratio and threshold voltage of P3HT-based OTFTs on silicon/glass substrates were summarized in Table 1 for comparision with literatures [14–19]. The field-effect mobilities' obtained here were lower than previously reported values for other high performance TFTs but it was expected that higher field-effect mobility could be further improved through the optimization of the device fabrication process by choosing appropriate solvents as previously mentioned.

3.4. Bending treatment to three-point bending conditions

Mechanical stability was the most important factor for flexible devices when dealing with the long-term application. We estimated the electrical properties of our OTFT after different bending times, convex and concave type bending stages to make sure the possibility for use in advanced flexible electronic devices. Fig. 5(A) showed the transfer characteristics for plasma treated high-k HfO_2 film followed by Si_3N_4 layer subjected to number of bending times. Inset of Fig. 5(A) presented an image of the setup of the frontward and backward bending tests and the number of bending times. For the initial measurement, the on/off currents ratio was calculated about to 10^4 and remained almost unchanged even after bending the TFT up to 100,500 and 1000 times. Here in our case, the P3HT as channel material and HfO_2 film as gate dielectric followed by Si_3N_4 layer over flexible organic PI substrate revealed superior stability even after bending the TFT device up to 1000 times. After the bending test, the on/off current ratio and threshold voltage remained almost the same as it was prior to initial bending. This observation indicated that the sol–gel spin-coating method to form OTFT by using high-k film as gate dielectric passivation provided superior electrical performance and stability on PI substrate.

Furthermore, we tested two additional features of our OTFT on PI to explore its feasibility for use in practical applications. Namely, we estimated the transfer characteristics in both convex (Fig. 5B) and concave (Fig. 5C) settings, varying the radii of curvature (denoted by R_c) for 2 and 4 cm. Prior to manufacturing process, a hard plastic foil was used as a substrate support to provide these specific bending conditions. As Fig. 5(A) and (B) suggested, the P3HT retained its transfer characteristics after the both convex and concave types bending conditions. All of the curves demonstrated the on/off current ratio to be about 10^4 at applied V_{DS} = −5 V. This value of on/off current ratio was consistent with the ratio of pristine device. This observation implied that the plasma treated HfO_2 film followed by Si_3N_4 passivation as gate dielectric over flexible organic PI substrate revealed superior stability after bending the OTFT device. After the bending measurement, the threshold voltage (V_{Th}) was almost in the same with no bending condition (i.e. −1.9 V). Therefore, the dielectric Si_3N_4 passivation film was supposed to enhance the electrical

Table 1
Comparison of various dielectric layers and corresponding electrical performance of P3HT-based OTFTs fabricated on silicon or glass substrates.

Refs.	Dielectric material	V_{Th} (v)	μ_{sat} (cm^2 V^{-1} s^{-1})	I_{on}/I_{off}	Substrate
This work	HfO_2–Si_3N_4	−1.9	0.041	2×10^4	Polyimide
[14]	SiO_2	−14	0.015	10^5	Silicon
[15]	Al_2O_3	−3.6	0.008	10^4	Silicon
[16]	PVP/TiO_2	1.14	0.014	10^3	Silicon
[17]	Ta_2O_5/PVP	1.7	0.032	–	Glass
[18]	HfO_x	−0.5	0.062	150	Silicon
[19]	TiO_2	1.0	0.054	10^2	Silicon

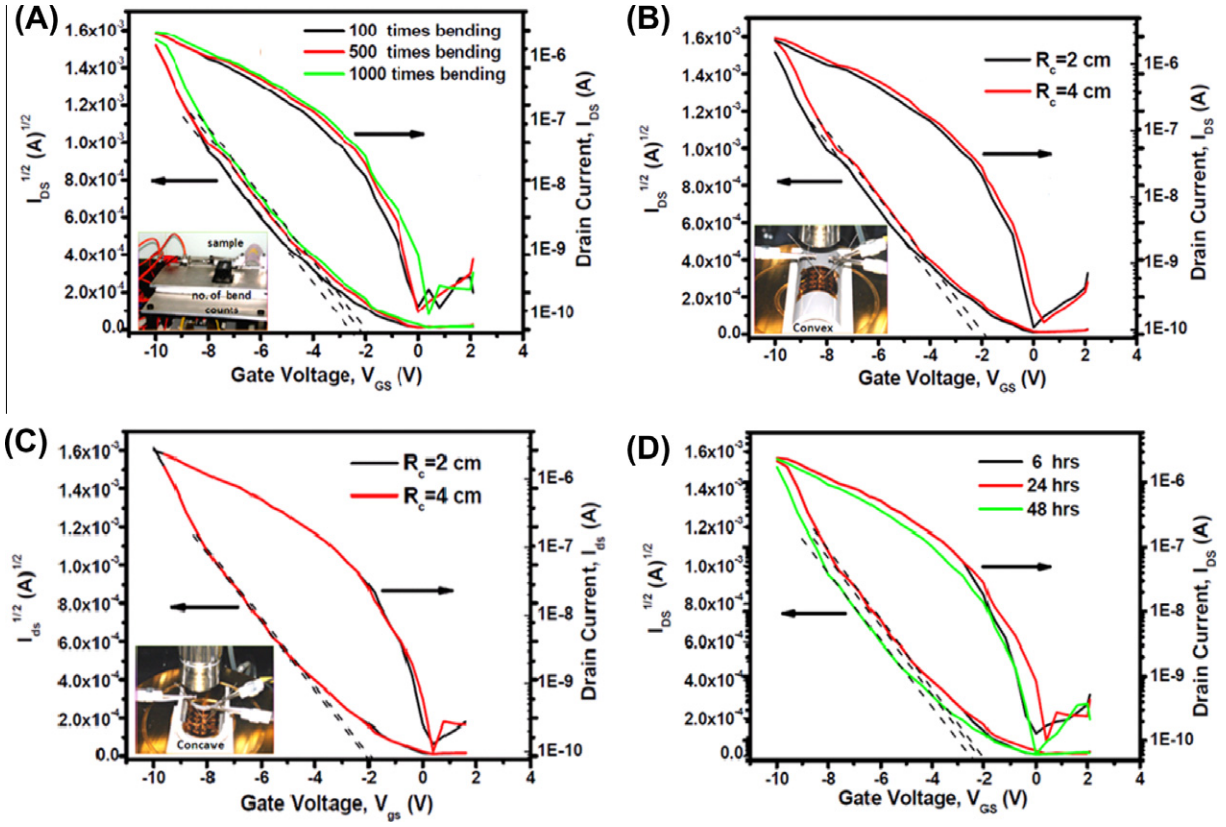

Fig. 5. I_{DS}–V_{GS} plots for P3HT-OTFT by using Si_3N_4–HfO_2 stacked film as gate dielectric on flexible PI substrate: (A) bending time test and inset of customized-homemade bending system, (B) convex shape test and inset of convex setting, (C) concave shape test and inset of concave setting, and (D) time-dependent I_{DS}–V_{GS} characteristics over 6 h, 1 day and 2 days.

characteristics of the TFT devices at low temperature manufacturing. Our results demonstrated better performance when compared to the report for flexible OTFTs [14,16]. Zhang's group had fabricated the flexible pentacene-based TFT arrays, whose mechanical flexibility represented the best values till date [20]. From this concave and convex examinations, we concluded that the P3HT based TFT device fabricated on plastic substrate had an excellent stability even bending the device up to 2 cm in convex or concave status.

3.5. Improved device stability in ambient air

The ambient stability of the TFT device was monitored through the time-dependent performance for the device. To evaluate the reliability of the P3HT-transistor device, environment dependent transfer characteristic measurements were carried out under normal environment. Time-dependent transfer characteristic was measured in Fig. 5(D) for the period of 6, 24, and 48 h. The resultant mobilities were calculated between 0.04–0.05 $cm^2\ V^{-1}\ s^{-1}$, on/off currents ratio 10^4, and threshold voltage about −2.0 V for our flexible P3HT-TFT device. This observation was very close with the illustration in Fig. 4(C). By considering the performance, the data suggested that over a day period of time, our flexible P3HT-TFT did not degrade the mobility. Meanwhile, we had pointed out that the device stability actually reduced for a long period of time over 10 days or more although it was not illustrated here. However, this was not a challenge issue because the commercial flexible device required the package process to avoid contamination. But, less than 48 h, the air stability of our flexible OTFT device without package was observed in comparison with the P3HT-FET on bare SiO_2 substrate. This subtle difference in on/off currents ratio and mobility meant that our flexible TFT had an excellent reliability after placing the devices in normal environment for 48 h and was able to use for advanced microelectronic devices. Our flexible TFT device showed a relatively excellent bias stability with the use of Si_3N_4 layer passivation on the HfO_2 film. O_2 plasma treated high-k film and following Si_3N_4 layer seemed to improve the P3HT-OTFT stability and reduce the absorption effect of humidity, and thereby retarded the degradation of the OTFTs under ambient condition. These results suggested that the possibility of using highly reliable Si_3N_4–HfO_2 stacked heterostructure to fully flexible poly-(3-hexylthiophene) thin-film transistor for future commercial manufacturing.

4. Conclusions

We have fabricated a new and fully flexible organic poly-3-hexylthiophene (P3HT) p-type thin-film transistor (TFT) on a transparent flexible polyimide substrate using high-k

HfO_2 as dielectric layer and Si_3N_4 as passivation layer via very simple and cost-effective sol–gel spin-coating technique. Defects in the HfO_2 films are expected to be rarely induced, because of the low temperature deposition process and plasma treatment. Current–voltage characteristics of the device in metal–insulator–metal structural device imply the success of using Si_3N_4 over HfO_2 to achieve the satisfactory leakage current. The fabricated devices exhibit good electrical performance with saturation mobility of 0.041 $cm^2 V^{-1} s^{-1}$. Moreover, the device demonstrates stable performance over the course of bending up to 1000 times and radii of curvature minimum down to 2 cm in both convex and concave type structures. Our results suggest that the P3HT semiconductor material in together with HfO_2 film followed by Si_3N_4 as passivation layer are promising materials for the low-cost flexible electronic devices.

Acknowledgements

The authors would like to thank the National Device Laboratories (NDL) for their support in device fabrication and the National Science Council of the Republic of China, Taiwan, for financially supporting this research under contract NSC98-2811-M-009-058.

References

[1] T. Sekitani, H. Nakajima, H. Maeda, T. Fukushima, T. Aida, K. Hata, T. Someya, Nat. Mater. 8 (2009) 494.
[2] K. Fukuda, T. Yokota, K. Kuribara, T. Sekitani, U. Zschieschang, H. Klauk, T. Someya, Appl. Phys. Lett. 96 (2010) 053302.
[3] O. Marinov, M.J. Deen, U. Zschieschang, H. Klauk, IEEE Trans. Electron Device 56 (2009) 2952.
[4] L. Jiang, J. Zhang, D. Gamota, C.G. Takoudis, Org. Electron. 11 (2010) 959.
[5] J. Vaillancourt, H. Zhang, P. Vasinajindakaw, H. Xia, X. Lu, X. Han, D.C. Janzen, W.-S. Shih, C.S. Jones, M. Stroder, M.Y. Chen, H. Subbaraman, R.T. Chen, U. Berger, M. Renn, Appl. Phys. Lett. 943 (2008) 243301.
[6] D. Maji, S.P. Duttagupta, V. Ramgopal Rao, Chia Ching Yeo Byung-Jin Cho, IEEE Electron Device Lett. 28 (2007) 731.
[7] D. Kaminishi, H. Ozaki, Y. Ohno, K. Maehashi, K. Inoue, K. Matsumoto, Appl. Phys. Lett. 86 (2005) 113115.
[8] J.H. Oh, M. Han, Y.H. Baek, S.W. Moon, J.K. Rhee, S.D. Kim, Semicond. Sci. Technol. 24 (2009) 025027.
[9] P.R. Emtage, W. Tantraporn, Phys. Rev. Lett. 8 (1962) 267.
[10] J.S. Meena, M.-C. Chu, S.-W. Kuo, F.-C. Chang, F.-H. Ko, Phys. Chem. Chem. Phys. 12 (2010) 2582.
[11] S.M. Goetz, C.M. Erlen, H. Grothe, B. Wolf, P. Lugli, G. Scarpa, Org. Electron. 10 (2009) 573.
[12] S.M. Sze, Physics of Semiconductor Devices;, Wiley-Interscience, NewYork, 1981.
[13] H.-L. Cheng, J.-W. Lin, M.-F. Jang, F.-C. Wu, W.-Y. Chou, M.-H. Chang, C.-H. Chao, Macromolecules 42 (2009) 8251.
[14] Y. Horii, M. Ikawa, K. Sakaguchi, M. Chikamatsu, Y. Yoshida, R. Azumi, H. Mogi, M. Kitagawa, H. Konishi, K. Yase, Thin Solid Films 518 (2009) 642.
[15] L. Fumagalli, D. Natali, M. Sampietro, E. Peron, F. Perissinotti, G. Tallarida, S. Ferrari, Org. Electron. 9 (2008) 198.
[16] F.-Y. Yang, K.-J. Chang, M.-Y. Hsu, C.-C. Liu, Org. Electron. 9 (2008) 925.
[17] J. Zhou, K. Yang, J. Zhou, Y. Liu, J. Peng, Y. Cao, Jpn. J. Appl. Phys. 46 (2007) 913.
[18] Y.R. Liu, L.F. Deng, R.H. Yao, P.T. Lai, IEEE Trans. Device Mater. Reliab. 10 (2010) 2.
[19] G. Wang, D. Moses, A.J. Heeger, H.-M. Zhang, M. Narasimhan, R.E. Demaray, J. Appl. Phys. 95 (2004) 306.
[20] F. Zhang, M. Funahashi, N. Tamaoki, Org. Electron. 11 (2010) 363.

Recently, improved performance of OPV cells with higher external quantum efficiency in the spectral range of 500–700 nm has been demonstrated by replacing C_{60} with fullerene C_{70} of higher visible light absorption arising from a relaxation of symmetry-forbidden transitions in C_{70} [18–20]. The C_{70} derivative, $PC_{70}BM$, is also utilized in polymer-based OPV devices to provide photocurrent enhancement over devices with $PC_{60}BM$ due to the greater long-wavelength absorption of $PC_{70}BM$ [21].

Besides the selection of effective OPV materials, it is well recognized that the electronic structures of organic interfaces, especially the energy level offsets at DA heterojunctions, play a crucial role in determining charge generation and transport processes in OPVs [22–25]. For instance, the open-circuit voltage (V_{OC}) is proposed to be dependent on energy level offset (ΔE_{DA}) between the highest occupied molecular orbital (HOMO) of the donor and the lowest unoccupied molecular orbital (LUMO) of the acceptor at the DA interface [26–28]. According to previous reports, the electronic structures at a planar DA bilayer interface differ from that of a mixed DA BHJ [23,24]. However, the related works are still scarce, and it is of interest to clarify the electronic properties of C_{70}-involved DA heterojunctions for the understanding and optimization of OPV cells. In this work, we report the detailed electronic structures and energy level alignment at DA heterojunctions consisting of C_{70} and copper phthalocyanine (CuPc) in the form of a planar C_{70}/CuPc bilayer structure and a mixed C_{70}:CuPc BHJ. The influence of thermal annealing on the mixed C_{70}:CuPc BHJ is also addressed.

2. Experimental

Interface studies were carried out in a Kratos AXIS Ultra-DLD ultrahigh vacuum photoemission spectroscopy system, which is composed of a fast entry air lock, a multiport carousel chamber, an evaporation chamber, and an analysis chamber. The base pressures in the four chambers were better than 1×10^{-8} Torr, 5×10^{-10} Torr, 5×10^{-10} Torr, and 3×10^{-10} Torr, respectively. Indium tin oxide (ITO) coated glass substrates (30 Ω/sq.) were *ex-situ* solvent cleaned and treated by UV-ozone for 20 min. Prior to film deposition, all the materials were entirely outgassed. CuPc and C_{70} were *in situ* thermally deposited onto the room-temperature substrates with a growth rate of 1–2 Å/s in the evaporation chamber. The C_{70}:CuPc mixture was formed by co-evaporating C_{70} and CuPc sources from separately Ta boats. Film thickness and deposition rate were monitored by a quartz crystal microbalance. The annealing procedure with a temperature ramp rate of ~10 °C/min was also carried out in the evaporation chamber with a heating stage. After each deposition or annealing step, samples were transferred to the analysis chamber without breaking vacuum for ultraviolet and X-ray photoelectron spectroscopy (UPS and XPS) measurements. UPS analysis was performed to characterize the valence states and vacuum level (VL) by using the HeI excitation line (21.2 eV) from a Helium discharge lamp with a total instrumental energy resolution of 100 meV, and samples were negatively biased to enable the observation of secondary electron cutoff. XPS measurements using a monochromatic Al Kα source (1486.6 eV) were carried out to study chemical reactions and the development of energy level bending. All the spectra were obtained at room temperature. The binding energy scale was calibrated by determining the $Au4f_{7/2}$ peak position and Fermi level (E_F) edge of the Au film, which was cleaned by Ar^+ ion sputtering. Fermi level is referred as the zero binding energy (BE) in all the UPS and XPS spectra.

OPV cells were fabricated on patterned ITO glass with a sheet resistance of 30 Ω/sq. The UV-ozone treated ITO substrates were loaded into a high-vacuum chamber with a base pressure of 1×10^{-7} Torr. The organic layers and metal cathode were thermally evaporated from separately Ta-heated quartz or BN crucibles. The mixture ratio of C_{70} and CuPc based on the wt% measured using the thickness monitor was fixed at 1:1, unless otherwise noted. A shadow mask was used to define the cathode and to make four 0.1 cm^2 devices on each substrate. Current density–voltage (J–V) characteristics of the PV cells without any device encapsulation were measured with a programmable Keithley model 2612 power source in the dark and under AM 1.5 solar illumination from a Newport 150 W solar simulator. Illumination intensity was measured with a calibrated Oriel radiant power meter.

3. Results and discussion

3.1. Electronic structures of the planar C_{70}/CuPc bilayer structure

The electronic structure evolution at the planar C_{70}/CuPc interface on UV-ozone treated ITO substrate was measured by UPS. Fig. 1 shows the HeI UPS spectra of the C_{70}/CuPc interface with increasing C_{70} overlayer on a 100 Å-thick CuPc layer deposited on ITO substrate. The

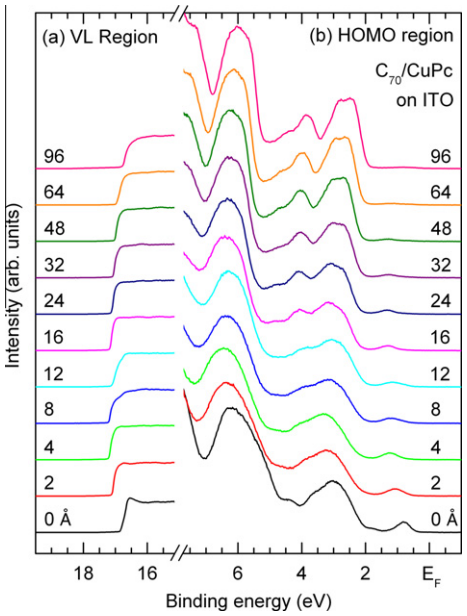

Fig. 1. Expanded UPS spectra of (a) the secondary electron cutoff and (b) the HOMO region for C_{70}/CuPc bilayer as a function of incremental C_{70} deposition on 100 Å-thick CuPc on ITO substrate.

top spectrum corresponds to the photoemission from a 96 Å-thick C_{70} layer. It is noted that upon deposition of C_{70}, the spectral features of CuPc are attenuated progressively, while those of C_{70} are concurrently increased and finally saturated. As shown in Fig. 1(a), the secondary electron cutoff at high BE region, from which the VL position can be inferred, exhibits a slight shift towards higher BE at the initial stage of C_{70} deposition, and then gradually shifts towards lower BE with increasing thickness of C_{70}. A similar shift is also observed for all the spectral features of both C_{70} and CuPc. Meanwhile, it is evident that there is no emergence of new features in the organic energy gap region with the deposition of C_{70} overlayer, implying a physical adsorption process at the C_{70}/CuPc interface. The slight BE shift of spectral features with respect to the increase of film thickness might be associated with electric dipoles produced in the film by a gradient change in the molecular orientation even if the molecule has no permanent electric dipole [29]. In addition, the collected UPS spectra were found not to be shifted or changed with irradiation time, which eliminate the influence of surface charging on the accuracy of the measurements for thick films. According to the Fig. 1(b), the HOMO onsets of CuPc and C_{70}, estimated by linear extrapolation at low binding energy side of the HOMO peak maximum, locate at 0.4 and 1.95 eV below E_F, respectively. The corresponding ionization potential (IP) values, which were determined by the energy difference between the VL position and HOMO onset, are 4.8 eV for CuPc and 6.35 eV for C_{70}, respectively.

XPS measurements were also taken after each deposition step. Fig. 2 displays the corresponding XPS C1s core level spectra at the C_{70}/CuPc interface, which are normalized to their peak maximum intensity. For CuPc, the C1s spectrum reveals three distinctive peaks as shown in the bottom spectrum of Fig. 2. As pointed out elsewhere, [25,30] these three peaks are associated with the aromatic carbon of the benzene rings, pyrrole carbon linked to nitrogen, and a π–π^* satellite feature from the pyrrole carbon, respectively. Correspondingly, the XPS spectrum of the C_{70} film is composed of the C1s main line and π–π^* shake-up structures caused by kinetic-energy losses of the photoelectrons due to simultaneously excited π–π^* transitions from the occupied to unoccupied molecular orbitals [31]. As shown in Fig. 2, there is neither additional component nor peak broadening except for the gradual changes of spectral intensity and positions. The results further confirm the absence of a chemical reaction at the C_{70}/CuPc interface, as demonstrated in the UPS measurements (see Fig. 1).

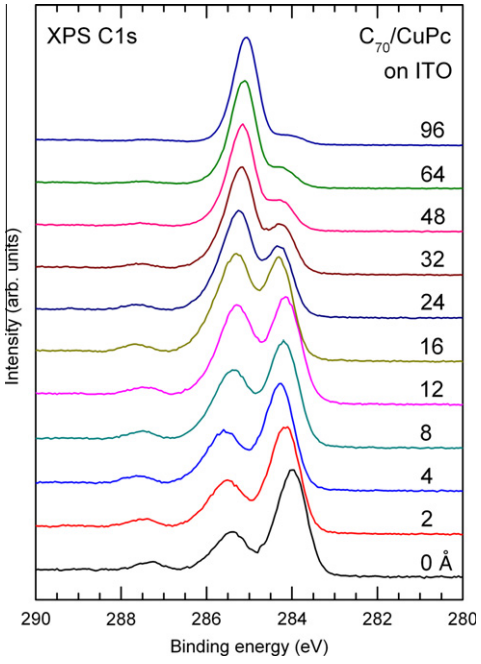

Fig. 2. XPS C1s core level spectra obtained upon formation of the C_{70}/CuPc bilayer on ITO substrate.

3.2. Electronic structures of the mixed C_{70}:CuPc BHJ

Fig. 3(a) and (b) shows the HeI UPS spectra of the incremental deposition of a mixed C_{70}:CuPc BHJ (1:1 by weight) on ITO substrate, where the C_{70}:CuPc thickness increases from submonolayer (~2 Å) to 100 Å. The bottom UPS spectrum in Fig. 3(a) and (b) was recorded from the UV-ozone treated ITO. It is noted that upon deposition of a 2 Å-thick C_{70}:CuPc mixed layer on ITO substrate, the VL cutoff exhibits a shift of ~0.3 eV towards higher BE, which is in good agreement with the formation of the CuPc/ITO interface [32]. With increasing mixed C_{70}:CuPc thickness, there is negligible shift for all the spectral features as well as VL cutoff, which is also observed in the XPS measurements (not shown here). More specifically, the UPS spectrum of 100 Å-thick C_{70}:CuPc layer is very similar to that of 16 Å-thick C_{70}/CuPc bilayer as shown in Fig. 1.

To accurately determine the HOMO onsets for C_{70} and CuPc in the mixed C_{70}:CuPc layer, the UPS spectrum of 100 Å-thick mixed C_{70}:CuPc layer is fitted with the spectral line shapes of pure CuPc and C_{70}, which are the same as those in Fig. 1. As evident in Fig. 3(c), the UPS spectrum of the deposited C_{70}:CuPc layer is deconvoluted into the superimposed spectra of CuPc (thin solid line) and C_{70} (thin dashed line). The HOMO onsets for C_{70} and CuPc in mixed C_{70}:CuPc layer are thus estimated to be at 1.7 and 0.4 eV below E_F, respectively.

3.3. Energy level alignment of C_{70}/CuPc and C_{70}:CuPc heterojunctions

According to the results from UPS and XPS measurements, the corresponding energy level alignments at the planar C_{70}/CuPc bilayer interface and the mixed C_{70}:CuPc BHJ are obtained and schematically illustrated in Fig. 4(a) and (b), respectively. Here, the charge transport gaps are taken to estimate the LUMO positions of C_{70} and CuPc, which were determined from UPS plus inverse photoemission spectroscopy (IPES) measurement (that is 2.1 eV for C_{70} and 1.9 eV for CuPc, respectively) [32,33]. The interface dipole (Δ) was determined from the VL cutoff shift. As shown in the energy level diagrams, the energy level lineup in the planar C_{70}/CuPc bilayer structure (Fig. 4(a)) is remarkably different from that in the mixed C_{70}:CuPc BHJ (Fig. 4(b)). In particular, the ΔE_{DA} between the donor-like

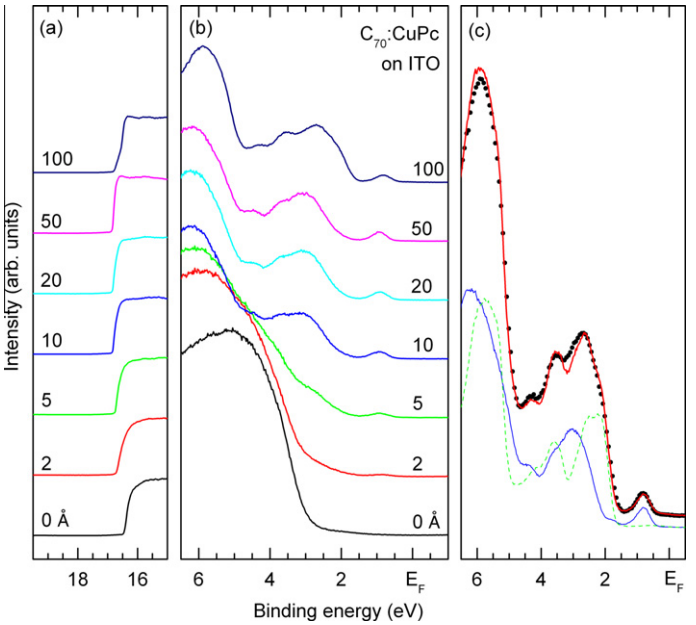

Fig. 3. Expanded UPS spectra of (a) VL region and (b) HOMO region for mixed C_{70}:CuPc BHJ for increasing thickness of C_{70}:CuPc on ITO substrate. (c) Decomposition of the UPS spectrum of C_{70}:CuPc BHJ with experimental data (open circles) and fitting curve (solid line).

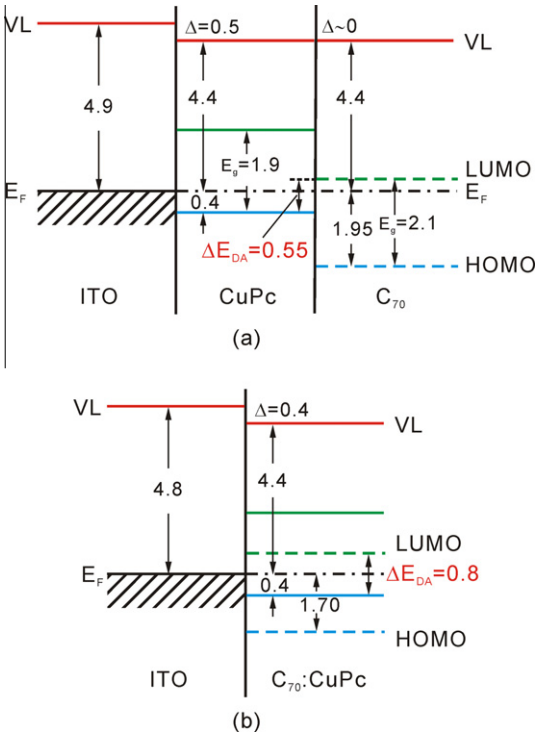

Fig. 4. Schematic energy level diagrams of (a) C_{70}/CuPc bilayer and (b) C_{70}:CuPc BHJ on ITO substrate, respectively. All the values shown are in unit of eV. The molecular levels of CuPc are presented in solid line, while that of C_{70} in dashed line. VL, E_F and HOMO energies are deduced from UPS measurements, and LUMO energies are derived from charge transport gaps plus HOMO.

CuPc and the acceptor-like C_{70} increases from 0.55 eV in the planar C_{70}/CuPc bilayer (Fig. 4(a)) to 0.8 eV (Fig. 4(b)) in mixed C_{70}:CuPc BHJ. Similar results have also been observed in other metal phthalocyanine–C_{60} systems, such as C_{60}–CuPc and C_{60}–ZnPc [23,24]. As ΔE_{DA} is related to the theoretical maximum of V_{OC} in OPV cells, it is expected that the mixed C_{70}:CuPc structure can induce a larger V_{OC} than the planar C_{70}/CuPc bilayer.

To validate the above analysis, the OPV devices using a planar C_{70}/CuPc bilayer and a mixed C_{70}:CuPc BHJ as the photoactive area were fabricated and compared. The OPV cells have a structure of ITO/CuPc (200 Å)/C_{70} (400 Å)/Bphen (100 Å)/LiF (5 Å)/Al (1000 Å) and ITO/CuPc (150 Å)/CuPc:C_{70} (150 Å)/C_{70} (300 Å)/Bphen (100 Å)/LiF (5 Å)/Al (1000 Å), respectively, where Bphen (4,7-diphenyl-1,10-phenanthroline) is used as exciton blocking layer, and LiF/Al as a bilayer cathode. Fig. 5 shows the *J*–*V* characteristics measured under simulated AM 1.5G solar illumination with an incident intensity of 100 mW/cm^2, and the parameters of the cells are summarized in Table 1. As evident in Fig. 5, the V_{OC} dramatically increased from 0.35 to 0.46 V with respect to the replacement of the C_{70}/CuPc bilayer with C_{70}:CuPc BHJ. In addition, J_{SC} of the cell with a C_{70}:CuPc BHJ is almost 2 times larger than that with a C_{70}/CuPc bilayer, resulting in a higher η_P of 1.51%. The results observed in Fig. 5 and Table 1 are consistent with the trend observed in Fig. 4, confirming the influence of the electronic structure at DA interface on the device performance.

It has been reported that the ΔE_{DA} increase in the C_{60}:CuPc BHJ was affected by the underlying substrate work function and charge transfer between two molecules [23], whereas the ΔE_{DA} increase for C_{60}:ZnPc system was attributed to the relatively small energy level bending

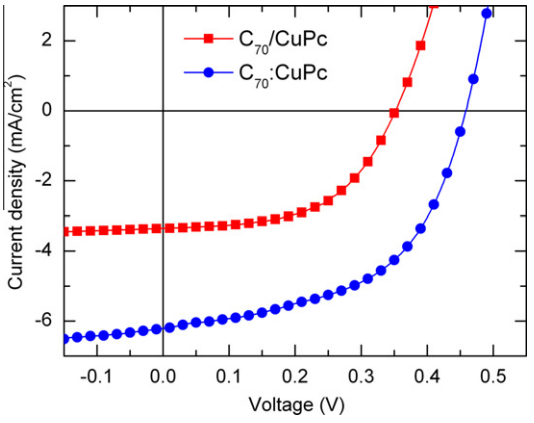

Fig. 5. Comparison of current density vs. voltage characteristics of the OPV cells with a C_{70}/CuPc bilayer (solid squares) and a C_{70}:CuPc BHJ (solid circles) under simulated AM1.5G solar illumination of 100 mW/cm^2.

Table 1
Structure and performance comparison of OPV cells incorporating a C_{70}/CuPc bilayer and a C_{70}:CuPc BHJ as the photoactive region, respectively, under AM1.5G simulated solar illumination with an intensity of 100 mW/cm^2.

Device configuration	V_{OC} (V)	J_{SC} (mA/cm^2)	FF	η_P (%)
ITO/CuPc (200 Å)/C_{70} (400 Å)/Bphen (100 Å)/LiF (5 Å)/Al (1000 Å)	0.35	3.35	0.55	0.64
ITO/CuPc (150 Å)/CuPc:C_{70} (150 Å) /C_{70} (300 Å)/Bphen (100 Å)/LiF (5 Å)/Al (1000 Å)	0.46	6.21	0.53	1.51

and doping effects (electron transfer from ZnPc to C_{60}) [24]. However, the observed difference in ΔE_{DA} between C_{70}/CuPc bilayer and C_{70}:CuPc mixture in Fig. 4(a) and (b) cannot be explained by the proposed mechanisms for C_{60}–CuPc or C_{60}–ZnPc systems. As shown in Fig. 4(b), the absence of a strong charge transfer in the C_{70}–CuPc couple suggests that the flat energy level lineup in the C_{70}:CuPc BHJ is different from the energy level bending occurring in C_{60}:CuPc and C_{60}:ZnPc. This can be understood in term of ΔE_{DA}. Since the CuPc HOMO level is 0.8 eV lower in energy than the C_{70} LUMO (see Fig. 4(b)), an energy barrier of 0.8 eV has to be overcome for charge transfer from CuPc to C_{70}. Moreover, the ΔE_{DA} increase in C_{70}:CuPc BHJ is because the energy level positions of C_{70} in the mixed layer differ from those in a bilayer structure, possibly due to the different polarizabilities of C_{70} and CuPc molecules in the mixed layer from that of pure films [34].

3.4. Thermal annealing effect on the electronic properties of mixed C_{70}: CuPc BHJ

To improve the performance of BHJ OPV cells, thermal annealing is extensively employed to modify the morphology and molecular arrangements of BHJs for governing the balance between exciton dissociation and charge transport property [2,10]. It has been revealed that annealing treatment at various temperatures results in lateral or vertical phase separation with different molecular arrangements in the BHJ [2,3,9,35]. Besides its influence on the morphology change, it is of importance to clarify the effect of thermal annealing on the electronic properties of mixed DA BHJ, e.g., C_{70}:CuPc.

Fig. 6 shows the HeI UPS spectra recorded from a 100 Å-thick C_{70}:CuPc BHJ after annealing treatment at different temperatures for 30 min. Fig. 6(a) and (b) display the zoom-in plots of the VL and HOMO regions. The bottom spectrum in Fig. 6 is the same as that of 100 Å-thick C_{70}:CuPc mixture in Fig. 3. To accurately distinguish the spectral contributions of C_{70} and CuPc to that of the C_{70}:CuPc mixture, the HOMO regions of UPS spectra (Fig. 6(c)) are fitted with the spectral line shapes of pure CuPc and C_{70} as used in Fig. 3. Relative to the spectral intensity of pure C_{70} and CuPc, the contribution ratio of C_{70} to CuPc is determined as shown in Fig. 3(c). It is evident that the spectral contribution of C_{70} to the C_{70}:CuPc mixture is gradually attenuated with increasing annealing temperature. However, increasing annealing temperature does not result in a shift of VL or HOMO, and thus the energy level offsets between C_{70} and CuPc remain almost constant during the thermal annealing process.

Fig. 7 displays the normalized XPS C1s core level spectra of the mixed C_{70}:CuPc layer annealed at different temperature, which are least-squares fitted with individual subspectra of CuPc (dashed area) and C_{70} (shadowed area) components to fit the C1s photoemission data. As depicted in Fig. 7, thermal annealing does not cause the appearance of additional component or the shift of spectral features in the C_{70}:CuPc mixture except for a continuous increase of CuPc peak intensity relative to that of C_{70} component, which is consistent with the UPS measurements (see Fig. 6). According to the decomposition of XPS C1s spectra, the C_{70} to CuPc molecular ratios at the C_{70}:CuPc surface upon different annealing temperatures can be obtained by comparing the integrated peak areas of C_{70} to CuPc as well as taking into account the number of carbon atoms per molecule. As summarized in the inset of Fig. 7, the C_{70}-to-CuPc molecular ratio is estimated to be ~1.2:1 for as-grown C_{70}:CuPc mixture, and decreases with increasing annealing temperature. As the XPS signals represent a weighted average collected from the sample surface, the lateral changes of the molecular ordering or morphology will not significantly influence the relative intensity change as observed in Fig. 7. The results in Figs. 6 and 7 are similar to the C_{60}:CuPc system [25], implying an annealing-induced vertical phase separation into a CuPc-rich region near the surface and a C_{70}-rich region adjacent to the substrate in the C_{70}:CuPc mixture. As previously proposed, the difference in the surface energy of CuPc and C_{70} might be the major factor contributing to the vertical segregation of components in the annealed mixture [25,36].

It has been reported that V_{OC} in C_{70}-involved BHJ OPV cells was increased after annealing [18]. As demonstrated in Figs. 6 and 7, thermal annealing has little effect on the electronic structures, especially ΔE_{DA}, of the C_{70}:CuPc BHJ, indicating that the theoretical maximum of V_{OC} remains unchangeable. Therefore, the increase in V_{OC} after annealing cannot be attributed to the change in ΔE_{DA}, rather it proba-

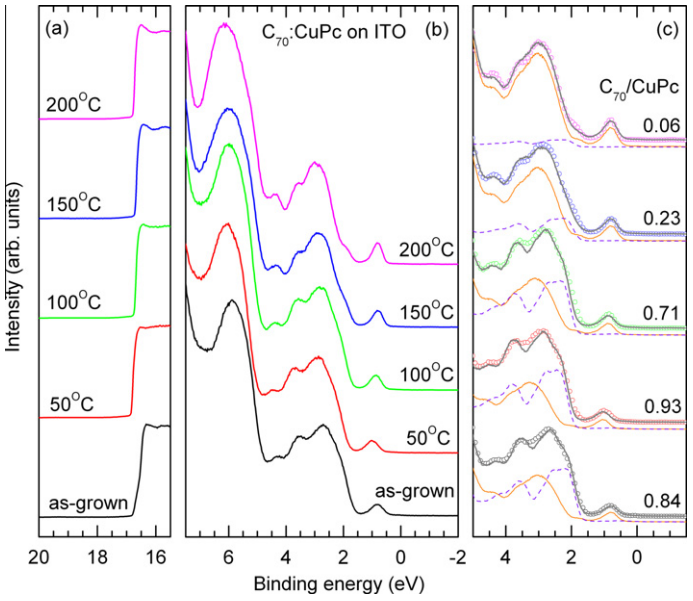

Fig. 6. UPS spectra of C_{70}:CuPc BHJ on ITO substrate upon thermal annealing with different temperatures. (a) VL region, (b) HOMO region, and (c) spectral decomposition.

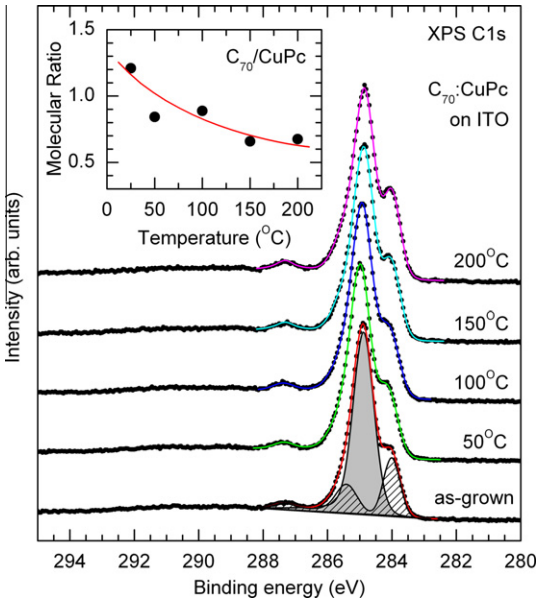

Fig. 7. XPS C1s core level spectra obtained upon thermal annealing of C_{70}:CuPc BHJ at various temperatures. Solid lines represent resultant fitting curves on the experimental date. Dashed and shadowed areas show the contributions of CuPc and C_{70}, respectively. Inset displays the various C_{70}-to-CuPc molecular ratios upon annealing.

bly arises from the decrease of cell series resistance. The major contributions to cell series resistance include the bulk resistances of organic materials and electrodes, and their contact resistance. An interpenetrating network of spatially distributed CuPc and C_{70} domains is formed during the annealing process, due to the spherical shape of the C_{70} molecules that allows close packing [35]. Consequently, the crystalline domains provides percolating pathways for the transport of dissociated holes and electrons to the respective electrodes, leading to the decrease of the cell series resistance. Still, more work is required to clarify the relation among ΔE_{DA}, V_{OC}, and cell series resistance.

4. Conclusions

The detailed electronic structures of planar C_{70}/CuPc bilayer and mixed C_{70}:CuPc BHJ have been studied by photoemission spectroscopy. The planar C_{70}/CuPc and mixed C_{70}:CuPc heterojunctions exhibit significantly different energy level alignments. The energy offset between donor-like CuPc HOMO and acceptor-like C_{70} LUMO is increased from 0.55 eV in the bilayer structure to 0.8 eV in the mixed BHJ. This increase is consistent with a V_{OC} enhancement in the OPV cells, and is possibly associated with the polarizability changes of C_{70} and CuPc molecules in the mixed materials. The influence of thermal annealing on the mixed C_{70}:CuPc heterojunction is also investigated, revealing annealing-induced vertical phase separation with compositional gradient along the cross-section. These results reported here are beneficial to the design of OPV cells with C_{70} as the acceptor.

Acknowledgements

The authors acknowledge the financial support by the National Natural Science Foundation of China (Nos. 910 27041, 61007020, 61036009, 60937001), the Major State Basic Research Development Program of China (973 program) (Nos. 2011CB808404, 2010CB934502), the National High-tech R&D Program of China (863 Program) (No. 2008AA03A327), and the Research Fund for the Doctoral

Program of Higher Education of China (Nos. 20093201120019, 20103201120019).

References

[1] P. Peumans, A. Yakimov, S.R. Forrest, J. Appl. Phys. 93 (2003) 3693.
[2] F. Yang, M. Shtein, S.R. Forrest, Nat. Mater. 4 (2005) 37.
[3] W.L. Ma, C.Y. Yang, X. Gong, K. Lee, A.J. Heeger, Adv. Funct. Mater. 15 (2005) 1617.
[4] J. Drechsel, B. Männig, F. Kozlowski, M. Pfeiffer, K. Leo, H. Hoppe, Appl. Phys. Lett. 86 (2005) 244102.
[5] G.P. Kushto, W. Kim, Z.H. Kafafi, Appl. Phys. Lett. 86 (2005) 093502.
[6] B.P. Rand, J. Genoe, P. Heremans, J. Poortmans, Prog. Photovoltaics Res. Appl. 15 (2007) 659.
[7] J.Y. Kim, K. Lee, N.E. Coates, D. Moses, T.-Q. Nguyen, M. Dante, A.J. Heeger, Science 317 (2007) 222.
[8] A. Hadipour, B. de Boer, P.W.M. Blom, Adv. Funct. Mater. 18 (2008) 169.
[9] Z. Xu, L.M. Chen, G. Yang, C.H. Huang, J. Hou, Y. Wu, G. Li, C.S. Hsu, Y. Yang, Adv. Funct. Mater. 19 (2009) 1227.
[10] L.M. Chen, Z.R. Hong, G. Li, Y. Yang, Adv. Mater. 21 (2009) 1434.
[11] G. Dennler, M.C. Scharber, C.J. Brabec, Adv. Mater. 21 (2009) 1323.
[12] M.D. Perez, C. Borek, P.I. Djurovich, E.I. Mayo, R.R. Lunt, S.R. Forrest, M.E. Thompson, Adv. Mater. 21 (2009) 1517.
[13] A.W. Hains, Z.Q. Liang, M.A. Woodhouse, B.A. Gregg, Chem. Rev. 110 (2010) 6689.
[14] S.H. Park, A. Roy, S. Beaupre, S. Cho, N. Coates, J.S. Moon, D. Moses, M. Leclerc, K. Lee, A.J. Heeger, Nat. Photonics 3 (2009) 297.
[15] Y. Liang, D. Feng, Y. Wu, S.-T. Tsai, G. Li, C. Ray, L. Yu, J. Am. Chem. Soc. 131 (2009) 7792.
[16] H. -Y. Chen, J. Hou, S. Zhang, Y. Liang, G. Yang, Y. Yang, L. Yu, Y. Wu, G. Li, Nat. Photonics 3 (2009) 649.
[17] <http://www.solarmer.com/newsevents.php>.
[18] J. Sakai, T. Taima, T. Yamanari, K. Saito, Sol. Energy Mater. Sol. Cells 93 (2009) 1149.
[19] S. Pfuetzner, J. Meiss, A. Petrich, M. Riede, K. Leo, Appl. Phys. Lett. 94 (2009) 223307.
[20] X. Xi, W.J. Li, J.Q. Wu, J.J. Ji, Z.R. Shi, G.H. Li, Sol. Energy Mater. Sol. Cells 94 (2010) 2435.
[21] M.M. Wienk, J.M. Kroon, W.J.H. Verhees, J. Knol, J.C. Hummelen, P.A. van Hal, R.A.J. Janssen, Angew. Chem. Int. Ed. 42 (2003) 3371.
[22] J.X. Tang, Y.C. Zhou, Z.T. Liu, C.S. Lee, S.T. Lee, Appl. Phys. Lett. 93 (2008) 043512.
[23] T.W. Ng, M.F. Lo, M.K. Fung, S.L. Lai, Z.T. Liu, C.S. Lee, S.T. Lee, Appl. Phys. Lett. 95 (2009) 203303.
[24] S.H. Park, J.G. Jeong, H.J. Kim, S.H. Park, M.H. Cho, S.W. Cho, Y.J. Yi, M.Y. Heo, H. Sohn, Appl. Phys. Lett. 96 (2010) 013302.
[25] H.X. Wei, J. Li, Z.Q. Xu, Y. Cai, J.X. Tang, Y.Q. Li, Appl. Phys. Lett. 97 (2010) 083302.
[26] B.P. Rand, D.P. Burk, S.R. Forrest, Phys. Rev. B 75 (2007) 115327.
[27] K. Vandewal, A. Gadisa, W.D. Oosterbaan, S. Bertho, F. Banishoeib, I. Van Severen, L. Lutsen, T.J. Cleij, D. Vanderzande, J.V. Manca, Adv. Funct. Mater. 18 (2008) 2064.
[28] M.D. Perez, C. Borek, S.R. Forrest, M.E. Thompson, J. Am. Chem. Soc. 131 (2009) 9281.
[29] H. Yamane, Y. Yabuuchi, H. Fukagawa, S. Kera, K.K. Okudaira, N. Ueno, J. Appl. Phys. 99 (2006) 093705.
[30] J.X. Tang, C.S. Lee, S.T. Lee, Appl. Surf. Sci. 252 (2006) 3948.
[31] B.Y. Han, L.M. Yu, K. Hevesi, G. Gensterblum, P. Rudolf, J.J. Pireaux, P.A. Thiry, R. Caudano, Ph. Lambin, A.A. Lucas, Phys. Rev. B 51 (1995) 7179.
[32] W.R. Salaneck, K. Seki, A. Kahn, J.J. Pireaux (Eds.), Conjugated Polymers and Molecular Interfaces: Science and Technology for Photonic and Optoelectronic Applications, Dekker, New York, 2002.
[33] P.J. Benning, D.M. Poirier, T.R. Ohno, Y. Chen, M.B. Jost, F. Stepniak, G.H. Kroll, J.H. Weaver, J. Fure, R.E. Smalley, Phys. Rev. B 45 (1992) 6899.
[34] J.G. Xue, S.R. Forrest, Phys. Rev. 69 (2004) 245322.
[35] A. Opitz, J. Wagner, W. Brütting, A. Hinderhofer, F. Schreiber, Phys. Stat. Solidi A 206 (2009) 2683.
[36] C.M. Björström, A. Bernasik, J. Rysz, A. Budkowski, S. Nilsson, M. Svensson, M.R. Andersson, K.O. Magnusson, E. Moons, J. Phys.: Condens. Matter 17 (2005) L529.

The similar idea of stacked OLED/OPV devices has also been explored for possible application in optical sensor and energy-circle optoelectronic components using ambient illumination, though such integration still faces some challenges [12–15]. One of them is to achieve an optical matching between the spectral responsivity of the OPV cell and the EL emission spectrum of the OLED in the integrated device. In other applications, when the OPV cell in an OLED/OPV structure is operated based on the absorption of the light emitted from the OLED component for application in optical sensors, it is then desired that the spectral responsivity of the photovoltaic component matches with the EL emission spectrum of the OLED [13]. The sensor platform technology, based on an integration of organic light transmissible devices, such as an OPV cell and an OLED with polymer waveguides [14], provides significant cost benefit as well as the functional superiority for application in low cost bioassay device, sign monitoring, and compact information systems.

We report here our efforts to develop a high performance organic optoelectronic device through the integration of a front semitransparent OPV cell [6,16,17] with a bottom OLED. In the integrated functional OPV/OLED systems, the photoactive materials used in the OPV cell are chosen in such a way that the OPV component has a very low absorption in the wavelength region of the light emitted by the integrated OLED unit. The front OPV cell is transparent to the EL emission of the underneath OLED. In this work, an 8-tris-hydroxyquinoline (Alq_3):10-(2-benzothiazolyl)-1,1,7,7-tetramethyl-2,3,6,7-tetrahydro-1H,5H,11H(1)benzopyrano(6,7,8-ij)-quinolizin-11-one (C545)-based OLED and a zinc phthalocyanine (ZnPc): fullerene (C_{60})-based OPV cell were used for fabrication of the integrated OPV/OLED device. Alq_3:C545-based OLED has a peak EL emission at ~530 nm, while the spectral response of ZnPc:C_{60}-based OPV cell has a very low photoresponse at the same wavelength, but relatively high absorption over the visible light wavelength range. Hence, the combination of a ZnPc:C_{60}-based semitransparent OPV cell and an Alq_3:C545-based OLED in an integrated OPV/OLED structure allows the light emitted from the OLED unit to pass through the front OPV cell without significant loss.

The integrated device was fabricated on an indium tin oxide (ITO) glass substrate with a sheet resistance of 12 Ω/sq. The organic and electrode materials were thermally evaporated in a vacuum system having a base pressure $<10^{-6}$ mbar. The ITO substrates were subjected to an O_2 plasma treatment at 100 W for 10 min. The OPV cell consists of a co-evaporated ZnPc:C_{60} layer (35 nm), a C_{60} acceptor layer (25 nm), a BPhen exciton-blocking layer (7 nm) and a semitransparent Ag cathode layer (30 nm). The Ag cathode was then modified with CF_X plasma, forming a plasma-polymerized CF_X fluorocarbon layer (~1 nm). The surface of the CF_X-modified Ag serves as an anode contact for the OLED [18]. The OLEDs consist of a *N*,*N*′-bis(l-naphthyl)-*N*,*N*′-diphenyl-1,l′-biphentl-4,4′-diamine (NPB) layer (55 nm), an emitting layer of Alq_3 doped with C545 (0.8%), and an electron-transporting layer of undoped Alq_3. Finally, a 150 nm thick of Al electrode was deposited on the organic layers through a shadow mask that defines an active area of 3 mm × 3 mm. The *J*–*V* characteristics of the OPV cells were measured using an AM1.5G solar simulator, calibrated by a KG-5 filtered photodiode.

In order to achieve an efficient light output, a microcavity OLED (MOLED) was used in the integrated device in order to achieve a narrow emission spectrum [19,20] to maximize the light output through the front semitransparent OPV cell. An optimization of the structure of semitransparent-OPV/MOLED thin film system was investigated. From optical point view, an integrated OPV/MOLED device can be considered as a multi-layer thin film system composed of absorbing and non-absorbing materials. Optical admittance analysis was utilized to optimize various parameters for enhanced light absorption in the front semitransparent OPV cell and output of the emitted light by the underneath MOLED. For a multilayered thin film system with m layers, assuming normal incidence, the total transmittance, $T(\lambda)$, of these m layers can be expressed as [21,22]:

$$T(\lambda) = [1 - R(\lambda)] \prod_{j=1}^{m} \Psi_j, \tag{1}$$

where $R(\lambda)$ is the total reflectance, and Ψ_j is the ratio of the real parts of the effective optical admittance for $(j+1)$th and jth layers, the net absorptance of the jth layer, $A_j(\lambda)$, in an m layered structure can be determined by:

$$A_j(\lambda) = \left[1 - R(\lambda)\right]\left[1 - \Psi_j(\lambda)\right] \prod_{i=1}^{j} \Psi_i. \tag{2}$$

Therefore the optical properties and optimal structure of a semitransparent-OPV/MOLED device can be investigated by applying optical admittance analysis technique, using Eqs. (1) and (2). This method has been applied successfully for the design of semitransparent heterojunction OPV cells [6,17]. In this work, the wavelength dependent refractive indices of indium tin oxide (ITO) and organic semiconducting layers in the semitransparent-PV/MOLED system were measured using the variable angle spectroscopic ellipsometry. An optimal structure of ZnPc:C_{60} (35 nm)/C_{60} (25 nm)/4,7-diphenyl-1,10-phenanthroline (Bphen) (7 nm)/Ag (30 nm)/CF_X /NPB (55 nm)/Alq_3:C545(25 nm)/Alq_3 (25 nm)/LiF (0.7 nm)/Al (150 nm) was thus optimized to enhance the absorption in the front semitransparent OPV cell and high output of the emitted light by the MOLED unit at 530 nm.

In addition to the device design and the materials selection, an optical transparent and electrical conductive inter electrode that functions simultaneously as a cathode for the front semitransparent OPV cell and an anode for the MOLED unit plays a critical role in determining the device performance. An ultra-thin plasma-polymerized fluorocarbon film (CF_X)-modified silver interlayer (Ag/CF_X) was used to vertically connect the front OPV cell and the rear MOLED unit. An Ag/CF_X bi-layer has been applied for making high performance top-emission OLEDs [18] and can be made easily without causing damage to the underlying organic layers. An optical admittance analysis was used to study the optical properties and optimize the structure of the semitransparent-OPV/MOLED devices. The performance

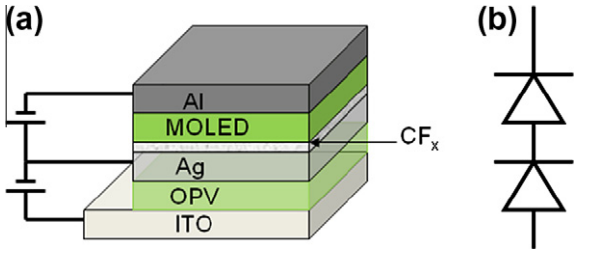

Fig. 1. Device structure and circuitry diagram of the device components. (a) Schematic diagram of an integrated OPV/MOLED device, with a layer configuration of glass/ITO/ZnPc:C_{60} (35 nm)/C_{60} (25 nm)/Bphen (7 nm)/Ag (30 nm)/CF_X/NPB (55 nm)/Alq_3:C545 (25 nm)/Alq_3 (25 nm)/LiF (0.7 nm)/Al (150 nm). (b) A schematic equivalent circuitry of the integrated device.

of the OLED and OPV components in the stacked devices was shown to have a luminous efficiency of 11.5 cd/A operated at 4.5 V and a PCE of 3.30%, achieving as high as 88% of the performance measured for the discrete control OPV cell. A cross sectional view of the structure of the integrated device is shown in Fig. 1(a). A schematic equivalent circuitry of the semitransparent-OPV/MOLED device is illustrated in Fig. 1(b).

The incident photon to current conversion efficiency (IPCE) measured for the semitransparent OPV cells and the EL spectra measured for the MOLEDs in the integrated device are plotted in Fig. 2(a). ZnPc:C_{60}-based semitransparent OPV cells thus fabricated have an optical transparency of >70% at 530 nm, allowing the emitted light from the bottom MOLED with a peak EL wavelength of 530 nm to pass through with a very low absorption lost. As shown in Fig. 2(a), the emission peak from the MOLED complementarily falls within the valley of the IPCE spectrum of the front semitransparent OPV cell. Such a result is achieved through an optical and optimal design of the device structure.

The results of the effect of the Ag interlayer thickness on the normalized absorbance of the front OPV cell and luminous efficiency of MOLED in the integrated device, with the normalization taken reference with the control OPV and MOLED devices, are presented in Fig. 2. The luminous efficiency of an OLED without microcavity structure is about 45%, as depicted by the dash line in Fig. 2(b). The calculation results indicate that the maximum luminous efficiency of the MOLED in the integrated devices can be achieved at an Ag interlayer thickness of 20 nm. On the other hand, the maximum light absorption by the front semitransparent OPV cell occurs when the thickness of the Ag layer is over 60 nm. A shaded region as depicted in Fig. 2(b) corresponds to the required Ag interlayer thickness to achieve high light absorption by the front semitransparent OPV cell and the high luminous efficiency of the rear MOLED in the integrated device. Based on the simulation results, an Ag interlayer thickness of 30 nm was selected as an optimal solution, corresponding to a light absorbance in the front OPV cell equivalent to 97% of a control OPV cell and, a luminous efficiency of a rear MOLED equivalent to 86% of a control MOLED, respectively.

The results of simulated and measured EL spectra obtained for a normal OLED, a discrete MOLED and an MOLED in the integrated devices are shown in Fig. 3(a) and (b). The wavelength of peak emission by the MOLED in the integrated device is located at 521 nm, which is hypsochromically shifted from 526 and 531 nm, the emission wavelengths for the single MOLED and the OLED, respectively. The full width at half maximum (FWHM) of the emission band is 33 nm, which is the same as that for the control MOLED and smaller than 58 nm for a conventional OLED.

The current density–voltage (J–V) characteristics of the OPV in the integrated device as well as that for a control cell, measured under air mass 1.5 global (AM1.5G) irradiation of 100 mW/cm^2, are shown in Fig. 4(a). The control cell, with a configuration of glass/ITO/ZnPc: C_{60}(35 nm)/C_{60}(25 nm)/Bphen(7 nm)/Ag(100 nm), was fabricated for comparison studies. The control device shows a PCE of 3.76%, a fill factor (FF) of 58.9% and a short-circuit current density (J_{SC}) of 11.4 mA/cm^2. The corresponding values for the upper OPV cell in the integrated semitransparent-OPV/MOLED device are 3.30%, 57.2% and 10.5 mA/cm^2. The open circuit voltages (V_{OC}) measured for the front OPV cell in the integrated device is the same as

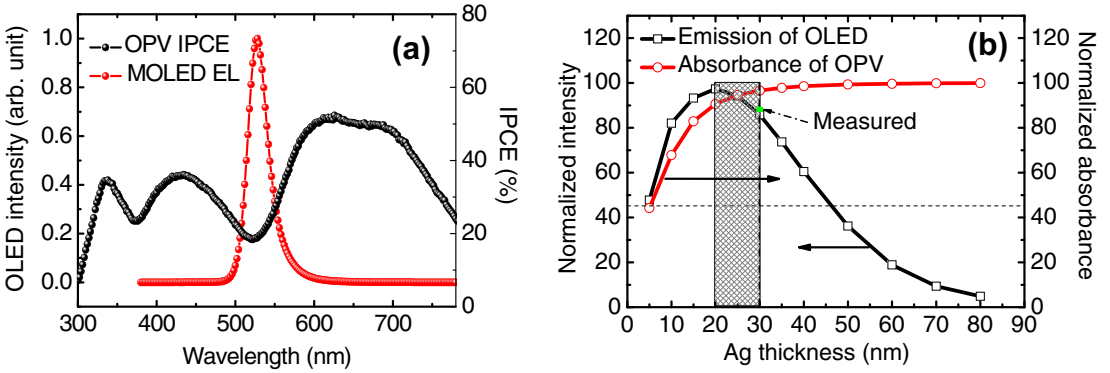

Fig. 2. Spectral response and electroluminescence characteristics of the device. (a) IPCE and EL emission spectra measured for the semitransparent OPV cell and the MOLED in the integrated device. (b) Calculated results showing the effect of Ag interlayer thickness on absorbance and emission of the integrated device (normalization is taken with reference to a discrete MOLED and a semitransparent OPV cell having identical structures used in the integrated device). The dash line refers to the normalized luminous efficiency measured for a normal OLED, which is equivalent to 45% of an MOLED.

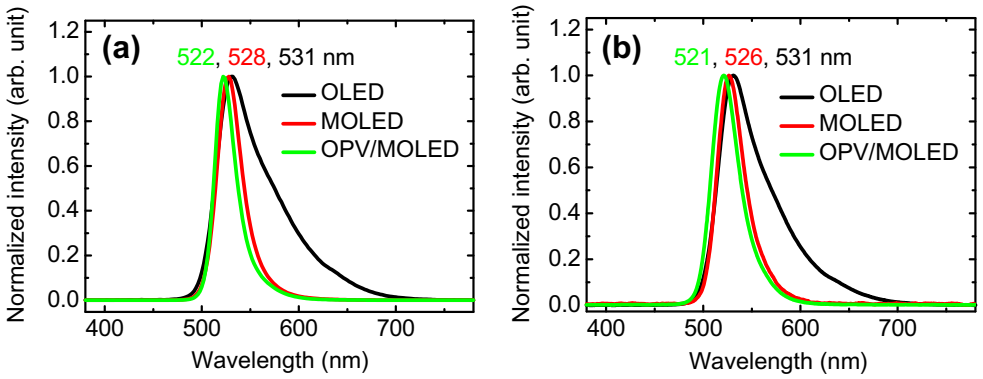

Fig. 3. Electroluminescence of OLEDs. (a) Simulated EL spectra obtained for a set of structurally identical light emitting diodes of a normal OLED, a discrete MOLED and an MOLED in an integrated device. (b) EL spectra measured for a normal OLED, a discrete MOLED and an MOLED in an integrated device.

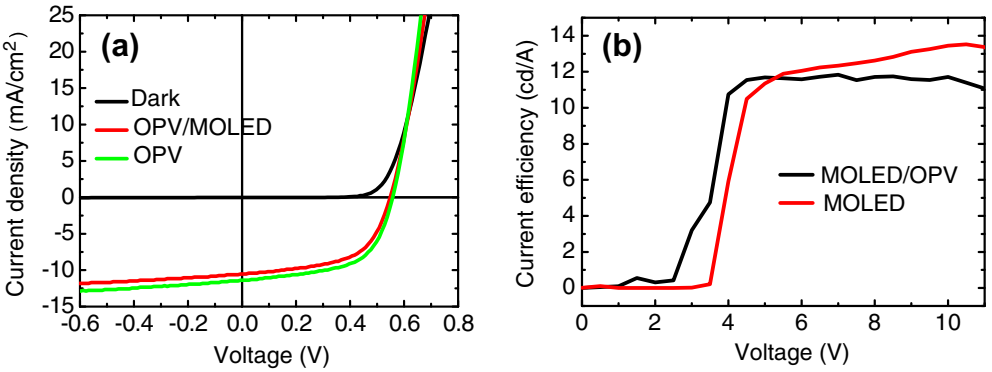

Fig. 4. Power conversion and luminous efficiency of the device, (a) *J–V* characteristics measured for a control OPV cell and a semitransparent OPV cell in the integrated device under AM1.5G. (b) Luminous efficiency measured for a control MOLED and an MOLED in the integrated MOLED/OPV device.

Table 1
A summary of luminous efficiency measured for a control MOLED and an MOLED in the integrated OPV/MOLED device at 4.5 V, and photovoltaic characteristics measured for a control OPV and a front semitransparent OPV in the integrated OPV/MOLED device under AM1.5G irradiation.

Device	EL peak position (nm)	FWHM (nm)	Luminous efficiency (cd/A)	
Control MOLED	526	32	10.5 (at 4.5 V)	
OPV/MOLED	521	33	11.5 (at 4.5 V)	
	V_{OC} (V)	FF (%)	J_{SC} (mA/cm^2)	PCE (%)
Control OPV	0.56	58.9	11.4	3.76
OPV/MOLED	0.55	57.2	10.5	3.30

the control device. It is interesting to note that the PCE obtained for the integrated device is as high as 88% of that for the reference OPV cell, labeled as "Measured" in Fig. 2(b). The results of the luminous efficiency measured for a discrete MOLED and an MOLED in the integrated device are given in Fig. 4(b). The luminous efficiency of the rear MOLED unit in the integrated device achieves 11.5 cd/A as compared to that of 10.5 cd/A for a control MOLED at 4.5 V, as shown in Fig. 4(b). Table 1 lists a summary of luminous efficiency measured for a control MOLED and an MOLED unit in the integrated OPV/MOLED device, as well as the photovoltaic characteristics measured for a control OPV and a front semitransparent OPV unit in the integrated OPV/MOLED device. The functional semitransparent-OPV/MOLED, based on an integration of organic light transmissible devices thus demonstrated, has the potential to create an organic optical sensor system capable of providing the power by absorption of the ambient illumination by the front semitransparent OPV cell. The accomplishment of this work would help to develop an organic sensor platform technology for application in organic electronics including organic optical switches and other organic photonic logic circuits.

In conclusion, a high performance integrated organic electronic device comprises of a ZnPc:C_{60}-based semitransparent OPV cell and an Alq_3:C545-based OLED was demonstrated. The front OPV cell is highly transparent to the emitted light from the underneath OLED unit. It serves as an ambient light absorbing coating to improve the optical signal/noise contrast of the OLED. The integrated functional semitransparent-OPV/OLED device possesses both a high power conversion efficiency of 3.30% measured under AM1.5G irradiation and a high luminous efficiency of 11.5 cd/A operated at 4.5 V.

Acknowledgments

The work of F.R. Zhu was supported by Hong Kong Baptist University Strategic Development Fund under Grant SDF10-0118-P01 and Faculty Research Grant FRG2/10-11/002.

References

[1] B. Walker, A.B. Tamayo, X.D. Dang, P. Zalar, J.H. Seo, A. Garcia, M. Tantiwiwat, T.C. Nguyen, Adv. Funct. Mater. 19 (2009) 3063.
[2] H.Y. Chen, J.H. Hou, S.Q. Zhang, Y.Y. Liang, G.W. Yang, Y. Yang, L.P. Yu, Y. Wu, G. Li, Nat. Photonics 3 (2009) 649.
[3] L.S. Liao, K.P. Klubek, Appl. Phys. Lett. 92 (2008) 223311.
[4] D. Han, H. Kim, S. Lee, M. Seo, S. Yoo, Optics Express 18 (2010) A513.
[5] Y. Galagan, M.G. Debije, P.W.M. Blom, Appl. Phys. Lett. 98 (2011) 043302.
[6] X. Wang, G.M. Ng, J.W. Ho, H.L. Tam, F.R. Zhu, IEEE J. Select. Topics Quant. Electron. 16 (2010) 1685.
[7] M. Thomschke, S. Hofmann, S. Olthof, M. Anderson, H. Kleemann, M. Schober, B. Lüssem, K. Leo, Appl. Phys. Lett. 98 (2011) 083304.
[8] L.W. Tan, C.C. Chum, K.S. Ong, X.T. Hao, E.C.W. Ou, F.R. Zhu, J. Mater. Sci. Mater. Electron. 18 (2007) 913.
[9] P. Peumans, S.R. Forrest, Appl. Phys. Lett. 76 (2000) 3855.
[10] C.J. Yang, T.Y. Cho, C.L. Lin, C.C. Wu, Appl. Phys. Lett. 90 (2007) 173507.
[11] C.J. Yang, T.Y. Cho, Y.Y. Chen, C.J. Yang, C.Y. Meng, C.H. Yang, P.C. Yang, H.Y. Chang, C.Y. Hsueh, C.C. Wu, S.C. Lee, Appl. Phys. Lett. 90 (2007) 233512.
[12] J. Park, J. Lee, D. Shin, J. Display Technol. 6 (2010) 247.
[13] J.G. Xue, S.R. Forrest, Appl. Phys. Lett. 82 (2003) 136.
[14] Y. Ohmori, H. Kajii, M. Kaneko, K. Yoshino, M. Ozaki, A. Fujii, M. Hikita, H. Takenaka, T. Taneda, IEEE J. Select. Top. Quantum Electron. 10 (2004) 70.
[15] C.J. Yang, T.Y. Cho, C.L. Lin, C.C. Wu, J. SID 16 (2008) 691.
[16] J.Y. Lee, S.T. Connor, Y. Cui, P. Peumans, Nano Lett. 10 (2010) 1276.
[17] G.M. Ng, E.L. Kietzke, T. Kietzke, L.W. Tan, P.K. Liew, F.R. Zhu, Appl. Phys. Lett. 90 (2007) 103505.
[18] Y.Q. Li, L.W. Tan, X.T. Hao, K.S. Ong, F.R. Zhu, L.S. Hung, Appl. Phys. Lett. 86 (2005) 153508.
[19] T. Nakayama, Y. Itoh, A. Kakuta, Appl. Phys. Lett. 63 (1993) 594.
[20] N. Takada, T. Tsutsui, S. Saito, Appl. Phys. Lett. 639 (1993) 2032.
[21] F.R. Zhu, P. Jennings, J. Cornish, G. Hefter, K. Luczak, Sol. Energy Mater. Sol. Cells 49 (1997) 163.
[22] H.A. Macleod, Adam Hilger Ttd, Bristol, second ed. 1986, p. 15.

as $CuInS_2$ and CdSe, the organic and inorganic phase are expected to contribute differently to charge carrier generation [9,14,15]. The resulting distribution of the carrier concentration and, consequently, the driving forces experienced by the charge carriers will be strongly dependent on the position within the device. In the organic phase, light absorption gives rise to the formation of excitons. As in all purely excitonic solar cells [1–3,16,17], these excitons need to diffuse to the heterojunction interface within their lifetime in order to dissociate into free charges. In the instant of dissociation, the hole remains in the organic phase, while the electron resides in the inorganic material. Then, a strong gradient in the chemical potential drives electrons and holes away from the exciton dissociation interface; in doing so, this gradient complements the action of the built-in voltage within the organic phase [18]. In the inorganic semiconductor, on the other hand, electron–hole pairs are photo-generated and separated directly in the bulk wherever a non-vanishing electric field is present. The such generated electrons and holes reside in the same material (i.e., chemical phase) and have a similar spatial distribution. Thus, the gradient of the chemical potential drives carriers in the same direction rather than selectively to the cathode or anode, respectively [18]. It is the interplay between this diffusional motion and the carrier drift due to the electric field that determines the output characteristic of the devices. Major processes determining the cell operation such as carrier separation, recombination, and transport, be that in the bulk or at the interface, have, at least in part, these driving forces in common. These forces depend, of course, on material-related transport parameters such as the carrier mobility μ and the static relative dielectric constant ϵ_r.

The values of these parameters that can be possibly achieved in inorganic materials are much larger than those associated to the organic materials. The values of ϵ_r for small band-gap inorganic materials exceed 8.0 in the crystal [12,13]; in some cases, such as PbS, also values beyond 100.0 can be reached. For typically employed organic materials, on the other hand, the values of ϵ_r range from 2.5 to ca. 4.0 [19,20].

In all hybrid inorganic–organic solar cells, the inorganic component nominally serves as electron transporting material due to low injection barriers towards common cathode materials and electron mobilities exceeding 250 $cm^2/V\,s$ in bulk samples [12]. When going to thin films, the electron mobility drops by at least an order of magnitude (e.g., $\mu_{Hall} = 30\ cm^2/V\,s$ at 300 K for CdS [21]) due to the presence of grain boundaries [21], local variations in stoichiometry, and impurities [22]. Nevertheless, such electron mobilities surpass the highest reported values for organic semiconductors, i.e., $\mu_{FET} = 3\ cm^2/V\,s$ for a perylene diimide single crystal [23]. The highest hole mobility value reported for organic semiconductors is $\mu_{FET} = 20\ cm^2/V\,s$ for a rubrene single crystal [24].

There has been considerable theoretical effort in elucidating the role of the carrier mobility in purely excitonic solar cells [25–31]. Macroscopic simulations based on a drift–diffusion model demonstrated the profound impact of the carrier mobility [27,28] and, more specifically, its field-dependence [25,26] on the *I–V* curve. As another quantity, that strongly depends on the carrier mobilities and ϵ_r, the bimolecular recombination rate was shown to be of significant importance for the understanding of the behavior of the devices [18,27]. The extent to which this rate influences the *I–V* characteristic was shown to depend on the heterojunction morphology, i.e., whether recombination occurs in a perfectly blended (i.e., effective medium) [28], in a partially blended [27], or an entirely phase-separated system [18,25]. Microscopic simulations have been employed to describe the interplay of carrier generation, recombination mechanisms, and transport processes in a given heterojunction geometry at a consistent level of theory [29–31]. Such studies point out that the device efficiency is predominantly determined by the *ratio* μ_p/μ_n of the majority carrier mobilities in their respective preferentially conducting material rather than being influenced by the absolute values of the mobilities [29–32]. Moreover, these works jointly state that any mismatch between the carrier mobilities, i.e., any ratio μ_p/μ_n differing from unity, detrimentally affects the PCE of the solar cell.

The scope of this work is to theoretically investigate the impact of the charge carrier mobilities μ and the dielectric constants ϵ_r on the operation of organic–small band gap inorganic hybrid devices. We particularly focus on comprehending the influence of the two distinct carrier generation mechanisms on the subsequent charge carrier transport and, hence, on relevant device output parameters, i.e., the open circuit voltage, V_{oc}, the short circuit current, j_{sc}, the shape of the *I–V* characteristic, and the power conversion efficiency (PCE). In addition to μ and ϵ_r, also the transport levels can be considered as material-related transport parameters. We demonstrated in a previous work, that the offset between hole transport levels (or the lack thereof) crucially influences the shape and V_{oc} of the *I–V* characteristic [15]. The inclusion of the transport level *offsets* into our study is, thus, pivotal to achieve a more detailed understanding of the relation between the material properties and the driving forces of the photocurrent. One major challenge in this context is to discriminate between the various effects that might be caused by changes in μ and ϵ_r; these two parameters were demonstrated to enter a subtle interplay of field-dependent mobilities, recombination rates, generation-, as well as morphology-determined processes in excitonic solar cells [25–32]. To conveniently monitor quantities and processes that depend on μ and ϵ_r, we utilize a two-dimensional drift–diffusion approach [15] rather than a microscopic description. In the framework of such a model, the generation of charges and its dependence on the heterojunction morphology can be controlled by introducing a spatially dependent generation rate. To further separate possible influences of the field-dependent mobilities and the recombination rates on the *I–V* curve from morphology-determined processes, we will concentrate on transport in a bilayer structure. The impact of the heterojunction geometry and the nature of the contacts, both representing two major efficiency-limiting factors, has already been studied in detail elsewhere [15].

Below, we will first introduce the details of the model. Then, a representative set of material parameters is presented that allows us to comprehensively study the extent to which changes in μ and ϵ_r (i) depend on the generation

mechanism and (ii) affect the I–V curves due to field-dependent mobilities and altered recombination rates. Based on the leading effects identified to that point, we will analyze different (fictitious) level alignment situations and, finally, heterojunctions formed by actual materials.

2. The device model

2.1. Model equations

To get a deeper understanding of the device behavior due to variations (i) of the transport level offsets between the donor and acceptor material and (ii) of the mobility and dielectric constants in the light of the interplay of bulk and interface carrier generation, a drift–diffusion model for the simulation of carrier transport in a two-dimensional device cross-section is proposed. Such a two-dimensional model offers, in principle, the possibility to regard the actual geometry of the heterojunction. The modeled cross-section, shown in Fig. 1(a), comprises a 100×100 nm active area containing the two semiconducting materials. Throughout this work, a flat heterojunction is placed at the center of the cell parallel to the electrodes (dotted line in Fig. 1(a)). In all devices considered in this work, ohmic contacts were assumed (cf. Appendix). Due to this choice of contacts, the carriers are instantaneously abstracted from the device when reaching the contact-semiconductor interface. The details of the system of model equations (comprising the continuity, current density, and Poisson equation) and the determination of the incoming photon flux $\Phi(\mathbf{r})$ are shown in Appendix.

For each position of the device, a generation $\mathbf{G}(\mathbf{r})$ rate needs to be specified to account for the appropriate generation mechanism. Upon photon absorption, charges are generated (i) indirectly via exciton formation in the organic phase and dissociation at the heterojunction and (ii) directly throughout the inorganic material. In order to get an overall understanding of the role of the two generation mechanisms, we explicitly introduce two scenarios that yield the boundaries of the possibly generated number of charge carriers, i.e., an upper limit and a lower limit. In both limits, incoming light is assumed to directly generate charge carriers. The upper limit can be expressed as

$$G_{(n,p)}(\mathbf{r}) = \Phi(\mathbf{r}) \tag{1}$$

with $\mathbf{r} = (x_i, y_j)$ being a discrete grid point anywhere within the device. Keeping in mind that our device is separated in two different parts (A: acceptor, D: donor) with different intrinsic parameters, a generation confined to the inorganic phase yields the following expression for the lower limit:

$$G_{(n,p)}(\mathbf{r}) = \begin{cases} 0 & \mathbf{r} = (x_i, y_j) \in D \\ \Phi(\mathbf{r}) & \mathbf{r} = (x_i, y_j) \in A. \end{cases} \tag{2}$$

Here, we assume that the charge carrier generation is driven thermodynamically in the inorganic phase due to low exciton binding energies [12]. Beyond these limiting cases, our model is capable to consider the actual carrier generation due to exciton formation in the bulk of the organic phase. The associated method aiming at modifying G due to exciton migration and dissociation at the *heterojunction* is shown in detail elsewhere [15]. Note that field-assisted exciton dissociation rates as introduced in [33,34] and used in [35,36], i.e., the possibility to generate carriers from excitons in the *bulk* of the organic phase, were not taken into account.

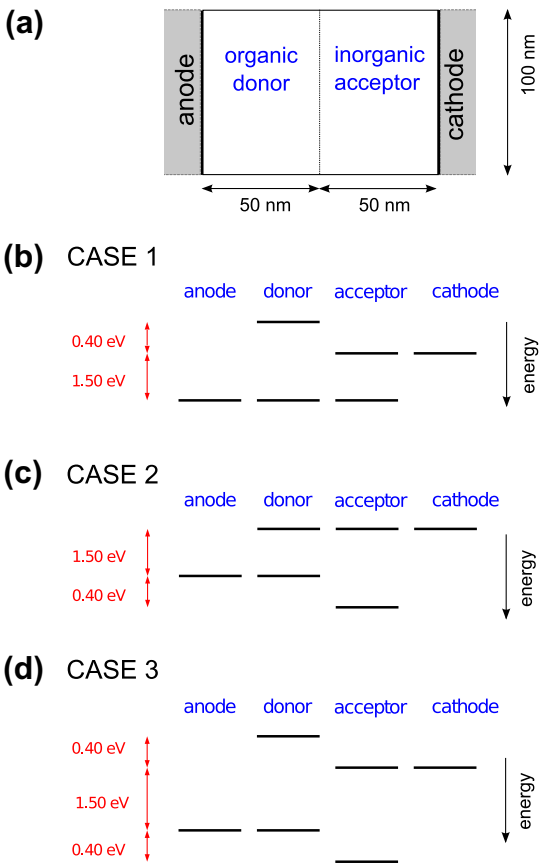

Fig. 1. (a) Schematic cross-section of the device containing the modeled area (solid rectangle), the location of the heterojunction (dotted line), and the location of the boundaries associated to Ohmic contacts (bold black lines). (b–d) Illustration of the energetic alignment of the transport levels for the model systems studied in this work. (b) Case 1, vanishing hole transport level offset ($\Delta E_p = 0$, $\Delta E_n = 0.4$ eV) (corresponds to P3EBT/$CuInS_2$). (c) Case 2, vanishing electron transport level offset ($\Delta E_p = 0.4$ eV, $\Delta E_n = 0$). (d) Case 3, equally set off transport levels $\Delta E_p = \Delta E_n = 0.4$ eV.

Also in the case of charge carrier recombination a distinction between the organic and the inorganic phase is necessary. The bimolecular charge carrier recombination in organic material is expressed by a Langevin-type rate

$$R_{(n,p)}(\mathbf{r}, \mathbf{E}, t) = k_r(\mathbf{r}, \mathbf{E}) n(\mathbf{r}, t) p(\mathbf{r}, t) \tag{3}$$

where the recombination rate constant k_r is given by [37]

$$k_r(\mathbf{r}, \mathbf{E}) = \frac{q}{\epsilon(\mathbf{r})} \left[\mu_n(\mathbf{r}, \mathbf{E}) + \mu_p(\mathbf{r}, \mathbf{E}) \right] \tag{4}$$

Recent investigations of the validity of this recombination rate quantitatively demonstrate how the relationship $k_r(\mu)$ depends on the structure of the material at the nanoscale [29]. Assuming a bimolecular recombination rate being proportional to $n(\mathbf{r}, t) p(\mathbf{r}, t)$, k_r according to Eq. (4)

represents the upper limit [29]. However, the overall deviation of k_r expressed by Eq. (4) from the actual value, that is known from microscopic simulations, becomes minimal for the ratio μ_e/μ_h of unity [29,38], i.e., the ratio that is used throughout this study (*vide infra*). Note that this ratio μ_e/μ_h must not be confused with the ratios $\mu_e^{\text{inorganic}}/\mu_e^{\text{organic}}$ and $\mu_h^{\text{inorganic}}/\mu_h^{\text{organic}}$, respectively. Reduced recombination rates as described by Deibel et al. [28,39] or Arkhipov and co-worker [40] were not taken into account.

Finding an appropriate description for the recombination in the inorganic phase is more involved, since the morphology of the inorganic layers can strongly vary depending on the processing conditions [4,5,7,9,42]. While there are studies with single- and polycrystalline layers available [5,9,42], also an agglomeration of nanoparticles served as inorganic layer [4,7]. One can readily expect that both cases have in common that recombination is strongly influenced by the probability of electron–hole encounter, since the motion of carriers is predominantly limited by hopping. The corresponding diffusion-limited recombination rate is, thus, proportional to $n(\mathbf{r},t)p(\mathbf{r},t)$. However, to the best of our knowledge, comprehensive theoretical models that supply an accurate expression for $k_r(\mu)$ in such disordered inorganic solids are not available. Yang et al. [14] suggested that Shockley–Read–Hall (SRH) recombination can become a dominating pathway for polycrystalline layers forming inorganic heterojunctions. Such SRH-type rates rely on cross-sections that describe the capture of mobile carriers by trap states. The concept of cross-sections is based on scattering theory [43] and is, thus, inherently inappropriate for disordered materials. Moreover, the parameters entering the cross-sections are largely undetermined due to the mostly unknown number and electronic nature of the traps involved. On the other hand, "classic" Langevin k_r (i.e., Eq. (4)) have been shown to profoundly overestimate the experimentally determined recombination rates [43]. Considering the arguments above, the most straight-forward and convenient way is, therefore, to consider (i) a Langevin rate according to Eqs. (3) and (4) and (ii) to consider this rate as an upper-limit for bimolecular recombination. Even with such significantly overestimated rates, the impact of recombination is far less pronounced than the influence of other parameters under study here (*vide infra*).

The field dependence of the charge carrier mobility is given in a Poole–Frenkel form ([44]) by

$$\mu_{(n,p)}(\mathbf{r},\mathbf{E}) = {}^0\mu_{(n,p)}(\mathbf{r})\exp(\gamma\mid\mathbf{E}\mid) \tag{5}$$

with ${}^0\mu_{(n,p)}(\mathbf{r})$ denoting the mobility at zero field and the constant $\gamma = 0.5\times10^{-4}\ \mathrm{m}^{-\frac{1}{2}}\mathrm{V}^{\frac{1}{2}}$ [36].

2.2. Material properties

The major material-intrinsic parameters relevant for the carrier transport are the electron and hole mobilities, the dielectric constants, and the relative position of the electron and hole transport levels. To capture the influence of the energetic alignment of the transport levels, we propose three representative model systems, whose specific level alignment is illustrated in Fig. 1. In the first model system, Case 1, depicted in Fig. 1(b), the hole transport levels lack an offset. This level alignment corresponds to an actual heterojunction consisting of P3EBT (poly[3-(ethyl-4-butanoat)tiophene-2,5-diyl] (Fig. 2) and $CuInS_2$ [15]. Moreover, fictitious systems with degenerate electron transport levels (Case 2) and transport levels with equivalent electron and hole barrier heights (Case 3) are proposed. The transport level offsets $\Delta E_n = |E_C - E_{LUMO}|$ and $\Delta E_p = |E_V - E_{HOMO}|$ are summarized in Table 1. In addition to these three model systems, two systems combining the polymer P3HT (poly(3-hexyltiophene-2,5-diyl)) or F8T2 (poly[(9,9-dioctylflourenyl-2,7-diyl)-co-(bitiophene)]), Fig. 2, with the inorganic acceptor $CuInS_2$ were studied. Their characteristic transport level alignment is given in Table 1 as well. All further default input-parameters for the simulations are given in Table 2. Note, that a default value of $\epsilon_r = 1$ in the organic layer yields the largest possible recombination rate (cf. Eq. (4)) with respect to the dielectric constant.

The mobilities ${}^0\mu(\mathbf{r})$ are varied such that both $\mu_e^{\text{inorganic}}$ and $\mu_h^{\text{inorganic}}$ remain larger or at least equal with respect to the values of μ_e^{organic} and μ_h^{organic}. By default, the inorganic mobilities are assumed to exceed the organic mobilities by two orders of magnitudes (cf. Table 2). However, we assume that μ_e equals μ_h within a phase.

3. Results and discussions

We study the three different energetic cases listed in Fig. 1 by varying the ratio of the mobilities and the dielectric constants between the organic and inorganic phase. The ohmic contacts ensure that the built-in voltage $V_{\text{built-in}}$, given by $E_C - E_{HOMO}$, is fixed at a value of 1.5 V. Further, we will have a look at (i) the two different charge carrier generation scenarios, Eqs. (1) and (2), and (ii) at the impact of field-dependent charge carrier mobilities and recombination rates on the device performance and the shape of the *I–V* characteristic. If not denoted differently, the default input parameters for all calculations can be found in Table 2. In the last section, we apply the model

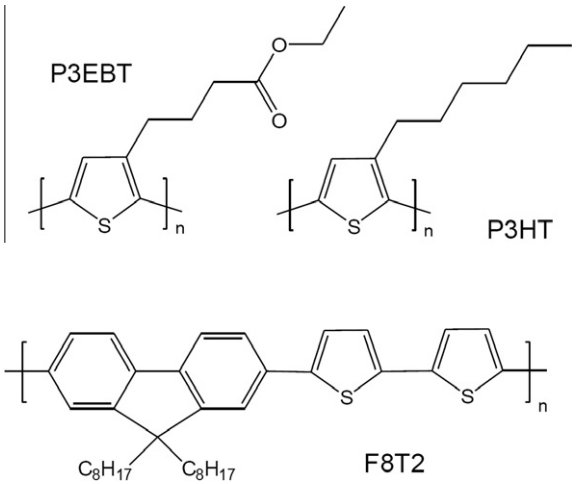

Fig. 2. Chemical structure of the polymers considered in this work.

Table 1
Energetic alignment of the transport levels for the actual and artificial materials considered in this work. The difference in the electron and hole transport levels are denoted by ΔE_n and ΔE_p, respectively.

	Case 1 (P3EBT/$CuInS_2$)	Case 2	Case 3	P3HT/$CuInS_2$	F8T2/$CuInS_2$
ΔE_n/eV	0.40	0.00	0.40	0.60	1.60
ΔE_p/eV	0.00	0.40	0.40	0.40	0.20

Table 2
Default input values of the temperature and the parameters zero-field mobility ${}^0\mu$, dielectric constant ϵ_r, and absorption coefficient α for the organic donor and the inorganic acceptor layer.

	Donor	Acceptor
${}^0\mu_n/\mathrm{cm}^2/\mathrm{V\,s}$	10^{-8}	10^{-6}
${}^0\mu_p/\mathrm{cm}^2/\mathrm{V\,s}$	10^{-8}	10^{-6}
ϵ_r	1	10
α/m^{-1}	2×10^7	2×10^7
T/K	298.15	298.15

to the three systems P3EBT/$CuInS_2$, P3HT/$CuInS_2$, and F8T2/$CuInS_2$.

3.1. Impact of generation profiles and recombination

To gain a better quantitative understanding of the interplay of charge carrier generation mechanisms that differ between the organic and inorganic materials, we discuss first two scenarios that limit the actual number of generated carriers from above and below: (i) in a best-case scenario, Eq. (1), all excitons formed in the polymer are assumed to dissociate instantaneously, i.e., all incident photons are directly converted to charge carriers. (ii) In the worst case scenario, the number of excitons that are formed and migrate towards the interface are assumed to give rise to negligible amount of mobile carriers. Thus, only carriers generated in the inorganic acceptor contribute to transport. This generation scenario is a valid lower limit due to an excitonic binding energy in inorganic materials being in the range of k_BT. Fig. 3 displays the I–V curves corresponding to the two generation scenarios in a Case 1-type device for varying mobilities μ and dielectric constants ϵ_r. During the variation of the ratio $\epsilon_r^{\mathrm{inorganic}}:\epsilon_r^{\mathrm{organic}}$, we keep the ratio $\mu_{p,n}^{\mathrm{inorganic}}:\mu_{p,n}^{\mathrm{organic}}$ at a default constant value of 10^2. Vice versa, the ratio $\epsilon_r^{\mathrm{inorganic}}:\epsilon_r^{\mathrm{organic}}$ is fixed at a value of 10 while changing $\mu_{p,n}^{\mathrm{inorganic}}:\mu_{p,n}^{\mathrm{organic}}$. In a first step (Fig. 3(a)–(d)), we omit (i) a possible field dependence of μ arising from local electric field changes and (ii) recombination effects the rate constant of which is indirectly proportional to the dielectric constant ϵ_r and directly proportional to the mobility.

A comparison of the set of curves displayed in Fig. 3(a), (b) and (c), (d) reveals that the photocurrent drops by at least a factor of ca. 4 when the carrier generation is confined to the inorganic material. The absolute value of the current density is, therefore, crucially determined by the efficiency of the charge generation in the organic material. The yield of charge carriers generated in the organic phase via exciton dissociation is limited by diffusion and therefore highly dependent on the interface structure of the solar cell [8,6,15,25]. Consequently, in the case of a flat interface as considered here, the second scenario according to Eq. (2) yields a more realistic number of photogenerated carriers than the first one, Eq. (1). When going to highly interpenetrated phases, such as observed, e.g., in polymer:PCBM blends [27,45] or nanoparticle:PCBM blends [7], carrier numbers approaching the first scenario need to be anticipated.

However, the qualitative trends in the *evolution* of the photocurrent–voltage dependence with varying transport parameters are independent from the actual generation scenario. The I–V curves change profoundly with increasing ϵ_r and μ in the inorganic phase (Fig. 3(a)–(d)). Inspecting the I–V curves in Fig. 3(b) and (d) corresponding to μ-ratios of 10^2 (squares) and 10^4 (diamonds) reveals an s-shaped section in the power quadrant. With increasing μ-ratio, this formation progresses, i.e., the slope of the curve at the inflection point becomes less steep. As can been seen further from the I–V curves in Fig. 3(c) (stars-circles), this s-shape appears to progress also with an increasing ratio of ϵ_r. Even though the I–V curves obtained for uniform generation (Fig. 3(a)) retain a diode-like shape, the maximum achievable slope in the power quadrant is reduced with increasing $\epsilon_r^{\mathrm{inorganic}}$. Such changes in the shape of the I–V curve result in photo-currents, in particular, short circuit currents j_{sc} that decrease with increasing ϵ_r- and μ-ratios. The open circuit voltage V_{oc}, on the other hand, remains (i) essentially unaffected by a change in the ϵ_r ratio and (ii) shifts only slightly towards lower values when increasing the μ-ratio (cf. curves stars-diamonds in Fig. 3(b) and (d)).

The trend in ϵ_r can be rationalized in terms of the electric field strength in the donor and acceptor phase that follows the condition $\epsilon_{\mathrm{D}}|\mathbf{E}|_{\mathrm{D}} = \epsilon_{\mathrm{A}}|\mathbf{E}|_{\mathrm{A}}$. When increasing the values of ϵ_r in the inorganic acceptor, the corresponding electric field $|\mathbf{E}|_{\mathrm{A}}$ is reduced with respect to its organic counterpart $|\mathbf{E}|_{\mathrm{D}}$. For $V_a < V_{\mathrm{oc}}$, the current density j, in particular the short circuit current density j_{sc}, decreases with increasing ϵ_r due to the smaller field in the inorganic phase (Fig. 3(a) and (c)). Values of ϵ_r as high as 10^2 limit the motion of the carriers almost to diffusion, since the drift force being proportional to $|\mathbf{E}|_{\mathrm{A}}$ becomes negligible. In the positive regime, i.e., $j > 0$, the current is determined by the amount of electrons that is able to pass the barrier of 0.4 eV into the organic phase (see Fig. 1(b)) at a given external voltage. This number is increased if the electric field $|\mathbf{E}|$ is higher in the organic than in the inorganic field phase, i.e., the ϵ_r-ratio exceeds 1:1. Beyond a certain ϵ_r-ratio, however, the electron current becomes insensitive to the actual field strength and saturates with $\epsilon_r^{\mathrm{inorganic}}$. Since this threshold is rather quickly reached, i.e., at an ϵ_r-ratio of ca. 5, j increases only slightly with increasing ϵ_r-ratio. The enhanced electric field $|\mathbf{E}|_{\mathrm{D}}$ is also responsible for the earlier onsets of the current increase and a slight increase of the open circuit voltage for higher dielectric constants.

Upon restricting generation to the acceptor, all I–V curves adopt an s-shape (Fig. 3(c) and (d)) apart from the one obtained for a μ-ratio of unity (stars). The appearance of the s-shape is due to the particular alignment of the

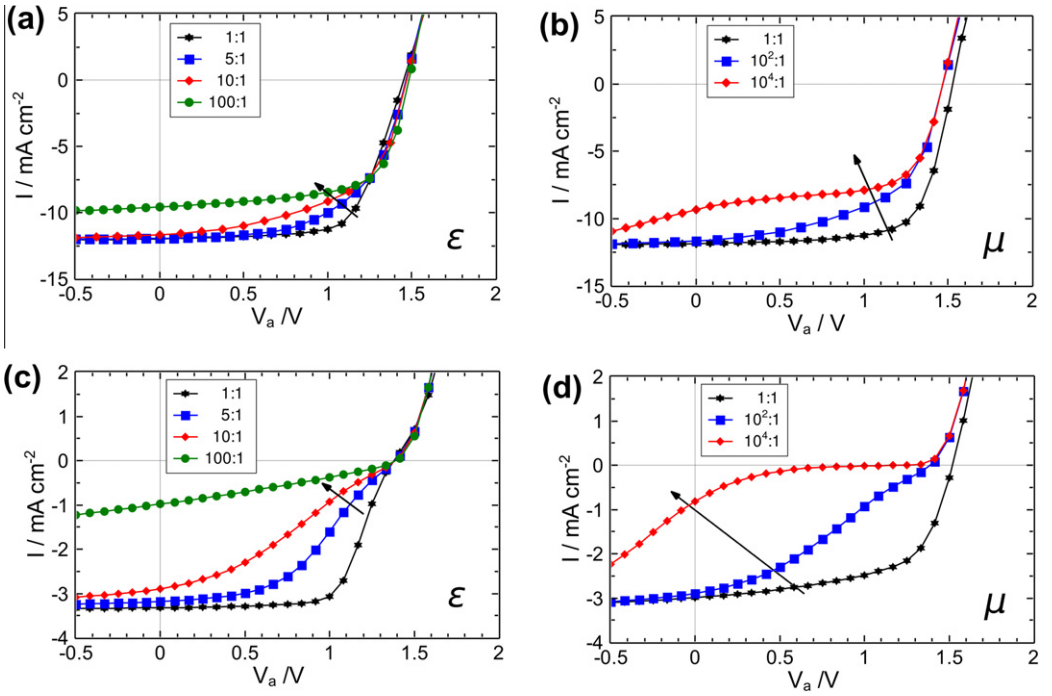

Fig. 3. *I–V* characteristics for a Case 1-type device (Fig. 1(b)) for different ratios of $\epsilon_r^{\text{inorganic}} : \epsilon_r^{\text{organic}}$ (left column) and $\mu_{(n,p)}^{\text{inorganic}} : \mu_{(n,p)}^{\text{organic}}$ (right column). Carrier generation is assumed to (i) occur homogeneously across the device (a), (b) and (ii) be confined to the inorganic phase (c), (d). The arrows indicate the evolution of the *I–V* curves with increasing ratios.

transport levels of the P3EBT/$CuInS_2$ system [15], as schematically indicated in Fig. 4(a). For biases approaching V_{oc} from below, the electric field can drive *holes* unhindered from anywhere in the device to the cathode due to the lack of an offset between the hole transport levels. This migration of holes is expected to occur even more pronounced in devices in which the energy E_V corresponding to the valence band edge of the inorganic component is less negative than the HOMO position E_{HOMO} of the organic material; such a situation is realized, e.g., in a ZnPc/n-Si hybrid solar cell [42]. However, electrons still cannot pass the energetic barrier (0.4 eV). Thus, their motion is determined by diffusion towards the cathode. As a result, electrons and holes move in the same direction and, therefore, lower the current density at voltages $V_a \approx V_{oc}$. This process is even supported by the fact, as we will discuss in detail below, that there is a higher charge carrier mobility in the acceptor phase which means that there is an *effective diffusional force* pointing from the anode to the cathode.

Increasing mobilities in the inorganic phase profoundly decreases the fill factor of the device Fig. 3(b) and (d). This is directly related to a mismatch in the hole mobilities $\mu_p^{\text{inorganic}}$ and μ_p^{organic}. Considering that diffusion is, according to the Einstein relation, determined by a diffusion constant being proportional to the mobility, holes diffuse faster through the inorganic layer than through the polymer. This spatial dependence of the diffusion constant is schematically indicated by arrows of differing lengths in Fig. 4(a). A hole located directly at the heterojunction experiences a diffusion constant being higher when facing the cathode than when facing the anode. Thus, there is an *effective diffusional force* drawing charge carriers into the inorganic phase [46]. It is important to note that this diffusion direction is not necessarily linked to the steepest gradient in carrier concentration. If the mobilities are assumed to be the same in both layers, there is no primarily preferred diffusion direction and, therefore, the motion is solely dominated by the drift term. It has to be emphasized that then also V_{oc} slightly increases (cf. Fig. 3(b) and (d)). For biases exceeding V_{oc}, the current increases due to higher mobilities in the inorganic phase.

When confining the carrier generation to the inorganic layer, any mobility ratio differing from 1:1 (i.e., $\mu_{(n,p)}^{\text{inorganic}} > \mu_{(n,p)}^{\text{organic}}$) yields an s-shape in the *I–V* characteristic (cf. Fig. 3(d)). We emphasize at this point that this particular shape arises solely due to the abovementioned diffusional advantage in the inorganic phase; neither recombination nor field-dependent mobilities were taken into account at this point.

Finally, we want to investigate to which extent the picture gained above is altered when field-dependent mobilities $\mu(\mathbf{E})$ and recombination effects R are taken into account. The situation is now more involved, since $\mu(\mathbf{E})$ (Eq. (5)) combines the influence of ${}^0\mu = \mu(\mathbf{E} = 0)$ and the ϵ_r-ratio due to the impact of the latter on the electric field distribution. Likewise, the recombination rate R, cf. Eqs. (3) and (4), is indirectly proportional to ϵ_r and directly proportional to the mobility $\mu(\mathbf{E})$. The corresponding *I–V* curves obtained for carrier generation confined to the inorganic phase are shown in Fig. 5(a) and (b). These *I–V* characteristics are clearly reminiscent to the curves obtained in Fig. 3(b) and (d); their qualitative evolution can be

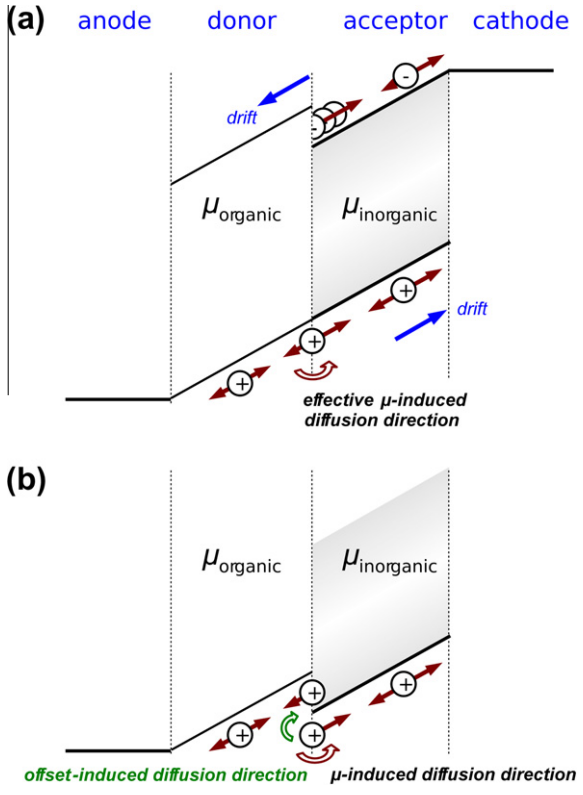

Fig. 4. Schematic illustration of the effective hole diffusion induced by (a) a difference in $\mu_p^{inorganic}$ and $\mu_p^{organic}$ and (b) by an offset in hole transport levels. Solid arrows at the charge carriers symbolize the diffusion current contribution for an acceptor-generated charge carrier at a given spot in the device for $V_a \lesssim V_{oc}$. Furthermore, the direction of motion dictated by the electric field is indicated by the "drift" arrows.

understood in terms of what has been discussed in Fig. 3(a), (c) and (b), (d). To better illustrate this behavior, the curves obtained in Fig. 3(c) and (d) are also indicated in Fig. 5(a) and (b) with open symbols and are connected to their respective counterparts (filled symbols) by an arrow.

When increasing the μ- or the ϵ_r-ratio, the values of the photocurrent do not follow the trend in the μ- and ϵ_r-ratio. This absence of an overall trend can be readily observed among the values of the short circuit current $j_{sc}(\mu, \epsilon_r)$ that are summarized in Table 5 in Appendix. Rather, two cases need to be distinguished due to the field-dependence of μ. (i) For a mobility ratio of 1:1 (Fig. 5(b), circles), the short circuit current (filled circles) becomes less negative compared to the ${}^0\mu$ case (open circles). Then, the *actual* mobilities associated to the two phases differ due to an electric field-strength $|\mathbf{E}|_D$ being larger than $|\mathbf{E}|_A$, i.e., an ϵ_r-ratio being larger than unity. (ii) For mobility ratios exceeding unity (squares and diamonds), the difference in electric field strengths gives rise to a *decrease* in the actual mobility ratio. As result, the short-circuit current becomes more negative. Moreover, this shift becomes more pronounced with increasing μ-ratio. The latter relationship has been already reported by Deibel et al. for effective media taken as a model for perfect donor–acceptor blends [28]. Along the same lines, the trend in the ϵ_r-ratios (Fig. 5(a)) can be rationalized: (i) an ϵ_r-ratio exceeding unity (squares and diamonds) enhances the difference in the electric field strength and, thus, decreases the actual $\mu(\mathbf{E})$ ratio. Then, more negative photo-currents are obtained (compare open and filled symbols). Increasing the ϵ_r-ratio (squares and diamonds) beyond unity increasingly enhanced this shift. (ii) Solely for the ϵ_r-ratio of 1:1 (circles) the behavior is reversed: due to a spatially constant field, the mobility-*ratio* becomes field-independent. The reduction of the photocurrent (closed circles) with respect to the ${}^0\mu$-case (open circles) is, thus, related to an enhanced recombination rate arising from the $\mu^{inorganic}(\mathbf{E})$ contribution.

3.2. Impact of the transport level alignment

Since, as discussed above, a vanishing hole transport level offset gives rise to a disadvantageous s-shaped *I–V* curve (Fig. 3(c) and (d)), it is interesting to compare these *I–V* curves to two other representative situations: (i) in Case 2 of Fig. 1, the electron transport levels are degenerate rather the hole ones. Based on previous experience in organic solar cells, material combinations with such a vanishing offset were avoided due to a small anticipated carrier generation efficiency. Until recently, it was considered an established fact that efficient exciton dissociation

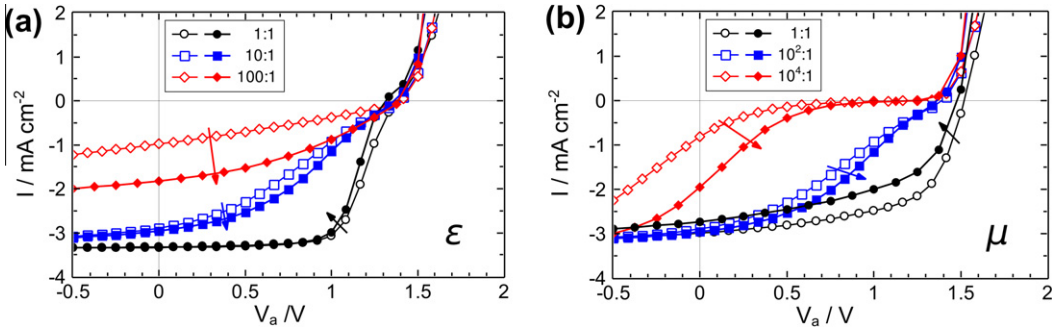

Fig. 5. *I–V* characteristics for a Case 1-type device (Fig. 1(b)) for different ratios of $\epsilon_r^{inorganic} : \epsilon_r^{organic}$ (left panel) and ${}^0\mu_{(n,p)}^{inorganic} : {}^0\mu_{(n,p)}^{organic}$ (right panel) with consideration of recombination and field-dependent mobilities. Carrier generation is assumed to be confined to the inorganic phase. For comparison, the *I–V* curves corresponding to field-independent mobilities and omitted recombination (Fig. 3(c) and (d)) are indicated with open symbols; arrows link the associated curves.

would require a minimum offset $\Delta E_n^{\min}$ [45,47,48]. However, efficient carrier generation was recently demonstrated in bulk heterojunction despite a very small offset in the electron transport levels [49]. It is, thus, worthwhile to investigate the impact of degenerate electron transport levels on carrier transport. (ii) Case 3 of Fig. 1 refers to non-vanishing offsets between the electron and the hole transport levels; this situation is realized for most combinations of materials. To be able to directly compare the values of the short circuit currents and open circuit voltages corresponding to these two level alignments with the P3EBT/$CuInS_2$ system (Case 1 of Fig. 1), we set non-vanishing level offsets to 0.4 eV.

In the following, we will restrict our discussion to the charge carrier generation in the inorganic acceptor according to Eq. (2). As shown in the previous section, this generation scenario reliably yields the major trends in the *I–V* curves upon parameter variation and, moreover, quantitative insights for flat heterojunctions. Also field-dependent mobilities and charge carrier recombination effects will not be considered, because they only have a minor influence on the dependence of the device performance when varying the dielectric constant and mobility ratio between the two different layers (cf. Fig. 5(a) and (b)). Thus, it needs to be stressed that *all* effects observed in the following are transport effects solely caused by the material specific parameters, i.e., the transport levels, the dielectric constants, and the mobilities.

In Fig. 6, one can see the *I–V* characteristics resulting from the variation of the material parameters μ and ϵ_r in the case of degenerate electron transport levels (Fig. 6(a) and (b)) and equidistantly set off transport levels (Fig. 6(c) and (d)). In comparison to the case of vanishing hole transport levels (Fig. 3(c) and (d), the variation of the *I–V* curves with μ and ϵ_r are considerably less marked. In strong contrast to Case 1, where the vanishing offset ΔE_p in the *hole* transport level leads to an s-shape in the *I–V* characteristic, the vanishing *electron* transport level offset ΔE_n preserves a diode-shaped *I–V* curve. The reason for this effect is twofold. (i) In order to contribute to the photo-current, electrons are required to diffuse to the cathode (cf. Fig. 4(a)). As the electrons are already generated next to the cathode, a level offset at the interface is not limiting the diffusion current. On the contrary, *electrons* are subject to a mobility-induced effective diffusion as observed before for holes; electrons that are trying to diffuse away from the cathode into the polymer are drawn back to the inorganic material and are, thus, enhancing the overall diffusion current. (ii) Holes contribute to the photo-current if they diffuse to the anode. As shown schematically in Fig. 4(b), holes located at the heterojunction consider migration into the polymer energetically favorably if a positive energetic offset is present. This effective diffusion of holes into the *donor* is enhancing the photocurrent.

Taking further the argument from above, we would immediately expect that the situation encountered in Case 1 is only recovered if the mobility is higher in the organic phase than in the inorganic phase, i.e., the μ-ratio becomes smaller than unity. Then, an effective μ-induced diffusion should decrease the photo-current, since it drives electrons away from the cathode. Indeed, the simulated *I–V* curve for a μ-ratio < 1 (not shown) exactly coincides with the

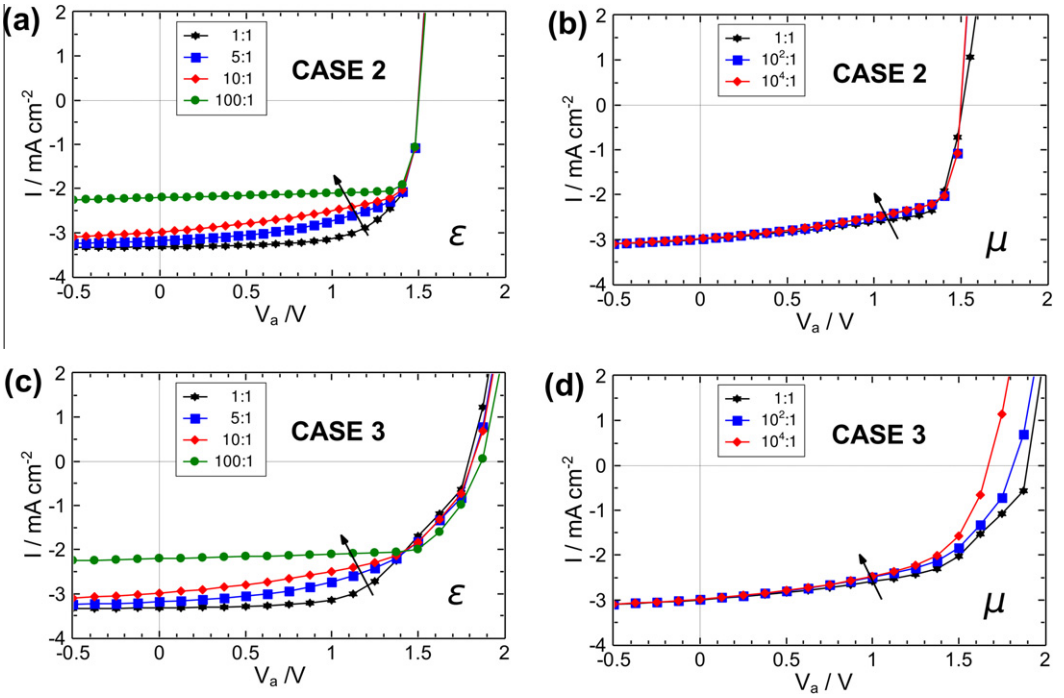

Fig. 6. *I–V* characteristics for generation of charge carriers only in the inorganic phase according to Lambert–Beer's law for different ratios of $\epsilon_r^{\text{inorganic}} : \epsilon_r^{\text{organic}}$ and $\mu_{(n,p)}^{\text{inorganic}} : \mu_{(n,p)}^{\text{organic}}$ corresponding to the energetic alignments Case 2 (upper panels) and Case 3 (lower panels) as illustrated in Fig. 1. The arrows indicate the evolution of the *I–V* curves with increasing ratios.

s-shaped *I–V* curve obtained for Case 1 with the inverse μ-ratio.

Thus, provided that the carriers are more mobile in the inorganic than in the organic material, the absence of an offset in the electron transport levels precludes a disadvantageous effect of μ or ϵ_r on the efficiency of the device. As in Case 1, the short-circuit current becomes less negative with increasing dielectric constant ratio, however, the device efficiency is almost not influenced by this fact (cf. Table 3). Increasing the mobility in the acceptor phase has even no influence on the device performance at all: electrons are not affected by a difference between $\mu^{\text{inorganic}}$ and μ^{organic} as they are already generated next to the cathode (cf. Fig. 4(a)). The migration of holes from the donor into the acceptor (cf. Fig. 4(b)) is aided by the level offset. This means that one is able to produce a very stable system with respect to the ratios of the dielectric constant and the mobilities between two different materials if (i) the inorganic material is situated at the cathode and (ii) the electron transport level offset vanishes.

The *I–V* characteristics resulting from the consideration of the third alignment configuration corresponding to Fig. 1(d) are shown in the Fig. 6(b) and (c). In this case we have the same non-zero energetic barrier for electrons and holes. As seen in the previous cases, an increase of the ϵ_r-ratio (Fig. 6(c), (stars-circles)) leads to decreasing short-circuit currents and increasing V_{oc}. However, the efficiency of the solar cell is almost unaffected by the change of the dielectric constant (cf. Table 3). A change in the mobility ratio, as shown in Fig. 6(d), has a marked impact on the V_{oc} value. The higher the ratio, the smaller V_{oc} becomes (Fig. 6(d), stars-diamonds). This sensitivity of V_{oc} to the μ-ratio relates to a μ-induced diffusion of *holes* into the acceptor (cf. Fig. 4). Moreover, Fig. 6(d) represents the first instant at which we encounter a V_{oc} profoundly exceeding the built-in voltage of 1.5 V. A qualitative and quantitative discussion and interpretation of this effect will follow in the next section.

Table 3
Evolution of the short circuit current (j_{sc}), open circuit voltage (V_{oc}), fill factor (FF), and power conversion efficiency (PCE) as a function of selected parameter ratios for carrier generation confined to the inorganic phase for the transport level alignments shown in Fig. 1. The default parameter ratios according to Table 2 are highlighted in bold numbers.

$\frac{\mu^{\text{inorganic}}}{\mu^{\text{organic}}}$	$\frac{\epsilon_r^{\text{inorganic}}}{\epsilon_r^{\text{organic}}}$	j_{sc}/mA cm^{-2}	V_{oc}/V	FF/%	PCE/%
Case 1/hole transport levels degenerate					
10^2	1	−3.32	1.38	66.7	3.1
10^2	**10**	−2.89	1.39	31.6	1.3
10^2	10^2	−0.98	1.39	29.8	0.4
1	10	−2.99	1.52	59.1	2.7
10^4	10	−0.81	1.26	8.9	0.1
Case 2/electron transport levels degenerate					
10^2	1	−3.32	1.50	68.2	3.4
10^2	**10**	−2.99	1.50	65.6	2.9
10^2	10^2	−2.21	1.50	83.2	2.8
1	10	−2.99	1.51	67.9	3.1
10^4	10	−2.98	1.50	62.5	2.8
Case 3/hole and electron transport levels non-degenerate					
10^2	1	−3.32	1.79	57.2	3.4
10^2	**10**	−2.99	1.82	54.3	2.9
10^2	10^2	−2.21	1.87	72.3	2.9
1	10	−3.00	1.89	55.7	3.2
10^4	10	−2.98	1.67	55.7	2.8

3.3. Comparison of donor materials

Now we will make use of the knowledge gained by analyzing the previous characteristics and apply it to the case of three different polymers, i.e., P3EBT, P3HT, and F8T2. Throughout the calculations, these polymers are assumed to differ in their particular HOMO/LUMO levels (see Table 2), while all other transport parameters were set to the default values given in Table 2. The resulting *I–V* curves are depicted in Fig. 7. The P3EBT/$CuInS_2$ curve (squares) possesses a saddle point at $V_a = V_{\text{oc}}$. The occurrence of such a saddle point relates in this case, as discussed above, to the vanishing offset between the hole transport levels. Uhrich et al. found such a behavior also for combinations of (purely organic) hole transporting materials [50].

Remarkably, all three donor materials yield approximately the same value of 1.4 V for V_{oc} (cf. Fig. 7), even though $V_{\text{built-in}}$ is not the same (cf. Table 4). This coincidence relates to a combination of individual, material-dependent contributions to the open circuit voltage: the value of V_{oc} in organic solar cells can be approximated by the sum of (i) the built-in voltage, (ii) the lowest band offset (which is in these three cases the hole transport level offset), and (iii) an additional term arising from diffusion [18]. In our particular case, the diffusion term should be sensitive towards the mobility ratio between the two different materials, i.e.,

$$qV_{\text{oc}}^{D/A} = V_{\text{built-in}}^{D/A} + \min_{D/A}(\Delta E_n, \Delta E_p) + \Delta E(\mu^{\text{inorganic}} : \mu^{\text{organic}}). \quad (6)$$

In the case of the three different polymers, the mobility ratio is always set to $\mu^{\text{inorganic}} : \mu^{\text{organic}} = 10^2 : 1$. Hence, the correction to V_{oc} due to diffusion should always be the same. Indeed, the inspection of the values of $V_{\text{built-in}}$ and $\min(\Delta E_n, \Delta E_p)$ entering V_{oc}, which are listed in Table 4, reveals that these two quantities sum up to

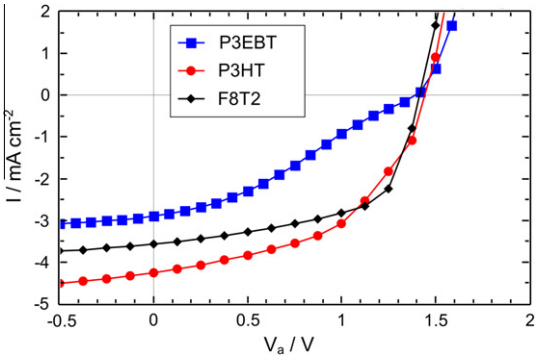

Fig. 7. Simulated *I–V* curves for the polymers P3EBT, P3HT, and F8T2 (Table 2) for a charge carrier generation confined to the inorganic $CuInS_2$ phase.

Table 4
Contributions to the open circuit voltage of polymer/$CuInS_2$ devices.

Polymer	$V_{\text{built-in}}$/V	ΔE_n/eV	ΔE_p/eV	$\min(\Delta E_n, \Delta E_p)$/eV	$qV_{\text{built-in}} + \min(\Delta E_n, \Delta E_p)$/eV	V_{oc}/V
P3EBT	1.5	0.4	0.0	0.0	1.5	1.4
P3HT	1.1	0.6	0.4	0.4	1.5	1.4
F8T2	1.3	1.6	0.2	0.2	1.5	1.4

1.5 eV for all donor materials (2nd column from the right in Table 4). Thus, there is a polymer-independent contribution $\Delta E/q$ to V_{oc} of -0.1 V.

To further test, whether ΔE can be related to the mobility-*ratio*, we try to predict V_{oc} for a material combination complying with the level alignment Case 3 (Fig. 1(d)) by using Eq. (6) and our empirical μ-dependent correction $\Delta E(100:1)/q$ of -0.1 V:

$$qV_{oc}^{\text{Case 3}} = V_{\text{built-in}}^{\text{Case 3}} + \min_{\text{Case 3}}(\Delta E_n, \Delta E_p) + \Delta E$$
$$(\mu^{\text{inorganic}} : \mu^{\text{organic}} = 100:1) \approx (1.5 + 0.4 - 0.1)\text{eV} = 1.8\text{eV}.$$

This value is in excellent agreement with the open circuit voltage associated to the *I–V* curve obtained for a μ-ratio of 100:1 (Fig. 6(d), squares).

From the arguments above, it is clear that $\Delta E(\mu^{\text{inorganic}} : \mu^{\text{organic}})$ must not be present in all systems in which mobility ratios larger than unity cannot induce a preferential diffusion direction, i.e., in systems with degenerate electron transport levels (Case 2). Indeed, the V_{oc} values (cf. Table 5) for Case 2 are almost entirely insensitive to the mobility ratio. Thus, it is possible to conclude that the diffusion correction to the open circuit voltage is mainly determined by the *ratio* of mobilities rather than their absolute values.

4. Conclusion

The carrier transport in inorganic–organic hybrid cells has been studied in the light of the interplay between carrier generation occurring at the heterojunction (due to dissociation of the donor excitons) *and* in the bulk of the acceptor material (due to direct generation in the small band gap inorganic material). Particular attention has been paid to the influence of (i) the carrier mobilities, (ii) the dielectric constants, and (iii) transport level offsets on the efficiency of collecting photogenerated carriers at the terminal contacts. Each of the three factors influences the power conversion efficiency of hybrid organic–inorganic solar cells. They predominantly affect the open circuit voltage, V_{oc}, and the shape of the *I–V* curve. The short circuit current, j_{sc}, is hardly affected by the transport-related phenomena studied here; in this context, slight variations that were nevertheless observed relate directly to the occurrence of s-shaped *I–V* characteristics. The leading effect originates from offsets in the transport levels and is, as shown in [15], comparable to the influence of non-ohmic contacts or more complex heterojunction morphologies on the PCE. All μ- and ϵ_r-induced changes have a significantly less marked impact on the *I–V* curve.

Due to the strongly differing nature of the two generation mechanisms, it is possible to judge the individual impact of the factors on the carrier transport in a semi-quantitative fashion solely on the basis of the directly generated carriers in the acceptor. In case flat heterojunctions are considered, this treatment becomes quantitative. As another striking consequence of the differing generation mechanisms, there is a pronounced asymmetry between level offsets formed for electrons and holes. A lack of a hole transport level offset ($\Delta E_p = 0$) represents the most serious loss factor encountered in this study; large variations in the PCE can be observed solely due to a pronounced sensitivity of the shape of the *I–V* curve towards μ and ϵ_r. In strong contrast, a degenerate electron transport level ($\Delta E_n = 0$) gives rise to values of V_{oc}, j_{sc}, and PCE that are almost insensitive towards actual mobility and ϵ_r values. Consequently, the mobilities cannot be used as a tuning handle to influence V_{oc}. Vice versa, a non-vanishing electron transport level offset is necessary to achieve a V_{oc} beyond $V_{\text{built-in}}$ at all.

The smaller the *mismatch* in μ *and* ϵ_r between organic and inorganic phase, i.e., the less their ratios differ from unity, the larger the short circuit current and, provided that $\Delta E_n > 0$, V_{oc} becomes. The variations due to ϵ_r are, however, much smaller than those caused by μ. Additionally, the effective mobility-induced diffusion of *holes* from the organic to the inorganic layer gives rise to a s-shaped section in the *I–V* curve. The steepness of this section increases when the μ-ratio is decreased. Such a minimal μ-mismatch requirement coincides with the findings for purely excitonic bulk heterojunction solar cells [30–32]. This result is probably not surprising, when we keep in mind that carrier generation predominantly occurs non-locally throughout a bulk phase both in such bulk heterojunctions and in the devices considered in this work.

From the considerations above, it is possible to derive the following guidelines to select suitable material combinations, provided that ohmic contacts can be formed: (i) to suppress the formation of an s-shaped *I–V* curve, holes need to be driven from the acceptor into the donor by means of a level offset-induced diffusion at the heterojunction. This is achieved for values of E_V being more negative than the value of E_{HOMO}. (ii) A non-vanishing offset ΔE_n between the electron transport levels is favorable, as then the open circuit voltage can exceed the built-in voltage due to a non-zero minimal offset term lessened by a diffusion term. In order to minimize the detrimental contribution from the mobility-dependent diffusion term, the mobility ratio should be as close to unity as possible. It should be noted at this point, however, that the requirement of $\Delta E_n \neq 0$ must not be confused with a minimum value $\Delta E_n^{\min}$ that has been demanded to guarantee

efficient exciton dissociation in purely excitonic cells [45,47,48].

Acknowledgments

This work has been supported by the Austrian Federal Ministry of Economy, Family, and Youth (bmwfj), ISOVOLTAIC AG, the Christian Doppler Research Association (CDG) and the Austrian Nanoinitiative (FFG) through the NILsimtos project as part of the NILaustria cluster.

Appendix A

In Table 5, the figures of merit for all simulated devices are listed as a function of mobility- and ϵ_r-ratios and transport level alignments.

Table 5
Short circuit current, open circuit voltage, fill factor, and power conversion efficiency for all simulated devices. The default parameter ratios according to Table 2 are highlighted in bold numbers.

$\frac{\mu^{\text{inorganic}}}{\mu^{\text{organic}}}$	$\frac{\epsilon_r^{\text{inorganic}}}{\epsilon_r^{\text{organic}}}$	j_{sc}/mA cm^{-2}	V_{oc}/V	*FF*/%	*PCE*/%
Case 1/carrier generation across device					
10^2	1	−11.99	1.46	67.3	11.7
10^2	5	−11.95	1.47	57.5	10.1
10^2	**10**	−11.67	1.47	55.3	9.5
10^2	10^2	−9.57	1.49	65.2	9.3
1	10	−11.87	1.53	70.7	12.8
10^4	10	−9.34	1.47	62.6	8.6
Case 1/carrier generation within inorganic phase					
10^2	1	−3.32	1.38	66.7	3.1
10^2	5	−3.18	1.39	44.6	1.9
10^2	**10**	−2.89	1.39	31.6	1.3
10^2	10^2	−0.98	1.39	29.8	0.4
1	10	−2.99	1.52	59.1	2.7
10^4	10	−0.81	1.26	8.9	0.1
Case 1/field-dependent mobilities and recombination					
10^2	1	−3.33	1.31	68.1	2.9
10^2	**10**	−2.96	1.36	37.5	1.5
10^2	10^2	−1.82	1.39	37.9	0.9
1	10	−2.73	1.49	51.4	2.1
10^4	10	−1.96	1.23	11.0	0.3
Case 2/electron transport levels degenerate					
10^2	1	−3.32	1.50	68.2	3.4
10^2	5	−3.18	1.50	63.6	3.0
10^2	**10**	−2.99	1.50	65.6	2.9
10^2	10^2	−2.21	1.50	83.2	2.8
1	10	−2.99	1.51	67.9	3.1
10^4	10	−2.98	1.50	62.5	2.8
Case 3/electron and hole transport levels non-degenerate					
10^2	1	−3.32	1.79	57.2	3.4
10^2	5	−3.18	1.82	52.5	3.0
10^2	**10**	−2.99	1.82	54.3	2.9
10^2	10^2	−2.21	1.87	72.3	2.9
1	10	−3.00	1.89	55.7	3.2
10^4	10	−2.98	1.67	55.7	2.8
donor polymers					
10^2	**10**	−4.25	1.44	50.2	3.1
10^2	**10**	−3.57	1.42	59.0	2.9

A.1. Model equations

The equations for the electron and hole drift–diffusion currents $\mathbf{J}_n(\mathbf{r},t)$ and $\mathbf{J}_p(\mathbf{r},t)$, respectively, at a particular position $\mathbf{r}=(x,y)$ and time $t \geqslant 0$ are given by ([51])

$$\mathbf{J}_n(\mathbf{r},t) = q\mu_n(\mathbf{r},\mathbf{E})n(\mathbf{r},t)\mathcal{E}_n(\mathbf{r}) + \mu_n(\mathbf{r},\mathbf{E})k_BT\nabla n(\mathbf{r},t), \quad (7)$$

$$\mathbf{J}_p(\mathbf{r},t) = q\mu_p(\mathbf{r},\mathbf{E})p(\mathbf{r},t)\mathcal{E}_p(\mathbf{r}) - \mu_p(\mathbf{r},\mathbf{E})k_BT\nabla p(\mathbf{r},t), \quad (8)$$

where $n(\mathbf{r},t)$ and $p(\mathbf{r},t)$ denote the electron and hole densities, and $\mu_{(n,p)}(\mathbf{r},\mathbf{E})$ the mobility of charge carriers as a function of the electric field $\mathbf{E}_{(n,p)}$. Further, k_B is Boltzmann's constant and T the temperature. The generalized electric field $\mathcal{E}_{n,p}(\mathbf{r})$ is related to the generalized potential $\Psi_{(n,p)}(\mathbf{r},t)$ that describes the motion of charge carriers under the influence of the material specific transport levels and the local charge carrier concentration [15,51]. It is given by the difference of the electrostatic potential $\psi(\mathbf{r},t)$ and the so-called band parameters $\Theta_{n(p)}$: $\Psi_{(n,p)}(\mathbf{r},t) = \psi(\mathbf{r},t) - \frac{\Theta_{(n,p)}(\mathbf{r})}{q}$. The electrostatic potential is gained by solving the Poisson equation

$$\nabla\cdot[\epsilon(\mathbf{r})\nabla\psi(\mathbf{r},t)] = -\rho(\mathbf{r},t), \quad (9)$$

where $\epsilon(\mathbf{r}) = \epsilon_0\epsilon_r(\mathbf{r})$ stands for the dielectric constant and $\rho(\mathbf{r})$ for the charge density given by $\rho(\mathbf{r},t) = q[p(\mathbf{r},t) - n(\mathbf{r},t)]$ with the elementary charge q. The additional terms $\Theta_{n(p)}(x,y)$ are associated to the spatial energetic alignment of the transport levels [51,52]. In disordered materials, $\Theta_{n(p)}(x,y)$ is directly given by the relative spatial alignment of the transport levels [52]. For convenience, we set the band parameters to zero in the organic donor, $\Theta_{n(p)} = 0$, and to the transport level offsets in the inorganic acceptor, i.e., $\Theta_n = E_C - E_{LUMO}$; $\Theta_p = E_V - E_{HOMO}$. Therein, $E_{C(/V)}$ refers to the conduction (/valence) band edge of the inorganic semiconductor and $E_{HOMO(/LUMO)}$ to the energy of the highest occupied (/lowest unoccupied) molecular orbital of the organic compound. The associated electric fields $\mathbf{E}_{(n,p)}$ and $\mathcal{E}_{n,p}(\mathbf{r})$ that were formally introduced in Eqs. (7) and (8), are given by

$$\mathbf{E}_{(n,p)} = -\nabla\psi(\mathbf{r},t) \quad \text{and} \quad \boldsymbol{\mathcal{E}}_{(n,p)} = -\nabla\Psi(\mathbf{r},t). \quad (10)$$

The continuity equations for electrons and holes are given by ([51])

$$\frac{\partial n(\mathbf{r},t)}{\partial t} = \frac{1}{q}\nabla\cdot\mathbf{J}_n(\mathbf{r},t) + \Gamma_n(\mathbf{r},t), \quad (11)$$

$$\frac{\partial p(\mathbf{r},t)}{\partial t} = -\frac{1}{q}\nabla\cdot\mathbf{J}_p(\mathbf{r},t) + \Gamma_p(\mathbf{r},t), \quad (12)$$

where $\Gamma_{(n,p)}(\mathbf{r},t)$ depict the corresponding generation and recombination terms, $\Gamma_{(n,p)}(\mathbf{r},t) = G_{(n,p)}(\mathbf{r},t) - R_{(n,p)}(\mathbf{r},t)$.

Assuming a Lambert–Beer type absorption profile across the device, the number of phonons absorbed per second and volume at position $\mathbf{r}$ in the device reads as

$$\Phi(\mathbf{r}) = \int_{\lambda_{min}}^{\lambda_{max}} d\lambda\,\Phi_0(\lambda)\,\alpha(\lambda)\exp[-\alpha(\lambda)d(\mathbf{r})], \quad (13)$$

where λ stands for the wavelength and is limited by λ_{min} and λ_{max} according to the band gap. Further, $\Phi_0(\lambda)$ is the incoming photon flux at a particular wavelength λ according to the reduced sun spectrum AM 1.5 with roughly 1000 W m^{-2} [53]. The absorption coefficient related to

the organic and inorganic species is denoted by α and $d(\mathbf{r})$ is the distance of a point within the device with position $\mathbf{r}$ to the surface in direction of the incident light.

In this formulation, Eq. (13) yields the photon number as a function of the material-dependent absorption and, in reasonable first approximation, the morphology of the device. As we intend to focus on solely investigating *carrier transport*-related phenomena, we will exclude additional effects that may originate from strongly spatially varying absorption profiles [54] by introducing the following simplifications: (i) α enters Eq. (13) as a wavelength- and material-independent parameter and (ii) the optical band gap $E_{gap} = 1.5$ eV is treated as material-independent. This means that both materials are considered to be capable of absorbing the same number of photons per volume and time. Then, the actual number of photons absorbed anywhere in the device is only determined by Lambert Beer's law, i.e., is solely dependent on the position of the considered volume element with respect to the transparent electrode. The coefficient α is set to the representative value of $2 \times 10^7\ m^{-1}$ according to [36]. With the help of the simplifications made above, we are able to quantitatively compare transport phenomena of materials, whose optical absorption profile is not identical.

The ohmic contacts are modeled by choosing appropriate boundary conditions [15]. The intrinsic charge carrier concentration at the contacts was set as $N_{cv} = 10^{22}\ \mathrm{m}^{-3}$. The resulting coupled system of equations given by the continuity equations, current density equations, and the Poisson equation is solved self-consistently on a two-dimensional mesh with variable grid spacing [15].

References

[1] B.M. Saunders, M.L. Turner, Adv. Colloid Interface Sci. 138 (2008) 1–23.
[2] A.C. Mayer, S.R. Scully, B.E. Hardin, M.W. Rowell, M.D. McGehee, Mater. Today 10 (2007) 28–33.
[3] S. Günes, H. Neugebauer, N.S. Sacriciftci, Chem. Rev. 107 (2007) 1324–1338.
[4] S. Günes, K.P. Fritz, H. Neugebauer, N.S. Sariciftci, S. Kumar, G.D. Scholes, Sol. Energy Mater. Sol. Cells 91 (2007) 420–423.
[5] D.O. Grynko, V.V. Kislyuk, P.S. Smertenko, O.P. Dimitriev, J. Phys. D: Appl. Phys. 42 (2009) 195104.
[6] I. Gur, N.A. Fromer, C.P. Chen, A.G. Kanaras, A.P. Alivisantos, Nano Lett. 7 (2007) 409–414.
[7] E. Arici, N.S. Sariciftci, D. Meissner, Adv. Funct. Mater. 13 (2003) 165.
[8] N.C. Greenham, X. Peng, A.P. Alivisatos, Phys. Rev. B 54 (1996) 17628.
[9] P.S. Smertenko, V.P. Kostylev, V.V. Kislyuk, A.F. Syngaevsky, S.A. Zynio, O.P. Dimitriev, Sol. Energy Mater. Sol. Cells 92 (2008) 976–979.
[10] E. Maier, T. Rath, W. Haas, O. Werzer, R. Saf, F. Hofer, D. Meissner, O. Volobujeva, S. Bereznev, E. Mellikov, H. Amenitsch, R. Resel, G. Trimmel, Sol. Energy Mater. Sol. Cells 95 (2011) 1354.
[11] M. Kruszynska, M. Knipper, J. Kolny-Olesiak, H. Borchert, J. Parisi, Thin Solid Films (2011), doi:10.1016/j.tsf.2010.12.102.
[12] R. Bhargava (Ed.), Wide Bandgap II–VI Semiconductors, Inspec, London, 1997.
[13] in D.R. Lide (Ed.), CRC Handbook of Chemistry and Physics, 76th ed., CRC Press, Boca Raton, 1995.
[14] L.G. Yang, F. Chen, H. Xu, M. Wang, H.Z. Chen, J. Appl. Phys. 106 (2009) 073701.
[15] M. Gruber, B.A. Stickler, G. Trimmel, F. Schürrer, K. Zojer, Org. Electron. 11 (2010) 1999–2011.
[16] P.W.M. Blom, V.D. Mihailetchi, L.J.A. Koster, D.E. Markov, Adv. Mater. 19 (2007) 1551–1566.
[17] M. Riede, T. Mueller, W. Tress, R. Schueppel, K. Leo, Nanotechnology 19 (2008) 424001.
[18] B.A. Gregg, M.C. Hanna, J. Appl. Phys. 93 (2003) 3605–3614.
[19] T. Blythe, D. Bloor, Electrical Properties of Polymers, second ed., Cambridge University Press, New York, 2005.
[20] For crystals of small molecules or conjugated polymers, this value typically corresponds to the isotropically averaged components of the ϵ_r-tensor.
[21] A. Waxman, V.E. Henrich, F.V. Shallcross, H. Borkan, P.K. Weimer, J. Appl. Phys. 36 (1965) 168;
A.L. Dawar, P.K. Shishodia, G. Chauhan, A. Kumar, P.C. Mathur, J. Mater. Sci. Lett. 9 (1990) 547–548.
[22] Y.B. He, T. Krämer, I. Österreicher, A. Polity, B.K. Meyer, M. Hardt, Semicond. Sci. Technol. 20 (2005) 685–692.
[23] A.S. Molinari, H. Alves, Z. Chen, A. Facchetti, A.F. Morpurgo, J. Am. Chem. Soc. 131 (2009) 2462–2463.
[24] C. Reese, Z. Bao, Mater. Today 10 (2007) 20–27.
[25] C.M. Martin, V.M. Burlakov, H.E. Assender, D.A.R. Barkhouse, J. Appl. Phys. 102 (2007) 104506.
[26] L.J.A. Koster, W.J. van Strien, W.J.E. Beek, P.W.M. Blom, Adv. Funct. Mater. 17 (2007) 1297–1302.
[27] K. Maturová, S. van Bavel, M.M. Wienk, R.A.J. Janssen, Nano Lett. 9 (2009) 3032–3037.
[28] C. Deibel, A. Wagenpfahl, V. Dyakonov, Phys. Status Solidi RRL 2 (2008) 175–177.
[29] C. Groves, N.C. Greenham, Phys. Rev. B 78 (2008) 155205.
[30] C. Groves, R.A. Marsh, N.C. Greenham, J. Chem. Phys. 129 (2008) 114903.
[31] F. Yang, S.R. Forrest, ACS Nano 2 (2008) 1022–1032.
[32] P. Peumans, S.R. Forrest, Chem. Phys. Lett. 398 (2004) 27–31.
[33] C.L. Braun, J. Chem. Phys. 80 (1984) 4157–4161.
[34] L. Onsager, J. Chem. Phys. 2 (1934) 599–615.
[35] L.J.A. Koster, V.D. Mihailetchi, P.W.M. Blom, Appl. Phys. Lett. 88 (2006) 052104.
[36] G.A. Buxton, N. Clarke, Model. Simul. Mater. Sci. Eng. 15 (2007) 13–26.
[37] P. Langevin, Ann. Chim. Phys. 28 (1903) 433.
[38] When assuming Koster-type recombination rates [35], i.e., the rate expression representing the lower limit [29], the deviation between the *I–V* curves obtained with Langevin and Koster-type rates was indiscernible.
[39] C. Deibel, A. Wagenpfahl, V. Dyakonov, Phys. Rev. B 80 (2009) 075203.
[40] G.J. Adriaenssens, V.I. Arkhipov, Solid State Commun. 103 (1997) 541.
[42] C.-H. Lin, S. Chattopadhyay, C.-W. Hsu, M.-H. Wu, W.-C. Chen, C.-T. Wu, S.-C. Tseng, J.-S. Hwang, J.-H. Lee, C.-W. Chen, C.-H. Chen, L.-C. Chen, K.-H. Chen, Adv. Mater. 21 (2009) 759–763.
[43] L. Jiang, J.H. Lyou, S. Rane, E.A. Schiff, Q. Wang, Q. Yuan, Mater. Res. Soc. Symp. Proc. 609 (2000).
[44] H. Bässler, Phys. Status Solidi B 175 (1993) 15–56.
[45] M.C. Scharber, D. Mühlbacher, M. Koppe, P. Denk, C. Waldauf, A.J. Heeger, C.J. Brabec, Adv. Mater. 18 (2006) 789–794.
[46] This effect is even more pronounced if carrier generation due to exciton dissociation at the interface is explicitly taken into account. Then, there is a strong gradient in the carrier concentration that drives charges from the heterojunction towards the contacts [18].
[47] J.L. Brédas, D. Beljonne, V. Coropceanu, J. Cornil, Chem. Rev. 104 (2004) 4917.
[48] S. Shoaee, T.M. Clarke, C. Huang, S. Barlow, S.R. Marder, M. Heeney, I. McCulloch, J.R. Durrant, J. Am. Chem. Soc. 132 (2010) 12919–12926.
[49] X. Gong, M.H. Tong, F.G. Brunetti, J.H. Seo, Y.M. Sun, D. Moses, F. Wudl, A.J. Heeger, Adv. Mater. 23 (2011) 2271.
[50] C. Uhrich, D. Wynands, S. Oltof, M.K. Riede, K. Leo, S. Sonntag, B. Maennig, M. Pfeiffer, J. Appl. Phys. 104 (2008) 043107.
[51] C.M. Snowden, Introduction to Semiconductor Device Modelling, World Scientific Publishing, Singapore, 1986.
[52] J.E. Sutherland, J.R. Hauser, IEEE Trans. Electron. Dev. 24 (1977) 363.
[53] Available from: <http://rredc.nrel.gov/solar/spectra/aml.5/>.
[54] The consideration of the actual distribution of the electrodynamic field is beyond the scope of this paper.

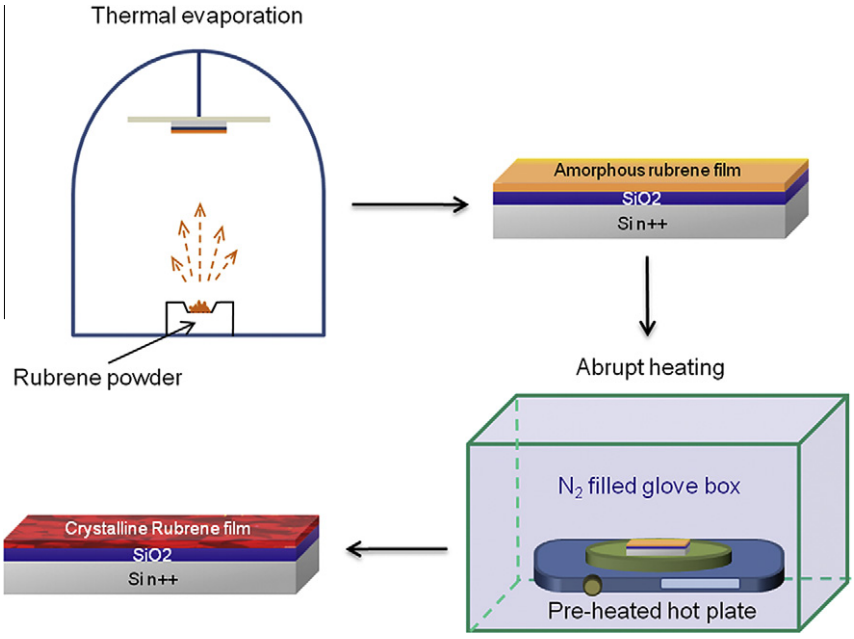

Fig. 1. Schematic illustration of the fabrication of the crystalline rubrene thin films.

rapid thermal annealing technique. Although this approach offers an alternative way to fabricate rubrene TFT without SAM treatment, the produced rubrene active layers still contain a number of undesired structures including discontinuous grains that is leading a relatively low device performance.

Here we present a very simple but effective approach to produce rubrene OTFTs with characteristics better than a-Si:H TFTs. Only by an abrupt heating process, the crystalline rubrene thin films that consist of highly ordered, uniaxially oriented single-crystalline grains are created, and the grains are interconnected with one another to form

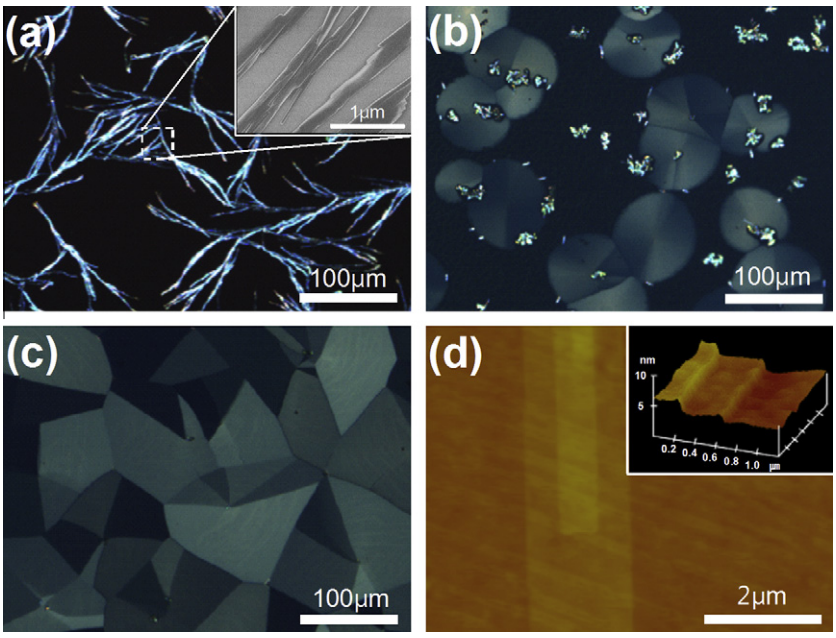

Fig. 2. POM images of the crystalline rubrene thin films fabricated by the abrupt heating process at various temperatures and time: (a) 125 °C for 5 min, (b) 150 °C for 5 min (c) 170 °C for 1 min. The inset in (a) is the magnified SEM image of the branch-like structures marked in the image. (d) AFM image and magnified three-dimensional AFM image (inset) of the crystalline rubrene thin film, corresponding to (c), prepared by the abrupt heating process at 170 °C for 1 min.

continuous films over the whole dielectric surfaces. Such high-quality crystalline rubrene thin films are remarkably rapidly produced in 1 min through this approach. Moreover, the approach does not require any surface modification of gate dielectrics of OTFTs, which is generally indispensable in the other methods developed to date for enhancing the performance of OTFTs.

2. Experimental

Rubrene powder (sublimed grade) was purchased from Sigma–Aldrich, Inc. Amorphous rubrene thin films were deposited on 100 nm thick SiO_2 dielectric surfaces underlying heavily doped *n*-type silicon substrates (2 cm × 2 cm) that were kept at room with a base pressure below 10^{-5}. The substrates were cleaned in isopropyl alcohol in an ultrasonic bath for 5 min, followed by drying under a nitrogen flow. The evaporation speed was ~5 nm/min. After the deposition, the as-deposited rubrene thin films were abruptly heated by placing the samples onto a pre-heated hot plate and taken out of the plates after the abrupt heating process. The abrupt heating process was carried out inside a nitrogen-filled glove box at various combinations of heating temperature (T_{ah}) and heating duration. In order to fabricate top-contact rubrene TFTs, gold was evaporated for source and drain electrodes through a shadow mask, and 16 TFTs were fabricated on a substrate.

Polarization images were captured using an Olympus BX51 microscope. The topographies and the thicknesses of the films were examined with an AFM (Veeco D3100) and a field-emission SEM (Hitachi S-4800). DSC of amorphous rubrene powder which was raked out from the as-deposited rubrene film was characterized on differential scanning calorimeter DSC-204 Phoenix (Netzsch). The TEM images and SAED patterns were taken with a Tecnai G2 Spirit BioTWIN (FEI Company) TEM operating at 120 kV. For TEM observation, rubrene films were prepared on SiO_2 coated TEM grids using the same abrupt heating method. GIXD measurements were performed using the 4C2 beam line at the Pohang Accelerator Laboratory (PAL), Pohang, Korea. The diffraction patterns were

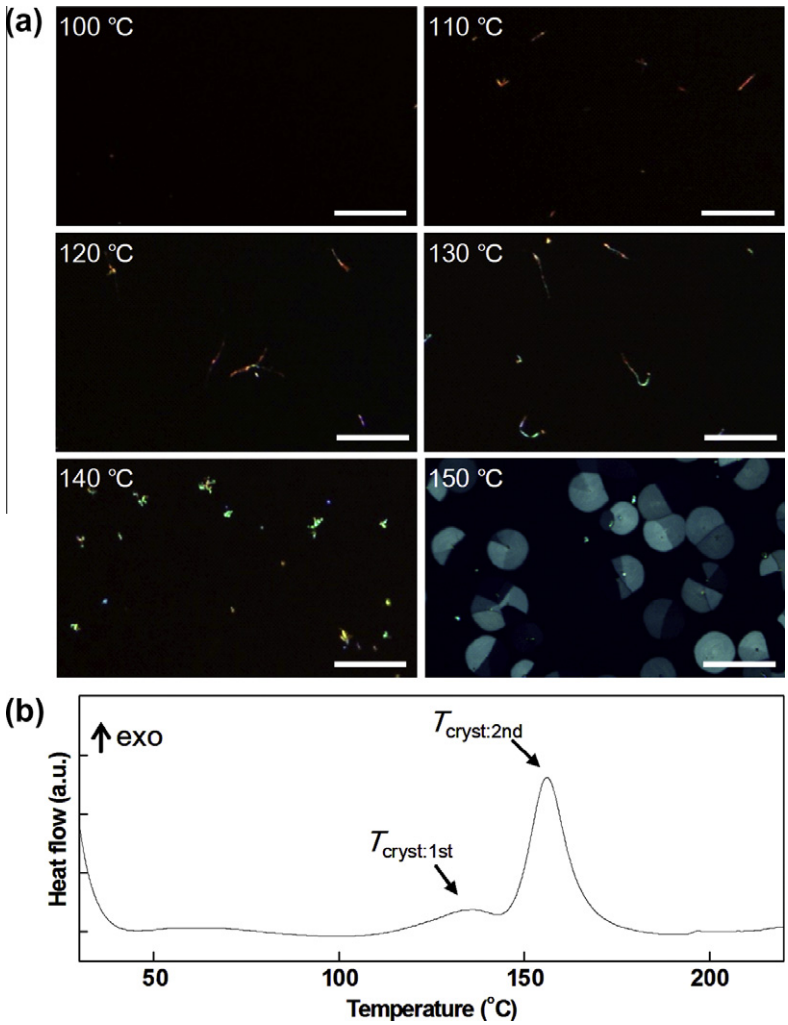

Fig. 3. (a) POM images of the rubrene thin films abruptly heated at temperatures corresponding to label in the image. The scale bars are all 30 μm. (b) DSC heating thermogram of amorphous rubrene (heating rate: 80 °C/min).

recorded using a MarCCD detector. The grazing-incidence angle of the X-ray beam (λ = 1.3807 Å) was varied between 0.14° and 0.25°, and the sample-to-detector distance (143.5 mm) was calibrated using a silver behanate standard sample and the footprint of the X-ray beam on the specimen surface was 1 mm × 5 mm. The diffraction data were displayed as an intensity map in which q_{xy} is the in-plane momentum transfer and q_z is the out-of-plane momentum transfer. The TFT characteristics were evaluated under ambient air conditions with a Keithley 4200 semiconductor characterization system.

3. Results and discussion

The high-quality crystalline rubrene thin films were produced simply by abrupt heating of amorphous rubrene films that were thermally evaporated on 100 nm thick SiO_2 dielectric layers underlying heavily doped *n*-type silicon substrate (Fig. 1) The abrupt heating process was carried out by placing as-deposited rubrene films on a pre-heated hot plate in a nitrogen environment for a short time. Fig. 2a–c shows the polarized optical microscopy (POM) images of the rubrene thin films (thickness: 20 nm) that

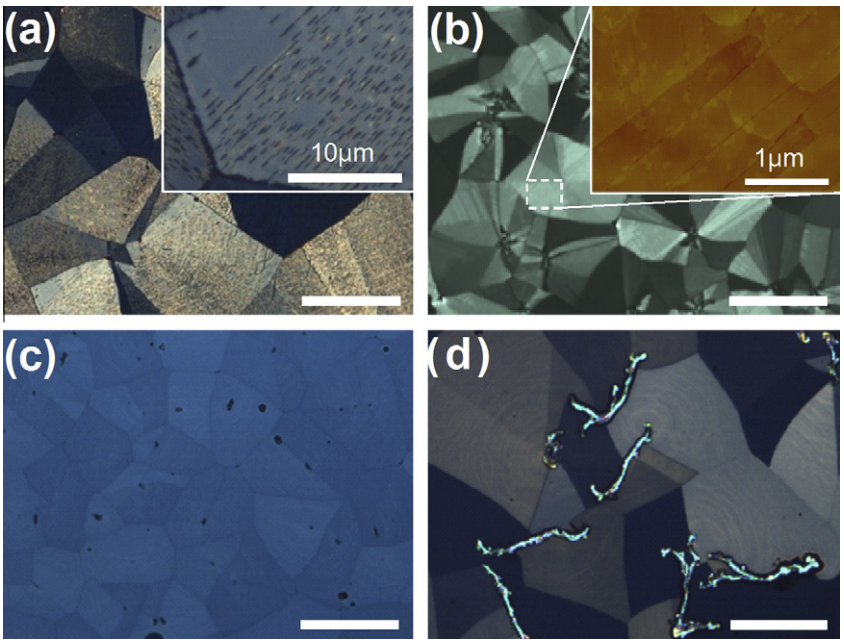

Fig. 4. (a) POM image of rubrene film abruptly heated at 170 °C for 10 min. (b) POM and AFM (inset) image of 50 nm thick crystalline rubrene film and (c) optical image of 10 nm thick crystalline rubrene film. (b and c) sample were fabricated by abrupt heating at 170 °C for 1 min. (d) POM image of gradually heated rubrene film from room temperature to 170 °C at heating rate of 40 °C/min. The scale bars are all 100 μm.

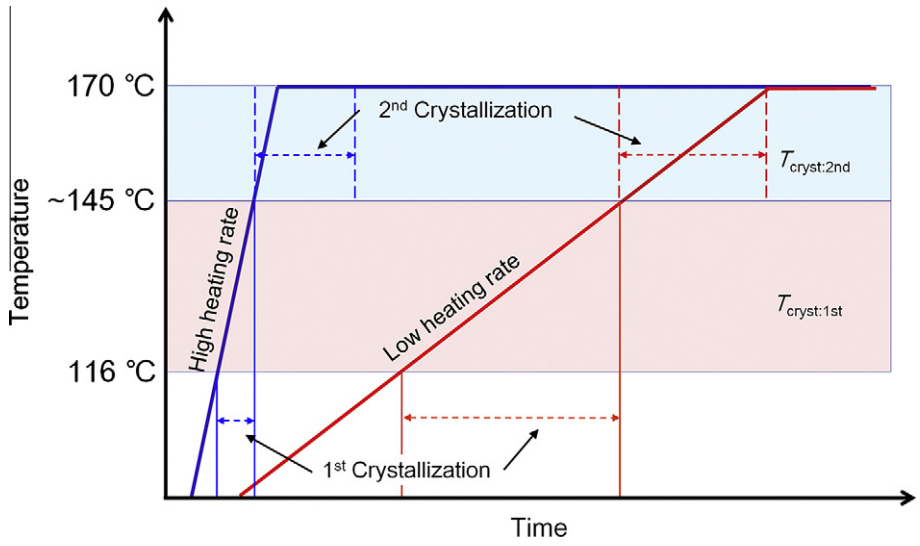

Fig. 5. Schematic time–temperature–transformation diagram of rubrene film heated at low and high heating rate, respectively.

were abruptly heated at different temperatures. The as-deposited rubrene film did not display a crystalline feature under polarized light (Supporting Information, Fig. S1a). However, the rubrene films that underwent the abrupt heating process exhibited strong birefringence in the POM images, indicating that crystalline structures were formed [22]. Upon abrupt heating at a relatively low temperature of 125 °C for 5 min, branch-like crystalline structures appeared (Fig. 2a). Scanning electron microscopy (SEM) images show that the branch-like crystallites with widths of a few 100 nm and lengths of several μm are embedded in an amorphous rubrene matrix (inset of Fig. 2a). Interestingly, when T_{ah} was increased to 150 °C, disk-shaped platelet crystallites with diameters of several tens μm were formed in addition to the branch-like crystallites (Fig. 2b). With a further increase of T_{ah} to 170 °C, novel crystalline rubrene films, that is, continuous crystalline films consisting of large-sized and well-faceted domains were created over the whole SiO_2 surfaces (Fig. 2c). No colour variation was observed within a single domain under POM investigation, suggesting that a domain is composed of a single crystalline grain. The average grain size was ca. 80 μm and the grains were interconnected with one another, as shown in the POM image of Fig. 2c [23]. These interconnected large grains are beneficial in OTFTs because large grains lead to a low density of grain boundaries that act as barriers on the carrier transport and because loosely connected grains prevent charge transport across grain boundaries [24]. Note that an OTFT can be prepared even on a single large grain in the film. Atomic force microscope (AFM) images show that the surfaces of the crystalline rubrene thin films are flat and smooth (the root mean square roughness was 0.36 nm for the flat area shown in Fig. 2d). Meanwhile, long platelets consisting of a few parallel layers were observed on the surface of the film, as shown in Fig. 2d. The layer spacing is ~1.3 nm, which corresponds to the half *c*-axis length of an orthorhombic rubrene unit cell [25].

For the systematic investigation of the evolution of crystalline structures during heat treatment, we examined thermal transition of the amorphous rubrene using POM and differential scanning calorimetry (DSC). Fig. 3a shows the POM images of abruptly heated rubrene film at various temperatures for 1 min. From this result, we found that branch-like crystalline structures begin to form in earnest at 110 °C and amount of the crystallites increase with the temperature elevation. Furthermore, the disk-shaped platelet crystallites were evoluted from T_{ah} of 150 °C. These

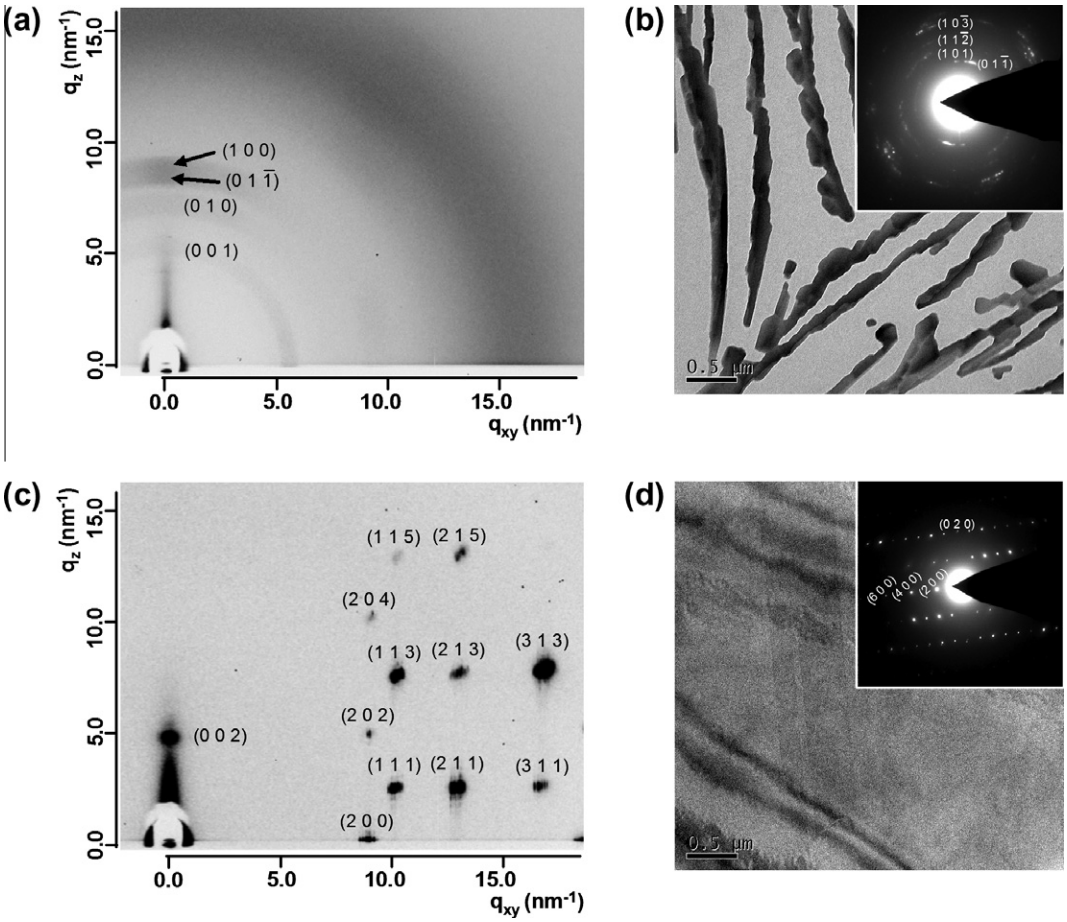

Fig. 6. Two dimensional GIXD patterns of the crystalline rubrene thin films produced at (a) 125 °C for 30 min, (c) 170 °C for 1 min. TEM images of the crystalline rubrene thin films prepared at (b) 125 °C for 30 min and (d) 170 °C for 1 min. The insets in (b and d) are the corresponding SAED patterns, respectively. The SAED pattern of the inset of (d) was recorded along the [0 0 1] zone axis of the orthorhombic rubrene.

temperature-dependent crystallization behaviours were consistent with the result of differential scanning calorimetry (DSC) analysis. As shown in the DSC heating thermogram (Fig. 3b), two distinct crystallization exotherms at 116–142 °C ($T_{cryst:1st}$) and 148–170 °C ($T_{cryst:2nd}$) were recorded. Combined with the results shown in Fig. 3a, the DCS analysis reveals that the branch-like crystallites and the disk-shaped platelet crystallites are formed at the temperature of the first and the second crystallization exotherms, respectively.

The high-quality crystalline rubrene thin films were incredibly rapidly produced in just 1 min by the abrupt heating process at 170 °C. We found that heating time, film thickness, and heating rate as well as T_{ah} were crucial parameters obtaining such high-quality crystalline rubrene films. The optimum T_{ah} was around 170 °C, and an insufficient heating time induced a partial coverage of the crystalline film over the SiO_2 surface, whereas an excessive heating time resulted in pores on the crystalline films (Fig. 4a). Furthermore, films thicker than the optimum value of 20 nm generated cracks on the crystalline films, while too thin films resulted in many discontinuities on the films (Fig. 4b and c). Particularly, we observed that when the amorphous rubrene film was heated at a low heating rate from room temperature to the optimum temperature of 170 °C, branch-like crystallites as well as platelet crystallites were always created (Fig. 4d). If the heating rate is low, the temperature of the film is slowly increased and thus the organic material can get enough time for the crystallization at the temperature zone of $T_{cryst:1st}$. Consequently, formation of the undesirable branch-like crystallites cannot be avoided. However, sufficiently high heating rate can prevent the formation of the branch-like crystallites because the organic material does not have enough time for the formation of the branch-like crystallites (Fig. 5). Therefore, high-quality rubrene crystalline films consisting of only platelet crystallites can be successfully fabricated by the abrupt heating process since it provides very high heating rate.

To identify the crystalline nature of the rubrene thin films produced by the abrupt heating process, transmission electron microscope (TEM) and two-dimensional grazing-incidence X-ray diffraction (2D GIXD) measurements were carried out. Selected area electron diffraction (SAED) patterns clearly confirm that as-deposited rubrene thin films are amorphous (Fig. S1b). However, a set of diffraction spots in the SAED pattern (Fig. 6b) and a highly scattered diffraction pattern along the Debye rings obtained from the 2D GIXD measurement (Fig. 6a) show that the branch-like structures prepared by the abrupt heating process at 125 °C, corresponding to the sample shown in Fig. 2a, are randomly oriented crystallites. The indexing of the 2D GIXD and the SAED patterns confirms that the branch-like crystallites have a triclinic (*P-1*) crystalline phase with lattice parameters of $a = 7.26$ Å, $b = 8.69$ Å, $c = 11.87$ Å, $\alpha = 97.5°$, $\beta = 104.7°$, and $\gamma = 98.8°$. In contrast, the GIXD pattern of the rubrene thin film prepared at 170 °C, corresponding to the sample shown in Fig. 2c, was indexed to an orthorhombic unit cell (*Cmca*) with the lattice parameters of $a = 14.14$ Å, $b = 6.86$ Å and $c = 25.91$ Å (Fig. 6c). Particularly, many strong and sharp reflection spots of the 2D GIXD pattern along the q_z at a given q_{xy} indicate that highly ordered crystals are formed in the film in both vertical and lateral directions.[26,27]. The 2D GIXD pattern further reveals that the *c*-axes of all the crystals in the film are uniaxially aligned perpendicular to the substrate surface, while *ab* planes of all the crystals in the film are perfectly oriented parallel to the substrate surface, which is desirable to obtain high charge carrier mobilities [28]. TEM images of the rubrene thin film clearly show that the film is composed of large grains well-connected with one another without discontinuity (Fig. S1c). The SAED patterns reveal that a single grain in the film has an orthorhombic rubrene single-crystalline phase (Fig. 6d). Therefore, from these analyses, combined with the POM and AFM results, we can conclude that continuous and highly-ordered crystalline rubrene thin films comprising large-sized grains with preferred molecular orientations can be rapidly and controllably fabricated by the abrupt heating approach.

To confirm the effectiveness of the abrupt heating method in actual devices, OTFTs were fabricated with the highly-quality crystalline rubrene thin films obtained by the illustrated method. The transfer and output characteristics of representative OTFT devices are presented in Fig. 7. The channel length and width were fixed at 50 and 1000 μm, respectively. The fabricated devices exhibited high performance with saturation mobilities as high as

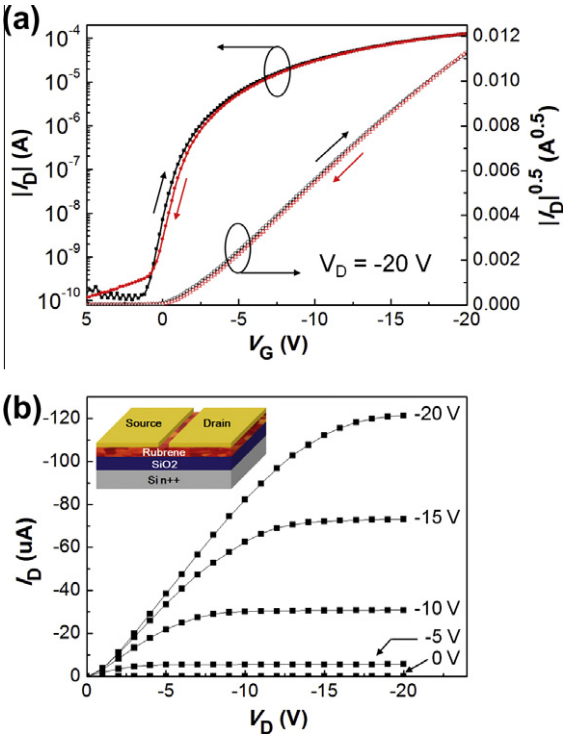

Fig. 7. (a) Drain current (I_D) and square root of the drain current versus gate voltage (V_G) curves scanned in the forward (black line) and reverse (red line) direction at a drain–source voltage of −20 V. (b) Drain current versus drain voltage characteristics for various gate voltages (V_D). The inset shows schematic transistor structure. (For interpretation of the references to colour in this figure legend, the reader is referred to the web version of this article.)

1.21 $cm^2 V^{-1} s^{-1}$ and on/off current ratios higher than 10^6 under ambient conditions. Threshold voltages deduced by the linear extrapolation of the saturation region in the square root of the drain current versus gate voltage were as small as −1.0 V. In addition, as shown in Fig. 5a, the devices showed little hysteresis between forward and reverse scans, and their subthreshold swings were as low as 0.62 V/decade. Both low hysteresis and small subthreshold swing indicate that the prepared high-quality crystalline rubrene films have a low density of traps [29]. It is noteworthy that the overall characteristics of our TFT devices are quite comparable to those of the state-of-the-art OTFTs [30,31]. From the random testing of 10 devices, a good uniformity in device performance was also observed: the average motility was 1.03 $cm^2 V^{-1} s^{-1}$ with a standard deviation of 0.11 $cm^2 V^{-1} s^{-1}$, and the average threshold voltage was −0.65 V with a standard deviation of 0.18 V.

4. Conclusions

We have presented a straightforward approach to fabricate high-quality crystalline rubrene active layers for OTFTs. Simply by an abrupt heating process, crystalline rubrene semiconductor thin films comprising large, highly ordered, and interconnected single-crystalline grains with desirable molecular orientation can be controllably fabricated. High-performance OTFTs with characteristics better than a-Si:H TFT devices were reproducibly produced using the rubrene thin films. Such high-quality crystalline rubrene thin films are remarkably rapidly produced without any surface modification of gate dielectrics, thereby demonstrating that the approach is a very simple yet effective route to produce high-performance OTFTs. Moreover, the approach is also compatible with polymeric substrates due to the short processing time at a relatively low temperature of 170 °C, as shown in our preliminary results (Fig. S2). We believe that our approach is very promising for practical applications of rubrene semiconductors to organic electronics.

Acknowledgement

This work was supported by the National Research Foundation of Korea (NRF) Grant funded by the Korea government (MEST) (No. 2010-0026150).

Appendix A. Supplementary data

Supplementary data associated with this article can be found, in the online version, at doi:10.1016/j.orgel.2011.05.015.

References

[1] G. Gelinck, P. Heremans, K. Nomoto, T.D. Anthopoulos, Organic transistors in optical displays and microelectronic applications, Adv. Mater. 22 (2010) 3778–3798.
[2] T. Sekitani, H. Nakajima, H. Maeda, T. Fukushima, T. Aida, K. Hata, T. Someya, Stretchable active-matrix organic light-emitting diode display using printable elastic conductors, Nat. Mater. 8 (2009) 494–499.
[3] E.C.P. Smits, S.G.J. Mathijssen, P.A. van Hal, S. Setayesh, T.C.T. Geuns, K. Mutsaers, E. Cantatore, H.J. Wondergem, O. Werzer, R. Resel, M. Kemerink, S. Kirchmeyer, A.M. Muzafarov, S.A. Ponomarenko, B. de Boer, P.W.M. Blom, D.M. de Leeuw, Bottom-up organic integrated circuits, Nature 455 (2008) 956–959.
[4] B. Crone, A. Dodabalapur, Y.Y. Lin, R.W. Filas, Z. Bao, A. LaDuca, R. Sarpeshkar, H.E. Katz, W. Li, Large-scale complementary integrated circuits based on organic transistors, Nature 403 (2000) 521–523.
[5] R. Rotzoll, S. Mohapatra, V. Olariu, R. Wenz, M. Grigas, K. Dimmler, O. Shchekin, A. Dodabalapur, Radio frequency rectifiers based on organic thin-film transistors, Appl. Phys. Lett. 88 (2006) 123502.
[6] D.J. Gundlach, Low power high impact, Nat. Mater. 6 (2007) 173–174.
[7] M.T. Martinez, Y.C. Tseng, N. Ormategui, I. Loinaz, R. Eritja, J. Bokor, Label-free DNA biosensors based on functionalized carbon nanotube field effect transistors, Nano Lett. 9 (2009) 530–536.
[8] T. Someya, T. Sekitani, S. Iba, Y. Kato, H. Kawaguchi, T. Sakurai, A large-area flexible pressure sensor matrix with organic field-effect transistors for artificial skin applications, Proc. Natl. Acad. Sci. USA 101 (2004) 9966–9970.
[9] G. Horowitz, Organic field-effect transistors, Adv. Mater. 10 (1998) 365–377.
[10] J. Rivnay, L.H. Jimison, J.E. Northrup, M.F. Toney, R. Noriega, S.F. Lu, T.J. Marks, A. Facchetti, A. Salleo, Large modulation of carrier transport by grain-boundary molecular packing and microstructure in organic thin films, Nat. Mater. 8 (2009) 952–958.
[11] V.C. Sundar, J. Zaumseil, V. Podzorov, E. Menard, R.L. Willett, T. Someya, M.E. Gershenson, J.A. Rogers, Elastomeric transistor stamps: reversible probing of charge transport in organic crystals, Science 303 (2004) 1644–1646.
[12] J. Takeya, M. Yamagishi, Y. Tominari, R. Hirahara, Y. Nakazawa, T. Nishikawa, T. Kawase, T. Shimoda, S. Ogawa, Very high-mobility organic single-crystal transistors with in-crystal conduction channels, Appl. Phys. Lett. 90 (2007) 102120.
[13] D. Braga, G. Horowitz, High-performance organic field-effect transistors, Adv. Mater. 21 (2009) 1473–1486.
[14] A.L. Briseno, S.C.B. Mannsfeld, M.M. Ling, S.H. Liu, R.J. Tseng, C. Reese, M.E. Roberts, Y. Yang, F. Wudl, Z.N. Bao, Patterning organic single-crystal transistor arrays, Nature 444 (2006) 913–917.
[15] L. Luo, G. Liu, L.W. Huang, X.Q. Cao, M. Liu, H.B. Fu, J.N. Yao, Solution-based patterned growth of rubrene nanocrystals for organic field effect transistors, Appl. Phys. Lett. 95 (2009) 263312.
[16] B. Park, I. In, P. Gopalan, P.G. Evans, S. King, P.F. Lyman, Enhanced hole mobility in ambipolar rubrene thin film transistors on polystyrene, Appl. Phys. Lett. 92 (2008) 133302.
[17] S.W. Park, J.M. Hwang, J.M. Choi, D.K. Hwang, M.S. Oh, J.H. Kim, S. Ima, Rubrene thin-film transistors with crystalline and amorphous channels, Appl. Phys. Lett. 90 (2007) 153512.
[18] Y. Chen, I. Shih, High mobility organic thin film transistors based on monocrystalline rubrene films grown by low pressure hot wall deposition, Appl. Phys. Lett. 94 (2009) 083304.
[19] C.H. Hsu, J. Deng, C.R. Staddon, P.H. Beton, Growth front nucleation of rubrene thin films for high mobility organic transistors, Appl. Phys. Lett. 91 (2007) 193505.
[20] Z.F. Li, J. Du, Q. Tang, F. Wang, J.B. Xu, J.C. Yu, Q.A. Miao, Induced crystallization of rubrene in thin-film transistors, Adv. Mater. 22 (2010) 3242–3246.
[21] N. Stingelin-Stutzmann, E. Smits, H. Wondergem, C. Tanase, P. Blom, P. Smith, D. De Leeuw, Organic thin-film electronics from vitreous solution-processed rubrene hypereutectics, Nat. Mater. 4 (2005) 601–606.
[22] Y. Luo, F. Gustavo, J.Y. Henry, F. Mathevet, F. Lefloch, M. Sanquer, P. Rannou, B. Grevin, Probing local electronic transport at the organic single-crystal/dielectric interface, Adv. Mater. 19 (2007) 2267–2273.
[23] X.N. Sun, C.A. Di, Y.Q. Liu, Engineering of the dielectric-semiconductor interface in organic field-effect transistors, J. Mater. Chem. 20 (2010) 2599–2611.
[24] R. Schmechel, H. von Seggern, Electronic traps in organic transport layers, Phys. Stat. Sol. (a) 201 (2004) 1215–1235.
[25] E. Menard, A. Marchenko, V. Podzorov, M.E. Gershenson, D. Fichou, J.A. Rogers, Nanoscale surface morphology and rectifying behavior of a bulk single-crystal organic semiconductor, Adv. Mater. 18 (2006) 1552–1556.
[26] J.A. Lim, W.H. Lee, H.S. Lee, J.H. Lee, Y.D. Park, K. Cho, Self-organization of ink-jet-printed triisopropylsilylethynyl pentacene via evaporation-induced flows in a drying droplet, Adv. Funct. Mater. 18 (2008) 229–234.
[27] H.C. Yang, T.J. Shin, M.M. Ling, K. Cho, C.Y. Ryu, Z.N. Bao, Conducting AFM and 2D GIXD studies on pentacene thin films, J. Am. Chem. Soc. 127 (2005) 11542–11543.

[28] G.J. Nan, X.D. Yang, L.J. Wang, Z.G. Shuai, Y. Zhao, Nuclear tunneling effects of charge transport in rubrene, tetracene, and pentacene, Phys. Rev. B 79 (2009).
[29] W.L. Kalb, T. Mathis, S. Haas, A.F. Stassen, B. Batlogg, Organic small molecule field-effect transistors with Cytop (TM) gate dielectric: eliminating gate bias stress effects, Appl. Phys. Lett. 90 (2007) 092104.
[30] H. Klauk, Organic thin-film transistors, Chem. Soc. Rev. 39 (2010) 2643–2666.
[31] W.P. Wu, Y.Q. Liu, D.B. Zhu, pi-Conjugated molecules with fused rings for organic field-effect transistors: design, synthesis and applications, Chem. Soc. Rev. 39 (2010) 1489–1502.

conductivities are still lacking [11–17]. Conductivity (σ) depends both on the carrier concentration (p) and the carrier mobility (μ), and these quantities are related by the simple relation $\sigma = pq\mu$, where q is the elementary charge [2]. Thus improvement in conductivities may arise from enhancements in both p and μ, or by p or μ alone. In this study, we present the effects of how TMOs dopants affect the conductivities of an archetype hole-transporting material N'-diphenyl-N,N'-bis(1-naphthyl)(1,1'-biphenyl)-4,4'diamine (NPB) [see Fig. 1, inset]. Three TMOs, namely, MoO_3, WO_3, and V_2O_5 were used in this study. Thin film transistor (TFT) configuration was employed to extract free both p or μ in one experiment. We show that after doping, there is a substantial increase in the hole concentration; in contrast, there is general reduction in the hole mobilities for all three TMOs. Thus the increase in conductivities of TMO-doped NPB can be solely attributed to the increase in the free carrier concentrations. Among the three TMOs, MoO_3 turns out to be the most effective dopant. At a doping concentration of 5% (by volume), conductivity of about 2.2×10^{-7} Scm^{-1} and a free carrier concentration of 1.4×10^{17} cm^{-3} was achieved.

2. Experimental

All TMOs, including molybdenum(VI) oxide (99.998%), tungsten(VI) oxide (99.9994%), and vanadium(V) oxide (99.995%), were purchased from Strem Chemical, Inc. NPB was purchased from E-Ray Optoelectronics Technology Co., Ltd. To evaluate the conductivities of pristine NPB and TMO-doped NPB, thin film transistors in top-contact configuration were fabricated. A p^+-Si wafer, with 300 nm of thermally grown SiO_2, was used as the substrate. Prior to TFT fabrication, the substrate was first cleaned by filtered acetone, followed by a UV–Ozone treatment. Doping was achieved by co-evaporating NPB and the TMO under high vacuum conditions. The doping concentration was 5 vol.% for all three oxides. The evaporation rates of the TMOs were between at 0.1–0.2 Å/s, and the total evaporation rate was kept at 2.0–4.0 Å/s depending on the kind of TMOs used. The active layer had a thickness of 100 nm. Subsequently, source (S) and drain (D) electrodes were coated on the active layer. Both the S and D electrodes are identical and consist of Au interposed by a thin layer (20 nm) of TMO between Au and the underlying organic layer [see Fig. 3(d)]. The channel width (W) and length (L) were 6 mm and 50 μm, respectively. After device fabrication, all TFTs were transferred immediately to a temperature-controlled cryostat for electrical measurements. The temperature of the sample can be regulated between 235 and 360 K. All measurements were performed in vacuum. In plane conductivities of the organic films were measured by holding $V_G = 0$ V while varying V_{DS}, and capturing I_{DS}. In addition to TFTs, UV–NIR absorption measurements (PerkinElmer Lambda Model 750 UV/NIR Spectrometer) were performed to analyze the interactions of the TMOs with NPB. Samples (100 nm) for absorption measurements were prepared on quartz substrates. Moreover, the structures of the organic films were checked by grazing incidence X-ray diffraction (Bruker AXS Model D8 Advance). All films remained amorphous before or after doping.

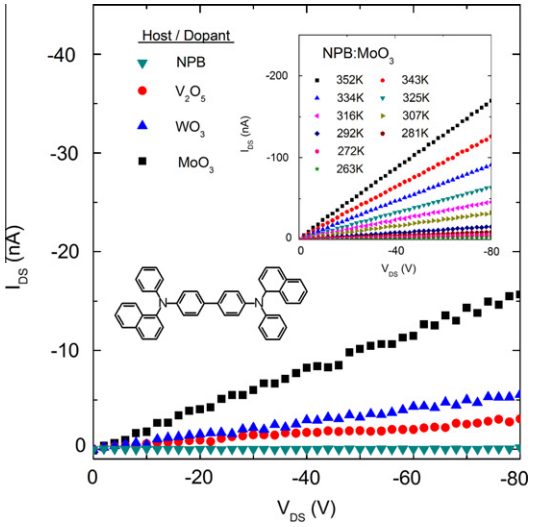

Fig. 1. Current–voltage characteristics of NPB and TMOs-doped NPB at $V_G = 0$ V. Inset: Temperature dependent I–V characteristics at $V_G = 0$ V for NPB:MoO_3 device; molecular structure of NPB is also shown.

3. Results and discussion

The room temperature current–voltage (I–V) characteristics of pristine and TMO-doped NPB samples were shown in Fig. 1. Only hole conduction is expected in all devices as there exists a large energy offset between the work functions of TMOs (>5 eV) and the LUMO of NPB (~2.4 eV). For pristine NPB, only background leakage currents of fractions of nA could be observed. After doping with TMOs, all samples exhibit clear and linear I–V characteristics, indicative of Ohmic conduction. The conductivity of each sample can be extracted from the slope of the I–V curve. Among the three TMOs, MoO_3 appears to be the most effective dopant as it results in a sample with the best conductivity. In contrast, V_2O_5 results in a sample with relative poor conductivity. For MoO_3-doped NPB, the conductivity at room temperature is 2.2×10^{-7} Scm^{-1}, followed by WO_3 (5.1×10^{-8} Scm^{-1}), and V_2O_5 (2.8×10^{-8} Scm^{-1}). The changes in conductivities after doping are comparable to recent reports of TMO-doped NPB [11–13]. The inset in Fig. 1 shows temperature dependent I–V characteristics of MoO_3-doped NPB between 263 and 352 K. A gradual increase in the conductivity with temperature is clearly observed. Similar observations were obtained for the other two TMO-doped samples. Fig. 2 shows a summary of temperature dependent conductivities. However, from the I–V curves alone, or from the conductivities data, one cannot determine if the improvement in conductivity is due to improvement in hole concentration or the hole mobility.

To differentiate the roles of the hole concentration and the mobility, we performed TFT measurements to extract the hole mobilities of the doped sample. Fig. 3 shows the results the TFT measurements at room temperature. For pristine NPB [Fig. 3(a)], well-defined p-channel field-effect

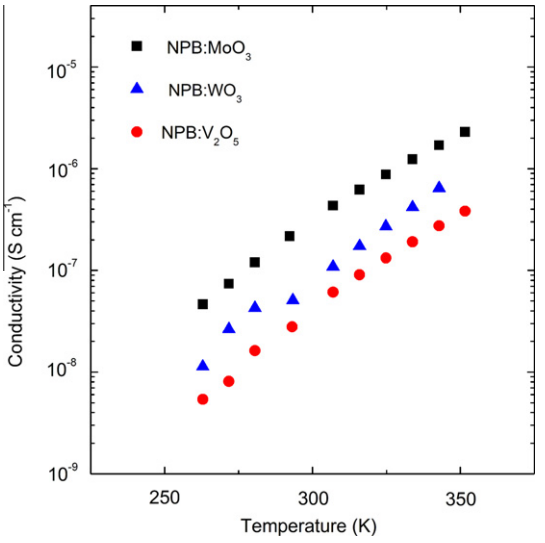

Fig. 2. Conductivity vs. temperature for NPB:MoO_3, NPB:WO_3, and NPB:V_2O_5.

behaviors with well-defined linear and saturation regions in the source-to-drain currents can be observed. The saturation (μ_{Sat}) and linear (μ_{Lin}) region mobilities can be evaluated by the standard equations: [3]

$$I_{DS} = \frac{W}{L}\mu_{Lin}C_i\left[V_{DS}(V_G - V_T) - \frac{V_{DS}^2}{2}\right] \quad (1)$$

$$I_{DS} = \frac{W}{2L}\mu_{Sat}C_i(V_G - V_T)^2 \quad (2)$$

where I_{DS} is the measured source to drain current, W is the channel width, L is the channel length, C_i is the capacitance of the gate dielectric per unit area; V_G, V_{DS} and V_T are the applied gate bias, the source to drain voltage, and the threshold voltage of the OTFT, respectively. For pristine NPB, the saturation and linear region mobilities are 1.1×10^{-5} cm^2/Vs and 7.8×10^{-6} cm^2/Vs, respectively. The results are essentially the same as our previous report [18]. After doping [Fig. 3(b)–(d)], field-effect behaviors can still be observed. However, the field-induced source-to-drain current, I_{DS}, is now on the top of a linear background current (the off-current). As a result, the resulting I_{DS} is now tilted upwards in the positive-x direction. The amount of tilt is clearly determined by the conductivities of the doped-sample in the "off-state" (with $V_G = 0$ V). A similar observation is also found in a previous report [14]. The TFT data can be modeled by a TFT in parallel with a leakage resistance R_{leak}. For the pristine case, R_{leak} is infinite as the amount of free carriers is negligible. For the doped-samples, R_{leak} depends only on the conductivity of the

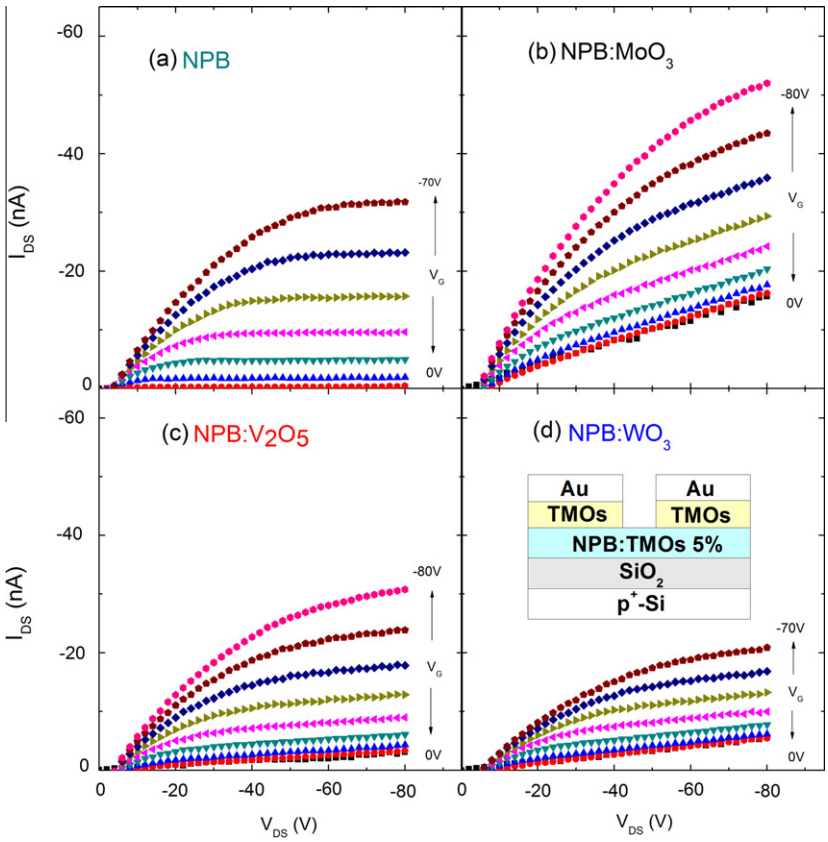

Fig. 3. Output characteristics of pristine NPB and TMOs-doped NPB OTFTs at room temperature. The gate voltage increased in steps of −10 V starting at $V_G = 0$ V. Inset: Bottom-gate top-contact OTFT device based on NPB:TMOs systems.

TMO-doped NPB. The field-effect mobility of a doped sample can, therefore, be extracted by removing the contribution of the background current (I_{DS} at $V_G = 0$ V) arising from a finite R_{leak}. Following this argument, we subtracted all I_{DS} from the background current. The resulting TFT characteristics can be fitted by Eqs. (1) and (2) again to extract both the linear and saturation mobilities. The results at room temperature are summarized in Table 1, columns 3 and 4. Generally, there is a slight reduction of the hole mobilities after doping. For MoO_3-doped NPB, the mobilities in the linear and saturation regions decrease to 9.4×10^{-6} cm^2/Vs and 7.5×10^{-6} cm^2/Vs, respectively. The reduction in the hole mobility is not surprising as ionized oxides (anions) are expected to be present in the doped-sample. The negatively charge oxides are fixed, but they have tendencies to trap holes temporarily, resulting in a reduction in hole mobilities. Trapping of holes was previously observed in the NPB:F4-TCNQ system [14].

As conductivity $\sigma = pq\mu$, we are now ready to extract free hole concentrations (p) in the doped samples using the conductivity data from Fig. 2 and the mobility data derived from Fig. 3. We use the FE mobilities extracted in the saturation regions as they are less susceptible to contact effects. For MoO_3-doped NPB, the free carrier concentration is 1.4×10^{17} cm^{-3} and is the highest among three TMOs. The free carrier concentrations for WO_3 (5.7×10^{16} cm^{-3}) and V_2O_5 (2.4×10^{16} cm^{-3}) doped samples are lower. To further explore the interactions of the three TMOs with NPB, we performed temperature dependent measurements. Fig. 4 shows the hole concentrations against the reciprocal of the absolute temperature T. It can be clearly seen that for each sample, all the temperature dependent data lie essentially on a straight line. The data can be fitted by the standard Arrehnius equation:

$$p = N_V \exp\left(-\frac{\Delta E}{k_B T}\right) \quad (3)$$

where p is the free hole concentration, k_B is the Boltzmann constant, N_V is the effective hole density of states, and ΔE is the activation energy. The solid lines in Fig. 4 are best fits to the data using Eq. (3). From the slope and the y-intercept, one can extract ΔE and N_V of each sample, respectively. These two parameters deserve additional comments. First, when TMO is doped into organic semiconductors, charge-transfer (CT) complexes can be formed [13,16]. In the case of TMO-doped NPB, due to the large electron affinities of the TMOs, NPB will partially donate some electron density to the oxide, resulting in a CT complex [19]. ΔE can be interpreted as the average energy required to ionize the CT complexes. The products are

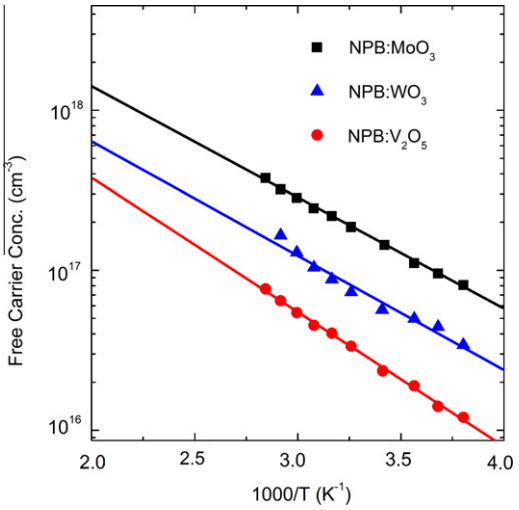

Fig. 4. Free hole concentrations vs. 1000/T plot for TMOs-doped NPB.

negatively charged TMO, and a free hole. Second, N_V, the prefactor in the exponential term in Eq. (3), can be interpreted as the number of states available for hole generation in the doped samples. For TMO-doped NPB, the oxide component tends to form nano-clusters [20]. Only those NPB molecules that are in the immediate neighborhood of the TMO nano-clusters are available for charge generation. As the three TMOs can conceivably have, on average, different sizes of nano-clusters in NPB, they may lead to different values of N_V. In our experiment, we found that both ΔE and N_V are the most favorable for the NPB:MoO_3 system in terms of carrier generation. The system has the lowest activation energy (138 meV) when compared to WO_3 (142 meV) and V_2O_5 (166 meV). Furthermore, N_V are between $\sim$2–3 $\times 10^{19}$ cm^{-3} for all doped samples, but is the largest for NPB:MoO_3. The results for ΔE and N_V are summarized in the last two columns in Table 1. Thus the temperature dependent data provide a thermo-dynamical explanation to the observation that MoO_3 is the best dopant among the TMOs.

To substantiate the temperature dependent data, we performed UV–NIR absorption spectra on pristine NPB and the three doping systems. Fig. 5 shows typical absorption spectra of 100 nm pristine and doped NPB on quartz substrates. Pristine NPB has a monotonically decreasing background from about 550–1300 nm. In contrast, after doping with TMOs, new absorption peaks can be found in the same spectral region. For the case of MoO_3-doped NPB, a well-defined peak occurs at about 500 nm.

Table 1
Conductivities (σ), field effect mobilities (μ_{Sat}, μ_{Lin}), free carrier concentrations (p), activation energies (ΔE) and the effective density of states (N_V) of NPB and TMOs-doped NPB.

	σ Conductivity (Scm^{-1})	μ_{Sat} (cm^2/Vs)	μ_{Lin} (cm^2/Vs)	p free carrier conc. (cm^{-3})	ΔE (meV)	N_V (cm^{-3})
NPB	–	1.1×10^{-5}	7.8×10^{-6}	–	–	–
NPB:V_2O_5 5%	2.8×10^{-8}	7.4×10^{-6}	6.6×10^{-6}	2.4×10^{16}	166	1.8×10^{19}
NPB:WO_3 5%	5.1×10^{-8}	5.6×10^{-6}	4.1×10^{-6}	5.7×10^{16}	142	1.8×10^{19}
NPB:MoO_3 5%	2.2×10^{-7}	9.4×10^{-6}	7.5×10^{-6}	1.4×10^{17}	138	3.5×10^{19}

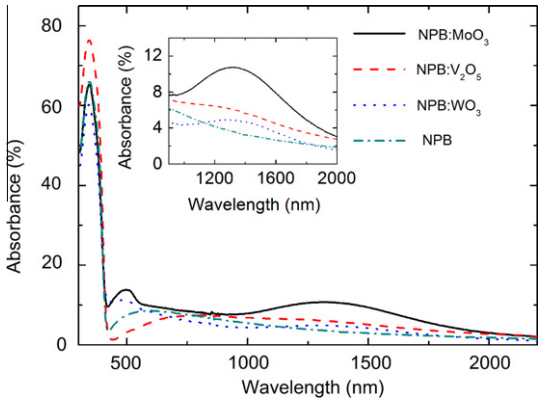

Fig. 5. Absorption spectra of NPB, NPB:MoO_3, NPB:V_2O_5, NPB:WO_3 films (100 nm) on quartz substrates. Inset shows the selected region from 900–2000 nm of the same spectra.

Furthermore, a broad peak, centered at about 1300 nm can be clearly observed (Fig. 5 inset). Similar broad peaks can be observed for the other two doped samples, but their intensities are significantly weaker. From the literatures, these peaks can be attributed to the charge transfer (CT) complex formed between the NPB and the TMOs molecules [13,16]. Their precise origins are still not known, but they may arise from resonant absorptions of the CT complexes. So their relationship with the activation energy ΔE is not clear. However, the absorption data do support again the observation that the reaction between MoO_3 with NPB is the strongest, resulting in the liberation of the largest amount of free carriers among the three TMOs.

4. Conclusions

The transport properties of NPB:TMOs systems were studied in details by field-effect transistors technique. After doping NPB with different TMOs, there is only a slight reduction in carrier mobilities in each case. Despite the reduction in carrier mobilities, the conductivities of all TMO doped systems were increased significantly. We concluded that this increase in conductivities is primarily due to an increase in the free carrier concentration when the oxide is doped into NPB. Among the three different oxides, MoO_3 is the most effective dopant as evidenced by its lowest activation energy of 138 meV and highest free carrier concentration of 1.4×10^{17} cm^{-3} in NPB. This is consistent with the independent UV–NIR absorption spectrum measurement, indicating that MoO_3 – NPB has the strongest interaction comparing with V_2O_5 and WO_3.

Acknowledgments

Supports of this research by the Research Committee of Hong Kong Baptist University and the Research Grant Council of Hong Kong under grant # HKBU211209E are gratefully acknowledged. Measurements of the GIXRD were supported by an equipment grant from the Research Grant Council of Hong Kong under grant # SEG HKBU06.

References

[1] F. So (Ed.), Organic Electronics: Materials, Processing, Devices and Applications, CRC Press, Francis and Taylor, 2010.
[2] C.W. Tang, S.A. VanSlyke, Appl. Phys. Lett. 51 (1987) 913.
[3] S.M. Sze, Physics of Semiconductor Devices, Wiley, New York, 1981.
[4] M. Pfeiffer, A. Beyer, T. Fritz, K. Leo, Appl. Phys. Lett. 73 (1998) 3202.
[5] S. Olthof, W. Tress, R. Meerheim, B. Lussem, K. Leo, J. Appl. Phys. 106 (2009) 103711.
[6] J. Kido, T. Matsumoto, Appl. Phys. Lett. 73 (1998) 2866.
[7] L.S. Hung, C.W. Tang, M.G. Mason, Appl. Phys. Lett. 70 (1997) 152.
[8] S.C. Tse, H.H. Fong, S.K. So, J. Appl. Phys. 94 (2003) 2033.
[9] S. Tokito, K. Noda, Y. Taga, J. Phys. D Appl. Phys. 29 (1996) 2750.
[10] M. Kröger, S. Hamwi, J. Meyer, T. Riedl, W. Kowalsky, A. Kahn, Appl. Phys. Lett. 95 (2009) 123301.
[11] X.F. Qiao, J.S. Chen, X.L. Li, D.G. Ma, J. Appl. Phys. 107 (2010) 104505.
[12] C.K. Suman, J.J. Yang, C.H. Lee, Mater. Sci. Eng. B 166 (2010) 147.
[13] J.H. Lee, D.S. Leem, J.J. Kim, Org. Electron. 11 (2010) 486.
[14] T. Matsushima, C. Adachi, Thin Solid Films 517 (2008) 874.
[15] C.C. Chen, B.C. Huang, M.S. Lin, Y.J. Lu, T.Y. Cho, C.H. Chang, K.C. Tien, S.H. Liu, T.H. Ke, C.C. Wu, Org. Electron. 11 (2010) 1901.
[16] W.J. Shin, J.Y. Lee, J.C. Kim, T.H. Yoon, T.S. Kim, O.K. Song, Org. Electron. 9 (2008) 333.
[17] C.I. Wu, C.T. Lin, G.R. Lee, T.Y. Cho, C.C. Wu, T.W. Pi, J. Appl. Phys. 105 (2009) 033717.
[18] C.H. Cheung, K.K. Tsung, K.C. Kwok, S.K. So, Appl. Phys. Lett. 93 (2008) 083307.
[19] S. Hamwi, J. Meyer, T. Winkler, T. Riedl, W. Kowalsky, Appl. Phys. Lett. 94 (2009) 253307.
[20] J. Meyer, S. Hamwi, S. Schmale, T. Winkler, H.H. Johannes, T. Riedl, W. Kowalsky, J. Mater. Chem. 19 (2009) 702.

quantum efficiency over 20.0% was demonstrated in the two color and three color PHWOLEDs using the PPO27 as the host material in the red:blue emitting layer. In addition, the effect of the thickness of each emitting layer in the red:blue/green stack structure was investigated.

2. Experimental

The basic device structure of the two color PHOLEDs was indium tin oxide (ITO, 50 nm)/N,N′-diphenyl-N,N′-bis-[4-(phenyl-m-tolyl-amino)-phenyl]-biphenyl-4,4′-diamine (DNTPD, 60 nm)/N,N′-di(1-naphthyl)-N,N′-diphenylbenzidine (NPB, 5 nm)/N,N′-dicarbazolyl-3,5-benzene (mCP, 10 nm)/PPO27:iridium(III) bis(4,6-(di-fluorophenyl)-pyridinato-N,C′) picolinate (FIrpic):iridium(III) bis(2-phenylquinoline) acetylacetonate (Ir(pq)$_2$acac) (30 nm, 15%:*x*% doping)/diphenylphosphine oxide-4-(triphenylsilyl)phenyl (TSPO1, 20 nm)/LiF (1 nm)/Al (200 nm). The doping concentration of FIrpic was 15%, while the doping concentrations of the Ir(pq)$_2$acac were varied as 0.7%, 1.0% and 1.5%. Three color PHWOLEDs had the device structure of ITO (150 nm)/DNTPD (60 nm)/NPB (5 nm)/mCP (10 nm)/PPO27:FIrpic:Ir(pq)$_2$acac (*x* nm, 15%:0.7%)/bis-9,9′-spirobi[fluoren-2-yl]-methanone (BSFM): tris(2-phenylpyridine) iridium (Ir(ppy)$_3$)(30 − *x* nm, 3%)/TSPO1 (20 nm)/LiF (1 nm)/Al (200 nm). The thickness of the red:blue and green emitting layers was changed to study the effect of the emitting layer thickness on the device performances of PHWOLEDs. The thicknesses of the red:blue emitting layer were 3, 4, 5, 10 and 20 nm. Chemical structures of the PPO27 and BSFM are shown in Fig. 1 in addition to the device structure and energy level diagram of WOLEDs fabricated in this work. The PPO27 host material was synthesized according to the method reported in other work [17]. BSFM was reported in other work showed high triplet energy of 2.6 eV for energy transfer to green phosphorescent dopant [18]. Energy levels of the BSFM are shown in the energy level diagram of Fig. 1. All devices were fabricated by thermal evaporation at a vacuum pressure of 7×10^{-7} torr. The evaporation rate of the charge transport layers and host materials was 0.1 nm/s and the doping concentration was controlled by managing the deposition rate of the dopant. All devices were encapsulated with a glass lid and a CaO getter after device fabrication. Electroluminescence (EL) characteristics and EL spectra of PHWOLEDs were measured with Keithley 2400 source measurement unit and CS 1000 spectroradiometer.

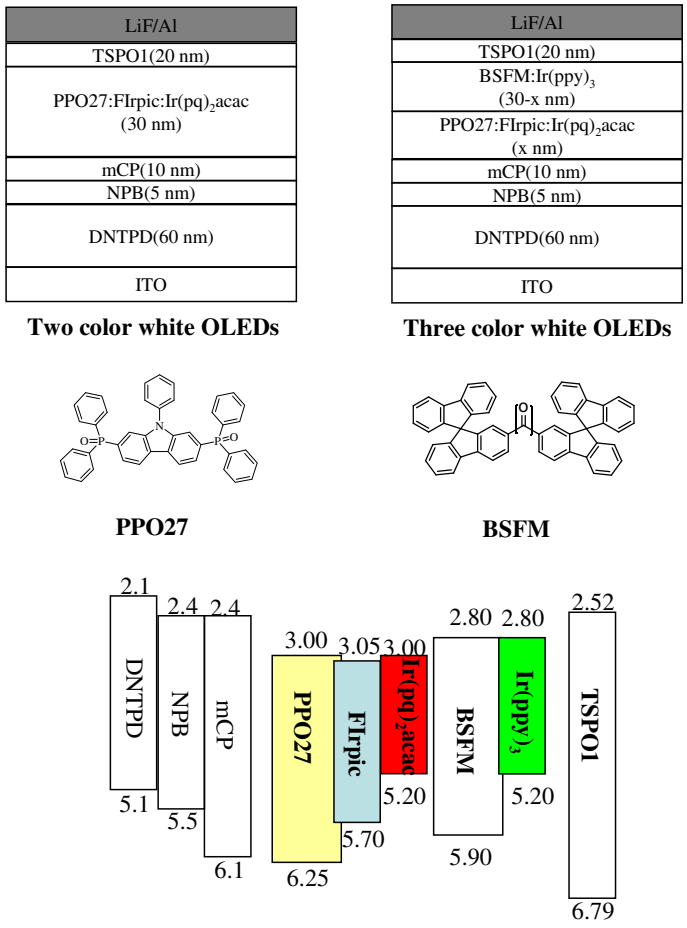

Fig. 1. Chemical structure of PPO27 host and BSFM host in addition to device structures of two color and three color PHWOLEDs.

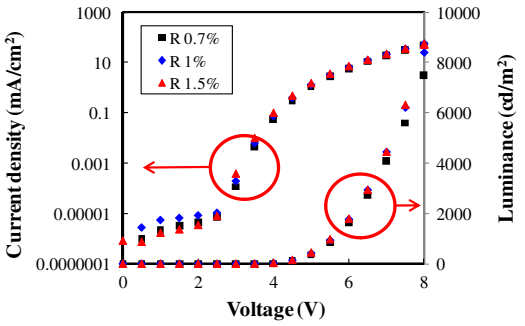

Fig. 2. Current density–voltage-luminance curves of two color PHWOLEDs according to red doping concentration. (For interpretation of the references to colour in this figure legend, the reader is referred to the web version of this article.)

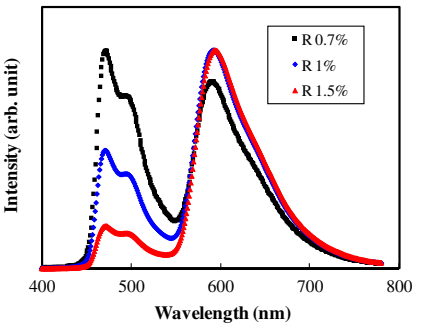

Fig. 4. Electroluminescence spectra of two color PHWOLEDs according to red doping concentration. (For interpretation of the references to colour in this figure legend, the reader is referred to the web version of this article.)

3. Results and discussion

The PPO27 was reported as the high triplet energy host material for blue PHOLEDs and was effective to improve the quantum efficiency and driving voltage of blue PHOLEDs [17]. A high quantum efficiency of 23.9% and a high power efficiency of 37.5 lm/W were reported in the blue PHOLEDs. Therefore, the PPO27 can be effectively used as the host material for the two color and three color PHWOLEDs.

Two color PHWOLEDs with a single emitting layer doped with red and blue triplet emitters were fabricated and the doping concentration of the red dopant was optimized. Fig. 2 shows the current density–voltage-luminance curves of the PHWOLEDs according to the doping concentration of the red dopant. The current density of the PHWOLEDs was similar irrespective of the doping concentration of the red dopant and the luminance showed the same tendency as the current density. As the doping concentration of the red dopant was low compared to that of the blue dopant, the doping concentration of the red dopant did not greatly affect the current density of the PHWOLEDs. The turn-on voltage of the device was 3.0 V and the driving voltage at 1000 cd/m^2 was 5.6 V.

Quantum efficiency–luminance curves of the PHWOLEDs are shown in Fig. 3. The quantum efficiency of the three PHWOLEDs was similar over all luminance range irrespective of the doping concentration. The maximum quantum efficiency of the PHWOLEDs was over 20.0% and the quantum efficiency at 1000 cd/m^2 was over 16.0% in all PHWOLEDs. The PHWOLEDs showed high quantum efficiency because of charge balance and efficient light emission of Ir(pq)$_2$acac in the emitting layer. It was reported that the PPO27 based blue PHOLEDs exhibited good charge balance due to bipolar charge transport properties of the PPO27 host, which also balances holes and electrons in the emitting layer of PHWOLEDs[17]. The efficient light emission of the Ir(pq)$_2$acac also contributes to the high quantum efficiency of the PHWOLEDs. The main light emission mechanism of the PHWOLEDs is the cascade energy transfer from PPO27 to FIrpic followed by energy transfer to Ir(pq)$_2$acac and charge trapping by the dopant. In particular, the charge trapping is important for the light emission of the red dopant material. Therefore, the Ir(pq)$_2$acac should have high quantum efficiency to obtain high quantum efficiency in the emitting layer. As reported earlier, the Ir(pq)$_2$acac based devices showed high quantum efficiency over 20%, which improved the quantum efficiency of the PHWOLEDs [19].

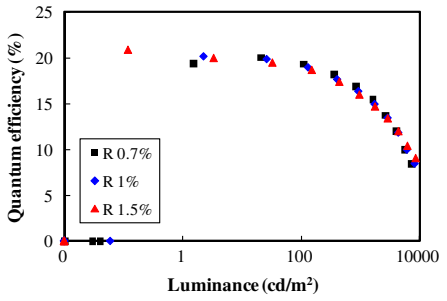

Fig. 3. Quantum efficiency–luminance curves of two color PHWOLEDs according to red doping concentration. (For interpretation of the references to colour in this figure legend, the reader is referred to the web version of this article.)

EL spectra of the PHWOLEDs are presented in Fig. 4 according to the doping concentration of the Ir(pq)$_2$acac. The red intensity was gradually increased according to the increase of the red doping concentration. As the energy transfer from FIrpic to Ir(pq)$_2$acac is the main light emission process for the single emitting layer PHWOLEDs, the increase of the Ir(pq)$_2$acac doping concentration intensified the red emission because of the blue absorption by the red dopant followed by red emission. The relative light intensity of the red and blue emission was balanced at a doping concentration of 0.7% and the color coordinate of the 0.7% Ir(pq)$_2$acac doped PHWOLEDs was (0.38, 0.37). Detailed device data are summarized in Table 1.

As high quantum efficiency could be obtained from the two color PHWOLEDs, three color PHWOLEDs were developed using the PPO27 based emitting layer. Red and blue co-doped PPO27 emitting layer was combined with phosphorescent green emitting layer to fabricate PHWOLEDs. Electron transport type host, BSFM, was adopted as the triplet host for the green emitting layer. As the optimum doping concentration of the BSFM based green PHOLED was 3%, the 3% Ir(ppy)$_3$ doped BSFM layer was used as the green emitting layer. The green emitting layer was

Table 1
Device performances of the two color PHWOLEDs with PPO27 as the host in red:blue phosphorescent emitting layer according to red doping concentration.

	Quantum efficiency (%)		Current efficiency (cd/A)		Power efficiency (lm/W)		Color coordinate	CRI
	Max	1000 cd/m^2	Max	1000 cd/m^2	Max	1000 cd/m^2		
R 0.7%	20.0	16.6	36.2	29.9	34.9	18.7	(0.38,0.37)	64
R 1.0%	20.1	16.1	36.1	29.1	35.9	18.3	(0.47,0.38)	61
R 1.5%	20.0	15.9	34.6	27.8	34.3	17.5	(0.54,0.39)	49

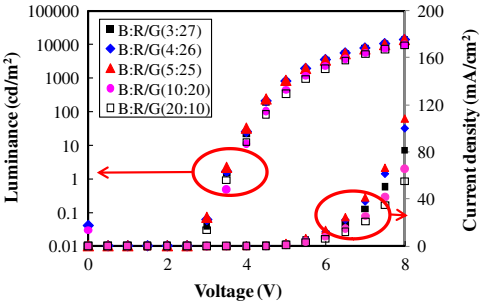

Fig. 5. Current density–voltage-luminance curves of three color PHWOLEDs with different red:blue and green emitting layer thicknesses. (For interpretation of the references to colour in this figure legend, the reader is referred to the web version of this article.)

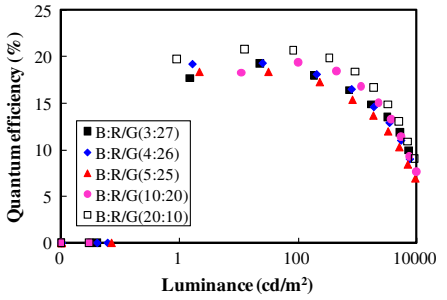

Fig. 6. Quantum efficiency–luminance curves of three color PHWOLEDs with different red:blue and green emitting layer thicknesses. (For interpretation of the references to colour in this figure legend, the reader is referred to the web version of this article.)

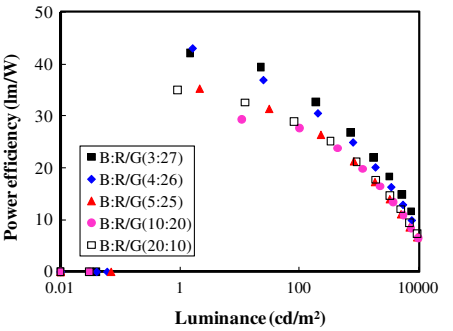

Fig. 7. Power efficiency–luminance curves of three color PHWOLEDs with different red:blue and green emitting layer thicknesses. (For interpretation of the references to colour in this figure legend, the reader is referred to the web version of this article.)

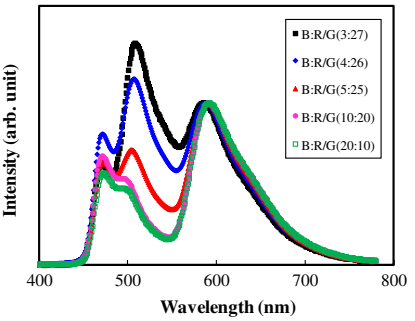

Fig. 8. Electroluminescence spectra of three color PHWOLEDs with different red:blue and green emitting layer thicknesses. (For interpretation of the references to colour in this figure legend, the reader is referred to the web version of this article.)

stacked on the red:blue emitting layer and the thickness of each emitting layer was changed to control the emission spectra and device performances of PHWOLEDs.

The thickness of the whole emitting layer was fixed at 30 nm and the thickness of the red:blue and green emitting layers was changed. Fig. 5 shows the current density–voltage-luminance curves of the three color PHWOLEDs according to the thickness of red:blue emitting layer. The current density was high in the device with 5 nm thick red:blue emitting layer and was reduced in the devices with less than 5 nm thick red:blue emitting layer. The reduced current density of the PHWOLED with thin red:blue emitting layer is caused by the poor hole injection properties originated from the incomplete film formation. It is difficult to form continuous film using the 3 nm and 4 nm thick red:blue emitting layer and the hole transport layer is partially covered by BSFM green emitting layer, leading to partially direct hole injection from the hole transport layer to the BSFM green emitting layer. As the BSFM is an electron transport type host, the hole injection from the hole transport layer to the BSFM is worse than that from the hole transport layer to the PPO27 layer. As the coverage of the red:blue emitting layer on the hole transport layer was increased, the current density was also increased. However, the current density was reduced again in the device with thick red:blue emitting layer (10 and 20 nm) due to rather poor charge transport properties of the red:blue emitting layer compared with those of green emitting layer. The poor charge transport properties of the red:blue emitting layer is mostly due to charge trapping by the red dopant [20]. The difference of the luminance data is caused by the different recombination efficiency of the PHWOLEDs depending on the thickness of each emitting layer.

Table 2
Device performances of the three color PHWOLEDs with PPO27 as the host in red:blue phosphorescent emitting layer.

	Quantum efficiency (%)		Current efficiency (cd/A)		Power efficiency (lm/W)		Color coordinate	CRI
	Max	1000 cd/m^2	Max	1000 cd/m^2	Max	1000 cd/m^2		
B:R/G(3/27)	19.3	16.0	45.4	37.2	42.2	25.1	(0.38,0.48)	65
B:R/G(4/26)	19.3	16.1	43.3	34.1	43.0	23.2	(0.38,0.44)	72
B:R/G(5/25)	18.4	14.9	36.1	29.3	35.3	20.2	(0.43,0.42)	74
B:R/G(10/20)	19.4	17.3	35.9	32.1	29.4	20.8	(0.43,0.39)	67
B:R/G(20/10)	20.8	18.2	37.6	33.0	35.0	20.7	(0.45,0.39)	63

The quantum efficiency–luminance data of the PHWOLEDs are presented in Fig. 6. The maximum quantum efficiency of the PHWOLED was in the range from 18.4% to 20.8%, while the range of quantum efficiency at 1000 cd/m^2 was from 14.9% to 18.2%. The quantum efficiency was minimized in the device with 5 nm thick red:blue emitting layer and was maximized in the device with 20 nm thick red:blue emitting layer. At high red:blue emitting layer thickness, the BSFM green emitting layer played a role of electron transport layer as shown in the EL spectra of the three color PHWOLEDs, resulting in quantum efficiency similar to that of the two color PHWOLEDs. As the BSFM has good electron transport properties and electrons are little trapped by the $Ir(ppy)_3$ in the BSFM emitting layer, the recombination zone was close to the hole transport side, leading to weak green emission in the three color PHWOLEDs. The quantum efficiency was reduced as the thickness of the red:blue emitting layer decreased up to 5 nm because of less electron injection into the red:blue emitting layer. The increase of the quantum efficiency below 5 nm can be explained by the high quantum efficiency of the green emitting layer. As the red:blue emitting layer cannot form continuous film on the hole transport layer, some part of the device has the device structure with only green emitting layer and the other part of the device has the device structure of red:blue and green emitting layers. Although the quantum efficiency of the red:blue and green stacked part is reduced at a thickness below 5 nm, the quantum efficiency of the green emitting part is as high as 25.1% (this was not shown here). Therefore, the quantum efficiency of the PHWOLEDs is increased again at a low red:blue emitting layer thickness. The efficiency value of the PHWOLEDs fabricated in this work is one of the best efficiency values reported in PHWOLEDs.

Power efficiency of the three color PHWOLEDs was plotted against luminance in Fig. 7. The power efficiency was maximized at the red:blue emitting layer thickness of 3 nm because of strong green emission. The green intensity was reduced at high red:blue emitting layer thickness, resulting in the decrease of the power efficiency. The maximum power efficiency value of the PHWOLEDs was 42.2 lm/W and the power efficiency at 1000 cd/m^2 was 25.1 lm/W.

EL spectra of the three color PHWOLEDs are shown in Fig. 8 according to the thickness of the red:blue emitting layer. All EL spectra were normalized to monitor the change of the relative emitting intensity of red, green and blue emissions. The green intensity was very weak in the PHWOLED with 20 nm thick red:blue emitting layer and it was not intensified although the thickness of the red:blue emitting layer was reduced up to 10 nm. The green intensity was a little increased at the red:blue emitting layer thickness of 5 nm and was sharply increased at the red:blue emitting layer thickness of 4 nm. It was even more intensified at the red:blue emitting layer thickness of 3 nm. As explained in the device data, the direct hole injection from the hole transport layer to the green emitting layer at low red:blue emitting layer thickness intensified the green emission. This indirectly proves the incomplete film formation of the red:blue emitting layer below 5 nm. The color coordinate of the three color PHWOLEDs was changed from (0.45,0.39) to (0.38,0.48) according to the decrease of the red:blue emitting layer thickness from 20 nm to 3 nm. Color coordinate of the PHWOLEDs is summarized in Table 2 in addition to other device data. The color rendering index (CRI) was high in the PHWOLED with 5 nm thick red:blue emitting layer and it was 74. CRI of all devices are summarized in Table 2.

4. Conclusions

In conclusion, high efficiency two color and three color PHWOLEDs with a emitting layer stack structure of red:blue/green could be effectively developed using PPO27 as the host material for the red:blue emitting layer. High quantum efficiency over 20.0% was achieved in both two color and three color PHWOLEDs using the PPO27 host material and the device performances could be effectively managed by changing the thickness of the emitting layer. It was found that the red:blue/green stacked PHWOLEDs with the PPO27 host is promising as the high efficiency PHWOLEDs in display and lighting applications.

References

[1] J. Kido, M. Kimura, K. Nagai, Science 267 (1995) 1332.
[2] Y.R. Sun, N.C. Giebink, H. Kanno, B.W. Ma, M.E. Thompson, S.R. Forrest, Nature 440 (2006) 908.
[3] G. Schwartz, M. Pfeiffer, S. Reineke, K. Walzer, K. Leo, Adv. Mater. 19 (2007) 3672.
[4] S.O. Jeon, K.S. Yook, C.W. Joo, J.Y. Lee, Opt. Lett. 34 (2009) 407.
[5] S. Gong, Y. Chen, C. Yang, C. Zhong, J. Qin, D. Ma, Adv. Mater. doi:10.1002/adma.201002732 (2011).
[6] S.J. Su, E. Gonmori, H. Sasabe, J. Kido, Adv. Mater. 20 (2008) 4189.
[7] S. Tokito, T. Iijima, T. Tsuzuki, F. Sato, Appl. Phys. Lett. 83 (2003) 2459.
[8] Q. Wang, J. Ding, D. Ma, Y. Cheng, L. Wang, X. Jing, F. Wang, Adv. Funct. Mater. 19 (2009) 84.
[9] X. Yang, Z. Wang, S. Makakumi, J. Li, G.E. Jabbour, Adv. Mater. 20 (2008) 2405.
[10] S. Reineke, F. Lindner, G. Schwartz, N. Seidler, K. Walzer, B. Lüssem, K. Leo, Nature 459 (2009) 234.
[11] Y. Sun, S.R. Forrest, Appl. Phys. Lett. 91 (2007) 263503.
[12] Y. Sun, S.R. Forrest, Org. Electron. 9 (2008) 994.
[13] B.W. D'Andrade, R.J. Holmes, S.R. Forrest, Adv. Mater. 16 (2004) 624.

[14] G. Cheng, Y. Zhang, Y. Zhao, Y. Lin, C. Ruan, S. Liu, T. Fei, Y. Ma, Y. Cheng, Appl. Phys. Lett. 89 (2006) 43504.
[15] H. Sasabe, J. Takamatsu, T. Motoyama, S. Watanabe, G. Wagenblast, N. Langer, O. Molt, E. Fuchs, C. Lennartz, J. Kido, Adv. Mater. doi:10.1002/adma.201002254 (2011).
[16] K.S. Yook, S.O. Jeon, C.W. Joo, J.Y. Lee, M.S. Kim, H.S. Choi, S.J. Lee, C.W. Han, Y.H. Tak, Org. Electron. 10 (2009) 681.
[17] H.S. Son, C.W. Seo, J.Y. Lee, J. Mater. Chem. 21 (2011) 5638.
[18] A. Gerhard, H. Vestweber, P. Stossel, S. Heun, H. Spreitzer, USP 7345301 (2008).
[19] S.O. Jeon, K.S. Yook, C.W. Joo, J.Y. Lee, Org. Electron. 11 (2010) 881.
[20] K.S. Yook, S.O. Jeon, C.W. Joo, J.Y. Lee, J. Ind. Eng. Chem. 15 (2009) 420.

addition of non-volatile additives to DCB can significantly improve the performance of P3HT:PCBM devices [7]. Thus, controlling the interactions between P3HT, PCBM, and solvent during the drying process appears to be an effective route to modulating device performance and could potentially enable fabrication of high performance devices without the use of halogenated solvents. The use of solvent mixtures of differing compositions provides one facile route to modulate the solvent quality.

In an attempt to rationally select candidate solvent mixtures, we have utilized Hansen solubility parameters (HSP), which describe the total cohesion energy, E by three contributions: the dispersion interactions, E_d, permanent dipole-permanent dipole molecular interactions, E_p, and the hydrogen bonding molecular interactions, E_h. This energy is directly related to the solubility parameters (δ), which are the square root of the cohesion energy density (E/V) [12]

$$\delta^2 = \delta_d^2 + \delta_p^2 + \delta_h^2 \quad (1)$$

The application of solubility parameters have been utilized in understanding the solubility of polymers [13] and pharmaceuticals [14] in solvent mixtures. Fig. 1 illustrates the HSP for a number of different solvents. The solvents that can dissolve the P3HT and PCBM mixture (chloroform [$CHCl_3$], ortho-dichlorobenzene [o-DCB], chlorobenzene [CB], biphenyl, mesitylene [MS], carbon tetrachloride [CCl_4], diethylbenzene, ethylbenzene, toluene and xylene) are grouped together in HSP space that define the interaction radius (R_0) wherein solvents dissolve the polymer and solvents outside of the volume defined by R_0 will not dissolve the polymer. As DCB tends to yield devices with better performance, a mixture that matches its solubility parameters (δ_d = 19.2, δ_p = 6.3, δ_h = 3.3 $MPa^{1/2}$) would be desired based upon these solubility arguments. As illustrated by the line in Fig. 1, a mixture of MS and AP can closely mimic DCB. In this work, we describe the use of MS/AP mixtures to fabricate BHJ solar cells based upon P3HT and PCBM blends. With proper choice of relative MS/AP composition, device efficiencies approaching that obtained from those cast from DCB can be obtained.

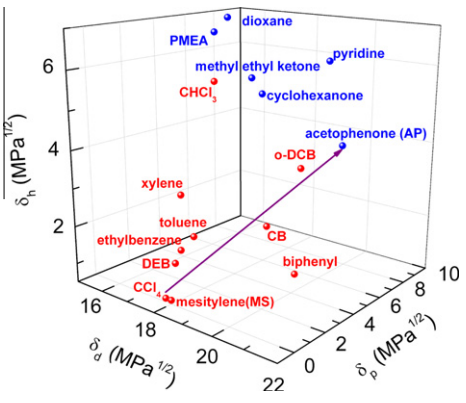

Fig. 1. Hansen solubility parameters (HSP) for selected solvents and solvent mixtures. Solvents in red are considered as good solvents for P3HT/PCBM blend and in blue are non-solvents. (For interpretation of the references in colour in this figure legend, the reader is referred to the web version of this article.)

2. Experimental details

2.1. Materials and device fabrication

Bulk-heterojunction solar cells based on P3HT/PCBM blend were fabricated in the following simple device stack structure: Indium tin oxide(ITO)/poly(3,4-ethylenedioxythiophene):poly(styrenesulfonate)(PEDOT:PSS)/P3HT:PCBM/bathocuproine(BCP)/Al. Regioregular P3HT (Rieke Metals, 4002E) and PCBM (99.5%, Solenne) were dissolved in a 1:1 ratio to 1.0 wt.% in mixtures of MS (99.0%, Sigma–Aldrich) and AP (99%, Sigma–Aldrich) by heating and stirring for 2 h at 75 °C in a nitrogen atmosphere. These solutions were then cooled slowly to ambient temperature. For comparison devices, the P3HT:PCBM blend (1.5 wt.%, 1:1 weight ratio) was dissolved in DCB (99%, Sigma–Aldrich) and stirred for 24 h at 40 °C. Before the fabrication of the devices, the substrates were cleaned by scrubbing with detergent and ultrasonic treatment in deionized water, acetone and isopropyl alcohol sequentially and UV-ozone (Jelight model 42) treatment for 40 min. The cleaned ITO-coated glass substrates were modified by spin-coating a thin layer (~40 nm) of PEDOT:PSS (Clevios, 4083) and cured at 200 °C for 30 min. The polymer blended films were spin-coated in a nitrogen-filled glove box onto the PEDOT:PSS modified substrate. The as-cast films were dried overnight in nitrogen atmosphere at ambient temperature. After drying, the samples were thermally annealed at 140 °C for 30 min. Finally, BCP (~14 nm) and Al cathode (~100 nm) layers were thermally deposited on top of the active layer and each device had an active area of 0.04 cm^2.

2.2. Device characterization

The current density–voltage characteristics were measured using a solar simulator (Newport, 150 W) with an AM 1.5G filter in a nitrogen filled glovebox at room temperature. The intensity of illumination was set for 100 mW/cm^2 using a Si reference Hamamatsu cell (Model C24 S1787-04) calibrated by the National Renewable Energy Laboratory (NREL), USA. The spectral mismatch of the solar simulator was estimated to be less than 10%. External quantum efficiency data were measured with monochromatic light by varying the excitation wavelength from 300 to 850 nm at intervals of 10 nm, under a white bias light of 100 mW cm^{-2} (Optronics Laboratories, Inc.). The surface morphology of the thin films was measured using atomic force microscopy (Park Systems XE-150) operating in non-contact mode with 2 μm × 2 μm scan size. The film thickness was measured using a Variable Angle Spectroscopic Ellipsometer (VASE M-2000, J.A. Woollam Co.).

3. Results and discussion

Fig. 2 shows the device performance with the use of pure MS and various MS/AP solvent mixtures. The J–V curves show a significant increase in the magnitude of short circuit current (J_{sc}) with the addition of AP to the MS solution. However, further increase of the AP concen-

tration from 20 vol.% to 30 vol.% lead to a negligible increase in J_{sc} and a small decrease in open-circuit voltage (V_{oc}). These changes in performance can be quantified by comparing the power conversion efficiency (PCE) of the devices as illustrated in Fig. 2b. The device fabricated from the 80–20 vol.% MS–AP mixture has a larger PCE than both 90–10 and 70–30 vol.% MS–AP mixtures. This result suggests that there is an optimal concentration for device performance. However, it may be noted that the composition of the solvent mixture (80–20 vol.% MS–AP) is far removed from the ideal composition (27–73 vol.% MS–AP with $\delta_d = 19.2$, $\delta_p = 6.3$, $\delta_h = 2.9$ MPa$^{1/2}$) that matches DCB based on the HSP selection rules. One explanation could be solvent electron density, which has been shown to be critical for surfactant solubility [15], is not explicitly addressed using HSP selection rules. Moreover, HSP does not account for any electrostatic interactions that will be important in this system. However, the normal boiling point difference between MS (165 °C) and AP (202 °C) results in significant concentrating of the AP during solvent evaporation in the film formation process. Thus during film formation, the solvent quality (from HSP arguments) would be evolving due to differential evaporation of the components in the solvent mixture. Thus, it would be expected that as the film forms the solvent quality will trend towards, and hopefully

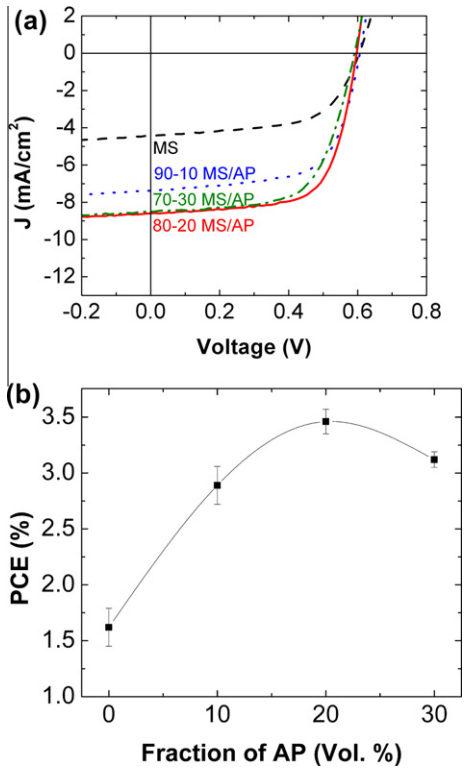

Fig. 2. (a) The *J–V* characteristics under illumination of 100 mW cm^{-2} (AM 1.5G) for devices fabricated from pure mesitylene and various MS/AP mixtures and (b) PCE values of devices fabricated from pure mesitylene and various MS/AP mixtures as a function of the amount of acetophenone (vol.%) in the solvent mixtures.

approach, that of DCB, due to comparably low boiling temperature of MS.

Nonetheless, this mixed solvent system of MS–AP does offer a route to improved device performance. Similarly, Bouman et al. [16] illustrated the potential of mixed solvent systems using chloroform–methanol mixtures and these mixtures have been shown to be effective in P3HT/PCBM system [8], but the origins of the improvement are not clear and halogenated solvent was still utilized. In this case, the HSP for methanol ($\delta_d = 15.1$, $\delta_p = 12.3$, $\delta_h = 22.3$ MPa$^{1/2}$) would not suggest an improvement in the match of the solvent quality to a system with well-known good performance such as DCB. Thus, the solubility parameters of the solvent are not be the only factors impacting performance; the wettability, solvent partitioning, solution aggregation and other factors will also be important. However, simply adding a poor solvent will not necessarily improve the performance. We have examined a mixture of MS with cyclohexanone; from the HSP arguments, it should be possible to form a mixture that is between chloroform and DCB (see Fig. 1). For all of these mixtures, the performance of the device was degraded in comparison to the pure MS. The overall solubility of the P3HT and PCBM decreased with the added cyclohexanone, but the cyclohexanone is also more volatile than MS. These two factors likely explain the degraded performance of this mixture as the solvent quality during film formation will evolve towards pure MS. Despite these differences, the performance of the device fabricated with 80–20 vol.% MS/AP mixture appears to be tremendously improved over typical devices fabricated from solely non-halogenated solvents. As this mixture provides the best performance with this solvent pair, it would be meaningful to compare its performances to analogous devices fabricated from the standard DCB.

Fig. 3 illustrates the difference in device performance obtained for the P3HT:PCBM blend depending upon the casting solvent used. First, the *J–V* curve illustrates the significant difference in the short circuit current for the device fabricated from MS in comparison to DCB as would be expected [9]. The performance of the device fabricated from DCB can be approached by addition of 20 vol.% AP to the MS with J_{SC} increased from 4.7 mA cm^{-2} to 8.9 mA cm^{-2}, R_{SA} decreased from 3.4 Ω cm^2 to 2.8 Ω cm^2, and the fill factor is increased from 59% to 66%. These changes in *J–V* characteristics results in a significant increase in PCE from 1.6% to 3.4% for MS and MS–AP mixture. Additionally, the external quantum efficiency (EQE) increases from a maximum of 35% at 500 nm for the device from MS by a factor of two up to 69% for the mixed solvent as shown in Fig. 3b. These are significant improvements in the device performance, although the performance for the pure MS is known to be poor. Thus, we have also compared the performance of the device formed from the mixed solvent system to those cast from DCB. From Fig. 3a, the short circuit current and open circuit voltage are both slightly larger for the 85 nm thick device from DCB, but at similar thickness (65 nm) the device performance is nearly indistinguishable between the device from DCB and from the MS–AP mixture. Similarly, the EQE for the thicker DCB sample is slightly larger at wavelengths exceeding 500 nm.

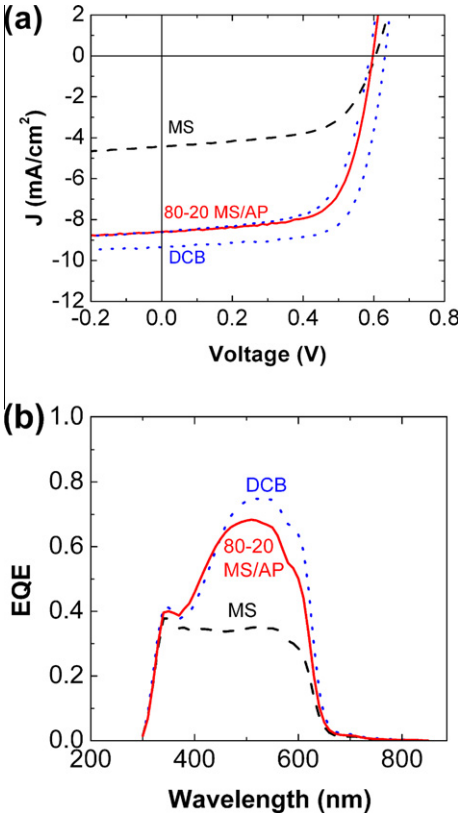

Fig. 3. (a) The *J–V* characteristics under illumination of 100 mW cm^{-2} (AM 1.5G) and (b) external quantum efficiency (EQE) measurements data for devices fabricated from DCB, MS, and 80 vol.% MS-20 vol.% AP mixture.

Table 1 summarizes the performance characteristics for devices from the three different solvents: pure MS, 80–20 MS–AP and pure DCB. One important point to note is that the performance is highly reproducible with at least 6 devices tested for each to calculate the standard deviations in performance characteristics. For the mixed solvent system, the PCE varies between 3.2% and 3.8%; for comparison, the performance for the 85 nm thick devices from DCB varies between 3.6% and 4.3%. However, it is well known that the efficiency for P3HT:PCBM solar cells is thickness sensitive for thin film less than 150 nm thick [17], which is consistent with the decrease in performance for the 65 nm thick devices from DCB. Difficulties in obtaining similar drying and spin coating conditions limited the ability to fully match the film thickness for the different solvent systems. However for thin films, the performance from the mixture closely mimics that obtained for DCB at similar active layer thickness. In addition to HSP arguments, one could also imagine that the relative solubility of P3HT and PCBM in each component of the solvent mixture would provide a route to control the structure. Recently, a mixture of pyridine and chlorobenzene, which good solvents for carboxylated polythiophenes and PCBM, respectively, has been utilized to fabricate OPV devices as the polymer is only marginally soluble in chlorobenzene [19]. For the MS–AP mixture, MS readily dissolves both P3HT and PCBM; the solubility of the components in AP is significantly less with PCBM soluble to >10 mg/mL and P3HT nearly insoluble in AP (<0.05 mg/mL).

We hypothesize that the improved device performance of the MS–AP mixed solvent system originates predominately from two contributions: a decrease in the series resistance (refer to Table 1) and the change in morphology of the active layer caused by the solvent quality upon phase separation of the PCBM and P3HT. The slower evaporation rate of the high boiling point component (AP) during spin coating and drying process may also facilitate reorganization in the blend to a more appropriate morphology for charge transport and exciton dissociation. However, the changes in device performance can generally be attributed to the morphology of the P3HT:PCBM that is dependent on the processing conditions [8,18]. To begin to understand the morphology of the blends processed with different solvents, the surface after annealing is interrogated using AFM. Fig. 4 illustrates the topography and phase images of the P3HT:PCBM films spun from the different solvents. It is clear from these micrographs that the morphology of the blend formed from the MS–AP mixed solvent closely resembles that of the film cast from DCB. For the film cast from MS, the surface is rough with large domains clearly visible in the micrograph. Conversely, no large domains are observed for the film formed from the solvent mixture or from DCB. We attribute this morphological change in the mixed solvent system to the solvent quality evolution during drying due to the lower vapor pressure of the AP that changes the thermodynamic interactions in the solution. Both the intramolecular interactions and interactions between P3HT and PCBM are

Table 1
Summary of device performance for various BHJ solar cell devices in the work.

	MS	80–20 vol.% MS/AP mix.	DCB (thin)	DCB (thicker)
Thickness (nm)	60	60	65	85
J_{sc}^{*} (mA cm^{-2})	4.68 ± 0.76	8.88 ± 0.67	8.34 ± 0.26	9.15 ± 0.15
V_{oc} (V)	0.56 ± 0.04	0.58 ± 0.02	0.59 ± 0.01	0.63 ± 0.01
R_{SA} (Ω cm^2)	3.44 ± 0.17	2.81 ± 0.14	2.49 ± 0.12	2.73 ± 0.13
FF (%)	58.9 ± 1.3	66.1 ± 1.4	65.3 ± 1.1	68.6 ± 2.0
PCE (%)	1.53 ± 0.16	3.38 ± 0.13	3.20 ± 0.10	3.92 ± 0.18
EQE (%)	3.45 ± 1.8	68.9 ± 1.3	62.6 ± 2.9	74.2 ± 1.2
J_{sc}^{**} (mA cm^{-2})	5.08 ± 0.68	9.04 ± 0.58	8.15 ± 0.15	10.4 ± 0.16

* J_{sc}: current density measured under similated solar illumination.
** J_{sc}: current density calculated based on EQE measurement.

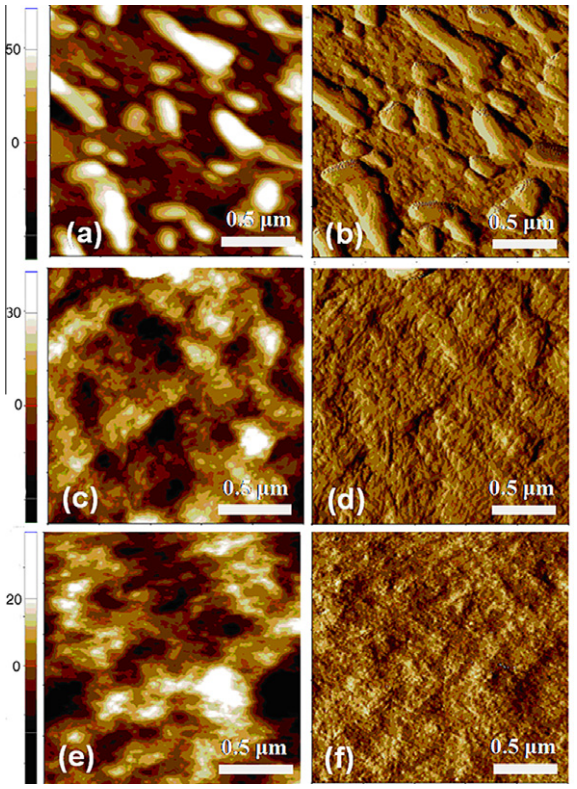

Fig. 4. AFM topography and phase images of P3HT/PCBM blend films cast from (a,b) MS, (c,d) 80 vol.% MS-20 vol.% AP mixture, and (e,f) DCB (scale bar for topology in nm).

mitigated by the solvent initially and the solvent quality upon crystallization of one phase or phase separation will dictate how the morphology evolves. The film cast from DCB exhibits the smallest domain size of the three films, but the surface morphology for the solvent mixture is very similar to that for the DCB. This similarity in morphology is in good agreement with the *J–V* characteristics of the analogous devices. These results suggest that high performance organic BHJ solar cells can be fabricated with proper choice of halogen-free solvent pairs. The elimination of the use of halogenated solvents without compromising the fabrication condition could prove to be important for the potential commercialization of polymer based BHJ solar cells. Future work will focus on extending these concepts to other donor–acceptor pairs that have higher theoretical efficiencies, especially when one component is not soluble in typical solvents (i.e. DCB).

4. Conclusion

In conclusion, we demonstrate the use of the non-halogenated solvent mixtures for the fabrication of BHJ organic solar cells. In comparison to a pure aromatic solvent, i.e. mesitylene, the use of a mixture containing 20 vol.% AP in MS results in more homogeneous morphology of the P3HT:PCBM film with a corresponding improvement in PCE from 1.6% to 3.4% and EQE from 35% to 69%. We find an optimal composition in this solvent mixture; either increasing to 30 vol.% AP or decreasing to 10 vol.% AP results in a decrease in PCE. The overall device performance of the device fabricated from the non-halogenated MS–AP mixed solvent system can be comparable to that of a standard device from DCB. Further optimization of this work could enable the use of fully, non-halogenated solvent mixture systems for scale-up manufacturing of high performance BHJ organic solar cells.

Acknowledgements

We thank B. O'Brien and J. Torres for assistance with AFM measurements. We acknowledge financial support from the Army Research Laboratory through the Flexible Display Center at ASU under Cooperative Agreement W911NF-04-2-0005. J. Li would like to acknowledge the partial support of the Advanced Photovoltaics Center, and the National Science Foundation (CBET-0756148).

References

[1] G. Yu, J. Gao, J.C. Hummelen, F. Wudl, A.J. Heeger, Polymer photovoltaic cells: enhanced efficiencies via a network of internal donor–acceptor heterojunctions, Science 270 (1995) 1789–1791.
[2] N.S. Sariciftci, D. Braun, C. Zhang, V.I. Srdanov, A.J. Heeger, G. Stucky, F. Wudl, Semiconducting polymer-buckminsterfullerene heterojunctions: diodes, photodiodes, and photovoltaic cells, Applied Physics Letters 62 (1993) 585–587.
[3] B.R. Saunders, M.L. Turner, Nanoparticle-polymer photovoltaic cells, Advances in Colloid and Interface Science 138 (2008) 1–23.
[4] R. Kroon, M. Lenes, J.C. Hummelen, P.W.M. Blom, B. de Boer, Small bandgap polymers for organic solar cells (polymer material development in the last 5 years), Polymer Reviews 48 (2008) 531–582.
[5] G. Li, Y. Yao, H. Yang, V. Shrotriya, G. Yang, Y. Yang, "Solvent Annealing" effect in polymer solar cells based on poly(3-hexylthiophene) and methanofullerenes, Advanced Functional Materials 17 (2007) 1636–1644.
[6] Y. Kim, S.A. Choulis, J. Nelson, D.D.C. Bradley, S. Cook, J.R. Durrant, Device annealing effect in organic solar cells with blends of regioregular poly(3-hexylthiophene) and soluble fullerene, Applied Physics Letters 86 (2005) 063502.
[7] C.S. Kim, L.L. Tinker, B.F. DiSalle, E.D. Gomez, S. Lee, S. Bernhard, Y.L. Loo, Altering the thermodynamics of phase separation in inverted bulk heterojunction organic solar cells, Advanced Materials 21 (2009) 3110–3115.
[8] A.J. Moulé, K. Meerholz, Morphology control in solution-processed bulk-heterojunction solar cell mixtures, Advanced Functional Materials 19 (2009) 3028–3036.
[9] M. Morana, P. Koers, C. Waldauf, M. Koppe, D. Muehlbacher, P. Denk, M. Scharber, D. Waller, C. Brabec, Organic field-effect devices as tool to characterize the bipolar transport in polymer-fullerene blends: the case of P3HT–PCBM, Advanced Functional Materials 17 (2007) 3274–3283.
[10] A.R. Campbell, J.M. Hodgkiss, S. Westenhoff, I.A. Howard, R.A. Marsh, C.R. McNeill, R.H. Friend, N.C. Greenham, Low-temperature control of nanoscale morphology for high performance polymer photovoltaics, Nano Letters 8 (2008) 3942–3947.
[11] S. Berson, R. DeBettignies, S. Bailly, S. Guillerez, Poly(3-hexylthiophene) fibers for photovoltaic applications, Advanced Functional Materials 17 (2007) 1377–1384.
[12] C.M. Hansen, The universality of the solubility parameter, Product R&D 8 (1969) 2–11.
[13] A.I. Imre, W.A. Van Hook, Liquid–Liquid demixing from solutions of polystyrene. 1. A review. 2. Improved correlation with solvent properties, Journal of Physical and Chemical Reference Data 25 (1996) 637.
[14] A. Martin, J. Newburger, A. Adjei, Extended Hildebrand solubility approach: solubility of theophylline in polar binary solvents, Journal of Pharmaceutical Sciences 69 (1980) 487–491.
[15] R.F. Tabor, S. Gold, J. Eastoe, Electron density matching as a guide to surfactant design, Langmuir 22 (2005) 963–968.

[16] M.M. Bouman, E.E. Havinga, R.A.J. Janssen, E.W. Meijer, Chiroptical properties of regioregular chiral polythiophenes, molecular crystals and liquid crystals science and technology, Section A: Molecular Crystals and Liquid Crystals 256 (1994) 439–448.
[17] L. Gang, S. Vishal, Y. Yan, Y. Yang, Investigation of annealing effects and film thickness dependence of polymer solar cells based on poly(3-hexylthiophene), Journal of Applied Physics 98 (2005) 043704.
[18] X. Yang, J. Loos, S.C. Veenstra, W.J.H. Verhees, M.M. Wienk, J.M. Kroon, M.A.J. Michels, R.A.J. Janssen, Nanoscale morphology of high-performance polymer solar cells, Nano Letters 5 (2005) 579–583.
[19] B.J. Worfolk, D.A. Rider, A.L. Elias, M. Thomas, K.D. Harris, J.M. Buriak, Bulk heterojunction organic photovoltaics based on carboxylated polythiophenes and PCBM on glass and plastic substrates, Advanced Functional Material 21 (2011) 1816–1826.

density; when there are enough carbon nanotubes mixed into the organic semiconductor film to drastically enhance mobility, the density of the CNTs appears to approach the percolation threshold, thus limiting the maximum mobility achievable before the percolation of CNT reduces the on/off ratio of such a hybrid organic/CNT transistor. Graphene, a two-dimensional lattice of carbon with single atom thickness, has generated significant attention due to its outstanding electronic, mechanical and physical properties [13]. As with the addition of CNTs, it is expected that few-layer and single-layer graphene flakes can provide good connection between the crystalline regions of the semiconductor film. Compare to CNTs, increased area in the conduction channel of an organic semiconductor transistor can be covered by graphene flakes before they start to percolate and reduce the on/off ratio. As a result, the mobility of organic transistors with graphene flakes would be expected to show higher values than what can be accomplished using CNTs before device on/off ratio drops.

Recent progress with liquid exfoliation of graphene provides cost efficient methods to prepare graphene dispersions [20–22]. Coleman et al. first reported the exfoliation of graphene in *N*-methyl-2-pyrrolidone (NMP) [20], and then the Tour and Barron groups reported exfoliation of graphene in ortho dichlorobenzene (ODCB) with higher graphene concentration [21]. In our method, graphite was exfoliated in ODCB. Not only is ODCB a good solvent for organic semiconductors, but also graphene flakes can be dispersed in ODCB without the aid of surfactants. Therefore ODCB appears to be a good solvent for hybrid organic semiconductor/graphene films. In this paper, we present a general approach for the preparation of solution processable organic semiconductor/graphene hybrid thin film transistors. Compared to FETs with pure organic semiconductors, hybrid FETs exhibit much higher effective mobility while keeping the on/off ratio of devices sufficiently high.

2. Materials and methods

In this work, poly(3,3-didodecylquaterthiophene) (PQT-12) was chosen as the organic semiconductor material because of its good air stability. Additionally, poly-(3-hexylthiophene) (P3HT), an organic semiconductor widely used for both organic transistor and organic photovoltaic device studies, was also studied to prove that our method is a general route to enhance the performance of polymer transistors.

We synthesized PQT-12 according to $FeCl_3$-mediated oxidative coupling polymerization [25]. Our PQT-12 showed almost the same thermal behavior in the differential scanning calorimetry (DSC) thermogram with Xerox's PQT-12 [26,27]. Regioregular P3HT (94.5%, M_n = 13,000 and M_w = 26,200 g/mol) was purchased from Merck and used without further purification. Graphene dispersions were prepared by an adaptation of the solution sonication method reported previously by the Tour and Barron groups [21]. Briefly, graphite (Asbury Graphite Mills Inc.) was added into ODCB at a concentration of 5 mg/ml. The mixture was then sonicated for 45 min with an ultrasonicator (Heilscher 400) at 50% power. After ultrasonication, graphene dispersions were left to settle for about 1 h to allow thick graphite flakes to sediment out of solution. The top portion of the solution was then centrifuged at 1500 rpm for 1 h. The supernatant from the top half of the solution yielded a graphene dispersion which contained single-layered and multi-layered graphene flakes. Three milligrams of PQT-12 or P3HT was then added to 1 ml of this graphene dispersion. The mixture was heated to allow the polymer to dissolve completely. The hot solution was then subjected to ultrasonic agitation and cooled to room temperature [24]. This yielded a dark-purple solution with polymer nanoparticles and graphene flakes suspended in ODCB. A heavily doped silicon wafer with 300 nm thermally grown SiO_2 was used as a substrate material. Wafers were cleaned by sonication in acetone, isopropanol and DI water, respectively, followed by N_2 drying. Some of the substrates were used as cleaned, while others were treated with an octyltrichlorosilane (OTS-8) self-assembled monolayer (SAM). OTS-8 self-assembled monolayer was deposited on a wafer surface by immersion into a 10 mM solution of OTS-8 in toluene at 60 °C for 15 min, subsequent rinsing with toluene and ethanol, and then blow-drying with nitrogen before use [24]. Hybrid field-effect transistors were fabricated by spin coating the PQT-12/graphene (or P3HT/graphene) composite solution onto a substrate at 1200 rpm for 60 s followed by vacuum drying to give 20–50-nm thick semiconductor layer. Control devices were fabricated with pure PQT-12 (or P3HT) films using the same procedures but without the addition of graphene flakes to the ODCB solution. Following deposition of the organic semiconductor films, gold source-drain electrodes were deposited by thermal evaporation through a shadow mask with channel length L = 130 μm and channel width W = 2 mm. As indicated in the text, some of the resulting devices were annealed in a vacuum oven at 140 °C for 20 min, followed by slow cooling.

All the current–voltage (I–V) curves were measured at room temperature under ambient conditions using a Cascade probe station connected to two Keithley 2400 source/measure units. The effective field-effect mobility of each transistor was extracted from the transfer characteristics using a linear fit to the plot of the square root of saturation source-drain current as a function of the gate voltage V_g.

3. Results and discussion

The concentration of graphene in the hybrid films was measured by two methods. First, graphene dispersion with known volume was slowly dropped onto a heated glass slide. After complete solvent evaporation, the mass change of the glass slide was carefully measured. With this method, the concentration of graphene in the dispersion was calculated to be about 0.055 mg/ml. In another method, the graphene concentration was determined by UV–vis–IR absorption spectroscopy (see Supplementary data). The spectra are featureless in the visible–IR region as expected [23]. An average absorption coefficient for graphene of 2460 L/g m at a wavelength of 660 nm was

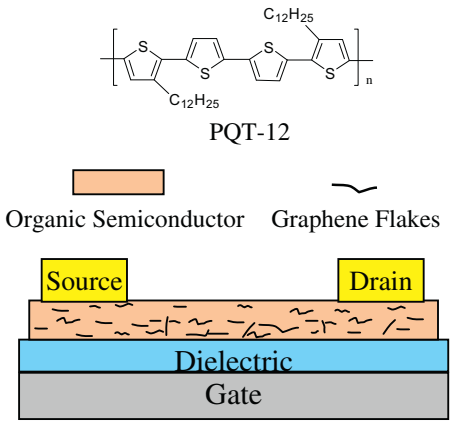

Fig. 1. Structure of organic semiconductor/graphene hybrid FET.

used for the calculation [20]. Therefore, optical methods can be employed to measure the concentration of graphene which was calculated to be about 0.045 mg/ml in the deposition dispersion. The first method gives a slightly higher concentration, which is believed to be due to the residual decomposed ODCB solvent on the heated glass slide.

As shown in Fig. 1, graphene flakes incorporated into an organic semiconductor film is expected to provide "fast lanes" for charge carriers within the conduction channel, enhancing the effective mobility of the entire transistor device. That is, the addition of graphene flakes might effectively reduces the conduction channel length, which acts to enhance the output source-drain current of the field-effect transistor. This activity is realized in the ambient laboratory atmosphere.

Transistors with and without substrate surface treatment or post-fabrication annealing process were all studied. For transistors fabricated without any substrate surface treatment or post annealing process, PQT-12/graphene hybrid FETs exhibited source-drain current about 10 times higher than that of a control device (containing only PQT-12 with no added graphene). Fig. 2 compares *I–V* characteristics of a control device and a PQT-12/graphene hybrid transistor both on a cleaned SiO_2 surface without any customized surface treatment. The mobility of the control device is 0.012 $cm^2 V^{-1} s^{-1}$, while the mobility of the PQT-12/graphene hybrid FET is 0.17 $cm^2 V^{-1} s^{-1}$. The on/off ratios of both devices are on the order of 10^3 but better on/off ratios could be achieved by post-fabrication annealing the devices as described below.

When substrate surface treatment and post-fabrication annealing process are performed, both PQT-12/graphene hybrid FETs and control devices exhibit better performance, but PQT-12/graphene hybrid FETs show significantly greater enhancement. Fig. 3 shows source-drain *I–V* curves and transfer curves for both control devices and hybrid FETs fabricated on substrate surfaces that were treated with octyltrichorosilane (OTS-8) and were vacuum annealed after fabrication. The effective mobility of the control device is 0.15 $cm^2 V^{-1} s^{-1}$, which is comparable to previously reported values [24]. In contrast, the effective mobility of the PQT-12/graphene hybrid FET is 0.55 $cm^2 V^{-1} s^{-1}$, which is remarkably high for a PQT-12 FET. In comparison, the highest prior report mobility for pure PQT-12 is 0.2 $cm^2 V^{-1} s^{-1}$ [24]. The on/off ratio of both devices are as high as 10^5 with the off current on the order 10^{-9} A when measured in air after vacuum annealing. The low off current obtained suggests that densities of graphene flakes in these PQT-12/graphene hybrid films are still lower than the percolation threshold of graphene.

To study the dependence of device performance on graphene dispersion concentration, hybrid PQT-12/graphene films containing higher densities of graphene flakes were also studied. Graphene dispersions at higher concentration can be prepared by first preparing graphene dispersion according to procedures described in Section 2, followed by removing some of the ODCB solvent either by rotary evaporation or by rapid heating in a shallow poly(tetrafluroethylene) (PTFE) dish. These high-concentration graphene dispersions are then mixed with PQT-12 semiconductor and deposited on substrates. It should be noted that if the graphene dispersion is heated in air for a long time (more than 10 min), graphene flakes will start to aggregate and precipitate, probably due to the adsorption of water into solution. This can be avoided by using a shallow dish with large surface area to reduce the time needed for the graphene dispersion to be exposed to air, or using a rotary evaporator to exclude water during the process. Sometimes during concentration, a small

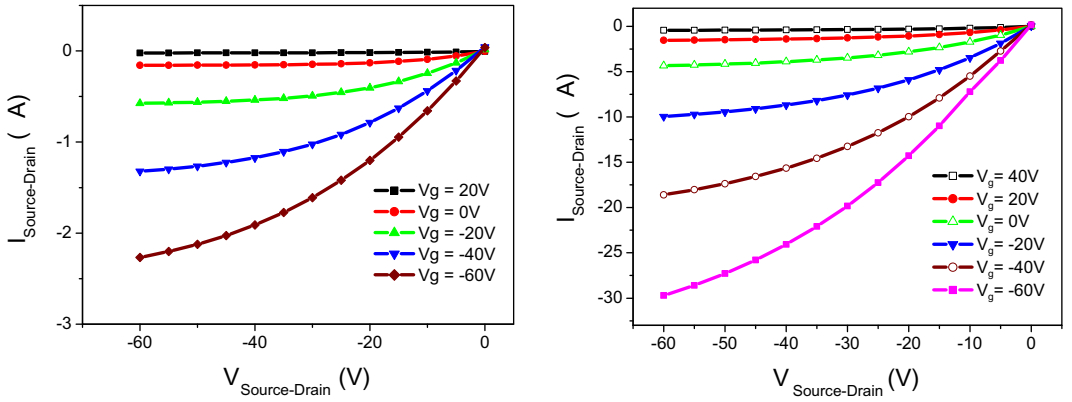

Fig. 2. Source-drain *I–V* curves of a pure PQT-12 FET (left) and a PQT-12/graphene hybrid FET (right).

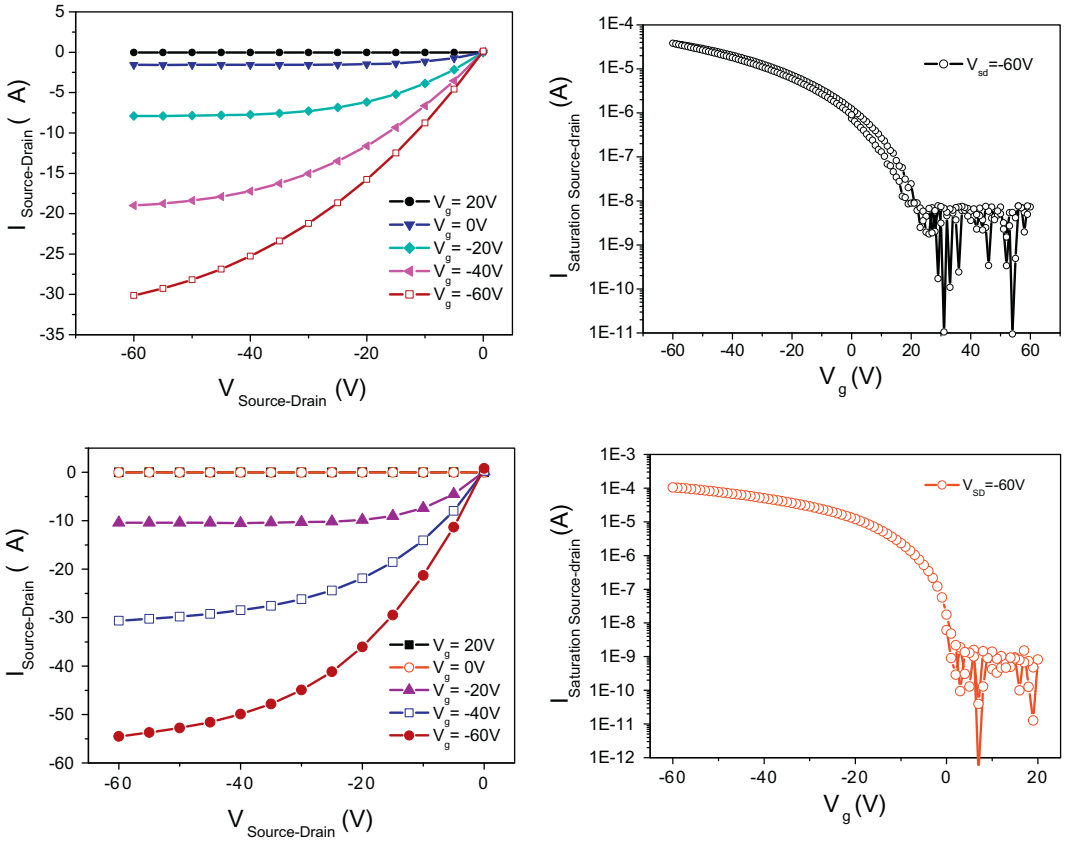

Fig. 3. Source-drain *I–V* curve (left) and transfer curve (right) of a PQT-12 FET (top) and a PQT-12/graphene hybrid FET (bottom) with OTS-8 surface treatment and vacuum annealing.

amount of graphene precipitates out, but can be re-dispersed into suspension by ultrasonication for 5 min. The resulting ink-like graphene dispersions at higher concentrations are only stable for a short time, and hence should be used right after preparation. For this study, graphene dispersions concentrated by 4 times and 10 times were prepared and mixed with PQT-12 semiconductor immediately after graphene dispersion preparation, followed by 5 min sonication. Hybrid transistors were then fabricated using these organic semiconductor/graphene composite solutions according to the same procedures as described above and are referred to below as PQT-12/4× graphene FETs and PQT-12/10× graphene FETs, respectively.

Fig. 4 summarizes the maximum mobilities, average mobilities and on/off ratios of all transistors measured. Error bars in the figure show the highest mobilities measured for each type of device, while the columns show averaged values. Field-effect transistors fabricated from 4× concentrated graphene dispersions exhibited average mobility of 0.32 $cm^2 V^{-1} s^{-1}$, which is lower than that of devices made from graphene dispersion at normal concentration. This is probably due to the fact that, when too many graphene flakes are present in PQT-12 film, the structural order in the PQT-12 is decreased. This is supported by X-ray diffraction results showing a loss of crystallinity with increasing graphene concentration, as

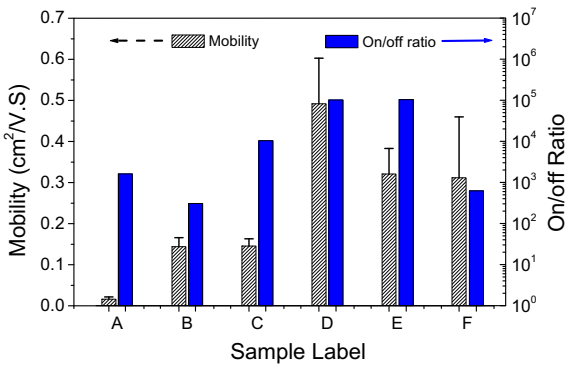

Fig. 4. Summary of mobilities and on/off ratio of all PQT-12 transistors with/without graphene: (A) PQT-12 FET no OTS8 and no annealing. (B) PQT-12/graphene FET no OTS-8 and no annealing. (C) PQT-12 FET with OTS-8 and annealing. (D) PQT-12/graphene FET with OTS-8 and annealing. (E) PQT-12/4×-graphene FET with OTS and annealing. (F) PQT-12/10×-graphene FET with OTS and annealing.

shown in the Supplementary data. Although more graphene flakes can provide more "fast lanes" for charge carriers in conduction channels, more disordered PQT-12 semiconductor layers ultimately reduce the effective mobility of devices. At this concentration, the density of graphene flakes in polymer is believed to be still lower than the percolation threshold, so that the on/off ratios of

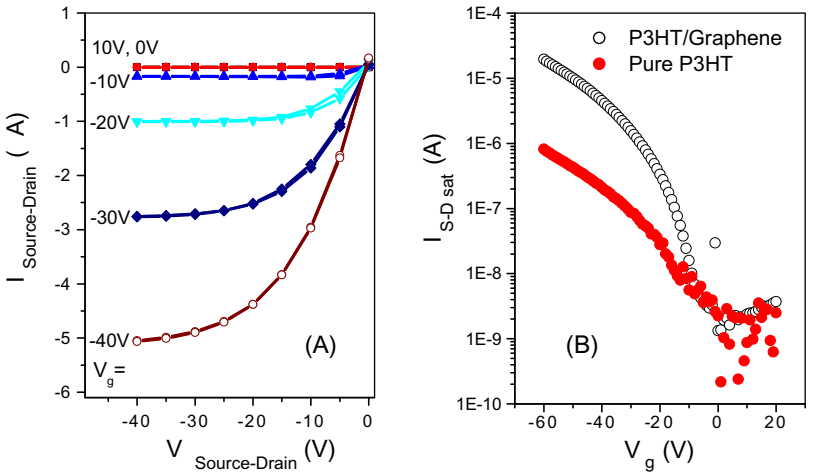

Fig. 5. (A) Source-drain *I–V* curve of a P3HT/graphene hybrid FET. (B) Transfer characteristics of pure P3HT and P3HT/graphene hybrid FET.

PQT-12/4× graphene FETs remain in the same order of magnitude as transistors with regular graphene concentration. However, when 10 times concentrated graphene dispersion was added into PQT-12 semiconductor, the on/off ratio of transistors was decreased significantly, suggesting that the density of graphene flakes in the polymer exceeds the percolation threshold. Off currents of these PQT-12/10× graphene FETs are on the order of 10^{-7} A, hundreds of times higher than that of PQT-12/graphene FETs with graphene dispersion at normal concentration.

Additionally, P3HT was also studied to demonstrate that our approach is a general route to enhance the performance of transistors made from polymer semiconductors. P3HT/graphene hybrid FETs were fabricated using the same methods on OTS-8 treated substrates, and again, all devices were fabricated and measured under ambient conditions. The measured current–voltage characteristics for P3HT/graphene FETs show well-defined gate modulation. As an example, Fig. 5A depicts the current–voltage characteristics of a P3HT/graphene FET, and Fig. 5B compares the transfer characteristics of a P3HT/graphene hybrid transistor to that of a pure P3HT FET. As can be seen, much higher current was obtained from the device with graphene. The P3HT/graphene FET exhibits mobility as high as 0.17 $cm^2\,V^{-1}\,s^{-1}$, which is more than 20 times higher than that from the pure P3HT FET (0.007 $cm^2\,V^{-1}\,s^{-1}$). The on/off ratio of the P3HT/graphene FET is on the order of 10^4, which is surprisingly an order of magnitude *higher* than that of the pure P3HT FET in contrast to what is observed in P3HT/carbon-nanotube composites. [14] This is because both devices exhibit similar off currents, while the P3HT/graphene FET shows much higher on current. These results suggest that our method is a general route to enhance the performance of polymer electronics.

4. Conclusions

In conclusion, we have developed composite field-effect transistors containing both polymer semiconductor materials and graphene flakes, and we have shown that effective mobilities of polymer/graphene hybrid FETs can be significantly higher than that of a pure polymer FET. When graphene dispersions with concentrations at about 0.05 mg/ml are mixed with PQT-12 semiconductor, effective mobilities as high as $0.5 \pm 0.1\ cm^2\,V^{-1}\,s^{-1}$ can be obtained in ambient conditions, while the on/off ratio of these devices can be on the order of 10^5 and was not reduced due to the addition of graphene flakes. This is attributed to the high percolation threshold of graphene. When the concentration of graphene flakes in the semiconductor film was increased by 4 times, the effective mobility was decreased to $0.32 \pm 0.06\ cm^2\,V^{-1}\,s^{-1}$ because the high density graphene flakes in the organic semiconductor layer probably resulted in a more disordered film. The on/off ratio of hybrid FETs significantly decreased when the concentration of graphene flakes in semiconductor film was increased by 10 times, which is believed to exceed the percolation threshold of graphene flakes. We also found that effective mobilities of P3HT/graphene hybrid FETs can be more than 20 times higher than that of pure P3HT FETs we fabricated. We expect that adding graphene flakes to organic semiconductors is a general route to enhance the performance of organic electronics, providing a low-cost avenue for enhancing OFET performance.

Acknowledgements

The authors acknowledge Dr. Christopher Richardson and Mingling Yeh for XRD measurements. H.E. Katz and B.J. Jung thank DOE, Office of Basic Energy Sciences, Grant No. DE-FG02-07ER46465 for the financial support.

Appendix A. Supplementary data

Supplementary data associated with this article can be found, in the online version, at doi:10.1016/j.orgel.2011.05.021.

References

[1] S.E. Burns, K. Reynolds, W. Reeves, M. Banach, T. Brown, K. Jacobs, A. Menon, S. Siddique, P. Too, C. Ramsdale, J. Watts, P. Cain, T. von Werne, J. Mills, C. Curling, H. Sirringhaus, K. Amindson, M.D. McCreary, J. Soc. Inf. Display 13 (2005) 583.
[2] T.W. Kelley, P.F. Baude, C. Gerlach, D.E. Ender, D. Muyres, M.A. Haase, D.E. Vogel, S.D. Theiss, Chem. Mater. 16 (2004) 4413.
[3] J. Huang, J. Miragliotta, A. Becknell, H.E. Katz, J. Am. Chem. Soc. 129 (2007) 9366.
[4] T. Someya, A. Dodabalapur, J. Huang, K.C. See, H.E. Katz, Adv. Mater. 22 (2010) 3799.
[5] J. Huang, T.J. Dawidcyk, B.J. Jung, J. Sun, A.F. Mason, H.E. Katz, J. Mater. Chem. 20 (2010) 2644.
[6] H.E. Katz, J. Huang, Annu. Rev. Mater. Res. 39 (2009) 71.
[7] J. Huang, J. Sun, H.E. Katz, Adv. Mater. 20 (2008) 2567.
[8] R. Parashkov, E. Becker, T. Riedel, H.H. Johannes, W. Kowalsky, Proc. IEEE 93 (2005) 1321.
[9] C. Reese, M. Roberts, M.M. Ling, Z. Bao, Mater. Today 7 (2004) 20.
[10] A. Salleo, Mater. Today 10 (2007) 38.
[11] M.S. Fuhrer, B.M. Kim, T. Durkop, T. Brintlinger, Nano Lett. 2 (2002) 755.
[12] E.S. Snow, J.P. Novak, P.M. Campbell, D. Park, Appl. Phys. Lett. 82 (2003) 145.
[13] A.K. Geim, K.S. Novoselov, Nat. Mater. 6 (2007) 183.
[14] X.Z. Bo, C.Y. Lee, M.S. Strano, M. Goldfinger, C. Nuckolls, G.B. Blanchet, Appl. Phys. Lett. 86 (2005) 182102.
[15] X.Z. Bo, N.G. Tassi, C.Y. Lee, M.S. Strano, C. Nuckolls, G.B. Blanchet, Appl. Phys. Lett. 87 (2005) 203510.
[16] J.X. Geng, B.S. Kong, S.B. Yang, S.C. Youn, S. Park, T. Joo, H.T. Jung, Adv. Funct. Mater. 18 (2008) 2659.
[17] S. Liu, S.C.B. Mannsfeld, M.C. LeMieux, H.W. Lee, Z. Bao, Appl. Phys. Lett. 92 (2008) 053306.
[18] Y.D. Park, J.A. Lim, Y. Jang, M. Hwang, H.S. Lee, D.H. Lee, H.J. Lee, J.B. Baek, K. Cho, Org. Electron. 9 (2008) 317.
[19] G.W. Hsieh, F.M. Li, P. Beecher, A. Nathan, Y. Wu, B.S. Ong, W.I. Milne, J. Appl. Phys. 106 (2009) 123706.
[20] Y. Hernandez, V. Nicolosi, M. Lotya, F.M. Blighe, Z.Y. Sun, S. De, I.T. McGovern, B. Holland, M. Byrne, Y.K. Gun'ko, J.J. Boland, P. Niraj, G. Duesberg, S. Krishnamurthy, R. Goodhue, J. Hutchison, V. Scardaci, A.C. Ferrari, J.N. Coleman, Nat. Nanotechnol. 3 (2008) 563.
[21] C.E. Hamilton, J.R. Lomeda, Z.Z. Sun, J.M. Tour, A.R. Barron, Nano Lett. 9 (2009) 3460.
[22] A.A. Green, M.C. Hersam, Nano Lett. 9 (2009) 4031.
[23] D.S.L. Abergel, V.I. Fal'ko, Phys. Rev. B 75 (2007) 155430.
[24] B.S. Ong, Y.L. Wu, P. Liu, S. Gardner, Adv. Mater. 17 (2005) 1141.
[25] B.S. Ong, Y.L. Wu, P. Liu, S. Gardner, J. Am. Chem. Soc. 126 (2004) 3378.
[26] N. Zhao, G.A. Botton, S.P. Zhu, A. Duft, B.S. Ong, Y.L. Wu, P. Liu, Macromolecules 37 (2004) 8307.
[27] J. Sun, B.J. Jung, T. Lee, L. Berger, J. Huang, Y. Liu, D.H. Reich, H.E. Katz, ACS Appl. Mater. Interfaces 1 (2009) 412.

inserting alkali-metallic materials, such as Cs_2CO_3, as an interfacial layer, and even by doping [9–11]. In our previous study, a self-assembled monolayer (SAM) was employed to modify a TiO_2 surface to tune the energy level of the conduction band [12]. Unfortunately, the inferior electron mobility of TiO_2 inhibited electron injection, reducing eletroluminescence (EL) efficiency. ZnO is an excellent alternative to TiO_2 because it has a similar bandgap but higher electron mobility. The resistivity of ZnO can be adjusted from $10^{-4}\,\Omega$ cm to $10^{12}\,\Omega$ cm by controlling the annealing conditions and doping[13]. Moreover, ZnO is widely utilized in organic optoelectronic devices such as O/PLEDs [6,10,14], and polymer photovoltaic cells [15].

In the present investigation, ZnO thin film was prepared using the sol–gel process and its energy level was modified by grafting thereon N-[3-(trimethoxysily)propyl]ethylenediamine (PEDA-TMS), which acted as an electron injection layer. The sol–gel-derived ZnO thin film was used to investigate the effect of heat treatment on the PLED performance. Following annealing at 300 °C, an inverted PLED exhibited a performance close to that of a conventional PLED. Furthermore, the effect of annealing on ZnO characteristics is determined in terms of the degree of grafting of PEDA-TMS and its relation to the amount of active –OH groups, the electron mobility owing to crystallinity of ZnO, and hole blocking effect, which enhances effective recombination.

2. Experimental

ZnO thin films were prepared using sol–gel technology [16]. Zinc acetate dehydrate (99.999%, J.T. Baker) as a precursor was dissolved in a mixture of 2-methoxyethanol and 0.1 M acetic acid aqueous solution at a 1:1 volume ratio. The concentration of zinc acetate was 0.1 g/ml. Before the zinc acetate solution was spin-coated, an ITO substrate (RITEK Corp., 15 Ω/square) was ultrasonically cleaned with detergent, deionized water, acetone, and isopropyl alcohol, sequentially. Contaminants on the ITO surface were removed using UV-ozone treatment. The mixing solution was spin-coated on ITO (approximately 100 nm) and the layers were subsequently annealed with different temperatures for 30 min. The modified ITO was immediately immersed in 1 wt.% PEDA-TMS (Aldrich, 97%) from a toluene solution for 2 min in an ultrasonic bath and cleaned. SAMs were bonded onto the ZnO surface using a hydrolyzed process described in a previous study [12]. Then, PLED devices with ITO/ZnO/SAMs/emissive layer/MoO_3/Au/Ag architecture were fabricated. Polyfluorene Green B (G-PF) (Dow Chemical Corp.) as an emissive layer (thickness of ca. 50 nm) was spin-coated on ZnO modification layer from a toluene solution, which was then baked at 65 °C for 30 min. The device was placed in a high vacuum chamber with a pressure of 10^{-6} Torr for the thermal evaporation of MoO_3 (6 nm), Au (20 nm), and Ag (80 nm). A conventional PLED was fabricated for comparison. ITO/PEDOT:PSS (Baytron P AI 4083) and Ca/Al were utilized as a anode and an cathode, respectively. Ca (60 nm)/Al (100 nm) was utilized as an anode in the electron-only device to characterize the electron injection ability.

The current density–voltage–luminescence (J–V–L) characteristics of the devices were measured with a Keithley 2400 source measure units and Keithley 2000 digital multimerter along with a silicon photodiode, calibrated using a Minolta LS-100 luminance meter. The capacitance–voltage (C–V) measurements were conducted with an Agilent 4284A precision LCR meter. C–V measurements were carried out under applied voltage of 0–3.8 V and a modulated voltage of 10 mV at 10 k Hz. The overall measurement was in an inert nitrogen atmosphere. Here, the threshold voltage (V_{th}) and turn-on voltage ($V_{turn\text{-}on}$) indicated the majority carrier injection point and luminescence point in J–V–L diagram.

Atomic force microscopy (AFM) was performed with a NanoScope IIIa (Digital Instruments Inc.) run in the tapping mode to observe the morphology of the ZnO surface. The vacuum level shifts of ZnO under various conditions were studied using ultraviolet photoelectron spectroscopy (UPS) with a VG CLAM4 surface analysis system equipped with a non-monochromatic He(I) UV source (21.2 eV) at the National Synchrotron Radiation Research Center. The UPS measurements were conducted at a base pressure of operated below 8×10^{-10} Torr.

3. Results and discussion

Annealing temperature affects the orientation and crystallinity of ZnO. Fig. S1 shows the X-ray diffraction patterns of ZnO thin film that has been annealed at various annealing temperatures. The extent of growth of the (0 0 2) orientation was directly proportional to the annealing temperature, indicating the presence of a Wurtzite structure with charge mobility [17,18]. AFM was used to investigate the surface morphologies. As shown in Fig. 1a–c, ZnO exhibits nano-ridge structures at various annealing temperatures. The root mean square (rms) roughness values following annealing at 150 °C, 300 °C, and 450 °C are 8.639 nm, 7.984 nm, and 25.422 nm, respectively. The roughest surface was obtained at an annealing temperature of 450 °C, indicating that the crystalline grains were largest at that temperature. When PEDA-TMS was grafted onto the ZnO electrode, the rms roughness did not change significantly (not shown), which finding is attributable to the coverage of only a monolayer on the ZnO surface.

Fig. 2a plots the current density–voltage–luminescence (J–V–L) curves of a conventional device and inverted devices with and without PEDA-TMS following annealing at 150 °C. From the J–V curves, the threshold voltage for the inverted devices without PEDA-TMS is unclear. The threshold voltage is a function of $\Delta\varphi + \phi$, where$\Delta\varphi$ is the build-in potential that results from the difference between the work function of the cathode and that of the anode and ϕ is the barrier height of majority carriers injection. In the device with an electron injection/buffer layer of ZnO, hole is regarded as the majority carrier owing to the inferior electron mobility of G-PF. The threshold voltage (V_{th}) for this device is indeterminable, attributing to the low build-in potential and high leakage current. However, the devices with the PEDA-TMS had a clear threshold voltage at 1.5 V. Since no substantial change occurred in the anode,

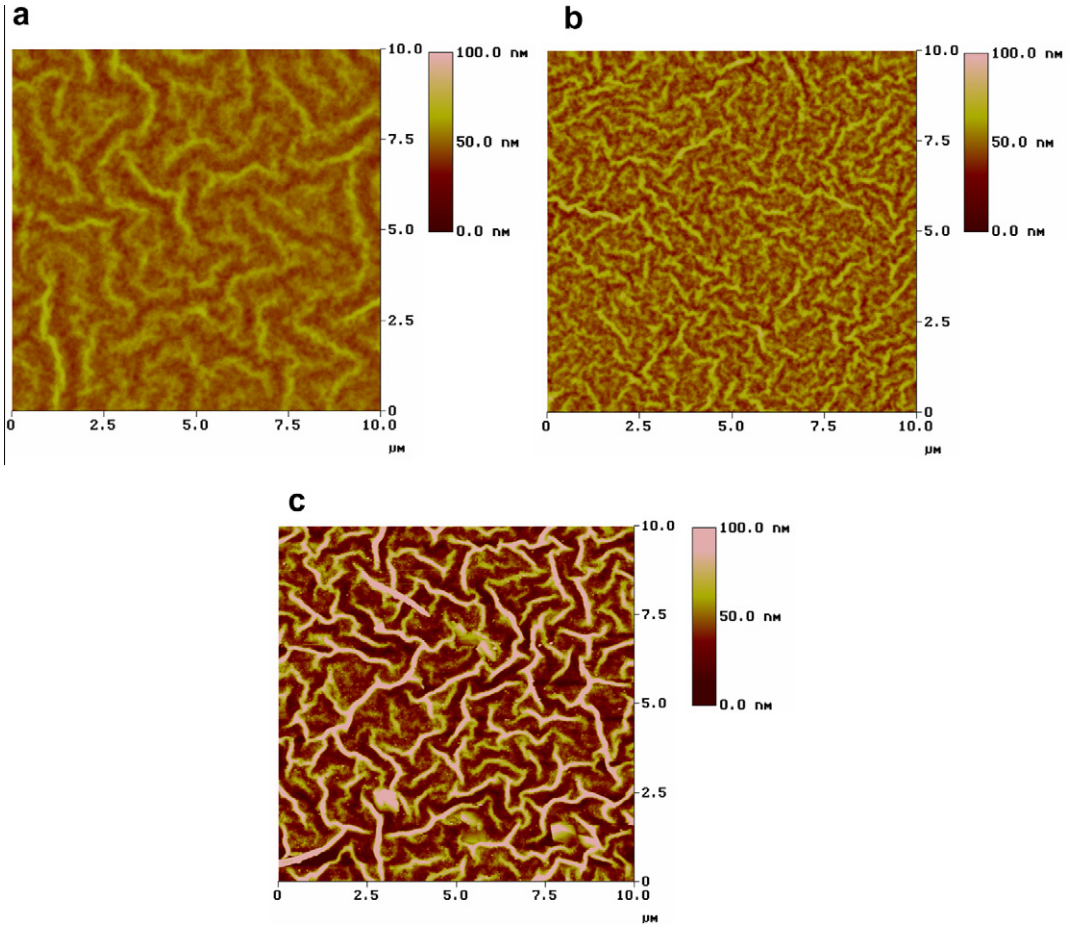

Fig. 1. AFM images of ZnO thin films annealed at various temperatures: (a) 150 °C, (b) 300 °C, and (c) 450 °C.

this result reflects the facts that the PEDA-TMS layer can effectively reduce the work function of ZnO, which increased the build-in potential of the device and modify its surface ZnO, which lowered the leakage current of the device. The luminescence is greatly increased by the presence of PEDA-TMS. The performance of a modified inverted device is close to that of a conventional device. Notably, the turn-on voltage ($V_{\text{turn-on}}$) is 0.5 V highly (conventional device: 2.3 V; inverted device: 2.8 V) because the formation of a space-charge field induces electron injection, indicating the build-up of hole accumulation near the G-PF/ZnO interface [5]. Fig. 2b presents the effect of ZnO annealing temperature on device performance. The current density increased with annealing temperature. Following annealing at 450 °C, the coarse surface of ZnO caused excess leakage current. A higher luminance value was observed following annealing at 300 °C. Fig. 3 plots the EL efficiencies of the devices. The EL efficiency gradually increased with voltage to a maximum of 7 cd A^{-1} for an inverted device that was annealed at 300 °C. This value is close to that of a conventional device. However, the EL efficiency of ZnO that was annealed at 450 °C was very low. The effects on device performance are related to the barrier height between ZnO and G-PF as well as the intrinsic electron mobility of the modified ZnO. The formation of dipole moments results in the decrease of barrier height by grafting self-assembled monolayer on the surface of ZnO. Consequently, X-ray photoelectron spectroscopic (XPS) and UPS measurements were made to analyze the interfacial characteristics of modified ZnO electrodes.

PEDA-TMS was bonded onto the surface of ZnO using a hydrolysis reaction [12]. The extent of conversion in the reaction depends on the number of —OH groups. The surface characteristics of ZnO were analyzed using XPS spectroscopy to investigate the oxidation states of both Zn and O. Fig. S2 presents the energy of the O 1s peak from as-modified ZnO that was annealed at various temperatures. The ratio of —OH to O (−2) were 1.14, 0.91, and 0.78 with increasing annealing temperatures of 150 °C, 300 °C, and 450 °C, respectively. The drop of the number of —OH groups reduced the amount of grafted PEDA-TMS. Fig. 4 shows the secondary cutoff edge regions of UPS spectra of ZnO with and without PEDA-TMS following annealing at various temperatures, to determine the shifts in the vacuum energy level. Herein, the HOMO edge region is not shown but the work function of the modified ZnO is carefully determined using the formula $\Phi = h\upsilon - \Delta E$, where $h\upsilon$ represents the photon energy (21.2 eV) and ΔE

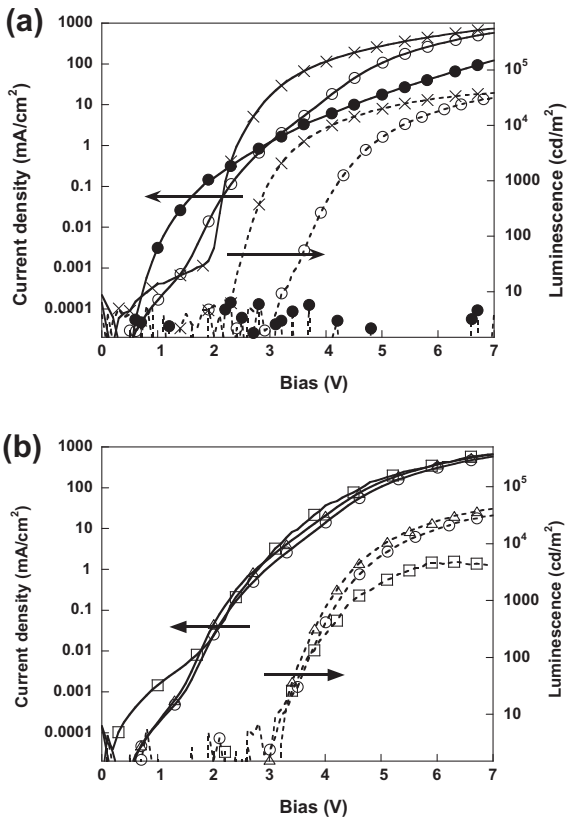

Fig. 2. *J–V–L* characteristics of PLED devices: (a) conventional device (X), inverted device without PEDA-TMS (●), and inverted device with PEDA-TMS (○); (b) inverted device with PEDA-TMS for various annealing temperatures: 150 °C (○), 300 °C (△), and 450 °C (□).

is determined from the distance between the binding energy at the secondary electron emission cutoff edge and that at the HOMO edge [19]. The values of l were 3.58, 3.52, and 3.77 eV following annealing at 150 °C, 300 °C, and 450 °C, respectively. When bare ZnO substrates were annealed at high temperatures, the cutoff edge slightly shifted toward higher binding energies, indicating that the conduction band of ZnO shifted toward a more positive energy owing to the increase of the direct band gap [20]. After PEDA-TMS was modified onto the ZnO surface, the vacuum energy level was shifted to a substantially lower binding energy, indicating that the barrier between ZnO and G-PF was lowered. The overall shifts of vacuum energy levels were 0.83 eV, 0.84 eV, and 0.58 eV following annealing at 150 °C, 300 °C, and 450 °C, respectively. Despite the fact that the number of —OH groups following annealing at 300 °C was slightly lower than that following annealing at 150 °C case, the work function of ZnO was changed by PEDA-TMS modification. The inferior shift associated with annealing at 450 °C case is attributable to the inadequacy of the number of —OH groups and the disordered dipole moment of PEDA-TMS that was grafted onto the coarse surface. The (ZnO/PEDA-TMS electrode that was annealed at 300 °C had an energy level that facilitated electron injection.

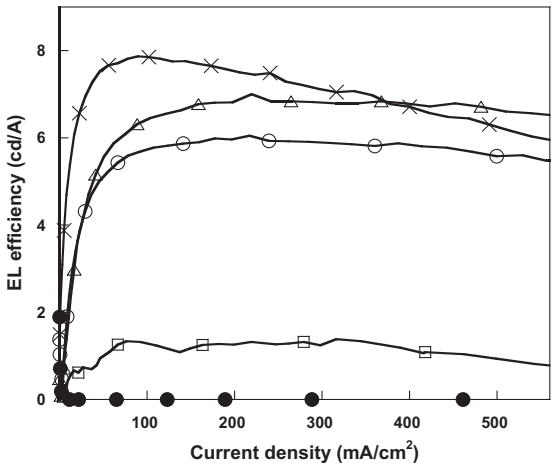

Fig. 3. EL efficiency as a function of current density: conventional device (X), inverted device without PEDA-TMS for 150 °C annealing temperature (●), inverted device with PEDA-TMS for various annealing temperatures: 150 °C (○), 300 °C (△), and 450 °C (□).

The electron mobility of intrinsic ZnO can influence device performance because electrons are regarded as the minor charges in an inverted device. Fig. 5 plots the *J–V* curves of an electron-only device following annealing at various temperatures. A comparison with a previous investigation [10] reveals that the inverted devices based on ZnO had a higher electron injection current than did those based on TiO_2, resulting in a significant improvement in device performance. Additionally, modified ZnO electrodes that are annealed at higher temperatures exhibit a higher electron injection ability because they have a greater crystallinity. However, poor device performance was observed following annealing at 450 °C, even though this temperature led to the greatest injection of electrons into the EL layer. This finding is inconsistent with the EL mechanism of a conventional device, indicating that the enhancement of minority charge injection increases EL efficiency.

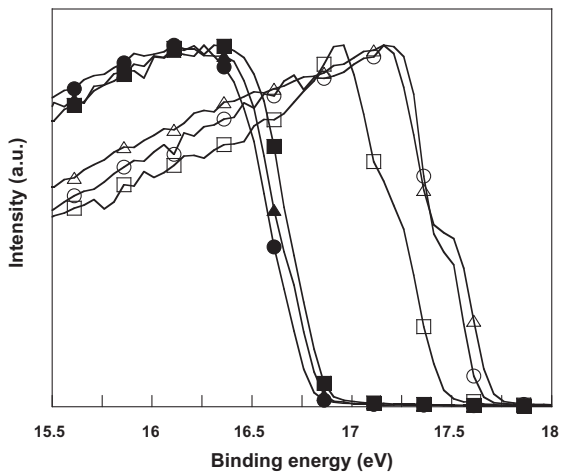

Fig. 4. Secondary cutoff edge regions of UPS spectra of ZnO with and without PEDA-TMS for various annealing temperatures: without PEDA-TMS at 150 °C (●), 300 °C (▲), and 450 °C (■); with PEDA-TMS at 150 °C (○), 300 °C (△), and 450 °C (□).

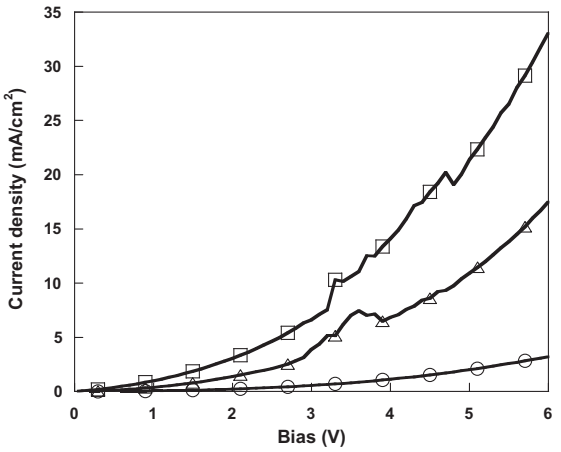

Fig. 5. *J–V* characteristics of electron-only devices for various annealing temperatures: 150 °C (○), 300 °C (△), and 450 °C (□).

The EL mechanism of inverted devices is considered to be based on metal oxide as an electron injection/buffer layer. A space-charge field is formed upon the accumulation of holes and then electrons are thus induced to enter the EL layer. To clarify the recombination condition of dual-carriers, Fig. 6 plots the capacitance–voltage (*C–V*) characteristics of the conventional device and inverted devices that were annealed at various temperatures. The *C–V* behaviors are correlated with the threshold voltage (majority charge injection) and turn-on voltage (minority charge injection). In the conventional device, the capacitance initially increased until the turn-on voltage was reduced due to the dark current and the injection of majority carriers (holes) and their accumulation in the G-PF layer. Then, the minority charge (electron) injection occurred, inducing the recombination of electrons and holes. The amount of charges in the G-PF layer was significantly diminished, and hence the capacitance sharply declined after the turn-on voltage was reached [21,22]. In contrast, the capacitance of the inverted device substantially increased after the threshold voltage was passed because the ZnO/G-PF interface blocked the majority charges (holes), so most charges accumulated in the polymer. Notably, the capacitance declined just before the turn-on voltage was reached about 2.4 V [21]. A few electrons are assumed to have been charge-induced to inject into the ZnO/G-PF interface. However, insufficient driving voltage led to electron and hole recombination in the ZnO region, which quenched exitons for radiative emission. Further increasing the bias caused the recombination region to shift into the G-PF layer. When the turn-on voltage was exceeded, the capacitance was substantially decreased by energetic charge recombination and effective photon emission. Following annealing at 300 °C, capacitance fluctuated significantly, presumably because of the increase in the intrinsic mobility of ZnO. However, the increase in capacitance associated with annealing at 450 °C is unobvious, indicating that ZnO does not mainly block holes or induce the injection of electrons into the G-PF layer for effective recombination because of its coarse morphology. The performance of ZnO annealed at 450 °C is inferior to that of ZnO annealed at 300 °C. The latter has high electron mobility and effectively blocks holes, supporting the favorable performance of the inverted device.

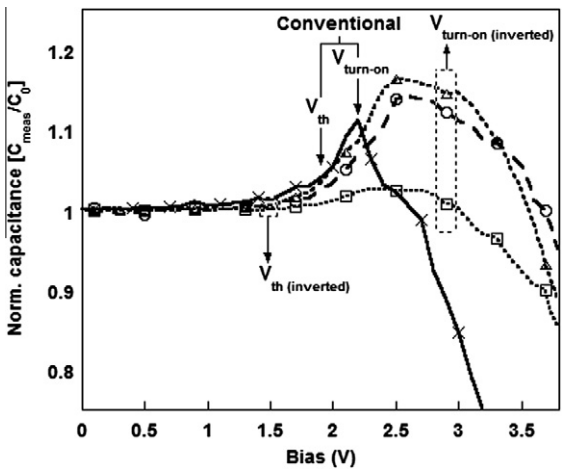

Fig. 6. Normalized *C–V* characteristics of conventional device (*X*) and inverted devices for various annealing temperatures: 150 °C (○), 300 °C (△), and 450 °C (□). Here, C_0 is the capacitance of the device at 0 V.

4. Conclusion

Inverted devices with high EL efficiencies were fabricated using stable ZnO/PEDA-TMS as electron injection/hole blocking layers. The effect of ZnO annealing temperature on device performance was analyzed in terms of charge injection barrier, electron injection ability of the modified electrode, and the recombination region of electrons and holes. The optimal annealing temperature of ZnO is about 300 °C. The adequate number of —OH groups on the surface of ZnO easily hydrolyze to form PEDA-TMS monolayer, reducing the barrier height between ZnO and the G-PF layer. The high crystallinity of ZnO associated with annealing temperature enhances the injection of minority carriers (electrons), helping to balance the ratio of electrons and holes in the active layer. The hole blocking effect dominates the region of recombination of electrons and holes in the G-PF polymer.

Acknowledgements

This work was supported by the National Science Council (NSC) of Taiwan under great NSC 99-2221-E-006-195 and by the Asian Office of Aerospace Research and Development (AOARD-10-4054). Dr. Y.C. Li would like to thank the Advanced Optoelectronic Technology Center of NCKU for providing postdoctoral fellow funding (HUA98-9-15-233-1). Ted Knoy is appreciated for his editorial assistance.

Appendix A. Supplementary material

Supplementary data associated with this article can be found, in the online version, at doi:10.1016/j.orgel.2011.05.022.

References

[1] T. Wakimoto, Y. Fukuda, K. Nagayama, A. Yokoi, H. Nakada, M. Tsuchida, IEEE Trans. Electron. Dev. 44 (1997) 1245.
[2] T.M. Brown, R.H. Friend, I.S. Millard, D.J. Lacey, T. Butler, J.H. Burroughes, F. Cacialli, J. Appl. Phys. 93 (2003) 6159.
[3] J. Huang, Z. Xu, Y. Yang, Adv. Funct. Mater. 17 (2007) 1966.
[4] Tsung-Hsun Lee, Jung-Chun-Andrew Huang, Georgi L'vovich Pakhomov, Tzung-Fang Guo,* Ten-Chin Wen, Yi-Shun Huang, Chuan-Cheng Tsou, Chia-Tin Chung, Ying-Chang Lin, and Yao-Jane Hsu, Adv. Funct. Mater. 18 (2008) 3036.
[5] H.J. Bolink, E. Coronado, D. Repetto, M. Sessolo, E.M. Barea, J. Bisquert, G.G. Belmonte, J. Prochazka, L. Kavan, Adv. Funct. Mater. 18 (2008) 145.
[6] H.J. Bolink, E. Coronado, D. Repetto, M. Sessolo, Appl. Phys. Lett. 91 (2007) 223501.
[7] N. Tokmoldin, N. Griffiths, D.D.C. Bradley, S.A. Haque, Adv. Mater. 21 (2009) 3475.
[8] H.J. Bolink, H. Brine, E. Coronado, M. Sessolo, J. Mater. Chem. 20 (2010) 4047.
[9] Katsuyuki Morii, Takeo Kawase and Satoshi Inoue, Appl. Phys. Lett. 92 (2008) 213304.
[10] H.J. Bolink, E. Coronado, J. Orozco, M. Sessolo, Adv. Mater. 21 (2009) 79.
[11] M.-H. Park, J.-H. Li, A. Kumar, G. Li, Y. Yang, Adv. Funct. Mater. 19 (2009) 1241.
[12] S.N. Hsieh, S.P. Chen, C.Y. Li, T.C. Wen, T.F. Guo, Y.J. Hsu, Org. Electron. 10 (2009) 1626.
[13] D. Raoufi, H.R. Fallah, A. Kiasatpour, Appl. Surf. Sci. 253 (2007) 9085.
[14] G. Shen, P.C. Chen, K. Ryu, C. Zhou, J. Mater. Chem. 19 (2009) 828.
[15] J.C. Wang, W.T. Weng, M.Y. Tsai, M.K. Lee, S.F. Horng, T.P. Perng, C.C. Kei, C.C. Yu, H.F. Meng, J. Mater. Chem. 20 (2010) 862.
[16] L. Van Heerden, R. Swanepoel, Thin Solid Films 299 (1997) 72.
[17] M.H. Koch, R.N. Lamb, G.L. Mar, P.Y. Timbrell, US Patent 6921, p. 552 (March 26, 2005).
[18] Y. Gu, X. Li, W. Yu, X. Gao, J. Zhao, C. Yang, J. Cryst. Growth 305 (2007) 36.
[19] C.Y. Li, T.C. Wen, T.H. Lee, T. F Guo, J.C.A. Huang, Y.C. Lin, Y.J. Hsu, J. Mater. Chem. 19 (2009) 1643.
[20] N. Bouhssira, S. Abed, E. Tomasella, J. Cellier, A. Mosbah, M.S. Aida, M. Jacquet, Appl. Surf. Sci. 252 (2006) 5594.
[21] I.H. Campbell, D.L. Smith, J.P. Ferraris, Appl. Phys. Lett. 66 (1995) 3030.
[22] V. Shrotriya, Y. Yang, J. Appl. Phys. 97 (2005) 054504.

[25]. Therefore, the general belief is that interaction between C_{60} and noble metal surfaces has an ionic character. However, Wang and Cheng reported that this interaction is covalent with some ionic features [28]. By comparison, there are far less studies for C_{60} evaporated onto HOPG [29–32]. Only one of them investigates the nature of the C_{60}-substrate interaction, and finds that C_{60} adsorbs on HOPG by van der Waals interactions [30].

Scanning tunneling spectroscopy (STS) is a unique technique that allows a direct measure of the local density of states (DOS) near the Fermi energy. In order to study the electronic structure, STS has been performed on thin films of C_{60} deposited by sublimation onto different substrates and changes in HOMO, LUMO and HOMO–LUMO gaps are studied. These values have been reported for single C_{60} molecules and ultrathin C_{60} films (thickness < 1 ML) on Si [25,33–35], Au [17,36–40] and HOPG [41], for different adsorption sites and surface conformations. The overall tendency is that the gap values for C_{60} on Si are smaller (*ca.* 1.7 eV) than those obtained on Au surfaces (*ca.* 2.55 ± 0.25 eV), due to charge transfer from Au to the C_{60} molecules.

In contrast to the large amount of literature concerning the C_{60} electronic properties at submonolayer or monolayer coverages, less attention has been paid to these properties for C_{60} films on Si, Au and HOPG at coverages above 4 ML. There is even less information on the electronic properties of thin C_{60} films exposed to ambient conditions, despite the fact that in many cases manipulation and applications of these films are performed under light and atmospheric oxygen levels. It is known that under these conditions, changes in macroscopic physical and chemical properties of C_{60} films take place [17,42–45]. For example, exposure to light and oxygen induces changes in the C_{60} films from diamagnetic to ferromagnetic [45]. Light and oxygen exposure of these films can also affect the electronic properties of these films [46–49]. Therefore, further knowledge on their electronic properties under these conditions is a key point for predicting their performance under normal ambient conditions, and could affect many technological developments.

In this paper, we present a study on the magnetic and electronic properties of C_{60} thin films (film thickness $\geqslant$ 4 ML) sublimated onto naturally oxidized Si(1 0 0), Au films, glass, and HOPG surfaces exposed to ambient conditions. The films are characterized by atomic force microscopy (AFM) and X-ray photoelectron spectroscopy (XPS) while magnetic and electronic properties are studied by magnetic force microscopy (MFM) and scanning tunneling spectroscopy (STS), respectively. In particular we estimate for the first time the gap energies for the above mentioned thin films allowing a direct comparison with the values reported at lower coverages and under vacuum conditions. We have also determined the influence of the substrate and thickness of the films on their morphology, electronic structure and adhesion strength/wear resistance. This article is organized as follows: first we explore the structure of the films by AFM, then, we characterize the systems by XPS and MFM, and finally we explore their electronic structure by STS.

2. Experimental

Fullerene films were grown by sublimation of C_{60} (Sigma–Aldrich Company, USA, 99.5%) on clean Au films deposited onto glass (250 nm gold thickness, Arrandees™), freshly cleaved highly oriented pyrolytic graphite (HOPG), naturally oxidized Si(1 0 0) surfaces and glass. An Edwards 360 metal coater operating at 10^{-6} Torr was used for the deposition. Films were simultaneously prepared on all four kinds of substrates mounted at the same distance and geometry from the C_{60} source, in single evaporation experiments, to assure similar preparation conditions at each given film thickness. The films were then stored in ambient conditions for several days and finally cleaned under nitrogen flux immediately before characterization.

Film morphology was characterized by imaging the samples with an atomic force microscope (Nanoscope IIIa, Digital Instrument/Veeco) operating in the contact mode, with silicon nitride tips. The chemical composition of the films and the nature of the chemical bonds of the species present were corroborated by X-ray photoelectron spectroscopy (XPS). Photoelectrons were excited with a Mg Kα source (XR50, Specs GmbH) and detected with a hemispherical electron energy analyzer (PHOIBOS 100, Specs GmbH). A two-point calibration of the energy scale was performed using sputter-cleaned gold (Au $4f_{7/2}$, binding energy BE = 84.00 eV) and copper (Cu $2p_{3/2}$, BE = 933.67 eV) foils.

Electronic properties of the films were determined by STS measurements using a scanning tunneling microscope (Nanoscope IIIa, Digital Instruments/Veeco) operating in air at room temperature. Pt–Ir tips were used for these measurements. The tunneling current vs bias voltage (I vs V) curves were averaged over at least three different regions of the samples. The dI/dV plots shown in this paper are the average of ten measurements. These measurements were taken under the same experimental conditions, but performed on different regions of each sample. Smoothening of the dI/dV plots was performed by using the Savitzky–Golay differentiation [50].

Film thickness was determined by AFM measurements of films grown by stencil lithography patterning through a hexagonal mask, in parallel with the other C_{60} films. The height difference between the masked and the exposed regions has been taken as a measure of the film thickness of the set of samples grown under the same experimental conditions, taking into account that once the film has nucleated, film thickness growth, on average, proceeds independent of the substrate employed [51].

Magnetic force gradient (MFM) and topographic sample images were obtained simultaneously with a NanoScope IIIa scanning probe microscope (Digital Instruments/Veeco) at room temperature in air. The microscope was operated in the tapping/lift™ scanning mode, i.e., the AFM tip was made to scan the sample at different heights above the topographic height of the sample at each point in order to separate short range topographic effects from long range magnetic signals. Lift-heights ranging from 25 to 100 nm were selected. Images were taken at a scanning rate of 1 Hz using a MESP (60–100 kHz, 1–5 N/m) scanning probe

coated with a magnetic CoCr alloy thin film. In addition, silicon FESP tips with the same range of frequency, force constant and dimensions, but uncovered (non magnetic) were used to compare the contrast phase signal obtained with both tips at different heights of the sample. This procedure was also applied with the bare substrates. Prior to acquiring images, the tips were exposed to a 0.3 T magnetic field.

3. Results and discussion

3.1. AFM characterization

Fig. 1 shows AFM images of C_{60} films of different thickness (h); that were grown by sublimation on the native SiO_x substrates. AFM images show that the films are formed by nanometric aggregates that entirely cover the SiO_x surface.

The average size (d) of the aggregates increases from ≈20 to ≈70 nm as h is increased from 3 nm (≈4 monolayers) to 70 nm (≈100 monolayers) and remains constant for thicker films, as determined by power spectral density analyses (right panel in Fig. 1). The mean square roughness (Rq) corresponding to the films with h of 3, 40, 70 and 100 nm are 1.06, 1.13, 2.75 and 3.46 nm, respectively.

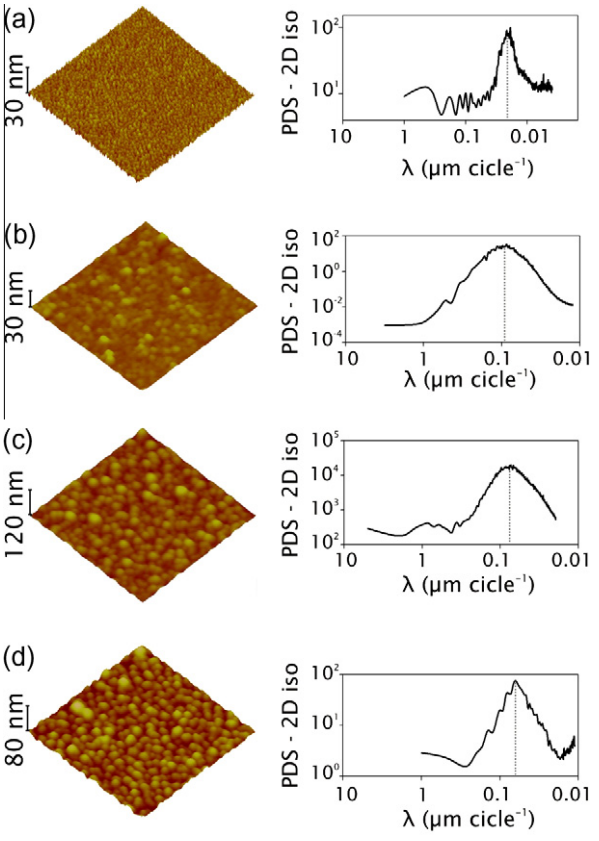

Fig. 1. Left: three-dimensional AFM images (1×1 μm^2, contact mode) of C_{60} films with different thickness (h) on silicon oxide substrates. Right: power spectral density (PSD) data corresponding to the AFM images on the left, after high-pass filtering. The grey lines indicate the average grain size (d). (a) h = 3 nm and d = 19 nm. (b) h = 40 nm and d = 55 nm. (c) h = 70 nm and d = 74 nm. (d) h = 100 nm and d = 60 nm.

Comparing h and Rq for each film, we note that for thin films (h = 3 nm) the roughness is 35.3% of the total film thickness, that is, the film topographical morphology is very irregular. On the other hand, the roughness parameter for the films with h of 40, 70 and 100 nm is 2.8%, 3.9% and 3.5% of the film thickness, respectively, which suggests a high degree of smoothness.

We observe that the films with h > 70 nm exhibit good adherence to the substrates, remaining stable under repetitive scanning with the AFM tip in the contact mode. In contrast, the adherence and wear resistance are poor for films with h = 3 nm, where repetitive scans with the tip finally open a window. In the irregular morphology present in the 3 nm thick films we expect that the outer C_{60} molecules exhibit weak van der Waals interactions so that the outer layer can be easily removed by the AFM tip. On the contrary, thicker films consist of large clusters where one expects stronger molecular interactions, and accordingly, the C_{60} molecules remain stable under tip scanning. We also note that the variations in the film thickness is accompanied by a change in the sample color from a pale brown (h = 3 nm) to green–blue (h > 40 nm). As we will see later, this color change is not related to the gap value and is mainly due to a light interference phenomenon.

Each film thickness was estimated by stencil lithography of a sample prepared in parallel with the continuous films (Fig. 2a). The height difference between the masked and exposed regions (Fig. 2b) has been taken as a measure of the film thickness for the set of samples grown during the same C_{60} sublimation experiment.

Fig. 3 shows high-pass filtered images for films of similar thicknesses grown in different sublimations on oxidized Si, HOPG, Au and glass. The images reveal a similar aggregate morphology irrespective of the substrate, but in the films grown on Au, the size of aggregates and the channels separating them are larger than on other substrates. While the high-pass filtered images allow a direct and easy comparison of the aggregate size, it loses the z-component of the image. The conventional top-view images in Fig. 4 illustrate the difference in film structure providing also information in the z-direction. Here we show C_{60} films prepared simultaneously in the same evaporation chamber on oxidized Si (Fig. 4a) and Au (Fig. 4b), both with a thickness of $h \approx 30$ nm. The images not only reveal larger aggregates for the C_{60} film grown on Au, but

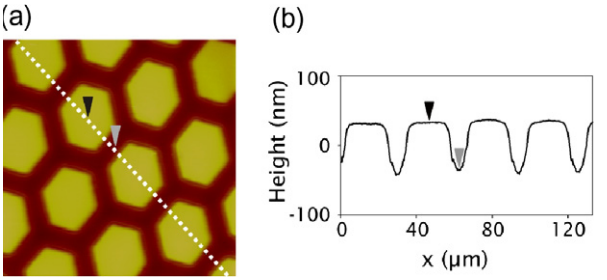

Fig. 2. (a) AFM image (2D view, 1×1 μm^2) of a patterned C_{60} film on SiO_x/Si. (b) Cross section profile across the dashed line in (a); the height difference between the black and grey arrows is h = 70 nm.

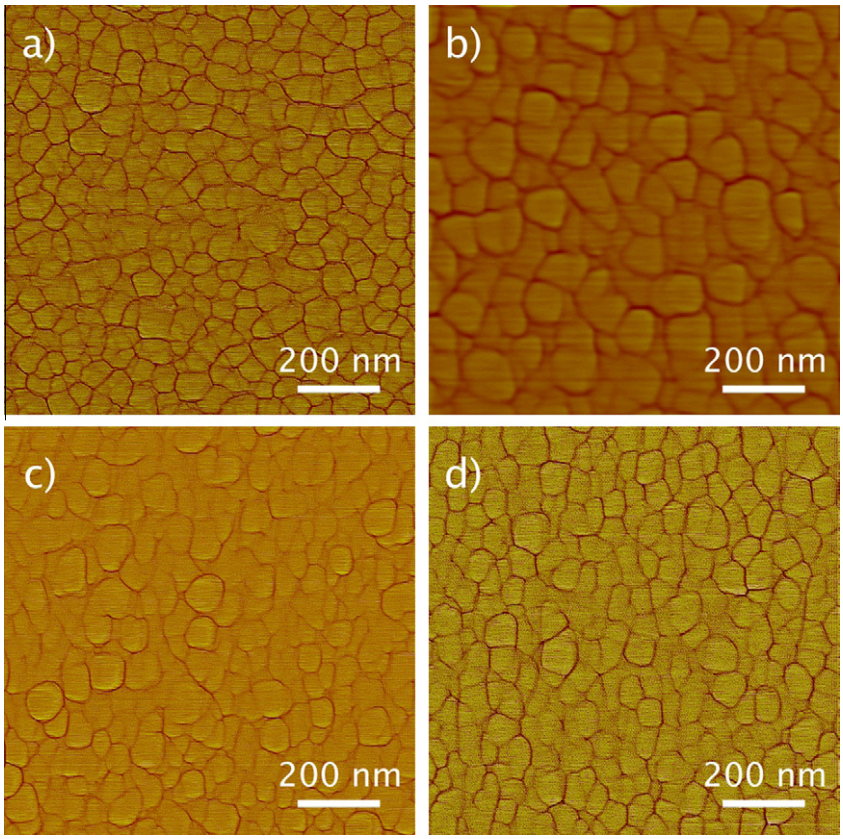

Fig. 3. AFM images (2D view, high pass filtered, $1 \times 1\ \mu m^2$) of C_{60} films grown in different sublimations on different substrates. (a) Si, $h = 100$ nm, (b) Au, $h = 140$ nm, (c) HOPG $h = 80$ nm, (d) glass, $h = 100$ nm.

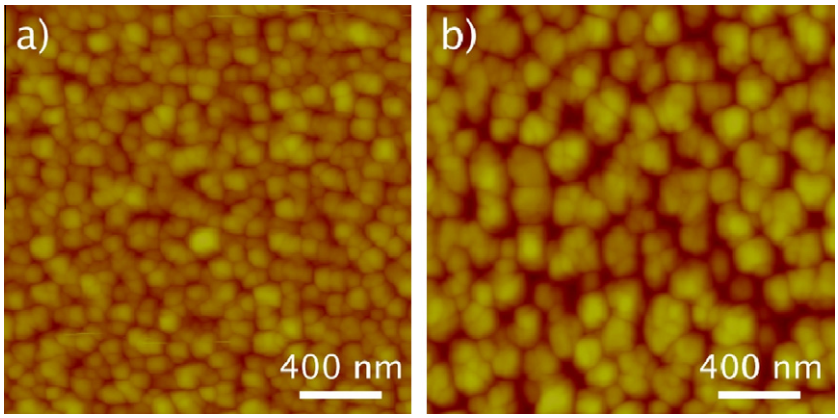

Fig. 4. AFM images (2D view, $2 \times 2\ \mu m^2$) of C_{60} films ($h = 30$ nm) prepared simultaneously on (a) oxidized Si(1 0 0) and (b) Au.

also a smaller connectivity between them, since they are separated by wider and deeper channels. The difference between aggregate size in Fig. 4, can be explained if we consider that, for submonolayer coverages, the C_{60} molecules have higher mobility on Au, facilitating the formation of large islands [21] and trenches, in contrast to what happens to the films grown on SiO_x, HOPG or glass where the first C_{60} molecules are isolated and dispersed on the surfaces, forming many more cluster seeds [15,52]. As a result, at higher coverages, the films grown on Au show larger clusters than those obtained on the others substrates (SiO_x, HOPG and glass).

3.2. XPS data

The XPS data for C_{60} films deposited onto SiO_x ($h = 70$ nm) are presented in Fig. 5. The survey spectrum (Fig. 5a) exhibits a strong C signal. Some O and only small

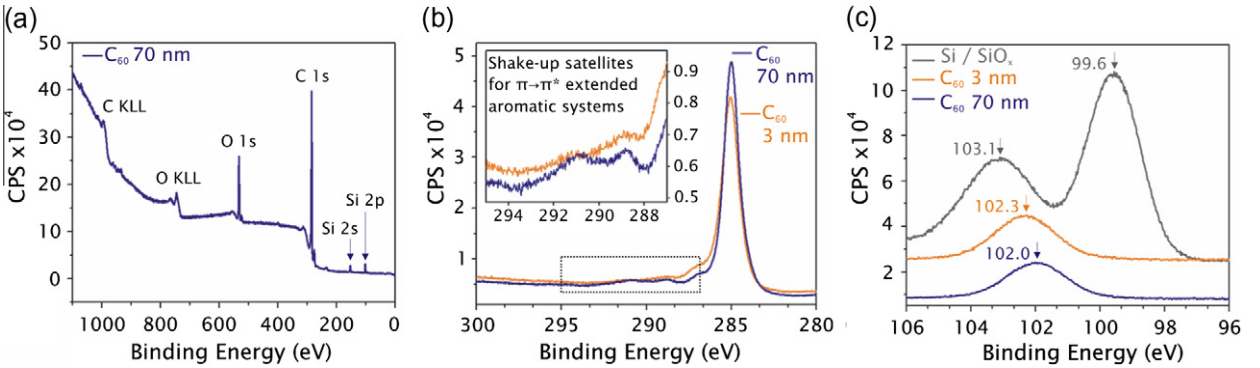

Fig. 5. XPS data for C_{60} films on oxidized silicon support: (a) survey spectrum (70-nm film), (b) C 1s spectra for 3 nm (orange) and 70 nm (blue) thick C_{60} films. Inset shows shake-up satellites attributable to C_{60} presence (c). Comparison Si 2p region between the same two C_{60} films and a SiO_x/Si reference (grey curve). C_{60} films interact with silicon substrate and show a kind of SiO_xC_y species (102.2 ± 0.1 eV) [56]. (For interpretation of the references to colour in this figure legend, the reader is referred to the web version of this article.)

amounts of Si are detected, in agreement with the film thickness and morphology (almost complete coverage of SiO_x by C_{60}) as determined by AFM. The atomic ratio between O and Si is roughly 4:1. The excess O can be associated with the extreme reactivity of C_{60} crystals to (atmospheric) oxygen [53], which quickly penetrates into the bulk fullerene. No traces of metallic contaminants can be observed in the spectra.

Fig. 5b shows XPS spectra of C 1s core level and shake-up satellites (inset in Fig. 5b) for C_{60} with film thicknesses of 3 nm (orange)[1] and 70 nm (blue),[1] and a large peak at 285 eV, typical for C_{60} films. The absence of components at energies below 283 eV is indicative of the lack of Si–C bonding in the films [17,25,54]. The inset in Fig. 5b illustrates the expanded region covering the C1s shake-up satellites. We resolved by high-resolution photoelectron spectroscopy two peaks for the deposited C_{60} film at 3.7 and 6 eV relative to the C1*s* binding energy; these results are consistent with two of the four peaks obtained in the report by Enkvist [55]. This result indicates that no significant degradation of the C_{60} films takes places under our experimental conditions.

Fig. 5c shows XPS spectra of the Si 2p core level region for a SiO_x/Si reference surface and C_{60} films of 3 and 70 nm thickness on SiO_x/Si(1 0 0). For the reference surface, two peaks are seen at 99.6 and 103.1 eV corresponding to Si^0 (Si–Si) and Si^{+4} (SiO), respectively. For the fullerene films, only one peak is found at 102.3 eV (3 nm film) or 102.0 eV (70 nm film) corresponding to Si^{+3}. By analogy with reports on oxidation of SiC [56], we can conclude that the SiO_x–C_{60} interface is mainly composed by SiO_xC_y.

3.3. MFM characterization

MFM was used to characterize magnetic properties of the C_{60} films. In order to enhance the magnetic contrast we used hexagonally patterned C_{60} films prepared by stencil lithography, as shown in Fig. 2. In Fig. 6 we show the topographic image (a) and magnetic phase contrast (b) of these films on glass. Magnetic contrast concentrated on the hexagons is evident in the C_{60} film as shown in Fig. 6b. On the other hand, the same experiments (Fig. 6c–d) under identical imaging conditions but using a non-magnetic tip give no evidence of the hexagons in the phase contrast magnetic image (Fig. 6d). Similar results are obtained for the C_{60} films deposited on the different substrates used in this work. Therefore, the MFM characterization indicates that our films are magnetic. While pristine van der Waals C_{60} crystals are diamagnetic, this behavior changes when the sample is exposed to oxygen under the action of the visible light [17]. These conditions apply to our films exposed to light under atmospheric conditions, since they contain excess amounts of oxygen as shown in the XPS data (Fig. 5a). It is known that light exposure during 2.5 h brings noticeable features of ferromagnetism: non-linear magnetization process at low fields and magnetization increases related to an increase in the exposure time [42,53].

The MFM images at high resolution (insets in Fig. 6a–b) show that the magnetic field corresponds closely to the C_{60} aggregates present on the glass substrate. However, a detailed analysis of these images indicates that the magnetic contrast does not directly map onto the aggregates, consistent with locally induced polymerization of C_{60} films [45]. After having verified that our films exhibit the ferromagnetic behavior expected for C_{60} exposed to oxygen and light we will characterize their electronic properties and discuss them in relation to previous work obtained under UHV conditions.

3.4. STS: electronic properties

Typical curves of tunneling current vs. bias voltage for C_{60} films prepared on three different substrates are shown in Fig. 7. We used metallic (Au), semi-metallic (HOPG) and semiconductor (oxidized Si) substrates in order to gain insight on the influence of the substrate on the electronic structure of C_{60} films on materials with different bulk electronic properties. As a way to calibrate our STS measurements, we first measured the averaged *I/V* curves for the bare substrates (Fig. 7, left panels). The *I/V* curve for Au shows an almost linear behavior,

[1] For interpretation of the references to colour in this figure, the reader is referred to the web version of this article.

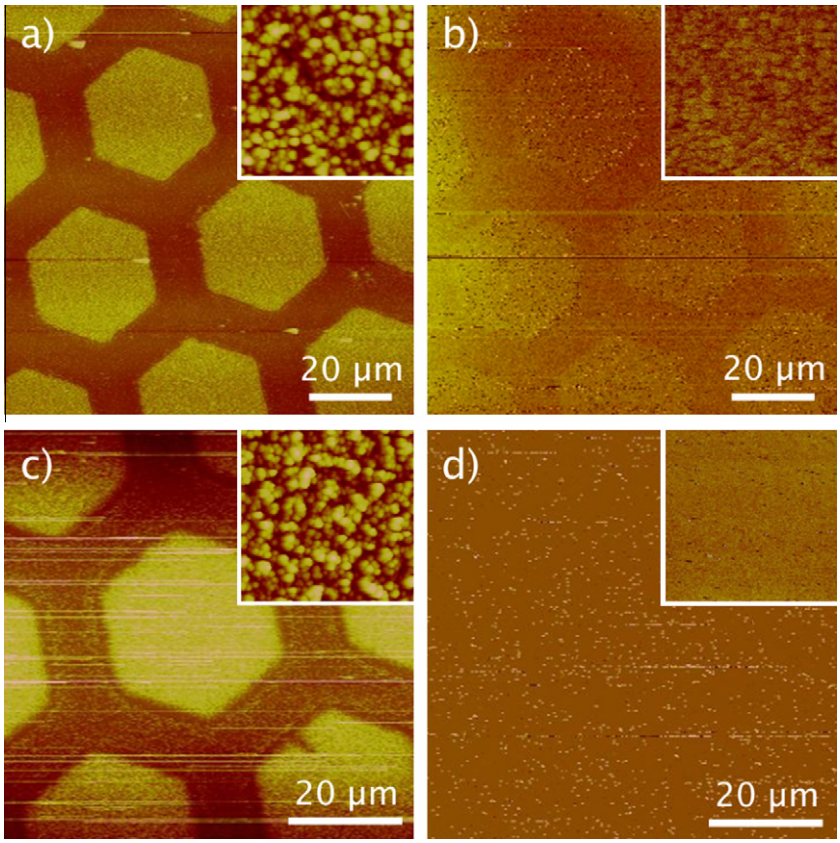

Fig. 6. (a and b) MFM images of patterned C_{60} films on glass. (a) Topographic image, 100 × 100 μm^2; inset: detail of the hexagon (3 × 3 μm^2) (b) magnetic phase contrast, 25 nm lift scan height, 100 × 100 μm^2; inset: detail of the hexagon (3 × 3 μm^2). (c and d) AFM images of patterned C_{60} films on glass. (c) Topographic image, tapping mode, 72.7 × 72.7 μm^2; inset: detail of the hexagon (3 × 3 μm^2). (d) Phase contrast, 25 nm lift scan height, 72.7 × 72.7 μm^2; inset: detail of the hexagon (3 × 3 μm^2).

as expected for metallic conductors [57]. In contrast, those recorded for SiO_x/Si(1 0 0) show zero current near the Fermi level, typical of semiconductors [58]. Meanwhile, the observed behavior for HOPG is intermediate between Au and SiO_x/Si(1 0 0). On the other hand, all *I/V* curves for the C_{60} films (Fig. 7, right panels) exhibit a response characteristic of semiconductor materials. Comparing the curves on the left of Fig. 7 with the curves on the right, it is clear that C_{60} masks the electronic properties of the pristine sample surfaces. For Au and HOPG, the change is very dramatic, while for SiO_x/Si(1 0 0) the only difference is that the width in the zero current response is greater for C_{60}/SiO_x/Si(1 0 0) than for SiO_x/Si(1 0 0), thus suggesting that the gap for the C_{60} film is larger than the corresponding for pristine support. The main difference observed between the three curves on the right is that the width of the linear response current region is greater for C_{60}/Au than for either C_{60}/HOPG or C_{60}/SiO_x/Si, which suggests that the gap width for the C_{60} film evaporated onto Au is higher than on either SiO_x or HOPG. While this same trend is observed for ultrathin C_{60} films (thickness < 1 ML) in UHV, where the gap is larger on Au [17,36–40] than on either Si [25,33–35], or HOPG [41]), it is very unlikely that STS can detect charge transfer from the substrate to films several layers high.

A better indication of the electronic state of a sample-surface and charge transfer processes involved can be obtained from the derivative tunneling spectra, *dI/dV*, (Fig. 8) which is a measure of the local density of states (LDOS) of a surface [59]. Our main objective was to quantify and compare the gap for all the fullerene films. The averaged derivative STS spectra for Au, HOPG and SiO_x/Si(1 0 0) were obtained at constant sample-tip separation conditions given by sample biases of 1.0, 0.5 and 2.0 V, respectively and a current of 1.0 nA.

The spectrum for Au (Fig. 8a) shows the expected metallic behavior, with a little curvature close to the Fermi level. On the other hand, the spectrum for HOGP (Fig. 8b) shows a slightly asymmetric parabolic shape of LDOS around the Fermi level as already reported for HOPG conductance data in ambient conditions [60,61].

Moreover, the spectrum for SiO_x/Si(1 0 0) exhibits a semiconductor behavior with a gap of 1.0 ± 0.1 eV. It shows good agreement with the values obtained in Refs. [62,63] and indicates that the average SiO_x thickness is at least 0.2 nm [62]. Our results are consistent with those reported in the literature, thus indicating that the ambient experimental conditions employed (open air and room temperature) are not responsible for the variations measured between bare and C_{60}-covered surfaces.

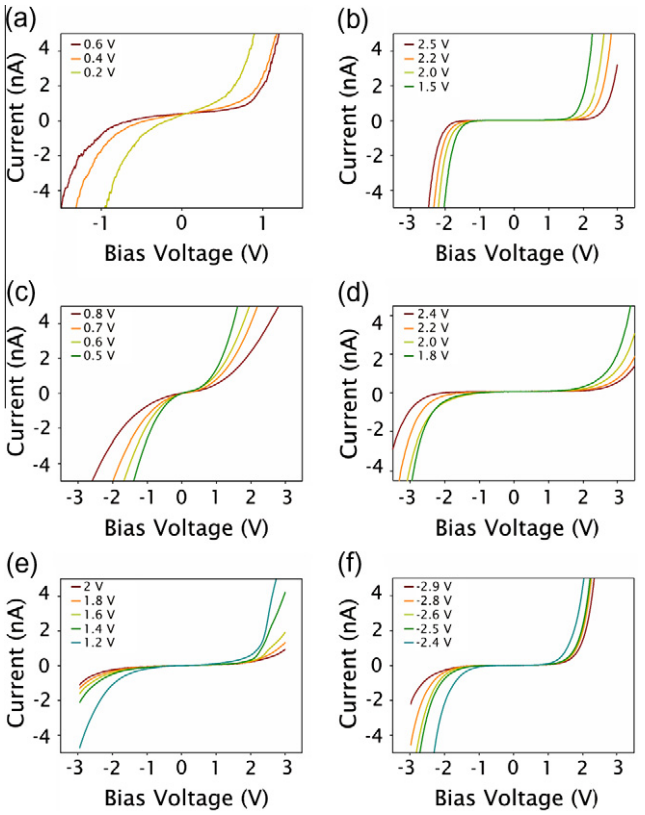

Fig. 7. *I*/*V* curves for bare substrates (left side) and C_{60} films (right side). All curves were taken at sample bias range from −3 V to +3 V and I = 1.0 nA. (a) Au, (b) C_{60}/Au, (c) HOPG, (d) C_{60}/HOPG, (e) SiO_x and (f) C_{60}/SiO_x.

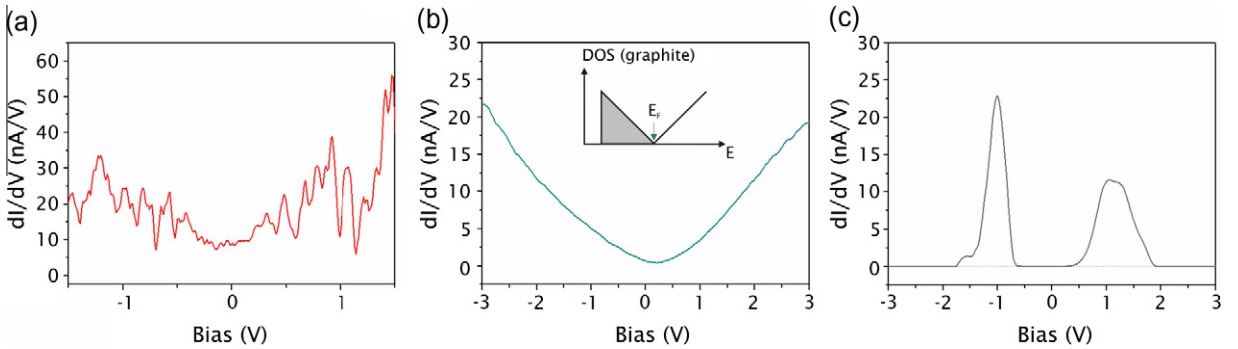

Fig. 8. The dI/dV curves measured for (a) Au (sample bias: 1 V), (b) HOPG (sample bias: 0.5 V) and (c) $Si0_x$/Si(1 0 0) (sample bias: 2 V) respectively. The current used in all spectra was 1.0 nA.

Fig. 9 shows *dI*/*dV* spectra for C_{60} films of different thicknesses prepared on SiO_x/Si(1 0 0). Our purpose was to address the electronic behavior of C_{60}/SiO_x/Si(1 0 0) system as the film thickness increases. Fig. 9(a) shows the STS spectrum for the 3 nm thick film (4 ML). The band gap obtained was 1.4 ± 0.1 eV with HOMO and LUMO at −1.0 and +0.4 eV, respectively. The Fermi level is shifted toward the LUMO band, which implies that there is a charge transfer from the SiO_x/Si(1 0 0) substrate to C_{60} consistent with the XPS data shown in Fig. 5c for the Si 2p signal, and in agreement with the results reported by Wang et al. for this system [17].

Fig. 9(b–d) summarizes STS data recorded for films thicker than 57 ML (40 nm). The gap values obtained are 1.6 ± 0.1, 1.6 ± 0.1 and 1.7 ± 0.1 eV, with HOMO energies of −0.7, −0.8 and −0.8 eV, and LUMO energies of 0.9, 0.8 and 0.9 eV for 40, 70 and 100 nm film-thicknesses, respectively. These results show that the gap is independent of thickness for smooth and thicker films and that their value correlates well with the gap for free C_{60} molecules [35], thus discarding the possibility that the film color could be caused by changes in the HOMO–LUMO position. In addition, we did not observe a LUMO shift towards the Fermi level (the spectra are symmetrical), suggesting that

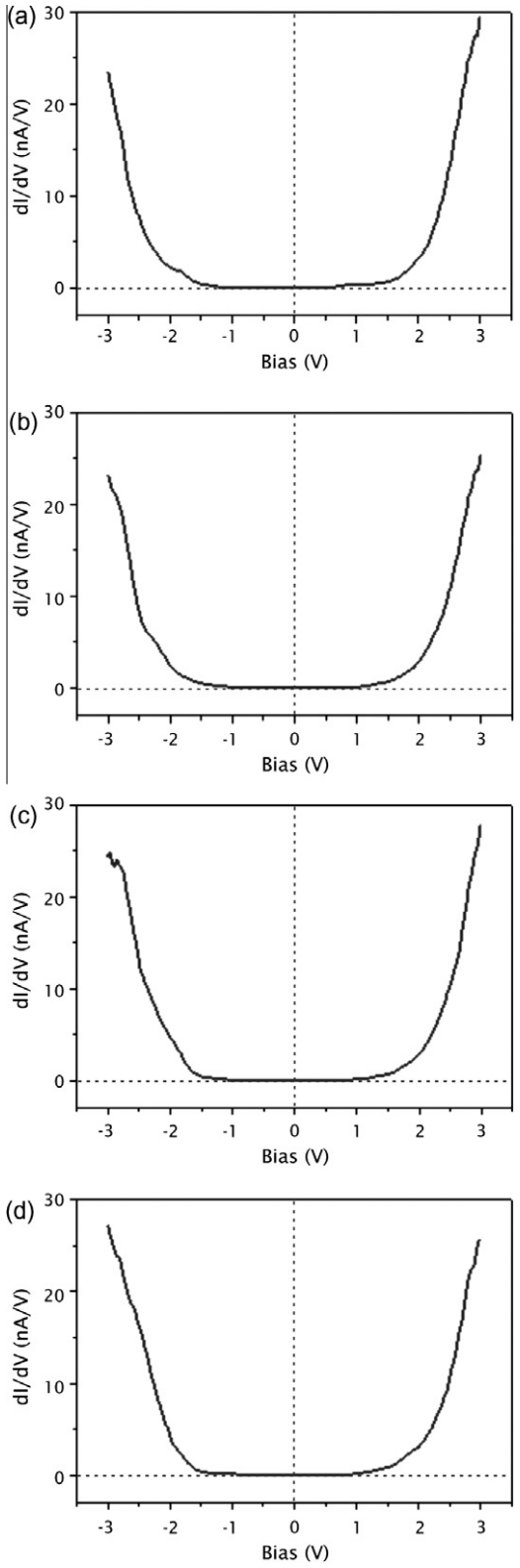

Fig. 9. STS spectra of $C_{60}/SiO_x/Si(1\,0\,0)$ for different film thicknesses: (a) 3 nm, (b) 40 nm, (c) 70 nm and (d) 100 nm. All curves were taken at sample bias of −3 V and current of 1.0 nA. The dashed line is shown to aid the gap visualization, and shows the symmetry with respect to the Fermi level.

there is no detectable charge transfer between Si and the outer C_{60} molecules, as expected for films with these thicknesses. In conclusion, we found that at high coverages (>57 ML) of C_{60} molecules deposited on $SiO_x/Si(1\,0\,0)$, the electronic characteristics of C_{60} films are very similar to those for C_{60}.

We have also tested the electronic properties of C_{60} films grown on Au and HOPG (Fig. 10). The clean Au and HOPG substrates exhibit ambient *dI/dV* curves typical of conducting materials (Fig. 8). However, after C_{60} deposition, the *dI/dV* plots show a semiconductor behavior with a gap of 1.6 ± 0.1 eV (HOMO = −0.8 eV and LUMO = +0.8 eV) and 2.5 ± 0.1 eV (HOMO = −1.3 eV and LUMO = +1.2 eV) for C_{60}/HOPG and C_{60}/Au, respectively. Both films have a thickness of 70 nm (100 ML of C_{60}) and show symmetrical behavior with respect to the Fermi level. The gap for C_{60}/HOPG is close to that obtained both for bulk C_{60}, and for the $C_{60}/SiO_x/Si$ film at the same coverage as above. In contrast, the gap of 2.5 ± 0.1 eV obtained for C_{60}/Au is higher than that for C_{60}/HOPG and Si substrate-surfaces, and comparable to those reported for single molecules and 1 ML of C_{60} deposited onto Au (gap values of 2.3–2.8 eV) [36–40]. The difference in the gap values measured for C_{60}/Au with respect to the C_{60} films

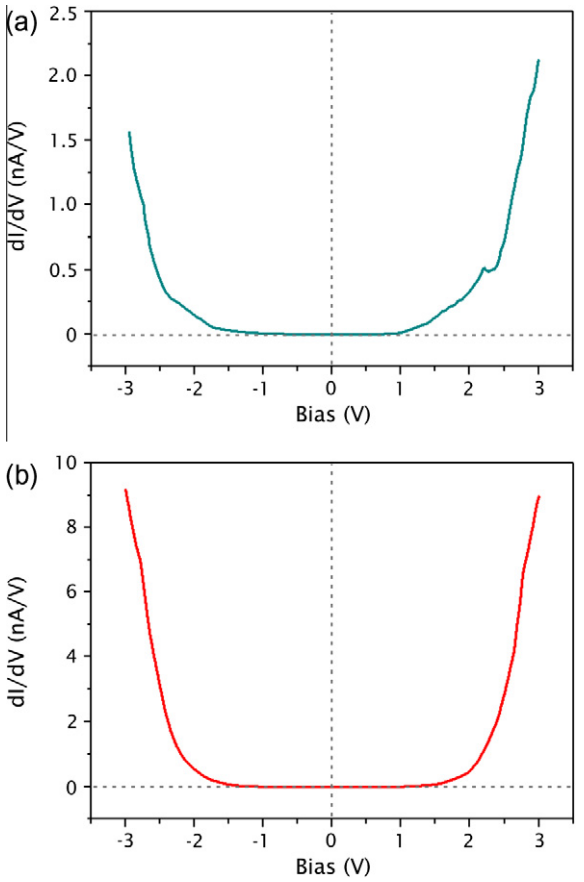

Fig. 10. STS spectra of (a) C_{60}/HOPG and (b) C_{60}/Au taken at sample bias of −3 V and current of 1.0 nA. The dashed line aids to visualize the gap of the film and shows the symmetry with respect to the Fermi level. The film thickness in both cases is 70 nm.

on the other substrates can, in principle, have multiple origins. While at first it is tempting to assign this value to charge transfer from Au to C_{60}, as for ultrathin C_{60} films, dI/dV curves are symmetric, essentially ruling out this possibility.

We next consider the structural differences in these films. Fernández-Torrente et al. [36] have shown that, for C_{60} films on Au(1 1 1), the gap obtained by STS changes in relation to the molecular environment. The differences in gap values measured for C_{60}/Au(1 1 1), with respect to the other substrates, seems to imply that the molecular environment for C_{60} on Au is different from the one in C_{60}/SiO_x/Si(1 0 0) and C_{60}/HOPG. If we take into account that the fullerene films were prepared simultaneously, in single evaporation experiments and with the same experimental setup, on all substrates, such preparation conditions imply that the mass of deposited fullerenes per unit surface area is the same for each sample, except perhaps during the very early stages of nucleation. However, once the steady growth state [51] is assumed to set in, (Fig. 4, $h \approx 30$ nm) the C_{60} films on Au (Fig. 4b) portray larger fullerene aggregates, and wider and deeper channels between them, than for example, on oxidized silicon (Fig. 4a). Bearing in mind that the mass of deposited fullerenes per unit surface area must be the same for each sample, under the same preparation conditions, the different morphologies could imply a local lowering of C_{60} density in the more extended grain-boundaries, resulting in a smaller number of C_{60} neighbors within the grain-boundaries. While this factor locally produces an increase in gap values, it is little likely that this change is detected by STS on an individual grain. Given that the initial thicknesses are comparable for all four kinds of substrates, these differences in gap values on Au could be a post-preparation effect, as we discuss below.

The fact that the electronic properties of the C_{60} films are not strongly modified by ambient conditions is at first surprising, particularly considering that their magnetic properties are modified. It has been reported that oxygen physisorbs (with a very small charge transfer) onto fullerene films, decreasing dramatically their conductivity [48]. Two distinct types of adsorbed oxygen were proposed [46]: oxygen incorporated at intergrain boundaries that rapidly quenches electronic transport, decreasing the intrinsic conductivity of C_{60} by one or two orders of magnitude, and oxygen at interstitial spaces of the C_{60} crystallites, resulting from slow diffusion, that lowers the conductivity of the material by about another two orders of magnitude. It has been shown, as well, that water diffusion is also important in C_{60} film degradation [49]. In principle, our results can be explained considering the kind of oxygen present in our C_{60} films and the different types of electronic measurements made by us and by other researchers. We propose that in our thicker film (where $d \approx h$) on Si, Au and HOPG, with nanometer sized grains, the dominant kind of physisorbed oxygen is at domain boundaries, so that it does not affect the molecular conductance measured by STS. Here we must recall that STS measures local properties resulting from electron transfer inside each nanometer-sized aggregate, and not the average properties of the films measured in other work, with non-local probes, where the contribution of domain boundaries is larger. In the case of C_{60}/Au, the larger grain boundary regions possibly enable a faster incorporation of oxygen at grain boundaries, that in turn could then interdiffuse into the grains, producing both swelling [45] and lowering of the conductivity, thus contributing to the increased gap of 2.5 eV observed for C_{60}/Au. In this case, the oxygen, initially incorporated into the more extended and deeper grain boundary regions of the film, can diffuse to interstitial C_{60} sites, thus effectively decreasing the local conductivity in the STS measurements. In summary, of the possible effects that could concurrently be responsible for the larger local band gap of C_{60} films on Au: charge transfer from the substrate to C_{60} molecules, as in ultra thin films; a local lowering of the grain-boundary packing density; and diffusion of oxygen to interstitial C_{60} sites; the latter is most probably the cause of the increase in the measured band gap on Au.

4. Conclusions

We have investigated the structure, chemical composition, magnetic and local electronic properties of thin C_{60} films (film thickness $\geqslant$ 4 ML) grown by sublimation on native silicon oxide, Au films, highly oriented pyrolytic graphite and glass, and subsequently exposed to ambient conditions. The films exhibit a structure consisting of nanometric aggregates, whose size increases with film thickness, irrespective of the substrate. Larger aggregates are systematically found on Au. The XPS data indicate no significant degradation of the C_{60} film although important amounts of oxygen are present in the films. The MFM data confirm that oxygen and light impact on the magnetic properties of C_{60}. In contrast, the STS measurements show little influence of ambient conditions on the local electronic properties. In fact, they are similar to those reported for ultrathin films grown and studied on the same substrates in UHV, i.e., in the absence of oxygen. For 4 ML of C_{60} on SiO_x, XPS data indicate the formation of a SiO_xC_y interface, in agreement with STS data showing charge transfer from SiO_x to C_{60}. The gap values for this film are close to those obtained in previous reports at lower coverages. On the other hand, thicker C_{60} films on SiO_x/Si and HOPG have gap values similar to those found for bulk C_{60}. In contrast, the electronic properties for C_{60} films on Au films show a larger gap value than those obtained on either HOPG or oxidized Si surfaces that, in our case, could be attributed to changes in the thin film structure, as a result of deep and extended domain boundaries. These extended boundaries on Au could facilitate the diffusion of oxygen to interstitial C_{60} sites, thereby increasing the band gap. The good adhesion and wear resistance of the thicker C_{60} films (40 nm < h < 100 nm), as well as the nearly constant local HOMO–LUMO gap on each substrate could become relevant for applications requiring manipulation, storage and operation under ambient conditions.

Acknowledgments

We acknowledge financial support from ANPCyT (Argentina, PICT06-621, PAE 22711, PICT-CNPQ 08-019), Gobierno de Canarias (ID20100152 ACIISI), MICIIN (Spain,

CTQ2008-06017/BQU), Spain, the National Autonomous University of Mexico (UNAM; grant DGAPA-IN100610), from the National Council of Science and Technology of Mexico (CONACYT; grant No. 127299) is greatly appreciated. O. A.-S. is grateful to the Posgrado en Ciencias Químicas UNAM and to CONACYT for a PhD fellowship.

References

[1] H.W. Kroto, J.R. Heath, S.C. O'Brien, R.F. Curl, R.E. Smalley, Nature 318 (1985) 162.
[2] W. Kratschmer, L.D. Lamb, K. Fostiropoulos, D.R. Huffman, Nature 347 (1990).
[3] S.A. Claridge, A.W. Castleman, S.N. Khanna, C.B. Murray, A. Sen, P.S. Weiss, ACS Nano 3 (2009).
[4] C.J. Brabec, S. Gowrisanker, J.J.M. Halls, D. Laird, S. Jia, S.P. Williams, Advanced Materials 22 (2010) 3839.
[5] L. Grausova, J. Vacik, V. Vorlicek, V. Svorcik, P. Slepicka, P. Bilkova, M. Vandrovcova, V. Lisa, L. Bacakova, Diamond and Related Materials 18 (2009) 578.
[6] D.M. Gruen, S. Liu, A.R. Krauss, J. Luo, X. Pan, Applied Physics Letters 64 (1994) 1502.
[7] D. Chen, R. Workman, D. Sarid, Surface Science 344 (1995).
[8] E. Radeva, V. Georgiev, L. Spassov, N. Koprinarov, S. Kanev, Sensors and Actuators B: Chemical 42 (1997) 11.
[9] J.-S. Shih, Y.-C. Chao, M.-F. Sung, G.-J. Gau, C.-S. Chiou, Sensors and Actuators B: Chemical 76 (2001) 347.
[10] N.-Y. Pan, J.-S. Shih, Sensors and Actuators B: Chemical 98 (2004) 180.
[11] H.-W. Chang, J.-S. Shih, Sensors and Actuators B: Chemical 121 (2007).
[12] R.M. Fleming, A.P. Ramirez, M.J. Rosseinsky, D.W. Murphy, R.C. Haddon, S.M. Zahurak, A.V. Makhija, Nature 352 (1991).
[13] H. Park, J. Park, A.K.L. Lim, E.H. Anderson, A.P. Alivisatos, P.L. McEuen, Nature 407 (2000).
[14] Y.Z. Li, M. Chander, J.C. Patrin, J.H. Weaver, L.P.F. Chibante, R.E. Smalley, Science 253 (1991) 429.
[15] T. Hashizume, X.D. Wang, Y. Nishina, H. Shinohara, Y. Saito, Y. Kuk, T. Sakurai, Japan Journal of Applied Physics 31 (1992) L880.
[16] H. Xu, D.M. Chen, W.N. Creager, Physical Review Letters 70 (1993) 1850.
[17] A.M. Rao, P. Zhou, K.A. Wang, G.T. Hager, J.M. Holden, Y. Wang, W.T. Lee, X.X. Bi, P.C. Ecklund, D.S. Cornett, M.A. Duncan, I.J. Amster, Science 259 (1993) 955.
[18] P. Moriarty, M.D. Upward, A.W. Dunn, Y.R. Ma, P.H. Beton, D. Teehan, Physical Review B 57 (1998) 362.
[19] K. Sakamoto, D. Kondo, Y. Ushimi, A. Kimura, A. Kakizaki, S. Suto, Surface Science 438 (1999) 248.
[20] J.I. Pascual, J. Gómez-Herrero, C. Rogero, A.M. Baró, D. Sánchez-Portal, E. Artacho, P. Ordejón, J.M. Soler, Chemical Physics Letters 321 (2000) 78.
[21] E.I. Altman, R.J. Colton, Surface Science 279 (1992) 49.
[22] A.J. Maxwell, P.A. Brühwiler, D. Arvanitis, J. Hasselström, M.K.-J. Johansson, N. Mårtensson, Physical Review B 57 (1998) 7312.
[23] C. Cepek, I. Vobornik, A. Goldoni, E. Magnano, G. Selvaggi, J. Kröger, G. Panaccione, G. Rossi, M. Sancrotti, Physical Review Letters 86 (2001) 3100.
[24] M. Grobis, X. Lu, M.F. Crommie, Physical Review B 66 (2002) 161408.
[25] A.W. Dunn, E.D. Svensson, C. Dekker, Surface Science 498 (2002).
[26] S. Suto, K. Sakamoto, T. Wakita, C.-W. Hu, A. Kasuya, Physical Review B 56 (1997) 7439.
[27] D. Kondo, K. Sakamoto, H. Takeda, F. Matsui, K. Amemiya, T. Ohta, W. Uchida, A. Kasuya, Surface Science 514 (2002) 337.
[28] L.-L. Wang, H.-P. Cheng, Physical Review B 69 (2004) 165417.
[29] H. Yu, J. Yan, Y. Li, W.S. Yang, Z. Gu, Y. Wu, Surface Science 286 (1993) 116.
[30] S. Suto, A. Kasuya, C.W. Hu, A. Wawro, K. Sakamoto, T. Goto, Y. Nishina, Thin Solid Films 281–282 (1996) 602.
[31] S. Szuba, R. Czajka, A. Kasuya, A. Wawro, H. Rafii-Tabar, Applied Surface Science 144–145 (1999) 648.
[32] D.J. Kenny, R.E. Palmer, Surface Science 447 (2000) 126.
[33] X. Yao, T.G. Ruskell, R.K. Workman, D. Sarid, D. Chen, Surface Science 366 (1996) L743.
[34] X. Yao, R.K. Workman, C.A. Peterson, D. Chen, D. Sarid, Applied Physics A: Materials Science & Processing 66 (1998) S107.
[35] H. Wang, C. Zeng, Q. Li, B. Wang, J. Yang, J.G. Hou, Q. Zhu, Surface Science 442 (1999) L1024.
[36] I. Fernández Torrente, K.J. Franke, J.I. Pascual, Journal of Physics: Condensed Matter 20 (2008) 184001.
[37] X. Lu, M. Grobis, K.H. Khoo, S.G. Louie, M.F. Crommie, Physical Review B 70 (2004) 115418.
[38] C. Rogero, J.I. Pascual, J. Gomez-Herrero, A.M. Baro, The Journal of Chemical Physics 116 (2002) 832.
[39] F. Schiller, M. Ruiz-Oses, J.E. Ortega, P. Segovia, J. Martinez-Blanco, B.P. Doyle, V. Perez-Dieste, J. Lobo, N. Neel, R. Berndt, J. Kroger, The Journal of Chemical Physics 125 (2006) 144719.
[40] G. Schull, N. Néel, M. Becker, J. Kröger, R. Berndt, New Journal of Physics 10 (2008).
[41] M. Nakaya, Y. Kuwahara, M. Aono, T. Nakayama, Small 4 (2008) 538.
[42] Y. Murakami, H. Suematsu, Pure and Applied Chemistry 68 (1996) 1463.
[43] A. Kumar, D.K. Avasthi, J.C. Pivin, Applied Physics Express 1 (2008) 125002.
[44] O.E. Kvyatkovskiia, I.B. Zakharovab, Fullerenes, Nanotubes, and Carbon Nanostructures 16 (2008) 574.
[45] T.L. Makarova, K.-H. Han, P. Esquinazi, R.R. Silva, Y. Kopelevich, I.B. Zakharova, B. Sundqvist, Carbon 41 (2003) 1575.
[46] B. Pevzner, A.F. Hebard, M.S. Dresselhaus, Physical Review B 55 (1997).
[47] M.S. Dresselhaus, G. Dresselhaus, R. Saito, Nanotechnology in carbon materials, in: G.L. Timp (Ed.), Nanotechnology, Springer-Verlag, New York, 1998, pp. 285–330.
[48] M. Foley, C. Ton-That, L. Kirkup, in: A. Barnhoorn, J.D. Fitz Gerald, I. Jackson, T.J. Senden (Eds.), 31st Annual Condensed Matter and Materials Meeting, Australian Institute of Physics, Wagga Wagga, 2007.
[49] H.B. Yang, Q.L. Song, C. Gong, C.M. Li, Solar Energy Materials and Solar Cells 94 (2010).
[50] A. Savitzky, M.J.E. Golay, Analytical Chemistry 36 (1964) 1627.
[51] P.C. dos Santos Claro, P.L. Schilardi, B. Blum, M.F. Castez, R.C. Salvarezza, Physical Review B 76 (2007).
[52] X.D. Wang, T. Hashizume, H. Shinohara, Y. Saito, Y. Nishina, T. Sakurai, Physical Review B 47 (1993) 15923.
[53] T.L. Makarova, B.B. Liu, B. Sundqvist, AIP Conference Proceedings 591 (2001).
[54] M. De Seta, N. Tomozeiu, D. Sanvitto, F. Evangelisti, Surface Science 460 (2000).
[55] C. Enkvist, S. Lunell, B. Sjogren, P.A. Bruhwiler, S. Svensson, The Journal of Chemical Physics 103 (1995) 6333.
[56] L. Charpentier, M. Balat-Pichelin, H. Glénat, E. Bêche, E. Laborde, F. Audubert, Journal of the European Ceramic Society 30 (2010).
[57] H. Yu, L.J. Webb, J.R. Heath, N.S. Lewis, Applied Physics Letters 88 (2006) 252111.
[58] K. Xue, H.P. Ho, J.B. Xu, Journal of Physics D: Applied Physics 40 (2007) 2886.
[59] J. Tersoff, D.R. Hamann, Physical Review B 31 (1985) 805.
[60] Z. Klusek, P. Kowalczyk, P. Byszewski, Vacuum 63 (2001) 145.
[61] Z.-Y. Yang, H.-M. Zhang, C.-J. Yan, S.-S. Li, H.-J. Yan, W.-G. Song, L.-J. Wan, Proceedings of the National Academy of Sciences 104 (2007) 3707.
[62] H. Ikegami, K. Ohmori, H. Ikeda, H. Iwano, S. Zaima, Y. Yasuda, Japanese Journal of Applied Physics 35 (1996) 1593.
[63] E. Nogales, B. Mendez, J. Piqueras, R. Plugaru, Semiconductor Science and Technology 16 (2001) 789.

been reported, including the mixing of polymers with different emission colors in single or multilayer devices, or the blending of small molecules in a appropriate ratio of red, green and blue (RGB), host–guest systems, in single or multiple layers [3,5–10]. The doping with phosphorescent complexes or fluorescent dyes in a polymer matrix or small molecule host exciplexes in bilayer devices or still a single polymer with different chromophores have also been reported [5,11–13].

The main issue for achieving white light through the blending of two or more chromophoric materials is the energy transfer among the various components. This energy transfer has to be incomplete, since all the colors should appear in the electroluminescence spectrum, requiring a judicious control in the concentration balance and miscibility of the mixture materials [14,15]. The basic operating mechanism involves the charge carriers injection, a partial energy transfer in order to avoid cascade non-radiative decays that will lead only to the lower-laying emission from the excited state [16,17]. The selected color in the donor–acceptor system is obtained by setting the appropriate dopant concentration. The range of dopant variation is limited, usually less than 1% and 10% for fluorescent and phosphorescent materials, respectively [10]. The upper limit is dictated by aggregate formation; since higher amounts lead to non-radiative self-quenching or intermolecular energy transfer processes [3,17]. Electroluminescent polymer blends are systems containing at least one active material which generally presents a better performance as compared to the material itself [18]. This effect can be explained by the synergic contribution of several factors, including the de-aggregation of associated species in the active medium (as ground state dimmers or excimers), the presence of heterojunctions between polymeric phases, improvement of the interfacial adhesion and of the optical properties, etc. These factors contribute to higher efficient exciton formation, charge transport and charge recombination [18–21]. When two or more active materials are blended, color tunability can also be obtained [19,20].

In this work a single layer device was explored, in which the blue emitter [poly(9,9-dihexyl-2,7-fluorene)] (LaPPS10) is the matrix host, and the green and red emitters poly[(9,9-dihexyl-9H-fluorene-2,7-diyl)-1,2-ethenediyl-1,4-phenylene-1,2-ethenediyl] (LaPPS16) and poly [2-methoxy-5-(2-ethylhexoxy)-1,4-phenylene vinylene] (MEH-PPV), respectively, were the guest components. The performance of this blend was compared with another using a second blue component, a copolymer of poly (methyl methacrylate-*co*-methyl antracenyl methacrylate), P(MMA-*co*-MMAnt) that was responsible by the improvement of the optical quality of the material [22]. The chemical structures are depicted in Fig. 1.

The choice of a polyfluorene for the main component was based on the fact that this class of polymer has emerged as an important class of blue emitter, with intense photoluminescence, good charge transport and thermal stability properties [23–26]. The other components, all of them also electroluminescent in a different spectral range, were chosen as an attempt to achieve white light emission. White light electroluminescent devices with organic materials can be built in multi-layer configuration composed by several different materials where each layer emits in a different region of the visible spectrum, generating white light output [27]. Here, single-layer devices were built, using blends with emitting materials of different band gap energies, exploring partial energy transfer [28]. Single layer devices are more attractive due to its ease of fabrication, large scale production and cost effective features, and according to published data they are more stable than those built with emitters in separated layers [20,29–31]. Therefore, for a system where the emission of one material spectrally overlaps with the absorption of another, a separating material had to be incorporated into the blend so as to prevent complete energy transfer and to give white emission with a wide spectral range [32]. To achieve this goal, morphology control of the polymer film is a crucial step and plays a main role on the device performance.

2. Experimental

2.1. Materials

The light emitting polymers poly(9,9-dihexyl-2,7-fluorene) (LaPPS10) poly[(9,9-dihexyl-9H-fluorene-2,7-diyl)-1,2-ethenediyl-1,4-phenylene-1,2-ethenediyl] (LaPPS16), poly(methylmethacrylate-*co*-methyl-antracenyl methacrylate P(MMA-*co*-MMAnt) (molar composition of 35:1 of MMA:MMAnt) were synthesized in our laboratory (LaPPS) as described in previous papers [20,22,33]. MEH-PPV was used as purchased from Sigma–Aldrich. Structures are in Fig. 1. The solvent chloroform (Vetec) was used without further purification. The solutions were mixed in different ratios, according to the blend's composition desired. LaPPS10:LaPPS16:MEH-PPV = 100:0.01:0.20 (w/w) (JF14) and LaPPS10:P(MMA-*co*-MMAnt):LaPPS16:MEH-PPV = 100:40:0.01:0.20 (w/w) (JF17). Blends were formed by casting from chloroform solutions and dried at room temperature for several days.

2.2. Samples for photophysical measurements

LaPPS10, LaPPS16, P(MMA-*co*-MMAnt) and MEH-PPV were dissolved in chloroform separately, in 10^{-5} mol L^{-1} concentration. Films were obtained from the solutions filtered through 0.2 μm Millex-FGS Filters (Millipore Co.), deposited by casting on quartz plates and allowed to dry slowly in a controlled solvent ambient. The film's thickness was adjusted in order to assure optical behavior according to Beer's Law.

2.3. Device preparation

The EL device fabrication with the configuration ITO/PEDOT-PSS/emissive layer/Al followed the procedure: the substrates were cleaned with detergent, acetone and isopropyl alcohol and subsequently underwent a process of hydrophylization with plasma ozone. Next a layer of PEDOT-PSS (Bayer) was deposited by spin coating at a speed of 4000 rpm, resulting in a 60 nm thick layer. The

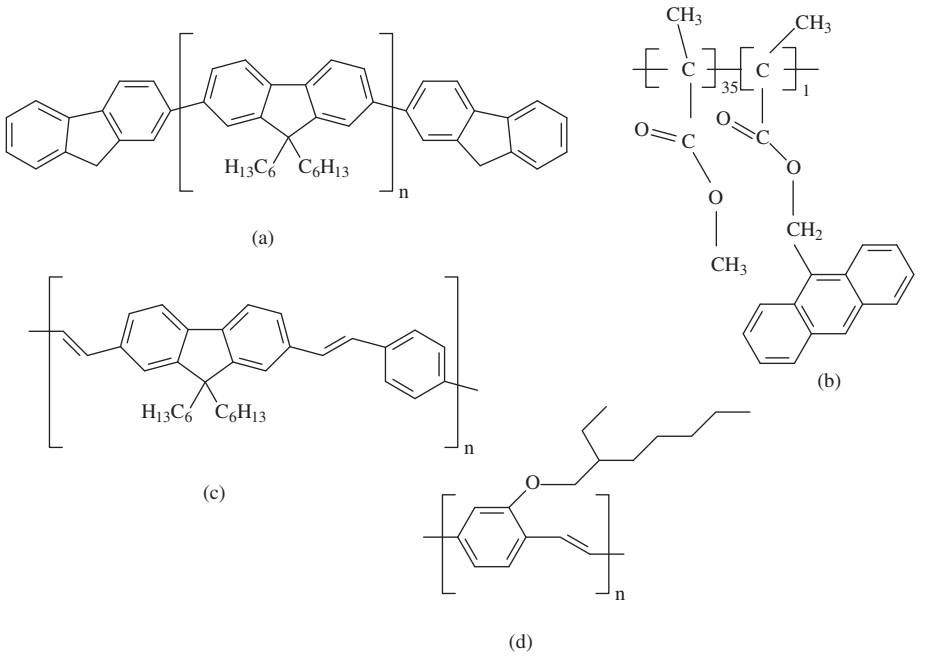

Fig. 1. Chemical structures of the emitting polymers: (a) LaPPS10 (blue), (b) P(MMA-*co*-MMAnt) (blue), (c) LaPPS16 (green) and (d) MEH-PPV (red). (For interpretation of the references to color in this figure legend, the reader is referred to the web version of this article.)

components of each material (polymer blend, JF14 and JF17) were dissolved in chloroform, with 25 mg/mL concentration. Films were obtained from the solutions filtered through 0.2 μm Millex-FGS Filters (Millipore Co.), deposited by spin coating using a rotation of 3000 rpm, forming films of 70 nm. The aluminum cathode was vacuum-deposited onto the blend layer under a pressure of about 10^{-6} mbar resulting in a layer 100 nm thick, completing the device preparation. The two devices are also named JF14 and JF17, according to their blends.

2.4. Optical analyses

UV–vis spectra were recorded on a Shimadzu model UV 2401 PC spectrophotometer, single beam, in the range of 250–750 nm. Steady-state emission spectra were acquired in a Shimadzu 5301 PC spectrofluorimeter, in the visible range of 390–780 nm. A 1.0 cm quartz square cuvette was used for solutions and a home-made optical support for film samples.

Fluorescence decays were recorded using time correlated single photon counting in an Edinburg Analytical Instruments FL 900 spectrofluorimeter using a pulsed hydrogen lamp, in a frequency rate of 40 kHz. Measurements were performed with wavelength excitation of λ_{exc} = 320 nm and the emission signals were collected in λ_{em} = 440 nm, respectively for solutions and for films. The sample cuvette was evacuated for 15 min and sealed under vacuum. The sample decay signal was deconvoluted from the lamp signal using the scattering from a Ludox® sample. The experimental curves were fitted using the software F900 provided by Edinburg. The analysis was performed by fitting the decays with multiple exponential functions using non-linear least-squares routines minimizing the χ^2. Good fits were obtained when χ^2 is close to 1.

$$I(t) = B_1 \exp\left(\frac{-t}{\tau_1}\right) + B_2 \exp\left(\frac{-t}{\tau_2}\right) + B_3 \exp\left(\frac{-t}{\tau_3}\right) + \ldots \quad (1)$$

τ_i is the fluorescence lifetime, B_i is the corresponding pre-exponential term and represents the contribution of each decay time to the total curve.

Epifluorescence optical images were recorded in a Leica DM IRB inverted microscope operating with a mercury lamp for UV–vis excitation in the transmission configuration. Pairs of optical filters for excitation and emission (dichroic mirrors) were selected in the range of λ_{exc} = 330–380 nm and λ_{em} > 440 nm, respectively. Photomicrographs were recorded using two microscope configurations: epifluorescence using UV-excitation and epifluorescence combined with lamp transmission to improve the image contrast. In this last configuration small bright domains could be visualized.

The CIE coordinates were calculated from data taken from the EL or PL emission, using the software CIE 31 xyz.xls.

2.5. Electroluminescence spectra, JxV and LxV measurements

The current–voltage measurements were performed using a 2400 Keithley Source. The EL spectra were acquired using a Labsphere Diode Array Spectrometer 2100 connected with Labsphere System Control 5500. The luminance–voltage was measured by 238 Keithley connected with a sensible photodiode. The samples were kept in a sealed Janis chamber with high vacuum.

3. Results and discussion

3.1. Photoluminescence properties

3.1.1. Solution properties

Fig. 2 presents the absorption and emission spectra of each polymer separately, recorded from the respective chloroform solutions (10^{-5} mol L^{-1}). Absorption of the P(MMA-*co*-MMAnt) is composed by a well defined vibronic structure in the range from 300 to 398 nm, characteristic of the anthracenyl moieties with the 0–0 band centered at $\lambda_{abs(0-0)}$ = 387.8 nm, and emission with the 0–0 band centered at $\lambda_{em(0-0)}$ = 393 nm [22,34,35]. Considering the 0–0 band for both absorption and emission, the Stokes shift is 341 cm^{-1}.

The LaPPS10 absorption band is broad and centered at $\lambda_{abs(0-0)}$ = 378.2 nm, strongly overlapped with that of P(MMA-*co*-MMAnt). Differently of the absorption, the LaPPS10 emission has a well resolved vibronic structure, with the 0–0 band at $\lambda_{em(0-0)}$ = 415.8 nm. The Stokes-shift taken as the difference between the absorption maximum and the 0–0 band of the emission is 2391 cm^{-1}. Absorption and emission spectra were not mirror images, indicating that the emission arises from a relaxed Franck–Condon state and are provided by energy transfer or by energy migration processes [37]. The LaPPS16 absorption band is also broader, two maxima were observed in the vibronic structure, at 430 nm and $\lambda_{abs(0-0)}$ = 454 nm. Its fluorescence emission has a partially resolved vibronic structure with the 0–0 band at $\lambda_{em(0-0)}$ = 472 nm. The Stokes-shift considering the 0–0 band in the absorption and emission spectra is 840 cm^{-1}. This smaller Stokes-shift suggests that Franck–Condon states with similar geometry are involved in the ground and electronic excited states due to the more rigid structure composed by a sequence of fluorene–vinylene alternated groups.

The MEH-PPV absorption band is also broader and centered at λ_{abs} = 491.5 nm. Emission is centered at $\lambda_{em(0-0)}$ = 554 nm, with a Stokes-shift of 2295 cm^{-1}. Therefore, taking this set of individual polymers, the absorption bands range from 325 to 550 nm, and the photoluminescence bands in solution that appears in the 400–600 nm range, cover almost the entire visible region.

3.1.2. Film properties

Fig. 3 presents the absorption and emission spectra of each component in the solid state. The P(MMA-*co*-MMAnt) absorption is composed by a well resolved vibronic

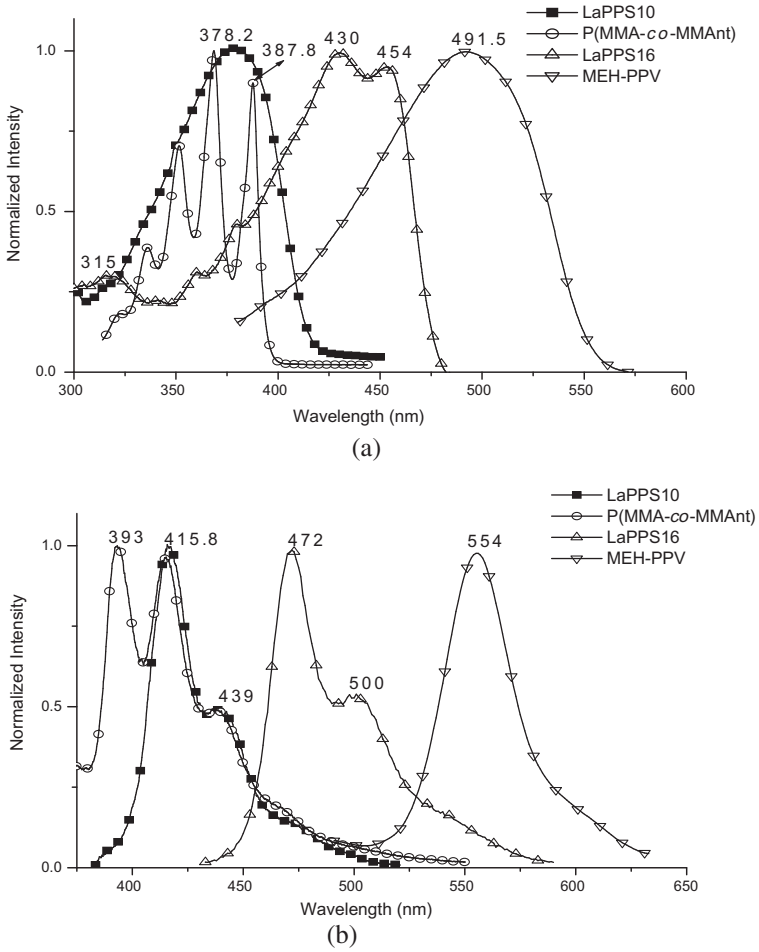

Fig. 2. Electronic absorption (a) and fluorescence (b) spectra of the polymers in 10^{-5} mol L^{-1} chloroform solutions. All samples were excited at λ_{exc} = 380 nm.

structure in the range of 300–420 nm, characteristic of the anthracenyl moieties, with the 0–0 band centered at $\lambda_{abs(0-0)}$ = 390.2 nm [22,34,35]. This spectrum is broader and red-shifted by 2.5 nm compared to the dilute solution. The lower energy peak at $\lambda_{abs(0-0)}$ = 410.4 nm can be attributed to ground state aggregates. Its emission is also broader with the 0–0 band centered at $\lambda_{em(0-0)}$ = 421.8 nm with a maximum located around 442.8 nm and

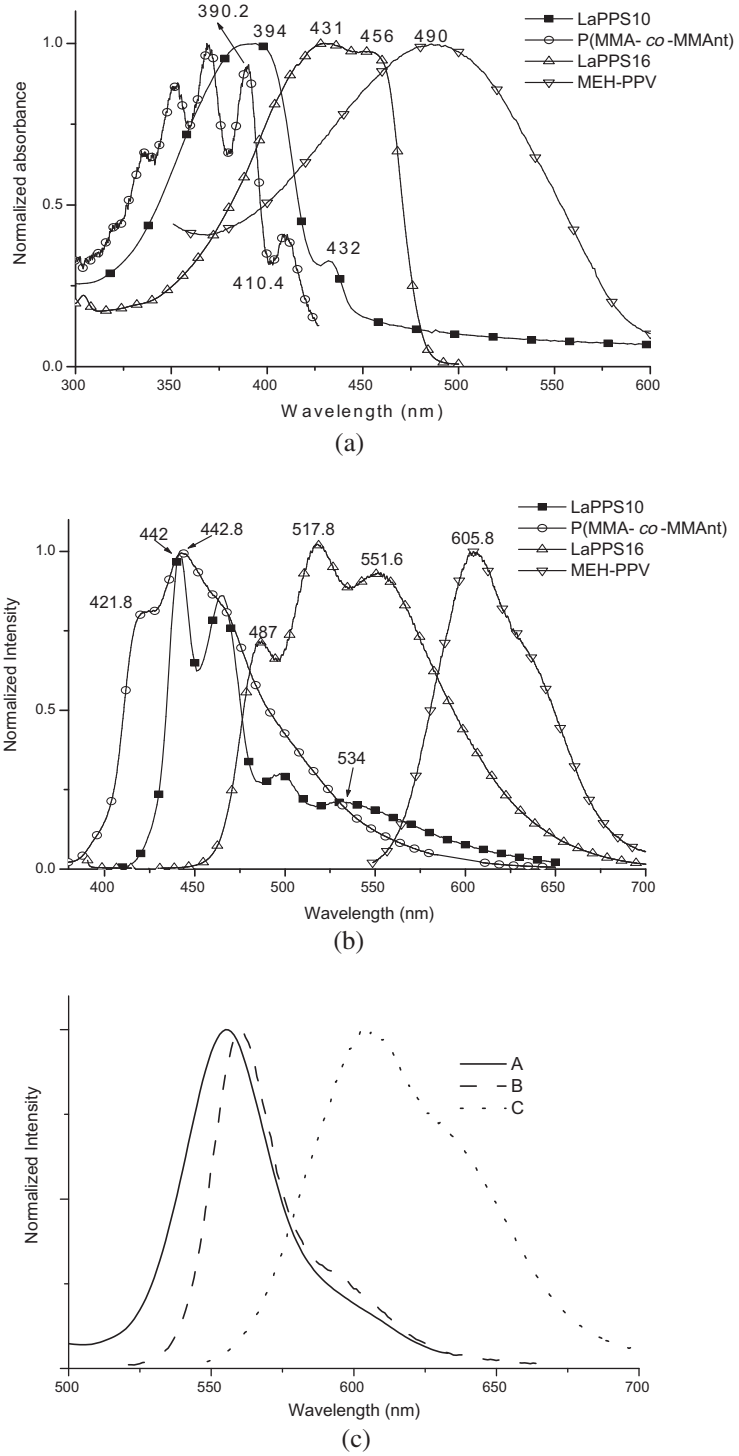

Fig. 3. Electronic absorption (a) and fluorescence (b) spectra of the polymers in film form. LaPPS10, LaPPS16 and P(MMA-*co*-MMAnt) were excited with λ_{exc} = 380 nm and MEH-PPV was excited with λ_{exc} = 490 nm. (c) Progresses red shift MEH-PPV emission with concentration, chloroform solutions (A) 10^{-7} mol L^{-1}, (B) 10^{-5} mol L^{-1} and (C) film.

with a Stokes-shift of 1920.0 cm^{-1}. The emission band has a red-edge tail, due to the presence of anthracenyl aggregates [22]. Generally, the presence of broad emission bands can be attributed to conformational disorders of the polymer chains where differences of microenvironment around every lumophore modifies their state densities [34]. Due to the large distance between two anthracenyl groups bonded to the main chain (35 MMA units) no excimer or aggregate emissions were observed in diluted solutions, and thus we ascribed the red-edge emission tail to aggregation of the lumophores in the solid state [34]. Emission of anthracenyl aggregates has been described and their formation requires very specific orientation of the polymer chains [37].

The LaPPS10 absorption band is broad and centered at λ_{abs} = 394 nm, red-shifted by 16 nm compared to the dilute solution. The presence of the low intensity band at λ_{abs} = 432 nm is a strong evidence that during the film formation some chains or chains segments are arranged in the β-conformation, a more planar orientation of the backbone [36,38–41]. The differences in the emission spectra of the blue emitter LaPPS10 in solution and in film form give further support for the presence of the β phase. The emission has a well resolved vibronic structure, with the 0–0 band at $\lambda_{em(0-0)}$ = 442 nm, with a Stokes-shift of 2756 cm^{-1}, red-shifted compared with the spectrum in solution by 27 nm. The emission in films of polyfluorenes in the 440 nm region has been assigned to the β-phase, and since its band gap is smaller than that of amorphous polymer, it may act as acceptors of resonance energy transfer [42]. That could be in part responsible for the absence of the higher energy bands seen in dilute conditions. The additional red-edge emission band at λ_{em} = 534 nm is characteristic of the LaPPS10 aggregates [41].

The LaPPS16 absorption band is also broader, with a poor resolved vibronic structure with two maxima at λ_{abs} = 431 nm and $\lambda_{abs(0-0)}$ = 456 nm. Its fluorescence emission is much broader than that in solution with the 0–0 band at $\lambda_{em(0-0)}$ = 487 nm, red-shifted by 15 nm compared to the dilute solution. In addition, two other strong bands at 517.8 and 551.6 nm are observed, possibly originated from aggregates [41]. Further, the LaPPS16 aggregate emission has a greater contribution to its total emission than that observed for LaPPS10.

The MEH-PPV absorption band is also broader compared to the solution and centered at $\lambda_{abs(0-0)}$ = 490 nm. Again, this spectral broadening can be ascribed to the inhomogeneous broadening in solid state produced by a larger distribution of states of individual chains in addition to the chain aggregation in more ordered regions. Its photoluminescence spectrum is not as broader as the absorption and centered at λ_{em} = 605.8 nm in the solid state, red-shifted by 52 nm compared to the solution spectra, with a larger Stokes-shift of 3985 cm^{-1}. Because of the relatively sharper and strongly red-shifted photoluminescence we suggest that its emission is occurring in more aggregated domains [43].

Putting all the individual absorption profiles together, we can see that they cover practically the entire visible spectral range (including part of the UV) whereas the photoluminescence ones also cover the entire visible spectrum, from the violet to the red (400–700 nm). Additionally, it can be seen from Fig. 3 that there is a strong overlap between the absorption from LaPPS16 and the photoluminescence from both LaPPS10 and P(MMA-*co*-MMAnt), as well as the absorption from MEH-PPV and the photoluminescence from LaPPS16. These spectral overlaps among the absorption and emission of the blend components play an important role on the photophysical properties of their polymer blends, since this is an important requirement for the resonant energy transfer process [44].

Fig. 4 shows the absorption and emission spectra of the blends: LaPPS10:LaPPS16:MEH-PPV = 100:0.01:0.20 (w/w) (JF14) and LaPPS10:P(MMA-*co*-MMAnt):LaPPS16:MEH-PPV = 100:40:0.01:0.20 (w/w) (JF17). The difference between the blends JF14 and JF17 is the presence of the methacrylic copolymer in JF17 as the second major component. The addition of this copolymer brings about at least three important consequences: it greatly enhances the optical quality of the films; there is an improvement of the film adhesion on the substrate leading to more flat surfaces; and there is a relative decrease of the contribution of the β-phase still present from the blue emitter LaPPS10 (absorption and emission bands at 432 and 442 nm, respectively). Dilution effect in polymer blends has been observed in several systems leading to a separation of the polymer chains and to the decrease of interchain interactions [33,45–47]. Moreover, the contribution of the β-phase in the JF17 blend seems to be less important than in the JF14, indicating that the improved optical quality produced by the inclusion of the acrylic copolymer is associated to the film morphology.

Fig. 4 also depicts the photoluminescence spectra of the blends. Emission in the higher energy edge is characteristic of the LaPPS10, where the 0–0 band occurs at 442 nm and a second vibronic peak appears at 465 nm, the same observed for this individual polymer in Fig. 3. However, the vibronic ratio is not constant for the three systems in solid state: LaPPS10, JF14 and JF17 blends. The lower vibronic ratio I_{465}/I_{442} observed for blend JF14 can be explained by a dilution effect which reduces the homopolymer interchain resonant energy transfer, whereas the higher vibronic ratio I_{465}/I_{442} and the spectral broadening observed for the JF17 can be explained by the contribution to the emission of the P(MMA-*co*-MMAnt) acrylic copolymer. Finally, the broad band at 540 nm present in both blends can be assigned to a contribution of the emission of LaPPS10 and LaPPS16 aggregates, along with that of MEHPPV. It is worthwhile to note that the emission of this polymer is very sensitive to concentration. In diluted solution (Fig. 2(b)) it peaks at 554 nm, whereas in the film the emission redshifts to 605.8 nm (Fig. 3(b)). Literature data reports r redshiftings of 100 nm for blends of MEHPPV with PMMA from concentrations of 12.5% in relation to the pure polymer film [48]. When diluted in polyfluorene, the emission around 600 nm which appears as a shoulder in the blends containing 3% to 1%, is no longer detected when MEHPPV is present in the concentration of 0.4% [20]. This progressive MEH PPV redshifting with concentration is illustrated in Fig. 3(c). Therefore, the broad band of the PL emission extending from 520 to 600 nm (see inset in

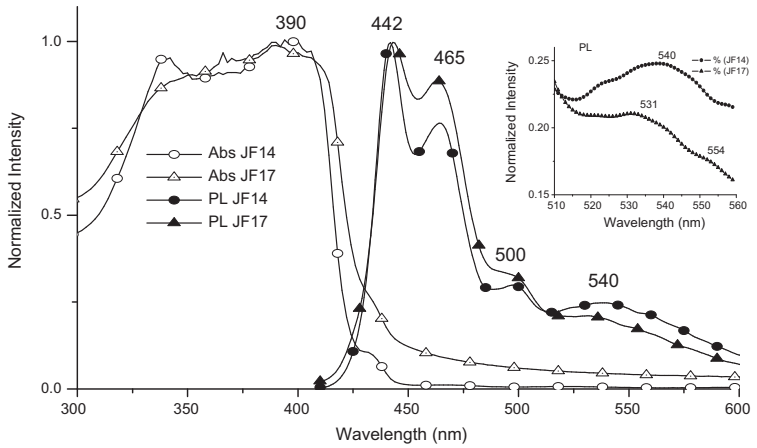

Fig. 4. Electronic absorption and emission spectra of blends JF14 and JF17 (λ_{exc} = 380 nm) in film form.

Fig. 4) can be attributed to the dopants LaPPS16 and MEH PPV, which do not appear separately due to their low concentration. It should be noted that the intensity in the region of 540 nm is higher for the JF14 than for JF17, characterizing a more efficient energy transfer in the former.

The spectral overlap among the absorption and emission of the blended components is a necessary condition for the resonant energy transfer from a donor polymer to an acceptor, which, in addition, also requires a close proximity between the components (distance within the Förster radium). Nevertheless, this condition must be avoided to some extent if a white emission is desired in a photoluminescent system. In other words, in a white emitting device, the resonant energy transfer process should not be completely efficient since the entire emission spectral range of white color must have contributions of the several chromatic components. Thus, from the photophysical point of view, to achieve white emission, only partial energy transfer processes and inner filter effects must be allowed in a photoluminescent system. Polymer blended systems with phase separation may undergo white emission because the domains are independent emissive sites, and the inner filter effect may be controlled by the thicknesses. Fig. 4 shows that the photoemission has a strong blue component, indicating that the energy transfer processes from the higher energy donors (LaPPS10 and P(MMA-*co*-MMAnt)) to the lower energy acceptors (LaPPS16 and MEH-PPV), are not complete suggesting that both blends underwent phase separation processes and the emission from the lower energy components are prevented by the inner filter, inhibiting their excitation.

In an attempt to explain the photoluminescence spectra observed for the two blends, we analyzed the morphology by epifluorescence optical microscopy. In Fig. 5a the morphology of the JF14 film under UV excitation (λ_{exc} = 330–380 nm, λ_{em} > 440 nm) is shown. A uniform blue emission over the entire samples is observed which is characteristic of LaPPS10, the major component, based on the emission spectra in Fig. 4. Nevertheless, more detailed images by combining the UV excitation with white lamp revealed also some blue spots of the LaPPS16 component (sizes smaller than 1 μm) (Fig. 5b) and under excitation with visible light (λ_{exc} = 480–500 nm, λ_{em} > 550 nm) red spots from the MEH-PPV component are the only one observed (Fig. 5c). Thus, the morphology of the JF14 blend can be described as a dispersion of the LaPPS16 and MEH-PPV domains in a blue matrix of LaPPS10. A phase separation is clearly seen. The morphology of the JF17 blend is completely different and since the only change is the addition of P(MMA-*co*-MMAnt), this is the responsible by the change. In Fig. 5d using UV excitation (λ_{exc} = 330–380 nm, λ_{em} > 440 nm), two types of blue domains can be seen: dispersed interconnected blue darker domains in a light blue matrix of LaPPS10. The dispersed domains are better visualized when with the combination of UV and white illumination (Fig. 5 – right side) and now, in addition to the interconnected domains we also identity dispersed spherical blue domains whose diameters are around 20 μm, which were ascribed to the P(MMA-*co*-MMAnt) (Fig. 5e). This combination also showed the presence of some interconnection of blue domains through a interphase, probably due to the LaPPS16 or some non-segregated P(MMA-*co*-MMAnt) components. Again the MEH-PPV red domains can be seen using visible light (λ_{exc} = 480–500 nm, λ_{em} > 550 nm) (Fig. 5f).

Therefore, from the morphological point of view, the components of these blends have a very low (if some) miscibility, forming a matrix of LaPPS10 and segregated domains of LaPPS16 and MEH-PPV in the case of JF14, and of LaPPS16, P(MMA-*co*-MMAnt) and MEH-PPV in the case of JF17. Even with phase separation, the acrylic copolymer played an important role on the film morphology, creating the possibility of interconnected domains formation in the JF17 blend. Nevertheless the changes of the photoluminescence spectra are not substantial. Because of this apparent poor miscibility in both JF14 and JF17 blends, we would not expect a complete energy transfer processes from the donors to the acceptors even though their absorption and emission are strongly overlapped. This result is an interesting example of the interplay between photophysical behavior and morphology. However, steady-state

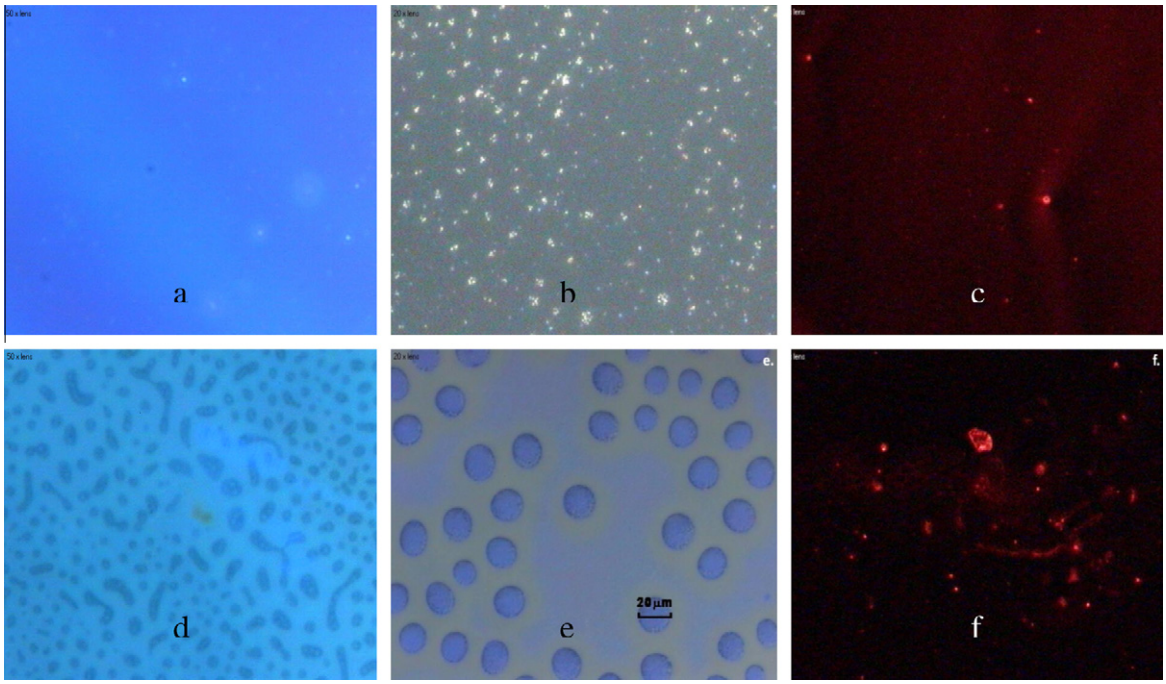

Fig. 5. Epifluorescence images of (a–c) JF14 and (d–f) JF17 and (d) UV excitation (λ_{exc} = 330–380 nm, λ_{em} > 440 nm); b and e (combining UV and white light to improve the contrast); c and f (λ_{exc} > 490 nm, λ_{em} > 550 nm). Amplification 22×.

fluorescence spectroscopy is not the most useful tool to evaluate the energy transfer processes when samples depict complex or overlapped emission spectra.

In order to get additional insight about the possibility of energy transfer processes from LaPPS10 and P(MMA-*co*-MMAnt) to LaPPS16 and MEH-PPV, fluorescence decays of the donors were measured in blends (in the presence of the acceptors), and compared these values with those of each isolated polymer in both solution and in film form. The LaPPS10 photoluminescence decays in degassed chloroform solution (10^{-5} mol L^{-1}) (λ_{exc} = 320 nm, λ_{em} = 440 nm) is bi-exponential with τ_1 = 0.48 ns (54%) and 0.79 ns (46%) (Table 1) and becomes mono-exponential in films with a lifetime of 0.31 ± 0.07 ns. This lifetime range is in accordance with those reported for polyfluorenes in diluted solution (from 0.08 to 5.0 ns) [36,49–52]. The decrease in lifetime in the solid state can be attributed to the formation of aggregates as well as to several possibilities of quenching processes in the solid state, apart from resonant energy transfer from disordered to β phases.

For the JF14 polymer blend in solution (λ_{exc} = 320 nm, λ_{em} = 440 nm), the decay is practically the same as the LaPPS10 in solution (bi-exponential with τ_1 = 0.48 ns (54%) and 0.76 ns (45%) (Table 1)), indicating that the presence of other components is not interfering with the LaPPS10 photophysics, and that no resonant energy transfer processes are occurring. Nevertheless, JF14 film exhibits a bi-exponential decay with the faster component of 0.41 ± 0.07 ns (86%), practically the same of the isolated LaPPS10 films and a longer component with τ_2 = 2.98 ± 0.01 ns with a smaller contribution (13%), that is absent in solution. Apart from a possible assignment of this longer decay to molecular aggregation in the ground state, as shown by the absorption and emission spectra, the complexity of the morphology makes the assignment of this transition very difficult.

Decays in JF17 blend-films, on the other hand, are mono-exponential, as also observed for solutions. Nevertheless, there is a pronounced decrease of the fluorescence lifetime in solid state (not observed in JF14) compared with the solution, which suggests that some non-radiative resonant energy transfer processes from LaPPS10 to the other components are occurring. It is very well documented in the literature that chain interpenetration favors the resonant energy transfer processes because the

Table 1
Fluorescence decays of the pure blend components in several conditions, using λ_{exc} = 320 nm, λ_{em} = 440 nm; *B* is the contribution of every lifetime to the entire decay, χ^2 measures the quality of the exponential fitting.

Materials	τ_1 (ns)	B_1 (%)	τ_2 (ns)	B_2 (%)	χ^2
LaPPS10 (solution)	0.48 ± 0.08	54	0.79 ± 0.06	46	1.041
LaPPS10 (film)	0.31 ± 0.07	100			1.089
P(MMA-*co*-MMAnt) (film) [22][c]	2.5	72	7.4	28	
JF14 (solution)	0.48 ± 0.07	55	0.76 ± 0.08	45	1.135
JF14 (film)[a]	0.41 ± 0,08	86	2.98 ± 0.01	13	1.161
JF17 (solution)[b]	0.62 ± 0.03	97			1.097
JF17 (film)	0.28 ± 0.08	97			1.080

[a] λ_{em} = 465 nm.
[b] λ_{em} = 410 nm.
[c] λ_{exc} = 370 nm, λ_{em} = 415 nm.

donor–acceptor distances approaches of that equivalent to the Förster radius [44]. This result can be correlated with the epifluorescence micrographs which showed the presence of interconnected domains that would lead to chain interpenetration. Based on this analysis we can conclude that the presence of the P(MMA-*co*-MMAnt) induces a better dispersion of the components, interferes with the interface energy, improves the optical quality of the films and facilitates the energy transfer from the donor to the acceptors.

3.2. Electroluminescence

Fig. 6 shows the electroluminescence spectra of LaPPS10 and of the JF14 and JF17 blends. The EL spectrum of LaPPS10 shows a band emission with vibronic structure, where the most intense band (0–0 band) is at 453.5 nm, 11 nm red-shifted as compared to the PL (Fig. 4). The vibronic progression occurred at 478.7 and 515.3 nm with a broad and less intense shoulder at 558 nm. It is particularly interesting that the relative intensities of the vibronic bands in the EL spectrum decrease at about half intensity on going the 0–0 to 0–1, from 0–1 to 0–2 and from the 0–2 to 0–3 vibronic bands which is completely different of the PL spectrum (Fig. 3), where systematic decrease of the emission was not observed. The EL spectrum is also sharper, showing, therefore, a better spectral resolution. These differences indicates that the EL is originated from other exciton species than those responsible for the PL. PL is originated from a very broad distribution of different species either by direct excitation or by several types of possible energy transfer processes. Moreover, considering the presence of the β-phase in the solid state identified by the sharper absorption band at 432 nm, red-shifted compared to the absorption of the amorphous disordered chains, and the emission band at 442 nm, we suggest that the EL is probably produced in the ordered β-phase of the LaPPS10.

Significant differences between EL and PL spectra were also observed for the JF14 and JF17 blends. The EL spectrum of the JF14 blend is similar to that of LaPPS10 in terms of spectral range, but significant differences were noted in the relative intensities of the red-edge peaks. The blue peak at 453 nm is present in all EL spectra (0–0 band of LaPPS10), but those at 514 nm (green) and 550–560 nm (yellow) were more intense, providing additional contribution to the visual color of the entire emission. The relative contributions of these red-edge peaks are greater in the EL compared with the PL spectra (Fig. 4). There are two possible explanations for the relatively more intense red-edge emission in EL. First, is that the excitation efficiency by photons in the PL is proportional to the amount of each component in the blend, in the absence of efficient energy transfer processes. Since we are using excitation in the blue region, the efficiency of the photoexcitation of the LaPPS16 and of the MEH-PPV are lower and thus their emissions are also relatively lower. This is not relevant for the EL spectrum. The second explanation is that the EL emission is proportional to the efficiency of the charge transport across each phase, to the charge recombination and to the efficiency of the exciton recombination. The first two processes are intrinsically associated with properties of each material and cannot be correlated with the PL. If they are more efficient for the LaPPS16 and for the MEH-PPV, it will be expected that the relative EL from these two components will be greater, as we effectively observed. Moreover, the band around 550–560 nm was attributed to the emission from the LaPPS16 aggregates, and again the EL seems to be more efficient at the more ordered crystalline phase of this polymer, as it does for LaPPS10. The EL is redshifted as compared to the PL, and that can be accounted for the charge trapping in the dopants domains, apart from energy transfer. The dopants emission in both JF14 and JF17 are enveloped the 500–700 nm region. In the EL spectrum of the JF14 blend a shoulder is seen at 590 nm which was attributed to the MEH-PPV domains, according to epifluorescence images. (See inset of Fig. 6). According to published data, the work function of the β phase regions is ca. 5.3 eV, i. e. 0.3 eV lower than that (5.65 eV) of the polyfluorene matrix [40], suggesting that hole carriers tend to be injected into the β phase rather than into the polyfluorene disordered matrix. It has been demonstrated that the β phase in poly(9,9-dioctylfluorene) is an energetically

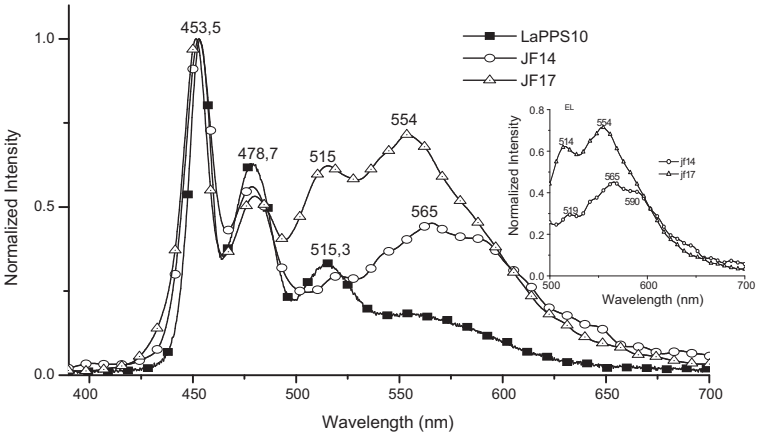

Fig. 6. EL spectra of the LaPPS10 film and JF14 and JF17 blends.

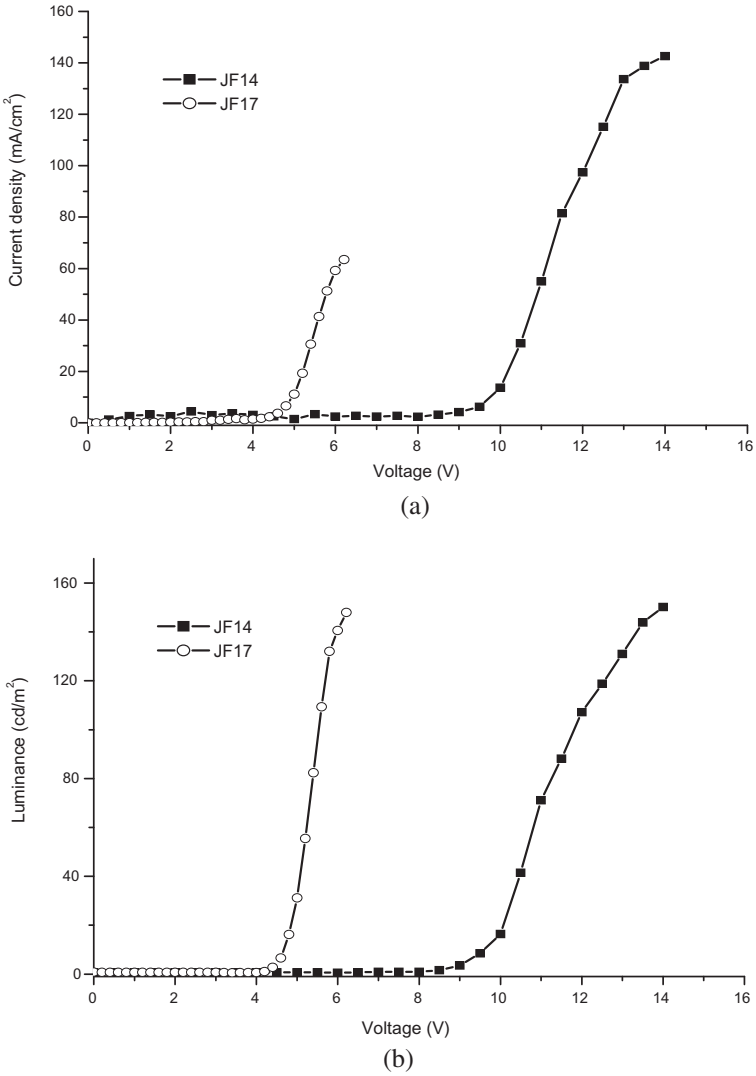

Fig. 7. (a) Current density × voltage and (b) luminance × voltage graphs of devices built with blends JF14 and JF17.

favorable environment for charge carriers, with an enhanced charge carrier mobility [53]. Due to its smaller band gap it can act also as traps for carriers, competing with other species in excitonic energy transfer processes, and more importantly, as carrier trapping/recombination sites.

The addition of P(MMA-*co*-MMAnt) in JF17 resulted in considerable differences in the EL profile as compared to LaPPS10 and JF14. There is a pronounced relative increase of the red-edge emission compared with the LaPPS10 and compared with the JF14. As previously mentioned, the EL emission is strongly correlated to the charge transport and charge recombination that seems to be enhanced by the addition of the acrylic copolymer. Taking into account the morphological and the photophysical properties, we can conclude that the formation of interconnected phases in JF17 are favoring not only the energy transfer processes (lifetime decreased) and the optical quality of the film but also the charge transport as already indicated for systems forming bulk heterojunctions [42]. Bulk heterojunctions are in JF17 enhancing the emission of LaPPS16, as indicated by the increase of the relative intensity of the bands at 515 and 554 nm. If the hypothesis of the heterojunction favoring the charge transport is correct, we should also expect changes on the electrical performance of these devices.

In the operation of an organic light-emitting diode (OLED) either the operating voltage or the luminance efficiency, depends firstly on the effective injection of carriers from both electrodes. It also strongly depends on the charge transport, the exciton generation and the recombination process. To achieve the lowest possible threshold voltage, the contact (cathode or anode) with the organic layer should approximate to ohmic condition. In general, this condition is easily reached with the anode, the transparent contact, in which the work function is close to the HOMO of the organic conjugated molecule. The injection of electrons, on the other hand, requires a more sophisticated technology to avoid the unbalance between electrons and holes.

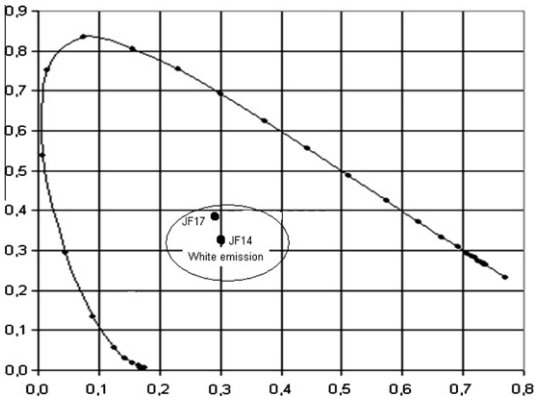

Fig. 8. CIE diagram relative to the electroluminescence of blends JF14 (0.30 and 0.32), JF17 (0.29 and 0.38).

In the present devices we used a simple structure, with a hole transport layer (PEDOT:PSS), and only one aluminum layer in the cathode (without an electron transport layer). Even so, both JF14 and JF17 devices showed a good performance as white OLED, as shown in Fig. 7. Fig. 7a shows the current–voltage curves for JF14 and JF17 devices, both exhibiting a diode characteristic. JF17 operates with lower voltage, having a threshold voltage below than 5 V and with a luminance, while the threshold voltage for JF14 was at about 10 V. Similar response was observed in the luminance vs. voltage curves. JF17 device reached 150 cd/m^2 at 6 V (60 mA/cm^2), while the JF14 presented the same luminance at 14 V (140 mA/cm^2). Therefore, the performance of JF17 was superior, since it achieved a luminance efficiency (cd/A) 2.5 higher, i.e. the same luminance at lower voltage and electric current. Fig. 8 exhibits the CIE coordinates of both devices (JF14 and JF17), and, as it can be seen in the CIE diagram, they emits in white region.

The HOMO and LUMO levels of the components used in the blends of JF14 and JF17 are shown in Table 2. The work functions of ITO and aluminum are about 4.8 and 4.1 eV, respectively. The values corresponding to LaPPS16 and MEHPPV were taken from Refs. [54,20], and those of poly(methyl methacrylate-*co*-methyl antracenyl methacrylate) were determined by cyclic voltammetry and UV–vis spectroscopy. The latter is in the same range of published data for poly(methyl methacrylate) copolymers with pendant chromophores: the reported HOMO and LUMO for the polymer with pendant azodyes are −6.08 and −3.21 eV, respectively [55].

Since the active layer of each luminescent diode is a blend composed by several components, it is not possible to sketch a sequence of energy barriers faced by the charge carriers, either for injection or transport mechanisms. The basic difference between JF17 and JF14 is that the blend of the former includes P(MMA- *co*-MMAnt), whose HOMO value is higher than the others. However, JF17 exhibited a better electrical and optical performance, as can be seen by the threshold voltage in the current and luminance curves (Fig. 7). Most probably this improvement brought about by P(MMA- *co*-MMAnt) to the blend is related to morphological modifications bringing the molecules in closer interactions one to another.

Table 2
HOMO and LUMO values in eV.

	PEDOT:PSS	P(MMA- *co*-MMAnt)	LaPPS10	LaPPS16	MEH-PPV
LUMO	3.50	3.90	2.60	3.04	2.80
HOMO	5.20	6.80	5.97	5.60	4.90

4. Conclusions

This study with the blends JF14 and JF17 showed that due to several mechanisms of energy transfer processes, an emission profile proportional the composition of every component is not the outcome of the device. The performance of the blends were compared, the segregated domains of the green and red emitters in the blue matrix brought about different behaviors. In the JF17 blend, the methacrylic non-conjugated copolymer was the predominant component in the dispersed phase, whereas for JF14 the MEH-PPV (red emitter polymer) was the main component of the domains. The differences in the EL and PL indicated that the mechanisms involved in the dynamics of excited states and/or in quenching processes are different in both cases. The EL emissions suggested that the cascade mechanism for the charge migration, charge recombination or energy transfer processes are incomplete, which opens possibility for more than one type of mechanism, resulting in emissions at different wavelengths. Spectroscopic data brought evidence of the formation of the β phase in the polyfluorene matrix, and due to differences in band gap, it was concluded that hole carriers tend to be injected into that phase rather than into the disordered one. The device with blend JF17 presented a better performance when compared with device JF14. Its turn on voltage was 4 V whereas that of JF14 was 9 V. The maximum luminance attained was 148 cd/m^2 at 6 V with current density maximum of 63 mA/cm^2 for JF17, compared to 142 cd/m^2 at 14 V for JF14.The behavior of the blue LED built with the pure matrix is inferior to those of the blends: turn on 13 V, maximum luminance 3.4 cd/m^2 at 20 V at 7.6 mA/cm^2. The CIE coordinates for EL emission of JF14 blend the coordinates are (0.30, 0.32) and for JF17 blend are (0.29, 0.38) corresponding to white light emission. It is worthwhile to note that these EL devices were not optimized; they were built in a standard configuration for comparison purposes, and focused in white light emission.

Acknowledgements

The authors are grateful to Dr.Paula C.Rodrigues for her contribution in the voltammetry measurements, and also to CNPq (Conselho Nacional de Pesquisas – Brazil), FAPESP (Fundação de Amparo à Pesquisa do Estado de São Paulo – Brazil) and National Institute on Organic Electronics (INEO/CNPq/FAPESP/CAPES) for financial support and fellowships.

References

[1] B.W. Andrade, S.R. Forrest, Adv. Mater. 16 (2004) 1585.
[2] L. Hou, L. Duan, J. Qiao, D. Zhang, G. Dong, L. Wang, Y. Qiu, Org. Electron. 11 (2010) 1344.

[3] D. Gupta, M.K. Deepak, Opt. Mater. 28 (2006) 295.
[4] J.M. Kang, M.J. Park, S.K. Kim, C. Lee, S.H. Jin, D.H. Hwang, Curr. Appl. Phys. 6 (2006) 756.
[5] J. Zou, J. Liu, H. Wu, W. Yang, J. Peng, Y. Cao, Org. Electron. 10 (2009) 843.
[6] B. Hu, F. Karasz, J. Appl. Phys. 93 (2003) 1995.
[7] Q.J. Sun, J.H. Hou, C.H. Yang, Y.F. Li, Y. Yang, Appl. Phys. Lett. 89 (2006) 153501.
[8] Q.L. Niu, Y.H. Xu, J.B. Peng, J. Lumin. 126 (2007) 531.
[9] J. Li, T. Sano, Y. Hirayama, K. Shibata, Synth. Met. 159 (2009) 36.
[10] A. Misra, P. Kumar, M.N. Kamalasanan, S. Chandra, Sci. Semicond. Technol 21 (2006) 35.
[11] M. Mazzeo, D. Pisignano, F. Della-Sala, J. Thompson, R.Y.R. Blyth, G. Gigli, R. Cingolani, G. Sotgiu, G.G. Barbarella, Appl. Phys. Lett. 82 (2003) 334.
[12] Q.J. Sun, B.H. Fan, Z.A. Tan, C.H. Yang, Y.F. Li, Y. Yang, Appl. Phys. Lett. 88 (2006) 163510.
[13] D.H. Hwang, J.H. Lee, J.I. Lee, C.H. Lee, Y.B. Kim, Mol. Cryst. Liq. Cryst. 405 (2003) 127.
[14] K.G. Ho, H.F. Meng, S.C. Lin, S.F. Horng, C.S. Hsu, L.C. Chen, S.M. Chang, Appl. Phys. Lett. 85 (2004) 4576.
[15] T.W. Lee, O.O. Park, H.N. Cho, J.M. Hong, C.Y. Kim, Synth. Met. 122 (2001) 437.
[16] Z. Tan, R. Tang, Q. Sun, C. Yang, F. Xi, Y. Li, Thin. Solid Films 516 (2007) 47.
[17] J.H. Park, T.W. Lee, Y.C. Kim, O.O. Park, J.K. Kim, Chem. Phys. Lett. 403 (2005) 293.
[18] G. He, Y. Li, J. Liu, Y. Yang, Appl. Phys. Lett. 80 (2002) 22.
[19] J.H. Park, O.O. Park, J.K. Kim, J.W. Yu, Y.C. Kim, Curr. Appl. Phys. 6 (2006) 640.
[20] F.Z. Shen, F. He, D. Lu, Z.Q. Xie, W.J. Xie, Y.G. Ma, B. Hu, Semicond. Sci. Technol. 21 (2006) 16.
[21] L. Akcelrud, Progr. Polym. Sci. 28 (2003) 875.
[22] J.F. Deus, M.L. Andrade, T.D.Z. Atvars, L. Akcelrud, Chem. Phys. 297 (2004) 177.
[23] X. Gong, D. Moses, A.J. Heeger, J. Phys. Chem. B 108 (2004) 8601.
[24] A.M. Assaka, P.C. Rodrigues, A.P.M. Oliveira, L. Ding, B. Hu, F.E. Karasz, L. Akcelrud, Polymer 45 (2004) 7071.
[25] J.I. Lee, H.Y. Chu, S.H. Kim, L.M. Do, T. Zyung, D.H. Hwang, Opt. Mater. 21 (2002) 205.
[26] J.F. Lee, S.L.C. Hsu, Polymer 50 (2009) 2558.
[27] Z.Y. Xie, Y. Liu, J.S. Huang, Y. Wang, C.N. Li, S.Y. Liu, J.C. Chen, Synth. Met. 106 (1999) 71.
[28] A. Dogariu, R. Gupta, A.J. Heeger, H. Wang, Synth. Met. 100 (1999) 95.
[29] J. Gmeiner, S. Karg, M. Meier, W. Rieb, P. Strohriegl, M. Schwoerer, Act. Polym. 44 (1993) 201.
[30] X.Y. Jiang, Z.L. Zhang, B.X. Zhang, W.Q. Zhu, S.H. Hong Xu, Synth. Met. 129 (2002) 9.
[31] G. Tu, Q. Zhou, Y. Cheng, L. Wang, D. Ma, X. Jing, F. Wang, Appl. Phys. Lett. 85 (2004) 2172.
[32] M. Granström, O. Inganäs, Appl. Phys. Lett. 68 (1996) 147.
[33] B. Nowacki, E. Iamazaki, A. Cirpan, F.E. Karasz, T.D.Z. Atvars, L. Akcelrud, Polymer 50 (2009) 6057.
[34] J.F. Deus, G.P. Souza, W.A. Corradini, T.D.Z. Atvars, L. Akcelrud, Macromolecules 37 (2004) 6938.
[35] M.L. Andrade, T.D.Z. Atvars, Macromolecules 37 (2004) 9096.
[36] A. Monkman, C. Rothe, S. King, F. Dias, in: U. Scherf, D. Neher (Eds.), Polyfluorenes, Advances in Polymer Science, vol. 212, Springer, Berlin, 2008, pp. 187–225.
[37] P.K. Lekha, E. Prasad, Chem. Eur. J. 16 (2010) 3699.
[38] M. Knaapila, M.J. Winokur, in: U. Scherf, D. Neher (Eds.), Polyfluorenes, Advances in Polymer Science, vol. 212, Springer, Berlin, 2008, pp. 293–318.
[39] M. Grell, D.D.C. Bradley, X. Long, T. Chamberlain, M. Inbasekaran, E.P. Woo, M. Soliman, Act. Polym. 49 (1998) 439.
[40] R.F. Cossiello, M.D. Susman, P.F. Aramendia, T.D.Z. Atvars, J. Lumin. 130 (2010) 415.
[41] J.R. Tozoni, F.E.G. Guimarães, T.D.Z. Atvars, B. Nowacki, L. Akcelrud, T.J. Bonagamba, Eur. Polym. J. 45 (2009) 2467.
[42] Y.C. Chang, C.C. Hsiao, T.H. Jen, J.L. Liao, A.C. Su, S.A. Chen, J. Chin. Chem. Soc. 57 (2010) 564.
[43] Nguyen, T.-Q.; Martini, I. B.; Liu, J.; Schwartz, B. J. J. Phys.Chem. B 104 (2000) 237.
[44] J.R. Lakowicz, Principles of Fluorescence Spectroscopy, Academic Press, New York, 1999.
[45] A. Babel, S.A. Jenekhe, Macromolecules 37 (2004) 9835.
[46] G.C. Oh, J.J. Yun, S.M. Park, S.H. Son, E.M. Han, H.B. Gu, S.H. Jin, Y.S. Yoon, Mol. Cryst. Liq. Cryst. 405 (2003) 43.
[47] R.F. Cossiello, A. Cirpan, F.E. Karasz, L. Akcelrud, T.D.Z. Atvars, Synth. Met. 158 (2008) 219.
[48] H.L. Chou, S.Y. Hsu, P.K. Wei, Polymer 46 (2005) 4967.
[49] J.F. Deus, A. Cirpan, F.E. Karasz, L. Akcelrud, Curr. Appl. Phys. 10 (2010) 365.
[50] H.P.M. Oliveira, R.F. Cossiello, T.D.Z. Atvars, L. Akcelrud, Quím. Nova 29 (2006) 286.
[51] R.F. Dias, J. Morgado, A.L. Maçanita, P.C. Costa, H.D. Burrows, A.P. Monkman, Macromolecules 39 (2006) 5854.
[52] H.L. Vaughan, F.M.B. Dias, A.P. Monkman, J. Chem. Phys. 122 (2005) 1492.
[53] P. Prins, F.C. Grozema, B.S. Nehls, T. Farrell, U. Scherf, L.D.A. Siebbeles, Phys. Rev. B 74 (2006) 113203.
[54] T.W. Lee, J.H. Park, O.O. Park, J. Lee, Y.C. Kim, Opt. Mater. 30 (2007) 486.
[55] L. Hua, L.J. Mei, L.N. Jun, X.Q. Feng, G.J. Feng, W.L. Hua, L.Z. Chang, Sci. China Chem. 53 (2010) 588.

as multifunctionality and miniaturization [39]. In contrast to these numerous applications of pyrene derivatives, regioregular polymeric systems with pyrene scaffold in the main chain are uncommon [40], albeit a few random copolymers of pyrene with pyrrole [41], 3,4-ethylenedioxythiophene [42] and bithiophene [43] have been reported.

In this paper, we wish to report the synthesis and properties of a novel processable regioregular PEC which is based on pyrene (**Py**) and didecylpropylenedioxythiophene (**P**). In this unique combination, **P** units provide solubility and low oxidation potential as well as electrochromic features whereas **Py** scaffold contributes with its fluorescence to this dual electrochromic and luminescent system. It is noteworthy that this novel processable PEC has a specific optical band gap (2.2 eV) to reflect or transmit the yellow color in the neutral state, which can be switched to a navy state upon doping. Furthermore, the optical and electrochemical features of this PEC were investigated.

2. Experimental details

All chemicals were purchased from Aldrich Chemical and used as received unless otherwise noted. 0.1 M tetrabutylammonium hexafluorophosphate (TBAH) dissolved in dichloromethane (DCM) and acetonitrile (ACN) was used as electrolyte solution. A platinum disk (0.02 cm^2) and a platinum wire were used as working and counter electrodes, respectively, as well as a Ag/ AgCl reference electrode (calibrated externally using 10 mM solution of ferrocene/ferrocenium couple which is an internal standard calibrated to be 0.44 V in ACN solution vs. Ag/AgCl). Repetitive cycling or constant potential electrolysis was used to obtain the polymer films. Electro-optical properties were investigated by using an indium tin oxide (ITO, Delta Tech. 8–12 Ω, 0.7 × 5 cm) electrode as well as a platinum wire as counter electrode and an Ag wire as a pseudo-reference electrode. For the spectroelectrochemical measurements, **P5** polymer film was coated on ITO electrode via cyclic voltammetry (between 0 and 1.15 V, 10 cycles) from a solution of **5** (5×10^{-3} M) in 0.1 M TBAH/ACN. In order to break in the polymer film, it was switched between 0.0 and 1.25 V in a monomer-free electrolytic solution during five cycles. Electroanalytical measurements were performed using a Gamry PCI4/300 potentiostat–galvanostat. The electro-optical spectra were monitored on a Hewlett–Packard8453A diode array spectrometer. FTIR spectra were recorded on Nicolet 510 FTIR with an attenuated total reflectance (ATR). High resolution mass spectrometry analysis of **5** was done via Water, Synapt HRMS instrument. GPC analysis of polymer was carried out with Polymer Laboratories PL-GPC 220 instrument. TGA analysis was done via Perkin Elmer Pyris 1 TGA under nitrogen atmosphere with 10 °C/minute heating rate. Bromination of pyrene (**1**) [44] and the synthesis of **4** [20] were carried out according to previously reported procedures.

2.1. Synthesis of 5

To an argon-degassed solution of **2** (150 mg, 0.417 mmol) and **4** (635 mg, 0.875 mmol) in dry toluene (30 mL) was added $Pd(PPh_3)_2Cl_2$ (62 mg, 0.0875 mmol) and the mixture was heated under reflux during 5 days. After being cooled to room temperature, the solvent was removed under reduced pressure. The crude mixture was chromatographed on silica gel by eluting with hexane: methylene chloride (10:1, v/v) to give **5**. 56% yield, yellow viscous liquid.

^{1}H NMR (400 MHz, $CDCl_3$, δ, ppm): 8.18–7.93 (m, 8H, Ar H), 6.55 (s, 2H, Ar H), 3.92 (s, 4H), 3.80 (s, 4H), 1.46–1.09 (m, 72H), 0.88–0.76 (m, 12H).

^{13}C NMR (100 MHz, $CDCl_3$, δ, ppm): 149.64, 146.35, 131.00, 129.89, 129.14, 129.11, 127.20, 126.26, 124.89, 124.56, 120.36, 103.98, 77.02, 49.56, 38.08, 31.92, 30.50, 29.65, 29.63, 29.56, 29.34, 22.96, 22.69, 14.11.

FTIR (ATR, cm^{-1}): 2926, 2950, 1609, 1509, 1487, 1467, 1405, 1375, 1270, 1176, 1042, 942, 849, 808, 732, 683.

2.2. Chemical polymerization of 5

Compound **5** (145 mg, 0.135 mmol) was dissolved in chloroform (50 mL). A solution of anhydrous $FeCl_3$ (110 mg, 0.675 mmol, 5 equiv) in nitromethane was added dropwise over a period of 45 min to the stirred monomer at room temperature (the bright yellow monomer solution turned progressively dark blue with addition of oxidizing agent). The mixture was stirred 48 h at room temperature. It was then precipitated into methanol (300 mL). The precipitate was filtered, redissolved in chloroform (300 mL), and stirred for 6 h with hydrazine monohydrate (6 mL) (the color of the solution was turned from dark blue to yellow after addition of the hydrazine monohydrate). After evaporation, the concentrate (dark blue) was precipitated into methanol (300 mL), the precipitate was filtered through a Soxhlet thimble and purified via Soxhlet extraction for 48 h with methanol. The polymer was extracted with chloroform and concentrated by evaporation. Then, the polymer was precipitated in methanol (300 mL) and collected as a black solid (52% yield).

3. Results and discussion

The synthesis of the target compound **5** (**PPyP**) started with the bromination of pyrene (**1**), as outlined in Scheme 1. This reaction yielded a mixture of 1,6- (**2**) and 1,4-dibromopyrene (**3**), from which 1,6-regioisomer (**2**) was isolated by repeated recrystallization from toluene [44,45]. Stille coupling reaction of 2 with tributyl(3,3-didecyl-3,4-dihydro-2H-thieno[3,4-b][1,4]dioxepin-8-yl)stannane (**4**) [20] in the next step provided **5** in a yield of 56% (Scheme 2). Compound **5** was initially characterized by spectral (^{1}H, ^{13}C NMR, FTIR, see supporting information Fig. S1–S3) data, which was in well aggreement with the structure.

UV–vis absorption and emission spectra of **5** were depicted in Fig. 1. It was found that **5** emits blue light (431 nm) in THF solution as it is the case for many pyrene derivatives. It should be noted that organic compounds with emissions in the solid state are quite rare, since even bright organic fluorophores pack very tightly in the crystalline state or amorphous solid phase (as thin films), leading to very significant quenching [46–48]. As π–π stacking is

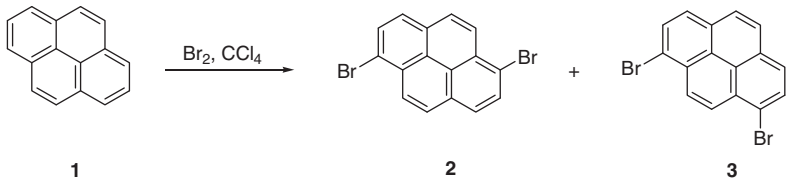

Scheme 1.

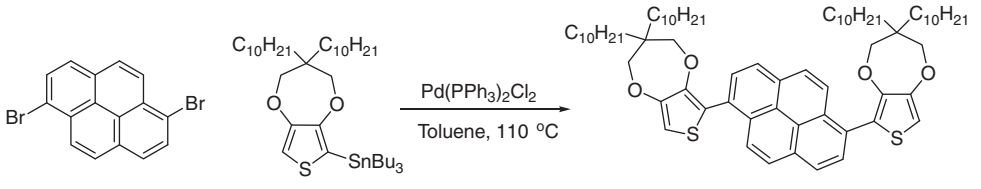

Scheme 2.

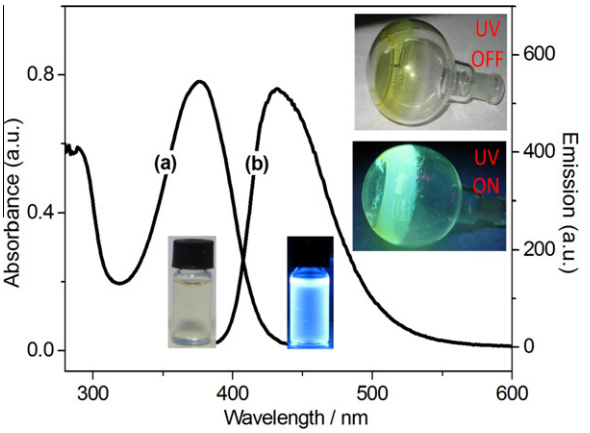

Fig. 1. (a) UV–vis absorption and (b) emission spectra (λ_{exc} = 377 nm) of **5** in THF. Inset: photographs of **5** under day (up) and UV (down) light.

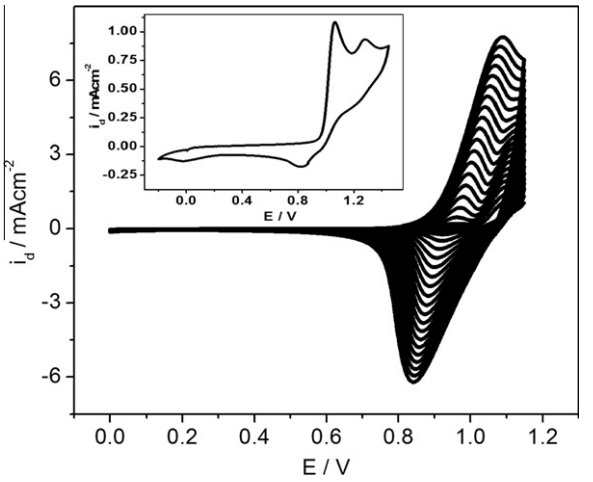

Fig. 2. Repetitive cyclic voltammogram of **5** (5×10^{-3} M) in order to obtain **P5** in 0.1 M TBAH/ 1:1 (v/v) DCM-ACN with a scan rate of 100 mV/s vs. Ag/AgCl. Inset: First anodic scan of **5** (5×10^{-3} M) under the same conditions.

mainly responsible for the quenching of the emission in the solid state for most of the aromatic fluorophores, it is assumed that **P** units on the core structure of **5** are effective in keeping the π-systems apart, where π–π stacking is hindered.

The electrochemical behavior of **5** was investigated by cyclic voltammetry in an electrolyte solution consisting of 0.1 M TBAH dissolved in DCM and ACN by 1:1 volume ratio. Upon anodic scan, two oxidation peaks were observed at 1.06 and 1.28 V, which were attributed to **P** and **Py** units, respectively (Fig. 2, inset). The second oxidation peak looks quite irreversible during the polymerization process (taking place at 1.06 V), which probably precludes the reversibility of the redox behavior of the pyrene units.

In order to get an electroactive polymer film, repetitive anodic scans were performed between 0.0 and 1.15 V. During this process, a new reversible redox couple was observed at 0.95 V. The increase in the current intensities of this redox couple clearly indicated the formation of the polymer film **P5** on the electrode surface (Fig. 2, Scheme 3).

When the as-prepared **P5** film (Scheme 3) was anodically scanned in a monomer free electrolyte solution of 0.1 M TBAH/ACN (Fig. 3), two reversible redox couples were observed at 1.02 and 1.28 V, which were ascribed to the **P** and **Py** units, respectively. Unlike monomer behavior, pyrene units have reversible redox couple since the polymerization was completed and the charges formed on polymer backbone do not prevent the reversibility. The onset potentials of this novel system, 0.91 and 1.07 V, were lower when compared to dodecylthiophene or fluorene based systems [40].

As shown in Fig. 3, inset, a linear increase in the peak currents as a function of the scan rates confirmed that the polymer film was tightly bounded to the electrode surface and the redox process is non-diffusional.

The oxidative polymerization of **5** was also carried out with $FeCl_3$ in order to get **P5** by chemical methods

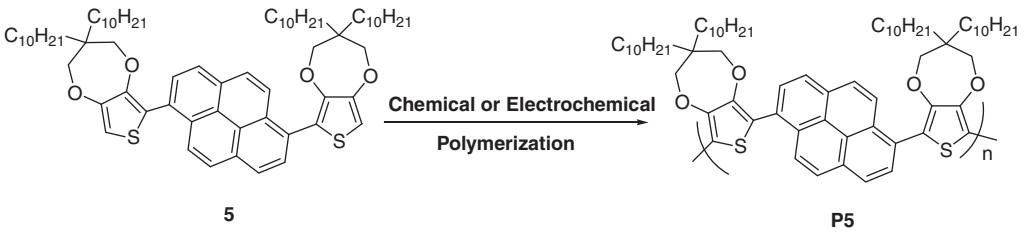

Scheme 3.

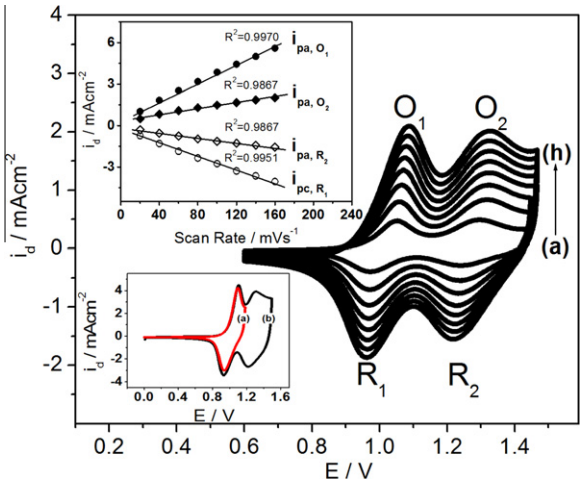

Fig. 3. Cyclic voltammogram of **P5** in 0.1 M TBAH/ACN with different scan rates: (a) 20, (b) 40, (c) 60, (d) 80, (e) 100, (f) 120, (g) 140, (h) 160 mVs^{-1}. Top inset: Peak current vs. scan rate in 0.1 M TBAH/ACN (i_{pa}: anodic peak current value, i_{pc}: cathodic peak current value). Bottom inset: Cyclic voltammogram of **P5** showing (a) first redox couple, (b) second redox couple (waveclipping).

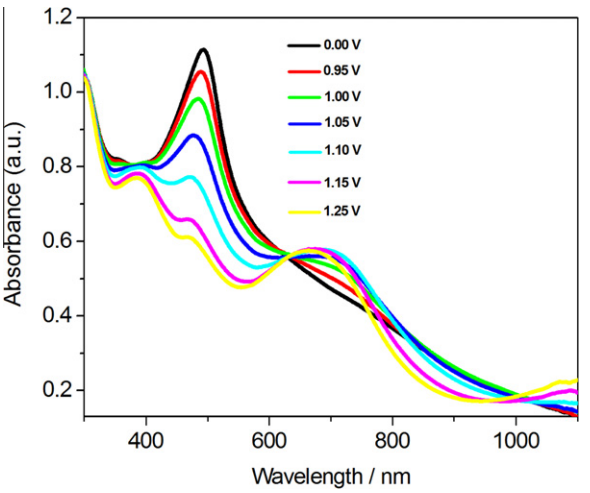

Fig. 5. Spectroelectrochemistry of **P5** film on an ITO coated glass slide in 0.1 M TBAH/CAN between 0.0 and +1.25 V vs. Ag wire.

(Scheme 3). It was found that both electrochemically and chemically obtained polymer, **P5**, was quite soluble in THF and partially soluble in common organic solvents: dichloromethane (DCM), $CHCl_3$, DMF (*N*,*N*-dimethylformamide). More importantly, **P5** reflects or transmits the yellow color in the neutral state. Note that soluble neutral state yellow PECs, which require a specific optical band gap (*vide infra*), are not enough. Additionally, the polymer has a maximum wavelength of emission resulting in yellowish green (524 nm) and yellow (545 nm) emission in the solution and in the solid phases, respectively (Fig. 4).

The molecular weight determination of the polymer was carried out by gel permeation chromatography (GPC) by using polystyrene as the standard and THF as the eluent.

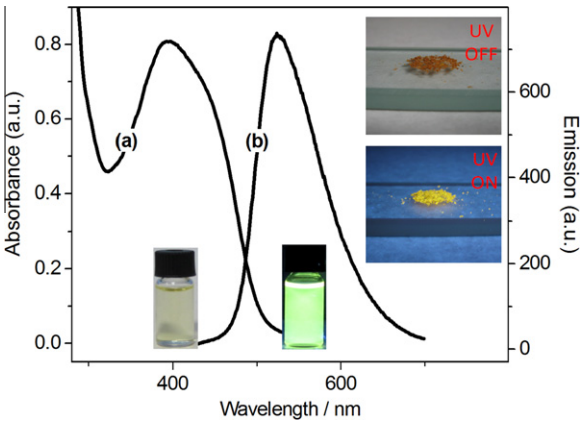

Fig. 4. (a) UV–vis absorption and (b) emission spectra (λ_{exc} = 391 nm) of **P5** in THF. Inset: photographs of **P5** under day (up) and UV (down) light.

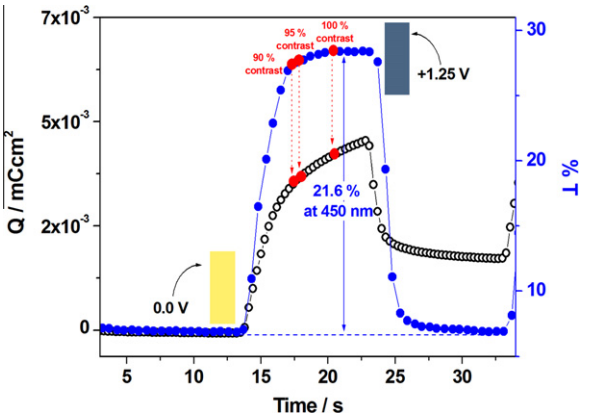

Fig. 6. Chronoabsroptometry and chronocoluolmetry tandem experiment of **P5** between 0.0 and +1.25 V at 495 nm.

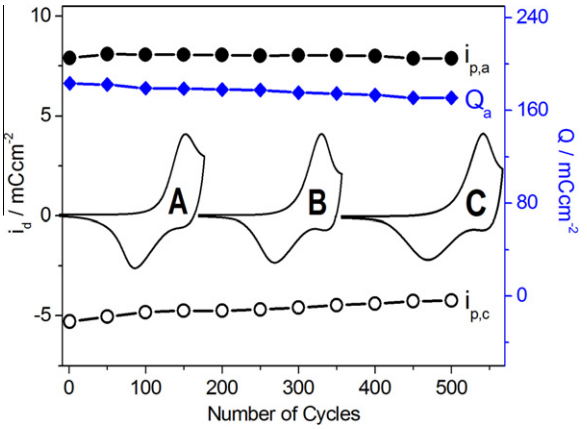

Fig. 7. Stability test for **P5** (5 mC/cm^2) film in 0.1 M TBAH/ACN via square wave potential switching between 0.0 and 1.3 V and cyclic voltammetry at 75 mVs^{-1}as a function of number of at: A: 1st; B: 100th, C: 500th. Q_a: Anodic charge stored; $i_{p,a:}$ Anodic peak current; $i_{p,c}$: Cathodic peak current.

The measurements indicated that **P5** had a weight-averaged molecular weight (Mw) of 9052 (*Mn* = 4316), with a polydispersity index (PDI) of 2.09, respectively. Although the Mw of **P5** was moderately low when compared to precedent analogs [40], it was evident that the polymer chain of **P5** consisted of approximately 25 repeating units.

In order to elucidate the electrochromic features of **P5**, a simple electrochromic device was constructed and the spectroelectrochemical behavior of the polymer film coated on ITO electrode was examined under a variety of voltage pulses between 0.95 and 1.25 V (p-doping). During p-doping, the higher energy absorbances at wavelengths shorter than 500 nm (π–$\pi*$ transition) started to decrease with an apparent new absorption band at around 680 nm, which was attributed to the formation of polaron charge (Fig. 5). Upon further oxidation, the polaron charge carriers turned into the bipolaron charge carriers above 1000 nm. In this process, it was assumed that charge carriers (polarons and bipolarons) were delocalized as the conformation of the polymer was planarized to an extent. As a result of these variations in the conformation and the absorption spectrum of **P5**, the color of the polymer changes from yellow in the neutral state to a navy state upon doping.

On that basis, the band gap (E_g) of polymer **P5** was calculated from the onset of π–$\pi*$ transition at 450 nm, and it was found to be 2.2 eV. The percentage transmittance change (Δ%T) and coloration efficiency (CE at 95% of the full optical switch, after which point the naked eyes couldn't sense the changes in the color) of the polymer film were also calculated to be 21.6% and 287 cm^2/C at 450 nm during p-doping, respectively. Also, the CE values were found as 252 and 298 cm^2/C for 100% and 90% of full optical switch (Fig. 6). The response time of the polymer film was found to be 3.4 s for 95% of full optical switch.

Stability of the material is a key parameter for any potential application of the polymers. For that reason, the electrochemical and thermal stability of the polymer were examined. First of all, the electrochemical stability of **P5** was tested by switching between neutral (0.0 V) and oxidized (1.25 V) states. It was found that **P5** retained 93% of its electroactivity even after 500 of cycles (Fig. 7).

Finally, the thermal stability of **P5** was determined by thermogravimetric analysis (TGA) as depicted in Fig. 8. Though light weight losses were observed during the analysis, the polymer shows the onset temperature of weight loss at 350 °C under nitrogen atmosphere. Note that polypyrene shows the onset temperature of weight loss at around 290 °C [42]. The data for **P5** suggested that the polymer would be thermally robust during metal deposition for optical device applications such as LED and solar cells, where thermal stability is very important. On the

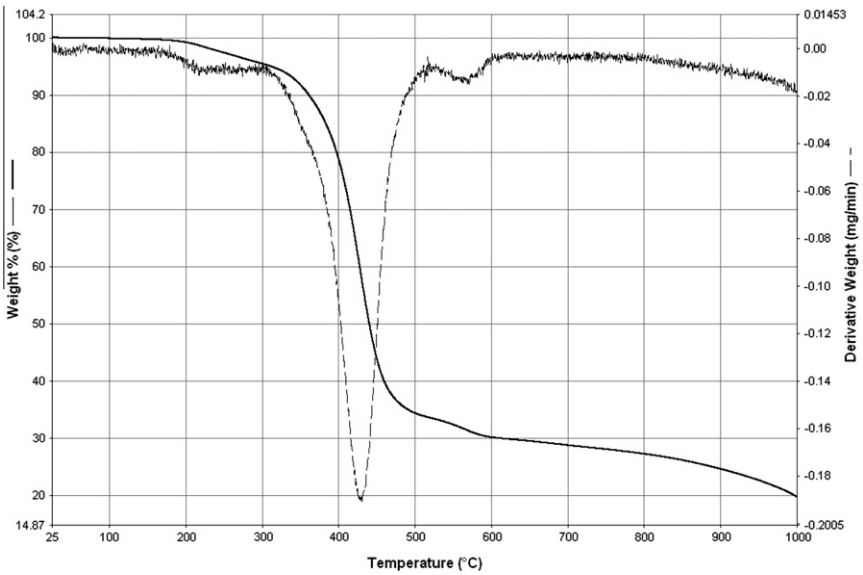

Fig. 8. Thermogravimetry curve of chemically prepared **P5**.

other hand, when the temperature was rised above 350 °C, the total weight loss was increased due to the decomposition of the material.

4. Conclusion

In conclusion, the design and synthesis of novel materials (**5** and **P5**) with pyrene scaffold were described. Interestingly, both of these systems were emissive in both solution and the solid states. It is assumed that **P** units on the core structure hinder π–π stacking thus rendering the emission in the solid state. Furthermore, a novel soluble PEC, **P5**, which has a specific optical band gap (2.2 eV) to reflect (or transmit) the yellow color in the neutral state was introduced herein to extend the repertoire of available colors of processable PECs (blue, green and black etc.), which are essential for full color displays [49]. The electrochemical and thermal stability of the polymer indicated that **P5** is a promising candidate for electrochromic applications. Work in this line is currently underway in our laboratories.

Acknowledgements

The authors gratefully acknowledge financial support from the Scientific and Technical Research Council of Turkey (TUBITAK) and European Cooperation in Science and Technology (Grant No. COST-108T959). Z. Ö. is indebted toTUBITAK for the scholarship.

Appendix A. Supplementary data

Supplementary data associated with this article can be found, in the online version, at doi:10.1016/j.orgel.2011.05.016.

References

[1] N.C. Greenham, S. Moratti, D.D.C. Bradley, R.H. Friend, A.B. Holmes, Efficient light-emitting diodes based on polymers with high electron affinities, Nature 365 (1993) 628–630.
[2] A. Goel, M. Dixit, S. Chaurasia, A. Kumar, R. Raghunandan, P.R. Maulik, R.S. Anand, Vapor-phase processable novel nonplanar donor-acceptor quateraryls for blue-OLEDs, Org. Lett. 10 (2008) 2553–2556.
[3] L. Schmidt-Mende, A. Fechtenkotter, K. Mullen, E. Moons, R.H. Friend, J.D. Mackenzie, Self-organized discotic liquid crystals for high-efficiency organic photovoltaics, Science 293 (2001) 1119–1122.
[4] D.P. Hagberg, J.-H. Yum, H. Lee, F. De Angelis, T. Marinado, K.M. Karlsson, R. Humphry-Baker, L. Sun, A. Hagfeldt, M. Grätzel, Md.K. Nazeeruddin, Molecular engineering of organic sensitizers for dye-sensitized solar cell applications, J. Am. Chem. Soc. 130 (2008) 6259–6266.
[5] M. Muccini, A bright future for organic field-effect transistors, Nat. Mater. 5 (2006) 605–613.
[6] C. Yang, J.Y. Kim, S. Cho, J.K. Lee, A.J. Heeger, F. Wudl, Functionalized methanofullerenes used as n-type materials in bulk-heterojunction polymer solar cells and in field-effect transistors, J. Am. Chem. Soc. 130 (2008) 6444–6450.
[7] I. Schwendeman, R. Hickman, G. Sonmez, P. Schottland, K. Zong, D. Welsh, J.R. Reynolds, Enhanced contrast dual polymer electrochromic devices, Chem. Mater. 14 (2002) 3118–3122.
[8] H. Meng, D. Tucker, S. Chaffins, Y. Chen, R. Helgeson, B. Dunn, F. Wudl, An unusual electrochromic device based on a new low-bandgap conjugated polymer, Adv. Mater. 15 (2003) 146–149.
[9] K. Bange, T. Gambke, Electrochromic materials for optical switching devices, Adv. Mater. 2 (1990) 10–16.
[10] A. Pennisi, F. Simone, G. Barletta, G. Di Marco, L. Lanza, Preliminary test of a large electrochromic window, Electrochim. Acta 44 (1999) 3237–3243.
[11] R. Rauh, Electrochromic windows: an overview, Electrochim. Acta 44 (1999) 3165–3176.
[12] R.G. Mortimer, Electrochromic materials, Chem. Soc. Rev. 26 (1997) 147–156.
[13] D.R. Rosseinsky, R.J. Mortimer, Electrochromic systems and the prospects for devices, Adv. Mater. 13 (2001) 783–793.
[14] P. Chandrasekhar, B.J. Zay, G.C. Birur, S. Rawal, E.A. Pierson, L. Kauder, T. Swanson, Large,switchable electrochromism in the visible through far-infrared in conducting polymer devices, Adv. Funct. Mater. 12 (2002) 95–103.
[15] S. Beaupré, A.-C. Breton, J. Dumas, M. Leclerc, Multicolored electrochromic cells based on poly(2,7-carbazole) derivatives for adaptive camouflage, Chem. Mater. 21 (2009) 1504–1513.
[16] P.M. Beaujuge, J.R. Reynolds, Color control in π-conjugated organic polymers for use in electrochromic devices, Chem. Rev. 110 (2010) 268–320.
[17] C.M. Amb, A.L. Dyer, J.R. Reynolds, Navigating the color palette of solution-processable electrochromic polymers, Chem. Mater. (2011) 23 397–415.
[18] C.M. Amb, P. Beaujuge, J.R. Reynolds, Spray processable blue to highly transmissive switching polymer electrochromes via the donor–acceptor approach, Adv. Mater. 22 (2010) 724–728.
[19] M. İçli-Özkut, S. Atak, A.M. Önal, A. Cihaner, A blue to highly transmissive soluble electrochromic polymer based on poly (3,4-propylenedioxyselenophene) with a high stability and coloration efficiency, J. Mater. Chem. 21 (2011) 5268–5272.
[20] M. İçli, M. Pamuk, F. Algi, A.M. Önal, A. Cihaner, Donor-acceptor polymer electrochromes with tunable colors and performance, Chem. Mater. 22 (2010) 4034–4044.
[21] G. Sonmez, H.B. Sonmez, C.K.F. Shen, R.W. Jost, Y. Rubin, F. Wudl, A processable green polymeric electrochromic, Macromolecules 38 (2005) 669–675.
[22] A. Durmus, G. Gunbas, P. Camurlu, L. Toppare, A neutral state green polymer with a superior transmissive light blue oxidized state, Chem. Commun. (2007) 3246–3248.
[23] P.M. Beaujuge, S. Ellinger, J.R. Reynolds, Spray processable green to highly transmissive electrochromics via chemically polymerizable donor–acceptor heterocyclic pentamers, Adv. Mater. 20 (2008) 2772–2776.
[24] P.M. Beaujuge, S.V. Vasilyeva, S. Ellinger, T.D. McCarley, J.R. Reynolds, Unsaturated linkages in dioxythiophene–benzothiadiazole donor–acceptor electrochromic polymers: the key role of conformational freedom, Macromolecules 42 (2009) 3694–3706.
[25] A. Cihaner, F. Algi, A novel neutral state green polymeric electrochromic with superior n- and p-doping processes: closer to red-blue-green (RGB) display realization, Adv. Funct. Mater. 18 (2008) 3583–3589.
[26] P.M. Beaujuge, S. Ellinger, J.R. Reynolds, The donor – acceptor approach allows a black-to-transmissive switching polymeric electrochrome, Nat. Mater. 7 (2008) 795–799.
[27] M. İçli, M. Pamuk, F. Algi, A.M. Önal, A. Cihaner, A new soluble neutral state black electrochromic copolymer via a donor – acceptor approach, Org. Electron. 11 (2010) 1255–1260.
[28] G. Öktem, A. Balan, D. Baran, L. Toppare, Donor – acceptor type random copolymers for full visible light absorption, Chem. Commun. 47 (2011) 3933–3935.
[29] P.M. Beaujuge, C.M. Amb, J.R. Reynolds, Spectral engineering in π-conjugated polymers with intramolecular donor–acceptor interactions, Acc. Chem. Res. 43 (2010) 1396–1407.
[30] C.M. Amb, J.A. Kerszulis, E.J. Thompson, A.L. Dyer, J.R. Reynolds, Propylenedioxythiophene (ProDOT)–phenylene copolymers allow a yellow-to-transmissive electrochrome, Polym. Chem. 2 (2011) 812–814.
[31] R. Huber, T. Fiebig, H.A. Wagenknecht, Pyrene as a fluorescent probe for DNA base radicals, Chem. Commun. 15 (2003) 1878–1879.
[32] K. Yamana, Y. Ohtani, H. Nakano, I. Saito, Bis-pyrene labeled DNA aptamer as an intelligent fluorescent biosensor, Bioorg. Med. Chem. Lett. 13 (2003) 3429–3431.
[33] B.J. Basu, C. Anandan, K.S. Rajam, Study of the mechanism of degradation of pyrene-based pressure sensitive paints, Sens. Actuators. B – Chem. 94 (2003) 257–266.
[34] H. Siu, J. Duhamel, Global analysis of the fluorescence decays of a pyrene-labeled polymer using a blob model, Macromolecules 37 (2004) 9287–9289.
[35] S. Kanagalingam, J. Spartalis, T.-M. Cao, J. Duhamel, Scaling relations related to the kinetics of excimer formation between pyrene groups

attached onto poly(*N*,*N*-dimethylacrylamide)s, Macromolecules 35 (2002) 8571–8577.
[36] C. Tang, F. Liu, Y.-J. Xia, L.-H. Xie, A. Wei, S.-B. Li, Q.-L. Fan, W. Huang, Efficient 9-alkylphenyl-9-pyrenylfluorene substituted pyrene derivatives with improved hole injection for blue light-emitting diodes, J. Mater. Chem. 16 (2006) 4074–4080.
[37] F. Liu, C. Tang, Q.-Q. Chen, S.-Z. Li, H.-B. Wu, L.-H. Xie, B. Peng, W. Wei, Y. Cao, W. Huang, Pyrene functioned diarylfluorenes as efficient solution processable light emitting molecular glass, Org. Electron. 10 (2009) 256–265.
[38] P. Anant, N.T. Lucas, J.M. Ball, T.D. Anthopoulos, J. Jacob, Synthesis and characterization of pyrene-centered oligothiophenes, Synthetic Metals 160 (2010) 1987–1993.
[39] N. Xie, Y. Chen, Combination of fluorescent switch and electrochemical switch based on a photochromic diarylethene, New J. Chem. 30 (2006) 1595–1598.
[40] H. Chen, X. Hu, S.-C. Ng, Synthesis and characterization of soluble conjugated polymers having pyrene moiety in the main chain, J. Poly. Sci. Part A 48 (2010) 5562–5569.
[41] S.-N. Ding, S. Cosnier, M. Holzinger, X. Wang, Electrochemical fabrication of novel fluorescent polymeric film: Poly(pyrrole–pyrene), Electrochem. Commun. 10 (2008) 1423–1426.
[42] C. Zhang, Y. Xu, N. Wang, C. Yu, W. Xiang, M. Ouyang, C. Ma, Electrosyntheses and characterizations of novel electrochromic copolymers based on pyrene and 3,4-ethylenedioxythiophene, Electrochem. Acta 55 (2009) 13–18.
[43] L. Xu, J. Zhao, R. Liu, H. Liu, J. Liu, H. Wang, Electrosyntheses and characterizations of novel electrochromic and fluorescent copolymers based on 2,2′-bithiophene pyrene, Electrochim. Acta 55 (2010) 8855–8862.
[44] H. Suenaga, K. Nakashima, T. Mizuno, M. Takeuchi, I. Hamachi, S. Shinkai, Pyrenylboronic acids as a novel entry for photochemical DNA cleavage: diradical-forming pyrene-1,6-diyldiboronic acid mimics the cleavage mechanism of enediyne antitumor antibiotics, J. Chem. Soc. Perkin Trans. 1 (1998) 1263–1268.
[45] J.E. Bullock, R. Carmieli, S.M. Mickley, J. Vura-Weis, M.R. Wasielewski, Photoinitiated charge transport through π-stacked electron conduits in supramolecular ordered assemblies of donor−acceptor triads, J. Am. Chem. Soc. 131 (2009) 11919–11929.
[46] T. Ozdemir, S. Atilgan, I. Kutuk, L.T. Yildirim, A. Tulek, M. Bayindir, E.U. Akaya, Solid-state emissive bodıpy dyes with bulky substituents as spacers, Org. Lett. 11 (2009) 2105–2107.
[47] Y. Ooyama, Y. Kagawa, Y. Harima, Synthesis and solid-state fluorescence properties of structural ısomers of novel benzofuro[2,3-c]oxazolocarbazole-type fluorescent dyes, Eur. J. Org. Chem. (2007) 3613–3621.
[48] Y. Ooyama, T. Okamoto, T. Yamaguchi, T. Suzuki, A. Hayashi, K. Yoshida, Heterocyclic quinol-type fluorophores: synthesis, x-ray crystal structures, solid-state photophysical properties of novel 5-hydroxy-5-substituent-benzo[b]naphtho[1,2-d]furan-6-one and 3-hydroxy-3-substituent-benzo[kl]xanthen-2-one derivatives, Chem. Eur. J. 12 (2006) 7827–7838.
[49] A.L. Dyer, M.R. Craig, J.E. Babiarz, K. Kiyak, J.R. Reynolds, Orange and red to transmissive electrochromic polymers based on electron-rich dioxythiophenes, Macromolecules 43 (2010) 4460–4467.

(by weight ratio, r) ranging from $r = 0\%$ (non-doped) to 6 wt.%. By separating the CR and TTA processes with quantitative analysis of MEL based on a theoretical rate model, we obtain simple analytical expressions allowing the estimation of the singlet yields from CR and TTA processes in the molecular fluorescent devices, respectively.

2. Experimental

The samples used for MEL measurements were fabricated in an organic molecular beam deposition system with bass pressure of $\sim 10^{-6}$ Pa. All organic layers of the 1×2 mm^2 devices were sandwiched between indium tin oxide (ITO) anode and lithium fluoride (LiF)/Al cathode. N,N′-Di(naphthalene-1-yl)-N,N′-diphenyl-benzidine (NPB) and pure Alq_3 layers are utilized as hole transport layer and electron transport layer, respectively. The emissive layer of DCM: Alq_3 with different DCM concentrations were co-evaporated by controlling the relative deposition rate of DCM and Alq_3. The device configurations then consisted of stacked thin films of ITO/NPB (50 nm)/Alq_3: DCM (0, 2, 3, 6 wt.%, 40 nm)/Alq_3 (30 nm)/LiF (0.7 nm)/Al (100 nm).

For the transient EL measurements, we used an Agilent pulse generator (8114A) to apply rectangular pulse voltage to our devices. The pulse repetition rate was 1 kHz with the width of 60 μs. Transient EL of the devices was measured with a Hamamatsu photomultiplier (H6780-P) and a digital oscilloscope (Tektronix DPO7104). The EL spectra were measured by SpectraPro-2300i spectrum units.

The MEL measurements were performed in a close-cycle cryostat system (Janis CCS-350s) which was located between the pole pieces of an electromagnet (Lakeshore EM647). During the measurement process, the samples were mounted on the cold finger of a close-cycle cryostat and operated at temperatures from 20 to 300 K. To exclude the effects of B-field enhanced current on the MEL, the devices were driven under constant current model. Current sourcing was performed using a Keithley 2400 source-measurement unit. The silicon photodetector for EL measurement was tested to make sure there was no field dependence on its output.

3. Results and discussion

Fig. 1(a) and (b) show the room temperature (300 K) MEL at different measuring current levels for the $r = 2$ wt.% and $r = 0\%$ devices, respectively. The MEL was defined as the relative change in EL intensity as a function of B-field, i.e. $\mathrm{MEL} = [I_{EL}(B) - I_{EL}(0)]/I_{EL}(0)$, where $I_{EL}(B)$ and $I_{EL}(0)$ are the EL intensity in the presence and absence of a B-field, respectively. The MEL always increases sharply at low B-field. After reaching the maximum value at around 45 mT, the MEL in the $r = 2$ wt.% device turns to decrease or level off with increasing B-field, depending on the current levels, while the MELs in the non-doped device for $r = 0\%$ turn to saturate over the current measurement range. In our previous work [15,17], the high-field decrease in MEL were qualitatively explained by B-field mediated TTA process. In fact, the room temperature TTA process in the DCM-doped device can be further confirmed by

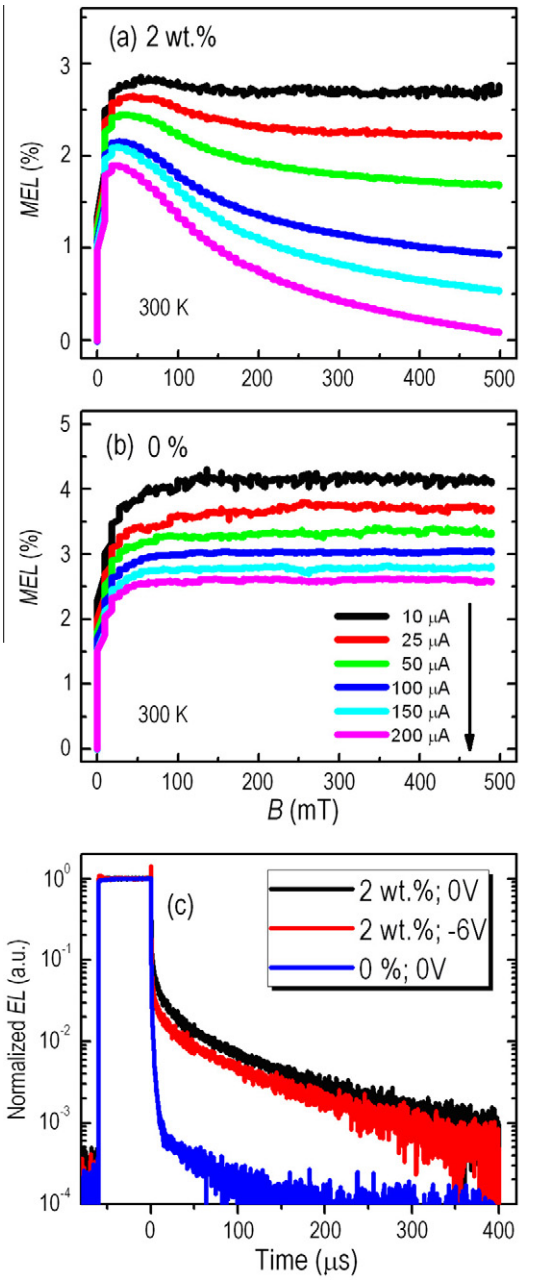

Fig. 1. MEL versus B-field in the 2 wt.% device (a) and non-doped device (b) under different driving current at 300 K. (c) Time-resolved EL intensity response of the $r = 0\%$ and $r = 2$ wt.% DCM-doped devices to 60 μs, 8 V excitation pulse, followed by 0 V or −6 V revise bias.

the transient EL measurements. Fig. 1(c) shows the time evolution of EL after a 60 μs excitation pulse was applied. It can be seen from the figure that the delayed fluorescence (DF) signal from the 2 wt.% device decays much slower than that from the non-doped device, which is consistent with the recent observation by Luo et al. [13]. In addition, nearly identical magnitudes and shapes of decay profiles in the 2 wt.% device after applying −6 V bias suggest the DF is caused by the TTA process [12,13]. Although these results

indicate that the TTA process plays an important role in the light generation in the small molecular fluorescent devices, the quantitative contribution of DF generated by TTA process to the EL intensity is still unresolved. The difficulty in distinguishing the DF from prompt fluorescence (PF) in the transient EL spectra makes the determination of the accurate relative rate of the DF very hard.

Fig. 2(a) shows the normalized current efficiencies of the $r = 2$ wt.% device measured at temperatures range from 20 to 300 K. MEL(B) curves of the $r = 2$ wt.% sample which are obtained under a large driving current of 200 μA at corresponding temperatures are compared in Fig. 2(b). It is found that higher current efficiency is corresponding with larger high-field decrease in MEL. In addition, the current efficiency is insensitive to the temperature lower than 200 K, which is similar to the situation for the high-field MEL. These results suggest some underlying correlations between the high current efficiency and TTA process since the high-field MEL is caused the B-field modulated TTA process [15,17].

In the presence of TTA, the EL intensity is the sum of the two components $I_{EL} = I_{PF} + I_{DF}$, where I_{PF} is the intensity of PF due to radiative decay of singlet excitons produced directly by CR process, and I_{DF} is intensity of DF which is generated by TTA process. Then the MEL can be expressed by

$$\mathrm{MEL} = \frac{\Delta I_{EL}}{I_{EL}} = \frac{m}{m+1}\frac{\Delta I_{PF}}{I_{PF}} + \frac{1}{m+1}\frac{\Delta I_{DF}}{I_{DF}} \quad (1)$$

with m being the ratio of PF to DF at zero field [i.e., $m = I_{PF}(0)/I_{DF}(0)$].

When electrons and holes are injected respectively from cathode and anode into the organic active layer, singlet and triplet intermolecular polaron pairs (*PP*s) are formed firstly according to spin configuration. Excitons with bound electron and hole on the same molecule are then formed after recombination of the intermolecular *PP*s [5]. Then, the direct singlet generation fraction α can be written as $\alpha = k_S/(k_S + 3k_T)$ [3], where k_S (k_T) is the recombination rate constant for singlet (triplet) exciton. In the absence of external B-field, singlet and triplet *PP*s are usually considered to be degenerate, causing a mixing between singlets and triplets through hyperfine interaction with rate k_{ISC} [18–20]. The k_{ISC} can be much faster than k_S and k_T in organic materials [21], leading to equal concentration for each level of singlet and triplet. Then the rate equation concerning the concentration of singlet *PP*s is [22]

$$\frac{d[^1\mathrm{PP}]_0}{dt} = -\frac{k_S + 3k_T}{4}[^1\mathrm{PP}]_0 + \frac{C_0}{4} \quad (2)$$

where C_0 is the formation rate constant of *PP*s and $[^1\mathrm{PP}]_0$ denotes the population of singlet *PP*s at zero field, respectively. Under the steady-state condition, we can obtain $[^1\mathrm{PP}]_0 = C_0/(k_S + 3k_T)$. When a B-field is turned on and the strength is larger than the hyperfine coupling interaction (about tens of mT), the degeneracy in triplet pairs is removed by Zeeman splitting and the hyperfine mixing remains only between ^{1}PP and $^3\mathrm{PP}_0$ (triplet *PP*s with sublevel of 0) states [18,19]. We then obtain $[^1\mathrm{PP}]_B = [^3\mathrm{PP}_0]_B = C_B/2(k_S + k_T)$ by resolving the rate equation for singlet *PP*s at external B-field [22], where C_B is the *PP* formation rate constant and $[\mathrm{PP}]_B$ is the pair populations of a species *PP* at B-field. Singlet excitons are then generated after singlet *PP*s recombined. The PF intensity is proportional to the concentration of singlet excitons from the CR process. Since the MEL measurements are made under constant current, the C_B/C_0 can be considered to be 1. Therefore, the $\Delta I_{PF}/I_{PF}$ can be written as

$$\frac{\Delta I_{PF}}{I_{PF}} = \frac{[^1\mathrm{PP}]_B}{[^1\mathrm{PP}]_0} - 1 = \frac{3}{2(2\alpha+1)} - 1 \quad (3)$$

Gärditz et al. [23] have measured the relative change of delayed EL intensity in Alq_3-based OLEDs and found that the $\Delta I_{DF}/I_{DF}$ fell to its zero-field level at about 125 mT and reached −2.5% at 200 mT. We then assume that the $\Delta I_{DF}/I_{DF}$ curves in our experiments have the same B-field dependence and take the $\Delta I_{DF}/I_{DF}|_{B=125\ \mathrm{mT}} = 0$, $\Delta I_{DF}/I_{DF}|_{B=200\ \mathrm{mT}} = -2.5\%$ as reference values. Therefore, the value of MEL at 125 mT can be regarded as the saturated magnitude of $m/(m+1)\cdot\Delta I_{PF}/I_{PF}$ [17] according to Eq. (1). In this case Eq. (1) then gives

$$\mathrm{MEL}|_{B=125\ \mathrm{mT}} = \frac{m}{m+1}\frac{\Delta I_{PF}}{I_{PF}}\bigg|_{B=125\ \mathrm{mT}} = \frac{m}{m+1}\frac{\Delta I_{PF}}{I_{PF}}\bigg|_{B=200\ \mathrm{mT}}$$

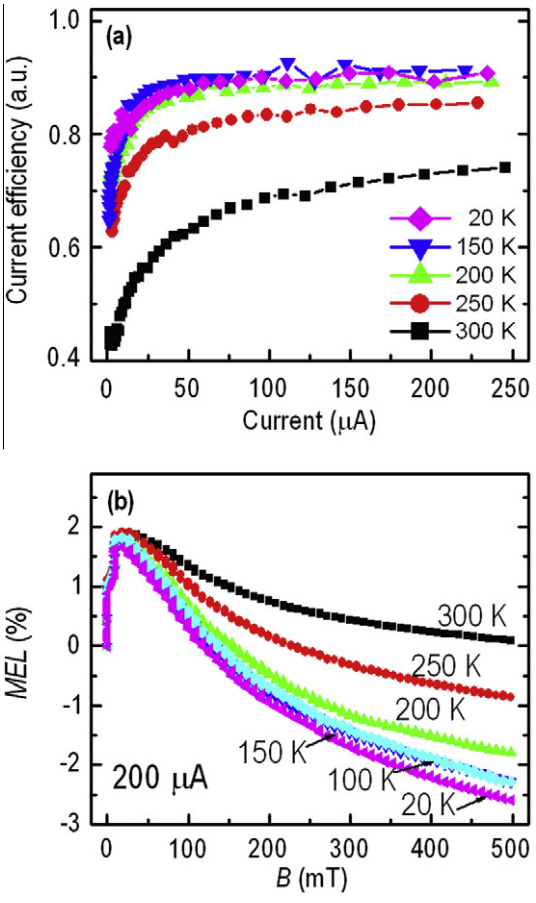

Fig. 2. (a) Normalized current efficiency for the $r = 2$ wt.% device versus current measured at temperature range from 20 to 300 K. (b) MEL versus B-field in the $r = 2$ wt.% device under different temperature at 200 μA.

$$\mathrm{MEL}|_{B=200\ \mathrm{mT}} - MEL|_{B=125\ \mathrm{mT}} = \frac{1}{m+1}\frac{\Delta I_{\mathrm{DF}}}{I_{\mathrm{DF}}}\Big|_{B=200\ \mathrm{mT}} \quad (4)$$

If the probability of radiative decay of singlet exciton is equal for PF and DF, we get $m = I_{\mathrm{PF}}(0)/I_{\mathrm{DF}}(0) = \alpha/\beta$, where the β denoting the generation fraction of extra singlet exciton via TTA process. The total singlet generation fraction is then represented by $\chi_S = \alpha + \beta$.

By using the values read out from the MEL curves which are displayed in Fig. 1 and also Fig. 2(b), m, α, β, and χ_S can be determined for each condition based on the above equations. For example, for the $r = 2$ wt.% sample at 200 μA, 300 K [see in Fig. 1(a)], by substituting $\mathrm{MEL}|_{B=125\ \mathrm{mT}} = 1.165\%$ and $\mathrm{MEL}|_{B=200\ \mathrm{mT}} = 0.743\%$ which are read out at 125 mT and 200 mT in the curve into Eq. (4), we obtain $m = 4.9$ and $\Delta I_{\mathrm{PF}}/I_{\mathrm{PF}} = 1.4\%$. These results give α of 0.240 according to Eq. (3), and then β and χ_S are determined to be 0.049 and 0.289, respectively.

It should be emphasized that these results should depend on the choosing of the reference values. The $\Delta I_{\mathrm{DF}}/I_{\mathrm{DF}}$ in organic materials under different excitation ways would show different B-field dependences. Mezyk et al. [11] have recently measured the sensitized $\Delta I_{\mathrm{DF}}/I_{\mathrm{DF}}$ in a DPA (9,10-diphenylanthracene):2% PtOEP [platinum(II) octaethylporphyrin] thin film and found that the $\Delta I_{\mathrm{DF}}/I_{\mathrm{DF}}$ fell to its zero field level at ~200 mT and reached −12% at 500 mT. To check the rationality of our method, we then take the $\Delta I_{\mathrm{DF}}/I_{\mathrm{DF}}|_{B=200\ \mathrm{mT}} = 0$ as reference value and use $\Delta I_{\mathrm{DF}}/I_{\mathrm{DF}}|_{B=500\ \mathrm{mT}} = -12\%$ to do the calculation. It gives $m = 17.2$, $\alpha = 0.244$, $\beta = 0.014$ and $\chi_S = 0.258$. Although departure is exhibited by varying the choice of the reference value, the contribution of TTA (β) can not be still ignored and the total singlet exciton yield χ_S can also exceed the classical 0.25 statistics limit. The biggest discrepancy is that the value of m calculated by using the reference values from PtOEP:DPA compound films is three times more than that calculated from Alq_3 EL device. This discrepancy can be explained by the different exciton environment in organic semiconductor between the two systems. Under laser excitation, the triplet states of PtOEP are rapidly populated due to the strong spin–orbit coupling and then the DPA triplets pile up because of energy transfer from PtOEP, leading to strong TTA in the compound [11]. The delayed EL would be much less because only a part of excitons (exciton with spin 1) are involved in TTA process in the Alq_3 EL device. Therefore, the decrease of sensitized DF with increasing B-field would be much sharper than the delayed EL, giving a large reference value at 500 mT and then the larger value of m. Given the above facts, the results which are calculated based on the reference values under electric excitation of Alq_3 device would be much more reasonable.

Fig. 3 shows the dependences of singlet generation fraction for the $r = 2$ wt.% device on measuring current and temperature. It can be seen from Fig. 3(a) that χ_S (black solid square) increases with enlarging the driving current and exceeds 0.25 spin statistics limit at current larger than 50 μA at 300 K. When the temperature decreases, the value of χ_S initially increases and then turns to saturate at temperatures lower than 150 K [see in Fig. 3(b)]. The average value of χ_S we obtain for the $r = 2$ wt.% sample driving by 200 μA at different

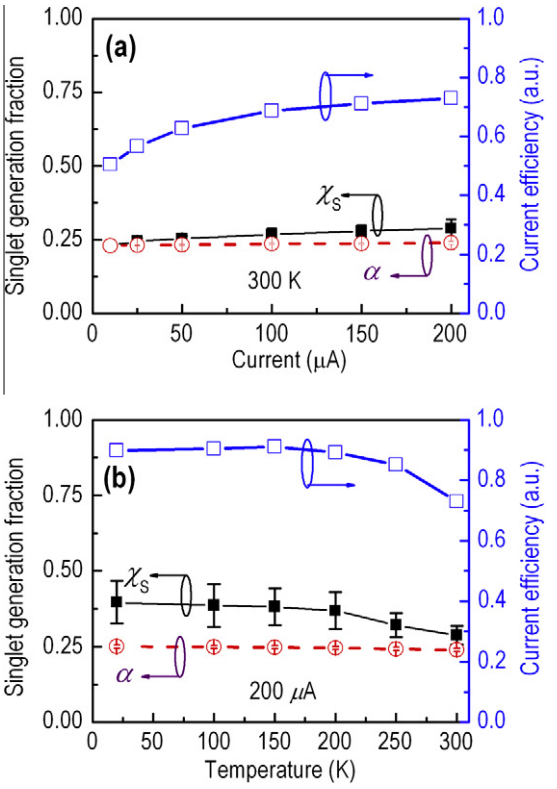

Fig. 3. The dependence of χ_S (black solid squares) and α (red open circles) on current at 300 K (a) and on temperature at 200 μA (b) for the 2 wt.% DCM-doped device. Normalized current efficiency values (blue open squares) are shown on the right y-axis of (a) and (b). (For interpretation of the references to colour in this figure legend, the reader is referred to the web version of this article.)

temperature is 0.36 ± 0.05. However, there is no significant variation in α with temperature and driving current over the measurement range [red open circle], suggesting that the probability of forming either a singlet or a triplet exciton via the CR process is independent of temperature and current density. This assumption is consistent with the observation of Wilson et al. [4] in a platinum-containing monomer. The average value of α for the sample at 300 K is 0.23 ± 0.02, which is in great agreement with the value of 0.22 ± 0.03 measured by Baldo et al. [2] for small molecular Alq_3. This result also confirms that CR process in the molecular fluorescent devices is spin-independent. The dependence of χ_S on current and temperature and the large value of χ_S exceeding the statistics limit might be caused by the TTA process since TTA heavily depends on the lifetime and concentration of triplet states in the devices [24]. At large driving current and low temperature, the triplet density is enlarged and the triplet lifetime is prolonged due to the reduced phonon-assisted decay of triplets, which causes a strong TTA and then a large value of β. Normalized current efficiency for the sample [blue open square] shows the same behavior against current and temperature as χ_S, suggesting that our discussion is consistent with the experimental results since the efficiency is proportional to the singlet yields in fluorescent devices.

We note that the reference B-field selected for $\Delta I_{DF}/I_{DF} = 0$ is an important parameter for the calculation and it would be varied with temperatures and materials, so it is necessary to discuss the validity of the assumption and the related results in this work. In order to test the dependence of the calculated results on the reference field, we do the calculation by using different fields ranging from 100 to 150 mT around 125 mT as the field for $\Delta I_{DF}/I_{DF} = 0$. The variation of α and χ_S are displayed in Fig. 3 as form of error bars. The value of α is found to be nearly independent on the reference field. Although the value of χ_S exhibits its departure with changing the reference field especially at low temperatures, two important conclusions are still unchanged. The first conclusion is that the total singlet exciton yield χ_S can exceed the classical 0.25 statistics limit, and the second one is that TTA process contributes an important component ($\beta = \chi_S - \alpha$) to the singlets.

In order to elucidate the control parameters for the extra singlet generation β via TTA process, devices with different dopant concentrations are studied at different temperatures and driving currents. Fig. 4(a) shows the MEL characteristics of 0%, 2 wt.%, 3 wt.% and 6 wt.% DCM-doped samples at 20 K, 200 μA. Normalized EL spectra of the doped and pure Alq_3 devices are compared in the inset. The peak position of EL spectra around 600 nm and the complete quenching of the Alq_3 emission indicate that light emission in the doped samples comes from DCM molecule. Compared to the non-doped sample, all doped devices show a larger high-field decrease in MEL, suggesting a stronger TTA in the doped devices [15]. Fig. 4(b) displays the extra singlet generation fraction β as a function of driving current for the samples with different DCM concentration at 300 K. For the non-doped (0%) device, β are constantly equal to zero, indicating that no TTA in the pure Alq_3 device at room temperature. The value of β for the doped devices increases with driving current. The maximum β at 300 K is obtained to be about 0.05 in 2 wt.% device, suggesting that DF intensity constitutes as high as ~17% (=0.05/0.289) to the total EL intensity at room temperature in this device [the χ_S is 0.289 as shown in Fig. 3(a)]. The dependence of β on temperature for different DCM concentration devices driving at 200 μA is shown in Fig. 4(c). A rise of the β is observed with decreasing the temperature. At temperatures lower than 150 K, the β for the non-doped device is not equal to zero any longer and reaches about 0.06 at 20 K, leading to the χ_S of 0.302 [the ratio of β to χ_S is then calculated to be ~19% (=0.06/0.302)]. This phenomenon indicates strongly that TTA process plays an important role in the emission of pure Alq_3-based OLEDs at low temperature. The maximum β of 0.146 is obtained in 2 wt.% device at 20 K, pushing the χ_S to 0.397 [see in Fig. 3(b)]. The contribution of extra singlets generated by TTA process to the total singlets under this condition is then calculated to be ~34% (=0.146/0.397). When the dopant concentration r is larger than 2 wt.%, the β decreases with further increasing r at a given measuring temperature or current level. This phenomenon might be caused by the aggregation of DCM molecule in the devices [25]. The aggregation of DCM molecule can trap carriers for self-quenching and also exciton quenching [25,26], resulting in a reduced TTA process and degradation of the devices. This argument is confirmed by the red-shifts of the emission peak of EL spectra with increasing the DCM concentration [see the inset in Fig. 4(a)]. The increasing aggregation of DCM causes the enhancement of the longer wavelength emission [26].

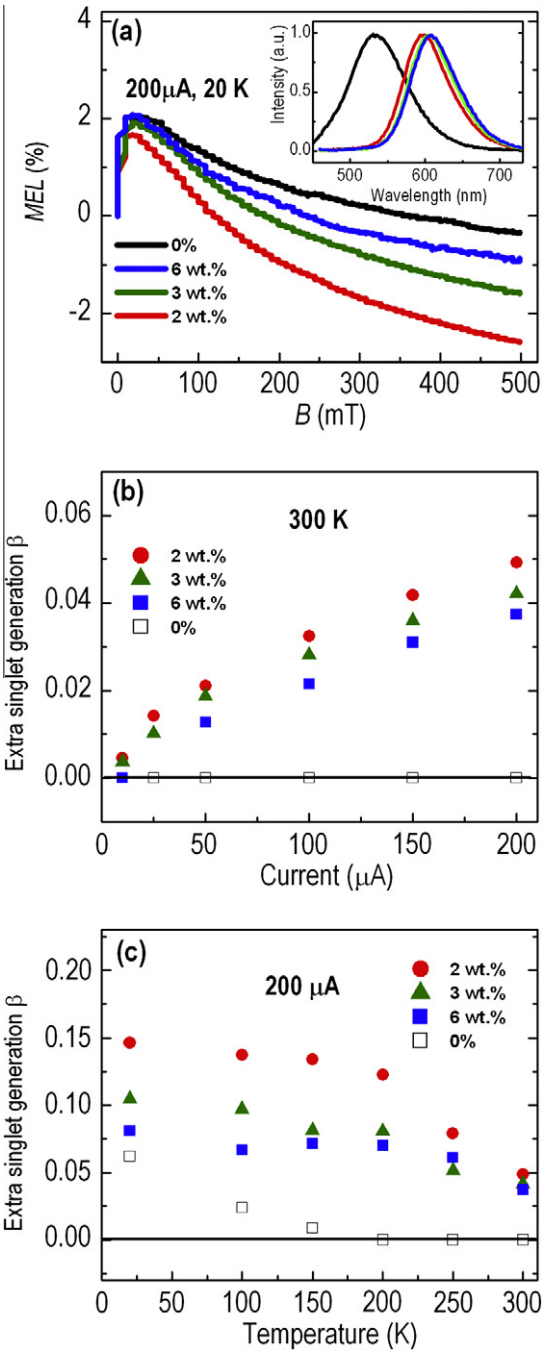

Fig. 4. (a) MEL versus B-field for 0%, 2 wt.%, 3 wt.% and 6 wt.% DCM-doped samples at 20 K, 200 μA. The normalized EL spectra for the doped and undoped devices are compared in the inset; The dependence of β on current at 300 K (b), and on temperature at 200 μA (c).

Following the above discussion, the β heavily depends on the dopant-induced exciton trapping [15,27]. Triplet excitons in the DCM-doped device are trapped in the

dopant molecules avoiding the quenching with thermal activation energy. Thus, the lifetime of triplet excitons in the DCM molecule would be long, which gives rise to a large population density of triplets and also large interaction time constant for TTA. In the non-doped devices triplets lifetime is strongly reduced due to the phonon-assisted quenching at room temperature, resulting in no TTA ($\beta = 0$) in the device even under large driving currents (high density of triplets). In the DCM-doped device with long lifetime of triplets, in contrast, TTA happens ($\beta > 0$) even at a small current level (low density of triplets). These phenomena also indicate that lifetime of triplet excitons (interaction time constant for TTA) is the primary factor for TTA, while population density of triplets is the secondary. Although the threshold value of interaction time constant for TTA is not yet exactly determined and it would depend on the triplet density, the high-field decrease in MEL can be utilized as a sensitive probe for TTA process in organic fluorescent devices.

4. Conclusions

We have demonstrated the generation fraction of singlet exciton in the small molecular based OLEDs by analyzing the MEL with a rate model. The results reveal that TTA process produces considerable extra singlets which account for as high as 19% of total singlets at 20 K in non-doped device, 34% at 20 K and 17% at room temperature in fluorescent dye doped device, causing the total singlet generation yields exceeding the classical 0.25 spin statistics limit. Of course, it should be noted that the most exact way to quantify the fraction of singlet generation in small molecular fluorescent devices should be based on quantum efficiency measurements. However, as yet, there would be still some difficulties to discern the contribution of the TTA process based on this quantum efficiency measurement. Much more research needs to be done to address this question properly. In summary, the results presented in this work can be used to understand the process of light generation in the small molecular based OLEDs, especially in the fluorescent host: guest systems with very high quantum efficiencies exceeding the classical 25% theoretical limit.

Acknowledgements

The authors thank the National Natural Science Foundation of China (10974157 and 10974159) and the NSF of Chongqing (CSTC, 2010BA6002) for their financial support.

References

[1] C.W. Tang, S.A. Vanslyke, Appl. Phys. Lett. 51 (1987) 913.
[2] M.A. Baldo, D.F. O'Brien, M.E. Thompson, S.R. Forrest, Phys. Rev. B 60 (1999) 14422.
[3] M. Wohlgenannt, K. Tandon, S. Mazumdar, S. Ramasesha, Z.V. Vardeny, Nature (London) 409 (2001) 494.
[4] J.S. Wilson, A.S. Dhoot, A.J.A.B. Seeley, M.S. Khan, A. Köhler, R.H. Friend, Nature (London) 413 (2001) 828.
[5] M. Segal, M.A. Baldo, R.J. Holmes, S.R. Forrest, Z.G. Soos, Phys. Rev. B 68 (2003) 075211.
[6] L.C. Lin, H.F. Meng, J.T. Shy, S.F. Horng, L.S. Yu, C.H. Chen, H.H. Liaw, C.C. Huang, K.Y. Peng, S.A. Chen, Phys. Rev. Lett. 90 (2003) 036601.
[7] A. Köhler, J. Wilson, Org. Electron. 4 (2003) 179.
[8] C. Rothe, S.M. King, A.P. Monkman, Phys. Rev. Lett. 97 (2006) 076602.
[9] J. Partee, E.L. Frankevich, B. Uhlhorn, J. Shinar, Y. Ding, T.J. Barton, Phys. Rev. Lett. 82 (1999) 3673.
[10] Z.D. Popovic, H. Aziz, J. Appl. Phys. 98 (2005) 013510.
[11] J. Mezyk, R. Tubino, A. Monguzzi, A. Mech, F. Meinardi, Phys. Rev. Lett. 102 (2009) 087404.
[12] D.Y. Kondakov, J. Appl. Phys. 102 (2007) 114504.
[13] Y.C. Luo, H. Aziz, Adv. Funct. Mater. 20 (2010) 1285.
[14] P. Chen, Y.L. Lei, R. Liu, Q.M. Zhang, Y. Zhang, Z.H. Xiong, Sci. China Phys. Astron. 53 (2010) 24.
[15] P. Chen, Y.L. Lei, Q.L. Song, Y. Zhang, R. Liu, Z.H. Xiong, Appl. Phys. Lett. 95 (2009) 213304.
[16] B. Hu, L. Yan, M. Shao, Adv. Mater. 21 (2009) 1500.
[17] Y.L. Lei, Y. Zhang, R. Liu, P. Chen, Q.L. Song, Z.H. Xiong, Org. Electron. 10 (2009) 889.
[18] J. Kalinowski, M. Cocchi, D. Virgili, P. Di Macro, V. Fattori, Chem. Phys. Lett. 380 (2003) 710.
[19] M. Segal, M. Singh, K. Rivoire, S. Difley, T. Van Voorhis, M.A. Baldo, Nat. Mater. 6 (2007) 374.
[20] T.D. Nguyen, G. Hukic-Markosian, F.J. Wang, L. Wojcik, X.G. Li, E. Ehrenfreund, Z.V. Vardeny, Nat. Mater. 9 (2010) 345.
[21] U.E. Steiaer, T. Ulrich, Chem. Rev. (Washington DC) 89 (1989) 51.
[22] Y. Iwasaki, T. Osasa, M. Asahi, M. Matsumura, Y. Sakaguchi, T. Suzuki, Phys. Rev. B 74 (2006) 195209.
[23] C. Gäditz, A. Mückl, M. Cölle, J. Appl. Phys. 98 (2005) 104507.
[24] A.H. Davis, K. Bussmann, J. Vac. Sci. Technol. A 22 (2004) 1885.
[25] G.Y. Zhong, Z. Xu, J. He, S.T. Zhang, Y.Q. Zhan, X.J. Wang, Z.H. Xiong, H.Z. Shi, X.M. Ding, W. Huang, X.Y. Hou, Appl. Phys. Lett. 81 (2002) 1122.
[26] S.W. Feng, M.C. Shih, C.J. Huang, C.T. Chung, Thin Solid Films 517 (2009) 2719.
[27] Y.C. Luo, H. Aziz, R. Klenkler, G. Xu, Z.D. Popovic, Chem. Phys. Lett. 458 (2008) 319.

films, reaching over 1400 S/cm at 89.5% transmission with solvent post treatment [5–8].

While PEDOT:PSS is most commonly used in commercial application, some alternative forms of PEDOT synthesis have been used in electrochemical polymerization (primarily for analytical studies) or in vapor phase polymerization (VPP) where a common polymerization catalyst is the Lewis acid Fe(III) p-toluene sulfonate or $Fe(tos)_3$ [9,10]. $Fe(tos)_3$ is also the most prominent oxidant used for in situ polymerization of PEDOT, where conductivities reach over 1000 S/cm when processed with the inhibitor pyridine and water for improved film quality and to extend pot life [11,12]. Ha et al. used relatively high concentrations of imidazole in the processing solution to reduce the high reactivity of $Fe(tos)_3$ prior to processing and to "[preserve] the EDOT in monomeric form after spin-casting", where polymerization is initiated by heating the substrate [13]. They report 750 S/cm with 81% transmission at 270 Ω/sq. With the aforementioned values, PEDOT is becoming more attractive as a flexible alternative electrode to brittle transparent conductive oxides, namely preeminent and expensive indium tin oxide.

For all its applications, PEDOT:PSS has some drawbacks. The inherent low pH (less than 3) and hygroscopic nature of PSS lead to degradation of surrounding interfaces [14,15]. To overcome corrosion issues, researchers at TDA Research developed a lauryl terminated bis-poly (ethyleneglycol) PEDOT doped with perchlorate, which is processed in nitromethane and reaches conductivities of 10–60 S/cm [16]. Additionally, Kim et al. produced an organic-processable, non-acidic solution of PEDOT using a hydrophobic, imidizolium-based polyionic liquid as a counterion for use as an HTL in OLEDs [15]. They reported conductivities of 10^{-2} S/cm.

To further address some of the problems associated with PEDOT:PSS, we have attempted the synthesis of a hydrophobic, matrix-assisted PEDOT thin film using the organic electron acceptor and dehydrogentating agent 2,3-dichloro-5,6-dicyanobenzoquinone (DDQ) as both the mediator for synthesis of PEDOT and for subsequent doping during spin coating. We also attempted synthesis of PEDOT with tetrachloro-1,4-benzoquinone, which has been used successfully in the synthesis of conductive polypyrrole along with other halogenated benzoquinones and in other oxidative coupling reactions requiring dehydrogenation [17–20]. However, within the chosen environment these reagents of lower oxidative potential relative to DDQ did not initiate an observable polymerization reaction with EDOT.

In our research, we developed a versatile procedure to process PEDOT:DDQ from solution using solvents with much lower dielectric constants than MeCN, such that significant polymerization is inhibited until the solvent evaporates and the reactants reach a critical concentration which drives polymerization. It has been shown that the formation of charge transfer (CT) complexes decreases with an increase in the dielectric constant of the solvent [21]. Therefore, it was believed that in solvents with high dielectric constants, the EDOT:DDQ CT complex dissociates into a radical cation and anion which drives polymerization in solution. Conversely, the CT state is more prevalent in less polar solvents (e.g. 1,4-dioxane, THF) such that the rate of dissociation and polymerization is significantly slowed and is largely governed by concentration.

When only solutions of EDOT and DDQ were spin coated in THF, a granular, highly resistive film was produced. However, upon the addition of PVAc or a related polymer to function as a templating matrix, smooth, conductive thin films were produced. Successful films turned from a pale brown–green to a bright blue after spin coating (Fig 1), which signals the formation of reduced PEDOT chains [22]. A subsequent rinse with MeCN after drying was necessary to further polymerize and oxidize the PEDOT chains as well as to remove excess PVAc, (un)reacted DDQ, and monomer.

As stated previously, conductive polypyrrole has been synthesized in the presence of halobenzoquinones. Bruno et al. reports a two order of magnitude increase in conductivity from pressed pellets of poly(EDOT-co-pyrrole) over PEDOT as a control [23]. Thin continuous films of the copolymer may give favorable results which this procedure could offer.

Thus far, we have achieved 17 S/cm with almost 87% transmission at 550 nm, where higher conductivities were achieved at a cost of decreased transmission. When comparing in situ processing procedures employing $Fe(tos)_3$/amine inhibitor or DDQ, PEDOT:DDQ conductivity and associated values are currently lower than those achieved by PEDOT:tos. Nevertheless, the processing procedure and properties of PEDOT:DDQ are still being investigated, and potential advantages include processing in non-polar solvents with organic-processable polymers. Further, the

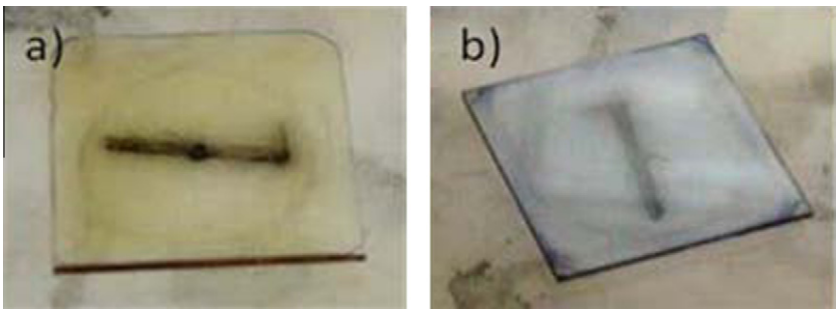

Fig. 1. THF solution of EDOT and DDQ (a) prior to spinning (b) after 2 s of spinning.

pot life of the $Fe(tos)_3$/amine inhibitor system varies. For pyridine solutions, the pot life can last up to a week whereas certain imidazole solutions are preserved indefinitely; however, in the latter, crystal formation in solution can occur and high temperatures are necessary for initiating polymerization [10]. The pyridine procedure presented by Clevios suggests processing the complete solution immediately to prevent gelling [24]. For PEDOT:DDQ, the processing solution has a relatively long pot life, and the resulting smooth, conductive film could take on a range of mechanical and optoelectronic properties dependent on the polymer additive.

2. Materials and methods

2.1. Spectroscopy

Solutions of approximately 73 μM DDQ (Aldrich 98%, stored under nitrogen) in a range of aprotic solvents (dry 1,4 dioxane, *n*-butyl acetate, dry THF, MeCN) were prepared and their spectra recorded. One molar equivalent of 3,4-ethylenedioxythiophene (EDOT, Aldrich) was added to the solutions, and the change in spectra was recorded over time.

2.2. Film formation

Multiple series of EDOT:DDQ solutions were prepared under ambient conditions in the following way: to a designated amount of PVAc (Aldrich, avg. M_w of 100,000) and DDQ was added reagent grade, dry 1,4-dioxane. After stirring for approximately 1 h to dissolve all contents, EDOT was added, and the solution was stirred for 1 h. For example, to 40.2 mg PVAc and 86.9 mg (0.38 mmol) DDQ was added 2 mL 1,4-dioxane. After 1 h of stirring, 29.9 μL EDOT (0.28 mmol) was added and stirred for another hour to give an overall concentration of 0.14 M EDOT with EDOT:DDQ in a 1:4/3 mol ratio and EDOT:PVAc in a 1:1 wt ratio. The solutions were spin coated on glass cleaned by sonication sequentially in baths of acetone and isopropanol and then oxygen plasma-treated prior to use. All films were spun at 1200 rpm for 5 s and immediately placed under a petri dish lid (9 cm diameter) for 2 h unless otherwise specified. This film recipe will be referred to as a standard film. After 2 h, films were carefully rinsed 2–3 times with MeCN and allowed to dry.

To a solution of PEDOT:PSS provided by H.C. Starck (Baytron PH 1000) was added 5% vol ethylene glycol (EG). The solution was filtered with a 0.45 μm Wattman membrane filter, spin coated at 2500 RPM for 30 s, and annealed at 120 °C for 1 h to serve as reference material – also referred to as standard.

2.3. Instrumentation

Absorption and transmission spectra were obtained by UV–vis spectroscopy (Shimadzu MPC-3100). Sheet resistance values were calculated and reported as an average of 10 values per film by 4-point probe measurements (Lucas Labs., tungsten carbide tips). X-ray photoelectron spectroscopy (XPS) and UV photoelectron spectroscopy (UPS) measurements were performed with a Poibos 100 setup (Specs) as described elsewhere [25]. Conductive AFM was performed on an AIST-NT Combiscope 1000 executed in contact mode with platinum or gold coated silicon tips at different bias voltages (PEDOT:PSS at −2.1 V, PEDOT:DDQ at 10 mV, tip radius ~50 nm).

3. Theory

In these experiments, we believe that the polymerization for conductive PEDOT with DDQ is based on the Diaz mechanism for polypyrrole [26–28]. One potential pathway to polymerization is illustrated in Scheme 1.

As benzoquinones are known to undergo one-electron reduction in aprotic solvents [29], one possible mechanism involves the initial formation of a CT complex following the collision of DDQ and EDOT. Dissociation of the complex – accelerated by solvent evaporation – and collision of the resulting radical cations could yield a cationic dimer. Once two EDOT radical cations couple, surrounding DDQ species can abstract α-hydrogen atoms. Scheme 1 represents one simplified pathway to polymer formation which shows the lifecycle of DDQ to $DDQH_2$. In this pathway a monoradical, cationic dimer is formed after hydrogen abstraction. Polymer chains grow by the addition of cationic species of EDOT.

Many pathways are possible to the formation of EDOT dimers with different oxidation states, radical number, and bond order. While we do not have experimental evidence for support, we believe that the $DDQH^{\bullet}$ radical found in these processes could perform subsequent oxidation of neutral PEDOT segments or that the $DDQH^{-}$ anion can become the counterion of an already-oxidized sulfur, leading to conductive polymer chains.

4. Results and discussion

4.1. Spectroscopy

Solutions of monomer, oxidant, and different solvents exhibited characteristic colors and color changes during processing. Common ethereal solvents were selected based on their solvating ability in search of a balance between charge-screening ability and vapor pressure relative to MeCN ($\varepsilon = 36.64$, $vp_{25} = 11.9$ kPa) and include: THF ($\varepsilon = 7.52$, $vp_{25} = 21.6$ kPa), 1,4-dioxane ($\varepsilon = 2.22$, $vp_{25} = 4.95$ kPa) and *n*-butyl acetate ($\varepsilon = 5.07$, $vp_{25} = 1.66$ kPa) [30].

A slower drying process was thought to lead to longer reaction times for increased polymerization and doping, thus, improving film quality. *N*-butyl acetate did not produce conductive films after drying and rinsing with MeCN, nor was a significant blue color change observed. Even after heating to remove more solvent, the films remained highly resistive, which was attributed to steric interference from the alkyl chain during the reaction. Films employing THF turned from a pale brown-green to a bright blue within seconds of spin coating (Fig. 1) while the rate of color change for 1,4-dioxane was slower. When spin coating films with 1,4-dioxane, polymerization on the pipette tip

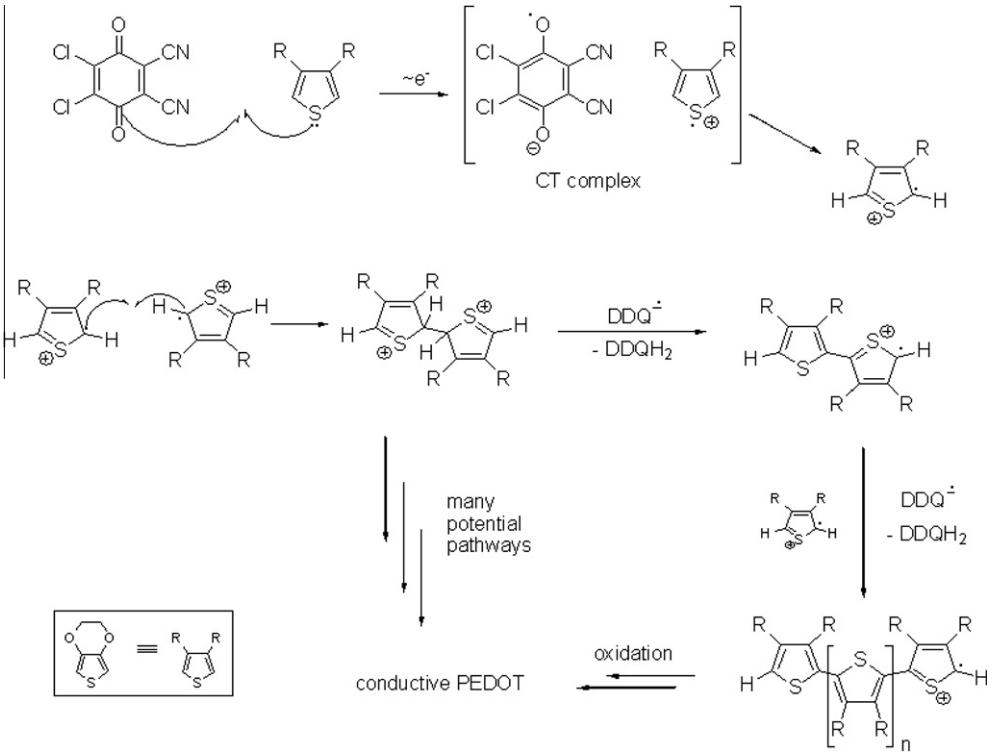

Scheme 1. One potential pathway for the formation of conductive PEDOT with DDQ as the oxidizing and dehydrogenating agent.

and on the substrate was slowed relative to THF due to the lower vapor pressure of the double ether. Further, THF produced films with holes after rinsing with MeCN while 1,4-dioxane did not. Thus, 1,4-dioxane was the solvent of choice in this study.

When adding EDOT to the bright yellow 1,4-dioxane DDQ solution at standard film concentrations, the solution turned dark initially and then faded to a clearer brown-green. At first, extensive polymerization was not observed in solution with the naked eye. However, in about a week, small crystals – believed to be DDQ – began to form on the bottom of the vial on which polymer grew. The addition of small amounts of toluene appeared to suppress this crystal growth which could extend the refrigerated shelf life to weeks or more.

With the same concentrations of reactants but using MeCN as the solvent, the solution turned dark immediately upon addition of EDOT and formed a significant amount of precipitate. A dark film began to coat the inside of the glass vial within a day. Thus, it is believed that such rapid polymerization was a result of the solvation of the CT-complex which initiated significant polymerization in solution.

To observe the solvent effect on DDQ and on DDQ in the presence of EDOT, UV–Vis absorption spectroscopy was performed in a polar (MeCN) and a non polar (1,4-dioxane) aprotic solvent (Fig. 2). Solutions containing only the monomer, 73 μM EDOT, show an absorption peak at around 260 nm and no other features in the observed wavelength range. Thus, the formation of a stable solution and there being little interaction of monomer and solvent were concluded. Solutions containing only 73 μM DDQ show quite different behavior depending on the solvent. For DDQ in MeCN a characteristic double peak was observed at 270 and 280 nm and for the radical anion (DDQ^{-}) at 346, 432, 457, 547, and 588 nm which are in agreement with previous reports [31,32]. This shows a strong interaction of DDQ with MeCN and supports the formation of radicals in solution. Upon addition of EDOT to the DDQ solution, the DDQ peaks reduced over time as the radical peaks increased, which indicates that MeCN supports the formation of radicals which could lead to polymerization. However, a peak around 265 nm appeared which is at the position of the sum of the original, separated EDOT and DDQ peaks.

Switching to a solvent with a much lower dielectric constant, 1,4-dioxane, the spectrum changed significantly. The combined EDOT and DDQ peak splits into separated peaks (around 264 nm and 290 nm, respectively), showing a further changing interaction with the solvent relative to MeCN. For higher wavelengths multiple peaks are visible with broad absorption bands centered around 500 and 682 nm which disappear upon the addition of EDOT. Sambhi reported the formation of charge transfer complexes of DDQ with the cyclic ethers 1,4-dioxane and THF which may account for such intense absorption peaks for this double ether [33].

For both solvents, the main peaks of EDOT and DDQ for short wavelengths were reasonably stable at this low concentration. The spectral characteristics differ between the solvents with regard to the interaction of DDQ and solvent as well as small temporal evolutions of the DDQ peaks upon the addition of EDOT. Definitive evidence for CT

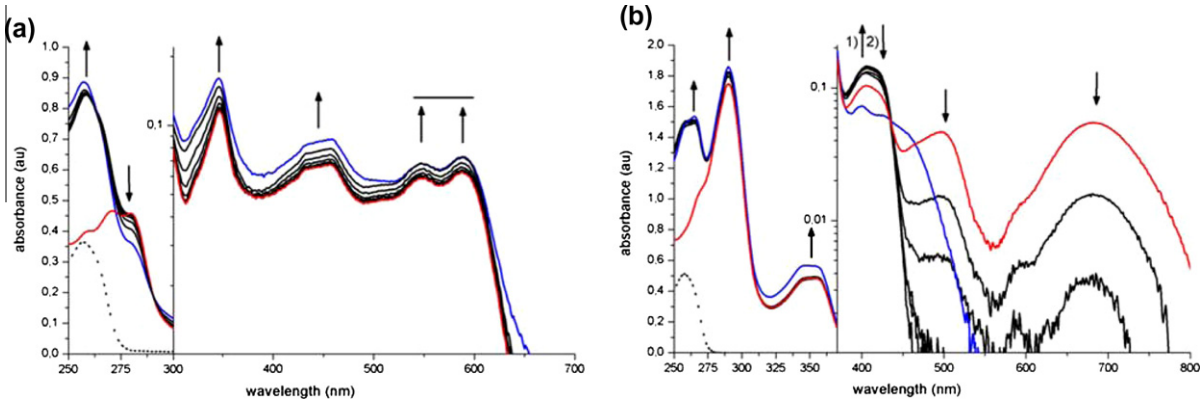

Fig. 2. UV–Vis absorption spectra, showing the temporal evolution of the solutions. Starting from 73 μM DDQ solutions (red) in aprotic solvents (a) MeCN and (b) 1,4-dioxane, the spectra begin to change upon the addition of 1 mol eq EDOT. The spectra were monitored for up to 2 h (black, several changing curves), and at 18 h post addition of EDOT (blue, last measurement). For comparison, the spectrum of 1 mol eq EDOT (dash) is given.(For interpretation of the references to colour in this figure legend, the reader is referred to the web version of this article.)

formation in either case could not be produced from these experiments, but it is inferred that much more stable CT formation occurs in 1,4-dioxane.

4.2. Film transmission

After spin coating a standard film, it was immediately transported for transmission measurements (T_0 = 30 s after spin coating). The evolution of transmission during drying can be found in Fig. 3.

The intense blue color observed immediately after spin coating was assumed to be reduced PEDOT which absorbs around 600 nm [22]. This dip in transmission reduced over time as absorption increased in the IR which suggests the formation of oxidized PEDOT and likely, longer chains. For shorter wavelengths, the curve shows a higher transmission initially and then evolves toward the shape of the absorption spectra of EDOT:DDQ in 1,4-dioxane around 350 and 450 nm found in Fig. 2. This dip in transmission is thus attributed to DDQ, indicating that unreacted DDQ and its other forms remain in the film. Once the film is rinsed with MeCN, the sharp absorption of DDQ around 300 nm is significantly reduced (Fig. 4).

Fig. 4 depicts the change in transmission of films containing varied concentrations of EDOT while the ratio of EDOT:DDQ was held at 1:4/3 and the wt ratio of EDOT:PVAc at 1:1. Films that followed this formulation had a greenish tinge after drying and were very resistive. A dramatic shift in transmission was observed after gently rinsing the films with MeCN, where acetone produced similar results but DMSO ruined the films. The shift is attributed to further polymerization and oxidation of PEDOT monomer and oligomers, accelerated by MeCN, while rinsing away excess (un)reacted DDQ, monomer and PVAc. The difference in magnitude of transmission is attributed to different film thicknesses, formed by the varying amounts of EDOT available. The transmission curves suggest that by these concentration changes the mechanism is not altered or limited somehow, so the chemical composition and the formation mechanism is nearly uniform for all ratios.

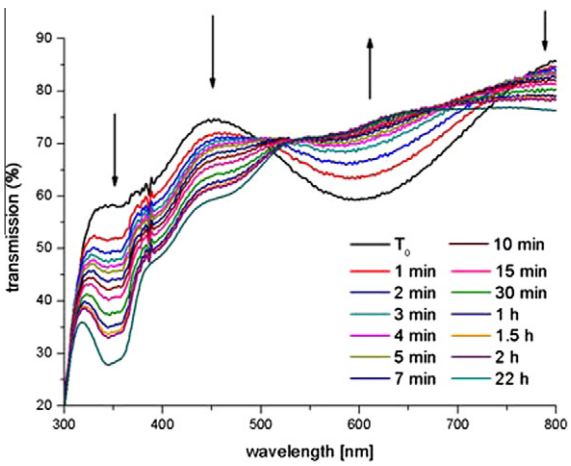

Fig. 3. Transmission measurements from the time evolution of drying a standard 0.14 M EDOT:DDQ film.

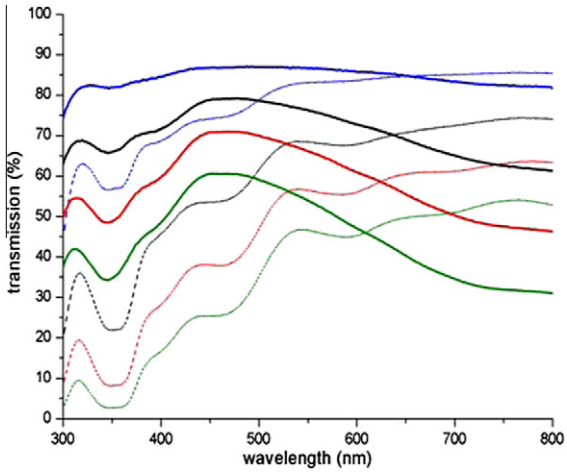

Fig. 4. Transmission spectra of EDOT:DDQ films at a ratio of 1:4/3 with an EDOT:PVAc wt ratio of 1:1. Before (dashed) and after rinsing (solid) with MeCN: 0.07 M EDOT (blue), 0.14 M EDOT (black), 0.21 M EDOT (red), 0.28 M EDOT (green) (For interpretation of the references to colour in this figure legend, the reader is referred to the web version of this article).

This uncontrolled secondary polymerization and oxidation during rinsing is a very important step in obtaining a conductive film. For the remainder of this paper, rinsing with MeCN was considered complete when the green tinge was visibly rinsed away (2–3 rinses). It should be noted that further improvement of this step has great potential and should be investigated further. A smooth PVAc:PEDOT layer, present after rinsing, suggests that as the PEDOT forms it migrates toward the bottom of the film due to its insolubility in common solvents. Similarly, as the film dries, it appears that DDQ and $DDQH_2$ may rise to the top with the evaporating solvent.

For films that were rinsed too hard with MeCN, the film peeled off of the glass surface but did not dissolve, maintaining film structure integrity. When water was added to the film surface, droplets condensed and ran off; contact angle measurements were not taken. It appears that the film material takes on the hydrophobic nature of PVAc while simultaneously taking on the insoluble nature of PEDOT. Such properties could be attractive when engineering mechanically robust, conductive plastics like those achieved by Hansen et al. by dissolving PEDOT:tos into a PMMA substrate [12].

4.3. Concentration effects

The effects of varying the EDOT:DDQ mol ratio, EDOT concentration, and the EDOT:PVAc wt ratio on film formation and on electronic properties were investigated. As can be expected, the films were much more resistive when one molar equivalent or less of DDQ was used, where excess oxidant is needed to dope the PEDOT (Table 1). Increasing the DDQ concentration to and above stoichiometric ratios produced an increase in film thickness and eventually a wavy surface morphology. Comparing ratios of 1:5/3 and 1:2, a decrease in sheet resistance concomitant with slightly higher transparency was observed which is contrary to the trend up to that point. An EDOT:DDQ ratio of 1:4/3 was chosen as the standard film for reproducibility.

Increasing the overall concentration of a standard film produced an increase in film thickness and a decrease in transmission (Table 2). The highest conductivity in this series was achieved with the standard film recipe. It appears that the act of rinsing with MeCN both polymerizes and oxidizes PEDOT while the rigid PEDOT structure continues to lock in PVAc as observed by the increase in film thickness in Table 2. There are slight differences in the values for the two standard films (separate solutions) in Tables 1 and 2. However, considering the non-standardized rinsing of the films, these values are remarkably similar.

Varying the amount of PVAc in a standard film did not produce a trend in film thickness, where the most transparent and conductive film was at a wt ratio of 1:5/4 (Table 3). This supports the idea that the PEDOT chains migrate to the bottom of the "wet" film as they form. The supporting polymer matrix species will likely impact many aspects of the film quality for its role may include aiding in both templating chain growth as well as in providing structural stability for the film itself.

4.4. Conductive AFM

Fig. 5 compares conductive AFM images of a standard PEDOT:DDQ film and a PEDOT:PSS film with 5% vol EG deposited on glass. Both layers are not treated further before measurement, so the surface depicted is as it was after several hours of exposure to atmosphere.

For both samples, the current appears to be centered on the grains. For PEDOT:PSS, the grain size can be adjusted by changing solvent concentration, where the size depicted in Fig. 5 is representative of PEDOT:PSS at approximately 750 S/cm [8,34]. Measuring local conductivity, both samples behaved quite differently. While the PEDOT:DDQ sample showed high currents at low bias

Table 1
Effects on film properties by varying the EDOT:DDQ molar ratio.

EDOT (M)	EDOT:DDQ (mol ratio)	EDOT:PVAc (wt ratio)	Transmission (%) 500 nm	700 nm	Sheet resistance (kΩ/sq)	Thickness (nm)	σ (S/cm)
0.14	1:2/3	1:1	86.8	81.8	1580	26	0.24
0.14	1:1	1:1	81.6	73.6	76.5	56	0.23
0.14	1:4/3	1:1	79.1	70.0	3.03	73	45
0.14	1:5/3	1:1	69.5	59.2	2.68	125 w_a	30
0.14	1:2	1:1	71.3	59.8	2.11	110 w_b	43

w = wavy surface, avg. thickness a = pk–pk ~12 nm b = pk–pk ~14 nm.

Table 2
Effects on film properties by varying the overall concentration of the film solutions.

EDOT (M)	EDOT:DDQ (mol ratio)	EDOT:PVAc (wt ratio)	Transmission (%) 500 nm	700 nm	Sheet resistance (kΩ/sq)	Thickness (nm)	σ (S/cm)
0.07	1:4/3	1:1.	86.6	83.3	16.4	33	17
0.14	1:4/3	1:1.	76.3	65.1	2.88	79	44
0.21	1:4/3	1:1.	61.2	50.3	3.68	142 w_c	19
0.28	1:4/3	1:1.	54.0.	34.6	6.10.	217 w_d	4.5

w = wavy surface, avg. thickness c = pk-pk ~30 nm d = pk-pk ~90 nm.

Table 3
Effect of film properties by varying the EDOT:PVAc weight ratio.

EDOT (M)	EDOT:DDQ (mol ratio)	EDOT:PVAc (wt ratio)	Transmission (%)		Sheet resistance (kΩ/sq)	Thickness (nm)	σ (S/cm)
			500 nm	700 nm			
0.14	1:4/3	1:1/2	76.1	67.4	3.90	80 r	32
0.14	1:4/3	1:3/4	75.5	65.3	4.54	92	24
0.14	1:4/3	1:5/4	78.3	69.5	2.12	80	59
0.14	1:4/3	1:3/2	77.4	68.2	2.72	85 s	43

r = rough, avg. s = tall spikes.

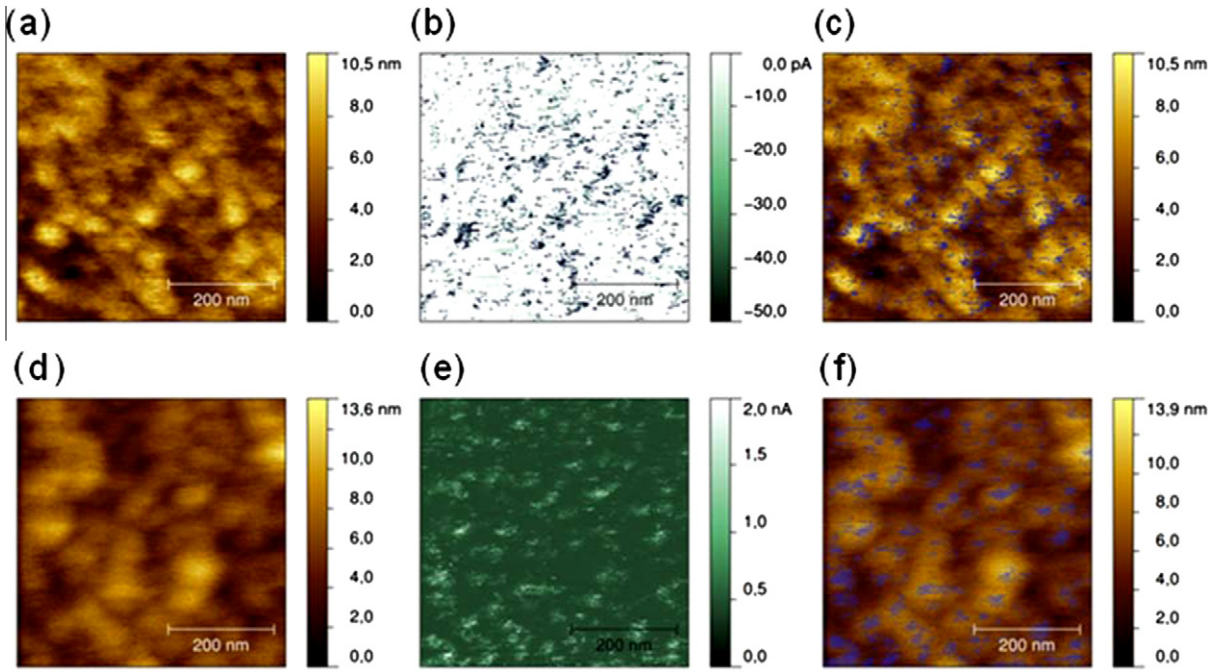

Fig. 5. Conductive AFM for standard (a–c) PEDOT:PSS and (d–f) PEDOT:DDQ. Tip bias was −2.1 V for PEDOT:PSS and 10 mV for PEDOT:DDQ. Images (c) and (f) are overlays of the subsequent images at certain current thresholds.

voltages, measuring currents on PEDOT:PSS required a relatively high bias voltage that was orders of magnitude higher than that of PEDOT:DDQ and which resulted in surface currents orders of magnitude lower. Thus, we believe there is a less conductive, PSS-rich phase present on the PEDOT:PSS surface which is in agreement with literature [35,36]. In combination with exposure to atmosphere, this results in an insulating top layer, causing poor contact properties. Such a surface layer is apparently not present on the PEDOT:DDQ film initially, resulting in significantly better contact properties. This difference in contact resistance was observed macroscopically when liquid metal was not needed to assist in sheet resistance measurements with a 4-point probe for PEDOT:DDQ while it was needed for macroscopically more conductive PEDOT:PSS.

4.5. UPS

To determine the work function (WF) and to further characterize the material, XPS and UPS measurements were performed. UP spectra of a standard PEDOT:DDQ film gave a work function of 4.62 eV. This rather low value compared to earlier measurements of 5.05 eV for PEDOT:PSS shows a significant shift of the work function due to a change of counteranion and suggests that DDQ is a weaker dopant [10,37]. However, both layers show similar intensities of occupied states near the Fermi level. Further, when comparing reported values for VPP PEDOT:tos of 4.3 ± 1 eV by UPS [38], the WF value is greater for PEDOT:DDQ. As the counterion of PSS and tosylate are identical, the surrounding chemical environment of a conductive polymer can also influence the WF which can be easily altered for PEDOT:DDQ (i.e. polymer matrix).

XPS was performed to compare PEDOT:DDQ to PEDOT:PSS. Unfortunately, our PEDOT:DDQ layers contain a rather large amount of PVAc with similar elemental and chemical structures, thus obscuring the signal. Nevertheless, some conclusions could be drawn (see Appendix A). Doping of PEDOT by DDQ was concluded, and a shift in surface chemistry toward a less PEDOT-rich top layer was observed over time.

5. Conclusion

Thin conductive films of PEDOT:DDQ were synthesized by delaying polymerization in ethereal solvents with low dielectric constants. The resulting smooth films produced by spin coating from 1,4-dioxane with PVAc as a stable, templating polymer and by rinsing with MeCN showed good structural integrity with decent conductivity and transparency. The feasibility of this approach has been proven, and a basic process has been established. Following our recipe, a film with a conductivity of 17 S/cm at 33 nm thick with 86.6% transmission at 550 nm was achieved. According to our observations, the processing solutions were sufficiently stable depending on solvent polarity, where significant polymerization is triggered by solvent evaporation in the spin-coated film. The as-coated layers still contained significant amounts of DDQ and partially reacted species, which can be reacted further by rinsing with MeCN which simultaneously removes by-products and enhances the degree of polymerization.

We are confident that the thin film properties can be improved further by optimizing many parameters such as the polymer matrix/template, solvents (and ratios), and the rinsing procedure or by changing the monomer. There is more potential for further exploration of this procedure due to its inherent versatility, where this system could rival that of the reference PEDOT:PSS. The attractive properties of this film formulation include: lower acidity relative to PSS, hydrophobic properties and structural support of the polymer additive, and a lower contact resistance relative to PEDOT:PSS. We believe PEDOT:DDQ has potential for many applications such as a hole transport layer or as a transparent electrode (e.g. in organic solar cells or other optoelectronic devices) and should be explored further.

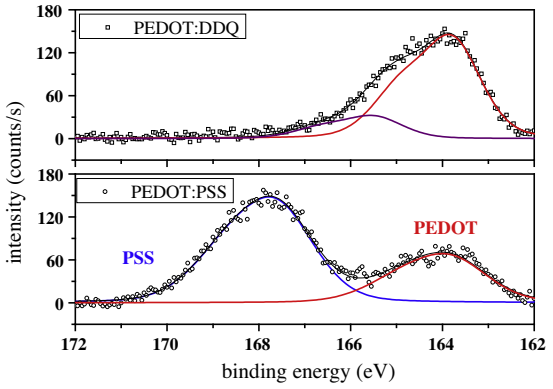

Fig. A1. Comparison of XPS spectra of sulfur S(2p) signal for standard PEDOT:DDQ and EG-treated PEDOT:PSS thin films.

Acknowledgments

The authors thank Olaf Hild and John Hofferberth for useful discussions and suggestions, H.C. Starck for supplying samples of Baytron PH 1000, Yong Hyun Kim and Christoph Sachse for support, and Christian May for supporting the DIZEeff. M. Machala thanks the German Federal Foreign Office for providing this experience through a Transatlantic Renewable Energy Fellowship and Dana C. Olson for suggesting this placement. This work was funded by the European Union (EFRE), the Free State of Saxony and the Fraunhofer Gesellschaft as part of the Dresdner Innovationszentrum für Energieeffizienz.

Appendix A

XPS spectra for the S(2p) signal of PEDOT:DDQ and PEDOT:PSS can be found in Fig. A1.

In both samples, the peak originating from PEDOT is at the same position within experimental error at 163.77 eV for PEDOT:DDQ and at 163.79 eV for PEDOT:PSS. For PEDOT:DDQ, a small subpeak – likely a positively charged sulfur atom – is visible. Whether this peak is present for PEDOT:PSS is unclear, since it might be hidden in the signal originating from the PSS peak. The positions of the S(2p) peak confirms the successful polymerization of EDOT and subsequent oxidation.

For a freshly prepared sample and after 2 days in ultra-high vacuum, the S(2s) signal, attributed to PEDOT and the Cl(2p) signal, attributed to DDQ, were recorded by XPS. The signal intensity for the S(2s) peak decreased by a factor of 2.4 while that of the Cl(2p) peak increases by a factor of 1.5 (Fig. A2).

From the relative peak intensities, the ratios between the different polymers/molecules in the upper few nanometers of the film can be estimated. The PEDOT:DDQ ratio was estimated by comparing Cl(2p) and S(2p) peak intensities. The values for PEDOT:PVAc and PVAc:DDQ are more error prone since the oxygen peak that is used for the calculation is present in PVAc as well as in DDQ and PEDOT. For PEDOT:PVAc, the S(2s) and O(1s) signals were

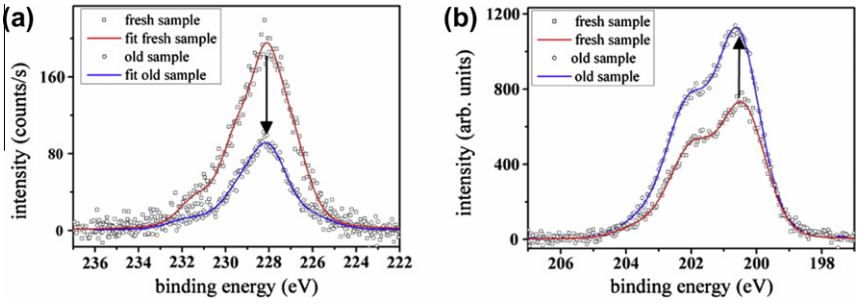

Fig. A2. XPS signals for a) S(2s) and b) Cl(2p) peaks in PEDOT:DDQ for a fresh sample and the same sample stored in ultra-high vacuum for 2 days.

Table A1
An estimation of ratios of various chemical species in PEDOT:DDQ films by XPS.

	PEDOT:DDQ	PEDOT:PVAc	PVAc:DDQ
Fresh sample	1.0	0.3	0.3
2-Day-old sample	0.3	0.1	0.3

compared whereby the O signal originating from PEDOT and DDQ was subtracted to get the fraction originating from PVAc. For PVAc:DDQ, the O(1s) and Cl(2p) signals were compared, and again the O signals from PEDOT and DDQ were subtracted Table A1.

In the older sample left in the vacuum chamber, the surface is essentially depleted of PEDOT which is not necessarily a bulk effect. This change on the surface indicates that diffusion and segregation may still be taking place, which could be controlled for improved performance. These results suggest that an investigation on long-term stability should be undertaken.

References

[1] G. Heywang, F. Jonas, Poly(alkylenedioxythiophene)s- new, very stable conducting polymers, Adv. Mat. 4 (1992) 116–118.
[2] L. Groenendaal, G. Zotti, P-H. Aubert, S.H. Waybright, J.R. Reynold, Electrochemistry of poly(3,4-alkylenedioxythiophene) derivatives, Adv. Mater. 15 (2003) 855–879.
[3] F. Jonas, G. Heywang, Technical applications for conductive polymers, Electrochim. Acta. 39 (1994) 1345–1347.
[4] S. Kirchmeyer, D. Rueter, Scientific importance, properties and growing applications of poly(3,4-ethylenedixoythiophene), J. Mater. Chem. 15 (2005) 2077–2088.
[5] J. Ouyanga, Q. Xua, C. Chua, Y. Yanga, G. Lib, J. Shinarb, On the mechanism of conductivity enhancement in poly(3,4-ethylenedioxythiophene):poly(styrene sulfonate) film through solvent treatment, Polymer 45 (2004) 8443–8450.
[6] A.M. Nardes, M. Kemerink, M.M. de Kok, E. Vinken, K. Maturova, R.A.J. Janssen, Conductivity, work function, and environmental stability of PEDOT:PSS thin films treated with sorbitol, Org. Elec. 9 (2008) 727–734.
[7] X. Crispin, S. Marciniak, W. Osikowicz, G. Zotti, A.W. Denier van der Gon, F. Louwet, M. Fahlman, L. Roenendaal, F. De Schryver, W.R. Salaneck, Morphology, interfacial chemistry, and stability of poly(3,4-ethylene dioxythiophene) – poly(styrene sunofonate): a photoelectron spectroscopy study, Part B: Polym. Phys. 41 (2003) 2561–2583.
[8] Y.H. Kim, C.Sachse;M.L. Machala, C. May, L. Mueller-Meskamp, K. Leo, Highly conductive pedot:pss electrode with optimized solvent and thermal post-treatment for ito-free organic solar cells, Adv. Funct. Mater. 21 (2011) 1076–1081.
[9] M. Fabretto, K. Zuber, C. Hall, P. Murphy, High conductivity pedot using humidity facilitated vacuum vapour phase polymerisation, Macromol. Rapid Commun. 2 (2008) 1403–1409.
[10] B. Winther-Jensen, D.W. Breiby, Keld West, Base inhibited oxidative polymerization of 3,4-ethylenedioxythiophene w/ iron (III) tosylate, Synth. Met. 152 (2005) 1–4.
[11] P.A. Levermore, L. Chen, X. Wang, R. Das, D.D.C. Bradley, Highly conductive poly(3,4-ethylenedioxythiophene) films by vapor phase polymerization for application in efficient organic light-emitting diodes, Adv. Mater. 19 (2007) 2379–2385.
[12] T.S. Hansen, K. West, O. Hassager, N.B. Larsen, Integration of conducting polymer nextwork in non-conductive polymer substrates, Synth. Met. 156 (2006) 1203–1207.
[13] Y.H. Ha, N. Nikolov, S.K. Pollack, J. Mastrangelo, B.D. Martin, R. Shashidhar, Towards transparent, highly conductive poly(3,4-ethylenedioxythiophene),, Adv. Funct. Mat. 14 (2004) 615–622.
[14] H. Okuzaki, H. Suzuki, T. Ito, Electromechanical properties of poly(3,4-ethylenedioxythiophene)/poly(4-styrene sulfonate) films, J. Phys. Chem. B. 113 (2009) 11378–11383.
[15] T.Y. Kim, M. Suh, S.J. Kwon, T.H. Lee, J.E. Kim, Y.J. Lee, J.H. Kim, M. Hong, K.S. Suh, Poly(3, 4-ethylenedioxythiophene) derived from poly(ionic liquid) for the use as hole-injecting material in organic light-emitting diodes, Macromol. Rapid Commun. 30 (2009) 1477–1482.
[16] TDA Research. http://www.tda.com/Products/products.htm, last accessed 02 May 2011.
[17] E.T. Kang, K.G. Neoh, T.C. Tan, Y.K. Ong, Polymerization and oxidation of pyrrole by organic electron acceptors,, Part A: Polym. Chem. 25 (1987) 2143–2153.
[18] E.T. Kang, K.G. Neo, Chemical polymerization and oxidation of pyrrole by Halobenzoquinones, Mol. Cryst. Liq. Cryst. 173 (1989) 141–150.
[19] O. Schäfer, S. Mang, E. Arici, G. Lussem, C. Unterlechner, J.H. Wendorff, A. Greiner, Simple poly(p-xylylene)s as precursor polymers for poly(p-phenylenevinylene)s and segmented poly(p-phenylenevinylene)s: synthesis, polymer analogous reactions, and thermal and optical properties, Macromol. Chem. Phys. 199 (1998) 807–813.
[20] Y. Zhang, C-J. Li, DDQ-mediated direct cross-dehydrogenative-coupling (cdc) between benzyl ethers and simple ketones, J. Am. Chem. Soc. 128 (2006) 4242–4243.
[21] M.M.A. Hamed, H.M.A. Salman, E.M. Abd-Alla, M.R. Mahmoud, Charge-transfer complexes of some Heteroarlythiourea derivatives with π-acceptors, Phosphorus Sulfur and Silicon. 80 (1993) 127–134.
[22] S. Sakamoto, M. Okumura, Z. Zhao, Y. Furukawa, Raman spectral changes in PEDOT-PSS in polymer light-emitting diodes upon operation, Chem. Phys. Lett. 412 (2005) 395–398.
[23] F.F. Bruno, S.A. Fossey, S. Nagarajan, R. Nagarajan, J. Kumar, L.A. Samuelson, Biomimetic synthesis of water-soluble conducting copolymers/homopolymers of pyrrole and 3,4-Ethylenedioxythiophene, Biomacromolecule 7 (2006) 586–589.
[24] Clevios TM sup http://www.clevios.com/index.php?page_id=115, last accessed 02 May 2011.
[25] S. Olthof, R. Meerheim, M. Schober, K. Leo, Energy level alignment at the interfaces in a multilayer organic light emitting diode structure, Phys. Rev. B. 79 (2009) 245308.
[26] R.J. Wattman, J. Bargon, A.F. Diaz, Electrochemical studies of some conducting polythiophene films, J. Phys. Chem. 87 (1983) 1459–1463.
[27] J. Roncali, Conjugated poly(thiophenes): synthesis, functionalization, and applications, Chem. Rev. 92 (1992) 711–738.
[28] J.P. Lock, S.G. Im, K.K. Gleason, Oxidative chemical vapor deposition of electrically conducting poly(3,4-ethylenedioxythiophene) films, Micromoles 39 (2006) 5326–5329.
[29] J.R.T.J. Wass, E. Ahlberg, I. Panas, D.J. Schiffrin, Quantum chemical modeling of the reduction of quinones, J. Phys.Chem. A. 110 (2006) 2005.
[30] D.R Lide, Handbook of Organic Solvents (Second Ed.), CRC Press, 1995. ISBN 0-8493-8930-5.
[31] J.S. Miller, P.J. Krusic, D.A. Dixon, W.M. Reiff, J.H. Zhang, E.C. Anderson, A.J. Epsteins, Radical ion salts of 2,3-dichloro-5,6-dicyanobenzoquinone and Metallocenes. A reexamination of their magnetic and spectroscopic properties, J. Am. Chem. Soc. 108 (1986) 4459–4466.
[32] M. Pandeeswaran, K.P. Elango, Spectroscopic and kinetic studies on the interaction of ketoconazole and povidone drugs with DDQ, Spectrochim. Acta, Part A 69 (2008) 1082–1088.
[33] M.S. Sambhi, Donor–acceptor complexes of 2,3-dichlor-5,6-dicyanobenzoquionone with Tetrahydrofuran, Tetrahydropyran, and 1,4-dioxane, J. Phys. Chem. 73 (1969) 1584–1586.
[34] H. Yan, H. Okuzaki, Effect of solvent on PEDOT/PSS nanometer-scaled thin films: XPS and STEM/AFM studies, Synth Met. 159 (2009) 2225–2228.
[35] H.J. Snaith, H. Kenrick, M. Chiesa, R.H. Friend, Morphological and electronic consequences of modifications to the polymer anode 'PEDOT:PSS', Polymer 46 (2005) 2573–2578.
[36] G. Greczynski, Th. Kugler, W.R. Salaneck, Characterization of the PEDOT-PSS system by means of X-ray and ultraviolet photoelectron spectroscopy, Thin Solid Films 354 (1999) 120–135.
[37] J. Meiss, C.L. Uhrich, K. Fehse, S. Pfuetzner, M.K. Riede, K. Leo, Transparent Electrode Materials for Solar Cells, Proceedings of SPIE. 7002 (2008) 700210–700211.
[38] A. Gadisa, K. Tvingstedt, S. Admassie, L. Lindell, X. Crispin, M.R. Andersson, W.R. Salaneck, O. Ingan, Transparent polymer cathode for organic photovoltaic devices, Synth. Met. 156 (2006) 1102–1107.

a high-k dielectric limits the insulating ability. Therefore, a metal oxide dielectric is suitable for low voltage OTFT application if the traps are passivated and the leakage current is reduced.

In this work, we demonstrated a bilayer dielectric structure consisting of random copolymer grafted room temperature sputtered metal oxide for an OTFT. The poly (styrene-co-methyl methacrylate) (PS-r-PMMA) random copolymer and hafnium oxide (HfO_x) were used as dielectrics. The PS-r-PMMA is a thoroughly studied material as a grafting layer for the template used in nanostructure patterning [17,18]. The thickness of PS-r-PMMA depends on the annealing conditions. The higher the temperature that is applied, the thicker the film that can be obtained [10,11]. For surface modification, a self-assembled monolayer (SAM) is commonly used in organic thin film transistors. The thickness of a SAM mainly depends on its chain length. Using the SAM layer usually obtains favorable device behavior. However, applying the monolayer structure in the large printing process is assumed to be difficult. Any region with few un-attached SAMs will cause the TFT to fail. Instead, long chain polymers form an "amorphous" random structure after grafting on the substrate. The substrate surface was completely covered by randomly crossover polymer chains. Consequently, the amounts of attached polymers may only affect the thickness of the dielectric with more effective process controllability. In the case of PS-r-PMMA, the film thickness of approximately several nanometers can be achieved through the temperature annealing process. The polymers that could graft on hydroxyl surface to passivate the hydroxyl surface may apply as well as PS-r-PMMA in this work. Owing to the only nanometer-thick polymer layer, the low voltage behavior of an OTFT with a high dielectric constant HfO_x could be retained.

2. Experimental

Fig. 1(a) illustrates the structure of the bottom gate and top contact OTFT used in this study. A heavily doped silicon wafer was utilized as the gate electrode. After the wafer was cleaned, an 80-nm-thick HfO_x dielectric was deposited by RF sputtering at room temperature. The HfO_x surface was then treated by O_2 plasma. The PS-r-PMMA random copolymer was dissolved in toluene with a concentration of 20 mg/ml. The PS-r-PMMA was then spin-coated on the HfO_x and heated by a hotplate in an N_2-filled glove box at 170 °C for 24 h. The chemical structure for PS-r-PMMA is shown in Fig. 1(b). High temperature annealing ensures that the PS-r-PMMA chains obtain sufficient energy to diffuse and end graft to the HfO_x surface by a condensation process [11]. After the heating process, the sample was rinsed with toluene to remove un-attached PS-r-PMMA chains, obtaining a desired thickness of PS-r-PMMA film (approximately 10 nm). The attachment of PS-r-PMMA is schematically shown in Fig. 1(c). For the organic channel layer, the pentacene was deposited by a thermal evaporator embedded in a glove box at a base pressure of 2×10^{-6} torr without substrate heating. The glove box is N_2-filled to avoid the oxygen and moisture effects on the organic semiconductor. The pentacene deposition rate was maintained at 0.1–0.2 nm/s to 40 nm thick. Finally, through a shadow mask, the gold source/drain electrodes with 30-nm-thick were deposited and defined, forming the ohmic contact between the active layer and source/drain regions. The OTFT channel length (L) and channel width (W) were 100 and 1000 μm, respectively. The pentacene for the OTFT was grown in the glove box, and the fabricated OTFTs were measured immediately after S/D formation. Additionally, the organic TFT is in a bottom gate structure, the dominant region for carrier transport is closed to the dielectric. Consequently, the additional donor-like or acceptor-like traps generated by the exposure of the OTFT to the environment are neglected.

3. Results and discussion

The transfer and output current–voltage (I–V) characteristics of the OTFT were measured by an HP 4145A

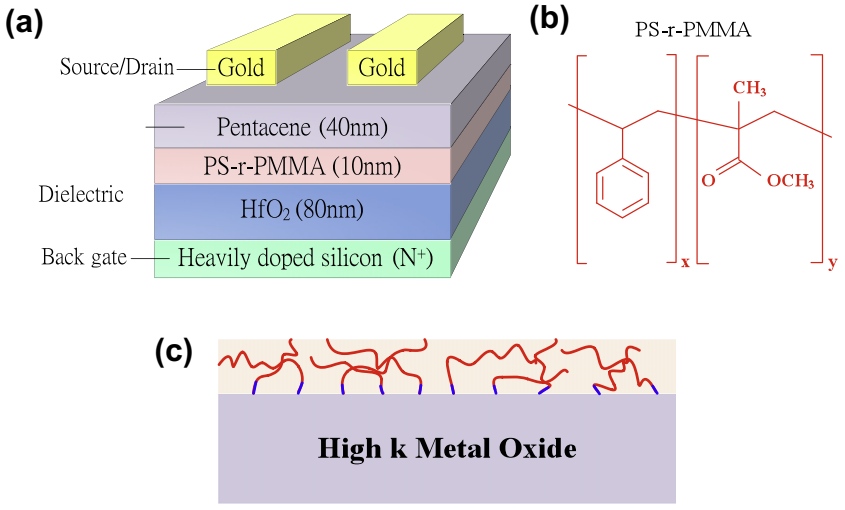

Fig. 1. (a) A schematic of the low voltage pentacene OTFT with PS-r-PMMA/HfO_x bi-layer dielectric. (b) Chemical structure of PS-r-PMMA and (c) the schematic arrangement of PS-r-PMMA on top of high k metal oxide.

semiconductor analyzer. All electrical characterizations were measured in ambient air immediately after the OTFT were made. Fig. 2(a) and (b) shows the transfer curves of pentacene-based OTFTs in which the HfO_x and PS-r-PMMA/HfO_x were each used as gate dielectrics. Details of electrical properties of a pentacene-based OTFT with PS-r-PMMA/HfO_x dielectrics and single HfO_x are listed in Table 1. The threshold voltage, subthreshold swing, and on/off current ratio (I_{on}/I_{off}) were each −1 V, 1.01 V/dec. and 10^3 for OTFT with HfO_x gate dielectrics. The equation of the drain current at the saturation regime for the Si-based MOSFET was usually used to describe the current behavior of an organic thin film transistor. The equation is expressed as follows:

$$I_d = \frac{WC_i\mu}{2L}(V_g - V_t)^2 \quad (1)$$

in which I_d is the drain current, W is the gate width, L is the gate length, C_i is the capacitance density, μ is the channel mobility, V_g is the gate voltage, and V_t is the threshold voltage. The mobility extracted from the saturation regime was 0.22 cm^2/V s. By grafting PS-r-PMMA onto the HfO_x, the off current was decreased to approximately two orders of magnitude from 10^{-9} to 10^{-11} A. Consequently, the I_{on}/I_{off} ratio was much improved to approximately 10^5 due to the leakage current reduction. In addition, the subthreshold behavior was also improved from 1.01 to 0.41 V/dec. The subthreshold swing (SS) indicates the ability of a TFT to switch from the off state to the on state. The improved SS may be due to the screening effect of PS-r-PMMA on the polarity of the HfO_x surface. The polar dielectric interface may broaden the distribution of density of states (DOS) [2]. The nonpolar PS-r-PMMA screens the dipoles of the HfO_x surface, usually leading to semiconductor/insulator interface improvement and concentrating the DOS distribution. The channel carriers can be accumulated at a small applied voltage. The improved interface may suggest higher mobility because of less interface scattering. However, the saturation mobility was not improved extensively in this work. For the TFT manufactured with different gate dielectrics, V_t might be different. Fig. 2(c) shows the output characteristics of OTFTs with the same

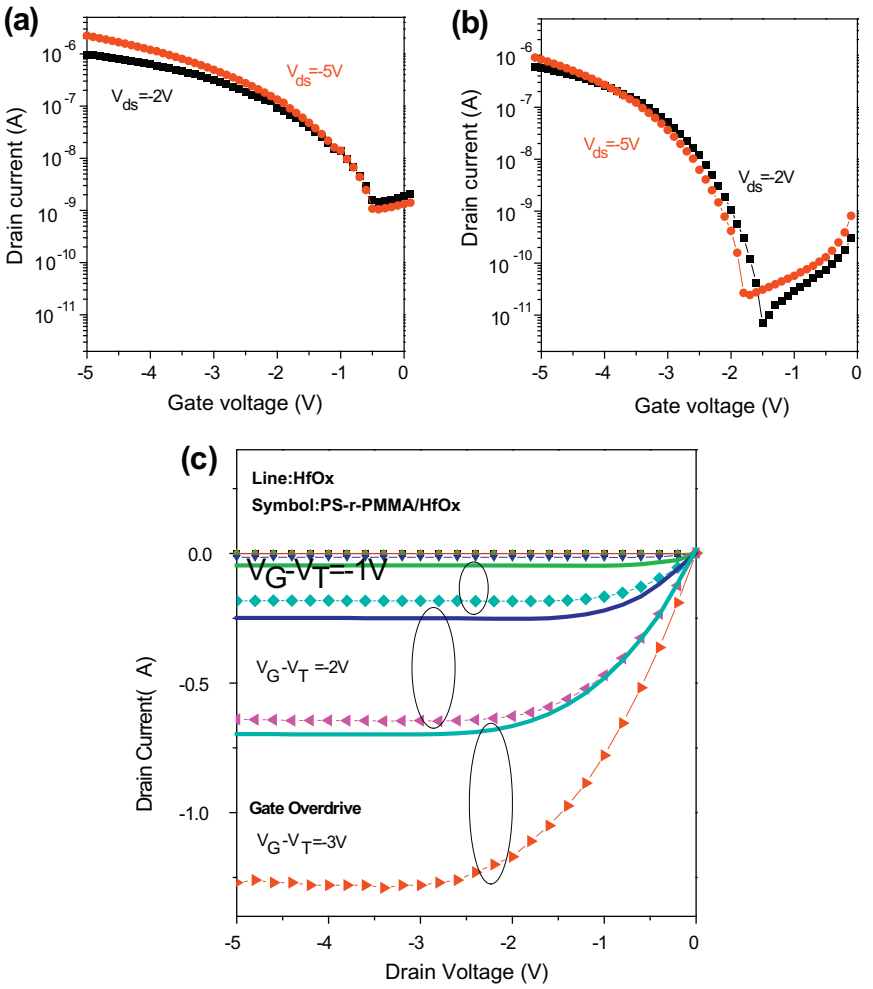

Fig. 2. Transfer curves of OTFT with (a) HfO_x and (b) PS-r-PMMA/HfO_x gate dielectrics and (c) output characteristics of OTFTs with the same gate overdrive. The gate overdrive means gate to source (V_{gs}) voltage in excess of the threshold voltage (V_t). It is the effective gate voltage applied in the TFT after threshold.

Table 1
Summary of OTFT's performance in this work and related references.

Dielectric (approach)	Rms (nm)	C_i (nF/cm^2)	V_t (V)	Mobility (cm^2/V s)	I_{on}/I_{off}	SS (V/dec.)	Ref.
OTS/SiO_2 (thermal oxide)[a]	N/A	~10	~0	1.5	10^8	1.6	[13]
PMMA/Ta_2O_5 (Solution/e-beam evaporation)[b]	N/A	74	−3.5	0.12	4.3×10^4	1.04	[14]
HfO_2 (solution)	1.3	52	−7.46	3.8	10^2	2.6	[15]
PS-r-PMMA (solution)	0.2	150	−2.5	0.12	5×10^3	0.27	[10]
HfO_x(sputtering)	~3	166	−1	0.22	10^3	1.01	This work
PS-r-PMMA/HfO_x(solution/sputtering)	~2	113	−3	0.28	10^5	0.41	This work

[a] OTS, octadecyltrichlorosilane.
[b] PMMA, polymer polymethylmethacrylate.

gate overdrive, V_g–V_t, to emphasize the gate controllability of the drain current for TFTs after threshold voltage. With higher mobility, higher I_{on}/I_{off}, and smaller SS, the output current for an OTFT with a PS-r-PMMA/HfO_x gate dielectric was largely increased. Furthermore, the OTFT (W/L = 500 μm/100 μm) with low PS-r-PMMA formation temperature, 130 °C, is also carried out to make sure the compatibility with the general plastic substrate. Fig. 3 shows the output curve and transfer curve based on PS-r-PMMA/HfO_x at process temperature of 130 °C for 24 h. The current–voltage characteristics are similar to the OTFT with high temperature fabricated PS-r-PMMA as gate dielectric. The OTFT has the performance with the threshold voltage of −1.5 V, the mobility of 0.19 cm^2/V s, subthreshold swing of 0.24 V/dec., and I_{on}/I_{off} of 10^5, respectively.

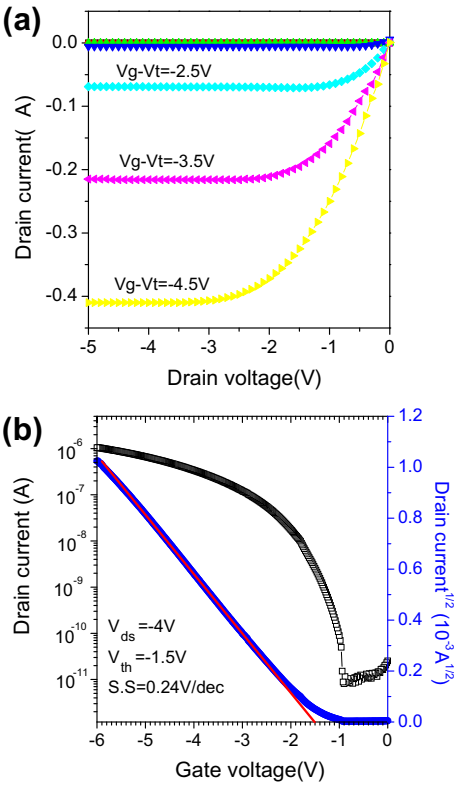

Fig. 3. Characteristics of OTFT with PS-r-PMMA/HfO_x, PS-r-PMMA layer was fabricated at 130 °C. (a) Output characteristics, (b) transfer characteristics.

To investigate the interface property, the capacitance–voltage (C–V) characteristic on an n$^+$-silicon/dielectrics/pentacene (MIS) structure was measured by an Agilent E4980A impedance analyzer at 1 MHz. The normalized capacitance for HfO_x and PS-r-PMMA/HfO_x dielectrics are shown in Fig. 4.

The transition from accumulation to depletion ranged from −2 to 1 V for the capacitor with a PS-r-PMMA/HfO_x dielectric. By contrast, the transition from accumulation to depletion for the HfO_x dielectric is much slower, ranging from −2 V to more than 5 V. The tardy transition is attributed to both the donor-like and acceptor-like states at pentacene/HfO_x interfaces that are occupied by holes in the accumulation region and electrons in the depletion region. During the voltage transition from negative to positive (accumulation to depletion), the trapped holes in the donor-like states escape gradually and contribute to the delay. Regarding the depletion behavior, electrons first fill the acceptor-like states provided by the hydroxyl groups and lead to slower transition of capacitance. Therefore, the rapid transition of an OTFT with PS-r-PMMA/HfOx dielectrics is regarded as a less interface state.The maximum interface state density, N_s, is approximated by the following equation [12]:

$$N_s = \left[\frac{SS}{\ln 10}\cdot\frac{q}{kT} - 1\right]\frac{C_i}{q} \quad (2)$$

in which the k is the Boltzmann constant, T is the absolute temperature, and C_i is the unit area capacitance. Based on this equation, the N_s for the HfO_x gate dielectric is

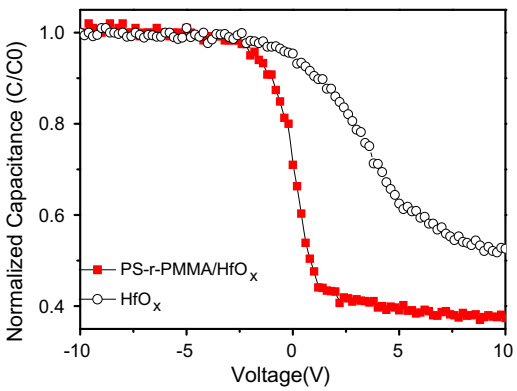

Fig. 4. Capacitance–voltage characteristics of metal/dielectrics/pentacene capacitors at 1 MHz.

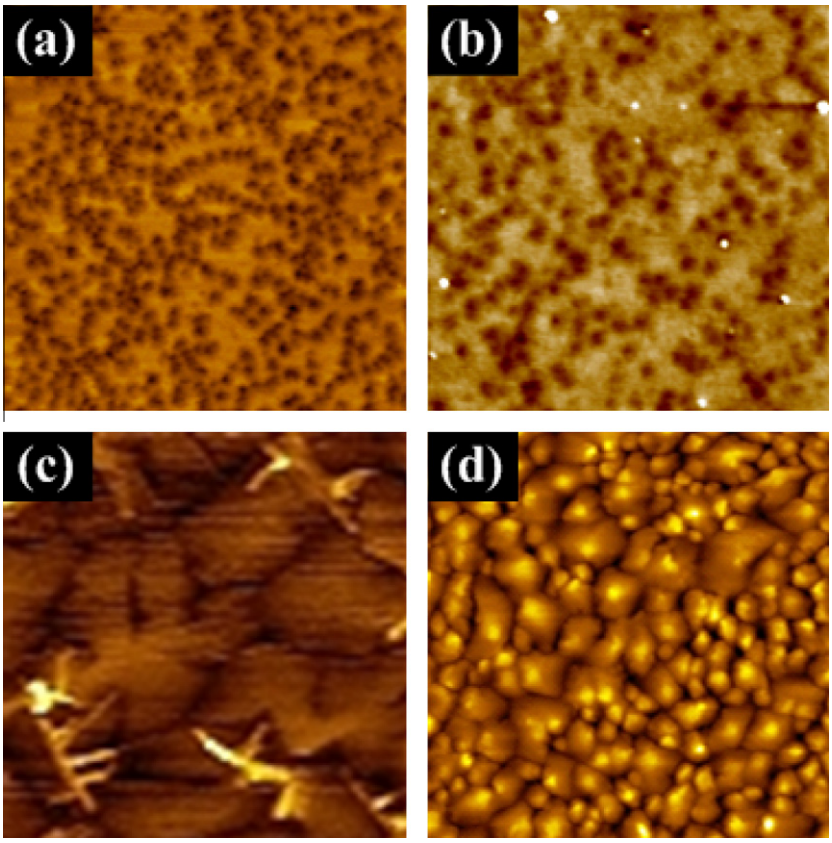

Fig. 5. AFM images of dielectrics (a) HfO_x ($2 \times 2\ \mu m^2$) (b) PS-r-PMMA/HfO_x ($2 \times 2\ \mu m^2$) and 40-nm-thick pentacene evaporated on (c) HfO_x dielectric ($3 \times 3\ \mu m^2$) (d) PS-r-PMMA/HfO_x bilayer dielectrics ($3 \times 3\ \mu m^2$).

approximately $1.65 \times 10^{13}\ cm^{-2}$. By applying a layer of PS-r-PMMA, the interface state density decreases to approximately $4.15 \times 10^{12}\ cm^{-2}$, nearly a one order magnitude of reduction.

By further investigating the leakage current reduction in the PS-r-PMMA/HfO_x dielectrics structure, the morphology of HfO_x and PS-r-PMMA/HfO_x were studied by atomic force microscopy (AFM), as shown in Fig. 5(a) and (b), respectively. For the HfO_x surface, a high density of observed pinhole-like cavities ($1.27 \times 10^6/cm^2$) caused an unsmooth dielectric surface with ~3 nm root mean square (RMS) roughness. After grafting the PS-r-PMMA layer, some pinhole-like cavities on the HfO_x surface were shielded and the density was reduced to $4.5 \times 10^5/cm^2$. The RMS roughness was decreased to ~2 nm. The application of the PS-r-PMMA layer could make the HfO_x surface smoother and partially filled the pinhole-like cavities. Therefore, the leakage current was suppressed as observed in the electrical analysis. For the organic semiconductor morphology observation, the AFM images of pentacene evaporated on the HfO_x and PS-r-PMMA/HfO_x dielectrics, as shown in Fig. 5(c) and (d), respectively. The grain size of approximately 300 nm of pentacene grown on the PS-r-PMMA is observed in Fig. 5(d). Conversely, the pentacene growth on the HfO_x results in a larger grain (~1 μm) with a dendrite structure. The grain size of pentacene on the PS-r-PMMA/HfO_x is much smaller than on the HfO_x. Due to the saturation mobility is similar for these two OTFTs. The grain size of pentacene on different dielectrics seems not strongly related to the saturation mobility in this work.

4. Conclusions

To summarize, we have demonstrated a low voltage OTFT based on PS-r-PMMA/HfO_x dielectrics. By stacking PS-r-PMMA on an HfO_x dielectric, the semiconductor/insulator interface was significantly improved. The leakage current and subthreshold swing were decreased. The OTFT with such low-*k*/high-*k* stack dielectrics can operate well below 5 V, with a sufficient on/off current ratio of 10^5, a subthreshold swing of 0.41 V/dec., and a mobility of $0.28\ cm^2/V\ s$.

Acknowledgements

The work was supported by National Science Council of Republic of China under Grant NSC-99-2628-E-005-004.

References

[1] H. Klauk, U. Zschieschang, J. Pflaum, M. Halik, Ultralow-power organic complementary circuits, Nature 445 (2007) 745.
[2] J. Veres, Simon D. Ogier, S.W. Leeming, D.C. Cupertino, S.M. Khaffaf, Low-k insulators as the choice of dielectrics in organic field-effect transistors, Adv. Funct. Mater. 13 (2003) 199.

[3] C. Bartic, H. Jansen, A. Campitelli, S. Borghs, Ta_2O_5 as gate dielectric material for low-voltage organic thin-film transistors, Org. Electron. 3 (2002) 65.
[4] F.-C. Chen, C.-W. Chu, J. He, Y. Yang, J.-L. Lin, Organic thin-film transistors with nanocomposite dielectric gate insulator, Appl. Phys. Lett. 85 (2004) 3295.
[5] O. Acton, G. Ting, H. Ma, J.W. Ka, H.-L. Yip, N.M. Tucker, A.K.-Y. Jen, π-σ-Phosphonic acid organic monolayer/sol–gel hafnium oxide hybrid dielectrics for low-voltage organic transistors, Adv. Mater. 20 (2008) 3697.
[6] Y. Lu, W.H. Lee, H.S. Lee, Y. Jang, K. Cho, Low-voltage organic transistors with titanium oxide/polystyrene bilayer dielectrics, Appl. Phys. Lett. 94 (2009) 113303.
[7] L. Manchanda, M. Gurvitch, Yttrium oxide/silicon dioxide: a new dielectric structure for VLSI/ULSI circuits, IEEE Electron Device Lett. 9 (1988) 180.
[8] S.H. Kim, S. Nam, J. Jang, K. Hong, C. Yang, D.S. Chung, C.E. Park, W.-S. Choi, Effect of the hydrophobicity and thickness of polymer gate dielectrics on the hysteresis behavior of pentacene-based field-effect transistors, J. Appl. Phys. 105 (2009) 104509.
[9] G. Gu, M.G. Kane, Moisture induced electron traps and hysteresis in pentacene-based organic thin-film transistors, Appl. Phys. Lett. 92 (2008) 053305.
[10] T.H. Huang, H.C. Huang, Z. Pei, Temperature-dependent ultra-thin polymer layer for low voltage organic thin-film transistors, Org. Electron. 11 (2010) 618.
[11] P. Mansky, Y. Liu, E. Huang, T.P. Russell, C. Hawker, Controlling polymer-surface interactions with random copolymer brushes, Science 275 (1997) 1458.
[12] C.A. Dimitriadis, P.A. Coxon, L. Dozsa, L. Papadimitriou, N. Economou, Performance of thin-film transistors on polysilicon films grown by low-pressure chemical vapor deposition at various pressures, IEEE Trans. Electron Devices 39 (1992) 598.
[13] Y.-Y. Lin, D.J. Gundlach, S.F. Nelson, T.N. Jackson, Stacked pentacene layer organic thin-film transistors with improved characteristics, IEEE Electron Device Lett. 18 (1997) 606.
[14] A.-L. Deman, J. Tardy, PMMA–Ta_2O_5 bilayer gate dielectric for low operating voltage organic FETs, Org. Electron. 6 (2005) 78.
[15] C.-Y. Wei, F. Adriyanto, Y.-J. Lin, Y.-C. Li, T.-J. Huang, D.-W. Chou, Y.-H. Wang, Pentacene-based thin-film transistors with a solution-process hafnium oxide insulator, IEEE Electron Device Lett. 30 (2009) 1039.
[16] W.-J. Yoon, P.R. Berger, Atomic layer deposited HfO2 gate dielectrics for low-voltage operating, high-performance poly-(3-hexythiophene) organic thin-film transistors, Org. Electron. 11 (2010) 1719.
[17] I.A. Zucchi, E. Poliani, M. Perego, Microdomain orientation dependence on thickness in thin films of cylinder-forming PS-b-PMMA, Nanotechnology 21 (2010) 185304.
[18] S. Ji, C.C. Liu, G. Liu, P.F. Nealey, Molecular transfer printing using block copolymers, ACS Nano 4 (2010) 599.

selected materials for devices. For our VS-CTFT inverter for logic and photo-gating, we used a thermally-evaporated p-channel pentacene layer, sputter-deposited n-channel GaZnSn-based oxide (GZTO), and atomic layer deposited (ALD) Al_2O_3 dielectric. As a more advanced hybrid approach, we also adopted a ferroelectric poly(vinylidene fluoride/trifluoroethylene) [P(VDF–TrFE)] layer for a CTFT nonvolatile memory inverter with a pentacene memory TFT which is vertically stacked on a top-gate GZTO TFT but sharing the Al gate electrode with the n-channel TFT. Our VS-CTFT inverter nicely displays effective photo- and electrical-gating with a high voltage gain, dynamically operating in the low-voltage regime of 3, 5, and 8 V (the thin pentacene channel receives blue photons), and the ferroelectric memory inverter as an ultimate hybrid device form demonstrates promising retention properties that are triggered by ±20 V gate pulses.

2. Experimental

2.1. Vertically stacked CTFT inverter Fabrication

Vertically stacked complementary TFT (VS-CTFT) inverters were fabricated on glass substrates (Corning, Eagle 2000). Substrate was cleaned with acetone, methanol, and de-ionized water, in that order. Aluminum (Al) source/drain (S/D) electrodes were deposited by thermal evaporation. Then a 60 nm thick GaZnSnO (GZTO) channel layer was formed by co-sputtering of a Ga-doped ZnO (Ga_2O_3 5.7 wt%) and a SnO_2 target with rf power of 110 and 40 W, respectively. The sputtering was performed in a working pressure of 5 mtorr with flowing Ar and O_2 mixed (5%) gas and the deposition temperature was maintained at 100 °C (The fraction of Sn in cationic elements of the prepared GZTO film was about 32 at.%). The GZTO layer was patterned through a shadow mask for patterning ($500 \times 500\ \mu m^2$). The nominal channel length (L) was 90 μm and the width (W) was 500 μm. As a dielectric, 40 nm-thick Al_2O_3 layers were deposited by atomic layer deposition (ALD; ForAll Co., Ozone100A) at a temperature of 200 °C. Then Al top gate electrodes were then deposited by thermal evaporation. (Fig. S1a and S1b shows the dielectric properties of our ALD Al_2O_3 layer.) By now, a half of VS-CTFT inverter process was completed. As the next half, bottom-gate p-channel TFT process was proceeded. As a gate dielectric, another 40 nm-thick Al_2O_3 layer was deposited on Al gate of GZTO-TFT by ALD with the same condition taken for the first half process. The dielectric layers were patterned by photolithography and wet etching (by 50× diluted 20:1 buffered HF) to open the S/D electrodes of GZTO-TFT. Pentacene (Aldrich Chem. Co., 99% purity, no other distillation) active channel layer was then patterned on the Al_2O_3 dielectric through a shadow mask at room temperature (RT) by thermal evaporation. Deposition rate was fixed to 1 Å/s using an effusion cell (ALPHA-PLUS Co., LTE-500S) in a vacuum chamber (base pressure of $\sim 1 \times 10^{-7}$ torr). The thickness of pentacene films was 50 nm as monitored by a quartz crystal oscillator and confirmed by ellipsometry. Au pads were finally deposited as S/D electrodes by thermal evaporation in a vacuum chamber; Au source contacted Al drain of n-TFT.

2.2. Vertically stacked CTFT memory inverter Fabrication

The first half process was the same as that of the top-gate GZTO-TFT with Al_2O_3. But then, for the next half process to realize a VS-CTFT memory inverter, 200 nm-thick films of P(VDF/TrFE) 75/25 mol% copolymer were coated on the GZTO-TFT by spin casting 6 wt% cyclohexanone solutions. The P(VDF/TrFE) polymer films were cured at 160 °C for 2 h in a vacuum oven and then subsequently quenched to the RT by blowing N_2 gas (99.9% purity). In order to open the S/D Al of GZTO-TFT, we utilized lithography and O_2 plasma to sequentially etch away P(VDF–TrFE) polymer ferroelectric and Al_2O_3 dielectric. Pentacene and Au S/D evaporation were then followed as in the same way stated above in VS-CTFT inverter process.

2.3. Characterization

After confirming the electrical isolation between top and bottom TFT devices, the electrical properties of n- and p-channel TFTs were separately measured. The dielectric strength of our 40 nm thick Al_2O_3 gate dielectric and all electrical characteristics of our vertically stacked CTFT inverters, CTFT memory inverters, unit GZTO TFT and unit pentacene TFT were measured with a semiconductor parameter analyzer (HP4155C, Agilent Technologies). The capacitance–voltage (C–V) measurements at 1 MHz were performed for our dielectric with an LCR meter (HP 4284, Agilent Technologies). Dynamic gating in VS-CTFT inverter was measured using pulse generator (AFG3022B, Tektronix) and oscilloscope (TDS2014, Tektronix). Additional gating effects such as photo-gating were obtained or measured by using red (λ = 650 nm), green (540 nm), and blue (440 nm) LEDs with an optical power of ~2 mW (irradiance ~0.2 mW/cm^2). Glancing incidence XRD analysis in the 2θ mode was carried out to characterize the crystallinity of the GZTO films: the as-grown and the annealed at 200 °C for 1 h (which corresponds to the heating condition during the subsequent ALD process).

3. Results and discussion

3.1. Device schemes

Fig. 1a and b displays the schematic cross section and photographic plan views of our VS-CTFT inverter that has pentacene- and amorphous GZTO-TFTs sharing the ALD Al_2O_3 layers for bottom- and top-dielectrics, respectively, while Fig. 1c shows the photo-gating experiment using a blue light as a probe. Our GZTO film was deposited by sputtering at 100 °C and exhibited an almost amorphous phase with few crystalline peaks according to X-ray diffraction spectra as shown in Fig. S2a. Our GZTO-TFT, which went through a 200 °C ALD process for the dielectric, displayed good device performances as shown in its output and transfer curves of Fig. S2b and S2c, respectively. The ALD temperature might cause a little bit of crystallization of amorphous GZTO (Fig. S1a), but according to the transfer curves of Fig. S1c the interface between GZTO channel and Al_2O_3 dielectric is still very stable causing only minimal electrical hysteresis. The saturation mobility (μ_{sat})

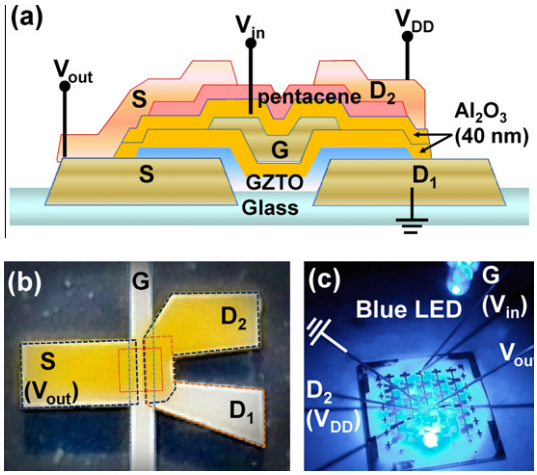

Fig. 1. (a) The schematic cross section and (b) photographic plan views of our VS-CTFT inverter that contains pentacene- and amorphous GZTO-channel TFTs using the same ALD Al_2O_3 layers for bottom- and top-dielectrics, respectively. (c) Photographic view of photo-gating experiment employing a blue light as a probe (440 nm). (For interpretation of the references to color in this figure legend, the reader is referred to the web version of this article.)

was $\sim$1.2 $cm^2\,V^{-1}\,s^{-1}$ for the top-gate TFT. (The mobility was 8.2 $cm^2\,V^{-1}\,s^{-1}$ for bottom-gate TFTs. This electron mobility difference between top- and bottom-gate configurations are addressed elsewhere, being considered to come from different channel geometries [15].)

3.2. Electrical gating of our VS-CTFT

According to the drain current–gate voltage (I_D–V_G) transfer curves of Fig. 2a, the curves from our bottom-gate pentacene- and top-gate GZTO-TFTs are quite symmetrical at their common threshold voltage (V_T) point of −0.4 V and show the maximum I_Ds of $\sim$1.5 and $\sim$4 μA at a drain voltage (V_D) of 5 V, respectively (pentacene-TFT has its saturation mobility of 0.4 $cm^2\,V^{-1}\,s^{-1}$). Pentacene-TFT showed some gate-hysteresis due to the electrons trapped by the OH groups on polar Al_2O_3 surface as the hysteresis direction indicates [16]. As a result of the symmetrical transfer curves, the voltage transfer characteristics (VTC) of our VS-CTFT inverter were nicely obtained with relatively high voltage gains of 20, 25, and 52 under respective supply voltages (V_{DD}) of 3, 5, and 8 V, as shown in Fig. 2b. (Inset shows a circuit diagram of the VS-CTFT inverter). Our CTFT inverter also dynamically operates, displaying a response time of 5–40 ms under 5 V input pulses; 5 ms rising and 40 ms falling times were recorded due to the different RC delays during p-channel and n-channel charging. (Fig. 2c and d) We actually fabricated another identical VS-CTFT inverter but with n-channel ZnO instead of amorphous GZTO, to confirm that our VS-CTFT inverter structure stably operates along with a high fabrication yield. (See Fig. S3a and S3b.) Our VS-CTFT inverter yield was over 50% either with ZnO- or with GZTO-channel, and the yield is far above that from planar CTFT inverters (less than 30%, in our experience, Ref. [8]).

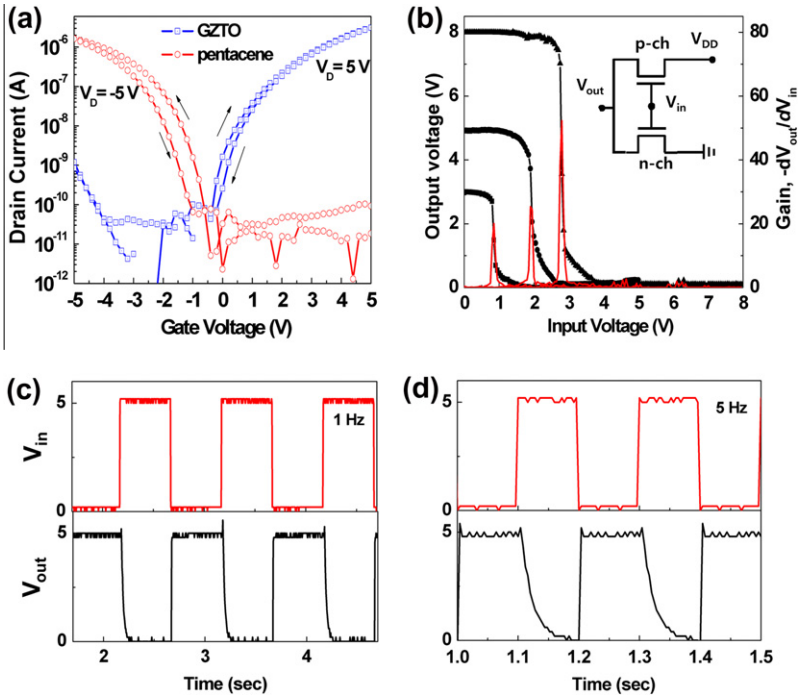

Fig. 2. (a) The drain current–gate voltage (I_D–V_G) transfer curves and b) the voltage transfer characteristics (VTC) of our VS-CTFT inverters under respective supply voltages (V_{DD}) of 3, 5, and 8 V. The curves from pentacene- and GZTO-TFTs are quite symmetrical. Inset of (b) shows a circuit diagram of the VS-CTFT inverter. Dynamic operating of our device under 5 V input pulses (c) at 1 Hz and (d) 5 Hz, respectively.

3.3. Photo-gating of VS-CTFT

Photo-gating was also implemented with our inverter since our device only exposes the pentacene-TFT on top so that the p-channel TFT may conveniently receive visible photons to collect photo-excited electrons and holes in a charge depletion state. According to the light-illuminated VTC curves of our device in Fig. 3a, the device only reacted with blue light when red, green, and blue lights were illuminated on our VS-CTFT inverter, although the highest occupied molecular orbital-lowest unoccupied molecular orbital (HOMO–LUMO) gap of solid crystalline pentacene is near 1.9 eV (which matches with red, but actual energy gap is 1.97 eV considering exciton binding energy) [17]. This photo-stability is possible with our pentacene channel layer as thin as only 50 nm. Similar results of pentacene TFT showing a weak photo-detection only on blue illumination were reported previously [8]. The dynamic photo-gating was successfully obtained near the transition voltage region (2 V) with monochromatic blue light. (For this operation our light-emitting-diode (LED) with 440 nm wavelength was pulsed at 5 V, to be periodically turned on). According to the time domain plot of Fig. 3b, the output voltage (V_{out}) in the light was clear enough to be used as an optical gating signal at the fixed input voltages (V_{in}) of 2.25 and 2.5 V but no signal was detected at exactly 2 V. In particular, the gating signal (photo-induced gain) at 2.5 V was only 0.8 V but is still regarded meaningful in that a minimum power consumption can be achievable at the V_{in} of 2.5 V, even though the photo-gain (0.8 V) was lower than that (V_{out} = 1.5 V) at 2.25 V where power consumption of the device should be quite large. The response time was around 80 ms.

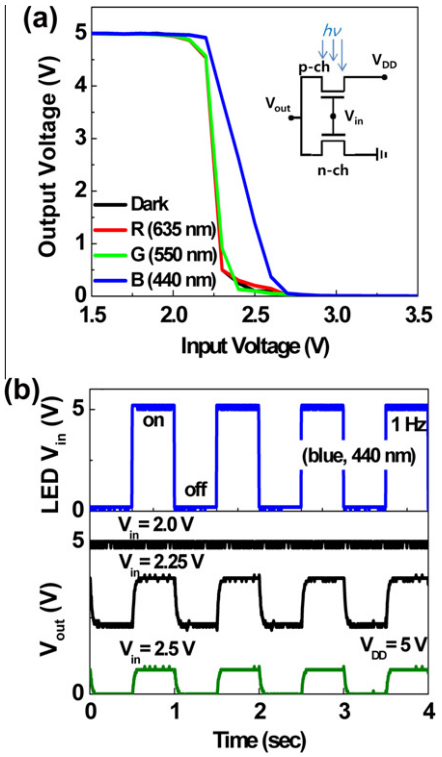

Fig. 3. (a) The light-illuminated VTC curves of our VS-CTFTs. Red (635 nm), green (550 nm), and blue (440 nm) lights were illuminated on our devices, which only reacted with blue light. (b) The dynamic photo-gating obtained near the transition voltage region (2 V) with monochromatic blue light. For this operation light-emitting-diode (LED) with 440 nm wavelength was pulsed by 5 V (LED input voltage), to be periodically turned on. The photo-induced V_{out} as an optical gating signal was obtained at the fixed V_{in} of 2, 2.25 and 2.5 V, respectively. No V_{out} signal was shown at 2 V V_{in}. (For interpretation of the references to color in this figure legend, the reader is referred to the web version of this article.)

3.4. Nonvolatile memory operation of ferroelectric VS-CTFT

For another hybrid device application, we deposited a ferroelectric polymer, P(VDF–TrFE) on the top-gate GZTO-TFT with ALD Al_2O_3 dielectric, so that our VS-CTFT inverter

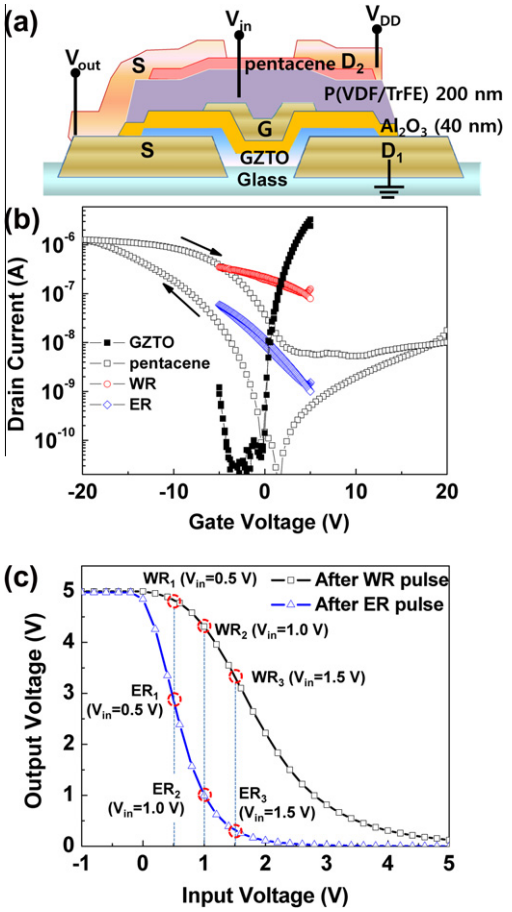

Fig. 4. (a) The schematic cross section of our CTFT memory inverter. (b) The transfer curves of top-gate GZTO-TFT and bottom-gate pentacene-TFT with ferroelectric polymer, where a large memory hysteresis is observed. As our pentacene memory TFT was pulsed with ±20 V for 1 s, write (WR, −20 V) and erase (ER, +20 V) states were clearly distinguished as red and blue I_D curves, respectively, in ±5 V V_G sweep range. (c) Inverter memory hysteresis in VTC was obtained at a V_{DD} of 5 V where we can achieve two separated V_{out} signals as WR and ER states at a fixed V_{in}. Three cases of V_{in} (0.5, 1, and 1.5 V) were marked by red circles. (For interpretation of the references to color in this figure legend, the reader is referred to the web version of this article.)

functions as a nonvolatile memory device based on the p-channel pentacene TFT with the ferroelectric polymer. Fig. 4a shows a schematic cross section of our CTFT memory inverter, which has a common gate for program pulse. Fig. 4b displays the transfer curves of our top-gate GZTO-TFT and bottom-gate pentacene-TFT with ferroelectric polymer, where a large memory hysteresis is observed. As our pentacene memory TFT was pulsed with ±20 V for 1 s (estimated coercive voltage = ~11 V for 200 nm-thick P(VDF–TrFE) according to Fig. S4a and S4b), write (WR, −20 V) and erase (ER, +20 V) states were clearly distinguished as red and blue I_D curves, respectively, in the ± 5 V V_G sweep range. Following the ±20 V pulse, inverter memory hysteresis in VTC was obtained at a V_{DD} of 5 V as shown in Fig. 4c, where we can achieve two separated V_{out} signals as WR and ER states at a fixed V_{in}. An optimum V_{in} may be selected as ~1 V, since the most clearly separated V_{out} states for WR and ER are obtained at this voltage.

Fig. 5a shows the 500 s retention properties of our nonvolatile memory inverter as measured at different V_{in} voltages of 0.5, 1, and 1.5 V after ±20 V 1 s pulse. The WR state more rapidly degrades than the ER state in general. WR and ER states were optimally maintained at a fixed V_{in} of 1 V while over time those two states became less distinguishable from each other at low V_{in} of 0.5 V or at high V_{in} of 1.5 V than at 1 V. In particular, the high V_{in} condition (1.5 V) led to the most rapid degradation of the WR state. It is because the WR state (hole accumulation in the p-TFT) obtained by −20 V pulse may not be easily retained under a (+) gate bias that would somewhat depolarize the pulse-aligned dipoles in our ferroelectric polymer. Expecting less depolarization effects, we determined 1 V as an optimum V_{in} for our memory inverter application. Therefore, 1 V was then confirmed as an optimum value according to the combined results of VTC memory hysteresis (Fig. 4c) and retention (Fig. 5a). Closer observation on the retention properties of our memory inverter was possible with the cyclic endurance test of Fig. 5b. The V_{out} as the WR signal rapidly decreases by 0.4 V for the initial 10 s after pulse although it is quite stabilized in the end, while V_{out} for the ER signal is well maintained without much increase. For the cyclic endurance test (Fig. 5b and c), sequential voltages per endurance cycle were applied on our ferroelectric memory inverter as programmed to be −20 V 1 s (WR pulse)/1 V 10 s (Reading)/+20 V 1 s (ER pulse)/1 V 10 s (Reading); V_{out} was read during the 10 s between WR and ER pulses at the optimum reading condition of 1 V-V_{in} and 5 V-V_{DD}. According to Fig. 5b and c, a very distinguished V_{out} was read as the WR and ER states, and it consistently maintained its respective values of ~4 and ~0.5 V during many cycles. We thus regard our VS-CTFT memory inverter as a unique hybrid device, to be quite useful for advanced memory applications on glass substrates.

4. Conclusion

In summary, we have fabricated organic/inorganic hybrid VS-CTFT inverters consisting of a bottom-gate

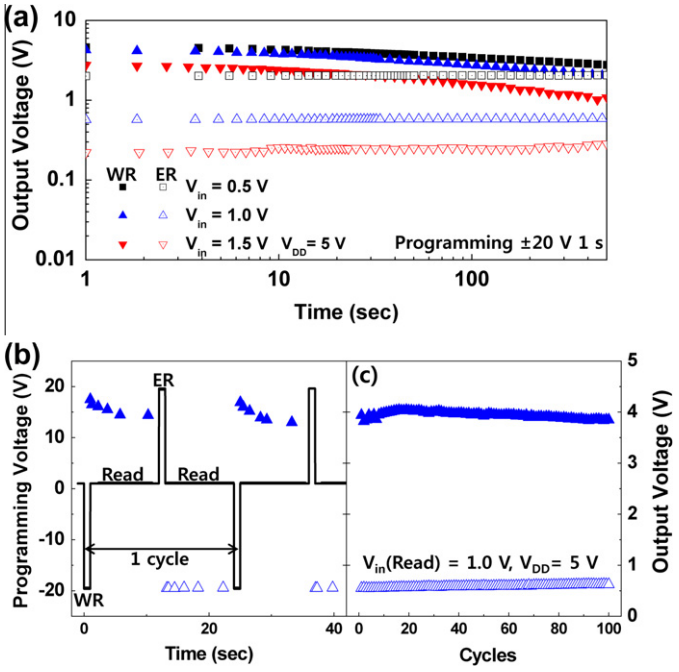

Fig. 5. (a) The 500 s retention properties of our nonvolatile memory (NVM) inverter as measured at different V_{in} voltages of 0.5, 1, and 1.5 V after ±20 V 1 s pulse. (b) Sequential programming voltages for one endurance cycle were programmed on our NVM inverters as composed of −20 V 1 s (WR)/1 V 10 s (READ)/+20 V 1 s (ER)/1 V 10 s (READ); V_{out} was read between WR and ER pulses at the optimum reading conditions of 1 V-V_{in} and 5 V-V_{DD}. (c) Results of the cyclic endurance test (100 cycles). WR and ER states were consistently maintained to be 4 and 0.5 V.

pentacene TFT and a top-gate amorphous GZTO TFT which are vertically connected with common gate. Our VS-CTFT device with Al_2O_3 dielectric well demonstrated electrical logic inverter functions and photo-gating under a blue LED, showing a maximum voltage gain of ~50, a good photo-gain of 0.8 V under 5 V-V_{DD}, and even good device yield. Our VS-CTFT device also displayed nonvolatile memory functions when we adopted P(VDF–TrFE) ferroelectric polymer for the p-channel pentacene; a more advanced organic/inorganic hybrid device form of organic ferroelectric memory TFT/oxide TFT hybrid was therefore demonstrated. We conclude that our VS-CTFT approach is quite promising in both aspects of advanced device applications and device yield.

Acknowledgments

The authors acknowledge the financial support from NRF (NRL program, No. 2011-0000375), BK21 Project, the 21st Century Frontier R&D Program funded by the MKE (Information Display R&D center, F0004022-2009). C.H. Park thanks for the Seoul Science Fellowship and Seoam Fellowship.

Appendix A. Supplementary data

Supplementary data associated with this article can be found, in the online version, at doi:10.1016/j.orgel.2011.06.001.

Reference

[1] K. Nomura, H. Ohta, A. Takagi, T. Kamiya, M. Hirano, H. Hosono, Nature 432 (2004) 488.
[2] E.M.C. Fortunato, P.M.C. Barquinha, A.C.M.B.G. Pimentel, A.M.F. Goncalves, A.J.S. Marques, L.M.N. Pereira, R.F.P. Martins, Adv. Mater. 17 (2005) 590.
[3] K. Song, J. Noh, T. Jun, Y. Jung, H.Y. Kang, J. Moon, Adv. Mater. 22 (2010) 4308.
[4] P. Görrn, M. Sander, J. Meyer, M. Kröger, E. Becker, H.H. Johannes, W. Kowalsky, T. Riedl, Adv. Mater. 18 (2006) 738.
[5] S.H.K. Park, C.S. Hwang, M. Ryu, S. Yang, C. Byun, J. Shin, J.I. Lee, K. Lee, M.S. Oh, Seongil Im, Adv. Mater. 21 (2008) 678.
[6] S.M. Yoon, S. Yang, C. Byun, S.H.K. Park, D.H. Cho, S.W. Jung, O.S. Kwon, C.S. Hwang, Adv. Funct. Mater. 20 (2010) 921.
[7] K.H. Lee, G. Lee, K. Lee, M.S. Oh, S. Im, S.M. Yoon, Adv. Mater. 21 (2009) 4287.
[8] K.H. Lee, H.S. Lee, K. Lee, T. Ha, J.H. Kim, S. Im, Adv. Mater. 23 (2011) 1231.
[9] B.N. Pal, J. Sun, B.J. Jung, E. Choi, A.G. Andreou, H.E. Katz, Adv. Mater. 20 (2008) 1023.
[10] M.S. Oh, K. Lee, K.H. Lee, S.H. Cha, J.M. Choi, B.H. Lee, M.M. Sung, S. Im, Adv. Func. Mat. 19 (2009) 726.
[11] A. Dodabalapur, J. Baumbach, K. Baldwin, H.E. Katz, Appl. Phys. Lett. 68 (1996) 2246.
[12] M. Bonse, D.B. Thomasson, H. Klauk, D.J. Gundlach, T.N. Jackson, I.E.D.M. Tech. Dig. 1998 (1998) 249.
[13] K. Nomura, T. Aoki, K. Nakamura, T. Kamiya, T. Nakanishi, T. Hasegawa, M. Kimura, T. Kawase, M. Hirano, H. Hosono, Appl. Phys. Lett. 96 (2010) 263509.
[14] J.B. Kim, C.F. Hernandez, D.K. Hwang, W.J. Potscavage Jr., H. Cheun, D.K. Hwang, B. Kippelen, Org. Electron. 12 (2011) 45.
[15] M.S. Oh, K. Lee, J.H. Song, B. Lee, M.M. Sung, D.K. Hwang, S. Im, J. Electrochem. Soc. H1009 (2008) 155.
[16] L.L. Chua, J. Zaumseil, J.F. Chang, E.C.W. Ou, P.K.H. Ho, H. Sirringhaus, R.H. Friend, Nature 434 (2005) 194.
[17] J. Lee, S.S. Kim, K. Kim, J.H. Kim, S. Im, Appl. Phys. Lett. 84 (2004) 1701.

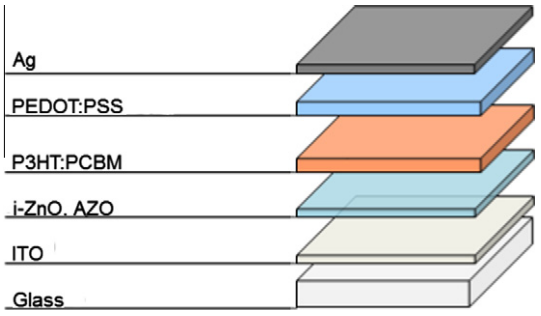

Fig. 1. Layer stack of the investigated solar cells.

using a metal oxide buffer layer between ITO and the semiconductor. One of the most intensely studied materials for this function is solution processed zinc oxide [3,8,9]. The energy levels of ZnO fit very well to the requirements for an electron injection layer. The work function is well matched to the PCBM lowest unoccupied molecular orbital (LUMO) and the valence band is deep below the highest occupied molecular orbital (HOMO) of most conjugated π-systems [10]. The wide bandgap of ZnO ensures high transmittance in the relevant spectral regime [11].

One of the few disadvantages of intrinsic ZnO (i-ZnO) is the restriction to a rather low film thickness of a few tens of nanometers due to the very low conductivity. Such a thin film imposes a major challenge for the manufacturing of polymer solar cells by high volume printing processes. On the one hand, complete coverage and a low density of pin-holes are challenging to achieve with thin film coatings. On the other hand, thin films may be less robust against mechanical stress being incurred during the subsequent printing processes. Such a robust electron injection layer is specifically important for the new generation of high performing semiconductors, which typically show the best efficiency with an active layer thickness of around or below 100 nm [12–17]. This concept is further applicable to multi-junction solar cells, where a reliable interface layer is essential to protect the lower half-cell [18].

In conclusion, we propose that thick interface layers are beneficial for enhanced device stability and increased production yield. The most straightforward way to enable thicker ZnO buffer layers is a conductivity increase via doping [11]. We are investigating aluminum (Al) as a dopant, because it is very cheap, non-toxic and resources are not limited. Vacuum processed aluminum-doped ZnO electrodes are used for various solar cell technologies like a-Si [19] or CIGS [20], and recently were also reported for organic solar cells [21].

In this work, we compare i-ZnO versus AZO, both processed from solution, as electron injection layers for organic solar cells. A dispersion of i-ZnO nanoparticles and an AZO precursor solution were prepared in organic solvents. The thin film properties of the two interface materials were characterized and the impact of their EIL thickness on the performance of the solar cells was compared. Overall, we found comparable device performance for thin i-ZnO and AZO layers. Increasing the EIL to ~100 nm results in significant performance loss in case of the i-ZnO, while cells with an AZO layer maintained their performance.

2. Materials and methods

The i-ZnO nanoparticles were prepared in methanol via hydroxylation of zinc acetate dihydrate ($ZnAc{\cdot}2H_2O$) by potassium hydroxide (KOH) adopting a method described by Harnack et al. [22] and afterwards dissolved in acetone at a concentration of 2 wt.%. The AZO solution was synthesized adopting a route described by Alam and Cameron [23] starting with a mixture of zinc acetate ($ZnAc{\cdot}2H_2O$) and aluminum hydroxide acetate ($HOAl(C_2H_3O_2)_2$) at a ratio of 1 at.%. Monoethanolamine (MEA) was added to the suspension to stabilize the Al doped ZnO complex.

The inverted photovoltaic devices were processed and characterized in ambient atmosphere. Pre-structured ITO coated glass substrates (as obtained from Osram) were subsequently cleaned in acetone and isopropyl alcohol for 10 min each. After drying, the substrates were coated with the organic precursor for AZO, respectively the i-ZnO solution, via doctor blading. Conversion of the precursor to AZO via hydrolysis was achieved by heating the samples to 260 °C for 10 min, while the i-ZnO film was dried at 150 °C for 10 min. Higher layer thicknesses were achieved via subsequent deposition steps. In case of AZO a calcination step was applied after each deposition. P3HT purchased from Merck and technical grade PCBM from Solenne were separately dissolved in chlorobenzene at a concentration of 2 wt.% and stirred for at least 1 h at 60 °C before being blended in a volume ratio of 1:1. The blended solution was stirred for at least another hour at 60 °C before use. The ca. 100 nm thick active layer was deposited via doctor blading. PEDOT:PSS (Clevios PH) from H.C. Starck was diluted in isopropyl alcohol (1:3 volume ratio) before deposition via doctor blading. The whole stack was annealed at 140 °C for 10 min on a hot plate before evaporation of a 100 nm thick Ag layer to form the top electrode. The active area of the investigated devices was 10.4 mm^2. Current density–voltage (j–V) characteristics were measured with a source measurement unit from BoTest. Illumination was provided by an Oriel Sol 1A solar simulator with AM1.5G spectra at 0.1 W/cm^2.

A UV–VIS-NIR spectrometer (Perkin Elmer – Lambda 950) was used for optical characterization of the thin films. The electrical conductivity was measured by a potentiostat (Autolab, Metrohm). Thickness of the thin films was measured by an interferometer (NanoFocus). X-ray diffraction (XRD) with CuKα radiation was done at an angle ranging from 20° to 80° by step-scanning with a step size of 0.02°.

3. Results and discussion

Table 1 compares the optical, electrical and crystalline properties of i-ZnO versus AZO. XRD spectra of AZO layers reveal a lattice stress in the 0 0 2 plane when aluminum is introduced, indicating that higher concentrations of aluminum are interstitially built into the lattice. i-ZnO particles are wurtzite type crystallites with an average crystal size of 4.2 nm while we find an average crystal size of 4.0 nm

for the converted AZO layers [24]. The optical band gap is determined by plotting $(\alpha h\nu)^2$ against $h\nu$ from UV/VIS absorption data. The optical bandgap can be found by extrapolating the linear portion of the curve to zero absorption [24]. The transmittance of the two materials is comparable. The most important difference is the increase in conductivity by about three orders of magnitude for AZO. A more detailed study of the ZnO layers will be published elsewhere [24].

Table 1
Comparison between the thin film properties of i-ZnO and AZO. The difference in the optical bandgap cannot be discussed in terms of the Moss-Burstein model due to the different synthesis, processing and conversion conditions of the i-ZnO versus the AZO film.

EIL	Crystallite size (nm)	Work function (eV)	Optical bandgap (eV)	Conductivity (S/cm)
i-ZnO	4.2	4.3	3.45	2.22×10^{-6}
AZO	4.0	4.2	3.34	2.35×10^{-3}

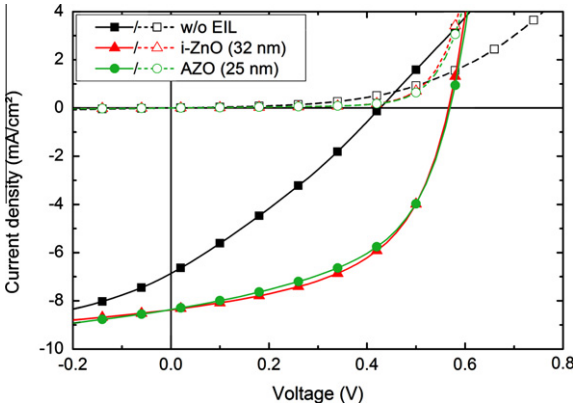

Fig. 2. j–V characteristics of solar cells without EIL, thin i-ZnO and AZO films.

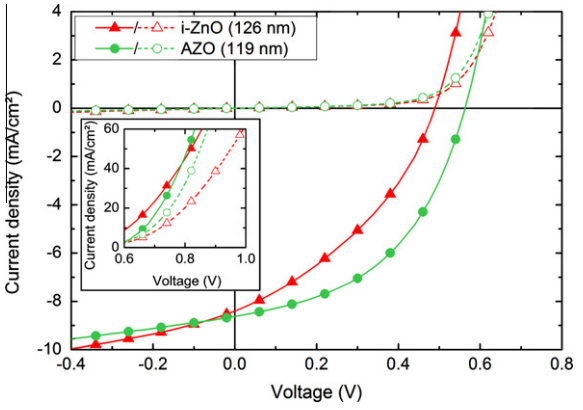

Fig. 3. j–V characteristics of solar cells with thick i-ZnO and AZO films. The inset shows the injection behavior in detail.

The layer stack of the investigated devices is shown in Fig. 1. The j–V characteristics of typical solar cells with thin i-ZnO and AZO layers (around 30 nm) are depicted in Fig. 2 and devices with thick EIL layers (above 100 nm) are shown in Fig. 3. The solar cell data for all configurations is summarized in Table 2.

A device without EIL is shown as reference in Fig. 2 as well. The j–V characteristics of the devices are dominated by a large, so-called photoshunt [25] and are further injection limited, which results in a nominal very high serial resistance of 23.6 Ω cm^2 (calculated from the slope around 1.25 V). Both loss mechanisms result from the non-selective ITO–PCBM interface. The photoshunt can be identified by the difference in slope of the illuminated versus the dark j–V curve at negative applied voltages. It originates from the several orders of magnitude higher charge carrier density of the active layer under illumination. The same mechanism is responsible for photoconductivity as well seen under forward bias as an increased injection current density. In case of the poorly charge selective ITO–PCBM interface, holes are more easily injected into the active layer at the nominal cathode. Therefore the shunt resistance scales with the conductivity of the active layer. Together with the ITO–PCBM contact resistance, this results in a decrease in the open circuit voltage (V_{OC}, 426 mV), short circuit current density (j_{SC}, −6.86 mA/cm^2), fill factor (FF, 29.2%) and consequently in a poor power conversion efficiency (PCE) of only 0.85%.

Thin layers (≈30 nm) of i-ZnO and AZO provide a much better electron selective interface and ohmic cathode contact. Losses at the cathode interface are minimized, because the electrons are extracted to i-ZnO or AZO, both at a higher work function than bare ITO. This results in increased FF, V_{OC} and j_{SC} and a significantly higher PCE of around 2.5% for both EILs. The series resistance of both device configurations is around 1.1 Ω cm^2 and well within expectations.

Increasing the layer thickness of the i-ZnO from around 30 to over 100 nm results in a severely reduced device performance from 2.5% to 1.5%. The main losses are a reduction of the FF from 53.9% to 37.7% and a reduction of the V_{OC} from 565 to 486 mV. These losses originate dominantly from three different mechanisms, which can be observed in the j–V-characteristics. First, an increase of the series resistance from 1.1 to 3.2 Ω cm^2 (see inset of Fig. 3), is

Table 2
Key parameters of the solar cells.

	V_{OC} (mV)	j_{SC} (mA/cm^2)	PCE (%)	FF (%)	R_S (Ω cm^2)	R_{Shunt} (kΩ cm^2)	$R_{Shunt/light}$ (kΩ cm^2)
w/o EIL	426	−6.86	0.85	29.2	23.6	3.0	0.29
i-ZnO (32 nm)	565	−8.41	2.56	53.9	1.1	6.2	0.59
i-ZnO (126 nm)	486	−8.40	1.54	37.7	3.2	3.1	0.33
AZO (25 nm)	569	−8.36	2.42	50.8	1.1	4.9	0.44
AZO (119 nm)	558	−8.69	2.40	49.4	1.2	3.9	0.50

caused by the thick i-ZnO layer. The higher R_S results dominantly in a FF loss. The V_{OC} loss is more subtle. The increased series resistance due to the i-ZnO layer is not expected to influence V_{OC} unless significant carrier recombination occurs in this region. Given the good charge selectivity of the ZnO layer, we exclude this loss mechanism. A contribution to the FF and V_{OC} loss originates from the already introduced photoshunt, which is much more strongly expressed in the case of thick i-ZnO layer. Photoshunts are a result of an interface-shunt, i.e. a defect shunting the electrode and the semiconductor. The photoshunt resistance is strongly dependent on the minority carrier blocking properties of the interface, the so called contact permeability of the buffer layers. This translates in our architecture to a defect, where holes become injected via the ZnO directly into the active layer [25]. We note that the photoshunt seems to emerge with increased i-ZnO layer thickness, as the shunt resistance under illumination is reduced from 0.59 kΩ cm^2 for the thin i-ZnO EIL down to 0.33 kΩ cm^2 for the thicker i-ZnO EIL (see Table 2). The dark shunt resistance also decreases from 6.0 to 3.1 kΩ cm^2. This is an indication for a reduced layer quality of the thick films. In summary, the photoshunt contributes to the losses in V_{OC} and FF. The third loss mechanism is associated with the photoconductivity of the EIL, which is much more significant for the i-ZnO based devices as compared to the AZO based devices. Illuminated i-ZnO is significantly more conductive, which leads to enhanced carrier injection under forward bias. Overall, this effect causes an increased current density under illumination (see inset of Fig. 3). This increased injected current does already compensate the photovoltaic current at lower bias, and in summary, the V_{OC} becomes reduced. This photoconductivity effect is responsible for the biggest part of the V_{OC} loss.

Solar cells with a thicker AZO EIL do not suffer from these defects. The series resistance of a device with a ~120 nm AZO layer is still as low as 1.2 Ω cm^2, which shows, that the contribution of the AZO EIL is negligible. For thicker AZO EIL the photoshunt is maintained at values larger than 0.45 kΩ cm^2, so the V_{OC} and the FF are not affected that much as for the thick i-ZnO EILs. All key parameters like FF, V_{OC}, j_{SC} and PCE remain constant for AZO layer thicknesses between 30 and 120 nm. In summary, doped ZnO opens the possibility to incorporate thick interface layers into the device architecture without sacrificing efficiency.

4. Conclusion

In this work we discussed the interface layer specifications as required from a reliable, large volume printing process for polymer solar cells. A thick electron injection layer using a solution processed aluminum-doped ZnO with high conductivity was suggested for this purpose. An increase of the intrinsic ZnO layer from 30 to ~120 nm reduced the device performance from initially 2.5% to 1.5%. The main losses are a reduction of the FF and V_{OC}, which are caused by the photoconductivity of the i-ZnO layer, the photoshunt behavior of the devices as well as its higher serial resistance. Aluminum doped ZnO could be processed as thick as 120 nm without causing losses. In the next step, the annealing temperature of the AZO films has to be reduced to around 150 °C, before these films can be processed on plastic substrates. Thick pin-hole free layers with good coverage are a prerequisite for the reliable large scale printing of organic solar cells with low shunts and high yield. In the presented concept, we incorporated thick electron injection layers into the devices. We propose that mechanically robust, thick EIL and hole injection layers (HIL) will be beneficial for the processing of thin active layers. This concept appears as an interesting strategy to optimize the lifetime and performance of single junction as well as tandem junction solar cells.

Acknowledgements

This work was funded by a German Research Foundation Project Grant (DFG; BR 4031/1-1) and the authors gratefully acknowledge the support of the Cluster of Excellence 'Engineering of Advanced Materials' at the University of Erlangen-Nuremberg, which is funded by the German Research Foundation (DFG) within the framework of its 'Excellence Initiative'. The authors would like to thank Lothar Sims, René Kogler and Jens Hauch from Konarka Technologies Inc., for the possibility to use the Kelvin Probe measurement setup.

References

[1] C.J. Brabec, N.S. Sariciftci, J.C. Hummelen, Plastic solar cells, Adv. Funct. Mater. 11 (1) (2001) 15–26.
[2] C.J. Brabec, Organic photovoltaics: technology and market, Sol. Energy Mater. Sol. Cells 83 (2–3) (2004) 273–292.
[3] S.K. Hau, H.-L. Yip, N.S. Baek, J. Zou, K. O'Malley, A.K.-Y. Jen, Air-stable inverted flexible polymer solar cells using zinc oxide nanoparticles as an electron selective layer, Appl. Phys. Lett. 92 (25) (2008) 253301–253303.
[4] C. Waldauf, M. Morana, P. Denk, P. Schilinsky, K. Coakley, S.A. Choulis, C.J. Brabec, Highly efficient inverted organic photovoltaics using solution based titanium oxide as electron selective contact, Appl. Phys. Lett. 89 (23) (2006) 233513–233517.
[5] B. Paci, A. Generosi, V.R. Albertini, P. Perfetti, R.D. Bettignies, C. Sentein, Time-resolved morphological study of organic thin film solar cells based on calcium/aluminium cathode material, Chem. Phys. Lett. 461 (1–3) (2008) 77–81.
[6] F.C. Krebs, Air stable polymer photovoltaics based on a process free from vacuum steps and fullerenes, Sol. Energy Mater. Sol. Cells 92 (7) (2008) 715–726.
[7] M. Jørgensen, K. Norrman, F.C. Krebs, Stability/degradation of polymer solar cells, Sol. Energy Mater. Sol. Cells 92 (7) (2008) 686–714.
[8] M.S. White, D.C. Olson, S.E. Shaheen, N. Kopidakis, D.S. Ginley, Inverted bulk-heterojunction organic photovoltaic device using a solution-derived ZnO underlayer, Appl. Phys. Lett. 89 (14) (2006) 143513–143517.
[9] S.K. Hau, H.-L. Yip, H. Ma, A.K.-Y. Jen, High performance ambient processed inverted polymer solar cells through interfacial modification with a fullerene self-assembled monolayer, Appl. Phys. Lett. 93 (23) (2008) 253301–253303.
[10] P. Ravirajan, A.M. Peiró, M.K. Nazeeruddin, M. Graetzel, D.D.C. Bradley, J.R. Durrant, J. Nelson, Hybrid polymer/zinc oxide photovoltaic devices with vertically oriented ZnO nanorods and an amphiphilic molecular interface layer, J. Phys. Chem. B 110 (15) (2006) 7635–7639.
[11] U. Ozgur, Y.I. Alivov, C. Liu, A. Teke, M.A. Reshchikov, S. Dogan, V. Avrutin, S.-J. Cho, H.A. Morkoc, Comprehensive review of ZnO materials and devices, J. Appl. Phys. 98 (4) (2005) 41103–41301.
[12] J. Hou, H.-Y. Chen, S. Zhang, G. Li, Y. Yang, Synthesis, characterization, and photovoltaic properties of a low band gap

polymer based on silole-containing polythiophenes and 2,1,3-benzothiadiazole, J. Am. Chem. Soc. 130 (48) (2008) 16144–16145.
[13] Y. Zou, A. Najari, P. Berrouard, S. Beaupré, B.R. Aích, Y. Tao, M.A. Leclerc, Thieno[3,4-c]pyrrole-4,6-dione-based copolymer for efficient solar cells, J. Am. Chem. Soc. 132 (15) (2010) 5330–5331.
[14] Y. Liang, Z. Xu, J. Xia, S.-T. Tsai, Y. Wu, G. Li, C. Ray, L. Yu, For the bright future – bulk heterojunction polymer solar cells with power conversion efficiency of 7.4%, Adv. Mater. 22 (20) (2010) 135–138.
[15] S.H. Park, A. Roy, S. Beaupre, S. Cho, N. Coates, J.S. Moon, D. Moses, M. Leclerc, K. Lee, A.J. Heeger, Bulk heterojunction solar cells with internal quantum efficiency approaching 100%, Nat. Photon. 3 (5) (2009) 297–302.
[16] J. Peet, J.Y. Kim, N.E. Coates, W.L. Ma, D. Moses, A.J. Heeger, G.C. Bazan, Efficiency enhancement in low-bandgap polymer solar cells by processing with alkane dithiols, Nat. Mater. 6 (7) (2007) 497–500.
[17] E. Wang, L. Wang, L. Lan, C. Luo, W. Zhuang, J. Peng, Y. Cao, High-performance polymer heterojunction solar cells of a polysilafluorene derivative, Appl. Phys. Lett. 92 (3) (2008) 33303–33307.
[18] G. Dennler, K. Forberich, T. Ameri, C. Waldauf, P. Denk, C.J. Brabec, K. Hingerl, A.J. Heeger, Design of efficient organic tandem cells: on the interplay between molecular absorption and layer sequence, J. Appl. Phys. 102 (12) (2007) 123106–123109.
[19] S. Ray, R. Das, A.K. Barua, Performance of double junction a-Si solar cells by using ZnO:Al films with different electrical and optical properties at the n/metal interface, Sol. Energy Mater. Sol. Cells 74 (1–4) (2002) 387–392.
[20] A.E. Delahoy, L. Chen, M. Akhtar, B. Sang, S. Guo, New technologies for CIGS photovoltaics, Sol. Energy 77 (6) (2004) 785–793.
[21] J. Hanisch, E. Ahlswede, M. Powalla, Contacts for semitransparent organic solar cells, EPJ Appl. Phys. 37 (3) (2007) 261–264.
[22] O. Harnack, C. Pacholski, H. Weller, A. Yasuda, J.M. Wessels, Rectifying behavior of electrically aligned ZnO nanorods, Nano Lett. 3 (8) (2003) 1097–1101.
[23] M.J. Alam, D.C. Cameron, Preparation and properties of transparent conductive aluminum-doped zinc oxide thin films by sol–gel process, J. Vac. Sci. Technol. (2001) 1642–1646.
[24] H. Oh, J. Krantz, I. Litzov, T. Stubhan, L. Pinna, C.J. Brabec, Comparison of various sol–gel derived metal oxide layers for inverted organic solar cells, Sol. Energy Mater. Sol. Cells 95 (8) (2011) 2194–2199.
[25] C. Waldauf, M.C. Scharber, P. Schilinsky, J.A. Hauch, C.J. Brabec, Physics of organic bulk heterojunction devices for photovoltaic applications, J. Appl. Phys. 99 (10) (2006) 104503–104506.

The intermolecular bound charge pairs, or charge transfer (CT) states, which are assumed to be formed after the ultrafast splitting of the Frenkel exciton, then needs to be dissociated as well. What determines the dissociation rate of this state, and the generation rate of fully free carriers is currently debated, but it has been suggested that larger domains appears to be beneficial [27,28]. Furthermore, bi-continuous paths or continuous donor and acceptor phases are needed for successfully transporting the free electrons and holes to the corresponding electrodes, and prevent them from recombining (bimolecularly). Therefore, the optimum morphology of the active layer is actually a trade-off between charge carrier generation and transport for solution-processed PSCs. However, ideal morphology of the active layers, which strongly depends on the solubility and miscibility of two components, can rarely be spontaneously formed during solution-processing. Therefore some treatments, such as thermal treatments, mixed solvents or adding suitable additives to solvents, are usually employed to tune the morphology of the active layers to optimize performance of PSCs [23,29–32]. For instances, significant morphology and performance changes could be achieved by mixing two solvents in APFO-3:PCBM system [30]; the PCE of PSCs based on PCPDTBT:$PC_{71}BM$ was doubled by adding high boiling point alkanethiols into chlorobenzene (CB) [32,33]. Recently, considerable improvement of PCEs in PSCs by tuning the morphology of active layers with various additives has been demonstrated and becomes a more attractive method due to its simplicity and production compatibility, compared with thermal treatment [21,34,35]. DIO is a most commonly used additive, which has been proved enhancing PCE in PSCs based on several different polymers. However, beyond morphology changes, how DIO enhances performance in different polymer fullerene systems has not been fully understood, yet. To the best of our knowledge, there is also no report regarding the impacts of DIO on device stability.

Following the demonstration of a PCE of 5.4% in the PSCs based on HXS-1 and $PC_{71}BM$ processed from DCB/DIO in our previous short communication [36], in this paper, the impacts of DIO on performance of PSCs are intensively investigated with the combination of several cutting edge methods. The clear connection between the morphology of the active layer with the charge generation, recombination and transport indicates that DIO improves PCE of PSCs through tuning the morphology of the active layer with specific stoichiometry (1:2.5 w/w), to an appropriate domain size and favorable vertical bulk interpenetrating distribution, which leads to a higher photocurrent (J_{sc}) and a fill factor (FF). In addition, the stability of PSCs is essential for commercialization. Therefore, the impact of DIO on shelf-stability is also studied in this paper.

2. Experimental

The device optimization was carried out in two labs. PSCs with the structure of ITO/PEDOT:PSS/HXS-1:$PC_{71}BM$/LiF/Al for investigation on DIO effects are mostly fabricated and characterized at Linköping University using the same setup and procedure as described in reference [37]. PSCs for shelf-stability study are fabricated and characterized at Freiburg Materials Research Centre as illustrated in reference [36]. All active layers of PSCs and blend films for PL, morphology study and transport measurement are spin-coated from either DCB or DCB/DIO (97.5:2.5, v/v). Detail descriptions of mobility measurements can be found in reference [38]. PL spectra of all films are recorded with a sensitive CCD Si array detector at wavelengths throughout the visible region and near IR region to 1050 nm [39].

The topographies of the active layers are imaged with AFM, using a Dimension 3100 system (Digital Instruments/Veeco) operating in tapping mode. Silicon cantilevers (NSG10) with a force constant of 5.5–22.5 N/m, a resonance frequency of 190–325 kHz, and a tip curvature radius of 10 nm are used. TEM specimens are prepared by detaching a BHJ film from the substrate in deionized water. The film is floating on the water surface, and is picked up with a copper grid. TEM images are obtained with a LEO 912 OMEGA (Zeiss) transmission electron microscopy operated at 30 kV under proper defocus conditions. The defocus value of TEM is about 700 nm for 40,000 × magnification, which corresponds to the TEM images with 100 nm scale bar and 8 μm for 8000 × magnification, which corresponds to the TEM images with 1 μm scale bar. Films for 3-D TEM are prepared by dissolution of the PEDOT:PSS layer and transfer of the films to a copper grid, as in the TEM-measurements. 10 nm gold particles are placed on the surface of the films and used for image alignment in the reconstruction process. Tilt series are obtained using a FEI CM200 FEG microscope with a CCD with 24 μm pixel size. Images are obtained with one degree increment from −65° to 65° for the film without DIO and from −68° to 68° for the film with DIO. Magnification and postmagnification are 20,000 times and 1.531, respectively. Underfocus is set to 2 μm. Three-dimensional reconstructions are produced with filtered back projection of the images, with software produced at Karolinska Institute (Stockholm, Sweden), and visualized with bob [40].

3. Results and discussion

3.1. The effect of additive on photovoltaic device performance

The external quantum efficiency (EQEs) of the two kinds of PSCs (without or with DIO) under monochromatic light illumination and *I-V* characteristics under AM1.5 (100 mW/cm^2) are recorded and shown in Fig. 1(a) and (b), respectively. EQE of the DCB cell is similar in shape to that of the DCB/DIO cell, but somewhat lower, which maybe caused by charge recombination and/or transport indicated by field dependence of I-V curve shown in Fig. 1(b). For comparison, the device performance parameters (J_{sc}, V_{oc}, FF and PCE) of the two kinds of PSCs are summarized in Table 1. With DIO, J_{sc} is increased from 8.3 to 9.8 mA/cm^2 and FF from 0.51 to 0.69, which lead to an enhancement of PCE from 3.6% to 5.4% (a higher PCE of 5.9% can be reached in diodes with a smaller active area of about 4 mm^2), though there is a small reduction of V_{oc} from 0.85 to 0.81 V. It is well known that J_{sc} of PSCs is sensitive to many factors, but FF is mainly determined by

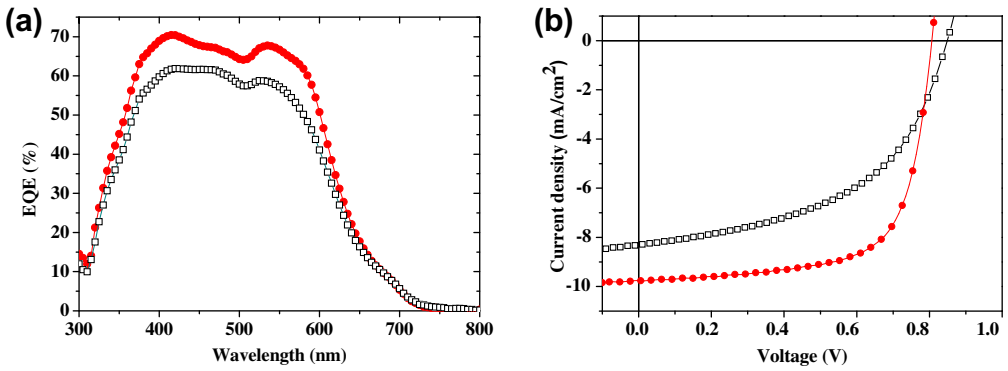

Fig. 1. (a) The EQEs and (b) I-V characteristics of PSCs spin-coated from DCB (open squares) and DCB/DIO (filled circles) under AM 1.5 illuminations.

Table 1
Parameters of HXS-1:$PC_{71}BM$ solar cell.

Solvent	J_{sc} [mA/cm^2]	V_{oc} [V]	FF	PCE	R_s [Ω cm^2]	R_{sh} [Ω cm^2]
DCB	8.3	0.85	0.51	3.6%	19	485
DCB/DIO	9.8	0.81	0.69	5.4%	7	2110

transport property of active layers and their contact with electrodes. A V_{oc} drop, in this case by 40 mV, suggests that ordering [32,41,42] of the active layer is induced by DIO, which is usually favorable for charge transport. Therefore, enlarged J_{sc} and FF combine with decreased V_{oc} imply that the following discussed morphology of the active layer in DCB/DIO cells enables more efficient charge carrier transport to the electrodes than DCB cells.

3.2. The effect of additive on the morphology of the active layers

Three kinds of microscopes are employed to examine the morphology variation between films cast from DCB and DCB/DIO. First, the topographies of pure HXS-1 films spin-coated from DCB and DCB/DIO are imaged with AFM where significantly different height images are observed (see Fig. 2(a) and (b)). The HXS-1 film from DCB/DIO exhibits much rougher surface with larger aggregations than in the film from DCB, This indicates that DIO can induce the formation of compact chain packing of HXS-1 and crystallization in aggregation form. The corresponding phase image of the HXS-1 film from DCB/DIO shown in Fig. 2(d) reveals fine fibril features contrasting with the featureless phase image of the HXS-1 film from DCB (Fig. 2(c)). This is in accordance with the finding in our previous communication [36]. HXS-1 is a planar polymer designed for facilitating polymer chain packing in solid film, which is realized by adding DIO into DCB [36]. The topographies of blends (HXS-1/$PC_{71}BM$) spin-coated from DCB and DCB/DIO are also imaged with AFM. The roughness of the blends cast from DCB/DIO increases also obviously in compare to that of the blends from DCB as shown in Fig. 2(e) and (f). As seen in the phase image, pronounced nanophase separation in the blend from DCB/DIO (Fig. 2(h)) and barely detectable phase separation of two components in the film from DCB (Fig. 2(g)) are consistent with the morphology of the pure HXS-1 due to its semi-crystalline property. This nanophase separation of HXS-1 and $PC_{71}BM$ may be a result of enhanced HXS-1 crystallization, which is again induced by DIO. The size of this feature is measured to be 10–25 nm.

To see the difference of bulk structures of two blends, the morphologies of blend films cast from two solutions are evaluated with TEM. To show both overall view and detailed information of the films, TEM images are recorded at two different scales, 1 μm (Fig. 3(a) and (c)) and 100 nm (Fig. 3(b) and (d)). Some large features bigger than 150 nm are observable. TEM images show contrast based on electron density in the thin film, so that the dark areas are assigned to the $PC_{71}BM$-rich phase. This image contrast is not caused by thickness difference because we know from AFM height image (Fig. 2e) that the film is very even and with a surface roughness being only 0.43 nm. Noticeably, the large phase separation possesses very broad and diffused interface between mixed $PC_{71}BM$-rich and HXS-1-rich phases as seen in Fig. 3(a) and (b). Such large features with indistinguishable phase interface can only be caused by inhomogeneous mixing of $PC_{71}BM$ and HXS-1 from the DCB only solution and they would not influence PSC performance. On the other hand, more homogeneously mixed blend with very fine structure from DCB/DIO can be distinguished in the overview image (Fig. 3c) and the zoomed image (Fig. 3d). This fine structure can also be seen in the film without $PC_{71}BM$ (TEM not shown), which means that the fine structure is induced by HXS-1 crystallization. This is in accordance with the AFM results. According the AFM phase images and TEM images, the thickness of the HXS-1 crystalline lamellae could be determined to be about 10–20 nm. Thereafter, $PC_{71}BM$ must be excluded from the HXS-1 crystal and reside between the lamellae, forcing a phase

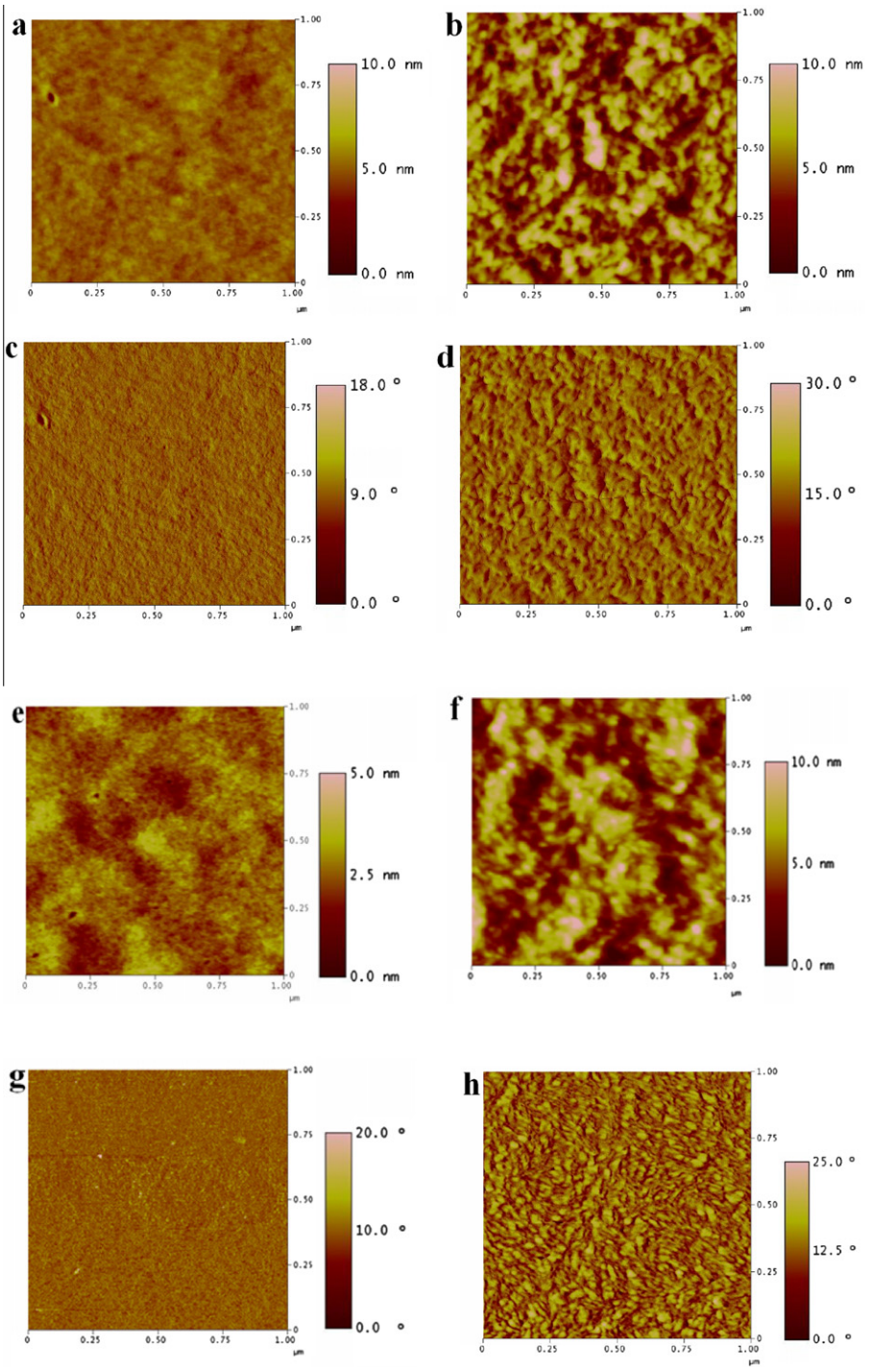

Fig. 2. (a) and (b) are the AFM height images of HXS-1 spin-coated from DCB and DCB/DIO (1 μm × 1 μm), The RMS of (a) and (b) are 0.430, 1.859 nm, respectively. (c) and (d) are the phase images corresponding to (a) and (b). (e) and (f) are AFM height images of HXS-1:$PC_{71}BM$ spin-coated from DCB and DCB/DIO. (g) and (h) are the phase images corresponding to (e) and (f). The RMS of (e) and (f) are 0.43 and 1.90 nm, respectively.

separation with the same size as the crystalline structure. To be clearly stated, the phase separation between $PC_{71}BM$ and HXS-1 is attributed to the unique crystallization of HXS-1 provoked by DIO. Another thing to be noticed, the film thickness investigated with TEM are about 150–200 nm, which means that features of 10–20 nm size seen here are stacks through the whole film. Therefore it is somewhat difficult to clearly separate the individual lamellae. Fortunately this problem can be solved with 3-D TEM investigation shown below.

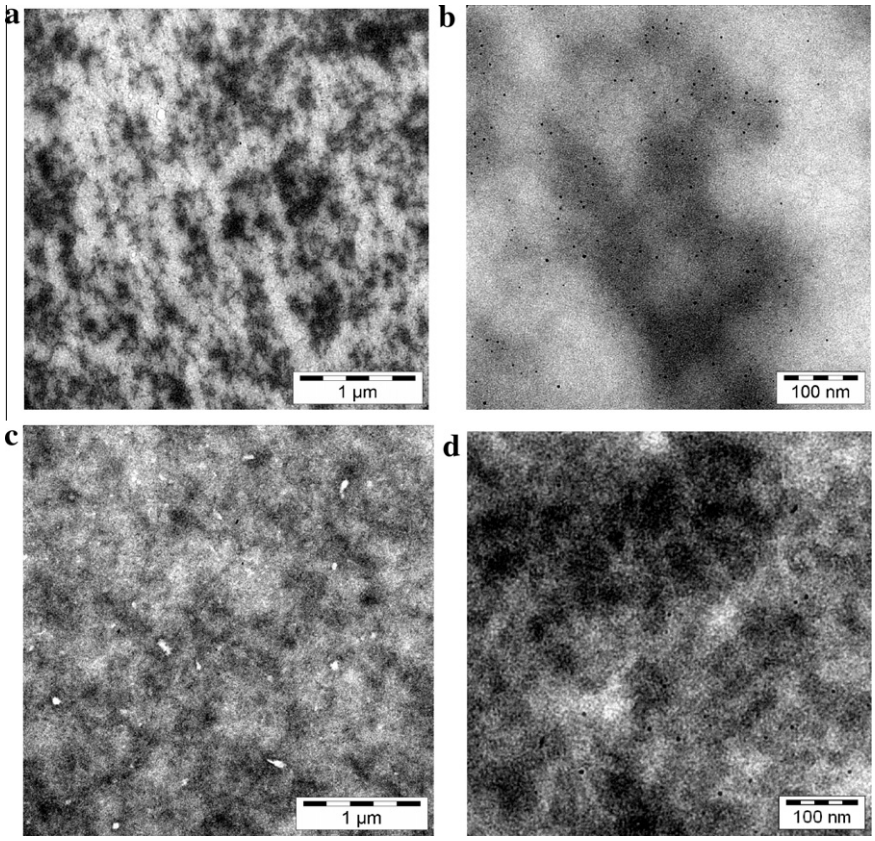

Fig. 3. The TEM images of HXS-1/$PC_{71}BM$ spin-coated from DCB (a and b) and DCB/DIO (c and d).

As the performance of PSCs depends on the vertical distribution of the two components in the active layers and free charges are transported in this direction to the collecting electrodes, it is very interesting to use a 3-D TEM to investigate the vertical distribution of HXS-1 and $PC_{71}BM$. Electron tomography reconstructions [43] are done on blend films cast from DCB and DCB/DIO (Fig. 4(a) and (b)), which show cross section overviews of the two films (ca. 310 nm wide and 60 nm deep). These reconstructions are low pass filtered at 10 nm [43]. In Fig. 4(c) and (d) the middle sections (ca 8 nm thick) in between anode and cathode interfaces of the same reconstructions are displayed, where a low pass filtering at 5 nm has been used. Light regions correspond to well scattering domains and dark regions to less scattering domains. The $PC_{71}BM$ is the more scattering material of the two [43]. Thus, the light volumes are attributed to the $PC_{71}BM$-rich domains while the dark volumes are the polymer rich domains. A coarser film structure in the film spin-coated from DCB/DIO is also found in these images shown in Fig. 4(b) and (d). The film without DIO exhibits smaller domains, which are evenly spread throughout the active layer (see Fig. 4(a) and (c)), while in the film with DIO the domains are larger and more clustered together (see Fig. 4(b) and (d)). Moreover, Fig. 4b shows more vertical continuous elongated clusters formed than that in Fig. 4a, which will facilitate charge carrier transport to collection electrodes.

3.3. The effect of additive on charge generation

Both charge generation and recombination depend strongly on the morphology of active layers. It is interesting to see how DIO influence these physical properties by comparing PL spectra under these two specific morphologies. Deteriorating charge generation is expected in DCB/DIO cells because the interface between HXS-1 and $PC_{71}BM$ is decreased due to increased domain size induced by DIO as shown in Figs. 2–4. To confirm that, the PL spectra of HXS-1:$PC_{71}BM$ films spin-coated from DCB and DCB/DIO excited by a monochromatic light with a wavelength of 405 nm is recorded (Fig. 5). Pure HXS-1 films show emission in the range of 600–900 nm, with a peak located at 685 nm (Fig. S2(B) in reference 36). The $PC_{71}BM$ film displays a relatively broad emission with a peak at 720 nm and also a shoulder at 800 nm. As expected, two morphologies result in two different PL spectra. As shown in Fig. 5, very weak emission in the region of 700 nm originated from pure HXS-1 and $PC_{71}BM$ is observed in the blend film of HXS-1:$PC_{71}BM$ from DCB indicating efficient charge transfer [36]. However, as a consequence of increasing domain size and lowering the amount of donor–acceptor interfaces by the addition of DIO, the emission peak at 710 nm dominates the PL of DCB/DIO films, which can most probably be explained by the combined emission from HXS-1 and $PC_{71}BM$ due to inefficient charge transfer

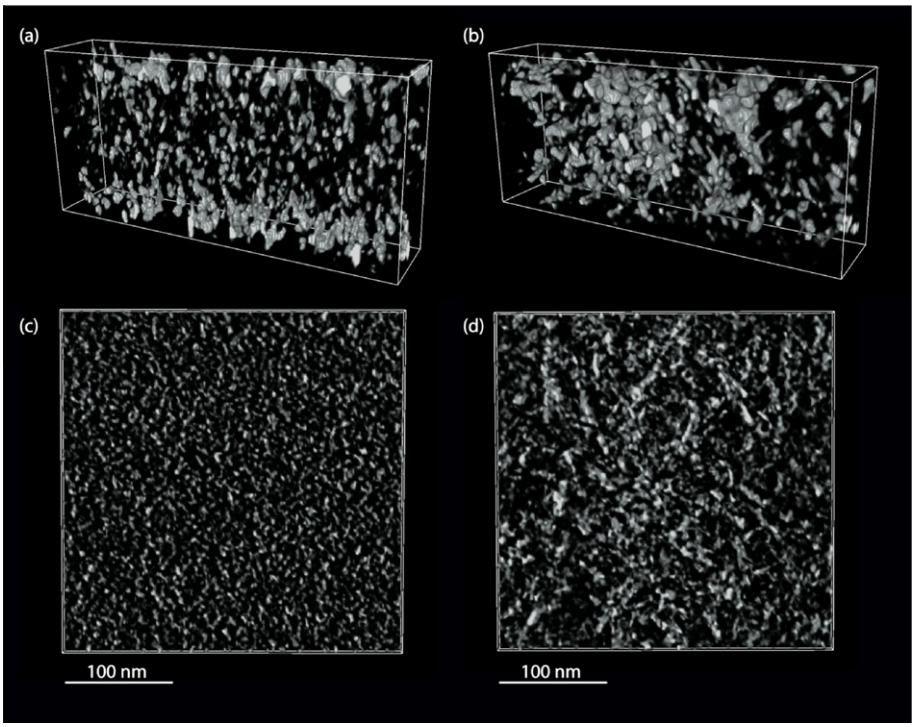

Fig. 4. The cross section overviews of the two blend films cast from DCB (a) and DCB/DIO (b). Image (c) and (d) are the middle sections (ca 8 nm thick) of the same reconstructions of (a) and (b).

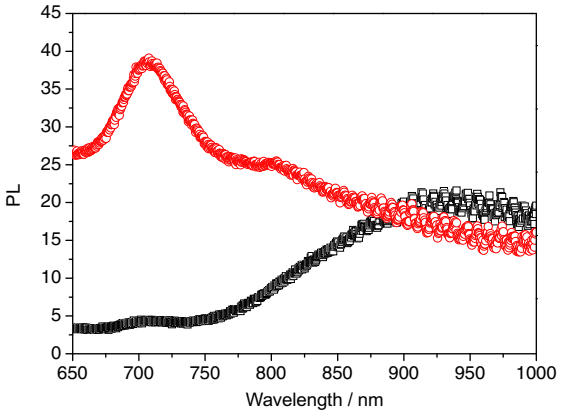

Fig. 5. The PL spectra of HXS-1/$PC_{71}BM$ film spin-coated from DCB (black squares) and DCB/DIO (red circles). The excitation wavelength is 405 nm.

since too big pure HXS-1 and $PC_{71}BM$ domains exist. So from a charge transfer point of view, DIO does not introduce a positive impact.

3.4. The effect of additive on charge carrier recombination

As shown in Fig. 5, a new broad emission with a peak located at 930 nm emerges in blend films from DCB, which is attributed to the recombination of interfacial charge transfer states (CTS) [39,44–49]. There appears to be less CTS emission from DCB/DIO films (Fig. 5), where it can only be seen as in the tail to the pure material emission. The reduced emission from the CTS in blend films from DCB/DIO compared to the blend film from DCB is interesting. Radiative recombination of CTS is a competitor to photocurrent generation in photovoltaic devices, so lower CTS emission is consistent with increased J_{sc} in DCB/DIO solar cells. Therefore, from a CTS recombination point of view, DIO introduces a positive impact, that is, decrease radiative recombination of CTS in DCB/DIO film, likely due to increasing phase separation in the active layer. Similar results have also been reported recently [47–49].

3.5. The effect of additive on transport property

The electrical properties of solar cells are very sensitive to the morphology of the active layers. To verify the different transport situations in the two kinds of PSCs, the R_s and the R_{sh} are evaluated and listed in Table 1. Upon adding DIO, the R_s of the PSC decreases significantly from 19 to 6 $\Omega\,cm^2$, which indicates that the geometry induced by DIO facilitates charge carrier transport in the active layer. Meanwhile, fourfold enhanced R_{sh} of the DCB/DIO cell implies smaller leak current or less recombination than that in DCB solar cells.

Hole and electron mobilities of the films from the two solutions are measured with FET and listed in Table 2. The hole mobility (μ_h) and electron mobility (μ_e) of DCB films are 3×10^{-5} and $1 \times 10^{-3}\,cm^2\,Vs^{-1}$, respectively. There appear to be a change in mobilities in the DCB/DIO film, where μ_h increases to $1 \times 10^{-4}\,cm^2\,Vs^{-1}$ and μ_e decreases to $6 \times 10^{-4}\,cm^2\,Vs^{-4}$, but this might be a measurement related effect. FET measurements might not be

Table 2
Hole and electron mobilities of the films from DCB and DCB/DIO.

Solvent	μ_h [cm^2 Vs^{-1}]	μ_e [cm^2 Vs^{-1}]	μ_e/μ_h
DCB	3×10^{-5}	1×10^{-3}	33.3
DCB/DIO	1×10^{-4}	6×10^{-4}	6

entirely appropriate for this material vis-à-vis solar cell performance due to the presence of ordering and spinodal decomposition [50], which may influence the correlation between FET and solar cell structures in terms of mobility. In particular, there might be an increase in PCBM concentration at the dielectric interface of the transistor in the DCB film compared to the DCB/DIO film as can be seen in Fig. 4(a) and (b), which may be responsible for the measured changes in mobility. Although an increase of the lower mobility agrees well with the increase in FF observed with additive [21], the rather small hole mobility increase and the fact that neither hole or electron mobility is particularly impressive, indicate that some other mechanism, e.g. enhanced charge separation or decreased recombination, is the main reason for the increased FF. This would also be consistent with the larger domains and the possible decrease in CTS emission seen in the films with DIO. From free charge generation and extraction perspective, a favorable morphology is thus probably more important than a high mobility in order to achieve a high FF.

3.6. The effect of DIO on the shelf-stability of the solar cells

To study the effect of additive on the shelf-stability of the solar cells, two substrates with 6 solar cells on each cast from DCB and DCB/DIO were fabricated in Freiburg Materials Research Centre. These cells are kept in a glove box filled with N_2 and their *I-V* curves are recorded for two years with different intervals in days, weeks and months after one day initial degradation. After two years, the average J_{sc}, V_{oc}, FF and PCE of 6 solar cells on the same substrate *vs* time are presented in the inset of Fig. 6 together with normalized corresponding performance parameters (Fig. 6). These 12 solar cells behave similar, V_{oc} increase, FF slightly decrease and J_{sc} clearly decrease, which result in an overall PCE decrease with time no matter if it is with or without DIO. The PCE and J_{sc} decrease by 10% for solar cells cast from DCB and 12% for those from DCB/DIO, respectively. The slightly difference (2%) in J_{sc} and PCE degradation between two groups of solar cells is in experimental error. These results indicate that DIO does not produce observable impact on the shelf-stability of solar cells. The major causes for performance degradation of these solar cells can be bleaching or/and morphology changes due to samples kept in the glove box filled with N_2. Bleaching in this case may not play a big role because the samples are only exposed to white light during I-V measurement. Therefore, the fact that degradation is only observable in the 1st year and no obvious degradation in the 2nd year indicates negligible morphology variation after one year initial relaxation.

4. Conclusions

In conclusion, the performance enhancement in the solar cells based on HXS-1:$PC_{71}BM$ by additive DIO is

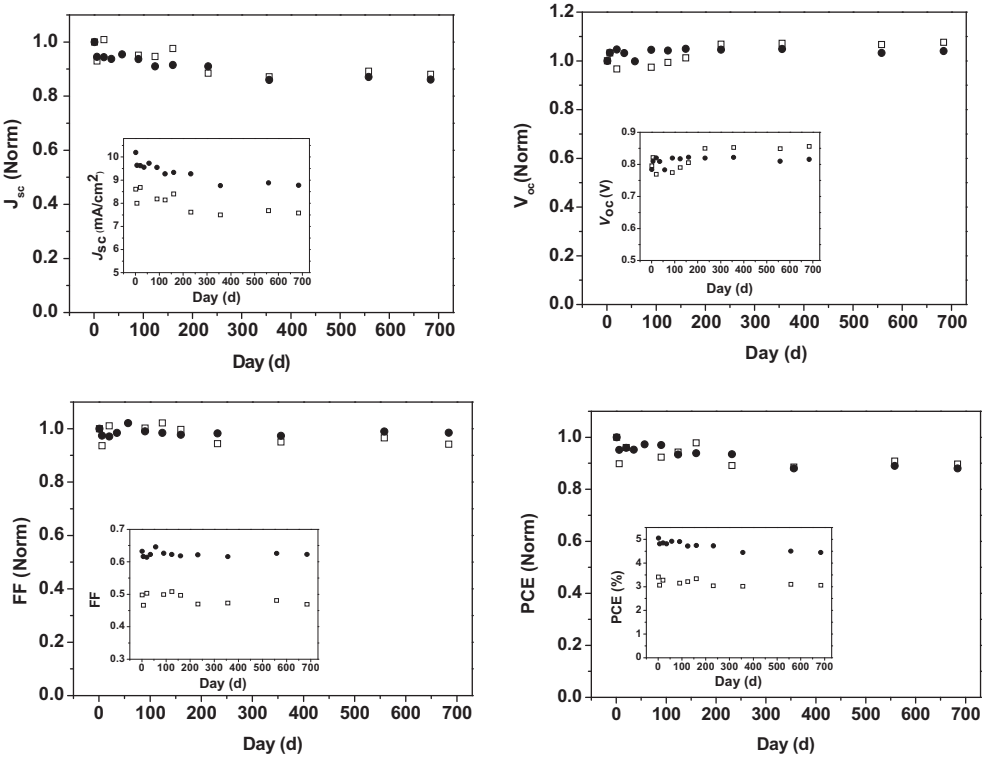

Fig. 6. Normalized and average (inset) performance parameters of HXS-1:$PC_{71}BM$ spin-coated from DCB (opened squares) and DCB/DIO (filled circles).

investigated with AFM, TEM, 3-D TEM, PL and FET. The observations from all these different techniques are well consistent with each other and make a clear connection between solar cell performance and morphology. The enhancement of J_{sc} from 8.3 to 9.8 mA/cm^2 and FF from 0.51 to 0.69 by introducing DIO into DCB is attributed to the pronounced morphology changes of the active layer induced by DIO. All of AFM, TEM and 3-D TEM images show big domains with sizes of 10–20 nm formed in the films of DCB/DIO. Specially, 3-D TEM images further demonstrate vertical continuous elongated clusters formed in DCB/DIO films. Lower PL intensity of CTS emission in the films from DCB/DIO than that from DCB, suggests that once excitons are dissociated at the interface between HXS-1 and $PC_{71}BM$ in the active layers, large domains (detected with AFM, TEM and 3-D TEM) are better at separating the holes and electrons in the two phases. All these results propose that beneficial morphology with domain size in 10–20 nm for inefficient charge recombination and vertical elongated clusters for assisting charge transport to the collecting electrodes in DCB/DIO films are the main reasons for the enhanced J_{sc} of 9.8 mA/cm^2, FF of 0.69 and PCE of 5.4%. The result of two year shelf-stability measurement indicates that DIO has no pronounced impact on the shelf-stability of the PSCs and the morphology is stable after one year initial relaxation.

Acknowledgement

Financial support by the NSF of China (20834006 and 50821062), and 863 Program (2008AA05Z425), Swedish Energy Agency, Swedish Research Council (VR) and VINNOVA are gratefully acknowledged. The collaboration between LiU and Fraunhofer ISE is also financed by Swedish Energy Agency. Funding of C. Veit and U. Würfel by the German Federal Ministry of Education and Research under the contract number 03SF0331 is gratefully acknowledged. We thank Dr. Sergej Masich at Karolinska Institute for assistance with electron tomography.

References

[1] F.C. Krebs, Solar Energy Materials and Solar Cells 93 (2009) 394.
[2] O. Inganäs, F.L. Zhang, M.R. Andersson, Accounts of Chemical Research 42 (2009) 1731.
[3] Y.F. Li, Y.P. Zou, Advanced Materials 20 (2008) 2952.
[4] E. Bundgaard, F.C. Krebs, Solar Energy Materials and Solar Cells 91 (2007) 954.
[5] Y.H. Zhou, F.H. Li, S. Barrau, W.J. Tian, O. Inganas, F.L. Zhang, Solar Energy Materials and Solar Cells 93 (2009) 497.
[6] F.C. Krebs, Solar Energy Materials and Solar Cells 93 (2009) 1636.
[7] Y.H. Zhou, F.L. Zhang, K. Tvingstedt, W.J. Tian, O. Inganäs, Applied Physics Letters 93 (2008) 033302.
[8] G. Dennler, M.C. Scharber, C.J. Brabec, Advanced Materials 21 (2009) 1323.
[9] A.M. Ballantyne, L. Chen, J. Dane, T. Hammant, F.M. Braun, M. Heeney, W. Duffy, I. McCulloch, D.D.C. Bradley, J. Nelson, Advanced Functional Materials 18 (2008) 2373.
[10] J. Gilot, M.M. Wienk, R.A.J. Janssen, Advanced Materials 22 (2010) E67.
[11] S. Sista, Z.R. Hong, M.H. Park, Z. Xu, Y. Yang, Advanced Materials 22 (2010) E77.
[12] F.L. Zhang, M. Johansson, M.R. Andersson, J.C. Hummelen, O. Inganas, Advanced Materials 14 (2002) 662.
[13] F. Huang, K.S. Chen, H.L. Yip, S.K. Hau, O. Acton, Y. Zhang, J.D. Luo, A.K.Y. Jen, J. Am. Chem. Soc. 131 (2009) 13886.
[14] Y.P. Zou, A. Najari, P. Berrouard, S. Beaupre, B.R. Aich, Y. Tao, M. Leclerc, J. Am. Chem. Soc. 132 (2010) 5330.
[15] E.G. Wang, L. Wang, L.F. Lan, C. Luo, W.L. Zhuang, J.B. Peng, Y. Cao, Applied Physics Letters 92 (2008) 033307.
[16] H.Y. Chen, J.H. Hou, S.Q. Zhang, Y.Y. Liang, G.W. Yang, Y. Yang, L.P. Yu, Y. Wu, G. Li, Nature Photonics 3 (2009) 649.
[17] J.H. Hou, H.Y. Chen, S.Q. Zhang, R.I. Chen, Y. Yang, Y. Wu, G. Li, Journal of the American Chemical Society 131 (2009) 15586.
[18] S.H. Park, A. Roy, S. Beaupré, S. Cho, N. Coates, J.S. Moon, D. Moses, M. Leclerc, K. Lee, A.J. Heeger, Nature Photonics 3 (2009) 297.
[19] D. Kitazawa, N. Watanabe, S. Yamamoto, J. Tsukamoto, Appl. Phys. Lett. 95 (2009) 053701.
[20] S.H. Chan, Y.S. Hsiao, L.I. Hung, G.W. Hwang, H.L. Chen, C. Ting, C.P. Chen, Macromolecules 43 (2010) 3399.
[21] Y.Y. Liang, Z. Xu, J.B. Xia, S.T. Tsai, Y. Wu, G. Li, C. Ray, L.P. Yu, Adv. Mater. 22 (2010) E135.
[22] M.A. Green, K. Emery, Y. Hishikawa, W. Warta, Progress in Photovoltaics 19 (2011) 84.
[23] W.L. Ma, C.Y. Yang, X. Gong, K. Lee, A.J. Heeger, Advanced Functional Materials 15 (2005) 1617.
[24] G. Li, V. Shrotriya, J.S. Huang, Y. Yao, T. Moriarty, K. Emery, Y. Yang, Nature Materials 4 (2005) 864.
[25] S.S. van Bavel, M. Barenklau, G. de With, H. Hoppe, J. Loos, Adv. Funct. Mater. 20 (2010) 1458.
[26] V.D. Mihailetchi, H.X. Xie, B. de Boer, L.J.A. Koster, P.W.M. Blom, Advanced Functional Materials 16 (2006) 699.
[27] T.M. Clarke, J.R. Durrant, Chemical Reviews 110 (2010) 6736.
[28] D.J.D. Moet, M. Lenes, M. Morana, H. Azimi, C.J. Brabec, P.W.M. Blom, Applied Physics Letters 96 (2010).
[29] R.B. Aich, Y.P. Zou, M. Leclerc, Y. Tao, Organic Electronics 11 (2010) 1053.
[30] F.L. Zhang, K.G. Jespersen, C. Bjorstrom, M. Svensson, M.R. Andersson, V. Sundstrom, K. Magnusson, E. Moons, A. Yartsev, O. Inganäs, Advanced Functional Materials 16 (2006) 667.
[31] H.W. Tang, G.H. Lu, L.G. Li, J. Li, Y.Z. Wang, X.N. Yang, J. Mater. Chem. 20 (2010) 683.
[32] J. Peet, J.Y. Kim, N.E. Coates, W.L. Ma, D. Moses, A.J. Heeger, G.C. Bazan, Nature Materials 6 (2007) 497.
[33] J. Peet, C. Soci, R.C. Coffin, T.Q. Nguyen, A. Mikhailovsky, D. Moses, G.C. Bazan, Appl. Phys. Lett. 89 (2006) 252105.
[34] J.S. Moon, C.J. Takacs, S. Cho, R.C. Coffin, H. Kim, G.C. Bazan, A.J. Heeger, Nano Letters 10 (2010) 4005.
[35] C.V. Hoven, X.D. Dang, R.C. Coffin, J. Peet, T.Q. Nguyen, G.C. Bazan, Advanced Materials 22 (2010) E63.
[36] R.P. Qin, W.W. Li, C.H. Li, C. Du, C. Veit, H.F. Schleiermacher, M. Andersson, Z.S. Bo, Z.P. Liu, O. Inganäs, U. Wuerfel, F.L. Zhang, Journal of the American Chemical Society 131 (2009) 14612.
[37] W.W. Li, C. Du, F.H. Li, Y. Zhou, M. Fahlman, Z.S. Bo, F.L. Zhang, Chemistry of Materials 21 (2009) 5327.
[38] L.J. Lindgren, F.L. Zhang, M. Andersson, S. Barrau, S. Hellstrom, W. Mammo, E. Perzon, O. Inganas, M.R. Andersson, Chemistry of Materials 21 (2009) 3491.
[39] Y. Zhou, K. Tvingstedt, F.L. Zhang, C.X. Du, W.X. Ni, M. Andersson, O. Inganäs, Advanced Functional Materials 19 (2009) 3293.
[40] s. t. w. http://www.3tag.com/bobicol.html.
[41] J.K. Lee, W.L. Ma, C.J. Brabec, J. Yuen, J.S. Moon, J.Y. Kim, K. Lee, G.C. Bazan, A.J. Heeger, Journal of the American Chemical Society 130 (2008) 3619.
[42] D. Di Nuzzo, A. Aguirre, M. Shahid, V.S. Gevaerts, S.C.J. Meskers, R.A.J. Janssen, Advanced Materials 22 (2010) 4321.
[43] B.V. Andersson, A. Herland, S. Masich, O. Inganas, Nano Lett 9 (2009) 853.
[44] K. Vandewal, K. Tvingstedt, A. Gadisa, O. Inganäs, J.V. Manca, Nature Materials 8 (2009) 904.
[45] I. Haeldermans, K. Vandewal, W.D. Oosterbaan, A. Gadisa, J. D'Haen, M.K. Van Bael, J.V. Manca, J. Mullens, Applied Physics Letters 93 (2008).
[46] D. Veldman, O. Ipek, S.C.J. Meskers, J. Sweelssen, M.M. Koetse, S.C. Veenstra, J.M. Kroon, S.S. van Bavel, J. Loos, R.A.J. Janssen, Journal of the American Chemical Society 130 (2008) 7721.
[47] K. Tvingstedt, K. Vandewal, A. Gadisa, F.L. Zhang, J. Manca, O. Inganäs, Journal of the American Chemical Society 131 (2009) 11819.
[48] M. Hallermann, I. Kriegel, E.D. Como, J.M. Berger, E.V. Hauff, J. Feldmann, Advanced Functional Materials 19 (2009) 3662.
[49] K. Tvingstedt, K. Vandewal, F.L. Zhang, O. Inganas, Journal of Physical Chemistry C 114 (2010) 21824.
[50] S. Nilsson, A. Bernasik, A. Budkowski, E. Moons, Macromolecules 40 (2007) 8291.

inorganic oxide layers separated by polymer layers. The results are promising but total thicknesses of 5–7 μm have been reported for the final device [18–20], largely exceeding the starting device thickness (a few hundred nm) and possibly modifying the final device flexibility. Another interesting approach has been recently suggested based on the introduction of a thin TiO*x* layer that acts both as a shielding and oxygen scavenging layer [21,22]; the carrier mobility of OTFTs encapsulated with TiO*x* remained stable in air for up to 500 h and degraded of one order of magnitude after 2000 h [22]. Indeed, the development of new methods for enhancing device lifetime is an important goal that must be accomplished either by developing novel packaging materials or by reducing the environment sensitivity of organic devices, without interfering with the mechanical properties and thin form factor peculiar to organic devices.

Previously obtained results on ion irradiation of polymers, showed that a controlled damage induced by the implanted ions can induce strong chemical and structural modifications of the material, altering its mechanical and electrical properties [23–25]. In particular, it was demonstrated that ion implantation not only changed the electrical conductivity of polyaniline but also significantly reduced its degradation to the moisture exposure by creating a dense, hermetic layer near the polyaniline surface through ion–polymer interactions [23]. However, the effects of ion implantation have never been investigated neither on small molecule organic semiconductors, such as pentacene, widely studied thanks to its excellent transport performance, nor on fully operating organic devices. The results here described focus on the lifetime-enhancing effects induced on pentacene OTFTs by a controlled low-energy implantation of Ne^+ and N^+ ions. These effects concern the main transport parameters of the material, such as its carrier mobility and threshold voltage, that are not only preserved after ion implantation but even stabilized on a longer time scale. Our results demonstrate that by accurately controlling the Ne^+ and N^+ ion energy and dose, it is possible to limit the ion penetration and action to the upper part of the semiconducting film, therefore preserving the device channel. Moreover, quite interestingly, the modifications induced by Ne^+ and N^+ ion implantation positively affect the stability of the electronic parameters of the device. In particular, we report on the formation of stable charged chemical species following implantation with N^+ ions that chemically react with the organic matrix and pin the device threshold voltage, thus assessing the potentiality of employing ion implantation to permanently modify the electrical transport properties of organic thin films.

2. Experimental

2.1. OTFT fabrication

Pentacene films of thickness of 50 nm and of 300 nm, were deposited on quartz slides to study by photocurrent and optical absorption spectroscopy the different relative weight of the "thin-film" and "bulk" phase (Fig. 1a). Pentacene OFETs were fabricated on highly conductive silicon substrate (acting as gate electrode) with a 500 nm thermally grown silicon dioxide layer, which acts as gate insulator. All devices have been realized using a bottom contact configuration with gold source and drain electrodes (W = 5 mm, L = 50 μm, being W and L channel width and length, respectively) patterned by means usual photolithographic process (Fig. 1b). Pentacene active layers were deposited by thermal evaporation and film thickness was monitored by a quartz crystal microbalance.

2.2. Ion implantation

Ion implantation was performed on Varian CF-3000 ion implanter at Ion Beam Materials Laboratory in Los Alamos national Laboratory. Monte Carlo SRIM code was used to estimate ion beam parameters that would produce the required damage thickness and ion profile in the pentacene. To minimize the sample exposure to the environment during the transportation, samples before and after the implantation were either packed under dry nitrogen atmosphere or sealed under vacuum. The implantation was performed under room temperature with two different ion species (N and Ne) to various fluencies. The beam flux was keep at a fixed value so that the flux effect is not a concern in these sets of experiments. The maximum ion energy was chosen so as not to completely damage the pentacene layer. According to Monte Carlo simulations by SRIM code, the thickness of the damaged layer is slightly thinner than the depth profile of the implanted ions. For example, under 25 keV (or 55 keV) N^+ ion bombardment, the damaged layer thickness in the pentacene is approximately 100 nm (or 200 nm), while the tail of the implanted N ions goes as deep as 130 nm (or 250 nm).

2.3. Photocurrent spectroscopy

Photocurrent spectroscopy analyses were carried out in the common mode planar configuration in air and at room temperature with a 150 W QTH lamp coupled to a SPEX monochromator and mechanically chopped at low frequency (<20 Hz), using a current amplifier connected to a digital lock-in amplifier (Stanford Research 850). The energy resolution was 0.01 eV at 2.40 eV. The photon flux was measured with a calibrated Si photodiode. The analyses were carried out under low-injection conditions (1×10^{13} photons/cm^2 at λ = 450 nm) and no variations were induced in the PC spectra by the incident photon beam, as assessed by comparing consecutively acquired spectra. Optical filters were used to avoid artifacts due to higher order harmonic wavelengths.

2.4. X-ray photoelectron spectroscopy

X-ray photoelectron spectroscopy (XPS) and ion sputter depth profiling analyses were done with a Physical Electronics 5600ci multi-technique surface science system. In profile mode XPS data was collected in medium energy resolution in order to increase signal intensity, and for the core level photoemission spectra shown here in high resolution (better than the intrinsic chemical linewidths) for more careful chemical analysis and assignments. Ion sputtering for the depth profile analysis was done using

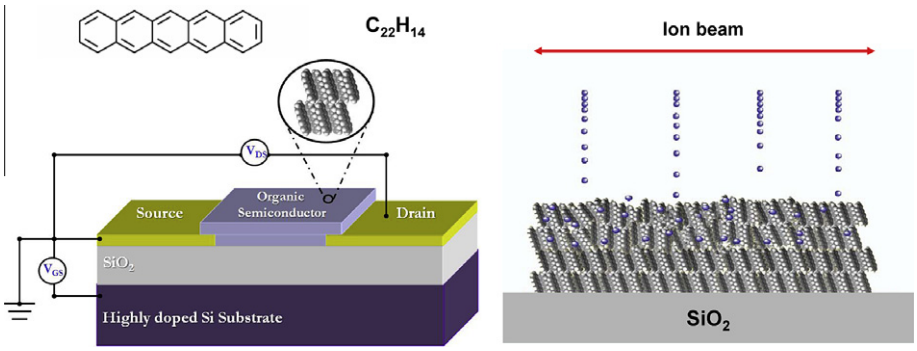

Fig. 1. Schematic layout of a pentacene organic thin film transistor.

4 keV Ar^+ ions at an approximate rate of 2 nm/minute erosion rate. XPS data acquisition was alternated with ion sputtering to obtain depth resolved information for the profile. Standard relativity sensitivity factors specific to the instrument were used to convert XPS peak area intensity to relative atomic concentration.

2.5. Electrical measurements

Drain-source current (I_D) measurements were carried out at room temperature in air and in dark. An Agilent HP 4155 Semiconductor Parameter Analyzer, provided with gold tips for contacting the electrodes, was used to control the gate voltage (V_G) and the drain-source voltage (V_D) and to measure I_D (the source being the common ground). For all devices, both mobility and threshold voltage were determined from the transfer characteristics in the saturation regime. Since the hysteresis was negligible for all devices, the device parameters are reported for the forward gate voltage sweep.

3. Results and discussion

3.1. Ion implantation effects

To achieve this goal we have implanted 300 nm thick pentacene OTFTs (the structure is shown in Fig. 1) with either Ne^+ and $^{14}N^+$ ions and we have observed by elastic recoil detection (ERD) and Fourier transform infrared (FTIR) analyses a strong modification induced in the C—H and C—C molecular bonds, forming a hydrogen-depleted carbon-rich matrix. Hydrogen loss occurs for both types of implanted ions and it increases with increasing implantation dose (more details in Supplementary Information, Figs. S1, S2).

The variations induced by ion implantation in the OTFT main electrical transport parameters, such as charge carrier mobility and threshold voltage, have been measured and Fig. 2 reports the values obtained as a function of dose for N^+ ion at 25 keV (the effects of N^+ ions as a function of increasing energy and of Ne^+ ions at 35 keV are reported in Supplementary Information, Figs. S3 and S4). The average carrier mobility and threshold voltage measured over 50 OTFTs before implantation were $\mu_0 = 0.02 \pm 0.01$ cm^2/Vs and $V_{t0} = -21 \pm 10$ V, respectively. We report in the SI section the characteristics of an investigated OTFTs (Fig. S5). Despite the large spread in μ_0 and V_{t0}, it is noteworthy that devices with very different starting μ_0 and V_{t0} values but implanted with the same dose/energy behave in a very reproducible way (as shown in more detail in the SI section, Tables T1 and T2). On the contrary, if we implant with a different (more than two orders of magnitude) ion dose two samples with an very similar initial mobility value, we record a huge difference in the mobility degradation (SI section, Fig. S6). These observations clearly indicate that the effects induced by ion implantation override the existing morphological/functional differences in the starting OTFT devices. The first value of the relative mobility of the not-implanted reference samples differs from one in Fig. 2a since it is determined using the mobility value of the reference samples re-measured after all the other samples had been exposed to ion implantation (there is a sizeable time-lag between the fabrication of the devices, their implantation and the measurement of their mobility). In this way, the mobility used to determine the first data point of Fig. 2a has been measured at the same time, both for the reference and the implanted ones. The same considerations apply to the non-zero value of the first data point for the not-implanted devices in Fig. 2b. The beam energy values have been chosen, following SRIM simulations [26], in order to limit the damage to the top portion of the active layer. The interesting result is that the OTFT performance is seriously affected only for doses higher than 5×10^{14} ions cm^{-2} for both types of ions. No particular trend can be detected in the mobility and threshold voltage variation as a function of the beam energy for N-implantation. The energy plots are not available for Ne^+ ions since for beam energies higher than 35 keV, the devices lose their field effect transistors behavior, indicating that these conditions severely damage the device active channel.

The molecular electronic density of states distribution has been investigated by photocurrent (PC) spectroscopy analyses to assess the modifications induced at the molecular level on the electronic transport properties [27–33]. PC analyses were carried out on all OTFTs except on those that have been implanted at the highest doses/energies and that, therefore, had completely lost their device behaviour (see Figs. 2, S3 and S4 in the SI section). PC spectra of OTFTs implanted with 25 keV N^+ ions at different doses are

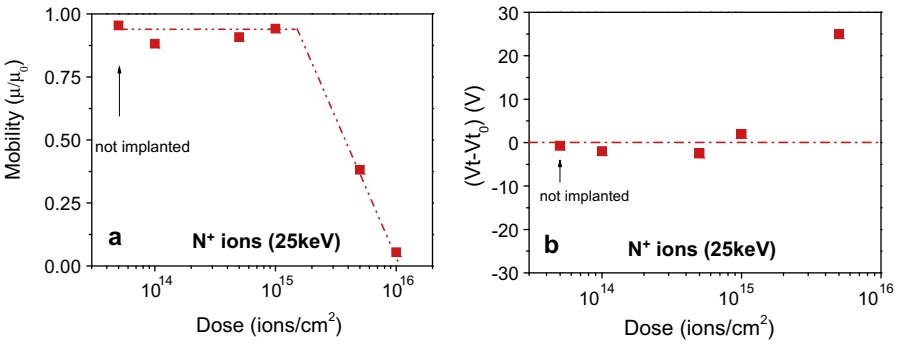

Fig. 2. Relative modification in the charge carrier mobility (μ) and threshold voltage (V_t) of OTFTs implanted with 25 keV N^+ ions as a function of the ion dose.

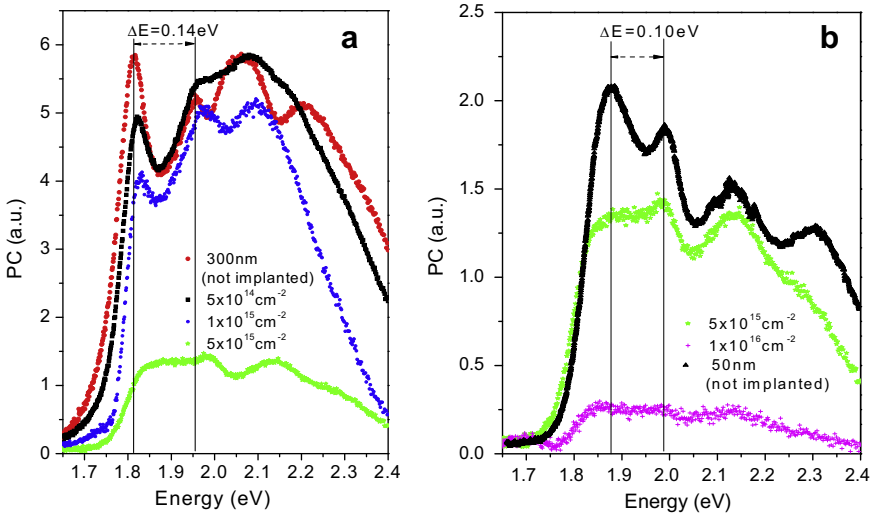

Fig. 3. Photocurrent spectra of OTFTs implanted at different N^+ ion doses. The ion energy is 25 keV. The spectrum of a not-implanted 300 nm thick reference sample is reported in (a) and the spectrum of a not-implanted 50 nm thick reference in (b). The reduction in the Davydov splitting as the pentacene layer thickness decreases is highlighted.

shown in Fig. 3 and provide a clear indication of the presence of an undamaged active pentacene film. In fact, two phases coexist in pentacene films, called the "thin-film" phase, characterized by a molecular spacing of 15.5 Å and dominant for thicknesses below 50 nm, and the "bulk" phase, characterized by a spacing of 14.5 Å and dominant for films over 150 nm thick [34,35]. The different molecular spacing derives from the different tilt angle of the molecular herringbone packing structure, which induces a different coupling of intermolecular π-electron systems. The density of states distribution obtained from PC spectra can provide information on the dominant phase of the pentacene film by assessing the Davydov splitting of the first absorption band. The Davydov splitting of the first absorption band is correlated to modifications in the film molecular structure and packing and it increases when passing from the "thin film" to the "bulk" phase [36–38]. Our measurements (Fig. 3) indicate that, as the implantation doses increase, the active layer passes from a "bulk phase" dominated (i.e. a film >150 nm thick to a "thin-film phase" dominated structure (i.e. about 50 nm thick). Fig. 3a shows the gradual decrease in the Davydov splitting with increasing implantation dose starting from the reference non-implanted sample (300 nm thick); its further evolution is highlighted in Fig. 3b, where the PC spectra of OTFTs implanted at the highest tested doses are compared with a non-implanted, 50 nm thick, reference sample. Similarly, also the mobility and threshold voltage are preserved. It is noteworthy that the PC spectrum of the highest dose implanted sample (1×10^{16} ions cm^{-2}) has an extremely poor quality and, correspondingly, the OTFT device functionality is completely lost. These PC results indicate that a thin undamaged layer of pentacene can still be preserved under the damaged top layer after ion implantation with selected doses and energies, and this layer grants the full functionality of the implanted OTFTs (see Fig. 2). Therefore, PC measurements confirm that it is possible to preserve the full functionality of the OTFT device by properly choosing ion implantation conditions. It is noteworthy that PC spectroscopy, that provides a "fingerprint" of the density of

states distribution on the pentacene film, allows identifying the actual thickness of the electrically active layer left undamaged after ion implantation, without affecting the operation of the device. Other techniques usually applied to obtain information on pentacene phases, such as X-ray diffraction, could not be easily applied to fully operational OTFTs that have also undergone ion implantation leaving their performance unaffected.

3.2. Evolution with time of OTFTs transport paramenters

We have then monitored the evolution of the transport parameters with time in ion implanted OTFTs to test the effects of the irradiation process on the aging and degradation of the device performance. The results are extremely promising since: (i) there is a clear stabilization effect induced on carrier mobility and/or in threshold voltage for at least up to 2000 h after the implantation process; (ii) implantation with $^{14}N^+$ or with Ne^+ ions induces different effects. In particular, low implantation doses (up to 3×10^{14} cm^{-2}) of 35 keV Ne^+ ions stabilize the carrier mobility (μ) (Fig. 4), while implantation with selected doses and energies of $^{14}N^+$ ions induce a stabilization of the OTFT threshold voltage (V_T) (Fig. 5). The stabilization of V_T is optimized (i.e. almost no V_T variations can be detected) for 25 keV ions and for doses up to 1×10^{15} cm^{-2}. It is noteworthy that higher doses and energies also induce a stabilization of V_T, even if it occurs at values that are largely shifted with respect to the reference, non-implanted device.

The reason for the different behavior induced by implantation with $^{14}N^+$ or with Ne^+ ions can be ascribed to the different reactivity of the two elements. In fact, Ne is not expected to chemically interact with the organic matrix, while N has a high probability of reacting with the organic matrix of pentacene once implanted within the film. We have carried out depth-resolved X-ray photoelectron spectroscopy (XPS) analyses to assess the chemical structure of both implanted species and the pentacene matrix layers by alternating XPS analyses with Ar ion sputter etching (4 keV) to form a sputter depth profile. Extensive XPS investigations were performed on both untreated and ion-implant treated specimens. This included replicate analysis, angle resolved XPS measurements in order to look for chemical differences in the near surface region (<10 nm) with depth into the material, and sputter ion XPS depth profiles to understand chemistry and elemental concentration through the thickness of the film, from the top, air exposed surface, through to the substrate where the primary electronic characteristics are active. The data shown in Fig. 6 are representative of various XPS analysis performed on the thin film pentacene system, and show unusual detail in the chemical composition of the film as a function of depth.

No Ne signal was detectable with sputter profile XPS analyses on Ne-implanted samples, indicating (as expected) that implanted Ne did not form bonds with the hydrocarbon matrix, and was thus lost into vacuum prior to, or during, XPS analyses. Fig. 6a shows the XPS depth profile for a N implanted layer (25 keV and 5×10^{16} cm^{-2} dose). The concentration of the implanted N in the pentacene is maximized at 4.5% atomic concentration (relative to carbon) at a depth of about 76 nm from the top surface in a Gaussian-like distribution as expected from the implant simulations. We have identified the presence of two main N-related chemical states, consistent with —C—N— (398.1 eV), and —C≡N (nitrile functional 399.7 eV) functional terminations on the aromatic rings (Fig. 6a inset) [39]. A minor third component at higher binding energy is indicative of the presence of $—NH_3^+$. This higher binding energy is consistent with ionic ammonium-like functionality. These observations confirm that N reacts with the hydrocarbon matrix and induces the activation/formation of both additional dipole layers (relative to virgin pentacene) and stable positive charge groups within the pentacene layer. The observed broadening of the C1s peak to higher binding energy when N is present in the organic matrix (Fig. 6b), is consistent with the activation of a C—N functionality. The only difference in the two C1s XPS traces in Fig. 6b is the presence (red trace) or absence (green trace) of implanted N in the virgin pentacene. An equivalent depth profile of the virgin pentacene does not

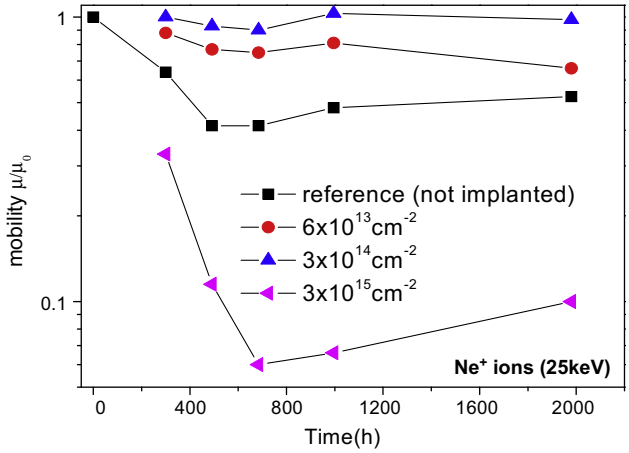

Fig. 4. Evolution with time of the relative charge carrier mobility (μ/μ_0) in Ne implanted OTFTs (ion energy 35 keV), for different ion doses.

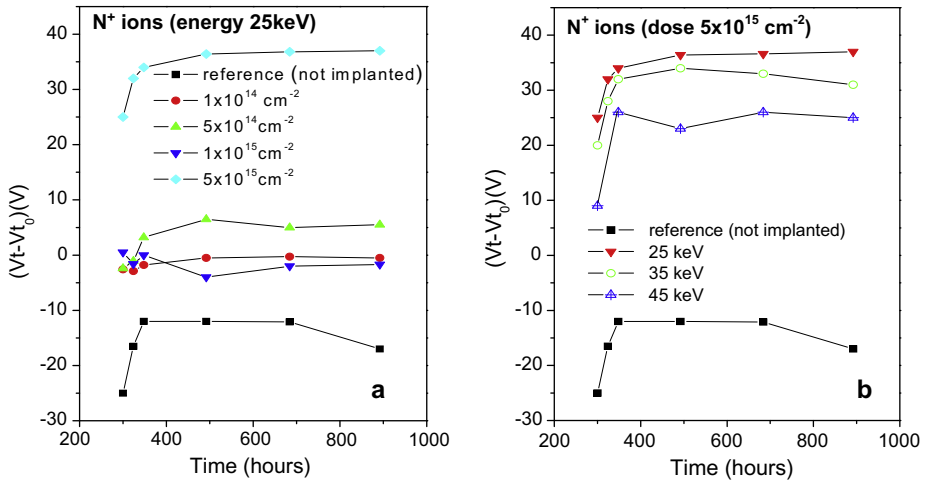

Fig. 5. Evolution with time of the relative threshold voltage ($V_t - V_{t0}$) in N^+ implanted OTFTs: (a) for different ion doses and same energy (25 keV); (b) for different ion energy and same dose (5×10^{15} cm^{-2}).

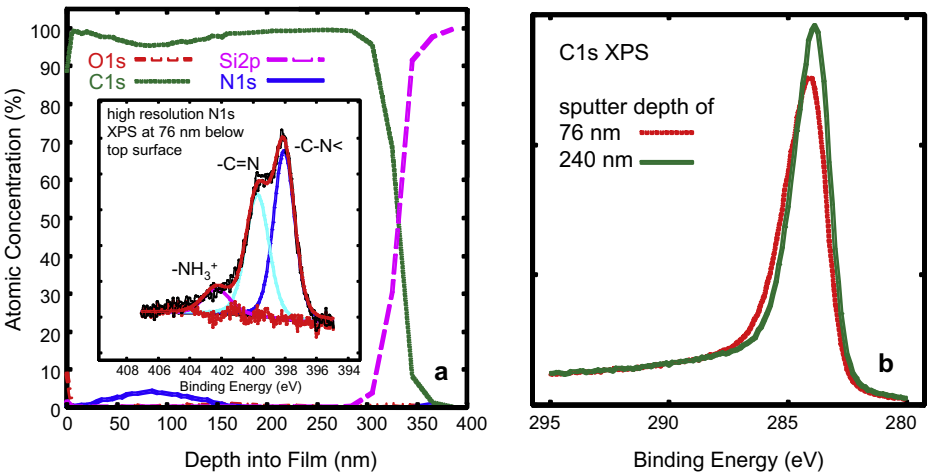

Fig. 6. Depth-resolved X-ray photoelectron spectroscopy (XPS) analyses for N^+ implanted OTFTs (ion energy 25 keV, dose 1×10^{16} cm^{-2}). The inset of (a) shows the deconvolution into the three main chemical components of the N1s peak at a film depth of 76 nm; (b) shows the modification in the chemical environment of C in the presence of N (depth of 76 nm). See text for Section 3.

show these differences, and as such, the differences are clearly due to chemical interaction (bonding) of N with C in the structure of pentacene. The N1s spectrum at the same depth (inset of 6a) also corroborates this by showing various chemical functionalities of N interacted with the C in the structure of pentacene. It is clear that the differences are due to N incorporation chemically with the pentacene matrix. These modifications lead to a different polarizability with respect to the pure pentacene that affects the material electrical behaviour.

Further interesting observations can be drawn from the V_T evolution with time; it is known that V_T in unaltered pentacene progressively degrades with time due to charge trapping effects at the semiconductor/dielectric interface. Many recent studies attribute this effect to the chemical surface structure of most dielectric layer (e.g. —OH terminations in SiO_2) [40]. In the investigated implanted devices, V_T does not significantly degrade with time (Fig. 5), indicating that these trapping effects could possibly be neutralized or masked by another effect. Since the semiconductor/dielectric interface in itself is not directly affected by the implantation process, a possible/reasonable explanation could rely on the effects induced on the OTFT active channel by the presence of charges or modification of the material polarizability, as suggested by XPS.

In particular, our XPS results indicate that N implantation gives rise to a positively charged layer that reaches different depths, controlled by the implant energy. The measured threshold voltage shift seems to be proportional to the thickness of the undamaged layer (Fig. 5b), i.e. to the difference between the film thickness and the implant depth. A simple effect can be invoked to qualitatively explain these data. The implanted charged layer induces an electric field that superposes to the gate field, thus pushing holes towards the insulating layer, i.e. into the device channel. As a consequence, it is necessary to apply a posi-

tive gate voltage in order to deplete the channel and to switch the device off. The same effect can also be obtained by keeping the energy constant (i.e. the implantation depth) and varying the dose (i.e. the density of the charges in the layer), as shown in Fig. 5a. The trend in V_t shift can be again quantified by considering the ratio between the implanted charge density and the undamaged layer capacitance. More interestingly, Fig. 5a shows how low doses ($1 \times 10^{14}\,cm^{-2}$, $5 \times 10^{14}\,cm^{-2}$, $1 \times 10^{15}\,cm^{-2}$) induce a clear stabilization effect on V_t and, on the contrary to what happens to the reference sample and to samples implanted with higher ion doses, V_t does not differ much from V_0 (the value before implantation). The stabilization effect on V_t, observed also in non V_t-shifted devices, suggests that it is this superposed electric field rather than the interface charged states that determines the effective charge carrier concentration and, as a consequence, the threshold voltage.

4. Conclusions

In summary, we have demonstrated how controlled, low energy ion implantation processes can enhance the lifetime of organic transistors, without resulting in increased thickness or modification of the electrical properties of the device. Ion implantation can be safely carried out on fully operational OTFTs, where it modifies the structure of the top portion of the organic active semiconductor layer, thus providing a barrier that reduces the sensitivity to oxygen and water vapor without affecting the functionality of the device. The air stabilization of the main electronic transport parameters of implanted OTFTs (i.e. carrier mobility and threshold voltage) has been assessed for up to 2000 h. Moreover, by selectively implanting with N^+ ions that can react with the hydrocarbon matrix, we observe effects that suggest a local modification of the charge distribution within the organic layer. These findings suggests how the effects induced by ion implantation on organic thin films extend well beyond the here reported lifetime-enhancing application and open up the way for novel and challenging developments in the realization of organic devices.

Acknowledgements

This work was performed, in part, at the Center for Integrated Nanotechnologies, a US Department of Energy, Office of Basic Energy Sciences user facility. Los Alamos National Laboratory, an affirmative action equal opportunity employer, is operated by Los Alamos National Security, LLC, for the National Nuclear Security Administration of the US Department of Energy under contract DE-AC52-06NA25396. A. B. and P. C. acknowledge financial support by the European Commission, VII FP, under the Project "Roboskin", Contract # 231500. PC acknowledges Regione Autonoma della Sardegna (RAS) for funding his research activity under the PO Sardegna FSE 2007-2013, L.R.7/2007 "Promozione della ricerca scientifica e dell'innovazione tecnologica in Sardegna" CRP Prot. No. 1399/207.

Appendix A. Supplementary data

Supplementary data associated with this article can be found, in the online version, at doi:10.1016/j.orgel.2011.05.018.

References

[1] G. Gelinck, H. Huitema, E. van Veenendaal, E. Cantatore, L. Schrijnemakers, J. van der Putten, T. Geuns, M. Beenhakkers, J. Giesbers, B. Huisman, E. Meijer, E. Benito, F. Touwslager, A. Marsman, B. van Rens, D. de Leeuw, Flexible active-matrix displays, shift registers based on solution-processed organic transistors, Nat. Mater. 3 (2004) 106.
[2] R. Street, Thin film transitors, Adv. Mater. 21 (2009) 2007.
[3] R. Rotzoll, S. Mohapatra, V. Olariu, R. Wenz, M. Grigas, K. Dimmler, Radio frequency rectifiers based on organic thin-film transistors, Appl. Phys. Lett. 88 (2006) 123502.
[4] A. Dediu, L. Hueso, I. Bergenti, C. Taliani, Spin routes in organic semiconductors, Nat. Mater. 8 (2009) 707.
[5] L. Torsi, G. Farinola, F. Marinelli, M.C. Tanese, O. Omar, L. Valli, F. Babudri, F. Palmisano, P. Zambonin, F. Naso, A sensitivity-enhanced field-effect chiral sensor, Nat. Mater. 7 (2008) 412.
[6] D. Simon, S. Kurup, K. Larsson, R. Hori, K. Tybrandt, M. Goiny, E. Jager, M. Berggren, B. Canlon, A. Richter-Dahlfors, Organic electronics for precise delivery of neurotransmitters to modulate mammalian sensory function, Nat. Mater. 8 (2009) 742.
[7] D. Knipp, R. Street, A. Voelkel, J. Ho, Pentacene thin film transistors on inorganic dielectrics: morphology, structural properties, and electronic transport, J. Appl. Phys. 93 (2003) 347.
[8] D. Knipp, J. Northrup, Electric-field-induced gap states in pentacene, Adv. Mater. 21 (2009) 2511.
[9] D. Gomes, P. Stallinga, F. Dinelli, M. Murgia, F. Biscarini, D. de Leeuw, Bias-induced threshold voltages shifts in thin-film organic transistors, Appl. Phys. Lett. 84 (2004) 3184.
[10] A. Salleo, F. Endicott, R. Street, Reversible and irreversible trapping at room temperature in poly(thiophene) thin-film transistors, Appl. Phys. Lett. 86 (2005) 263505.
[11] Y. Qiu, Y. Hu, G. Dong, L. Wang, J. Xie, Y. Ma, H_2O effect on the stability of organic thin-film field-effect transistors, Appl. Phys. Lett. 83 (2003) 644.
[12] D. Lang, X. Chi, T. Siegrist, A. Sergent, A. Ramirez, Amorphous like density of gap states in single-crystal pentacene, Phys. Rev. Lett. 93 (2004) 86802.
[13] J. Northrup, M. Chabinyc, Gap states in organic semiconductors: Hydrogen- and oxygen-induced states in pentacene, Phys. Rev. B 68 (2003) 41202.
[14] A. Vollmer, O. Jurchescu, I. Arfaoui, I. Salzmann, T. Palstra, P. Rudolf, J. Niemax, J. Pflaum, J. Rabe, N. Koch, The effect of oxygen exposure on pentacene electronic structure, Eur. Phys. J. E17 (2005) 339.
[15] S. Ogawa, T. Naijo, Y. Kimura, H. Ishii, M. Niwano, Photoinduced doping effect of pentacene field effect transistor in oxygen atmosphere studied by displacement current measurement, Appl. Phys. Lett. 86 (2005) 252104.
[16] P.E. Burrows, V. Bulovic, S. Forrest, L. Sapochak, D. McCarthy, M. Thompson, Reliability and degradation of organic light emitting devices, Appl. Phys. Lett. 65 (1994) 2922.
[17] M. Weaver, L. Michalski, K. Rajan, M. Rothman, J. Silvernail, J. Brown, P. Burrows, G. Graff, M. Gross, P. Martin, M. Hall, E. Mast, C. Bonham, W. Bennett, M. Zumhoff, Organic light-emitting devices with extended operating lifetimes on plastic substrates, Appl. Phys. Lett. 81 (2002) 2929.
[18] A. Chwang, M. Rothman, S. Mao, Thin film encapsulated flexible organic electroluminescent displays, Appl. Phys. Lett. 83 (2003) 413.
[19] M. Rapisarda, D. Simeone, G. Fortunato, A. Valletta, L. Mariucci, Pentacene thin film transistors with (polytetrafluoroethylene) PTFE-like encapsulation layer, Org. Electron. 12 (2011) 219.
[20] S.H. Kwon, S.Y. Paik, O.J. Kwon, J.S. Yoo, Triple-layer passivation for longevity of polymer light-emitting diodes, Appl. Phys. Lett. 79 (2001) 4450.
[21] K. Lee, J.Y. Kim, S.H. Park, S.H. Kim, S. Cho, A. Heeger, Air-stable polymer electronic devices, Adv. Mater. 19 (2007) 2445.
[22] S. Cho, K. Lee, A. Heeger, Extended lifetime of organic field-effect transistors encapsulated with titanium sub-oxide as an 'active' passivation/barrier layer, Adv. Mater. 21 (2009) 1941.
[23] Y.P. Feng, D. Robey, Y. Wang, R. Giedd, Conductivity and stability in ion-implanted polyaniline, Mater. Lett. 71 (1993) 167.

[24] Y.Q. Wang, L. Bridwell, R. Giedd, in: R. Arshady (Ed.), Modification of Polymers by Ion Implantation, ACS Book Publisher, 1997, pp. 371–404.
[25] J. Kleiman, Surface modification technologies for durable space polymers, MRS Bull. 35 (2010) 55.
[26] J. Ziegler, J. Biersack, U. Littmark, The Stopping and Range of Ions in Solids, Pergamon Press, New York, 1985. WWW.SRIM.ORG (Version 2003).
[27] R. Bube, Photonductivity of Solids, Wiley & Sons, New York, 1960.
[28] B. Fraboni, A. Matteucci, A. Cavallini, E. Orgiu, A. Bonfiglio, Photocurrent studies of stress and aging in pentacene thin film transistors, Appl. Phys. Lett. 89 (2006) 222112.
[29] Y. Ahn, J. Dunning, J. Park, Scanning photocurrent imaging and electronic band studies in silicon nanowire field effect transistors, Nano Lett. 5 (2005) 1367.
[30] R. Zhang, X. Chen, J. Lu, W. Shem, J. Appl. Phys. 102 (2007) 123708.
[31] S. Shamuilia, V. Afanasev, A. Stesmans, I. McCarthy, S. Campbell, M. Boutchich, M. Roeckerath, T. Heeg, J. Lopes, J. Schubert, Photoconductivity of Hf-based binary metal oxide systems, J. Appl. Phys. 104 (2008) 114103.
[32] M. Breban, D. Romero, S. Mezhenny, V. Ballarotto, E. Williams, Photocurrent probe of field-dependent mobility in organic thin-film transistors, Appl. Phys. Lett. 87 (2005) 203503.
[33] B. Fraboni, DiPietro, A. Cavallini, P. Cosseddu, A. Bonfiglio, J.O. Vogel, Photocurrent studies of sexythiophene-based OFETs, Appl. Phys. A 95 (2009) 37.
[34] C. Mattheus, A. Dros, J. Baas, G. Oostergetel, A. Meetsma, J. de Boer, T. Palstra, Identification of polymorphs of pentacene, Synth. Met. 138 (2003) 475.
[35] D. Faltermeier, B. Gompf, M. Dressel, A. Tripathi, J. Pflaum, Optical properties of pentacene thin films and single crystals, Phys. Rev. B 76 (2006) 125416.
[36] T. Jentzsch, H. Juepner, K. Brzezinka, A. Lau, Efficiency of optical second harmonic generation from pentacene films of different morphology and structure, Thin Solid Films 315 (1998) 273.
[37] H.L. Cheng, W. Chou, C. Kuo, Y. Wang, Y. Mai, F. Tang, Influence of electric field on microstructures of pentacene thin films in field-effect transistors, Adv. Funct. Mater. 108 (2008) 285.
[38] B. Fraboni, A. Scidà, A. Cavallini, P. Cosseddu, A. Bonfiglio, S. Milita, M. Nastasi, Spectroscopic investigation of the semiconductor molecular packing in fully operational organic thin-film transistors, Appl. Phys. Lett. 96 (2010) 163302.
[39] J.F. Moulder, W.F. Stickle, P.E. Sobol, K.D. Bomben, Handbook of X-Ray Photoelectron Spectroscopy, in: J. Chastain (Ed.), Perkin Elmer Corporation, Physical Electronics Division, Eden Prairie, MN, USA, 1992.
[40] L.-L. Chua, R. Friend, P. Ho, General observation of n-type field-effect behaviour in organic semiconductors, Nature 434 (2005) 194.

carriers, although the experimental evidence was insufficient [20]. Furthermore, Liang et al. recently demonstrated the estimation of the carrier mobility in a model OFET device by analyzing the time dependence of the current peak in DCM curves [21].

In principle, the observed current in DCM includes both capacitive and transient terms. The current in metal–insulator–semiconductor (MIS) devices with a time dependent voltage stimulus V is expressed by

$$I = \frac{dQ}{dt} = C_{\text{eff}}\frac{dV}{dt} + i_{\text{tra}}, \tag{1}$$

where C_{eff} is the effective capacitance of the device, Q is the charge, and V is the applied voltage. i_{tra} is the transient current which reflects the dynamic behavior of carrier. Thus, the observed current in DCM includes information in both the quasi-static and transient states as shown in Eq. (1). However, understanding of the second term is still limited. This is mainly because it is not easy to separate the transient contribution in a conventional DCM experiment.

In this study, we propose a new DCM scanning mode, called combined waveform DCM method, using a triangular wave with a plateau region which allows to successfully separate the quasi-static and dynamic DCM currents. By applying combined waveform DCM to pentacene (Pn) MIS devices, we demonstrate that the current peak in the DCM curve reported by Ogawa et al. actually originates from the transient contribution owing to the carrier-spreading process in this device. In addition, the decay time of the transient current in the DCM corresponds to the inverse of the relaxation frequency which is obtained from capacitance–frequency (C–f) measurement. The combined waveform DCM allows us to simultaneously collect information about the effective capacitance and the inverse of the relaxation frequency of the organic device. This advantage will be useful when investigating the device physics in organic electronics.

2. Method

As mentioned above, the current in the MIS device (Fig. 1a) is expressed by Eq. (1). We briefly explain the basics of a typical DCM curve, assuming that the device is in a quasi-static state (corresponding to conventional C–V measurements). Since the organic and insulator layers beneath the top electrode work as capacitor dielectrics without carrier injection, the observed current is governed by the serially combined capacitance of the organic and insulator layers. The current is given by

$$I = C_{\text{eff}}\frac{dV}{dt} = \frac{C_{\text{org}}C_{\text{ins}}}{C_{\text{org}} + C_{\text{ins}}}\frac{dV}{dt}. \tag{2}$$

Here, C_{org} and C_{ins} are the capacitance of the organic and insulator layers, respectively. As shown in Fig. 1b and c, the start voltage of the triangular wave is set as 0 V, and we assume that the MIS device is completely depleted at the 0 V (Fig. 1c region 1 and 2). When holes are injected from the top electrode to the organic layer at the negative voltage (Fig. 1c region 3), they accumulate at the organic/insulator interface as shown in Fig. 1a. Assuming that the current flows through the organic layer without a significant voltage drop, only the insulator layer works as a capacitor dielectric, and hence the displacement current can be expressed as

$$I = C_{\text{ins}}\frac{dV}{dt}. \tag{3}$$

Since the capacitance of the insulator layer is larger than the combined capacitance, the current increases owing to a hole injection in the backward scan ($dV/dt < 0$).

At the beginning of the forward voltage scan ($dV/dt > 0$), the holes are discharged from the organic layer to the electrode (Fig. 1c region 4); then, the organic layer is depleted and back to its initial state. As a result, I–V curves of the typical MIS structure are obtained, as shown in Fig. 1c, when the dynamic current is negligibly small.

Conventional DCM is not suited to analyze the dynamic current for devices in a transient state, because the shape of the curve is often complicated owing to the coexistence of the two terms. In order to separate the transient term, we use a voltage waveform with a ramp and plateau region as shown in Fig. 1d. In this scanning mode, first a applied voltage is kept at the start voltage (V_{str}). Then, a ramp voltage is applied and both the quasi-static and dynamic currents are observed. At the hold voltage (V_{hold}), the ramp is switched to the plateau voltage, and only the transient term is observed due to $dV/dt = 0$. By changing the V_{hold}, we can directly examine the carrier properties in various states of the device.

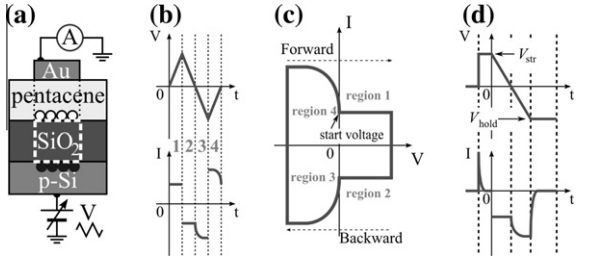

Fig. 1. (a) Schematic illustration of device structure and experimental setup. (b) Top: Applied voltage waveform in conventional DCM. Bottom: Current response with hole injection. (c) A typical C–V curve for a p-type semiconductor with hole injection. (d) Top: Applied voltage waveform in combined waveform DCM. Bottom: Current response with hole injection and transient current.

3. Experiment

The structure of the device under study is Au (50 nm)/Pn (100 nm)/SiO_2 (100 nm)/p-type Si (resistivity ~0.02 Ω cm). The organic layer and the Au electrode were successively fabricated using a conventional vacuum evaporation technique on a highly doped p-type Si substrate covered with SiO_2. The evaporation rate of the organic and metal layers was about 0.5 Å/s. The devices were transferred to a vacuum probe station and DCM was performed in the dark at room temperature. During the transfer of the device from the fabrication chamber to the vacuum probe station, the devices were exposed to air for a short time. We fabricated two kinds of devices, denoted as devices A

and B. The electrode area of device A is the same as the Pn area (2.4 mm^2), while that of device B (1.77 mm^2) is smaller than the Pn area (4.91 mm^2). Table 1 shows the area of Au (S_{Au}) and Pn (S_{Pn}), and the effective capacitances estimated from the device structure (dielectric constant of $\varepsilon_{Pn} = 4.0$ [22] and $\varepsilon_{SiO_2} = 3.8$). C_{dep} shows the geometrical capacitance of the device in depletion, normalized by the electrode area, and corresponds to the capacitance of Region (a) in Fig. 2. C_{inj} shows the capacitance of the device with the carrier injection from the Au electrode to the Pn layer and corresponds to the capacitance of Region (b) in Fig. 2. C_{acc} shows the capacitance of the device in which carriers accumulate over the entire Pn/SiO_2 interface and corresponds to the capacitance of Region (d) in Fig. 2.

DCM measurements were performed using the FCE-1 measurement system for ferroelectrics (Toyo Corp.) at Chiba University. The DCM curves were measured by applying biases within ±20 V to the p-type Si layer, with reference to the Au electrode. To investigate the frequency dependence of the DCM curve, the ramp rate of a triangular wave voltage was changed from 80 V/s to 800 kV/s. Impedance measurements were performed using a frequency response analyzer (Solartron SI 1260 Impedance/Gain-Phase Analyzer) combined with a dielectric interface (Solartron 1296) at University of Augsburg. The amplitude of the AC bias was set to 0.1 V for the *C–f* measurement and the DC bias was varied from −20 to 20 V.

4. Results and discussion

4.1. Analysis of DCM curves in conventional mode

Fig. 2 shows the typical DCM curves of devices A and B at a ramp rate of 80 V/s. The inset shows the comparison of the results between DCM and *C–V* measurement. Vertical axis is the current which is normalized by the electrode area divided by the ramp rate, corresponding to C_{eff} of a device with unit area. As shown in the inset (Fig. 2), the peak structure can only be observed for DCM. This is a unique feature of DCM and we will discuss its results in detail below.

In device A, the capacitance is equal to C_{dep} at voltages larger than 2 V, indicating that the device is depleted. In the backward scan, the negative current increases at 2 V owing to the hole injection from the Au electrode to the Pn layer. C_{eff} at voltages below −1 V is consistent with C_{inj} (Table 1). Then, in the forward scan, the injected carriers are discharged from the Pn to the Au electrode. Finally, the Pn layer is fully depleted and back to its initial state. In device A, the shape of the DCM curve in the forward scan is almost the same as that in the backward scan.

At voltages larger than 12 V in the backward scan, the DCM curve of device B is precisely equal to that of device A. When scanning the voltage to the negative side, the increase of the negative current owing to the hole injection appears in Region (b). The voltage of hole injection for device B is different from that for device A. This is maybe due to the effect of oxygen on Pn layer: since the Pn layer of device B is not fully covered by the top electrode, the hole injection property may be affected by the oxygen penetrated into the device. Finally, a larger capacitance about 0.8 mF/m^2 is observed in Region (d) after the current peak (Fig. 2 Region (c)). The capacitance estimated from the DCM curves indicates that the charge sheet is formed over the Pn/SiO_2 interface. After the sweep direction of the applied voltage is changed to forward at −20 V, the current gradually decreases owing to hole discharge (Fig. 2 Region (e)). The current continues to decay even in the positive bias region in device B, while the carrier discharges around the zero bias region in device A.

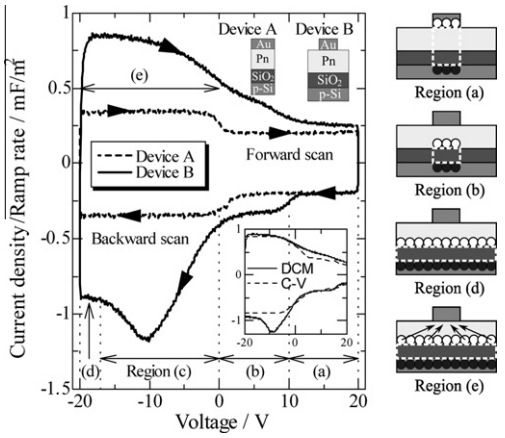

Fig. 2. Device structure dependence in DCM curves of an MIS diode (device A: dashed line, device B: solid line). Region (a): Without carrier injection. Region (b): Carrier injection from Au electrode to Pn layer. Region (c): Injected carrier spreading along the Pn/SiO_2 interface. Region (d): Carrier accumulation over the interface. Region (e): Carrier discharge from Pn layer to Au electrode. Inset: Comparison of DCM (solid line) with *C–V* curves (dashed line) for device B.

Table 1
Area and capacitance of devices A and B. The units of area and capacitance are mm^2 and mF/m^2, respectively.

	S_{Au}	S_{Pn}	C_{dep}	C_{inj}	C_{acc}
Device A	2.4	2.4	0.17	0.34	–
Device B	1.77	4.91	0.17	0.34	0.93

A peak structure is observed in Region (c), and it appears only in the DCM curve of device B. In device A, since the area of the Pn layer is the same as that of the top electrode, no carrier spreading along the Pn/SiO_2 interface can be expected after the carrier injection. Thus, we conclude that the current peak originates from the carrier-spreading effect at the Pn/SiO_2 interface. In addition, the slow discharge process in device B is also owing to its device structure because it is expected that the holes injected farther from the electrode will take longer to discharge.

Fig. 3 shows the DCM curves as a function of the frequency of the applied voltage in device A (left) and device B (right). The ramp rate of the triangular wave voltage is changed from 80 V/s to 800 kV/s. In device A, although there is no difference in the DCM curves from 80 V/s to 8 kV/s, the hole injection voltage shifts slightly to the negative voltage side at 80 and 800 kV/s with the increasing frequency (Fig. 3a). On the other hand, the peak structure in device B strongly depends on the ramp rate and finally disappears at 800 kV/s (Fig. 3c). This result implies that

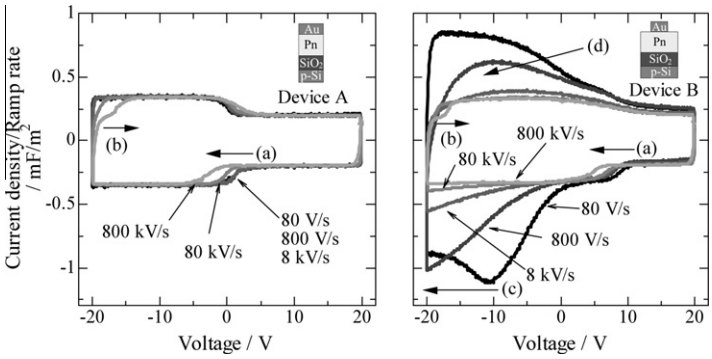

Fig. 3. DCM curves as a function of frequency of applied voltage in device A (left) and device B (right). Ramp rate is varied from 80 V/s to 800 kV/s. The curves showed characteristic changes with increasing frequency: (a) Shift of the hole injection voltage. (b) Shift of the start voltage of hole discharge. (c) Shift of the peak structure. (d) Rounded structure with hole discharge.

the relaxation time of the carrier-spreading process at the Pn/SiO_2 interface is longer than that of the carrier injection process from the electrode to the Pn layer.

In device B, we can observe the terrace structure, $-0.35\ mF/m^2$, corresponding to the C_{inj} at 80 V/s in the backward scan, that is, the injected holes first accumulate only under the electrode area and then start to spread laterally along the Pn/SiO_2 interface. This result indicates that the injected holes do not spread smoothly along the Pn/SiO_2 interface; this behavior can be explained as follows. When the voltage is applied to the sample, the electric field far from the electrode is not enough to drive the carriers laterally. Therefore, the potential difference between just under and far from the electrode prevents the injected holes from spreading at the Pn/SiO_2 interface. With increasing carrier density, the diffusion effect helps the holes to spread.

At the beginning of the forward scan in device A, the injected holes are discharged smoothly at a lower ramp rate than those discharged at 8 kV/s. In comparison, the shape of the DCM curves does not rise sharply at the apex of the triangular voltage (−20 V) for higher ramp rates, and the start voltage of the discharge shifts to the positive voltage side in Fig. 3b. This characteristic feature is also observed in device B at 800 kV/s. In addition, the rounded structure is observed only for device B when the holes which are located at the Pn/SiO_2 interface far from the electrode are discharged in the forward scan. These results indicate that the injected holes cannot follow the high frequency of the applied voltage.

4.2. Transient current characteristics during carrier spreading

Next, we discuss the results of the combined waveform DCM method. Fig. 4a and b show the combined waveform DCM curves for devices A and B, respectively. Vertical axis is the logarithm of the absolute value of current normalized by the electrode area. The measurement was performed while changing the hold voltage (V_{hold}) from 8 to −10 V in device A and from 14 to −18 V in device B, and the V_{str} of device A and B is set to 10 and 20 V, respectively. The V_{hold} is indicated by the bold number in Fig. 4a and b. The current density in the ramp region (before the voltage is held) corresponds to that measured by the traditional scanning mode in the backward scan.

In device A, while the V_{hold} is higher than 2 V, the Pn layer is completely depleted, as shown in Fig. 4a. At a V_{hold} lower than 0 V, the holes are injected from the electrode and accumulate at the Pn/SiO_2 interface. Just after the voltage is held, the current with various V_{hold} values decays immediately. If we define that t_{rel} is the time required for the current to decay less than $0.1\ mA/m^2$ from the beginning of the plateau voltage region, t_{rel} is less than 0.1 s in device A.

In Fig. 4b, the Pn layer is fully depleted around 14 V (depletion). While decreasing the V_{hold}, the current increases with a hole injection at 10 V (injection), and then, at V_{hold} = 2 V, the injected holes start to spread laterally along the Pn/SiO_2 interface. Finally, the charge sheet is completed over the interface at a V_{hold} lower than −10 V (accumulation). Note that the transient currents in the quasi-static, for example, depletion, injection, and accumulation states, decay immediately just after the voltage is held. On the other hand, it takes about 1 s for the transient current to decay at V_{hold} = 2 and −2 V in device B. This t_{rel} is much longer than that in the quasi-static state.

The above result demonstrates that we succeeded in extracting the dynamic current by using the combined waveform DCM method. The dynamic current with a large t_{rel} continues to flow during the hole-spreading at the Pn/SiO_2 interface, clearly indicating that the peak structure originates from the dynamic current. After the charge sheet is formed completely at the Pn/SiO_2 interface ($V < -10$), t_{rel} becomes much smaller. In this way, DCM is able to evaluate both quasi-static and dynamic carrier behavior in organic devices.

Fig. 4c and d show the capacitance-frequency (C–f) curves of devices A and B, respectively. The DC bias is changed from −20 to 20 V and is indicated by bold numbers. For frequencies higher than 10^3 Hz, the capacitance of device A almost agrees with the C_{dep}, because the injected holes cannot follow the frequency of the applied voltage. As the frequency slows, if the DC bias is larger than the hole injection voltage, the capacitance of the device increases and corresponds to C_{inj}. The frequency at the inflection point is called the relaxation frequency (f_{rel}). The f_{rel} at DC bias = −10 and −5 V is 129 Hz. In device A, one f_{rel} is ob-

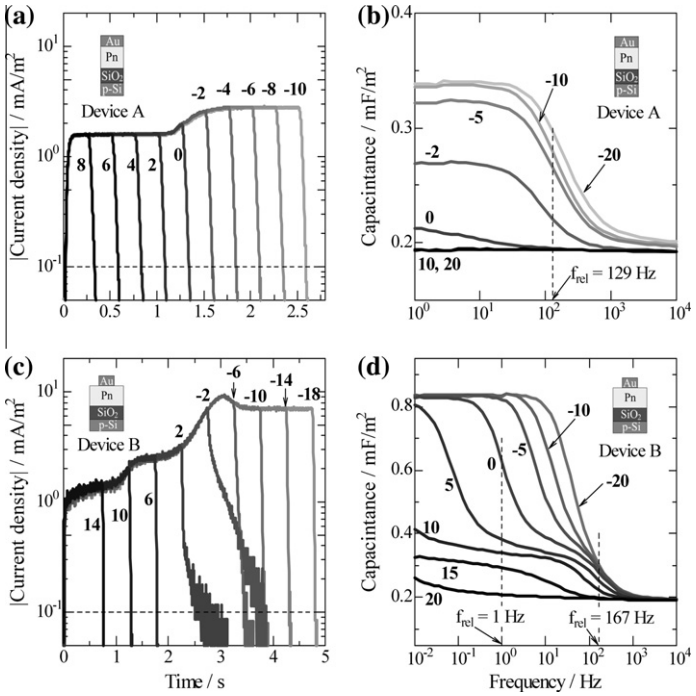

Fig. 4. Combined waveform DCM curves of device A (a) and device B (b) with the various V_{hold}. Ramp rate is 8 V/s and bold numbers show the V_{hold}. C–f curves of device A (c) and device B (d). Bold numbers show the DC bias and f_{rel} shows the relaxation frequency.

served between the depletion and injection states and reflects the hole injection speed from the electrode to the Pn layer.

In device B, the Pn layer is also depleted at frequencies higher than 10^3 Hz, as in device A. For lower frequencies, the capacitance starts to increase from a few hundred hertz; for example, f_{rel} = 167 Hz at DC bias = −5 and 0 V. This f_{rel} is comparable to that estimated for device A; this result indicates that the holes accumulated just under the electrode are following the frequency of the applied voltage. When lowering the frequency, a second increase of the capacitance can be observed at DC bias = 0 V. Since the capacitance almost corresponds to C_{acc} at the low frequency region, this second f_{rel} reflects the hole spreading speed along the Pn/SiO_2 interface. The inverse of the relaxation frequency is about 1 s, by inverting the observed f_{rel} of 1 Hz. This value corresponds well with t_{rel} of combined waveform DCM. This result demonstrates that the combined waveform DCM method is a useful tool to observe not only the effective capacitance of a device but also the relaxation time, as impedance spectroscopy.

The carrier spreading effect has been observed in some reports about inorganic FET [23,24] and organic devices [4,5,20,25–28]. By analyzing the admittance spectra, Ullah et al. suggest that the observed C–V behavior originates from a parasitic, lateral conduction effect occurring at the perimeter of the electrode [28]. In principle, the conventional C–V measurements detect the carrier behavior in static state under each step of DC voltage, which does not correspond to dynamic processes such as formation and annihilation of charge sheet under sweeping voltage. The latter is important to discuss switching properties of OFETs. On the other hand, DCM can investigate the carrier injection, accumulation and discharging processes separately. Actually, the peak structure due to transient current including information about the speed of carrier spreading (dC/dt) was observed only in the formation process (backward scan). The area of the charge sheet is changing with finite dC/dt during the formation, but almost constant in the annihilation (forward scan). From these viewpoints, DCM is a useful tool to investigate the channel behavior of OFETs, especially the switching process.

5. Conclusion

In the DCM of a Pn MIS structure, the carrier injection from the electrode to the organic layer, spreading along the Pn/SiO_2 interface, and the accumulation at the interface were clearly observed. The combined waveform DCM method was proposed and the quasi-static and dynamic currents of DCM were successfully separated in the plateau voltage region. We demonstrated that a current peak observed in the DCM curve originates from the carrier spreading along the Pn/SiO_2 interface. The transient current with a very long decay time was found during the formation of the charge sheet at the Pn/SiO_2 interface. Its decay time is consistent with t_{rel} estimated from the C–f measurement. These results indicate that DCM is a powerful tool for investigating the quasi-static and dynamic behavior of carriers in organic devices. By using various

types of combined waveforms, we can expect further extensions of DCM to investigate carrier behavior in detail.

Acknowledgments

We thank Dr. S. Ogawa for his helpful suggestions. This work was supported by the Global-COE program at Chiba University (Advanced School for Organic Electronics, G-03, MEXT), KAKENHI (Grant Nos. 21245042 and 22750167), and the Funding Program for World-Leading Innovative R&D on Science and Technology (FIRST). YT gratefully acknowledges JSPS Research Fellowships for Young Scientists (Grants No. 22·7042). WB also acknowledges financial support by JSPS.

References

[1] G. Horowitz, Adv. Mater. 10 (1998) 365–377.
[2] C.D. Dimitrakopoulos, P.R.L. Malenfant, Adv. Mater. 14 (2002) 99–117.
[3] S.A. DiBenedetto, A. Facchetti, M.A. Ratner, T.J. Marks, Adv. Mater. 21 (2009) 1407–1433.
[4] S. Ogawa, Y. Kimura, H. Ishii, M. Niwano, Jpn. J. Appl. Phys. 42 (2003) L1275–L1278.
[5] S. Ogawa, T. Naijo, Y. Kimura, H. Ishii, M. Niwano, Synth. Met. 153 (2005) 253–256.
[6] Y. Suzue, T. Manaka, M. Iwamoto, Jpn. J. Appl. Phys. 44 (2005) 561–565.
[7] T. Manaka, E. Lim, R. Tamura, M. Iwamoto, Thin Solid Films 499 (2006) 386–391.
[8] S.M. Sze, Physics of Semiconductor Devices, second ed., John Wiley & Sons, New York, 1981.
[9] S. Scheinert, W. Schliefke, Synth. Met. 139 (2003) 501–509.
[10] Y.-M. Chen, C.-F. Lin, J.-H. Lee, J. Huang, Solid-State Electron 52 (2008) 269–274.
[11] T. Manaka, C.-Q. Li, X.-M. Cheng, M. Iwamoto, J. Chem. Phys. 120 (2004) 7725–7732.
[12] T. Manaka, E. Lim, R. Tamura, D. Yamada, M. Iwamoto, Appl. Phys. Lett. 89 (2006) 072113.
[13] T. Manaka, E. Lim, R. Tamura, M. Iwamoto, Nat. Photon. 1 (2007) 581–584.
[14] A.J. Twarowski, A.C. Albrecht, J. Chem. Phys. 70 (1979) 2255–2261.
[15] K. Iriyama, M. Shiraki, K. Thuda, A. Okada, M. Sugi, S. Iizima, K. Kudo, S. Shiokawa, T. Moriizumi, T. Yasuda, in: Proc. First Photovoltaic Science and Engineering Conf. Japan, Tokyo, 1979, Jpn. J. Appl. Phys. 19(Suppl. 19-2) (1980) 173.
[16] S. Egusa, N. Gemma, M. Azuma, J. Appl. Phys. 71 (1992) 2042–2044.
[17] S. Egusa, A. Miura, N. Gemma, M. Azuma, Jpn. J. Appl. Phys. 33 (1994) 2741–2745.
[18] Y. Noguchi, N. Sato, Y. Tanaka, Y. Nakayama, H. Ishii, Appl. Phys. Lett. 92 (2008) 203306.
[19] Y. Noguchi, N. Sato, Y. Miyazaki, H. Ishii, Appl. Phys. Lett. 96 (2010) 143305.
[20] S. Ogawa, T. Naijo, Y. Kimura, H. Ishii, M. Niwano, Appl. Phys. Lett. 86 (2005) 252104.
[21] Y. Liang, C.D. Frisbie, H.-C. Chang, P.P. Ruden, J. Appl. Phys. 105 (2009) 024514.
[22] A. Bolognesi, M. Berliocchi, M. Manenti, A.D. Carlo, P. Lugli, K. Lmimouni, C. Dufour, IEEE T. Electron Dev. 51 (2004) 1997–2003.
[23] H.-A.-R. Jung, K.-H. Park, J.-H. Lee, IEEE Electr. Device L. 28 (2007) 12.
[24] S. Dhar, S. Haney, L. Cheng, S.-R. Ryu, A.K. Agarwal, J. Appl. Phys. 108 (2010) 054509.
[25] E. Itoh, I. Torres, C. Hayden, D.M. Taylor, Synth. Met. 156 (2006) 129–134.
[26] K.-D. Jung, C.A. Lee, D.-W. Park, B.-G. Park, H. Shin, J.D. Lee, IEEE Electr. Device L. 28 (2007) 3.
[27] D.M. Taylor, N. Alves, J. Appl. Phys. 103 (2008) 054509.
[28] M. Ullah, D.M. Taylor, R. Schwodiauer, H. Sitter, S. Bauer, N.S. Sariciftci, Th. B. Singh, J. Appl. Phys. 106 (2009) 114505.

formed on flexible substrates have been particularly attractive due to their potential applications in environment-friendly nonvolatile memory devices with low-power consumption and with flexible storage elements.

This letter reports data on the electrical bistability properties and the memory mechanisms of OBDs fabricated utilizing CIS/ZnS core–shell QDs blended with a PVK layer on indium-thin-oxide (ITO)-coated polyethylene terephthalate (PET) substrates by using a spin-coating method. Transmission electron microscopy (TEM) measurements were performed to investigate the structural properties of the colloidal CIS/ZnS core–shell QDs blended with a PVK layer. Current–voltage (I–V) measurements and data fitting were carried out to investigate the electrical bistability and the memory mechanisms of the Al/PVK + [CIS/ZnS QDs]/ITO/PET devices, and the memory mechanisms of the OBDs fabricated on flexible PET substrates are described on the basis of the I–V results.

The inorganic/organic nanocomposites consisting of colloidal CIS/ZnS QDs and a PVK conducting polymer layer used in this study were prepared on ITO-coated PET substrates by using a spin-coating technique. The PVK polymer was purchased from the Sigma–Aldrich Co., and the molar mass of the PVK was approximately 25,000 g/mol. The substrates were ultrasonically cleaned by using acetone and methanol and were thoroughly rinsed in deionized water. The chemically-cleaned substrates were then dried by using N_2 gas with a purity of 99.9999% in order to avoid interaction with air. The formation process of the CIS/ZnS QDs solution was started by using a CIS core solution. That solution consisting of 8 ml of octadecene (ODE), 0.1 mmol of indium acetate, and 0.3 mmol of miristic acid was mixed in a 25-ml three-neck flask. Then, the mixed solution was degassed at 110 °C for 2 h, and a Cu-thiol stock solution at 250 °C was added. Subsequently, the solution was heated at 200–210 °C for 2 h. Copper iodide, 0.3 mmol, was mixed with dodecanethiol, 3 ml, for the synthesis of the Cu-thiol stock solution. Then, the mixed solution, while being stirred, was slightly heated on a hot plate. When the synthesis of the CIS core solution was finished, the synthesized solution was in situ cooled to form the ZnS shell at room temperature. Zn acetate, 0.5 mmol, was added to the CIS core solution, and the solution was heated to 230 °C. Then, the solution was aged for 1.5 h at 230 °C.

To fabricate the CIS/ZnS core–shell QDs blended with a PVK layer, we added 2 mg of a $CuInS_2$/ZnS QDs solution to 50 mg of PVK dissolved in 5 ml of toluene. Then, the mixed solution was ultrasonicated for 30 min to obtain a uniform solution. After the substrate had been mounted onto a susceptor in the spin coater, the mixed solution was coated on the substrate by using a spin-coating method at 2500 rpm for 25 s. Then, the solvents existing on the samples were removed by putting the samples onto a hot plate at 90 °C for 30 min. Finally, Al top electrodes with thicknesses of 180 nm were thermally deposited through a metal mask at a system pressure of 1×10^{-6} torr. The diameter of the top Al electrode was approximately 0.3 mm, and the area of the bottom electrode was 2 cm × 2 cm. A schematic diagram of the OBDs fabricated utilizing CIS/ZnS QDs blended with a PVK layer is shown in Fig. 1(a).

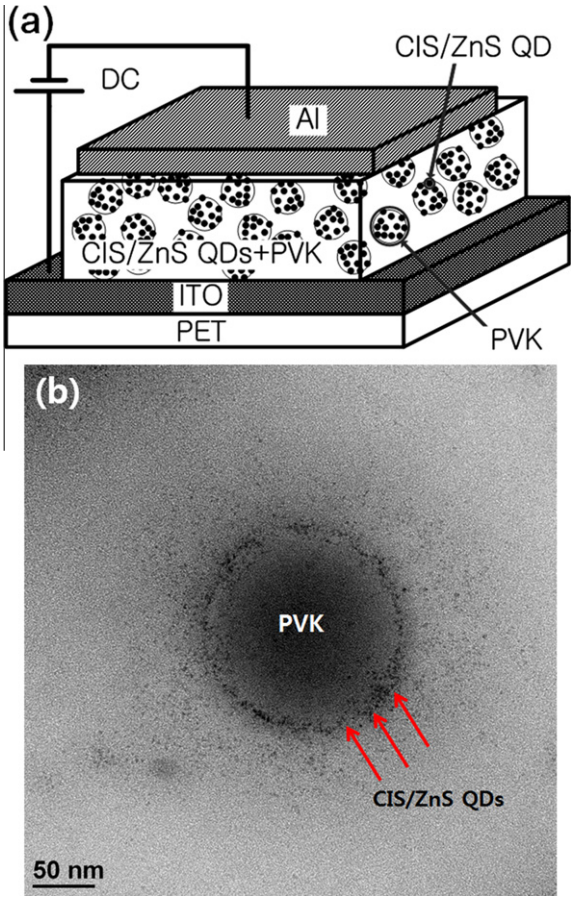

Fig. 1. (a) Schematic diagram of the OBDs based on CIS/ZnS core–shell QDs blended with a PVK polymer. (b) Plane-view bright-field transmission electron microscopy image of CIS/ZnS core–shell QDs blended with a PVK polymer.

TEM measurements (model: STEM/TEM (CM30)) were done at 200 kV. The samples for the TEM measurements were prepared by cutting and polishing with diamond paper to a thickness of approximately 30 μm and then argon-ion milling at liquid-nitrogen temperature to electron transparency. I–V measurements were performed by using a HP 4140B I–V meter at room temperature in an atmosphere.

Fig. 1(b) shows a plane-view bright-field TEM image of the CIS/ZnS QDs blended with a PVK polymer matrix. An apparent aggregation of the CIS/ZnS QDs appears around the surfaces of the PVK molecules. The TEM image indicates that the PVK has particle-like features with diameters of about 150 nm. Fig. 1(b) shows that the CIS/ZnS QDs, indicated by arrows, were attached to the surface of a PVK particle-like structure. The average diameter of the CIS/ZnS QDs is approximately 3 nm.

Fig. 2 shows the I–V curves for the Al/PVK + [CIS/ZnS QDs]/ITO/PET device. The voltage across the device was varied from −3.5 to 3.5 to −3.5 V in all cases, as shown in Fig. 2. When the bottom ITO layer is biased positive, the bias condition is forward. The I–V curves for the device clearly show current hysteresis behaviors, which are

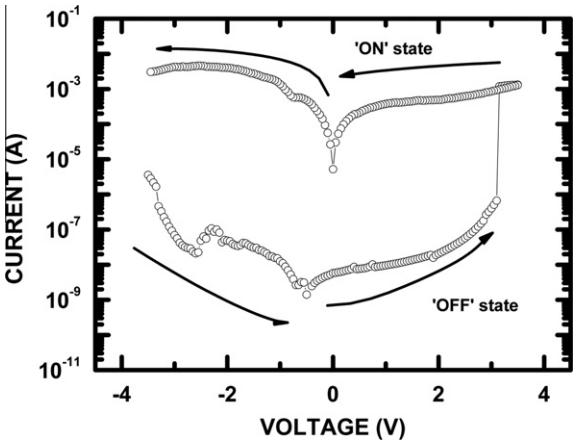

Fig. 2. Current–voltage curves for the Al/PVK + [CIS/ZnS QDs]/ITO/PET device. The scanning step of the applied voltage is 0.05 V.

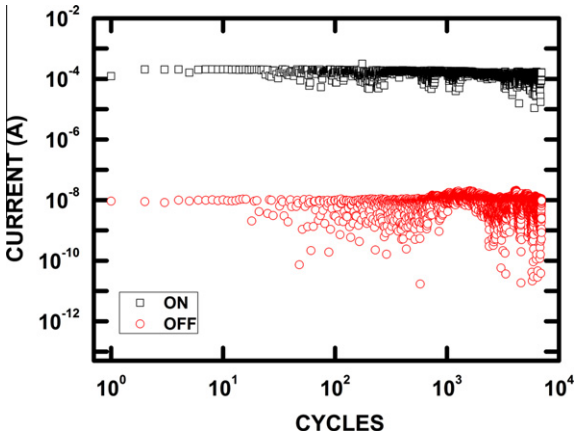

Fig. 3. Cycling stress test of the Al/PVK + [CIS/ZnS QDs]/ITO/PET device under a reading bias of 1 V.

essential features of bistable devices. The "ON" and the "OFF" states correspond to relatively high-conductivity and relatively low-conductivity states, respectively [21]. The maximum current ratio between the "ON" and the "OFF" states for the device at 1 V is as large as 3.9×10^4. The device without an applied voltage at an initial stage maintains an "OFF" state with a current below 10^{-6} A. The current of the device gradually increases with increasing applied voltage. The current of the device at 3.1 V abruptly increases to 10^{-3} A, indicative of a state transition to the "ON" state in the device. The transition from the "OFF" state to the "ON" state is equivalent to the "writing" process in a digital memory cell. After the transition has been achieved, the "ON" state current is maintained, with currents between 10^{-4} and 10^{-2} A, even after turning off the external power, which is evident from the *I–V* curves under a reverse bias sweep, as shown in Fig. 2. The "OFF" state can be achieved by applying a reverse bias of −3.5 V, at which the device returns to the "OFF" state from the "ON" state, indicative of the completion of the "erasing" process in a digital memory cell.

Fig. 3 shows the currents as functions of the number of cycles for the "ON" and the "OFF" states of the Al/PVK + [CIS/ZnS QDs]/ITO/PET device. A sequence of pulses lasting less than 1 ms was employed to confirm the memory endurance for the write/erase stress. An endurance larger than 5×10^3 ON/OFF switchings, together with a rewritable capability, is clearly observed. The current fluctuations in the "ON" and the "OFF" states for a large number of cycles are attributed to incomplete writing and erasing operations [6]. However, even though a state fluctuation appears, the ON/OFF ratio in the device is always larger than 10^3.

To investigate the carrier transport mechanisms in the device, we fitted the data for the *I–V* curves by using three conduction models: thermionic emission (TE), space-charge-limited current (SCLC), and Fowler–Nordheim (FN) tunneling models [22–24]. Fig. 4(a) is a log–log plot of the current as a function of the applied voltage for the entire voltage sweep range. Fig. 4(a) shows the fitting data for various current transport models in different voltage regions. The *I–V* curves exhibit three regions with different

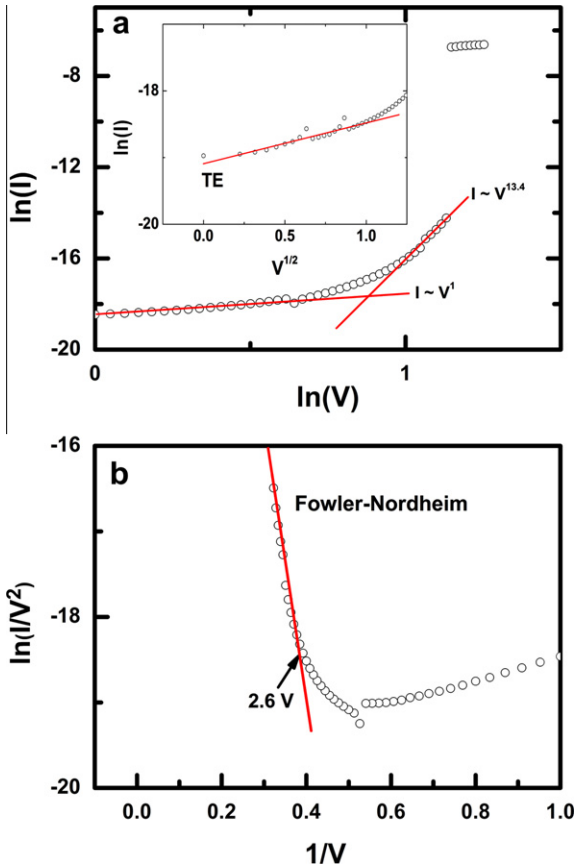

Fig. 4. (a) A log–log plot of the current as a function of the voltage for an Al/PVK + [CIS/ZnS QDs]/ITO/PET device, and the curves are fitted for the space-charge-limited current mechanism. The inset represents the ln(*J*) vs. $V^{1/2}$ characteristics at lower voltages, and the curve is fitted for the thermionic-emission conduction mechanism. (b) Fowler–Nordheim plot for OBDs with CIS/ZnS QD–PVK nanocomposites.

behaviors. The data at lower voltages up to 1 V can be well fitted with the TE model, as shown in the inset of Fig. 4(a), where ln(*I*) is plotted against $V^{1/2}$. The small current in the

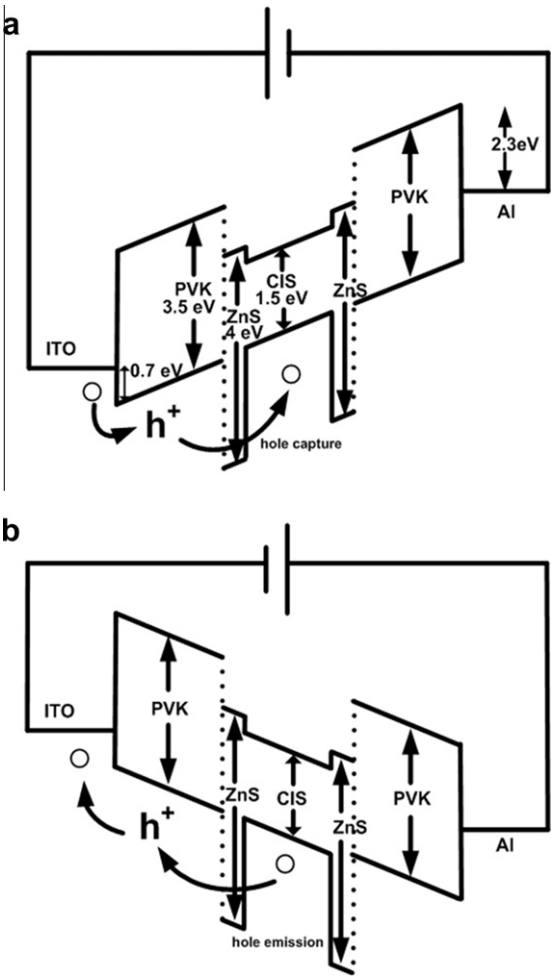

Fig. 5. Schematic diagrams of the electronic structures corresponding to the operating mechanisms of the (a) writing and (b) erasing processes for the Al/PVK + [CIS/ZnS QDs]/ITO/PET device. The energy levels for the CIS core are taken from Ref. [27], and those for the ZnS shell and the PVK layer are taken from Refs. [29,26], respectively.

region might be attributed to thermally-generated electrons from the PVK layer or from the interface between the electrode and the PVK layer [25]. Two distinct regions with different linear slopes are clearly observed at voltages above 1 V, with a changeover at 2 V. The equation $I \propto V^{\alpha}$ was used for the SCLC behavior, where α is an exponential fitting parameter. The exponential fitting parameter, α, is about 1 for the voltage range between 1 and 2 V, indicating that the electrical conduction is dominantly governed by Ohm's law in this range. The *I–V* characteristics in the applied voltage range between 2 and 3.1 V show a large linear slope of $\alpha = 13.7$, and the response follows a dominant, exponential trap SCLC ($\alpha \gg 2$). This result indicates that the traps are distributed exponentially within a forbidden gap. At voltages above 3.1 V, the magnitude of the current starts to significantly increase to higher values. Because the plot of $\ln(I/V^2)$ as a function of $1/V$ at voltages above 2.6 V is linear, as shown in Fig. 4(b), the carrier conduction in this region is dominantly attributed to FN tunneling.

Fig. 5 shows schematic diagrams of the electronic structures corresponding to the mechanisms of the writing and the erasing operations for the Al/PVK + [CIS/ZnS QDs]/ITO/PET device under (a) positive and (b) negative voltages. The LUMO and the HOMO represent the energy levels of the lowest unoccupied molecular orbital and the highest occupied molecular orbital of the PVK layer, respectively [26]. The HOMO of the PVK layer and the energy bands of the CIS core at the writing operation bend downward with increasing positive voltage, so holes injected from the ITO are tunneled through the PVK layer. The injected electron cannot tunnel through the barrier because of the relatively high barrier height at the interface between the electrode and the PVK layer. After the injection of holes via FN tunneling, the holes existing at the HOMO are transported to the CIS core along the direction of the applied voltage by hopping among the PVK molecules [27,28]. The ZnS shell around the CIS core suppresses the leakage of the captured holes due to its high energy barrier, as shown in Fig. 5(a). This results in the writing operation of the memory devices, which is transited from the OFF to the ON states. When a negative voltage is applied to the ITO electrode, the device remains in an ON state until the critical voltage of -3.5 V is reached, at which the CIS cores are discharged. The discharge of the holes captured in the CIS core about -3.5 V results in a significant decrease in the current, and the current of the device again goes to a low-current-conducting OFF state, as shown in Fig. 5(b). This results in the erasing process of the devices, which is transited from the ON to the OFF states.

In summary, OBDs based on CIS/ZnS core–shell QDs blended with a PVK layer were fabricated on flexible substrates by using a simple spin-coating method. TEM images showed that the CIS/ZnS core–shell QDs were attached to the surfaces of PVK molecules. The *I–V* curves at 300 K for the devices exhibited electrical bistabilities due to the existence of the CIS/ZnS core–shell QDs embedded in a PVK layer. The maximum ON/OFF ratio of the current bistability for the OBDs was as large as 3.9×10^4, and the cycling endurance of the ON/OFF switching for the OBDs was larger than 5×10^3. The fitting data of the *I–V* curves demonstrated that the carrier transport mechanisms related to the memory effects of the devices for the writing process were attributed to the TE and the SCLC processes while the corresponding mechanisms for the erasing process were related to the FN tunneling process.

Acknowledgments

This work was supported by the National Research Foundation of Korea (NRF) Grant funded by the Korea Government (MEST) (No. 2010-0018877).

References

[1] Y. Zhang, G.M. Dalpian, B. Fluegel, S.-H. Wei, A. Mascarenhas, X.-Y. Huang, J. Li, L.-W. Wang, Novel approach to tuning the physical properties of organic–inorganic hybrid semiconductors, Phys. Rev. Lett. 96 (2006) 026405-1–026405-4.
[2] S. Blumstengel, S. Sadofev, C. Xu, J. Puls, F. Henneberger, Converting Wannier into Frenkel excitions in an inorganic/organic hybrid semiconductor, Phys. Rev. Lett. 97 (2006) 237401-1–237401-4.

[3] S. Coe, W.-K. Woo, M. Bawendi, V. Bulovic, Electroluminescence from single monolayers of nanocrystals in molecular organic devices, Nature 420 (2002) 800–803.
[4] C.-J. Sun, Y. Wu, Z. Xu, B. Hu, J. Bai, J.-P. Wang, J. Shen, Enhancement of quantum efficiency of organic light emitting devices by doping magnetic nanoparticles, Appl. Phys. Lett. 90 (2007) 232110-1–232110-3.
[5] S.H. Kim, K.S. Yook, J.Y. Lee, J. Jang, Organic light emitting bistable memory device with high on/off ratio and low driving voltage, Appl. Phys. Lett. 93 (2008) 053306-1–053306-3.
[6] T.-Y. Chang, Y.-W. Cheng, P.-T. Lee, Electrical characteristics of an organic bistable device using an Al/Alq_3/nanostructured MoO_3/Alq_3/p^+-Si structure, Appl. Phys. Lett. 96 (2010) 043309-1–043309-3.
[7] F. Huguenin, D.S. dos Santos Jr., A. Bassi, F.C. Nart, O.N. Oliveira Jr., Charge storage capability in nanoarchitectures of V_2O_5/chitosan/poly(ethylene oxide) produced using the layer-by-layer technique, Adv. Funct. Mater. 14 (2004) 985–991.
[8] A.K. Cuentas-Gallegos, M. Lica-Cantu, N. Casan-Pastor, P. Gomez-Romero, Nanocomposite hybrid molecular materials for application in solid-state electrochemical supercapacitors, Adv. Funct. Mater. 15 (2005) 1125–1133.
[9] A. Tang, F. Teng, Y. Hou, Y. Yang, F. Tan, S. Qu, Z. Wang, Optical properties and electrical bistability of CdS nanoparticles synthesized in dodecanethiol, Appl. Phys. Lett. 96 (2010) 163112-1–163112-3.
[10] H. Kind, H. Yan, B. Messer, M. Law, P. Yang, Nanowire ultraviolet photodetectors and optical switches, Adv. Mater. 14 (2002) 158–160.
[11] X. Li, Y. Wu, D. Steel, D. Gammon, T.H. Stievater, D.S. Katzer, D. Park, C. Piermarocchi, L.J. Sham, An all-optical quantum gate in a semiconductor quantum dot, Science 301 (2003) 809–811.
[12] J.H. Kim, J.Y. Jin, J.H. Jung, I. Lee, T.W. Kim, S.K. Lim, C.S. Yoon, Y.-H. Kim, Formation and electrical properties of $Ni_{1-x}Fe_x$ nanocrystals embedded in a polyimide layers for applications as nonvolatile flash memories, Appl. Phys. Lett. 86 (2005) 032904-1–032904-3.
[13] N.J. Craig, J.M. Taylor, E.A. Lester, C.M. Marcus, M.P. Hanson, A.C. Gossard, Tunable nonlocal spin control in a coupled-quantum dot system, Science 304 (2004) 565–567.
[14] F. Li, D.-I. Son, J.-H. Ham, G.-J. Kim, J.H. Jung, T.W. Kim, Memory effect of nonvolatile bistable devices based on CdSe/ZnS nanoparticles sandwiched between C_{60} layers, Appl. Phys. Lett. 91 (2007) 162109-1–162109-3.
[15] Official Journal of the European Union L037 0019-0023, 2003, 0019.
[16] L. Ma, J. Liu, S. Pyo, Y. Yang, Organic bistable light-emitting devices, Appl. Phys. Lett. 80 (2002) 362–364.
[17] L. Ma, S. Pyo, J. Ouyang, Q. Xu, Y. Yang, Nonvolatile electrical bistability of organic/metal–nanocluster/organic system, Appl. Phys. Lett. 82 (2003) 1419–1421.
[18] A. Prakash, J.Y. Ouyang, J.L. Lin, Y. Yang, Polymer memory device based on conjugated polymer and gold nanoparticles, J. Appl. Phys. 100 (2006) 054309-1–054309-5.
[19] W.T. Kim, J.H. Jung, D.I. Son, T.W. Kim, Current bistability and carrier transport mechanisms of organic bistable devices based on hybrid Ag nanoparticle–polymethyl methacrylate polymer nanocomposites, Appl. Phys. Lett. 96 (2010) 253301-1–253301-3.
[20] P.-T. Lee, T.-Y. Chang, S.-Y. Chen, Tuning of the electrical characteristics of organic bistable devices by varying the deposition rate of Alq_3 thin film, Org. Electron. 9 (2008) 916–920.
[21] L. Ma, J. Liu, Y. Yang, Organic electrical bistable devices and rewritable memory cells, Appl. Phys. Lett. 80 (2002) 2997–2999.
[22] M.A. Lampert, P. Mark, Current Injection in Solids, Academic Press, New York, 1970.
[23] S.M. Sze, Physics of Semiconductor Devices, second ed., John Wiley and Sons, New York, 1981.
[24] K.C. Kao, W. Hwang, Electrical transport in solids, in: B.R. Pamplin (Ed.), International Series in the Science of Solid State, vol. 14, Pergamon Press, New York, 1981, pp. 64–144.
[25] H.T. Lin, Z. Pei, Y.J. Chan, Carrier transport mechanism in a nanoparticle-incorporated organic bistable memory device, IEEE Electron Device Lett. 28 (2007) 569–571.
[26] S.-C. Chang, G. He, F.-C. Chen, T.-F. Guo, Y. Yang, Degradation mechanism of phosphorescent-dye-doped polymer light-emitting diodes, Appl. Phys. Lett. 79 (2001) 2088–2090.
[27] E. Arici, N.S. Sariciftci, D. Meissner, Hybrid solar cells based on nanoparticles of $CuInS_2$ in organic matrices, Adv. Funct. Mater. 13 (2003) 165–171.
[28] J. Wu, L. Ma, Y. Yang, Single-band Hubbard model for the transport properties in bistable organic/metal nanoparticle/organic devices, Phys. Rev. B 69 (2004) 115321-1–115321-9.
[29] H. Mattousssi, L.H. Radzilowski, B.O. Dabbousi, E.L. Thomas, M.G. Bawendi, M.F. Rubner, Electroluminescence from heterostructures of poly(phenylene vinylene) and inorganic CdSe nanocrystals, J. Appl. Phys. 83 (1998) 7965–7974.

(TBADN) are used as neat green and blue fluorescent materials, respectively. Indium-Tin-Oxide (ITO) and LiF/Al are used as the two electrodes between which the organic material is sandwiched. All samples are fabricated by the deposition of the organic materials and metals at a rate of 1.5–3 Å/s using thermal evaporation at a base pressure of $\sim 5 \times 10^{-6}$ torr on UV ozone-cleaned ITO-coated glass substrates. For photo-degradation, monochrome illumination from a 200 W Hg–Xe lamp equipped with Oriel-77200 monochromator is used. All tests are carried out in a nitrogen atmosphere.

3. Results and discussion

A group of samples of structure ITO/AlQ_3(50 nm)/LiF(x)/Al(100 nm) are fabricated and tested. In theses samples, the thickness of the LiF, x, is varied from 0 to 20 nm. Fig. 1 shows the changes in FL yield (as evident from changes in FL intensity normalized to the initial value at the same excitation power density) of these samples versus time elapsed during which the samples are either left in the dark or exposed to 365 nm illumination of power density $\sim$0.5 mW/cm^2. The temperature of the samples is kept at 22 ± 1 °C during the measurements to eliminate any thermal effects on FL yield. As the figure shows, the sample without LiF (solid triangle) shows no detectable decrease in FL yield after exposure to illumination for a period of 5 h, indicating that any photo-degradation in AlQ_3 molecules under these irradiation conditions must be insignificant in the given time frame. On the other hand, the ones containing LiF show a significant decrease in FL yield under the same conditions. More notably, the decrease in FL becomes faster as the thickness of the LiF layer increases from 1 to 20 nm. Furthermore, the decrease in FL from a sample with 100 nm AlQ_3 and 1 nm LiF (solid square) is found to be slower than that from a sample with 50 nm AlQ_3 and 1 nm LiF (hollow triangle). These observations suggest that the decrease in FL of the samples incorporating LiF may be due to the diffusion of certain species at the AlQ_3/LiF interface to bulk AlQ_3 which acts as FL quenchers, hence the less pronounced effect in samples with thicker AlQ_3 and/or thinner LiF. It should be pointed out that keeping a sample of the structure ITO/AlQ_3(50 nm)/LiF(5 nm)/Al(100 nm) in the dark (solid diamond) leads to no detectable change in FL yield, indicating that the change in FL is induced by illumination. The observations therefore suggest that the diffusing species behind the decrease in FL must be the product of some photo-induced interactions between LiF and AlQ_3.

The inset of Fig. 1 displays the percentage change in FL yield observed in these samples after 1 h of illumination versus the thickness of the LiF layer. From the figure, the faster deterioration in FL with LiF thickness appears to proceed less rapidly as thickness increases, possibly reaching saturation at a thickness of about 20 nm. This can perhaps be explained in terms of the fact that the LiF/AlQ_3 interface is not abrupt but rather diffuse possibly due to the disparate molecular sizes of AlQ_3 and LiF [15], which would allow for significant interpenetration between molecules of the two materials at the interface. Therefore, the FL loss increases quickly with LiF thickness initially (when LiF is less than 5 nm) as a result of an increasing effective AlQ_3–LiF interface, yet gradually saturates when LiF exceeds 10 nm when AlQ_3 "valleys" have been filled with LiF and no more AlQ_3–LiF interface is formed.

To further investigate the nature of the processes behind the behavior observed in Fig. 1, we study the effect of applying electric fields on the photo-induced changes in the FL yield. Fig. 2a shows the changes in FL yield of a sample of structure ITO/AlQ_3(50 nm)/LiF(1 nm)/Al(100 nm) versus time elapsed during which the samples are subjected to one of the following stress scenarios: (i) irradiation only (denoted by L), during which the sample is exposed to 405 nm illumination of power density $\sim$0.6 mW/cm^2, (ii) reverse bias only (denoted by R), during which a reverse bias of −6 V is applied across the ITO and the Al electrodes of the sample (with ITO at a more negative potential relative to Al), and (iii) irradiation and reverse bias together

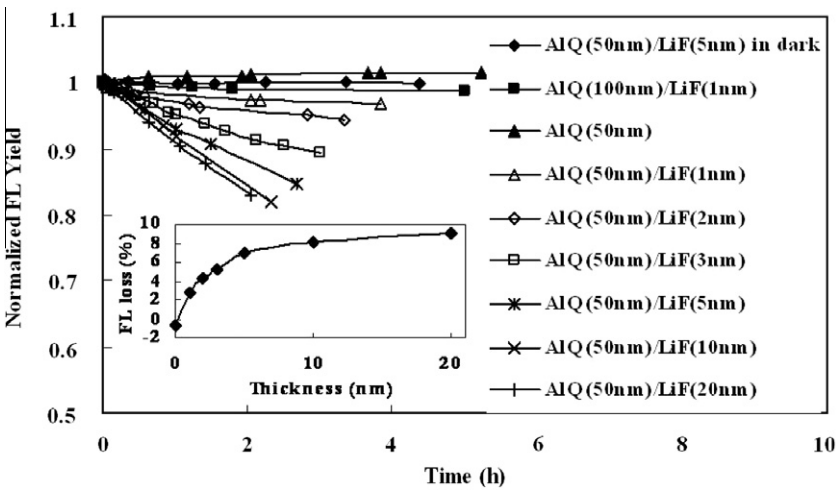

Fig. 1. The changes in FL yield versus time elapsed during which the samples are either left in the dark or exposed to 365 nm illumination of power density $\sim$0.5 mW/cm^2. Inset: the percentage change in FL yield after 1 h of illumination versus the thickness of the LiF layer.

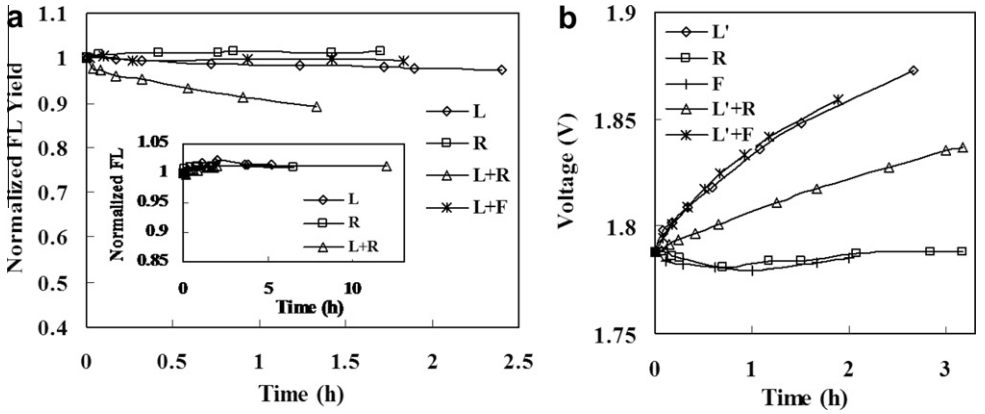

Fig. 2. (a) The changes in FL yield of samples of the structure ITO/AlQ_3(50 nm)/LiF(1 nm)/Al(100 nm) versus time elapsed during which the samples are subjected to stress scenario L, R, L + R and L + F. Inset: the changes in FL yield of samples of the structure ITO/AlQ_3(50 nm)/Al(100 nm) versus time elapsed during which the samples are subjected to stress scenario L, R and L + R. (b) The changes in V_d of the samples versus time elapsed during which the samples are subjected to scenario L' (535 nm illumination, 1 mW/cm^2), R, F, L' + R and L' + F, respectively.

(denoted by L + R), during which the sample is subjected to the conditions of (i) and (ii) simultaneously, and (iv) irradiation and forward bias together (denoted by L + F), during which the sample is subjected to the conditions of applying a forward bias of +4 V and (ii) simultaneously. A lower voltage is used in case of the forward bias in order to minimize electrical aging effects which could result from the higher current flow in this case [16]. Despite the voltage difference, the electric field across the AlQ_3/LiF interface is expected to be similar in both forward and reverse bias. This is in view of the fact that carrier concentration in the AlQ_3 will be much higher in case of forward bias (due to the good electron injection characteristics of the AlQ_3/LiF/Al contact and the much higher mobility of electrons in AlQ_3 versus that of holes [17]); hence an expectedly much lower field across the AlQ_3 layer itself in this case. As Fig. 2a depicts, exposing the sample to illumination (scenario i) leads to a gradual decrease in its FL yield, which is consistent with the results in Fig. 1, and exposing it to illumination in the presence of reverse bias (scenario iii) significantly accelerates such change. In contrast, applying a reverse bias alone (i.e. without irradiation) (scenario ii) does not bring about any detectable change in FL yield, again verifying that the underlying mechanisms are photo-induced in nature. The fact that a reverse bias can accelerate the photo-induced deterioration in FL yield suggests that the underlying processes are also electrochemical in nature. Interestingly, applying a forward bias during irradiation (scenario iv) appears to have a little bearing on the changes in FL yield, evident in the fact that the decrease in FL yield in this case is very similar to that obtained by irradiation alone without bias (i.e. similar to that obtained from scenario i). This suggests that the diffusing species, produced by some photo-induced interactions between LiF and AlQ_3 at the AlQ_3/LiF interface, may be positively charged, hence its faster migration into the AlQ_3 layer under reverse bias. In this regard, the slow decrease in FL yield observed in case of scenario i (i.e. L only) can be attributed to the diffusion of these positively charged species from the AlQ_3/LiF interface (where it is formed by photo-induced interactions) into the AlQ_3 layer, driven by concentration gradients. In scenario iii (i.e. L + R), the application of a reverse bias during illumination significantly accelerates the migration of these positively charged species into the AlQ_3 layer, hence the much faster deterioration in FL in this case. As the formation and/or release of these species from the AlQ_3/LiF interface depends on photo-induced processes, the behavior is not observed with scenario ii (R only, no illumination), and the FL yield remains essentially unchanged in this case. According to this model, we would expect the application of an opposite (i.e. forward) bias to slow down the diffusion of these species. A close examination of the FL trends in the figure indeed supports this notion, where the application of a forward bias during illumination (scenario iv, L + F) can be seen to result in a slower decrease in FL yield versus that observed under scenario i (L only). Although the difference between the two trends on the figure is small, additional work shows that using a thicker LiF layer enhances the difference.

It should be pointed out that the faster degradation in FL yield in case of scenario iii may, in principle, be alternatively attributed to an increased concentration of photogenerated carriers of AlQ_3, due to electric field-induced dissociation of AlQ_3 excitons [18], and hence to a subsequent increase in exciton–carrier interactions [19] or to a higher concentration of the unstable AlQ_3 cations [16]. In order to investigate this alternative hypothesis, we tested other samples that do not contain the LiF layer. The results are shown in the inset of Fig. 2a. As shown in the figure, subjecting the samples of the structure ITO/AlQ_3(50 nm)/Al(100 nm) to scenarios i, ii and iii leads to no detectable change in FL yield, indicating that the changes observed above are associated with LiF and are not merely due to a higher concentration of photogenerated carriers in the AlQ_3 layer. The results therefore rule out this alternative degradation mechanism.

Besides the degradation in FL yield of the bulk organic layer, the AlQ_3/LiF/Al contact also degrades as the samples

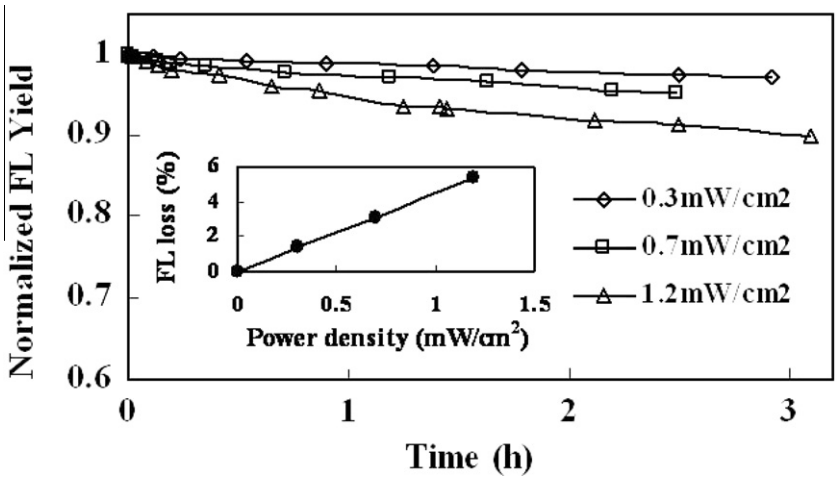

Fig. 3. Normalized FL yield of samples of structure ITO/AlQ_3(50 nm)/LiF(3 nm)/Al(100 nm) as a function of time during which the samples are exposed to 405 nm illumination at three different power densities; ~0.3, 0.7 and 1.2 mW/cm^2. Inset: the FL loss after 1 h of illumination versus the illumination power density.

are subjected to irradiation. Fig. 2b shows the changes in V_d of the samples at current density 0.3 mA/cm^2 versus time elapsed during which the samples are subjected to scenario L' (535 nm illumination, 1 mW/cm^2), R, F, L'+ R and L' + F, respectively. As the figure depicts, exposing the sample to illumination (scenario L', L' + R and L' + F) leads to a gradual increase in V_d, suggesting a deteriorated electron injection from the cathode and thus a degraded AlQ_3/LiF/Al contact.

We have also investigated the dependence of this behavior on the illumination power density and on the optical absorbance of the organic layer. Fig. 3 shows normalized FL yield of samples of structure ITO/AlQ_3(50 nm)/LiF(3 nm)/Al(100 nm) as a function of time during which the samples are exposed to 405 nm illumination at three different power densities; ~0.3, 0.7 and 1.2 mW/cm^2. As the figure shows, increasing the power density brings about a faster degradation in FL yield. The inset in Fig. 3 shows the FL loss after 1 h of illumination versus the illumination power density. Clearly, the figure shows a linear correlation, indicating that the effect depends linearly on the density of AlQ_3 excited states. Fig. 4a shows normalized FL yield versus time for a sample of structure ITO/AlQ_3(50 nm)/LiF(5 nm)/Al(100 nm) subjected to monochromatic illumination of various wavelengths in the range 365–640 nm. We note that there are small variations in the illumination power density at the different wavelengths. We therefore also normalize the data to the same illumination power density, using the linear correlation as established from Fig. 3. Fig. 4b displays the same data after being normalized to the same illumination power density. Fig. 4c displays the FL loss after 1 h of illumination according to the results in

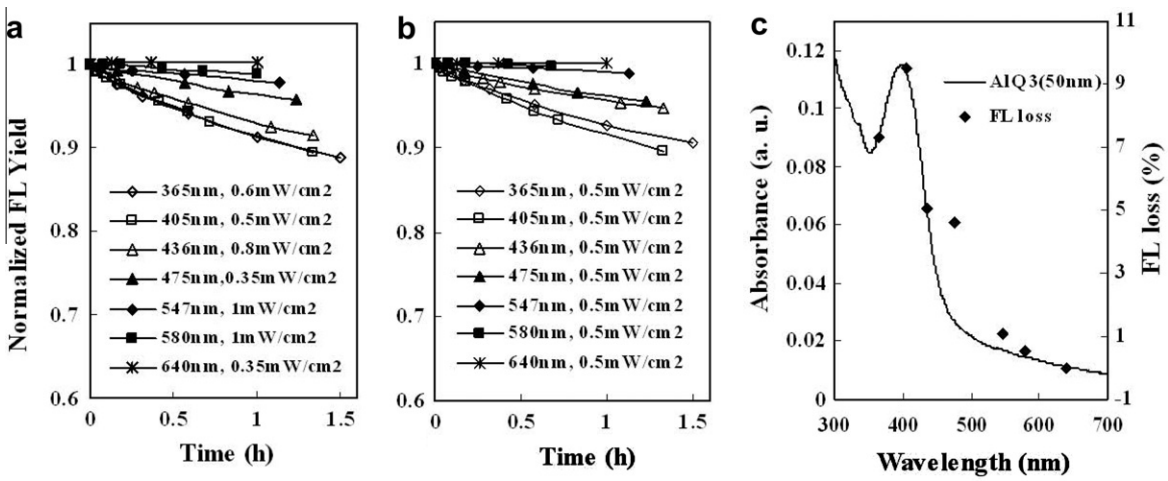

Fig. 4. (a) Normalized FL yield versus time for samples of structure ITO/AlQ_3(50 nm)/LiF(5 nm)/Al(100 nm) subjected to monochromatic illumination of various wavelengths. (b) The same data after being normalized to the same illumination power density. (c) The FL loss after 1 h of illumination according to the results in Fig. 4b and the UV–Vis absorption spectrum of neat AlQ_3.

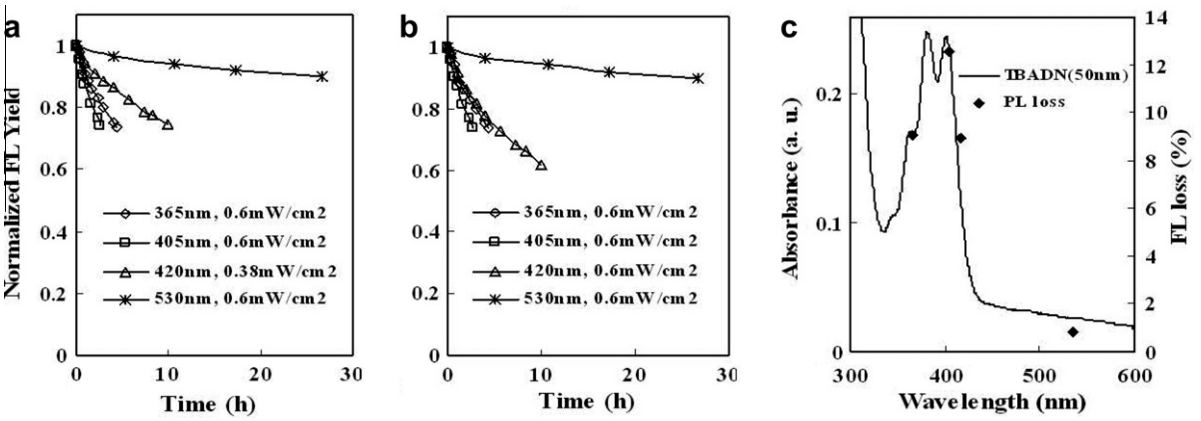

Fig. 5. (a) Normalized FL yield versus time for samples of structure ITO/TBADN(50 nm)/LiF(5 nm)/Al(100 nm) subjected to monochromatic illumination of various wavelengths. (b) The same data after being normalized to the same illumination power density. (c) The FL loss after 1 h of illumination according to the results in Fig. 4b and the UV–Vis absorption spectrum of neat TBADN.

Fig. 4b. It also shows UV–Vis absorption spectrum of neat AlQ_3. Clearly, the results show a strong correlation between the FL loss and the absorption spectrum of AlQ_3, evident in the fact that illumination at wavelengths where AlQ_3 has stronger absorption lead to a faster degradation in FL yield. The results indicate that absorption of light by the AlQ_3 layer, rather than by other species at the contact, is behind the photo-induced processes. To further confirm this conclusion, a parallel study is carried out on another set of samples that utilize another organic material TBADN. Clearly, Fig. 5c also shows a strong correlation between the FL loss and the absorption spectrum of TBADN in this case. These results convincingly indicate that the photo-induced interactions at organic/LiF/Al contact involve interactions between LiF (or some LiF species) and adjacent organic molecules that are in an excited state; possibly due to some photo-chemical reactions, and which can lead to the release of some positively charged quenchers that can diffuse into the organic layers, and, subsequently reduce the FL yield. It should be pointed out that in case of OLEDs, the effect of the diffusion of the FL quenchers could be less serious due to the applied forward bias; however, the photo-degradation of the organic/LiF/Al contacts by the device own EL leads to a deteriorated electron injection and thus poor stability [14].

4. Summary

In summary, we study the photo-stability of the organic/LiF/Al contacts widely used in organic optoelectronic and photovoltaic devices. Exposing organic/LiF/Al to illumination is found to lead to a decrease in FL yield of the organic layer. The decrease in FL is found to be due to the diffusion of certain positively charged species, possibly resulting from photochemical interactions with the LiF layer. Evidence of the correlation between the density of the excited states in the organic material and the rate of photo-degradation of the organic/LiF/Al contact is also reported. The results reveal that these widely used contacts suffer poor photo-stability.

Acknowledgements

Support by DALSA Corporation and the Natural Science and Engineering Research Council of Canada is acknowledged.

References

[1] L.S. Hung, C.W. Tang, M.G. Mason, Appl. Phys. Lett. 70 (1997) 2.
[2] L.S. Hung, C.W. Tang, M.G. Mason, P. Raychaudhuri, J. Madathil, Appl. Phys. Lett. 78 (2001) 4.
[3] S.E. Shaheen, G.E. Jabbour, M.M. Morrell, Y. Kawabe, B. Kippelen, N. Peyghambarian, J. Appl. Phys. 84 (1998) 4.
[4] G.E. Jabbour, B. Kippelen, N.R. Armstrong, N. Peyghambarian, Appl. Phys. Lett. 73 (1998) 9.
[5] S.E. Shaheen, C.J. Brabec, N.S. Sariciftci, Appl. Phys. Lett. 78 (2001) 6.
[6] C.J. Brabec, S.E. Shaheen, C. Winder, N.S. Sariciftci, Appl. Phys. Lett. 80 (2002) 7.
[7] F. Padinger, R.S. Rittberger, N.S. Sariciftci, Adv. Funct. Mater. 13 (2003) 1.
[8] D. Grozea, A. Turak, X.D. Feng, Z.H. Lu, D. Johnson, R. Wood, Appl. Phys. Lett. 81 (2002) 17.
[9] T. Mori, H. Fujikawa, S. Tokito, Y. Taga, Appl. Phys. Lett. 73 (1998) 19.
[10] M.G. Mason, C.W. Tang, L.-S. Hung, P. Raychaudhuri, J. Madathil, D.J. Giesen, L. Yan, Q.T. Le, Y. Gao, S.-T. Lee, L.S. Liao, L.F. Cheng, W.R. Salaneck, D.A. dos Santos, J.L. Brédas, J. Appl. Phys. 89 (2001) 5.
[11] H. Heil, J. Steiger, S. Karg, M. Gastel, H. Ortner, H. von Seggern, J. Appl. Phys. 89 (2001) 1.
[12] R. Schlaf, B.A. Parkinson, P.A. Lee, K.W. Nebesny, G. Jabbour, B. Kippelen, N. Peyghambarian, N.R. Armstrong, J. Appl. Phys. 84 (1998) 12.
[13] P. He, S.D. Wang, S.T. Lee, L.S. Hung, Appl. Phys. Lett. 82 (2003) 19.
[14] Q. Wang, Y. Luo, H. Aziz, Appl. Phys. Lett. 97 (2010) 063309.
[15] C. Shen, A. Kahn, J. Schwartz, J. Appl. Phys. 89 (2001) 1.
[16] H. Aziz, Z.D. Popovic, N. Hu, A. Hor, G. Xu, Science 283 (1999) 1900.
[17] S. Berleb, W. Brutting, Phys. Rev. Lett. 89 (2002) 28.
[18] Z.D. Popovic, H. Aziz, J. Appl. Phys. 98 (2005) 13510.
[19] N.C. Giebink, B.W. D'Andrade, M.S. Weaver, J.J. Brown, S.R. Forrest, J. Appl. Phys. 105 (2009) 124514.

be advantageous as a charge injecting electrode for AS since it possesses a high work function of up to >6.1 eV, but does not introduce any series impedance into the device structure. As we will show the hole mobility of N,N′-diphenyl-N,N′-bis-(1-naphthyl)-1-1′-biphenyl-4,4′-diamine (α-NPD) measured using AS with a Cl-ITO anode is found to be closer to the value measured by TOF than for an equivalent measurement with a MoO_3 charge injection layer.

2. Experimental

Single carrier devices for the AS measurements were fabricated in a Kurt J. Lesker LUMINOS® cluster tool on commercially patterned ITO coated glass with a sheet resistance less than 15 Ω/□. Substrates were ultrasonically cleaned with a standard regiment of Alconox®, acetone, and methanol followed by UV ozone treatment for 15 min. The standard device structure is as follows: anode/α-NPD (536 nm)/Ag. The anodes used in this work were bare ITO, Cl-ITO, and ITO coated with 0.75 nm of MoO_3. The active area for all devices was 2 mm^2. Cl-ITO was produced by treatment of pre-cleaned substrates with 1,2-dichlorobenzene vapor for 3 min in a sealed Pyrex Petri dish in a UV photo surface processor (SEN Lights Corporation), followed by UV ozone treatment for 3 min [10]. The thickness of the organic layer was measured using a quartz crystal microbalance calibrated using spectroscopic ellipsometry and were verified for each device using capacitance-voltage measurements. The frequency-dependent capacitance of the devices was measured using an HP4192A impedance analyzer in a vacuum cryostat [11]. Ultraviolet photoelectron spectroscopy (UPS) measurements were performed using a PHI 5500 Multi-Technique system (base pressure of $\sim 10^{-10}$ Torr) with attached organic deposition chamber using He Iα ($h\nu$ = 21.22 eV).

3. Theory

The theory behind the AS technique has been extensively discussed in the literature [1,2,4]. A very thorough summary of the technique complete with all derivations is provided in Ref. [4]. In short the AS technique is based on the measurement of the frequency-dependent capacitance of an organic thin film. The capacitance is found to exhibit a characteristic minimum as a function of frequency, which is indicative of the carrier transit time τ_{dc} across the organic film. Typically the frequency-dependent capacitance is re-plotted as the negative differential susceptance,

$$-\Delta B = -\omega(C - C_{geo}), \tag{1}$$

where $\omega = 2\pi f$ is the angular frequency, C is the capacitance and $C_{geo} = \varepsilon A/d$ is the geometric capacitance. This plot typically yields a maximum in $-\Delta B$ at a characteristic frequency $f_r = \tau_r^{-1}$. Simulation results have shown that $\tau_{dc} = 0.56\tau_r$ for non-dispersive transport [4]. The dc mobility is then given by,

$$\mu_{dc} = \frac{d^2}{\tau_{dc}(V - V_{bi})}, \tag{2}$$

where d is the device thickness, V is the applied voltage and V_{bi} is the built-in potential, which can be measured using photovoltaic measurements [12].

4. Results and discussion

Fig. 1 shows the room temperature (300 K) current-voltage (*IV*) characteristics of α-NPD single carrier devices with ITO, ITO/MoO_3, and Cl-ITO anodes. As expected the device with bare ITO anode has the lowest current density due a large injection barrier at the ITO/α-NPD interface. The current density of the devices with ITO/MoO_3 or Cl-ITO anodes is ~2 orders of magnitude higher than the device with bare ITO anode. Transition metal oxides, such as MoO_3, have been reported to lower the injection barrier into HTL molecules due to their high work function [13]. Cl-ITO also has a high work function of up to >6.1 eV (measured by the authors using photoelectron spectroscopy), which allows for a lower injection barrier into α-NPD, which has a HOMO of 5.4 eV as measured by UPS. The current density of the device with Cl-ITO anode is slightly higher than that of the device with ITO/MoO_3 anode, particularly at higher currents. This suggests that there is a series impedance introduced by the MoO_3 layer. The mobility extracted from devices with ITO/MoO_3 anode using AS might therefore be influenced by this series impedance.

To confirm that the difference in the *IV* characteristics is a result of series impedance and not due to a difference in injection barrier, we measured the energy-level alignment of α-NPD with ITO/MoO_3 and Cl-ITO using UPS. Fig. 2 shows the UPS valence band spectra of ITO/MoO_3 and Cl-ITO with and without a 3 nm thick layer of α-NPD. As expected there is no density of states at the Fermi level for ITO/MoO_3, which indicates that the MoO_3 layer is a semiconductor and hence will contribute a finite series

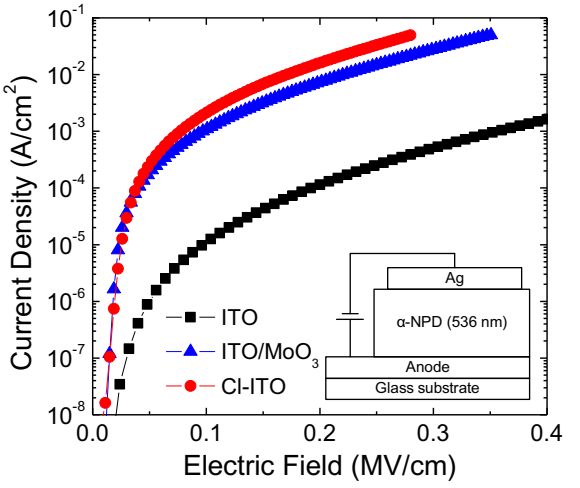

Fig. 1. Current density as a function of electric field for α-NPD single carrier devices with ITO, ITO/MoO_3, and Cl-ITO anodes. The inset shows the device structure. The electric field (F) is taken as $F = (V - V_{bi})/d$, where V is the applied voltage, V_{bi} is the built-in potential determined from photovoltaic measurements and d is the device thickness (536 nm).

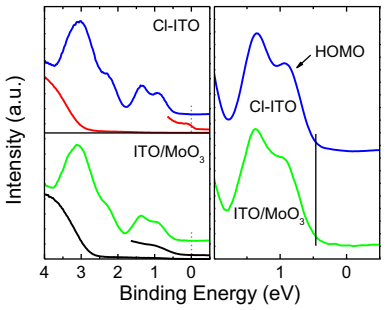

Fig. 2. Valence band spectra of ITO/MoO_3 (bottom left) and Cl-ITO (top left) with and without a 3 nm thick layer of α-NPD measured using UPS. An enlargement of the density of states near the Fermi level (indicated by the vertical dashed line) for ITO/MoO_3 and Cl-ITO is shown on the left. An enlargement of the HOMO derived peak of α-NPD on both samples is also shown on the right.

impedance to the device. The valence band of the Cl-ITO is nearly identical to that of UV ozone treated ITO (not shown). The finite density of states at the Fermi level of ITO is clearly visible in the Cl-ITO valence band spectra (ITO is a degenerate semiconductor). After deposition of α-NPD the work function of the ITO/MoO_3 and Cl-ITO decreased to 4.9 eV for both samples from 5.9 eV and 6.1 eV, respectively, indicating a large interfacial dipole at both interfaces. The HOMO derived peak of α-NPD deposited on ITO/MoO_3 and Cl-ITO are also shown in Fig. 2. The HOMO of α-NPD is found to be ~0.45 eV on both samples, which indicates that the injection barriers are the same. We have previously measured a much higher barrier of ~0.6 eV for bare UV ozone treated ITO [15], which is consistent with the *IV* characteristics shown in Fig. 1. Hence the difference in the *IV* characteristics should be the result of the series impedance introduced by the MoO_3 layer.

Fig. 3 shows the frequency-dependent capacitance and conductance of α-NPD single carrier devices with Cl-ITO anode as a function of applied bias. At zero applied bias the capacitance is nearly constant with frequency and is representative of the geometric capacitance C_{geo}. The decline in capacitance at high frequency is due to the parasitic capacitance of the test fixture and does not affect the present analysis. With increasing applied bias the characteristic minimum in the capacitance curve shifts to higher frequency, indicative of the field dependent mobility of the organic. Fig. 4 shows the negative differential susceptance $-\Delta B$ as a function of voltage for the same device. The characteristic frequency $f_r = \tau_r^{-1}$, indicated by the arrows, shifts to higher frequency with increasing applied bias. This trend indicates that the carrier transit time is shorter at higher applied bias and hence the mobility increases with electric field.

Fig. 5 shows the hole mobility as a function of electric field extracted from the negative differential susceptance of α-NPD single carrier devices with ITO, ITO/MoO_3, and Cl-ITO anodes. The mobility measured by TOF is also shown as reference [15]. As expected the mobility extracted from the device with ITO anode using AS is significantly lower than the value measured using TOF. What is

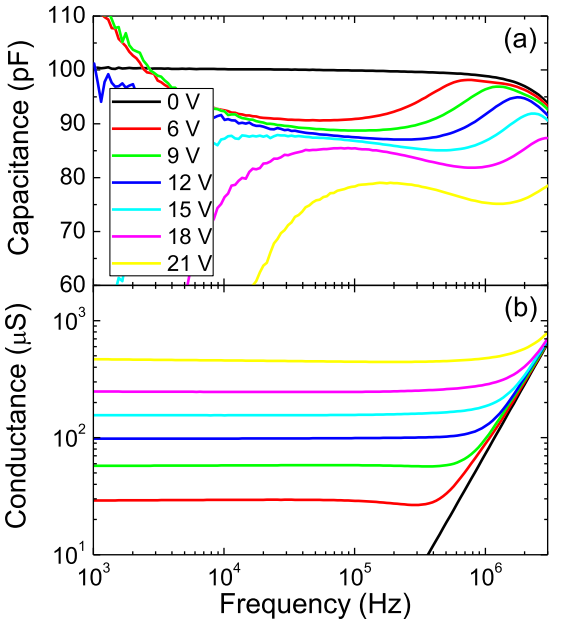

Fig. 3. Admittance spectra as a function of applied bias for α-NPD single carrier devices with Cl-ITO anode showing (a) the frequency-dependent capacitance and (b) the frequency-dependent conductance.

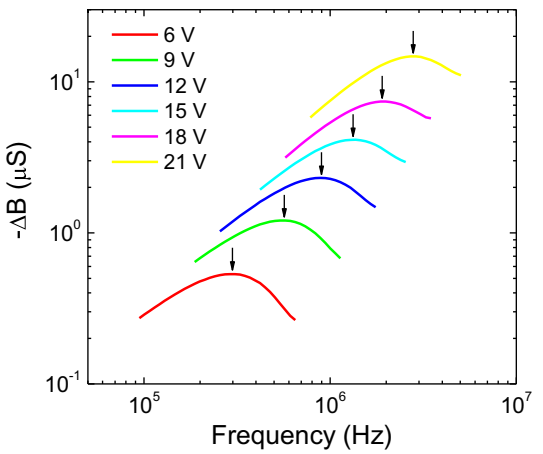

Fig. 4. Frequency-dependent negative differential susceptance as a function of applied bias for α-NPD single carrier devices with Cl-ITO anode. The arrows indicate the characteristics relaxation time $f_r = \tau_r^{-1}$.

more, the field dependence is also significantly different than the TOF results. This can be easily understood as there is a significant injection barrier of ~0.6 eV at the ITO/α-NPD interface [14]; as discussed above AS requires an Ohmic contact at the injecting electrode. The mobility extracted from the device with ITO/MoO_3 anode using AS is much closer to the value measured using TOF, but is still noticeably lower. Since MoO_3 has been reported to form an Ohmic contact with α-NPD [16] this implies that the impedance of the MoO_3 layer does indeed affect the AS measurements. On the other hand, the mobility extracted from the device with Cl-ITO anode using AS is nearly identical to the value measured using TOF, since the Cl-ITO

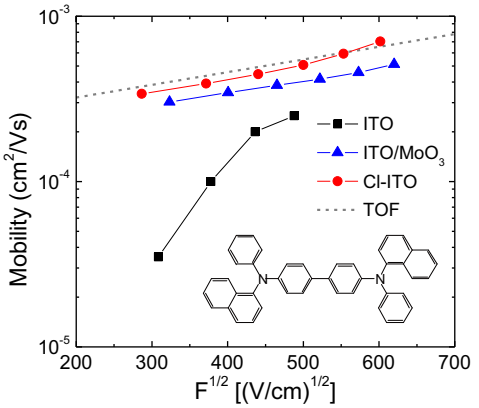

Fig. 5. The field dependent hole mobility as a function of the square root of electric field extracted from α-NPD single carrier devices with ITO, ITO/MoO_3, and Cl-ITO anodes using AS. The electric field (F) is taken as $F = (V - V_{bi})/d$, where V is the applied voltage, V_{bi} is the built-in potential determined from photovoltaic measurements and d is the device thickness (536 nm). The dashed line is the mobility measured by TOF shown as Ref. [14].

electrode does not introduce any series impedance into the device. Clearly, Cl-ITO is an advantageous charge injecting electrode for mobility measurements using AS.

5. Conclusion

In summary, we have shown that Cl-ITO can be used as a charge injecting electrode for mobility measurements using AS. The mobility extracted from devices with Cl-ITO anode using AS is found to be closer to the value measured by TOF than for devices with ITO/MoO_3 anode. The lower value of the mobility measured for the devices with ITO/MoO_3 anode is attributed to the effect of the series impedance introduced by the MoO_3 layer. Cl-ITO is therefore found to be an ideal charge injecting electrode for mobility measurements using AS since it possesses a high work function, but does not introduce any series impedance into the device structure.

Acknowledgment

We wish to acknowledge funding for this research from Natural Sciences and Engineering Research Council (NSERC) of Canada.

References

[1] H.C.F. Martens, H.B. Brom, P.W.M. Blom, Phys. Rev. B 60 (1999) R8489.
[2] S. Berleb, W. Brütting, Phys. Rev. Lett. 89 (2002) 286601.
[3] D. Poplavskyy, F. So, J. Appl. Phys. 99 (2006) 033707.
[4] S.W. Tsang, S.K. So, J.B. Xu, J. Appl. Phys. 99 (2006) 013706.
[5] O.J. Weiss, R.K. Krause, A. Hunze, J. Appl. Phys. 103 (2008) 043709.
[6] S.E. Debebe, W. Mammo, T. Yohannes, F. Tinti, A. Zanelli, N. Camaioni, Appl. Phys. Lett. 96 (2010) 082109.
[7] K.K. Tsung, S.K. So, J. Appl. Phys. 106 (2009) 083710.
[8] S.W. Tsang, S.C. Tse, K.L. Tong, S.K. So, Org. Electron. 7 (2006) 474.
[9] M. Hoping, C. Schildknecht, H. Gargouri, T. Riedl, M. Tilgner, H.H. Johannes, W. Kowalsky, Appl. Phys. Lett. 92 (2008) 213306.
[10] M.G. Helander, Z.B. Wang, J. Qiu, M.T. Greiner, D.P. Puzzo, Z.W. Liu, Z.H. Lu, Science 332 (2011) 944.
[11] M.G. Helander, Z.B. Wang, M.T. Greiner, J. Qiu, Z.H. Lu, Rev. Sci. Instrum. 80 (2009) 033901.
[12] G.G. Malliaras, J.R. Salem, P.J. Brock, J.C. Scott, J. Appl. Phys. 84 (1998) 1583.
[13] H. Lee, S.W. Cho, K. Han, P.E. Jeon, C.-N. Whang, K. Jeong, K. Cho, Y. Yi, Appl. Phys. Lett. 93 (2008) 043308.
[14] Z.B. Wang, M.G. Helander, M.T. Greiner, J. Qiu, Z.H. Lu, J. Appl. Phys. 107 (2010) 034506.
[15] S.W. Tsang, M.W. Denhoff, Y. Tao, Z.H. Lu, Phys. Rev. B 78 (2008) 081301.
[16] T. Matsushima, Y. Kinoshita, H. Murata, Appl. Phys. Lett. 91 (2007) 253504.

Unfortunately, the fabrication of polymer thin film transistors and diodes in which both the semiconductor and the dielectric layer are solution processable polymers has been limited. This limitation is due to the inherent fabrication problem whereby an underlying dielectric layer can be damaged by spincoating the overlying semiconducting layer, in the case of bottom-gate architecture or where an underlying semiconducting layer can be damaged by spincoating the overlying dielectric layer, in the case of top-gate device architecture.

Sun et al. [10] have reported baking their PMMA dielectric film at a high temperature of 220 °C for 30 min in nitrogen gas environment in order to make the film resistant to swelling and dissolution by trichlorobenzene (TCB) used to dissolve the overlying semiconducting layer. They observed that for PMMA films baked at lower temperatures, spincoating with TCB resulted in changes in film color and increase in surface roughness. Also the difficulty in finding an orthogonal and stable solvent that does not dissolve the underlying semiconducting film when spincoated has been identified as one of the obstacles in applying crosslinkable polymer thin gate dielectrics in top-gate transistor architectures [11]. The use of solution processable semiconductor with divinyltetramethylsiloxane-bis(bisbenzocyclobutene) derivative (BCB), as a solution processable dielectric has been reported [12,13], but it turns out that BCB requires a very high curing temperature (250 °C), which is difficult to handle at times.

This work introduces matrix-assisted pulsed-laser evaporation (MAPLE) [14–16], a derivative of pulsed laser deposition (PLD), as an alternative fabrication technique that circumvents the inherent solvent selectivity problem encountered in the fabrication of organic field-effect transistors (FET) and metal–insulator–semiconductor (MIS) diodes via spincoating. It has several advantages over traditional spincoating/dipcoating techniques. Since the organic molecules arrive at the substrate free of solvent molecules, the wettability issue is eliminated. Moreover, it allows homogenous film coverage of high molecular weight organic materials for layer-by-layer growth without any laser induced damage, and provides enhanced adhesion to the substrate. Besides offering the advantage of good layer-by-layer film control, remarkable features of this technique are its solvent non-selectivity and its ability to not cause the swelling and dissolution of polymer dielectrics and semiconductors, common inherent problems associated with spincoating.

Here, an organic semiconducting material, 9,9-dioctylfluorene-co-bis-N-N-(4-butylphenyl)-bis-N,N-phenyl 1,4-phenylenediamine (PFB) was dissolved in a toluene solvent and frozen at liquid nitrogen temperature. Then the frozen target is irradiated by a pulsed laser beam (e.g. KrF excimer laser), whose energy is absorbed by the toluene and is pumped away, thereby leaving the PFB molecules to be gently evaporated and deposited without causing any swelling or dissolution of the PMMA film on the substrate. Our prior studies of MAPLE deposited polyfluorene films show that the optical and structural properties of the films remain unchanged comparable to spincoated films [17].

2. Experimental

The organic FETs and MIS diodes employed in this work are of bottom-gate with PFB as the semiconductor and PMMA as the gate dielectric. In order to fabricate the devices, glass substrates were ultrasonically cleaned in water, acetone and alcohol after which 80 nm thick aluminum electrodes were evaporated onto them inside a glove box at a rate of 3 Å/s. PMMA (molecular weight (Mw): 996,000 g/mol) purchased from Sigma–Aldrich and dissolved in three different solvents: butylacetate, toluene, and anisole, were spincoated onto the cleaned glass substrates at 2000 rpm for 1 min resulting in film thicknesses of between 500 and 550 nm as measured using a reflectometer (Mprobe). Thereafter, the samples were baked at 100 °C for 1 h in order to achieve solvent evaporation. PFB was deposited using the MAPLE technique on top of the PMMA film. Details of the MAPLE technique are reported elsewhere [17]. Briefly, a PFB/toluene solution (2 mg/ml) was filtered through a 0.22 μm pore size polytetrafluoroethylene (PTFE) membrane syringe before use. The solution was poured into a target cup and cooled to liquid nitrogen temperature. The frozen target was then installed inside a vacuum chamber evacuated to $\sim 10^{-5}$ mbar. A KrF excimer laser (Lambda Physik COMPex, $\lambda = 248$ nm; pulse duration of 20 ns) at a pulse rate of 10 Hz and an energy density of 0.9 J/cm^2 was directed at 45° angle of incidence on the cold target (2 mm × 1 mm spot size). The target was rotated with a constant speed to avoid excessive heating and erosion of a single spot on the frozen sample (target). The majority of the laser intensity was initially absorbed by the solvent molecules (toluene) causing them to vaporize; the kinetic energy of the solvent molecules is then transferred to PFB through collective collisions, resulting in the polymer to evaporate and deposit on the substrate. All the PFB films were deposited at room temperature. The growth rate was ~0.6 nm/min.

The gold source and drain electrodes, which define a channel length, $L = 50$ μm and channel width, $W = 500$ μm for FETs, and top gold contacts for MIS diodes, were deposited though metallic shadow masks. The area of the MIS diodes was determined with the aid of a scanning electron microscopy to be 7.85×10^{-3} cm^2. The electrical characterization of the FETs and MIS diodes were carried out under ambient conditions with Keithley 2400 and 236 source/measure units and HP 4284A LCR meter, respectively. The dielectric/polymer film morphologies were determined with an atomic force microscope (AFM); the measurements were carried out in tapping mode. Each of our devices contains both FET and MIS diode with Al/PMMA/PFB/Au structure and is named according to the solvent used to dissolve PMMA: butylacetate (Sample A), toluene (Sample B), and anisole (Sample C).

3. Results and discussion

3.1. Dielectric film: morphology and electrical properties

The surface morphology of the films resulting from dissolving PMMA in butylacetate, toluene, and anisole,

obtained by means of AFM (Cypher scanning probe microscope) in tapping mode are shown in Fig. 1. The films exhibited very smooth surfaces with root mean square (rms) values of 2.18, 2.35, and 2.55 Å for butylacetate, toluene, and anisole, respectively. Parallel plate capacitor structures (Al/PMMA/Al) were fabricated to investigate the dielectric properties of PMMA. The leakage current density of the films is in the low 10^{-8} A cm^{-2} for applied fields of up to 1.4 MV cm^{-1} and measurements of the dielectric constant of PMMA dissolved in the different solvents revealed a decrease of the observed dielectric constant from approximately 3.50 at 5 kHz to 2.81 at 1 MHz. This range of values is in good agreement with other published reports [18,19].

The morphology of the PFB films on PMMA in this work is similar to MAPLE-deposited PF films on SiO_2, as reported in our earlier work [17]. The average rms value of the surface roughness of PFB films is ~10 to 15 nm in an area of 2×2 μm.

3.2. MIS diode characteristics

Fig. 2(a–c) shows capacitance–voltage (*C–V*) characteristics of PFB MIS diodes with PMMA dielectric dissolved in butylacetate, toluene, and anisole measured at four different frequencies in the low kHz range. Observable is the existence of frequency dispersions in the accumulation and depletion regions. The *C–V* curves are typical of p-type organic MIS behavior characterized by an accumulation of holes at the dielectric/semiconductor interface at large negative bias, a depletion of holes from the dielectric/semiconductor interface at less negative bias, and a deep depletion of holes from the dielectric/semiconductor interfacial region at positive bias, corresponding to the accumulation, depletion, and deep depletion regimes. No inversion is observed, which is typical of organic MIS diodes. The amount of frequency dispersion in accumulation capacitance, ΔC_{OX} is approximately 0.5%, 0.8%, and 0.9% for Samples A, B, and C, respectively. These values are smaller than similar observations involving inorganic devices [20]. The dispersion in the accumulation region may arise from a difference in the response of trapped and mobile charges in the interface and the bulk.

The insets of Fig. 2(a–c) shows the hysteresis effects observed by measurement of the devices at 5 kHz by sweeping the gate bias continuously in a staircase shape with a 0.4 V step, starting from −40 V, passing through 40 V, and finally back to −40 V. The magnitude of the hysteresis, Δ, is approximately 3.47, 8.62, and 3.97 V for Samples A, B, and C, respectively. The magnitude of hysteresis observed here with PMMA as the insulator is far less than observed with the use of SiO_2 [21]. It has been noted that polar groups in PMMA result in a slow polarization of the bulk dielectric [22]. A reduced hysteresis in PMMA compared

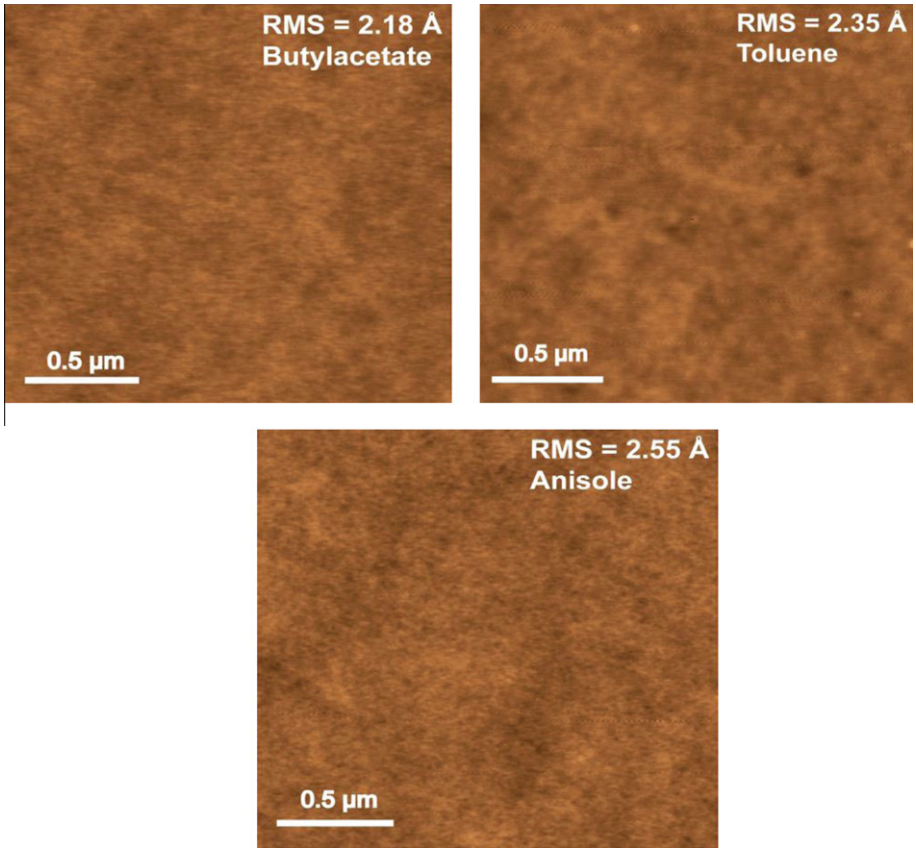

Fig. 1. Atomic force micrographs of PMMA films prepared in different solvents.

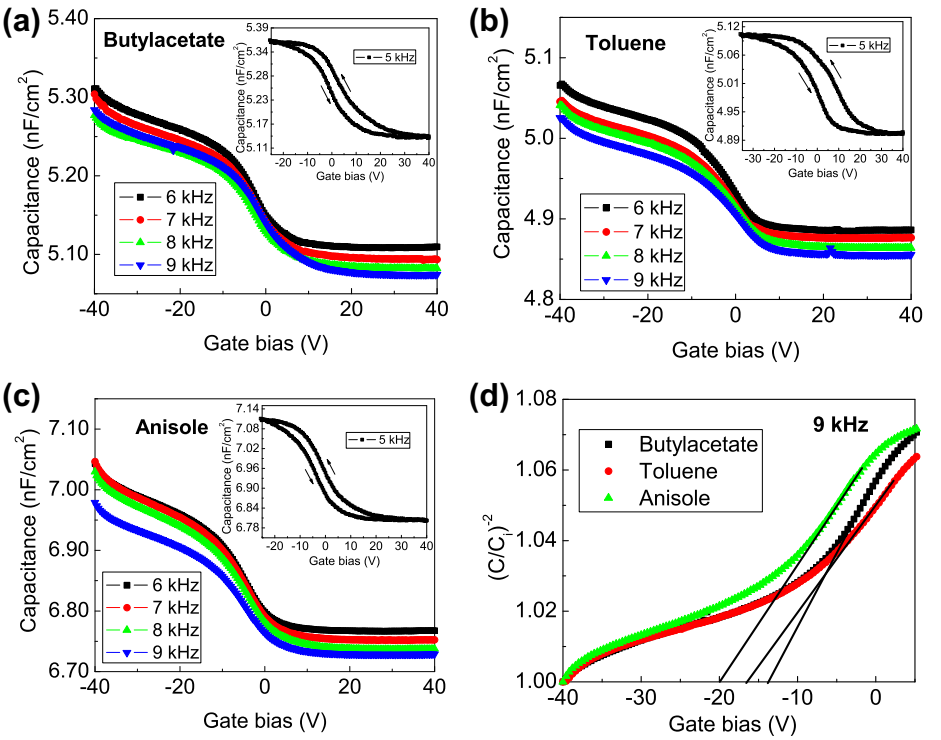

Fig. 2. *C–V* characteristics between 6 and 9 kHz for Al/PMMA/PFB/Au structure and *C–V* characteristics of Al/PMMA/PFB/Au MIS diodes at 5 kHz (insets) for (a) butylacetate (Sample A), (b) toluene (Sample B), (c) anisole (Sample C) solvents and (d) plots of $(C/C_i)^{-2}$ versus gate bias for Samples A, B, and C.

to SiO_2 may originate from a cancellation of the dipole-induced slow polarization with charge trapping; the two typically have opposite directions. The net hysteresis direction reveals the nature of charge injection. The counterclockwise loop of the hysteresis in the *C–V* curve indicates a positive carrier injection into the PFB layer with subsequent trapping [23]. The difference in the accumulation capacitance/area is due to the variations in PMMA thickness for the three MIS diodes. According to the standard Schottky–Mott analysis, the unintentional doping density can be extracted using the relation [23]

$$\frac{\partial(1/C^2)}{\partial V_G} = \frac{2}{q\varepsilon_{semi}\varepsilon_0 N_A A^2}, \tag{1}$$

where C is the capacitance in the depletion region, V_G is the gate bias, ε_{semi} is the relative permeability of the semiconductor, ε_0 is the permittivity of vacuum, A is the area of the device, and N_A is the doping density. The acceptor doping density (N_A) was estimated to be 2.6×10^{17}, 2.9×10^{17}, and 4.9×10^{17} cm^{-3} for Samples A, B, and C, respectively.

From the plot of $(C/C_i)^{-2}$ versus gate bias taken at a frequency of 9 kHz (Fig. 2(d)), flat band voltages (V_{FB}) of −14, −16.6, and −21 V were deduced for Samples A, B, and C, respectively, by extrapolating to the *x*-intercept at $(C/C_i)^{-2} = 1$. Here, C_i is the capacitance of the PMMA layer. Noticeable from this plot is the negative occurrence and the obvious shifts in V_{FB} of the three devices. While the difference in the metal and semiconductor work functions (ϕ_{ms}) and the existence of positive interface traps (Q_i) at the semiconductor–insulator interface are known to account for negative V_{FB} in non-ideal MIS capacitors as given by the relation [24]

$$V_{FB} = \phi_{ms} - \frac{Q_i}{C_i}, \tag{2}$$

our observed shifts in V_{FB} are not due to ϕ_{ms} since it is presumably similar for the three devices. Therefore, considering our calculated values for density of interface states (D_{it}) at flat band (insets of Fig. 3) for the various devices
(Sample A = 2.8×10^{12} eV^{-1} cm^{-2},
Sample B = 3.9×10^{12} eV^{-1} cm^{-2},
Sample C = 5.0×10^{12} eV^{-1} cm^{-2}),
the details of which are found below, and making use of Eq. (2), we can conclude that the shifts in V_{FB} are due to the differences in the density of holes trapped at the semiconductor–insulator interfaces of these devices. The lower the D_{it} at flat band, the less negative is the shift in flat band voltage.

Fig. 3(a–c) shows conductance–voltage (*G–V*) characteristics of the Al/PMMA/PFB/Au MIS diodes. The devices undergo a gate bias independent loss which results from the bias independence of electron and hole densities at the point where the Fermi level crosses bulk trap levels located near the mid gap [25]. This bias independent loss evidenced by the absence of conductance peaks suggests that loss in the devices is mainly dominated by generation and recombination through bulk states. Interface states usually give rise to confined energy levels at the semiconductor–insulator interface. The use of the conductance technique, as suggested by Nicollian and Brews [25] in the depletion

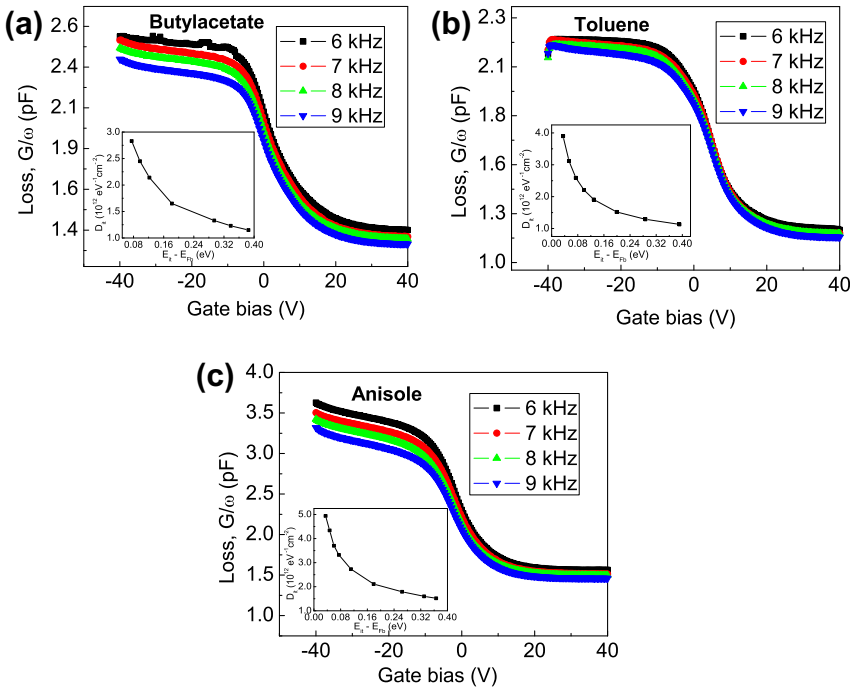

Fig. 3. Frequency dependence of loss (conductance/angular frequency) versus gate bias for PFB MIS diodes and density of interface traps, D_{it}, at the PFB/PMMA interface plotted as a function of energy above bulk Fermi level $E_{it} - E_{Fb}$ (insets) for (a) Sample A, (b) Sample B, and (c) Sample C.

region enables the extraction of interface states density, capture probability and time constant dispersion of the majority carriers (holes in this case) from the real component of the admittance.

The interface trap states change occupancy over a few k_BT/q (where k_B is the Boltzmann constant) wide centered about the Fermi level by interacting with the semiconductor bands via the emission and capture of carriers. A small ac signal applied to the gate of an MIS diode results in an alternate movement of the band edges toward or away from the Fermi level. Using the conductance technique, interface trap states are detected through the loss resulting from changes in their occupancy due to small variations in dc gate bias. Usually, a conductance peak is observed as a result of the ac loss due to capture and emissions of carriers by these interface states. An equivalent parallel conductance (G_p) extracted at different biases from the measured capacitance and conductance data is employed to estimate the density of interface traps, D_{it} using the continuum of states model given by [25]

$$\frac{G_p}{\omega} = \frac{qD_{it}}{2\omega\tau}\ln(1+\omega^2\tau^2), \tag{3}$$

where τ is interface state time constant. The capacitance and equivalent parallel conductance for a distributed or a continuum of trap states are broadened along the $\omega\tau$ axis in comparison to single-level trap states and the maximum of G_p/ω occurs at $\omega\tau = 1.98$ (while for single-level trap states, $\omega\tau = 1$). A determination of the interface trap energy states (E_{it}) can be easily carried out by calculating the degree of band bending induced by the applied bias, by solving the Poisson equation in the depletion approximation:

$$E_{it} - E_{Fb} = \frac{qN_A\varepsilon\varepsilon_0A^2}{2C_d^2}, \tag{4}$$

where q is the electronic charge, N_A is the acceptor doping density, ε is the semiconductor dielectric constant, ε_0 is the permittivity of free space, and C_d is the depletion capacitance estimated at the relevant voltage. Insets of Fig. 3(a–c) show plots of interface state density (D_{it}) versus energy for Samples A, B, and C. The results of the analyses show a non-linear decrease of the interface trap density as one moves away from the bulk Fermi level. For Sample A, D_{it} was found to decrease from approximately 2.8×10^{12} to 1.2×10^{12} eV^{-1} cm^2 over an energy range of 0.075–0.385 eV with a flat band value of 2.8×10^{12} eV^{-1} cm^2. D_{it} decreased from approximately 3.9×10^{12} to 1.1×10^{12} over an energy range of 0.035–0.395 eV in Sample B, with a calculated flat band value of 3.9×10^{12} eV^{-1} cm^{-2}. The D_{it} at flat band for Sample C was calculated to be 5.0×10^{12} eV^{-1} cm^{-2} and it decreased to approximately 1.5×10^{12} eV^{-1} cm^2 over an energy range of 0.035–0.366 eV above the bulk Fermi level. A comparison of D_{it} versus energy plots for the three samples shows that D_{it} at flat band is least in Sample A.

3.3. FET characteristics

Fig. 4(d) shows the output characteristics of the PFB-based FET prepared using butylacetate, which is typical of transistor devices. This device exhibits leakage current of the order of about 0.1 nA. Also shown in Fig. 4(a–c) are the FET transfer characteristics from all three Samples (A–C) in the saturation region ($V_D = -40$ V). The square root of the drain current is also plotted for all three.

According to theoretical prediction [23], above the threshold voltage, these transfer plots should yield a straight line whose slope is proportional to the carrier mobility (μ), as well as a threshold voltage (V_T) which is equal to the intercept. Using the standard saturation regime current–voltage FET characteristics [23],

$$\mu_{sat} = \frac{2L}{WC}\left(\frac{\partial\sqrt{I_D}}{\partial V_G}\right)^2, \tag{5}$$

where C is the capacitance per unit area of the polymer insulator, W is the channel width, L is the channel length, I_D is the drain current, and V_G is the gate voltage. The field-effect mobility in the saturation regime can be obtained by fitting the linear region of the transfer plot. Since the plots show a linear behavior at values of V_G above the threshold voltage, the calculated mobility is independent of the specific range of V_G used for the linear fit. We point out that the toluene sample shows a slight non-linear behavior at high gate voltages indicating a gate-dependent mobility; the fit region was thus restricted to V_G below -30 V. The highest average field-effect mobility of 0.2×10^{-4} cm^2 V^{-1} s^{-1} and the lowest threshold voltage of -0.2 V, respectively were obtained for Sample A. For Sample B, the average field-effect mobility was calculated to be 0.4×10^{-5} cm^2 V^{-1} s^{-1} and a threshold voltage of -3.3 V was obtained. Sample C yielded an average field-effect mobility and a threshold voltage of 0.2×10^{-5} cm^2 V^{-1} s^{-1} and -7.2 V, respectively. The FET mobilities here are higher than MAPLE deposited PFB on as-is SiO_2 as the dielectric layer [21].

The threshold voltage (V_T) is negative for all the devices, which is typical of p-channel devices and is given by the relation [24]

$$V_T = V_{FB} + \frac{Q_d}{C_i} - 2\phi_F, \tag{6}$$

where Q_d/C_i accommodates the charge in the depletion region, and ϕ_F defined as $(E_i - E_F)/q$ in the neutral substrate, is the bulk potential. From the above relation, it is understandable that an applied negative voltage higher than V_T is needed in order to achieve flat band condition. The depletion charge is proportional to the acceptor concentration (N_A), and as such, should be least for Sample A and highest for Sample C. Also looking at the obtained values for N_A, it is immediately obvious that ϕ_F is least in Sample A and highest in Sample C. Therefore, considering our aforementioned extracted values for V_{FB} (in the MIS diodes) and making use of Eq. (6), it is observable that the trend in the threshold voltage becomes easily explainable. Therefore, we can conclude that the behavior of V_T in FETs is predictable from knowledge of the doping concentration and the behavior of V_{FB} in MIS capacitors, in accordance with theory.

Considering that FETs based on polymer dielectrics typically show some hysteresis (shifts in threshold voltage depending on the sweep direction of the gate voltage) in I_D, remarkably, our FETs exhibited no hysteresis for Sample A and little hysteresis in only the off regime for Samples B and C. Hysteresis in organic thin film transistors has been linked with dielectric bulk trapping of electrons and holes injected from the gate [26,27]. It could be deduced that the absence of hysteresis in Sample A and little hysteresis in Samples B, and C are very likely due to suppressed gate injection of carriers and subsequent trapping in the PMMA bulk. The device characteristics for our FETs and MIS diodes are summarized in Table 1.

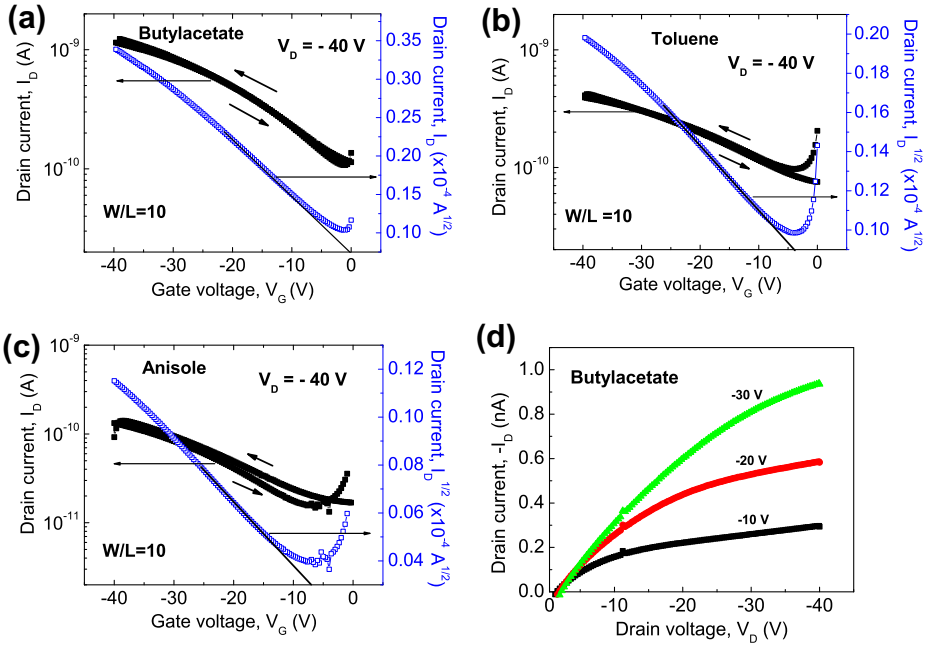

Fig. 4. Electrical transfer characteristics of the OFETs for various solvents: (a) butylacetate (Sample A), (b) toluene (Sample B), (c) anisole (Sample C), and (d) electrical output characteristics of Sample A.

Table 1
Field-effect mobilities in saturation regime, threshold voltages, root mean square values, density of interface state at flat band (D_{it}), and solubility parameters for various solvents.

	Mobility ($cm^2 V^{-1} s^{-1}$)	Threshold voltage (V)	PMMA film rms (Å)	D_{it} at flatband ($eV^{-1} cm^{-2}$)	Solubility parameters[a] $(MPa)^{1/2}$
Butylacetate	0.2×10^{-4}	−0.2	2.18	2.8×10^{12}	17.4
Toluene	0.4×10^{-5}	−3.8	2.35	3.9×10^{12}	18.1
Anisole	0.2×10^{-5}	−7.2	2.55	5.0×10^{12}	19.5

[a] Ref. [30].

As is evident from Table 1, the type of solvent used in dissolving the dielectric has quite noticeable effects on the performance of the devices. The morphology of the dielectric layer onto which the semiconducting layer is formed has been observed to play an important role in the performance of polymer devices [28]. Similarly, surface roughness of polymer dielectric films, which is very closely related to the solubility parameter, could be dependent on the type of solvent used [29]. It is well known that the less the difference between the solubility parameters of a polymer and its solvent, the more soluble the polymer is in the solvent and vice versa. Table 1 contains the solubility parameters of the various solvents used, while the solubility parameter for PMMA is 22.5 $(MPa)^{1/2}$ [30].

While the FET mobility decreased with increasing PMMA film roughness, D_{it} at flat band of the MIS diodes followed the same trend as the PMMA film roughness. Earlier reports have shown that a rougher surface leads to increase in voids and defects giving rise to increase in interface trap states at the semiconductor–dielectric interface and consequent adverse effects on field-effect mobility and molecular ordering [31–33]. Our results point in the direction that there is a trade-off between solubility and swelling of the dielectric layer in the actual device performance. Although PMMA is most soluble in anisole, the device performance is worse compared to the other two solvents. It has been observed that the degree of swelling in a polymer increases with the decrease in the difference between the solubility parameters of the polymer and the solvent [28,29]; anisole is thus most likely to leave behind the roughest PMMA film surface on evaporation, and as such, the lowest average field-effect mobility, followed by toluene, then butylacetate.

4. Conclusion

In summary, we have demonstrated the success of the MAPLE technique in overcoming the solvent selectivity and inherent swelling and dissolution problems associated with fabricating device-quality polymer FETs and MIS diodes via traditional spincoating technique especially when non-orthogonal solvents are used. It is observed that the higher the difference between the solubility parameters of the solvent and PMMA, the less rough the PMMA surface, and consequently, the better the device performance. Negative shifts of the threshold voltage in the FETs were correlated with differences in acceptor doping density and similar shifts in flat band voltage of the MIS diodes, which was found to be due to difference in the density of interface states at flat band. PFB-based FETs exhibited a hysteresis-free operation, a low threshold voltage of −0.2 V, and field-effect mobility of $0.2 \times 10^{-4} cm^2 V^{-1} s^{-1}$. The density of interface trap states in the MIS diodes was found to decrease non-linearly and is distributed over an energy range of 0.075–0.385 eV above the bulk Fermi level; the energy loss was found to be dominated by the emission and capture of carriers through bulk states. We are currently exploring other MAPLE-deposited solution processable polymers that have inherently higher charge carrier mobilities with polymer dielectrics in FET and MIS structures.

Acknowledgments

We gratefully acknowledge the support of this work through the National Science Foundation under Grant No. ECCS-0823563. We thank Dr. Gavin King, Raghavendar Gari, and Keshab Paudel for the AFM measurements.

References

[1] C.D. Sheraw, L. Zhou, J.R. Huang, D.J. Gundlach, M.G. Kane, I.G. Hill, M.S. Hammond, J. Campi, B.K. Greening, J. Franci, J. West, T.N. Jackson, Appl. Phys. Lett. 80 (2002) 1088.
[2] H.E.A. Huitena, G.H. Gelinck, J.B.P.H. van der Puttan, K.E. Kuijk, K.M. Hart, E. Cantatore, D.M. de Leeuw, Adv. Mater. 14 (2002) 1201.
[3] P. Mach, S.J. Rodriguez, R. Wortrup, P. Wiltzius, J.A. Rogers, Appl. Phys. Lett. 78 (2001) 3592.
[4] H. Sirringhaus, T. Kawase, R.H. Friend, T. Shimoda, M. Inbrasekaran, W. Wu, E.P. Woo, Science 290 (2002) 2123.
[5] T. Kawase, H. Sirringhaus, R.H. Friend, T. Shimoda, Adv. Mater. 13 (2001) 1601.
[6] Y. Jang, D.H. Kim, Y.D. Park, J.H. Cho, M. Hwang, K. Cho, Appl. Phys. Lett. 88 (2008) 072101.
[7] T.-S. Huang, Y.-K. Su, P.-C. Wang, Appl. Phys. Lett. 91 (2007) 092116.
[8] M. Yun, R. Ravindran, M. Hossain, S. Gangopadhyay, U. Scherf, T. Bunngel, F. Galbrecht, M. Arif, S. Guha, Appl. Phys. Lett. 89 (2006) 013506.
[9] G. Wang, J. Swensen, D. Moses, A.J. Heeger, J. Appl. Phys. 93 (2003) 6137.
[10] Y. Sun, X. Lu, S. Lin, J. Kettle, S.G. Yeates, A. Song, Org. Electron. 11 (2010) 351.
[11] Y.-Y. Noh, H. Sirringhaus, Org. Electron. 10 (2009) 174.
[12] F. Todescato, R. Capelli, F. Dinelli, M. Murgia, N. Camaioni, M. Yang, R. Bozio, M. Muccini, J. Phys. Chem. B 112 (2008) 10130.
[13] L.-L. Chua, J. Zaumseil, J.-F. Chang, E.C.-W. Ou, P.K.-H. Ho, H. Sirringhaus, R.H. Friend, Nature 434 (2005) 194.
[14] A. Pique, R.A. McGill, D.B. Chrisey, Ind. Phys. 6 (2000) 20.
[15] B. Toftmann, M.R. Papantonakis, R.C.Y. Auyeung, W. Kim, S.M. O'Malley, D.M. Bubb, J.S. Horwitz, J. Schou, P.M. Johansen, R.F. Haglund Jr., Thin Solid Films 453–454 (2004) 177.
[16] A. Pique, R.A. McGill, D.B. Chrisey, D. Leonhardt, T.E. Mslna, B.J. Spargo, J.H. Callahan, R.W. Vachet, R. Chung, M.A. Bucaro, Thin Solid Films 355–356 (1999) 536.
[17] R.K. Gupta, K. Ghosh, P.K. Kahol, J. Yoon, S. Guha, Appl. Surf. Sci. 254 (2008) 7069.
[18] Y. Yun, C. Pearson, M.C. Petty, J. Appl. Phys. 105 (2009) 034508.
[19] G. Horowitz, F. Deloffre, F. Garnier, R. Hajlaoui, M. Hmyene, A. Yassar, Synth. Met. 54 (1993) 435.

[20] G.K. Dalapati, Y. Tong, W.Y. Loh, H.K. Mun, B.J. Cho, Appl. Phys. Lett. 90 (2007) 183510.
[21] D. Adil, N.B. Ukah, R.K. Gupta, K. Ghosh, S. Guha, Synth. Met. 160 (2010) 2501.
[22] D.K. Hwang, M.S. Oh, J.M. Hwang, J.H. Kim, S. Im, Appl. Phys. Lett. 92 (2008) 013304.
[23] S.M. Sze, Physics of Semiconductor Devices, second ed., Wiley Interscience, New York, 1981.
[24] B.G. Streetman, S.K. Banerjee, Solid State Electronic Devices, sixth ed., Prentice Hall Inc., 2006.
[25] E.H. Nicollian, J.R. Brews, MOS Physics and Technology, Wiley, New York, 2003.
[26] C. An Lee, D.W. Park, S.H. Jin, I.H. Park, J.D. Lee, B.-G. Park, Appl. Phys. Lett. 88 (2006) 252102.
[27] S.Y. Park, M. Park, H.H. Lee, Appl. Phys. Lett. 85 (2004) 2283.
[28] J. Park, S.Y. Park, S.-O. Shim, H. Kang, H.H. Lee, Appl. Phys. Lett. 85 (2004) 3283.
[29] J.E. Mark, Physical Properties of Polymers Handbook, American Institute of Physics, Woodbury, New York, 1996.
[30] C.M. Hansen, Hansen Solubility Parameters; A User's Handbook, CRC Press, Boca Raton, Florida, 2000.
[31] I. Kymissis, C.D. Dimitrakopoulos, S. Purushotham, IEEE Trans. Electron Devices 48 (2001) 1060.
[32] D.J. Gundlach, L. Jia, T.N. Jackson, IEEE Electron Device Lett. 22 (2001) 571.
[33] B.M.W. Langeveld-Voss, A.J.H. Spiering, R.A.J. Janssen, E.W. Meijer, P. Herwig, D.M. de Leeuw, Nature (London) 401 (1999) 685.

In this paper we report strong p-type surface transfer doping of C_{60}, due to formation of space charge in the C_{60} layer at the C_{60}/MoO_x interface. We investigated the interface formation of ITO, MoO_x, and C_{60} using ultraviolet photoemission spectroscopy (UPS) and inverse photoemission spectroscopy (IPES). We monitored the changes in the valence electronic structure, WF, and ionization potential of the surface as C_{60} was deposited layer by layer on a MoO_x/ITO substrate. We found that the MoO_x inter-layer substantially increased the surface WF, due to which all the energy levels of C_{60} moved up, and making C_{60} strongly p-type at the C_{60}/MoO_x interface. With further C_{60} deposition energy levels gradually relax down, resulting in an extremely thick layer of band-bending-like region. We also investigated the effect of exposing MoO_x to air and then depositing C_{60}. In this case almost no band bending was observed in C_{60}. The study therefore reveals a method of turning organic materials which on most of the metals behave as n-type, to be p-type without any intentional intermixing of materials.

2. Experimental

UPS and IPES studies were performed using a VG ESCA Lab, an ultrahigh vacuum (UHV) system equipped with a He I discharge lamp. The UHV system consists of a spectrometer chamber, an in situ oxygen plasma (OP) treatment chamber, and an evaporation chamber all interconnected. The base pressure of the spectrometer chamber is typically 8×10^{-11} torr. The base pressure of the evaporation chamber is typically 1×10^{-6} torr. The UPS spectra were recorded by using unfiltered He I (21.22 eV) excitation as the excitation source with the sample biased at −5.00 V to observe the low-energy secondary cutoff. The UV light spot size on the sample is about 1 mm in diameter. The typical instrumental resolution for UPS measurements ranges from 0.03 to 0.1 eV with the photon energy dispersion of less than 20 meV. Two substrates of size about 9 mm × 9 mm were cut from borosilicate glass sheet from Corning, coated with 250 nm thick conducting ITO, with resistivity 15 Ω per square. The substrates were treated separately in situ in oxygen ambience [11] of 600 m torr at bias voltage about −500 V for about 30 s. Both MoO_x and C_{60} were thermally evaporated layer-by-layer. Thicknesses of deposited films were monitored by quartz crystal microbalance. The 50 Å MoO_x substrate was exposed to 7.2×10^{14} Langmuir (about 10 days in atmospheric pressure) air and again inserted inside the UHV system for measurements. One Langmuir (L) exposure is equal to the 10^{-6} torr s exposure. The surface topography data were obtained with Nanoscope III (from Digital/Vecco) atomic force microscope (AFM) in tapping mode with silicon tips. All the measurements were performed at room temperature.

3. Results and discussion

In Fig. 1, the UPS spectra of C_{60} on MoO_x/ITO are presented as a function of the thickness of C_{60} over-layer. Shown in Fig. 1a and b, are the cut off and the HOMO regions of the UPS data, respectively. The WF of ITO was measured to be 5.78 eV [15,16,20–22]. Upon the deposition of 30 Å MoO_x, the surface WF became 6.8 eV. As it is clearly visible from Fig. 1a, with the C_{60} deposition the surface WF kept gradually decreasing. The WF after 1.2, 2.3, 4.7, 37.2, 74.4, 407, and 581.4 Å C_{60} deposition were measured to be 6.55, 6.49, 6.46, 6.08, 5.98, 5.64 and 5.58 eV, respectively. From Fig. 1b, we notice that there is a strong valence band peak of MoO_x at the binding energy (BE) of about 3.8 eV with respect to the Fermi level. The two occupied levels closest to the Fermi level appear right after 1.2 Å C_{60} deposition. There is a visible shift in the MoO_x valence band peak upon the deposition of C_{60} towards the higher BE. We measured this shift to be about 0.3 eV at 4.7 Å C_{60} deposition. The occupied molecular levels of C_{60} become prominent between 4.7 and 9.3 Å of C_{60} deposition. It is obvious from Fig. 1b, that all the occupied level peaks of C_{60} keep shifting towards the higher binding energy (BE). The HOMO onset BE of C_{60} after 4.7, 9.3, 37.2, 74.4, 407, and 581.4 Å C_{60} deposition were measured to be 0.21, 0.23, 0.38, 0.46, 0.81, and 0.85 eV, respectively. It is important to mention that no significant sample charging was observed during the measurements.

In Fig. 2a and b, changes in the WF and the shift in C_{60} HOMO level onset BE are presented as a function of increasing C_{60} thickness. From Fig. 2a, we observe the WF increase from 5.78 eV of the ITO to 6.8 eV upon deposition of 30 Å MoO_x, indicating an interface dipole of 1.02 eV at the MoO_x/ITO interface. With deposition of C_{60} on MoO_x/ITO we observe a slow WF change. As discussed in the previous section, if we take into account the 0.3 eV initial shift of the characteristic MoO_x peak by C_{60} deposition, there is a negligibly small surface dipole moment at the C_{60}/MoO_x interface. As C_{60} thickness increases we observe gradual WF change causing an extremely large band bending region of over 400 Å. 580Å C_{60} thickness appears to be in quasi-equilibrium state. From Fig. 2b, we observe a gradual HOMO level BE shift towards the higher BE with increasing thickness of C_{60}. Overall about 0.6 eV shift was observed in the C_{60} HOMO level onset spanning over 580 Å thickness. Both WF and HOMO level shift have similar trend of change.

The UPS data indicate that the high WF of MoO_x is causing charge transfer and surface transfer doping of C_{60}. It is further verified by reducing the WF of the MoO_x by air exposure and observed C_{60} behavior deposited on the exposed MoO_x. In Fig. 3, the UPS spectra of the C_{60} on air exposed MoO_x/ITO are presented as a function of C_{60} thickness. Fig. 3a and b, show the cut off and HOMO regions of the UPS data, respectively. Upon the deposition of 50 Å MoO_x the surface WF became 6.75 eV. After MoO_x deposition the substrate underwent an air exposure of 7.2×10^{14} L, and the substrate WF was measured to be 4.85 eV, which is 1.9 eV below the WF of an unexposed MoO_x surface. The contrast in the WF and occupied levels evolution with the C_{60} deposition is clearly visible from Fig. 3a and b, in comparison with Fig. 1a and b. The surface WF gradually increases up to 16 Å of C_{60} deposition, and saturates thereafter. From Fig. 1b, we notice that a strong valence band peak of MoO_x at the BE of ~3.75 eV. After the air exposure the valence band peak of MoO_x was ob-

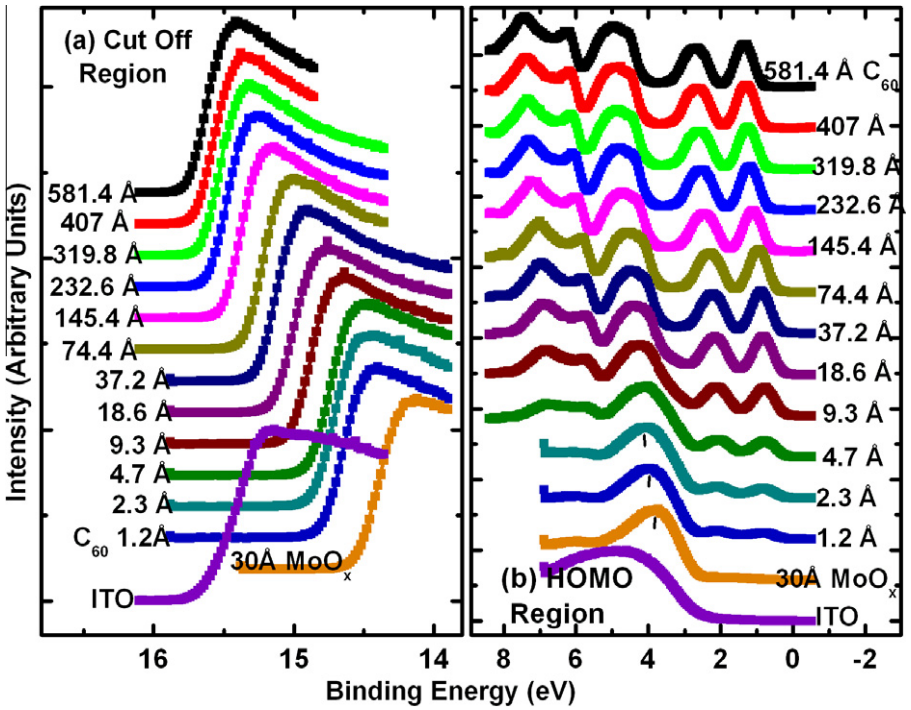

Fig. 1. UPS data for 0–581.4 Å C_{60}/30 Å MoO_x/ITO. (a) The cut-off region and (b) the HOMO region.

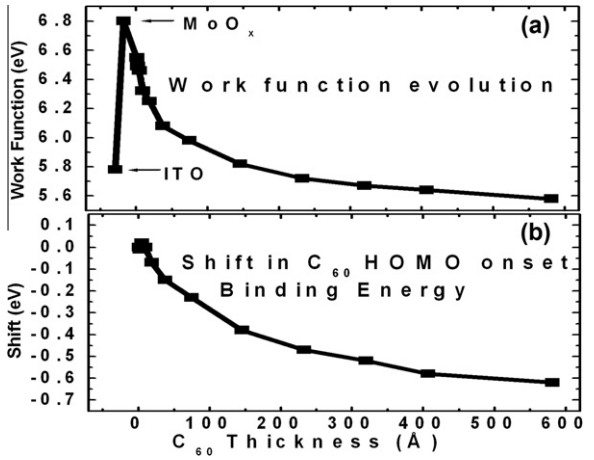

Fig. 2. Workfunction evolution (a) and HOMO onset binding energy shift (b) values for 0–581.4 Å C_{60}/30 Å MoO_x/ITO.

served at BE of ~4.3 eV, which corresponds to ~0.55 eV shift in peak position towards the higher BE than the unexposed MoO_x surface. The HOMO level peak appeared right after the 2 Å of C_{60} deposition. The occupied molecular levels feature of C_{60} became prominent between 4 and 8 Å of C_{60} deposition. It is obvious from Fig. 1b, that all the occupied level peaks of C_{60} remain almost intact with further C_{60} deposition. The HOMO onset BE of C_{60} after 4, 8, 16, 32, 64, and 128 Å C_{60} deposition were measured to be 1.25, 1.29, 1.25, 1.30, 1.37, and 1.38 eV, respectively.

In order to further demonstrate strong surface p-doping in C_{60} with pristine thermally evaporated MoO_x, we performed IPES and UPS together on an another MoO_x film and compared that with 7.2 L air exposed MoO_x substrate. Occupied and unoccupied energy levels of C_{60} near Fermi level with increasing C_{60} thickness are presented in Fig. 4. Four set of data presented in the bottom to middle of Fig. 4, are for 5, 20, 100 and 450 Å C_{60} thickness on 30 Å MoO_x/ITO substrate, 5 Å thickness one being at the bottom of Fig. 4. It is straightforward to state that the HOMO level onset is less than 0.2 eV from the Fermi level. On the unoccupied side though features are not completely develop for 5 Å coverage but the LUMO onset is about 2 eV from the Fermi level. As we increase C_{60} thickness the entire spectrum shifts towards the higher BE. At 450 Å C_{60} coverage we calculated the HOMO edge to be 0.7 eV while the LUMO peak also shifts rigidly with the HOMO one. The LUMO edge is about 1.5 eV, indicating that C_{60} is p-type even after 450 Å coverage. On top of the Fig. 4, the UPS and IPES spectrum of 128 Å C_{60} thickness are presented on 7.2 L air exposed 30 Å MoO_x/ITO substrate. The HOMO edge is measured to be 1.38 eV while the LUMO edge is about ~0.9 eV. As presented in the Fig. 4, the polaron gap (HOMO–LUMO peak to peak separation) observed to be almost fixed which further corroborates our claim. Polaron gap values are measured to be 3.93, 3.8, 3.72 and 3.79 eV for 5, 20, 100 and 450 Å C_{60} thicknesses on unexposed MoO_x substrate. It was found to be 3.78 eV for 128 Å C_{60} on the air exposed MoO_x film.

Energy level diagrams for C_{60}/30 Å MoO_x/ITO and C_{60}/(7.2×10^{14} L air exposed) 50 Å MoO_x/ITO, interfaces are depicted in Fig. 5a and b, respectively. In Fig. 5a, the interface

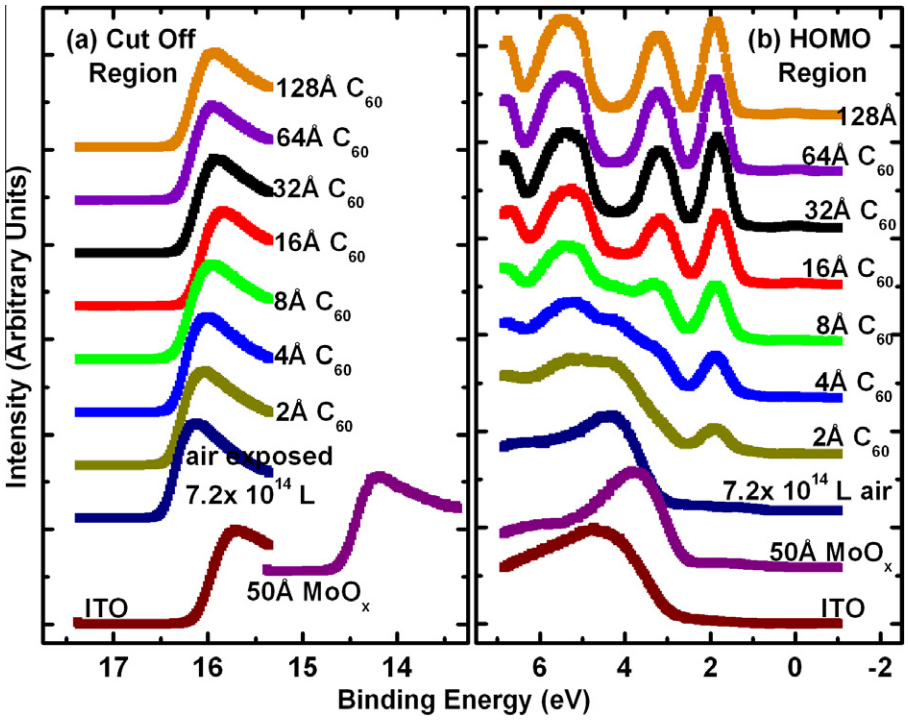

Fig. 3. UPS data for 0–128 Å C_{60}/(7.2×10^{14} L air exposed) 50 Å MoO_x/ITO. (a) The cut-off region and (b) the HOMO region.

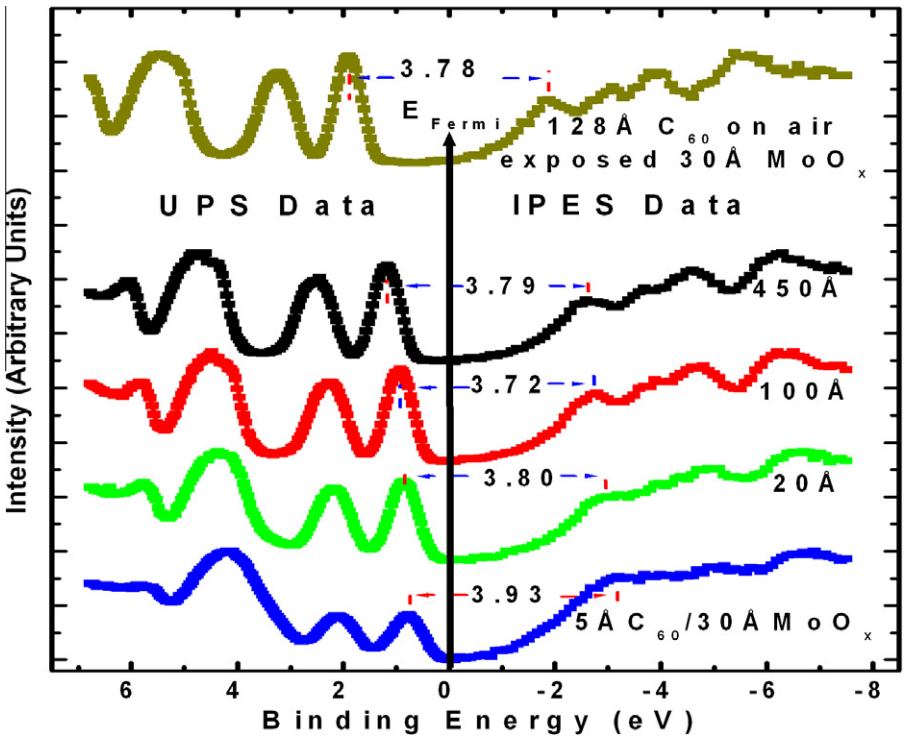

Fig. 4. UPS-IPES combined data for 5, 20, 100, 450 Å C_{60} on /30 Å MoO_x/ITO and 128 Å C_{60} on (7.2×10^{14} L air exposed) 50 Å MoO_x/ITO.

between ITO and MoO_x has an interface dipole 1.36 eV and HOMO onset BE of MoO_x was measured to be 2.63 eV. The high WF of MoO_x lifted up the C_{60} energy levels, resulting in a strong electron attraction towards the MoO_x layer from

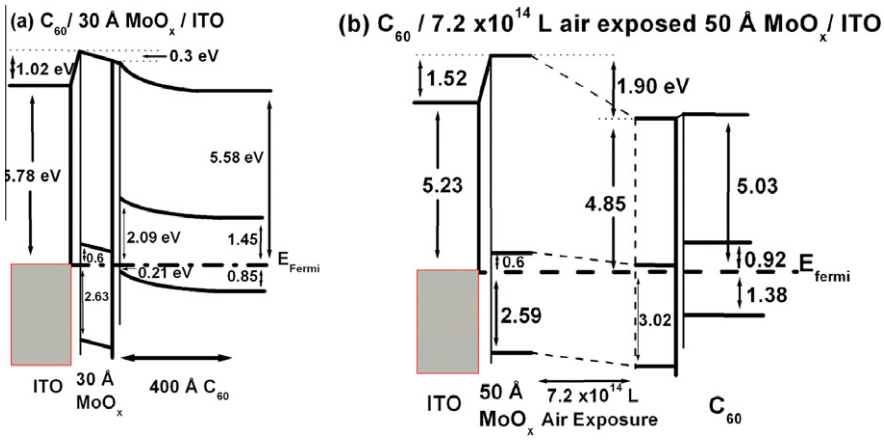

Fig. 5. Energy level alignment at, (a) C_{60}/30 Å MoO_x/ITO, and (b) C_{60}/(7.2×10^{14} L air exposed) 50 Å MoO_x/ITO.

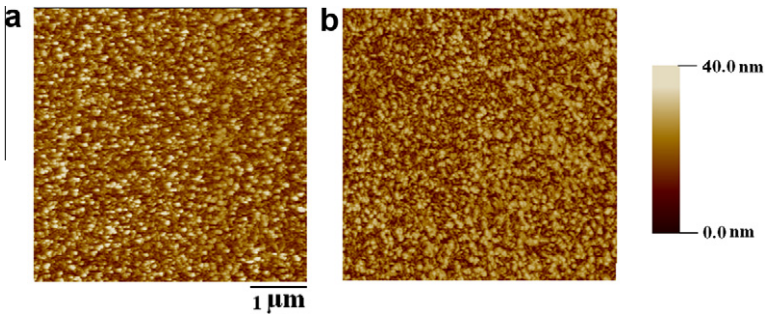

Fig. 6. AFM images of, (a) oxygen plasma treated ITO and (b) 50 Å MoO_x.

the C_{60} side. Due to the strong attraction of electrons from the C_{60} layer to the MoO_x side, C_{60}^+ is produced, as space charge in the C_{60} layer. Close to the C_{60}/MoO_x interface the C_{60} HOMO level was observed to be almost pinned to the Fermi level, and after 4.7 Å C_{60} deposition the onset BE was measured to be 0.21 eV, indicating a strong inversion. With further C_{60} deposition a gradual relaxation was observed, resulting in a large band bending region of ~400 Å. At 581.4 Å the surface WF and the HOMO onset BE were measured to be 5.58 and 0.85 eV respectively. With the Poisson equation it is always possible in principle to calculate the charge density from the potential change, but for taking the derivative it requires fine film thickness steps, not performed in the current experiment. If we assume C_{60}^+ ions are uniformly distributed in the organic side, as reported by Ishii et. al., [23] the estimated density of C_{60}^+ ions ($N_D = (2\varepsilon_0 \cdot \varepsilon_r \cdot V_{bi})/(ed^2)$) would be 8.7×10^{16} cm^{-3}, where V_{bi} = 0.6 eV, ε_r = 4.4, and d = 580 Å.

From Fig. 5b, the ITO WF was measured to be 5.23 eV. After 50 Å of MoO_x deposition the surface FW becomes 6.75 eV. The HOMO onset BE was measured to be 2.59 eV. The difference in the ITO WF in Fig. 5a and b, is the result of variation of ITO surfaces after the O_2 plasma treatment. It is inconsequential for the subsequent experiments as the surface becomes dominated by the MoO_x overlayer with the same saturated WF. The substrate then underwent an air exposure of 7.2×10^{14} L. The exposure renders the surface WF and HOMO onset BE to be 4.85 and 3.02 eV, respectively. With C_{60} deposition almost no band bending was observed and all the energy levels remained more or less flat. Meyer et al. recently observed [24] that even after air exposure of MoO_x interlayer device performance did not suffer, as lowering of MoO_x WF only reduced the interface dipole between MoO_x and the organic hole transport layer (HTL), almost by the amount of MoO_x WF reduction due to the air exposure. The present work shows that the reported insensitivity of MoO_x to air exposure is not a general case.

Based on our previous reported device data, [17] there are noticeable differences in the open-circuit voltage (V_{oc}) and short-circuit current (I_{sc}) that can be attributed to the variation in MoO_x inter-layer thickness. The cell with an unexposed MoO_x layer produces a V_{oc} of 1.2 V and an I_{sc} of 1.3 mA/cm^2, whereas the cell with an air exposed MoO_x layer has substantial degradation both in V_{oc} and I_{sc} with values of 0.85 V and 0.92 mA/cm^2, respectively. The cause for the variation in V_{oc} and I_{sc} in the OPV cells with different MoO_x inter-layer thickness can be understood with reference to the energy level diagram in Fig. 5. The high WF of unexposed MoO_x produces a relatively high built-in potential with an extended band bending region in the C_{60} layer. Presumably this governs photogeneration of electrons and holes in the bulk of C_{60} and the observed field dependence of photocurrent in the

MoO_x/C_{60} cells. For MoO_x/C_{60} cells with an air exposed MoO_x layer, a lower built-in potential in C_{60} is to be expected because of the lower workfunction measured for the air exposed MoO_x films. Indeed, this is consistent with the lower V_{oc} and I_{sc} obtained for OPV cells with air exposed MoO_x.

We also studied surface morphology for ITO, MoO_x and C_{60} films. In Fig. 6, atomic force microscope (AFM) data are presented for 30 s oxygen plasma (OP) treated ITO and 50 Å MoO_x film, respectively. Topography in images are from selected area of 5 μm × 5 μm from each sample. Root mean square (RMS) roughness of surfaces were measured to be 55 and 56 Å, respectively. The RMS roughness for C_{60} film was measured to be 68 Å (data not presented). These results indicate that while MoO_x grows smoothly on ITO, ~600 Å of C_{60} deposition does increase the surface roughness by about 10 Å. Given the total thickness, the small increase of the roughness should not affect the morphology and our general estimate of the layer thickness.

4. Conclusions

In conclusion, we have measured the electronic structure evolution of C_{60} on MoO_x/ITO. We observed that the high workfunction of MoO_x inter-layer strongly lift up the energy levels of C_{60} towards lower binding energy at the interface, resulting in an strong p-doping and inversion of C_{60}. The HOMO edge of C_{60} was observed at 0.21 eV below the Fermi level at the interface. We observed an exceptionally long band bending of 400 Å in the organic material, such long band bending has not been reported so far, for the organic/insulator (MoO_x) interface. With exposed MoO_x this inversion and the long band bending was not observed. This lead us to conclude that the workfunction reduction for air exposed MoO_x films does affect the energy level alignment in general. Our work suggests a method of turning organic materials which on most of the metals behave as n-type to be p-type without any intentional intermixing of materials.

Acknowledgments

The authors would like to acknowledge the support of the National Science Foundation Grant No. DMR-1006098. Help of Semyon Papernov, a scientist at Laboratory for Laser Energetics, University of Rochester, for AFM measurements is gratefully acknowledged.

References

[1] G. Yu, J. Gao, J.C. Hummelen, F. Wudl, A.J. Heager, Science 270 (1995) 1789.
[2] J. Xue, S. Uchida, B.P. Rand, S.R. Forrest, Appl. Phys. Letts. 84 (2004) 3013.
[3] R.C. Haddon, A.S. Perel, R.C. Morris, T.T.M. Palstra, A.F. Hebard, R.M. Fleming, Appl. Phys. Letts. 884 (2004) 3013.
[4] K. Tanigaki, T.W. Ebbesen, S. Saito, J. Mizuki, J.S. Tsai, Y. Kubo, S. Kuroshima, Nature 352 (1991) 222.
[5] R.W. Lof, M.A. Veennendaal, B. Koopmans, H.T. Jonkman, G.A. Sawatzky, Phys. Rev. Letts. 68 (1992) 3924.
[6] T.R. Ohno, Y. Chen, S.E. Harvey, G.H. Kroll, J.H. Weaver, R.E. Haufler, R.E. Smalley, Phys. Rev. B 44 (1991) 13747.
[7] Z.T. Liu, M.F. Lo, H.B. Wang, T.W. Ng, V.A.L. Roy, C.S. Lee, S.T. Lee, Appl. Phys. Letts. 95 (2009) 093307.
[8] R.C. Haddon, A.F. Hebard, M.J. Rosseinsky, D.W. Murphy, S.J. Duclos, K.B. Miller, J.M. Rosamilia, R.M. Fleming, A.R. Kortan, S.H. Glarum, A.V. Makhija, R.H. Eick, S.M. Zahurak, R. Tycko, G. Dabbagh, F.A. Thiel, Nature 350 (1991) 320.
[9] D. Claves, J. Nanosci. Nanotech. 7 (2007) 1221.
[10] W. Maser, S. Roth, J. Anders, J. Reichenbach, M. Kaiser, H. Byrne, H. Schier, M. Filzmoser, E. Sohmen, J. Fink, P. Bernier, A. Zahab, H.U. Siehl, M. Hanack, Syn. Met. 51 (1992) 103.
[11] A.M. Panich, P.K. Ummat, W.R. Datars, Sol. State Comm. 121 (2002) 367.
[12] P. Strobel, M. Riedel, J. Ristein, L. Ley, Nature 95 (2004) 093301.
[13] W. Chen, D. Qi, X. Gao, A.T.S. Wee, Prog. Surf. Sci. 84 (2009) 279.
[14] V. Shrotriya, G. Li, Y. Yao, C. Chu, Y. Yang, Appl. Phys. Letts. 88 (2006) 073508.
[15] D.Y. Kim, J. Subbiah, Franky So, H. Ding, Irfan, Y. Gao, Appl. Phys. Letts. 2009, 95, 093301.
[16] Irfan, H. Ding, Y. Gao, D.Y. Kim, J. Subbiah, Franky So, Appl. Phys. Letts. 96 (2010) 073304.
[17] M. Zhang, Irfan, H. Ding, Y. Gao, C.W. Tang, Appl. Phys. Letts. 2010, 96, 183301.
[18] Irfan, H. Ding, Y. Gao, C. Small, D.Y. Kim, J. Subbiah, Franky so, Appl. Phys. Letts. 96 (2010) 243307.
[19] J. Hou, J. Wu, Z. Xie, L. Wang, Appl. Phys. Letts. 95 (2009) 203508.
[20] M. Kroger, S. Hamwi, J. Meyer, T. Riedle, W. Kowalsky, A. Kahn, Appl. Phys. Lett. 95 (2009) 123301.
[21] M. Kroger, S. Hamwi, J. Meyer, T. Riedle, W. Kowalsky, A. Kahn, Appl. Phys. Lett. 10 (2009) 932.
[22] Y. Nakayama, K. Morii, Y. Suzuki, H. Machida, S. Kera, N. Ueno, H. Kitagawa, Y. Noguchi, H. Ishii, Adv. Funct. Mat. 19 (2009) 3746.
[23] H. Ishii, N. Hayashi, E. Ito, Y. Washizu, K. Sugi, Y. Kimura, M. Niwano, Y. Ouchi, K. Seki, Phys. Stat. Sol. A 201 (2004) 1075.
[24] J. Meyer, A. Shu, M. Kroger, A. Kahn, Appl. Phys. Lett. 96 (2010) 133308.

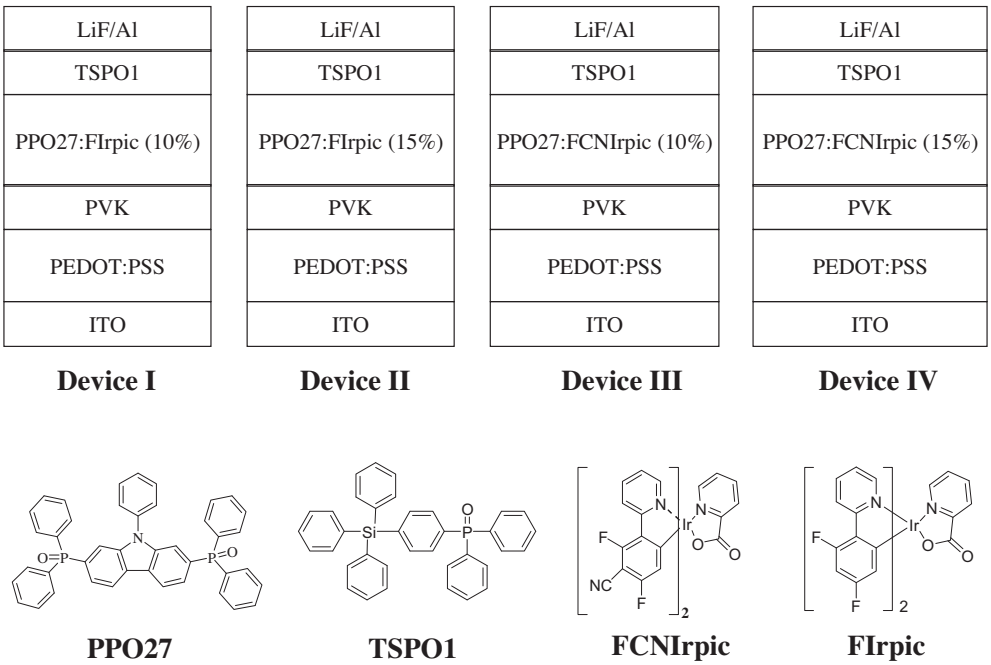

Fig. 1. Device structures of the solution processed blue PHOLEDs and chemical structures of materials used.

efficiency of 14.6% with a color coordinate of (0.15, 0.37) and high quantum efficiency of 13.4% with a color coordinate of (0.15, 0.26) were demonstrated in the solution processed PPO27:FIrpic and PPO27:FCNIrpic blue PHOLEDs.

2. Experimental

The device structure of the soluble PHOLEDs was indium thin oxide (ITO)/poly-3,4-ethylenedioxythiophene:polystyrenesulfonate (PEDOT:PSS, 60 nm)/PVK (15 nm)/PPO27:FIrpic or PPO27:FCNIrpic (40 nm)/diphenylphosphineoxide-4-(triphenylsilyl)phenyl (TSPO1, 35 nm)/LiF (1 nm)/Al (100 nm). The doping concentrations of the FIrpic and FCNIrpic were 10% and 15%. Device structures and chemical structures of organic materials are shown in Fig. 1. The PEDOT:PSS layer was spin coated at a thickness of 60 nm and was baked at 150 °C for 10 min to remove residual solvent. The PVK was spin coated from 0.3 wt.% chlorobenzene solution at a spin speed of 2000 rpm to make 15 nm thick hole transport layer. It was baked at 120 °C for 10 min after spin coating. The PPO27 host was dissolved in isopropanol at a concentration of 1.0 wt.% and the dopant materials were mixed in the isopropanol solution according to the doping concentration. After drying at 80 °C for 10 min, TSPO1 was deposited as the exciton blocking electron transport layer by thermal evaporation followed by LiF and Al deposition. Film morphology of the PPO27:FIrpic and PPO27:FCNIrpic was analyzed using atomic force microscope (AFM, Digital Instrument Co. Multimode Nanoscope IIIa). Current density–voltage–luminance characteristics and electroluminescence (EL) spectra of the devices were measured with Keithley 2400 source measurement unit and Minolta CS 1000A spectroradiometer.

3. Results and discussion

The synthesis of the PPO27 was reported in our previous work and the PPO27 was effective as the host material for the blue PHOLEDs doped with FIrpic and FCNIrpic [13]. It was reported that the PPO27 was suitable as the host for blue PHOLEDs because of low singlet energy of 3.25 eV and high triplet energy of 2.81 eV. In addition, it showed high glass transition temperature of 117.6 °C and stable amorphous film formation was observed in the PPO27. Therefore, the PPO27 can be used as the host material for solution processed blue PHOLEDs. In particular, the PPO27 is soluble in highly polar alcohol solvent because of highly polar diphenylphosphine oxide groups. The good solubility in alcohol solvent is advantageous because a multilayer structure can be formed using the solubility difference between the emitting layer and charge transport layers. Therefore, multilayer structure solution processed blue PHOLEDs can be fabricated using the PPO27 host material.

The PPO27 was spin coated from 2-propanol solution and the morphology of the spin coated PPO27 film was studied. Fig. 2 shows the AFM pictures of spin coated PPO27, PPO27:FIrpic and PPO27:FCNIrpic films. The surface roughnesses of the PPO27, PPO27:FIrpic and PPO27:FCNIrpic films were 0.22, 0.24 and 0.19 nm, respectively, indicating that the spin-coated films show smooth surface morphology even after spin coating from 2-propanol solution. The FIrpic and FCNIrpic were also soluble in 2-propanol and well dispersed in the PPO27 matrix. No large scale aggregation of the FIrpic and FCNIrpic was observed after spin coating. Therefore, the PPO27:FIrpic and PPO27:FCNIrpic can be used as the alcohol soluble

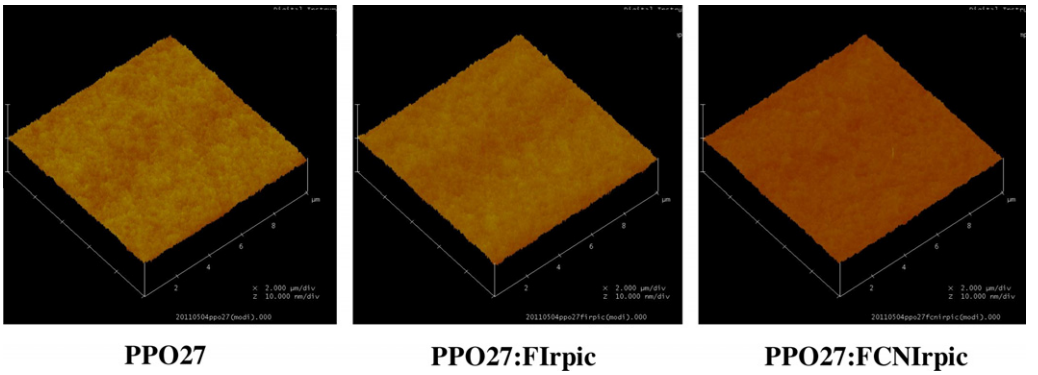

Fig. 2. Atomic force microscopic pictures of spin coated PPO27, PPO27:FIrpic and PPO27:FCNIrpic films.

phosphorescent emitting layer in solution processed blue PHOLEDs.

Fig. 3 shows the current density–voltage–luminance curves of the PPO27:FIrpic and PPO27:FCNIrpic devices. The current density was little affected by the doping concentration and similar current density was observed at 10% and 15% doping concentrations. The current density of the blue PHOLEDs was sharply increased from 4.0 V and the turn on voltage of the device was 4.0 V. The rather higher current density of the PPO27:FIrpic device than that of the PPO27:FCNIrpic device is due to good electron transport properties of FIrpic. Holes and electrons are partially transported by the dopant materials at high doping concentration, leading to high current density in the PPO27:FIrpic devices.

Quantum efficiency–current density curves of the solution processed PPO27:FIrpic and PPO27:FCNIrpic blue PHOLEDs are shown in Fig. 4. The quantum efficiency of the device II was slightly higher than that of the device I over all current density range. The maximum quantum efficiency of the device II was 14.6% at 0.71 mA/cm^2 which corresponds to the luminance of 200 cd/m^2. The device IV also showed higher quantum efficiency than the device III and the maximum quantum efficiency of the device IV was 13.4% at 0.10 mA/cm^2 which corresponds to the luminance of 21 cd/m^2. The color coordinates of the device II and device IV were (0.15, 0.36) and (0.15, 0.26). All blue PHOLEDs fabricated in this work showed high quantum efficiency compared with other solution processed blue PHOLEDs reported in the literature. In particular, the quantum efficiency of the device IV is the best efficiency value reported in the solution processed deep blue PHOLEDs with y color coordinate less than 0.30.

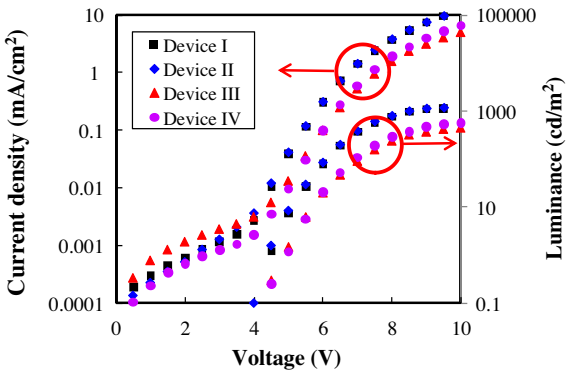

Fig. 3. Current density–voltage–luminance curves of the solution processed blue PHOLEDs with PPO27:FIrpic and PPO27:FCNIrpic emitting layers.

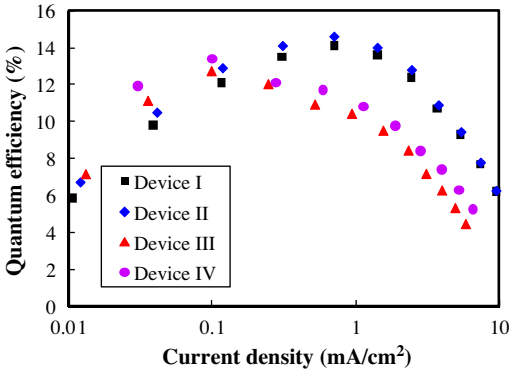

Fig. 4. Quantum efficiency–current density curves of the solution processed blue PHOLEDs with PPO27:FIrpic and PPO27:FCNIrpic emitting layers.

The high quantum efficiency of the PPO27 based blue PHOLEDs can be explained by effective charge injection and confinement, triplet exciton confinement, and stable film morphology in the emitting layer. In general, it is difficult to confine charges and triplet excitons inside the emitting layer in solution processed blue PHOLEDs because multilayer structure formation is limited by the intermixing of organic materials during solution coating process. Hole transport type exciton blocking material should be inserted between common PEDOT:PSS layer and phosphorescent emitting layer to confine charges and triplet excitons inside the emitting layer. However, most hole transport materials and phosphorescent emitting materials are soluble in organic solvents such as benzene, toluene and chlorobenzene, which limits the orthogonal film formation. However, the PPO27 host material used in this work was soluble in highly polar 2-propanol solvent and could be spin-coated on organic soluble PVK hole transport

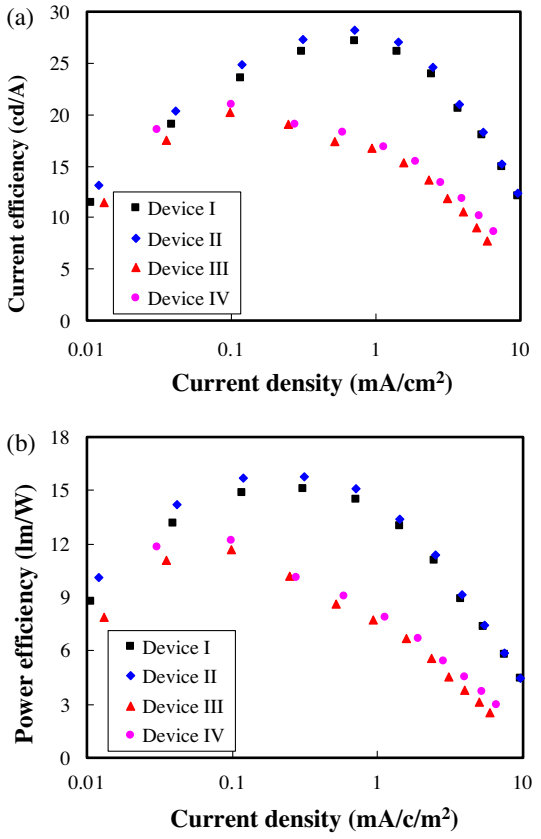

Fig. 5. (a) Current efficiency–current density and (b) power efficiency–current density curves of the solution processed blue PHOLEDs with PPO27:FIrpic and PPO27:FCNIrpic emitting layers.

layer without any intermixing. The PVK is a well-known hole transport material with the HOMO/LUMO level of 5.9/2.4 eV and a high triplet energy of 2.9 eV. The PVK injects holes into the PPO27 emitting layer and prevents the electron leakage from the emitting layer to the hole transport layer. The energy barrier for hole injection was 0.35 eV, while the energy barrier for electron leakage was 0.60 eV. Therefore, the PVK hole transport layer could effectively inject holes and block electron leakage, contributing to the improvement of recombination efficiency in the emitting layer. In addition, the high triplet energy of the PVK blocks the triplet exciton diffusion into the hole transport layer, confining triplet excitons inside the emitting layer. The triplet energy of the PVK (2.90 eV) was higher than that of FIrpic (2.65 eV) and FCNIrpic (2.74 eV), which blocked the triplet exciton leakage. Therefore, the triplet excitons of the PPO27:FIrpic and PPO27:FCNIrpic emitting layers can be confined in the emitting layer by the PVK hole transport layer. The orthogonal film formation by the spin coating of the alcohol soluble PPO27:FIrpic and PPO27:FCNIrpic emitting layers on the PVK hole transport layer improved the device performances of blue PHOLEDs.

The stable film morphology of the PPO27:FIrpic and PPO27:FCNIrpic films was also critical to the high quantum efficiency of the solution processed blue PHOLEDs. As the

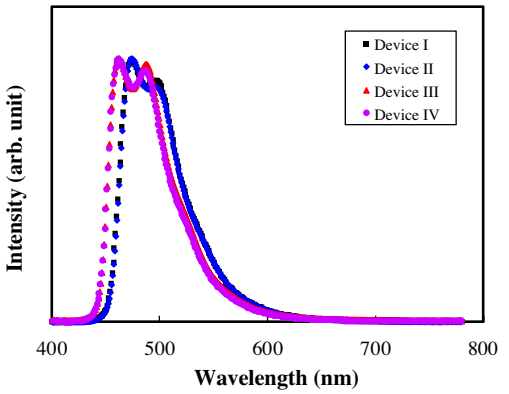

Fig. 6. Electroluminescence spectra of the solution processed blue PHOLEDs with PPO27:FIrpic and PPO27:FCNIrpic emitting layers.

FIrpic and FCNIrpic were well dispersed in the alcohol soluble PPO27 host material, little aggregation and crystallization were observed in the spin coated film, resulting in high quantum efficiency in the PPO27 based blue PHOLEDs.

Current efficiency–current density and power efficiency–current density curves of the PPO27:FIrpic and PPO27:FCNIrpic based blue PHOLEDs are shown in Fig. 5. The current efficiency and power efficiency showed similar relationship to the quantum efficiency depending on the device structure. The maximum current efficiency and power efficiency of the device II with PPO27:FIrpic emitting layer was 28.2 cd/A and 15.8 lm/W, while that of the device IV with PPO27:FCNIrpic emitting layer was 21.0 cd/A and 12.2 lm/W.

Electroluminescence (EL) spectra of the PPO27:FIrpic and PPO27:FCNIrpic devices are shown in Fig. 6. The maximum emission peak of the PPO27:FCNIrpic device was blue shifted by 12 nm compared with that of PPO27:FIrpic device because of the deep blue emission of the FCNIrpic. The color coordinate of the device IV was (0.15, 0.26) compared with (0.15, 0.36) of device II. Therefore, solution processed deep blue PHOLEDs could be effectively fabricated using the alcohol soluble PPO27:FCNIrpic emitting layer.

4. Conclusions

In conclusion, high quantum efficiency was achieved in the solution processed sky blue and deep blue PHOLEDs using alcohol soluble phosphorescent emitting layer. A multilayer device structure with an exciton blocking layer was fabricated by the spin-coating of the alcohol soluble PPO27:FIrpic and PPO27:FCNIrpic emitting layers on toluene soluble PVK exciton blocking layer. The approach to fabricate multilayer device structure using the solubility difference between the emitting layer and charge transport layers can be useful to improve the device performances of the solution processed PHOLEDs.

References

[1] T. Earmme, E. Ahmed, S.A. Jenekhe, Adv. Mater. 22 (2010) 4744.

[2] M.K. Mathai, V. Choong, S.A. Choulis, B. Krummacher, F. So, Appl. Phys. Lett. 88 (2006) 243512.
[3] S. Lamansky, P.I. Djurovich, F.A. Razzaq, S. Garon, D.L. Murphy, M.E. Thompson, J. Appl. Phys. 92 (2002) 1570.
[4] K.S. Yook, S.O. Jeon, O.Y. Kim, J.Y. Lee, Electrochem. Solid-State Lett. 13 (2010) J71.
[5] X. Yang, D.C. Müller, D. Neher, K. Meerholz, Adv. Mater. 18 (2006) 948.
[6] S. Tokito, M. Suzuki, F. Sato, M. Kamachi, K. Shirane, Org. Electron. 4 (2003) 105.
[7] X.H. Yang, F. Jaiser, S. Klinger, D. Neher, Appl. Phys. Lett. 88 (2006) 021107.
[8] K.S. Yook, S.E. Jang, S.O. Jeon, J.Y. Lee, Adv. Mater. 22 (2010) 4479.
[9] S. Ye, Y. Liu, K. Lu, W. Wu, C. Du, Y. Liu, H. Liu, T. Wu, G. Yu, Adv. Funct. Mater. (2010), doi:10.1002/adfm.201000474.
[10] W. Jiang, L. Duan, J. Qiao, D. Zhang, G. Dong, L. Wang, Y. Qiu, J. Mater. Chem. 20 (2010) 6131.
[11] L.D. Hou, L. Duan, J. Qiao, W. Li, D.Q. Zhang, Y. Qiu, Appl. Phys. Lett. 92 (2008) 263301.
[12] J.-H. Jou, W.-B. Wang, S.-Z. Chen, J.-J. Shyue, M.-F. Hsu, C.-W. Lin, S.-M. Shen, C.-J. Wang, C.-P. Liu, C.-T. Chen, M.-F. Wu, S.-W. Liu, J. Mater. Chem. 20 (2010) 8411.
[13] H.S. Son, C.W. Seo, J.Y. Lee, J. Mater. Chem. 21 (2011) 5638.

surface energy between the hydrophilic ITO surface and the hydrophobic HTL [5], allowing a good compatibility of the ITO surface and HTL, and hence a reduced turn-on voltage. The SAM-modified interface suppresses the crystallization of the overlaying HTL upon heating even above the glass transition temperatures of HTL materials [6]. The suppression of crystallization is an additional advantage brought about by using SAMs as a modifier.

As physically-adsorbed modifiers, chloride and acid derivatives, including phosphonic, sulfonic, and carboxylic acids, have been used [3,7–12]. For more stable SAM-ITO interfaces, chemically-bonded modifiers are considered to be preferable, because the rigid covalent bond prevents the exfoliation at the interface. Organo-alkoxysilane [4,13–19], silazane [20], and chlorosilane [21–23] have been used as modifiers, for which facile sol–gel reactions have often been used. Vapor phase reactions are also often used for the silanization [24]. However, they require high temperatures in many cases. This also limits kinds of modifiers, since the modifier should have a high thermal stability and a sufficiently high vapor pressure. In the sol−gel silanization, diluted silane molecules are immobilized on ITO surface in organic solvents, such as toluene [13–16,19], ethanol [16], and hexane [22]. The silanization includes two reaction steps [24–26]. The first step is the hydrolysis of silanes with water molecules adsorbed on a substrate surface or incorporated in a solvent to generate a silanol (Si–OH). The second step is the condensation of two silanols to form a siloxane bond on the ITO surface. The rate of hydrolysis significantly depends on the amount of water, and hence, the amount of water considerably influences on the resultant SAM structure on the ITO surface. Also, pH in a reaction solution has a significant impact on the SAM structure, because the mechanism and the kinetics of condensation reaction are completely different between under acidic and basic conditions [27,28]. When the hydrolysis and the condensation proceed via base-catalyzed mechanism, ramified silane polymers with widely-distributed molecular weights are formed, and the polymers subsequently form isolated particles. On the other hand, when the hydrolysis and the condensation proceed via acidic-catalyzed mechanism, homogeneous polymerization leads to mostly linear silane polymers with narrowly-distributed molecular weights. In addition to these factors, the rate of the condensation also depends on the amount of the silane molecule in a system. Therefore, the control of the three factors, i.e., catalytic condition, water amount, and the concentration of silane, is crucial for precise formation of SAMs and, therefore, for achieving excellent charge-injection properties of devices.

As described above, there are a number of studies targeting superior device performances by using novel modifiers. However, the systematic studies on preparation conditions for the SAM formation on ITO have not been reported. This may partly be because the amount of water and the pH are hardly controllable in hydrophobic solvents frequently used in the previous studies, such as toluene and hexane, which are immiscible with water. In this study, we investigated SAM formations of an alkylsilane, pentyltriethoxysilane (PTES), on ITO in an amphiphilic solvent, tetrahydrofuran (THF), which is miscible with water and can precisely control the amount of water and catalytic conditions. We, for the first time, systematically studied how the SAM structure and the resultant hole-injection property depend on amount of water, concentration of PTES, and catalytic condition in the reaction solution. The results obtained here would provide a benefit clue on the conditions of SAM formation for the high-performance OLEDs.

2. Experimental

2.1. Substrate preparation

We used an ITO patterned glass substrate, 55 nm ITO deposited on a soda-lime–silica glass with 0.7 mm thickness covered with 23 nm SiO_2 layer, sheet resistance of 50 Ω/sq, and an one subnanometer average roughness, as a cathode. The substrate was swabbed with acetone, followed by ultrasonic cleaning in detergent, ultrapure water, acetone, and isopropyl alcohol. The substrate was then boiled in isopropyl alcohol and placed in an ultraviolet−ozone treatment chamber (PL16-110, Sen Lights Co.). For the silane SAM formation, a freshly treated substrate was used without storage.

2.2. Silane SAM formation

Nitric acid (HNO_3: Nacalai Tesque Inc., 0.1 M) and ammonium hydroxide (NH_3: Hayashi Pure Chemical Industries, 28 wt%) were used as catalysts after being diluted with ultrapure water. Tetrahydrofuran (THF: Wako Pure Chemicals Industries, dehydrated, no stabilizer) and pentyltriethoxysilane (PTES: Tokyo Chemical Industry Co. Ltd.) were used as a solvent and a silica source, respectively.

First, THF and a given concentration of HNO_3 or NH_3 aqueous solution were mixed in a glass vessel. Under stirring in an ice water bath, PTES was added and kept stirring for 5 min. After stirring was stopped, the freshly treated ITO substrate was soaked in the solution, sealed, and kept at 40 °C for 24 h. The substrate was retrieved, rinsed with chloroform, and supersonically cleaned in chloroform for 10 min. Finally, the substrate was baked at 100 °C under vacuum to remove volatile residuals. The SAM-modified ITO substrates were used for device fabrication immediately. Hereafter, a H_2O/PTES ratio and a PTES concentration in a THF solvent are denoted as r and C_{PTES}, respectively. The value of r was controlled with the amount of catalytic aqueous solution, and thus the catalytic aqueous solutions were employed as a water source as well as a catalyst. In the present study, the sample prepared with C_{PTES} = 0 mM denoted as bare-ITO.

2.3. Silane SAM characterization

Contact angles, θ, of SAM-modified ITO substrates were measured with a contact-angle meter (Drop Mater 700, Kyowa Interface Science Co. Ltd.) using distilled water. The measurements were performed at five different points for respective substrates and the data were averaged. Surface morphology of the substrates was observed by an atomic force microscope (AFM: SPA400 + SPI3800 N, SII

Nano Technology Inc.) operating in a dynamic force mode (DFM).

2.4. Device fabrication and characterization

We used *N*, *N*′-di(1-naphthy)-*N*, *N*′-diphenylbenzidine (α-NPD) as a hole-transporting layer, tris(8-hydroxyquinoline) aluminum(III) (Alq_3) as a emissive and electron-transporting layer, lithium fluoride (LiF: Furuuchi Chemical Co. Ltd., 99.99%) as a electron-injection layer, and aluminum (Al: Kojundo Chemical Lab. Co. Ltd., 99.999%) as a cathode material. All the reagents were used as received.

Hole only devices (HODs) and OLED devices were fabricated on the SAM-modified ITO substrate by successive vapor deposition of organic layers, followed by the deposition of LiF and Al. HODs were composed of ITO-SAM/NPD 100 nm/Al 100 nm, whereas OLED devices were composed of ITO-SAM/NPD 50 nm/Alq_3 50 nm/LiF 0.6 nm/Al 100 nm. The deposition was carried out under 10^{-5} Pa. The deposition rates were 3 Å s^{-1} for the organic layers and Al, and 0.1 Å·s^{-1} for LiF. The devices thus fabricated have four active areas with 4 mm^2 each. Current density–voltage–luminance (*J*–*V*–*L*) characterization was performed using a computer-controlled source meter (Source Meter 2400, Keithley Instruments Inc.) equipped with a spectroradiometer (SR-3, TOPCON Co.). The characterization was carried out on all of the four active areas, providing information about reproducibility of the SAM formation on the ITO surfaces.

3. Results and discussion

First, we conducted a surface modification of ITO substrates with SAM and fabricated OLEDs with using the modified substrates. Fig. 1 shows the optical microscope images of the electroluminescence from the OLEDs. The images clearly indicate that in-plane uniformity of emission was considerably influenced by the catalytic condition for the SAM formation. Homogeneous emission was observed when the SAM was formed under the acidic condition (Fig. 1a), while significantly inhomogeneous emission was observed when it was formed under the basic condition (Fig. 1b). The luminance for the acidic condition (601 cd/m^2) was much larger than that for the basic condition (<100 cd/m^2) at an applied voltage of 6 V for the devices in Fig. 1. Namely, the luminescence was stronger and more homogeneous for the acidic condition than the basic condition. Fig. 2 shows the current density–voltage (*J*–*V*) and luminance–voltage (*L*–*V*) characteristics of the two OLEDs shown above (with the SAM formation under the acidic and basic conditions). For each sample, the measurements were performed on the four active areas (2 × 2 mm) and all the four data are plotted. The *J*–*V* (Fig. 2a) and *L*–*V* (Fig. 2b) plots reveal that the acidic condition led to lower turn-on voltages and higher luminance than the basic condition. Moreover, the four data for the basic condition were scattered, while those for the acidic condition were more reproducible. Thus, the in-plane uniformity of *J*–*V* and *L*–*V* characteristics highly depends on the catalytic conditions.

Fig. 3 shows the *J*–*V* plots of HODs for the 0.1, 0.01, and 0.001 M HNO_3, and 0.1 and 0.01 M NH_3 catalytic conditions. The acidic conditions exhibited higher hole-injection properties than the basic conditions, as in the case of OLEDs. In the studied case, the highest hole-injection property was achieved with 0.01 M HNO_3. The difference in the hole-injection property would be related to the surface morphologies of SAM-modified ITO substrates, as discussed below.

Fig. 4 shows the AFM images of the SAM-modified ITO substrates prepared with (a) acidic (0.01 M HNO_3) and (b) basic (0.01 M NH_3) catalysts. In the acidic condition (Fig. 4a), the roughness of the SAM was virtually the same as that of the bare ITO, indicating the coverage of a homogeneous silane layer on the ITO substrate. On the other hand, the basic condition (Fig. 4b) resulted in an inhomogeneous formation of coarse particles with the size of several micrometers in length and 30 nm in thickness. This confirms that the different luminance in Fig. 1 originates from the different homogeneity of the silane layers on the respective ITO surfaces. The contact angles of the modified surfaces were 93.6 ± 1.8° and 84.4 ± 0.5° with 0.01 M HNO_3 and 0.01 M NH_3, respectively, confirming a higher coverage of hydrophobic PTES on the ITO substrate under the acidic condition. The observation of coarse particles in Fig. 4b is explained by the fact that base-catalyzed condensation of silicate species produces ramified polymers with widely-distributed molecular weights [27,28]. The coarse particles are derived from the well-grown polymeric silicates which are formed on the ITO surface and/

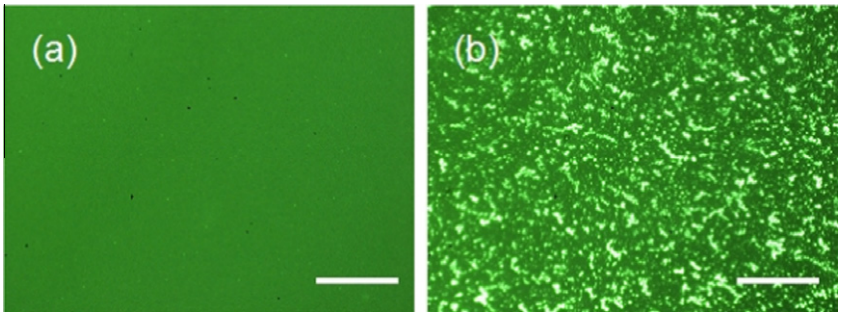

Fig. 1. Optical microscope images of the OLEDs under the applied voltage of 9 V. The SAM layers were formed with (a) acidic (0.01 M HNO_3) and (b) basic (0.01 M NH_3) catalysts under the condition of $r = 15$ and $C_{PTES} = 250$ mM. The OLEDs consist of ITO-SAM/NPD 50 nm/Alq_3 50 nm/LiF 0.6 nm/Al 100 nm. White bar = 100 μm in both the images.

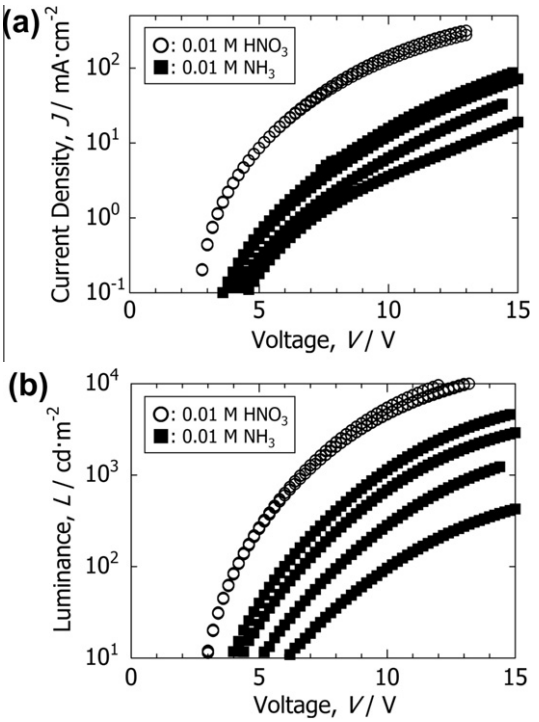

Fig. 2. (a) J–V and (b) L–V characteristics of the OLEDs composed of ITO-SAM/NPD 50 nm/Alq_3 50 nm/ LiF 0.6 nm/Al 100 nm. The SAM layers were prepared with 0.01 M HNO_3 (open circles) and 0.01 M NH_3 (closed squares) as catalysts, under the condition of $r = 15$ and $C_{PTES} = 250$ mM. The measurements were performed on the four active areas and all the data are plotted for both the devices.

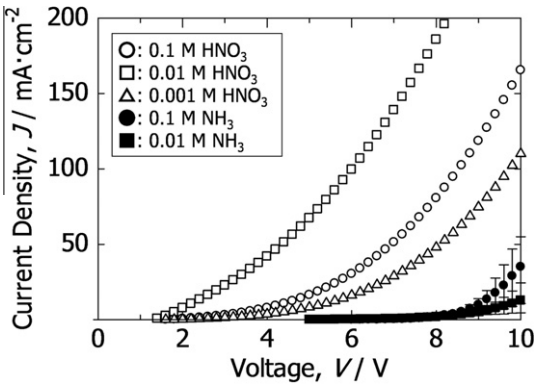

Fig. 3. J–V characteristics of HODs composed of ITO-SAM/NPD 100 nm/Al 100 nm. SAM formation was performed with the condition of $r = 10$ and $C_{PTES} = 250$ mM using various catalysts; open circles: 0.1 M HNO_3, open squares: 0.01 M HNO_3, open triangles: 0.001 M HNO_3, closed circles: 0.1 M NH_3, closed squares: 0.01 M NH_3. Error bars are depicted for HODs fabricated on the base-catalyzed SAMs, caused by the inhomogeneous characteristics among the respective four active areas.

or attached onto the surface. On the other hand, acid-catalyzed condensation of silicate species is favorable for the formation of homogenous polymer networks [27,28], which leads to the coverage of SAM on the ITO surface without segregation. Moreover, it is well-known that the rate of condensation is minimized around isoelectric point (IEP) of polymerizing silicates [29,30]. For example, the rate of condensation becomes extremely slow at pH 2.0–2.5 and 4 for silica and methylsilsesquioxane ($MeSiO_{1.5}$), respectively. In this study, the use of the condition, 0.01 M HNO_3, realized a relatively moderate condensation reaction of PTES, leading to the formation of a homogeneous silane layer.

Fig. 5 shows the J–V plots of the HODs at various r values under an acidic (0.01 M HNO_3) condition. With an increase of r, the hole-injection property was improved gradually from $r = 3$ to $r = 15$. The J increased from 11.9 mA cm^{-2} at $r = 3$ to 219 mA cm^{-2} at $r = 15$ at an applied voltage of 6 V. Further increase in r lowered the hole-injection property. For PTES, $r = 1.5$ is the stoichiometric condition for hydrolysis and condensation. However, the reactions generally take long reaction times to complete at $r = 1.5$ [27]. Thus, the excessive amount of water ($r > 1.5$) was required for the complete coverage of the ITO surface for the present reaction time, 24 h, and at the present reaction temperature, 40 °C. The best r was 15 in this case. The contact angles were 91.8 ± 0.7° at $r = 15$ and 79.9 ± 0.5 ° at $r = 30$. From the contact angles, the coverage of PTES for $r = 15$ and $r = 30$ can be roughly estimated as 88 ± 5% and 11 ± 3%, respectively. The small contact angle at $r = 30$ suggests that the condensation reaction occurred in the solvent phase rather than the ITO surface. The enhanced condensation in the solvent phase can be related to the formation of oligomers with the low connectivity to an ITO surface. A previous report [31] revealed that the oligomers with a cage structure tended to form with increasing r in a organosiloxane sol–gel system. Since the oligomers with a cage structure have no contribution to the formation of SAMs, they are isolated in a solvent. The insufficiently-modified ITO would explain the observed decrease in the hole-injection property at $r > 15$. Also, the small contact angle at $r = 30$ would be related to the increased silanols on the immobilized modifiers. An increase in r enhances the hydrolysis of PTES and produces hydrophilic silanols more effectively, leading to the small contact angle of ITO surface. Thus, the calculated coverage for $r = 30$, 11 ± 3%, would somewhat underestimate the coverage of PTES on ITO.

Fig. 6 shows the J–V plots of the HODs at various C_{PTES} values in an acidic (0.01 M HNO_3) condition at $r = 15$. The hole-injection property was improved with an increase of C_{PTES}. The J at applied voltage of 6 V increased from 3.94 to 206 mA cm^{-2}, as C_{PTES} increased from 0 to 250 mM. Fig. 7 shows the contact angle, θ, of the SAM-modified ITO surface as a function of C_{PTES}. The θ decreased from $C_{PTES} = 0$–42 mM and increased from $C_{PTES} = 42$–250 mM. The decrease in θ in the low C_{PTES} regime suggests the immobilization of hydrophilic species on ITO surface. Since the low C_{PTES} is an insufficient condition for the SAM formation, the silane layer unlikely developed on the entire surface of ITO. Thus, the immobilization of hydrolyzed PTES with hydrophilic silanols would decrease θ, as depicted in the inset of Fig. 7. In fact, the presence of silanols in silica networks was evidenced in the silica gels prepared under the acid-catalyzed condensations [27,32,33]. Whereas, in the condition of C_{PTES} from 42 to 252 mM,

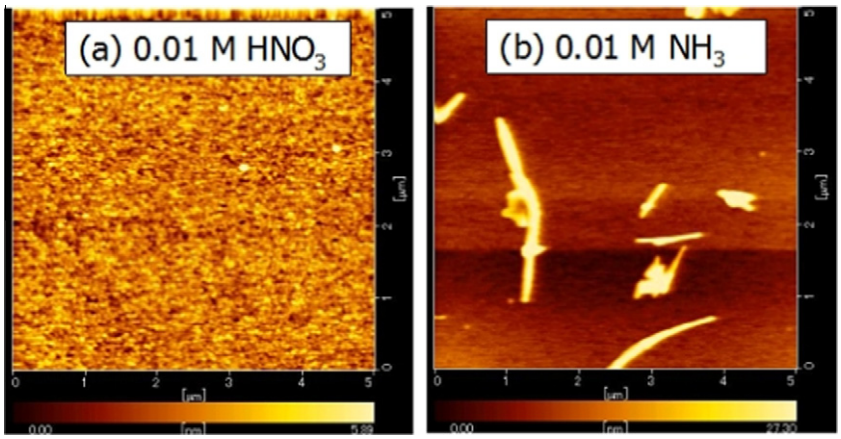

Fig. 4. AFM images of SAM-modified ITO substrates prepared under the condition of $r = 10$ and $C_{PTES} = 250$ mM with (a) acidic (0.01 M HNO_3) and (b) basic (0.01 M NH_3) catalysts. The image areas correspond to 5×5 μm.

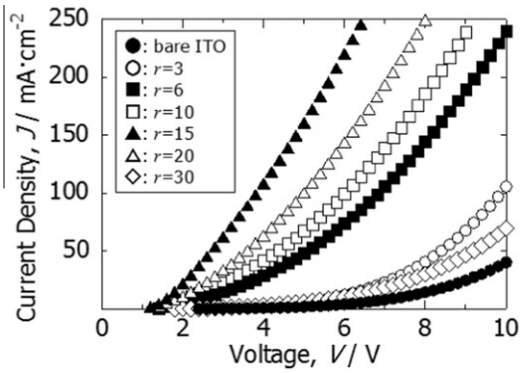

Fig. 5. The r-dependence of J–V characteristics of HODs composed of ITO-SAM/NPD 100 nm/Al 100 nm. 0.01 M HNO_3 was used as a catalyst and $C_{PTES} = 250$ mM for all the devices. closed circle: bare ITO, open circle: $r = 3$, closed square: $r = 6$, open square: $r = 10$, closed triangle: $r = 15$, open triangle: $r = 20$, open rhombus: $r = 30$.

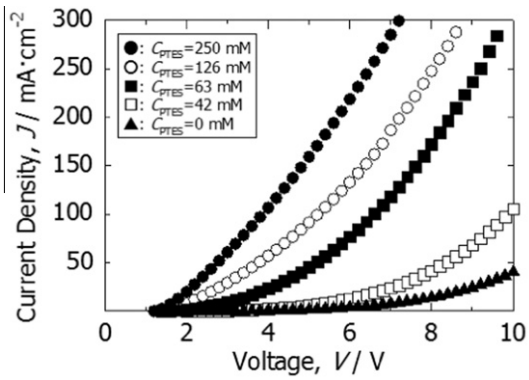

Fig. 6. Influence of C_{PTES} on J–V characteristics of HODs composed of ITO-SAM/NPD 100 nm/Al 100 nm; closed circles: 250 mM, open circles: 126 mM, closed squares: 63 mM, open squares: 42 mM, closed triangles: 0 mM. 0.01 M HNO_3 was used as a catalyst and $r = 15$ for all the devices.

θ increased due to the formation of siloxane network and the coverage of the ITO surface with the hydrophobic silane layer. At $C_{PTES} = 250$ mM, θ value virtually reached a value expected for the full coverage of PTES [4,34], meaning that 250 mM is large enough to fully cover the ITO surface.

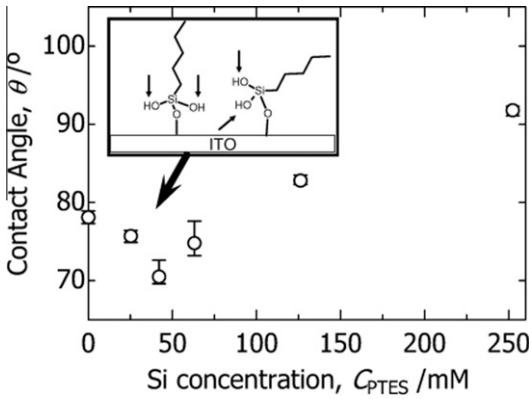

Fig. 7. Contact angles as a function of C_{PTES}.

In this way, with an appropriate pH (0.01 M HNO_3), water amount ($r = 15$), and PTES concentration ($C_{PTES} = 250$ mM), the acidic condition reproducibly provided a remarkably uniform PTES-modified ITO surface, which cannot be achieved in basic conditions. The OLEDs fabricated under this condition exhibited excellent J–V and L–V characteristics. The homogeneous PTES layer covalently-bonded to the ITO surface works as a good compatible layer with HTL, helping the hole-injection significantly. Thus, the acid-catalyzed silanization can be a very useful method for the precise modification of ITO substrates for the applications to OLED and other electronic devices. We used THF as a solvent in this work. PTES forms organosiloxane network on ITO with the formula of $RSiO_{1.5}$ through the hydrolysis and condensation reactions. Due to its hydrophobicity, oligomeric compounds of organosiloxanes easily phase separate from an aqueous solution or lower alcohols, resulting in the precipitation of amorphous compounds [35,36]. The use of THF as a solvent allows an accurate control of the

water content without the precipitation of silane compounds. Although the variation of the hole-injection property can be explained on the basis of the coverage of SAM on the ITO surface, the thickness of the silane layer should also influence on the hole-injection property; the silane layer on the ITO surface works as an insulator, and hence, the formation of a thick silane layer is undesirable. Considering the reaction mechanisms of PTES, the formation of a thick silane layer is unavoidable in the case of the base-catalyzed reactions. Therefore, the acid-catalyzed reactions would be preferable also in this sense.

4. Conclusions

By using facile sol–gel route, the conditions for SAM formation on ITO were systematically studied. The relationship between the preparation conditions of SAM and the resultant device properties was investigated by using OLEDs and HODs fabricated on SAM-modified ITO substrates. The emissions from OLEDs and the hole-injection properties of HODs revealed that the acidic conditions are favorable for the reproducible formation of SAM on the ITO surface. The SAM formation under the acidic conditions allows the homogeneous coverage of a silane layer on the ITO substrates, which leads to improved hole-injection properties from the anode. On the other hand, the use of basic conditions results in the inhomogeneous coverage of a silane layer on the ITO substrates and the decreased hole-injection from the anode. The choice of r and C_{PTES} also affect the kinetics of hydrolysis and condensation reactions of PTES, and hence the resultant SAM structures and hole-injection properties. The hole-injection property of HODs depends on the coverage of SAM on the ITO surface; the hole-injection property improved with increased coverage of SAM on the ITO surface. As a result, the highest hole-injection was achieved when SAM formation was performed under $r = 15$ and $C_{PTES} = 250$ mM, with 0.01 M HNO_3 as a catalyst. The results obtained here suggest that the device performance of OLEDs and HODs can improve drastically by choosing appropriate SAM formation conditions.

Acknowledgment

We thank financial supports by Grant-in-Aids for Scientific Research (A) (No. 21245044) and by Funding Program for World-Leading Innovative R&D on Science and Technology (FIRST Program), Japan Society for the Promotion of Science (JSPS). The present work was partly supported by the Global COE Program "Integrated Materials Science" (No. B-09) of the Ministry of Education, Culture, Sports, Science and Technology (MEXT), administrated by JSPS. Y. T. thanks the Grant-in-Aid for Fellow (No. 21-607) from JSPS. The authors thank Professor Tsujii, Mr. Nomura, and Mr. Nakanishi, Institute for Chemical Research in Kyoto University, for the AFM observations and the contact-angle measurements.

References

[1] C.W. Tang, S.A. VanSlyke, Appl. Phys. Lett. 51 (1987) 913–915.
[2] F. Nüesch, L. Si-Ahmed, B. François, L. Zuppiroli, Adv. Mater. 9 (1997) 222–225.
[3] F. Nüesch, F. Rotzinger, L. Si-Ahmed, L. Zuppiroli, Chem. Phys. Lett. 288 (1998) 861–867.
[4] Q. Huang, G.A. Evmenenko, P. Dukka, P. Lee, N.R. Armstrong, T.J. Marks, J. Am. Chem. Soc. 127 (2005) 10227–10242.
[5] H. Klauk, Chem. Soc. Rev. 39 (2010) 2643–2666.
[6] J.G.C. Veinot, T.J. Marks, Acc. Chem. Res. 38 (2005) 632–643.
[7] S.F.J. Appleyard, S.R. Day, R.D. Pickford, M.R. Willis, J. Mater. Chem. 10 (2000) 169–173.
[8] C. Ganzorig, K.-J. Kwak, K. Yagi, M. Fujihira, Appl. Phys. Lett. 79 (2001) 272–274.
[9] M. Carrara, F. Nüesch, L. Zuppiroli, Synth. Met. 121 (2001) 1633–1634.
[10] J. Morgado, N. Barbagallo, A. Charas, M. Matos, L. Alcácer, F. Cacialli, J. Phys, D: Appl. Phys. 36 (2003) 434–438.
[11] S. Khodabakhsh, D. Poplavskyy, S. Heutz, J. Nelson, D.D.C. Bradley, H. Murata, T.S. Jones, Adv. Funct. Mater. 14 (2004) 1205–1210.
[12] S. Besbes, H. Ben Ouada, J. Davenas, L. Ponsonnet, N. Jaffrezic, P. Alcouffe, Mater. Sci. Eng. C 26 (2006) 505–510.
[13] J. Lee, B.-J. Jung, J.-I. Lee, H.Y. Chu, L.-M. Do, H.-K. Shim, J. Mater. Chem. 12 (2002) 3494–3498.
[14] P. Sigaud, J.-N. Chazalviel, F. Ozanam, J. Appl. Phys. 92 (2002) 992–996.
[15] Q. Huang, J. Li, G.A. Evmenenko, P. Dutta, T.J. Marks, Chem. Mater. 18 (2006) 2431–2442.
[16] L.-W. Chong, Y.-L. Lee, T.-C. Wen, Thin Solid Films 515 (2007) 2833–2841.
[17] T. Mori, S. Nishino, T. Nishikawa, S. Ogawa, Org. Electron. 9 (2008) 63–69.
[18] O.P. Khatri, K. Murase, H. Sugimura, Jpn. J. Appl. Phys. 47 (2008) 5048–5052.
[19] O.P. Khatri, K. Murase, H. Sugimura, Langmuir 24 (2008) 3787–3793.
[20] C.-C. Hsiao, C.-H. Chang, M.-C. Hung, N.-J. Yang, S.-A. Chen, Appl. Phys. Lett. 86 (2005) 2235051–2235053.
[21] Y. Koide, Q. Wang, J. Cui, D.D. Benson, T.J. Marks, J. Am. Chem. Soc. 122 (2000) 11266–11267.
[22] R.A. Hatton, S.R. Day, M.A. Chesters, M.R. Willis, Thin Solid Films 394 (2001) 292–297.
[23] B. Choi, J. Rhee, H.H. Lee, Appl. Phys. Lett. 79 (2001) 2109–2111.
[24] J. Duchet, B. Chabert, J.P. Chapel, J.F. Gérard, J.M. Chovelon, N. Jaffrezic-Renault, Langmuir 13 (1997) 2271–2278.
[25] M.E. McGovern, K.M.R. Kallury, M. Thompson, Langmuir 10 (1994) 3607–3614.
[26] A. Ulman, An Introduction to Ultrathin Organic Films from Langmuir–Blodgett to Self-Assembly, Academic Press, San Diego, 1991.
[27] C.J. Brinker, G.W. Scherer, Sol–Gel Science. The Physics and Chemistry of Sol–Gel Processing, Academic Press, San Diego, 1990.
[28] R.K. Iler, The Chemistry of Silica, Willy, New York, 1979.
[29] A.H. Boonstra, J.M.E. Baken, J. Non-Cryst. Solids. 122 (1990) 171–182.
[30] H. Dong, M.A. Brook, J.D. Brennan, Chem. Mater. 17 (2005) 2807–2816.
[31] L.-H. Lee, W.-C. Chen, W.-C. Liu, J. Polym. Sci., Part A: Polym. Chem. 40 (2002) 1560–1571.
[32] H. Kaji, K. Nakanishi, N. Soga, T. Inoue, N. Nemoto, J. Non-Cryst. Solids 181 (1995) 16–26.
[33] H. Kaji, K. Nakanishi, N. Soga, J. Non-Cryst. Solids 185 (1995) 18–30.
[34] A.V. Rao, M.M. Kulkarni, D.P. Amalnerkar, T. Seth, Appl. Surf. Sci. 206 (2003) 262–270.
[35] M. Park, S. Komarneni, J. Choi, J. Mater. Chem. 33 (1998) 3817–3821.
[36] D.A. Loy, B.M. Baugher, C.R. Baugher, D.A. Schneider, K. Rahimian, Chem. Mater. 12 (2000) 3624–3632.

the dopant. However, most of theoretical studies only focused on the electronic property or zero bias conductance. The transport properties of the bilayer GNRs under finite bias are rarely discussed. As we know, the electronic devices always work under a finite bias voltage. For the purpose of practical applications, it is important to investigate the transport properties of bilayer GNRs under a wide range of finite bias voltages. In the present work, by applying first-principles quantum transport calculations, we investigate the electronic transport properties of a bilayer GNR device. The results show that the electronic transport properties can be modulated by changing weak interaction between two GNR molecules.

This letter is organized as follows: Section 2 gives a brief description of the model and the formulas used in calculations. The calculated results are presented in Section 3 with discussions. Finally, a summary is made in Section 4.

2. Model and formalism

In Fig. 1, we show a typical nanoelectronic device based on the bilayer GNR. Here we choose bilayer armchair GNR (AB-α stacking) [28] with the width of $N_a = 5$ as a typical system. The system is divided into three regions: the left and right electrodes and the scattering region. Each electrode is described by a supercell with two repeated carbon unit cells along the transport direction. In the scattering region, the bilayer GNR is connected to two monolayer GNR. When the intermolecular distance (D) is 5 Å, the top GNR is rotated around its main axis with 0, $\pi/4$, $\pi/3$, and $\pi/2$, which correspond to $M0$, $M1$, $M2$, and $M3$, respectively. When the D is 3 Å (3.5 Å), the top GNR is shifted along its main axis (towards the right side) with 0, 4.26, and 8.52 Å, which correspond to $M4$ ($M7$), $M5$ ($M8$), and $M6$ ($M9$), respectively. $M4$–$M6$ ($M7$–$M9$) are arranged with same stacking configure in the overlapping region of the scattering region, namely, AB-α stacking configure. Previous studies have shown that this arrangement is energetically favorable configure for bilayer GNR [28,29]. The geometrical optimizations and the electronic transport properties are all performed by the first-principles method based on the fully self-consistent *ab initio* density-functional theory [30,31]. The nonlinear current through the device is calculated using the Landauer formula [32]:

$$I(V_b) = \frac{2e}{h}\int T(E, V_b)[f_l(E-\mu_l) - f_r(E-\mu_r)]dE \quad (1)$$

where $\mu_{l(r)}$ are electrochemical potentials of the left and right electrodes and the difference of them is $\mu_l - \mu_r = eV_b$. The energy region of the transmission spectrum that contributes to the current is referred to as the bias window. The total transmission probability

$$T(E, V_b) = Tr[\Gamma_l G^R \Gamma_r G^A] \quad (2)$$

where $G^{R(A)}$ is the retarded (advanced) Green functions of the central region, $\Gamma_{l(r)}$ is the contact broadening functions associated with the left (right) electrodes. In calculation, the valence electrons are expanded in a numerical atomic-orbital basis set of double-ζ plus polarization type. The core electrons are described by norm-conserving pseudopotentials and the local-density approximation (LDA) is used to the exchange-correlation potential. The k-point sampling is 1, 1, and 100 in the x, y, z direction, respectively, and the cutoff energy is set to 150 Ry. In our model, we have assumed that the electron transport through the device is so quick that there is no time for the GNR molecules to deform [2,3,33–35].

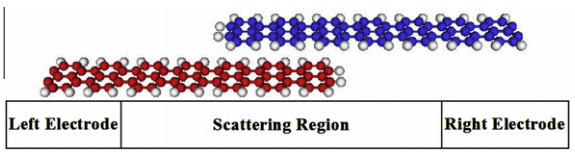

Fig. 1. Schematic view of the bilayer graphene nanoribbon device. All edge carbon atoms are saturated with hydrogen atoms.

3. Numerical results and discussion

In Fig. 2a–c, we give the current as a function of applied bias for the bilayer GNR systems. From the figure, some distinct features of calculated I–V curves can be addressed as follows: (i) For all systems, there exists a threshold voltage which can be attributed to the intrinsic semiconducting nature of armchair GNR ($N_a = 5$). (ii) When we increase the dihedral angle between two GNR molecules, the current values increase obviously with the increasing dihedral angle at same bias. Rectifying behavior can be found in $M1$, $M2$, and $M3$. From the inset of Fig. 2a, it can be found that $M2$ shows the best rectifying performance as compared with the others. The rectifying ratio in $M2$ is comparable to that in the recently reported double-silane chains system [3]. (iii) If we take the device $M5$ ($M8$) as OFF state, and $M4$ ($M7$) and $M6$ ($M9$) as ON states, the most interesting result is the appearance of the successive switch process [36] (ON–OFF–ON) when we reduce the size of overlapping region with fixed intermolecular distance. From the insets of Fig. 2b and c, the maximum value of ON–OFF ratio between $M4$ ($M7$) and $M5$ ($M8$) reaches 216 (51) at 0.45 V, and between $M6$ ($M9$) and $M5$ ($M8$) it is about 61 (25) at 0.45 V.

In Fig. 3a–d, we give the transmission spectra of $M0$–$M3$ at zero bias. From Fig. 3a, we can clearly see that the transmission coefficient is essentially zero in the energy region and a large HOMO–LUMO gap can be observed, which means very weak π–π interaction. It is known that the interaction between two molecules can lead to the splitting of the level and the magnitude of the splitting is dependent on the relative position of the interacting molecules [37]. When the dihedral angle between two GNR molecules is $\pi/4$, obvious level splitting for the frontier molecular levels can be observed. For instance, the LUMO and LUMO + 1 (splitting = 0.1 eV) in $M1$ originate from the LUMO splitting. More interestingly, we can find that the transmission coefficients and the amplitudes of the level splitting are strongly correlated, namely, the stronger the level splitting, the larger the corresponding transmission coefficient. This indicates that the molecular levels originating from large level splitting can be more effective

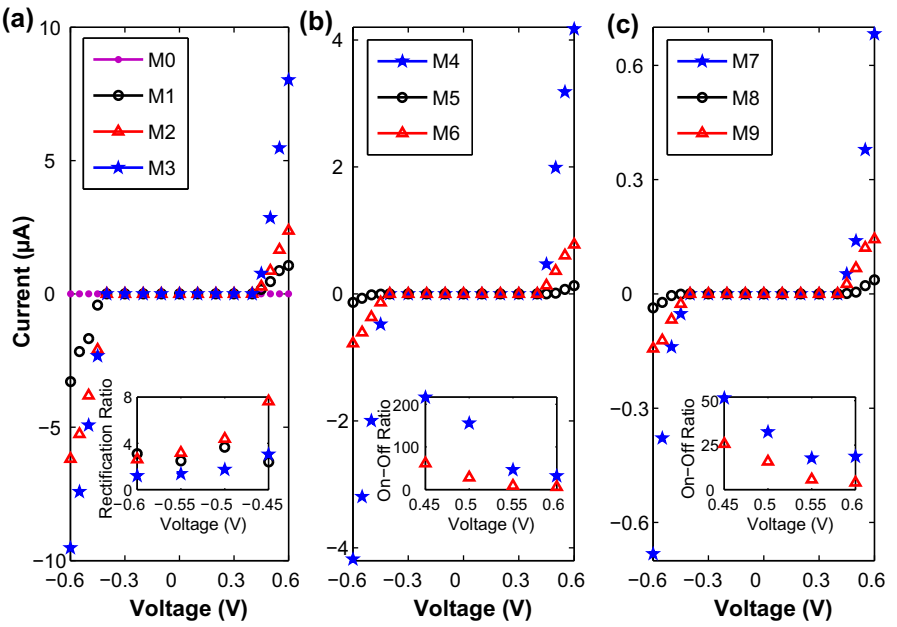

Fig. 2. (a) Calculated current as a function of the applied bias of *M*0–*M*3. The inset is the changes of rectifying ratio with the applied bias for *M*1–*M*3, respectively. (b) Calculated current as a function of the applied bias of *M*4–*M*6. The inset shows the ON/OFF ratio between *M*4 and *M*5 (blue) and between *M*6 and *M*5 (red). (c) Calculated current as a function of the applied bias of *M*7–*M*9. The inset shows the ON/OFF ratio between *M*7 and *M*8 (blue) and between *M*9 and *M*8 (red). (For interpretation of the references to color in this figure legend, the reader is referred to the web version of this article.)

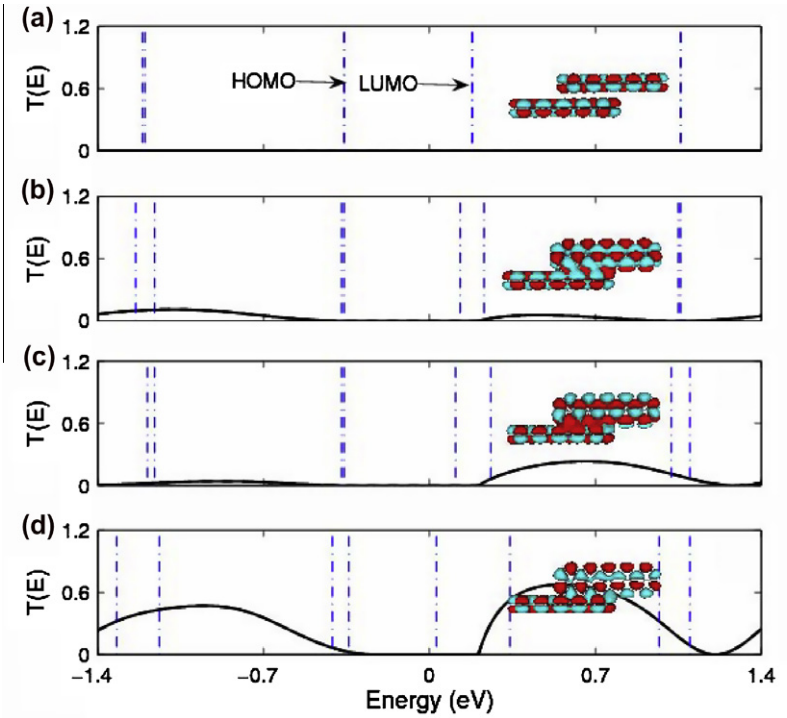

Fig. 3. (a)–(d) The transmission coefficients (solid lines) at zero bias for systems *M*0–*M*3, respectively. The vertical dash-doted curves stand for frontier molecular levels, and the Fermi level is set to be the origin of energy. The insets of (a)–(d) give the molecularly projected self-consistent Hamiltonian (MPSH) of the LUMO for *M*0–*M*3 at zero bias, respectively.

transport channels for electron transport. From the Fig. 3b–d, we can clearly see that the level originating from the LUMO splitting is very close to the Fermi level, indicating that the electron transport at low bias is mainly

determined by the amplitudes of LUMO splitting. From *M*1–*M*3, we can find that the splitting for LUMO is monotonically increasing as the dihedral angle increases. As a result, the conductivity of the system is obviously enhanced with the increase of dihedral angle even if the size of the overlapping region between two GNR molecules is reduced in the process. To explore the possibility about the formation of bilayer molecular junction in experiment, in the insets of Fig. 3a–d, we also plot the molecular projected self-consistent Hamiltonian (MPSH) of the LUMO for *M*0–*M*3 at zero bias, respectively. From the inset of Fig. 3a, we can find that when the vertical distance between two GNR molecules is 5 Å, the electronic density for two molecules cannot overlap each other due to large spatial distance. Thus, the molecular orbit shows the character of a single molecule's orbit. However, from the insets of Fig. 3b–d, we can find that when the dihedral angle is larger than or equal to $\pi/4$, there exists obvious overlapping of electronic density between two GNR molecules and thus these orbitals show a unitary behavior related to the two GNR molecules, indicating that π–π coupling between two molecules is efficient enough to induce the formation of bilayer GNR junction [38].

In order to understand the rectifying performance in *M*1–*M*3, we take *M*2 as an example to explore the origin of this phenomenon. As we know, the frontier molecular levels can be renormalized by bias potential, which modulates the electron transport in the two probe system [39]. In Fig. 4a–d, we demonstrate the rearrangement of the LUMO respect to the bands of left and right electrodes at $V_b = \pm 0.5$ V and $V_b = \pm 0.6$ V, respectively. From the Fig. 4a–d, we can find the LUMO is the unique conducting channel in the energy region [−0.2, 0.2] eV, and it lies in different positions at same positive and negative bias. As we use the semiconductor electrodes, the transmission coefficients in the bias window cannot be observed until the conductance band minimum matches with the valence band maximum at the Fermi level. Then, further increase in bias will develop the narrow the transmission region. From previous reports [18,19,40], it is known that the match or mismatch between the molecular states and the electrode states play a vital role in the changes of the conductivity of the systems. From Fig. 4a and c, we can clearly see that when the positive bias is applied, the LUMO level overlaps with the upper part of the valence band of the right electrode, but falls into the band gap of the left electrode. Thus, the hybridization between the LUMO and electrode states can be weakened so that the electron transport ability is weak in the bands matching region [19,40]. When the corresponding negative bias is applied, the LUMO overlaps with the lower part of the conductance band of the right electrode. Meanwhile, it is interesting to find that here the LUMO level overlaps with the valence band of the left electrode, especially obvious at $V_b = -0.6$ V. This leads to the enhancement of the electron transport ability compared with the case of the positive bias. As a result, the current value at negative bias is much larger than that at corresponding positive bias and rectification appears correspondingly, as shown in Fig. 2a. From above results, we can infer that when the positive bias is applied, the bad match between the LUMO state and the bands matching region might be main origin of the rectifying behavior.

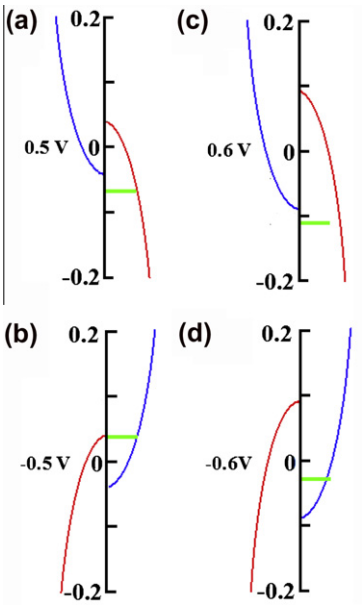

Fig. 4. The schematic diagram of the position of the LUMO in the scattering region relative to the bands of left and right electrodes at $V_b = \pm 0.5, \pm 0.6$ V. The blue and red curves indicate the conductance band and the valence band, respectively. The short lines (green) represent the position of the LUMO. (For interpretation of the references to color in this figure legend, the reader is referred to the web version of this article.)

For *M*4 (*M*7), *M*5 (*M*8), and *M*6 (*M*9), the bilayer GNR are arranged with the same intermolecular distance and stacking form in the scattering region so that the smaller the size of overlapping region, the weaker the intermolecular interaction. However, from Fig. 2b and c, we can find the currents are *M*4 (*M*7) > *M*6 (*M*9) > *M*5 (*M*8) for the same bias voltage, which means that the ON–OFF–ON process occurs when the top GNR is shifted along its main axis with fixed intermolecular distance. To understand this interesting phenomena, in Fig. 5, we present the change of the HOMO and LUMO with the bias voltage and the MPSH of the LUMO at $V_b = 0.45$ V for *M*4, *M*5, and *M*6, respectively. From Fig. 5a–c, it is found that when same bias is applied, the decrease of overlapping region can lead to the shift of the levels. Furthermore, we can clearly see that for *M*4–*M*6, the LUMO always lies inside the bias window. For the HOMO, however, a high bias voltage is necessary to drive it into the bias window. So, the electron transport through the bilayer GNR device mainly depends on the LUMO at low bias. This is similar to the cases of *M*1−*M*3. Comparing Fig. 5d and e with f, it is found that the LUMO of *M*4 and *M*5 has a high density on the overlapping region, indicating stronger coupling between two GNR molecules which plays an important role in the transport behaviors of these two systems. Comparing Fig. 5e with d, we can clearly see that the electron transport ability getting weaker in *M*5 is mainly due to the decrease of the strength of intermolecular coupling and molecule–electrode coupling. For LUMO of *M*6, although there is a low density on the overlapping region, the orbital covers

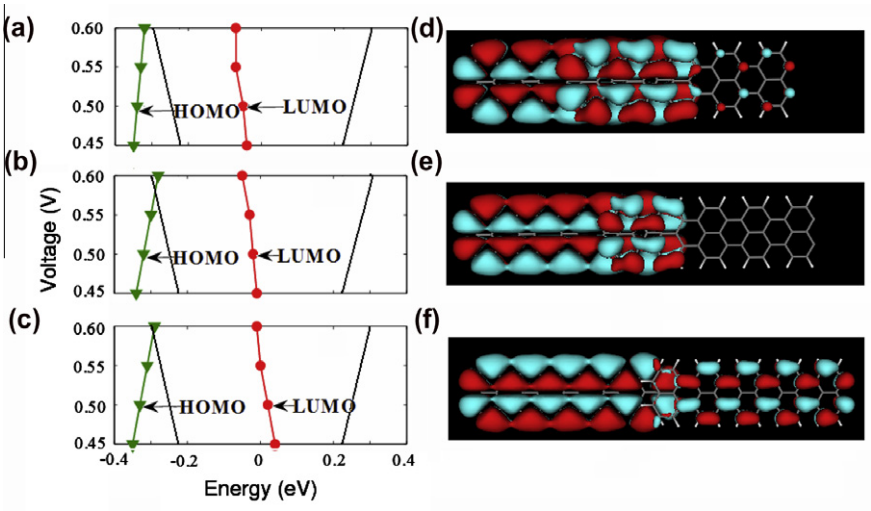

Fig. 5. (a)–(c) The shift of the HOMO and LUMO levels with the increase of bias voltage for *M*4–*M*6, respectively. (d)–(f) The molecularly projected self-consistent Hamiltonian (MPSH) of the LUMO for *M*4–*M*6 at V_b = 0.45 V, respectively.

the entire system and shows delocalized characteristic, resulting in the enhancement of the electron transport ability. As a result, the current of *M*6 is bigger than that of *M*5. However, its current is still smaller than that of *M*4. This may be due to the fact that compared with the *M*4, the slight delocalization of the LUMO in *M*6 cannot compensate for the loss of electron transport induced by the drastic decrease of the overlapping region.

4. Summary

In conclusion, we investigate the electronic transport properties of a bilayer GNR device. When we change the dihedral angle between two GNR molecules, the rectifying behavior can be observed. It is suggested that when the positive bias is applied, the bad match between the LUMO state and the bands matching region might be main origin of the rectifying behavior in *M*2. More importantly, a successive switch behavior can be realized by adjusting the overlapping region between two GNR molecules, namely by changing interaction between two GNR molecules. This can be attributed to the fact that the change of the intermolecular interaction leads to the shift of the molecular orbitals, and then leads to the change of the coupling strength between molecules and electrodes. It is suggested that we can adjust the electronic transport properties of the molecular devices by changing the weak intermolecular interaction between molecules, which provides a way for the design of molecular devices.

Acknowledgements

This work was supported by the National Natural Science Foundation of China (No. 60871065), by the National Basic Research Program of China (No. 2011CB606405), by the Specialized Research Fund for the Doctoral Program of Higher Education of China (No. 200805320011), and by Aid Program for Science and Technology Innovative Research Team in Higher Educational Institutions of Hunan Province.

References

[1] S. Wu, M.T. González, R. Huber, S. Grunder, M. Mayor, C. Schönenberger, M. Calame, Nat. Nanotechnol. 3 (2008) 569.
[2] M.Q. Long, K.Q. Chen, L.L. Wang, B.S. Zou, Z. Shuai, Appl. Phys. Lett. 91 (2007) 233512.
[3] X.Q. Deng, Z.H. Zhang, J.C. Zhou, M. Qiu, Appl. Phys. Lett. 97 (2010) 143103.
[4] Q.M. Yan, G. Zhou, S.G. Hao, J. Wu, W.H. Duan, Appl. Phys. Lett. 88 (2006) 173107.
[5] K.S. Novoselov, A.K. Geim, S.V. Morozov, D. Jiang, Y. Zhang, S.V. Dubonos, I.V. Grigorieva, A.A. Firsov, Science 306 (2004) 666.
[6] D.A. Areshkin, C.T. White, Nano Lett. 7 (2007) 3253.
[7] T. Mori, Y. Kikuzawa, H. Takeuchi, Org. Electron. 9 (2008) 328.
[8] M. Choe, B.H. Lee, G. Jo, J. Park, W. Park, S. Lee, W.K. Hong, M.J. Seong, Y.H. Kahng, K. Lee, T. Lee, Org. Electron. 11 (2010) 1864.
[9] Z.Y. Li, H.Y. Qian, J. Wu, B.L. Gu, W.H. Duan, Phys. Rev. Lett. 100 (2008) 206802.
[10] H.Y. Yang, D.I. Son, T.W. Kim, J.M. Lee, W.I. Park, Org. Electron. 11 (2010) 1313.
[11] J. He, K.Q. Chen, Z.Q. Fan, L.M. Tang, W.P. Hu, Appl. Phys. Lett. 97 (2010) 193305.
[12] X.R. Wang, Y.J. Ouyang, X.L. Li, H.L. Wang, J. Guo, H.J. Dai, Phys. Rev. Lett. 100 (2008) 206803.
[13] Q.M. Yan, B. Huang, J. Yu, F.W. Zheng, J. Zang, J. Wu, B.L. Gu, F. Liu, W.H. Duan, Nano Lett. 7 (2007) 1469.
[14] B. Huang, Q.M. Yan, G. Zhou, J. Wu, B.L. Gu, W.H. Duan, F. Liu, Appl. Phys. Lett. 91 (2007) 253122.
[15] Z.F. Wang, Q.X. Li, Q.W. Shi, X.P. Wang, J.G. Hou, H.X. Zheng, J. Chen, Appl. Phys. Lett. 92 (2008) 133119.
[16] M.G. Zeng, L. Shen, M. Yang, C. Zhang, Y.P. Feng, Appl. Phys. Lett. 98 (2011) 053101.
[17] Y. Ren, K.Q. Chen, J. Appl. Phys. 107 (2010) 044514.
[18] H. Ren, Q.X. Li, Y. Luo, J.L. Yang, Appl. Phys. Lett. 94 (2009) 173110.
[19] H. Fang, R.Z. Wang, S.Y. Chen, M. Yan, X.M. Song, B. Wang, Appl. Phys. Lett. 98 (2011) 082108.
[20] Z.F. Wang, Q.X. Li, Q.W. Shi, X.P. Wang, J.L. Yang, J.G. Hou, J. Chen, Appl. Phys. Lett. 92 (2008) 133114.
[21] X.H. Zheng, R.N. Wang, L.L. Song, Z.X. Dai, X.L. Wang, Z. Zeng, Appl. Phys. Lett. 95 (2009) 123109.
[22] J. Kang, F.M. Wu, J.B. Li, Appl. Phys. Lett. 98 (2011) 083109.
[23] R.Y. Oeiras, F.M. Araújo-Moreira, E.Z. da Silva, Phys. Rev. B 80 (2009) 073405.
[24] A. Saffarzadeh, R. Farghadan, Appl. Phys. Lett. 98 (2011) 023106.
[25] W.Y. Kim, K.S. Kim, Nat. Nanotechnol. 3 (2008) 408.

[26] F. Muñoz-Rojas, J. Fernández-Rossier, J.J. Palacios, Phys. Rev. Lett. 102 (2009) 136810.
[27] R. Qin, J. Lu, L. Lai, J. Zhou, H. Li, Q.H. Liu, G.F. Luo, L.N. Zhao, Z.X. Gao, W.N. Mei, G.P. Li, Phys. Rev. B 81 (2010) 233403.
[28] B. Sahu, H. Min, A.H. MacDonald, S.K. Banerjee, Phys. Rev. B 78 (2008) 045404.
[29] K.T. Lam, G. Liang, Appl. Phys. Lett. 92 (2008) 223106.
[30] J. Taylor, H. Guo, J. Wang, Phys. Rev. B 63 (2001) 245407.
[31] M. Brandbyge, J.L. Mozos, P. Ordejón, J. Taylor, K. Stokbro, Phys. Rev. B 65 (2002) 165401.
[32] M. Büttiker, Y. Imry, R. Landauer, S. Pinhas, Phys. Rev. B 31 (1985) 6207.
[33] H. Geng, S.W. Yin, K.Q. Chen, Z.G. Shuai, J. Phys. Chem. B 109 (2005) 12304.
[34] L.H. Wang, Y. Guo, C. Zhu, C.F. Tian, X.P. Song, B.J. Ding, Phys. Lett. A 374 (2010) 778.
[35] M.Q. Long, L.L. Wang, K.Q. Chen, X.F. Li, B.S. Zou, Z. Shuai, Phys. Lett. A 365 (2007) 489.
[36] Q. Liu, Y. Jia, Phys. Rev. E 70 (2004) 041907.
[37] J.L. Brédas, J.P. Calbert, D.A. da Silva Filho, J. Cornil, Proc. Natl. Acad. Sci. USA 99 (2002) 5804.
[38] L.L. Lin, J.C. Leng, X.N. Song, Z.L. Li, Y. Luo, C.K. Wang, J. Phys. Chem. C 113 (2009) 14474.
[39] B. Larade, J. Taylor, Q.R. Zheng, H. Mehrez, P. Pomorski, H. Guo, Phys. Rev. B 64 (2001) 195402.
[40] W.C. Lu, V. Meunier, J. Bernholc, Phys. Rev. Lett. 95 (2005) 206805.

conductivity which at the same time substantially reduces transmissivity of the entire device [5]. As most of the organic layers are very brittle and temperature sensitive, the choice of transparent top electrode material and processing conditions are very restricted and additionally essential in all cases where an opaque substrate like foils of stainless steel for OPV is used to allow for efficient illumination of the OPV. Thin metal films like silver (Ag) allow "soft" processing conditions and exhibit a high conductivity but only a limited transmittance in the visible part of the spectrum (T_{VIS}) [6]. In contrast, transparent conductive oxides (TCOs) such as indium tin oxide (ITO) show a high T_{VIS} but relatively poor electrical properties when deposited with a gentle sputter process at room temperature [7]. In general, sputter deposition of metal-oxides on top of organic devices is related with serious issues. Recently, thin films of thermally evaporated transition metal oxides (TMO) such as tungsten oxide (WO_3) or molybdenum oxide (MoO_3) have been demonstrated as efficient buffer layers which protect the organic layers from damages induced by sputter deposition of the top electrode [3,8,9]. A severe limitation is given by the fact, that TCOs typically require some high-temperature (>300 °C) post deposition thermal treatment in order to improve their conductivity, which is not possible on top of organic devices. Therefore, the combination of the high T_{VIS} of TCOs and the excellent conductivity of metals by sandwiching a thin metal layer between two TCO layers appears to be an attractive approach. Due to their high T_{VIS} and high reflectance in the infrared region these multilayer structures are used in window glasses for thermal insulation as low-emissivity coatings [10]. Compared to a bare ITO film which achieves a low sheet resistance (R_s) of 13 Ω/sq and about T_{VIS} = 90% after annealing at 350 °C various TCO/metal/TCO structures yield similar values deposited at room temperature [11,12]. For the embedding TCO, both excellent optical and electrical properties are required. Moreover, it is favorable to use amorphous TCO materials, concerning reproducibility and homogeneity on a large active area. Additionally, amorphous film growth provides a low roughness which is essential to avoid electrical shorts in thin film technology. The requirements listed above are fulfilled by zinc tin oxide (ZTO). In recent years, ZTO has been used as the channel semiconductor in transparent thin film transistors (TFT) [2,14]. In contrast to the crystalline compound zinc-stannate (Zn_2SnO_4) which can be formed by substrate heating during deposition or thermally post deposition treatment [15], ZTO prepared at low temperatures has been shown to provide an entirely amorphous structure over a wide range of deposition parameters which is preferred in oxide TFTs to improve homogeneity on a large area [16]. ZTO layers deposited at room temperature exhibit carrier concentrations in a wide range of 10^{12}–10^{19} cm^{-3} and a Hall mobility greater than 10 $cm^2(Vs)^{-1}$ [17]. In comparison, zinc oxide (ZnO) deposited at room temperature shows significantly lower electrical conductivity and a strong tendency to form polycrystalline layers [18]. Recently, a multilayer electrode including ZTO and sputtered Ag has been shown as bottom contact for opaque OSCs especially for use on flexible substrates [19].

In this communication, we report on the origin of the high conductivity and the high transparency of a multilayer electrode, in which a thin thermally evaporated Ag layer is sandwiched by layers of ZTO, prepared by RF-sputtering. By a thorough study of structural, electrical and optical properties, we clearly evidence that the ZTO/Ag/ZTO (ZAZ) multilayer electrode is uniquely advantageous for two reasons:

The favorable interface energy of ZTO and Ag allows closed Ag layers at an Ag thickness as low as 6 nm. By comparing sputtered ZTO and evaporated MoO_3, we found that closed Ag films and therefore higher conductivity are achieved at lower Ag thickness when deposited on ZTO as on MoO_3. Thereby, conductivities in optimized ZAZ multilayers are an order of magnitude higher than that of ITO and a concomitantly high T_{VIS} can be achieved.

Furthermore, the ZTO cap on top of ultrathin Ag not only improves the overall transmissivity of the electrode but, even more importantly, enables the stabilization of electrical characteristics of the electrode by suppressing Ag diffusion. It is well known that a severe issue of many TCO/Ag/TCO electrodes is their long term stability. The tendency of thin silver layers to form agglomerates and discontinuous layers over time has been reported [13]. We show, that owing to the stabilizing effect of the sputtered ZTO cap, ZAZ is substantially more robust than ZTO/Ag (ZA).

Finally, we demonstrate the application of our novel transparent electrode as top contact for semitransparent bulk hetero junction (BHJ) OSCs with an active area in excess of 2 cm^2. For semitransparent OSCs with an ITO top electrode the efficiency drops from 2.5% to 1.5% when the active area is increased from 0.2 to 2.25 cm^2. For the 2.25 cm^2 ZAZ based devices a substantially higher efficiency of 2% is found at a concomitant high transmissivity of more than 60% for $\lambda > 650$ nm.

2. Experimental

ZAZ structures were deposited on glass substrates (17×17 mm^2, Borofloat) using a RF magnetron sputtering system and a thermal evaporation chamber under UHV conditions. The ZTO target had a size of 10 cm in diameter and existed of SnO_2/ZnO (50:50 at.%) with a purity of 99.9%. The RF process was run with a power density of 0.2 W/cm^2 in a pure argon (Ar) gas atmosphere with an Ar flow of 40 sccm at a process pressure of 12 μbar. Base pressure of the system is 10^{-8} mbar. Sputtering was performed at room temperature without any post process treatment. The distance between target and substrate was 70 mm and substrate oscillation speed was set to 17.1 min^{-1} angular velocity. Intermediate silver films were deposited from a common thermal evaporation system using molybdenum boats at a base pressure of 10^{-6} mbar. ZAZ multilayer films were fabricated without vacuum break.

R_s, carrier concentration and Hall mobility was estimated using Van-der-Pauw and Hall measurement, respectively. T_{VIS} was measured by a UV–vis spectrophotometer (Perkin-Elmer Lambda 9) in reference to glass substrates.

Film thickness was measured by a surface profilometer (Veeco Dektak 4). The surface morphology was investigated by non-contact AFM (Danish Micro Engineering). SIMS depth profiling was performed and analyzed with a 500 eV Cs^- ion beam. Cross-sectional TEM was carried out in a Philips CM 200 FEG microscope operated at 200 kV.

Details of the preparation of inverted OSCs (regioregular of poly(3-hexylthiophene):(6,6)-phenyl C61 butyric acid methyl ester) and the ITO sputter process are given in [3]. *I–V* curves were measured by a Keithley 2400 sourcemeter. Photocurrent was measured under illumination from a 300 W solar simulator with an AM1.5G filter (Newport Corp.) considering the transient characteristics of cells incorporating Titania layers [20]. Efficiencies were determined without correction for spectral mismatch.

3. Results and discussion

3.1. Transparent ZAZ multilayer structure

3.1.1. Electrical characteristics

Initially, the electrical properties of our ZAZ multilayer structures were studied by varying the thickness of the ZTO and Ag layers, respectively. ZTO layers prepared in this study exhibit a carrier concentration of 10^{17} cm^{-3} and a Hall mobility of 6 $cm^2(Vs)^{-1}$ leading to a specific resistivity of about 50 Ω cm. To determine the influence of the embedded metal film on R_s, the thickness of Ag was varied from 4 to 10 nm whereas the thickness of both ZTO layers was kept constant at 39 nm. As shown in Fig. 1, R_s of ZAZ decreases exponentially from 250 to 5 Ω/sq with increasing Ag thickness. The percolation threshold (formation of a closed and continuous film) for sputtered Ag films on top of zinc-stannate was found at a thickness of 5–6 nm [6,21]. Owing to the electronic structure of Ag and ZTO, a transfer of electrons may lead to doping of the adjacent ZTO layers [22]. As a result, for discontinuous Ag layers (<6 nm) the sheet conductivity will be governed by separated Ag islands connected via doped ZTO claddings. It is essential to note, that we did not observe any significant influence of the thickness of the ZTO cladding layers on R_s. This is in agreement with previous reports on oxide/metal/oxide multilayers [23,24].

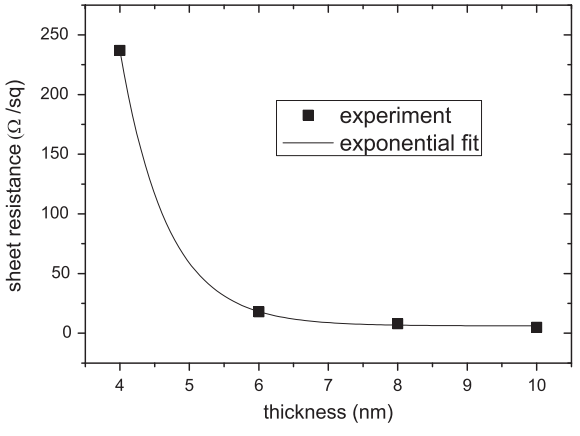

Fig. 1. Sheet resistance and exponential fit of a ZAZ multilayer structure as a function of Ag thickness. Thickness of ZTO layers sandwiching the Ag film was fixed to 39 nm each.

3.1.2. Origin of structural and morphological properties

The microstructure of Ag and ZTO films has been studied by cross sectional transmission electron microscopy (TEM). The analyzed structure consists of two ZTO layers (60 nm) and an intermediate Ag layer (6 nm) deposited on a silicon substrate (covered with 2 nm of native silicon oxide). Fig. 2(a) shows the TEM cross section of the ZAZ stack along with a magnified view of the interface. As an estimate from the TEM image, the roughness of the structure is 2–3 nm, in agreement with AFM data (not shown here). Obviously, the Ag film is continuous whereas its thickness is not homogeneous. Aside from polycrystalline growth of Ag, the inset of Fig. 2(a) confirms the completely amorphous structure of ZTO. Secondary ion mass spectroscopy (SIMS) was used to verify that there is no significant penetration or migration of Ag into the surrounding ZTO layers represented by Fig. 3. Our findings are in contrast to previous reports on Ag diffusion into an adjacent ZnO layer in case of a sputtered Ag film [25].

Fig. 2(b) shows a ZTO (60 nm)/Ag (6 nm) (ZA) structure (not capped with a second sputtered ZTO layer) after storage for 500 h in air. Strikingly, we evidence separated Ag islands in contrast to the findings for the capped Ag layer in the ZAZ stack. By carrying out conductivity measurements over several days in nitrogen atmosphere, given in Table 1(a), we found that in case of the ZAZ structure the R_s remains constant (11 Ω/sq) over 480 h whereas R_s of un-capped ZA structures increases by three orders of magnitude (20 kΩ/sq). As these experiments have been done under inert atmosphere, any oxidation of Ag due to the ambient oxygen can be ruled out. Fig. 2(c) verifies the completely amorphous growth of ZTO on top of the amorphous MoO_3 by showing the FFT images of the films in comparison to that of the crystalline Si substrate. Furthermore, it seems that there is no abrupt transition between MoO_3 and ZTO indicating an intermixing of the interface caused by highly energetic ZTO particles in the sputter process. This strikingly justifies the necessity of a buffer layer to protect the subjacent organic layers against sputter damages [3,8]. The growth of ZTO on top of MoO_3 is of paramount interest for the application as top contact on organic devices.

Taking these electrical properties and the TEM image of Fig. 2(b) into account, we conclude that island formation of silver on top of ZTO is due to a slowly proceeding surface diffusion process of Ag leading to formation of an aggregated and discontinuous Ag layer over time. Essentially, this diffusion of Ag appears to be suppressed by the second sputtered ZTO cladding layer on top of Ag. As the initial values ($t = 0$ h) of R_s of ZAZ and ZA are similar (about 10 Ω/sq), we infer that the sputter process of ZTO on top does not directly affect the Ag layer. Interestingly, if we replace both sputtered ZTO layers by thermally evaporated MoO_3 layers, we obtain significantly higher R_s of 580 Ω/sq for the MoO_3/Ag/MoO_3 (MAM) structure. Replacing the capping MoO_3 layer with ZTO (MAZ) leads to a slightly

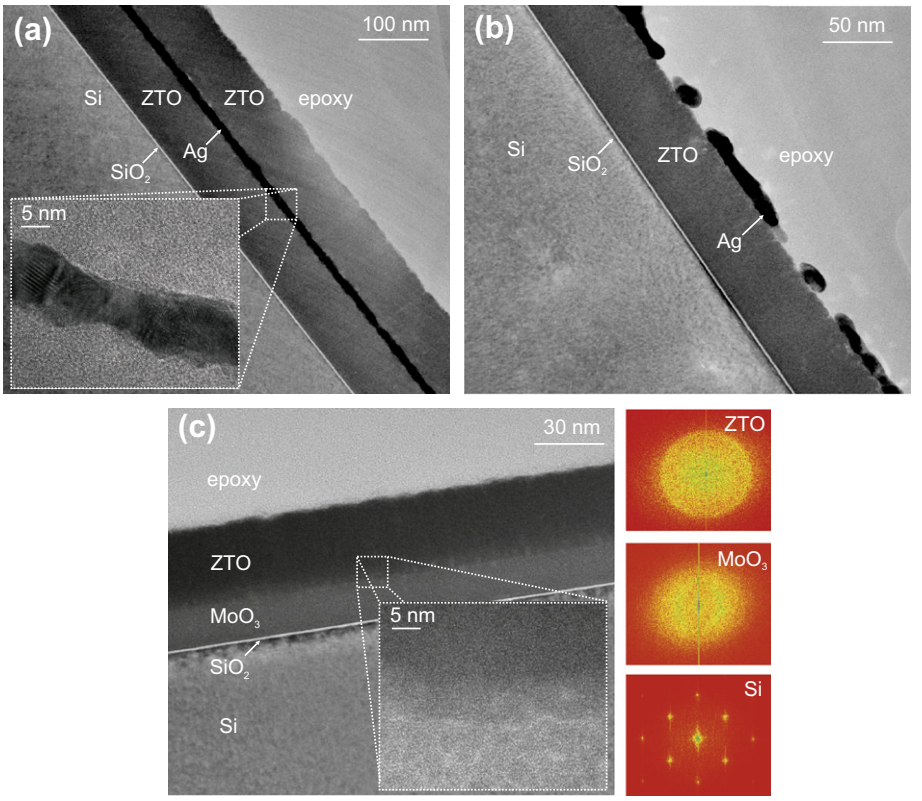

Fig. 2. (a) Cross sectional TEM image of ZAZ multilayer structure. Inset: magnified view on the constriction of Ag. (b) ZA structure deposited on silicon substrate at room temperature, showing the agglomeration of an Ag layer after storage for 500 h in air. Nominal thicknesses of the layers are 6 nm (Ag) and 60 nm (ZTO). (c) ZTO deposited on MoO_3 with FFT (fast Fourier transformation) images of Si, MoO_3 and ZTO.

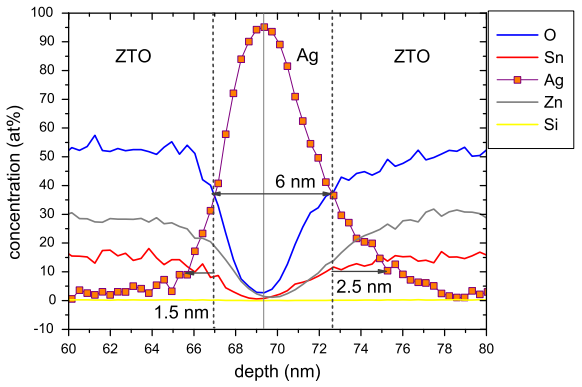

Fig. 3. Secondary ion mass spectrum (SIMS) of a ZAZ structure with a nominal layer thickness of 6 nm (Ag) and 60 nm (ZTO) deposited at room temperature on a silicon substrate.

lower R_s of 150 Ω/sq, which is still an order of magnitude higher than that of ZAZ (see Table 1(a)). The lower R_s of MAZ compared to MAM is attributed to the doping effect of ZTO as discussed above [22], which is, however, not as significant as the influence of the two metal oxides on the morphology of the subsequently grown Ag layer. In order to obtain values of R_s similar to those of ZA ($t = 0$) with 6 nm Ag interlayer, thicker Ag layers of about 10 nm are required in MA (see Table 1(b)). Thus, the deposition of silver on top of ZTO seems to be beneficial and inevitable for a low R_s and a high transparency of the multilayer electrodes.

3.1.3. Optical and overall performance

The spectral transmittance of a single ZTO layer (30 nm), a single Ag layer (12 nm) and a ZTO/Ag/ZTO sandwich structure (20/8/40 nm) is shown in Fig. 4. All layers were deposited on glass substrates. Due to high reflectivity and absorption losses, the bare Ag film shows low T_{VIS} of about 25%. By inserting Ag between two ZTO layers transmittance can be dramatically increased up to 83%. Inset of Fig. 4 demonstrates the spectral shift of the transmission maximum of ZAZ to higher wavelength by increasing the ZTO capping layer from 39 to 59 nm.

To compare the performance of several transparent conductive films on basis of optical and electrical properties, we used a figure of merit (FOM) Φ_{TC} defined by Haacke et al. [26]. The FOM is calculated by $\Phi_{TC} = T^{10}/R_s$, where T is the optical transmittance (at 550 nm in our study). A maximum of $\Phi_{TC} = 2.0 \times 10^{-2}\,\Omega^{-1}$ is reached for an optimized ZAZ structure and is an order of magnitude larger than that of an ITO film ($\Phi_{TC} = 2.4 \times 10^{-3}\,\Omega^{-1}$). The higher FOM of ZAZ is predominantly caused by its substantially lower R_s compared to ITO. Specifically, the ITO layer in this study was deposited at room temperature without any post deposition annealing according to the constraints

Table 1
(a) Time dependent measurement of R_s of various sandwich structures (ZTO/Ag (ZA), ZTO/Ag/ZTO (ZAZ), MoO_3/Ag/MoO_3 (MAM) and MoO_3/Ag/ZTO (MAZ)). Layer thicknesses are 10 nm (ZTO), 6 nm (Ag) and 20 nm (MoO_3). (b) Time dependent measurement of R_s of MoO_3 (10 nm)/Ag structures with varied Ag thickness on top.

(a) Structure	ZA		ZAZ		MAM		MAZ	
Time (h)	0	480	0	480	0	432	0	432
R_s (Ω/sq)	12.2	20 k	11.7	10.9	580	550	150	138
(b) MoO_3Ag (×) nm	Ag (6)		Ag (8)		Ag (10)		Ag (12)	
Time (h)	0	192	0	192	0	192	0	192
R_s (Ω/sq)	170 M	–	22	39.2	2.5	2.8	1.6	1.6

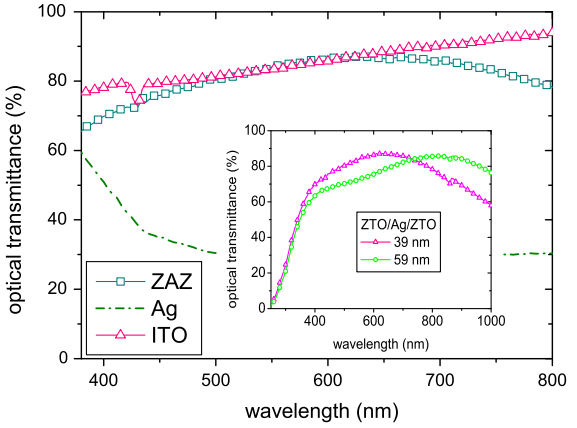

Fig. 4. Optical transmittance spectra of ZAZ (20/8/39 nm) compared to bare Ag (10 nm) and ITO (60 nm) films. Inset: Transmittance spectra of ZAZ structures with different ZTO thicknesses at a silver layer thickness of 8 nm. The bottom ZTO layer thickness was fixed at 20 nm.

Table 2
Results of sheet resistance R_s, FOM Φ_{TC} and average transmittance for symmetrical and asymmetrical ZAZ structures with varying Ag and ZTO thickness.

ZTO/Ag/ZTO (nm)	R_s (Ω/sq)	Φ_{TC} (Ω^{-1})	Average transmittance 380–780 nm (%)
20/8/20	10	3.7×10^{-4}	68
39/8/39	8.9	8.3×10^{-3}	73
20/10/20	5.3	7.0×10^{-3}	67
39/10/39	5.7	1.1×10^{-2}	71
20/8/39	8.8	2.0×10^{-2}	82
20/8/59	8.8	4.6×10^{-3}	75
ITO 60	83.3	2.4×10^{-3}	85

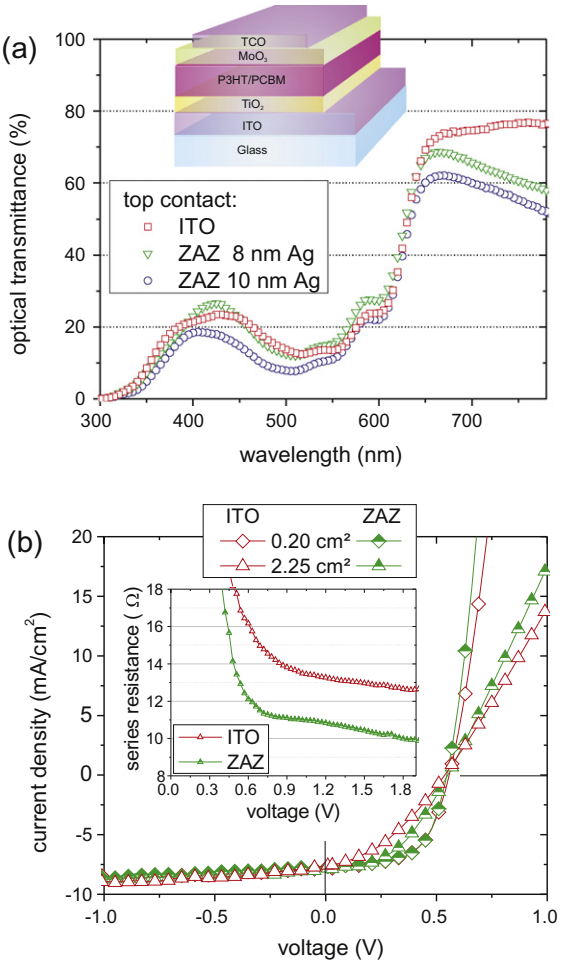

Fig. 5. (a) Transmission of semitransparent OSCs with different top contacts. Inset: layer sequence of the semitransparent solar cell device, (b) *J–V* characteristics of semitransparent OSCs with ITO and ZAZ top electrode with varied active area. Inset: series resistance of ITO and ZAZ determined from the slope of *J–V* in forward bias.

given by the application as top contact of temperature sensitive organic devices [3,18]. A summary of some specific examples of ZAZ multilayers compared to bare ITO concerning R_s, Φ_{TC} and T_{VIS} is given in Table 2.

3.2. Transparent top electrode for semitransparent OSCs

To expose the outstanding performance of ZAZ we used optimized highly transparent and conductive ZAZ electrodes as top side contacts in semitransparent OSCs. Fig. 5(a) displays the spectral transmission of the entire device. Obviously, the transmission is higher at wavelengths $\lambda > 600$ nm due to the specific absorption features of P3HT:PCBM BHJ [3]. The transmission of devices with ITO as top contact is 69% at 650 nm. Compared to that, the transmission of devices with ZAZ top contact is 67% (8 nm Ag) and 60% (10 nm Ag) at 650 nm, respectively.

Table 3
Performance results of solar cell devices with different top electrodes and varied size of active area separately illuminated from both sides of the device.

Top electrode	Active area (cm^2)	Glass side				Top side			
		PCE (%)	V_{oc} (V)	J_{sc} (mA/cm^2)	FF (%)	PCE (%)	V_{oc} (V)	J_{sc} (mA/cm^2)	FF (%)
ITO	0.2	2.5	0.56	7.8	58	2.1	0.55	6.2	61
	0.8	2.3	0.56	7.8	54	2	0.55	6.2	57
	2.25	1.5	0.54	7.6	37	1.3	0.54	5.8	42
ZAZ (8 nm Ag)	0.2	2.5	0.55	7.7	60	2.1	0.54	6.2	63
	0.8	2.6	0.55	7.9	61	2.2	0.55	6.4	62
	2.25	2	0.55	7.9	46	1.7	0.55	6.3	49
Al	0.2	2.5	0.55	8.5	56	–	–	–	–
	2.25	2.2	0.54	9.1	45	–	–	–	–

In Fig. 5(b) current density versus voltage (*J–V*) of devices with varied active area is shown. For devices with smaller active area of 0.2 cm^2 the difference between cells with ZAZ or ITO is small. The work function (WF) of ZTO was determined by Kelvin Probe measurements to 4.3 eV and is therefore smaller than that of ITO (WF = 4.7 eV). However, the difference in WF of the electrodes does not seem to play an important role possibly due to the subjacent high-WF molybdenum oxide layer, which is consistent to results shown by Schulze et al. [27]. The main advantage of the ZAZ top electrodes compared to ITO becomes obvious for devices with increasing active area. Obviously, cells with ZAZ top contact show higher current densities under forward bias owing to a lower series resistance compared to cells with ITO. The inset of Fig. 5(b) shows the series resistance of the cells with ITO or ZAZ top contact and an area of 2.25 cm^2 determined from the slope of the *J–V* characteristics in forward bias. As expected from the sheet resistance results of the pure electrode layers the sheet resistance of the cells with ITO top contact is higher. The series resistance plays an important role in controlling the fill factor [28]. With an optimized ZAZ top contact the semitransparent OSCs maintain a high FF even for cells with a larger device area as required for serious applications.

Table 3 summarizes the performance of devices with an active area between 0.2 and 2.25 cm^2. In general, we find higher power conversion efficiency (PCE) when devices are illuminated from glass side. This is due to a lower absorption of the bottom ITO electrode compared to optical losses in the top electrodes. Note the bottom ITO electrode is substantially more transparent due to some post deposition thermal treatment by the manufacturer. For a small active area, values for PCE, V_{oc}, J_{sc} and *FF* of cells with ITO and ZAZ top contact are similar. As a general trend, the performance of the cells decreases towards larger active area. Most strikingly, the devices with an ITO top electrode suffer from a loss in PCE for 2.25 cm^2 cells by 60% compared to PCE of devices with the smallest area used (0.2 cm^2). Opposed to that, ZAZ cells show a 30% higher PCE than ITO devices. An efficiency of 2% for semitransparent OSC states the highest efficiency with an active area larger than 2 cm^2, so far.

To figure out if the bottom ITO electrode already contributes to some limitation for the 2.25 cm^2 devices, the ZAZ top electrodes have been coated with a thick (opaque), highly conductive Ag layer. Surprisingly, the resulting cells also show lower efficiencies compared to small area devices. Furthermore opaque cells with ITO bottom and aluminum top contact show a similar decrease in FF and PCE with increasing cell area as cells with ZAZ top contact. This result hints to some limit added by R_s of the ITO bottom electrode. In further work the bottom ITO electrode could be replaced by an optimized ZAZ layer, as well.

4. Conclusion

In conclusion, we have demonstrated highly efficient transparent electrodes which are especially suitable for the use as transparent contacts on top of organic devices. An optimized (ZAZ) multilayer structure deposited at room temperature achieves a maximum transmittance of 85% at 550 nm similar to ITO under comparable process conditions. At the same time R_s is about an order of magnitude lower than that of ITO prepared at room temperature. Additionally, closed films leading to lower R_s can be achieved at lower Ag thickness when deposited on top of ZTO compared to MoO_3. We have evidenced that formation of islands and discontinuous layers due to the typically occurring surface diffusion of Ag on top of oxide materials can be effectively suppressed by using a sputtered ZTO layer on top of thin Ag films. Owing to the low R_s and a concomitantly high transmissivity, semitransparent OSCs comprising an optimized ZAZ top electrode show a 30% higher efficiency at large active device areas (>2 cm^2) compared to cells with ITO top electrode. Therefore, the presented ZAZ electrodes pave the way towards organic optoelectronic devices with substantially relaxed limitations due to resistive losses even for a larger active area, required for serious applications.

References

[1] G. Parthasarathy, C. Adachi, P.E. Burrows, S.R. Forrest, Appl. Phys. Lett. 76 (2000) 15.
[2] P. Görrn, M. Sander, J. Meyer, M. Kröger, E. Becker, H.-H. Johannes, W. Kowalsky, T. Riedl, Adv. Mater. 18 (2006) 738–741.
[3] H. Schmidt, H. Flügge, T. Winkler, T. Bülow, T. Riedl, W. Kowalsky, Appl. Phys. Lett. 94 (2009) 243302.
[4] R. Koeppe, D. Hoeglinger, P. Troshin, R.N. Lyubovskaya, V.F. Razumov, N.S. Sariciftci, CemSusChem 2 (2009) 309–313.
[5] T. Ameri, G. Dennler, C. Waldauf, H. Azimi, A. Seemann, K. Forberich, J. Hauch, M. Scharber, K. Hingerl, C.J. Brabec, Adv. Funct. Mater. 20 (2010) 1592.

[6] K. Seal, Mark A. Nelson, Z. Charles Ying, Phys. Rev. B 67 (2003) 035318.
[7] T.C. Gorjanc, D. Leong, C. Py, D. Roth, Thin Solid Films 413 (2002) 181–185.
[8] J. Meyer, T. Winkler, S. Hamwi, S. Schmale, H.-H. Johannes, T. Weimann, P. Hinze, W. Kowalsky, T. Riedl, Adv. Mater. 20 (2008) 3839.
[9] H. Schmidt, T. Winkler, M. Tilgner, H. Flügge, S. Schmale, T. Bülow, J. Meyer, H.-H. Johannes, T. Riedl, W. Kowalsky, Proc. SPIE 7416 (2009) 741611.
[10] B. Karlsson, E. Valkonen, T. Karlsson, C.-G. Ribbing, Thin Solid Films 86 (1981) 91–98.
[11] R.N. Joshi, J.M.V.P. Singh, Thin Solid Films 257 (1995) 32–35.
[12] A. Indluru, T.L. Alford, J. Appl. Phys. 105 (2009) 123528.
[13] M. Fahland, in: C. Brabec, V. Dyakonov, U. Scherfeds (Eds.), Organic Photovoltaics, Wiley-VCH, Weinheim, 2008.
[14] H.Q. Chiang, J.F. Wager, R.L. Hoffman, J. Jeong, D.A. Keszler, Appl. Phys. Lett. 86 (2005) 013503.
[15] D.L. Young, H. Moutinho, Y. Yan, T.J. Coutts, J. Appl. Phys. 92 (2001) 310.
[16] P. Görrn, P. Hölzer, J. Wang, T. Weimann, P. Hinze, S. Kipp, T. Riedl, W. Kowalsky, Appl. Phys. Lett. 90 (2007) 063502.
[17] M.K. Jayaraj, K.J. Saji, K. Nomura, T. Kamiya, H. Hosono, J. Vac. Sci. Technol., B 26 (2008) 2.
[18] E.M.C. Fortunato, P.M.C. Barquinha, A.C.M.B.G. Pimentel, A.M.F. Gonçalves, A.J.S. Marques, L.M.N. Pereira, R.F.P. Martins, Adv. Mater. 17 (2005) 5.
[19] Y.-Y. Choi, K.-H. Choi, H. Lee, H. Lee, J.-W. Kang, H.-K. Kim, Sol. Energy Mater. Sol. Cells 95 (2011) 1615–1623.
[20] H. Schmidt, K. Zilberberg, S. Schmale, H. Flügge, T. Riedl, W. Kowalsky, Appl. Phys. Lett. 96 (2010) 243305.
[21] M. Arbab, Thin Solid Films 381 (2001) 15–21.
[22] H. Han, N.D. Theodore, T.L. Alford, J. Appl. Phys. 103 (2008) 013708.
[23] D.R. Sahu, J.-L. Huang, Thin Solid Films 515 (2006) 876–879.
[24] M. Fahland, P. Karlsson, C. Charton, Thin Solid Films 392 (2001) 334–337.
[25] D. Sahu, J.-L. Huang, Appl. Surf. Sci. 252 (2006) 7509–7514.
[26] G. Haacke, J. Appl. Phys. 47 (1976) 4086–4089.
[27] K. Schulze, B. Maennig, K. Leo, Y. Tomita, C. May, J. Hüpkes, E. Brier, E. Reinold, P. Bäuerle, Appl. Phys. Lett. 91 (2007) 073521.
[28] M.-S. Kim, B.G. Kim, J. Kim, Appl. Mater. Interfaces 1 (2009) 1264.

energy transfer and confinement of triplet excitons on the triplet emitters. But, if the E_g of the host is too large, deep and strong charge traps will be induced on the dopant emitters, resulting in poor conductivity of the host and a high driving voltage of the device [13]. There exists also an inherent tradeoff between E_T, E_g, and the π-conjugation length, since longer π-conjugation will lead to lower E_T and E_g but higher charge mobility for lower driving voltage and higher device efficiency [14]. The large difference in HOMO and/or LUMO level between the charge-transporting and the emitting layers will also cause energetically unfavorable charge injection and a high driving voltage. Due to the large E_g and E_T of the blue phosphorescent emitters, the search for a suitable host material is urgent and challenging. The host material used for blue PHOLEDs must have a large E_T (>2.7 eV) which results in an even wider E_g (>3.0 eV) that may act as energy barriers for the carriers transport from nearby hole or electron-transporting layer to the emitting layer, leading to high driving voltage of the FIrpic-based devices [15]. One approach to solve the problematic high driving voltage of blue PHOLEDs is to design and synthesis suitable host materials that possess both the high triplet excited state, the superior carrier-transporting property, and the appropriate energy levels (HOMO and LUMO). Up to now, researches directed toward the molecular design of host materials with high E_T, relatively narrow E_g, and good carrier-transporting properties were rather limited [8,16–17].

Heterofluorenes (HF) [18] such as nitrogafluorene (carbazole, NF) [19], sulfurafluorene (SF) [20], silafluorene (SiF) [21–23], germafluorene (GeF) [24], and phosphafluorene (PF) [25] have received a number of interests in many fields due to their particular physical and optoelectronic properties, since the breakthrough of their synthetic methods [26]. Recently, we designed and successfully prepared a serial of carbazole end-capped heterofluorenes (CzHFs) via Ullmann C—N coupling reaction in high yields [27] by mimicking the molecular structure of 4,4′-*N*,*N*′-dicarbazole-biphenyl (CBP). CBP is the most popular and famous carbazole-based host material for green and red phosphorescent emitters, but its E_T (2.56 eV) [13] is too low for blue emitters even the sky-blue phosphor, FIrpic. Our innovation is to connect the biphenyl of CBP with the bridging heteroatoms, which results in a planar heterofluorene in the centre of CBP [28]. And, this marriage of carbazole and heterofluorene in a manner as that in CBP is expected to produce interesting host materials for blue PHOLEDs with the more desirable localization and energy level of HOMOs and LUMOs and also higher E_T (∼3.0 eV) compared with those of CBP, with the aid of the great impact of the heteroatoms on the optoelectronic properties [18]. This heterofluorene-based host material benefits both from the heterofluorene which has very particular optoelectronic properties and from the carbazole which is very popular building block for host materials.

In this paper, FIrpic-based PHOLEDs using *meta*-CzHFs (*m*-CzHFs) as the host material were fabricated and the devices exhibit driving voltages lower than 3.9 V at the luminance of 1000 cd m^{-2}. With such low driving voltages, the power efficiency of the CzHF-based devices are dramatically enhanced up to 30.9 and 30.2 lm W^{-1} (with very little variation) at the practical operation brightness from 100 to 1000 cd m^{-2}. The high efficiency with the EQE of 18.4%, and the highly stable CIE (0.16, 0.31) of the *m*-CzHFs-based PHOLEDs at a wide range of brightness were also observed. This novel concept to combine carbazole and heterofluorene by structurally mimicking CBP turns out to be very effective in the molecular design of the high-performance host materials.

2. Results and discussion

2.1. Synthesis and photophysical properties of m-CzHFs

CzHFs were synthesized as reported in our previous publication [27]. An optimized Ullmann C—N cross-coupling reaction between the carbazole and dibromoheterofluorene was adopted to attach the 9-position of the carbazole moiety to the terminal ends of the heterofluorene cores in high yields (∼70%) [29]. CzHFs have good solubility in common solvents and excellent thermal properties (see Table 1) with the glass-transition temperature (T_g) above 97 °C and that of *m*-CzSF and *m*-CzOF are even higher than 110 °C, which are significantly improved in comparison with that of CBP (T_g = 62 °C) [30]. The melting point (T_m) of these materials are also high, which are all above 200 °C, and *m*-CzSF and *m*-CzOF are even nearly 300 °C. High T_g is highly desirable for host materials in OLEDs to prevent morphological changes and to suppress the formation of aggregation upon exposure to the heat produced during the device operation.

The *m*-CzHFs show two main absorption bands both in THF solution and in solid film (see Fig. S7a in S.I.), the first absorption band around 290 nm can be assigned to the carbazole-centered n-π* transition, while the other longer absorption around 320–340 nm is attributed to the π–π* transition of the entire conjugated backbone. The optical energy band gaps of the *m*-CzHFs determined from the onset of the UV–vis spectra in solid film are very similar (3.34–3.41 eV), which is very close to that of CBP (3.4 eV). The PL spectra of the host materials are between 350 and 500 nm, which are well overlapped with the metal-to-ligand charge-transfer absorption peaks of the FIrPic around 380 and 420 nm [15], indicating that efficient and rapid Förster energy transfer from the host materials to the blue phosphorescent emitter.

2.2. Triplet energy and molecular simulations

From the highest-energy 0–0 phosphorescence emissions of *m*-CzHFs (see Fig. S7b in S.I.), we estimated that their values of E_T are 2.84, 2.97, and 2.87 eV respectively, as listed in Table 1. Because *m*-CzHFs possesses significantly higher E_T than CBP resulted from the bridging of the heteroatoms, we would expect that (1) *m*-CzHFs can be good host for FIrpic (2.62 eV), (2) the energy of the triplet excitons would be transferred effectively from the host to the guest emitter, and (3) the reversing pathway (backward energy transfer) was prohibited. The HOMO and LUMO levels of *m*-CzHFs were measured using cyclic voltammetry (CV) (see Table 1 and Fig. S8 in S.I.). *m*-CzHFs

Table 1
Thermal and Electrochemical properties, triplet energy (E_T), and dipole moment of *m*-CzHFs.

Compound	Thermal analysis [°C]		Electrochemical analysis [eV]			E_T	Dipole moment
	T_g	T_m	HOMO	LUMO	E_g	[eV]	
CBP [30]	62	–	−5.5	−2.0	3.7	2.56	0.0003
m-CzNF	97	213	−5.34	−2.22	3.12	2.84	4.80
m-CzOF	114	285	−5.40	−2.26	3.14	2.97	1.62
m-CzSF	121	293	−5.42	−2.26	3.16	2.87	1.65

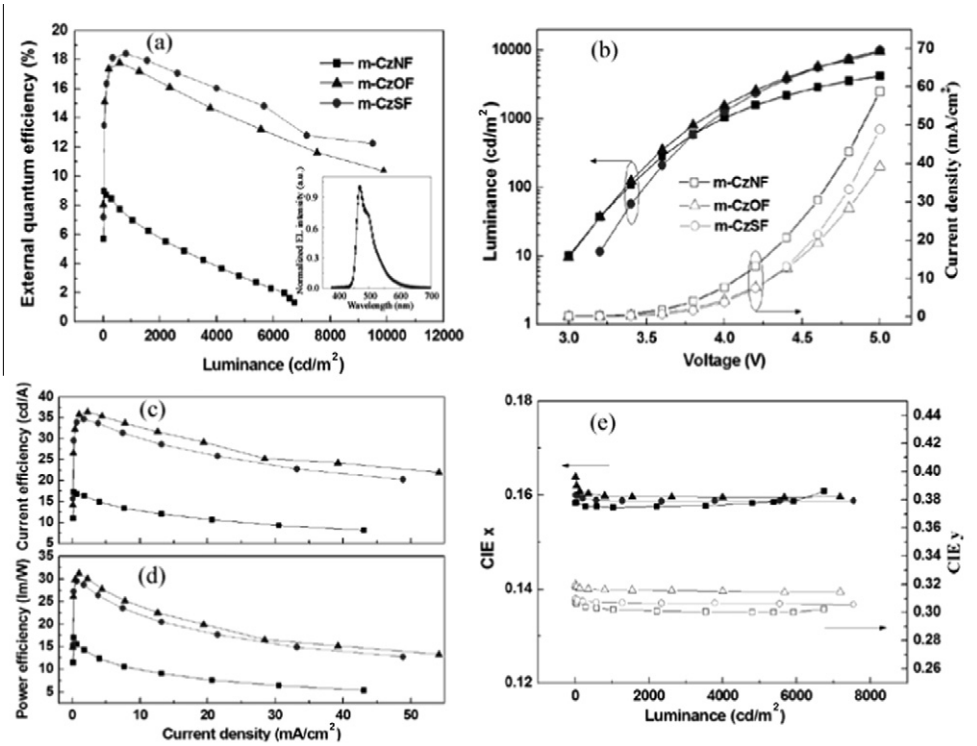

Fig. 2. (a) External quantum efficiency–Luminance curves. Inset: the corresponding normalized EL spectra; (b) Luminance-voltage-current density (L-V-J) curves; (c) and (d) Current efficiency (c) and Power efficiency (d) versus current density curves; e) CIE (*x*, *y*) versus luminance curves of *m*-CzHFs-based PHOLEDs.

have very close HOMOs (−5.34 – −5.42 eV) and LUMOs (−2.22 ∼ −2.26 eV), and their band gaps are also quite similar (3.12–3.22 eV). Their higher band gaps than that of FIrpic (3.1 eV) ensure the exothermic energy transfer from the host to the guest. It is interesting that *m*-CzHFs have E_Ts higher than that of CBP although their bandgaps are lower, showing the great modification abilities of the heteroatom linkage. The higher HOMOs, lower LUMOs, but still higher E_Ts, compared with those of CBP, make CzHFs attractive host materials for blue triplet emitters. To gain insight into the electronic states of *m*-CzHFs, molecular simulations via ab initio density-functional theory (DFT) calculation were performed. The results show that their HOMOs are mainly determined by carbazole, whereas LUMOs are predominately localized on and are primarily determined by the central heterofluorenes (see S.I. Table S2). The separated electron density distribution between the HOMO and LUMO of CzHFs is preferable for efficient hole- and electron-transporting properties and the prevention of reverse energy transfer, enabling CzHFs the excellent host materials for PHOLEDs [31].

2.3. Device performance of the m-CzHFs as hosts for FIrpic

To evaluate the performance of the *m*-CzHFs as host materials for blue phosphorescent emitters, we fabricated the devices with the following configurations (see Fig. 1): ITO/MoO_x(2 nm)/m-MTDATA:MoO_x(15 wt.%, 30 nm)/m-MTDATA(10 nm)/Ir(ppz)$_3$(10 nm)/*m*-CzHFs:FIrpic (10 wt.%, 10 nm)/BPhen (40 nm)/LiF(1 nm)/Al (100 nm). In these devices, MoO_x acts as hole-injecting layers, 4,4′,4″-tris(3-methylphenylphenylamino)-triphenylamine (m-MTDATA) as hole-transporting layer (HTL), tris(phenylpyrazole) Iridium (Ir(ppyz)$_3$) as electron-blocking layer (EBL), and 4,7-dipheyl-1,10-phenanthroline (BPhen) as hole-blocking (HBL) and electron-transporting layer

Table 2
Performance of *m*-CzHFs-based PHOLEDs[a].

Host compoud	EL [nm]	η_{ext} [%]	V_{on}[b] [V]	η_c [cd/A]	η_p [lm/W]	L[c] (cd/m^2)	CIE, (x,y)[d]
m-CzNF	468	9.0	3.0	17.3	17.0	4186	(0.157,0.301)
m-CzOF	472	17.8	3.0	36.4	31.2	9504	(0.160,0.316)
m-CzSF	468	18.4	3.2	34.8	29.6	9884	(0.159,0.306)

[a] Maximum external quantum efficiency (η_{ext}), current efficiency (η_c), and power efficiency (η_p).
[b] The applied voltage (Von) required for brightness of 10 cd m^{-2}.
[c] The luminescence (L) at 5 V.
[d] CIE (*x*,*y*) at the brightness of 1000 cd m^{-2}.

(ETL). From Fig. 2, holes can be effectively injected into the host with small barrier (<0.3 eV) and be blocked by BPhen with the energy barrier about 0.9 eV; whilst the electron is injected into the host with the similar barrier as that of hole (0.3–0.4 eV) and is blocked by Ir(ppz)$_3$ with the barrier over 0.5 eV. In such a device construction, the holes and electrons can be effectively confined in the host layer to form host excitons, which subsequently transfer exothermicly to FIrpic for the blue phosphorescence. The device performance, as summarized in Table 2, is extraordinary with low turn-on voltages (<3.0 V), and high maximum external quantum efficiency, current efficiency, and power efficiency, up to 18.4%, 36.4 cd A^{-1}, and 31.2 lm W^{-1}, respectively. At a brightness level of 1000 and 5000 cd m^{-2}, the driving voltages are still lower than 4.5 V with the external quantum efficiencies retain as high as 18.1% and 16.8%. The performance is comparable with the previously reported highest values for FIrpic-based devices [10,11].

From Fig. 2a, the electroluminescence (EL) spectra of the *m*-CzHFs-based devices show identical FIrpic emission without any residue emission from the host and/or adjacent layer, even at high current densities, indicating complete energy transfer from the host to the guest upon electrical excitation and excellent confinement of charge carriers and excitons in the emitting layer. FIrpic is a greenish-blue emitter with a typical emission peak around 472 nm and a shoulder at 500 nm with CIE (*x*, *y*) around (0.17, 0.34), depending on the emission band profile [15]. One advantage of the EL spectra of our devices is that they all displayed bluer emission with an emission peak at 468 (*m*-CzNF and *m*-CzSF) and 472 nm (*m*-CzOF) and a vibrational peak around 495–498 nm with a narrow full-width at half maximum (FWHM) of 55 nm and a CIE (*x*, *y*) around (0.16, 0.30). The bluer emission and improved color purity are probably attributed to the excellent miscibility and morphological stability of CzHFs, which effectively separated and clamped the doped FIrpic, depressing the ground-state association and leaving single molecule emission of the dopant in the solid solution (host) [15].

Fig. 2b displays the current density–voltage-luminance characteristics of these devices and obvious advantages of our devices lie in the very low turn-on and driving voltages. Remarkably, the driving voltages required for brightness of 10, 100, and 1000 cd m^{-2} are 3.0–3.2, 3.4–3.5, and 3.8–4.0 V with corresponding current density of 1.1–1.2, 1.3–1.4, 1.9–3.3 mA cm^{-2}, respectively. And at 5 V, our devices show high luminance from 4186 to 9884 cd/m^2. With such low driving voltages and current densities, the efficiency of the CzHFs-based PHOLEDs is dramatically enhanced. In Fig. 2(c and d), the highest current efficiency of 36.4 cd A^{-1} is reached at 4.0 V, with the corresponding brightness of 1613 cd m^{-2} and current density of 2.24 mA cm^{-2}, while the highest power efficiency of 31.2 lm W^{-1} is observed at 3.6 V, with brightness of 360 cd m^{-2} and current density of 1.02 mA cm^{-2}. The efficiency roll-off of the devices is greatly reduced in the blue PHOLEDs with *m*-CzHFs as the host material (see Fig. 2a). For example, the external quantum efficiency of the *m*-CzSF-based device is 15.8%, 18.4% (maximum), 18.2%, and 15.3% at 100, 791, 1000, and 5000 cd m^{-2}, respectively, suggesting the balanced charge transporting in our devices. Color stability of PHOLEDs with different host materials were monitored according to luminance, as shown in Fig. 2e. The color coordinate of (0.16, 0.30) was little affected within the luminance range, indicating good color stability of the devices. And, their normalized EL spectra are identical over the range of the current density from 10 to 50 mA cm^{-2}, which further assures the stability of our devices. The low driving voltage, high efficiency, and high stability of the *m*-CzHFs-based devices at practical brightness are mainly resulted from the low charge injection barrier, the balanced charge transport, and the reduced triplet–triplet annihilation of the CzHFs-based devices due to the proper device structural design (see Fig. 1).

The *m*-CzNF-based device shows lower brightness, efficiency, and color stability due to two main reasons. One is its high dipole moment (see Table 1) which results in low carrier mobilityand increased triplet–triplet annihilation [32]. The other is the alkyl linked to the N atom, which influences the molecular packing of the thin film, resulting in low charge mobility. The relatively lower T_g of *m*-CzNF (97 °C) is also an important reason for its lower device performance. *m*-CzOF and *m*-CzSF have comparable device performances due to their similar photophysical and electrochemical properties. Considering the higher triplet energy of *m*-CzOF, it may find further applications in deep blue PHOLEDs. In comparison with the device results of Seidler [33] and Wu [34] based on the host materials that are very similar to *m*-CzNF (with only different substituents on the carbazole core), which showed efficiencies up to 15%, 31 cd A^{-1}, and 28 lm W^{-1} under a different device structure, the performance of our *m*-CzNF based device is a little lower, suggesting that our devices based on *m*-CzOF and *m*-CzSF can be further improved by optimizing device structures. The high performance of the FIrpic-based blue PHOLEDs using *m*-CzHFs as the host material in this research proves the validity of our approach to design host materials by connecting the biphenyl of CBP with heteroatoms.

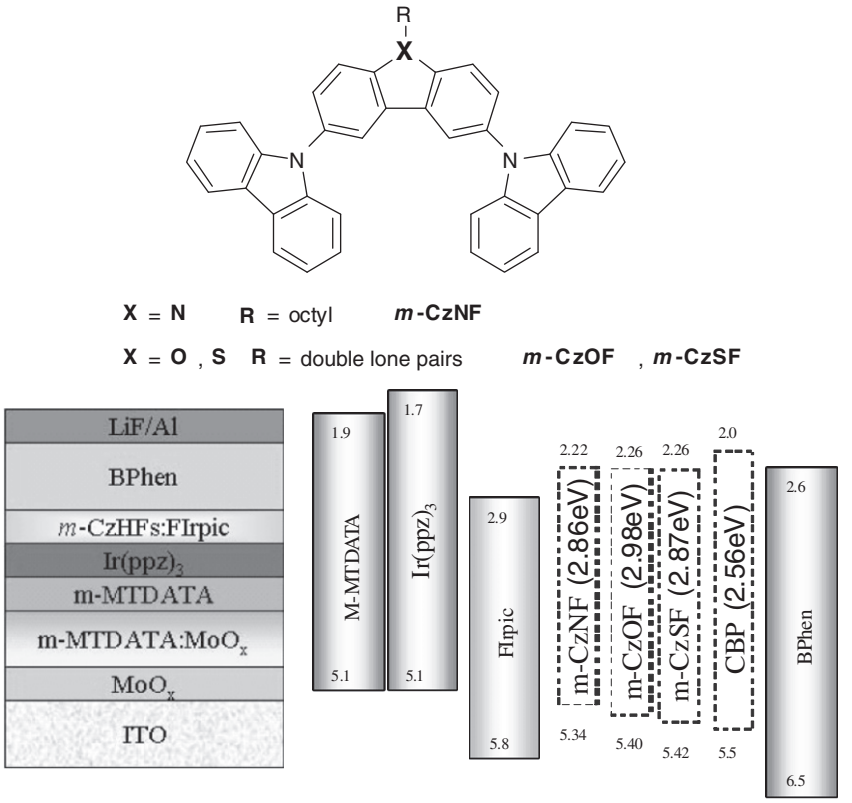

Fig. 1. Device structure and energy level diagrams of the *m*-CzHFs-based PHOLEDs.SYNOPSIS TOC.

3. Conclusions

In summary, *m*-CzHFs of *m*-CzNF, *m*-CzOF, and *m*-CzSF, which possess superior localization and energy level of HOMOs and LUMOs and also higher E_T (~3.0 eV) compared with CBP, were reported for use as blue phosphorescent hosts. Their superiorities in high-efficiency and low-voltage blue PHOLEDs have been demonstrated. The extraordinary device performance of *m*-CzOF was observed with low turn-on voltages (<3.0 V), and high maximum external quantum, current, and power efficiencies, up to 18.4%, 36.4 cd A^{-1}, and 31.2 lm W^{-1}, respectively. At the brightness level of 5000 cd m^{-2}, the driving voltages are still lower than 4.5 V with the external quantum efficiencies retain as high as 16.8%. The important concept of combining carbazole and heterofluorene via structurally mimicking CBP has proven to be successful in the rational molecular design of the high-performance host materials for PHOLEDs. *m*-CzHFs that can be prepared easily in high yields, are ideal host materials for blue PHOLEDs and their excellent device performance enables them to be good choice in the next-generation flat-panel displays and lighting technologies.

4. Experimental

The OLEDs were fabricated using a vacuum thermal evaporation chamber with high-vacuum (~10^{-4} Pa) at a rate of 0.1–0.2 nm/s. The devices without encapsulation were measured in ambient atmosphere at room temperature. Electroluminescent (EL) spectra and CIE corrdinates of the devices were measured by a PR650 spectroscan spectrometer, as well as the luminance-voltage and current–voltage characteristics were measured simultaneously with a programmable Keithley 2400 voltage-current source. The cyclic voltammetry (CV) measurements were performed at room temperature on a CHI660E system in a typical three-electrode cell. The phosphorescence spectra of the compounds were measured using an Edinburgh LFS920 fluorescence spectrophotometer at 77 K, with a 5 ms delay time. All computations were done with Gaussian03 program package with B3LYP/6–31G(d) for structure optimizations and vibrational analysis.

Acknowledgment

This work was financially supported by the National Basic Research Program of China (973 Program, 2009CB930601 and 2010CB327701), National Natural Science Foundation of China (20804020, 60976019, 20974046, and 60977024), and Scientific Research Foundation of Nanjing University of Posts and Telecommunications (NY210017).

References

[1] M.C. Gather, A. Köhnen, K. Meerholz, Adv. Mater. 23 (2011) 233–248.
[2] Q. Wang, D. Ma, Chem. Soc. Rev. 39 (2010) 2387.
[3] U. Mitschke, P. Bauerle, J. Mater. Chem. 10 (2000) 1471.

[4] C.W. Tang, S.A. VanSlyke, Appl. Phys. Lett. 51 (1987) 913.
[5] S. Reineke, F. Lindner, G. Schwartz, N. Seidler, K. Walzer, B. Lussem, K. Leo, Nature 459 (2009) 116.
[6] Y. Sun, N.C. Giebink, H. Kanno, B. Ma, M.E. Thompson, S.R. Forrest, Nature 440 (2006) 908.
[7] M.A. Baldo, B.D. O, Y. You, A. Shoustikov, S. Sibley, M.E. Thompson, S.R. Forrest, Nature 395 (1998) 151.
[8] H.H. Chou, C.H. Cheng, Adv. Mater. 22 (2010) 2468.
[9] L. Xiao, Z. Chen, B. Qu, J. Luo, S. Kong, Q. Gong, J. Kido, Adv. Mater. 23 (2011) 926.
[10] L.X. Xiao, S.J. Su, Y. Agata, H.L. Lan, J. Kido, Adv. Mater. 21 (2009) 1271.
[11] H. Sasabe, E. Gonmori, T. Chiba, Y.J. Li, D. Tanaka, S.J. Su, T. Takeda, Y.J. Pu, K.I. Nakayama, J. Kido, Chem. Mater. 20 (2008) 5951.
[12] S.P. Huang, T.H. Jen, Y.C. Chen, A.E. Hsiao, S.H. Yin, H.Y. Chen, S.A. Chen, J. Am. Chem. Soc. 130 (2008) 4699.
[13] Z.Q. Gao, M. Luo, X.H. Sun, H.L. Tam, M.S. Wong, B.X. Mi, P.F. Xia, K.W. Cheah, C.H. Chen, Adv. Mater. 21 (2009) 688.
[14] [a] M.T. Chu, M.T. Lee, C.H. Chen, M.R. Tseng, Org Electron. 10 (2009) 1158;
[b] D.P. Tsang, M. Chan, A.Y. Tam, V.W. Yam, Org Electron. 12 (2011) 1114.
[15] [a] S. Ye, Y. Liu, J. Chen, K. Lu, W. Wu, C. Du, Y. Liu, T. Wu, Z. Shuai, G. Yu, Adv. Mater. 22 (2010) 4167;
[b] W. Jiang, L.A. Duan, J. Qiao, D.Q. Zhang, G.F. Dong, L.D. Wang, Y. Qiu, J. Mater. Chem. 20 (2010) 6131.
[16] [a] S.O. Jeon, K.S. Yook, C.W. Joo, J.Y. Lee, Adv. Mater. 22 (2010) 1872;
[b] S.E. Jang, C.W. Joo, S.O. Jeon, K.S. Yook, J.Y. Lee, Org. Electron. 11 (2010) 1059.
[17] E. Polikarpov, J.S. Swensen, N. Chopra, F. So, A.B. Padmaperuma, Appl. Phys. Lett. (2009) 94.
[18] R.F. Chen, C. Zheng, Q.L. Fan, W. Huang, J. Comput. Chem. 28 (2007) 2091.
[19] P.T. Boudreault, S.B. Eacute, M. Leclerc, Polym. Chem. (2010) 127.
[20] S.M. King, I.I. Perepichka, I.F. Perepichka, F.B. Dias, M.R. Bryce, A.P. Monkman, Adv. Funct. Mater. 19 (2009) 586.
[21] R.F. Chen, Q.L. Fan, S.J. Liu, R. Zhu, K.Y. Pu, W. Huang, Synth. Met. 156 (2006) 1161.
[22] K.L. Chan, M.J. McKiernan, C.R. Towns, A.B. Holmes, J. Am. Chem. Soc. 127 (2005) 7662.
[23] W.W. Wong, J.F. Hooper, A.B. Holmes, Aust. J. Chem. 62 (2009) 393.
[24] R.F. Chen, R. Zhu, C. Zheng, S.J. Liu, Q.L. Fan, W. Huang, Sci. China. Ser. B 52 (2009) 212.
[25] R.F. Chen, R. Zhu, Q.L. Fan, W. Huang, Org. Lett. 10 (2008) 2913.
[26] [a] R.F. Chen, Q.L. Fan, C. Zheng, W. Huang, Org. Lett. 8 (2006) 203;
[b] Y.Q. Mo, R.Y. Tian, W. Shi, Y. Cao, Chem. Commun. (2005) 4925.
[27] S. Zhang, R. Chen, J. Yin, F. Liu, H. Jiang, N. Shi, Z. An, C. Ma, B. Liu, W. Huang, Org. Lett. 12 (2010) 3438.
[28] J. Yin, S.-L. Zhang, R.-F. Chen, Q.-D. Ling, W. Huang, Phys. Chem. Chem. Phys. 12 (2010) 15448.
[29] V. Promarak, S. Saengsuwan, S. Jungsuttiwong, T. Sudyoadsuk, T. Keawin, Tetrahedron. Lett. 48 (2007) 89.
[30] C.H. Chen, F.I. Wu, C.F. Shu, C.H. Chien, Y.T. Tao, J. Mater. Chem. 14 (2004) 1585.
[31] I. Avilov, P. Marsal, J.L. Bredas, D. Beljonne, Adv. Mater. 16 (2004) 1624.
[32] [a] T. Chu, M. Ho, J. Chen, C.H. Chen, Chem. Phys. Lett. 415 (2005) 137;
[b] K.L. Tong, S.K. So, H.F. Ng, L.M. Leung, M.Y. Yeung, C.F. Lo, Synth. Met. 147 (2004) 199.
[33] N. Seidler, S. Reineke, K. Walzer, B. Lussem, A. Tomkeviciene, J.V. Grazulevicius, K. Leo, Appl. Phys. Lett. 96 (2010) 933049.
[34] M.H. Tsai, Y.H. Hong, C.H. Chang, H.C. Su, C.C. Wu, A. Matoliukstyte, J. Simokaitiene, S. Grigalevicius, J.V. Grazulevicius, C.P. Hsu, Adv. Mater. 19 (2007) 862.

to tune the electrochemical and the optical properties of π-conjugated polymers. The first is the increasing the conjugation length. An increase in the conjugation length results in decreasing the band gap (E_g), limited by Peierls distortion [18]. A second strategy is to change the electron density via incorporation of electron donating or withdrawing groups onto the polymer. The third method is to modify the steric interaction between repeat units within the polymer backbone, using more planar systems result in better orbital overlap, thereby lowering the band gap. The fused-ring units allow fine-tuning of the polymer band gap due to the enhanced π–π stacking between the polymeric chains. Following this strategy, we previously reported the synthesis of thienyl and ethylenedioxybenzene functionalized thieno[3,4-b]pyrazines [19] as precursors to investigate the effect of changes in π-conjugated terthienyls on the electronic and optoelectronic properties of the resulting polymers.

In an earlier work, a series of polymers with a conjugated core building block containing dibenzo[*a,c*]phenazine moiety as the acceptor unit and thiophene based donor units were synthesized [20]. In the present study, three new donor–acceptor–donor polymers with 10,11, 12,13-tetrahydrodibenzo[*a,c*]phenazine moiety as the acceptor unit and thiophene, 3-hexyl thiophene and 3,4-ethylenedioxythiophene as the donor units were synthesized. The effect of replacing the 10,11,12,13-tetrahydrodibenzo[*a,c*]phenazine moiety with dibenzo[*a,c*]phenazine as the acceptor unit on the electrochemical and spectroelectrochemical properties of the resulting polymers were analyzed.

2. Experimental

2.1. Materials

Dichloromethane (DCM), chloroform ($CHCl_3$), hexane, ethanol, *N*-bromosuccinimide (NBS), cyclohexane-1,2-diamine, dichlorobis(triphenyl phosphine)palladium(II) ($Pd(PPh_3)_2Cl_2$), *p*-toluene sulfonic acid (PTSA) were purchased from Sigma–Aldrich. Silica gel was purchased from Merck and tetrahydrofuran (THF) was purchased from Fisher Scienific UK Limited. Tributylstannane compounds [21–23] and 2,7-dibromophenanthrene-9,10-dione [24] were prepared according to literature method. THF was dried and distilled over benzophenone–sodium under nitrogen before use.

2.2. Instrument

^{1}H-NMR and ^{13}C-NMR spectra of compounds were recorded in $CDCl_3$ using Bruker Spectrospin Avance DPX-400 Spectrometer and chemical shifts were given relative to tetramethylsilane. Voltalab 50 potentiostat was used for the investigation of the redox behavior of monomers. Electropolymerizations were carried out in a three-electrode cell consisting of indium tin oxide (ITO, Delta technologies, 8–12 Ω/cm^2) coated glass as the working electrode, platinum wire as the counter electrode, and Ag wire as the pseudo-reference electrode (0.3 V vs Fc/Fc^+). UV–Vis-NIR spectra of the polymers were recorded on a Varian Cary 5000 spectrophotometer. Minolta CS-100 spectrophotometer was used for colorimetry measurements.

2.3. Synthesis

2.3.1. 2,7-Dibromo-10,11,12,13-tetrahydrodibenzo[a,c]phenazine (3)

2,7-Dibromophenanthrene-9,10-dione (300 mg, 0.82 mmol), ethanol (50 mL), catalytic amount PTSA and cyclohexane-1,2-diamine (0.82 mmol) were placed in a round-bottomed flask fitted with a condenser. The mixture was heated under reflux. At the end of the reaction, cloudy mixture was observed. Upon cooling, filtration of the reaction mixture followed by washing with ethanol afforded the desired product, 2,7-dibromo-10,11,12,13-tetrahydrodibenzo[*a,c*]phenazine. To purify the dibrominated compound, column chromatography was performed over silica gel, eluting with 1:5 ($CHCl_3$:Hexane).

White solid (180 mg, 49%) IR υ = 3074, 2931, 1878, 1598, 1479, 1427, 1371, 1323, 1263, 1197, 1074, 955, 898, 797, 733, 655, 526 cm^{-1}. ^{1}H-NMR (400 MHz $CDCl_3$): δ (ppm) 9.04 (d, 2H, J = 2.2 Hz), 8.12 (d, 2H, J = 8.7 Hz), 7.64 (dd, 2H, J = 8.7, 2.2 Hz), 3.08–3.10 (m, 4H), 1.99–2.02 (m, 4H) ^{13}C-NMR (100 MHz, $CDCl_3$): δ (ppm) 153.3, 137.4, 131.7, 131.4, 128.7, 127.6, 124.1, 122.1, 32.7, 22.8.

2.3.2. General procedure for the synthesis of 4, 5, 6 via Stille coupling

2,7-Dibromo-10,11,12,13-tetrahydrodibenzo[*a,c*]phenazine (100 mg, 0.23 mmol), and tributylstannane compound (0.92 mmol) were dissolved in anhydrous THF (80 ml), the solution was purged with argon for 30 min and $Pd(PPh_3)_2Cl_2$ (40 mg, 0.057 mmol) was added at room temperature. The mixture was refluxed over night under argon atmosphere. The crude products were purified by column chromatography using DCM – Hexane as the eluent.

2.3.2.1. 2,7-Bis(4-hexylthiophen-2-yl)-10,11,12,13-tetrahydro dibenzo[a,c] phenazine (4, HTBP). The crude product was purified by column chromatography (DCM:Hexane 1:3) to give 4, HTBP (82 mg, 58%) as pale yellow solid. IR υ = 3055, 2925, 2852, 1611, 1460, 1371, 1323, 903, 810, 724, 580 cm^{-1}. ^{1}H-NMR (400 MHz $CDCl_3$): δ (ppm) 9.21 (s, 2H), 8.33 (d, 2H, J = 8.5 Hz), 7.79 (d, 2H, J = 8.5 Hz), 7.34 (s, 2H), 6.88 (s, 2H), 3.10–3.18 (m, 4H), 2.60 (t, 4H, J = 7.6 Hz), 1.88–2.03 (m, 4H), 1.63 (p, 4H), 1.26–1.35 (m, 12H), 0.84 (t, 6H, J = 7.0 Hz) ^{13}C-NMR (100 MHz, $CDCl_3$): δ (ppm) 152.8, 144.8, 144.1, 138.9, 133.8, 130.4, 129.9, 126.6, 125.5, 123.4, 121.6, 120.2, 33.0, 32.0, 31.0, 30.8, 29.3, 23.2, 22.9, 14.4. HRMS *m/z* calcd for $C_{40}H_{44}N_2S_2$ 617.3024 found 617.3046 $[M+H]^+$.

2.3.2.2. 2,7-Bis(2,3-dihydrothieno[3,4-b][1,4]dioxin-5-yl)-10, 11,12,13-tetrahydrodibenzo [a,c]phenazine (5, DTBP). The crude product was purified by column chromatography (DCM:Hexane 3:1) to give 5, DTBP (86 mg, 66%) as a yellow solid. IR υ = 3112, 2932, 1610, 1503, 1437, 1365, 1168, 1071, 897, 810, 755, 605 cm^{-1}. ^{1}H-NMR (400 MHz $CDCl_3$): δ (ppm) 9.31 (d, 2H, J = 1.8 Hz), 8.37 (d, 2H, J = 8.7 Hz), 7.99 (dd, 2H, J = 8.7, 1.8 Hz), 6.30 (s, 2H), 4.32–4.33 (m, 4H),

4.22–4.24 (m, 4H), 3.10–3.16 (m, 4H), 1.97–1.99 (m, 4H). ^{13}C-NMR (100 MHz, $CDCl_3$): δ (ppm) 151.3, 141.3, 137.7, 137.6, 131.1, 129.1, 128.1, 125.5, 121.8, 120.5, 116.6, 97.0, 63.8, 63.4, 31.8, 21.9. HRMS *m/z* calcd for $C_{32}H_{24}N_2O_4S_2$ 565.1256 found 565.1250 $[M+H]^+$.

2.3.2.3. 2,7-Di(thiophen-2-yl)-10,11,12,13-tetrahydrodibenzo [a,c]phenazine (6, TTBP). The crude product was purified by column chromatography (DCM:Hexane 5:1) to give 6, TTBP (68 mg, 66%) as yellow solid. IR υ = 3067, 2934, 1898, 1610, 1446, 1371, 1193, 1075, 903, 811, 696, 592 cm^{-1}. ^{1}H-NMR (400 MHz $CDCl_3$): δ (ppm) 9.35 (d, 2H, J = 1.9 Hz), 8.49 (d, 2H, *J* = 8.5 Hz), 7.91 (dd, 2H, *J* = 8.5, 1.9 Hz), 7.53 (dd, 2H, *J* = 3.5, 1.0 Hz), 7.30 (dd, 2H, *J* = 5.1, 1.0 Hz), 7.10 (dd, 2H, *J* = 5.1, 3.5 Hz), 3.18–3.21 (m,4H), 2.02–2.05 (m, 4H). HRMS *m/z* calcd for $C_{28}H_{20}N_2S_2$ 449.1146 found 449.1139 $[M+H]^+$.

3. Results and discussion

3.1. Synthesis of monomers

Syntheses of the monomers are depicted Scheme 1. In literature, there are a number of methods [25–28] for the synthesis of 2,7-dibromophenanthrene-9,10-dione 2 starting from phenanthrene-9,10-dione or 2,7-dibromophenanthrene. With the help of one of them [24], it was synthesized starting from phenanthrene-9,10-dione 1 in the presence of NBS and concentrated H_2SO_4. Condensation reaction of 2 with cyclohexane-1,2-diamine afforded 3 in 49% yield, to obtain which reflux in EtOH for 5 h. To increase the reaction yields, *p*-toluene sulfonic acid was utilized as the catalyst. If the reaction medium is kept at room temperature without catalyst, there is no aromatization in the phenazine ring. However, this product is highly unstable and undergoes rearrangement with heat or light [25]. Finally, condensation product 3 was reacted with related stannane compounds in the presence of $Pd(PPh_3)_2Cl_2$ to obtain target monomers 4 (HTBP), 5 (DTBP) and 6 (TTBP) in moderate yields (58–66%).

3.2. Electropolymerization

The electrochemical behavior of HTBP, DTBP and TTBP were investigated by cyclic voltammetry technique. Cyclic voltammetry (CV) is a very useful method that reveals the electroactivity of the compounds in concern. It also gives evidence on the reversibility of the electron transfer reactions during the electropolymerization. Electrochemical polymerizations of the monomers were studied via CV in a solution of 10^{-2} M monomer on an ITO working electrode.

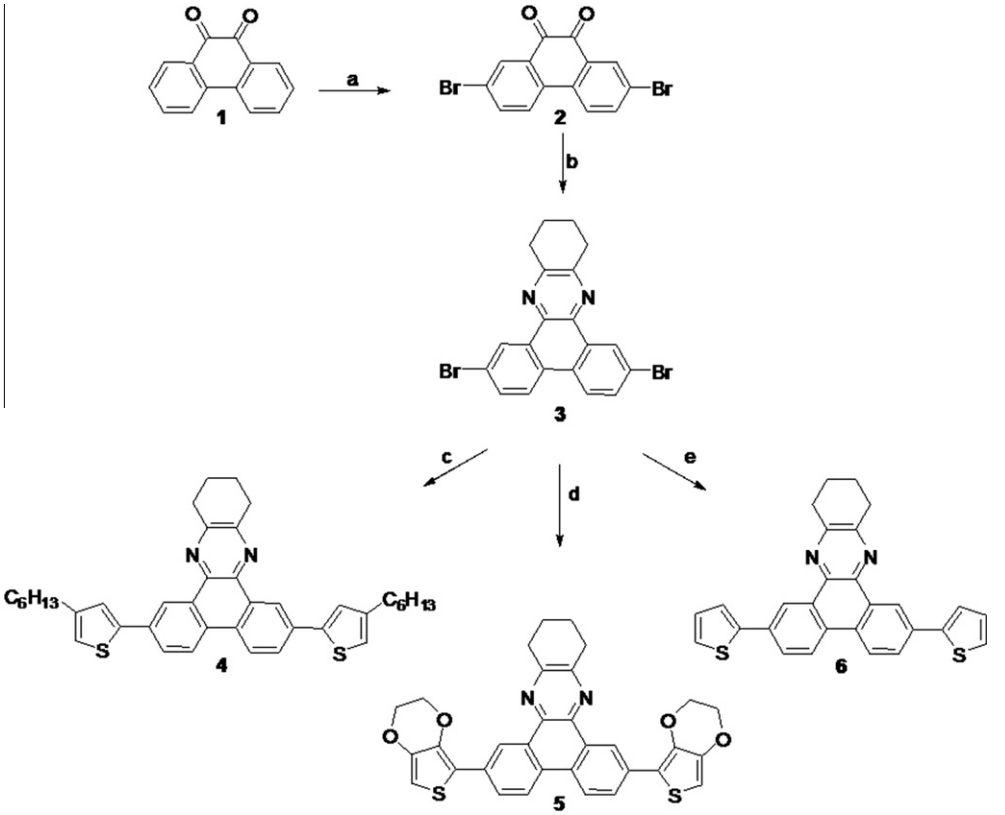

Scheme 1. The synthetic route of the monomers. (a) NBS, conc. H_2SO_4, rt, 3h (b) Cyclohexane-1,2-diamine, PTSA, EtOH, reflux, 5h (c–e) $Pd(PPh_3)_2Cl_2$, stannanes(tributyl(4-hexylthiophen-2-yl)stannane)(c), tributyl(2,3-dihydrothieno[3,4-*b*][1,4]dioxin-5-yl)stannane(d) and tributyl(thiophen-2-yl)stannane(e), dry THF, overnight reflux.

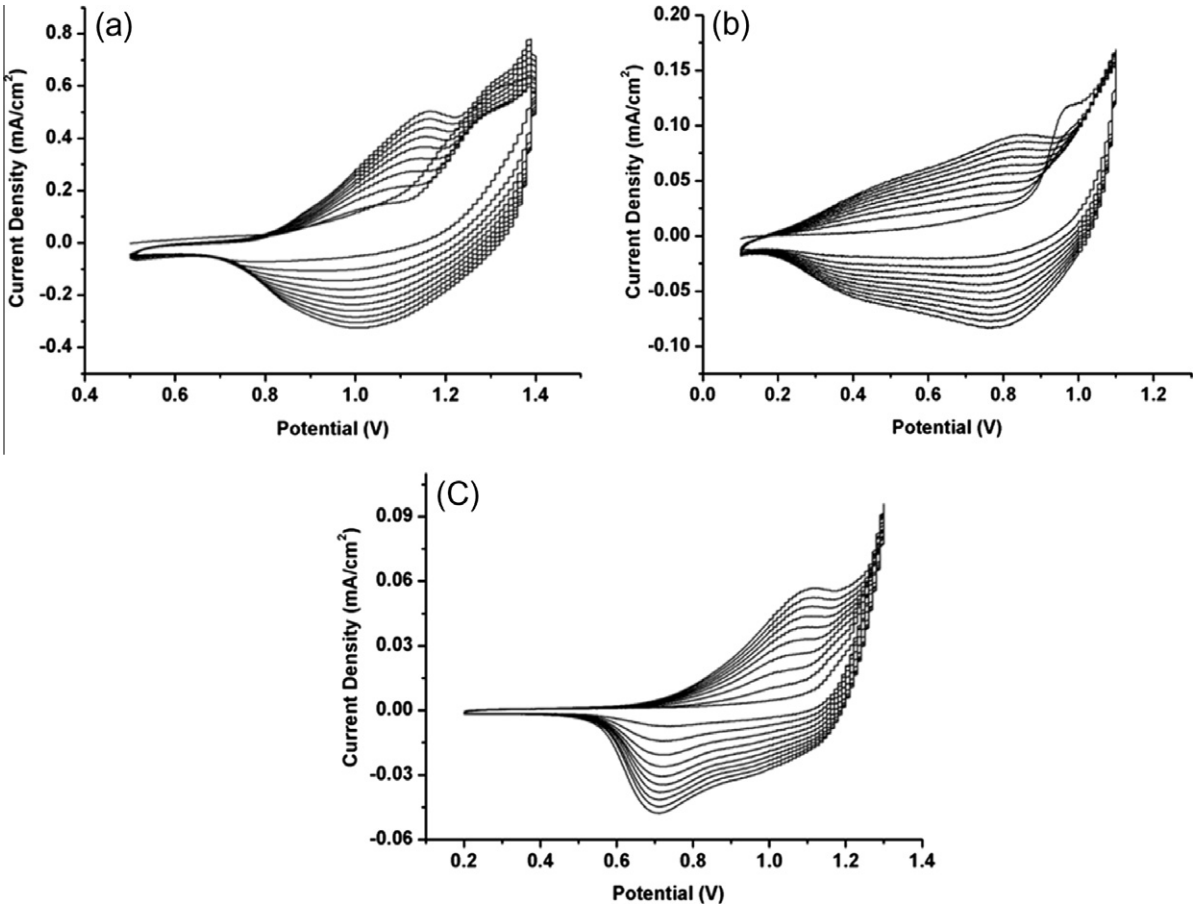

Fig. 1. Cyclic voltammogram of (a) PHTBP (b) PDTBP (c) PTTBP in DCM (for PDTBP, DCM/ACN(5/95)) solution containing 0.1 M $TBAPF_6$, scan rate 100 mV s^{-1}.

Cyclic voltammograms showed both an irreversible oxidation wave corresponding to the oxidation of the monomers and the reversible redox couple for the polymers (Fig. 1). While the monomer oxidation potential of DTBP was observed at 0.97 V, they were at 1.28 V for HTBP and >1.3 V for TTBP. Comparing the onsets of monomer oxidation, DTBP was much more easily oxidized than both HTBP and TTBP. The presence of electron-donating ethylene-dioxy bridge on EDOT units lowers the oxidation potential compared to those of thiophene and 3-hexyl thiophene substituted monomers. The oxidation peak potentials of polymers vary from 0.83 to 1.16 V vs Ag wire pseudo reference electrode, whereas the reduction peak potentials were in a range of 0.70–1.00 V. As the cyclic scan proceeded, intensities of anodic and cathodic currents of the polymer films gradually increased, indicating the presence of a conductive polymer on the electrode.

Our previous work where dibenzo[*a,c*]phenazine moiety was used as the acceptor unit, 2,7-di(thiophen-2-yl)dibenzo[a,c]phenazine (TTP) did not produce an adherent thin polymer film on ITO-coated electrode surface [19]. Introduction of alkyl bridge on the backbone of π-conjugated system leads to obtain a polymer film on the surface of working electrode. It seems like that the presence of alkyl bridge enhanced the solubility of the resulting oligomer, thereby the polymer film grows on the surface of electrode.

3.3. Spectroelectrochemistry

Polymers were prepared by repetitive potential-sweep anodic oxidation of the corresponding monomers HTBP and TTBP on ITO coated glass slides in DCM. For DTBP, a DCM/ACN mixture (5:95) was utilized with 0.1 M $TBAPF_6$ at a scan rate 100 mV s^{-1}. After electropolymerization, the polymer coated electrode was washed with acetonitrile to remove unreacted monomer. To investigate spectroscopic changes, UV–Vis-NIR spectrophotometer was used in a monomer free system. The spectra of polymers were recorded continuously versus time while applying a constant potential. Fig. 2 illustrates the optoelectrochemistry of PHTBP, PDTBP and PTTBP. Stepwise oxidation of the PHTBP shows the fading of absorbance at 395 nm which belongs to π–π* transition. As polymer film gets oxidized, typical evolution of peaks at 620 nm and 1500 nm occurred corresponding to polaronic and bipolaronic bands, respectively. The band gap of PHTBP, onset of the π–π* transition for the neutral polymer was calculated as 2.5 eV using the absorption band centered at 395 nm. The absorbance assigned to π–π* transition for PDTBP is at

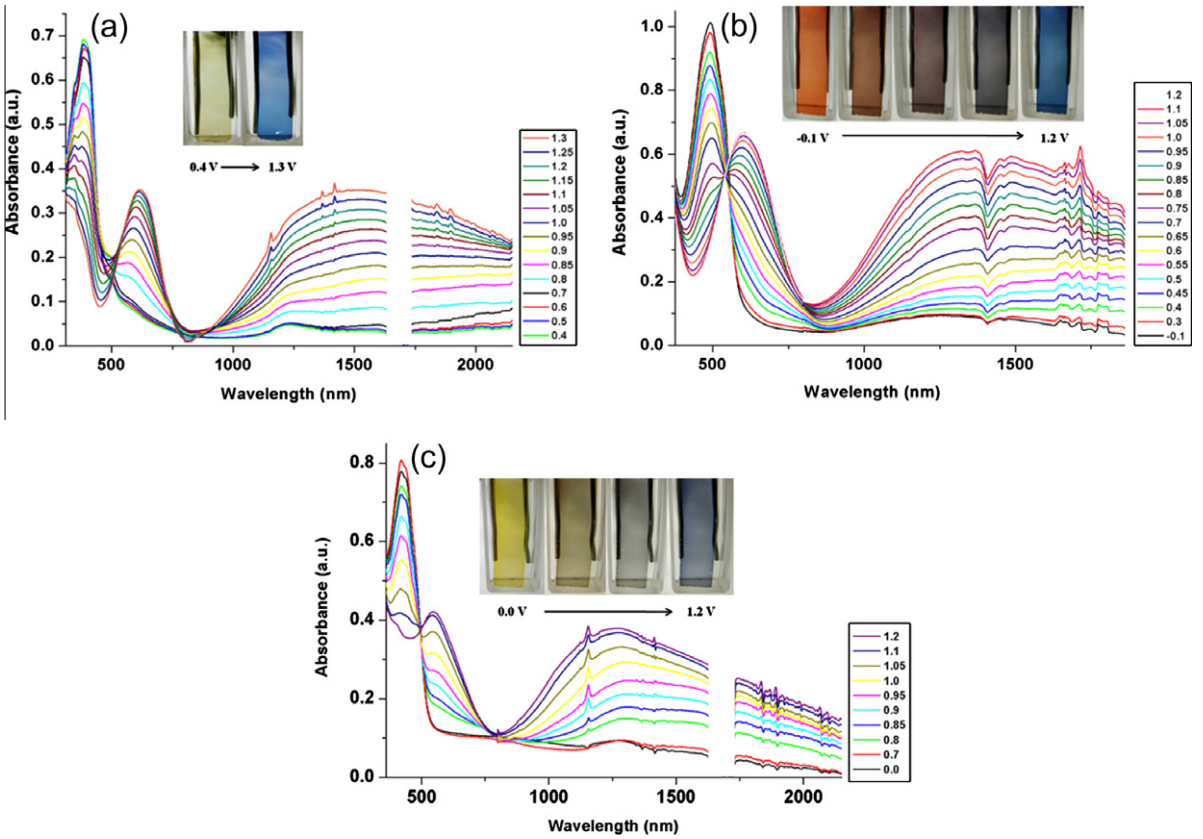

Fig. 2. Spectroelectrochemical spectra of (a) PHTBP with applied potential between +0.4 and +1.3 V in DCM/$TBAPF_6$ (b) PDTBP with applied potential between −0.1 and +1.2 V in ACN/DCM/$TBAPF_6$ (c) PTTBP with applied potential between 0.0 and +1.2 V in DCM/$TBAPF_6$.

490 nm and this transition was observed at 430 for PTTBP. The band gap of PDTBP was calculated as 2.0 eV and that of PTTBP was calculated as 2.2 eV using the wavelength value at the onset of the π–π^* transition. The difference in band gap, 0.5 eV, between PHTBP and PDTBP can be explained by distortion of backbone planarity. Presence of alkyl chains at the β-position of thiophene ring causes steric interactions between repeat units within the polymer backbone, resulting in decreasing π orbital overlap.

The π–π^* transition for 10,11,12,13-tetrahydrodibenzo[*a,c*]phenazine containing polymers takes place at an higher energy than those of the dibenzo[*a,c*]phenazine derivatives [20]. Introduction of alkyl bridge on the backbone of π-conjugated system instead of aromatic unit leads to deviation from the planarity, resulting in decreasing π-orbital overlap, thereby the absorption band of π–π^* transition shifts to shorter wavelength.

3.4. Colorimetry

Color and luminance (L) changes were monitored as the potential was increased. According to the CIE (Commission Internationale de I'Eclairage) system of colorimetry, the color is made up of three attributes; luminance (Y), hue (x), and saturation (y).

Polymers of PDTBP and PTTBP reveal several distinct colors since the polaron bands of the polymers are still in the visible region (Table 1, colors refer to polymer thicknesses between 0.5 and 1 microns). Polymers of PDTBP and PTTBP have the ability to achieve multi-colors with small structural modifications. Multicolored electrochromism observed in a polymer is a promising property since these types of materials can be utilized as active layers in many device applications especially in the information technologies. On the other hand, PHTBP film changes from a yellow neutral state to a blue oxidized state.

PDTBP is orange in its neutral state. Upon oxidation, the orange color of the polymer turns into brown. Further oxidation results in purple. A gray color was observed when +0.7 V potential was applied. When the potential is further increased the polymer turns into a blue color.

The color of the PTTBP film is yellow in its neutral state. Its color switches from yellow to greenish brown due to further oxidation. When +0.9 V potential is applied, the polymer turns into gray. Further oxidation causes blue color.

3.5. Electrochemical switching

Electrochromic switching studies were carried out to obtain changes in the transmittance (optical contrast). A square-wave potential step method coupled with optical spectroscopy is used to obtain the switching times and the contrast for these polymers. For that matter, polymer

Table 1
Electronic and electrochromic properties of the polymers.

Polymer	λ_{max} (nm)	Redox state	Y	x	y	Color	E_g (eV)
PHTBP	395	Neutral	99.9	0.320	0.366	Yellow	2.5
		Oxidized	48.7	0.258	0.297	Blue	
PDTBP	490	Neutral	38.9	0.4S9	0.398	Orange	2.0
		Half Ox.	32.9	0.437	0398	Brown	
		Half Ox.	32.7	0.376	0.385	Purple	
		Half Ox	34,8	0316	0.329	Dark gray	
		Oxidized	34.8	0.209	0.219	Blue	
PTTBP	430	Neutral	79.8	0.353	0.397	Yellow	2.2
		Oxidized	62.5	0.353	0.399	Gray	
			49.9	0.321	0.363	Brown	
			44.6	0.2S0	0.312	Blue	

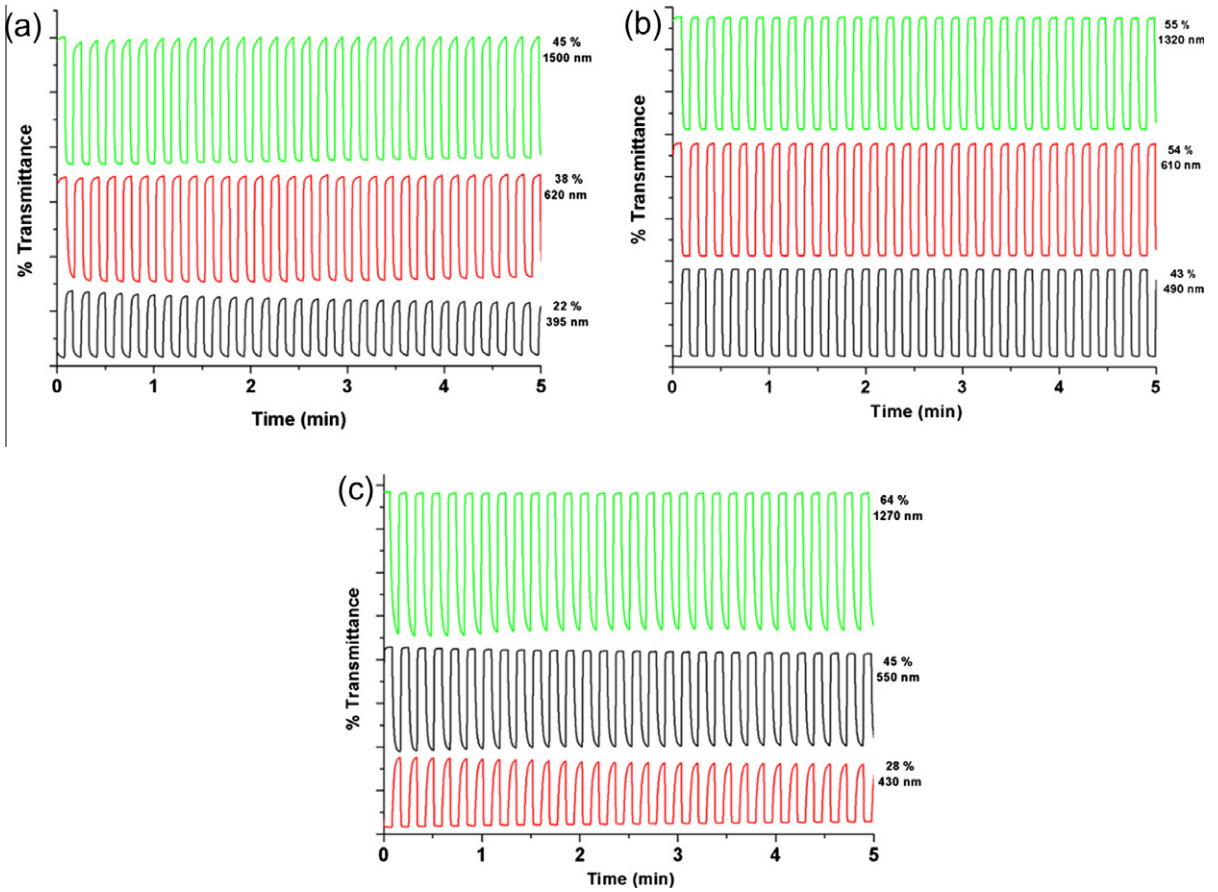

Fig. 3. Electrochromic switching, optical absorbance change monitored (a) at 395, 620 and 1500 nm for PHTBP between +0.4 and +1.3 V (b) at 490, 610 and 1320 nm for PDTBP between −0.1 and +1.2 V (c) at 430, 550 and 1270 nm for PTTBP between 0.0 and +1.2 V.

Table 2
Switching properties of polymers.

Polymer	PHTBP			PDTBP			PTTBP		
λ_{max} (nm)	395	620	1500	490	610	1320	430	550	1270
Switching time (s)	1.7	1 5	1.8	0.8	0.7	06	2.3	0.5	0.5

films were switched between their neutral and oxidized states with a time interval of 5 s to monitor their stability, optical contrasts and switching times both in visible and NIR regions. The results were displayed in Fig. 3 where transmittance–time profiles of the polymers were recorded during double step spectrochronoamperometry.

In Near-IR region, PTTBP film has the maximum contrast ratio (% ΔT) as 64% at 1270 nm. The corresponding data are given in Fig. 3.

The switching time from oxidized state to reduced state of an electrochromic polymer is yet another important parameter to determine its potential application in electrochromic windows. The time required for full oxidized state from full reduced state is defined as the response time. The switching time data for polymers are given in Table 2.

4. Conclusion

A series of π-conjugated monomers based on 10,11, 12,13-tetrahydrodibenzo[*a,c*]phenazine as the acceptor unit was synthesized to understand the effects of donor strength on the optoelectronic and redox properties of the electropolymerized materials. Multicolored polymers from PDTBP and PTTBP were successfully synthesized via electrochemical methods. Spectroelectrochemical studies and electrochromic characterization demonstrated that the polymer containing EDOT unit in the polymer backbone not only decreased the band gap (E_g) but also enhanced the electrochromic properties such as optical contrast, switching time and multicolor properties. The polymer films with their electrochromic property, comparatively fast switching time and high optical contrast, are expected to be useful for practical use in smart windows.

References

[1] V. Seshadri, J. Padilla, H. Bircan, B. Radmard, R. Draper, M. Wood, T.F. Otero, G.A. Sotzing, Optimization, preparation, and electrical short evaluation for 30 cm^2 active area dual conjugated polymer electrochromic windows, Org. Electron. 8 (2007) 367.

[2] M. De Paoli, W.A. Gazotti, Electrochemistry, polymers and optoelectronic devices: a combination with a future, J. Braz. Chem. Soc. 13 (2002) 410.

[3] R.J. Mortimer, Organic electrochromic materials, Electrochim. Acta 44 (1999) 2971.

[4] T.L. Rose, S. D'Antonio, M.H. Jillson, A.B. Kon, R. Suresh, F. Wang, A microwave shutter using conductive polymers, Synth. Met. 85 (1997) 1439.

[5] Y.A. Udum, A. Durmus, E.G. Gunbas, L. Toppare, Both p- and n-type dopable polymer toward electrochromic applications, Org. Electron. 9 (2008) 501.

[6] P. Topart, P. Hourquebie, Infrared switching electroemissive devices based on highly conducting polymers, Thin Solid Films 352 (1999) 243.

[7] G. Sonmez, H. Meng, F. Wudl, Organic polymeric electrochromic devices: polychromism with very high coloration efficiency, Chem. Mater. 16 (2004) 574.

[8] S.A. Sapp, G.A. Sotzing, J.R. Reynolds, High contrast ratio and fast-switching dual polymer electrochromic devices, Chem. Mater. 10 (1998) 2101.

[9] A. Kumar, D.M. Welsh, M.C. Morvant, F. Piroux, K.A. Abboud, J.R. Reynolds, Conducting poly(3,4-alkylenedioxythiophene) derivatives as fast electrochromics with high-contrast ratios, Chem. Mater. 10 (1998) 896.

[10] G. Sonmez, H.B. Sonmez, C.K.F. Shen, F. Wudl, Red, green, and blue colors in polymeric electrochromics, Adv. Mater. 16 (2004) 1905.

[11] B.C. Thompson, P. Schottland, K. Zong, J.R. Reynolds, In situ colorimetric analysis of electrochromic polymers and devices, Chem. Mater. 12 (2000) 1563.

[12] B.C. Thompson, P. Schottland, G. Sonmez, J.R. Reynolds, In situ colorimetric analysis of electrochromic polymer films and devices, Synth. Met. 119 (2001) 333.

[13] G. Sonmez, C.K.F. Shen, Y. Rubin, F. Wudl, A. Red, Green, and blue (RGB) polymeric electrochromic device (PECD): the dawning of the PECD era, Angew. Chem. Int. Edit. 43 (2004) 1498.

[14] I. Schwendeman, R. Hickman, G. Sonmez, P. Schottland, K. Zong, D. Welsh, J.R. Reynolds, Enhanced contrast dual polymer electrochromic devices, Chem. Mater. 14 (2002) 3118.

[15] G. Sonmez, C.K.F. Shen, Y. Rubin, F. Wudl, The unusual effect of bandgap lowering by C60 on a conjugated polymer, Adv. Mater. 17 (2005) 897.

[16] F. Ozyurt, E.G. Gunbas, A. Durmus, L. Toppare, Processable and multichromic polymer of bis-3-hexylthiophene substituted 4-tert-butylphenyl quinoxaline, Org. Electron. 9 (2008) 296.

[17] H.S. Nalwa, Handbook of Organic Conductive Molecules and Polymers, John Wiley and Sons, New York, 1997.

[18] C.Q. Wu, Y.G. Zhang, H.Q. Lin, Peierls bond distortion in substituted polyacetylenes, Synth. Met. 119 (2001) 219.

[19] S. Tarkuc, E.K. Unver, Y.A. Udum, C. Tanyeli, L. Toppare, The effect of changes in π-conjugated terthienyl systems using thienyl and ethylenedioxybenzene functionalized thieno[3,4b] pyrazine precursors: multicolored low band gap polymers, Electrochim. Acta 55 (2010) 7254.

[20] E.K. Unver, S. Tarkuc, Y.A. Udum, C. Tanyeli, L. Toppare, Effect of conjugated core building block dibenzo[a,c]phenazine unit on p-conjugated electrochromic polymers: red-shifted absorption, J. Polym. Sci., Part A: Polym. Chem. 48 (2010) 1714.

[21] J.T. Pinhey, E.G. Roche, The chemistry of organolead(IV) tricarboxylates. Synthesis and electrophilic heteroarylation reactions of 2- and 3-thienyl-, and 2- and 3-furyl-lead tricarboxylates, J. Chem. Soc. Perkin Trans. 1 (1988) 2415.

[22] E. Bundgaard, F.C. Kreb, A comparison of the photovoltaic response of head-to-head and head-to-tail coupled poly{(benzo-2,1,3-thiadiazol-4,7-diyl)-(dihexyl)[2,2′]dithiophene-5,5′-diyl}, Polym. Bull. 55 (2005) 157.

[23] E. Kim, M. Kim, K. Kim, Diarylethenes with intramolecular donor–acceptor structures for photo-induced electrochemical change, Tetrahedron 62 (2006) 6814.

[24] M. Hanif, P. Lu, M. Li, Y. Zheng, Z. Xie, Y. Ma, D. Li, Synthesis, characterization, electrochemistry and optical properties of a novel phenanthrenequinone-alt-dialkylfluorene conjugated copolymer, J. Polym. Int. 56 (2007) 1507.

[25] M. Putala, N.K. Pustet, A. Mannschreck, Diastereoselective reaction of (MP)-pentahelicene-7,8-dione with trans-cyclohexane-1,2-diamine, thermal and photochemical transformations of its product, Tetrahedron Asymmetr. 12 (2001) 3333.

[26] B. He, H. Tian, Y. Geng, F. Wang, K. Mullen, Facile synthesis of 9,10-diarylphenanthrenes and poly(9,10-diarylphenanthrenes), Org. Lett. 10 (2008) 773.

[27] F. Dewhurst, P. Shah, Iodination of fluorenone by *N*-iodosuccinimide, J. Chem. Soc. C 11 (1969) 1503.

[28] J. Gautrot, P. Hodge, M. Helliwell, J. Raftery, D. Cupertino, Synthesis of electron-accepting polymers containing phenanthra-9,10-quinone units, J. Mater. Chem. 19 (2009) 4148.

and the high-conductivity state, with the difference in the conductivity on several orders of magnitude. These two conductivity states can thus be used to represent and memorize the logic "1" and logic "0" states.

In our previous work, we reported ONBM devices adopting polymer-chain-stabilized gold (Au) nanoparticles dispersed in the host polymer as the active memory layer. Being stabilized with polymer chains, the Au nanoparticles were well dispersed in the host polymer and the ONBM devices exhibited promising memory characteristics and endurance [4]. We also suggested the trap-filling space-charge-limited current (SCLC) as the transport mechanism for the bistable operation of the Au nanoparticle ONBM devices [5]. In such a mechanism, with a large enough voltage applied, a large number of injected carriers can completely fill the traps existing in the nanoparticle-dispersed host layer, and the device enters the higher-conductivity trap-filled conduction state [6]. On the other hand, if the traps are not completely filled, the current conduction is limited by the traps and the device is in the trap-limited SCLC (low-conductivity) state [6]. In addition, we noticed that the device current is not proportional to the device area. In our and other nanoparticle-based or nanomaterial-based ONBM devices, the bistable operation is all highly related to the distributed nanoparticles. Since the dispersion of nanoparticles in a host to some degree is random, it is therefore reasonable to speculate that the current conduction in such nanoparticle-based ONBM devices might not be uniform over the whole device area. Yet, such an issue had not been thoroughly investigated and possible localized current transport paths had not been clearly visualized before. In this work, we report that the spatial distribution of the current transport paths in Au nanoparticle ONBM devices can be investigated by the so-called the optical beam induced resistance change (OBIRCH) method [23], in which the thermal energy transferred by a scanning laser beam was used to resolve the spatial distribution of electric conduction in the memory devices. Through adoption of the OBIRCH technique, the localized current transport paths in ONBM devices can be clearly visualized for the first time, demonstrating that the OBIRCH technique might be an useful method to characterize localized current transport paths in organic devices.

2. Experiment

2.1. Device preparation and characterization

The active layer of the memory device consists of the host polymer material and the polymer-stabilized Au nanoparticles [4]. Fig. 1 shows the schematic structure of the polymer-stabilized Au nanoparticle. The polymer chains are attached with a sulfur atom at one end, which stabilizes the Au clusters with an S–Au bond to form the Au nanoparticles. The polymer used to prepare polymer-stabilized Au nanoparticles was [4-Cyano-2,4,4-trimethyl-2-methylsulfanylthiocarbonylsulfanyl-poly (butyric acid 1-adamantan-1-yl-1-methyl-ethyl ester)] or the so-called PCm. The chemical structure of the PCm is also shown in Fig. 1. The polymer-stabilized Au nanoparticles are considered immobile in the same host polymer material (i.e. PCm) during fabrication and electrical operation of devices, thus beneficial to the stability and endurance of the memory devices [4]. The properties of the polymer-stabilized Au nanoparticles and films had been discussed in details previously [4].

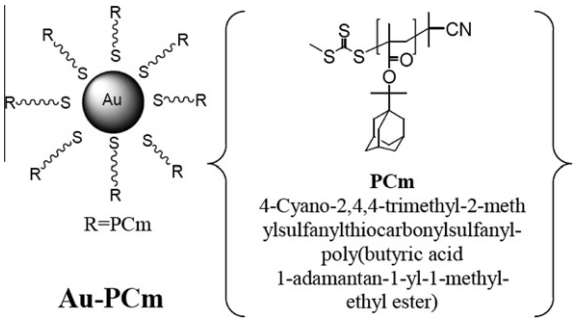

Fig. 1. The schematic structure of the polymer-stabilized Au nanoparticle and the host polymer PCm.

The memory devices were fabricated using the following procedures. First, glass substrates were cleaned by detergent solution, de-ionized water, acetone, and isopropanol (IPA) sequentially in the ultrasonic cleaner and then were dried in a vacuum oven at 100 °C. A 75-nm-thick aluminum (Al) was then deposited by a thermal evaporator with a base pressure of 2×10^{-6} Torr, using a shadow mask to pattern the bottom electrodes. Subsequently, the ultraviolet (UV)-ozone treatment was applied to treat the Al surface to enhance the adhesion of the subsequent polymer layer onto the electrode. The solution containing the active-layer materials was spin-coated onto the bottom electrode in a glove box filled with N_2. The solution was prepared by dissolving the polymer-stabilized Au nanoparticles (Au-NP) (0.05 wt.%) and the host polymer PCm (2.4 wt.%) in 1,2-dichlorobenzene [4]. The particle sizes of Au nanoparticles were 3–5 nm. The thickness of the dried active layer had been determined by transmission electron microscopy (TEM) to be about 50 nm. Finally, the Al top electrode was deposited by thermal evaporation using the shadow mask. The completed memory cell had a device structure of Al/PCm + Au-NP/Al, as shown in Fig. 2. The area of the memory cell was 2×2 mm^2. The current–voltage (I–V) characteristics of the ONBM devices were measured by an HP 4156C semiconductor analyzer under the ambient condition.

2.2. OBIRCH measurement

The distribution of current transport paths in ONBM was investigated by using a scanning laser beam as a source of thermal energy transfer to induce local changes of the temperature and the electronic/conduction properties. This method is usually called the optical beam induced resistance change (OBIRCH) method [23], which is often used in semiconductor devices and integrated circuits to detect localization of current paths and abnormal current paths. Fig. 3 shows the schematic setup of the OBIRCH measurement. An OBIRCH system μAMOS-200 of

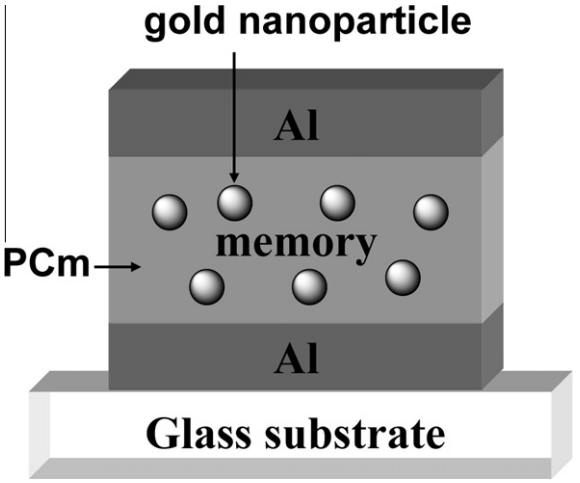

Fig. 2. The schematic structure of the device.

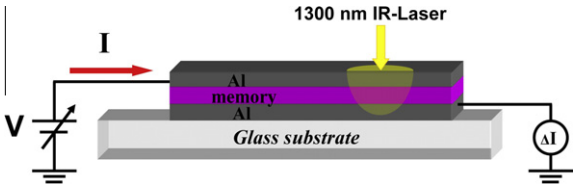

Fig. 3. The schematic setup of the OBIRCH measurement.

Hamamatsu Photonics was used in this study. In the measurement, a constant voltage (e.g. 1 V) was applied to the memory device under test (which was pre-set in either the "1" state or the "0" state) and a laser beam was scanned over the top surface of the device. An IR laser (1.3 μm, 370 mW) was utilized and the spot size of the laser beam was ~6 μm. Because the spot size of the laser beam is much smaller than the device area, the device thickness is very small (50 nm) compared to both the device area and the laser beam, and the laser beam stays at each location only for a short time, the heating and thermal diffusion in the vertical direction (to the active layer) can be considered effective but meanwhile localized in the lateral direction. In scanning the IR laser beam, simultaneously the current (I) and the current change (ΔI) of the device (under the constant bias voltage) at each scanning step were measured and recorded. The recorded current change (ΔI) along with the laser scanning can then be displayed as a two-dimensional image over the device area to visualize the distribution of electronic properties/conduction. The OBIRCH method has the particular advantage that it is a non-destructive characterization method.

3. Results and discussions

3.1. I–V characteristics of the ONBM devices

The current–voltage (I–V) characteristics of the Al/PCm + Au–NP/Al device are shown in Fig. 4. Two distinct conducting states were observed in the I–V characteristics.

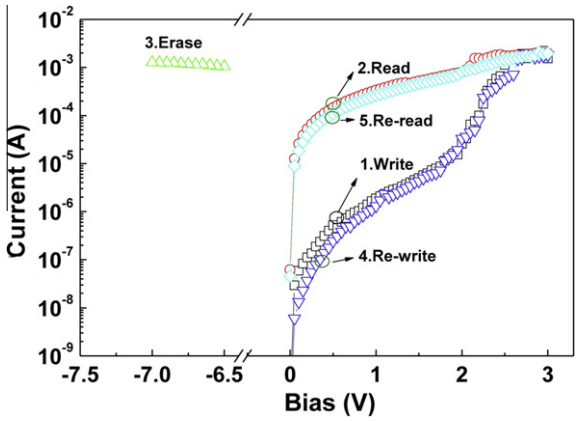

Fig. 4. The current–voltage (I–V) characteristics of the Al/PCm + Au-NP/Al device.

A low-conductivity state with a low current of approximately 10^{-7}–10^{-6} A was recorded in the voltage range of 0–1 V for the first voltage sweep. It corresponds to the "0" state of the bistable memory. When the applied voltage approached 2.3 V (the writing voltage), a remarkably abrupt current increase from 10^{-5} to 10^{-3} A was observed. Once the writing voltage was applied, the device remained in the high-conductivity state (with a current being several orders of magnitude higher than that before writing) even when the writing voltage was removed and a lower bias voltage (e.g. 1 V, i.e. the reading voltage) was subsequently applied. Such behaviors clearly manifested the nonvolatile memory characteristics. This high-conductivity state corresponds to the "1" state of the memory device. In addition, the device can be switched from the high-conductivity state back to the low-conductivity state by applying a high enough negative bias voltage of −6.5–−7 V (i.e. the erasing voltage). After the device was restored to its low-conductivity state, once again, it could be switched to the high-conductivity state by applying a positive voltage sweep again, exhibiting I–V characteristics similar to the first voltage sweep (i.e. the "rewrite" curve in Fig. 4). Similarly, the reading and erasing actions could be repeated, also showing similar I–V characteristics (e.g. the "re-read" curve in Fig. 4). Thus, this device clearly shows the characteristics of a rewritable nonvolatile bistable memory. For the purpose of this present work, only the basic I–V characteristics of the device are discussed here. More information on the endurance and retention characteristics of the device could be fund in our previous work [4].

3.2. OBIRCH analysis of the ONBM devices

The distribution of current transport paths in ONBM was investigated by using a scanning laser beam as a source of thermal energy transfer to induce local changes of the temperature and the electronic/conduction properties. This method is usually called the optical beam induced resistance change (OBIRCH) method [23]. In OBIRCH measurements as shown in Fig. 3, when a spot in the device is illuminated by the laser beam, part of the

laser energy is absorbed and is converted into heat, rendering the local temperature change (rise) in the illuminated area. The local temperature change could affect the local electronic properties/conduction. When there is a spatial non-uniformity in local electronic properties/conduction, the local temperature change at different locations would induce different changes in local electronic properties/conduction. If a constant bias is applied to the device, different changes in local electronic properties/conduction in turn would result in a spatial distribution of the current change ΔI (or resistance change) in scanning the laser beam. In principle, $\Delta I(x) \propto [\Delta R(x)/R(x)]J(x) \propto [\Delta R(x)/V]J(x)^2$, where $\Delta I(x)$ is the current change induced by a laser beam at the position x, $J(x)$ is the current density at x, $R(x)$ is the local resistance (i.e. $V/J(x)$) at x, $\Delta R(x)$ is the change of local resistance at x induced by the laser beam at x, and V is the applied constant voltage. The two-dimensional image of ΔI thus visualizes the distribution of electronic properties/conduction over the device area. This mapping would be particularly sensitive when the device current paths are highly localized to some spots, since ΔI would be more significant when the laser beam is scanned over these spots (note $\Delta I(x)$ is proportional to $J(x)^2$ under a constant bias voltage). In this study, the property of interest is the distribution of the current conduction paths for the "on" state (high-conductivity state) of the ONBM device. The OBIRCH method has the particular advantage that it is a non-destructive characterization method.

Fig. 5(a) shows the OBIRCH ΔI image of the ONBM device (which is superimposed with the optical microscopic image of the device taken simultaneously) recorded upon applying a writing voltage of nearly 3 V. At this writing voltage, a relatively high current (1.05 mA) was recorded, which corresponded to the logic "1" state. Several green[1] points in Fig. 5(a) indicate the locations of large ΔI in scanning the IR laser. Such an image indicates that upon applying a writing voltage (i.e. in the writing mode), the current conduction was localized. After the writing process, a smaller reading voltage (1 V) was applied to read the ONBM. In this reading mode, still a relatively large current of 0.126 mA was recorded, indicating the ONBM remained in the logic "1" (or "on") state. Furthermore, upon applying the reading voltage (i.e. in the reading mode) subequently, the OBIRCH ΔI image of the device was also recorded and is shown in Fig. 5(b). Again, some green points (locations of large ΔI) occur in the image, indicating also localized current conduction in the reading mode. Interestingly, one notices that locations of large ΔI in the reading mode almost coincide with locations of large ΔI in the writing mode. Overall, these results suggest that in the ONBM devices using polymer-stabilized Au nanoparticles, the current transport paths for the "on" state during the writing mode or the reading mode are localized and that once the localized current transport paths are established in the writing mode, the current transport in the subsequent reading mode would basically follow the same paths. Such localized current transport paths resemble "filament formation" suggested by some previous works [4–22], which may be associated with thermal evaporation of the metal electrode or with points where the film thickness is less or there are more nanoparticles. Yet, in a reference device with the structure of Al/PCm/Al, the current was low and it did not show conductance switching. It thus suggests that the memory effect and localized current transport paths in the present device are highly associated with Au nanoparticles.

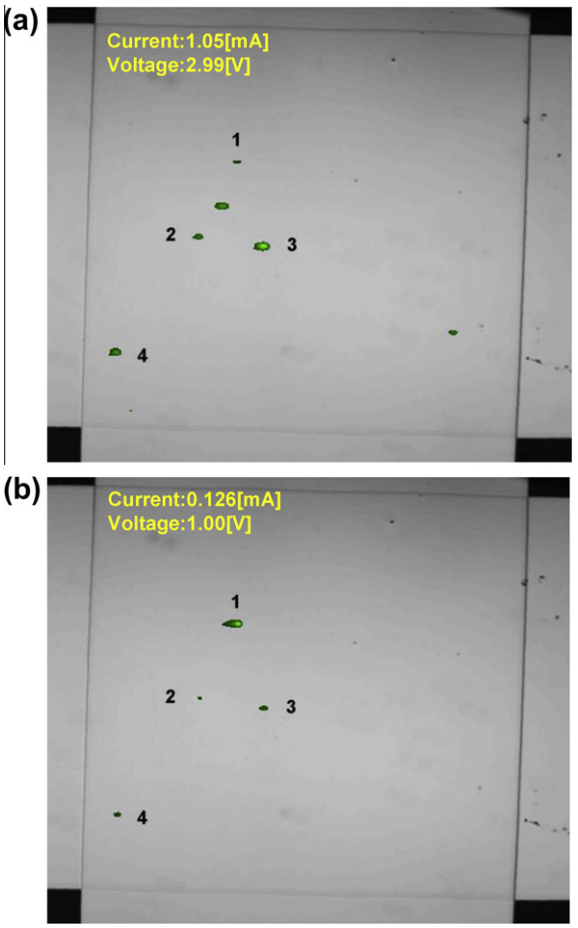

Fig. 5. OBIRCH ΔI images of the ONBM device (which is superimposed with the optical microscopic image of the device taken simultaneously): (a) recorded upon applying a writing voltage of nearly 3 V, and (b) recorded upon applying the 1-V reading voltage (i.e. in the reading mode) after the writing process.

To further investigate how the current transport paths would vary in repeated write–read–erase–write processes, a voltage of −6.5–−7 V was further applied to erase the ONBM device of Fig. 5. After erasing, a 1-V reading voltage was again applied to read the ONBM and a very small current of 1.3 μA was recorded, indicating the ONBM be switched back to the logic "0" (or "off") state. Upon applying the reading voltage, the OBIRCH ΔI image of the device under the "0" state was also recorded and is shown in Fig. 6(a). In contrast to the OBIRCH image in the "1" state, the "0" state image is homogeneous and no singular points (i.e. locations of relatively significant thermally induced

[1] For interpretation to color in the text, the reader is referred to the web version of this article.

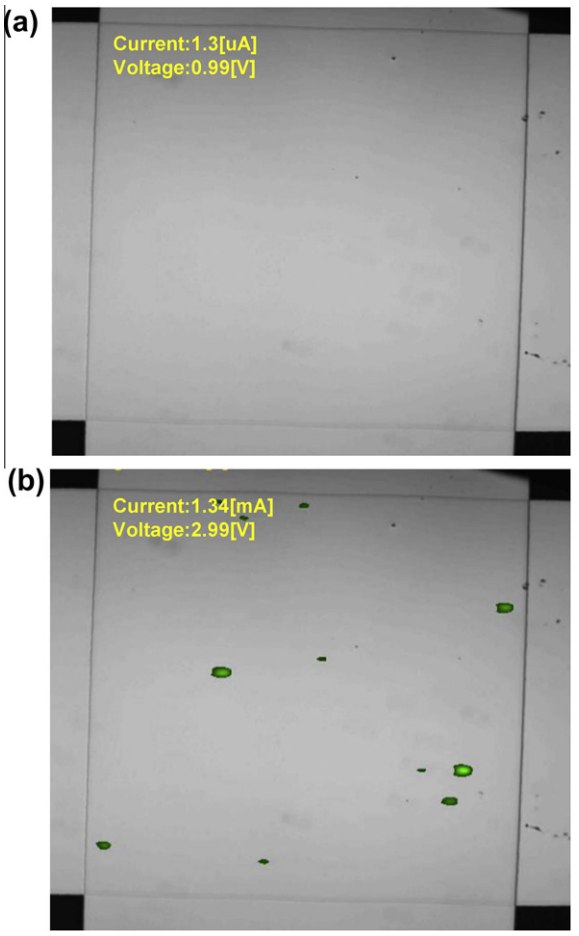

Fig. 6. OBIRCH ΔI images of the ONBM device in Fig. 5: (a) recorded upon applying the 1-V reading voltage (i.e. in the reading mode) after the erasing process, and (b) recorded upon subsequently applying a writing voltage of nearly 3 V again.

ΔI) occur in the image. When a writing voltage of nearly 3 V was applied again, in addition to the relatively large current (1.34 mA), localized current paths (marked as green[2] points in the OBIRCH ΔI image Fig. 6(b) recorded simultaneously) were found again. Similar localized current transport paths were also observed in the subsequent reading mode (e.g. with applying a smaller bias voltage of 1 V after writing). However, locations of the current paths in Fig. 6(b) are different from the previous current paths found in Fig. 5(a) and (b). Such results indicate that although the localized current transport paths established in each writing process would remain for the ONBM device to sustain the "1" state till the subsequent erasing operation, yet the localized current transport paths established vary from writing to writing. According to the previous model we established for the Au nanoparticle ONBM, the current conduction state is associated with the filling status of the trap levels of Au nanoparticles. During each erasing process, filled trap levels would be evacuated. The established conduction paths would be eliminated and the device would return to the low-conductivity state. In the subsequent writing process, some trap-filled high -conductivity paths would be established again, somehow randomly and varied from writing to writing, with filling trap levels of Au nanoparticles along the conduction paths. Such phenomena might have significant implications to operation or applications of such or similar devices. For instance, it may have impacts on how much one can shrink the device size. When the device area is largely reduced, such phenomena may affect the device-to-device variation in a memory array, the writing to writing variation of a device, or the long-term operation of devices. It may be worthy of further studies.

[2] For interpretation to color in the text, the reader is referred to the web version of this article.

4. Conclusions

In summary, the so-called optical beam induced resistance change (OBIRCH) method, which is a non-destructive characterization method, was adopted to investigate the spatial distribution of current transport paths in Au nanoparticle nonvolatile bistable memory devices. With using a scanning laser beam as a thermal source to induce local changes of the temperature and the electronic/conduction properties, simultaneously the current change of the device (under the constant bias voltage) at each scanning step was recorded to visualize the distribution of the current conduction paths in devices. The results reveal that in the bistable memory devices using polymer-stabilized Au nanoparticles, the current transport paths during the writing mode or the subsequent reading mode (of the "on" state) are localized, and that once the localized current transport paths are established in the writing mode, the current transport in the subsequent reading mode (of the "on" state) would basically follow the same paths. The established conduction paths would be eliminated in the erasing process and re-established in the next writing process. Yet, the current conduction paths established for the "on" state are somehow random and vary from writing to writing. Results of this work might have significant implications to operation or applications of such memory devices. This work demonstrates that the OBIRCH technique might be an useful method to characterize localized current transport paths in organic devices.

Acknowledgements

The authors gratefully acknowledge the financial support from the Ministry of Economic Affairs, Taiwan, ROC.

References

[1] J.H. Burroughes, D.D.C. Bradley, A.R. Brown, R.N. Marks, K. Mackay, R.H. Friend, P.L. Burns, A.B. Holmes, Nature 347 (1990) 539.
[2] H. Sirringhuas, N. Tessler, R.H. Friend, Science 280 (1998) 1741.
[3] G. Tu, J. Gao, J.C. Hummelen, F. Wudl, A.J. Heeger, Science 270 (1995) 1789.
[4] H.T. Lin, Z. Pei, J.R. Chen, G.W. Hwang, J.F. Fan, Y.J. Chan, IEEE Electron Device Letters 28 (2007) 951.
[5] H.T. Lin, Z. Pei, Y.J. Chan, IEEE Electron Device Letters 28 (2007) 569.
[6] M.A. Lampert, P. Mark, Current injection in Solids, Academic Press, New York, 1970.

[7] Y. Li, H. Zhong, R. Li, Y. Zhou, C. Yang, Y. Li, Advanced Functional Materials 16 (2006) 1705.
[8] K. Mohanta, S.K. Majee, S.K. Batabyal, A.J. Pal, Journal of Physical Chemistry B 110 (2006) 18231.
[9] J. Chen, M.A. Reed, A.M. Rawlett, J.M. Tour, Science 286 (1999) 1550.
[10] C.P. Collier, E.W. Wong, M. Belohradsky, F.M. Raymo, J.F. Stoddart, P.J. Kuekes, R.S. Williams, J.R. Heath, Science 285 (1999) 391.
[11] Z.J. Donhauser, B.A. Mantooth, K.F. Kelly, L.A. Bumm, J.D. Monnell, J.J. Stapleton, D.W. Price Jr., A.M. Rawlett, D.L. Allara, J.M. Tour, P.S. Weiss, Science 292 (2001) 2303.
[12] A. Bandyopadhyay, A.J. Pal, Applied Physics Letters 82 (2003) 1215.
[13] T. Oyamada, H. Tanaka, K. Matsushige, H. Sasabe, C. Adachi, Applied Physics Letters 83 (2003) 1252.
[14] C.C. Chang, Z. Pei, Y.J. Chan, Applied Physics Letters 93 (2008) 143302.
[15] H.T. Lin, Z. Pei, J.R. Chen, C.P. Kung, Y.C. Lin, C.M. Tseng, Y.J. Chan, IEDM Technical Digest (2007) 233.
[16] R.J. Tseng, J. Huang, J. Ouyang, R.B. Kaner, Y. Yang, Nano Letters 5 (2005) 1077.
[17] D.T. Simon, M.S. Griffo, R.A. Dipietro, S.A. Swanson, S.A. Carter, Applied Physics Letters 89 (2006) 133510.
[18] L.D. Bozano, B.W. Kean, V.R. Deline, J.R. Salem, J.C. Scott, Applied Physics Letters 84 (2004) 607.
[19] S. Möller, C. Perlov, W. Jackson, C. Taussig, S.R. Forrest, Nature 426 (2003) 166.
[20] J. Wu, L. Ma, Y. Yang, Physical Review A 69 (2004) 115321.
[21] J. Ouyang, C. Chu, C. Szmanda, Y. Yang, Nature Materials 3 (2004) 918.
[22] L.D. Bozano, B.W. Kean, M. Beinhoff, K.R. Carter, P.M. Rice, J.C. Scott, Advanced Functional Materials 15 (2005) 1933.
[23] K. Nikawa, C. Matsumoto, S. Inoue, Japaneese Journal of Applied Letters 34 (1995) 2260.

tum efficiency due to charge balance in the emitting layer. The highly efficient deep-blue OLEDs can surely be realized by using bipolar host materials without employing a DEL structure, and thus, one of the key methods of simplifying the device structure of deep-blue POLEDs is the development of a suitable host material. It has been difficult to synthesize a bipolar host material with high E_T to confine the triplets of deep-blue dopant in the guest. The only molecular architecture that combines high E_T and bipolar carrier transport properties has been realized by combining a hole-transporting carbazole substituent and an electron-transporting phosphine oxide (phosphine sulfide) substituent [19–23]. The novel molecular architecture should be proposed to discuss more about the effect of such a bipolar host material on the efficiency of simplified deep-blue POLEDs.

In this paper, we report on a new bipolar host material for use in simply structured, deep-blue POLEDs, 2-[(4-carbazolyl-9-yl)phenyl]-2-[(4-pyridoindolyl-9-yl)phenyl]adamantane (Ad-CzPd). The simplified POLED consists of only three layers, namely, a hole-transporting layer, an emitting layer, and an electron-transporting layer, yet the η_{EQE} of the FIr6-based POLED is 13% at a current density (J) of 0.1 mA/cm^2. This efficiency is three times higher than the previously reported value for the same device structure [14]. The new host has both a hole-transporting carbazole substituent [16] and an electron-transporting pyridoindole substituent [18]. By combining these two substituents, an ideal host for a blue POLED, which exhibits both high E_T and bipolar transportability, can be realized. We have found that this novel molecular architecture is useful for simplifying and fabricating highly efficient, deep-blue POLED devices, since it distributes the carrier recombination region within the emitting layer.

2. Experimental

2.1. Preparation of Ad-CzPd

Ad-CzPd was synthesized by the reactions outlined in Scheme 1. 2,2-Bis(4-aminophenyl)damantane **1** was synthesized by adapting the dehydration method [24]. The reaction of 2-adamantanone with aniline and aniline hydrogen chloride in refluxing produced bis-aminophenyl product 1. Bis-iodophenyl product 2 was synthesized by the Sandmeyer reaction, in which aromatic amino compounds were converted into halogeno benzene derivatives. The nucleophilic aromatic substitution of 2 with 5H-pyrido[4,3-b]indole in the presence of Cu furnished monoiodophenyl intermediate 3. Furthermore, nucleophilic aromatic substitution of 3 with carbazole in the presence of Cu furnished the desired product Ad-CzPd.

The structure of Ad-CzPd was identified using NMR. The following 37 hydrogen signals were detected by ^{1}H NMR ($CDCl_3$, 600 MHz): δ 9.4 (1H, s), 8.5 (1H, d, J = 5.5 Hz), 8.2 (1H, d, J = 7.6 Hz), 8.1 (2H, d, J = 7.6 Hz), 7.7 (4H, dd, J = 19.2, 7.8 Hz), 7.5–7.4 (6H, m), 7.4–7.3 (4H, m), 7.3 (4H, dd, J = 19.2, 7.8 Hz), 3.4 (2H, s), 2.2 (4H, t, J = 13.7 Hz), 2.0 (2H, s), 1.9 (4H, d, J = 12.4 Hz), 1.8 (2H, d).

Ad-CzPd showed excellent thermal properties with a glass transition temperature (T_g) of 165 °C and a melting point of 345 °C, both of which are determined by differential scanning calorimetry. The purity of Ad-CzPd confirmed to be over 99% from high performance liquid chromatography.

2.2. Device fabrication

To clarify the carrier transportability of Ad-CzPd, we compared the hole and electron transport properties of Ad-CzPd, Ad-Cz and Ad-Pd thin films in the hole-only and electron-only devices, as shown in Fig. 1a and b. Furthermore, we compared the carrier transport properties of Ad-CzPd and 4,4′-bis(*N*-carbazolyl)-1,1′-biphenyl (CBP), which is a well-known bipolar host material [19]. The structure of the hole-only device is ITO/PEDOT:PSS (35 nm)/α-NPD (8 nm)/Ad-CzPd or Ad-Cz or Ad-Pd or CBP (60 nm)/α-NPD (8 nm)/Al (100 nm) (ITO: indium-tin oxide; PEDOT:PSS: poly(3,4-ethylenedioxythiophene)/poly(styrene sulfonic acid); α-NPD: 4,4′-bis[*N*-(1-naphthyl)-*N*-phenyl-amino]biphenyl). The structure of the electron-only device is ITO/PEDOT:PSS (35 nm)/UGH2 (10 nm)/Ad-CzPd or Ad-Cz or Ad-Pd or CBP (40 nm)/TmPyPB (20 nm)/LiF (1 nm)/Al (100 nm) (UGH2: *p*-bis(triphenylsilyly) benzene; TmPyPB: 1,3,5-tris(*N*-phenylbenzimidazol-2-yl)benzene) [11,13]. Then, we developed three types of FIr6-based OLEDs as shown in Fig. 1c. The device structure is ITO/PEDOT:PSS (35 nm)/TAPC (40 nm)/3 wt.% FIr6 in Ad-Cz or Ad-Pd or Ad-CzPd (35 nm)/TmPyPB (40 nm)/LiF (1 nm)/Al (100 nm) (TAPC: 1,1-bis[(di-4-tolylamino)phenyl] cyclohexane). Since TmPyPB has a relatively high E_T in a commercially available electron-transporting material, we selected it as the electron-transporting/hole-blocking layer [11]. The hole-only and electron-only devices, and POLEDs were developed on a glass substrate coated with a 150-nm-thick indium-tin oxide (ITO) layer. Prior to the fabrication of the organic layers, the substrate was cleaned with ultra-purified water and organic solvents, and treated with a UV-ozone ambient. To reduce the possibility of electrical shorts within the device, PEDOT:PSS, diluted in water, was spun onto the substrate to form a 35-nm-thick PEDOT:PSS layer after being baked for 1 h at 180 °C. The other organic layers were sequentially deposited onto the substrate without breaking the vacuum at a pressure of about 10^{-5} Pa. After cathode formation, the devices were encapsulated using a UV-epoxy resin and a glass cover within a nitrogen atmosphere. The electroluminescent (EL) spectra and luminance were measured with a spectroradiometer (Minolta CS-1000). A digital source meter (Keithley 2400) and a desktop computer used to operate the devices were connected. We assumed that the emission from the OLED device was isotropic, such that the luminance was Lambertian, and calculated the η_{EQE} from the luminance (L), J, and EL spectra.

3. Results and discussion

Fig. 2 shows the molecular structure and absorption spectrum of Ad-CzPd. The optical band gap (E_g) of Ad-CzPd was estimated to be 3.5 eV from the cutoff wavelength of the absorption peak (354 nm). The ionization potential (IP) of Ad-CzPd was estimated to be 5.9 eV (close to that

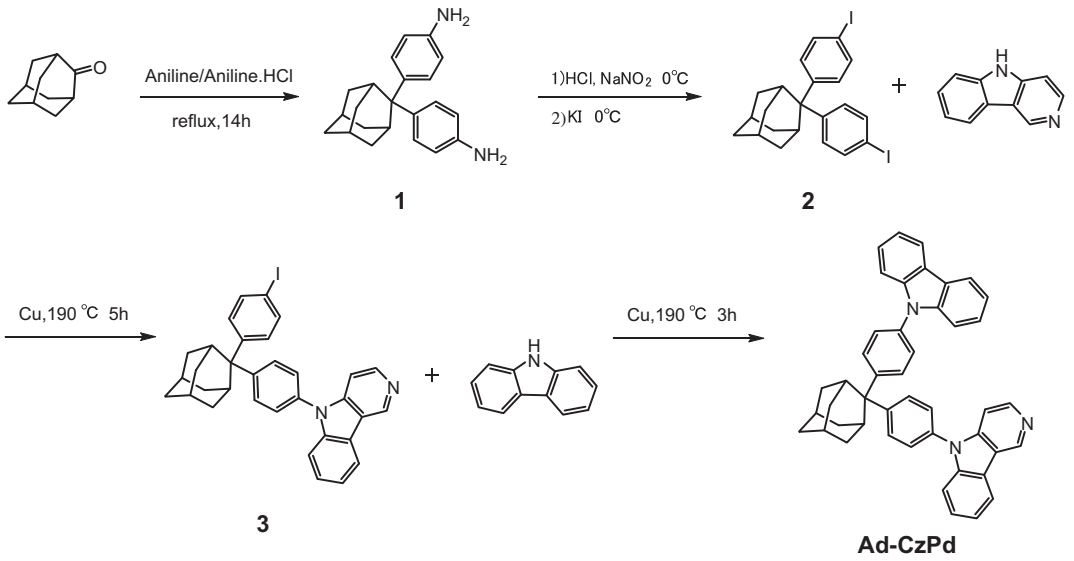

Scheme 1. Synthesis of Ad-CzPd.

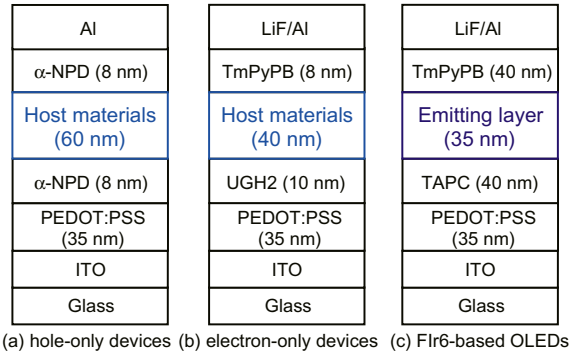

Fig. 1. Structures of (a) hole-only and (b) electron-only devices, and (c) FIr6-based OLEDs.

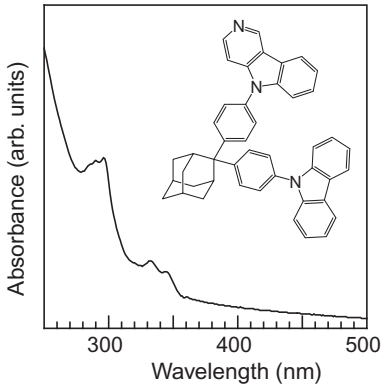

Fig. 2. UV–vis absorption spectrum of Ad-CzPd.

of 2,2-bis(4-carbazolyl-9-ylphenyl)adamantane (AdCz)) from spectroscopic measurements of the photoemission in air (AC-3, Rikenkeiki) [16]. We estimated the electron affinity of Ad-CzPd to be 2.4 eV (close to that of 2,2-bis(4-pyridoindolyl-9-ylphenyl)adamantane (Ad-Pd)) by subtracting E_g from IP [18]. The photoluminescence (PL) efficiency (Φ_{PL}) of the FIr6-doped Ad-CzPd film was measured using an absolute PL quantum yield measurement system (C9920, Hamamatsu), and it was found that the Φ_{PL} of the 6 wt.% film (82%) is higher than that of the FIr6-doped Ad-Cz film [16]. From this observation, we confirmed that the triplet energy transfer from FIr6 to Ad-CzPd is completely suppressed and the energy is confined in FIr6.

Fig. 3 shows the current density-applied voltage (J–V) characteristics of (a) a hole-only device and (b) an electron-only device. The Ad-Cz-based device shows the highest current density in the hole-only device, while the corresponding electron-only device shows the lowest current density. In contrast, the Ad-Pd-based device shows the highest current density at a low electric field in the electron-only device, while the corresponding hole-only device shows the lowest current density. These results clearly demonstrate that the carbazole substituent transports holes and the pyridoindole substituent transports electrons [16,18]. It is evident that the Ad-CzPd-based device has a similar current density to the CBP-based device, indicating the bipolar carrier transportability of Ad-CzPd [25]. Thus, Ad-CzPd is likely to be a suitable host for a simply structured blue POLED because of its high E_T and bipolar transportability.

The J–V–L characteristics of three types of FIr6-based OLED device are shown in Fig. 4a. The Ad-Cz-based device appears to have a higher current density than the Ad-Pd-based device. This difference is expected to be caused by the differences in carrier injection/transport properties. Not only is the carrier injection barrier at the anode/organic layer interface smaller than that at the cathode/organic

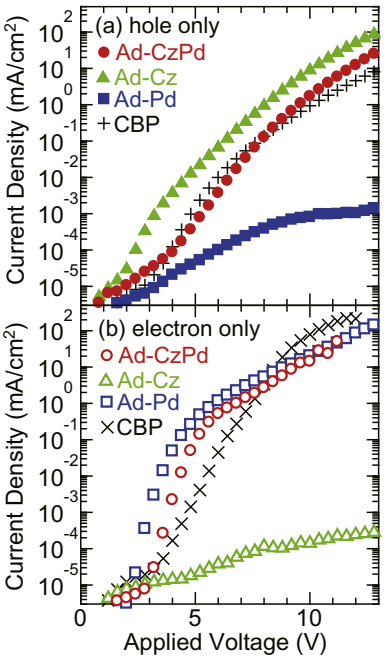

Fig. 3. Current density–voltage characteristics of (a) hole-only and (b) electron-only devices.

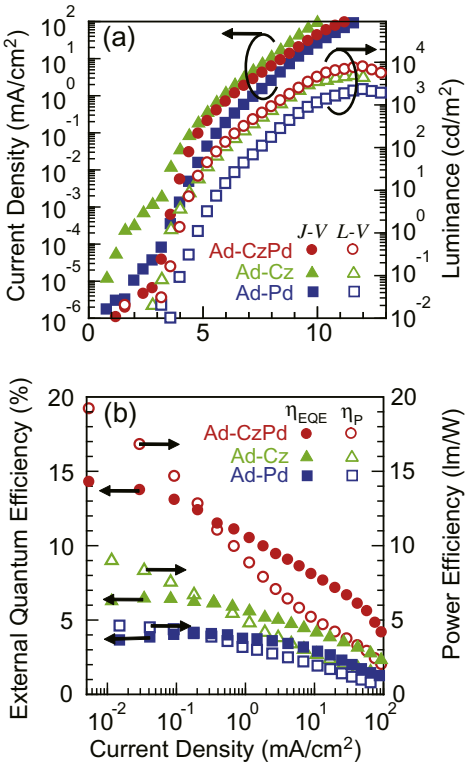

Fig. 4. (a) Current–density (J, left) and luminance (L, right) voltage characteristics of three devices. (b) External quantum efficiency (η_{EQE}, left) and power efficiency (η_P, right) current density characteristics of three devices.

layer interface, but also the hole mobility of TAPC is higher than the electron mobility of TmPyPB [11,26]. Thus, it is reasonable to suppose that the Ad-Cz-based device, the host material of which can transport holes, has an advantage in carrier recombination. The current density of the Ad-CzPd-based device is between those of the other two devices. Fig. 4b shows the η_{EQE} and power efficiency (η_P) of each device. The Ad-CzPd-based device has the largest maximum η_{EQE} of 14%. This efficiency can be explained by the distribution of the carrier recombination region within the emitting layer [16].

Fig. 5 shows the EL spectra of the Ad-Pd and Ad-CzPd-based devices driven at 1 mA/cm^2. In both OLEDs, the shape of the EL spectrum is almost independent of current density. The EL spectrum of the Ad-Pd-based device shows a residual emission at around 570 nm. Although the vibrational peak was intensified in the Ad-Pd-based device because of the difference in recombination zone [20,27], the small change in the intensity of the vibrational peak at 570 nm is expected [14,20]. Thus, the emission can be attributed to the emission from the electromer of TAPC, since the carrier recombination region is localized at the TAPC/emission layer interface because of the electron transportability of Ad-Pd [28]. In fact, the Ad-Pd-based device shows η_{EQE} of about 10% by inserting the thin Ad-Cz layer (10 nm) between TAPC and the emitting layer, where the residual emission is not observed (not shown). As we have reported on the Ad-Cz-based device, residual emissions not from the guest material reduce the efficiency of POLEDs [16]. Unlike the EL spectrum of the Ad-Pd-based device, the EL spectrum of the Ad-CzPd-based device does not show any residual emissions from the host and/or adjacent layer, indicating an almost complete energy and/or charge transfer from the host exciton to the guest upon the electrical excitation and excellent confinement of charge carriers and excitons in the emitting layer. By employing a bipolar host material with high E_T, the carrier recombination region is distributed over the emitting layer. Such a distribution of the recombination region was previously achieved by employing a DEL structure [15–18] and/or bipolar host materials that consist of carbazole and phosphine oxide (phosphine sulfide) substituents

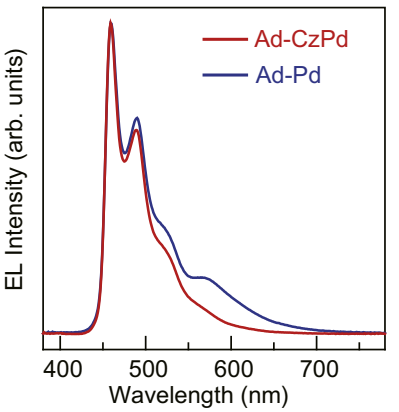

Fig. 5. EL spectra for two types of FIr6-based OLED devices. The host of one device is Ad-CzPd, and that of the other is Ad-Pd.

Table 1
Comparison of turn-on voltage, external quantum efficiency (η_{EQE}), power efficiency (η_P) values, and CIE coordinates of three different devices. The efficiencies are for a current density of 0.1 mA/cm^2. η_{EQE}, η_P: value at current density of 0.1 mA/cm^2.

Configuration (number) of organic layer	Turn-on voltage (V)	η_{EQE} (%)	η_P (lm/W)	CIE (x, y)	Ref.
TAPC/Ad-CzPd:FIr6/TmPyPB (three)	3.6	13	15	(0.16, 0.26)	This work
TAPC/UGH2:FIr6/BCP (three)	–	5	5	–	Ref. [14]
TAPC/mCP/UGH2:FIr6/BCP (four)	4.1	15	14	(0.16, 0.27)	Ref. [14]

[19–23]. Here, we have demonstrated that the distribution of the carrier recombination region in deep-blue POLEDs can be achieved by employing a bipolar host material that consists of carbazole and pyridoindole substituents. An efficient FIr6 emission is obtained in the simply structured POLED by using a bipolar host material with a novel molecular architecture.

Table 1 shows the device structures (organic layer configurations), turn-on voltages, efficiencies, and Commission Internationale de L'Eclairage (CIE) coordinates of an Ad-CzPd-based POLED and other FIr6-doped POLEDs. Turn-on voltage is defined as the voltage corresponding to a luminance of 0.1 cd/m^2. The efficiencies of the Ad-CzPd-based device are approximately three times higher than those of a similarly structured device [14]. Although its η_{EQE} is slightly lower than that of the four-layer device, its η_P is slightly higher [14]. This difference in η_P is caused by the difference in turn-on voltage (driving voltage). The turn-on voltage of the conventional device is higher because of the use of the poor electron-transporting material UGH2 [18]. The bipolar host material with high E_T not only is very efficient, but also reduces the driving voltage by not using a low conductivity material.

Finally, we discuss the efficiency of the Ad-CzPd-based POLED in the high-current–density region. Although the Ad-CzPd exhibits bipolar carrier transportability, a roll-off of efficiency is observed, as shown in Fig. 4b. Such a roll-off of efficiency is observed not only in our Ad-CzPd-based POLED but also in other bipolar-host-based deep-blue POLEDs [19–22]. On the other hand, Jeon et al. have realized a deep-blue POLED with high quantum efficiency and low efficiency roll-off [23]. They proposed that the important parameters for realizing high efficiency and low efficiency roll-off are bipolar charge transport properties of the host, balanced charge injection, triplet exciton confinement in the emitting layer and triplet exciton confinement by carrier-transporting layers. If we take these parameters into consideration, the triplet exciton should be confined by the carrier-transporting layer in our Ad-CzPd-based OLED to suppress the roll-off of efficiency. Although the E_T of TAPC is sufficiently high to confine the triplet excitons of FIr6, the E_T of TmPyPB is similar to that of FIr6, which leads to triplet exciton quenching [11,14,23,29,30]. Unlike the DEL-structured device, the carrier recombination region is directly located in the carrier-transporting layer in simply structured device. Thus, the development of the carrier transporting layer with high E_T is another problem in the simplification of the device structure of efficient blue POLEDs.

4. Summary

We succeeded in developing a simply structured, deep-blue POLED by using a bipolar host material with high E_T. The novel molecular architecture that combines high E_T and bipolar carrier transport properties was realized by combining a hole-transporting carbazole substituent with an electron-transporting pyridoindole substituent. The simplified device consists of three organic layers, and it had a maximum η_{EQE} of about 13% and η_P of about 15 lm/W at a current density of 0.1 mA/cm^2. Residual emissions were prevented by distributing the carrier recombination region within the emitting layer. The efficiency of the three-layer POLED was found to be comparable to that of a conventional four-layer POLED. We believe that the bipolar host material with high E_T will be useful for fabricating simple, highly efficient, deep-blue POLEDs.

References

[1] M.A. Baldo, D.F. O'Brien, Y. You, A. Shoustikov, S. Sibley, M.E. Thompson, S.R. Forrest, Nature 395 (1998) 151.
[2] M.A. Baldo, M.E. Thompson, S.R. Forrest, Nature 403 (1998) 750.
[3] C. Adachi, M.A. Baldo, M.E. Thompson, S.R. Forrest, J. Appl. Phys. 90 (2001) 5048.
[4] M. Pfeiffer, S.R. Forrest, K. Leo, M.E. Thompson, Adv. Mater. 14 (2002) 1633.
[5] S. Watanabe, N. Ide, J. Kido, Jpn. J. Appl. Phys. 46 (2007) 1186.
[6] T.J. Park, W.S. Jeon, J.J. Park, S.Y. Kim, Y.K. Lee, J. Jang, J.H. Kwon, R. Pode, Appl. Phys. Lett. 92 (2008) 113308.
[7] Z.Q. Gao, M. Luo, X.H. Sun, H.L. Tam, M.S. Wong, B.X. Mi, P.F. Xia, K.W. Cheah, C.H. Chen, Adv. Mater. 21 (2009) 688.
[8] C. Adachi, R.C. Kwong, P. Djurovich, V. Adamovich, M.A. Baldo, M.E. Thompson, S.R. Forrest, Appl. Phys. Lett. 79 (2001) 2082.
[9] S. Tokito, T. Iijima, T. Tsuzuki, F. Sato, Appl. Phys. Lett. 83 (2003) 2459.
[10] D. Tanaka, Y. Agata, T. Takeda, S. Watanabe, J. Kido, Jpn. J. Appl. Phys. 46 (2007) L117.
[11] S.J. Su, T. Chiba, T. Takeda, J. Kido, Adv. Mater. 20 (2008) 2125.
[12] R.J. Holmes, S.R. Forrest, Y.-J. Tung, R.C. Kwong, J.J. Brown, S. Garon, M.E. Thompson, Appl. Phys. Lett. 82 (2003) 2422.
[13] R.J. Holmes, B.W. D'Andrade, S.R. Forrest, X. Ren, J. Li, M.E. Thompson, Appl. Phys. Lett. 83 (2003) 3818.
[14] Y. Zheng, S.H. Eom, N. Chopra, J. Lee, F. So, J. Xue, Appl. Phys. Lett. 92 (2008) 223301.
[15] S.H. Eom, Y. Zheng, N. Chopra, J. Lee, F. So, J. Xue, Appl. Phys. Lett. 93 (2008) 133309.
[16] H. Fukagawa, K. Watanabe, T. Tsuzuki, S. Tokito, Appl. Phys. Lett. 93 (2008) 133312.
[17] S.H. Eom, Y. Zheng, E. Wrzesniewski, J. Lee, N. Chopra, F. So, J. Xue, Org. Electro. 10 (2009) 686.
[18] H. Fukagawa, N. Yokoyama, S. Irisa, S. Tokito, Adv. Mater. 22 (2010) 4775.
[19] S.O. Jeon, K.S. Yook, C.W. Joo, J.Y. Lee, Adv. Funct. Mater. 19 (2009) 3644.
[20] S.O. Jeon, K.S. Yook, C.W. Joo, J.Y. Lee, Adv. Mater. 22 (2010) 1.
[21] H. Chou, C. Cheng, Adv. Mater. 22 (2010) 2468.
[22] H. Sasabe, J. Takamatsu, T. Motoyama, S. Watanabe, G. Wagenblast, N. Langer, O. Molt, E. Fuchs, C. Lennartz, J. Kido, Adv. Mater. 22 (2010) 5003.
[23] S.O. Jeon, S.E. Jang, H.S. Son, J.Y. Lee, Adv. Mater. 23 (2011) 1436.
[24] M.H. Yi, W. Huang, B.J. Lee, K.Y. Cho, J. Poly. Sci., Part A: Poly. Chem. 37 (1999) 3449.
[25] S. Liu, B. Li, L. Zhang, H. Song, H. Jiang, Appl. Phys. Lett. 97 (2010) 083304.

[26] P. Strohriegl, J.V. Grazulevicius, Adv. Mater. 14 (2002) 1439.
[27] B.D. Chin, N.S. Kang, J.-W. Yu, S.M. Jo, J.Y. Lee, J. Appl. Phys. 102 (2007) 024506.
[28] J. Kalinowski, G. Giro, M. Cocchi, V. Fattori, P. Di Marco, Appl. Phys. Lett. 76 (2000) 2352.
[29] M. Ikai, S. Tokito, Y. Sakamoto, T. Suzuki, Y. Taga, Appl. Phys. Lett. 79 (2001) 156.
[30] V.I. Adamovich, S.R. Cordero, P.I. Djurovich, A. Tamayo, M.E. Thompson, B.W. D'Andrade, S.R. Forrest, Org. Electron. 4 (2003) 77.

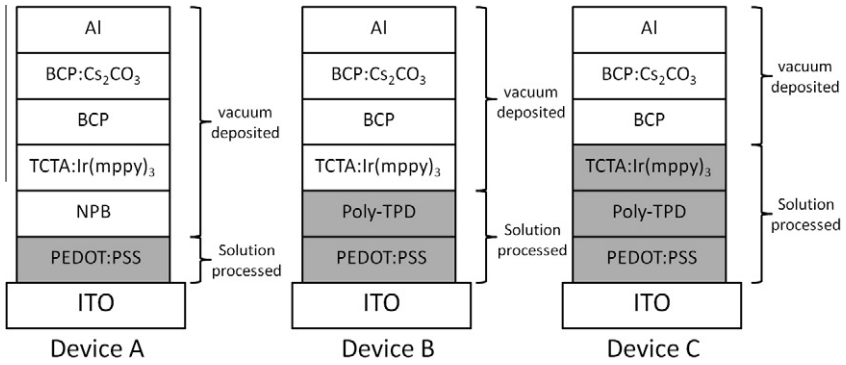

Fig. 1. The device architectures of the OLEDs fabricated in these experiments. The reference device A consists of a spincoated PEDOT:PSS hole injection layer (HIL) and evaporated small molecules. For device B the NPB hole transport (HTL) layer is replaced with a spincoated poly-TPD HTL and device C in which the first three layers including the emissive layer (EML) are solution processed.

ethylenedioxythiophene):poly(styrenesulfonic acid) (PEDOT:PSS) was used as hole injection layer (HIL). The main purpose of using a solution processed PEDOT:PSS HIL is the planarizing of the patterned ITO, while improving the injection into the subsequently deposited layers due to its relatively high work function (5.2 eV) [9]. In addition, the use of a heavily doped HIL eliminates the need for high work function anode materials, which allows the replacement of ITO by less expensive materials. For the reference device 10 nm of *N*,*N*′-bis(1-naphtalenyl)-*N*-*N*′-bis(phenylbenzidine) (NPB) was deposited on top of the PEDOT:PSS layer by thermal evaporation. For the hybrid devices a thin layer of a polyarylamine poly(*N*,*N*,(diphenyl)-*N*′,*N*′di-(4-hexylphenyl)-4,4′-biphenyldiamine (pTPD) was used as the hole transporting and electron blocking layer. It was spincoated on top of the PEDOT:PSS layer, annealed and rinsed twice with its solvent. After this treatment a thin insoluble layer of pPTD remains on which the light emitting layer can be deposited by spincoating from the same solvent. For the monochrome devices the emissive layer consisted either of a combination of a 2,2′,7,7′-tetrakis-(*N*,*N*-diphenylamino)-9,9′-spirobifluoren (s-TAD) host doped with 10 wt.% of Iridium(III)bis(2-methyldibenzo-[f,h]quinoxaline)(acetylacetonate) (ADS076) red phosphorescent emitter or a 4,4′,4″-tris(carbazol-9-yl)triphenylamine (TCTA) host doped with 10 wt.% Iridium(III)tris(2-(4-tolyl)pyridinato-N,C) (Ir(mppy)$_3$) green phosphorescent emitter. ADS076 and Ir(mppy)$_3$ were chosen as emitter for their high luminescence and commercial availability. [10,11]. S-TAD and TCTA were chosen as the matrix molecules for their amorphous behavior after spincoating, ensuring good film forming properties [4]. For the monochrome devices, following the deposition of the emissive layer 10 nm layer of 2,9-dimethyl-4,7-diphenyl-1,10-phenanthroline (Bathocuproine, BCP) was thermally evaporated on top, which serves as a hole blocking layer. Subsequently, Cs_2CO_3 was co-evaporated with BCP in a 1 to 5 ratio (by wt.), forming a 30 nm doped electron injection/transport layer. An aluminum cathode was evaporated in a separate vacuum chamber to finish the devices, serving as both a top electrode and an optical mirror to increase the luminance through the transparent bottom contact. In the case of the white light emitting devices, prior to the hole blocking layer additional (green and blue) light emitting layers were deposited using thermal vacuum deposition techniques.

The organic layers were evaporated using thermal vacuum deposition at a base pressure of 10^{-6} mbar in a high-vacuum chamber integrated in an inert-atmosphere (<0.1 ppm O_2 and H_2O) glove box. The aluminum cathode was thermally evaporated at a pressure of 10^{-6} mbar in a separate chamber in the same glove box. Current density and luminance versus voltage characteristics were measured using a Keithley 2400 source meter and a photodiode coupled to a Keithley 6485 pico-amperometer using a Minolta LS100 for calibration of the photodiode. The EL spectrum was measured using an Avantes luminance spectrometer. The thicknesses of the solution processed layers were determined using an Ambios XP1 profilometer. The thicknesses of the evaporated layers were monitored by calibrated quartz-crystal sensors.

3. Results and discussion

3.1. Replacement of hole transport layer

The current density *(J)* and luminance *(L)* versus voltage *(V)* characteristics of the reference device are shown in Figs. 2 and 3. Low turn-on voltages were obtained while the luminous efficiencies of 40 cd/A (see Fig. 4) and 40 lm/W are in the range of what can be expected using an Ir(mppy)$_3$ emitter. As a first step to investigate the influence of replacing thermally evaporated layers by solution processed layers, the NPB hole transport layer (HTL) was replaced by a spincoated poly[*N*,*N*′-bis(4-butylphenyl)-*N*,*N*′-bis(phenyl)benzidine] (poly-TPD) layer. The chemical structures and energy levels of poly-TPD and NPB resemble each other closely, making poly-TPD an appropriate substituent. An important benefit of using poly-TPD as a solution processed HTL is that it forms an insoluble interlayer of a few nm when spincoated on PEDOT:PSS and annealed subsequently, a feature also observed in similar polymers [12–14]. This allows solution processing on top of the HTL, which is not possible using a HTL consisting of NPB. Furthermore, the thickness of the insoluble interlayer depends only on the annealing time and temperature, and

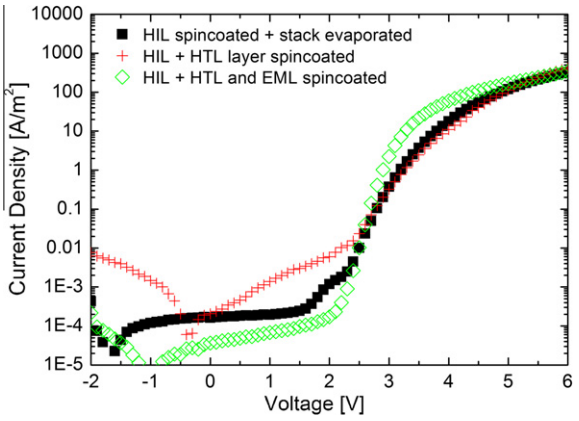

Fig. 2. Current density to voltage characteristics of the fabricated green OLEDs. Filled squares: the reference device A. Crosses: device B where the hole transport (HTL) layer is replaced with a spincoated poly-TPD HTL and finally device C (open diamonds) in which the first three layers including the emissive layer (EML) are solution processed. (For interpretation of the references to color in this figure legend, the reader is referred to the web version of this article.).

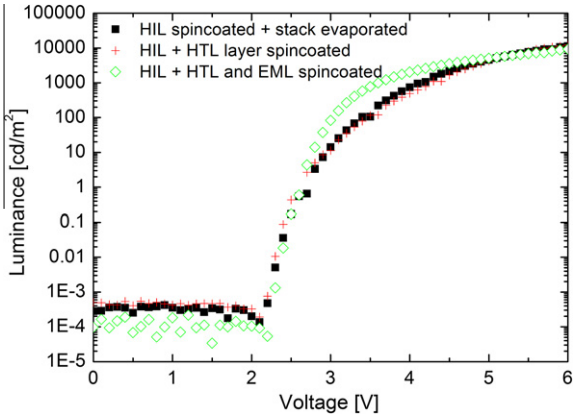

Fig. 3. Luminance versus voltage of the fabricated green OLEDs. Filled squares: the reference device A. Crosses: device B where the hole transport (HTL) layer is replaced with a spincoated poly-TPD HTL and finally device C (open diamonds) in which the first three layers including the emissive layer (EML) are solution processed. (For interpretation of the references to color in this figure legend, the reader is referred to the web version of this article.).

is independent on the initial thickness of the as-cast layer. This is advantageous for practical considerations, since the preparation of defect free layers at these thicknesses is challenging. Poly-TPD was spincoated on top of PEDOT:PSS from a chlorobenzene solution to give layers of approximately 20 nm. The layers were annealed at 150 °C for 30 min immediately after deposition. Subsequently, the soluble part of the poly-TPD layer was removed with a double chlorobenzene wash, leaving only the insoluble interlayer to remain. The subsequent layers were thermally evaporated following the procedure of the reference device. The *J–L–V* characteristics of the device with a poly-TPD HTL in comparison with the reference device are depicted in Figs. 2 and 3. The current density and luminance are in close resemblance. Moreover, there seems to be no loss in current efficiency when the NPB HTL is replaced by the poly-TPD HTL. Omission of a HTL does lead to a slight decrease in current efficiency whereas both the current density and luminance are higher (not shown).

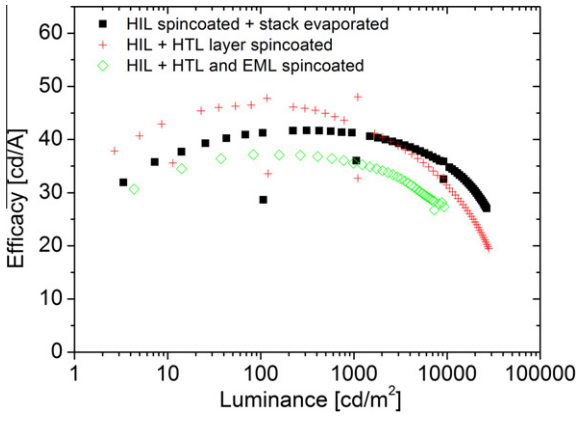

Fig. 4. Efficacy versus luminance of the fabricated green OLEDs. Filled squares: the reference device A. Crosses: device B where the hole transport (HTL) layer is replaced with a spincoated poly-TPD HTL and finally device C (open diamonds) in which the first three layers including the emissive layer (EML) are solution processed. (For interpretation of the references to color in this figure legend, the reader is referred to the web version of this article.).

3.2. Replacement of emitting layer

As the obtained poly-TPD interlayer is insoluble, the emitting layer (EML) can be solution processed on top of the HTL. For green emitting devices, a 20 nm layer of TCTA doped with $Ir(mppy)_3$ (16 wt.%) was spincoated from toluene solution on top of the HTL, followed by the evaporation of the subsequent layers. The obtained light emission is uniform for the whole device area, indicating that the thin emissive layer is defect-free. The feasibility of solution processing very thin and homogenous layers is indispensable to reduce the voltage drop and hence allow for high power efficiencies of wet-processed multilayer OLEDs, which is shown to be achieved using the small molecular TCTA host. From the *J–L–V* characteristics for this device and the reference device, as shown in Figs. 2 and 3, it can be observed that both the current densities as well as the luminance are in close resemblance. The similarity in performance can also be seen in the efficacy (Fig. 4), reaching maximum values close to 40 cd/A for all three described devices at a luminescence of 1000 cd/m^2.

To verify if these partially solution processed OLEDs can also yield competitive white light emitting diodes, a hybrid white light emitting device was prepared. First, in a similar approach to the green emitting device, a red emitting device was fabricated in which the first three layers are processed by spincoating. Here, a 20 nm layer of s-TAD doped with ADS076 (10 wt.%) was spincoated from a toluene solution on top of the HTL and HIL. Again, devices were completed by the evaporation of the hole blocking, electron injecting layers and the cathode resulting in similar

performances as obtained for a fully evaporated reference devices. Next, the emissive layer was complimented by subsequent thermal evaporation of green and blue emitter layers yielding a white OLED. Fig. 5 shows the *J–L–V* characteristics of the combined evaporated and solution processed device together with the fully evaporated reference device. The turn-on voltage for the two devices is identical. Also the luminance and current density versus voltage curves are very similar for the two devices, with the only difference the slightly lower current density and luminance values at higher voltages obtained for the partially solution processed device. This slightly lower luminance is reflected in the lower current efficiency values, reaching 8 cd/A versus 10 cd/A for the reference device. In both cases the current efficiency values remains practically the same up to high luminance values (2000 cd/m^2), which is an indication that in both devices the hole and electron current are quite well balanced. The electro-emission spectra for the partially solution processed device is practically the same as that of the reference device (Fig. 6, inset). For these white light emitting devices the effect of the different processing methods on the lifetime has been investigated. In Fig. 7 the luminance versus time characteristics are depicted with an initial luminance level of 700 cd/m^2. A similar stability for the devices with one layer and two layers out of solution is observed. For the device in which the first three layers are solution processed a stable long-term trend is observed as well. However, in contrast to the first two hybrid devices, where a negative burn-in effect is apparent, here a positive burn-in effect is evident followed by a more rapid degradation. Such an increase of the luminance with time was also reported in [15] but less pronounced. We ascribe the observed increase to morphology changes of the solution processed emitting layer, i.e. to some reorientations of the small molecules in the red emissive layer which are favored due to a rise in temperature during operation mode and potential out gassing of residual solvent. The inset of Fig. 6 shows the

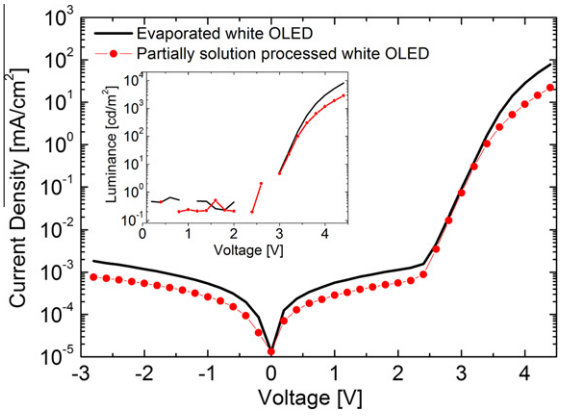

Fig. 5. Current density versus voltage characteristics of the fabricated white OLEDs. Black line: the evaporated reference device. Red dots: the partially solution processed device in which the first three layers including the red emissive layer (EML) are solution processed. Inset: luminance versus voltage characteristics. (For interpretation of the references to color in this figure legend, the reader is referred to the web version of this article.)

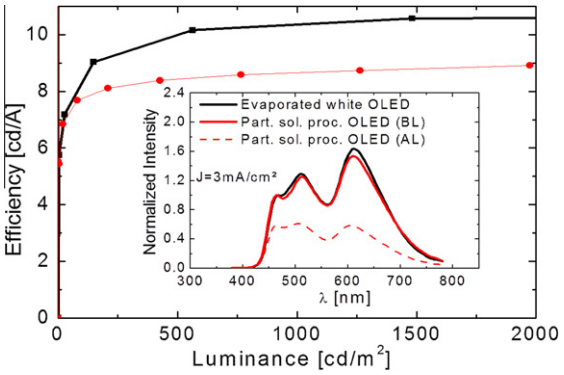

Fig. 6. Luminance efficiency versus luminance characteristics of the fabricated white OLEDs. Black line: the evaporated reference device. Red dots: the partly solution processed device in which the first three layers including the red emissive layer (EML) are solution processed. Inset: the electroluminescence profile of both devices obtained at a current density of 3 mA/cm^2, and the electroluminescence profile (red dotted line) for the partly solution processed device after having reached the half of the initial luminance value. (For interpretation of the references to color in this figure legend, the reader is referred to the web version of this article.)

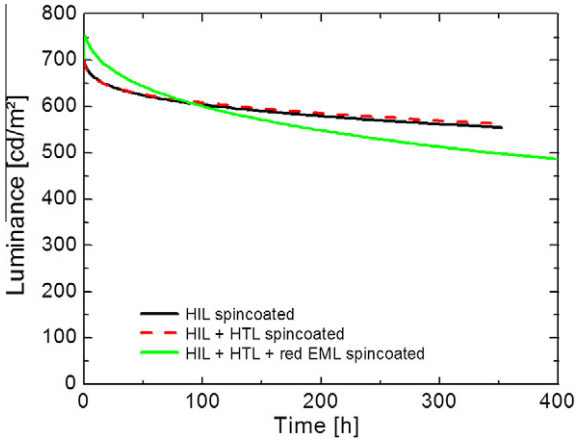

Fig. 7. Luminance versus time characteristics for the white OLEDs with an initial luminance level of 700 cd/m^2.

electroluminescence spectrum for the three layer from solution device after a luminance decay of more than 50%. What can be observed is that the red emission has decreased slightly more than the blue and green emission, indicating that the solution processed red layer is the least stable part. And although not studied in detail this implies that device C (Fig. 1) most likely has a similar or higher lifetime. We would like to point out that even the three layer approach shows stable and promising lifetime results. Lifetimes (time to reach 50% of initial luminance) can be extrapolated to more than 1000 h for the OLED containing three layers processed from solution and approximately 2000 h for both references. To the best of our knowledge these are the best lifetime values found for white hybrid architectures based on solution processed polymers and small molecules so far. Considering these results, a partly

solution processed device can be a competitive alternative to completely evaporated OLEDs.

4. Conclusions

In conclusion, we have shown the fabrication of highly efficient, partly solution processed phosphorescent OLEDs with small molecular host materials. Evaporated layers in an optimized reference device were stepwise replaced by solution processed layers. Replacing the evaporated NPB HTL by a solution processed poly-TPD interlayer did not affect the performance and allows spincoating of the emissive layer after annealing. Comparable results for a solution processed and evaporated EML were obtained for a red and green emitting device and for the red emitting layer of a white OLED with lifetime in excess of 1000 h. This shows that solution processing can be a promising alternative to thermal evaporation, in order to reduce production costs.

Acknowledgement

This work has been supported by the European Union (CombOLED, STRP 215934) and the Generalitat Valenciana.

References

[1] S. Reineke, F. Lindner, G. Schwartz, N. Seidler, K. Walzer, B. Lüssem, K. Leo, Nature 459 (2009) 234.
[2] F. So, J. Kido, P. Burrows, MRS Bulletin 33 (2008) 663.
[3] N. Rehmann, D. Hertel, K. Meerholz, H. Becker, S. Heun, Applied Physics Letters 91 (2007) 103507.
[4] F. So, B. Krummacher, M.K. Mathai, D. Poplavskyy, S.A. Choulis, V.-E. Choong, Journal of Applied Physics 102 (2007) 091101.
[5] C.D. Müller, A. Falcou, N. Reckefuss, M. Rojahn, V. Wiederhirn, P. Rudati, H. Frohne, O. Nuyken, H. Becker, K. Meerholz, Nature 421 (2003) 829.
[6] J.J. Park, T.J. Park, W.S. Jeo, R. Pode, J. Jang, J.H. Kwon, E.-S. Yu, M.-Y. Chae, Organic Electronics 10 (2009) 189.
[7] H. Kim, Y. Buyn, R.R. Das, B.K. Choi, P.S. Ahn, Applied Physics Letters 91 (2007) 093512.
[8] H. Fukagawa, K. Watanabe, S. Tokito, Organic Electronics 10 (2009) 798.
[9] T.M. Brown, J.S. Kim, R.H. Friend, F. Cacialli, R. Daik, W.J. Feast, Applied Physics Letters 75 (1999) 1679.
[10] X. Yang, D. Neher, D. Hertel, T.K. Däubler, Advanced Materials 161 (2004) 161.
[11] X. Yang, D.C. Müller, D. Neher, K. Meerholz, Advanced Materials 18 (2006) 948.
[12] J.-S. Kim, R.H. Friend, I. Grizzi, J.H. Burroughes, Applied Physics Letters 87 (2005) 023506.
[13] S.A. Choulis, V.-E. Choong, M.K. Mathai, F. So, Applied Physics Letters 87 (2005) 113503.
[14] X.H. Yang, F. Jaiser, B. Stiller, D. Neher, F. Galbrecht, U. Scherf, Advanced Functional Materials 16 (2006) 2156.
[15] M. Ooe, S. Naka, H. Okada, H. Onnagawa, Japanese Journal of Applied Physics 45 (1A) (2006) 250–254.

expected in the direction parallel to the aligned grains [11]. The higher mobility was interpreted as better connectivity due to the existence of elongated polymer chains connecting two neighboring grains. These observations indicate that in addition to the appearance of crystalline grains, the connectivity between the grains is an important factor for charge transport.

Various microstructures have been realized by modifying chemical designs (e.g., regioregularity [12,13] and MW [10,14]), by applying different processing methods (e.g., using various boiling-point solvents [15,16] and changing deposition conditions [5,17]), or by employing different post-treatments [18,19]. Within liquid crystalline polymers in particular, thermal annealing – a typical example of post-treatment – plays an important role in self-healing, that is, in reducing the grain boundaries and increasing the average grain size. For instance, annealing of poly(2,5-bis(3-alkylthiophen-2-yl)thieno[3,2-b]thiophene) (PBTTT) thin films induces an extraordinary three-dimensional (3D) terrace structure that is composed of lamellar sheets stacked by interdigitated side chains in between [18,20].

The annealed film is then cooled down in order to form the solid thin film from the liquid crystalline phase. The recrystallization is a non-isothermal process, and accordingly, the cooling rate through the transition may affect the recrystallization process and the resultant microstructures of the thin films. This non-isothermal process is, however, not extensively studied; therefore, the correlation between the cooling rate and the microstructure is not yet known.

In this paper, we report that the cooling rate in the recrystallization from the liquid crystalline mesophase to the solid phase strongly influences on the microstructural morphology of PBTTT thin films and charge transport characteristics. Non-isothermal behavior in the recrystallization process is monitored by differential scanning calorimetry (DSC) measurements at various cooling rates. Microstructures of the films with different cooling rates are examined using AFM and two-dimensional grazing incidence wide-angle X-ray scattering (2D GIWAXS) experiments. Thin-film transistors (TFTs) with each resulting film as an active layer are fabricated. The transport characteristics show the dependence of charge transport on cooling rate from room temperature down to low temperatures.

2. Material and methods

Commercially available PBTTT-C14 (Merck Chemical Co.) was used as is. Thermal analysis of PBTTT was implemented using a differential scanning calorimeter (DSC 204 F1, NETZSCH). Powder PBTTT (3.69 mg) was used; it was heated at a rate of 10 °C/min and cooled at various rates under N_2 gas flow. Thin-film fabrication was performed in a glove box filled with N_2 gas. A heavily n-doped silicon (Si) wafer with a thermally grown 200 nm silicon dioxide (SiO_2) layer was used as a substrate. Before fabrication, substrates were completely dried at 120 °C on a hot plate in the glove box after sonication with acetone followed by ethanol. The substrates were treated with octatrichlorosilane (OTS) to make the surface hydrophobic. PBTTT solution was prepared at 0.5 wt% concentration in chlorobenzene. The heated solution (125 °C) was spin cast onto the substrate at 3000 rpm resulting in approximately 30 nm-thick films.

For an accurate measurement of sample annealing/cooling temperature at its equilibrium, a thermometer was attached to a large-mass metal plate which was placed on a conventional hot plate. Samples were placed on the metal plate and annealed at 150 °C above the liquid crystalline phase transition temperature for 10 min. Average cooling rates over the exothermic region were determined by monitoring temperature of the metal plate. AFM images were taken with Dimension 3100 (Veeco Instruments) operating in the tapping mode.

2D GIWAXS measurements were conducted at the 4C2 beamline of the Pohang Accelerator Laboratory at Pohang University of Science & Technology [21]. A monochromatized X-ray radiation source of 8.979 keV (wavelength $\lambda = 0.138$ nm) with a size of 0.5 mm (height) × 0.8 mm (width) was used. A 2D charge-coupled device (CCD) detector (MAR USA) producing 2D data of 2084 × 2084 pixel was used (where each pixel size is 57.6 × 57.6 μm^2). Samples were loaded on a homemade z-axis goniometer in a vacuum chamber. The exposure time for the measurements was 60 s.

TFT devices were fabricated with conventional top-contact geometry. The heavily n-doped substrate worked as a gate electrode. Source and drain electrodes were formed on the spin-coated polymer layer by thermal evaporation of 70 nm Au using a patterned shadow mask. The channel length (L) and channel width (W) were 50 μm and 2000 μm, respectively, with W/L = 40. All electrical measurements were performed with the Keithley 2636 Dual-Channel System SourceMeter. For temperature dependent transport measurements, samples were mounted on the cold head of a GM refrigerator (130GM, Leybold Cryogenics) where a Si thermometer (LakeShore Cryotronics) was attached. Every measurement was conducted after full thermal equilibrium was reached.

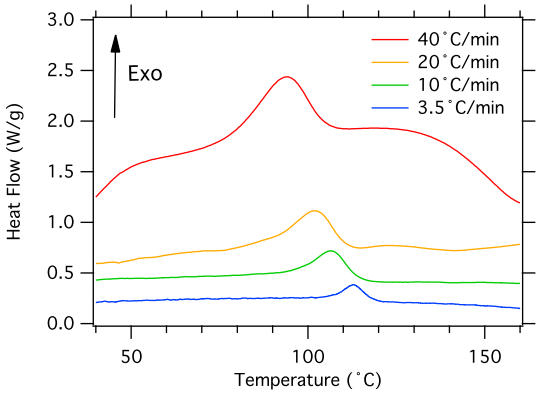

Fig. 1. DSC curves of PBTTT powder for various cooling rates.

Table 1
Exothermic peak parameters for various cooling rates.

Cooling rate (°C/min)	Peak position (°C)	ΔH (J/g)
40	77.6	15.21
20	90.3	20.87
10	97.5	26.48
3.5	112.9	26.02

3. Results and discussion

3.1. Non-isothermal recrystallization behavior

When a PBTTT film is formed on the substrate by deposition, innate defects hinder the construction of ordered microstructure. Annealing these films above the liquid crystalline phase transition temperature (T_H) induces side-chain melting and freely moving polymer backbones. Subsequent cooling of the films induces the well-ordered structures because defects in the films are removed, resulting in a 3D terrace structure with domains of typically several hundred nanometers in lateral size. This is the basic mechanism of self-healing via thermal treatment in the liquid crystalline polymers. Upon cooling below the recrystallization temperature (T_C), most of the high-quality structural order formed in the liquid crystalline phase is preserved by side chain interdigitation, which is attributed to the origin of the exceptional 3D registry between the layers in PBTTT. Simultaneous X-ray diffraction (XRD) measurements along the thermal cycle show that a reorganized structure is maintained throughout the recrystallization process [22].

We systematically studied the recrystallization process by measuring the thermal properties of PBTTT powder by DSC. The samples were first heated at a fixed rate of 10 °C/min and subsequently cooled at various cooling rates from 3.5 to 40 °C/min. The exothermic heat flow curves for various cooling rates are shown in Fig. 1. The exothermic behavior at a cooling rate of 10 °C/min is consistent with previously reported results [18,22]. When the sample is cooled from the liquid crystalline phase, the DSC curve shows a peak owing to the recrystallization transition, which is strongly dependent on the cooling rate. The key parameters of the recrystallization transition are listed in Table 1. Fast cooling through the recrystallization

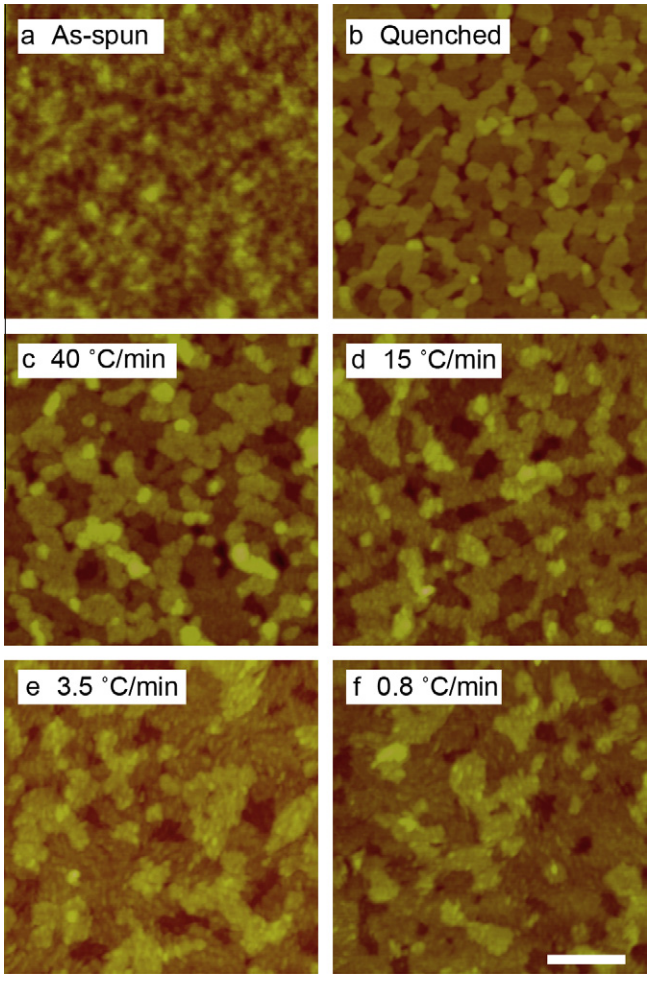

Fig. 2. AFM images of PBTTT films with various cooling rates. Scale bar denotes 500 nm.

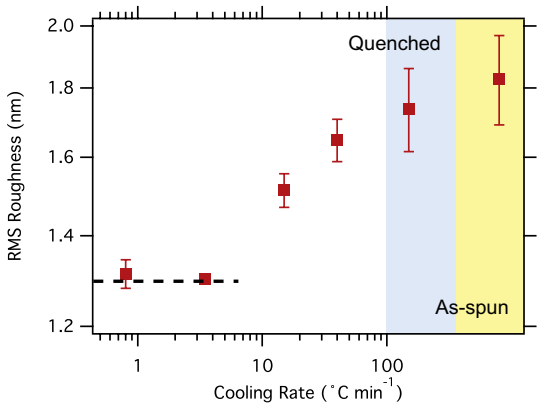

Fig. 3. RMS roughness values obtained from the AFM surface images for the films with various cooling rates.

temperature prohibits the release of sufficient heat for the recrystallization and homogenous interdigitation of the polymers. Thus, as the cooling rate increases, the exothermal peak shifts to lower temperatures, which is the typical characteristic of the meta-stability in the first-order phase transition. The enthalpy change (ΔH) of the recrystallization for the fast-cooled sample does not reach the value obtained from the slow-cooled sample. The insufficient recrystallization time probably leads to poor interdigitation and inhomogeneous recrystallization (see Supplementary data). We performed the measurements with powdered PBTTTs and presumed that the recrystallization process in the polymer thin films is not unusually different from that of powdered polymers.

3.2. Effect of cooling rate on PBTTT microstructure

In order to directly study the effect of recrystallization rate on the microstructure of PBTTT thin films, the topography images were obtained using AFM (Fig. 2). All the samples were annealed at 150 °C for 10 min and cooled at various rates. Small (50–100 nm) water-droplet-like domains were observed in the fast-cooled sample in Fig. 2b. In the slow-cooled samples, on the other hand, relatively large (several hundred nanometers) and flat domains were observed, as shown in Fig. 2e and f. Recent TEM studies showed that the large lateral domains in the terrace structure are composed of crystalline subunits (~10 nm in size) [7]. Thus the large domains are not directly characterizing the size of grains but reflecting possibly enhanced connectivity between the grains with relatively small angles. A variety of domain sizes displayed in Fig. 2 can be

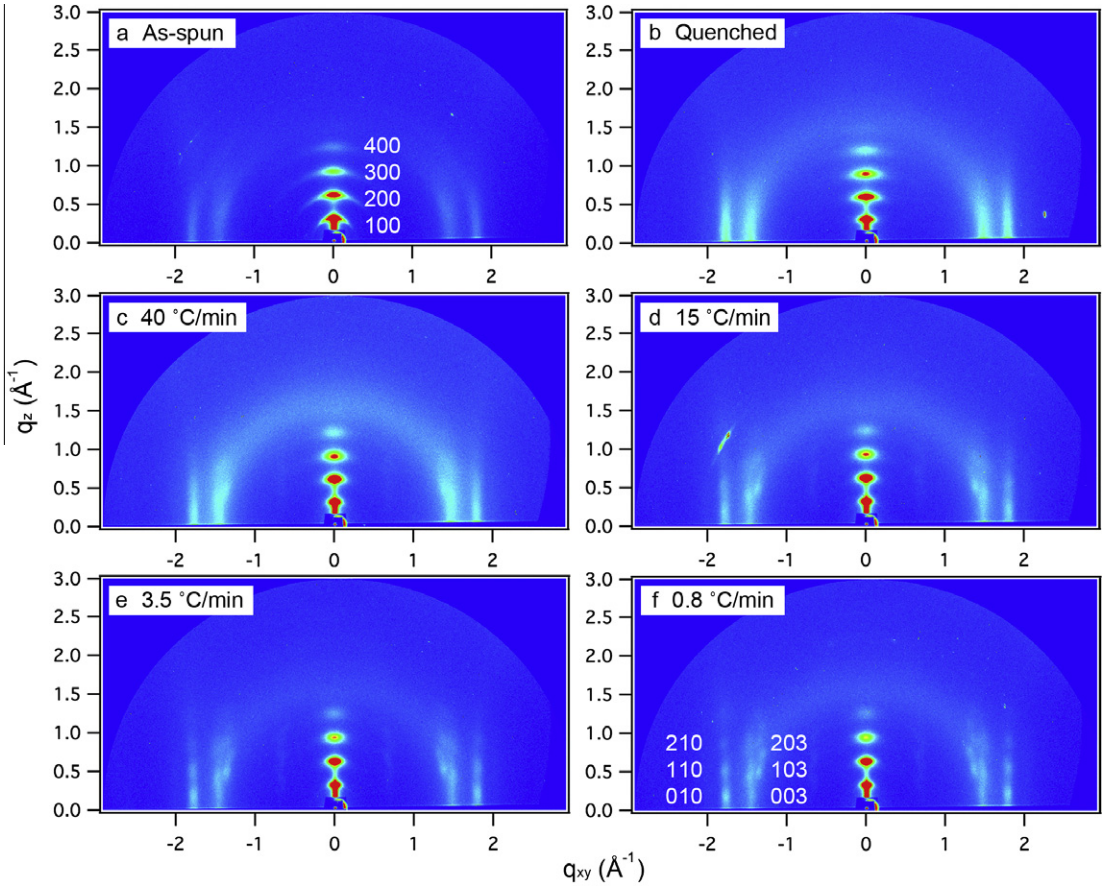

Fig. 4. 2D X-ray scattering at the grazing incidence of PBTTT films with various cooling rates. (a) (h 0 0) peaks and (f) mixed index peaks (e.g., (h 1 0) and (h 0 3)) are labeled.

interpreted by the indication that slow recrystallization leads to better connectivity among PBTTT molecules and consequently larger ordered domains, as is proposed in the previous section. Samples cooled at intermediate cooling rates show progressive improvement in morphology.

Another noticeable effect of slow cooling on the terrace structure is the flattening of surface layers to smoother surface morphologies. While the quenched sample exhibits rough surface morphology with small domains distributed over five or more layers, slow-cooled samples show smoother morphology with mostly one or two layers appearing on the surface. The root-mean-square (RMS) roughness of the films, shown in Fig. 3, quantitatively indicates the improvement of the surface morphology as the cooling rate decreases. Finally, RMS roughness saturates to about 1.3 nm with a cooling rate less than 15 °C/min. The substrate roughness was found to reduce the lateral domain size and the extent of long-range order, prevent the terrace formation, and suppress the field-effect mobility [17]. From this perspective, formation of large and smooth domains in the 3D terrace structure is likely to be an essential component for realization of high-performance polymer thin films.

The effect of the cooling rate on the long-range order in the polymer was determined by 2D GIWAXS measurements. The 2D diffraction patterns for the various samples shown in Fig. 4 exhibit several noticeable differences. One is the *d*-spacing in the normal direction to the substrate.

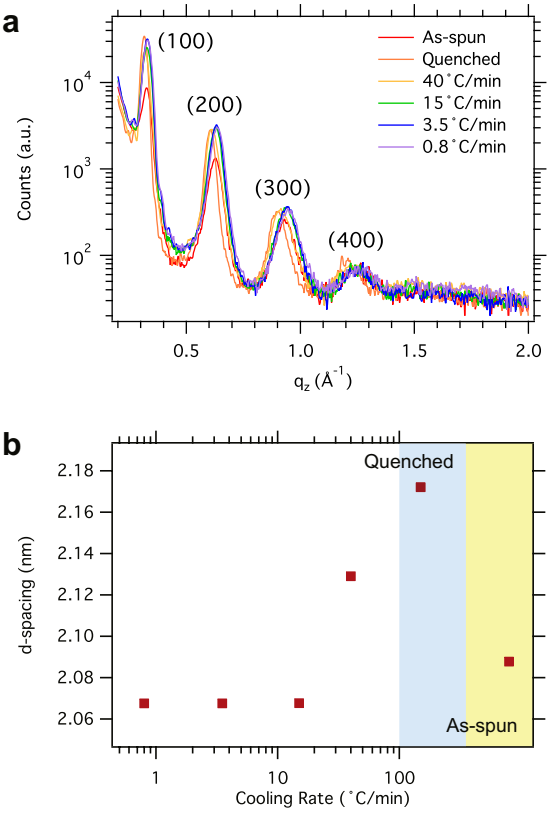

Fig. 5. (a) Out-of-plane X-ray scattering from PBTTT films for various cooling rates and (b) corresponding lamellar spacing distances.

The *d*-spacing can be obtained from the out-of-plane diffraction peak position, i.e., the q_z direction slice at $q_{xy} = 0$, as shown in Fig. 5. The *d*-spacing of the diffraction peak in the fastest cooled film was 21.7 Å. As the cooling rate decreased, the *d*-spacing decreased and saturated to 20.7 Å for samples cooled slower than 15 °C/min, which is consistent with the results of the previously reported XRD analysis showing that the layer spacing changes with the thermal cycle [22]. The cooling rate dependence of the *d*-spacing can be explained by the different recrystallization times of melted side-chains. Above T_H, side-chain melting expands the vertical layer spacing, and subsequent cooling down through T_C leads to the formation of interdigitated side-chains, reducing the layer-to-layer distance. It can be inferred that if melted side-chains have insufficient time to recrystallize, layer packing does not occur sufficiently; in contrast, sufficient recrystallization time guarantees relatively close-packing of the layers. It is worthwhile to mention that in-plane diffraction patterns show negligible cooling rate dependence (not shown here), which is consistent with the previous literatures [19]. This suggests that annealing modifies only the lamellar stacking and not the π-stacking.

Another prominent feature found in the 2D GIWAXS measurements is the shape and the intensity of Bragg peaks, from which the extent of layer ordering and tilting orientations can be compared. Figs. 6a–c show the 2D patterns of the (2 0 0) Bragg peaks of polymer films for different cooling rates. A perfectly aligned structure would exhibit an elliptical pattern in the Bragg peak, whereas a misaligned structure would exhibit an arc-shaped pattern [17,23]. The elliptical shape of the Bragg peak in the slow-cooled sample clearly demonstrates the lack of tilted layers in this sample in comparison to the as-spun sample or the quench-cooled sample. We also examined at the horizontal (q_{xy}-direction) slice of the (2 0 0) peak intensity, as shown in Fig. 6d. The width of the peak is related to the lateral length of the ordered structure along the surface, in other words, the lateral domain size. The tilting of domains broadens the width of the horizontal peak intensity. The sharp and narrow peak of the slow-cooled sample indicates the highly oriented large in-plane domains. Since each layer is mutually supported by adjacent layers during recrystallization, side-chain interdigitation also enhances the lateral ordering, resulting in formation of large-size domains [22].

In addition, the higher-order mixed-index Bragg peaks, which are an index of 3D ordering, exhibit strong dependence on the cooling rate in the direct comparison of the (h 1 0) peaks, as depicted in Fig. 7. The intensity data were collected from the slice of the 2D diffraction patterns at the (0 1 0) peak point along the q_z direction. Although higher-order mixed-index peaks are indistinguishable in the as-spun sample and the fast-cooled samples, they become discernable in the slow-cooled samples, as (h 1 0) and (h 0 3) peak series labeled in Fig. 4f.

We did not study the microstructures of TFT at the dielectric interface which dominates the 2D transport in TFT. However, it is not unnatural to think that the cooling rate influences overall film structure of about 30 nm thickness including the dielectric interface.

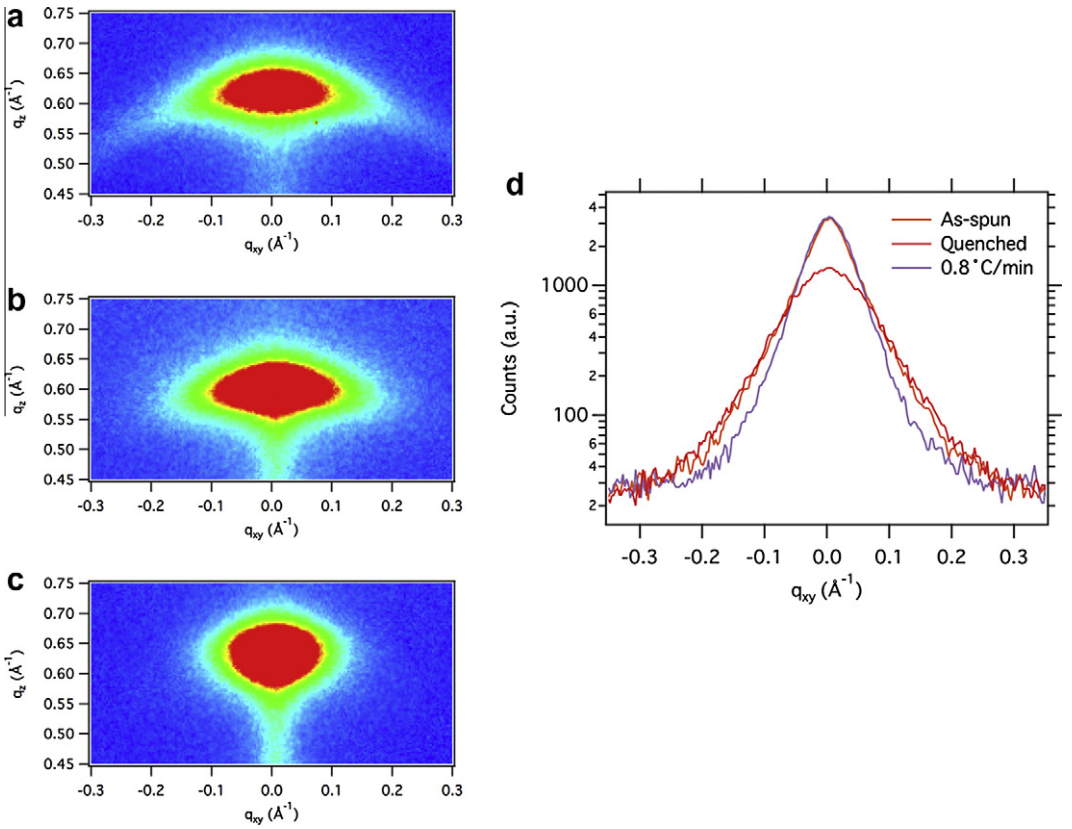

Fig. 6. 2D X-ray scattering near the (2 0 0) Bragg peak of a film of PBTTT (a) as-spun, (b) quenched and (c) slowly cooled at 0.8 °C/min. The peak patterns were plotted on the same intensity scale. (d) q_{xy} scan of the (2 0 0) peak for the corresponding films.

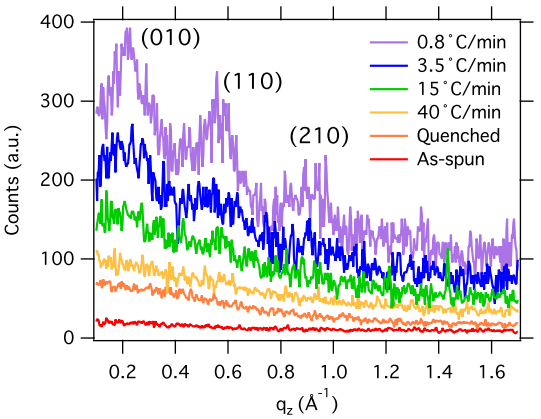

Fig. 7. q_z Scan along the (h 1 0) peak series for various cooling rates.

3.3. Effect of cooling rate on charge transport in TFT device

In order to study the effect of different morphologies on charge transport, the transfer characteristics of PBTTT TFTs with a top-contact configuration were investigated (Fig. 8a). All the devices exhibited high performance p-type TFT characteristics operating in the accumulation mode. The cooling-rate-dependent charge carrier mobility measured in the saturation region is shown in Fig. 8b. The mobility tends to increase as the cooling rate decreases. When the cooling rate is sufficiently low (lower than 15 °C/min), the mobility saturates at a certain value and becomes unaffected by further decrease in the cooling rate. The saturated mobility obtained from the slow-cooled samples is few times higher than the mobility from the quench-cooled sample.

To investigate the relationship between the recrystallization rate and the charge transport further, transport measurement was carried out at various temperatures. All the mobilities were measured in the saturation region at fixed effective gate bias, i.e., $V_g - V_t = -20$ V. The mobility monotonically decreases as temperature decreases. This temperature dependence becomes stronger with increasing cooling rate, as shown in Fig. 8b. The activation energy, i.e., the slope of mobility as a function of temperature, is calculated and plotted in Fig. 8c, showing a clear increase with increasing cooling rate. All the activation energy values are in reasonable agreement with those in previous work [7]. The activation energy also saturates for a sufficiently slow cooled sample, which is consistent with the behavior of raw mobility as a function of the cooling rate.

The relatively small mobility in the fast-cooled PBTTT film is closely related to its higher activation energy, which can be treated as an effective energy barrier that obstructs

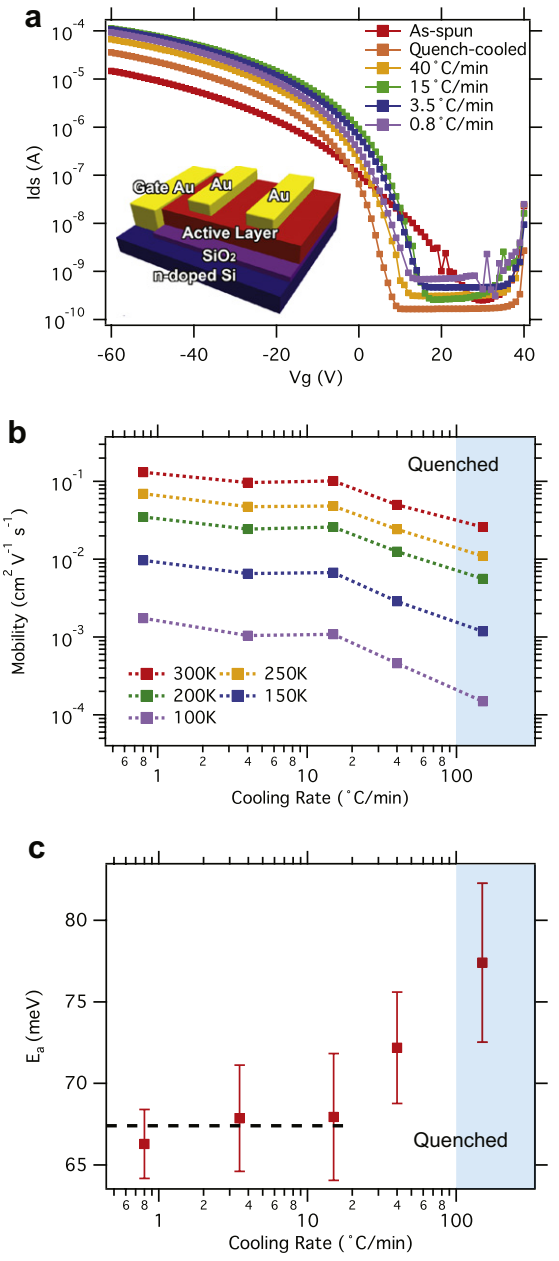

Fig. 8. (a) Cooling rate dependent transfer characteristics of PBTTT TFTs. The inset depicts the TFT configuration used in this study. (b) Cooling-rate-dependent mobility measured at various temperatures. (c) Activation energies are obtained for various cooling rates.

the charge transport. The dominant source of charge transport obstruction is grain boundaries, which is proliferated upon faster cooling. In other words, smaller mobility with higher activation energy can be attributed to its microstructure, which contains small and rough domains with worse connectivity induced by fast recrystallization. Sufficiently slow cooling results in well-connected, smooth, and large-size domains; the critical value of the cooling rate is found to be around 15 °C/min.

4. Conclusions

We have demonstrated the effect of recrystallization rate on the morphology and charge transport properties of a PBTTT thin film. DSC measurements at various cooling rates confirmed that the cooling rate plays an essential role in the recrystallization process. The connectivity between domains increases through recrystallization, resulting in larger domains. The microstructures obtained at various cooling rates were extensively studied by AFM and 2D GI-WAXS. Slower cooling leads to well-connected large domains with 3D ordering, whereas faster cooling induces misaligned small domains. The charge carrier mobility increases with decreasing cooling rate and saturates for a cooling rate slower than the critical value of 15 °C/min. The activation energy obtained from the temperature dependent transport measurement showed that the charge transport obstruction tends to reduce as the cooling rate reaches the critical value. The smaller activation energy observed in the sufficiently slow cooled sample is attributed to the improved microstructure of the thin film.

Acknowledgements

We gratefully acknowledge the financial support from the National Research Foundation of Korea through the Creative Research Initiatives (CSQR). We would also like to thank Dr. Hyuongsoon Choi and Dr. Shinuk Cho for helpful discussions and suggestions, and Mr. Yecheol Rho for assisting 2D GIWAXS measurements.

Appendix A. Supplementary data

Supplementary data associated with this article can be found, in the online version, at doi:10.1016/j.orgel.2011.06.013.

References

[1] H. Klauk, Chem. Soc. Rev. 39 (2010) 2643.
[2] A. Salleo, R.J. Kline, D.M. DeLongchamp, M.L. Chabinyc, Adv. Mater. 22 (2010) 3812.
[3] L.A. Lucas, D.M. DeLongchamp, B.M. Vogel, E.K. Lin, M.J. Fasolka, D.A. Fischer, I. McCulloch, M. Heeney, G.E. Jabbour, Appl. Phys. Lett. 90 (2007) 012112.
[4] H.N. Tsao, K. Mullen, Chem. Soc. Rev. 39 (2010) 2372.
[5] R.J. Kline, D.M. DeLongchamp, D.A. Fischer, E.K. Lin, M. Heeney, I. McCulloch, M.F. Toney, Appl. Phys. Lett. 90 (2007) 062117.
[6] R. Zhang, B. Li, M.C. Iovu, M. Jeffries-EL, G. Sauve, J. Cooper, S.J. Jia, S. Tristram-Nagle, D.M. Smilgies, D.N. Lambeth, R.D. McCullough, T. Kowalewski, J Am. Chem. Soc. 128 (2006) 3480.
[7] C.C. Wang, L.H. Jimison, L. Goris, I. McCulloch, M. Heeney, A. Ziegler, A. Salleo, Adv. Mater. 22 (2010) 697.
[8] K.A. Singh, G. Sauve, R. Zhang, T. Kowalewski, R.D. McCullough, L.M. Porter, Appl. Phys. Lett. 92 (2008) 263303.
[9] R.J. Kline, M.D. Mcgehee, M.F. Toney, Nat. Mater. 5 (2006) 222.
[10] R.J. Kline, M.D. McGehee, E.N. Kadnikova, J.S. Liu, J.M.J. Frechet, Adv. Mater. 15 (2003) 1519.
[11] L.H. Jimison, M.F. Toney, I. McCulloch, M. Heeney, A. Salleo, Adv. Mater. 21 (2009) 1568.
[12] H. Sirringhaus, P.J. Brown, R.H. Friend, M.M. Nielsen, K. Bechgaard, B.M.W. Langeveld-Voss, A.J.H. Spiering, R.A.J. Janssen, E.W. Meijer, P. Herwig, D.M. de Leeuw, Nature 401 (1999) 685.
[13] B.S. Ong, Y.L. Wu, Y.N. Li, P. Liu, H.L. Pan, Chem-Eur. J. 14 (2008) 4766.
[14] A. Zen, J. Pflaum, S. Hirschmann, W. Zhuang, F. Jaiser, U. Asawapirom, J.P. Rabe, U. Scherf, D. Neher, Adv. Funct. Mater. 14 (2004) 757.
[15] J.F. Chang, B.Q. Sun, D.W. Breiby, M.M. Nielsen, T.I. Solling, M. Giles, I. McCulloch, H. Sirringhaus, Chem. Mater. 16 (2004) 4772.

[16] H.C. Yang, T.J. Shin, L. Yang, K. Cho, C.Y. Ryu, Z.N. Bao, Adv. Funct. Mater. 15 (2005) 671.
[17] Y. Jung, R.J. Kline, D.A. Fischer, E.K. Lin, M. Heeney, I. McCulloch, D.M. DeLongchamp, Adv. Funct. Mater. 18 (2008) 742.
[18] I. Mcculloch, M. Heeney, C. Bailey, K. Genevicius, I. Macdonald, M. Shkunov, D. Sparrowe, S. Tierney, R. Wagner, W.M. Zhang, M.L. Chabinyc, R.J. Kline, M.D. Mcgehee, M.F. Toney, Nat. Mater. 5 (2006) 328.
[19] M.L. Chabinyc, M.F. Toney, R.J. Kline, I. McCulloch, M. Heeney, J. Am. Chem. Soc. 129 (2007) 3226.
[20] D.M. DeLongchamp, R.J. Kline, E.K. Lin, D.A. Fischer, L.J. Richter, L.A. Lucas, M. Heeney, I. McCulloch, J.E. Northrup, Adv. Mater. 19 (2007) 833.
[21] J. Yoon, K.W. Kim, J. Kim, K. Heo, K.S. Jin, S. Jin, T.J. Shin, B. Lee, Y. Rho, B. Ahn, M. Ree, Macromol. Res. 16 (2008) 575.
[22] D.M. DeLongchamp, R.J. Kline, Y. Jung, E.K. Lin, D.A. Fischer, D.J. Gundlach, S.K. Cotts, A.J. Moad, L.J. Richter, M.F. Toney, M. Heeney, I. McCulloch, Macromolecules 41 (2008) 5709.
[23] M.L. Chabinyc, Polym. Rev. 48 (2008) 463.

P3HT degrade rapidly [10–13]. A number of studies report that this is related to formation of a charge transfer complex between O_2 and the polymer (CTC-P/O_2). This charge transfer complex can act as a precursor for formation of a charge pair consisting of a positively charged radical cation (or polaron) on the polymer chain (P^+) in combination with O_2^- [12]. It has also been found that electronic excitation of the charge transfer complex by light strongly enhances the charge formation [12–15]. This provides a possible explanation for the rapid degradation of P3HT in the presence of both light and O_2 [12–18]. Presently it is not fully clear, which wavelengths promote charge generation from the charge transfer complex. Furthermore, one might expect rapid recombination of the photogenerated P^+ and O_2^- to reform the ground state charge transfer complex CTC-P/O_2. Finally it is not clear whether the generated O_2^- directly initiates a radical chain reaction leading to large scale degradation. One study has indicated that photoinduced degradation as probed by fluorescence quenching is still partly reversible in the initial stage [14].

In this study we focus on the initial stages of photoinduced changes in films of π-conjugated polymers. We investigate P3HT and also a poly(cyclopentadithiophene-alt-benzothiadiazole) derivative, PCPDTBT, which shows higher power conversion efficiencies in bulk heterojunctions with PCBM than P3HT. The highest reported efficiency for PCPDTBT:PCBM is 5.5% [19]. By combining results from several spectroscopic techniques (infrared and visible optical spectroscopy and electron paramagnetic resonance (EPR) we find unambiguous evidence that in the first stage of the photoinduced degradation persistent charge pairs P^+ O_2^- are generated. These are stable in the dark for hours but disappear again upon removal of O_2 by applying a vacuum. This charge formation also occurs in the presence of PCBM. The fact that no other photochemical reaction products could be identified in this early stage of photodegradation, combined with the stability of the photoinduced charges, indicates that the P^+ and O_2^- charge pair is stabilized by chemical interactions and needs to be reactivated to initiate chemical degradation of the polymer.

2. Experimental

P3HT was obtained from Rieke Metals (Sepiolid P200) and was regioregular; PCBM was obtained from Solenne BV; poly[2,6-(4,4-bis(2-ethylhexyl)-4H-cyclopenta[2,1-*b*;3,4-*b*′] dithiophene)-alt-4,7-(2,1,3-benzothiadiazole) (PCPDTBT) was obtained from Konarka.

Absorption spectra of spin coated (from chloroform solutions) films on quartz substrates were recorded with a Perkin Elmer Lambda 40 UV–vis Spectrometer. Controlled exposure to oxygen of the samples was achieved using a bath cryostat (Oxford Instruments) at room temperature that controlled the atmosphere around the sample. The illumination was performed in situ with a 365 nm UV lamp (Spectroline, model CM-10, Spectronics Corporation). The optical data were corrected by subtraction of the absorption spectrum of the P3HT film in the dark. Data points in Fig. 2c were calculated subtracting the optical density at 700 nm from the optical density at the mentioned wavelength.

Electron paramagnetic resonance (EPR) at 9.44 GHz (X-band) was measured with a Bruker ESP 300E spectrometer using a cavity with a 50% transmission grid for illumination. The films for EPR experiments in the solid state were drop cast on glass substrates, dried in an oxygen free atmosphere, peeled off the substrates and inserted in the EPR sample tubes. The illumination in the EPR experiments was done by focusing the filtered ($\lambda > 510$ nm for vis experiments and $250 < \lambda < 450$ nm for UV illumination) white light from a 500 W Xe light source. Samples were irradiated for a known period of time, ranging from 5 s to several hours. The evolution of the peak-to-peak EPR intensity was monitored as a function of illumination time and oxygen exposure. In all the measurements the microwave power used was 10 mW. A time constant of 326 ms and conversion time of 162 ms were used. The field was modulated with an amplitude of 1 G at a frequency of 100 kHz. The microwave frequency and magnetic field were measured using a HP 5350B microwave frequency counter and a ER 035 M NMR gauss meter. Single scans were sufficient to obtain an acceptable signal-to-noise ratio.

FT-IR measurements were performed in drop cast films from chlorobenzene solutions (thicknesses in the range of μm). Infrared spectra were measured on a Perkin Elmer Spectrum One UATR FT-IR spectrophotometer. Illumination of the samples was performed with a desktop lamp and a cutoff ($\lambda > 510$ nm) filter. Chemical doping of P3HT

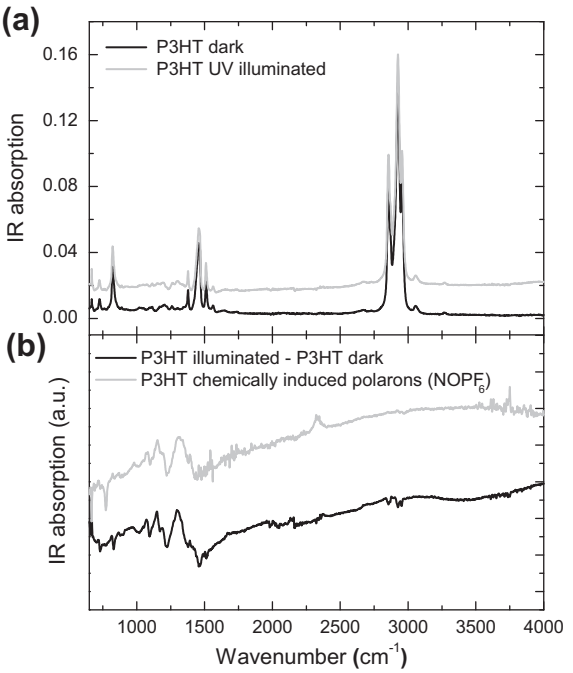

Fig. 1. (a) FT-IR absorption spectra of a P3HT film prior to and after illumination with UV light in ambient air for several minutes. (b) Corresponding difference spectrum for P3HT before and after illumination (black line). For comparison also the difference spectrum upon chemical oxidation of P3HT with $NOPF_6$ is shown (grey line).

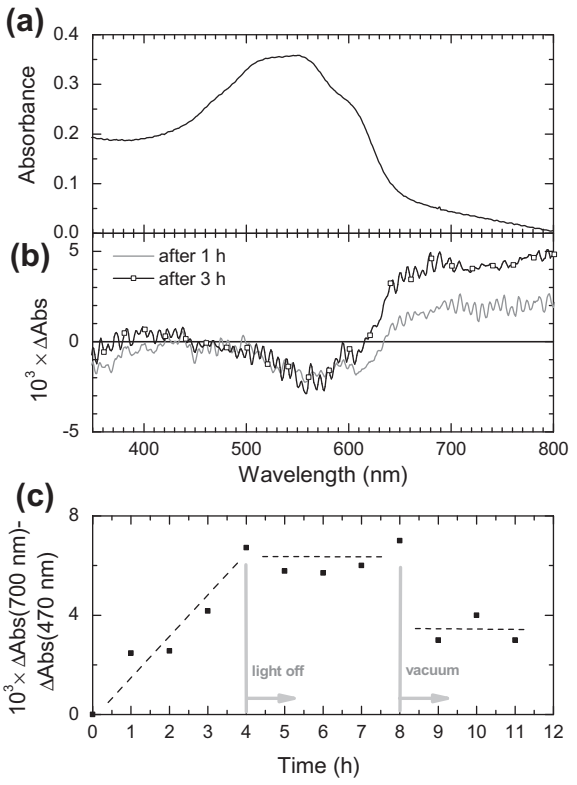

Fig. 2. (a) Optical absorption of a P3HT film. (b) Differential absorption (ΔAbs) after UV illumination for 1 and 3 h in air with respect to the initial 'dark' absorption. (c) Difference of ΔAbs at 700 nm and at 470 nm as function of illumination time. The illumination was ended after 4 h and the sample chamber was evacuated after 8 h.

in film was achieved by adding nitrosyl hexafluorophosphate ($NOPF_6$) to a P3HT solution followed by drop casting.

3. Results and discussion

In Fig. 1a we show the FT-IR spectra of a P3HT film before and after illumination in ambient air. As can be seen, illumination induces a new broad absorption band with a maximum near or above 4000 cm^{-1}. This feature is clearly visible in the difference spectrum, obtained by subtracting the spectrum taken before illumination from the spectrum after illumination, as shown in Fig. 1b. Besides the broad 4000 cm^{-1} band, a few narrower features are induced in the range below 1500 cm^{-1}. Surprisingly, no new infrared bands appear due to photochemical degradation products such as e.g. carbonyl moieties in the range of 1800–1650 cm^{-1} [20] or sulfonyl groups (between 1400 to 1300 and 1100 to 1000 cm^{-1}). The photoinduced species in the P3HT film can be identified unambiguously by comparing with the differential absorption induced by oxidative doping of the polymer with the strong electron acceptor $NOPF_6$. Oxidative doping of P3HT induces a low-energy electronic absorption (P_1 band) with a maximum around 4000 cm^{-1} corresponding to the $D_1 \leftarrow D_0$ transition of the radical cation on the polymer chain [21]. Associated with this transition are characteristic infrared active vibrational (IRAV) modes occurring below 1500 cm^{-1} as a consequence of symmetry breaking in the charged state [22,23]. The close match between doping and photoinduced spectra show that illumination results in formation of radical cations in the film. We stress that the photoinduced changes appear gradually during the long illumination period and persist for hours after turning off the illumination. Hence, we conclude that in the first stage of photodegradation, stable radical cations on P3HT are formed before any photochemical degradation products become detectable via IR.

The photoinduced radical cations in the P3HT film can also be detected via optical spectroscopy in the visible and near infrared spectral range. In Fig. 2 we show the UV–vis absorption spectrum of a film of P3HT before illumination, together with the differential absorbance induced by irradiation with UV light for 1 and 3 h of illumination in ambient air. As can be seen, the ground state absorption of the polymer in the 450-650 nm range, corresponding to the S_0–S_1 optical transition, is bleached upon illumination. A new absorption band appears in the 650–800 nm wavelength range that can be interpreted as the high energy electronic absorption (P_2 band) of P3HT corresponding to the $D_2 \leftarrow D_0$ transition of the radical cation on the polymer [21]. The time evolution of the number density of radical cations can be visualized by plotting the difference of the photoinduced absorption probed at 700 and 470 nm (Fig. 2c). This procedure minimizes the influence of small shifts in the baseline of the spectral measurement. During illumination the density of radical cations increases slowly over the course of hours and after terminating the illumination, the charges persist. However, upon evacuation of the sample chamber, the photoinduced changes can to a large extent be reversed. This indicates that the persistent charges owe their stability to the presence of molecular oxygen and that upon removal of O_2, they recombine.

To investigate the recombination of charges upon removal of O_2 in detail, we have used EPR spectroscopy. This technique allows us to probe the radical cations directly without interference of the EPR silent neutral polymer. As can be seen in Fig. 3, illumination of a P3HT sample in air at temperature $T = 293$ K induces an EPR signal with a g-value of 2.00158. This g-value is slightly different from the free electron g-value (2.0023), indicating delocalization of electrons along the polymer backbone. The intensity of this EPR signal rises steadily with the illumination time. In the dark the signal persists for at least 4 h (Fig. 3).

By varying the experimental conditions it can be proven that the formation of radicals on the polymer chains is a light induced process associated with the presence of molecular oxygen. This is illustrated in Fig. 4. Here we show changes in the peak-to-peak intensity with time for the EPR signal centered on $g = 2.00158$, for different experimental conditions. Generally, the g-value and line width of this signal remain unaltered during the experiment.

We find that both UV and visible illumination induce radicals. Furthermore illumination of films of P3HT cast, dried, mounted, and illuminated in absence of oxygen (sample type A, Fig. 4 squares) does not result in the formation of radicals. Merely exposing these pristine films

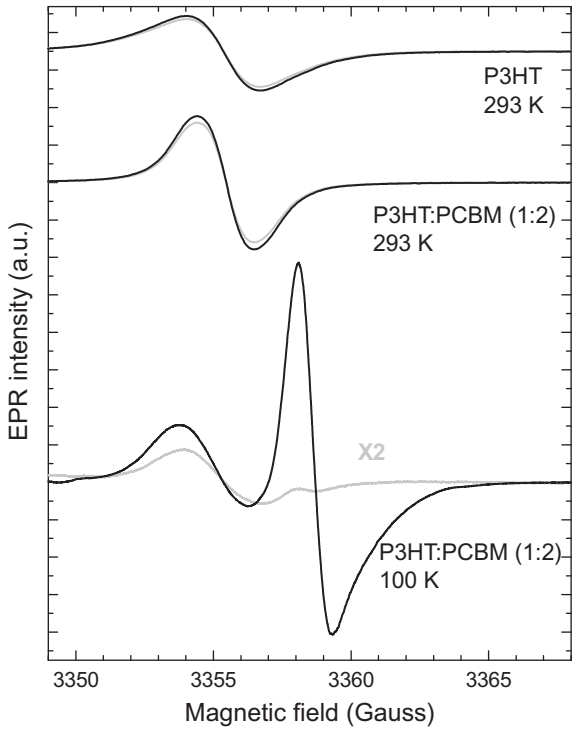

Fig. 3. (Top) Black line: EPR spectrum of P3HT at room temperature during UV illumination, with the film having been illuminated continuously in the 4 h prior to the measurement. Grey line: EPR spectrum of the same film after having been in the dark for 4 h after recording the spectrum shown as the black line. (Middle) Black and grey line: Same measurements as above but now for a P3HT:PCBM (1:2) mixed film at room temperature. (Bottom): Black and grey line same but now for a P3HT:PCBM (1:2) mixed film at $T = 100$ K. The 'light off' spectrum of P3HT:PCBM at 100 K has been multiplied by 2 for a better comparison.

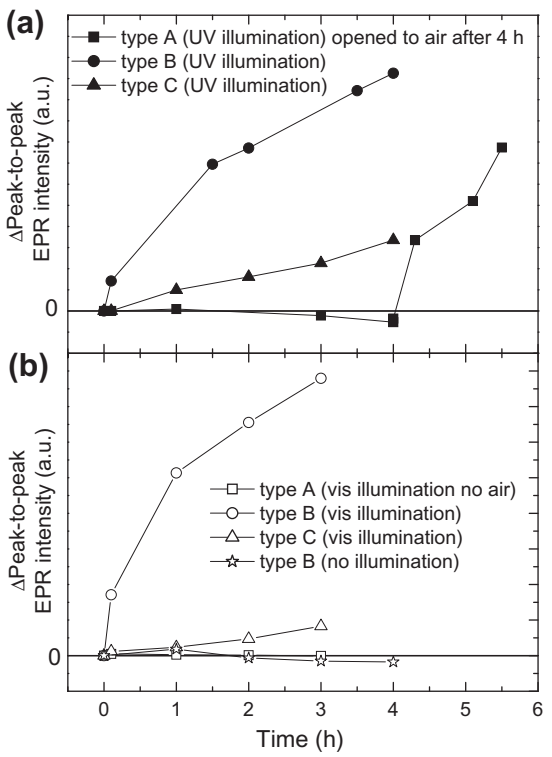

Fig. 4. Peak-to-peak EPR intensity vs. illumination time for P3HT films at 298 K. (a) UV ($\lambda < 420$ nm) illumination. (b) Visible ($\lambda > 510$ nm) illumination. Sample type A: film dried and mounted in absence of oxygen. Type B: dried in absence of oxygen and mounted in oxygen. Type C: dried and mounted in oxygen (type C). All samples were measured in air except sample type A that was kept oxygen free in a sealed tube. In the top graph the effect of opening the sealed tube containing A to air after 4 h of illumination is shown.

to oxygen at the start of the measurements series does also not result in formation of radical as long as no oxygen is present during illumination. On the other hand samples cast and dried in the absence of oxygen – but mounted and measured in air – (type B, Fig. 4 circles) do show formation of P3HT radical cations in EPR when illuminated, but not in the absence of light (type B, Fig. 4 stars). This proves that radical formation is the result of photoinduced electron transfer from P3HT to O_2. Unfortunately, the EPR signal from the superoxide radical anion (O_2^-) is too broad to be detectable at atmospheric pressures [23]. An indirect indication for the formation of O_2^- upon illumination of P3HT could be obtained from EPR experiments on solutions using a spin trap that reacts with O_2^- (experimental results not shown).

Surprisingly, samples of type B show significantly larger changes in the peak-to-peak intensity upon illumination than samples cast, dried, mounted and measured in air (type C, Fig. 4 triangles). We explain this influence of sample preparation as follows. Due to inadvertent exposure to light during sample preparation, films prepared and mounted in air contain already a larger density of radical cations at the start of the EPR experiment. As the density of radical cations seems to have an asymptotic maximal limit, samples mounted in presence of oxygen show a smaller increase in signal intensity than samples prepared under oxygen free conditions.

The EPR measurements confirm the observation that the persistent radical cations on P3HT recombine upon removal of O_2 from the sample. This is illustrated in Fig. 5. Upon evacuation of the EPR tube, the signal intensity due the P3HT radical cations drops dramatically.

Formation of persistent radical cations on the P3HT also occurs in the presence of the electron acceptor PCBM. In these mixtures illumination primarily results in the formation of $P3HT^+/PCBM^-$ charge pairs. At low temperature, during illumination, negative radical EPR signal of PCBM with a g-value of 1.9996 can be clearly resolved (Fig. 3). The $P3HT^+/PCBM^-$ charge pairs are known to be metastable and after terminating the illumination, the intensity of the PCBM radical anion signal decreases rapidly. After 4 h in the dark at low temperature, the PCBM signal has almost completely vanished from the EPR spectrum. A signal of P3HT radical cations however remains under these conditions. We attribute this signal to $P3HT^+/O_2^-$ charge pairs. At room temperature due to rapid spin relaxation and charge recombination the PCBM radical anion signal is hardly visible in the EPR spectra. Under these conditions, the persistent radical cations on P3HT formed via interaction with O_2 can easily be identified from the EPR spectra.

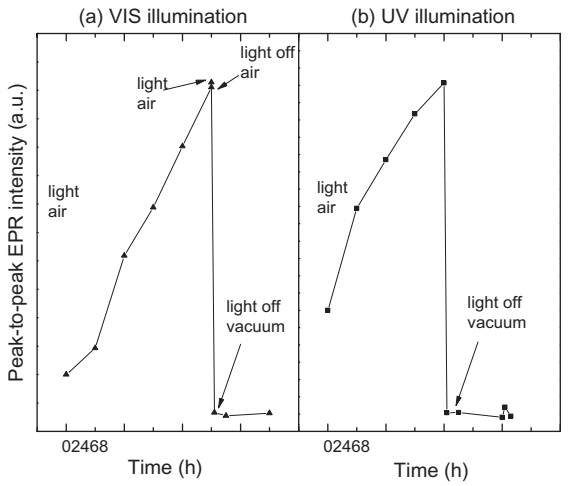

Fig. 5. Peak-to-peak EPR ($T = 298$ K) intensity vs. illumination time for P3HT film samples (type B) in oxygen atmosphere under illumination. (a) Visible illumination($\lambda > 510$ nm). (b) UV illumination ($\lambda < 420$ nm). After 5 and 4 h, respectively, the illumination was switched off and the sample was evacuated to 3×10^{-5} mbar.

The time evolution of the P3HT radical cation signal in mixed films containing also PCBM is further illustrated in Fig. 6.

The experiments described here involve the influence of air on photoinduced processes. Experiments focusing on

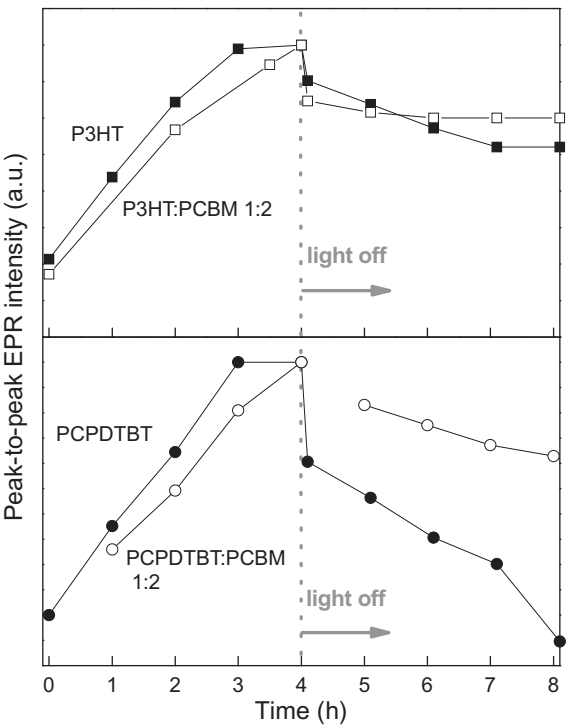

Fig. 6. Normalized peak-to-peak EPR ($T = 298$ K) intensity vs. UV illumination time for P3HT, PCPDTBT, P3HT:PCBM, and PCPDTBT:PCBM film samples (prepared as type B) in oxygen atmosphere. $t = 0$ h corresponds to the first moment of illumination and oxygen exposure of the samples.

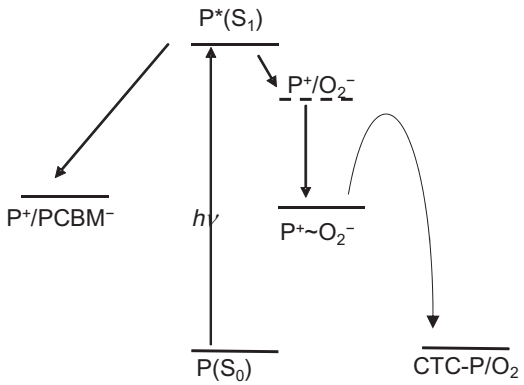

Fig. 7. Diagram illustrating the energy levels and transitions after photoexcitation of the polymer (P) in presence of PCBM or O_2 as electron acceptors. P* is the excited singlet state; P^+/O_2^- represents the initial excited charge transfer state of polymer with oxygen; $P^+ \sim O_2^-$ a relaxed excited charge transfer state; CTC-P/O_2 is the ground state charge transfer complex of P and O_2.

the influence of moisture contained in the air on the photoinduced changes, have shown that water without molecular oxygen does not give rise to formation of metastable photoinduced charges as observed in presence of O_2. Furthermore photoinduced charges are also observed in absence of H_2O [17].

Formation of persistent radical cations in the presence of light and oxygen is a property that is not restricted to films of P3HT. Also for PCPDTBT, EPR experiments indicate the formation of persistent radical cations in the presence of air (Fig. 6).

4. Conclusions

In summary, we find that illumination of the π-conjugated polymers P3HT and PCPDTBT in the presence of air leads to formation of persistent radical cations on the polymer chain. Charge formation is interpreted as the result of a photoinduced electron transfer from photoexcited polymer (P^*) to O_2 to form an excited charge transfer state (P^+/O_2^-). For P3HT the energy of the excited charge transfer state with O_2 is estimated at 1.9 eV ± 0.1 above the ground state [24]. In order to explain the persistent nature of the photoinduced charges, we postulate an energy barrier separating the excited charge transfer state (P^+/O_2) from the ground state charge transfer complex (CTC) between O_2 and polymer (CTC-P/O_2) (Fig. 7). This barrier may arise from stabilization of the excited charge transfer state and may be the result of chemical interactions between the O_2 and the polymer, leading to a 'relaxed' charge transfer state ($P^+ \sim O_2$). Because merely lowering the atmospheric pressure in the sample tube is enough to break up the charge pair, it seems unlikely that a completely covalent bond is formed between these two species in the relaxed charge transfer state. Given the acidity of alkylaromatic cation radicals [25], the basicity of the superoxide radical [26] and the reversible nature of the interaction, an acid-base reaction between cationic polymer and superoxide radical (e.g. coupled photoinduced electron and proton

transfer) seems a possibility. Formation of persistent charges also takes place in the presence of PCBM.

Acknowledgements

This work was financially supported by the German Ministry for Education and Research (BMBF project "OPV Stability", FKZ 03SF0334). The work of AA was supported by the European Commission through the Human Potential Program Marie Curie Research Training Network NANOMATCH (Grant No. MRTN-CT-2006-035884).

References

[1] Y.Y. Liang, Z. Xu, J.B. Xia, S.T. Tsai, Y. Wu, G. Li, C. Ray, L.P. Yu, For the Bright future – bulk heterojunction polymer solar cells with power conversion efficiency of 7.4%, Adv. Mater. 22 (2010) E135–E138.
[2] H.Y. Chen, J.H. Hou, S.Q. Zhang, Y.Y. Liang, G.W. Yang, Y. Yang, L.P. Yu, Y. Wu, G. Li, Polymer solar cells with enhanced open-circuit voltage and efficiency, Nat. Photon. 3 (2009) 649–653.
[3] M.A. Green, K. Emery, Y. Hishikawa, W. Warta, Solar cell efficiency tables (version 37), Prog. Photovolt: Res. Appl. 19 (2011) 84–92, 10.1002/pip.1088
[4] M. Jørgensen, K. Norrman, F.C. Krebs, Stability/degradation of polymer solar cells, Sol. Energy. Mater. Sol. Cells 92 (2008) 686–714.
[5] X. Yang, J.K.J. van Duren, R.A.J. Janssen, M.A.J. Michels, J. Loos, Morphology and thermal stability of the active layer in poly(*p*-phenylenevinylene)/methanofullerene plastic photovoltaic devices, Macromolecules 37 (2004) 2151–2158.
[6] B. Paci, A. Generosi, V.R. Albertini, R. Generosi, P. Perfetti, R. de Bettignies, C. Sentein, Time-resolved morphological study of bulk heterojunction films for efficient organic solar devices, J. Phys. Chem. C 112 (2008) 9931–9936.
[7] K. Kawano, R. Pacios, D. Poplavskyy, J. Nelson, D.D.C. Bradley, J.R. Durrant, Degradation of organic solar cells due to air exposure, Sol. Energy. Mater. Sol. Cells 90 (2006) 3520–3530.
[8] M.O. Reese, A.J. Morfa, M.S. White, N. Kopidakis, S.E. Shaheen, G. Rumbles, D.S. Ginley, Pathways for the degradation of organic photovoltaic P3HT:PCBM based devices, Sol. Energy Mater. Sol. Cells 92 (2008) 746–752.
[9] M.O. Reese et al., Consensus stability testing protocols for organic photovoltaic materials and devices, Sol. Energy Mater. Sol. Cells 95 (2011) 1253–1267.
[10] L. Lüer, H.J. Egelhaaf, D. Oelkrug, G. Cerullo, G. Lanzani, B.H. Huisman, D. de Leeuw, Oxygen-induced quenching of photoexcited states in polythiophene films, Org. Electron. 5 (2004) 83–89.
[11] E.J. Meijer, A.V.G. Mangnus, B.H. Huisman, G.W. 't Hooft, D.M. de Leeuw, T.M. Klapwijk, Photoimpedance spectroscopy of poly(3-hexyl thiophene) metal–insulator–semiconductor diodes, Synth. Met. 142 (2004) 53–56.
[12] J. Schafferhans, A. Baumann, A. Wagenpfahl, C. Deibel, V. Dyakonov, Oxygen doping of P3HT:PCBM blends: influence on trap states, charge carrier mobility and solar cell performance, Org. Electron. 11 (2010) 1693–1700.
[13] M.O. Reese, A.M. Nardes, B.A. Rupert, R.E. Larsen, D.C. Olson, M.T. Lloyd, S. Shaheen, D.S. Ginley, G. Rumbles, N. Kopidakis, Photoinduced degradation of polymer and polymer–fullerene active layers: experiment and theory, Adv. Funct. Mater. 20 (2010) 3476–3483.
[14] D.M. Taylor, H.L. Gomes, A.E. Underhill, S. Edge, P.I. Clemenson, Effect of oxygen on the electrical characteristics of field effect transistors formed from electrochemically deposited films of poly(3-methylthiophene), J. Phys. D 24 (1991) 2032–2038.
[15] M. Sandberg, S. Tanaka, K. Kaeriyama, Photo-oxidation of freely suspended submicron films of poly(3-nonylthiophene), Polymer 35 (1994) 468–474.
[16] H. Hintz, H.-J. Egelhaaf, H. Peisert, T. Chassé, Photo-oxidation and ozonization of poly(3-hexylthiophene) thin films as studied by UV/VIS and photoelectron spectroscopy, Polym. Degrad. Stab. 95 (2010) 818–825.
[17] A. Seemann, T. Sauermann, C. Lungenschmied, O. Armbruster, S. Bauer, H.J. Egelhaaf, J. Hauch, Reversible and irreversible degradation of organic solar cell performance by oxygen, Solar Energy 85 (2011) 1238–1249, doi:10.1016/j.solener.2010.09.007.
[18] H. Hintz, H.-J. Egelhaaf, L. Lüer, J. Hauch, H. Peisert, T. Chassé, Photodegradation of P3HT – A systematic study of environmental factors, Chem. Mater. 23 (2011) 145–154.
[19] J. Peet, J.Y. Kim, N.E. Coates, W.L. Ma, D. Moses, A.J. Heeger, G.C. Bazan, Efficiency enhancement in low-bandgap polymer solar cells by processing with alkane dithiols, Nat. Mater. 6 (2007) 497–500.
[20] M. Manceau, A. Rivaton, J.L. Gardette, S. Guillerez, N. Lemaître, The mechanism of photo – and thermooxidation of poly(3-hexylthiophene) (P3HT) reconsidered, Polym. Degrad. Stabil. 94 (2009) 898–907.
[21] T. Drori, J. Holt, Z.V. Vardeny, Optical studies of the charge transfer complex in polythiophene/fullerene blends for organic photovoltaic applications, Phys. Rev. B 82 (2010) 075207/1–8.
[22] K.H. Lee, R.A.J. Janssen, N.S. Sariciftci, A.J. Heeger, Direct evidence of photoinduced electron transfer in conducting polymer-C_{60} composites by infrared photoexcitation spectroscopy, Phys. Rev. B 49 (1994) 5781–5784.
[23] R. Beringer, J.G. Castle, Microwave magnetic resonance absorption in oxygen, Phys. Rev. 75 (1949) 1963.
[24] M.S.A. Abdou, F.P. Orfino, Y. Son, S. Holdcroft, Interaction of oxygen with conjugated polymers: Charge transfer complex formation with poly(3-alkylthiophenes), J. Am. Chem. Soc. 119 (1997) 4518–4524.
[25] E. Baciocchi, T. Del Giacco, F. Elisei, Proton-transfer reactions of alkylaromatic cation radicals. The effect of (α-substituents on the kinetic acidity of p-methoxytoluene cation radicals, J. Am. Chem. Soc. 115 (1993) 12290–12295.
[26] I. Dzidic, D.I. Carroll, R.N. Stillwell, E.C. Homing, Gas phase reactions. Ionization by proton transfer to superoxide anions, J. Am. Chem. Soc. 96 (1974) 5258–5259.

the cavity ($q \rightarrow q_{eff}$). Finally, only a fraction of the internally generated photons can leave the structure, as described by the outcoupling factor η_{out}.

The emissive process is considered as a dipole transition with the transition dipole moment having a certain orientation ϑ with respect to the normal of the surrounding layered system [7]. The emission of any arbitrarily oriented emitter can be decomposed into contributions of three orthogonal dipoles (||TE, ||TM, ⊥TM), as illustrated in Fig. 1a. These orthogonal dipoles are specified according to their orientation with respect to the interfaces of the layered system (parallel "||" with $\vartheta = \pi/2$, perpendicular "⊥" with $\vartheta = 0$) and the corresponding polarization of the emitted radiation (transverse-electric "TE", transverse-magnetic "TM"). Note that q_{eff} and η_{out} severely depend on the emitter position within the active layer as well as on the emitter orientation [14]. The OLED emission originates from an ensemble of emissive sites with an angular distribution $g(\vartheta)$ of their transition dipole moments. Then, only the relative contributions of parallel and perpendicular dipoles $p_{||}$:$p_{\perp}$ according to the integral quantities

$$p_{||} = \int_0^{\pi/2} g(\vartheta) \cdot \sin^2(\vartheta) \cdot \sin(\vartheta) d\vartheta \quad (2)$$

$$p_{\perp} = \int_0^{\pi/2} g(\vartheta) \cdot \cos^2(\vartheta) \cdot \sin(\vartheta) d\vartheta \quad (3)$$

enter the calculation [7] and will be determined experimentally in this paper.

In order to optimize the efficiency of OLEDs, the material specific electrical (γ) and optical ($\eta_{S/T}$ and q) properties as well as the layered system specific parameters (q_{eff} and η_{out}) need to be maximized. In state-of-the-art OLEDs the recombination zone is confined within a narrow layer by applying appropriate blocking materials and thus, recombination of all charge carriers is achieved ($\gamma = 1$) [15]. Utilizing phosphorescent emissive materials allows for both, singlet and triplet excitons, to decay radiatively into the ground state, yielding $\eta_{S/T} = 1$ [5]. Furthermore, emitter systems with short triplet-lifetimes and with reduced phonon mediated non-radiative relaxation processes promise the possibility of $q = 1$ [16]. However, the energy of an excited emitter can be radiated into different optical channels and only a small part of the light is finally emitted to the outside medium air, thus fundamentally limiting η_{out}. Optimizing an OLED stack enhances the emission of dipoles lying parallel to the plane of the OLED layers as this global optimum allows for extracting most power into air. Unfortunately, this optimized stack architecture tends to trap almost all light generated by perpendicularly oriented dipoles inside the layered system or the substrate glass, since perpendicular emitters undergo opposite interference conditions compared to the parallel ones [7,14]. As a result, analyzing and optimizing OLED systems require the knowledge of the emitter orientation distribution, that is generally assumed to be predominantly parallel for polymers and perfectly isotropic (a superposition of parallel and perpendicular dipoles with a ratio of $p_{||}$:$p_{\perp}$ = 2:1) for

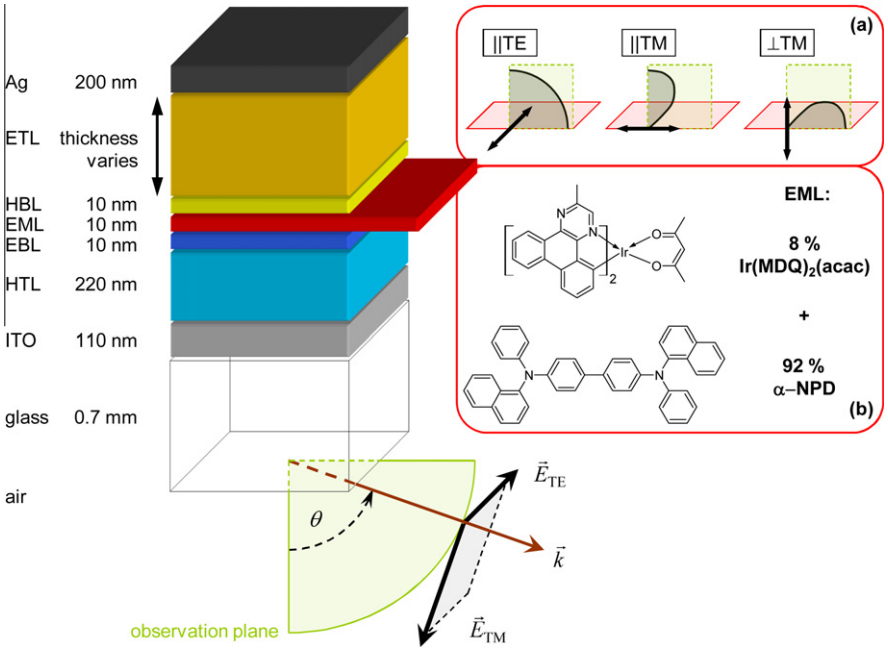

Fig. 1. Sketch of the thin film stack consisting of indium-tin oxide (ITO) as transparent anode on a glass substrate, covered by a thermally evaporated stack of hole transport (HTL), electron blocking (EBL), emitting (EML), hole blocking (HBL), and electron transport layer (ETL), contacted by a silver (Ag) cathode. The EML is prepared by co-evaporating the α-NPD matrix material with 8 wt.% of the red emitting phosphorescent dye $Ir(MDQ)_2(acac)$ as indicated in the inset. (b). An OLED series with varying ETL thicknesses from about 40 nm up to almost 400 nm has been analyzed. For angular resolved experiments, emission pattern in air has been scanned in one dimension (angle θ). The observation direction k and the orientations of the two perpendicular electric field polarization components TE and TM are drawn for convenience. The inset (a) illustrates the three basic dipoles and corresponding emission patterns assuming an infinite emitting medium. (For interpretation of the references to color in this figure legend, the reader is referred to the web version of this article.)

small molecule guest–host systems [6,7,17–23]. The simple fact that the optical outcoupling efficiency for exclusively parallel oriented emitters is about 50% larger than for emitters with isotropic orientation [6,7], suggests a highly promising OLED optimization approach.

2. Material and methods

In this paper the emitter orientation of the well-known red triplet-emitting material Iridium(III)bis(2-methyldibenzo-[f,h]quinoxaline)(acetylacetonate) [$Ir(MDQ)_2$(acac), 8 wt.%] in a *N*,*N*′-bis(naphthalen-1-yl)-*N*,*N*′-bis(phenyl)-benzidine [α-NPD] matrix is studied. The chemical structures of $Ir(MDQ)_2$(acac) and α-NPD as well as the architecture of the OLED stack are shown in Fig. 1.

2.1. OLED fabrication

OLED samples, comprising several individually addressable circular pixels of 4 mm^2 area, have been prepared by thermal evaporation of organic materials onto commercial ITO coated substrates. The layered structure (Fig. 1) was fabricated using standard evaporation techniques at a base pressure of 10^{-7} mbar and an evaporation rate of 0.05 nm/s. Doped ETL and HTL were used in order to improve electron and hole transport, respectively, introducing the dopant by co-evaporation. This technique was also used for incorporating red emitters into the EML matrix. After cathode evaporation all devices were encapsulated with a glass lid containing a getter. Analogous structures, but without getter and without cathode, have been prepared for photoluminescence experiments.

2.2. Electroluminescence (EL) emission pattern measurement

In order to access the optical far-field of the OLED, polarized angular radiation patterns have been recorded utilizing a rotational stage (CR1/M-Z7E, Thorlabs) where the OLED was mounted, and an optical detection system consisting of a wire grid linear polarizer (NT47-101, Edmund Optics) with attached achromatic waveplate (AQWP05M-630, Thorlabs), combined with a fiber coupled calibrated spectrometer (SD2000, Ocean Optics). The resulting experimental intensity data $I(\theta,\lambda)$ possess a wavelength resolution of $\Delta\lambda < 5$ nm and an angular resolution of $\Delta\theta < 0.5^\circ$, as well as an intensity uncertainty below 2%. The OLED was driven at a current density of $j = 50$ mA/cm^2 using a constant current source (GS610, Yokogawa). Radiation patterns recorded at $j = 1$ mA/cm^2 and $j = 100$ mA/cm^2 show identical relative characteristics.

2.3. Photoluminescence (PL) radiation pattern measurement

An OLED stack without cathode and comprising 31 nm and 65 nm thick HTL and ETL layers, respectively, has been encapsulated without getter in order to enable for optically excited luminescence experiments using an almost linearly polarized continuous wave laser ($\lambda = 375$ nm). Polarized emission patterns inside the substrate have been measured by mounting the sample with an immersion coupled fused silica half cylinder on a computer controlled rotational stage. The angular dependent PL spectrum was measured with a calibrated fiber optical spectrometer and a polarizer to distinguish between TE and TM polarized emission. The measured cross sections are normalized to the values at small angles because the emission in this range occurs exclusively from parallel dipoles. Emission patterns have been shown to be independent of both, the incident angle and the polarization of the illuminating laser beam.

2.4. Radiation pattern analysis

Prior to any analysis, the wavelength-dependent, complex dispersion data ($n + i\kappa$) of all materials involved have been measured utilizing dispersion-model-free reflection–transmission-spectroscopy, a method published previously [24]. Subsequent spectral reflectivity analysis enables for exact determination of layer thicknesses. Device emission has been simulated by means of a self-developed software tool, based upon the theory of Chance, Prock, and Silbey [25–27]. By analyzing TE polarized emission following approaches presented previously [7,14], we determined the emitter's internal EL spectrum to be identical to the PL spectrum and the emission zone to be constant.

3. Results

Varying the distance between the emissive sites and the cathode by adjusting the electron transport layer (ETL) thickness imposes the most pronounced effects onto the optical device properties because of interference effects arising due to the reflection at the mirror like metal cathode. As previously demonstrated [7,14], the presence of perpendicularly oriented emitters can be visualized by adapting the ETL thickness. For the system under study, a 160 nm thick ETL induces destructive interference for emitters aligned parallel to the layers, while enhancing the emission of perpendicularly oriented emitters into the air half space, thus being a particularly sensitive probe for studying the presence of perpendicular dipoles. Fig. 2a shows the experimentally observed radiation pattern for TM polarized emission. Knowing the optical constants and layer thicknesses of all materials, the radiation pattern $I(\theta,\lambda)$ of the device is calculated according to classical theory [25], where further details can be found in previous publications [14,21,26,27]. Obviously, the experimental emission pattern is well described assuming a ratio of $p_{||}:p_{\perp} = 2:(0.63 \pm 0.07)$ for parallel vs. perpendicularly oriented emitters. Thus, the amount of perpendicularly oriented active sites is significantly lower compared to the common isotropic assumption ($p_{||}:p_{\perp} = 2:1$). Note that this result is obtained in an operating OLED differing from an optimized stack only in the increased ETL thickness.

In order to prove this surprising result, the emitter orientation has been determined independently using optically excited luminescence from an essentially identical stack without the metal cathode, following the approach presented in Ref. [6]. Again, the quantitative analysis in Fig. 3 yields a fraction of $p_{||}:p_{\perp} = 2:(0.67 \pm 0.05)$ for parallel vs. perpendicular emitters well within the confidence

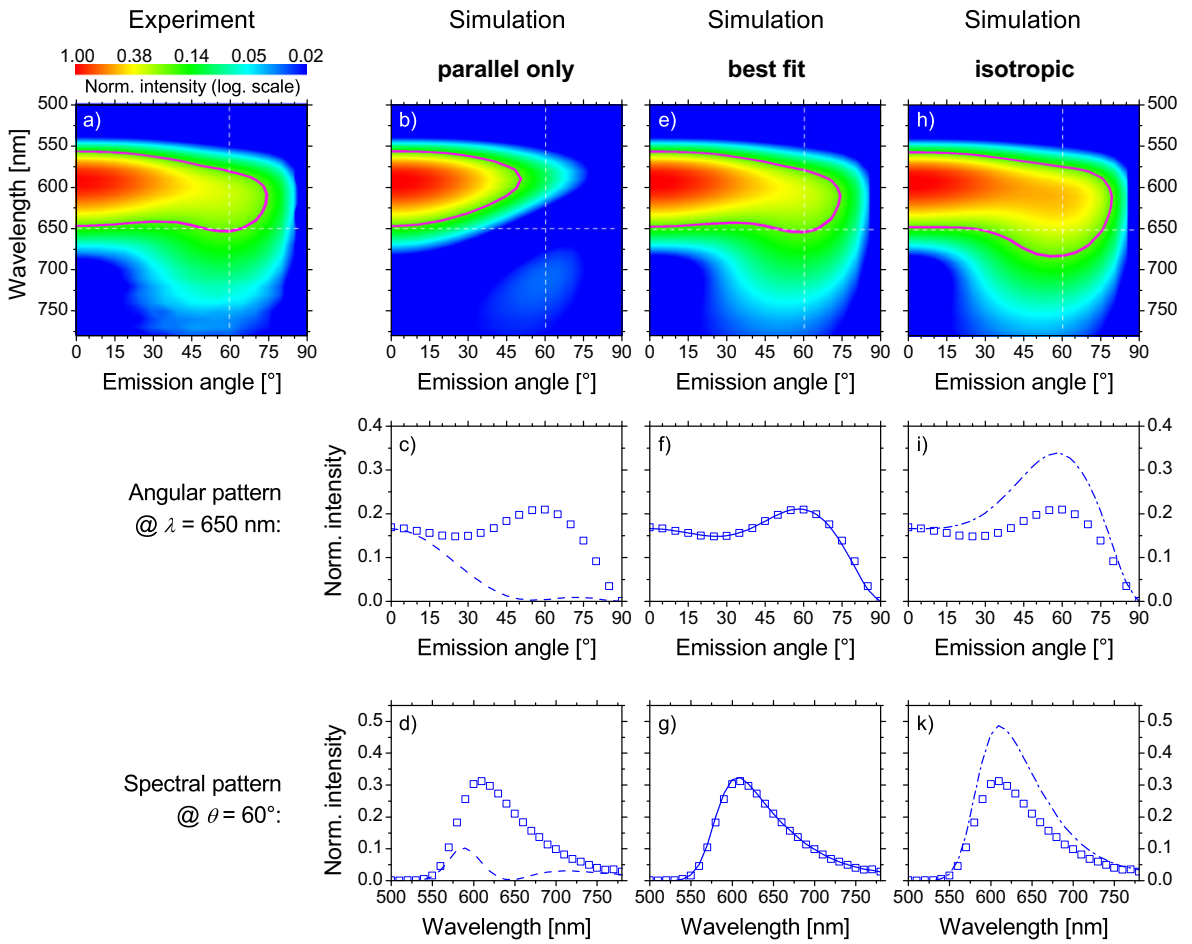

Fig. 2. Experimental and theoretical results obtained for the TM-polarized, spectral and angular resolved emission pattern $I(\theta,\lambda)$ in air of the adapted OLED comprising 160 nm ETL thickness. False color plots containing the entire spectral and angular pattern (top row; a, b, e, h) exhibit a logarithmic intensity scale to better visualize low intensity data. The value 0.2 is accentuated by a magenta line, the cross sections at angle $\theta = 60°$ and wavelength $\lambda = 650$ nm are indicated by white dashed lines. Cross section data for one fixed wavelength ($\lambda = 650$ nm; middle row; c, f, i) and one fixed angle ($\theta = 60°$; bottom row; d, g, k) are plotted with experimental results (squares) as well as the theoretical predictions (lines). Simulation results for three different emitter orientations are shown: An emitter alignment strictly parallel to the interfaces is assumed for the left "parallel" column (b, c, d); and an isotropic distribution for the right "isotropic" column (h, i, k). These two assumptions fail to yield a match to the experimental data, resulting in a "best fit" (middle column; e, f, g) assuming a fraction of 2:(0.63 ± 0.07) for parallel and perpendicular emitter contributions.

interval of the result in electrical operation, and clearly demonstrating a significant difference to the commonly assumed isotropic case.

So far, the discussion is based on a single device comprising the adapted ETL thickness of 160 nm. Additionally, quantitative radiation pattern analysis as well as emission lifetime measurements have been performed with a series of similar devices with varying ETL thickness in the 40–400 nm range (results not shown). The relative amount of perpendicular emitters could be confirmed with a device comprising a 333 nm thick ETL layer that is the second optimum for coupling of perpendicular emitters into air. Thus, the preferred parallel orientation is valid for all reasonable emitter–cathode distances, including devices which are optimized for maximum efficiency. Furthermore, no effect of pump current density on the determined orientation distribution was apparent up to 100 mA/cm^2 current density. Additionally, the internal luminescence quantum efficiency extrapolated to zero current was measured to be $q_0 = (74 \pm 4)\%$ utilizing previously published methods [22,23]. In result, we conclude that this particular emissive system is precisely described by quantitative optical simulation.

4. Discussion

The orientation distribution of Ir(MDQ)$_2$(acac) in α-NPD has been determined by two different optical methods with and without electrical excitation, both yielding identical results. The presence of non-isotropically distributed emitter ensembles in this phosphorescent guest–host system is concluded. We attribute this truly surprising result to the morphology of the α-NPD matrix blended with

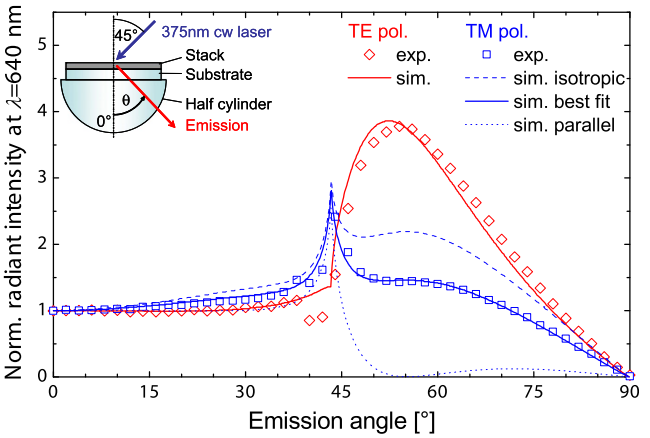

Fig. 3. Angular and polarization resolved photoluminescence emission pattern $I(\theta,640\,\text{nm})$ obtained by optical excitation at 375 nm and detection at 640 nm wavelength. An OLED stack according to Fig. 1 with HTL thickness of 31 nm and ETL thickness of 65 nm, but without the Ag cathode was used. The experimental geometry is illustrated in the inset. Data are normalized to perpendicular emission ($\theta = 0°$). Obviously, TM polarized emission is overestimated when assuming an isotropic emitter ensemble. The fit reveals a relative contribution of 2:(0.67 ± 0.05) parallel vs. perpendicular emitters.

the $Ir(MDQ)_2(acac)$ chromophore. The interaction of the asymmetric molecules during co-evaporation and the resulting predominantly parallel orientation of the dipole transition moments are not fully understood yet. We consider additional investigations potentially utilizing more sophisticated spectroscopic techniques in order to understand and to further exploit this effect.

It is worth to note that a slight birefringence of the α-NPD matrix has been observed [28] previously. Taking this effect into account yields an even more pronounced parallel emitter contribution but still within the confidence limits given.

The emitter orientation distribution obtained for the investigated small-molecular OLED emitter system reveals: the active sites in phosphorescent small molecule guest–host systems are not necessarily distributed isotropically. While the common assumption of isotropy yields a $p_{||}:p_{\perp} = 2:1$ ratio of parallel vs. perpendicularly aligned emitters, our result corresponds to a ratio of $p_{||}:p_{\perp} = 2:0.63$, i.e., a predominantly parallel orientation. Consequently, one generally accepted argument applied to discussions of triplet emitting OLED devices must be revised. Beyond doubt, there are triplet emitters with isotropic orientation, but this attribute cannot be assumed generally. By contrast, emitter orientation based optimization of OLED devices seems to be within reach, since parallel emitters preferably emit into air and, therefore, reduce the effect of surface plasmon polariton excitation at the cathode as optical loss channel. This optimization potential is illustrated by the calculations shown in Fig. 4. Assuming an optimized stack with the emitter properties obtained in this work yields 22.5% *EQE* (green curve in Fig. 4). A further emitter based optimization towards high quantum efficiency ($q = 0.95$) and an improved, predominantly parallel emitter orientation (with a ratio of $p_{||}:p_{\perp} = 2:0.14$ according to a realistic angular distribution with ±22° total width) could boost this efficiency by a factor of 1.5 to reach *EQE* = 35% (red curve in Fig. 4). Note that these efficiency values are given for the planar OLED system according to

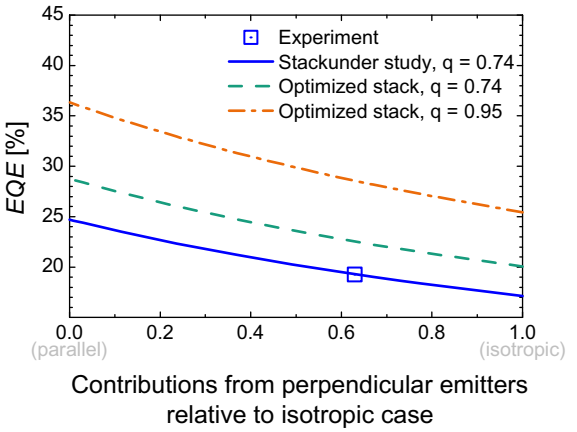

Fig. 4. OLED external quantum efficiencies vs. the relative amount x of perpendicular emitters as given in the text ($p_{||}:p_{\perp} = 2:x$). The square indicates the best value reached within this study at an ETL thickness of 250 nm. Plotting *EQE*-values simulated for this system with different amounts of perpendicular emitters yields the blue curve. Optimizing the OLED stack by varying ETL (~250 nm), HTL (~90 nm), and ITO (~90 nm) thicknesses yields the green curve with potential device efficiencies of 20–30%. Extending the simulation towards nearly ideal emitters ($q = 0.95$, red curve) provides planar devices with the highest possible efficiencies, potentially exceeding 30% *EQE*. (For interpretation of the references to color in this figure legend, the reader is referred to the web version of this article.)

Fig. 1, avoiding more or less expensive internal or external outcoupling structures.

Interestingly, *EQE*-values in excess of 30% – definitely impossible with isotropic emitters (see Fig. 4) – have been reported recently [29], but without giving a sound explanation for this unexpected high number. Our results clearly demonstrate that an *EQE*-value in this range is feasible without any outcoupling enhancement structures by using phosphorescent emitters with their transition dipole moments being preferentially oriented in the substrate plane. This opens up novel approaches for OLED efficiency improvement by using smart emissive materials with

advantageous molecular orientation. Materials design, the influence of the matrix material, and the substrate as well as film deposition conditions are just a few parameters that need to be studied further to exploit the huge potential of the dipole emitter orientation in OLEDs.

Acknowledgments

The authors thank the German Federal Ministry of Education and Research (BMBF) for funding part of this work under contract FKZ 13N10474 (TOPAS 2012). M.F. is indebted to S. Roth and T. Kümpfel for experimental assistance at Fraunhofer IOF Jena.

References

[1] C.W. Tang, S.A. VanSlyke, Organic electroluminescent diodes, Applied Physics Letters 51 (1987) 913–915.
[2] B. D'Andrade, White phosphorescent LEDs offer efficient answer, Nature Photonics 1 (2007) 33–34.
[3] S. Reineke, F. Lindner, G. Schwartz, N. Seidler, K. Walzer, B. Lüssem, K. Leo, White organic light-emitting diodes with fluorescent tube efficiency, Nature 459 (2009) 234–239.
[4] J.H. Burroughes, D.D.C. Bradley, A.R. Brown, R.N. Marks, K. Mackay, R.H. Friend, P.L. Burns, A.B. Holmes, Light-emitting diodes based on conjugated polymers, Nature 347 (1990) 539–541.
[5] M.A. Baldo, D.F. O'Brien, Y. You, A. Shoustikov, S. Sibley, M.E. Thompson, S.R. Forrest, Highly efficient phosphorescent emission from organic electroluminescent devices, Nature 395 (1998) 151–154.
[6] J. Frischeisen, D. Yokoyama, C. Adachi, W. Brütting, Determination of molecular dipole orientation in doped fluorescent organic thin films by photoluminescence measurements, Applied Physics Letters 96 (2010) 073302.
[7] M. Flämmich, M.C. Gather, N. Danz, D. Michaelis, A.H. Bräuer, K. Meerholz, A. Tünnermann, Orientation of emissive dipoles in OLEDs: quantitative in situ analysis, Organic Electronics 11 (2010) 1039–1046.
[8] J. Clark, G. Lanzani, Organic photonic for communications, Nature Photonics 4 (2010) 438–446.
[9] M.C. Gather, K. Meerholz, N. Danz, K. Leosson, Net optical gain in a plasmonic waveguide embedded in a fluorescent polymer, Nature Photonics 4 (2010) 457–461.
[10] I. De Leon, P. Berini, Amplification of long-range surface plasmons by a dipolar gain medium, Nature Photonics 4 (2010) 382–387.
[11] K.G. Lee, X.W. Chen, H. Eghlidi, P. Kukura, R. Letow, A. Renn, V. Sandoghdar, S. Götzinger, A planar dielectric antenna for directional single-photon emission and near-unity collection efficiency, Nature Photonics 5 (2011) 166–169.
[12] R.H. Friend, R.W. Gymer, A.B. Holmes, J.H. Burroughes, R.N. Marks, C. Taliani, D.D.C. Bradley, D.A. Dos Santos, J.L. Bredas, M. Lögdlund, W.R. Salaneck, Electroluminescence in conjugated polymers, Nature 397 (1999) 121–128.
[13] M.A. Baldo, D.F. ÓBrien, M.E. Thompson, S.R. Forrest, Excitonic singlet–triplet ratio in a semiconducting organic thin film, Physical Review B 60 (1999) 14422–14428.
[14] M. Flämmich, D. Michaelis, N. Danz, Accessing OLED emitter properties by radiation pattern analyses, Organic Electronics 11 (12) (2011) 83–91.
[15] M. Pfeiffer, K. Leo, X. Zhou, J.S. Huang, M. Hofmann, A. Werner, J. Blochwitz-Nimoth, Doped organic semiconductors: physics and application in light emitting diodes, Organic Electronics 4 (2003) 89–103.
[16] Yersin, H, Highly Efficient OLEDs with Phosphorescent Materials (Wiley-VCH Verlag GmbH & Co. KGaA, Weinheim, 2008).
[17] J.A.E. Wasey, A. Safonov, I.D.W. Samuel, W.L. Barnes, Effects of dipole orientation and birefringence on the optical emission from thin films, Optics Communication 183 (2000) 109–121.
[18] J.-S. Kim, P.K.H. Ho, N.C. Greenham, R.H. Friend, Electroluminescence emission pattern of organic light-emitting diodes: implications for device efficiency calculations, Journal of Applied Physics 88 (2000) 1073–1081.
[19] L.H. Smith, J.A.E. Wasey, W.L. Barnes, Light outcoupling efficiency of top emitting organic light-emitting diodes, Applied Physics Letters 84 (2004) 2986–2988.
[20] J.M. Ziebarth, M.D. McGehee, A theoretical and experimental investigation of light extraction from polymer light-emitting diodes, Journal of Applied Physics 97 (2005) 064502.
[21] S. Nowy, B.C. Krummacher, J. Frischeisen, N.A. Reinke, W. Brütting, Light extraction and optical loss mechanisms in organic light-emitting diodes: influence of the emitter quantum efficiency, Journal of Applied Physics 104 (2008) 123109.
[22] B.C. Krummacher, S. Nowy, J. Frischeisen, M. Klein, W. Brütting, Efficiency analysis of organic light-emitting diodes based on optical simulation, Organic Electronics 10 (2009) 478–485.
[23] M. Flämmich, M.C. Gather, N. Danz, D. Michaelis, K. Meerholz, In situ measurement of the internal luminescence quantum efficiency in organic light-emitting diodes, Applied Physics Letters 95 (2009) 263306.
[24] M. Flämmich, N. Danz, D. Michaelis, A. Bräuer, M.C. Gather, J.H.-W.M. Kremer, K. Meerholz, Dispersion-model-free determination of optical constants: application to materials for organic thin film devices, Applied Optics 48 (2009) 1507–1513.
[25] R.R. Chance, A. Prock, R. Silbey, Molecular fluorescence and energy transfer near interfaces, Advances in Chemical Physics 37 (1978) 1–65.
[26] N. Danz, R. Waldhäusl, A. Bräuer, R. Kowarschik, Dipole lifetime in stratified media, Journal of the Optical Society of America B: Optical Physics 19 (2002) 412–419.
[27] N. Danz, J. Heber, A. Bräuer, R. Kowarschik, Fluorescence lifetimes of molecular ensembles near interfaces, Physical Review A 66 (2002) 063809.
[28] D. Yokoyama, A. Sakaguchi, M. Suzuki, C. Adachi, Horizontal molecular orientation in vacuum-deposited organic amorphous films of hole and electron transport materials, Applied Physics Letters 93 (2008) 173302.
[29] P. A. Levermore, V. Adamovich, K. Rajan, W. Yeager, C. Lin, S. Xia, G. S. Kottas, M. S. Weaver, R. Kwong, R. Ma, J. J. Brown, M. Hack, Highly efficient phosphorescent OLED lighting panels for solid-state lighting. presentation at 48th Society for Information Display Symposium (Seattle, May 27, 2010); Hack, M. Phosphorescent OLED Technology for Energy Efficient Solid State Lighting. Presentation at 6th Global Plastic Electronics Conference & Exhibition (Dresden, October 21, 2010).

In recent years, PEDOT:PSS sheet resistance could be decreased to around 100 Ω/sq and even less and consequently also grid free organic solar cells with a transparent polymer electrode [5,7–10] were fabricated, including large scale deposition techniques like spray-coating [10,11]. Since the increased sheet resistance of the polymer electrode compared to ITO (10–30 Ω/sq) affects the solar cell fill factor, these kinds of devices are usually less efficient than ITO reference samples. So far, the impact of a polymer electrode on organic photodetector performance, significant at reverse bias voltage, is not reported in literature. In this work we show the applicability of a highly conductive and transparent PEDOT:PSS layer as top electrode for a top-absorbing organic photodetector and we report on the device performance with varying anode sheet resistance.

2. Experimental

All devices were fabricated in a nitrogen-filled glovebox. The layer sequence of an inverted photodiode is shown in Fig. 1. The aluminum bottom electrode with an area size of 7 mm^2 and a thickness of around 100 nm was thermally evaporated through a shadow mask on a glass substrate. The photoactive material PCBM:P3HT (ratio 0.75:1 by weight) was solved in 1,2-dichlorobenzene (46 mg/ml) and spin-coated on the substrates with a thickness of about 300 nm. To overcome the problem of spin-coating the water-based electron-blocking layer PEDOT:PSS (Clevios™ P VP CH 8000) on top of the hydrophobic blend layer, a sensible oxygen plasma treatment was performed creating polar oxygen species on the blend as described in [2]. The thickness of this low-conductive PEDOT:PSS layer is around 170 nm.

The conductive top electrode was prepared by adding ethylene glycol to PEDOT:PSS Clevios™ PH 1000 with a mixing ratio of 10:100 (by weight) which we determined as optimal ratio for high conductive films. Since the wetting ability of this PEDOT:PSS mix is significantly reduced compared to pure PEDOT:PSS films, about 0.3% of the wetting agent Dynol™ 604 was added to the mix to improve adhesion. After stirring for several hours, the formulation was spin-coated on top of the first PEDOT:PSS layer. Without Dynol™ we obtained similar results for the sheet resistance of spin-coated PEDOT:PSS layers but reproducibility suffered due to layer inhomogeneities. The annealing of the PEDOT:PSS layer was performed at 140 °C for 10 min on a hot plate.

Before characterization the devices were encapsulated with thin glass sheets and an epoxy resin.

Electrical characterization was performed by using a Keithley 2600 sourcemeter. The samples were illuminated with an halogen lamp with a power density of 100 mW/cm^2. The spectral resolved external quantum efficiency (EQE) and the transmission spectra were measured by lock-in-technique (Merlin Digital Lock-in Radiometry System), using a solar simulator with 300 W power and an Oriel Cornerstone 260 monochromator. The sheet resistance of the conductive PEDOT:PSS formulation was determined by 4-point-probe measurements of spin-coated films on glass substrates, using a Keithley 4200-SC System.

For determination of the cut-off frequency the organic photodiode were illuminated with square light pulses which were generated by a waveform generator Keithley 2602. The photocurrent of the diode was then amplified by a FEMTO Current Amplifier DHPCA-100 and the decrease of transient voltage by increasing pulse frequency was measured by a 1.5 GHz digital sampling oscilloscope (LeCroy Wavepro 715zi).

3. Results

3.1. Top-electrode transmission and sheet resistance

In Fig. 2 the transmission spectra of conductive PEDOT:PSS layers with different layer thicknesses are shown. For comparison, two alternative anode materials, commercially available indium-tin-oxide (ITO) and a

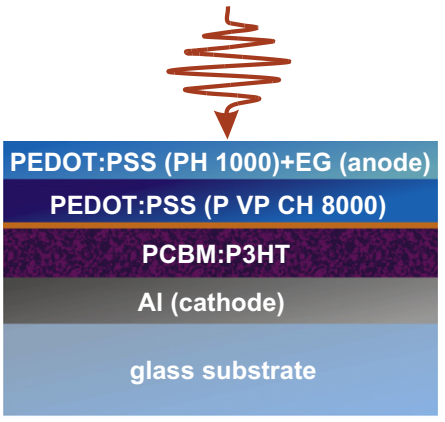

Fig. 1. Layer structure of a top-absorbing inverted photodiode with a polymeric top-contact layer. The thin layer between the photoactive layer (PCBM:P3HT) and PEDOT:PSS indicates the introduced oxide layer due to plasma treatment.

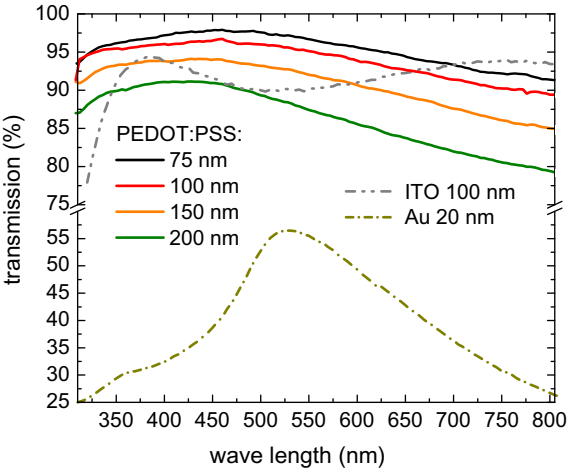

Fig. 2. Transmission spectra of PEDOT:PSS layers (with different thicknesses), commercially available ITO and a 20 nm thick gold layer electrode.

20 nm thick gold layer, are added to Fig. 2. Whereas ITO is a standard anode material used for non-inverted diodes, deposition on organic layers can decrease the inverted device performance because of the high temperatures and kinetic energies involved [12]. Instead a thin semi-transparent gold layer (work function: 5.1 eV) can be thermally evaporated on top of an inverted structure [2] but with poor transmission properties. Compared to these materials, the modified PEDOT:PSS exhibits a very high transmission even for thick layers. In Fig. 3 the increase of PEDOT:PSS transmission at a wave length of 450 nm is measured as a function of the sheet resistance and the layer thickness d which are related by $R_{sheet} \propto 1/d$. The wave length of 450 nm corresponds to the PEDOT:PSS maximum transmission and is also near to the absorption maximum of the PCBM:P3HT blend in the visible region. Even for the thickest investigated layers (up to 260 nm) shown in Fig. 3 the transmission is still >90%.

Compared with ITO, the transmission properties of the modified PEDOT:PSS layers up to a thickness of about 150 nm (see Fig. 2) are superior for a device with a PCBM:P3HT blend in the visible region of the spectrum, minor losses appear for the red region near the absorption edge of PCBM:P3HT at about 650 nm.

3.2. I–V curves

In Fig. 4 *I–V* characteristics of two inverted photodetectors with different anode materials are shown. The device structure with a gold layer as top electrode material was first proposed in [2] and improved here by using 1,2-dichlorobenzene (1,2-DCB) as solvent for the photoactive layer. 1,2-DCB, featuring a high boiling point, enables spin-coating of thick photoactive layers reducing the dark current to state-of-the-art values [13,14]. Furthermore, compared to the results in [2], 1,2-DCB improves the space charge limited current transport through the plasma-treated blend, comprising interfacial oxide states, to the

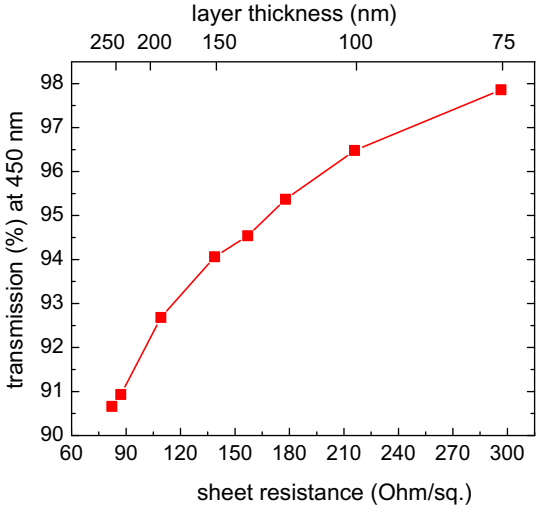

Fig. 3. Transmission change at a wave length of 450 nm (max. transmission) of PEDOT:PSS layers as a function of their sheet resistance and layer thickness.

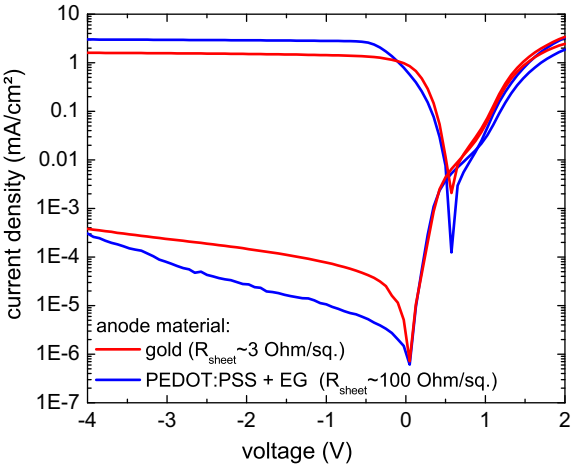

Fig. 4. Typical *I–V* curves of inverted diodes with a gold respective polymer electrode under dark and illuminated conditions. The applied light intensity was 100 mW/cm^2.

PEDOT:PSS layer. Going from forward to reverse bias, the photocurrent plateau value is reached at about −0.5 V as shown in Fig. 4, compared to −1 V for using toluene as solvent [2]. This solvent dependence of the space charge limited current is still not clear but might be related to an increased number of hopping paths since the overall P3HT concentration on the blend surface can be increased by the slow evaporation of 1,2-DCB [15].

The second *I–V* characteristic shown in Fig. 4 results when replacing the semi-transparent gold anode with a polymer electrode comprising a sheet resistance of 100 Ω/sq. The device sustains a similar low dark current for high reverse bias (2×10^{-4} mA/cm^2 at −4 V), but even one order of magnitude lower current for smaller reverse bias (1×10^{-5} mA/cm^2 at −1 V). The current density under illumination increases about 50% due to the enhanced transparency of the polymer layer thus improving the photocurrent on/off-ratio at −4 V to four orders of magnitudes. The forward current density, strongly influenced by deep traps introduced by the plasma treatment as described in [2], is slightly reduced due to the higher resistance of the polymer electrode (100 Ω/sq) compared to the gold electrode (3 Ω/sq).

Comparing the impact of different layer thicknesses and according sheet resistances of the anode on the *I–V* characteristics, we found that by increasing R_{sheet} from 100 to 300 Ω/sq neither the for a photodetector relevant dark nor light backward current are influenced within accuracy of fabrication and characterization, whereas the forward current density slightly decreases. Since a photodetector is operated in reverse bias, the increased serial resistance introduced by the polymer electrode, even if deposited as a thin layer with lower conductance, does not limit the electrical detector performance.

3.3. EQE

The improved light transmittance of the inverted diode with PEDOT:PSS anode instead of gold manifests itself by

remarkable values of the external quantum efficiency (EQE). In Fig. 5 the EQEs of inverted photodetectors with gold (20 nm thick) respective polymer anode (200 nm thick) are shown. Whereas the narrow transmission spectrum of a 20 nm thick gold layer with a transmission maximum of about 55% showed in Fig. 2 is responsible for an EQE inhibiting a maximum of only about 45% at 530 nm (−4 V) and efficiency losses at the short wave length range, the replacement with PEDOT:PSS increases the short wave length part of the EQE and shifts the maximum over 70% (−4 V). This value is comparable to the EQE of state-of-the-art non-inverted ITO photodetectors [13,14].

The dependence of the EQE on the sheet resistance is shown in the inset of Fig. 5. With increasing R_{sheet} (decreasing layer thickness) from 100 to 300 Ω/sq the EQE decreases about 7.5%. This is interesting since the transmission at the same wavelength (see Fig. 3) increases by 6.5% when increasing R_{sheet} from 100 to 300 Ω/sq. Consequently, decreasing the sheet resistance has bigger impact on device performance than increasing the transmission. An optimal layer thickness for the inverted photodetector could not be determined since lowering of the spin-coating speed results in the formation of inhomogenous PEDOT:PSS films and consequently large EQE variations.

3.4. Cut-off frequency

The cut-off frequency is a measure of the photodiode response to time-modulated incident light. Commonly, it is defined as the frequency at which the photocurrent pulse height is attenuated by a factor of $\frac{1}{\sqrt{2}}$, the so called −3 dB cut-off frequency f_c. It is influenced by the transit time t_{tr} of the light generated carriers traveling through blend and PEDOT:PSS to the electrodes. The transit time is given by $t_{tr} = d^2/\mu V$ with layer thicknesses d, carrier mobility μ and voltage drop V. For inverted photodetectors with different conductive electrodes but with the same layer structure in between, the transit time towards the electrodes is constant. The serial resistance of the electrodes, proportional to the sheet resistance R_{sheet}, plus additional load resistances sum up to a total resistance R. The time constant $t_{rc} = RC$ takes this resistance into account, together with the photodiode capacitance $C \propto A/d$ (with diode area A).

The overall device time constant t is the root-sum-square value of the individual time constants [16]:

$$t = \sqrt{t_{tr}^2 + t_{rc}^2} \quad (1)$$

It is related to the cut-off frequency $f_c \propto 1/2\pi t$.

Since the sheet resistance of a polymer electrode can be about two orders of magnitude higher than that of a metal electrode, also t_{rc} can increase remarkably. To investigate the impact of the sheet resistance on the dynamic behavior of photodiodes with a polymer top electrode, the cut-off frequencies were measured.

In Fig. 6 the frequency response of an inverted diode with a polymer electrode (100 Ω/sq) on illuminating it with square light pulses (light intensity 0.8 mW/cm², duty cycle 50%) is shown. At about 420 kHz the −3 dB attenuation is reached. This is a state-of-the-art −3 dB cut-off frequency for organic photodiodes [2,14,17]. Increasing R_{sheet} from 100 to 300 Ω/sq results in a cut-off frequency decrease to about 260 kHz.

Considering this experimentally determined dependence between sheet resistance and cut-off frequency in the inset of Fig. 6 and assuming that C is equal for each diode, it is possible to determine a proportional factor $x = t_{tr}/t_{rc}$ for different t_{rc} respective R_{sheet} with Eq. (1). Assuming $R \propto R_{sheet}$, a change of R_{sheet} also causes a proportional change of t_{rc}. For the device with the lowest sheet resistance, R_{sheet} = 100 Ω/sq, $x = 2$ follows, which means that t_{tr} contributes about four times more (see Eq. (1)) to the overall time constant than t_{rc}. In addition, also an upper limit of the cut-off frequency of the photodetectors with polymer electrodes can be estimated with Eq. (1) and the data of the inset of Fig. 6. With $RC = 0$ only the transit time determines the overall time constant t, resulting in an

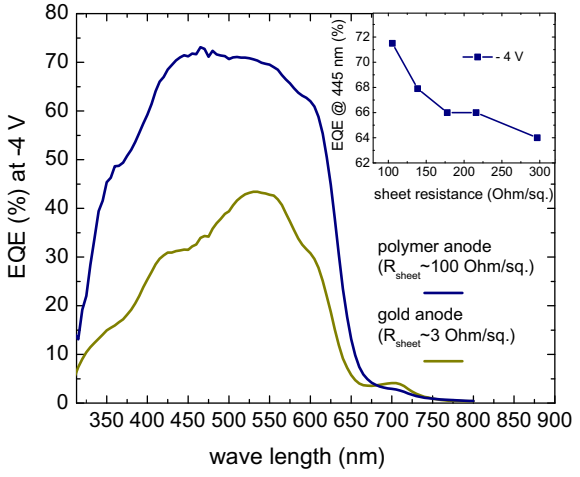

Fig. 5. External quantum efficiency (EQE) of devices with gold respective polymer electrodes. The inset shows the EQE decrease with increasing anode sheet resistance.

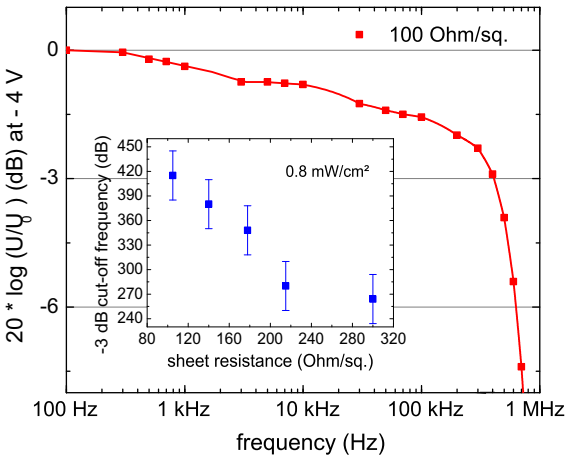

Fig. 6. Frequency response of an photodiode with electrode sheet resistance of 100 Ω/sq at −4 V. The inset shows the dependence of the −3 dB cut-off frequency on the electrode sheet resistance.

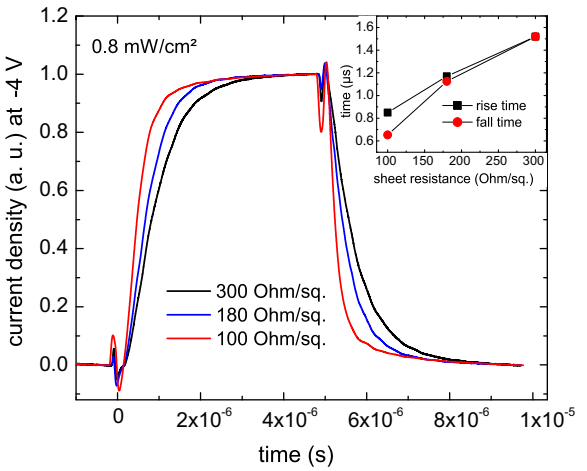

Fig. 7. Dynamic photocurrent response for diodes with different sheet resistances. The applied light pulse length was 5 µs and the frequency 100 kHz. The inset shows the decrease of rise and fall time with decreasing sheet resistance. Overshoots are dedicated to capacitive effects arising from cables.

upper cut-off frequency limit of about 470 kHz which is barely higher as the highest cut-off frequency measured in Fig. 6.

In Fig. 7 typical light pulse responses of the photodetectors with different anode sheet resistances are shown for a light pulse frequency of 100 kHz. The shape of the response changes for the different resistances, meaning that also rise and fall time (the fall time is defined as time required for a pulse to decrease from 90% to 10% of the peak value) change accordingly. This is shown in the inset of Fig. 7 where the response times double for increasing R_{sheet} from 100 to 300 Ω/sq. The behavior is consistent with the trend shown before in Fig. 6 where the cut-off frequency reduces approximately by half.

4. Conclusion

In conclusion, we have demonstrated the fabrication of an ITO-free inverted organic photodetector with state-of-the-art performance regarding the low dark current, the high on/off-ratio (four orders of magnitude at −4 V) and the high EQE of 70% (at 500 nm, at −4 V). The higher sheet resistance of the transparent polymer electrode, containing ethylene glycol as conductivity enhancer, does not significantly affect the photodetector performance. Comparing photodetectors with different electrode sheet resistances between 100 and 300 Ω/sq, we found out that the thickest and most conductive electrode lead to the highest EQE in spite of higher transmission losses compared with the lower conductive electrodes. This implies that a further conductivity enhancement could even increase the EQE to higher values. The highest cut-off frequency we measured was around 400 kHz, which is in spite of the high anode sheet resistance of 100 Ω/sq a state-of-the-art value.

The solution-processability of all layers except for the cathode makes this organic photodiode suitable for an easy deposition and integration on top of inorganic read-out-electronics such as CMOS-circuits.

Acknowledgments

Financial support by the German Exchange Service through the Vigoni-program and by the "Fondazione Bruno Kessler (FBK)" in Trient (Italy) is gratefully acknowledged.

References

[1] S. Tedde, E.S. Zaus, J. Fürst, D. Henseler, P. Lugli, IEEE Electron Device Lett. 11 (2007) 893–895.
[2] D. Baierl, B. Fabel, P. Gabos, L. Pancheri, P. Lugli, G. Scarpa, Org. Electron. 11 (2010) 1199–1206.
[3] X. Crispin, F. Jakobsson, A. Crispin, P. Grim, P. Andersson, A. Volodin, C. Van Haesendonck, M. Van Der Auweraer, W. Salaneck, M. Berggren, Chem. Mater. 18 (2006) 4354.
[4] J. Ouyang, C.W. Chu, F.C. Chen, Q. Xu, Y. Yang, Adv. Funct. Mater. 15 (2005) 203.
[5] S.-I. Na, S.-S. Kim, J. Jo, D.-Y. Kim, Adv. Mater. 20 (2008) 4061–4067.
[6] S.-I. Na, G. Wang, S.-S. Kim, T.-W. Kim, S.-H. Oh, B.-K. Yu, T. Leea, D.-Y. Kim, J. Mater. Chem. 19 (2009) 9045–9053.
[7] Y. Kim, C. Sachse, M.L. Machala, C. May, L. Müller-Meskamp, K. Leo, Adv. Funct. Mater. 21 (2011) 076–1081.
[8] S.K. Hau, H.-L. Yip, J. Zou, A.K.-Y. Jen, Org. Electron. 10 (2009) 1401–1407.
[9] Y. Zhou, F. Zhang, K. Tvingstedt, S. Barrau, F. Li, W. Tian, O. Inganäs, Appl. Phys. Lett. 92 (2008) 233308.
[10] S.-I. Na, B.-K. Yu, S.-S. Kim, D. Vak, T.-S. Kim, J.-S. Yeo, D.-Y. Kim, Sol. Energy Mater. Sol. Cells 94 (2010) 1333–1337.
[11] Y.-F. Lim, S. Lee, D.J. Herman, M.T. Lloyd, J.E. Anthony, G.G. Malliaras, Appl. Phys. Lett. 93 (2008) 193301.
[12] H. Schmidt, H. Flügge, T. Winkler, T. Bülow, T. Riedl, W. Kowalsky, Appl. Phys. Lett. 94 (2009) 243302.
[13] S.F. Tedde, J. Kern, T. Sterzl, J. Fürst, P. Lugli, O. Hayden, Nano Lett. 9 (2009) 980–983.
[14] M. Ramuz, L. Bürgi, C. Winnewisser, P. Seitz, Org. Electron. 9 (2008) 369–376.
[15] J.-N. Audinot, P. Leveque, R. Bechara, N. Leclerc, J. Guillot, H.-N. Migeon, G. Hadziioannouc, T. Heiserb, Surf. Interface Anal. 42 (2010) 1010–1013.
[16] R.M. Walker, H. Wallman, in: G.E. Valley, H. Wallman (Eds.), Vacuum-Tube Amplifiers, McGraw-Hill, New York, 1948.
[17] M. Punke, S. Valouch, S.W. Kettlitz, N. Christ, C. Gärtner, M. Gerken, U. Lemmer, Appl. Phys. Lett. 91 (2007) 071118.

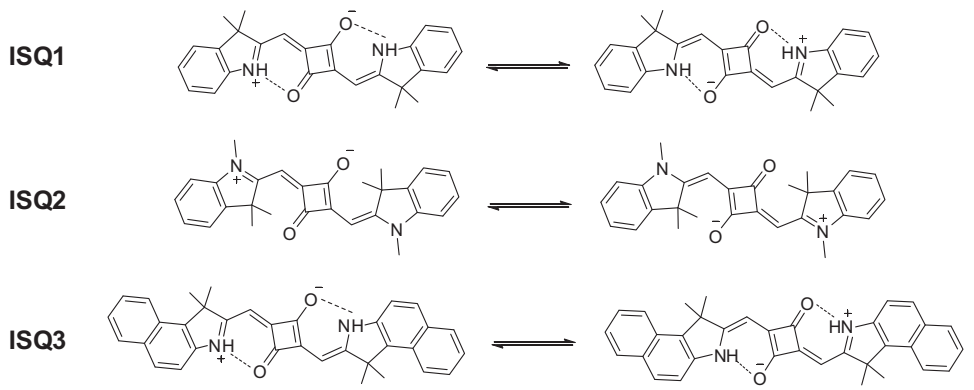

Fig. 1. Resonant structure of the squarylium dyes.

because of the crystallization occurring upon annealing. In 2010, Anthopoulos et al. continued this work and demonstrated the suitability of squarylium dyes as ambipolar semiconductors [20].

Although to date the mobility of squarine based transistor is not as high as ordinary semiconductors, the enhancement via simple and cheap post-process such as annealing is a potential advantage. In this paper, we fabricated p-type transistors based on a series of indolium squarine dyes, ISQ1, ISQ2 and ISQ3 (Fig. 1), and compared the effect of structural factors, such as intramolecular H-bondings and steric hindrance, on the phase transition and electrical properties enhancement of the semiconducting layer. The mobility of solution processed device came up to 4.8×10^{-3} cm^2/Vs and the highest mobility of 0.2 cm^2/Vs was achieved in single crystal device.

2. Experimental

2.1. General description

All commercial available materials were used as received without further purification unless otherwise stated. All reactions were heated in refluxing under Ar atmosphere with anhydrous solvents. ^1H NMR data were collected on JEOL JNM-ECA 600 MHz spectrometer with chemical shifts reference to tetramethylsilane in $CDCl_3$. Mass spectrometry was performed with Thermo Fisher LTQ LCMS spectrometer. Material purity was analyzed with Agilent 1100 High Performance Liquid Chromatograph (HPLC). Thermal gravimetric analysis was performed in nitrogen with TA Instrument TGA Q5000 (heating rate of 10 °C/min). Optical images were taken via Olympus BX51M microscope. The dynamic atomic force microscopy (DFM) of the ISQ film was taken by Seiko SPI 3800 Series SPA-400 scanning probe microscope.

2.2. Material synthesis

The octadecyltrichlorosilane (OTS) and 3,4-dihydroxy-3-cyclobutene-1,2-dione was purchased from Acros. 2,3,3-trimethyl-4,5-benzo-3H-indole was purchased from Alfa Aesar. The remaining chemicals and solvents were purchased from Sigma–Aldrich. 2,4-bis(3,3-dimethyl-2-benzoindolinylidenemethyl)cyclobutenediylium-1,3-diolate (ISQ3) was synthesized by a modified procedure accordi ng to previously published methods [21]. 3,4-dihydroxy-3-cyclobutene-1,2-dione and 2,3,3-trimethyl-4,5-benzo-3H-indole in molar ratio 1:2 were heated in toluene:*n*-butanol for 6 h and then heated azeotropically using a Dean–Stark trap for 2 h. The extra solvents were removed by vacuum distillation. The precipitate was isolated and purified by column chromatography and recrystallization to get dark green crystals with a yield of 84%. The purity was assessed by NMR and HPLC and found to be higher than 99.5%. ^1H NMR ($CDCl_3$): δ 13.13 (s, 2H, NH), 7.39–7.96 (d or t, 12H, benzoindole), 5.60 (s, 2H, CH), 1.74 (s, 12H, CH_3). MS-ESI (CH_2Cl_2) *m/z*: 495.45 (M–H); calcd for $C_{34}H_{28}N_2O_2$: 496.22. Anal. found: C 81.75, H 5.66, N 5.58; Anal. calcd: C 82.23, H 5.68, N 5.64. The other ISQ compounds were synthesized and purified by similar procedures.

2.3. X-ray diffraction

The purple prism crystal of ISQ2 and dark green platelet crystal of ISQ3 were grown by slow evaporation from the ISQ/dichloromethane solution at room temperature. X-ray crystallography was performed on a Bruker CCD diffractometer for ISQ2 at 293 K and on a Rigaku CrystalClear CCD diffractometer for ISQ3 at 153 K. Computations were performed using the Shelxtl NT ver. 5.10 program package [22] on an IBM PC 586 computer [22]. Analytic expressions of atomic scattering factors were employed, and anomalous dispersion corrections were incorporated [23]. Crystal drawings were produced with XP [22].

The film samples were prepared by vacuum deposition of 50 nm ISQ on silicon wafers. X-ray diffraction patterns were collected by Rigaku-2500 diffractometer equipped with a Cu target. 2θ scan ranged from 3° to 100° at a speed of 6°/min.

The film samples were prepared by vacuum deposition of 50 nm ISQ on silicon wafers. X-ray diffraction patterns were collected by Rigaku-2500 diffractometer equipped with a Cu target. 2θ scan ranged from 3° to 100° at a speed of 6°/min.

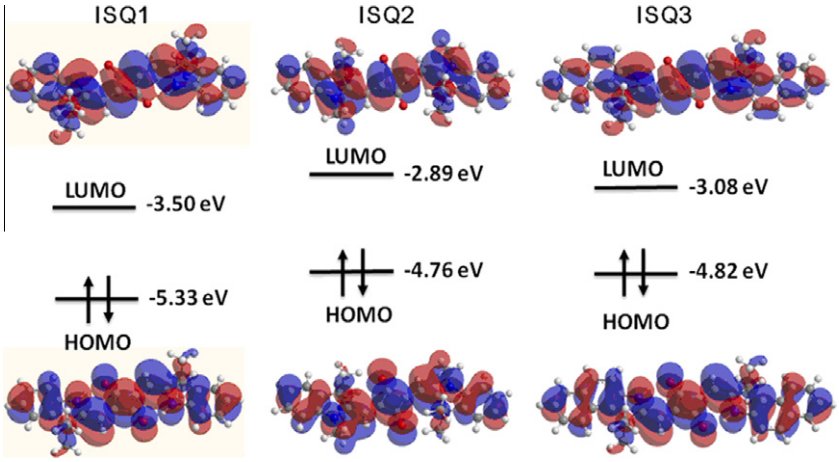

Fig. 2. HOMO and LUMO of the singlet ground-state ISQ.

2.4. Energy band

Absorption spectra of 10^{-3} M ISQ/CH_2Cl_2 solution in a quartz cuvette were recorded with Aglient 8453 UV–Vis spectrophotometer. The maximum absorption edges were observed at 664 nm for ISQ2 and 713 nm for ISQ3, from which the band gaps of ISQ2 and ISQ3 were estimated to be 1.87 and 1.74 eV respectively. The electrochemical properties were investigated by cyclic voltammetry. The measurement was performed on a Princeton Applied Research Potentiostat/Galvanostat model 283 voltammetric analyzer in dichloromethane at a scan rate of 100 mV/s and a range from −2 to 2 V. Ferrocene was added as an internal reference. From the oxidation with peaks for ISQ and ferrocene, the highest occupied molecular orbital (HOMO) level of ISQ2 and ISQ3 was estimated to be −4.76 and −4.80 eV. According to the spectrum data, the lowest unoccupied molecular orbital (LUMO) level of ISQ2 and ISQ3 was deduced to be −2.89 and −3.08 eV.

2.5. Device fabrication and characterization

Bottom gate top contact field-effect transistors were fabricated on heavily n^+ doped silicon wafer with a 300 nm thermally grown SiO_2 gate dielectric. The wafers were subsequently cleaned by sonication in toluene, acetone and isopropynol. SiO_2 surface was treated by piranha solution and then modified with OTS. Forty-five nanometers ISQ were thermally deposited at a rate of 1 Å/s under a pressure of 10^{-4} Pa. For solution processed devices, 0.4 wt% ISQ/$C_2H_4Cl_2$ solution was spin coated onto the substrate in glove box. Forty-five nanometers films were obtained and then baked at 40 °C for 10 min. For single crystal devices, the ISQ crystal strips were in situ assembled on the OTS modified substrates by immersing the substrates into 10^{-3} M ISQ/CH_2Cl_2 solution and then slowly evaporating the solvent in a saturated hexane atmosphere for two weeks. Finally 50 nm Au was vacuum deposited through a shadow mask as drain and source electrodes. Electrical characteristics of the transistors were measured with Keithley 4200 in air and without encapsulation.

3. Results and discussion

3.1. π–π packing mode on intermolecular electrostatic interaction

Due to the recomposition effect of squaric acid, 1,3-sysmetrically substituted squarines hold separate charge centers. Through rapid configuration resonance, positive charges are averagely dispersed on both side groups (Fig. 1) [24]. ISQ1 was studied as a basic structure. ISQ2 and ISQ3 were employed as comparison. For ISQ1 and ISQ3, the intramolecular H-bondings between squaric ring and the indole ring help constructing a quasi-heptatomic ring and benefitted the flat structure. For ISQ2, as the hindrance of attached methyls on nitrogens, no H-bondings formed between the indole ring and the squaric ring. There is also a 180° reversal in the plane of the side groups [25]. For ISQ3, the conjugated area was enlarged by extending aromatic rings on indole groups, which also increased rigidity and the hindrance of molecular motion. Geometrical configurations were explored by theoretical calculation at B3LYP/6-311+G(d,p) level and verified by crystal structural diffraction. Fig. 2 shows the profiles and the relative energy levels of HOMO and LUMO. As the frontier orbital was delocalized among the whole molecular plane, a close face to face packing would benefit the π–π carrier transport between neighboring molecules.

The crystal packing of ISQs was shown in Fig. 3. Face to face packing was found in the cell. The closest interplanar distance of ISQ1 is 3.6 Å. For ISQ2 this value is 3.9 Å, larger than 3.6 Å, the upper limit of general π–π interaction. For ISQ3 it is only 3.3 Å, indicating better conjugated transport efficiency. Twenty-five- and eighteen degree torsions of side groups were observed in ISQ2 and ISQ3 respectively, which is different with the near planar structure of ISQ1.

To characterize the distribution of electron-rich and electron-deficient parts, net charge calculation was

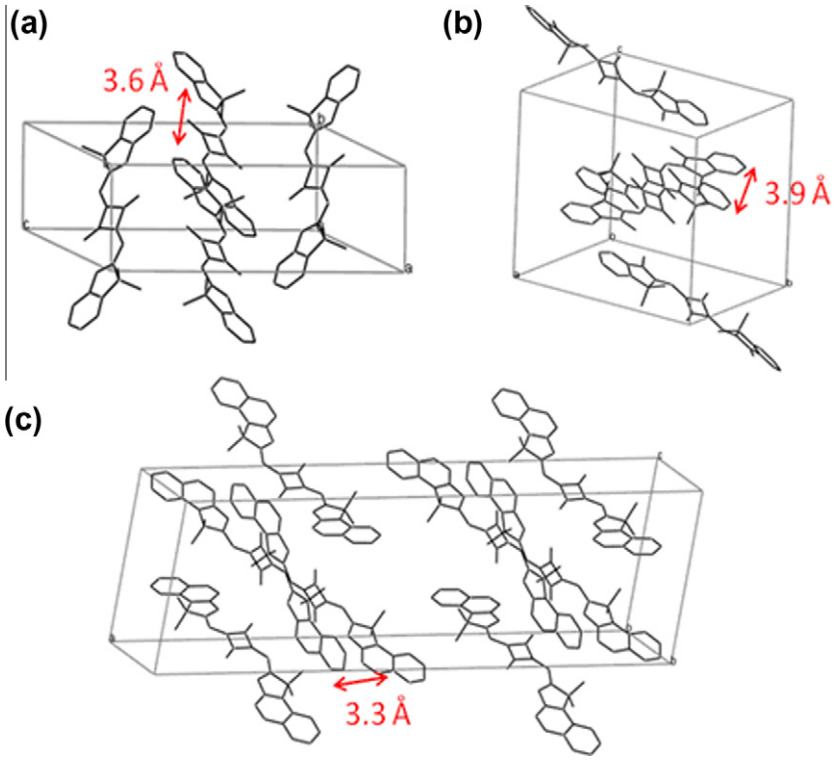

Fig. 3. Crystal packing of ISQ1 (a), ISQ2 (b) and ISQ3 (c) in a single cell (hydrogens omited).

performed by natural bond orbital population at PBE1PBE/6–311+G(d, p) level. It was found the central squaric ring with two oxygen atoms carried more negative charges and the two side groups carried more positive charges. Remarkably, the staggered packing of squaric rings and side groups for adjacent molecules accorded with this result. The electrostatic interaction, marked by double arrows in Fig. 4, also indicated that the torsion originated from the mismatch of the charge centers.

In ISQ1, the positive centers face well against the negative centers. Besides the intramolecular H-bondings, the electrostatic attraction of opposite charge centers helps keeping planar packing. However, for ISQ2, no H-bondings assist in limiting the rotation of indole groups and the hindrance of N-methyls prevents fine packing between inverse centers. The shift of the relative positions causes partly overlapped positive areas. The direction of the electrostatic repulsion is consistent with the observed torsion. Though ISQ3 is structurally similar to ISQ1, the extended benzene rings of side groups intruded into the positive region where repulsion took place.

To investigate whether the contrary charge centers could enable ambipolar transport, inner reorganization energy (λ_h and λ_e) was calculated based on the result of energy and geometrical optimization for ISQ ions at B3LYP/6-311+G(d,p) level: $\lambda_h = E^+/E - E + E/E^+ - E^+$, $\lambda_e = E^-/E - E + E/E^- - E^-$, where E, E^+ and E^- are the optimized energy of neutral, positive and negative molecules, E^+/E means the static energy of positive molecule based on the geometrically optimized configuration of neutral molecule; E/E^+, E^-/E and E/E^- are defined correspondingly. For ISQ1, $\lambda_h = 0.168$ eV, $\lambda_e = 0.271$ eV; for ISQ2, $\lambda_h = 0.208$ eV, $\lambda_e = 0.266$ eV; for ISQ3, $\lambda_h = 0.134$ eV, $\lambda_e = 0.264$ eV. The

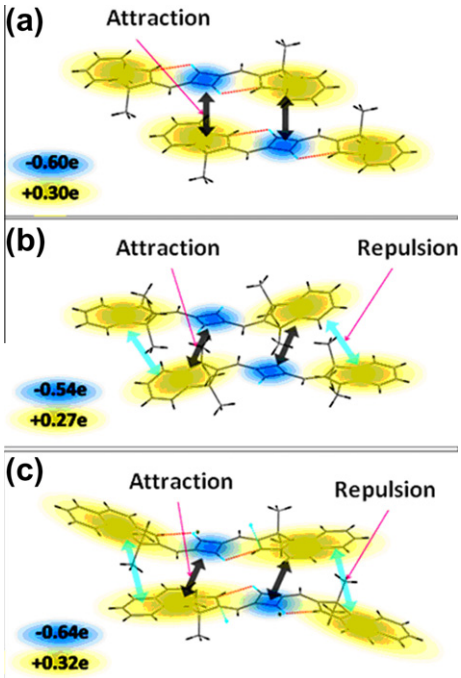

Fig. 4. The intermolecular packing mode and electrostatic interaction: (a) ISQ1, (b) ISQ2, (c) ISQ3.

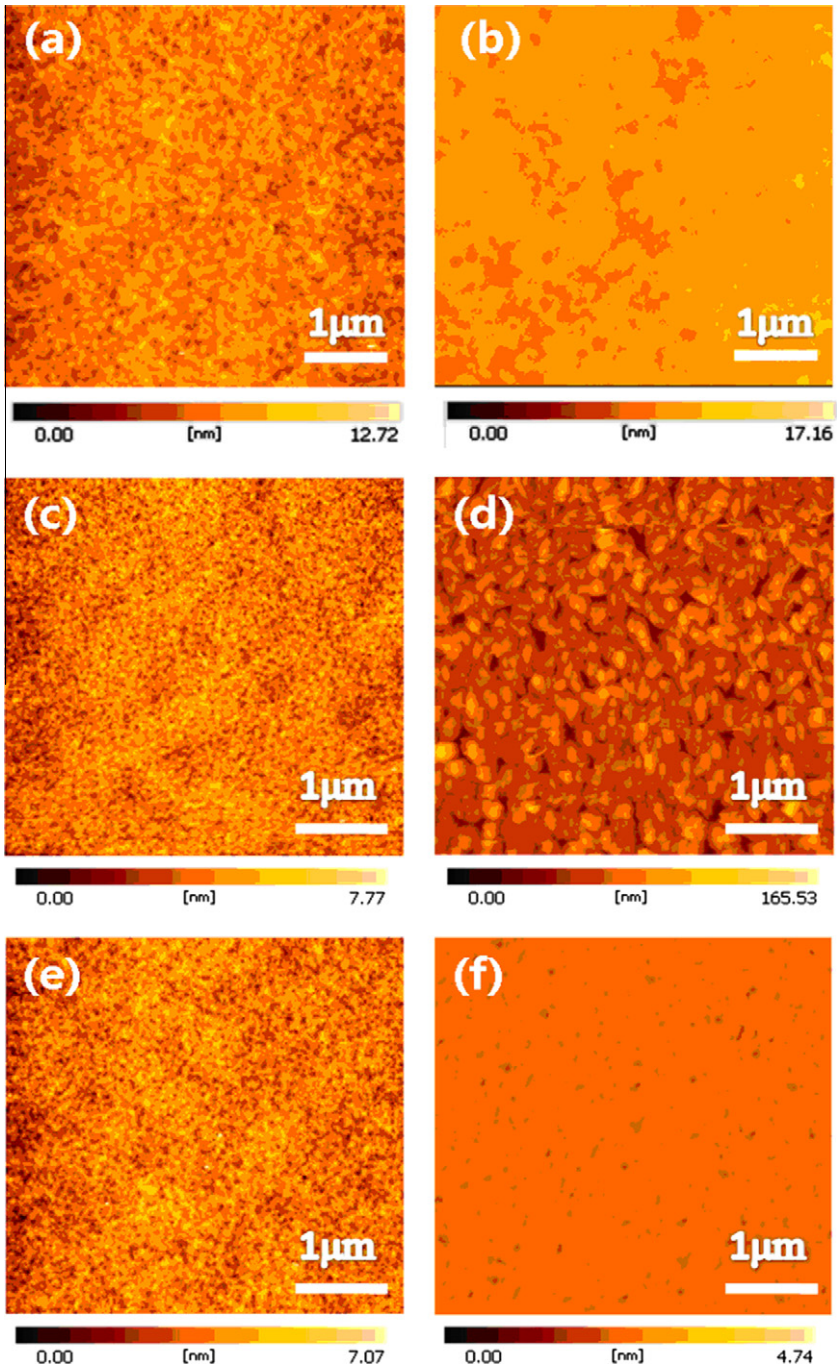

Fig. 5. DFM morphology on SiO_2 substrate: (a) thermal evaporated film of ISQ1, RMS = 0.6 nm, (b) spin coated film of ISQ1, RMS = 0.4 nm, (c) thermal evaporated film of ISQ2, RMS = 0.7 nm, (d) spin coated film of ISQ2, RMS = 18 nm, (e) thermal evaporated film of ISQ3, RMS = 0.5 nm, and (f) spin coated film from of ISQ3, RMS = 0.3 nm.

results predicted ISQs are mainly hole-transporters and ISQ3 might have higher mobility than ISQ1.

3.2. ISQ field-effect transistors

The processability of three ISQ compounds is similar. The decomposition temperatures were estimated to 265 °C for ISQ2 and 288 °C for ISQ3, and both have good solubility in halohyrocarbons. The film quality via vacuum thermal deposition and solution process was investigated by DFM (Fig. 5). The root mean square (RMS) roughness is generally less than 1 nm, except ISQ2 spin-coated film because crystallization during spin coating caused rather coarse surface.

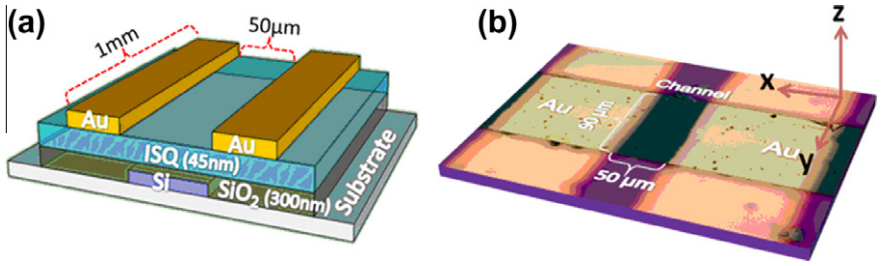

Fig. 6. (a) Architecture of ISQ field-effect transistor and (b) optical image of ISQ3 single crystal transistor.

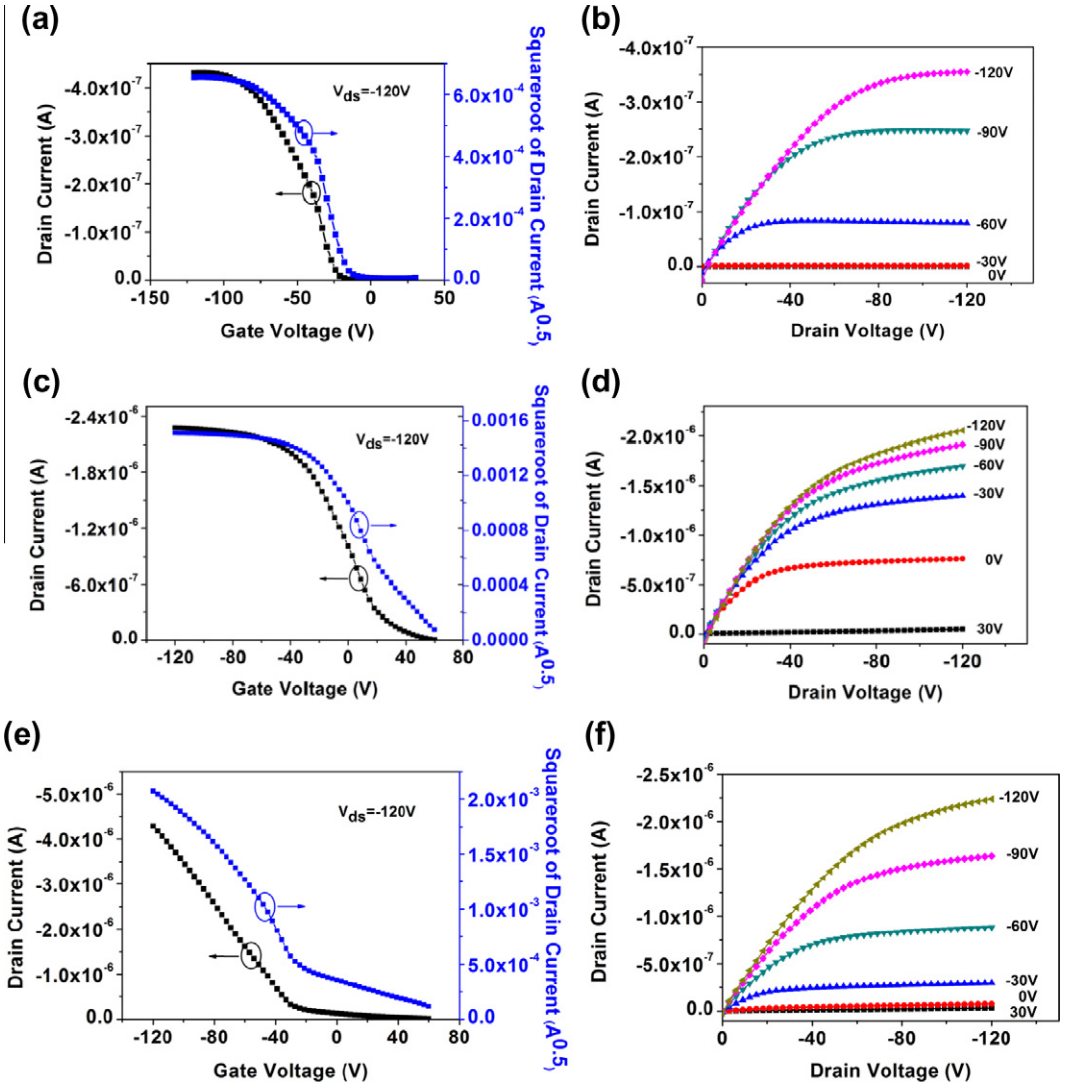

Fig. 7. Transistor characteristic curves: (a, b) ISQ1 by thermal evaporation; (c, d) ISQ3 by spin coating, with *W*/*L* of 20; (e, f) ISQ3 single crystal with *W*/*L* of 1.8.

Top-contact bottom-gate transistors based on thermally deposited and spin coated films of ISQ2 and ISQ3 were fabricated on Si/SiO_2 wafers (Fig. 6a). In addition, single crystal device of ISQ1 and ISQ3 was also obtained by solution growth (Fig. 6b). Except spin coated device of ISQ2, all ISQ transistors exhibited typical p-type field effect characteristics with saturated output. Post annealing in the N_2-filled glove box at 80 °C for 8 h accelerated the crystallization of the ISQ films, and consequently enhanced the device performance. The highest mobility for thermal

Table 1
Electrical parameters of ISQ transistors.

Material	Process	Annealing temp (°C)	μ[cm^2/(Vs)][a]	On/off ratio[a]	V_T[V][a]
ISQ1	Evaporation	–	5.0×10^{-5}	2×10^2	−10
	Evaporation	80	7.1×10^{-3}	2×10^4	−16
	Solution	–	1.1×10^{-6}	10	0
	Solution	80	6.8×10^{-4}	8×10^3	38
	Crystal	–	0.078	10^2	−37
ISQ2	Evaporation	–	1.8×10^{-4}	8×10^2	35
	Evaporation	80	3.1×10^{-3}	5×10^3	20
ISQ3	Evaporation	–	5.4×10^{-4}	10^4	29
	Evaporation	80	8.7×10^{-4}	10^4	4
	Solution	–	1.8×10^{-6}	40	45
	Solution	80	4.8×10^{-3}	10^3	75
	Crystal	–	0.2	3×10^2	−14

[a] The listed values are derived from the devices with the best mobility.

evaporated devices was achieved by ISQ1. The best spin-coated device and single crystal device were achieved by ISQ3. Representative transfer and output curves of these devices were displayed in Fig. 7. The best electrical parameters for all kinds of devices were summarized in Table 1.

3.3. Mobility dependence on crystallization and morphology of the channel

As estimated by inner reorganization energy, the performance of ISQ2 devices is lower than the ISQ1 and ISQ2. This could be explained by the large π–π interplanar distance and the hindrance from N-methyls. ISQ3 was expected to have better performance than ISQ1. Its evaporated device has mobility of 5.4×10^{-4} cm^2/Vs and on/off ratio of 10^4, which is the highest among all samples before annealing. However, no visible crystalline regions formed after annealing, and thus little performance improvement was detected. To compare the speed of crystallization, 50 nm ISQs were thermally deposited on silicon wafers and characterized by XRD. Initially all samples had same diffraction pattern as pure silicon wafers (Fig. 8a). In the test 24 h later, diffractional peaks appeared only in ISQ1 and ISQ2 films, which indicated a trend from amorphous state to polycrystalline state (Fig. 8b). The difficulty for evaporated ISQ3 films to reorder its micro structure into crystal phase could be explained by the large hindrance from the structural rigidity.

For solution processed ISQ3 device, solvent in the films counteracted the effect of the steric hindrance and made the films' polycrystallization possible. From the optical image (Fig. 9b), we can find that the annealed channels contained the light blue area (region 1) and the dark blue area (region 2). The magnified images show that, in region 1, the polycrystalline film is continuous (Fig. 9c), while region 2 was filled with large and separate crystal particles (Fig. 9d). As the two regions are parallely connected between the electrodes, assuming that the threshold voltages of the two regions are uniform, the total saturated drain current could be expressed as

$$I = I_1 + I_2 = \frac{\mu_1 W_1 C_0 (V_G - V_T)^2}{2L} + \frac{\mu_2 W_2 C_0 (V_G - V_T)^2}{2L} \quad (1)$$

where μ_1, W_1 and μ_2, W_2 are the mobilities and the channel widths of region 1 and 2, respectively. Assuming φ_1 and φ_1

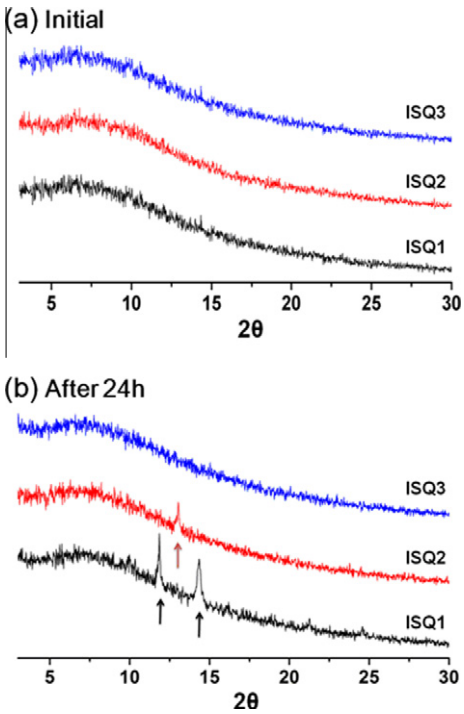

Fig. 8. XRD patterns of 50 nm ISQ films on silicon. (a) Initial; (b) 24 h later.

were the fractions of region 1 and region 2 in the whole channel width, respectively, then

$$W_1 = W \cdot \varphi_1 \quad (2)$$

$$W_2 = W \cdot \varphi_2 \quad (3)$$

From Eqs. (1)–(3), we can get Eq. (4):

$$I = \frac{WC_0 (V_G - V_T)^2}{2L} (\mu_1 \varphi_1 + \mu_2 \varphi_2) \quad (4)$$

Therefore the effective mobility (μ_e) of the whole channel could be written as

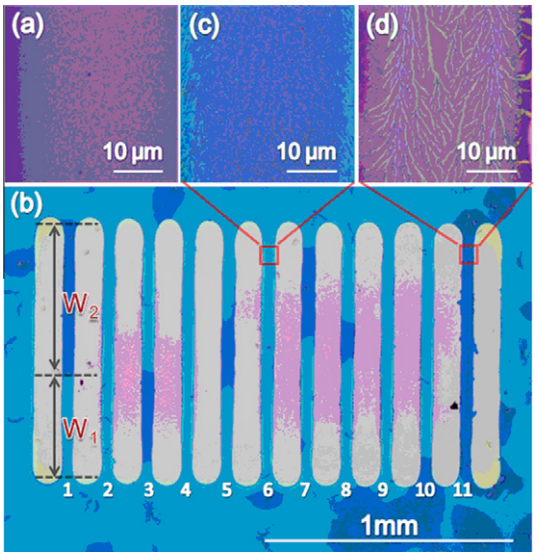

Fig. 9. Optical images of the spin coated ISQ3 device: (a) the channel before annealing; (b) the total 11 channels after annealing; the morphology of (c) region 1 and (d) region 2.

$$\mu_e = \mu_1\varphi_1 + \mu_2\varphi_2 \tag{5}$$

Since $\varphi_1 + \varphi_2 = 1$, supposing the mobility of region 1 in all channels is uniform and the mobility of region 2 in all channels is uniform, Eq. (5) could be changed into Eq. (6).

$$\mu_e = (\mu_1 - \mu_2)\varphi_1 + \mu_2 \tag{6}$$

According to Eq. (6), we know the effective channel mobility is linearly dependent on the percentage of each region.

The data of all the 11 channels on one substrate were listed in Table 2. It was found the linear fitting of Eq. (6) conformed well to the experimental values (Fig. 10). The average mobilities of region 1 and 2 in this device were thus determined as 2.8×10^{-3} and 4.6×10^{-5} cm^2/Vs respectively from the fitting parameters. We think the higher mobility of region 1 resulted from the better transport in polycrystalline phase and fine continuity. In region 2, excessive crystallization caused discontinuity and large grain boundaries, which prohibited the transport of the carriers and resulted in the low mobility. Therefore, the channel status of the best mobility (4.8×10^{-3} cm^2/Vs) in our experiments should consist of region 1. Our analysis indicated that annealing condition and structural property of semiconductors are important factors of the channel structure, and should be carefully controlled to improve the device performance.

In single crystal device of ISQ3, the highest mobility of 0.2 cm^2/Vs was obtained with an on/off ratio of 3×10^2, better than ISQ1 (0.078 cm^2/Vs and 10^2). One possible reason for this improvement is the enlargement of side conjugated groups. However, according to the stacking modes and the interplanar distances of ISQ1 and ISQ3 crystals (shown in Fig. 3), the anisotropies of the transport efficiency should exist. At present, mobilities of ISQ1 and ISQ2 crystals were measured only in *x*–*y* plane as shown in Fig. 6b and the molecular orientation along the channel is not clear yet. Therefore, more research works on the anisotropic transport are necessary in our follow-up works for understanding the mechanisms of charge transport in ISQ crystals. Meanwhile, it was noticed that large thickness of crystal (50 μm for ISQ3 and 30 μm for ISQ1) weakened field induction and the top contact structures increased the off current. The potentiality of ISQ dyes has not been adequately exploited yet.

Table 2
The effective channel mobilities of spin coated ISQ3 transistors after annealing.

Channel No.	φ_1(%)	φ_2(%)	μ[cm^2/(Vs)]
1	42	58	1.14×10^{-3}
2	100	0	2.96×10^{-3}
3	65	35	1.83×10^{-3}
4	100	0	2.75×10^{-3}
5	75	25	1.97×10^{-3}
6	100	0	2.85×10^{-3}
7	67	27	1.87×10^{-3}
8	83	17	2.53×10^{-3}
9	100	0	2.74×10^{-3}
10	89	11	2.55×10^{-3}
11	0	100	1.11×10^{-4}

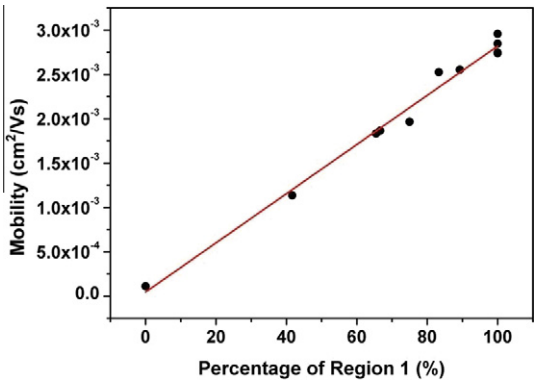

Fig. 10. Linear fitting of mobility versus area percentage of region 1.

3.4. Stability

All the annealed devices were kept in air without encapsulation. The mobility in a period of 4 months was shown in Fig. 11. Generally there was no break down and severe aging for these devices. The mobility of thermal vacuum deposition device of ISQ1 decayed fast in the first few months. Ambient H_2O and O_2 were thought to be the predominant physical reasons. The sudden degradation of ISQ3 single crystal device from the 3rd month may result from the natural airslake and the wear of Au electrodes in repeating measurements. As the compact structure of crystal phase is effective in carrier transport and preventing the infiltration of ambient impurity, the rising mobility in ISQ2 thermal evaporated and ISQ3 spin-coated devices could be related with the gradual completion of spontaneous crystallization process.

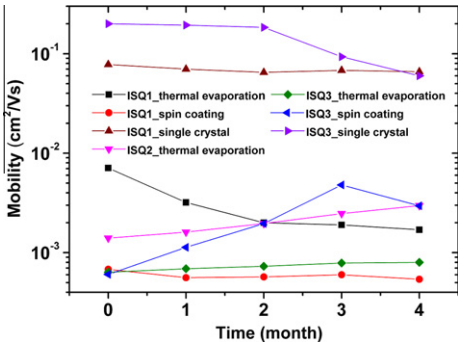

Fig. 11. The stability of ISQ transistors in air.

4. Conclusion

In summary, a series of ISQ compounds were systematically investigated as semiconductors in OFETs. The comparison between structure and performance clarified the relation of the intermolecular electrostatic interaction to the packing configuration in crystal phase. The crystallization speed and morphology of polycrystalline film could be controlled by adjusted the structural rigidity. Highest mobility of 0.2 cm^2/Vs was obtained, which could be improved by further optimization. Moreover, the application of ISQ compounds broadens the scale for stable semiconductors in OFETs.

Acknowledgments

The authors greatly appreciate the help from Prof. Ruji Wang, Prof. Yongge Wei and Prof. Huizhong Kou in the analysis of crystal structure. This work was financially supported by the National Natural Science Foundation of China (60877026 and 50990062), the National Key Basic Research and Development Program of China under Grant (2009CB930602).

References

[1] G. Horowitz, Organic field-effect transistors, Advanced Materials 10 (1998) 365.
[2] Z.N. Bao, A.J. Lovinger, Soluble regioregular polythiophene derivatives as semiconducting materials for field-effect transistors, Chemistry of Materials 11 (1999) 2607.
[3] C.D. Dimitrakopoulos, D.J. Mascaro, Organic thin-film transistors: a review of recent advances, IBM Journal of Research and Development 45 (2001) 11.
[4] S.R. Forrest, The path to ubiquitous and low-cost organic electronic appliances on plastic, Nature 428 (2004) 911.
[5] P. Sonar, S.P. Singh, S. Sudhakar, A. Dodabalapur, A. Sellinger, High-mobility organic thin film transistors based on benzothiadiazole-sandwiched dihexylquaterthiophenes, Chemistry of Materials 20 (2008) 3184.
[6] Y. Didane, G.H. Mehl, A. Kumagai, N. Yoshimoto, C. Videlot-Ackermann, H. Brisset, A "kite" Shaped styryl end-capped benzo[2,1-b:3,4-b′]dithiophene with high electrical performances in organic thin film transistors, Journal of American Chemical Society 130 (2008) 17681.
[7] D. Song, H.B. Wang, F. Zhu, J.L. Yang, H.K. Tian, Y.H. Geng, D.H. Yan, Phthalocyanato tin(IV) dichloride: an air-stable high-performance n-type organic semiconductor with a high field-effect electron mobility, Advanced Materials 20 (2008) 2142.
[8] Y. Ito, A.A. Virkar, S. Mannsfeld, J.H. Oh, M. Toney, J. Locklin, Z.N. Bao, Crystalline ultrasmooth self-assembled monolayers of alkylsilanes for organic field-effect transistors, Journal of American Chemical Society 131 (2009) 9396.
[9] A.A. Virkar, S.C.B. Mannsfeld, Z.N. Bao, Energetics and stability of pentacene thin films on amorphous and crystalline octadecylsilane modified surfaces, Journal of Materials Chemistry 20 (2010) 2664.
[10] Y.D. Park, J.A. Lim, H.S. Lee, K. Cho, Interface engineering in organic transistors, Material Today 10 (2007) 46.
[11] H. Yan, Z.H. Chen, Y. Zheng, D. Newman, J.R. Quinn, F. Dötz, M. Kastler, A. Facchetti, A high-mobility electron-transporting polymer for printed transistors, Nature 457 (2009) 679.
[12] A.L. Briseno, S.C.B. Mannsfeld, M.M. Ling, S.H. Liu, R.J. Tseng, C. Reese, M.E. Roberts, Y. Yang, F. Wudl, Z.N. Bao, Patterning organic single-crystal transistor arrays, Nature 444 (2006) 913.
[13] Y. Qiu, Y.C. Hu, G.F. Dong, L.D. Wang, J.F. Xie, Y.N. Ma, H_2 O effect on the stability of organic thin-film field-effect transistors, Applied Physics Letters 83 (2003) 1644.
[14] M.E. Roberts, S.C.B. Mannsfeld, M.L. Tang, Z.N. Bao, Influence of molecular structure and film properties on the water-stability and sensor characteristics of organic transistors, Chemistry of Materials 20 (2008) 7332.
[15] M. Mas-Torrent, M. Durkut, P. Hadley, X. Ribas, C. Rovira, High mobility of dithiophene-tetrathiafulvalene single-crystal organic field effect transistors, Journal of American Chemical Society 126 (2004) 984.
[16] A. Treibs, K. Jacob, Cyclotrimethine dyes derived from squaric acid, Angewandte Chemie-international edition 699 (1965) 153.
[17] Z.Y. Li, S. Xu, L. Huang, X. Huang, L.H. Niu, Z.H. Chen, Z. Zhang, F.S. Zhang, K. Kasatani, Large third-order optical nonlinearities of centrosymmetric squaraines with heterocyclic donor groups measured by femtosecond degenerate four-wave mixing technique, Chemical Physics Letters 441 (2007) 123.
[18] A. Burke, L. Schmidt-Mende, S. Ito, M. Grätzel, A novel blue dye for near-IR 'dye-sensitised' solar cell applications, Chemical Communcations 234 (2007).
[19] E.C.P. Smits, S. Setayesh, T.D. Anthopoulos, M. Buechel, W. Nijssen, R. Coehoorn, P.W.M. Blom, B. Boer, D.M. Leeuw, Near-infrared light-emitting ambipolar organic field-effect transistors, Advanced Materials 19 (2007) 734.
[20] P.H. Wobkenberg, J.G. Labram, J.M. Swiecicki, K. Parkhomenko, D. Sredojevic, J.P. Gisselbrecht, D.M. Leeuw, D.D.C. Bradley, J.P. Djukic, T.D. Anthopoulos, Ambipolar organic transistors and near-infrared phototransistors based on a solution-processable squarilium dye, Journal of Materials Chemistry 20 (2010) 3673.
[21] Bruker, SHELXTL, Structure Determination Programs, Version 5.10, Bruker AXS Inc., Madison, WI, USA, 1997.
[22] G. M. Sheldrick, Shelxtl-97, Universitaet Goettingen, Goettingen, Germany, 1998.
[23] International Tables for X-ray Crystallography, vol. C, Kluwer Academic Publishers, Dordrecht, 1989. (Tables 4.2.6.8 and 6.1.1.4).
[24] R. West, D.L. Powell, New aromatic anions -3 molecular orbital calculations on oxygenated anions, Journal of American Chemical Society 85 (1963) 2577.
[25] Y. Kobayashi, M. Goto, M. Kurahashi, The crystal-structure of a squarylium dye, 2,4-bis(1,3,3-trimethyl-2-indolinylidenemethyl) cyclobutenediylium-1,3-diolate, Bulletin of the chemical society of japan 59 (1986) 311.

Light-Emitting Diodes (PhOLEDs). Specificity of LEDs compared to LECs is that light emission is instantly observed upon application of a sufficient voltage. PhOLEDs have been without contest the most widely investigated devices [12] even if use of neutral metal complexes limits the possibilities offered by coordination chemistry. As drawbacks, PhOLEDs are highly sensitive to the doping concentration and devices suffer from reduced emission efficiency while increasing the concentration of phosphorescent emitters, thus rendering their elaboration more difficult than LECs [13]. Recently, new devices involving the use of iridium soft salts based on an equimolar mixture of cationic and anionic iridium complexes have been reported [14]. Even if charged iridium complexes are included in the active layer, size of iridium (III) ions prevents their motions and resulting devices thus behave like a conventional diode.

Herein, we report on the synthesis of a new iridium (III) soft salt combining a cationic heteroleptic iridium complex prepared with a bipyridine as the ancillary ligand and an anionic iridium complex bearing thiocyanate anions as ligands. Soft salt was investigated as emitter in PhOLEDs and device characteristics of the corresponding device are reported. Cationic complex was also used as single emitter in LEC device and relevant data are summarized. Electrochemical, UV–visible absorption and photoluminescence properties were also investigated. DFT results obtained for soft salt **C·A** and cationic complex **C·PF$_6$** allowed us to rationalize the effect of the substituent on the optical properties and to assign the nature of the relevant excited states involved in the electroluminescence process.

2. Experimental

2.1. General informations

Electrochemical measurements were performed in a three electrode cell equipped with a 1 mm diameter carbon disk as the working electrode, platinum wire as the counter electrode and $Hg_2Cl_{2(s)}/Hg_{(l)}$ (saturated calomel electrode SCE) as the reference electrode. The supporting electrolyte was tetrabutylammonium perchlorate (TBAP) 0.1 M (Fluka, puriss.) and the solutions were deaerated by argon bubbling prior each experiment. Cyclic voltammograms (CVs) were recorded with a 600 CH Instruments potentiostat connected to a PC. Mass spectroscopy was performed by the Spectropole of the Université Paul Cézanne (Marseille). ESI mass spectral analyses were recorded with a 3200 QTRAP (Applied Biosystems SCIEX) mass spectrometer. The HRMS mass spectral analysis was performed with a QStar Elite (Applied Biosystems SCIEX) mass spectrometer. UV–visible spectra were recorded using a CARY 500 UV–visible–NIR spectrophotometer (Varian). Each sample was analyzed in a similar way: about 10 μL of a 1 mM solution of the chromophore were introduced into the cell (1 cm optical path) and diluted with an appropriate volume of solvent (spectroscopic grade), in order to obtain absorbance values lower than 1. Measurements of the molar absorption coefficient were made by recording the spectra corresponding to several aliquots of 10 μL of the chromophore solution in 2 mL of solvent, and then drawing a Beer–Lambert plot. Fluorescence spectral analyses were carried out with a Cary Eclipse spectrofluorimeter (Varian). Optical density was adjusted below 0.1 to avoid reabsorption artifacts. The fluorescence decay curves were obtained with a time-correlated single-photon-counting method using a titanium/sapphire laser (82 MHz, fundamental wave: 695–1000 nm, repetition rate lowered to 4 MHz by a pulse-peaker, 1 ps pulse width) pumped by an argon ion laser. A doubling crystal was used to reach 495 nm excitation. Solid state spectroscopic data were obtained on thin films of material deposited by sublimation under secondary vacuum (10^{-6} mbar) from organic-designed temperature-controlled thermal oven with alumina beds. Thickness of approx. 50 nm was controlled using built-in piezoelectric sensor assuming a material density of 1.25. Solid state absorption and emission spectra were recorded with a UV MC2 spectrophotometer from the SAFAS Monaco society and a Photon Technology International spectrofluorimeter. ^{1}H and ^{13}C NMR spectra were determined on a Bruker Advance DPX 300 MHz spectrometer: ^{1}H (300 MHz) and ^{13}C (75.5 MHz). The ^{1}H chemical shifts were referenced to the solvent peak: $CDCl_3$ (7.26 ppm), and the ^{13}C chemical shifts were referenced to the solvent peak: $CDCl_3$ (77.0 ppm). ^{1}H and ^{13}C NMR spectra were also obtained at room temperature in 5 mm o.d. tubes on a Bruker Avance 300 spectrometer equipped with a QNP probe head at the University of Versailles. All calculations were performed with the Gaussian03 program [15] in vacuo on a Nec TX7 with 32 processors Itanium 2 of the MESO center of the ENS Cachan. Orbitals were generated with the cubgen module of Gaussian and visualized with GaussView 3.0 of Gaussian Inc. GaussSum 2.1 [16,17] was used for the electronic spectrum simulation. The equation employed by the program to calculate the theoretical spectrum and the extinction coefficients is based on Gaussian convolution and is reported in the open source code of the program (available at http://gausssum.svn.sf.net/viewvc/gausssum/Trunk/src/gausssum/).

All starting materials and solvents were purchased from Aldrich and used as supplied commercially. Dimers Ir_2(ppy)$_4$μ-Cl$_2$ [18,19] (ppy = 2-phenylpyridine) and Ir_2(dfppy)$_4$ μ-Cl$_2$ [20,21] (dfppy = 2-(2′,4′-difluorophenylpyridine) were synthesized in a inert atmosphere according to the Nonoyama route by refluxing $IrCl_3 \cdot 3H_2O$ with 2–2.5 equivalents of cyclometalating ligand in a 3:1 mixture of 2-ethoxyethanol and water. Heteroleptic complexes $NBu_4 \cdot [Ir(dfppy)_2(SCN)_2]$ [22,23] (**NBu$_4$·A**) was synthesized from procedures adapted from the literature with tetrabutylammonium thiocyanate. Ir(ppy)$_2$(4,4′-dinonyl-2,2′-bipyridine)·PF$_6$ (**C·PF$_6$**) [24] was synthesized from a procedure reported in the literature without modification and with similar yield.

2.2. General procedure for the synthesis of the anionic complex *NBu$_4$·A*

A mixture of dichlorobridged iridium (III) dimer Ir_2(dfppy)$_4$μ-Cl$_2$ (1 eq.) was stirred with tetra *n*-butylammonium thiocyanate (10 eq.) in a mixture MeOH/$CHCl_3$ (50/50) with a few drops of DMF. The reaction mixture was stirred at reflux overnight. The solvent was removed under reduced pressure and addition of ether precipitated a solid which was filtered off and dried. Anionic complex **NBu$_4$·A** was obtained in 72% yield. Noticeably, significant

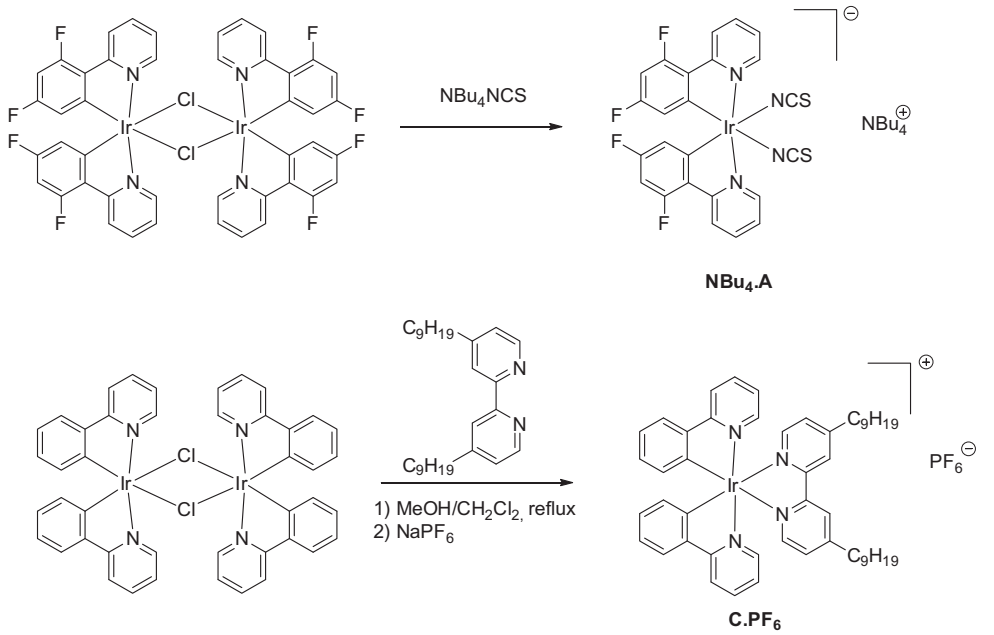

Scheme 1. Synthetic pathways and structures of complexes **C·PF$_6$** and **NBu$_4$·A**.

differences with the ^{1}H NMR spectrum previously reported in $CDCl_3$ were evidenced [22].

^{1}H NMR (400 MHz, $CDCl_3$, ppm): 0.96 (t, 12H, J = 6.4 Hz), 1.34–1.45 (m, 8H), 1.59–1.83 (m, 8H), 3.34 (t, 8H, J = 7.8 Hz), 5.49 (d, 2H, J = 7.1 Hz), 6.29 (t, 2H, J = 11.8 Hz), 7.20 (t, 2H, J = 6.3 Hz), 7.80 (t, 2H, J = 7.8 Hz), 8.22 (d, 2H, J = 8.6 Hz), 9.19 (d, 2H, J = 5.4 Hz).

HRMS (TOF MS ES-) m/z: theor: 689.0069 exp: 689.0107 (M^- detected).

Anal. Calcd. for $C_{40}H_{48}F_4IrN_5S_2$: C, 51.59; H, 5.20; N, 7.52; S, 6.89. Found: C, 51.84; H, 5.31; N, 7.59; S, 7.04.

2.3. General procedure for the synthesis of soft salt C·A

A mixture of **C·PF$_6$** (50 mg, 0.0474 mmol, 1.07 eq.), **NBu$_4$·A** (33 mg, 0.0439 mmol) were stirred at room temperature for one hour in a mixture of water/THF/$CHCl_3$: 10/7/5. Organic solvents were removed under reduced pressure and the residue was extracted several times with DCM. The organic phases were combined, dried over magnesium sulfate and the solvent removed under reduced pressure. Yellow solid was used without any further purification.

Table 1
Physical data of the compounds.

Complex	λ_{em}[a] (nm)	Φ_F[b]	Solid-state λ_{em} (nm)
C·PF$_6$	559	0.390	556
NBu$_4$·A	466, 502	0.574	555, 597
C·A	552	0.073	564

[a] Emission maximum in CH_2Cl_2.
[b] Fluorescence quantum yield in CH_2Cl_2. Ru(bpy)$_3$·PF$_6$ was used as a standard (λ_{ex} = 450 nm, Φ_F = 0.028 in CH_2Cl_2).

^{1}H NMR (400 MHz, $CDCl_3$, ppm): 0.86 (t, 6H, J = 6.6 Hz), 1.24–1.45 (m, 24H), 1.68 (qt, 4H, J = 7.6 Hz), 2.81 (t, 4H, J = 8.0 Hz), 5.47 (dd, 2H, J = 1.3 Hz, J = 8.8 Hz), 6.21 (dd, 2H, J = 2.2 Hz, J = 9.3 Hz), 6.29 (d, 2H, J = 7.4 Hz), 6.90 (t, 2H, J = 6.3 Hz), 6.99–7.09 (m, 4H), 7.19 (d, 2H, J = 5.1 Hz), 7.53 (d, 2H, J = 5.3 Hz), 7.67–7.80 (m, 8H), 7.89 (d, 2H, J = 8.0 Hz), 8.17 (d, 2H, J = 8.7 Hz), 8.46 (s, 2H), 9.17 (d, 2H, J = 4.8 Hz).

Anal. Calcd. for $C_{74}H_{72}F_4Ir_2N_8S_2$: C, 55.62; H, 4.54; N, 7.01; S, 4.01. Found: C, 55.73; H, 4.58; N, 6.81; S, 3.58.

2.4. OLED fabrication and measurements

PhOLEDs were fabricated onto cleaned indium tin oxide (ITO) glass substrates with sheet resistance of 10–12 Ω/cm^2. Prior to organic layer deposition, the ITO substrates were successively washed with acetone, ethanol and isopropanol under ultrasonic for 15 min, and finally exposed to UV-ozone 20 min. A poly(3,4-ethylenedioxythiophene):polystyrene sulfonate (PEDOT:PSS) layer was spin-coated in ambient atmosphere at a rate of 3000 rpm for 90 s and then dried by baking in air at 120 °C for 1 h. A filtered solution of poly(vinylcarbazole) (PVK, average M_n = 25,000–50 000, 20 mg/mL in 1,2-dichlorobenzene) was spin-coated at a rate of 3000 rpm for 40 s on top of the PEDOT:PSS layer. The light-emitting layers (soft salts) were then spin-coated from the 1,2-dichlorobenzene solution (30 or 60 mg/mL). The assembly was transferred into a deposition chamber where the calcium cathode was deposited by thermal evaporation under secondary vacuum, followed by the deposition of aluminum. The Ca (300 nm)/Al (60 nm) bilayer cathode of the device was formed with a shadow mask. Current density–voltage–luminescence (J–V–L) characteristics of the PhOLEDs and LECs were measured with a Keithley 4200 Semiconductor analyzer coupled with a Hamamatsu

Light sensor calibrated with a Minolta CS-100 luminancemeter. The EL spectra were collected with an Ocean Optics HR2000 Spectrometer. Chromatic Coordinates were calculated from the EL spectra and reported following the CIE-1964 chromaticity diagram. From the electrode deposition step, devices are stored and characterized in nitrogen filled gloveboxes (0_2 and H_2O < 0.1 ppm) without encapsulation.

3. Results and discussion

3.1. Synthesis and characterization

Syntheses of cationic iridium (III) complex **C·PF$_6$**, anionic iridium (III) complex **NBu$_4$·A** and corresponding soft salt **C·A** are schematically presented in the Scheme 1 and described in detail in the experimental section. Anion **NBu$_4$·A** was conveniently synthesized by reaction of the corresponding dichloro-bridged iridium (III) dimer [Ir(dfppy)$_2$(Cl)]$_2$ with 2 equivalents of tetra *n*-butylammonium thiocyanate in refluxing dichloromethane. Precipitation in ether provided **NBu$_4$·A** in 72% yield. Preparation of the mononuclear cationic complex **C·PF$_6$** was carried out under inert atmosphere through reaction of the dimer [Ir(ppy)$_2$(Cl)]$_2$ with 2 equivalents of bipyridine ligand in 75% yield. Choice of this bipyridine (4,4′-dinonyl-2,2′-bipyridine) as the ancillary ligand for **C·PF$_6$** was motivated by previous results published on light-emitting devices highlighting that addition of alkyl substituents on the bipiridyl ligand efficiently inhibited self-quenching of the excited states in charged complexes [25].

3.2. UV–visible absorptions and photoluminescence properties

The absorption and photoluminescence (PL) spectra of complexes **C·PF$_6$** and **NBu$_4$·A**, soft salt **CA**, recorded in the solid state and in solution, are shown in Figs. 1 and 2 for absorption, Figs. 3 and 4 for emission, respectively. Absorption spectra displayed the typical intense bands observed for iridium complexes in the Ultraviolet part of the spectrum between 200 and 300 nm, assigned to spin-allowed $^1\pi$–π^* ligand-centered transitions in both the 4,4′-dinonyl-2,2′-bipyridine and the 2′,4′-difluorophenylpyridine ligands. The less-intense, lower-energy absorption features extending from 300 to 450 nm were attributed to both spin-allowed and spin-forbidden metal-to-ligand charge transfer (MLCT) transitions [26,27]. Interestingly, charged complexes **C·PF$_6$**, **NBu$_4$·A**, and soft salt **C·A** exhibited similar absorption spectra in solution and in the solid state.

Fig. 3 shows a comparison of the emission spectra of complexes **C·PF$_6$**, **NBu$_4$·A** and soft salt **C·A** measured in the solid state at 298 K. When excited within the π–π^* and MLCT absorption band, solid films of all complexes **C·PF$_6$**, **NBu$_4$·A** and **C·A** exhibited a main peak with emission maxima centered at 558, 555 and 564 nm, respectively, followed by a shoulder at 597 nm for **NBu$_4$·A** (see Table 1). In contrast, the same experiments performed in deaerated solutions evidenced a slight blue shift of the emission maximum for **C·A** with maximum centered at 552 nm whereas maximum remained unchanged for **C·PF$_6$** (559 nm). On the opposite, emission maximum of anionic complex **A** strongly blue shifted in solution with maximum detected at 466 nm ($\Delta\lambda$ = 89 nm). Hypsochromic shift of the photoluminescence in solution for **NBu$_4$·A** compared to **C·PF$_6$** originates from the presence of electron-withdrawing fluorine on the ligands, therefore raising the Lowest Unoccupied Molecular Orbitals (LUMO) levels and increasing the band gap. Spectral blue shifts observed for the solution spectra of **NBu$_4$·A** and **C·A** relative to their solid-state photoluminescence can be attributed to aggregation-induced emissions and was notably previously reported for anionic iridium complexes by Graetzel and co-workers [28]. With reference to previous work on mixed-ligand cationic iridium complexes, nature of the emissive excited states in solution can be assigned

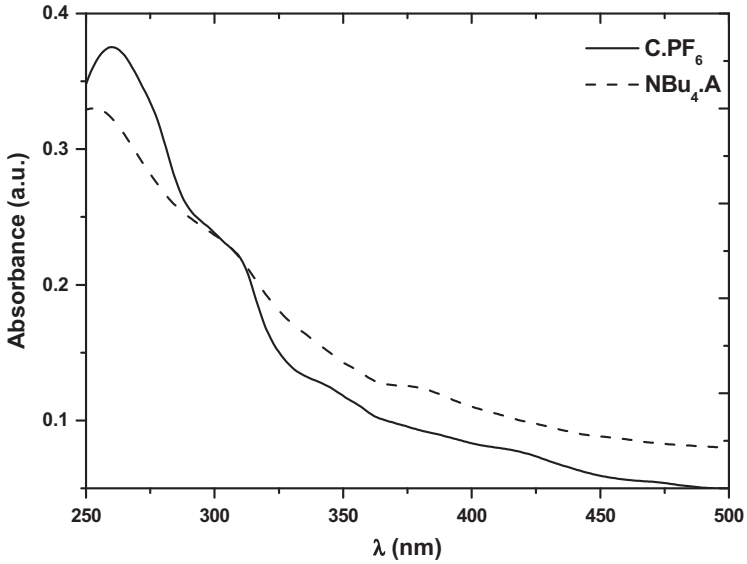

Fig. 1. UV–visible absorption spectra of complexes **C·PF$_6$** (solid line) and **NBu$_4$·A** (dashed line) in the solid state.

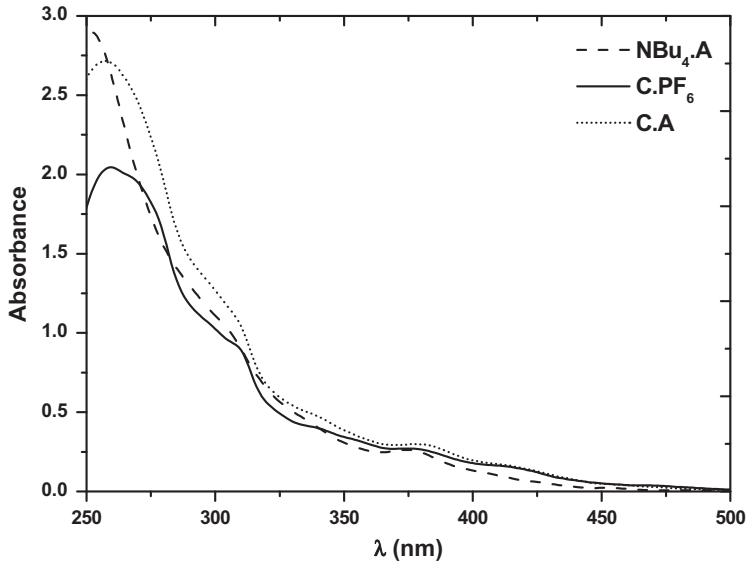

Fig. 2. UV–visible absorption spectra of complexes **C·PF$_6$**, **NBu$_4$·A** and **C·A** in CH_2Cl_2.

for **C·PF$_6$** to both metal-to-ligand and ligand-to-ligand charge transfer characters (^{3}MLCT and ^{3}LLCT, respectively) mixed with a ^{3}LC π–π^* character [19,29–32]. Concerning **NBu$_4$·A**, luminescence was assigned to the emission state of ^{3}MLCT. Interestingly, a lower photoluminescence is observed for anionic complex **NBu$_4$·A** compared to **C·PF$_6$**, as clearly demonstrated on the spectrum of **C·A** in solution by the intensity of the shoulder related to the anionic contribution at 466 nm. Noticeably, a strong red shift of the solid state emission wavelength for **NBu$_4$·A** was evidenced compared to that previously reported in the literature for the same complex without fluorines. (λ_{em}(NBu_4[Ir(ppy)$_2$(NCS)$_2$]) = 500 nm, $\Delta\lambda_{em}$ = 55 nm) [27].

3.3. Electrochemical properties

In order to investigate the frontier orbitals of the two complexes, their electrochemical behavior was investigated by cyclic voltammetry (CV) in acetonitrile on a carbon electrode. The results are presented in Fig. 5 and their respective redox data gathered in the Table 2. Highest Occupied Molecular Orbital (HOMO) and Lowest Unoccupied Molecular Orbitals (LUMO) levels of each complex were determined by using the correspondence between the electrode potentials values measured vs. Standard Hydrogen Electrode (SHE) and the redox Fermi energy values measured vs. electron energy in vacuum (see equation) [33]:

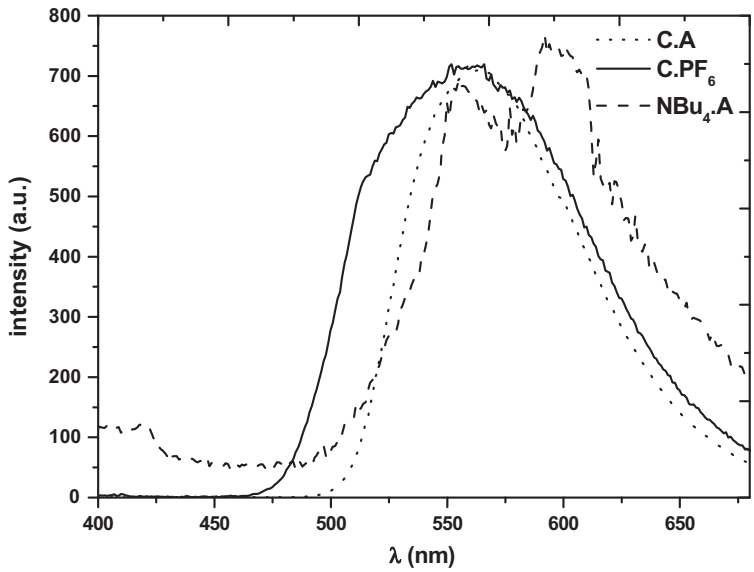

Fig. 3. Normalized photoluminescence spectra of complexes **C·PF$_6$**, **NBu$_4$·A** and **C·A** in thin films (λ_{ex} = 350 nm) at 298 K.

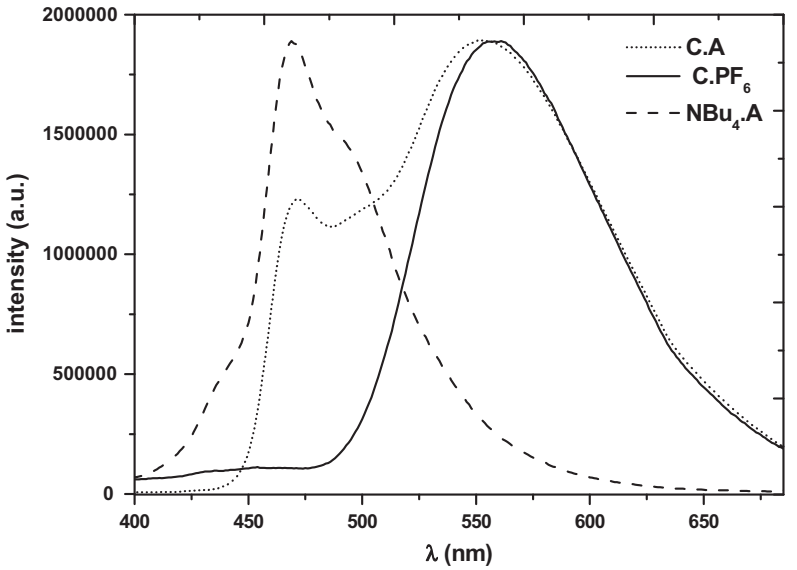

Fig. 4. Normalized photoluminescence spectra of complexes **C·PF$_6$**, **NBu$_4$·A** and **C·A** in argon-degassed CH_2Cl_2 (λ_{ex} = 350 nm) at 298 K.

$$E^{redox}_{F,0}\ (eV) = -E\ (V) - 4.4$$

The HOMO and the LUMO energy of the soft salts were then determined by the lowest energy potential of the pair of iridium complexes.

All complexes showed oxidation processes in the range of +1.01 to +1.28 V corresponding to the metal centered $Ir^{III/IV}$ process. The one-electron oxidation process was assigned to the removal of an electron from the metal-centered HOMO and complex **C·PF$_6$** only showed reversible oxidation. As expected, **NBu$_4$·A** was the easiest complex to oxidize, as a result of the negative charge on the complex. Concerning reduction processes, **C·PF$_6$** displayed one reversible reduction wave at −1.41 V. This reduction process can be attributed to ligand-based $bpy^{0/-}$ process and consisted in the addition of one electron on bpy-centered LUMO. Reduction process was more difficult for **NBu$_4$·A** due to the negative electric charge of the anionic complex and the phenylpyridine instead of bpy involved ligand (see DFT calculations). When combined in the soft salt, cyclic voltammogram of **C·A** displayed an overlap of the voltammograms of both individual components. As a result, **C·A** soft salt exhibited the lowest energy oxidation originating from the HOMO of the anion and the reduction process was issued from the LUMO of the cation, respectively.

Determination of the HOMOs and LUMOs of each iridium partner by electrochemistry confirmed the origin of the yellow photoluminescence observed for the soft salt **C·A** (see Fig. 7). Introduction of the negatively charged thiocyanate ligands on **Bu$_4$N·A** destabilized its HOMO (−5.2 eV) by releasing electron density from the ligand to the metal and also increased the energy of the LUMO (−2.7 eV). On the opposite, positive charge of the cationic complex stabilizes its HOMO (−5.6 eV) by removing electron density from the metal and also lowers its LUMO (−3.1 eV). Therefore, as the MLCT state of the cationic complex is stabilized compared to the MLCT state of the anionic one, yellow emission for the soft salt is thus observed in agreement with the measured HOMO–LUMO gap (2.2 eV).

3.4. Electroluminescent properties of PhOLEDs

In the only previous report concerning the incorporation of soft salt in light-emitting devices [14], iridium soft salts were tested both as emitters in single layered LECs and in multilayered OLED devices. Careful study of the resulting devices evidenced that soft salts behave as neutral complexes and that OLEDs were obtained as no delay between turn-on time and emission was observed. In our case, poly(*N*-vinylcarbazole) (PVK) was used as a hole-injection layer because of its good solubility in common organic solvents, excellent film-forming properties, high glass-transition-temperature (200 °C) and high triplet energy (3.0 eV) [34]. As previously mentioned by Thompson and co-workers, PVK layer was also introduced to lower the hole-injection barrier while preventing the agglomeration or the crystallization of the soft salt layer [14]. Structure of the investigated device was the following: ITO/PEDOT:PSS (40 nm)/PVK (20 nm)/iridium complexes/Ca (300 nm)/Al (60 nm) (Scheme 2). In particular, best performances of the PhOLED devices were obtained in our case when the iridium-containing layer was spin-coated onto the surface of PVK rather than blended with PVK, thus traducing that PVK was more efficiently acting as a hole-injection layer than as a host in a host–guest strategy. Thickness of the emissive layer was also optimized to improve the device performances. Fig. 6 shows the current–voltage–luminance curves obtained for the optimized PhOLED. Noticeably, in our case and contrarily to the previously reported deposition process, soft salt layer was deposited in a 1,2-dichlorobenzene solution to avoid the dissolution of the PVK underlayer, this polymer being highly soluble in acetonitrile.

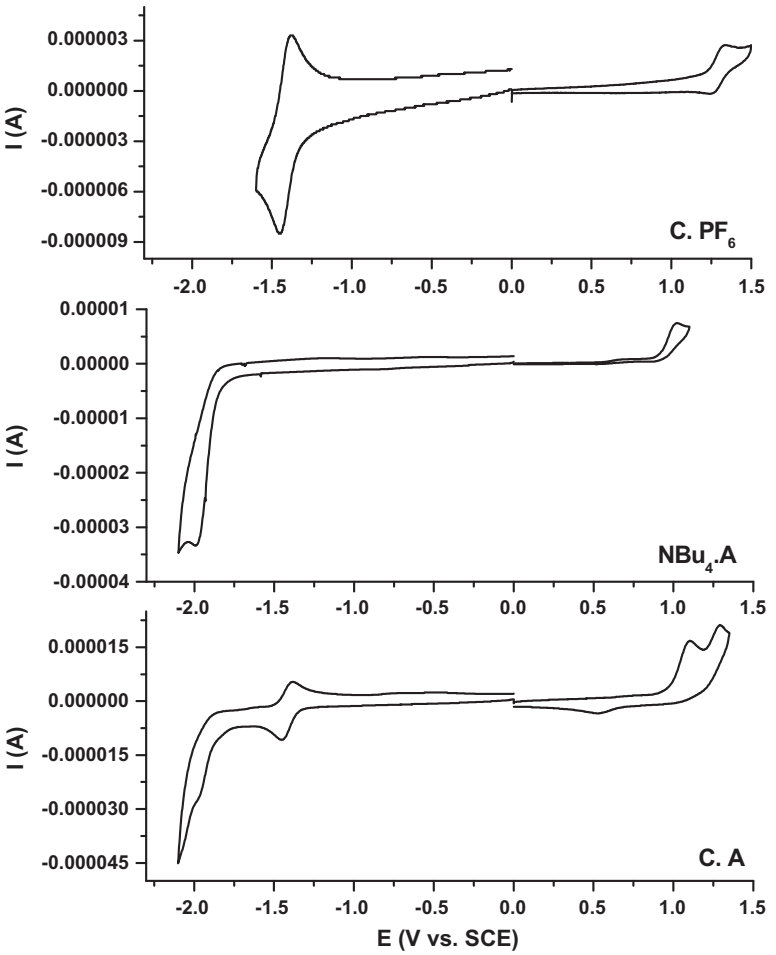

Fig. 5. Cyclic voltammograms of **C·PF$_6$** (top), **NBu$_4$·A** (middle) and soft salt **C·A** (down). CV in acetonitrile on carbon electrode vs. SCE with TBAP (0.1 M) as the supporting electrolyte. Scan rate: 50 mV/s.

Table 2
Redox potentials, energy levels of the soft salt **C·A**, **C·PF$_6$** and **NBu$_4$·A**.

Complex	$E^{\circ}_{red}(2)$ (V)[a]	$E^{\circ}_{red}(1)$ (V)[a]	$E_{ox}(1)$ (V)[a]	$E_{ox}(2)$ (V)[a]	Energy levels (eV) HOMO/LUMO
C·PF$_6$	–	−1.41	1.28[b]	–	−5.6/−3.1
NBu$_4$·A	–	−1.98^{irr}	1.01^{irr}	–	−5.2/−2.7
C·A	−1.96^{irr}	−1.41 −1.40^{irr}	1.09^{irr}	1.28^{irr}	−5.3/−3.1

[a] CV in acetonitrile on carbone electrode vs. SCE, with TBA.ClO$_4$ (0.1 M) as supporting electrolyte. Scan rate: 50 mV/s. E°_{red} is the reduction standard potential.
[b] $E^{\circ}_{ox}(½)$.

Detailed performances of OLEDs and LECs are summarized in Table 3. Double-layered active devices exhibited a peak current efficiency of 0.66 cd A^{-1} and a maximum brightness of 1114 cd m^{-2} for an optimal active layer thickness of 73 nm. Dramatic decrease of the device efficiency was evidenced with increasing the thickness of the active layer. Thickness of the emissive layer was controlled by mean of the concentration of the deposited solution. The corresponding CIE chromaticity coordinates were $x = 0.43$, $y = 0.54$, indicating that the device showed nearly saturated yellow emission. The EL spectrum of the PhOLED displayed an emission peak centered at 553 nm (see inset in Fig. 6) almost identical to that observed in the photoluminescent spectrum (λ_{em} = 552 nm). Compared to results previously reported for devices with the similar soft salt **C′·A′** (see the Scheme 2), our devices displayed higher turn-on voltage but higher brightness at low voltage. However, whatever the thickness of the emissive layer was, all devices displayed current efficiencies significantly lower to what expected. Low performance of our devices originates

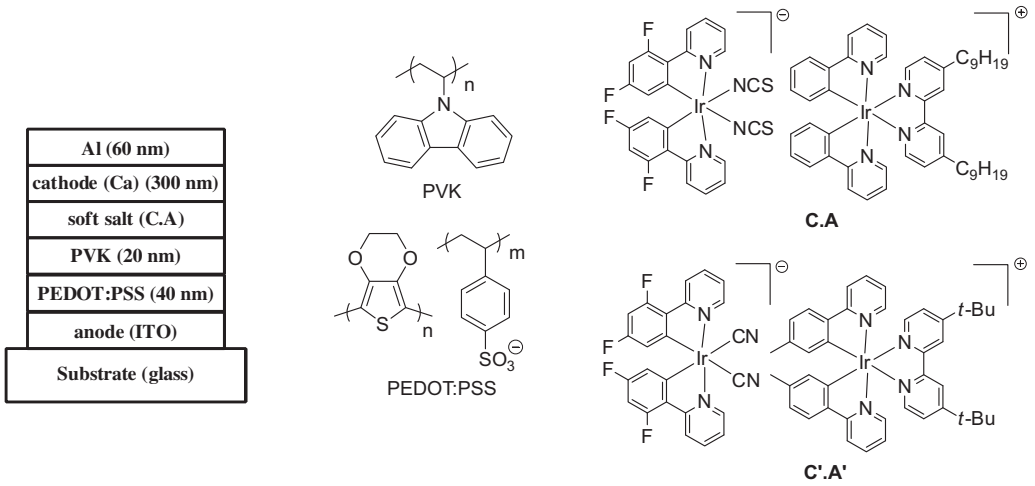

Scheme 2. The device structure of PhOLEDs and the molecular structures of the materials.

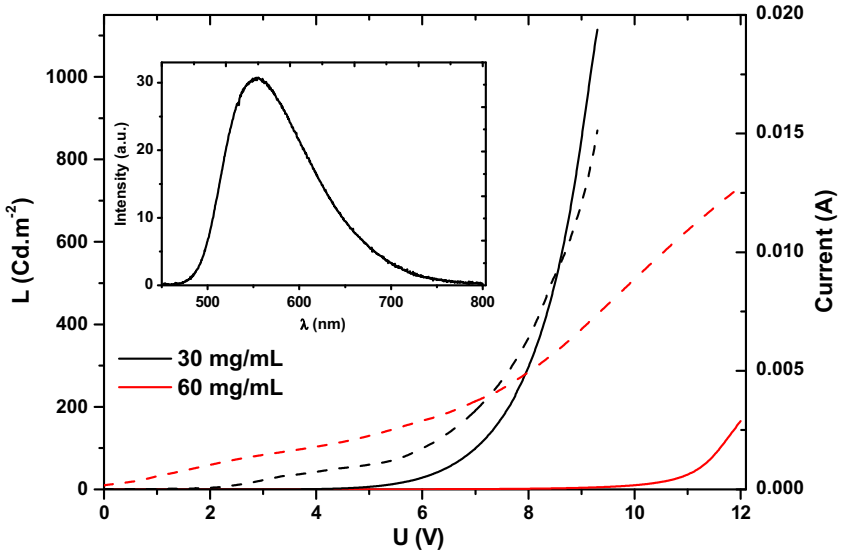

Fig. 6. *J–V–L* curves of OLEDs with increasing **C·A**. layer thicknesses, with both different concentrations used for the deposition of the emissive layer (brightness: solid line, current: dashed line). Inset: electroluminescence spectrum of the device.

Table 3
Characteristics of OLEDs and LECs as a function of the thickness.

Complex	[*C*] (mg/mL)	Thickness (nm)	V^{a} (V)	$\eta_{c\ max}{}^{b}$ (cd A^{-1})	$\eta_{e\ max}{}^{c}$ (lm W^{-1})	$L_{max}{}^{d}$ (cd m^{-2})	EL[e] λ (nm)	CIE (x, y)
C·A	30	73	6	0.66	0.23	1114 (9.3 V)	553	(0.43, 0.54)
C·A	60	150	9	0.092	0.024	165 (12 V)	553	(0.43, 0.54)
C′·A′	30	–	2.5	–	–	7428 (21 V)	586	–
C·PF$_6$	30	48	4.2	0.55	0.28	1223 (6.3 V)	567	(0.44, 0.52) (0.30, 0.60)
C·PF$_6$	60	74	5.2	0.47	0.21	1075 (9.6 V)	567	(0.44, 0.52) (0.30, 0.60)

[a] Luminous threshold voltage.
[b] Maximal external quantum efficiency.
[c] Maximal power efficiency.
[d] Maximal brightness.
[e] Electroluminescence peak wavelength.

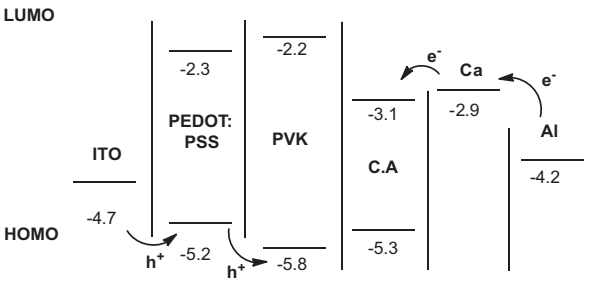

Fig. 7. Energy level diagram of the materials and Fermi levels of the electrodes used in OLEDs. The Highest and Lowest Occupied Molecular Orbitals (HOMO and LUMO) levels of **C·A** were calculated from its oxidation potentials.

from the poor matching existing between the two HOMOs and LUMOs of the soft salt. By the quite high energy barrier existing between the two HOMOs and LUMOs (0.4 eV), carriers exchange was impeded and exciton formation hindered.

3.5. Electroluminescent properties of LECs

Cationic iridium complex was also investigated as emitter in LEC devices. LEC devices were prepared with **C·PF$_6$** using the following configuration: ITO/PEDOT:PSS (40 nm)/PVK (20 nm)/cationic iridium complex/Ca (300 nm)/Al (60 nm). All solutions were spin-coated in 1,2-dichlorobenzene as solvent. In LEC devices, size of the counterions is reported to strongly impact the turn-on time by the production rate of the electric field at the electrodes due to ion motion. Therefore, we expected that the small anion PF_6^- could produce the electric field faster than larger counter anions. As first experiments, the light output vs. voltage was investigated for each fabricated devices. By applying voltage, **C·PF$_6$** emitted light above a turn-on voltage determined as being over 3.8 V (see inset in Fig. 8). The turn-on voltage was significantly higher than the electrochemical gap (ΔE = 2.29 eV). As expected, as the thickness of the functional layer increased, the turn-on voltage increased as well and was assigned to an enhanced resistivity of the emissive layer. Above this turn-on voltage, the emission intensity increased with increasing the applied voltage as evidenced in the Fig. 8. Another specificity of LECs is that they can be operated at a bias voltage higher than their electrochemical bandgap. As the band-gap for **C·PF$_6$** was electrochemically determined to be 2.29 eV and to investigate its time-dependent brightness, devices were tested under the applied bias of 7 V. Under application of this voltage, light emission was observed within a few minutes. Brightness reached a maximum luminance of 128 cd m^{-2} after 33 min. Then, a slow decay of the brightness was evidenced as a result of the low operational stability of LECs arising from various detrimental side-reaction processes [35,36]. Half-life of the device, defined as the time for the brightness of the device to decay half-maximum under a constant bias was determined to be 167 min. Surprisingly, investigation of the electroluminescence spectrum of the device evidenced a modification of the emission color over time under a constant applied voltage (see Fig. 10). When the device was switched on at 5 V, the emission color profoundly changed from green to yellow within a few minutes (see Fig. 9). Variation of the color emission over time was ascribed to a temperature-induced modification of the molecular packing or to the degradation of the active layer. Under application of the bias, temperature dissipation induced a temperature rise of the active layer and the micro and/or nanostructures of the light emissive layer changed. As a result, the emitted color was modified. This color tunability of OLEDs has notably previously been reported by acting on various parameters

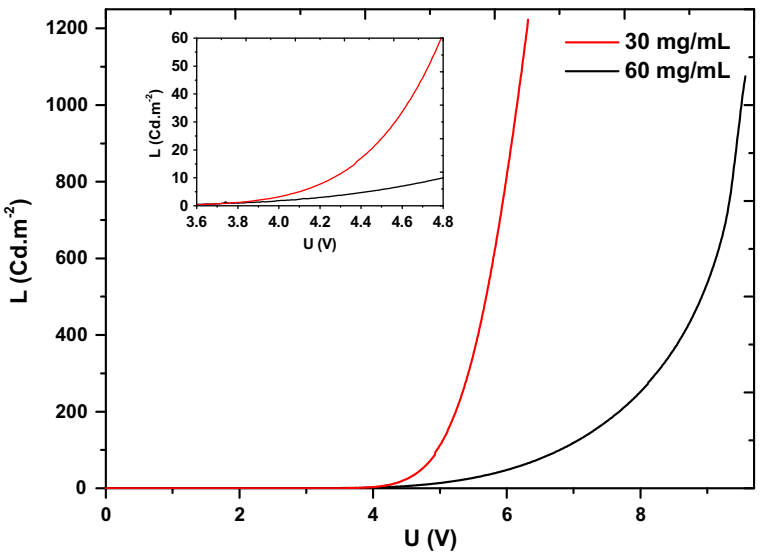

Fig. 8. Plot of the luminance vs. voltage at two different concentrations of **C·PF$_6$** used for the deposition of the emissive layer. The inset shows a magnification of the turn-on region.

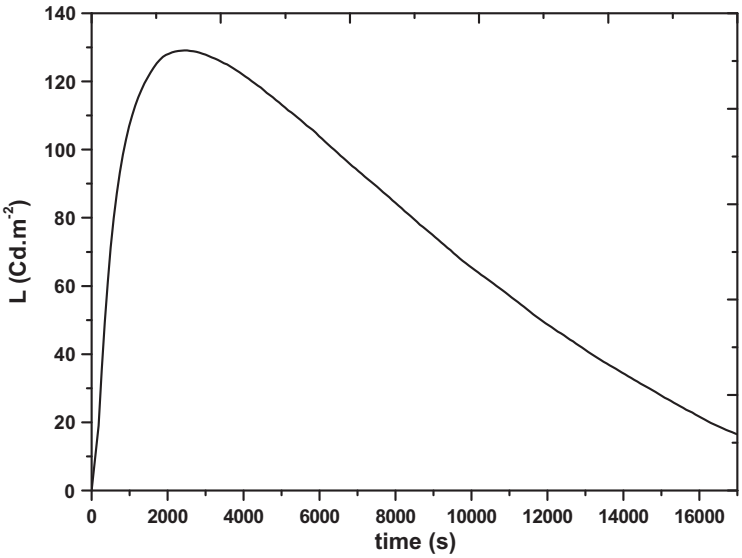

Fig. 9. Time-dependent luminance of the LEC driven at 7 V for the emissive layer deposited at 30 mg/mL in 1,2-dichlorobenzene.

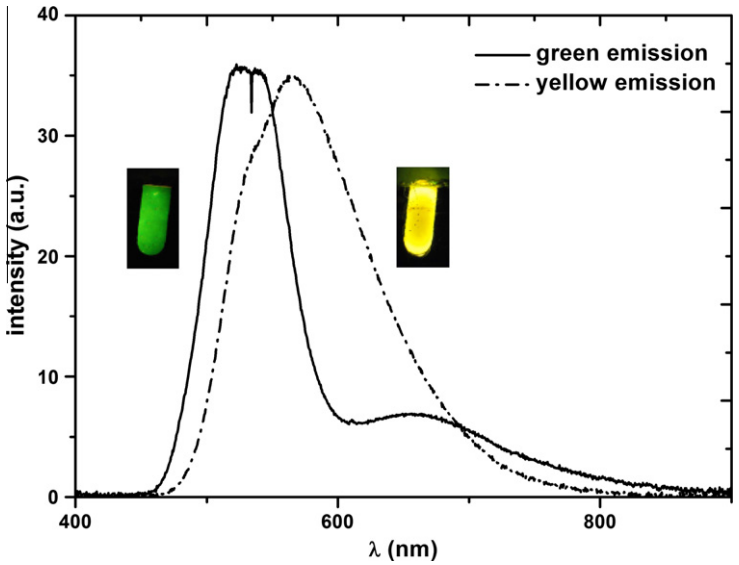

Fig. 10. Electroluminescence spectra of the LEC over time with initial emission (green color) and final emission (yellow color). (For interpretation of the references to color in this figure legend, the reader is referred to the web version of this article.)

such as the driving voltage, current [37–39] and temperature [40,41].

3.6. DFT calculations

Density functional theory (DFT) calculations at the B3LYP level of the hybrid functional theory were performed with a mixed basis set (double ξ quality LANL2 and the corresponding pseudo-potential for the metal and 6−31+G(d) for all other atoms) to optimize the geometry of both complexes and generate orbitals. The contour plots depicted in Fig. 11 clearly show that the HOMO of **C·PF$_6$** mainly comprises a contribution of the d_π orbitals of the Ir^{III} center and some π-orbital contributions of the two phenylpyridine ligands. In contrast, the LUMO is mainly localized on the ancillary bipyridine unit and consists of pyridyl π^* orbitals. Similarly, the HOMO of **NBu$_4$·A** is a mixture of Ir^{III} d_π orbitals and π orbitals of the two thiocyanate units. However, contrarily to **C·PF$_6$**, the LUMO distribution of **NBu$_4$·A** primarily resides on the phenylpyridine units of the complex and not on the ancillary ligand, as observed for **C·PF$_6$**. Therefore, introduction of the electron-releasing anionic thiocyanate ligand and the fluorine atoms on the phenylpyridine ligands in **NBu$_4$·A** inverted the contribution of both the cyclometallating ligands and the ancillary ligand in the HOMO and LUMO orbitals compared to **C·PF$_6$**. From Fig. 11, it was also possible to determine that the alkyl chain on the bipyridine ligand was essentially not contributing to the HOMO of **C·PF$_6$**, thus

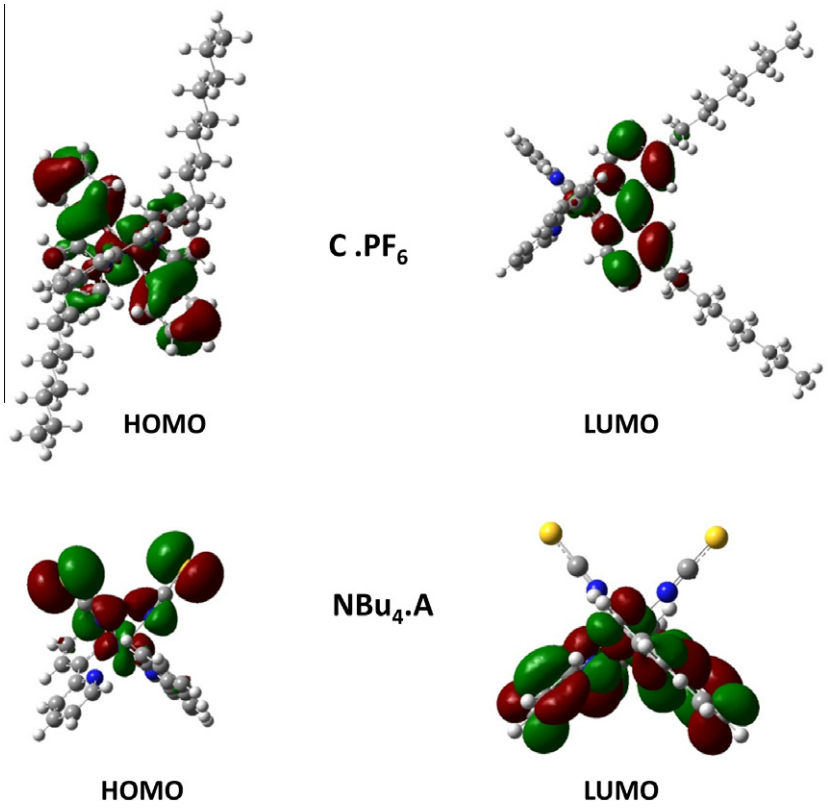

Fig. 11. Contour plots of the frontier orbitals of **C·PF$_6$** and **NBu$_4$·A** in the ground state as determined by the DFT calculations. Counteranion or countercation were not taken into consideration during geometry optimization.

suggesting the little dependence of the HOMO and LUMO level of **C·PF$_6$** to the variation of the alkyl chain length. Alkyl chains on the complex mostly contribute to render the complex more soluble in common organic solvents while limiting its crystallization within the active layer.

4. Conclusions

In conclusion, efficient electrophosphorescent devices were fabricated using the cationic complex **C·PF$_6$** as a single emitter in LECs or mixed with an anionic complex (**C·A**) in soft salt-based PhOLEDs. Interestingly, LECs demonstrated a color-variability attributed to a modification of the emissive layer with the temperature, i.e. molecular packing and/or degradation. Electroluminescent PhOLED fabricated by the spin-coating technique showed higher-performances compared to that previously reported in the literature by a higher luminance at low voltages, thus demonstrating that soft salt-based PhOLEDs constitute a promising alternative to conventional PhOLEDs based on neutral complexes.

Acknowledgments

The authors gratefully thank the C'NANO IdF, CNRS, the University of Provence and the ANR Agency (ANR-07-JCJC-040, AURUS Program) for financial supports.

References

[1] K. Ziemelis, Nature 399 (1999) 408–411.
[2] I.D.W. Samuel, A. Beeby, Nature 403 (2000) 710–711.
[3] E. Holder, B.M.W. Langeveld, U.S. Schubert, Adv. Mater. 17 (2005) 1109–1121.
[4] A. Misra, P. Kumar, M.N. Kamalasanan, S. Chandra, Semicond. Sci. Technol. 21 (2006) R35–R47.
[5] B.W. D'Andrade, S.R. Forrest, Adv. Mater. 16 (2004) 1585–1595.
[6] A. Kraft, A.C. Grimsdale, A.B. Holmes, Angew. Chem. Int. Ed. 37 (1998) 402–428.
[7] R.H. Friend, R.W. Gymer, A.B. Holmes, J.H. Burroughes, R.N. Marks, C. Taliani, D.D.C. Bradley, D.A. Dos Santos, J.L. Brédas, M. Lögdlund, W.R. Salaneck, Nature 397 (1999) 121–128.
[8] J.L. Segura, Acta. Polym. 49 (1998) 319–344.
[9] C.H. Chen, J.M. Shi, Coord. Chem. Rev. 171 (1998) 161–174.
[10] L. De Cola, M. Mauro, R. Prétôt, PCT Int. Appl. WO2010037668 A1.
[11] R.D. Costa, A. Pertegas, E. Ortı, H.J. Bolink, Chem. Mater. 22 (2010) 1288–1290.
[12] H. Yesin, Highly Efficient OLEDs with Phosphorescent Materials, Wiley-VCH, 2008.
[13] C. Rothe, S. King, A.P. Monkman, Phys. Rev. B 73 (2006) 245208.
[14] C. Wu, H.-F. Chen, K.-T. Wong, M.E. Thompson, J. Am. Chem. Soc. 132 (2010) 3133–3139.
[15] M. Frisch et al., Gaussian 03, Revision D0.1, Gaussian Inc., Wallingford, CT, 2004.
[16] N.M. O'Boyle, A.L. Tenderholt, K.M. Langner, J. Comput. Chem. 29 (2008) 839–845.
[17] N.M. O'Boyle, J.G. Vos, GaussSum, Version 2.1, Dublin City University, Dublin, Ireland, 2007, Available at: <http://gausssum.sourceforge.net>.
[18] M. Nonoyama, Bull. Chem. Soc. Jpn. 47 (1974) 767–768.
[19] S. Sprouse, K.A. King, P.J. Spellane, R.J. Watts, J. Am. Chem. Soc. 106 (1984) 6647–6653.

[20] Y.H. Park, G.Y. Park, Y.S. Kim, Mol. Cryst. Liq. Cryst. 462 (2007) 197–207.
[21] P. Coppo, E.A. Plummer, L. De Cola, Chem. Commun. (2004) 1774–1775.
[22] H. Yang, J. Qian, L. Li, Z. Zhou, D. Li, H. Wu, S. Yang, Inorg. Chim. Acta 363 (2010) 1755–1759.
[23] M.K. Nazeeruddin, R.T. Wegh, S. Klink, M. Graetzel, C.N. Klein, PCT Int. Appl., WO2007004113 A2.
[24] F. Neve, M. La Deda, A. Crispini, A. Bellusci, F. Puntoriero, S. Campagna, Organometallics 23 (2004) 5856–5863.
[25] H. Rudman, S. Shimada, M.F. Rubner, J. Am. Chem. Soc. 124 (2002) 4918–4921.
[26] M.S. Lowry, J.I. Goldsmith, J.D. Slinker, R. Rohl, R.A. Pascal Jr., G.G. Malliaras, S. Bernhard, Chem. Mater. 17 (2005) 5712–5719.
[27] A.B. Tamayo, S. Garon, T. Sajoto, P.I. Djurovich, I.M. Tsyba, R. Bau, M.E. Thompson, Inorg. Chem. 44 (2005) 8723–8732.
[28] M.K. Nazeeruddin, R. Humphry-Baker, D. Berner, S. Rivier, L. Zuppiroli, M. Graetzel, J. Am. Chem. Soc. 125 (2003) 8790–8797.
[29] M.G. Colombo, T.C. Brunold, T. Riedener, H.U. Güdel, M. Förtsch, H.B. Bürgi, Inorg. Chem. 33 (1994) 545–550.
[30] M.G. Colombo, H.U. Güdel, Inorg. Chem. 32 (1993) 3081–3087.
[31] M.G. Colombo, A. Hauser, H.U. Güdel, Inorg. Chem. 32 (1993) 3088–3092.
[32] M.S. Lowry, W.R. Hudson, R.A. Pascal Jr., S. Bernhard, J. Am. Chem. Soc. 126 (2004) 14129–14135.
[33] A.J. Bard, L.R. Faulkner, Electrochemical Methods: Fundamentals and Applications, J. Wiley and Sons, 2001 (Chapter 2).
[34] J. Pina, J. Seixas de Melo, H.D. Burrows, A.P. Monkman, S. Navaratnam, Chem. Phys. Lett. 400 (2004) 441–445.
[35] J. Fang, P. Matyba, N.D. Robinson, L. Edman, J. Am. Chem. Soc. 130 (2008) 4562–4568.
[36] T. Wågberg, P.R. Hania, N.D. Robinson, J.H. Shin, P. Matyba, L. Edman, Adv. Mater. 20 (2008) 1744–1746.
[37] M. Hamaguchi, K. Yoshino, Appl. Phys. Lett. 69 (1996) 143–145.
[38] S. Welter, K. Brunner, J.W. Hofstraat, L. De Cola, Nature 421 (2003) 54–57.
[39] K. Nakamura, T. Ishikawa, D. Nishioka, T. Ushikubo, N. Kobayashia, Appl. Phys. Lett. 97 (2010) 193301.
[40] M. Berggren, O. Inganas, G. Gustafsson, J. Rasmusson, M.R. Andersson, T. Hjertberg, O. Wennerstrom, Nature 372 (1994) 444–446.
[41] M. Berggren, G. Gustafsson, O. Inganäs, M.R. Andersson, O. Wennerström, T. Hjertberg, Appl. Phys. Lett. 65 (1994) 1489–1491.

realized as a nanoscale electronic power source [8]. Recently, single NW photovoltaic devices using coaxial NWs consisting of ZnO and P3HT exhibited a η value of 0.036% [9]. The nanoscale photovoltaic cells using the coaxial NWs, composite NWs, or various nanostructures must be studied to fabricate high-efficiency future energy harvesting systems.

In this study, we report on the nanoscale optical and photoresponsive electrical characteristics of composite NWs of *p*-type P3HT and *n*-type PCBM materials. The P3HT:PCBM composite NWs were fabricated through a wetting process based on an alumina (Al_2O_3) nanoporous template. The nanoscale phase separation of the P3HT and PCBM materials in the composite NWs was observed by optical absorption spectra and laser confocal microscope Raman and photoluminescence (PL) spectra. For the photoresponsive electrical properties of an isolated single strand of the P3HT:PCBM composite NWs, the Au–Al electrodes were patterned using an electron beam (E-beam) lithography technique, and the current–voltage (I–V) characteristic curves with and without light illumination were measured and analyzed. The current levels of the single NW at a high bias ($\geqslant$10 V) were enhanced by light illumination because of the contribution of the photogenerated charges in the *p*-type P3HT materials. The photovoltaic effect was observed for the cells using P3HT:PCBM composite NWs.

2. Experimental

The P3HT:PCBM composite NWs were fabricated through a wetting method by using Al_2O_3 nanoporous templates (Whatman International Ltd.) with a pore size of 100 nm [10]. Regio-regular P3HT and PCBM powders were purchased from Sigma–Aldrich Co. and Nanobest Co., respectively, and they were used without further purification. The molecular weight and regio-regularity of the P3HT materials were 50 kDa and 90–93%, respectively. The P3HT and PCBM were simultaneously dissolved in dichlorobenzene ($C_6H_4Cl_2$) with stirring for 12 h at 100 °C. The relative concentration (wt.%) of the P3HT and PCBM materials varied from 1:1 to 1:2 and 1:4 wt.%. The composite solution was dropped onto the Al_2O_3 nanoporous templates placed on a hotplate at 60 °C in an air atmosphere. The composite solution with the Al_2O_3 template was annealed in a vacuum oven at 150 °C for 1 h. The Al_2O_3 nanoporous template was removed only by using 2.0 M NaOH solvent. Fig. 1(a) shows the schematic illustration of the fabrication process of the P3HT:PCBM composite NWs. The P3HT and PCBM NWs themselves were also fabricated through the same wetting method using Al_2O_3 nanoporous templates.

The formation of the P3HT:PCBM composite NWs was visualized using SEM images (Hitachi S-4300). The ultraviolet and visible (UV/Vis) absorption spectra (Agilent 8453) of the NWs were measured for optical properties. The nanoscale PL and Raman spectra for an isolated single strand of the NW were measured by using a laser confocal microscope (LCM) (NanoFocus Inc., Albatross SPM). For LCM PL spectra, the incident laser power with an excitation wavelength of 488 nm and the acquisition time were fixed at about 10 μW and 0.5 s, respectively. For the LCM Raman

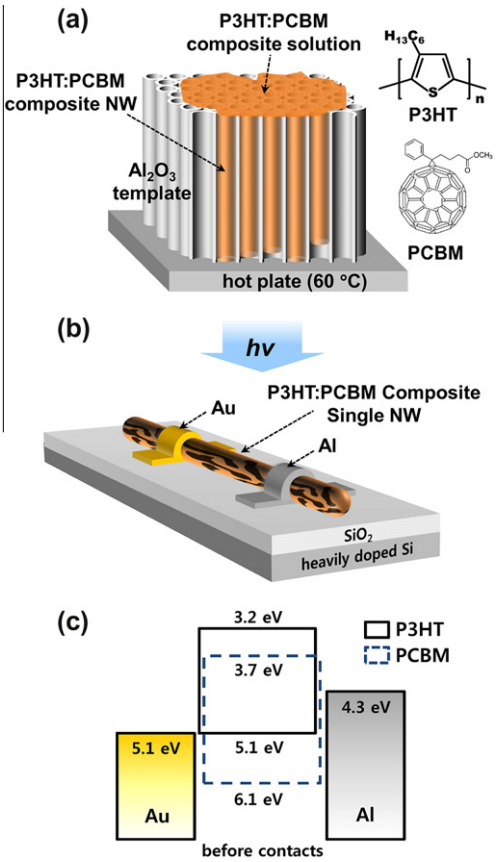

Fig. 1. Schematic illustrations of (a) the fabrication process of the P3HT:PCBM composite NWs and (b) the nanodevice with Au and Al electrodes using the P3HT:PCBM single NW. (c) Energy band diagram of the P3HT and PCBM materials and the Fermi levels of Au and Al electrodes.

spectrum of the single NW, the incident laser power with an excitation wavelength of 488 nm and the acquisition time were at about 20–40 μW and 60 s, respectively. The detailed method of the LCM experiment was reported earlier [11].

To investigate the photoresponsive electrical characteristics of the P3HT:PCBM single NW, an E-beam lithography technique was employed to fabricate two-probe electrodes of Au and Al. Fig. 1(b) shows a schematic illustration of the nanodevice using the P3HT:PCBM single NW. The distance between the Au and Al electrodes was about 1 μm. The SiO_2 dielectric layer with a thickness of 250 nm was grown by the chemical vapor deposition method onto the heavily doped Si substrate. Fig. 1(c) shows the energy band diagram of the highest occupied molecular orbital (HOMO) and the lowest unoccupied molecular orbital (LUMO) levels of the P3HT and PCBM materials and the Fermi levels of the electrodes for the nanodevice [12]. Before measurements were performed, the single NW device was annealed one more time in a vacuum oven at 150 °C for 1 h. The current–voltage (I–V) characteristic curves of the single NW were measured under a vacuum condition at 10^{-3} Torr, using a Keithley 237 SMU and Keithley 487 picoammeter. The incident light (λ = 455 nm) power from

a correlated LED (Thorlabs) was 8.5 mW at the sample location and the distance between the device and the light source was about 5 cm. The leakage current was negligible due to the relatively low current level ($\leqslant$1 nA) both with and without light illumination.

Photovoltaic cells were fabricated by using the P3HT:PCBM composite NWs with the concentration of 1:1 wt.%. The poly (3,4-ethylenedioxythiophene):poly(styrenesulfonate) (PEDOT:PSS) layer was spin-coated onto the ITO glass. The P3HT:PCBM composite NWs dispersed in methanol solvent were deposited onto the PEDOT:PSS layer through the spin coating. The P3HT:PCBM composite NW layer was covered by an insulating poly (methyl methacrylate) (PMMA) before the deposition of the Al electrode.

3. Results and discussion

Fig. 2(a) shows the SEM image of the P3HT:PCBM composite NWs, in which the formation of the NWs was confirmed and the diameter and length of the NWs was about 200 nm and 50 μm, respectively. To study the structural properties of the NWs, the LCM Raman spectra were measured for a single strand of the P3HT NWs, the PCBM NWs, and the P3HT:PCBM composite NWs, as shown in Fig. 2(b). For the P3HT single NW, LCM Raman characteristic peaks of P3HT material corresponding to the $C_\alpha = C_\beta, C_\beta{-}C_{\beta'}$, and $C_{\alpha'} = C_{\beta'}$ stretching modes in the thiophene ring were observed at 1429, 1359, and 1492 cm^{-1}, respectively [13]. For the PCBM single NW, two broad Raman peaks with a relatively low intensity were observed at 1424 and 1600 cm^{-1}. The Raman mode of the C_{60} molecules at 1465 cm^{-1} corresponding to the tangential stretching mode of the PCBM material was downshifted to 1424 cm^{-1}. The broad and weak LCM Raman peaks for the PCBM single NW may originate from the polymerization of the C_{60} due to exposure of the focused laser beam during the LCM Raman measurement [14,15]. For the P3HT:PCBM composite single NW, the Raman characteristic peaks corresponding to P3HT and PCBM materials were simultaneously observed at 1429, 1359, 1492, and 1600 cm^{-1}, as shown in Fig. 2(b). From the results of the LCM Raman spectra, both P3HT and PCBM phases existed in the P3HT:PCBM composite single NW.

Fig. 2(c) shows normalized UV/Vis absorption spectra for the P3HT NWs, the PCBM NWs, and the P3HT:PCBM composite NWs dispersed in methanol. For the P3HT NWs, the UV/Vis absorption characteristic peaks of the regio-regular P3HT material were observed at 525, 570, and 620 nm. The relatively strong absorption band at the longer wavelengths of 570 and 620 nm implies a longer π-conjugation length [16], because of the enhanced interchain interactions and ring planarity during the formation of NWs in the limited nanopore space [17–19]. For the PCBM NWs, the maximum absorption peak was observed at 327 nm with broad absorption in the visible range [20]. For the P3HT:PCBM composite NWs, the absorption peaks corresponding to the P3HT and PCBM materials were simultaneously observed at 327, 525, 570, and 620 nm. The UV/Vis absorption spectra for the P3HT:PCBM composite NWs with various weight ratios of the P3HT and PCBM materials were measured, as shown in Fig. 2(c). Below 500 nm, the relative intensity of the UV/Vis absorption for the composite NWs increased as the concentration of the PCBM material increased. The intensity of the absorption at 620 nm due to the P3HT material increased as the concentration of the PCBM material decreased. These results are attributed to the reduction of the interchain interaction of the P3HT main chains through the blending of the PCBM molecules, which are consistent with previous reports of the P3HT:PCBM composite nanoparticles (NPs) [21–23].

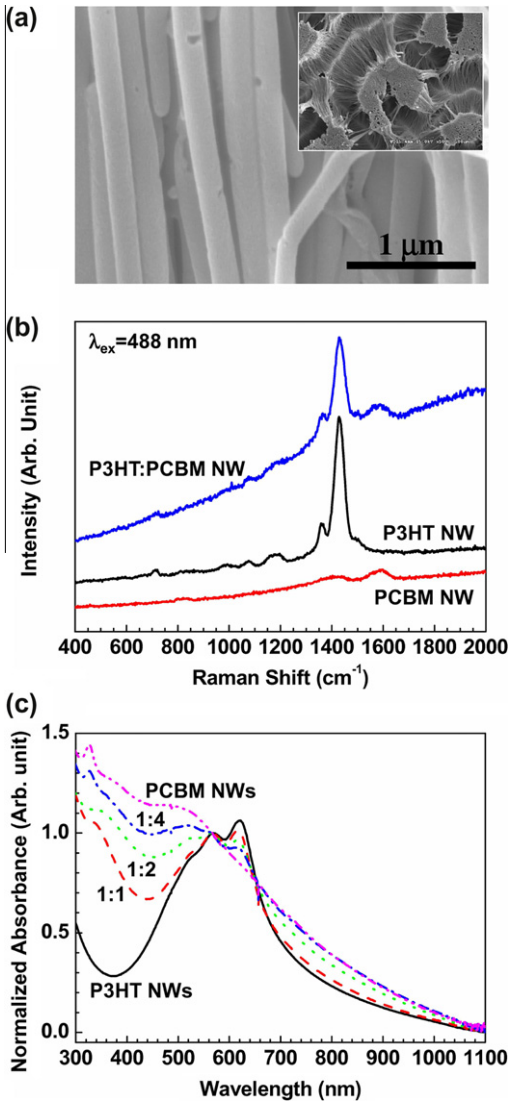

Fig. 2. (a) SEM image of the P3HT:PCBM composite NWs. Inset: SEM image of the bundle of P3HT:PCBM NWs. (b) LCM Raman spectra for the single NW of the P3HT and PCBM materials, and of the P3HT:PCBM composites. (c) Normalized UV/Vis absorption spectra for the P3HT NWs, the PCBM NWs, and the P3HT:PCBM composite NWs (with various concentrations of 1:1, 1:2, and 1:4 wt.%) dispersed in methanol.

To investigate the nanoscale luminescence and phase separation, the LCM PL spectra of single NWs were measured. Fig. 3(a) shows normalized LCM PL spectra (λ_{ex} = 488 nm) for the single NW of the P3HT, PCBM, and

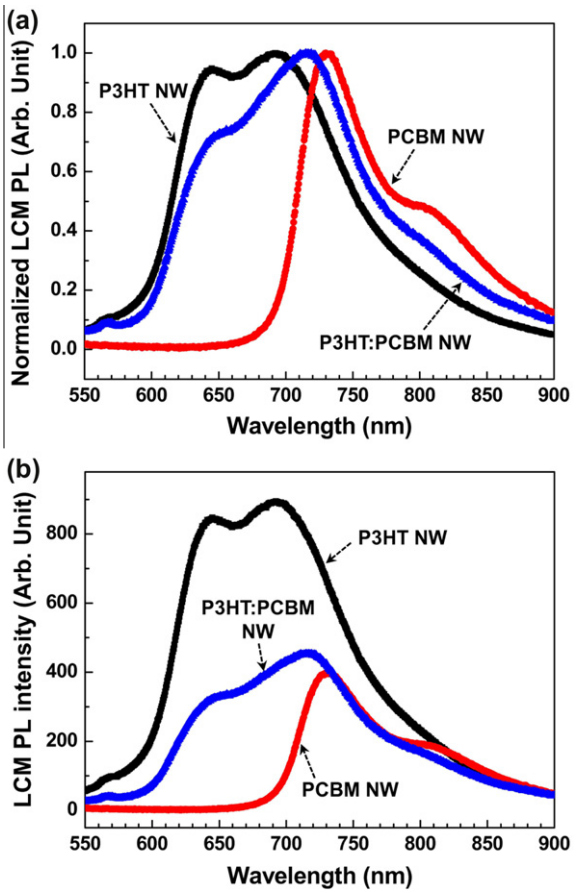

Fig. 3. (a) Normalized LCM PL spectra (λ_{ex} = 488 nm) for the single NWs of the P3HT, PCBM, and P3HT:PCBM composite. (b) LCM PL spectra with an absolute intensity for the single NWs of the P3HT, PCBM, and P3HT:PCBM composite.

P3HT:PCBM composite (1:1 wt.%). The LCM PL spectra were measured at 30 different positions in the same NW, and then, the averaged LCM PL spectrum was obtained for each single NW. For the P3HT single NW, the LCM PL peaks corresponding to the 0–0 and 0–1 transitions of the P3HT material were observed at 650 and 700 nm, respectively, which was due to two crystalline regions of the interdigitated alkyl side chains and the tilted alkyl side chains between neighboring π-stacks, respectively [22,23]. The two observed LCM PL peaks due to the two crystalline configurations for the P3HT NWs were qualitatively consistent with the UV/Vis absorption peaks with the strong interchain interaction. The LCM PL peak of the PCBM single NW was observed at 730 nm with a shoulder peak at 810 nm. For the P3HT:PCBM composite single NW, the maximum LCM PL peak at 725 nm with shoulder peaks at 650 and 810 nm were observed, indicating the coexistence of P3HT and PCBM phases in the single NW. It is noted that the main LCM PL peak at 725 nm for the composite NW was relatively red-shifted as compared with that (700 nm) of the P3HT NW. The results of the LCM PL spectra for the P3HT:PCBM composite single NW are consistent with the previous results for the P3HT:PCBM single NP [22,23].

The absolute intensities of LCM PL spectra for the single NWs of the P3HT, PCBM, and P3HT:PCBM composite were measured under the same experimental conditions, as shown in Fig. 3(b). The LCM PL characteristic peaks of the P3HT and PCBM materials were observed in the composite single NW. The LCM PL intensity of the P3HT:PCBM single NW relatively decreased compared with that of the P3HT single NW, because of the charge transfer from the P3HT to the PCBM (i.e., PL quenching). The results of the LCM Raman and PL spectra and UV/Vis absorption spectra suggest that, for the P3HT:PCBM composite single NW, the P3HT and PCBM materials were well phase-separated on the nanoscale.

Fig. 4(a) represents the SEM image of the nanodevice using the P3HT:PCBM composite single NW with Au and Al electrodes. The I–V characteristic curve of the P3HT:PCBM single NW with the P3HT:PCBM concentration of 1:2 wt.% in the dark condition shows diode-like behavior, as shown in Fig. 4(b). In the case of the reverse bias, energy barriers of 1.4 eV existed for electron injection between the Fermi energy level (E_F) of Au and the LUMO level of PCBM and barriers of 0.8 eV existed for hole injection between the E_F of Al and the HOMO level of P3HT. However, in the case of the forward bias, there was no energy barrier for the hole injection from the Au electrode, and a relatively lower barrier of 0.6 eV existed for the electron injection from the Al electrode. These induce the diode-like behavior of the nanodevice using the P3HT:PCBM composite single NW in the dark condition. Under light illumination, the current levels of the P3HT:PCBM single NW were clearly enhanced at a relatively high bias ($V \geqslant 10$ V), as shown in Fig. 4(b). Excitons were created in the major P3HT and minor PCBM materials, and they dissociated to electrons and holes due to the applied electric field near the interface of the P3HT and PCBM [24]. The increased ratios of the currents with the light illumination were estimated to be ~3.5 at −50 V and ~3.2 at 50 V, as shown in Fig. 4(b) and its inset. To study photocurrent (I_{ph}) behavior of the single P3HT:PCBM NWs with different concentrations of P3HT and PCBM such as 1:1, 1:2, and 1:4 wt.%, the I_{ph} was obtained from difference between currents with and without light illumination (i.e., $I_{ph} = I_{light} - I_{dark}$) [24]. It is noted that these NWs are new batch samples compared to those in Fig. 4(b). The I_{ph}'s were plotted as a function of applied bias, as shown in Fig. 4(c). The I_{ph} values of the single composite NW decreased as the concentration of PCBM increased, which is due to the reduction of the interchain interaction of the P3HT main chains through the blending of the PCBM molecules. These results were supported by the UV/Vis absorption spectra of the composite NWs (Fig. 2(c)). The decay of the photocurrent (after the light was turned off; I) for the P3HT:PCBM single composite NW exhibited a slow relaxation (i.e., relatively long relaxation time), which was fitted to a double exponential decay of the photocurrent after the light was turned off, as shown in the inset of Fig. 4(c). The fitted curves have a form of $I(t) = I_1 \exp(-t/\tau_1) + I_2 \exp(-t/\tau_2) + I_0$. Here, I_1 and I_2 are the amplitudes of the processes and τ_1 and τ_2 are the time constants. With the applying bias of 50 V, the fitting parameters of the P3HT:PCBM single NW with the concentration of 1:1 wt.% were estimated to be I_1 ~3.52×10^{-10} A, τ_1 ~0.92 s, I_2

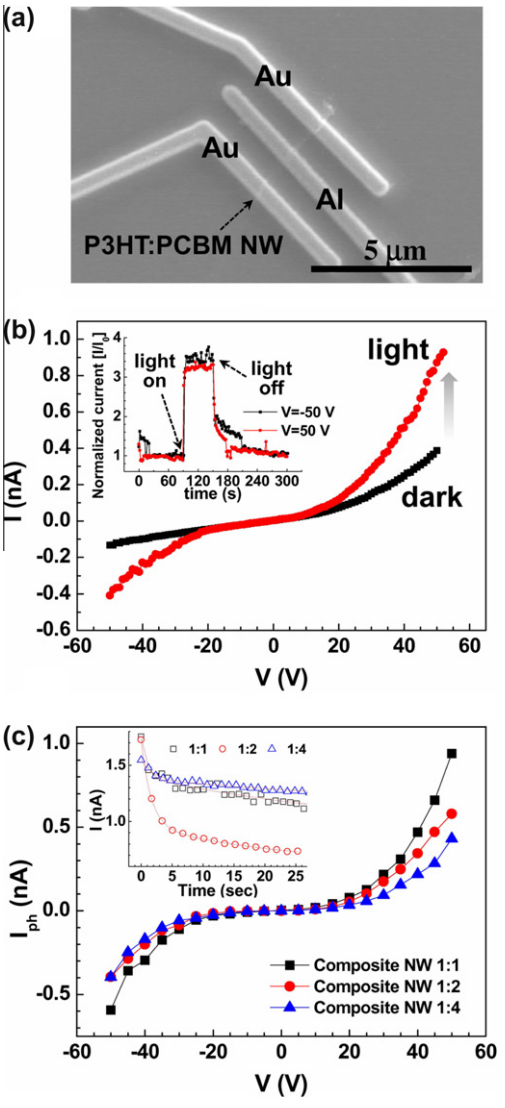

Fig. 4. (a) SEM image of the nanodevice using a single NW with Au and Al electrodes. (b) I–V characteristic curves for the P3HT:PCBM single NW with a P3HT:PCBM concentration of 1:2 wt.% with and without light irradiation. Inset: Normalized currents of the composite NW with and without light illumination, as a function of time. (c) The I_{ph}–V characteristic curves for the P3HT:PCBM single NWs with different concentrations of 1:1, 1:2, and 1:4 wt.%. Inset: Decay curves of photocurrent (at V = 50 V) for the P3HT:PCBM single NWs with different concentrations of 1:1, 1:2, and 1:4 wt.%, based on double exponential decay.

$\sim 4.76 \times 10^{-10}$ A, τ_2 ~37.46 s, and I_0 $\sim 9.23 \times 10^{-10}$ A. For the NW with 1:2 wt.%, I_1 $\sim 7.59 \times 10^{-10}$ A, τ_1 ~1.58 s, I_2 $\sim 3.61 \times 10^{-10}$ A, τ_2 ~23.18 s, and I_0 $\sim 6.08 \times 10^{-10}$ A were estimated. For the NW with 1:4 wt.%, I_1 $\sim 1.71 \times 10^{-10}$ A, τ_1 ~1.93 s, I_2 $\sim 2.64 \times 10^{-10}$ A, τ_2 ~50.39 s, and I_0 $\sim 1.11 \times 10^{-9}$ A were estimated. The relaxation time τ_2 was considerably longer than τ_1 for all NWs. The relaxation time τ_1 of the single composite NW increased as the concentration of PCBM increased. The observed double exponential decay of the photocurrent suggests a bipolar transport mechanism of the photogenerated electrons and holes through two photoactive traps [25]. Therefore, the photocurrent of the P3HT:PCBM composite NW can be caused by two photoactive traps and distinct charge carriers at the interface. The use of high crystalline organic semiconductors with low trap density can improve the switching speed of the photocurrent [26]. It is noted that the photovoltaic effect of the nanodevices using the composite single NW was measured at a low bias region (⩽0.5 V) for 2 nanodevices among 25 different ones, in which the power conversion efficiencies (η's) were 0.016% and 2.03%. The average value of the η's was estimated to be 1.62 (±1.42)%.

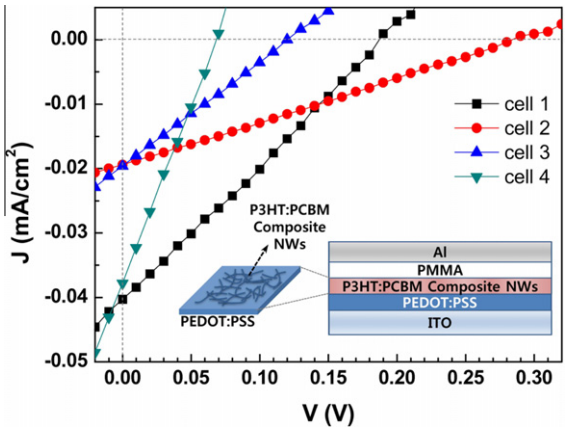

Fig. 5. J–V characteristic curves of the OPVCs using P3HT:PCBM composite NWs.

The OPVCs were fabricated by using the P3HT:PCBM composite NWs with a concentration of 1:1 wt.%, as shown in the inset of Fig. 5. The photovoltaic (current density)–V characteristic curves of the cells were consistently observed, as shown in Fig. 5. The power conversion efficiency [$\eta = FF \cdot (J_{sc}V_{oc}/P_{in})$] of the cells was 0.04–0.14% with a 100 mW/cm^2 simulated solar spectrum (1 SUN AM 1.5G). The average value of the η's was estimated to be 0.068 (±0.051)%. The various η's and J–V characteristics of the OPVCs using the composite NWs might be due to the different distributions of the composite NWs. For the OPVC with a maximum η = 0.14%, the J_{sc} and V_{oc} were measured to be about 1.94×10^{-2} mA/cm^2 and 0.28 V, respectively. The fill factor ($FF = J_{max}V_{max}/J_{sc}V_{oc}$) of the cell was 0.27. The pristine area overlapped by the ITO and Al electrodes was used to estimate the current density. When the effective area contributed by the composite NWs only is used for the current density, the J_{sc} and η of OPVCs using the P3HT:PCBM composite NWs can be expected to be higher. Therefore, the results suggest that the p-type P3HT and n-type PCBM materials of the composite NW were phase separated on the nanoscale, which contributed to the photovoltaic effect.

4. Conclusion

Composite NWs with heterojunctions of P3HT and PCBM materials were fabricated using a wetting method. From the UV/Vis absorption spectra, the coexistence of the P3HT and PCBM materials in the P3HT:PCBM composite NWs was observed. From the LCM Raman and PL spectra of the P3HT:PCBM single NW, the nanoscale phase

separation of P3HT and PCBM materials was observed. The LCM PL intensity of the P3HT:PCBM composite NWs decreased due to the efficient charge transfer. The $I-V$ characteristics of the nanodevices using the P3HT:PCBM single NW exhibited diode-like behaviors in the dark. With light illumination, the current level of the composite NW was clearly enhanced at a high bias. The photovoltaic effect was observed for the OPVCs using the P3HT:PCBM composite NWs.

Acknowledgment

This work was supported by a National Research Foundation of Korea (NRF) grant funded by the Korean government (MEST) (No. R0A-2007-000-20053-0).

References

[1] A.J. Heeger, Chem. Soc. Rev. 39 (2010) 2354.
[2] G. Yu, J. Gao, J.C. Hummelen, F. Wudl, A.J. Heeger, Science 270 (1995) 1789.
[3] W. Ma, C. Yang, X. Gong, K. Lee, A.J. Heeger, Adv. Funct. Mater. 15 (2005) 1617.
[4] Y. Kim, S. Cook, S.M. Tuladhar, S.A. Choulis, J. Nelson, J.R. Durrant, D.D.C. Bradley, M. Giles, I. Mcculloch, C.-S. Ha, M. Ree, Nat. Mater. 5 (2006) 197.
[5] M. Campoy-Quiles, T. Ferenczi, T. Agostinelli, P.G. Etchegoin, Y. Kim, T.D. Anthopoulos, P.N. Stavrinou, D.D.C. Bradley, J. Nelson, Nat. Mater. 7 (2008) 158.
[6] S.H. Park, A. Roy, S. Beaupré, S. Cho, N. Coates, J.S. Moon, D. Moses, M. Leclerc, K. Lee, A.J. Heeger, Nat. Photonics 3 (2009) 297.
[7] A.J. Mozer, G. Dennler, N.S. Sariciftci, M. Westerling, A. Pivrikas, R. Österbacka, G. Juška, Phys. Rev. B 72 (2005) 035217.
[8] B. Tian, X. Zheng, T.J. Kempa, Y. Fang, N. Yu, G. Yu, J. Huang, C.M. Lieber, Nature 449 (2007) 885.
[9] A.L. Briseno, T.W. Holcombe, A.I. Boukai, E.C. Garnett, S.W. Shelton, J.J.M. Fréchet, P. Yang, Nano Lett. 10 (2010) 334.
[10] M. Steinhart, J.H. Wendorff, A. Greiner, R.B. Wehrspohn, K. Nielsch, J. Schilling, J. Choi, U. Gősele, Science 296 (2002) 1997.
[11] D.H. Park, M.S. Kim, J. Joo, Chem. Soc. Rev. 39 (2010) 2439.
[12] C.-Y. Nam, D. Su, C.T. Black, Adv. Funct. Mater. 19 (2009) 3552.
[13] M. Baibarac, M. Lapkowski, A. Pron, S. Lefrant, I. Baltog, J. Raman Spectrosc. 29 (1998) 825.
[14] V.A. Karachevtsev, P.V. Mateichenko, N.Y. Nedbailo, A.V. Peschanskii, A.M. Plokhotnichenko, O.M. Vovk, E.N. Zubarev, A.M. Rao, Carbon 42 (2004) 2091.
[15] A. Dzwilewski, T. Wágberg, L. Edman, J. Am. Chem. Soc. 131 (2009) 4006.
[16] T.-A. Chen, X. Wu, R.D. Rieke, J. Am. Chem. Soc. 117 (1995) 233.
[17] B.J. Schwartz, Annu. Rev. Phys. Chem. 54 (2003) 141.
[18] P.J. Brown, D.S. Thomas, A. Kohler, J.S. Wilson, J.S. Kim, C.M. Ramsdale, H. Sirringhaus, R.H. Friend, Phys. Rev. B 67 (2003) 064203.
[19] J. Clark, C. Silva, R.H. Friend, F.C. Spano, Phys. Rev. Lett. 98 (2007) 206406.
[20] S. Cook, H. Ohkita, Y. Kim, J.J. Benson-Smith, D.D.C. Bradley, J.R. Durrant, Chem. Phys. Lett. 445 (2007) 276.
[21] V. Shrotriya, J. Ouyang, R.J. Tseng, G. Li, Y. Yang, Chem. Phys. Lett. 411 (2005) 138.
[22] Z. Hu, A.J. Gesquiere, Chem. Phys. Lett. 476 (2009) 51.
[23] Z. Hu, D. Tenery, M.S. Bonner, A.J. Gesquiere, J. Luminescence 130 (2010) 771.
[24] V.D. Mihailetchi, H.X. Xie, B. de Boer, L.J.A. Koster, P.W.M. Blom, Adv. Funct. Mater. 16 (2006) 699.
[25] P. Baveliuk, B. Ruiz, R. Duchowicz, N. Bolognini, IEEE J. Quantum Electron. 36 (2000) 692.
[26] I. Hwang, C.R. McNeill, N.C. Greenham, J. Appl. Phys. 106 (2009) 094506.

have been reported [13]. These attachments, based on the electronic properties of the neutral semiconducting form of conjugated systems, have had a great effect on the chemistry of these systems. This new formation has created a strong change in point of view regarding the molecular engineering of the electronic properties of materials derived from conjugated systems and hence on the structural control of their band gap [10].

In particular, thiophene and carbazole containing polymers have been of recent attraction due to their interesting electrochemical and optical behavior, and electrochromic properties [14]. Using these materials in electrochromic applications that possess the ability to reversibly color change by altering redox state has emerged [15]. Besides, polycarbazole is well-known as a good hole transport and photonic material for optoelectronic devices [16]. Polycarbazoles are known as not only an efficient short wavelength emitter but also as a strong electro-donating (p-type) chromophore [17]. Another advantage of carbazole is that it can be easily functionalized at its (3,6-) [18], (2,7-) [19] or *N*-positions [20] and then covalently linked into polymeric systems, both in the main chain [21] as building blocks and in a side chain as pendant unit [22]. Furthermore, poly(3,6-carbazole)s show interesting electrochromic properties because of the conjugation breaks that are present due to the inclusion of a 3,6-linkage. These broken conjugation lengths generate radical cations, which are separated from one another and do not combine. Therefore, the ability of poly(3,6-carbazole) derivatives to form two distinct oxidation states further ability to exhibit many colors on the ITO/glass surface upon applied positive potentials [15a,23].

Since 2,7-carbazoles were theoretically found to have smaller energy gaps than the 3,6-carbazoles, the small energy gaps of these monomers are expected to contribute to a lowering of the band gaps in the resulting polymers [17b–e]. Due to easily synthesized, there are many reports about poly(3,6-carbazole)s [24]. For instance, direct oxidative polymerization or electropolymerization of carbazoles resulted in just oligomeric materials linked at the 3,6- positions [23,25]. On the other hand, the synthesis of poly(2,7-carbazole)s was not straightforward due to unreactive the 2 and 7 positions of carbazole. Several approaches have been developed to overcome the barrier to obtaining various poly(2,7-carbazole) derivatives [19].

Herein, we synthesized a new poly(2,7-carbazole) derivative bearing electro-withdrawing $-NO_2$ substituent that could easily be polymerized electrochemically to give stable, electroactive and electrochromic materials (Scheme 1). When compared to the poly-9-phenyl-2,7-di-2-thienyl-9H-carbazole (poly(TCT)) standard molecule, as a result of the attachment of $-NO_2$ moiety to the structure, it gain many useful properties such as multi-electrochromic behavior, high redox stability, and high coloration efficiency.

2. Experimental

2.1. Materials

All chemicals purchased from Aldrich, Merck and Fluka and used without further purification. 2-Azido-4,4′-dinitrobiphenyl (1), 2,7-dinitro-9*H*-carbazole (2), 2,7-diamino-9*H*-carbazole (3), 2,7-diiodo-9*H*-carbazole (4) were prepared from previously published procedures [19].

2.2. Synthesis of 2,7-di-2-thienyl-9H-carbazole (**5**)

Compound **4** (0.5 g, 0.95 mmol) was dissolved in acetic anhydride (20 mL) and added boron trifluoride diethyl etherate (0.15 mL) with refluxing for 1 h to yield 9-acetyl-2,7-diiodocarbazole as a residue. A mixture of 9-acetyl-2,7-diiodocarbazole (0.44 g, 1 mmol) 2-thiopheneboronic-acid (0.27 g, 2 mmol), 20 mL THF and 3 M 5 mL of Na_2CO_3 solution was stirred at room temperature for 2 h under argon atmosphere. Then $Pd(PPh_3)_4$ (0.02 g) was added to this solution as catalyst and the reaction was refluxed for 24 h. The mixture was cooled to room temperature and then poured into a large amount of methanol (500 mL), and the mixture of 9-acetyl-2,7-di-2-thienylcarbazole was obtained by filtration. Finally the residue was dissolved in THF (50 mL), DMSO (10 mL), H_2O (5 mL), and then KOH (9.72 g, 0.173 mol) was added, and the mixture was refluxed for 24 h. The reaction mixture was cooled to room temperature, neutralized by HCl, and then poured into water to give the final product. Remaining solid was crystallized in methanol two times. The solid was dried at 50 °C under vacuum. *Yield: 0.34 g, 87%, brown color product.*

FT-IR (cm^{-1}): 3397 (–NH); 3063, (C–H aromatic); 1605, (C=C aromatic), 685 (thienyl C–H) (^{1}H NMR, $CHCl_3$-d, ppm): δ, 11.96, (s, 1H, N–H); 7.94 (d, 2H, Ar-$H_{ff'}$); 7.62 (d, 2H, Ar-$H_{cc'}$); 7.55, (s, 2H, Ar-$H_{dd'}$); 7.39, (d, 2H, Ar-$H_{aa'}$); 7.14, (m, 4H, Ar-$H_{ff'}$, Ar-$H_{bb'}$).

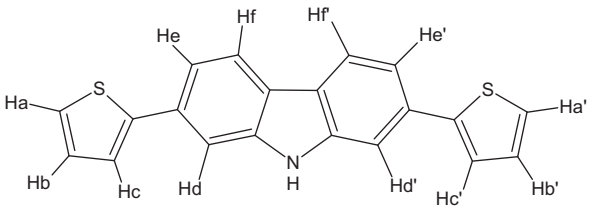

2.3. Synthesis of 9-(4-nitrophenyl)-2,7-di-2-thienyl -9H-carbazole (TCT-N)

Compound **5** (0.18 g, 0.54 mmol), K_2CO_3 (0.15 g, 1.0 mmol), Cu powder (0.05 g) and 1-iodo-4-nitrobenzene (0.135 g, 0.54 mmol) were added to 30 mL nitrobenzene and heated to reflux temperature for 48 h under argon atmosphere. Then the reaction mixture was cooled, filtered through a pad of celite and nitrobenzene was removed under vacuum. Remaining solid was dissolved in DMF and poured into cold water. The precipitated product was filtered, recrystallized from a mixture of chloroform/hexane (1/3; v/v) dried at 60 °C under vacuum. *Yield: 0.1 g, 41%, yellow color product.*

FT-IR (cm^{-1}): 3093, 3068, (C–H aromatic); 1594 (C=C aromatic); 1522, 1340 ($-NO_2$), (^{1}H NMR, $CHCl_3$-d, ppm): δ, 8.18, (d, 2H, $H_{hh'}$); 7.89 (d, 2H, Ar-$H_{ee'}$); 7.57 (d, 2H, Ar-

$H_{cc'}$); 7.37, (d, 2H, Ar-$H_{gg'}$); 7.35, (d, 2H, Ar-$H_{aa'}$); 7.28, (d, 2H, Ar-$H_{ff'}$); 7.22, (s, 2H, Ar-$H_{dd'}$); 7.13, (dd, 2H, Ar-$H_{bb'}$).

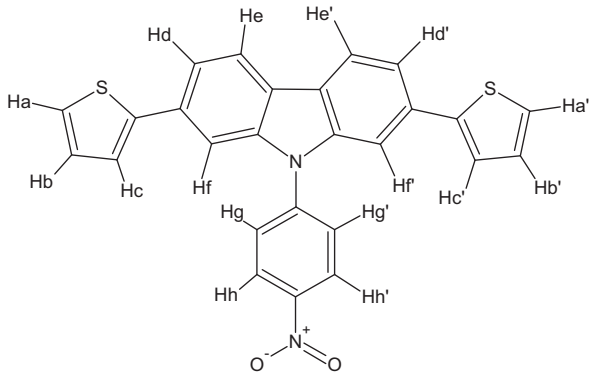

2.4. Synthesis of 9-phenyl-2,7-di-2-thienyl -9H-carbazole standard molecule (TCT)

2,7-Di-2-thienyl-9*H*-carbazole (0.09 g, 0.27 mmol), K_2CO_3 (0.075 g, 0.05 mmol), Cu powder (0.05 g) and iodobenzene (0.2 g, 0.49 mmol) were added to 20 mL nitrobenzene and heated to reflux temperature for 48 h under argon atmosphere. Then the reaction mixture was cooled, filtered through a pad of celite and nitrobenzene was removed under vacuum. Remaining solid was dissolved in DMF and poured into cold water. The precipitated product was filtered, recrystallized from a mixture of chloroform/hexane (1/2; v/v) dried at 60 °C under vacuum. *Yield: 0.08 g, 70%, light yellow color product.*

FT-IR (cm^{-1}): 3088, 3045, (C–H aromatic); 1592, 1450 (C=C aromatic); (^{1}H NMR, DMSO-d_6, ppm): δ, 7.98, (d, 2H, $H_{ff'}$); 7.52 (d, 2H, Ar-$H_{aa'}$); 7.41 (t, 2H, Ar-$H_{hh'}$); 7.37, (d, 2H, Ar-$H_{gg'}$); 7.24, (d, 2H, Ar-$H_{cc'}$); 7.16, (d, 2H, Ar-$H_{ii'}$); 7.13, (s, 2H, Ar-$H_{dd'}$); 6.97, (d, 2H, Ar-$H_{bb'}$); 6.77, (d, 2H, Ar-$H_{bb'}$).

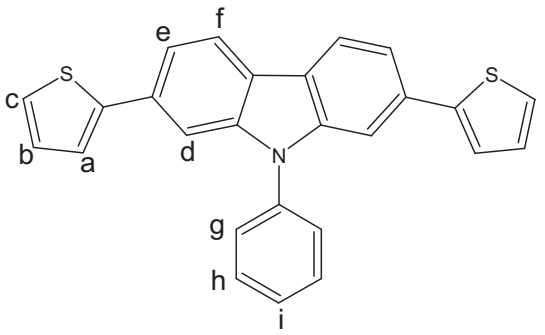

2.5. Electrochemical polymerization

Electrochemical polymerization of TCT-N and TCT were carried out in a dichloromethane solution of 2.0×10^{-3} M monomers and 0.1 M $TBAPF_6$ by repetitive cycling at a scan rate of 100 mV/s. A platinum wire was used as a counter electrode and Ag wire as a pseudo reference. The polymer was directly coated onto platinum disk (0.02 cm^2) or indium–tin oxide (ITO, 8–12 Ω, 0.8 cm × 5 cm) and then the film was rinsed with acetonitrile to remove from electrolyte salt.

2.6. Instrumentation

FT-IR spectra were recorded by a Perkin Elmer FT-IR Spectrum One by using ATR system (4000–650 cm^{-1}). ^{1}H NMR (Bruker Avance DPX-400) spectra were recorded at 25 °C in deuterated chloroform and TMS as internal standard.

Cyclic voltammetry (CV) technique used for electrochemical measurements was performed using Biologic SP50 potentiostat–galvanostat system. The electrochemical cell includes an Ag/AgCl as reference electrode (RE), Pt wire as counter electrode (CE) and glassy carbon as working electrode (WE) immersed in 0.1 M $TBAPF_6$/acetonitrile as the supporting electrolyte. CV measurements were carried under argon atmosphere. HOMO and LUMO energy levels of polymer were calculated according to the inner reference ferrocene redox couple E (Fc/Fc+) = +0.41 V (*vs.* Ag/AgCl) in acetonitrile by using the formula EHOMO = $-e(E_{ox}-E_{Fc})$ + (−4.8 eV) [26]. Onset values of oxidation potentials were taken into account while calculating HOMO energy levels. LUMO energy levels of TCT and poly-TCT were calculated by subtracting the optical band gap from HOMO level.

UV–Vis spectra were recorded by Analytic Jena-Speedcord S600 spectrophotometer. The absorption spectra of monomer and polymer were recorded in dichloromethane. The optical band gap (E_g) of products were calculated from their low energy absorption edges (λ_{onset}) ($E_g = 1241/\lambda_{onset}$) [27].

Spectro-electrochemical measurements were carried out to consider absorption spectra of this polymer film under applied potential [28]. The spectroelectrochemical cell consisted of a quartz cell, an Ag wire (RE), Pt wire counter electrode (CE) and ITO/glass as transparent working electrode (WE). Measurements were carried out in the 0.1 M $TBAPF_6$ as supporting electrolyte in acetonitrile.

Colorimetric measurements were performed by using Konica Minolta CS-200 chromameter with viewing geometry as recommended by CIE. According the CIE system, the color is made up of three attributes; luminance (L), hue (a), and saturation (b) [29]. These parameters were measured at neural and oxidized state of the poly-TCT-N and poly-TCT on the ITO/glass surface.

3. Results and discussion

3.1. Synthesis and characterization

The new 2,7-carbazole derivative bearing –NO_2 pendant was synthesized in six steps. Starting from 2-amino-4,4′-dinitrobiphenyl, 2,7-dinitro functionalized carbazoles typically obtained from the Cadogan ring-closure reactions were firstly synthesized by Morin and Leclerc [19]. Reduction of nitro group of this intermediate product was performed by using Pd/C and hydrazine monohydrate, a different reducing conditions used by Morin and Leclerc

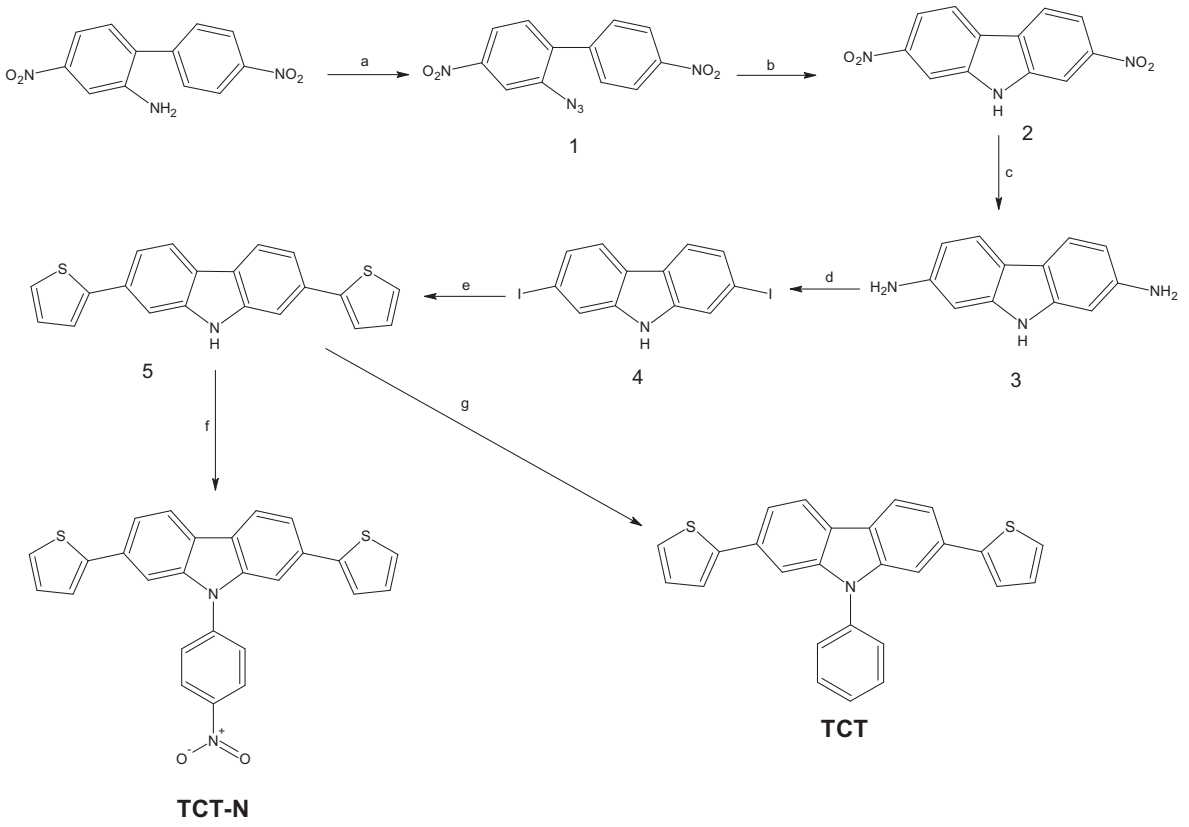

Scheme 1. (a) (i) $NaNO_2$, H_2SO_4, AcOH 0 °C, 2 h, (ii) NaN_3, r.t., 18 h; (b) Kerosene, 250 °C, 6 h; (c) Pd/C, N_2H_5OH, EtOH, reflux, 24 h; (d) (i) $NaNO_2$, AcOH, 0 °C, 2 h, (ii) KI, r.t.,18 h; (e) (i) Acetic anhydride, BF_3-Et_2O, reflux, 1 h, (ii) 2-thiopheneboronic acid, $Pd(Ph_3P)_4$, THF-Water (4:1), Na_2CO_3, reflux 24 h, (iii) KOH, THF–DMSO–Water (10:2:1), reflux, 24 h; (f) Cu powder, 18-Crown-6, K_2CO_3, 1-iodo-4-nitrobenzene, nitrobenzene, reflux, 24 h; (g) Cu powder, 18-Crown-6, K_2CO_3, iodobenzene, nitrobenzene, reflux, 24 h.

[19]. 2,7-Diiodo-*9H*-carbazole (**4**) was synthesized in two steps. In the first step, 2,7-diamino-9*H*-carbazole (**3**) was converted to diaazonium salt and then to give **4** adding KI to this solution [19]. After that, the diiodo compound coupled with thiophene was carried out by using Suzuki type coupling reaction to get 2,7-dithienyl-*9H*-carbazole (**5**). Consequently, the electroactive monomers (TCT-N and TCT) were synthesized by Ullman type condensation of 5 and iodophenyl derivatives in nitrobenzene in the presence of CuI as catalyst and K_2CO_3. The reaction yields of TCT-N and TCT were found to be 41% and 70%, respectively.

After completion of the synthetic works, chemical structure of TCT-N was identified by FT-IR, and ^{1}H NMR. Significant changes were observed in the spectral properties of the initial compounds and the products. In FT-IR spectrum of **1**, characteristic triple bond vibration exerted by azide ($-N_3$) groups was observed at 2123 cm^{-1} and also characteristic $-NH_2$ vibrations at about 3200–3400 cm^{-1} were disappeared. In the next step, as a result of the ring closure reaction, characteristic N–H vibration band for secondary amines of obtained carbazole derivative was observed at 3339 cm^{-1}. Then, **3** obtained from reduction of **2** was identified from its characteristic $-NH_2$ bond vibration at 3306 and 3205 cm^{-1}. In the FT-IR spectra of **4** characteristic $-NH_2$ vibration attributed to **3** disappeared. The FT-IR spectrum of 5 obtained with the attached thienyl moiety on the structure exhibits characteristic strong peak at 685 cm^{-1} (for α-hydrogens of thiophene rings). Finally, TCT-N synthesized from Ullmann condensation of **F10** with 1-iodo-4-nitrobenzene, their characteristic unsymmetric and symmetric $-NO_2$ vibrations were observed at 1522 and 1340 cm^{-1}, respectively. Also characteristic –NH vibration for secondary amines was removed in this spectrum (see Electronic Supplementary information).

In the ^{1}H NMR spectrum of TCT-N monomer, the phenylene proton signals neighboring $-NO_2$ moiety were observed at higher ppm (8.09 ppm) than that of other proton signals due to electro-withdrawing effect of $-NO_2$ substituent. Besides characteristic thienyl β-H doublet signal was observed at 7.12 ppm. Furthermore, other signals attributed to thiophene and carbazole moieties were observed as expected. Finally, FT-IR and ^{1}H NMR spectroscopy results proved that all chemical reactions were completed successfully (Fig. 1).

Electrochemical polymerization was carried out in a reaction medium containing 2.0×10^{-3} M TCT-N or TCT monomer and 0.1 M TBAPF6/dichloromethane via repetitive cycling at a scan rate of 100 mV s^{-1}. The electroactive

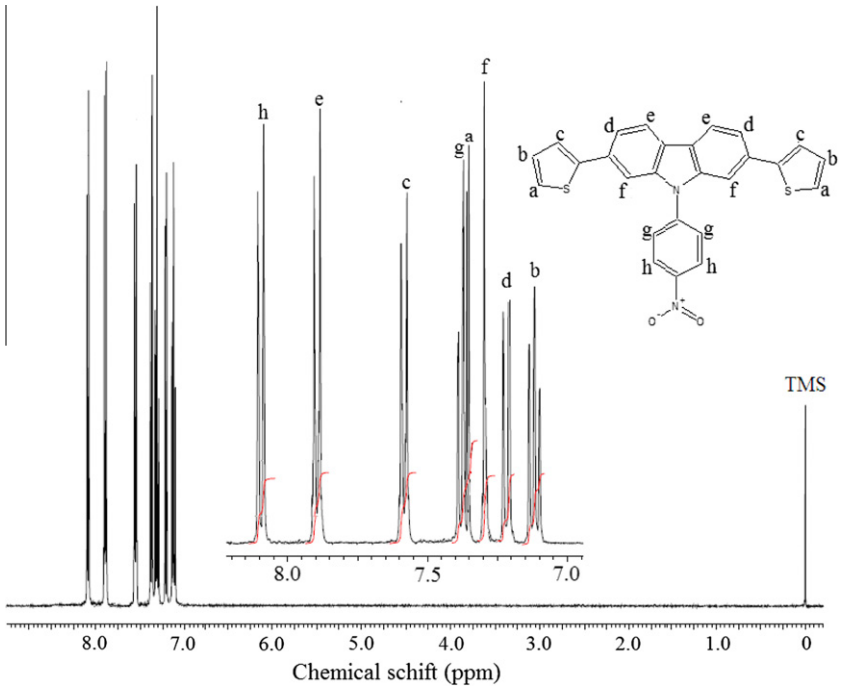

Fig. 1. ^{1}H NMR spectrum of TCT-N.

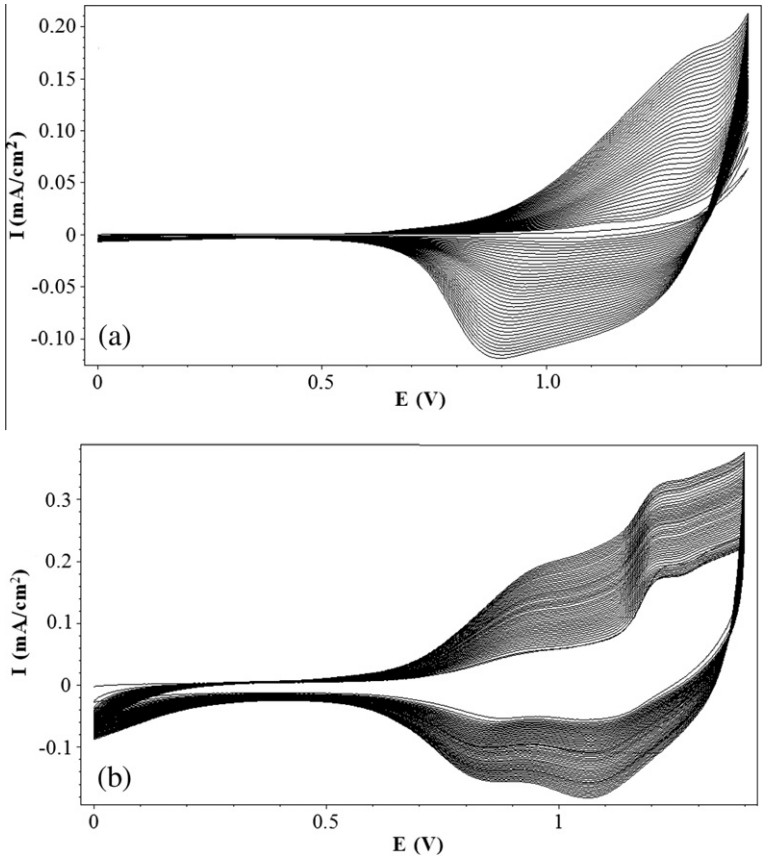

Fig. 2. Repeated potential scan of TCT-N between 0 and 1.45 V (a) TCT (b) between 0 and 1.45 V in 0.1 M $TBAPF_6$/dichloromethane, scan rate 100 mV/s, *vs.* Ag/AgCl.

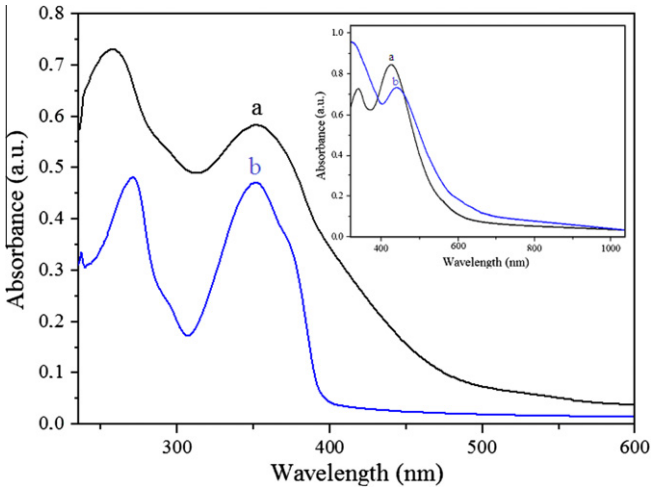

Fig. 3. UV–Vis absorbtion spectra of TCT-N (a) and TCT (b) *inset:* poly-TCT-N (a) and poly-TCT (b) in dichloromethane.

polymers were directly coated onto the working electrode (platinum disk or ITO/glass surface). Potentiodynamic electrochemical polymerization of TCT-N was carried out repetitive cycling at a potential between 0 and 1.45 V exhibited a new redox couple at 0.89–1.31 V ($E^{ox}_{p,1/2}$ = 1.12) (Fig. 2a). Due to presence of $-NO_2$ moiety, electrochemical polymerization of TCT-N requires to reach higher potentials compared with TCT standard molecule. Because of this reason, the electrochemical polymerization of TCT was carried out by repetitive cycling at a potential between 0 and 1.40 V exhibited two new redox couples at 0.85–0.95 V ($E^{ox1}_{p,1/2}$ = 0.90 V), and 1.08–1.22 V ($E^{ox2}_{p,1/2}$ = 1.15 V) (Fig. 2b). These two redox couple may be attributed to polaronic and bipolaronic formation of the occurred polymer chain by the electrochemical process [30]. Due to electro-withdrawing effect of the $-NO_2$ substituent on the poly(TCT-N), the two redox states could not be observed at this potential of 1.40 V. In addition, all peaks were increased current density after each successive cycle clearly indicated the formation of poly(TCT-N) and/or poly(TCT) deposited onto the surface of the working electrode. Prepared polymer films on ITO/glass surface was dedoped electrochemically in monomer free-electrolyte solution to equilibrate the redox behavior after washing with an acetonitrile to remove the unreacted monomers and/or oligomeric species. Then, the polymers on ITO/glass surface partly dissolved in dichloromethane by using ultrasonic bath for UV–Vis absorption measurements.

3.2. Optical and electrochemical properties

The UV–Vis absorption spectra of TCT-N and TCT monomers and polymers were recorded in dichloromethane (Fig. 3). The lowest energy bands of TCT-N and TCT standard molecule at about λ_{max} = 350 nm attributed to thiophene-carbazole-thiophene (TCT) π-conjugated system. Although λ_{max} of TCT-N and TCT are the same, the absorption band of TCT-N is broadened than that of TCT. Thus, TCT-N has an onset value of 472 nm corresponding to a 76 nm red shift with respect to that of the TCT. This significant bathochromic shift is attributed to the $-NO_2$ electro-withdrawing effect. According to these results, the optical band gap values of TCT and TCT-N were found to be 3.13 and 2.63 eV. On the other hand, the lowest energy transition band (λ_{max}) of poly(TCT-N) was observed at about 415 nm. This significant bathochromic shift is attributed to resulting the polymer with extended π-system. Due to TCT-N consist of $-NO_2$ moiety, the molecule require for higher potential than that of TCT and thus reduced both the length of chain and degree of conjugation with respect to that of the TCT. Because of this effect, 20 nm red shift of λ_{max} was observed in the λ_{max} of TCT. Finally, for poly(TCT-N), the onset absorption is 580 nm corresponding to an energy band gap of 2.13 eV. Besides, the poly-TCT has an onset value of 615 nm (equal to a band gap of 2.01 eV) corresponding to a 35 nm red shift with respect to that of the poly(TCT-N).

The electrochemical properties of TCT-N and TCT monomer and their polymers were investigated by cyclic voltammetry (CV). An explicit difference in redox behavior of the TCT-N and TCT can be deduced from the CV which was depicted in Fig. 4. During CV scan in the anodic regime of TCT-N and TCT monomer, TCT-N exhibited an irreversible oxidation peak at $E^{ox}_{m,a}$ = 1.46 V *vs.* Ag/AgCl during an anodic scan, and this oxidation potential is higher than that of TCT (semi reversible; $E^{ox}_{m,a}$ = 1.25 and $E^{ox}_{m,c}$ = 1.11 V; $E^{ox}_{m,1/2}$ = 1.19 V *vs.* Ag/AgCl). As expected, this result indicated that TCT has a more electron rich nature than TCT-N when attaching the $-NO_2$ moiety in a similar system. On the other hand, to record the cyclic voltammogram of poly(TCT-N) and poly(TCT), the polymer films prepared by repetitive potential cycling were rinsed in a monomer-free-electrolyte solution. Due to the extended conjugation in the polymers backbone, the oxidation potentials were observed as reversible and at lower potential with compared to corresponding monomers. On the other hand, in the cathodic regime, cyclic voltammogram of TCT-N exhibits characteristic reversible reduction couple with potentials of $E^{red}_{m,c}$ = −0.93 V $-E^{red}_{m,a}$ = −0.85 V and $E^{red}_{m,1/2}$ = −0.89 V which reflects the reduction process of $-NO_2$

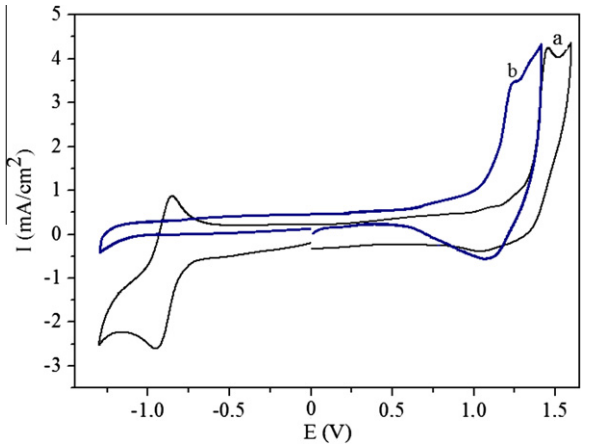

Fig. 4. Cyclic voltammogram of TCT-N (a) TCT (b) in the 0.1 M $TBAPF_6$/dichloromethane, scan rate 100 mV/s, *vs.* Ag/AgCl.

moiety. In comparison to the monomer, the reduction couple of poly(TCT-N) broadened and slightly shifted positively ($E^{red}_{p,c} = -0.91$ V – $E^{red}_{p,a} = -0.77$ V and $E^{red}_{m,1/2} = -0.84$ V) and the conjugated backbone is still sufficiently conducting to allow electron transfer at potentials. Besides, HOMO–LUMO energy levels of TCT-N and poly(TCT-N) were calculated according to the onset values of their oxidation and reduction potentials. The LUMO energy levels of TCT and poly(TCT) were calculated by adding the optical band gap from their HOMO levels (Table 1). As a result of the data in Table 1, optical and electrochemical properties of the molecules were greatly influenced by the addition of electro-withdrawing $–NO_2$ as subunit in the structure.

The spectro-electrochemical properties of the poly(TCT-N) film were determined upon doping process (Fig. 5) and compared to poly-TCT (Fig. 6) in order to get further support for the effect of $–NO_2$ electro-withdrawing moiety. In the neutral state, the poly(TCT-N) had one maximum absorption at 418 nm (λ_{max}, π–π^* transition). The optical band gap (E_g) of poly(TCT-N) was found to be 2.18 eV from the onset of absorption, which is somewhat higher than the E_g of poly-TCT (2.06 eV). Upon oxidation, the intensity of the λ_{max} was simultaneously decreased up to a certain first and second broad bands intensified at about 762 (0–1.0 V) and 1000 nm (1.0–1.6 V) indicated the formation of polarons and bipolarons on poly(TCT-N) film, respectively (Fig. 5). Thus, NIR region, above 700 nm, was strongly absorbed at the fully oxidized state. Based on foregoing results, the orange color of the film with Commision Internationale de l'Eclairage (CIE) color parameters (Luminance $L = 60$, hue $a = 7$, and saturation $b = 57$) turned into green (L: 54; a: −20; b: 43), turquoise (L: 42; a: −16; b: 2), and dark blue (L: 38; a: −2; b: −10), respectively, upon oxidation (Fig. 5). On the other hand, when the intensity of the π–$\pi*$ transition band of poly(TCT) film ($\lambda_{max} = 422$ nm) decreased, a new broad absorption band at about 790 nm started to intensify due to the polaron formation (0–0.8 V). Upon further oxidation, a broad band between 400 and 1000 nm also intensified (1–1.4 V). Thus all visible and near-IR regions were absorbed by the poly(TCT) film at fully oxidized state. The yellow color of the film with CIE color parameters (L: 75; a: −11; b: 64) turned into dark gray (L: 39; a: −6; b: 13), upon oxidation (Fig. 6).

Double step chronoamperometry technique was used to monitor the changes in the electro-optical responses during switching. Electrochromic parameters of the polymer

Table 1
HOMO and LUMO energy levels, electrochemical (E'_g) and optical band gaps (E_g) values of TCT-N and TCT standard molecules.

Molecules	Reduced group and its peak potential (V)	Oxidized group and its peak potential (V)	HOMO (eV)	LUMO (eV)	$E_{g'}$, Electrochemical band gap (eV)	E_g, Optical band gap (eV)
	$–NO_2$	TCT (Ring)				
TCT-N	$E^{red}_{m,c} = -0.93$ $E^{red}_{m,c} = -0.85$ *reversible* $E^{red}_{m,on} = -0.76$	$E^{ox}_{m,a} = 1.46$ *Irreversible* $E^{ox}_{m,on} = 1.25$	−5.64	−3.63	2.01	2.63
TCT	–	$E^{ox}_{m,a} = 1.25$ $E^{ox}_{m,c} = 1.11$ *Semi-reversible* $E^{ox}_{m,on} = 1.04$	−5.43	−2.30[a]	–	3.13
Poly-TCT-N	$E^{red}_{p,c} = -0.91$ $E^{red}_{p,a} = -0.77$ *reversible* $E^{red}_{m,on} = -0.71$	$E^{ox}_{p,a} = 1.31$ $E^{ox}_{p,c} = 0.89$ *reversible* $E^{ox}_{m,on} = 0.91$	−5.30	−3.68	1.62	2.18
Poly-TCT	–	$E^{ox1}_{p,a} = 0.95$ $E^{ox1}_{p,c} = 0.85$ *reversible* $E^{ox2}_{p,a} = 1.22$ $E^{ox2}_{p,c} = 1.08$ *reversible* $E^{ox2}_{m,on} = 0.73$	−5.12	−3.06[a]	–	2.06

[a] Calculated by the addition of the optical band gap to the HOMO level.

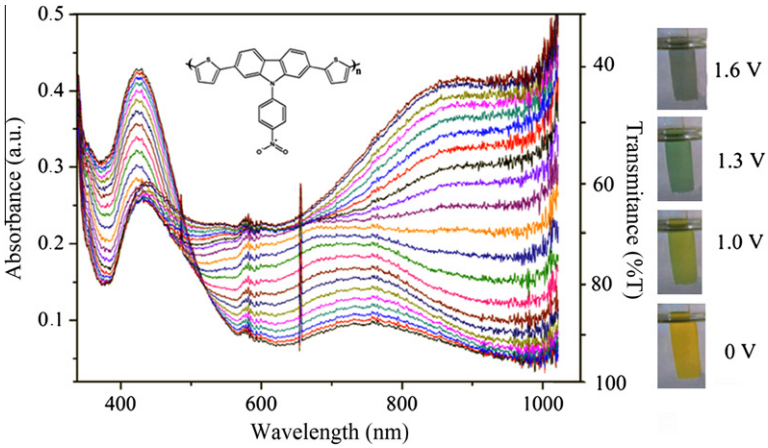

Fig. 5. Spectro-electrochemical behavior of poly-TCT-N film on the ITO/glass surface.

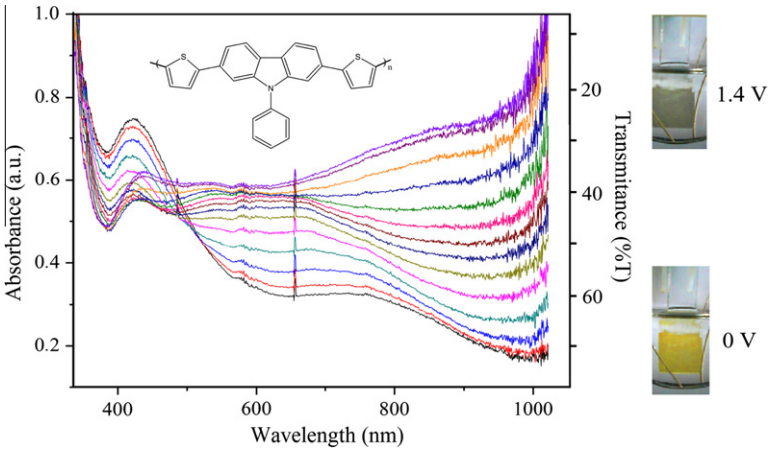

Fig. 6. Spectro-electrochemical behavior of poly-TCT film on the ITO/glass surface.

films were analyzed by changes that occurred in the transmittance (increments and decrements of the absorption band at 420 and 1000 nm with respect to time) while switching the potential step wisely between neutral and oxidized states with a residence time of 10 s [28a]. The percentage transmittance changes (%ΔT) of poly(TCT-N) between the neutral (at 0 V) and oxidized states (at 1.6 V) were found to be 22% for 420 nm and 57% for 1000 nm (Fig. 5). For poly(TCT), these values were found as 8% for 420 nm and 55% for 1000 nm (Fig. 6). Besides, the oxidation and reduction response times were measured to be 4.3 and 1.3 s for poly(TCT-N) and 0.8 and 1.8 s for poly(TCT) (Fig. 7). Optical activities of the poly(TCT-N) and poly(TCT) polymer film were retained by 92% and 77% even after 1000 cycles of operation, respectively (Fig. 7). Although the response times were relatively slow, the polymer film of TCT-N was more stable than that of TCT upon repetitive cycles.

On the other hand, the coloration efficiency (CE) was calculated by using $CE = \Delta OD/Q_d$ and $\Delta OD = \log (T_{colored}/T_{bleached})$, where Q_d is the injected/ejected charge between neutral and oxidized states, $T_{colored}$ and $T_{bleached}$ are the transmittance in the oxidized and neutral states, respectively. Using this equation, CE of poly(TCT-N) and poly(TCT) was measured to be 264 and 126 $cm^2\,C^{-1}$ by chronoamperometry, while switching the polymer films between oxidized and reduced states. The results clearly show that the coloration efficiency of poly(TCT-N) is two times greater than that of poly(TCT). Toppare et al. reported the multi-electrochromic polymer of thiophene-pyrrole-thiophene (SNS) analogue containing electro-withdrawing $-NO_2$ substituent [31]. Based on previous results, it can be easily seen that the prepared polymer film of TCT-N has much better electrochromic performance than that of its SNS analogue and poly(TCT) standard.

4. Conclusion

Herein, we have reported the synthesis of a new multi-electrochromic 2,7 linked thiophene-carbazole-thiophene (TCT) derivative containing an electro-withdrawing $-NO_2$ substituent. It has been determined that the optical and the electrochemical properties of the monomer were

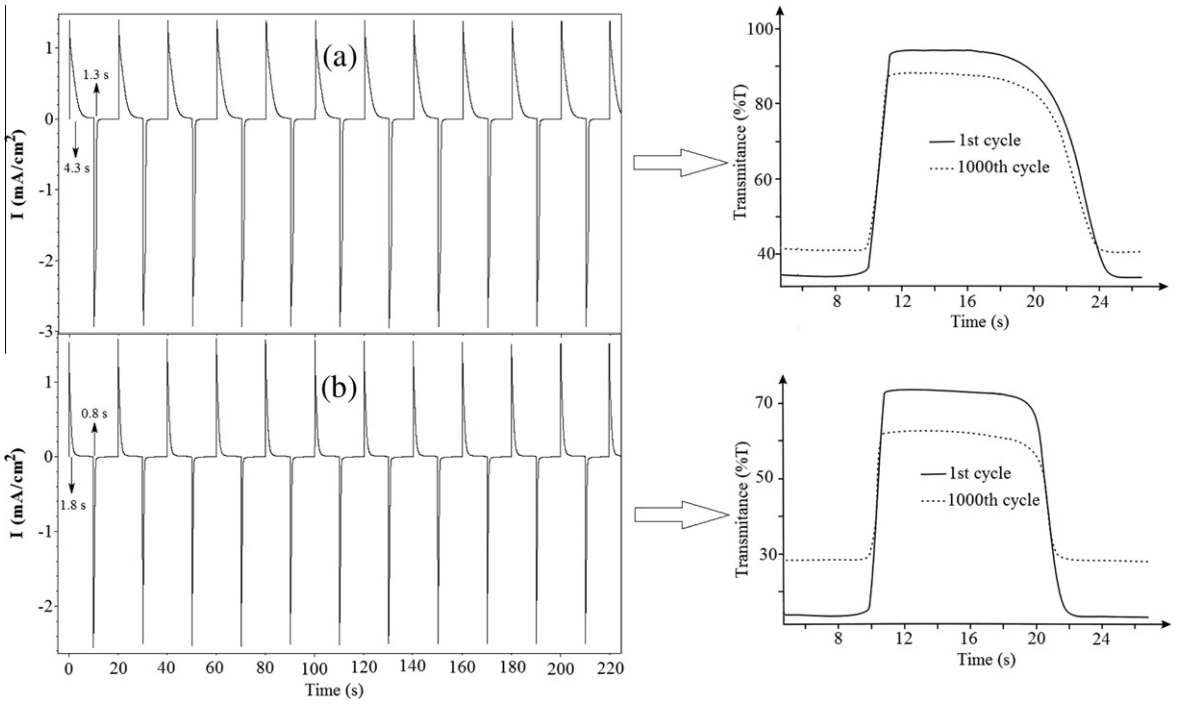

Fig. 7. Electrochemical switching, optical absorbance monitored at 1000 nm for poly-TCT-N (a) and poly-TCT (b) film between 0 and 1.6 V.

greatly influenced the presence of the electro-withdrawing $-NO_2$ as subunit in the structure. TCT-N monomer was electrochemically polymerized onto transparent ITO/glass surface to give a quite stable multi-electrochromic polymer with a high contrast ratio in the NIR region (ΔT = 57% at 1000 nm). In comparison to TCT standard reference, polymer film of TCT-N has much better electrochromic performance in terms of multielectrochromic behavior, high resistance to over oxidation and high contrast ratio at near-IR region. With a high contrast ratio and an impressive electrochemical stability, TCT-N is a possible good candidate for electrochromic applications.

Acknowledgements

We gratefully acknowledge the supports from Çanakkale Onsekiz Mart University Grants Commission (Project Number: 2009/17) and also grateful to Scientific and Technical Research Council of Turkey (TUBITAK, project #: 109T516) for financial support.

Appendix A. Supplementary data

Supplementary data associated with this article can be found, in the online version, at doi:10.1016/j.orgel.2011.06.023.

References

[1] C.K. Chiang, Y.W. Park, A.J. Heeger, H. Shirakawa, E.J. Louis, A.G. MacDiarmid, J. Chem. Phys. 69 (1978) 5098–5104;
T.A. Skotheim, J.R. Reynolds, Handbook of Conducting Polymers, CRC Pres-Taylor Francis, 2006.

[2] M.J. Cho, D.H. Choi, P.A. Sullivan, A.J.P. Akelaitis, L.R. Dalton, Prog. Polym. Sci. 33 (2008) 1013–1058.

[3] A. Agrawal, S.A. Jenekhe, Chem. Mater. 5 (1993) 633–640.

[4] A.B. Holmes, J.H. Burroughes, D.D.C. Bradley, A.R. Brown, R.N. Marks, K. MacKay, R.H. Friend, P.L. Burn, Nature 347 (1990) 539–541;
L. Akcelrud, Prog. Polym. Sci. 28 (2003) 875–962;
Y.J. Cheng, S.H. Yang, C.S. Hsu, Chem. Rev. 109 (2009) 5868–5923;
A.C. Grimsdale, K.L. Chan, R.E. Martin, P.G. Jokisz, A.B. Holmes, Chem. Rev. 109 (2009) 897–1091;
S. Chen, L. Deng, L. Peng, L. Xie, Q. Fan, W. Huang, Adv. Mater. 22 (2010) 5227–5239;
A. Kraft, A.C. Grimsdale, A.B. Holmes, Angew. Chem. Int. Ed. 37 (1998) 402–428.

[5] G. Yu, J. Gao, J.C. Hummelen, F. Wudl, A.J. Heeger, Science 270 (1995) 1789–1791;
L. Chen, D. Godovsky, O. Inganas, J.C. Hummelen, R.A.J. Janssen, M. Svensson, M.R. Andersson, Adv. Mater. 12 (2000) 1367–1370;
A. Cravino, G. Zerza, M. Maggini, S. Buchella, M. Svensson, M.R. Andersson, H. Neugebauer, C.J. Brabec, N.S. Sariciftci, Monatshefte für Chemie 134 (2003) 519–527;
K. Colladet, S. Fourier, T.J. Cleij, L. Lutsen, J. Gellan, D. Vanderzande, L.H. Nguyen, H. Neugebauer, N.S. Sariciftci, A. Aguierre, G. Janssen, E. Goovaerts, Macromolecules 40 (2007) 65–72;
J.A. Mikroyannidis, M.M. Stylianakis, G.D. Sharma, P. Balraju, M.S. Roy, J. Phys. Chem. C 113 (2009) 7904–7912;
J.A. Mikroyannidis, A.N. Kabanakis, P. Balraju, G.D. Sharma, Macromolecules 43 (2010) 5544–5553.

[6] M. Morana, P. Koers, C. Aldauf, M. Koppe, D. Muehlbacher, P. Denk, A. Scharber, D. Waller, C. Brabec, Adv. Funct. Mater. 17 (2007) 3274–3283;
R.D. Champion, K.-F. Cheng, C.-L. Pai, W.-C. Chen, S.A. Jenekhe, Macromol. Rapid Commun. 26 (2005) 1835–1840.

[7] G. Sonmez, H.B. Sonmez, J. Mater. Chem. 16 (2006) 2473–2477.

[8] S. Panero, P. Prosperi, B. Klaptse, B. Scrosati, Electrochim. Acta 31 (1986) 1597–1600;
K. Kaneto, K. Yoshino, Y. Inuishi, Jpn. J. Appl. Phys. 22 (1983) 567–568. Part 2;
T. Yamamoto, J. Chem. Soc. Chem. Commun. 4 (1981) 187–188.

[9] P.M. Beaujuge, J.R. Reynolds, Chem. Rev. 110 (2010) 268–320;
C.M. Amb, A.L. Dyer, J.R. Reynolds, Chem. Mater. 23 (2011) 397–415;
G. Sonmez, H.B. Sonmez, C.K.F. Shen, R.W. Jost, Y. Rubin, F. Wudl, Macromolecules 38 (2005) 669–675;

I. Schwendeman, R. Hickman, G. Sonmez, P. Schottland, K. Zong, D.M. Welsh, J.R. Reynolds, Chem. Mater. 14 (2002) 3118–3122;
A. Durmus, G.E. Gunbas, P. Camurlu, L. Toppare, Chem. Commun. 31 (2007) 3246–3248;
G.S. Liou, S.H. Hsiao, N.K. Huang, Y.L. Yang, Macromolecules 39 (2006) 5337–5346;
H.-M. Wang, S.H. Hsiao, G.S. Liou, C.H. Sun, J. Polym, Sci. Part A: Polym. Chem. 48 (2010) 4775–4789.

[10] J. Roncali, Chem. Rev. 97 (1997) 173–206;
J. Roncali, Macromol. Rapid Commun. 28 (2007) 1761–1775.

[11] P.M. Beaujuge, C.M. Amb, J.R. Reynolds, Acc. Chem. Res. 43 (2010) 1396–1407;
L. Biniec, S. Fall, C.L. Chochos, D.V. Anokhin, D.A. Ivanov, N. Leclerc, P. Leveque, T. Heiser, Macromolecules 43 (2010) 9779–9786.

[12] D. Asil, A. Cihaner, F. Algi, Am. Onal, J. Electroanal. Chem. 618 (2008) 87–93;
T.L. Lambert, J.P. Ferraris, J. Chem. Soc. Chem. Commun. (1991) 752–754;
J.M. Toussaint, J.L. Brédas, Synth. Met. 61 (1993) 103–106;
K.H. Hsieh, K.S. Ho, Y.Z. Wang, S.D. Ko, S.C. Fu, Synth. Met. 123 (2001) 217–224;
D.T. McQuade, A.E. Pullen, T.M. Swager, Chem. Rev. 100 (2000) 2537–2574.

[13] J. Roncali, Chem. Rev. 92 (1992) 711–738;
R.D. McCullough, Adv. Mater. 10 (1998) 93–116.

[14] S.A. Sapp, G.A. Sotzing, J.L. Reddinger, J.R. Reynolds, Adv. Mater. 8 (1996) 808–811;
S.A. Sapp, G.A. Sotzing, J.R. Reynolds, Chem. Mater. 10 (1998) 2101–2108;
J. Padilla, V. Seshadri, J. Filloramo, W.K. Mino, S.P. Mishra, B. Radmard, A. Kumar, G. Sotzing, T.F. Otero, Synth. Met. 157 (2007) 261–268.

[15] D. Witker, J.R. Reynolds, Macromolecules 38 (2005) 7636–7644;
S. Beaupre, A.-C. Breton, J. Dumas, M. Leclerc, Chem. Mater. 21 (2009) 1504–1513;
K. Kawabata, H. Goto, Synth. Met. 160 (2010) 2290–2298;
S. Koyuncu, C. Zafer, E. Sefer, F. Baycan Koyuncu, S. Demic, I. Kaya, E. Ozdemir, S. Icli, Synth. Met. 159 (2009) 2013–2021.

[16] O. Usluer, S. Demic, D.A.M. Egbe, E. Birckner, C. Tozlu, A. Pivrikas, A.M. Ramil, N.S. Sariciftci, Adv. Funct. Mater. 20 (2010) 4152–4161;
V. Promarak, M. Ichikawa, T. Sudyoadsuk, S. Saengsuwan, S. Jungsuttiwong, T. Keawin, Synth. Met. 157 (2007) 17–22;
S. Koyuncu, O. Usluer, M. Can, S. Demic, N.S. Sariciftci, J. Mater. Chem. 21 (2011) 2684–2693.

[17] J.V. Grazulevicius, P. Stroghriegl, J. Pielichowski, K. Pielichowski, Prog. Polym. Sci. 28 (2003) 1297–1353;
N. Blouin, M. Leclerc, Acc. Chem. Res. 41 (2008) 1110–1119;
S. Walkim, B.-R. Aich, Y. Tao, M. Leclerc, Polym. Rev. 48 (2008) 432–462;
N. Bloudin, A. Michaud, M. Leclerc, Adv. Mater. 19 (2007) 2295–2300;
J.V. Grazulevicius, I. Soutar, L. Swanson, Macromolecules 31 (1998) 4820–4827;
S. Tirapattur, M. Belletête, N. Drolet, M. Leclerc, G. Duroche, Chem. Phys. Lett. 370 (2003) 799–804.

[18] M. Grigoras, M.C. Antonia, Eur. Poly. J. 41 (2005) 1079–1089.

[19] J.-F. Morin, M. Leclerc, Macromolecules 34 (2001) 4680–4682.

[20] M. Watanabe, M. Nishiyama, T. Yamamoto, Y. Koie, Tetrahedron Lett. 41 (2000) 481–483.

[21] J.P. Chen, A. Natansohn, Macromolecules 32 (1999) 3171–3177.

[22] G. Bubniene, T. Malinauskas, V. Getautis, A. Stanisauskaite, V. Jankauskas, J. Sidaravicus, Synth. Met. 158 (2008) 670–675.

[23] S. Koyuncu, B. Gultekin, C. Zafer, H. Bilgili, M. Can, S. Demic, I. Kaya, S. Icli, Electrochim. Acta 54 (2009) 5694–5702;
O. Usluer, S. Koyuncu, S. Demic, R.A.J. Janssen, J. Polym, Sci. Part B: Polym. Phys. 49 (2011) 333–341.

[24] J.-F. Morin, M. Leclerc, D. Ades, A. Siove, Macromol. Rapid Commun. 26 (2005) 761–778.

[25] A. Desbene-Monvernay, P.C. Lacaze, J.E. Dubois, P. Desbene, J. Electroanal. Chem. 152 (1983) 87–96;
K. Faid, D. Ades, A. Siove, C. Chevrot, J. Chim. Phys. 89 (1992) 1019–1026;
K. Faid, A. Siove, D. Ades, C. Chevrot, Synth. Met. 55–57 (1993) 1656–1661;
K. Faid, D. Ades, A. Siove, C. Chevrot, Synth. Met. 63 (1994) 89–99.

[26] G. Yu, Y. Yang, Y. Cao, Q. Pei, C. Zhang, A.J. Heeger, Chem. Phys. Lett. 259 (1996) 465–468.

[27] A.O. Patil, A.J. Heeger, F. Wudl, Chem. Rev. 88 (1988) 183–200.

[28] F. Wudl, H. Meng, G.Sonmez, Chem. Mater. 16 (2004) 574–580;
W. Kaim, J. Fiedler, Chem. Soc. Rev. 38 (2009) 3373–3382.

[29] B.C. Thompson, P. Schottland, G. Sonmez, J.R. Reynolds, Synth. Met. 119 (2001) 333–334.

[30] A. Chaner, O. Mert, A.S. Demir, Electrochim. Acta 54 (2009) 1333–1338.

[31] S. Varis, M. Ak, C. Tanyeli, I.M. Akhmedov, L. Toppare, Eur. Polym. J. 42 (2006) 2352–2360.

the soluble blue PHOLEDs is not suitable for display application. Deep blue color with *y* color coordinate below 0.20 is required for display application, but no solution processed deep blue PHOLED has been fabricated. High triplet energy host materials with a triplet energy over 2.90 eV and morphological stability after solution film coating are required to develop deep blue PHOLEDs. In addition, soluble deep blue emitting phosphorescent dopant materials are needed to obtain deep blue color. However, there has been no report fabricating soluble deep blue PHOLEDs because no soluble host and dopant material was available for application in deep blue PHOLEDs. Therefore, it is important to develop solution processed deep blue PHOLEDs using soluble host and dopant materials.

Phosphine oxide type compounds can be a candidate as a high triplet energy soluble host materials. Our group reported high external quantum efficiency in deep blue PHOLEDs using phosphine oxide type host materials [19–21]. In particular, *N*,*N*′-Dicarbazolyl-3,5-benzene based phosphine oxide compound showed above 20% external quantum efficiency in deep blue PHOLEDs [19]. Therefore, the phosphine oxide type host materials can be useful as the host materials for soluble deep blue PHOLEDs.

In this work, solution processed deep blue PHOLEDs were developed using a soluble high triplet energy host material and a deep blue emitting phosphorescent dopant. High quantum efficiency of 22.1% and a deep blue color coordinate of (0.14, 0.19) were demonstrated from solution processed deep blue PHOLEDs. The quantum efficiency is one of the best efficiency values reported in solution processed blue PHOLEDs and this work is the first paper reporting deep blue PHOLEDs fabricated by solution process.

2. Experimental

The synthesis of the mCPPO1 was described in our previous work [19]. The device structure of the blue PHOLED was indium thin oxide (ITO)/poly-3,4-ethylenedioxythiophene:polystyrenesulfonate (PEDOT:PSS) (60 nm)/PVK (10 nm)/(9-(3-(9H-carbazol-9-yl)phenyl)-9H-carbazol-3-yl)-diphenylphosphine oxide (mCPPO1):bis((3,5-difluoro-4-cyanophenyl)pyridine) iridium picolinate (FCNIrpic) (20 nm, 3%)/4-(triphenylsilyl)phenyldiphenylphosphine oxide (TSPO1) (35 nm)/LiF(1 nm)/Al(200 nm). The soluble deep blue PHOLED with PVK host instead of mCPPO1 was also fabricated for comparison. The mCPPO1:FCNIrpic emitting layer was spin coated from toluene solution and the concentration of the mCPPO1 solution was 1.0 wt.%. The mCPPO1:FCNIrpic film was baked at 80 °C for 10 min to remove residual solvent after spin coating. PVK hole transport layer was formed by spin coating from 0.3 wt.% chlorobenzene solution at a spin speed of 1000 rpm. The PVK layer was baked at 110 °C for 10 min after spin coating. TSPO1 was vacuum deposited at a vacuum pressure of 8.0×10^{-7} torr at a deposition rate of 0.1 nm/s. All devices were encapsulated with a CaO getter and a glass lid after device fabrication. Current density–voltage–luminance performances of the soluble blue PHOLEDs were measured with a Keithley 2400 source measurement unit and a CS 1000 spectroradiometer. Surface morphology of the spin coated mCPPO1:FCNIrpic film was analyzed using atomic force microscope.

3. Results and discussion

There are several requirements for the soluble host materials for solution processed high efficiency deep blue PHOLEDs. The host material should form uniform film with low surface roughness less than 1 nm, which is comparable to that of vacuum deposited film. The solution coated film should also be stable and form amorphous film. In addition to the smooth surface morphology after coating, high triplet energy and bipolar charge transport properties are important to obtain high efficiency in soluble deep blue PHOLEDs. Other than these, good solubility in common aromatic solvents such as toluene, chlorobenzene and dichlorobenzene is also required for good mixing with blue phosphorescent dopant.

A high triplet energy host material, mCPPO1, was reported to be effective as the host material for vacuum deposited blue PHOLEDs [19]. It has a high triplet energy of 3.00 eV and bipolar charge transport properties. In addition, the asymmetric molecular structure of the mCPPO1 is suitable for amorphous film formation. Therefore, the mCPPO1 is suitable as the host material for solution processed deep blue PHOLEDs. A deep blue emitting phosphorescent dopant, FCNIrpic, was reported in other works and gave high efficiency [19]. It has highly polar substituents and picolinic acid as the ancillary ligand. Although the dopant with three main ligands without any ancillary ligand was not soluble in aromatic solvent, the FCNIrpic was soluble in chlorobenzene and dichlorobenzene. Therefore, the FNCIrpic can be used as the soluble deep blue emitting dopant in solution processed deep blue PHOLEDs. Chemical structures of host and dopant materials are shown in Fig. 1.

The mCPPO1 and FNCIrpic were mixed in toluene solvent and was spin coated on Si substrate and PVK film to study the morphology of the mCPPO1:FNCIrpic film. Atomic force microscope pictures of spin coated mCPPO1:FCNIrpic and PVK/mCPPO1:FCNIrpic films are shown in Fig. 1. The mCPPO1:FCNIrpic and PVK/mCPPO1:FCNIrpic films showed smooth morphology with a surface roughness of 0.47 and 0.48 nm, respectively. The mCPPO1:FCNIrpic film could be stably coated on the PVK layer with little intermixing because the high molecular weight PVK layer shows poor solubility in toluene. There was little aggregation of the FCNIrpic dopant and uniform morphology was observed in spin coated mCPPO1:FCNIrpic film. The surface roughness of the mCPPO1:FCNIrpic film was comparable to that of the vacuum deposited mCPPO1:FCNIrpic film. This indicates that the mCPPO1:FCNIrpic film forms stable morphology after spin coating from toluene solution. The low surface roughness of the mCPPO1:FCNIrpic film was maintained even after thermal annealing at 110 °C for 10 min, indicating morphological stability of the mCPPO1:FCNIrpic film. The high temperature morphological stability of the mCPPO1:FCNIrpic film is due to the thermal and morpho-

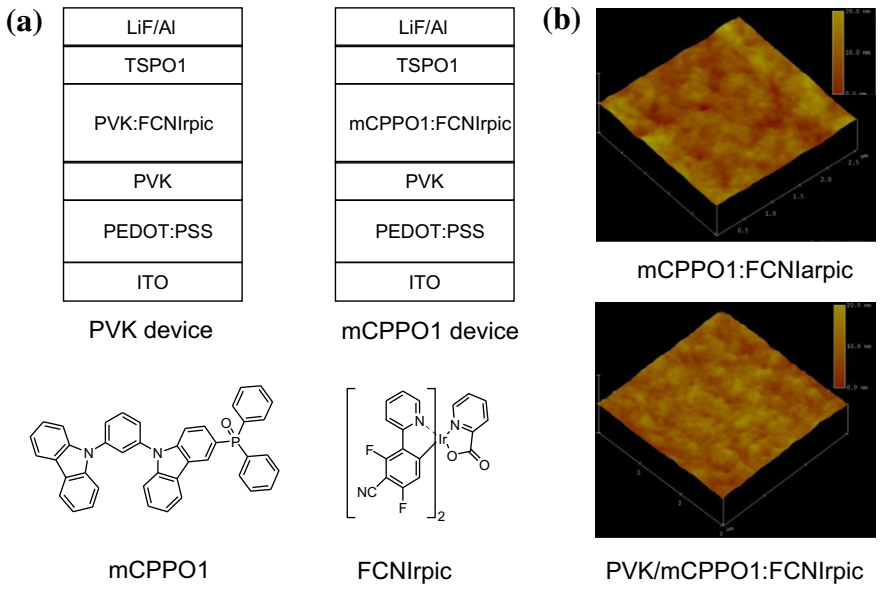

Fig. 1. Device structures and chemical structures of mCPPO1 and FCNIrpic (a) and atomic force microscope image of the spin coated mCPPO1:FCNIrpic and PVK/mCPPO1:FCNIrpic films (b).

logical stability of the mCPPO1. The mCPPO1 has a high glass transition temperature of 115 °C, which contributed to the morphological stability at high temperature.

Deep blue PHOLEDs with a basic device structure of ITO/PEDOT:PSS/PVK/mCPPO1:FCNIrpic/TSPO1/LiF/Al was fabricated. Annealing temperature to remove residual solvent was changed from 80 to 140 °C to optimize the process. Fig. 2 shows the device performances of the deep blue PHOLEDs according to the annealing temperature of the emitting layer. The current density and luminance of the deep blue PHOLEDs were not greatly affected by the annealing temperature up to 110 °C, but they were significantly reduced at 140 °C. This indicates that the spin coated mCPPO1:FCNIrpic emitting layer is degraded at 140 °C. The emitting layer was stable up to 110 °C in the morphology study of the mCPPO1:FCNIrpic film, resulting in stable device performances at 110 °C. The quantum efficiency was also very low after 140 °C thermal treatment. The quantum efficiency of the 80 and 110 °C treated deep blue PHOLEDs was similar. The maximum quantum efficiency of the two devices was 19.5%. However, the quantum efficiency at high luminance was better in the device thermally annealed at 80 °C than the device annealed at 110 °C. The efficiency was dropped at high luminance after thermal annealing at 110 °C, which may be due to slight aggregation of the FCNIrpic dopant. Therefore, the thermal annealing of the emitting layer was performed at 80 °C.

The device performances of the deep blue PHOLEDs with the mCPPO1:FCNIrpic emitting layer were further optimized by changing the thickness of the emitting layer from 30 to 20 nm. A deep blue PHOLED with PVK host instead of mCPPO1 was also fabricated for comparison. Device performances of the solution processed deep blue PHOLEDs are shown in Fig. 3. It can be shown that the current density of the mCPPO1 device is higher than that of the PVK device. PVK has the highest occupied molecular orbital (HOMO) of 5.9 eV and the lowest unoccupied molecular orbital (LUMO) of 2.4 eV. Although the PVK

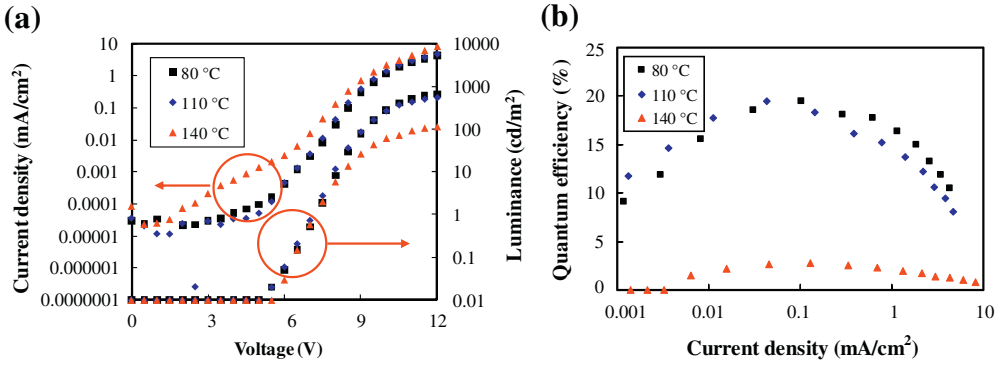

Fig. 2. Current density–voltage–luminance curves (a) and quantum efficiency–current density curves of spin coated mCPPO1:FCNIrpic devices according to annealing temperature (b).

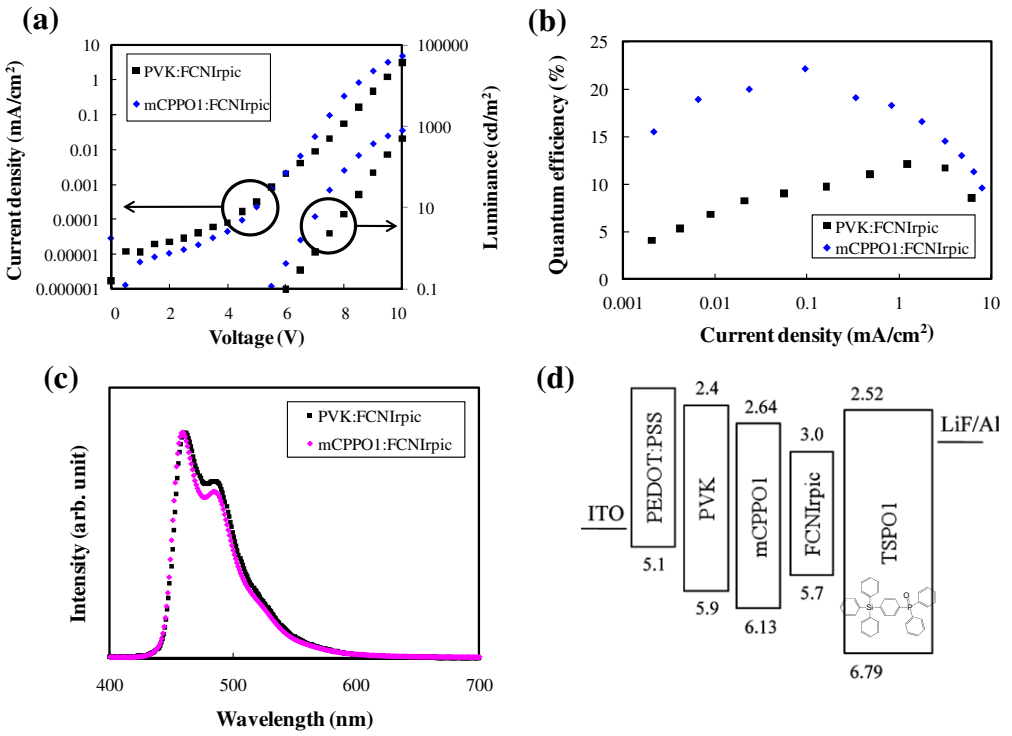

Fig. 3. Current density–voltage–luminance (a), quantum efficiency–current density (b), and electroluminescence (c) curves of mCPPO1and PVK based blue phosphorescent organic light-emitting diodes in addition to the energy level diagram of the device and chemical structure of TSPO1 (d).

shows good hole injection and transport properties, poor electron injection and transport properties of PVK reduced the current density of the PVK device. The mCPPO1 has hole transport carbazole unit and electron transport diphenylphosphine oxide unit in the molecular structure. Therefore, it shows good hole transport and electron transport properties, which resulted in high current density in the mCPPO1 device. In addition, the HOMO level of mCPPO1 was 6.13 eV for good hole injection from PVK and the LUMO level was 2.64 eV for electron injection from TSPO1 with the LUMO level of 2.52 eV for efficient electron injection into the mCPPO1. Energy level diagram and chemical structure of TSPO1 are shown in Fig. 3(d). The luminance of the mCPPO1 device was also high in the mCPPO1 device, which is due to high current density and high recombination efficiency of the mCPPO1 device.

The quantum efficiency–current density curves of the solution processed deep blue PHOLEDs are shown in Fig. 3(b). The quantum efficiency of the mCPPO1 device was much higher than that of the PVK device over all current density range. The maximum quantum efficiency of the mCPPO1 device was 22.1% and the quantum efficiencies at 0.42 mA/cm^2 (100 cd/m^2) and 2.61 mA/cm^2 (500 cd/m^2) were 18.9% and 15.1%, respectively. This quantum efficiency is one of the best efficiency values reported in soluble blue PHOLEDs. The maximum quantum efficiency of the PVK:FCNIrpic device was only 12.1%. The high quantum efficiency of the mCPPO1:FCNIrpic device can be explained by the high triplet energy and bipolar charge transport properties of the mCPPO1. The FCNIrpic dopant has a triplet energy of 2.74 eV and the host should have higher triplet energy than the dopant material. The mCPPO1 has higher triplet energy than FCNIrpic dopant and the triplet energy can be effectively transferred from mCPPO1 host to FCNIrpic dopant. As mentioned above, bipolar charge transport properties of the mCPPO1 balanced holes and electrons in the emitting layer, inducing high recombination efficiency in the emitting layer. In the case of the PVK, poor electron transport properties of the PVK limited the quantum efficiency. Maximum current efficiency and current efficiency at 100 cd/m^2 of the mCPPO1:FCNIrpic device were 28.4 and 23.9 cd/A.

Electroluminescence (EL) spectra of mCPPO1:FCNIrpic and PVK:FCNIrpic devices are shown in Fig. 3(c). Maximum emission peak of the blue PHOLEDs was observed at 457 nm and a color coordinate of (0.14, 0.19) was obtained in the soluble deep blue PHOLEDs. Within our knowledge, this is the first work reporting deep blue color in solution processed blue PHOLEDs. No emission other than FCNIrpic emission was detected in the EL spectra, indicating effective exciton confinement and energy transfer to FCNIrpic in the emitting layer.

4. Conclusions

In conclusion, a high efficiency solution processed deep blue PHOLED with a deep blue color coordinate of (0.14, 0.19) was developed using a soluble emitting layer of mCPPO1 and FCNIrpic. A maximum quantum efficiency of 22.1% and a quantum efficiency of 18.9% at 100 cd/m^2 were achieved in the soluble deep blue PHOLEDs. High effi-

ciency soluble deep blue PHOLEDs were realized using the mCPPO1:FCNIrpic emitting layer for the first time and further development of soluble host and dopant materials may enhance the quantum efficiency of soluble blue PHOLEDs further.

References

[1] H.B. Wu, J.H. Zou, F. Liu, L. Wang, A. Mikhailovsky, G.C. Bazan, W. Yang, Y. Cao, Adv. Mater. 20 (2008) 696.
[2] J.S. Huang, W.J. Hou, J.H. Li, G. Li, Y. Yang, Appl. Phys. Lett. 89 (2006) 133509.
[3] H. Kim, Y. Byun, R.R. Das, B.–K. Choi, P.-S. Ahn, Appl. Phys. Lett. 91 (2007) 093512.
[4] A.W. Freeman, S.C. Koene, P.R.L. Malenfant, M.E. Thompson, J.M.J. Fréchet, J. Am. Chem. Soc. 122 (2000) 12385.
[5] J.Q. Ding, J. Gao, Y.X. Cheng, Z.Y. Xie, L.X. Wang, D.G. Ma, X.B. Jing, \F.S. Wang, Adv. Funct. Mater. 16 (2006) 575.
[6] T. Earmme, E. Ahmed, S.A. Jenekhe, Adv. Mater. 22 (2010) 4744.
[7] M.K. Mathai, V. Choong, S.A. Choulis, B. Krummacher, F. So, Appl. Phys. Lett. 88 (2006) 243512.
[8] S. Lamansky, P.I. Djurovich, F.A. Razzaq, S. Garon, D.L. Murphy, M.E. Thompson, J. Appl. Phys. 92 (2002) 1570.
[9] K.S. Yook, S.O. Jeon, O.Y. Kim, J.Y. Lee, Electrochem. Solid-State Lett. 13 (2010) J71.
[10] X. Yang, D.C. Müller, D. Neher, K. Meerholz, Adv. Mater. 18 (2006) 948.
[11] S. Tokito, M. Suzuki, F. Sato, M. Kamachi, K. Shirane, Org. Electron. 4 (2003) 105.
[12] X.H. Yang, F. Jaiser, S. Klinger, D. Neher, Appl. Phys. Lett. 88 (2006) 021107.
[13] K.S. Yook, S.E. Jang, S.O. Jeon, J.Y. Lee, Adv. Mater. 22 (2010) 4479.
[14] .S. Ye, Y. Liu, K. Lu, W. Wu, C. Du, Y. Liu, H. Liu, T. Wu, G. Yu, Adv. Funct. Mater. (2011), doi:10.1002/adfm.201000474.
[15] W. Jiang, L. Duan, J. Qiao, D. Zhang, G. Dong, L. Wang, Y. Qiu, J. Mater. Chem. 20 (2010) 6131.
[16] L.D. Hou, L. Duan, J. Qiao, W. Li, D.Q. Zhang, Y. Qiu, Appl. Phys. Lett. 92 (2008) 263301.
[17] J.-H. Jou, W.-B. Wang, S.-Z. Chen, J.-J. Shyue, M.–F. Hsu, C.-W. Lin, S.-M. Shen, C.-J. Wang, C.-P. Liu, C.-T. Chen, M.-F. Wu, S.-W. Liu, J. Mater. Chem. 20 (2010) 8411.
[18] I. Takasu, Y. Mizuno, S. Uchikoga, S. Enomoto, T. Sawabe, A. Amano, A. Wada, J. Yoshida, T. Ono, SPIE 7415 (2009) 74150B.
[19] S.O. Jeon, S.E. Jang, H.S. Son, J.Y. Lee, Adv. Mater. 23 (2011) 1436.
[20] S.O. Jeon, K.S. Yook, C.W. Joo, J.Y. Lee, Adv. Mater. 22 (2010) 1872.
[21] S.O. Jeon, K.S. Yook, C.W. Joo, J.Y. Lee, Adv. Funct. Mater. 19 (2009) 3644.

Among the blue-emitting materials, anthracene derivatives are particularly attractive due to their excellent photoluminescence and electroluminescence properties [12–16]. Such as, triarylamines [17,18], or the other moieties [19–21] have been incorporated into anthracene unit to improve hole injection and charge carrier transport properties. Although a number of vacuum-deposited anthrance-based molecules have been reported as efficient blue electroluminescent materials [22,23], solution-processed analogs remain rare and largely unexplored in OLEDs for its poor solubility and aggregating properties. In our previous work [24], we have demonstrated that 1,3,5-tri (9-anthracene) benzene is a good core emitter, and its centered starburst oligofluorenes show robust blue light emission in an OLED device. Although these materials exhibit deep blue emission, and the current efficiency is up to 1.8 cd/A, but the values of T_g are only about 110 °C for the oligofluorenes possessing long alkyl chains.

Here, we report the design and synthesis of four symmetric dendrimer molecules based on the following two principles. Firstly, the propeller-like, and highly rigid 1,3,5-tri (9-anthracene) benzene group was used as the core, which can reduce strong intermolecular interactions and suppress fluorescence quenching. Secondly, using stilbenzene as a conjugated bridge, the different electron donor dendrons (naphthalene, diphenylbenzene, carbazole, and diphenylamine) were introduced at the peripheries of the core to improve solubility in common organic solvents, influence the charge transporting properties, enhance the morphological stability and the thermal stability and improve color purity. As we expected, all of these materials possess high glass transition temperatures (T_g) and good morphological properties, and exhibit good EL performance with low driving voltages in solution-processed double-layer OLED devices. These materials are a promising class of solution-processable blue emitters for practical applications.

2. Experimental section

2.1. Material and methods

All reagents and solvents were used as purchased from Aldrich and were used without further purification. ^{1}H NMR spectra were recorded using a Bruker-AF301 AT 400 MHz. High resolution mass spectrometric measurements were carried out using a Bruker autoflex MALDI-TOF mass spectrometer. Fluorescence spectra were obtained on a Perkin Elmer LS55 Luminescence spectrometer and UV–Vis spectra were measured using a Shimadzu-3150 UV–Vis–NIR spectrophotometer. The differential scanning calorimetry (DSC) analysis was performed under a nitrogen atmosphere at a heating rate of 10 °C/min using a PE Instruments DSC 2920. Thermogravimetric analysis (TGA) was undertaken using a SEIKO EXSTAR 6000 TG/DTA 6200 unit under nitrogen atmosphere at a heating rate of 10 °C/min. To measure the PL quantum yields (Φ_f), degassed solutions of the compounds in CH_2Cl_2 were prepared. The concentration was adjusted so that the absorbance of the solution would be lower than 0.1. The excitation was performed at 360 nm and 9,10-diphenylanthracene(DPA) in CH_2Cl_2 (Φ_f = 0.9 in CH_2Cl_2) or solid film(η_{DPA} = 1) was used as a standard [25,26]. Cyclic voltammetry measurements were carried out in a conventional three electrode cell using a Pt button working electrode of 2 mm in diameter, a platinum wire counter electrode, and a Ag/AgCl (0.1 M) reference electrode on a computer-controlled EG&G Potentiostat/Galvanostat model 283 at room temperature. Reductions CV of all compounds were performed in dichloromethane containing 0.1 M tetrabutylammoniumhexafluorophosphate (Bu_4NPF_6) as the supporting electrolyte.

2.2. Synthesis

The structures and synthetic routes of the four well-defined compounds are shown in Scheme 1. 1,3,5-tri(anthracen-9-yl)benzene (**1**) and 1,3,5-tris(10-bromo anthracen-9-yl)benzene (**2**) were synthesized according to the literature [24].

2.2.1. Synthesis of compound (**3**)

A 100 ml round-bottomed flask was charged with compound **2** (422 mg, 0.5 mmol), toluene (20 ml), and ethanol (10 ml) under nitrogen atmosphere. Subsequently, 4-formylphenylboronic acid (375 mg, 2.5 mmol), tetrabutylammonium bromide (0.96 g, 2.98 mmol) and aqueous potassium carbonate (15.0 ml, 30 mmol) were added slowly to the solution. 10 min later, tetrakis (triphenylphosphine) palladium (0) (173 mg, 0.15 mmol) was added and the reaction mixture was stirred under reflux for 24 h in the absence of light. After cooling to room temperature, the precipitate was filtrated and washed with distilled water and methanol, a yellow powder was obtained. Yield 0.34 g (74%). ^{1}H NMR: ($CDCl_3$, 400 MHz): δ (ppm) 10.21 (s, 3H), 8.30–8.28 (d, J = 8.8 Hz, 6H), 8.15–8.13 (d, J = 8.0 Hz, 6H), 7.90 (s, 3H), 7.68–7.56 (m, 18H), 7.43–7.40 (t, J = 7.6 Hz, 6H). ^{13}C NMR (100 MHz, $CDCl_3$) δ 191.98, 145.92, 139.21, 136.94, 135.86, 135.77, 133.98, 132.18, 129.93, 129.87, 129.60, 126.85, 126.64, 125.72, 125.63. MS (FAB): 919.3 (m/z), calcd for $C_{69}H_{42}O_3$: 919.3. Anal. Calcd. For $C_{69}H_{42}$ O_3: C 90.17, H 4.61, O, 5.22; found: C 90.14, H 4.56, O 5.30.

2.2.2. Synthesis of compound (**4**)

A 500 ml three-neck round-bottomed flask was charged with 4-bromobenzylphosphonium bromide (5.21 g, 10.0 mmol), sodium hydride (0.75 g, 30.0 mmol) and THF (200 ml) under nitrogen atmosphere. After stirring for 1 h, at 40 °C, compound **3** (2.3 g, 2.5 mmol) was added. The solution was continuously stirred for 4 h at room temperature and the product was precipitated by the addition of methanol (200 ml). The precipitated solid was filtrated and washed with methanol, a light yellow solid powder was obtained. Yield 3.2 g (93%). ^{1}H NMR: ($CDCl_3$, 400 MHz): δ (ppm) 8.30–8.28 (d, J = 8.0 Hz, 6H), 7.89 (s, 3H), 7.78–7.75 (m, 12H), 7.56–7.39 (m, 33H), 7.26–7.21 (m, 3H). ^{13}C NMR (100 MHz, $CDCl_3$) δ 136.34, 132.20, 132.10, 131.98, 131.89, 131.82, 131.51, 131.41, 130.81, 130.59, 130.01, 128.58, 128.47, 128.07, 127.85, 127.13, 126.82, 126.62, 125.55, 125.16. MS (MALDI-TOF): 1378.1999 (m/z), calcd for

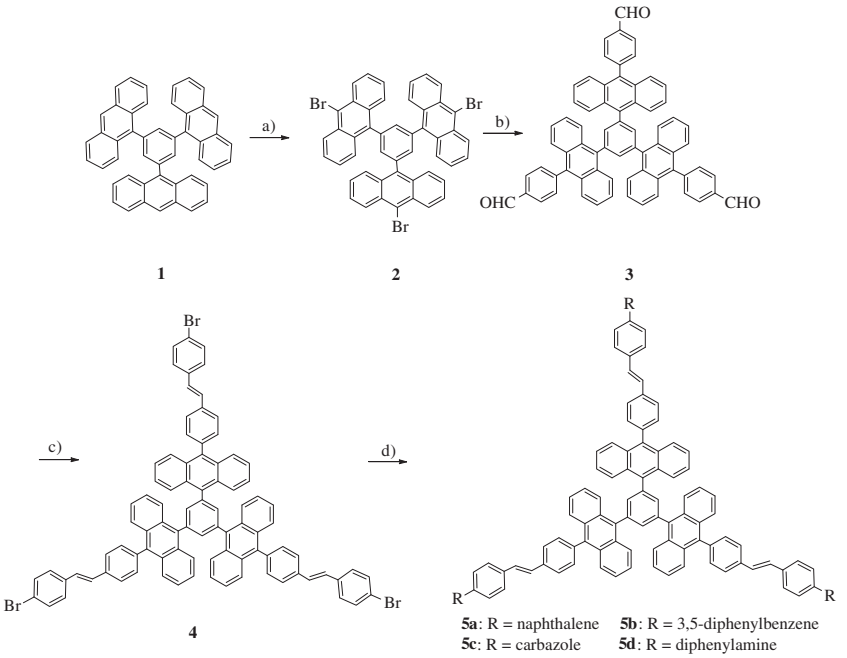

Scheme 1. Synthetic route of **5a, 5b, 5c** and **5d**. Reagents and conditions: (a) NBS, DMF, 30 °C; (b) toluene, K_2CO_3, ethanol, (4-formylphenyl)boric acid, $Pd(PPh_3)_4$, reflux; (c) 4-bromobenzyl-phosphonium bromide, 40 °C, NaH, THF, 1 h; (d) (i) 1-naphthylboronic acid or 3,5-diphenylbenzeneboronic acid, $Pd(PPh_3)_4$, toluene, EtOH; (ii) carbazole or diphenylamine, 18-crown-6, CuI, DMPU, K_2CO_3, 180 °C.

$C_{90}H_{57}Br_3$: 1378.1994. Anal. Calcd. For $C_{90}H_{57}Br_3$: C 78.44, H 4.17, Br, 17.39; found: C 78.50, H 4.15, Br, 17.35.

2.2.3. Synthesis of compound (*5a*)

A 500 ml three-neck round-bottomed flask was added compound **4** (137.8 mg, 0.1 mmol), 1-naphthaleneboronic acid (111 mg, 0.5 mmol), toluene (20 ml), ethanol (10 ml), 2 M K_2CO_3 (15 ml, 30 mmol) aqueous solution and tetrakis-(triphenylphosphine) palladium (0) (173 mg, 0.15 mmol) in turn, then the reaction mixture was refluxed under nitrogen for 24 h in the absence of light. After cooling to the room temperature, the precipitate was collected by filtration and washed with distilled water and methanol. The crude product was purified by column chromatography and dried under vacuum to yield a yellowish solid. Yield: 92%. ^{1}H NMR: ($CDCl_3$, 400 MHz): δ (ppm) compound **5a**: 8.30–8.28 (d, J = 8.0 Hz, 6H), 8.00–7.81 (m, 26H), 7.74–7.72 (m, 6H), 7.58–7.26 (m, 40H). ^{13}C NMR (100 MHz, $CDCl_3$) δ 140.24, 139.87, 139.32, 138.46, 137.20, 136.67, 136.41, 134.05, 133.88, 131.79, 131.58, 130.50, 130.05, 128.75, 128.60, 128.24, 128.13, 127.87, 127.74, 127.21, 126.88, 126.61, 126.51, 126.09, 125.99, 125.96, 125.82, 125.56, 125.41, 125.17. MS (MALDI-TOF): 1519.6144 (m/z), calcd for $C_{120}H_{78}$: 1519.6132. Anal. Calcd. For $C_{120}H_{78}$: C 94.83, H 5.17; found: C 94.58, H 5.42.

2.2.4. Synthesis of compound (*5b*)

The compound was synthesized using a similar procedure as for compound **5a**, yield: 85%. ^{1}H NMR: ($CDCl_3$, 400 MHz): δ (ppm) 8.32–8.30 (d, J = 8.8 Hz, 6H), 7.91–7.72 (m, 50H), 7.57–7.35 (m, 40H). ^{13}C NMR (100 MHz, $CDCl_3$) δ 142.45, 141.79, 141.15, 140.36, 139.28, 138.47, 137.17, 136.71, 136.59, 136.41, 131.78, 130.01, 129.17, 128.87, 128.79, 128.60, 128.55, 127.64, 127.59, 127.38, 127.25, 127.18, 127.11, 126.81, 126.60, 126.12, 125.54, 125.32, 125.17, 124.94 MS (MALDI-TOF): 1825.7515 (m/z), calcd for $C_{144}H_{96}$: 1825.7546. Anal. Calcd. For $C_{144}H_{96}$: C 94.70, H 5.30; found: C 94.85, H 5.15.

2.2.5. Synthesis of compound (*5c*)

A mixture of compound **4** (689 mg, 0.5 mmol), carbazole (376 mg, 2.25 mmol), CuI (14.25 mg, 0.075 mmol), 18-crown-6 (19 mg, 0.25 mmol), K_2CO_3 (310.5 mg, 2.25 mmol) and 1,3-di-methyl-3,4,5,6-tetrahydro-2(1H)-pyrimidinone (DMPU, 2.0 ml) was heated to 190 °C for 24 h under a nitrogen atmosphere. After cooling down to room temperature, the mixture was quenched with 1 N hydrochloric acid, then extracted with dichloromethane, washed with $NH_3{\cdot}H_2O$ and water. The combined organic phases were dried ($MgSO_4$) and concentrated under reduced pressure. The residue was purified by column chromatography on silica gel using hexane as the eluent to give compound **5c** as a yellow solid. Yield: 80%. ^{1}H NMR: ($CDCl_3$, 400 MHz): δ (ppm) 8.33–8.31 (d, J = 9.2 Hz, 6H), 8.17–8.15 (d, J = 7.6 Hz, 6H), 7.92 (s, 3H), 7.83–7.80 (m, 18H), 7.63–7.38 (m, 42H), 7.33–7.29 (m, 6H). ^{13}C NMR (100 MHz, $CDCl_3$) δ 140.80, 140.70, 139.30, 138.69, 137.12, 137.00, 136.51, 136.44, 136.42, 134.04, 131.84, 130.42, 130.03, 129.25, 128.08, 127.90, 127.27, 127.18, 126.84, 126.68, 125.98, 125.57, 125.20, 123.46, 120.35, 120.02. MS (MALDI-TOF): 1636.6458 (m/z), calcd for $C_{126}H_{81}N_3$: 1636.6461. Anal. Calcd. For $C_{126}H_{81}N_3$: C 92.45, H 4.99, N 2.57; found: C 92.31, H 5.17, N 2.52.

*2.2.6. Synthesis of compound (**5d**)*

The compound was synthesized using a similar procedure as for compound **5c**. Yield: 74%. 8.30–8.28 (d, J = 8.8 Hz, 6H), 8.17–8.15 (d, J = 7.6 Hz, 6H), 7.89–7.88 (s, 3H), 7.78–7.72 (m, 18H), 7.60–7.37 (m, 48H), 7.27–7.21 (m, 6H). ^{13}C NMR (100 MHz, $CDCl_3$) δ 139.25, 138.68, 137.19, 136.62, 136.36, 136.29, 134.01, 131.86, 131.79, 131.72, 131.49, 130.57, 129.99, 129.30, 129.10, 128.87, 128.75, 127.81, 127.44, 126.80, 126.54, 126.31, 125.53, 125.17, 124.55, 121.45. MS (MALDI-TOF): 1641.6924 (m/z), calcd for $C_{126}H_{87}N_3$: 1641.6900. Anal. Calcd. For $C_{126}H_{87}N_3$: C 92.11, H 5.34, N 2.56; found: C 92.10, H 5.39, N 2.51.

2.3. Device fabrication

To investigate the electroluminescent (EL) properties of the symmetric starburst compounds containing different surface groups, double layer OLEDs were fabricated via solution processing according to the previous literature.[27] The device structures of the OLEDs were as follows: ITO/PEDOT:PSS/**5a–5d** or (doping **DPAVBi**) /TPBI/LiF/Al. Polyethylene dioxythiophene-polystyrene sulfate (PEDOT-PSS) and 2,2′,2″-(1,3,5-benzenetriyl)tris[1-phenyl-1H-benzimidazole] (TPBI) were used as hole injection and hole-blocking/electron-transporting layer, respectively. The active layer was spin-coated from toluene solution, and TPBI layer was deposited by means of conventional vacuum deposition onto the ITO-coated glass substrates. The *J–V–L* characteristics of the EL devices were measured using a Keithley 2400 source meter and a Keithley 2000 source multimeter equipped with a calibrated silicon photodiode. The EL spectra were measured using a JY SPEX CCD3000 spectrometer. The thicknesses of the films were measured using the instrument of Profiler DEKTAK150. All of the measurements were carried out at room temperature under ambient conditions.

3. Results and discussion

3.1. Synthesis, Thermal, Film-forming, Optical and Electrochemical properties

Four target compounds, **5a, 5b, 5c** and **5d,** were prepared as shown in Scheme 1. Detailed synthesis of the 1,3,5-tris(10-bromoanthracen-9-yl)benzene (**2**) has been described in previous work [24]. The intermediate **3** was synthesized by the Pd-catalyzed Suzuki cross-coupling of formylated benzene boric acid with compound **2** with excellent yields, and were easily purified by a simple filtration and washed with distilled water and methanol. Then Wittig reaction of 4-bromobenzyl-phosphonium bromide and compound **3** gave the compound **4** in 93% yield at 40 °C. The target compounds **5a** and **5b** were obtained in 92% and 85% of isolated yield, by an easy Suzuki coupling reaction, respectively. The target compound **5c** and 5**d** were obtained in 80% and 74% of isolated yield by the CuI-catalyzed Ullman reaction, respectively. All the four target compounds were soluble in common organic solvents (CH_2Cl_2, toluene), and characterized fully by ^{1}H and ^{13}C NMR, MALDI-TOF, and elemental analysis.

Thermal properties of these compounds were studied using DSC and TGA. The thermal properties were measured under N_2 gas condition at heating rates of 10 °C/min, and the related data are listed in Table 1. As shown in Fig. 1a, compounds **5a–5d** exhibit a high glass transition temperature (T_g) at 166, 189, 260, and 231 °C, respectively. The high T_g are attributed to the rigid core and the star shaped dendrons can effectively suppress the crystallization (or arm aggregation). High decomposition temperatures (T_d, 5% weight loss) of these compounds were also observed at 484, 504, 497, and 427 °C (Fig. 1b), respectively, which may be due to the highly stability of the 1,3,5-tri (9-anthracene) benzene core and the side groups. The stable aromatic side group can supply electron to the styryl group and enhance the thermal stability of material.[28] The relatively high T_g and T_d of these star shaped compounds is very desirable for high performance OLED applications.

Efficient film-forming properties of light emitting materials used in OLEDs are crucial for the performance of the devices, so the surface morphologies of thin films of the four compounds (**5a**, **5b**, **5c** and **5d**) were examined. As showed in Fig. 2, the AFM images show smooth and amorphous thin films formed by spin-coating the compounds (**5a**, **5b**, **5c** and **5d**) from toluene solution. The deposited films were annealed under N_2 gas condition at 150 °C for 0.5 h. The annealed film exhibits a fairly smooth surface morphology with a root-mean-square (rms) roughness of 0.5539, 0.6211, 0.5202 and 0.6565 nm for **5a, 5b, 5c** and **5d**, respectively. This suggests that all of the compounds possess excellent thermal and amorphous stability, which indicates that the rigid propeller core influences the arrangement of the molecules in the thin films, and 1,3,5-tri(9-anthracene)benzene is a good core emitter for star-shaped fluorophore.

Fig. 3 shows the normalized UV–Vis and fluorescence spectra of compounds **5a, 5b, 5c** and **5d** in a CH_2Cl_2 solution and in the thin film. The related photophysical properties were listed in Table 1. All of these compounds have similarly structured absorption spectra (range: 330–440 nm) and emission spectra (range: 400–550 nm) in solution. This indicates that the photophysical properties are mainly determined by the core 1, 3, 5-tri(9-anthracene)benzene. The absorption in the range 330–440 nm is assigned to the $S_1 \leftarrow S_0$ transition of the anthracene moiety. In the solid state, all of them show strong pure-blue emission with a main peak at 448, 453, 451 and 460 nm, respectively, which shows that the introduction of dipenylamine results in a notable red-shift in PL spectra and peripheral dendrons can affect the molecular interaction. The quantum yields of compound **4a**-**4d** in CH_2Cl_2 were 0.68, 0.66, 0.67 and 0.64, respectively, which is even higher than the typical blue material m-ADN [25]. The quantum yield in solid state was also measured, the relative high values indicated that no obviously aggregating or quenching phenomena appeared. In order to further investigate the morphological stability of these materials, the Abs and PL spectra before/after annealing state (see Figure S4.) was also researched, the absorbance and PL emission have no clearly change after annealing (150 °C for 1 h), which showed that the morphological stability of material is excellent. The optical energy bandgaps of the compound

Table 1
The optical, photophysical and thermal properties of **5a–5d**.

	HOMO	LUMO	Φ^a/η^b	E_g (eV)	PL (nm)		Abs (nm) in solution	T_g/T_d (°C)
					Solution	Film		
5a	−5.57	−2.65	0.68/0.69	2.92	436	448	331,358,380,401	166/484
5b	−5.54	−2.59	0.66/0.68	2.95	436	453	340,358,380,401	189/504
5c	−5.52	−2.58	0.67/0.64	2.94	436	451	344,358,380,401	260/497
5d	−5.50	−2.57	0.64/0.61	2.93	437	460	320,358,380,401	231/427

[a] Using DPA as a standard; λex = 360 nm (Φ = 0.9 in CH_2Cl_2).
[b] Using DPA as a standard; λex = 360 nm (η = 1 in thin film).

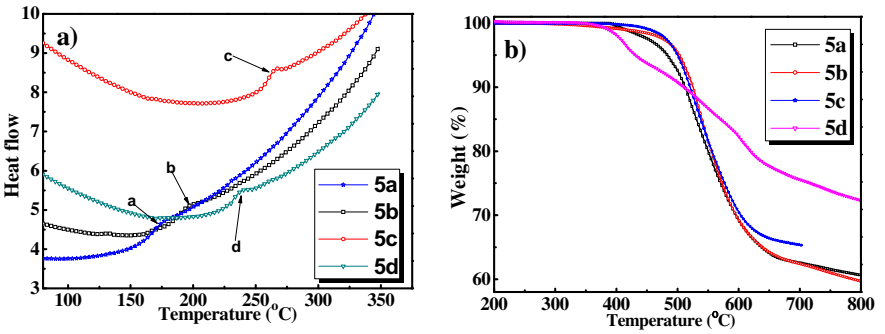

Fig. 1. (a) DSC curves of compounds **5a**, **5b**, **5c** and **5d** measured under nitrogen at a heating rate of 10 °C/min; (b) TGA curves of star-shaped compounds measured at a heating rate of 10 °C/min under nitrogen.

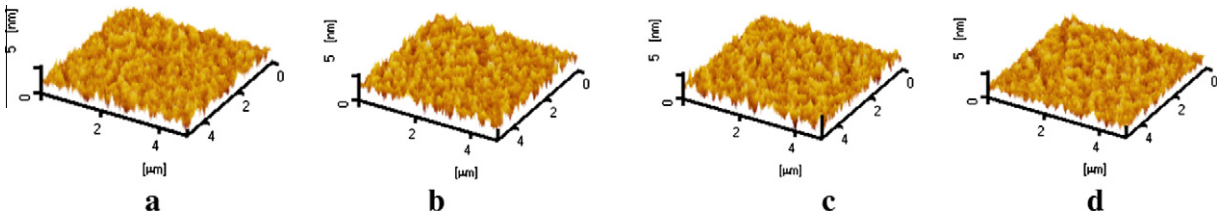

Fig. 2. AFM topographic images of the four compounds (**5a**, **5b**, **5c** and **5d**) in thin solid films (ca. 40 nm thick).

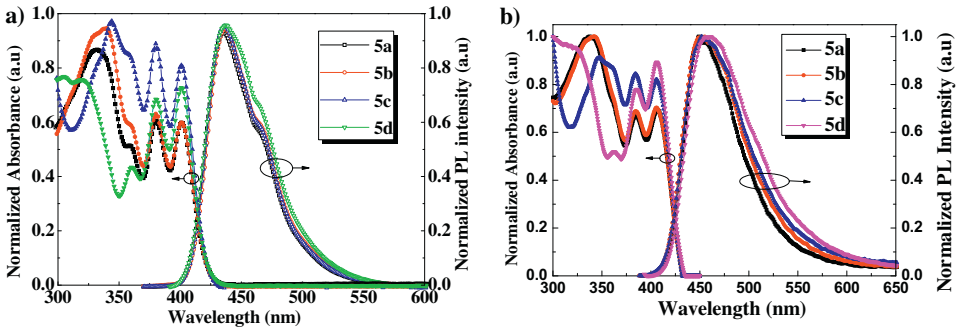

Fig. 3. (a) Absorption and photoluminescence spectra of compound **5a, 5b, 5c** and **5d** in CH_2Cl_2; (b) Absorption and PL spectrum of the compounds **5a, 5b, 5c** and **5d** in thin film (ca. 40 nm).

5a, **5b**, **5c**, and **5d** are 2.92, 2.95, 2.94, and 2.93 eV, respectively, which is calculated from the threshold of the optical absorption.

In addition to the photophysical properties, the electrochemical properties are also very important in evaluating a material usefulness for optoelectronic applications. The electrochemical behaviors of the compounds **5a**, **5b**, **5c** and **5d** were examined by cyclic voltammetry using a standard three-electrode electrochemical cell in an electrolyte solution of 0.1 M tetrabutylammoniumhexafluorophosphate ($TBPAPF_6$) dissolved in dichloromethane [29]. The onset oxidation peaks (E_{ox}) for **5a–5d** were 1.26, 1.23,

Table 2
Electroluminescence Characteristics of the Devices.[a]

Device	Emitter	L_{max}[b] (cd/m^2) voltages (V)	$\eta_{c.max}$[c] (cd/A)	$\eta_{p.max}$[d] (lm/W)	CIE (x, y)[e]	V_{on} (1 cd/m^2) (V)	EL(peak) (nm)
1	5a	3366, 11.3	1.7	1.10	(0.15,0.17)	4.8	468
2	5b	2740, 11.1	1.6	1.14	(0.15, 0.14)	4.5	456
3	5c	4754, 8.5	2.0	1.71	(0.16, 0.19)	3.4	468
4	5d	1562, 11.5	2.4	1.54	(0.18, 0.28)	4.9	476
5	5a:DPAVBi	3635, 8.6	3.6	2.40	(0.16, 0.31)	3.2	472
6	5b:DPAVBi	6807, 12.4	4.2	2.81	(0.16, 0.30)	3.6	472
7	5c:DPAVBi	7470, 11.6	3.6	2.25	(0.17, 0.33)	3.6	476
8	5d:DPAVBi	11204, 11.4	4.9	3.22	(0.17, 0.31)	3.4	472

[a] Devices configuration: ITO/PEDOT:PSS (40 nm)/ **5a–5d** (40 nm) or **5a–5d**: **DPAVBi** (5%)(40 nm)/TPBI (40 nm) /LiF (1 nm) /Al (100 nm).
[b] Maximum luminance.
[c] Maximum current efficiency.
[d] Maximum powder efficiency.
[e] Commission International de l'Eclairage coordinates.

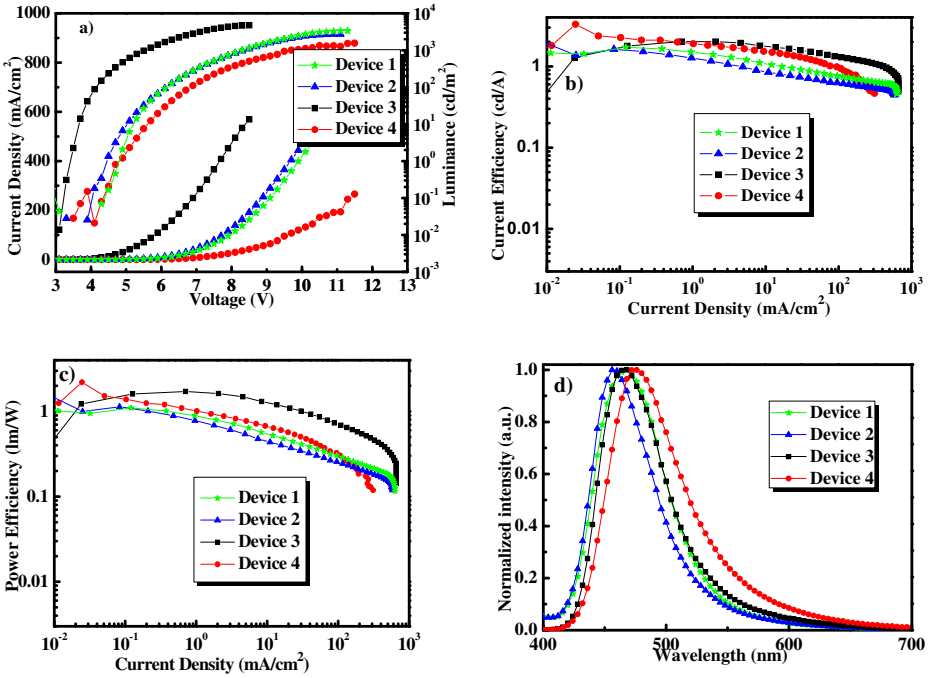

Fig. 4. (a) *J–V–L* curve of the four devices; (b) current efficiency-current density characteristics; (c) powder efficiency-current density characteristics; (d) EL spectra of the four devices.

1.21 and 1.19 eV, respectively (see Figure S3). Thus, the HOMO levels were determined to be −5.57, −5.54, −5.52 and −5.50 eV by the method $-(E_{ox} + 4.31)$ eV reported by Li et al. [25] (Table 1). The values were very close to that of 9,10-diphenylanthracene (5.54 eV), which indicates the HOMO level of these compounds were mainly decided by 1,3,5-tri(9-anthracene)-benzene center and the side groups were only finely tune the energy gap and the HOMO level. Generally speaking, the electrochemical properties and photophysical properties of compound **5a**–**5d** in dilute solution are very similar, mirroring the anthracene unit's characteristics. It shows every individual arm's electrochemical properties are remained unperturbed for the propeller topology serving as a spacer to effectively block conjugation.

3.2. Device performance

To study the EL properties of these compounds, double-layered devices with the configuration ITO/PEDOT:PSS (40 nm)/**5a–5d** (40 nm)/TPBI (40 nm)/LiF (1 nm) /Al (100 nm) (emitter: **5a**, Device 1; **5b**, Device 2; **5c**, Device 3; **5d**, Device 4) were fabricated by spin-coating from a toluene solution (ca. 7 mg/ml). The EL performances of these compounds are listed in Table 2. Double-layer devices utilizing compounds **5a** and **5b** exhibit a maximum brightness of 3366, 2740 cd/m^2, luminous efficiency of 1.7, 1.6 cd/A, with CIE coordinates **5a** (0.15, 0.17), **5b** (0.15, 0.14). For compounds **5c** and **5d**, the double-layer devices showed a maximum brightness of 4754, 1562 cd/m^2, luminous efficiency of 2.0, 2.4 cd/A, with CIE coordinates **5c**

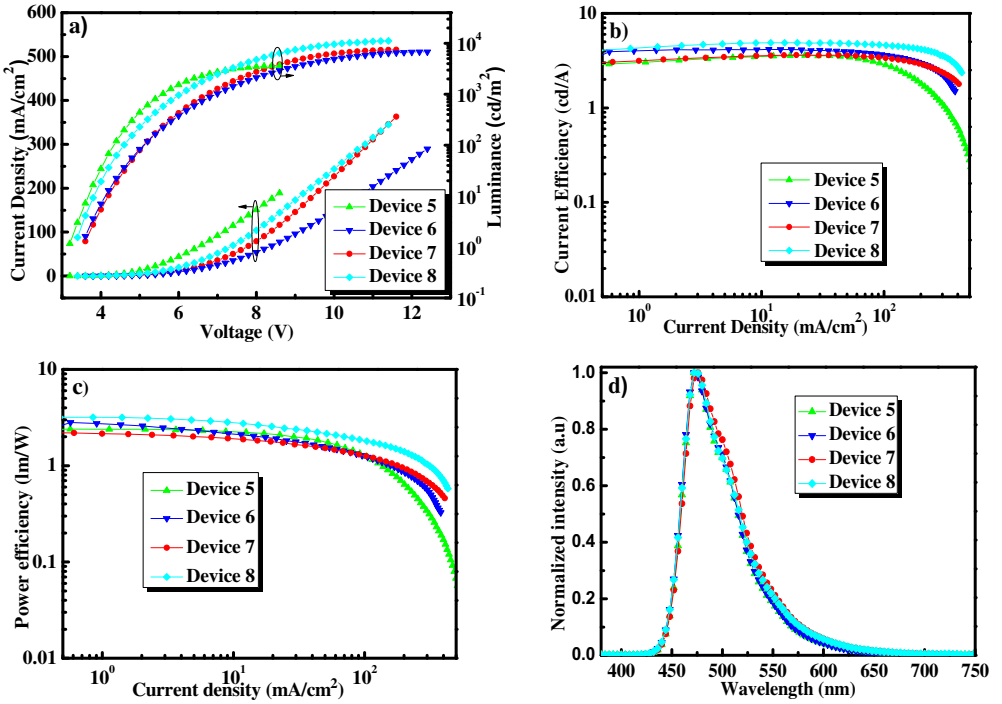

Fig. 5. (a) J–V–L curve of the four doped devices; (b) current efficiency-current density characteristics; (c) powder efficiency-current density characteristics; (d) EL spectra of the four doped devices.

(0.16, 0.19), **5d** (0.18, 0.28). Fig. 4 shows the EL spectra, the current density–voltage-brightness and the current density-efficiency characteristics of the devices (**1**, **2**, **3**, **4**). EL spectra of the devices based on the emitters **5c** and **5d** have obviously red-shift compared to the compounds **5a** and **5b**, it is induced by the carbazole and diphenylamine group's electronic-donating properties. Especialy, the EL spectrum of the device 4 has a red shift about 20 nm compared to that of device four. Additionally, the electroluminescence (EL) of all devices remained quite stable under different driving voltages (see Figure S1).

In order to further improve the device efficiency, we adopted a host-dopant system using these materials as the host and a highly fluorescent blue dye, DPAVBi, as dopant at a concentration of 5%. Table 2 summarizes the key EL performance of doped devices (**5**, **6**, **7**, **8**), all of them show a strong blue emission with current efficiency of 3.6–4.9 cd/A. Fig. 5. shows the EL spectra, the current density–voltage-brightness and the current density-efficiency characteristics of devices (**5**, **6**, **7**, **8**). The device **8** exhibits a maximum brightness of 11204 cd/m^2 at 11.4 V, and a maximum current efficiency of 4.9 cd/A with CIE coordinates of (0.17, 0.31). We ascribe the higher efficiency to the more efficient Förster energy transfer because there is more overlap between the emission of compound **5d** and the absorption of DPAVBi. As shown in Fig. 5d, the EL spectra of all DPAVBi doped devices (**5**, **6**, **7**, **8**) exhibit bright blue emissions at 472 nm with a shoulder at around 496 nm, which is the intrinsic characteristic of the emissions from the dopant DPAVBi. This result indicates completed energy transfer from the host to dopant. From the Fig. 6, it is obviously that the quantum efficiency of the doped device has been improved, which indicated that the better device performance in the doped device is not due to the change of emission colors. More interestingly, the driving voltage of all the devices is low (ca. 3.6 eV), in which device **5** exhibits the lowest driving voltage of 3.2 V. This indicates that the energy levels of the host materials and the dopant DPAVBi are well matched. Additionally, the dopant DPAVBi can also act as the hole trapper in all of doped devices, so the turn on voltage of the most of doped devices are lower than the undoped devices(see Table 2) [30]. Excellent EL stability (see Figure S2) and the efficient color purity render these materials promising candidates for display applications. We believe that optimization could further improve the device

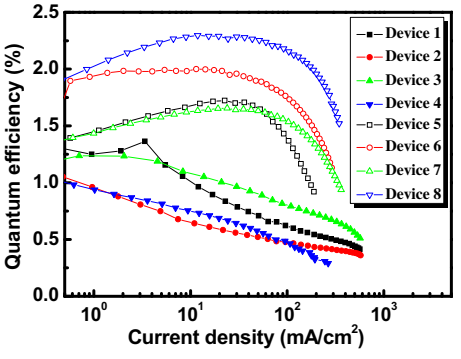

Fig. 6. Quantum efficiency-current density characteristics of devices **1–8**.

performance and fully explore the potential of these starburst materials.

4. Conclusion

In summary, we present a series of novel blue star-shaped molecules, in which the propeller core 1,3,5-tri(9-anthracene)benzene and the different dendrons were bridged by the stilbenzene. These materials exhibit high thermal stability (high glass transition temperature in the range 166–231 °C) with good film forming properties. Meanwhile, their optical and electronic properties can be tuned by adjusting the appropriated surface groups. The nondoped OLED devices fabricated using compound **5c** exhibits a maximum brightness of 4754 cd/m^2 and maximum current efficiency of 2.0 cd/A (corresponding to a power efficiency of 1.71 lm/W) with CIE$_{x,y}$ color coordinates of (x = 0.16, y = 0.19) and the devices' threshold voltage are only 3.4 eV. Compound **5d** shows an even higher efficiency of up to 4.90 cd/A with CIE$_{x,y}$ color coordinates of (x = 0.17, y = 0.31). These results will be beneficial for the molecular design of blue dendritic materials.

Acknowledgements

We thank the Donghu New & High Technology Development Zone of Wuhan City and Doctoral Fund of Ministry of Education of China (20100142120049) for financial support and thank the Analytical and Testing Centre of Huazhong University of Science and Technology for measurements.

Appendix A. Supplementary data

Supplementary data associated with this article can be found, in the online version, at doi:10.1016/j.orgel.2011.06.025.

References

[1] O. Usluer, S. Demic, D.A.M. Ebge, E. Birckner, C. Tozlu, A. Pivrikas, A.M. Ramil, N.S. Sariciftci, Adv. Funct. Mater. 20 (2010) 4152.
[2] J.L. Wang, Y. Zhou, Y.F. Li, J. Pei, J. Org. Chem. 74 (2009) 7449.
[3] S.C. Lo, R.E. Harding, C.P. Shipley, S.G. Stevenson, P.L. Burn, I.D.W. Samuel, J. Am. Chem. Soc. 131 (2009) 16681.
[4] S.H. Hwang, C.N. Moorefield, G.R. Newkome, Chem. Soc. Rev. 37 (2008) 2543.
[5] L. Wang, Y. Jiang, J. Luo, Y. Zhou, J.H. Zhou, J. Wang, J. Pei, Y. Cao, Adv. Mater. 21 (2009) 4854.
[6] S.H. Ye, Y.Q. Liu, K. Lu, W.P. Wu, C.Y. Du, Y. Liu, H.T. Liu, T. Wu, G. Yu, Adv. Funct. Mater. 20 (2010) 3125.
[7] S. Sax, N.R. Penkalla, A. Neuhold, S. Schuh, E. Zojer, E.J.W. List, K. Müllen, Adv. Mater. 22 (2010) 2087.
[8] H. Sasabe, E. Gonmori, T.Y. Chiba, Y.J. Li, D.K. Tanaka, S.J. Su, T. Takeda, Y.J. Pu, K.C. Nakayama, J.J. Kido, Chem. Mater. 20 (2008) 5951.
[9] W.Y. Lai, Q.Y. He, R. Zhu, Q.Q. Chen, W. Huang, Adv. Funct. Mater. 18 (2008) 265.
[10] F. Liu, W.Y. Lai, C. Tang, H.B. Wu, Q.Q. Chen, B. Peng, W. Wei, W. Huang, Y. Cao, Macromol. Rapid. Commun. 29 (2008) 659.
[11] S.C. Lo, R.N. Bera, R.E. Harding, P.L. Burn, I.D.W. Samuel, Adv. Funct. Mater. 18 (2008) 3080.
[12] J.H. Huang, J.H. Su, X. Li, M.K. Lam, K.M. Fung, H.H. Fan, K.W. Cheah, C.H. Chen, H. Tian, J. Mater. Chem. 21 (2011) 2957.
[13] J.H. Park, D.H. Lee, H. Kong, M.J. Park, I.H. Jung, C.E. Park, H.K. Shim, Org. Electron. 11 (2010) 820.
[14] J. Shi, C.W. Tang, Appl. Phys. Lett. 80 (2002) 3201.
[15] S.K. Kim, B. Yang, Y. Ma, J.H. Lee, J.W. Park, J. Mater. Chem. 18 (2008) 3376.
[16] Y.T. Lyu, J. Kwak, O. Kwon, S.H. Lee, D. Kim, C. Lee, K. Char, Adv. Mater. 20 (2008) 2720.
[17] Z.H. Li, M.S. Wong, Y. Tao, M. D'Iorio, J. Org. Chem. 69 (2004) 921.
[18] S.B. Jiao, Y. Liao, X.J. Xu, L.P. Wang, G. Yu, L.M. Wang, Z.M. Su, S.H. Ye, Y.Q. Liu, Adv. Funct. Mater. 18 (2008) 2335.
[19] K. Albrecht, Y.T. Kasai, K. Yamamoto, J. Inorg. Organomet. Polym. 118 (2009) 118.
[20] H.Q. Zhang, S.M. Wang, Y.Q. Li, B. Zhang, C.X. Du, X.J. Wan, Y.S. Chen, Tetrahedron 65 (2009) 4455.
[21] C.J. Zheng, W.M. Zhao, Z.Q. Wang, D. Huang, J. Ye, X.M. Ou, X.H. Zhang, C.S. Lee, S.T. Lee, J. Mater. Chem. 20 (2010) 1560.
[22] L. Wang, W.Y. Wong, M.F. Lin, W.K. Wong, K.W. Cheah, H.L. Tam, C.H. Chen, J. Mater. Chem. 18 (2008) 4529.
[23] Y.H. Yu, C.H. Huang, J.M. Yeh, P.T. Huang, Org. Electron. 12 (2011) 694.
[24] H. Huang, Q. Fu, S.Q. Zhuang, Y.K. Liu, L. Wang, J.S. Chen, D.G. Ma, C.L. Yang, J. Phys. Chem. C. 115 (2011) 4872.
[25] J.H. Seo, K.H. Lee, B.M. Seo, J.R. Koo, S.J. Moon, J.K. Park, S.S. Yoon, Y.K. Kim, Org. Electron. 11 (2010) 1605.
[26] J.A. Osaheni, S.A. Jenekhe, J. Am. Chem. SOC. 117 (1995) 7389.
[27] J. Luo, L. Xiao, Z. Chen, Q. Gong, Appl. Phys. Lett. 93 (2008) 133301.
[28] J.Y. Park, S.Y. Jung, J.Y. Lee, Y.G. Baek, Thin. Solid. Films. 516 (2008) 2917.
[29] Q. Sun, H. Wang, C. Yang, Y.F. Li, J. Mater. Chem. 13 (2003) 800.
[30] C.W. Tang, S.A. Van Slyke, C.H. Chen, J. Appl. Phys. 65 (1989) 3610.

In this work, we provide new insight into the light generation mechanism of an AC-driven light-emitting device in a transistor configuration. The semiconductor para-hexaphenylene (p6P) with a wide band-gap (3 eV) acts as the active material. By combining time-resolved EL experiments with a study of the influence of the biasing parameters (gate voltage amplitude and DC potential of the drain voltage) on the light emission intensity, we reveal a device operating mechanism that combines hole injection and SCF assisted electron tunneling from an individual metal electrode. A theoretical calculation on the basis of Arkhipov's charge injection model [16] predicts an increasing hole injection probability with increasing temperature, which is qualitatively in agreement with our low temperature experiments. Our proposed device operating mechanism can explain well the light emission from a unipolar transistor platform driven by AC gate voltage. This operating approach has implication for the development of nano-scale light-emitting devices [15] and can assist in the design of facile fabricated OLED architectures, which constitute a promising component of novel full color displays [17].

2. Experimental

2.1. Device fabrication

300 nm thermally grown SiO_2 formed the gate dielectric while the underlying highly *n*-doped silicon ($\rho = 0.025$ Ω cm) served as back gate electrode. Titanium/gold (2 nm/30 nm) source and drain electrodes were fabricated on the SiO_2 by optical lithography, electron-beam deposition and lift-off. The total channel width was 2.66 cm and the channel length *L* was either 2.5, 10, or 25 μm. After substrate fabrication and cleaning, a 50 nm thick p6P film was deposited (rate approx. 0.2 Å s^{-1}) with the substrate at room temperature under high-vacuum conditions ($\sim 10^{-7}$ mbar). Fig. 1a illustrates the device configuration and the operating circuit used for light emission experiments together with the p6P molecular structure. Although each metal contact is actually acting sequentially as electron "drain" and electron "source" during AC-driven operation, we have used the conventional terms "drain" and "source" as labels in order to distinguish between the metal contacts on the transistor platform.

2.2. Characterization methods

Electrical DC measurements (not shown here) were conducted under ambient conditions to confirm that the p6P transistor acts as a *p*-type device. The leakage current was found to be negligible compared with the injection current, which is assumed to be the situation as well for AC biasing. The light emission experiments were performed under vacuum conditions ($\sim 10^{-4}$ mbar) by symmetrically biasing the source and drain electrodes relative to ground, while an AC voltage was applied to the gate electrode. The spatial distribution of the emission (Fig. 1b and c) was recorded by a camera mounted on a microscope while the spectrum (Fig. 1d) was recorded with an ARC SpectraPro-150 spectrometer. A He-Cd laser with wavelength of 325 nm was used as the excitation source to record photoluminescence (PL) spectra. Time-resolved data were recorded by a photomultiplier tube (Hamamatsu R943–02) connected to a digital storage oscilloscope (Instek GDS-2102) via a DC preamplifier (Hamamatsu C7319). Low temperature measurements (down to 30 K) were made under vacuum conditions ($\sim 10^{-5}$ mbar) in a cryocooler (Sumitomo CNA-11 Helium Compressor Unit).

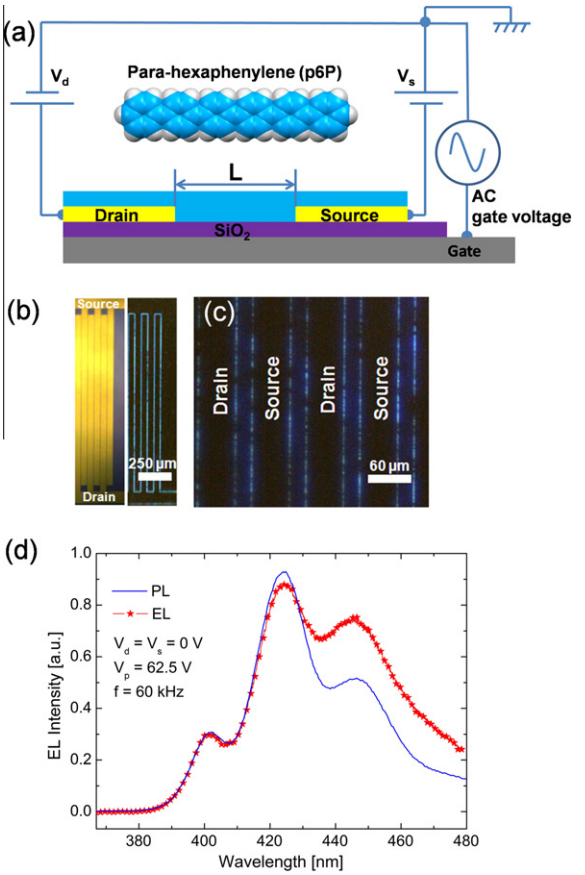

Fig. 1. (a) Schematic diagram of the operating circuit for light emission experiments along with the device configuration. Inset: molecular structure of p6P. (b) Optical microscope image of AC-driven light emission when only the drain electrode is biased while the source electrode is floating. (c) AC-driven light emission when both the drain and source electrodes are biased (channel length is 25 μm). (d) EL spectrum from a p6P OLET under gate voltage amplitude of 62.5 V. A scaled PL spectrum is shown for comparison.

3. Results and discussion

Fig. 1b and c show AC-driven light emission from a p6P film. In Fig. 1b, only the drain electrode was biased while the source electrode was floating. This gives rise to light emission close to the interface between the drain electrode and the p6P film. When both the drain and the source electrodes were biased, light emission from both sides of the channel (i.e., from both electrode-p6P interfaces) can be observed as seen from Fig. 1c. No light emission was observed when the gate terminal was biased by a DC voltage.

This must be due to high electron injection barrier in our p6P-based device under DC biasing. Fig. 1d shows the electroluminescence spectrum obtained with an amplitude of the sinusoidal gate voltage (V_p) of 62.5 V (frequency was 60 kHz and drain and source electrodes were grounded). A scaled PL spectrum is provided for comparison. The similarity of EL and PL spectra with three main peaks at 401, 422, and 448 nm corresponding to the $(0 \rightarrow 0)$, $(0 \rightarrow 1)$, and $(0 \rightarrow 2)$ vibronic transitions [18], respectively, indicates that identical excitonic transitions take place in both cases although with different relative intensities.

Since the light emission in our devices occurs from the circumference of a single biased electrode and from both sides of the device channel when both electrodes are biased, this indicates that charge transport across the channel does not play a role in the light generation process. Instead, the emitted photons must be caused by the radiative recombination of holes and electrons injected from the same metal electrode. However, the work function of gold used for the electrode is 5.1 eV while the electron affinity of p6P is 3 eV; this leads to an estimated electron barrier height of more than 2 eV (neglecting a possible interface dipole). This suggests the hole injection probability is much higher than the electron injection probability. This is in accordance with the previously reported transistor output characteristics, in which no *n*-type behavior was observed [15]. Our transistor therefore constitutes a unipolar device, however without any charge transport across the channel during AC operation.

The time-resolved EL intensity measurements in Fig. 2a and b show how the light emission is correlated to the instantaneous gate voltage. The gate voltage waveforms in Fig. 2a and b are square wave and sinusoidal, respectively, and the amplitude in both cases is 50 V with a frequency of 20 kHz. Two distinct peaks can be observed within one period both for square wave and sinusoidal gate voltage. The larger EL peak appears when the gate voltage shifts from a negative to a positive value. In contrast, the smaller EL peak appears when the gate voltage shifts from a positive to a negative value. Using a light source with a known intensity, we calibrated our photomultiplier setup in order to quantify the emission intensity. The ratio of collected to emitted light was estimated by assuming a Lambertian emitter, while the emission area was found as the full width at half maximum of the emission zone multiplied by the emission zone length. This provides an estimate of the averaged intensity of 8×10^{-8} (estimated uncertainty: -3×10^{-8},$+7 \times 10^{-8}$) W cm^{-2} for the data presented in Fig. 2b. To compare the averaged EL intensity generated from square wave and sinusoidal gate voltage, the amplitude of the gate voltage V_p was varied from 40 to 60 V in steps of 5 V, while the drain electrode was grounded and the source electrode was floating. Fig. 2c shows how the EL intensity increases as V_p increases both for square wave and sinusoidal gate voltages. The EL intensity has been determined by summing up from 380 to 480 nm of the corresponding spectrum. The inset shows the ratio of the EL intensities for square wave to sinusoidal gate voltages. A constant ratio of 1.73 is obtained. Since the effective value of a square wave is 1.41 times higher than the effective value of a sine wave with the same amplitude,

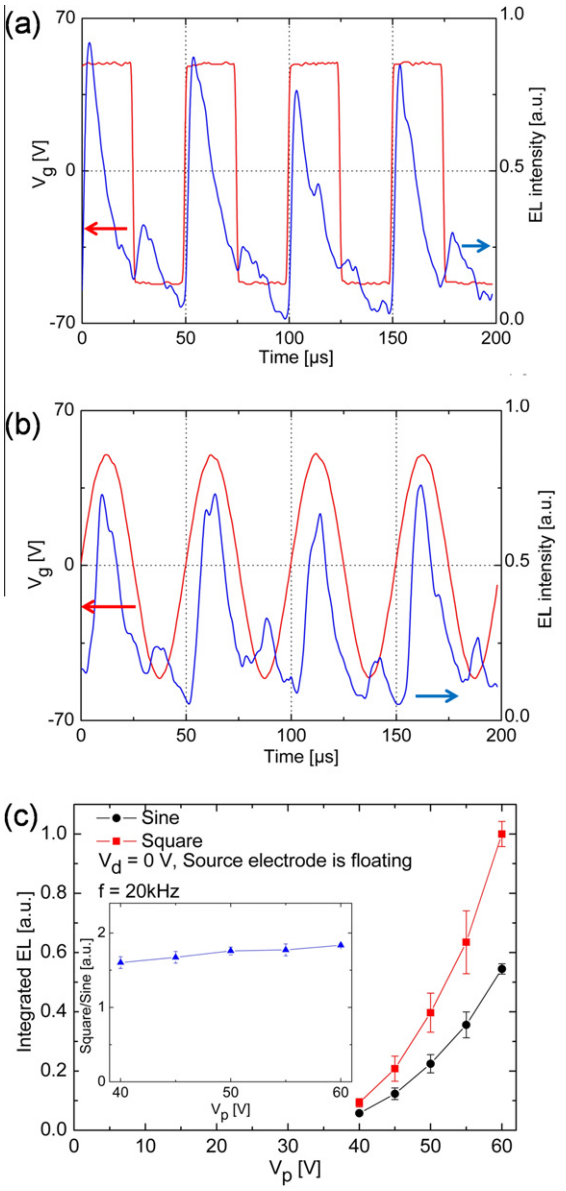

Fig. 2. Time dependence of EL emission intensity (blue curve) as a function of (a) square wave gate voltage (red curve) and (b) sinusoidal gate voltage. (c) Integrated EL emission intensity as a function of (square wave and sinusoidal) gate voltage amplitude V_p. Inset: ratio of EL intensity obtained from square wave gate voltage to the intensity from sinusoidal gate voltage.

a ratio higher than 1 is expected, however, this simplistic view cannot account for non-linear processes involved in charge injection across an energy barrier. A more appropriate analysis would be to study the effects of the gate voltage waveform using a theoretical model based on thermally assisted tunneling. We will elaborate on this aspect below.

In order to investigate the influence of the drain voltage V_d on the emission intensity, a series of measurements were conducted, in which V_d was varied while the amplitude and frequency of the square wave gate voltage were

fixed and the source electrode was floating. As shown in Fig. 3, the integrated EL intensity increases when the drain electrode is positively biased while a negative drain potential causes a reduced EL intensity. Two measurement sequences were made in either direction: one from negative V_d to positive V_d and one in the other direction. This shows that the observed EL variations are indeed caused by the drain potential and are not due to a possible degradation effect. In our previous work, we have investigated the frequency dependence of the light emission intensity under AC biasing [14,15]. The emission intensity generally increased with increasing frequency until saturation or even a small reduction was observed around a few hundred kHz.

On the basis of these results, we propose the following device operating mechanism: As mentioned above, charge transport across the channel is not part of the light generation process. Rather, the two types of charge-carriers are sequentially injected from the same contact. This must mean that one type of charge is piled up in the organic film close to the electrode interface during one half-period of the gate voltage effectively forming a space-charge region at this position. During the subsequent half-period of the gate voltage, the opposite charge-carrier is injected, recombines with the first type of carrier, and thereby causes light emission. Since the injection of holes is much more probable than the injection of electrons in our device, the space-charge region must be formed by holes piling up either due to deep hole traps or short hole transport distance under high frequency operation. The positive space-charge region is therefore formed during the negative half-period of the gate voltage, as illustrated in Fig. 4a. In the next (positive) half-period, electrons are injected into the organic material to recombine with the previously injected holes. Since the injection barrier of electrons between Au and p6P is very high, the electrons are most likely to tunnel into the p6P. The electron tunneling process is primarily influenced by the positive space-charge region rather than the positive gate voltage (Fig. 4b). This can be argued as follows: During the negative half-period of the gate voltage, holes are injected. If the DC potential of the drain electrode is increased (positive V_d), this leads to an increased hole injection and therefore a larger space-charge. In the following, positive half-period of the gate voltage, electrons are tunneling into the organic material. The positive value of V_d means that the drain to gate voltage difference is effectively reduced. If the main factor driving the electron tunneling would be the gate voltage, then the electron tunneling and thus also the emission intensity should be less than at zero V_d. On the contrary, if the main driving mechanism for electron injection is tunneling assisted by the positive SCF, then the additionally injected holes caused by the positive V_d should enhance electron tunneling and thereby emission intensity. Since positive V_d causes increased EL intensity as shown in Fig. 3, the second explanation must be correct.

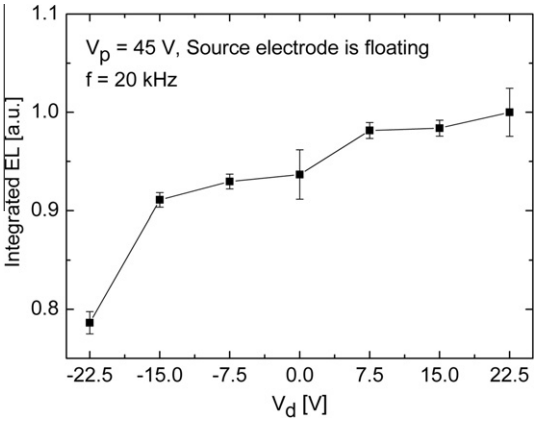

Fig. 3. Integrated EL intensity as a function of drain electrode voltage V_d (source electrode was floating). The gate voltage amplitude was $V_p = 45$ V and the frequency was $f = 20$ kHz.

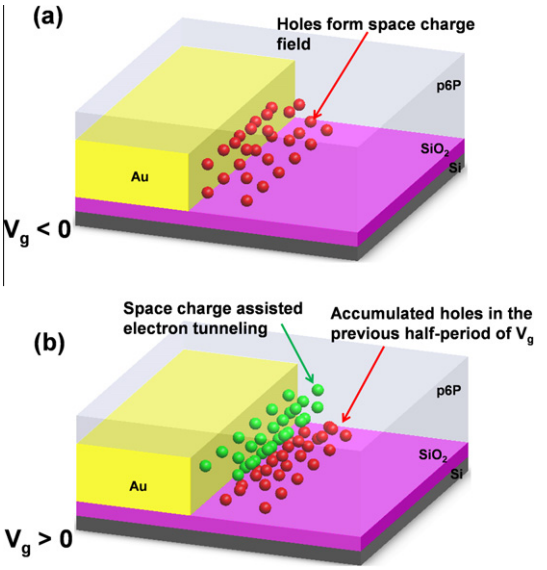

Fig. 4. Schematic illustration of the device operating mechanism (red indicates holes; green indicates electrons). (a) Holes are injected from Au into semiconductor to form positive SCF. (b) In the next half-period of AC gate biasing, electrons tunnel into the semiconductor assisted by the previously formed positive SCF.

The time-resolved EL intensity illustrated in Fig. 2a and b can be explained by this model. The majority of the light emission occurs when the gate voltage shifts from a negative to a positive value, corresponding to the shift from hole to electron injection. This means the electron injection is significantly enhanced due to the positive SCF, which is formed by holes injected in the previous half-period of the AC gate voltage. The decay of the emission intensity after reaching its maximum must be caused by the recombination process that reduces the hole intensity. Upon elimination of the SCF by electron–hole recombination, electron injection continues at a lower rate caused only by the positive gate voltage. When the AC gate voltage shifts polarity, a smaller EL peak can be observed, which is caused by the recombination of the electrons injected in the previous positive gate regime and the holes injected during this negative gate bias.

Since the electron tunneling is enhanced by the positive SCF formed by previously injected holes, the hole injection

is an important factor to determine the overall light emission of the p6P device. We therefore focus on the hole injection aspects in the following discussion and assume the EL intensity to be proportional to the magnitude of the hole injection. Our previous work showed that the relationship between the EL intensity and the gate voltage amplitude corresponds to a straight line in a Fowler–Nordheim (F–N)-type plot [14]. However, F–N theory describes charge-carrier tunneling through an energy barrier into a delocalized state, which is typically not the case in organic materials, in which the charge-carriers form localized polarons. F–N theory is therefore not applicable for the present system [19]. Instead, we have applied a model based on thermally assisted tunneling developed by Arkhipov et al. [16] in order to study hole injection into the hopping state distribution of the p6P semiconductor. In this model, the hole injection occurs over/through a potential barrier $U(x)$ given by

$$U(x) = \phi - \frac{q^2}{16\pi\varepsilon_0\varepsilon_r x} - qFx \tag{1}$$

where x is distance from the metal electrode, ϕ is the energy difference between the work function of gold and the HOMO (highest occupied molecular orbital) level of p6P, $\varepsilon_0\varepsilon_r$ is the dielectric constant, q is the elementary charge, and F is the external field strength. The hole injection is considered including either the return of the charge-carrier to the metal electrode or the diffusive escape from the image potential to the semiconductor bulk. Therefore, the injected current I_{inj} can be described in terms of the tunneling probability $\exp(-2\overline{\Gamma}x_0)$ (x_0 is the distance from the contact the charge-carrier made the first jump) and the escape probability $w_{\text{esc}}(x_0)$

$$I_{\text{inj}} \propto \int_a^\infty dx_0 \exp(-2\overline{\Gamma}x_0)\cdot w_{\text{esc}}(x_0)\cdot \int_{-\infty}^{\infty} dE Bol(E) g[U(x_0) - E] \tag{2}$$

where $\overline{\Gamma}$ is the inverse localization radius and a is the nearest neighbor distance. $Bol(E)$ is a Boltzmann factor defined as

$$Bol(E) = \begin{cases} \exp(-\frac{E}{k_B T}) & E > 0; \\ 1 & E < 0. \end{cases} \tag{3}$$

The Gaussian energy distribution with an energy width σ is given by

$$g(E) = \frac{N_0}{\sqrt{2\pi}\cdot\sigma}\cdot\exp\left(-\frac{E^2}{2\cdot\sigma^2}\right) \tag{4}$$

where N_0 is the density of p6P molecules.

Applying this model, we calculated the hole injection from a gold electrode to p6P with the external electric field generated either by a square wave or a sinusoidal gate voltage (with parameters ϕ = 0.9 eV, σ = 0.27 eV, T = 295 K, ε_r = 1.9, a = 5.57 Å, $\overline{\Gamma}$ = (3Å)$^{-1}$, and $N_0 = 1.71\times10^{21}$ cm^{-3} [20]). Only one half-period of gate voltage is considered in the calculation due to the waveform repetition of the gate voltage. For simplicity, the external electric field near the vicinity of the injecting gold electrode was estimated simply as the gate voltage divided by the thickness of SiO_2 gate dielectric. We have performed finite element analysis calculations to verify that this assumption is reasonable. The amplitude of the gate voltage was varied from 40 to 60 V, with steps of 5 V. The resulting ratio of hole injection generated by square wave gate voltage to that generated by sinusoidal gate voltage is approximately 2.2, which is 27% larger than the experimental value shown in Fig. 2c. This difference could be due to the neglect of the suppressing effect of the positive SCF on the further hole injection during the negative half-cycle of the AC gate voltage. This suppressing effect is larger for the square wave case resulting in an overestimation of the EL ratio.

In order to better understand the underlying operating mechanism, we characterized the temperature dependence of the PL and EL output. As illustrated in Fig. 5a, both the PL and EL intensity increase as the temperature decreases from 295 to 30 K. With increasing temperature, the probability for coupling to phonon modes and thus in general for non-radiative decay process increases, as observed by an increase of the Huang–Rhys factor for p6P nanofiber films [21]. In addition, it can be seen that the PL increases more than the EL. The ratio of the normalized EL intensity to the normalized PL intensity $W_{\text{EL}}(T)/W_{\text{PL}}(T)$ is also shown in Fig. 5a. The temperature dependence of this ratio can be correlated with the temperature dependence of the hole injection as follows: The detected EL intensity $W_{\text{EL}}(T)$ is given by:

$$W_{EL}(T) = k_1\cdot\eta_{\text{ext}}(T)\cdot I_{\text{inj}}(T) \tag{5}$$

where $I_{\text{inj}}(T)$ is the injected current, $\eta_{\text{ext}}(T)$ is the temperature-dependent external quantum efficiency, and the temperature-independent proportionality constant k_1 includes the unit charge, the photon energy and collection efficiency of the detector. From [22] we describe $\eta_{\text{ext}}(T)$ by:

$$\eta_{\text{ext}}(T) = R_{\text{st}}\cdot\gamma\cdot\Phi_{\text{outc}}\cdot\Phi_{\text{PL}}(T) \tag{6}$$

where $\Phi_{\text{PL}}(T)$ is the efficiency of radiative decay, R_{st} is the singlet to triplet ratio (typically 0.25), γ is the charge balance factor, Φ_{outc} is the outcoupling efficiency. The detected PL intensity $W_{\text{PL}}(T)$ is given by:

$$W_{\text{PL}}(T) = k_2\cdot\Phi_{\text{outc}}\cdot\alpha(T)\cdot\Phi_{\text{PL}}(T) \tag{7}$$

where the proportionality constant k_2 includes the intensity of the stimulating light, the photon energy, and the collection efficiency of the detector. Since the temperature dependence of the absorption cross section $\alpha(T)$ is very weak for p6P films [23], we neglect its temperature dependence here, i.e., $\alpha(T) = \alpha$. By combining Eq. (5-7), the ratio of the EL and PL intensities is found to be

$$\frac{W_{\text{EL}}(T)}{W_{\text{PL}}(T)} = \frac{k_1}{k_2\cdot\alpha}\cdot R_{\text{st}}\cdot\gamma\cdot I_{\text{inj}}(T). \tag{8}$$

Since all factors in Eq. (8) except the injected current have negligible temperature dependence, the ratio $W_{\text{EL}}(T)/W_{\text{PL}}(T)$ should therefore have the same temperature dependence as the injected current.

Fig. 5b shows the temperature dependence of the current injection calculated using the approach based on Arkhipov's model, and the ratio derived from experiment is again illustrated for comparison. The calculated current

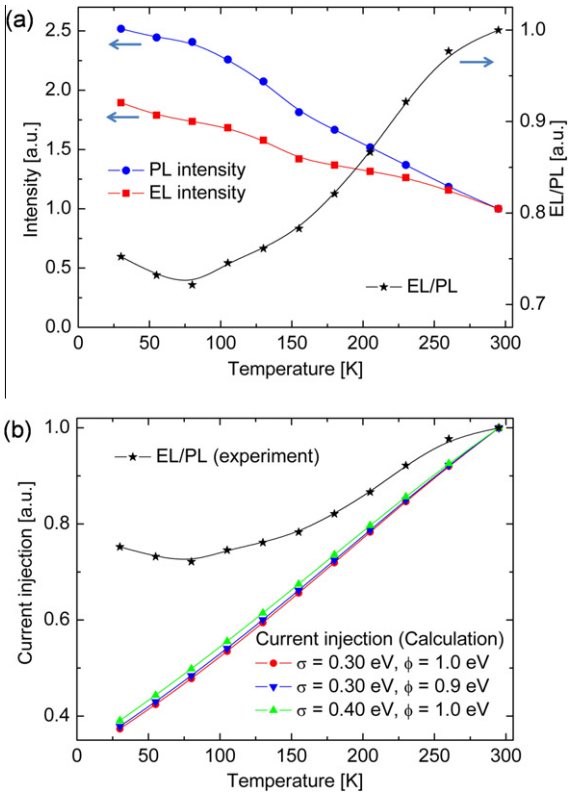

Fig. 5. (a) Temperature dependence of PL and EL intensity (data have been normalized at $T = 295$ K) of a p6P light-emitting device. The square wave gate voltage amplitude was 37.5 V; the biasing frequency was 15 kHz. (b) Theoretical calculation of current injection compared with experiment.

injection varies only slightly if the hole injection barrier ϕ or the energy width σ is varied. Also, it can be seen that the theory predicts a stronger temperature dependence than what is observed experimentally. This large deviation could be due to the inadequacy of the Gaussian energy distribution of the hopping state [24]. Nevertheless, the calculation based on Arkhipov's model reproduces qualitatively the trend observed experimentally, which is not captured by the F–N formalism.

We have focused on the hole injection between gold and p6P because the hole injection barrier in this case (typically 0.9 eV) is much lower than the electron injection barrier (2.1 eV). In contrast, electron injection should be mainly studied for the organic materials which possesses lower electron injection barrier with respect to the injecting electrodes.

To rule out the possibility that impact ionization could be involved in the light generation process, similar substrates but with aluminum rather than gold electrodes were fabricated. Since aluminum electrodes oxidize under ambient conditions, there will be an insulating layer of aluminum oxide between the electrode and the p6P, and light emission would under such circumstances only be possible via impact ionization [25]. Based on the sensitivity of our detection system, we estimate that the light emission from aluminum electrode devices is at least two orders of magnitude lower than that from gold electrode devices under similar biasing parameters, indicating that impact ionization plays an insignificant role for the light generation.

4. Conclusions

In this study, we have investigated the operating mechanism of organic light-emitting devices based on a transistor platform driven by an AC gate voltage. The holes and electrons are sequentially injected from the same metal electrode under the AC gate biasing. Positive SCF is dominant if the hole injection barrier is much lower than the electron injection barrier, and this positive SCF assists in the subsequent electron injection. Therefore, electrically driven light emission can be obtained in a *p*-type unipolar organic field-effect transistor platform, from which light emission is difficult to derive under traditional DC gate voltage. We assume this charge-carrier injection assisted by SCF is also valid for *n*-type organic transistors and that a similar model would therefore be applicable.

Further appropriate metal/semiconductor interface modification could help enhance the light emission output from the light-emitting devices by changing the interface dipole and morphology [26], thus leading to possible improvement towards the realization of electrically driven organic laser diodes. Besides, the better understanding of the operating mechanism can assist in the design of future light-emitting devices when attempting to localize the light emission.

Acknowledgments

The authors thank Henrik H. Henrichsen for valuable assistance, the VILLUM KANN RASMUSSEN FONDEN for a VELUX Visiting Professor scholarship, and the BHJ-Foundation for financial support.

References

[1] C.D. Müller, A. Falcou, N. Reckefuss, M. Rojahn, V. Wiederhirn, P. Rudati, H. Frohne, O. Nuyken, H. Becker, K. Meerholz, Multi-colour organic light-emitting displays by solution processing, Nature 421 (2003) 829–833.
[2] J. Zaumseil, H. Sirringhaus, Electron and ambipolar transport in organic field-effect transistors, Chem. Rev. 107 (2007) 1296–1323.
[3] R. Capelli, S. Toffanin, G. Generali, H. Usta, A. Facchetti, M. Muccini, Light-emitting transistors with an efficiency that outperforms the equivalent light-emitting diodes, Nat. Mater. 9 (2010) 496–503.
[4] I.D.W. Samuel, G.A. Turnbull, Organic semiconductor lasers, Chem. Rev. 107 (2007) 1272–1295.
[5] T. Yamao, Y. Sakurai, K. Terasaki, Y. Shimizu, H. Jinnai, S. Hotta, Current-injected spectrally-narrowed emissions from an organic transistor, Adv. Mater. 22 (2010) 3708–3712.
[6] A. Hepp, H. Heil, W. Weise, M. Ahles, R. Schmechel, H. von Seggern, Light-emitting field-effect transistor based on a tetracene thin film, Phys. Rev. Lett. 91 (2003) 157406.
[7] C. Santato, I. Manunza, A. Bonfiglio, F. Cicoira, P. Cosseddu, R. Zamboni, M. Muccini, Tetracene light-emitting transistors on flexible plastic substrates, Appl. Phys. Lett. 86 (2005) 141106.
[8] T.-H. Ke, R. Gehlhaar, C.-H. Chen, J.-T. Lin, C.-C. Wu, C. Adachi, High efficiency blue light emitting unipolar transistor incorporating multifunctional electrodes, Appl. Phys. Lett. 94 (2009) 153307.
[9] H. Kajii, K. Koiwai, Y. Hirose, Y. Ohmori, Top-gate-type ambipolar organic field-effect transistors with indium–tin oxide drain/source electrodes using polyfluorene derivatives, Org. Electron. 11 (2010) 509–513.

[10] T. Yamao, Y. Shimizu, K. Terasaki, S. Hotta, Organic light-emitting field-effect transistors operated by alternating-current gate voltages, Adv. Mater. 20 (2008) 4109–4112.
[11] T. Yamao, K. Terasaki, Y. Shimizu, S. Hotta, Organic-crystal light-emitting field-effect transistors driven by square-wave gate voltages, J. Nanosci. Nanotechnol. 10 (2010) 1017–1020.
[12] T. Katagiri, Y. Shimizu, K. Terasaki, T. Yamao, S. Hotta, Light-emitting field-effect transistors made of single crystals of an ambipolar thiophene/phenylene co-oligomer, Org. Electron. 12 (2011) 8–14.
[13] Y. Ohshima, H. Kohn, T. Manaka, M. Iwamoto, Space charge field effect on light emitting from tetracene field-effect transistor under AC electric field, Thin Solid Films 518 (2009) 583–587.
[14] X. Liu, I. Wallmann, H. Boudinov, J. Kjelstrup-Hansen, M. Schiek, A. Lützen, H.-G. Rubahn, AC-biased organic light-emitting field-effect transistors from naphthyl end-capped oligothiophenes, Org. Electron. 11 (2010) 1096–1102.
[15] J. Kjelstrup-Hansen, X. Liu, H.H. Henrichsen, K. Thilsing-Hansen, H.-G. Rubahn, Conduction and electroluminescence from organic continuous and nanofiber thin films, Phys. Status Solidi C 7 (2010) 2763–2766.
[16] V.I. Arkhipov, U. Wolf, H. Bässler, Current injection from a metal to a disordered hopping system. II. Comparison between analytic theory and simulation, Phys. Rev. B 59 (1999) 7514.
[17] J. Sung, Y.S. Choi, S.J. Kang, S.H. Cho, T.-W. Lee, C. Park, AC field-induced polymer electroluminescence with single wall carbon nanotubes, Nano Lett. 11 (2011) 966–972.
[18] S. Guha, J.D. Rice, Y.T. Yau, C.M. Martin, M. Chandrasekhar, H.R. Chandrasekhar, R. Guentner, P. Scanduicci de Freitas, U. Scherf, Temperature-dependent photoluminescence of organic semiconductors with varying backbone conformation, Phys. Rev. B 67 (2003) 125204.
[19] J.C. Scott, Metal–organic interface and charge injection in organic electronic devices, J. Vac. Sci. Technol., A 21 (2003) 521–531.
[20] J. Kjelstrup-Hansen, P. Bøggild, H.-G. Rubahn, Charge injection and transport in organic nanofibers, J. Phys: Conf. Ser. 61 (2007) 565–569.
[21] F. Balzer, A. Pogantsch, H.-G. Rubahn, Temperature dependent analysis of three classes of fluorescence spectra from p-6P nanofiber films, J. Lumin. 129 (2009) 784–789.
[22] C. Adachi, M.A. Baldo, M.E. Thompson, S.R. Forrest, Nearly 100% internal phosphorescence efficiency in an organic light-emitting device, J. Appl. Phys. 90 (2001) 5048.
[23] A. Piaggi, G. Lanzani, G. Bongiovanni, A. Mura, W. Graupner, F. Meghdadi, G. Leising, M. Nisoli, Emission properties of para-hexaphenyl polycrystalline films, Phys. Rev. B 56 (1997) 10133.
[24] M.D. Hanwell, T.A. Madison, G.R. Hutchison, Charge transport in imperfect organic field effect transistors: effects of explicit defects and electrostatics, J. Phys. Chem. C 114 (2010) 20417–20423.
[25] J. Kalinowski, Electronic processes in organic electroluminescence, in: S. Miyata, H.S. Nalwa (Eds.), Organic Electroluminescent Materials and Devices, OPA, Amsterdam, 1997, pp. 1–72.
[26] G. Heimel, F. Rissner, E. Zojer, Modeling the electronic properties of π-conjugated self-assembled monolayers, Adv. Mater. 22 (2010) 2494–2513.

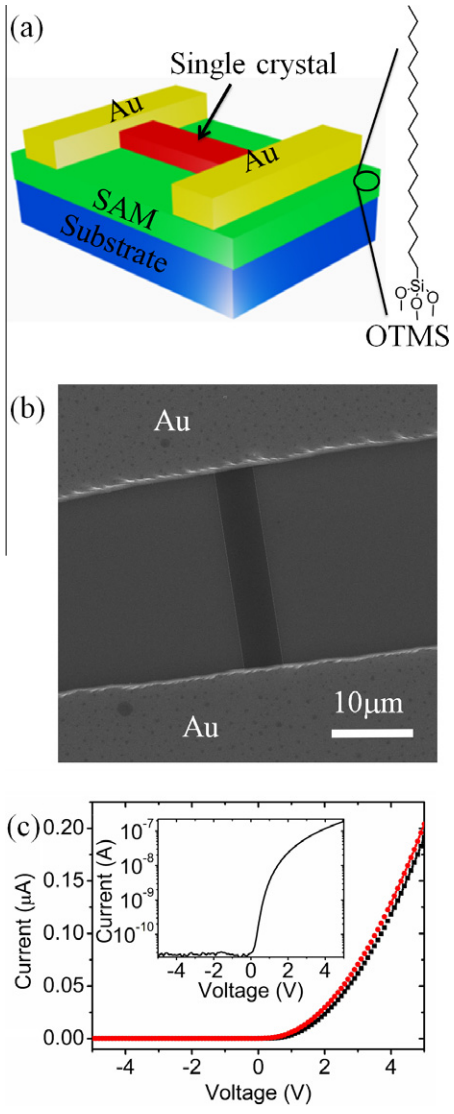

Fig. 1. (a) Schematic diagram of the devices used in this communication; (b) scanning electron microscopy (SEM) images of a typical device; (c) current–voltage curves of rubrene devices on OTMS substrates (inset: logarithmic plot of the *I*–*V* curve). For comparison, the electrical connection to the two Au contacts is switched and the measured *I*–*V* curve is plotted in red (original curve: black). (For interpretation of the references to colour in this figure legend, the reader is referred to the web version of this article.)

and b). The devices were obtained with the following three steps: (i) the Si substrates (with 300 nm SiO_2) were modified by the octadecyltrimethoxysilane (OTMS) monolayer through spin-casting method [20], which was used to passivate the traps at the semiconductor/insulator interface; (ii) rubrene single crystals were grown onto the surface via physical vapor transport (PVT) technique; (iii) the electrodes were fabricated by gluing Au-films onto the single crystals directly from pre-deposited Au film [3,21] with channel formed simultaneously (a pre-deposited Au-film (about 100 nm thick on another substrate) was firstly cut into small pieces (usually about tens of micrometers in width and hundreds of micrometers in length) and secondly a small piece of Au-film was glued by a probe of a micromanipulator station and then was placed onto the single crystals). As shown in Fig. 1b, the channel length was about 20 μm and the channel width was dependent on the size of single crystals, ranging from several to tens of micrometers. The "gluing Au-films" technique is used as it is free from lithography and thermal radiation during metal deposition which has been shown to result in better contact between the semiconductor and the electrodes [21]. The current–voltage curve was measured using only the two gold electrodes, and the silicon substrate was disconnected from the measurement electrical circuit. It is important to point out that the reason that we select silicon substrate is due to its commercial availability, smooth surface and convenience to be modified by self assembled monolayers (SAMs). Therefore, the silicon substrate is not used as gate electrode as in other conventional OFET structure. That is, the device is characterized under a two-terminal condition.

The current–voltage characteristics of a typical device are shown in Fig. 1c. Interestingly, the current-curves displays rectifying properties with rectification ratio as high as 10^5–10^6 at ±5 V in most devices, and exchanging electrodes results in the same rectifying characteristics (Fig. 1c). Although formation of Schottky contact between organic semiconductor and the electrodes could lead to a rectifying behavior, several evidences reveal that it is not the dominant mechanism for the observed *I*–*V* characteristics. Firstly, the highest occupied molecular orbital (HOMO) energy level (−5.1 to −5.36 eV) matches well with the Fermi level of Au electrodes (∼−5.1 eV) [18,22], and therefore a low injection barrier of holes is expected. Secondly, when we measured the device in a FET mode, we did not observe any suppression of drain current at low drain voltages, suggesting that the contact between the semiconductor and the electrodes is Ohmic one instead of the Schottky contact (see Supplementary data). Thirdly, the measured *I*–*V* curves do not obey the exponential law that is commonly used to describe the *I*–*V* relation for Schottky diodes (see Fig. 1c inset and descriptions below). To further investigate the mechanism of the rectifying behavior, we varied the intrinsic carrier density in the rubrene crystals via two methods: (1) to modify the substrate surface with (tridecafluoro-1,1,2,2-tetrahydrooctyl)trichlorosilane (FTS) (through chemical vapor deposition (CVD) method [23]), which has been used previously to dope organic semiconductors via charge transfer mechanism [23,24]; and (2) to measure the device under illumination [17,25]. (Note that a gate-voltage is required in this case to dissociate the photo-induced electron-hole pairs [26].) In both cases, the rectifying behavior disappeared and the devices showed almost symmetric *I*–*V* relations at low voltages (Fig. 2a and b, inset). The fact that the increasing of carrier density could eliminate the rectifying properties suggests again that the rectifying property is unlikely originated from the Schottky contact.

Instead of the metal-semiconductor Schottky barrier, we propose that the rectifying effect is a consequence of the simultaneously formed vertical and lateral distributed electric fields throughout the organic semiconductor:

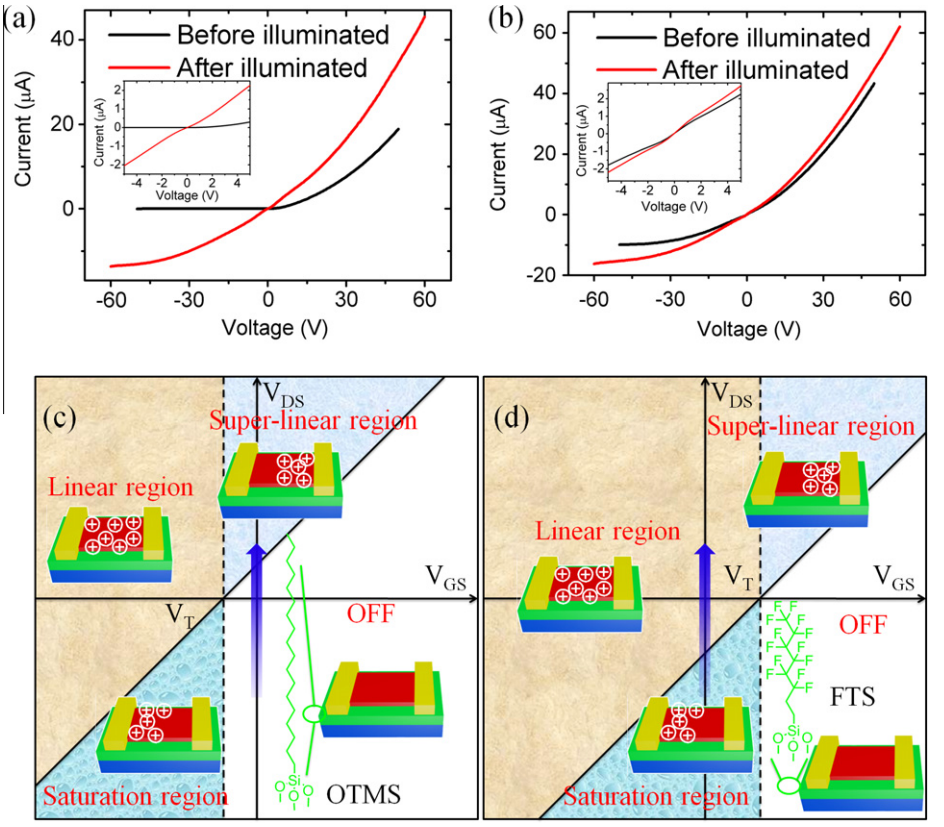

Fig. 2. Current–voltage curves of rubrene devices (a) on OTMS and (b) FTS modified substrates, (inset, amplification curves around low voltage). Four operation regimes of p-channel FET: off-state, saturation, linear and super-linear regimes in the situation for (c) OTMS and (d) FTS modified substrates. The blue arrows indicate the measurement condition of our devices (note that $V_{GS} = 0$ is assumed for two-terminal devices). Adapted with permission from Ref. [27]. Copyright© 2010 Elsevier B.V. All rights reserved. (For interpretation of the references to colour in this figure legend, the reader is referred to the web version of this article.)

applying a bias voltage between two gold electrodes not only varies the lateral electrostatic potential linearly along the channel but also creates a vertical potential drop between the top and bottom surfaces of the semiconductor, which is similar to applying a gate voltage. Once this potential drop exceeds the threshold voltage V_T, an accumulation layer is formed in the semiconductor and the device is turned on. Different from the regular on-state of an FET where the channel potential is modulated by the gate voltage, in our devices, the channel potential is modulated by the laterally applied voltages. The channel is always "pinched-off" at the grounded electrode, since the potential in this region is close to zero. As a consequence, the device is operated in a "saturation region". This operation mode is also known as super-linear region as shown in Fig. 2c and d, which is often observed in ambipolar OFETs [27,28]. In our two-terminal devices, the "gate voltage V_{GS}" can be considered as fixed at zero and the rectifying property is strongly dependent on the threshold voltage. For the OTMS modified substrates, the density of trap states at the rubrene/OTMS interface is low and therefore V_T is close to 0 V (see Supplementary data); applying a relatively small positive voltage across the lateral electrodes (equivalent to "V_{DS}") can turn the device from "off" to the super-linear region. For the FTS modified devices, on the other hand, due to the presence of the electron-withdrawing groups, a layer of fixed charges is formed at the rubrene/FTS interface [24] which shifts the V_T towards positive voltage. In this case, when "V_{DS}" is changed from negative to positive voltage, the device is switched from the saturation region to the linear region. At last, when the devices are illuminated, the concentration of charges [17,25] in the semiconductor is further increased, and the V_T is shifted to a much more positive voltage value. As a result, only linear operation mode can be observed for "V_{DS}" in the range of −5 to +5 V.

In order to verify the above model, we fit the experimental data to the equations that describe the super-linear and linear models, respectively. For the OTMS modified devices, when a positive voltage bias is applied, the devices are considered to be operated in the super-linear region. Fig. 3a plots the fitting results of measured I–V curves using the equation $I_{DS} = I_s(V_{DS} - V_T)^2(1 - \lambda V_{DS})$, where λ is the channel-length modulation parameter according to Shichman–Hodges model. Good fitting results are obtained as shown in the figure. We also tried to fit the data with the models for other operation modes, but the fittings are poorly coincident and require using physically irrational fitting parameters. Different from the OTMS modified devices, the FTS treated ones have I–V curves that are best

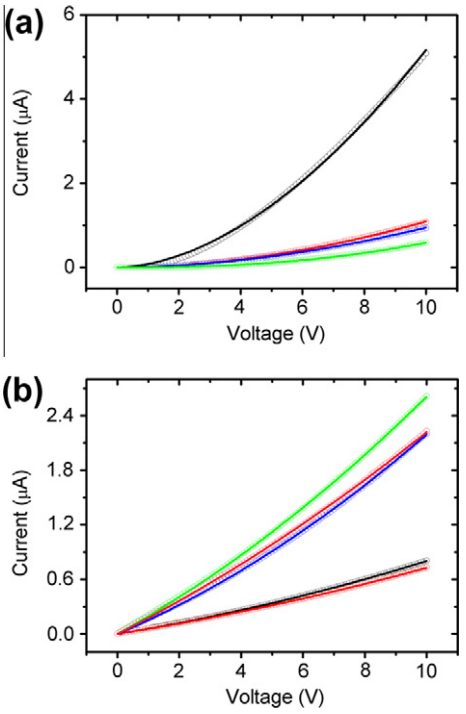

Fig. 3. Open circles: experimental data of different devices (a) on OTMS modified substrates and (b) on FTS modified substrates at positive voltage. Solid lines: fitting curves by using equation of (a) super-linear and (b) linear regimes.

fitted with the linear region model $I_{DS} = I_s[V_T V_{DS} - (V_{DS})^2/2]$, as plotted in Fig. 3b. In summary, the current–voltage characteristics of the two terminal devices can be well described by one of the operation models of field-effect transistors, and the position of V_T, which is dependent on the intrinsic carrier density at the rubrene/substrate interface, determines the cross point of the different operation modes.

3. Conclusions

In conclusion, we observed a rectifying behavior in lateral, symmetrical two-terminal device based on rubrene single crystals. We have showed that the rectifying property of the device was originated from a mechanism that is similar to the super-linear operation of field-effect transistors. We have also demonstrated that we can turn on or off this rectifying behavior by changing the density of space charge in the organic semiconductor/substrate interface, which essentially affects the threshold voltage V_T. These results demonstrated a simple approach that could potentially be used to fabricate organic rectifiers, oscillator, etc. without application of multi-layer device structure such as MOSFET diode.

4. Experimental

All solvents and reagents were obtained from commercial source and used as received unless ultra noted. The substrates (Si with 300 nm-thick SiO_2 layer, 11 nF cm^{-2}) were first rinsed with water, acetone and isopropanol, respectively. Then they were cleaned by oxygen plasma for 10 min. The FTS monolayer modified substrates were obtained by CVD method (self-assembled in vacuum at 100 °C for 1 h) according to literature [23]. And then the FTS modified substrates were rinsed by acetone and isopropanol respectively. The OTMS modified substrates were obtained via spin-coating method according to literature [20]. And then the OTMS modified substrates were washed by toluene and isopropanol respectively. Single crystals of rubrene were grown onto the OTMS or FTS-modified SiO_2/Si substrate by PVT method at sublimation temperature of 245 °C (Ar, 100 sccm). Then devices were fabricated by attaching Au-films onto single crystals as two-terminal electrodes [21]. Device fabrication and characteristics were obtained with a Keithley 4200 SCS and Wentworth Labs probe station in a clean and shielded box at room temperature in air. SEM was performed on a FEI field-emission scanning electron microscope.

Acknowledgements

The authors acknowledge the support by the Research Grants Council of Hong Kong SAR, particularly, under Grant Nos. CUHK2/CRF/08 and 418209. The authors also thank the technical support by Dr. N. Ke and Mr. W.K. Chan. J.B. Xu thanks the National Science Foundation of China (Grants Nos. 60990314 and 60928009) for support.

Appendix A. Supplementary data

Supplementary data associated with this article can be found, in the online version, at doi:10.1016/j.orgel.2011.06.024.

References

[1] C. Reese, Z. Bao, Mater. Today 10 (2007) 20.
[2] H. Najafov, B. Lee, Q. Zhou, L.C. Feldman, V. Podzorov, Nat. Mater. 9 (2010) 938.
[3] R. Li, W. Hu, Y. Liu, D. Zhu, Acc. Chem. Res. 43 (2010) 529.
[4] Z. Rang, M.I. Nathan, P.P. Ruden, V. Podzorov, M.E. Gershenson, C.R. Newman, C.D. Frisbie, Appl. Phys. Lett. 86 (2005) 123501.
[5] Y. Zhou, L. Wang, J. Wang, J. Pei, Y. Cao, Adv. Mater. 20 (2008) 3745.
[6] D.H. Kim, J.T. Han, Y.D. Park, Y. Jang, J.H. Cho, M. Hwang, K. Cho, Adv. Mater. 18 (2006) 719.
[7] Y. Yamamoto, T. Fukushima, Y. Suna, N. Ishii, A. Saeki, S. Seki, S. Tagawa, M. Taniguchi, T. Kawai, T. Aida, Science 314 (2006) 1761.
[8] V.C. Sundar, J. Zaumseil, V. Podzorov, E. Menard, R.L. Willett, T. Someya, M.E. Gershenson, J.A. Rogers, Science 303 (2004) 1644.
[9] V. Podzorov, V.M. Pudalov, M.E. Gershenson, Appl. Phys. Lett. 82 (2003) 1739.
[10] A.F. Stassen, R.W.I. de Boer, N.N. Iosad, A.F. Morpurgo, Appl. Phys. Lett. 85 (2004) 3899.
[11] A.L. Briseno, R.J. Tseng, M.M. Ling, E.H.L. Talcao, Y. Yang, F. Wudl, Z.N. Bao, Adv. Mater. 18 (2006) 2320.
[12] Y. Zhang, H. Dong, Q. Tang, Y. He, W. Hu, J. Mater. Chem. 20 (2010) 7029.
[13] M. Haemori, J. Yamaguchi, S. Yaginuma, K. Itaka, H. Koinuma, Jpn. J. Appl. Phys. Part 1 44 (2005) 3740.
[14] Z. Li, J. Du, Q. Tang, F. Wang, J.-B. Xu, J.C. Yu, Q. Miao, Adv. Mater. 22 (2010) 3242.
[15] N. Stingelin-Stutzmann, E. Smits, H. Wondergem, C. Tanase, P. Blom, P. Smith, D. De Leeuw, Nat. Mater. 4 (2005) 601.

[16] T. Takahashi, T. Takenobu, J. Takeya, Y. Iwasa, Appl. Phys. Lett. 88 (2006) 033505.
[17] H. Najafov, I. Biaggio, V. Podzorov, M.F. Calhoun, M.E. Gershenson, Phys. Rev. Lett. 96 (2006) 056604.
[18] T. Kaji, T. Takenobu, A.F. Morpurgo, Y. Iwasa, Adv. Mater. 21 (2009) 3689.
[19] D. Braga, M. Campione, A. Borghesi, G. Horowitz, Adv. Mater. 22 (2010) 424.
[20] Y. Ito, A.A. Virkar, S. Mannsfeld, J.H. Oh, M. Toney, J. Locklin, Z. Bao, J. Am. Chem. Soc. 131 (2009) 9396.
[21] Q. Tang, Y. Tong, H. Li, Z. Ji, L. Li, W. Hu, Y. Liu, D. Zhu, Adv. Mater. 20 (2008) 1511.
[22] Y. Wang, R. Kumashiro, R. Nouchi, N. Komatsu, K. Tanigaki, J. Appl. Phys. 105 (2009) 124912.
[23] S. Kobayashi, T. Nishikawa, T. Takenobu, S. Mori, T. Shimoda, T. Mitani, H. Shimotani, N. Yoshimoto, S. Ogawa, Y. Iwasa, Nat. Mater. 3 (2004) 317.
[24] M.F. Calhoun, J. Sanchez, D. Olaya, M.E. Gershenson, V. Podzorov, Nat. Mater. 7 (2008) 84.
[25] N. Mathews, D. Fichou, E. Menard, V. Podzorov, S.G. Mhaisalkar, Appl. Phys. Lett. 91 (2007) 212108.
[26] Q. Tang, L. Li, Y. Song, Y. Liu, H. Li, W. Xu, W. Hu, D. Zhu, Adv. Mater. 19 (2007) 2624.
[27] J.B. Kim, C. Fuentes-Hernandez, S.J. Kim, W.J. Potscavage Jr., S. Choi, B. Kippelen, Org. Electron. 11 (2010) 1351.
[28] E.C.P. Smits, T.D. Anthopoulos, S. Setayesh, E. van Veenendaal, R. Coehoorn, P.W.M. Blom, B. de Boer, D.M. de Leeuw, Phys. Rev. B 73 (2006) 205316.

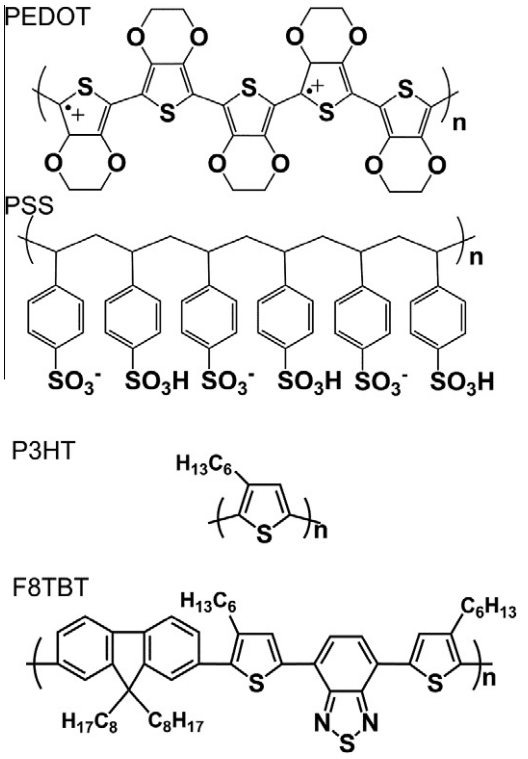

Fig. 1. Chemical structures of polymers used.

Generally these colloidal particles are described as entanglements of PSS chains with PEDOT oligomer units adsorbed to them. When in aqueous solution, the hydrophobicity of the adsorbed PEDOT causes preferential orientation of the hydrophilic sulfate groups to the outside and the PEDOT-rich parts of the chain to the inside of the entangled polymer chain, causing a micelle-like formation. From the macroscopic point of view this results in a particle with a PEDOT-rich conductive core and an insulating PSS-rich shell, which has been verified in numerous investigations on dried films, e.g. via XPS [5,13,14]. While the particles are in a swollen state when in aqueous solution, they shrink drastically during drying (water content up to ~95%) [12]. The PSS content in these solutions may be altered to tune the electric properties of PEDOT:PSS films. Up to a certain concentration, the PSS dopant enhances PEDOT:PSS film conductivity (up to ~10 S/cm). It decreases again for higher PSS content, due to the formation of PSS insulating cover layers or lamellae [15,16].

In this work we study the influence of thermal treatment on the PEDOT:PSS solution and resulting effects on the device performance of solar cells made from P3 HT (poly(3-hexylthiophene)) and F8TBT (poly((9,9-dioctylfluorene)-2,7-diyl-alt-[4,7-bis(3-hexylthiophen-5-yl)2,1,3-benzothiadiazole]-2′,2″-diyl)) (Fig. 1) [17]. Besides electrical characterization of photovoltaic cells we employ photoelectron spectroscopy (both X-ray photoelectron spectroscopy (XPS) and ultraviolet photoelectron yield spectroscopy (PEYS)), atomic force microscopy (AFM) and electrical conductivity measurements to characterize solid PEDOT:PSS thin films, and ion activity measurement (pH) and photon correlation spectroscopy (Dynamic Light Scattering (DLS)) on solutions to reveal the interplay between thermal treatment of PEDOT:PSS, resulting thin film properties and photovoltaic performance.

2. Experimental details

2.1. Materials

All substrates used (Spectrosil quartz glass, indium-tin oxide (ITO) coated sodium silicate glass) were cleaned by sonication in acetone and isopropanol (20 min. each), followed by oxygen plasma etching (250 W, 10 min). The aqueous colloidal PEDOT:PSS solution used has a PEDOT-to-PSS ratio of 1:16 (Clevios P VP AI 4083, H.C. Starck GmbH, subsequently enriched with PSS). Its nominal solid content is 2.2% and the particle size in the swollen state (in solution) is characterized by d_{50} of 80 nm and d_{90} of 100 nm (d_n implies that n wt.% of the particles are below the given size). The molecular weight of PSS in *Clevios P* is M_W = 313,000 and M_n = 134,000. The aqueous PSS solution (Scientific Polymer Products Inc.) has a solid content of 20 wt.% and the PSS a molecular weight of M_W = 70,000. Powdered In_2O_3 (99.99 % Sigma–Aldrich) was added to PEDOT:PSS solution for some pH measurements at a concentration of 1.21 mg/mL.

For the solar cell active layers a binary all-polymer blend was used, consisting of poly((9,9-dioctylfluorene)-2,7-diyl-alt-[4,7-bis(3-hexylthien-5-yl)-2,1,3-benzothiadiazole]-2′,2″-diyl) (F8TBT) supplied by Cambridge Display Technology Ltd. with a molecular weight (M_W) of 55,000 and poly(3-hexylthiophene) (P3HT) supplied by Rieke Metals Inc. with a molecular weight (M_W) of 46,000 and a regioregularity of 93% (electronic grade). The photoactive polymers were used without further purification. The P3HT:F8TBT system has been intensively studied previously in photodetector or photovoltaic applications [18,19] and in solar cells gave external quantum efficiencies up to 26% and power conversion efficiencies of 1.8% under solar simulator conditions [2].

2.2. Preparation

The PEDOT:PSS solutions were sonicated (10 min) before use. The solution heating was carried out in a metal hot block to ensure homogeneous heat distribution and the heated solutions were filtered with a preheated 0.25 μm filter (Whatman PP w/GMF polypropylene membrane syringe filter with glass microfiber prefilter) before film deposition or solution characterization. Sonicated PEDOT:PSS solutions were modified by heating at temperatures between 20 °C and 90 °C for at least 10 min before further processing. The warm solutions were filtered and characterized either undiluted (pH value determination) or diluted (to a ratio of 1:50 for PEDOT:PSS) with water of the same temperature (dynamic light scattering). Undiluted, heated, filtered PEDOT:PSS solutions were deposited as thin films for further characterization (photovoltaic studies, conductivity, photoelectron spectroscopy, AFM, profilometer). This was done via spin-coating in ambient

air to yield a final thickness of about 70 nm. Note that the spin-coating chuck and substrate were at room temperature, so that the polymer solution cooled during spin-coating. The spin-cast samples were annealed at 230 °C while purged with dry N_2 gas (<1 ppm H_2O) for 30 min to remove residual water. This temperature was found to be optimum for device performance in our previous study [11]. Samples were then cooled to room temperature in dry N_2 atmosphere and immediately sealed in separate small containers (additionally to glovebox storage) until further processing or measurement to avoid water or oxygen uptake. For conductivity determination gold channels with 80 μm channel width (sets of two parallel 3 mm-long gold stripes with a spacing of 80 μm) were evaporated (thickness: 50 nm) onto clean glass substrates, followed by deposition of PEDOT:PSS on top. For photoelectron spectroscopy studies (PEYS and XPS), the heated PEDOT:PSS solution was spun on fully covered ITO glass substrates. Profilometer and AFM imaging samples were prepared on Spectrosil quartz glass substrates. Photovoltaic devices were fabricated spinning a continuous layer of PEDOT:PSS on patterned ITO glass substrates. These were transferred to a nitrogen-filled glovebox for subsequent device fabrication steps. Firstly, the photoactive polymer layer was deposited on top by spin-coating from a 70 °C *o*-xylene solution of a 1:1 blend of P3HT:F8TBT (20 mg/mL) to give an active layer thickness of 70 nm. Then a 100 nm aluminum cathode was evaporated, followed by annealing of the device at 140 °C for 10 min. Finally devices were encapsulated with an epoxy-glass combination, prior to any air exposure and testing. All devices had an active area of 4.5 mm^2.

2.3. Methods

Surface imaging was performed using atomic force microscopy (Veeco Dimension 3100 AFM) operated in tapping mode and with a probe tip of radius of curvature R_C < 10 nm. Film thickness was measured using a stylus profilometer (Veeco Dektak 6 M). Monitoring of the pH values in solution was performed using a Jenway 370 pH meter, high-temperature-stable quartz-glass-bodied combination electrode and connected thermo element. The pH measurement was performed with automatic temperature compensation after two-point calibration. For device characterization, external quantum efficiency (EQE) was measured as a function of wavelength, using a monochromatic light source (250 W tungsten filament lamp, passed through a monochromator), with a final spot size smaller then the device active area. The short-circuit current was recorded with a Keithley 2635 source measure unit (SMU). Incident light intensity was continuously monitored during measurement and calibrated by a Thorlabs SM5PD1A photodiode. Current–voltage characteristics were recorded in the dark and under the same illumination as used for EQE measurements using the Keithley 2635 SMU. Current–voltage characteristics were also acquired under simulated solar conditions (intensity equivalent to 100 mW/cm^2, AM 1.5 G, after correction for spectral mismatch) using a solar simulator light source (Oriel 81160-1000) calibrated to a silicon reference cell. The hydrodynamic diameter of particles was determined by dynamic light scattering measurements using a Malvern Zetasizer. Measurements were performed on aqueous PEDOT:PSS solutions in the diluted regime (below overlap concentration). Two different concentrations, namely of 50 or 100 μg/ml were used to ensure independence of the data from solution concentration. Three independently prepared solutions were measured for each temperature with at least 20 runs each (number of runs was setted by the Zetasizer software, dependent on the signal quality). The statistical particle size distribution for each measurement was calculated by the Malvern Zetasizer software. The program also takes temperature dependent parameters (e.g. solvent viscosity) into account. Resistance of the PEDOT:PSS films was measured under a N_2 atmosphere, using a two-point-probe setup on a Karl Suss probe station connected to an HP 4155B semiconductor parameter analyzer. The measurement was performed in-plane, across the PEDOT:PSS-covered evaporated 80 μm gold channel, by penetrating the polymer to make contact with the gold electrodes. XPS measurements were performed in an ultra-high-vacuum system with a Kratos Axis Ultra DLD XPS with a monochromated Al K_α X-ray gun ($h\nu$ = 1486.69 eV) and a delay line detector. XPS data were analysed with *CasaXPS* (spectral data processing and analysis software). The core-level spectra were fitted with a combination of Gaussian and Lorentzian peaks after Shirley-background subtraction. Work functions were determined with photoelectron yield spectroscopy (PEYS) in air using a Riken-Keiki AC-2 surface analyzer (Riken Keiki Co., Ltd.). Full details of the AC-2 measurement can be found in the literature [20]. Briefly, film work function is determined by detecting the photoelectrons emitted from the film while the energy of incident UV light from a deuterium lamp (here operating at 250 nW) is varied between 4.5 and 6.2 eV with a monochromator. The work function is equal to the onset of photoelectron emission. For organic solids it is extracted from the linear fit of $Y^{1/3}$ on a plot of $Y^{1/3}$ versus $h\nu$ since $Y \sim (h\nu - W_f)^3$, where Y is the photoelectron yield, $h\nu$ the incident photon energy and W_f the material work function [21]. PEYS is advantageous compared to common UPS, because no vacuum is required and no charging of the sample occurs. Since also slower electrons are detected, the probing depth is 20–30 nm, much larger than for UPS (~10 nm), so surface effects have less impact on the measurement. This latter feature is useful to draw conclusions about the existence and thickness of thin dielectric surface layers on top of the samples from analysis of the yield slope [22]. If the photoelectron emission is retarded by such a damping surface layer, the slope will be smaller.

3. Results

For the investigation of heating effects on PEDOT:PSS solution and the consequences on solar cell performance we follow two different approaches. On the one hand physicochemical modifications occuring within the solution upon heating can be expected. On the other hand solution characteristics will affect the morphology and properties of solid thin films produced from such solutions via spin-coating. By examining in-depth the temperature

dependent properties of both solution and film, insight into the impact on photovoltaic device performance may be derived.

3.1. Effects on solution

One observation from PEDOT:PSS solution heating is the considerable change of particle size in solution, as determined by dynamic light scattering (DLS). Fig. 2a shows the distributions of hydrodynamic diameters in colloidal PEDOT:PSS solutions at various solution temperatures. We note that repeated measurements (as described in Section 2) yielded very similar distributions. It can be seen that the average particle size (Fig. 2b) remains stable at values of about 230 nm up to a solution temperature of 50 °C. With further heating from 60 °C up to 90 °C the particle size decreases rapidly to a new lower plateau at around ~40 nm, representing a size reduction of 83%. In thickness measurements on spun films for different solution temperatures we achieved similar values for all films of 71 ± 4 nm, confirming the absence of significant alterations of the solid content of the filtered solutions [23,24]. We further found that the size alterations are reversible, with larger particles reforming in solution upon cooling. Associated effects occurring under spin-coating conditions will be discussed later.

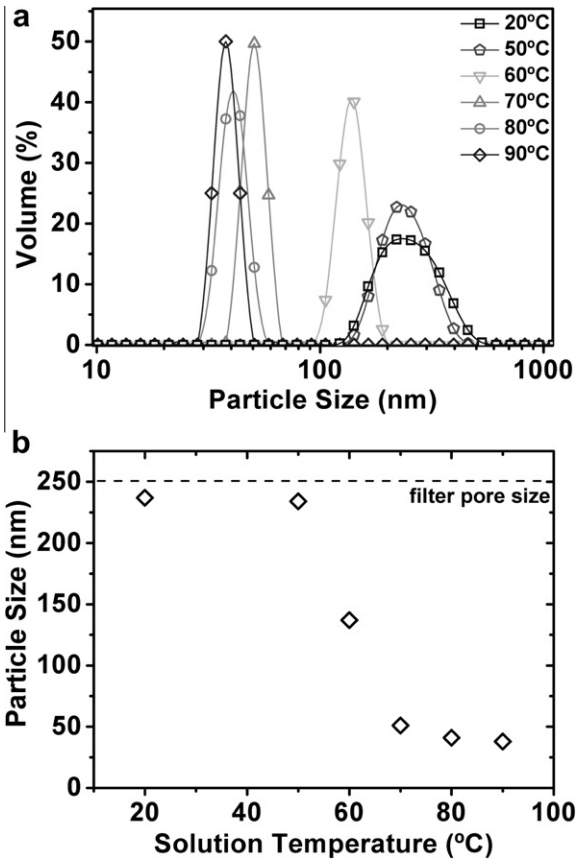

Fig. 2. Size distribution (a) and average particle diameters (b) in colloidal PEDOT:PSS solutions as a function of solution temperature as determined via dynamic light scattering.

Physicochemical processes in solution, especially in the presence of electrolytes like PSS, can be accompanied by changes in pH, since the concentration of hydrogen ions is affected. We found, however, no change in solution pH with heating, with a value of 1.23 ± 0.05 measured independent of solution temperature (between 20 °C and 90 °C) and in agreement with specifications provided by the supplier of 1.2–1.8. Thus we can discount any temperature-induced ion exchanges involving hydrogen. We note that since solution deposition involves contact with the ITO electrode, there may be a corrosive interaction during the brief spin-coating period before the film dries. To exclude any ITO-induced change in pH we have also measured the pH of PEDOT:PSS solutions with In_2O_3 powder added. A concentration of 1.21 mg/mL was used to simulate the maximum likely concentration of dissolved In_2O_3 in a 60 μl solution that is dispensed onto an ITO electrode (dimensions of ITO stripe: 12 mm × 7 mm × 120 nm) during spin-coating. However, we saw no change in pH with In_2O_3 added, remaining at pH 1.23 ± 0.05 independent of temperature. We note that this is contrast to the results of Chang and Chen [25], who observed an increase in pH value by adding In_2O_3 to PEDOT:PSS solution at room temperature, however the reaction was observed to take several hours, much longer than the time window of a few minutes used here to mimic spin-coating conditions. These observations show that whatever reactions may take place between PEDOT:PSS and ITO (such as the release of indium into the PEDOT:PSS solution), they do not significantly affect the concentration of the hydrogen ions.

3.2. Effects on films

We firstly look for possible chemical modifications of films spin-coated at different solution temperatures with X-ray photoelectron spectroscopy. Having a probing depth of less than 10 nm, XPS is used to quantify the elemental surface composition and provides information about the chemical environment. Survey scans covering binding energies of 0–1400 eV were first performed to identify elements in the film, with significant amounts of sodium (1070 eV), oxygen (532 eV), indium (446 eV), carbon (284 eV) and sulfur (170 eV) found. As discussed above, the presence of indium is most likely caused by diffusion of indium ions induced by the high acidity of the PEDOT:PSS solution [26]. Sodium is a trace component in PEDOT:PSS solutions (here less than 400 ppm after ion-exchange purification, as stated by the supplier), caused by the preparation process, involving Na^+PSS^-. The nominal concentrations of the elements detected near the surface of a standard room temperature spun PEDOT:PSS film were: 1.1% sodium (Na 1s), 19.3% oxygen (O 1s), 1.8% indium (In 3d), 70.6% carbon (C 1s) and 7.2% sulfur (S 2p). A comparison between sample films spun from differently heated solutions showed slightly varying compositions (changes <2%), but no obvious trends. High-resolution scans of oxygen (O 1s) and sulfur (S 2p) peaks were recorded to check for any changes in chemical environment of these two elements, which are of specific interest for PEDOT:PSS, such as changes in chemical bonds [8,27]. According to the work of Greczynski et al. [5] the sulfur

and oxygen peaks of PEDOT:PSS may have multiple components originating from PEDOT, PSSH and $PSS^{-}Na^{+}$ species that all have slightly shifted characteristic energies. The sulfur and oxygen core-level spectra for our PEDOT:PSS films spun from solutions heated between 20 °C and 90 °C are shown in Fig. 3.

The sulfur spectra obtained (Fig. 3a) are all consistent with one chemical species, namely the PSSH doublet located at 169.9 eV (S $2p_{1/2}$) and 168.7 eV (S $2p_{3/2}$). No indications of $PSS^{-}Na^{+}$ or PEDOT were found. We note that the effective energy values slightly differ from those reported in literature [5], which may result from the calibration of the spectrometer. We did not observe any change in the sulfur core-level spectra with heating of the PEDOT:PSS solutions. Analysis of the oxygen core-level spectra (Fig. 3b) showed only two contributions; one is attributed to oxygen—sulfur double bonds (O═S) in the sulfonate group in PSSH at 532.2 eV and the other to hydroxyl groups (O—H) at 533.4 eV from PSSH and residual water [5]. The hydroxyl peak appears to be rather broad, possibly caused by hydroxyl groups participating in hydrogen bonds [5]. A peak intensity ratio between O—H bonds and O═S bonds of 1:9 was observed (measured composition 10.5% O—H and 89.5% O═S). We suggest that the comparatively low amount of O—H bonds is mainly caused by our post-deposition film annealing at 230 °C, which firstly might have removed most inter- and intra-particle water and additionally condensated (dehydrolysed) a large quantity of the existing hydroxyl groups in the solid film. No further contributions of either $PSS^{-}Na^{+}$ or PEDOT were found. Just as for the sulfur, no significant changes between the films spun from solution at different temperatures were observed in the oxygen core-level spectra. It should be mentioned that our 230 °C film annealing step is below the temperature at which the rupture of the sulfonate group from PSS takes place [5,11]. This has been supported by further XPS studies which we have performed on PEDOT:PSS films annealed at temperatures between 140 °C and 300 °C in N_2 (graphs not shown). Only for films annealed above 260 °C we could observe additional contributions due to the presence of PEDOT at the surface (at 165.4 eV (S $2p_{1/2}$), 164.2 eV (S $2p_{3/2}$) and 533.6 eV (O 1s)) and an energy-shift in the PSS sulfur doublet, indicating the predominance of $PSS^{-}Na^{+}$ due to PSSH degradation. Both effects were already reported in the literature [5].

For most optoelectronic applications, as in organic photovoltaic devices, the work function of the electrode is crucial and can be one of the factors limiting performance. We have therefore determined the work function changes of films spun from PEDOT:PSS solutions heated at different temperatures via (ultraviolet) photoelectron yield spectroscopy (PEYS). Additionally the yield slopes have been analyzed which can indicate an increase or decrease in the thickness of dielectric surface layers such as excess PSS. Fig. 4a shows the baseline-corrected plots of the photoelectron yield $Y^{1/3}$ plotted against photon energy for different solution temperatures.

At first sight the absence of obvious onset shifts or changes of slope implies that there are only subtle differences upon variation of solution temperature. The work function values and slopes, obtained from linear fits to $Y^{1/3}$, are displayed in Fig. 4b. Despite the comparatively high experimental uncertainty of the measurement ($\Delta W_f = \pm 0.05$ eV), there appears to be a trend in the work function development with solution temperature. Up to 70 °C the work function W_f remains at a stable value of around 5.38 eV; with higher solution temperatures it increases up to 5.50 eV for the 90 °C sample. The slopes of the photoemission yield curves, which represent a measure of the photoelectron emission rates, do not follow the same trend. The highest emission rate within the studied temperature range was found for films spun from room-temperature solution. With increasing solution temperature the emission rate drops, with a minimum for the 70 °C sample. Temperatures above 70 °C cause rising emission rates (higher slopes) from the films. This could be an indication for a variation in thickness of the excess PSS surface layer with solution temperature or changing film density. It should be noted that the short exposure to air during the measurement might have slightly influenced the data due to the strongly hygroscopic nature of PSS. However, apart from a control sample that had been exposed to air for several hours, none of the films shows signs of strong water uptake, which is typically reflected by a strongly lowered work function of around 5.05 eV [6,7,28].

Conductivity is likely to be one of the most important characteristics of an electrode material in a solar cell. PEDOT:PSS films were spun from solutions at different temperatures and subsequently annealed for conductivity measurement. The corresponding development of in-plane conductivity with solution temperature is shown in Fig. 5.

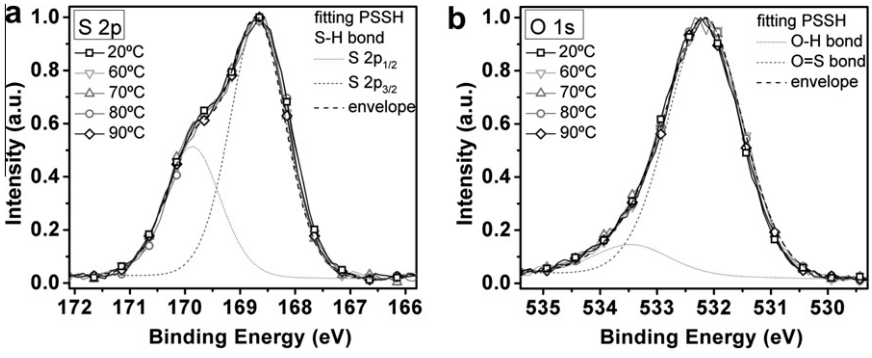

Fig. 3. (a) Sulfur (S 2p) and (b) oxygen (O 1s) XPS core-level spectra of PEDOT:PSS films spun from differently heated solutions.

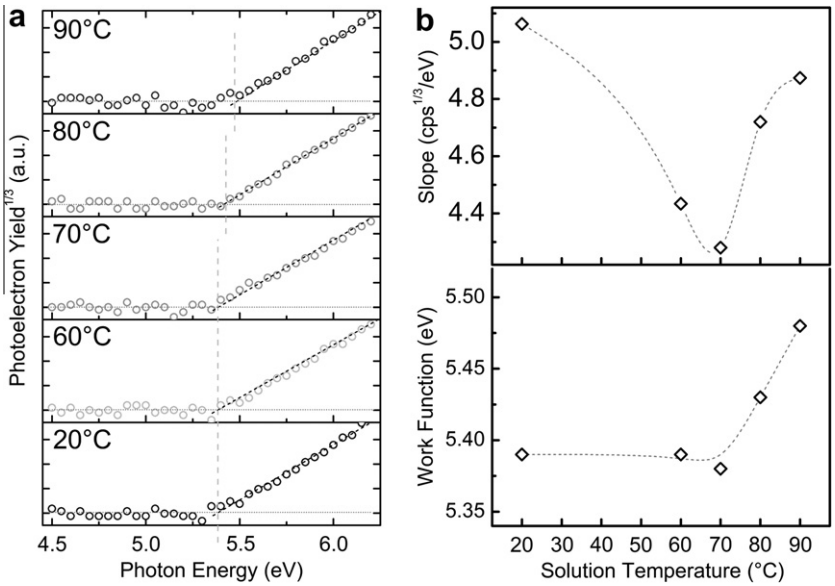

Fig. 4. (a) Cube root plot of the photoelectron yield from PEDOT:PSS films prepared from heated solution. (b) Slope extracted from linear fit to yield (top) and measured work function (bottom) as a function of PEDOT:PSS solution temperature (the dashed lines are a guide to the eye).

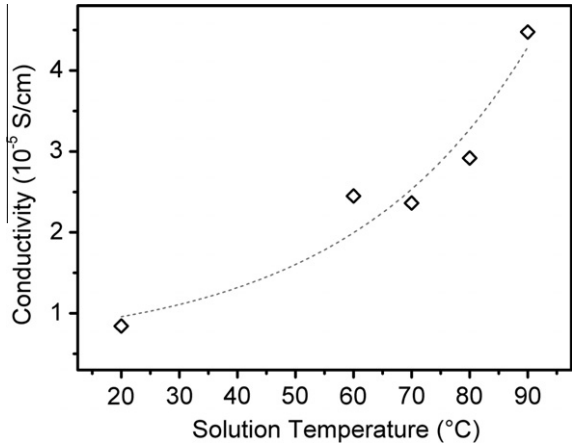

Fig. 5. In-plane conductivity of equally annealed PEDOT:PSS films spun from differently heated aqueous colloidal PEDOT:PSS solutions (the dashed line is meant as guide to the eye).

We found that the in-plane bulk conductivity is enhanced by a factor of five with increasing solution temperature from 20 °C to 90 °C. This is in good agreement with results reported by Tsai et al. [29], who found 2–3 times higher conductivity in films spun from PEDOT:PSS solutions heated from 20 to 160 °C.

The morphology of PEDOT:PSS solid films, spun from solution at different temperatures has been investigated with AFM. Fig. 6a shows the height images for PEDOT:PSS films spun from heated solutions between 20 °C and 90 °C, after subsequent annealing.

It is apparent that although the macroscopic roughness of all films is very similar, there is a refinement in the microscopic structure for films spun at 60 °C and higher. There are obviously considerable changes in particle dimension depending on the PEDOT:PSS solution temperature. The average particle size (Fig. 6b), as acquired from statistical feature size analysis of AFM cross-sectional line scans of the different films, reveals a trend similar to that one seen from DLS on PEDOT:PSS solutions (Fig. 2b). The feature size remains stable at about 55 nm for films up to 50 °C solution temperature and then drops quickly for higher temperatures to a new plateau at around 20 nm. It should be mentioned that a further size decrease might not be detectable as AFM resolution is limited by the tip size (R_C < 10 nm).

3.3. Effects on solar cells

Finally the effect of PEDOT:PSS solution temperature on the performance of P3HT:F8TBT solar cells has been studied. Fig. 7 plots external quantum efficiency *EQE* (Fig. 7a), current–voltage characteristics under solar simulator conditions (AM1.5G) (Fig. 7b) and specific key solar cell parameters (Fig. 7c) (namely short-circuit current density, J_{sc}, open-circuit voltage, V_{oc}, fill factor, *FF*, and power conversion efficiency, η) as a function of PEDOT:PSS solution temperature. As expected, the *EQE* curves (Fig. 7a) do not show any significant spectral change since the active layer is kept constant. However, there are variations in the magnitude of *EQE* with maximum *EQE* increasing with increasing PEDOT:PSS solution temperature to a maximum at 70 °C, then falling again as temperature is increased to 90 °C. A similar trend is seen in the current–voltage characteristics. Fig. 7c shows that all key parameters are optimized with a solution temperature of 70 °C, which is most apparent for J_{sc} and η, while V_{oc} and *FF* only change slightly.

4. Discussion

Among the numerous publications addressing the optimization of PEDOT:PSS films for use in organic

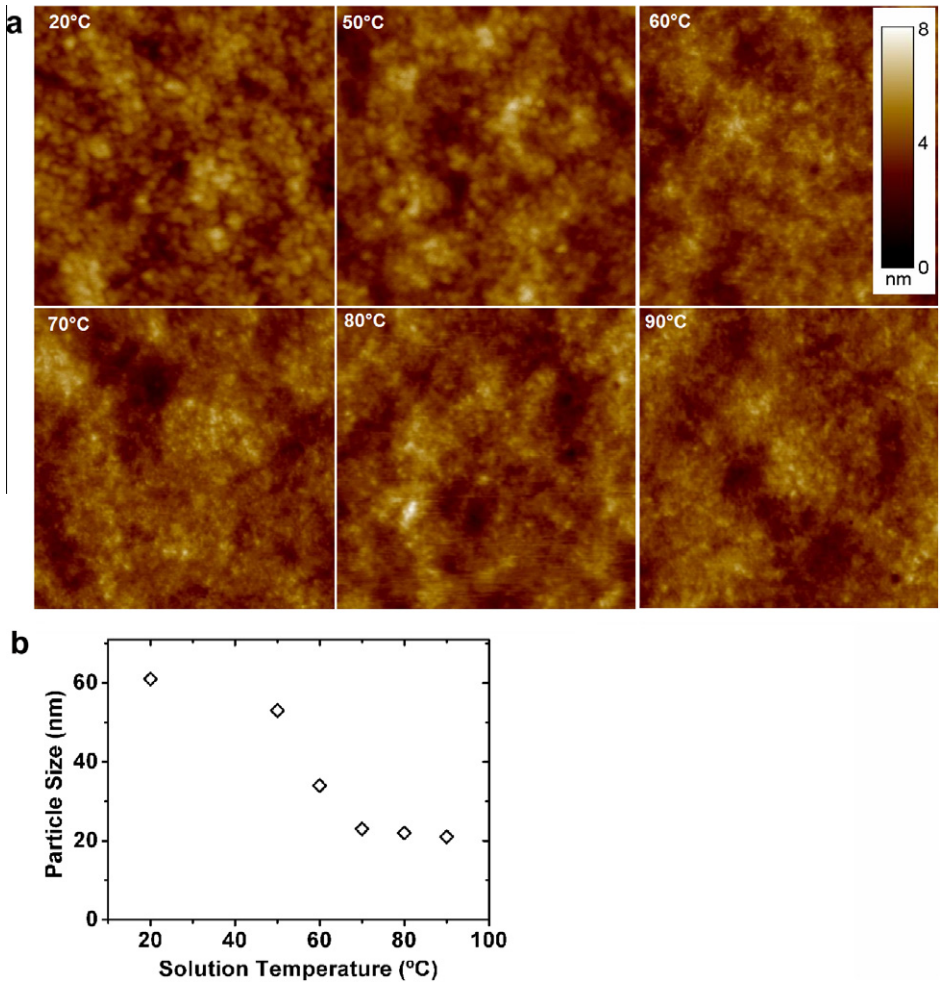

Fig. 6. (a) AFM height images (2 μm × 2 μm) of the surface morphology for PEDOT:PSS films spun from heated solutions. (b) Temperature dependent development of average feature size in these films.

optoelectronic devices, changes in particle/grain size by addition of dopants or co-solvents, have occasionally been addressed. Usually these have been attributed to agglomerate formation [30–32], e.g. due to dominating Van-der-Waals forces facilitated by partial removal of the repulsive negatively charged surface PSS layer (e.g. by solvent additives) [33]. We found in our experiments that the size variations could be detected within a few minutes in highly diluted solutions. This makes agglomeration as a cause for a size increase unlikely, since the required diffusion processes for interparticle contacts take place on a much longer time scale (days or weeks). Furthermore the particles could not be broken down by ultrasonication, which also speaks against agglomeration effects. We suggest that the observed solution-temperature-induced size effects are rather associated with the phase behavior of PEDOT:PSS, which has not been reported in this context so far.

The solubility of PEDOT:PSS in aqueous solution is mainly determined by the presence of the charged sulfonate groups on the polystyrene backbone, since PEDOT and polystyrene are both hydrophobic on their own. Experimental and theoretical approaches reported in literature have shown that phase behavior of PSS crucially depends on the degree of sulfonation, the distribution of the sulfonate groups along the backbone, the presence and strength of counter ions or the presence of salts in solution [34–37], information which was not fully available, either for commercial PSS solution or for the PSS used in PEDOT:PSS, making it difficult to compare the two systems. Although some values could have been determined experimentally, that is beyond the scope of this publication.

The size dependence of NaPSS with temperature has been the subject of only few earlier studies, finding an increase of hydrodynamic size of the chains with increasing solution temperature from 5 nm up to 18 nm and demixing with an upper critical solution temperature (UCST) [38,34]. Fig. 2 shows an opposite trend, with a decrease in size of PEDOT:PSS particles with increasing solution temperature. This indicates phase separation of the polymer solution at high solution temperatures. Microscopically this means that the polymer chains are most extended at low temperatures and contract/collapse towards higher temperatures. A phase behavior of this kind is typical for a lower critical

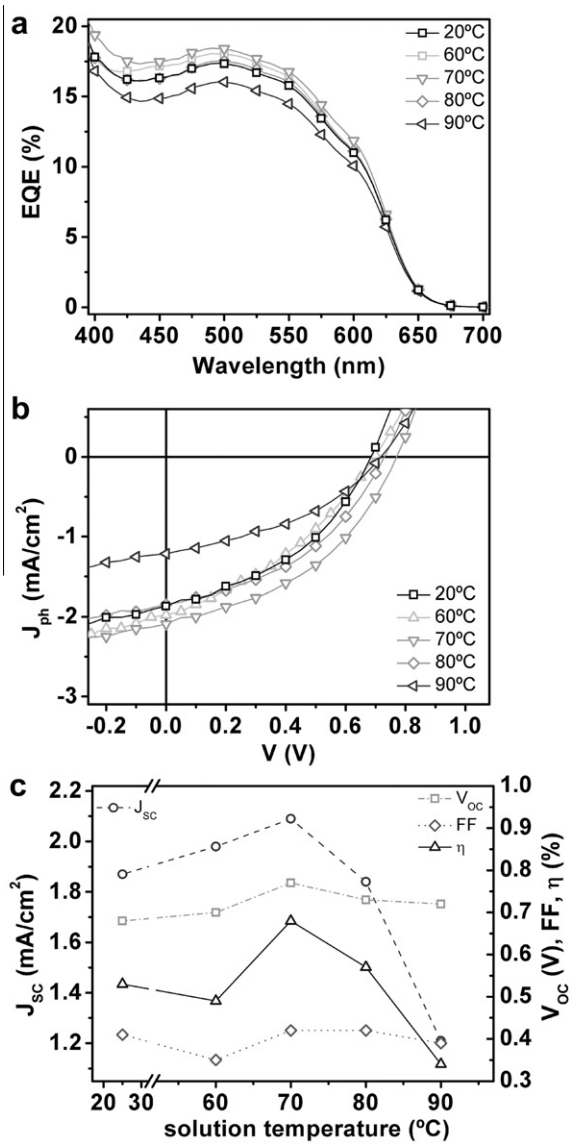

Fig. 7. Characteristics of solar cell devices with PEDOT:PSS films spun from differently heated PEDOT:PSS solutions, (a) external quantum efficiency, (b) photocurrent density (AM1.5G) and (c) key photovoltaic parameters.

solution temperature (LCST), similar to the phase behavior of other polymer solutions [39a]. The variation of particle size in the dry PEDOT:PSS films shows an very similar behavior. Although this trend could also arise from the change of other solution parameters during spin-coating, the similarity of Figs. 2b and 6b suggests the dominance of an LCST behavior of PEDOT:PSS on the particle size in the film. Fig. 8 summarizes the two data sets and schematically indicates the trajectories in phase space of the two experiments. Heating a solution at fixed concentration is indicated by the red dashed (vertical) arrow. Phase separation occurs when the trajectory crosses the binodal line (boundary between polymer–solvent miscibility and immiscibility). In a dilute solution this is accompanied by a step decrease in the hydrodynamic diameter, as observed in the DLS experiments (Fig. 8, right), caused by a collapse of the polymer chains. This process is fully reversible. Spin-coating, on the other hand ideally occurs at constant temperature. Solvent evaporation increases the solution concentration, indicated by the blue dashed (horizontal) arrow in the phase diagram. Horizontally crossing the binodal gives rise to a similar step in particle size, as observed in the as-cast films (Fig. 8, left). In practice, the trajectory for spin-coating from heated solutions is slightly more complex. In addition to a rapid concentration change, the temperature also changes, by casting the solution onto a cold substrate and through evaporative cooling. While this implies a diagonal trajectory in the phase diagram (indicated by the purple (diagonal) arrows), the description for the ideal spin-coating process remains qualitatively valid. Both trends for the hydrodynamic and solid diameter agree well with this scenario. Preheating the substrates, while feasible, substantially changes the evaporation rate of the solution, possibly causing additional changes in the films. The very similar cross-over temperatures of the two data sets in Fig. 8 suggest, however, that film formation occurs much more quickly than a change in particle size. This is in agreement with recent results showing a very slow change in the conformation of polymer brushes upon crossing a LCST [39b].

A further interesting observation arises from the comparison of Figs. 2b and 6b. The particle diameter decreased from 230 nm in solution to 55 nm in the film (i.e. by a factor of 4) when the casting from a 20 °C solution, compared to a size change from 40 nm to 20 nm (by a factor of 2) when the spin coating was above 70 °C. This observation indicates that the coils were less swollen in solution at the high temperatures compared to room temperature, in good agreement with the LCST assumption mentioned above. This result also matches well recent non-equilibrium effects in spin-cast polystyrene films reported by Thomas et al. [40], showing that that solution coil conformations are substantially preserved in the film after spin-coating [41].

In the case of the PEDOT:PSS micellar solution, the signature of an LCST behavior is as follows: Because most PSS chains are localized around PEDOT cores, the phase transition leads to a change in micellar size, which leads to the observations in Fig. 8. Secondly macroscopic phase separation of the suspension into polymer-rich and polymer poor phases should set in at high temperatures. This second process, which is much slower (on the time scale of many hours), was not investigated in detail.

LCST phase behavior of polymer solutions is less common than the UCST type, but often occurs for polymers that can form hydrogen bonds with the solvent [42]. In the case of PEDOT:PSS the presence of hydrogen bridges between sulfonate groups has been reported [31], which could be responsible for the observed LCST phase behavior. It is worth mentioning that hydrated PSS-chains are to some degree extended into the aqueous medium, while they are fully collapsed in the dry film. Macroscopically this is observed when swollen particles in solution shrink during drying, leading to the reported dried PEDOT:PSS grains with PEDOT-rich core, covered by a thin insulating PSS layer [37,38].

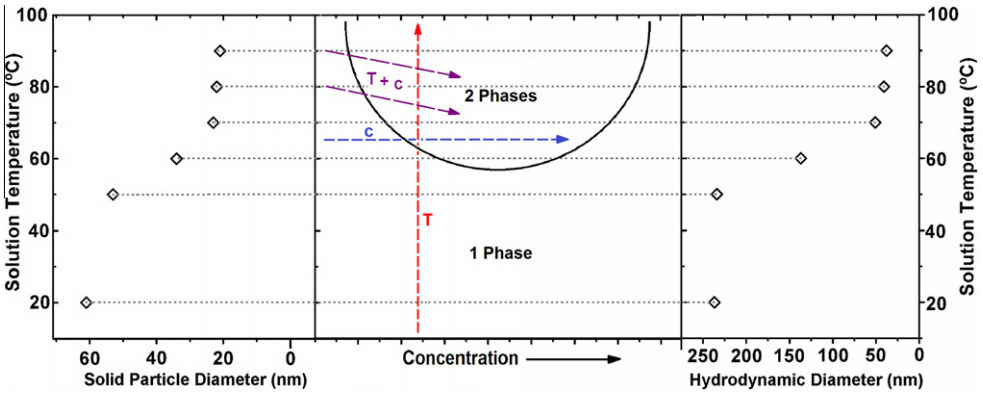

Fig. 8. Schematic LCST-phase diagram illustrating trajectories of solution heating and spin-coating, associated with the obtained trends of average particle diameters as determined from DLS from PEDOT:PSS colloidal solutions (right) and in solid films (left) as a function of solution temperature.

We did not observe any variation in pH value of the PEDOT:PSS solution during heating, neither in pure solution nor involving indium oxide. This is not indicative of PEDOT:PSS-induced ITO corrosion during film formation, which is suspected to cause damage of the organic active layer by indium diffusion already during device fabrication.

The temperature-induced shrinkage of the PEDOT:PSS particles was accompanied by a considerable effect on the film conductivity which was quadrupled by solution heating. It has been reported that smaller PEDOT:PSS particles actually cause lower film conductivity [12], since PEDOT:PSS conductivity is determined by the extension of the conducting PEDOT-rich domains and the hopping distance/frequency across the insulating PSS phases. We found that the interface properties are characterized by an increasingly refined structure and densification of the PEDOT:PSS film, leading to shorter hopping distance between the conductive PEDOT-rich units, the consequence of which is a lower bulk resistance and enhanced interlayer contact.

However, the fact that even for small particles the PSS-shell is at least 10 nm thick, explains why no PEDOT was detected from the films via XPS within the nominal probing depth of 10 nm, independent of the solution temperature. Nor was any other evidence for chemical changes found near the surface.

The observed increase in film work function for solutions exceeding 70 °C is probably caused by the densification of the film causing considerable changes in the interface properties. Even more significant is the behavior of the photoelectron emission rates, represented by the yield slope. The rate starts at a high level, because for low solution temperatures the films are porous and in spite of the thicker damping PSS shell surrounding the particles, more electrons can be detected. When the film density grows towards 70 °C, the rates go down, due to increasingly hindered signal from the depth of the film. Exceeding 70 °C, the emission rates raise again, because the dimensions of the PSS shell of the particles are significantly reduced.

When films from solution-heated PEDOT:PSS are incorporated into a P3HT:F8TBT solar cell, we find that actually most of the key characteristics peak at a PEDOT:PSS solution temperature of 70 °C. It seems obvious that the largest improvement is caused by the enhanced conductivity of the PEDOT:PSS films. However, it is still questionable why the PV performance does not improve beyond 70 °C while the conductivity is still rising. Possible reasons include changes in work function or other interface properties, and changes in vertical charge transport (as opposed to the lateral conductivity measured here). Although the observed work function shift is not large ($\Delta W_f = 0.1$ eV), it could be just sufficient to form a barrier for hole extraction from P3HT. Accordingly the performance would go down for higher solution temperatures. It has been reported earlier [43], that vertical charge transport in PEDOT:PSS can be up to three orders of magnitude lower than in-plane, due to layers of segregated excess PSS. Though we cannot prove this by our spectroscopic or imaging data, it is possible that the phase transitions seen in PEDOT:PSS are accompanied by alterations of the amount of electrostatically bound excess PSS. In that case the release or withdrawal of free PSS into/from solution could certainly change the presence and extension of insulating horizontal PSS interlayers in the resulting films.

5. Conclusions

In this work, the influence of heating on PEDOT:PSS colloidal solutions and its consequence on the performance of polymer–polymer photovoltaic devices has been investigated. We found reversible heat-induced reduction in size of PEDOT:PSS particles by solution heating between 20 °C and 70 °C. We associated this transition with LCST-type phase behavior of PEDOT:PSS. This transition from large particles with a thicker (expanded) insulating PSS-shell to smaller particles covered with a thin (contracted chains) PSS layer causes property alterations in resulting films. In particular, increasing the solution temperature results in films with finer structure, higher density, increased conductivity and work function. Solar cell performance was found to improve, but only up to 70 °C. Above 70 °C, device performance deteriorated alongside an increase in PEDOT:PSS work function, suggesting the formation of a hole

extraction barrier. Based on our observations, we conclude that PEDOT:PSS solutions heated at 70 °C deliver the most beneficial film properties for P3HT:F8TBT solar cells. These results may have implications in the roll-to-roll manufacture of organic photovoltaics, where the liquid film deposited by printing is heated to aid drying [44,45]. Changes in PEDOT:PSS particle size during this process may have a direct impact on device performance.

Acknowledgment

We are grateful to Cambridge Display Technology Ltd. (CDT) for the supply of materials, to the Technology Strategy Board for funding, as part of the OPALS (TP/K2512F) collaborative project with CDT and Molecular Vision Ltd., and to Dr. J.J.M. Halls, Dr. R.J. Wilson and Dr. A.B. Doust for useful discussions. T.J.K.B. and C.R.M. thank the EPSRC for support through Grant no. EP/E051804/1.

References

[1] A.C. Mayer, S.R. Scully, B.E. Hardin, M.W. Rowell, M.D. McGehee, Mater. Today 10 (2007) 28–33.
[2] C.R. McNeill, J.J.M. Halls, R. Wilson, G.L. Whiting, S. Berkebile, M.G. Ramsey, R.H. Friend, N.C. Greenham, Adv. Funct. Mater. 18 (2008) 2309–2321.
[3] Y. Liang, Z. Xu, J. Xia, S.T. Tsai, Y. Wu, G. Li, C. Ray, L. Yu, Adv. Mater. 22 (2010) E135–E138.
[4] H.Y. Chen, J.H. Hou, S.Q. Zhang, Y.Y. Liang, G.W. Yang, Y. Yang, L.P. Yu, Y. Wu, G. Li, Nat. Photonics 3 (2009) 649–653.
[5] G. Greczynski, T. Kugler, M. Keil, W. Osikowicz, M. Fahlman, W.R. Salaneck, J. Electron Spectrosc. Relat. Phenom. 121 (2001) 1–17.
[6] A.M. Nardes, M. Kemerink, M.M. de Kok, E. Vinken, K. Maturova, R.A.J. Janssen, Org. Electron. 9 (2008) 727–734.
[7] J.S. Huang, P.F. Miller, J.S. Wilson, A.J. de Mello, J.C. de Mello, D.D.C. Bradley, Adv. Funct. Mater. 15 (2005) 290–296.
[8] T.P. Nguyen, S.A. de Vos, Appl. Surf. Sci. 221 (2004) 330–339.
[9] E. Vitoratos, S. Sakkopoulos, E. Dalas, N. Paliatsas, D. Karageorgopoulos, F. Petraki, S. Kennou, S.A. Choulis, Org. Electron. 10 (2009) 61–66.
[10] Y. Kim, A.M. Ballantyne, J. Nelson, D.D.C. Bradley, Org. Electron. 10 (2009) 205–209.
[11] B. Friedel, P.E. Keivanidis, T.J.K. Brenner, A. Abrusci, C.R. McNeill, R.H. Friend, N.C. Greenham, Macromolecules 42 (2009) 6741–6747.
[12] S. Kirchmeyer, K. Reuter, J. Mater. Chem. 15 (2005) 2077–2088.
[13] X. Crispin, S. Marciniak, W. Osikowicz, G. Zotti, A.W.D. Van der Gon, F. Louwet, M. Fahlman, L. Groenendaal, F. De Schryver, W.R. Salaneck, J. Polym. Sci. Pt. B-Polym. Phys. 41 (2003) 2561–2583.
[14] M. Kemerink, S. Timpanaro, M.M. de Kok, E.A. Meulenkamp, F.J. Touwslager, J. Phys. Chem. B 108 (2004) 18820–18825.
[15] S.G. Im, E.A. Olivetti, K.K. Gleason, Surf. Coat. Technol. 201 (2007) 9406–9412.
[16] J. Hwang, F. Amy, A. Kahn, Org. Electron. 7 (2006) 387–396.
[17] C.R. McNeill, A. Abrusci, J. Zaumseil, R. Wilson, M.J. McKiernan, J.H. Burroughes, J.J.M. Halls, N.C. Greenham, R.H. Friend, Appl. Phys. Lett. 90 (2007) 193506.
[18] B. Friedel, C.R. McNeill, N.C. Greenham, Chem. Mat. 22 (2010) 3389–3398.
[19] T.J.K. Brenner, I. Hwang, N.C. Greenham, C.R. McNeill, J. Appl. Phys. 107 (2010) 114501.
[20] H. Kirihata, M. Uda, Rev. Sci. Instrum. 52 (1981) 68–70.
[21] Y. Nakayama, S. Machida, T. Minari, K. Tsukagishi, Y. Noguchi, H. Ishii, Appl. Phys. Lett. 93 (2008) 173305.
[22] T. Kagiyama, Y. Saito, K. Otobe, S. Nakajima, Appl. Surf. Sci. 216 (2003) 542–548.
[23] Y.J. Min, M. Akbulut, K. Kristiansen, Y. Golan, J. Israelachvili, Nat. Mater. 7 (2008) 527–538.
[24] G.V. Franks, Chem. Eng. Res. Des. 83 (2005) 937–945.
[25] C.H. Chang, S.A. Chen, Appl. Phys. Lett. 91 (2007) 103514.
[26] M.P. de Jong, L.J. van Ijzendoorn, M.J.A. de Voigt, Appl. Phys. Lett. 77 (2000) 2255–2257.
[27] G. Greczynski, T. Kugler, W.R. Salaneck, Thin Solid Films 354 (1999) 129–135.
[28] N. Koch, A. Vollmer, A. Elschner, Appl. Phys. Lett. 90 (2007) 043512.
[29] K.H. Tsai, S.C. Shiu, C.F. Lin, Proc. SPIE 7052 (2008) 70521B.
[30] H.J. Snaith, H. Kenrick, M. Chiesa, R.H. Friend, Polymer 46 (2005) 2573–2578.
[31] U. Lang, E. Muller, N. Naujoks, J. Dual, Adv. Funct. Mater. 19 (2009) 1215–1220.
[32] H. Yan, S. Arima, Y. Mori, T. Kagata, H. Sato, H. Okuzaki, Thin Solid Films 517 (2009) 3299–3303.
[33] H. Yan, H. Okuzaki, Synth. Met. 159 (2009) 2225–2228.
[34] S. Kanai, M. Muthukumar, J. Chem. Phys. 127 (2007) 244908.
[35] A.V. Dobrynin, M. Rubinstein, Prog. Polym. Sci. 30 (2005) 1049–1118.
[36] J.M.Y. Carrillo, A.V. Dobrynin, J. Phys. Chem. B 114 (2010) 9391–9399.
[37] S. Block, C.A. Helm, J. Phys. Chem. B 112 (2008) 9318–9327.
[38] E. Serhatli, M. Serhatli, B.M. Baysal, F.E. Karasz, Polymer 43 (2002) 5439–5445.
[39] [a] I. Teraoka, Polymer Solutions: An Introduction to Physical Properties, John Wiley & Sons, 2002;
[b] R. Poetes, PhD Thesis, University of Cambridge 2010.
[40] K.R. Thomas, A. Chenneviere, G. Reiter, U. Steiner, Phys. Rev. E 83 (2011) 021804.
[41] D.R. Barbero, U. Steiner, Phys. Rev. Lett. 102 (2009) 248303.
[42] T. Tsubouchi, K. Nishida, T. Kanaya, Colloids and Surfaces B: Biointerphases 56 (2007) 265–269.
[43] A.M. Nardes, M. Kemerink, R.A.J. Janssen, Phys. Rev. B 76 (2007) 085208.
[44] F.C. Krebs, T. Tromholt, M. Jørgensen, Nanoscale 2 (2010) 873.
[45] F.C. Krebs, S.A. Gevorgyan, J. Alstrup, J. Mater. Chem. 19 (2009) 5442–5451.

cathode) and hole (at the anode) transport level in the organic semiconductor. From then on, electrons and holes are injected in the active layer. The ions react by (electrostatically) compensating the injected charge, in other words the anions and cations respectively stabilize the oxidation and reduction of the polymer. This process is called electrochemical doping [4].

In wide-gap planar LECs, this electrochemical doping can be visualized by monitoring the PL of the active layer under UV illumination; [16] in the presence of doping, PL is quenched in the active layer [17]. Particularly interesting is the way in which this doping occurs. Starting from the electrodes, doped regions expand towards each other. During this expansion, doping fronts are visible as sharp transitions between the undoped region and the n- and p-doped regions. These fronts have been observed to accelerate. Fig. 1a (blue symbols) shows a typical measurement [18] of the front position versus time.

Several experimental studies [19–21] have been performed on these fronts as well as analytical [22,23] and numerical modeling [24]. Robinson and co-workers developed an analytical model that predicts the position of the doping fronts and the resultant switch-on time. They assumed that both the potential over the shrinking undoped region and the conductivity through this region remain equal. The first assumption is however not necessarily true in LECs. Recent measurements of the electrostatic potential have shown that the potential does not strongly evolve during doping front progression [25]. Results presented in the present work confirm these findings.

Here we demonstrate by numerical modeling [4] that a doping dependent mobility [26] is required to generate the accelerating doping fronts observed experimentally (Fig. 1b, blue symbols). In addition the ion mobility with respect to the electron/hole mobility is critical for front formation as well as for other transient properties like the formation of electric double layers (EDLs) [27] and a light-emitting p–n junction. For formation of accelerating doping fronts, the ion mobility needs to be approximately equal to the electron/hole mobility in the undoped polymer. In simulations that obey these criteria, the doping front propagation shows an excellent agreement with experimentally observed doping fronts as shown in Fig. 1a (black solid line) [18]. As opposed to the t^2 dependency of the front position obtained by Robinson et al. [22] (Fig. 1a, red solid line) our model shows a less strong time dependence of the front position. Next to this fundamental understanding of the formation of doping fronts, also the transient behavior and the switch-on time in LECs are rationalized by means of numerical modeling. The simulations indicate that the switch on time is mostly related to the time an ion needs to cross approximately half the device.

2. Material and methods

2.1. Computational details

A 1-dimensional model was used in which an active layer with a length of 2 μm was divided in discrete, equidistant grid points [4,25]. The numerical model solves the drift–diffusion equations for electrons, holes, anions and cations and Poisson's equation on this grid by forward integration in time. Devices with a bandgap $E_g = 2$ eV were simulated during operation at a bias voltage $V_{bias} = 5$ V. A detailed description of the numerical model can be found in the Supplementary Information sections A and B. Simulations were ran for devices with an initial homogeneous ion concentration $c_0 = 1 \times 10^{-1}$ nm^{-3}. No binding energy was assumed between anions and cations. The electrodes were ionically-blocking and electrons and holes were injected from the contacts according to a dedicated injection model that gives rise to field dependent injection [4]. The injection model is described in detail in the Supplementary Information and has the advantage that injection is not affected by grid-point spacing. At the start of the simulations, no electrons and holes are present in the device. The hole and electron injection barriers were set at 0.5 and 1.5 eV respectively to simulate an asymmetric device. Such an asymmetry is realistic for actual planar LECs, in which both the anode and the cathode are made from a single material, e.g. Au. Bimolecular electron–hole

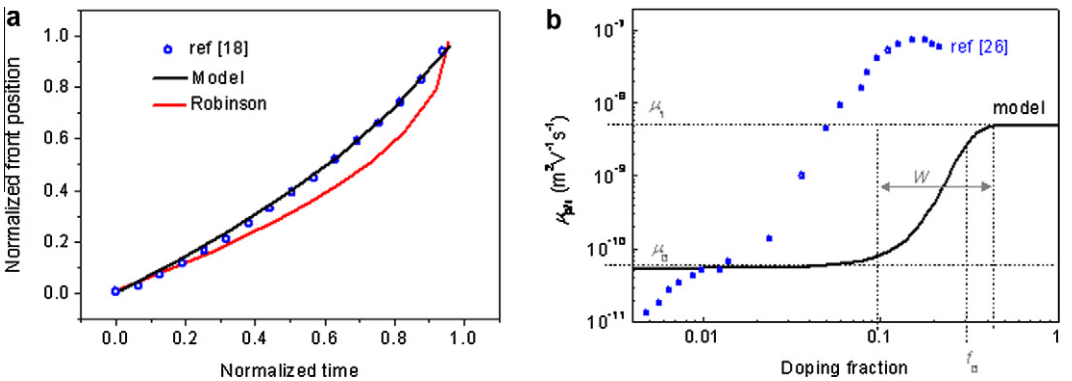

Fig. 1. (a) Front position during switch-on in an LEC as obtained experimentally (blue markers) [18], analytically (red line) [22] and by numerical modeling (black line). The model curve follows from modeling of a planar LEC with a doping dependent $\mu_{p/n}$ according to Eq. (1) for $\mu_0 = 5 \times 10^{-11}$ m^2 V^{-1} s^{-1}, $\mu_1 = 5 \times 10^{-8}$ m^2 V^{-1} s^{-1}, $f_0 = 0.13$ and $W = 0.015$. (b) The electron/hole mobility as a function of the doping fraction. The blue graph was experimentally determined by Shimotani et al. [26] in regioregular P3HT (here the mobility values are divided by 10^2) and the black graph follows from Eq. (1) for $\mu_0 = 5{\cdot}10^{-11}$ m^2 V^{-1} s^{-1}, $\mu_1 = 5 \times 10^{-9}$ m^2 V^{-1} s^{-1}, $f_0 = 0.3$ and $W = 0.04$. (For interpretation of the references to color in this figure legend, the reader is referred to the web version of this article.)

recombination was described by a Langevin process and the electrostatic potential was determined by Poisson's equation. Furthermore, energetic and spatial disorder, as present in real polymers, were omitted for convenience, as were charge traps. In addition, we set the relative dielectric constant $\varepsilon = 3$ and the temperature $T = 300$ K.

To implement a doping density dependency of the electron/hole mobility ($\mu_{p/n}$) the following expression was used:

$$\mu_{p/n}(f) = \frac{\mu_{p/n.1} - \mu_{p/n,0}}{1 + \exp\left(\frac{f_0 - f}{W}\right)} + \mu_{p/n,0}. \quad (1)$$

Here f is the doping fraction which is equal to the carrier density divided by the density of states (=0.3 nm^{-3}). This approximation of the doping fraction is justified by the observation (see Supplementary Information Fig. C.1) that the net ion density always equals the net electronic charge density in the doped regions. Regarding the other parameters, $\mu_{p/n,1}$ is the mobility at maximal doping ($f = 1$), $\mu_{p/n,0}$ is the mobility in the absence of doping ($f = 0$), and f_0 and W are two parameters that set the transition from μ_0 and μ_1:f_0 determines at which doping fraction the mobility increases and W determines the range of doping fractions over which this increase occurs. Fig. 1b shows a typical plot of the doping dependent mobility that follows from Eq. (1) for $f_0 = 0.3$, $W = 0.04$, $\mu_0 = 5 \times 10^{-11}$ m^2 V^{-1} s^{-1} and $\mu_1 = 5 \times 10^{-9}$ m^2 V^{-1} s^{-1}. The anion and cation mobilities were chosen to be equal to each other and doping independent. Ion mobilities ranged from 5×10^{-12} to 5×10^{-9} m^2 V^{-1} s^{-1}.

Since our interest is the transient behavior of LECs, calculations started with the application of a bias voltage on a homogeneous device and were continued until steady state was reached. At $t = 0$ the electron and hole density equals zero and the anion and cation density equals c_0. It was checked that the inter-electrode gap and meshing did not affect the outcome of the calculations in any non-trivial manner (see Supplementary Information A).

3. Results and discussion

Multiple simulations were performed to analyze the effect of the electronic and ionic mobilities on the transient behavior in LECs. The time-evolution of the electron and hole density profiles that follow from these simulations are shown in Fig. 2. The absence (Fig. 2a–d) and presence (Fig. 2e–f) of a doping dependent mobility was studied as well as the effect of the ion mobility. The doping dependent mobility that is shown in Fig. 1b (model) was used in these simulations. It will be shown below that the qualitative behavior in these simulations only depends on the relative values of the mobilities of the electronic and ionic species.

Starting from $t = 0$, the processes in these devices are similar: anions and cations move towards the anode and cathode respectively forming EDLs (see Supplementary Information Fig. S4). When the resultant potential drop at the interfaces has become similar in size to the injection barriers, charge carriers start being injected. During EDL formation, the anion and cation concentrations in the bulk remain equal to maintain charge neutrality. Only at the electrodes this neutrality is broken because of depletion of one type of ion and accumulation of the other. During the subsequent injection of either electrons or holes, a third type of charge carrier comes into play. To maintain charge neutrality in the bulk, the anion and cation densities start to differ. At this stage, where injection of carriers is initiated, differences in the transient processes arise when ion or carrier mobilities are altered.

When interpreting the results shown in Fig. 2, the discussion focuses on two characteristics: (1) the collision of the p- and n-doped regions and (2) the saturation of doping at each grid-point after the doping front has passed. Here, doping is saturated when a doping fraction of approximately 0.2–0.3 is reached, i.e. at a charge density of $2–3 \times 10^{-1} \times 0.3$ nm^{-3} in Fig. 2. Note that in experiments, strong PL quenching is observed when the doping density reaches a threshold level; PL quenching is not necessarily linear with doping fraction [16].

As a first example, we show in Fig. 2b, the time evolution of the doping of the active layer assuming a doping-independent mobility of $\mu_{ion} = \mu_{p/n} = 5 \times 10^{-11}$ m^2 V^{-1} s^{-1}. No sharp transitions are observed from doped to undoped regions: the doped regions already connect to each other while the doping density in roughly half the cell is far from saturated. However, in case of a doping dependent mobility $\mu_{p/n}$ (Fig. 2f), the transition between the doped and undoped regions becomes sharper; the increased mobility of electrons and holes injected behind the front results in a faster saturation of doping compared to the progression of the doped region through the intrinsic region. The enhanced mobility behind the front also ensures a sufficient supply of carriers towards the fronts to prevent a decrease of the doping rate at the front. In contrast to the situation for a doping-independent mobility (panel b), the time needed to completely dope the active layer in panel f is limited by the front progression and not by the process of saturating the doping behind the fronts.

When the ion mobility is decreased by a factor 10 ($\mu_{ion} = 5 \times 10^{-12}$ m^2 V^{-1} s^{-1}, panels a and e) both doping regions come into contact even before doping has saturated at any position in the cell. No sharp transitions are observed from doped to undoped regions. These observations are the result of the relative immobility of the ions compared to the electrons and holes, which mainly hampers the actual doping of the active layer. Since $\mu_{p/n,0} > \mu_{ion}$ progression of the electronic charges through the device is fast relative to the actual doping at any fixed position in the device. Consequently there is a small doping density difference between the front and the doped regions just behind it, which results in only a minor carrier mobility enhancement behind the front. Therefore, the carriers behind the front are not propelled towards the front as was observed in Fig. 2f. For that reason, the two doping fronts have already moved across the active layer while the doping process is far from finished. After the doped regions have met, doping saturates more or less evenly throughout the LEC. This result indicates that if $\mu_{ion} < \mu_{p/n,0}$ homogeneous doping of the active layer is found rather than doping by doping fronts.

On the other hand, when the ion mobility is increased by a factor 10 ($\mu_{ion} = 5 \times 10^{-10}$ m^2 V^{-1} s^{-1}, panels c and g),

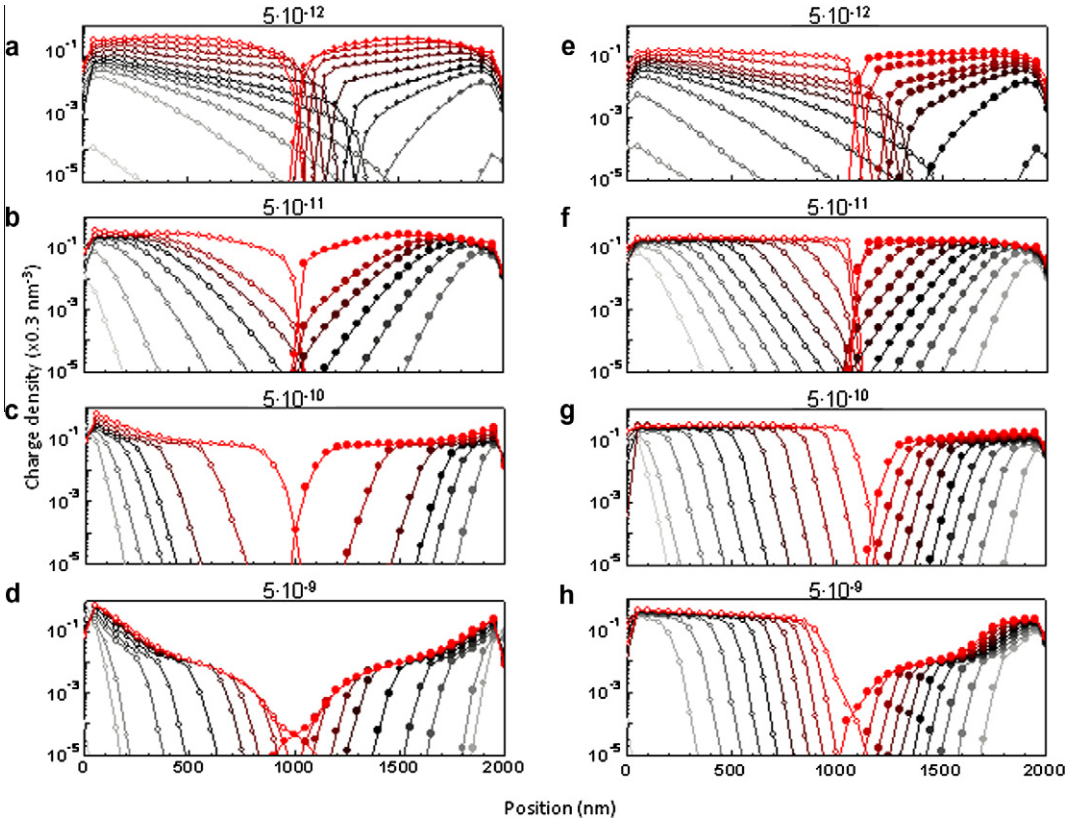

Fig. 2. Transient carrier concentration profiles in LECs for (a)–(d) a constant $\mu_{p/n}$ equal to 5×10^{-11} $m^2 V^{-1} s^{-1}$ and (e)–(h) a doping dependent $\mu_{p/n}$ (see Fig. 1b, model). Holes (open circles) are injected from the left and electrons (closed circles) from the right. The corresponding values of μ_{ion} are shown at the top of each graph expressed in $m^2 V^{-1} s^{-1}$. The movement in time is expressed by the color change of the graphs from light gray to black followed by red. The final red graphs are not the steady state distributions but represent the moment the p–n junction has formed. (For interpretation of the references to color in this figure legend, the reader is referred to the web version of this article.)

sharp doping fronts are formed for both a density dependent and a density independent $\mu_{p/n}$. The origin of the formation of these sharp fronts is however different as compared to the fronts formed in Fig. 2f. In case a constant $\mu_{p/n}$ is chosen (panel c) anions and cations always move faster than the injected carriers. As a result, the available anions and cations are able to electrostatically compensate the injected carriers relatively fast. As shown in our previous publication, [4] in the absence of injected carriers, because of e.g. relatively poor carrier injection, the ions tend to screen the bulk from the electric field. Here this tendency is observed during doping of the active layer: the electric field E_i in the intrinsic region, that drives the doping front, is reduced by ion screening (see Supplementary Information Fig. D.1). Accordingly the carriers at the fronts are slowed down, while newly injected carriers in the already doped regions are accelerated because of a locally enhanced field. (see Supplementary Information Fig. D.2c for the potential evolution). This combination results in a sharp doping front. For a doping dependent mobility (panel g), the same behavior of the ions is observed; ions accumulate at the front to screen the intrinsic region from the applied field. In addition, in this case the doping-enhanced mobility of injected carriers is larger than the ion mobility. Hence, these carriers can more easily approach the carriers at the front, which further sharpens the doping front in panel g as compared to panel c. (see Supplementary Information Fig. D.3 for an evaluation of the sharpness of the n-type doping front during propagation).

In case the ion mobility is increased even more, i.e. 5×10^{-9} $m^2 V^{-1} s^{-1}$, the effects of a reduction of E_i become more pronounced, as shown by relatively large doping density close to the electrodes in panels d and h. Furthermore, the strong depletion of ions from the intrinsic region becomes a limiting factor. The regions close to the electrodes absorb most of the ions and hence they are not directly available for electrochemical doping. Consequently, the doping fronts slow down as no more ions are available in the intrinsic region. After that, ions from the already doped regions are transported backwards to the front to complete the doping (the ion density profiles are shown in Supplementary Information Fig. D.4). This backward ion transport is driven by the inward movement of electrons and holes.

It is important to point out that the steady state carrier distributions and potential profiles are the same for each ion mobility as the ion mobility only affects the transient characteristics in LECs, not the steady state characteristics [4]. The graphs in Fig. 2 are plotted until the p–n junction

has formed, hence the red curves do not represent complete equilibrium.

The positions of the sharp doping fronts observed in Fig. 2 are plotted vs. time in Fig. 3a. For each doping profile in Fig. 2 the position at which the doping density equaled a constant, arbitrarily chosen value of 3×10^{-3} nm^{-3} was taken to produce Fig. 3a. A different choice of this value hardly affects the doping front propagation profiles in Fig. 3a, because the shape of the doping density profile is more or less constant during doping front propagation (see e.g. Fig. 2g). The observed acceleration (superlinear behavior in Fig. 3a and c) or deceleration (sublinear behavior) of the sharp doping fronts can be related to the origins of sharp front formation as discussed above. A reduction of the electric field and/or ion density in the intrinsic region was found to underlay the fronts observed in panels c, d, g, and h of Fig. 2. Both these effects directly lead to a deceleration of the doping front. Consequently, newly injected carriers have time enough to dope the region behind the front and thus maintain a constant doping density from the electrodes towards the fronts, which is perceived as a sharp doping front. In case sharp doping fronts are formed because the mobility of newly injected carriers is enhanced (Fig. 2f), the doping front velocity is observed to slightly increase with time because of the large supply of injected carriers. These effects or combinations of these effects can be observed in the front position vs. time plots in Fig. 3a. Consider the front position vs. time graphs for a doping-dependent mobility (gray–black lines). For $\mu_{ion} = 5 \times 10^{-9}$ m^2 V^{-1} s^{-1} (light gray line) the front speed declines because of a reduction of both E_i and ion density in the intrinsic region. For $\mu_{ion} = 5 \times 10^{-10}$ m^2 V^{-1} s^{-1} (dark gray line) the front speed is constant, being the sum of opposite effects: a reduction of E_i and an enhancement of $\mu_{p/n}$ in the doped regions. For $\mu_{ion} = \mu_{p/n,0} = 5 \times 10^{-11}$ m^2 V^{-1} s^{-1} (black line), the front speed increases, because $\mu_{p/n}$ is enhanced. The latter, an increasing front speed, is in agreement with published experimental data, see Fig. 1a [22]. In case $\mu_{p/n}$ is doping-independent (red lines), the front speed mainly declines because of the reduction of E_i and ion density in the intrinsic regions.

To study the effect of a sharper mobility increase as a function of doping, simulations were performed in which parameters W and f_0 in Eq. (1) were decreased. The used mobility curves are shown in Fig. 3b. Simulations of the front propagation were performed for all these curves while $\mu_{ion} = 5 \times 10^{-11}$ m^2 V^{-1} s^{-1}. The results are shown in Fig. 3c. If the mobility increase becomes sharper with respect to an increased doping density, the time needed for both fronts to meet each other clearly decreases. Further-

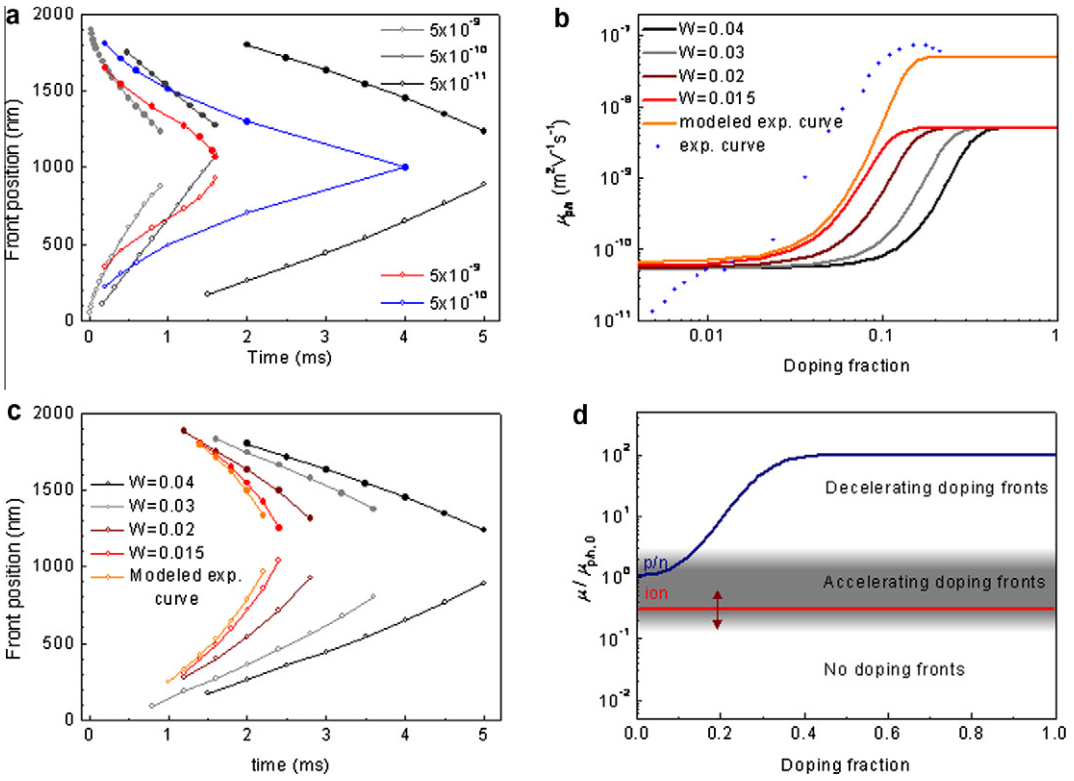

Fig. 3. Calculated doping front position vs. time plots in LECs for different carrier mobility functions. The p- and n-type doping fronts are denoted by the open and closed circles respectively. (a) The doping front propagation for different values of μ_{ion} as indicated in the legend in m^2 V^{-1} s^{-1}. The gray–black lines and red lines correspond to a density dependent and independent $\mu_{p/n}$ respectively. (b) Different doping dependent mobility functions for which $\mu_0 = 5 \times 10^{-11}$ m^2 V^{-1} s^{-1}, $\mu_1 = 5 \times 10^{-9}$ m^2 V^{-1} s^{-1}, $W = 0.04/0.03/0.02/0.015$ and $f_0 = 0.3/0.22/0.14/0.10$. For the orange line, $W = 0.015$, $f_0 = 0.13$ and $\mu_1 = 5 \times 10^{-8}$ m^2 V^{-1} s^{-1}. (c) The doping front propagation for the different doping dependent mobility functions shown in (b). (d) Schematic of the ion mobility criteria with respect to the doping dependent electron and hole mobility (blue line) that result in the formation of accelerating doping fronts in LECs during switch-on. (For interpretation of the references to color in this figure legend, the reader is referred to the web version of this article.)

more, also a larger acceleration of the fronts is observed. These observations are related to the enhanced carrier mobility at progressively lower doping levels: the higher carrier mobility behind the front results in an increased supply of carriers for doping at the fronts, enabling the front to move faster through the active layer. Also a simulation was performed with a doping dependency of the mobility that mimics the experimental mobility curve in Fig. 1b (see orange line in Fig. 3b). The resultant front position vs. time curve is shown in Fig. 3c. This result was normalized and plotted in Fig. 1a to enable comparison with the experiment [22]. A striking similarity is observed, constituting the validity of the model. Furthermore, it shows that the chosen mobility dependency seems qualitatively correct in describing front propagation in LECs. More comparisons of the experimental and modeled front position vs. time plots are shown in the Supplementary Information (Fig. E.1b, d and e). To ensure the device length did not qualitatively influence the results, simulations of a longer device were performed that showed qualitatively similar behavior (see Supplementary Information Fig. E.1c). Furthermore, the results are qualitatively not strongly dependent on the ion concentration c_0. Quantitatively, an increase of c_0 results in faster movement of the fronts through the device (see Supplementary Information Fig. E.1a). This effect originates from the availability of more ions to dope the organic semiconductor, thereby increasing the rate of doping behind the fronts. The consequently increased doping density results in an increased supply rate of carriers towards the fronts that effectively increases the doping front propagation.

The phase diagram shown in Fig. 3d summarizes the results shown in Figs. 2 and 3a–c. In the diagram the doping dependent $\mu_{p/n}$ is shown relative to $\mu_{p/n,0}$. Dependent on the ratio between μ_{ion} and $\mu_{p/n,0}$, three regions can be identified: (1) if $\mu_{ion} \ll \mu_{p/n,0}$ no doping fronts are formed; (2) if $\mu_{ion} \approx \mu_{p/n,0}$ accelerating doping fronts are formed; and (3) if $\mu_{ion} \ll \mu_{p/n,0}$ decelerating doping fronts are formed. For a constant $\mu_{p/n}$ the central region disappears so either no or decelerating doping fronts are formed. As already mentioned, experiments on planar LECs have indicated the formation of doping fronts during turn-on that accelerate when closing in on each other [18]. Combination of these experimental results with our numerical modeling strongly indicates that $\mu_{p/n}$ depends similarly on doping and that μ_{ion} is of the same order as $\mu_{p/n,0}$.

From the simulations presented in Fig. 2e–h current vs. time plots were made to study the transient behavior in LECs with a doping dependent mobility for different ion mobilities. A typical plot is shown in Fig. 4a. The ionic and electronic contributions to the current are plotted separately as well to make the total current transient more comprehensive. At $t = 0$, the current is completely carried by the ions. These ions first form the EDLs at the electrodes, resulting in injection of holes (marked with arrow 1 in Fig. 4a) and electrons (arrow 2). Electron injection is delayed compared to hole injection because of the larger injection barrier that needs to be overcome by formation of a larger EDL. This injection results in an increased electronic current. Following this injection, the active layer is doped, during which the ionic current is observed to slowly decrease and the electronic current to increase. The initiation of recombination (orange line in Fig. 4a) indicates that the doping fronts have met (arrow 3). After this, both recombination and the electronic current increase [28]. This indicates the further doping of the active layer until at some time the current as well as the recombination suddenly drop (arrow 4). This is related to a change in the electric field distribution after which the externally applied electric field becomes concentrated in the recombination region rather than being distributed over the entire active layer: The p–n junction has formed. Hence, meeting of the doping front does not coincide with but precedes the formation of a p–n junction. The appearance of a sharp potential drop in the p–n junction arises from the anions and cations being completely removed from the junction region [4]. These ions have been used to maximize doping in the surrounding regions. Because of the relatively small density of carriers in the recombination region, the conductivity is relatively low compared to the doped regions. Therefore, in order to fulfill current conservation, a larger field in the junction region is needed then in the doped regions.

The time between the application of a bias and the injection of holes, the injection of electrons, the doping front meeting and the p–n junction formation is plotted in Fig. 4b as a function of μ_{ion} relative to $\mu_{p/n,0}$. The time is normalized by the time an ion needs to travel across the device in the presence of an (average) field equal to $((V_{bias} - E_g))/L$. A horizontal line in this graph indicates that the time needed for the corresponding process depends linearly on μ_{ion} and bias. Accordingly, the graph shows that the time needed for the initiation of electron and hole injection linearly depends on μ_{ion}. This can also be easily deduced from the fact that injection of carriers is directly related to the formation of EDLs, which results from a reorganization of the ion density across the device. The meeting of the doping fronts that follows after injection of carriers is however not linearly related to μ_{ion}. Doping of the active layer is related to both $\mu_{p/n}$ and μ_{ion}. This is unlike the conclusion drawn by Robinson et al. that mainly ionic movement in the intrinsic region determines the time needed to dope the active layer [22]. Rather, the doping front propagation is determined on one hand by the electron/hole transport in the doped regions and at the doping front, and on the other hand by the ion transport in the intrinsic region. Formation of a light-emitting p–n junction is observed to be linearly dependent on μ_{ion} at small values of $\mu_{ion}/\mu_{p/n,0}$, for the used parameters <10. As discussed above this time is related to ion depletion from the recombination zone. This, in turn, can only occur when the transfer of mobile anions (cations) from the n (p)-doped region to the p (n)-doped region is completed. For this to complete, the largest distance ions need to travel in a mostly symmetric device is a bit more than half the device length. A value of ~0.6 is found in the modeling shown in Fig. 4b (orange graph). For large $\mu_{ion}/\mu_{p/n,0}$, i.e. slow electronic carriers, the formation of a light-emitting p–n junction becomes limited by the meeting of the doping fronts. In this case, the ions are already depleted from the recombination region before the fronts have met, which is determined by the slow electronic charge carriers.

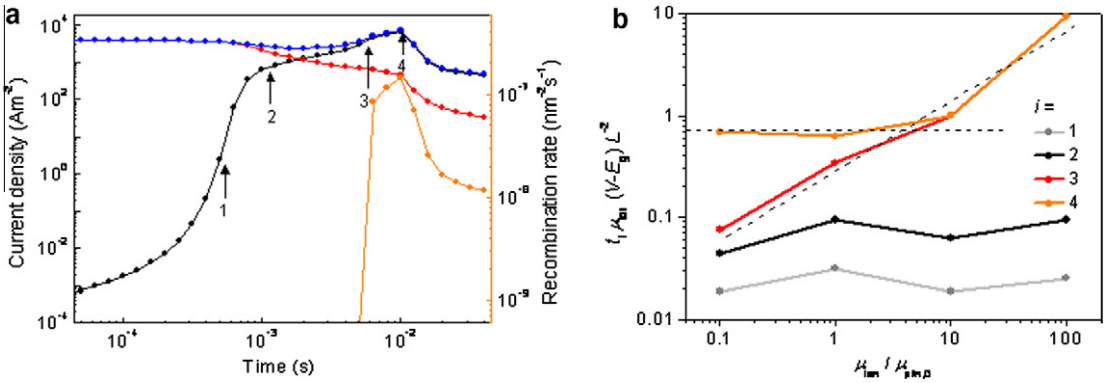

Fig. 4. Calculated transient behavior in LECs in case a doping dependent $\mu_{p/n}$ is chosen (c.f. Fig. 1b). (a) Calculated J, t and R, t characteristics in an LEC for $\mu_{ion} = 5 \times 10^{-11}$ m^2 V^{-1} s^{-1} (c.f. Fig. 2f). The blue, red, black and orange graphs represent the total current density J_{total}, the ion current density J_{ion}, the electron and hole current density $J_{p/n}$ and the recombination rate R respectively. (b) Time scale comparison for four characteristic processes in LECs for different values of $\mu_{ion}/\mu_{p/n,0}$. One, two, three, and four refer to initiation of hole injection, initiation of electron injection, front meeting and formation of a light-emitting p–n junction respectively. In (b) the dashed lines highlight the transition in behavior of the time needed for junction formation (4) around $\mu_{ion}/\mu_{p/n,0} \approx 5$. (For interpretation of the references to color in this figure legend, the reader is referred to the web version of this article.)

The transition point (in this case at $\mu_{ion}/\mu_{p/n,0} \approx 10$) at which the switch-on time in LECs becomes dependent on the doping front propagation is related to the choice of the doping dependency of $\mu_{p/n}$. In the simulations from which Fig. 4b is constructed, the doping fractions in case doping is nearly saturated lies in between 0.2 and 0.3, which can be translated to $\mu_{p/n} \approx 10 \cdot \mu_{p/n,0}$. This effective mobility in the doped regions determines the transition point. In case of a doping independent $\mu_{p/n}$, the effective mobility is equal to $\mu_{p/n}$ and the transition point is thus expected at $\mu_{ion}/\mu_{p/n,0} = 1$. This is indeed the case in our model (see Fig. F.1 in Supplementary Information).

In our previous publication [25] results on a planar ion rich LEC were published in which a significant amount of time was observed between initiation of light emission (10 s), i.e. meeting of the doping fronts, and the formation of a p–n junction (~20 s). Comparison of those results with the modeling presented here in Fig. 4b indicates that $\mu_{ion}/\mu_{p/n,0} < 10$, as the 10 s time difference proves that p–n junction formation was not limited by doping front propagation. Therefore, the switch-on time of this LEC can be used to estimate the ion mobility, as $t_{switch\text{-}on}\mu_{ion}(V_{bias} - E_g)L^{-2} \approx 0.6$ must hold. For $L = 100$ μm and $V_{bias} = 8$ V and $E_g \approx 2$ eV, the ion mobility is then estimated to be 5×10^{-11} m^2 V^{-1} s^{-1} at a temperature of 323 K. The conclusion that $\mu_{ion}/\mu_{p/n,0} < 10$ is also consistent with the discussion of Fig. 3b since in these devices accelerating doping fronts are typically observed. More particularly, from the parameter window for accelerating doping fronts it can, with some caution, be estimated that the electronic charge carrier mobility in PPV-based LECs is also of the order of 5×10^{-11} m^2 V^{-1} s^{-1}, which is surprisingly close to typical values for pure PPV derivatives [29,30]. A further comparison can be done between the experimental results on the planar ion rich LEC in Ref. [25] and the simulation results shown in Figs. 2f and 4a and Supplementary Information Fig. B.2f. First of all the potential profile evolution is similar: The potential distribution (see Supplementary Information Fig. B.2f) hardly changes during doping front propagation. Also the current response to an applied bias voltage (see Fig. 4a) is the same in both experiment and model. These results further prove that the experiment is adequately modeled.

One deviating experiment in literature is reported in which the doping fronts were found to have a constant speed [31]. Gao et al. did measurements on such an LEC, which has an inter-electrode distance of 2 mm and is biased at 200 V. Our modeling shows that in case a constant front speed is encountered, μ_{ion} must be large relative to $\mu_{p/n,0}$ (see Figs. 2g and 3a). Inspection of Fig. 4b furthermore shows that the doping process in such an LEC is not limited by the ion redistribution, but by the electronic carrier mobility.

A side-note on the mobility discussion above is that rather than a single, constant ion mobility, a range of ion mobilities is expected in actual LECs, which further may differ for anions and cations. The determined ion mobility therefore applies to the most mobile fraction of ions. This hypothesis is in agreement with the finding in Ref. [25] that the actual amount of *mobile* ions is far less than the amount of ions put into the active layer.

4. Conclusions

Numerical modeling has shown that the time needed for LECs to electrochemically dope the active layer and switch-on is dependent on a combination of the ion mobility, the electron/hole mobility, the applied bias voltage and the thickness of the active layer.

Regarding the doping process three regimes were identified, related to the mobilities of all present charge carriers. If $\mu_{ion} > \mu_{p/n}$, the active layer is doped by decelerating doping fronts sweeping the active layer, whereas if $\mu_{ion} < \mu_{p/n}$ the active layer is doped homogeneously across the complete device. Only in case a doping dependent $\mu_{p/n}$ is chosen in addition to μ_{ion} being approximately equal to $\mu_{p/n}$ in the undoped state ($\mu_{p/n,0}$), accelerating doping fronts are formed.

The switch-on time in LECs is shown to become independent of $\mu_{p/n}$ when the ratio between $\mu_{ion}/\mu_{p/n}$ becomes

small enough. For a doping independent $\mu_{p/n}$ this critical ratio is unity, whereas in case of a doping dependent $\mu_{p/n}$, $\mu_{ion} < \sim 10\ \mu_{p/n,0}$. Generally the latter occurs in planar LECs where accelerating doping fronts are often observed. This enables the extraction of the ion mobility from the switch-on time of LECs. Further experiments are required to check whether the extracted ion mobility is indeed correct.

Acknowledgements

This research is supported by the High Tech Systems and Materials (HTS&M) program of the Dutch ministry of economic affairs.

Appendix A. Supplementary data

Supplementary data associated with this article can be found, in the online version, at doi:10.1016/j.orgel.2011.07.005.

References

[1] Q.B. Pei, G. Yu, C. Zhang, Y. Yang, A.J. Heeger, Polymer light-emitting electrochemical-cells, Science 269 (1995) 1086–1088.
[2] C.W. Tang, S.A. Vanslyke, Organic electroluminescent diodes, Appl. Phys. Lett. 51 (1987) 913–915.
[3] P. Matyba, K. Maturova, M. Kemerink, N.D. Robinson, L. Edman, The dynamic organic p–n junction, Nat. Mater. 8 (2009) 672–676.
[4] S. van Reenen, P. Matyba, A. Dzwilewski, R.A.J. Janssen, L. Edman, M. Kemerink, A unifying model for the operation of light-emitting electrochemical cells, J. Am. Chem. Soc. 132 (2010) 13776–13781.
[5] D.B. Rodovsky, O.G. Reid, L.S.C. Pingree, D.S. Ginger, Concerted emission and local potentiometry of light-emitting electrochemical cells, Acs Nano. 4 (2010) 2673–2680.
[6] Q. Pei, A.J. Heeger, Operating mechanism of light-emitting electrochemical cells, Nat. Mater. 7 (2008) 167.
[7] G.G. Malliaras, J.D. Slinker, J.A. DeFranco, M.J. Jaquith, W.R. Silveira, Y.W. Zhong, J.M. Moran-Mirabal, H.G. Craighead, H.D. Abruna, J.A. Marohn, Direct measurement of the electric-field distribution in a light-emitting electrochemical cell, Nat. Mater. 6 (2007) 894–899.
[8] S. Tang, L. Edman, Quest for an appropriate electrolyte for high-performance light-emitting electrochemical cells, J. Phys. Chem. Lett. 1 (2010) 2727–2732.
[9] L. Edman, T. Wagberg, P.R. Hania, N.D. Robinson, J.H. Shin, P. Matyba, On the limited operational lifetime of light-emitting electrochemical cells, Adv. Mater. 20 (2008) 1744–1749.
[10] M. Lenes, G. Garcia-Belmonte, D. Tordera, A. Pertegas, J. Bisquert, H.J. Bolink, Operating modes of sandwiched light-emitting electrochemical cells, Adv. Funct. Mater. 21 (2011) 1581–1586.
[11] C.V. Hoven, H.P. Wang, M. Elbing, L. Garner, D. Winkelhaus, G.C. Bazan, Chemically fixed p–n heterojunctions for polymer electronics by means of covalent B–F bond formation, Nat. Mater. 9 (2010) 249–252.
[12] H.J. Bolink, R.D. Costa, A. Pertegas, E. Orti, Improving the turn-on time of light-emitting electrochemical cells without sacrificing their stability, Chem. Mater. 22 (2010) 1288–1290.
[13] R.D. Costa, E. Orti, H.J. Bolink, S. Graber, C.E. Housecroft, E.C. Constable, Efficient and long-living light-emitting electrochemical cells, Adv. Funct. Mater. 20 (2010) 1511–1520.
[14] J.F. Fang, P. Matyba, L. Edman, The design and realization of flexible, long-lived light-emitting electrochemical cells, Adv. Funct. Mater. 19 (2009) 2671–2676.
[15] S. Tang, L. Edman, On-demand photochemical stabilization of doping in light-emitting electrochemical cells, Electrochim Acta, doi:10.1016/j.electacta.2011.01.073.
[16] J. Gao, J. Dane, Visualization of electrochemical doping and light-emitting junction formation in conjugated polymer films, Appl. Phys. Lett. 84 (2004) 2778–2780.
[17] A.L. Holt, J.M. Leger, S.A. Carter, Electrochemical and optical characterization of p- and n-doped poly[2-methoxy-5-(2-ethylhexyloxy)-1,4-phenylenevinylene], J. Chem. Phys. 123 (2005) 044704.
[18] J.H. Shin, N.D. Robinson, S. Xiao, L. Edman, Polymer light-emitting electrochemical cells: doping concentration, emission-zone position, and turn-on time, Adv. Funct. Mater. 17 (2007) 1807–1813.
[19] J. Gao, J. Dane, Imaging the doping and electroluminescence in extremely large planar polymer light-emitting electrochemical cells, J. Appl. Phys. 98 (2005) 063513.
[20] D. Hohertz, J. Gao, How electrode work function affects doping and electroluminescence of polymer light-emitting electrochemical cells, Adv. Mater. 20 (2008) 3298–3302.
[21] J.F. Fang, Y.L. Yang, L. Edman, Understanding the operation of light-emitting electrochemical cells, Appl. Phys. Lett. 93 (2008) 063503.
[22] N.D. Robinson, J.H. Shin, M. Berggren, L. Edman, Doping front propagation in light-emitting electrochemical cells, Phys. Rev. B 74 (2006) 155210.
[23] N.D. Robinson, J.F. Fang, P. Matyba, L. Edman, Electrochemical doping during light emission in polymer light-emitting electrochemical cells, Phys. Rev. B 78 (2008) 245202.
[24] M. Modestov, V. Bychkov, G. Brodin, D. Valiev, M. Marklund, P. Matyba, L. Edman, Model of the electrochemical conversion of an undoped organic semiconductor film to a doped conductor film, Phys. Rev. B 81 (2010) 081203.
[25] S. van Reenen, P. Matyba, A. Dzwilewski, R.A.J. Janssen, A. Edman, M. Kemerink, Salt concentration effects in planar light-emitting electrochemical cells, Adv. Funct. Mater. 21 (2011) 1795–1802.
[26] H. Shimotani, G. Diguet, Y. Iwasa, Direct comparison of field-effect and electrochemical doping in regioregular poly(3-hexylthiophene), Appl. Phys. Lett. 86 (2005) 022104.
[27] J.C. deMello, N. Tessler, S.C. Graham, R.H. Friend, Ionic space-charge effects in polymer light-emitting diodes, Phys. Rev. B 57 (1998) 12951–12963.
[28] J. Gao, Y.F. Hu, Direct imaging and probing of the p–n junction in a planar polymer light-emitting electrochemical cell, J. Am. Chem. Soc. 133 (2011) 2227–2231.
[29] E. Lebedev, T. Dittrich, V. PetrovaKoch, S. Karg, W. Brutting, Charge carrier mobility in poly(p-phenylenevinylene) studied by the time-of-flight technique, Appl. Phys. Lett. 71 (1997) 2686–2688.
[30] E. Pinotti, A. Sassella, A. Borghesi, R. Tubino, Electrical characterization of organic semiconductors by transient current methods, Synthetic Met. 122 (2001) 169–171.
[31] J. Dane, C. Tracy, J. Gao, Direct observation of a frozen junction in polymer light-emitting electrochemical cells, Appl. Phys. Lett. 86 (2005).

for device optimization. More importantly many researches have been reported that the film morphology and carrier mobility are significantly affected by the MW of poly(3-hexylthiophene) (P3HT) [31–33]. For example, Heeger et al. found that the optimum annealing temperature for bulk heterojunction material is related to the MW of P3HT [31]. The devices made of higher MW P3HT exhibits higher performance because of the persistence conjugation length of polymer chain and the proper interconnections within bicontinuous network. However, P3HT is not the ideal polymer due to its relatively large bandgap. It is essential to obtain low band gap material so light-harvesting abilities of polymers can be enhanced to improve BHJ device efficiencies. One successful approach to low bandgap materials involved donor–acceptor (D–A) copolymers, in which electron-rich units and electron-deficient moieties are integrated into a single conjugated polymeric system. Furthermore, replacing the bridge carbon atom in cyclopentadithiophene (CPDT)-based copolymers with a silicon atom has been shown to be an efficient way to improve solar cell performance [34–36]. The silole-based polymer is found to feature better crystallinity, lower bimolecular recombination, favorable morphology and higher carrier mobility compared with its carbon counterpart. While D–A copolymers have been developed for efficient BHJ solar cells, the differences in their MW and their impact on the film morphology and the opto-electronic properties have not been thoroughly addressed. In this article, we investigated the influence of MW on various optical and physico-chemical properties of Si-PCPDTTBT:PCBM films. We have also correlated the morphology and exciton lifetime distribution for the Si-PCPDTTBT:PCBM films with various MWs. Finally, the photovoltaic performances of the devices based on the hybrids with different MWs are also presented.

2. Experimental

2.1. Material

Monomers M1 and M2 were synthesized according to a reported procedure [36], and the characterization is described as follows. The synthetic route of copolymer Si-PCPDTTBT is shown in Schemes 1, and the procedure is described as follows:

M1. Yield: 65%. ^{1}H NMR: δ 7.03 (d, 2H), 6.92 (d, 2H), 2.86 (t, 4H), 1.72 (m, 4H), 1.40–1.15 (m, 12H), 0.86 (t, 6H). EI-MS: m/z 656. M2. Yield: 92%. ^{1}H NMR: δ 7.06 (s, 2H), 1.68 (m, 2H), 1.4–1.13 (m, 16H), 0.90 (t, 6H), 0.83 (t, 6H), 0.74 (m, 4H), 0.32 (s, 18H).

2.2. General procedure of polymerzation

A solution of M1 (2.00 g, 2.68 mmol) and M2 (1.70 g, 2.68 mmol) in toluene (40 mL) was purged with Ar for 10 min and then $Pd(PPh_3)_4$ (0.150 g, 0.134 mmol) and triphenylphosphine (0.21 g, 0.80 mmol) were added. After purging with Ar for 20 min, the mixture was heated under reflux in an oil bath set at 110 °C under an Ar atmosphere. The mixture was cooled to room temperature, MeOH (100 mL) was added, and the precipitated polymer was filtered out. After Soxhlet extraction with MeOH, hexane, and $CHCl_3$, the polymer was recovered from the $CHCl_3$ phase through reprecipitation with MeOH and then dried under vacuum for 1 day. The MW of polymer was controlled by changing the reaction time, which was monitored by GPC. In this study, Si-PCPDTTBT with four different MWs was synthesized. The reaction times were 6, 10, 24, and 48 h, respectively. The detail information of the MWs for the as-prepared polymers are shown in Table 1.

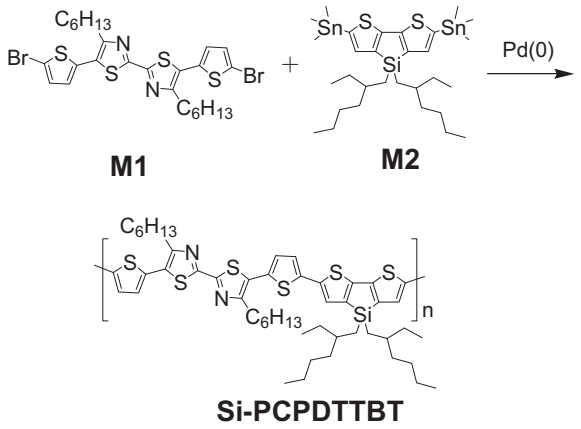

Scheme 1. Synthetic Route of Si-PCPDTTBT Copolymer.

2.3. Device fabrication

The polymer solar cells are consisted of a layer of the Si-PCPDTTBT/PCBM blend thin film sandwiched between a transparent anode (ITO) and a metal cathode. Prior to device fabrication, the ITO glasses (1.5×1.5 cm^2) were cleaned ultrasonically in detergent, deionized water, acetone, and isopropyl alcohol. After routine solvent cleaning, the substrates were treated with UV ozone for 15 min. The modified ITO surface was then obtained by spin-coating a layer of PEDOT:PSS (ca. 30 nm). Subsequently, the active layer, Si-PCPDTTBT/PCBM (1:2 w/w), was spin-coated from DCB onto the PEDOT:PSS-modified ITO surface. Finally, layers of Ca (30 nm) and Al (100 nm) were thermally evaporated under vacuum (pressure: $<6 \times 10^{-6}$ torr) through a shadow mask. The active area of the device was 0.12 cm^2. In the hole-only devices, Ca was replaced with MoO_3

Table 1
Summary of the MWs, polydispersities (PDI) and yields of Si-PCPDTTBT samples in this study.

Sample of Si-PCPDTTBT	Reaction Time (hours)	M_n[a] (kg/mol)	M_w[a] (kg/mol)	PDI	Yield (%)
Low MW	6	6.3	12.2	1.93	61
Medium MW	10	12.7	15.7	1.23	55
	24	22.9	27.3	1.19	57
High MW	48	33.6	38.9	1.15	56

[a] Molecular weights and polydispersity were measured by GPC, using THF as an eluent, polystyrene as a standard. *M*n, number average molecular weight. *M*w, weight average molecular weight.

Table 2
Summary of the transition temperature of Si-PCPDTTBT with various MWs.

Sample of Si-PCPDTTBT	T_g[a] (°C)	T_m[a] (°C)	T_c[a] (°C)	T_d[b] (°C)
Low MW	163	239	n.d.[c]	375
Medium MW	167	245	n.d.[c]	390
	165	251	227	429
High MW	166	253	234	430

[a] The T_g, T_m and T_c were measured by DSC at a heating rate of 10 °C/min.
[b] Temperature (°C) at 5% weight loss measured by TGA at a heating rate of 10 °C/min under nitrogen.
[c] No noticeable transition temperature was observed.

because its higher work function (Φ = 5.3 eV) provided a better hole injection contact for Si-PCPDTTBT/PCBM. A layer of 20 nm thick MoO_3 was thermally evaporated and then it was capped with a layer of Al (50 nm). For the electron-only devices, the PEDOT:PSS layer was replaced with $CsCO_3$ (Φ = 2.9 eV), which is an efficient electron injection layer. This layer of Cs_2CO_3 was thermally evaporated to a thickness of 2 nm. The active layers were then annealed at 130 °C for 20 min to provide the final hole- and electron-only devices.

2.4. Characteriaztion

The cell performance was tested under simulated AM 1.5 G irradiation at 100 mW cm^{-2} using a Xe lamp-based solar simulator (Thermal Oriel 1000 W). The light intensity was calibrated using a mono-silicon photodiode equipped with a Hamamatsu KG-5 color filter. The whole measurement process was performed at room temperature in a glove box filled with N_2. The absorption spectra were obtained from Jasco-V-670 UV-visible spectrophotometer. X-ray diffraction (XRD) studies were performed by Philips X'Pert/MPD. For the fluorescence measurements, the samples were excited with light (wavelength: 470 nm) from a picosecond laser (LDH-P-C-470, PicoQuant); the fluorescence lifetime signal was measured using time-correlated single photon counting (TCSPC). To map the lifetime images, the samples were scanned using an Olympus FV300 confocal optical microscope equipped with a PicoQuant PDM single photon avalanche diode detector and a PicoQuant PicoHarp 300 USB interface for TCSPC. The fluorescence signal was improved using an edge filter (REF-473.0-25, CVI). The acquisition time for each lifetime image (pixel size: 512 × 512) was 20 min. The surface morphologies of the polymer films were investigated using an atomic force microscope (Digital Instrument NS 3a controller equipped with a D3100 stage). The EQE action spectra were obtained under short-circuit conditions. The light source was a 450-W Xe lamp (Oriel Instrument, model 6266) equipped with a water-based IR filter (Oriel Instrument, model 6123NS). The light output from the monochromator (Oriel Instrument, model 74100) was focused onto the photovoltaic cell under test.

3. Results and discussion

Scheme 1 shows the chemical structure and the synthetic route of Si-PCPDTTBT. On the basis of the electron donor–acceptor concept, the strong electron–accepting

Table 3
List of electron and hole mobility of devices based on Si-PCPDTTBT:PCBM with various MWs.

Sample	Low MW	Medium MW		High MW
	6.3	12.7	22.9	33.6
μ_e (m^2 V^{-1} s^{-1})	9.7×10^{-8}	1.1×10^{-7}	1.5×10^{-7}	2.7×10^{-7}
μ_h (m^2 V^{-1} s^{-1})	4.5×10^{-8}	6.4×10^{-8}	9.6×10^{-8}	1.9×10^{-7}
μ_e/μ_h	2.2	1.7	1.6	1.4

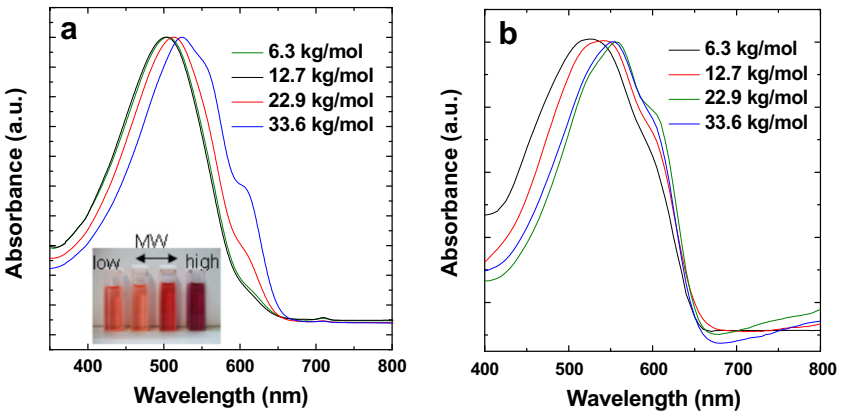

Fig. 1. Optical absorption of Si-PCPDTTBT with various MWs (a) in chlorobenzene solution, and (b) in solid films (spin-coated from chlorobenzene solution). The red-shift of the absorption indicates the larger orbital delocalization by virtue of longer conjugated polymer chains. (Inset: corresponding solution image).

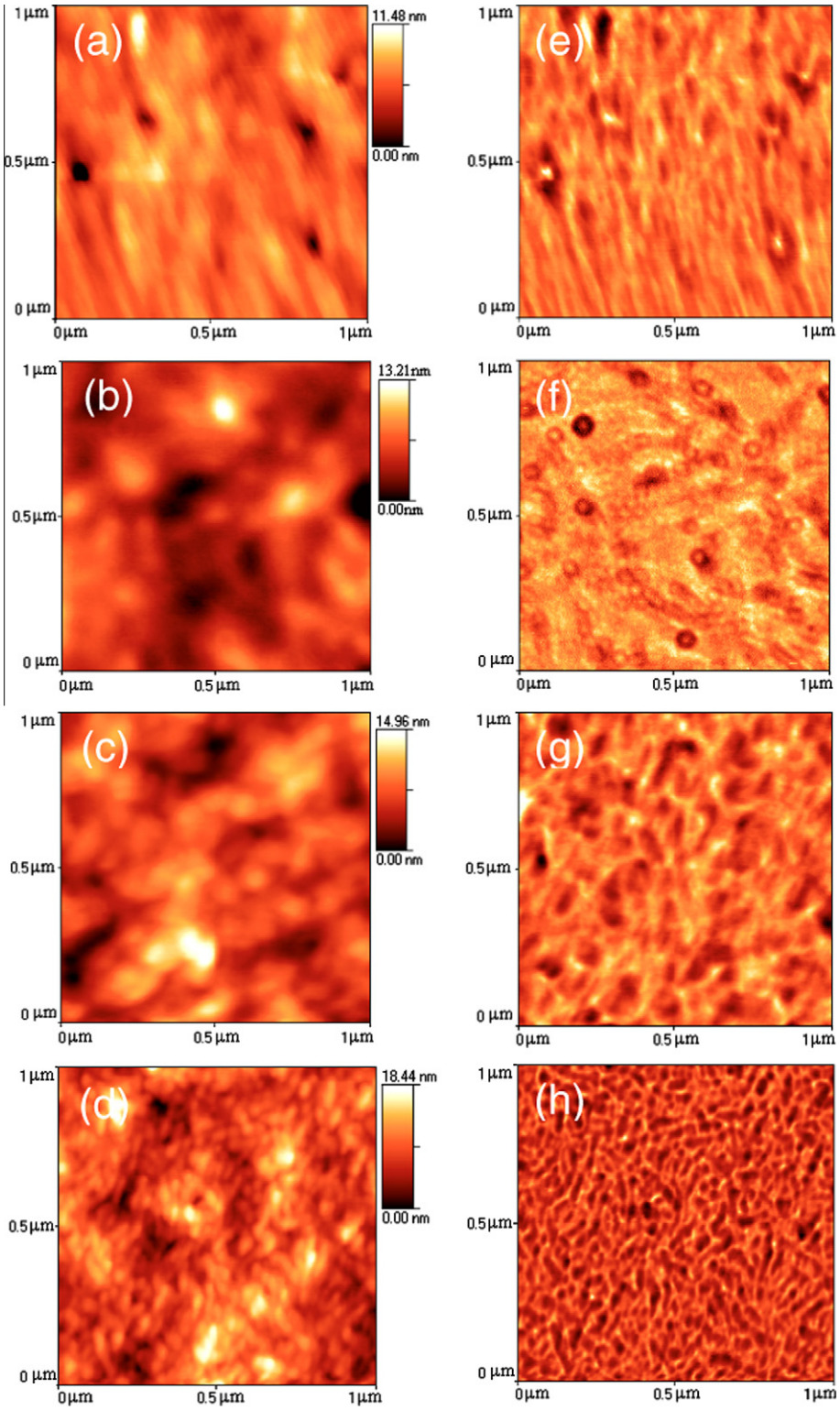

Fig. 2. The AFM images of Si-PCPDTTBT:PCBM films with various MWs for surface morphology (a) 6.3 kg/mol, (b) 12.7 kg/mol, (c) 22.9 kg/mol, (d) 33.6 kg/mol and phase images (e) 6.3 kg/mol, (f) 12.7 kg/mol, (g) 22.9 kg/mol, (h) 33.6 kg/mol.

dialkyl-bithiazole unit and electron-donating thiophene moieties were utilized to synthesize the low bandgap copolymer. Combining with the coplanar siloles, the process of self-organization of polymer into two-dimensional

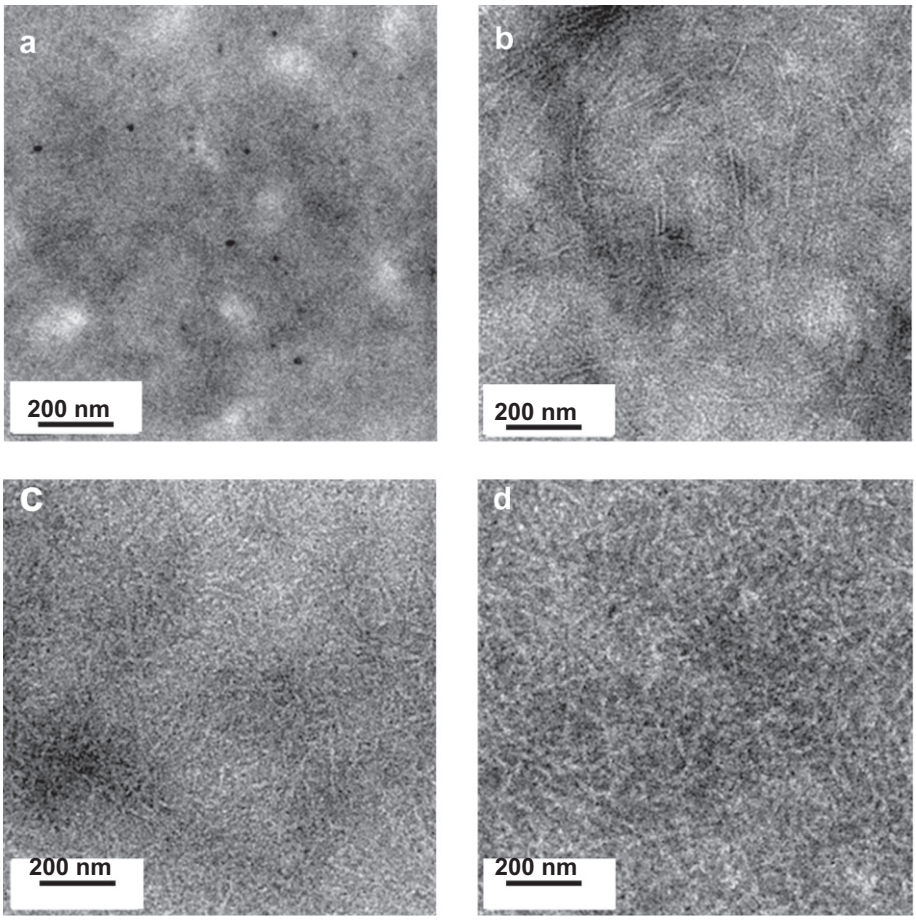

Fig. 3. TEM images of Si-PCPDTTBT:PCBM (1:1) blend films with various MWs. (a) 6.3 kg/mol, (b) 12.7 kg/mol, (c) 22.9 kg/mol, (d) 33.6 kg/mol.

(2D) sheets can be significantly enhanced by means of interchain stacking leading to an enhancement in device efficiency.

Table 1 summarizes the MWs, polydispersities (PDI) and yield of the pristine Si-PCPDTTBT samples used in this study. It should be mentioned that the solubility of Si-PCPDTTBT becomes very poor with MW larger than 33.6 kg/mol (M_n). The thermal stabilities and phase transition temperatures of Si-PCPDTTBT, including 5% weight loss temperatures (T_d), glass transition temperatures (T_g), melting temperatures (T_m), and crystallization temperatures (T_c) characterized by Thermogravimetric analyses (TGA) and differential scanning calorimetry (DSC) are summarized in Table 2. All copolymers are thermally stable up to 375–430 °C upon heating and show T_g values over 163 °C. The T_d and T_g for Si-PCPDTTBT are found to increase with increasing MWs. The increase of thermal stability with higher MW is attributed from stronger π−π interaction and polymer chain entanglement as observed in many polymer systems. In addition, the detectable melting temperatures (T_m) and crystallization temperatures (T_c) of Si-PCPDTTBT suggested that it has great potential in organic solar cells application since their high ordering capabilities can enhance the formation of phase-separated ordered nanostructures in the photovoltaic layer desirable for charge transport and separation.

As shown in the absorption spectra (Fig. 1), with the increase of Si-PCPDTTBT MW, a significant red shift of the absorption for the edge of Si-PCPDTTBT from solution (10^{-6} M in chlorobenzene), together with more pronounced vibronic absorption shoulders is observed. The result indicates that charge carriers and excitons in the higher MW Si-PCPDTTBT can delocalize over a larger extent as a result of π–π stacking and a stronger wave function overlap, and the absorbance band extend from 500 to 525 nm is attributed to a fully delocalized excitonic π–π* transition. The corresponding images for the polymer solution with various MWs are shown in the inset of Fig. 1a. On the other hand, the solid film exhibited an absorption pattern similar to that recorded in solution, except that a slight red-shift occurred in the solid state as a result of interchain association and aggregation. It is worthy to mention that the polymer with higher MWs reveal a pronounced vibronic peak. This indicates that aggregation already occurs for the high MW Si-PCPDTTBT due to the strong π–π interaction in the solution state.

Since morphology has been shown to affect mobility, efforts were made in this study to conduct a comprehensive

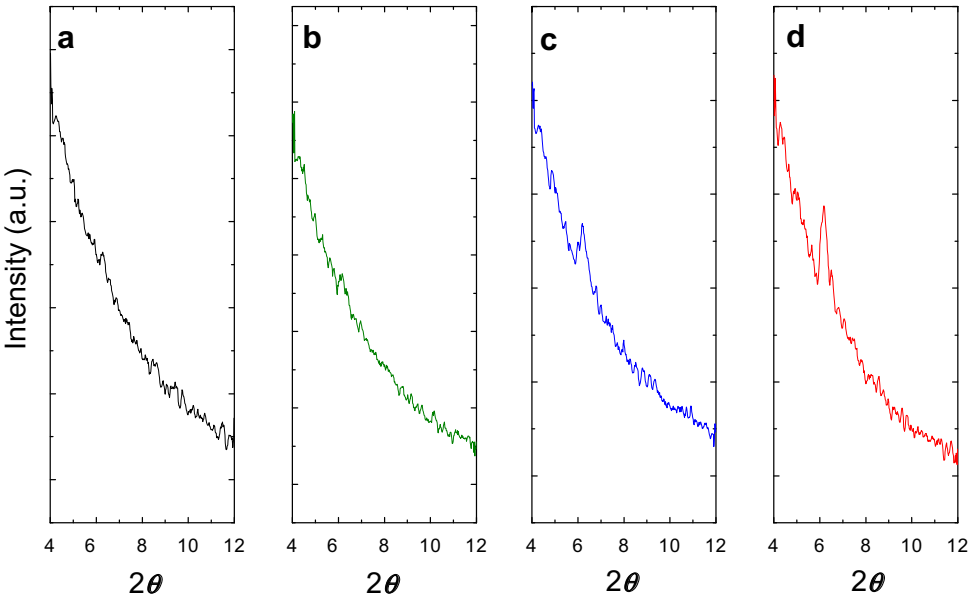

Fig. 4. XRD spectra of Si-PCPDTTBT:PCBM films with various MWs. (a) 6.3 kg/mol, (b) 12.7 kg/mol, (c) 22.9 kg/mol, (d) 33.6 kg/mol.

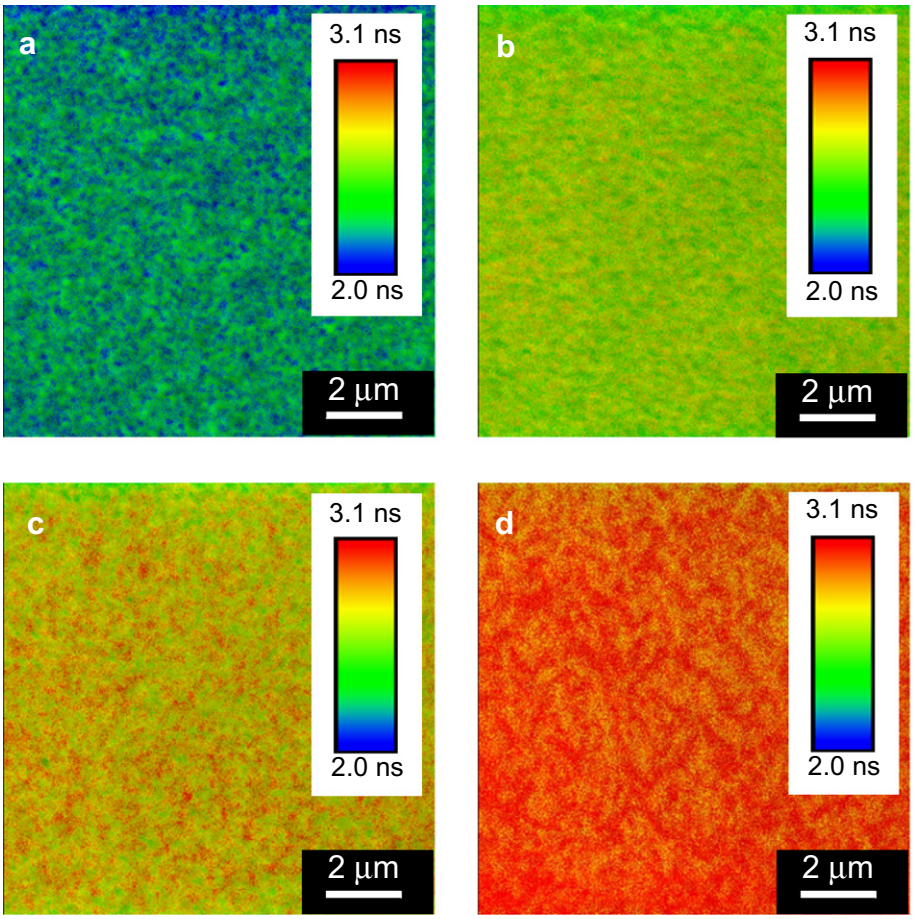

Fig. 5. Exciton lifetime images of the Si-PCPDTTBT:PCBM film with various MWs, (a) 6.3 kg/mol, (b) 12.7 kg/mol, (c) 22.9 kg/mol, (d) 33.6 kg/mol. measured after excitation at 470 nm using a picosecond laser microscope (512 × 512 pixels).

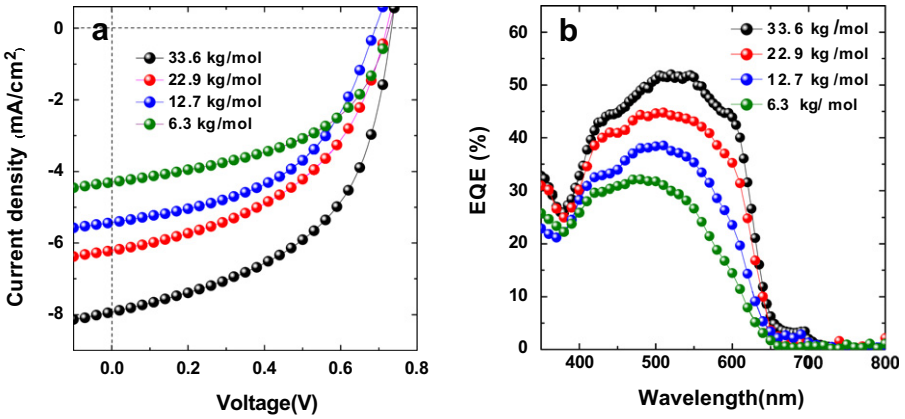

Fig. 6. (a) *J–V* curves and (b) EQE spectra of Si-PCPDTTBT:PCBM-based BHJ solar cells with various MWs.

characterization in terms of MW dependency by AFM and TEM analysis. It has been reported that P3HT with lower MW polymer chains are more able to pack into crystals forming a rod-like morphology [32]. It is interesting; however, the low MW Si-PCPDTTBT reveals very smooth morphology. This can be explained by a much more complicated structure such as Si-PCPDTTBT instead of P3HT, which prevent the polymer chains from stacking. With increasing polymer MW, Si-PCPDTTBT:PCBM films reveal rougher surface morphology with stronger crystallinity. For the 33.6 kg/mol Si-PCPDTTBT/PCBM film, the morphology exhibits coarse, chainlike features, having an average size of 30 nm, running across the surface as shown in Fig. 2d. The corresponding phase images in Fig. 2h also features many channels with a diameter of 20 nm distributed throughout the film originated from the separation between the Si-PCPDTTBT and PCBM. Because the exciton diffusion length in organic materials typically ranges from 10 to 30 nm depending on the mobility, the feature size can offer a certain degree of segregation for the two components to maintain suitable mixing for charge transport and exciton dissociation.

The MW impact on nanoscale morphology is also confirmed by TEM as shown in Fig. 3. In the TEM images, polymer nanofibers look bright and PCBM-rich regions appear dark because of the lower density of polymer crystals compared to PCBM. The TEM images are consistent with the AFM results. For the 6.3 kg/mol Si-PCPDTTBT, hardly any polymer fibers can be discerned. The TEM image of the blending films processed with higher MWs shows phase separation clearly with the appearance of interconnected fibers which are surrounded by darker fullerene-rich regions. With the increase of the polymer MWs, the amount and diameter of Si-PCPDTTBT fibers become larger and coarser. Since the J_{SC} and FF are strongly dependent on the transport properties of the networks in the BHJ film, it can be expected that, at least in part, the formation of the larger domains with wider connective cross sections within the high MW Si-PCPDTTBT network can leads to an improved device performance.

Further investigation of the crystalline nature of Si-PCPDTTBT is accomplished using XRD of polymer films as shown in Fig. 4. The low MW Si-PCPDTTBT exhibits an amorphous pattern indicating the disorder structure. Increased intensity is observed with increasing MW for the peak at $2\theta = 6.17°$, which corresponds to the layering distance, $d_{100} = 14.3$ Å, between the sheets of Si-PCPDTTBT chains associated with the plane perpendicular to their longitudinal axes. The features are in good agreement with the results of AFM and TEM images. It is known that long polymer chains are more prone to entanglement [37]. Hiorns has suggested the entanglement of P3HT may cause the alignment of conjugated segments to be more difficult to achieve, leading to disorder structure [38]. This proposal does not obviously agree with the results displayed here. For the high MW Si-PCPDTTBT, the polymer chains tend to stack and aggregate forming a preferential orientation of the polymer domains. This can be further supported by the charge mobility as shown in Table 3. The charge mobility calculated by space-charge limited current reveals that the holes mobility increases with increasing MW leading to more balanced charge mobility. It is likely that mobility could increase with MW because the closer organization of the polymer chains. Moreover, the charge carriers can travel farther along longer chains before they have to hop to another chain. The net reduction in hopping events could result in an increased mobility. In order to further investigate the optophysical properties of Si-PCPDTTBT/PCBM film with various MWs, we performed the exciton lifetime mapping using time-resolved PL measurement system combining with a confocal laser scanning microscopy [39,40]. This technique enabled us to examine the distribution of the exciton lifetimes within a wide range. Fig. 5 shows the exciton lifetime images (10×10 μm) with the corresponding statistical histograms for these samples. All the samples reveal a uniform exciton lifetime distribution throughout the films. This behavior suggests that good mixing exists between the polymer and the fullerene, leading to a more-efficient energy transfer. The average value of exciton lifetime increases from 2.3 to 3.2 ns with respect to the increase in polymer MW. The slight increase in exciton lifetime can be explained by the better crystallinity of the high MW Si-PCPDTTBT. The enhanced stacking of Si-PCPDTTBT

expels some PCBM molecules from the polymer domain, leading to demixing between the two components which impedes the efficiency of exciton dissociation. Therefore, the average value of exciton lifetime increases with high MW Si-PCPDTTBT.

Fig. 6 presents the current–voltage (J–V) curves and external quantum efficiencies (EQEs) of solar cells incorporating Si-PCPDTTBT blended with PCBM. The V_{OC} remains unchanged at about 0.71 ± 0.02 V even with different MWs of Si-PCPDTTBT. However, the J_{SC} and PCE of the devices vary significantly with polymer MWs as seen from Fig. 6a. The J_{SC} varies from as low as 4.29 mA/cm^2 (for 6.3 kg/mol Si-PCPDTTBT) to as high as 8.7 mA/cm^2 (for 33.6 kg/mol Si-PCPDTTBT). Consistent with the trend in J_{SC}, the EQE magnitude generally increases from 29.3% (6.3 kg/mol Si-PCPDTTBT) to 51.6% (33.6 kg/mol Si-PCPDTTBT). Combining 0.73 V of V_{OC} and 51.9% FF, an efficiency of 3.33% is achieved for the device based on 33.6 kg/mol Si-PCPDTTBT. The correlation between the solar cell performance and the MW of the Si-PCPDTTBT is similar to that of P3HT:PCBM system. The main difference in PCE arises from the better charge mobility and more favorable morphology. For high MW Si-PCPDTTBT, the long polymer chains tend to form the appropriate aggregation in the solution. With such partially aggregated solution, the blending of Si-PCPDTTBT and PCBM can easily produce phase separation during spin coating process to create continuous percolation pathways for charge transport.

4. Conclusion

In conclusion, we have shown the effect of MW on the performance of photovoltaic devices based on Si-PCPDTTBT:PCBM. Morphological analysis indicates that higher MW Si-PCPDTTBT tends to form stacked aggregation and produce better interconnections within the bicontinuous network which can enhance the charge transport. Based on our device performance, the aggregation of Si-PCPDTTBT is an essential process to guarantee high solar cell performance. The PCE can be enhanced from 1.54% to 3.33% for the 6.3 and 33.6 kg/mol Si-PCPDTTBT, respectively. However, the MW of Si-PCPDTTBT cannot be further increased due to the solubility problems. Thus, considering carrier mobility, materials solubility, crystallinity and morphology, the cell performance can be further improved by using mixture of Si-PCPDTTBT with different molecular weights.

Acknowledgements

The authors are grateful to the National Science Council (NSC), Taiwan (NSC 98-2221-E-001-002 and 99-2120-M-009-008-), and Academia Sinica for financial support.

References

[1] G. Yu, J. Gao, J.C. Hummelen, F. Wudl, A.J. Heeger, Science 270 (1995) 1789–1791.
[2] F. Padinger, R.S. Rittberger, N.S. Sariciftci, Adv. Funct. Mater. 13 (2003) 85–88.
[3] H. Kim, M. Shin, Y. Kim, J. Phys, Chem. C 113 (2009) 1620–1623.
[4] Y. Liu, E.N. Mills, R.J. Composto, J. Mater. Chem. 19 (2009) 2704–2709.
[5] S.S. van Bavel, E. Sourty, G. de With, S. Veenstrabd, J. Loos, J. Mater. Chem. 19 (2009) 5388–5393.
[6] J.H. Huang, C.Y. Yang, Z.Y. Ho, D. Kekuda, M.C. Wu, F.C. Chien, P. Chen, C.W. Chu, K.C. Ho, Org. Electron. 10 (2009) 27–33.
[7] H. Tang, G. Lu, L. Li, J. Li, Y. Wang, X. Yang, J. Mater. Chem. 20 (2010) 683–688.
[8] J. Peet, J.Y. Kim, N.E. Coates, W.L. Ma, D. Moses, A.J. Heeger, G.C. Bazan, Nat. Mater. 6 (2007) 497–500.
[9] H.Y. Chen, H. Yang, G. Yang, S. Sista, R. Zadoyan, G. Li, Y. Yang, J. Phys. Chem. C 113 (2009) 7946–7953.
[10] J. Liu, S. Shao, H. Wang, K. Zhao, L. Xue, X. Gao, Z. Xie, Y. Han, Org. Electron. 11 (2010) 775–783.
[11] J.H. Huang, H.Y. Wei, K.C. Huang, C.L. Chen, R.R. Wang, F.C. Chen, K.C. Ho, C.W. Chu, Energy Environ. Sci. 3 (2010) 654–658.
[12] H. Yang, Q. Song, Z. Lu, C. Guo, C. Gong, W. Hu, C.M. Li, Energy Environ. Sci. 3 (2010) 1580–1586.
[13] M. Shin, H. Kim, S. Nam, J. Park, Y. Kim, Energy Environ. Sci. 3 (2010) 1538–1543.
[14] A.W. Hains, C. Ramanan, M.D. Irwin, J. Liu, M.R. Wasielewski, T.J. Marks, A.C.S. Appl, Mater. Interfaces 2 (2010) 175–185.
[15] S.K. Hau, Y.J. Cheng, H.L. Yip, Y. Zhang, P.H. Ma, A.K.Y. Jen, ACS Appl. Mater. Interfaces 2 (2010) 1892–1902.
[16] J.H. Huang, D. Kekuda, C.W. Chu, K.C. Ho, J. Mater. Chem. 19 (2009) 3704–3712.
[17] X. Chen, J. Yang, L.Y.X.C. Haley, J. Lu, F. Zhu, K.P. Loh, Org. Electron. 11 (2010) 1942–1946.
[18] H.W. Tsai, Z. Pei, T.H. Huang, P.W. Li, Y.J. Chan, Org. Electron. 11 (2010) 1796–1801.
[19] P. de Bruyn, D.J.D. Moet, P.W.M. Blom, Org. Electron. 11 (2010) 1419–1422.
[20] G.D. Sharma, P. Suresh, J.A. Mikroyannidis, Org. Electron. 11 (2010) 731–742.
[21] Y.I. Lee, J.H. Youn, M.S. Ryu, J. Kim, H.T. Moon, J. Jang, Org. Electron. 12 (2011) 353–357.
[22] I. Sasajima, S. Uesaka, T. Kuwabara, T. Yamaguchi, K. Takahashi, Org. Electron. 12 (2011) 113–118.
[23] T. Sakurai, T. Ohashi, H. Kitazume, M. Kubota, T. Suemasu, K. Akimoto, Org. Electron. 12 (2011) 966–973.
[24] S. Wang, Z. Bian, X. Xia, C. Huang, Org. Electron. 11 (2010) 1909–1915.
[25] S. Sarkar, J.H. Culp, J.T. Whyland, M. Garvan, V. Misra, Org. Electron. 11 (2010) 1896–1900.
[26] J.H. Kim, J.H. Park, J.H. Lee, J.S. Kim, M. Sim, K. Cho, J. Mater. Chem. 20 (2010) 7398–7405.
[27] C. Müller, E. Wang, L.M. Andersson, K. Tvingstedt, Y. Zhou, M.R. Andersson, O. Inganäs, Adv. Funct. Mater. 20 (2010) 2124–2131.
[28] D.J.D. Moet, M. Lenes, J.D. Kotlarski, S.C. Veenstra, J. Sweelssen, M.M. Koetse, B. de Boer, P.W.M. Blom, Org. Electron. 10 (2009) 1275–1281.
[29] M.C. Wu, C.H. Chang, H.H. Lo, Y.S. Lin, Y.Y. Lin, W.C. Yen, W.F. Su, Y.F. Chen, C.W. Chen, J. Mater. Chem. 18 (2008) 4097–4102.
[30] M.K. Siddiki, J. Li, D. Galipeau, Q. Qiao, Energy Environ. Sci. 3 (2010) 867–883.
[31] W. Ma, J.Y. Kim, K. Lee, A.J. Heeger, Macromol. Rapid Commun. 28 (2007) 1776–1780.
[32] A.M. Ballantyne, L. Chen, J. Dane, T. Hammant, F.M. Braun, M. Heeney, W. Duffy, I. McCulloch, D.D.C. Bradley, J. Nelson, Adv. Funct. Mater. 18 (2008) 2373–2380.
[33] R.J. Kline, M.D. McGehee, E.N. Kadnikova, J. Liu, J.M.J. Fréchet, Adv. Mater. 15 (2003) 1519–1522.
[34] M.C. Scharber, M. Koppe, J. Gao, F. Cordella, M.A. Loi, P. Denk, M. Morana, H.J. Egelhaaf, K. Forberich, G. Dennler, R. Gaudiana, D. Waller, Z. Zhu, X. Shi, C.J. Brabec, Adv. Mater. 21 (2009) 1–4.
[35] H.Y. Chen, J. Hou, A.E. Hayden, H. Yang, K.N. Houk, Y. Yang, Adv. Mater. 22 (2010) 371–375.
[36] J.H. Huang, C.M. Teng, Y.S. Hsiao, F.W. Yen, P. Chen, F.C. Chang, C.W. Chu, J. Phys. Chem. C 115 (2011) 2398–2405.
[37] J.M.G. Cowie, Polymer: Chemistry and Physics of Modern Materials, 2nd. Ed., Blackie Academic & Professional, Glasgow, 1991.
[38] R.C. Hiorns, R. de Bettignies, J. Leroy, S. Bailly, M. Firon, C. Sentein, A. Khoukh, H. Preud'homme, C. Dagron-Lartigau, Adv. Funct. Mater. 16 (2006) 2263–2273.
[39] J.H. Huang, F.C. Chien, P. Chen, K.C. Ho, C.W. Chu, Anal. Chem. 82 (2010) 1669–1673.
[40] J.H. Huang, K.C. Li, F.C. Chien, Y.S. Hsiao, D. Kekuda, P. Chen, H.C. Lin, K.C. Ho, C.W. Chu, J. Phys. Chem. C 114 (2010) 9062–9069.

between the electrode and an organic layer [2,6–14], although other interfaces are also important in the inverted device structure [15].

In this paper, we demonstrate, based on the energy levels and the current density–voltage (*J–V*) characteristics of electron only devices, that the interface between an n-doped ETL (n-ETL) and an ETL is as important as the interface between the cathode and the n-ETL for efficient electron injection to an emitting layer. By properly selecting an ETM to have no energy barrier for electron injection between the n-ETL and the ETL, we could realize a high performance IBOLED with the maximum EQE of 20% and the maximum power efficiency of 80 lm/W.

2. Experimental

The inverted bottom emission OLEDs we fabricated have the structure of ITO/n-doped ETL (20 nm)/undoped ETL (30 nm)/8 wt.% Ir(ppy)$_3$ doped 4,4′-*N*,*N*′-dicarbazole-biphenyl (CBP) (15 nm)/undoped 1,1′-bis-(4-bis(4-methyl-phenyl)-amino-phenyl)-cyclohexane (TAPC) (30 nm)/8 wt.% ReO_3 doped TAPC (20 nm)/Al. The organic layers and the metal anode were successively deposited on pre-cleaned 150 nm-thick-indium tin oxide (ITO) patterned glass substrates. Three different *ETMs* of bis-4,6-(3,5-di-3-pyridylphenyl)-2-methylpyrimi-dine (B3PYMPM), 4,7-diphenyl-1,10-phenanthroline (Bphen), and 2,2′,2″-(1,3,5-benzenetriyl)tris-[1-phenyl-1H-benzimidazole] (TPBi) were selected to investigate their effects on the performance of the inverted OLEDs. Rb_2CO_3 was used as the n-dopant in the n-doped ETLs with a doping concentration of 15% for all the devices [16,17]. ReO_3 was used as the p-dopant in the devices [18–20]. The current density–voltage–luminance (*J–V–L*) characteristics of the devices were measured using a Keithley 237 semiconductor parameter analyzer and a Photo Research spectrophotometer (PR-650).

3. Results and discussion

Fig. 1 shows the *J–V–L* characteristics of the inverted OLEDs. Among the three ETMs, B3PYMPM resulted in the lowest charge injection and turn-on voltages of 1.9 V and 2.4 V, respectively. The injection voltage was defined as the voltage where the charge injection begins to rise, and the turn-on voltage was defined as the voltage at the luminance of 1 cd/m^2. The driving voltage at 1000 cd/m^2 is only 4.3 V for the device with the B3PYMPM ETL followed by 5.4 V for the BPhen ETL and 7.4 V for TPBi ETL. These facts indicate that electrons are more easily injected and transported from the bottom cathode to the light emitting layer in the B3PYMPM device than the others because the hole injection layer and the hole transport layer are the same in the three devices. It is interesting to note that the difference between the injection voltage and the turn-on voltage is very small (0.5 V) for the B3PYMPM device but it is large, i.e. about 1.5 V, for the other devices, indicating a more balanced injection of electrons and holes in the B3PYMPM device than the other devices.

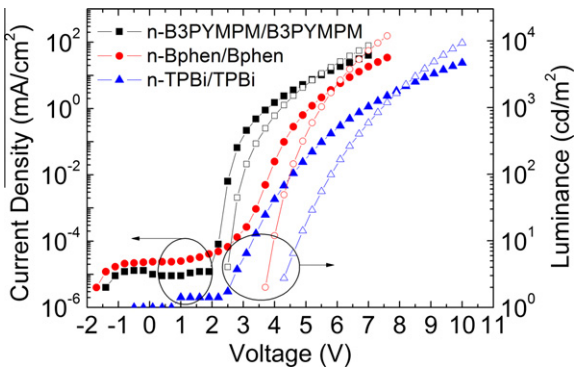

Fig. 1. The current density–voltage–luminance (*J–V–L*) characteristics of the three different inverted OLEDs.

The electron injection and transport characteristics of the devices were interpreted using two different electron only devices: (a) ITO/n-ETL (50 nm)/Al; and (b) ITO/n-ETL (20 nm)/undoped ETL (30 nm)/Al. The three different ETMs were used as the ETLs and the doping concentration was 15% in all the devices. Negative bias was applied on the ITO electrode for the electron injection from ITO to the ETLs. Fig. 2 shows the *J–V* characteristics of the devices. It is very interesting to note that the *J–V characteristics* of the electron only devices with the structure (a) are not consistent with the *J–V* characteristics of the IBOLEDs. In the electron only devices, the BPhen device shows the highest current among the three devices followed by the B3PYMPM and the TPBi devices. In the OLEDs, however, the B3PYMPM device showed the higher current and *luminance* in the low voltage region than the BPhen device.

The difference can be understood using the electron only devices with the structure (b). Insertion of the intrinsic ETL between the n-*ETL* and the Al electrode in the electron only devices modified the *J–V* characteristics significantly as shown in Fig. 2. It lowers the current density by orders of magnitude in low voltage (Ohmic current) region. Also, all the *J–V* curves showed a transition from the Ohmic current where *J* is linearly proportional to applied voltage to the trap charge limited current (TCLC).

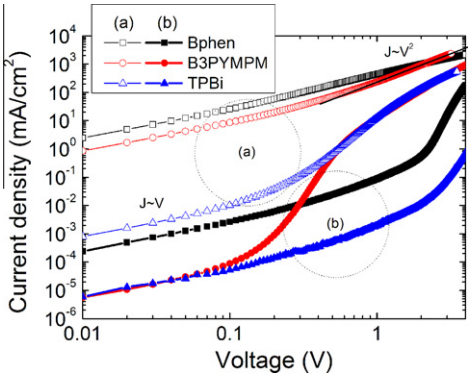

Fig. 2. Current density–voltage characteristics of electron-only devices with the inverted structures of (a) ITO/Rb_2CO_3 doped ETL (50 m, 15 wt.%)/Al (open symbol) or (b) ITO/Rb_2CO_3 doped ETL (20 m, 15 wt.%)/undoped ETL (30 nm)/Al (solid symbol).

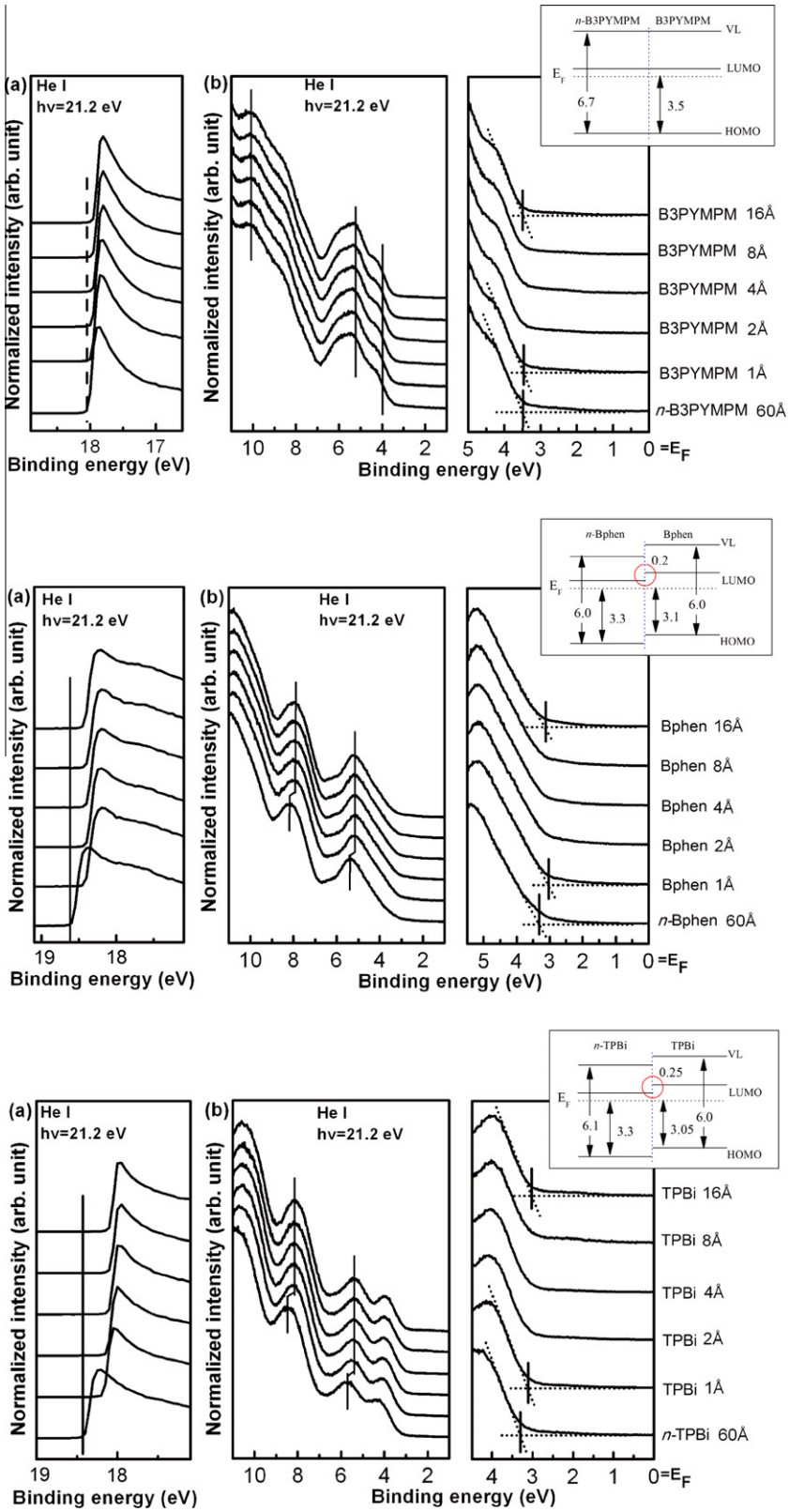

Fig. 3. UPS spectra near (a) the onset and (b) the valence band region of (1) ITO/n-B3PYMPM/B3PYMPM, (2) ITO/n-Bphen/Bphen, and (3) ITO/n-TPBi/TPBi structures. The insets show the resulting energy level diagrams and all binding energies are referenced to the Fermi level (E_F) of ITO. Vertical lines address the position of featured states. n-Doped ETL is gradually deposited on ITO followed by the deposition of an undoped ETM on the n-doped ETL.

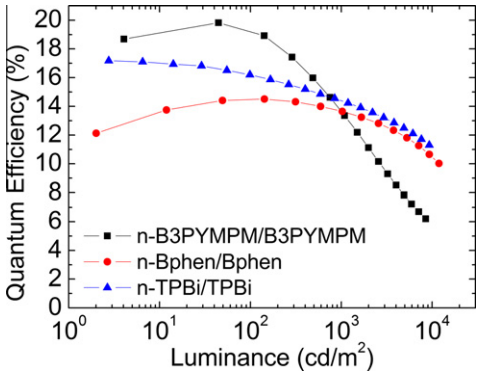

Fig. 4. External quantum efficiencies (EQEs) vs. luminance of three-different inverted OLEDs.

Interestingly enough, the B3PYMPM layer exhibited the transition at a much lower voltage than the other two materials. The current density in the B3PYMPM based electron only device dramatically increases as the voltage increases over 0.1 V. This fact suggests that the barrier height for electron injection from the n-B3PYMPM layer to the undoped B3PYMPM layer is lower than for other materials.

The injection characteristics and the energy band alignment at the interfaces of the devices were further investigated by ultraviolet photoelectron spectroscopy (UPS). UPS measurements were carried out with He I (21.2 eV) and He II (40.8 eV) as excitation sources at a base pressure at 10^{-10} Torr. The detailed experimental procedures were described in the previous reports [21,22]. Fig. 3-1–3 shows the evolutions of UPS spectra near (a) the onset and (b) the valence band region during junction formation between undoped ETLs and n-doped ETLs. All binding energies are referenced to the Fermi level (E_F) of ITO. The vacuum level (VL) shift and highest occupied molecular orbital (HOMO) level position can be analyzed with increment of thickness of the organic materials from the figures, and they are indicated by vertical lines, respectively. The position of HOMO is determined by interpolating the shoulder of HOMO signal and background of the spectra. Fig. 3-1 shows little change in the onset spectra (a) and the valence band spectra (b) when pristine B3PYMPM is deposited on n-doped B3PYMPM, indicating that there is no interface dipole and HOMO offset between n-doped B3PYMPM and pristine B3PYMPM. In contrast, however, Bphen and TPBi exhibit the shift of 0.2 and 0.25 eV toward the lower binding energy, respectively, both in the vacuum level and the HOMO level between the n-doped and the undoped layers as shown in Fig. 3-2 and 3. It is interesting to note that the shifts are abrupt at the junctions, implying the existence of interface dipole.

The energy level diagrams of the ITO/n-ETL/ETL structure extracted from the UPS spectra for the three ETMs are displayed in the insets of Fig. 3-1–3. Lowest unoccupied molecular orbital (LUMO) energy levels are included in the diagrams by adding the optical band gap of the materials obtained from the lowest energy absorption edge of the UV–Vis absorption spectra to the HOMO levels. Since the optical band gap of a doped organic film is similar to that of the pristine film [23], the complete energy level diagrams were constructed in both n-doped ETL and undoped ETL regions using the optical band gap of 3.6 eV for B3PYMPM [24], 3.4 eV for Bphen [25], and 3.5 eV for TPBi [26]. The energy barriers for electron injection between ITO and the n-ETLs are 0.1 eV for B3PYMPM and Bphen, and 0.2 eV for TPBi, respectively. All the devices have relatively low energy barriers because of the doping effect of Rb_2CO_3 [16,17]. However, the energy barriers between the n-ETL and the ETL are significantly different from each other. B3PYMPM showed no energy barrier while the energy barrier in Bphen was 0.2 eV, and that in TPBi was 0.25 eV. These results are consistent with the *J–V* characteristics of the IBOLEDs and the electron only devices where the lowest injection and turn on voltage (Fig. 1) and the lowest transition voltage (Fig. 2) were observed in the devices with B3PYMPM ETL. The current density of the electron only device with the homo-junction of n-B3PYMPM and B3PYMPM dramatically increases at the lowest voltage about 0.1 V as shown in Fig. 2, resulting from the lowest electron injection barrier at the interface of the homo-junction among three different systems.

The energy barrier between n-ETL and ETL significantly influences the performance of the inverted OLEDs as shown in Fig. 4. The B3PYMPM based device exhibited the maximum external quantum efficiency of 19.8% (at 45 cd/m^2) which is the highest efficiency reported up to now in the IBOLEDs to the best of our knowledge. It is more than a 30% increase from the previous best efficiency of 15% [14]. The maximum power efficiency (η_{power}) of the device with the B3PYMPM ETL is very high with the value of 79.8 lm/W, and it is 1.8 times higher than that of 42.7 lm/W for TPBi ETL and 37.3 lm/W for Bphen ETL as summarized in Table 1. However, the η_{power} of the device with the B3PYMPM rapidly decreases after 100 cd/m^2, and finally reached 33.3 lm/W at 1000 cd/m^2. It is just 1.2 times higher than that of 27.2 lm/W for the device with Bphen ETL, indicating that roll off in the device with B3PYMPM is much larger than the other devices due to the formation of an exciplex observed in the emission spectrum of the device at high luminance (not shown).

Table 1
Characteristics of the IBOLEDs with three different ETMs.

ETM	$V_{Injection}$	V_{1cd/m^2}	EQE (%)			η_{power} (lm/W)	
			Max.	@ 100 cd/m^2	@ 1000 cd/m^2	Max.	@ 1000 cd/m^2
B3PYMPM	1.9 V	2.4 V	19.8	19.2	13.5	79.8	33.3
Bphen	2.2 V	3.6 V	14.2	14.5	13.6	37.3	27.2
TPBi	2.4 V	4.0 V	17.1	16.1	14.3	42.7	21.2

4. Conclusion

In summary, we developed a high performance inverted OLED and investigated the effect of the n-ETL/ETL interface on the performance of inverted OLEDs. Among the three ETMs, B3PYMPM resulted in the lowest injection and turn-on voltages of 1.9, and 2.4 V, respectively, and the highest maximum EQE of 19.8% at low voltage. UPS measurements showed that there is no energy barrier for electron injection between n-B3PYMPM and B3PYMPM, while Bphen and TPBi have energy barriers of 0.2 and 0.25 eV, respectively. As a result, the electron only device exhibited a large increase in current at a much lower voltage than the other two materials. The energy barrier between n-ETL and ETL is one of the most important factors for high performance inverted OLEDs.

Acknowledgement

This work was supported by the Industrial strategic technology development program [10035225, Development of core technology for high performance AMOLED on plastic] funded by MKE/KEIT.

References

[1] C.C. Wu, C.W. Chen, C.L. Lin, C.J. Yang, J. Disp. Technol. 01 (2005) 248.
[2] T.-Y. Chu, S.-Y. Chen, J.-F. Chen, C.H. Chen, Jpn. J. Appl. Phys. 45 (2006) 4948.
[3] X. Zhou, M. Pfeiffer, J.S. Huang, J.B. Nimoth, D.S. Qin, A. Werner, J. Drechsel, B. Maenning, K. Leo, Appl. Phys. Lett. 81 (2002) 922.
[4] J. Meyer, P. Görrn, S. Hamwi, H.-H. Johannes, T. Riedl, W. Kowalsky, Appl. Phys. Lett. 93 (2008) 073308.
[5] T.-Y. Chu, J.-F. Chen, S.-Y. Chen, C.-J. Chen, C.H. Chen, Appl. Phys. Lett. 89 (2006) 053503.
[6] F. Wang, T. Xiong, X. Qiao, D. Ma, Org. Electron. 10 (2009) 266.
[7] P.-S. Wang, I.-W. Wu, C.-I. Wu, J. Appl. Phys. 108 (2010) 103714.
[8] C. Yun, H. Cho, H. Kang, Y.M. Lee, Y. Park, S. Yoo, Appl. Phys. Lett. 95 (2009) 053301.
[9] J. Hou, J. Wu, Z. Xie, L. Wang, Appl. Phys. Lett. 95 (2009) 203508.
[10] H. Choi, S. Kim, W. Kim, K. Hong, J. Lee, J. Appl. Phys. 100 (2006) 064106.
[11] H. Lee, I. Park, J. Kwak, D.Y. Yoon, C. Lee, Appl. Phys. Lett. 96 (2010) 153306.
[12] S.Y. Ryu, C.H. Lee, I.S. Oh, S.Y. Song, K.H. Hwang, H.S. Hwang, M.H. Han, B.H. Hwang, H.K. Baik, Y.S. Kim, J.Y. Lee, Electrochem. Solid-State Lett. 13 (2010) J43.
[13] Q. Wang, Z. Deng, D. Ma, Opt. Express 17 (2009) 17269.
[14] M. Thomschke, S. Hofmann, S. Olthof, M. Anderson, H. Kleemann, M. Schober, B. Lüssem, K. Leo, Appl. Phys. Lett. 98 (2011) 083304.
[15] S. Braun, M.P. de Jong, W. Osikowicz, W.R. Salaneck, Appl. Phys. Lett. 91 (2007) 202108.
[16] D.-S. Leem, S.-Y. Kim, J.-J. Kim, M.-H. Chen, C.-I. Wu, Electrochem. Solid-State Lett. 12 (2009) J8.
[17] M.-H. Chen, Y.-H. Chen, C.-T. Lin, G.-R. Lee, C.-I. Wu, D.-S. Leem, J.-J. Kim, T.-W. Pi, J. Appl. Phys. 105 (2009) 113714.
[18] D.-S. Leem, H.-D. Park, J.-W. Kang, J.-H. Lee, J.W. Kim, J.-J. Kim, Appl. Phys. Lett. 91 (2007) 011113.
[19] J.-H. Lee, D.-S. Leem, H.-J. Kim, J.-J. Kim, Appl. Phys. Lett. 94 (2009) 123306.
[20] J.-H. Lee, D.-S. Leem, J.-J. Kim, Org. Electron. 11 (2010) 486.
[21] C.-I. Wu, C.-T. Lin, Y.-H. Chen, M.-H. Chen, Y.-J. Lu, C.-C. Wu, Appl. Phys. Lett. 88 (2006) 152104.
[22] C.-I. Wu, G.-R. Lee, T.-W. Pi, Appl. Phys. Lett. 87 (2005) 212108.
[23] M.Y. Chan, S.L. Lai, K.M. Lau, C.S. Lee, S.T. Lee, Appl. Phys. Lett. 89 (2006) 163515.
[24] D. Tanaka, H. Sasabe, Y.-J. Li, S.-J. Su, T. Takeda, and J. Kido, Jpn. J. Appl. Phys., Part 2 46, L10 (2007).
[25] D.-S. Leem, S.O. Jung, S.-O. Kim, J.-W. Park, J.W. Kim, Y.-S. Park, Y.-H. Kim, S.-K. Kwon, J.-J. Kim, J. Mater. Chem. 19 (46) (2009) 8824–8828.
[26] Z.Q. Gao, C.S. Lee, I. Bello, S.T. Lee, Appl. Phys. Lett. 74 (1999) 865.

polythiophene OFETs annealed in solvent vapors exhibit higher μ_{FET} compared to virgin samples [13].

Obtaining polycrystalline or amorphous molecular films is possible with a variety of deposition methods described in the literature. Spin coating, drop casting and vacuum evaporation are chosen most often [17] but one should also turn attention to spray coating – a method very convenient for cost-efficient large scale production and appropriate for a great number of materials [18–21]. The spray deposition has been applied in fabrication of organic OFETs [19–21], solar cells [18,22], light emitting diodes [23], and for electrode deposition [24]. Being a fast and simple technique for large-area application, the spray coating technique has nevertheless an important drawback: the homogeneity of the layers so obtained is inferior to that of layers fabricated by spin coating.

Three regimes of spray coating can be distinguished: wet, intermediate and dry [19,25]. In the wet regime, the solution flow is high and nozzle-substrate distance is short enough to avoid drying of solution droplets before reaching the substrate. This results in formation of a wet layer of polymer on the substrate. In the dry regime, when the nozzle-substrate distance is long, the solvent evaporates before reaching the sample and a polymer powder is cast on the substrate. The intermediate regime seems to be most suitable for the deposition of organic thin films. In this case wet droplets reach the substrate surface but they get dry before a next droplet accesses the film. The thickness can be easily controlled in this regime by adjusting the spraying time. Deposition parameters: temperature, solvent volatility, geometry of spraying system, nozzle speed and diameter, flow of solution may be adjusted to obtain required type of spraying.

In this work, we present results of a comparative study of spray and spin coated P3HT films deposited from fresh and aged solutions, acting as active layers of OFETs. Our main interest was the effect of the deposition technique and of the solution used on the morphology, and optical and electrical properties of the films.

2. Experimental

Regioregular P3HT was purchased from Ossila Ltd. (electronic grade, M_W = 65.5 kDa, regioregularity 96.6%). Chloroform solutions of P3HT (10 mg/ml), either freshly made or aged for 2 months, were used for thin film deposition. During the aging period, the solutions were kept in tightly closed vessels at ambient temperature. The films of P3HT were deposited by spin coating or by spray coating in ambient air. The spin coated samples were deposited at 900 rpm. For the spray coating, we used the Badger airbrush spray gun, the nozzle – substrate distance being controlled manually. We exploited the intermediate regime of spraying (a wet droplet comes to the substrate surface, getting dry before the next droplet reaches the film), claimed to be optimum for homogeneity of the films [19,25]. The following working parameters were employed: the nozzle – substrate distance amounted to (12 ± 2) cm, the total spraying time was equal to (5 ± 1) s, the deposition was carried out at ambient atmosphere, at room temperature ((23 ± 2) °C). The substrate was also kept at room temperature.

Four groups of samples (spin coated from fresh solution, spin coated from aged solution, spray coated from fresh solution, spray coated from aged solution) were compared.

The surface morphology of P3HT films was investigated using an atomic force microscope (AFM, NanoScope V, Veeco). AFM was also used for determination of film thicknesses. Absorption spectra of the films deposited on quartz substrates as well as of the solutions were measured with Perkin Elmer Lambda 20 UV–Vis spectrophotometer.

Silicon(n+)/SiO_2 wafers with deposited gold interdigital electrodes (purchased from Fraunhofer Institute for Photonic Microsystems, Dresden, Germany) were used as substrates for OFETs (Fig.1). The SiO_2 layer was 230 nm thick, the thicknesses of gold electrodes amounted to 30 nm (with additional 10 nm of ITO underneath). The length, L, and width of the FET channel, W, amounted to 10 μm and 1 cm, respectively. The surface capacitance of the insulator, C, was equal to 15 nF/cm^2.

The electrical characteristics were measured using a PC controlled system consisting of two Keithley 6517 electrometers, both capable of sourcing a dc voltage to source and gate electrodes. The experiments were performed in vacuum (p < 3 Pa).

The mobilities of charge carriers, μ_{FET}, have been determined from current–voltage characteristics measured in OFETs with active P3HT layers, fabricated according to each of the four procedures mentioned above (spin and spray casting, fresh and aged solutions). Over 15 transistors of each type of samples were employed in order to obtain more reliable data minimizing accidental errors. The FET mobilities have been calculated from the transfer current–voltage characteristics in the saturation regime employing the equation [26]:

$$I_{SD} = \mu_{FET}\frac{WC}{2L}(U_G - U_T)^2, \quad (1)$$

I_{SD} standing for the source–drain current, and U_G and U_T being gate and threshold voltages, respectively.

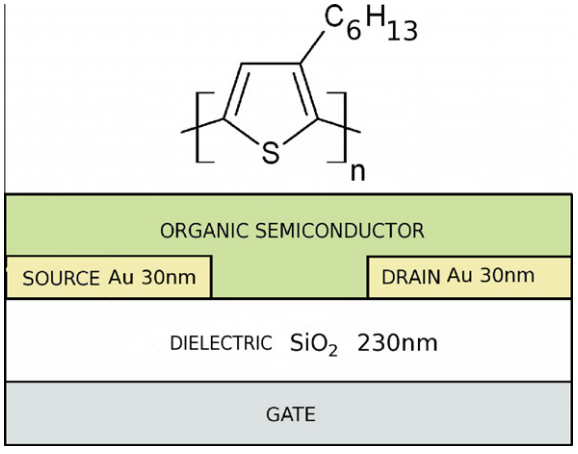

Fig. 1. Schematic representation of the structures under study. The chemical formula of P3HT is given on the top of the scheme.

3. Results and discussion

P3HT solutions, stored for a sufficiently long time, undergo aging, the process manifesting itself in changes of color and consistence. Freshly made chloroform solutions were clear orange-reddish liquids of low viscosity; after 2 months of aging the solutions became opaque, gel-like and dark brown. It should be mentioned that the rate of the process depends on solvent used: aging of the chloroform solution of P3HT occurs much slower than of solutions in other solvents (e.g., toluene or xylene). The difference can be rationalized taking into account a better solubility of P3HT in chloroform compared to that in other solvents. The difference in solubilities can be expressed by respective differences in their solubility parameters [9,27] ($\delta_{P3HT} = 19.27\ J^{0.5}\ cm^{-1.5}$; $\delta_{P3HT} - \delta_{chloroform} = 0.31\ J^{0.5}\ cm^{-1.5}$) compared to the solubility parameters of toluene ($\delta_{P3HT} - \delta_{toluene} = 1.00\ J^{0.5}\ cm^{-1.5}$) or xylene ($\delta_{P3HT} - \delta_{xylene} = 1.32\ J^{0.5}\ cm^{-1.5}$). Admixture of a solvent which does not dissolve P3HT (for example, anisole [3,28]) speeds up the aging of the solution to a few days instead of months. In this work, however, neat chloroform solutions of P3HT were used because of the high values of μ_{FET} observed in OFETs deposited from chloroform [8].

Surfaces of spin coated films were reasonably smooth; their thicknesses, measured by AFM, amounted to (130 ± 10) nm. The surfaces of the spray coated films appeared quite rough, the thicknesses of individual samples varying locally between 70 and 200 nm. It is believed, however, that the surface roughness of the sprayed films affects the quality of the organic films near the semiconductor–insulator interface to a lesser degree [20] since the channel thickness in OFETs is limited to a few nm close to the interface. Thus any inhomogeneity above this limit is not expected to matter in performance of bottom contact FETs.

AFM images of surfaces of the studied P3HT films are presented in Fig. 2. The surfaces of sprayed films appear highly nonuniform, with small areas but also with abundance of regions containing pinholes, lumps and craters. Similar irregularities were also observed earlier in sprayed films of P3HT [19].

The morphology of films fabricated using freshly made chloroform solutions of P3HT was found dramatically different from those fabricated from aged solutions. The difference is demonstrated on AFM images (Fig. 2) showing nanofeatures on the surface of the films. The films fabricated from fresh solution did not exhibit any specific features on the surfaces (Fig.2, top images) whereas nanofibers are clearly visible in the films deposited from aged solutions (Fig.2, bottom images). A particularly high concentration of the nanofibers can be observed in the spin coated films, their length reaching a few μm (Fig. 2, left bottom image). The nanofibers on the surfaces of the spray coated films (Fig. 2, right bottom image) appear less discernible compared to the spin coated ones. The nanofiber width amounts to ca. 40 nm regardless the deposition technique applied.

The difference between the lengths of nanofibers in spin- and spray-coated films may be explained by analyzing technological aspects of the film formation. In the spin coated films, the nanofibers are extended, nearly parallel to the sample surfaces and oriented to some degree by the centrifugal force acting on them during the deposition (*vide infra*) whereas one cannot notice any privileged orientation in the spray coated films.

A further insight into the process of formation of the nanofibers can be obtained from the analysis of spectra of the solutions and thin films in the visible region. The spectra shown in Figs. 3a and 4 exhibit distinct differences between freshly made and aged solutions, as well as between films fabricated from these solutions. The absorption spectra of fresh chloroform solution of P3HT (concentration amounting to 0.5 mg/ml) exhibit a maximum at 457 nm (Fig. 3a, curve 1), typical of solutions of non-aggregated polythiophene [3,9]. Increasing concentration of the polymer results in appearance of a new band peaking at 610 nm (Fig. 3a, curves 2 and 3). The latter band appears more pronounced in the spectra of the aged solution (curves 4–6); one can also identify another band peaking at 553 nm as well as a small spectral feature around 510 nm (Fig. 3a, curve 4). These bands have been assigned to an electronic transition and its vibrational satellites in the ordered P3HT [9].

The process of aggregation of P3HT in chloroform solutions was followed by monitoring the temporal evolution of the 610 nm peak in the solutions of the lowest and the highest concentrations used in our experiments (0.5 and 10 mg/cm^3, respectively). Within the time span of the experiment (6 days), we noticed a continuous increase of the intensity, its rate depending on the concentration of the solution. The results are shown in Fig. 3b. The rates of the process (processes) responsible for the build-up of the peak strongly depend on the concentration of the solution; in order to place the temporal dependencies for both concentrations on a common diagram, we adopted an auxiliary variable z, linearly dependent on the absorbance at 610 nm (A) and defined as

$$z = \frac{A(t) - A(t_o)}{c^2}, \tag{2}$$

where t_o is the time of the start of the experiment, and c is the concentration of the solution. It should be stressed, however, that the linear courses of the increase of the peak height do not mean that the kinetic process responsible for the changes be of the order 0; it rather shows that our measurements cover the initial period only. The process (processes) occurring in the solutions should result in an equilibrium established beyond the time scale of the present experiment. The slopes of the lines displayed in Fig. 3b ($(1/c^2)(dA/dt)$) do not differ much thus suggesting that the process may be governed by the second order kinetics. Hence, the rate of formation of the fibers should rapidly increase with the concentration as was indeed found in our experiments. The time necessary to attain the equilibrium in the experiments reported in this paper (P3HT in chloroform solutions) is of the order of weeks/months. It is worth noting that the aged solutions, stored over the period of 9 months are quite stable: their spectra were found essentially identical with those taken after 2 months of aging. Finally, it should be stressed that the rate of nanofiber

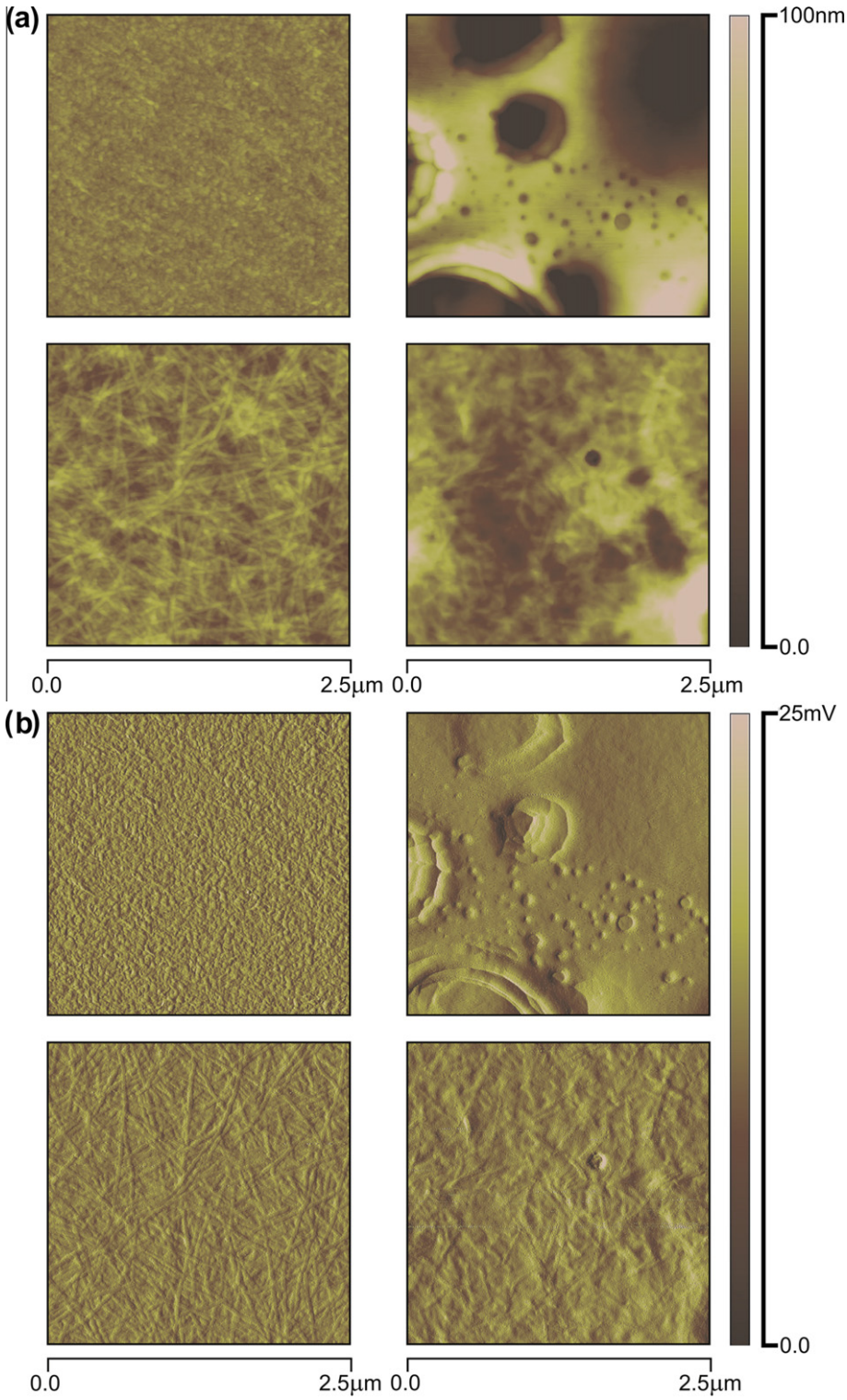

Fig. 2. AFM images of surface morphologies of spin coated (left side) and spray coated (right side) P3HT films deposited from fresh (top) and aged (bottom) solutions: (a) heights (amplitude signals); (b) amplitude error signals.

formation can be substantially increased by using another solvent or a suitable mixture of solvents [9,10].

The peaks characteristic of nanofibers are dominating features in the spectra of P3HT films shown in Fig. 4a.

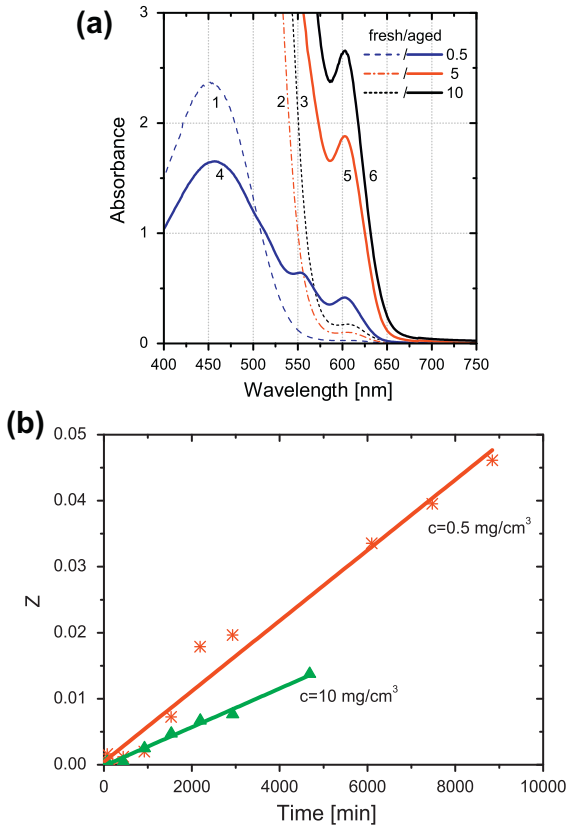

Fig. 3. (a) Absorption spectra of fresh (curves 1–3) and aged (curves 4–6) solutions of P3HT. The concentrations amount to 0.5 mg/ml (curves 1 and 4), 5 mg/ml (curves 2 and 5), and 10 mg/ml (curves 3 and 6). (b) Temporal evolution of the 610 nm peak. The concentration of the solution amounted to 0.5 mg/cm^3 (asterisks) and 10 mg/cm^3 (triangles). The parameter z, linearly dependent on the absorbance, has been defined in the text.

The spectra of the films fabricated in various conditions are similar in their general appearance but different in details; for example, the absorbance at the 610 nm peak in films deposited from fresh solutions is lower than that in spectra of the films made of aged solutions. For a more detailed analysis, the spectra were deconvoluted into 6 Gaussian peaks (cf. Fig. 4b and Table 1). The first five peaks, with narrow halfwidths (0.056–0.085 eV), can be attributed to electronic transitions in ordered (π-stacked) P3HT aggregates, whereas the broad component with the halfwidth amounting to 0.36–0.44 eV, is due to absorption in non-aggregated P3HT. It should be noted that the energies of the deconvoluted peaks come reasonably close to the values reported by Morfa et al. [29] (see Table 1).

An interesting conclusion can be drawn from a comparison of the heights of the deconvoluted peaks (cf. Table 1). The heights of the peaks associated with the P3HT aggregates are apparently more pronounced in the spectra of the films deposited from aged solutions. On average, the amplitudes of the five narrow peaks are 8% higher in the spray coated films and as much as 16% higher in spin coated ones. One may relate this result to the presence of nanoaggregates of P3HT in the samples, their concentration being higher in samples deposited from the aged solutions, and particularly high in spin-coated ones.

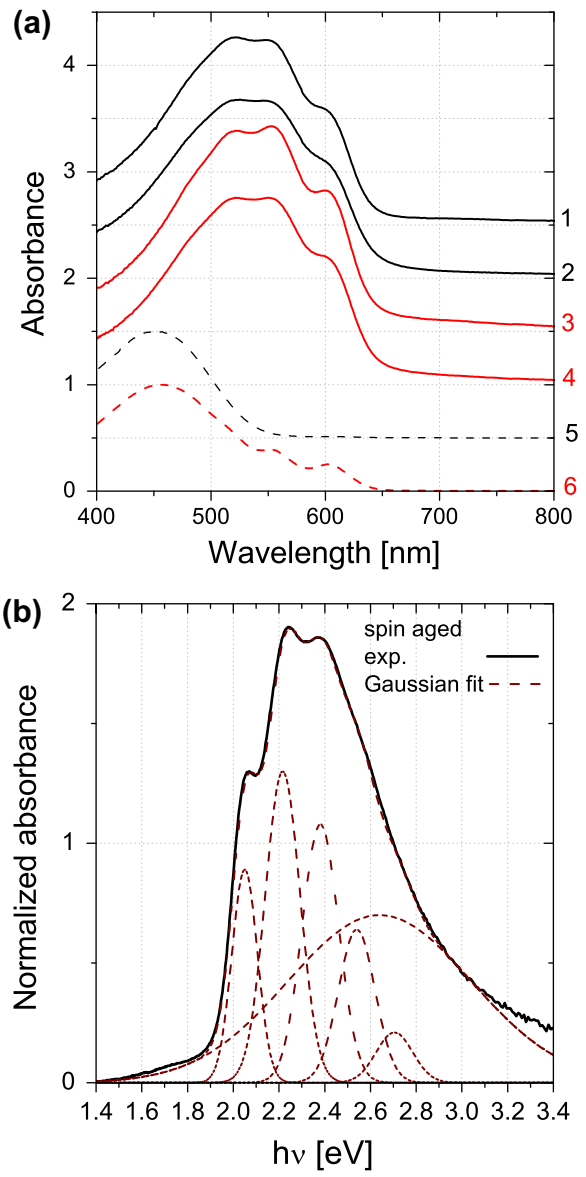

Fig. 4. (a) Absorption spectra of spin coated (curves 1 and 3) and spray coated (curves 2 and 4) films fabricated from fresh (curves 1 and 2) and aged (curves 3 and 4) solutions. Thicknesses of the films ranged from 120 to 140 nm. Curves 5 and 6 are spectra of the fresh and aged solutions, respectively. All spectra have been normalized at 457 nm and vertically displaced. (b) Absorption spectrum of a spin coated film deposited from the aged solution, fitted with 6 Gaussian curves. Solid line – experimental curve; dashed lines – deconvoluted Gaussian bands.

Aiming at elucidating a possible effect of presence and orientation of nanofibers on transport of charge carriers, we determined the carrier mobilities in OFETs fabricated using the four methods of deposition mentioned in the preceding section. Examples of output and transfer current–voltage characteristics of the studied OFETs are shown in Fig. 5a and b, respectively. The characteristics were measured for gate and source-drain voltages ranging

Table 1
Energies and heights of peaks obtained after deconvolution of absorption spectra of P3HT films. Energies of peaks reported by Morfa et al. [29] are given for comparison.

Gaussian peak No		1	2	3	4	5	6
Maximum (eV)		2.050	2.216	2.381	2.540	2.705	2.713
Amplitude (arb. u.)	*Spin coated samples*						
	Fresh solution	0.72	1.20	1.05	0.65	0.25	0.65
	Aged solution	0.99	1.43	1.20	0.73	0.25	0.65
	Spray coated samples						
	Fresh solution	0.71	1.11	0.96	0.61	0.28	0.65
	Aged solution	0.80	1.20	1.01	0.67	0.30	0.65
Energies of peaks given in Ref. [29]		2.0458	2.2045	2.3633	2.5220	2.6808	

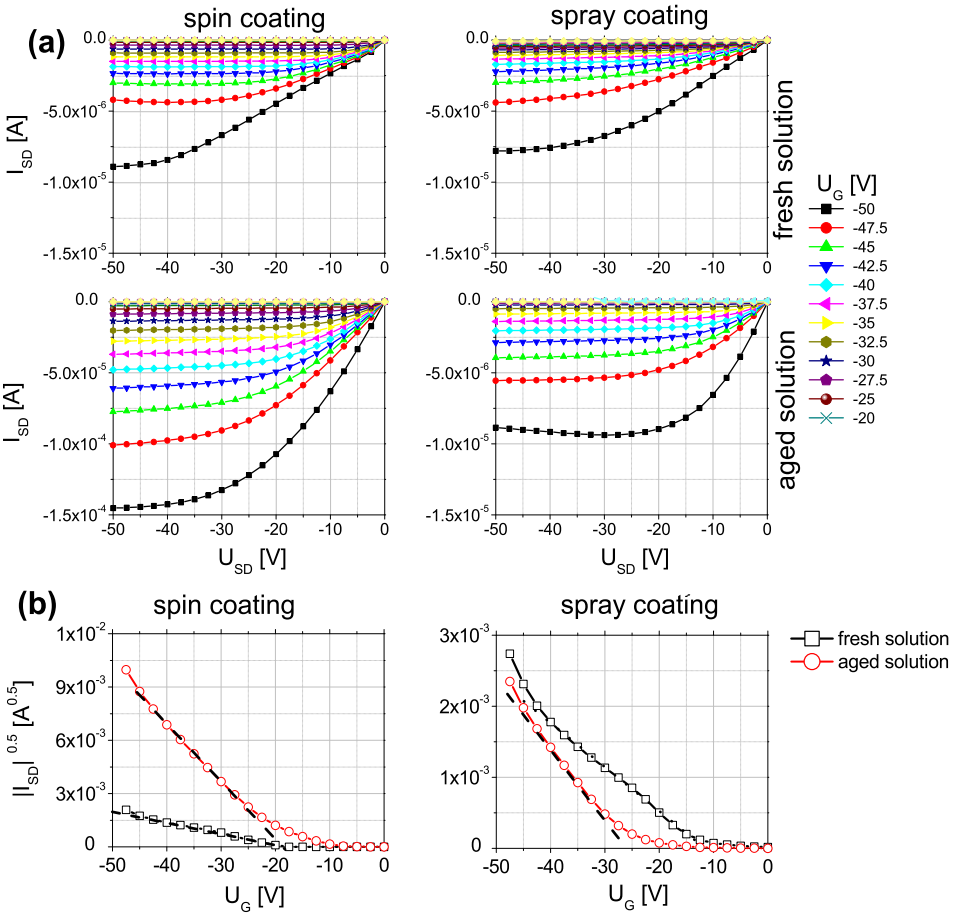

Fig. 5. (a) Output current–voltage characteristics in P3HT OFETs fabricated by spin coating (left) and spray coating (right) using fresh (top) and aged (bottom) solutions. Note the different scale of source-drain current in the left bottom diagram. (b) Exemplary transfer current–voltage characteristics in four groups of P3HT OFETs. Note the different scales of the current.

from −50 to 0 V. The threshold voltages in studied OFETs ranged between −15 and −25 V.

A histogram demonstrating the statistics of values of μ_{FET} determined from our experiments, shown in Fig. 6, points to an important effect of the character of the used solution and method of deposition (see also Table 2). Average mobilities in P3HT OFETs obtained from the fresh solution were practically the same for spin coated and spray coated samples ((0.5 ± 0.1) and $(0.4 \pm 0.2) \times 10^{-3}\,cm^2\,V^{-1}\,s^{-1}$, respectively). Spray coating using the aged solution yielded devices exhibiting significantly higher mobilities ($(1.5 \pm 0.5) \times 10^{-3}\,cm^2\,V^{-1}\,s^{-1}$). Even higher hole mobilities were determined in spin coated samples deposited from the aged solution: the average value amounted to $(7 \pm 5) \times 10^{-3}\,cm^2\,V^{-1}\,s^{-1}$. The high average mobility was accompanied by an exceptionally large

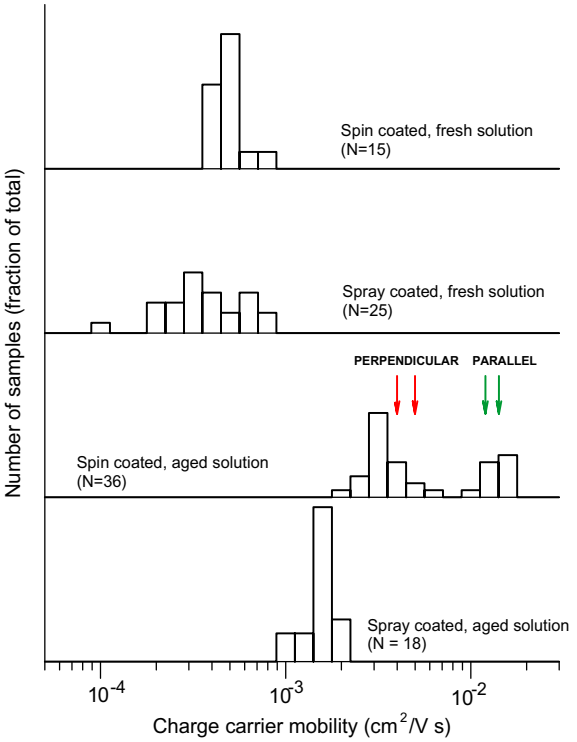

Fig. 6. Statistics of mobilities for the four groups of samples. Total numbers of measured samples of each group are given in the figure. The arrows indicate the mobilities determined in OFETs fabricated with the channels oriented parallel or perpendicular to the direction of the centrifugal force. Note the logarithmic scale of mobilities.

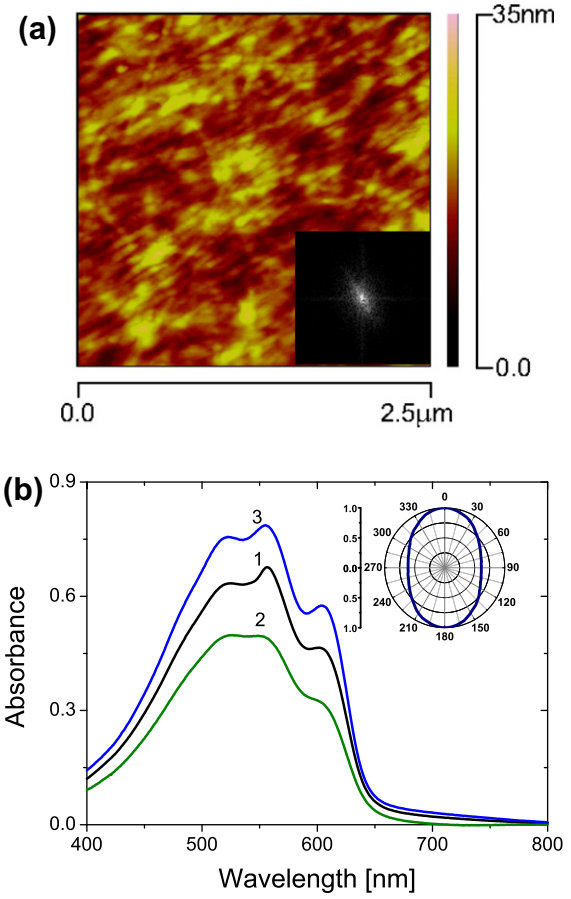

Fig. 7. (a) AFM image of surface morphology of a spin coated P3HT film deposited from an aged chloroform solution. The direction of the centrifugal force was from left to right. Inset: Fourier transform of the main image. The long axis of the shape shown in the insert is perpendicular to the preferred orientation of the nanofibers. (b) Absorption spectra of a P3HT film deposited by the spin coating of an aged solution. (1) Spectrum taken with unpolarized light; (2) light polarized along the preferential orientation of the fibers; (3) light polarized perpendicular to the fibers. Inset: angular dependence of the transmittance at 514.5 nm. The polarization angle was changed every 4° between 0° and 180° (the zero point was set in the direction of minimum absorbance).

spread of the results: the highest mobilities exceeded in some samples 10^{-2} cm^2 V^{-1} s^{-1} being over 1 order of magnitude higher than typical mobilities in FETs fabricated from the fresh solution.

The large scatter of the mobilities in OFETs fabricated by spin coating of the aged solution needs a comment. The results shown in Fig. 6 point to an interesting difference between the samples spin coated using the aged solution and those belonging to the three remaining groups: while the results obtained for the latter three groups of samples are spread around single maxima, spin coating of the aged solution yields results grouped around two maxima. It is tempting to associate this feature with the morphology of the spin coated samples; indeed, a closer inspection of the AFM pictures reveals a certain degree of orientation of the nanofibers along the direction of the centrifugal force acting on the samples during the spin coating. In order to verify this hypothesis, we prepared additional two pairs of samples,

Table 2
Average and maximum values of field effect mobilities of charge carriers, μ_{FET}.

	Average μ_{FET}[a] (10^{-3} cm^2 V^{-1} s^{-1})	The highest μ_{FET} (10^{-3} cm^2 V^{-1} s^{-1})	Nanofibers on the surface (AFM)
Spin coating			
Fresh solution	0.5 ± 0.1	0.73	No
Aged solution	7 ± 5	15.6	High concentration, partly oriented
Spray coating			
Fresh solution	0.4 ± 0.2	0.76	No
Aged solution	1.5 ± 0.5	1.92	High concentration, no preferred orientation

[a] $\pm\sigma$ – standard deviation.

with the channels in each pair oriented parallel or perpendicular to the direction of the centrifugal force. The resulting mobilities are indicated by the arrows in Fig. 6.

Moreover, additional samples were fabricated for AFM inspection and spectroscopic measurements using polarized light, with a determined orientation with respect to the centrifugal force, using the same aged solution and employing identical conditions of deposition. The surface morphology is shown in Fig. 7a, the spectra taken with the polarized light – in Fig. 7b. In both cases, the results point to an anisotropy of the samples, thus confirming validity of our hypothesis about the ordering of P3HT nanofibers by the centrifugal force and its influence on the carrier mobility.

4. Conclusions

We carried out a comparative study of OFETs fabricated of P3HT, relating their performance to their morphology dependent on the consistency of solutions used and deposition technique. Mobilities of charge carriers in samples fabricated using fresh solutions have been found of the order of $10^{-4}\,cm^2\,V^{-1}\,s^{-1}$, irrespective of the deposition technique. Use of aged solutions results in an increase of the carrier mobilities in the devices by ca. one order of magnitude or more. The mobilities in spray coated OFETs have been found of the order of $10^{-3}\,cm^2\,V^{-1}\,s^{-1}$, on the same level as the values reported by Abdellah et al. [19] and one order of magnitude lower than those in P3HT FETs fabricated with an optimized fabrication technique by Chan et al. [20]. Spin coated P3HT films deposited using aged solutions exhibit even higher mobilities, particularly high in samples with some degree of orientation of the nanofibers parallel to the channel length.

Our results confirm that the presence of nanofibers, their length and their orientation are decisive factors for achieving high carrier mobilities in OFETs. We have also demonstrated that use of the spray coating technique, albeit simple and technologically convenient, has its price: lack of orientation of nanofibers, and their shorter lengths result in lower mobilities.

Acknowledgements

This work was supported by the European Commission through the Human Potential Programme (Marie-Curie RTN BIMORE, Grant No. MRTN-CT-2006-035859) and, in part, by the Wroclaw University of Technology.

References

[1] A. Tsumura, H. Koezuka, T. Ando, Macromolecular electronic device: field effect transistor with a polythiophene thin film, Appl. Phys. Lett. 49 (1986) 1210–1212.
[2] A. Salleo, Morphology, microstructure and charge transport in polymeric thin-film transistors, Mater. Today 10 (2007) 38–45 (and references therein).
[3] S. Samitsu, T. Shimomura, S. Heike, T. Hashizume, K. Ito, Effective production of poly(3-alkylthiophene) nanofibers by means of whisker method using anisole solvent: structural, optical, and electrical properties, Macromolecules 41 (2008) 8000–8010.
[4] Y.D. Park, D.H. Kim, J.A. Lim, J.H. Cho, Y. Jang, W.H. Lee, J.H. Park, K. Cho, Enhancement of field-effect mobility and stability of poly(3-hexylthiophene) field-effect transistors by conformational change, J. Phys. Chem. C 112 (2008) 1705–1710.
[5] R. Zhang, B. Li, M.C. Iovu, M. Jeffries-EL, G. Sauvé, J. Cooper, S. Jia, S. Tristram-Nagle, D.M. Smilgies, D.N. Lambeth, R.D. McCullough, T. Kowalewski, Nanostructure dependence of field-effect mobility in regioregular poly(3-hexylthiophene) thin film field effect transistors, J. Am. Chem. Soc. 128 (2006) 3480–3481.
[6] J.-M. Verilhac, G. LeBlevennec, D. Djurado, F. Rieutord, M. Chouiki, J.-P. Travers, A. Pron, Effect of macromolecular parameters and processing conditions on supramolecular organisation, morphology and electrical transport properties in thin layers of regioregular poly(3-hexylthiophene), Synth. Met. 156 (2006) 815–823.
[7] B. Meredig, A. Salleo, R. Gee, Ordering of poly(3-hexylthiophene) nanocrystallites on the basis of substrate surface energy, ACS Nano 3 (2009) 2881–2886.
[8] H. Yang, T.J. Shin, L. Yang, K. Cho, C.Y. Ryu, Z. Bao, Effect of mesoscale crystalline structure on the field-effect mobility of regioregular poly(3-hexyl thiophene) in thin-film transistors, Adv. Funct. Mater. 15 (2005) 671–676.
[9] C.-Y. Chen, S.-H. Chan, J.-Y. Li, K.-H. Wu, H.-L. Chen, J.-H. Chen, W.-Y. Huang, S.-A. Chen, Formation and thermally-induced disruption of nanowhiskers in poly(3-hexylthiophene)/xylene gel studied by small-angle x-ray scattering, Macromolecules 43 (2010) 7305–7311.
[10] S. Sun, T. Salim, L. Wong, Y. Foo, F. Boey, Y. Lam, A new insight into controlling poly(3-hexylthiophene) nanofiber growth through a mixed-solvent approach for organic photovoltaic applications, J. Mater. Chem. 21 (2011) 377–386.
[11] D. Fichou (Ed.), Handbook of Oligo- and Polythiophenes, Wiley-VCH, Weinheim, 1999.
[12] B.S. Ong, Y. Wu, P. Liu, S. Gardner, Structurally ordered polythiophene nanoparticles for high-performance organic thin-film transistors, Adv. Mater. 17 (2005) 1141–1144.
[13] J.-H. Huang, C.-Y. Yang, C.-Y. Hsu, C.-L. Chen, L.-Y. Lin, R.-R. Wang, K.-C. Ho, C.-W. Chu, Solvent-annealing-induced self-organization of poly(3-hexylthiophene), a high-performance electrochromic material, ACS Appl. Mater. Interfaces 1 (2009) 2821–2828.
[14] S. Samitsu, T. Shimomura, S. Heike, T. Hashizume, K. Ito, Field effect carrier transport in poly(3-alkylthiophene) nanofiber networks and isolated nanofibers, Macromolecules 43 (2010) 7891–7894.
[15] L. Xue, X. Gao, K. Zhao, J. Liu, X. Yu, Y. Han, The formation of different structures of poly(3-hexylthiophene) film on a patterned substrate by dip coating from aged solution, Nanotechnology 21 (2010) 145303-1–145303-9.
[16] L. Qiu, X. Wang, W.H. Lee, J.A. Lim, J.S. Kim, D. Kwak, K. Cho, Organic thin-film transistors based on blends of poly(3-hexylthiophene) and polystyrene with a solubility-induced low percolation threshold, Chem. Mater. 21 (2009) 4380–4386.
[17] F. Garnier, G. Horowitz, D. Fichou, A. Yassar, Molecular order in organic-based field-effect transistors, Synth. Met. 81 (1996) 163–171.
[18] R. Green, A. Morfa, A.J. Ferguson, N. Kopidakis, G. Rumbles, S.E. Shaheen, Performance of bulk heterojunction photovoltaic devices prepared by airbrush spray deposition, Appl. Phys. Lett. 92 (2008) 033301-1–033301-3.
[19] A. Abdellah, B. Fabel, P. Lugli, G. Scarpa, Spray deposition of organic semiconducting thin-films: towards the fabrication of arbitrary shaped organic electronic devices, Org. Electron. 11 (2010) 1031–1038.
[20] C.K. Chan, L.J. Richter, B. Dinardo, C. Jaye, B.R. Conrad, H.W. Ro, D.S. Germack, D.A. Fischer, D.M. DeLongchamp, D.J. Gundlach, High performance airbrushed organic thin film transistors, Appl. Phys. Lett. 96 (2010) 133304-1–133304-3.
[21] N.A. Azarova, J.W. Owen, C.A. McLellan, M.A. Grimminger, E.K. Chapman, J.E. Anthony, O.D. Jurchescu, Fabrication of organic thin-film transistors by spray-deposition for low-cost, large-area electronics, Org. Electron. 11 (2010) 1960–1965.
[22] K.-J. Kim, Y.-S. Kim, W.-S. Kang, B.-H. Kang, S.-H. Yeom, D.-E. Kim, J.-H. Kim, S.-W. Kang, Inspection of substrate-heated modified PEDOT:PSS morphology for all spray deposited organic photovoltaics, Solar Energy Mater. Sol. Cells 94 (2010) 1303–1306.
[23] S. Seki, M. Wakana, Y. Kasahara, Y. Seki, T. Kondo, M. Wang, T. Uchida, K. Haga, Y. Sawada, Fabrication of organic light-emitting devices with indium-tin-oxide anode prepared by spray chemical vapor deposition, Jpn. J. Appl. Phys. 46 (2007) 6837–6841.
[24] S.K. Hau, H.-L. Yip, K. Leong, A. K.-Y. Jen, Spraycoating of silver nanoparticle electrodes for inverted polymer solar cells, Org. Electron. 10 (2009) 719–723.
[25] D. Vak, S. Kim, J. Jo, S. Oh, S. Na, J. Kim, D. Kim, Fabrication of organic bulk heterojunction solar cells by a spray deposition method for

low-cost power generation, Appl. Phys. Lett. 91 (2007) 081102-1–081102-3.
[26] S.M. Sze, Physics of Semiconductor Devices, second ed., Wiley-Interscience, New York, 1981.
[27] D.W. van Krevelen, Properties of Polymers, third ed., Elsevier, Amsterdam, 1997.
[28] S. Sun, T. Salim, L. Wong, Y. Foo, F. Boey, Y. Lam, A new insight into controlling poly(3-hexylthiophene) nanofiber growth through a mixed-solvent approach for organic photovoltaic applications, J. Mater. Chem. 21 (2011) 377–386.
[29] A.J. Morfa, T.M. Barnes, A.J. Ferguson, D.H. Levi, G. Rumbles, K.L. Rowlen, J. van de Lagemaat, Optical characterization of pristine poly(3-hexyl thiophene) films, J. Polym. Sci. B: Polym. Phys. 49 (2011) 186–194.

The organic/polymer rectifiers may be formed with the vertical Schottky diodes or the diode-configured thin-film transistors (TFTs) [11]. The appealing property of a transistor-based rectifier is its ease of integration with the logic gates [12,13]. Yet, its response frequency may be limited by the longer carrier transport path (i.e. the channel length) [11,14]. On the other hand, the active layer thickness of the vertical Schottky diode can be easily reduced, thereby having a larger potential to achieve much higher operating frequencies [15]. The requirements for implementing high-speed organic rectifying diode in general include high current density under the forward bias for faster charging of the load circuits, low current density under the reverse bias to reduce charge leakage of the load capacitor during the reverse-bias half cycle, and low turn-on voltage to reduce voltage drop on the diode and to produce higher voltage output. In recent years, there have been reports on progresses in operation frequencies of organic/polymer rectifiers [11,15–20]. Yet except for few cases of vacuum-deposited small-molecule organic rectifying devices showing operation frequencies around or exceeding 13.56 MHz [15,20], in general there is still difficulty for solution-processed polymer devices to achieve such high operating frequencies.

In this work, we report the implementation of flexible high-frequency rectifying diodes using the polythiophene-based semiconducting polymers and the polycarbonate substrates. We show how the intermediate hole-injection layer between the anode and the semiconducting polymer and the semiconducting polymer itself affect the characteristics/performances of the rectifying diodes. Furthermore, we integrate the polymer-based vertical Schottky diode rectifier, antenna and capacitors to demonstrate a flexible wireless power-transmission sheet that can convert a 13.56 MHz electromagnetic wave into the dc power.

2. Experiment

2.1. Fabrication and characterization of polymer diodes

Two types of device structures on polycarbonate (PC) substrates, as shown in Fig. 1, were studied in this work. The device structure for type-I devices is: PC/IZO/semiconducting polymer/Al, while the device structure for type-II devices is: PC/IZO/PEDOT:PSS/semiconducting polymer/Al. In both devices, transparent and conducting indium zinc oxide (IZO) was used as the anode and Al was used as the cathode. IZO was reported to provide good optical/electrical performances even by low-temperature deposition and exhibit low internal stress and etching stability when deposited on plastic substrates [21], making it attractive for applications in flexible electronics. PC/IZO substrates used in this work were purchased from Teijin Ltd. and had a sheet resistance of 30 Ω/square and light transmittance of 87%.

The chemical structures of semiconducting polymers and conducting polymers used in this work are shown in Fig. 2. Two types of semiconducting polymers, poly(3-hexylthiophene) (P3HT) and poly(3,3‴didodecylquaterthiophene) (PQT-12) shown in Fig. 2, were used in devices. P3HT is a widely used semiconducting polymer for polymer devices [22], while PQT-12 is a polythiophene-based polymer that had been reported to exhibit higher carrier mobilities than P3HT in polymer devices [22–26]. P3HT was purchased from Rieke Metals, Inc. and was used as received. PQT-12 was purchased from American Dye Source, Inc. and was used either as received or after in-house purification. The polydispersity index (PDI) of PQT-12 decreased from 1.6 (Mw = 19 kg/mol) to 1.4 (Mw = 26 kg/mol) after purification by gel-permeation chromatography (GPC). In type-II devices, the conducting polymer (3,4-ethylenedioxy thiophene)poly(styrene sulfonate) (PEDOT:PSS) as shown in Fig. 2 was inserted between the IZO anode and the semiconducting polymer as the hole-injection layer [27]. Two models of PEDOT:PSS, one having a higher conductivity (Baytron P HCV4, resistivity = 10^3 Ω cm) and one having a lower conductivity (Baytron P VP AI 4083, resistivity = 10^4 Ω cm), were purchased from H.C. Stark and were used in this study. Fig. 2(d) shows the energy levels of PEDOT, P3HT, and PQT-12 used in this work [28–30].

In fabrication of devices, polycarbonates coated with IZO was first cleaned by sonification in de-ionized water, acetone and isopropyl alcohol sequentially, and then dried in an oven at 100 °C for 30 min. After the wet cleaning, the substrate was further subjected to a dry cleaning in UV ozone for 25 min. For type-I devices, a semiconducting polymer (e.g. P3HT) was then directly spin-coated onto IZO. For type-II devices, prior to deposition of the semiconducting polymer (P3HT or PQT-12), a hole-injection layer of PEDOT:PSS was spin-coated onto the PC/IZO substrate at 4000 rpm to form a 50-nm-thick film. The PEDOT:PSS coated substrate was then baked on a hotplate at 110 °C for 20 min. The 160-nm-thick semiconducting polymer, P3HT or PQT-12, were coated onto IZO or PEDOT:PSS by spin-coating. P3HT was spin-coated under the N_2 environment, followed by annealing at 110 °C. PQT-12 was spin-coated under the ambient environment, followed by annealing at 145 °C. Finally, the aluminum electrode was deposited by thermal evaporation. The area of each Schottky diode was 0.07 mm^2, as defined by the shadow mask. We found the small device area is one of the important

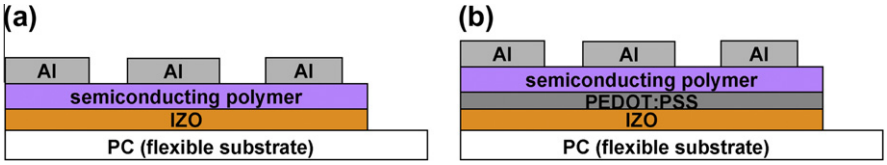

Fig. 1. Two types of device structures on polycarbonate (PC) substrates studied in this work: (a) type-I devices, (b) type-II devices.

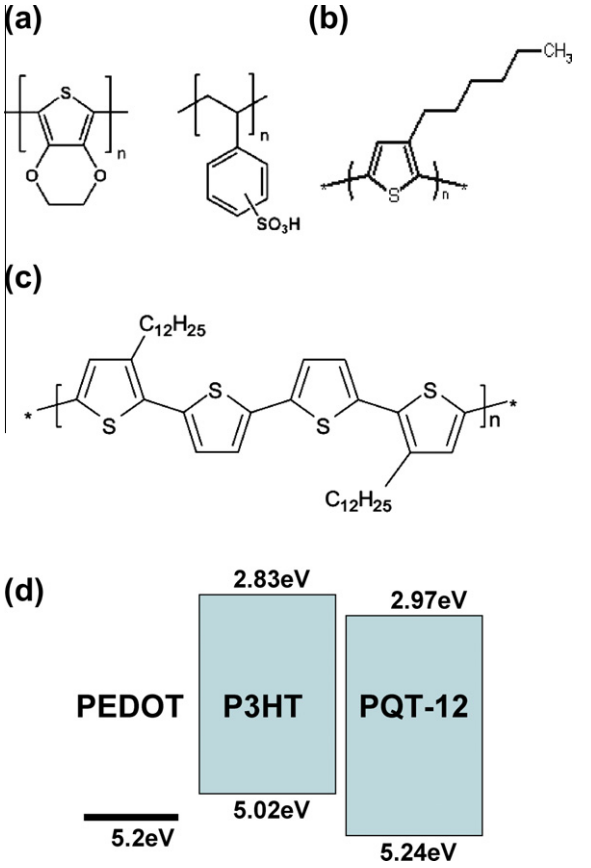

Fig. 2. Chemical structures and energy levels of the materials used: (a) PEDOT:PSS, (b) P3HT, (c) PQT-12, (d) energy levels of PEDOT, P3HT and PQT-12.

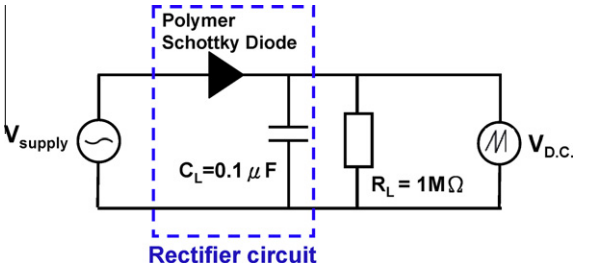

Fig. 3. The schematic circuit configuration for measuring the frequency response of the diode rectifier.

factors to achieve high-frequency operation of the device. After device fabrication, the current–voltage characteristics of the diodes were measured using an Agilent 4156C Semiconductor Parameter Analyzer.

2.2. Frequency response measurements

Fig. 3 shows the schematic circuit configuration for measuring the frequency response of the diode rectifier. It consisted of a function generator (to provide the ac input signal V_{supply} of various frequencies), the polymer diode, a load capacitance (C_L), a load resistance (R_L), and an oscilloscope (to measure the dc output signal $V_{D.C.}$). The function generator Agilent 3120A was used to feed the input ac signal into the rectifier circuit. The output of the diode rectifier was recorded by a Tektronix TDS3052B oscilloscope with the input impedance set to 1 MΩ. A 0.1 μF capacitor was used as the load capacitor.

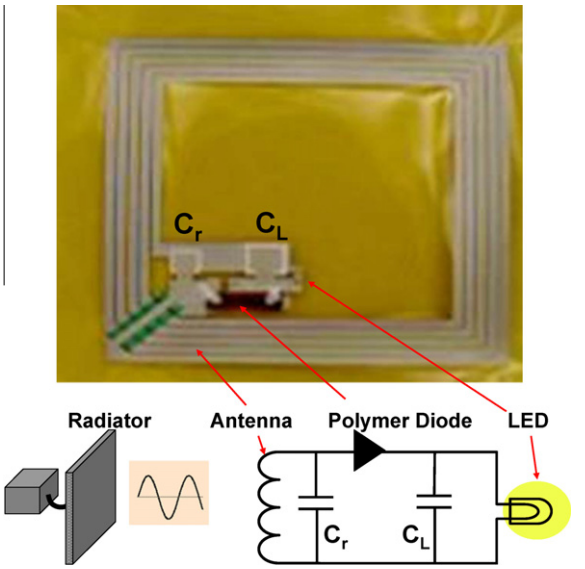

Fig. 4. The schematic configuration of the flexible wireless power-transmission sheet/system and a photo of the power-transmission sheet.

2.3. Flexible wireless power-transmission sheet

To demonstrate the use of the high-speed polymer rectifying diode in wireless power transmission, the polymer rectifying diode developed in this work was integrated into a flexible wireless power-transmission sheet and system. Fig. 4 shows the schematic configuration of the flexible wireless power-transmission sheet and system. The flexible wireless power-transmission sheet on plastics consisted of a printed metal-coil antenna (4.6 × 4.6 cm, L = 2.281 μH), a resonant capacitance (C_r = 60.4 pF), a polymer diode, a load capacitance (C_L = 201 pF), and a commercial inorganic light emitting diode (LED) as the load. The antenna and bottom electrodes of capacitors were screen-printed on polyimide substrates. Then, the polymer dielectrics (for capacitors) and the top electrodes of capacitors were coated by screen printing in sequence. Finally, the polymer Schottky diode and commercial inorganic LED were mounted on the sheet having patterned antenna and capacitors. The darker area in Fig. 4 represents the color of the PQT-12 film, but the actual active area of the polymer diode used was 0.07 mm^2, as determined by the overlap of the bottom IZO electrode and the top Al electrode.

3. Results and discussion

3.1. Effects of PEDOT:PSS intermediate layer

First, the effects of the intermediate layer (i.e. PEDOT:PSS) between the IZO anode and the semiconducting

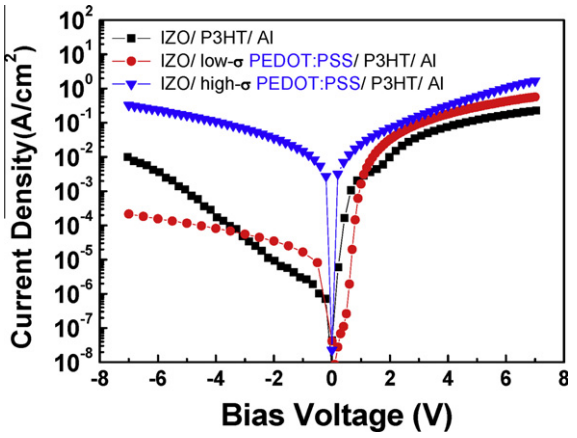

Fig. 5. *I–V* characteristics of P3HT diodes having the structures of: IZO/P3HT/Al, IZO/lower-conductivity (low-σ) PEDOT:PSS/P3HT/Al, and IZO/higher-conductivity (high-σ) PEDOT:PSS/P3HT/Al.

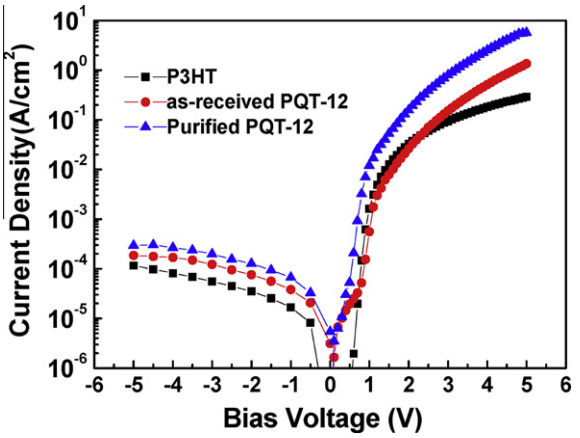

Fig. 6. *I–V* characteristics of the IZO/low-σ PEDOT:PSS/semiconducting polymer/Al diodes using P3HT, as-received PQT-12, and in-house purified PQT-12.

layer was studied. Fig. 5 shows the *I–V* characteristics of P3HT diodes having no PEDOT:PSS intermediate layer, having the lower-conductivity (low-σ) PEDOT:PSS intermediate layer, and having the higher-conductivity (high-σ) PEDOT:PSS intermediate layer. Diodes with either high-conductivity or low-conductivity PEDOT:PSS exhibit higher forward current densities than the diode without PEDOT:PSS, indicating that the adoption of PEDOT:PSS is effective in providing a better contact and enhancing hole injection to the semiconducting polymer in consideration of energy levels of materials shown in the Fig. 2(d). The diode using the higher-conductivity PEDOT:PSS, however, exhibits much higher reverse leakage current than the other two diodes. Such much larger reverse leakage current may due to fringing and lateral conductivity associated with the higher PEDOT:PSS conductivity. Therefore, the conductivity of the PEDOT:PSS hole-injection layer should be judiciously tuned to obtain both enhanced forward current and yet also low reverse leakage current, thus achieving high rectification desired for high-performance diode rectifiers. In the three devices shown in Fig. 1, indeed the diode adopting the lower-conductivity PEDOT:PSS shows both enhanced forward current and yet also low reverse leakage current, consequently giving the enhanced diode rectification ratio.

3.2. Effects of different semiconductor polymers

After investigating effects of the anode intermediate layers, we then studied characteristics of diodes using different semiconducting polymers. Due to the effectiveness of the low-σ PEDOT:PSS in both enhancing the forward current and suppressing the reverse leakage current, the same device structure of IZO/low-σ PEDOT:PSS/semiconducting polymer/Al was extended to test different semiconducting polymers (i.e. both P3HT and PQT-12). Fig. 6 shows the *I–V* characteristics of the diode using P3HT, the diode using the as-received PQT-12, and the diode using the in-house purified PQT-12. It is seen that with adopting the PQT-12, the forward current of the diode is increased. The diode current is further enhanced when using the purified PQT-12. The current enhancement (at 5 V) is more than one order of magnitude, when compared to the P3HT diode. Simultaneously, the rectification ratio of the diode is also enhanced. It is supposed that the better performance of the PQT-12 diodes is owing to the higher mobility of PQT-12, which in general can show a mobility (0.1–0.7 cm^2/Vs) about one order higher than that of P3HT (0.01–0.1 $cm^2/V\,s$) [22–26]. Overall, a forward current density up to ~6 A/cm^2 at 5 V and a rectification ratio up to 2×10^4 at ±5 V were achieved with the rectifying diodes using purified PQT-12. The high current density observed for the PQT-12 diode is comparable to those of high-performance organic diodes using vacuum-deposited organic semiconductors [15,20,31].

In addition to better electrical characteristics, PQT-12 diodes also exhibit better environmental stability in comparison with P3HT diodes. Fig. 7(a) shows the *I–V* characteristics of a same P3HT diode measured when freshly made and after being stored in the air for 120 h. Clearly the diode characteristics had degraded dramatically after extended exposure to the ambient. On the other hand, after a same storage test, the characteristics of the PQT-12 diode only varied slightly, as shown in Fig. 7(b). It had been reported that the HOMO energy level of PQT-12 is higher than that of P3HT due to the difference in conjugation structures, thus making it less susceptible to oxidative doping associated with ambient gases (e.g. humidity, etc.) and more environmentally stable [32,33].

3.3. Frequency response of the polymer diode rectifier

The frequency response of the diode rectifier was measured using the basic rectifier circuit configuration shown in Fig. 3, which consists of the polymer diode, a load capacitance (C_L), and a load resistance (R_L). The load resistance of 1 MΩ and load capacitance of 0.1 μF were used in this study, which were chosen to make $R_L \times C_L$ much larger than the period of the input ac voltage to avoid/reduce the output voltage ripples [34]. Fig. 8 shows the frequency

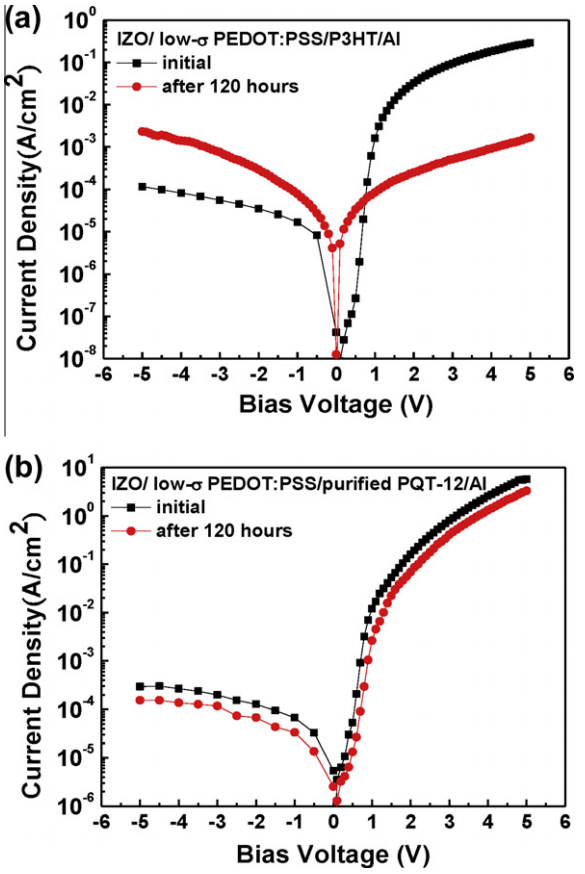

Fig. 7. *I–V* characteristics of IZO/low-σ PEDOT:PSS/semiconducting polymer/Al diodes measured when freshly made and after being stored in the air for 120 h: (a) P3HT diode, (b) purified PQT-12 diodes.

response, i.e. the dc output voltage vs. the frequency of the input ac signal (with an amplitude of 10 V), of the diode rectifiers using the three polymer diodes of IZO/low-σ PEDOT:PSS/P3HT/Al, IZO/low-σ PEDOT:PSS/as-received PQT-12/Al, and IZO/low-σ PEDOT:PSS/purified PQT-12/Al. The rectifier using the purified PQT-12 exhibits the highest operation frequency. The 3-dB frequency of the rectifier using the purified PQT-12 is higher than 14 MHz (which is beyond the upper frequency limit of our instrument). Indeed, the output voltage remains rather constant up to 14 MHz. The maximum operation frequency (f_{MAX}) of the rectifying diode is determined by the transition time (t_t) of carriers traveling through the polymer diode during the forward-bias half cycle, i.e. roughly speaking $f_{MAX} \approx \mu(V_A - V_{dc})/L^2$, where V_A is the amplitude of the input ac voltage, V_{dc} the output dc voltage at the load capacitance, μ the bulk material mobility, and L the diode thickness [15]. With the same active-layer thickness and the same applied ac voltage, the purified PQT-12 diode gives the highest operation frequency, presumably due to its higher carrier mobility. Fig. 9 shows the output voltage waveform of the purified PQT-12 diode rectifier along with the 13.56 MHz/10 V input ac signal. When operated at 13.56 MHz/10 V, the purified PQT-12 diode rectifier outputs a dc voltage of ~4 V.

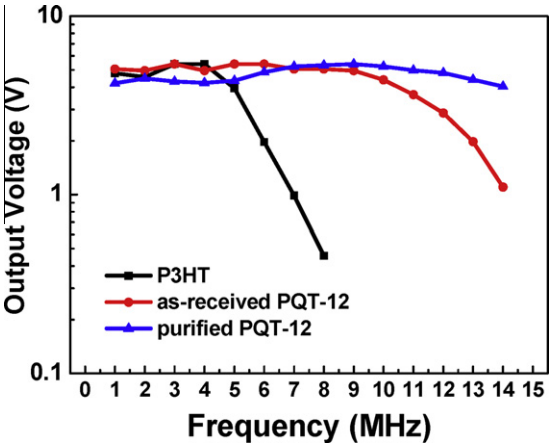

Fig. 8. The frequency response, i.e. the dc output voltage vs. the frequency of the input ac signal (with an amplitude of 10 V), of the diode rectifiers using the three polymer diodes of: IZO/low-σ PEDOT:PSS/P3HT/Al, IZO/low-σ PEDOT:PSS/as-received PQT-12/Al, and IZO/low-σ PEDOT:PSS/purified PQT-12/Al.

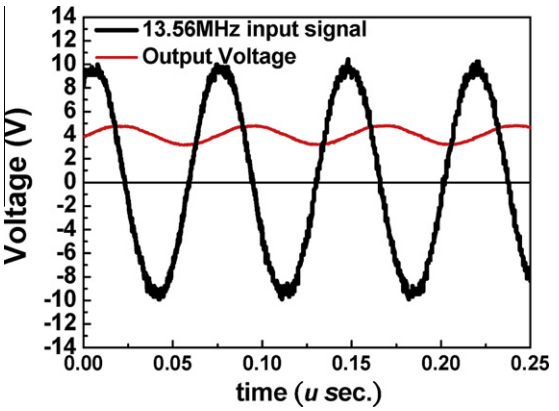

Fig. 9. The output voltage waveform of the purified PQT-12 diode rectifier along with the 13.56 MHz/10 V input ac signal.

3.4. Use of the polymer diode rectifier in flexible wireless power-transmission sheet

To demonstrate the use of the high-speed polymer rectifying diode in wireless power transmission, the polymer rectifying diode developed in this work was integrated into a flexible wireless power-transmission sheet and system, whose configuration and photo are shown in Fig. 4. The wireless power-transmission sheet consists of a resonant circuit and a rectifier circuit. The resonant circuit receives the energy from the radiator and the rectifier circuit converts the ac signal from the resonant circuit to dc voltage. The resonant circuit is composed of a resonant capacitor (C_r) and the inductor coil (L) of the antenna. The resonant frequency of the resonant circuit has been tuned at the carrier frequency of the radiator (13.56 MHz in the present case) to obtain the best performance. The rectifier circuit is composed of a polymer diode and a filter capacitor (C_L). A commercial inorganic LED was mounted onto the sheet to demonstrate the function of the power-transmission sheet. The photograph in Fig. 10 shows that a flexible

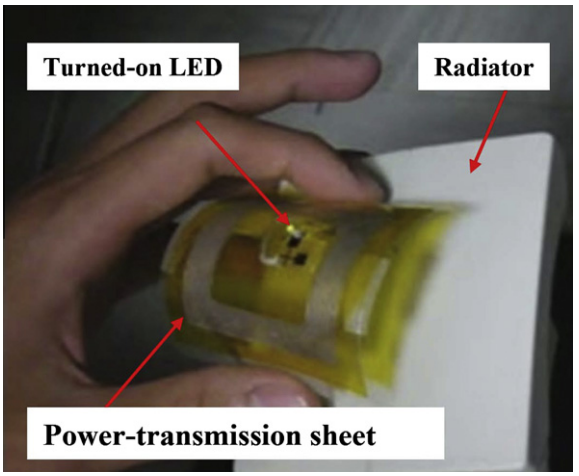

Fig. 10. A photograph showing that a flexible wireless power-transmission sheet (under the bending status) was receiving 13.56 MHz RF power from the radiator and converting it into dc voltage to drive the LED (the bright spot in the photo).

wireless power-transmission sheet was receiving 13.56 MHz RF power from the radiator and converting it into dc voltage to drive the LED. In Fig. 10, it is seen that even under the bending state, the wireless power-transmission sheet remained normally functional, clearly demonstrating the flexibility and the functionality of wireless power transmission.

4. Conclusions

In summary, we successfully implemented flexible high-frequency rectifying diodes on polycarbonate substrates using the polythiophene-based semiconducting polymers. We show that the appropriate conductivity of the intermediate hole-injection layer PEDOT:PSS between the anode and the semiconducting polymer is critical to simultaneously achieve enhanced forward currents and rectification ratios. Among the semiconducting polymers studied (P3HT and PQT-12), the diodes based on carefully purified PQT-12 exhibited higher forward currents, higher rectification ratios, much better environmental stability, and much higher operation frequencies. A forward current density up to $\sim$6 A/cm^2 at 5 V, a rectification ratio up to 2×10^4 at ±5 V, and an operation frequency of the diode rectifier over 14 MHz were achieved with the PQT-12 rectifying diodes. Finally, to demonstrate the use of the high-speed polymer rectifying diode in wireless power transmission, we integrate the polymer-based vertical Schottky diode rectifier, printed antenna and capacitors on plastic substrates to demonstrate a flexible wireless power-transmission sheet that can convert a 13.56 MHz electromagnetic wave into the dc power to drive load devices.

Acknowledgements

The authors gratefully acknowledge the financial support from the Ministry of Economic Affairs, and the Electronics and Optoelectronics Research Laboratories of the Industrial Technology Research Institute (EOL/ITRI), Taiwan, ROC.

References

[1] T.-H. Chuang, H.-H. Hsieh, C.-K. Chen, C.-C. Wu, C.-C. Lin, P.-T. Chou, T.-H. Chao, T.J. Chow, Organic Letters 10 (2008) 2869.
[2] C.-K. Chen, H.-H. Hsieh, J.-J. Shyue, C.-C. Wu, IEEE/OSA Journal of Display Technology 5 (2009) 515.
[3] S.H. Ko, H. Pan, C.P. Grigoropoulos, C.K. Luscombe, J.M.J. Fŕechet, D. Poulikakos, Nanotechnology 18 (2007) 345202.
[4] V. Subramanian, P.C. Chang, J.B. Lee, S.E. Molesa, S.K. Volkman, IEEE Transactions on Components and Packaging Technologies 28 (2005) 742.
[5] B. Lee, B. Yu, Microwave and Optical Technology Letters 50 (2008) 232.
[6] J. Krumm, E. Eckert, W.H. Glauert, A. Ullmann, W. Fix, W. Clemens, IEEE Electron Device Letters 25 (2004) 399.
[7] A. Kurs, A. Karalis, R. Moffatt, J.D. Joannopoulos, P. Fisher, M. Soljacic, Science 317 (2007) 83.
[8] H. Abe, H. Sakamoto, K. Harada, IEEE Transactions on Industry Applications 36 (2000) 444.
[9] W.C. Brown, IEEE Transactions on Microwave Theory and Techniques MTT 32 (1984) 1230.
[10] T. Sekitani, M. Takamiya, Y. Noguchi, S. Nakano, Y. Kato, T. Sakurai, T. Someya, Nature Materials 6 (2007) 413.
[11] S. Steudel, S.D. Vusser, K. Myny, M. Lenes, J. Genoe, P.H.K. Kaneto, W. Takashima, Journal of Applied Physics 99 (2006) 114519.
[12] A.R. Brown, A. Pomp, C.M. Hart, D.M. de Leeuw, Science 270 (1995) 972.
[13] H. Klauk, D.J. Gundlach, J.A. Nichols, T.N. Jackson, IEEE Transactions on Electron Devices 46 (1999) 1258.
[14] N. Stutzmann, R.H. Friend, H. Sirringhaus, Science 299 (2003) 1881.
[15] S. Steudel, K. Myny, V. Arkhipov, C. Deibel, S.D. Vusser, J. Genoe, P. Heremans, Nature Materials 4 (2005) 597.
[16] C.-M. Kang, S. Kim, Y. Hong, C. Lee, Thin Solid Films 518 (2009) 889.
[17] K.E. Lilja, T.G. Backlund, D. Lupo, T. Hassinen, T. Joutsenoja, Organic Electronics 10 (2009) 1011.
[18] L.A. Majewski, C. Balocco, R. King, S. Whitelegg, A.M. Song, Materials Science and Engineering B 147 (2008) 289.
[19] A.D.L.F. Vornbrock, D. Sung, H. Kang, R. Kitsomboonloha, V. Subramanian, Organic Electronics 11 (2010) 2037.
[20] Y. Ai, S. Gowrisanker, H. Jia, I. Trachtenberg, E. Vogel, R.M. Wallace, B.E. Gnade, R. Barnett, H. Stiegler, H. Edwards, Applied Physics Letters 90 (2007) 262105.
[21] G. Gonçalves, P. Barquinha, L. Raniero, R. Martins, E. Fortunato, Thin Solid Films 516 (2008) 1374.
[22] H. Sirringhaus, P.J. Brown, R.H. Friend, M.M. Nielsen, K. Bechgaard, B.M.W. Langeveld-Voss, A.J.H. Spiering, R.A.J. Janssen, E.W. Meijer, P. Herwig, D.M. de Leeuw, Nature 401 (1999) 685.
[23] G. Wantz, F. Lefevre, M.T. Dang, D. Laliberté, P.L. Brunner, O.J. Dautel, Solar Energy Materials and Solar Cells 92 (2008) 558.
[24] Y. Wu, P. Liu, B.S. Ong, T. Srikumar, N. Zhao, G. Bolton, S. Zhu, Applied Physics Letters 86 (2005) 142102.
[25] I. McCulloch, M. Heeney, C. Bailey, K. Genevicius, I. Macdonald, M. Shkunov, D. Sparrowe, S. Tierney, R. Wagner, W. Zhang, M.L. Chabinyc, R.J. Kline, M.D. Mcgehee, M.F. Toney, Nature Materials 5 (2006) 328.
[26] H. Pan, Y. Li, Y. Wu, P. Liu, B.S. Ong, S. Zhu, G. Xu, Journal of the American Chemical Society 129 (2007) 4112.
[27] A. Elschner, F. Bruder, H.-W. Heuer, F. Jonas, A. Karbach, S. Kirchmeyer, S. Thurm, R. Wehrmann, Synthetic Metals 111 (2000) 139.
[28] M.J. Yang, S.L. Lu, Y. Li, Journal of Materials Science Letters 22 (2003) 813.
[29] B.S. Ong, Y. Wu, P. Liu, S. Gardner, Advanced Materials 17 (2005) 1141.
[30] G. Agalyaa, C. Lva, X. Wanga, M. Koyamaa, M. Kuboa, A. Miyamoto, Applied Surface Science 244 (2005) 195.
[31] J. Sun, B.N. Pal, B.J. Jung, H.E. Katz, Organic Electronics 10 (2009) 1.
[32] D. Li, E.-J. Borkent, R. Nortrup, H. Moon, H. Katz, Z. Bao, Applied Physics Letters 86 (2005) 042105.
[33] B.S. Ong, Y. Wu, P. Liu, Proceedings of the IEEE 93 (2005) 1412.
[34] A.S. Sedra, K.C. Smith, Microelectronic Circuits, fifth ed., Oxford University Press, New York, 2004. p.180.

organic metal–chelate complexes such as tris(8-hydroxyquinoline) aluminum (Alq_3) and its beryllium derivatives, e.g., $Bebq_2$ and Beq_2 [9]. Organic metal–chelate complexes have been widely used as electron-transporting and host emitting materials in OLEDs because they are thermally and morphologically stable that can be evaporated into thin films, they are easily synthesized and purified, and their molecular geometry can be designed to avoid exciplex formation, e.g. with 4,4′-bis(*N*-(1-naphthyl)-*N*-phenylamino)biphenyl (NPB) at the interface. For example, utilizing Alq_3 as the electron-transporting host material, phosphorescent dyes were for the first time successfully incorporated in OLEDs, achieving high electro-luminescence (EL) efficiencies by utilizing both the singlet and triplet state energies [1b]. Recently, several efficient PHOLEDs have been reported that use bis(2-(2-hydroxyphenyl)-pyridine)beryllium ($Bepp_2$) as an electron-transporting host material and either combine it with another layer of hole-transporting host layer in a double layer structure or use a *p-i-n* structure with multiple-doped-layer system [10], due to the excellent charge transport ability of this beryllium complex [11]. Here, we present a simple and highly efficient single-emitting-layer PHOLED that uses $Bepp_2$ as the electron-transporting host material and bis(7,8-benzoquinolinato) iridium(III) (*N*,*N*′-diisopropyl-benzamidine) ($(bzq)_2Ir(dipba)$) [12] as the phosphorescent dye to enhance the electro-luminescence performance. This PHOLED device exhibits substantially lower driving voltage (2.8 V) and higher EL efficiencies than those based on the CBP host. It shows dramatically enhanced peak values of more than 70 cd A^{-1} for luminous efficiency, 55 lm W^{-1} for power efficiency, and 23% for external quantum efficiency. The high EL performance is attributed to the well-matched energy levels of $Bepp_2$ with the hole-/electron- transporting (HT/ET) materials as well as the highly efficient and complete energy transfer between the host and the guest.

2. Experimental section

2.1. Materials

NPB, CBP and 1,3,5-tris(*N*-phenylbenzimidazol-2-yl)benzene (TPBI) were commercially available. $Bepp_2$ and $(bzq)_2Ir(dipba)$ were prepared according to literature procedures [11,12], and their structures are shown in Fig. 1. Hexane was distilled over sodium benzophenone ketyl under a nitrogen atmosphere and degassed by three freeze–pump–thaw cycles. All glassware, syringes, magnetic stirring bars and needles were dried in a convection oven for at least 4 h before use. Reactions were monitored with thin layer chromatography (TLC) using commercial TLC plates (Silica gel 60 F254, Merck Co.) under either 254 or 365 nm UV light. Silica column chromatography was done with silica gel 60 G (particle size 5–40 μm, Merck Co.). ^{1}H NMR spectra were recorded on a Bruker AVANVE 300 MHz spectrometer with tetramethylsilane as an internal standard. Mass spectra were measured on a GC/MS mass spectrometer. Elemental analyses were performed on a flash EA 1112 elemental analyzer.

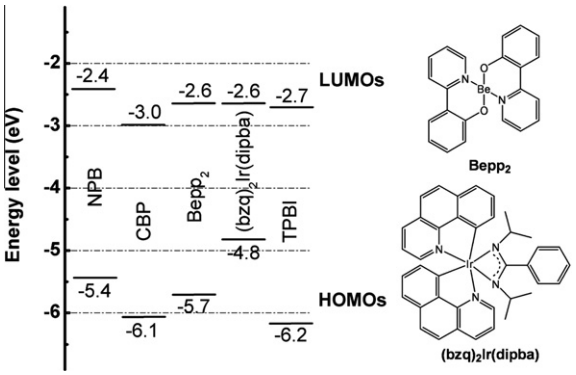

Fig. 1. Proposed energy diagram of the materials used in OLEDs (left) and the chemical structures of the host and emitting materials (right).

2.1.1. Bis(2-(2-hydroxyphenyl)-pyridine)beryllium ($Bepp_2$)

MS: *m/z* 349 (M^+). Anal. Calcd for $C_{22}H_{16}N_2O_2Be$: C: 75.62%, H: 4.62%, N: 8.02%. Found: C: 75.54%, H: 4.71%, N: 7.89%. ^{1}H NMR (300 MHz, $CDCl_3$) δ 8.52 (d, *J* = 2.5 Hz, 2H), 7.93 (d, *J* = 4.25 Hz, 2H), 7.84 (t, *J* = 8.75 Hz, 2H), 7.80 (d, *J* = 4.75 Hz, 2H), 7.31 (t, *J* = 8.5 Hz, 2H), 7.25 (t, *J* = 6.25 Hz, 2H), 7.04 (d, *J* = 4 Hz, 2H), 6.92 (t, *J* = 8 Hz, 2H).

2.1.2. Bis(7,8-benzoquinolinato) iridium(III) (*N*,*N*′-diisopropyl-benzamidine) ($(bzq)_2Ir(dipba)$)

MS: m/z 753 (M^+). Anal. Calcd for $C_{39}H_{35}IrN_4$: C, 62.29; H, 4.69; N, 7.45. Found: C, 62.12; H, 4.78; N, 7.55. ^{1}H NMR (300 MHz, $CDCl_3$) δ 9.63 (d, *J* = 5.10, 2H), 8.19 (d, *J* = 8.1 Hz, 2H), 7.74 (d, *J* = 9.0 Hz, 2H), 7.62 (t, *J* = 7.2, 2H), 7.60 (d, *J* = 9.0 Hz, 2H), 7.44 – 7.33 (m, 5H), 7.30 (d, *J* = 8.1 Hz, 2H), 6.91 (t, *J* = 7.2 Hz, 2H), 6.38 (d, *J* = 7.2 Hz, 2H), 3.23–3.16 (m, 2H), 0.65 (d, *J* = 6.0 Hz, 6H), −0.47 (d, *J* = 6.0 Hz, 6H).

2.2. Absorption, PL and electrochemical measurements

Absorption spectra were obtained using a Shimadzu UV-2550 UV–vis spectrometer. The PL spectra were recorded by a Perkin–Elmer LS-55 fluorescence spectrometer with a Xe arc lamp excitation source. All solvents were degassed via three freeze–pump–thaw cycles before use.

Electrochemical measurements were performed on a BAS 100 W Bioanalytical electrochemical work station, using Pt as the working electrode, platinum wire as the auxiliary electrode, and a porous glass wick Ag/Ag^+ as the reference electrode, standardized against ferrocene/ferrocenium couple, scan rate 100 mV s^{-1}. Due to the limitation [13] in measuring reduction potentials in the range of −2.7 to −3.5 V in CH_2Cl_2, only the oxidation potentials for $Bepp_2$ and $(bzq)_2Ir(dipba)$ were obtained, and no reduction wave was detected within the electrochemical window of CH_2Cl_2. The highest occupied molecular orbital (HOMO) and the lowest unoccupied molecular orbital (LUMO) energy levels of both complexes were calculated from the cyclic voltammetry (CV) data as well as their absorption spectra. The proposed energy diagram of the materials used in OLEDs is shown in Fig. 1, where the values for NPB, CBP and TPBI are taken from the literature [14].

2.3. Fabrication of the OLEDs and EL measurements

The devices were grown on a glass slide precoated with indium tin oxide (ITO) that has a sheet resistance equal to 20 Ω cm^{-2}. The ITO glass was routinely cleaned by sonicating in detergent solutions, rinsing with acetone, boiling in isopropanol, rinsing with methanol, and then de-ionized water. The glass was dried in vacuum oven between each cleaning step above. To reduce the possibility of electrical shorts on the ITO anode and increase the value of its work function, the ITO substrate was treated using a Plasma Cleaner (PDC-32G-2, 100 W) with the oxygen ambient. Prior to the deposition, all the organic materials were purified by sublimation. The organic layers were sequentially deposited onto the substrate without breaking vacuum at a pressure of about 10^{-4} Pa. A very thin layer of LiF was used to enhance electron injection from aluminum cathode. A shadows mask with 2×3 mm^2 openings was used to define the cathode. The EL spectra, brightness, CIE coordinates and the current–brightness–voltage characteristics of the devices were measured with a rapid scan system using a spectrophotometer (PR-650, Photo Research) and a computer-controlled, programmable, direct-current (DC) source (Keithley 2400). Luminance–voltage and current–voltage characteristics of the EL devices were measured at room temperature under an ambient atmosphere.

3. Results and discussion

3.1. Absorption and photoluminescent (PL) properties

To investigate the energy-transfer properties of the host–guest system, a series of evaporated-film and solution samples of $Bepp_2$ and $(bzq)_2Ir(dipba)$ were prepared, and their UV–vis absorption and PL emission spectra are shown in Fig. 2. The $(bzq)_2Ir(dipba)$ neat film exhibits a typical metal-to-ligand charge transfer (MLCT) absorption band centered at 520 nm and a strong orange emission at 600 nm. The PL spectrum of the $Bepp_2$ neat film shows an emission peak at 445 nm at room temperature and this peak blue shifts to 430 nm at 77 K (the glass state) with a phosphorescence shoulder at 470 nm [15]. From these spectroscopic data, the corresponding triplet energy (T_1) of $Bepp_2$ was estimated to be 2.6 eV, higher than the value (2.2 eV) estimated for $(bzq)_2Ir(dipba)$. The fact that the phosphorescence spectrum of $Bepp_2$ and the MLCT absorption band of $(bzq)_2Ir(dipba)$ significant overlaps together with a triplet energy alignment suggest that an efficient triplet energy transfer from $Bepp_2$ to $(bzq)_2Ir(dipba)$ is possible. Indeed, this efficient triplet energy transfer has been demonstrated by the unique emission observed in the PL spectrum of the $Bepp_2$: $(bzq)_2Ir(dipba)$ thin film with the doping concentration of 8 wt%.

3.2. EL properties

To examine the EL properties of $Bepp_2$ as an electron-transporting host material, a series of PHOLEDs (devices I–III) were fabricated with a device configuration of ITO/NPB (40 nm)/doping EML (8 wt%, 15 nm)/ETL and HBL (35 nm)/LiF (1 nm)/Al. In devices I and III, 1,3,5-tris(*N*-phenylbenzimidazol-2-yl)benzene (TPBI) was used as the electron-transporting layer (ETL) and hole-blocking layer (HBL) [16], whereas in device II a neat film of $Bepp_2$ was used as the ETL. To test the EML property of $Bepp_2$, in devices I and II, a film of $Bepp_2$ doped with $(bzq)_2Ir(dipba)$ was used as the emitting layer. For comparison, device III using CBP instead of $Bepp_2$ as the host was fabricated.

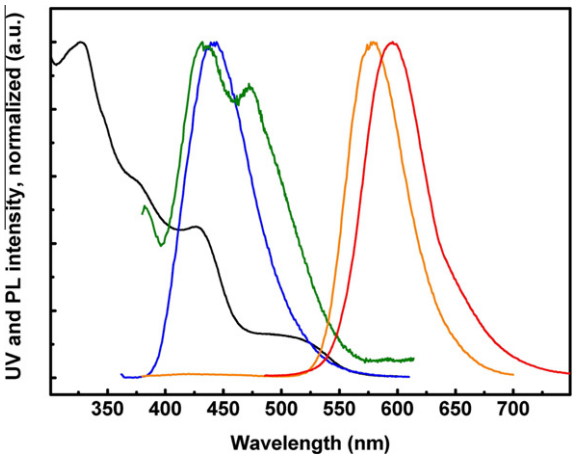

Fig. 2. UV absorption spectrum (black line) and PL spectrum (red line) of neat $(bzq)_2Ir(dipba)$ film, PL spectrum of neat $Bepp_2$ film (blue line), PL spectrum in solution (THF, 77 K) (green line) and PL spectrum of $(bzq)_2Ir(dipba)$ doped in $Bepp_2$ film (8 wt%) (orange line). (For interpretation of the references to color in this figure legend, the reader is referred to the web version of this article.)

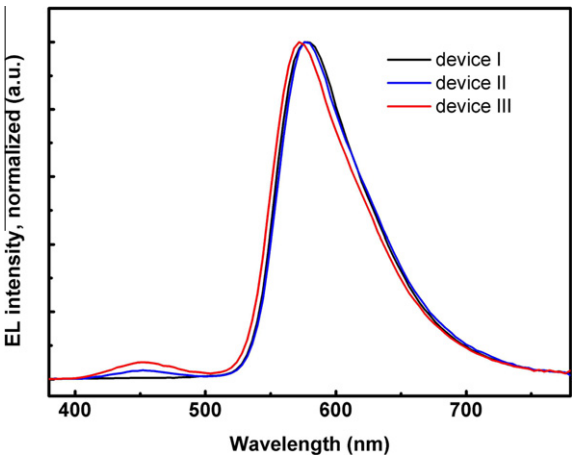

Fig. 3. EL spectra of device I, II and III at the brightness of 10,000 cd m^{-2}.

As shown in Fig. 3, the normalized EL spectra of device I, II, and III at high brightness of 10,000 cd m^{-2} all have similar emission peaks at around 575 nm. The lack of a host emission in the EL spectrum of device I indicates a complete energy transfer from $Bepp_2$ to $(bzq)_2Ir(dipba)$. This is as expected under the doping concentration of 8 wt% and is consistent with the characteristic PL spectra of the doped film shown in Fig. 2. In device II, where neat $Bepp_2$ film is utilized as the ETL, a slight shoulder emission at

around 450 nm is observed as the brightness gradually increased above 5000 cd m^{-2}. Because devices I and II use the same host:dopant combination as well as the doping concentration and thickness, the slight change of their EL spectra at high brightness, i.e., high driving voltages, indicates that the recombination zone in device II is extended to the ETL region made of neat $Bepp_2$. This extension of the recombination zone in device II is consistent with the fact that a HBL such as a TPBI film is not present in device II but is present in device I. In device III, a weak emission at 450 nm was also observed that can be attributed to the emission from CBP that originates from incomplete energy transfer and/or charge transfer from the host to the guest [17]. The presence of this weak emission from CBP suggests that it is not a favorable host for this specific phosphorescent guest emitter, i.e., $(bzq)_2Ir(dipba)$.

As shown in the current density–brightness–voltage plots (Fig. 4), devices I and II exhibited similar and very low turn-on voltage of 2.8 and 2.7 V, respectively, much lower than the 3.5 V value of the CBP-based device III. Moreover, devices I and II show a fast rise of the EL intensity and the current density as the voltage increases. The driving voltages of the $Bepp_2$-based devices I and II at a brightness of 100 cd m^{-2} and a current density of 100 mA cm^{-2} are ~3.7 and 7–8 V, respectively. These values are much lower than those of the CBP-based device, i.e., 5.0 and 11.0 V, respectively. At a driving voltage of 9.5 V, devices I and II reached their peak radiance at 36,110 and 31,170 cd m^{-2}, respectively, whereas devices III needed a higher voltages of 13.5 V to achieve the same brightness levels (37,110 cd m^{-2}). The relatively low driving voltages and the linear response of brightness with current density for devices I and II indicate that they are highly efficient PHOLEDs that have a suitable host–guest system. Since both devices I and II use $Bepp_2$ as the host material, this high efficiency can be attributed to the higher HOMO levels of the beryllium complex than that of CBP (See Fig. 1 for the energy-level diagrams). The low driving voltages of devices I and II may also result from the well-matched energy levels of $Bepp_2$ with HTL that enhances the holes injection from the HTL to the EML. When compared with device I, device II shows a slightly faster rise in the current density and a slower rise in the EL intensity as the driving voltage increases. This trend becomes more obvious as the driving voltage increases further and further (Fig. 4). This phenomenon supports our previous hypothesis that the holes or excitons may have leaked into the ETL in device II. As a result, the triplet excitons could have been quenched in the neat $Bepp_2$ ETL of device II, leading to lower EL performance.

The LE (luminous efficiency)–EQE (external quantum efficiency)–PE (power efficiency)–brightness characteristics for devices I, II and III are shown in Fig. 5. As expected, both devices based on $Bepp_2$ show much higher EL efficiencies than those of CBP-based device III. Devices I and II exhibit the exciting peak LE of 70.9 cd A^{-1} (23.4% for EQE, 4.4 V) and 62.8 cd A^{-1} (21.4% for EQE, 4.0 V) at the reliable brightness of 605 and 270 cd m^{-2}, respectively. In comparison, device III exhibit a much lower peak value of 38.1 cd A^{-1} (12.4% for EQE) at the brightness of 245 cd m^{-2} (5.5 V). In addition, as a result of the low driving voltages, the PE of $Bepp_2$-based devices are dramatically enhanced. The maximum PE and the corresponding values at the practical brightness of 100 and 1000 cd m^{-2} are 56.3, 56.1 and 46.8 lm W^{-1} for device I and 51.9, 51.5 and 36.5 lm W^{-1} for device II, respectively. These PE values are significantly better than those of device III, i.e., 23.0, 23.0 and 17.6 lm W^{-1}, respectively.

These data showed that there are at least three properties of $Bepp_2$ make it to construct an OLED with high EL efficiency and relatively low driving voltages. First, the HOMO levels of $Bepp_2$ in ETL and NPB in HTL match very well. Second, the relatively high energy of the triplet state of $Bepp_2$ together with a well overlap of the phosphorescence spectrum of $Bepp_2$ and the MLCT absorption band of $(bzq)_2Ir(dipba)$ ensure that an exothermic energy transfer from the host to the guest can occur. Third, the similar LUMO energy levels of $Bepp_2$, TPBI and $(bzq)_2Ir(dipba)$ (shown in Fig. 1) can facilitate a smooth injection of electrons from TPBI to $Bepp_2$ and also possibly a direct electron injection and exciton formation from TPBI onto

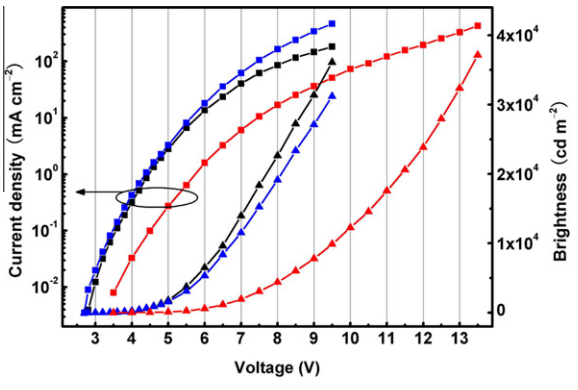

Fig. 4. Current density–brightness–driving voltage curves of device I (black), II (blue) and III (red). (For interpretation of the references to color in this figure legend, the reader is referred to the web version of this article.)

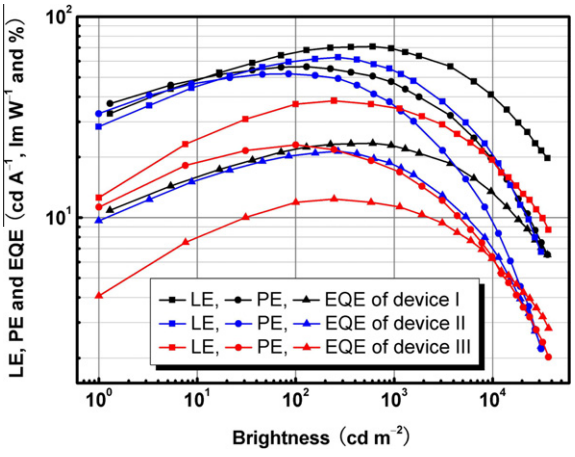

Fig. 5. LE (luminous efficiency)–, EQE (external quantum efficiency)– and PE (power efficiency)–brightness characteristics for the device I, II and III.

$(bzq)_2Ir(dipba)$ [18]. We have previously demonstrated the direct electron injection and exciton formation mechanism can improve EL efficiencies [12,15b]. In comparison with $Bepp_2$, CBP used in device III has a much lower LUMO level that can act as trapping sites for electrons. This electron trapping could reduce the EL performance of the corresponding devices also.

4. Conclusions

In summary, highly efficient PHOLEDs employing a classical beryllium metal–chelate complex $Bepp_2$ as a host material have been successfully developed. The $Bepp_2$-based devices exhibit significantly enhanced EL performance with low driving voltages and high EL efficiencies compared with the device that uses CBP as the host as well as those PHOLEDs reported in the literature that use fluorescent metal–chelate complexes at electron-transporting-type host material [1b,9]. The excellent EL performance of the $Bepp_2$-based devices is attributed to the well-matched energy levels of $Bepp_2$ with HT and ET (or HB) materials together with the efficient triplet energy transfer from $Bepp_2$ to the $(bzq)_2Ir(dipba)$ guest. This efficient transfer of triplet energy between $Bepp_2$/$(bzq)_2Ir(dipba)$ is especially important because our host/guest system of $Bepp_2$/$(bzq)_2Ir(dipba)$ show a much better EL performance than the systems based on $Bepp_2$ and other phosphorescence guests such as $Ir(ppy)_3$ [10]. These findings demonstrate that $Bepp_2$ is a promising host material to replace the commonly used CBP because of its higher EL efficiency and its relative high triplet energy (~2.6 eV). This high triplet energy should facilitate the development highly efficient PHOLEDs based on green-, orange- and red-phosphorescent guest emitters.

Acknowledgements

This work was partly supported by National Basic Research Program of China (973 Program, 2009CB623600), Natural Science Foundation of China (50733002 and 50903036), Provincial Science and Technology Bureau of Jilin Province (201105010).

References

[1] (a) C.W. Tang, S.A. VanSlyke, C.H. Chen, J. Appl. Phys. 65 (1989) 3610;
(b) M.A. Baldo, D.F. O'Brien, Y. You, A. Shoustikov, S. Sibley, M.E. Thompson, S.R. Forrest, Nature 395 (1998) 151.
[2] (a) M.A. Baldo, S. Lamansky, P.E. Burrows, M.E. Thompson, S.R. Forrest, Appl. Phys. Lett. 75 (1999) 4;
(b) M.K. Nazeeruddin, R. Humphry-Baker, D. Berner, S. Rivier, L. Zuppiroli, M. Graetzel, J. Am. Chem. Soc. 125 (2003) 8790;
(c) L.Q. Chen, H. You, C.L. Yang, D.G. Ma, J.G. Qin, Chem. Commun. (2007) 1352.
[3] V. Adamovich, J. Brooks, A. Tamayo, A.M. Alexander, P. Djurovich, B.W. D'Andrade, C. Adachi, S.R. Forrest, M.E. Thompson, New J. Chem. 26 (2002) 1171.
[4] M. Ikai, S. Tokito, Y. Sakamoto, T. Suzuki, Y. Taga, Appl. Phys. Lett. 79 (2001) 156.
[5] (a) Y.T. Tao, Q. Wang, C.L. Yang, C. Zhong, K. Zhang, J.G. Qin, D.G. Ma, Adv. Func. Mater. 20 (2010) 304;
(b) Y.T. Tao, Q. Wang, C.L. Yang, C. Chong, J.G. Qin, D.G. Ma, Adv. Func. Mater. 20 (2010) 2923.
[6] (a) H. Antoniadis, M.A. Abkowitz, B.R. Hsieh, Appl. Phys. Lett. 65 (1994) 2030;
(b) S.C. Tse, K.C. Kwok, S.K. So, Appl. Phys. Lett. 89 (2006) 262102;
(c) K.K. Tsung, S.K. So, Appl. Phys. Lett. 92 (2008) 103315;
(d) D.D. Zhang, J. Feng, Y.F. Liu, Y.Q. Zhong, Y. Bai, Y. Jin, G.H. Xie, Q. Xue, Y. Zhao, S.Y. Liu, H.B. Sun, Appl. Phys. Lett. 94 (2009) 223306;
(e) D.D. Zhang, J. Feng, H. Wang, Y. Bai, Q.D. Chen, S.Y. Liu, H.B. Sun, Appl. Phys. Lett. 95 (2009) 263303.
[7] C. Adachi, M.A. Baldo, M.E. Thompson, S.R. Forrest, J. Appl. Phys. 90 (2001) 5048.
[8] (a) R.J. Holmes, B.W. D'Andrade, S.R. Forrest, X. Ren, J. Li, M.E. Thompson, Appl. Phys. Lett. 83 (2003) 3818;
(b) X. Ren, J. Li, R.J. Holmes, P.I. Djurovich, S.R. Forrest, M.E. Thompson, Chem. Mater. 16 (2004) 4743.
[9] L.S. Hung, C.H. Chen, Mater. Sci. Eng. R 39 (2002) 143.
[10] (a) W.S. Jeon, T.J. Park, J.J. Park, S.Y. Kim, J. Jang, J.H. Kwon, R. Pode, Appl. Phys. Lett. 92 (2008) 113311;
(b) W.S. Jeon, T.J. Park, S.Y. Kim, R. Pode, J. Jang, J.H. Kwon, Appl. Phys. Lett. 93 (2008) 063303;
(c) S.Y. Kim, W.S. Jeon, T.J. Park, R. Pode, J. Jang, J.H. Kwon, Appl. Phys. Lett. 4 (2009).
[11] (a) Y.Q. Li, Y. Liu, W.M. Bu, Da Lu, Y. Wu, Y. Wang, Chem. Mater. 12 (2000) 2672;
(b) Y. Liu, J.H. Guo, J. Feng, H.D. Zhang, Y.Q. Li, Y. Wang, Appl. Phys. Lett. 78 (2001) 2300.
[12] T. Peng, Y. Yang, Y. Liu, D.G. Ma, Z.M. Hou, Y. Wang, Chem. Commun. 47 (2011) 3150.
[13] S. Jung, Y.J. Kang, H.S. Kim, Y.H. Kim, C.L. Lee, J.J. Kim, S.K. Lee, S.K. Kwon, Eur. J. Inorg. Chem. 17 (2004) 3415.
[14] (a) T. Tsuzuki, S. Tokito, Adv. Mater. 19 (2007) 276;
(b) C.-H. Chien, C.-K. Chen, F.-M. Hsu, C.-F. Shu, P.-T. Chou, C.-H. Lai, Adv. Func. Mater. 19 (2009) 560.
[15] (a) K. Goushi, R. Kwong, J.J. Brown, H. Sasabe, C. Adachi, J. Appl. Phys. 95 (2004) 7798;
(b) T. Peng, Y. Yang, H. Bi, Y. Liu, Z.M. Hou, Y. Wang, J. Mater. Chem. 21 (2011) 3551.
[16] (a) K.R.J. Thomas, J.T. Lin, Y.-T. Tao, C.-W. Ko, J. Am. Chem. Soc. 123 (2001) 9404;
(b) B.W. D'Andrade, S.R. Forrest, Adv. Mater. 16 (2004) 1585.
[17] Z.Q. Gao, M. Luo, X.H. Sun, H.L. Tam, M.S. Wong, B.X. Mi, P.F. Xia, K.W. Cheah, C.H. Chen, Adv. Mater. 21 (2009) 688.
[18] Q. Wang, J.Q. Ding, D.G. Ma, Y.X. Cheng, L.X. Wang, X.B. Jing, F.S. Wang, Adv. Func. Mater. 19 (2009) 84.

morphology for organic BHJ solar cells is where the lateral dimensions of the donor and acceptor domains correspond to roughly twice the exciton diffusion lengths while the domains form continuous pathways for electrons and holes along the current direction.

Various parameters such as: solvents [7,11,12], drying time of the active layer [13,14], techniques used for deposition [14], ratio between electron donor and electron acceptor materials [15] and the post-annealing [6] affect extensively the morphology and the performance of polymer BHJ solar cells. Due to large variation in material properties, an optimized processing recipe for one polymer:fullerene system cannot be extrapolated directly to another polymer:fullerene system. Generally, if the polymer:fullerene system is changed, the optimum processing conditions have to be determined again.

However, it has been shown that regardless of the polymer:fullerene system used, a nano-scale interpenetrating network of electron-donor and electron-acceptor is unquestionably a common feature that is required for an efficient BHJ cells [16].

Besides optimizing the aforementioned processing parameters to gain control of the nano-scale structure of polymer solar cells, several other approaches have also been used to fine tune the phase morphology of BHJ films with some success. These include the addition of processing additives to the blend of polymer:fullerene to enhance the phase separation between the two materials [17], and the vertical modulation of the nano-scale morphology by modifying the distribution of donors and acceptors to make the BHJ layers richer in donors and acceptors near the anode and the cathode respectively [18].

Recently, poly(2,7-carbazole) derivatives have gained momentum as a class of promising alternative materials to poly(3-hexylthiophene) (P3HT) in organic solar cell applications. Among them, poly[N-9″-hepta-decanyl-2,7-carbazole-alt-5,5-(4′,7′-di-2-thienyl-2′,1′,3′-benzothiadiazole)] (PCDTBT) has a relatively deeper highest occupied molecular orbital (HOMO) of 5.45 eV compared to the HOMO of 5.1 eV of the P3HT. As a result, a high open circuit voltage (V_{oc}) of 0.9 V was reached in PCDTBT:fullerene devices [5]. In addition, the HOMO level of the PCDTBT is below the air oxidation threshold of 5.27 eV, which ensures better air-stability [19]. Park et al. reported a power conversion efficiency (PCE) of 6.1% on devices with an active area of 0.127 cm^2 prepared by spin-coating a dichlorobenzene solution of PCDTBT:$PC_{70}BM$ (1:4) as the active layer, and a thin TiOx layer as an optical spacer [7]. We demonstrated the importance of optical interference in PCDTBT/$PC_{70}BM$ device optimization and the need to consider the whole layer stack as a system in optical design, and obtained a PCE of 5.7% on cells with an active area of 1.0 cm^2. However, efforts to further improve the device efficiency were hampered by the fact that PCDTBT is an amorphous polymer, and responds poorly to thermal or solvent annealing, and to the use of common additives.

In this paper, we report the effect of processing conditions on the performance of PCDTBT:$PC_{70}BM$ based cells, and the fine tuning of the nano-scale morphology of PCDTBT:$PC_{70}BM$ BHJ active layers by using a mixed solvent. In the first part of the experiment, the active layers with different PCDTBT:$PC_{70}BM$ ratios were spin cast using two solvents: chloroform (CF) and 1,2-dichlorobenzene (ODCB). These solvents were chosen primarily due to the good solubility of PCDTBT and $PC_{70}BM$ in them. However, as chloroform and 1,2-dichlorobenzene have respectively a low (60 °C) and a high (178 °C) boiling point, the PCDTBT:$PC_{70}BM$ films prepared using CF or ODCB exhibit very different morphologies, possibly due to the slow and fast evaporation rate of solvents. These observations are correlated to the organic field effect transistor (OFET) transport measurements to explain the variations in photovoltaic (PV) performance. The electron mobility in the BHJ films prepared with ODCB is very close to that in pure $PC_{70}BM$ film, and the hole mobility is close to that in pure PCDTBT film, indicating the formation of a more or less continuous donor and acceptor network. As a result, the devices prepared using ODCB show better overall photovoltaic performance than the ones prepared using CF.

For the second part of the experiment, the nano-scale morphology of the PCDTBT:$PC_{70}BM$ BHJ film was further tuned by using a mixed solvent of chloroform and 1,2-dichlorbenzene. At a CF:ODCB ratio of 50%:50%, a high PCE of 6.1% was achieved on PCDTBT:$PC_{70}BM$ (1:3) devices with an active area of 1 cm^2, under AM 1.5 G irradiation of 100 mW/cm^2, where an optimal phase separation led to low exciton recombination rate and the highest short-circuit current density. This PCE, obtained without using an optical spacer and antireflective coating on the glass, approaches the theoretical limit of 6.5% as estimated from the Scharber diagram [20,21].

2. Experimental

Pre-patterned indium tin oxide (ITO)-coated glass slides, purchased from Luminescence Technology Corp., were used as substrates. The sheet resistance and thickness of the ITO are 12 Ω/sq and 150 nm, respectively. The ITO substrates were first cleaned with detergent, ultrasonicated in acetone and isopropyl alcohol for 15 min, and dried in an oven at 120 °C. UV-ozone treatment was then performed for 15 min. A film of poly(ethylene dioxythiophene) (PEDOT:PSS-Baytron® P) was spin cast on top of the ITO substrates and was dried for 15 min at 140 °C. Afterwards, chloroform and 1,2-dichlorobenzene solutions of PCDTBT:$PC_{70}BM$ with different weight ratios (1:2, 1:3, 1:4) were spin cast in a nitrogen-filled glove-box, onto the PEDOT:PSS film to form the active layer. The thickness of the PEDOT:PSS layer (30 nm) and the active layer (80 nm) were optimized in our previous work [5]. Finally, a bilayer cathode consisting of 100 nm Al on top of 2 nm LiF was thermally evaporated through a shadow mask on the active layer to form cells with an active area of 1 cm^2. More than 70 devices cast from CF, ODCB and a mixture of CF and ODCB in different ratios were fabricated and characterized.

The photovoltaic parameters were extracted from the current–voltage (J–V) characteristics measured in air with a Keithley 2400 Digital SourceMeter and the photocurrent was generated under AM 1.5 G irradiation of 100 mW/cm^2 from a ScienceTech SS 500 W solar simulator. The light intensity was adjusted using a calibrated Si photodiode with a KG-5 filter purchased from PV Measurements, Inc.

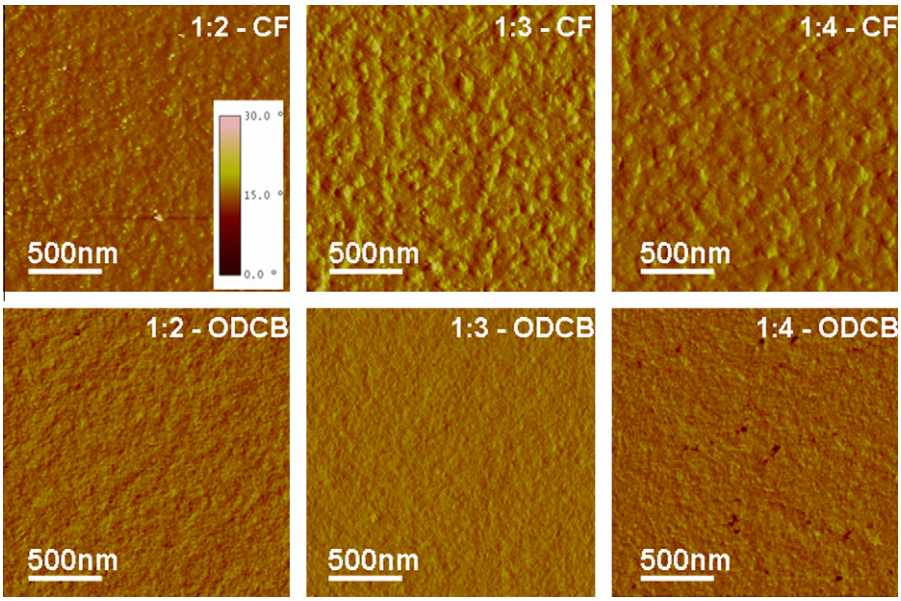

Fig. 1. Tapping-mode atomic force microscopy images of PCDTBT:$PC_{70}BM$ films cast from chloroform and 1,2-dichlorobenzene with different PCDTBT:$PC_{70}BM$ weight ratios on PEDOT:PSS layer.

The thickness of the polymer films were measured by a Dektak profilometer.

For OFET measurement, a heavily doped n-Si wafer with an overlayer of SiO_2 (230 nm, Ci = 15nF/cm^2) was used as a substrate. With bottom contact configuration, sputtered gold films were used as Source and Drain electrodes. An interdigitated layout was used for the OFET where channel length and width are 20 μm and 10 mm, respectively. PCDTBT:$PC_{70}BM$ solutions, like the PV devices, were spin cast to cover the Source and Drain electrodes.

The hole and the electron mobilities were deduced from the saturation regime of the *J–V* characteristics, which were performed with a computer-controlled semiconductor parameter analyzer (HP4145A).

3. Results and discussion

Fig. 1 displays the surface topography, investigated by the atomic force microscopy (AFM), of PCDTBT:$PC_{70}BM$ films with various weight ratios, cast from CF and ODCB solutions on the PEDOT:PSS layer. The PV parameters of corresponding devices are shown in Table 1.

The ODCB-films exhibit a smooth surface and small domains, while the CF-films exhibit a structured surface with large domains. Surface roughness values measured for 1:2, 1:3 and 1:4 PCDBTB:$PC_{70}BM$ weight ratios were: ~1.17, 1.21 and 1.22 nm for CF-films; ~0.89, 0.90 and 0.86 nm for ODCB-films, respectively. The increase of domains size with increasing ratio of $PC_{70}BM$ in the CF-films is presumably the reason for the decrease of the short circuit current density in CF-devices (see Table 1); as large domains in BHJ layer not only increase the distance for excitons to reach an heterojunction, but also reduce the interfaces between the polymer and the fullerene, leading to a low exciton dissociation efficiency. The short-circuit current density (J_{sc}) of ODCB-devices remains constant (around 10.7 mA/cm^2) for different PCDBTB:$PC_{70}BM$ ratios. This trend has also been observed with the J_{sc} values calculated from the external quantum efficiency (EQE) data (Fig. 2). The J_{sc} values calculated from the EQE data of CF-devices with 1:2, 1:3 and 1:4 ratios are 10.3, 9.8, and 8.9 mA/cm^2, respectively. For ODCB-devices, the values are 10.2, 10.3, and 10.2 mA/cm^2. These values are about 3.7–5.5% lower than those obtained from *J–V* characteristics, indicating a possible spectral mismatch within this error range.

Table 1
Photovoltaic parameters and OFET mobility of devices based on PCDTBT:$PC_{70}BM$ active layer cast from chloroform and 1,2-dichlorobenzene with different PCDTBT:$PC_{70}BM$ weight ratios.

Active layer spun-cast from	Ratio *D*:*A*	J_{sc} (mA/cm^2)	V_{oc} (V)	FF (%)	η (%)	μ_H	μ_E	μ_E/μ_H
						(*10^{-4} cm^2/V s)		
Chloroform	1:2	10.7	0.91	59	5.7	5.84	1.75	0.30
	1:3	10.3	0.89	61	5.6	5.51	3.70	0.67
	1:4	9.3	0.88	61	5.0	6.11	5.44	0.89
1,2-Dichlorobenzene	1:2	10.7	0.91	58	5.6	1.98	9.27	4.68
	1:3	10.8	0.89	62	6.0	1.92	20.1	10.5
	1:4	10.8	0.88	63	6.0	1.99	29.1	14.6

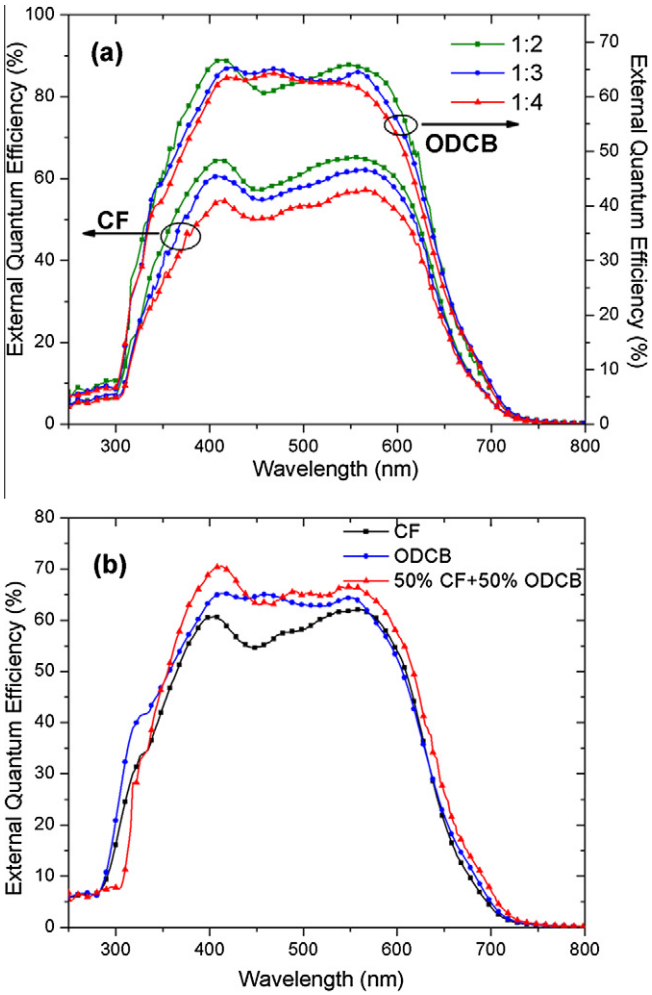

Fig. 2. Comparison of external quantum efficiencies of PCDTBT:$PC_{70}BM$ devices cast from chloroform and 1,2-dichlorobenzene with different weight ratios (a) and mixed CF:ODCB solvent for a PCDTBT:$PC_{70}BM$ weight ratio of 1:3 (b).

It is worth noting that at the same PCDTBT:$PC_{70}BM$ ratio there is no difference in the total light absorption by the devices prepared by CF or ODCB, as revealed by small angle reflectance (data not shown) measurement. Therefore the difference in their J_{sc} at the same PCDTBT:$PC_{70}BM$ ratio for the CF and ODCB-devices is not caused by light absorption.

A small reduction in V_{oc} was observed with the increase of $PC_{70}BM$ concentration in both CF and ODCB-devices. This trend was previously observed in other polymer:fullerene system devices [22,23]. The exact reason for the reduction in V_{oc} is not clear. It might be caused by the increase in leakage current with increasing $PC_{70}BM$ concentration [24]; or by the energetic losses of the dissociated charges due to the band bending at the electrodes [25], which is probably affected by $PC_{70}BM$ concentration. Another possibility is that at higher PCBM concentration the charge transfer state may shift to a lower energy as a result of increased permittivity, causing a reduction in V_{oc}, as shown in polyfluorene copolymer/fullerene devices [23].

We attempt to correlate the nano-scale morphology of the active layers and the PV parameters of the devices to the charge carrier mobility data measured from OFET mobility tests, shown in Table 1. The electron and hole mobilities are assigned to the electron acceptor ($PC_{70}BM$) and electron donor (PCDTBT) materials respectively.

Three observations ensue from OFET data. Firstly the electron mobility increases with the ratio of $PC_{70}BM$ for both CF- and ODCB-films. This illustrates an enhanced electron transport in the BHJ films due to improved connections between $PC_{70}BM$ molecules, leading to a higher fill factor in PV devices. But the ODCB-films exhibit much finer domain structure and relatively higher electron mobility, and at PCDTBT:$PC_{70}BM$ ratio of 1:4, the electron mobility approaches the value in pure $PC_{70}BM$ film (3.5×10^{-3} cm^2/V s), demonstrating a much better connection between $PC_{70}BM$ molecules and domains, as compared with the CF-films. Secondly, the hole mobility remains approximately constant at different ratios of PCDTBT:$PC_{70}BM$, proving that even with high concentration of $PC_{70}BM$, a continuous network of PCDTBT is maintained. Thirdly, the domain size plays a critical role in determining the exciton dissociation efficiency, and thus the short circuit current. As shown by the device prepared from CF solution at a PCDTBT:$PC_{70}BM$ weight ratio of 1:4, although the electron mobility is much

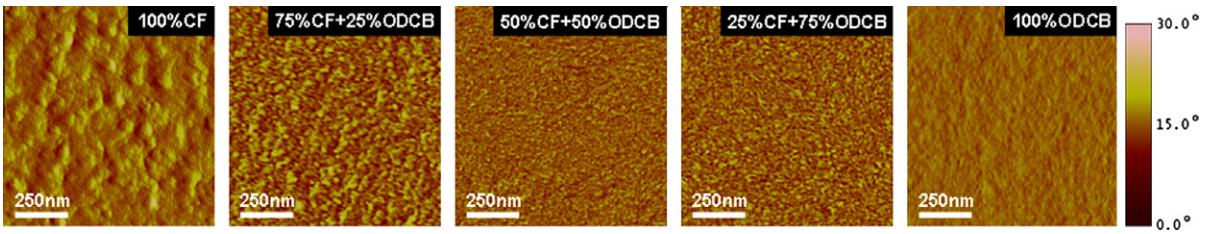

Fig. 3. Comparison of atomic force microscopy images of PCDTBT:$PC_{70}BM$ (weight ratio 1:3) spin cast from various CF:ODCB ratios on PEDOT:PSS layer.

Table 2
Photovoltaic parameters of devices based on PCDTBT:$PC_{70}BM$ (1:3) active layer cast from chloroform, 1,2-dichlorobenzene, and a mixture of chloroform and 1,2-dichlorobenzene with different ratios.

Active layer spun-cast from	J_{sc} (from EQE) (mA/cm^2)	V_{oc} (V)	FF (%)	η (%)
CF	10.3 (9.8)	0.89	61	5.6
75% CF + 25% ODCB	10.5 (10.3)	0.90	59	5.6
50% CF + 50% ODCB	11.0 (10.7)	0.91	61	6.1
25% CF + 75% ODCB	11.0 (10.8)	0.89	59	5.8
ODCB	10.7 (10.3)	0.89	62	5.9

higher as compared to the devices prepared at 1:2 and 1:3 ratios, the device has the lowest J_{sc} (~9.3 m mA/cm^2) and overall low performance due to the large $PC_{70}BM$ domains. This demonstrates the need of maintaining proper domain size when trying to improve the charge carrier mobilities in BHJ films for high performance.

Fig. 3 shows the AFM images of PCDTBT:$PC_{70}BM$ films (weight ratio 1:3) prepared using mixed CF and ODCB of different ratios (100%:0%, 75%:25%, 50%:50%, 25%:75%, 0%:100%). The domains size becomes progressively finer with increasing ODCB ratio. The corresponding short circuit current densities are 10.3, 10.5, 11.0, 11.0 and 10.7 mA/cm^2 respectively (see Table 2). This trend has also been observed for the short-circuit current densities calculated from the EQE data. Fig. 2b shows the EQE spectra of devices cast from CF, ODCB, and mixed CF and ODCB at 50%:50% ratio.

The J_{sc} is higher for devices cast from 50%:50% and 25%:75% solutions, corresponding presumably to the optimal domain sizes. Larger domains, as in the case of devices cast from 100%:0%, 75%:25% solutions, lead to a larger exciton recombination rate. The domain sizes in films cast from pure ODCB are probably smaller than the exciton diffusion length. Although a small domain structure is very efficient for exciton dissociation, it is not very effective in separating the charge transfer complex and transporting free charge carriers. The highest PCE of 6.1% was obtained from PCDTBT:$PC_{70}BM$ (1:3) devices prepared using a CF:ODCB mixing ratio of 50%:50%, with J_{sc} of 11.0 mA/cm^2, V_{oc} of 0.91 V, and a fill factor of 61% (Table 2). This improvement is attributed to the optimized nano-scale morphology for efficient exciton dissociation and charge transport.

The films prepared using different CF:ODCB ratios were also investigated by using transmission electron microscopy (TEM). The images are shown in Fig. 4. The films cast from mixed CF:ODCB solvent at ratios of 50%:50%, 25%:75% present similar morphology to the film cast from pure ODCB, with fine and indistinguishable domain structure. But domains are clearly discerned in films cast from pure CF solution and they probably correspond to the domains in the AFM images. From the energy dispersive X-ray (EDX) measurement, no sulfur signal was detected from these domains, indicating these are $PC_{70}BM$-rich domains, because PCDTBT contains sulfur and $PC_{70}BM$ does not. This clarifies the AFM results (Fig. 1), where the domain size becomes larger with increasing $PC_{70}BM$ ratio in the blend film.

We believe that the domains are discernable in 100%:0%, 75%:25% films because of their size (>100 nm) is larger than the thickness of the film (~80 nm). When the size becomes smaller than the film thickness (probably the case in 50%:50%, 25%:75%, 0%:100% films), the domains vertically overlap and are hardly distinguishable by transmission electron microscopy.

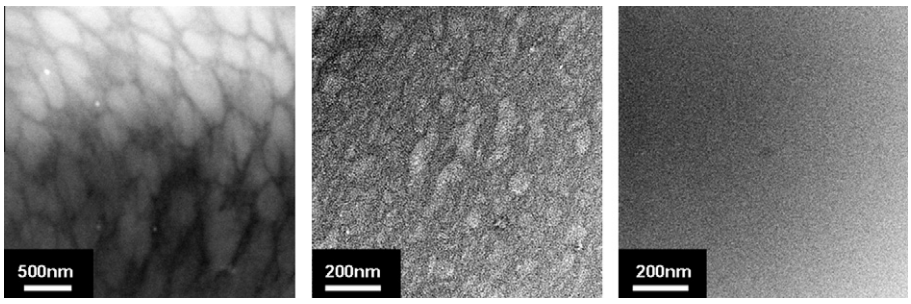

Fig. 4. Transmission electron microscopy images of PCDTBT:$PC_{70}BM$ (weight ratio 1:3) spin cast from 100% CF (left), 75% CF:25% ODCB (center), 100% ODCB (right) on carbon-coated copper TEM grids.

4. Conclusion

In conclusion, PCDTBT:$PC_{70}BM$ active layer spin cast from chloroform solution shows a structured surface with large domains as compared to the films spin cast from 1,2-dichlorobenzene solution. The high values of electron mobility in 1,2-dichlorobenzene devices prove that the 1,2-dichlorobenzene films ensure a better connection between $PC_{70}BM$ domains. The domain size in PCDTBT:$PC_{70}BM$ films can be further tuned by using a mixture of chloroform and 1,2-dichlorobenzene with different ratios. At a CF:ODCB mixing ratio of 50%:50%, a PCE of 6.1% was obtained from PCDTBT:$PC_{70}BM$ (1:3) devices with an active area of 1 cm^2.

Acknowledgments

The authors thank Dr. Xiaohua Wu for the TEM and EDX work, Eric Estwick and Hiroshi Fukutani for their technical support. This project was supported by the Sustainable Development Technology Canada (SDTC).

References

[1] N.S. Sariciftci, L. Smilowitz, A.J. Heeger, F. Wudl, Photoinduced electron transfer from a conducting polymer to buckminsterfullerene, Science 258 (1992) 1474–1476.
[2] G. Yu, A.J. Heeger, Charge separation and photovoltaic conversion in polymer composites with internal donor/acceptor heterojunctions, Journal of Applied Physics 78 (1995) 4510–4515.
[3] G. Yu, J. Gao, J.C. Hummelen, F. Wudl, A.J. Heeger, Polymer photovoltaic cells: enhanced efficiencies via a network of internal donor–acceptor heterojunctions, Science 270 (1995) 1789–1791.
[4] H.-Y. Chen, J. Hou, S. Zhang, Y. Liang, G. Yang, Y. Yang, L. Yu, Y. Wu, G. Li, Polymer solar cells with enhanced open-circuit voltage and efficiency, Nature Photonics 3 (2009) 649–653.
[5] T.-Y. Chu, S. Alem, P.G. Verly, S. Wakim, J. Lu, Y. Tao, S. Beaupré, M. Leclerc, F. Bélanger, D. Désilets, S. Rodman, D. Waller, R. Gaudiana, Highly efficient polycarbazole-based organic photovoltaic devices, Applied Physics Letters 95 (2009) 063304.
[6] W. Ma, C. Yang, X. Gong, K. Lee, A.J. Heeger, Thermally stable, efficient polymer solar cells with nanoscale control of the interpenetrating network morphology, Advanced Functional Materials 15 (2005) 1617–1622.
[7] S.H. Park, A. Roy, S. Beaupre, S. Cho, N. Coates, J. Sun Moon, D. Moses, M. Leclerc, K. Lee, A.J. Heeger, Bulk heterojunction solar cells with internal quantum efficiency approaching 100%, Nature Photonics 3 (2009) 297–302.
[8] W. Cai, X. Gong, Y. Cao, Polymer solar cells: recent development and possible routes for improvement in the performance, Solar Energy Materials and Solar Cells 94 (2010) 114–127.
[9] S. Gunes, H. Neugebauer, N.S. Sariciftci, Conjugated polymer-based organic solar cells, Chemical Reviews 107 (2007) 1324–1338.
[10] Y. Yao, J. Hou, Z. Xu, G. Li, Y. Yang, Effects of solvent mixtures on the nanoscale phase separation in polymer solar cells, Advanced Functional Materials 18 (2008) 1783–1789.
[11] S.E. Shaheen, C.J. Brabec, N.S. Sariciftci, F. Padinger, T. Fromherz, J.C. Hummelen, 2.5% Efficient organic plastic solar cells, Applied Physics Letters 78 (2001) 841–843.
[12] M. Al-Ibrahima, O. Ambacher, S. Sensfuss, G. Gobsch, Effects of solvent and annealing on the improved performance of solar cells based on poly(3-hexylthiophene): fullerene, Applied Physics Letters 86 (2005) 201120.
[13] G. Li, Y. Yao, H. Yang, V. Shrotriya, G. Yang, Y. Yang, "Solvent annealing" effect in polymer solar cells based on poly(3-hexylthiophene) and methanofullerenes, Advanced Functional Materials 17 (2007) 1636–1644.
[14] S.A. Arnautov, E.M. Nechvolodova, A.A. Bakulin, S.G. Elizarov, A.N. Khodarev, D.S. Martyanov, D.Yu. Paraschuk, Properties of MEH-PPV films prepared by slow solvent evaporation, Synthetic Metals 147 (2004) 287–291.
[15] S. Alem, R. de Bettignies, J.-M. Nunzi, M. Cariou, Efficient polymer-based interpenetrated network photovoltaic cells, Applied Physics Letters 84 (2004) 2178–2180.
[16] H. Hoppe, N.S. Sariciftci, Morphology of polymer/fullerene bulk heterojunction solar cells, Journal of Materials Chemistry 16 (2006) 45–61.
[17] J.K. Lee, W.L. Ma, C.J. Brabec, J. Yuen, J. Sun Moon, J.Y. Kim, K. Lee, G.C. Bazan, A.J. Heeger, Processing additives for improved efficiency from bulk heterojunction solar cells, Journal of American Chemical Society 130 (2008) 3619–3623.
[18] A. Kumar, G. Li, Z. Hong, Y. Yang, High efficiency polymer solar cells with vertically modulated nanoscale morphology, Nanotechnology 20 (2009) 165202.
[19] S. Wakim, S. Beaupré, N. Blouin, B.-R. Aich, S. Rodman, R. Gaudiana, Y. Tao, M. Leclerc, Highly efficient organic solar cells based on a poly(2,7-carbazole) derivative, Journal of Materials Chemistry 19 (2009) 5351–5358.
[20] M.C. Scharber, D. Mühlbacher, M. Koppe, P. Denk, C. Waldauf, A.J. Heeger, C.J. Brabec, Design rules for donors in bulk-heterojunction solar cells – towards 10% energy-conversion efficiency, Advanced Materials 18 (2006) 789–794.
[21] N. Blouin, A. Michaud, D. Gendron, S. Wakim, E. Blair, R. Neagu-Plesu, M. Belletete, G. Durocher, Y. Tao, M. Leclerc, Toward a rational design of poly(2,7-carbazole) derivatives for solar cells, Journal of American Chemical Society 130 (2008) 732–742.
[22] H. Hoppe, M. Niggemann, C. Winder, J. Kraut, R. Hiesgen, A. Hinsch, D. Meissner, N.S. Sariciftci, Nanoscale morphology of conjugated polymer/fullerene-based bulk-heterojuction solar cells, Advanced Functional Materials 14 (2004) 1005–1011.
[23] D. Veldman, O. Ipek, S.C.J. Meskers, J. Sweelssen, M.M. Koetse, S.C. Veenstra, J.M. Kroon, S.S. van Bavel, J. Loos, R.A.J. Janssen, Compositional and electric field dependence of the dissociation of charge transfer excitons in alternating polyfluorene copolymer/fullerene blends, Journal of American Chemical Society 130 (2008) 7721–7735.
[24] S.M. Sze, Physics of semiconductor devices, Wiley, New York, 1981.
[25] V.D. Mihailetchi, P.W.M. Blom, J.C. Hummelen, M.T. Rispens, Cathode dependence of the open-circuit voltage of polymer:fullerene bulk heterojunction solar cells, Journal of Applied Physics 94 (2003) 6849–6854.

Like the 'standard' OFET, the device current – and therefore light emission – can be controlled through suitable application of gate and drain voltages, i.e. addressing on a 2D plane. The combination of addressability and efficient light emission into a single device could be advantageous in a display application, but despite such technological potential, the LH-FEBT remains relatively unexplored and much can be done to better understand them. In particular, their current–voltage curves (which are closely tied to light emission) have a distinctive shape that clearly depends on device dimensions and the properties of its constituent semiconductors, and so we explore how these parameters relate to the curves and see if simple rules could be found.

2. Device fabrication

Organic semiconductors combining high mobility with light emission are few and far between. In this study on the current–voltage characteristics of LH-FEBTs, high mobilities took precedence over light emission, and an LH-FEBT based on pentacene (p-type) and zinc oxide (n-type) was studied. The device was fabricated on n^+-Si/SiO_2 (200 nm) substrates by first depositing ZnO by thermal decomposition of zinc acetate precursor [13], which resulted in a roughly 10 nm film. This process was repeated another five times to ensure good ZnO coverage. One half of the ZnO film was then protected with adhesive tape while the exposed half was etched away in dilute acetic acid. The tape was then removed and pentacene was deposited on the bare half of the substrate by thermal evaporation through a shadow mask, which resulted in a slight overlap of pentacene on top of the ZnO. Another shadow mask was aligned onto the sample for deposition of the gold source and drain contacts via evaporation. Fig. 1 (top) shows the schematic device structure.

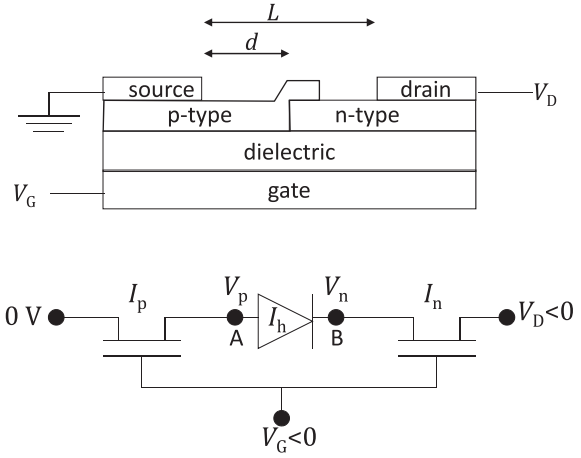

Fig. 1. (Top) Schematic diagram of a pentacene/ZnO LH-FEBT, showing the heterojunction within the transistor channel. L is the total transistor length, and d defines the location of the heterojunction. (Below) An equivalent circuit model of an LH-FEBT consisting of a diode sandwiched between a p-type transistor and an n-type transistor. Points A and B represent virtual contacts between the transistors and the diode, which are at voltages V_p and V_n, respectively. The p-type transistor current depends on V_p and V_G, the diode current depends on $(V_p - V_n)$, and the n-type transistor current depends on V_n, V_D and V_G.

3. Experimental current–voltage curves

Fig. 2A shows the current–drain voltage I_D–V_D curves of the pentacene/ZnO LH-FEBT, as measured by a Keithley 4200 semiconductor analyser, at gate voltages ranging from −10 to −70 V in 10 V steps. Using the curve with a gate voltage of −20 V as an example, the current was low at low drain voltages due to a discontinuous hole accumulation layer. As the drain voltage increased, the hole accumulation layer became continuous and conductivity rose, but the current eventually saturated when the electron accumulation layer was 'pinched off'. Fig. 2B shows the current–gate voltage I_D–V_G curves of the device at drain voltages of −10 to −70 V. These curves all exhibit remarkably similar asymmetric bell-shaped profiles: starting at a low current near 0 V, the current 'turns on' at a gate voltage of roughly −10 V, then increases rapidly to a maximum before attenuating more gradually to zero at a 'turn-off' voltage that depends on the drain voltage. As the drain voltage V_D increases (in magnitude), the peaks increase while also shifting gradually to the right. The I_D–V_G curves are visually more distinctive than the I_D–V_D curves, and the following analysis will therefore address the key features of the I_D–V_G curves: the 'turn-on' and 'turn-off' voltages, the slope before and after the peak, and the peak itself.

4. Equivalent circuit model

Analysis of the current–gate voltage curves of the pentacene/ZnO LH-FEBT is based on an equivalent circuit model, shown in Fig. 1 (bottom). The source contact of the LH-FEBT is grounded, and the drain contact held at a negative drain voltage V_D. The model treats the heterojunction as a diode with 'virtual' contacts at points A and B, with voltages of V_p and V_n, respectively. The diode is thus forward-biased by $\Delta V = (V_p - V_n)$. The virtual contact A also acts as the virtual drain electrode for the p-type transistor on the left of the heterojunction, while virtual contact B acts as the virtual source electrode for the n-type transistor on the right. Since the p- and n-type semiconductors are deposited on a single gate/dielectric substrate, the two transistors must share a gate voltage V_G.

4.1. Mathematical representation

A well-established model (based on the gradual channel approximation) for the current–voltage behaviour of thin film transistors such as OFETs is:

$$I_D = \frac{CW\mu}{L}\left(V_G - V_T - \frac{V_D}{2}\right)V_D \quad (1)$$

in the linear, or non-saturation, regime, where I_D is the current flowing from source to drain, C is the capacitance per unit area of the gate dielectric layer, W is the channel width, μ is the carrier mobility, L is channel length from source to drain, and V_T is the threshold voltage. When the drain voltage increases to $(V_G - V_T)$ and beyond, the vertical field arising from the gate ceases to support a

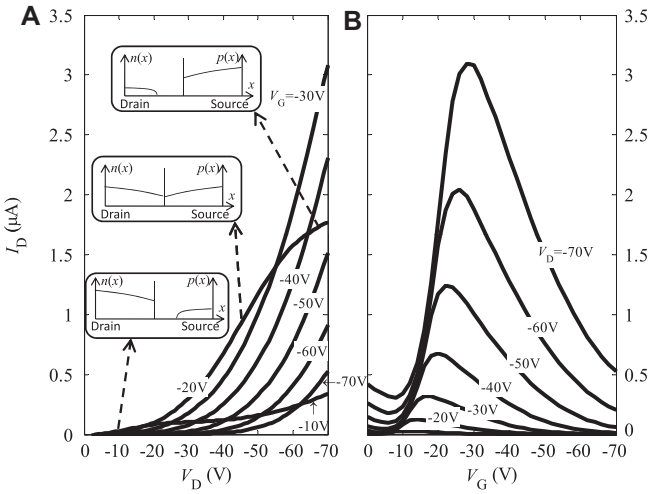

Fig. 2. (A) Current–drain voltage characteristics of a pentacene/ZnO LH-FEBT with gate voltages of −10 to −70 V in 10 V steps. At V_G = −20 V, the output curve began at a low current due to a discontinuous p-channel even though the n-channel is complete. As V_D increased, the p-channel grew to reach the interface so that a complete conduction channel formed and conductivity rose. When V_D increased further, the n-channel became pinched-off and conductivity fell, leading to current saturation. (B) Current–gate voltage characteristics of the same device with drain voltages of −10 to −70 V in 10 V steps. The curves all possess the same asymmetric bell-shaped profile.

continuous conduction channel, and the transistor operates in the saturation regime:

$$I_D = \frac{CW\mu}{2L}(V_G - V_T)^2 \tag{2}$$

We now apply Eqs. (1) and (2) to the model LH-FEBT. Referring to Fig. 1, the source contact of the left-hand-side p-type transistor is at 0 V, while the virtual negative contact is at V_p. Substituting into Eqs. (1) and (2) yields the current I_p in the p-type virtual transistor:

$$I_p = \begin{cases} \frac{CW\mu_p}{d}\left(V_G - V_{Tp} - \frac{V_p}{2}\right)V_p, & V_G - V_{Tp} < V_p \leqslant 0 \\ \frac{CW\mu_p}{2d}(V_G - V_{Tp})^2, & V_p \leqslant V_G - V_{Tp} \leqslant 0 \\ 0, & 0 < V_G - V_{Tp} \end{cases} \tag{3}$$

where μ_p is the hole mobility, V_{Tp} is the threshold voltage for the p-type virtual transistor and d is its channel length, taken to be the length between the positive contact and the heterojunction. Here we have assumed the length of the heterojunction diode to be negligibly small relative to the channel length. For now, we defer discussion of the diode to a later part of the manuscript. From top to bottom, the inequality conditions correspond to the linear regime, the saturation regime and when the transistor is in an 'off' state, respectively.

In the case of the virtual n-type transistor on the right of the heterojunction (see Fig. 1), both the gate voltage V_G and the voltage V_n at the virtual positive contact must be shifted relative to the drain voltage V_D before substitution into Eqs. (1) and (2). This yields the current in the n-type virtual transistor:

$$I_n = \begin{cases} \frac{CW\mu_n}{L-d}\left(V_G - V_D - V_{Tn} - \frac{V_n - V_D}{2}\right)(V_n - V_D), & V_D \leqslant V_n < V_G - V_{Tn} \\ \frac{CW\mu_n}{2(L-d)}(V_G - V_D - V_{Tn})^2, & V_D \leqslant V_G - V_{Tn} \leqslant V_n \\ 0, & V_G - V_{Tn} < V_D \end{cases} \tag{4}$$

where μ_n is the electron mobility and V_{Tn} is the threshold voltage of the n-type virtual transistor.

Illustrative plots of Eqs. (3) and (4) are shown in Fig. 3 for a fixed drain voltage V_D, with Fig. 3A–C each corresponding to a different gate voltage V_G. Fig. 3A corresponds to a regime when V_G is low (close to zero). The I_p and I_n curves are functions of the floating voltages V_p and V_n respectively, and the currents flowing through the two transistors, $I_p(V_p)$ and $I_n(V_n)$, must also equal the diode current $I_h(V_p–V_n)$. Without detailed knowledge of the current–voltage characteristics of the heterojunction diode, a possible operating point of the device can be represented by the dotted tie-line in Fig. 3A, which specifies the current as well as both floating voltages V_p and V_n (crosses).

4.2. Analysis of peak voltage and other key features

Due to saturation behaviour of the p-type transistor, the length of the tie-line, which is also the diode voltage drop, does not affect its vertical position (i.e. device current) appreciably. One can then infer that in the low V_G regime, the LH-FEBT current is effectively the p-type transistor saturation current. Therefore from Eq. (3), the 'turn-on' voltage in the current–gate voltage curves must be the p-type threshold voltage V_{Tp}, while the slope in the low V_G regime is proportional to μ_p/d (see Supplementary information, for more detail).

Fig. 3B shows device operation at an increased V_G while keeping V_D constant. If we make the reasonable assumption that the diode voltage drop (i.e. length of the tie-line) changes negligibly over small current changes, then it becomes clear that Fig. 3B represents device operation at the peak, since deviation from this particular gate voltage in either direction leads to the tie-line moving downwards. At this point, the saturation currents of both virtual transistors equate, but the actual LH-FEBT current still depends

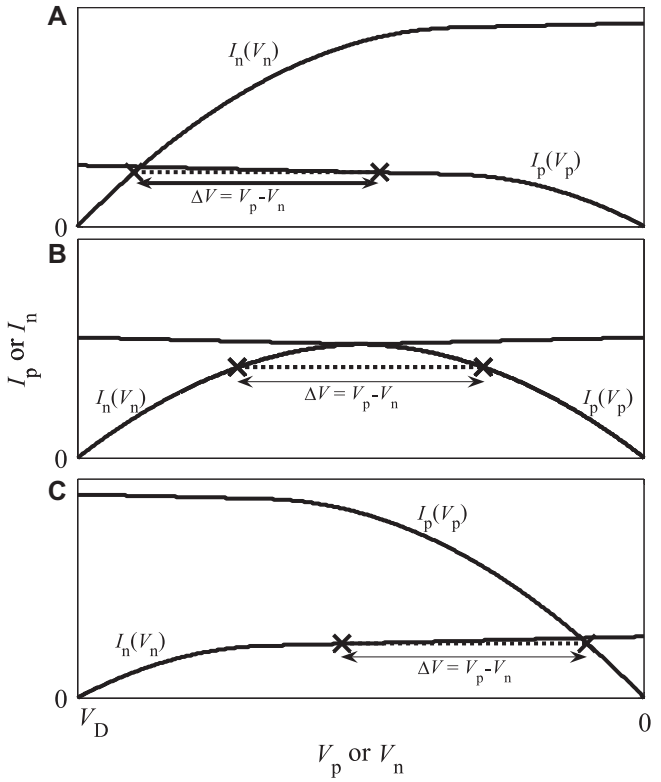

Fig. 3. (A) A graphical representation of Eqs. (3) and (4), showing the current $I_p(V_p)$ and $I_n(V_n)$ in each virtual transistor when V_G is small. The operating point can be represented by the dotted tie-line, which specifies the floating voltages V_p and V_n as well as the common current value. As V_G increases, $I_p(V_p)$ will increase in magnitude, leading to current increase. (B) When the device is operating at peak current, V_G must be at a value where both virtual transistors have equal saturation currents, regardless of ΔV. (C) A representation of $I_p(V_p)$ and $I_n(V_n)$ when V_G is large. As V_G increases further, $I_n(V_n)$ will decrease in magnitude, leading to attenuation in current.

on V_p–V_n, and so the peak current cannot be calculated without knowledge of the diode characteristics. We can still, however, calculate the *voltage* position of the peak $V_{G,peak}$ by equating the saturation currents from Eqs. (3) and (4):

$$\frac{CW\mu_p}{2d}\left(V_{G,peak} - V_{Tp}\right)^2 = \frac{CW\mu_n}{2(L-d)}\left(V_{G,peak} - V_D - V_{Tn}\right)^2 \tag{5}$$

Solving for $V_{G,peak}$ gives:

$$V_{G,peak} = \frac{\sqrt{\frac{\mu_p}{d}}V_{Tp} + \sqrt{\frac{\mu_n}{L-d}}(V_{Tn} + V_D)}{\sqrt{\frac{\mu_p}{d}} + \sqrt{\frac{\mu_n}{L-d}}} \tag{6}$$

In Fig. 3C, the gate voltage has been increased further still. Following an argument similar to that accompanying Fig. 3A, the LH-FEBT current in the high V_G regime is effectively the n-type transistor saturation current. This leads us to deduce that, in the high V_G regime of the I_D–V_G curves, the 'turn-off' voltage is $V_D + V_{Tn}$, and the slope of the curve is proportional to $\mu_n/(L-d)$.

4.3. Comparison with experiment

To verify our analysis, unipolar pentacene OFETs and ZnO FETs were used to estimate the hole and electron mobility of each material (see Supplementary information). The pentacene films have a hole mobility of about 0.16 cm^2/V s with a threshold voltage of −17 V, and the ZnO film has an electron mobility of about 0.051 cm^2/V s with a threshold voltage of −23 V. The heterojunction of the LH-FEBT is closer to the source contact such that d = 25 μm, with L = 200 μm. Substituting these values into Eq. (6), the predicted peak voltage when V_D = −70 V is $V_{G,peak}$ = −29 V, which is remarkably close to the corresponding experimental value of −28 V (see Fig. 2B).

The 'turn-on' voltage is predicted to be −17 V, which is an overestimate of the actual, which appears to be around −10 V. The 'turn-on' voltage has been partially obscured by a background current, which is likely due to current flowing to the gate. Possible explanations for this current include the presence of pinholes in the dielectric film, and a lateral field extending outside the channel between the source and drain, leading to spreading of current. Because the n-type transistor has a *negative* threshold voltage (i.e. depletion mode), the 'turn-off' voltages for V_D = −70, −60 and −50 V lie beyond the V-axis of Fig. 2B. However, for V_D = −40 V, the 'turn-off' voltage is calculated as $V_D + V_{Tn} = -63$ V, which again agrees well with the data.

Lastly, by comparing the values μ_p/d = 6.4 cm/V s and $\mu_p/(L-d)$ = 0.29 cm/V s, we expect the I_D–V_G curves to be

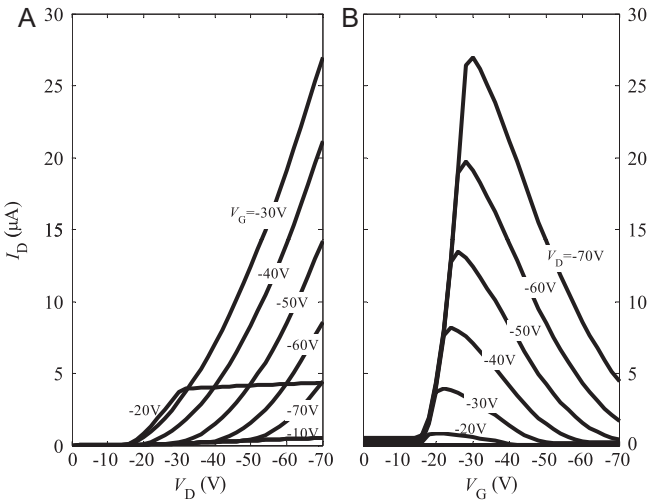

Fig. 4. (A) Simulated current–drain voltage curves for a pentacene/ZnO LH-FEBT based on Eqs. (3), (4) and (7), with gate voltages of −10 to −70 V in 10 V steps. (B) Simulated current–gate voltage curves with drain voltages of −10 to −70 V in 10 V steps. The curves in both subfigures clearly reproduce the general features seen in the experimental data (Figs. 2A and B).

steep at low gate voltages but gentle at high gate voltages, which is indeed the case observed in Fig. 2B.

5. Numerical solution

The arrangement of energy levels and band-bending effects for organic–inorganic interfaces – and by extension, heterojunction charge transport – are in general unclear. A possible mechanism for the injection of carriers across the LH-FEBT heterojunction is Schottky emission [14,15], which has a current density given by:

$$J_s = \frac{4\pi m_e e}{h^3}(kT)^2 \exp\left[\frac{1}{kT}\left(-\phi + \sqrt{\frac{e^3E}{4\pi\epsilon_0}}\right)\right] \quad (7)$$

where m_e is the electronic mass, h is Planck's constant, k is Boltzmann's constant, T is the temperature, ϵ_0 is the vacuum permittivity and E is the electric field strength. ϕ is the offset between the appropriate energy levels of the two semiconductors when injecting carriers from one to the other. Each semiconductor pair has two energy level offsets, but because of the exponential nature of Eq. (7), the larger of the two offsets can be considered negligible, i.e. we assume, in this case, that electrons are injected from ZnO into pentacene (conduction band-LUMO offset is roughly 1.4 eV), whereas hole injection from pentacene into ZnO occurs at a comparatively negligible rate (HOMO-valence band offset is roughly 2.6 eV).

Eqs. (3), (4) and (7) form a system of equations which can be solved to obtain full current–voltage characteristics. However, Eq. (7) requires a conduction channel cross-sectional area, and the electric field strength E at the heterojunction. The conducting channel in FETs is a very thin layer at the semiconductor/dielectric interface; we therefore assumed its thickness as 1 nm. For simplicity, we also made the approximation $E = (V_p - V_n)/l$, where l is a constant length over which the potential drops, which assumes a constant field at the heterojunction over a region of length l. Recent surface potential measurements on a P3HT:NTCDI LH-FEBT [2] showed the region of potential drop at the heterojunction to be smaller than the 100 nm resolution of the instrument. Therefore in our calculations, we used a value of l = 10 nm.

The numerical solution to the system of Eqs. (3), (4) and (7) was computed for the pentacene/ZnO LH-FEBT, using a simple self-written iterative procedure. The calculated curves are shown in Fig. 4A and B, and they clearly reproduce the features seen in experimental data (Fig. 2A and B). In particular, the calculated I_D–V_G curves bear close resemblance to the skewed bell-shaped profile seen in Fig. 2B. De Vusser et al. used the Silvaco Atlas software to model an LH-FEBT. Their model was two-dimensional and allowed for slightly ambipolar transport in the constituent semiconductors; however, they did not consider energy level offsets at the heterojunction. Despite these differences, the simulated I_D–V_D curves from their group appear similar to those reported here.

To validate the applicability of our analysis, we have simulated LH-FEBTs based on other semiconductor combinations such as pentacene/PTCDI, DH-BTZ-4T/NTCDA, etc., and found similar levels of agreement between experimental and simulated curves. However, we found that overestimation of device peak current (by up to a factor of about 10, as is the case of pentacene/ZnO) was a common discrepancy. To address this discrepancy, mobility values were obtained from the low-current region (reflective of the LH-FEBT peak current) of the unipolar FET I_D–V_G curves, which are lower than those reported under Section 4.3. However, these lower mobilities only account for less than half of the discrepancy. Increasing the length of the diode region over which the potential drops resulted in reduction of the simulated current, but before it could

reach experimental levels, the I_D–V_G curves took on a semi-circular appearance and lost resemblance to the experimental curves. The simulated curves were also found to be virtually independent of the conducting channel thickness, even when a value of 100 nm was used.

6. Conclusion

Lateral heterostructure field-effect bipolar transistors (LH-FEBTs) are still relatively new to the field of organic electronics, and their properties remain largely unexplored. Using a simple equivalent circuit model of an LH-FEBT, we have shown the origins of key features in the current–voltage curves: the 'turn-on' and 'turn-off' voltages, the slopes, and the peak. We recognise that there are limitations in the model, but despite these, we have found simple rules relating these features to the mobilities and threshold voltages of the constituent semiconductors – rules that will surely be useful in the design of LH-FEBTs in potential applications. A summary of these rules and their applications are as follows:

1. The turn-on voltage of an LH-FEBT is determined solely by the threshold voltage of the p-type semiconductor. To operate the device at the lowest voltages possible, we therefore need to reduce the p-type threshold voltage.
2. The slope of the I_D–V_G curve between its turn-on and peak voltages depends mostly on the mobility of the p-type semiconductor. In an application requiring good control of the current using the gate voltage, such as for displays, a gentle slope is sought. In this case, μ_h has to be lower than μ_e such that the peak voltage is pushed further away from the turn-on voltage.
3. For a pair of p- and n-type semiconductors whose mobilities and threshold voltages are known, we can then use the peak voltage Eq. (6) to determine the necessary operating range (to switch from 'off' to peak) of the LH-FEBT.

Acknowledgement

The authors are grateful for financial support provided by the Science and Engineering Research Council (SERC), A*STAR, Singapore.

Appendix A. Supplementary data

Supplementary data associated with this article can be found, in the online version, at doi:10.1016/j.orgel.2011.06.026.

References

[1] S.D. Vusser, S. Schols, S. Steudel, S. Verlaak, J. Genoe, W.D. Oosterbaan, L. Lutsen, D. Vanderzande, P. Heremans, Appl. Phys. Lett. 89 (2006) 223504.
[2] B.M. Dhar, G.S. Kini, G. Xia, B.J. Jung, N. Markovic, H.E. Katz, Proc. Natl. Acad. Sci. USA 107 (2010) 3972.
[3] S.P. Singh, P. Sonar, A. Sellinger, A. Dodabalapur, Appl. Phys. Lett. 94 (2009) 013308.
[4] P.H. Wobkenberg, J.G. Labram, J.-M. Swiecicki, K. Parkhomenko, D. Sredojevic, J.-P. Gisselbrecht, D.M. deLeeuw, D.D.C. Bradley, J.-P. Djukic, T.D. Anthopoulos, J. Mater. Chem. 20 (2010) 3673.
[5] Z. Chen, H. Lemke, S. Albert-Seifried, M. Caironi, M.M. Nielsen, M. Heeney, W.M. Zhang, I. McCulloch, H. Sirringhaus, Adv. Mater. 22 (2010) 2371.
[6] P. Sonar, S.P. Singh, Y. Li, M.S. Soh, A. Dodabalapur, Adv. Mater. 22 (2010) 5409.
[7] M.A. Loi, C. Rost-Bietsch, M. Murgia, S. Karg, W. Reiss, M. Muccini, Adv. Funct. Mater. 16 (2006) 41.
[8] C. Lombardo, A. Dodabalapur, Appl. Phys. Lett. 97 (2010) 233302.
[9] A. Dodabalapur, H.E. Katz, L. Torsi, R.C. Haddon, Appl. Phys. Lett. 68 (1995) 1108.
[10] M.-J. An, H.-S. Seo, Y. Zhang, J.-D. Oh, J.-H. Choi, Appl. Phys. Lett. 97 (2010) 023506.
[11] F. Dinelli, R. Capelli, M.A. Loi, M. Murgia, M. Muccini, A. Facchetti, T.J. Marks, Adv. Mater. 18 (2006) 1416.
[12] J. Zaumseil, R.H. Friend, H. Sirringhaus, Nat. Mater. 5 (2006) 69.
[13] L.E. Greene, M. Law, D.H. Tan, M. Montano, J. Goldberger, G. Samorjai, P. Yang, Nano Lett. 5 (2005) 1231.
[14] W. Schottky, Z. Phys. 15 (1914) 872.
[15] L.W. Swanson, G.A. Schwind, Review of ZrO/W Schottky cathode, in: J. Orloff (Ed.), Handbook of Charged Particle Optics, second ed., CRC Press, Boca Raton, 2009, pp. 6–7.

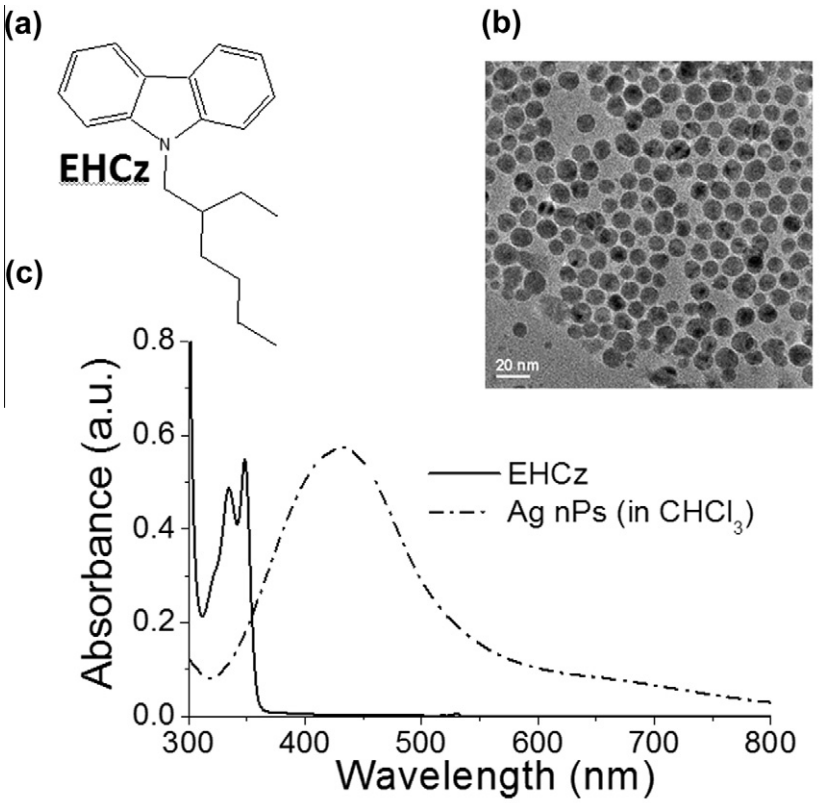

Fig. 1. (a) Chemical structure of the liquid carbazole, (b) TEM image of Ag-nPs coated with hexanethiol ligands, (c) normalized absorbance spectra of a liquid EHCz layer sandwiched between two fused silica substrates and Ag-nPs coated with hexanethiol ligands in $CHCl_3$ solution.

of mechanical flexibility, device reliability and control of the degradation processes. In addition it also offers original potentials to regenerate or to renew the active parts of the devices without disposing of the whole device simply by injecting a fresh batch of liquid electronic materials, an aspect which is impossible to achieve with polymer and small molecules thin films obtained by solution or evaporation processing. The demonstration of an organic rewritable nonvolatile bistable memory based on a liquid carbazole host is an important step towards the development of organic liquid optoelectronic devices.

2. Experimental

The silver nPs presented in Fig. 1b were synthesized at room temperature and in toluene by chemical reduction by hydrazine monohydrate of silver acetate mixed with dodecyl amine and decanoic acid [15]. After 15 min, the as-formed nPs were mixed with hexane thiol and extracted from the reaction media by centrifugation and redissolution in a blend of ethanol and chloroform. After repeating the extraction step several times, the resulting nPs of about 10 nm diameter were finally redispersed in pure chloroform. The absorption spectra of the EHCz layer and the silver nPs solution are shown in Fig. 1c and were measured using a UV–visible-near infrared scanning absorption spectro-photometer (Shimadzu UV-3100PC). Liquid carbazole is fully transparent in the visible and presents strong absorption features in the UV. The two peaks between 310 and 360 nm are characteristic of the carbazole monomer unit. The spectrum of the silver nPs shows an absorption peak centered at about 430 nm resulting from the surface plasmon excitation moderated by the Ag-thiol bonding. The concentration of silver nPs in chloroform solutions was determined based on the absorbance of the nPs solution and their molar extinction coefficient at 410 nm. Appropriate volumes of these stock solutions were then mixed with known volumes of EHCz. By neglecting the volumes of the coated nPs, once the chloroform had been evaporated the concentration of nPs in EHCz was calculated from the concentration of the stock solution and a straightforward volume ratio. Once blended, the low concentration of the silver nPs in the devices and the low absorption coefficients of the EHCz and indium tin oxide (ITO) in the visible, make the organic bistable liquid memory devices fabricated in this study nearly transparent, which can be of strong interest for practical electronic applications.

The schematic structure of the organic liquid bistable memory devices is shown in Fig. 2a. ITO glass substrates ($10\ \Omega/cm^2$) were patterned through standard etching techniques followed by ultrasound cleaning in pure water, 2-propanol, acetone and chloroform baths finalized by an UV-ozone treatment. Empty cells were prepared by clipping tightly the two ITO glass substrates together. The thickness of the sample was controlled using silica spheres with a diameter of 5 μm (Sekisui Chemical Ltd) and dispersed into

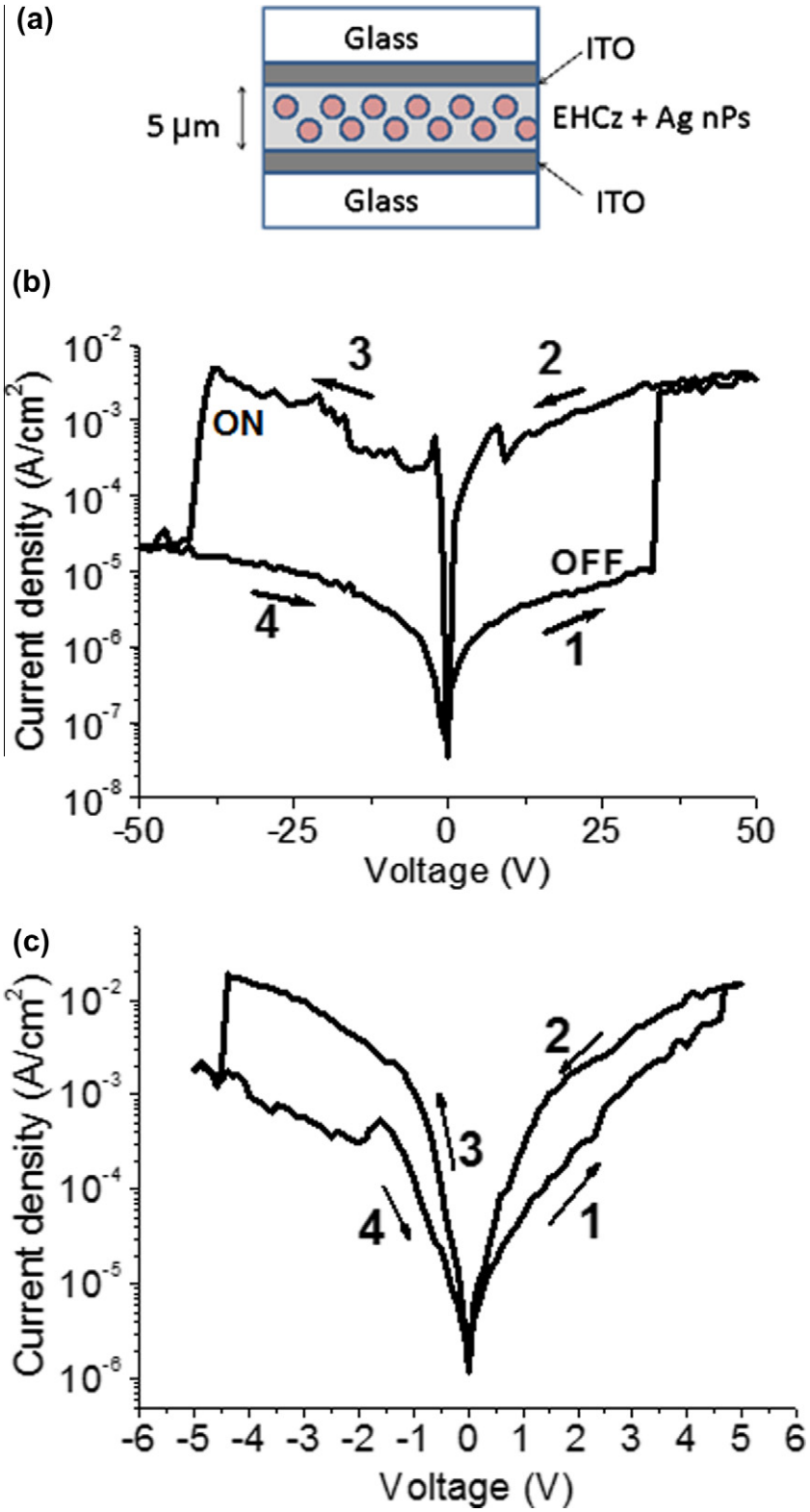

Fig. 2. (a) Schematic of the hybrid memory devices, (b) current density–voltage curve of the ITO/EHCz + Ag-nPs/ITO device fabricated with [Ag-nP] = 8.5×10^{-10} M. (c) current density–voltage curve of a device using [Ag-nP] = 8.5×10^{-9} M. The arrows indicate the voltage-scanning direction.

a silicon paste (Dow Corning). The top and bottom ITO electrodes were aligned perpendicularly to define an active area of 3×3 mm^2. Solution of silver nPs coated with hexanethiol ligands was prepared in chloroform at specific concentrations (8.5×10^{-10} and 8.5×10^{-9} M) and then mixed into 10 mg of the liquid carbazole host. Note that these concentrations lead to a mass ratio between the nPs and the organic host comparable to those used in a recent work on bistable memories based on a PVK/Ag-nPs colloidal film [16]. After evaporation of the residual solvent, the empty cells were filled with the liquid carbazole/nPs blends by capillarity. The current–voltage characteristics of the organic liquid bistable memories were measured using a picoammeter/voltage source unit (Keithley 6487) interfaced and controlled by a computer. A typical sweep speed of 3.5 V/s was used for all the measurements of the *I–V* characteristics to reduce the influence of this parameter on the hysteresis behavior and to allow meaningful comparison between devices. Noticeably the device fabrication and all the characterization were performed in air.

3. Results and discussion

A typical current density–voltage curve of the organic liquid bistable memory device is shown in Fig. 2b. The response shows a strong electrical hysteresis behavior which is essential for the operation of a bistable memory device. It can also be seen that the bistable behavior is nearly symmetric which is consistent with the symmetric structure of our devices. A very low current can be measured during the forward bias scan from 0 to 35 V where a very sharp increase in the current is observed. When the bias voltage is further increased above 38 ± 3 V, the sample exhibits a very high current density. The abrupt transition between the low and high conductance levels corresponds to the switching from the OFF state to the ON state of the memory device. The ratio of the conductivities associated with these two states in our liquid memory devices was found to be of the order of 2×10^2. The device shows a good stability in the ON state during the subsequent voltage scan from 50 to −40 V. At a reverse applied external bias of −40 V, the current suddenly drops and the high conductivity of the ON state is changed back to the low conductivity of the OFF state. The device is then stable in the OFF state during the scan from −50 to 0 V. No hysteresis is observed in samples which do not contain silver nPs, which indicates that the nPs play a key role on the bistability mechanism observed in this memory device. The nP concentration in the liquid EHCz has a strong impact on the hysteresis and the values of the current densities in both the ON and OFF states. The comparison of the current density–voltage curves displayed in Fig. 2b and c shows that an increase in the nP concentration leads to higher conductivity in both ON and OFF states, lower switching threshold voltage and lower ON/OFF ratio. This result suggests that the performance of these liquid memory devices could be further optimized. It is also worth noticing that the maximum applied electric field across our devices is on the order of 1×10^5 V/cm, which is lower than the fields previously used to measure the charge carrier mobilities in EHCz by the time-of-flight technique [11]. Thus, any heating effects generated when applying voltage up to 50 V on the charge transport properties and the characteristics of the devices can be neglected. In addition, whereas the present work used voltage values when compared with the literature, it should be mentioned that the applied electric field required for the transition between the OFF and ON states is nonetheless comparable with those reported in bistable thin film memories based on metallic nanoparticles blended into a polymer host all of which are of the order of 10^5 V/cm [6,16].

As shown in Fig. 3, the device exhibits an ohmic behavior in the OFF state and a space-charge limited current (SCLC) behavior in the ON state. The [Ag-nP] = 8.5×10^{-10} M device presents a current density, *J*, associated with the OFF state proportional to the applied voltage *V*, as expected when the current is injection limited and results from thermally generated free carriers [17]. The slope was found to be about $2.5 \pm 0.5 \times 10^{-7}$ Ω/cm. In the ON-state, the *J* and *V* average relationship is different, non-linear and can be better described by a $J \propto V^{1.8}$ law. This is consistent with a trap-free space charge limited conduction where trapping sites in the active layer are filled as the voltage is increased. This result strongly suggests that the memory effect in our devices is related to charge storage within the hexanethiol capped silver nPs which act as charge carrier trap centers [17,18]. The observation of different conduction mechanisms in the two states of the organic memory indicates that the electronic structure of the device is modified through the electrical transition [19]. The highest occupied molecular orbital (HOMO) and lowest unoccupied molecular orbital LUMO levels of EHCz have been measured to be around 5.8 and 2.3 eV, respectively [14], while silver has a work function of about 4.7 eV. Thus, the silver nPs can act as charge traps in the EHCz host. Similarly to what has been reported in devices based on gold nPs doping at similar concentrations a semiconducting polymer host, including PVK, the bistability can be attributed to electric-field-induced charge transfer between silver nPs and EHCz involving charges tunneling through the insulating coating of the nPs [6,16,20]. When blending the nPs into the EHCz host, the liquid carbazole plays the role of electron donor and the nPs act as electron acceptor. When applying a high electric field across the device, an electric-field-induced charge transfer can occur between the liquid carbazole and the nPs, resulting in EHCz being positively charged and the nPs being negatively charged. As previously demonstrated [6,16], this effect leads to a decrease of the bandgap and a significant improvement of the conductivity of the hybrid material, which is associated to the ON-state of the memory devices. For the transition from the ON- to the OFF-state, a reverse bias is then required to make the electric-field-induced charge transfer complexes return back to their initial state. Note that the stability of the negative charges trapped on the silver nPs in the ON state is certainly associated with the insulating hexanethiol ligands surrounding the nPs, which eliminate the possibility for the charges to recombine in the absence of an applied electric field.

Other key characteristics of organic bistable memory devices are evidently their stability characteristics in both ON and OFF state under a constant applied voltage stress as

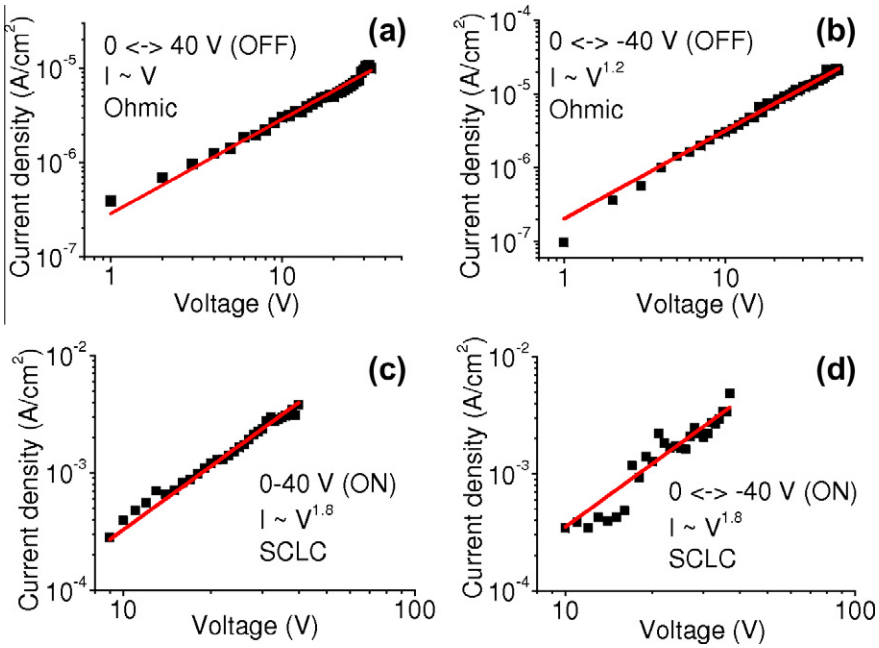

Fig. 3. Fitting results of the current density–voltage curves of the memory device with [Ag-nP] = 8.5×10^{-10} M in log–log scale and deduced mechanisms: ohmic [(a) and (b)], SCLC [(c) and (d)].

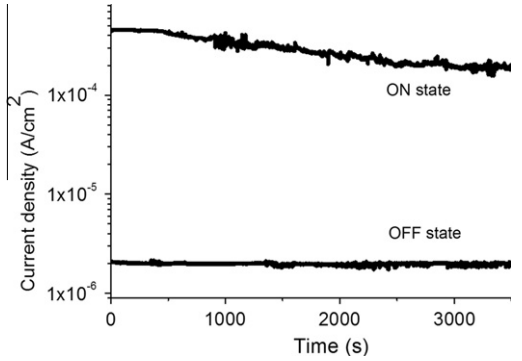

Fig. 4. Stability of an organic liquid bistable memory device in the ON and OFF states under a constant bias of 10 V, [Ag-nP] = 8.5×10^{-10} M.

well as their ability to read, write and erase data. Fig. 4 shows the stability of the device in both the ON and OFF states under a continuous constant voltage of 10 V for 1 h. A slow decrease of the ON state current is observed but overall the device shows little degradation over time.

Write–read–erase cycle tests were also performed on the device. As shown in Fig. 5a, different bias voltages were used for the writing to the ON state (+50 V), the reading (+10 V) and the erasing (−50 V) processes. The corresponding absolute value of the current response is plotted in Fig. 5b and is found to follow the applied write–read–erase–read cycles. Consequently, the results provide clear evidences that hybrid organic–inorganic liquid bistable devices can be electrically programmed for rewritable non-volatile memory applications. For further development of the organic liquid memories, it is evident that the switching threshold voltage and the ON/OFF ratio of the devices

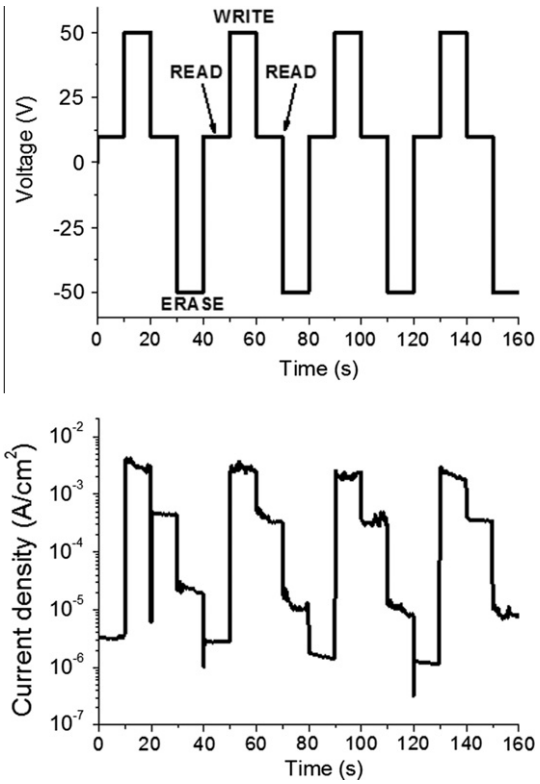

Fig. 5. Write–read–erase–read voltage cycles measured in an hybrid liquid bistable memory: (a) input applied voltages and (b) output currents as a function of time. [Ag-nP] = 8.5×10^{-10} M.

need to be improved for practical applications. For this purpose, devices with much thinner hybrid active layers could be envisaged along with efforts towards materials design and optimization.

4. Conclusion

In conclusion, a liquid hybrid organic-inorganic bistable memory device based on a blend of hexanethiol capped silver nPs and liquid carbazole EHCz was demonstrated. The device can be electrically switched between two states which conductivities are more than two orders of magnitude apart of one another. The repeatable and nonvolatile electrically bistable properties observed in our liquid memories are attributed to an electric-field-induced charge transfer between the liquid carbazole and the silver nPs. This study opens a very promising way for organic electronic memory devices and supports the concepts that liquid carbazole and that blending organic and inorganic materials to complement each other electronic properties have strong potentials for the development of soft optoelectronic.

Acknowledgements

P.A. gratefully acknowledges the *Scottish Universities Physics Alliance* for funding his *SUPA Advanced Research Fellowship*. P.A. and J.C.R. would like to acknowledge funding from the Royal Society (International Joint Project Ref. JP0869934).

References

[1] D.V. Talapin, J.S. Lee, M.V. Kovalenko, E.V. Shevchenko, Chem. Rev. 110 (2010) 389.
[2] V.L. Colvin, M.C. Schlamp, A.P. Alivisatos, Nature 370 (1994) 354.
[3] N.S. Sariciftci, L. Smilowitz, A.J. Heeger, F. Wudl, Science 258 (1992) 1474.
[4] L.P. Ma, J. Liu, Y. Yang, Appl. Phys. Lett. 80 (2002) 2997.
[5] R.J. Tseng, J.X. Huang, J. Ouyang, R.B. Kaner, Y. Yang, Nano Lett. 5 (2005) 1077.
[6] Y. Yang, J. Ouyang, L.P. Ma, R.J.H. Tseng, C.W. Chu, Adv. Funct. Mater. 16 (2006) 1001.
[7] D.T. Simon, M.S. Griffo, R.A. DiPietro, S.A. Swanson, S.A. Carter, Appl. Phys. Lett. 89 (2006) 133510.
[8] D.Y. Yun, J.K. Kwak, J.H. Jung, T.W. Kim, D.I. Son, Appl. Phys. Lett. 95 (2009) 143301.
[9] B. Cho, T.W. Kim, M. Choe, G. Wang, S. Song, T. Lee, Org. Electr. 10 (2009) 473.
[10] W.T. Kim, J.H. Jung, T.W. Kim, D.I. Son, Appl. Phys. Lett. 96 (2010) 253301.
[11] J.C. Ribierre, T. Aoyama, T. Muto, Y. Imase, T. Wada, Org. Electr. 9 (2008) 396.
[12] J.C. Ribierre, T. Aoyama, T. Kobayashi, T. Sassa, T. Muto, T. Wada, J. Appl. Phys. 102 (2007) 033106.
[13] D.H. Xu, C. Adachi, Appl. Phys. Lett. 95 (2009) 053304.
[14] S. Hirata, K. Kubota, H.H. Jung, O. Hirata, K. Goushi, M. Yahiro, C. Adachi, Adv. Mater. 23 (2011) 889.
[15] N.R. Jana, X. Peng, J. Am. Chem. Soc. 125 (2003) 14280.
[16] D.I. Son, D.H. Park, J.B. Kim, J.W. Choi, T.W. Kim, B. Angadi, Y. Yi, W.K. Choi, J. Phys. Chem. C 115 (2011) 2341.
[17] M. Arif, M. Yun, S. Gangopadhyay, K. Ghosh, L. Fadiga, F. Galbrecht, U. Scherf, S. Guha, Phys. Rev. B 75 (2007) 195202.
[18] D.I. Son, D.H. Park, W.K. Choi, S.H. Cho, W.T. Kim, T.W. Kim, Nanotechnology 20 (2009) 195203.
[19] J.Y. Ouyang, C.W. Chu, D. Sieves, Y. Yang, Appl. Phys. Lett. 86 (2005) 123507.
[20] A. Tang, S. Qu, Y. Hou, F. Teng, H. Tan, J. Liu, X. Zhang, Y. Wang, Z. Wang, J. Appl. Phys. 108 (2010) 094320.

Perylene bisimides (PBIs) have been demonstrated n-type semiconductors which have large conjugated structures and strong electron affinities [18–21]. Because of the representative geometric, electronic and transport properties, PBIs show the promising applications in optical and electronic devices [22–24]. Attaching substituents, such as perfluoroalkyl, fluorine, chlorine, cyanide, etc. to the conjugated perylene bisimide core could stabilize molecular orbitals and facilitate electron transport successfully [25–28]. This kind of functionalization of material will improve device performance and increase lifetime of the device. The similar substituents have been investigated and demonstrated practical for device design [18,29,30]. Two kinds of substituents referred in our theoretical work: substituents at imide nitrogen positions with fluorinated groups and substituents at bay positions with different electron-withdrawing atoms. The compounds with substituents of fluoroalkyl and fluorophenyl groups, such as $-CH_2C_3F_7$ and $-C_6F_5$ at imide nitrogen position of perylene bisimide have been demonstrated to perform the air-stable electron mobilities with the improved solubility [30,31]. The molecular models in the present work – a series of n-type electron-withdrawing derivatives based on perylene bisimide are shown in Scheme 1. Mobility is the intrinsic property of organic crystal and it is the most important characteristic when evaluate the material performance. Some groups have investigated this kind of functionalization of PBI, Chen et al. have measured the highest mobility $0.068\ cm^2\ V^{-1}\ s^{-1}$ of fluorine substituents [30] and $0.35\ cm^2\ V^{-1}\ s^{-1}$ have been reported by Schmidt et al. of the derivatives with both bay and imide nitrogen substituents of PBI [27]. Delgado et al. have investigated considerable PBI derivatives and found that the important impact of the intermolecular packing on the charge transport properties [18]. Here we provide the theoretical study of detailed influences of these electron-withdrawing substituents on geometric structures, electronic properties, especially the carrier mobilities. We developed a method to simulate the angular-resolution mobility and investigated the anisotropic behaviors of organic material [32].

In the present work, both hole and electron hopping motions are considered and the related electronic and transport properties of the two kinds of hoppings are discussed. Density functional theory (DFT) calculations have been performed to investigate the geometries, molecular orbitals, electron affinities and reorganization energies of PBI monomers. The absorption spectra of all the derivatives in the tetrahydrofuran solution have been simulated with time-dependent density functional theory (TDDFT) method. The intermolecular electronic couplings and charge transport mobilities at room temperature have been deduced with the available single crystal structures. The anisotropic mobility is simulated with our angular-resolution expression. The functionalized derivatives of perylene bisimides have been compared systematically in terms of these charge transport properties. The theoretical analysis is helpful to understand the influence of the structure variations on the transport properties of these organic conjugated molecules and direct the high-performance material design.

2. Theoretical methodology

Density functional theory (DFT) has been employed to calculate the structural, electronic and transport properties of these organic semiconductors. It has been demonstrated reliable to study the organic conjugated molecules [4,10,33]. In the solid state the reorganization energy is mostly from the internal energy relaxation when charge transport and the contribution from the environment to the reorganization energy could be neglected [34–36]. Thus the reorganization energy could be expressed as:

$$\lambda_{hole} = \lambda_0^+ + \lambda_+ = (E_0^* - E_0) + (E_+^* - E_+) \quad (1)$$

$$\lambda_{electron} = \lambda_0^- + \lambda_- = (E_0^* - E_0) + (E_-^* - E_-) \quad (2)$$

where E_0 and E_+/E_- denote the energies of the neutral and cation/anion molecules in their lowest energy geometries, E_0^* and E_+^* E_-^* are the energies of the neutral and cation/anion monomers with the cation/anion and neutral geometries, respectively. The calculations of reorganization

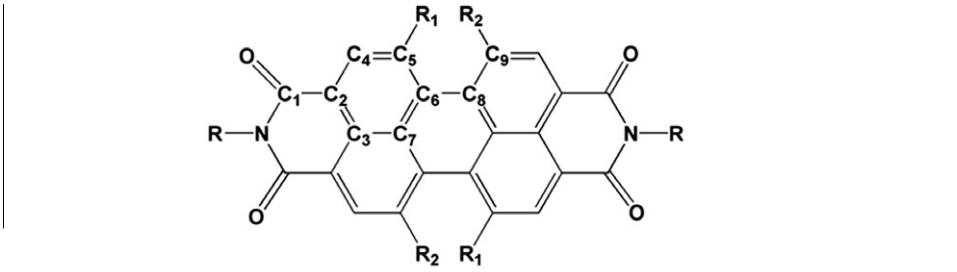

A1: R=C_4H_9, R_1=R_2=H
A2: R=$CH_2C_3F_7$, R_1=R_2=H
A3: R=C_6F_5, R_1=R_2=H

B1:R=$CH_2C_3F_7$ R_1=R_2=F
B2:R=$CH_2C_3F_7$ R_1=R_2=Cl
B3:R=$CH_2C_3F_7$ R_1=R_2=Br
B4:R=C_6F_5 R_1=R_2=Cl

C1:R=$CH_2C_3F_7$ R_1=F, R_2=H
C2:R=$CH_2C_3F_7$ R_1=CN, R_2=H
C3:R=C_6F_5 R_1=F, R_2=H

Scheme 1. Schematic of the structures of investigated PBI derivatives.

energy are performed with B3LYP functional with 6-311G** basis set. Time-dependent density functional theory (TDDFT) is also employed to simulate the absorption spectra of investigated semiconductors. These calculations are carried out with Gaussian 09 program package [37].

The evolution of electronic coupling t is based on the molecular orbitals of the conjugated molecules. The coupling matrix element could be deduced as Eq. (3).

$$t = \frac{J_{12} - S_{12}(E_1 + E_2)/2}{1 - S_{12}^2} \tag{3}$$

The electronic coupling t could be written with charge transfer integral J, overlap matrix S and site energy of monomer E, as described in the reference [38]. The monomer orbitals with proper orthogonalization are used as basis sets for the Hamiltonian of this dimer system. Assuming h is the Kohn–Sham Hamiltonian of a dimer pair system and $\varphi_1^{H/L}$, $\varphi_2^{H/L}$ are the localized molecular orbitals of adjacent monomers. For hole transport the highest occupied molecular orbitals (HOMOs) of monomers are used as the basis function while for electron transport the lowest unoccupied molecular orbitals (LUMOs) are used correspondingly, and then S, J and E could be expressed as:

$$\begin{aligned} J_{12} &= \langle \varphi_1^{H/L} | h | \varphi_2^{H/L} \rangle \\ S_{12} &= \langle \varphi_1^{H/L} | \varphi_2^{H/L} \rangle \\ E_1 &= \langle \varphi_1^{H/L} | h | \varphi_1^{H/L} \rangle \\ E_2 &= \langle \varphi_2^{H/L} | h | \varphi_2^{H/L} \rangle \end{aligned} \tag{4}$$

In the calculation of electronic coupling, the fragment orbital approach is applied with Amsterdam density functional (ADF) software [39]. The local density functional VWN combined with PW91 gradient corrections and TZ2P basis set are selected as the calculation method.

There are two widely used models to describe the charge transport in organic semiconductors: the band-like model and the hopping model [40]. The former is usually applied at very low temperature. At room temperature the charge carriers in organic single crystals are localized and the charge transport in a sequential hopping mode between neighboring molecules which could be described by Marcus theory. Hutchison and Bromley et al. have demonstrated that for organic oligomers the thermally assisted polaron hopping mechanism is reasonable [41–43]. Here we mainly investigate the electron and hole transport behaviors of PBI derivatives at room temperature and employ the hopping mechanism. According to Marcus–Hush theory the hopping rate k could expressed as [44–46]:

$$k = \frac{t^2}{\hbar}\left(\frac{\pi}{\lambda k_B T}\right)^{1/2} \exp\left(-\frac{\lambda}{4k_B T}\right) \tag{5}$$

where k_B is the Boltzmann constant and T is the temperature which is 298 K in our calculation. The reorganization energy λ and electronic coupling t between two adjacent molecules are key parameters for the charge hopping rate.

The hopping mobility μ could be evaluated from the Einstein relation:

$$\mu = \frac{eD}{k_B T} \tag{6}$$

where D is the diffusion efficient. Assuming the hopping motion is an isolated random walk and there is no correlation between charge hopping motions, the diffusion coefficient D could be evaluated from the hopping rate:$D = \frac{1}{2n}\sum_i r_i^2 k_i P_i$, n is the spatial dimensionality, k_i denotes the hopping rate along the specific hopping path i, r_i is the intermolecular center-of-mass distance between two neighboring molecules and P_i is the hopping probability for the specific path i which can be calculated by: $P_i = k_i/\sum_i k_i$.

The mobility orientation function is deduced to simulate the angular-resolution anisotropic mobility, see details in reference [32].

$$\mu_\Phi = \frac{e}{2k_B T}\sum_i k_i r_i^2 P_i \cos^2\gamma_i \cos^2(\theta_i - \Phi) \tag{7}$$

here γ_i is the angle of hopping path relative to the plane of interest, ϕ is the orientation angle of the transistor channel relative to the specific crystallographic axis and θ_i is the angle of the projected hopping path relative to the specific axis. These calculations are based on the detailed analysis of the molecular packing of organic single crystals.

3. Results and discussion

3.1. Geometry and molecular orbital

Some selected optimized geometric parameters, including bond lengths, bond angles and dihedral angles of A1, A2, B1, C1 and C3 molecules both in neutral and anion states are listed in Table A. 1 in the Supporting Information. From the calculated results, we could tell that most bond lengths have visible change between neutral and anion states. The modification of C–C bond lengths in anion state are very big except for the ones located in two conjugated cores, e.g. the bond length difference of C_1–C_2 is 0.023 Å while the one of C_2–C_3 is only 0.002 Å for compound A1. The C–N bonds lengthen 0.006 Å in the anion state. The strengths of C–O bonds are weaker in the anion states and the bond lengths are all increased by about 0.012 Å. The electron transport also induces the bond angle change, e.g. the bond angle C_2–C_3–C_7 of investigated molecules decrease by about 0.2° in anion state. For different PBI derivatives we could detect the geometric conformation change induced by attaching electron-withdrawing groups. When substituents are attached to nitrogen atom of perylene bisimide core, the C–N bond is lengthened by 0.01 Å and other bonds are almost changeless. However, substituents at the bay positions of perylene bisimide core bring the obvious geometric differences. The bonds have stretching vibration and the angles C_5–C_6–C_8 increases by more than 2°. With the calculated geometries we could find that the conformation change of these compounds when electrons transport are considerable which directly induce the large reorganization energies. Compound A1 and A2 keep a relatively planar conjugated core with the dihedral angles less than 1°. The compounds with substituents at the bay positions have the visible twist, and also the planarity of the conjugated structure for this kind of derivatives is influenced by electron transport. For B1, it

is more planar in anion state than in neutral state. However, for compound C1, the dihedral angles of conjugated structure are increased significantly in the radial-anion state and the torsion is enhanced. The geometric structure of the isolated molecule plays an important role in determining the molecular arrangement of the single crystal.

Fig. 1 shows the calculated molecular orbital levels of all the investigated PBI compounds. General n-type organic semiconductor materials are air sensitive and the electrons are easily trapped by the ambient oxidants. Because of instability of these materials, the device lifetime and performance have been limited. Attaching electron-withdrawing substituents to conjugated semiconductor could lower the molecular orbitals and improve the stability of materials. In the figure we could find both HOMOs and LUMOs have been stabilized by at least 0.3 eV for these PBI derivatives. The energy gaps, which mean the energy difference between HOMO and LUMO, are very close for these compounds. The HOMO and LUMO plots of all the investigated monomers at B3LYP/6-311G** calculation level are shown in Fig. A.1–A.10 in the Supporting Information. The charges are strongly located in the conjugated perylene bisimide center for all the compounds. All these derivatives are practical to produce semiconductors with improved stability. It is an effective strategy to decrease the electrons trapping by the ambient oxygen and moisture and obtain the air-stable materials. When realizing the application of organic material in electronic devices, solution process is an important operation. However, most organic conjugated semiconductors have poor solubility, thus increasing the solubility is also an object in molecular design. The added electron-withdrawing substituents in our investigated system would improve the solubility efficiently because the polarity has been increased with the introduced polar atoms.

3.2. Ionization potential, electron affinity and reorganization energy

Adiabatic ionization potentials and electron affinities of all considered compounds are calculated with DFT method at the level of B3LYP/6-311G**, as shown in Fig. 2. The ionization potential and electron affinity relate to the ability of holes and electrons coming across the energy barrier and injecting the metal electrodes or empty orbitals. The introduction of electron-withdrawing substituents increases the ionization potential and electron affinity obviously. According to Newman, a practical requirement for n-type material is that organic conjugated semiconductor have electron affinity between 3 eV and 4 eV [47]. These substituents are favorable for n-type semiconductors in respect of the electron affinity. An increase of electron affinity (cal. 0.3–0.9 eV) has been observed from our calculation. The enhanced electron affinity facilitates the electrons injecting into LUMOs of semiconductors effectively.

Reorganization energy is the relaxation of site energy by vibrations [38]. The calculations of reorganization energies of hole and electron transport are based on the idea of adiabatic potential energy surface at the level of B3LYP/6-311G** as well, shown in Table 1. When the substituented groups are attached to compound A1, the obvious increases of reorganization energies are observed. These increases are not helpful for charge carriers transport and the hopping rate will be decreased according to Marcus theory. The electron transport will induce larger structural relaxation than hole transport. A main reason why the mobility of n-type semiconductor is usually lower than

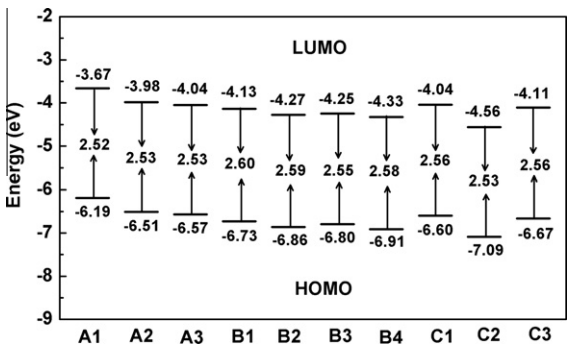

Fig. 1. Energy levels (in eV) of HOMO and LUMO of PBI derivatives (the upper ones are LUMOs and the lower ones are HOMOs) with the method B3LYP/6-311G**.

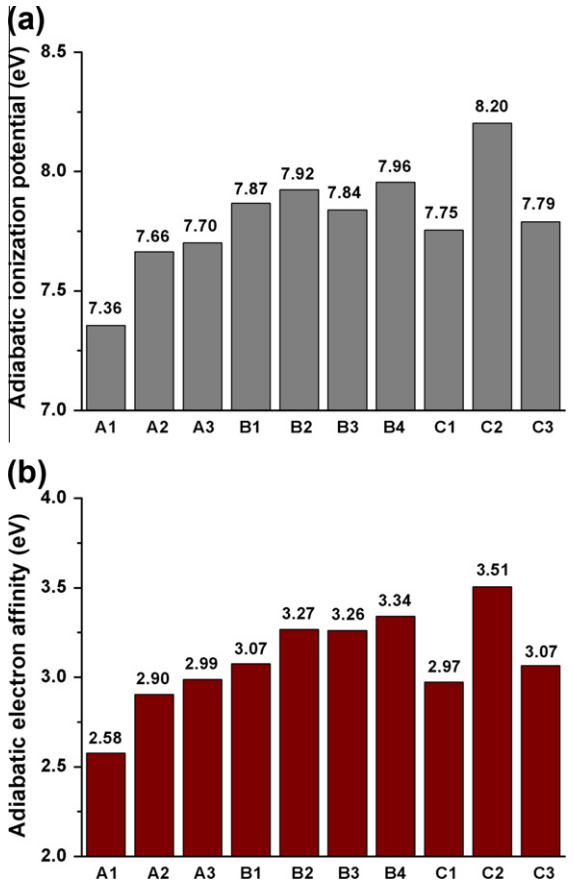

Fig. 2. Calculated adiabatic ionization potentials and electron affinities (in eV) of all the investigated PBI compounds for (a) adiabatic ionization potentials, (b) adiabatic electron affinities.

Table 1
Calculated reorganization energies (in eV) of the hole and electron transport of PBI derivatives with the B3LYP/6-311G** method.

	Hole			Electron		
	λ_0^+	λ_+	λ_{hole}	λ_0^-	λ_-	$\lambda_{electron}$
A1	0.084	0.082	0.166	0.140	0.140	0.280
A2	0.098	0.093	0.191	0.152	0.156	0.308
A3	0.089	0.087	0.176	0.152	0.149	0.301
B1	0.127	0.127	0.254	0.166	0.167	0.333
B2	0.122	0.121	0.243	0.164	0.163	0.327
B3	0.120	0.113	0.233	0.163	0.158	0.321
B4	0.115	0.106	0.221	0.162	0.159	0.321
C1	0.109	0.110	0.219	0.159	0.162	0.321
C2	0.095	0.096	0.191	0.142	0.145	0.287
C3	0.103	0.101	0.204	0.156	0.156	0.312

p-type one is the difference of the reorganization energy when electron and hole transport.

The variation of the substituents at the bay positions has obvious influence on the charge transport reorganization energy. Fig. 3 shows the evolution of electron transport reorganization energy with electronegativity of the substituented atoms at the bay positions. A2, B1, B2 and B3 have the similar geometries only the different subsituented atoms at the bay positions. According to Pauling definition the electronegativity of H, F, Cl and Br are 2.10, 4.00, 3.16 and 2.96, respectively. The evolution of reorganization energy has been analyzed which follows a straight line expression. As the electronegativity increase the electron transport reorganization energy increase, correspondingly. When PBI molecule is substituted with F which has the largest electronegativity, the electron transport reorganization energy could come to 0.333 eV. With the fitting line we could deduce the reorganization energy substituted with other atoms. These electron-withdrawing groups could improve the stability and electron injection effectively though they would introduce the obvious increase of reorganization energy which is not expected by device design.

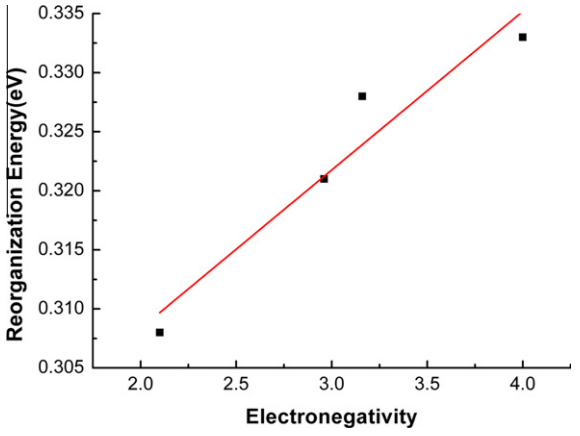

Fig. 3. Correlation of reorganization energy of electron transport with electronegativity of substituented atom at the bay positions.

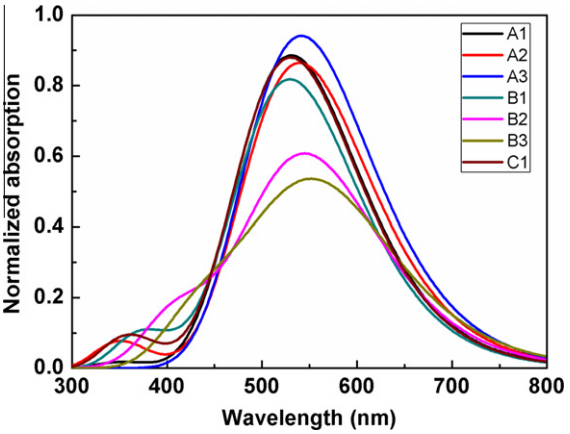

Fig. 4. UV-Vis absorption spectra of A2, B1, B2, B3 and C1 in tetrahydrofuran (THF) solution.

3.3. Absorption spectra

Time-dependent DFT calculations at B3LYP/6-311G** level are performed to simulate the absorption spectra of these PBI derivatives. The theoretical simulations of absorption spectra are performed in tetrahydrofuran solution with SCM model. From the simulated spectra in Fig. 4, we find that the PBI derivatives have broad and strong absorption in the UV-Visible region especially from 400 to 700 nm. The perylene cores are the chromophore centers for these compounds and all the derivatives have the maximum absorption peak almost in the same area near 530 nm which assigns to the π–π^* transition. It reflects that these derivatives need almost the same optical transition energy. Attaching the strong electron-withdrawing fluorine atoms on the core positions will induce the blue shift of the absorption spectra which means the energy increase needed for the optical transition. Relative to the absorption maximum of B1, the red shift of 9 nm for B2 and the red shift of 18 nm for B3 have been observed. Though the structures of B1 and C1 have evident differences from Table A.1, the absorption spectra of the two compounds show almost the same shape and distribution only a tiny difference in the absorption strength. The calculated results are in good agreement with the corresponding experimental ones by Chen et al. [30] and Jones et al. [48]. These results indicate that the organic conjugated PBI compounds have advantages in terms of absorption spectra and they have potential to realize the application in organic solar cell.

3.4. Electronic coupling and anisotropic mobility

Fig. 5 shows the molecular packings of compound A2, B3 and C1 as well as the torsion angles of perylene bisimide plane. The dimers of molecule D with adjacent molecules in single crystal are marked as D_1, D_2, D_3, D_p (D_p denotes the dimer in two neighboring packing layers) ..., and the center-of-mass distance of the two closest conjugated molecules is presented. The theoretical analysis are based on the single crystals from Schmidt et al. [49]. If

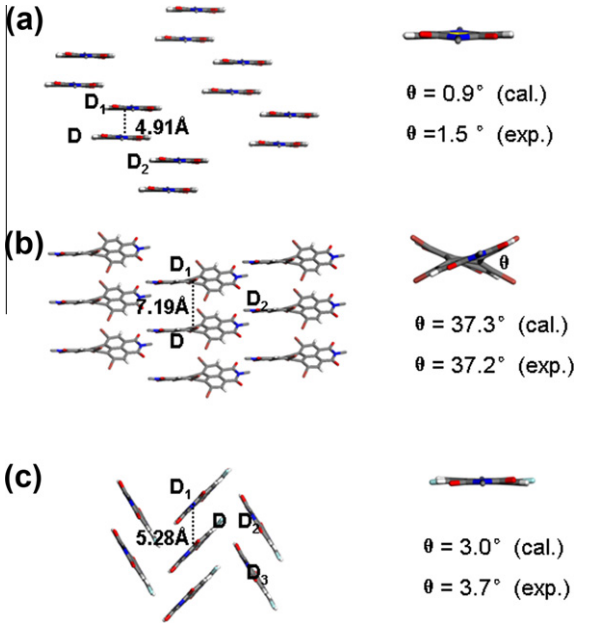

Fig. 5. Molecular packings of compounds (a) A2, (b) B3 and (c) C1 [49] with the center-of-mass distance between the conjugated centers and the torsion angles of the perylene bisimide plane by DFT calculation (cal.) as well as the experimental results (exp.). Fluoroalkyl groups have been removed for clarity.

there is no substituent at the bay position, the conjugated perylene bisimide part is almost planar, like A1, A2 and A3. The torsion angle from calculation by DFT method (0.9°) and experiment measurement (1.5°) [49] of compound A2 indicate the good planarity of this kind of molecule. The electron-withdrawing substituents at 1, 6, 7, and 12 positions can make a twisting angle as large as 35° and the conjugated PBI skeletons have been largely distorted. The calculated torsion angle of B3 molecule is 37.3 ° which is in good agreement with 37.2 ° from experiment [49].

The molecular arrangement in crystal structure is mostly determined by molecular conformation and intermolecular interactions. From the comparison of B1 and C1, we find that the addition of fluorine atoms at the bay positions enlarge the torsion of perylene backbone out of planarity which would not facilitate the dense packing and hence the intermolecular electronic coupling. The packing modes are mainly affected by the molecular conformation. The face-to-face stacking with a short distance with the large coupling area could contribute to the high mobility. The molecular packing of A2 crystal keeps a slipped stack while C1 crystal changes to a herringbone one with an increased intermolecular center-to-center distance. The charge mobility is partly dependent on the molecular distance of the conjugated compounds. The centroid distance is 4.91 Å of the closest conjugated molecules for A2 while it is 7.19 Å for B3 and 5.28 Å for C1. The planar torsion hinders the approach of the molecules and obstructs the molecule packing densely.

With the known crystal structures, the electronic couplings of neighboring molecules of compounds A2, B2, B3, B4 and C1 are calculated, listed in Table A.2 in the Supporting Information. For the most organic single crystals the electronic couplings between the molecules in the same organic packing layer are much stronger than that between the molecules in two neighboring layers. For A2 crystal, the electronic couplings for dimer D_p is far less than the ones for dimer D_1 and D_2. The weak electronic coupling along layer-to-layer molecules contributes negligibly to mobility. The large variation of electronic couplings along directions will give rise to a 2D mobility distribution in the packing layer. For our studied PBI derivatives the electronic couplings of LUMOs could come to the same order of the ones of HOMOs. Table 2 list the maximum mobilities of hole and electron of some PBI derivatives. In these PBI derivatives A2 has the preferred transport properties for both hole and electron, with the hole and electron mobilities as large as 0.552 and 0.123 $cm^2 V^{-1} s^{-1}$. The close packing of the molecules in the solid state allows the strong electronic couplings of the π-conjugated orbitals which determines the high mobility. When attaching the two fluorine atoms at the bay position of the perylene core, electronic coupling between LUMOs has been enhanced significantly, about two orders of magnitude larger than that for HOMOs. The compound C1 shows favorable electron transport properties. The LUMOs of conjugated molecules show strong coupling interaction and the mobility for electrons can come to 0.514 $cm^2 V^{-1} s^{-1}$. For compound C1 the experimentally measured electron mobility is 0.35 $cm^2 V^{-1} s^{-1}$ by Schmidt [49] and our theoretical simulation provides the reliable results. For the PBI derivatives with four electron-withdrawing atoms, B2, B3 and B4, the charge transport mobilities are not satisfying. Because of the repulsion of the introduced electron-withdrawing atoms, the regular molecular packing of the PBI compounds has been distorted and the distance of the conjugated center has been lengthened. The mobilities measured in experiments are very sensitive to the experimental conditions. Schmidt et al. reported that the organic thin film transistor measurements of mobility are varied a lot when the substrate is modified or the temperature is changed [49]. Our theoretical charge transport investigation is under the ideal conditions at room temperature which could provide the reasonable results and assist to understand the detailed transport behaviors of the charge carriers.

The highly anisotropic character of molecular packing of organic single crystals gives rise to the highly anisotropic

Table 2
The calculated hole and electron transport mobility (in $cm^2 V^{-1} s^{-1}$) of some PBI derivatives. (The corresponding experimental values from reference [49] are in parentheses).

	A2	B2	B3	B4	C1
μ_{hole}	0.552	0.005	0.137	0.014	0.019
$\mu_{electron}$	0.123 (0.67)	0.002 (0.0005)	0.024 (0.0003)	0.002 (0.025)	0.514 (0.35)

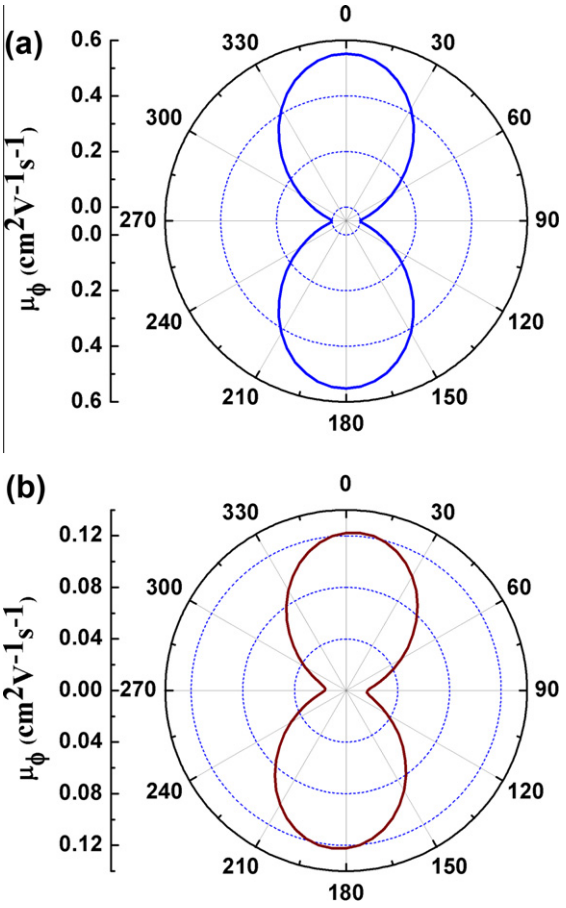

Fig. 6. The angular-resolution anisotropic mobility of A2 crystal: (a) hole mobility and (b) electron mobility.

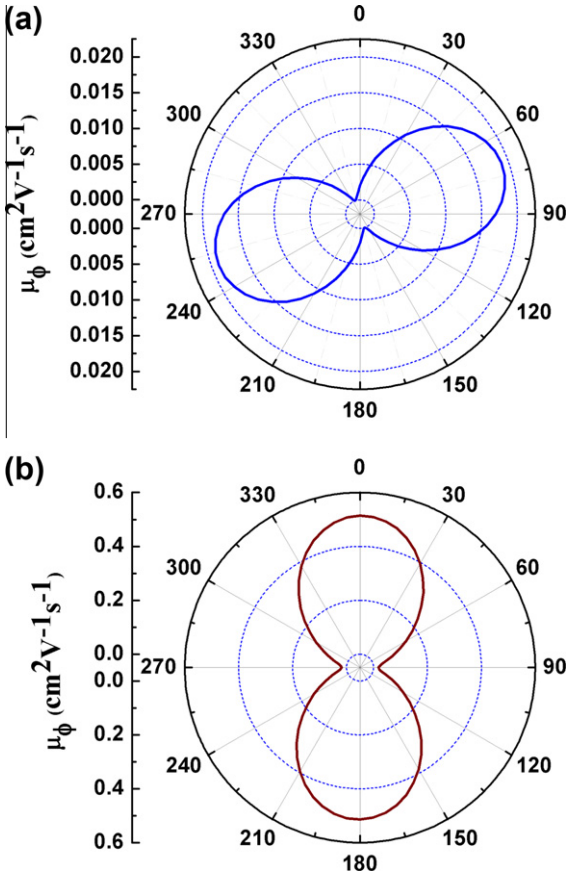

Fig. 7. The angular-resolution anisotropic mobility of C1 crystal: (a) hole mobility and (b) electron mobility.

mobility. Understanding the anisotropic mobility can assist in controlling the directions of transistor channel relative to reference direction of molecular crystal to obtain the highest charge mobility [50–52]. Figs. 6 and 7 describe the angular-resolution anisotropic mobilities of both hole and electron transport of compounds A2 and C1. We choose the direction of strongest electronic couplings of LUMOs as the reference direction (the 0° direction in the angular-resolution figures) and all the vectors of mobility project to this direction and then deduce the corresponding angular-resolution formula.

For the hole transport of compound A2, since the electronic coupling of HOMOs for dimer D_1 is very strong, the mobility maximum 0.552 $cm^2\ V^{-1}\ s^{-1}$ appears in this dimer direction. Differently the electronic coupling of LUMOs for dimer D_2 is comparable to the one for D_1, it will contribute to the mobility distribution. Thus the mobility maximum of electron transport is along about 5° in the angular-resolution figure. For compound C1 we could find the obvious difference of the angular-resolution mobility, it is because the strongest coupling of HOMOs occurs in D_2 while the strongest coupling of LUMOs occurs in D_1. The hole transport mobility maximum is 0.019 $cm^2\ V^{-1}\ s^{-1}$ when the angle is 71° in the angular-resolution figure and the electron transport mobility maximum is 0.514 $cm^2\ V^{-1}\ s^{-1}$ along dimer D_1 vector. Understanding the angular-resolution distribution of mobility and making use of the anisotropy of mobility can help us to improve the charge transport and get high-performance materials.

4. Conclusions

In summary we theoretically investigated the perylene diimde derivatives with electron-withdrawing substituents. These derivatives show the promising performance in terms of electronic, optical and charge transport properties. Attaching the electron-withdrawing substituents at the proper positions could improve the stability of the materials, enhance the electronic coupling and facilitate the hopping motions, efficiently, though these substituents would induce the increase of the reorganization energy inevitably. All the investigated derivatives have the strong absorption in the UV-Visible area which is highly desired by the organic solar cell applications. The molecular conformation of the organic semiconductor plays a significant role in determining the electronic properties, molecular stackings and transport behaviors. In all these derivatives, compound C1 which has two fluorine substituents at the bay positions shows the favorable electron transport ability with the mobility as large as 0.514 $cm^2\ V^{-1}\ s^{-1}$. Although the derivatives with

four halogen substituents at the bay positions, B1, B2, B3 and B4, stabilize the LUMO levels and increase the electron affinities, the distorted molecular geometries are adverse to the close packings, and hence leading to the low mobilities. The charge carriers mostly transport in the basal stacked organic layer which give rise to a 2D mobility distribution. The angular-resolution anisotropic mobility analysis shows the importance to control the directions of crystals in applications to improve the material performance. The theoretical investigations of the organic semiconductors are helpful to understand the intramolecular and intermolecular charge transport behaviors and beneficial to the materials design for the electronic applications.

Acknowledgment

We thank the supercomputer center of Virtual Laboratory of Computational Chemistry, Computer Network Information Center, Chinese Academy of Sciences for the computational resources. This work is supported by the Natural Science Foundation of China (No. 20833008) and NKBRSF (Grant 2007CB815202).

Appendix A. Supplementary data

Supplementary data associated with this article can be found, in the online version, at doi:10.1016/j.orgel.2011.07.008.

References

[1] Y. Ie, T. Uto, N. Yamamoto, Y. Aso, Dendritic oligothiophene bearing perylene bis(dicarboximide) groups as an active material for photovoltaic device, Chem. Commun. 23 (2009) 1213–1215.
[2] J.E. Anthony, Functionalized acenes and heteroacenes for organic electronics, Chem. Rev. 106 (2006) 5028–5048.
[3] M.L. Tang, T. Okamoto, Z.N. Bao, High-performance organic semiconductors: asymmetric linear acenes containing sulphur, J. Am. Chem. Soc. 128 (2006) 16002–16003.
[4] M.Y. Kuo, C.C. Liu, Molecular design toward high hole mobility organic semiconductors: Tetraceno [2,3-c] thiophene derivatives of ultrasmall reorganization energies, J. Phys. Chem. C 113 (2009) 16303–16306.
[5] Z.Y. Yuan, Y. Xiao, X.H. Qian, A design concept of planar conjugated ladder oligomers of perylene bisimides and efficient synthetic strategy via regioselective photocyclization, Chem. Commun. 46 (2010) 2772–2774.
[6] H.X. Li, R.H. Zheng, Q.A. Shi, Theoretical study on charge carrier mobilities of tetrathiafulvalene derivatives, Phys. Chem. Chem. Phys. 13 (2011) 5642–5650.
[7] R. Chesterfield, C. Newman, T. Pappenfus, P. Ewbank, M. Haukaas, K. Mann, L. Miller, C. Frisbie, High electron mobility and ambipolar transport in organic thin-film transistors based on a π-stacking quinoidal terthiophene, Adv. Mater. 15 (2003) 1278–1282.
[8] M.E. Gershenson, V. Podzorov, A.F. Morpurgo, Colloquium: electronic transport in single-crystal organic transistors, Rev. Mod. Phys. 78 (2006) 973–989.
[9] D. Braga, G. Horowitz, High-performance organic field-effect transistors, Adv. Mater. 21 (2009) 1473–1486.
[10] W.Q. Deng, W.A. Goddard, Predictions of hole mobilities in oligoacene organic semiconductors from quantum mechanical calculations, J. Phys. Chem. B 108 (2004) 8614–8621.
[11] D. Nabok, P. Puschnig, C. Ambrosch-Draxl, O. Werzer, R. Resel, D.M. Smilgies, Crystal and electronic structures of pentacene thin films from grazing-incidence X-ray diffraction and first-principles calculations, Phys. Rev. B 76 (2007).
[12] L.B. Roberson, J. Kowalik, L.M. Tolbert, C. Kloc, R. Zeis, X.L. Chi, R. Fleming, C. Wilkins, Pentacene disproportionation during sublimation for field-effect transistors, J. Am. Chem. Soc. 127 (2005) 3069–3075.
[13] S.H. Wen, W.Q. Deng, K.L. Han, Revealing quantitative structure-activity relationships of transport properties in acene and acene derivative organic materials, Phys. Chem. Chem. Phys. 12 (2010) 9267–9275.
[14] H. Klauk, U. Zschieschang, J. Pflaum, M. Halik, Ultralow-power organic complementary circuits, Nature 445 (2007) 745–748.
[15] P.F. Baude, D.A. Ender, M.A. Haase, T.W. Kelley, D.V. Muyres, S.D. Theiss, Pentacene-based radio-frequency identification circuitry, Appl. Phys. Lett. 82 (2003) 3964–3966.
[16] M.-H. Yoon, S.A. DiBenedetto, A. Facchetti, T.J. Marks, Organic thin-film transistors based on carbonyl-functionalized quaterthiophenes: High mobility n-channel semiconductors and ambipolar transport, J. Am. Chem. Soc. 127 (2005) 1348–1349.
[17] Y. Ie, M. Nitani, M. Karakawa, H. Tada, Y. Aso, Air-stable n-type organic field-effect transistors based on carbonyl-bridged bithiazole derivatives, Adv. Funct. Mater. 20 (2010) 907–913.
[18] M.C.R. Delgado, E.G. Kim, D.A. da Silva, J.L. Brédas, Tuning the charge-transport parameters of perylene diimide single crystals via end and/or core functionalization: a density functional theory investigation, J. Am. Chem. Soc. 132 (2010) 3375–3387.
[19] M. Scholz, R. Schmidt, S. Krause, A. Scholl, F. Reinert, F. Würthner, Electronic structure of epitaxial thin films of bay-substituted perylene bisimide dyes, Appl. Phys. A 95 (2009) 285–290.
[20] B.L. Liang, Y.X. Zhang, Y.F. Wang, W. Xu, X.Y. Li, Structures and properties of 1,7-disubstituted perylene tetracarboxylic diimides: The substitutional effect study based on density functional theory calculations, J. Mater. Chem. 917 (2009) 133–141.
[21] F. Pichierri, Substitution effects on the frontier orbitals of 3,4,9,10-perylene bis(dicarboximide). A computational quantum chemistry study with insights into the electronic properties of organic semiconductors, J. Mol. Struc-Theochem 686 (2004) 57–63.
[22] L. Schmidt-Mende, A. Fechtenkotter, K. Mullen, E. Moons, R.H. Friend, J.D. MacKenzie, Self-organized discotic liquid crystals for high-efficiency organic photovoltaics, Science 293 (2001) 1119–1122.
[23] Z.Y. Yuan, J. Li, Y. Xiao, Z. Li, X.H. Qian, Core-perfluoroalkylated perylene diimides and naphthalene diimides: versatile synthesis, solubility, electrochemistry, and optical properties, J. Org. Chem 75 (2010) 3007–3016.
[24] A.L. Briseno, S.C.B. Mannsfeld, C. Reese, J.M. Hancock, Y. Xiong, S.A. Jenekhe, Z. Bao, Y. Xia, Perylenediimide nanowires and their use in fabricating field-effect transistors and complementary inverters, Nano Lett. 7 (2007) 2847–2853.
[25] Z.J. Chen, M.G. Debije, T. Debaerdemaeker, P. Osswald, F. Würthner, Tetrachloro-substituted perylene bisimide dyes as promising n-type organic semiconductors: Studies on structural, electrochemical and charge transport properties, Chem. Phys. Chem. 5 (2004) 137–140.
[26] H.E. Katz, A.J. Lovinger, J. Johnson, C. Kloc, T. Siegrist, W. Li, Y.Y. Lin, A. Dodabalapur, A soluble and air-stable organic semiconductor with high electron mobility, Nature 404 (2000) 478–481.
[27] R. Schmidt, M.M. Ling, J.H. Oh, M. Winkler, M. Könemann, Z.N. Bao, F. Würthner, Core-fluorinated rerylene bisimide dyes: Air stable n-channel organic semiconductors for thin film transistors with exceptionally high on-to-off current ratios, Adv. Mater. 19 (2007) 3692–3695.
[28] J.H. Oh, S.L. Suraru, W.-Y. Lee, M. Könemann, H.W. Höffken, C. Röger, R. Schmidt, Y. Chung, W.-C. Chen, F. Würthner, Z. Bao, High-performance air-stable n-type organic transistors based on core-chlorinated naphthalene tetracarboxylic diimides, Adv. Funct. Mater. 20 (2010) 2148–2156.
[29] M.M. Shi, H.Z. Chen, J.Z. Sun, J. Ye, M. Wang, Fluoroperylene diimide: a soluble and air-stable electron acceptor, Chem. Commun. (2003) 1710–1711.
[30] H.Z. Chen, M.M. Ling, X. Mo, M.M. Shi, M. Wang, Z. Bao, Air stable n-channel organic semiconductors for thin film transistors based on fluorinated derivatives of perylene diimides, Chem. Mater. 19 (2007) 816–824.
[31] B.A. Jones, M.J. Ahrens, M.H. Yoon, A. Facchetti, T.J. Marks, M.R. Wasielewski, High-mobility air-stable n-type semiconductors with processing versatility: dicyanoperylene-3,4:9,10-bis(dicarboximides), Angew. Chem. Int. Ed. 43 (2004) 6363–6366.
[32] S.H. Wen, A. Li, J.L. Song, W.Q. Deng, K.L. Han, W.A. Goddard, First-principles investigation of anistropic hole mobilities in organic semiconductors, J. Phys. Chem. B 113 (2009) 8813–8819.
[33] J.-D. Huang, S.-H. Wen, W.-Q. Deng, K.-L. Han, Simulation of hole mobility in α-oligofuran crystals, J. Phys. Chem. B 115 (2011) 2140–2147.

[34] T. Yamada, T. Sato, K. Tanaka, H. Kaji, Percolation paths for charge transports in N,N′-diphenyl-N,N′-di(m-tolyl)benzidine (TPD), Org. Electron. 11 (2010) 255–265.
[35] I. Vilfan, Small polaron model of electron motion in organic molecular-crystals, Phys. Stat. Sol. B 59 (1973) 351–360.
[36] J.J. Kwiatkowski, J. Nelson, H. Li, J.L. Brédas, W. Wenzel, C. Lennartz, Simulating charge transport in tris(8-hydroxyquinoline) aluminium (Alq3), Phys. Chem. Chem. Phys. 10 (2008) 1852–1858.
[37] M.J. Frisch, G.W. Trucks, H.B. Schlegel, G.E. Scuseria, M.A. Robb, J.R. Cheeseman, G. Scalmani, V. Barone, B. Mennucci, G.A. Petersson, H. Nakatsuji, M. Caricato, X. Li, H.P. Hratchian, A.F. Izmaylov, J. Bloino, G. Sonnenberg, J.L. Zheng, M, Hada, M. Ehara, K. Toyota, R. Fukuda, J. Hasegawa, M. Ishida, T. Nakajima, Y. Honda, O. Kitao, H. Nakai, T. Vreven, J.A. Montgomery, Jr., J.E. Peralta, F. Ogliaro, M. Bearpark, J.J. Heyd, E. Brothers, K.N. Kudin, V.N. Staroverov, R. Kobayashi, J. Normand, K. Raghavachari, A. Rendell, J.C. Burant, S.S. Iyengar, J. Tomasi, M. Cossi, N. Rega, N.J. Millam, M. Klene, J.E. Knox, J.B. Cross, V. Bakken, C. Adamo, J. Jaramillo, R. Gomperts, R.E. Stratmann, O. Yazyev, A.J. Austin, R. Cammi, C. Pomelli, J.W. Ochterski, R.L. Martin, K. Morokuma, V.G. Zakrzewski, G.A. Voth, P. Salvador, J.J. Dannenberg, S. Dapprich, A.D. Daniels, Ö. Farkas, J.B. Foresman, J.V. Ortiz, J. Cioslowski, D.J. Fox, R.A. Gaussian 09, Gaussian, Inc., Wallingford, CT, 2009.
[38] V. Coropceanu, J. Cornil, D.A. da Silva, Y. Olivier, R. Silbey, J.L. Brédas, Charge transport in organic semiconductors, Chem. Rev. 107 (2007) 926–952.
[39] G.T. Velde, F.M. Bickelhaupt, E.J. Baerends, C.F. Guerra, S.J.A. Van Gisbergen, J.G. Snijders, T. Ziegler, Chemistry with ADF, J. Comput. Chem. 22 (2001) 931–967.
[40] R.M. Glaeser, R.S. Berry, Mobilities of electrons and holes in organic molecular solids. Comparison of band and hopping models, J. Chem. Phys. 44 (1966) 3797–3810.
[41] G.R. Hutchison, M.A. Ratner, T.J. Marks, Effects of heteroatom and molecular packing on hopping transport in organic semiconductors, J. Am. Chem. Soc. 127 (2005) 16866–16881.
[42] S.T. Bromley, M. Mas-Torrent, P. Hadley, C. Rovira, Importance of intermolecular interactions in assessing hopping mobilities in organic field effect transistors: Pentacene versus dithiophene-tetrathiafulvalene, J. Am. Chem. Soc. 126 (2004) 6544–6545.
[43] G.R. Hutchison, M.A. Ratner, T.J. Marks, Hopping transport in conductive heterocyclic oligomers: Reorganization energies and substituent effects, J. Am. Chem. Soc. 127 (2005) 2339–2350.
[44] R.A. Marcus, On the theory of oxidation-reduction reactions involving electron transfer, J. Chem. Phys. 24 (1956) 966–978.
[45] R.A. Marcus, Theory of oxidation-reduction reactions involving electron transfer .5. Comparison and properties of electrochemical and chemical rate constants, J. Phys. Chem. 67 (1963) 853–857.
[46] R.A. Marcus, Electron-transfer reactions in chemistry – theory and experiment, Rev. Mod. Phys. 65 (1993) 599–610.
[47] C.R. Newman, C.D. Frisbie, D.A. da Silva Filho, J.-L. Brédas, P.C. Ewbank, K.R. Mann, Introduction to organic thin film transistors and design of n-channel organic semiconductors, Chem. Mater. 16 (2004) 4436–4451.
[48] B.A. Jones, A. Facchetti, M.R. Wasielewski, T.J. Marks, Theory of oxidation-reduction reactions involving electron transfer .5. Comparison and properties of electrochemical and chemical rate constants, J. Am. Chem. Soc. 129 (2007) 15259–15278.
[49] R. Schmidt, J.H. Oh, Y.S. Sun, M. Deppisch, A.M. Krause, K. Radacki, H. Braunschweig, M. Konemann, P. Erk, Z.A. Bao, F. Würthner, High-performance air-stable n-channel organic thin film transistors based on halogenated perylene bisimide semiconductors, J. Am. Chem. Soc. 131 (2009) 6215–6228.
[50] S.H. Wen, W.Q. Deng, K.L. Han, Ultra-low resistance at TTF-TCNQ organic interfaces, Chem. Commun. 46 (2010) 5133–5135.
[51] V.C. Sundar, J. Zaumseil, V. Podzorov, E. Menard, R.L. Willett, T. Someya, M.E. Gershenson, J.A. Rogers, Elastomeric transistor stamps: reversible probing of charge transport in organic crystals, Science 303 (2004) 1644–1646.
[52] S.C.B. Mannsfeld, J. Locklin, C. Reese, M.E. Roberts, A.J. Lovinger, Z. Bao, Probing the anisotropic field-effect mobility of solution-deposited dicyclohexyl-α-quaterthiophene single crystals, Adv. Funct. Mater. 17 (2007) 1617–1622.

performances of the ISFET device. A pH sensor that combined the commercial MOSFET and an extended-gate concept using V_2O_5 xerogel, tin oxide (SnO_2) and indium tin oxide (ITO) as the pH sensing material was investigated by various authors [10–12]. The pH probe coated with V_2O_5, SnO_2, and ITO as the pH sensing materials electrically connects with the extended gate electrode of the commercial MOSFET devices. The reference electrode used for the measurement of the FET characteristics is used as a floating electrode, while both the reference electrode and pH probe are immersed in the electrolyte. However, the selectivity of these sensing layers to other ions including K^+ and Ca^{2+} was not measured.

Despite the various advantages of the Si ISFET device, it also has some limitations, due to the rigidity and opacity of the Si substrate and difficulty of achieving monolithic integration with microfluidic components for lab-on-a-chip (LOC) or micro-total analysis systems (μ-TAS) for clinical use. For the facile integration of ISFET devices into the new concepts of LOC or μ-TAS based on transparent polymeric or glass substrates having the capability of electrochemical and optical detection, new ISFET devices based on thin film transistor technologies from the display industry look promising. Among the various ISFETs based on non-single crystalline Si channels [13–15], the organic FET (OFET) is a good candidate, because the OFET has shown considerable potential in many electronics applications, due to its light weight, low cost, mechanical flexibility, optical transparency, compatibility for large area applications, and simple fabrication compared to conventional MOSFET devices based on silicon [16,17]. Bio-chemical sensors based on OTFTs have been developed by functionalizing an organic semiconductor sensing layer to specific target species. Some groups have also developed organic ISFETs for H^+ sensing [18,19]. However, the application of organic ISFETs is still limited, because of their limited dynamic pH range from 4–10 [18–20], poor linear sensitivity behavior [18–20], slow response [19], and poor stability [18]. These issues are related to the inherent degradation of the organic semiconductor layers which are sensitive to moisture and oxygen. However, in the above-mentioned cases, the organic dielectric or semiconductor layers are directly exposed to the electrolyte. Also, organic ISFETs with a top gate structure have difficulties in terms of the fabrication of the H^+ sensing gate dielectric on top of the organic semiconductor layer, because of the damage incurred during the formation of the gate dielectric. The damage to the organic semiconductor can be prevented by using organic gate dielectrics layers, such as parylene or polyvinyl alcohol (PVA) layers. However, choosing oxide gate materials for H^+ sensing is challenging in this case, due to the large difference in the thermal expansion coefficients of inorganic and organic materials. Furthermore, the ions can be transported through the gate insulator, which gives rise to a leakage current, due to the formation of cracks in the sensing layer under the influence of the large electric field in the solution during the measurement. These factors will affect the stability of the sensor performance.

In our work, a bottom–gate OTFT structure with ITO-extended gate sensing electrode was successfully fabricated. The side-effects caused by the fabrication process were minimized to improve the stabilty of the organic ISFET for pH sensing. This structure could be used to develop a stable pH sensor with good linearity over a wide dynamic pH range of 2–12, high sensitivity of 57–59 mV/pH, and fast response. The ITO-extended gate electrode in the organic ISFET could be used for sensing the pH selectively in K^+ and Ca^{2+} containing solutions.

2. Experiments

Fig. 1 shows the cross-section view (a) and top view (b) of the pH sensor based on the ITO-extended gate OFET. The ITO glass substrates were purchased from Fine Chemicals Co., Ltd., (Korea). The resistivity of ITO is below 20 ohm/sq, its thickness is 80 nm, and its transmittance is 87%. The ITO-extended gate OFET with a channel length of 40 μm was fabricated on an ITO-coated glass substrate. The ITO layer on the ITO-coated glass substrate was selectively etched by an etchant solution consisting of 24 wt.% HCl followed by a photo lithography process for patterning to form a gate electrode for the OFET as well as H^+ sensing layer. Then, poly(4-vinylphenol) (PVP) was deposited by the spin coating pro-

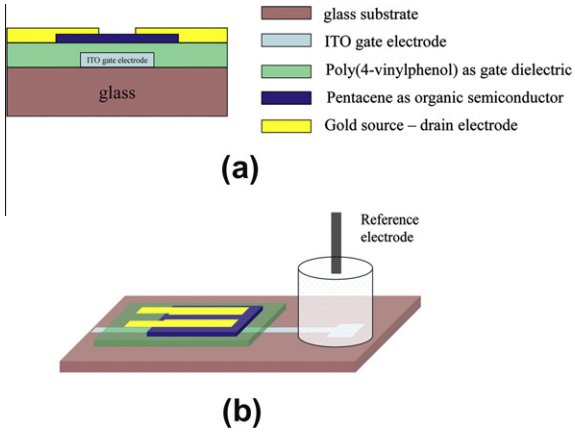

Fig. 1. Schematic of cross-section and top view of ITO-extended gate OFET device.

cess as a gate dielectric with a thickness of 250 nm. Pentacene as an organic semiconductor was formed by thermal evaporation at 80 °C with a thickness of 60 nm. Finally, gold was deposited with a thickness of 60 nm for use as the source and drain electrodes. To monitor the sensitivity of the ITO layer to H^+ ions, a polydimethylsiloxane (PDMS) well designed to contain the electrolyte was attached to the substrate, which has an extended-gate part attached using epoxy glue for sealing.

3. Results and discussion

Fig. 2 shows the electrical properties of a standard ITO bottom gate OFET, having a current on/off ratio of 10^5, field-effect mobility, μ, of 0.45 $cm^2 V^{-1}s^{-1}$, and threshold voltage, V_T, of −10.5 V. In the buffer solution, the measurement of the OFET using a saturated calomel electrode (SCE) as the floating gate electrode, the electrical properties were similar to those obtained for the standard device with the bottom gate electrode. To determine the sensitivity of the ITO-extended-gate electrode to H^+ ions, electrolytes with different pH values of 2, 4, 6, 8, 10, and 12 were placed one by one in the PDMS well. Due to the effect of bias stress on the pentacene OTFT [21–23] caused by the trapping of carriers from the gate bias-induced conduction channel into localized electronic states, a pre-measurement stabilization step should be performed to obtain the stable baseline of the electrical properties. As shown in Fig. 3(a), the measured drain current, I_{SD}, versus elapsed time at a source–drain voltage V_{SD} = −40 (V), voltage of the reference electrode V_{RE} = −40 (V), and pH of the solution of 7 shows that the I_{SD} value is stabilized after a measurement time of 10 minutes. At the initial stage, I_{SD} slightly increased from −116 μA to −140 due to the increase in the number of charges accumulated in the conduction channel under reference electrode bias. Then, I_{SD} decreases rapidly from −140 μA to −30 μA in 10 minutes because of the increase in the number of carriers trapped at the applied V_{RE} voltage [21,22]. From this point, the rate of decrease of I_{SD} over time is small. Therefore, it can be neglected and the investigation of the sensitivity of the ITO material to H^+ is carried out at this point.

The mechanism of H^+ ion sensing of the ITO-extended gate OFET can be explained based on the theoretical operation of the OFET and behavior of the ITO surface in the electrolyte, which are described by the Gouy–Chapman–Stern–Graham and Site-binding models [2]. The ITO material is a solid solution of indium (III) oxide (In_2O_3) and tin (IV) oxide (SnO_2), typically 90% In_2O_3 and 10% SnO_2 by weight. Thus, the ITO surface has various ionic states, including InOH, InO^-, $InOH_2^+$, SnOH, SnO^-, and $SnOH_2^+$.

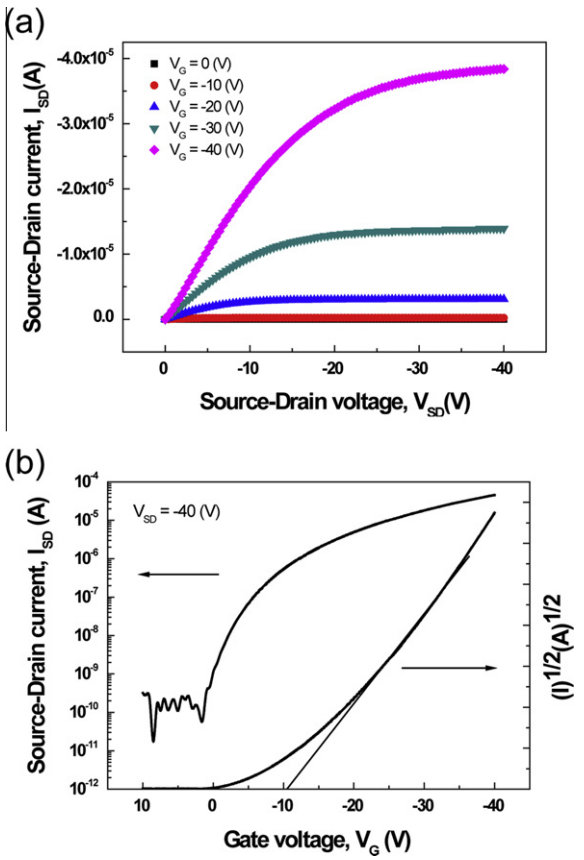

Fig. 2. The output and transfer characteristics of the standard ITO-extended bottom gate OFET device.

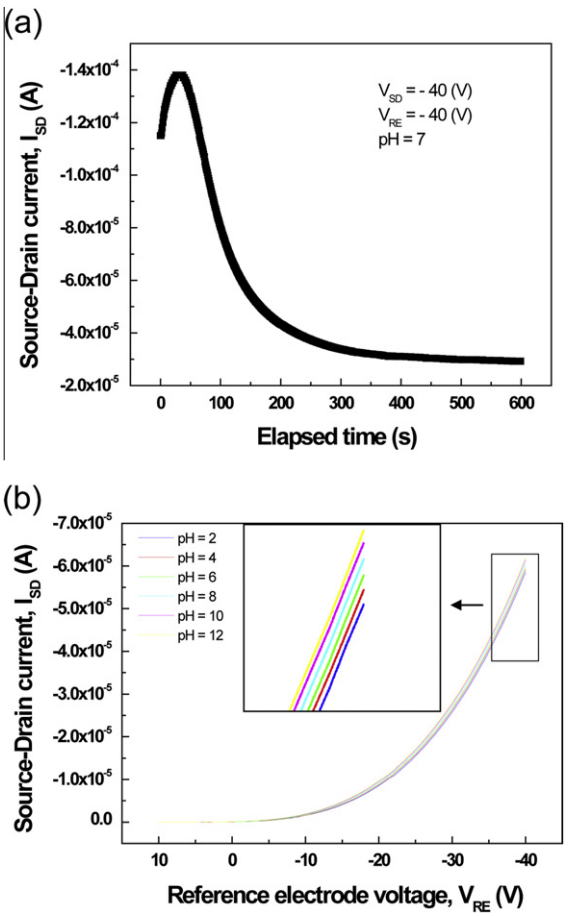

Fig. 3. Source–Drain current (I_{DS}) versus elapsed time at condition of V_{SD} = −40 (V), V_{RE} = −40 (V), and electrolyte with pH value of 7 in 10 min (a), and transfer characteristics of OFETs in various pH solutions (b).

Therefore, the interaction between the ITO surface and electrolyte can be explained by the above models. These models can be referenced elsewhere [2]. According to these models, there is an electrochemical surface potential, ψ, of ITO in the electrolyte solution. This potential decays exponentially within the critical distance given by $\lambda_D = \sqrt{\frac{\varepsilon\varepsilon_0 kT}{N_A q^2 \sum_i z_i^2 C_i}}$, where ε is the dielectric constant of the electrolyte, ε_0 is the permittivity of a vacuum, N_A is the Avogadro constant, C_i is the concentration of species i in the electrolyte, and z_i the corresponding ionic charge. Actually, the physicochemical change in the electrolyte can only be detected when it causes a change within the Debye length and, as a result, a change in the electrochemical potential at the interface [24]. Therefore, in the buffer solution, the H^+ ions exert a significant effect on the oxide surface, instead of on the companion negative groups.

To calculate the surface potential between the sensitive layer and the electrolyte, the equations given in references [25] and [26] can be used. From those equations, the pH sensitivity of the structure based on the ISFET is given by, $\frac{\delta\psi}{\delta pH} = 2.303\frac{kT}{q}\alpha$, where α is a dimensionless parameter that varies between 0 and 1. If α is 1, the ISFET has an ideal sensitivity of 59 mV per pH at 25 °C.

The OFET operates almost entirely in accumulation mode, which can be divided into two regions, in which the currents are in the linear and saturation regimes, as described by equations, $I_{linear} = \frac{\mu CW(V_G - V_T)V_{SD}}{L}$ and $I_{sat} = \frac{\mu CW}{2L}(V_G - V_T)^2$,respectively, where μ is the field-effect mobility, C the capacitance of the gate insulator, W the channel width, L the channel length, and V_T the threshold voltage. An important parameter for any FET device is the threshold voltage. It is the gate voltage required to turn the transistor "on" and is given by $V_T = V_{FB} + 2\psi_B + \frac{\sqrt{2\varepsilon_s qN(2\psi_B)}}{C}$ where the flat-band voltage, $V_{FB} = \frac{\phi_m}{q} - \frac{\phi_s}{q}$, ϕ_m is the metal work function, ϕ_s the semiconductor work function, ε_s the permittivity of free space, q the uinit charge, N the semiconductor doping concentration, and ψ_B the Fermi level from the intrinsic Fermi level ($\psi_B = |E_F - E_i|/q$). In the case where a reference electrode is used as the floating gate electrode instead of a metal gate electrode, the term $\frac{\phi_m}{q}$ is replaced by the terms that represent the reference electrode voltage (V_{RE}) and electrolyte ($\chi_{sol} - \psi$). At that time, the flat-band voltage is defined as: $V_{FB} = V_{RE} + \chi_{sol} - \psi - \frac{\phi_s}{q}$, where χ_{sol} is the surface dipole of the electrolyte and ψ is the ITO surface potential. Therefore, the threshold voltage is $V_T = V_{RE} + \chi_{sol} - \psi - \frac{\phi_s}{q} + 2\psi_B + \frac{\sqrt{2\varepsilon_s qN(2\psi_B)}}{C}$. Therefore, at the same applied V_{RE}, $\Delta V_T = -\Delta\psi$. This equation can be used for the calculation of the pH sensitivity, while plotting the transfer characteristics of the ITO-extended gate OTFT with various pH values of the electrolyte.

After the pre-measurement stabilization step, the transfer characteristics of the ITO-extended gate OTFT were measured with electrolytes having various pH values in the range from 2 to 12, as shown in Fig. 3(b). It can be seen that I_{SD} increased as the pH value of the solution increased. This can be easily explained by the fact that the increase in pH value means a decrease in the proton ion concentration. As a result, the proton ion concentration on the ITO surface decreases according to the Boltzman equation describing the relationship between the H^+ concentration on the solid surface $[H_s^+]$ and that in the electrolyte solution $[H_b^+]$, $[H^+]_s = [H^+]_b \exp(\frac{-q\psi}{kT})$ [2]. Therefore, the negative charge density will increase on the ITO gate surface as the pH value increases. This is equivalent to the increase in the negative bias value of the ITO bottom gate electrode causing the increase in I_{SD} due to the p-type semiconductor behavior of pentacene.

As mentioned above, the H^+ ions in the buffer electrolyte have an electrochemical interaction with the ITO surface, resulting in the change in V_T of the FET device. The change in V_T is equal to the change of the surface electrochemical potential of ITO (but with the opposite sign). Fig. 4(a) shows the curves of $(I_{SD})^{1/2}$ versus V_{RE} with varying pH from 2 to 12. From these curves, the threshold voltage can be extracted for each pH solution as shown in Fig. 4(b). From this data, if the pH of the buffer is changed from 2 to 4, the V_T value is changed from −10.78 to −10.664. Therefore, the difference in the threshold voltage, $\Delta V_T = 116$mV. This means that the difference in the ITO surface potential is −116 mV. This agrees with the theory

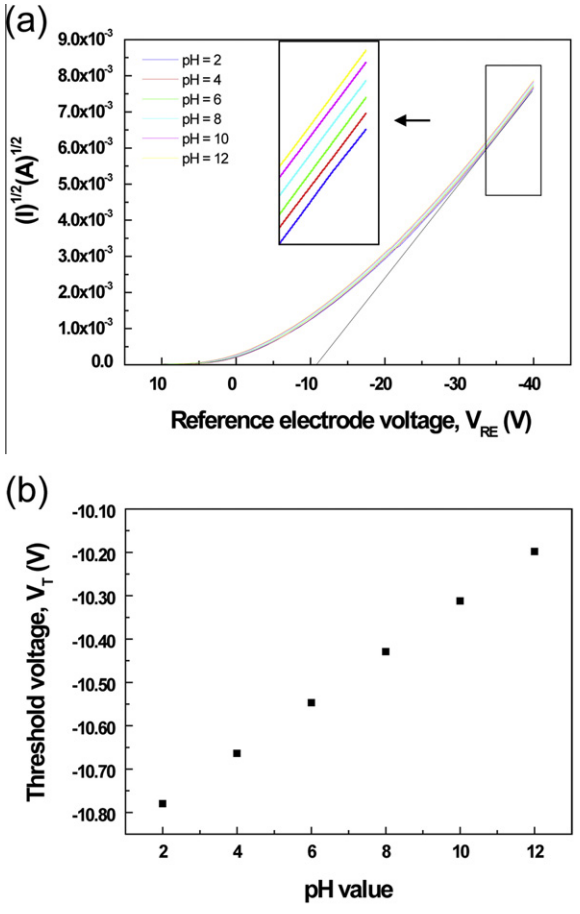

Fig. 4. Curves of $(I_{SD})^{1/2}$ versus V_{RE} with various pH solutions (a), and threshold voltage, V_T, in different pH solutions (b).

that as the pH value increases, the positive surface charge decreases. Fig. 4(b) shows the linear behavior of V_T versus the pH of the buffer solution and sensitivity of 57–59 mV/pH.

Actually, a pH sensor for real applications in biochemical engineering needs to have good selectivity to protons without any interference from other ions such as K^+, Ca^{2+}, Na^+, etc. Therefore, in this study, we investigated the selectivity of the ITO layer to K^+ and Ca^{2+} ions. Fig. 5(a) and (b) show the transfer characteristics of the ITO-extended gate OTFT for various K^+ and Ca^{2+} ion concentrations. The data show that the ITO surface is insensitive to the variation of the K^+ and Ca^{2+} ion concentrations, because there is no change in the V_T value obtained from the transfer characteristics. For the quantitative estimation of the interference of K^+ and Ca^{2+} ions to the pH measurement, the selectivity coefficient is measured. The selectivity is characterized by determining the selectivity coefficient, which is defined in the Nicolsky–Eisenman equation [27,28], $E = E_0 + \frac{RT}{z_A F} \ln\left[a_A + K^{pot}_{A,B}(a_B)^{z_A/z_B}\right]$, where z_A and z_B are the charge numbers of the primary ion, A, and of the interfering ion, B, respectively; a_A and a_B are the activities of the primary ion, A, and of the interfering ion, B, respectively; R is the gas constant (8.31 J $K^{-1}mol^{-1}$); F is the Faraday constant (96,485 C mol^{-1}); T is the temperature (K). The activity is related to the concentration by the activity coefficient, γ, as $a = \gamma c$ [29], where γ can be calculated from the Debye–Huckel equation which estimates the effects of interaction between ions in a solution. The Debye–Huckel equation is given by, $-\log\gamma = \frac{Az^2\sqrt{I}}{1+B\alpha\sqrt{I}}$ [29], where A and B are constants from the Debye–Huckel theory with value of 0.51 and 3.3×10^7, respectively at room temperature, I is the ionic strength, and α is the ion size parameters. The α values of 600 and 900 pm for Ca^{2+} and H^+ ions, respectively, and 300 pm for both K^+ and OH^- ions were used [29]. The ionic strength, I, is a measure of the total ions in the solution, weighted according to their charges, and affects the dissociation and solubility of different salt. It is defined by, $I = \frac{1}{2}\sum_i^n c_i z_i^2$ [29], where c_i and z_i are the molar concentration and charge number of ion i. The selectivity coefficient value $K^{pot}_{A,B}$ indicates the sensing selectivity to primary ion A compared to interfering ion B. The selectivity coefficient value depends on the nature of sensing layer or selective membrane as well as the experimental conditions such as ion concentration and methods of determination [27–29]. The traditional methods include the separate solution method (SSM) [28] and mixed solution method (MSM) [28]. In the SSM method, the electrochemical potentials are measured separately in solutions containing only primary ions A or interfering ions B. In the case of the MSM method, the electrochemical potentials are measured both in only primary ions A and in a mixed solution containing the primary ions A and interfering ions B with various concentrations. Based on Nicolsky–Eisenman equation, the selectivity coefficient in the MSM method can be calculated as, $K^{pot}_{A,B} = a_A\left(e^{\frac{(E_{AB}-E_A)z_A F}{RT}} - 1\right) / (a_B)^{z_A/z_B}$ [28].

The measurements for obtaining sensing selectivity of H^+ to K^+ and Ca^{2+} were carried out in both acid (pH 2 solution) and base (pH 12 solution) medium. The pH 2 and 12 solutions with presence of various KCl and $CaCl_2$ concentrations of 10^{-2}, 10^{-3} and 10^{-4} M, respectively, were used for investigations. Fig. 6 shows the transfer curves of the pH 2 solutions and pH 2 solutions in the presence of various KCl concentrations of 10^{-2}, 10^{-3} and 10^{-4} M. This data indicates that the K^+ ions have low interference to H^+ ions

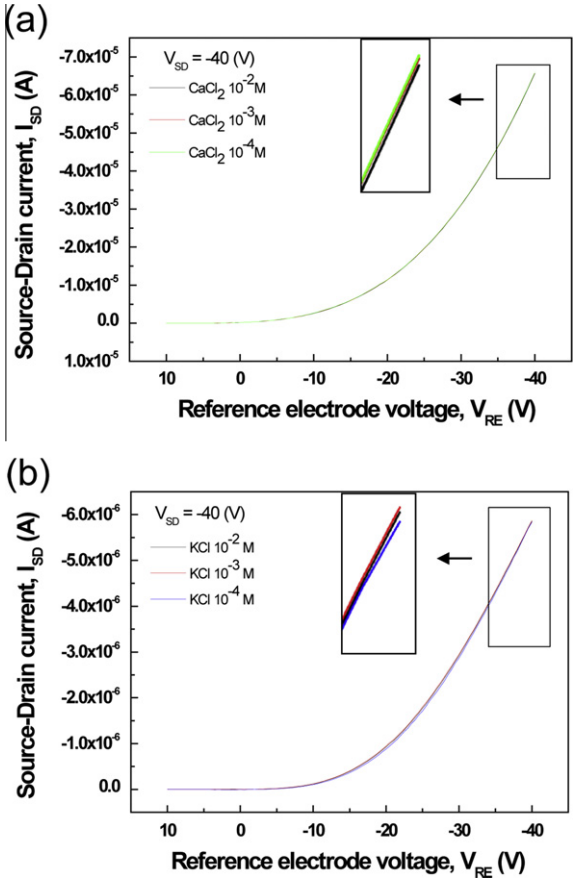

Fig. 5. Transfer characteristics in the solutions with various (a) $CaCl_2$ and (b) KCl concentrations.

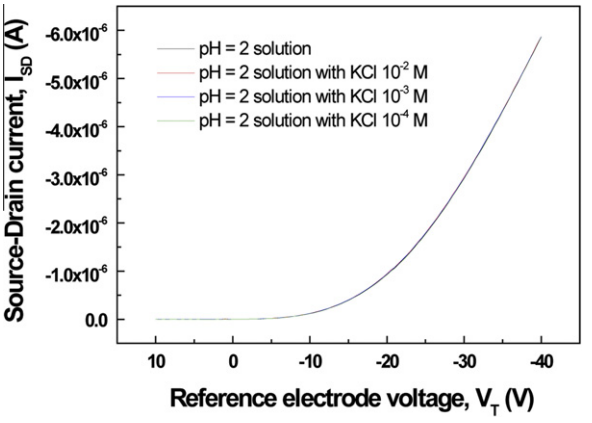

Fig. 6. Transfer characteristics of the OFET in the pH 2 solution, pH 2 solution with 10^{-2}, 10^{-3}, and 10^{-4} M KCl, respectively.

Table 1
The ionic strength and activity coefficient calculation of experimented solutions.

Solution	Ionic strength (M)	Activity coefficient			
		$\gamma(H^+)$	$\gamma(K^+)$	$\gamma(oh^-)$	$\gamma(Ca^{2+})$
pH 2 solution	0.01	0.8895			
pH 2 solution with KCl 10^{-2} M	0.02	0.8475	0.8471		
pH 2 solution with KCl 10^{-3} M	0.011	0.8844	0.8842		
pH 2 solution with KCl 10^{-4} M	0.0101	0.8889	0.8887		
pH 12 solution	0.01			0.8893	
pH 12 solution with KCl 10^{-2} M	0.02		0.8471	0.8471	
pH 12 solution with KCl 10^{-3} M	0.011		0.8842	0.8842	
pH 12 solution with KCl 10^{-4} M	0.0101		0.8887	0.8887	
pH 2 solution with $CaCl_2$ 10^{-2} M	0.04	0.7917			0.3922
pH 2 solution with $CaCl_2$ 10^{-3} M	0.013	0.8750			0.5860
pH 2 solution with $CaCl_2$ 10^{-4} M	0.0103	0.8879			0.6214
pH 12 solution with $CaCl_2$ 10^{-2} M	0.04			0.7910	0.3922
pH 12 solution with $CaCl_2$ 10^{-3} M	0.013			0.5860	0.5860
pH 12 solution with $CaCl_2$ 10^{-4} M	0.0103			0.6214	0.6214

in the pH 2 solution due to the shift voltage between each curve is smaller than 1 mV at constant current. Based on activity coefficient values of each ion in the mixed solution, presented in the Table 1, the selectivity coefficient could be calculated according to the aforementioned equations. In the case of selectivity to K^+, in both acid and base medium (pH 2 and 12), the selectivity coefficient value is as low as 2×10^{-2}. An analogous measurement in the solutions of pH 2 and 12 containing $CaCl_2$ was carried out. The results show the Ca^{2+} ions had low interference effect on the pH 2 and pH 12 solutions. The selectivity coefficient value was measured to be 5×10^{-2}. As compared to the selectivity coefficient values of the order of 10^{-3} reported from the measurements using ion-selective electrode (ISE) for selectively H^+ sensing to Ca^{2+} and K^+ ions [27–29], the obtained values from the pH sensor with no selective membrane in our work are slightly higher but appropriate for selective H^+ sensing in the electrolyte containing Ca^{2+} and K^+ ions with no large interference.

4. Conclusion

In this work, an ITO-extended gate OFET pH sensor was successfully fabricated and showed good performance. Its sensitivity was as high as 57–59 mV/pH in the pH range of 2–12. The interfering effects of K^+ and Ca^{2+} ions were investigated. The results indicated weakly interfering effects exerted by the K^+ and Ca^{2+} ions showing the selectivity coefficient to K^+, K_H^+, $_K^+$, of 2×10^{-2} and to Ca^{2+}, K_H^+, Ca^{2+}, of 5×10^{-2}. Therefore, the ITO-extended gate FET device can be used as an ion selective sensor device for pH measurements in multi-ion electrolytes and cell-based biosensors without an ion-selective membrane. Furthermore, organic FETs with an extended gate structure can be used as a potentiometric transducer for bio-chemical applications, since the surface of the extended gate ITO can be easily modified with different sensing layers.

Acknowledgments

This research was supported by the Basic Science Research Program (Grant No. 2010-0015035) and the WCU Program (Grant No. R32-2008-000-10124-0) through the National Research Foundation of Korea (NRF) funded by the Ministry of Education, Science and Technology (MEST).

References

[1] P. Bergveld, IEEE Transactions on Biomedical Engineering BME-17 (1970) 70.
[2] M.W. Shinwari, M.J. Deen, D. Landheer, Microelectronics Reliability 47 (2007) 2025.
[3] SA Instrument & Control, Technews Publishing (Pty) Ltd., http://instrumentation.co.za/article.aspx?pklarticleid=2201 (2003).
[4] L. Bousse, S. Mostarshed, B.V.D. Schoot, N.F. de Rooij, Sensors and Actuators B: Chemical 17 (1994) 157.
[5] S. Yoshida, N. Hara, K. Sugimoto, Journal of the Electrochemical Society 151 (2004) H53.
[6] T.M. Pan, K.M. Liao, Sensors and Actuators B: Chemical 127 (2007) 480.
[7] T.M. Pan, K.M. Liao, Sensors and Actuators B: Chemical 133 (2008) 97.
[8] A. Fog, R. Buck, Sensors and Actuators 5 (1984) 137.
[9] J.V.D. Spiegel, I. Lauks, P. Chan, D. Babic, Sensors and Actuators 4 (1983) 291.
[10] J.C. Chou, P.K. Kwan, Z.J. Chen, Japan Journal of Applied Physics 42 (2003) 6790.
[11] J.C. Chou, J.L. Chiang, C.L. Wu, Japan Journal of Applied Physics 44 (2005) 4838.
[12] E.M. Guerra, G.R. Silva, M. Mulato, Solid State Sciences 11 (2009) 456.
[13] A. Cohen, M.E. Spira, S. Yitshaik, G. Borghs, O. Shwartzglass, J. Shappir, Biosensors and Bioelectronics 19 (2004) 1703.
[14] S. Meyburg, M. Goryll, J. Moers, S. Ingebrandt, S.B. Meffert, H. Luth, A. Offenhausser, Biosensors and Bioelectronics 21 (2006) 1037.
[15] M.H. Asif, O. Nur, M. Willander, B. Danielson, Biosensors and Bioelectronics 24 (2009) 3379.
[16] A. Bonfiglio, F. Mameli, O. Sanna, Applied Physics Letters 82 (2003) 3550.
[17] C. Bartic, G. Borghs, Analytical and Bioanalytical Chemistry 384 (2006) 354.
[18] K. Diallo, M. Lemiti, J. Tardy, F. Bessueille, N.J. Renault, Applied Physics Letters 93 (2008) 183305.
[19] A. Loi, I. Manunza, A. Bonfiglio, Applied Physics Letters 86 (2005) 103512.
[20] A. Caboni, E. Orgiu, E. Scavetta, M. Barbaro, A. Bonfiglio, Applied Physics Letters 95 (2009) 123304.
[21] D. Kawakami, Y. Yasutake, H. Nishizawa, Y. Majima, Japan Journal of Applied Physics 45 (2006) L1127.
[22] U. Zschieschang, R.T. Weitz, K. Kern, H. Klauk, Applied Physics A 95 (2009) 139.
[23] T.N. Ng, J.H. Daniel, S. Sambandan, A.C. Arias, M.L. Chabinyc, R.A. Street, Applied Physics 103 (2008) 044506.

[24] M.J. Spijkman, J.J. Brondijk, T.C.T. Geuns, E.C.P. Smits, T. Cramer, F. Zerbetto, P. Stoliar, F. Biscarini, P.W.M. Blom, D.M. de Leeuw, Advanced Fucntional Materials 20 (2010) 898.
[25] P. Bergveld, Sensors and Actuators B: Chemical 88 (2003) 1.
[26] L. Bousse, N.F. de Rooij, P. Bergveld, IEEE Transactions on Electron Devices 30 (1983) 1263.
[27] E. Bakker, P. Buhlmann, E. Pretsch, Electroanalysis 11 (1999) 915.
[28] C.A. Grimes, E.C. Dickey, M.V. Pishko, Encyclopedia of Sensors 5 (2006) 133.
[29] B.R. Eggins, Chemical Sensors and Biosensors, John Wiley & Sons Ltd., West Sussex, 2002.

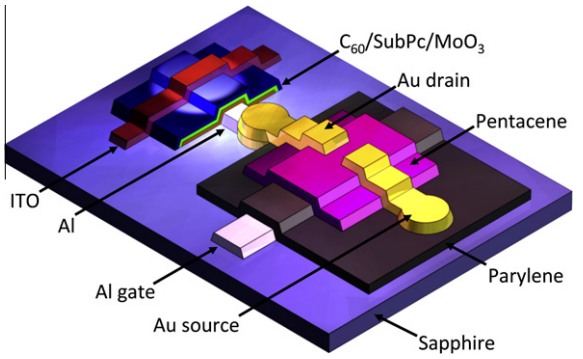

Fig. 1. Schematic diagram of the integrated passive pixel sensor consisting of a top-illuminated organic photodetector with an indium-tin-oxide (ITO) top contact in series with a pentacene organic thin film transistor. Layer compositions are indicated.

structure (500 Å C_{60}/90 Å SubPc/300 Å MoO_3) was thermally evaporated at a rate of 1 Å/s. A 500 Å-thick ITO anode was sputtered at a power of 20 W (rate = 0.1 Å/s) using an Argon plasma at a pressure of 2 mTorr. In Fig. 2c, inset, is a molecular structural formula of the donor, SubPc. After depositing the OPD layers, the samples were loaded into a parylene deposition system where 0.70 g of parylene C (dielectric constant, $\varepsilon_r = 3.15$) was coated onto the OTFT gate contact, forming a 2700 Å-thick insulator. Finally, the 500 Å-thick pentacene channel and the 400 Å-thick Au source and drain contacts were sequentially evaporated at the rates of 0.5 and 0.3 Å/s, respectively, to complete the OTFT. All features were defined using shadow masks attached in a high-purity N_2 ambient (<1 ppm H_2O and O_2), with the exception of a brief exposure to air before and after parylene deposition. The OPD dimensions (100 μm × 800 μm) and OTFT channel width-to-length ratio (W/L = 500 μm/30 μm) were set by shadow-masking during ITO and Au deposition, respectively.

Device performance was measured in air using a semiconductor parameter analyzer. Incident light for measuring the circuit dynamic range (*DR*) was provided by a mercury lamp with a spectral bandpass filter at a center wavelength of $\lambda = 580 \pm 2$ nm, matching a Hg emission peak as well as the absorption maximum of SubPc. The illumination intensity was varied using neutral density filters and measured using a calibrated Si photodetector. External quantum efficiency (*EQE*) was measured using a lock-in amplifier and monochromated light from a tungsten-halogen lamp chopped at ~200 Hz. Voltage was applied to the detector with a current amplifier at the input to the lock-in for biased *EQE* measurement. The circuit

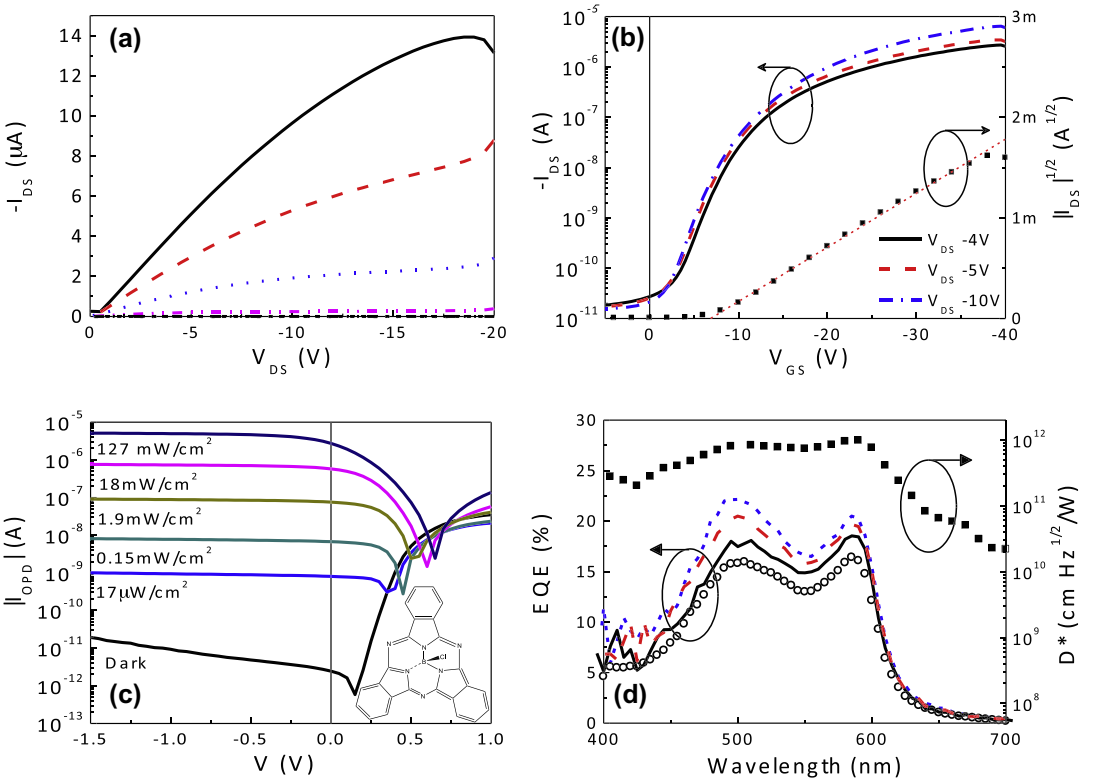

Fig. 2. Performance of discrete components comprising the integrated passive pixel sensor. (a) Output characteristics of the pentacene OTFT for V_{GS} = 0 V (short-dashed line), −10 V (dash-dotted line), −20 V (dotted line), −30 V (dashed line), and −40 V (solid line). (b) Transfer characteristics of drain current (I_{DS}) vs. gate-source voltage (V_{GS}) of the organic thin film transistor (OTFT) at a drain-source voltage of V_{DS} = −4 V (solid line), −5 V (dashed line), and −10 V (dash-dotted line). The square-root of the drain-source current (squares) and the fit (short-dashed line) are shown on the right-hand axis. (c) Current–voltage characteristics (I_{OPD}–V) of the organic photodetector (OPD) in the dark and under illumination at several different intensities. The incident wavelength is $\lambda = 580 \pm 2$ nm. *Inset*: Molecular structural formula of SubPc. (d) External quantum efficiency (*EQE*) of the integrated SubPc/C_{60} OPD under 0 V bias (solid line), −1 V (dashed line), and −2 V reverse bias (short-dashed line), compared to that of a control inverted OPD (open circles). The specific detectivity (D^*) at −1.5 V is shown on the right-hand axis (squares).

transient response was measured using an oscilloscope and a pulse generator with rise and fall times of 2 ns controlling the transistor gate.

The characteristics of the discrete pixel components were individually measured with results shown in Fig. 2. The OTFT output characteristic is shown in Fig. 2a. The drain OFF current is $I_{DS} = 27 \pm 3$ pA at $V_{DS} = -4$ V, and the ON/OFF ratio is 10^5 (Fig. 2b). The OFF current is comparable to that of a BC-OTFT[3] at small V_{DS}, while the ON current is improved by more than two orders of magnitude. The field-effect hole mobility, $\mu = 0.09 \pm 0.02$ cm^2/V s, was obtained using $I_{DS} = [\mu WC/2L](V_{GS} - V_{th})^2$ in the saturation region, where C is the gate-insulator capacitance, V_{GS} is the gate-source voltage, and V_{th} is the threshold voltage. The OTFT ON current is comparable to previously reported bottom-gate pentacene transistors employing a polymer gate dielectric, while the low OFF current is achieved with much smaller dielectric thickness (270 nm) than a previously reported thickness of >500 nm [10]. This is attributed to reduced gate leakage due to small gate-source overlap (<350 μm × 500 μm).

The current–voltage (I_{OPD}–V) response of the OPD is shown in Fig. 2c. Under a reverse bias of −1.5 V, the OPD dark current is $I_{Dark} = 20$ pA. Also, $EQE = 18.2\%$ at $\lambda = 580$ nm, and increases to 19.9% at −2 V due to increased polaron-pair dissociation at higher voltages [11] (Fig. 2d). The *EQE* of an analogous inverted discrete OPD is also shown in Fig. 2d. The *EQE* of both devices is within typical device-to-device variations. Over the range of incident optical powers used for this work (from 2.6 to 151 mW/cm^2), the OPD photocurrent is linear, resulting in a high detection *DR*. The photodetector specific detectivity (D^*) at −1.5 V is shown in Fig. 2d). Now, D^* is calculated using $D^* = \sqrt{A\Delta f}/NEP$, where A is the detector area, Δf is the bandwidth, and *NEP* is the noise equivalent power [2]. Under reverse bias, shot noise dominates the *NEP*, giving $D^* = \sqrt{A\Delta f} \cdot R/\sqrt{2qI_{Dark}}$, where R is the responsivity, and q is the elementary charge. At $\lambda = 580$ nm, $D^* = 9.4 \times 10^{11}$ cm Hz$^{1/2}$ W^{-1}.

The integrated pixel performance was characterized by measuring the current between the anode of the OPD and the source of the OTFT (I_{AS}) under various light intensities and V_{GS} (Fig. 3a). The pixel has a dark OFF current of $I_{AS} = 31 \pm 5$ pA and dark ON current of 950 ± 130 pA. The dark OFF current is consistent with that of the discrete OTFT within measurement error. The slight difference is due to the change in V_{DS} across the sample from testing the discrete OTFT ($V_{DS} = -4$ V) vs. testing the integrated pixel ($V_{AS} = -4$ V). The dark ON current of the pixel at $V_{AS} = -4$ V is noticeably higher than that of the OPD at −1.5 V in Fig. 2c. Nevertheless, this pixel performance is sufficient for application to a 30 × 30 sensor array.

The lowest detectable light intensity is 17 μW/cm^2, as shown in Fig. 3a, establishing a lower limit to the *DR*. Since the OPD photocurrent does not saturate within the testing range used, the upper limit is determined by the ON current (4.6 ± 0.05 μA) of the OTFT at light intensities >130 mW/cm^2. Furthermore, ΔI_{AS} is the difference between the ON current under illumination and in the dark at a gate bias, $V_{GS} = -39.5$ V. Fitting the pixel photocurrent ΔI_{AS} vs. incident power P gives $R = 0.083 \pm 0.003$ A/W, consistent with the *EQE* result (see Fig. 3b). The pixel showed a 12-bit dynamic range (corresponding to $DR = \Delta I_{AS,MAX}/\Delta I_{AS,MIN} = 4.1 \times 10^3$). The improved performance is due to the enhanced ON current of TC-OTFTs compared with previously reported BC transistors [3].

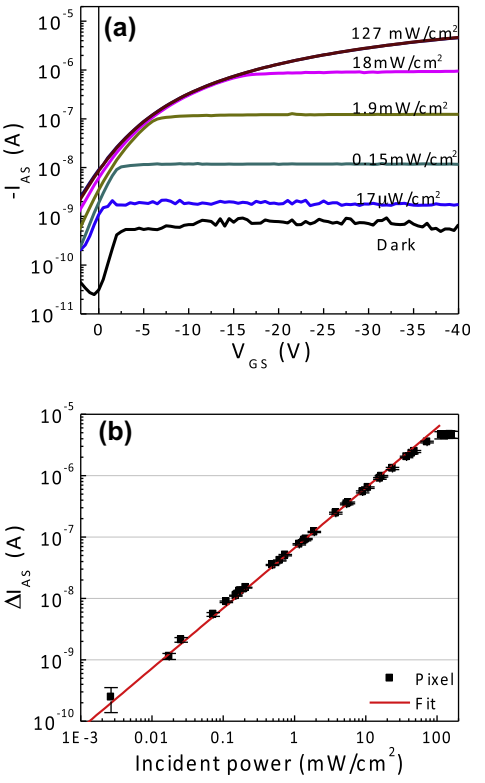

Fig. 3. (a) Transfer characteristics of anode-source current (I_{AS}) vs. V_{GS} of the pixel at an anode-source voltage of −4 V for various illumination intensities at $\lambda = 580 \pm 2$ nm. (b) Pixel photocurrent response, ΔI_{AS}, as a function of illumination power intensity (P) extracted from the transfer characteristics at $V_{GS} = -39.5$ V, where ΔI_{AS} is the difference between I_{AS} under illumination and in the dark. The line is a linear fit of to the data. The extent of the linear range of data gives the circuit dynamic range, equal to 12-bit.

The pixel response time was determined by measuring the voltage across a resistor between the source of the OTFT and ground. A pulsed V_{GS} from +2 V (OFF state) to −40 V (ON state) was applied while the device was kept under a constant $V_{AS} = -4$ V and an illumination intensity of 49 mW/cm^2. The resulting data were modeled by a bi-exponential decay following $-I_{AS} = I_0 + A_1 \exp[-(t - t_0)/\tau] + A_2 \exp[-(t - t_0)/t_{RO}]$, where I_0 is the steady state pixel current when the gate is ON, and t_0 is the time when the pulse is applied (Fig. 4). The read-out time was found to be $t_{RO} = 0.4 \pm 0.05$ ms. The resistance-capacitance charging time constant is $\tau = 29 \pm 8$ μs when using a 37.7 kΩ load, corresponding to the fast decay initially observed. Previously, it has been found that the optical response of analogous SubPc/C_{60} OPDs is on the order of nanoseconds [3,12], indicating that the circuit response time, t_{RO}, is limited by the discharging time through the OTFT channel. Note that t_{RO} is larger than the charge transit time across the channel (25 μs) as derived from the hole mobility, indicating that t_{RO} is primarily determined by charge trapping in the

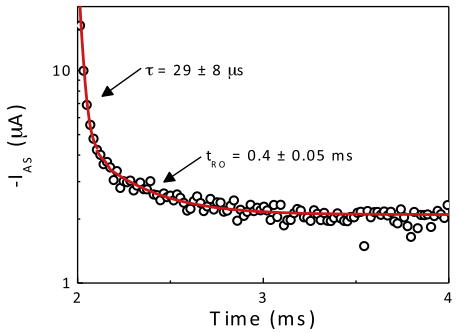

Fig. 4. Transient response of the pixel to a square voltage pulse applied at the transistor gate electrode measured using a 37.7 kΩ load. Also shown (dashed line) is a bi-exponential decay fit to the data. The time constants extracted from the fit are the read-out time of t_{RO} = 0.4 ± 0.05 ms, and the *RC* time constant of τ = 29 ± 8 μs.

pentacene layer. This response can be further improved by using a transistor with a higher mobility employing, for example, self-assembled monolayers at the insulator–channel interface that result in improved crystal orientation [10,13,14].

In conclusion, an organic integrated pixel based on a bottom-gate, top-contact pentacene transistor and an inverted SubPc/C_{60} photodetector has been demonstrated. It has a 12-bit dynamic range, an OFF current of 31 ± 5 pA, and a read-out time of 0.4 ± 0.05 ms. The circuit performance is adequate for use in video-rate, high-sensitivity focal plane arrays with dimensions of at least 30 × 30 pixels.

Acknowledgments

The authors thank Dr. X. Xu and C.K. Renshaw for helpful discussions, and Universal Display Corporation for financial support.

References

[1] X. Xu, M. Davanco, X. Qi, S.R. Forrest, Org. Electron. 9 (2008) 1122–1127.
[2] X. Xu, M. Mihnev, A. Taylor, S.R. Forrest, Appl. Phys. Lett. 94 (2009) 043313.
[3] C.K. Renshaw, X. Xu, S.R. Forrest, Org. Electron. 11 (2010) 175–178.
[4] K.-D. Jung, Y.C. Kim, H. Shin, B.-G. Park, J.D. Lee, E.S. Cho, S.J. Kwon, Appl. Phys. Lett. 96 (2010) 103305.
[5] D. Gupta, M. Katiyar, D. Gupta, Org. Electron. 10 (2009) 775–784.
[6] M. Nakamura, H. Ohguri, N. Goto, H. Tomii, M. Xu, T. Miyamoto, R. Matsubara, N. Ohashi, M. Sakai, K. Kudo, Appl. Phys. A 95 (2008) 73–80.
[7] I. Nausieda, Ryu Kyungbum, I. Kymissis, A.I. Akinwande, V. Bulovic, C.G. Sodini, IEEE Trans. Electron Devices 55 (2008) 527–532.
[8] T. Someya, Y. Kato, Shingo Iba, Y. Noguchi, T. Sekitani, H. Kawaguchi, T. Sakurai, IEEE Trans. Electron Devices 52 (2005) 2502–2511.
[9] X. Tong, B.E. Lassiter, S.R. Forrest, Org. Electron. 11 (2010) 705–709.
[10] T. Sekitani, S. Iba, Y. Kato, Y. Noguchi, T. Sakurai, T. Someya, J. Non-Cryst. Solids 352 (2006) 1769–1773.
[11] N.C. Giebink, G.P. Wiederrecht, M.R. Wasielewski, S.R. Forrest, Phys. Rev. B 82 (2010) 155305.
[12] M.S. Arnold, J.D. Zimmerman, C.K. Renshaw, X. Xu, R.R. Lunt, C.M. Austin, S.R. Forrest, Nano Lett. 9 (2009) 3354–3358.
[13] M. Shtein, J. Mapel, J.B. Benziger, S.R. Forrest, Appl. Phys. Lett. 81 (2002) 268.
[14] D.K. Hwang, K. Lee, J.H. Kim, S. Im, C.S. Kim, H.K. Baik, J.H. Park, E. Kim, Appl. Phys. Lett. 88 (2006) 243513.

metal phthalocyanines (MPcs) [18–22], and 1,5-diaminoanthraquinone [23–25] – has been used to prepare various nanostructures for applications in organic electronics, especially photovoltaic devices and field emitters, with the advantages of low-cost, low-temperature processing and mechanical flexibility. Among those materials, MPcs, which feature a central metal atom bound to a π-conjugated ligand, have particularly attractive properties for their application in optoelectronic devices (e.g., light emitting diodes [26], gas sensors [27–29], field-effect transistors [30–33], solar cells [34–36], and field emission devices [20,21]). Most active layers of MPcs have been fabricated using deposition methods, including organic vapor-phase deposition (OVPD) [1,18,37,38], thermal evaporation [19,21], and molecule beam epitaxy (MBE) [39]. It has been reported [1,21,22,25] that the morphologies of thin films of MPcs depend on the type of deposition technique, the heat-treatment temperature, and the conditions of the substrates during the deposition process. Tuning these various growth conditions can have a dramatic effect on the resulting morphologies and electronic properties, thereby requiring further investigation of the potential use of such structures in optoelectronic devices.

When developing field emitters, the inter-fiber distance, the aspect ratio, and the density of the nanofibers are theoretically and experimentally important parameters for achieving efficient field emission (FE) performance. Under practical conditions, however, it can be difficult to control the inter-fiber distance at an ideal fiber density. Although higher-density nanofibers provide higher electron currents, electrostatic screening effects are observed in such films; therefore, high-density nanofiber films do not possess appropriate FE properties [40]. To decrease the screening effect, forming a pattern array of aligned nanofibers is a facile method of enhancing FE properties [41]. Moreover, a recent study found that the electric field gradient at the edge of an emission bundle is significantly higher than that at its center [42]. Therefore, the ability to design patterns of nanofiber films should allow efficient increases in FE performance.

In this present study, we used FePc as a starting material, instead of a precursor of the catalyst for CNT growth [43], to fabricate FePc nanostructures on Si and Ag substrates. Because the surface energy and temperature of a substrate are both important factors affecting the morphologies of FePc films, we sought appropriate conditions for the direct growth of FePc films featuring planar structures on Si surfaces (higher surface energy) and fiber-like structures on Ag surfaces (lower surface energy). We used scanning electron microscopy (SEM) and high-resolution transmission electron microscopy (HRTEM) to characterize these 1D FePc nanofiber films. By taking advantage of such selective growth at various substrate temperatures, we used micropatterned Ag/Si substrates to obtain the fine growth of FePc nanofibers on the patterned Ag regions and in-plane FePc structures on the remaining open areas of the Si surfaces. To study the enhancement in FE performance when using field emitters with such micropatterned geometries, we used a vacuum emission measurement (VEM) system to compare the FE characteristics and device stability tests relative to those of corresponding unpatterned devices.

2. Experimental details

FePc thin films were deposited using a thermal evaporator operated at a base pressure of 7×10^{-6} torr. A commercially available FePc powder (purity: 96%; Tokyo Chemical Industry) was used as received without further purification; it was sublimed onto two kinds of substrates (Si and Ag). The Ag substrates were prepared by depositing Ag films onto Si (1 0 0) substrates using an electron beam (e-beam) evaporator. Prior to e-beam evaporation of the Ag film, a Ti layer (thickness: 300 Å) was deposited on a cleaned Si substrate as an adhesion layer. Without breaking the vacuum, a thin layer of Ag (thickness: 1000 Å) was then deposited. The influence of the substrate temperature (T_{sub}) on the FePc film morphology during FePc thermal evaporation was tested at values of T_{sub} of 25, 120, 180, and 240 °C. The sublimation of the FePc powder was performed at a crucible temperature of 180 °C; the corresponding deposition rate, controlled by a quartz crystal microbalance, was 0.4 Å/s.

Top and cross-sectional views of the morphologies of the FePc thin films were investigated using a JEOL JSM-6500F scanning electron microscope. The profiles and fine structure of nanofibers were imaged and analyzed using a JEOL-2010 high-resolution transmission electron microscope. The phase and crystallinity of the FePc nanofibers were characterized using grazing-incidence X-ray diffraction (GIXRD), employing a Bruker D8 system with Cu Kα radiation. The incident angle of the X-ray beam was fixed at 0.2°. Contact angles and surface energies were determined on each substrate using a Krüss universal surface tester (model GH-100), the geometric mean approximation, and three standard liquids: water (H_2O), diiodomethane (CH_2I_2), and ethylene glycol [$C_2H_4(OH)_2$]. The surface energies of the substrates were measured using the Owens and Wendt method. The valence band [highest occupied molecular orbital (HOMO)] of the FePc materials was surveyed using photoelectron spectroscopy in air (PESA; AC-2 photoelectron spectrometer); the Riken Keiki apparatus detected the number of photo-emitted electrons per second (CPS) as a function of the photon energy, using a UV light source for excitation and a gas-flow Geiger counter. The relationship between CPS and the photon energy is described using the approximate equation [44]:

$$\mathrm{CPS}^{1/2} = \frac{M}{k}(h\nu - \phi) \quad (1)$$

where M is an emission constant, k is the Boltzmann constant, $h\nu$ is the photon energy, and ϕ is the work function. When the surface materials were bombarded under a gradually increasing amount of UV light, photoelectrons were emitted from the surface (from a depth of several to hundred angstroms) at a certain energy level, due to the photoelectron effect. These emitted photoelectrons were then counted by a detector and open counter. The value of ϕ was determined through linear extrapolation of $\mathrm{CPS}^{1/2}$ to zero yield [44], when the PESA data were fitted using the software supplied with the spectrometer. UV–Visible (UV–Vis) spectra (300–1100 nm) were recorded using a Shimadzu UV-3600 spectrophotometer.

The FE characteristics of the FePc nanofibers were determined using a VEM system under a base pressure of 5×10^{-6} torr. Indium tin oxide (ITO) plate glasses were used as anodes, positioned above the substrate surfaces at a distance of 60 μm. The FE instrument featured a plate-to-plate geometry; the active area of the FePc nanofibers was 0.06 cm^2 for the unpatterned devices and 0.006156 cm^2 for the micropatterned devices featuring 171 (19×9) squares, each with a width of 60 μm. Current density–electric field (J–E) curves of the FE devices were measured using a Keithley 237 instrument (accuracy: 10^{-13} A). The emission currents of the FePc nanofibers were monitored as a function of the sweep bias. Stability tests were performed for 3000 s under a constant applied field of 11 V/μm at room temperature. The patterned FE devices are denoted herein as "**FE-X-P**," where **X** refers to the FePc nanofiber films were prepared at the value of T_{sub}. In addition, the unpatterned FE devices are denoted as "**FE-X-N**".

3. Results and discussion

The growth mechanisms of organic thin films on substrates are complicated because of specific issues related to each type of organic molecule; for example, the effects of the surface energy of the substrate, noncovalent interactions at the molecule–substrate interface, and intermolecular forces between molecules. Stranski–Krastanov growth tends to be the mode most frequently observed for small organic molecules under thermal evaporation conditions [45]. Previous studies [21,34–36] have revealed that the surface energy and substrate temperature are both important factors controlling the morphologies of films of small organic molecules. Therefore, in this study, we selected Ag and Si, with surface energies of 34.8 and 41.3 mJ/m^2, respectively, as electrodes for the selective growth of micropatterned FePc nanofiber films for FE applications. Fig. 1 displays SEM images of the FePc films deposited on the Si and Ag substrates at various values of T_{sub}. At a value of T_{sub} of 25 °C, all of the FePc thin films on the Si and Ag substrates exhibited analogous and contiguous granular crystals with smooth morphologies [Fig. 1(A, E, and I)]. When we increased the value of T_{sub} from 120 to 240 °C, elongated FePc grain-like films were formed with the in-plane morphology on the Si surface [Fig. 1(B–D)]. In contrast, when the FePc layers were deposited on the Ag substrate at values of T_{sub} in the range 120–240 °C, we obtained high-quality FePc fiber-like films featuring out-of-plane 1D nanostructural morphologies [Fig. 1(F–H) (top-view) and (J–L) (cross-sectional view)]. Notably, we found a high-density of aligned FePc nanofibers in the films deposited on the Ag surface at a value of T_{sub} of 240 °C [Fig. 1(H, L)]. The variation in FePc morphology that occurred upon increasing the value of T_{sub} can be explained by considering the following equation [46]:

$$\gamma_s = \gamma^0[1 - (T_s/T_c)]^n \quad (2)$$

where γ_s is the surface energy at the substrate temperature T_s and γ^0 is the surface energy at the critical temperature (T_c); the value of n may be close to unity for cathodes. This formula suggests that the surface energy of the substrate (γ_s) decreases as the substrate temperature increases, thereby favoring the desorption and surface diffusion of FePc molecules. A decrease in surface energy weakens the molecule–substrate interactions, causing the molecule–molecule interactions (i.e., π–π and van der Waals interactions) to become dominant. When nonpolar molecules (e.g., Alq_3, PY, coronene) form 1D nanofibers, molecular stacking occurs mainly through π–π and van der Waals interactions. In the 1D nanostructure of the stacked planar FePc molecules, we suspect that both face-to-face (π stacking) and edge-to-edge (van der Waals interaction) intermolecular forces play an important role in the 1D self-assembly of the stacking molecules [4–9].

At the device level of field emitters, the field enhancement factor (β) is approximated by the aspect ratio (AR; length-to-radius ratio) of a 1D nanostructure, defined as AR = (mean length; L)/(mean radius; r_m). A 1D nanostructure having a higher AR will exhibit a larger geometrical field enhancement and a lower turn-on field [47]. In this study, we found that changing the deposition time adjusted the lengths of the nanofibers. Besides, both high-density and high-AR of aligned FePc nanofiber films can be easily achieved on the Ag surface at a value of T_{sub} of 240 °C. To further investigate the influence of AR effect on FE properties, we prepared FePc nanofiber films with different ARs by changing values of T_{sub} of 180 and 240 °C [Fig. 2(A and E)]. Furthermore, the histograms of the fiber length, radius, and AR [Fig. 2(B and F), (C and G), and (D and H)] were obtained for comparison, respectively, which were based on the cross-sectional SEM images of those structures. In the fabrication condition of T_{sub} of 180 and 240 °C, the values of L of these FePc nanofibers with an apparent difference were found to be 124 ± 41 and 699 ± 216 nm, while the values of r_m of these FePc nanofibers were analogous to be 21.9 ± 4.0 and 22.2 ± 4.3 nm, respectively. In addition, the mean values of ARs of individual FePc nanofibers were calculated to be 6.0 ± 2.6 and 30.3 ± 3.6, respectively.

Fig. 3(A) displays a TEM image and the corresponding selected area electron diffraction (SAED) pattern of a single FePc nanofiber, which we had deposited on the Ag substrate at a value of T_{sub} of 240 °C. The TEM image of this FePc nanofiber exhibits fringes, suggesting that the FePc molecules were stacked in short-range order at the edges of the nanofiber, but entangled randomly within the nanofiber. The SAED pattern presented in the inset indicates that the FePc nanofibers were polycrystalline. From studies of several polymorphs of phthalocyanine materials, it is well established that the processing conditions can result in different phase formations (e.g., polymorphs of α and β phases), which exhibit slightly different structural and electrical characteristics [18]. The structural difference between these two polymorphs is the tilt angle of the molecular plane with respect to the stacking b-axes, with the tilt angle of the α phase being smaller than that of the β phase [39]. In addition, the α-form of a FePc film can transform to the β-form during subsequent annealing or when deposited at higher temperature [48,49]. Fig. 3(B) presents GIXRD patterns of commercial FePc powders and the FePc thin films that we deposited on the Ag surface at various

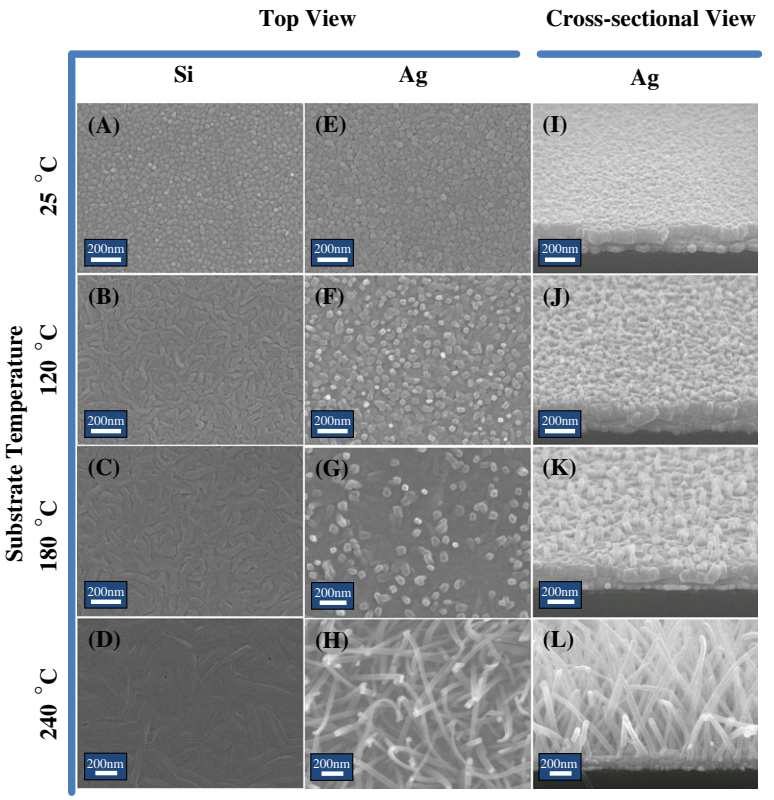

Fig. 1. Top-view and cross-sectional SEM images of FePc thin films deposited on Si and Ag substrates at values of T_{sub} of 25 (A, E, and I), 120 (B, F, and J), 180 (C, G, and K), and 240 °C (D, H, and L).

values of T_{sub}. The commercial FePc powders were crystalline in character; a single peak appeared at a value of 2θ of 6.96°, corresponding to the (2 0 0) peak of the α-FePc phase. The diffraction patterns of the thin films deposited on the Ag substrate at a value of T_{sub} of 25 °C suggested that they featured the same polymorphs as those deposited on sapphire at the same temperature [39]. The absence of diffraction patterns of the β-FePc phase (peaks at 7.01° and 9.6°) [39] suggested that the structure of the FePc nanofibers deposited on the Ag surfaces at a value of T_{sub} of 240 °C was that of the α phase, with preferential orientation along the (2 0 0) direction.

To further understand the energy levels of the FePc materials for FE applications, we used photoelectron spectroscopy [Fig. 4(A)] and UV–Vis spectroscopy [Fig. 4(B)] to measure the HOMO energy levels and obtain the energy gap. Using the supplied software, we fitted the PESA data through linear extrapolation of the value of $CPS^{1/2}$ to zero yields, obtaining a HOMO energy level for FePc of 5.01 eV relative to the vacuum level. The Q-band in Fig. 4(B), between 500–800 nm in the UV–Vis spectrum of the FePc films, revealed overlapping of the three main bands with maxima at 570, 630, and 710 nm. From the onset wavelength at 817 nm, we derived the energy gap and LUMO energy level for the FePc materials of 1.52 and 3.49 eV. Fig. 4(C) displays a schematic representation of the energy level diagram; the work function of the Ag cathode substrate was 4.8 eV. Therefore, electrons injected from the Ag substrate into the LUMO of the FePc materials would have to conquer an energy gap of 1.31 eV.

Next, we performed the selective growth of micropatterned FePc nanofiber arrays on the patterned Ag/Si substrates. In this electrode system, the Ag region would induce the formation of the fiber-like structure of FePc and the Si region would result in the flat grain-like structure. We prepared the patterned Ag substrate in three steps: (i) First, a purpose-made shadow mask was placed on the surface of Si substrate [Fig. 5(A and B)]. The pattern of this purpose-made mask featured a total of 171 (19×9) squares, each with a width of 60 μm. The active area of the device was 0.006156 cm^2. (ii) Next, 100-nm-thick Ag films were deposited on the substrate through e-beam evaporation [Fig. 5(C)]. (iii) Finally, the FePc nanofiber arrays were formed at a certain substrate temperature via thermal evaporation [Fig. 5(D)]. Fig. 6(A–D) display top-view and cross-sectional SEM images of the FePc thin films deposited on the patterned Ag substrate at 240 °C. In Fig. 6(B–C), it is evident that the vertical growth of nanofibers was restricted to the areas presenting the Ag film, where the pattern of the cathode featured nanofiber arrays with each square having a width of 60 μm and an interval of 45 μm between neighboring squares. From the point of view of practical applications, the fabrication of FePc nanofiber arrays on patterned Ag substrates at low temperature (<250 °C) through simple patterning method should be suitable for developing electronic devices. Fig. 6(D) pro-

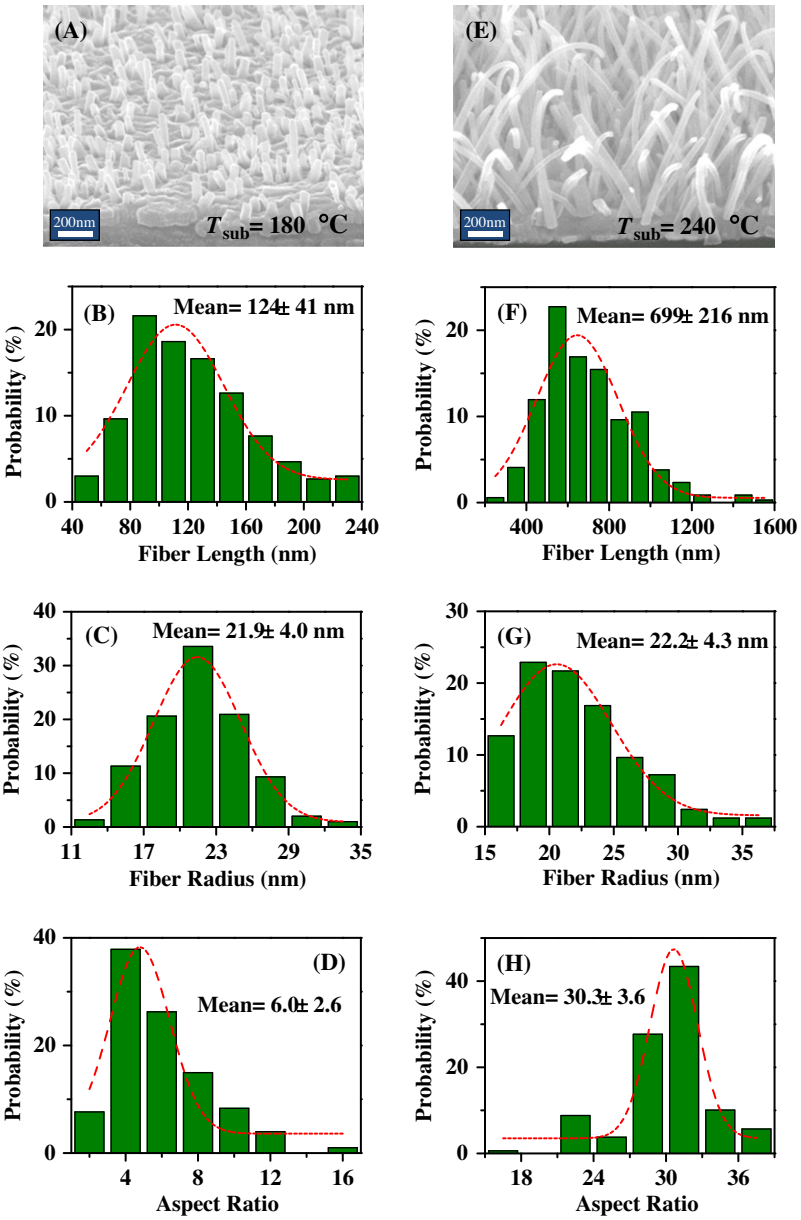

Fig. 2. Cross-sectional SEM images and histograms of FePc nanofiber films deposited on Ag substrates at values of T_{sub} of 180 (A–D) and 240 °C (E–H). Histograms of (B and F) fiber length, (C and G) fiber radius, and (D and H) aspect ratio of these two FePc nanofiber films.

vides a tilted-view, magnified SEM image of a FePc film grown on a region between Ag square patterns.

We examined the FE properties of the FePc nanofiber devices using a parallel-plate configuration with a spacing of 60 μm in a vacuum chamber under a pressure of 5×10^{-6} torr. The anode (ITO glass) was connected to the source monitor unit (SMU) of a Keithley 237 instrument; the cathode of the Ag substrate beneath the FePc nanofibers was grounded. We measured the emission current while increasing the applied voltage from 0 to 720 V with a sweep step of 20 V. To investigate the AR effect of FE properties, we examined the FE characteristics (J–E curve) of the patterned FePc nanofiber devices prepared at values of T_{sub} of 180 (**FE-180-P**) and 240 °C (**FE-240-P**), as shown in Fig. 7(A and B). The turn-on fields (defined as the applied field required for a current density of 10 μA/cm^2) of these patterned FE devices were 10 and 7.7 V/μm, respectively; at an applied field of 12 V/μm, the maximum current densities were 0.26 and 6.77 mA/cm^2, respectively. The Fowler–Nordheim (FN) equation describes the dependence of the emission current of a field emitter on the applied field [50]:

$$\ln\left(\frac{J}{E^2}\right) = \ln\left(\frac{A\beta^2}{\phi}\right) + \left(\frac{-B\phi^{3/2}}{\beta}\right)\left(\frac{1}{E}\right) \quad (3)$$

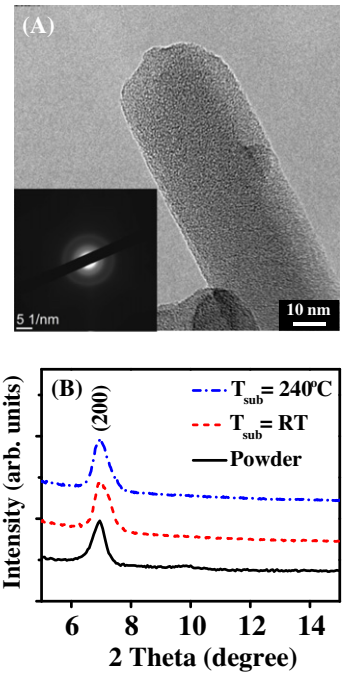

Fig. 3. (A) HRTEM image of FePc nanofibers formed on a Ag substrate; inset: corresponding SAED pattern; (B) XRD patterns of FePc commercial powder and thin films deposited on Ag surfaces at values of T_{sub} of 25 and 240 °C.

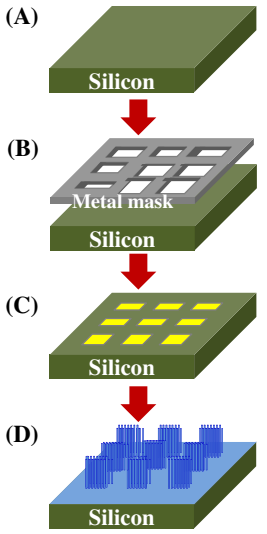

Fig. 5. Flow chart of the growth of micropatterned FePc nanofiber arrays: (A) a P-type Si (1 0 0) wafer (heavy doped); (B) a purpose-made metal mask for Ag layer deposition using an e-beam evaporator; (C) the resulting patterned Ag arrays; (D) the well-aligned FePc nanofibers grown selectively on the patterned Ag arrays through thermal deposition.

where A and B are constants (1.54×10^{-6} A eV/V^2 and 6.83×10^3 V/eV$^{3/2}$/μm, respectively), J is the current density, E is the applied field, and ϕ is the local work function of the emitter material. By plotting $\ln(J/E^2)$ with respect to $1/E$, the slope of the line of best fit can be used to deduce the field enhancement factor (β):

$$\beta = -\frac{6.83 \times 10^3 \phi^{3/2}}{S} \tag{4}$$

where S is the slope of the FN plot. The linear FN plots of **FE-180-P** and **FE-240-P** reveal that the J–E characteristics of the FePc nanofibers followed the FN field emission mechanism, indicating that cold electrons tunneled

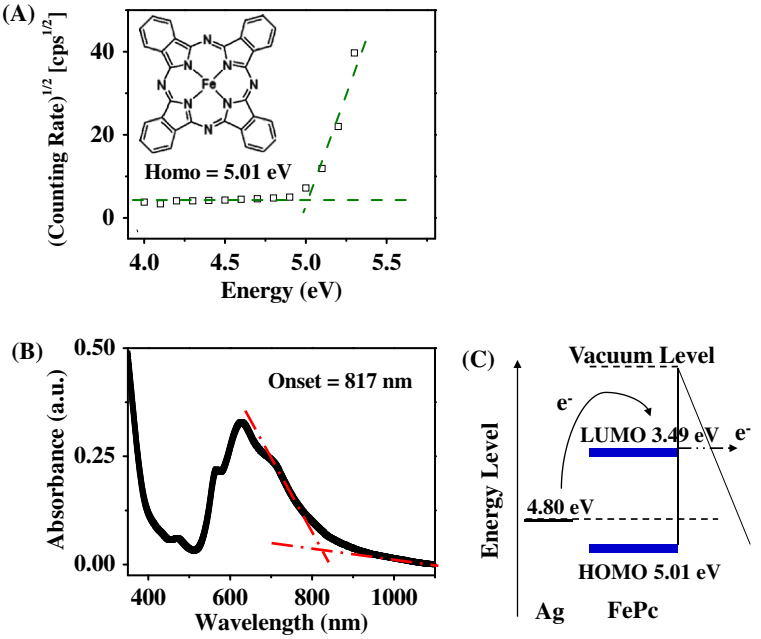

Fig. 4. (A) PESA analysis of the FePc thin films. Inset: molecular structure of FePc. (B) UV–Vis absorption spectra of the FePc thin films. (C) Schematic representation of the energy levels and electrons field-emitting through the FePc nanofibers.

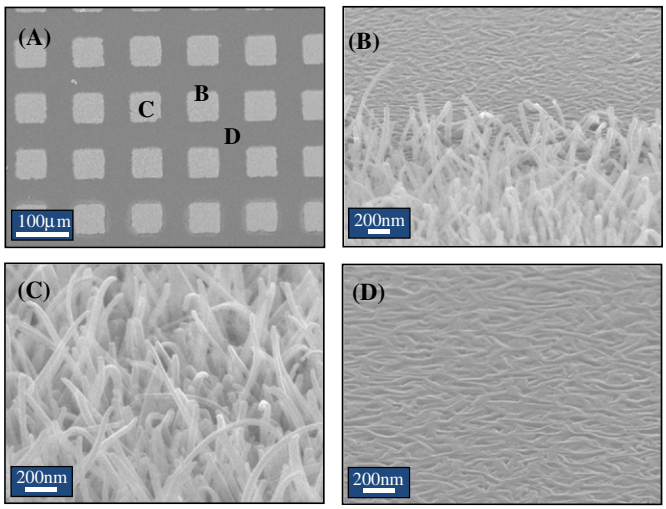

Fig. 6. (A) Top-view SEM images of (A) patterned FePc nanofiber arrays. (B–D) Higher-magnification tilted-view images of (B) the margin of the patterned nanofibers grown on the substrate, (C) the patterned square, and (D) the FePc thin films grown on the Si region in the absence of a Ag layer.

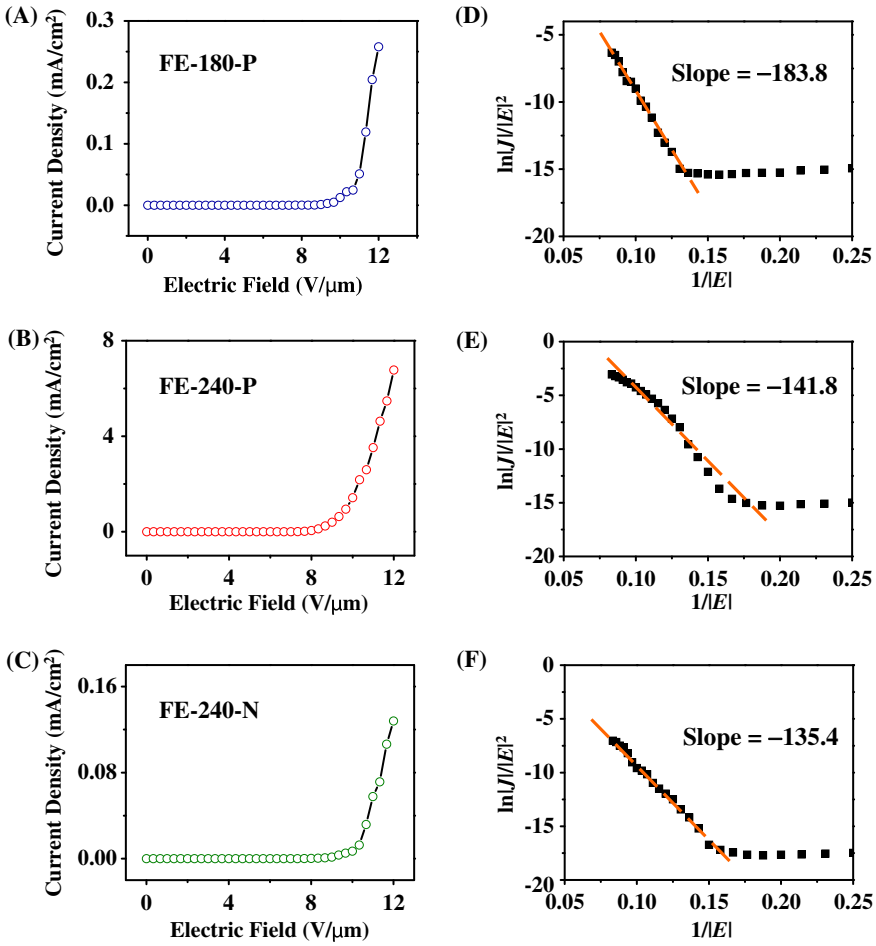

Fig. 7. Field emission *J*–*E* curves and corresponding FN plots of (A and D) **FE-180-P**, (B and E) **FE-240-P**, and (C and F) **FE-240-N**.

through the quantum energy barrier (i.e., quantum tunneling process) under an applied field [Fig. 7(D and E)]. The slopes of the FN plots for **FE-180-P** and **FE-240-P** were −183.8 and −141.8, respectively. Because the LUMO en-

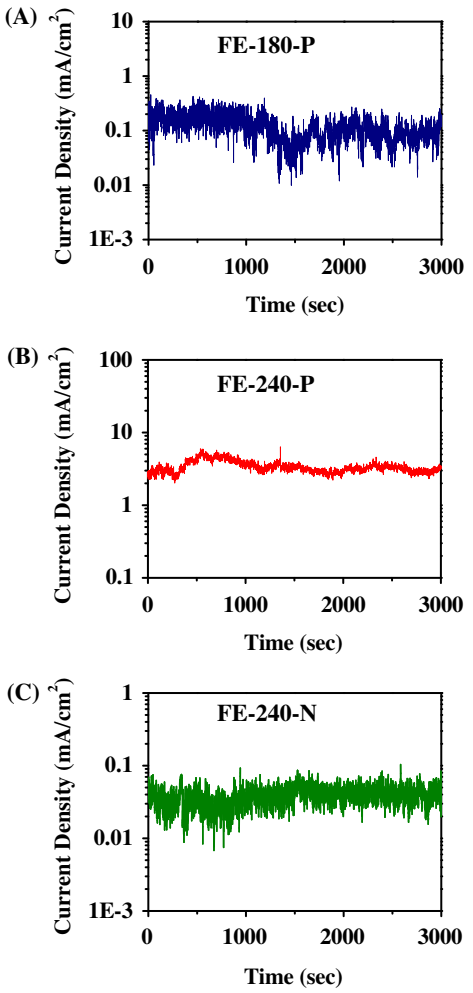

Fig. 8. Emission current stability plots of (A) **FE-180-P**, (B) **FE-240-P**, and (C) **FE-240-N** recorded for 3000 s under a constant applied field.

ergy level (ϕ) of FePc was 3.49 eV, we estimated the values of β of these patterned FE devices to be 242 and 314, respectively. According to FN theory, β is strongly dependent on the geometric structure [51–54] (i.e., shape, size, alignment, crystallinity, AR) and density of the nanofibers grown on the cathode. In our system, **FE-240-P** exhibited efficient FE performance, in terms of a lower turn-on field, higher emission current and larger value of β, relative to that of **FE-180-P**, suggesting the higher AR of patterned devices were suitable for the FE application. To study the enhancement of patterned geometries in FE performance, we also performed the FE measurements of the unpatterned FePc nanofiber devices prepared at 240 °C (**FE-240-N**) as a reference. In the Fig. 7(C), the turn-on field of **FE-240-N** was 10.3 V/μm, and the maximal current density of that was 0.13 mA/cm^2 at an applied field of 12 V/μm. Fig. 7(F) reveals the slope of the linear FN plot for **FE-240-N**, getting that the value of β of **FE-240-N** was approximately 329. Notably, the maximal current density of **FE-240-P** was over 50 times greater than that of **FE-240-N**; that is to say, its FE properties had obviously improved. When the number-density of the nanofibers in each square pattern is sufficiently high [41], the individual nanofiber can be replaced by the square pattern, which can be considered as a single emitter in FE fabrication. In this study, the patterned FePc nanofiber arrays exhibited enhanced emission characteristics that resulted from the pattern design decreasing the screening effect [40]. Each FePc nanofiber square pattern could be regarded as an independent field emitter. Moreover, each individual FePc nanofiber square pattern, as an isolated emitter, allows the emission of electrons from the edges of the square pattern. The highly efficient FE current can be attributed to the edge effect at a certain level [42].

We performed stability tests of our aligned FePc nanofibers for 3000 s under an applied field of 11 V/μm at room temperature. Fig. 8 presents the plots of the FE current density versus testing time for **FE-180-P**, **FE-240-P**, and **FE-240-N**. The calculated mean current density was ca. 0.12 mA/cm^2 for **FE-180-P** [Fig. 8(A)], ca. 3.39 mA/cm^2 for **FE-240-P** [Fig. 8(B)], and ca. 0.04 mA/cm^2 for **FE-240-N** [Fig. 8(C)]. Particularly, **FE-240-P** exhibited remarkably stable emission current with fluctuations of less than 20%. Furthermore, we observed slowly increasing emission currents from all emitters over time. Relative to other organic FE devices [5,20,21], the comparable properties of the FePc nanofibers prepared at a low fabrication temperature and exhibiting a low turn-on field suggest their potential application in organic field emitters. The pattern design of the well-aligned 1D FePc nanostructures has advantages over other nanomaterials in that it allows FE improvement. Thus, this promising organic nanomaterial sustained a stable FE current, without any decay, during the measurement period, demonstrating that the patterned FePc nanofiber arrays, prepared at the value of T_{sub} of 240 °C, have great applicability for use in cold field electron-emitting devices.

4. Conclusions

By varying the surface energy and the temperature of the substrates during vacuum evaporation, the morphology of self-assembled FePc films can be controlled to form in-plane structures on Si surfaces (higher surface energy) and out-of-plane structures on Ag surfaces (lower surface energy). These temperature-enhanced and well-aligned 1D FePc nanofibers exhibited FE characteristics and followed FN behavior. Using such morphological control, we grew the patterned FePc nanofibers selectivity on previously patterned Ag/Si substrates; moreover, the higher AR of the patterned device (**FE-240-P**) exhibited better FE performance than **FE-180-P**. In the optimal growth condition of T_{sub} of 240 °C, the emission current of the device improved dramatically from 0.13 mA/cm^2 for the unpatterned device to 6.77 mA/cm^2 for the patterned device (when biased at an applied field of 12 V/μm), while the turn-on electric field of the device decreased accordingly from 10.3 to 7.7 V/μm. In FE stability tests, the current densities of **FE-240-P** exhibited fluctuations of less than 20%, revealing its stable and superior property within the duration of the measurement process. The enhanced FE performance and the stability of the emission current sug-

gest that this facile method for fabricating patterned FePc nanofiber arrays is suitable for their application in electron-emitting devices.

Acknowledgment

We thank for National Science Council of Taiwan, ROC, for financial support (project NSC 97-2221-E-009-012-MY3).

References

[1] A.B. Djurišić, A.M.C. Ng, K.Y. Cheung, M.K. Fung, W.K. Chan, Journal of Materials Science and Technology 24 (2008) 563.
[2] Y.S. Zhao, H. Fu, A. Peng, Y. Ma, D. Xiao, J. Yao, Advanced Materials 20 (2008) 2859.
[3] Y.S. Zhao, H. Fu, A. Peng, Y. Ma, Q. Liao, J. Yao, Accounts of Chemical Research 43 (2010) 409.
[4] J.J. Chiu, C.C. Kei, T.P. Perng, W.S. Wang, Advanced Materials 15 (2003) 1361.
[5] C.P. Cho, T.P. Perng, Organic Electronics 11 (2010) 115.
[6] W. Chen, Q. Peng, Y. Li, Advanced Materials 20 (2008) 2747.
[7] Y.S. Zhao, C. Di, W. Yang, G. Yu, Y. Liu, J. Yao, Advanced Functional Materials 16 (2006) 1985.
[8] H. Liu, Y. Li, S. Xiao, H. Gan, T. Jiu, H. Li, L. Jiang, D. Zhu, D. Yu, B. Xiang, Y. Chen, Journal of the American Chemical Society 125 (2003) 10794.
[9] S.C. Suen, W.T. Whang, B.W. Wu, Y.F. Lai, Applied Physics Letters 84 (2004) 3157.
[10] H. Liu, Q. Zhao, Y. Li, Y. Liu, F. Lu, J. Zhuang, S. Wang, L. Jiang, D. Zhu, D. Yu, L. Chi, Journal of the American Chemical Society 127 (2005) 1120.
[11] S. Cui, Y. Li, Y. Guo, H. Liu, Y. Song, J. Xu, J. Lv, M. Zhu, D. Zhu, Advanced Materials 20 (2008) 309.
[12] F. Tian, W. Liu, C.R. Wang, Journal of Physical Chemistry C 112 (2008) 8763.
[13] H. Liu, X. Wu, L. Chi, D. Zhong, Q. Zhao, Y. Li, D. Yu, H. Fuchs, D. Zhu, Journal of Physical Chemistry C 112 (2008) 17625.
[14] C. Ouyang, Y. Guo, H. Liu, Y. Zhao, G. Li, Y. Li, Y. Song, Y. Li, Journal of Physical Chemistry C 113 (2009) 7044.
[15] H. Liu, Z. Liu, X. Qian, Y. Guo, S. Cui, L. Sun, Y. Song, Y. Li, D. Zhu, Crystal Growth & Design 10 (2010) 237.
[16] K. Zheng, X. Li, X. Mo, G. Chen, Z. Wang, G. Chen, Applied Surface Science 256 (2010) 2764.
[17] C. Ye, K. Zheng, W. You, G. Chen, Nanoscale Research Letters 5 (2010) 1307.
[18] W.Y. Tong, A.B. Djurišić, M.H. Xie, A.C.M. Ng, K.Y. Cheung, W.K. Chan, Y.H. Leung, H.W. Lin, S. Gwo, Journal of Physical Chemistry B 110 (2006) 17406.
[19] S. Karan, B. Mallik, Journal of Physical Chemistry C 111 (2007) 7352.
[20] W.Y. Tong, Z.X. Li, A.B. Djurišić, W.K. Chan, S.F. Yu, Materials Letters 61 (2007) 3842.
[21] S.C. Suen, W.T. Whang, F.J. Hou, B.T. Dai, Organic Electronics 7 (2006) 428.
[22] W.Y. Tong, A.B. Djurišić, A.M.C. Ng, W.K. Chan, Thin Solid Film 515 (2007) 5270.
[23] Y.S. Zhao, J. Wu, J. Huang, Journal of the American Chemical Society 131 (2009) 3158.
[24] Y.S. Zhao, P. Zhan, J. Kim, K. Sun, J. Huang, ACS Nano 4 (2010) 1630.
[25] K.J. Huang, Y.S. Hsiao, W.T. Whang, Organic Electronics 12 (2011) 686.
[26] J. Blochwitz, M. Pfeiffer, T. Fritz, K. Leo, Applied Physics Letters 73 (1998) 729.
[27] M. Bouvet, Analytical and Bioanalytical Chemistry 384 (2006) 366.
[28] T. Nagasawa, K. Murakami, K. Watanabe, Molecular Crystals and Liquid Crystals 316 (1998) 389.
[29] M.I. Newton, T.K.H. Starke, M.R. Wills, G. McHale, Sensors and Actuators B-Chemistry 67 (2000) 307.
[30] J. Zhang, H. Wang, X. Yan, J. Wang, J. Shi, D. Yan, Advanced Materials 17 (2005) 1191.
[31] R.W.I. de Boer, A.F. Stassen, M.F. Craciun, C.L. Mulder, A. Molinari, S. Rogge, A.F. Morpurgo, Applied Physics Letters 86 (2005) 262109.
[32] J. Wang, H. Wang, X. Yan, H. Huang, D. Yan, Applied Physics Letters 87 (2005) 093507.
[33] Q. Tang, H. Li, M. He, W. Hu, C. Liu, K. Chen, C. Wang, Y. Liu, D. Zhu, Advanced Materials 18 (2006) 65.
[34] F. Yang, M. Shtein, S.R. Forrest, Journal of Applied Physics 98 (2005) 014906.
[35] F. Yang, M. Shtein, S.R. Forrest, Nature Materials 4 (2005) 37.
[36] Y.S. Hsiao, W.T. Whang, S.C. Suen, J.Y. Shiu, C.P. Chen, Nanotechnology 19 (2008) 415603.
[37] J.W. Chung, B.K. An, J.W. Kim, J.J. Kim, S.Y. Park, Chemical Communications (2008) 2998.
[38] Y.S. Zhao, D. Xiao, W. Yang, A. Peng, J. Yao, Chemistry of Materials 18 (2006) 2302.
[39] A.K. Debnath, S. Samanta, A. Singh, D.K. Aswal, S.K. Gupta, J.V. Yakhmi, S.K. Deshpande, A.K. Poswal, C. Sürgers, Physica E: Low-dimensional Systems and Nanostructures 41 (2008) 154.
[40] L. Nilsson, O. Groening, C. Emmenegger, O. Kuettel, E. Schaller, L. Schlapbach, H. Kind, J.-M. Bonard, K. Kern, Applied Physics Letters 76 (2000) 2071.
[41] M. Katayama, K.Y. Lee, S.I. Honda, T. Hirao, K. Oura, Japan Journal of Applied Physics 43 (2004) L774.
[42] S. Fujii, S.I. Honda, H. Machida, H. Kawai, K. Ishida, M. Katayama, Applied Physics Letters 90 (2007) 153108.
[43] S. Huang, A.H.W. Mau, Applied Physics Letters 82 (2003) 796.
[44] T. Sakurai, Y. Momose, K. Nakayama, E.-J. Surf, Science Nanotechnology 3 (2005) 179.
[45] J.A. Venables, G.D.T. Spiller, M. Hanbücken, Reports on Progress in Physics 47 (1984) 399.
[46] A.W. Adamson, Physical Chemistry of Surfaces, 5th ed., John Wiley & Sons Publishers, 1990, pp. 55.
[47] F.G. Tarntair, C.Y. Wen, L.C. Chen, J.J. Wu, K.H. Chen, P.F. Kuo, S.W. Chang, Y.F. Chen, W.K. Hong, H.C. Cheng, Applied Physics Letters 76 (2000) 2630.
[48] S.I. Shihub, R.D. Gould, Thin Solid Films 290–291 (1996) 390.
[49] P. Ballirano, R. Caminiti, C. Ercolani, A. Maras, M.A. Orru, Journal of the American Chemical Society 120 (1998) 12798.
[50] R. Fowler, L.W. Nordheim, Proceedings of the Royal Society of London 119 (1928) 173.
[51] Y.W. Zhu, H.Z. Zhang, X.C. Sun, S.Q. Feng, J. Xu, Q. Zhao, B. Xiang, R.M. Wang, D.P. Yu, Applied Physics Letters 83 (2003) 144.
[52] J. Chen, S.Z. Deng, N.S. Xu, S.H. Wang, X.G. Wen, S.H. Yang, C.L. Yang, J.N. Wang, W.K. Ge, Applied Physics Letters 80 (2002) 3620.
[53] B.Y. Li, Y. Bando, D. Golberg, K. Kurashima, Applied Physics Letters 81 (2002) 5048.
[54] C.J. Lee, T.J. Lee, S.C. Lyu, Y. Zhang, H. Ruh, H.J. Lee, Applied Physics Letters 81 (2002) 3648.

organic film. All these models are based on an assumption that the localized carriers (charged polarons) are spin sensitive to the external magnetic field and the internal hyperfine field of the hydrogen nucleus [13]. For the Zeeman mechanism, researchers seem to be also puzzled that why an extremely small Zeeman energy ($|-g\mu_B\vec{S}\cdot\vec{B}| \sim 10^{-5}$ eV for 1 T) can beat the thermal energy ($k_BT \sim 0.026$ eV at room temperature) to generate this OMFE. It is regretful that none of these models can give a quantitative explanation on the OMFE. Maybe a dynamic response theory of the spin to the magnetic field is needed to understand the OMFE, which there is not yet a report up to now. Recently the field-induced hopping mechanism has also been suggested [14], which believes that the hopping transport in OSCs is changed due to the Lorentz charge-magnetic field interaction but not the Zeeman spin-magnetic field one. However, the field-induced hopping mechanism still needs a further confirmation quantitatively for actual organic materials. In this paper, we try to give an analysis on the OMFE by calculating the magnetoresistance of an OSC based on the Zeeman mechanism. In our picture, the distinct properties of OSCs from that of inorganic counterparts are focused and it is found that the OMR is tightly related with these properties. We believe that this mechanism plays an important role in the understanding of OMFE. In the following section, the model and the method are presented. The results and discussions are shown in Section 3. Finally, in Section 4 a summary is given.

2. Model and method

Organic materials usually appear amorphous structure in the fabrication progress, such as spin coating or thermal evaporation. Theoretical investigation on the transport in an organic material or device is considered in two ways: one is based on the band transport mechanism and the disordered is partly included by considering the atomic position fluctuation [15]. Another is based on the hopping mechanism. In this mechanism, the transport is reflected by the Marcus formula of the hopping rate

$$\kappa_{ij} = \frac{2\pi}{\hbar}\tau^2 \frac{1}{\sqrt{4k_BT\pi\lambda}} \exp\left(-\frac{(\lambda+\varepsilon_j-\varepsilon_i)^2}{4k_BT\lambda}\right) \quad (1)$$

where τ_{ij} is the transfer integral and $\varepsilon_{i(j)}$ is the on-site energy. We give a simple estimate for MR based on the hopping mechanism. When an external magnetic field is applied, the on-site energy will become $\varepsilon_i \to \varepsilon_i \pm g\mu_B S_Z B$, due to the Zeeman effect. In this case, there exist four hoppings of π-electrons, i.e., from spin up to up, from spin down to down, from spin up to down and from spin down to up. Suppose the four hoppings take place with the same probability. The total hopping rate is

$$\kappa_{ij} = \frac{2\pi}{\hbar}\tau^2 \frac{1}{\sqrt{4k_BT\pi\lambda}} \exp\left(-\frac{(\lambda+\varepsilon_j-\varepsilon_i)^2}{4k_BT\lambda}\right) \times \left\{1+\left[\left(\frac{\lambda+\varepsilon_j-\varepsilon_i}{2k_BT\lambda}\right)^2 - \frac{1}{2k_BT\lambda}\right](g\mu_B S_Z)^2B^2\right\} \quad (2)$$

Assume the conductance is in proportional to the hopping rate, i.e., $\sigma \propto \langle\kappa_{ij}\rangle$, then the MR is obtained

$$MR = \frac{\sigma(0)-\sigma(B)}{\sigma(B)} = \frac{B^2}{B_0^2+B^2} \quad (3)$$

where $B_0^2 = \frac{1}{\left[\left(\frac{-(\lambda+\langle\varepsilon_j-\varepsilon_i\rangle)}{2k_BT\lambda}\right)^2 - \frac{1}{2k_BT\lambda}\right]g^2\mu_B^2S_Z^2}$. Although the expression is similar to the observed Lorentz fitting, the B_0 value in present formula is too large, which will result in an unobservable MR. Therefore, it seems to be difficult to obtain an apparent OMR based on present hopping picture. Of course here it is just a crude estimation. We have to take a much more comprehensive consideration on OMR in the frame work of hopping mechanism in the future.

Now let us consider the transport based on the band theory. To explain the large MR in silver chalcogenides, Xiong et al. considered the Zeeman splitting of the density of states (DOS) under an external magnetic field [16]. They showed that a nonmagnetic material could have a large MR when the DOS at Fermi level is sensitive to an external magnetic field (they also assumed a large Lande factor g in the calculation to enlarge the theoretical picture). As analyzed below, organic semiconductors should satisfy the condition and a large MR could be obtained even we do not take a large Lande factor.

Firstly we give the transport formula in organic semiconductors under a magnetic field. The conductance is mainly contributed from carriers at the Fermi level E_F, i.e., $\sigma \propto \rho(E_F)$, where $\rho(E)$ is the DOS of the system. For organic materials, the one-dimension model has been usually adopted. We give a schematic description of DOS in Fig. 1 for easier comprehension. In general, the spin of

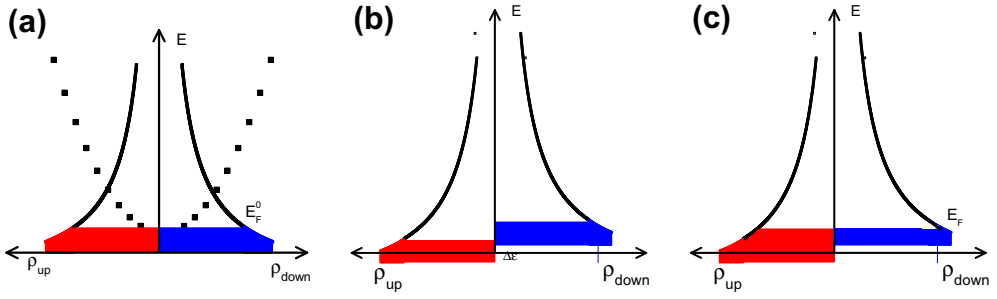

Fig. 1. Schematic description of the energy levels: (a) without an external magnetic field, the electrons of spin up and down are same, the dashed line is for the three-dimensional case; (b) apply an external magnetic field, the electron states are in nonequilibrium; and (c) after redistribution, a new Fermi level is formed.

electron can be divided into two parts, spin up and down and the corresponding DOS defined as $\rho_0(E)$ are degenerated in the absence of magnetic field, as shown in Fig. 1a, then the conductance $\sigma(0) \propto \rho(E_F) = 2\rho_0(E)$. When an external magnetic field is applied, energy levels of different spin would have opposite shifts by the Zeeman energy,

$$\Delta\varepsilon = -g\mu_B \vec{S}\cdot\vec{B} \tag{4}$$

where g is the Lande factor, μ_B is the Bohr magneton and $\vec{S}$ is the spin angular momentum. In some materials, such as silver chalcogenides, the Lande factor g is as large as 10^2 [16], its value in organic materials is 2 [17], the same as free electron. Of course a large g factor may enlarge the theoretical result. As Zeeman energy is a constant for the same spin, the shape of the DOS for spin-up and spin-down remain the same, which is shown in Fig. 1b. Due to the Zeeman energy splitting, some electrons shifting upwards will be converted into the electron shifting downwards. So the Fermi level of the material will change due to the redistribution of electrons as shown in Fig. 1c. The density of states will also change from $\rho_0(E)$ to $\rho_B(E)$. Then the MR is obtained,

$$MR = \frac{\sigma^{-1}(B) - \sigma^{-1}(0)}{\sigma^{-1}(0)} = \frac{2\rho_0(E_F^0) - \rho_B(E_F)}{\rho_B(E_F)} \tag{5}$$

where E_F and E_F^0 are the Fermi level with and without the magnetic field separately. The total DOS at the new Fermi level E_F under a magnetic field is given by,

$$\begin{aligned}\rho_B(E_F) &= \rho_\uparrow(E_F) + \rho_\downarrow(E_F) \\ &= \rho_0(E_F - |\Delta\varepsilon|) + \rho_0(E_F + |\Delta\varepsilon|)\end{aligned} \tag{6}$$

and E_F is derived from the conservation of the total electrons through the following relation,

$$\begin{aligned}\int_0^{E_F^0} 2\rho_0(E) &= \int_{-|\Delta\varepsilon|}^{E_F} \rho_0(E - |\Delta\varepsilon|)dE + \int_{|\Delta\varepsilon|}^{E_F} \rho_0(E + |\Delta\varepsilon|)dE \\ &= \int_0^{E_F+|\Delta\varepsilon|} \rho_0(E)dE + \int_0^{E_F-|\Delta\varepsilon|} \rho_0(E)dE\end{aligned} \tag{7}$$

From Eq. (5) we can see that MR is sensitive to the difference of DOS at Fermi level with and without the magnetic field.

To get MR of an organic semiconductor, we have to calculate the DOS with a concrete material. Here we take the most common small molecule Alq_3 as an example, which can be considered as a one-dimensional stack of planar conjugated molecules due to the highly one-dimensional motion of charge carriers [18]. Therefore a one-dimensional model can be adopted within which each molecule is reduced to a site with one molecular orbital, similar to the model for pentacene proposed by Troisi and Orlandi [15], so the Hamiltonian can be written as,

$$H = -\sum_j [\tau - \alpha(u_{j+1} - u_j)](|j\rangle\langle j+1| + |j+1\rangle\langle j|) \tag{8}$$

where $|j\rangle$ is the jth molecular orbital. The charge-transfer integral τ between the consecutive orbitals $|j\rangle$ and $|j+1\rangle$ is modulated by the term $\alpha(u_{j+1} - u_j)$ with α the electron–phonon coupling constant, and u_j is the jth molecular displacement from its equilibrium position. This model is almost identical to the SSH (Su–Schrieffer–Heeger) model used for a conducting polymer and can be solved with a self-consistently iteration method [19]. As indicated by the α term, there exists a strong electron–phonon interaction in organic semiconductors. The band structure obtained from Eq. (8) is tightly related to the doping or carrier concentration. We have to solve Eq. (8) with a given carrier concentration $n_e = N_e/N$. In addition, due to the feature of self-generation of carriers, the carrier concentration in organic materials is very low [18], in the following calculation, we consider a dilute doping with $n_e \leqslant 0.25$.

In OSCs, we suppose $\varepsilon_i = \varepsilon_j$, from the hopping rate of Marcus formula equation (1) and the Einstein–Smoluchowski relation, we have the charge carrier mobility,

$$\mu = \frac{e}{k_B T} P d^2 \tag{9}$$

where d is the average distance between neighboring localization sites, i.e., the stacking distance between two adjacent molecules. So the charge-transfer integral is given,

$$\tau = \left(\frac{k_B T \hbar \mu}{2ed^2\pi}\right)^{1/2} (4k_B T \pi\lambda)^{1/4} \left[\exp\left(\frac{\lambda}{4k_B T}\right)\right]^{1/2} \tag{10}$$

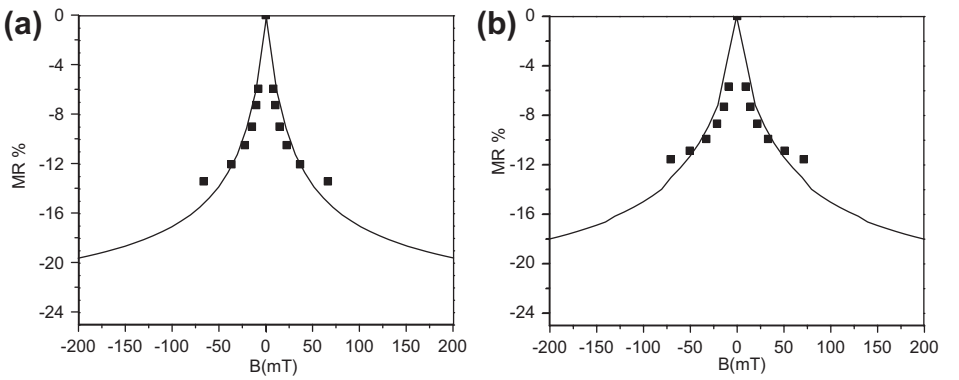

Fig. 2. Comparison between experimental measurements and our theoretical results (a) solid curve for carrier concentration $n_e = 0.2$, square corresponding to the bias 5 V; (b) solid curve for carrier concentration $n_e = 0.24$, circle corresponding to the bias 5.5 V. The charge-transfer integral τ is chosen as 20 meV and the electron–phonon coupling constant α is 110 meV/Å. Experimental data is extracted from Fig. 2 in Ref. [8].

We see that the charge-transfer integral is dependent on the carrier mobility and the distance between adjacent Alq_3 molecules in the stack. For most OSCs, the mobility is very small in the range of 10^{-6}–10^{-3} $cm^2/V \cdot S$. For example, polyparaphenylenevinylene (PPV) derivatives have a mobility of about 10^{-6} $cm^2/V \cdot S$ [20] and Alq_3 of about 10^{-5}–10^{-2} $cm^2/V \cdot S$ [18]. If we take the average distance $d = 4 - 7$ Å between two adjacent molecules and the reorganization energy $\lambda = 0.1$–0.3 eV [21], it is deduced a charge-transfer integral of tens meV near the room temperature. The electron–phonon coupling constant α is in the range of 80–140 meV/Å [15].

3. Results and discussion

For a given carrier concentration n_e, the electronic eigenvalues ε_μ are solved with a self-consistently iteration method. The DOS is obtained by the Lorentz line shape formula,

$$\rho(\varepsilon) = \sum_\mu \frac{1}{\pi} \frac{\delta}{(\varepsilon - \varepsilon_\mu)^2 + \delta^2} \tag{11}$$

where δ is the Lorentz parameter and $\sum_\mu$ is sum over all the eigenvalues. The Fermi level of the system is determined by the total number of iterant electrons (carriers) and the MR is calculated from Eq. (5). In the following calculations, the electron–phonon coupling constant α is chosen as 110 meV/Å which is a moderate value for organic materials. Fig. 2 shows the dependence of MR on the magnetic field. We see that (1) the MR is negative. The reason is the one-dimensional model adopted in present approach. From the quantum theory we know that the DOS $\rho_d(\varepsilon) \sim \varepsilon^{d/2-1}$ for a free electron system, where d is the spatial dimension. Apparently, $\rho_2(\varepsilon) \sim C$ and we obtain MR = 0 for a two-dimensional electron system from above formula. For a three-dimensional system, it has been derived MR > 0 [16]. For a one-dimensional system we obtain MR < 0. So we believe that most of the negative MR observed in experiments is due to the one-dimensional characteristic of organic materials; (2) the MR is sensitive to the carrier concentration or the doping (or injection from electrodes) of an OSC. It is found that a large MR value could be obtained in dilute doping case. For example, in Fig. 2a we can see that, under a magnetic field of 100 mT, for a fixed charge-transfer integral $\tau = 20$ meV, a MR value of 17 % can be obtained with the concentration of $n_e = 0.2$. However the MR value will decrease to 14.8% when n_e increases to 0.24 as shown in Fig. 2b; (3) the MR is also sensitive to the charge-transfer integral. As shown in Fig. 3, under a magnetic field of 100 mT, for the same carrier concentration $n_e = 0.2$, |MR| = 10% with the charge-transfer integral $\tau = 30$ meV, while this value will increase to 17% with the charge-transfer integral $\tau = 20$ meV. We give a comparison between our theoretical results and the experimental ones. It has been shown that the polyfluorene can have a well-defined chemical regularity [22] and its crystallinity is also explicitly pointed [23]. Therefore it is reasonable to adopt a band theory to describe the carrier transport in polyfluorene. The symbol in Fig. 2 shows the magnetoresistance of polyfluorene measured at different

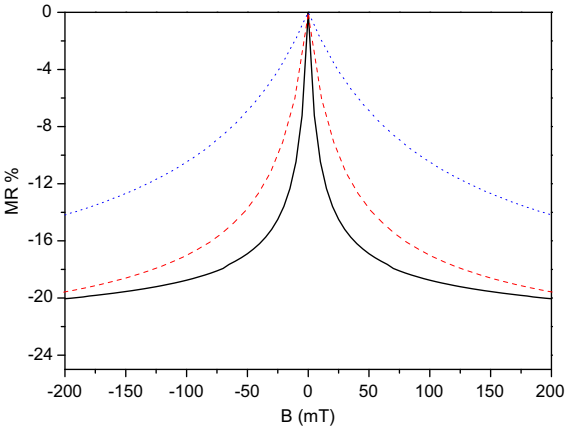

Fig. 3. Dependence of MR on the magnetic field with different charge-transfer integral. Dot: $\tau = 30.0$ meV, dash: $\tau = 20.0$ meV, solid: $\tau = 10.0$ meV. The electron–phonon coupling constant α is 110 meV/Å and the carrier concentration $n_e = 0.2$.

voltages [8]. A qualitatively consistency can be obtained and we can see that both the experimental measurements and our theoretical calculation show the two most prominent features of OMR: (I) its absolute value increases rapidly with B in the range of weak magnetic field, and (II) the OMR will reach a saturated value with a strong magnetic field.

Dependence of the OMR on the charge-transfer integral τ and carrier concentration n_e is easily understood. In the tight-binding model, the energy band width is about 4τ. If we wake $\tau = 20meV$, then the band width is about 80 meV, which is basically consistent to that in Refs. [20,24] based on the hopping mechanism. A small τ means a narrow band width and so a large DOS. As indicated in the investigation of SSH model, unless the full-band case (with $n_e = 2$), the energy band will be split into some subbands due to the strong electron–phonon interaction in organic materials. And only the lowest subband is fully occupied, which constitutes the valence band of an organic semiconductor. As indicated by the schematic of DOS in Fig. 1, with the decrease of the charge-transfer integral τ, the DOS changes more rapidly with energy; on the other hand, for a smaller carrier concentration, the valence band is narrower and the original Fermi level is closer to the edge of the band, then the differential of DOS with respect to energy is larger. As mentioned above, there is a large MR in materials with a narrow energy band and the DOS changing abruptly near the Fermi level. Therefore, a comprehensive MR is predicated in present mechanism in an OSC with a low mobility and small carrier concentration.

A fascinating and incomprehensible feature of the OMR is that it is weakly dependent on the temperature and still persists at room temperature. This is also a promising feature for practical utility in the future. From Eq. (10), we can see that in the range of room temperature, the charge-transfer integral τ increases slowly with the temperature. In Fig. 3 we can see that even there is a little increase in the charge-transfer integral τ, the absolute value of MR can still be sizable. Of course, in actual OSs, thermal effect

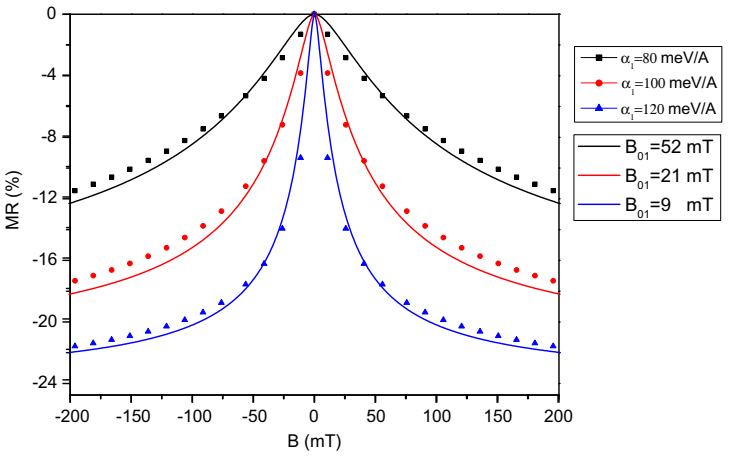

Fig. 4. The MR of an organic semiconductor with different electron–phonon coupling strength and the corresponding fitting curves. τ is chosen as 20 meV and $n_e = 0.2$. The symbols represent our theoretical results and solid curves are the fitting curves with $\Delta R(B)/R \propto B^2/(|B| + B_0)^2$. α_i (meV/Å) represents different electron–phonon coupling strength and B_i (mT) is the corresponding fitting constant.

will also affect the spin relaxation and so the MR. Here we only consider its influence on the charge-transfer integral. Our study shows that even the thermal effect is included, an observable MR can still be obtained in organic materials.

It has been mentioned that the OMR is well fitted with empirical formula $\Delta R(B)/R \propto B^2/(|B| + B_0)^2$ or $\Delta R(B)/R \propto B^2/(B^2 + B_0^2)$ depending on the material. In Fig. 4, we give the comparison between fitting curves of the empirical formula and our theoretical results. We can see that a well consistency is obtained between the non-Lorentzian shape empirical formula and our theoretical results. From Fig. 4 it is also find that the OMR is sensitive to the electron–phonon coupling α. In the present model $\alpha = 0$ means a rigid system or an inorganic one, and in this case there is nearly no MR. This result seems to coincide with the present observation that MR is difficult to appear in inorganic materials with such a small magnetic field of mT. With the increase of electron–phonon coupling, the value of MR will increase. From Fig. 4 we can see that, when the electron–phonon coupling α increases from 80 meV/Å to 120 meV/Å, the corresponding magnitude of OMR increases from 12% to 22%. As the electron–phonon coupling is an internal characteristic of organic materials, it is understandable to appear a large MR in OSCs. Furthermore, it is also found that the fitting parameter B_0 is relative to the electron–phonon coupling parameter α, which is an interesting conclusion, as, up to now, the exact source of B_0 seems to be unknown. It should be noticed that, in different experimental investigations, the fitting constant B_0 is dependent upon the concrete materials [25]. From our results, a large fitting constant corresponds to a weak electron–phonon coupling. Therefore, we speculate that MR in organic materials should be phonon dependent. It is also noted that a spin–phonon interaction model was suggested recently to explain OMR, which believes that the presence of a local bosonic environment is important in understanding the anomalous OMR [26]. In a recent article, Rybicki et al. also predicated that the spin precession must be a phonon-assisted progress in π-conjugated polymers [27].

4. Summary

In summary, we have performed a theoretical study on the mechanism of OMR based on the magnetic field-spin Zeeman interaction. Firstly we give a preliminary discussion based on the hopping mechanism and could not get a desired result. Then we performed a thorough investigation on the OMR based on the band conduction. It is found that the peculiar properties of the organic materials are important factors in the explanation of OMR. Also the value of OMR is found to be dependent on the charge-transfer integral and the concentration of carriers. It is known that the charge-transfer integral is different in various organic materials, and the carrier concentration can also be changed under different conditions. So the diversity of OMR obtained by different groups, though sometimes in the same organic material, could be explained by the dependence on the charge-transfer integral τ and (or) carrier concentration n_e. According to our model, the two most prominent features of OMR can be obtained. The peculiar electron–phonon interaction is crucial to help understanding the details of OMR. We fit our results to the empirical formula and find that the fitting parameter B_0 is phonon dependent.

Acknowledgments

The authors would like to acknowledge the financial support from the National Basic Research Program of China (Grant Nos. 2009CB929204 and 2010CB923402) and the National Natural Science Foundation of the People's Republic of China (Grant No. 10874100).

References

[1] H. Nakanotani, C. Adachi, Appl. Phys. Lett. 96 (2010) 053301.
[2] K. Kawano, C. Adachi, Appl. Phys. Lett. 96 (2010) 053307.
[3] J.J.M. Halls, R.H. Friend, Synth. Metals 85 (1997) 1307.
[4] V. Dediu, M. Murgia, F.C. Matacotta, C. Taliani, S. Barbanera, Solid State Commun. 122 (2002) 181.
[5] Z.H. Xiong, D. Wu, Z.V. Vardeny, J. Shi, Nature 427 (2004) 821.

[6] F. Luo, W. Song, Z.M. Wang, C.H. Yan, Appl. Phys. Lett. 84 (2004) 1719.
[7] A.H. Davis, K. Bussmann, J. Vac. Sci. Technol. A 22 (2004) 1885.
[8] Ö. Mermer, G. Veeraraghavan, T.L. Francis, Y. Sheng, T.D. Nguyen, M. Wohlgenannt, A. Köhler, M.K. Al-Sutí, M.S. Khan, Phys. Rev. B 72 (2005) 205202.
[9] B. Hu, L. Yan, M. Shao, Adv. Mater. 21 (2009) 1500.
[10] V.N. Prigodin, J.D. Bergeson, D.M. Lincoln, A.J. Epstein, Synth. Metals 156 (2006) 57.
[11] P. Desai, P. Shakya, T. Kreouzis, W.P. Gillin, Phys. Rev. B 75 (2007) 094423.
[12] P.A. Bobbert, T.D. Nguyen, F.W.A. van Oost, B. Koopmans, M. Wohlgenannt, Phys. Rev. Lett. 99 (2007) 216801.
[13] P.A. Bobbert, T.D. Nguyen, W. Wagemans, F.W.A. van Oost, B. Koopmans, M. Wohlgenannt, Synth. Metals 160 (2010) 23.
[14] X.R. Wang, S.J. Xie, Europhys. Lett. 92 (2010) 57013.
[15] A. Troisi, G. Orlandi, Phys. Rev. Lett. 96 (2006) 086601.
[16] G. Xiong, S.D. Wang, X.R. Wang, Phys. Rev. B 61 (2000) 4335.
[17] G.N. Kurochkina, V.G. Gaidalovich, F.I. Khakimov, Eurasian Soil Sci. 39 (2006) 727.
[18] A.J. Drew, F.L. Pratt, J. Hoppler, L. Schulz, V. Malik-Kumar, N.A. Morley, P. Desai, P. Shakya, T. Kreouzis, W.P. Gillin, K.W. Kim, A. Dubroka, R. Scheuermann, Phys. Rev. Lett. 100 (2008) 116601.
[19] Å. Johansson, S. Stafström, Phys. Rev. B 65 (2002) 045207.
[20] V. Coropceanu, C. Jérôme, D.A.S. Filho, Y. Olivier, R. Silbey, J.L. Brédas, Chem. Rev. 107 (2007) 926.
[21] Y. Olivier, V. Lemaur, J.L. Brédas, J. Cornil, J. Phys. Chem. A 110 (2006) 6356.
[22] M. Redecker, D.D.C. Bradley, M. Inbasekaran, E.P. Woo, Appl. Phys. Lett. 73 (1998) 1565.
[23] M. Grell, D.D.C. Bradley, G. Ungar, J. Hill, K.S. Whitehead, Macromolecules 32 (1999) 5810.
[24] S.L.M. van Mensfoort, R. Coehoorn, Phys. Rev. B 78 (2008) 085207.
[25] T.D. Nguyen, Y. Sheng, J. Rybicki, G. Veeraraghavan, M. Wohlgenannt, J. Mater. Chem. 17 (2007) 1995.
[26] Y. Yao, W. Si, X.Y. Hou, C.Q. Wu (2010), arxiv:cond-mat/1008.1437v2.
[27] J. Rybicki, T.D. Nguyen, Y. Sheng, M. Wohlgenannt, Synth. Metals 160 (2010) 280.

ratio, and it is mainly originated from improper current suppression and imperfect carrier depletion in off state [12]. To reduce off-state current effectively and to enhance on/off ratio, it is essential to make current channel openings smaller and more uniform. Therefore, making gate pattern with shadow mask and evaporation technique is not feasible because obtaining sub-micron feature through vacuum evaporation method is extremely difficult and highly ordered patterns like porous shape cannot be acquired with shadow mask. Although conventional e-beam lithography has been used to make channel opening patterns with sub-micron feature size [13], it is an intrinsically expensive process. Polystyrene sphere based shadow mask method has also been used to obtain sub-micron porous channel opening patterns, namely colloidal lithography technique [14], but it is very difficult to obtain uniform channel opening patterns through this method. Therefore, in this study, we report a laser holography lithography method to form highly uniform nanoscale two-dimensional channel openings for VOFET devices. The laser holography has been recently used to make uniform photonic crystal structure in various optical applications like light-emitting diodes (LEDs) and photonic crystal slab waveguides [15,16]. It is a simple and maskless lithography technique which has many advantages in making well-aligned nanoscale reciprocal structures, but it has not been much used to make electrical device applications yet.

2. Experimental

The simplified process flow and schematic configuration of the fabricated VOFETs are illustrated in Fig. 1. Fig. 2 shows scanning electron microscope (SEM) images of top and cross-section views of the fabricated devices at several process steps. On a heavily doped silicon substrate which would act as a drain electrode, the first silicon nitride (SiN_x) layer, aluminum (Al) gate electrode layer, the second SiN_x layer, and chrome (Cr) hardmask layer have been sequentially deposited. Each SiN_x layer was formed by a plasma enhanced chemical vapor deposition (PECVD) process and its thickness was about 50 nm. Each metal layer (Al, Cr) was deposited with an e-gun evaporator. The thicknesses of Al gate and Cr hardmask layers were about 100 and 40 nm, respectively. After photoresist was spun-coated (Fig. 1a), the sample was exposed to the periodical line-shaped interference patterns generated from a laser holography system [15,16]. Negative type photoresist was used to make two dimensional (2-D) nanoscale patterns. After exposing the substrate to the laser holography line-shaped image two times in orthogonal directions and developing it in AZ®300 MIF developer, 2-D interference patterns (or holes) were formed in the unexposed area (Fig. 2a). The pitch between each channel opening could be controlled in 200 nm–1 μm range by adjusting the angle of stage where the sample is located. In this work, we fixed the pitch in 500 nm to obtain small and uniform porous patterns having holes with about 250 nm diameters. We expect that the gate controllability would be further enhanced by making channel openings smaller, because

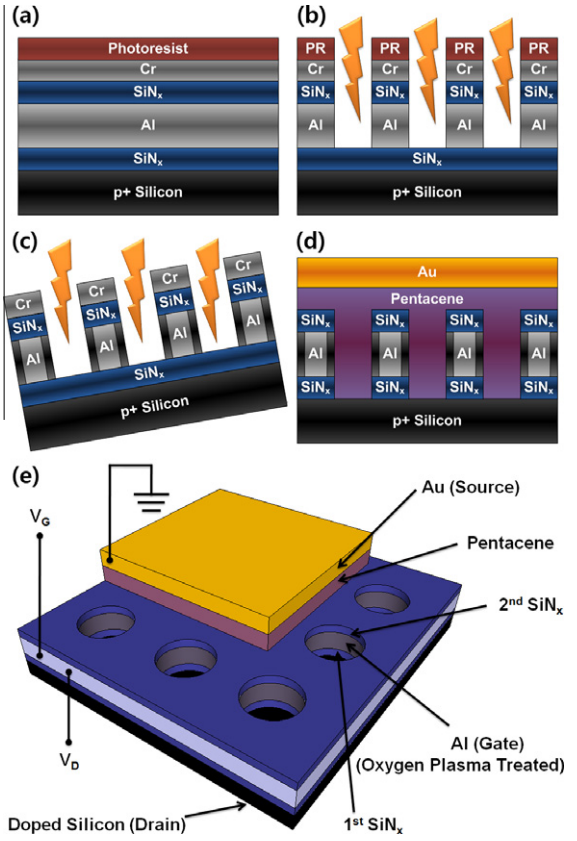

Fig. 1. (a)–(d) Fabrication processes and (e) a schematic configuration of vertical organic field effect transistors. (a) Photoresist coating after aluminum, chrome hardmask and two silicon nitride layers deposition. (b) Etching each layers after holography lithography process. (c) Plasma oxidation of gate electrode surfaces after removing photoresist. (d) Pentacene active layer and gold source electrode deposition after etching silicon nitride layer and removing hardmask.

the portion of the effective depletion region to the whole channel area, which is controlled by applied gate voltage, would be increased [14]. Since we need to perform additional plasma treatment process, however, the channel openings were maintained to be greater than 250 nm diameter considering overall device thickness, which is about 200 nm in this study.

By using these patterns, we etched the device structure through a reactive ion etching (RIE) process, producing the same holographic patterns for the vertical stack of Cr etch hardmask, the second SiN_x and Al gate layers (Fig. 1b). To reduce gate leakage current we have oxidized the Al gate sidewall surfaces. To effectively oxidize the sidewall, the sample was tilted in the plasma chamber during the plasma oxidation process. The oxygen plasma treatment (now O_2 plasma for 10 min) was performed four times for the same sample tilted in four different directions to equally oxidize the surface of the Al gate electrode sidewall (Fig. 1c). After removing the first SiN_x layer (Fig. 2b) with RIE process, pentacene (Tokyo Chemical Industry, P0030, 240 nm, @ 3 Å/s) and gold (Au, 100 nm, @ 2 Å/s) source electrode layers have been sequentially deposited using a thermal evaporation method (Figs. 1d and 2c and d). The

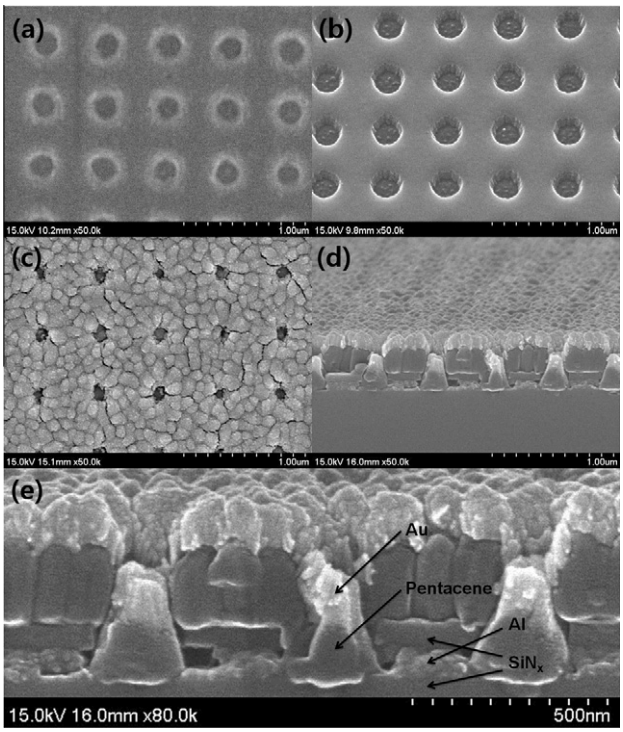

Fig. 2. SEM images of (a) top view of photoresist layer with two dimensional well-aligned porous patterns, (b) top-view of the vertical stack after oxygen plasma and etching of the first SiN_x layer, (c) top and (d), (e) cross-section views after depositing pentacene and gold electrode layers.

fabricated VOFETs were measured with a semiconductor parameter analyzer (Agilent 4155C) in air under dark conditions.

3. Results and discussion

Fig. 3a and b show the transfer characteristics and output characteristics of the fabricated VOFETs, respectively. Size of the measured device, i.e. size of Au source electrode was about 2×2 mm^2 for this result. Because VOFETs have short channel length, they can be operated even in low drain voltage region below 1 V. We investigated the transfer characteristics as we swept the gate voltage (V_G) from 2 to -2 V with -0.02 V step and increased the drain voltage (V_D) from 0 to -1 V with -0.2 V step. Current flow between source and drain electrodes (I_D) was effectively suppressed when positive V_G was applied. When positive voltage is applied to the gate electrode, energy barrier near the gate electrode is enhanced and the effective depletion region is expanded, which inhibits the current flow between source and drain electrode. On the other hands, when negative voltage is applied to the gate electrode, the current is increased due to the lowered energy barrier near the gate electrode and reduced effective depletion region. On/off ratio was obtained up to about 10^3 when -0.1 V was applied to V_D. It is noted that no additional ultra-thin organic semiconductor layers were inserted before pentacene deposition, which is known to improve on/off ratio [17] of the VOFETs. Therefore, on/off ratio can be further improved if organic multilayer approach is used. We also obtained output characteristics of the fabricated VOFETs for the same voltage range as in the transfer curves. Drain voltage was swept from 0 to -1 V with -0.01 V step, and the gate voltage was changed from 2 to -2 V with -0.4 V step. Like other VOFETs, our devices did not show saturation behavior when large V_D was applied [6,11]. Gate leakage current was maintained under hundreds of nano-amperes for relatively large V_G values. The mobility of pentacene in VOFETs was estimated by the space charge limited current (SCLC) model [8] because the conventional mobility extraction method which is widely used in OTFTs cannot be applied in VOFETs. Our current density to the applied drain voltage (J–V_D) was fitted quite well to the SCLC model, and the mobility extracted with SCLC model was estimated as 1.2×10^{-4} cm^2/Vs, which is a quite low value compared with conventional OTFTs, but common in vertical type transistor devices. Although VOFETs have shown low mobilities compared with lateral-type OTFTs, the short channel length of VOFETs which is 240 nm in current devices, and a number of channel openings covering each VOFET devices enable a large current driving capability even in low voltage regimes.

Fig. 4 shows the effect of plasma oxidation on Al gate sidewall surfaces of VOFETs, which in this case have channel openings with 1 μm diameter. It is indicated that the oxidized gate surfaces can suppress the gate leakage current levels originated from high gate bias exceeding Schottky barrier and improper Schottky junction formation between gate electrode and active layer. Especially, the effect of plasma oxidation is more prominent in an off-state, when positive voltages are applied to gate electrodes,

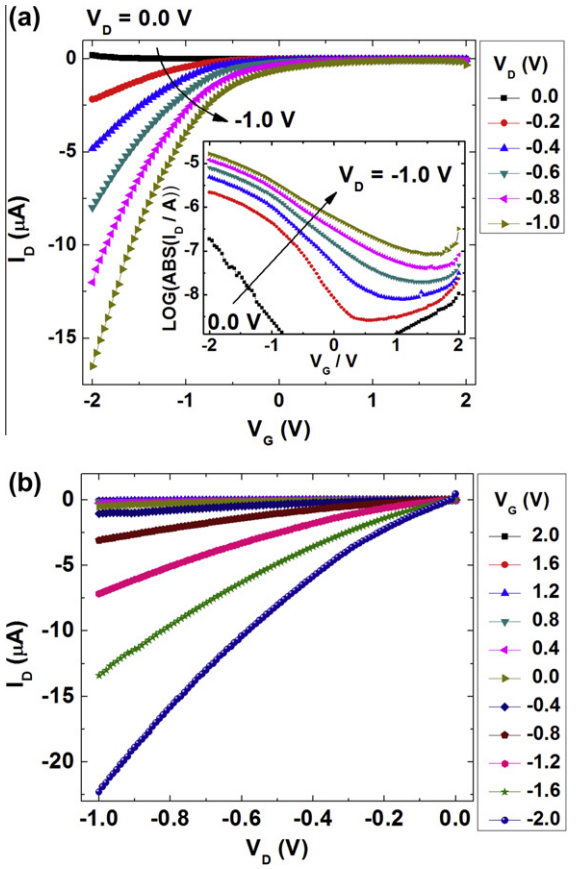

Fig. 3. (a) Transfer characteristics and (b) output characteristics of VOFETs with channel openings of about 250 nm diameter.

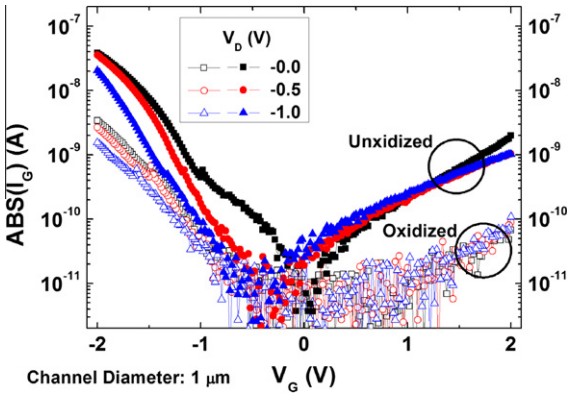

Fig. 4. Suppressed gate leakage current levels after plasma oxidation of gate electrode surfaces.

and this contributes to on/off ratio enhancement due to lower leakage current levels. Without these additional insulation structures, it is typically challenging to obtain proper transistor characteristics because maintaining Schottky contact for various semiconductor materials is challenging. An insertion of additional insulating structure by oxidizing gate electrode surface may allow us to use many semiconductor materials in the active layer. Although we can produce 2-D patterns only over 3×3 cm^2 area due to equipment limitation, it is noted that the laser holography lithography can produce reciprocal patterns over large area (>50×50 cm^2) [18]. Therefore, if this plasma oxidation process is combined together, our method can produce uniform 2-D nanoscale patterns for high performance VOFET arrays over large area substrate. Furthermore, adjusting exposure times and direction enables making various reciprocal lateral patterns such as lines and squarely or hexagonally aligned hole arrays. Since these patterns are well-aligned and have uniform shape generally, devices with minimal performance variation can be easily made.

4. Conclusion

In summary, we have used a laser holography lithography technique to make 2-D channel opening patterns in fabricating VOFET structures. Holographically generated small channel opening patterns were well-aligned and quite uniform in size and shape. The gate electrode sidewall was oxidized with oxygen plasma to further reduce gate leakage. The pentacene VOFET with the channel opening size of about 250 nm in diameter showed on/off ratio of about 10^3 without any further treatment. We believe that by introducing better gate electrode sidewall oxidation process and optimizing the channel opening size, the device performance can be further improved.

Acknowledgment

This work was supported by the Industrial Strategic Technology Development Program (KI002104, Development of Fundamental Technologies for Flexible Combined-Function Organic Electronic Device) funded by the Ministry of Knowledge Economy (MKE, Korea).

References

[1] U. Haas, H. Gold, A. Haase, G. Jakopic, B. Stadlobera, Appl. Phys. Lett. 91 (2007) 043511.
[2] K. Tsukagoshi, K. Shigeto, I. Yagi, Y. Aoyagi, Appl. Phys. Lett. 89 (2006) 113507.
[3] J. Collet, O. Tharaud, A. Chapoton, D. Vuillaume, Appl. Phys. Lett. 72 (2000) 1941.
[4] M. Leufgen, U. Bass, T. Muck, T. Borzenko, G. Schmidt, J. Geurts, V. Wagner, L.W. Molenkamp, Synth. Met. 146 (2004) 341.
[5] M. Leufgen, O. Rost, C. Gould, G. Schmidt, J. Geurts, L.W. Molenkamp, N.S. Oxtoby, M. Mas-Torrent, N. Crivillers, J. Veciana, C. Rovira, Org. Electron. 9 (2008) 1101.
[6] K. Kudo, M. Iizuka, S. Kuniyoshi, K. Tanaka, Thin Solid Films 393 (2001) 362.
[7] T. Takano, H. Yamauchi, M. Iizuka, M. Nakamura, K. Kudo, Appl. Phys. Exp. 2 (2009) 071501.
[8] S. Cheng, Y. Chuang, D. Kekuda, C. Ou, M. Wu, C. Chu, Adv. Mater. 21 (2009) 1860.
[9] Y. Yang, A.J. Heeger, Nature 372 (1994) 344.
[10] S. Li, Z. Xu, L. Ma, C. Chu, Y. Yang, Appl. Phys. Lett. 91 (2007) 083507.
[11] F. Pu, Y. Watanabe, H. Yamauchi, M. Nakamura, K. Kudo, Thin Solid Films 518 (2009) 514.
[12] S. Zorba, Y. Gao, Appl. Phys. Lett. 86 (2005) 193508.
[13] H. Yamauchi, Y. Watanabe, M. Iizuka, M. Nakamura, K. Kudo, IEICE Trans. Electron. E91-C (2008) 1852.
[14] K. Fujimoto, T. Hiroi, M. Nakamura, e-J. Surf. Sci. Nanotech. 3 (2005) 327.

[15] C. Cho, Y. Roh, Y. Park, H. Jeon, B. Lee, H. Kim, Y. Choe, Jpn. J. Appl. Phys. 43 (2004) 1384.
[16] D. Kim, C. Cho, Y. Roh, H. Jeon, Y. Park, Appl. Phys. Lett. 87 (2005) 203508.
[17] Y. Watanabe, H. Iechi, K. Kudo, Jpn. J. Appl. Phys. 45 (2006) 3698.
[18] J.P. Spallas, R.D. Boyd, J.A. Britten, A. Fernandez, A.M. Hawryluk, M.D. Perry, D.R. Kania, J. Vac. Sci. Technol., B 14 (1996) 2005.

mode can be effectively controlled through the voltages applied independently to the top and bottom TFT gate electrodes. We also report on the characteristics of dual-gate devices made with indenofluorene–phenanthrene copolymer semiconductor.

2. Experimental

Fig. 1 shows the chemical structure of the indenofluorene–phenanthrene copolymer as well as the schematic cross-section of organic TFTs based on indenofluorene–phenanthrene copolymer semiconductor using recessed source/drain electrodes and dual-gate geometry. Device fabrication started with an n-type silicon substrate with a resistivity of 1–10 Ωcm, also used as the bottom-gate electrode. This is thermally oxidized to result in a 160 nm thick silicon dioxide gate insulator. All samples were sonicated in acetone, methanol and isopropyl alcohol for 5 min each, dried with nitrogen gas, baked in a 120 °C oven for 10 min to remove remaining water, and then exposed to UV ozone treatment for 5 min. Source/drain regions were patterned via a photolithographic process for all samples. In half the samples, the silicon dioxide was first etched to a depth of 40 nm for 1 min by a reactive ion etching to facilitate the formation of recessed source/drain contact. A 2.5 nm chrome adhesion layer and a 37.5 nm gold layer were blanket deposited by thermal evaporation to define the source/drain electrodes by a standard lift-off process on all samples (both regular and recessed source/drain). Sets of devices from each group of samples were then treated with nitrobenzenethiol (NBT) to form a SAM [16,17]. These samples were immersed in a dilute NBT solution in chloroform (10 mM) for 1 h, rinsed with ethanol to remove residual NBT, and then annealed at 120 °C for 30 min. The samples were exposed to hexamethyldisilazane (HMDS) vapor at room temperature for 16 h to improve the interface between the silicon dioxide gate dielectric and the organic polymeric semiconductor [18]. Both NBT and HMDS treatments were performed under an inert atmosphere.

The indenofluorene–phenanthrene copolymer solution was formed using toluene as the solvent (5 mg/mL concentration) with magnetic stirring at 50 °C for 10 h in an inert environment. The synthesis of the indenofluorene–phenanthrene copolymer has been described in detail by Schulte et al. [5]. The semiconductor film was formed by spin-coating for 45 s at 1600 rpm and then was pre-annealed at 110 °C for 30 min. The thickness of semiconductor layer measured by elipsometer is ~70 nm. The as-supplied polymeric dielectric Merck® D139 was employed as a passivation layer. D139 was spin-coated onto the semiconductor layer for 5 s at 500 rpm and then 50 s at 1000 rpm. After the spinning, the samples were cured by increasing the annealing temperature from 25 to 130 °C over 1 h.

To fabricate the dual-gate devices, a 50 nm titanium and gold–palladium double layer as gate electrode was deposited onto a silicon dioxide barrier layer on a silicon substrate by e-beam evaporation. A poly(vinyl cinnamate) dielectric layer (0.5 wt.% concentration in cyclopentanone) as bottom gate insulator was formed by spin-coating for 60 s at 1000 rpm. This layer was pre-annealed at 130 °C for 25 min in nitrogen atmosphere and then cross-linked by exposing to UV radiation source of e-beam aligner (7.5 mW/cm^2 of intensity and 365 nm of wave length) for 10 min. After deposition of a 40 nm chrome and gold double layer as source/drain electrodes, the indenofluorene–phenanthrene copolymer semiconductor layer and D139 layer as top gate insulator were spin-coated in order. Finally, a 50 nm gold layer as top gate electrode was deposited by thermal evaporation. The device fabrication was completed with a thermal post-anneal at 140 °C for 10 h. The spin-coating and thermal annealing of semiconductor and D139 layers were performed under nitrogen atmosphere.

3. Results and discussion

Fig. 2a and b shows the output characteristics of an amorphous indenofluorene–phenanthrene copolymer TFT using elevated source/drain electrodes and recessed source/drain electrodes without surface treatment. With the recessed source/drain electrodes, the on-current level increased by about a factor of 4 and the field-effect mobility increased from 0.018 to 0.055 cm^2/V-s as compared to

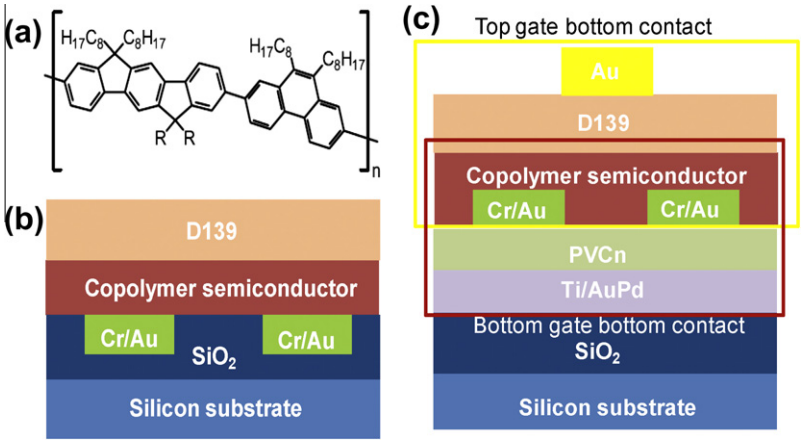

Fig. 1. (a) The chemical structure of indenofluorene–phenanthrene copolymer and a schematic cross-section of an amorphous polymeric thin film transistor based on indenofluorene–phenanthrene copolymer (b) using recessed source/drain electrodes (c) using dual-gate structure.

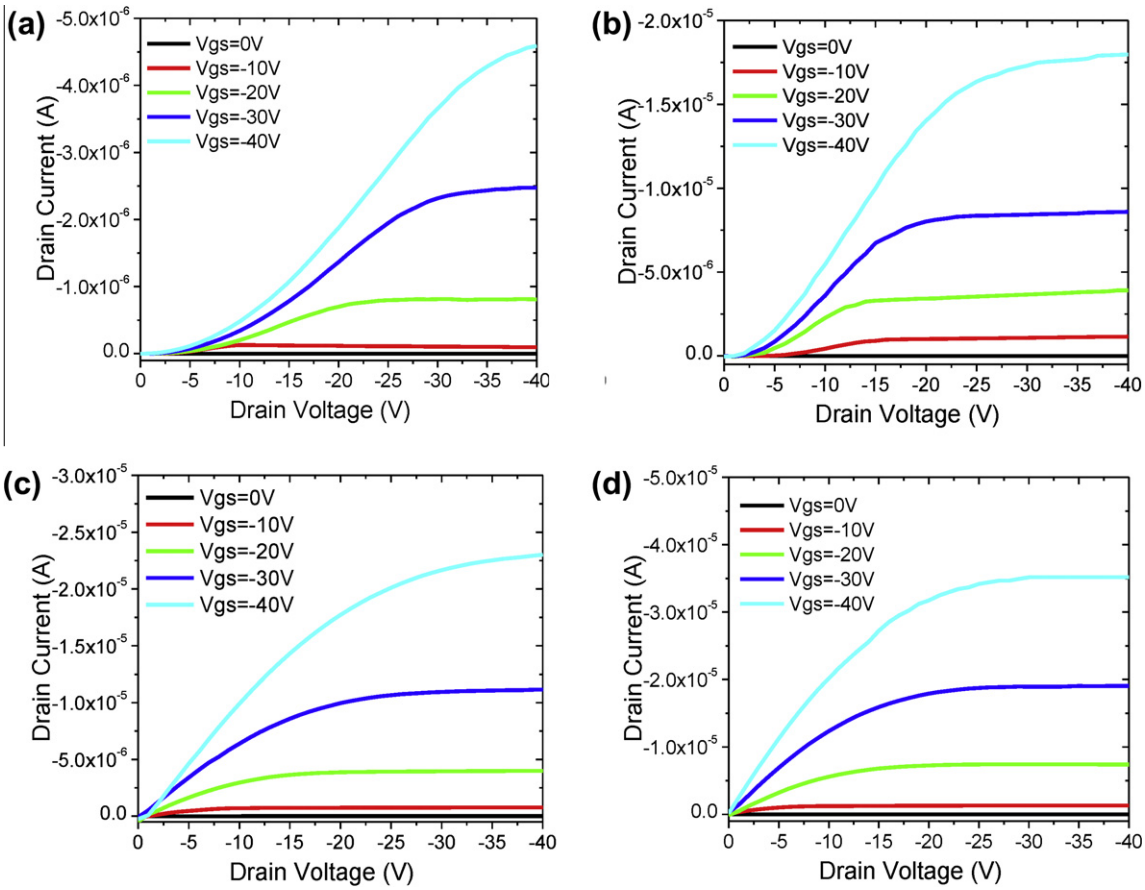

Fig. 2. The output characteristics of amorphous indenofluorene–phenanthrene copolymer TFT using (a) elevated source/drain electrodes without treatment (b) recessed source/drain electrodes without treatment (c) elevated source/drain electrodes with NBT treatment (d) recessed source/drain electrodes with NBT treatment.

the elevated structure. The super-linear behavior seen as low drain voltages in the elevated contact structure is attributed to a high injection barrier, which is reduced substantially by the adoption of recessed contacts as shown in Fig. 2. In order to further investigate the combination effect of recessed source/drain electrodes and the surface treatment of the electrodes, non-treated and NBT-treated samples based on both recessed and elevated source/drain structure have been compared. SAM surface treatments are expected to reduce contact resistance by improving the physical contact between the metal and semiconductor [10,11]. After applying surface treatments, the device performance for surface-treated samples is improved in both the recessed and elevated source/drain geometries as shown in Fig. 2c and d. The device employing surface-treated, recessed source/drain possesses a field-effect mobility of 0.144 cm^2/V-s, sub-threshold swing (S.S.) of 1.25 V/decade and on–off current ratio in excess of 10^5 in air. Fig. 3a shows the square root of drain current versus gate voltage with different conditions. Effective mobilities extracted by Fig. 3a increase due to the improved electrical contact. The use of NBT surface treatment, as shown in Fig. 3, improves hole injection between gold source/drain electrodes and the organic semiconductor layer [16,17]. Significantly, the combination of the use of surface treatments and the recessed source/drain geometry improves the effective mobility of amorphous indenofluorene–phenanthrene copolymer TFTs, which is about nine times higher than the non-treated, elevated source/drain sample.

The total resistance in TFT devices is the sum of the contact resistance and channel resistance [19,20]. If channel length decreases, the intrinsic channel resistance decreases and the relative influence in the contact resistance increases. Therefore, device characteristics such as the apparent field-effect mobility are influenced by significant contact resistance [20–22]. In order to investigate the dependence of contact resistance on channel length, a transmission line method can be used to extract the value of contact resistance [20,21]. The contact resistance can be calculated by determining the device on-resistance from the linear region mode operation and plotting the width-normalized on-resistance as a function of channel length for different gate voltages. The width-normalized contact resistance is extracted at the y-axis intercept of the extrapolated linear fits of the different gate voltages. Fig. 3b shows the width-normalized device resistance as a function of channel length at the gate voltages of −20, −30 and −40 V with the drain-source voltage of −2 V. This

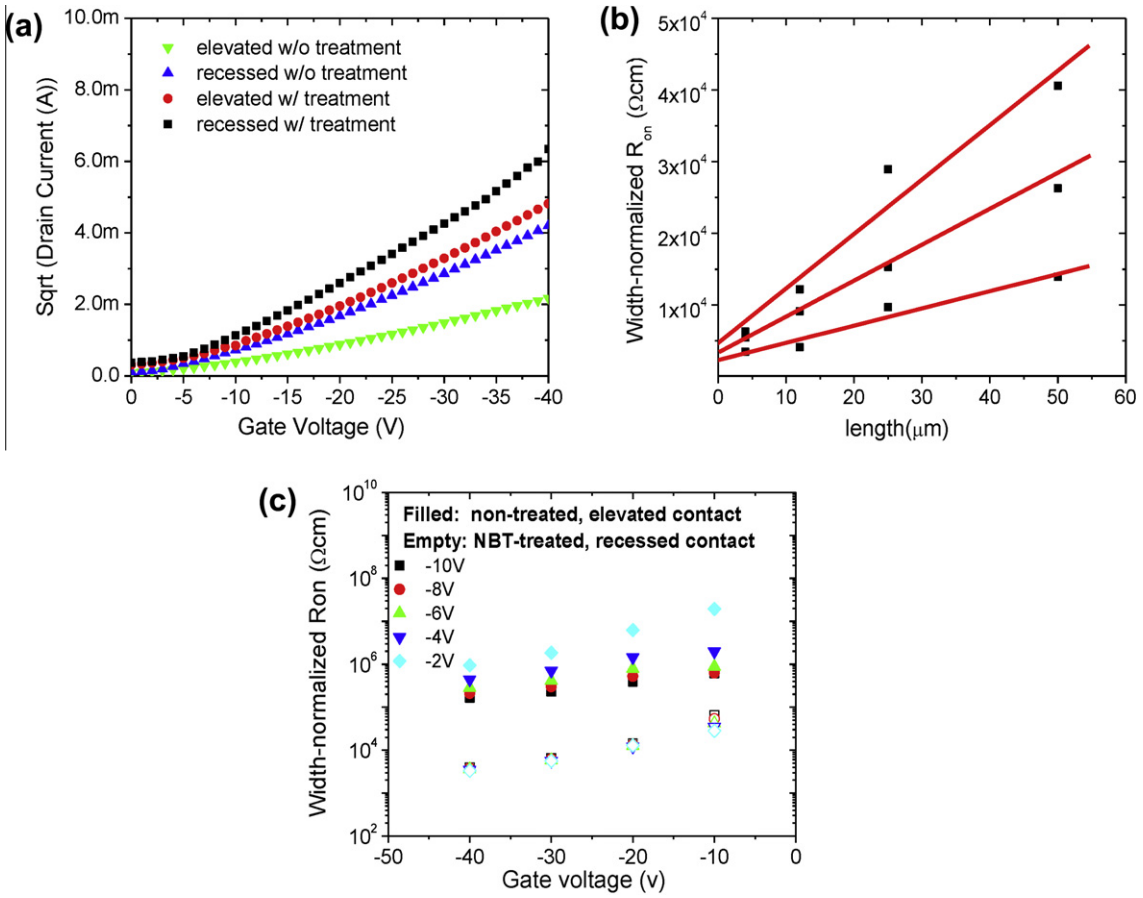

Fig. 3. (a) Square root of drain current vs. gate voltage with different conditions. (b) Width normalized resistance as a function of channel length at the gate voltages with fixed drain voltage using recessed source/drain electrodes with treatment. (c) Width-normalized resistances as a function of gate and drain voltage in recessed source/drain with treatment (filled) and elevated source/drain without treatment (empty).

was extracted from output characteristics curves on devices with channel lengths ranging from 4 to 50 μm. The width-normalized contact resistance was extrapolated from the graph to be 1275 Ωcm for devices employing recessed contacts modified with NBT surface treatment. Fig. 3c shows the width-normalized resistances as a function of gate and drain voltages in recessed source/drain with surface treatment and elevated source/drain without surface treatment. Width-normalized resistances of a non-treated TFT with elevated contacts are strongly influenced by drain voltage in linear mode operation. The schottky barrier is attributed to a high injection barrier, which influences the effective mobility. Furthermore, width-normalized resistances decrease with increasing drain voltage compared to surface-treated, recessed source/drain TFT, indicating there is the point of certain threshold of injection barrier.

Fig. 4a shows the transfer characteristics in the top-gate, bottom-gate and dual-gate modes of a dual-gate indenofluorene–phenanthrene copolymer TFT at the gate voltages ranging from −40 to 40 V with the drain-source voltage of −40 V. These TFTs possess a field-effect mobility of 0.2$cm^2V^{-1}s^{-1}$ when measured in the top-gate mode and 0.09$cm^2V^{-1}s^{-1}$ in the bottom-gate mode in air. The current of the top-gate device is lower than that of the bottom-gate device because polymer gate dielectric as top-gate insulator is thicker and has a lower capacitance per unit area (4 nF/cm^2) compared to silicon dioxide as bottom-gate insulator (20 nF/cm^2). The characteristics of the interface have a significant influence on the measured mobility [23,24]. The fabrication sequence of the top-gate device allows the use of an in situ process in which the semiconductor layer and the top-gate insulator layer can be deposited sequentially under an inert environment. For this reason, better quality interfaces can be obtained from top-gate devices. In addition, the effective area for charge injection in the top-gate bottom-contact device is larger than that in BGBC device, leading to improved contact properties.

Dual-gate mode operation results in improved performance such as increased on-current, reduced threshold voltage (V_{th}), improved S.S. and increased on–off current ratio compared to either single gate mode as shown in Fig. 4a. This is because interaction between charge carriers and interface between a semiconductor and a gate insulator layer is reduced. Fig. 4b shows the schematic illustration of interfacial energy band diagram in case of single-gate mode vs. dual-gate mode. In single-gate devices, charge carriers are more highly confined, leading to enhanced

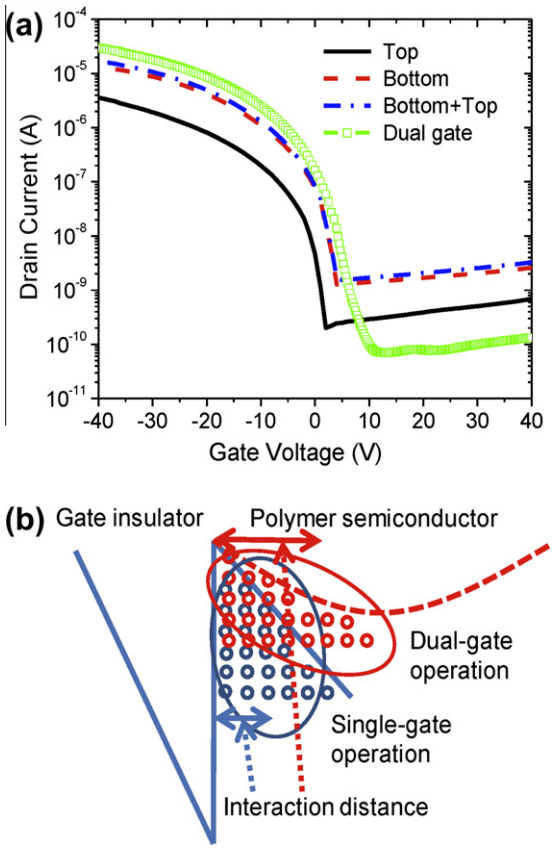

Fig. 4. (a) The transfer characteristics of top-gate, bottom-gate and dual-gate mode in indenofluorene–phenanthrene copolymer TFTs. (b) The schematic illustration of interfacial energy band diagram in case of single-gate mode vs. dual-gate mode.

interaction with interface. When the other gate bias is applied, interaction distance between charge carriers and interface in dual-gate mode becomes increased over singe-gate mode due to the band bending. It means that interface characteristics in dual-gate mode are improved due to the reduced interaction of charge carriers. Horowitz et al. reported that the mobility of charge carriers in organic FETs is lower closer to the interface compared to the bulk [25]. This is because of a greater interaction with the interface. The same effect is one of the factors responsible for the improved performance of dual-gate mode operation. Improved interface characteristics lead to improved S.S. and reduced V_{th} including increased on-current and on–off current ratio. Improved S.S. and reduced V_{th} can also explain why the current density from a dual-gate device is larger than the sum of current densities of both top- and the bottom-gate devices, as shown in Fig. 4a. We note that other reasons have been provided for improved performance of dual-gate devices such as gate screening effects and shift of V_{th} [13,26]. Such effects also result in improved performance of dual-gate devices. After the electric bias-stress is applied on each mode of operation, dual-gate mode exhibits greater stability than the single-gate modes. This is also a consequence of improved interface characteristics due to the reduced interaction of charge carriers with the interfaces. These results demonstrate that high mobilities can be achieved in amorphous polymer field-effect transistors. The mobility values we report are comparable to those reported for regioregular poly(3-hexyl thiophene), a liquid crystalline semiconductor that has been extensively investigated for over a decade by many groups [2–4,27]. Our work further demonstrates the importance of contact engineering on device performance for this class of materials. We have in previous work shown the effects of recessed source/drain regions on the performance of pentacene FETs [12]. The mobilities achieved at channel lengths of 4 μm suggest that such semiconductors will be useful in a number of applications such as displays.

4. Conclusion

In summary, the bottom gate bottom contact amorphous polymer semiconductor TFT based on indenofluorene–phenanthrene copolymer exhibits a field-effect mobility of 0.144 cm^2/V-s and a width-normalized contact resistance of 1275 Ωcm in air. In addition, we fabricated dual-gate indenofluorene–phenanthrene copolymer TFTs, which possess enhanced gate control as well as less instability caused by electrical bias stress compared to single gate TFT mode operation. Interface characteristics in dual-gate mode were improved due to the reduced interaction of charge carriers. The combination of suitable surface treatments of source/drain contact electrodes and the recessed source/drain geometry and device architecture of dual-gate configuration are the key to realizing such better device performances required for flexible electronic circuits and fabrication.

Acknowledgment

The work on device fabrication and characterization were performed at The University of Texas and supported by NSF-ECCS Division. The authors thank Soumya Dutta and Brain Cobb for helpful discussion.

References

[1] J. Veres, S.D. Ogier, S.W. Leeming, D.C. Cupertino, S.M. Khaffaf, Adv. Funct. Mater. 13 (2003) 199.
[2] B.S. Ong, Y. Wu, P. Liu, S. Gardner, J. Am. Chem. Soc. 126 (2004) 3378.
[3] B.H. Hamadani, D.J. Gundlach, I. McCulloch, M. Heeney, Appl. Phys. Lett. 91 (2007) 243512.
[4] Z. Bao, A. Dodabalapur, A.J. Lovinger, Appl. Phys. Lett. 69 (1996) 3066.
[5] H. Kim, N. Schulte, G. Zhou, K. Mullen, F. Laquai, Adv. Mater. 23 (2011) 894.
[6] L. Torsi, A. Dodabalapur, H.E. Katz, J. Appl. Phys. 78 (1995) 1088.
[7] K. Shibata, H. Wada, K. Ishikawa, H. Takezoe, Appl. Phys. Lett. 90 (2007) 193509.
[8] T.J. Richards, H. Sirringhaus, J. Appl. Phys. 102 (2007) 094510.
[9] R.A. Street, A. Salleo, Appl. Phys. Lett. 81 (2002) 2887.
[10] I. Kymissis, C.D. Dimitrakopoulos, S. Purushothaman, IEEE Trans. Electron Devices 48 (2001) 1060.
[11] A. Jakubowicz, H. Jia, R.M. Wallace, B.E. Gnade, Langmuir 21 (2005) 950.
[12] C.-G. Lee, S. Park, R.S. Ruoff, A. Dodabalapur, Appl. Phys. Lett. 95 (2009) 023304.
[13] F. Maddalena, M. Spijkman, J.J. Brondijk, P. Fonteijin, F. Brouwer, J.C. Hummelen, D.M. de Leeuw, P.W.M. Blom, B. de Boer, Org. Electron. 9 (2008) 839.

[14] G.H. Gelinck, E. van Veenendaal, R. Coehoorn, Appl. Phys. Lett. 87 (2005) 073508.
[15] M. Spijkman, E.C.P. Smits, P.W.M. Blom, D.M. de Leeuw, Y. Bon Saint Come, S. Setayesh, E. Cantatore, Appl. Phys. Lett. 92 (2008) 143304.
[16] D.J. Gundlach, L. Jia, T.N. Jackson, IEEE Electron Device Lett. 22 (2001) 571.
[17] J. Takeya, C. Goldmann, S. Haas, K.P. Pernstich, B. Ketterer, B. Batlogg, J. Appl. Phys. 94 (2003) 5800.
[18] A. Salleo, M.L. Chabinyc, M.S. Yang, R.A. Street, Appl. Phys. Lett. 81 (2002) 4383.
[19] P.V. Necliudov, M.S. Shur, D.J. Gundlach, T.N. Jackson, Solid State Electron. 47 (2003) 259.
[20] J. Zaumseil, K.W. Baldwin, J.A. Rogers, J. Appl. Phys. 93 (2003) 6117.
[21] M. Kim, J.H. Jeong, H.J. Lee, T.K. Ahn, H.S. Shin, J.-S. Park, J.K. Jeong, Y.-G. Mo, H.D. Kim, Appl. Phys. Lett. 90 (2007) 212114.
[22] N. Yoneya, M. Noda, N. Hirai, K. Nomoto, M. Wada, J. Kasahara, Appl. Phys. Lett. 85 (2004) 4663.
[23] S. Georgakopoulos, D. Sparrowe, F. Meyer, M. Shkunov, Appl. Phys. Lett. 97 (2010) 243507.
[24] C.D. Dimitrakopoulos, P.R.L. Malenfant, Adv. Mater. 14 (2002) 99.
[25] G. Horowitz, M. Mottaghi, P. Lang, F. Rodriguez, A. Yassar, S. Lenfant, D. Vuillaume, Proc. SPIE 6336 (2006) 63360.
[26] H. Marien, M.S.J. Steyaert, E.V. Veenendaal, P. Heremans, IEEE J. Solid-State Circuits 46 (2011) 276.
[27] H. Yang, T.J. Shin, L. Yang, K. Cho, C.Y. Ryu, Z. Bao, Adv. Funct. Mater. 15 (2005) 671.

used to measure the difference between the Fermi level (E_F) and the highest occupied molecular orbital (HOMO). UPS with a resolution of 0.15 eV was measured using He I (21.22 eV) photon line from discharge source. The hole concentration as a function of the MoO_x mole percentage in the various MoO_x-doped pentacene channel layers was also investigated to study the doping mechanisms. Furthermore, the crystalline quality of the various MoO_x-doped pentacene channel layers was analyzed using an X-ray diffraction (XRD) system. The contact resistance was estimated using the gated-transmission line method (gated-TLM).

2. Experimental

Fig. 1 shows the schematic structure of the top contact organic thin-film transistors, in which the LiF buffer layer was inserted between the MoO_x-doped pentacene channel layer and the gold (Au) source/drain electrodes. The aluminum (Al) was deposited as the gate electrode on cleaned glass substrates. A 170-nm-thick polymethylmethacrylate (PMMA) was spread as dielectric layer using a spin-coated method. To investigate the influence of the various MoO_x-doped pentacene channel layers, a 30-nm-thick undoped pentacene and a 30-nm-thick MoO_x-doped pentacene with various MoO_x mole percentages were fabricated as the channel layer of the OTFTs. The former one is named as the conventional OTFTs and the latter ones are named as the MoO_x-doped OTFTs. The various MoO_x-doped pentacene channel layers were deposited by the co-evaporation system, and the mole percentage of carbon and molybdenum was determined by the X-ray photoemission spectroscopy (XPS). A 1-nm-thick LiF buffer layer was then deposited on the pentacene channel layer. Finally, a 100-nm-thick Au layer was thermally evaporated to fabricate the source and drain electrodes. The 1-nm-thick LiF buffer layer was deposited to modulate the work function and enhance the carrier tunneling behaviors [13]. All the deposition processes were performed under a base pressure of about 4×10^{-4} Pa. The channel length (L) and width (W) of the OTFTs were 50 and 400 μm, respectively. The electrical characteristics of the OTFTs were measured using an HP4156 semiconductor parameter analyzer.

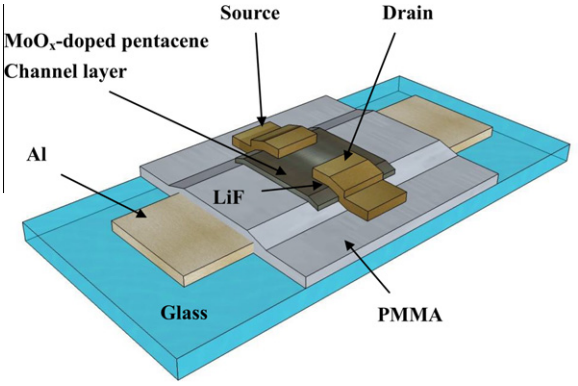

Fig. 1. The schematic structure of top contact organic thin-film transistors.

3. Results and discussion

The output drain-source current-drain-source voltage (I_{DS}–V_{DS}) characteristics of the conventional OTFTs and the 0.50% MoO_x-doped OTFTs were shown in Fig. 2. The associated transfer characteristics were shown in Fig. 3(a and b), respectively. According to the experimental measurement results, Table 1 listed the performances of the OTFTs with the conventional and the various MoO_x-doped

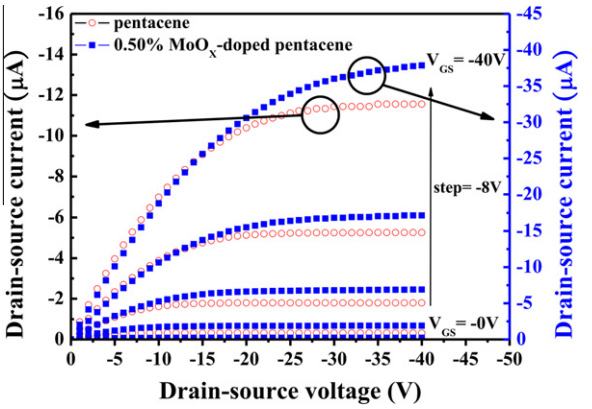

Fig. 2. Output characteristics of conventional OTFTs and 0.50% MoO_x-doped OTFTs.

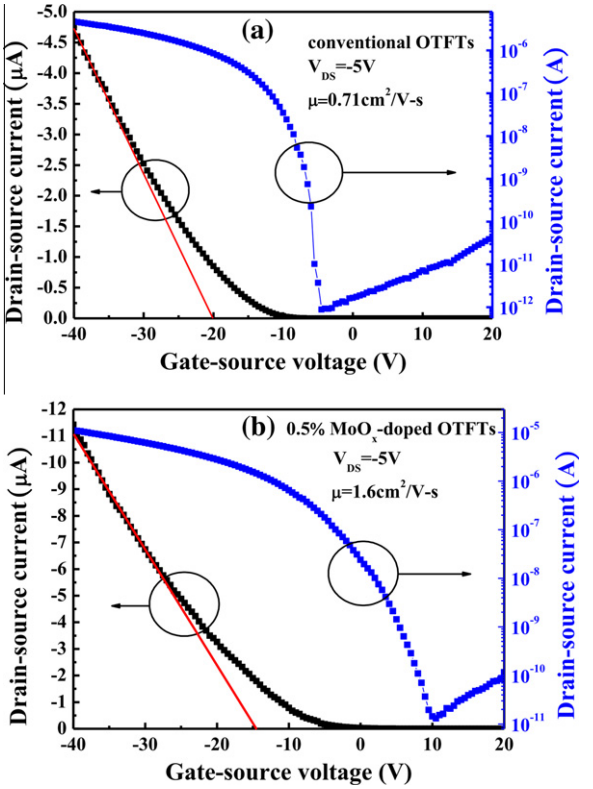

Fig. 3. Transfer characteristics of: (a) conventional OTFTs and (b) 0.50% MoO_x-doped OTFTs.

pentacene channel layers. It was found that the maximum output current was −11.6 μA of the conventional OTFTs operated at $V_{DS} = V_{GS} = -40$ V, where V_{GS} was the gate-source voltage. For operating at the same V_{DS} and V_{GS} conditions, the maximum output current of the OTFTs with the 0.50% MoO_x-doped pentacene channel layer increased by 3.2 times (−37.9 μA). As could be seen from Fig. 3(a and b) and Table 1, when the OTFTs with the MoO_x doping mole percentage varied from 0% to 0.50% operated at $V_{DS} = -5$ V and varied the V_{GS} from 20 to −40 V, the effective field-effect mobility changed from 0.71 to 1.60 cm^2/V-s, the threshold voltage changed from −21.2 to −14.8 V, and the on–off current ratio changed from 3.6×10^6 to 1.2×10^6. These experimental results indicated that the effective field-effect mobility of the 0.50% MoO_x-doped OTFTs increased 2.25 times compared with the conventional OTFTs. The decrease of the threshold voltage meant that the needed operation energy of the OTFTs decreased. The on–off current ratio of the OTFTs with 0.50% MoO_x-doped pentacene channel layer slightly decreased due to an increase of the off-current. Fig. 4(a and b) shows the drain-source current-gate-source voltage characteristics of the conventional OTFTs and 0.5% MoO_x-doped OTFTs by varying the drain-source voltage, respectively. As shown in Fig. 4(a and b), when the OTFTs with the MoO_x doping mole percentage varied from 0% to 0.50% operated at $V_{DS} = -40$ V and varied the V_{GS} from 20 to −40 V, the on–off current ratio changed from 5.0×10^5 to 3.8×10^3. It was deduced that the channel conductivity increased by doping MoO_x. Because OTFTs usually operated in the linear region, it is effective to improve the performance of OTFTs by using co-thermal method to dope MoO_x into pentacene as the channel layer.

Table 1
The device performances of OTFTs with various MoO_x-doped pentacene channel layers.

MoO_x doping (mol%)	I_{DS} (μA)	μ_{eff} (cm^2/V-s)	V_{TH} (V)	I_{on}/I_{off}
0	−11.6	0.71	−21.2	3.6×10^6
0.21	−34.7	1.22	−17.1	2.0×10^6
0.50	−37.9	1.60	−14.8	1.2×10^6
0.68	−37.5	1.50	−13.2	7.5×10^5
1.39	−32.8	0.88	−7.8	3.4×10^3

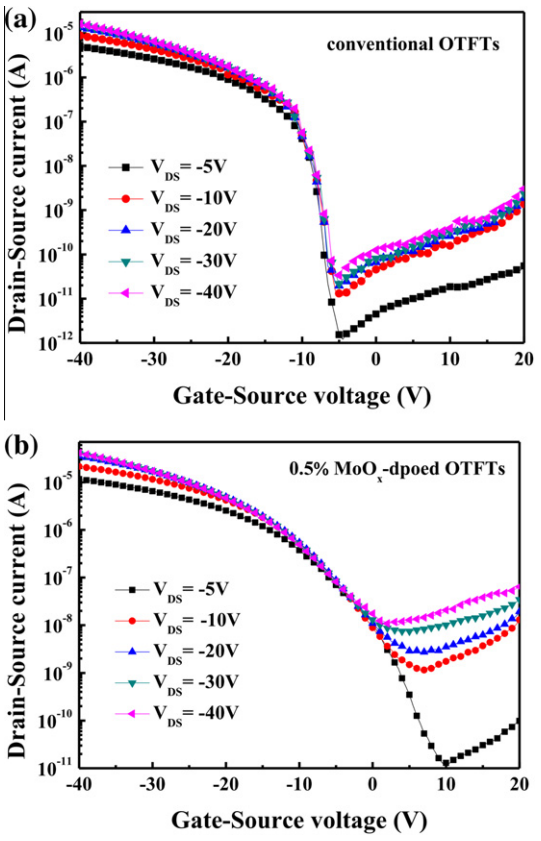

Fig. 4. Drain-source current-gate-source voltage characteristics of: (a) conventional OTFTs and (b) 0.50% MoO_x-doped OTFTs.

Based on the shift of the HOMO relative to the Au work function, the UPS was used to analyze the various MoO_x-doped pentacene channel layers. Since the conduction band energy (6.7 eV) of MoO_x was lower than the HOMO (5.20 eV) of pentacene, the energy difference led electron to transfer. For stabilization, the electrons on the HOMO of pentacene would transfer to the conduction band of the MoO_x. As shown in Fig. 4(b), the turn-on voltage ($V_{turn\text{-}on}$) of the 0.5% MoO_x-doped OTFT is a positive value. It verified that the OTFTs revealed normally turn-on depletion type characteristics. Therefore, the electrons on pentacene would transfer to the doped MoO_x. Consequently, the hole density of the MoO_x-doped pentacene increased with the doping concentration of MoO_x. The UPS experimental results were shown in Fig. 5(a). To clearly show the experimental results, the extended larger scale results were shown in Fig. 5(b). As shown in Fig. 5(b), the energy shift was 0.66, 0.36, and 0.30 eV respect to the Fermi level (E_F) corresponded to the MoO_x-doped mole percentage of 0%, 0.50% and 1.39%, respectively. The UPS measurement results verified that the HOMO of the MoO_x-doped pentacene increased with the doping percentage of MoO_x and gradually approached to the work function value of the Au. Therefore, the p-type characteristics were enhanced and the hole density and the hole mobility were increased for the MoO_x-doped pentacene channel layer with a higher mole percentage of MoO_x. However, when the mole concentration of MoO_x increased to a certain amount and the produced carrier concentration satisfied the thermal equilibrium condition, the hole concentration gradually approached to saturation with an increase of the MoO_x mole concentration due to the Fermi level pinning effect [14–16].

To investigate the carrier injection of Au/LiF/pentacene and Au/LiF/0.50% MoO_x-doped pentacene junction. The contact resistance of pentacene and 0.50% MoO_x-doped pentacene channel layer was estimated using the gated-TLM. Contact resistance (R_C) was extracted from the dependence of the total resistance (R_T) on the channel length (L). Fig. 6(a and b) shows the R_T as a function of L extracted from the measured results of the gated-TLM test structure of the pentacene and the 0.50% MoO_x-doped pentacene channel layers operated at $V_{DS} = -5$ V and

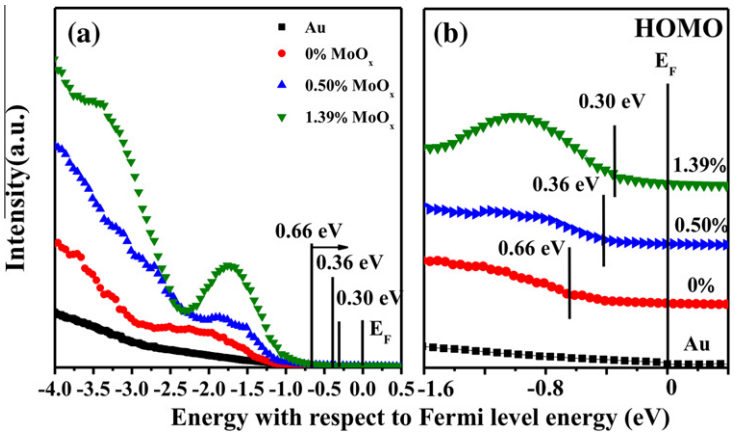

Fig. 5. (a) The energy shift of HOMO related to Au work function based on pentacene with various MoO_x doping percentages and (b) HOMO of MoO_x-doped pentacene thin films respected to Fermi level (E_F) for various MoO_x doping percentages.

various V_{GS} voltages, respectively. By fitting the line to the $L = 0$ of the R_T vs. L characteristics, the contact resistance R_C can be extrapolated. The contact resistance R_C of the OTFTs with the pentacene and the 0.50% MoO_x-doped pentacene channel layers operated at a gate voltage of -40 V was 1.57×10^7 and $8.12 \times 10^6\ \Omega$, respectively. These experimental results indicated that the contact resistance could be reduced in the OTFTs with the MoO_x-doped pentacene channel layer. Fig. 6(c) shows the dependence of the contact resistance (R_C) on the gate-source-voltage (V_{GS}) of the OTFTs with the pentacene and the 0.50% MoO_x-doped pentacene channel layers. According to the previous reports [10,17,18], the deep-lying electronic states of MoO_3 could enhance the hole hopping and hole-injection in organic thin films. Therefore, the reduction of R_C was attributed to that part of holes injected through the doped MoO_x.

Fig. 7 shows the XRD results of the 30-nm-thick various MoO_x-doped pentacene thin films. It could be seen that the crystallinity of the MoO_x-doped pentacene channel layer was kept at the similar performance until the MoO_x doping mole percentage was larger than 0.50%. Table 1 indicated that the output current and mobility of the OTFTs increased, when the doping mole percentage was lower than 0.50%. The performances of these behaviors were mainly affected by an increase of the hole concentration. When the MoO_x doping mole percentage was higher than 0.50%, it could be found that the associated crystallinity significantly degraded with increasing the MoO_x doping amount. When the MoO_x doping percentage increased, the influence of the crystallinity degradation was gradually serious. Therefore, the hole concentration and the hole mobility decreased with an increase of the MoO_x doping mole percentage larger than 0.50% due to the crystallinity degradation. Furthermore, when the MoO_x doping mole percentage was higher than 0.50%, the associated output current and the effective field-effect mobility of the OTFTs decreased with an increase of the MoO_x doping percentage due to the Fermi level pinning effect and the crystallinity degradation. The performance of the OTFTs was mainly affected by the degradation of crystallinity. The maximum output current and the hole mobility were obtained for the 0.50% MoO_x-doped pentacene. It was attributed to the trade-off between the increasing hole concentration and the crystallinity degradation. The results showed that the proper doping percentage of MoO_x could improve the performances of the pentacene-base OTFTs.

The threshold voltage (V_{TH}) of the OTFTs can be calculated using the following equation [19]:

$$V_{TH} = (\Phi_M - \Phi_s) - \frac{1}{C_{OX}}\left(Q_s + \int_0^t \frac{x}{t}\rho_{OX}(x)dx\right), \quad (1)$$

where Φ_M and Φ_s are the work function of the metal and the semiconductor, respectively, C_{OX} is the capacitance of the insulator, Q_s is the interface charge density between the semiconductor channel and the insulator, and $\int_0^t \frac{x}{t}\rho_{OX}(x)dx$ is the insulator charge density per unit volume. From Eq. (1), the V_{TH} value was mainly affected by the work function difference between the metal and the semiconductor channel, and the interface charge density of the semiconductor channel and the insulator. Fig. 5(a) shows that a rigid shift of all these features towards lower binding energy occurs as increasing the doping mole percentage. This phenomenon indicated that a corresponding shift of the Fermi level within the gap approached to the HOMO edge. It revealed that the hole density increased with an increase of the MoO_x mole percentage in the MoO_x-doped pentacene channel layer. Therefore, the increase of the hole concentration of the MoO_x-doped pentacene channel could compensate the crystallinity degradation and decreased the V_{TH} value. The V_{TH} value (-7.8 V) of the OTFTs with 1.39% MoO_x-doped pentacene was about one third of the conventional OTFTs (-21.2 V).

In this study, the electronic structure of the MoO_x was examined using XPS. The XPS spectrum of the Mo 3d was fitted and shown in Fig. 8. The spectrum was characterized by the complex mixture of Mo 3d(3/2) and Mo 3d(5/2) spin doublets molybdenum. The peaks of 228 and 232 eV are Mo 3d(5/2) and Mo 3d(3/2), respectively. The simulation spectra constructed by using Shirley fitting for peaks corresponding Mo 3d(5/2) and Mo 3d(3/2) were also shown in Fig. 8. The Mo 3d(5/2) binding energies of the oxidation

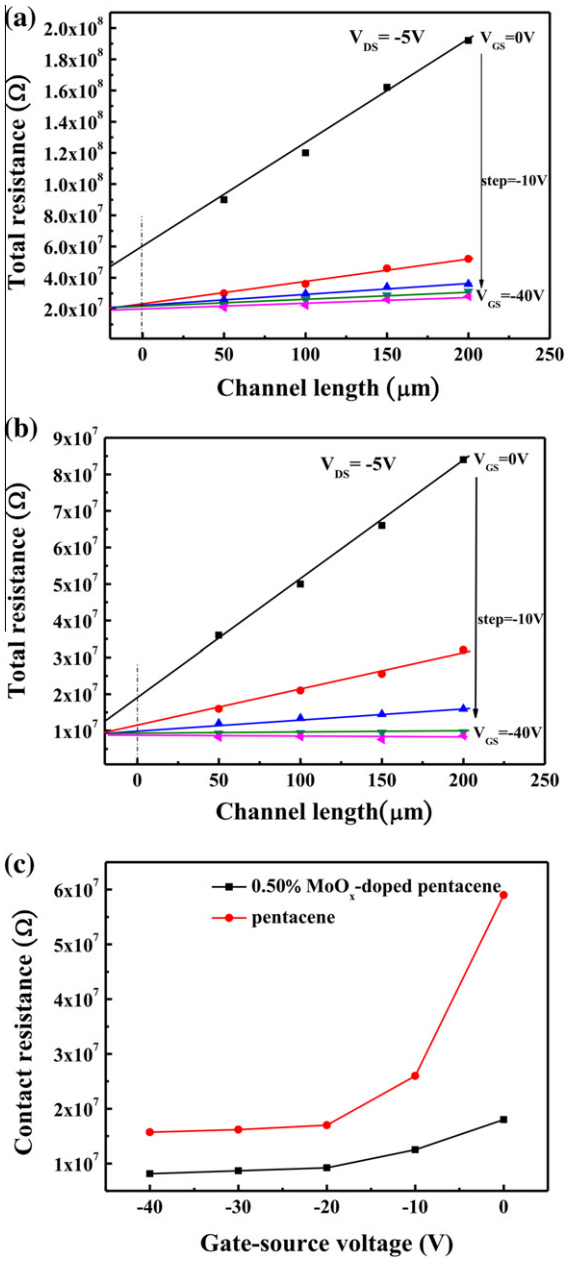

Fig. 6. Total resistance R_T vs. channel length L of: (a) pentacene channel layer and (b) 0.50% MoO_x-doped pentacene channel layer operated at $V_{DS} = -5$ V. (c) Contact resistance as a function of gate-source voltage of pentacene channel layer and 0.50% MoO_x-doped pentacene channel layer.

state of Mo^0, $Mo^{\delta+}$, Mo^{4+}, Mo^{5+}, and Mo^{6+} were located at 227.8, 228.7, 230.0, 231.2, and 232.6 eV, respectively [20–24]. A splitting energy of ~3.1 eV was used for Mo 3d(3/2) and Mo 3d(5/2) doublet [22]. Therefore, the Mo 3d(3/2) binding energies of Mo^0, $Mo^{\delta+}$, Mo^{4+}, Mo^{5+}, and Mo^{6+} were located at 230.9, 231.8, 233.1, 234.3 and 235.7 eV, respectively. The distribution area percentage of the Mo^0, $Mo^{\delta+}$, Mo^{4+}, Mo^{5+}, and Mo^{6+} was about 11.27%, 47.53%, 5.67%, 24.24%, and 11.29% of the total molybdenum, respectively. Based on the above mentioned

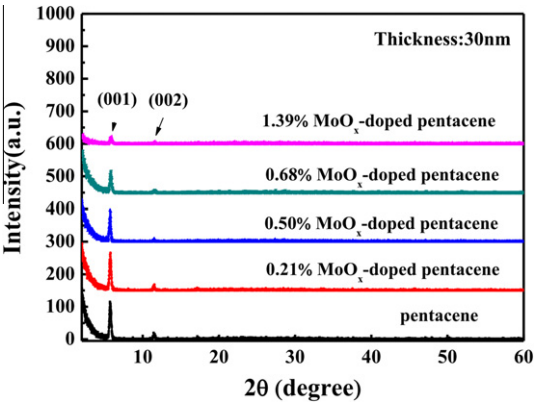

Fig. 7. X-ray diffraction spectra of 30 nm-thick various MoO_x-doped pentacene thin films.

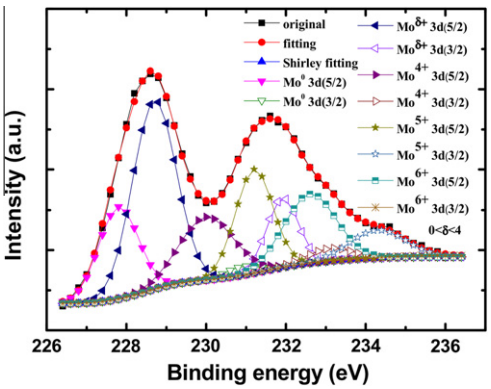

Fig. 8. The XPS spectrum of Mo 3d energy region for Mo oxide.

experimental results, the OTFTs with 0.50% MoO_x-doped pentacene channel layer exhibited the optimal effective field-effect mobility. In the optimal structure of OTFTs, the mole percentage of the Mo^0, $Mo^{\delta+}$, Mo^{4+}, Mo^{5+}, and Mo^{6+} in the 0.50% MoO_x-doped pentacene channel layer was 0.056%, 0.24%, 0.028%, 0.12%, and 0.056%, respectively. It could be found that the mole percentage of MoO_3 was 0.056% in the 0.50% MoO_x-doped pentacene channel layer.

4. Conclusions

Co-thermal evaporation system was used to dope MoO_x into pentacene as the MoO_x-doped pentacene channel layer of the OTFTs. Compared the OTFTs with the 0.50% MoO_x-doped pentacene with the conventional OTFTs, the maximum output current was increased from −11.6 to −37.9 μA, the effective field-effect mobility was enhanced from 0.71 to 1.60 cm^2/V-s, the threshold voltage was reduced from −21.2 to −14.8 V, and the on/off current ratio was slightly decreased from 3.6×10^6 to 1.2×10^6. The performance improvement was attributed to that the HOMO of the MoO_x-doped pentacene gradually approached to the Au work function with increasing the doping percentage of MoO_x, which led to reduce the

contact resistance and to enhance the p-type characteristics of the MoO_x-doped OTFTs by increasing the hole density and enhancing the hole-injection efficiency. However, when the MoO_x doping mole percentage was higher than 0.50%, the associated output current and the effective field-effect mobility of the OTFTs decreased with an increase of the MoO_x doping percentage due to the Fermi level pinning effect, the gradual increase of hole concentration, and significant degradation of crystallinity.

Acknowledgment

This work was supported by the National Science Council of Taiwan, Republic of China under Contract No. NSC 99-2221-E006-106-MY3.

References

[1] W. Fix, A. Ullmann, J. Ficker, W. Clemens, Appl. Phys. Lett. 81 (2002) 1735.
[2] J.H. Oh, P. Wei, Z. Bao, Appl. Phys. Lett. 97 (2010) 243305.
[3] J. Collet, O. Tharaud, A. Chapoton, D. Vuillaume, Appl. Phys. Lett. 76 (2000) 1941.
[4] B.K. Crone, A. Dodabalapur, R. Sarpeshkar, A. Gelperin, H.E. Katz, Z. Bao, J. Appl. Phys. 91 (2002) 10140.
[5] J. Lee, K. Kim, J.H. Kim, S. Im, D.Y. Jung, Appl. Phys. Lett. 82 (2003) 4169.
[6] H. Klauk, M. Halik, U. Zschieschang, G. Schmid, W. Radlik, W. Weber, J. Appl. Phys. 92 (2002) 5259.
[7] M. Halik, H. Klauk, U. Zschieschang, G. Schmid, C. Dehm, M. Schütz, S. Maisch, F. Effenberger, M. Brunnbauer, F. Stellacci, Nature 431 (2004) 963.
[8] Y. Jang, D.H. Kim, Y.D. Park, J.H. Cho, M. Hwang, K. Cho, Appl. Phys. Lett. 88 (2006) 072101.
[9] P.S. Kumar, P. Rai, G.N. Mathur, V.K. Varadan, Proc. SPIE 7646 (2010) 76460M.
[10] M. Kröger, S. Hamwi, J. Meyer, T. Riedl, W. Kowalsky, A. Kahn, Appl. Phys. Lett. 95 (2009) 123301.
[11] H. Nakanotani, H. Kakizoe, C. Adachi, Solid State Commun. 151 (2011) 93.
[12] H. Nakanotani, M. Saito, H. Nakamura, C. Adachi, Appl. Phys. Lett. 95 (2009) 103307.
[13] Y.J. Lin, Y.C. Li, T.C. Wen, L.M. Huang, Y.K. Chen, H.J. Yeh, Y.H. Wang, Appl. Phys. Lett. 93 (2008) 043305.
[14] M. Kröger, S. Hamwi, J. Meyer, T. Riedl, W. Kowalsky, A. Kahn, Org. Electron. 10 (2009) 932.
[15] X. Qiao, J. Chen, X. Li, D. Ma, J. Appl. Phys. 107 (2010) 104505.
[16] H. Ishii, K. Sugiyama, E. Ito, K. Seki, Adv. Mater. 11 (1999) 605.
[17] J. Li, X.W. Zhang, L. Zhang, H. Zhang, X.Y. Jiang, K. Haq, W.Q. Zhu, Z.L. Zhang, Synth. Met. 160 (2010) 376.
[18] D. Kumaki, T. Umeda, S. Tokito, Appl. Phys. Lett. 92 (2008) 013301.
[19] S.M. Sze, K.K. Ng, Physics of Semiconductor Devices, John Wiley & Sons, Inc., Hoboken, NJ, 2007.
[20] P. Marcus, I. Olefjord, Corros. Sci. 28 (1988) 589.
[21] J. Goldwasser, S.M. Fang, M. Houalla, W.K. Hall, J. Catal. 115 (1989) 34.
[22] J.G. Choi, L.T. Thompson, Appl. Surf. Sci. 93 (1996) 143.
[23] A. Cimino, B.A. De Angelis, J. Catal. 36 (1975) 11.
[24] E.J. Markel, J.W. Van Zee, J. Catal. 126 (1990) 643.

that the work function of the cathode metals could be tuned on a large scale by the individual molecular dipoles and the interface dipole formed upon chemisorption of the SAM organic molecules [19,20,26,27], leading to the improvement of device performances.

In our contribution, we discovered that by spin-casting the solvents commonly used to dissolve CPEs and SAMs on top of the organic layer before the deposition of the metal layer, the device performance was significantly enhanced. The quantum efficiency is increased by as large as 58% for low work function Ba/Al cathode. An interface dipole between the cathode and the EL layer induced by the solvent (either from the solvent's intrinsic dipole or the interaction between the solvent and the cathode metal), is identified by the Kelvin Probe Force Microscopy (KPFM) to be responsible for the reduction of the electron injection barrier, and further verified by the photovoltaic measurements. The process of solvent treatment to modify the organic/metal interface is simple, efficient, cost-effective and easy to be adopted in industrial manufacturing.

2. Experiments

Three conjugated polymers PFO ADS 329 (from American Dye Sources, Inc.), P-PPV, and MEH-PPV (both from Canton OLedking Optoelectric Materials Co. Ltd.), were used for device fabrication. While the solvent treatments work for all the polymer devices, we select P-PPV as the representative to demonstrate our work.

Before making the light emitting devices, the ITO substrates were thoroughly cleaned in sequence in ultrasonic bath of acetone, isopropyl alcohol, detergent, de-ionized water, isopropyl alcohol, and went through O_2 plasma for 20 min. A thin layer of PEDOT:PSS was spin-casted in air followed by 10 min' baking at 200 °C in nitrogen. After PEDOT:PSS annealing, a 75 nm thick poly[2-(4-(3′,7′-dimethyloctyloxy)-phenyl)-*p*-phenylenevinylene] (P-PPV) layer was spin-casted from *p*-xylene solution. To treat the organic/metal interface by solvent, 60 μL of the selected solvent were spin-coated on top of the P-PPV layer with the spinning speed of 2000 rpm for 1 min. The device was completed by thermally evaporating the metal cathode consisting of either 4 nm Ba covered by a 120 nm Al in vacuum under a pressure of 3×10^{-4} Pa.

Samples for KPFM measurements were prepared by spin-coating P-PPV on stainless steel pucks 12 mm in diameter, and spin-coating respective solvent on top of the P-PPV film. The KPFM measurements were performed with both single-pass mode and lift-mode on Bruker's Multimode® 8 scanning probe microscope in a customized glove-box (MBraun). SCM-PIT probes (platinum–iridium coating, Bruker) were used throughout the measurements. All the sample preparations and KPFM measurements were carried out inside a nitrogen filled glove-box with both O_2 and H_2O below 0.1 ppm to minimize surface contamination. The CPD images were obtained on a 1×1 μm area, over which the averaged CPD values are used.

For other experiments' details, please refer to the Supplementary data.

3. Results and discussions

To demonstrate the effect of solvent treatment on OLEDs, the green light-emitting conjugated polymer P-PPV, was selected, and two solvents most widely used to dissolve CPEs and SAMs: methanol and ethanol, were chosen with the device structure of ITO/PEDOT (45 nm)/P-PPV (75 nm)/Ba (4 nm)/Al (120 nm). The current density (*J*)–bias (*V*)–luminance (*L*) characteristics, and the luminous efficiency's (LE) dependence on the current density are illustrated in Fig. 1a and b, respectively. Compared with the device without solvent treatment, which has the maximum quantum efficiency (QE) of 6%, LE of 17.0 cd A^{-1} and brightness of 57,291 cd m^{-2}, the device treated with ethanol has the maximum QE of 9.5%, LE of 26.9 cd A^{-1} and brightness of 83,575 cd m^{-2}. The device with methanol treatment exhibits similar performance improvement with the highest brightness of 74,663 cd m^{-2}, LE of 25.3 cd A^{-1} and QE of 9.0%. After modifying the organic/metal interface by ethanol, the maximum quantum efficiency was increased by 58%. Even at high working brightness (3000 cd m^{-2}), the devices treated with ethanol and methanol show a quantum efficiency of 8.5% and 6.6%, respectively.

In order to understand the functions of the organic/metal interface after solvent treatment, electron-only devices were fabricated with structure of ITO/Sn (130 nm)/P-PPV (75 nm)/Ba (4 nm)/Al (120 nm). The *J*–*V* characteristics are depicted in Fig. 1c. With methanol or ethanol treatment, the devices exhibits higher electron current than the device without solvent treatment at the same operation voltage after turn-on. The results indicate that using solvent can greatly improve the electron injection, leading to balanced charge density inside the active layer.

The electron injection improvement is due to the reduction of the electron injection barrier. Photovoltaic measurement is a direct measurement of the built-in potential which scales with the electron injection barrier height on the cathode side, when the anode and the organic layers are identical for all the devices [28]. Fig. 2 shows the *J*–*V* characteristics of the devices under white-light illumination (100 mW cm^{-2}). The open-circuit voltage (V_{OC}) increased from 1.85 V for the untreated Ba/Al device, to 2.10 and 2.20 V for ethanol and methanol treated devices, respectively. The significant enhancement of V_{OC} (0.25 V from ethanol and 0.35 V from methanol) clearly confirms that the electron injection barrier is substantially lowered at the organic/metal interface after interface modification. Reducing electron injection barrier helps electron injection and makes electron and hole density balanced inside the EL layer, improving the device performance as evidenced in Fig. 1b.

Some groups have reported that a change in molecular orientation can affect the work function/ionization energy [29]. In our studies, the polymers are PPV and PFO based which are nonpolar or low polar materials. They form stable and smooth films by spin-coating their solutions in the non-polar solvents such as *p*-xylene. Moreover, those polymers are not soluble in either ethanol or methanol. Therefore, it is highly unlikely that spin-coating a small amount of ethanol/methanol on a dense solid film could change the

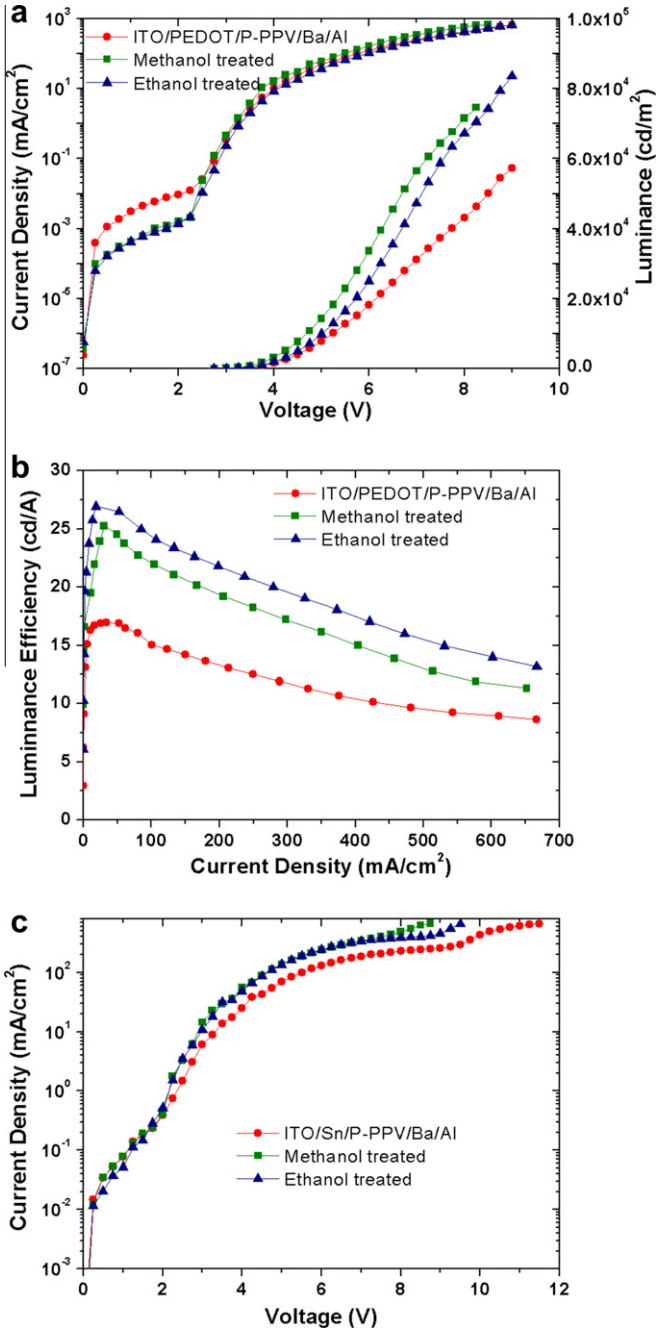

Fig. 1. (a) *J*–*L*–*V* and (b) LE–*J* characteristics of light-emitting devices with and without solvent treatment. (c) *J*–*V* characteristics of electron-only devices.

polymer molecule's orientation. We believe that the origin of the electron barrier reduction could be attributed to an interface dipole induced by the solvent. The dipole raises the vacuum level of the cathode, thereby reducing the electron injection barrier [30,31].

There are three possible mechanisms for dipole formation at the organic/metal interface: (1) interaction between the solvent and the polymer; (2) the solvent's intrinsic dipole; and (3) interaction between the solvent and the cathode. To study the interaction between the solvent and the polymer, the UV–Visible absorption, photoluminescence (PL) and electroluminescence (EL) spectra are carefully examined. The indistinguishable UV–Visible spectra obtained from the polymer films with and without solvent treatment (Fig. S1a) indicates that the solvent treatment did not change the ground-states of the bulk light-emitting materials. The identical PL spectra (Fig. S1a) and EL spectra (Fig. S1b) suggest that the application of solvent did not alter the excited-states of the bulk light-emitting materials. No difference in the atomic force microscopy (AFM) images and roughness of the active layer surface was found in the films with and without solvent treatment, implying that

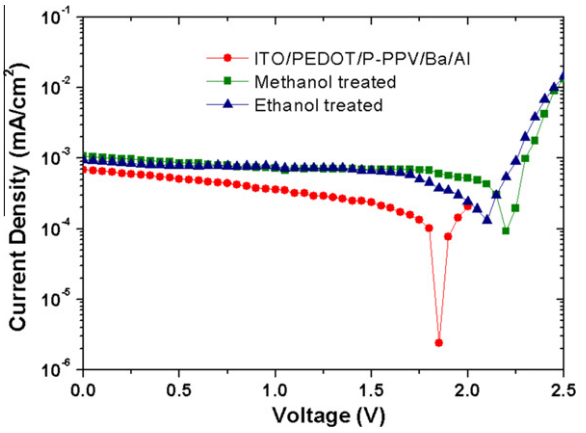

Fig. 2. Photovoltaic characteristics of the devices with and without solvent treatment.

the solvent did not modify the polymer film's morphology (Fig. S2). The film thickness also remained unchanged after solvent treatment. Adding the fact that the PL efficiencies of the neat P-PPV film with and without exposure to the methanol or ethanol are the same (Table S1), we conclude that even if there is interaction between the solvent and the polymer, the interaction is neither powerful enough to alter the polymer's bulk properties, nor strong enough to be detected by our currently available characterization techniques.

The existence of the solvent's intrinsic dipole on the organic surface can be directly verified by Kelvin Probe Force Microscopy. KPFM is used extensively to measure the surface potential at nanometer scale on various materials [32,33]. Before the solvent treatment, the contact potential difference (CPD) between the KPFM tip and the P-PPV surface is 0.499 V. After spin-coating the solvents, the CPD became 0.753 and 0.849 V for ethanol and methanol treated surfaces, respectively. The CPD images are shown in

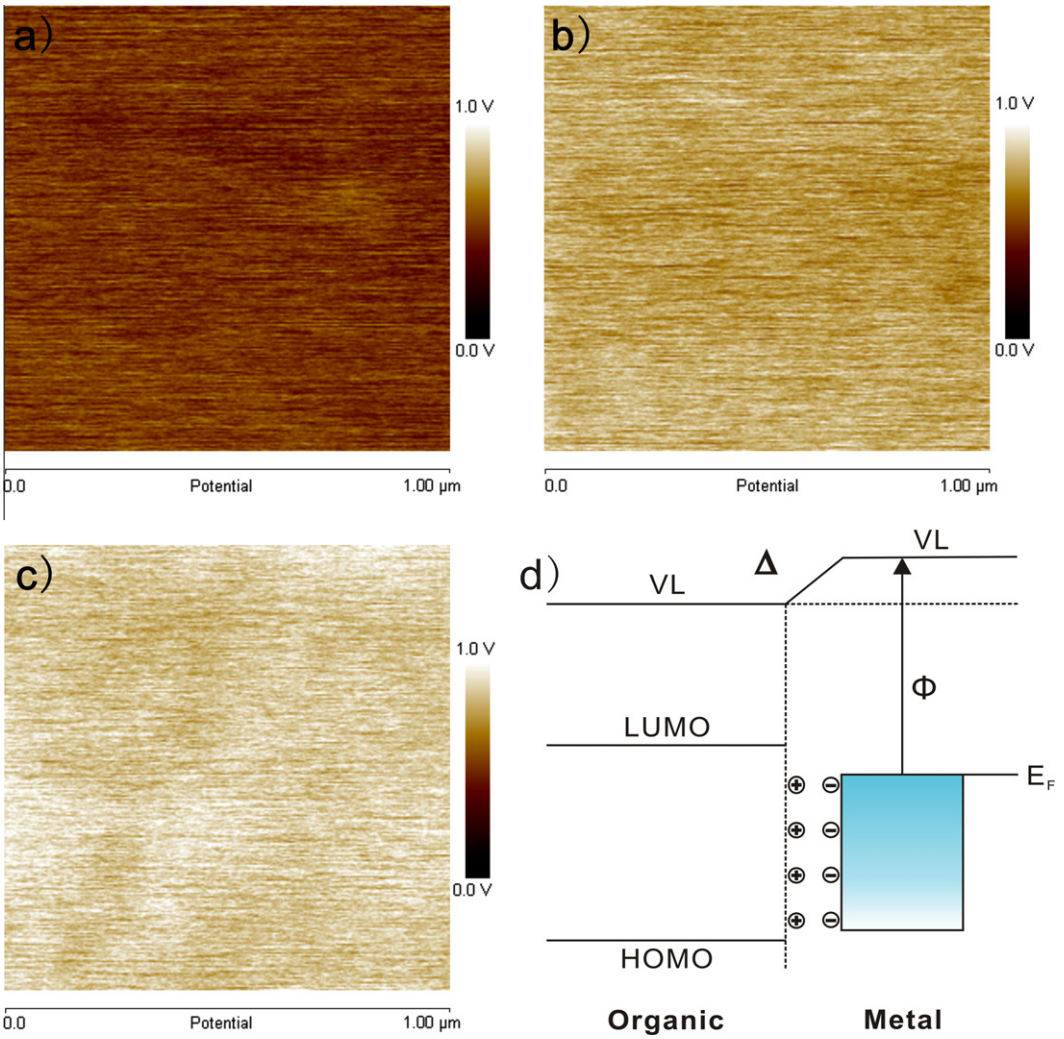

Fig. 3. Contact potential difference (CPD) images of P-PPV films (a) without solvent treatment, (b) with ethanol and (c) with methanol treatment. (d) The interfacial energy diagram of organic/metal interface with solvent treatment obtained from KPFM. Δ is the shift of VL and Fermi level (E_F) of the cathode by the interface dipole, and Φ denotes the metal's work function.

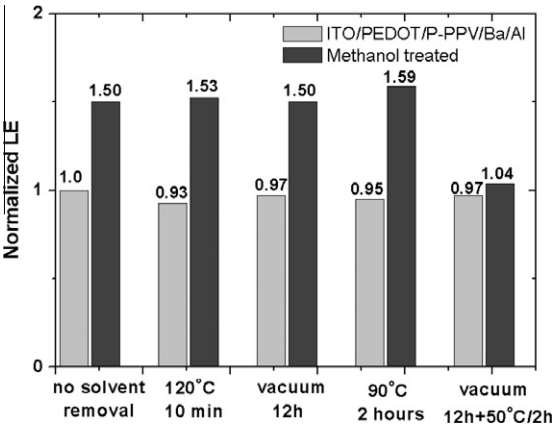

Fig. 4. Luminous efficiency of the light emitting devices with and without methanol treatment undergoing different solvent removal processes. All the LEs are normalized to the LE of the device without methanol treatment or any solvent removal process.

Fig. 3. The increase of CPD shows the surface potential of P-PPV is increased suggesting that the vacuum level (VL) of the cathode is correspondingly elevated by the solvent's intrinsic dipole as schematically illustrated in Fig. 3d. Of note, the 0.254 and 0.35 V surface potential increases are in precise agreement with the exact results of the photovoltaic measurements, which clearly demonstrates the solvent's dipole formation at the organic/metal interface.

It is well-known that the solvent can react with metal to release the metal ions. For example, the alcohol can react with low work function metal, such as Ba or Ca, to produce metal salt. Since the interaction between the solvents and the metal cannot be excluded, the interface dipole induced by the solvents is probably a result of the combined effects of the interaction between the solvent and the cathode metal, and the solvent's intrinsic dipole. Further experiments are being carried out to pin down the exact dipole formation mechanism.

Though the solvent did not change the polymer's bulk properties, it is difficult to remove the solvent completely from the organic surface. The most common solvent removal processes are vacuuming for 12 h [24], baking at either 80 or 120 °C for 10 min, and annealing at 90 °C for 2 h [15,34,35] before the cathode deposition. Our experiments showed that those solvent removal processes did not succeed in removing solvent. As depicted in Fig. 4, after spin-casting the methanol, the devices which went through the said solvent removal processes exhibited almost the same performances as those from the devices without undergoing the solvent removal processes. We found out that only by vacuuming the solvent treated devices at 10^{-4} Pa for 12 h followed by vacuum baking at 50 °C for 2 h before cathode deposition, the improved performance of devices treated with methanol returned to that of the devices without solvent treatment.

4. Summary

Reducing the electron injection barrier at the organic/metal interface to improve the OLED efficiency, and modifying that interface through surface engineering materials, such as CPE, SAM, surfactants, or metal compounds, become a hot research area. Our discovery shows that solvent treatment on the organic active layer can effectively modify organic/metal interface and improve the electron injection. In Ba/Al cathode devices, the quantum efficiency could be increased by 58%. KPFM and photovoltaic measurements demonstrate the existence of the interface dipole which lifts the vacuum level on the metal side, hence reducing the electron injection barrier, and enhancing the device performance.

Acknowledgments

The authors are deeply grateful to the Ministry of Science and Technology (973 Program 2009CB623604, 2009CB930604, and 863 Program 2008AA03A311), and National Nature Science Foundation of China (61076116) for their financial supports.

Appendix A. Supplementary data

Supplementary data associated with this article can be found, in the online version, at doi:10.1016/j.orgel.2011.07.021.

References

[1] J.H. Burroughes, D.D.C. Bradley, A.R. Brown, R.N. Marks, K. Mackay, R.H. Friend, P.L. Burns, A.B. Holmes, Nature 347 (1990) 539.
[2] Y. Cao, I.D. Parker, G. Yu, C. Zhang, A.J. Heeger, Nature 397 (1999) 414.
[3] R.H. Friend, R.W. Gymer, A.B. Holmes, J.H. Burroughes, R.N. Marks, C. Taliani, D.D.C. Bradley, D.A. Dos Santos, J.L. Bredas, M. Logdlund, W.R. Salaneck, Nature 397 (1999) 121.
[4] D. Braun, A.J. Heeger, Appl. Phys. Lett. 58 (1991) 1982.
[5] I.D. Parker, Y. Cao, C.Y. Yang, J. Appl. Phys. 85 (1999) 2441.
[6] L.S. Hung, C.W. Tang, M.G. Mason, Appl. Phys. Lett. 70 (1997) 152.
[7] X.H. Yang, Y.Q. Mo, W. Yang, G. Yu, Y. Cao, Appl. Phys. Lett. 79 (2001) 563.
[8] F. Li, H. Tang, J. Anderegg, J. Shinar, Appl. Phys. Lett. 70 (1997) 1233.
[9] Q.F. Xu, J.Y. Ouyang, Y. Yang, T. Ito, J. Kido, Appl. Phys. Lett. 83 (2003) 4695.
[10] J.S. Huang, G. Li, E. Wu, Q.F. Xu, Y. Yang, Adv. Mater. 18 (2006) 114.
[11] Y. Cao, G. Yu, A.J. Heeger, Adv. Mater. 10 (1998) 917.
[12] Y.H. Niu, H. Ma, Q.M. Xu, A.K.Y. Jen, Appl. Phys. Lett. 86 (2005) 083504.
[13] Y.H. Niu, A.K.Y. Jen, C.F. Shu, J. Phys. Chem. B 110 (2006) 6010.
[14] C.V. Hoven, A. Garcia, G.C. Bazan, T.Q. Nguyen, Adv. Mater. 20 (2008) 3793.
[15] Y.H. Xu, R.Q. Yang, J.B. Peng, A.A. Mikhailovsky, Y. Cao, T.Q. Nguyen, G.C. Bazan, Adv. Mater. 21 (2009) 584.
[16] Y. Zhang, F. Huang, Y. Chi, A.K.Y. Jen, Adv. Mater. 20 (2008) 1565.
[17] F. Huang, Y. Zhang, M.S. Liu, A.K.Y. Jen, Adv. Funct. Mater. 19 (2009) 2457.
[18] I.H. Campbell, S. Rubin, T.A. Zawodzinski, J.D. Kress, R.L. Martin, D.L. Smith, N.N. Barashkov, J.P. Ferraris, Phys. Rev. B. 54 (1996) 14321.
[19] P.C. Rusu, G. Brocks, Phys. Rev. B. 74 (2006) 073414.
[20] G. Heimel, L. Romaner, E. Zojer, J.L. Bredas, Nano. Lett. 7 (2007) 932.
[21] H.B. Wu, F. Huang, Y.Q. Mo, W. Yang, D.L. Wang, J.B. Peng, Y. Cao, Adv. Mater. 16 (2004) 1826.
[22] H.B. Wu, F. Huang, J.B. Peng, Y. Cao, Org. Electron. 6 (2005) 118.
[23] L. Wang, B. Liang, F. Huang, J.B. Peng, Y. Cao, Appl. Phys. Lett. 89 (2006) 151115.
[24] C.V. Hoven, R.Q. Yang, A. Garcia, V. Crockett, A.J. Heeger, G.C. Bazan, T.Q. Nguyen, Proc. Natl. Acad. Sci. 105 (2008) 12730.
[25] C. Hoven, R. Yang, A. Garcia, A.J. Heeger, T.Q. Nguyen, G.C. Bazan, J. Am. Chem. Soc. 129 (2007) 10976.
[26] B. de Boer, A. Hadipour, M.M. Mandoc, T. van Woudenbergh, P.W.M. Blom, Adv. Mater. 17 (2005) 621.
[27] M.L. Sushko, A.L. Shluger, J. Phys. Chem. B 111 (2007) 4019.

[28] C.J. Brabec, A. Cravino, D. Meissner, N.S. Sariciftci, T. Fromherz, M.T. Rispens, L. Sanchez, J.C. Hummelen, Adv. Funct. Mater. 11 (2001) 374.
[29] M.P. Nikiforov, U. Zerweck, P. Milde, C. Loppacher, T.-H. Park, H.T. Uyeda, M.J. Therien, L. Eng, D. Bonnell, Nano. Lett. 8 (2008) 110.
[30] H. Ishii, K. Sugiyama, E. Ito, K. Seki, Adv. Mater. 11 (1999) 605.
[31] S. Braun, W.R. Salaneck, M. Fahlman, Adv. Mater. 21 (2009) 1450.
[32] W. Melitz, J. Shen, A.C. Kummel, S. Lee, Surf. Sci. Rep. 66 (2011) 1.
[33] M. Nonnenmacher, M.P. Oboyle, H.K. Wickramasinghe, Appl. Phys. Lett. 58 (1991) 2921.
[34] F. Huang, Y.H. Niu, Y. Zhang, J.W. Ka, M.S. Liu, A.K.Y. Jen, Adv. Mater. 19 (2007) 2010.
[35] W.L. Ma, P.K. Iyer, X. Gong, B. Liu, D. Moses, G.C. Bazan, A.J. Heeger, Adv. Mater. 17 (2005) 274.

and the interfacial layer. For example, charge trapping by the nanosized domains in the ZnO or TiO_2 layer fabricated by the sol–gel process can reduce the photovoltaic efficiency. Cs_2CO_3 and Al_2O_3 are insulators, so they can form an energy barrier for the electron transport from the active layer to ITO if they are too thick.

Here, we report inverted PSCs with PbO-modified ITO as the cathode. PbO was selected as the interfacial material because PbO is a semiconductor and has interesting optical properties [23–26]. It exhibits photoactivity over a wide range of wavelengths, so it can be used in imaging devices, electrophotography and electroradiography. It will be interesting to integrate this optically active material in solar cells. In addition, PbO can be easily processed by thermal evaporation [27–29]. Wang et al. used PbO/Al as the electron injection electrode in highly efficient organic light-emitting diodes [29]. We found that a high-quality PbO film could be readily deposited on ITO and it could effectively reduce the work function of ITO to 3.8 eV. The optimal inverted PSCs of P3HT:PCBM (P3HT = poly(3-hexylthiophene), PCBM = [6,6]-phenyl-C_{61}-butyric acid methyl ester) with PbO-modified ITO as the cathode exhibited a photovoltaic efficiency of 4.0%, which was even higher than that (3.5%) of control PSCs with normal architecture.

2. Experimental

2.1. Materials and fabrication of inverted PSCs

ITO glass with a sheet resistance of 15 Ω/v was purchased from Nikko Materials Co. All chemical regents, including P3HT, PCBM and PbO with a light yellow color and a purity of 99.999%, were obtained from Sigma–Aldrich. All chemicals were used as received.

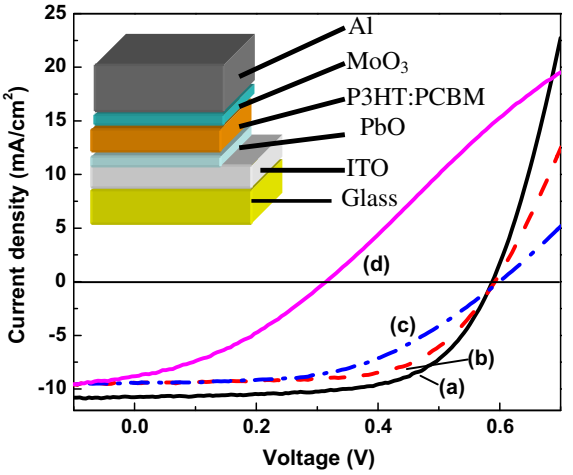

Fig. 1. *J–V* characteristics of PSCs under simulated AM1.5G illumination. (a) Inverted PSC, ITO/PbO/P3HT:PCBM (230 nm)/MoO_3/Al, (b) normal PSC, ITO/PEDOT:PSS/P3HT:PCBM (180 nm)/LiF/Al, (c) normal PSC, ITO/PEDOT:PSS/P3HT:PCBM (230 nm)/LiF/Al, and (d) inverted PSC, ITO/P3HT:PCBM (230 nm)/MoO_3/Al. The PbO thickness was 1 nm for device (a). The active layer of devices (a), (c) and (d) was prepared from 1,2-dichlorobenzene solution consisting of 25 mg ml^{-1} P3HT and 25 mg ml^{-1} PCBM, while the active layer of device (b) was coated from 1,2-dichlorobenzene solution consisting of 17 mg ml^{-1} P3HT and 17 mg ml^{-1} PCBM. The inset shows the architecture of inverted PSCs.

The architecture of inverted PSCs is presented in the inset of Fig. 1. The devices were fabricated through the following process. ITO glass substrates patterned with only half of the substrate surface covered with ITO were successively rinsed with detergent, de-ionized water, acetone, and isopropyl alcohol. Each rinsing step was carried out in an ultrasonic bath for 10 min. The cleaned and dried ITO glass substrates were treated with UV-ozone (JeLight UV Ozone cleaner 42) for 15 min before the deposition of PbO. A thin PbO layer was thermally deposited on ITO in a chamber of 1.6×10^{-6} mbar. The thickness of the PbO layer was controlled from 0.5 to 2.5 nm. Then, the ITO glass substrates deposited with PbO were transferred into a glove box filled with dried nitrogen. A 1,2-dichlorobenzene solution consisting of 25 mg ml^{-1} P3HT and 25 mg ml^{-1} PCBM was spin coated at 600 rpm for 40 s. The P3HT:PCBM films were slowly dried in covered petri dishes at room temperature. The dried P3HT:PCBM films had a thickness of *ca.* 230 nm. The P3HT:PCBM films were subsequently annealed at 120 °C for 10 min. The devices were completed by thermally depositing a 5 nm-thick MoO_3 layer and subsequently a 100 nm-thick Al layer on the P3HT:PCBM layer.

2.2. Characterizations of PSCs and materials

The PSCs were encapsulated in the glove box with a UV-curable epoxy and glass sheets and then taken out for the electrical testing. The photovoltaic performance of the devices was measured with a computer-programmed Keithley 2400 source/meter under a Newport Oriel class A solar simulator, which simulated the AM1.5G sunlight (100 mW cm^{-2}) and was certified to the JIS C 8912 standard. A Schott visible-color glass-filtered (KG5 color filtered) Si diode (Hamamatsu S1133) was used as a reference cell to correct the mismatch between the lamp and the AM1.5G solar spectrum. The active area of each device is 0.11 cm^2. Incident photon-to-current conversion efficiencies (IPCEs) of PSCs were measured with a 300 W Xenon Lamp (Oriel 6258) and a Cornerstone 260 Oriel 74125 monochromator.

The UV–Vis absorption spectra were acquired with a Shimadzu UV-1800 spectrometer. The X-ray diffraction (XRD) data were obtained with a Bruker D8 powder XRD diffractometer system. The Raman spectra were collected in a back scattering configuration with a Jobin Yvon Horiba LabRam HR800 Raman system using a 514.5 nm Ar^+ laser as the excitation source. The laser power was 2 mW, and the resolution was 2.4 cm^{-1}. The accumulation time for each sample was 900 s. X-ray photoelectron spectra (XPS) were taken using an Axis Ultra DLD X-ray photoelectron spectrometer with an Al K_α X-ray source (1486.6 eV). Ultraviolet photoelectron spectra (UPS) were collected using a VG ESCA 220i-XL Imaging UPS with the He I emission (21.2 eV) as the light source. The resolution of both XPS and UPS was 0.1 eV. Atomic force microscopic (AFM) images were acquired using a Veeco NanoScope IV Multi-Mode AFM with the tapping mode. The thicknesses of the polymer films were measured using an Alpha-Step IQ surface profiler.

Table 1
Photovoltaic performance of inverted and normal PSCs.

PSC	J_{sc} (mA cm^{-2})	V_{oc} (V)	*FF*	*PCE* (%)	R_s (Ω cm^2)	R_{sh} (Ω cm^2)
ITO/P3HT:PCBM/MoO_3/Al	8.80	0.31	0.355	0.98	22.3	102
ITO/PbO/P3HT:PCBM/MoO_3/Al[a]	10.8	0.59	0.632	4.00	3.70	9700
ITO/PEDOT:PSS/P3HT:PCBM/LiF/Al[b]	9.43	0.60	0.510	2.89	14.3	1000
ITO/PEDOT:PSS/P3HT:PCBM/LiF/Al[c]	9.42	0.59	0.625	3.50	6.20	2370

[a] The PbO thickness was 1 nm.
[b] The P3HT:PCBM layer was spin coated from a 1,2-chlorobenzene solution consisting of 25 mg ml^{-1} P3HT and 25 mg ml^{-1} PCBM.
[c] The P3HT:PCBM layer was spin coated from a 1,2-chlorobenzene solution consisting of 17 mg ml^{-1} P3HT and 17 mg ml^{-1} PCBM.

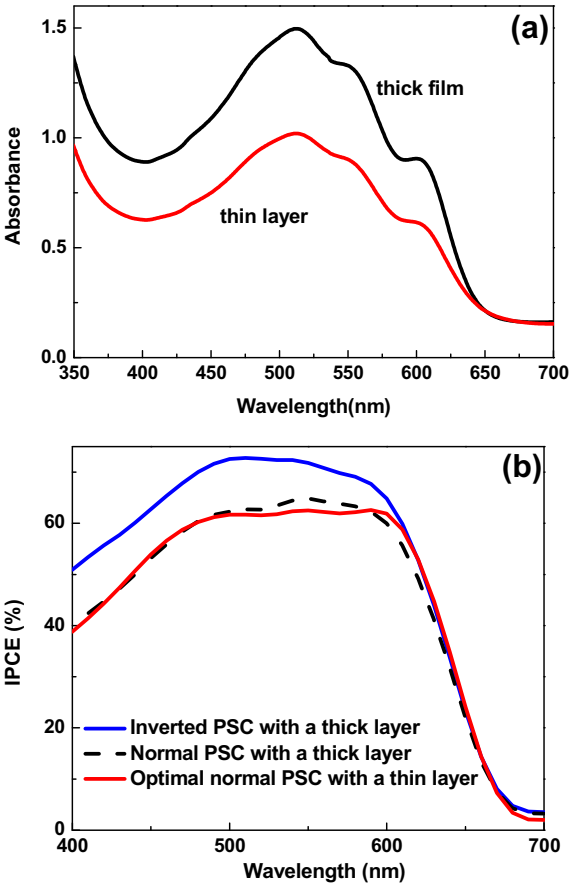

Fig. 2. (a) UV–Vis absorption spectra of P3HT:PCBM films. The thick film was prepared from 1,2-dichlorobenzene solution consisting of 25 mg ml^{-1} P3HT and 25 mg ml^{-1} PCBM, and the thin film from a solution of 17 mg ml^{-1} P3HT and 17 mg ml^{-1} PCBM. (b) IPCEs of inverted and normal PSCs. The thick and thin P3HT:PCBM layers of PSCs were prepared by spin coating the same solutions as for the thick and thin P3HT:PCBM films in (a).

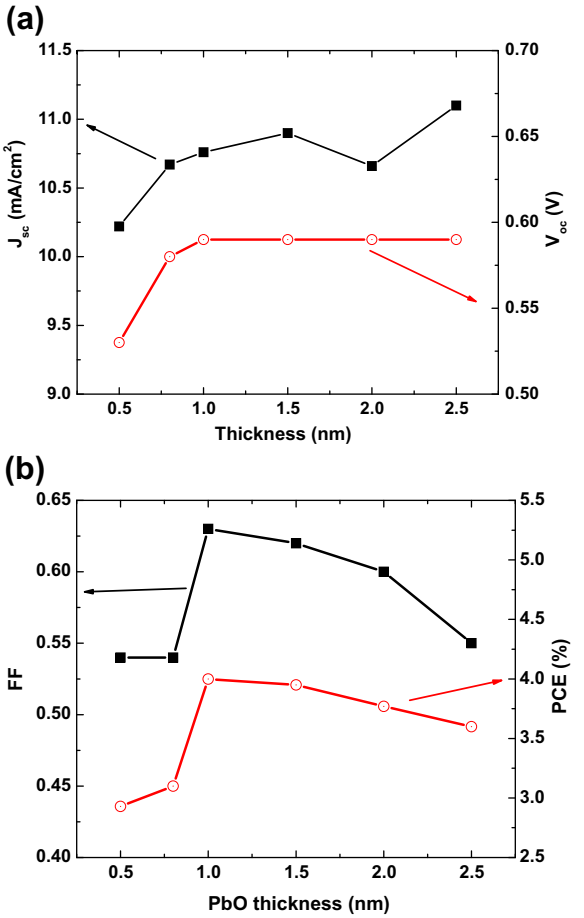

Fig. 3. Variations of (a) J_{sc} and V_{oc} and (b) FF and PCE of inverted PSCs ITO/PbO/P3HT:PCBM/MoO_3/Al with the thickness of the PbO layer.

3. Results and discussion

3.1. Inverted PSCs with PbO-modified ITO as the cathode

More than 50 inverted PSCs were investigated. Their photovoltaic performance had good reproducibility. Fig. 1 shows the current density (*J*)–voltage (*V*) curves of an inverted PSC with ITO modified with a 1 nm-thick PbO layer as the cathode under AM 1.5G illumination (curve *a*). The *J*–*V* curve of a control inverted PSC with unmodified ITO as the cathode is also presented for comparison (curve *d*). The photovoltaic performances of these devices, including open-circuit voltage (V_{oc}), short-circuit current density (J_{sc}), fill factor (FF) and PCE, are summarized in Table 1. The inverted PSC with PbO-modified ITO exhibited high ph otovoltaic performances: V_{oc} = 0.59 V, J_{sc} = 10.8 mA cm^{-2}, FF = 0.632, and PCE = 4.00%. The photovol ta ic performance is much higher than the control inverted PSC. The PbO layer on ITO particularly improves the V_{oc} and FF values, which are only 0.314 V and 0.355 for the control inverted PSC.

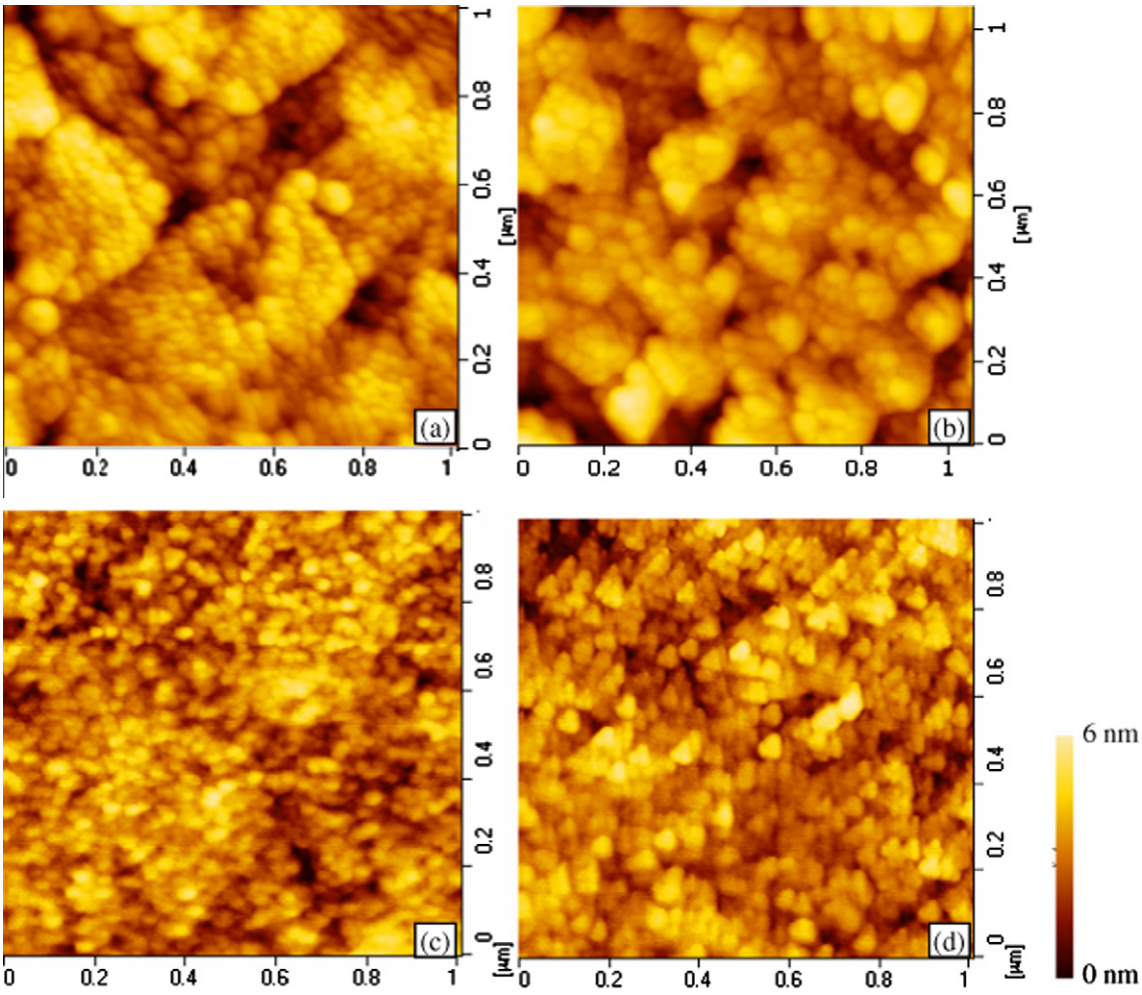

Fig. 4. AFM images of ITO substrates (a) unmodified and modified with a PbO layer of (b) 0.5 nm, (c) 1 nm, and (d) 2.5 nm in thickness.

The effect of the ITO surface modification on the photovoltaic performance is related to its effect on the shunt (R_{sh}) and series resistances (R_s) [30,31]. R_{sh} and R_s were estimated in terms of the slopes of the *J*–*V* curves at 0 and 0.7 V, respectively. The low V_{oc} value of the PSC with unmodified ITO indicates the non-ohmic contact between the active layer and the ITO electrode. The deviation of the *J*–*V* curve from the ideal solar cell model suggests that the R_s and R_{sh} values obtained in terms of the slopes at 0 and 0.7 V of the *J*–*V* curves are not so meaningful. But we still present these values in Table 1 to get some sense about the dependence of the apparent R_s and R_{sh} values on the work function of the electrode. They are 103 and 22.3 $\Omega\,cm^{-2}$, respectively, for the control inverted PSC with unmodified ITO. R_s decreases to 2.3 $\Omega\,cm^{-2}$, whereas R_{sh} increases to 9700 $\Omega\,cm^{-2}$ for the inverted PSC with PbO-modified ITO. These changes suggest that PbO helps the electron collection while suppresses the leakage current.

Fig. 1 also illustrates the *J*–*V* curves of two control PSCs with normal architecture. They were fabricated through a similar process. They have ITO coated with PEDOT:PSS as the anode and LiF/Al as the cathode. The active layers of the two normal PSCs were prepared from solutions of different P3HT and PCBM concentrations. One was coated from the same solution as for the inverted PSCs, whereas another was prepared from a 1,2-dichlorobenzene solution consisting of 17 mg ml^{-1} P3HT and 17 mg ml^{-1} PCBM. The latter solution is the optimal one for the normal PSCs. The PCEs of the two normal PSCs are 2.89% and 3.50%, respectively (Table 1). The efficiency of 3.50% is reasonable for normal P3HT:PCBM PSCs, though it is lower than that reported by Li et al. [32]. Both PCEs are remarkably lower than that of the inverted PSC with PbO-modified ITO. The main differences in the photovoltaic performances between the normal and inverted PSCs are the J_{sc} and FF values.

Presumably, the high PCE of the inverted PSC is related to the thick P3HT:PCBM layer [33]. It is thicker than the optimal thickness (180 nm) of the active layer for normal PSCs, so that more light can be absorbed. As shown in Fig. 2a, the absorption of the thick P3HT:PCBM film prepared from the 1,2-dichlorobenzene solution consisting of 25 mg ml^{-1} P3HT and 25 mg ml^{-1} PCBM is remarkably higher than that

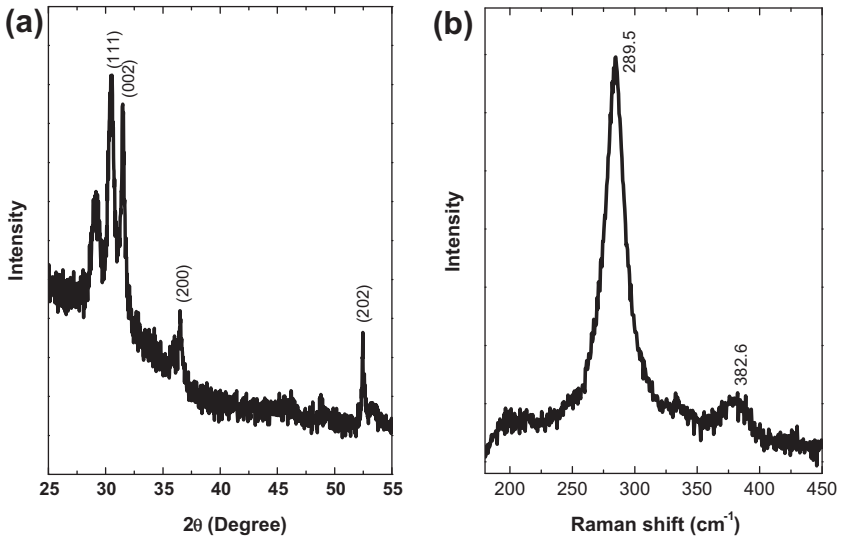

Fig. 5. (a) XRD and (b) Raman spectrum of a PbO film thermally deposited.

of the thin P3HT:PCBM film prepared from the solution consisting of 17 mg ml^{-1} P3HT and 17 mg ml^{-1} PCBM.

IPCE of the inverted PSC is saliently higher than that of the normal PSC with the P3HT:PCBM active layer of the same thickness (Fig. 2b). Because the integration of the product of the IPCE with the photon flux density over the whole range is related to J_{sc} of a PSC, the IPCEs of the two PSCs are consistent with their J_{sc} values. The main reason for the difference in the photovoltaic performances of inverted and normal PSCs is related to the distribution of P3HT and PCBM in the active layer along the vertical direction. As reported in literature, there is a vertical phase separation in the active layer [34–36]. The vertical phase separation is related to the difference in the surface energies of the polymer donor and organic acceptor. P3HT has a lower surface energy than PCBM, so it tends to accumulate at the air surface while PCBM is rich at the bottom of the active layer. The vertical phase separation can become more significant on ITO/PbO than ITO/PEDOT:PSS, because the former is more hydrophilic than the latter. As the results of the vertical phase separation, both the hole transport along P3HT into the top electrode and the electron transport along PCBM into the bottom electrode are promoted. Thus, the inverted architecture can benefit both the electron and hole collections.

Though the thick P3HT:PCBM film can absorb more light than the thin P3HT:PCBM film, the IPCEs of the normal PSCs with the thick and thin P3HT:PCBM active layers are comparable. This is also consistent with their J_{sc} values. The different PCEs for these two normal PSCs can be attributed to the low charge carrier mobilities. As mentioned above, there is a vertical phase separation in the active layer of both normal and inverted PSCs. PCBM accumulates at the bottom while P3HT accumulates at the top. Thus, the electrons transporting along PCBM to the bottom electrode can have a higher mobility than to the top electrode, while the holes transporting along P3HT to the top electrode is easier than to the bottom electrode. This can explain that the optimal P3HT:PCBM thickness of normal PSCs is lower

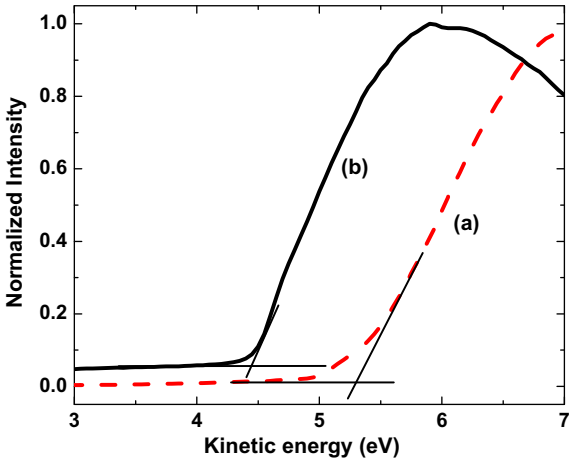

Fig. 6. UPS spectra of ITO substrates (a) unmodified and (b) modified with a 1 nm-thick PbO layer.

than that of inverted PSCs. The normal PSC with a thick P3HT:PCBM layer has higher R_s than that with a thin P3HT:PCBM layer. Though more light can be absorbed in the thicker layer, more charges get lost, giving rise to lower FF and PCE [37].

PbO films with different thicknesses were deposited on ITO substrates to study the PbO thickness effect on the photovoltaic performance of the inverted PSCs. Fig. 3 illustrates the variations of J_{sc}, V_{oc}, FF and PCE of the inverted PSCs with the thickness of the PbO layer. All four parameters increase with the increase of the PbO thickness when the thickness is below 1 nm. Presumably, PbO can fully cover all the ITO surface after its thickness is 1 nm or above. When the PbO layer is thicker than 1 nm, J_{sc} becomes insensitive to the further increase in the PbO thickness, and V_{oc} becomes flat. But both FF and PCE decrease with the further increase of the PbO layer. This can be

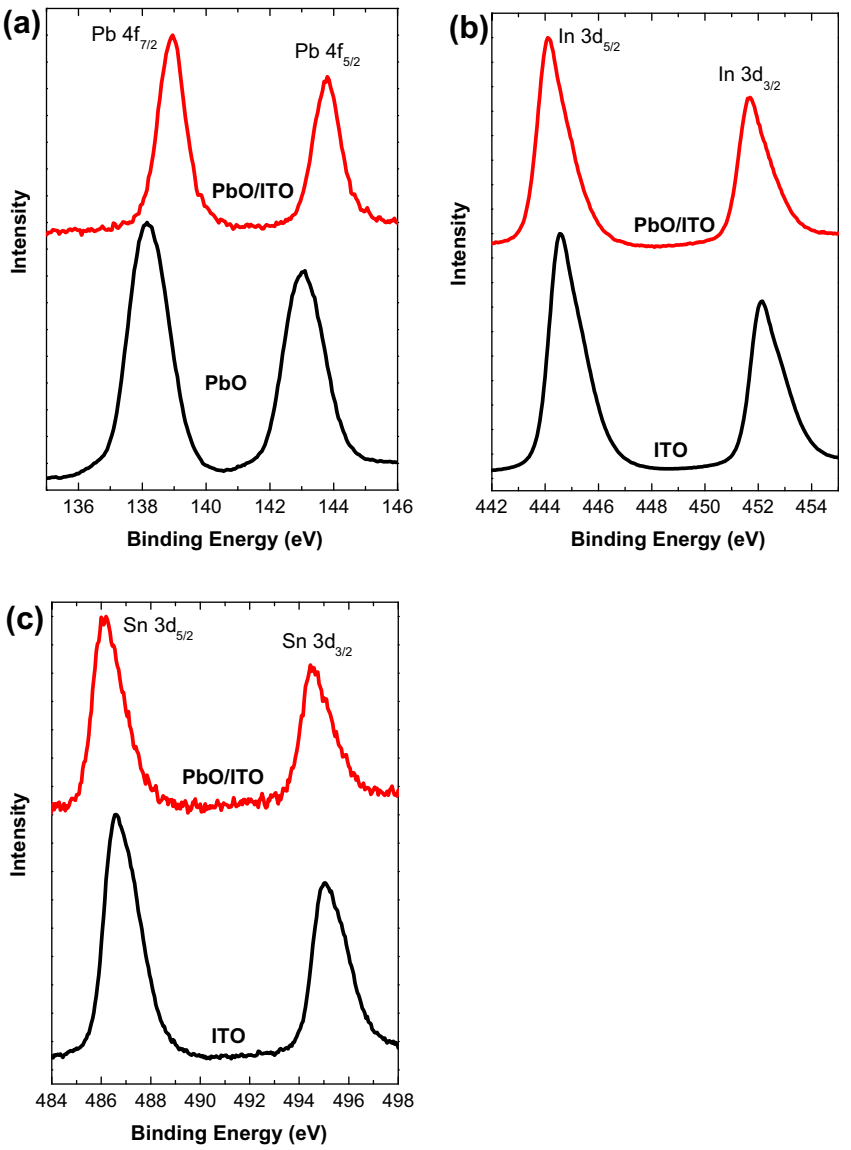

Fig. 7. XPS spectra of (a) Pb $4f_{7/2}$ and $4f_{5/2}$ of PbO and PbO/ITO, (b) In $3d_{5/2}$ and $3d_{3/2}$ of PbO/ITO and ITO, and (c) Sn $3d_{5/2}$ and $3d_{3/2}$ of PbO/ITO and ITO.

attributed to the resistance for the charge transport through the PbO layer.

Photovoltaic performance of PSCs depends on the charge collections at the anode and cathode. They are affected by the surface morphology of the cathode [38,39]. The morphology of the blank and PbO-modified ITO substrates was studied by AFM (Fig. 4). The blank ITO has a quite rough surface with a RMS roughness of 3.3 nm. The ITO surface becomes smoother after the deposition of a PbO layer. The RMS roughness reduces to 3.0, 0.9, and 1.0 nm for ITO substrates deposited with a PbO layer with a thickness of 0.5, 1.0 and 2.5 nm, respectively. These AFM images suggest that a 0.5 nm-thick PbO layer cannot fully cover the ITO surface while a PbO layer with a thickness of 1 nm or above can fully cover the surface. They are consistent with the photovoltaic performance of the corresponding inverted OPVs.

3.2. Mechanism for PbO on the work function of ITO

The high V_{oc} and PCE of the inverted PSCs suggest that the PbO-modified ITO can effectively collect electrons. There are two possible reasons accounting for it. One reason is that PbO can collect electrons like TiO_2 and ZnO, and another is that the work function of ITO is reduced through the PbO modification.

PbO has two kinds of crystalline structures, α-PbO with a tetragonal structure and β-PbO with an orthorhombic structure. The two PbO structures have different electronic structures. β-PbO has a band gap of 2.5–2.7 eV, whereas α-PbO has a band gap of 1.8–2.0 eV [40–42]. The two crystalline structures can be distinguished by XRD and Raman spectroscopy. XRD data indicate that PbO used in this study is β-PbO (Fig. 5a) [43,44]. This is confirmed by the

Raman spectrum of PbO (Fig. 5b) [45]. The Raman bands at 289.5 and 382.6 cm^{-1} are the A_g and B_{1g} modes of β-PbO.

The conduction and valence bands of β-PbO are 4.02 and 6.82 eV, respectively [46]. The conduction band is lower than the LUMO of PCBM that is 3.7–3.9 eV [47,48]. Thus, the hot electron transport from PCBM into a layer of β-PbO alone can cause energy loss during the electron collection. The work function of PbO-modified ITO substrates was investigated by UPS (Fig. 6). The cut-off edge of the PbO-modified ITO has a kinetic energy lower than that of the unmodified ITO by 0.9 eV. This indicates that the work function of the PbO-modified ITO is lower than that of unmodified ITO by 0.9 eV. Because the work function of unmodified ITO is 4.4–4.7 eV [49,50], the PbO-modified ITO substrates should have a work function of 3.5–3.8 eV. Thus, the effective electron collection by the PbO-modified ITO is not due to the conduction band of PbO but the surface modification of ITO, that is, it is related to the interactions between PbO and ITO.

The interactions between PbO and ITO were studied by XPS. Fig. 7 presents the XPS spectra of a blank ITO, a 1 nm-thick PbO deposited on ITO (PbO/ITO), and a PbO layer which was deposited on Si and had a thickness of 10 nm. The Pb $4f_{7/2}$ and $4f_{7/2}$ XPS bands appear at 138.2 and 143.1 eV, respectively, for PbO. They shift to 139.0 and 143.8 eV for PbO/ITO. The binding energies increase after the deposition of PbO on ITO. On the other hand, the XPS bands of In and Sn of ITO exhibited opposite shifts after the deposition with PbO. The two In $3d_{5/2}$ and $3d_{3/2}$ XPS bands appear at 444.6 and 452.1 eV, respectively, for the blank ITO. They shift to 444.1 and 451.6 eV, respectively, for PbO/ITO. The binding energies decrease after the deposition of the 1 nm-thick PbO layer on ITO. The binding energies of the two Sn 3d XPS bands also shift to red after the deposition of PbO on ITO. They are at 486.6 and 495 eV, respectively, for the blank ITO, and shift to 486.1 and 494.5 eV after the deposition of PbO. The XPS spectra of PbO and ITO suggest that electrons may transfer from PbO to ITO. This electron transfer may push up the Fermi level at the ITO surface and consequently lower the work function. The lone $6s^2$ electron pair of Pb^{2+} may take part in the electron transfer [42]. In addition, it has been understood that the lone $6s^2$ electron pair of Pb^{2+} give rise to a high dipole moment in PbO [51]. This dipole moment may also contribute to the reduction of the PbO-modified ITO.

4. Conclusions

In conclusion, a thin PbO layer can effectively lower the work function of ITO. The inverted PSCs with the PbO-modified ITO as the cathode show high photovoltaic performance. The optimal performances are: V_{oc} = 0.59 V, J_{sc} = 10.8 mA cm^{-2}, FF = 0.632, and PCE = 4.00% under simulated AM1.5G illumination. The optimal PCE of the inverted PSCs is significantly higher than the inverted PSCs with unmodified ITO and even higher than the optimal PCE (3.5%) of normal PSCs. The lowering in the work function of ITO by the PbO modification is attributed to the interactions between ITO and PbO.

Acknowledgment

This research work was financially supported by a grant from the National University of Singapore (R-284-000-059-123/101).

References

[1] R.F. Service, Science 332 (2011) 293.
[2] J.Y. Kim, K. Lee, N.E. Coates, D. Moses, T.Q. Nguyen, M. Dante, A.J. Heeger, Science 317 (2007) 222.
[3] Y. Yuan, T.J. Reece, P. Sharma, S. Poddar, S. Ducharme, A. Gruverman, Y. Yang, J. Huang, Nat. Mater. 10 (2011) 296.
[4] Z. Wu, B. Fan, A. Li, F. Xue, J. Ouyang, Org. Electron. 12 (2011) 993.
[5] G. Zhao, Y. He, Y. Li, Adv. Mater. 22 (2010) 4355.
[6] Z. Wu, B. Fan, F. Xue, C. Adachi, J. Ouyang, Sol. Energy Mater. Sol. Cells 94 (2010) 2230.
[7] J. Ouyang, Y. Xia, Sol. Energy Mater. Sol. Cells 93 (2009) 1592.
[8] J.H. Huang, C.Y. Yang, Z.Y. Ho, Dhananjay, M.C. Wu, Z.Y. Chu, K.C. Ho, Org. Electron. 10 (2009) 27.
[9] J.C. Hummelen, P.W.M. Blom, Adv. Mater. 20 (2008) 2116.
[10] J. Peet, J.Y. Kim, N.E. Coates, W.L. Ma, D. Moses, A.J. Heeger, G.C. Bazan, Nat. Mater. 6 (2007) 497.
[11] Z. Wu, A. Li, B. Fan, F. Xue, C. Adachi, J. Ouyang, Sol. Energy Mater. Sol. Cells 95 (2011) 2516.
[12] C.J. Brabec, S.E. Shaheen, C. Winder, N.S. Sariciftci, P. Denk, Appl. Phys. Lett. 80 (2002) 1288.
[13] M.P. de Long, L.J. van IJzendoom, M.A. de Voigt, Appl. Phys. Lett. 77 (2000) 2255.
[14] V. Shrotriya, G. Li, Y. Yao, C.W. Chu, Y. Yang, Appl. Phys. Lett. 88 (2006) 073508.
[15] K. Takanezawa, K. Tajima, K. Hashimoto, Appl. Phys. Lett. 93 (2008) 063308.
[16] Y.J. Cheng, C.H. Hsieh, Y. He, C.S. Hsu, Y. Li, J. Am. Chem. Soc. 132 (2010) 17381.
[17] M.S. White, D.C. Olson, S.E. Shaheen, N. Kopidakis, D.S. Ginley, Appl. Phys. Lett. 89 (2006) 143517.
[18] S.K. Hau, H.L. Yip, N.S. Baek, J. Zou, K. O'Malley, A. Jen, Appl. Phys. Lett. 92 (2008) 25330.
[19] H.H. Liao, L.M. Chen, Z. Xu, G. Li, Y. Yang, Appl. Phys. Lett. 92 (2008) 173303.
[20] H.M. Zhang, J. Ouyang, Appl. Phys. Lett. 97 (2010) 063509.
[21] G.K. Mor, K. Shankar, M. Paulose, O.K. Varghese, C.A. Grime, Appl. Phys. Lett. 91 (2007) 152111.
[22] R. Steim, S.A. Choulis, P. Schilinsky, C.J. Brabec, Appl. Phys. Lett. 92 (2008) 093303.
[23] E.F. de Haan, A. van der Drift, P.P.M. Schampers, Philips Tech. Rev. 25 (1967) 133.
[24] J.R. Clark, A.K. Weiss, J.L. Donovan, J.E. Green, R.E. King, J. Vac. Sci. Technol. 14 (1977) 219.
[25] S. Radhakrishnan, M.N. Kamalasan, P.C. Mehendra, J. Mater. Sci. 18 (1983) 1912.
[26] R. Clasen, J. Photogr. Sci. 28 (1980) 226.
[27] R.C. Hughes, R.J. Sokel, J. Appl. Phys. 52 (1981) 6743.
[28] R. Dalven, Infrared Phys. 9 (1969) 141.
[29] Q. Wang, Z. Deng, D. Ma, Opt. Express 17 (2009) 17269.
[30] Y.K. Do, S. Galileo, F. So, Sol. Energy Mater. Sol. Cells 93 (2009) 1452.
[31] J.D. Servaites, S. Yeganeh, T.J. Marks, M.A. Ratner, Adv. Funct. Mater. 20 (2010) 97.
[32] G. Li, V. Shrotriya, J. Huang, Y. Yao, T. Moriarty, K. Emery, Y. Yang, Nat. Mater. 4 (2005) 864.
[33] S.K. Hau, H.L. Yip, N.S. Baek, J. Zou, K. O'Malley, A.K.Y. Jen, Appl. Phys. Lett. 92 (2008) 253301.
[34] Z. Xu, L.M. Chen, G.W. Yang, C.H. Huang, J.H. Hou, Y. Wu, G. Li, C.S. Hsu, Y. Yang, Adv. Funct. Mater. 19 (2009) 1227.
[35] C.M. Björström, A. Bernasik, J. Rysz, A. Budkowski, S. Nilsson, M. Svensson, K.O. Magnusson, E. Moons, J. Phys. Condens. Matter 17 (2005) L529.
[36] S.Y. Heriot, R.A.L. Jones, Nat. Mater. 4 (2005) 782.
[37] S.H. Park, A. Roy, S. Beaupre, S. Cho, N.I. Coates, J.S. Moon, D. Moses, M. Leclerc, K. Lee, A.J. Heeger, Nat. Photon. 3 (2009) 297.
[38] A.C. Mayer, S.R. Scully, B.E. Hardin, M.W. Rowell, M.D. McGehee, Mater. Today 10 (2007) 28.
[39] G. Dennler, K. Forberich, M.C. Scharber, C.J. Brabec, I. Tomiš, K. Hingerl, T. Fromherz, J. Appl. Phys. 102 (2006) 054516.
[40] S.P. Gabuda, S.G. Kozlova, V.V. Terskikh, C. Dybowski, G. Neue, D.L. Perry, Chem. Phys. Lett. 305 (1999) 353.

[41] H. Mizoguchi, H. Kawazoe, Chem. Mater. 8 (1996) 2769.
[42] H.J. Terpstra, R.A. de Groot, C. Haas, Phys. Rev. B 52 (1995) 11690.
[43] B. Jia, L. Gao, Mater. Chem. Phys. 100 (2006) 351.
[44] M.I. Baleva, L.N. Bozukov, V.D. Tuncheva, J. Phys. Chem. 98 (1994) 13308.
[45] M. Baleva, V. Tuncheva, J. Solid State Chem. 110 (1994) 36.
[46] Y. Xu, A.A. Schoonen, Am. Mineralogist 85 (2000) 543.
[47] C.J. Brabec, A. Cravino, D. Meissner, N.S. Sariciftci, T. Fromherz, M.T. Rispens, L. Sanchez, J.C. Hummelen, Adv. Funct. Mater. 11 (2001) 374.
[48] Y. He, Y. Li, Phys. Chem. Chem. Phys. 13 (2011) 1970.
[49] Y. Park, V. Choong, Y. Gao, B.R. Hsieh, C.W. Tang, Appl. Phys. Lett. 68 (1996) 2699.
[50] I.D. Parker, J. Appl. Phys. 75 (1994) 1656.
[51] J.R. Tessman, A.H. Kahn, W. Shockley, Phys. Rev. 92 (1953) 890.

us to use the same thermal evaporation process that is needed for organic light-emitting layers. Namely, it does not involve any damage to organic layers and the photolithography process as well. Those organic insulating molecules can be placed right on the ITO anode, just below the aluminum (Al) cathode, or both on the ITO anode and below the Al cathode (Fig. 1). Those evaporated right on the ITO anode prevent hole leakage via the spikes existing on the ITO edges. To suppress it effectively, the hole mobility of those organic insulating molecules should be as low as possible. Meanwhile, those evaporated just below the Al cathode block off the electron-leak pathway. As such, organic insulating molecules that have very low electron mobility are preferred. In practice, however, it is unknown which device configuration (Fig. 1) shows higher performance. To clarify it, we make a performance comparison among those devices in Fig. 1 in terms of the current efficiency and lifetime. With attempt to understand the complex device behaviors, especially the carrier transport, we also perform the numerical simulations of those configurations. It is demonstrated that blocking off both hole- and electron-leak pathways is highly desired to enhance the current efficiency and lifetime of the sputter-patterned ITO-based OLEDs.

2. Experiment and simulation

For systematic inquiries, we have fabricated two different OLED devices. A fluorescent green bilayer OLED that is composed of 50-nm-thick 4,4′-bis[*N*-(1-nathyl)-*N*-phenylamino]biphenyl (NPB) for a hole transport layer (HTL)

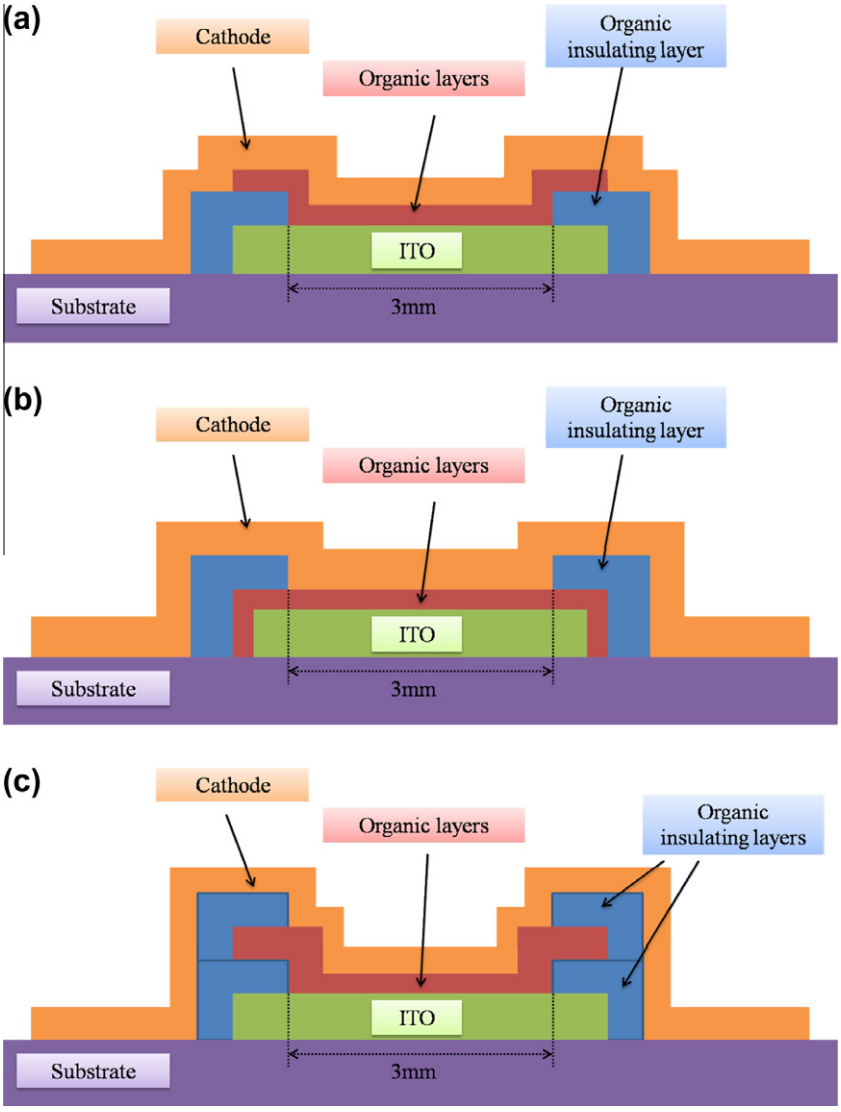

Fig. 1. Cross-sectional view of OLEDs with organic insulating molecules (a) on the ITO anode, (b) below the Al cathode, and (c) both on the ITO anode and below the Al cathode (the width of ITO is 4 mm).

and 45-nm-thick Tris-(8-hydroxyquinoline) aluminum (Alq_3) for an electron transport layer (ETL) was fabricated to make a numerical and experimental investigation of the leakage current cut-off capability of those organic insulating molecules. In this work, Alq_3 is used to prevent hole leakage, which has very low hole mobility ($\sim 1.2 \times 10^{-7}$ cm^2/Vs) [16], whereas NPB is used to block off the electron-leak pathway, which exhibits very low electron mobility ($\sim 1.0 \times 10^{-8}$ cm^2/Vs) [16]. For fluorescent green bilayer OLEDs, we used the commercial ITOs purchased from GEOMATEC Co., Ltd. and patterned them using the standard photolithography process with a patterned PI insulation layer (TORAY, Photoneece™ DL-1602). We intentionally covered the whole emission area (2 mm × 2 mm) with those organic insulating layers and then conducted numerical and experimental investigations of their leakage current cut-off capability. The other device we fabricated is a phosphorescent green multi-layer OLED device that consists of a 10-nm-thick LG-101 for a hole injection layer (HIL), 40-nm-thick NPB for a HTL, 30-nm-thick *N*,*N*′-dicarbazolyl-3,5-benzene (mCP) doped with tris(2-phenylpyridinate) iridium(III) ($Ir(ppy)_3$, 8 wt.%) for an emitting layer (EML), 7-nm-thick *m*-bis-(triphenylsilyl)benzene (UGH3) for a hole blocking layer (HBL), 30-nm-thick (2,9-dimethyl-4,7-diphenyl-1,10-phenanthroline) (Bphen) for an ETL, 1-nm-thick lithium fluoride (LiF) for an electron injection layer (EIL), and 100-nm-thick aluminum (Al). Unlike fluorescent green bilayer OLEDs, we have fabricated the ITO anodes for phosphorescent green multi-layer OLEDs using a sputtering deposition system (SUNICOAT-IS3000, SUNIC SYSTEM) with a metal open mask under the DC power of 500 W and at the substrate heater temperature of 240 °C. The sputtered ITO films show the sheet resistance of 25Ω/□. For phosphorescent green OLEDs, those organic insulating molecules (NPB and Alq_3) were thermally evaporated using a metal open mask that covers the sputter-patterned ITO edges. As such, the total emission area of those devices is 3 mm × 4 mm (the width of ITO is 4 mm, which is the same as that of Al).

For numerical simulations, we have implemented a 1D numerical model that is composed of Poisson's equation, drift–diffusion equation, and singlet exciton rate equation [16,17]. This model is capable of capturing the current injection into organic materials, the hopping transport of carriers, the locally generated excited states (excitons), the radiative decay of excitons, as well as the interactions among the electric field, the carrier mobility, and the current injection. We have used this model to visualize the carrier density distribution over the device, which facilitates the analysis of the experiment results. To obtain steady-state solutions, we truncated the iteration when the average local deviation was a small fraction (10^{-5}) of the total current [16]. More details as to the model and its numerical implementation can be found in [16,17].

3. Results and discussion

Presented in Fig. 2 is the surface morphology of the patterned ITO edges. As discussed in [15], the sputter-patterned ITO edge has a very gentle slope and its surface roughness is very poor due to the emergence of a number of spikes. Once spikes exist over an emission area, then a short-circuit problem arises because an instant current crowding takes place right at the spikes. Namely, such spikes appeared on the slope of the ITO edges act as leak channels that increase non-emissive current component. As a result, the injected current into OLED lighting panels at a fixed driving voltage is getting increased without saturation. It appears more seriously for large-area OLED lighting panels [3]. Such an increase of the injected current brings in local heat generation during operation, causing a device failure and thus raising a reliability issue. Therefore, the sputter-patterned ITO edges should be covered with those organic insulating molecules.

We have first investigated the feasibility of using those organic molecules (NPB, Alq_3) as an insulating material. To this end, we fabricated three different fluorescent green bilayer OLEDs with those organic insulating layers, the energy level diagrams of which are depicted in Fig. 3, To make a comparative study, we also fabricated a bilayer OLED without any organic insulating layer included (Fig. 3a). In Fig. 3b, the leakage hole cut-off layer (HCl, i.e., Alq_3 layer for blocking off hole transport) is placed before HTL. Owing to a large energy barrier for holes between ITO and the HCl layer along with a low hole mobility of the HCl layer, the hole transport would be effectively hindered. On the contrary, the leakage electron cut-off layer (ECL, i.e., NPB layer for blocking off electron transport) is placed before the Al cathode in Fig. 3c. Similarly, the electron transport would be effectively blocked due to a large energy barrier for electrons between the ECL layer and the Al cathode along with a low electron mobility of the ECL layer.

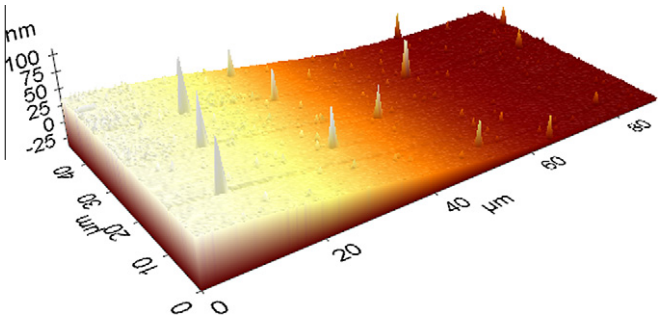

Fig. 2. AFM image of sputter-patterned ITO measured on the slope of the patterned edge.

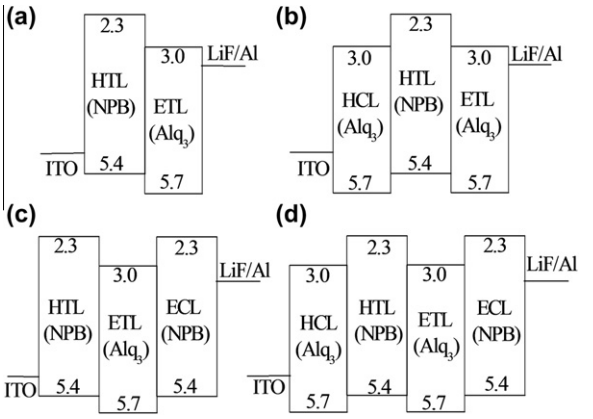

Fig. 3. Energy level diagram of fluorescent green bilayer OLEDs (a) without organic insulating molecule, (b) with leakage hole cut-off layer (HCl), (c) with leakage electron cut-off layer (ECL), and (d) with both HCl and ECL layers.

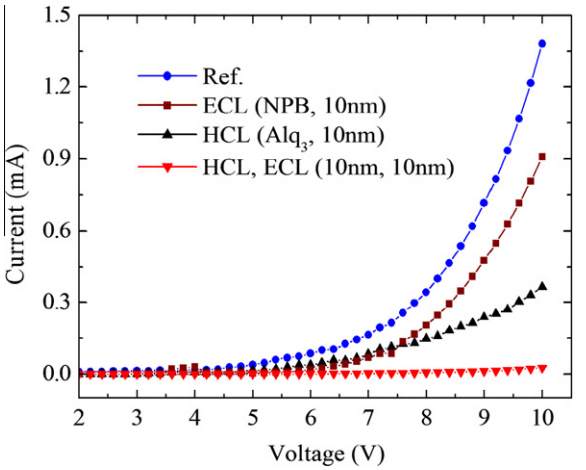

Fig. 4. Measured current versus voltage from fluorescent green bilayer OLEDs in Fig. 3.

Meanwhile, both hole and electron cut-off layers are placed in Fig. 3d. Shown in Fig. 4 are the *IV* curves measured from those OLED devices. As expected, the current flow is clogged the most in OLED with both hole and electron cut-off layers, followed by OLED with the single HCl layer (10 nm) and then OLED with the single ECL layer (10 nm). Though the current cut-off capability of OLEDs with the single insulation layer is higher than that of

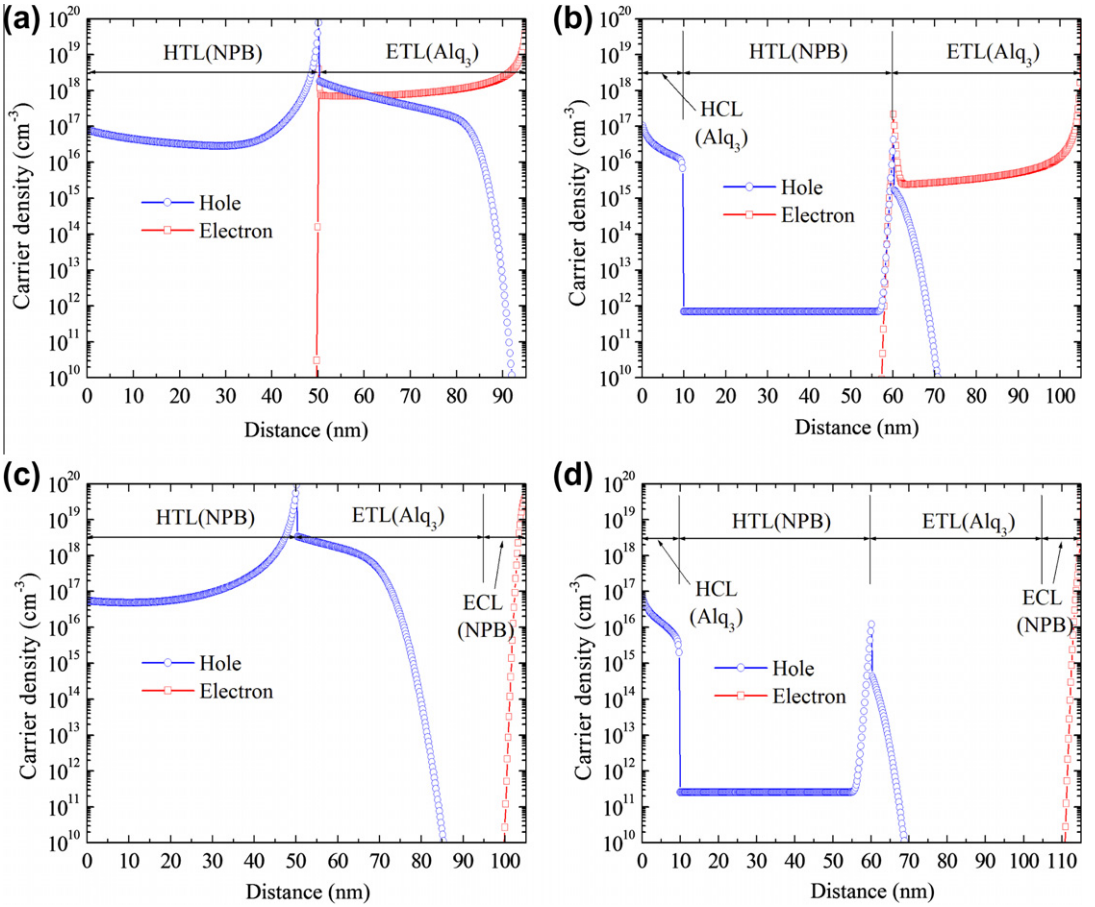

Fig. 5. Simulation results of carrier density distribution of fluorescent green bilayer OLEDs in Fig. 3 under the bias voltage of 9 V.

OLEDs without any organic insulating layer involved, yet it is not comparable with that of OLEDs with the dual (HCl and ECL) insulation layer. Meanwhile, the OLED structure with the single ECL layer shows poorer current cut-off property, compared with the OLED structure with the single HCl layer, the reason for which is uncertain. Furthermore, we have found that light emission occurs only from the bilayer OLED with the single HCl layer under a high bias condition. To find out these reasons, we performed the numerical simulations of those devices in Fig. 3 and presented the results of carrier density distribution in Fig. 5. As seen in Fig. 5a, when no organic insulating layer is involved, holes and electrons reach the HTL/ETL interface. Moreover, holes penetrate into the ETL layer since the hole mobility of HTL is almost two orders of magnitude higher than the electron mobility of ETL [16]. When the HCl (Alq_3) layer is presented, holes that reach the HTL/ETL interface are dramatically reduced as evident in Fig. 5b. Even so, some holes exist near the HTL/ETL interface, generating light emission through hole-electron recombination under a high bias condition. Similarly, when the ECL (NPB) layer is placed, electrons hardly reach the HTL/ETL interface. However, the hole density in Fig. 5c is observed to be much higher than the electron density in Fig. 5b near the HTL/ETL interface. Therefore, the OLED structure with the single ECL layer may show the poorest current cut-off capability, which is consistent with the experiment result in Fig. 4. When both HCl and ECL layers are presented, the carrier density at the interface is negligibly low as apparent in Fig. 5d. This result indicates that both hole- and electron-leak pathways should be blocked off to effectively suppress the leakage current that may occur in the sputter-patterned ITO-based OLEDs.

The current cut-off capability can be boosted by increasing their thickness. As shown in Fig. 6 where experiment and simulation results of *IV* curves are presented, the current flow is much reduced with increasing thickness of the ECL (NPB) layer. This result implies that one can improve the current cut-off capability using a single but thick organic insulating layer. However, it is observed that more current flows through OLED with the thicker (30-nm-thick) and single (ECL) insulation layer (Fig. 6), compared with current flowing through OLED with the thinner (totally 20-nm-thick) and dual (HCl and ECL) insulation layer (Fig. 4). This result also supports our conclusion that not only electron flow but also hole flow should be clogged because the total current density is determined by both hole and electron current densities flowing through the device.

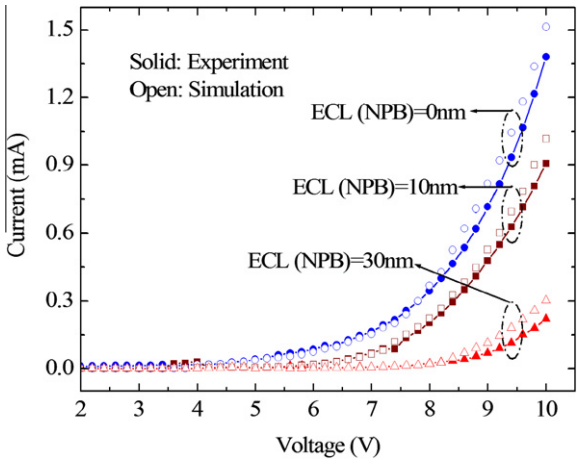

Fig. 6. Measured and simulated *IV* curves from the OLED structure with the ECL layer for different ECL layer thicknesses.

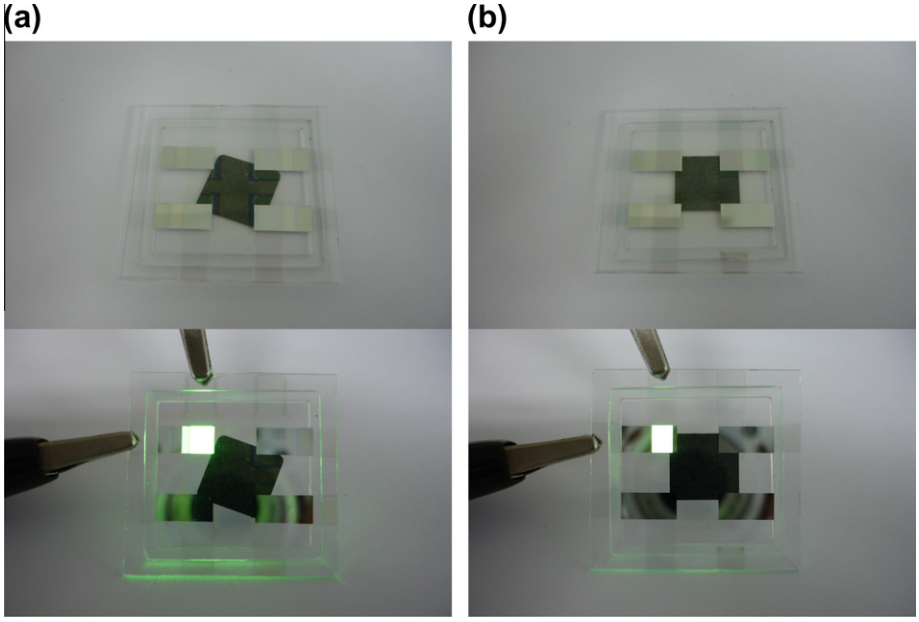

Fig. 7. Images of (a) OLED device with the HCl layer (top) and its green light emission (bottom) and (b) OLED device with the dual insulation layer (top) and its green light emission (bottom). The image of green light emission from OLED device with the ECL layer is similar to that (b) of OLED device with the dual insulation layer. (For interpretation of the references to colour in this figure legend, the reader is referred to the web version of this article.)

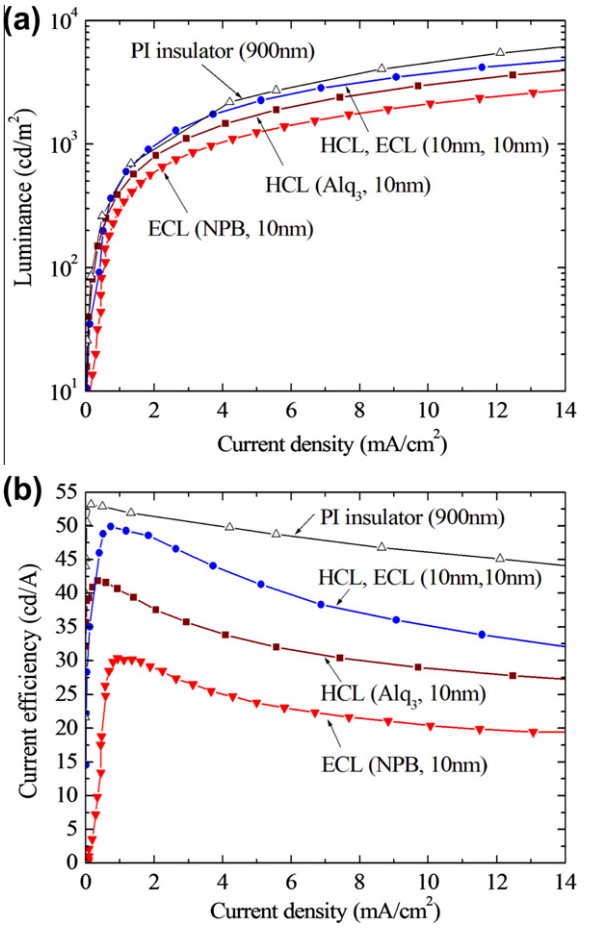

Fig. 8. Measured (a) luminance and (b) current efficiency versus current density of those OLED devices (Fig. 1) with organic insulating molecules.

For the practical applications of those organic insulating molecules, we have fabricated phosphorescent green multi-layer OLED devices where the sputter-patterned ITO edges are covered with the HCl or ECL layers. Fig. 7 shows the images of green light emission from those devices biased at 10 V. It is clearly seen to the naked eye that the emission area of OLED with the HCl layer is larger than that (3 mm × 4 mm) of OLED with the dual insulation layer. As discussed earlier, some holes existing near the HTL/ETL interface of OLED with the HCl layer in Fig. 5(b) generate green light emission through recombination with electrons, thereby blurring the boundaries between the real emission and non-emission areas. We have measured the luminance and current efficiency of those devices (Fig. 1) as a function of the current density and presented the results in Fig. 8. For comparison, we have also fabricated the OLED device based on the sputtered ITO and patterned PI insulation layer. The PI insulation layer is as thick as 900 nm, possibly exhibiting an excellent electrical insulation capability. Summarized in Table 1 are the luminance and current efficiency of those devices at a current density of 10 mA/cm^2. As expected, the OLED structure with the PI insulation layer shows the best device performance. Of those three devices with leakage current cut-off layers, however, the OLED structure with the dual insulation layer is shown to have the highest luminance (3784 cd/m^2 at 10 mA/cm^2) and current efficiency (35 cd/A at 10 mA/cm^2). At the same current density, the current efficiency of OLED with the single HCl layer is reduced to 29 cd/A, while it is further reduced to 20 cd/A for OLED with the single ECL layer. Such a large reduction in the current efficiency is due most likely to the presence of leak channels and poor leakage current cut-off capability. Since the leakage current originates dominantly from holes rather than electrons in OLEDs, the current efficiency of OLED with the single ECL (NPB) layer is reduced further. Therefore, it is more desired to place such an organic insulating layer right on the sputter-patterned ITO edges. However, the best use of them is to deploy them both on the ITO edges and below the Al cathode. Namely, one needs to prevent both hole and electron leakage in order to suppress effectively the overall leakage current and thus boost the device performance.

Table 1
Measured luminance and current efficiency of phosphorescent green multi-layer OLEDs (Fig. 1) at a current density of 10 mA/cm^2.

@10 mA/cm^2	OLED with ECL layer	OLED with HCl layer	OLED with both HCl and ECL layers	OLED with PI insulator
Luminance (cd/m^2)	2127	3042	3784	4556
Current efficiency (cd/A)	20	29	35	46

We have also measured the lifetime of those devices and presented the results in Fig. 9. At an initial luminance of 1000 cd/m^2, we measured T_{50} (in h), representing the duration from the start of testing to the time at which luminance is decreased to 50% of its initial value. As expected, the OLED structure with the PI insulation layer shows the longest lifetime. Of those three devices with

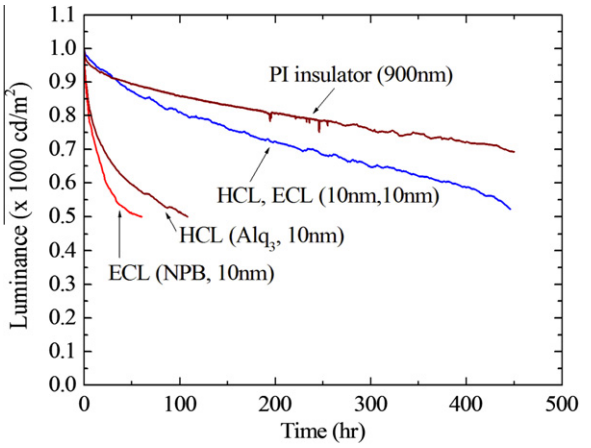

Fig. 9. Luminance as a function of time measured at an initial luminance of 1000 cd/m^2.

leakage current cut-off layers, however, the OLED structure with the dual insulation layer shows the longest lifetime (T_{50} of 446 h), followed by OLED with the single HCl layer (T_{50} of 108 h) and then OLED with the single ECL layer (T_{50} of 60 h). Such a lifetime reduction occurring on OLEDs with the single insulation layer is attributed to the leakage current. Namely, OLEDs with the single insulation layer should be operated at a higher bias voltage to compensate for the increased non-emissive current component (i.e., to exhibit the same luminance (1000nit)).

4. Conclusion

We have demonstrated the cost-effective fabrication of OLEDs using a sputter-patterned ITO and thermal evaporation of organic insulating molecules. We have found that organic insulating molecules are desired to be positioned right on the patterned ITO edges to suppress the leakage current dominated by holes. However, the best way to reduce the overall leakage current was to block off both hole- and electron-leak pathways by placing those organic insulating molecules both on the ITO edges and below the Al cathode. The OLED structure based on this scheme exhibited much higher current efficiency and longer lifetime, compared with OLED having the single insulation layer.

References

[1] Y. Sun, N. Giebink, H. Kanno, B. Wa, M.E. Thompson, S.R. Forrest, Nature (London) 440 (2006) 908.
[2] K. Leo, Science 310 (2005) 1762.
[3] Joerg Amelung, Available from: <http://www.spie.org/x23960.xml>.
[4] J. Kido, SID 08 (2008) 931.
[5] J.W. Park, D.C. Shin, S.H. Park, Semicond. Sci. Technol. 26 (2011) 034002.
[6] T. Uchida, M. Wakana, M. Yahata, S. Dangtip, T. Osotchan, T. Satoh, Y. Sawada, IEEE J. Disp. Tech. 5 (2009) 188.
[7] G. Parthasarathy, C. Adachi, P.E. Burrows, S.R. Forrest, Appl. Phys. Lett. 76 (2000) 2128.
[8] S.Y. Ryu, J.H. Noh, B.H. Hwang, C.S. Kim, S.J. Jo, J.T. Kim, H.S. Hwang, H.K. Baik, H.S. Jeong, C.H. Lee, S.Y. Song, S.H. Choi, S.Y. Park, Appl. Phys. Lett. 92 (2008) 023306.
[9] K.S. Yook, S.O. Jeon, C.W. Joo, J.Y. Lee, Appl. Phys. Lett. 93 (2008) 013301.
[10] C.-J. Yang, T.-Y. Cho, C.-L. Lin, C.-C. Wu, Appl. Phys. Lett. 90 (2007) 173507.
[11] C.-Y. Yang, T.-Y. Cho, Y.-Y. Chen, C.-J. Yang, C.-Y. Meng, C.-H. Yang, P.-C. Yang, H.-Y. Chang, C.-Y. Hsueh, C.-C. Wu, S.-C. Lee, Appl. Phys. Lett. 90 (2007) 233512.
[12] T. Komine, M. Nakagawa, IEEE Trans. Consum. Electron. 49 (2003) 71.
[13] T. Komine, M. Nakagawa, IEEE Trans. Consum. Electron. 50 (2004) 100.
[14] J.W. Park, IEEE/OSA J. Lightwave Tech. 28 (2010) 2873.
[15] H.K. Ham, J.W. Park, D.C. Shin, Org. Electron. 12 (2011) 745–750.
[16] B. Ruhstaller, S.A. Carter, S. Barth, H. Riel, W. Riess, J.C. Scott, J. Appl. Phys. 89 (2001) 4575.
[17] B. Ruhstaller, T. Beierlein, H. Riel, S. Karg, J.C. Scott, Walter Riess, IEEE J. Sel. Top. Quantum Electron. 9 (2003) 723.

semiconductors. The problem there is that these two parameters cannot be obtained independently in a single measurement. It also does not yield the spatial distribution. While it can be done with an effort, it is not straightforward to obtain energetic distribution of states in the band gap from this type of measurement. Secondary ion mass spectroscopy (SIMS), which is the conventional method to study depth profiling of semiconductor with known doping agents, is not applicable to many organic semiconductors because the chemical species responsible for doping are not known. The popular methods to measure mobility in bulk organic semiconductors [8] are the well-established time-of-flight (TOF) [9–12], the space-charge limited current [13,14] (SCLC), and the charge extraction by linearly increasing voltage [15–17] (CELIV), and more recently the susceptance analysis techniques [18]. TOF requires relative thick films and large bias therefore it may suppress some features of real devices. In addition, determining mobilities for materials having a high carrier density, such as P3HT, is difficult because diffusive charge carriers will affect the drift of photogenerated charge carriers under an electric field. The SCLC method, on the other hand, is based on the analysis of current density versus applied voltage (J–V) characteristics in the dark and it is applicable to regular devices ($\sim$200 nm thick active layer). The SCLC method is usually applied to the large electric field regime where the carrier concentration is altered and the extracted mobility may not be accurate. The CELIV technique is the only one known method up to date to directly measure the charge carrier mobility in semiconductors with dispersive transport (disordered media). However, the CELIV technique requires a minimum amount of dark carrier concentration (10^{14}–10^{15} cm^{-3}) a requirement that is not always reached. Recently, there have been reports on mobility extraction based on susceptance analysis [18]. The validity of that method is established by complex fitting and simulation and limited to materials with non-dispersive transport only. It is worth mentioning that none of the aforementioned methods provides independent measurement of the carrier density.

The classic method to measure the carrier density in inorganic semiconductors is the capacitance–voltage (C–V) technique [1]. Unlike the conductivity method, the C–V technique is an independent measurement of carrier density (assuming the permittivity ε and the device area A are known). An inherent advantage of C–V technique is the depth profiling of carrier density in a planar device structure. Moreover, it is straightforward to integrate other methods associated with the C–V method such as admittance spectroscopy [19] and deep level transient spectroscopy [20] to obtain the energetic distribution of states in the bandgap. However, there have been very few applications of the C–V method to measure the carrier density in organic semiconductors [21–23]. We think the reason may lie in the frequency dependence of the capacitance. In this work, we present a method integrating the C–V and voltage-dependent admittance spectroscopy analysis to measure both the carrier density and mobility. We apply the method to the regioregular poly(3-hexylthiophene) (P3HT), a model polymetric semiconductor [24–26] as a proof of principle. After carefully analyzing the frequency effect on C–V measurement, we arrive at a general guideline on the measurement frequency for reliable measurement of carrier density. Furthermore, we take advantage of the frequency dependence to extract the carrier mobility from the same set of capacitance data.

2. Sample preparation

P3HT was obtained from Rieke Metals (90–93% regioregularity) and used as received. Preparation of P3HT film samples was carried out in a N_2 atmosphere glovebox. P3HT ($\sim$20 mg/mL) was dissolved in anhydrous chlorobenzene with heating (60 °C) and stirring overnight. Films were prepared by solution-casting on the substrate. Film thickness was measured on an Alpha-step profilometer (Veeco Dektak 8 Advanced Development Profiler). Indium tin oxide (ITO) substrates were cleaned sequentially in an ultrasonic solvent bath of detergent, acetone, deionized water, and isopropyl alcohol. A PEDOT–PSS (Clevios) layer of $\sim$30 nm was spin-coated onto the ITO at 4000 rpm for 30 s and then baked on a hot plate at 120 °C for 1 h. In order to obtain relative thick films, we drop-casted the P3HT onto the PEDOT–PSS-coated ITO substrate, followed by slow solvent evaporation. We note that the thick films prepared by such a method, while smooth with a roughness $\sim$6 nm confirmed by an atomic force microscope scan of 20 by 20 μm^2, yield non-uniform film thickness (varying by as much as $\sim\pm$1 μm across an area of 2.5 by 4.0 mm^2 as confirmed by a Dektak profilometer). Lastly, an Al (100 nm) layer was deposited by thermal evaporation through a shadow mask at a rate of 2 Å/s. The shadow mask was used to define six pixels per substrate where the active area is defined by the overlap of ITO anode and Al cathode as $\sim$0.11 cm^2.

It is generally accepted that the PEDOT–PSS layer forms a good ohmic contact with the P3HT layer [27,28]. The carrier transport in the device is then dominated by the Al/P3HT Schottky junction. The Schottky junction can be replaced by a p–n junction without affecting the validity of the discussion in this study. Since Schottky and p–n junction are basic building blocks of many practical devices, we can extend the applicability of this study to any actual planar diode-like devices such as solar cells and light-emitting diodes. We note that this ease-of-use is advantageous over the time-of-flight and susceptance analysis methods which generally exclude device structures with Schottky or p–n junctions.

3. Experimental methods

We used an Agilent 4294A impedance analyzer to measure the capacitance data. An automated program was developed to acquire capacitance and conductance data at various temperature (100–300 K), modulation frequency (40 Hz to 4 MHz), and DC bias (-3 to +0.5 V). We used an AC modulation voltage of 45 mV$_{rms}$ for all the data presented here. For temperature dependent measurements, the devices were mounted in a He-cooled cryostat. The temperature of the device was taken from a temperature sensor directly attached to the top of the device.

For completeness' sake, we briefly summarize the physics of C–V technique and then extend the discussion to our new method. The capacitance measurement relies upon the existence of a space-charge region in a p–n or Schottky junction. The capacitance, essentially the transfer function of charge response to small AC modulation of bias voltage, is inversely proportional to the width of the space charge region:

$$W = \sqrt{\frac{2\varepsilon}{qN}(V_{bi} - V)}, \tag{1}$$

where ε is the permittivity, q is the elementary charge, V_{bi} is the built-in potential, N is the carrier density, and V is the bias voltage. It is worth noting that when many trapped charges are present, this equation may overestimate W and lead to an underestimate of N [29]. Because V_{bi} is a constant at a specific temperature, W only depends on N and V, the latter being experimentally controllable. It is then possible to solve for N from the bias voltage dependence of capacitance. In the case of uniform doping, i.e., N is a constant, the C^{-2} versus V curve is a straight line. N can be calculated from the slope of this line and V_{bi} from its intercept with the horizontal axis. In case of non-uniform doping, one can obtain the carrier density depth profile $N(W)$ by calculating W from $1/C$ and N from the local slope (derivative) of C^{-2} versus V.

In a typical C–V measurement, an AC modulation voltage with frequency ω is combined with a DC bias voltage which is gradually swept across certain range. The range for DC bias voltage sweeping is typically in the reverse bias regime. Occasionally, it may overlap with the low forward bias regime. One should avoid the high forward bias regime where additional capacitance (e.g., due to diffusion of minority carriers or other means of carrier injection) and excessive conductance interfere with proper measurement and interpretation of capacitance data. We note that the susceptance analysis method has to be carried out at a forward bias [18] sometimes up to 12 V, which may invoke some measurement challenges in actual application.

The choice of modulation frequency ω is critical. The prerequisite of the C–V technique is that carriers are mobile and can respond to the AC bias at the modulation frequency. Due to the low conductivity, the dielectric relaxation frequency of organic semiconductors puts an upper limit to the usable modulation frequency. Recall that a semiconductor material characterized by conductivity σ and permittivity ε exhibits a dielectric relaxation at frequency $\omega_{dr} = \sigma/\varepsilon$. For a hypothetical organic semiconductor with carrier density $\sim 1 \times 10^{15}\ \mathrm{cm}^{-3}$, mobility $\sim 1 \times 10^{-4}\ \mathrm{cm}^2/\mathrm{V/s}$, and $\varepsilon = 4\varepsilon_0$ the dielectric relaxation frequency is $\sim$50 kHz. Below ω_{dr}, the carriers can keep up with the AC bias modulation therefore the semiconductor behaves like a conductor with $G_g = A\sigma/t$, where A is the area and t is the thickness. Above ω_{dr}, the carriers cannot keep up with the AC bias modulation therefore the semiconductor behaves like a capacitor $C_g = \varepsilon A/t$.

The dielectric relaxation frequency is further modified by the presence of a p–n or Schottky junction, which contributes to a depletion capacitance C_d. The equivalent-circuit model becomes the series connection of C_d with the parallel connection of the geometrical conductance $A\sigma/(t–W)$ and capacitance $\varepsilon A/(t–W)$ of the quasi-neutral region. The frequency dependence of the total capacitance C is:

$$C = C_d \frac{\omega^2\varepsilon^2 C_d/\sigma^2 C_g + 1}{\omega^2\varepsilon^2 C_d^2/\sigma^2 C_g^2 + 1}. \tag{2}$$

The frequency dependence of capacitance thus exhibits a step at a transition frequency ω_p, below which C approaches C_d and above which C approaches C_g. By taking the derivative of C with respect to ω, we arrive at the differential capacitance $\omega dC/d\omega$ whose negative peak corresponds to the transition frequency:

$$\omega_p = \frac{C_g\sigma}{C_d\varepsilon} = \frac{W}{t}\frac{\sigma}{\varepsilon}. \tag{3}$$

We see that the ω_p is the dielectric relaxation frequency ω_{dr} modified by the factor W/t. Because $W/t < 1$, ω_p is always less than ω_{dr}. This means that upper ceiling for usable modulation frequency in C–V measurement is further lowered by a factor of W/t. For our experiment, a more convenient parameter to use is the square of the inflection frequency:

$$\omega_p^2 = \frac{W^2}{t^2}\frac{\sigma^2}{\varepsilon^2} = \frac{2\sigma^2}{q\varepsilon N t^2}(V_{bi} - V). \tag{4}$$

It is obvious that ω_p^2 depends linearly on the bias voltage V. All variables in the linear coefficient are physical constants except σ and t, the latter can be independently measured by observing the geometrical capacitance under full depletion or by mechanical means such as a profilometer. If one plots ω_p^2 against bias V, the slope of the resulting line can be used to determine the conductivity σ and in turn mobility μ.

4. Results and discussion

Fig. 1 shows the capacitance measured at 100 Hz modulation frequency at room temperature. As a result of the evolution of depletion width with bias, C increases with

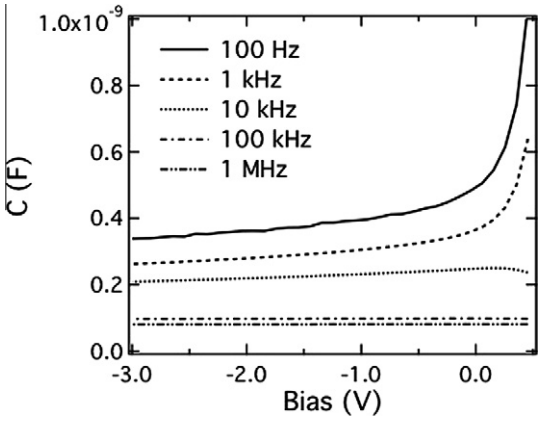

Fig. 1. The voltage dependence of capacitance measured in drop-casted P3HT device. Data were taken at $T = 295$ K and various modulation frequencies.

forward bias and decreases with reverse bias. The Mott-Schottky plot is shown in Fig. 2 based on capacitance data taken at 100 Hz. The built-in voltage (0.57 V) is extracted from the linear part of the Mott-Schottky plot [1]. Using conventional *C–V* analysis [1], i.e., from the derivative of $C^{-2}(V)$, one can obtain the carrier density *N* as a function of depletion width *W* (Fig. 3). Because *W* is measured from the metallurgical junction whose location in the device may be known, one can convert *W* to a measure of depth below the surface of a planar device structure. The *N* versus *W* plot is therefore one version of the carrier density depth profile, i.e., carrier density *N* as a function of depth from the surface. This valuable information is not available in other experimental methods discussed in Section 1. The gradual increase of *N* with *W* may be the real carrier density profile due to chemical and physical evolutions occurred during the formation of the P3HT thin film and the device. It could also be indicative of defect states within the bandgap, as observed in inorganic semiconductors [30] The determination of actual mechanism responsible for the depth profile of carrier density is subject to further study.

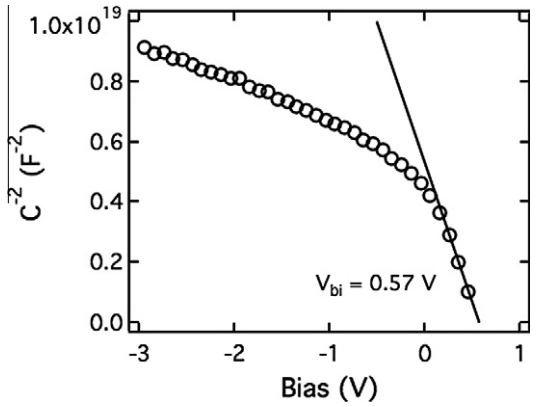

Fig. 2. The Mott-Schottky plot (C^{-2} versus bias) based on data measured in drop-casted P3HT at modulation frequency $\omega/2\pi$ of 100 Hz and $T = 295$ K. The line fitting is used to extract built-in voltage $V_{bi} = 0.57$ V.

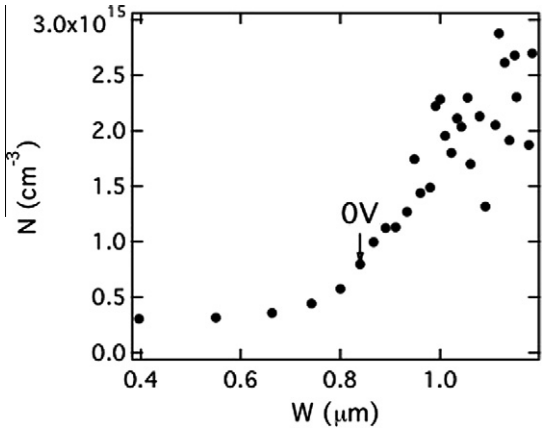

Fig. 3. The carrier density *N* versus depletion width *W* extracted by capacitance–voltage technique. Data were measured in drop-casted P3HT at modulation frequency $\omega/2\pi$ of 100 Hz and $T = 295$ K. The arrow marks 0 V bias.

The *C–V* data taken at 1 kHz (Fig.1, dashed) shows similar trend as that taken at 100 Hz (solid). The *C–V* data taken at 10 kHz (Fig. 1, dotted), however, is drastically different. This is because 10 kHz is approximately the modified dielectric relaxation frequency ω_p. The frequency effect is even more pronounced at 100 kHz (Fig. 1, dash-dotted) and 1 MHz (Fig. 1, dash-double-dotted) where the *C–V* data show little voltage dependence. At frequencies higher than ω_p, the carriers in P3HT cannot respond to the AC bias modulation. As a result, the *C–V* technique becomes ineffective as a probe for carrier density in P3HT. At very high frequencies (~1 MHz), only those carriers in the two contacts (i.e., in Al and PEDOT–PSS layers, as opposed to P3HT) can respond to the AC modulation. Because the P3HT layer is effectively "insulating" at these frequencies, the measured capacitance is nothing but the geometrical capacitance of a classic parallel plate capacitor consisting of two metallic contacts separated by the thickness of the P3HT layer. This geometrical capacitance does not vary with the bias voltage or measurement frequency, as shown by the *C–V* data taken at 100 kHz and 1 MHz.

The breakdown of assumptions in *C–V* technique is reflected in the extracted carrier density *N*. The frequency dependence of *N* (bias = 0 V) is plotted in Fig. 4 (filled dots). Below 2 kHz, the extraction of carrier density is consistent within a reasonable range: $6–10 \times 10^{14}$ cm^{-3}. The carrier density increases slightly with lower measurement frequency, indicating the existence of defect states within the bandgap. Because the emission of carriers from deep states obey the Boltzmann statistics [31,32], increasing the measurement frequency progressively excludes the deeper states from contributing to the "free" carrier density. Consequently, the apparent carrier density decreases slightly with frequency. As the frequency approaches 10 kHz, however, the extracted "carrier density" increases drastically. As we discussed earlier, extraction of *N* at these frequencies above the modified dielectric relaxation frequency is invalid. The very high carrier density extracted there is therefore reflective of

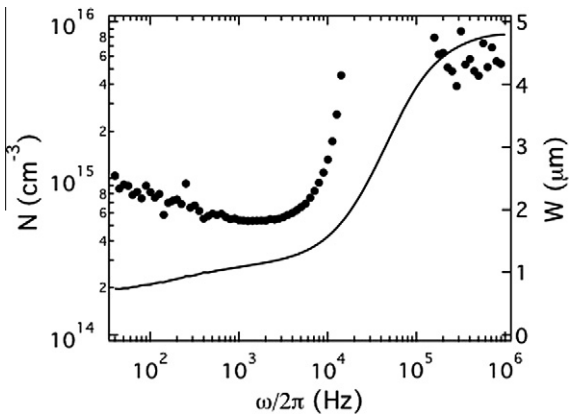

Fig. 4. The carrier density *N* (dots) and depletion width (line) extracted by capacitance–voltage technique plotted against the modulation frequency at which the data were taken. Data were measured in drop-casted P3HT at $T = 295$ K and 0 V bias.

the carrier density in the less conductive of the two contact layers, in our case, PEDOT–PSS.

The frequency dependence of depletion width W (Fig. 4, line) provides additional evidence of dielectric relaxation at high frequencies. Below 10 kHz, W is reasonable ($\sim$1 μm) and consistent with solution of Poisson equation. Above 10 kHz, W increases drastically before eventually reaching a plateau ($\sim$4.8 μm). This plateau agrees approximately with the low end of the physical thickness of the P3HT film confirmed by a Dektak profilometer (data now shown). This is direct proof that: at frequencies ($\sim$1 MHz) much higher than the modified dielectric relaxation frequency, the carriers in P3HT cannot respond to the AC modulation. At that point, the "depletion width" is essentially the thickness of the now "insulating" P3HT film.

The above frequency dependent data of C, N, and W show that it is important to keep below the modified dielectric relaxation frequency ω_p in order to obtain valid C–V measurement. We note that the upper ceiling of usable measurement frequency imposed by ω_p is a few orders of magnitude lower than that in the conventional inorganic semiconductors (e.g., 10^9–10^{12} Hz in Si). As a result, frequencies that are routinely used for C–V measurement in other semiconductors (10^5 Hz is considered quite normal for Si) may be too high for organic semiconductors. A corollary of this conclusion is that the measurement frequency (1 MHz) used in most deep-level transient spectroscopy [20] systems is also too high for organic semiconductors.

Now that we have reliably and independently extracted the carrier density N, we turn our attention to extracting carrier mobility from the bias dependence of the modified dielectric frequency. Fig. 5 shows the frequency dependence of the raw capacitance (solid) and differential capacitance $\omega dC/d\omega$ (dashed). The raw capacitance exhibits a step at certain transition frequency ω_p. Below ω_p, the data represent a reliable measurement of the depletion capacitance albeit with secondary modification by the defect states in the bandgap as discussed above. Above ω_p, the data instead represent a measurement of geometrical capacitance between the two contacts. The transition frequency ω_p is clearly identified as the position of the negative peak in the differential capacitance spectrum.

The transition frequency ω_p exhibits a monotonic decrease with forward bias. This is clearly visible in the shift of the negative peak of the differential capacitance spectrum (Fig. 6). As expected, the square of the transition frequency ω_p^2 exhibits a linear dependence on the bias voltage (Fig. 7). From the slope of this line, we can extract the conductivity σ and mobility μ using Eq. (4).

The conductivity and mobility of the same device are measured at a number of temperatures (Fig. 8). From the Arrhenius plots (Fig. 9), one sees that both parameters appear to be thermally activated. The activation energies are 0.24 ± 0.03 and 0.15 ± 0.01 eV for conductivity and mobility, respectively. It appears that that most of the contribution to thermal activation of conductivity comes from the temperature dependence of mobility [33]. The temperature dependence data of carrier density, although showing

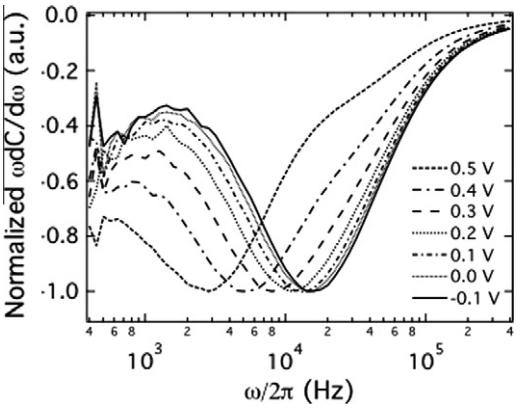

Fig. 6. The differential capacitance measured from a drop-casted P3HT device at 295 K and various biases. The transition frequency ω_p decreases with forward bias.

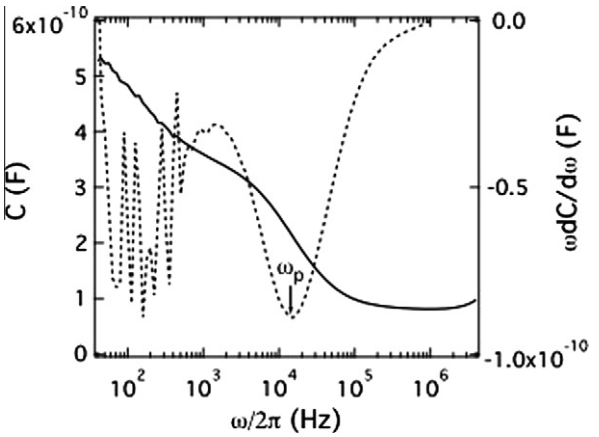

Fig. 5. The frequency dependence of capacitance (solid) and differential capacitance (dashed) measured from a drop-casted P3HT device at 295 K and 0 V bias. The arrow indicates the transition frequency ω_p at which the capacitance exhibits a step transition and differential capacitance exhibits a negative peak.

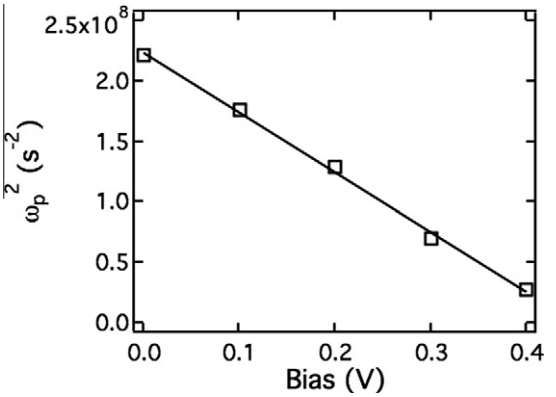

Fig. 7. The square of the transition frequency ω_p^2 identified from Fig. 6 exhibits linear dependence on bias voltage. From the slope (Eq. (4)), the conductivity $(4.9 \pm 2\%) \times 10^{-8}$ 1/Ω cm and mobility $(3.8 \pm 2\%) \times 10^{-4}$ cm^2/V/s were calculated using $N = 8.2 \times 10^{14}$ cm^{-3}, which was measured at 100 Hz at the same temperature.

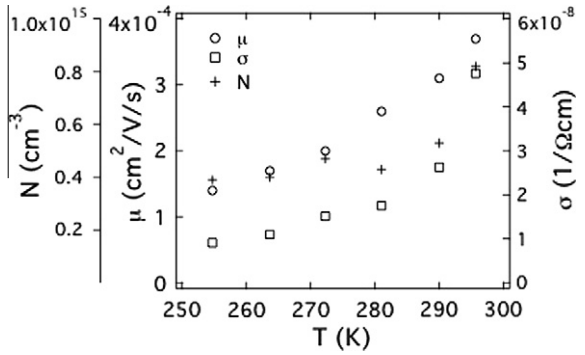

Fig. 8. The temperature dependence of carrier density, conductivity, and mobility in drop-casted P3HT. The relative error of conductivity and mobility is ±4%.

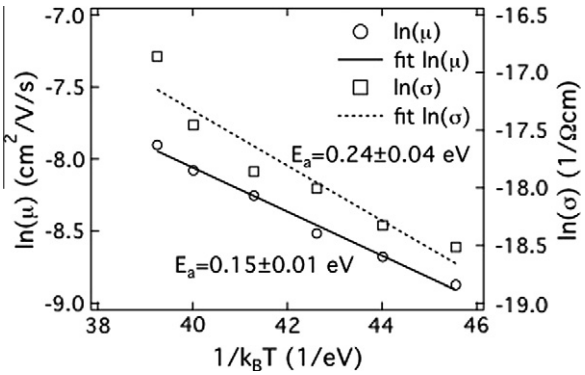

Fig. 9. The activation energies for the conductivity and mobility measured in drop-casted P3HT are extracted from the respective Arrhenius plots.

a general trend consistent with those of mobility and conductivity, are not good enough to extract a reliable activation energy. One possible mechanism for the temperature dependence of mobility in the measured temperature range is trap-limited mobility [34,35].

We note that there is a fair amount of scattering in the extracted carrier density (high 10^{14} to low 10^{16} cm^{-3}) and mobility (high 10^{-6} to low 10^{-4} $cm^2/V/s$). The reason for this wide scattering is mostly likely the lack of control in chemical and physical uniformity during the drop casting process and following fabrication of contacted devices. Our measurement results are consistent with previous reports on P3HT [7], where the origin of the free carriers has been attributed to the intrinsic defects susceptible to chemical treatment. We expect the method presented in this work to be applicable to a wide range of organic semiconductor materials and devices. Unlike the previously reported susceptance analysis method [18], our method does not rely upon any complex simulation and is applicable to materials of both dispersive and non-dispersive transport nature.

Our method requires the co-existence of a space charge region and a quasi-neutral region. Because most of the bias voltage is dropped over the space charge region, the voltage drop over the quasi-neutral region is assumed to be negligible. The extracted mobility is that of the quasi-neutral region which is under zero electric-field. In fact, the electric-field in the quasi-neutral region can not be experimentally adjusted without breaking the basic assumptions of our method. Therefore, our method is not suitable for studying the electric-field dependence of mobility. We note that other methods (e.g., TOF, susceptance analysis, CELIV, and SCLC) are suitable for measuring mobility in an electric-field.

For some techniques such as TOF, a very thick layer is required. The same is not true for our method. We use relatively thick P3HT layer because the depletion region width W at equilibrium is $\sim$1 μm (for a free carrier density N of $\sim 10^{15}$ cm^{-3}). The only necessary condition for our method to be applicable is that the layer of interest is not completely depleted. In other words, the layer thickness t needs to be larger than W. Because W roughly scales with $N^{1/2}$, it is possible to use thinner layers if free carrier density is higher. We have applied our method to layer thickness $\sim$300 nm for material with high free carrier density (e.g., $\sim 10^{17}$ cm^{-3} in P3HT:PCBM mixture, data not shown).

The range of bias useful for our method has two limiting values in forward and reverse biases, respectively. In reverse bias direction, the limit is reached when the layer of interest is completely depleted. At that point, the quasi-neutral region vanishes. In forward bias direction, a few things can happen: (i) there may be minority carrier injection which results in a diffusion capacitance. In a conventional p–n junction, this diffusion capacitance is proportional to the current density under forward bias, which increases exponentially with bias voltage. In other words, the diffusion capacitance [36] quickly outweighs the depletion capacitance (which increases roughly with the square root of bias voltage) at certain bias voltage. Beyond that point, the analysis in this work (as well as that in the conventional C–V measurement) is invalid because the capacitance is no longer dominated by the depletion mechanism. It is worth mentioning that other useful information such as carrier lifetime can be extracted from diffusion capacitance measurement [36]. (ii) The conductivity of the device increases rapidly. (In a conventional p–n junction, the conductivity is also proportional to the current density under forward bias, which increases exponentially with bias voltage.) At some point, the impedance analyzer can no longer measure capacitance accurately. In other words, the phase angle (ideally 90°) of the capacitance measurement becomes too small to be reliable. Admittedly, the carrier transport mechanism in OPV devices differ from that of a classical p–n junction. Nevertheless, the general guideline still holds to avoid using capacitance data at large forward bias for any depletion-capacitance-based analysis.

5. Conclusions

We have developed a method based on the capacitance–voltage–frequency experiment to simultaneously measure both the carrier density and mobility in organic semiconductors from the capacitance–voltage–frequency

experiment. Measurement using the P3HT as an example demonstrates the applicability of this method. Careful inspection of the frequency effect reveals that the conventional capacitance–voltage technique can provide reliable measurements of carrier density and its depth profile in organic semiconductors provided that certain conditions are satisfied. In particular, one needs to make sure that the measurement frequency is below the modified dielectric relaxation frequency, which is much lower in most organic semiconductors than in inorganic semiconductors. By exploiting the voltage dependence of the modified dielectric relaxation frequency, the conductivity and carrier mobility can also be extracted from the same experiment data. Mobility data measured from P3HT show positive temperature dependence within the measurement range (from 250 to 300 K). The activation energies of mobility and conductivity of P3HT are calculated as 0.15 ± 0.01 and 0.24 ± 0.03 eV, respectively. Our mobility extraction method is general and easy to apply because it does not assume any particular dispersive model of mobility *a priori* and it requires no complex fitting or simulation.

Acknowledgments

This work was funded by the US Department of Energy, Office of Science, Basic Energy Science, Division of Chemical Sciences, Geosciences and Biosciences, under Contract No. DE-AC36-08GO28308 to NREL.

References

[1] S.M. Sze, Physics of Semiconductor Devices, John Wiley and Sons, 1981.
[2] R.A. Smith, Semiconductors, Cambridge University Press, 1978.
[3] M. Pope, C.E. Swenberg, Electronic Processes in Organic Crystals and Polymers, Oxford University Press, 1999.
[4] M. Lonergan, Charge transport at conjugated polymer–inorganic semiconductor and conjugated polymer–metal interfaces, Annu. Res. Phys. Chem. 55 (2004) 257–298.
[5] A. Pivrikas, N.S. Sariciftci, G. Juska, R. Osterbacka, A review of charge transport and recombination in polymer/fullerene organic solar cells, Prog. Photovolt.: Res. Appl. 15 (2007) 677–696.
[6] J.F. Rubinson, Y.P. Kayinamura, Charge transport in conducting polymers: insights from impedance spectroscopy, Chem. Soc. Rev. 38 (2009) 3339–3347.
[7] Z. Liang, A. Nardes, D. Wang, J.J. Berry, B.A. Gregg, Defect engineering in pi-conjugated polymers, Chem. Mater. 21 (2009) 4914–4919.
[8] S. Tiwari, N.C. Greenham, Charge mobility measurement techniques in organic semiconductors, Opt. Quant. Electron. 41 (2009) 69–89.
[9] P.M. Borsenberger, L. Pautmeier, H.J. Bässler, Charge transport in disordered molecular-solids, Chem. Phys. 94 (1991) 5447–5454.
[10] T. Kreouzis, D. Poplavskyy, S.M. Tuladhar, M. Campoy-Quiles, J. Nelson, A.J. Campbell, D.D.C. Bradley, Temperature and field dependence of hole mobility in poly(9,9-dioctylfluorene), Phys. Rev. B 73 (2006) 235201.
[11] S.A. Choulis, J. Nelson, Y. Kim, D. Poplavskyy, T. Kreouzis, J.R. Durrant, D.D.C. Bradley, Investigation of transport properties in polymer/fullerene blends using time-of-flight photocurrent measurements, Appl. Phys. Lett. 83 (2003) 3812–3814.
[12] N. Kopidakis, E.A. Schiff, N.-G. Park, J. van de Lagemaat, A.J. Frank, Ambipolar diffusion of photocarriers in electrolyte-filled, nanoporous TiO_2, J. Phys. Chem. B 104 (2000) 3930–3936.
[13] M.A. Lampert, P. Mark, Current Injection in Solids, Academic Press, 1970.
[14] P.W.M. Blom, M.J.M. de Jong, J.J.M. Vleggaar, Electron and hole transport in poly(*p*-phenylene vinylene) devices, Appl. Phys. Lett. 68 (1996) 3308–3310.
[15] G. Juška, K. Arlauskas, M. Viliunas, K. Genevicius, R. Osterbacka, H. Stubb, Charge transport in pi-conjugated polymers from extraction current transients, Phys. Rev. B 62 (2000) 16235–16238.
[16] A.J. Mozer, N.S. Sariciftci, L. Lutsen, D. Vanderzande, R. Österbacka, M. Westerling, G. Juška, Charge transport and recombination in bulk heterojunction solar cells studied by the photoinduced charge extraction in linearly increasing voltage technique, Appl. Phys. Lett. 86 (2005) 112104.
[17] A.J. Mozer, N.S. Sariciftci, A. Pivrikas, R. Österbacka, G. Juška, L. Brassat, H. Bässler, Charge carrier mobility in regioregular poly(3-hexylthiophene) probed by transient conductivity techniques: a comparative study, Phys. Rev. B 71 (2005) 035214.
[18] S.W. Tsang, S.K. So, J.B. Xu, Application of admittance spectroscopy to evaluate carrier mobility in organic charge transport materials, J. Appl. Phys. 99 (2006) 013706.
[19] D.L. Losee, Admittance spectroscopy of impurity levels in Schottky barriers, J. Appl. Phys. 46 (1975) 2204–2214.
[20] D.V. Lang, Deep-level transient spectroscopy – new method to characterize traps in semiconductors, J. Appl. Phys. 45 (1974) 3023–3032.
[21] E.J. Lous, P.W.M. Blom, L.W. Molenkamp, D.M. de Leeuw, Schottky contacts on a highly doped organic semiconductor, Phys. Rev. B 51 (1995) 17251–17254.
[22] Y. Zhang, B. de Boer, P.W.M. Blom, Controllable molecular doping and charge transport in solution-processed polymer semiconducting layers, Adv. Funct. Mater. 19 (2009) 1901–1905.
[23] M. Lehnhardt, S. Hamwi, M. Hoping, J. Reinker, T. Riedl, W. Kowalsky, Charge carrier densities in chemically doped organic semiconductors verified by two independent techniques, Appl. Phys. Lett. 96 (2010) 193301.
[24] R.D. McCullough, The chemistry of conducting polythiophenes, Adv. Mater. 10 (1998) 93.
[25] Z. Bao, A. Dodabalapur, A.J. Lovinger, Soluble and processable regioregular poly(3-hexylthiophene) for thin film field-effect transistor applications with high mobility, Appl. Phys. Lett. 69 (1996) 4108–4110.
[26] H. Sirringhaus, P.J. Brown, R.H. Friend, M.M. Nielsen, K. Bechgaard, B.M.W. Langeveld-Voss, A.J.H. Spiering, R.A.J. Janssen, E.W. Meijer, P. Herwig, D.M. de Leeuw, Two-dimensional charge transport in self-organized, high-mobility conjugated polymers, Nature 401 (1999) 685–688.
[27] L.B. Groenendaal, F. Jonas, D. Freitag, H. Pielartzik, J.R. Reynolds, Poly(3,4-ethylenedioxythiophene) and its derivatives: past, present, and future, Adv. Mater. 12 (2000) 481–494.
[28] S. Kirchmeyer, K. Reuter, Scientific importance, properties and growing application of poly(3,4-ethylenedioxythiophene), J. Mater. Chem. 15 (2005) 2077–2088.
[29] J.D. Cohen, D.V. Lang, Calculation of the dynamic response of Schottky barriers with a continuous distribution of gap states, Phys. Rev. B 25 (1982) 5321–5350.
[30] L.C. Kimerling, Influence of deep traps on the measurement of free-carrier distributions in semiconductors by junction capacitance techniques, J. Appl. Phys. 45 (1974) 1839–1845.
[31] T. Walter, R. Herberholz, C. Muller, H.W. Schock, Determination of defect distributions from admittance measurements and application to $Cu(In,Ga)Se_2$ based heterojunctions, J. Appl. Phys. 80 (1996) 4411–4420.
[32] P.P. Boix, G. Garcia-Belmonte, U. Munecas, M. Neophytou, C. Waldauf, R. Pacios, Determination of gap defect states in organic bulk heterojunction solar cells from capacitance measurements, Appl. Phys. Lett. 95 (2009) 233302.
[33] C. Goh, R.J. Kline, M.D. McGehee, E.N. Kadnikova, J.M.J. Frechet, Molecular-weight-dependent mobilities in regioregular poly(3-hexyl-thiophene) diodes, Appl. Phys. Lett. 86 (2005) 122110.
[34] Z. Chiguvare, V. Dyakonov, Trap-limited hole mobility in semiconducting poly(3-hexylthiophene), Phys. Rev. B 70 (2004) 235207.
[35] A.W. Hains, Z. Liang, M.A. Woodhouse, B.A. Gregg, Molecular semiconductors in organic photovoltaic cells, Chem. Rev. 110 (2010) 6689–6735.
[36] G. Garcia-Belmonte, P.P. Boix, J. Bisquert, M. Sessolo, H.J. Bolink, Simultaneous determination of carrier lifetime and electron density-of-states in P3HT:PCBM organic solar cells under illumination by impedance spectroscopy, Solar Energy Mater. Solar Cells 94 (2010) 366–375.

omy of scale both through straight-forward synthesis and processing. While a limited number of high mobility, environmental stable materials have been advanced [7,25–30], one of the key challenges, which remains and limits further progress, is the provision of straight-forward and meaningful comparisons between the electronic properties of different compounds. Such comparisons would allow for efficient materials design and screening but necessitates high reproducibility in synthesis, processing and reliable device fabrication and characterization.

Blending of organic semiconductors with insulating (semi-crystalline) polymers has been shown to be a useful strategy to address, among other things, the latter two issues [31–38]. In addition, blending with properly selected commodity polymers to the semiconducting material(s) should enable control over melt- and solution viscosity. In the case of small-molecular semiconductors, a suitable polymer matrix may furthermore be mandatory to meet the ink rheology requirements for specific printing steps in solution-processed devices. From a device point of view, blending is an interesting approach, as it may also lead to multi-component structures with a property matrix that is often not accessible with the individual components. The latter is possibly best exemplified by organic semiconductor:insulator blends, which – under appropriate processing conditions – feature excellent performance in organic field-effect transistors (OFETs) and organic photovoltaics (OPVs) at remarkably low semiconductor contents combined with highly desirable mechanical properties when a tough insulating component is utilized [31]. Besides improved and reliable film formation, blending promises the prospect for major cost reduction, truly "flexible" electronics and, often, significantly enhanced environmental stability of devices produced with them.

In the present study we explored bi-component blends comprising arylacetylenes and the insulating poly(vinylidene fluoride) (PVDF). PVDF was selected as the insulating component as this polymer has been shown to allow film processing at room temperature of, for instance, poly(3-hexylthiophene) (P3HT):PVDF binaries [33]; this in contrast to, e.g., blends based on high-density polyethylene which require deposition temperatures above ~70 °C [31,32]. For the semiconducting species, we focused on *small-molecular* arylacetylenes [39–50]. From a synthetic point of view these compounds exhibit a number of advantages, including availability of efficient synthetic protocols [51–59] that offer the possibility to access in large quantities a broad variety of molecules with specific geometries and flexibility in new conceptions of steric and conformational structures. In addition, their shape-persistent rod-like structures may be of beneficial use for the construction of a broad spectrum of nano and microstructures. A further major advantage of arylacetylenes is that they can be readily synthesized from easily accessible precursors, do not require exotic, rare materials, reducing risks regarding materials supply or costs; their production can easily be scaled up; and, finally, the compounds can readily be isolated in high purity.

Here, we concentrate on arylacetylenes with an anthracene [60,61] backbone, since this core may enable enhanced solubility and stability when compared to, for instance, pentacene, which has become a benchmark in the organic electronics field. Moreover, the anthracene core is a beneficial chromophore unit. Importantly, their chemical structure allows for derivatization with flexible chains at the terminal phenyl-ring systems to modulate the phase behavior and solubility of the resulting arylacetylenes. Those latter attributes permit to manipulate their solid-state structure over a large range of length scales, the influence of which on simple electronic characteristics being the subject of this study.

2. Experimental

2.1. Materials

9,10-Bis(phenylethynyl)anthracene (**1**) was purchased from Alfa Aesar GmbH & Co KG, Karlsruhe, Germany, and used as received. 9,10-Bis[3,4-bis(hexyloxy)phenylethynyl]anthracene (**2**) was synthesized according to a previously reported procedure [44]. Poly(vinylidene fluoride) (PVDF) (M_w = 534 kg/mol) was acquired from Aldrich, Steinheim, Germany. Cyclohexanone was purchased from Acros, Geel, Belgium, and used as received.

2.2. Sample preparation

Blends for thermal analysis and optical microscopy were prepared by co-dissolving the semiconducting species and PVDF in cyclohexanone (~2 wt.% total solids content) at 100 °C, followed by solvent evaporation at ambient conditions or at ~100 °C. Blends for OFETs were prepared by co-dissolving the different materials in cyclohexanone (~6 wt.% solids content) at 100 °C, followed by subsequent adjustment of the solution temperatures to the respective processing temperatures of 25, 50, 75 or 100 °C. To allow film fabrication under isothermal conditions, solutions, metal substrate holders and substrates (doped silicon–silicon oxide (Si–SiO_2)) were equilibrated for ca. 10 min at the designated temperature before spin-drop-casting active layers with a Laurell WS-400B-6NPP/LITE spin-coater at 500 rpm. Note, however, that dissolution temperatures below 100 °C could have been applied, if required, as indicated by the crystallization temperature/composition diagrams of the blend components (*cf.* Figs. 1 and 2b). In addition, the substituted derivative **2** allows fabrication of solutions that are stable under ambient conditions and, hence, can be stored at room temperature without featuring precipitation of the solutes.

2.3. Characterization

Differential scanning calorimetry (DSC) was conducted under N_2 atmosphere at a scan rate of 10 °C/min with a Mettler Toledo DSC 822^e instrument. For DSC analysis of **1**, **2** and PVDF in cyclohexanone, medium pressure 120 μl Mettler stainless steel crucibles sealed with Viton O-rings were utilized. The total sample weight varied between 20 and 40 mg. For characterization of the dried blend films, amounts of ~5 mg were sealed in Al standard 40 μl crucibles.

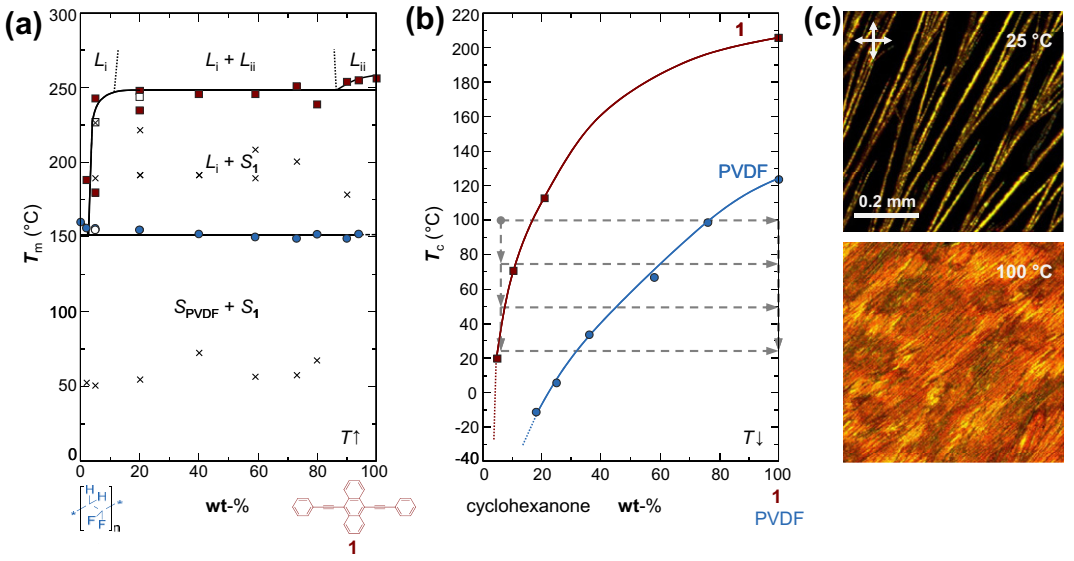

Fig. 1. (a) Binary non-equilibrium temperature/composition diagram of **1**:PVDF blends produced by co-dissolution in cyclohexanone, followed by solvent evaporation at ambient. The diagrams were constructed with peak temperatures recorded during first heating in differential scanning calorimetry (DSC, filled symbols) and polarized optical microscopy (open symbols). L_i, L_{ii} denote liquid phases and S_1, S_{PVDF} solid phases of compound **1** and PVDF, resp.; x indicates exceedingly minor endothermic transitions. (b) Superimposed crystallization temperature/composition diagrams of **1**:cyclohexanone and PVDF:cyclohexanone constructed with DSC peak crystallization temperatures in second cooling thermograms. The gray dashed lines indicate different processing routes applied for **1**:PVDF binaries with solvent removal at 25, 50, 75 or 100 °C, followed by cooling to room temperature. (c) Polarized optical micrographs of **1**:PVDF 40:60 blends solidified at 25 °C (top) and 100 °C (bottom), respectively (polarizer/analyzer indicated with white arrows).

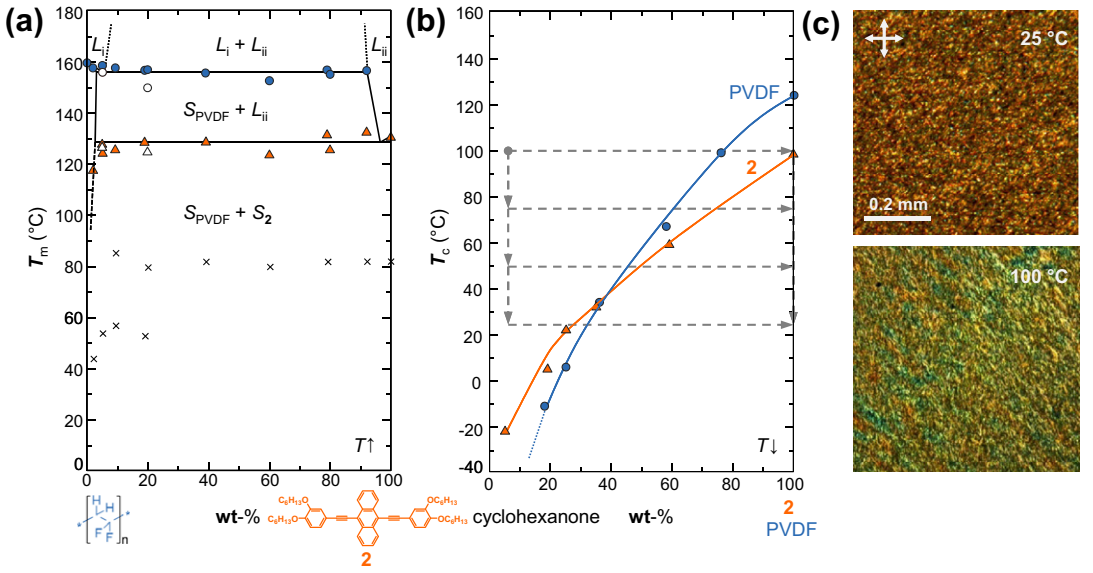

Fig. 2. (a) Binary non-equilibrium temperature/composition diagram of **2**:PVDF blends. L_i, L_{ii} denote liquid phases and S_2, S_{PVDF} solid phases of compound **2** and PVDF, resp.; x indicates exceedingly minor endothermic transitions. (b) Superimposed crystallization temperature/composition diagrams of **2**:cyclohexanone and PVDF:cyclohexanone constructed with DSC peak crystallization temperatures in second cooling thermograms. (c) Polarized optical micrographs of **2**:PVDF 40:60 blends solidified at 25 °C (top) and 100 °C (bottom), respectively (polarizer/analyzer indicated with white arrows).

Room temperature optical microscopy was carried out with a Leica DM4000M polarizing microscope. Variable temperature polarized optical microscopy was performed with a Leica DMRX microscope equipped with a Mettler Toledo FP82HT hot stage. For construction of temperature/composition diagrams of binaries of low semiconductor contents, blend films were heated at 10 °C/min in the hot stage under N_2 atmosphere; in these cases transition temperatures were deduced from the disappearance of birefringence of the respective crystalline phases. At higher

arylacetylene contents, peak endo- and exotherm temperatures recorded by DSC were employed.

Bottom-gate bottom-contact organic field-effect transistors were fabricated on highly doped Si-wafers with a thermally grown ~250 nm SiO_2 layer. The two layers served as the gate electrode and gate insulator, respectively. Au source and drain electrodes (30 nm thick) were defined by standard photolithography (channel length, $L = 10$ μm; channel width, $W = 10$ mm). Prior to use, the Si–SiO_2 substrates were cleaned in an ultrasonic bath with acetone and isopropyl alcohol, followed by drying with a nitrogen flow. Electronic characterization of the OFETs was carried out in a N_2 atmosphere with a Keithley 4200 semiconductor parameter analyzer.

3. Results and discussion

3.1. 9,10-Bis(phenylethynyl)anthracene:PVDF

In a first set of experiments, the phase behavior of blends of the commercially available 9,10-bis(phenylethynyl)anthracene **1** ($T_m = 256$ °C) and PVDF was explored. For this purpose, the non-equilibrium temperature/composition diagram of the **1**:PVDF binary was determined by differential scanning calorimetry (DSC) and variable-temperature polarized optical microscopy – see Fig. 1a. As is evident from this diagram, the small-molecular semiconductor and polymer insulator are largely incompatible, resulting in a classical monotectic behavior featuring an extremely large miscibility gap. The significant difference between the melting temperatures between the two components resulted in a $L_i + S_1$ two-phase region that extended over more than 100 °C.

The phase behavior of blends of **1**:PVDF naturally has a significant influence also when processing them from solution. This is illustrated with a 40:60 wt.% **1**:PVDF blend, the composition of which was selected to provide a good compromise between electronic characteristics and film forming properties. When cast at 25 °C from cyclohexanone (~2 wt.% total material content), the semiconducting:insulating binary formed a microstructure comprised of crystalline arylacetylene needles of hundreds of microns length coarsely distributed throughout a PVDF matrix (Fig. 1c). The formation of this solid-state structure is readily understood on the basis of the superimposed crystallization temperature/composition diagrams of the two respective components and the solvent cyclohexanone, presented in Fig. 1b. These diagrams indicate that during evaporation of the solvent from this blend, **1** solidified prior to PVDF essentially at all compositions. Due to the relatively large gap between the solidus of the two components, *i.e.* the significant difference in supercooling that is required for the semiconductor and insulator to solidify from cyclohexanone, a coarse, highly phase separated structure resulted, combining features of the microstructures that are observed when processing the neat blend components at that same temperature.

Not unexpectedly, increasing the rate of solidification of the two components by applying higher deposition temperatures, causing an enhanced rate of solvent evaporation, yielded a much finer and more homogeneous microstructure (*cf.* Fig. 1c), similar to those observed for α-quaterthiophene:polyethylene blends reported previously [32]. However, from a processing point of view – particularly with respect to printing – high-temperature operations are not particularly desirable, and, therefore we explored influencing the microstructure formation not by thermal means but by chemical modification of the semiconducting species.

3.2. 9,10-Bis[3,4-bis(hexyloxy)phenylethynyl]anthracene:PVDF

In order to beneficially alter the phase- and solidification behavior of the semiconducting:insulating arylacetylene:PVDF blends through adjustment of the physicochemical properties of the small-molecular compound by chemical modification, we elected to introduce four flexible hexyloxy side-chains at the terminal phenyl-ring systems. This compound **2**, consequently, featured a considerably lower melting temperature ($T_m = 131$ °C), and associated enhanced solubility in common solvents, compared to its unsubstituted counterpart **1**. The **2**:PVDF temperature/composition diagram is shown in Fig. 2a. From this diagram, it is clear that also this compound, like **1**, is largely incompatible with PVDF. However, due to its lower melting temperature, the temperature range between liquidus and solidus lines in the two systems is significantly reduced, *i.e.* from ΔT ~100 °C for **1**:PVDF blends to ~30 °C for the **2**:PVDF binaries.

The significantly increased solubility of **2** in cyclohexanone also resulted in a distinct shift of its solidus not only to lower temperatures but also higher concentrations (Fig. 2b). As a consequence, the (superimposed) crystallization temperature/composition diagrams of **2**:cyclohexanone and PVDF:cyclohexanone feature a crossover of the two solidus lines; and, hence, there exist two distinct regimes in which, in principle, the semiconductor can either crystallize prior to, or after the polymer. In either case, however, at any given concentration or temperature, below their liquidus the difference in supercooling experienced by both components is relatively small when compared to the above described binary. As a consequence, invariably the organic semiconductor **2** and PVDF solidified virtually simultaneously, yielding fine grained structures. Accordingly, in this system, the semiconductor solidified in a much finer microstructure than that observed for the neat species, both at room temperature and 100 °C (*cf.* Fig. 2c). Note, however, that above and below 40–50 °C the sequence of solidification reversed.

3.3. Electronic properties

Having the chemical means and corresponding processing protocols to readily adjust arylacetylenes:PVDF blend microstructure by either controlling composition or deposition temperature, we sought to elucidate the influence of solid-state morphology on the performance of devices fabricated with them, and also probed if their electronic characteristics were affected by the solubilizing side-chain substitutions. For this purpose, bottom-gate, bottom-

contact field-effect transistors were fabricated with binaries of PVDF comprising 40 wt.% of, respectively, **1** and **2**, casting them at 25, 50, 75 or 100 °C. Electronic characteristics of these devices are presented in Fig. 3 and in the Supplementary data.

What is immediately evident from the OFET data presented is that the performance of devices with **1**:PVDF binaries increased steadily with the deposition temperature. By contrast, processing conditions had only a minor influence on OFET performance of **2**:PVDF blends; however an optimum casting temperature was observed around 50 °C. These observations can be directly correlated with the superimposed temperature/composition diagrams presented in Figs. 1 and 2. As shown above for **1**:PVDF blends, a rapid solidification sequence of the two components, realized through thermal control of the rate of solvent evaporation, resulted in a finely phase-separated blend microstructure, apparently, enhancing device performance. In the case of compound **2**, the reduced melting temperature and increased solubility resulting from the introduction of side-chains, caused the two components under most conditions to solidify rapidly after each other, if not simultaneously, even when casting the active layer at room temperature. The resulting finely phase-separated bi-component layers invariably lead to good device characteristics. Deposition at more elevated temperatures (>50 °C), however, (slightly) affected OFET performance of **2**:PVDF blends in a negative manner, despite the observation that the degree of phase segregation in the binary film was not significantly different. We attributed this to the fact that in these cases the sequence of crystallization of the components is reversed at elevated temperatures, with the insulating polymer crystallizing *prior* to the active species. The latter observation is in agreement with previous work in which it was shown that this solidification mode not only does not promote the necessary percolation of the semiconducting species, but might even prevent that [31,62].

From the above it is clear that very similar device characteristics (charge-carrier mobility $\mu_{FET} \sim 5 \times 10^{-4}$ cm^2/Vs; ON–OFF ratio $\sim 10^3$) can be obtained for both arylacetylenes, provided that a finely phase-separated blend structure is induced. For all blend systems explored, devices were injection limited, resulting in a sub-linear dependence of source–drain currents, I_{sd}, at small source–drain bias, V_{sd} in the output characteristics (*cf.* Fig. 3). However, as the contact resistance seems to be comparable for arylacetylenes:PVDF OFETs, the electronic characteristics still allow meaningful comparison, even though, as a consequence of the limited charge injection, mobility values determined might be underestimated. Importantly, the melting-temperature-reducing and solubilizing hexyloxy side-chains in compound **2** did not negatively affect charge transport. Furthermore, this study shows that a key for providing meaningful comparisons between different semiconducting species – even simple derivatives – is to

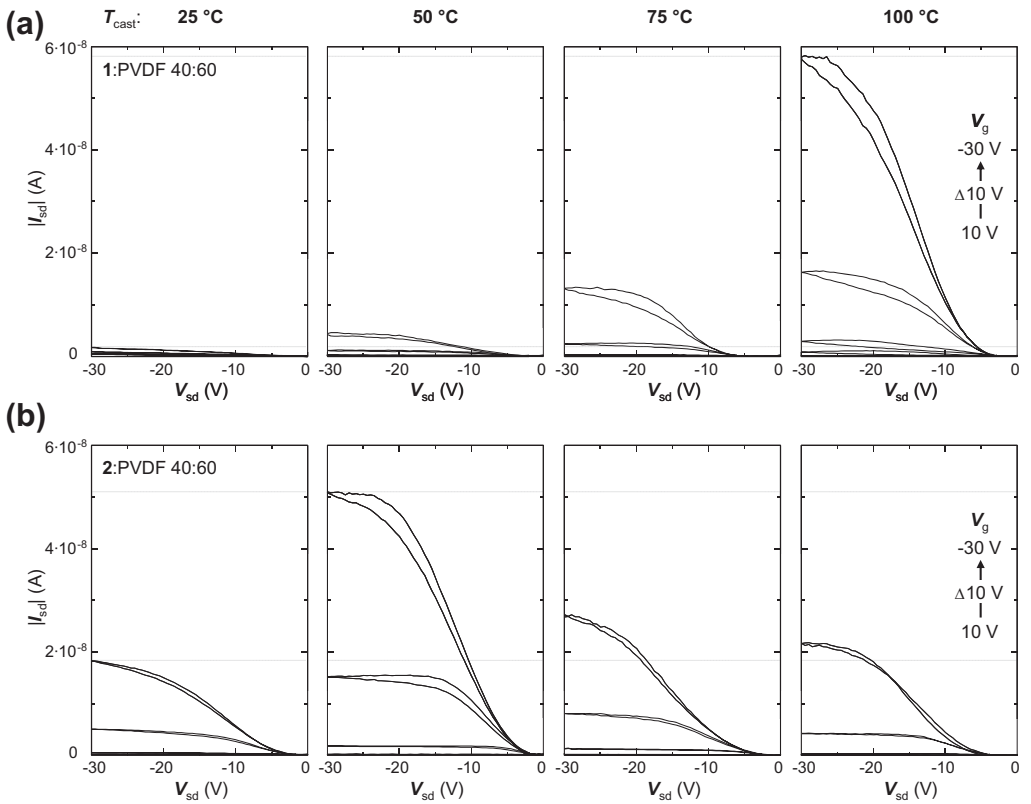

Fig. 3. (a) Output characteristics of bottom-gate bottom-contact OFETs (L = 10 μm; W = 10 mm) of **1**:PVDF and (b) **2**:PVDF 40:60 blend films fabricated at 25, 50, 75 and 100 °C. In all graphs, forward and backward scans are shown. Gray dotted lines indicate $I_{sd,max}$ of OFETs comprising **1**:PVDF blend films produced via solvent evaporation at 100 and 25 °C, respectively and **2**:PVDF binaries fabricated at 50 and 25 °C, respectively.

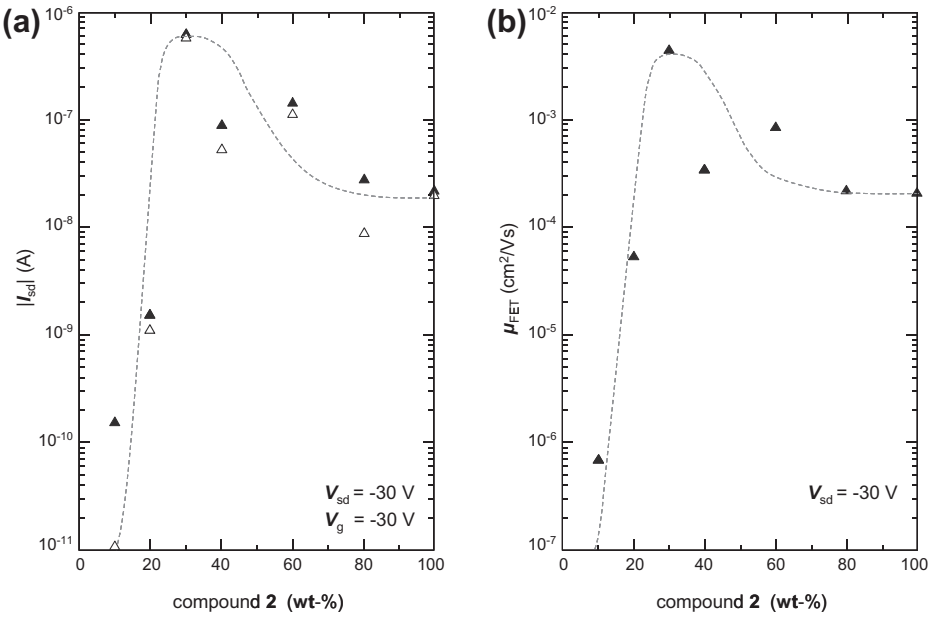

Fig. 4. (a) Source–drain currents, I_{sd}, of **2**:PVDF binaries of different compositions solidified at 50 °C at $V_{sd} = V_g = -30$ V, deduced from OFET transfer (filled symbols) and output characteristics (open symbols). (b) Corresponding field-effect mobilities deduced from the saturated regime in OFET transfer characteristics (dashed lines are a guide to the eye only).

select processing conditions that are adjusted to the phase behavior of the respective system to yield comparable structures of their solid state. Simple binary crystallization temperature/composition diagrams of the individual component in the solvent selected are useful to understand solidification kinetics and to identify a suitable processing window, both with respect of selection of deposition temperatures and solution concentrations.

3.4. Percolation

After having established optimum processing conditions of typical blends of PVDF with both semiconducting compounds **1** and **2**, we proceeded to explore the maximum content of the insulating polymer that could be added without dramatically deteriorating the electronic properties of such blends. For this purpose we concentrated on **2**:PVDF binaries as they allow for a significantly broader processing window both with respect of deposition temperature and composition when compared to the **1**:PVDF system. Thus, OFETs were fabricated with active layers of a range of compositions *via* solvent evaporation at 50 °C.

Remarkably, the electronic performance of the devices was found to *increase* by more than one order of magnitude when certain amounts of PVDF were added to the semiconductor, as indicated by the significantly increased source–drain currents and field-effect mobilities (Fig. 4). Maximum device performance was reached for a blend comprising only ~30 wt.% of the semiconductor **2**; the latter featured ON-currents of $\sim 5 \times 10^{-7}$ A, field-effect mobilities in the saturation regime of $\sim 4 \times 10^{-3}$ cm^2/Vs and ON–OFF ratios of 10^3 compared to corresponding values of, resp. $\sim 2 \times 10^{-8}$ A, $\sim 2 \times 10^{-4}$ cm^2/Vs and 10^2 for the neat compound **2**. Evidently, adding the insulating polymer PVDF to the small-molecular semiconductor enhanced the electronic performance of the latter species. We attribute this beneficial phenomenon to improved film-forming properties of such blends. At high small molecule content ($\geqslant$80 wt.%), film formation is dominated by that species and the amount of polymeric material appears to be insufficient to provide for the generation of continuous and homogenous active layers. As a consequence, the resulting brittle and discontinuous films featured negatively affected charge transport. On the other hand, blends comprising >70 wt.% of the insulating polymer appeared to feature a solid-state structure in which the organic semiconducting compound increasingly failed to form a percolating network required for electronic transport.

4. Conclusions

In summary, we presented blends of two small-molecular arylacetylene derivatives with the semi-crystalline, insulating polymer PVDF that exhibit FET characteristics comparable to those of the neat semiconductors. The chemical design of the two semiconducting compounds was selected in such a way that it allows facile synthesis protocols with readily accessible up-scaling options and permits control of their thermal properties. Beneficially, selection of processing controls was found to be more critical in obtaining optimum device performance than molecular design, which indicates that electronic characteristics can be tailored from the outset while processing parameters can be adjusted according to the phase behavior of the active compound.

Acknowledgements

This research was funded by the European Community's Seventh Framework Programme (FP7/2007-2013) under grant agreement No. 212311 of the ONE-P project. N.S. in addition acknowledges support from UK's Engineering and Physical Sciences Research Council (EPSRC) EP/G060738/1. L.V. and A.M. gratefully acknowledge the Ministero dell'Istruzione, dell'Università e della Ricerca (MIUR) and University of Perugia for support of this research through the *FIRB-Futuro in Ricerca (Projects RBFR08TTWW and RBFR08J78Q)* and *PRIN 2008* initiatives.

Appendix A. Supplementary data

Supplementary data associated with this article can be found, in the online version, at doi:10.1016/j.orgel.2011.07.018.

References

[1] C.K. Chiang, C.R. Fincher, Y.W. Park, A.J. Heeger, H. Shirakawa, E.J. Louis, S.C. Gau, A.G. MacDiarmid, Phys. Rev. Lett. 39 (1977) 1098–1101.
[2] Y. Cao, P. Smith, A.J. Heeger, Synth. Met. 48 (1992) 91–97.
[3] J.H. Burroughes, D.D.C. Bradley, A.R. Brown, R.N. Marks, K. Mackay, R.H. Friend, P.L. Burns, A.B. Holmes, Nature 347 (1990) 539–541.
[4] J.J.M. Halls, C.A. Walsh, N.C. Greenham, E.A. Marseglia, R.H. Friend, S.C. Moratti, A.B. Holmes, Nature 376 (1995) 498–500.
[5] G. Yu, J. Gao, J.C. Hummelen, F. Wudl, A.J. Heeger, Science 270 (1995) 1789–1791.
[6] M. Mushrush, A. Facchetti, M. Lefenfeld, H.E. Katz, T.J. Marks, J. Am. Chem. Soc. 125 (2003) 9414–9423.
[7] C.R. Newman, C.D. Frisbie, D.A. da Silva Filho, J.-L. Brédas, P.C. Ewbank, K.R. Mann, Chem. Mater. 16 (2004) 4436–4451.
[8] J.E. Anthony, Angew. Chem. Int. Ed. 47 (2008) 452–483.
[9] H.E. Katz, Z. Bao, S.L. Gilat, Acc. Chem. Res. 34 (2001) 359–369.
[10] K.M. Coakley, M.D. McGehee, Chem. Mater. 16 (2004) 4533–4542.
[11] S. Allard, M. Forster, B. Souharce, H. Thiem, U. Scherf, Angew. Chem. Int. Ed. 47 (2008) 4070–4098.
[12] I. McCulloch, M. Heeney, C. Bailey, K. Genevicius, I. MacDonald, M. Shkunov, D. Sparrowe, S. Tierney, R. Wagner, W. Zhang, M.L. Chabinyc, R.J. Kline, M.D. McGehee, M.F. Toney, Nature Mater. 5 (2006) 328–333.
[13] A.R. Murphy, J.M.J. Fréchet, Chem. Rev. 107 (2007) 1066–1096.
[14] D.M. de Leeuw, M.M.J. Simenon, A.R. Brown, R.E.F. Einerhand, Synth. Met. 87 (1997) 53–59.
[15] K. Kawano, R. Pacios, D. Poplavskyy, J. Nelson, D.D.C. Bradley, J.R. Durrant, Sol. Energy Mater. Sol. Cells 90 (2006) 3520–3530.
[16] M. Jorgensen, K. Norrman, F.C. Krebs, Sol. Energy Mater. Sol. Cells 92 (2008) 686–714.
[17] T.D. Anthopoulos, G.C. Anyfantis, G.C. Papavassiliou, D.M. de Leeuw, Appl. Phys. Lett. 90 (2007) 122105-1–122105-3.
[18] D.J. Gundlach, Y.Y. Lin, T.N. Jackson, S.F. Nelson, D.G. Schlom, IEEE Electron Device Lett. 18 (1997) 87–89.
[19] C.D. Dimitrakopoulos, D.J. Mascaro, IBM J. Res. Dev. 45 (2001) 11–27.
[20] D. Knipp, R.A. Street, A. Volkel, J. Ho, J. Appl. Phys. 93 (2003) 347–355.
[21] R. Ruiz, D. Choudhary, B. Nickel, T. Toccoli, K.-C. Chang, A.C. Mayer, P. Clancy, J.M. Blakely, R.L. Headrick, S. Iannotta, G.G. Malliaras, Chem. Mater. 16 (2004) 4497–4508.
[22] G. Dennler, C. Lungenschmied, H. Neugebauer, N.S. Sariciftci, A. Labouret, J. Mater. Res. 20 (2005) 3224–3233.
[23] F.C. Krebs, H. Spanggard, T. Kjaer, M. Biancardo, J. Alstrup, Mater. Sci. Eng., B 138 (2007) 106–111.
[24] A. Facchetti, T.J. Marks, Transparent Electronics, in: From Synthesis to Applications, Wiley, Chichester, UK, 2010.
[25] J.E. Anthony, D.L. Eaton, S.R. Parkin, Org. Lett. 4 (2002) 15–18.
[26] B.A. Jones, M.J. Ahrens, M.-H. Yoon, A. Facchetti, T.J. Marks, M.R. Wasielewski, Angew. Chem. Int. Ed. 43 (2004) 6363–6366.
[27] K. Takimiya, Y. Kunugi, T. Otsubo, Chem. Lett. 36 (2007) 578–583.
[28] H. Yan, Z. Chen, Y. Zheng, C. Newman, J.R. Quinn, F. Dötz, M. Kastler, A. Facchetti, Nature 457 (2009) 679–687.
[29] J. Smith, A. Bashir, G. Adamopoulos, J.E. Anthony, D.D.C. Bradley, R. Hamilton, M. Heeney, I. McCulloch, T.D. Anthopoulos, Adv. Mater. 22 (2010) 3598–3602.
[30] X. Guo, R.P. Oritz, Y. Zheng, Y. Hu, Y.-Y. Noh, K.-J. Baeg, A. Facchetti, T.J. Marks, J. Am. Chem. Soc. 133 (2011) 1405–1418.
[31] S. Goffri, C. Müller, N. Stingelin-Stutzmann, D.W. Breiby, C.P. Radano, J.W. Andreasen, R. Thompson, R.A.J. Janssen, M.M. Nielsen, P. Smith, H. Sirringhaus, Nature Mater. 5 (2006) 950–956.
[32] P. Wolfer, C. Müller, P. Smith, M.A. Baklar, N. Stingelin-Stutzmann, Synth. Met. 157 (2007) 827–833.
[33] D. Sparrowe, M. Baklar, N. Stingelin, Org. Electron. 11 (2010) 1296–1300.
[34] J. Smith, R. Hamilton, I. McCulloch, N. Stingelin-Stutzmann, M. Heeney, D.D.C. Bradley, T.D. Anthopoulos, J. Mater. Chem. 20 (2010) 2562–2574.
[35] M.-B. Madec, D. Crouch, G.R. Llorente, T.J. Whittle, M. Geoghegan, S.G. Yeates, J. Mater. Chem. 18 (2008) 3230–3236.
[36] T. Ohe, M. Kuribayashi, R. Yasuda, A. Tsuboi, K. Nomoto, K. Satori, M. Itabashi, J. Kasahara, Appl. Phys. Lett. 93 (2008) 053303-1–053303-3.
[37] J. Kang, N. Shin, D.Y. Jang, V.M. Prabhu, D.Y. Yoon, J. Am. Chem. Soc. 130 (2008) 12273–12275.
[38] W.H. Lee, J.A. Lim, D. Kwak, J.H. Cho, H.S. Lee, H.H. Choi, K. Cho, Adv. Mater. 21 (2009) 4243–4248.
[39] R.E. Martin, F. Diederich, Angew. Chem. Int. Ed. 38 (1999) 1350–1377.
[40] J.M. Tour, Acc. Chem. Res. 33 (2000) 791–804.
[41] J. Cornil, Y. Karzazi, J.L. Brédas, J. Am. Chem. Soc. 124 (2002) 3516–3517.
[42] V.A.L. Roy, Y.-G. Zhi, Z.-X. Xu, S.-C. Yu, P.W.H. Chan, C.-M. Che, Adv. Mater. 17 (2005) 1258–1261.
[43] T. Yasuda, K. Kashiwagi, Y. Morizawa, T. Tsutsui, J. Phys. D: Appl. Phys. 40 (2007) 4471–4475.
[44] L. Valentini, D. Bagnis, A. Marrocchi, M. Seri, A. Taticchi, J.M. Kenny, Chem. Mater. 20 (2008) 32–34.
[45] Q. Meng, J. Gao, R. Li, L. Jiang, C. Wang, H. Zhao, C. Liu, H. Li, W. Hu, J. Mater. Chem. 19 (2009) 1477–1482.
[46] A. Marrocchi, F. Silvestri, M. Seri, A. Facchetti, A. Taticchi, T.J. Marks, Chem. Commun. (2009) 1380–1382.
[47] A. Marrocchi, M. Seri, C. Kim, A. Facchetti, A. Taticchi, T.J. Marks, Chem. Mater. 21 (2009) 2592–2594.
[48] M. Kivala, F. Diederich, Acc. Chem. Res. 42 (2009) 235–248.
[49] F. Silvestri, A. Marrocchi, Int. J. Mol. Sci. 11 (2010) 1471–1508.
[50] F. Silvestri, A. Marrocchi, M. Seri, C. Kim, T.J. Marks, A. Facchetti, A. Taticchi, J. Am. Chem. Soc. 132 (2010) 6108–6123.
[51] R.R. Schrock, Polyhedron 14 (1995) 3177–3195.
[52] K. Weiss, A. Michel, E.-M. Auth, E.H.F. Bunz, T. Mangel, K. Mullen, Angew. Chem. Int. Ed. Engl. 36 (1997) 506–509.
[53] K. Sonogashira, Metal Catalyzed Cross-Coupling Reactions, Wiley-VCH, Weinheim, Germany, 1998.
[54] P. Siemsen, R.C. Livingston, F. Diederich, Angew. Chem. Int. Ed. 39 (2000) 2633–2657.
[55] W. Zhang, S. Kraft, J.S. Moore, J. Am. Chem. Soc. 126 (2004) 329–335.
[56] B. Liang, M. Dai, J. Chen, Z. Yang, J. Org. Chem. 70 (2005) 391–393.
[57] F. Monnier, F. Turtaut, L. Duroure, M. Taillefer, Org. Lett. 10 (2008) 3203–3206.
[58] Y.Y. Kuang, F.E. Chen, Helv. Chim. Acta 92 (2009) 897–902.
[59] D.A. Fulmer, W.C. Shearouse, S.T. Mendonza, J. Mack, Green Chem. 11 (2009) 1821–1825.
[60] H. Meng, F. Sun, M.B. Goldfinger, G.D. Jaycox, Z. Li, W.J. Marshall, G.S. Blackman, J. Am. Chem. Soc. 127 (2005) 2406–2407.
[61] J.E. Anthony, Chem. Rev. 106 (2006) 5028–5048.
[62] C. Müller, S. Goffri, J.W. Andreasen, D.W. Breiby, H.D. Chanzy, R.A.J. Janssen, M.M. Nielsen, C.P. Radano, H. Sirringhaus, P. Smith, N. Stingelin-Stutzmann, Adv. Funct. Mater. 17 (2007) 2674–2679.

In this work, a phosphine oxide based high efficiency green phosphorescent host material was synthesized for optimum charge balance in the emitting layer and it was combined with high efficiency deep blue emitting layer to obtain high quantum efficiency in PHWOLEDs. A high quantum efficiency over 25% was obtained from the green PHOLEDs, and a quantum efficiency of 21.6% and power efficiency of 47.0 lm/W were demonstrated from the PHWOLEDs using the new green host material. The quantum efficiency value achieved in this work is comparable to that the efficiency values reported in green PHOLEDs and WOLEDs without any out-coupling enhancement and p-i-n doping structure [15–17].

2. Experimental

2.1. Synthesis

The synthetic route of the 2,7-bis(diphenylphosphoryl)-3′-phenyl-9,9′-spirobi[fluorene] (BPSBF) is shown in Scheme 1.

2.2. Synthesis of 2-bromo-m-terphenyl (1)

A solution of *o*-bromoiodobenzene (5.14 g, 18.1 mmol), 3-biphenylboronic acid (3 g, 15 mmol), tetrakis(triphenylphosphine)palladium(0) (0.86 g, 0.75 mmol) and THF (30 mL) were stirred in a two-necked flask under nitrogen atmosphere for 30 min. Potassium carbonate (8.29 g, 2 M solution) was added to a reaction mixture dropwise over a period of 20 min. The resulting solution was refluxed overnight at 80 °C. The reaction mixture was extracted with dichloromethane and water, and the organic layer was evaporated with a rotary evaporator. The resulting powdery product was purified by column chromatography from n-hexane to give a white crystalline solid. The 2,7-dibromo-3′-phenyl-9,9′-spirobi[fluorene] (2) was synthesized according to the method that described in previous work [18].

2.3. Synthesis of 2,7-bis(diphenylphosphoryl)-3′-phenyl-9,9′-spirobi[fluorene] (BPSBF)

2,7-Dibromo-3′-phenyl-9,9′-spirobi[fluorene] (2) (1.35 g, 2.43 mmol) was dissolved in 30 mL of anhydrous tetrahydrofuran under argon and cooled to −78 °C and 1.2 eq. of *n*-butyllithium (2.5 M in hexanes, 2.43 mL) was added dropwise to give a bright yellow solution that thickened to a slurry. The stirring was continued for 3 h at −78 °C after which 1.12 mL (6.08 mmol) of chlorodiphenylphosphine was added giving a clear, pale yellow solution. The reaction was stirred for 10 h at room temperature before quenching with 10 mL of degassed methanol. Volatiles were removed under a reduced pressure to give an off-white solid that was digested in methanol, filtered, then digested in water, and filtered. The crude material was purified by column chromatography. The purified compound was reacted with 2 mL of 30% hydrogen peroxide in 10 mL of methylene chloride. The mixture was stirred overnight at room temperature. The organic layer was separated and washed with water and then brine. The extract was evaporated to dryness affording a white solid.

BPSBF Yield 40%. Tg 119 °C. ^{1}H NMR (200 MHz, $CDCl_3$): δ 7.78 (d, 2H, J = 7.6 Hz), 7.64–7.29 (m, 28H), 7.03 (t, 1H, J = 7.3 Hz), 6.88–6.81 (m, 2H), 6.58–6.47 (m, 3H), 5.98 (d, 2H, J = 7.0 Hz). ^{13}C-NMR (100 MHz, $CDCl_3$) δ 150.4, 150.3, 146.9, 144.4, 143.2, 141.8, 140.4, 139.2, 133.8, 133.3, 132.9, 131.7, 131.2, 129.9, 129.1, 128.3, 128.1, 127.8, 127.0, 126.3, 121.0, 120.7, 120.3, 66.1. MS (FAB) m/z 792 [(M + H)$^+$]. Anal. Calcd. for $C_{55}H_{38}O_2P_2$: C, 83.32; H, 4.83. Found: C, 83.16; H, 4.86.

2.4. General analysis

The ^{1}H and ^{13}C nuclear magnetic resonance (NMR) spectra were recorded on a Varian 200 (200 MHz) and 400 (400 MHz) spectrometers. The photoluminescence (PL) spectra were recorded on a fluorescence spectrophotometer (HITACHI, F-7000) and the ultraviolet–visible (UV–Vis) spectra were obtained using UV–vis spectropho-

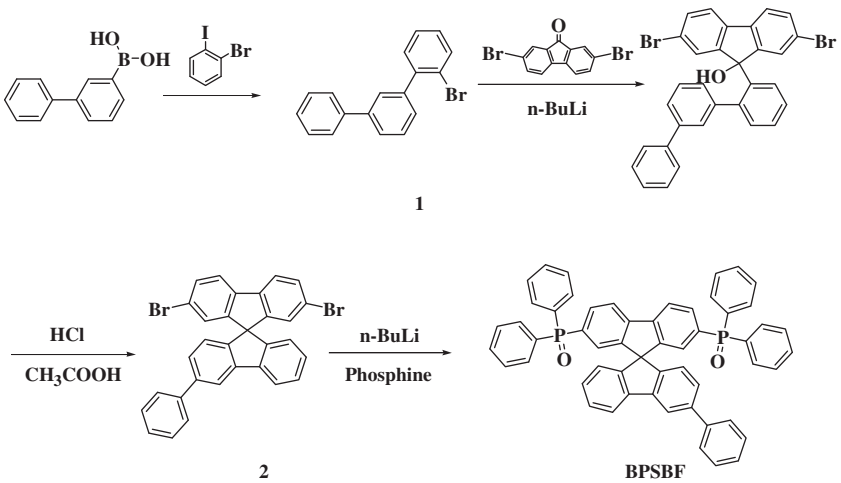

Scheme 1. Synthetic scheme of BPSBF.

tometer (Shimadzu, UV-2501PC). Samples were dissolved in tetrahydrofuran at a concentration of 1.0×10^{-4} M. The differential scanning calorimetry (DSC) measurements were performed on a Mettler DSC 822 under nitrogen at a heating rate of 10 °C/min. The mass spectrometric analysis was performed using a JEOL, JMS-AX505WA spectrometer in fast atom bombardment mode. Cyclic voltametry measurement of organic materials was carried out in acetonitrile solution with tetrabutylammonium perchlorate at 0.1 M concentration. Ag was used as the reference electrode and Pt was the counter electrode. Organic materials were coated on indium tin oxide substrate and were immersed in electrolyte for analysis. Scan rate was 0.1 mV/s. Elemental analysis of the materials was carried out using EA1110 (CE instrument).

2.5. Device preparation and measurements

The device structure of green PHOLEDs was indium tin oxide (ITO, 150 nm)/*N*,*N*′-diphenyl-*N*,*N*′-bis-[4-(phenyl-*m*-tolyl-amino)-phenyl]-biphenyl-4,4′-diamine (DNTPD)/*N*,*N*′-di(1-naphthyl)-*N*,*N*′-diphenylbenzidine (NPB, 5 nm)/*N*,*N*′-dicarbazolyl-3,5-benzene (mCP, 10 nm)/BPSBF:iridium(III) tris(2-phenylpyridine) ($Ir(ppy)_3$) (30 nm, 5% or 10%)/diphenylphosphine oxide-4-(triphenylsilyl)phenyl (TSPO1, 25 nm)/LiF (1 nm)/Al (200 nm). The PHWOLED had a device structure of ITO (150 nm)/poly-(3,4-ethylenedioxythiophene):polystyrenesulfonate (PEDOT:PSS, 60 nm)/NPB (5 nm)/mCP (10 nm)/9-(3-(9H-carbazole-9-yl)-phenyl)-3-(dibromophenylphosphoryl)-9H-carbazole (mCPPO1): bis((3,5-difluoro-4-cyanophenyl)pyridine) iridium picolinate (FCNIrpic) (10 nm, 3%)/BPSBF:$Ir(ppy)_3$: iridium(III) bis(2-phenylquinoline) acetylacetonate ($Ir(pq)_2acac$) (25 nm, 10%:0.7%)/TSPO1 (25 nm)/LiF/Al. A blue PHOLED with the device structure of ITO (150 nm)/PEDOT:PSS (60 nm)/NPB (5 nm)/mCP (10 nm)/mCPPO1:FCNIrpic (30 nm)/TSPO1 (25 nm)/LiF/Al was also fabricated as the standard deice. The device structure is shown in Fig. 1. A green PHOLED and a PHWOLED with mCPPO1 instead of BPSBF as the host material were also fabricated to compare BPSBF and mCPPO1 as the host material for green PHOLEDs. All devices were encapsulated with CaO getter and a glass lid after device fabrication. The device performances of the green and blue PHOLEDs were measured with Keithley 2400 source measurement unit and CS1000 spectroradiometer. The quantum efficiency of the devices was calculated from the device performances of green and white devices.

3. Results and discussion

It was reported in our previous work that high efficiency deep blue PHOLEDs can be fabricated using mCPPO1 as the host material in the emitting layer [14]. Deep blue emitting FCNIrpic was doped into the mCPPO1 and high quantum efficiency over 20% could be achieved. Therefore, the mCPPO1:FCNIrpic emitting layer can be used as the deep blue emitting layer in PHWOLEDs. The mCPPO1 host has the highest occupied molecular orbital (HOMO) of 6.13 eV and the lowest unoccupied molecular orbital (LUMO) of 2.64 eV. However, the mCPPO1 showed poor performances in green PHOLEDs and it cannot be used in PHWOLEDs with multilayer emitting structure. Therefore, a new green triplet host material is required to develop high efficiency PHWOLEDs with deep blue phosphorescent emitters.

A new green phosphorescent host material, BPSBF, was synthesized to develop high efficiency PHWOLEDs. Synthetic scheme of the BPSBF is shown in Scheme 1. The phenyl substituted bromobiphenyl group was prepared as the intermediate compound and the BPSBF was synthesized by ring closing reaction followed by phosphorylation. The BPSBF was designed as the electron transport type host material to fabricate high efficiency green PHOLEDs and stacked emitting layer structure for PHWOLEDs. It has a rigid phenyl substituted spirobifluorene core structure and diphenylphosphine oxide groups for efficient electron transport [19,20]. Therefore, the BPSBF can be stacked on blue phosphorescent emitting layer as the electron transport type green/red emitting layer due to electron transport properties of the BPSBF.

Density functional theory calculation was carried out using a suite of Gaussian 09 program to study the HOMO and LUMO distribution of the BPSBF. The nonlocal density functional of Becke's 3-parameters employing Lee–Yang–Parr functional (B3LYP) with 6-31G* basis sets was used for the calculation. As shown in the molecular orbital distribution of BPSBF in Fig. 2, the HOMO was dispersed over the phenyl group and the fluorene unit without the diphenylphosphine oxide, while the LUMO was distributed over the

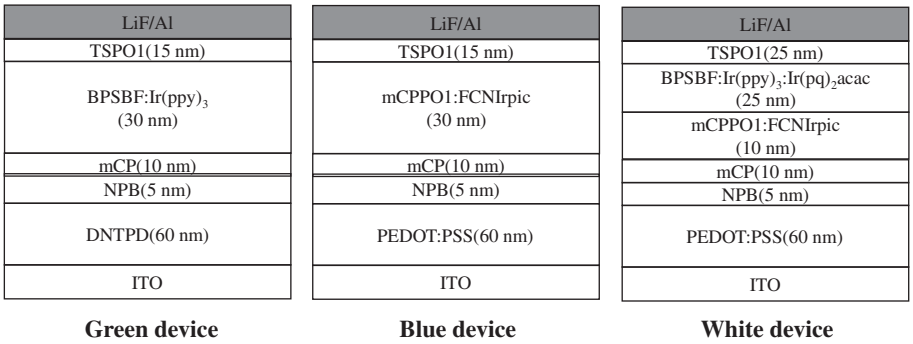

Fig. 1. Device structure of green, blue and white devices.

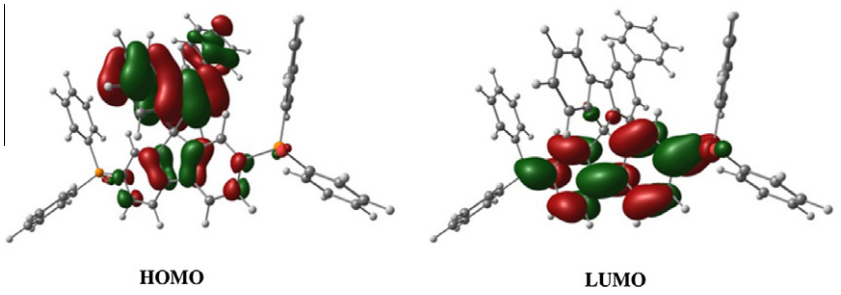

Fig. 2. HOMO and LUMO molecular orbital distribution of BPSBF.

fluorene unit substituted with the diphenylphosphine oxide groups. As the diphenylphosphine oxide unit has strong electron withdrawing properties, the HOMO was localized on the fluorene unit without the diphenylphosphine oxide and the LUMO was localized on the fluorene unit with the diphenylphosphine oxide. Compared with the spirobifluorene host without the phenyl substituent, the BPSBF showed uniform dispersion of the HOMO over the fluorene and phenyl substituent [21].

Photophysical properties of the BPSBF host material were studied using UV–Vis and PL spectra. UV–Vis and PL spectra of BPSBF host material are shown in Fig. 3. The BPSBF showed strong absorption peaks at 295 nm and 327 nm which are assigned to the absorption of the phenyl substituted spirobifluorene core. The bandgap was calculated from the absorption edge of the UV–Vis spectrum and it was 3.66 eV.

The PL emission was also originated from the phenyl substituted spirobifluorene core and it was observed at 356 nm. Low temperature PL spectrum of the BPSBF was also obtained to measure the triplet energy of the BPSBF and the triplet energy was 2.71 eV. The triplet energy of the BPSBF was high enough for energy transfer to green emitting phosphorescent dopant with a triplet energy around 2.40 eV. The triplet emission of the BPSBF was well overlapped with the metal to ligand charge transfer absorption peak of the green emitting $Ir(ppy)_3$ around 450 nm. Therefore, the BPSBF can be effective as the host material for green PHOLEDs. The HOMO energy level of the BPSBF was 6.53 eV from cyclic voltametric measurement and the LUMO level was 2.87 eV from the HOMO and bandgap from the UV–Vis measurement.

Green PHOLEDs with the BPSBF as the host material were fabricated to investigate the performances of BPSBF. Fig. 4 shows the device performances of BPSBF based green PHOLEDs. There was little change of the current density and luminance according to doping concentration. The quantum efficiency of the two devices was also similar irrespective of the doping concentration. The maximum quantum efficiency of the BPSBF green device with 10% doping concentration was 25.3% and the quantum efficiency at 1000 cd/m^2 was 22.0%. Although the efficiency value was not state of the art external quantum efficiency, high efficiency above 20% was obtained [15–17]. The high efficiency of the BPSBF based green PHOLEDs is due to balanced charge injection,

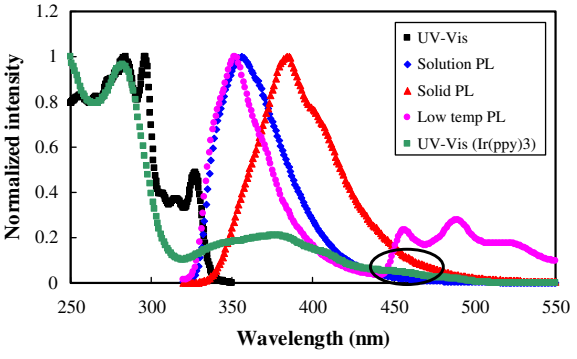

Fig. 3. UV–Vis and PL spectra of BPSBF.

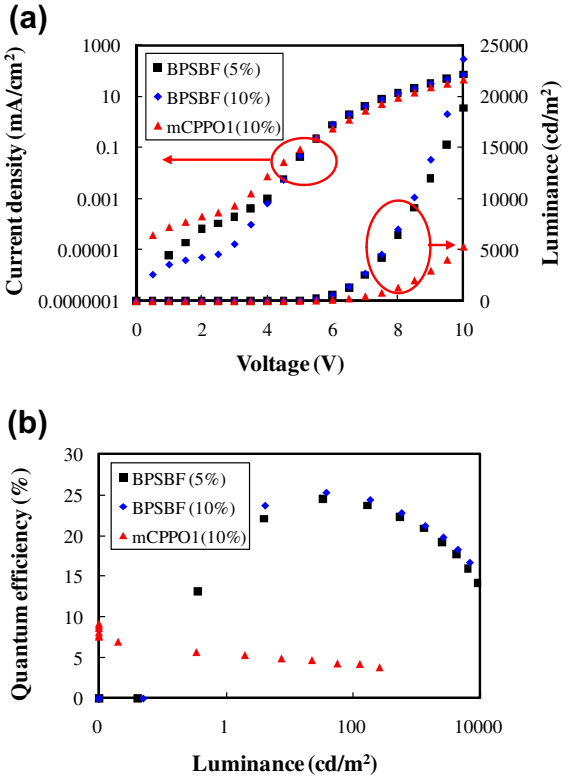

Fig. 4. Current density–voltage–luminance (a) and quantum efficiency–luminance (b) curves of BPSBF based green PHOLEDs.

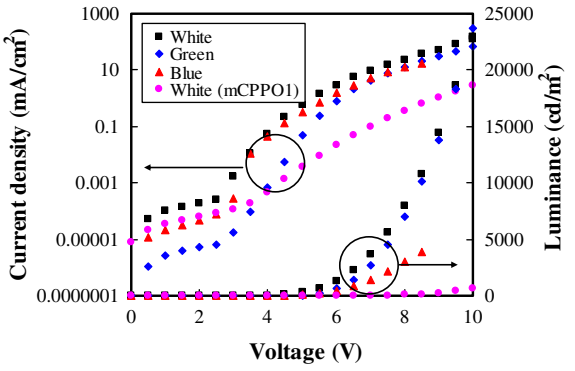

Fig. 5. Current density–voltage–luminance curves of green, blue and white PHOLEDs.

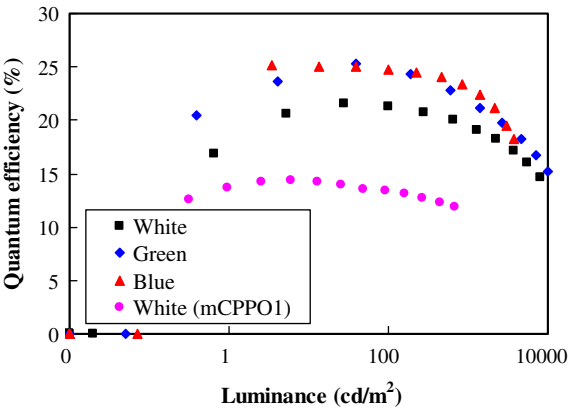

Fig. 7. Quantum efficiency–luminance curves of green, blue and white PHOLEDs.

efficient energy transfer and exciton confinement. Compared with the mCPPO1 host which was reported as the high triplet host for deep blue PHOLEDs, the BPSBF showed much higher quantum efficiency in green PHOLEDs.

As the BPSBF showed high quantum efficiency in green PHOLEDs, it was applied as the host material for PHWOLEDs with stacked blue/red:green emitting layer structure. Deep blue mCPPO1:FCNIrpic emitting layer was used to cover wide spectrum range and red/green BPSBF:Ir(ppy)$_3$:Ir(pq)$_2$acac emitting layer was stacked on the deep blue emitting layer. Fig. 5 shows the device performances of the PHWOLEDs with the deep blue emitting layer combined with BPSBF based red/green emitting layer. Blue device performances were also added for comparison. The current density and luminance of the PHWOLEDs were a little higher than those of the blue PHOLED, which is due to efficient electron injection though the BPSBF red/green emitting layer. The electron injection from TSPO1 electron transport layer to the BPSBF emitting layer is better than electron injection from TSPO1 layer to the mCPPO1 emitting layer, resulting in high current density and luminance in the PHWOLEDs. Energy level diagram of the PHWOLEDs is shown in Fig. 6. The current density and luminance of the PHWOLEDs with mCPPO1 as the host for red:green emitting layer were much lower than those of the PHWOLEDs with BPSBF as the host for red:green emitting layer.

Quantum efficiency–luminance curve of PHWOLEDs is shown in Fig. 7. Although the quantum efficiency of the PHWOLEDs was a little reduced compared with that of the blue or green PHWOLEDs, the PHWOLEDs showed high

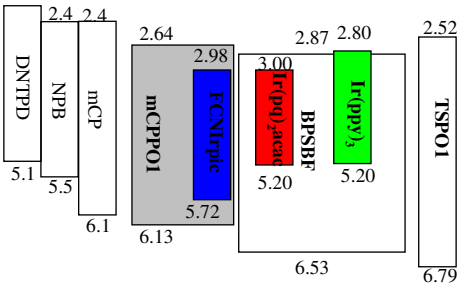

Fig. 6. Energy level diagram of white PHOLEDs.

quantum efficiency over 20%. The maximum quantum efficiency of the PHWOLEDs was 21.6% and the quantum efficiency at 1000 cd/m^2 was 19.6%. High quantum efficiency above 20% was obtained in PHWOLEDs without any tandem or outcoupling device structure [5]. In particular, this device showed much higher quantum efficiency than other WOLEDs with deep blue emitting material [3]. The high quantum efficiency of the PHWOLEDs with the mCPPO1:FCNIrpic and BPSBF:Ir(ppy)$_3$:Ir(pq)$_2$acac is due to high quantum efficiency of each emitting layer and device architecture for charge balance. The BPSBF based green PHOLED showed high quantum efficiency when mCP and TSPO1 were used as the hole transport layer and electron transport layer, respectively. In the PHWOLEDs, holes are injected from the mCPPO1 layer to the BPSBF layer, while electrons are injected from TSPO1 layer to the BPSBF layer. The mCPPO1 has similar HOMO level to mCP and hole density in the BPSBF emitting layer can be maintained similarly although it can be slightly decreased because of rather weak hole transport properties of mCPPO1 and hole trapping by FCNIrpic. In the case of the mCPPO1 emitting layer, the hole injection structure was not changed in the PHWOLEDs, while electron injection structure was changed. The BPSBF is better than TSPO1 in terms of electron injection due to two diphenylphosphine oxide groups. However, electrons are trapped by the red and green dopants, which do not increase the electron density in the mCPPO1 emitting layer. Therefore, the hole and electron density in each emitting layer is not greatly changed, resulting in charge balance in the whole emitting layer. In the case of the PHWOLEDs with mCPPO1 as the host for red:green emitting layer, the quantum efficiency was low due to low quantum efficiency in red:green emitting layer.

Power efficiency–luminance data of the PHWOLED are shown in Fig. 8. The maximum power efficiency of the PHWOLED was 47.0 lm/W and the power efficiency at 1000 cd/m^2 was 26.1 lm/W. Although no p type or n type doped charge transport layer was adopted in the device structure, high power efficiency was achieved because of high quantum efficiency of the PHWOLED. The maximum power efficiency of the green PHOLED could reach 59.0 lm/W. However, the power efficiency of the PHWOLEDs with the

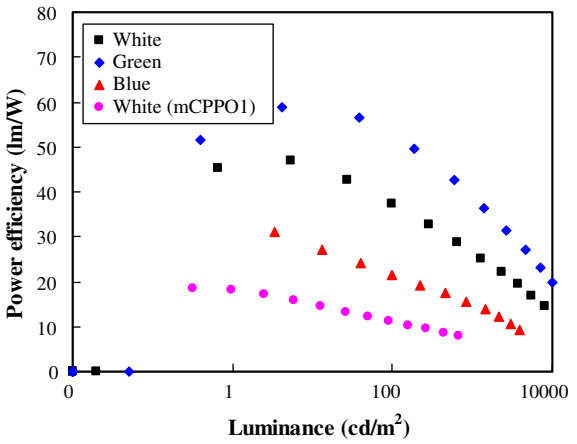

Fig. 8. Power efficiency–luminance curves of green, blue and white PHOLEDs.

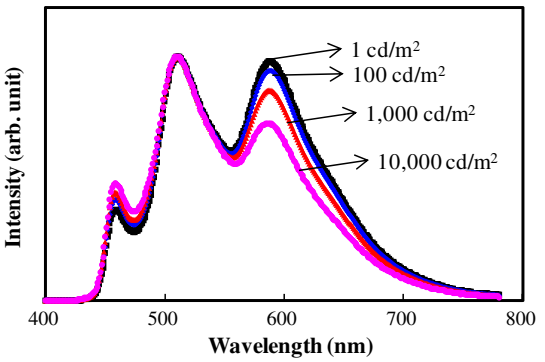

Fig. 9. Electroluminescence spectra of PHWOLED with BPSBF host.

mCPPO1 as the host for red:green emitting layer was low due to high driving voltage and low quantum efficiency.

Electroluminescence (EL) spectra of the PHWOLEDs are shown in Fig. 9. The PHWOLED covered wide spectral range from 440 nm to 750 nm. As the deep blue emitting FCNIrpic was used in the PHWOLEDs, deep blue emission with a peak maximum at 458 nm was observed in addition to green and red emission. Although green emission was a little stronger than red and blue emission, warm white spectrum for lighting application could be obtained. The color coordinate of the PHWOLED was (0.38,0.46) at 1000 cd/m^2. The change of the EL spectra according to the luminance is also shown in Fig. 9. The red emission was weakened at high luminance and the color coordinate was changed from (0.39,0.46) at 100 cd/m^2 to (0.35,0.46) at 10,000 cd/m^2. The color rendering index of the PHWOLEDs at 1000 cd/m^2 was 74.

4. Conclusions

In conclusion, high efficiency green and white PHOLEDs could be effectively fabricated using electron transport type BPSBF host materials. Above 20% quantum efficiency was achieved both in green and white PHOLEDs and the BPSBF type materials can be useful in future applications as the host for green and white PHOLEDs. Further study for the derivatives of BPSBF will follow for application as the host for PHWOLEDs.

References

[1] J. Kido, M. Kimura, K. Nagai, Science 267 (1995) 1332.
[2] S. Reineke, F. Lindner, G. Schwartz, N. Seidler, K. Walzer, B. Lussen, K. Leo, Nature 459 (2009) 234.
[3] Y. Sun, N.C. Giebink, H. Kanno, B. Ma, M.E. Thompson, S.R. Forrest, Nature 440 (2006) 908.
[4] E.L. Williams, K. Haavisto, J. Li, G.E. Jabbour, Adv. Mater. 19 (2007) 197.
[5] S.-H. Eom, Y. Zheng, E. Wrzesniewski, J.I. Lee, N. Chopra, F. So, J. Xue, Appl. Phys. Lett. 94 (2009) 153303.
[6] 6. H. Sasabe, J. Takamatsu, T. Motoyama, S. Watanabe, G. Wagenblast, N. Langer, O. Molt, E. Fuchs, C. Lennartz, J. Kido, Adv. Mater. DOI:10.1002/adma.201002254 (2010).
[7] S.-J. Su, E. Gonmori, H. Sasabe, J. Kido, Adv. Mater. 20 (2008) 4189.
[8] S.O. Jeon, K.S. Yook, C.W. Joo, J.Y. Lee, Opt. Lett. 34 (2009) 407.
[9] G. Cheng, Y. Zhao, Y. Zhang, S. Liu, F. He, H. Zhang, Y. Ma, Appl. Phys. Lett. 84 (2004) 4457.
[10] K.S. Yook, S.O. Jeon, C.W. Joo, J.Y. Lee, M.S. Kim, H.S. Choi, S.J. Lee, C.W. Han, Y.H. Tak, Org. Electron. 10 (2009) 681.
[11] G. Schwartz, M. Pfeiffer, S. Reineke, K. Walzer, K. Leo, Adv. Mater. 19 (2007) 3672.
[12] M.E. Kondakova, J.C. Deaton, T.D. Pawlik, D.J. Giesen, D.Y. Kondakov, R.H. Young, T.L. Royster, D.L. Comfort, J.D. Shore, J. Appl. Phys. 107 (2010) 014–515.
[13] K.S. Yook, S.O. Jeon, J.Y. Lee, K.H. Lee, Y.S. Kwon, S.S. Yoon, J.H. Yoon, Org. Electron. 10 (2009) 1378.
[14] S.O. Jeon, S.E. Jang, H.S. Son, J.Y. Lee, Adv. Mater. 23 (2011) 1436.
[15] Y. Tao, Q. Wang, C. Yang, Q. Wang, Z. Zhang, T. Zou, J. Qin, D. Ma, Ang. Chem. Int. Ed. 47 (2008) 8104.
[16] C. Adachi, M.A. Baldo, M.E. Thompson, S.R. Forrest, J. Appl. Phys. 90 (2001) 5048.
[17] M. Ikai, S. Tokito, Y. Sakamoto, T. Suzuki, Y. Taga, Appl. Phys. Lett. 79 (2001) 156.
[18] S.O. Jeon, K.S. Yook, C.W. Joo, J.Y. Lee, Org. Electron. 11 (2010) 881.
[19] A.B. Padmaperuma, L.S. Sapochak, P.E. Burrows, Chem. Mater. 18 (2006) 2389.
[20] S.O. Jeon, K.S. Yook, C.W. Joo, J.Y. Lee, Adv. Funct. Mater. 19 (2009) 3644.
[21] S.E. Jang, C.W. Joo, J.Y. Lee, Thin Solid Films 519 (2010) 906.

Fluorescent microscopy is conventionally used to detect Zn^{2+} with the help of fluorescent indicators since techniques such as nuclear magnetic resonance and electron paramagnetic resonance spectroscopy cannot be utilized to detect spectroscopically silent Zn^{2+} with a closed-shell $4s^2 3d^{10}$ electronic configuration [14]. The fluorescence of Zn^{2+} indicators can be varied upon Zn^{2+} binding. Although the fluorescent microscope is suitable for fundamental research, however, it cannot be used to monitor Zn^{2+} in the human body. Besides, a fluorescent indicator has to be used before the examination, and the indicator might influence cell functions. A small-sized semiconductor optoelectronic device is therefore needed for a real-time and indicator-free detection of Zn^{2+} in liquid environment.

Using organic optoelectronic devices as components of sensors has been demonstrated to be a way to reduce the size of sensors [15–19]. Organic photodiodes (PDs) were used as optical detectors to monitor chemiluminescence reactions in microfludic systems [16,17]. Integrated sensors, utilizing a microfluidic system, an organic light-emitting diode (OLED), an organic PD, and two polarizers, were also demonstrated in a front detection geometry [18,19]. The microfluidic system was sandwiched between the OLED and the organic PD. The polarizers were utilized to suppress the excitation light at the detector. However, the integrated sensors in a front detection geometry are less compact than the one in a back detection geometry. Recently, real-time and indicator-free detection of oxygen and glucose has been demonstrated by an integrated sensor in a back detection geometry, composing of an OLED, a PD, filters, and a sensing unit as shown in Fig. 1(a) [15]. The sensing unit is a film made of a host polymer and a fluorescent indicator for certain analyte. The OLED is used to excite the sensing unit, and the PD is used to detect the photoluminescence (PL) of the sensing unit. However, there is no such sensing unit specific to Zn^{2+} and hence the integrated semiconductor device for a real-time and indicator-free detection of Zn^{2+} is still lacking.

In this work, a Zn^{2+} sensing film is developed by incorporating a fluorescent Zn^{2+} indicator 11,16-bis(phenyl)-6,6,21,21-tetramethyl-*m*-benzi-6,21-porphodimethene (BPDM-H) into a hydrogel host polymer poly(2-hydroxyethyl methacrylate) (pHEMA). The water permeable nature of pHEMA enables Zn^{2+} in liquid environment to diffuse into interior of the sensing film and react with BPDM-H. The surface area of the sensing film is increased by fabricating a micron-sized pillar array on the surface. The sensing film shows high stability, sensitivity and selectivity to Zn^{2+}. The response time is 30 s for 10^{-4} M Zn^{2+} concentrations and 3 s for 10^{-3} M Zn^{2+} concentrations. This sensing film is able to be used as the sensing unit in the integrated semiconductor optoelectronic devices for Zn^{2+} sensing.

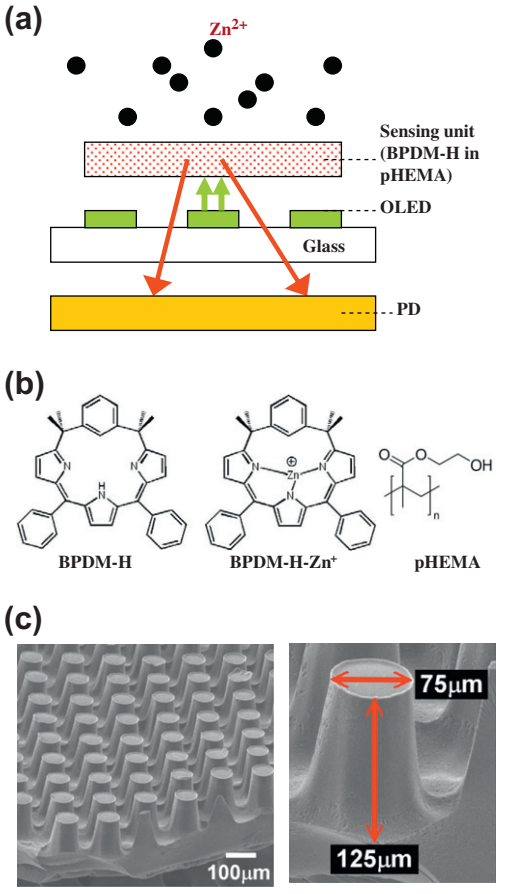

Fig. 1. (a) Schematic structure of an integrated semiconductor optoelectronic device with a sensing unit for detecting analyte, an organic light-emitting diode for excitation, and a photodiode for recording signal from the sensing unit. The sensing film is composed of BPDM-H and pHEMA. (b) Molecular structures of BPDM-H, BPDM-H–Zn^+, and pHEMA. (c) Scanning electron microscope images of the sensing film with a micron-sized pillar array on the surface.

2. Experimental

The Zn^{2+} sensing film is prepared from a mixture of BPDM-H, 2-hydroxyethyl methacrylate (HEMA), ethylene glycol dimethacrylate (EGDMA), and azobisisobutyronitrile (AIBN). BPDM-H is synthesized through an acid catalyzed condensation reaction at room temperature [20]. pHEMA with a three-dimensional network is synthesized by utilizing HEMA as a hydrophilic monomer, EGDMA as a hydrophobic cross-linker, and AIBN as a thermal initiator. The chemical structures of BPDM-H and pHEMA are shown in Fig. 1(b). HEMA is blended with EGDMA in the weight ratio 12:1, and then AIBN (1%) and BPDM-H (0.08%) are added. The sensing film of 180 μm with planar surface is prepared by pouring the blending solution into a cell and annealing at 80 °C for 10 min. As for the sensing film with a high surface area, a micron-sized pillar array on the surface is molded from a polydimethylsiloxan (PDMS) master which is replicated from a microfabricated SU-8 2100 (Shipley) film. To prepare the microfabricated SU-8 2100 film, the SU-8 2100 is spin coated on the glass substrate, and ultra-violet light (365 nm) is employed for exposure from the glass side with a mask [21]. After development, a patterned SU-8 structure with a pillar array is obtained. A layer of Ti(100 nm)/Au(100 nm) is then sputtered on the surface of a patterned SU-8 as an anti-adhesion layer. PDMS prepared in a 10:1 weight ratio of a silicone elasto-

mer with a curing agent (Dow Corning) is poured on the patterned SU-8 and baked at 65 °C for 1 h. The cured PDMS is peeled off and pressed on a mixture of BPDM-H, HEMA, EGDMA, and AIBN in a cell. After annealing at 80 °C for 10 min and demolding, the pattern on SU-8 is transferred to the surface of the sensing film, and the sensing film with a micron-sized pillar array on the surface is obtained as shown in Fig. 1(c). The PL spectra of the sensing film are monitored by a Hitachi F-4500 fluorescence spectrophotometer. Solutions of metal ions are prepared from $Zn(CH_3COO)_2$, $CaCl_2$, NaCl, $MnCl_2$, $CoCl_2$, and $MgCl_2$. The real-time detection of Zn^{2+} is carried out with a PDMS microfluidic channel with a sensing film inside the channel as shown in the inset of Fig. 4(a). A 635 nm laser is used for excitation and a fiber optic spectrometer (EPP2000, StellarNet) is used for monitoring PL with time.

3. Results and discussions

The fluorescent Zn^{2+} indicator BPDM-H in methanol has a broad absorption from 450 to 580 nm and a low background emission from 600 to 800 nm as shown in Fig. 2(a). After adding Zn^{2+} to the BPDM-H solution, the zinc(II) 11,16-bis(phenyl)-6,6,21,21-tetramethyl-*m*-benzi-6,21-porphodimethene cation complex (BPDM-H–Zn^+) is formed with a maximum chelation-enhanced fluorescence at 670 nm [16]. The chemical structures of BPDM-H–Zn^+ is shown in Fig. 1(b). As for the sensing film composed of BPDM-H and pHEMA, PL changes similar to the one of the BPDM-H solution in the presence of Zn^{2+}. Fig. 2(b) shows the PL spectra of the sensing film before and after introducing Zn^{2+}. Even if BPDM-H is trapped in pHEMA, BPDM-H functions still well and the formation of BPDM-H–Zn^+ after the addition of Zn^{2+} is not influenced. The sensing film is initially stabilized in water overnight without an apparent PL feature. BPDM-H could not be measured in water which means that BPDM-H is tightly trapped inside pHEMA without a detectable leakage. When Zn^{2+} is added, PL increases with time. The increase in PL stops once the sensing film is resettled in water without Zn^{2+}.

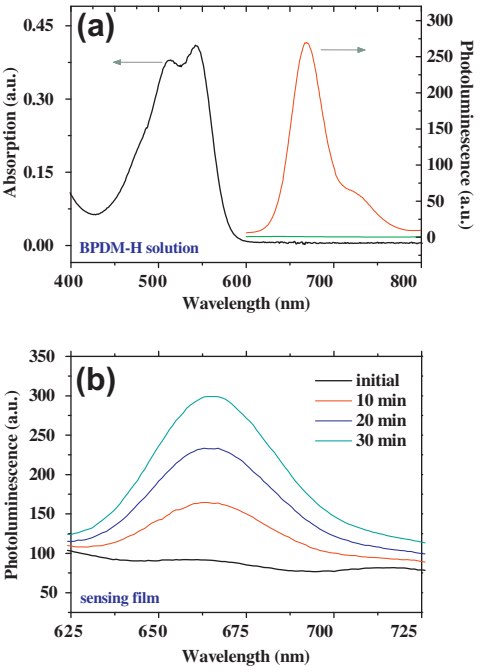

Fig. 2. (a) Absorption (black line) and PL spectra of BPDM-H in methanol. BPDM-H does not fluorescent itself (green line) until binding to Zn^{2+} (red line). (b) PL spectra of the sensing film before and after Zn^{2+} addition. (For interpretation of the references to color in this figure legend, the reader is referred to the web version of this article.)

Since selectivity is an essential characteristic of a sensing film to be utilized in a biological system, physiologically important metal ions are used to investigate the selectivity of the sensing film. Fig. 3 shows the PL spectra of the planar sensing films treated with aqueous solutions of various metal ions (5×10^{-3} M) for 30 min. The sensing film is also treated by solutions with different pH values to understand its stability, and it is observed that the PL spectrum of the sensing film will not change from pH 5 to pH 7. Since the pH values of the various metal ion solutions are in the range from pH 5.5 to pH 6.5, the change in PL will not be caused by the pH values of the various metal ion solutions but by the metal ions in the solutions. The largest PL is observed in the presence of Zn^{2+} as shown in Fig. 3. Other ions do not induce remarkable increase in PL. The sensing film is very specific to Zn^{2+}, and such high selectivity of the sensing film makes it a reliable component to be used as the sensing unit of the integrated semiconductor optoelectronic devices.

The real-time detection ability of the sensing film is then investigated. The microfluidic channel is utilized to produce Zn^{2+} pulses, and PL at 670 nm is recorded with time. Hanks' balanced salt solution (HBSS) is used here since it is an important buffer maintaining osmotic balance and pH. The response time of the sensing film is defined as the time needed for PL larger than the noise level. As shown in Fig. 4(a), the PL intensity of the planar sensing film is initially stable in HBSS. When 10^{-4} M Zn^{2+} solution is injected into the microfluidic channel, PL is increased immediately and continually. The increase in PL is ceased after injecting HBSS into the microfluidic channel to replace Zn^{2+} solution. PL increases again when the channel is refilled with 10^{-3} M Zn^{2+} solution. PL increases faster for the sensing film in 10^{-3} M Zn^{2+} solution than in

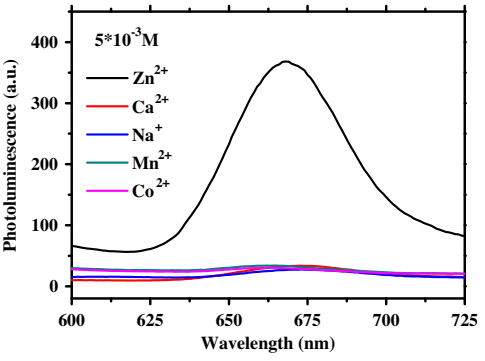

Fig. 3. The PL spectra of the sensing film submerged in a solution of various metal ions for 30 min.

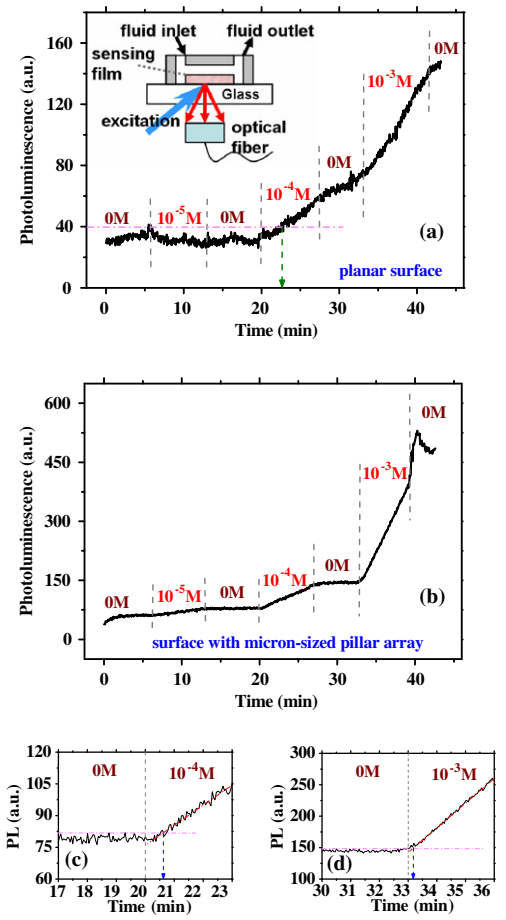

Fig. 4. PL variation with time of (a) the planar sensing film and (b) the sensing film with a micron-sized pillar array. Different Zn^{2+} concentration is injected at different time. The inset in (a) shows the experimental setup. The PL response of the sensing film with a micron-sized pillar array while (c) 10^{-4} M and (d) 10^{-3} M Zn^{2+} are injected.

10^{-4} M Zn^{2+} solution. The slope of the PL–time curve can therefore be used to identify Zn^{2+} concentration. The response time is 3 min for the Zn^{2+} concentration of 10^{-4} M for the planar sensing film. The long response time and low sensitivity of the planar sensing film make the sensor consume more time to give an accurate readout. To improve the response time of the sensing film, the surface area of the sensing film is increased by fabricating a micron-sized pillar array on the surface. The real-time detection characteristics of the sensing film with a micron-sized pillar array on the surface is shown in Fig. 4(b). In the presence of Zn^{2+}, the PL increment of the sensing film with a micron-sized pillar array is larger than that of the planar sensing film. As indicated in Fig. 4(c) and in Fig. 4(d), the response time is 30 and 3 s as Zn^{2+} concentration is 10^{-4} and 10^{-3} M, respectively. Increasing the surface area of the sensing film increases sensitivity. Fast response Zn^{2+} sensing film is realized.

4. Conclusion

In summary, a hydrogel sensing film with a micron-sized pillar array on the surface is realized for a real-time and indicator-free detection of Zn^{2+}. This sensing film shows high selectivity, sensitivity, as well as stability. A response time of 3 s is obtained while Zn^{2+} concentration is 10^{-3} M. The hydrogel sensing film is able to be used as the sensing unit in a solid-state Zn^{2+} biosensor.

Acknowledgements

This work is supported by the National Science Council of Taiwan (NSC99-2628-M-009-001-), Academia Sinica (AS-100-TP-B03), and the Veterans General Hospitals and University System of Taiwan Joint Research Program (VGHUST100-G5-1-1). Authors are grateful to the members in the biomimetic system research center, National Chiao Tung University.

References

[1] E.L. Que, D.W. Domaille, C.J. Chang, Chem. Rev. 108 (2008) 1517.
[2] C.J. Frederickson, Int. Rev. Neurobiol. 31 (1989) 145.
[3] E.H. Cox, G.L. McLendon, Curr. Opin. Chem. Biol. 4 (2000) 162.
[4] G.K. Andrews, Biometals 14 (2001) 223.
[5] M. Murakami, T. Hirano, Cancer Sci. 99 (2008) 1515.
[6] S. Yamasaki, K. Sakata-Sogawa, A. Hasegawa, T. Suzuki, K. Kabu, E. Sato, T. Kurosaki, S. Yamashita, M. Tokunaga, K. Nishida, T. Hirano, J. Cell Biol. 177 (2007) 637.
[7] D. Glesne, S. Vogt, J. Maser, D. Legnini, E. Huberman, J. Struct. Biol. 155 (2006) 2.
[8] H. Haase, J.L. Ober-Blöbaum, G. Engelhardt, S. Hebel, A. Heit, H. Heine, L. Rink, J. Immunol. 181 (2008) 6491.
[9] A.Q. Truong-Tran, J. Carter, R.E. Ruffin, P.D. Zalewski, Biometals 14 (2001) 315.
[10] M.P. Cuajungco, G.J. Lees, Brain Res. Rev. 23 (1997) 219.
[11] C. Devirgiliis, P.D. Zalewski, G. Perozzi, C. Murgia, Mutat. Res. 622 (2007) 84.
[12] D.T. Dexter, A. Carayon, F. Javoy-Agid, Y. Agid, F.R. Wells, S.E. Daniel, A.J. Lees, P. Jenner, C.D. Marsden, Brain 114 (1991) 1953.
[13] G.A. Qureshi, A.A. Qureshi, S.A. Memon, S.H. Parvez, J. Neural Transm. 71 (2006) 229.
[14] P. Jiang, Z. Cuo, Coord. Chem. Rev. 248 (2004) 205.
[15] J. Shinar, R. Shinar, J. Phys. D 41 (2008) 133001.
[16] O. Hofmann, P. Miller, P. Sullivan, T.S. Jones, J.C. deMello, D.D.C. Bradley, A.J. deMello, Sens. Actuat. B: Chem. 106 (2005) 878.
[17] X. Wang, M. Amatatongchai, D. Nacapricha, O. Hofmann, J.C. deMello, D.D.C. Bradley, A.J. deMello, Sens. Actuat. B: Chem. 140 (2009) 643.
[18] A. Pais, A. Banerjee, D. Klotzkin, I. Papautsky, Lab Chip 8 (2008) 794.
[19] E. Kraker, A. Haase, B. Lamprecht, G. Jakopic, C. Konrad, S. Köstler, Appl. Phys. Lett. 92 (2008) 033302.
[20] C.H. Hung, G.F. Chang, A. Umar, G.F. Lin, L.Y. Luo, W.M. Ching, E.W.G. Diau, Chem. Commun. (2008) 978.
[21] W.C. Yang, C.C. Fu, J. Micromech. Microeng. 17 (2007) 393.

Radiation sensors are an emerging application for semiconducting polymers [16]. The use of polymers – in the place of conventional inorganic semiconductors – opens up the possibility for large-area fabrication of sensors using low-cost, wet processing techniques, such as spin-casting, spray-casting, ink-jet or roll-to-roll printing [17]. Radiation sensors made from polymers exhibit greater mechanical flexibility in comparison to inorganic solids [5]. Furthermore, the elemental composition of most polymers (C, H, N and O) makes them an ideal candidate for dosimeters in medical applications, in which the detector requires a "human tissue-equivalent" interaction with radiation. (The average atomic number of muscle tissue is 7.4 [18].) Although radiotherapy and medical applications would benefit greatly from the improved accuracy of tissue-equivalent dosimeters, there are currently no low-cost, large-area devices with tissue-equivalence available.

Here, we present the first-ever measured charge transport properties of PTAA:TIPS-pentacene blends using a time-of-flight (TOF) photocurrent measurement technique. We correlate the raised mobility of the device with a four-fold increase in the X-ray detection sensitivity. Our results point to benefits in using TIPS-pentacene/polymer blends in applications that require high charge transport, such as light-emitting diodes, solar cells, and light sensors, to raise their performance to a higher level.

2. Materials and methods

The sensors employ layers (*ca.* 10 μm thick) of the polymer/molecule blend in a diode geometry. The details of the device preparation can be found elsewhere [19,20]. Briefly, slides of ITO-coated glass (Delta Technology Ltd., USA (CB-60IN)) were cleaned with acetone and deionised water. A 3 wt.% solution of PTAA (with an average molecular weight of 31 kg/mol) was prepared in toluene (99.99% purity, Sigma–Aldrich). Various concentrations TIPS pentacene (Sigma–Aldrich) were then added to the solution. It was homogenized for 10 min by stirring. Five different solutions were made: pure PTAA and PTAA blended with TIPS-pentacene with PTAA:TIPS molar ratios of 1:1, 1:10, 1:17 and 1:25. The solutions were spin-cast at 50 rpm for 30 s onto a clean substrate to provide a single layer of polymer. The films were dried under atmospheric conditions. Vacuum annealing was then performed at 100 °C for 12 h at pressure of 10^{-3} mbar, ensuring the temperature was kept below the solid-to-solid phase transition temperature of TIPS-pentacene at 124 °C [21]. Then, the thickness and average surface roughness of the active layer was measured using profilometry (Dektak Veeco). The device fabrication was completed by thermal evaporation of thin aluminum contacts on top of the active layer to create a Schottky contact.

A Leica DM 2500P microscope was employed to take polarized optical images. For energy dispersive X-ray analysis, an electron beam (Hitachi S-3200N electron microscope) with accelerating voltage of 20 kV and an X-ray detector (silicon drift detector, Oxford Instruments) was used.

For TOF measurements, an Al contact thickness of 50 nm and area of 9.6 mm^2 was deposited by thermal evaporation. The sample was held in a vacuum-tight steel box and was illuminated through the semi-transparent Al electrode. The 10 ns, 355 nm pulse of a Nd:YAG laser (Surelite Lasers, Continuum) was chosen to induce the optical excitation of the charge carriers. The intensity of the laser was attenuated by a neutral density filter in order to minimize the space-charge effect. To limit charge injection, the device was operated under a reverse bias by applying a negative voltage to the ITO electrode through a blocking resistor (10 kΩ). The resulting photocurrent pulses were recorded using a digital oscilloscope with a 50 Ω input terminal (Tektronix TDS 3032). Signal averaging and dark current subtraction were carried out to improve the quality of the data. The TOF experiments were performed in the dark, at room temperature, and under vacuum (3×10^{-1} mbar).

For X-ray photocurrent measurements, Al top contacts with a thickness of 100 nm and an area of 25 mm^2 were deposited via thermal evaporation. To prevent oxidation, the sensors were dip-coated in molten paraffin wax to create a barrier coating. The sensors were irradiated by 17.5 keV Kα X-rays from a molybdenum target X-ray tube (XF50 11, Oxford instruments, UK). While operating in a reverse bias, the sensor was exposed to the X-ray beam through the metal top electrode. The induced photocurrent was then measured using a voltage source-picoammeter (487, Keithley Instruments, UK). The dark current was subtracted from the measured X-ray photocurrent in order to provide a corrected value of the photocurrent. During exposure, the sensors were mounted in a steel box, in the dark and at room temperature, 10 cm from the X-ray source. Sensor sensitivity was calculated from the slope of a graph of X-ray photocurrent against dose rate and dividing by the active volume under the contact (see Supplementary data, Fig. 1A and B) [5].

3. Results and discussion

Fig. 1A–C show images obtained from polarized optical microscopy of films of PTAA blended with various concentrations of TIPS-pentacene. There is obvious crystallization of the TIPS-pentacene (confirmed separately via X-ray diffraction). The images reveal a needle-like crystal structure in which the crystal size increases with an increasing amount of TIPS-pentacene. The long-axis of the crystals lies in the plane of the film. Analysis of the Si distribution in the blend film using energy dispersive X-ray analysis in a mapping mode (not shown here) has revealed that crystals are uniformly distributed throughout the depth of the film. The average surface roughness of the films increases from 0.28 μm in a pure PTAA film to 5.3 μm for a film of PTAA blended with TIPS-pentacene in a 1:17 molar ratio. This roughening, which is also apparent in optical microscopy, is attributed to faceting from the TIPS-pentacene crystal formation.

Typical room-temperature transient hole TOF photocurrent measurements at two different applied voltages are presented in Fig. 2A for a device whose active layer consists of PTAA blended with TIPS-pentacene in a 1:17 molar ratio. Analysis over a range of applied voltages found an increase in the total collected charge (*i.e.* the area under the

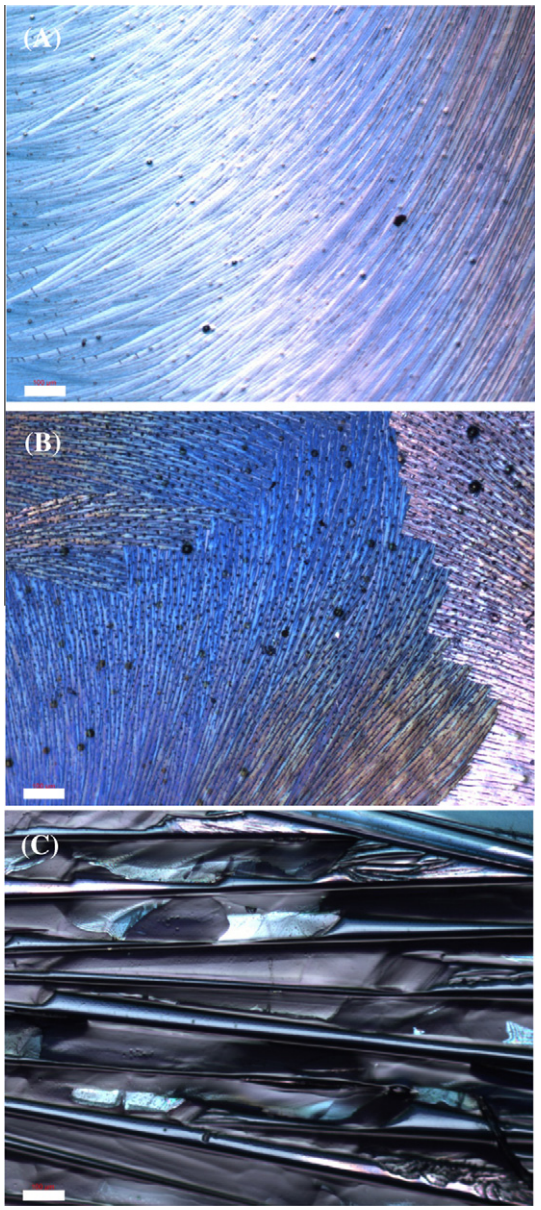

Fig. 1. Polarized optical images of PTAA blended with TIPS-pentacene in molar ratios of (A) 1:1, (B) 1:10 and (C) 1:17. The long axis of the crystals lies in the plane of the film. Scale bar is 100 μm.

transient curves) with an increase in the applied voltage. This observation is attributed to the field dependence of the carrier drift length, as has been found elsewhere [7,22]. The transient photocurrents in our devices exhibit some dispersive behavior, which is commonly observed in polymer-based systems [7,8,22–24]. An effective lifetime (τ) was found on a double logarithmic plot as the intersection of asymptotes to the plateau and the linear region of transient's trailing edge [25,26], as is shown in the inset of Fig. 2A. It is apparent in Fig. 2B that the reciprocal of the effective lifetime ($1/\tau$ depends linearly on the applied voltage (V) for all samples. The transit time for charge-carrier transport, τ_{tr}, is expected to be proportional to the applied field strength, E. Hence, the inverse linear trends in Fig. 2B are consistent with dispersive transport. However, in the limit of E approaching 0, then $1/\tau_{tr}$ is expected to approach 0. The data in Fig. 2B do not extrapolate through the origin, and hence there is evidence for lifetime-limited transport.

For films of film thickness, d, the charge carrier mobility, μ, can be calculated by

$$\mu = \frac{d^2}{\tau_{tr} V}. \quad (1)$$

In our system, there is a convolution of the effects of transit-limited and lifetime-limited transport in our measurements of τ, such that

$$\frac{1}{\tau} = \frac{1}{\tau_{lt}} + \frac{1}{\tau_{tr}}, \quad (2)$$

where τ_{lt} is the lifetime of the charge carrier and is independent of E. The intercept of the y-axis obtained from the best fit to the data in Fig. 2B will therefore provide an estimate of τ_{lt}. For the PTAA, τ_{lt} is approximately 1.7 ms. For the blend materials, there is some variation in τ_{lt}, but their average value is 460 μs. The $1/\tau_{lt}$ contribution to τ can be subtracted to provide τ_{tr}, and the gradient of the linear best-fit to the data in Fig. 2B provides μ via Eq. (1). The fact that the data fall on a linear trend over field strengths ranging from 3×10^4 to 4×10^5 V cm^{-1} indicates that there is not a strong field dependence of μ.

Ideally, the thickness, d, of a TOF sample should be in the range from 1 to 5 μm [27,28]. For the pure PTAA film and the blend film with a PTAA:TIPS-pentacene molar ratio of 1:1, d is 3 and 4 μm, respectively. However, a short circuit developed with the higher concentrations of TIPS-pentacene in thin devices, because of the high conductivity of the TIPS-pentacene and possible film imperfections. Therefore, in order to avoid this problem, thicker films were used in the TOF experiments for the 1:10, 1:17 and 1:25 samples (8, 12 and 12 μm, respectively). Furthermore, according to profilometry analysis, there is a large variation of the thickness in the 1:10, 1:17 and 1:25 sample because of the crystallization of the TIPS-pentacene leading to a range of crystal sizes, especially in the 1:17 and 1:25 samples. Hence, it should be noted that these are only average thicknesses.

Fig. 3 shows the increasing trend in the mobility with increasing TIPS-pentacene concentration. The field-averaged mobility in the 1:25 sample is 2.2×10^{-5} cm^2 V^{-1} s^{-1}, which is about 17 times higher compared to the value of 1.3×10^{-6} cm^2 V^{-1} s^{-1} in the PTAA device. The mobilities for the other three blends are consistently higher than that of the pure PTAA but lower than that of the 1:25 of PTAA:-TIPS-pentacene device.

To our knowledge, there has never been a report on the mobility measurement of TIPS-pentacene using the TOF technique. The reference mobility values for TIPS-pentacene have been obtained from measurements of field -effect transistor (FET) structures, which provide a different mobility value compared to TOF measurements because of the different charge carrier densities in the two types of device. It has been shown elsewhere that the

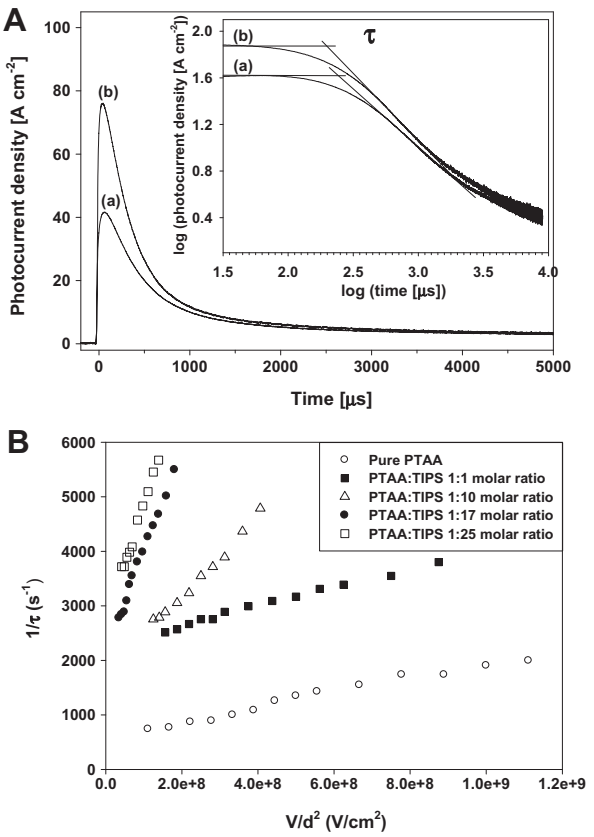

Fig. 2. (A) Transient photocurrent for hole transport in the PTAA blended with TIPS-pentacene of 1:17 by molar ratio at (a) 160 V, and (b) 260 V. The inset shows a double logarithmic plot at these two applied voltages. (B) Plots of the inverse effective lifetime, τ, as a function of the applied voltage over the square of the film thickness for pure PTAA (○), and PTAA blended with TIPS-pentacene in molar ratios of 1:1 (■), 1:10 (Δ), 1:17 (●) and 1:25 (□).

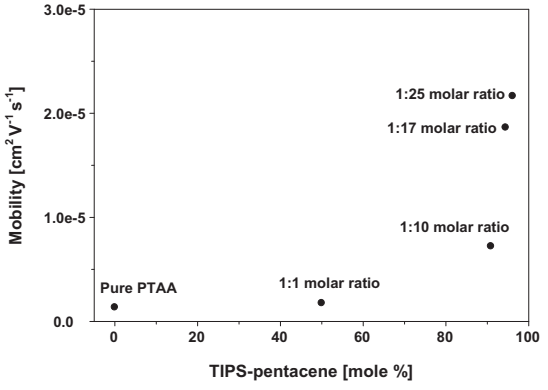

Fig. 3. Hole mobility as a function of TIPS-pentacene concentration in mole%. The average mobility values for field strengths, ranging from 3×10^4 to 4×10^5 V cm^{-1}, are reported here.

charge carrier density greatly affects the mobility [29]. The charge-carrier density is higher in a transistor configuration compared to a diode, and hence, in some materials, the measured mobilities are also higher. For instance, in P3HT, the hole mobility is found to be in the range of 0.1–0.3 cm^2 V^{-1} s^{-1} in a transistor [30,31] but only 10^{-4} cm^2 V^{-1} s^{-1} in a diode structure [9,28].

Moreover, in FET measurements charge transport is in the plane of the film, whereas it is "out of plane" for TOF measurements. The TIPS crystals are aligned in the plane of the film, and charge transport is measured in the TOF experiment in a direction normal to the crystal orientation. Therefore, field-effect mobility of TIPS-pentacene cannot be used as a reference value for measurements in a diode structure, as in solar cells or sensors. Hamilton et al. have reported the field-effect mobility value in the linear regime of about 0.7 cm^2 V^{-1} s^{-1} (1.1 cm^2 V^{-1} s^{-1} in the saturation regime) for the 1:1 by weight (1:50 molar ratio) of the PTAA:TIPS-pentacene blend system [15]. Based on their argument, the mobility of the blend system in the diode configuration is expected to be three orders of magnitude lower than in the field-effect structure or about 7×10^{-4} cm^2 V^{-1} s^{-1}. This number is about 30 times greater than the field-averaged mobility value found in our 1:25 PTAA:TIPS-pentacene device: 2.2×10^{-5} cm^2 V^{-1} s^{-1}.

Charge transport in conjugated polymer systems occurs through the hopping of charge carriers from one site to another. Barard et al. [22] have employed the correlated disorder model [32,33] to analyze the time-of-flight mobility data of a PTAA-based device. The effect of the positional disorder was found to be greater than the energetic disorder at room temperature and the mobility showed a weak negative field dependence. A large amount of positional disorder in our device could come from the microstructure of the PTAA:TIPS-pentacene blend film. In the optical images (Fig. 1), it is apparent that TIPS-pentacene is crystallized and forms ordered regions when the film is left to dry at room temperature. The ordered TIPS-pentacene crystals are embedded in the PTAA amorphous phase, creating a large PTAA/TIPS-pentacene interface. Due to better electronic coupling, the mobility in the TIPS-pentacene crystals is significantly higher than in the amorphous PTAA phase.

It is apparent in Fig. 3 that the introduction of TIPS-pentacene into PTAA has clearly resulted in an increase in the mobility of the device. At higher TIPS-pentacene concentrations, the mobility increases sharply. An increase in the mobility with increasing TIPS-pentacene concentration is expected from a shift of charge transport domination from PTAA to TIPS-pentacene, when the latter phase occupies a greater volume fraction. If the densities of the two phases are approximated as being equal, then weight fraction will equal the volume fraction. It can be estimated that the 1:25 composition will have a crystal volume fraction of 35%, which is 17 times higher than that of the 1:1 composition. The 1:25 system consists of a high fraction of polycrystalline TIPS-pentacene. Each TIPS-pentacene molecule in a crystal is strongly electronically coupled to its neighboring molecules, providing a faster route for charge carriers. The mobility of PTAA is negligible in comparison to that of a network of connected TIPS-pentacene crystals.

The question now arises as to how an increase in mobility in the blend will translate into device performance. Fig. 4A demonstrates the d.c. dark current–voltage characteristics for the PTAA-based diodes containing increasing

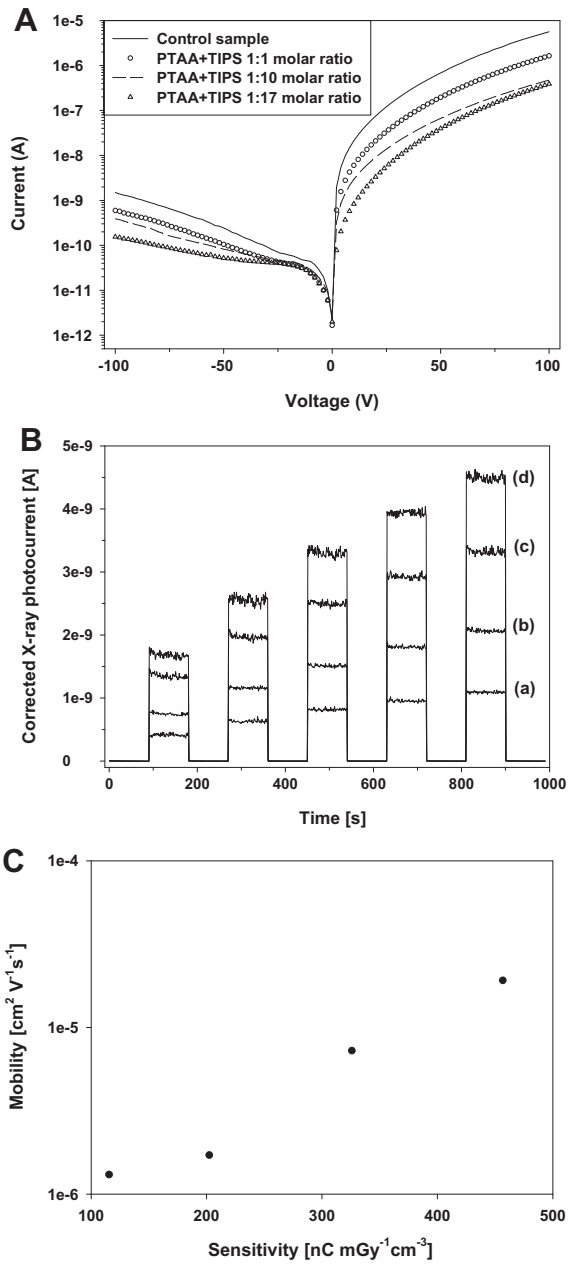

Fig. 4. (A) Semi-log current–voltage characteristics for the ITO/PTAA-based active layer/Al diodes when active layers are pure PTAA (solid line), PTAA blended with TIPS-pentacene of 1:1(○), 1:10 (dashed line), and 1:17 (Δ) by molar ratio. (B) Dynamic X-ray photocurrent for the ITO/PTAA-based/Al sensors with an active layer (10 μm thick) of (a) pure PTAA, and PTAA blended with TIPS-pentacene of in molar ratios of (b) 1:1, (c) 1:10, and (d) 1:17, when operated at 40 V. The devices were irradiated by 17.5 keV X-rays through an Al top contact with increasing dose rate from left to right: 13, 27, 40, 54 and 66 mGy s^{-1}. (C) Positive correlation between the X-ray sensitivity of the sensors and the charge-carrier mobility of their active material (PTAA or PTAA/TIPS-pentacene blend).

concentrations of TIPS-pentacene. According to surface profilometry, the thickness of the active layer for every sample is approximately 10 μm. Voltages ranging from −100 to 100 V were applied through the ITO back electrode. For the ITO/pristine PTAA/Al diode, the *I–V* curve shows a rectifying behavior with a reverse bias leakage current density of 6.12 nA/cm^2 at −100 V (field strength of 100 kV/cm). For the devices with the blend material of PTAA and TIPS-pentacene, the *I–V* characteristics still show a distinct Schottky rectification with a low leakage current in reverse bias. The reverse bias leakage current density for the devices with 1:1, 1:10 and 1:17 by molar ratio of PTAA:TIPS-pentacene are found to be 2.4, 1.56 and 0.6 nA/cm^2 at −100 V, respectively.

For device applications, experiments on X-ray sensors were conducted in which diode devices were irradiated through an Al top contact by an X-ray beam. The induced photocurrent was measured as a function of the dose rate to evaluate the performance of the sensor. Fig. 4B demonstrates dynamic photocurrent responses for devices biased at 40 V which have an active layer made of PTAA-doped with different concentrations of TIPS-pentacene. The dose rate was systematically increased from 13 to 66 mGy/s in increments of 13 mGy/s. The induced photocurrent from the sensors increases proportionally to the increasing of the X-ray dose rate, which can be attributed to a higher number of generated charge carriers. The rise and fall times are both less than the sampling rate of the instrument (<0.25 s).

The data confirm that the induced photocurrent can be significantly increased when the active layer contains TIPS-pentacene. For all applied dose rates and operational voltages, the X-ray photocurrent increases as the amount of TIPS-pentacene increases. For instance, at the X-ray dose rate of 66 mGy/s, it increases from about 1.8 nA for the PTAA sensor to approximately 9 nA for the 1:17 PTAA:-TIPS-pentacene sensor, at an operational voltage of −100 V.

The dependence of the X-ray photocurrent on the dose rate is used to define the sensitivity. A positive correlation between the radiation sensor's sensitivity and the charge carrier mobility for the PTAA and the PTAA:TIPS-pentacene devices is revealed in Fig. 4C. The sensitivity of the 1:17 device is highest, and its active material has the greatest mobility (Table 1). At the highest field strength, the sensitivity of the 1:17 device is 457 nC/mGy/cm^3, which is nearly four times that obtained for PTAA (116 nC/mGy/cm^3). As TIPS-pentacene has a relatively high charge carrier mobility, the rise in the sensitivity in the blend device can be assigned to an increase of the ability of the active material to transport charge carriers. However, even higher concentrations of TIPS-pentacene increase the conductivity of the blend too much to enable its use in a rectifying diode (with a low dark current) in a sensor. Thus, there is an upper limit to the increase in X-ray sensitivity that is possible through

Table 1
Charge-carrier mobility and X-ray sensitivity of PTAA and TIPS/PTAA Diodes.

Composition of active material	Charge-carrier mobility (10^{-6} cm^2 V^{-1} s^{-1})	X-ray sensitivity (nC mGy^{-1} cm^{-3})
PTAA	1.3	116
TIPS:PTAA = 17:1	19	457

the addition of TIPS-pentacene. Note that although the X-ray sensitivity of the 1:17 blend device is below what has been reported elsewhere for tissue-equivalent diamond detectors [34], polymers offer the distinct advantages of being lower in cost and able to coat large areas.

4. Conclusions

We have determined, for the first time, the influence of TIPS-pentacene on charge transport in PTAA/TIPS-pentacene blends using a time-of-flight technique. Our results have demonstrated that the mobility of the device increases with an increasing amount of TIPS-pentacene The value of mobility was found to be $2.2 \times 10^{-5}\,cm^2\,V^{-1}\,s^{-1}$, averaged for field strengths between 3×10^4 and $4 \times 10^5\,V\,cm^{-1}$ for the 1:25 PTAA:TIPS-pentacene blend, which is about 17 times higher than in PTAA over the same range of field strengths. Increasing mobility correlates very well with a fourfold increase in the X-ray detection sensitivity in the PTAA:TIPS-pentacene devices. The blend material presents the highest sensitivities reported to-date for organic, *tissue-equivalent* direct radiation sensors. The higher sensitivity and charge-carrier mobility are attributed to TIPS-pentacene crystals that provide a fast path for charge transport. The organic blends offer the potential for processing mechanically-flexible, large-area sensors for use in radiation protection and imaging applications. These diode structures also offer attractive properties for other applications, including light-emitting diodes, solar cells, and light sensors.

Acknowledgements

A.I. acknowledges a scholarship from the Office of the Higher Education Commission, the Royal Thai Government. Dr. Heiko Thiem (Evonik Degussa GmbH, Germany) kindly supplied the PTAA. The authors thank Dr. Veeramani Perumal, John-William Brown, Gary Strudwick, Violeta Dukova and John Dear (Department of Physics, University of Surrey) for help with sample preparation and characterization. We are very grateful to helpful comments from T. Kreouzis (Queen Mary University) and from an anonymous reviewer.

Appendix A. Supplementary data

Supplementary data associated with this article can be found, in the online version, at doi:10.1016/j.orgel.2011.08.003.

References

[1] O.D. Jurchescu, M. Popinciuc, B.J. van Wees, T.T.M. Palstra, Adv. Mater. 19 (2007) 688–692.
[2] S.R. Forrest, Nature 428 (2004) 911–918.
[3] S. Günes, H. Neugebauer, N.S. Sariciftci, Chem. Rev. 107 (2007) 1324–1338.
[4] F.A. Boroumand, M. Zhu, A.B. Dalton, J.L. Keddie, P.J. Sellin, J.J. Gutierrez, Appl. Phys. Lett. 91 (2007) 033509.
[5] C.A. Mills, A. Intaniwet, M. Shkunov, J.L. Keddie, P.J. Sellin, Proc. SPIE 7449 (2009) 74491.
[6] H. Sirringhaus, Adv. Mater. 17 (2005) 2411–2425.
[7] W. Tang, V. Chellappan, M. Liu, Z.K. Chen, L. Ke, ACS Appl. Mater. Interfaces 1 (2009) 1467–1473.
[8] T. Kreouzis, D. Poplavskyy, S.M. Tuladhar, M.C. Quiles, J. Nelson, A.J. Campbell, D.D.C. Bradley, Phys. Rev. B 73 (2006) 235201.
[9] R. Mauer, M. Kastler, F. Laquai, Adv. Funct. Mater. 20 (2010) 2085–2092.
[10] S.K. Park, T.N. Jackson, J.E. Anthony, D.A. Mourey, Appl. Phys. Lett. 91 (2007) 063514.
[11] T. Sakanoue, H. Sirringhaus, Nat. Mater. 9 (2010) 736–740.
[12] S.I. Shin, J.H. Kwon, H. Kang, B.K. Ju, Semicond. Sci. Technol. 23 (2008) 085009.
[13] M.B. Madec, D. Crouch, G.R. Llorente, T.J. Whittle, M. Geoghegan, S.G. Yeates, J. Mater. Chem. 18 (2008) 3230–3236.
[14] R.L. Headrick, S. Wo, F. Sansoz, J.E. Anthony, Appl. Phys. Lett. 92 (2008) 063302.
[15] R. Hamilton, J. Smith, S. Ogier, M. Heeney, J.E. Anthony, I. McCulloch, J. Veres, D.D.C. Bradley, T.D. Anthopoulos, Adv. Mater. 21 (2009) 1166–1171.
[16] J.W. Kingsley, A.J. Pearson, L. Harris, S.J. Weston, D.G. Lidzey, Org. Electron. 10 (2009) 1170–1173.
[17] A.C. Arias, J.D. Mackenzie, I. McCulloch, J. Rivnay, A. Salleo, Chem. Rev. 110 (2010) 3–24.
[18] M. Bruzzi, M. Bucciolini, F. Nava, S. Pini, S. Russo, Nucl. Instrum. Methods A 485 (2002) 172–177.
[19] A. Intaniwet, C.A. Mills, M. Shkunov, H. Thiem, J.L. Keddie, P.J. Sellin, J. Appl. Phys. 106 (2009) 064513.
[20] A. Intaniwet, C.A. Mills, P.J. Sellin, M. Shkunov, J.L. Keddie, ACS Appl. Mater. Interfaces 2 (2010) 1692–1699.
[21] J. Chen, J. Anthony, D.C. Martin, J. Phys. Chem. B 110 (2006) 16397–16403.
[22] S. Barard, M. Heeney, L. Chen, M. Cölle, M. Shkunov, I. McCulloch, N. Stingelin, M. Philips, T. Kreouzis, J. Appl. Phys. 105 (2009) 013701.
[23] S.A. Choulis, Y. Kim, J. Nelson, D.D.C. Bradley, M. Giles, M. Shkunov, I. McCulloch, Appl. Phys. Lett. 85 (2004) 3890–3892.
[24] Q. Shi, Y. Hou, H. Jin, Y. Li, J. Appl. Phys. 102 (2007) 073108.
[25] H. Scher, E.W. Montroll, Phys. Rev. B 12 (1975) 2455–2477.
[26] Y. Shirota, H. Kageyama, Chem. Rev. 107 (2007) 953–1010.
[27] R. Pacios, J. Nelson, D.D.C. Bradley, C.J. Brabec, Appl. Phys. Lett. 83 (2007) 4764.
[28] A.M. Ballantyne, L. Chen, J. Dane, T. Hammant, F.M. Braun, M. Heeney, W. Duffy, I. McCulloch, D.D.C. Bradley, J. Nelson, Adv. Funct. Mater. 18 (2008) 2373–2380.
[29] C. Tanase, E.J. Meijer, P.W.M. Blom, D.M. de Leeuw, Phys. Rev. Lett. 91 (2003) 216601.
[30] Z. Bao, A. Dodabalapur, A.J. Lovinger, Appl. Phys. Lett. 69 (1996) 4108.
[31] H. Sirringhaus, N. Tessler, R.H. Friend, Science 280 (1998) 1741–1744.
[32] S.V. Novikov, D.H. Dunlap, V.M. Kenkre, P.E. Parris, A.V. Vannikov, Phys. Rev. Lett. 81 (1998) 4472–4475.
[33] V. Coropceanu, J. Cornil, D.A.D.S. Filho, Y. Olivier, R. Silbey, J.L. Brédas, Chem. Rev. 107 (2007) 926–952.
[34] A. Lohstroh, P.J. Sellin, F. Boroumand, J. Morse, Phys. Status Solidi A 204 (2007) 3011–3016.

zinc- and indium-based oxides deposited by vacuum techniques, mainly by sputtering and atomic layer deposition [9–14]. In contrast to vacuum-based techniques, solution-based semiconductor deposition allows a simple and high throughput fabrication of inexpensive and large-area electronics. For this reason, solution-based metal oxide semiconductors recently gained a lot of attention. Several solution-based AOS materials have been reported as active channel layers in n-TFTs [15–18]. However, the applied annealing temperature to convert the soluble precursors into high performance AOS films lies mostly in the range of 350–500 °C. Applying lower annealing temperatures dramatically lowers TFT performance and often hardly results in functioning transistors [19]. Although complementary inverters have been reported with solution-processed ZnO and organic p-type TFTs [20], no scalable integration technology has been demonstrated yet, using solution-based metal oxide n-TFTs and organic p-TFTs for more complex complementary circuitry.

Here, we report on high performance n-type oxide TFTs based on solution-processable indium-based oxide formulations and processed at a maximum temperature of only 250 °C, which is compatible with flexible substrates such as polyimide. Using these oxide n-TFTs, we show a completely scalable integration process for hybrid inorganic–organic complementary logic superior to other complementary low-temperature processes.

2. Experimental

A schematic cross-section of the complete inorganic–organic inverter integration process is shown in Fig. 1. All transistors and hybrid inorganic–organic complementary circuits were fabricated on Si/SiO_2 substrates with a thermally evaporated and patterned gold layer, acting as the gate for both the organic p- and inorganic n-TFTs. Atomic layer deposition was performed to deposit 100 nm of Al_2O_3 high-k gate dielectric ($\varepsilon_r = 8$), which was subsequently patterned by photolithography and wet etching.

A 10 nm thick indium-based metal oxide active layer was deposited in air under ambient conditions by sequentially spin-coating and post-annealing a metal-organic precursor formulation (iXsenic S, developed by Evonik Industries). The post-annealing was performed on a hotplate for 2 h at 250 °C to remove residual solvents and to form the metal oxide film. Photolithography and wet etching were used to pattern the n-type channel regions. Next, a bilayer of Ti and Au (2–30 nm) was deposited by thermal evaporation and patterned by a lift-off process. The Ti–Au bilayer forms top source–drain contacts for the oxide n-TFTs and bottom source–drain contacts for the pentacene p-TFTs. In this way, the amount of processing and mask steps required for circuit fabrication is minimized.

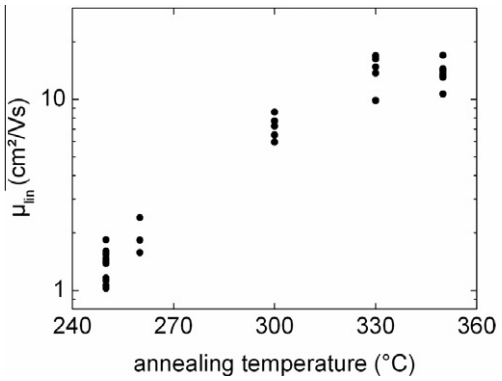

Fig. 2. The linear mobility values of discrete n-type metal-oxide TFTs after baking out at different temperatures (W/L = 2000/20 μm/μm). The distribution of the average linear mobility is shown over five successive experiments.

Subsequently, a 2 μm thick layer of the negative photoresist SU-8 2002 (purchased from MicroChem Corp.) is spin-coated over the entire substrate to protect the n-TFTs. Next, openings are photolithographically defined in the SU-8 layer above the active transistor areas of the p-channel TFTs. Because of the negative slopes of these SU-8 edges, the openings act as an integrated shadow mask and define isolated islands of pentacene after the deposition of 30 nm pentacene by thermal evaporation in ultrahigh vacuum [21]. To improve the pentacene film growth, the Ti–Au contacts and the Al_2O_3 dielectric were treated with self-assembled monolayers, respectively pentafluorothiophenol (PFTP) and phenethyltrichlorosilane (PETS) [22,23] before pentacene deposition. Then the entire substrate was capped with an encapsulation layer consisting of 3 μm parylene C, deposited by a vapor polymerization process. Finally, via holes are opened by photolithography and dry etching on the contact pad areas.

The current–voltage characteristics of the individual TFTs were measured with a HP 4156 parameter analyzer. The output characteristics of the ring-oscillators were examined with an oscilloscope. All measurements were performed under nitrogen atmosphere and under dark conditions.

3. Results and discussion

Fig. 2 shows the typical linear mobility values of the metal-organic precursor formulation iXsenic S before the integration and optimization of the inorganic–organic

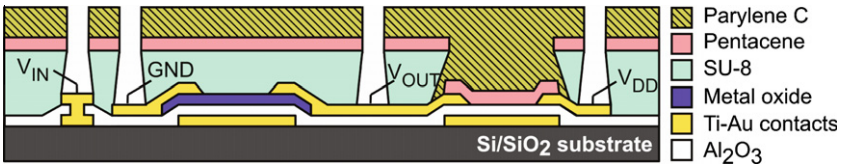

Fig. 1. Schematic cross-section of an encapsulated pentacene–metal oxide inverter.

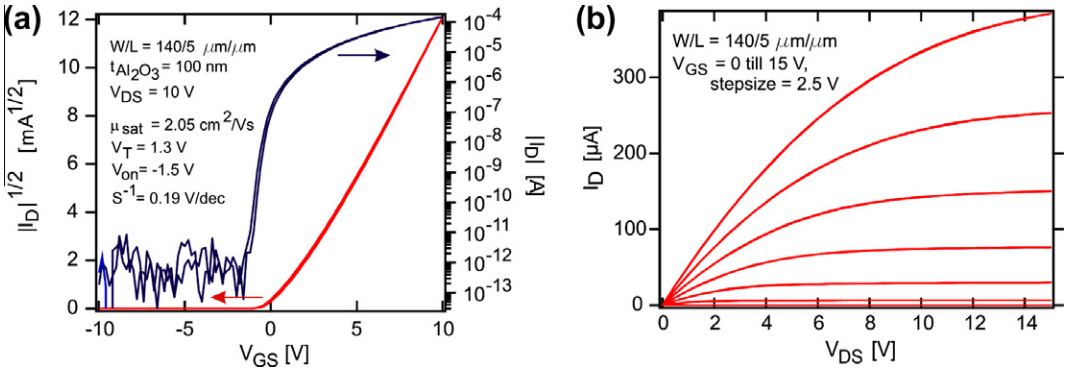

Fig. 3. (a) Transfer characteristics and (b) output characteristics for an integrated oxide n-type bottom gate – top contact TFT.

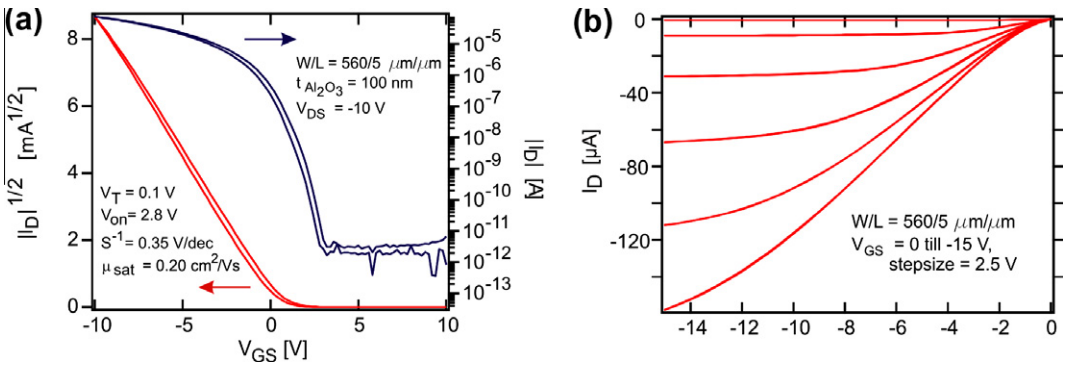

Fig. 4. (a) Transfer characteristics and (b) output characteristics for an integrated pentacene p-type bottom gate – bottom contact TFT.

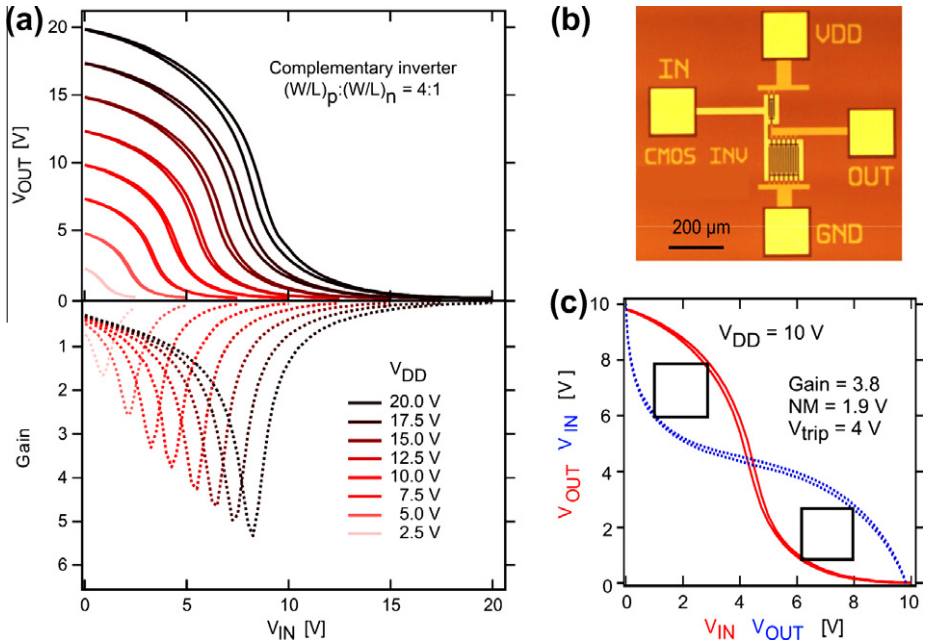

Fig. 5. (a) The voltage transfer curves as function of the supply voltage and their corresponding gain curves of a complementary inverter. (b) An optical microscope image of a complementary inverter. (c) The voltage transfer curve and its inverted curve at a V_{DD} of 10 V.

hybrid process. A steady increase of the electron mobility is observed as the annealing temperature increases from 250 to 330 °C, after which the mobility plateaus at around 15 cm^2/V s. In this work the lower processing range at

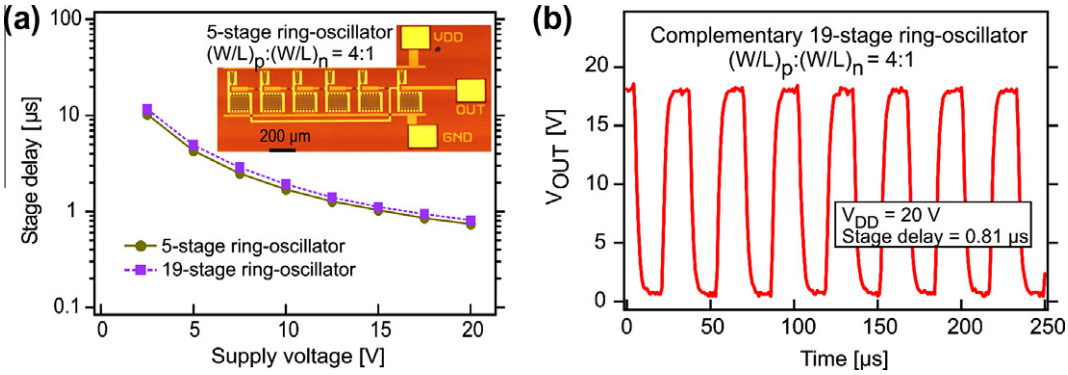

Fig. 6. (a) The stage delay of a 5-stage and 19-stage complementary ring-oscillator as function of the supply voltage. (b) Output characteristics of a 19-stage complementary ring-oscillator at a V_{DD} of 20 V.

250 °C was used for the development of the complementary technology, as the mobility reached at this temperature matches that of the organic p-type semiconductor.

Fig. 3a and b shows the typical transfer and output characteristics of a metal oxide n-TFT after integration. We were able to achieve high performance n-TFTs with saturation mobilities of ~2 $cm^2/(V\,s)$, an onset voltage of ~−1.5 V, a subthreshold swing of only ~0.19 V/decade, and an on–off current ratio of ~10^7. The channel length (L) and width (W) of the n-TFTs were 5 and 140 µm, respectively. The transfer and output characteristic of a discrete pentacene p-TFT is shown in Fig. 4a and b, the W/L ratio is 560/5 µm/µm. The integrated pentacene p-TFT exhibits a saturation hole mobility of 0.20 $cm^2/(V\,s)$, an onset voltage of ~2.8 V, and a subthreshold swing of ~0.35 V/decade. In both transistor types the off-current is below 10 pA.

The complementary circuits were designed with a $(W/L)_p$:$(W/L)_n$ ratio of 4:1, as shown in the optical microscope image of Fig. 5b. The resulting voltage transfer curves and corresponding gain curves of a complementary inverter are shown in Fig. 5a for different supply voltages. Good inverter behavior was obtained at supply voltages (V_{DD}) down to 2 V, making the presented hybrid technology well-suited for future low-voltage applications. The voltage transfer curve and its inverted curve at V_{DD} of 10 V are shown in Fig. 5c. The inverter transition point (V_{trip}) was at 4 V and a DC gain and noise margin (NM) of, respectively 3.8 and 1.9 V were obtained. In complementary logic the least performing transistor dictates the overall performance, in our case this is the pentacene p-TFT. Consequently, the inverter transition points of all transfer curves are below $V_{DD}/2$.

Fig. 6a shows the stage delay of a 5-stage complementary ring-oscillator as a function of the supply voltage. Excellent stage delays as low as 0.74 µs, corresponding to 113 kHz, were measured at a V_{DD} of 20 V. Also the spread of seven different 5-stage ring-oscillators, measured on the same substrate at a V_{DD} of 10 V was minimal, i.e. 1.78 ± 0.05 µs. The 19-stage ring-oscillators operate at 30.8 kHz, corresponding to a stage delay of only 0.81 µs at a V_{DD} of 20 V as shown in Fig. 6b. These results demonstrate that our hybrid technology has reached the level of reliability and yield required to fabricate more complex circuits in the future.

4. Conclusion

In summary, we fabricated state-of-the-art solution-based oxide n-type TFTs with saturation electron mobilities up to 2.05 $cm^2/(V\,s)$ after post-annealing at only 250 °C in air. Based on these high-performance n-TFTs and thermally evaporated pentacene p-TFTs, a completely scalable hybrid organic–inorganic complementary technology was developed.

Using this technology, hybrid complementary circuit building blocks, such as inverters and ring-oscillators were realized. Because the integrated p-TFT on-current was much lower compared to its n-type counterpart, a $(W/L)_p$:$(W/L)_n$ ratio of 4:1 was selected for the complementary circuits. Supply voltages as low as 2 V resulted in good circuit behavior, indicating that the presented technology is suited for future low-voltage applications. The 5-stage ring-oscillators operated up to 113 kHz, corresponding to stage delays as low as 0.74 µs at a V_{DD} of 20 V. Moreover 19-stage ring-oscillators were shown to operate at more than 30 kHz. This robust complementary thin-film technology holds promise for the realization of more complex circuitry in the future.

Acknowledgements

M. Rockelé thanks the Agency for Innovation by Science and Technology in Flanders (IWT-Vlaanderen) for financial support. This work was carried out in the frame of the Holst Centre. The research leading to these results has received funding from the European Community's Seventh Framework Program FP7-ICT-2009-4 under Grant Agreement No. 247798 of the ORICLA project.

References

[1] E. Cantatore, T.C.T. Geuns, G.H. Gelinck, E. van Veenendaal, A.F.A. Gruijthuijsen, L. Schrijnemakers, A.F.A. Gruijthuijsen, L. Schrijnemakers, S. Drews, D.M. de Leeuw, A 13.56-MHz RFID system based on organic transponders, IEEE J. Solid-State Circ. 42 (2007) 84–92.

[2] K. Myny, S. Steudel, P. Vicca, M.J. Beenhakkers, N.A.J.M. van Aerle, G.H. Gelinck, J. Genoe, W. Dehaene, P. Heremans, Plastic circuits and tags for 13.56 MHz radio-frequency communication, Solid-State Electron. 53 (2009) 1220–1226.

[3] J.E. Anthony, A. Facchetti, M. Heeney, S.R. Marder, X. Zhan, N-Type organic semiconductors in organic electronics, Adv. Mater. 22 (2010) 3876–3892.
[4] A. Nathan, P. Servati, K.S. Karim, D. Striakhilev, A. Sazonov, Device physics, compact modeling, and circuit applications of a-Si:H TFTs, in: Y. Kuo (Ed.), Thin film transistors, Materials and Processes, vol. I, Kluwer Academic Publishers, Boston, 2004, pp. 79–181.
[5] C.-S. Yang, L.L. Smith, C.B. Arthur, G.N. Parsons, Stability of low-temperature amorphous silicon thin film transistors formed on glass and transparent plastic substrates, J. Vac. Sci. Technol. B 18 (2000) 683–689.
[6] D. Bode, K. Myny, B. Verreet, B. van der Putten, P. Bakalov, S. Steudel, S. Smout, P. Vicca, J. Genoe, P. Heremans, Organic complementary oscillators with stage-delays below 1 μs, Appl. Phys. Lett. 96 (2010) 133307.
[7] H. Yan, Y. Zheng, R. Blache, C. Newman, S. Lu, J. Woerle, A. Facchetti, Solution processed top-gate n-channel transistors and complementary circuits on plastics operating in ambient conditions, Adv. Mater. 20 (2008) 3393–3398.
[8] H. Hosono, Ionic amorphous oxide semiconductors: material design. Carrier transport, and device application, J. Non-Cryst. Solids 352 (2006) 851–858.
[9] M.S. Oh, D.K. Hwang, K. Lee, W.J. Choi, J.H. Kim, S. Im, S. Lee, Pentacene and ZnO hybrid channels for complementary thin-film transistor inverters operating at 2 V, J. Appl. Phys. 102 (2007) 076104.
[10] J.H. Na, M. Kitamura, Y. Arakawa, Organic/inorganic hybrid complementary circuits based on pentacene and amorphous indium gallium zinc oxide transistors, Appl. Phys. Lett. 93 (2008) 213505.
[11] D.A. Mourey, S.K. Park, D.A. Zhao, Y.V. Li, S. Subramanian, S.F. Nelson, D.H. Levy, J.E. Anthony, T.N. Jackson, J. Sun, Fast, simple ZnO/organic CMOS integrated circuits, Org. Electron. 10 (2009) 1632–1635.
[12] P.-T. Liu, Y.-T. Chou, L.-F. Teng, C.-S. Fuh, High-gain complementary inverter with InGaZnO/pentacene hybrid ambipolar thin film transistors, Appl. Phys. Lett. 97 (2010) 083505.
[13] K. Nomura, H. Ohta, A. Takagi, T. Kamiya, M. Hirano, H. Hosono, Room-temperature fabrication of transparent flexible thin-film transistors using amorphous oxide semiconductors, Nature 432 (2004) 488–492.
[14] P. Barquinha, L. Pereira, G. Gonçalves, R. Martins, E. Fortunato, Toward high-performance amorphous GIZO TFTs, J. Electrochem. Soc. 156 (3) (2009) H161–H168.
[15] S.-J. Seo, C.G. Choi, Y.H. Hwang, B.-S. Bae, High performance solution-processed amorphous zinc tin oxide thin film transistor, J. Phys. D: Appl. Phys. 42 (2009) 035106.
[16] C.Y. Koo, D. Kim, S. Jeong, J. Moon, C. Park, M. Jeon, Sol–gel derived Ga–In–Zn–O semiconductor layers for solution-processed thin-film transistors, J. Korean Phys. Soc. 53 (2008) 218–222.
[17] S.K. Park, Y.-H. Kim, J.-I. Han, All solution-processed high-resolution bottom-contact transparent metal-oxide thin film transistors, J. Phys. D: Appl. Phys. 42 (2009) 125102.
[18] G. Adamopoulos, A. Bashir, S. Thomas, W.P. Gillin, S. Georgakopoulos, M. Shkunov, M.A. Baklar, N. Stingelin, R.C. Maher, L.F. Cohen, D.D.C. Bradley, T.D. Anthopoulos, Spray-deposited Li-doped ZnO transistors with electron mobility exceeding 50 cm^2/V s, Adv. Mater. 22 (2010) 4764–4769.
[19] S. Jeong, Y.-G. Ha, J. Moon, A. Facchetti, T.J. Marks, Role of gallium doping in dramatically lowering amorphous-oxide processing temperatures for solution-derived indium zinc oxide thin-film transistors, Adv. Mater. 21 (2009) 1–5.
[20] J. Smith, A. Bashir, G. Adamopoulos, J.E. Anthony, D.C. Bradley, R. Hamilton, M. Heeney, I. McCulloch, T.D. Anthopoulos, Air-stable solution-processed hybrid transistors with hole and electron mobilities exceeding 2 $cm^2 V^{-1} s^{-1}$, Adv. Mater. 22 (2010) 3598–3602.
[21] S. De Vusser, S. Steudel, K. Myny, J. Genoe, P. Heremans, Integrated shadow mask method for patterning small molecule organic semiconductors, Appl. Phys. Lett. 88 (2006) 103501.
[22] I. Kymissis, C.D. Dimitrakopoulos, S. Purushothaman, High-performance bottom electrode organic thin-film transistors, IEEE Trans. Electron. Dev. 48 (2001) 1060–1064.
[23] K.S. Pyo, C.K. Song, The effects of simultaneous treatment of SiO_2 gate and Au electrode with octadecyltrichlorosilane and charge transfer molecules on characteristics of pentacene thin film transistors, Thin Solid Films 485 (2005) 230–234.

one novel blue-emitting molecule bis(2-(2-hydroxyphenyl)-4-methyl-pyridine)beryllium ($Be(4\text{-}mpp)_2$) is designed by introducing a sterically hindered methyl group onto the pyridyl ring of the ligand in the original complex $Bepp_2$, which leads to both the desired enhancement for the luminescent and charge carriers transporting properties of $Be(4\text{-}mpp)_2$, and the considerable optimization for the organic-solid interfacial characteristic between the hole transporting layer and the emitting layer. As expected, the simple double-layer device based on $Be(4\text{-}mpp)_2$ exhibits excellent pure and stable blue light with CIE (Commission International de I' Eclarirage) coordinates of (0.14, 0.09), and shows very high EL efficiency with the peak external quantum efficiency (EQE) of 5.4% and peak power efficiency (PE) of 4.2 lm W^{-1}, which are better overall than the EL performance of $Bepp_2$-based device [8]. The details about the corresponding synthesis, crystal packing structure, photophysical properties and EL performance of the new beryllium complex are reported herein.

2. Experimental

2.1. Materials and synthesis

NPB and Alq_3 were commercially available. The 2-(2-hydroxyphenyl)-5-metheyl-pyridine (4-mppH) and the beryllium complex were prepared following the synthetic route shown in Scheme 1 [9,8b]. The starting materials obtained from commercial suppliers were used without further purification. Anhydrous hexane was distilled with sodium benzophenone ketyl under nitrogen atmosphere, degassed by the freeze–pump–thaw method. All glass wares, syringes, magnetic stirring bars and needles were dried in a convection oven at least 4 h. Reactions were monitored with thin layer chromatography (TLC). Commercial TLC plates (Silica gel 60 F254, Merck Co.) were developed and the spots were seen under UV light at 254 and 365 nm. Silica column chromatography was done with silica gel 60 G (particle size 5–40 μm, Merck Co.). ^{1}H NMR spectra were recorded on a Bruker AVANVE 300 MHz spectrometer with tetramethylsilane as an internal standard. Mass spectra were measured on a GC/MS mass spectrometer. Elemental analyses were performed on a flash EA 1112 spectrometer.

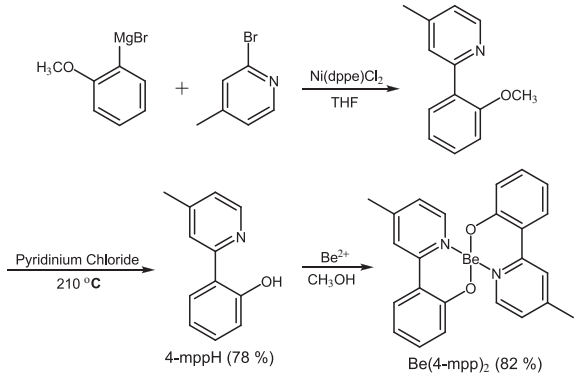

Scheme 1. Synthesis of $Be(4\text{-}mpp)_2$.

2.1.1. Synthesis of 4-mppH

To an ice-cold mixture of $[Ni(dppe)Cl_2]$ (dppe = $Ph_2PCH_2CH_2PPh_2$) (0.52 g, 1 mmol) and 2-bromo-4-methyl-pyridine (5.1 g, 30 mmol) in dry THF (30 ml) under a nitrogen atmosphere was added dropwise a solution of Grignard reagent prepared from 2-bromoanisole (6.74 g, 36 mmol). The mixture solution was allowed to attain room temperature and stirred for 12 h. The reaction was then quenched by addition of aqueous NH_4Cl and the THF was removed under reduced pressure. The resulting white precipitate was filtered off, washed with water and dried in air to give the product 2-(2-methoxyphenyl)-4-methyl-pyridine. It is sufficiently pure for use in the subsequent step. 2-(2-Methoxyphenyl)-4-methyl-pyridine was added in molten pyridinium chloride (from 30 ml pyridine and 35 ml concentrated HCl) under nitrogen for 3 h at 210 °C. After addition of water to the mixture and neutralization with aqueous KOH, the crude product was extracted with CH_2Cl_2 (3 × 60 ml), and the organic phase was washed twice with water (2 × 30 ml) and then dried over Na_2SO_4. The solvent was removed under reduced pressure. The residual yellow solid was purified by chromatography (silica, CH_2Cl_2) to give the light yellow powder product in 78% yield. MS: m/z = 185 (M^+). Anal. Calcd. for $C_{12}H_{11}NO$: C, 77.81; H, 5.99; N, 7.56. Found: C, 77.68; H, 5.79; N, 7.63. ^{1}H NMR in $CDCl_3$ (δ, ppm): 12.96 (1H, broad, s), 8.32 (1H, d, J = 5.2 Hz), 7.72 (1H, d, J = 5.2 Hz), 7.68 (1H, s), 7.32–6.74 (4H, m), 2.40 (3H, s).

2.1.2. Synthesis of $Be(4\text{-}mpp)_2$

In a 100-ml round bottom flask fitted with magnetic stirrer, $BeSO_4{\cdot}5H_2O$ (0.9 g, 5 mmol) and 30 ml methanol was slowly added to 4-mppH (1.85 g, 10 mmol) dissolved in 30 ml of methanol. Then the mixed solution was adjusted to pH 12 using NaOH and was stirred for 5 h at room temperature. Colorless solid precipitated from the solution. The solid product was collected by filtration and purified by recrystallization and sublimation methods (82% yield). MS: m/z = 377 (M^+). Anal. Calcd. for $C_{24}H_{20}N_2O_2Be$: C, 76.37; H, 5.34; N, 7.42. Found: C, 76.59; H, 5.26; N, 7.58. ^{1}H NMR in $CDCl_3$ (δ, ppm): 8.46 (2H, d, J = 5.2 Hz), 7.82 (2H, d, J = 5.2 Hz), 7.50 (2H, s), 7.15 (2H, t, J = 4.8 Hz), 6.95–6.76 (6H, m), 2.35 (6H, s).

2.2. Absorption, PL and electrochemical measurements

Absorption spectrum was obtained using a Shimadzu UV-2550 UV–vis spectrometer. PL spectra were recorded by a Perkin-Elmer LS-55 fluorescence spectrometer with a Xe arc lamp excitation source. The PL quantum yields were measured by use of quinine sulfate in 1 M sulfuric acid as a standard (Φ = 0.546) [10]. All solvents were degassed via three freeze–pump–thaw cycles. Electrochemical measurements were performed in anhydrous CH_2Cl_2 with a BAS 100 W bioanalytical electrochemical work station, using Pt as the working electrode, platinum wire as the auxiliary electrode, and a porous glass wick Ag/Ag^+ as the reference electrode. It was standardized against a ferrocene/ferrocenium couple with a scan rate of 100 mV s^{-1}. The highest occupied molecular orbital (HOMO) and the lowest unoccupied molecular orbital (LUMO) energy levels

of the emitting materials were calculated from the cyclic voltammetry (CV) data together with their absorption spectra. The proposed energy diagram of the materials used in OLEDs is shown in Fig. 2 (inset), where the values for NPB and Alq_3 are taken from literature [11].

2.3. Fabrication of the OLEDs and EL measurements

The devices were grown on a glass, which was precoated with indium tin oxide (ITO) having a sheet resistance equal to 20 $\Omega\,cm^{-2}$. The ITO glass was routinely cleaned by ultrasonic treatment in detergent solutions, followed by rinsed with acetone, boiled in isopropanol, rinsed in methanol, and then in de-ionized water. The glass was dried in vacuum oven between each cleaning step above. To reduce the possibility of electrical shorts on the ITO anode and increase the value of its work function, the ITO substrate was treated using a Plasma Cleaner (PDC-32G-2, 100 W) with the oxygen ambient. Prior to the deposition, all the organic materials were purified by sublimation method. The organic layers were sequentially deposited onto the substrate without breaking vacuum at a pressure of about 10^{-4} Pa. A very thin layer of LiF could enhance electron injection from aluminum cathode. A shadows mask with $2 \times 3\ mm^2$ openings was used to define the cathodes. The EL spectrum, brightness, CIE coordinates and the current-brightness–voltage characteristics of the devices were measured with a rapid scan system using a spectrophotometer (PR-650, Photo Research) and a computer-controlled, programmable, direct-current (DC) source (Keithley 2400). Luminance–voltage and current–voltage characteristics were measured at room temperature under an ambient atmosphere.

3. Results and discussion

3.1. π–π packing properties

Single X-ray diffraction study (CCDC reference number is 827923) revealed that there are strong intermolecular π–π stacking between 4-mpp ligands of the adjacent beryllium molecules in the solid state (Fig. 1), and the interplanar distance is approximately 3.3 Å, which is shorter than that shown in $Bepp_2$ (3.4 Å) [8b], and it is one rather short π–π interaction. Our earlier studies demonstrated that the high electron mobility of EL materials is due to the intermolecular interactions and intermolecular aromatic stacking could offer the charge transfer pathway [8a]. Therefore, the results above suggest that $Be(4\text{-mpp})_2$ should possess good charge transport property, which is an essential property for an excellent EL material, and indicates that it may be even higher than that of $Bepp_2$ for their interplanar distance alignment.

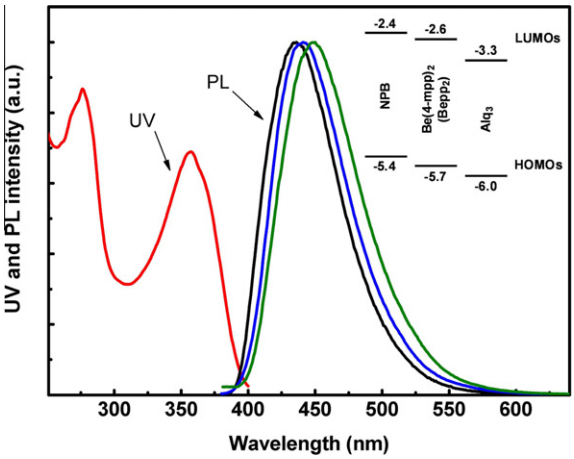

Fig. 2. UV absorption spectrum (red line) and PL spectrum (black line) of $Be(4\text{-mpp})_2$ in the chloroform solution. PL spectra of $Be(4\text{-mpp})_2$ (blue line) and $Bepp_2$ (green line) in the neat film. Inset: the proposed energy diagram of the materials used in OLEDs.

3.2. Photophysical properties

The UV/vis and photoluminescent (PL) spectra of $Be(4\text{-mpp})_2$ in chloroform solution and the PL spectra of $Be(4\text{-mpp})_2$ and $Bepp_2$ in their solid thin films deposited on quartz substrates were measured and shown in Fig. 2. The UV absorption spectrum of $Be(4\text{-mpp})_2$ in solution has maxima at around 360 nm, and under the excitation of UV-light of wavelength 365 nm, this complex shows strong blue emission at around 435 nm with the relative quantum yield of 0.37, which is much higher than that of $Bepp_2$ (0.27). In solid films, both complexes exhibits strong blue fluorescence with the similar half-maximum width about 65–70 nm, but the emission peak of $Be(4\text{-mpp})_2$

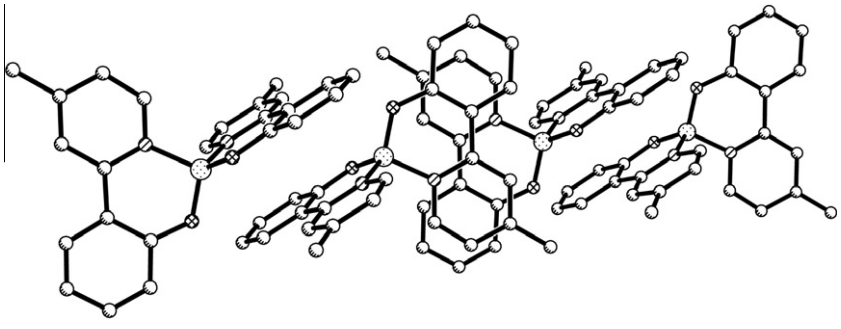

Fig. 1. Crystal packing diagrams of $Be(4\text{-mpp})_2$.

shows a slight blue shift compared with $Bepp_2$ due to the introduction of one methyl onto the ligand. It is consistent with the results studied on the emission characteristic of the metal–chelate complexes based on the pyridyl and hydroxyphenyl system reported previously [7a,d], where inserting an electron donating group at the 2- or 4-position of the pyridyl ring can achieve blue-shift in the emission spectrum. Nevertheless, the relatively weak electron donating ability of the methyl group could not lead to significantly detectable difference between the values of the corresponding HOMO and LUMO energy levels of $Bepp_2$ and $Be(4\text{-mpp})_2$ shown in Fig. 2 (inset).

3.3. EL properties

To investigate the EL properties, series of EL devices were fabricated. $Be(4\text{-mpp})_2$ acts as the neat emitting layer (EML) as well as the electron transporting layers (ETL) in device I, where NPB (4,4-bis(*N*-(1-naphthyl)-*N*-phenylamino)biphenyl) was used as a hole transport layer (HTL). For comparison, device II based on $Bepp_2$ with the same device structure and device III using $Be(4\text{-mpp})_2$ as the EML and Alq_3 as the ETL were prepared also, respectively. All the device structures are shown as follows:

(I) [ITO/NPB (40 nm)/$Be(4\text{-mpp})_2$ (50 nm)/LiF (1 nm)/Al].
(II) [ITO/NPB (40 nm)/$Bepp_2$ (50 nm)/LiF (1 nm)/Al].
(III) [ITO/NPB (40 nm)/$Be(4\text{-mpp})_2$ (20 nm)/Alq_3 (30 nm)/LiF (1 nm)/Al].

Fig. 3 shows the normalized EL spectra of device I–III at the brightness of 1000 cd m^{-2}. All of them have the similar emission peak at around 450 nm, but show much variation in the half-maximum width ranging from 60 to 110 nm. Compared with device II based on $Bepp_2$, which just show a sky-blue emission with the CIE coordinates of (0.16, 0.18) and obviously broader EL spectrum relative to the corresponding PL spectrum of $Bepp_2$ in the solid film shown in Fig. 2, device I using $Be(4\text{-mpp})_2$ as the neat EML display very narrow spectral shape that is consistent well with

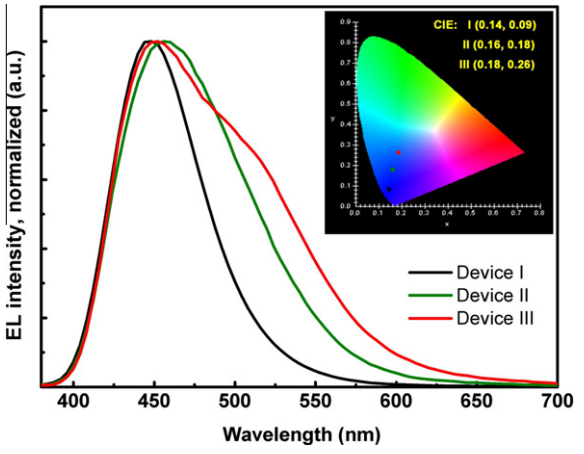

Fig. 3. EL spectra of device I, II and III at the brightness of 1000 cd m^{-2}. Inset: the corresponding CIE coordinates of device I, II and III at the brightness of 1000 cd m^{-2}.

the PL spectral characteristics of this complex (Fig. 2). The EL emission from device I is saturated blue light with CIE (0.14, 0.09) at the brightness of 1000 cd m^{-2} as shown in Fig. 3 (inset), which matches closely to the NTSC (National Television Standards Committee) blue standard (0.14, 0.08) and remain almost unchanged in the driving voltage range from 4 to 10 V. The possible reason for this enhancement in the blue-light quality is through introducing a sterically hindered methyl onto the pyridyl ring of the beryllium complex, which can optimize the organic-solid interface properties between the layers of NPB and $Be(4\text{-mpp})_2$ and then prevent the possible exciplex formation [3a,7c,12] that could lead to a broader EL spectrum such as in the NPB/$Bepp_2$ interface of device II. In the device III using Alq_3 as the ETL, an additional emission in the wavelength region from 500 to 550 nm is observed and increases as the applied voltage increased together with the dominant blue emission at 450 nm, which leads to a greenish-blue EL emission with the CIE coordinates of $x \geqslant 0.18$ and $y \geqslant 0.22$. The clear shoulder is attributed to the emission of Alq_3, which should come from such emission mechanism in this Alq_3-based device: because there is a large barrier height of 0.7 eV for electron injection from the LUMO (the lowest unoccupied molecular orbital) of Alq_3 to the LUMO of $Be(4\text{-mpp})_2$ (as shown in Fig. 2, inset), some electrons are confined within the Alq_3 layer and lead to the recombination of certain number of holes and electrons occurred at the ETL. The gradual increase in the emission intensity of the Alq_3 suggests that more holes can leak into the ETL and form more excitons with electrons in this layer as the voltage increased. This phenomenon indicates that Alq_3 is not a very favorable ET material for a blue emitter due to the inevitable green emission that will lead to a poor-purity blue EL emission.

The current density–voltage and luminance–voltage characteristics of device I, II and III were plotted in Fig. 4 (top) and Fig. 4 (bottom), respectively. Device I and II exhibit similar turn-on voltage of 3.0 V (recorded at 1 cd m^{-2}), which is lower than that of device III (3.5 V). Compared with device II and III, device I shows faster rise of the EL intensity and the current density after the onset voltages, and such trend becomes more obvious along with the driving voltage increased. The driving voltage of device I at the brightness of 100, 1000 and 10,000 cd m^{-2} are 4.7, 6.2 and 9.0 V, respectively, which are lower than those of device II (4.8, 6.4 and 9.7 V, respectively) and device III (5.3, 7.1 and 10.7 V, respectively). The faster response of the EL intensity as well as the current density of device I than those of device II should partly be attributed to the relatively higher quantum yield of $Be(4\text{-mpp})_2$ than that of $Bepp_2$, but also supports the hypothesis mentioned above that $Be(4\text{-mpp})_2$ might possess better electron-transporting ability than $Bepp_2$. In addition, the much lower LUMO level of Alq_3 than that of $Be(4\text{-mpp})_2$ causes a high election–injection barrier in device III, and thus leads to the higher driving voltage of device III than those of device I and II.

As a result, device I based on $Be(4\text{-mpp})_2$ as the EML and ETL exhibits the best overall EL performance, in terms of not only the improved color purity mentioned above, but also the significantly enhanced EL efficiency relative to the $Bepp_2$-based device II and Alq_3-based device III.

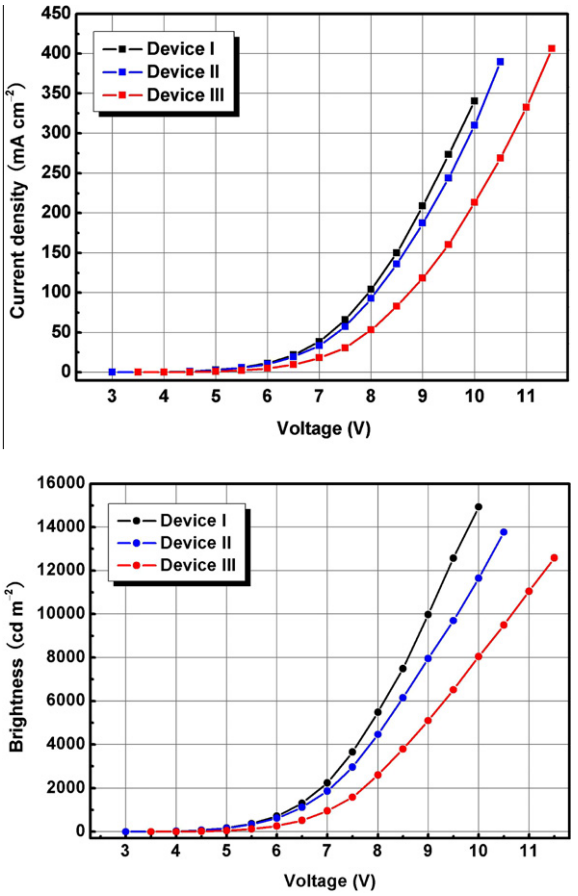

Fig. 4. Current density–voltage and brightness–voltage characteristics of device I, II and III.

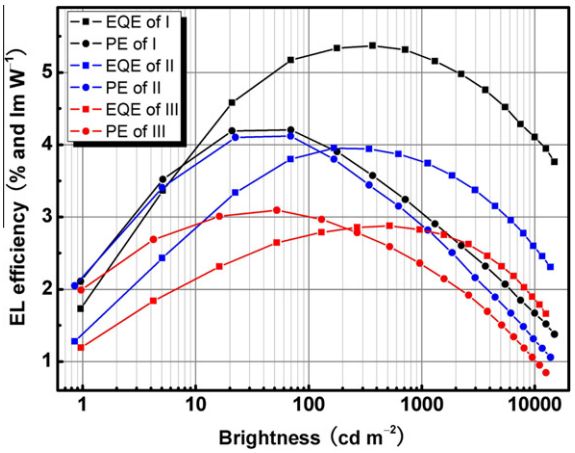

Fig. 5. EQE (external quantum efficiency)–brightness and PE (power efficiency)–brightness characteristics for the device I, II and III.

Fig. 5 shows the EQE (external quantum efficiency)–brightness and PE (power efficiency)–brightness characteristics for the device I, II and III. Device I shows the highest EL efficiency with the maximum EQE of 5.4% at 370 cd m^{-2} (5.5 V) and maximum PE of 4.2 lm W^{-1} at the brightness of 70 cd m^{-2} (4.5 V), compared with the corresponding peak values of device II (3.9% at 340 cd m^{-2} and 5.5 V, 4.1 lm W^{-1} at 70 cd m^{-2} and 4.5 V) and device III (2.9% at 520 cd m^{-2} and 6.5 V, 3.1 lm W^{-1} at 50 cd m^{-2} and 5.0 V). Obviously, although the PE level of device I shows just a little higher than that of device II, the EQE level device I is dramatically enhanced and exhibits much higher than that of device II within the whole range of the driving voltages. This should be attributed to the perfect blue EL emission with the CIE coordinates of (0.14, 0.09) of device I that is much bluer than that of device II, which leads to device I can release more photons than device II based on the similar lumen output of two devices [13]. Notably, the EQE values of device I at the practical brightness of 100 and 1000 cd m^{-2} in the fields of flat panel displays and solid-state lighting, remain as high as 5.0% that is much higher than those of device II, which indicates the better charge carrier balance and more efficient confinement of the excitons generated within the emitting layer in device I than in device II [11a,14]. These values of device I mentioned above are the highest EL efficiencies ever reported for such saturated and stable OLED (CIE: $x < 0.15$, $y < 0.10$) to the best of our knowledge, even including the devices utilizing doped [4,16] and non-doped emitting systems [4a,15]. In addition, it is noteworthy that the brightness– and current density–voltage curves of device I show no significant saturation behavior at high driving voltages and its EQE keeps more than 4.0% in very wide the brightness range (10–10,000 cd m^{-2}) corresponding to the current density range (0.2–200 mA cm^{-2}), which suggest that this simple and efficient double-layer device displays very good operational stability also. The fact that NPB is a well-known hole transporting material and no conventional ETM such as Alq_3 is required to achieve the highly efficient and deep-blue EL emission in Be(4-mpp)$_2$-based device demonstrates that Be(4-mpp)$_2$ can act as a desired bifunctional material: not only a bright blue emitter, but also a suitable ETM in EL devices, especially for the blue-emission OLEDs that need perfect color purity.

4. Conclusions

In summary, the high-performance blue OLED using one novel beryllium complex Be(4-mpp)$_2$ as the EML as well as the ETL has been developed. The simple double-layer device shows pure and stable blue emission with the CIE coordinates of (0.14, 0.09) and exhibits very high EL efficiency in terms of both the peak values (5.4% for EQE and 4.2 lm W^{-1} for PE) and the good operational stability. The dramatically enhanced EL properties of Be(4-mpp)$_2$ is realized easily through the minor modification for the molecular structure, which has proven to be a simple and effective strategy to improve both the luminescent and the charge carriers transporting properties of the host emitting materials. The gratifying bifunctional property suggests that this new beryllium complex has high potential as both an efficient deep-blue emitter or host and a competent electron transporting material, for the applications in large flat panel displays and solid-state lighting in future.

Acknowledgements

This work was partly supported by National Basic Research Program of China (973 Program, 2009CB623600), Natural Science Foundation of China (50733002, 50903036 and 51173064), Provincial Science and Technology Bureau of Jilin Province (201105010).

Appendix A. Supplementary data

Supplementary data associated with this article can be found, in the online version, at doi:10.1016/j.orgel.2011.08.006.

References

[1] C.W. Tang, S.A. Vanslyke, Appl. Phys. Lett. 51 (1987) 913.
[2] (a) R.J. Holmes, S.R. Forrest, Y.-J. Tung, R.C. Kwong, J.J. Brown, S. Garon, M.E. Thompson, Appl. Phys. Lett. 82 (2003) 2422;
(b) S.-C. Lo, G.J. Richards, J.P.J. Markham, E.B. Namdas, S. Sharma, P.L. Burn, I.D.W. Samuel, Adv. Funct. Mater. 15 (2005) 1451;
(c) J.-J. Lin, W.-S. Liao, H.-J. Huang, F.-I. Wu, C.-H. Cheng, Adv. Funct. Mater. 18 (2008) 485;
(d) K.S. Yook, S.O. Jeon, C.W. Joo, J.Y. Lee, Org. Electron. 10 (2009) 170;
(e) C.-H. Chang, C.-C. Chen, C.-C. Wu, C.-H. Yang, Y. Chi, Org. Electron. 10 (2009) 1364.
[3] (a) Y.Z. Wu, X.Y. Zheng, W.Q. Zhu, R.G. Sun, X.Y. Jiang, Z.L. Zhang, S.H. Xu, Appl. Phys. Lett. 83 (2003) 5077;
(b) M.-T. Lee, C.-H. Liao, C.-H. Tsai, C.H. Chen, Adv. Mater. 17 (2005) 2493;
(c) S.-L. Jeon, Y.-M. Jeon, J.-W. Kim, C.-W. Lee, M.-S. Gong, Org. Electron. 19 (2008) 522;
(d) T.Z. Yu, P. Zhang, Y.L. Zhao, H. Zhang, J. Meng, D.W. Fan, Org. Electron. 10 (2009) 653;
(e) G.S. Samal, K.N. Narayanan Unni, S. Bharat, S. Gupta, Deepak, Org. Electron. 10 (2009) 1201;
(f) Q.J. Qi, X.M. Wu, Y.L. Hua, Q.C. Hou, M.S. Dong, Z.Y. Mao, B. Yin, S.G. Yin, Org. Electron. 11 (2010) 503.
[4] (a) C.J. Tonzola, A.P. Kulkarni, A.P. Gifford, W. Kaminsky, S.A. Jenekhe, Adv. Funct. Mater. 17 (2007) 863;
(b) P.-I. Shih, C.-Y. Chuang, C.-H. Chien, E.W.-G. Diau, C.-F. Shu, Adv. Funct. Mater. 17 (2007) 3141;
(c) K.-C. Wu, P.-J. Ku, C.-S. Lin, H.-T. Shih, F.-I. Wu, M.-J. Huang, J.-J. Lin, I.-C. Chen, C.-H. Cheng, Adv. Funct. Mater. 18 (2008) 67;
(d) S. Park, J. Seo, S.H. Kim, S.Y. Park, Adv. Funct. Mater. 18 (2008) 726;
(e) S.J. Lee, J.S. Park, K.-J. Yoon, Y.-I. Kim, S.-H. Jin, S.K. Kang, Y.-S. Gal, S. Kang, J.Y. Lee, J.-W. Kang, S.-H. Lee, H.-D. Park, J.-J. Kim, Adv. Funct. Mater. 18 (2008) 3922;
(f) T.-C. Tsai, W.-Y. Hung, L.-C. Chi, K.-T. Wong, C.-C. Hsieh, P.-T. Chou, Org. Electron. 10 (2009) 158.
[5] (a) L.-H. Chan, R.-H. Lee, C.-F. Hsieh, H.-C. Yeh, C.-T. Chen, J. Am. Chem. Soc. 124 (2002) 6469;
(b) R.C. Chiechi, R.J. Tseng, F. Marchioni, Y. Yang, F. Wudl, Adv. Mater. 18 (2006) 325;
(c) Z.Q. Gao, Z.H. Li, P.F. Xia, M.S. Wong, K.W. Cheah, C.H. Chen, Adv. Funct. Mater. 17 (2007) 3194;
(d) C.-G. Zhen, Y.-F. Dai, W.-J. Zeng, Z. Ma, Z.-K. Chen, J. Kieffer, Adv. Funct. Mater. 21 (2011) 699.
[6] (a) W.L. Jia, X.D. Feng, D.R. Bai, Z.H. Lu, S. Wang, G. Vamvounis, Chem. Mater. 17 (2005) 164;
(b) D.D. Zhang, J. Feng, Y.F. Liu, Y.Q. Zhong, Y. Bai, Y. Jin, G.H. Xie, Q. Xue, Y. Zhao, S.Y. Liu, H.B. Sun, Appl. Phys. Lett. 94 (2009) 223306;
(c) D.D. Zhang, J. Feng, H. Wang, Y. Bai, Q.D. Chen, S.Y. Liu, H.B. Sun, Appl. Phys. Lett. 95 (2009) 263303.
[7] (a) X.T. Tao, H. Suzuki, T. Wada, S. Miyata, H. Sasabe, J. Am. Chem. Soc. 121 (1999) 9447;
(b) N.-X. Hu, M. Esteghamatian, S. Xie, Z. Popovic, A.-M. Hor, B. Ong, S. Wang, Adv. Mater. 11 (1999) 1460;
(c) S.-F. Liu, Q. Wu, H.L. Schmider, H. Aziz, N.-X. Hu, Z. Popović, S. Wang, J. Am. Chem. Soc. 122 (2000) 3671;
(d) L.M. Leung, W.Y. Lo, S.K. So, K.M. Lee, W.K. Choi, J. Am. Chem. Soc. 122 (2000) 5640;
(e) F.S. Liang, J.S. Chen, L.X. Wang, D.G. Ma, X.B. Jing, F.S. Wang, J. Mater. Chem. 13 (2003) 2922.
[8] (a) Y. Wang, W.X. Zhang, Y.Q. Li, L. Ye, G.D. Yang, Chem. Mater. 11 (1999) 530;
(b) Y.Q. Li, Y. Liu, W.M. Bu, D. Lu, Y. Wu, Y. Wang, Chem. Mater. 12 (2000) 2672;
(c) Y. Liu, J.H. Guo, J. Feng, H.D. Zhang, Y.Q. Li, Y. Wang, Appl. Phys. Lett. 78 (2001) 2300.
[9] L. Kaczmarek, R. Balicki, J. Lipkowski, P. Borowicz, A. Grabowska, Chem. Soc., Perkin Trans. 2 (1994) 1603.
[10] J.N. Demas, G.A. Crosby, J. Phys. Chem. 75 (1971) 991.
[11] (a) Y. Liu, K.Q. Ye, Y. Fan, W.F. Song, Y. Wang, Z.M. Hou, Chem. Commun. (2009) 3699;
(b) H. Bi, K. Ye, Y. Zhao, Y. Yang, Y. Liu, Y. Wang, Org. Electron. 11 (2010) 1180.
[12] (a) Y.Q. Li, Y. Liu, W.M. Bu, J.H. Guo, Y. Wang, Chem. Commun. (2000) 1551;
(b) T.-H. Liu, W.-J. Shen, C.-K. Yen, C.-Y. Iou, H.-H. Chen, B. Banumathy, C.H. Chen, Synth. Met. 137 (2003) 1033.
[13] "The luminous (power) efficiency of a device accounts for a spectral sensitivity of a human eye. Therefore, two devices with similar quantum efficiencies can have different luminous performance." See: M. Stolka, Optoelectronics Industry Development Association (OIDA): Organic Light Emitting Diodes (OLEDs) for General Illumination Update 2002, 2002, p. 25.
[14] M. Ikai, S. Tokito, Y. Sakamoto, T. Suzuki, Y. Taga, Appl. Phys. Lett. 79 (2001) 156.
[15] P.-I. Shih, C.-Y. Chuang, C.-H. Chien, E.W. Guang Diau, C.-F. Shu, Adv. Funct. Mater. 17 (2007) 3141.
[16] T. Peng, G.F. Li, Y. Liu, Y. Wu, K.Q. Ye, D.D. Yao, Y. Yuan, Z.M. Hou, Y. Wang, Org. Electron. 12 (2011) 1068.

For Alq3 thin films sandwiched between Mg:Ag and either Al or Mg:Ag electrodes, Baldo and Forrest [8] observed very unique temperature and thickness dependent I/V characteristics that required implementation of a new model of injection into a disordered solid [8]. In the Baldo and Forrest model, it was hypothesized that disorder was enhanced near the metal–organic interface in such a way that the limiting charge injection process was not direct injection from the metal electrode into the disordered Alq3 film but rather injection from a highly disordered interfacial molecular layer into the somewhat less disordered bulk film. A possible physical origin of the interfacial disorder was suggested to be random variations in orientations of Alq3 molecules that result in strongly varying local interfacial dipoles [14] in the plane of the metal–organic interface.

Only a few scanned probe experiments directed at visualizing Alq3 film structure at the molecular level have been attempted. Alvarado and co-workers found that Alq3 diffused too rapidly on the surface to image by scanning tunneling microscopy (STM) at room temperature on Au(1 1 1) [15]. However, they were able to estimate the transport gap for Alq3/Au(1 1 1) using tip distance-versus-voltage spectroscopy [15,16]. More recently, linear Alq3 nanostructures were observed on ultrathin KBr films, but intermolecular distances were not reported [17]. Numerous studies have used atomic force microscopy to image the nanometer scale morphology of thick Alq3 films [18–20].

In the present paper we report scanning tunneling microscopy observations of the first layer of Alq3 on a Cu(1 1 0) surface that achieve single molecule resolution. These experiments show a poorly ordered interface that results from growth on a room temperature substrate and that persists after annealing up to about 590 K. While no long range order is observed in this first monolayer, intermolecular interactions are revealed by the formation of randomly-oriented chain-like aggregates of Alq3 molecules. We describe the origin of these disordered chain structures from anisotropic intermolecular interactions using model density functional theory (DFT) calculations.

2. Experimental methods

Experiments were carried out in an ultrahigh vacuum system with two interconnected chambers. One chamber (base pressure $<7 \times 10^{-11}$ torr) houses facilities for substrate cleaning and STM characterization. Another chamber (base pressure $\sim 1 \times 10^{-8}$ torr) is separated from the first by a gate valve and houses home-built organic evaporators and a quartz oscillator for flux monitoring.

The substrate was a Cu(1 1 0) single crystal (Princeton) cleaned by repeated cycles of 1 keV Ar^+ sputtering following by annealing for 20 min at ~700 K. During deposition, the Cu(1 1 0) crystal was held at room temperature. Powdered tris-(8-hydroxyquinoline) – Aluminum (“Alq3”, Sigma–Aldrich – 99.995%) was loaded as received into a degassed quartz crucible that could be heated by a tightly wrapped Tantalum filament coil. The Alq3 was outgassed for several hours in the deposition chamber prior to film growth. The stability of Alq3 flux was monitored with a quartz oscillator before and after deposition. Absolute flux calibration was carried out by direct STM imaging with molecular resolution.

STM imaging was carried out at room temperature with a commercial instrument (Omicron VT-STM-XA) operated in constant current mode with electrochemically-etched tungsten tips. Annealing experiments after Alq3 deposition were performed by heating the sample in the cleaning/STM chamber manipulator with an integrated PBN heater. Temperature was monitored by a K-type thermocouple attached near the sample and corrected by adding 120 K to estimate the real sample temperature. This correction is based on infrared pyrometry at temperatures greater than 820 K and is expected to be accurate only to about ±30 K.

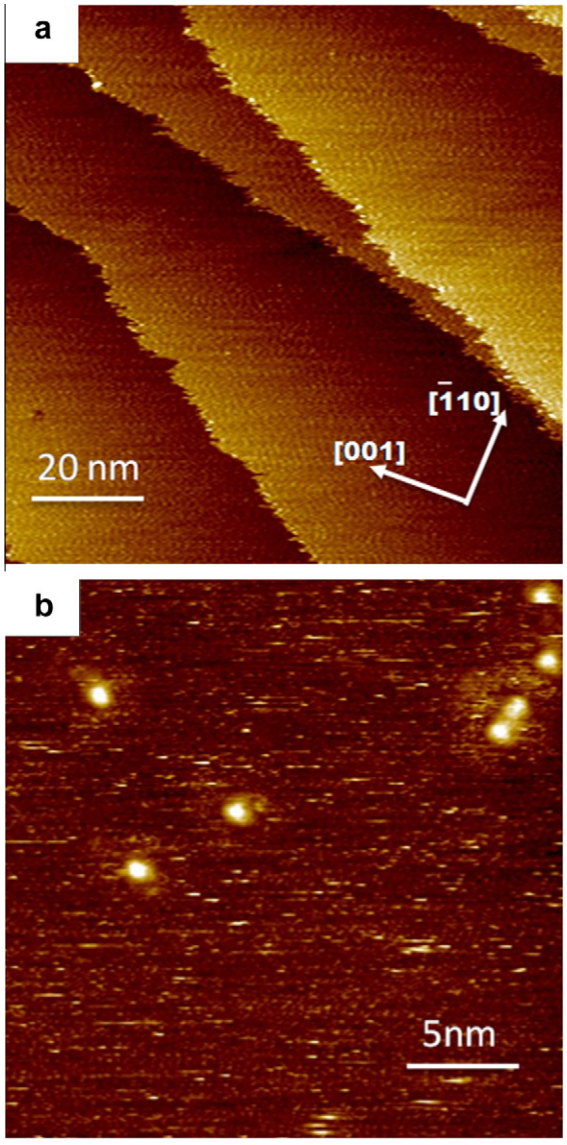

Fig. 1. (a) STM image (100 nm × 95 nm, −0.8 V, 30 pA) of the clean Cu(1 1 0) substrate; (b) STM image (25 nm × 25 nm, −1.0 V, 2 pA) after deposition of a small quantity (90 s deposition time) of Alq3. Single molecules are imaged as bright protrusions as indicated by the arrow.

3. Results

In Fig. 1a, an STM image of the large scale morphology of the Cu(1 1 0) substrate surface is shown. Relatively flat terraces separated by single-atom high steps can be seen. After a very short deposition of Alq3, it is possible to see a number of uniformly sized approximately circular protrusions on the terraces that are single Alq3 molecules (Fig. 1b).

Upon further deposition, Alq3 molecules begin to aggregate, displaying a strong tendency to form pairs as shown in Fig. 2a. These pairs are spaced typically just under 1 nm apart (center to center), which is a distance consistent with near-neighbor spacings in bulk Alq3 crystals [6]. We note that the pairing direction does not show any strong preference with respect to crystallographic directions in the plane of the Cu(1 1 0) surface. At these low coverages, there is apparently a significant mobility of some surface species as evidenced by the streaky noise surrounding bright molecular protrusions in STM images.

As the coverage of Alq3 increases in the first monolayer, a tendency to form chain-like aggregates is observed building from the paired molecules in Fig. 2a. This is shown in Fig. 2b–d where randomly-oriented chains of 3–7 Alq3 molecules can be seen. The spacing (0.8–1.0 nm) between near neighbor molecules in chains is similar to the spacing in pairs. The lack of long-ranged order and the tendency toward chain formation persist upon annealing up to 590 K as shown in Fig. 3. Fig. 3a shows an STM image of a Alq3 film deposited at room temperature and Fig. 3b shows the result of annealing the same film to 590 K. This observation indicates that the amorphous monolayer created by deposition of Alq3 on Cu(1 1 0) is a relatively stable structure. Despite significant open space on the surface, it was never observed to convert to an ordered molecular layer.

4. Discussion

4.1. Interfacial disorder

The most significant observation reported above is that the first monolayer of Alq3 is highly disordered when deposited onto a room temperature Cu(1 1 0) surface. Many other organic semiconductors exhibit ordered monolayers on this surface, templated by strong substrate–molecule interactions. For example, pentacene forms an ordered first layer with intermolecular spacings that have been argued to be determined by substrate-mediated interactions [21]. In addition, PTCDA has been shown to form ordered monolayers [22] (accompanying substrate surface reconstruction) followed by beautifully crystalline 3D islands [23,24].

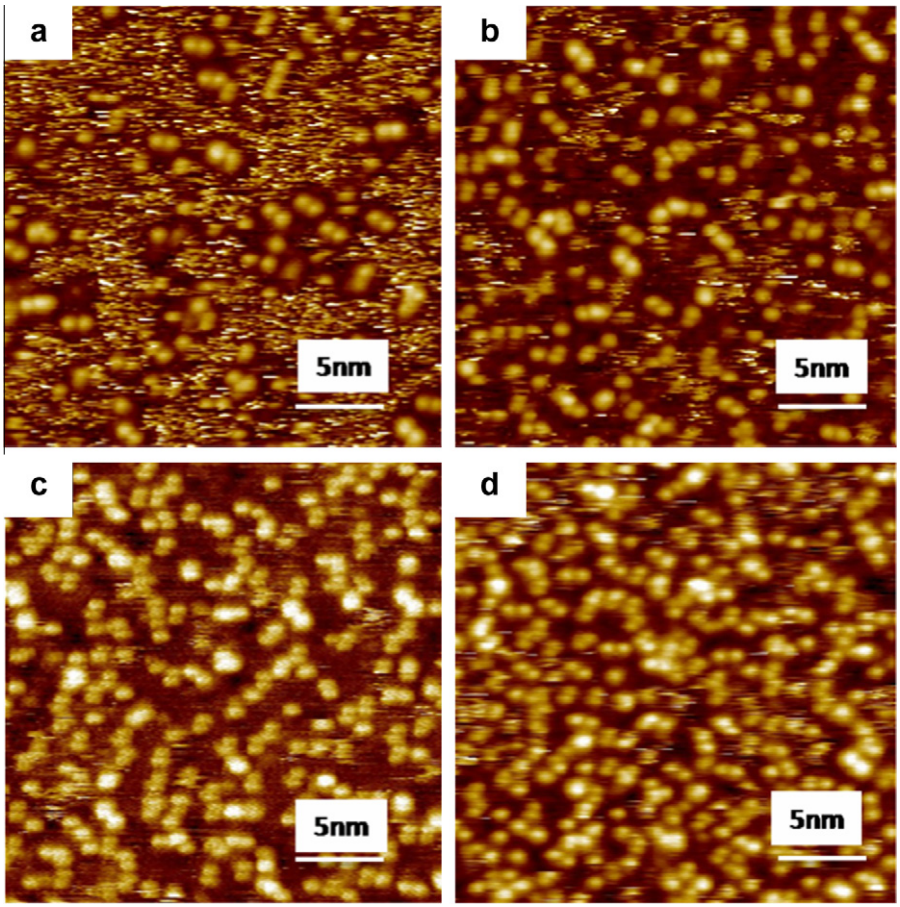

Fig. 2. Coverage-dependent STM images (all 25 nm × 25 nm) during the growth of the first monolayer of Alq3 on Cu(1 1 0); (a) 0.16 nm^{-2} (−1.3 V, 1 pA); (b) 0.33 nm^{-2} (−1.2 V, 5 pA); (c) 0.49 nm^{-2} (−1.4 V, 3 pA); (d) 0.63 nm^{-2} (−0.6 V, 1 pA).

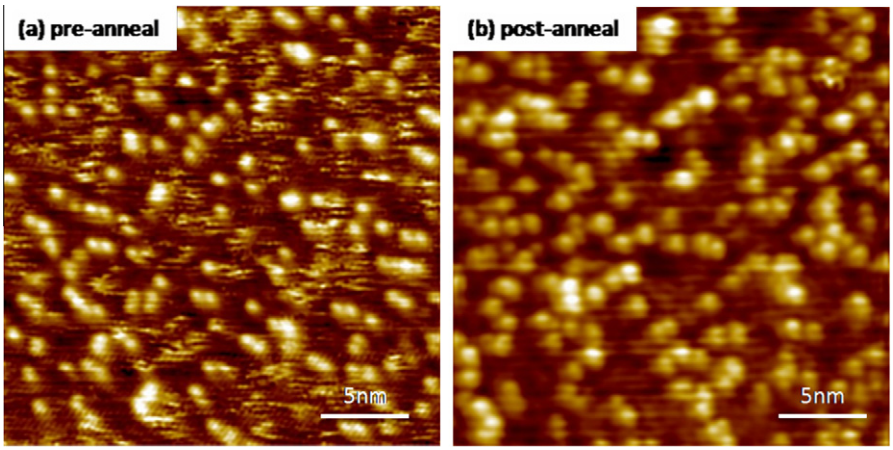

Fig. 3. (a) STM image (25 nm × 24 nm, −1.3 V, 10 pA) of an as-deposited Alq3 film with coverage of 0.25 ± 0.02 nm^{-2}; (b) STM image (25 nm × 24 nm, −1.2 V, 20 pA) of the same film as in (a) after annealing to 590 K. The coverage is 0.24 ± 0.02 nm^{-2}.

The fact that disorder in the first Alq3 layer is not easily removed by annealing suggests that it is the dominant structural motif on Cu(1 1 0) and that the well-known amorphous structure of Alq3 films can begin in the first layer. As mentioned in the Section 1, Baldo and Forrest suggested an Alq3 diode device model that included strong electronic disorder in the first few layers near the metal–organic interface [8]. Our observations are consistent with such a picture, since the observed structural disorder should translate into significant disorder in electronic density of states. This could result from random local electronic polarization environments due to variable local coordination number [25–27]. Alternatively, it could result from random local interface dipoles due to disorder in either molecular orientations or site location [28].

4.2. Alq3 chain formation

The single molecule resolution afforded by STM measurements allows an elaboration of the subtle details of disorder at the Alq3/Cu(1 1 0) interface. The prominence of linear structures in the disordered first monolayer of Alq3 on Cu(1 1 0) shows that intermolecular interactions are important enough to establish significant *local* molecular correlations at the metal–molecule interface. Such local ordering has been argued to be important in determining optoelectronic properties of thick organic films. [29] In addition, aggregation on the scale of a few molecules has been shown to influence exciton dynamics. [30].

In this section, we address the origin of the chain-like Alq3 structures using density functional theory (DFT) calculations of intermolecular interactions designed to capture some important aspects of the direct intermolecular interactions that are likely to be operative on a metal surface. In order to explain the observed tendency to form chain-like aggregates, it is necessary that intermolecular interactions are anisotropic to some degree. Such anisotropy is intuitively plausible for Alq3 since the molecule has a relatively low symmetry (C_1 point group for the most stable "meridional" isomer) and a large (∼5D) intrinsic dipole moment [31].

Previously, the adsorption configuration of Alq3 on aluminum surfaces has been studied using density functional theory by Yanagisawa et al. [31,32]. These calculations illustrate that the intrinsic dipole moment of the molecule is only slightly reduced when adsorbed on a Al(1 1 1) surface [31]. We hypothesize that adsorbed Alq3 molecules are not completely free to rotate out of the plane of the surface (i.e. they cannot change the orientation of their intrinsic dipole moment with respect to the surface normal). In this case, the crucial direct intermolecular interactions on a surface occur between Alq3 molecules each with a fixed orientation with respect to the surface plane. This orientation may vary from molecule to molecule on the surface but cannot change to optimize intermolecular interactions to achieve a bulk-like crystal structure [6].

Density functional theory calculations were carried out using the Gaussian 09 software package [33]. We optimized the geometry of an isolated *meridional* Alq3 molecule using Hartree–Fock calculations with a 3-21G basis set. This method was chosen based on reports that Hartree–Fock most accurately produces the experimentally-determined molecular geometry and dipole moment [34]. After single molecule optimization, we calculated single point energies (i.e. with no further optimization permitted) for pairs of molecules in different configurations as described below. These calculations were carried out using density functional theory (DFT) with a 3-21G basis set and the hybrid B3LYP functional in order to capture some aspects of non-covalent intermolecular interactions. This methodology is not ideal for highly accurate calculations of most non-covalently bound systems [35] and the binding energies that we report are likely to be underestimated. The goal of the calculations is to understand the anisotropy of intermolecular interactions for molecules that are geometrically constrained to mimic some effects of a substrate surface even though metal substrate atoms are not explicitly included in the DFT calculation.

Substrate-defined molecular orientation is implemented in our model DFT calculation (which does not include the substrate atoms) by maintaining the dipole moment vectors of adjacent molecules rigidly fixed in direction with respect

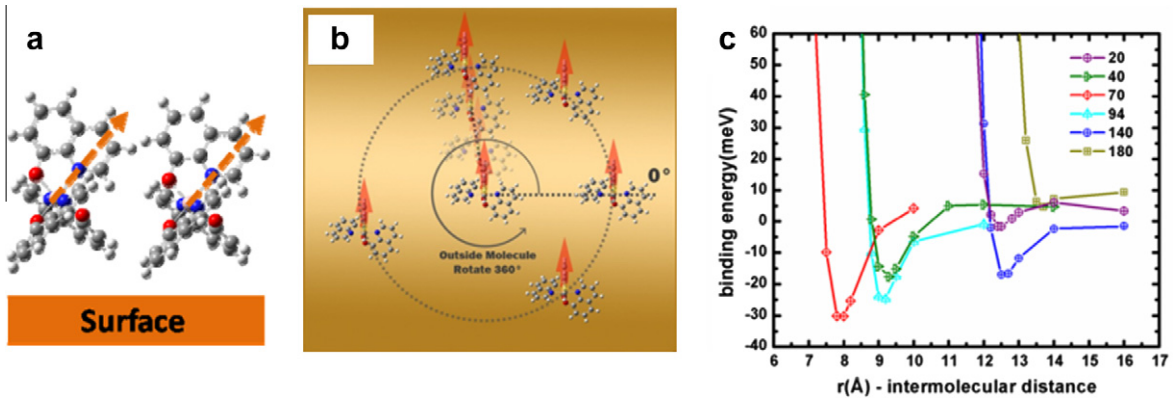

Fig. 4. (a) Schematic of relative orientation of dipoles for identically oriented molecules with respect to an imaginary surface plane; (b) Schematic depiction of model DFT calculations of the interaction between two Alq3 molecules with dipole oriented as indicated in part (a); (c) Binding energy as a function of intermolecular distance for different angular displacement of one molecule with respect to the other.

to an imaginary plane (Fig. 4a). We then rotated one molecule about the other as indicated schematically in Fig. 4b to determine whether there is an anisotropic intermolecular interaction given this orientation constraint. At each angular position, we calculated binding energy as a function of separation between molecules. The separation is reported here as the distance between central Al atoms on different molecules and the binding energy is calculated as the difference between the calculated total energy of a pair at each (r, θ) position and twice the energy of the single molecule (each calculated with 3-21G, B3LYP).

Two different relative orientations of adjacent molecules were considered to explore the favorable adsorption geometries (either dipole "up" or dipole "down") in the DFT studies of Yanagisawa et al. [31]. The first is shown in Fig. 4a and corresponds to adjacent dipole moment vectors both pointed in the same direction. This configuration mimics adsorption geometries in which adjacent molecules are either both "dipole up" or both "dipole down". The binding energy curves for different angles for this configuration are shown in Fig. 4c and exhibit an energy minimum at an angle near 70°. The intermolecular distance at the binding energy minimum in Fig. 4c is about 0.8 nm, consistent with intermolecular spacing observed in our STM studies. Due to the symmetry of this relative arrangement of two Alq3 molecules, only angles between 0° and 180° were calculated since angles from 180° to 360° would be repeat configurations with the roles of the two molecules reversed.

The second configuration considered is shown in Fig. 5a and corresponds to one molecule with an "up" dipole moment and the other with a "down" dipole moment (or *vice versa*). As shown in the calculated binding energies in Fig. 5b, the most significant favorable interaction occurs at an angle of 60° and in the range of about 200–240°. Intermolecular spacings of just under 0.7–1.0 nm at the binding energy minima are again consistent with STM experiments. In this case, the lower symmetry of the pair requires direct calculation for all angles between 0° and 360° since configurations do not repeat.

The anisotropic intermolecular interactions in these calculations are evident by reference to the polar plots in Fig. 6. Points in this figure correspond to the energy at the minimum in the binding energy curve along the radial coordinate (e.g. extracted from Figs. 4 and 5c) as a function of the angular displacement of the rotating molecule. In Fig. 6a, there is a clear set of angles within ±20° about 0°

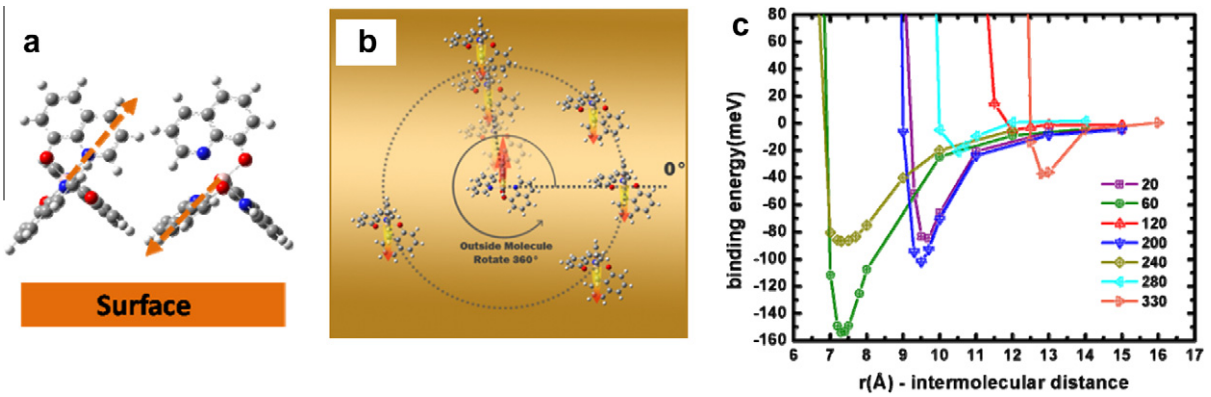

Fig. 5. (a) Schematic of the relative orientation of dipole moments of adjacent molecules differently-oriented with respect to an imaginary surface plane; (b) Schematic depiction of model DFT calculations of the interaction between two Alq3 molecules with differently-oriented dipoles as indicated in part (a); (c) Binding energy as a function of intermolecular distance for different angular displacement of one molecule with respect to the other.

where the interactions are least favorable or possibly repulsive. For most other angles there is a weak binding energy with a maximum at 70° and 250°. Fig. 6b shows a slightly different and weaker anisotropy for configurations with oppositely-oriented dipoles. In this case, there are favored orientations at 60°, 200°, and 240°. Weaker favorable interactions occur for other angles.

The anisotropy seen in Fig. 6 can explain the propensity for disordered chain formation observed in our STM studies. For the two adsorption configurations considered, there is a range of angles for which intermolecular interactions are least favorable. In addition, the range of angles where favorable interactions can occur is relatively broad. This would be expected to lead to anisotropic aggregation where the direction of linear aggregation is somewhat random due to the large angular range of favorable interactions. Our model calculations suggest that this mechanism for chain formation does not demand strict orientational order of Alq3 with respect to the substrate. Molecules could have several random orientations "frozen in" upon arrival at the surface and the general anisotropy inherent in intermolecular interactions would still favor quasi-linear aggregation as opposed to purely random adsorption.

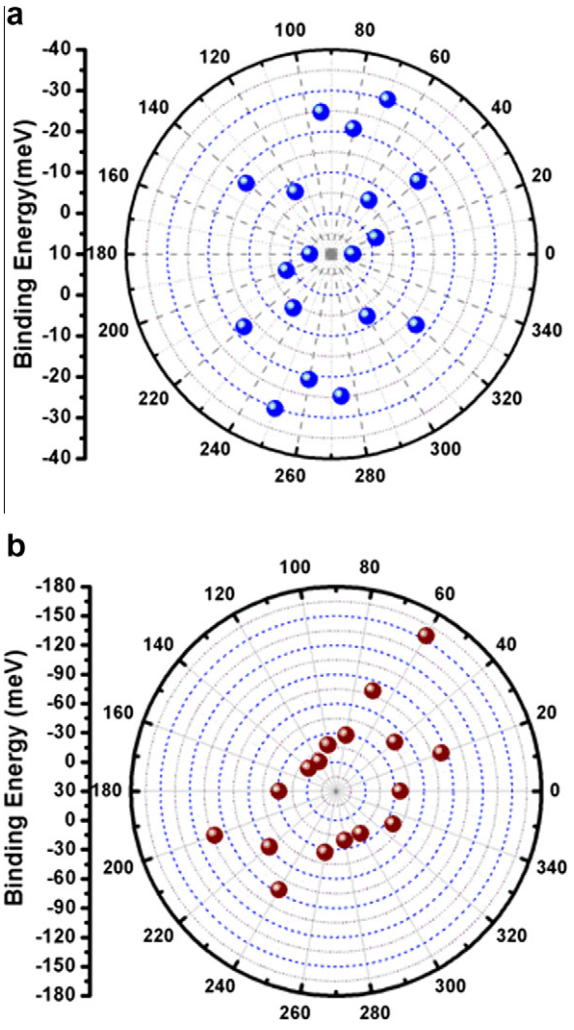

Fig. 6. (a) Polar plot of the depth of the energy of the minimum in each curve from Fig. 4c as a function of angular displacement; (b) Similar polar plot of the minima from Fig. 5c along with other angles.

From a more microscopic perspective, it is plausible that the anisotropic interactions partially originate from direct electrostatic dipole interactions between adjacent Alq3 molecules. The range of angles with favorable binding energies in the model DFT calculations in Fig. 4 suggests nearly head-to-tail dipolar interactions. In fact, the angular pattern of binding energies is reminiscent of the general shape of an electrostatic dipole potential. However, it is important to recognize that the molecular geometry is strongly anisotropic and would lead to chain like aggregation even in the absence of intrinsic molecular dipole moments. In particular, steric effects due to the propeller shape of the molecule will lead to anisotropic interactions even in the absence of a permanent dipole moment.

Direct electrostatic multipole interactions between molecules in the first monolayer on a metal surface have only been reported to drive structure formation in a few cases [36,37]. In general, such interactions would be expected to be strongly screened by the metallic substrate. This can be viewed as an interaction with induced "image dipoles" in the metal surface. However, in the case of Alq3, the charge separation within the molecule is associated with the chemical bonds between the ligands and the central Al atom. These bonds may be sufficiently separated from the metal surface that electrostatic screening does not significantly reduce electrostatic dipole interactions. We have checked that a simple model of screening does not qualitatively change the conclusions about anisotropy drawn from Fig. 6 by calculating the binding energy of a system that includes mirror image molecules to represent image dipoles at selected angles (not shown here). The image dipoles have the effect of making most binding energies more positive, but does not significantly change the general anisotropy of intermolecular interactions.

A complete microscopic understanding of the mechanism of intermolecular interactions would require further calculations that explicitly include the substrate. Of particular importance in such calculations would be the consideration of *substrate-mediated* intermolecular interactions that could result from the formation of hybrid metal–molecule interface states [38,39]. Furthermore, if there is charge transfer between the metal and the molecule, the resulting change in interface dipole could strongly modify intermolecular interactions. Strong charge transfer has recently been found to be a crucial consideration in determining intermolecular interactions at metal molecule interfaces [40].

5. Summary and conclusions

In summary, the growth of the first layer of Alq3 on a Cu(1 1 0) surface has been directly visualized with scanning tunneling microscopy. Strong disorder is observed in the first layer with no tendency toward long range ordering even for films annealed up to 590 K. However, a clear tendency for aggregation of molecules into dimers at low

coverage and randomly wandering chains at high coverage is observed. The formation of chain-like aggregates is attributed to the strong anisotropy of intermolecular interactions that is illustrated by model DFT calculations. Anisotropic interactions may have an electrostatic dipole contribution as well as contributions from intrinsic molecular shape anisotropy.

These observations are significant to ongoing consideration of the most accurate modeling approach for Alq3 device operation. In particular, the observation of strong disorder at the metal–organic interface is in accord with the suggestion of its crucial role in explaining macroscopic device current–voltage characteristics [8]. However, the film structure we observe is not completely random. Our STM measurements show chain-like aggregates that suggest the possibility of *correlated disorder* at the metal–Alq3 interface. Long range spatial correlations in electronic states in disordered organic films have been shown to be a crucial consideration for device modeling [41,42] and should be considered for injection limited transport in Alq3 films.

Acknowledgment

This work was supported by the NSF Center for Chemical Innovation: Center for Molecular Spintronics (NSF CHE-0943975).

References

[1] C.W. Tang, S.A. van slyke, Appl. Phys. Lett. 51 (12) (1987) 913–915.
[2] S.E. Shaheen, D.S. Ginley, G.E. Jabbour, MRS Bull. 30 (1) (2005) 10–19.
[3] C. Shen, A. Kahn, Org. Electron. 2 (2) (2001) 89–95.
[4] L. Yan, M.G. Mason, C.W. Tang, Y. Gao, Appl. Surf. Sci. 175–176 (2001) 412–418.
[5] W. Brütting, S. Berleb, A.G. Mückl, Org. Electron. 2 (1) (2001) 1–36.
[6] M. Brinkmann, G. Gadret, M. Muccini, C. Taliani, N. Masciocchi, A. Sironi, J. Am. Chem. Soc. 122 (21) (2000) 5147–5157.
[7] N. Tessler, Y. Preezant, N. Rappaport, Y. Roichman, Adv. Mater. 21 (27) (2009) 2741–2761.
[8] M.A. Baldo, S.R. Forrest, Phys. Rev. B 64 (8) (2001) 17.
[9] A.L. Burin, M.A. Ratner, J. Chem. Phys. 113 (10) (2000) 3941–3944.
[10] A.L. Burin, M.A. Ratner, J. Polym. Sci. Pt. B-Polym. Phys. 41 (21) (2003) 2601–2621.
[11] M.C. Blum, M. Pivetta, F. Patthey, W.D. Schneider, Phys. Rev. B 73 (19) (2006) 7.
[12] S. Barth, U. Wolf, H. Bassler, P. Muller, H. Riel, H. Vestweber, P.F. Seidler, W. Rie, Phys. Rev. B 60 (12) (1999) 8791.
[13] B.N. Limketkai, M.A. Baldo, Phys. Rev. B 71 (8) (2005) 9.
[14] Y. Tanaka, K. Kanai, Y. Ouchi, K. Seki, Org. Electron. 10 (5) (2009) 990–993.
[15] S.F. Alvarado, L. Libioulle, P.F. Seidler, Synth. Met. 91 (1–3) (1997) 69–72.
[16] S.F. Alvarado, P.F. Seidler, D.G. Lidzey, D.D.C. Bradley, Phys. Rev. Lett. 81 (5) (1998) 1082–1085.
[17] U. Zerweck, C. Loppacher, L.M. Eng, Nanotechnology 17 (7) (2006) S107–S111.
[18] P.T. Lee, T.Y. Chang, S.Y. Chen, Org. Electron. 9 (5) (2008) 916–920.
[19] G.F. Wang, X.M. Tao, H.M. Huang, Appl. Surf. Sci. 253 (10) (2007) 4463–4466.
[20] D.S. Zheng, H.R. Li, Y.Y. Wang, F.J. Zhang, Appl. Surf. Sci. 183 (3–4) (2001) 165–172.
[21] S. Lukas, G. Witte, C. Woll, Phys. Rev. Lett. 88 (2002) 2–4.
[22] M. Stohr, M. Gabriel, R. Moller, Surf. Sci. 507 (2002) 330–334.
[23] M. Stohr, M. Gabriel, R. Moller, Europhys. Lett. 59 (3) (2002) 423–429.
[24] T. Wagner, A. Bannani, C. Bobisch, H. Karacuban, M. Stohr, M. Gabriel, R. Moller, Org. Electron. 5 (1–3) (2004) 35–43.
[25] D.B. Dougherty, W. Jin, W.G. Cullen, G. Dutton, J.E. Reutt-Robey, S.W. Robey, Phys. Rev. B 77 (7) (2008) 4.
[26] E.V. Tsiper, Z.G. Soos, Phys. Rev. B 64 (19) (2001) 12.
[27] E.V. Tsiper, Z.G. Soos, W. Gao, A. Kahn, Chem. Phys. Lett. 360 (1–2) (2002) 47–52.
[28] S.V. Novikov, G.G. Malliaras, Phys. Rev. B 73 (3) (2006) 4.
[29] M.A. Baldo, Z.G. Soos, S.R. Forrest, Chem. Phys. Lett. 347 (4–6) (2001) 297–303.
[30] S. Reineke, G. Schwartz, K. Walzer, M. Falke, K. Leo, Appl. Phys. Lett. 94 (16) (2009) 3.
[31] S. Yanagisawa, Y. Morikawa, Chem. Phys. Lett. 420 (4–6) (2006) 523–528.
[32] S. Yanagisawa, K. Lee, Y. Morikawa, J. Chem. Phys. 128 (24) (2008) 13.
[33] G.W.T.M.J. Frisch, H.B. Schlegel, G.E. Scuseria, M.A. Robb, J.R. Cheeseman, G. Scalmani, V. Barone, B. Mennucci, G.A. Petersson, H. Nakatsuji, M. Caricato, X. Li, H.P. Hratchian, A.F. Izmaylov, J. Bloino, G. Zheng, J.L. Sonnenberg, M. Hada, M. Ehara, K. Toyota, R. Fukuda, J. Hasegawa, M. Ishida, T. Nakajima, Y. Honda, O. Kitao, H. Nakai, T. Vreven, J.A. Montgomery Jr., J.E. Peralta, F. Ogliaro, M. Bearpark, J.J. Heyd, E. Brothers, K.N. Kudin, V.N. Staroverov, R. Kobayashi, J. Normand, K. Raghavachari, A. Rendell, J.C. Burant, S.S. Iyengar, J. Tomasi, M. Cossi, N. Rega, J.M. Millam, M. Klene, J.E. Knox, J.B. Cross, V. Bakken, C. Adamo, J. Jaramillo, R. Gomperts, R.E. Stratmann, O. Yazyev, A.J. Austin, R. Cammi, C. Pomelli, J.W. Ochterski, R.L. Martin, K. Morokuma, V.G. Zakrzewski, G.A. Voth, P. Salvador, J.J. Dannenberg, S. Dapprich, A.D. Daniels, Ö. Farkas, J.B. Foresman, J.V. Ortiz, J. Cioslowski, D.J. Fox, Gaussian, Inc., Wallingford, CT, 2009 (Gaussian, Inc., Wallingford, CT, 2009).
[34] M.D. Halls, H.B. Schlegel, Chem. Mater. 13 (8) (2001) 2632–2640.
[35] Y. Zhao, D.G. Truhlar, J. Chem. Theory Comput. 3 (1) (2006) 289–300.
[36] A.E. Baber, S.C. Jensen, E.C.H. Sykes, J. Am. Chem. Soc. 129 (20) (2007) 6368.
[37] P. Han, E.C.H. Sykes, T.P. Pearl, P.S. Weiss, J. Phys. Chem. A 107 (40) (2003) 8124–8129.
[38] A. Calzolari, W. Jin, J.E. Reutt-Robey, M.B. Nardelli, J. Phys. Chem. C 114 (2) (2010) 1041–1045.
[39] A.N. Caruso, D.L. Schulz, P.A. Dowben, Chem. Phys. Lett. 413 (4–6) (2005) 321–325.
[40] I. Fernandez-Torrente, S. Monturet, K.J. Franke, J. Fraxedas, N. Lorente, J.I. Pascual, Phys. Rev. Lett. 99 (17) (2007) 176103.
[41] S.V. Novikov, D.H. Dunlap, V.M. Kenkre, P.E. Parris, A.V. Vannikov, Phys. Rev. Lett. 81 (20) (1998) 4472–4475.
[42] M. Bouhassoune, S.L.M. van Mensfoort, P.A. Bobbert, R. Coehoorn, Org. Electron. 10 (3) (2009) 437–445.

semiconductors. However, these approaches are difficult to apply to OLEDs because organic materials are generally soluble in the solvents used in lithography, and they experience optical and/or electrical deterioration when exposed to water, oxygen or high-energy electrons.

In order to avoid the degradation of the OLEDs, microstructuring has to start from the substrate, so that corrugation transmits through the organic layer to the opposite electrode. Periodic corrugation [22] on silica substrates by holographic lithography followed with RIE (reactive-ion etching) dry etching, and spontaneously formed quasi-periodic structure on glass substrate [23,24] have been reported. Although trapped optical modes were found coupled out, the substrate pattern transmission approach is encountered with problems such as electronic degradation since the ITO anode has to be sputtered on the corrugated substrates, which increase its surface roughness. It is obvious that the problem may be solved if microstructures are induced into a certain organic functional layer without affecting the flatness of the ITO film. Efforts have been paid along this line, for example, micromoulding [25,26] dendrimers above the ITO anode [27,28]. However, the complexity of the fabrication process and the high fluidity requirement to the polymer limits the practical application of the technology. Periodic change of the refractive index has been inscribed in the active materials without surface-relief structure in the OLEDs by holographic setup, and output characteristics of the OLEDs have been modified [29]. However, this method is restricted by realizing a polymer with both photosensitive and charge-transporting qualities to undergo a photoisomerization and act as functional layer in OLEDs. In addition, a necessity of large difference in the periodic changed refractive index for the highly efficient Bragg scattering is another limitation.

In this communication, we solve this problem by employing a one-step fabrication approach to introduce a

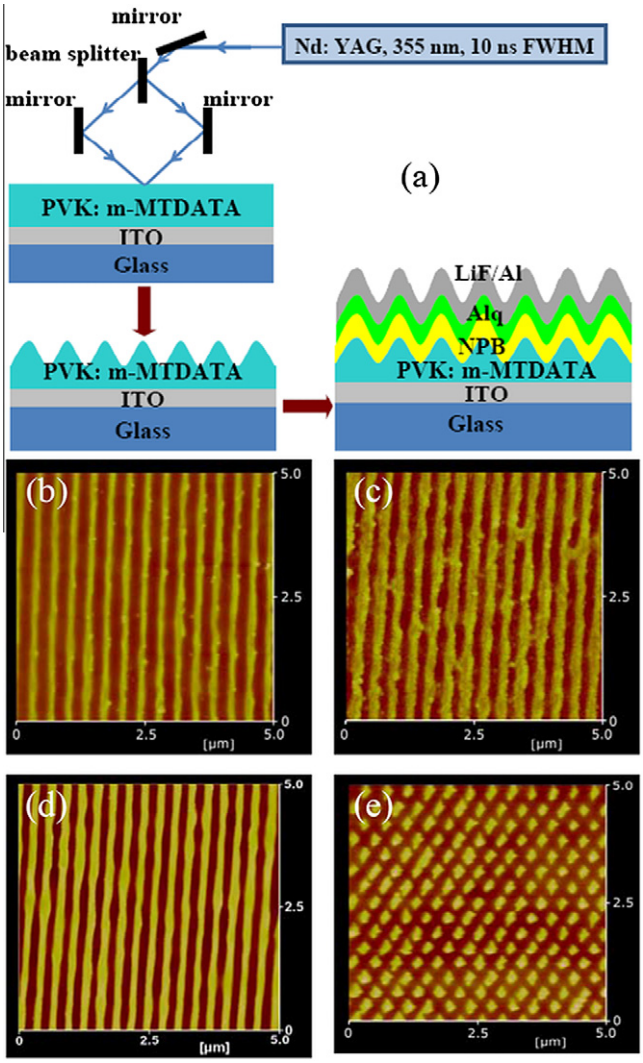

Fig. 1. Scheme of introducing periodic corrugation into OLED by laser ablation (a), and AFM images of the ablated corrugation. 1-D grating with period of 350 nm on the HTL (b) and the cathode surface of the OLED (c), the 1-D grating with period of 250 nm (d) and 2-D grating with 350-nm period on the HTL surface (e).

grating onto the functional layers of the OLEDs. Most polymers show a strong sensitivity to UV laser ablation condition and possess low ablation thresholds, so that a periodic grating can be directly recorded on the hole-transport layer (HTL) of OLEDs via laser ablation by two interference beams. Gratings with appropriate period and depth for Bragg scattering in OLEDs are easily obtained by adjusting the angle of the two beams and the laser fluence. Experimentally, three times enhancement in the current efficiency has been observed from the corrugated OLEDs with appropriate grating period. Theoretical simulations demonstrate that the power lost to both WG and SPP modes have been recovered. This one-step laser ablation on HTL provides a simple and facile approach with high resolution, high controllability and reproducibility to obtain periodically corrugated OLEDs.

2. Experimental details

2.1. Preparation of periodic microstructure by laser ablation

A conducting polymer widely used in polymer LEDs as a hole-transport material, poly(*N*-vinyl carbazole) (PVK) is chosen and it is spin-coated on the ITO glass for the fabrication of the corrugated HTL in OLEDs. 4,4′,4″-Tris(3-methylphenylphe-nylamino)triphenylamine (*m*-MTDATA) [30] was doped into the PVK with a concentration of 10% by weight to enhance the hole injection and transport of the HTL. The experimental scheme for laser ablation on PVK:*m*-MTDATA film and fabrication sequence of the corrugated OLED is illustrated in Fig. 1(a). The ablation experiments used a frequency-tripled Nd:YAG laser (Spectra-physics Company) with 3 nm pulse width, 10 ns pulse length, 10 Hz repetition rate and 355 nm wavelength. An ITO coated glass substrate was cleaned with acetone and ethanol. The HTL was spin-coated at 4000 rpm/s speed for 70 nm thicknesses. The sample was prebaked in vacuum for 30 min at 60 °C to evaporate the organic solvent. Then, the sample was exposed by two beams which were split from the UV laser with beam size of ~6 mm in diameter. The microstructure recorded on the polymer film with different period and depth was obtained by adjusting the writing angle and the laser power. The microstructure fabrication was conducted in air at room temperature using single laser pulse. The morphologies of the microstructure were characterized by an atomic force microscopy (AFM, Digital Instruments Nanoscope IIIA) in the contact mode and field emission scanning electron microscope (SEM, JSM-7500F, JEOL).

2.2. OLED fabrication and evaluation

Prepared ITO substrates coated with corrugated HTL were immediately brought into a thermal evaporation chamber. The 20 nm thick hole transporting layer of *N*,*N*′-diphenyl-*N*,*N*′-bis(1,1′-biphenyl)-4,4′-diamine (NPB), 50 nm thick emitting layer of tris-(8-hydroxyquinoline) aluminum (Alq_3) and cathode of LiF (1 nm)/Al (100 nm) were evaporated sequentially. Here, all layers were prepared by thermal evaporation in a high vacuum system with the pressure of less than 5×10^{-4} Pa. The active area of the devices was 2×2 mm^2. Their current density–voltage–luminance (*J*–*V*–*L*) characteristics were measured by Keithley 2400 programmable voltage–current source and Photo Research PR-655 spectrophotometer. The emission spectra at different observation angle were collected with a lens and then collimated and focused into the entrance slit of a 300-mm monochromator/spectrograph (SR-3031-A, Andor) to limit the angular acceptance to ~1°. The spectrogram of the emission was recorded using a charge coupled device (iDus, Andor). The OLEDs were placed on a rotation stage with the grooves parallel to the rotation axis. All of the measurements were conducted in air at room temperature.

3. Results and discussion

3.1. Investigation of periodically corrugated HTL by laser ablation

Laser ablation has been extensively studied, both theoretically and experimentally [31–33]. Several models have been proposed for ablation of polymers, involving photochemical effects (direct bond breaking) [34], photothermal effects (thermally broken bonds) [35], photophysical (mechanical stress) [36] or a combination of them. Although the chemical nature of the reaction that are involved is still not clearly verified, it does offer an alternative, simple and fast technique of direct generation of the microstructure on organic functional materials. Through combining with a multi-beam interference, the one-step fabrication of the microstructure can be faster and highly reproducible with the period from microns to sub 100 nm [37–39]. Shown in Fig. 1(b)–(e) is the atom force microscopy (AFM) images of a laser ablated grating on the PVK:*m*-MTDATA film and the cathode surfaces after deposition of organic and metallic cathode layers by thermal evaporation. As can be seen, the profile of the top surface was essentially a replication of the underlying nanostructure, therefore, forming a periodic corrugation throughout all the layers on the ITO substrate.

Due to the scattering and diffraction of the grating, the structured surface shows varied colors from structures of different periods, which are clearly observed by the naked human eyes as shown in Fig. 2(a). The microstructure on the PVK:*m*-MTDATA film in a large scale is investigated by scanning electron microscope (SEM) and shows homogeneous profile (the inset of Fig. 2(b). A 6-mm diameter area of uniform corrugation was produced with single-shot laser exposure, in another word, the exposure duration is only 10 ns. Provided that the laser pulse energy is sufficient after laser beam expansion, and assumed the laser repetition rate of 10 Hz, and the wafer transferring time of 0.1 s in a production line, the introduction of the microstructures in an entire wafer by single-pulse exposure takes only 0.1 s and as a result, the cost would be very low.

The controllability of the microstructure parameters is quite high. Experimentally, we found the groove depth is fully determined by the laser fluence at low laser energy

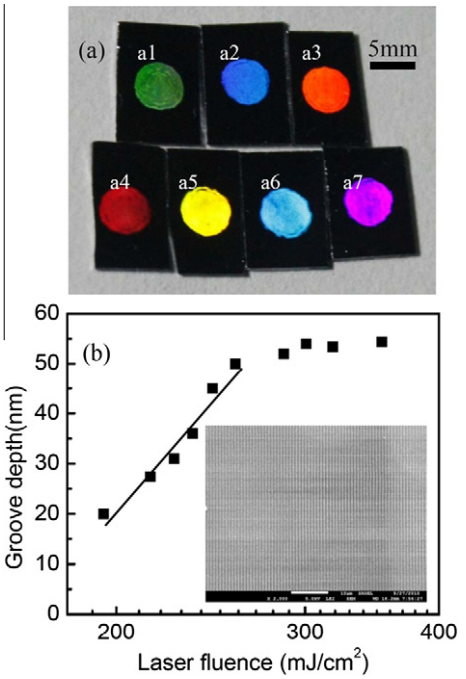

Fig. 2. (a) Photograph of the periodic corrugation on the PVK:*m*-MTDATA film with various period of a1 2000 nm, a2 1500 nm, a3 1000 nm, a4 800 nm, a5 600 nm, a6 400 nm, and a7 350 nm. (b) Etch depth by one-pulse laser ablation as a function of the laser fluence for 70 nm PVK:*m*-MTDATA film. The inset in (b) shows the large-scale SEM image of the grating on the PVK:*m*-MTDATA film with period of 800 nm and the scale bar represents 10 μm.

density (<270 mJ/cm^2), and it follows Beer's law [31], which sums up the light energy absorbed by the layer:

$$x_f = (1/\alpha)\ln(F/F_0) \quad (1)$$

where, x_f is the ablation depth per pulse. Other symbols denote: α, the linear absorption coefficient; F, the laser fluence, and F_0, the fluence threshold. The linear dependence of the ablation depth on the logarithm of the fluence is shown in Fig. 2(b), which is deviated, and is gradually saturated to ~55 nm after $F > 270$ mJ/cm^2. This derivation at high fluence is due to limitation of the ablation depth by the film thickness. The threshold fluence for the ablation of the two-beam interference on a 70-nm thick PVK:*m*-MTDATA film is $F_0 = \sim 180$ mJ/cm^2 (1.8×10^{11} W/m^2). This level of the laser irradiation, almost four-order lower than the laser-induced damage threshold of typical transparent solids, for example, 10^{15} W/m^2 for most fused silica [40], induce no any damage to the ITO substrate.

3.2. EL performance of the corrugated OLEDs

The tris-(8-hydroxyquinoline) aluminum (Alq_3)-based OLEDs with one-dimensional (1-D) periodic corrugation were fabricated according to the design in Fig. 1(a). Various grating period from 200 to 400 nm have been tested, and the grating depth is fixed at 40 nm. The devices structure is ITO/PVK:*m*-MTDATA (70 nm)/NPB (20 nm)/Alq_3 (50 nm)/LiF (1 nm)/Al (100 nm). To investigate the effect

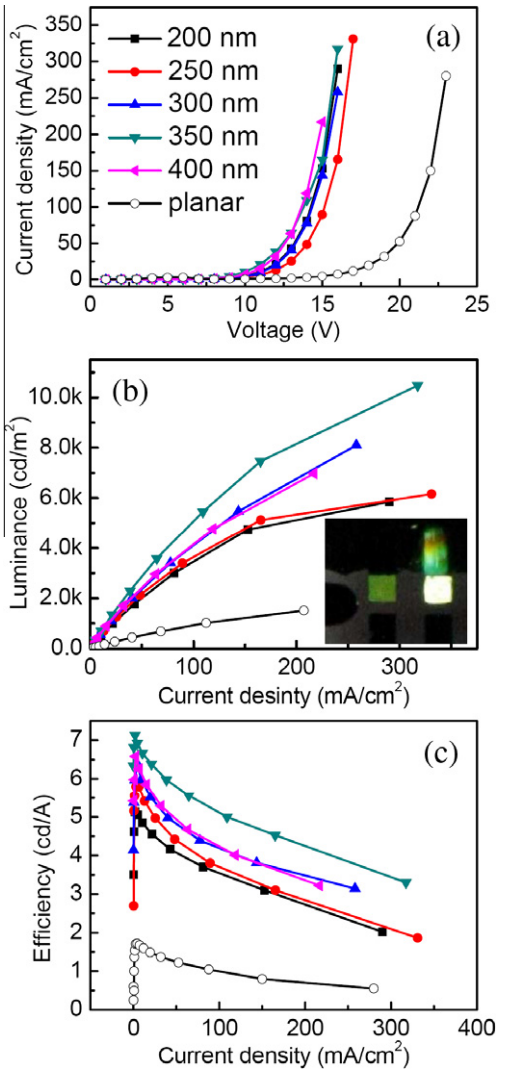

Fig. 3. EL performance of the corrugated and planar OLEDs. Current density–voltage (a), current density–luminance (b), current density–efficiency (c) characteristics. Inset in (b) shows the photograph of the operating corrugated and planar OLEDs at the same substrate and under same driving voltage.

of the grating, flat OLEDs were fabricated on the planar region of the ITO glass substrate. Considering that the average thickness of the corrugated HTL is decreased from 70 to 50 nm after laser ablation, the thickness of the HTL for the planar devices is designed to 50 nm to be equal to that of the corrugated HTL, so that the effect of the HTL thickness on the hole transport could be excluded. Actually, a 20-nm average difference between the HTL thickness before and after ablation has no much effect on the planar OLED performance through the comparison with experiment. The corrugated OLEDs show increased current density as shown in Fig. 3(a). The introduction of the corrugation has the effect on increasing the effective area of the operating devices, which would result in the increased current density. On the other hand, the ablation on the HTL has probably influenced the hole-transport

ability of the material, for which further study is needed. It can be clearly seen in Fig. 3(b) and (c) that the corrugated OLEDs exhibit much higher luminance and current efficiency than that of the planar devices and shows grating-period dependence. Both luminance and efficiency increase with the increasing grating period, and reach the maximum at 350 nm, and then decrease with further increment to 400 nm. In case of 350 nm, the luminance at the current density of 100 mA/cm^2 is 5100 cd/m^2 and the maximum current efficiency is 7.2 cd/A, respectively, while it is 910 cd/m^2, and 1.8 cd/A, respectively, for the planar devices. This corresponds to three times enhancement in the maximum current efficiency. The photograph of the operating OLEDs at the same substrate and under same driving voltage of 12 V (inset in Fig. 3(b)) indicates that much brighter emission can be obtained from the corrugated OLED.

3.3. EL spectra from the corrugated OLEDs

Understanding of the enhancement mechanism starts from analyzing the scattering of guided modes from a device by measuring its emission spectra as a function of observation angle. The scattered modes appear as additional emission peaks in intensity which shifts in wavelength as the angle varies. Fig. 4 shows the electroluminescent (EL) spectra measured from the experimental devices employing different grating period at several observation angles off to the surface normal. The EL spectra from the corrugated devices are more complex than that from the flat devices. Additional peaks with different wavelength are observed from the devices with varied grating period. The EL spectra at normal direction from the devices with different grating periods are summarized in Fig. 4(f) together with an EL spectrum from a planar

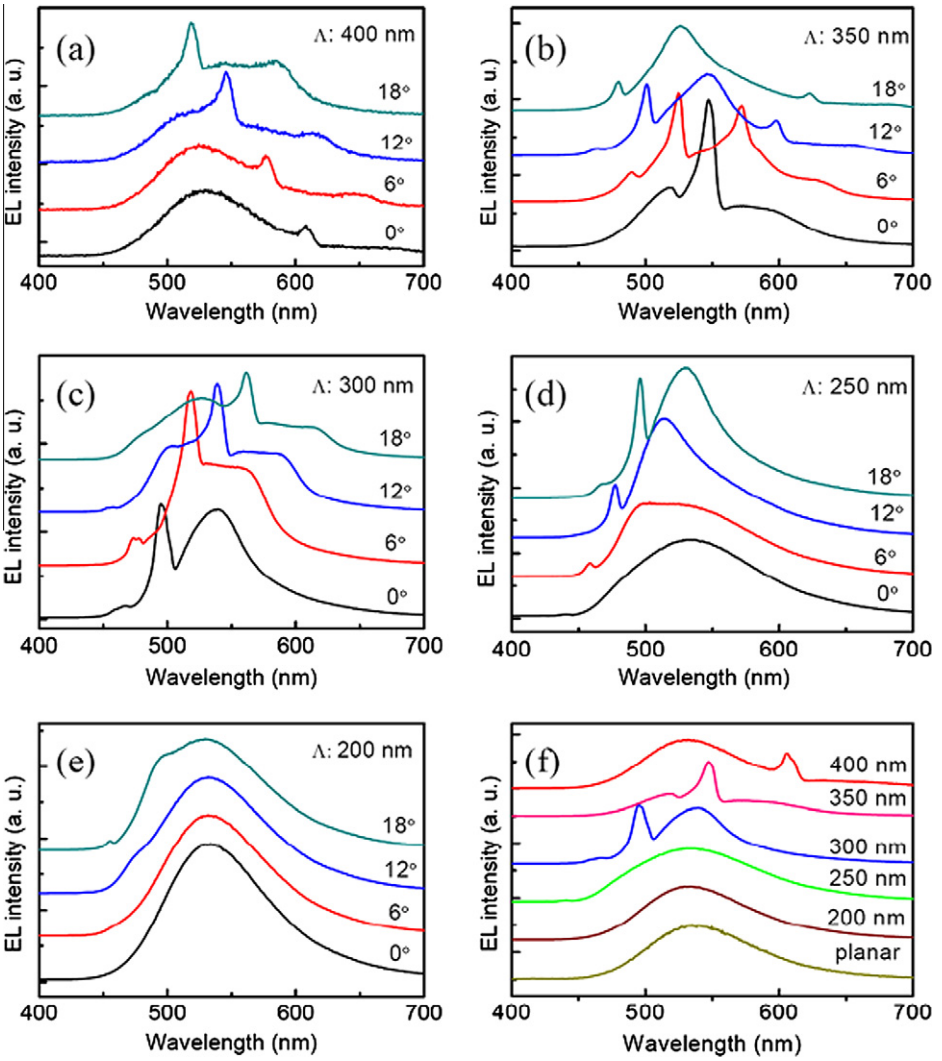

Fig. 4. The EL spectra at different observation angle from the corrugated OLEDs with various grating period (Λ). (a) 400 nm, (b) 350 nm, (c) 300 nm, (d) 250 nm, and (e) 200 nm. Their EL spectra at normal direction are summarized in (f).

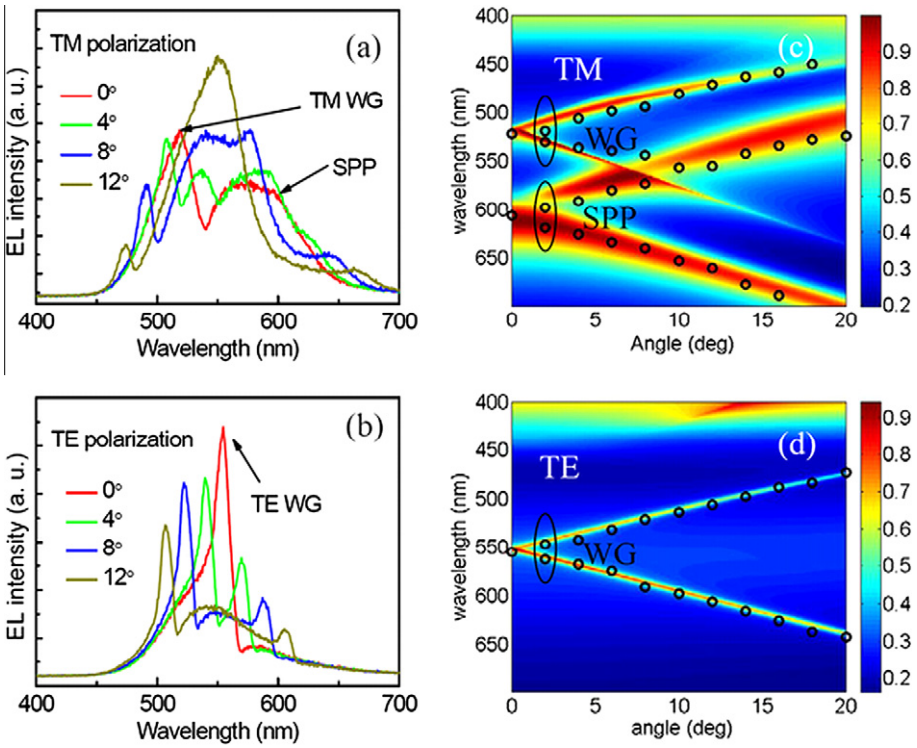

Fig. 5. Measured EL spectra with TM (a) and TE (b) polarization at different observation angle from the corrugated OLEDs with 350-nm grating. And the wavelength versus incident angle for the calculated dispersion relation of the corrugated OLEDs for TM (c) and TE (d) polarization. The measured dispersion relation extracted from the EL spectra (circles) is also shown in (c) and (d).

device at normal direction. All the additional peaks exhibit obvious blueshift with the decreasing grating period, and some of them then move out of the EL spectra for the grating period less than 250 nm. For the devices with 350 nm grating period, peaks at around 520, 547 and 595 nm are observed at normal direction, and the bandwidth of the peak at 595 nm is broader than that of the others. Each of them splits into two peaks, which shifts in wavelength with the increasing observation angle. Both TM and TE polarized EL spectra are also measured and shown in Fig. 5(a) and (b), which indicate that the modes corresponds to the emission peaks of 520 and 595 nm at the normal direction are TM polarized and that of 547 nm are TE polarized.

4. Simulated optical modes in the corrugated OLEDs

To establish the optical modes supported by the microstructured OLEDs, absorption spectra are simulated. A number of absorption maxima could be seen, if the incident light is coupled into modes supported by the structure. We apply the scattered matrix approach [41] to deal with our periodically microstructured OLED with metal and organic multilayered structure. The overall scattering of the OLEDs is determined by first evaluating a matrix of scattering parameters for each individual layer through the solving of Maxwell's equation, and then forming a scattering matrix for the entire structure by the relevant boundary conditions. As high as fifty orders spatial harmonics are taken into consideration. Given an incoming wave from the ITO glass side, the reflection waves have been computed. Absorption spectra are obtained from complementary relation between reflection and absorption. The grating with rectangular cross section and fill factor of 50% was employed and the refractive index of the organic materials employed in the OLEDs was measured by ellipsometry for the simulation. The dispersion map derived from the simulated absorption spectra for the corrugated device with 350 nm grating period and for both TM and TE polarization is shown in Fig. 5(c) and (d), in which the absorption intensity appears as a function of both incident angles and absorption wavelength. The dispersion relation curve constructed from the experimental EL emission spectra with both TM and TE polarization (Fig. 5(c) and (d)) are also plotted. It can be seen that there is excellent agreement between the theoretical calculation and experimental measurement. Actually both the calculated peak position at different angle and bandwidth of the emission spectra coincide with that of measured data very well. The optical modes within the device structure appear as EL maxima indicates an efficiently outcoupling of light from those optical modes, which are normally non-radiative, by the addition of the appropriate wavelength scale microstructure.

Both SPP and WG modes could be coupled out by the microstructure. The spatial magnetic field (H_y) distribution across the device structure as a function of position with

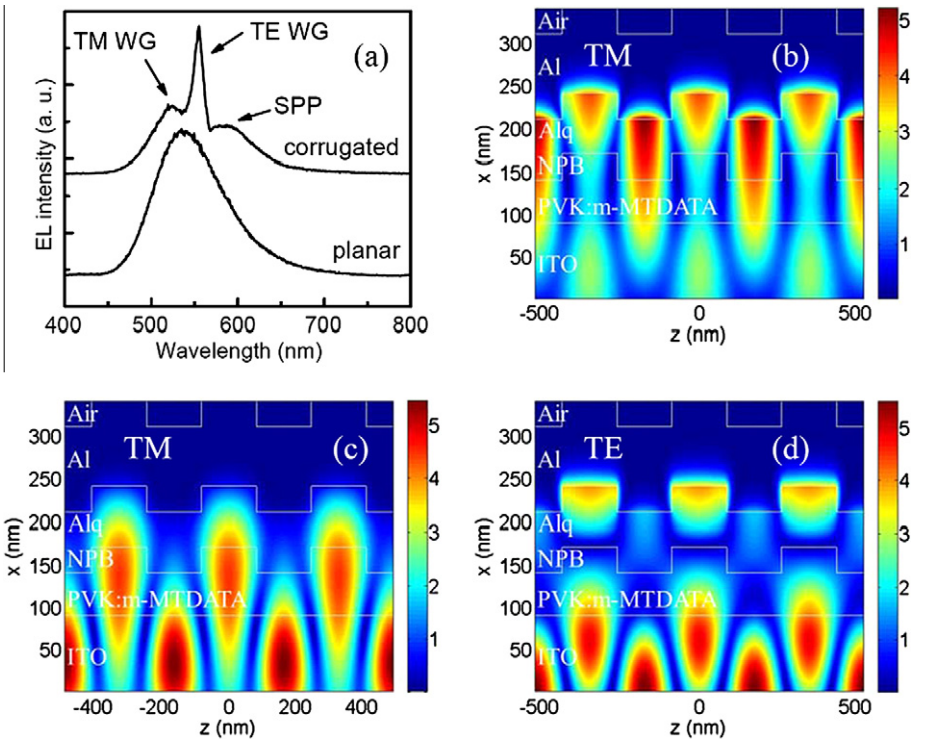

Fig. 6. EL spectra from both corrugated OLED with 350-nm grating and planar devices at normal direction (a), and distribution of the magnetic field intensity in the corrugated OLEDs at the wavelength of incident polarized light of 595 nm (b), 547 nm (c) and 520 nm (d), respectively.

the normal incident light is calculated to identify the optical modes for the devices with 350 nm grating period. Fig. 6 shows the field distribution at the illumination wavelength of 595, 547 and 520 nm, respectively, which corresponds to the three peak wavelength of the EL emission at normal direction. The field intensity is with maximum at the Al/Alq_3 interface and decay along the direction perpendicular to it at the wavelength of 595 nm

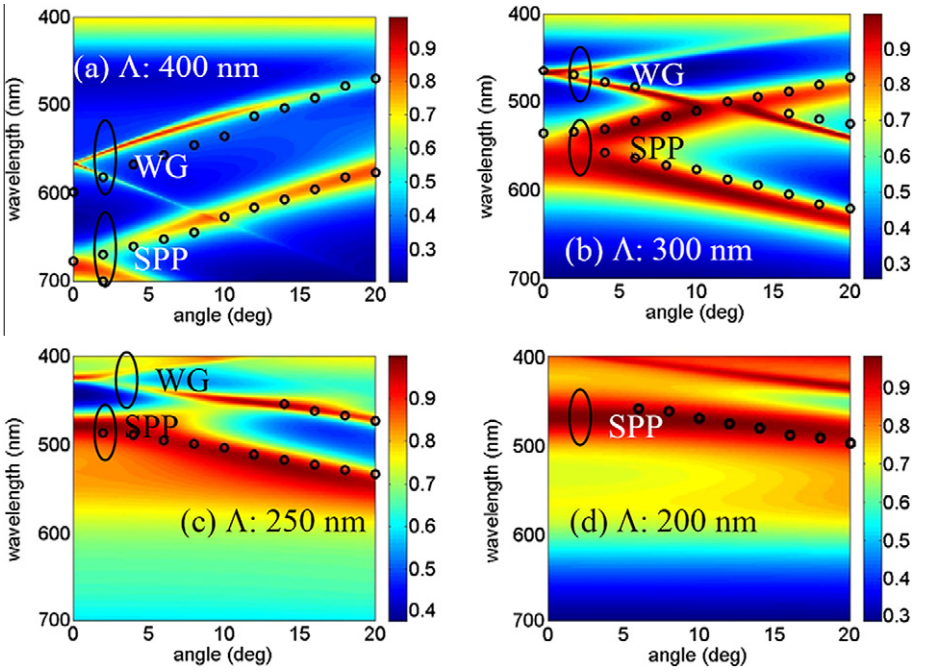

Fig. 7. Wavelength versus incident angle for the calculated dispersion relation of the corrugated OLEDs with various grating period (Λ) and for TM polarization. The measured dispersion relation extracted from the EL spectra (circles) is also shown.

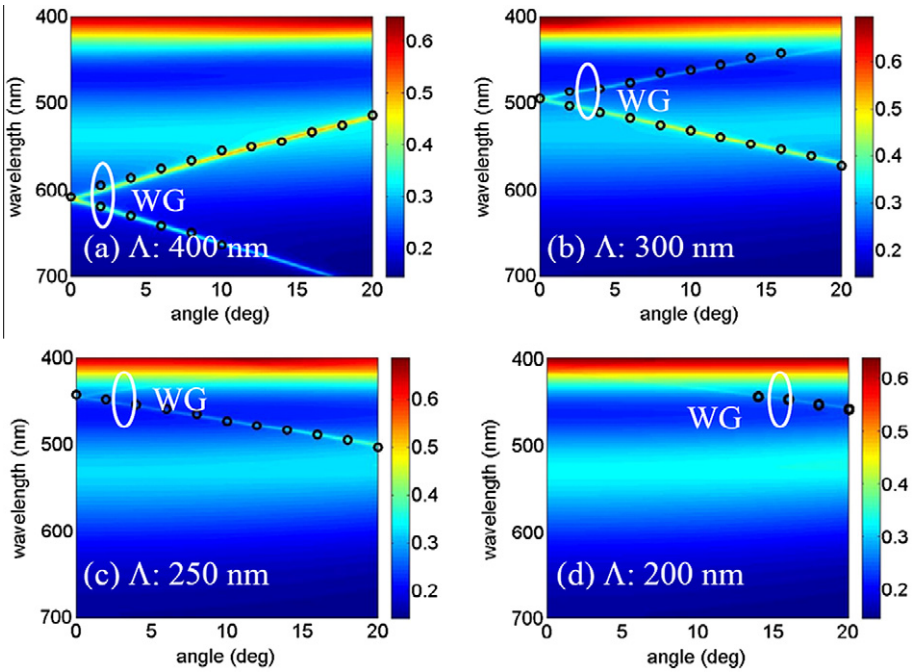

Fig. 8. Wavelength versus incident angle for the calculated dispersion relation of the corrugated OLEDs with various grating period and for TE polarization. The measured dispersion relation extracted from the EL spectra (circles) is also shown.

as shown in Fig. 6(b). We can conclude from this field distribution that the emission peak at 595 nm originates from SPP modes, since SPPs are surface wave and propagating along an interface between a metal and dielectric [42–46]. On the other hand, the field at the wavelength of 547 and 520 nm is mainly confined within the ITO and organic layers (Fig. 6(c) and (d)), which should be assigned to the TM and TE polarized WG modes due to the high refractive index of ITO and organic layers. Therefore the additional peaks shown in the EL spectra in Fig. 6(a) is identified as the SPP mode associated with the Al cathode/organic interface, and WG mode confined within the ITO and organic layers, respectively. This conclusion is applicable to the corrugated OLEDs with the various periods, except that the peak wavelength corresponding to the SPP and WG modes is shift with the different period, which has been verified by the following simulations.

The dispersion map derived from the simulated absorption spectra for the corrugated device with 400, 300, 250 and 200 nm grating period and for both TM and TE polarization is shown in Figs. 7 and 8, respectively, which also show agreement with the experimentally measurement extracted from the EL spectra. The extracted light emission from both the SPP and WG modes show blueshift with the decreasing of the grating period. Comparing the EL spectra from the corrugated and flat OLEDs at the normal direction (Fig. 4(f)), we can see that both the extracted SPP and WG modes located within the emission wavelength region of the Alq_3 emission for the device with the 350 nm grating period at the normal direction, which contribute to a more efficient outcoupling of the optical modes trapped in the devices and result in the highest EL efficiency for this OLED. Both the TM and TE polarized WG modes move out of the emission region of Alq_3 in case of the 200 and 250 nm grating period, while the emission band from the SPP mode becomes flat, which results in a smaller shift of the EL spectra at different observation angle and has been verified in Fig. 4(d) and (e). Therefore an improved viewing characteristic is expected. Our experimental and simulated data indicate that the power lost to both SPP and WG modes has been successfully recovered as light in far field for the corrugated OLEDs, which contributes to a much enhanced light extraction. It is possible to obtain a further improved light outcoupling by employing a 2-D grating due to its higher efficiency in coupling SPPs to far-filed radiation [47]. 2-D grating on the PVK:*m*-MTDATA by laser ablation has been realized (Fig. 1(e)), and further investigation are needed to explore its effect on the light outcoupling.

5. Conclusions

A periodic wavelength-scale corrugation has been introduced into OLEDs by one-step laser ablation of two interference beams, and enhanced outcoupling of radiation has been demonstrated. The introduction of this microstructure has allowed the observation of the emission originating from the SPP and WG modes, which are usually trapped within planar devices. An enhanced EL efficiency from the corrugated OLEDs has been observed. The microstructure has been directly formed on the HTL of the OLEDs by laser ablation without degradation of the device performance. While combining with the two-beam interference, both the period and the groove depth of the grating can be easily and precisely controlled, so that it is applicable to

OLEDs with different emission wavelength. With beam expansion, an entire wafer could be structured with one-shot nanosecond laser ablation, implying a broad industrial application prospect of the one-step efficient large-area approaches for OLEDs with much enhanced light outcoupling efficiency.

Acknowledgments

The authors gratefully acknowledge support from 973 Project (Grant Nos. 2010CB327701 and 2011CB013005), NSFC (Grant Nos. 60977025, 61177024 and 90923037) and NCET (Grant No. 070354).

References

[1] T. Chiba, Y.J. Pu, R. Miyazaki, K. Nakayama, H. Sasabe, J. Kido, Org. Electron. 12 (2011) 710–715.
[2] Y. Yang, T. Peng, K. Ye, Y. Wu, Y. Liu, Y. Wang, Org. Electron. 12 (2011) 29–33.
[3] L.H. Smith, A.E. Wasey, I.D.W. Samuel, W.L. Barnes, Adv. Funct. Mater. 15 (2005) 1839–1844.
[4] P.A. Hobson, S. Wedge, J.A.E. Wasey, I. Sage, W.L. Barnes, Adv. Mater. 14 (2002) 1393–1396.
[5] G. Gu, D.Z. Garbuzov, P.E. Burrows, S. Venkatesh, S.R. Forrest, M.E. Thompson, Opt. Lett. 22 (1997) 396–398.
[6] D.H. Kim, C.O. Cho, Y.G. Roh, H. Jeon, Y.S. Park, J. Cho, J.S. Im, C. Sone, Y. Park, W.J. Choi, Q.H. Park, Appl. Phys. Lett. 87 (2005) 203508.
[7] A.A. Erchak, D.J. Ripin, S. Fan, P. Rakich, J.D. Joannopoulos, E.P. Ippen, G.S. Petrich, L.A. Kolodziejski, Appl. Phys. Lett. 78 (2001) 563–565.
[8] T. Tsutsui, M. Yahiro, H. Yokogawa, K. Kawano, M. Yokoyama, Adv. Mater. 13 (2001) 1149–1152.
[9] S. Möller, S.R. Forrest, J. Appl. Phys. 91 (2002) 3324–3327.
[10] Y. Sun, S.R. Forrest, Nat. Photon. 2 (2008) 483–487.
[11] F. Li, X. Li, J. Zhang, B. Yang, Org. Electron. 8 (2007) 635–639.
[12] Y.R. Do, Y.C. Kim, Y.W. Song, C.O. Cho, H. Jeon, Y.J. Lee, S.H. Kim, Y.H. Lee, Adv. Mater. 15 (2003) 1214–1218.
[13] B.J. Matterson, J.M. Lupton, A.F. Safonov, M.G. Salt, W.L. Barnes, I.D.W. Samuel, Adv. Mater. 13 (2001) 123–127.
[14] A.H. Stephen, J.A.E. Easey, I. Sage, W.L. Barnes, Adv. Mater. 14 (2002) 1393–1396.
[15] B.J. Eggleton, R.E. Slusher, C.M. de Sterke, P.A. Krug, J.E. Sipe, Phys. Rev. Lett. 76 (1996) 1627–1630.
[16] C. Kallinger, M. Hilmer, A. Haugeneder, M. Perner, W. Spirkl, U. Lemmer, J. Feldmann, U. Scherf, K. Müllen, A. Gombert, V. Wittwer, Adv. Mater. 10 (1998) 920–923.
[17] H.A. Atwater, A. Polman, Nat. Mater. 9 (2010) 205–213.
[18] T. Okamoto, F. H'Dhili, S. Kawata, Appl. Phys. Lett. 85 (2004) 3968–3970.
[19] E. Hwang, I.I. Smolyaninov, C.C. Davis, Nano Lett. 10 (2010) 813–820.
[20] S. Nien, N. Chiu, Y. Ho, J. Lee, C. Lin, K. Wu, C. Lee, J. Lin, M. Wei, T. Chiu, Appl. Phys. Lett. 94 (2009) 103304.
[21] C.C. Chang, Y.D. Sharma, Y.S. Kim, J.A. Bur, R.V. Shenoi, S. Krishna, D. Huang, S.Y. Lin, Nano Lett. 10 (2010) 1704–1709.
[22] J. Feng, T. Okamoto, S. Kawata, Opt. Lett. 30 (2005) 2302–2304.
[23] K. Hong, H.K. Yu, I. Lee, K. Kim, S. Kim, J.L. Lee, Adv. Mater. 22 (2010) 4890.
[24] W.H. Koo, S.M. Jeong, F. Araoka, K. Ishikawa, S. Nishimura, T. Toyooka, H. Takezoe, Nat. Photon. 4 (2010) 222–226.
[25] E. Kim, Y. Xia, X.M. Zhao, G.M. Whitesides, Adv. Mater. 9 (1997) 651–654.
[26] J.R. Lawrence, G.A. Turnbull, I.D.W. Samuel, Appl. Phys. Lett. 82 (2003) 4023–4025.
[27] C.J. Yates, I.D.W. Samuel, P.L. Burn, S. Wedge, W.L. Barnes, Appl. Phys. Lett. 88 (2006) 161105.
[28] J. Wang, X. Sun, L. Chen, S.Y. Chou, Appl. Phys. Lett. 75 (1999) 2767–2769.
[29] T. Höfler, M. Weinberger, K. Wolfgang, S. Rentenberger, A. Pogantsch, Adv. Funct. Mater. 16 (2006) 2369–2373.
[30] Y. Shirota, Y. Kuwabara, H. lnada, T. Wakimoto, H. Nakada, Y. Yonemoto, S. Kawami, K. lmai, Appl. Phys. Lett. 65 (1994) 807–809.
[31] E. Sutcliffe, R. Srinivasan, J. Appl. Phys. 60 (1986) 3315–3322.
[32] N. Bityurin, B.S. Luk'yanchuk, M.H. Hong, T.C. Chong, Chem. Rev. 103 (2003) 519–552.
[33] T.C. Chong, M.H. Hong, L.P. Shi, Laser Photon. Rev. 4 (2010) 123–143.
[34] M. Prasad, P.F. Conforti, B.J. Garrison, J. Appl. Phys. 101 (2007) 103113.
[35] G. Bounos, A. Selimis, S. Georgiou, E. Rebollar, M. Castillejo, N. Bityurin, J. Appl. Phys. 100 (2006) 114323.
[36] B. Luk'yanchuk, N. Bityurin, S. Anisimov, A. Malyshev, N. Arnold, D. Bäuerle, Appl. Surf. Sci. 106 (1996) 120–125.
[37] D.Y. Kim, S.K. Tripathy, L. Li, J. Kumar, Appl. Phys. Lett. 66 (1995) 1166–1168.
[38] T. Lippert, T. Gerber, A. Wokaun, D.J. Funk, H. Fukumura, M. Goto, Appl. Phys. Lett. 75 (1999) 1018–1020.
[39] F. Yu, P. Li, H. Shen, S. Mathur, C.M. Lehr, U. Bakowsky, F. Mücklich, Biomaterials 26 (2005) 2307–2312.
[40] L.D. Merkle, M. Bass, R.T. Swimm, Opt. Eng. 22 (1983) 405–410.
[41] R.C. Hall, R. Mittra, K.M. Mitzner, IEEE T. Antenn. Propag. 36 (1988) 511.
[42] W.L. Barnes, A. Dereux, T.W. Ebbesen, Nature 424 (2003) 824–830.
[43] D. Oosten, M. Spasenović, L. Kuipers, Nano Lett. 10 (2010) 286–290.
[44] H. Gao, J. Henzie, T.W. Odom, Nano Lett. 6 (2006) 2104–2108.
[45] W.C. Liu, D.P. Tsai, Phys. Rev. B 65 (2002) 155423.
[46] J. Li, C.Z. Ning, Phys. Rev. Lett. 93 (2004) 087402.
[47] P.T. Worthing, W.L. Barnes, Appl. Phys. Lett. 79 (2001) 3035–3037.

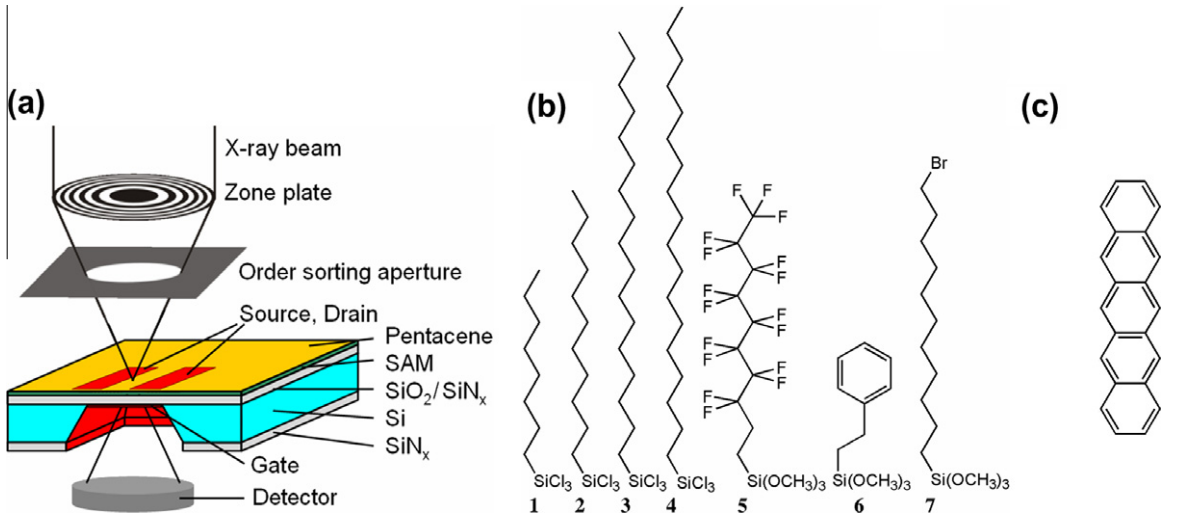

Fig. 1. (a) Schematic of the experimental setup (side view). The pentacene TFT is prepared on a SiN_x membrane. The X-rays are focused on the sample and raster scan over the window area. A photo detector on the backside subsequently produces a two dimensional image of the sample. (b) Lewis structures of used SAMs and (c) of pentacene.

Table 1
Statistical data of pentacene films on different types of SAMs.

System	1	2	3	4	5	6	7
Mobility ($cm^2V^{-1}s^{-1}$)	0.20	0.40	0.44	0.60	$<10^{-3}$	$<10^{-3}$	$<10^{-3}$
Average grain area (μm^2)	0.54	0.98	1.04	1.50	0.06	0.10	0.15
Ratio of GB to total surface area	0.20	0.10	0.06	0.05	0.24	0.20	0.28
Ratio of low-angle GB	0.15	0.15	0.15	0.15	0.15	0.15	0.15

phase separation, domain size, and molecular orientation from electron diffraction [8], sample preparation for TEM measurements can be difficult. It requires deposition on a TEM grid which does not represent the actual morphology of the device. Cross-sectioning of the actual device may damage organic materials or alter their native morphology. Other major factors which limit accuracies are the beam damage and the strong charging of the molecular film when exposed to accelerated electrons especially when the substrate is an insulating gate oxide.

The X-ray absorption technique used here keeps electronic charging effects relatively low and can be even applied to insulating materials [9]. Scanning transmission X-ray microscopy (STXM) has recently been used to investigate the molecular orientation and composition/structure of thin films. It can be adapted to a wide range of sample environments, such as in magnetic fields [10], variable temperature [11], polymer [12] and environmental samples in aqueous media [13]. Moreover, the radiation damage caused by soft X-rays was shown to be low [14]. STXM has also been used to obtain information about the composition of organic materials [15] and their molecular orientation [9]. This information can be derived from the variation in the photon flux and the change in polarization in the carbon K edge region, based on the near edge X-ray absorption fine structure (NEXAFS) effect [16].

Recently, we used STXM to map the molecular orientation of pentacene underneath the Au contacts and in the channel regions of organic TFTs [9]. The goal of this current work is to investigate the effect of surface modification on the pentacene grain orientation distribution. We correlate the structural information with electronic information of pentacene TFTs. Pentacene was chosen because of its high charge carrier mobility and its strong linear dichroism effect for the π^* resonances at the carbon K edge between 283 and 287 eV. A pentacene molecule consists of five linearly fused aromatic rings. The two molecules in the unit cell of pentacene form a herringbone pattern with an angle of 53° [17]. In thin films, the long axis of the pentacene molecules were observed to only deviate by 6° from the substrate normal [17].

2. Results and discussion

The experimental setup is shown in Fig. 1. The transistor devices were built up on a SiO_2 coated SiN_x membrane which was used as a gate oxide. The SiO_2 was modified with the following silane molecules: octyltrichlorosilane (**1**), undecyltrichlorosilane (**2**), heptadecyltrichlorosilane (**3**), octadecyltrichlorosilane (**4**), as well as with (heptadecafluoro-1,1,2,2,-tetrahydrodecyl)trimethoxysilane (**5**), phenethyltrimethoxysilane (**6**), and 11-bromoundecyltrimethoxysilane (**7**). A pentacene film (30 nm thick, measured with a quartz crystal monitor) was then deposited on top. The transistor was completed by Au electrode

deposition as the source, drain, and gate electrodes as reported earlier [9]. The charge carrier mobility for pentacene TFTs on different surfaces is shown in Table 1.

The transistor devices are used directly for STXM studies. The X-ray beam was focused by a zone plate and after passing an order sorting aperture, a 30 nm large X-ray spot raster scans the sample area. The transmitted X-rays are detected by a photo detector. Through this approach, a two-dimensional image of the sample can be obtained. Linearly polarized X-ray radiation was used to study the molecular in-plane orientation.

A schematic top view on the pentacene molecules is shown in Fig. 2(a). The angles between the short unit cell axis "a" and the transition dipole moments $\mathbf{p}_1$ and $\mathbf{p}_2$ of the π^* orbitals are represented by δ with 2δ approximately 53° [3]. The absorbance $A(x,y)$ is maximal when the electric field vector of the X-rays **E** is parallel to the transition dipole moment of the molecule. The relation between $A(x,y)$, the polarization angle of the X-rays α_p, and the angle $\beta(x,y)$ between the short molecule axis "a" and the electric field vector **E** can be written as:

$$A(x,y) = a_0 t\left(1 + a_1 \cos^2(\alpha_p - \beta(x,y) - \delta) + a_1 \cos^2(\alpha_p - \beta(x,y) + \delta)\right) \quad (1)$$

Herein, a_0 is the absorption of the pentacene film with a thickness t, a_1 the strength of the linear dichroism effect, and α_p the X-ray polarization angle [9]. In the following the angle $\alpha_p - \beta(x,y)$, i.e. the orientation of the short unit cell axis "a" with respect to the horizontal axis, will be illustrated by different colors according to the color wheel scheme in Fig. 3(d).

Fig. 2(b) shows the X-ray absorption spectrum of a pentacene grain for two different polarization angles $\alpha_p = 0°$ and 90°. In the energy range of 283–287 eV the difference in the X-ray absorption intensity is very pronounced and is suitable for the determination of the molecular orientation. These resonances correspond to transitions of core electrons in carbon into unoccupied π^* states of the sp^2-hybridized carbon atoms [16].

The angular dependence of the absorbance for two single grains at 285.5 eV is plotted in Fig. 2(c). The X-ray polarization angle was varied between 0° and 90° with 10° step width. The data were fitted using Eq. (1). The STXM images on the bottom of Fig. 2(c) illustrate the changes in the X-ray absorption characteristic for every 30° and show which grains have been selected for plotting the angular dependent absorption behavior. Both the grains A and B show different angular dependences due to their different in-plane orientation. Even though there are two independent molecules in the pentacene unit cell, only one local minimum or maximum in the X-ray absorption spectrum between 0° and 90° was observed. The reason can be explained through the following trigonometric relation:

$$\cos^2(\alpha_p - \beta(x,y) - \delta) + \cos^2(\alpha_p - \beta(x,y) + \delta) = \cos^2(\alpha_p - \beta(x,y))\cos(2\delta) \quad (2)$$

where $\cos(2\delta)$ is constant since the angle between two adjacent molecules is fixed. This finding is important for the interpretation of X-ray microscopy data because regardless of the number of molecules present in the unit cell, there will only be one "average" signal from the

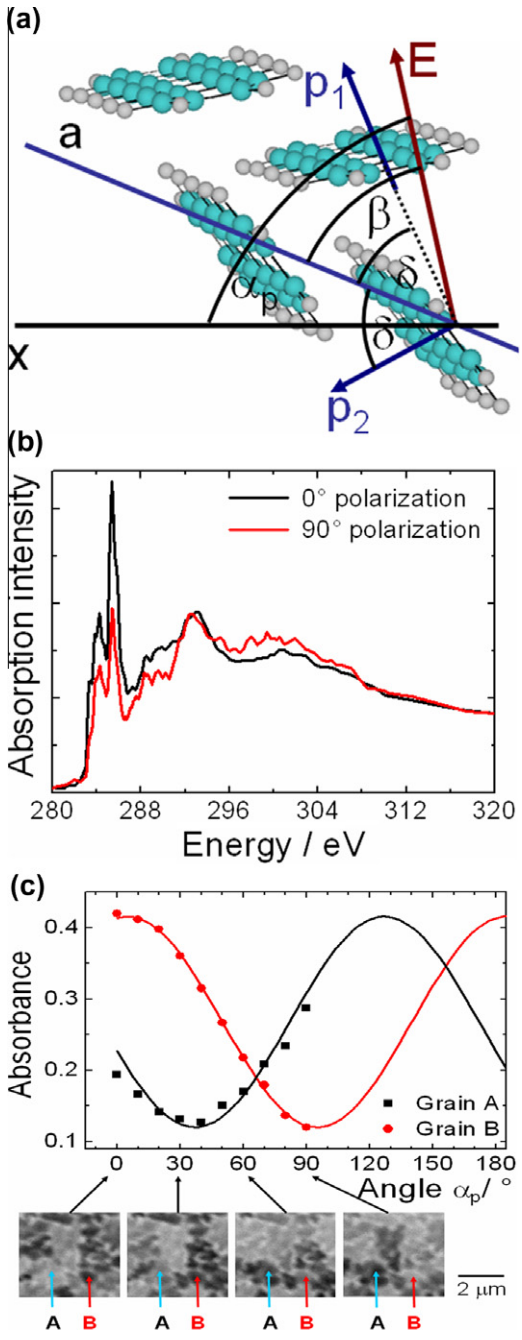

Fig. 2. (a) Top view on four pentacene molecules. The electric field vector **E** of the X-rays interacts with the transition dipole moments $\mathbf{p}_1$ and $\mathbf{p}_2$ of the π^* orbitals of the pentacene molecules. The X-ray polarization angle α_p is varied between 0 and 90°. The absorption intensity reaches its maximum when **E** and the short unit cell axis "a" are parallel to each other ($\beta = 0$). (b) X-ray absorption spectrum of a pentacene grain taken at two different polarization angles $\alpha_p = 0$ and 90°. (c) Angular dependency of the X-ray absorbance at the energy 285.5 eV for linearly polarized X-rays with angles α_p going from 0° to 90° in 10° steps. STXM images for 0°, 30°, 60°, and 90° are shown on the bottom. Measured values were fitted using Eq. (1). Absorbance values from 90° to 180° were extrapolated.

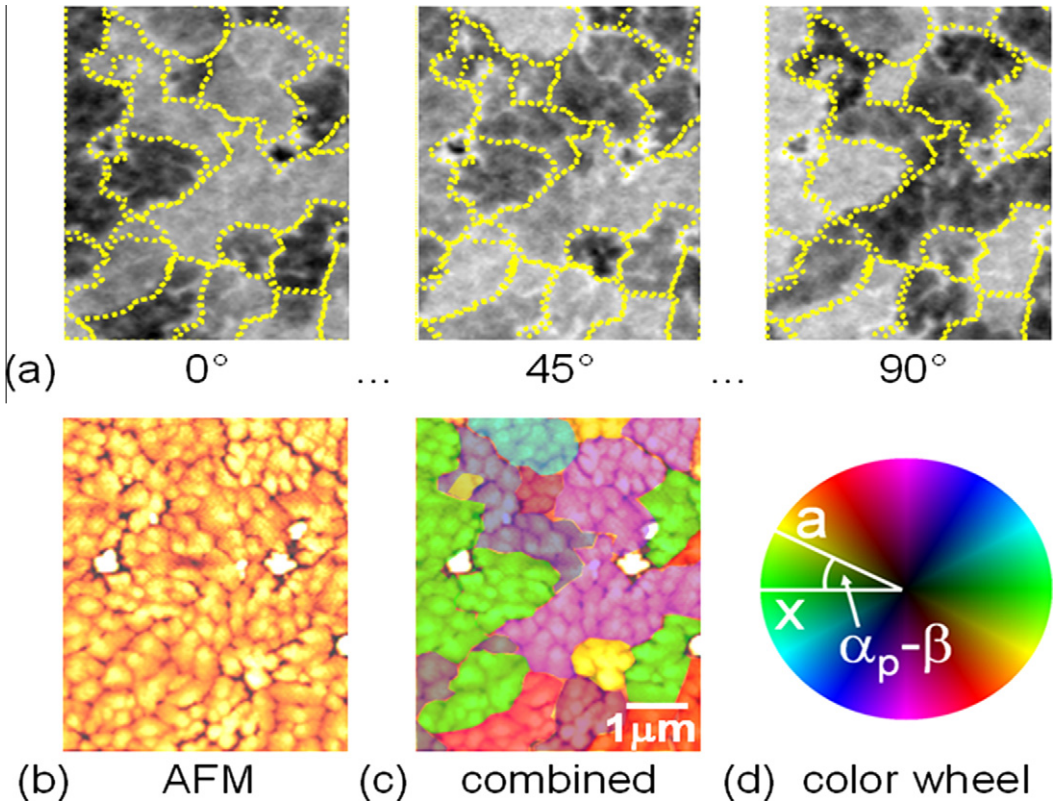

Fig. 3. (a) STXM images of a 30 nm thick pentacene film on a SiN_x membrane, coated with **4**. The measurements were performed using linearly polarized X-rays with $\alpha_p = 0°$, 45°, and 90°. The broken lines in the images illustrate the grain boundaries as determined by STXM. (b) An AFM image was recorded at the place where the STXM images were taken. (c) The gained information from the STXM measurements about the molecular orientation is combined with the AFM image. The different colors represent the in-plane orientation according to the color wheel scheme in (d). All images are on the same length scale, see bar in (c). (d) Color wheel scheme to illustrate the angle $\alpha_p - \beta$ between "*a*" and "*x*" where, e.g., green stands for 0°, red for 60°, and blue for 120°. (For interpretation of the references in color in this figure legend, the reader is referred to the web version of this article.)

X-ray absorption. The fitting procedure leads to $\alpha_p - \beta(x,y) = (127 \pm 2)°$ and $(5 \pm 2)°$ for grain A and grain B, respectively with $a_0 t = 0.268$ and $a_1 = 0.552$.

Fig. 3(a) shows the STXM images for three different linear polarizations. For the determination of the molecular orientation all data sets discussed herein consist of images taken in 15° increments from 0° to 90°. All the images collected are summarized in the supplementary material. The angle of the grains can be read according to the color wheel scheme in Fig. 3(d) where the colors green[1], red, and blue illustrate the angle of the short unit cell axis "*a*" of pentacene with an angle 0°, 60°, and 120°, respectively. Fig. 3(b) was recorded at the same position where the STXM images in Fig. 3(a) were taken. The AFM data themselves do not allow a determination of the real grain size due to crystal lobes and overgrowth. Only the combination with the STXM data provides clear evidence about the molecular orientation and, consequently, the grain size. Fig. 3(c) combines the topography information of the AFM with the information about the molecular orientation from the STXM measurements. From this image the average grain size can be determined and can be compared when changing, for example, the SAM on which the pentacene is grown.

Fig. 4 shows the grain orientation for pentacene films deposited on four alkyl silanes with different chain lengths (**1**–**4**), as well as silanes with different end groups of different polarity such as **5**–**7**. The grain size was observed to increase as the molecular chain length increases. The pentacene grains on fluorine **5**, phenyl **6**, and bromine **7** functionalized surfaces were observed to be much smaller in size (notice different length scales in the second line in Fig. 4). This trend was found to correlate with the surface roughness of the samples we prepared. For example, as the SAM surface roughness decreases in the sequence **5** → **2** → **3** → **4** (cf. Fig. S4 of the supplementary material), the grain size of the pentacene, deposited on top of the corresponding surface, increased.

The results of the statistical evaluation, performed on the images in Fig. 4, are shown in Fig. 5. The grain area varies strongly for different surfaces. The average values for the grain size are summarized in Table 1, together with the charge carrier mobility values of the corresponding transistor devices. The average grain size values increased from 0.54 µm^2 (**1**) to 1.5 µm^2 (**4**). The smallest values were

[1] For interpretation of color in Fig. 3, the reader is referred to the web version of this article.

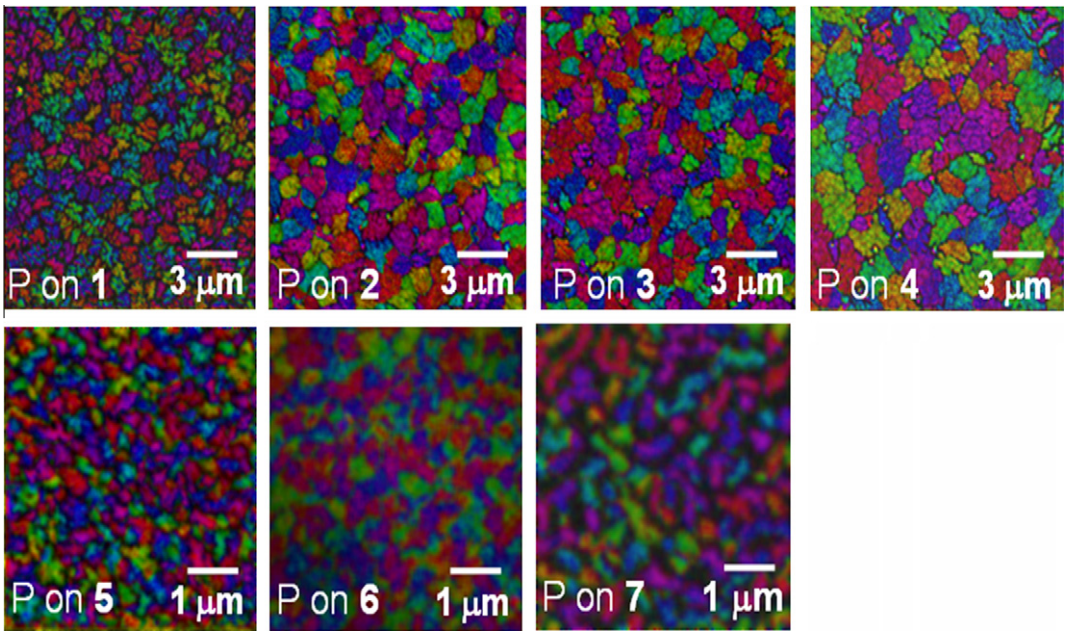

Fig. 4. Grain orientation, derived from STXM measurements, for pentacene (P) deposited on octyltrichlorsilane (**1**), undecyltrichlorsilane (**2**), heptadecyltrichlorosilane (**3**), octadecyltrichlorosilane (**4**), as well as with (heptadecafluoro-1,1,2,2,-tetrahydrodecyl)trimethoxysilane (**5**), phenethyltrimethoxysilane (**6**), and 11-bromoundecyltrimethoxysilane (**7**). Please notice the different length scales in the first and in the second row.

found for **5**, **6**, and **7** ranging from 0.06 to 0.15 μm^2 average grain size.

The charge carrier mobility, grain size, and relative grain boundary area for **1**–**4** are plotted in Fig. 6(a). The ratio of low- to high-angle grain boundaries is plotted in Fig. 6(b). The charge carrier mobility values are observed to be in the range of 0.2–0.6 $cm^2 V^{-1} s^{-1}$ for **1**–**4**, with **1** having the lowest value. With corresponding increase in the alkyl chain length, the grain size increased from **1** to **4**, as well as the corresponding mobility. In the same sequence, the ratio of the GB area to the total area covered by the grains decreased significantly. The ratio of low- to high-angle grain boundaries is nearly identical for pentacene grains grown on different SAMs. This is a clear indication that the charge carrier mobility is mainly influenced by the grain size or the area occupied by the grain boundaries.

The different chain lengths and polarities of the end groups are expected to affect the packing density and conformation of the molecular chain and the ultimate structure depends on all possible interactions [18]. Surfaces with alkyl chains less than about ten carbon atoms are mostly disordered due to the lack of cohesive interaction between the molecules. For longer alkyl chains the cohesive forces are sufficiently strong to force the SAM molecules in an upright position, resulting in dense monolayers with a very smooth surface, leading to very good conditions for the pentacene growth and a better performance of the OFETs. Previously, we have shown that the performance of organic semiconductors is directly related to their molecular packing, crystallinity, growth mode, and purity. Therefore, it is critical to understand how organic semiconductors nucleate and grow [19].

Our results are in agreement with recent findings, that large grains and consequently a smaller amount of grain boundaries leads to a higher performance of pentacene field-effect transistors. It is also known that the major part of the charge transport happens at the gate interface [20], therefore, imaging techniques are required which unravel the structure throughout the entire device and not only at the surface.

3. Summary

STXM was employed to unravel the grain size and orientation of pentacene based field-effect transistors. The transistor devices were built on a SiN_x membrane coated with SiO_2. The pentacene thin films were grown on different self assembled monolayers (SAMs) used to modify the SiO_2 dielectric surface. It was shown that the STXM technique allows determining the molecular in-plane angle with an accuracy of ±4° and it could be performed in tandem with AFM measurements. As the chain length of the SAMs increases, its surface roughness decreases. Therefore, the grain size of the pentacene, deposited on top, increases. In the same sequence, the ratio of grain boundaries to the total surface area is getting smaller resulting in an increase of the charge carrier mobility of the respective transistor device.

Previously it was inconsistent in literature whether a larger or smaller grain size will result in high charge carrier mobility. It was recognized that the grain size determined by AFM, which only looks at the top surface of the grains, could not be used to fully explain the observed trends. We have shown STXM to be a promising technique which

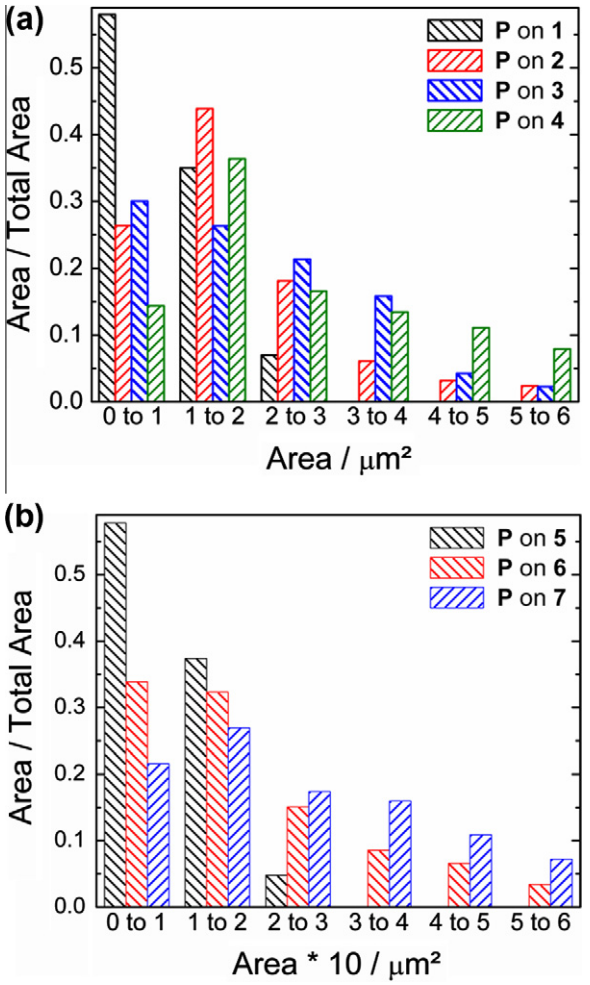

Fig. 5. Grain size distribution of pentacene (P) on different SAMs (**1**–**7**).

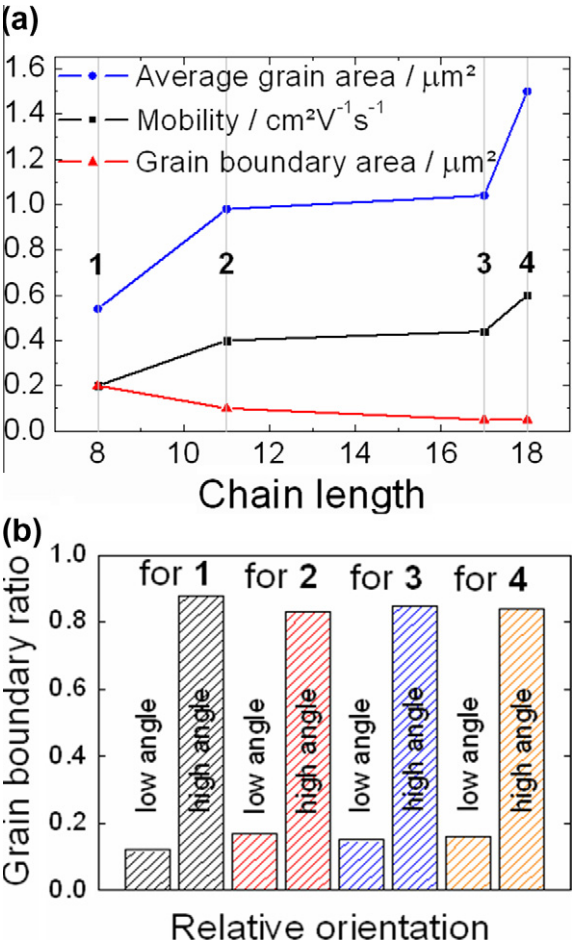

Fig. 6. Dependency of the charge carrier mobility, grain size, and grain boundary area on the chain length of the self assembled monolayer (a) and the grain boundary ratio (b).

can be used to image the grain size through the entire film. In this case, the determined grain size is indeed correlated with the charge carrier mobility. Therefore, we have demonstrated the utility of STXM for understanding charge transport in organic semiconductor materials.

4. Experimental

Materials: All trichlorosilanes were purchased from Gelest Inc. and used as received. Pentacene was purchased from Sigma–Aldrich and sublimed once prior to usage. Device substrates consisted of highly doped Si wafers with 100 nm silicon nitride as the gate dielectric.

Fabrication: The SiN_x membrane substrates were prepared at the Stanford Nanofabrication Facility from SiN_x coated Si wafers. After the membranes were prepared by wet etching a SiO_2 film (50 nm) was grown by chemical vapor deposition. The roughness of the SiO_2 film was determined by atomic force microscopy and is the same for all the substrates used in this paper. The substrates were cleaned with isopropanol and treated with UV ozone for 10 min. They were then modified with a monolayer of commercial available octyltrichlorsilane (**1**), undecyltrichlorsilane (**2**), heptadecyltrichlorosilane (**3**), octadecyltrichlorosilane (**4**), as well as with (heptadecafluoro-1,1,2,2,-tetrahydrodecyl)trimethoxysilane (**5**), phenethyltrimethoxysilane (**6**), and 11-bromoundecyltrimethoxysilane (**7**). For this purpose, the cleaned membrane substrates were placed in a desiccator with a heated metal block (200 °C). About 0.5 ml of **1**–**7**, respectively, were filled in a beaker and placed onto the block. The desiccator was pumped down to approx. 25 mTorr. The substrates were washed with isopropanol and dried with a nitrogen gun prior to deposition of pentacene. Pentacene (30 nm) was subsequently deposited at 60 °C on top of the coated membrane. The gate consists of aluminum (20 nm) and gold (5 nm) and was deposited on the backside of the membrane. [21]. Gold (30 nm) was deposited on the front side as source and drain electrode using the shadow mask technique (channel width: 0.3 mm, channel length: 0.05 mm).

Characterization: STXM measurements were carried out at beamline 11.0.2 at the Advanced Light Source in Berkeley, California, USA (Photon energy range: 280–320 eV;

zone plate resolution: approx. 35 nm) [22]. STXM measurements were performed at room temperature in He atmosphere. The electrical measurements on the organic devices were performed under ambient conditions using a Keithley 4200SCS semiconductor parameter analyzer. The atomic force microscope images of pentacene thin films were collected using a Park XE-70.

Acknowledgements

B.B. would like to thank the German Research Foundation (DFG) for a postdoctoral- and the Funds of Chemical Industry for a Liebig-scholarship. H.B.A. acknowledges the Netherlands Organisation for Scientific Research (NWO) for support. A.V. and Z.B. thank the financial support from the NSF sponsored MRSEC (DMR 0213618) and NSF Solid State Chemistry (DMR 0705687). The Advanced Light Source is supported by the Director, Office of Science, Office of Basic Energy Sciences, of the US Department of Energy under Contract No. DE-AC02-05CH11231.

Appendix A. Supplementary data

Supplementary data associated with this article can be found, in the online version, at doi:10.1016/j.orgel.2011.08.007.

References

[1] A. Virkar, S. Mannsfeld, J.H. Oh, M.F. Toney, Y.H. Tan, G. Liu, J.C. Scott, R. Miller, Z. Bao, Adv. Funct. Mater. 19 (2009) 1962.
[2] Z. Bao, A. Lovinger, A. Dodabalpur, Adv. Mater. 9 (1997) 42.
[3] S.F. Nelson, Y.-Y. Lin, D.J. Gundlach, T.N. Jackson, Appl. Phys. Lett. 72 (1998) 1854.
[4] (a) G. Horowitz, M.E. Hajlaoui, Adv. Mater. 12 (2000) 1046;
(b) T.W. Kelley, C.D.J. Frisbie, Phys. Chem. B 105 (2001) 4538;
(c) T. Someya, H.E. Katz, A. Gelperin, A.J. Lovinger, A. Dodabalapur, Appl. Phys. Lett. 81 (2002) 3079;
(d) A. Di Carlo, F. Piacenza, A. Bolognesi, B. Stadlober, H. Maresch, Appl. Phys. Lett. 86 (2005) 263501;
(e) J. Zhang, J.P. Rabe, N. Koch, Adv. Mater. 20 (2008) 3254;
(f) B. Bräuer, Y. Vaynzof, W. Zhao, A. Kahn, W. Li, D.R.T. Zahn, C.J. Fernández, C. Sangregorio, G.J. Salvan, Phys. Chem. B 113 (2009) 4565;
(g) B. Bräuer, M. Grobosch, M. Knupfer, F. Weigend, Y. Vaynzof, A. Kahn, T. Rüffer, G.J. Salvan, Phys. Chem. B Lett. 113 (2009) 10051;
(h) B. Bräuer, D.R.T. Zahn, T. Rüffer, G. Salvan, Chem. Phys. Lett. 432 (2006) 226;
(i) B. Bräuer, M. Fronk, D. Lehmann, D.R.T. Zahn, G. Salvan, J. Phys. Chem. B 113 (2009) 14957;
(j) M. Fronk, B. Bräuer, J. Kortus, O.G. Schmidt, D.R.T. Zahn, G. Salvan, Phys. Rev. B 79 (2009) 235305.
[5] J. Rivnay, L.H. Jimison, J.E. Northrup, M.F. Toney, R. Noriega, S. Lu, T.J. Marks, A. Facchetti, A. Salleo, Nat. Mater. 8 (2009) 952.
[6] P.E.J. Flewitt, R.K. Wild, Grain. Boundaries, Grain Boundaries: Their Microstructure and Chemistry, Wiley, New York, 2001.
[7] V. Kalihari, E.B. Tadmor, G. Haugstad, C.D. Frisbie, Adv. Mater. 20 (2008) 4033.
[8] X. Zhang, S.D. Hudson, D.M. DeLongchamp, D.J. Gundlach, M. Heeney, I. McCulloch, Adv. Funct. Mater. XX (2010) 1–9.
[9] B. Bräuer, A. Virkar, S.C.B. Mannsfeld, D.P. Bernstein, R. Kukreja, K.W. Chou, T. Tyliszczak, Z. Bao, Y. Acremann, Chem. Mater. 22 (2010) 3693.
[10] Y. Acremann, J.P. Strachan, V. Chembrolu, S.D. Andrews, T. Tyliszczak, J.A. Katine, M.J. Carey, B.M. Clemens, H.C. Siegmann, J. Stöhr, Phys. Rev. Lett. 96 (2006) 217202.
[11] Y. Wang, C. Jacobsen, J. Maser, A. Osanna, J. Microsc. 197 (2000) 80.
[12] C.R. McNeill et al., Nanoscale quantitative chemical mapping of conjugated polymer blends, Nano Lett. 6 (2006) 1202.
[13] (a) U. Neuhäusler, S. Abend, C. Jacobsen, G. Lagaly, Soft X-ray spectromicroscopy on solid-stabilized emulsions, Colloid Polym. Sci. 277 (1999) 719.;
(b) G.E. Mitchell, et al., Quantitative characterization of microscopic variations in the cross-link density of gels, Macromolecules 35 (2001) 1336.
[14] (a) E.G. Rightor, et al., Spectromicroscopy of poly(ethylene terephthalate): comparison of spectra and radiation damage rates in X-ray absorption and electron energy loss. J. Phys. Chem. B 101 (1997) 1950.;
(b) Coffey, T., Urquhart, S.G., Ade, H. Characterization of the effects of soft X-ray irradiation on polymers. J. Electron. Spectrosc. Relat. Phenom. 122 (2002) 65.
[15] (a) C.R. McNeill et al., Macromolecules 40 (2007) 3263–3270;
(b) C.R. McNeill et al., Nanotechnology 19 (2008) 424015;
(b) K.B. Burke et al., Macromolecules 42 (2009) 3098.
[16] J. Stöhr, NEXAFS Spectroscopy, first ed., Springer, New York, 1992.
[17] S.C.B. Mannsfeld, A. Virkar, C. Reese, M.F. Toney, Z. Bao, Adv. Mater. 21 (2009) 2294.
[18] (a) J. Yu-Tai Tao, Am. Chem. Soc. 115 (1993) 4350;
(b) K. Fukuda, T. Hamamoto, T. Yokota, T. Sekitani, U. Zschieschang, H. Klauk, T. Someya, Appl. Phys. Lett. 95 (2009) 203301.
[19] Ajay A. Virkar, Stefan Mannsfeld, Zhenan Bao, Natalie Stingelin, Adv. Mater. 22, 34 (2010) 3857–3875.
[20] Z. Bao, J. Locklin, Organic Field-Effect Transistors, Taylor and Francis, 2007.
[21] C. Hub, M. Burkhardt, M. Halik, G. Tzvetkov, R. Fink, J. Mater. Chem. 20 (2010) 4884.
[22] A.L.D. Kilcoyne, T. Tyliszczak, W.F. Steele, S. Fakra, P. Hitchcock, K. Franck, E. Anderson, B. Harteneck, E.G. Rightor, G.E. Mitchell, A.P. Hitchcock, L. Yang, T. Warwick, H. Ade, J. Synchrotron Radiat. 10 (2003) 125.

to ~5.4 eV for CF_X-modified Ag nanoparticles/ITO, which is advantageous to charge collection at the anode/organic interface in organic photovoltaic cells. Hence, a CF_X-Ag nanoparticles/ITO anode has advantages of (i) improved charge collection efficiency at anode/organic interface, and (ii) enhanced light absorption in the active layer of ZnPc:C_{60}-based OPV devices through broadband scattering of Ag nanoparticles.

2. Experimental

The thin film ZnPc:C_{60}-based OPV devices have a layer configuration of glass/ITO(160 nm)/Ag(1.5 nm)/CF_X-(~0.3 nm)/ZnPc:C_{60}(35 nm, 1:1)/C_{60}(25 nm)/4,7-diphenyl-1,10-phenanthroline (BPhen) (7 nm)/Ag(100 nm), in which the CF_X-modified Ag nanoparticles/ITO forms a composite anode. The composite anode is formed by the thermal evaporation of an ultra-thin Ag layer on ITO/glass followed by the subsequent modification of the Ag/ITO contact by an ultra-thin CF_X layer, deposited by a C_4F_8 plasma processing method [11]. After the formation of the composite electrode of CF_X-modified Ag nanoparticles/ITO, the active layer of ZnPc:C_{60}, electron transport layer of BPhen and cathode of Ag were then deposited through thermal evaporation. The OPV cells had an active area of 3.0 mm × 3.0 mm.

The current density–voltage (*J*–*V*) characteristics of the OPV cells were measured under air mass 1.5 global (AM1.5G) irradiation of 100 mW/cm^2 (300 W SAN-EI XEC-301S solar simulator; beam size: 4 inch diameter). The light intensity was determined by a monosilicon detector (with KG-5 visible color filter) calibrated by the National Renewable Energy Laboratory to minimize spectral mismatch. The surface work function of bare ITO and CF_X-modified Ag nanoparticles/ITO was examined using ultraviolet photoelectron spectroscopy with the Helium line (21.2 eV).

3. Results and discussion

ITO has been widely used as anode for applications in organic light-emitting diodes (OLEDs) and OPV cells. However, device formed on a bare ITO surface usually shows imperfection in device performance. The mitigation of this problem has involved ITO surface modification, e.g., using oxygen/UV-ozone plasma treatments or interposing an appropriate intermediate ultra-thin interlayer between the organic and ITO anode. A CFx-modified Ag surface was manifested to be an effective anode for OLEDs [11]. In this work, the modification of ITO using an ultra-thin Ag layer for application in OPV was investigated. It is found that CF_X-modified Ag nanoparticles/ITO forms an excellent anode for application in OPV cells. The performance of OPV devices involved an ultra-thin Ag layer can be influenced quite substantially as the Ag layer thickness increases, a Ag-based electrode with appropriate surface electronic and optical properties are desired for efficient operation of the OPV cells [12].

Scanning electron microscopy (SEM) images for the bare ITO and the CF_X-modified Ag nanoparticles/ITO surfaces are shown in Fig. 1 (a)–(d). The average size of the Ag nanoparticles ranges from ~10 nm to ~20 nm as the thickness of the Ag film increases from 1.5 nm to 10 nm – a consequence of coalescence with increasing time of deposition. As a thick Ag layer is expected to increase the energy loss attributable to reflection or scattering from the metallic layer, a 1.5 nm thick ultra-thin Ag layer which is non-continuous as shown in Fig. 1(b), was chosen such that the resulting anode retains a relatively high level of optical transparency and the beneficial contribution of plasmonic effect to enhance the light absorption in the active layer of the OPV devices.

In order to better understand the changes in surface work function of the ITO anode, the surface electronic properties of the modified ITO were studied using UPS measurement to determine the electronic structures on both bare ITO and CF_X-modified Ag nanoparticles/ITO surfaces. Fig. 2 shows the secondary electron edge in the UPS spectra measured for bare ITO, Ag nanoparticles/ITO and CF_X-modified Ag nanoparticles/ITO surfaces, which can provide information on the work function of the ITO surface. The spectra show that the work function of ITO (~4.4 eV) is reduced to ~4.1 eV with the incorporation of a 1.5 nm-thick Ag layer in ITO/Ag, but the combinatory layer of ITO/Ag/CF_X significantly increased the anode work function to ~5.4 eV. The work functions of ITO after UV-ozone and O_2 plasma treatments (not shown here) are about 5.1 eV and 5.4 eV, respectively.

In a previous work, a CF_X-modified Ag anode has been applied to improve carrier injection properties in organic light-emitting diodes [11]. In this work, we found that CF_X-modified Ag nanoparticles/ITO also exhibited a similar high surface work function nature. This clearly reveals that modification of ITO through Ag nanoparticles/CF_X conferred superior high surface work function suited for application in OPV devices. It is known that the interfacial energy level alignment at organic/electrode interface has a crucial impact on the device performance. The offset between the lowest-unoccupied-molecular-orbital of organic films and the Fermi level of an anode, e.g., ITO, is important for efficient charge collection in the OPV devices. The inset in Fig. 2 illustrates the schematic energy diagram of a ZnPc:C_{60}-based OPV cell studied in this work. As shown in the inset of Fig. 2, the difference in energy level between the work function of an ITO anode (~4.4 eV) and the highest occupied molecular orbital of ZnPc (5.17 eV [13]) at the ITO/ZnPc:C_{60} interface, can be reduced significantly after the ITO anode is modified with Ag nanoparticles/CF_X. The reduced electronic barrier at the ITO/CF_X-Ag nanoparticles/ZnPc:C_{60} interface may be favorable for charge extraction in OPV cells.

The OPV devices of ITO/Ag/CF_X/ZnPC:C_{60}/C_{60}/BPhen/Ag were fabricated along with two other control devices of ITO/ZnPc:C_{60}/C_{60}/BPhen/Ag, each with different surface treatment of the ITO anode prior to thermal evaporation of the organic layers. The two OPV control devices prepared for comparison studies are made with (i) an ITO anode treated with UV-ozone (control device-1) and (ii) an ITO anode treated with *in situ* O_2 plasma (control device-2). The incident photon to electron conversion efficiencies (IPCE) of the OPV devices and the two control devices over

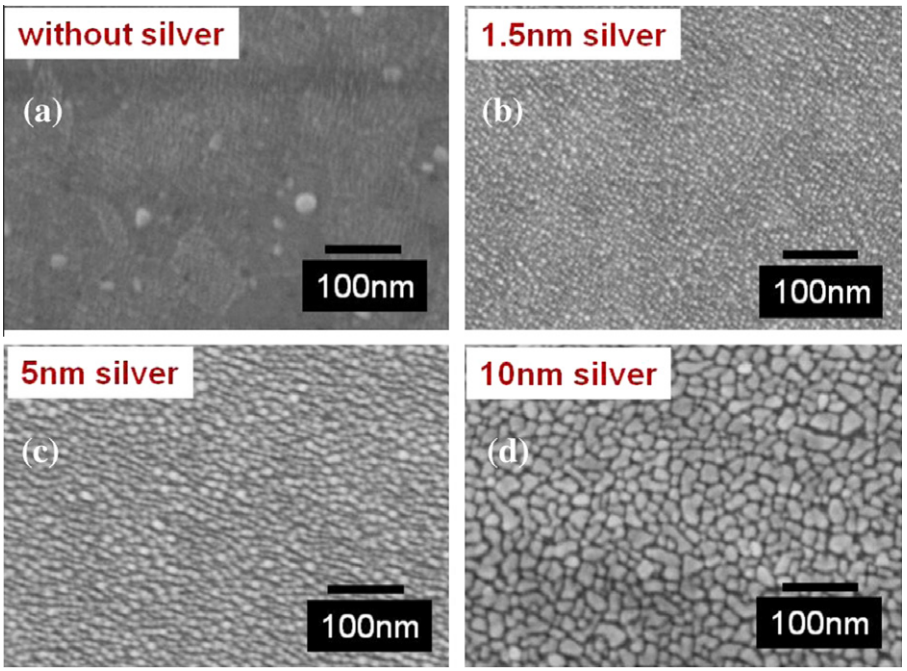

Fig. 1. SEM images of bare ITO and Ag nanoparticles modified ITO surfaces: (a) ITO/glass, (b) 1.5 nm-thick Ag on ITO/glass, (c) 5 nm-thick Ag on ITO/glass, and (d) 10 nm-thick Ag on ITO/glass.

the wavelength range from 300 nm to 800 nm were measured and the results are shown in Fig. 3. The general trend of the IPCE spectra of the OPV devices made with UV-ozone treated, O_2 plasma treated and CF_X-modified Ag nanoparticles/ITO electrodes is similar, consisting of two broad peaks (each divided into two local peaks) and a trough at 480 nm to 580 nm. With the exception of the trough where the IPCE of all OPV devices are similar, the IPCE of the OPV devices is notably higher than that of the O_2 plasma processed device which is in turn greater than that of the UV-ozone case. The *J–V* characteristics of the OPV devices are shown in Fig. 4. The short-circuit current density (J_{SC}), open circuit voltage (V_{OC}), fill factor (FF) and power conversion efficiency (PCE) of the OPV devices measured under AM1.5G irradiation are summarized in Table 1. It can be seen that the OPV devices with CF_X-Ag nanoparticles/ITO composite electrode has the best performance.

The work function measured for ITO treated with *in situ* O_2 plasma is about 5.4 eV, which is similar to that of a CF_X-modified Ag nanoparticles/ITO anode based on our UPS measurement (See schematic energy level diagram given as the inset of Fig. 2). This implies that the anode/organic interface in OPV devices with *in situ* O_2 plasma (control device-2) and the modified-ITO (OPV cell) would have very similar charge collection efficiency. Hence, similar IPCE for both OPV devices would be expected if this accounts for the main contribution to the improvement in device performance. Evidently, this has not been the case. Moreover, for the same surface work function, the incorporation of the Ag metallic layer would, in all likelihood, reduce the admission of light into the device and lower the IPCE. Therefore, an explanation involving only improved contact properties at anode/organic interface is not sufficient to account for the improved performance of the device concerned.

The increase in the power conversion efficiency of the OPV cells with an CF_X-modified Ag nanoparticles/ITO anode can be attributed to combinatory effects of (1) improved charge collection properties at the modified ITO/organic interface, and (2) enhanced absorption in the active layer of OPV cells through the advantages of broadband plasmonic enhancement effect [14,15]. From the SEM image (Fig. 1(b)) of the 1.5 nm-thick non-continuous Ag layer on ITO surface, it can be seen that the Ag nanoparticles have an average lateral dimension of ~10 nm. Localized plasmon resonance of Ag nanoparticles is known to be excited by incident light, the wavelength of plasmon resonance being dependent on the size and shape of the Ag nanoparticles and the permittivity of the surrounding dielectric background. Under conditions of plasmon resonance, the local electric field (tens of nm) around the Ag nanoparticles is strongly enhanced. The strong field aids the absorption of light in the organic photovoltaic devices, leading to enhanced device performance.

The optical absorption spectra measured for 1.5 nm-thick Ag nanoparticles on ITO are shown in Fig. 5. Deposition of Ag nanoparticles on ITO/glass evidently leads to higher absorption of the glass/ITO/Ag sample (*black curve*). As the Ag nanoparticles have a range of lateral dimensions of ~10 nm, the absorption is relatively broad extending over a wavelength range below ~550 nm. The mean size of the Ag nanoparticles at ~10 nm accounts for the broad absorption peak at $\lambda \sim 480$ nm. In comparison, the absorption peak is further shifted to 510 nm in the ZnPc:C_{60} blend layer deposited on CF_X-modified Ag nanoparticles/ITO (*blue curve*).

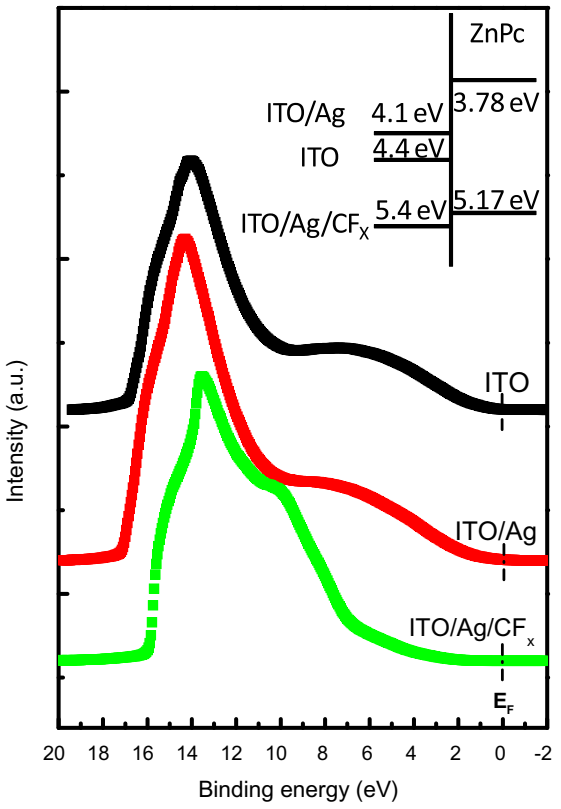

Fig. 2. Evolution of the secondary electron edge in UPS spectra measured for bare ITO, Ag nanoparticles/ITO, and CF_X-modified Ag nanoparticles/ITO surfaces (from top to bottom). The inset illustrates the schematic diagram of energy levels in ZnPc:C_{60}-based OPV devices with different anode contacts of ITO, Ag nanoparticles/ITO and CF_X-modified Ag nanoparticles/ITO.

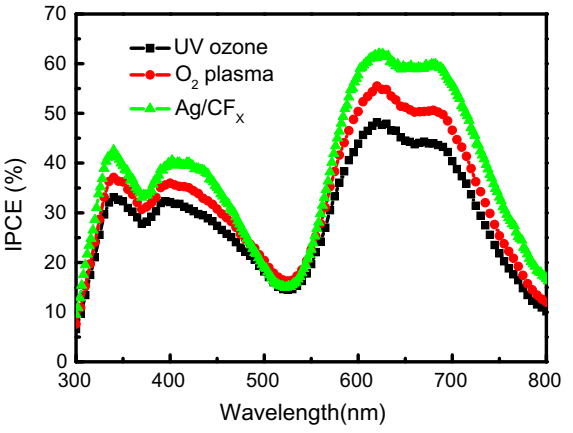

Fig. 3. Comparison of IPCE spectra measured for ZnPc:C_{60}-based OPV devices with different anode contacts: ITO with UV-ozone surface treatment (black square), ITO with *in situ* O_2 plasma treatment (red diamond) and CF_X-modified Ag nanoparticles/ITO anode (green triangle). (For interpretation of the references to color in this figure legend, the reader is referred to the web version of this article.)

As shown in Fig. 5, it can be gleaned that the incorporation of the ultra-thin Ag layer significantly improves the

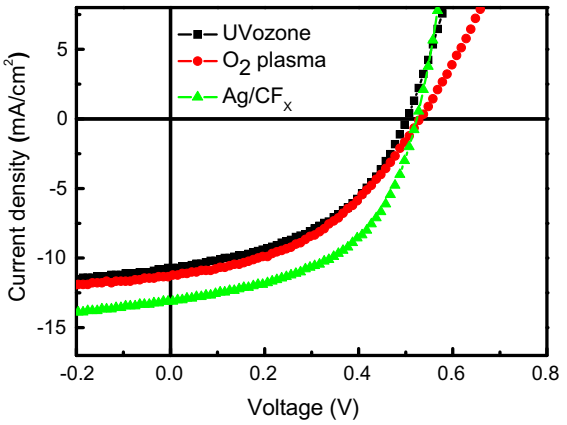

Fig. 4. *J–V* characteristics measured for ZnPc:C_{60}-based OPV devices fabricated on ITO treated with: UV-ozone surface treatment (black square), *in situ* O_2 plasma treatment (red diamond) and CF_X-modified Ag nanoparticles/ITO anode (green triangle). (For interpretation of the references to colors in this figure legend, the reader is referred to the web version of this article.)

Table 1
Photovoltaic characteristics of the ZnPc:C_{60}-based OPV devices with ITO anode treated with UV-ozone, O_2 plasma and modified with Ag nanoparticle/CF_X.

Anode	UV-ozone (Control device-1)	O_2 plasma (Control device-2)	Ag/CF_X
J_{SC} (mA/cm^2)	10.72 ± 0.50	11.13 ± 0.50	13.10 ± 0.50
V_{OC} (V)	0.50 ± 0.05	0.52 ± 0.05	0.52 ± 0.05
FF (%)	0.46 ± 0.05	0.47 ± 0.05	0.51 ± 0.05
PCE (%)	2.4 ± 0.1	2.7 ± 0.1	3.5 ± 0.1

absorption in an active ZnPc:C_{60} layer on the modified ITO anode over the wavelength range from ~420 nm to ~800 nm (*blue & green curve*[1]). The relative low absorption of ZnPc:C_{60} layer on CF_X/ITO over the wavelength range from ~420 nm to ~550 nm (*red curve*[1]) culminates to a local peak in the ZnPc:C_{60} layer on CF_X/Ag nanoparticles/ ITO (*blue curve*[1]), while the double peaks over the wavelength range from ~580 nm to ~800 nm is further enhanced. The absorption spectra of ZnPc:C_{60} on Ag nanoparticle/ITO (*green curve*[1]) show a similar trend. Examining the absorption spectra of ZnPc:C_{60} in greater detail reveals that a slightly higher absorption is observed for the ZnPc:C_{60} blend layer on Ag nanoparticles/ITO (*green curve*[1]) than the case with CF_X/Ag nanoparticles /ITO (*blue curve*[1]) for wavelength >610 nm, implying that the former would induce a higher absorption in devices. However, the work function of a bare ITO/Ag anode (Fig. 2) is not favorable to an efficient charge extraction at ITO/Ag/organic interface. The modification of the surface of Ag nanoparticles with CF_X is desired (*blue curve*[1]).

Comparing the absorption spectra of the glass/ITO/CF_X/ZnPc:C_{60} and glass/ITO/Ag/CF_X/ZnPc:C_{60} samples with the IPCE of the finished devices (glass/ITO/ZnPc:C_{60}/C_{60}/

[1] For interpretation to colour in the text, the reader is referred to the web version of this article.

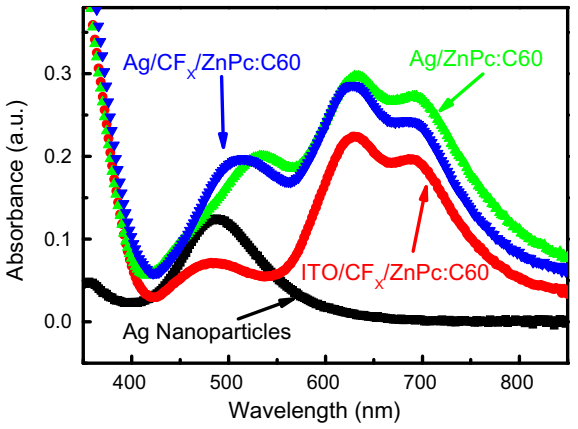

Fig. 5. Absorption spectra for Ag nanoparticles on ITO, 35 nm-thick ZnPc:C_{60} blend layer deposited on ITO/CF_X, on ITO/Ag nanoparticles, and ITO/Ag nanoparticles/CF_X.

BPhen/Ag and glass/ITO/Ag/CF_X/ZnPc:C_{60}/C_{60}/BPhen/Ag), a good correspondence in the broad absorption peaks over the wavelength range from ~580 nm to ~800 nm can be observed. It is obvious that the enhanced absorption brought on by the incorporation of the Ag nanoparticles layer translates into an improved spectral responsivity and hence the enhancement in the power conversion efficiency of the OPV devices. It is clear that the IPCE of the OPV devices with Ag nanoparticles/CF_X-modified anode remains higher than those with the bare ITO anode. This allows a notably higher short-circuit current density of 13.10 ± 0.50 mA/cm^2 to be achieved compared to 10.72 ± 0.50 mA/cm^2 in control device-1 and 11.13 ± 0.50 mA/cm^2 in control device-2, as summarized in Table 1. Our results reveal that the composite anode of Ag nanoparticles with inclusion of CF_X enhanced the performance of OPV cells through improved light harvesting in the OPV devices.

4. Conclusion

In summary, performance enhancement in ZnPc:C_{60}-based OPV devices is achieved through the composite CF_X-modified Ag nanoparticles/ITO anode. The CF_X-modified Ag nanoparticles/ITO is favorable for application in OPV devices due to its advantages of broadband plasmonic enhancement effect and improved charge collection efficiency at anode/organic interface. The CF_X-modified Ag nanoparticles/ITO anode yielded a promising power conversion efficiency of $3.5 \pm 0.1\%$ for ZnPc:C_{60} OPV devices, notably higher than that with a bare ITO anode ($2.4 \pm 0.1\%$ with UV-ozone treatment and $2.7 \pm 0.1\%$ with O_2 plasma treatment).

Acknowledgements

F.R. Zhu acknowledges support by the Strategic Development Fund of Hong Kong Baptist University under Grant SDF10-0118-P01 and Faculty Research Grant FRG2/09-10/022.

References

[1] D.H. Ko, J.R. Tumbleston, L. Zhang, S. Williams, J.M. Desimone, R. Lopez, E.T. Samulski, Nano Letters 9 (2009) 2742–2746.
[2] W.L. Barnes, A. Dereux, T.W. Ebbesen, Nature 424 (2003) 824–830.
[3] H.A. Atwater, A. Polman, Nature Materials 9 (2010) 205–213.
[4] H. Shen, P. Bienstman, B. Maes, Journal of Applied Physics 106 (2009) 073109.
[5] F.C. Chen, J.L. Wu, C.L. Lee, Y. Hong, C.H. Kuo, M.H. Huang, Applied Physics Letters 95 (2009) 013305.
[6] S.S. Kim, S.I. Na, J. Jo, D.Y. Kim, Y.C. Nah, Applied Physics Letters 93 (2008) 073307.
[7] A.P. Kulkarni, K.M. Noone, K. Munechika, S.R. Guyer, D.S. Ginger, Nano Letters 10 (2010) 1501–1505.
[8] K. Tvingstedt, N. Krister, O. Ingnas, A. Rahachou, I.V. Zozoulenko, Applied Physics Letters 91 (2007) 113514.
[9] N.C. Lindquist, W.A. Luhman, S.H. Oh, R.J. Holmes, Applied Physics Letters 93 (2008) 123308.
[10] R.A. Pala, J. White, E. Barnard, J. Liu, M.L. Brongersma, Advanced Materials 21 (2009) 3504–3509.
[11] Y.Q. Li, L.W. Tan, X.T. Hao, K.S. Ong, F.R. Zhu, L.S. Hung, Applied Physics Letters 86 (2005) 153508.
[12] X.Z. Wang, H.L. Lam, K.S. Yong, Z.K. Chen, F.R. Zhu, Organic Electronics 12 (2011) 429.
[13] F.T. Reisa, D. Mencaraglia, S. Oould Saad, I. Seguy, M. Oukachmih, P. Jolinat, P. Destruel, Synthetic Metals 138 (2003) 33.
[14] J.R. Cole, N.J. Halas, Applied Physics Letters 89 (2006) 153120.
[15] A. Aubry, D.Y. Lei, S.A. Maier, J.B. Pendry, Physics Review B 82 (2010) 125430.

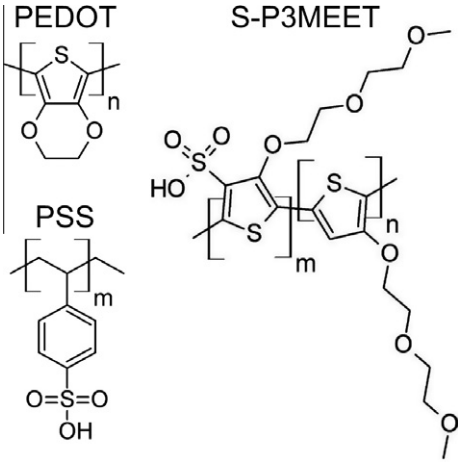

Fig. 1. Chemical structures of PEDOT:PSS and S-P3MEET.

with PEDOT:PSS, the barrier has been shown to be lower than expected in some cases [9].

Despite the widespread use of PEDOT:PSS, it is not without problems. It is highly acidic (pH = 1.2) and corrodes the ITO anode [10,11]. PEDOT:PSS is also hygroscopic and the water it uptakes can diffuse into the active layer or the cathode, reducing efficiency and device lifetime [12]. Additionally, the hole injection barrier could be limiting the performance of blue emitting OLED devices [13]. Another problem for OLEDs is that PEDOT:PSS's high parallel conductivity could lead to crosstalk between pixels in displays [14]. As a result, other materials have been investigated as replacements for PEDOT:PSS. OPV devices made with conductive oxide HTLs such as V_2O_5, MoO_3, and NiO have shown efficiencies comparable or better than PEDOT:PSS HTL devices [15–17]. The problem with oxides is that they do not work for all HOMO levels like PEDOT:PSS. There has also been significant work studying doped small molecules for OLEDs and OPVs [18,19]. The problem with organic small molecules is that they must be deposited under vacuum, which is not compatible with high-throughput manufacturing. A solution processable polymer/small molecule blend that has shown better hole selectivity is a blend of 4,4-bis[(*p*-trichlorosilylpropylphenyl)-phenylamino]biphenyl ($TPDSi_2$) and poly[9,9-dioctylfluorene-co-*N*-[4-(3-methlypropyl)]-diphenylamine (TFB) [20]. The problem with all of these alternatives is that because they are semiconductors, and not quasimetallic like PEDOT:PSS, they must be tuned for each donor/acceptor system, whereas PEDOT:PSS can accept holes from any polymer in an OPV. Despite this bevy of replacements, PEDOT:PSS is still used in almost all published results.

PEDOT:PSS is commercially available as an aqueous colloidal solution. In solution, the colloids are rich in hydrophilic PSS at the surface with PEDOT-rich centers. When these films are cast by spin coating this structure is maintained [6]. Scanning tunneling microscopy (STM) and cross-section atomic force microscopy (AFM) were used to show that spin-cast PEDOT:PSS films consist of a phase-separated structure [14]. Under the forces of spin coating the colloids flatten to form PEDOT rich layers that are vertically segregated by PSS-rich layers. In the PEDOT-rich lamella, PEDOT-rich "pancakes" are laterally separated by very thin or incomplete PSS-rich lamellas. This morphology results in anisotropic conductivity in PEDOT:PSS films. In the plane of the film, holes are conducted via three-dimensional variable range hopping, and normal to the film, conduction is via nearest-neighbor hopping [21]. Due to the different conduction mechanisms, the parallel ($\sigma_{||}$, in-plane) conductivity of PEDOT:PSS is three orders of magnitude larger than the perpendicular ($\sigma_{\perp}$, out-of-plane) conductivity [21].

In addition to having anisotropic conductive properties, PEDOT:PSS films also display anisotropic optical properties. The films are uniaxially anisotropic with the ordinary complex refractive index ($N_o = n_o + ik_o$) in the plane of the film and the extraordinary complex refractive index ($N_e = n_e + ik_e$) normal to the film and parallel to the optical axis, where n_i is the refractive index and k_i is the extinction coefficient ($i = o, e$) [22,23]. PEDOT films doped with iron (III) tris-*p*-toluenesulfonate also display uniaxial optical constants [24]. In each case, k_o looks metallic as it increases with increasing wavelength, which is attributed to free charge carrier absorption [22,24]. Free carrier absorption is based in the Drude model where the dielectric function is dependent on the number of free carriers per unit volume [25]. This model is consistent with band structure of PEDOT:PSS, which has a non-zero density of states at the Fermi energy [21]. In each of these studies, $\sigma_{||}$ was different, ranging from 10^{-3}–500 S/cm and as $\sigma_{||}$ increases so does the amplitude of the free charge absorption. From a classical perspective, this correlation between conductivity and free carrier absorption is expected as both are dependent on the number of free electrons. These studies also show varying levels of anisotropy between N_e and N_o. In contrast to N_o, N_e looks more like a dielectric than a metal [24]. Again we see a correlation between conductivity and optical properties as the low $\sigma_{\perp}$ of PEDOT:PSS would correspond to a low free charge density which would not result in a Drude model of the dielectric function.

The focus of this article is a new conductive polymer, sulfonated poly (thiophene-3-[2-(2-methoxyethoxy) ethoxy]-2,5-diyl) (S-P3MEET). Samples of all S-P3MEET solutions were generously provided by Plextronics, Inc. S-P3MEET is a copolymer whose structure is shown in Fig. 1. Like PEDOT, S-P3MEET is a conjugated polythiophene. The most significant difference between S-P3MEET and PEDOT:PSS is that S-P3MEET is self-doped by the sulfonate moieties that are bonded to some of the thiophene rings instead of having the dopant in solution. The sulfonate moieties dope the polymer by oxidizing it and generating a hole that can be delocalized over the conjugated backbone. Having the sulfonate moieties linked to the polymer has multiple advantages. One is that the sulfonate concentration is much lower in S-P3MEET than PEDOT:PSS, leading to a pH above 2. Also, the pure S-P3MEET films do not have any mobile dopants, which can have unintended results in devices. Our group recently showed that the high concentration of PSS at the HTL/active layer interface results in an oxidation of poly (3-hexylthiophene-2,5-diyl) (P3HT) upon heating and alters the electrical characteristics of OPV devices [8].

In this study we characterize three different preparations of spin coated S-P3MEET thin films. All of the solutions

contain S-P3MEET in a solution of water and ethylene glycol butyl ether. The solution containing only S-P3MEET is Plexcore® OC CFAJ10-100, hereto referred as AJ10. The two other solutions studied are Plexcore® OC CFAJ20-100 and CFAJ30-100. The AJ20 and AJ30 solutions have proprietary additives in the mixture, with AJ20 having the highest additive concentration. In this article, we characterize the electrical and optical properties of all films and determine how the additives alter the optical, electrical, and morphological properties of these films.

2. Experimental details

2.1. Materials and sample preparation

All substrates were rinsed with chloroform then ultrasonically cleaned in successive baths of acetone, Mucasol, and deionized water followed by rinsing and drying in a FSI Phoenix spin-rinse-dryer. Prior to spin coating all substrates were placed in a UV/Ozone plasma cleaner for 30 min. Thin films of PEDOT:PSS (Clevios P VP AI 4083; Heraeus), AJ10 (Plexcore® OC CFAJ10-100; Plextronics, Inc.), AJ20(Plexcore® OC CFAJ20-100; Plextronics, Inc.), and AJ30 (Plexcore® OC CFAJ30-100; Plextronics, Inc.) were prepared by spin coating (Specialty Coating Systems 6800) onto the substrates.[1] The polymer solutions were dispensed from a syringe fitted with a 0.45 μm filter. Spinning speed and time were varied to achieve the desired film thickness. After coating, the samples were placed on a hot plate set to 110 °C for 5 min to remove any remaining solvent from the films.

2.2. Measurements

1×1 in^2 glass substrates were cleaned as described in Section 2.1. For parallel (in-plane, $||$) measurements the slides were scored using a steel cutting wheel to divide the glass into nine (0.33×0.33 in^2) subsections. Following light rinsing with acetone, Mucasol, and deionized water, the substrates were transfered to a high vacuum chamber (MBraun). Four electrodes (1×5 mm^2, 1 mm spacing) composed of 5 nm of chromium followed by 95 nm of gold were deposited by thermal evaporation. Following electrode deposition the samples were rinsed again and cleaned in the UV/ozone plasma. For perpendicular (out-of-plane, $\perp$) measurements, one Cr/Au electrode was deposited onto glass. After electrode deposition, the substrates were lightly rinsed and UV/ozone cleaned. Films were spin-coated as described in Section 2.1 for both geometries. The perpendicular samples were returned to the high vacuum chamber and 100 nm of gold was deposited to give an active area of 0.35 cm^2. Electrical measurements were performed with a Keithely 2420 source measurement unit.

For ellipsometry measurements, silicon wafers with 300 nm of thermally grown oxide were used as the substrates. Films were spin-coated and annealed prior to measurement. Measurements were performed using a VASE model ellipsometer from the J.A. Woollam Co., Inc. Scans were performed at multiple angles of incidence from 55° to 85° in steps of 5°. The measurement range was 300 nm to 1000 nm in steps of 5 nm. Depolarization was measured and used to fit film thickness nonuniformity to improve modeling accuracy. Modeling of the optical properties of the substrate materials and polymer films was carried out using WVASE32® ellipsometric analysis software from the J.A. Woollam Co., Inc. All optical data was recorded in air and at room temperature. The oxide thickness was measured using published values of the optical constants of Si and SiO_2 [26]. The refractive index of the quartz was modeled using a Cauchy dispersion model and the extinction coefficient was modeled using a point-by-point fit.

Transmittance measurements of of the films on quartz slides were performed using a Perkin Elmer Lambda 750 UV/vis/NIR spectrophotometer. Measurements were recorded at wavelengths from 190 nm to 1700 nm in steps of 5 nm.

Atomic force microscopy (AFM) measurements were conducted in tapping mode using a Veeco Multimode 3 microscope. Silicon tips (K-Tech) with a spring constant of 5 N/m were used for imaging. Images were analyzed and processed using Veeco's Nanoscope Analysis software.

Work function values of polymer films were measured with a Kelvin probe (KP Technologies, Inc.). Samples were prepared by spin-coating films onto glass substrates coated with ITO. Work function values for aluminum with native oxide and UV/ozone cleaned gold were used to calibrate the work function of the probe tip [27].

Contact angle measurements were performed on a leveled goniometer stage. A droplet of deionized water was placed on the sample surface and the contact angle between the droplet and the surface was measured with the goniometer.

Thickness measurements of polymer films were performed using a Veeco Dektak 150 Stylus Profiler. Films were scratched with a knife blade to create a measurement step. The profiler was calibrated with two certified step-height standards from VLSI Standards, Inc.

3. Results and discussion

In the following sections, we use AFM along with Kelvin probe and contact angle measurements to study the film morphology and surface properties of S-P3MEET thin films. Then using conductivity measurements and spectroscopic ellipsometry we determine how the film morphology affects the conductive and optical properties of the S-P3MEET films. All measurements of S-P3MEET films are compared to standard PEDOT:PSS films.

3.1. Atomic force microscopy

The first step in the characterization of the S-P3MEET films is to measure the morphology of the surfaces using tapping mode AFM (TM–AFM). In TM–AFM, the cantilever tip is oscillated near its resonance frequency as it is scanned

[1] All Plexcore solutions used is this study are commercially available from Plextronics, Inc., 2180 William Pitt Way, Pittsburgh, PA 15238, USA. Tel.: +1 412 423 2030; fax: +1 412 423 2039, www.plextronics.com.

over the sample. The amplitude of this oscillation changes with surface topography and this change is used to generate the height image. An image of the phase of the oscillation of the cantilever can also provide useful information about a film's surface. Changes in surface forces will result in differences in phase lag between the cantilever oscillation and the feedback signal. This makes the phase image sensitive to changes in the surface composition.

TM–AFM scans were performed on the polymer films and the topography and phase images are shown in Fig. 2. Also, the root-mean-square roughness values for the topography (r_z) and phase (r_p) images are reported in Table 1. From the topography images and r_z values we can see that all of the AJ films are rougher than PEDOT:PSS, which is very smooth due to the thin PSS top layer that forms upon annealing [28,29]. Stylus profiler measurements also show that the AJ films are rougher than PEDOT:PSS films. On closer inspection of Fig. 2b and c, one notices that the areas of the different height regions are much smaller for AJ30 than for AJ20. In Fig. 2b we see

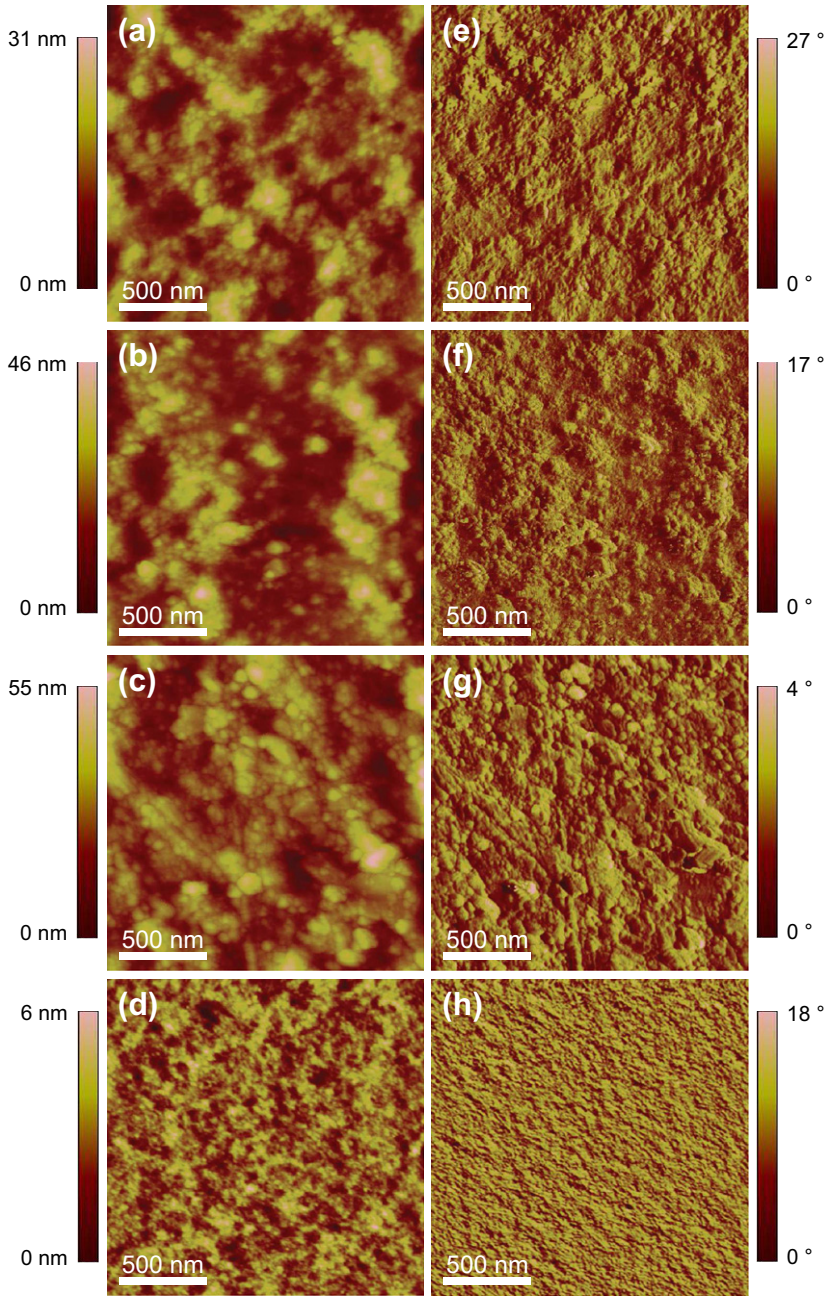

Fig. 2. $2 \times 2\ \mu m^2$ topography and phase AFM images of (a and e) AJ10, (b and f) AJ20, (c and g) AJ30, and (d and h) PEDOT:PSS on glass. Height and phase scales vary between samples.

Table 1
Topography (r_z) and phase (r_p) RMS roughness values from TM–AFM, work function (ϕ) values measured using the Kelvin probe method, and contact angle (θ_c) measurements measured between a water drop and film surface for AJ10, AJ20, AJ30, and PEDOT:PSS.

	r_z (nm)	r_p (°)	ϕ (eV)	θ_c (°)
AJ10	4.38	4.04	5.2 ± 0.1	22 ± 1
AJ20	6.52	2.35	5.3 ± 0.1	32 ± 1
AJ30	7.54	0.61	5.6 ± 0.1	46 ± 1
PEDOT:PSS	0.80	2.54	5.1 ± 0.1	14 ± 1

two ridges running vertically on the left and right sides of the images. Looking at the "valley" region in the phase data in Fig. 2f one can see islands of a lighter phase surrounded by a darker phase. This indicates that there may be some phase separation on the surface of the AJ20 film. A common feature between AJ20 and AJ30 is that the topography images both show a granular morphology. STM microscope images of PEDOT:PSS films also show a granular morphology [14]. The commonality of a granular morphology between AJ20, AJ30 and PEDOT:PSS further suggests that the additives may be causing a phase separated morphology in AJ20 and AJ30.

When comparing the data for the AJ films an interesting trend is noticeable. While AJ10 has the lowest r_z it also has highest r_p. On the other hand, AJ30 has the highest r_z but has the lowest r_p. It might seem counterintuitive that AJ10, which contains only S-P3MEET, would exhibit the largest range in the phase images until one considers the structure of the polymer. S-P3MEET (shown in Fig. 1) is a copolymer with two different repeat units. One contains only an ether side group, but the other has the addition of a sulfonate group. These groups will exert different attractive/repulsive forces on the the AFM tip, meaning that the different sections of the S-P3MEET polymer will have a different phase leading to an inhomogeneous phase image. We interpret the increase in homogeneity in the phase images of AJ20 and AJ30 to be caused by a high concentration of additives on the surface that make the surface more uniform in material content.

To confirm this we use two different techniques that are sensitive to the surface composition: Kelvin probe and contact angle (θ_c) measurements. A Kelvin probe measures the work function (ϕ), i.e. the energy required to remove an electron from the surface, giving a measure of the surface's electronic make up [30]. Measuring θ_c between a drop of deionized water and a material gives a measure of the hydrophobicity of the surface. The results from these two measurements are summarized in Table 1. For AJ10, the value of ϕ (5.2 eV) is close to PEDOT:PSS (5.1 eV), but PEDOT:PSS has a lower θ_c due to the layer of hyrdrophylic PSS on the surface. For AJ20 and AJ30 we see an increase in ϕ and θ_c. The increase in θ_c either means that the additives are hydrophobic or hydrophobic parts of the S-P3MEET polymer are at the surface. The increase in ϕ may also indicate that the additives are fluorinated. In a study of blue OLEDs the addition of a perfluorinated ionomer to PEDOT:PSS increased the work function by 0.20–0.65 eV depending on the ionomer concentration [13]. The authors also showed that the device efficiencies were improved when a higher work function PEDOT:PSS layer was used. This indicates that AJ30 may be preferable for use in OLEDs because its ϕ will result in a lower hole injection barrier into the HOMO of the polymer.

3.2. Conductivity

We next measured the conductivity of the S-P3MEET films. If S-P3MEET is to be used as a HTL in OPV or OLED devices it must be sufficiently conductive to efficiently transport charges between the anode and active/emissive layer. For these measurements shadow masks were designed so that the electrode geometries produced electric fields parallel or perpendicular to the surface normal. For the parallel conductivity measurements the shadow mask was modeled after the mask used by Nardes et al. [14] to allow for detection of any in-plane anisotropy. For all of the films, no in-plane anisotropy was found. All conductivity values reported represent an average of nine individual four-point conductivity measurements.

The parallel ($\sigma_{||}$) and perpendicular ($\sigma_{\perp}$) conductivity values measured in N_2 and at room temperature are reported in Table 2. PEDOT:PSS shows the highest $\sigma_{||}$ and is consistent with previously reported values [21]. For the S-P3MEET films we see a trend of decreased conductivity as the additive concentration increases (the additive concentration is highest in AJ20). This is not without precedent, as in PEDOT:PSS films conductivity decreases

Table 2
Conductivities of polymer thin films, parallel ($\sigma_{||}$) and perpendicular ($\sigma_{\perp}$) to the surface normal measured in a DC field in N_2 and at room temperature.

	$\sigma_{||}$ (S/cm)	$\sigma_{\perp}$ (S/cm)
AJ10	$(7.3 \pm 0.4) \times 10^{-4}$	$(1.2 \pm 0.1) \times 10^{-5}$
AJ20	$(5.3 \pm 2.1) \times 10^{-6}$	$(1.2 \pm 0.1) \times 10^{-5}$
AJ30	$(2.6 \pm 0.1) \times 10^{-4}$	$(1.1 \pm 0.1) \times 10^{-5}$
PEDOT:PSS	$(1.1 \pm 0.1) \times 10^{-3}$	$(0.7 \pm 0.1) \times 10^{-5}$

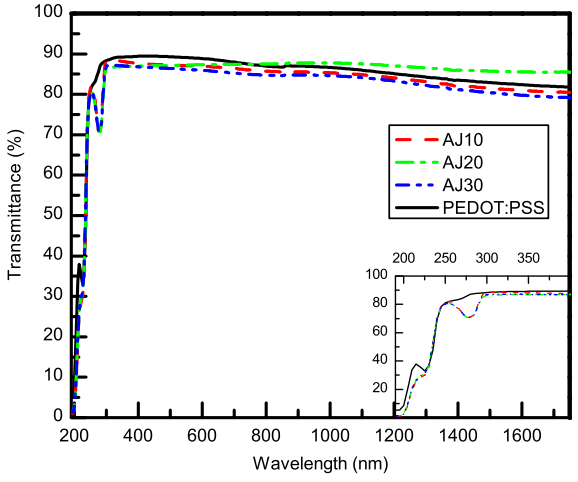

Fig. 3. Wavelength dependent transmittance spectra for films AJ10 (red, dash), AJ20 (green, dash-dot), AJ30 (blue, dash-dot-dot), and PEDOT:PSS (black, solid) of equal thickness (70 nm) on quartz in the spectral range of 190–1750 nm. The inset figure highlights the spectral range from 190 to 400 nm. (For interpretation of the references in colour in this figure legend, the reader is referred to the web version of this article.)

as the ratio of PSS to PEDOT increases [31]. We conclude that the decrease in conductivity is due to the additives separating the conductive domains as was indicated by the TM–AFM images. Based on the relatively high conductivity of AJ30 it does not appear that the conductive domains are completely isolated from each other, however, the data for AJ20 indicates complete separation of conductive domains. The complete separation will prohibit any long-range hopping transport and limit conduction to a nearest-neighbor hopping mechanism, as is seen in $\sigma_{\perp}$ of PEDOT:PSS. The data for AJ30 suggests that the lower additive concentration diminishes long-range hopping, but does not eliminate it. The low $\sigma_{||}$ of AJ20 may make it preferable for use in pixilated OLED displays as crosstalk between neighboring pixels will be less likely than in displays with PEDOT:PSS.

Based on our interpretation of the parallel conductivity data, the conductive domains in AJ20 are fully separated from each other, but, in AJ30 films the conductive domains are only partially separated. The vertical separation between the conductive S-P3MEET domains is thick like the PSS-rich shells in PEDOT:PSS films. This is supported by the perpendicular conductivity values for AJ20 and AJ30 which are close to that of PEDOT:PSS. Interestingly, AJ10 displays similar vertical conductivity values to AJ20, AJ30, and PEDOT:PSS even though it does not have any mobile additives that are separating the conductive domains. It is possible that the different parts of the S-P3MEET

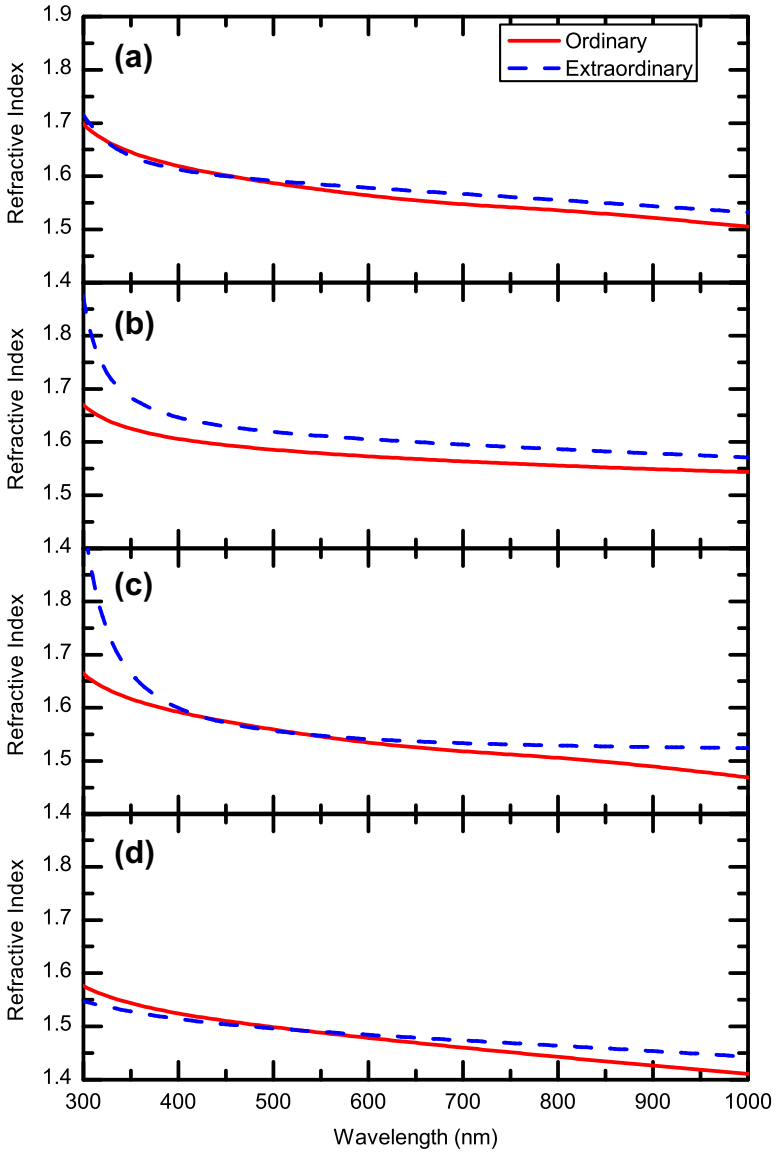

Fig. 4. Wavelength dependent ordinary (n_o, solid) and extraordinary (n_e, dashed) refractive indexes for (a) AJ10, (b) AJ20, (c) AJ30, and (d) PEDOT:PSS calculated from ellipsometric and transmission measurements of thin-films on Si/SiO_2 wafers and quartz slides.

polymer are segregating and the nonconductive regions are separating the conductive regions.

3.3. Optical properties

In addition to measuring the conductivity of the S-P3MEET films the complex optical properties were also measured. In this study we determined the optical properties of the S-P3MEET and PEDOT:PSS thin films using variable angle spectroscopic ellipsometry (VASE). Since none of the films have transparent regions it is not possible to fit the film thickness independently of absorption. In order to accurately fit the thickness and the optical properties a multiple sample analysis (MSA) was performed to reduce the correlation between film thickness and optical absorption. In an MSA experiment, samples with different film thicknesses are measured and fit simultaneously. In the fitting, the optical properties are assumed to be independent of film thickness. Through this procedure, the correlation between thickness and absorption is minimized. Measuring at multiple angles of incidence also reduces the correlation between fitting parameters because thickness is independent of wavelength. The thickness values derived from the fits were checked against the measured thickness from stylus profilometry. N_o is probed by s-polarized light at all angles and partially by p-polarized light at low angles. In contrast, N_e is only probed by p-polarized light at high angles of incidence. Since N_e is not probed strongly, models of it are less accurate than models of N_o.

In addition to VASE measurements, transmission spectroscopy, at normal incidence, was performed on the films on quartz substrates. By measuring at normal incidence

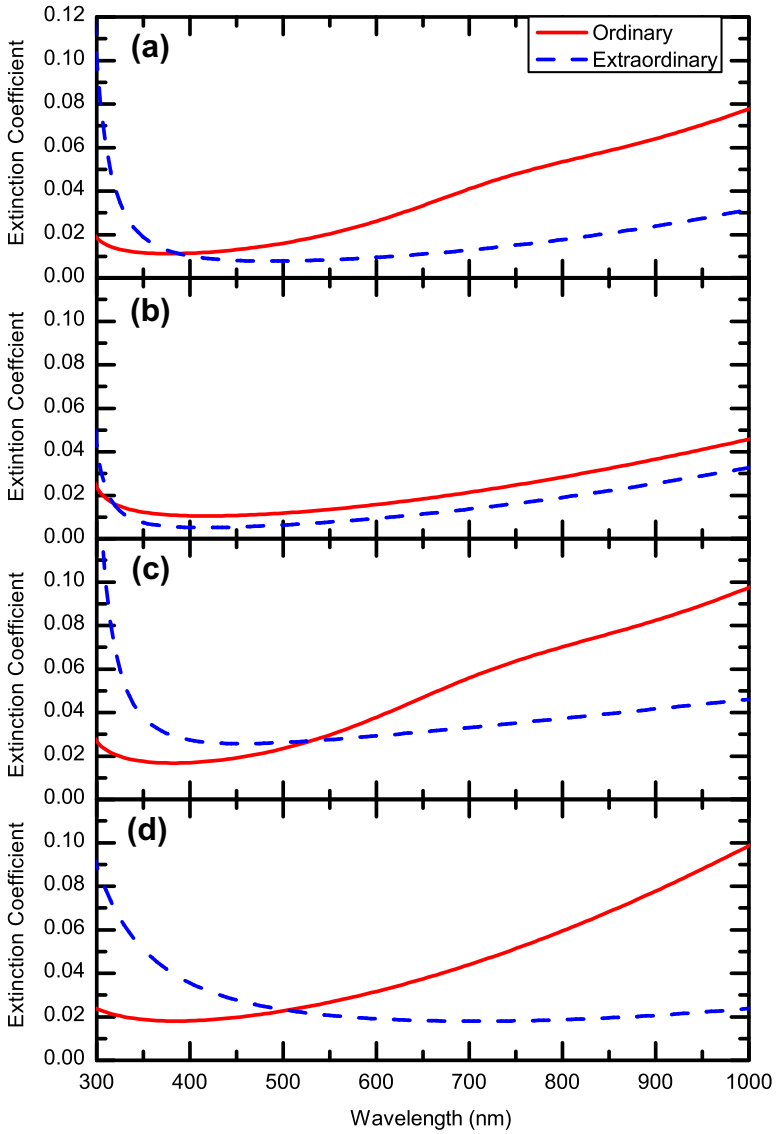

Fig. 5. Wavelength dependent ordinary (k_o, solid) and extraordinary (k_e, dashed) extinction coefficients for (a) AJ10, (b) AJ20, (c) AJ30, and (d) PEDOT:PSS calculated from ellipsometric and transmission measurements of thin-films on Si/SiO_2 wafers and quartz slides.

only N_o is probed. Quartz was selected as the substrate for these measurements because it is transparent much further into the UV than glass and allows the detection of peaks that would be obscured by the strong absorption of glass in the UV. The transmittance spectra for all of the films are presented in Fig. 3. All films exhibit high transparency in the visible region. We see that all films have peaks at 193 nm and 225 nm, which can be seen more clearly in the inset figure. The spectrum for PEDOT:PSS has a small shoulder from 250 to 280 nm, while the AJ films have a peak at 280 nm. These peaks can be attributed to π–π^* transitions in both S-P3MEET and PEDOT:PSS [22]. The transmittance spectra of AJ10, AJ30, and PEDOT:PSS show a broad absorption feature above 400 nm that increases into the infrared (IR), which is due to absorption from free charges. In contrast to AJ10, AJ30, and PEDOT:PSS, AJ20 does not have a free charge absorption feature as seen by flat transmittance above 400 nm. The lack of free charge absorption correlates well with the conductivity data as $\sigma_{||}$ for AJ20 is very low and thus has few free charges.

To fit the optical properties of the thin films, models were constructed using the WVASE32® software package from J.A. Woollam Co., Inc. The optical properties as a function of $h\nu$ were fit using multiple Lorentz oscillators as:

$$N = n + ik = \varepsilon^{1/2} = \left(\varepsilon_1(\infty) + \sum_{j=1}^{J} \frac{A_j}{E_n^2 - (h\nu)^2 - i\Gamma_j h\nu}\right)^{1/2}, \quad (1)$$

where A_j is the amplitude, Γ_j is the broadening, and E_j is the center energy of oscillator j, and $\varepsilon_1(\infty)$ is the dielectric function at infinite energy. When fitting, A_j, Γ_j, E_j, and $\varepsilon_1(\infty)$, Eq. (1) can be fixed or used as fit parameters to minimize the mean square error (MSE) between the generated values and experimental experimental. All films were initially modeled assuming an isotropic layer on top of layers of SiO_2 and Si, however, this model did not produce acceptable fits to the experimental data. To improve the fitting a uniaxial anisotropic layer was selected to model the polymer films.

To model N_o for all films, two oscillators had their energies fixed at 6.4 eV and 5.5 eV to account for the π–π^* transitions. All of the AJ polymers also had an oscillator with a fixed energy of 4.45 eV. Fixing the oscillator energies removes fitting parameters, decreasing correlations. For PEDOT:PSS, AJ10, and AJ30 an oscillator had its energy fixed at 0 eV (Drude oscillator) to account for the free charge contribution. For AJ20, the best fit was achieved without a free charge oscillator. For $\lambda < 300$ nm, only transmittance data was fit because of the limitations of the ellipsometer wavelength range. Also when fitting the data between 300 nm and 400 nm, the transmittance data was weighted at 400% of the ellipsometric data because the fiber optic cables in the ellipsometer have absorption peaks in the UV. In total, five oscillators were used to model N_o for AJ10, AJ30, and PEDOT:PSS while four were used for AJ20.

To fit N_e, only two oscillators were used in the models. Because it is not possible to measure the extraordinary axis with transmittance spectroscopy it is not possible to measure below 300 nm. As a result only the oscillator with its energy fixed at 4.5 eV was used to account for absorption in the UV. For the second oscillator, A_j, Γ_j, and E_j were used as fitting parameters. As was mentioned previously, the extraordinary refractive index is only probed slightly at oblique angles by p-polarized light resulting in less accurate fitting.

The ordinary and extraordinary refractive indices and extinction coefficients generated from the best fits are displayed in Figs. 4 and 5, respectively. The results for PEDOT:PSS are consistent with previously published optical constants for the same formulation [23]. Both figures show that AJ10, AJ30, and PEDOT:PSS are more anisotropic, especially when comparing k_o and k_e, than AJ20. This correlates well with the different amounts of anisotropy in the conductivity measurements as AJ20 has only slight conductive anisotropy when compared to the other films. For PEDOT:PSS, AJ10, and AJ30 the amplitude of the free electron oscillators are similar, again agreeing with the conductivity data. The similarities can also be seen in the k_o values shown in Fig. 5. In Fig. 4c, both n_o and n_e of AJ20 look similar to a Cauchy dispersion model, which is commonly used to model the refractive index of dielectrics. This, too, is consistent with the low conductivity of AJ20.

4. Conclusions

In conclusion, we have shown that all of the AJ solutions produce films that have anisotropic conductive and optical properties. The pure S-P3MEET films from the AJ10 solution have conductive and optical properties that are similar to PEDOT:PSS films, indicating that it may be a suitable replacement for PEDOT:PSS in OPV devices. Additives to the solutions are found to alter the morphology of the films. In AJ20 films, there is complete isolation of the conductive S-P3MEET domains, resulting in a low parallel conductivity and optical properties that look similar to a dielectric material. AJ20 may be well suited for use in pixelated OLED displays as its low parallel conductivity will limit crosstalk between pixels. The lower concentration of additives in AJ30 causes the conductive domains to only be partially separated, which slightly decreases the parallel conductivity of the film relative to AJ10, where as the optics are not significantly affected. The surfaces of AJ20 and AJ30 are also shown to be rich in additive molecules. The high work function of AJ30 films indicates it may be best suited for use in OPV devices with high open circuit voltage and in blue emitting OLEDs due to the lowered hole injection barrier. Future studies will seek to better understand the properties of S-P3MEET and the effect of additives on surface and bulk properties.

Acknowledgments

This work was supported by the US Department of Energy EERE Solar America Initiative under Contract No. DE-FG36 08GO18018. We thank Plextronics, Inc. for donating the materials used in this study. We would also like to thank Andre Knoesen and Diego Yankelevich for support with ellipsometry measurements.

References

[1] R.F. Service, Outlook brightens for plastic solar cells, Science 332 (6027) (2011) 293.

[2] J.G. Xue, S.R. Forrest, Carrier transport in multilayer organic photodetectors: Ii. effects of anode preparation, Journal of Applied Physics 95 (4) (2004) 1869–1877.

[3] M.G. Helander, Z.B. Wang, J. Qiu, M.T. Greiner, D.P. Puzzo, Z.W. Liu, Z.H. Lu, Chlorinated indium tin oxide electrodes with high work function for organic device compatibility, Science 332 (6032) (2011) 944–947.

[4] Y. Yang, A.J. Heeger, Polyaniline as a transparent electrode for polymer light-emitting diodes: lower operating voltage and higher efficiency, Applied Physics Letters 64 (10) (1994) 1245–1247.

[5] S. Karg, J.C. Scott, J.R. Salem, M. Angdopoulos, Increased brightness and lifetime of polymer light-emitting diodes with polyaniline anodes, Synthetic Metals 80 (2) (1996) 111–117.

[6] G. Greczynski, T. Kugler, M. Keil, W. Osikowicz, M. Fahlman, W.R. Salaneck, Photoelectron spectroscopy of thin films of pedot-pss conjugated polymer blend: a mini-review and some new results, Journal of Electron Spectroscopy and Related Phenomena 121 (1-3) (2001) 1–17.

[7] H. Yan, B.J. Scott, Q. Huang, T.J. Marks, Enhanced polymer light-emitting diode performance using a crosslinked-network electron-blocking interlayer, Advanced Materials 16 (21) (2004) 1948–1953.

[8] D.M. Huang, S.A. Mauger, S. Friedrich, S.J. George, D. Dumitriu-LaGrange, S. Yoon, A.J. Moul, The consequences of interface mixing on organic photovoltaic device characteristics, Advanced Functional Materials 21 (9) (2011) 1657–1665.

[9] S. Bange, A. Kuksov, D. Neher, A. Vollmer, N. Koch, A. Ludemann, S. Heun, The role of poly(3,4-ethylenedioxythiophene): poly(styrene-sulphonate) as a hole injection layer in a blue-emitting polymer light-emitting diode, Journal of Applied Physics 104 (10) (2008) 104506–104510.

[10] M.P. de Jong, L.J. van Ijzendoorn, M.J.A. de Voigt, Stability of the interface between indium-tin-oxide and poly(3,4-ethylenedioxy-thiophene)/poly(styrenesulfonate) in polymer light-emitting diodes, Applied Physics Letters 77 (14) (2000) 2255–2257.

[11] K.W. Wong, H.L. Yip, Y. Luo, K.Y. Wong, W.M. Lau, K.H. Low, H.F. Chow, Z.Q. Gao, W.L. Yeung, C.C. Chang, Blocking reactions between indium-tin oxide and poly (3,4-ethylene dioxythiophene): poly(styrene sulphonate) with a self-assembly monolayer, Applied Physics Letters 80 (15) (2002) 2788–2790.

[12] M. Jorgensen, K. Norrman, F.C. Krebs, Stability/degradation of polymer solar cells, Solar Energy Materials and Solar Cells 92 (7) (2008) 686–714.

[13] T.W. Lee, O. Kwon, M.G. Kim, S.H. Park, J. Chung, S.Y. Kim, Y. Chung, J.Y. Park, E. Han, D.H. Huh, J.J. Park, L. Pu, Hole-injecting conducting-polymer compositions for highly efficient and stable organic light-emitting diodes, Applied Physics Letters 87 (23) (2005) 231106–231113.

[14] A.M. Nardes, M. Kemerink, R.A.J. Janssen, J.A.M. Bastiaansen, N.M.M. Kiggen, B.M.W. Langeveld, A. van Breemen, M.M. de Kok, Microscopic understanding of the anisotropic conductivity of PEDOT:PSS thin films, Advanced Materials 19 (9) (2007) 1196–1200.

[15] V. Shrotriya, G. Li, Y. Yao, C.W. Chu, Y. Yang, Transition metal oxides as the buffer layer for polymer photovoltaic cells, Applied Physics Letters 88 (7) (2006) 073508.

[16] M.D. Irwin, B. Buchholz, A.W. Hains, R.P.H. Chang, T.J. Marks, p-Type semiconducting nickel oxide as an efficiency-enhancing anode interfacial layer in polymer bulk-heterojunction solar cells, Proceedings of the National Academy of Sciences of the United States of America 105 (8) (2008) 2783–2787.

[17] K.X. Steirer, J.P. Chesin, N.E. Widjonarko, J.J. Berry, A. Miedaner, D.S. Ginley, D.C. Olson, Solution deposited nio thin-films as hole transport layers in organic photovoltaics, Organic Electronics 11 (8) (2010) 1414–1418.

[18] B. Maennig, J. Drechsel, D. Gebeyehu, P. Simon, F. Kozlowski, A. Werner, F. Li, S. Grundmann, S. Sonntag, M. Koch, K. Leo, M. Pfeiffer, H. Hoppe, D. Meissner, N.S. Sariciftci, I. Riedel, V. Dyakonov, J. Parisi, Organic p-i-n solar cells, Applied Physics A – Materials Science and Processing 79 (1) (2004) 1–14.

[19] K. Walzer, B. Maennig, M. Pfeiffer, K. Leo, Highly efficient organic devices based on electrically doped transport layers, Chemical Reviews 107 (4) (2007) 1233–1271.

[20] A.W. Hains, J. Liu, A.B.F. Martinson, M.D. Irwin, T.J. Marks, Anode interfacial tuning via electron-blocking/hole-transport layers and indium tin oxide surface treatment in bulk-heterojunction organic photovoltaic cells, Advanced Functional Materials 20 (4) (2010) 595–606.

[21] A.M. Nardes, M. Kemerink, R.A.J. Janssen, Anisotropic hopping conduction in spin-coated PEDOT:PSS thin films, Physical Review B (Condensed Matter and Materials Physics) 76 (8) (2007) 085208–085217.

[22] L.A.A. Pettersson, S. Ghosh, O. Inganas, Optical anisotropy in thin films of poly(3,4-ethylenedioxythiophene)-poly(4-styrene sulfonate), Organic Electronics 3 (3–4) (2002) 143–148.

[23] D.S. Germack, C.K. Chan, R.J. Kline, D.A. Fischer, D.J. Gundlach, M.F. Toney, L.J. Richter, D.M. DeLongchamp, Interfacial segregation in polymer/fullerene blend films for photovoltaic devices, Macromolecules 43 (8) (2010) 3828–3836.

[24] L.A.A. Pettersson, F. Carlsson, O. Inganas, H. Arwin, Spectroscopic ellipsometry studies of the optical properties of doped poly(3,4-ethylenedioxythiophene): an anisotropic metal, Thin Solid Films 313 (1998) 356–361.

[25] J. Singh, Optical Properties of Condensed Matter and Applications, John Wiley and Sons, New York, 2006.

[26] C.M. Herzinger, B. Johs, W.A. McGahan, J.A. Woollam, W. Paulson, Ellipsometric determination of optical constants for silicon and thermally grown silicon dioxide via a multi-sample, multi-wavelength, multi-angle investigation, Journal of Applied Physics 83 (6) (1998) 3323–3336.

[27] C. Tengstedt, W. Osikowicz, W.R. Salaneck, I.D. Parker, C.H. Hsu, M. Fahlman, Fermi-level pinning at conjugated polymer interfaces, Applied Physics Letters 88 (5) (2006) 053502.

[28] X. Crispin, S. Marciniak, W. Osikowicz, G. Zotti, A.W.D. van der Gon, F. Louwet, M. Fahlman, L. Groenendaal, F. De Schryver, W.R. Salaneck, Conductivity, morphology, interfacial chemistry, and stability of poly(3,4-ethylene dioxythiophene) poly(styrene sulfonate): a photoelectron spectroscopy study, Journal of Polymer Science Part B: Polymer Physics 41 (21) (2003) 2561–2583.

[29] A.M. Higgins, S.J. Martin, P.C. Jukes, M. Geoghegan, R.A.L. Jones, S. Langridge, R. Cubitt, S. Kirchmeyer, A. Wehrum, I. Grizzi, Interfacial structure in semiconducting polymer devices, Journal of Materials Chemistry 13 (11) (2003) 2814–2818.

[30] D. Cahen, A. Kahn, Electron energetics at surfaces and interfaces: concepts and experiments, Advanced Materials 15 (4) (2003) 271–277.

[31] Heraeus, Clevios General Properties, August 2007, 2011.

compared to inorganic alkali metal compounds /Al, such as LiF/Al [13–14]. It was found out that the organic aromatic alkali metal complexes bilayer cathode could achieved high efficiency device even matching to chemical stable material such as 2-methyl-9,10-di-(2-naphthyl)-anthracene (MADN) as electron transport layer without n-doping [15–16]. The authors ascribed it to the better conductivity of alkali metal complexes and smaller LUMO differences between them and MADN. Meanwhile, in the advances within the OLED research field, the non-aromatic alkali complexes are believed to be difficult for the injection of electrons when it matches with the chemical stable material. Tris(8-quinolino-lato)aluminium (Alq_3), once a widely used electron transport materials, is no longer suitable for high-efficiency OLEDs due to its high highest occupied molecular orbital (HOMO) energy and instability in air [17–18]. If the electron can be injected from the simple alkali metal salts into the chemical stable materials, it will be beneficial for the development of novel electron transport material and constructing homogenous device.

Here we report a new alkali metal complex cesium pivalate ($(CH_3)_3CCOOCs$), which can be sublimated at low temperature and match with chemical stable materials such as MADN and chemical reactive material such as Alq_3, and also exhibits good electron injection properties.

2. Experimental section

2.1. Material and methods

All reagents and solvents were used as purchased from Aldrich and were used without further purification. ^1H NMR spectra were recorded on a Bruker-AF301 AT 400 MHz NMR spectrometer. Mass spectra were obtained on a 1100 LC/MSD Trap (positive and negative) mode. Thermal gravimetric analysis (TGA) experiments were performed under a nitrogen atmosphere on a SEIKO EXSTAR 6000 TG/DTA 6200.

2.2. Preparation of compounds

Pivalic acid (2.04 g, 20 mmol) was added into a solution of hydroxycesium (3.1 g, 20 mm) in dry $CHCl_3$ (50.0 mL). The reaction mixture was stirred at room temperature for 4 h. Then the mixture was poured into hexane. The precipitate was filtered to afford white solid powder, then they were purified by procedure sublimation in vacuum (1.0×10^{-4} Pa) at 180 °C. Yield: 85% (4 g). ^1H-NMR: (400 MHz, $CDCl_3$): δ (ppm) 4.65 (s, 9H), MS (APCI):132.79 $(m/z)^+$, 100.9$(m/z)^-$, calcd for $C_5H_9CsO_2$: 233.97.

2.3. Device fabrication

The device structure used for the evaluation of cesium pivalate complex as an electron injection material was indium-tin-oxide (ITO)/NPB (60 nm)/Alq_3 (50 nm)/$(CH_3)_3$ CCOOCs/Al (150 nm). Moreover, the device with structure of ITO/2-TNATA (60 nm)/NPB (10 nm)/Alq_3:2% C545T (40 nm)/MADN or Alq_3 (15 nm)/$(CH_3)_3CCOOCs$/Al was also constructed for the further investigation. 4,4′,4″-*tris*[*N*-(1-naphthyl)-*N*-phenylamino]triphenylamine (2-TNATA), *N*, *N*′-bis-(1-naphthyl)-*N*,*N*′-diphenyl,1,1′-biphenyl-4,4′-diamine (NPB), tris(8-quinolino-lato)aluminium (Alq_3) and 2,3,6,7-tetrahydro-1,1,7,7,-tetramethyl-1H,5H,11H-10-(2-benzothiazolyl) quinol (C545T) were used as the hole injection, hole transport, electron transport and green dopant materials, respectively. To rigorously evaluate the device performance, reference OLEDs with LiF as electron injection layer (EIL) were also prepared for the comparison. In the fabrication of devices, prior to the deposition of organic materials, the indium-tin-oxide (ITO)/glass was cleaned with a routine cleaning procedure and pretreated with UV–Ozone [19]. The structures of all the OLED devices are shown in Table 1. The current density–voltage–luminance characteristics of the devices were measured with a diode array rapid scan system using a Photo Research PR650 spectrophotometer and a computer-controlled, programmable, direct-current (DC) source. The interface electronic structure and variation in the work function were performed by XPS with Al Ka X-ray source (1486.6 eV) and UPS with He discharge lamp (UV light of 21.22 eV) (Thermo ELECTRON CORPORATION, ESCALAB 250).

3. Results and discussion

Cesium pivalate was prepared using pivalic acid and the hydroxylcesium, then further purified by train sublimation at around 180 °C, and characterized with ^1H NMR and ESI. The complex exhibits a high decomposition temperature (424 °C) (see SFig. 1) and low Ts around 180 °C, while LiF showed a high Ts of 717 °C. The Ts of $(CH_3)_3CCOOCs$ is nearly 244 °C lower than its decomposition temperature, suggesting that the complex does not decompose during the thermal evaporation process. To the best of our knowledge, there is no other non-aromatic organic salt has been reported that acts as an electron injection layer without decomposition and sublimating at so low temperature, which will be beneficial for the development new type electron injection material and process of industry.

The device with simple configuration ITO/NPB (60 nm)/Alq_3 (50 nm)/EIL/Al (150 nm) was fabricated firstly. As we know, the thickness of the EIL is critical to forming both

Table 1
Layers structure of OLED devices.

1	ITO/NPB (60 nm)/Alq_3 (50 nm)/LiF (1 nm)/Al
2	ITO/NPB (60 nm)/Alq_3 (50 nm)/$(CH_3)_3CCOOCs$ (2 nm)/Al
3	ITO/2-TNATA (60 nm)/NPB (10 nm)/Alq_3:2% C545T (40 nm)/Alq_3 (15 nm)/LiF (1 nm)/Al
4	ITO/2-TNATA (60 nm)/NPB (10 nm)/Alq_3:2% C545T (40 nm)/Alq_3 (15 nm)/$(CH_3)_3CCOOCs$ (2 nm)/Al
5	ITO/2-TNATA (60 nm)/NPB (10 nm)/Alq_3:2% C545T (40 nm)/MADN (15 nm)/LiF (4 nm)/Al
6	ITO/2-TNATA (60 nm)/NPB (10 nm)/Alq_3:2% C545T (40 nm)/MADN (15 nm)/$(CH_3)_3CCOOCs$ (2 nm)/Al

interfaces and the energy band bending region. In these research works, when Alq_3 was used as electron transport layer (ETL), the optimized thickness for $(CH_3)_3CCOOCs$ (device **2**) and LiF (device **1**) is 2 nm and 1 nm, respectively. As shown in Fig. 1a, the typical two layer device with $(CH_3)_3CCOOCs$ as electron injection material exhibits higher power efficiency than device with LiF, device power efficiency has been improved by 19% (1.97 lm/W for device **2** and 1.66 lm/W for device **1**) at the current density of 50 mA/cm^2. Also, the turn on voltage and drive voltage of the device **2** are both lower than that of the device **1** (See Fig. 1b), which means $(CH_3)_3CCOOCs$ has better electron injection ability than LiF.

Typical three layer OLED devices **3**, **4**, **5**, **6** were prepared for further evaluation of cesium pivalate as EIL (see Table 1). The EL properties of these devices are summarized in Table 2, with all devices showing good green light. As expected, device **4** shows higher power efficiency than device **3**. The improvement can be attributed to lowering of the work function of the cathode and n-doping of Alq_3 with alkali metals that were formed by the higher reactivity of $(CH_3)_3CCOOCs$ than LiF with hot Al atoms impinging on these salts during the vapor deposition. Interestingly, when MADN was used as the electron transport layer (device **6**), in the optimized thickness (2 nm), the bilayer cathodes $(CH_3)_3CCOOCs$/Al also exhibits good electron injection properties, the maximum current efficiency is up to 20 cd/A with Commission Internationale d'Eclairage ($CIE_{x,y}$) color coordinates of ($x = 0.30$, $y = 0.65$) at current density of 140 mA/cm^2. As to literatures [15–16], the MADN is an anthracene derivative which is difficult to be chemically reduced by alkali ions and be injected electron by non-aromatic salt. Is it the special properties of $(CH_3)_3CCOO^-$ ions? In order to demonstrate it, we further fabricated the devices with similar structure by varying the thickness of LiF (see SFig. 2). With the optimized LiF thickness of 4 nm, the device **5** also shows good performance despite its efficiency is lower than the device **6**. The reasonable explanation is that the optimized thickness of LiF changed dramatically (1–4 nm) when MADN was used to instead of Alq_3 as ETL and its electron inject properties to MADN were ignored by the authors [15]. In fact, cathode can inject electron through LiF into ETL for tunneling effect when the thickness of LiF arriving a reasonable level. This result indicates even when the ETL is a chemical stable material, the non-aromatic salts can also act as efficient EIL by varying the thickness of the layer. Anyway, as shown in Fig. 2b, devices **6** and **4** also show lower driving voltage than devices **5** and **3** for better electron injection ability. Meanwhile, the optimized thickness of $(CH_3)_3CCOOCs$ was stable when matching with different ETL, which means it possess more widely usage in electronic device than LiF. By the way, considering that high efficiency of device **4** and **6** may be caused by the high reactive Cs ion, the similar device structure using CsF as EIL is also tested. The result indicates that the device using $(CH_3)_3CCOOCs$ as EIL has much higher power efficiency than device with CsF when MADN was used ETL (see SFig. 3).

In order to explore the injection mechanism of MADN/LiF/Al and MADN/$(CH_3)_3CCOOCs$/Al interfaces, "electron-only" devices Al/MADN (150 nm)/EIL (x nm)/Al were fabricated. Here we use aluminum as the anode to avoid light emission, which can be assumed that only electrons are injected. Fig. 3 shows the J–V characteristics of the electron-only devices. It can be seen that the current density of the devices increases dramatically at the same voltage when the electron injection layer was changed from LiF to $(CH_3)_3CCOOCs$. Meanwhile, for LiF, the electron injection ability changed dramatically with the thickness from 1 nm

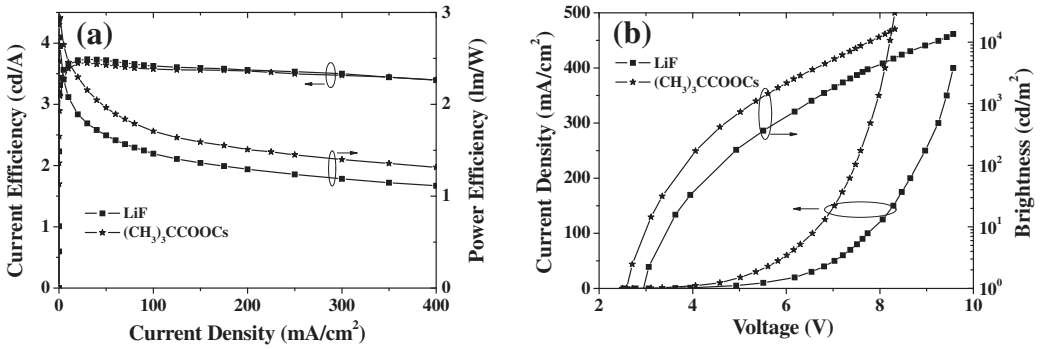

Fig. 1. (a) Dependence of efficiency on the drive current density for **device 1**, **2**; (b) J–V–B curve of the device **1**, **2**.

Table 2
The EL performance of the device **3**, **4**, **5**, **6** at the current density of 20 mA/cm^2.

Device	Voltage (V)	Voltage on (V)	CE (cd/A)	PE (lm/W)	EQE (%)	CIE
3	8.62	2.55	18.54	6.75	4.73	(0.32, 0.64)
4	7.71	2.55	19.25	7.84	5.00	(0.29, 0.65)
5	9.2	2.7	16.21	5.53	4.22	(0.30, 0.65)
6	8.27	2.52	18.38	6.98	4.79	(0.29, 0.66)

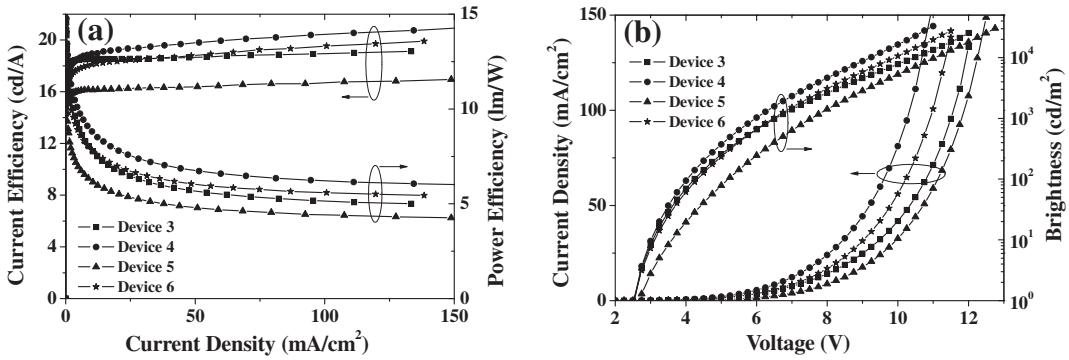

Fig. 2. (a) Dependence of efficiency on the drive current density for device **3**, **4**, **5**, **6**; (b) *J–V–B* curve of the device **3**, **4**, **5**, **6**.

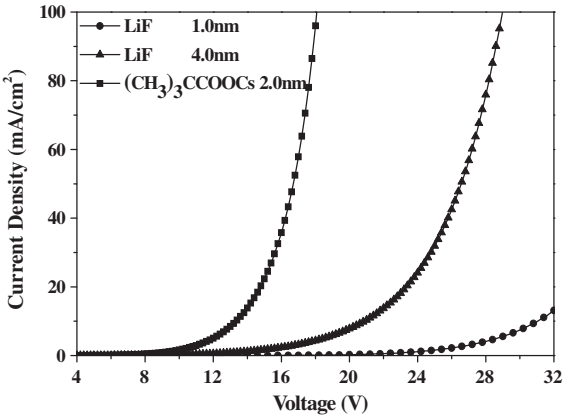

Fig. 3. Current density–voltage (*J–V*) curve of electron-only device for $(CH_3)_3CCOOCs$ and LiF in device Al/MADN (150 nm)/EIL/Al.

to 4 nm, which is consistent with the OLED performance in device **5** (SFig. 2).

Efficient film-forming properties of electron injection layer used in OLEDs are crucial for the performance of the devices, so the surface morphologies of thin films of the two EIL $(CH_3)_3CCOOCs$ and LiF were also examined. The deposited EIL films were sublimated on MADN (150 nm) with ITO as the substrate. As showed in Fig. 4, the AFM phase image of $(CH_3)_3CCOOCs$ shows a smooth and amorphous thin film, but the LiF film exhibits slight crystallization. The root-mean-square (rms) roughness of $(CH_3)_3CCOOCs$ and LiF films are 0.97 and 1.94 nm, respectively. This suggests that $(CH_3)_3CCOOCs$ possess better amorphous stability and film-forming properties than LiF, which indicates that the rigid t-butyl group influences the arrangement of the molecules in the thin films, and $(CH_3)_3CCOO^-$ ion is as excellent group in instructing electron injection materials.

To further understand the mechanism for enhanced electron injection at the atomic scale, the interface of Alq_3/$(CH_3)_3CCOOCs$, MADN/$(CH_3)_3CCOOCs$, and $(CH_3)_3CCOOCs$/Al have been studied by XPS and UPS. Fig. 5a shows the Cs $3d_{5/2}$ core level peaks of pure $(CH_3)_3CCOOCs$, Alq_3/$(CH_3)_3CCOOCs$, Alq_3/$(CH_3)_3CCOOCs$/Al film respectively. Compared with pure $(CH_3)_3CCOOCs$ film, it can be seen that after the deposition of $(CH_3)_3CCOOCs$ onto Alq_3, the peaks of Cs $3d_{5/2}$ shift towards high binding energy by 0.1 eV, which indicates that electron transfer from $(CH_3)_3CCOOCs$ to Alq_3 forming a n-doping ETL. When Al is deposited onto Alq_3/$(CH_3)_3CCOOCs$, the peaks shift towards high binding energy by 0.2 eV, indicating the n-doping is enhanced and ohmic connection may be formed at the Alq_3/Al interface because of the high reactivity of $(CH_3)_3CCOOCs$ with hot Al. Fig. 5b shows the Cs $3d_{5/2}$ core level peaks of pure $(CH_3)_3CCOOCs$,

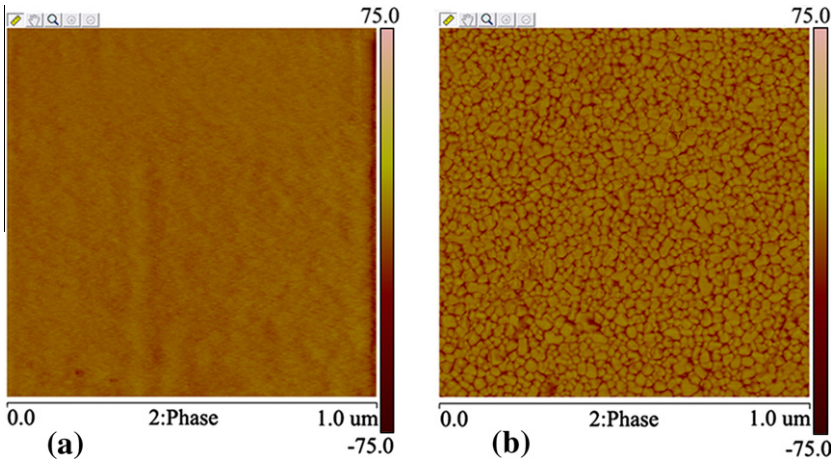

Fig. 4. AFM topographic images of $(CH_3)_3CCOOCs$ (a) and LiF (b) in thin solid films (ITO/MADN (150 nm)/EIL (5 nm).

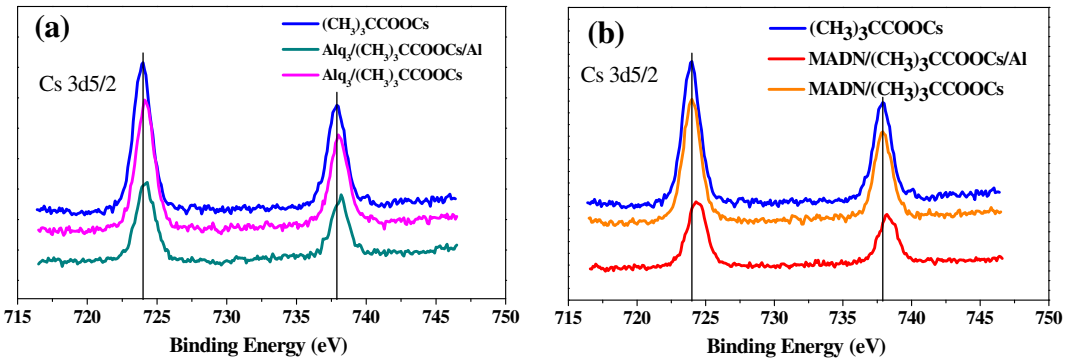

Fig. 5. XPS spectra of (a) $(CH_3)_3CCOOCs$, $Alq_3/(CH_3)_3CCOOCs$, and $Alq_3/(CH_3)_3CCOOCs/Al$ film; (b) $(CH_3)_3CCOOCs$, $MADN/(CH_3)_3CCOOCs$, and $MADN/(CH_3)_3CCOOCs/Al$ film.

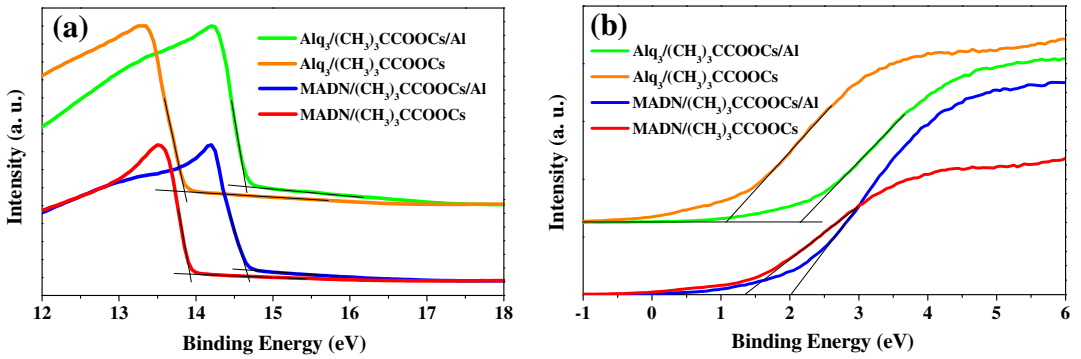

Fig. 6. UPS spectrum around (a) the secondary electron cut-off, and (b) the Fermi energy for a 2 nm thermally deposited film of $(CH_3)_3CCOOCs$, before and after the deposition of 2 nm Al.

$MADN/(CH_3)_3CCOOCs$, $MADN/(CH_3)_3CCOOCs/Al$ film, respectively. Different from that in Fig. 5a, after deposition of $(CH_3)_3CCOOCs$ onto MADN, there is no shift of the binding energy peaks, which indicate there is no electron transfer from $(CH_3)_3CCOOCs$ to MADN because MADN is a chemical stable compounds. However, when Al is deposited onto $MADN/(CH_3)_3CCOOCs$, the peaks shift towards the high binding energy by 0.3 eV, which means that electron transferring occurred and n-doping appeared. This also explains that why $(CH_3)_3CCOOCs$ has good match with the chemical stable compound and exhibits good electron injection properties in device **6**.

Fig. 6 shows the UPS spectrum for secondary electron cutoff region and the Fermi energy of the Alq_3, $MADN/(CH_3)_3CCOOCs$ (2 nm) and Alq_3, $MADN/(CH_3)_3CCOOCs$ (2 nm)/Al (2 nm), respectively. It can be clearly seen from Fig. 6a that the vacuum level shifted downwards after the deposition of Al onto $(CH_3)_3CCOOCs$ no matter using Alq_3 or MADN as ETL, which indicate the work function of cathode is reduced and the energy barrier for electron injection becomes small. Making two tangent lines along each curve in Fig. 6a, the variation of binding energy versus the intersection indicate the variation of vacuum level. It can be estimated that after the deposition of Al, the work function of cathode is reduced by about 0.82 and 0.73 eV for $Alq_3/(CH_3)_3CCOOCs$ and $MADN/(CH_3)_3CCOOCs$, respectively. By the way, it is obviously obtained from Fig. 6b that the Fermi energy of Alq_3, $MADN/(CH_3)_3CCOOCs$ (2 nm) also shifted toward a higher binding energy by about 1.1 and 0.71 eV, which indicated that the Alq_3, MADN become n-doped with the electron transfer because of the high reactivity of $(CH_3)_3CCOOCs$ with hot Al, this result is consistent with the XPS results.

4. Conclusions

In summary, a new electron injection material $(CH_3)_3CCOOCs$ was synthesized and evaluated by fabricating OLED devices using different electron transport materials in the device. $(CH_3)_3CCOOCs/Al$ cathode shows obviously enhanced electron injection ability into the electron transport material as compared to LiF/Al. Specifically, interposing of thin layer of $(CH_3)_3CCOOCs$ between the Al cathode and the MADN layer leads to a low driving voltage and higher efficiency device performance. It should be noted that, this non-aromatic alkali metal complex matching with chemical stable electron transport material properties was never be reported. At last, the EIL material can be sublimated under vacuum at about 180 °C, which is beneficial for the process of device fabrication. Further investigation on the mechanism of $(CH_3)_3CCOOCs$ as efficient EIL matching with MADN, and effect of $(CH_3)_3CCOOCs$ in the homojunction devices is ongoing.

Acknowledgements

This work was supported by the central allocation grant from Dong hu New & High Technology Development Zone of Wuhan City, the Research Grants Council of Hong Kong SAR (GHP/057/05) and Faculty Research Grant (FRG/05-06/II-43) of HKBU.

Appendix A. Supplementary data

Supplementary data associated with this article can be found, in the online version, at doi:10.1016/j.orgel.2011.08.005.

References

[1] Y.J. Pu, M.S. Miyamoto, K.I. Nakayama, T. Oyama, Y. Masaaki, J.J. Kido, Org. Electron. 10 (2009) 228.
[2] J.S. Huang, Z. Xu, Y. Yang, Adv. Func. Mater. 17 (2007) 1966.
[3] C.W. Tang, S.A. VanSlyke, Appl. Phys. Lett. 51 (1987) 913.
[4] Y. Li, D.Q. Zhang, L. Duan, R. Zhang, L.D. Wang, Y. Qiu, Appl. Phys. Lett. 90 (2007) 012119.
[5] L.S. Hung, C.W. Tang, M.G. Mason, Appl. Phys. Lett. 70 (1997) 152.
[6] G.E. Jabbour, B. Kippelen, N.R. Armstrong, N. Peyghambarian, Appl. Phys. Lett. 73 (1998) 1185.
[7] C.H. Lee, Synth. Met. 91 (1997) 125.
[8] Y.J. Yi, S.J. Kang, K. Cho, J.M. Koo, K. Han, K.J. Park, M.K. Noh, C.N. Whang, K.H. Jeong, Appl. Phys. Lett. 86 (2005) 213502.
[9] C. Ganzorig, K. Suga, M. Fujihira, Mater. Sci. Eng. B85 (2001) 140.
[10] P.C. Kao, J.H. Lin, J.Y. Wang, C.H. Yang, S.H. Chen, Synth. Met. 160 (2010) 1749.
[11] C. Ganzorig, M. Fujihira, Appl. Phys. Lett. 85 (2004) 4774.
[12] C. Schmitz, H.W. Schmidt, M. Thelakkat, Chem. Mater. 12 (2000) 3012.
[13] K. Xie, J. Qiao, L. Duan, Y. Li, D.Q. Zhang, G.F. Dong, L.D. Wang, Y. Qiu, Appl. Phys. Lett. 93 (2008) 183302.
[14] S.H. Kim, J. Jang, J.Y. Lee, Appl. Phys. Lett. 91 (2007) 103501.
[15] D.Y. Zhou, S.D. Cai, W. Gu, L.S. Liao, S.T. Lee, Appl. Phys. Lett. 97 (2010) 223302.
[16] X. Sun, D.Y. Zhou, L.H. Qiu, L.S. Liao, F. Yan, J. Phys. Chem. C 115 (2011) 2433.
[17] H. Aziz, Z.D. Popovic, S. Xie, A. Hor, N. Hu, C.P. Tripp, G. Xu, Appl. Phys. Lett. 72 (1998) 756.
[18] L.S. Liao, X.H. Sun, L.F. Cheng, N.B. Wong, C.S. Lee, S.T. Lee, Chem. Phys. Lett. 333 (2001) 212.
[19] L. Wang, Z.Y. Wu, W.Y. Wong, K.W. Cheah, H. Huang, C.H. Chen, Org. Electron. 12 (2011) 595.

to limited exciton dissociation [21]. On the other hand, having eliminated phase separation as a morphological parameter of consideration, these devices represent model systems with which we can probe how constituent crystallization affects device characteristics. Yet, planar-heterojunction polymer solar cells, especially those derived from solution processing [16–20], are notoriously difficult to fabricate as the need to create pristine interfaces between the organic semiconductors necessitates solvent orthogonality during deposition.

In this paper, we employ a combination of soft-contact lamination and polymer transfer techniques [16,17,22–24] to fabricate planar-heterojunction polymer solar cells having solution-processed components. More specifically, the electron donor and electron acceptor are deposited from solution onto independent substrates and processed in isolation before they are laminated to establish the charge transfer interface. Thermal annealing is intentionally avoided after lamination to prevent constituent interdiffusion [25]. This procedure obviates the need for solvent orthogonality during the deposition of the active layers. More importantly, it allows the independent processing of the electron donor from the electron acceptor; the constituent organic semiconductors can thus be subjected to different thermal annealing conditions before they are brought together. The ability to independently process the individual organic semiconductor layers in polymer solar cells having one pristine exciton dissociation interface provides an opportunity for us to elucidate how such processing conditions influence structural development, and uniquely allows us to correlate quantitative structural changes in the active layers with planar-heterojunction device performance without having to take complications associated with phase separation into account.

2. Experimental

The experiments reported herein were conducted with commonly studied poly(3-hexyl thiophene), P3HT, as the polymer donor and [6,6]-phenyl-C_{61}-butyric acid methyl ester, PCBM, as the electron acceptor. To elucidate how processing history influences constituent crystallization of P3HT and PCBM, and to assess how changes in their crystallinity affect device performance, we fabricated planar-heterojunction devices comprising P3HT and PCBM by soft-contact lamination and polymer transfer [16,17,22–24]. We have previously shown this soft-contact lamination and polymer transfer procedure to be highly versatile; planar-heterojunction devices comprising P3HT and a polymer acceptor of poly{[*N*,*N*′-bis(2-octyldodecyl)-naphthalene-1,4,5,8-bis(dicarboximide)-2,6-diyl]-alt-5,5′-(2,2′-bithiophene)}, P(NDI2OD-T2), have also been successfully fabricated [16].

Starting with the inverted device geometry [26,27], Fig. 1 illustrates schematically the procedure by which we fabricated P3HT/PCBM planar-heterojunction polymer solar cells. Pre-patterned ITO on glass substrates (15 Ω/sq.; Colorado Concept Coatings) were cleaned by sonication in acetone and isopropyl alcohol for 10 min each. A 1 wt.% titanium isopropoxide ($Ti[OCH(CH_3)_2]_4$; Aldrich; 99.999%) in isopropyl alcohol solution was then spin coated uniformly on the pre-cleaned ITO on glass substrates at 3000 rpm for 30 s. Hydrolysis at room temperature for 1 h and at 170 °C for 10 min resulted in a 40 nm-thick titania electron transport layer [26–29]. A 1 wt.% PCBM (American Dye Source, Inc.) solution in chloroform was spin coated directly on the titania electron transport layer at 3000 rpm for 60 s to create the electron acceptor layer. This procedure completed the construction of the bottom half of the planar-heterojunction polymer solar cells. To create the top half of the polymer solar cells, we first spin coated a 1.5 wt.% P3HT (Merck Chemicals, Ltd.) solution prepared in chlorobenzene at 500 rpm for 60 s on UV-ozone treated silicon wafers. This P3HT layer was then placed in direct contact with a featureless poly(dimethyl siloxane), PDMS, stamp (Dow Corning Sylgard 184 formulation). The thicknesses of the P3HT and PCBM layers were separately optimized; they were kept constant at 160 and 95 nm, respectively, in this present study. The entire assembly of P3HT sandwiched between PDMS and the silicon wafer was then immersed in water. Since water selectively wicks into the interface between hydrophobic P3HT and hydrophilic silicon [22], removal of the stamp subsequent to immersion resulted in the complete transfer of P3HT from

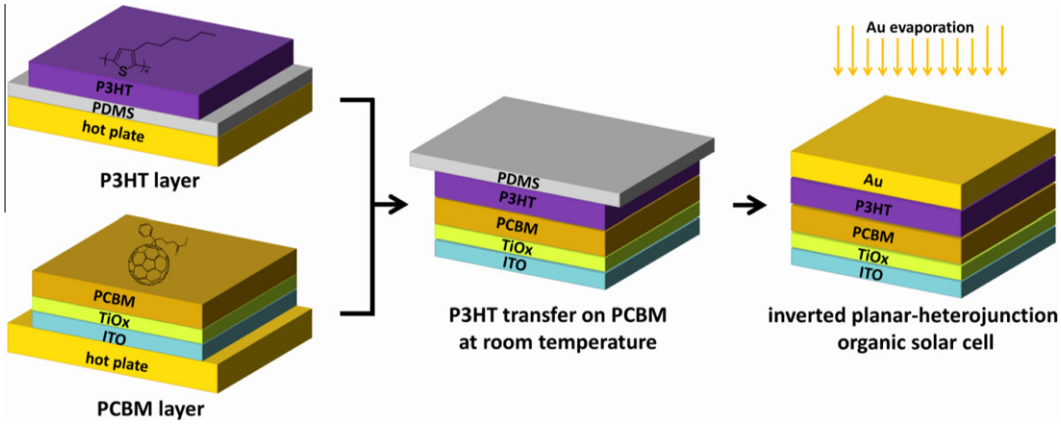

Fig. 1. Schematic illustration for fabricating planar-heterojunction polymer solar cells. The P3HT and PCBM layers are deposited and processed independently before they are brought together at room temperature to make electrical contact.

the silicon wafer onto PDMS. We then subjected the two components of the planar-heterojunction device – PCBM on titania and P3HT on PDMS – to independent thermal annealing at 170 °C for varying durations (from 1 to 10 min) in air and in a nitrogen-filled glove box before they were laminated against each other to establish the electron donor-electron acceptor charge transfer interface. Upon lamination, the PDMS stamp was carefully removed to complete the transfer of the P3HT layer onto PCBM. We can routinely transfer P3HT that is 2.5 cm × 1.5 cm onto PCBM though larger areas are possible. XPS measurements conducted on the polymer surface upon removal of the PDMS stamp reveal an absence of silicon signal; we therefore surmise that transfer of residual siloxane oligomers from PDMS to the polymer surface is negligible. Finally, we thermally evaporated 100 nm thick gold through a stencil mask on the active layer to define the anode with which holes are collected. The active area of our planar-heterojunction polymer solar cell is 0.18 cm^2. All the devices were tested in air. Given the rapid diffusion of PCBM into amorphous P3HT even at modest temperatures [25], the planar-heterojunction devices were not subjected to any additional thermal annealing after soft-contact lamination and polymer transfer to maintain the pristine interface between electron donor and electron acceptor.

Planar-heterojunction polymer solar cells were tested with a Keithley Model 2400 source measurements unit under AM 1.5 G 100 mW/cm^2 illumination. Current density–voltage (J–V) characteristics were acquired 10 min after flood illumination to fill shallow electron traps in the titania electron transport layer [26].

To characterize the structural changes associated with the constituent organic semiconductors upon thermal annealing, grazing-incidence X-ray diffraction (GIXD) was carried out on thin films of P3HT and PCBM prepared under the same conditions employed for device fabrication. GIXD measurements were conducted on beam line 11-3 at the Stanford Synchrotron Radiation Lightsource with an incident angle of 0.11° and an incident X-ray energy of 12.7 keV. An area detector was used to acquire the scattered X-rays. In addition to X-ray diffraction in the grazing geometry, we also acquired local specular scans on the P3HT (100) reflection (q = 0.37 $Å^{-1}$) by rocking the samples about its corresponding Bragg angle – from 1.55° to 1.80° – to capture all scattered intensity. For both grazing incidence and local specular data, the diffracted intensity was first background-subtracted before it was integrated along an annular region that contains the reflection of interest to derive the one-dimensional intensity as a function of the polar angle, χ. This one-dimensional trace is known as a pole figure. The pole figures extracted from the grazing incidence data and the local specular data were then stitched together to obtain the full pole figure [30,31], which we used to quantify the relative crystallinity of P3HT [30,32]. The polarization correction factor estimated for the P3HT (100) reflection is near unity (>0.99), so polarization correction was not applied to our analysis. The absorbance correction was also omitted since X-ray absorption in thin polymer films is small [30]. The full pole figure was then normalized with sample thickness to allow for comparison between samples [31]. The relative crystallinity is proportional to the integrated intensity according to $D_0C \propto 2\pi \int_0^{\pi/2} I(\chi)\sin(\chi)d\chi$. Local specular scans, however, were only acquired for P3HT and not PCBM because the incident angle required to acquire local specular data on PCBM is too high (q = 1.4 $Å^{-1}$; corresponding to a Bragg angle of 6.2°) [32]. Experiments conducted at such incident angles are compounded by non-negligible background contributions due to substrate penetration of X-rays and the lower intensity from the film resulting from the large incidence angle [32].

To assess charge transport along the vertical and lateral directions of PCBM thin films, we also fabricated single-carrier diodes and thin-film transistors comprising PCBM, respectively. Single-carrier diodes were fabricated and tested on pre-patterned ITO on glass according to previously published procedures [33,34]. Pre-patterned ITO on glass substrates were cleaned by sonication in acetone followed by in isopropyl alcohol for 10 min each, upon which the substrates were subjected to UV-ozone exposure for 10 min. We then spin coated an aqueous dispersion of poly(ethylene dioxythiophene) that is templated on poly(styrene sulfonate), PEDOT:PSS (Clevios P; used as-purchased from H.C. Starck), at 2000 rpm for 120 s. The PEDOT:PSS layer, ca. 140 nm thick, was then subjected to thermal annealing at 150 °C for 20 min. Following thermal annealing, a 1 wt.% PCBM solution in chloroform was spin coated at 3000 rpm for 60 s, resulting in an active layer that is 95 nm thick. To mirror the thermal treatments imposed during planar-heterojunction device fabrication, PCBM was also subjected to thermal annealing at 170 °C for varying durations in air and in a nitrogen-filled glove box. Thermal evaporation of 1 nm thick LiF and 40 nm aluminum completed the fabrication of single-carrier diodes comprising PCBM. These diodes have the same active area as the planar-heterojunction devices. These devices were tested with a Keithley Model 2400 source measurement unit under nitrogen to prevent oxidation of the aluminum contacts. Thin-film transistors comprising PCBM were fabricated in the bottom-gate, top-contact geometry using highly doped silicon and 300 nm thick silicon dioxide (Process Specialties, Inc.) as gate and gate dielectric, respectively. The wafers were initially subjected to a sequential solvent cleaning of sonication in acetone and isopropyl alcohol for 10 min each, and then exposed to UV-ozone for 10 min. To passivate the silicon dioxide surface, we spin coated 1,1,1,3,3,3-hexamethyldisilazane, HMDS (Seidler Chemical) on the pre-cleaned wafer at 3000 rpm for 60 s. The electrically-active channel was created by spin coating a 1 wt.% PCBM solution in chloroform at 3000 rpm for 60 s on the HMDS-treated surface. The PCBM layer was subjected to thermal annealing analogous to conditions imposed during planar-heterojunction solar cell and single-carrier diode fabrication. After thermal annealing, the substrates were transferred into a nitrogen-filled glovebox in which 60 nm of aluminum was thermally evaporated through a stencil mask as source and drain electrodes. The channel length and width were 100 and 1000 μm, respectively. Electrical characterization of PCBM thin-film transistors was carried out using an Agilent 4145B Parameter Analyzer in the same nitrogen-filled glove box to avoid oxidation of aluminum contacts.

Ultra-violet photoelectron spectroscopy (UPS) measurements were carried out on thin films of as-cast and thermally annealed PCBM. Thermal annealing occurred at 170 °C for 10 min either in air or in a nitrogen-filled glovebox. The base pressure of the ultrahigh vacuum chamber that is equipped with a He discharge lamp and a double-pass cylindrical mirror analyzer was 2×10^{-10} Torr. The photon energy for UPS measurements was 21.2 eV for HeI and 40.8 eV for HeII. These measurements provided estimates for the work function and the energy level of the highest occupied molecular orbital (HOMO) of PCBM. We also assessed the electronic band gap of PCBM thin films before and after thermal annealing by carrying out optical spectroscopy measurements on as-cast and thermally annealed PCBM across a UV–vis/NIR spectral range of 190–1100 nm using an Agilent 8453 spectrophotometer with 1 nm resolution. Thermal annealing was carried out in air or in nitrogen for 10 min.

3. Results and discussion

Fig. 2 shows the current density–voltage (J–V) characteristics of P3HT/PCBM planar-heterojunction polymer solar cells that were fabricated by soft-contact lamination and polymer transfer. Here, we explored the influence of thermal annealing of P3HT for varying durations in air and in nitrogen on solar cell device characteristics. As-spun as well as thermally annealed thin P3HT films were thus transferred onto unannealed PCBM according to the procedures outlined above and shown schematically in Fig. 1. P3HT films were annealed at 170 °C for 1, 5, and 10 min in air (top portion of Fig. 2a) and in a nitrogen-filled glovebox (bottom portion of Fig. 2a) prior to transfer. As-spun P3HT spontaneously contacted the underlying PCBM film upon transfer; thermally annealed P3HT films were slightly stiffer and required some external pressure to establish contact with PCBM upon transfer. The J–V characteristics of a representative planar-heterojunction polymer solar cell having unannealed P3HT and PCBM are shown with open squares in Fig. 2a. Of five devices tested, the open-circuit voltage (V_{oc}) was -0.41 ± 0.01 V and the short-circuit current density (J_{sc}) was 0.73 ± 0.01 mA/cm^2, resulting in an average efficiency of 0.13 ± 0.01%. While the V_{oc} of these devices are lower than those of conventional bulk-heterojunction devices [35,36], it is comparable to the V_{oc} reported for bulk-heterojunction polymer solar cells constructed in the inverted architecture tested immediately after device fabrication [26]. Previously, we found that prolonged exposure (>days) of inverted solar cells to air induces oxidation of P3HT, effectively increasing V_{oc} [26]. We believe this mechanism will be at play in our inverted planar-heterojunction devices as well. To eliminate potential complications due to extensive oxidation of P3HT in our present study, however, all the planar-heterojunction devices were tested immediately after fabrication. We further note that these planar-heterojunction devices exhibit efficiencies that are significantly lower than those typically reported for P3HT:PCBM bulk-heterojunction solar cells, presumably due to an extensive reduction in the density of donor–acceptor interface at which exciton dissociation and charge transfer occur in the planar-heterojunction

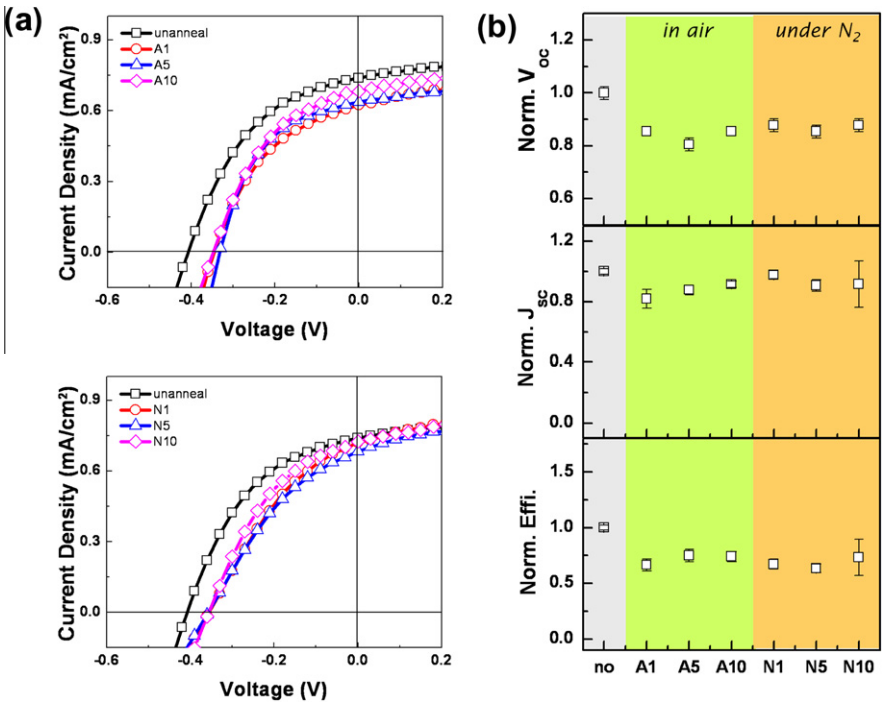

Fig. 2. (a) J–V characteristics of P3HT/PCBM planar-heterojunction solar cells in which the P3HT layer was annealed at 170 °C for 0, 1, 5 and 10 min in air (a; top graph) and in a nitrogen-filled glovebox (a; bottom graph) prior to polymer transfer. Normalized device characteristics are summarized in (b).

architecture [21]. Despite their low efficiencies, these devices represent model devices with which we can elucidate processing–structure–function relationships of P3HT and PCBM.

The *J–V* characteristics of planar-heterojunction devices comprising transferred P3HT that had been thermally annealed in air and in nitrogen are represented by open circles (annealing for 1 min at 170 °C), open triangles (5 min) and open diamonds (10 min). The characteristics of devices comprising thermally annealed P3HT appear to be largely independent of the processing history imposed upon P3HT prior to transfer. Specifically, of all devices tested, the average V_{oc} = 0.35 ± 0.01 V; the average J_{sc} = 0.66 ± 0.04 mA/cm^2, resulting in an average efficiency of 0.092 ± 0.006%. The normalized device characteristics are plotted in Fig. 2b; error bars represent standard deviations from five devices tested. We observe a small difference (about 10%) between the V_{oc} of devices comprising as-cast P3HT and those containing thermally annealed P3HT; this difference resulted in the lower efficiency we observe with devices having thermally annealed P3HT in Fig. 2b. We speculate that this difference may arise from changes in the dipole strength at the interface of as-spun and annealed P3HT with PCBM or to conformational changes in P3HT. Given that the V_{oc} change is small and the UPS resolution is 0.1 eV, we were not able to directly measure the changes in the energy level of P3HT. Consistent with our speculation, however, we previously measured interfacial dipoles as high as 0.3–0.4 eV at the interface between P3HT and PCBM domains in bulk-heterojunction active layers [37,38]. The J_{sc} of devices comprising thermally annealed P3HT is statistically the same as that extracted from devices comprising as-spun P3HT. This observation was initially surprising given that the thermal annealing of bulk-heterojunction polymer solar cells is reported to increase J_{sc} due to increases in P3HT and PCBM crystallinities within the active layers [16,39,40].

To understand why the J_{sc} of our planar-heterojunction solar cells does not change with P3HT annealing, we carried out GIXD experiments on thin films of P3HT prepared under the same conditions as those that were transferred for device fabrication. Fig. 3a contains X-ray diffraction patterns acquired on an as-cast P3HT thin film, as well as on those that were thermally annealed at 170 °C in nitrogen for 1, 5, and 10 min. The X-ray diffraction patterns look qualitatively similar; we observe intensities along the meridian at q = 0.37, 0.74, and 1.11 Å^{-1} in all P3HT films corresponding to the (100), (200) and (300) reflections of the lamellar stacks of P3HT; these lamellae are oriented in-plane, with the stacking periodicity out-of-plane [41]. Integrating the intensities in the X-ray diffraction patterns radially yielded the 1-D X-ray traces in Fig. 3b. The (h00) reflections, along with the (010) reflection of P3HT are highlighted for clarity. All the P3HT films are semi-crystalline, as evinced by the multiple higher-order reflections present in the X-ray diffraction traces. To quantify the relative crystallinity of the P3HT films, we acquired data in the local specular geometry and constructed full pole figures at q = 0.37 ± 0.1 Å^{-1} corresponding to the (100) reflection of P3HT. This procedure allows us to capture all the scattered intensities from the P3HT crystallites within the sample volume; see full pole figures in Supplementary material (Fig. S1). As such, the integrated intensities of the full pole figures provide relative

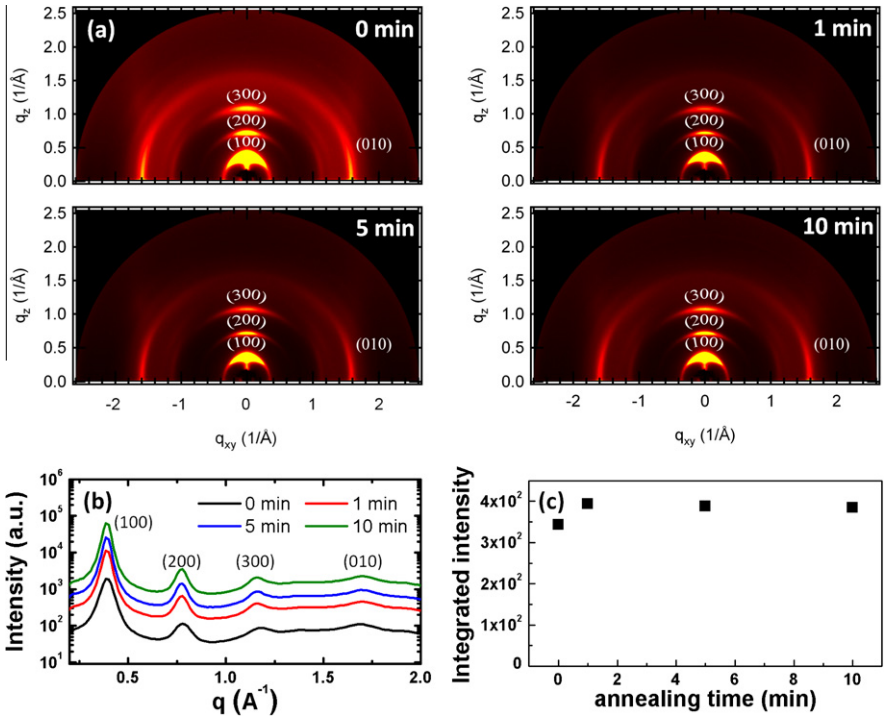

Fig. 3. (a) GIXD patterns of P3HT annealed at 170 °C for 0, 1, 5 and 10 min in nitrogen and (b) 1-D X-ray traces acquired by radially averaging across the X-ray patterns. (c) Integrated intensity of the full pole figure collected on the (100) reflection of P3HT indicates relative crystallinity in each film.

comparisons for the extent of crystallinity of P3HT films that were annealed for varying durations [30–32]. The integrated intensities extracted from the full pole figures are plotted in Fig. 3c. The integrated intensity increases by 15% when the P3HT film is subjected to thermal annealing at 170 °C for 1 min, reflecting a small increase in the extent of P3HT crystallinity. Subsequent annealing for longer durations does not alter the extent of crystallinity significantly, as indicated by the near-constant integrated intensity of the full pole figures. This observation is somewhat different from some reports of thermal annealing of bulk-heterojunction active layers comprising P3HT and PCBM where the crystallinity of P3HT has been reported to increase significantly [16,39,40]; the extent of which depends on the solvent from which the active layers were cast [42]. Rather, our experiments indicate that as-spun P3HT exhibits non-negligible crystallinity. Subjecting the thin film to a 1 min annealing increases P3HT crystallinity modestly, beyond which extended annealing does not further improve P3HT crystallinity. Our experiments thus suggest that P3HT – in the absence of PCBM – crystallizes readily and quickly upon solvent evaporation when cast from chlorobenzene; subsequent annealing does not significantly increase its crystallinity. Accordingly, the planar-heterojunction devices comprising these films exhibit near-constant J_{sc}'s that are independent of the duration P3HT was annealed.

The ability to independently process the constituent layers of the planar-heterojunction device also provides us with the opportunity to examine the effects of thermally annealing PCBM on solar cell performance. In this set of experiments, as-spun P3HT was transferred onto either as-spun PCBM or thermally annealed PCBM on titania for device construction. Analogous to the example above, PCBM was annealed at 170 °C for 1, 5, and 10 min in air and in a nitrogen-filled glovebox prior to P3HT transfer. We observe intimate molecular contact upon the transfer of P3HT onto both unannealed and annealed PCBM; the application of external pressure was thus not necessary.

Fig. 4a contains *J–V* characteristics of representative planar-heterojunction solar cells in which PCBM has been thermally annealed at 170 °C for varying durations in air (top graph) and in nitrogen (bottom graph). The *J–V* characteristics of the representative device having as-spun PCBM are shown as open squares; the *J–V* characteristics of representative devices comprising PCBM thin films that had been annealed for 1, 5, and 10 min are shown as open circles, triangles and diamonds, respectively. Of five devices with unannealed PCBM tested, the average J_{sc} was 0.73 ± 0.01 mA/cm^2 and the average V_{oc} was −0.41 ± 0.01 V, resulting in an average efficiency of 0.13 ± 0.01%. Unlike thermal annealing of P3HT, thermal annealing of PCBM results in drastically different device characteristics. The J_{sc} of these devices, for example, decreased drastically to 0.33 ± 0.01, 0.076 ± 0.003 and 0.049 ± 0.001 mA/cm^2 for devices in which PCBM was thermally annealed in air for 1, 5 and 10 min, respectively, prior to lamination. Accordingly, the fill factor for these devices also decreased with increasing annealing times (see Fig. S2 in Supplementary material). Planar-heterojunction devices in which PCBM was thermally annealed in nitrogen for 1 min showed a modest increase in J_{sc}; the J_{sc} decreased progressively upon subsequent annealing. Annealing PCBM in nitrogen thus

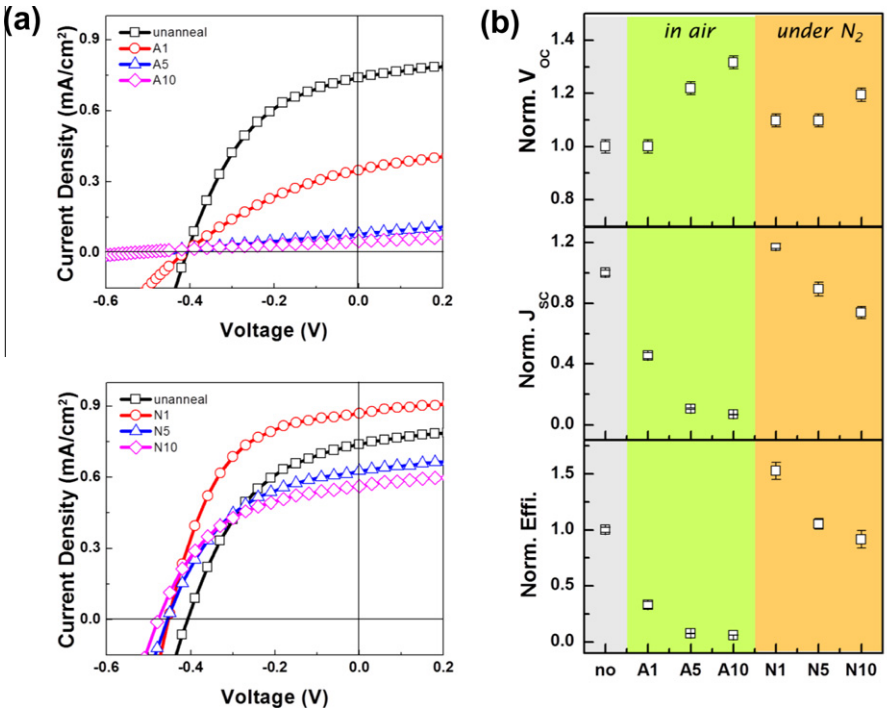

Fig. 4. (a) *J–V* characteristics of P3HT/PCBM planar-heterojunction solar cells in which the PCBM layer was annealed at 170 °C in air (a; top graph) and in nitrogen (a; bottom graph) for 0, 1, 5 and 10 min prior to polymer transfer. Normalized device characteristics are summarized in (b).

appears to impose the same fate to the devices as annealing PCBM in air, although the decrease in J_{sc} is less pronounced, presumably because irreversible chemical oxidation is avoided [43,44]. Compared to devices in which the processing of P3HT was explored, the present planar-heterojunction devices also show changes in V_{oc}'s when thermally annealed PCBM thin films are employed as the electron-accepting layer. The incorporation of PCBM that had been thermally annealed in air resulted in planar-heterojunction devices with increased V_{oc}. This trend of increasing V_{oc} is also observed in devices in which PCBM was thermally annealed in nitrogen, albeit to a smaller extent. For ease in comparison, we have plotted the normalized device characteristics in Fig. 4b. Given that the variations in J_{sc} (and accordingly, variations in fill factor) are more dramatic with thermal annealing of PCBM, the efficiencies of these devices mirror the trends of decreasing J_{sc}, as shown in the bottom panel of Fig. 4b. Collectively, the testing of our devices indicates the characteristics of our planar-heterojunction solar cells are more sensitive to the processing of PCBM compared to that of P3HT. This qualitative observation is in agreement with our prior study during which the structuring of PCBM and P3HT was quantified for a myriad of different processing conditions [32].

Thermal annealing of PCBM thin films prior to lamination can cause surface roughening due to structural rearrangement (e.g., crystallization). To verify that the decrease in J_{sc} is not due to poor electrical contact at the organic–organic charge transfer interface attributable to surface roughness upon P3HT transfer, we measured the J_{sc} of these same devices with increasing illumination intensity. Over the range of illumination intensity examined (50–250 mW/cm^2), we observe the same linear intensity dependence for all our devices regardless of PCBM annealing conditions; see Fig. S3 in Supplementary material. This observation strongly suggests that current generation in our devices is not limited by differences in exciton dissociation at the organic–organic planar-heterojunction interface. Rather, the decrease in J_{sc} observed in Fig. 4 stems from structural changes that are brought about by thermal annealing the electron acceptor thin films.

To quantify the structural development that has occurred with thermal annealing of PCBM, we turned to GIXD. Fig. 5 contains GIXD images acquired on PCBM thin films that were prepared under nitrogen using the same conditions as those in planar-heterojunction devices. The X-ray diffraction pattern acquired on unannealed PCBM appears featureless. After thermal annealing at 170 °C for 1 min, we observe the emergence of a broad halo at 1.4 Å^{-1} (see Fig. S4 in Supplementary material). Although this broad halo suggests that the film is largely amorphous, we cannot preclude the beginnings of nanoscale (2–3 nm sized) crystallites formation [45]. That the J_{sc} increases with a 1 min annealing in nitrogen is consistent with enhanced charge transport stemming from the presence of nanocrystallites of PCBM. This broad halo sharpens with further annealing of PCBM. Strikingly, we observe the development of six sharp spots coexisting with the amorphous halo in the X-ray diffraction pattern acquired on PCBM annealed for 10 min. The series of X-ray diffraction patterns in Fig. 5 therefore suggest progressive crystallization of PCBM with thermal annealing; the 1-D radially integrated plots of these X-ray diffraction patterns are provided in Supplementary material for completeness (Fig. S5). This crystallization behavior is consistent with that of PCBM cast from chloroform reported by Verploegen et al. [13]. Unfortunately, further quantification of the relative extent of PCBM crystallinity is challenging as local specular scans cannot be effectively carried out because the required X-ray incident angle of 6.2° brings about large background contributions [32]. There remain, however, large qualitative differences among the X-ray patterns presented in Fig. 5. In particular, the X-ray pattern acquired on PCBM that had been annealed for 10 min shows that the PCBM crystallites in this film are preferentially oriented. Tracing the scattered intensity at $q = 1.4$ Å^{-1} (through the sharp peaks) azimuthally reveals increases in intensity at $\chi = \pm 26°$ from the meridian (see Supplementary material, Fig. S4). While we are unable to determine the crystal structure and preferential orientation adopted by PCBM with only one diffraction peak, we note that the peak position observed here is consistent with one of the peaks observed of crystallized PCBM in

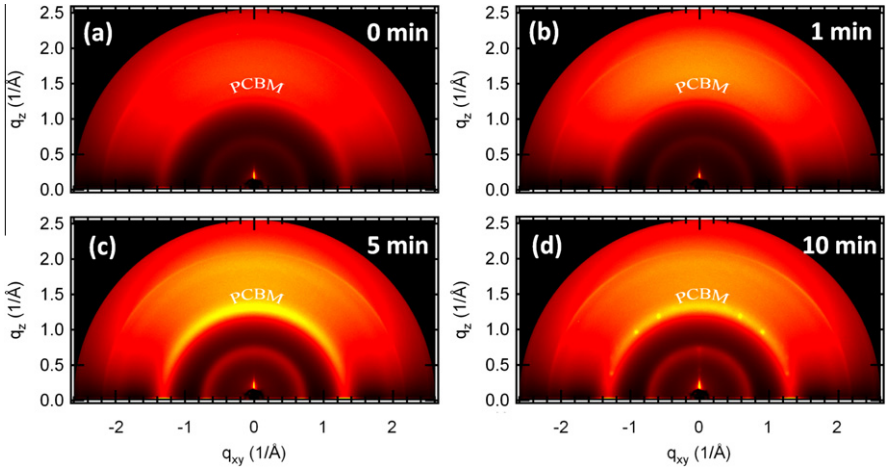

Fig. 5. GIXD images of PCBM layers (a) before and (b–d) after thermal annealing at 170 °C in nitrogen for (b) 1 min, (c) 5 min and (d) 10 min.

bulk-heterojunction polymer solar cells comprising P3HT and PCBM [16]. The sharpness of the spots in our present X-ray diffraction patterns, however, suggests that PCBM is substantially more oriented in the absence of P3HT. We further speculate that it may be the preferential orientation of the crystalline portions of PCBM that dramatically hinders vertical charge transport in our planar-heterojunction devices, ultimately resulting in reduced J_{sc}.

To validate our hypothesis, we evaluated the vertical charge transport of similarly prepared PCBM in single-carrier diodes. PCBM single-carrier diodes were fabricated according to previously published procedures and the electron mobility of PCBM was evaluated in the space charge limited current regime; representative data from one such single-carrier diode and its corresponding fit to extract out-of-plane electron mobility is shown in Fig. S6 of Supplementary material [33,34]. For reference, we also prepared thin-film transistors comprising similarly processed PCBM as active channels to evaluate its in-plane charge transport. The extracted electron mobility from these experiments is summarized in Fig. 6. Of four single-carrier diodes comprising unannealed PCBM, the average electron mobility is $1.56 \times 10^{-3} \pm 0.59 \times 10^{-3}$ cm^2/V s. With thermal annealing in air, we observe a progressive decrease in electron mobility. With thermal annealing in nitrogen, we observe first an increase in electron mobility before subsequent decreases upon further annealing. The electron mobility trends of the diodes comprising PCBM mirror those of the J_{sc} observed in our planar-heterojunction devices exactly. We thus attribute the initial increase in electron mobility in diodes to the development of nanocrystallinity of PCBM on annealing in nitrogen for 1 min; subsequent annealing induces a preferential orientation of PCBM crystals that hinders charge transport in the vertical. The absolute magnitude of the electron mobility (and the J_{sc} of planar-heterojunction devices in Fig. 5) is uniformly lower in diodes in which PCBM was annealed in air as opposed to in nitrogen, presumably because of chemical oxidation of PCBM at ambient conditions [43,44]. Interestingly, thin-film transistors comprising PCBM that were processed under nominally the same conditions exhibit comparable electron mobilities. Given that the mobilities of thin-film transistors can easily depend on dielectric treatment and the details of processing conditions, it is difficult for us to assign any real significance to the difference in the absolute values of the electron mobilities extracted single-carrier diodes and transistors. Collectively, our experiments indicate that thermal annealing of thin films of PCBM induces large-scale structural rearrangement; PCBM crystallizes with annealing at 170 °C and adopts a preferential orientation that we believe to hinder charge transport in the vertical, but not the lateral direction, on further annealing. Given that charge transport in thin-film transistors only occurs in the several nanometers near the dielectric surface [46], we thus speculate that the transistor electron mobility is less sensitive to PCBM crystallinity that develops on thermal annealing in the bulk of the film. The results in Fig. 6 also indicate that the electron mobility extracted from thin-film transistors – unlike that extracted from single-carrier diodes or planar-heterojunction solar cells – are largely independent of PCBM exposure to air. Again, since charge transport in thin-film transistors only occurs near the dielectric surface [46], our results suggest that the thermal annealing conditions in our study do not induce chemical oxidation of PCBM at the charge transport interface.

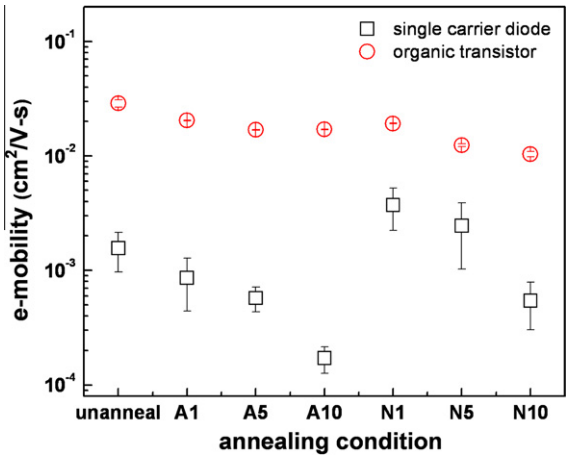

Fig. 6. Electron mobility of PCBM extracted from single-carrier diodes and thin-film transistors. PCBM was annealed at 170 °C in air and in a nitrogen-filled glovebox for varying times.

To assess the changes in V_{oc} observed in Fig. 4, we carried out UPS experiments on thin films of PCBM. Fig. 7a contains UPS data acquired on thin films of PCBM that were unannealed, and those that were annealed at 170 °C in air and in nitrogen for 10 min. UPS measurements on unannealed PCBM indicate a cut-off energy of 16.8 eV and a highest occupied molecular orbital (HOMO) edge that is 2.0 eV below the Fermi level (E_F), as extracted from the intersection between the steepest slope and the baseline. UPS measurements conducted on thermally annealed PCBM reveal similar shifts in both the cut-off energy and the HOMO edge. PCBM that had been annealed in air exhibits a cut-off energy of 16.5 eV and a HOMO edge of 1.7 eV below E_F. Thermal annealing in nitrogen as opposed to air also resulted in comparable shifts; the cut-off energy and the HOMO edge were estimated to be 16.4 and 1.7 eV below E_F, respectively. The energy levels of PCBM before and after thermal annealing are schematized in Fig. 7b. We observe a shift in the ionization potential of PCBM with thermal annealing. Optical spectroscopy experiments on the same films reveal the same absorption spectra for PCBM thin films before and after thermal annealing at 170 °C for 10 min in air and in nitrogen (see Fig. S7 in Supplementary material); these experiments indicate that the electronic band gap of PCBM is not altered with thermal annealing. Collectively, the UPS and absorption spectroscopy experiments thus imply a shift in the lowest unoccupied molecular orbital (LUMO) of PCBM corresponding to the shift observed in the HOMO with respect to E_F on thermal annealing. If this trend holds up when PCBM is brought into contact with P3HT, this shift would result in a larger difference between the HOMO energy level of P3HT and the LUMO energy level of PCBM, and accordingly, a higher V_{oc} in our planar-heterojunction devices. This energy level shift in PCBM with thermal annealing is independent of exposure to oxygen but appears to be highly dependent on its structural development. This

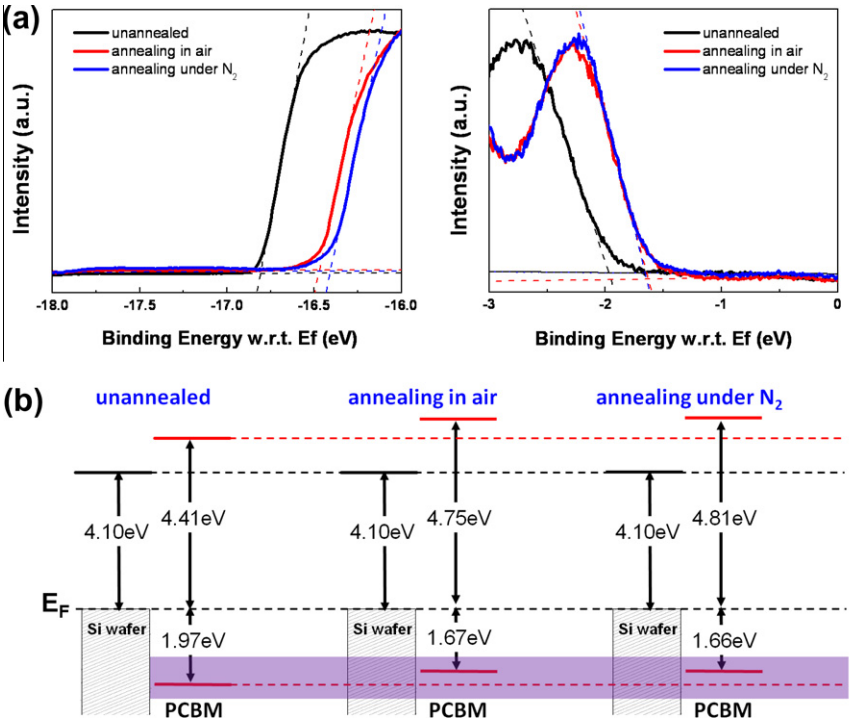

Fig. 7. (a) UPS spectra of PCBM before and after thermal annealing at 170 °C for 10 min. (b) Energy diagrams generated from UPS measurements indicate a shift in the HOMO energy level of PCBM after thermal annealing.

observation is reminiscent of prior reports in which the energy levels of organic semiconductor thin films are highly dependent on the details of structural order and preferential orientation [47].

4. Conclusions

The ability to laminate organic semiconductors and establish effective and efficient charge transfer interfaces has enabled us to fabricate model planar-heterojunction devices in which the processing of the constituent organic semiconductors can be systematically varied. Thermal annealing after lamination is intentionally avoided to eliminate constituent interdiffusion and maintain the pristine charge transfer interface. In our study, we showed the effective decoupling of the contributions of constituent crystallization to devices characteristics. In particular, thermally annealing P3HT thin films prior to lamination does not significantly alter J_{sc} because as-spun P3HT is already sufficiently crystalline to support charge transport. Thermal annealing PCBM, on the other hand, resulted in reduced J_{sc}. Our experiments indicate that PCBM partly crystallizes and hinders vertical charge transport on annealing, effectively reducing J_{sc}. This structural development is also correlated with a shift in the energy levels of PCBM, resulting in changes in V_{oc} in our planar-heterojunction devices.

Acknowledgments

This work was supported by the Photovoltaics Program at ONR (N00014-11-10328) and the SOLAR Initiative at the NSF (DMR-1035217). Partial funding by an NSF-sponsored MRSEC through the Princeton Center for Complex Materials (DMR-0819860) and by the Department of Energy (DE-FG02-04ER46165) is also gratefully acknowledged. Portions of this research were carried out at the Stanford Synchrotron Radiation Lightsource user facility operated by Stanford University on behalf of the US Department Energy, Office of Basic Energy Sciences.

Appendix A. Supplementary data

Supplementary data associated with this article can be found, in the online version, at doi:10.1016/j.orgel.2011.08.011.

References

[1] Y. Liang, Z. Xu, J. Xia, S.-T. Tsai, Y. Wu, G. Li, C. Ray, L. Yu, Adv. Mater. 22 (2010) E135.
[2] S.H. Park, A. Roy, S. Beaupre, S. Cho, N. Coates, J.S. Moon, D. Moses, M. Leclerc, K. Lee, A.J. Heeger, Nat. Photonics 3 (2009) 297.
[3] J. Peet, J.Y. Kim, N.E. Coates, W.L. Ma, D. Moses, A.J. Heeger, G.C. Bazan, Nat. Mater. 6 (2007) 497.
[4] B. Stuart, Solarmer Achieves 8.13% OPV Efficiency, PV Magazine, July 28, 2010 (Accessed 03.06.11).
[5] G. Dennler, M.C. Scharber, C.J. Brabec, Adv. Mater. 21 (2009) 1323.
[6] S. Günes, H. Neugebauer, N.S. Sariciftci, Chem. Rev. 107 (2007) 1324.
[7] G. Yu, J. Gao, J.C. Hummelen, F. Wudl, A.J. Heeger, Science 270 (1995) 1789.
[8] P.W.M. Blom, V.D. Mihailetchi, L.J.A. Koster, D.E. Markov, Adv. Mater. 19 (2007) 1551.
[9] S.R. Forrest, MRS Bull. 30 (2005) 28.
[10] X. Yang, J. Loos, S.C. Veenstra, W.J.H. Verhees, M.M. Wienk, J.M. Kroon, M.A.J. Michels, R.A.J. Janssen, Nano Lett. 5 (2005) 579.
[11] S.S. Lee, Y.-L. Loo, Annu. Rev. Chem. Biomol. Eng. 1 (2010) 59.
[12] P. Peumans, S. Uchida, S.R. Forrest, Nature 425 (2003) 158.

[13] E. Verploegen, R. Mondal, C.J. Bettinger, S. Sok, M.F. Toney, Z. Bao, Adv. Funct. Mater. 20 (2010) 3519.
[14] M.M. Alam, S.A. Jenekhe, Chem. Mater. 16 (2004) 4647.
[15] S. Heutz, P. Sullivan, B.M. Sanderson, S.M. Schultes, T.S. Jones, Sol. Energy Mater. Sol. Cells 83 (2004) 229.
[16] J.B. Kim, S. Lee, M.F. Toney, Z. Chen, A. Facchetti, Y.S. Kim, Y.-L. Loo, Chem. Mater. 22 (2010) 4931.
[17] K.-H. Yim, Z. Zheng, Z. Liang, R.H. Friend, W.T.S. Huck, J.-S. Kim, Adv. Funct. Mater. 18 (2008) 1012.
[18] L. Chen, P. Degenaar, D.D.C. Bradley, Adv. Mater. 20 (2008) 1679.
[19] J.-H. Huang, Z.-Y. Ho, T.-H. Kuo, D. Kekuda, C.-W. Chu, K.-C. Ho, J. Mater. Chem. 19 (2009) 4077.
[20] H. Yan, S. Swaraj, C. Wang, I. Hwang, N.C. Greenham, C. Groves, H. Ade, C.R. McNeill, Adv. Funct. Mater. 20 (2010) 4329.
[21] A. Tada, Y. Geng, Q. Wei, K. Hashimoto, K. Tajima, Nat. Mater. 10 (2011) 450.
[22] D.C. Hyun, G.D. Moon, E.C. Cho, U. Jeong, Adv. Funct. Mater. 19 (2009) 2155.
[23] Y.-L. Loo, T. Someya, K.W. Baldwin, Z. Bao, P. Ho, A. Dodabalapur, H.E. Katz, J.A. Rogers, Proc. Natl. Acad. Sci. USA 99 (2002) 10252.
[24] H. Wang, E.D. Gomez, J. Kim, Z. Guan, C. Jaye, D.A. Fischer, A. Kahn, Y.-L. Loo, Chem. Mater. 23 (2011) 2020.
[25] N.D. Treat, M.A. Brady, G. Smith, M.F. Toney, E.J. Kramer, C.J. Hawker, M.L. Chabinyc, Adv. Energy Mater. 1 (2011) 82.
[26] C.S. Kim, S.S. Lee, E.D. Gomez, J.B. Kim, Y.-L. Loo, Appl. Phys. Lett. 94 (2009) 113302.
[27] J.B. Kim, C.S. Kim, Y.S. Kim, Y.-L. Loo, Appl. Phys. Lett. 95 (2009) 183301.
[28] C.S. Kim, J.B. Kim, S.S. Lee, Y.S. Kim, Y.-L. Loo, Org. Electron. 10 (2009) 1483.
[29] J.B. Kim, K. Allen, S.J. Oh, S. Lee, M.F. Toney, Y.S. Kim, C.R. Kagan, C. Nuckolls, Y.-L. Loo, Chem. Mater. 22 (2010) 5762.
[30] J.L. Baker, L.H. Jimison, S. Mannsfeld, S. Volkman, S. Yin, V. Subramanian, A. Salleo, A.P. Alivisatos, M.F. Toney, Langmuir 26 (2010) 9146.
[31] L.H. Jimison, A. Salleo, M.L. Chabinyc, D.P. Bernstein, M.F. Toney, Phys. Rev. B 78 (2008) 125319.
[32] E.D. Gomez, K.P. Barteau, H. Wang, M.F. Toney, Y.-L. Loo, Chem. Commun. 47 (2010) 436.
[33] G.J. Matt, T. Fromherz, H. Neugebauer, N.S. Sariciftci, AIP Conf. Proc. 786 (2005) 530.
[34] V.D. Mihailetchi, J.K.J. van Duren, P.W.M. Blom, J.C. Hummelen, R.A.J. Janssen, J.M. Kroon, M.T. Rispens, W.J.H. Verhees, M.M. Wienk, Adv. Funct. Mater. 13 (2003) 43.
[35] J.Y. Oh, W.S. Jang, T.I. Lee, J.-M. Myoung, H.K. Baik, Appl. Phys. Lett. 98 (2011) 023303.
[36] P. Vanlaeke, A. Swinnen, I. Haeldermans, G. Vanhoyland, T. Aernouts, D. Cheyns, C. Deibel, J. D'Haen, P. Heremans, J. Poortmans, J.V. Manca, Sol. Energy Mater. Sol. Cells 90 (2006) 2150.
[37] Z.-L. Guan, J.B. Kim, H. Wang, C. Jaye, D.A. Fischer, Y.-L. Loo, A. Kahn, Org. Electron. 11 (2010) 1779.
[38] Z.-L. Guan, J.B. Kim, Y.-L. Loo, A. Kahn, J. Appl. Phys. 110 (2011) 043719.
[39] G. Li, V. Shrotriya, Y. Yao, J. Huang, Y. Yang, J. Mater. Chem. 17 (2007) 3126.
[40] S.S. van Bavel, M. Bärenklau, G. de With, H. Hoppe, J. Loos, Adv. Funct. Mater. 20 (2010) 1458.
[41] H.J. Kim, J.H. Park, H.H. Lee, D.R. Lee, J.-J. Kim, Org. Electron. 10 (2009) 1505.
[42] D. Chen, A. Nakahara, D. Wei, D. Nordlund, T.P. Russell, Nano Lett. 11 (2011) 561.
[43] Y.-G. Guo, L.-J. Wan, C.-J. Li, D.-M. Chen, C. Wang, C.-R. Wang, C.-L. Bai, Y.-G. Wang, J. Mater. Chem. 14 (2004) 914.
[44] M. Kaiser, W.K. Maser, H.J. Byrne, A. Mittelbach, S. Roth, Solid State Commun. 87 (1993) 281.
[45] M. Reyes-Reyes, K. Kim, J. Dewald, R. López-Sandoval, A. Avadhanula, S. Curran, D.L. Carroll, Org. Lett. 7 (2005) 5749.
[46] A. Dodabalapur, L. Torsi, H.E. Katz, Science 268 (1995) 270.
[47] S. Duhm, G. Heimel, I. Salzmann, H. Glowatzki, R.L. Johnson, A. Vollmer, J.P. Rabe, N. Koch, Nat. Mater. 7 (2008) 326.

Table 1
Physical properties of host materials.

Host	T_1 (eV)[a]	$E_{HOMO/LUMO}$ (eV)[b]	Charge mobility (cm/V s)[c]	$T_g/T_c/T_m$ (°C)[d]
3PCBP	3.04	−6.02/−2.46	9.9×10^{-5}	71//123
2MCBP	3.04	−6.05/−2.50	3.5×10^{-4}	99/−/274
MCBP	3.04	−6.01/−2.49	1.1×10^{-3}	155/−/328
SiTAZ	2.84	−6.45/−2.50	6.2×10^{-4}[e]	115/185/294

[a] In MTHF (@ 77 K).
[b] The HOMO and LUMO levels were determined by cyclovoltametry.
[c] Under an electric field of 5×10^5 V/cm.
[d] Determined by differential scanning calorimetry (DSC).
[e] Under an electric field of 2×10^5 V/cm.

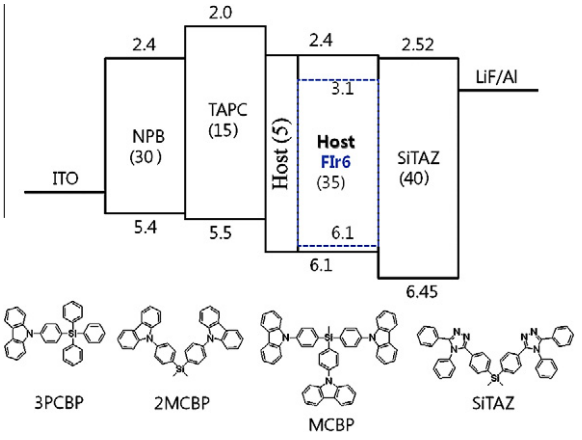

Fig. 1. Schematic energy level diagram of the single host emissive layer phosphorescent organic light-emitting devices (PHOLEDs) and molecular structures of the three different p-type hosts (3PCBP, 2MCBP, and MCBP) and electron transporting material (SiTAZ).

host [27]. Chopra et al. [28] and Lee et al. [29] reported on an efficient mixed-host system for a light blue PHOLED. Because of the scarcity of p-type host materials with high hole mobility and high T_1, they used a hole transporting material (TAPC, or TCTA) for the p-type host. However, highest occupied molecular orbital (HOMO) levels of the materials are too shallow to accommodate deep blue emitters, and moreover, the T_g of the materials are too low for practical applications. Therefore, the development of mixed host system with p-type host materials with high T_g, high T_1, high hole mobility, and deep HOMO level is urgently needed for real application of a mixed-host system in deep blue PHOLEDs. In this study, a carbazole-based p-type host material tris(4-(*N*-carbazolyl)phenyl)methylsilane (MCBP), exhibiting a high T_1 value of 3.05 eV, high T_g of 155 °C, and high hole mobility of 1.1×10^{-3} cm^2 V^{-1} s^{-1}, is introduced [30] for use in a mixed-host system. When it is used as a p-type material in a mixed-host system, a maximum external quantum efficiency of 19.0%, power efficiency of 23.5 lm/W, and deep blue color coordinates of (0.15, 0.23) are obtained, which are one of the best results ever reported for a mixed-host system in deep blue PHOLEDs. To address the origin of the high performance of the device using this material, three different p-type host materials are systematically examined.

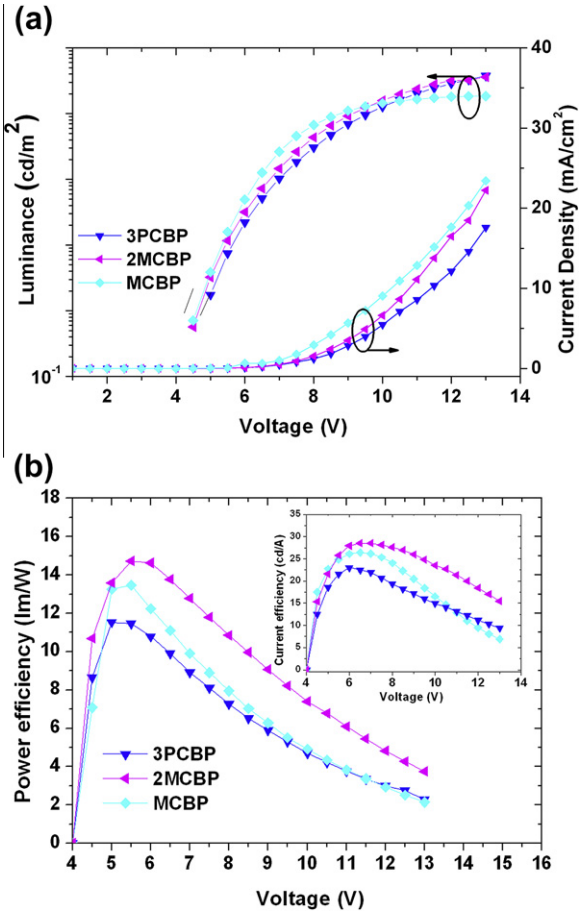

Fig. 2. Device characteristics of the PHOLEDs using single host systems with the device structure of ITO/NPB (30 nm)/TAPC (15 nm)/host (5 nm)/host:FIr6 (30 nm, 10 wt.%)/SiTAZ (40 nm)/LiF (0.5 nm)/Al (60 nm). (a) Current–voltage and luminance–voltage curves. (b) Power efficiency–voltage curves (inset: current efficiency–voltage).

2. Experimental section

Mono(4-(*N*-carbazolyl)phenyl)triphenylsilane (3PCBP), bis(4-(*N*-carbazolyl)phenyl)dimethylsilane (2MCBP), tris(4-(*N*-carbazolyl)phenyl)methylsilane (MCBP), and bis(4-(4,5-diphenyl-4H-1,2,4-triazol-3-yl)phenyl)dimethylsilane (SiTAZ) were prepared using methods reported in the literature [30–36], and purified by train sublimation under

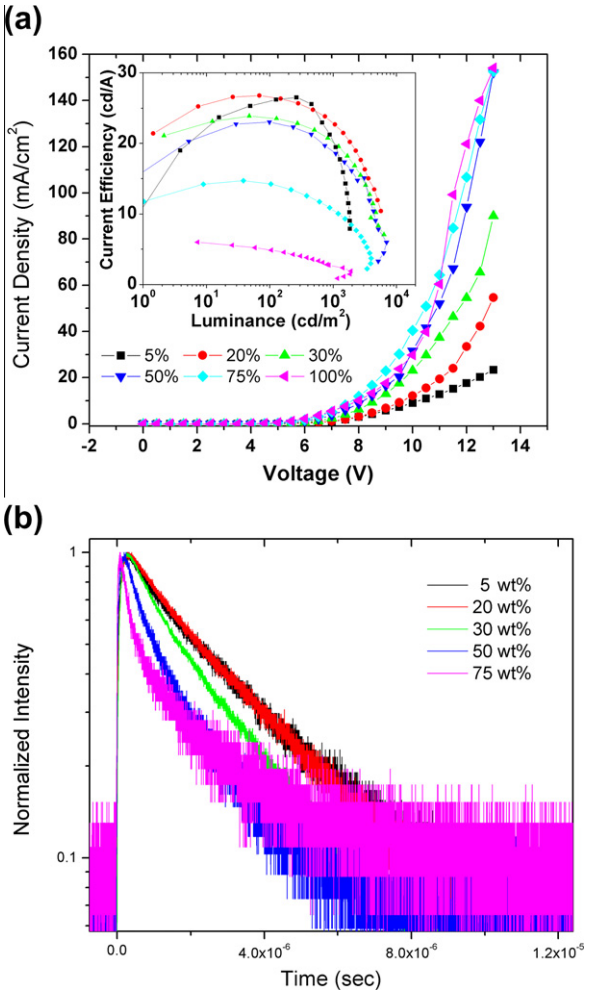

Fig. 3. (a) Current density–voltage and current efficiency–luminance curves of the device ITO/NPB/TAPC/MCBP/MCBP:FIr6 *x* wt.%/SiTAZ/LiF/Al as a function of FIr6 doping ratio. (b) Transient phosphorescence decay curves as a function of the doping ratio of FIr6 in MCBP films on fussed silica substrate.

5.4×10^{-5} Torr. Commercially obtainable organic materials were used as received for the experiments.

The hole mobility was measured by time of flight (TOF) transient photocurrent method. A nitrogen laser (GL-3300, Photon Technology International) was used as the pulsed light source. A 1 GHz digital oscilloscope (LC 572A, LeCroy) was used to measure the transient photocurrent signal.

For the transient photoluminescent decay measurements, a nitrogen laser (GL-3300, PTI) was used as an excitation light source and the phosphorescence light was passed through a monochromator (Oriel 77200), to which a photomultiplier tube (Oriel 77346) was attached at the exit slit.

The OLED devices were fabricated on glass substrates precoated with a 150 nm ITO layer with a sheet resistance of 10 Ω/square. The ITO glass was precleaned using a conventional solvent cleaning method. The ITO surface was cleaned again with a UV ozone treatment immediately before depositing the HTL. To confine triplet excitons into the EML, a thin interlayer of TAPC was inserted between the NPB and EML as a triplet exciton blocking layer because TAPC has a high triplet energy ($E_T \sim 2.9$ eV) and high hole mobility, as reported by Zheng et al. [37] As a deep blue emitter, iridium(III)[bis(4,6-difluorophenyl)pyridinato-N,C$^{2'}$]tetrakis(1-pyrazolyl)borate (FIr6) was chosen because it has high quantum yield and is commercially available. The ETL material, SiTAZ, was used for its high triplet energy (2.84 eV), deep HOMO level (6.45 eV), and high LUMO level (2.5 eV). The HOMO level is deeper than those of carbazole based hosts and FIr6 (6.1 eV), which is an important factor for hole blocking, whereas, the LUMO level is high enough to accommodate that of FIr6 (3.1 eV). The organic, LiF, and Al layers were deposited sequentially onto the substrate without breaking the vacuum. The current–voltage characteristics of OLEDs were measured using a source measure unit (Keithley 236). The electroluminescence spectra, luminance, and the CIE color coordinates were measured using a spectroradiometer (Photo Research PR650). Assuming Lambertian emission, the external quantum efficiency (EQE) was calculated from the luminance, current density, and electroluminescence spectrum.

3. Results and discussion

As summarized in Table 1, the materials exhibited various charge mobilitiy in the range of 10^{-5}–10^{-3} cm/V s [30,32,33]. Interestingly, carbazole based materials show systematic increase of hole mobility values in order of 3PCBP (9.9×10^{-5} cm/V s) < 2MCBP (3.5×10^{-4} cm/V s) < MCBP (1.1×10^{-3} cm/V s), as the number of 4-(*N*-carbazolyl)phenyl groups at the silicon core increases. MCBP is expected to be the most promising host material for deep blue PHOLEDs among the three materials studied, because of its high charge mobility, high thermal stability, and high triplet energy. In particular, the high hole mobility of MCBP would result in a high density of hole current due to its enhanced transporting properties. Therefore, high power efficiency would be expected if MCBP is used as a host for deep blue PHOLEDs. To examine the effects of hosts on device characteristics, a series of FIr6-based PHOLEDs were fabricated using three different host materials. As shown in Fig. 1, the PHOLEDs had the following device structure: ITO/NPB (30 nm)/TAPC (15 nm)/host (5 nm)/host:FIr6 (30 nm, 10 wt.%)/SiTAZ (40 nm)/LiF (0.5 nm)/Al (60 nm). Three different host materials were used in a single-host system with FIr6 10 wt.% doped EML layers, where the hosts are 3PCBP, 2MCBP, and MCBP, respectively. As shown in Fig. 2, all of the devices show efficient exothermic energy transfer from hosts to FIr6, which is evident from the high current efficiency of the devices, ranging from 23.6 to 28.9 cd/A. The devices exhibited driving voltages in the range of 6.4–7.7 V at 100 cd m^{-2}, which are high considering the mobilities of the host materials. The relatively high driving voltage can be ascribed to three causes. First, the thickness of EML (35 nm) of our device is relatively thick compared to the other reported devices [28]. Second, electron injection barrier from cathode into ETL is relatively high due to the high LUMO level of SiTAZ

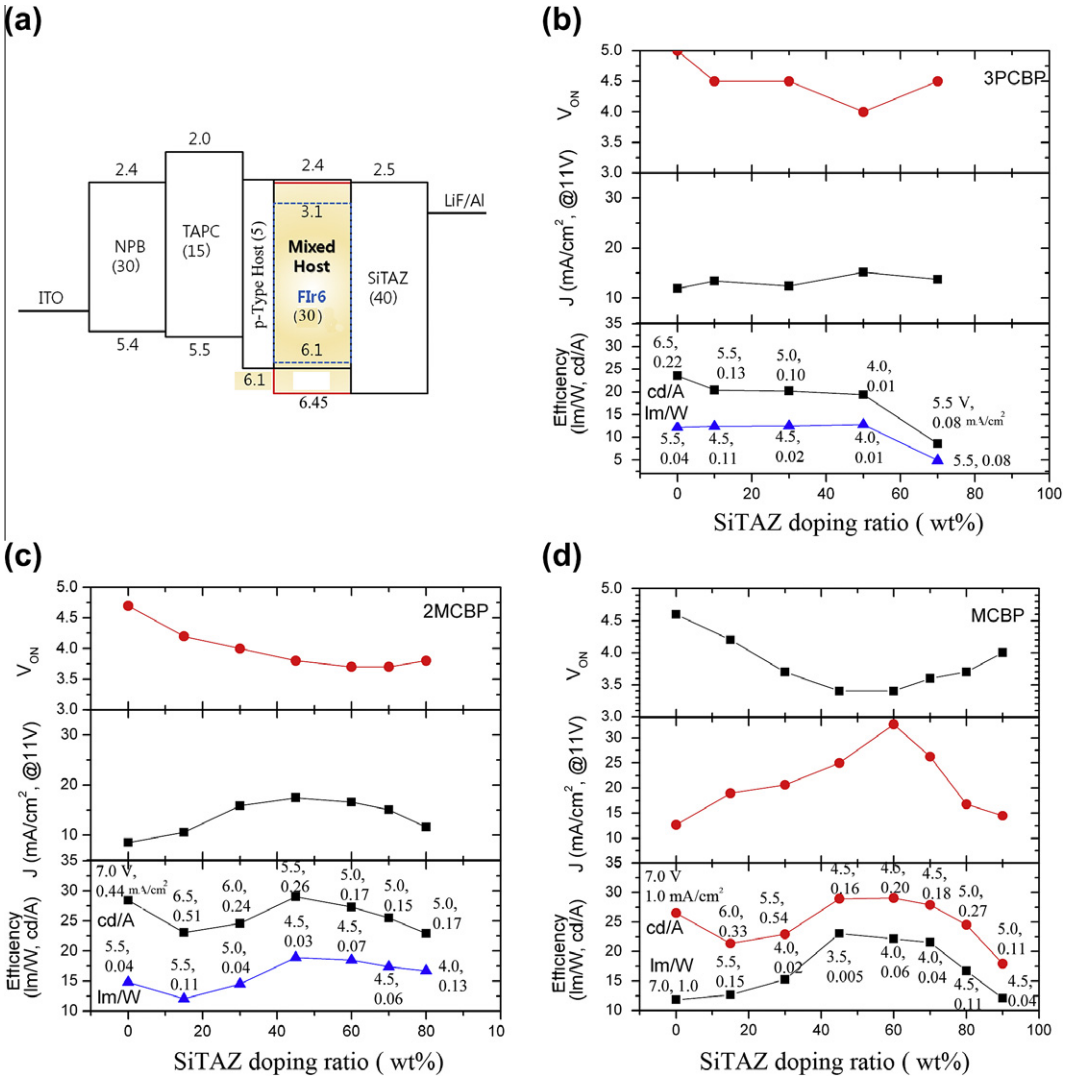

Fig. 4. (a) Schematic energy level diagram of the mixed-host emissive layer PHOLEDs. Dependence of V_{ON}, J, and maximum efficiencies on the doping ratio of SiTAZ for p-type hosts of (b) 3PCBP (c) 2MCBP and (d) MCBP, respectively. The device structure is ITO/NPB (30 nm)/TAPC (15 nm)/p-type host (5 nm)/mixed host:FIr6 (30 nm, 5 wt.%)/SiTAZ (40 nm)/LiF (0.5 nm)/Al (60 nm).

(2.5 eV), which is higher than that of conventional ETL materials in the range of 2.7–3.0 eV [36]. And the last one is low electron mobility of carbazole based host materials. The major way of electron current is by the recombination with holes carried by hosts or FIr6. For low doping concentration of FIr6, the recombination zone is limited near the interface of EML and ETL, resulting in accumulation of holes and electrons in this narrow region, and this may lower the overall conductance of current of the device [37].

The devices showed maximum power efficiency in the range of 12.3–15.0 lm/W. However, the differences in power efficiency are not as significant as expected from the hole mobility properties. These results could be anticipated from the point of view of the charge balance between hole and electron, or from the confinement of the emission zone in the EML layer [28]. The carbazole-based host materials show high hole mobility whereas most of the electron charges are carried by FIr6 as reported by Wee et al. [34]. At a low doping ratio of FIr6, the electron mobility is low and the emission zone is confined near the EML/ETL interface. To get high efficiency, the hole current should be balanced with the electron current in the emission zone, which is low at low doping ratios of FIr6. If we increase the doping ratio of FIr6 to get a high electron current in the emission zone, this may induce a stability problem due to repeated oxidation and reduction stress of the FIr6 [21]. Moreover, the doping ratios of FIr6 should not be increased over 30 wt.%, due to the self-quenching effect of Ir-based emitters [35]. Fig. 3 shows the dependence of doping ratio on the device characteristics. If the doping ratio of FIr6 is increased the current is increased accordingly. The current efficiency is increased until the doping ratio of 20 wt.%. However, from 30 wt.%, the current

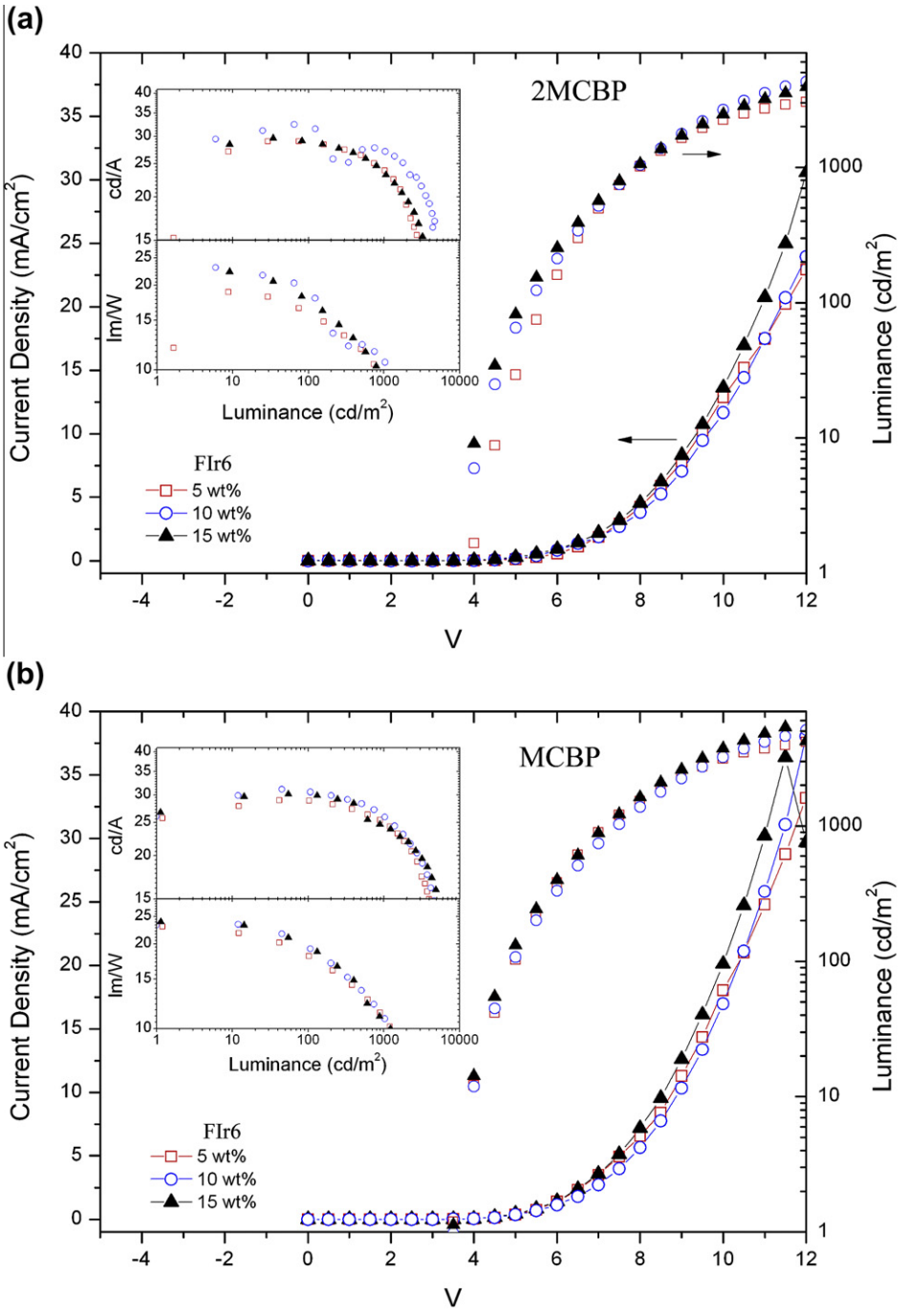

Fig. 5. Device characteristics as a function of FIr6 doping ratios in a mixed host of (a) 2MCBP:SiTAZ (1:1), and (b) MCBP:SiTAZ (1:1). The device structure is ITO/NPB (30 nm)/TAPC (15 nm)/p-type host (5 nm)/mixed host:FIr6 (30 nm, *x* wt.%)/SiTAZ (40 nm)/LiF (0.5 nm)/Al (60 nm).

efficiency decreases. The reason of decrease of current efficiency is supposed to be due to the self quenching of FIr6. Fig. 3(b) shows the transient photoluminescence decay of FIr6-doped MCBP films deposited on fused silica substrates at a wavelength of 460 nm and room temperature. Mono exponential decay curves were observed up to the doping ratio of 20 wt.%. However from 30 wt.%, the decay curve starts to be deviated from mono exponential curve, which is the evidence of self quenching of triplet energy. As a result, in a single-host device structure, hole mobility of the host material does not significantly influence on the power efficiency.

To circumvent the above problem, an n-type material, bis(4-(4,5-diphenyl-4H-1,2,4-triazol-3-yl)phenyl)dimeth-

Table 2
Device characteristics of carbazole host-based PHOLEDs.

Device	V_{ON} (V)[c]	Max. eff.		Eff. @ 100 cd/m^2		Eff. @ 1000 cd/m^2		CIE @ 100 cd/m^2 (x, y)
		CE cd/A	PE lm/W	CE cd/A (V)	PE lm/W	CE cd/A (V)	PE lm/W	
Single-3PCBP[a]	4.8	23.6	12.3	23.3 (7.7)	10.4	19.6 (9.6)	6.5	0.16, 0.23
Single-2MCBP[a]	4.7	28.9	15.0	28.9 (6.7)	13.5	26.0 (9.1)	9.0	0.16, 0.22
Single-MCBP[a]	4.6	26.5	13.0	25.6 (6.4)	12.6	21.9 (8.8)	7.3	0.15, 0.23
45% Mix-2MCBP[b]	3.9	29.0	18.9	28.7 (5.7)	15.7	24.4 (7.8)	9.9	0.15, 0.23
60% Mix-MCBP[b]	3.4	28.9	23.1	28.9 (4.9)	19.1	24.8 (7.2)	10.8	0.15, 0.23
Opt-2MCBP[a]	3.7	32.4	22.5	31.0 (5.3)	18.5	27.1 (8)	10.6	0.15, 0.23
Opt-MCBP[a]	3.4	31.5	23.5	30.6 (4.9)	19.3	25.9 (7.2)	11.1	0.15, 0.23

[a] 10 wt.% Fir6 doping device.
[b] 5 wt.% Fir6 doping device.
[c] Defined as the voltage required to give a brightness of 1 cd m^{-2}.

ylsilane (SiTAZ) [36] is doped into p-type host materials, in which a low density of FIr6 (5 wt.%) is co-doped. SiTAZ has a high electron mobility of 6×10^{-4} cm^2 V^{-1} s^{-1}, a high triplet energy (E_T = 2.84), and wide band gap of 3.93 eV. Therefore, SiTAZ is expected to act as an n-type host. However, due to its deep HOMO level (6.45 eV), hole injection into this material is not easy. As a result this material does not show high efficiency when it is used as a single host of FIr6.

Fig. 4 shows the device characteristics of mixed-host systems with the device structure of ITO/NPB (30 nm)/TAPC (15 nm)/p-type host (5 nm)/mixed host:FIr6 (30 nm, 5 wt.%)/SiTAZ (40 nm)/LiF (0.5 nm)/Al (60 nm). In mixed host, SiTAZ is doped into three different p-type hosts, 3PCBP, 2MCBP and MCBP. The current density increases as the doping ratio of SiTAZ increases, shows a maximum value at a certain doping ratio, and decreases as the ratio increases over that value. The devices using 3PCBP show relatively poor characteristics, which is attributed to the low hole mobility of 3PCBP. Therefore, hereafter, only the other two materials are discussed in detail. The optimum doping ratios are between 45 wt.% and 60 wt.%. The same trends are observed for current and power efficiency. The maximum current and power efficiencies are 29.0 cd/A and 18.9 lm/W for 2MCBP, and 28.9 cd/A and 23.1 lm/W for MCBP. The current efficiencies are similar in the two systems, and efficiency roll-offs are commonly very small, showing high values of about 25 cd/A even at 1000 cd/m^2. In the case of power efficiency, the MCBP system shows higher value. This is the result of the higher current value of the MCBP system (32.67 mA/cm^2) than that of 2MCBP (17.47 mA/cm^2) at the same driving voltage of 11 V. The changes in turn-on voltages are more distinct. The turn-on voltage is reduced from 4.7 V down to 3.9 V, as the doping ratio of SiTAZ increases in the 2MCBP host. The same trends are also observed for MCBP, however, the minimum value is lower (3.4 V) than that of 2MCBP. The effects of co-doping of SiTAZ in the two hosts can be summarized as follows. First, turn-on voltages are lowered by 0.8 and 1.2 V for 2MCBP and MCBP, respectively. Second, the maximum current density increased by about 10 and 20 mA/cm^2 at the same driving voltage of 11 V, respectively. The differences in device characteristics can be attributed to the differences in hole mobility of the two hosts. The electron mobility of SiTAZ is higher than the hole mobility of 2MCBP and lower than that of MCBP. If SiTAZ is doped at the same amount in both of the hosts, the resultant hole mobility of the SiTAZ:2MCBP layer would be lower than that of SiTAZ:MCBP layer. The increased electron current is compensated for by the reduced hole current and vice versa. Therefore, the balanced net current is expected to be lower for 2MCBP than for MCBP. This results in enhanced hole and electron currents for the SiTAZ:MCBP layer with respect to those of the SiTAZ:2MCBP layer, and results in lower turn-on voltage of the device due to faster supply of enough current required to produce the light of 1 cd/m^2.

The device is finally optimized using 2MCBP and MCBP as p-type hosts and SiTAZ as n-type host in mixed host system as shown in Fig. 5a and b. In both of the devices, the ratios of SiTAZ in mixed host are set to 45 wt.%, because both devices show maximum power efficiency at this doping ratio. All of the device structures are the same as that of Fig. 4, except the doping ratio of FIr6. The optimum doping ratio of FIr6 is found to be 10 wt.% for both of the systems. Because most of the electron current is driven by SiTAZ, the increase in current caused by the increase of FIr6 doping ratio is not remarkable. 2MCBP device shows maximum current efficiency of 32.4 cd/A (EQE 19.5%), and maximum power efficiency of 22.5 lm/W. The MCBP device shows maximum current efficiency of 31.5 cd/A (EQE 19.0%), and maximum power efficiency of 23.5 lm/W. Even though the 2MCBP device shows higher current efficiency than that of MCBP device, the power efficiency of MCBP device show higher value than that of 2MCBP device, which is the direct result of higher current maintaining charge balance between electron and hole in the MCBP device (Table 2).

4. Conclusion

In conclusion, a series of p-type host materials with different hole mobility were tested in mixed-host system for use in efficient deep blue PHOLEDs, in which SiTAZ was used as a n-type host material. A maximum external quantum efficiency of 19.0% and maximum power efficiency of 23.5 lm/W was achieved at a low driving voltage and deep blue color coordinates of (0.15, 0.23), using MCBP as a p-type host. The origin of the enhanced device result was addressed systematically. The high hole mobility of MCBP could accommodate more electron current for maintaining

charge balance than the other carbazole-based materials, when it is mixed with an n-type material, SiTAZ, in a mixed-host EML. Moreover, together with its high hole mobility (1.1×10^{-3} cm^2 V^{-1} s^{-1}), its high glass transition temperature of 155 °C makes this material a promising candidate for achieving commercialization of deep blue PHOLEDs with high thermal stability.

Acknowledgments

This research was supported by the Basic Science Research Program through the National Research Foundation of Korea (NRF) funded by the Ministry of Education, Science, and Technology (MEST) of Korea (2011-0018595) and by the Center for Next Generation Dye-Sensitized Solar Cells (No. 2011-0001055). We also acknowledge the Industrial Strategic Technology Development Program (10030814, Development of Organic Materials for OLED) funded by the Ministry of Knowledge Economy (MKE, Korea).

References

[1] M.A. Baldo, D.F. O'Brien, Y. You, A. Shoustikov, S. Sibley, M.E. Thompson, S.R. Forrest, Nature 395 (1998) 151–154.
[2] C. Adachi, M.A. Baldo, M.E. Thompson, S.R.J. Forrest, Appl. Phys. 90 (2001) 5048–5051.
[3] Y.Y. Lyu, J. Kwak, W.S. Jeon, Y. Byun, H.S. Lee, D. Kim, C. Lee, K. Char, Adv. Funct. Mater. 19 (2009) 420–427.
[4] H. Sasabe, T. Chiba, S.-J. Su, Y.J. Pu, K.I. Nakayama, J. Kido, Chem. Comm. (2008) 5821–5823.
[5] N. Chopra, J. Lee, Y. Zheng, S.-H. Eom, J. Xue, F. So, Appl. Phys. Lett. 93 (2008) 143307.
[6] L. Xiao, S.-J. Su, Y. Agata, H. Lan, J. Kido, Adv. Mater. 21 (2009) 1271–1274.
[7] S.O. Jeon, K.S. Yook, C.W. Joo, J.Y. Lee, Adv. Mater. 22 (2010) 1872–1876.
[8] L. Xiao, Z. Chen, B. Qu, J. Luo, S. Kong, Q. Gong, J. Kido, Adv. Mater. 23 (2011) 926–952.
[9] W.D. Andrade, S.R. Forrest, Adv. Mater. 16 (2004) 1585–1595.
[10] R.J. Holmes, S.R. Forrest, Y.-J. Tung, R.C. Kwong, J.J. Brown, S. Garon, M.E. Thompson, Appl. Phys. Lett. 82 (2003) 2422–2424.
[11] X. Ren, J. Li, R.J. Holmes, P.I. Djurovich, S.R. Forrest, M.E. Thompson, Chem. Mater. 16 (2004) 4743–4747.
[12] M.-H. Tsai, Y.-H. Hong, C.-H. Chang, H.-C. Su, C.-C. Wu, A. Matoliukstyte, J. Simokaitiene, S. Grigalevicius, J.V. Grazulevicius, C.-P. Hsu, Adv. Mater. 19 (2007) 862–866.
[13] W. Wei, P.I. Djurovich, M.E. Thompson, Chem. Mater. 22 (2010) 1724–1731.
[14] C.-H. Yang, Y.-M. Cheng, Y. Chi, C.-J. Hsu, F.-C. Fang, K.-T. Wong, P.-T. Chou, C.-H. Chang, M.-H. Tsai, C.-C. Wu, Angew. Chem. Int. Ed. 46 (2007) 2418–2421.
[15] K. Goushi, R. Kwong, J.J. Brown, H. Sasabe, C.J. Adachi, Appl. Phys. 95 (2004) 7798–7802.
[16] Y. Agata, H. Shimizu, J. Kido, Chem. Lett. 36 (2007) 316–317.
[17] H. Sasabe, E. Gonmori, T. Chiba, Y.-J. Li, D. Tanaka, S.-J. Su, T. Takeda, Y.-J. Pu, K.-I. Nakayama, J. Kido, Chem. Mater. 20 (2008) 5951–5953.
[18] S.J. Su, Y. Takahashi, T. Chiba, T. Takeda, J. Kido, Adv. Mater. 20 (2008) 2125–2130.
[19] S.-J. Su, H. Sasabe, Y.-J. Pu, K.-I. Nakayama, J. Kido, Adv. Mater. 22 (2010) 3311–3316.
[20] H. Sasabe, D. Tanaka, D. Yokoyama, T. Chiba, Y.-J. Pu, K.-I. Nakayama, M. Yokoyama, J. Kido, Adv. Funct. Mater. 21 (2011) 336–342.
[21] A.B. Padmaperuma, L.S. Sapochak, P.E. Burrows, Chem. Mater. 18 (2006) 2389–2396.
[22] S.-J. Su, Y. Takahashi, T. Chiba, T. Takeda, J. Kido, Adv. Funct. Mater. 19 (2009) 1260–1267.
[23] S.O. Jeon, S.E. Jang, H.S. Son, J.Y. Lee, Adv. Mater. 23 (2011) 1436–1441.
[24] Y. Tao, Q. Wang, C. Yang, Q. Wang, Z. Zhang, T. Zou, J. Qin, D. Ma, Angew. Chem. Int. Ed. 47 (2008) 8104–8107.
[25] S. Gong, Y. Chen, C. Yang, C. Zhong, J. Qin, D. Ma, Adv. Mater. 22 (2010) 5370–5373.
[26] S. Gong, Y. Chen, J. Luo, C. Yang, C. Zhong, J. Qin, D. Ma, Adv. Funct. Mater. 21 (2011) 1168–1178.
[27] M.E. Kondakova, T.D. Pawlik, R.H. Young, D.J. Giesen, D.Y. Kondakov, C.T. Brown, J.C. Deaton, J.R. Lenhard, K.P.J. Klubek, Appl. Phys. 104 (2008) 094501.
[28] N. Chopra, J.S. Swensen, E. Polikarpov, L. Cosimbescu, F. So, A.B. Padmaperuma, Appl. Phys. Lett. 97 (2010) 033304.
[29] J. Lee, J.-I. Lee, J.Y. Lee, H.Y. Chu, Appl. Phys. Lett. 95 (2009) 253304.
[30] W.-S. Han, H.-J. Son, K.-R. Wee, K.-T. Min, S. Kwon, I.-H. Suh, S.-H. Choi, D.-H. Jung, S.O.J. Kang, Phys. Chem. C 113 (2009) 19686–19693.
[31] M.-H. Tsai, H.-W. Lin, H.-C. Su, C.-C. Wu, F.-C. Fang, Y.-L. Liao, K.-T. Wong, C.-I. Wu, Adv. Mater. 18 (2006) 1216–1220.
[32] M.-F. Wu, S.-J. Yeh, C.-T. Chen, H. Murayama, T. Tsuboi, W.-S. Li, I.-T. Chao, S.-W. Liu, J.-K. Wang, Adv. Funct. Mater. 17 (2007) 1887–1895.
[33] M.-H. Tsai, T.-H. Ke, H.-W. Lin, C.-C. Wu, S.-F. Chiu, F.-C. Fang, Y.-L. Liao, K.-T. Wong, Y.-H. Chen, C.-I.A.C.S. Wu, Appl. Mater. Interfaces 1 (2009) 567–574.
[34] K.-R. Wee, W.-S. Han, H.-J. Son, S. Kwon, S.O.J. Kang, Phys. D: Appl. Phys. 42 (2009) 235107.
[35] Y. Kawamura, J. Brooks, J.J. Brown, H. Sasabe, C. Adachi, Phys. Rev. Lett. 96 (2006) 017404.
[36] S. Kwon, K.-R. Wee, A.-L. Kim, S.O.J. Kang, Phys. Chem. Lett. 1 (2010) 295–299.
[37] Y. Zheng, S.-H. Eom, N. Chopra, J. Lee, F. So, J. Xue, Appl. Phys. Lett. 92 (2008) 223301.

transport through the device and can adversely affect the carrier mobility. Attempts to fabricate aligned organic nanostructures by template-assisted synthesis and field-assisted assembly have been reported [23–25]. But both of these processes require additional steps, either to remove the templates after the synthesis process (template-assisted) or involving an external electric or magnetic field (field-assisted). To cope up with this problem and to reveal the performance limits of organic semiconductor, various types of micro/nano sized organic single crystals based on π-conjugated aromatic molecules have been extensively studied [26–28]. Recent reports of selective growth of organic crystals by modification of surface properties by self-assembly [29] point to the need to move from a top down engineering approach of patterning to a bottom-up approach of self-organization. Still, the problem of crystal orientation and crystal morphology is mostly unresolved and requires particular attention. Aligned layers of small organic molecules can be grown by zone casting technique [30–32] for long range ordering or on rubbed dielectric substrates [33] or by techniques such as solution shearing and dip coating [34,35]. Self-aligned crystals with highly ordered crystalline structure can be developed by inkjet printing [36] or by the stamping (soft lithography) technique [37]. The growth and self-organization of organic crystals by a method based on isothermal evaporation of the solvent in a two-liquid system, similar to ink-jet printing, also led to the formation of aligned organic crystal [38].

In this study, we describe a novel method, where capillary induced force is used to grow ordered crystalline array of π-conjugated molecules from the solution phase and its use in fabricating different optoelectronic devices. The simple, cost-effective, solution based self-assembly approach to grow ordered crystalline array is suitable for large area fabrication and compatible with rigid as well as flexible substrates. This is rather impressive considering the fact that no additional surface treatment is required for the growth of aligned crystals array. Moreover, the proposed method to manipulate crystal morphology can be extended to other π–π stacked soluble organic molecules. The focus is on the method whose simplicity, flexibility in patterning, and demonstrated applications strengths suggest potentially broad utility and applicability. A systematic study of the orientation of crystals at the contact line during the drying process can further improve the theoretical understanding of pattern formation induced by solvent evaporation. Such knowledge may lead to a facile method of patterning and alignment of organic crystals, which is critical for many device applications [39,40].

2. Experimental section

The active organic semiconductors, 7,7,8,8-tetracyanoquinodimethane (TCNQ) and tetrathiafulvalene (TTF) were purchased from Aldrich Chemicals and were used as received. The substrate, which was used for the fabrication of ordered crystalline array, is indium tin oxide (ITO) coated glass substrate over which a polymer dielectric was deposited. To deposit the crystals, a 3–4 cm long glass capillary tube of outer wall diameter 1.0–1.1 mm was placed on top of the dielectric film. 5–10 μL TCNQ solution (having different solvents) was poured dropwise atop the tube which immediately spread along the length of the tube, also covering its sides. The film with the capillary tube was then placed on a hot plate, preset at temperature of 100 °C and baked for 1 h under ambient conditions. After complete evaporation of the solvent, crystals had grown on both sides of the tube in directions normal to its length. The details of the crystal growth technique was described in our earlier communication [41,42]. For the fabrication of OFET, we have used patterned ITO coated glass substrates as gate electrode. Cross-linked poly(4-vinyl phenol) (CL-PVP) was used as the gate dielectric. The precursor solution of CL-PVP was prepared by mixing poly(4-vinylphenol) (PVP) (M_w = 20,000 g/mol) (10 wt%) with a cross linking agent, poly(melamine-co-formaldehyde) (M_n = 511 g/mol) (5 wt%) and butanol (85 wt%). The mixture was stirred for 3 h at room temperature before use. The precursor solution of the dielectric was spun-cast over the ITO gate electrode. The spun cast films were soft-baked at 90 °C for 10 min on a hot plate in ambient conditions and baked further at 175 °C in a vacuum oven (10^{-3} Torr) for 45 min. The thickness of the dielectric film was measured to be around 400 nm (Dektak 3030). On top of the dielectric (or on the glass substrate), ordered arrays of TCNQ and TTF crystals were grown using a glass capillary tube. To complete the device fabrication, gold (Au) was thermally evaporated on top of the crystals to make the top contact source-drain electrodes (50 nm) under a high vacuum (5×10^{-6} Torr) at a rate of 0.3 Å/s. A shadow mask, used during the Au deposition ensured the rod shaped TCNQ crystals lying within the channel region and defined the channel length (L) and channel width (W) as 50 and 1000 μm, respectively. For the fabrication of photodetectors (PDs), the TCNQ and TTF crystalline arrays were grown on cleaned glass substrate by the same method and the top contact Au electrodes were deposited thermally with a channel separation of 30 μm. A HP4145B semiconductor parameter analyzer controlled by locally written LabView codes through a GPIB interface was used for the characterization of the devices under ambient conditions. X-ray diffraction measurement of the crystals was carried out using an X'pert Pro (Pananalytical) X-ray diffractometer (with Cu-Kα radiation). Atomic Force Microscopic (AFM) measurements were done with Nanoscope IIIa (Veeco, digital instruments). For the characterization of the devices under illumination, a common incandescent lamp (white LED) was employed as a light source.

3. Results and discussion

Fig. 1 shows the molecular structure of the compounds used in this study. Four different organic solvents, namely, acetone, chloroform, acetonitrile and toluene, were used to prepare several TCNQ solutions with equal concentrations (1 mg/ml) and to grow TCNQ crystals on dielectric coated glass substrates. Polarized optical microscopic (POM) images (Fig. 2) showed that dense arrays of long (micron-sized), elongated crystals were formed from each solvent, which is important from the standpoint of homogeneously covering a substrate in large area. Interestingly, it is found that the needle-shaped crystals grown in lower tempera-

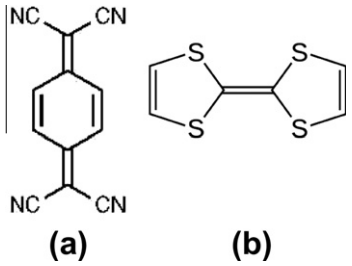

Fig. 1. Chemical structure of (a) 7,7,8,8-tetracyanoquinodimethane (TCNQ) and (b) tetrathiafulvalene (TTF) molecules.

ture (*ca.* 40 °C) are sparsely dispersed and isolated, making it difficult for any practical device fabrication. In contrast, crystals produced at higher temperature (*ca.* 100 °C) are longer, densely packed, regular and better aligned. With increasing evaporation of the solvent and shrinking of the solid/liquid interfacial area, the interaction between adjacent TCNQ molecules induced the formation of crystalline structures, while the gradient of concentration of the active material drives the formation of unidirectional growth of ordered microstructure.

When the temperature is raised, solvent evaporation at the edges is enhanced, which increases the diffusion of

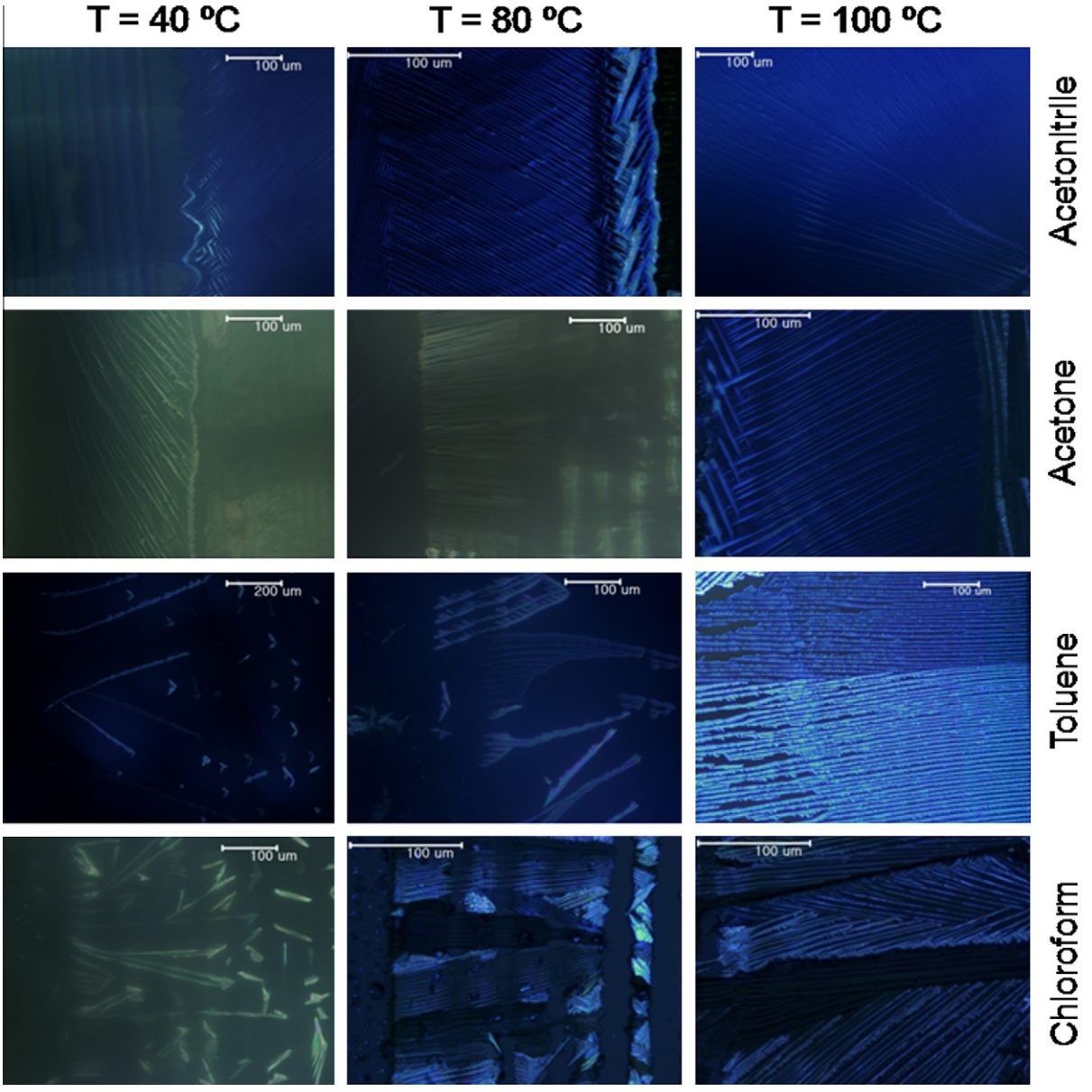

Fig. 2. (Color online) Optical microscopy (OM) images of TCNQ crystals grown on PVP-CL coated glass substrate under different conditions. The baking temperature (*T*) is constant along column-wise while solvent is constant along row-wise.

crystallites seeds towards the contact line and results in the nucleation of crystals and the self-assembly of molecules from the peripheral edge to the contact line of the solution with the tube. It is clear from Fig. 2 that, by casting from TCNQ solution with different solvent, densely packed crystal fibers having homogeneous width and lengths exceeding 200 μm are formed. Moreover, it is found that the use of acetonitrile as the solvent leads to thinner crystal fibers formation as compared to that with toluene or chloroform. The crystals grown at 100 °C from the solvent with lower boiling point, such as, acetone, acetonitrile are thinner than those grown from the solvent with higher boiling point (toluene), probably due to higher evaporation rate of the former, thus getting smaller time for the TCNQ crystallite seeds to self-assemble. On the other hand, toluene solution of TCNQ produced thicker crystals, because, higher boiling point (110–112 °C) of the solvent allowed more time and hence more crystallite seeds to diffuse and self-assembled for producing thicker micro crystalline structures. Additionally, the solubility of TCNQ in different solvents might play some role in forming different crystals. TCNQ, being non-polar molecule, has greater solubility in toluene and chloroform (non-polar) solvents compared to that in acetonitrile and acetone (polar solvent). As a result, toluene solution of TCNQ will contain more number of molecules than the acetone/acetonitrile solution of TCNQ, enabling more diffusion and assembling of crystal seeds for producing thicker crystal structures. All these results indicate that the dynamics of crystal growth is dependent significantly on the solvent used for the preparation of TCNQ solution.

To get more insight into the crystal formation and to find the dependence of the crystals growth on the concentration of TCNQ solutions, we have used toluene solutions of TCNQ having concentrations 1, 0.5, and 0.1 mg/ml. The crystals were grown in identical conditions with temperature setting at 100 °C. The results have been summarized in Fig. 3. It is found that when the concentration of TCNQ in the solution is low, short-length crystals with partial alignment are grown, whereas, higher concentration of TCNQ produced highly oriented and densely packed long, needle-shaped crystals which is highly essential for developing any practical circuitry.

To verify the crystallinity of the microrods of TCNQ, we have performed X-ray diffraction (XRD) analysis. Fig. 4 shows the XRD spectrum of TCNQ crystals grown over the dielectric coated ITO substrate. The peak at 25.88° arises solely due to the TCNQ crystals and is attributed to the (0 2 1) reflection for the crystals, corresponding to a lattice plane distance of 3.43 Å. The other peaks, which arise due to the bottom ITO surface, are well known and are widely reported [43]. The single peak in the XRD spectrum clearly indicates that the crystals formed by this capillary force method is single crystalline. For further investigation of TCNQ crystal structure, 2-dimensional grazing incidence X-ray diffraction (2D-GIXD) measurements were carried out. Simulated diffraction pattern based on a monoclinic structure belonging to $C_{2/c}$ space group and having unit cell parameters, $a = 8.906$, $b = 7.060$, $c = 16.395$ Å, and $\beta = 98.54°$ [44] are well consistent with the experimentally measured peaks. In our previous communication [41], we have shown from

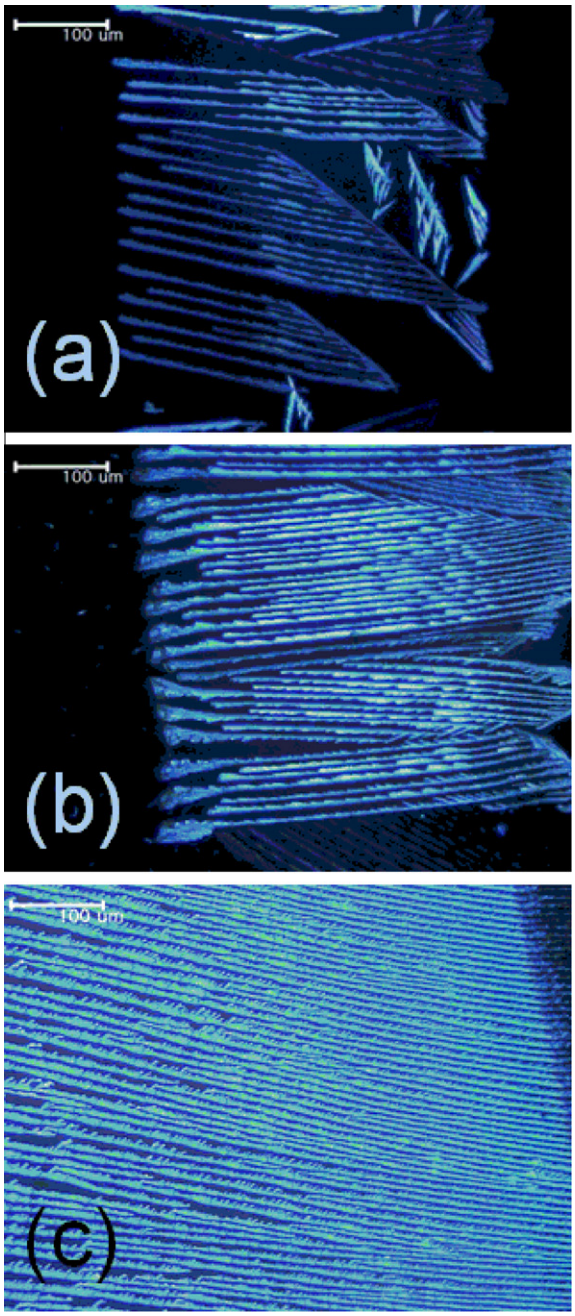

Fig. 3. (Color online) OM images of TCNQ Crystals deposited at 100 °C for various concentrations of TCNQ in toluene. TCNQ concentrations were (a) 0.1 mg/ml (b) 0.5 mg/ml and (c) 1 mg/ml.

the GIXD measurements that the growth of TCNQ crystals preferred along (0 2 1) direction and the diffraction patterns measured at parallel and perpendicular geometry (with respect to *c*-axis), indicated that the TCNQ crystals have highly preferred crystal orientation along the *c*-axis. As a result, 2-D GIXD analysis strongly suggests that the TCNQ crystals prepared by the proposed method have one directionally grown single crystalline nature.

Atomic force microscope (AFM) image of the TCNQ crystals shows that the crystals are aligned in one direction

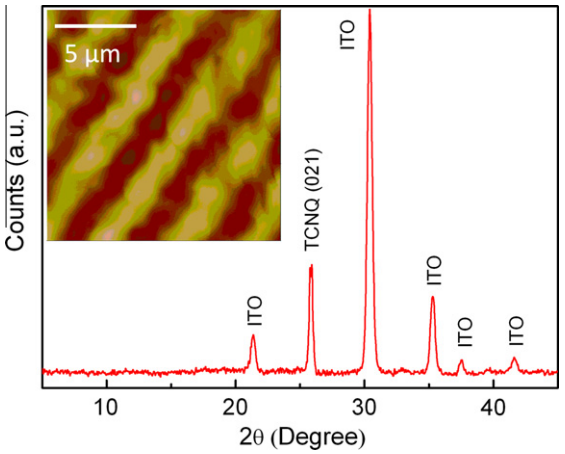

Fig. 4. (Color online) XRD spectra of TCNQ crystals grown on polymer dielectric deposited ITO substrate. (inset) Tapping mode AFM (phase) image of the TCNQ crystals.

and are well oriented. Fig. 4 (inset) shows the tapping mode AFM (phase) image of the ordered TCNQ micro crystals grown over the polymer dielectric surface. The typical height of the crystals as measured from the AFM height profile was ~25–29 nm and the length was found to be >200 μm.

Although the formation and growth of the ordered crystalline film may need further elucidation of its mechanism, it invariably represents a novel, facile approach for one-step fabrication of highly ordered organic micro-crystalline array. Significantly, this technique is applicable to preparing oriented crystals array of other organic compounds. For example, by using an identical procedure, aligned crystals of tetrathiafulvalene (TTF) (Fig. 5a) can be obtained. In this case also, the concentration of TTF was fixed at 1 mg/ml with a drying temperature of 100 °C. It is evident from the figure that the present method affords the formation of ordered microstructures for other molecules also. In order to verify the necessity and suitability of the capillary tube in the present method for best production of oriented and ordered crystals, we have performed a control experiment. We deposited TTF crystals from the same solution by drop cast (Fig. 5b) and spin cast (Fig. 5c) method and baked at 100 °C. It has been observed that, in both the cases, curved fibrillar structures (Fig. 5b and c) having no ordering and with random orientation of crystals domain have been developed. These results clearly indicate the necessity of the use of capillary tube for the production of ordered array of organic microcrystals.

To demonstrate the potential application of the present technique, we constructed photodetectors (PDs) from the TCNQ and TTF crystalline arrays. *I–V* measurements were performed on the device by a two-probe method under ambient conditions. Fig. 6a shows the typical *I–V* curves of TCNQ crystals based PD obtained in the dark and under continuous illumination by light. It shows that the photocurrent under illumination is markedly higher than that obtained in the dark. Moreover, the linear *I–V* characteristics both in dark and under light indicated that ohmic contact has been established at the semiconductor metal junction. Fig. 6b reveals that the time response of the device, where the light source was switched on and off periodically, is reversible and reproducible. It can be seen from the figure that as soon as the light was turned on, the current sharply increased to a high value demonstrating fast response of the device. The maximum current level is, however, same for all the cycles exhibiting highly stable photo characteristics. Under illumination, the device current increased to a value which is much higher compared to that in the dark. The ratio between the currents under light and in dark states was found to be ~40. The photoswitching characteristics of devices based on TTF crystals arrays is shown in Fig. 6c. With an applied bias of 10 V between the electrodes, when the light was switched alternately on and off, it caused the current of

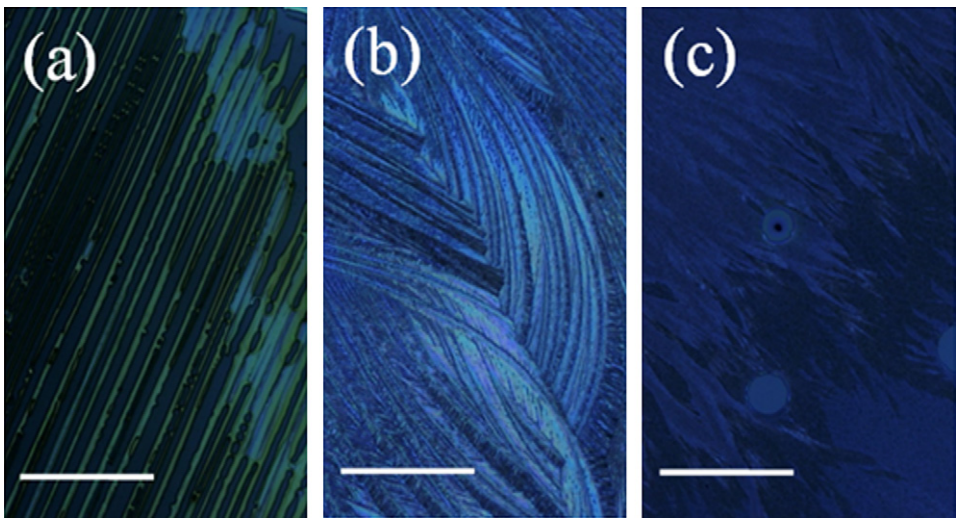

Fig. 5. (Color online) OM image of (a) TTF crystals on glass substrate prepared by capillary method and TTF crystal fibers produced by (b) drop cast (c) spin cast method. The scale bar is 100 μm.

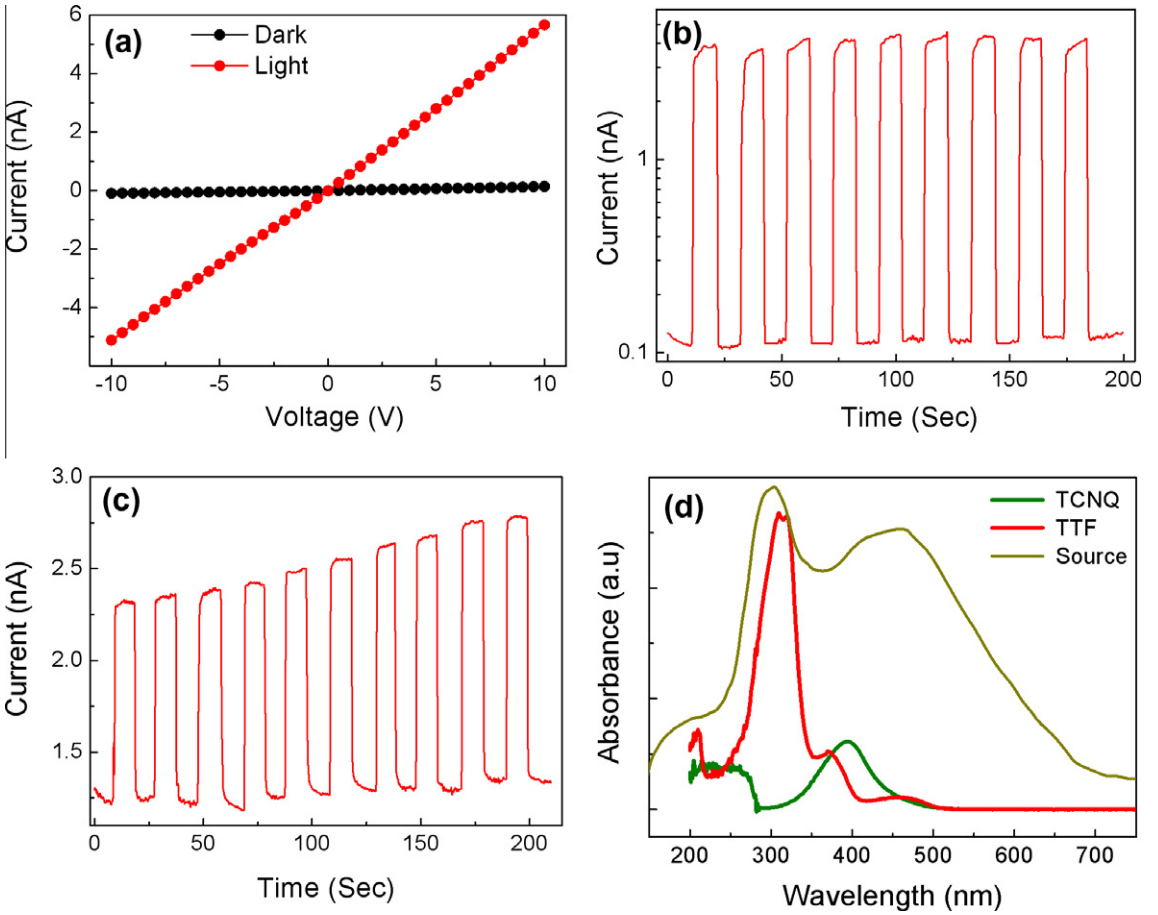

Fig. 6. (Color online) Typical photoresponsive behavior from ordered crystalline array. (a) *I–V* characteristics of the TCNQ crystals array based photodetector (PD) measured in the dark and under illumination. (b) Time response of the device biased at 10 V under excitation with pulsed light of fixed intensity. (c) Photoswitching characteristics of TTF crystals based PD with electrode bias 10 V. (d) UV–Vis absorption spectra of TCNQ and TTF in toluene along with the spectral response of the light source.

the devices to show two distinct states: the "low" current state in the dark and the "high" current state in the light. The variation between these two states was fast and reversible, making it possible for the device to act as a high quality photosensitive switch. Here, we have observed a little persistent current effect (Fig. 6c) which may be ascribed to the remaining of some photocarriers even after switching off the light source.

To overrule the possibility of current increase due to temperature rise of the sample as a result of long time light exposure, we have compared the spectral characteristics of the light source with the absorption spectrum of the samples (Fig. 6d). The spectrum of the light source has a peak around 300 nm, where TTF has large absorption and a broad hump around 400 nm, where TCNQ has maximum absorption. The lamp used for the optical illumination was made of white LEDs and the power was adjusted to 4 mW/cm^2. Such a low power can not produce much heating effect to switch the conductivity of the sample. If the increase in current of the device under illumination occurred due to heating (temperature increase) of the sample, the current for a particular cycle would become higher than the corresponding current of the previous cycle. Thus, there would be gradual increase in current value in every cycle due to gradual increase in temperature. Moreover, upon switching the light off, the current would not have decreased sharply; rather, there would be slow and gradual decay of the current. Furthermore, we have observed the photoswitching characteristics of the sample for light pulses of very short duration (10 ms) also. These results indicate that the observed photoswitching characteristic of the device is a molecular phenomena, which occurs due to the absorption of photons, not due to the heating effect of the sample. Another possible reason for the photoswitching effect may be photoinjection from the electrodes. However, the photoinjection/photoemission of carriers from the metal (Au) electrode requires that the photon energy must at least be equal to the work function of Au (*ca.* 5.1 eV). However, the maximum energy of the illumination corresponding to minimum wavelength, *ca.* 300 nm, was found to be (4.1 eV) less than the work function of Au electrode. Also, TCNQ has maximum light absorption at ~400 nm which corresponds to energy ~3.1 eV, much less than that required for photoemission from Au electrode. These results proves that the observed photoswitching effect is not due to the photoinjection/photoemission from

the electrodes, rather it is an intrinsic effect, arising due to the absorption of photons by the TCNQ/TTF crystals and exciton dissociation at the metal/semiconductor interface.

When light with photon energy greater than the band gap of the material is absorbed, a number of excitons are generated which subsequently dissociated into free electrons and holes. Fig. 6d illustrates the UV–Vis absorption spectra of TCNQ and TTF showing that the maximum absorption of light occurred in the visible region of the spectrum. These, in turn, imply that upon illumination of light, additional mobile charge carriers (photocarriers) are generated, namely, holes in the highest occupied molecular orbital (HOMO) and electrons in the lowest unoccupied molecular orbital (LUMO) levels which will contribute to the resulting transport properties. The photocurrent generation in the crystals, which is indicative of the irradiation induced enhancement of carrier concentration, resulted in increase of the device current. All the results in Fig. 6 suggest the potential of the organic crystalline array to act as high quality optoelectronic switches.

Additionally, we have demonstrated that it is possible to design organic field-effect transistors based on these ordered crystalline arrays. Among the different architectures for measuring the organic field effect, we chose the bottom-gate, top contact architecture with ITO as the gate electrode and CL-PVP as the gate dielectric. The output (I_{DS}–V_{DS}) characteristics of TCNQ (*n-type*) and TTF (*p-type*) crystals based OFETs is shown in Fig. 7a. The characteristics of representative OFETs showed excellent gate modulation along with current saturation (Fig. 7a). The characteristics for TTF crystalline OFETs exhibited *p-type* (hole dominant) conduction (left panel, Fig 7a), whereas, the OFET based on TCNQ crystals showed *n-type* (electron dominant) conduction (right panel, Fig 7a). With increase in V_G, more charge carriers are accumulated in the interface between organic crystals and the gate dielectric near the channel region resulting in increase of the drain current (I_{DS}). From the transfer (I_{DS}–V_G) characteristics of the OFETs (Fig. 7b), we have estimated an on/off current ratio $\sim 10^3$ for both OFETs and saturation charge carrier mobility (μ) $\sim$0.02 and 0.05 $cm^2\ V^{-1}\ s^{-1}$, respectively, for TCNQ and TTF crystals based OFETs. The threshold voltage (V_{Th}) for TCNQ and TTF OFETs fabricated in this study were found to be 5 and −18 V, respectively. The performance (in terms of mobility, threshold voltage) of the current device is impressive and superior than the early report of TCNQ thin-film transistors [45,46], indicating that the intrinsic material performance was not fully realized in previous TCNQ OFETs with the polycrystalline films, presumably because of extrinsic influences, such as from grain boundaries, defects and traps.

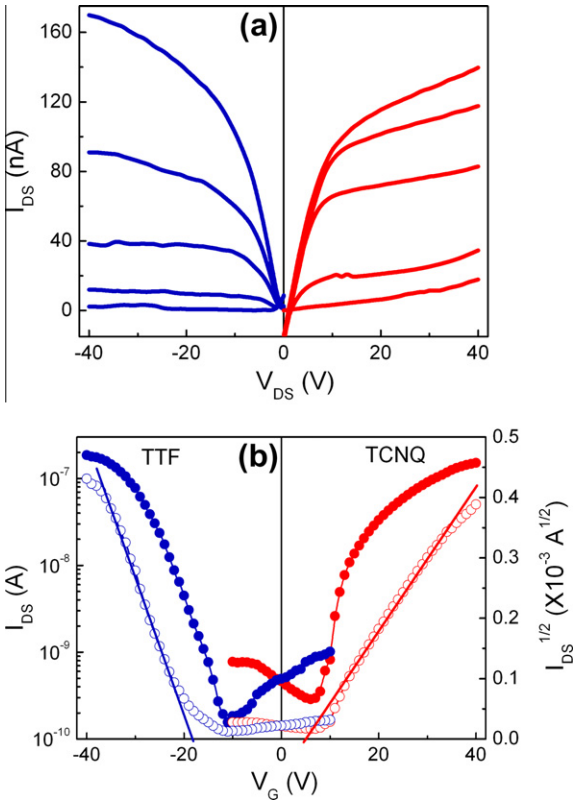

Fig. 7. (Color online) (a) Typical output characteristics of TTF (left panel) and TCNQ (right panel) crystalline array based OFET with $|V_G|$ ranging from 0 to 40 V (step 10 V). Absolute value of current is plotted in the vertical scale. (b) Transfer characteristics of the OFETs measured at $|V_{DS}|$ = 30 V.

4. Conclusions

In conclusion, we have shown that oriented array of different organic crystals can be prepared by a simple capillary force induced solution process. The microcrystalline structure can be prepared by solvent evaporation, and then self-aligned and -assembled into ordered films through one-step self-assembly method, requiring no additional surface treatment. Different processing conditions have been examined to understand the optimum solution for growing dense array of oriented crystals. The crystal dimensions and morphology depend not only on the active materials, but on solvent used, material concentration, and annealing temperatures also. In general, it can be concluded that higher material concentrations and higher temperatures lead to the formation of longer and well aligned micro crystalline arrays. This one-step method of combining growth and self-assembly of microcrystalline array in large-area is highly applicable for fabricating high performance optical and electronic devices. TCNQ and TTF micro crystalline array based devices including photodetectors and high-mobility organic transistors with good field-effect characteristics were demonstrated. This method for the fabrication of ordered organic micro/nanostructures could have significant potential for large-scale and low-cost optoelectronic applications. Additionally, the current method of patterning of a range of organic semiconductors for various device applications elucidates its potential broad utility and applicability.

Acknowledgement

We acknowledge the support and help from Prof. S. Pyo, Konkuk University, Seoul, Korea.

References

[1] E.W. Meijer, A.P.H.J. Schenning, Nature 419 (2002) 353.
[2] Q. Tang, H. Li, Y. Liu, W. Hu, J. Am. Chem. Soc. 128 (2006) 14634.
[3] Y. Yamamoto, T. Fukushima, Y. Suna, N. Ishii, A. Saeki, S. Seki, S. Tagawa, M. Taniguchi, T. Kawai, T. Aida, Science 314 (2006) 1761.
[4] A.L. Briseno, S.C.B. Mannsfeld, X. Lu, Y. Xiong, S.A. Jenekhe, Z. Bao, Y. Xia, Nano Lett. 7 (2007) 668.
[5] G.H. Heilmeier, L.A. Zanoni, J. Phys. Chem. Solids 25 (1964) 603.
[6] G. Horowitz, X.Z. Peng, D. Fichou, F. Garnier, Solid State Commun. 72 (1989) 381.
[7] E. Ebisawa, T. Kurokawa, S. Nara, J. Appl. Phys. 54 (1983) 3255.
[8] J.H. Burroughes, C.A. Jones, R.H. Friend, Nature 335 (1988) 137.
[9] C.J. Bettinger, Z. Bao, Adv. Mater. 22 (2010) 651.
[10] T. Sekitani, U. Zschieschang, H. Klauk, T. Someya, Nat. Mater. 9 (2010) 1015.
[11] L.A. Majewski, R. Schroeder, M. Voigt, M. Grell, J. Phys. D 37 (2004) 3367.
[12] M.H. Yoon, A. Facchetti, T.J. Marks, Proc. Natl. Acad. Sci. USA 102 (2005) 4678.
[13] H. Klauk, U. Zschieschang, J. Pflaum, M. Halik, Nature 445 (2007) 745.
[14] H. Sirringhaus, L. Buergi, T. Kawase, R.H. Friend, in: C.R. Kagan, P. Andry (Eds.), Thin Film Transistors, Marcel Dekker, New York, 2003, p. 427.
[15] S.R. Forrest, Nature 428 (2004) 911.
[16] C.S. Kim, S. Lee, E.D. Gomez, J.E. Anthony, Y. Loo, Appl. Phys. Lett. 93 (2008) 103302.
[17] S.K. Park, T.N. Jackson, J.E. Anthony, D.A. Mourey, Appl. Phys. Lett. 91 (2007) 063514.
[18] N. Liu, Y. Zhou, L. Wang, J. Peng, J. Wang, J. Pei, Y. Cao, Langmuir 25 (2009) 665.
[19] J.A. Lim, W.H. Lee, H.S. Lee, J.H. Lee, Y.D. Park, K. Cho, Adv. Funct. Mater. 18 (2008) 229.
[20] K.C. Dickey, J.E. Anthony, Y.-L. Loo, Adv. Mater. 18 (2006) 1721.
[21] D.J. Gundlach, J.E. Royer, S.K. Park, S. Subramanian, O.D. Jurchescu, B.H. Hamadani, A.J. Moad, R.J. Kline, L.C. Teague, O. Kirillov, C.A. Richter, J.G. Kushmerick, L.J. Richter, S.R. Parkin, T.N. Jackson, J.E. Anthony, Nat. Mater. 7 (2008) 216.
[22] I. Mcculloch, Nat. Mater. 4 (2005) 583.
[23] L. Zhi, T. Gorelik, J. Wu, U. Kolb, K. Müllen, J. Am. Chem. Soc. 127 (2005) 12792.
[24] J.S. Hu, Y.G. Guo, H.P. Liang, L.J. Wan, L. Jiang, J. Am. Chem. Soc. 127 (2005) 17090.
[25] L. Sardone, V. Palermo, E. Devaux, D. Credgington, M.de. Loos, G. Marletta, F. Cacialli, J.V. Esch, P. Samorí, Adv. Mater. 18 (2006) 1276.
[26] Q. Tang, L. Jiang, Y. Tong, H. Li, Y. Liu, Z. Wang, W. Hu, Y. Liu, D. Zhu, Adv. Mater. 20 (2008) 2947.
[27] A.L. Briseno, S.C. Mannsfeld, S.A. Jenekhe, Z. Bao, Y. Xia, Mater. Today 11 (2008) 38.
[28] C. Reese, Z. Bao, Mater. Today 10 (2007) 20.
[29] A.L. Briseno, S.C.B. Mannsfield, M.M. Ling, S. Liu, R.J. Tseng, C. Reese, M.E. Roberts, Y. Yang, F. Wudl, Z. Bao, Nature 444 (2006) 913.
[30] W. Pisula, A. Menon, M. Stipputat, I. Lieberwirth, U. Kolb, A. Tracz, H. Sirringhaus, T. Pakula, K. Müllen, Adv. Mater. 17 (2005) 684.
[31] S. Kotarba, J. Jung, A. Kowalska, T. Marszalek, M. Kozanecki, P. Miskiewicz, M.M. Torrent, C. Rovira, J. Veciana, J.P. Luis, J. Ulanski, J. Appl. Phys. 108 (2010) 014504.
[32] C.M. Duffy, J.W. Andreasen, D.W. Breiby, M.M. Nielsen, M. Ando, T. Minakata, H. Sirringhaus, Chem. Mater. 20 (2008) 7252.
[33] S.J. Kang, Y.Y. Noh, K.J. Baeg, J. Ghim, J.H. Park, D.Y. Kim, J.S. Kim, J.H. Park, K. Cho, Appl. Phys. Lett. 92 (2008) 052107.
[34] H.A. Becerril, M.E. Roberts, Z.H. Liu, J. Locklin, Z.N. Bao, Adv. Mater. 20 (2008) 2588.
[35] R.L. Headrick, S. Wo, F. Sansoz, J.E. Anthony, Appl. Phys. Lett. 92 (2008) 063302.
[36] J. Lim, W. Lee, D. Kwak, K. Cho, Langmuir 25 (2009) 5404.
[37] Y.N. Xia, J.A. Rogers, K.E. Paul, G.M. Whitesides, Chem. Rev. 99 (1999) 1823.
[38] J.P. Hong, S. Lee, Angew. Chem. Int. Ed. 48 (2009) 3096.
[39] Z. Nie, D. Fava, E. Kumacheva, S. Zou, G.C. Walker, M. Rubinstein, Nat. Mater. 6 (2007) 609.
[40] K.T. Nam, D.W. Kim, P.J. Yoo, C.Y. Chiang, N. Meethong, P.T. Hammond, Y.M. Chiang, A.M. Belcher, Science 312 (2006) 885.
[41] B. Mukherjee, T.J. Shin, K. Sim, M. Mukherjee, J. Lee, S.H. Kim, S. Pyo, J. Mater. Chem. 20 (2010) 9047.
[42] B. Mukherjee, M. Mukherjee, K. Sim, S. Pyo, J. Mater. Chem. 21 (2011) 1931.
[43] R.A. Gilstrap Jr., C.J. Capozzi, C.G. Carson, R.A. Gerhardt, C.J. Summers, Adv. Mater. 20 (2008) 4163.
[44] R.E. Long, R.A. Sparks, K.N. Trueblood, Acta Crystallogr. 18 (1965) 932.
[45] A.R. Brown, D.M. de Leeuw, E.J. Luos, E.E. Havinga, Synth. Met. 66 (1994) 257.
[46] M. Lizuka, Y. Shiratori, S. Kuniyoshi, K. Kudo, K. Tanaka, Appl. Surf. Sci. 130 (1998) 914.

A first order rate does not always exist. It is defined only if the "reactants" had time to equilibrate and the energy distribution over all degrees of freedom of the reactants follows the equilibrium distribution for that species. All rate theories, including for example transition state theory [5] for adiabatic reaction or Marcus theory for non-adiabatic charge [6] transfer reactions assume that the reactants are equilibrated. Thermal equilibration of the reactants guarantees that the process is memoryless, i.e. the probability of occurring does not depend on the particular way the reactants are generated. In condensed phase, the degrees of freedoms that need to be equilibrated are the vibrational degrees of freedom. For this reason the hopping rate is defined only if the vibrational relaxation rate $k_{vib-rel}$ is (much) larger than the hopping rate i.e.

$$k_{vib-rel} > k_{hop} \tag{2}$$

We know a lot about vibrational relaxation time in different environments thanks to a large number of spectroscopic measurements, which included measurements on organic solids [7]. In particular, at low temperature ($T \to 0$), there is a simple relation between the vibrational relaxation rate and the Raman line broadening $\tilde{\delta}$ (in cm^{-1}), namely $k_{vib-rel} = 2\pi c\tilde{\delta}$ with c being the speed of light (few papers discussing this relation are given in Refs. [7–9]). The broadenings are not identical for all vibrational modes, so there is not a single $k_{vib-rel}$, but sufficiently similar (within a factor of 2–3) to be considered a single experimental parameter for our purpose [9,10]. Moreover, for molecules with center of inversion the modes involved in the hopping are totally symmetric and Raman active, so that it is even possible to specifically consider the lifetime of the most relevant vibrational modes if desired. Note that, not surprisingly, the vibrational relaxation rate is much slower in solids than in liquids.

The inequality (2) can be written as $2\pi c\tilde{\delta} > \mu_{hop} k_B T/eL^2$ and can be better analyzed in the form

$$\mu_{hop} < \frac{2\pi c\tilde{\delta} eL^2}{k_B T} \tag{3}$$

which is the main result we want to discuss. All the quantities appearing in the equation above are experimentally accessible. If the measured charge mobility in a material is larger than the quantity in the right hand side of the equation, the transport cannot be described by hopping. In fact, mobilities that are faster than this threshold correspond to hypothetical hopping rates that are too fast compared to the vibrational relaxation and cannot be considered independent events.

To be more practical, we can set to $L = 6 \cdot 10^{-8}$ cm, a typical center-to-center distance between pi-stacked molecules (some experimental values are 3.6, 5.1, 7.2, and 7.6 Å for hexabenzocoronene [11], pentacene [12], rubrene [13] and TIPS-pentacene [14], respectively), $k_B T = 0.026$ eV, as at room temperature, and $\tilde{\delta} = 3\ cm^{-1}$ (a rather generous broadening, considering that the largest low temperature broadening in naphthalene is $\tilde{\delta} = 1.2\ cm^{-1}$ [9]) we obtain that, in order to be able to consider a hopping mechanism, we must have

$$\mu_{hop} \sim< 0.08\ cm^2\ V^{-1}\ s^{-1} \tag{4}$$

This is indeed a very low mobility, considering that the record mobility for crystalline semiconductors at room temperature is of the order of $\sim 10\ cm^2\ V^{-1}\ s^{-1}$ [13,15] and liquid crystalline materials can achieve mobility of $0.1\ cm^2\ V^{-1}\ s^{-1}$ [2]. The mobility value in Eq. (4) is not to be considered a rigid cut-off and the value must be adapted for molecules with a larger center-to-center distance or different Raman linewidths. The maximum value of μ_{hop} refers to the crystal direction with the largest mobility which is usually the direction with a relatively short intermolecular distance L.

The appropriate way of describing charge transport in organic solid has been discussed by theoreticians with a wealth of methods each valid under a number of conditions and the specialized literature analyzes how to compute the mobility from first principles in different regimes [16]. These theories also analyze from the point of view of quantum statistical mechanics and electronic structure calculations under what condition hopping transport is possible. The interesting aspect of the inequality in (3) is that it is valid regardless of all the technicalities of formal theories and, indeed, it bypasses them providing an immediate relation that can be used (and understood) to rule out the possibility of hopping transport in molecular materials.

To exemplify how useful such a relation can be, it may be worth summarizing the different methods used to compute the hopping mobility from first principles. In a large number of papers it was assumed that, in analogy with what happens in solution, Marcus equation can be used to describe the charge hopping process [11,17]. Marcus theory is not very accurate is solid phases, because it is valid when the nuclear degrees of freedom involved in the reaction can be treated classically and if the electronic coupling between molecules is so small that the process is non-adiabatic [6]. It is possible to use rate expressions that incorporate the quantum nature of the nuclear degrees of freedom [18] or that take into account the fact that the electronic coupling between molecules is relatively strong [19]. Virtually under any condition one can obtain a (more or less complicated) hopping rate expression, only provided that such rate exists! It is not uncommon that the rate of hopping between two molecules cannot be defined, as we have verified by inserting the appropriate numerical values in Eq. (3). In all the references given in this paragraph the experimental mobility is just too high to support a hopping mechanism and so it does not matter what the rate expression used is: the charge simply does not propagate by hopping and any theoretical effort made to improve the hopping rate is misplaced. It should be noted, incidentally, that hopping theories describe in a qualitatively correct way how the electronic structure is related to the mobility and they retain the ability to rationalize the differences between similar materials even when they are not the most suitable model.

The impossibility of describing the transport in terms of a sequence of hopping does not mean, of course, that it cannot be described in a different way. Chemical physicists are not unprepared to the situation of thermal relaxation

processes being not fast enough [20] and it is possible to study the quantum dynamics in this case using a variety of techniques, mostly based on the propagation of the density matrix [5]. The essential point for this paper is that, if the thermal relaxation is not fast enough, it is not possible to describe simply the time evolution of the probability of finding a system in a particular state (chemical kinetics approach). The charge dynamics is described instead by the evolution of the wavefunction which can be scattered, as a classical wave, by the crystal impurities and vibration creating genuinely quantum effects like the interference between wavefunctions propagating in different directions [21]. All the methods used to describe long range and long time evolution based on a collection of rates for individual processes (e.g. kinetic Monte Carlo methods) are bound to fail when interference and dephasing have to be taken into account. The inequality above (valid also if the molecules in the material are not all equivalent because of some static disorder effect) can be seen as a limiting condition for the applicability of any of these methods.

The considerable attraction of the chemistry community to the idea of charge transport as a series of hopping events is deeply rooted in the experimental evidence that, with very few exceptions [15,22], the transport is thermally activated, i.e. the mobility increases with temperature following Arrhenius law [23]. Thanks to few experiments on ultrapure samples [15] we now know that the activation energy in crystalline samples is not related to the hopping rate between adjacent molecules but to the rate of escape of charge carrier trapped by impurities [24] into delocalized states of the molecular crystal [25] (a mechanism that cannot be described as simple hopping).

In summary, we have shown in this paper that there is a maximum value of charge mobility compatible with a hopping transport model where the charge is transferred from molecule to molecule in independent events. We demonstrated a simple inequality, which involves only experimentally accessible quantities, without using any detailed knowledge of the system or involving any technicalities from quantum dynamics (see Fig. 1). The simple hopping transport model, made very common in chemistry by its simplicity and by the analogy with redox chemistry, is in practice never valid for the highest mobility crystalline materials. We purposely presented only results that can be fully justified with elementary arguments and avoided to take any position with respect to the actual transport mechanism in crystalline materials which is currently under debate in the technical literature [16]. Fortunately, as this paper shows, it is still possible to establish at least a firm point without even entering in the debate.

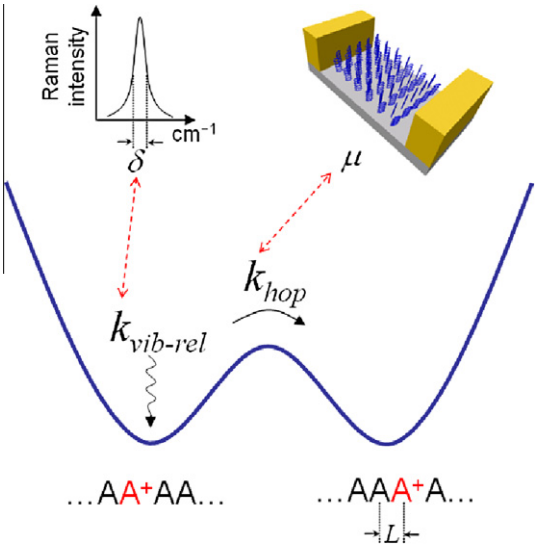

Fig. 1. Schematics of the argument presented in the main text. If one can define a hopping rate between two states such that the charge in the two states is localized in adjacent molecules (separated by a distance L), the hopping k_{hop} rate must be slower than the vibrational relaxation rate $k_{vib-rel}$. The first can be related to the experimentally measurable charge mobility μ and the second to the linewidth δ of vibrational spectroscopic measurements.

Acknowledgment

The author is grateful to the Levelhulme Trust for supporting this work.

References

[1] J.E. Anthony, Angew. Chem. Int. Ed. 47 (2008) 452;
M.H. Yoon, A. Facchetti, C.E. Stern, T.J. Marks, J. Am. Chem. Soc. 128 (2006) 5792.
[2] A.M. van de Craats, J.M. Warman, A. Fechtenkötter, J.D. Brand, M.A. Harbison, K. Müllen, Adv. Mater. 11 (1999) 1469.
[3] M.T. Rispens, A. Meetsma, R. Rittberger, C.J. Brabec, N.S. Sariciftci, J.C. Hummelen, Chem. Commun. (2003) 2116.
[4] Y. Yamamoto, T. Fukushima, Y. Suna, N. Ishii, A. Saeki, S. Seki, S. Tagawa, M. Taniguchi, T. Kawai, T. Aida, Science 314 (2006) 1761;
M.J. Frampton, H.L. Anderson, Angew. Chem. Int. Ed. 46 (2007) 1028.
[5] A. Nitzan, Chemical Dynamics in Condensed Phases, Oxford University Press, New York, 2006.
[6] R. Marcus, Annu. Rev. Phys. Chem. 15 (1964) 155.
[7] J.C. Bellows, P.N. Prasad, J. Chem. Phys. 70 (1979) 1864.
[8] J.C. Owrutsky, D. Raftery, R.M. Hochstrasser, Annu. Rev. Phys. Chem. 45 (1994) 519;
P. Ranson, R. Ouillon, S. Califano, Chem. Phys. Lett. 86 (1984) 115;
S. Califano, V. Schettino, Int. Rev. Phys. Chem. 7 (1988) 19.
[9] C. Panero, R. Bini, V. Schettino, J. Chem. Phys. 100 (1994) 7938.
[10] The line broadening at room temperature can be few times larger than the broadening at low temperature because of the effect of pure dephasing (see Refs. [8,9]). If, for a particular system, one only knows the line broadening at room temperature the magnitude of can be still estimated with reasonable accuracy.
[11] X.L. Feng, V. Marcon, W. Pisula, M.R. Hansen, J. Kirkpatrick, F. Grozema, D. Andrienko, K. Kremer, K. Mullen, Nat. Mater. 8 (2009) 421.
[12] R.B. Campbell, J.M. Robertson, J. Trotter, Acta Crystallogr. 15 (1962) 289.
[13] V.C. Sundar, J. Zaumseil, V. Podzorov, E. Menard, R.L. Willett, T. Someya, M.E. Gershenson, J.A. Rogers, Science 303 (2004) 1644.
[14] J.E. Anthony, D.L. Eaton, S.R. Parkin, Org. Lett. 4 (2002) 15.
[15] O.D. Jurchescu, J. Baas, T.T.M. Palstra, Appl. Phys. Lett. 84 (2004) 3061.
[16] (a) V. Coropceanu, J. Cornil, D.A. da Silva, Y. Olivier, R. Silbey, J.L. Bredas, Chem. Rev. 107 (2007) 926;
(b) F. Ortmann, F. Bechstedt, K. Hannewald, Phys. Status Solidi B-Basic Solid State Phys. 248 (2011) 511;
(c) A. Troisi, Chem. Soc. Rev. 50 (2011) 4039.
[17] (a) S.W. Yin, Y.F. Lv, Org. Electron. 9 (2008) 852;
(b) S.H. Wen, A. Li, J.L. Song, W.Q. Deng, K.L. Han, W.A. Goddard, J. Phys. Chem. B 113 (2009) 8813;
(c) M. Rossi, K. Sohlberg, J. Phys. Chem. C 113 (2009) 6821.
[18] S. Di Motta, E. Di Donato, F. Negri, G. Orlandi, D. Fazzi, C. Castiglioni, J. Am. Chem. Soc. 131 (2009) 6591.
[19] G.J. Nan, L.J. Wang, X.D. Yang, Z.G. Shuai, Y. Zhao, J. Chem. Phys. 130 (2009) 024704.
[20] H. Ma, M. Gruebele, J. Comput. Chem. 27 (2006) 125.

[21] D.P. McMahon, A. Troisi, Chem. Phys. Chem. 11 (2010) 2067.
[22] O. Ostroverkhova, D.G. Cooke, F.A. Hegmann, J.E. Anthony, V. Podzorov, M.E. Gershenson, O.D. Jurchescu, T.T.M. Palstra, Appl. Phys. Lett. 88 (2006) 162101.
[23] C.D. Dimitrakopoulos, P.R.L. Malenfant, Adv. Mater. 14 (2002) 99.
[24] H. Sirringhaus, Adv. Mater. 21 (2009) 3859.
[25] D.P. McMahon, A. Troisi, Phys. Chem. Chem. Phys. 13 (2011) 10241.

dyes for DSSCs application. Using this strategy, many novel D–π–A metal-free dyes with various donor moieties, such as coumarin [4], indoline [5], triarylamine [6], [bis(dimethylfluorenyl)amino]phenyl [7], phenothiazine [8], tetrahydroquinoline [9], carbazole [10], porphyrin [11], dithieno[3,2-*b*:2′,3′-*d*]thiophene [12], and pyrrole [13], have been designed and synthesized as efficient sensitizers for DSSCs in recent years. PCEs up to ~9% have been achieved for DSSCs using these metal-free dyes [4]. Moreover, highly impressive PCEs (~10%) and excellent stability were also reported in very recent publications [14]. Developing novel and highly efficient metal-free organic dyes applied in DSSCs is thus an area of strong current research activity [3].

The π-conjugated bridge connecting the donor and acceptor in the dye influences not only the region of light absorbed by the DSSCs but also the degree of electron injection from the dye's excited state to the TiO_2 surface. Aromatic moiety is usually used as efficient bridge in the design of dye molecules. Thiophene-based aromatic compounds have been demonstrated as the effective π-conjugated bridges by several research groups [15], including ours [6g]. Imahori et al. [16] investigated the effects of 5-membered heteroaromatic bridges on structures of porphyrin films and photovoltaic properties of porphyrin-based DSSCs. Recently, Wang and co-workers [17] also studied the influence of different heteroaromatic bridges on photovoltaic properties of triphenylamine-based organic dyes.

Aromatic hydrazone compounds are widely studied and used as organic nonlinear optical materials [18] and organic hole-transport materials for electrophotographic photoreceptors [19]. The main advantages of such compounds are the simple synthesis and high enough charge mobilities [19b]. Many triphenylamine- [20], carbazole- [21] and thiophene-based hydrazone [22] compounds were synthesized and used as glass-forming hole-transport materials. Squaraine-based compounds containing *N*,*N*-diphenylhydrazone moiety were synthesized and applied as efficient small molecule donors in bulk-heterojunction solar cells [23]. In addition, Tran-Van et al. recently reported on the synthesis and application of biscarbazole and terthiophene derivatives containing hydrazone functional groups as hole-transport materials in solid-state DSSCs [24]. However, aromatic hydrazones compounds until now are few studied as photoactive dyes for DSSCs. Therefore, we became interested in constructing metal-free organic dyes with hydrazone moiety to make use of its excellent hole-transport property for the electron donor.

Expanding on the foregoing points and as another try of our efforts to explore new metal-free dyes, we herein report on the design and synthesis of four D–π–A dyes (**HB**, **HP**, **HF**, and **HT**, as shown in Fig. 1) consisting of an *N*,*N*-diphenylhydrazone donor, a 2-cyanoacetic acid acceptor, and a different aromatic bridge, i.e., benzene, pyrrole, furan, and thiophene. The effects of the π-conjugated bridges on the photophysical, electrochemical and photovoltaic properties of these dyes were investigated in detail. To the best of our knowledge, this is the first time to develop hydrazones-based compounds as metal-free organic dyes used in DSSCs. Once again, our results indicate that π-conjugated bridge would have a large impact on photoelectronic properties of the metal-free dyes sensitized TiO_2 cells.

2. Experimental

2.1. Materials and reagents

1,1-Diphenylhydrazine hydrochloride, terephthalaldehyde, 2-furaldehyde, 2-thienaldehyde, thiophene, pyrrole, and 2-ethylhexyl bromide were purchased from commercial suppliers (Pacific ChemSource and Alfa Aesar) in analytical grade. 2-Carbaldehyde-*N*-ethylhexyl-pyrrole was synthesized according to the previous published procedure [25]. Toluene was dried and distilled over sodium/benzophenone. DMF, $CHCl_3$, and CH_3CN were dried over by accustomed methods and distilled before using. All other solvents and chemicals used in this work were analytical grade and used without further purification. All chromatographic separations were carried out on silica gel (200–300 mesh).

2.2. Characterization

^1H NMR spectra was recorded on a Bruker Avance 400 instrument. Ultraviolet–visible (UV–vis) spectra of the dyes were measured on a Perkin-Elmer Lamada 25 spectrometer. The PL spectra were obtained using Perkin-Elmer LS-50 luminescence spectrometer. FT-IR spectra were obtained on Perkin-Elmer Spectra One spectrophotometer. The elemental analysis of all compounds were performed with a Perkin-Elmer 2400 analyzer for C, H, N, and S determination. Electrochemical redox potentials were obtained by cyclic voltammetry (CV) using a three-electrode cell and an electrochemistry workstation (CHI830B, Chenhua Shanghai). The working electrode was a Pt ring electrode; the auxiliary electrode was a Pt wire, and saturated calomel electrode (SCE) was used as reference electrode. Tetrabutylammonium hexafluorophosphate (Bu_4NPF_6) 0.1 M was used as supporting electrolyte in dry acetonitrile. Ferrocene was added to each sample solution at the end of the experiments, and the ferrocenium/ferrocene (Fc^+/Fc) redox couple was used as an internal potential reference. The potentials of dyes versus NHE were calibrated by addition of 0.63 V to the potentials versus Fc^+/Fc [6a]. The solutions were purged with argon and stirred for 15 min before the measurements. Electrochemical impedance experiments for DSSCs were carried out in the dark with an electrochemical workstation (ZAHNER ZENNIUM) at room temperature. Electrochemical impedance spectra (EIS) were scanned in a frequency range of 10^{-1}–100 kHz with applied potential set at open-circuit. The alternate current (AC) amplitude was set at 10 mV. Geometry optimization and electronic structure calculations of the hydrazone-based dyes were performed using B3LYP functional and 3-21G* basis set implemented in the Gaussian 03 program package. Molecular orbitals were visualized by GaussView 3.0 software.

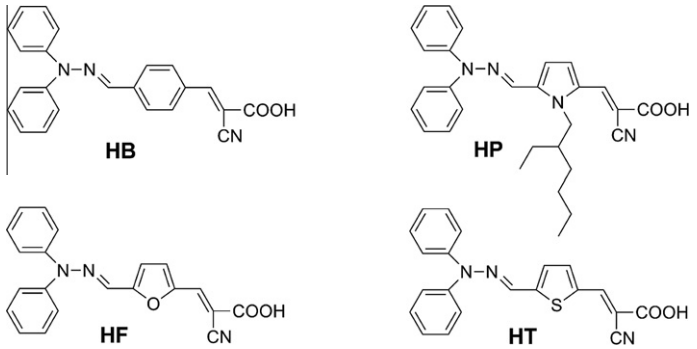

Fig. 1. Molecular structures of the dyes **HB**, **HP**, **HF**, and **HT**.

2.3. General procedure for fabrication and characterization of DSSCs

Fluorine-doped SnO_2 conducting glass (FTO) were cleaned and immersed in aqueous 40 mM $TiCl_4$ solution at 70 °C for 30 min, then washed with water and ethanol, sintered at 450 °C for 30 min. The TiO_2 colloid was prepared from 12 g P25 (Degussa AG, Germany) following the literature procedure [4]. First the 20–30 nm particles sized TiO_2 colloid was coated onto the above FTO glass by sliding glass rod method to obtain a TiO_2 film of 14 μm thickness after drying. Subsequently, the 200 nm particles sized TiO_2 colloid was coated on the electrode by the same method, resulting in a TiO_2 light-scattering layer of 5 μm thickness. The double-layer TiO_2-coated FTO glass were sintered at 450 °C for 30 min, then treated with $TiCl_4$ solution and calcined at 450 °C for 30 min again. After cooling to 100 °C, the TiO_2 electrodes were soaked in a CH_3CN solution with 0.5 mM dyes (and 1 mM chenodeoxycholic acid as a coadsorbent) and kept at room temperature under dark for 24 h.

The dye-adsorbed TiO_2 electrode washed with ethanol and dried. A drop of electrolyte solution was deposited onto the surface of the electrode and a Pt foil counter electrode was clipped onto the top of the TiO_2 electrode to assemble a dye sensitized solar cells for photovoltaic performance measurements. The electrolyte consisted of 0.5 M LiI, 0.05 M I_2, and 0.5 M 4-*tert*-butylpyridine (TBP) in 3-methoxypropionitrile and the efficient irradiated area of cell was 0.196 cm^2. The photocurrent–voltage (*J*–*V*) characteristics of solar cells were measured using a Keithley 2602 Source meter under the 100 Mw/cm^2 irradiation of a 500 W Xe lamp with a global AM 1.5 filter for solar spectrum simulation. Meanwhile, the photoelectric conversion efficiency was calculated. The measurement of monochromatic incident photon-to-current conversion efficiencies (IPCE) was performed by a Zolix DCS300PA Data acquisition system and other optical system.

2.4. Synthesis

The synthetic routes to the four dyes were shown in Scheme 1. The detailed synthetic procedures were as follows.

2.4.1. 4-Carbaldehyde-benzene-N,N-diphenylhydrazone (**1**)

Under nitrogen atmosphere, a solution of *N*,*N*-diphenylhydrazine hydrochloride (0.88 g, 4 mmol) in 30 mL of THF was added dropwise into the mixture of terephthalaldehyde (0.94 g, 7 mmol), sodium acetate (0.82 g, 10 mmol) and anhydrous MeOH (20 mL) at the room temperature. The mixture was refluxed for 24 h and the color changed gradually from yellow to dark brown. After cooling, the resulting mixture was quenched with 40 mL distilled water and extracted with chloroform. The combined organic layer was washed with distilled water and brine, dried over anhydrous $MgSO_4$. The solvent was removed by rotary evaporation. The crude product was purified by silica gel column chromatography with petroleum ether/dichloromethane (5/1, v/v) as eluent to yield **1** as a yellow solid. Yield: 67% (0.85 g). FT-IR (KBr, cm^{-1}): 1667 ($\nu_{C=O}$). ^1H NMR (400 MHz, $CDCl_3$): δ (ppm) 9.97 (s, 1H), 7.83–7.85 (d, 2H, *J* = 8.0 Hz), 7.73–7.75 (d, 2H, *J* = 8.0 Hz), 7.48–7.44 (m, 4H), 7.25–7.23 (m, 6H), 7.15 (s, 1H). Elem. Anal. Calcd. for $C_{20}H_{16}N_2O$: C, 79.98%; H, 5.37%; N, 9.33%. Found: C, 79.70%; H, 5.85%; N, 9.56%.

2.4.2. The general synthetic procedure of (**2**)

In a 100 mL three-necked flask, a solution of *N*-ethylhexylpyyrole-2-carbaldehyde (or 2-furaldehyde or 2-thienaldehyde, 5 mmol) in 30 mL of THF was added dropwise into the mixture of *N*,*N*-diphenylhydrazine hydrochloride (1.54 g, 7 mmol), sodium acetate (0.82 g, 10 mmol) and anhydrous MeOH (20 mL) under nitrogen atmosphere. The mixture was refluxed for 24 h and the color turned gradually from yellow to dark brown. After cooling, the resulting mixture was quenched with 40 mL distilled water and extracted with chloroform. The combined organic layer was washed with distilled water and brine, dried over anhydrous $MgSO_4$. The solvent was removed by rotary evaporation. The crude product was purified by silica gel column chromatography with petroleum ether/dichloromethane (4/1, v/v) as eluent.

*2.4.2.1. N-Ethylhexylpyrrole-2-carbaldehyde-N,N-diphenylhydrazone (**2a**).* Yield: 76% (1.42 g). ^1H NMR (400 MHz, $CDCl_3$): δ (ppm) 7.46–7.42 (m, 5H), 7.24–7.17 (m, 5H), 7.10 (s, 1H), 6.88 (s, 1H), 6.67–6.65 (m, 2H), 4.34 (d, 2H, *J* = 5.6 Hz), 1.31–1.01 (m, 9H), 0.85 (t, 3H, *J* = 7.3 Hz), 0.72 (t, 3H, *J* = 7.2 Hz). Elem. Anal. Calcd. for $C_{25}H_{31}N_3$: C, 80.39%; H, 8.37%; N, 11.25%. Found: C, 80.40%; H, 8.47%; N, 11.66%.

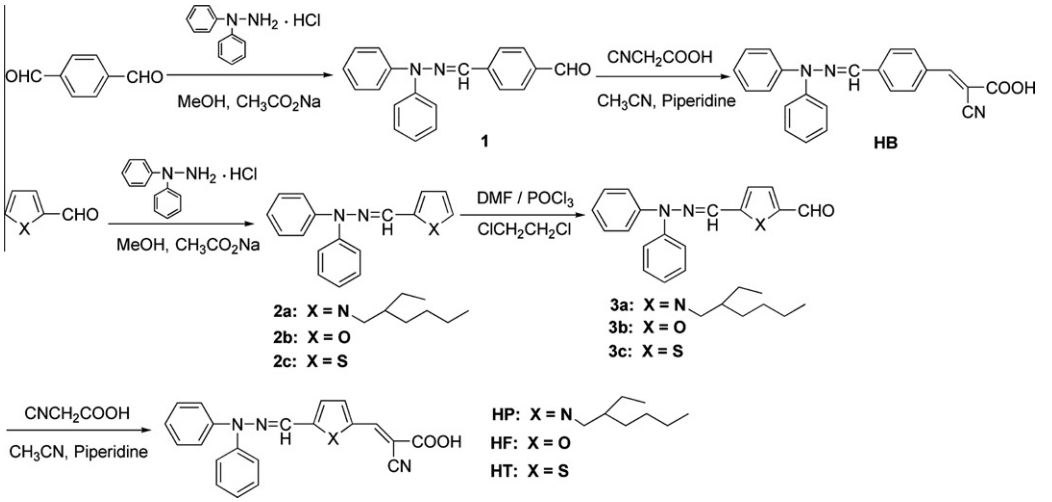

Scheme 1. Synthesis of the **HB**, **HP**, **HF**, and **HT** dyes.

*2.4.2.2. Furan-2-carbaldehyde-N,N-diphenylhydrazone (**2b**).* Yield: 70% (0.92 g). ^{1}H NMR (400 MHz, $CDCl_3$): δ (ppm) 7.43–7.39 (m, 6H), 7.20–7.27 (m, 5H), 7.08 (s, 1H), 6.46–6.42 (m, 2H). Elem. Anal. Calcd. for $C_{17}H_{14}N_2O$: C, 77.84%; H, 5.38%; N, 10.68%. Found: C, 77.52%; H, 5.47%; N, 10.80%.

*2.4.2.3. Thiophene-2-carbaldehyde-N,N-diphenylhydrazone (**2c**).* Yield: 72% (1.0 g). ^{1}H NMR (400 MHz, $CDCl_3$): δ (ppm) 7.44–7.42 (m, 4H), 7.31 (s, 1H), 7.27 (s, 1H), 7.22–7.20 (m, 6H), 7.97–7.93 (m, 2H). Elem. Anal. Calcd. for $C_{17}H_{14}N_2S$: C, 73.35%; H, 5.07%; N, 10.06%; S, 11.52%. Found: C, 73.50%; H, 5.07%; N, 10.50%; S, 11.58%.

*2.4.3. The general synthetic procedure of (**3**)*

In a 100 mL three-necked flask, compound **2** (2 mmol) and dried DMF (0.23 mL, 3 mmol) were dissolved into 1,2-dichloroethane (20 mL). After the solution was cooled to 0 °C, $POCl_3$ (0.27 mL, 3 mmol) was added dropwise. The mixture was stirred at room temperature for 0.5 h and then heated up to reflux for another 12 h. After cooling to room temperature, saturated aqueous solution of NaOAc (20 mL) was added into the reaction mixture and stirred violently for 1 h. Then the resulting mixture was extracted with chloroform. The combined organic layer was washed with distilled water and brine, dried over anhydrous $MgSO_4$. Solvent was removed by rotary evaporation, and the crude product was purified by silica gel column chromatography with petroleum ether/dichloromethane (5/1, v/v) as eluent.

*2.4.3.1. 5-Formyl-N-ethylhexypyrrolel-2-carbaldehyde-N,N-diphenylhydrazone (**3a**).* Yield: 83% (0.67 g). FT-IR (KBr, cm^{-1}): 1666 ($\nu_{C=O}$). ^{1}H NMR (400 MHz, $CDCl_3$): δ (ppm) 9.45 (s, 1H), 7.46–7.42 (m, 5H), 7.24–7.17 (m, 5H), 7.09 (s, 1H), 6.90 (d, 1H, J = 4.1 Hz), 6.67 (d, 1H, J = 4.2 Hz), 4.33 (d, 2H, J = 5.8 Hz), 1.26–1.03 (m, 9H), 0.83 (t, 3H, J = 7.1 Hz), 0.70 (t, 3H, J = 7.4 Hz). Elem. Anal. Calcd. for $C_{26}H_{31}N_3O$: C, 77.77%; H, 7.78%; N, 10.46%. Found: C, 77.40%; H, 7.97%; N, 10.66%.

*2.4.3.2. 5-Formyl-furan-2-carbaldehyde-N,N-diphenylhydrazone(**3b**).* Yield: 81% (0.39 g). FT-IR (KBr, cm^{-1}): 1665 ($\nu_{C=O}$). ^{1}H NMR (400 MHz, $CDCl_3$): δ (ppm) 9.56 (s, 1H), 7.46–7.43 (m, 6H), 7.26–7.23 (m, 4H), 7.19 (d, 1H, J = 3.5 Hz), 7.07(s, 1H), 6.81 (d, 1H, J = 3.2 Hz). Elem. Anal. Calcd. for $C_{18}H_{14}N_2O_2$: C, 74.47%; H, 4.86%; N, 9.65%. Found: C, 74.32%; H, 4.77%; N, 9.80%.

*2.4.3.3. 5-Formyl-thiophene-2-carbaldehyde-N,N-diphenylhydrazone (**3c**).* Yield: 85% (0.52 g). FT-IR (KBr, cm^{-1}): 1668 ($\nu_{C=O}$). ^{1}H NMR (400 MHz, $CDCl_3$): δ (ppm) 9.86 (s, 1H), 7.63 (d, 1H, J = 3.5 Hz), 7.62 (s, 1H), 7.48 (d, 1H, J = 3.5 Hz), 7.47–7.45 (m, 4H), 7.27–7.21 (m, 2H), 6.99–6.98 (m, 4H). Elem. Anal. Calcd. for $C_{18}H_{14}N_2OS$: C, 70.56%; H, 4.61%; N, 9.14%; S, 10.47%. Found: C, 70.50%; H, 4.67%; N, 9.16%; S, 10.53%.

2.4.4. The general synthetic procedure of sensitizers

Under nitrogen atmosphere, a mixture of compound **1** (or **3**, 1.2 mmol), 2-cyanoacetic acid (0.21 g, 2.4 mmol), piperidine (0.5 mL), and CH_3CN (30 mL) was refluxed at 80 °C for 24 h. After cooling, most of solvent was removed under vacuum and the residue was dropped into a mixture of petroleum ether and HCl (0.1 M) to form a precipitation. The crude product was further purified by silica gel column chromatograph eluted with dichloromethane/methanol (15/1, v/v) to obtain dyes.

2.4.4.1. 5-(2-Cyanoacrylicacid-3-yl)-benzene-2-carbalde-hyde-N,N-diphenylhydrazone (HB). Yield: 72% (0.32 g). FT-IR (KBr, cm^{-1}): 2227 ($\nu_{C\equiv N}$), 1693 ($\nu_{C=O}$). ^{1}H NMR (400 MHz, $CDCl_3$): δ (ppm) 8.27 (s, 1H), 7.85 (s, 1H), 7.76–7.55 (m, 4H), 7.30–7.26 (m, 6H), 7.24–7.19 (m, 4H). Elem. Anal. Calcd. for $C_{23}H_{17}N_3O_2$: C, 75.19%; H, 4.66%; N, 11.44%. Found: C, 75.30%; H, 4.97%; N, 11.60%.

2.4.4.2. 5-(2-Cyanoacrylicacid-3-yl)-N-ethylhexylpyrrole-2-carbaldehyde-N,N-diphen-ylhydrazone (HP). Yield: 74% (0.42 g). FT-IR (KBr, cm^{-1}): 2210 ($\nu_{C\equiv N}$), 1670 ($\nu_{C=O}$). ^1H NMR (400 MHz, $CDCl_3$): δ (ppm) 8.04 (s, 1H), 7.84 (d, 1H, J = 4.5 Hz), 7.08 (s, 1H), 7.52–7.44 (m, 4H), 7.21–7.17 (m, 6H), 6.82 (d, 1H, J = 4.6 Hz), 4.05 (d, 2H, J = 7.4 Hz), 1.55–1.11 (m, 9H), 0.84 (t, 3H, J = 7.0 Hz), 0.75 (t, 3H, J = 7.3 Hz). Elem. Anal. Calcd. for $C_{29}H_{32}N_4O_2$: C, 74.33%; H, 4.88%; N, 11.96%. Found: C, 74.10%; H, 4.97%; N, 11.60%.

2.4.4.3. 5-(2-Cyanoacrylicacid-3-yl)-furan-2-carbaldehyde-N,N-diphenylhydrazone (HF). Yield: 72% (0.31 g). FT-IR (KBr, cm^{-1}): 2221 ($\nu_{C\equiv N}$), 1685 ($\nu_{C=O}$). ^1H NMR (400 MHz, $CDCl_3$): δ (ppm) 7.96 (s, 1H), 7.48–7.44 (m, 6H), 7.28–7.26 (m, 4H), 7.22 (d, 1H, J = 3.5 Hz), 7.03 (s, 1H), 6.82 (d, 1H, J = 3.5 Hz). Elem. Anal. Calcd. for $C_{21}H_{15}N_3O_3$: C, 70.58%; H, 4.43%; N, 11.76%. Found: C, 70.30%; H, 4.57%; N, 11.80%.

2.4.4.4. 5-(2-Cyanoacrylicacid-3-yl)-thiophene-2-carbalde-hyde-N,N-diphenylhydrazone (HT). Yield: 74% (0.33 g). FT-IR (KBr, cm^{-1}): 2213 ($\nu_{C\equiv N}$), 1673 ($\nu_{C=O}$). ^1H NMR (400 MHz, DMSO-d_6): δ (ppm) 8.36 (s, 1H), 7.82 (d, 1H, J = 3.4 Hz), 7.52 (s, 1H), 7.50 (d, 1H, J = 3.5 Hz), 7.37–7.26 (m, 6H), 7.19–7.17 (m, 4H). Elem. Anal. Calcd. for $C_{21}H_{15}N_3O_2S$: C, 67.54%; H, 4.05%; N, 11.25%; S, 8.59%. Found: C, 67.58%; H, 4.07%; N, 11.60%; S, 8.63%.

3. Results and discussion

3.1. Synthesis and characterization of sensitizers

The synthesis of the four hydrazone-based organic dyes **HB**, **HP**, **HF**, and **HT** is outlined in Scheme 1. The three dyes **HP**, **HF**, and **HT** were synthesized by the similar stepwise synthetic protocol. Firstly, the five-membered heterocyclic aldehyde (2-furaldehyde, 2-thienaldehyde or 2-carbaldehyde-*N*-ethylhexyl-pyrrole) reacted with *N*,*N*-diphenylhydrazine hydrochloride to afford five-membered heterocycle-based hydrazone **2a**, **2b** or **2c** according to the previous reports [22,23] in high yields. Then Vilsmeier formylation of **2a**, **2b** and **2c** afforded the key intermediates **3a**, **3b** and **3c** with good yields (81–85%), respectively. Finally, Knoevenagel condensation reactions of aldehyde derivatives **3a**, **3b** or **3c** with twofold excess of cyanoacetic acid afforded the target dyes **HP**, **HF**, or **HT** in acetonitrile using piperidine as catalyst. Compared to the former three dyes, the dye **HT** with the phenyl unit as the conjugated bridge was synthesized by a relatively simple procedure. *N*,*N*-Diphenylhydrazine hydrochloride was reacted with excess terephthalaldehyde to afford compound **1**. Then **1** reacted with cyanoacetic acid by Knoevenagel condensation to give the dye **HT**. The structures of all dye molecules were characterized unambiguously with FT-IR, ^1H NMR spectroscopy and elemental analyze.

3.2. Optical properties

In DSSCs, sensitizer is a key and unique component with a function of light harvesting. Its spectral response overlapped with the solar emission will affect the device photocurrent to a large extent; thus, we measured the ultraviolet–visible (UV–vis) absorptions of the dyes **HB**, **HP**, **HF**, and **HT** both in THF solutions and on TiO_2 films (Fig. 2 and Fig. 3, respectively). The characteristic data are collected in Table 1.

All the dyes exhibit two distinct absorption bands (Fig. 2): one absorption band is in the UV region (280–350 nm) corresponding to the π–$\pi*$ electron transitions of the conjugated molecules; and the other is in the visible region (380–550 nm) that can be assigned to an intramolecular charge transfer (ICT) between the *N*,*N*-diphenylhydrazone donating unit and the cyanoacrylic acid acceptor moiety [26]. It can be seen that the maximum absorption (λ_{max}) of the visible region red-shifts from 425 nm to 452 nm, 465 nm, and 469 nm for **HB**, **HF**, **HT** and **HP**, respectively. This red-shifted phenomenon may be ascribed to the different aromatic ability of the three five-membered heteroaromatic bridges. The aromatic ability of furan is larger than that of thiophene and pyrrole due to the stronger electronegative of oxygen element than that of nitrogen and sulphur elements. We can see that the λ_{max} values in the visible region shift to a lower energy with the decreased electronegativity of heteroatoms, which is in accordance with results of Wang et al. [17].

As depicted in Table 1, the molar extinction coefficient (ε) of the ICT bands of the four dyes ($15.9–24.6 \times 10^3$ M^{-1} cm^{-1}) are higher than that of the standard N719 sensitizer (14.2×10^3 M^{-1} cm^{-1}) [27], indicating a better ability of light harvesting of these new *N*,*N*-diphenylhydrazone-based metal-free organic dyes than that of classical organometallic dyes. Moreover, the ε of the ICT bands increases in the order of **HB** < **HT** < **HF** < **HP**, which suggests that **HP** should hold the best ability of light harvesting. The higher ε of the organic dyes allows a correspondingly thinner nanocrystalline film so as to avoid the decrease of the film mechanical strength. This also benefits the electrolyte diffusion in the film and reduces the recombination possibility of the light-induced charges during transportation [28].

When the dyes were attached on TiO_2 films, the absorption spectra may shift more or less as compared with that

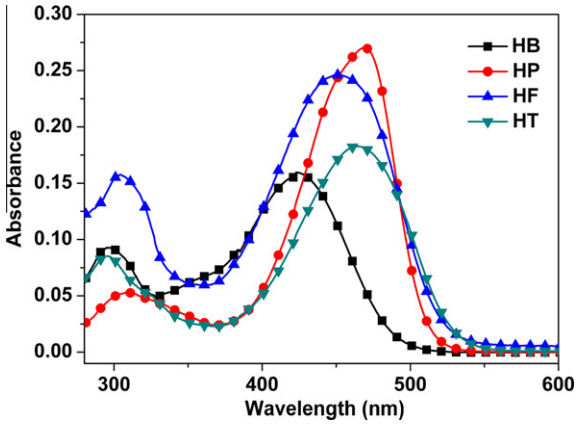

Fig. 2. Absorption spectra of the four dyes in THF solutions (10^{-5} M) at 25 °C.

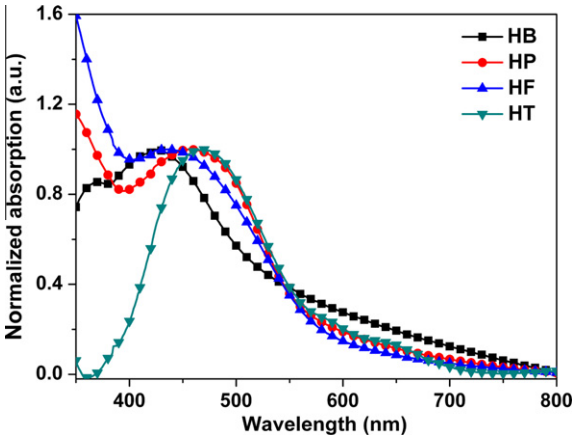

Fig. 3. Absorption spectra of the four dyes adsorbed on TiO_2 surface.

Table 1
Maximum absorption and emission data of the four dyes.

Dye	λ_{max}[a] ([c]ε/M^{-1} cm^{-1})		λ_{max}[b]/nm
HB	425(15,900)	295(9300)	418
HP	469(27,000)	310(5300)	457
HF	452(24,600)	304(15,800)	437
HT	465(18,300)	295(8500)	469

[a] Maximum absorption in THF solutions (10^{-5} M).
[b] Maximum absorption on TiO_2 films.
[c] ε is the molar extinction coefficient at λ_{max} of maximum absorption.

in solutions because of strong interactions between the dyes and the semiconductor surface, which can lead to form aggregates of the dyes on semiconductor surface, such as *H*-aggregation for the blue shift or *J*-aggregation for the red shift. From Figs. 2 and 3 and Table 1, it can be seen that absorption spectra of the dyes **HB**, **HP**, and **HF** on TiO_2 films displayed broader and a blue shift of 7 nm, 12 nm, and 15 nm, respectively, compared to those in THF solutions due to *H*-aggregation. However, the absorption spectrum of **HT** on TiO_2 film red shifted (4 nm) slightly in comparison with that in solution, indicating the dye possesses the *J*-aggregation on semiconductor surface. Another noteworthy feature in the spectra of dyes adsorbed on TiO_2 surfaces is an apparent tailing toward longer wavelength region (Fig. 3). In solutions the low energy edge of absorption bands does not exceed 550 nm (Fig. 1), yet on TiO_2 the absorption threshold extends to 750 nm. The long wavelength absorption should be result from the formation of a certain degree of aggregates on the surface of TiO_2. The absorption of aggregates is responsible for the induction of photocurrent in the regions of $\geqslant$600 nm (Fig. 5).

3.3. Electrochemical properties

While a good light absorption is an essential requirement for photovoltaic cells, the following charge generation from the closely bound electron–hole pair (Frenkel exciton) confined in a single organic molecule [29] also determines device operation. This process is triggered at the interface between a donor component and an acceptor component (dye and titania in DSSC), featuring a favorite energy alignment, although a hot electron injection is also possible [30]. Here we measured the oxidation potential of the four dyes by means of cyclic voltammetry (CV) to evaluate the possibility of electron transfer from the excited dye molecule to the conductive band of TiO_2. CV was performed in CH_3CN with 0.1 M Bu_4NPF_6 as a supporting electrolyte (Fig. 4). Table 2 summarizes all the electrochemical properties of the four dyes.

The first oxidation potential vs. NHE (E_{ox}), which corresponds to the highest occupied molecular orbital (HOMO vs. NHE), was calibrated by addition of 0.63 V to the potential (vs. SCE) vs. Fc/Fc^+ by CV (Table 2). The first oxidation potentials of the four dyes **HB**, **HP**, **HF**, and **HT** were measured as 1.23, 1.15, 1.28, and 1.29 V, respectively. It is easy to see that the negative shifts of the E_{ox} (0.08, 0.13, and 0.14 V) were observed for **HB**, **HF**, and **HT** vs. **HP**, respectively, which means that **HP** has the lowest HOMO level among the four dyes. The decrease of HOMO levels of the dyes could show a positive effect on the DSSCs performance due to the narrower gap between the HOMO level and the redox potential of iodine/iodide leading to less waste of energy [17]. We also can see that all the HOMO levels of four dyes are more positive than the iodide/triiodide redox couple (~0.42 V vs. NHE), indicating that the oxidized dyes formed after electron injection into the conduction band of TiO_2 could accept electrons from I^- ions in the electrolyte thermodynamically.

By neglecting any entropy change during light absorption, the reduction potential vs. NHE (E_{red}), which corresponds to the lowest unoccupied molecular orbital (LUMO vs. NHE), can be obtained from E_{ox} and E_{0-0} value determined from the intersection of absorption and emission spectra, namely, $E_{ox}-E_{0-0}$. The calculated LUMO levels of **HB**, **HP**, **HF**, and **HT** were −1.33, −1.36, −1.21, and −1.09 V vs. NHE (Table 2), respectively, which all are sufficiently higher than that of the conduction band (CB) level of TiO_2 (−0.5 V vs. NHE). Provided that energy gap (E_{gap}) between LUMO levels and CB level of TiO_2 of 0.2 eV is necessary for efficient electron injection [4a], these driving

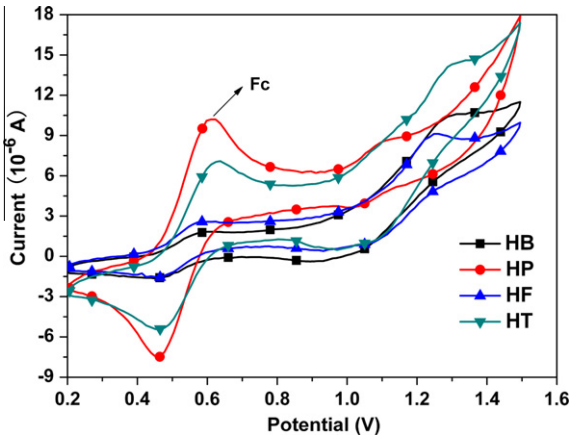

Fig. 4. Cyclic voltammograms of the three dyes: working electrode, Pt ring; auxiliary electrode, Pt wire; reference electrode, Hg/Hg_2Cl_2; scanning rate is 100 mV/s.

Table 2
Electrochemical data of the four dyes [a].

Dye	λ_{int}/nm	E_{0-0}/eV	E_{ox}/V vs. NHE	E_{red}/V vs. NHE	E_{gap}/V
HB	485	2.56	1.23	−1.33	0.83
HP	495	2.51	1.15	−1.36	0.86
HF	498	2.49	1.28	−1.21	0.71
HT	520	2.38	1.29	−1.09	0.59

[a] E_{0-0} values were calculated from intersection of the normalized absorption and the emission spectra (λ_{int}): $E_{0-0} = 1240/\lambda_{int}$. The first oxidation potential (vs. NHE), E_{ox} was measured in acetonitrile and calibrated by addition of 0.63 V to the potential versus Fc/Fc^+. The reduction potential, E_{red}, was calculated from $E_{ox}-E_{0-0}$. E_{gap} is the energy gap between the E_{red} of dye and the CB level of TiO_2 (−0.5 V vs. NHE).

forces are sufficiently large for effective electron injection. Therefore, the four dyes used as sensitizers will have sufficient driving force for electron transfer from the excited dye molecules to the CB of TiO_2 electrode. Noticeably, the relatively large E_{gap} of the dyes allow for the addition of the 4-tertbutylpyridine (TBP) into the electrolyte, which can shift the conduction band of TiO_2 negatively about 0.3 V and consequently improve the open-circuit voltage (V_{oc}) and total power energy conversion efficiency (PCE) [31]. The E_{gap} of the four dyes ranges from 0.59 (**HT**) to 0.86 eV (**HP**) (Table 2). Accordingly, an increased E_{gap} may yield higher V_{oc} and enhance the PCE considerably, which predicts the dye **HP** may give a higher V_{oc} and PCE.

These above-discussed results indicate that the introduction of aromatic cycles (benzene, pyrrole, furan and thiophene) in π-conjugated bridges could easily tune the absorption spectra and HOMO and LUMO energy levels of the dyes.

3.4. Molecular orbital calculations

In order to gain an insight into the molecular structure and electron distribution, density functional theory (DFT) calculations were performed on the four dyes using the Gaussian 03 program package. In particular we used B3LYP as exchange-correlation functional and 3-21G* as basis set. The electron distribution of the HOMO and LUMO of the dye**s** is shown in Table 3. It is obvious that the electron density of HOMO is localized mainly on the *N*,*N*-diphenylhydrazone moiety and is extended along the π-conjugated bridge to the central region of the molecule. On the other hand, the LUMO is localized over the cyanoacrylic unit through aromatic bridges. We notice that the HOMO–LUMO excitation induced by light irradiation could move the electron distribution from the *N*,*N*-diphenylhydrazone unit to the cyanoacrylic acid moiety via aromatic π-conjugated bridges and the photo-induced electron transfer from the dyes to the TiO_2 electrode can occur efficiently by the HOMO–LUMO transition.

3.5. Photovoltaic performance of DSSCs

DSSCs were fabricated using these dyes as the sensitizers, with an effective area of 0.196 cm^2, TiO_2 particles on FTO, and the electrolyte composed of 0.5 M LiI, 0.05 M I_2, and 0.5 M 4-*tert*-butyl-pyridine (TBP) in 3-methoxy-propionitrile. Fig. 5 shows incident photon-to-electron conversion efficiency (IPCE) as a function of the wavelength for the sandwiched DSSCs based on the four dyes as sensitizers. As shown in Fig. 5, the IPCE of **HP** sensitizer exceeds 60% in the spectral region from 400 to 520 nm, reaching its maximum over 80% at 425 nm, while other three dyes produce maximum IPCE about 60%. The relatively higher maximum IPCE for **HP** compared with other three dyes is well in agreement with the tendency of UV–vis absorption properties. In comparison with **HB** and **HF**, **HT** exhibits a broader IPCE spectrum. These results imply that **HP** and **HT** would show a relatively large photocurrent in DSSCs. Additionally, it should be noted that the four dyes still show weak IPCE response at the range of long wavelength region (650–750 nm), as shown in Fig. 5. We believe that this feature should be ascribed two reasons: one is the weak absorption band of the dyes on TiO_2 films at the range of 650–750 nm (see Fig. 3), which is consistent with our and the other reports [32]; the other is the effect of light scattering by TiO_2 nanoparticles, which increases the photocurrents for the weak absorption in that region.

Fig. 6 shows current density–voltage (*J*–*V*) characteristics of devices based on the four dyes. The detailed photovoltaic parameters of the short-circuit photocurrent density (J_{sc}), open-circuit photovoltage (V_{oc}), fill factor (FF), and power conversion efficiency (PCE) are listed in Table 4. According to Fig. 6, it is clear that the photovoltaic performances of the DSSCs can be evidently affected by the aromatic bridges in the dye molecules. The PCE increases in the order of **HB** (4.39%) < **HF** (4.66%) < **HT** (5.29%) < **HP** (7.18%). **HP** exhibits the best PCE due to both the highest J_{sc} (14.76 mA/cm^2) and V_{oc} (0.69 V) values. Obviously, the tendency of a gradually increased PCEs for the four dyes with various aromatic bridges shows be along with the increase of J_{sc}. Consistent with the increased tendency of IPCE, the measured J_{sc} increases in the order of **HB** (9.64 mA/cm^2) < **HF** (10.62 mA/cm^2) < **HT** (11.04 mA/cm^2) < **HP** (14.76 mA/cm^2). In view of the similar configuration and anchoring mode of the four sensitizers, we compare their ratios of molar extinction coefficients and the absorptivities of dye coated titania films, deducing that **HB** has a lower surface coverage than those of other three dyes. In addition, the remarkably increased J_{sc} value of **HP** compared with other three dyes can be ascribed to its relatively better light harvesting ability, reflecting in its better IPCE spectrum.

Generally, V_{oc} becomes low along with the decrease of aromatic ability of aromatic π-conjugated bridges. The improved V_{oc} value (0.69 V) of **HP** compared to other three dyes (0.61–0.67 V) could be attributed to the following two aspect reasons. One is that the additional hydrophobic alkyl chain of pyrrole bridge in **HP** can effectively retard the charge recombination between injected electron and I_3^- ions in the electrolyte, which is favorable for increasing the electron lifetimes and hence to improve V_{oc} [33a,6i,6h,11b]. We will discuss it in detail as the following electrochemical impedance spectroscopy studies. The other reason can be attributed to the comparatively lower-lying HOMO of the **HP** (estimated from the CV), which offers enough larger driving force for the reduction of the oxidized dye. This, in turn, will lead to a slower back

Table 3
Frontier molecular orbitals of the HOMO and LUMO calculated with DFT on a B3LYP/3-21G* level of the four dyes.

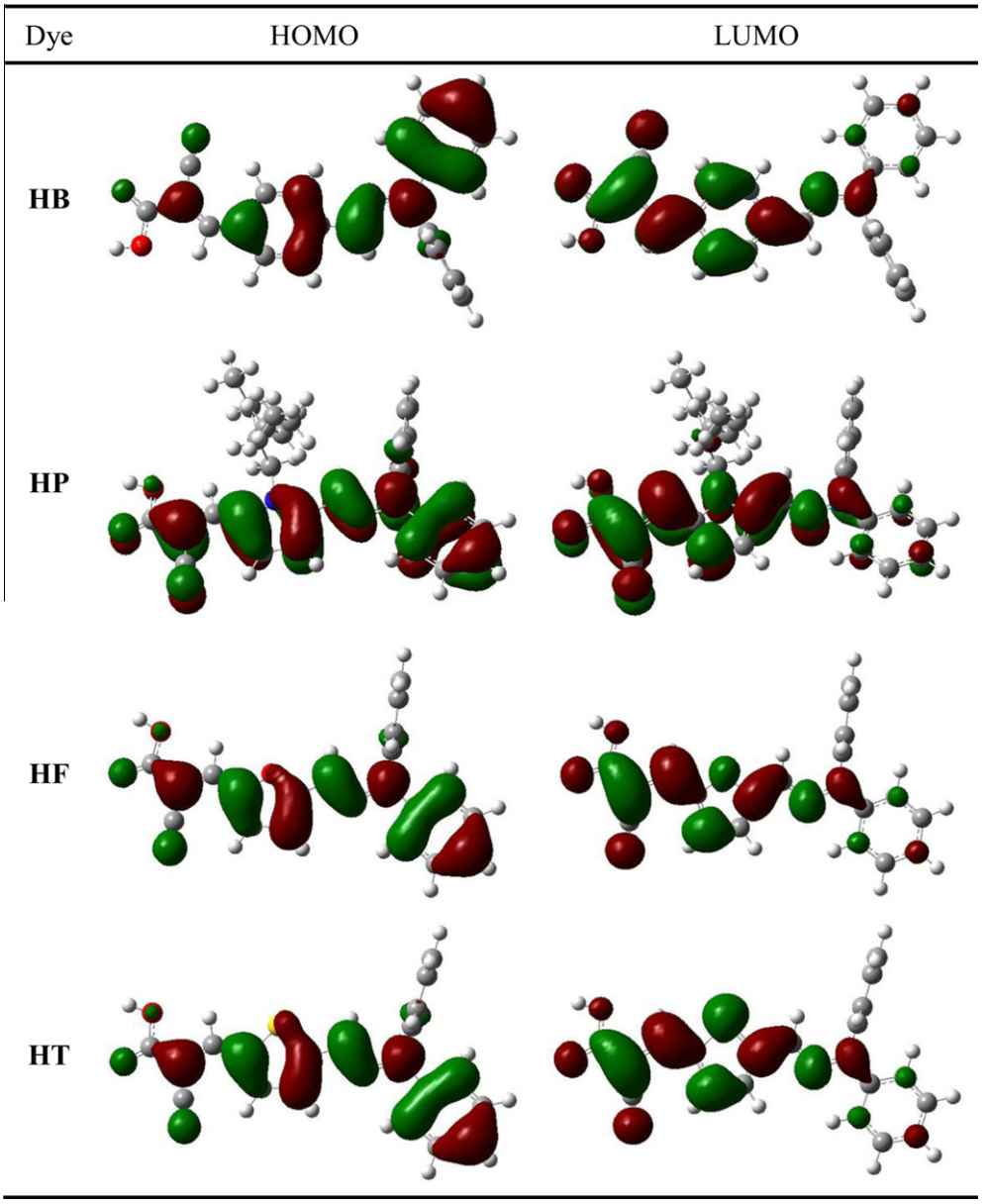

electron transfer from TiO_2 to the dye and result in a lager V_{oc} value [33b].

It has been reported that chenodeoxycholic acid (CDCA) can enhance the performance of the DSSCs because CDCA can reduce the aggregation of the dyes on the TiO_2 surface [6g,8b,9a,34]. To investigate the influence of aggregation of dyes on the photovoltaic performance, CDCA was added into the dye solution as a coadsorbent and the relative photovoltaic data are also collected in Table 4. As shown in Table 4, after the addition of CDCA (1 mM) to the dye bath, PCEs of DSSCs based on the four dyes are increased by 16%, 8%, 19%, and 10% for **HB**, **HP**, **HF**, and **HT** respectively, which results from the significant improvement of J_{sc} values. The obviously improved PCEs of **HB** (5.11%) and **HF** (5.54%) indicate that CDCA plays a important role in suppressing the aggregation conformation of dyes on TiO_2 surface. In the case of **HP** (7.74%), the relatively little increase implies that the CDCA has a slight impact on the aggregation the dye, which can be ascribe to effectively inhibiting aggregation of alkyl group to pyrrole unit [6g,10a,33a]. The above photovoltaic results indicate strongly that coadsorption of CDCA is effective to improve solar cell performance by suppressing the aggregation conformation of dyes on TiO_2 surface.

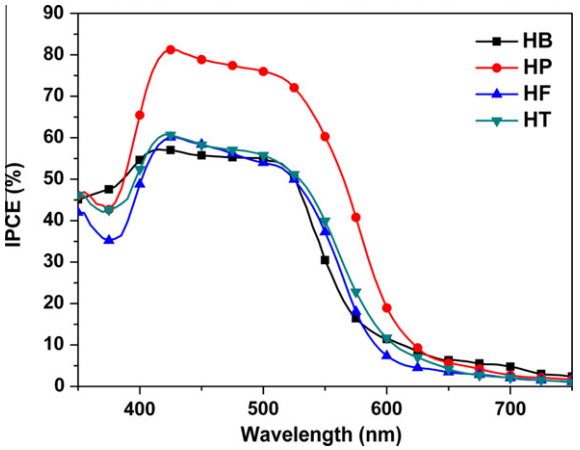

Fig. 5. IPCE plots for the DSSCs based on the four dyes.

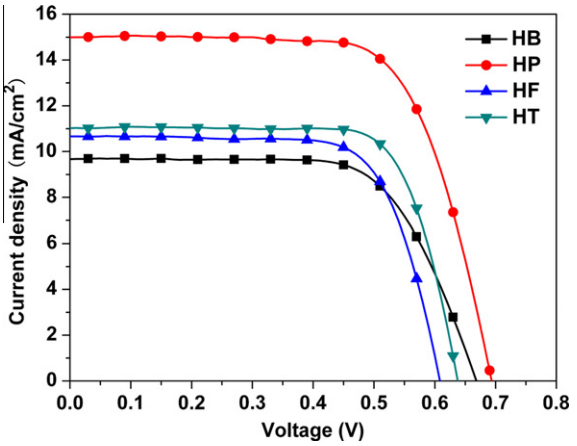

Fig. 6. The *J–V* characteristics for DSSCs based on the four dyes.

Table 4
Photovoltaic performance of DSSCs based on the four dyes.

Dye	J_{sc} (mA/cm^2)	V_{oc} (V)	FF	PCE (%)
HB[a]	9.64	0.67	0.680	4.39
HB[b]	11.35	0.66	0.682	5.11
HP[a]	14.76	0.69	0.705	7.18
HP[b]	16.17	0.69	0.694	7.74
HF[a]	10.62	0.61	0.719	4.66
HF[b]	12.78	0.62	0.699	5.54
HT[a]	11.04	0.64	0.749	5.29
HT[b]	12.69	0.65	0.707	5.83

[a] Dye bath: CH_3CN solution (0.5 mM).
[b] Dye bath: CH_3CN solution (0.5 mM) with addition of CDCA (1 mM). For all cells, the double-layer TiO_2 films are composed of ~14 μm transparent layer and ~5 μm scatter layer.

3.6. Electrochemical impedance spectroscopy studies

Electrochemical impedance spectroscopy (EIS) is a powerful technique of characterizing the important interfacial charge transfer processes in a DSSC. The EIS was measured in the dark to elucidate correlation of V_{oc} with those dyes. The Nyquist plots of DSSCs with four dyes are shown in Fig. 7. Three semicircles are observed in the Nyquist plots. The small and large semicircles respectively located in the high- and middle-frequency regions, are assigned to the charge transfer at Pt/electrolyte and TiO_2/dye/electrolyte interface, respectively [33]. Another small semicircle, which should have appeared at the low-frequency region, is overlapped by the middle-frequency large semicircle. The charge recombination resistance (R_{rec}) at the TiO_2 surface can be deduced by fitting curves from the range of the middle-frequency using a Z-view software. R_{rec} is related to the charge recombination rate between injected electron and electron acceptor (I_3^-) in the electrolyte, estimated by the large semicircle width. A large R_{rec} means the small charge recombination rate and vice versa. The R_{rec} values for **HP** and **HB** were estimated to be 186 and 97 Ω, respectively. In contrast, **HF** and **HT** were found to have relatively smaller R_{rec} values at 84 and 57 Ω, respectively. The result appears to be consistent with the larger V_{oc} values for the dyes **HP** (0.69 V) and **HB** (0.67 V). The significantly increased R_{rec} values of **HP** and **HB** imply the retardation of the charge recombination between injected electron and I_3^- ions in the electrolyte, with a consequent increase of V_{oc}.

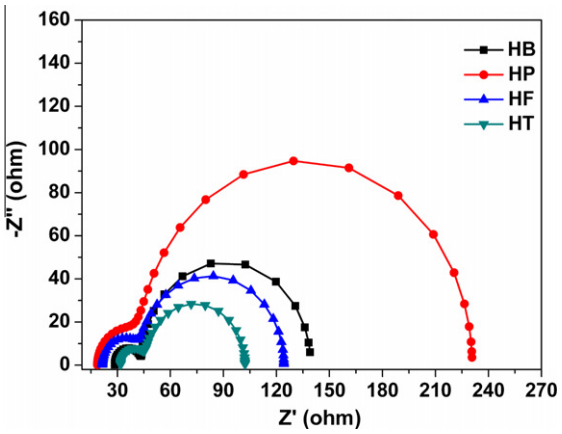

Fig. 7. EIS Nyquist plots for DSSCs based on the four dyes measured in the dark under −0.65 V bias.

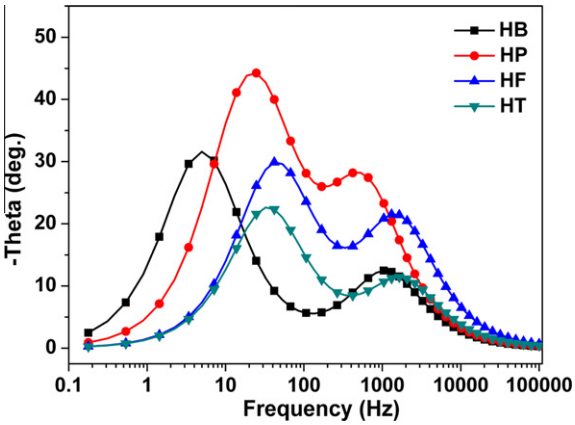

Fig. 8. EIS Bode plots for DSSCs based on the four dyes measured in the dark under −0.65 V bias.

At the same time, DSSCs based on **HP** and **HB** produced higher V_{oc} than **HF** and **HT**, which can be explained by the

electron lifetime. Fig. 8 shows the Bode plot for DSSCs based on **HB**, **HP**, **HF**, and **HT**. Two peaks in Fig. 8 located at the high-frequency (right) and middle-frequency (left) respectively correspond to the small semicircle (left) and large semicircle (right) in the Nyquist plots (Fig. 7). The reciprocal of the peak frequency for the middle-frequency peak is regarded as the electron lifetime since it represents the charge transfer process at the TiO_2/dye/electrolyte interface. It is evident that the electron lifetime for the DSSC based on **HT** and **HF** is smaller than those for DSSCs based on **HP** and **HB**, thereby explaining the V_{oc} increase from **HT** and **HF** to **HP** and **HB**.

4. Conclusions

In summary, we have designed and synthesized a series of novel hydrazone-based D–π–A dyes (**HB**, **HP**, **HF**, and **HT**), by employing different aromatic π-conjugated bridges such as benzene, pyrrole, furan, and thiophene in combination with the hydrophobic *N*,*N*-diphenylhydrazone donor and the hydrophilic cyanoacrylic acid acceptor. The effects of the aromatic π-conjugated bridges on the photophysical, electrochemical and photovoltaic properties of these dyes were extensively investigated. It was found that the absorption spectra and HOMO and LUMO energy levels can be conveniently tuned by alternating the aromatic bridges. Molecular orbital calculations showed that the HOMO–LUMO excitation could readily move the electron distribution from the *N*,*N*-diphenylhydrazone donor to the cyanoacrylic acid acceptor via aromatic π-conjugated bridges. We have also studied the influence of aromatic bridges on photovoltages through the electrochemical impedance experiments and achieved a preliminary conclusion that the high V_{oc} of **HP** based DSSC resulted from the relatively small charge recombination rate and long electron lifetime due to the additional hydrophobic alkyl chain of pyrrole bridge. DSSCs based on these dyes have achieved 5.11–7.74% PCEs when CDCA (1 mM) was added into the dye bath as a coadsorbent. For the first time we have proved that *N*,*N*-diphenylhydrazone and *N*-(2-ethylhexyl)-substituted pyrrole units can be employed as the effective and promising donor and π-conjugated bridge, respectively in D–π–A dyes, which expands the selection scope of building blocks for further dye design. Further structural modification of the π-conjugated bridge based on the series sensitizers to improve the photovoltaic performance is just ongoing.

Acknowledgements

This work was supported by the General Program of the Education Department of Hunan Province (No. 09C946), National Natural Science Foundation of China (No. 50973092, 21004050, 51003089), and National Natural Science Foundation of Hunan Province (No. 10JJ4007).

References

[1] M. Grätzel, Nature 414 (2001) 338.
[2] Q. Yu, Y. Wang, Z. Yi, N. Zu, J. Zhang, M. Zhang, P. Wang, ACS Nano 4 (2010) 6032.
[3] Y. Ooyama, Y. Harima, Eur. J. Org. Chem. (2009) 2903;
(b) A. Mishra, M.K.R. Fischer, P. Büerle, Angew. Chem. Int. Ed. 48 (2009) 2474;
(c) A. Hagfeldt, G. Boschloo, L. Sun, L. Kloo, H. Pettersson, Chem. Rev. 110 (2010) 6595.
[4] (a) K. Hara, T. Sato, R. Katoh, A. Furube, Y. Ohga, A. Shinpo, S. Suga, K. Sayama, H. Sugihara, H. Arakawa, J. Phys. Chem. B 107 (2003) 597;
(b) Z. Wang, Y. Cui, K. Hara, Y. Dan-oh, C. Kasada, A. Shinpo, Adv. Mater. 19 (2007) 1138;
(c) Z. Wang, Y. Cui, Y. Dan-oh, C. Kasada, A. Shinpo, K. Hara, J. Phys. Chem. C 111 (2007) 7224.
[5] (a) S. Ito, M. Zakeeruddin, R. Hummphrey-Baker, P. Liska, R. Charvet, P. Comte, M.K. Nazeeruddin, P. Péchy, M. Takata, H. Miura, S. Uchida, M. Grätzel, Adv. Mater. 18 (2006) 1202;
S. Ito, H. Miura, S. Uchida, M. Takata, K. Sumioka, P. Liska, P. Comte, P. Pechy, M. Grätzel, Chem. Commun. (2008) 5194.
[6] (a) D.P. Hagberg, T. Edvinsson, T. Marinado, G. Boschloo, A. Hagfeldt, L. Sun, Chem. Commun. (2006) 2245;
(b) S. Hwang, J.H. Lee, C. Park, H. Lee, C. Kim, C. Park, M.H. Lee, W. Lee, J. Park, K. Kim, N.G. Park, C. Kim, Chem. Commun. (2007) 4887;
(c) D.P. Hagberg, T. Marinado, K.M. Karlsson, K. Nonomura, P. Qin, G. Boschloo, T. Brinck, A. Hagfeldt, L. Sun, J. Org. Chem. 72 (2007) 9550;
(d) W. Xu, B. Peng, J. Chen, M. Liang, F. Cai, J. Phys. Chem. C 112 (2008) 874;
(e) G. Zhang, Y. Bai, R. Li, D. Shi, S. Wenger, S.M. Zakeeruddin, M. Grätzel, P. Wang, Energy Environ. Sci. 2 (2009) 92;
(f) L.-Y. Lin, C.-H. Tsai, K.-T. Wong, T.-W. Huang, L. Hsieh, S.-H. Liu, H.-W. Lin, C.-C. Wu, S.-H. Chou, S.-H. Chen, A.-I. Tsai, J. Org. Chem. 75 (2010) 4778;
(g) P. Shen, Y. Liu, X. Huang, B. Zhao, N. Xiang, J. Fei, L. Liu, X. Wang, S. Tan, Dyes Pigm. 83 (2009) 187;
(h) H. Chen, H. Huang, X. Huang, John N. Clifford, A. Forneli, E. Palomares, X. Zheng, L. Zheng, X. Wang, P. Shen, B. Zhao, S. Tan, J. Phys. Chem. C 114 (2010) 3280;
(i) W. Zhu, Y. Wu, S. Wang, W. Li, X. Li, J. Chen, Z. S Wang, H. Tian, Adv. Funct. Mater. 21 (2011) 756.
[7] (a) S. Kim, J.K. Lee, S.O. Kang, J. Ko, J.H. Yum, S. Fantacci, F. DeAngelis, D. Dicenso, M.K. Nazeeruddin, M. Grätzel, J. Am. Chem. Soc. 128 (2006) 16701;
(c) I. Jung, J.K. Lee, K.H. Song, K. Song, S.O. Kang, J. Ko, J. Org. Chem. 72 (2007) 3652;
H. Choi, J.K. Lee, K. Song, S.O. Kang, J. Ko, Tetrahedron 63 (2007) 3115;
(d) H. Choi, C. Baik, S.O. Kang, J. Ko, M.S. Kang, M.K. Nazeeruddin, M. Grätzel, Angew. Chem. Int. Ed. 47 (2008) 327.
[8] (a) H.N. Tian, X.C. Yang, R.K. Chen, Y.Z. Pan, L. Li, A. Hagfeldt, L. Sun, Chem. Commun. (2007) 3741;
(b) D. Cao, J. Peng, Y. Hong, X. Fang, L. Wang, H. Meier, Org. Lett. 13 (2011) 1610.
[9] (a) R. Chen, X. Yang, H. Tian, X. Wang, A. Hagfeldt, L. Sun, Chem. Mater. 19 (2007) 4007;
(b) R. Chen, X. Yang, H. Tian, L. Sun, J. Photochem. Photobiol. A Chem. 189 (2007) 295.
[10] (a) N. Koumura, Z.S. Wang, S. Mori, M. Miyashita, E. Suzuki, K. Hara, J. Am. Chem. Soc. 128 (2006) 14256;
[b] D. Kim, J.K. Lee, S.O. Kang, J. Ko, Tetrahedron 63 (2007) 1913;
(c) C. Zafer, B. Gultekin, C. Ozsoy, C. Tozlu, B. Aydin, S. Icli, Sol. Energ. Mater. Sol. Cells 94 (2010) 655.
[11] (a) S.-L. Wu, H.-P. Lu, H.-Ti.Yu, S.-H. Chuang, C.-L. Chiu, C.-W. Lee, E.W.-G. Diau, C.-Y. Yeh, Energy Environ. Sci. 3 (2010) 949;
(b) Y. Liu, N. Xiang, X. Feng, P. Shen, W. Zhou, C. Weng, B. Zhao, S. Tan, Chem. Commun. (2009) 2499;
(c) C.-P. Hsieh, H.-P. Lu, C.-L. Chiu, C.-W. Lee, S.-H. Chuang, C.-L. Mai, W.-N. Yen, S.-J. Hsu, Eric W.-G. Diau, C.-Y. Yeh, J. Mater. Chem. 20 (2010) 1127;
(d) T. Bessho, S.M. Zakeeruddin, C.-Y. Yeh, Eric W.-G. Diau, M. Grätzel, Angew. Chem. Int. Ed. 49 (2010) 6646.
[12] H.-Y. Yang, Y.-S. Yen, Y.-C. Hsu, H.-H. Chou, J.T. Lin, Org. Lett. 12 (2010) 16.
[13] (a) Y.-S. Yen, Y.-C. Hsu, J.T. Lin, C.W. Chang, C.-P. Hsu, D. Yin, J. Phys. Chem. C 112 (2008) 12557;
(b) J.A. Mikroyannidis, M.S. Roy, G.D. Sharma, J. Power Sources 19 (2010) 5391.
[14] (a) G. Zhang, H. Bala, Y. Cheng, D. Shi, X. Lv, Q. Yu, P. Wang, Chem. Commun. (2009) 2198;
(b) W. Zeng, Y. Cao, Y. Bai, Y. Wang, Y. Shi, M. Zhang, F. Wang, C. Pan, P. Wang, Chem. Mater. 22 (2010) 1915.
[15] (a) W.-H. Liu, I.-C. Wu, C.-H. Lai, P.-T. Chou, Y.-T. Li, C.-L. Chen, Y.-Y. Hsu, Y. Chi, Chem. Commun. (2008) 5152;

(b) H. Qin, S. Wenger, M. Xu, F. Gao, X. Jing, P. Wang, S.M. Zakeeruddin, M. Grätzel, J. Am. Chem. Soc. 130 (2008) 9202;
(c) M. Xu, S. Wenger, H. Bala, D. Shi, R. Li, Y. Zhou, S.M. Zakeeruddin, M. Grätzel, P. Wang, J. Phys. Chem. C 113 (2009) 2966.
[16] S. Eu, S. Hayashi, T. Umeyama, A. Oguro, M. Kawasaki, N. Kadota, Y. Matano, H. Imahori, J. Phys. Chem. C 111 (2007) 3528.
[17] R. Li, X. Lv, D. Shi, D. Zhou, Y. Cheng, G. Zhang, P. Wang, J. Phys. Chem. C 113 (2009) 7469.
[18] O.-P. Kwon, M. Jazbinsek, H. Yun, J.-I. Seo, E.-M. Kim, Y.-S. Lee, P. Günter, Cryst. Growth Des. 8 (2008) 4021.
[19] (a) V. Getautis, M. Daskeviciene, T. Malinauskas, V. Gaidelis, V. Jankauskas, Z. Tokarski, Synth. Met. 155 (2005) 599;
(b) J.V. Grazulevicius, Polym. Adv. Technol. 17 (2006) 694;
(c) R. Lygaitis, V. Getautis, J.V. Grazulevicius, Chem. Soc. Rev. 3 (2008) 770.
[20] R. Budreckiene, G. Buika, J.V. Grazulevicius, V. Jankauskas, Z. Tokarski, Synth. Met. 156 (2006) 677.
[21] (a) G. Bubnienea, T. Malinauskasa, A. Stanisauskaitea, V. Jankauskasb, V. Getautis, Synth. Met. 159 (2009) 1695;
(b) A. Michaleviciute, J. Ostrauskaite, G. Buika, R. Lygaitis, J.V. Gražulevičius, V. Jankauskas, Synth. Met. 159 (2009) 218.
[22] (a) R. Lygaitis, J.V. Gražulevičius, F. Tran Van, C. Chevrot, V. Jankauskas, D. Jankunaite, J. Photochem. Photobiol. A: Chem. 181 (2006) 67;
(b) A. Michalevičiutė, R. Lygaitis, J.V. Gražulevičius, G. Buika, V. Jankauskas, A. Undzėnas, E. Fataraitė, Synth. Met. 159 (2009) 223.
[23] F. Silvestri, M.D. Irwin, L. Beverina, A. Facchetti, G.A. Pagani, T. Marks, J. Am. Chem. Soc. 130 (2008) 1764.
[24] R. Aich, F. Tran-Van, F. Goubard, L. Beouch, A. Michaleviciute, J.V. Gražulevičius, B. Ratier, C. Chevrot, Thin Solid Films 516 (2008) 7260.
[25] D.X. Liu, B. Zhao, P. Shen, H. Huang, L.M. Liu, S.T. Tan, Sci. China Ser. B-Chem. 52 (2009) 1198.
[26] S. Roquet, A. Cravino, P. Leriche, O. Alévêque, P. Frère, J. Roncali, J. Am. Chem. Soc. 128 (2006) 3459.
[27] P. Wang, B. Wenger, R. Humphry-Baker, J.-E. Moser, J. Teuscher, W. Kantlehner, J. Mezger, E.V. Stoyanov, S.M. Zakeeruddin, M. Grätzel, J. Am. Chem. Soc. 127 (2005) 6850.
[28] (a) A.C. Khazraji, S. Hotchandani, S. Das, P.V. Kamat, J. Phys. Chem. B 103 (1999) 4693;
(b) K. Sayama, K. Hara, N. Mori, M. Satsuki, S. Suga, S. Tsukagoshi, Y. Abe, H. Sugihara, H. Arakawa, Chem. Commun. (2000) 1173.
[29] M. Pope, C.E. Swenberg, Electronic Processes in Organic Crystals and Polymers, 2nd ed., Oxford University Press, Oxford, 1999.
[30] (a) R.T. Ross, A.J. Nozik, J. Appl. Phys. 53 (1982) 3813;
(b) S. Ardo, G.J. Meyer, Chem. Soc. Rev. 38 (2009) 115.
[31] K. Hara, T. Sato, R. Katoh, A. Furube, T. Yoshihara, M. Murai, M. Kurashige, S. Ito, A. Shinpo, S. Suga, H. Arakawa, Adv. Funct. Mater. 15 (2005) 246.
[32] (a) P. Shen, Y. Tang, S. Jiang, H. Chen, X. Zheng, X. Wang, B. Zhao, S. Tan, Org. Electron. 12 (2011) 125;
(b) Y.J. Chang, T.J. Chow, Tetrahedron 65 (2009) 9626.
[33] (a) Z. Wang, N. Koumura, Y. Cui, M. Takahashi, H. Sekiguchi, A. Mori, T. Kubo, A. Furube, K. Hara, Chem. Mater. 20 (2008) 3993;
(b) K.R.J. Thomas, Y.-C. Hsu, J.T. Lin, K.-M. Lee, K.-C. Ho, C.-H. Lai, Y.-M. Cheng, P.-T. Chou, Chem. Mater. 20 (2008) 1830;
(c) C. Longo, A.F. Nogueira, M.-A. De Paoli, H. Cachet, J. Phys. Chem. B 106 (2002) 5925;
(d) R. Kern, R. Sastrawan, J. Ferber, R. Stangl, J. Luther, Electrochim. Acta 47 (2002) 4213;
(e) F. Fabregat-Santiago, G. Garcia-Belmonte, I. Mora-Seró, J. Bisquert, Phys. Chem. Chem. Phys. 13 (2011) 9083.
[34] W. Xu, J. Pei, J. Shi, S. Peng, J. Chen, J. Power Sources 183 (2008) 792.

FTO conductors having varied textures were characterized for their physical, electrical and optical properties and were subjected to device studies to establish the correlation between FTO textures and device characteristics/performances.

2. Experiments

2.1. Characterization of textured FTO

Six FTO transparent conductors on glass substrates (samples #1–#6) having different textures and properties were purchased from commercial sources (Solaronix, Hartford Glass, and Nippon Sheet Glass). Their properties obtained from characterizations described below are summarized in Table 1.

Scanning electron microscopy (SEM) and atomic force microscopy (AFM) were used to characterize the morphology, surface topography and roughness of FTO films. The sheet resistances of FTO films were measured by the Van der Pauw method. A UV–Vis spectrophotometer equipped with an integrating sphere was used to characterize the transmittance and scattering properties of the FTO films. In this work, two types of transmittance were characterized: the total transmittance (T_{total}) and the direct transmittance (T_{direct}). T_{total} was measured by using a monochromatic light beam normally incident onto sample and then using an integrating sphere to collect transmitted light over all angles. On the other hand, T_{direct} was measured by using a monochromatic light beam normally incident onto the sample and then collecting transmitted light only in the normal direction (within a 5° collection angle). The haze values of FTO films, which are defined as the ratio of the diffusively transmitted light against the total transmitted light [25], were then obtained by Haze = $(T_{total} - T_{direct})/T_{total}$ at some specific wavelength, which is useful indication of the optical scattering capability of a thin film.

2.2. DSSC fabrication

Fig. 1 shows the schematic device structure of the DSSC using the textured FTO as the transparent conductor for the incident light. In fabrication of devices, the FTO glass substrates were first cleaned in a detergent solution using an ultrasonic bath and then were rinsed with water and ethanol. A layer of 20-nm-sized anatase TiO_2 nanoparticles was then coated on the FTO by the doctor-blade method. After drying the film at 120 °C, another layer of 400-nm-sized anatase TiO_2 nanoparticles was then coated as the light scattering layer. The resulting working electrode was composed of a 12-μm-thick transparent TiO_2 nanoparticle layer (average particle size: 20 nm) and a 4-μm-thick TiO_2 scattering layer (average particle size: 400 nm) [26]. The thickness of the TiO_2 nanoparticle layer had been optimized by

Table 1
Characteristics of different textured FTO films and characteristics of DSSCs fabricated on these different FTO films.

Characteristics of FTO films							Characteristics of DSSCs				
FTO sample	Thickness (nm)	Grain size (nm)	Roughness (nm)	Sheet resistance (Ω/□)	T_{total} (550 nm) (%)	Haze (550 nm) (%)	J_{sc} (mA/cm^2)	V_{oc} (V)	FF	Eff. (%)	Rct (Ω)
#1	~400	~100–200	9.14	15	85	2	14.87	0.80	0.69	8.18	63.6
#2	~400	~100–200	9.91	15	84	4	15.19	0.80	0.70	8.51	62.4
#3	~600	~300–400 + ~100–200	23.72	7	82	9	16.46	0.79	0.70	9.10	50.6
#4	~600	~400 + ~100–200	28.34	8	79	13	17.62	0.77	0.70	9.5	49.6
#5	~800	~400 + ~100–200	36.41	10	80	16	18.26	0.78	0.69	9.88	43.7
#6	~800	~400 + ~100–200	38.42	10	80	17	18.56	0.79	0.69	10.1	43.1

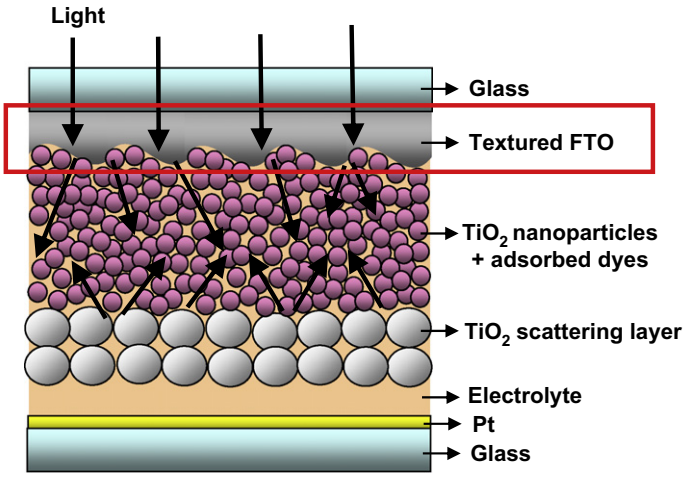

Fig. 1. The schematic device structure of the DSSC using the textured FTO as the transparent conductor for the incident light.

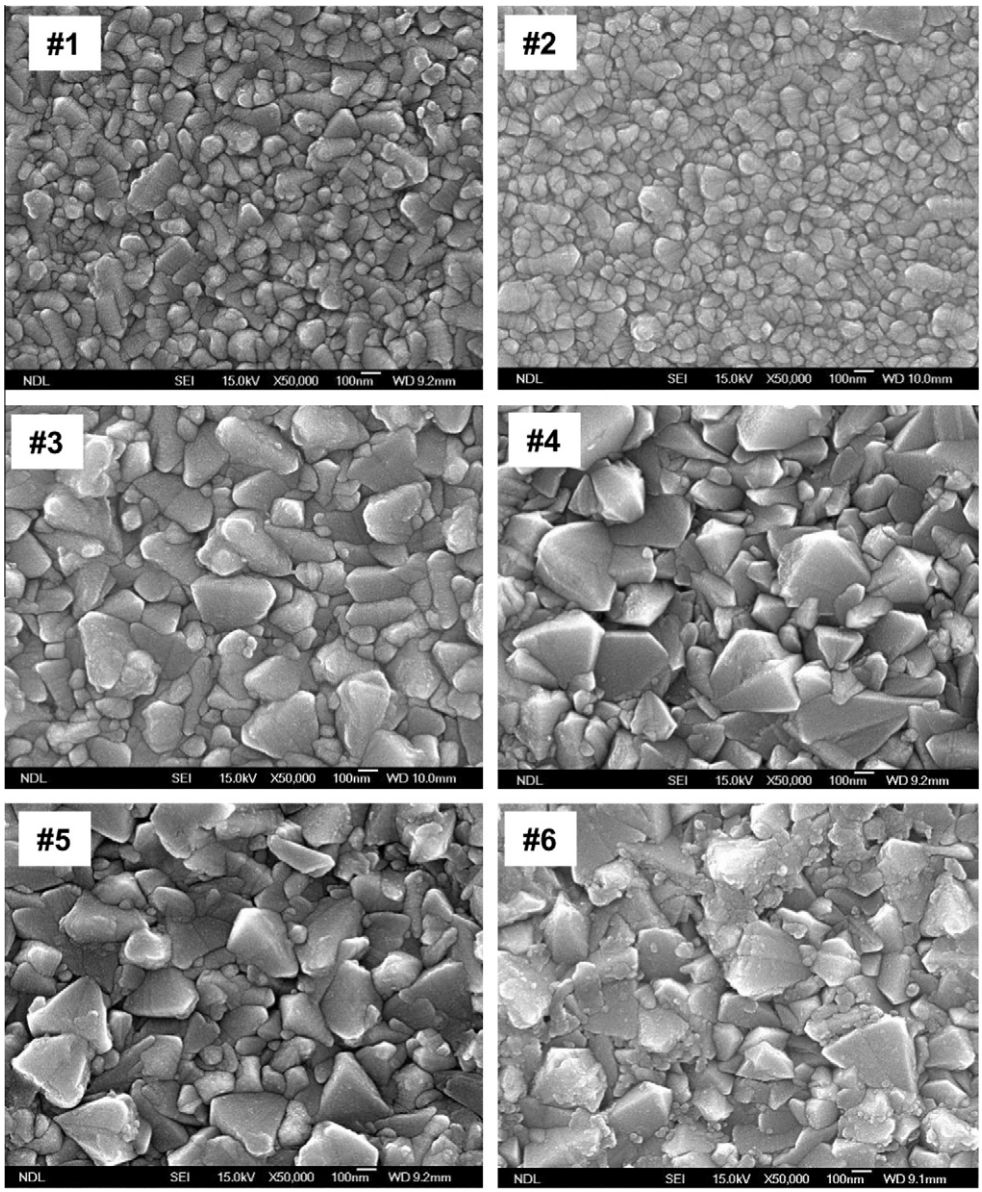

Fig. 2. SEM images of textured FTO samples #1–#6.

balancing the tradeoff between optical absorption and the electrical transport properties. The nanoporous TiO_2 electrodes were then heated in an atmospheric oven first by gradually ramping the temperature from 150 to 500 °C and then at 500 °C for 30 min. After cooling, the nanoporous TiO_2 electrodes were immersed into a dye solution at room temperature for 24 h for dye adsorption. The dye solution was composed of 0.5 mM ruthenium dye **N719**, [cis-di(thiocyanato)-N-N′-bis(2,2′-bipyridyl-4-carboxylic acid-4′-tetrabutyl-ammonium carboxylate) ruthenium (II)] [27], and 0.5 mM chenodeoxycholic acid (CDCA, as a co-adsorbent) in the acetonitrile/*tert*-butanol mixture (1:1) [28].

Counter electrodes of the DSSC were prepared by depositing 40-nm-thick Pt films on another glass substrates by e-beam evaporation. The dye-adsorbed TiO_2 working electrode and a counter electrode were then assembled into a sealed DSSC cell with a sealant spacer between the two electrode plates. A drop of the electrolyte solution [0.6 M 1-butyl-3-methylimidazolium iodide (BMII), 0.03 M I_2, 0.5 M 4-*tert*-butylpyridine, and 0.1 M guanidinium thiocyanate in a mixture of acetonitrile–valeronitrile (85:15, v/v)] was injected into the cell through a drilled hole [29]. Finally, the hole was sealed. An active device areas of 0.125 cm^2 was used for the device characterization.

2.3. DSSC characterization

The photocurrent–voltage (*I*–*V*) characteristics of the DSSCs were measured under illumination of the simulated

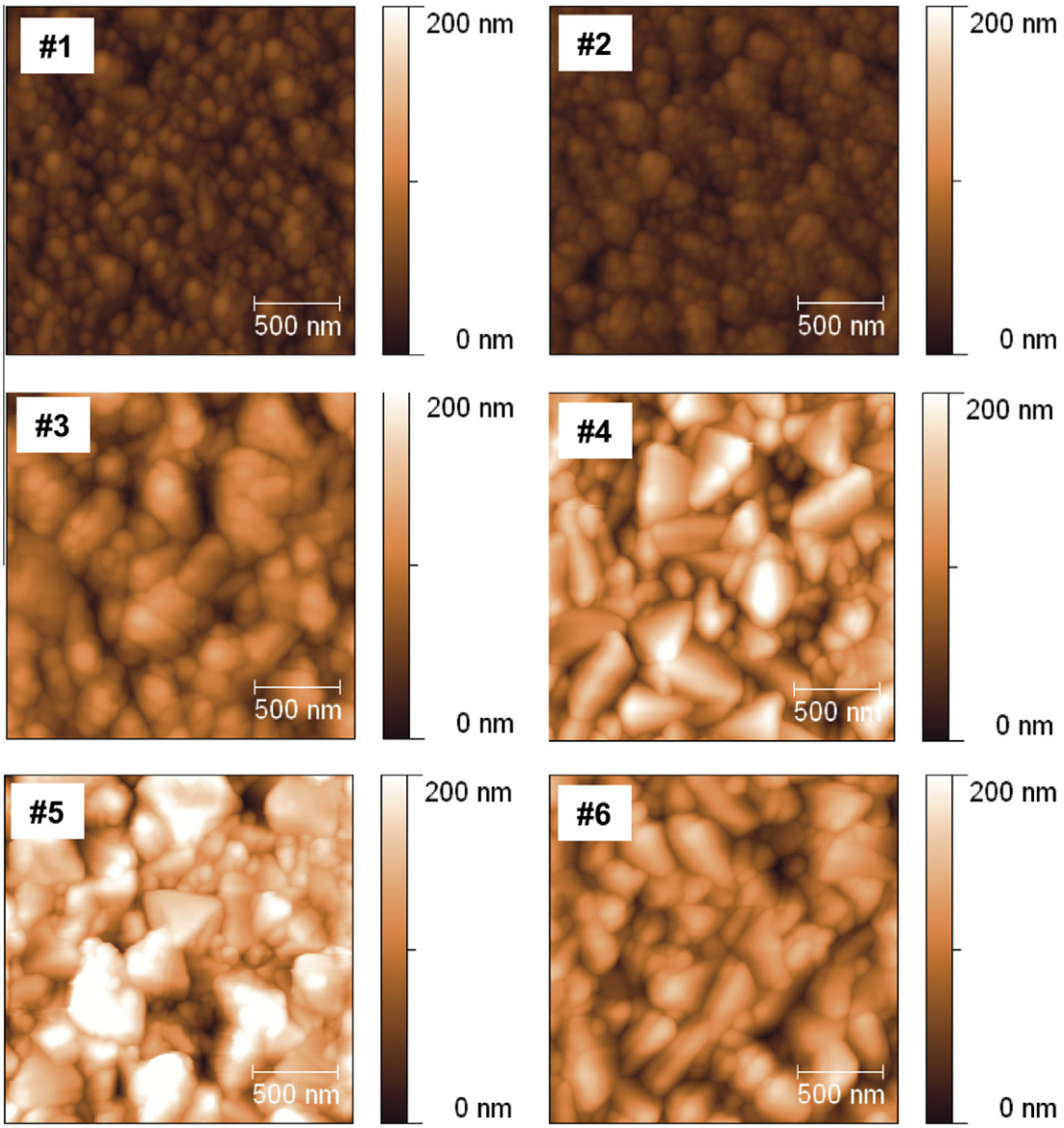

Fig. 3. AFM images of textured FTO samples #1–#6.

AM1.5G solar light from a 300-W Xenon lamp solar simulator. The incident light intensity was calibrated as 100 mW/cm^2. Photocurrent-voltage curves were obtained by applying an external bias voltage to the cell and measuring the generated photocurrent. The current–voltage characteristics of DSSCs were used to extract the short-circuit current density (J_{SC}), open-circuit voltage (V_{OC}), fill factor (FF), and power conversion efficiency (Eff.) of the DSSCs [30–32]. The incident photon-to-current conversion efficiency (IPCE) spectra of the devices were measured by using a 75-W Xenon arc lamp as the light source coupled to a monochromator. The IPCE data were taken by illuminating monochromatic light on the solar cells (with the wavelength from 300 to 800 nm) and measuring the short-circuit current of the solar cells [33]. The IPCE measurement was performed with a lock-in amplifier, a low speed chopper, and a bias light source under the full computer control.

In addition to the standard *I–V* and IPCE characterization of solar cells, in this study, the electrochemical impedance spectroscopy (EIS) was also used to analyze the internal impedance properties of DSSCs [34–36]. The electrochemical impedance spectroscopy of the cells was measured by using an impedance analyzer with a frequency range of 20–1 MHz. In this study, during the impedance measurement, the cell was under the constant AM 1.5G 100 mW/cm^2 illumination. The impedance of the cell (throughout the frequency range of 20–1 MHz) was then measured by applying a bias at the open-circuit voltage V_{OC} of the cell (namely, under the condition of no dc electric current) and by using an ac amplitude of 10 mV.

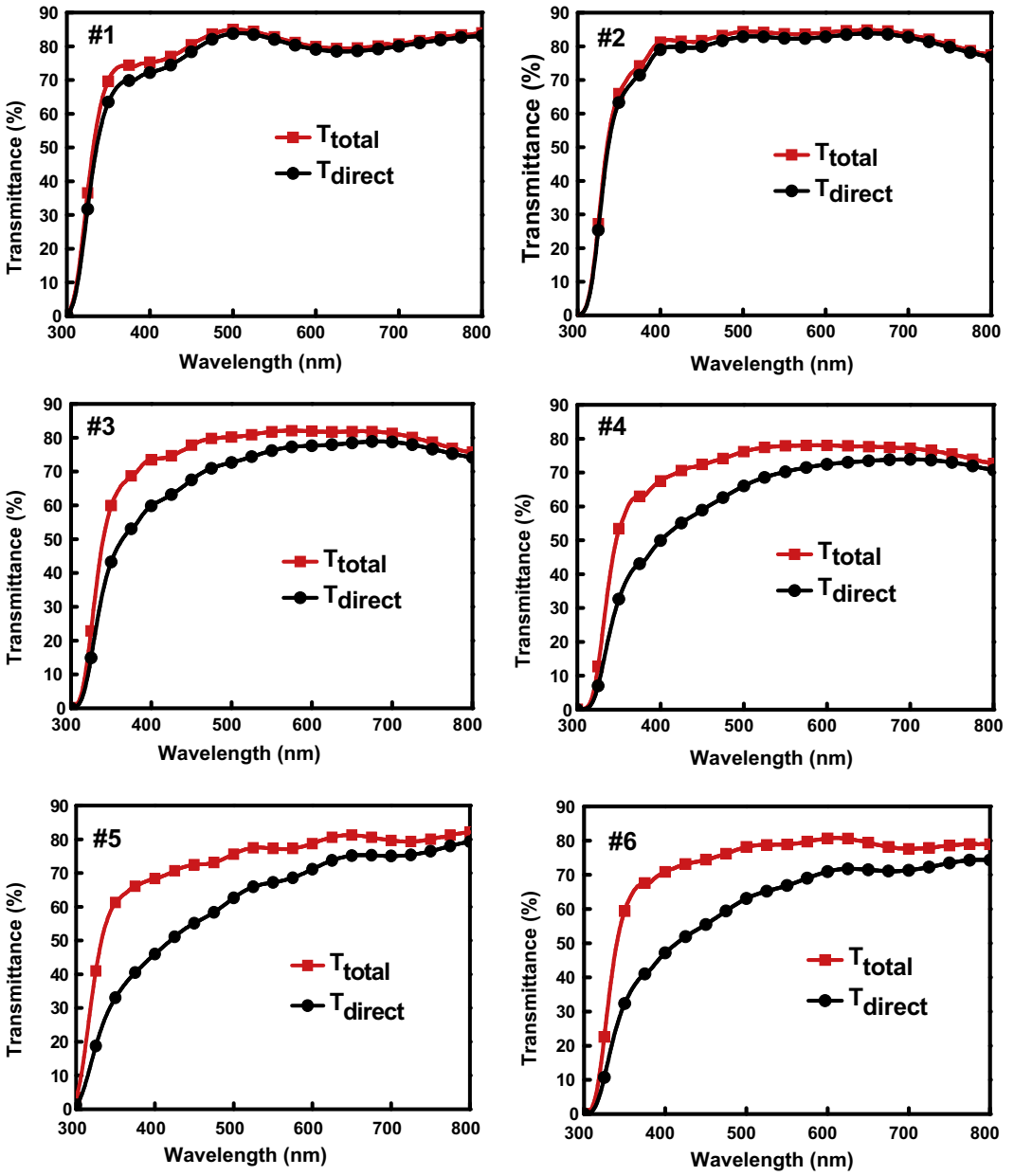

Fig. 4. Total transmittance (T_{total}) and the direct transmittance (T_{direct}) spectra of FTO samples #1–#6.

3. Results and discussions

3.1. Properties of textured FTO

Figs. 2 and 3 show the SEM and AFM images of the textured FTO samples #1–#6, respectively. In SEM images of Fig. 2, one sees that all FTO samples show grainy structures (textures) in the films. Samples #1 and #2 have smaller grain sizes of about 100–200 nm, while #3–#6 samples are composed of a mixture of larger grains and smaller grains. In #3, the sizes for smaller grains and larger grains are ~100–200 nm and ~300–400 nm, respectively. In #4–#6, the sizes of larger grains, with an average size of ~400 nm and with some grains even larger than 400 nm, are slightly larger than those in #3. Furthermore, larger grains in all #3–#6 samples exhibit the distinct pyramidal shape. While the sizes of the smaller grains in #4–#6 are also ~100–200 nm, they tend to show the pyramidal shape, in contrast with smaller grains in samples #1–#3. With the size of larger grains in #3–#6 (~400 nm) being similar to the optical wavelengths, one may expect a stronger scattering effect from these samples, compared to #1 and #2 samples. Topographical characteristics examined by AFM for #1–#6 samples are similar to/consistent with those observed by SEM. Yet the surface roughness can now be quantitatively determined from the AFM results.

#1 and #2 FTO films show smaller surface roughnesses of 9.14 and 9.91 nm, respectively, while samples #3, #4, #5 and #6 containing larger grains show significantly greater surface roughnesses of 23.72, 28.34, 36.41, and 38.42 nm, respectively. Indeed, the numbering of the FTO samples was based on their surface roughness (and haze as will be described). The grain sizes and surface roughnesses of all samples are summarized in Table 1, together with their sheet resistances measured by the Van der Pauw method and optical properties to be described below. All six FTO samples have small sheet resistances of 7–15 Ω/□.

Fig. 4 shows the total transmittance (T_{total}) and the direct transmittance (T_{direct}) spectra of FTO samples #1–#6. T_{total} and Haze (calculated from T_{total} and T_{direct} spectra) of FTO films #1–#6 at the wavelength of 550 nm are also summarized in Table 1. As can be seen in Fig. 4 and Table 1, the occurrence of larger grains (~400 nm, samples #3–#6) largely raises Haze values, and thus the optical scattering capability. From sample #1 to sample #6 (with increased surface roughness), the haze increases from 2% to 17%. The Haze tends to increase with the surface roughness and the highest haze of 17% was obtained in the FTO sample with the largest surface roughness (i.e. #6). The integrated total transmittance T_{total} of the textured FTO films is also critical for the overall efficiency of the DSSCs. A low T_{total} implies most of the incident light cannot transmit through the film (either directly or by scattering), but be scattered backward instead, not good for device efficiency. Therefore upon tuning the haze (and thus the scattering capability), simultaneously maintaining a high enough T_{total} is also important. In results of Fig. 4, it is seen that all six FTO samples exhibit rather high T_{total} of ~70–85% for a wide wavelength range above 400 nm. As shown in Table 1, at the wavelength of 550 nm, T_{total} of the six samples is in the range of 79–85%. Thus for these FTO samples, one acquires a haze value significantly varying from 2% to 17%, and yet still keeps similarly high total transmittance, making it possible to study effects of the haze/scattering of textured FTO films on DSSC characteristics without worrying about adverse effects of lowered overall transmittance.

3.2. Device characteristics of DSSCs using textured FTO

Fig. 5(a) and (b) shows the *I–V* and IPCE characteristics of six DSSCs fabricated on the six FTO samples, respectively. The photovoltaic characteristics of the six devices, including the short-circuit current J_{SC}, the open-circuit voltage V_{OC}, the fill factor FF, and the conversion efficiency (Eff.), are summarized in Table 1 and are also plotted versus the haze value of FTO in Fig. 6. From Figs. 5 and 6 and Table 1, one sees that the open-circuit voltage V_{OC} and the fill factor FF do not differ much among these six devices. Yet, the J_{SC} and power conversion efficiency of the six devices in general increases significantly with the texture sizes, the surface roughness, and the haze ratio of the FTO. The J_{SC} and the power conversion efficiency of DSSCs increased from (14.87 mA/cm^2, 8.18%) of the device on #1 FTO (haze = 2%) to (18.56 mA/cm^2, 10.1%) of the device on #6 FTO (haze = 17%). An enhancement of the conversion efficiency by ~24% was obtained with using the highly textured, large-roughness and high-haze FTO as

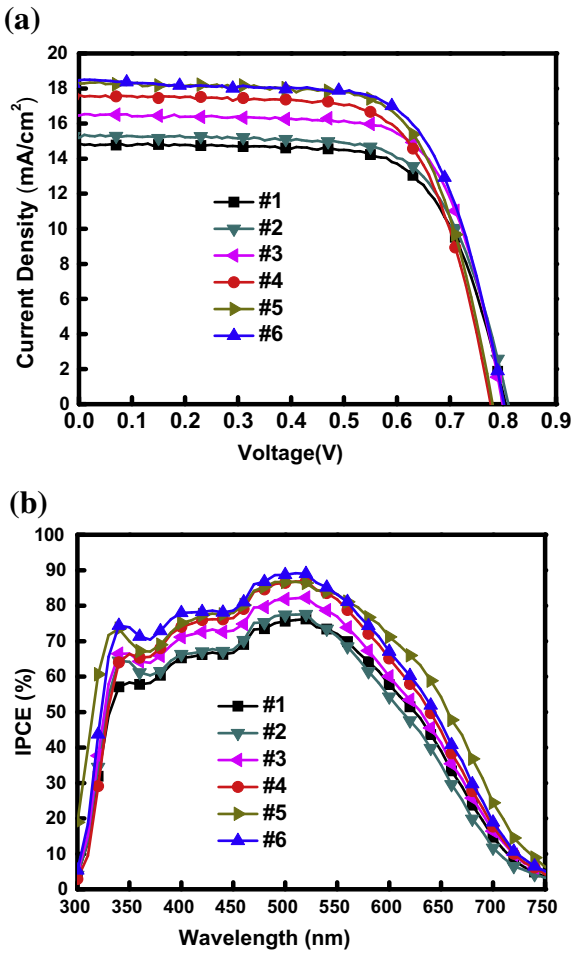

Fig. 5. (a) *I–V*, and (b) IPCE characteristics of DSSCs fabricated on the FTO samples #1–#6.

the bottom transparent conductor. Due to the availability of FTO substrates with even higher hazes, the highest haze tested in this work was 17%. Nevertheless, the trend in Fig. 6 suggests the possible direction for further enhancement. If one could prepare FTO substrates with even higher hazes and in the meantime maintain high total transmittance (it is noted that the total transmittance of the FTO samples gradually decrease with the haze), the DSSC efficiency may be further enhanced and/or optimized.

Since the surface texture, roughness, and the optical haze had no significant effects on the V_{OC} and the fill factor FF and all devices had the same TiO_2 thickness and device processing, the enhanced conversion efficiency must result from enhanced optical absorption in the devices. This is well supported by IPCE results shown in Fig. 5(b), in which one sees that the IPCE in generally increases with the optical haze of the FTO used over the broad absorption range, except for few situations. For instance, IPCE of device #5 is higher than that of device #6 for the short and long wavelength ranges, which may be associated with the detailed morphological and optical properties of the FTO samples. Yet even in this case, device #6 exhibits higher IPCE than device #5 for the major wavelength range of

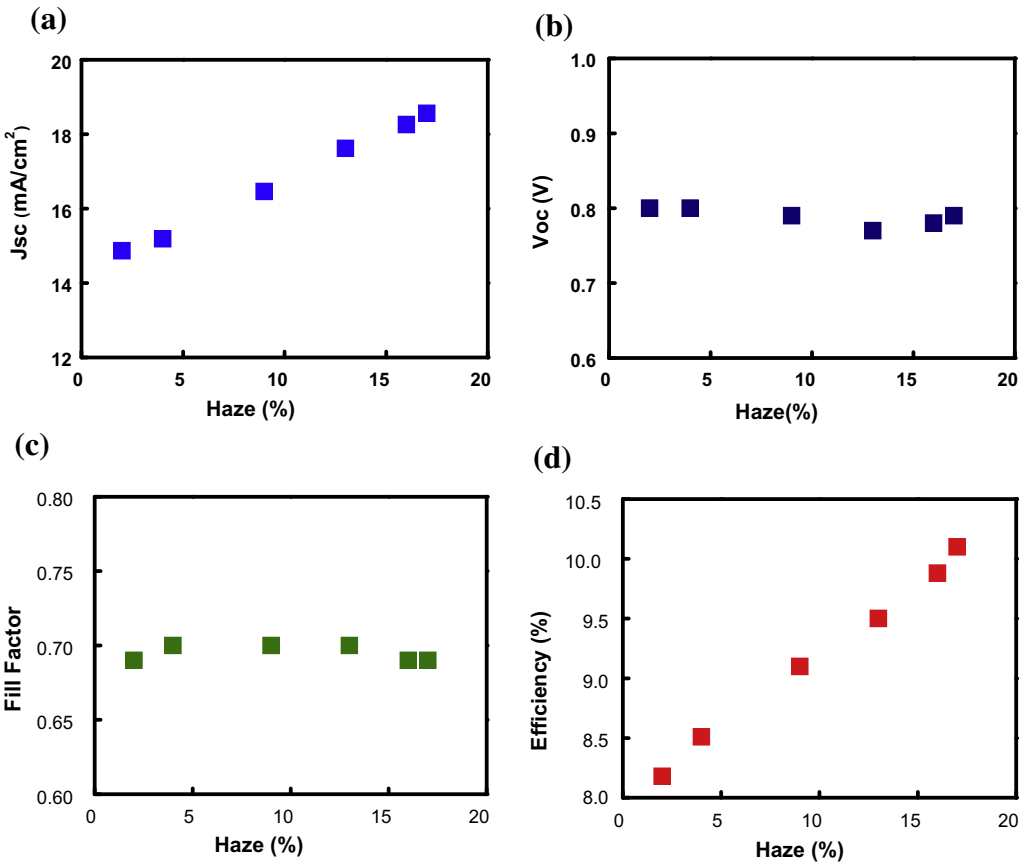

Fig. 6. (a) Short-circuit current J_{SC}, (b) open-circuit voltage V_{OC}, (c) fill factor FF, and (d) conversion efficiency (Eff.) are plotted versus the haze value of FTO samples.

350–550 nm, and it can be shown that integrating (IPCE spectrum × solar spectrum) over the wavelengths yields a higher calculated J_{sc} value for device #6. In general, the peak IPCE increases from ~75% of the device on a flatter/less textured FTO (#1, haze = 2%) to ~90% of the device on a much rougher/highly textured FTO (#6, haze = 17%). As a result, the short-circuit current J_{sc} (Fig. 5(a), Table 1) also shows a corresponding enhancement. These results suggest the highly textured and high-haze FTO can effectively scatter a portion of the incident light into larger oblique angles in the device, increasing the traveling distance of the incident light in the device. The highly textured and high-haze FTO may also effectively reflect (or backward scatter) the light reflected (or backward scattered) from the back scattering layer composed of large TiO_2 nanoparticles (~400 nm), enhancing the light trapping within the device. These factors together can contribute to significant enhancement of absorption (and thus J_{SC} and power conversion efficiency) in the device configuration.

3.3. Electrochemical impedance spectroscopy of devices

The effects of textured FTO on photovoltaic characteristics of DSSCs were further investigated by electrochemical impedance spectroscopy (EIS). EIS is a useful tool for characterizing interfacial charge-transfer processes in DSSCs, such as the charge recombination at the TiO_2/dye/electrolyte interface, electron transport in the TiO_2 electrode, electron transfer at the counter electrode, and ion transport in the electrolyte etc. [37]. In this study, EIS was conducted by subjecting the cell to the constant AM 1.5G 100 mW/cm^2 illumination and to the bias at the open-circuit voltage V_{OC} of the cell (namely, the condition of no DC current).

Fig. 7 shows the measured and simulated EIS Nyquist plots (i.e., minus imaginary part of the impedance $-Z''$ vs. the real part of the impedance Z' when sweeping the frequency) for DSSCs using various FTO samples. In the frequency range investigated (20–1 MHz), a larger semicircle occurs in the lower frequency range (~20–1 kHz) and a smaller semicircle occurs in the higher frequency range. The larger semicircles in the lower frequency range (~20–1 kHz) are not complete due to the limited frequency range of our instrument (the lowest frequency is not low enough). With the bias illumination and voltage applied, the larger semicircle at lower frequencies corresponds to the charge transfer processes at the TiO_2/dye/electrolyte interface [38], while the smaller semicircle at higher frequencies corresponds to the charge transfer processes at the Pt/electrolyte interface [39]. The intercept on the horizontal axis (Z') represents the series resistance of the device [35], which is associated with the sheet resistance of FTO. Consistently, FTO samples with larger sheet

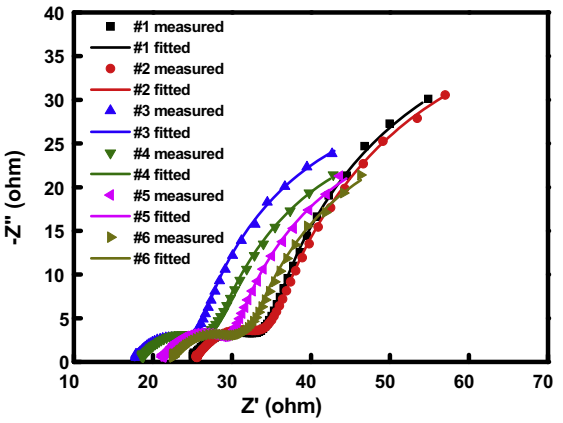

Fig. 7. Measured (symbols) and fitted (lines) EIS Nyquist plots for DSSCs fabricated on FTO samples #1–#6.

resistances show larger series resistances. Yet in general, the series resistances detected were still relatively small, not significant enough to produce visible difference in FF or J_{sc} of cells. The smaller semicircles corresponding to the platinum electrode show no difference between devices except for the varied parallel shifts caused by the series resistances of different devices. It indicates that the impedance at the Pt/electrolyte interface was not quite affected by the different textured FTO samples used (as one would expect).

On the other hand, the shape (width) of the larger lower-frequency semicircles somehow differs between devices. By fitting the measured impedance characteristics of Fig. 7 with equivalent circuits of DSSCs [40], the charge-transfer resistances R_{ct} (for the TiO_2/dye/electrolyte interface) for DSSCs fabricated on FTO samples #1–#6 can be extracted and are summarized in Table 1. The extracted R_{ct} decreases from 63.6 Ω of the device on #1 FTO (smallest texture, roughness, and optical haze; lowest conversion efficiency) to 43.1 Ω of the device on #6 FTO (largest texture, roughness, and optical haze; highest conversion efficiency). The decrease of R_{ct} with the increase of the DSSC efficiency indicates electron generation and transportation at the TiO_2/dye/electrolyte interface is enhanced with larger FTO textures and larger device efficiencies [41]. Among the six FTO samples, #6 FTO gives the smallest R_{ct}, which corresponds to the optimal light harvesting and electron generation due to the larger textural structures and strongest light scattering. Thus, the EIS results are in good agreement with results of the shot-circuit currents and the overall power conversion efficiencies of the DSSCs.

4. Conclusions

In conclusion, we investigated the influences of textures in the transparent conductor fluorine-doped tin oxides (FTO) on characteristics and performances of DSSCs. FTO conductors having varied textures were characterized for their physical, electrical and optical properties and were subjected to device studies to establish the correlation between FTO textures and device characteristics/performances. The results suggest that the highly textured and high-haze FTO can effectively scatter a portion of the incident light into larger angles in the device, enhancing the propagation length and trapping of the incident light within the device and contributing to significant enhancement of absorption (and thus J_{SC}, IPCE, and power conversion efficiency) in the device configuration. As a result, the conversion efficiency of the DSSC was enhanced from 8.18% to 10.1%, an improvement by 24%, with using the highly textured, large-roughness and high-haze FTO as the transparent conductor.

Acknowledgements

The authors gratefully acknowledge the financial support from AU Optronics Corporation and National Science Council of Taiwan.

References

[1] B. O'Regan, M. Grätzel, Nature 353 (1991) 737.
[2] J. Jiu, S. Isoda, F. Wang, M. Adachi, J. Phys. Chem. B 110 (2006) 2087.
[3] A. Hagfeldt, M. Grätzel, Acc. Chem. Res. 33 (2000) 269.
[4] Y. Chiba, A. Islam, Y. Watanabe, R. Komiya, N. Koide, L. Han, Jpn. J. Appl. Phys. 25 (2006) 638.
[5] C.Y. Chen, M. Wang, J.Y. Li, N. Pootrakulchote, L. Alibabaei, C. Ngoc-le, J. Decoppet, J. Tsai, C. Grätzel, C.G. Wu, S.M. Zakeeruddin, M. Grätzel, ACS Nano 3 (2009) 3103.
[6] T. Bessho, S.M. Zakeeruddin, C.Y. Yeh, E.W.G. Diau, M. Grätzel, Angew. Chem. Int. Ed. 49 (2010) 6646.
[7] K.O. Ott, Prog. Nucl. Energy 29 (1995) 81.
[8] L.L. Kazmerski, Renewable Sustainable Energy Rev. 1 (1997) 71.
[9] M. Grätzel, Nature 414 (2001) 338.
[10] M.K. Nazeeruddin, A. Kay, I. Rodicio, R. Humphry-Baker, E. Müller, P. Liska, N. Vlachopoulos, M. Grätzel, J. Am. Chem. Soc. 115 (1993) 6382.
[11] W. Kubo, S. Kambe, S. Nakade, T. Kitamura, K. Hanabusa, Y. Wada, S. Yanagida, J. Phys. Chem. B 107 (2003) 4374.
[12] U. Bach, D. Lupo, P. Comte, J.E. Moser, F. Weissortel, J. Salbeck, H. Spreitzer, M. Grätzel, Nature 395 (1998) 583.
[13] R.W. Siegel, S. Ramasamy, H. Hahn, Zi. Li, T. Lu, R. Gronsky, J. Mater. Res. 3 (1988) 1367.
[14] J.C. Bijleveld, A.P. Zoombelt, S.G.J. Mathijssen, M.M. Wienk, Mathieu Turbiez, D.M. de Leeuw, R.A.J. Janssen, J. Am. Chem. Soc. 131 (2009) 16616.
[15] S. Pelet, J.E. Moser, M. Grätzel, J. Phys. Chem. B 104 (2000) 1791.
[16] S.S. Kim, K.W. Park, J.H. Yum, Y.E. Sung, J. Photochem. Photobiol. A 189 (2007) 301.
[17] J.H. Yoon, S.R. Jang, R. Vittal, J. Lee, K.J. Kim, J. Photochem. Photobiol. A. 180 (2006) 184.
[18] E. Palomares, J.N. Clifford, S.A. Haque, T. Lutz, J.R. Durrant, J. Am. Chem. Soc. 125 (2003) 475.
[19] P. Wang, C. Klein, J.E. Moser, R.H. Baker, N. Le, C. Ha, R. Charvet, P. Comte, S.M. Zakeeruddin, M. Grätzel, J. Phys. Chem. B 108 (2004) 17553.
[20] L.Y. Lin, C.H. Tsai, K.T. Wong, T.W. Huang, C.C. Wu, S.H. Chou, S.H. Chen, A.I. Tsai, J. Mater. Chem. 21 (2011) 5950.
[21] X. Fang, T. Ma, G. Guan, M. Akiyama, T. Kida, E. Abe, J. Electroanal. Chem. 570 (2004) 257.
[22] P.I. Rovira, A.S. Ferlauto, C.R. Wronski, R.W. Collins, J. Non-Cryst. Solids. 266 (2000) 279.
[23] J. Muller, B. Rech, J. Springer, M. Vanecek, Solar Energy 77 (2004) 917.
[24] Y. Nasuno, N. Kohama, K. Nishimura, T. Hayakawa, H. Taniguchi, M. Shimizu, Appl. Phys. Lett. 88 (2006) 071909.
[25] J. Krc, M. Zeman, F. Smole, M. Topic, J. Appl. Phys. 92 (2002) 749.
[26] L. Andrade, S.M. Zakeeruddin, M.K. Nazeeruddin, H.A. Ribeiro, A. Mendes, M. Grätzel, Chem. Phys. Chem. 10 (2009) 1117.
[27] M.K. Nazeeruddin, F.D. Angelis, S. Fantacci, An. Selloni, G. Viscardi, P. Liska, S. Ito, B. Takeru, M. Grätzel, J. Am. Chem. Soc. 127 (2005) 16835.
[28] S. Ito, N.L.C. Ha, G. Rothenberger, P. Liska, P. Comte, S.M. Zakeeruddin, P. Pechy, M.K. Nazeeruddin, M. Grätzel, Chem. Commum. (2006) 4004.
[29] M. Grätzel, Photovolt. Res. Appl. 8 (2000) 171.

[30] N. Vlachopoulos, P. Liska, J. Augustynski, M. Grätzel, J. Am. Chem. Soc. 110 (1988) 1216.
[31] H.W. Lin, S.Y. Ku, H.C. Su, C.W. Huang, Y.T. Lin, K.T. Wong, C.C. Wu, Adv. Mater. 17 (2005) 2489.
[32] R. Eichberger, F. Willig, Chem. Phys. 141 (1990) 159.
[33] C.J. Yang, T.Y. Cho, C.L. Lin, C.C. Wu, J. Soc. Inf. Display 16 (2008) 691.
[34] C.J. Lin, W.Y. Yu, S.H. Chien, Appl. Phys. Lett. 91 (2007) 233120.
[35] M. Adachi, M. Sakamoto, J. Jiu, Y. Ogata, S. Isoda, J. Phys. Chem. B 110 (2006) 13872.
[36] C.C. Chen, B.C. Huang, M.S. Lin, Y.J. Lu, T.Y. Cho, C.H. Chang, K.C. Tien, S.H. Liu, T.H. Ke, C.C. Wu, Org. Electron. 11 (2010) 1901.
[37] L.Y. Lin, C.H. Tsai, T.W. Huang, L. Hsieh, S.H. Liu, H.W. Lin, K.T. Wong, C.C. Wu, S.H. Chou, S.H. Chen, A.I. Tsai, J Org. Chem. 75 (2010) 4778.
[38] Q. Wang, J. Moser, M. Grätzel, J. Phys. Chem. B. 109 (2005) 14945.
[39] J. Zhang, G. Yang, Q. Sun, J. Zheng, P. Wang, Y. Zhu, X. Zhao, J. Renewable Sustainable Energy 2 (2010) 013104.
[40] L. Han, N. Koide, Y. Chiba, A. Islam, R. Komiya, N. Fuke, A. Fukui, R. Yamanaka, Appl. Phys. Lett. 86 (2005) 213501.
[41] J.J. Wu, G.R. Chen, H.H. Yang, C.H. Ku, J.Y. Lai, Appl. Phys. Lett. 90 (2007) 213109.

its polarization even after the external electric field was removed, and thus the feFETs were non-volatile. The ferroelectric transistors allowed reprogrammability and non-destructive read-out, and this offered an advantage over using ferroelectric capacitors, for which the read-out process would erase the polarization states.

The current performance of solution-processed organic memory has been sufficient to meet the requirement of short-term applications, including a pressure-sensor system [2] and a wireless communication sheet [4]. When incorporating memory devices into circuit systems, one of the main challenges involves device isolation and proper signal routing. In a memory array, there is potential cross-talk between neighboring devices. Addressing switches such as transistors or diodes are needed to isolate the neighboring cells. Previously in Ref. [4], memory cell isolation was achieved by combining one memory transistor with two addressing transistors, in which one addressing transistor controls the input voltage and the second one selects the readout signal. In this paper we describe a memory array design that uses only one addressing transistor in each memory cell, simplifying array design and reducing footprint requirements. This design can be applied as non-volatile random-access memory [5] to reduce power consumption. We have also examined device variations among the memory transistors, to determine how array performance could be improved.

Each memory cell is comprised of two transistors: one feFET (memory element) and one addressing transistor (signal switch). Both the feFET and the addressing transistors were in top-gate configuration and with p-type semiconductors. The typical transfer characteristics of an addressing transistor and of a memory feFET are plotted in Fig. 1(a) and (b), respectively. The transistors showed average saturation mobility of 0.2 $cm^2/V\,s$ for Flexink and 0.01 $cm^2/V\,s$ for PQT [23]. No significant hysteresis was observed in the addressing transistors during gate-voltage V_g sweeps, as shown by the measurement in Fig. 1(a). To use the feFETs as memory devices, the polarization of the ferroelectric dielectric was set by an input V_g. The remnant polarization affected the transistor source–drain current I_{sd}, and thus the I_{sd} hysteresis in Fig. 1(b) served as a record of the applied gate voltage. As the V_g pulse time was increased in Fig. 1(c), the output I_s became saturated. A V_g pulse length of 1 ms was the minimum switching time required for a feFET current to reach the plateau value. This timing requirement may be different depending on polarization direction (switching from positive to negative V_g versus negative to positive V_g) [21] and dielectric thickness [24]. The gate current in Fig. 1(d) shows peaks at ±25 V, indicating the coercive voltage where the ferroelectric dielectric switched polarization.

The effect of strain on feFET was examined for use in mechanically flexible applications. The transfer characteristics in Fig. 1(e) shows that current was reduced with tensile bending at 0.4% strain where radius of curvature = 1.5 cm. Nevertheless the characteristics recovered when the device was laid flat again and released from strain. The current reduction with bending has been previously observed in non-ferroelectric organic transistors [25], in which mechanical strain led to changes in dielectric capacitance and semiconductor mobility. The current in Fig. 1(f) was measured with source–drain voltage $V_{sd} = -10$ V and $V_g = 0$ V under tensile bending, after the feFET had been polarized at $V_g = +30$ V. Since PVDF-TrFE is a ferroelectric polymer, piezoelectric voltage was generated during bending and was observed as spikes at transitions. After the spikes, the I_{sd} was decreased by <5% under tensile strain of 0.4%, and the I_{sd} partially recovered when the substrate was relaxed to 0% strain. The reason for incomplete recovery was that, besides mechanical bending, the feFET current was also affected by electrical bias stress under constant V_{sd} bias. Without mechanical bending, electrical bias stress [26] alone would reduce I_{sd}, as indicated by the dashed line in Fig. 1(f). The measured feFET current change under constant V_{sd} is ~5% over 15 min, and this level of bias stress is comparable to the current change in previous studies [27,28] and is due to traps at the semiconductor–dielectric interface. The feFET remained functional up to tensile strain of 0.6% (radius of curvature of 1 cm) before it broke down with open circuit. The above results were promising for applying feFETs to mechanically flexible systems, but more detailed studies are needed to thoroughly characterize the influence of strain on feFET parameters and to elucidate the long-term effects of repetitive strain cycles on memory retention time.

To place the memory feFETs into an array, neighboring devices were isolated by addressing switches such as transistors or diodes preventing potential cross-talk. The schematics and the photograph of an active matrix array are shown in Fig. 2. The addressing transistor regulated the input voltage to a memory feFET within each cell. Although the cells in a column were connected to a common data-line, the input voltage was passed only to a specific feFET, by turning on its addressing switch through applying a voltage pulse to its select-line. The addressing transistors of neighboring rows were turned off by holding their select-lines at ground or positive voltage. The bus-lines B_N and the readout-lines R_N were maintained at ground during the memory input process. For the read-out process, the key to minimize cross-talk relied on that the readout-lines and bus-lines of feFETs were arranged perpendicular to each other and located on separate layers as shown in Fig. 2. To determine the memory state of cell C_{11}, a voltage pulse was applied to the bus-line B_1, and the feFET current or charge was measured from the read-out line R_1. The other bus-lines $B_2 \ldots B_N$ were maintained at ground potential. The measured current depended on the state of the feFET at cell C_{11} only and was not affected by other feFETs connected to the same readout line, because their bus-lines were grounded to not generate current.

The input signal to an addressed feFET and to its neighbor down the column is shown in Fig. 3(a) and (b), respectively, by monitoring the voltage at the feFET gate-electrode pad with a picoprobe [29]. The input voltage was transmitted to the intended feFET through its addressing transistor within 1 ms. The voltage at the neighboring feFET gate electrode has remained below 2.5 V (less than 20% of the input voltage at the data-line), indicating that neighboring cell was sufficiently isolated from cross-talk disturbance. Voltage overshoot due to capacitance feed-through [15] was observed during potential change in Fig. 3(a), but it was not deleterious to the signal routing

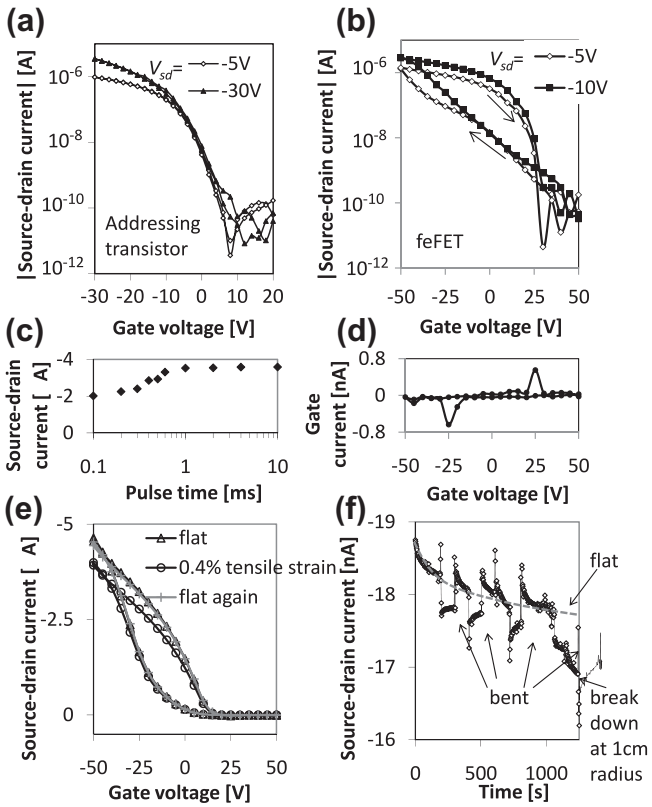

Fig. 1. Transfer characteristics of (a) an addressing transistor and (b) a memory ferroelectric transistor (feFET). (c) Current output of a feFET versus duration of the gate-voltage pulse, with $V_{sd} = -10$ V and $V_g = -30$ V. (d) Gate current of a feFET where $V_{sd} = 0$ V. (e) Transfer characteristics of a feFET with $V_{sd} = -10$ V in different strain conditions. (f) Source–drain current of a feFET under tensile strain cycles, measured at $V_{sd} = -10$ V and $V_g = 0$ V. The feFET had been previously polarized at $V_g = +30$ V. The sample was bent to radius of curvature = 1.5 cm, corresponding to 0.4% tensile strain. The voltage spikes were piezoelectric response of the ferroelectric dielectric. The dashed gray line indicates feFET current at 0% strain; the decrease in current is due to bias-stress effects.

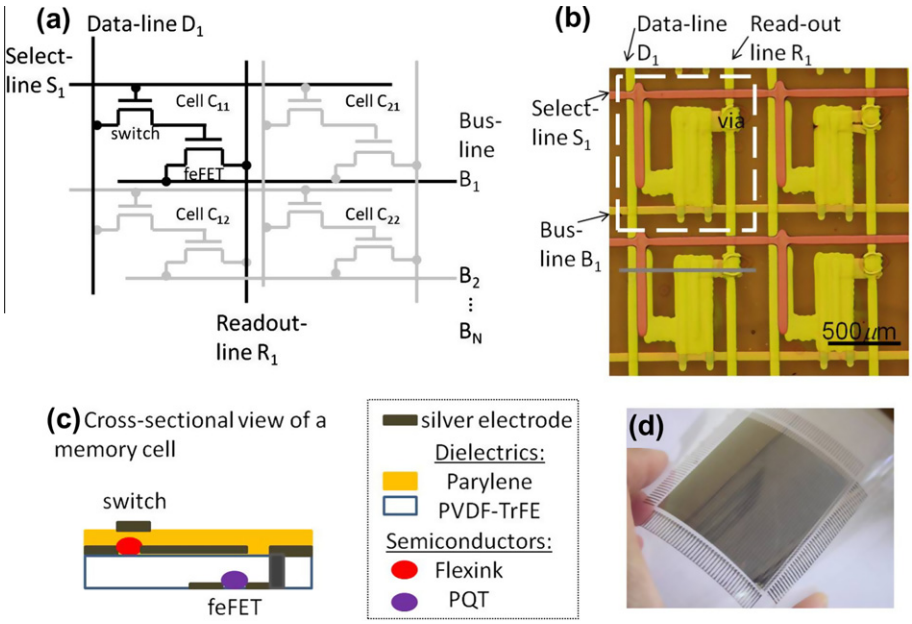

Fig. 2. (a) Schematics and (b) photograph of an active matrix memory array. The black lines in (a) and the white dash box in (b) indicate an individual cell. (c) Cross-sectional view at the location indicated by the gray line in (b). (d) A flexible memory array on plastic substrate.

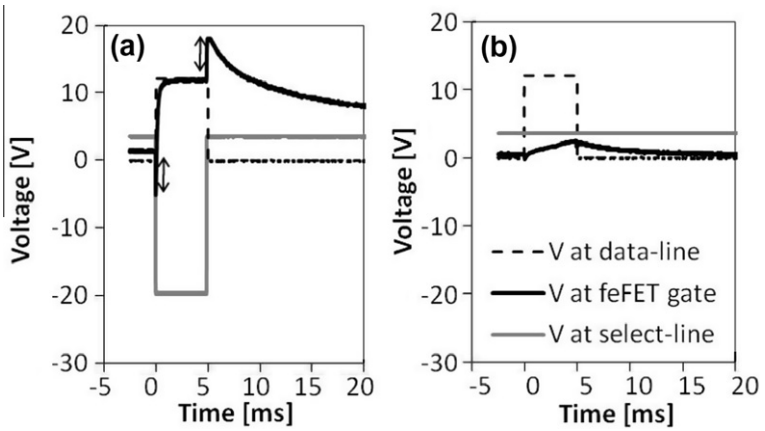

Fig. 3. Comparison between the oscilloscope traces of (a) an addressed feFET and (b) a neighboring feFET down the column. Voltage overshoot due to capacitance feed-through [15] was indicated by the arrows in (a).

process. It was observed that the rise and fall time of the feed-through voltage were not the same because of the difference in channel resistance at respective gate voltages ($V_g = -20$ V during rise, $V_g = 0$ V during fall). The feed-through voltage was due to the overlap between the gate and source electrodes and may be reduced by minimizing the overlapping area.

To write into a memory array as shown in Fig. 4, the select-line voltage was −15 V for turning an addressing transistor on and +10 V for off, and the input data-line voltage was a 5 ms pulse at −30 V for polarized state or at 0 V for unpolarized state, applied according to a checkerboard pattern. Eight hours after the pattern was recorded, the difference in dielectric polarization was obtained by charge amplifiers [30–32]. The read-out electronics applied a 130 μs pulse at −5 V to the bus-line of a selected cell and measured the feFET charge via the corresponding read-out line, while the remaining lines were held at ground. The results in Fig. 4(a) shows distinguishable memory states between neighboring feFETs in a 7 × 8 array. Signals of the two memory states differed by ~6000 readout units or 0.77 pC as seen in Fig. 4(b) (one readout unit corresponded to 800 electrons or 0.13 fC as explained in Ref. [30]). The histogram indicates signal variations of the two polarization states, with standard deviation of 580 units for unpolarized states and 1120 units for polarized states, indicating larger variation after polarization. In this proof-of-concept demonstration, the yield of working memory cells was low (~3.5%, since only the cells in Fig. 4(a) were detectable for a 40 × 40 array). The memory feFETs have been damaged during via processing step, in which solvent was printed to dissolve via holes in the dielectric [33]. Via holes were formed by printing solvent droplets, and eleven drops per site was required to dissolve the PVDF-TrFE film. In the photo in Fig. 2(b), the shape of via were oval instead of circular, due to misalignment of solvent drops. More severe misalignment caused shorts between the feFET gate and source–drain electrodes and was the main reason for low array yield. This misalignment issue can be mitigated by redesigning the cell layout and providing wider area for via process tolerance, or alternative via process such as laser ablation can be used. It should be feasible to improve the array yield in the future by improving layout design and equipment capability.

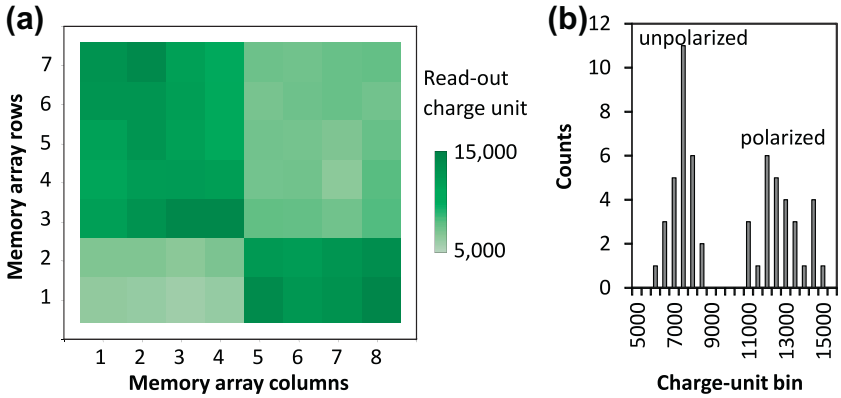

Fig. 4. (a) Memory states of a 7 × 8 array measured by charge sensors 8 h after the feFETs were polarized in a checkerboard pattern. The input voltages were 5 ms pulses at −30 V for the polarized state (dark green) or at 0 V for the unpolarized state (light green). One readout-charge unit corresponded to 800 electrons or 0.13 fC as explained in Ref. [30]. (b) Histogram of the memory cells in part (a). (For interpretation of the references to color in this figure legend, the reader is referred to the web version of this article.)

Fig. 5 compared the output characteristics of twenty inkjet-printed feFETs that were fabricated in an array. The data were all obtained with $V_g = 0$ V and were taken by directly probing the electrodes of the feFETs. A polarization voltage of $V_g = -30$ V was used as it was the voltage limit for our array test setup. This voltage exceeded the coercive voltage of the ferroelectric dielectric Fig. 1(d) and enabled polarization switch, but it was still relatively low and the ferroelectric polarization was not saturated. The addressing transistors were not used for routing in these measurements, in order to only evaluate variations among the memory devices independent of other circuit components. Before polarization, the output current varied by a factor of 2 among the cells Fig. 5(a). After the polarization voltage was applied, the output characteristics varied by a factor of 3 and showed an increase in current variations among the cells Fig. 5(b). The polarized dielectric increased channel charge accumulation, and the feFETs reached saturation regime ($V_g - V_T < V_{sd}$) due to positive threshold voltage V_T. After two weeks since polarization, the output current was no longer saturated in Fig. 5(c), indicating shifts in threshold voltage due to charge trapping [27,28,34–36]. In Fig. 5(d), the values of output current at $V_{sd} = -20$ V showed the I_{sd} ratio between the polarized and unpolarized states was >25 (between 25 and 100). Although the feFET current has decreased to 50% of the initial values after a two-week interval, the memory states were still distinguishable. The decrease in current corresponded to the results from our previous study [36] of similarly inkjet-printed feFETs, in which the memory retention time was extrapolated to be roughly one month, with device variations taken into account.

Achieving consistent characteristics across an array is important for estimating the data-storage time of an array, because it will be limited by the cell with the worst retention time unless the low-performing cells are identified and excluded. Thus, in addition to improving the performance of individual feFETs, it is also desirable to understand and mitigate array variations in memory integration. Before polarization, the variations in output characteristics of Fig. 5(a) were mainly due to differences in mobility among the devices [15]. After the feFETs were polarized, the output characteristics became even less uniform with time. There were different rates of charge trapping among the polarized devices, leading to a widening range of output characteristics in Fig. 5(b) and (c) and larger variations for polarized states in Fig. 4(c). Therefore, besides semiconductor mobility, charge-trapping effects must be controlled to improve array uniformity. Techniques such as template annealing [37] or nano-embossing [38] might reduce charge-trapping effects in the dielectric to extend both the memory retention time and array uniformity.

In summary, inkjet-printed active-matrix memory arrays were demonstrated to show less than 20% cross-talk between neighboring cells. The readout signal from each feFET was isolated by using bus-lines and readout-lines on different layers to enable a memory design with two transistors per cell. The memory arrays were shown to retain data for at least 8 h and remained functional below 0.6% tensile strain. Array uniformity was reduced with time by different charge-trapping rates among the transistors. Thus, better control of charge trapping will improve the performance of individual feFETs as well as enhance array uniformity, to advance organic memory for flexible electronics.

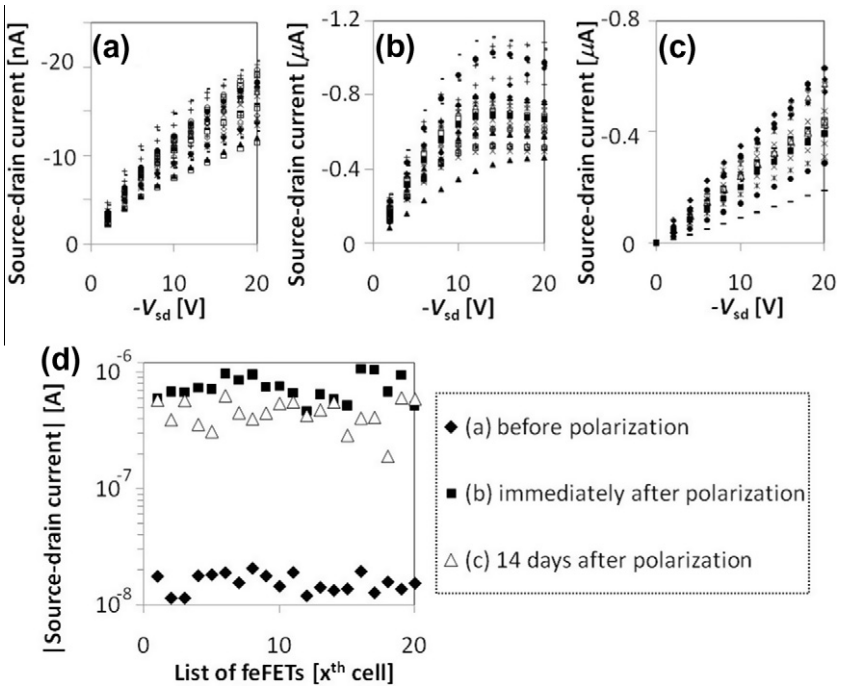

Fig. 5. Output characteristics of 20 feFETs (a) before polarization, (b) immediately after polarization at $V_g = -30$ V, and (c) after two weeks in the polarized state. These output characteristics were taken with $V_g = 0$ V. The graph (d) compares the values of output current at $V_{sd} = -20$ V.

2. Array fabrication

The memory devices were fabricated either on glass or on 125 μm poly(ethylenenapthalate) substrates. Both the addressing transistors and the memory feFETs were in top-gate configuration and were patterned with channel length L of 40 μm. The metal electrodes were inkjet-printed using a silver-nanoparticle solution from Cabot Corporation. The memory feFETs had channel width W of 1 mm and consisted of p-type semiconductor polythiophene (PQT). The memory gate dielectric was spin-coated from a solution of ferroelectric co-polymer poly(vinylidene fluoride-co-trifluoroethylene) (PVDF-TrFE, 65:35 ratio) in methyl-ethyl-ketone to form a 600 nm film with capacitance $C_f = 16$ nF/cm^2 and was processed as described in Ref. [36]. Interconnects through the PVDF-TrFE dielectric were made by inkjet-printing the solvent methyl-ethyl -ketone to locally dissolve away the dielectric to form via openings, yielding vias with resistance of 150 Ω, similar to the procedure in Ref. [33]. Subsequent layers for the addressing transistors were fabricated with $W/L = 15$ using the polymer blend semiconductor FS12 from Flexink and vacuum-deposited parylene-N as the gate dielectric (film thickness = 400 nm and capacitance = 5 nF/cm^2).

Acknowledgments

The authors would like to thank Jurgen Daniel, Raj Apte, and Chris Paulson for experimental assistance with the read-out electronics. We express our gratitude to Sanjiv Sambandan, Robert Street Gregory Whiting, and Leah Lavery for helpful discussions. We are very grateful to Xerox Research Center Canada for providing PQT, Iain McCulloch and Martin Heeney for providing Flexink, W.A. MacDonald of Dupont-Teijin Films for supplying the polyethylene naphthalate substrates, and E-ink for the electrophoretic media. This work is partially supported by Sensor Tape Program of the Defense Advanced Research Projects Agency (Contract No: W81XWH-08-0065). This document has been approved for public release by DARPA for unlimited distribution.

References

[1] M. Takamiya, T. Sekitani, Y. Kato, H. Kawaguchi, T. Someya, T. Sakurai, An organic FET SRAM with back gate to increase static noise margin and its application to Braille sheet display, IEEE J. Solid-St. Circ. 42 (1) (2007) 93–100.
[2] T. Sekitani, T. Yokota, U. Zschieschang, H. Klauk, S. Bauer, K. Takeuchi, M. Takamiya, T. Sakurai, T. Someya, Organic nonvolatile memory transistors for flexible sensor arrays, Science 326 (2009) 1516–1519.
[3] R. Blache, J. Krumm, W. Fix, Organic CMOS circuits for RFID applications, ISSCC Dig. Tech. Pap. (2009) 208–209.
[4] T. Sekitani, K. Zaitsu, Y. Noguchi, K. Ishibe, M. Takamiya, T. Sakurai, T. Someya, Printed nonvolatile memory for a sheet-type communication system, IEEE Trans. Electron Dev. 56 (5) (2009) 1027–1035.
[5] K.-H. Kim, J.-P. Han, S.-W. Jung, T.-P. Ma, Ferroelectric DRAM (FEDRAM) FET with metal/SrBi2Ta2O9/SiN/Si gate structure, IEEE Electron. Device Lett. 23 (2) (2002) 82–84.
[6] H. Kimura, T. Hanyu, M. Kameyama, Multiple-valued logic-in-memory VLSI using MFSFETs and its applications, J. Mult.-Valued Logic Soft Comput. 9 (2003) 23–42.
[7] K. Galatsis, K. Wang, Y. Botros, Y. Yang, Y.-H. Xie, J.F. Stoddart, R.B. Kaner, C. Ozkan, J. Liu, M. Ozkan, C. Zhou, K.W. Kim, Emerging memory devices, IEEE Circuits Dev. 22 (3) (2006) 12–21.
[8] J.C. Scott, L.D. Bozano, Nonvolatile memory elements based on organic materials, Adv. Mater. 19 (11) (2007) 1452–1463.
[9] R.C. Naber, K. Asadi, P.W.M. Blom, D.M. de Leeuw, B. de Boer, Organic nonvolatile memory devices based on ferroelectricity, Adv. Mater. 22 (9) (2010) 933–945.
[10] P. Heremans, G.H. Gelinck, R. Muller, K.-J. Baeg, D.-Y. Kim, Y.-Y. Noh, Polymer and organic nonvolatile memory devices, Chem. Mater. doi:10.1021/cm102006v.
[11] A. Jedaa, M. Halik, Toward strain resistant flexible organic thin film transistors, Appl. Phys. Lett. 95 (10) (2009) 103309.
[12] T.N. Ng, W.S. Wong, R.A. Lujan, R.A. Street, Characterization of charge collection in photodiodes under mechanical strain: comparison between organic bulk heterojunction and amorphous silicon, Adv. Mater. 21 (18) (2009) 1855–1859.
[13] M. Singh, H.M. Haverinen, P. Dhagat, G.E. Jabbour, Inkjet printing-process and its applications, Adv. Mater. 22 (6) (2010) 673–685.
[14] G.H. Gelinck, H.E.A. Huitema, E. van Veenedaal, E. Cantatore, L. Schrijnemakers, J.B.P.H. van der Putten, T.C.T. Geuns, M. Beenhakkers, J.B. Giesbers, B. Huisman, E.J. Meijer, E.M. Benito, F.J. Touwslager, A.W. Marsman, B.J.E. van Rens, D.M. de Leeuw, Flexible active-matrix displays and shift registers based on solution-processed organic transistors, Nature Mater. 3 (2) (2004) 106–110.
[15] A.C. Arias, S.E. Ready, R. Lujan, W.S. Wong, K.E. Paul, A. Salleo, M.L. Chabinyc, R. Apte, R.A. Street, Y. Wu, P. Liu, B. Ong, All jet-printed polymer thin-film transistor active-matrix backplanes, Appl. Phys. Lett. 85 (15) (2004) 3304–3306.
[16] J. Daniel, A.C. Arias, W.S. Wong, R. Lujan, S. Ready, B. Krusor, R.A. Street, Jet-printed active-matrix backplanes and electrophoretic displays, Jpn. J. Appl. Phys. 46 (3B) (2007) 1363–1369.
[17] A.C. Arias, J.D. MacKenzie, I. McCulloch, J. Rivnay, A. Salleo, Materials and applications for large area electronics: solution-based approaches, Chem. Rev. 110 (1) (2010) 3–24.
[18] W.S. Wong, A. Salleo (Eds.), Flexible Electronics: Materials and Applications, Springer, NY, 2009.
[19] Y. Kuo, Thin-film transistor and ultra-large scale integrated circuit: competition or collaboration, Jpn. J. Appl. Phys. 47 (3) (2008) 1845–1852.
[20] S.L. Miller, P.J. McWhorter, Physics of the ferroelectric nonvolatile memory field effect transistor, J. Appl. Phys. 72 (12) (1992) 5999–6010.
[21] R.C.G. Naber, C. Tanase, P.W.M. Blom, G.H. Gelinck, A.W. Marsman, F.J. Touwslager, S. Setayesh, D.M. de Leeuw, High-performance solution-processed polymer ferroelectric field-effect transistors, Nature Mater. 4 (3) (2005) 243–248.
[22] Y.J. Park, H.J. Jeong, J. Chang, S.J. Kang, C. Park, Recent development in polymer ferroelectric field effect transistor memory, J. Semicond. Technol. Sci. 8 (1) (2008) 51–56.
[23] B.S. Ong, Y. Wu, P. Liu, S. Gardner, High-performance semiconducting polythiophenes for organic thin-film transistors, J. Am. Chem. Soc. 126 (11) (2004) 3378–3379.
[24] R.C.G. Naber, P.W.M. Blom, A.W. Marsman, D.M. de Leeuw, Low voltage switching of a spin cast ferroelectric polymer, Appl. Phys. Lett. 85 (11) (2004) 2032–2034.
[25] T. Sekitani, Y. Kato, S. Iba, H. Shinaoka, T. Someya, T. Sakurai, S. Takagi, Bending experiment on pentacene field-effect transistors on plastic films, Appl. Phys. Lett. 86 (7) (2005) 073511.
[26] T.N. Ng, M.L. Chabinyc, R.A. Street, A. Salleo, Bias stress effects in organic thin film transistors, in: Proc. IEEE International Reliability Physics Symposium, 2007, pp. 243–247.
[27] K.N.N. Unni, R. de Bettignies, S. Dabos-Seignon, J. Nunzi, A nonvolatile memory element based on an organic field-effect transistor, Appl. Phys. Lett. 85 (10) (2004) 1823–1825.
[28] G. Gu, M.G. Kane, J.E. Doty, A.H. Firester, Electron traps and hysteresis in pentacene-based organic thin-film transistors, Appl. Phys. Lett. 87 (24) (2005) 243512.
[29] A high-impedance picoprobe from GGB Industries (model 18C-2-50-HV) was used. Positive source-drain voltage was applied due to the probe's voltage limits. Please note that this was different from the input voltages used in Fig. 4.
[30] R.A. Street (Ed.), Technology and Applications of Amorphous Silicon, Springer, New York, 2000. pp. 147–221.
[31] K.S. Karim, A. Nathan, Readout circuit in active pixel sensors in amorphous silicon technology, IEEE Electron. Device Lett. 22 (10) (2001) 469–471.
[32] The electronic noise in this charge-readout systems is about 1000–2000 electrons.
[33] T. Kawase, H. Sirringhaus, R.H. Friend, T. Shimoda, Inkjet printed via-hole interconnections and resistors for all-polymer transistor circuits, Adv. Mater. 13 (21) (2001) 1601–1605.

[34] C.H. Seager, D.C. McIntyre, W.L. Warren, B.A. Tuttle, Charge trapping and device behavior in ferroelectric memories, Appl. Phys. Lett. 68 (18) (1996) 2660–2662.
[35] T.P. Ma, J.-P. Han, Why is nonvolatile ferroelectric memory field-effect transistor still elusive? IEEE Electron. Device Lett. 23 (7) (2002) 386–388.
[36] T.N. Ng, B. Russo, A.C. Arias, Degradation mechanisms of organic ferroelectric field-effect transistors used as non-volatile memory, J. Appl. Phys. 106 (9) (2009) 094504.
[37] Y.J. Park, S.J. Kang, C. Park, E. Woo, K. Shin, K.J. Kim, Recovery of remanent polarization of poly(vinylidene fluoride-co-trifluoroethylene) thin film after high temperature annealing using topographically nanostructured aluminum bottom electrode, Appl. Phys. Lett. 90 (22) (2007) 222903.
[38] Z. Hu, M. Tian, B. Nysten, A.M. Jonas, Regular arrays of highly ordered ferroelectric polymer nanostructures for non-volatile low-voltage memories, Nature Mater. 8 (1) (2009) 62–67.

characterizations. Moreover, one should note that the tip/probe measures the potential at the free surface of the organic semiconductor (OSC) film and not at active channel/dielectric interface, implying systematic errors [10]. Therefore, in this paper we propose a TLM based on the dissipated power in the whole device, namely the Power TLM (P-TLM), which allows the evaluation of the contact resistance in linear region as well as in saturation regime, by means of usual *I–V* measurements. Thus, one can investigate the contact resistance with respect to not only gate bias but also drain voltage.

2. Experimental

Two types of organic transistors are employed in this work. One is the poly-triarylamine (PTAA) OFETs fabricated on gold-plated 125 μm-thick polyethylene-naphthalate (PEN), using a top-gate (TG) structure [11]. The 30 nm gold layer is patterned by photolithography with a line/space resolution down to 5 μm, forming the source and drain electrodes as well as the 1st level of interconnection lines between gates. Organic semiconductor (poly-triarylamine derivative) is deposited in solution by direct printing methods, defining patterns corresponding to individual devices and annealed under ambient atmosphere at 100 °C, leading to a final thickness in the range of 50–200 nm. The gate dielectric polymer is printed on the top of semiconductor and then annealed, leaving open areas for via holes with a final thickness of 1 μm, corresponding to the unit area capacitance $C_i = 1.5 \times 10^{-9}$ F/cm^2. Finally, a silver-ink conductor is printed on the top of dielectric and annealed at 100 °C, forming in the same step the gate electrodes for devices and the 2nd level for interconnection. The measured mobility (μ) is about 0.035 cm^{2}V^{-1}s^{-1} and threshold voltage (V_T) is around −9 V.

Another type is top-contact (TC) and bottom-contact (BC) pentacene OFETs [12]. They were fabricated on heavily doped Si (100) wafers covered with a 50 nm thick SiO_2 layer, which ultimately serve as the gate electrode and the gate insulator ($C_i \approx 8 \times 10^{-8}$ F/cm^2), respectively. After the surface was ultrasonically cleaned with acetone and isopropyl alcohol, the substrates were immersed in a mixture of sulfuric acid and hydrogen peroxide to fully remove organic contaminants. After that, the substrates were immersed in 10 Mmol chloroform solution of octadecyltrichlorosilane (OTS) to form a self-assembled monolayer (SAM) on the SiO_2 surface. For the BC OFETs, the source and drain electrodes are deposited directly on the SiO_2 surface. Here that was done by a sequential evaporation of 5-nm-thick MoO_3 and 35-nm-thick gold through a metal mask, where MoO_3 was used as an adhesion or charge injection layer. Next a pentacene (Aldrich, purified using temperature gradient sublimation) layer was vacuum-deposited (rate of 0.01 nm/s at room temperature, final thickness of 50 nm). In the TC devices the pentacene layer was deposited first and then the source and drain electrodes were formed by thermal evaporation of Cu through a metal mask. The observed $\mu \approx 0.3$–0.4 cm^{2}V^{-1}s^{-1}(TC)/0.04–0.1 cm^{2}V^{-1}s^{-1}(BC) and $V_T \approx -2$ V $-$ 0.7 V(TC)/0.7 V $-$ 2.3 V(BC).

3. Methods

The Power-TLM relies on the fact that the total power dissipated P_{tot} in the whole device volume can be calculated, according to Joule's law as [13]:

$$P_{tot} = \int_{\Omega} \rho J^2 d\Omega \tag{1}$$

where ρ and J are the local resistivity and current density, respectively. The advantage of using Eq. (1) for evaluating the dissipated power is that it is independent of the specific conductor shape and thus of the current flow distribution. Therefore, one can separately evaluate the power dissipated in each region of the device, i.e., contact and channel regions such as,

$$P_{tot} = P_s + P_{ch} + P_d \tag{2}$$

where P_s, P_d and P_{ch} are the power contribution coming from source, drain and channel regions, respectively. So, for a given drain current I_D circulating in the device, one can calculate an equivalent total resistance by normalizing Eq. (2) as,

$$R_{tot} \equiv \frac{P_{tot}}{I_D^2} = \frac{V_D}{I_D} = \frac{P_s}{I_D^2} + \frac{P_{ch}}{I_D^2} + \frac{P_d}{I_D^2} = R_s + R_{chEq} + R_d \tag{3}$$

where R_{chEq} is the channel equivalent resistance. In the absence of contact resistance ($R_{sd} = 0$), it would simply be equal to V_D/I_D and, by turn, scales as (L/W). In the presence of contact resistances, the channel power reads $P_{ch} = V_{Deff}I_D$, where V_{Deff} is the effective (intrinsic) drain voltage applied to the channel, we have $R_{chEq} = V_{Deff}/I_D$. As I_D is governed by the effective (intrinsic) gate voltage (V_{Geff}) and the effective drain voltage, one can simply denote $I_D = (W/L)F(V_{Geff}, V_{Deff})$ with F being the intrinsic transistor characteristics per unit aspect ratio and hence, $R_{chEq} = (L/W)[V_{Deff}/F(V_{Geff}, V_{Deff})]$. In other words, R_{chEq} of different transistors always varies $\sim(L/W)$, for the same gate and drain biasing.

In linear regime, the channel can be regarded as a linear resistance $R_{ch} = L/[W\mu C_i(V_G - V_T)]$ if μ (the effective mobility) is constant but it sometimes reveals a power law dependence of $(V_G - V_T)$ [4,12], e.g., in amorphous polymer OFETs where the carrier transport is nearly via hopping. In this case, Eq. (3) is nothing but the base of the conventional TLM since the total output resistance is a linear superposition of channel and contact resistance, i.e., $R_{tot} = R_s + R_{ch} + R_d$, where the unique channel length dependent contribution is $R_{ch} \sim (L/W)$.

In non-linear regime, the channel cannot be treated as a linear resistance but could be still equivalent to $R_{chEq} = P_{ch}/{I_D}^2$ also scaling as $\sim(L/W)$, as discussed above. Therefore, one can find that Eq. (3) is a universal expression for power TLM (P-TLM): R_{chEq} varies as L/W but R_{sd} only follows $\sim(1/W)$, irrespective of linear/saturation operation. Hence R_{sd} can be extracted from the plot of the W normalized R_{tot} with respect to L, if the channel width is not uniform in the transistors' group, similar to the conventional TLM.

4. Results and discussion

4.1. Application to PTAA OFETs

Fig. 1a shows typical output characteristics for a PTAA OFET. At small V_D, the $R_{tot}(=V_D/I_D)$ represented by the reciprocal of the slope of illustrated straight lines is constant, indicating the ohmic operation. As V_D is increased over the limit of $V_{Dsat} = (V_G - V_T)$, the normalized $R_{tot} \times W$ increases also with V_D, as shown in Fig. 1b for a set of devices with various L and at fixed $V_G = -30$ V. Fig. 1c clearly shows that these $R_{tot} \times W$ (at $V_D = -30$ V) exhibit a linear variation with respect to L, providing $R_{sd} \times W$ in the y-axis intercept. However, we frequently encounter difficulties in applying P-TLM as found in the conventional TLM, mainly obtaining negative $R_{sd} \times W$, in particular at small gate voltages. This is due to the parameter variation from transistors-to-transistor (e.g., μ, C_i and V_T), and it is even amplified in saturation regime and in longer channel devices [6]. Hence the modified-power TLM (MP-TLM) becomes useful, $R_{tot} \times W/L$ are plotted as a function of $1/L$ and $R_{sd} \times W$ is evaluated from the slope of the fitting line, instead of the intercept [6]. Indeed, the linear regression giving the slope versus $1/L$ minimizes the impact of channel parameters scattering and maximizes the influence of small L, i.e., large $1/L$ values where the contact resistance plays an important role in the overall output resistance. In addition, compared to the channel resistance the contact resistance generally exhibits much smaller dispersion from transistor-to-transistor. Fig. 1d shows the MP-TLM for the same extraction seen in Fig. 1c, one can readily find a better linear regression, implying greater accuracy.

The two power TLM extractions are applied at various V_D, as shown in Fig. 2a and b. The obtained $R_{sd} \times W$ is shown in Fig. 2c. Note that the contact resistance represented by the intercepts in y-axis (P-TLM, cf. Fig. 2a) or the slopes (MP-TLM, cf. Fig. 2b) for this transistors' group of linear fitting lines remain constant at small V_D and afterward increases with V_D. The former constant $R_{sd} \times W$ in linear regime is reasonable because the small drain voltage doesn't significantly affect the source and drain access resistance. However, as V_D is much increased, the channel will be pinch-off on the drain side and thereby, R_d increases with V_D while R_s remains the same [9,14]. One may notice the large deviation between the results obtained by the two power-TLMs, as seen in Fig. 2c. This might be due to the drain voltage dependences of the channel equivalent resistance R_{chEq} and it causes an additional variation in various transistors of different channel length while V_D is changing. This dispersion in R_{chEq} is reduced in MP-TLM extraction where the linear regression slope is directly governed by the contact resistance and its dispersion arising from V_D dependences is smaller than R_{chEq} for a same basing condition and as a result, the contact resis-

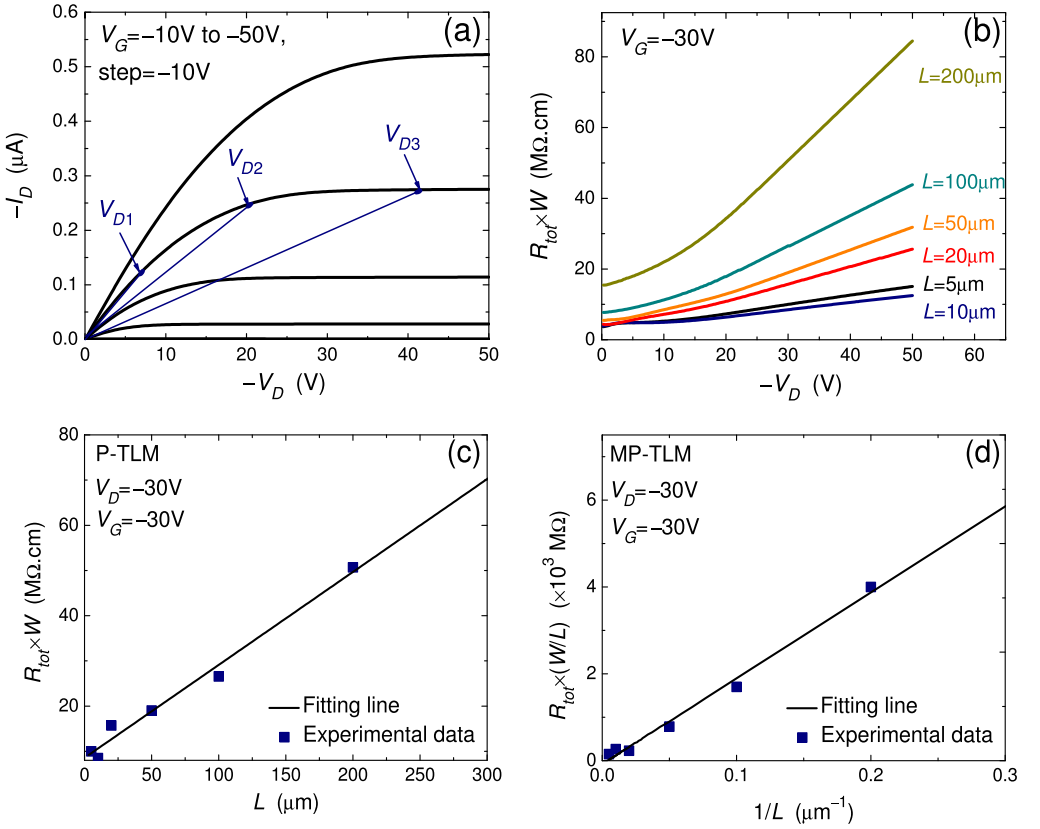

Fig. 1. (a) Output characteristics of a PTAA OFET (W = 1000 μm, L = 100 μm), where three data points at various V_D are chosen to illustrate the output resistance ($R_{tot} = V_D/I_D$, represented by the reciprocal of the straight lines' slope) variation versus V_D, as shown in (b), for a set of transistors with various L. (c) and (d) are the P-TLM and the MP-TLM extraction, respectively, at a fixed V_G and V_D.

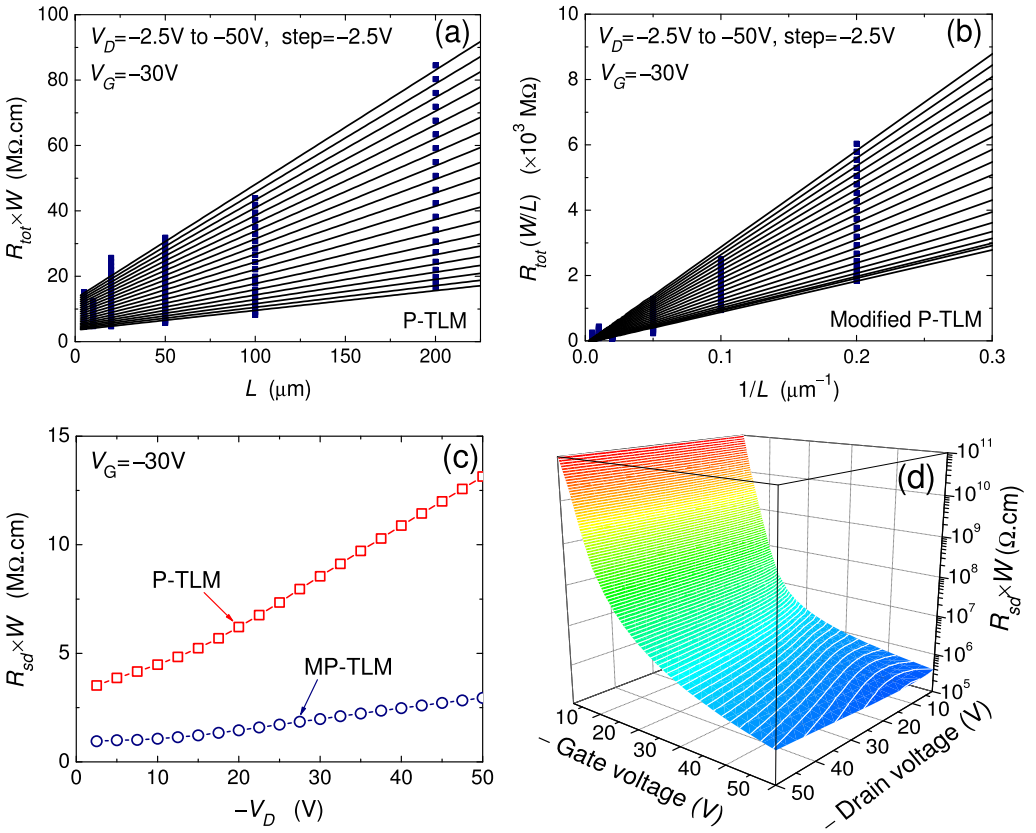

Fig. 2. (a and b) are P-TLM and MP-TLM extractions for the above PTAA OFETs, respectively, at various drain voltages and at fixed $V_G = -30$ V. (c) Shows the extracted results by the two power TLMs. (d) Shows the global contact resistance extracted by MP-TLM, at various V_G and V_D.

tance dependences on V_D and V_G can be more reliably reflected in MP-TLM extractions. Moreover, in view of the greater accuracy and higher stability of MP-TLM, it is preferred for the next analysis. The overall $R_{sd} \times W$ (at various V_D and V_G) are shown in Fig. 2d, strong gate-voltage dependence and relatively weak drain-voltage dependence can be observed.

4.2. Application to pentacene OFETs

Next, the same procedure is applied on two groups of TC/BC pentacene OFETs (with bottom-gate and uniform $W = 500$ μm). The evaluated R_{sd} is shown in Fig 3a and b, for TC and BC group, respectively. Compared to BC counterparts (cf. Fig. 3c), the TC OFETs show much stronger gate-voltage dependence, consistently with the literature [9,12,15,16]. In staggered transistors (e.g., TC/BG OFETs here), carriers must traverse the entire semiconductor film in the contact region where the bulk conductivity strongly depends on the carrier density modulated by the gate voltage. This bulk resistance dominates the overall contact resistance, manifesting a strong gate-voltage dependence [9,16,17]. In coplanar devices (e.g., BC/BG OFETs here), the channel directly connects the two electrodes. Thus R_{sd} is predominantly controlled by the contribution in a low conductive access region in the immediate vicinity of the contacts, in which a large number of defects reside in [10,14,18]. Such a defect-rich access region is sometimes characterized as a depletion area at negative gate biases. Its width is varied by V_G, leading to an R_{sd} gate-voltage dependence [18]. However, its variation range is much smaller than that for the bulk resistance (dominant component in TC OFETs) and hence, the TC contact resistances quickly decrease with V_G and become smaller than those for BC devices at higher gate voltages, in line with our previous results [12]. Note also that the TC OFETs show stronger drain-voltage dependence than BC ones, cf. Fig. 3c and d. This is because in staggered transistors increasing V_D weakens the channel accumulation in the drain region and thus lowers the contact bulk conductivity at drain contact. This feature is not significant for coplanar devices due to the directly connected channel and/or the depletion space screening from the lateral electrical field. One may find a rapid increase in BC contact resistance with V_G at small gate voltages and high drain voltages (e.g., Fig. 3b and c), this might be due to an extraction error or could result from a significant decrease of R_s at weak accumulation and in saturation regime, as reported in Ref. [14].

5. Summary

In summary, a power-TLM for full biasing contact resistance evaluation has been presented. By estimating the dissipated power in access region and in the channel, the

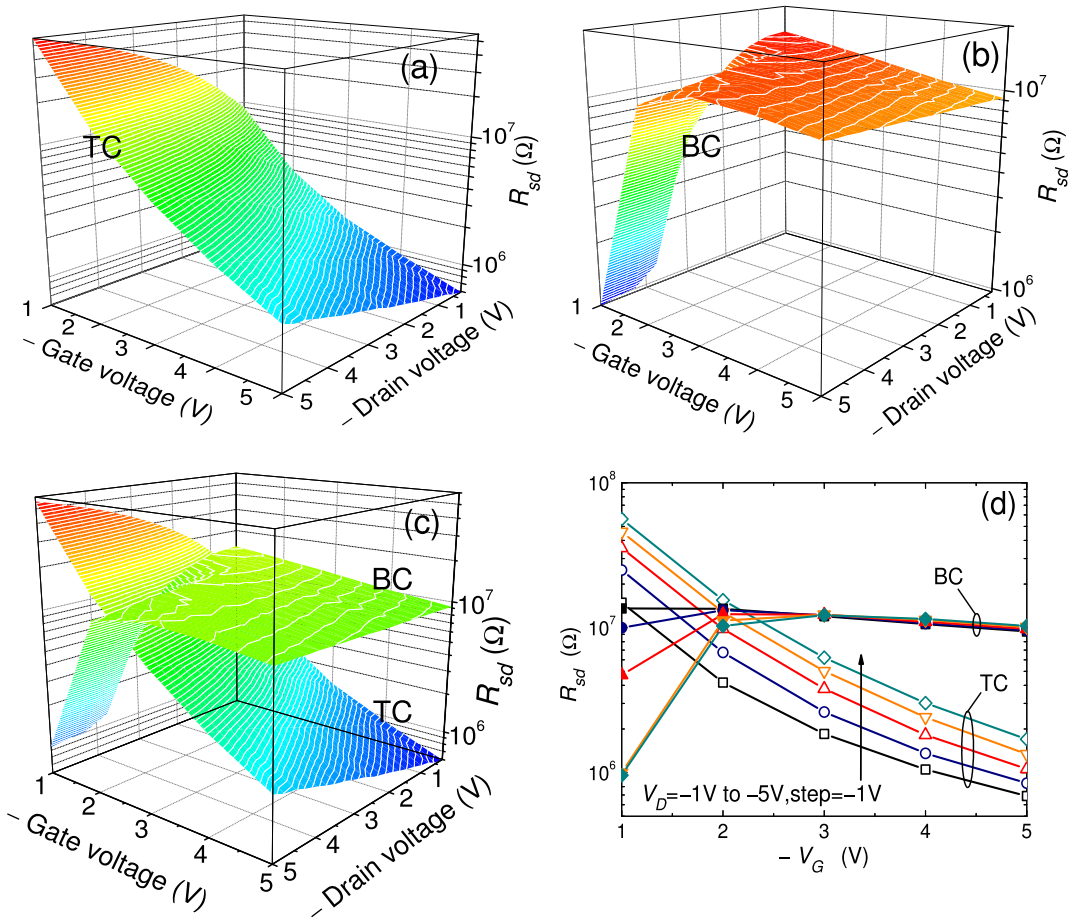

Fig. 3. Contact resistance obtained by MP-TLM in a set of TC (a) and BC (b) pentacene OFETs. (c) Shows the comparison of the contact resistance in TC and BC group. (d) Shows the gate-voltage dependence at various V_D.

channel equivalent resistance is found to always scale as $\sim(L/W)$ and the contact resistance follows $\sim(1/W)$, no matter whether the organic transistors operate in linear regime or not. This result reveals that the conventional TLM can be also applied to non-linear regime, and thus enabling a full biasing (i.e., all range of gate/drain voltages) contact resistance extraction. To ensure stable application of this power-TLM, particularly at small gate voltages, and in order to improve the extraction accuracy its modified form (i.e., MP-TLM) becomes mandatory. The contact resistance in PTAA OFETs is found to be strongly attenuated by the gate voltage but slightly increased with the drain voltage, due to the channel pinch-off at drain contact. The results of pentacene OFETs indicate that compared to the BC counterparts the contact resistance in TC OFETs exhibit much stronger gate- and drain- voltage dependences. Therefore, MP-TLM is proved as a useful approach to directly investigate the gate and drain bias dependences of contact resistance by using output characteristic measurements.

References

[1] J. Zaumseil, K.W. Baldwin, J.A. Rogers, Contact resistance in organic transistors that use source and drain electrodes formed by soft contact lamination, Journal of Applied Physics 93 (2003) 6117–6124.
[2] D.J. Gundlach, L. Zhou, J.A. Nichols, T.N. Jackson, P.V. Necliudov, M.S. Shur, An experimental study of contact effects in organic thin film transistors, Journal of Applied Physics 100 (2006) 024509.
[3] H. Klauk, G. Schmid, W. Radlik, W. Weber, L.S. Zhou, C.D. Sheraw, J.A. Nichols, T.N. Jackson, Contact resistance in organic thin film transistors, Solid-State Electronics 47 (2003) 297–301.
[4] G. Horowitz, Organic thin film transistors: from theory to real devices, Journal of Materials Research 19 (2004) 1946–1962.
[5] K. Ryu, I. Kymissis, V. Bulovic, C. Sodini, Direct extraction of mobility in pentacene OFETs using *C–V* and *I–V* measurements, IEEE Electron Device Letters 26 (2005) 716–718.
[6] Y. Xu, R. Gwoziecki, I. Chartier, R. Coppard, F. Balestra, G. Ghibaudo, Modified transmission-line method for contact resistance extraction in organic field-effect transistors, Applied Physics Letters 97 (2010) 063302.
[7] L. Bürgi, H. Sirringhaus, R. Friend, Noncontact potentiometry of polymer field-effect transistors, Applied Physics Letters 80 (2002) 2913.
[8] P.V. Pesavento, R.J. Chesterfield, C.R. Newman, C.D. Frisbie, Gated four-probe measurements on pentacene thin-film transistors: contact resistance as a function of gate voltage and temperature, Journal of Applied Physics 96 (2004) 7312–7324.
[9] T.J. Richards, H. Sirringhaus, Analysis of the contact resistance in staggered, top-gate organic field-effect transistors, Journal of Applied Physics 102 (2007) 094510.
[10] T. Li, P. Ruden, I. Campbell, D. Smith, Investigation of bottom-contact organic field effect transistors by two-dimensional device modeling, Journal of Applied Physics 93 (2003) 4017.
[11] J.M. Verilhac, M. Benwadih, A.L. Seiler, S. Jacob, C. Bory, J. Bablet, M. Heitzman, J. Tallal, L. Barbut, P. Frere, G. Sicard, R. Gwoziecki, I. Chartier, R. Coppard, C. Serbutoviez, Step toward robust and reliable amorphous polymer field-effect transistors and logic functions made

by the use of roll to roll compatible printing processes, Organic Electronics 11 (2010) 456–462.
[12] Y. Xu, T. Minari, K. Tsukagoshi, J.A. Chroboczek, G. Ghibaudo, Direct evaluation of low-field mobility and access resistance in pentacene field-effect transistors, Journal of Applied Physics 107 (2010) 114507.
[13] L.K.J. Vandamme, G. Trefan, 1/*f* Noise in homogeneous and inhomogeneous media, IEE Proceedings – Circuits Devices and Systems 149 (2002) 3–12.
[14] K.P. Puntambekar, P.V. Pesavento, C.D. Frisbie, Surface potential profiling and contact resistance measurements on operating pentacene thin-film transistors by Kelvin probe force microscopy, Applied Physics Letters 83 (2003) 5539–5541.
[15] I.G. Hill, Numerical simulations of contact resistance in organic thin-film transistors, Applied Physics Letters 87 (2005) 163505.
[16] V. Vinciguerra, M. La Rosa, D. Nicolosi, G. Sicurella, L. Occhipinti, Modeling the gate bias dependence of contact resistance in staggered polycrystalline organic thin film transistors, Organic Electronics 10 (2009) 1074–1081.
[17] T. Minari, T. Miyadera, K. Tsukagoshi, Y. Aoyagi, H. Ito, Charge injection process in organic field-effect transistors, Applied Physics Letters 91 (2007) 053508.
[18] L. Burgi, T.J. Richards, R.H. Friend, H. Sirringhaus, Close look at charge carrier injection in polymer field-effect transistors, Journal of Applied Physics 94 (2003) 6129–6137.

successfully demonstrated [5]. However, single layer blue PhOLEDs [2,5a,6] reported as far were not satisfactory yet, giving challenges for material scientists. The most popular blue emitter FIrpic has revealed its bipolar charge carrier transport behavior by using the time-of-flight (TOF) transient photocurrent technique [7]. Accordingly, highly efficient single layer blue PhOLED should be feasible if one uses FIrpic dispersed into a tailor-made high triplet energy host with suitable energy levels for direct carriers injection. In this paper, we report a novel high triplet energy host material: 3,3′,3″-phosphoryl tris(9-phenyl-9H-carbazole) (POCz3) for efficient single-layer blue PhOLEDs. The device: ITO/PEDOT:PSS/POCz3 (3 nm)/POCz3:FIrpic 20 wt.% (80 nm)/LiF/Al gives a maximum external quantum efficiency (η_{ext}) of 9%, power efficiency (η_p) of 10.4 lm/W, and current efficiency (η_c) of 21.3 cd/A. To the best of our knowledge, this work represents an unprecedented example of realizing a single-layer blue PhOLED with remarkable device characteristics.

2. Results and discussion

2.1. Materials

The most successful host materials used for FIrpic are carbazole derivatives [8]. Without extended π-conjugation from the carbazole core, carbazole-based host materials usually exhibit high triplet energies. Thus, the triplet excitons can be efficiently confined within the emitting layer. However, typical FIrpic-based blue PhOLEDs incorporated with carbazole-based hosts require multilayer structures for facilitating the hole/electron injections into the emitting layer. In order to enhance the electron injection capability of carbazole, structural modification by introducing electron deficient moiety onto the carbazole core is necessary. Recently, triarylphosphine oxides have been reported to perform facile electron injection and transport properties [9–11]. The combination of the structural features of carbazole and phosphine oxide had led to promising bipolar hosts for blue PhOLEDs with excellent device characteristics [12]. The HOMO level of carbazole compound can be modulated by introducing appropriate substitutions at the C3 and/or C6 positions of carbazole [13–14], giving the opportunity of developing potential host materials for single layer device. Scheme 1 depicts the structure of the new bipolar host material POCz3, which was synthesized in one step with reasonable yield from a known precursor. The 3-bromo-9-phenylcarbazole reacted with magnesium turning in THF to give a Grignard solution, which was then quenched with $POCl_3$ to give the desired product POCz3 in 55% yield. The structural identity of POCz3 was confirmed by satisfactory ^1H, ^{13}C and ^{31}P NMR spectra, high-resolution mass spectrometry (HRMS).

2.2. Physical properties characterizations

POCz3 exhibits a high thermal tolerance [5% weight loss occurred at 395 °C, determined by thermogravimetric analysis (TGA)] and a distinct glass transition temperature (T_g) of 163 °C analyzed by differential scanning calorimetry (DSC). Therefore, POCz3 can form homogeneous and stable amorphous films upon thermal evaporation, which is a crucial criterion for OLED application.

The photophysical property of POCz3 as compared to that of parent compound 9-phenyl carbazole is shown in Fig. 1. Apparently, the introduction of phosphine oxide onto the carbazole ring only brings out limited perturbation on the photophysical property of carbazole. In solution, POCz3 exhibits a strong absorption band range from 260 to 300 nm that is attributed to the typical π–π* electronic transition of carbazole, whereas the weak absorption bands (300–350 nm) are ascribed to the n–π* transitions of carbazole. The emission spectrum of POCz3 is almost superimposable to that of 9-phenyl carbazole. The phosphorescent spectrum of POCz3 was obtained at 77 K (in EtOH). Again, there is no significant difference on the triplet energy upon introducing the electron deficient phosphine oxide to the carbazole as compared to that of 9-phenyl carbazole. The difference between the fluorescence (351 nm) and phosphorescence (408 nm) spectra corresponds to an exchange energy of ca. 0.67 eV between the singlet and triplet of POCz3. The triplet energy (E_T) of 3.03 eV (defined as the 0–0 transition in phosphorescent spectrum) is sufficiently high for POCz3 to confine the triplet excitons of the blue phosphorescence emitter FIrpic (E_T = 2.7 eV) within the emitting layer.

Fig. 2 displays the cyclic voltammograms of POCz3 and 9-phenyl carbazole in CH_2Cl_2 using a glassy carbon electrode with 0.1 M of nBu$_4$NPF$_6$ as electrolyte. The oxidation of POCz3 showed typical electrochemical behavior of C3

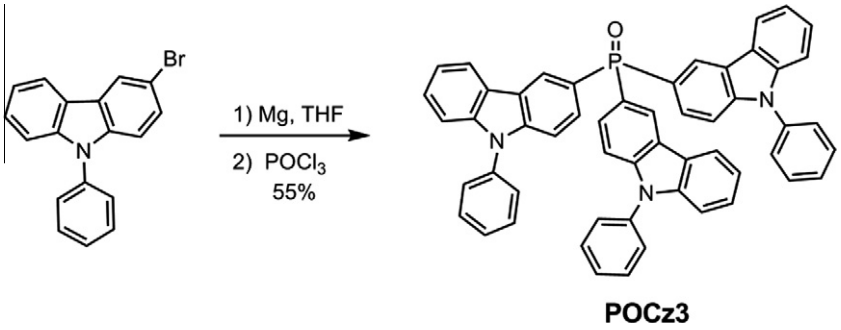

Scheme 1. The structure and synthesis of bipolar host POCz3.

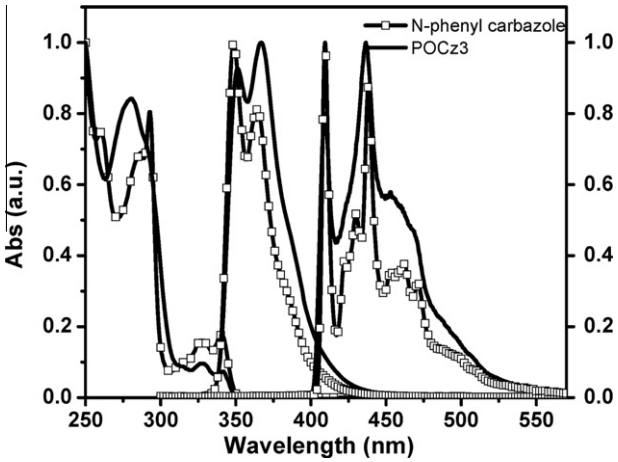

Fig. 1. A comparison of UV–vis absorption, photoluminescence (PL) (CH_2Cl_2), and phosphorescence (EtOH, 77 K) spectra of POCz3 and its parent counterpart N-phenyl carbazole.

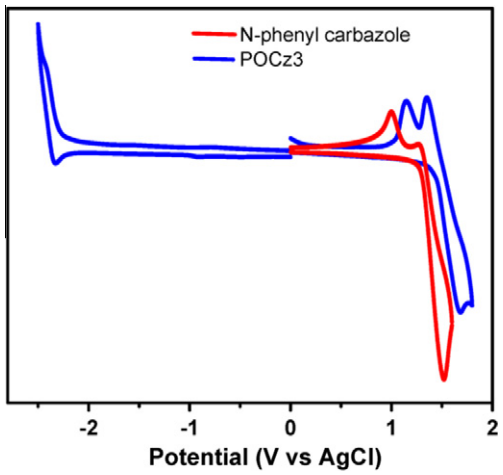

Fig. 2. The cyclic voltammogram of POCz3 as compared to that of parent compound 9-phenylcarbazole.

and C6 unprotected carbazole derivatives, which usually performed a lower reduction peak originated from the more conjugated dimeric species generated from the coupling of carbazole cationic radicals. It is noteworthy that the oxidation onset of POCz3 is evidently shifted from 1.28 V of 9-phenyl carbazole to 1.44 V. Thus, the highest occupied molecular orbital (HOMO) energy of POCz3 is strongly affected by introducing the electron-withdrawing phosphine oxide. The electron deficient substituent is also beneficial to the reduction behavior of POCz3, in which one quasi-reversible reduction potential, onset potential at −2.25 V, was observed in dimethylformamide (DMF) using a glassy carbon electrode with 0.1 M of nBu$_4$NClO$_4$ as electrolyte. For practical evaluation, the HOMO of POCz3 were measured using UV photoemission spectroscopy (AC-2) to be −5.5 eV, and the lowest unoccupied molecular orbital (LUMO) energy was deduced to be −1.8 eV by adding the energy gap of POCz3 to the HOMO energy.

To further understand the charge-carrier transport properties of POCz3, we used the time-of-flight (TOF) technique [15] to evaluate the carrier mobilities. Fig. 3(a) displays representative TOF transient for electrons of POCz3. The transit time, t_T, can be evaluated from the intersection point of two asymptotes in the double-logarithmic representation of the TOF transient. It is then used to determine the carrier mobilities, according to the equation $\mu = d^2/Vt_T$, where d is the sample thickness and V is the applied voltage. Fig. 3(b) reveals that the field dependence of the electron mobility follows the nearly universal Poole–Frenkel relationship, with values in the range from 1.4×10^{-6} to 6.4×10^{-6} cm^2/Vs for fields varying from 4×10^5 to 6.8×10^5 V/cm.

In contrast, the TOF transient for holes exhibited weak photocurrent signals, which could not be used to determine the hole mobility. From the chemical structure of POCz3 (Scheme 1), the carbazole unit is a good hole transport unit and is effective in improving the hole transport property of the organic material. Hence, we also prepared hole- and electron-only single-carrier devices, to evaluate the bipolar transport behavior. We used high-LUMO 4,4′-bis[*N*-(1-naphthyl)-*N*-phenylamino]biphenyl (NPB, μh of 10^{-3} cm^2/Vs order) [16] to limit the electron carrier in hole-only devices and low-HOMO 2,9-dimethyl-4,7-diphenyl-1,10-phenanthroline (BCP, μe of 10^{-7} cm^2/Vs order) [17] to limit the hole carrier in electron-only devices. As shown in Fig. 4, POCz3 shows bipolar transport property. However, the current density of electron-only device is larger than that of hole-only device at the same voltage, indicating the superior capability of POCz3 to transport electron other than hole-transport. This result is in agreement with the observed TOF mobility that only electron mobility can be resolved.

2.3. Device characteristics

The energy levels diagram of single-layer blue PhOLEDs with host molecule POCz3 and blue emitter FIrpic is depicted in Fig. 5. It is obvious that the energy level alignment allows energetically favorable electron injection from cathode directly into FIrpic (energy barrier ∼0.1 eV) instead of POCz3 which gives an energy barrier ∼1.2 eV.

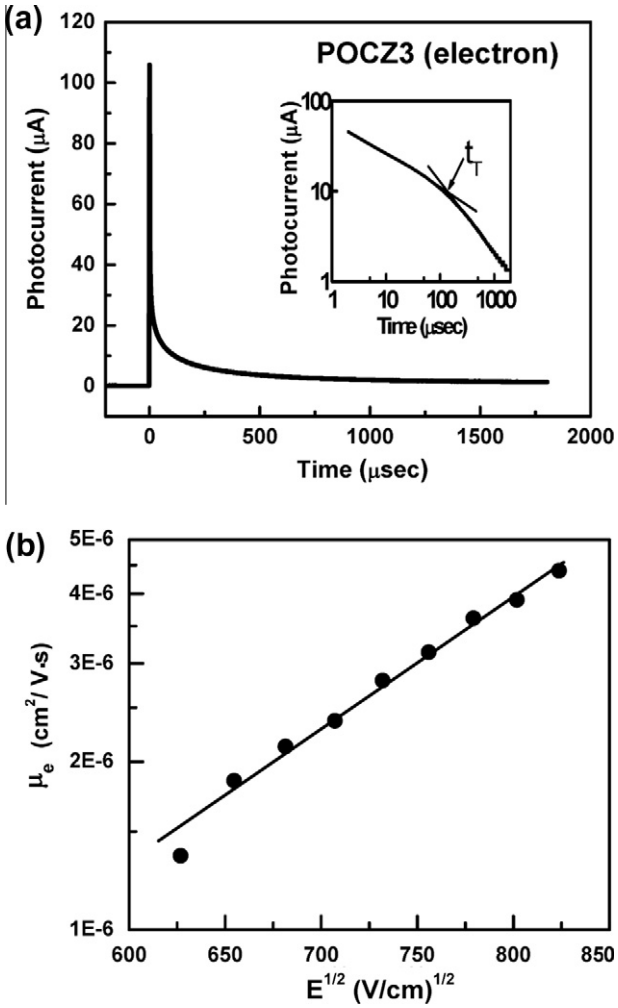

Fig. 3. Typical transient photocurrent signals for POCZ3 (2.8 μm thick): (a) electron at $E = 5.4 \times 10^5$ V/cm. Insets are the double logarithmic plots of (a). (b) Electron mobility plotted with respect to $E^{1/2}$ at ambient temperature.

In contrast, the HOMO energy level of POCz3 allows hole injection from anode and transporting by way of host to reach to FIrpic. Based on the promising physical properties of POCz3, a single layer blue PhOLEDs with POCz3 as host for FIrpic was fabricated with the device configuration as ITO/PEDOT:PSS/POCz3:FIrpic/LiF/Al.

It is inevitable that the recombination zone should be as away as possible from both electrodes for avoiding exciton quenching. Thus, the thickness of the single layer device needs to be carefully optimized. We used the typical doping concentration 10 wt.% of FIrpic for devices configured as ITO/PEDOT:PSS/POCz3:FIrpic (x nm)/LiF/Al, where the thicknesses x were varied as 70 nm, 80 nm, and 90 nm, respectively. The J–V and efficiency characteristics of these devices are shown in Fig. 6.

It is clear that the devices have higher driving voltages as the thickness of POCz3:FIrpic layer increases. Among these three devices, the single-layer device with thickness of 80 nm gave the optimal maximum external quantum efficiency (EQE) of 7.1% at brightness of 100 cd/m^2, and showed slow efficiency roll-off as the EQE keeps at 6.4% at the brightness of 1000 cd/m^2. As a consequence, we utilized 80 nm as the optimal thickness of the emitting layer in the following experiments. It should be noted that the hole-injection material PEDOT:PSS may act as a strong quencher of blue phosphorescence, rendering low device efficiency. In order to suppressing the possible triplet exciton diffusion, a neat thin film of POCz3 was introduced between the PEDOT:PSS and emitting layer comprised of POCz3 and FIrpic. Thus, we fabricated two devices with device configuration of ITO/PEDOT:PSS/POCz3 (x nm)/ POCz3:FIrpic 10.0 wt.% (80 nm)/LiF/Al, where the thickness x of POCz3 is 3 and 5 nm, respectively. Fig. 7 shows the J–V and external quantum efficiency-brightness characteristics of these two devices as compared to those of the parent device. Fig. 7(b) shows the EL spectra of the devices with and without introducing a thin film of POCz3 as exciton confinement layer. As shown, all devices have almost identical EL spectra which gave blue light originating from the FIrpic, indicating that the triplet excitons of FIrpic are

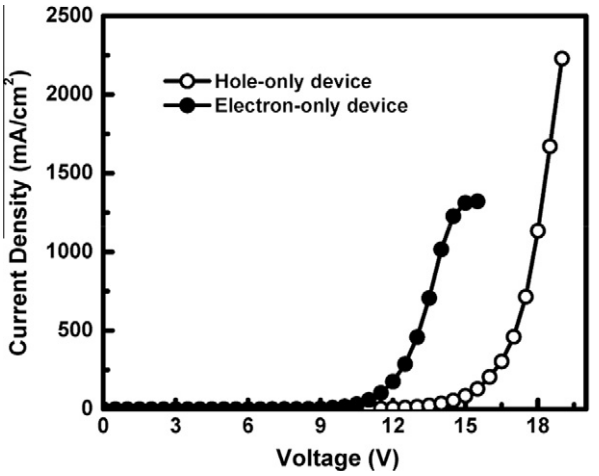

Fig. 4. Current density–voltage (I–V) characteristics of carrier-only device: hole-only device (ITO/NPB (10 nm)/POCz3 (30 nm)/NPB (10 nm) /LiF/Al and electron-only device: (ITO/BCP (10 nm)/POCz3 (30 nm)/BCP (10 nm)/LiF/Al.

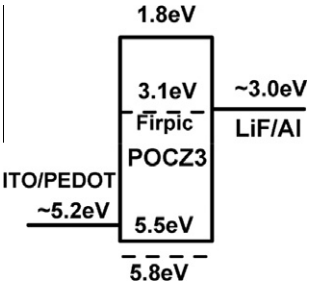

Fig. 5. Relative energy levels of a single-layer PhOLED device with blue emitter FIrpic and host POCz3.

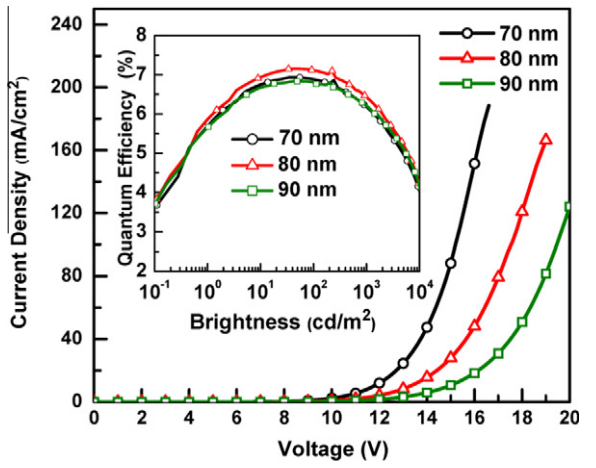

Fig. 6. Current–voltage and external quantum efficiency characteristic of POCz3:FIrpic based single layer blue PHOLEDs as a function of device thickness.

efficiently confined within the POCz3:FIrpic layer. The device with POCz3 as the interfacial layer (5 nm) achieves higher efficiency of 7.7% as compared to that of the parent

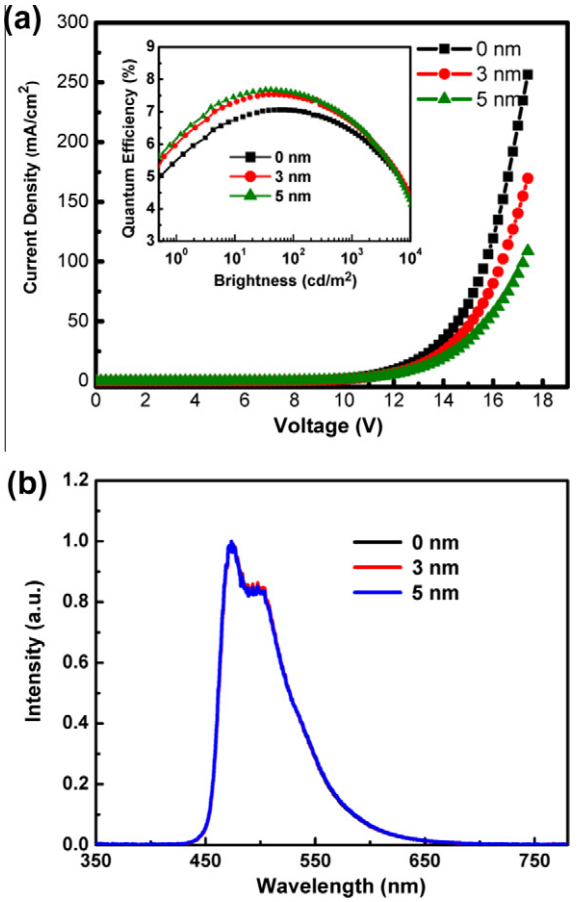

Fig. 7. (a) Current–voltage and external quantum efficiency–brightness characteristic of the exciton confined devices, (b) EL spectra of the devices with different thickness of exciton confinement layer.

device due to the exciton confinement effect. However, due to the low hole transport ability of POCz3, the driving voltages are higher with the thickness of interfacial POCz3 layer increases. As a consequence, a 3 nm neat thin film of POCz3 was utilized as the exciton confinement layer in the following experiments.

In the case of direct injection and transport on the dopant, the increase of the doping concentration may lead to enhanced probability of carrier injection and transport channels, resulting in higher device efficiency [6]. In order to improve device efficiency, four devices of varied concentrations of FIrpic were fabricated with a configuration of ITO/PEDOT:PSS/POCz3(3 nm)/POCz3: FIrpic *x* wt.% (80 nm)/LiF/Al, where the doping concentration *x* was varied as 10, 15, 20, and 25 wt.%, respectively, in order to determine the optimal dopant concentration. J–V–L curve and efficiency characteristics of these devices are shown in Fig. 8. The driving voltage decreases as the concentration of dopant concentration increases from 10 to 20 wt.%. There was limited difference on driving voltage between the doping concentration of 20 and 25 wt.%. This result indicates that device with higher FIrpic concentration imparts better carrier injection and more transport channels. Fig. 8(b) shows that maximum external quantum efficiency (power efficiency) enhanced

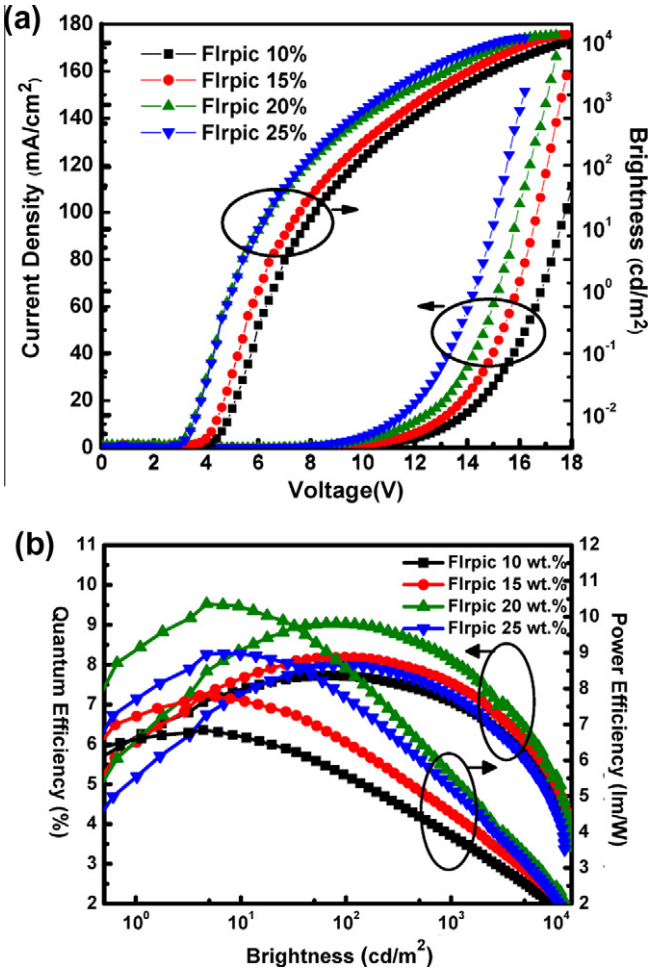

Fig. 8. (a) Current–voltage–brightness characteristic, (b) external quantum efficiencies and power efficiencies of single layer blue PhOLEDs.

from 7% (6.7 lm/W) to 9% (10.4 lm/W), when the FIrpic concentration increases from 10 to 20 wt.%. At higher doping concentration, more carriers can be directly injected and transported on FIrpic, leading to better device efficiency. However, at dopant concentration reaches to 25 wt.%, the efficiency decreased dramatically due to the triplet–triplet annihilation and concentration quenching effects. With the optimized dopant concentration of 20 wt.%, the device

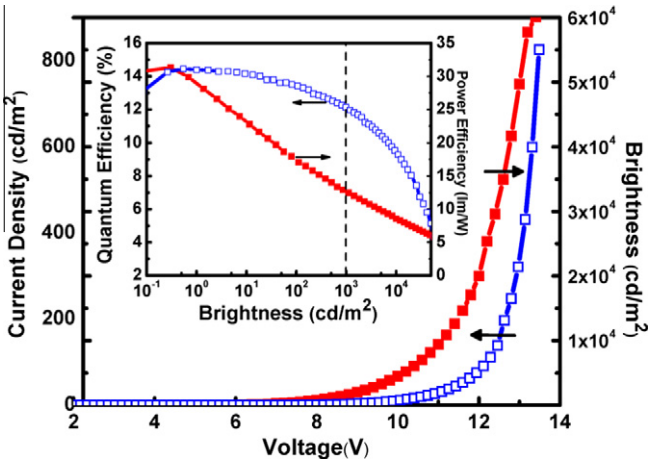

Fig. 9. Current–voltage–brightness and efficiency characteristic of POCz3 hosted three-layer blue PhOLEDs.

achieves the best performance, yielding maximum external quantum efficiency 9%, power efficiency 10.4 lm/W, and current efficiency 21.3 cd/A. The efficiencies of this optimized device show low roll-off effect with comparably high η_{ext} (8.1%), η_p (5.6 lm/W), and η_c (19.6 cd/A) when the brightness was increased to 1000 cd/m^2.

For evaluate the potential usefulness of POCz3 as a suitable host in multilayer OLEDs, a three-layer device using hole transport material 1,1-bis[4-[*N*,*N*-di(4-tolyl)-amino] phenyl]cyclohexane (TAPC) with high hole mobility (1×10^{-3} cm^2/Vs) and electron transport material 1,3,5-tri(m-pyrid-3-yl-phenyl)benzene (TmPyPB) with high electron mobility (1×10^{-3} cm^2/Vs) were fabricated. Considering the triplet exciton confinement within the FIrpic (E_T = 2.65 eV), a thin neat film of POCz3 (E_T = 3.03 eV) was introduced between TmPyPB (E_T = 2.78 eV) and POCz3:FIrpic. After optimizing charge balance by tuning the thickness of TAPC and TmPyPB, the J–V–L and efficiency characteristics of a three-layer device was shown in Fig. 9 with device configuration: ITO/TAPC (40 nm)/POCz3:FIrPic 8.0 wt.% (25 nm)/POCz3 (5 nm)/TmPyPB (50 nm)/LiF (0.8 nm)/Al. This device exhibits maximum luminance 60098 cd/m^2 and maximum external quantum efficiency and power efficiency of 14.5% and 31.3 lm/W, respectively. This device shows slow efficiency roll-off as the η_{ext} retains at 12.1% as the brightness is 1000 cd/m^2.

3. Conclusion

In summary, an efficient one-step synthesis gives a new bipolar host material POCz3 with high triplet energy and good thermal/morphological stabilities useful for efficient single-layer and tri-layer blue PhOLED devices. The introduction of electron-withdrawing phosphine oxide renders POCz3 to give a shallow HOMO energy suitable for injecting hole from anode and transporting through to reach to the bipolar blue phosphorescence dopant FIrpic, and recombining with the electrons direct-trap from the cathode. This strategy was evidenced by the higher device efficiency as doping concentration of FIrpic increased due to enhanced probability of carrier injection and transporting channels. With the optimized dopant concentration of 20 wt.%, and incorporates a thin POCz3 film as exciton diffusion blocking layer between PEDOT:PSS and the emitting layer comprised of POCz3:FIrpic, the single-layer blue PhOLED achieves maximum external quantum efficiency of 9%, power efficiency of 10.4 lm/W, and current efficiency of 21.3 cd/A which are comparable to the common multilayer PhOLEDs devices. A three-layer device with a double confinement effect exhibits maximum luminance 60098 cd/m^2 and maximum EQE (power efficiency) of 14.5% (31.3 lm/W). We believe that these results can trigger the molecular design of new bipolar host materials for more cost-effective PhOLEDs.

4. Synthesis of POCz3

Mg (243 mg, 10 mmol) in a 50 mL double-necked round-bottomed flask, equipped with a reflux condenser and an addition funnel, under an atmosphere of argon, few anhydrous THF was added in the flask. 3-bromo-9-phenylcarbazole (3.22 g, 10 mmol) and anhydrous THF (10 mL) in the addition funnel were added dropwise to the flask and the reaction mixture was refluxed until Mg is disappeared. Return to room temperature, $POCl_3$ (0.28 mL, 3 mmol) was added in the Grignard reagent. The resulting pale-yellow solution was stirred for 8 h. The mixture was quenched with saturated aqueous solution of NH_4Cl (10 mL). The aqueous layer was extracted with dichloromethane (3×20 mL), and the combined organic layers were washed with water (2×20 mL), dried ($MgSO_4$), and concentrated under reduced pressure. The residue was purified through column chromatography (SiO_2; EtOAc/hexane 1:1) to yield POCz3 as a white yellow solid (4.3 g, 55%) ^{1}H NMR (400 MHz, $CDCl_3$) δ 8.67 (d, *J* = 12 Hz, 3H), 8.09 (d, *J* = 7.6 Hz, 3H), 7.76 (td, *J* = 10, 1.6 Hz, 3H), 7.62–7.55 (m, 12H), 7.50–7.41 (m, 12H), 7.27 (td, *J* = 7.2, 2.4 Hz, 3H); ^{13}C NMR (100 MHz, $CDCl_3$) δ 142.5, 141.2, 136.9, 129.8, 129.7, 129.6, 129.4, 127.8, 127.0, 126.5, 125.3, 125.2, 124.7, 123.6, 123.3, 123.1, 122.9, 120.7, 120.5, 110.0, 109.8, 109.6; ^{31}P NMR (161 MHz, $CDCl_3$) δ 33.9; HRMS(M/z, FAB$^+$) Calcd. For $C_{54}H_{36}N_3OP$ 774.2596, found 774.2674.

References

[1] M.A. Baldo, D.F. O'Brien, Y. You, A. Shoustikov, S. Sibley, M.E. Thompson, S.R. Forrest, Nature 395 (1998) 151–154.
[2] L.D. Hou, L. Duan, J. Qiao, W. Li, D.Q. Zhang, Y. Qi, Appl. Phys. Lett. 92 (2008) 263301–263301-3.
[3] C.W. Joo, S.O. Jeon, K.S. Yook, J.Y. Lee, Org. Electron. 11 (2010) 36–40.
[4] W.S. Jeon, T.J. Park, K.H. Kim, R. Pode, J. Jang, J.H. Kwon, Org. Electron. 11 (2010) 179–183.
[5] (a) M.-Y. Lai, C.-H. Chen, W.-S. Huang, J.T. Lin, T.-H. Ke, L.-Y. Chen, M.-H. Tsai, C.-C. Wu, Angew. Chem. Int. Ed. 47 (2008) 581–585;
(b) W.-Y. Hung, T.-C. Tsai, S.-Y. Ku, L.-C. Chi, K.-T. Wong, Phys. Chem. Chem. Phys. 10 (2008) 5822–5825;
(c) W.-Y. Hung, T.-C. Wang, H.-C. Chiu, H.-F. Chen, K.-T. Wong, Phys. Chem. Chem. Phys. 12 (2010) 10685–10687;
(d) C.-H. Chen, W.-S. Huang, M.-Y. Lai, W.-C. Tsao, J.T. Lin, Y.-H. Wu, T.-H. Ke, L.-Y. Chen, C.-C. Wu, Adv. Funct. Mater. 19 (2009) 2661–2670;
(e) X. Qiao, Y. Tao, Q. Wang, D. Ma, C. Yang, L. Wang, J. Qin, F. Wang, J. Appl. Phys. 108 (2010) 034508–034508-8;
(f) Y. Tao, C. Yang, J. Qin, Chem. Soc. Rev. 40 (2011) 2943–2970;
(g) S. Gong, Y. Chen, C. Yang, C. Zhong, J. Qin, D. Ma, Adv. Mater. 22 (2010) 5370–5373;
(h) Y. Tao, Q. Wang, C. Yang, Q. Wang, Z. Zhang, T. Zou, J. Qin, D. Ma, Angew. Chem., Int. Ed. 47 (2008) 8104–8107.
[6] Z. Liu, M.G. Helander, Z. Wang, Z. Lu, Org. Electron. 10 (2009) 1146–1151.
[7] N. Matsusue, Y. Suzuki, H. Naito, Jpn. J. Appl. Phys. 44 (2005) 3691–3694.
[8] M.-H. Tsai, H.-W. Lin, H.-C. Su, T.-H. Ke, C.-C. Wu, F.-C. Fang, Y.-L. Liao, K.-T. Wong, C.–I. Wu, Adv. Mater. 18 (2006) 1216–1220.
[9] F.-M. Hsu, C.-H. Chien, P.-I. Shih, C.-F. Shu, Chem. Mater. 21 (2009) 1017–1022.
[10] A.B. Padmaperuma, L.S. Sapochak, Paul E. Burrows, Chem. Mater.18 (2006) 2389–2396.
[11] P.E. Burrows, A.B. Padmaperuma, L.S. Sapochak, P. Djurovich, M.E. Thompson, Appl. Phys. Lett. 88 (2006) 183503–183503-3.
[12] (a) H.-H. Chou, C.-H. Cheng, Adv. Mater. 22 (2010) 2468;
(b) S.O. Jeon, K.S. Yook, C.W. Joo, J.Y. Lee, Adv. Funct. Mater. 19 (2009) 3644–3649;
(c) S.O. Jeon, S.E. Jang, H.S. Son, J.Y. Lee, Adv. Mater. 23 (2011) 1436–1441;
(d) J. Ding, Q. Wang, L. Zhao, D. Ma, L. Wang, X. Jing, F. Wang, J. Mater. Chem. 20 (2010) 8126–8133;
(e) S.O. Jeon, K.S. Yook, C.W. Joo, J.Y. Lee, Adv. Mater. 22 (2010) 1872–1876;
(f) F.-M. Hsu, C.-H. Chien, C.-F. Shu, C.-H. Lai, C.-C. Hsieh, K.-W.

Wang, P.-T. Chou, Adv. Funct. Mater. 19 (2009) 2834–2843;
(g) C.-H. Chien, F.-M. Hsu, C.-F. Shu, Y. Chi, Org. Electron. 10 (2009) 871–876;
(h) P.A. Vecchi, A.B. Padmaperuma, H. Qiao, L.S. Sapochak, P.E. Burrows, Org. Lett. 8 (2006) 4211–4214;
(i) X. Cai, A.B. Padmaperuma, L.S. Sapochak, P.A. Vecchi, P.E. Burrows, Appl. Phys. Lett. 92 (2008) 083308–082208-3;
(j) E. Polikarpov, J.S. Swensen, N. Chopra, F. So, A.B. Padmaperuma, Appl. Phys. Lett. 94 (2009) 223304–223304-3.

[13] P. Marsal, I. Avilov, D.A. da Silva Filho, J.L. Gredas, D. Beljonne, Chem. Phys. Lett. 392 (2004) 521–528.
[14] K. Brunner, A. Van Dijken, H. Brrner, J.J.A.M. Bastiaansen, N.M.M. Kiggen, B.M.W. Langeveld, J. Am. Chem. Soc. 126 (2004) 6035–6042.
[15] P.M. Borsenberger, D.S. Weiss, Org. Photorecep. Imag. Sys., Marcel Dekker, New York, 1993.
[16] S.C. Tse, K.C. Kwok, S.K. So, Appl. Phys. Lett. 89 (2006) 262102.
[17] Z.-Y. Xie, T.-C. Wong, L.-S. Hung, S.-T. Lee, Appl. Phys. Lett. 80 (2002) 1477–1479.

wearability comfort [6]; the aim of many research groups has therefore become the development of a specific treatment on cotton yarns with the purpose of obtaining conductive fibres while preserving cotton's unique set of physical and comfort properties.

Several different methods for the realization of conductive cellulose fibres have already been described in the literature [7–14]. These procedures may be roughly grouped into two different categories. On one hand, cotton's conductivity was increased by incorporating metal particles onto cotton modified with polymer brushes [7] or carbon nanotubes (CNTs) [8] into cellulose yarns. With these techniques, very high values of conductance per length unit (up to 1 S cm^{-1}) were achieved. The majority of reported works on conductive cotton, however, have focused on grafting conductive polymers (CPs) onto cellulose fibres by in-situ, liquid-phase polymerization [9–13] or simple soaking the cellulosic substrates in polymeric aqueous solutions [14]. The most commonly used CPs are π-conjugated polymers including polythiophenes (such as PEDOT) [9,12,14], polypyrrole [10,13] and polyaniline [11]. Incorporation of CPs into cotton fibres has shown to raise the conductance per length unit of the native fibre from $\sim 10^{-12}$ to 10^{-1} S cm^{-1}.

Surprisingly enough, even though it has been shown that the incorporation of metallic (e.g. Au, Ag, Pt) nanoparticles (NPs) into CPs films may result in the formation of highly conductive layers, characterized by conductivities several orders of magnitude greater than the values obtained for the CPs alone [15,16], the deposition of such composites on cotton substrates has not yet been attempted.

In this paper, we present a novel technique in which conductive Au NPs are deposited onto the cotton surface and subsequently interconnected with a layer of conductive polymer. The electrical properties of these samples are compared to those of yarns on which only Au NPs or only a CP layer was deposited, in order to evaluate the effect on the electrical behaviour of the combination of the two deposition processes.

We will show that the deposition of a metal NPs/CP composite on plain cotton yarns determines a dramatic increase of its conductivity so that treated yarns may be used as electrical connectors in order to bias or to interconnect electronic devices, behaving thus as relatively low resistance resistors.

Moreover, to demonstrate practically the possibility of using cotton fibres to fabricate organic textiles circuits, two different kinds of transistors have been realized.

The first device is based on the concept of OECT, first developed in planar form [17] and also realized in form of yarn based on a nylon fibre [18] and more recently on silk [19].

An OECT is made up of two electrodes, source and drain, connected by an active layer called channel realized using a conductive polymer which can be electrochemically doped/de-doped [20]. The channel conductivity is modulated by applying a voltage on a third electrode, the gate, immersed in an electrolyte solution in contact with the channel. The gate voltage drives the electrolyte cations into the channel where they cause its de-doping and, as a consequence, a decrease of the current flowing between the source and drain terminals. Channel de-doping is a reversible process: when the gate voltage is brought back to zero, the channel conductivity increases again.

The second example of active device realized on a cotton yarn is based on the concept of organic field effect transistor (OFET). In this case, the conductivity of the channel, made of a semiconductor deposited between two metal contacts (source and drain), is modulated by the voltage applied to a gate electrode, capacitively coupled with the device channel [21]. The transistor current is modulated by varying the voltage on the gate. To realize a yarn-shaped OFET, a multilayered structure based on a conductive yarn (that acts as the gate of the device) is used. This cylindrical structure is able to act as a transistor, according to a model that takes into account its geometrical characteristics [22] giving rise to results very similar to those obtained with planar structures.

2. Materials and methods

2.1. Preparation of Au NPs/PEDOT:tos coated conductive cotton yarns

The procedure for the deposition of Au nanoparticles on cellulosic substrates has been already reported in previous publications [23].

After conformally coating cotton yarns with high packing surface density of Au NPs, a thin layer of tosylate-doped PEDOT (PEDOT:tos) was deposited on the yarns by means of a vapour phase polymerization (VPP) process. Such a procedure has already been described in detail in the literature [24,25] for the deposition of thin PEDOT:tos films on planar substrates. In our case, we prepared a solution of 125:25:1 wt% of isopropanol:Fe(III)–tosylate:pyridine in which the yarns were soaked for 10 min and then dried on a hot plate at 80 °C for 3 min.

After polymerization of EDOT monomer into PEDOT, the samples were dried in an oven at 50 °C for 30 min. Then they were rinsed into ethanol for 10 min and finally dried in a vacuum oven at room temperature for 12 h.

This procedure is described in the cartoon presented in the Supplementary data.

Conductive cotton fibres were used as source, drain and gate electrodes in the assembly of cotton-made electrochemical transistors (see Section 2.6).

2.2. Preparation of PEDOT:poly(styrenesulphonate) coated semiconductive yarns

The cotton yarns were soaked in an aqueous dispersion of PEDOT:poly(styrenesulphonate) (PEDOT:PSS) (CLEVIOS™ PH 500, H.C. Starck, used as received) for 48 h at 6 °C. Samples were then baked on a hotplate at 145 °C for 60 min. After baking, samples were soaked in ethylene glycol (EG) (anhydrous, 99.8%, Sigma–Aldrich, used as received) for 3 min at room temperature. Then they were baked on a hotplate at 145 °C for 60 min. Such semiconductive yarns were used for the realization of the channel of organic electrochemical transistors.

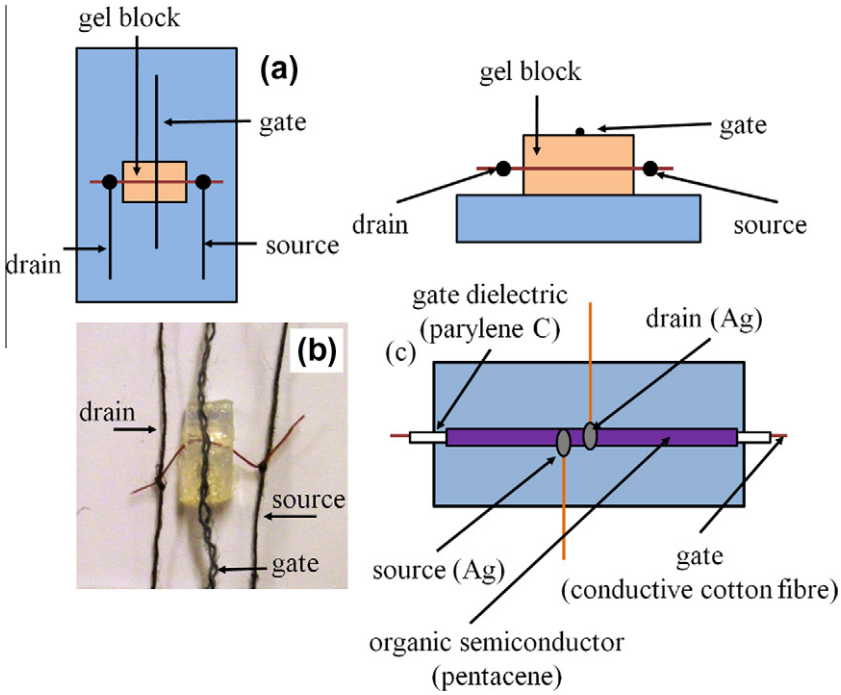

Fig. 1. Organic transistors realized on a cotton fibre. (a) Scheme of an OECT on cotton yarns seen both from the above (left) and from a lateral perspective (right). (b) Actual picture of the transistor. (c) Scheme showing the structure of an OFET fabricated on a cotton yarn.

2.3. Microscopic and spectroscopic analysis of conductive cotton yarns

Short pieces (1 cm) of conductive cotton yarns were immersed into small blocks of epoxy resin and baked at 80 °C for 24 h in order to achieve the complete solidification of the resin. Such blocks were then sectioned by means of a microtome (Dupont Sorvall MT500 Ultramicrotome) obtaining slices with a thickness of approximately 90 nm. The samples slices were placed onto a copper microgrid and analysed with a Tecnai FEI F20 TEM STEM microscope. This instrument is also equipped with a Gatan tridium spectrometer for electron energy loss spectroscopic analysis, so that on the samples treated with both Au NPs and PEDOT:tos an energy-dispersive X-ray spectrum (EDX) was acquired.

2.4. Electrical characterization of conductive cotton yarns

Resistance per unit length was measured using a four probe method, performed using a couple of Keithley 2636 SYSTEM Source Meters. More in detail, a current of 10 μA was injected by means of a couple of electrodes (outer electrodes) connected to the yarn and placed at a distance of 2 cm. Another couple of electrodes (inner electrodes) was inserted between the external electrodes, connected to the yarn and placed at a distance of 1 cm in order to measure the voltage drop resulting from the current passage; resistance was measured as the ratio between this potential drop and the current injected. For each yarn type, 10 samples were acquired.

2.5. Mechanical characterization of conductive cotton yarns

Conductive cotton fibres were characterized by means of stress–strain measurements performed using a TA Instruments DMA Q800 Dynamic Mechanical Thermal Analysis (DMTA) equipment. The samples measured were 4 cm long, the stress applied varied from 0 to 18 N with steps of 0.3 N. Percentage elongation was measured with respect to the sample's original length.

2.6. Cotton-based organic electrochemical transistors assembly

First, a 250 mM solution of KCl in deionized water was prepared. Bacto™ Agar (DIFCO Microbiology) was employed as gelling agent (3.75% in weight). The solution was heated up at 90 °C and vigorously stirred for 60 min. To improve solidification, the gel was stored at 6 °C for 24 h before being used. The gel is used in the OECT assembly to realize the ionic bridge between the gate and the channel. A piece of semiconductive yarn (1 cm, prepared as described in Section 2.2) was inserted into the centre of a small parallelepiped of electrolyte gel (approximately: 6 mm^3) with the help of a needle. Two conductive yarns (2 cm long, prepared as described in Section 2.1) were fixed at the end of the semiconductive yarn with a simple knot and then connected to the power supply by means of a couple of micrograbbers (Fig. 1a and b). Another conductive yarn was fixed on the top of the electrolyte gel block and used as the gate electrode.

2.7. Cotton-based organic field effect transistors assembly

The core of the organic field effect transistors (OFET) is a yarn treated with PEDOT:PSS/EG (prepared as described in Section 2.2), which acts as the gate electrode of the final device. The gate dielectric layer was realized by depositing a thin film of poly(chloro-p-xylylene) (usually known as Parylene C) with a nominal thickness of 1.5 μm on the entire yarn surface through a chemical vapour deposition (CVD) process performed using a PDS 2010 LABCOTER deposition system. Such a dielectric film was obtained starting from 3.3 g of dichloro-[2,2]-paracyclophane (dimer), vapourized at 175 °C at a pressure of around 1 mmHg. The dimer vapours are then pyrolized at 690 °C at a pressure of around 0.5 mmHg to form the gaseous monomer which is eventually deposited at room temperature at a pressure of around 0.1 mmHg on the substrate surface, where polymerization of monomers occurs. After that, a thin pentacene (nominal thickness 50 nm) film was deposited by thermal evaporation at pressure below 2×10^{-5} mbar, at a constant rate of ca. 4 Å min^{-1}. Source and drain electrodes have been realized by depositing two drops of conductive silver paint on the previously realized structure. The silver paint drops have been placed by means of a very sharp needle, in this way, a typical channel length of approximately 200 ± 50 μm have been obtained, whereas the channel width is usually given by the average semicircumference of the employed yarn (Fig. 1c).

2.8. Electrical characterization of OECTs and OFETs

Each transistor was characterized by acquiring the Ids–Vds curves. The source electrode was grounded while the voltage applied to the drain was:

- Varied from 0.5 to −0.5 V with steps of −0.01 V (forward curve) and then again from −0.5 to 0.5 V with steps of 0.01 V (backward curve) for OECTs.
- Varied from 0 V to −60 V with steps of −1 V for OFETs.

During the acquisition of each curve, the gate voltage was fixed at a specific value and then increased in correspondence with the acquisition of the next curve (gate voltage range: $0 \div 0.4$ V, step width: 0.1 V for OECTs; $20 \div -100$ V, step width −20 V for OFETs).

OECT samples were also characterized by the acquisition of drain current vs. time curve. In this case, drain voltage was kept constant at −0.5 V while gate voltage varied abruptly from 0 to 0.4 V (square wave) every 60 s.

3. Results and discussion

Fig. 2 shows a example of the use of the described conductive cotton yarn for connecting a LED to a battery. It is noteworthy that the flexibility of this yarn (made according to the procedure described in Section 2.1) is such that the connection is made through a simple knot. The described yarn treatment in fact modifies the yarn conductivity without significantly compromising its mechanical features.

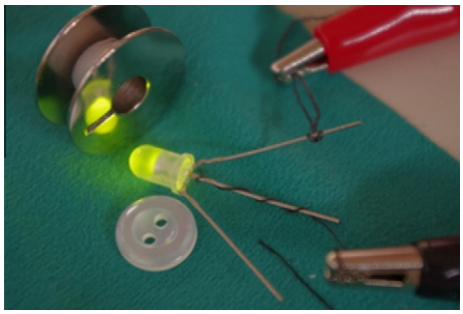

Fig. 2. Light emitting diode (LED) biased by means of conductive cotton yarns.

To investigate the modifications induced in the conductive yarn structure, transmission electron microscopy (TEM) analysis of the cross section of the treated yarns was performed and the obtained results are shown in Fig. 3. Gold nanoparticles clearly appear as an external coating (Fig. 3a). Conversely, it was found that PEDOT:tos is not confined to the yarn's external surface but penetrates among the yarn inner fibres in a very irregular way (Fig. 3b). For this reason, it was not possible to obtain a precise measurement of the samples' cross-sectional conductive area.

Fig. 3d shows an energy-dispersive X-ray spectroscopy (EDX) spectrum of a sample treated with both Au NPs and PEDOT:tos (cross section shown in Fig. 3c). EDX was performed to identify the chemical composition of the materials deposited on the cotton yarn surface: the spectrum confirmed the presence of both Au NPs (Au peaks) and PEDOT:tos (S peaks, caused by the sulphur atoms contained into the thiophene rings). The sharp Cu peak which appears in the spectrum is due to the copper grid on which the samples slices were placed during the analysis.

All conductive cotton samples were electrically characterized with a four-point probe method in order to eliminate possible contributions of contact resistances.

The following types of samples were compared:

Type 1: Cotton yarns as received;
Type 2: Cotton yarns covered with Au NPs;
Type 3: Cotton yarns covered with PEDOT:tos;
Type 4: Cotton yarns covered with Au NPs and subsequently covered with a layer of PEDOT:tos.

Since, as previously mentioned, a precise determination of the samples cross section was not possible, the electrical performance of the different fibres has been compared in terms of resistance per unit length.

The mean values of the electrical resistance of all samples types are summarized in the first column of Table 1: the most conductive samples were type 4. The unmodified cotton specimens show a resistance of $(3.1 \pm 0.9) \times 10^8\ \Omega\ cm^{-1}$; the deposition of nanoparticles onto the cotton fibres does not seem significantly influence the resistance value, which remains of the same order of magnitude. However, when PEDOT:tos layers are deposited over plain cotton yarns, the resistance value of the modified fibre is reduced by three orders of magnitude.

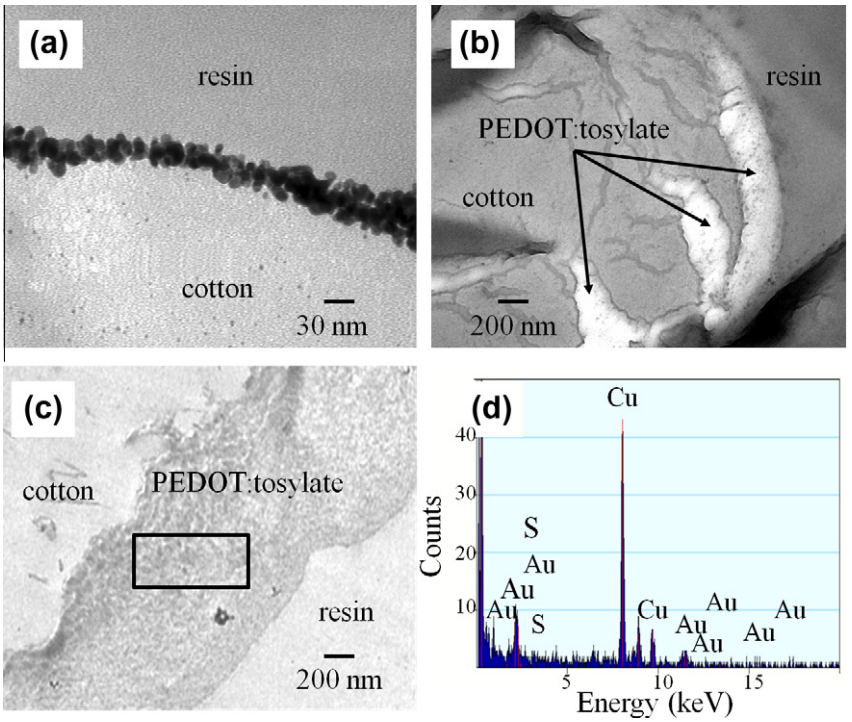

Fig. 3. Transmission electron microscope (TEM) analysis of the cross section of the conductive cotton fibres. (a) Cross section of a cationic cotton fibre uniformly coated with Au nanoparticles. (b) (Bright Field TEM image) Cross section of a fibre coated with PEDOT:tos. (c) (Dark Field TEM image) Cross section of a fibre treated with Au nanoparticles and a conductive polymer layer (PEDOT:tos). The rectangle in the conductive layer indicates the area in which the EDX spectrum (see inset d) was acquired. (d) EDX analysis performed on the area shown in (c).

Table 1
Electrical and mechanical data of the conductive cotton yarns.

Yarn type	Resistance per unit length ($\Omega\,cm^{-1}$)	Young's modulus (MPa)	Stress at break (MPa)	Elongation to break (%)
1. Plain cotton	$(3.1 \pm 0.9) \times 10^8$	342 ± 75	10.3 ± 3.3	4.4 ± 1.8
2. Cotton + Au NPs	$(1.1 \pm 0.1) \times 10^8$	140 ± 60	8.2 ± 1.9	11.0 ± 5.3
3. Cotton + PEDOT:tos	$(186.8 \pm 0.2) \times 10^3$	331 ± 82	4.0 ± 1.3	2.5 ± 1.0
4. Cotton + Au NPs + PEDOT:tos	$(24.7 \pm 0.3) \times 10^3$	142 ± 18	4.3 ± 1.0	4.4 ± 0.9

An unexpected further reduction of one order of magnitude in resistance is then achieved when PEDOT:tos is deposited on NPs coated cotton fibres, which clearly proves a Au NPs-enhanced conductivity phenomenon. These experimental results demonstrate that a natural cotton fibre can be made conductive by a conformal coating with thin layers of a conductive polymer, hence increasing the conductance by about three orders of magnitude. More importantly, when the PEDOT:tos layers are deposited on a Au NPs previously treated substrate, a further increase, up to four orders of magnitude, in conductance is observed.

Further investigations are being performed to establish the exact nature of the electrical transport mechanism in the treated fibres and the synergistic role of the Au NPs.

Such treated yarns were then mechanically characterized by measuring static stress vs. strain curves. Three mechanical parameters were acquired: Young's modulus, stress at break and elongation before breaking (also called elongation to break, indicated as εb); the mean values of such parameters for the different types of conductive yarns are reported in Table 1 (see Supplementary data for the full statistical analysis). On a typical curve of a yarn treated with Au NPs + PEDOT:tosylate compared to plain cotton, shown in Fig. 4, two main observations can be made: first

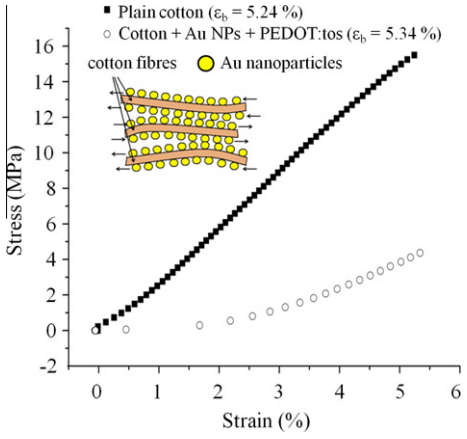

Fig. 4. Stress strain curves on conductive cotton yarns.

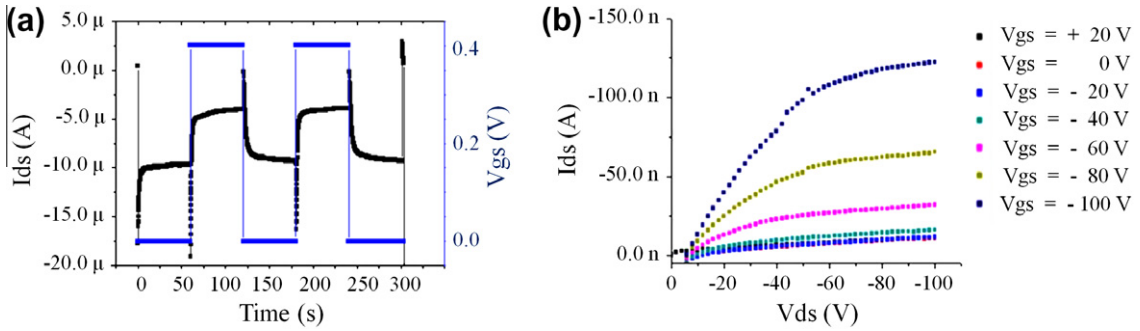

Fig. 5. Electrical characteristics of organic transistors on cotton yarns. (a) Drain current and gate voltage vs. time characteristics of an all cotton-made OECT. (b) Id–Vd curves acquired on a cotton-made OFET.

the maximum elongation before breaking appears to be similar for both samples, thus indicating that the main mechanical property of interest for evaluating the ability of the yarn to be woven or knit are preserved in treated yarns. Secondly, the treated yarn can reach larger strain values before starting to experience elongational stress (represented by the slope of the curve in the initial phase). This unusual effect, that was observed only in NPs-treated samples (with and without PEDOT:tos, see the full statistical analysis of all kinds of yarns in Table 1) may be tentatively attributed to a "lubricant" effect due to the conformal nature of the NPs coating which seems to enable them to slide on one another following the application of the mechanical stimulus (see the inset in Fig. 4). These observations demonstrate that the proposed treatment does not stiffen the cotton yarns that, at the same time, still possess mechanical properties apt for weaving purposes.

Finally, active electronic devices have been made starting from natural cotton fibres.

As for the transistors characterization, it can be seen from Fig. 1a and b that the OECT structure includes an electrolyte in gel form. Being this based on water, it is strictly necessary that the OECT channel (in this case the yarn) is impermeable to water. Cotton yarns simply soaked in PEDOT:PSS cannot be used as such as the contact with a water-based electrolyte solution would cause on one hand the dissolution of PEDOT:PSS and on the other hand, the possible absorption of water and the consequent ionic conduction of the yarn through the adsorbed water: in any case, the loss of the transistor action. To avoid this problem, after the deposition of PEDOT:PSS, the samples were treated with ethylene glycol (EG). The effect of this treatment is twofold: on one hand it dramatically decreases PEDOT:PSS solubility in water, on the other EG is also able to increase its conductivity [26,27]. In the SD section, the comparison (in terms of electrical resistance and water-resistance) between yarns soaked in PEDOT:PSS with and without ethylene glycol treatment is presented.

Fig. 5a shows the electrical characteristics of the cotton-made OECT. It is noteworthy that source and drain contacts were made by a simple knot between the yarn that acts as the device channel (i.e. the semiconductive yarn obtained with the procedure described in Section 2.2) and two conductive cotton yarns (i.e. the conductive yarns obtained with the procedure described in Section 2.1) used to connect the device to the source/measure units. This is a very basic example of textile circuit entirely based on cotton yarns. Despite the non optimal ratio between the on and off currents, the transistor effect is clearly achieved. It is noticeable that we have attempted also to obtain an OECT device using the conductive cotton yarn (i.e. the conductive yarn obtained with the procedure described in Section 2.1) but we never obtained a transistor action with this yarn, i.e. its conductivity cannot be modulated by the exchange of ions with the electrolytic solution. This aspect is under further investigation.

The structure of the yarn-shaped organic field effect transistor (OFET) is shown in Fig. 1c. The core of the OFETs is a yarn treated with PEDOT:PSS/EG as described above, which acts as the gate electrode of the final device. Even if the PEDOT:PSS/EG yarn nominally behaves as a semiconductor, its resistance per unit length ($2 \times 10^3\ \Omega\ cm^{-1}$), is such that at the voltage values used for operating the gate in the OFETs, it may be considered as a conductor. In addition, the contact with any external agent able to modulate its conductivity is prevented in the OFET, as the gate is coated with an insulating layer. Clearly, also conductive cotton yarns based on Au NPs and PEDOT:tos could be used for this function but the yarn treated with PEDOT:PSS was preferred because its external surface is smoother and this feature improves the quality of the dielectric layer deposition. Fig. 5b shows an example of the electrical characteristics of the OFETs. The insulating layer capacitance was measured and found to be 2.17 nF cm^{-2} (corresponding to an estimated thickness of the insulating layer of 1.5 µm). The OFET mobility mean value (over 20 devices measured) is $1.3 \pm 1.0 \times 10^{-2}\ cm^2\ (V^{-1}\ s^{-1})$ and the threshold voltage is -24 ± 5 V. These values are not too different from those taken from typical curves of planar OFETs with comparable aspect ratios. Relatively high values of the threshold voltage may be attributed to the thickness of the insulating layer.

4. Conclusions

In conclusion, we presented an innovative method based on the combination of two deposition processes which can be used in order to obtain conductive yarns starting from common cotton fibres, which are by

themselves intrinsically insulating. The electrical and mechanical characterization of these fibres showed that these yarns can be successfully used as conductors, in order to bias electronic devices. Cotton was also successfully employed as a basis for realizing two kinds of active devices based respectively on the concept of organic electrochemical transistor and of organic field effect transistor. Our study demonstrates the possibility of realizing a fully textile circuit, including passive and active elements, and paves the way for a future complete integration between electronics and textiles.

Acknowledgements

Prof. Ennio Bonetti is gratefully acknowledged for the fruitful discussions about the mechanical measurements conducted on the yarns.

G.M. would like to thank Dr. Sang Yang for the fruitful discussions concerning the polarization of OECTs and Alwin Wan for the help with the polymerization of PEDOT:tosylate process.

A.B. and G.M. gratefully acknowledge EU Commission for funding the Integrated Project #26987 "Proetex".

G.G.M. would like to thank ReynoldsTech for building the tool for vapour deposition of conducting polymers.

J.P.H. acknowledges the US Department of Agriculture for partially funding this work under projects NRI-NCZ09462 and CRIS-Hatch NYC-329433.

P.C. acknowledges Regione Autonoma della Sardegna (RAS) for funding his research activity under the PO Sardegna FSE 2007-2013, L.R.7/2007, CRP Prot. No. 1399/207.

This work made use of the electron microscopy facility of the Cornell Center for Materials Research (CCMR) with support from the National Science Foundation Materials Research Science and Engineering Centers (MRSEC) program (DMR 0520404). This work was performed in part at the Cornell NanoScale Facility, a member of the National Nanotechnology Infrastructure Network, which is supported by the National Science Foundation (ECS-0335765).

Appendix A. Supplementary data

Supplementary data associated with this article can be found, in the online version, at doi:10.1016/j.orgel.2011.09.001.

References

[1] J. Berzowska, Electronic textiles: wearable computers reactive fashion and soft computation, Textile: J Cloth Culture 3 (2005) 58–75.
[2] D. De Rossi, Electronic textiles: a logical step, Nat. Mater. 6 (2007) 328–329.
[3] D. De Rossi, F. Carpi, F. Lorussi, A. Mazzoldi, R. Paradiso, E.P. Scilingo, A. Tognetti, Electroactive fabrics and wearable biomonitoring devices, AUTEX Res. J. 3 (2003) 180–185.
[4] J.B. Lee, V. Subramanian, Organic transistors on fibre: a first step towards electronic textiles, IEEE Int. Electron Device Meet. Techn. Digest 8 (2003) 1–4.
[5] M. Maccioni, E. Orgiu, P. Cosseddu, S. Locci, A. Bonfiglio, Towards the textile transistor: assembly and characterization of an organic field effect transistor with a cylindrical geometry, Appl. Phys. Lett. 89 (143515) (2006) 1–3.
[6] M.R. Chaudry, Cotton production and processing, in: J. Müssig, C. Stevens (Eds.), Industrial Applications of Natural Fibres: Structure, Properties and Technical Applications, John Wiley and Sons Ltd., Chichester, 2010, pp. 219–220.
[7] X. Liu, H. Chang, Y. Li, W.T.S. Huck, Z. Zheng, Polyelectrolyte-bridged metal/cotton hierarchical structures for highly durable conductive yarns, ACS Appl. Mater. Inter. 2 (2010) 529–535.
[8] B.S. Shim, W. Chen, C. Doty, C.L. Xu, N.A. Kotov, Smart electronic yarns and wearable fabrics for human biomonitoring made by carbon nanotube coating with polyelectrolytes, Nano Lett. 8 (2008) 4151–4157.
[9] I. Wistrand, R. Lingstrom, L. Wagberg, Preparation of electrically conducting cellulose fibres utilizing polyelectrolyte multilayers of poly(3,4-ethylenedioxythiophene):poly(styrene sulphonate) and poly(allylamine), Eur. Polym. J. 43 (2007) 4075–4091.
[10] S.N. Bhadani, M. Kumari, S.K. Sen Gupta, G.C. Sahu, Preparation of conducting fibers via the electrochemical polymerization of pyrrole, J. Appl. Pol. Sci. 64 (1997) 1073–1077.
[11] A.C. Aksit, N. Onar, M.F. Ebeoglugil, I. Birlik, E. Celik, I. Ozdemir, Electromagnetic and electrical properties of coated cotton fabric with barium ferrite doped polyaniline film, J. Appl. Polym. Sci. 113 (2009) 358–366.
[12] D. Knittel, E. Schollmeyer, Electrically high-conductive textiles, Synth. Met. 159 (2009) 1433–1437.
[13] A. Varesano, A. Aluigi, L. Florio, R. Fabris, Multifunctional cotton fabrics, Synth. Met. 159 (2009) 1082–1089.
[14] Y. Ding, M.A. Invernale, G.A. Sotzing, Conductivity trends of PEDOT–PSS impregnated fabric and the effect of conductivity on electrochromic textile, ACS Appl. Mater. Inter. 2 (2010) 1588–1593.
[15] S.H. Cho, S. Park, Electrochemistry of conductive Polymers 39. Contacts between conducting polymers noble metal nanoparticles studied by current-sensing atomic force microscopy, J. Phys. Chem. B 110 (2006) 25656–25664.
[16] B.C. Sih, M.O. Wolf, Metal nanoparticles – conjugated polymer nanocomposites, Chem. Commun. 27 (2005) 3375–3384.
[17] H.S. White, G.P. Kittelsen, M.S. Wrighton, Chemical derivatization of an array of three gold microelectrodes with polypyrrole: fabrication of a molecule-based transistor, J. Am. Chem. Soc. 106 (1984) 5375–5377.
[18] M. Hamedi, R. Forchheimer, O. Inganäs, Towards woven logic from organic electronic fibres, Nat. Mater. 6 (2007) 357–362.
[19] C. Müller, M. Hamedi, R. Karlsson, R. Jansson, R. Marcilla, M. Hedhammar, O. Inganäs, Woven electrochemical transistors on silk fibers, Adv. Mater. 23 (2011) 898.
[20] M. Berggren, R. Forchheimer, J. Bobacka, P.O. Svensson, D. Nilsson, O. Larsson, A. Ivaska, PEDOT:PSS-based electrochemical transistors for ion-to-electron transduction and sensor signal amplification, in: D.A. Bernards, R.M. Owens, G.G. Malliaras (Eds.), Organic Semiconductors in Sensor Applications, Springer Publications, New York, 2008, pp. 261–263.
[21] G. Horowitz, F. Deloffre, F. Garnier, R. Hajlaoui, M. Hmyene, A. Yassar, All-organic field-effect transistors made of (-conjugated oligomers and polymeric insulators, Synth. Met. 54 (1993) 435–445.
[22] S. Locci, M. Maccioni, E. Orgiu, A. Bonfiglio, An analytical model for cylindrical thin-film transistors, IEEE Trans. Electron Devices 54 (2007) 2362–2368.
[23] H. Dong, J.P. Hinestroza, Metal nanoparticles on natural cellulose fibres: electrostatic assembly and in situ synthesis, ACS Appl. Mater. Inter. 1 (2009) 797–803.
[24] B. Winther-Jensen, K. West, Vapour-phase polymerization of 3,4-ethylenedioxythiophene: a route to highly conducting polymer surface layers, Macromolecules 37 (2004) 4538–4543.
[25] B. Winther-Jensen, B.W. Breiby, K. West, Base inhibited polymerization of 3,4-ethylenedioxythiophene with iron(III)tosylate, Synth. Met. 152 (2005) 1–4.
[26] J. Ouyang, Q. Xu, C. Chu, Y. Yang, G. Li, J. Shinar, On the mechanism of conductivity enhancement in PEDOT:PSS films through solvent treatment, Polymer 45 (2004) 8443–8450.
[27] X. Crispin, S. Marciniak, W. Osikowicz, G. Zotti, A.W. Denier Van Der Gon, F. Louwet, M. Fahlman, L. Groenendaal, F. De Schryver, W.R. Salaneck, Conductivity morphology interfacial chemistry and stability of PEDOT:PSS: a photoelectron spectroscopy study, J. Polym. Sci. Pol. Phys. 41 (2003) 2561–2583.

molecules can obtain high energy from the applied electric field. These highly excited molecules are easily ionized, which causes leakage current and dielectric breakdown [31,32]. In practical applications, curing is crucial to make the dielectric layer insoluble in the liquid deposition of soluble organic semiconductors. Other effective paths to reduce hysteresis include addition of SiO_2 buffer layer, which blocks the electron injection from the gate electrode [33], but the addition of an inorganic layer is not advantageous due to the undermined flexibility and the high cost of vacuum process.

The current polymer/cross-linker system complicates the manufacturing process, and requires high processing temperatures [33,34]. High curing temperatures above 180 °C are generally required to eliminate hysteresis in polymer insulated FETs, preventing the use of conventional plastic films (T_g < 150 °C), such as polycarbonate and polyethylene naphthalate as a substrate for flexible OFETs. The commonly used PVP/poly(methylated melamine-co-formaldehyde) blends require 180–200 °C to achieve hysteresis-free OFETs [28,29]. Our previous report about acid/epoxide functioned polyacrylate (PB174) gate insulator was effectively cured at 230 °C to eliminate hysteresis behavior [35]. Most recently, several cross-linking agents such as dianhydrides [2] and chlorosilanes [36] were proposed to cross-link PVP at low temperatures around 110 °C, but no successful elimination of hysteresis behavior was demonstrated. Hysteresis-free FETs with organosiloxane-based organic–inorganic hybrid dielectrics of poly(methyl silsesquioxane) (PMSQ) were reported [10] while low-temperature curable polymer gate dielectric for hysteresis-free OFETs is still under investigation.

Here we report a novel low-temperature curable polyacrylate type copolymer (L-PA) gate dielectric, and the investigation of its favorable curing condition to permit hysteresis-free OFETs and MIS (metal–insulator–semiconductor) capacitors. Reaction mechanisms and related temperature ranges, surface properties of the gate dielectric and the morphological features of semiconductor layers were also studied and correlated to electrical performance. Optimal conditions were identified that produce hysteresis-free OFETs through low-temperature curing.

2. Experimental

L-PA (sample name: TAB18-binder, supplied by LG Chem. Co., Ltd.) was dissolved in propylene glycol methyl ether acetate (PGMEA) to obtain 10 wt.% polymer solution. The molecular structures of each repetitive unit and corresponding mass ratios of the random copolymer L-PA are demonstrated in Fig. 1. The film was formed with spin-coating on piranha cleaned n-type heavily doped silicon wafers at 3000 rpm for 1 min inside the high purity Ar-filled glove box. And then the film was baked in an annealing furnace for 30 min at various temperatures of 110 °C, 140 °C and 170 °C to study the temperature effects on the

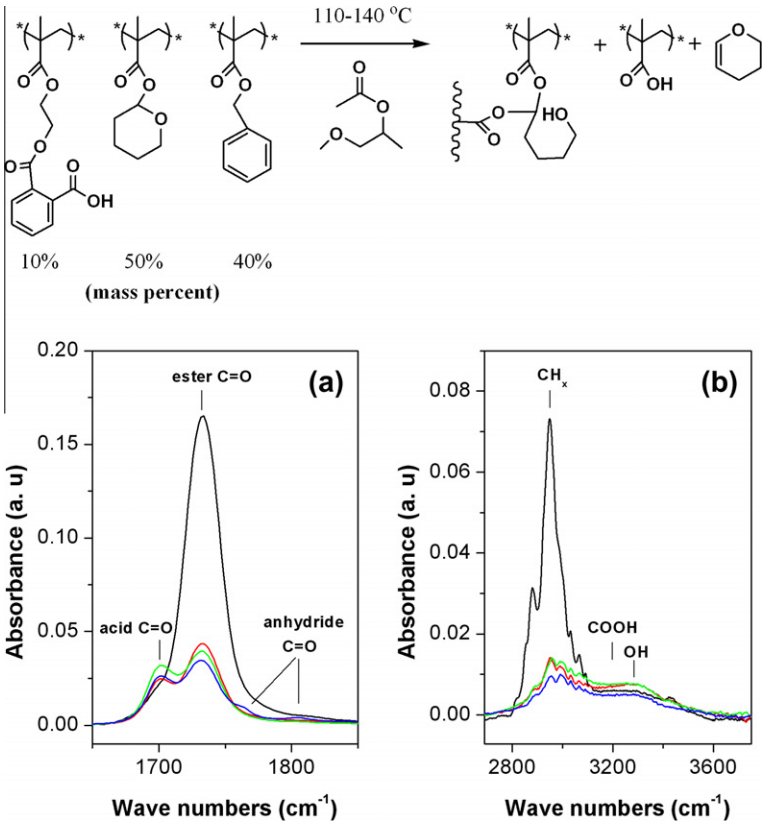

Fig. 1. Repetitive units, mass percents and reaction mechanisms for L-PA copolymer as well as FT-IR spectra of as deposited (—), 110 °C (—), 140 °C (—) and 170 °C (—) baked L-PA films: (a) C=O vibrations at low wave numbers and (b) O–H, C–H vibrations at high wave numbers.

film properties and device performance. The unbaked and baked films were correspondingly referred to as L-PA-as dep., L-PA-110, L-PA-140 and L-PA-170. It was expected that cross-linking reaction as illustrated in Fig. 1 occurred during the bake. Pentacene, which was purchased from Aldrich Chemical Co., was deposited onto the gate dielectric using an organic molecular beam deposition system at a rate of 0.2–0.3 Å/s and a moderate substrate temperature of 50 °C. The thickness of the pentacene layer was 60 nm for OFETs and for morphology study with AFM. For MIS capacitors and metal/insulator/metal structures (MIM), Au top electrode was deposited with evaporation through a shadow mask to make a circular dot area of 8.02×10^{-4} cm^2. For OFETs, Au electrodes were deposited in an evaporator and patterned by a shadow mask with a channel width of 1500 μm and a channel length of 150 μm.

FT-IR (Nicolet 700) spectra of the solid films were recorded in a transmission mode. Contact angle measurements were conducted using a face contact angle meter (Model CA-A, manufactured by Kyowa Kaimenkagaku Co., Ltd.). Thickness was obtained from Woolham Co. VASE32 ellipsometer. To study the roughness of the dielectric surface as well as pentacene morphology, AFM (Dimension™ 3100 microscope, Digital Instruments) was adopted. Capacitance–voltage (*C*–*V*) characteristics of the MIS capacitors were measured to study the hysteresis behavior, using HP 4284A Precision LCR meter (Agilent Tech.) at 1 MHz. Leakage current density and electrical performance were characterized with HP5270A (Agilent Tech.).

3. Results and discussion

3.1. Reaction mechanism

FT-IR in a transmission mode was used to monitor reactive functional group changes in the cross-linking process, as demonstrated in Fig. 1a and b. As seen in Fig. 1a, the bands between 1650 cm^{-1}–1850 cm^{-1} were attributed to the stretching vibrations of different carbonyl groups (C═O). Peaks centered at 1701 cm^{-1} and 1733 cm^{-1} were assigned to carboxylic acid and ester groups, and the double peak centered at 1762 cm^{-1} and 1805 cm^{-1} was from anhydride groups. Under 110 °C and 140 °C, ester groups partially broke up into carboxylic acids and vacuum-removable small molecules. At the same time, carboxylic acid groups attacked the precursor, producing cross-linked structures, with reaction mechanism demonstrated in Fig. 1. The resultant hydroxyl (OH) group centering at ~3300 cm^{-1} and the broad band carboxylic acid dimmers between 2800–3500 cm^{-1} were observed as shown in Fig. 1b. When baking temperature was increased up to 170 °C, carboxylic acids were converted into an ambient-unstable anhydride species as a side reaction.

To further confirm the reaction mechanisms, DSC and TGA were carried out for L-PA bulk polymer. DSC analysis was conducted to investigate the temperature ranges of heat adsorption or release during heating. As shown in Fig. 2, two major regions were confirmed with a sharp peak centered at 148.2 °C and a broad peak centered at 244.0 °C.

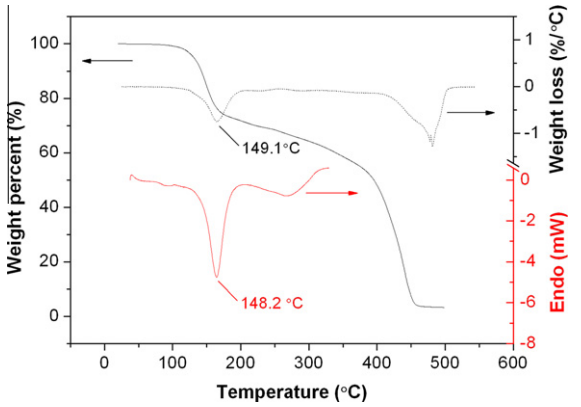

Fig. 2. Thermogravimeric analysis (TGA) (in black) and differential scanning calorimetry (DSC) (in red) characteristics for L-PA bulk polymer. (For interpretation of the references to color in this figure legend, the reader is referred to the web version of this article.)

This implied two major chemical reactions with heat release within the two temperature ranges.

TGA was adopted to confirm reaction temperature ranges by monitoring the weight loss during heating, which was caused by the release of gaseous product during chemical reactions. A 25% weight loss within 100–160 °C was correlated to 2H-pyrrane removal from the weight loss of 6-membered ester ring in the copolymer. The film thickness was drastically reduced from 293 nm (L-PA-as dep.) to 241 nm for L-PA-110, 221 nm for L-PA-140, and 208.2 nm for L-PA-170, further confirming the two weight loss processes.

3.2. Film properties

As displayed in Fig. 3a and b, AFM images of the dielectric surface exhibited root-mean-square (RMS) roughness between 0.22–0.32 nm, which was smooth enough to have negligible affects on pentacene deposition mode [17]. Fig. 3c and d shows the AFM images of 60 nm pentacene films deposited on L-PA-as dep. and L-PA-140. The relatively small pentacene grains on L-PA-as dep. were due to the higher dielectric surface energy, which caused stronger interactions between the dielectric surface and the pentacene molecules during the deposition. High dielectric surface polarity was reported to lead to smaller grains [37] with larger grain boundary area, which is considered to be a trap site disrupting the charge transport in organic semiconductors [38]. In contrast, pentacene exhibited well defined terraces and larger dendritic grains on L-PA-140, whose surface energy was relatively low. Surface energy, which was reported to drive molecular stacking mode in pentacene deposition [39], was determined from the contact angle measurement using distilled water and diiodomethane as the probe liquids [40]. As summarized in Table 1, the surface energy was decreased with the heat treatment.

3.3. Metal–insulator–metal structures

Dielectric strength and leakage current density are two key parameters to evaluate electrical robustness of a gate

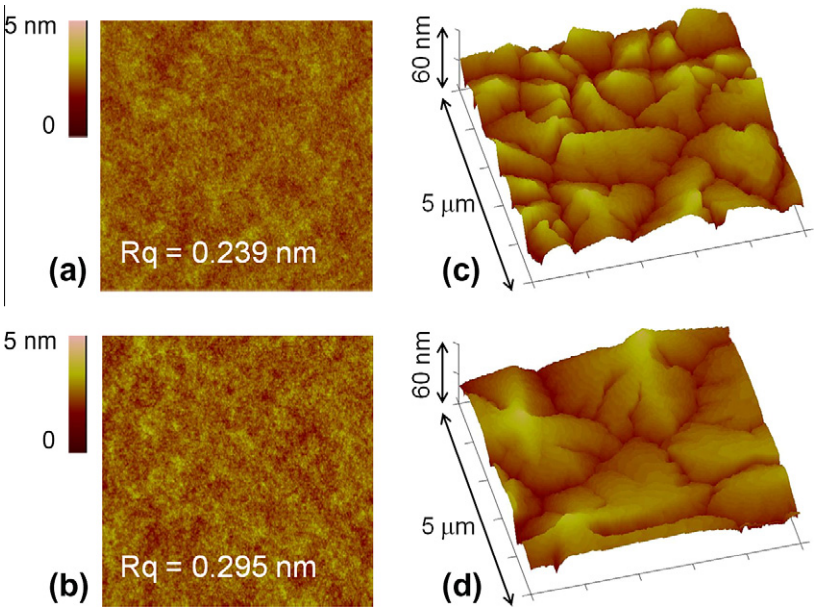

Fig. 3. 5 × 5 μm² AFM images of dielectric surfaces, (a) L-PA-as dep., (b) L-PA-140, and pentacene grains on (c) L-PA-as dep. and (d) L-PA-170.

Table 1
Roughness, contact angle and surface energy of the dielectric surface.

Temperature (°C)	Roughness (nm)	Contact angle (°)		Surface energy (mJ/cm²)
		(H_2O)	(CH_2I_2)	
As dep.	0.239	72.2	27.2	46.4
110	0.278	75.2	30.4	44.8
140	0.295	75.4	31.0	44.5
170	0.314	79.5	31.6	44.2

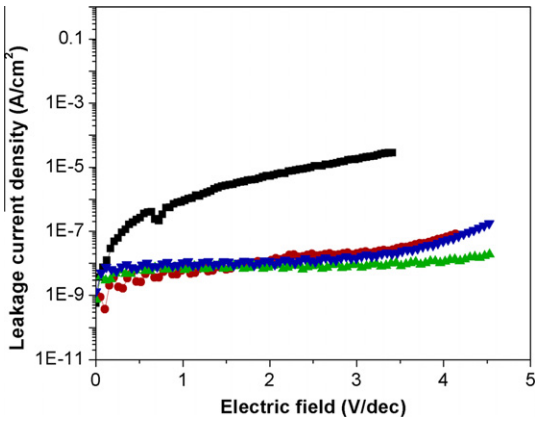

Fig. 4. Leakage current density–electric field (*J*–*E*) characteristics of Au/insulator/n + Si type MIM structures with as deposited (└■─), 110 °C (-○-), 140 °C (-▲-) and 170 °C (-▼-) baked L-PA films. (For interpretation of the references to color in this figure legend, the reader is referred to the web version of this article.)

dielectric, which can be examined from typical current density–electric field (*J*–*V*) curves, as displayed in Fig. 4. No observable electrical breakdown within our instrumental limit of 4.5 MV/cm implied a high dielectric strength for the film. Leakage current densities at 1 MV/cm were as low as 5×10^{-9}–10^{-8} A/cm² for cured L-PA110–L-PA170, which was superior to other polymer dielectric and even comparable with some inorganic materials [35]. The high dielectric strength and low electrical leakage were attributed to both the linear type polymeric chain and effective cross-linked structures. Linear type chains can aggregate into a dense film with low free volume. The migration and discharge of the ionized molecules cause degradation to carbon and gaseous products, acting as the most popular polymer dielectric breakdown mechanism [35]. Effective cross-linking further densified the dielectric film and produced a network through chemical bonding between polymeric chains reducing the possibility of electrical penetration. This could be achieved at the low processing temperature down to 110 °C.

3.4. Metal–insulator–semiconductor capacitors

By measuring the *C*–*V* (capacitance–voltage) characteristics with MIS capacitor, hysteresis can be observed as seen in Fig. 5. From the shift of the flat band voltage (ΔV_{FB}) in the forward and backward sweep, the charge trap density (N_{trap}) at insulator/semiconductor interface and in the bulk of insulators can be calculated [41–43]. As seen in Fig. 5, the forward and backward curves nearly overlapped with each other, and hence exhibited negligible hysteresis. In the previous reports [28,29,35,44,45], processing temperatures higher than 180 °C were required to reduce the hysteresis behavior for cross-linked polymer.

The maximum capacitance (C_{max}) values in *C*–*V* curve was 6.92 pF, 7.37 pF, 7.62 pF and 7.65 pF for L-PA-as dep., L-PA-110, L-PA-140 and L-PA-170 and the dielectric constant was 4.65, 4.01, 3.78, and 3.65, respectively.

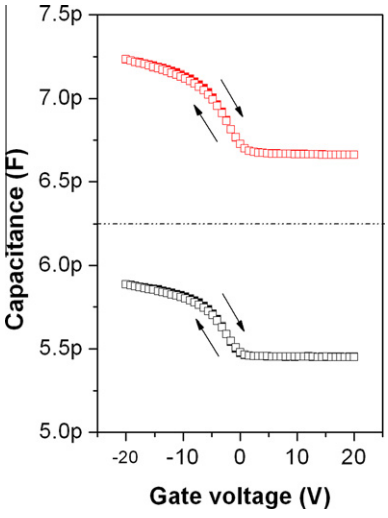

Fig. 5. Forward (└■—) and backward (○) sweeps for *C–V* characteristics of n + Si/insulator/pentacene/Au MIS capacitors with as deposited (in black) and 140 °C baked (in red) L-PA films. (For interpretation of the references to color in this figure legend, the reader is referred to the web version of this article.)

3.5. Organic field-effect transistors

Top-contact pentacene FETs were fabricated utilizing as deposited and baked L-PA copolymer thin films as a gate insulator. The transfer and output curves of OFET with L-PA-as dep. and L-PA-140 are compared in Fig. 6a–c and the electrical parameters of the OFETs are summarized in Table 2.

OFET with L-PA-as dep. showed μ of 0.27 $cm^2/V\,s$, on/off current ratio (I_{on}/I_{off}) of 10^4, and subthreshold slope (SS) of 3.58 V/dec, while these parameters were evidently improved with baked dielectrics. OFET with L-PA-140 showed optimized μ of 0.91 $cm^2/V\,s$, I_{on}/I_{off} of 10^6 and SS of 1.81 V/dec and it was confirmed that the optimum curing temperature was 140 °C. The significant improvement in μ was due to the larger pentacene grains, as confirmed in Fig. 3c and d [46]. The relationship between the dielectric surface energy of L-PA-as dep., L-PA-110 and L-PA-140 and the corresponding device field-effect mobility is shown in Fig. 7. The degraded electrical parameters of OFET with L-PA-170 may be attributed to ambient-unstable species, such as anhydrides, which were formed from the side reaction at higher temperature. Also a processing temperature higher than 150 °C is less attractive for fabricating devices on low-cost flexible plastic substrates. The optimized I_{on}/I_{off} of the OFET with L-PA-140 confirmed the most effective cross-linking reactions at 140 °C. As compared in Fig. 6c, the saturated drain current in the output characteristics for L-PA-140 device was almost 4 times higher than L-PA-as dep. This current level satisfied the requirement of the driving transistor for OLED displays (larger than 10 μA) [47,48].

Also the device with cured dielectrics exhibited negligible hysteresis during the full voltage sweep (from 10 to −40 V and then from −40 to 10 V) in both transfer and output characteristics, as shown in Fig. 6a–c. As shown

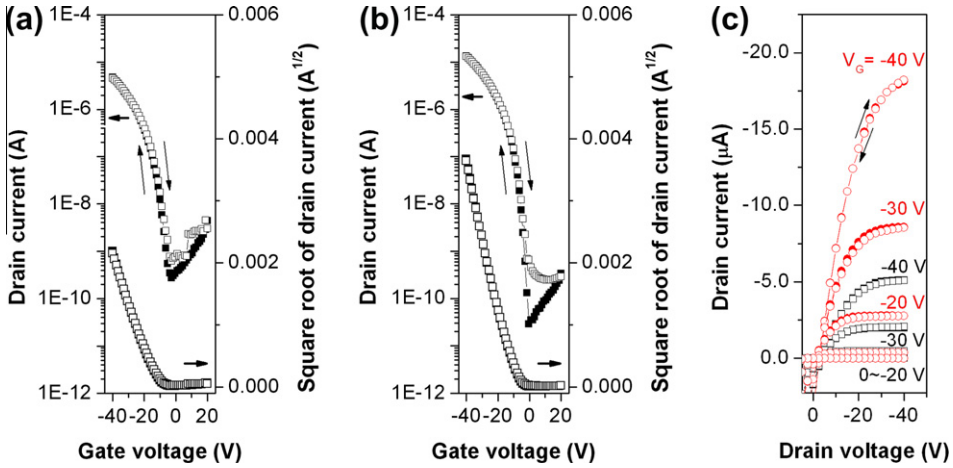

Fig. 6. (a) Output characteristics for OFET with L-PA-as dep. and (b) L-PA-140 with forward (└■—) and backward (○) sweeps. (c) Comparison of output characteristics for OFET with L-PA-as dep. (in black) and OFET-L-PA-140 (in red). (For interpretation of the references to color in this figure legend, the reader is referred to the web version of this article.)

Table 2
Electrical characteristics of OFETs with as deposited and baked gate dielectrics.

Temperature (°C)	Curing time (h)	μ ($cm^2/V\,s$)	I_{on}/I_{off}	V_{th} (V)	ΔV_{th} (V)	SS (V/dec)	N_{trap}^{max} ($10^{12}/cm^2$)
As dep.	0.5	0.27	$\sim 10^4$	−14.7	1.41	3.58	2.55
110	0.5	0.84	$\sim 10^5$	−13.0	0.64	2.74	1.32
140	0.5	0.91	$\sim 10^6$	−12.2	0.43	1.81	0.93
170	0.5	0.72	$\sim 10^5$	−13.3	0.45	2.14	1.06

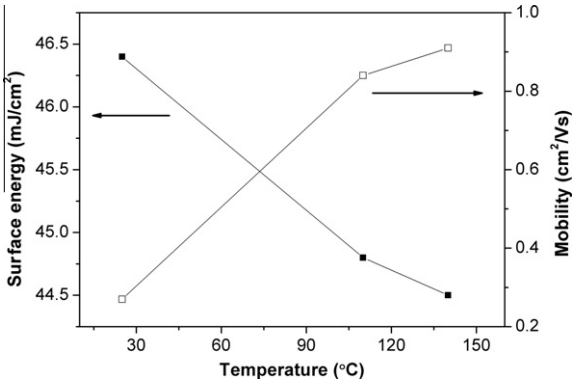

Fig. 7. Surface energy and field-effect mobility as a function of the curing temperature.

in Table 2, ΔV_{th} for L-PA insulated OFETs is small and the optimal ΔV_{th} of 0.43 V was achieved with the 140 °C baked dielectric. The L-PA film baked at 110 °C for 2 h produced small hysteresis gap of ~0.40 V in the transistor transfer characteristics with comparable electrical properties: μ of 0.90 $cm^2/V\,s$, I_{on}/I_{off} ~10^6 and even smaller SS of 1.13 V/dec.

The SS values are closely associated with charge trap density at the pentacene/dielectric interface [49], and the upper limit of the trapped charge density (N_{trap}^{max}) were estimated to be $2.55 \times 10^{12}/cm^2$, $1.32 \times 10^{12}/cm^2$, $9.32 \times 10^{11}/cm^2$, $1.06 \times 10^{12}/cm^2$ for L-PA-as dep., L-PA-110, L-PA-140 and L-PA-170 devices, respectively. Charge trap from electronic defect states at the semiconductor/gate dielectric interface, should be as small as possible, since it causes instability in the threshold voltage of OFET. N_{trap} was decreased as the curing temperature increased up to 140 °C.

4. Conclusion

We reported hysteresis-free pentacene FETs with low-temperature self-curable L-PA copolymer as a gate insulator. Negligible hysteresis could be achieved with thermal cross-linking reaction under a low temperature range between 110–140 °C. The optimized L-PA cured at 140 °C showed high dielectric strength (>4.5 MV/cm) and low leakage current density (5×10^{-9} A/cm^2 at 1 MV/cm) and OFET with this dielectric showed the mobility of ~0.91 $cm^2/V\,s$, on/off current ratio of ~10^6 and low inverse subthreshold slope of 1.13 V/dec. This result showed that L-PA gate dielectric is a promising candidate for low-temperature curable, hysteresis free OFETS.

Acknowledgments

This research was supported by the Korea Research Foundation (KRF) through the National Research Laboratory Project and Polymer Gel Cluster group (RT1-04-04-04) of the Korean government. The author Wentao Xu is grateful to Hyunjin Park, researcher at NCNT for supporting AFM analysis.

References

[1] Y.-G. Ha, S. Jeong, J. Wu, M.-G. Kim, V.P. Dravid, A. Facchetti, T.J. Marks, J. Am. Chem. Soc. 132 (2010) 17426.
[2] M.E. Roberts, S.C.B. Mannsfeld, N. Queraltó, C. Reese, J. Locklin, W. Knoll, Z. Bao, Proc. Natl. Acad. Sci. USA 105 (2008) 12134.
[3] L. Wang, D. Fine, D. Sharma, L. Torsi, A. Dodabalapur, Anal. Bioanal. Chem. 384 (2006) 310.
[4] L. Miozzo, A. Yassar, G. Horowitz, J. Mater. Chem. 20 (2010) 2513.
[5] C. Di, G. Yu, Y. Liu, D. Zhu, J. Phys. Chem. B 111 (2007) 14083.
[6] T.W. Kelley, L.D. Boardman, T.D. Dunbar, D.V. Muyres, M.J. Pellerite, T.P. Smith, J. Phys. Chem. B 107 (2003) 5877.
[7] H. Yang, T.J. Shin, M.M. Ling, K. Cho, C.Y. Ryu, Z. Bao, J. Am. Chem. Soc. 127 (2005) 11542.
[8] M.M. Payne, S.R. Parkin, J.E. Anthony, C.-C. Kuo, T.N. Jackson, J. Am. Chem. Soc. 127 (2005) 4986.
[9] H. Ebata, T. Izawa, E. Miyazaki, K. Takimiya, M. Ikeda, H. Kuwabara, T. Yui, J. Am. Chem. Soc. 129 (2007) 15732.
[10] T. Nagase, T. Hamada, K. Tomatsu, S. Yamazaki, T. Kobayashi, S. Murakami, K. Matsukawa, H. Naito, Adv. Mater. 22 (2010) 4706.
[11] C.D. Dimitrakopoulos, P.R.L. Malenfant, Adv. Mater. 14 (2002) 99.
[12] J. Veres, S. Ogier, G. Lloyd, D.D. Leeuw, Chem. Mater. 16 (2004) 4543.
[13] H. Sirringhaus, T. Kawase, R.H. Friend, T. Shimoda, M. Inbasekaran, W. Wu, E.P. Woo, Science 290 (2000) 2123.
[14] Y. Wu, Y. Li, B.S. Ong, P. Liu, S. Gardner, B. Chiang, Adv. Mater. 17 (2005) 184.
[15] S.P. Li, D.P. Chu, S.J. Newsome, D.M. Russell, T. Kugler, M. Ishida, T. Shimoda, Appl. Phys. Lett. 87 (2005) 232111.
[16] Y. Liu, K. Varahramyan, T. Cui, Macromol. Rapid Commun. 26 (2005) 1955.
[17] T.-W. Lee, Y. Byun, B.-W. Koo, I.-N. Kang, Y.-Y. Lyu, C.H. Lee, L. Pu, S.Y. Lee, Adv. Mater. 17 (2005) 2180.
[18] M. Matters, D.M. de Leeuw, M.J.C.M. Vissenberg, C.M. Hart, P.T. Herwig, T. Geuns, C.M.J. Mutsaers, C.J. Drury, Opt. Mater. 12 (1999) 189.
[19] S. Scheinert, G. Paasch, M. Schrodner, H.-K. Roth, S. Sensfub, J. Appl. Phys. 92 (2002) 330.
[20] H. Klauk, M. Halik, U. Zschieschang, F. Eder, G. Schmid, C. Dehm, Appl. Phys. Lett. 82 (2003) 4175.
[21] G. Horowitz, F. Deloffre, F. Garmier, R. Hajlaoui, M. Hmyene, A. Yassar, Synthetic Met. 54 (1993) 435.
[22] R. Schroeder, L.A. Majewski, M. Grell, Appl. Phys. Lett. 84 (2004) 1004.
[23] C.D. Sheraw, D.J. Gundlach, T.N. Jackson, Mater. Res. Soc. Symp. Proc. 558 (2000) 403.
[24] Y. Kato, S. Iba, R. Teramoto, T. Sekitani, T. Someya, H. Kawaguchi, T. Sakurai, Appl. Phys. Lett. 84 (2004) 3789.
[25] L.-L. Chua, P.K.H. Ho, H. Sirringhaus, R.H. Friend, Appl. Phys. Lett. 84 (2004) 3400.
[26] A. Facchetti, M.-H. Yoon, T.J. Marks, Adv. Mater. 17 (2005) 1705.
[27] D.K. Hwang, M.S. Oh, J.M. Hwang, J.H. Kim, S. Im, Appl. Phys. Lett. 92 (2008) 013304.
[28] S.C. Lim, S.H. Kim, J.B. Koo, J.H. Lee, C.H. Ku, Y.S. Yang, T. Zyung, Appl. Phys. Lett. 90 (2007) 173512.
[29] D.K. Hwang, K. Lee, J.H. Kim, S. Im, J.H. Park, E. Kim, Appl. Phys. Lett. 89 (2006) 093507.
[30] J. Jang, S.H. Kim, S. Nam, D.S. Chung, C. Yang, W.M. Yun, C.E. Park, J.B. Koo, Appl. Phys. Lett. 92 (2008) 143306.
[31] S.H. Kim, S.Y. Yang, K. Shin, H. Jeon, J.W. Lee, K.P. Hong, C.E. Park, Appl. Phys. Lett. 89 (2006) 183516.
[32] V.A. Zakrevskii, N.T. Sudar, A. Zaopo, Y.A. Dubitsky, J. Appl. Phys. 93 (2003) 2135.
[33] C.A. Lee, D.-W. Park, K.-D. Jung, B.-J. Kim, Y.C. Kim, J.D. Lee, B.G. Park, Appl. Phys. Lett. 89 (2006) 262120.
[34] S.Y. Yang, S.H. Kim, K. Shin, H. Jeon, C.E. Park, Appl. Phys. Lett. 88 (2006) 173507.
[35] W. Xu, S.-W. Rhee, Org. Electron. 11 (2010) 836.
[36] C. Kim, Z. Wang, H.-J. Choi, Y.-G. Ha, A. Facchetti, T.J. Marks, J. Am. Chem. Soc. 130 (2008) 6867.
[37] K. Shin, S.Y. Yang, C. Yang, H. Jeon, C.E. Park, Org. Electron. 8 (2007) 336.
[38] A. Bolognesi, M. Berliocchi, M. Manenti, A.D. Carlo, P. Lugli, K. Lmimouni, C. Dufour, IEEE Trans. Electron Devices 51 (2004) 1997.
[39] M. Taniguchi, T. Kawai, Appl. Phys. Lett. 85 (2004) 3298.
[40] F.M. Fowkes, Treatise on Adhesion and Adhesives, Edited by R.L. Patrick, Marcel Dekker, New York, 1967. pp. 352–353.
[41] L. Lan, J. Peng, M. Sun, J. Zhou, J. Zou, J. Wang, Y. Cao, Org. Electron. 10 (2009) 346.
[42] K.P. Pernstich, S. Haas, D. Oberhoff, C. Goldmann, D.J. Gundlach, B. Batlogg, A.N. Rashid, G. Schitterb, J. Appl. Phys. 96 (2004) 6431.

[43] Dhananjay, S.B. Krupanidhi, J. Appl. Phys. 101 (2007) 123717.
[44] W. Xu, S.-W. Rhee, J. Mater. Chem. 19 (2009) 5250.
[45] W. Xu, S.-W. Rhee, Org. Electron. 11 (2010) 996.
[46] W. Xu, S.-W. Rhee, J. Mater. Chem. 21 (2011) 998.
[47] I. Yagi, N. Hirai, M. Noda, A. Imaoka, Y. Miyamoto, N. Yoneya, K. Nomoto, J. Kasahara, A. Yumoto, T. Urabe, SID Symp. Digest 38 (2007) 1753.
[48] M. Mizukami, N. Hirohata, T. Iseki, K. Ohtawara, T. Tada, S. Yagyu, T. Abe, T. Suzuki, Y. Fujisaki, Y. Inoue, S. Tokito, T. Kurita, I.E. EE, Electron Device Lett. 27 (2006) 249.
[49] A. Rolland, J. Richard, J.-P. Kleider, D. Mencaraglia, J. Electrochem. Soc. 140 (1993) 3679.

structure allows for an extended conjugation of the carbazole units over the biphenyl structure leading to a decrease in triplet energy to around 2.56 eV [13]. If the conjugation between the constituting units in carbazole derivatives is minimised the triplet energy can be maintained at a high level. Many approaches to confine the conjugated system in carbazole derivatives have been described in literature. One way to minimise the conjugation in carbazole based host materials introduced by Tokito et al. is to attach two methyl groups in the 2,2′-positions of the central biphenyl in CBP leading to the host material 4,4′-bis(9-carbazolyl)-2,2′-dimethylbiphenyl (CDBP) [14,15]. Due to the steric hindrance the biphenyl is forced into a tilted conformation which reduces the conjugation in the molecule and concomitantly enlarges the triplet energy to 2.79 eV. We recently reported a series of CBP-based materials with high triplet energies using a similar concept by introducing methyl and trifluoromethyl substituents in the 2,2′-positions of the central biphenyl unit [16,17]. Another design concept is to choose different linkers between the carbazole units such as a single phenyl ring instead of biphenyl in *N*,*N*′-dicarbazolyl-3,5-benzene (mCP) [18,13] or non-conjugated units as, for example, an aliphatic cyclohexyl ring, an oxygen-bridge [19] or a diphenylsilane linker [20]. In mCP another effect reduces the conjugation: instead of the *para*-connection, the two carbazole moieties are *meta*-linked over the phenyl ring [21,22]. A major drawback of mCP however is its high crystallinity. Matrix materials with carbazole units linked to a biphenyl in the 3,3′-positions have been described in a patent of Adachi and Forrest [23] and a number of following patents. In the scientific literature *meta*-linked CBP derivatives are to the best of our knowledge only reported in a theoretical study about heterofluorene linker groups between the two carbazoles as alternatives to biphenyl [24]. Besides the high triplet energy a host material has to reveal a stable amorphous phase at device operating temperatures [25]. This ensures homogeneous mixing of the emitter within the matrix material and minimises the effects of concentration quenching. In addition the use of organic glasses in OLEDs helps to avoid

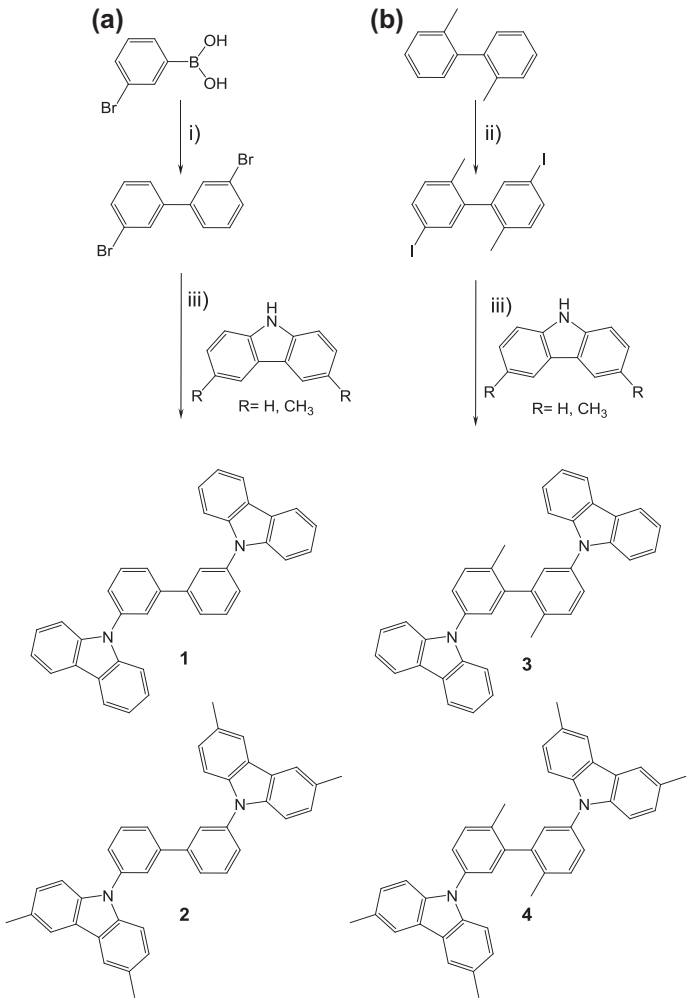

Fig. 1. Chemical structures and synthetic routes to (a) *meta*-linked CBP derivatives **1** and **2** and (b) twisted *meta*-linked CBP derivatives **3** and **4**. Reagents and conditions: (i) $Cu(OAc)_2$, DMF, 100 °C, 90 min; (ii) I_2, HIO_3, H_2SO_4, H_2O, CCl_4, acetic acid, 80 °C, 18 h; (iii) Cu, K_2CO_3, 18-crown-6, *o*-dichlorobenzene, reflux, 24 h.

grain boundaries which may act as trap states [26,27]. Organic glasses can be obtained by avoiding strong intermolecular forces like hydrogen bonding or π–π stacking between the molecules. A very common design concept for molecular glasses is the space-filling star-shaped topology, as in the well-known hole transporting organic glass 4,4′,4″-tris(carbazol-9-yl)triphenylamine (TCTA) [28]. Furthermore, the introduction of bulky substituents leads to a larger intermolecular distance and a hindrance in packing and therefore to amorphous behaviour. For example, in 9-(4-tert-butylphenyl)-3,6-bis(triphenylsilyl)-carbazole (CzSi) [29] and 3,5-di(*N*-carbazolyl)-tetra-phenylsilane (SimCP) [30] packing of the molecules is avoided by introducing bulky triphenylsily groups. However, the separation of the conducting units usually leads to a decrease in charge carrier mobility.

In this work we describe the preparation, the thermal and optical characterisation of four *meta*-linked CBP-derivatives. Materials revealing high triplet energies and amorphous behaviour with high glass transition temperatures are achieved by attaching the carbazole units at the *meta*-position of the phenyl rings of the biphenyl moiety in combination with a selective methyl substitution at the *meta*-CBP structure. The high triplet energy allows the use as host materials for the pure blue carbene emitter *mer*-tris(*N*-dibenzofuranyl-*N*′-methylimidazole)iridium (III) (Ir(dbfmi)). The molecular structures of the host materials **1**–**4** are depicted in Fig. 1.

2. Experimental

2.1. Materials

All chemicals and reagents were used as received from commercial sources without further purification. The solvents for reactions and purification were all distilled before use.

2.2. Characterisation

^{1}H and ^{13}C NMR spectra were recorded with a Bruker AC 300 (300, 75 MHz) and $CDCl_3$ as solvent. All data are given as chemical shifts δ (ppm) downfield from $Si(CH_3)_4$. For optical measurements, 10^{-5} M cyclohexane (Ultrasolv®) solutions of the materials as well as thin films on quartz substrates were prepared by spincoating. The UV/Vis spectra were measured in solution and on neat films with a Hitachi U-3000 spectrometer. Fluorescence spectra in solution were obtained from a Shimadzu spectrofluorophotometer RF-5301PC using excitation at 300 nm. Phosphorescence spectra of thin films have been measured at 5 K (Helium cryostat Optistat CF from Oxford Instruments) applying the technique of time-gated spectroscopy (with fluorescence and phosphorescence lifetime spectrometer FLSP 920 from Edinburgh Instruments). For differential scanning calorimetry measurements (DSC) a Diamond DSC apparatus from Perkin Elmer was used (heating/cooling rate 10 K min^{-1}, nitrogen). Thermogravimetric analysis (TGA) was performed on a Mettler Toledo TGA/SDTA815e machine at a heating rate of 10 K/min under nitrogen. Cyclic voltammetry measurements were carried out in absolute solvents measuring at a platinum working electrode versus a $Ag/AgNO_3$ reference electrode. Each measurement was calibrated against an internal standard (ferrocene/ferrocenium redox system). The purity of the target compounds was checked with a Waters size exclusion chromatography system (SEC) for oligomers (analytical columns: cross-linked polystyrene gel (Polymer Laboratories), length: 2 × 60 cm, width: 0.8 cm, particle size: 5 μm, pore size 100 Å, eluent THF (0.5 mL/min, 80 bar), polystyrene standard).

2.3. Computational methods

The transport levels of the materials used were determined via density functional calculations. For the ionisation potential and the electron affinity first the geometry of the neutral as well as the charged states were optimised using the BP86-functional [31,32] in combination with a split-valence basis set (SV(P)) including polarisation functions on all heavy atoms [33]. For iridium an effective core potential was employed [34]. For the energetics we performed single point calculations at the optimised geometries using the same functional in combination with a TZVP-basis set [35]. To account for dielectric solid state effects a UPS/IEPS-calibrated version of the conductor like screening model (COSMO) [36] was used in conjunction with these single point calculations. All calculations were carried out with the turbomole program package [37].

2.4. Synthetic procedures

The synthesis of tris[(3-phenyl-1*H*-benzimidazol-1-yl-2(3H)-yliden-1,2-phenylene]-irdidium (DPBIC) [38], 2,8-bis(triphenylsilyl)-dibenzofuran (DBFSi) [39], *mer*-tris(*N*-dibenzofuranyl-*N*′-methylimidazole)-iridium (III) (Ir(dbfmi)) [5,39] and 3,6-dimethyl-carbazole [16] is described in literature.

3,3′-Dibromobiphenyl was synthesized according to a procedure reported by Demir et al. [40] Yield: 43%. EI-MS *m/z*: 312 (100, M$^+$), 232 (5), 152 (95). ^{1}H NMR (300 MHz, $CDCl_3$), δ (ppm): 7.70 (dd, 2H), 7.52–7.46 (m, 4H), 7.31 (dd, 2H). ^{13}C NMR (75 MHz, $CDCl_3$), δ (ppm): 142.11, 131.16, 130.74, 130.50, 126.09, 123.33.

5,5′-Diiodo-2,2′-dimethylbiphenyl: 2,2′-Dimethylbiphenyl (9.9 g, 54 mmol) in 120 mL of acetic acid and 5.5 mL of water were heated to 90 °C to get a clear solution. After the addition of iodine (10.9 g, 43 mmol), iodic acid (5.7 g, 32 mmol), 5.5 mL of sulphuric acid and 5.5 mL of tetrachloromethane the solution was stirred at 80 °C for 18 h. The excess of iodine was removed by adding a solution of sodium hydrogen sulphide. The product was extracted with dichloromethane and washed several times with water. After drying the organic layer over anhydrous sodium sulphate, the solvent was evaporated. The resulting yellowish oily product was recrystallised from ethyl acetate to yield 6.9 g (16 mmol, 30%) of a white solid. EI-MS *m/z*: 434 (100, M+), 180 (50), 165 (47). ^{1}H NMR (300 MHz, $CDCl_3$), δ (ppm): 7.58 (dd, 2H), 7.42 (ds, 2H), 7.00 (d, 2H). 1.99 (s,

6H). ^{13}C NMR (75 MHz, $CDCl_3$), δ (ppm): 142.30, 137.65, 136.56, 135.48, 131.83, 90.41, 19.38.

2.5. General procedure for the Ullmann- type reaction

Dihalogenobiphenyl (2.3 mmol), carbazole (5.06 mmol), potassium carbonate (2.5 g, 18.4 mmol), copper powder (0.58 g, 9.2 mmol) and 18-crown-6 (0.12 mg, 0.46 mmol) were refluxed in 15 mL of *o*-dichlorobenzene in an argon atmosphere for 24 h. Copper and inorganic salts were filtered off and the solvent was evaporated. Column chromatography on silica gel with mixtures of hexane/tetrahydrofurane as eluent yielded the products **1**–**4** as white solids.

3,3′-Bis(carbazolyl)biphenyl (**1**): Yield: 47%. EI-MS *m*/*z*: 484 (100, M+), 316 (10), 234 (39). ^{1}H NMR (300 MHz, CDCl3), δ (ppm): 8.17 (d, 4 H), 7.88 (m, 2H), 7.75 (dt, 2H), 7.70 (dd, 2 H), 7.60 (dt, 2H), 7.51 (d, 4H), 7.43 (dt, 4H), 7.31 (dt, 4H). (^{13}C NMR (75 MHz, CDCl3), δ (ppm): 142.42, 141.19, 138.82, 130.84, 126.80, 126.52, 126.39, 126.10, 123.79, 120.71, 120.40, 110.08.

3,3′-Bis(3,6-dimethylcarbazolyl)biphenyl (**2**): Yield: 55%. EI-MS *m*/*z*: 540 (100, M+), 345 (5), 270 (24). ^{1}H NMR (300 MHz, $CDCl_3$), δ (ppm): 7.92 (m, 4H), 7.86 (m, 2H), 7.70 (dt, 2H), 7.66 (dd, 2H), 7.57 (dt, 2H), 7.38 (d, 4H), 7.24 (dd, 4H), 2.56 (s, 3H). ^{13}C NMR (75 MHz, $CDCl_3$), δ (ppm): 142.38, 139.63, 139.24, 130.70, 129.55, 127.52, 126.41, 126.05, 125.76, 123.84, 120.56, 109.75, 21.74.

3,3′-Bis(carbazolyl)-6,6′-dimethylbiphenyl (**3**): Yield: 50%. EI-MS *m*/*z*: 512 (100, M^+), 329 (8), 257 (17), 166 (12). ^{1}H NMR (300 MHz, $CDCl_3$), δ (ppm): 8.15 (d, 4H), 7.55–7.39 (m, 14H), 7.32–7.26 (m, 4H), 2.33 (s, 6H). ^{13}C NMR (75 MHz, $CDCl_3$), δ (ppm): 142.51 141.25 135.65, 135.46, 131.85, 127.96 126.45, 126.26, 123.67, 120.65, 120.20, 110.09, 20.11.

3,3′-Bis(3,6-dimethylcarbazolyl)-6,6′-dimethylbiphenyl (**4**): Yield: 55%. EI-MS *m*/*z*: 568 (100, M^+), 358 (15), 284 (29), 192 (24). ^{1}H NMR (300 MHz, $CDCl_3$), δ (ppm): 7.90 (s, 4H), 7.52–7.45 (m, 4H), 7.41–7.38 (m, 4H), 7.33 (d, 4H), 7.21(d, 4H), 2.55 (s, 12H), 2.30 (s, 6H). ^{13}C NMR (75 MHz, $CDCl_3$), δ (ppm): 142.47, 139.72, 136.06, 134.98, 131.70, 129.30, 127.69, 127.39, 126.10, 123.70, 120.49, 109.74, 21.73, 20.06.

2.6. OLED fabrication

The organic layers were deposited by thermal evaporation in high vacuum (<10^{-6} mbar) onto indium-tin-oxide (ITO, 10 ohm/square) precoated glass substrates. Prior to use the ITO glass was degreased using organic solvents and cleaned using an UV-ozon oven for 30 min. The organic layers and the metal cathode were evaporated without breaking the vacuum. The current density–luminance–voltage (J–L–V) characteristics of the OLEDs were measured by a Keithley source meter 2400 and a Konica Minolta CS-200, respectively. EL spectra were taken by a CCD spectral analyser by Zeiss. EQEs were calculated from the luminance, current density, and EL spectrum, assuming a Lambertian distribution.

3. Results and discussion

3.1. Synthesis

In Fig. 1a the synthetic route to the *meta*-linked CBP derivatives **1** and **2** is depicted. In a copper-mediated homocoupling reaction 3-bromophenylboronic acid reacts to 3,3′-dibromobiphenyl [40]. An Ullmann-type reaction of dibromobiphenyl with carbazole or 3,6-dimethylcarbazole [16] yields the host materials.

To obtain the twisted *meta*-linked CBP-derivatives **3** and **4**, first, 5,5′-diiodo-2,2′-dimethyl-biphenyl was prepared by direct iodination [41] of 2,2′-dimethylbiphenyl with iodine and iodic acid in acetic acid (Fig. 1b). Via 2D ^{1}H NMR experiments (see Supporting Information) the selective iodination at the 5- and 5′-positions of the biphenyl could be confirmed. Here, the inductive effect of the methyl groups in the 2- and 2′-positions of the biphenyl increases the electron density in the 5- and 5′-positions and favours the electrophilic attack of I^+. We consider this 5,5′-diiodo-2,2′-dimethylbiphenyl unit as a versatile building block for the synthesis of materials with confined conjugation which, to the best of our knowledge, has not been described in the literature before. The tilted *meta*-linked CBP derivatives **3** and **4** were prepared via the Ullmann-type reaction of 5,5′-diiodo-2,2′-dimethylbiphenyl with carbazole or 3,6-dimethylcarbazole [16].

Mass spectrometry, ^{1}H and ^{13}C NMR spectroscopy were used to identify the materials. The data are given in the experimental part. All materials were purified by repeated zone sublimation.

3.2. Thermal properties

We examined the thermal properties of the *meta*-linked CBP derivatives **1**–**4** by thermal gravimetric analysis (TGA) and differential scanning calorimetry (DSC) in nitrogen atmosphere at a scanning rate of 10 K min^{-1}. All results are summarised in Table 1.

Both the *para*-linked CBP and the *meta*-linked **1** show crystalline behaviour in the DSC experiment. For the *meta*-derivative **1** the melting and the crystallisation are observed at around 10 °C lower temperatures than for CBP. Methyl substitution at the pendant carbazoles in **2** leads to a material with a much lower tendency to crystal-

Table 1
Thermal properties of CBP and the *meta*-linked host materials **1**–**4**.

	T_g (°C)	T_m (°C)	T_{cr} (°C)	T_{id}[a] (°C)
CBP	–	283	205[b]	365
1	–	271	191[b]	315
2	107	270	184[c]	349
3	108	237	176[c]	319
4	120	212	–	319

T_g: glass-transition temperature, T_m: melting temperature, T_{cr}: crystallisation temperature and T_{id}: initial decomposition temperature.

[a] T_{id} is the temperature at which an initial mass loss was observed in a thermogravimetric experiment with a heating rate of 10 K min^{-1} in a nitrogen atmosphere.

[b] Observed during cooling scan.

[c] Observed only during the heating scan.

lise. The glass transition of **2** is observed at 107 °C and the recrystallisation is observed at a high temperature of 184 °C. In compound **3** the introduction of methyl groups only at the central biphenyl unit leads to nearly the same glass transition temperature of 109 °C and nearly the same recrystallisation temperature of 176 °C. The biphenyl substitution in combination with the methyl substitution at the carbazoles increases the T_g even to 120 °C for compound **4**. Moreover, for compound **4** crystallisation is observed neither in the cooling nor in the heating cycle which renders **4** the derivative of the series with the highest tendency to form a molecular glass. This thermal investigation shows that the introduction of additional methyl groups at the central biphenyl and/or the adjacent carbazole moieties of the *meta*-linked molecular structure has beneficial effects on the thermal properties, i.e. amorphous materials with high T_gs in the range of 107–120 °C are obtained.

3.3. Optical properties

The room temperature UV/Vis absorption and fluorescence spectra of 10^{-5} M cyclohexane solutions of **1**–**4** are depicted on top of Fig. 2. Compounds **1** and **3** as well as compounds **2** and **4** show very similar spectra. In each compound the absorption and photoluminescence behaviour is dominated by optical transitions localised on the carbazole units. Since the chromophore in compounds **1** and **3** and in compounds **2** and **4** are identical it is not surprising that these two pairs of materials show nearly the same absorption and fluorescence spectra. For compound **2** and **4** the additional methyl substituents on the chromophore 3,6-dimethylcarbazole cause a bathochromic shift of 13 nm in the absorption and emission spectra compared to compounds **1** and **3**.

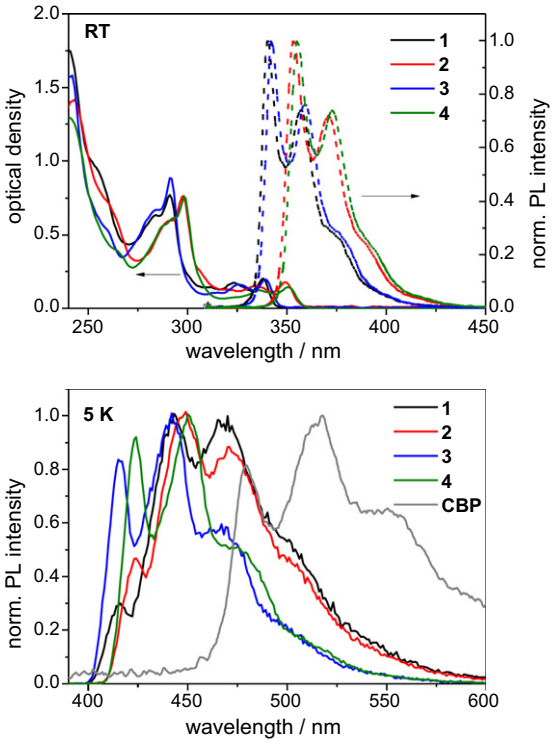

Fig. 2. Top: absorption and fluorescence spectra of **1**–**4** taken in 10^{-5} M solutions in cyclohexane at 300 K. Bottom: normalised phosphorescence spectra of CBP and **1**–**4** measured in 2 wt.% solid solution of the compounds in PMMA at 5 K.

As a prerequisite for the application of **1**–**4** as host materials, their triplet energy has to be higher compared to that of the blue phosphorescent emitter. By measuring phosphorescence at low temperatures the triplet energies can be experimentally determined as the highest energy peak of luminescence.

In order to understand how the *meta*-linkage of the carbazole units affects the triplet energy we compare the phosphorescence spectra of the *para*-linked CBP and the *meta*-linked derivative **1**–**4**. The most striking difference in the normalised spectra (see Fig. 2, bottom) is the remarkable blue shift in phosphorescence of **1**–**4** compared with CPB. The emission of **1**, for example, is shifted to lower wavelengths by 65 nm compared with CBP, corresponding to triplet energies ($\Delta E(T_1–S_0)$) of 2.98 eV for **1** and 2.58 eV for CBP. This is a proof of the design concept of *meta*-connection to achieve high triplet energies. In fact, the methyl substitution at the central biphenyl moiety is expected to lead to even higher triplet energies by introducing torsion between the phenyl rings of the biphenyl unit as is well known from CDBP. However, in the case of the *meta*-linked host materials the additional twisted molecular structure has only minor effects on the emission characteristics. Similar to the emission at room temperature, compounds **1** and **3** and compounds **2** and **4** reveal the highest energy peaks at the same wavelength, while the shape of the phosphorescence spectra is different. In the case of the twisted methyl substituted biphenyl containing compounds **3** and **4** the 0–0 transition is more pronounced and the width of the spectra is smaller than for **1** and **2**. As an effect of the methyl substitution at the 3- and 6-positon of the carbazole units we observe again a small bathochromic shift of ca. 10 nm for compounds **2** and **4** compared to **1** and **3**.

All results of the photo physical investigations of CBP and the *meta*-linked matrix materials **1**–**4** are summarised in Table 2.

3.4. Cyclic voltammetry

The electrochemical behaviour of **1**–**4** was investigated by cyclic voltammetry in a conventional three-electrode setup using a platinum working electrode, a platinum wire as counter electrode, and a $Ag/AgNO_3$ reference electrode. Particularly, the oxidation behaviour of **1**–**4** in dichloromethane solutions was studied. From the half-wave potential of the first oxidation relative to ferrocene the HOMO value of the compounds can be deduced. By adding the optical band gap to the HOMO value the LUMO value can be estimated. As the cyclic voltammetry is measured in solution and not in the solid state the values of HOMO and LUMO may differ from the solid state values in an OLED. Both the experimentally received and the calculated values for the energy levels of CBP and of **1**–**4** are listed in

Table 2
Optical properties and energy levels of CBP and the *meta*-linked host materials 1–4.

	Solution	Film	Solution	Film	Film	Calculated		Experimental	
	λ_{EA}[a] (nm)	λ_{EA}[b] (nm)	λ^{RT}_{em}[c] (nm)	λ^{5K}_{em}[d] (nm)	λ^{5K}_{em}[e] (nm)	HOMO (eV)	LUMO (eV)	HOMO[g] (eV)	LUMO[h] (eV)
CBP	350	357	356, 374	484	477	−5.58	−1.78	−5.63	−2.16
1	344	354	340, 357	421	415	−5.71	−1.77	−5.65	−2.15
2	357	365	353, 370	452[f]	421	−5.48	−1.71	−5.56	−2.17
3	346	354	342, 359	423	415	−5.64	−1.51	−5.65	−2.16
4	358	369	355, 373	431	421	−5.44	−1.47	−5.53	−2.17

[a] Absorption edge measured in 10^{-5} M cyclohexane solutions at room temperature.
[b] Absorption edge measured on neat films at room temperature.
[c] Wavelengths of the intensity maxima of the fluorescence at 300 nm excitation of 10^{-5} M cyclohexane solutions at room temperature.
[d] Measured on film samples (100%) at 5 K.
[e] Measured in 2 wt.% PMMA at 5 K.
[f] No 0–0 transition is observed.
[g] Estimated from the half-wave potential of the first oxidation in the cyclic voltammetry experiment.
[h] Estimated from the HOMO values and the optical band gap (determined from the UV/Vis absorption onset of neat films).

Table 2. The *meta*-linked compounds **1** and **3** with unsubstituted carbazole units reveal almost the same energy levels as for CBP. In contrast, **2** and **4** show ca. 10 mV higher HOMO levels which can be attributed to the inductive effect of the additional methyl groups in the 3- and 6-positons of the carbazole units. The cyclic voltammetry experiments show that the behaviour upon oxidation is clearly dominated by the molecules' site with the highest electron density, i.e. the carbazole moieties. Contrary to the theoretical expectations, the substitution on the central biphenyl unit does not affect the HOMO levels and fairly no effects of the different substitution pattern on the LUMO levels are observed.

Charge transport processes in organic semiconductors involve the formation of radical anions and cations. Thus, investigations of the electrochemical stability can give information about the stability of the materials in OLED devices. To evaluate the electrochemical stability of the materials we carried out multicycle experiments. The cyclic voltammograms showing five repeated oxidation cycles of **1** and **2** in 2×10^{-3} M dichloromethane solutions are given as Supporting Information. In the case of **1**, the oxidation cycles are not reproducible. After the first reduction into the uncharged molecule at 0.88 V an additional reduction at around 0.59 V is observed. The latter can be attributed to new oligomeric species formed during dimerisation reactions at the active 3- and 6-positions of the carbazole units after the first oxidation of the molecule [42,43]. As the oligomeric species is oxidised more easily the corresponding oxidation process takes place at a lower voltage of around 0.70 V. In contrast, **2** reveals a fully reversible oxidation behaviour. The methyl substitution at the adjacent carbazole units blocks the electroactive 3- and 6-positions and renders the oxidised species stable against dimerisation in solution. The same stability of the radical cations was also found for compound **4** in contrast to **3**.

3.5. Blue phosphorescent organic light-emitting diodes

Common blue phosphors as for example FIrpic and FIr6 show blue emission tailing to the green region with emission maxima at 472 nm (CIE colour coordinates $x = 0.17$, $y = 0.34$) [14] and 458 nm (CIE colour coordinates $x = 0.16$, $y = 0.26$) [44], respectively. For solid state lighting, phosphors with a more saturated blue emission would be beneficial. Due to the high triplet energy of more than 2.9 eV the host materials **1**–**4** should be suitable for saturated blue emitters. Thus, we have tested the host materials with the pure blue carbene emitter Ir(dbfmi) with a $\lambda_{em} = 450$ nm and CIE colour coordinates of $x = 0.16$, $y = 0.18$.

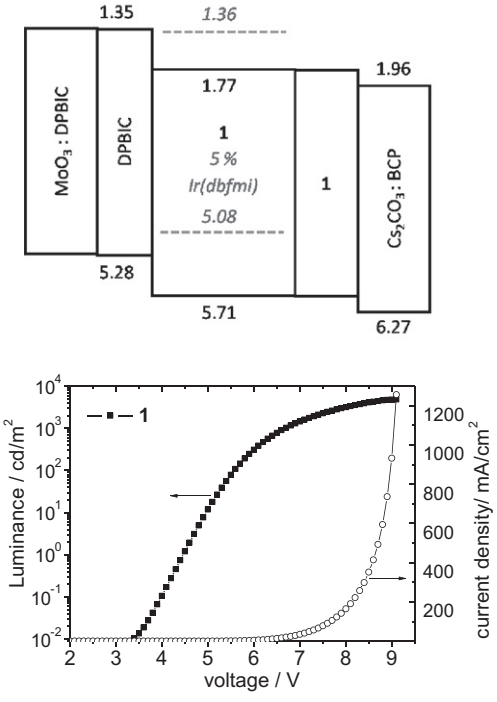

Fig. 3. Top: energy level diagram of the OLED device with the configuration ITO/PEDOT:PSS/MoO_3-doped DPBIC (10 nm)/DPBIC (10 nm)/**1**: Ir(dbfmi) (5 %, 20 nm)/**1** (10 nm)/Cs_2CO_3-doped BCP (20 nm)/Cs_2CO_3 (1 nm)/Al (100 nm) employing **1** as host for Ir(dbfmi); ionisation potentials and electron affinities obtained from calculations are indicated. The grey dotted lines represent the levels of the emitter Ir(dbfmi). Bottom: luminance-voltage plot (filled symbols) and current density–voltage characteristic (open symbols).

The first OLED device setup is shown in Fig. 3. On top of the ITO glass substrate poly(3,4-ethylene-dioxythiophene):poly(styrenesulphonate) (PEDOT:PSS) was applied by spin coating as hole injection layer followed by 10 nm DPBIC p-doped with molybdenum(VI) oxide as hole transporting layer. An additional 10 nm thick layer of DPBIC followed as exciton and electron blocker. The 20 nm emission layer consisted of 5% Ir(dbfmi) doped into the *meta*-linked CBP host materials. Ten nanometer of the host material were deposited as hole and exciton blocking layer followed by 20 nm of caesium carbonate doped 2,9-dimethyl-4,7-diphenyl-1,10-phenanthroline (BCP) as electron transporting layer. As cathode 1 nm Cs_2CO_3 and 100 nm aluminium were deposited.

The turn-on voltage at 1 cd m^{-2} of 4.5 V is quite high and luminances of 100 and 1000 cd m^{-2} are achieved at voltages of 5.6 and 6.8 V, respectively. In some cases we observed a small contribution of the hole transporting material DPBIC to the emission. This indicates that the exciton formation is shifted towards the hole conducting layer. We attribute this to the high energy barrier for hole injection from the DPBIC into the emission layer causing as well the high turn-on voltage. In contrast, electrons do not have to overcome major energy barriers.

To improve the hole injection into the emission layer we coevaporated the hole transporting DPBIC into the emission layer providing a barrier free path for holes. The optimised device setup and the molecular structures of the materials used are shown on top of Fig. 4. Ten nanometer molybdenum(VI) oxide doped DPBIC as hole transporting layer and an additional 10 nm thick layer of DPBIC were used as exciton and electron blocker. The 20 nm thick emission layer comprises a mixed matrix system of the carbazole containing host materials **1**–**4** with DPBIC and the blue emitter Ir(dbfmi) in the ratio 75:20:5. 2,8-Bis (triphenylsilyl)-dibenzofuran (DBFSi) (5 nm) was used as exciton and hole blocking material followed by 5 nm BCP and 40 nm BCP n-doped with Cs_2CO_3. As cathode 1 nm Cs_2CO_3 and 100 nm aluminium were deposited.

In the electroluminescence spectrum of the optimised device setup the pure emission of the phosphor Ir(dbfmi) can be observed with CIE-coordinates of $x = 0.16$ and $y = 0.18$ (Fig. 4, bottom). The CIE-coordinates do not change within the voltage range between 4.2 and 8.2 V. By decreasing the hole injection barrier in the mixed matrix

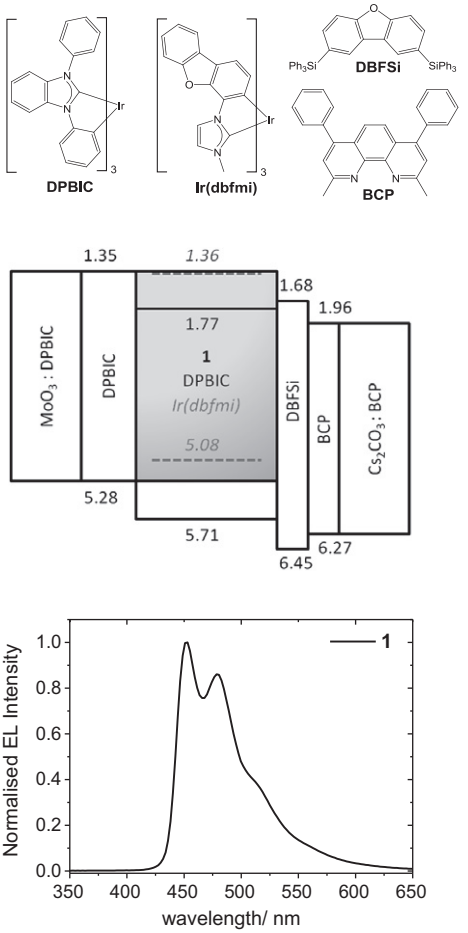

Fig. 4. Top: energy level diagram of the optimised OLED device with the configuration ITO/PEDOT:PSS/MoO_3-doped DPBIC (10 nm)/DPBIC (10 nm)/**1**: DPBIC:Ir(dbfmi) (75:20:5, 20 nm)/DBFSi (5 nm)/BCP (5 nm)/Cs_2CO_3-doped BCP (40 nm)/Cs_2CO_3 (1 nm)/Al (100 nm) employing **1** as host for Ir(dbfmi) with chemical structures of the materials used; Ionisation potentials and electron affinities obtained from calculations are indicated. The grey dotted lines represent the levels of the emitter Ir(dbfmi). Bottom: electroluminescence spectrum of the devices with **1** as host material for Ir(dbfmi) at 4.25 V. CIE coordinates: $x = 0.16$, $y = 0.18$.

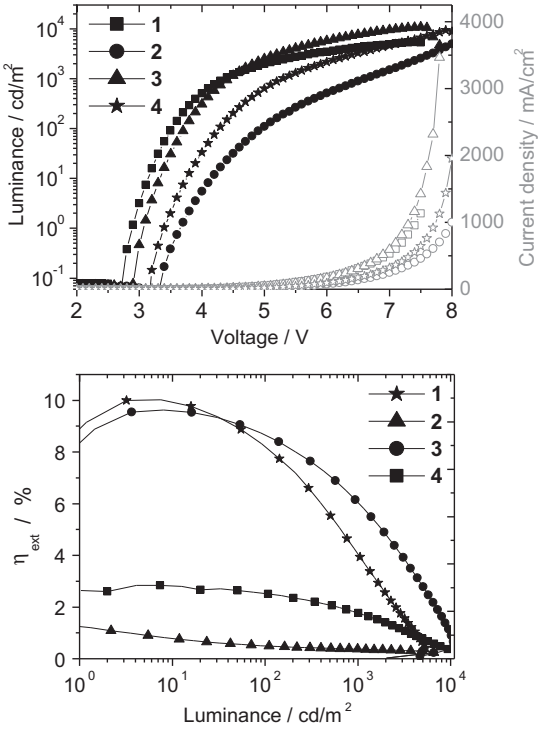

Fig. 5. Top: luminance–voltage curves (black filled symbols) and current density–voltage characteristics (grey open symbols) of the optimised device setup. Bottom: external quantum efficiency–luminance curves of the devices with **1**–**4** as host material for Ir(dbfmi).

Table 3
Performance data at 100 cd m^{-2} and 1000 cd m^{-2} using **1**–**4** as host materials for the blue emitter Ir(dbfmi).

	At 100 cd m^{-2}				At 1000 cd m^{-2}			
	Voltage (V)	η_C (cd A^{-1})	η_P (lm W^{-1})	η_{ext} (%)	Voltage (V)	η_C (cd A^{-1})	η_P (lm W^{-1})	η_{ext} (%)
1	3.5	11.5	10.2	8.2	4.4	5.7	4.1	4.1
2	4.9	0.9	0.6	0.5	6.6	0.6	0.3	0.4
3	3.7	12.2	10.2	8.7	4.4	8.5	6.0	6.1
4	4.3	4.5	3.3	2.6	5.3	3.1	1.9	1.8

η_C: Current efficiency; η_P: power efficiency; η_{ext}: external quantum efficiency.

system the exciton formation zone could be successfully separated from the hole transporting layer. Moreover, the applied voltages at 100 and 1000 cd m^{-2} could be significantly lowered, to 3.5 and 4.4 V, respectively, in the case of host **1** (see Fig. 5).

Peak luminances are 5300 cd m^{-2} for **1**, 5000 cd m^{-2} for **2**, 10,800 cd m^{-2} for **3** and 9300 cd m^{-2} for **4**. For hosts **1** and **3** higher luminances are reached at lower voltages than for **2** and **4**. Comparing the efficiencies of the four *meta*-linked CBP-derivatives **1**–**4**, the compounds **2** and **4** with methyl substituents at the 3- and 6-positions of the carbazole units show significantly lower efficiencies than **1** and **3**. As evident from the current density–voltage-plot in Fig. 5, higher operation voltages are needed in the devices employing the host materials **2** and **4**. One possibility might be that the transport properties of **2** and **4** with methyl substituents at the carbazole units are worse compared to **1** and **3** with unsubstituted carbazole units. In contrast, **1** and **3** give similar performances with slightly better values for **3** at higher luminances. The highest efficiency was achieved for **3** with an external quantum efficiency of 8.7% and a power efficiency of 10.2 lm W^{-1} at 100 cd m^{-2} and 6.1% and 6.0 lm W^{-1} at 1000 cd m^{-2}. These efficiencies are comparable to those of Ir(dbfmi) in the phosphine oxide based host material PO9 recently reported by Sasabe et al. [5] At a brightness of 1000 cd m^{-2} they reported an external quantum efficiency of 6.2% which compares well with the external quantum efficiency of 6.1% we found for the host material **3**. All performance data are summarised in Table 3.

The large differences in device performance as evident from Table 3 are quite surprising as the chemical structures of all hosts **1**–**4** are very similar. These findings show that each combination of emitter and host needs to be chosen very carefully as the host-emitter-system is very sensitive to even small structural variations which may change the charge-carrier balance in the device or the chemical compatibility of host and emitter. Both effects in conjunction with the relatively long triplet lifetime of Ir(dbfmi) of ~20 μs [5] could negatively influence the device performance.

4. Conclusions

We have described a series of CBP derivatives with a *meta*-linkage of the carbazole moieties to the central biphenyl unit. By selective methyl substitution at two sites of the basic *meta*-CBP structure, the 3- and 6-position of the pendant carbazoles and at the 6- and 6′-position of the biphenyl unit, the tendency to crystallise could be lowered. Glass transition temperatures in the range of 107–120 °C were achieved. The *meta*-linkage reduces the conjugation of the molecules effectively, leading to high triplet energies in the range of 2.93–2.98 eV compared with 2.58 eV for CBP. Here, the additional twist by the methyl substitution at the biphenyl unit does not increase the triplet energy any further, but narrows the phosphorescence spectra of **3** and **4** compared with **1** and **2**. Introducing methyl groups at the 3- and 6-position of the pendant carbazole units in the matrix materials **2** and **4** leads to electrochemical stability of the oxidised species in cyclic voltammetry. First results from OLED tests show that *meta*-linked CPB-derivatives are suited host materials for blue emitters, e.g., Ir(dbfmi), with pure blue emission at 450 nm. The highest efficiencies were achieved with the twisted *meta*-linked derivative **3** giving external quantum efficiencies of 8.7% and 6.1% and power efficiencies of 10.2 and 6.0 lm W^{-1} at 100 and 1000 cd m^{-2}, respectively.

Acknowledgements

We thank Irene Bauer for the help during synthesis and characterisation of the host materials and Christian Bonsignore and Mustapha Al-Helwi for their support during the device fabrication and characterisation. We also thank Dr. Ingo Münster, Dr. Evelyn Fuchs and Dr. Soichi Watanabe for scientific discussions. Financial support from the BMBF project TOPAS 2012 (FKZ 13N 10447) is gratefully acknowledged. P.S. thanks the Universität Bayern e.V. for a grant. Supporting Information is available online.

Appendix A. Supplementary data

Supplementary data associated with this article can be found, in the online version, at doi:10.1016/j.orgel.2011.08.012.

References

[1] M.A. Baldo, D.F. O'Brian, Y. You, A. Shoustikov, S. Sibley, M.E. Thompson, S.R. Forrest, Nature 395 (1998) 151–154 (London, U. K.).
[2] D.F. O'Brian, M.A. Baldo, M.E. Thompson, S.R. Forrest, Appl. Phys. Lett. 74 (4) (1999) 442–444.
[3] M.A. Baldo, S. Lamansky, P.E. Burrows, M.E. Thompson, S.R. Forrest, Appl. Phys. Lett. 75 (1999) 4–6.
[4] H. Sasabe, J. Kido, Chem. Mater. 23 (2011) 621–630.
[5] H. Sasabe, J. Takamatsu, T. Motoyama, S. Watanabe, G. Wagenblast, N. Langer, O. Molt, E. Fuchs, C. Lennartz, J. Kido, Adv. Mater. 22 (2010) 5003–5007.
[6] C. Adachi, M.A. Baldo, M.E. Thompson, S.R. Forrest, J. Appl. Phys. 90 (2001) 5048–5051.

[7] A.B. Padmaperuma, L.S. Sapochak, P.E. Burrows, Chem. Mater. 18 (2006) 2389–2396.
[8] P.-I. Shih, C.-L. Chiang, A.K. Dixit, C.-K. Chen, M.-C. Yuan, R.-Y. Lee, C.-T. Chen, E.W.-G. Diau, C.-F. Shu, Org. Lett. 8 (2006) 2799–2802.
[9] M.-H. Tsai, Y.-H. Hong, C.-H. Chang, H.-C. Su, C.-C. Wu, A. Matoliukstyte, J. Simokaitiene, S. Grigalevicius, J.V. Grazulevicius, C.-P. Hsu, Adv. Mater. 19 (2007) 862–866.
[10] H. Fukagawa, K. Watanabe, T. Tsuzuki, S. Tokito, Appl. Phys. Lett. 93 (2008) 133312–133314.
[11] J.-H. Jou, W.-B. Wang, S.-M. Shen, S. Kumar, I.-M. Lai, J.-J. Shyue, S. Lengvinaite, R. Zostautiene, J.V. Grazulevicius, S. Grigalevicius, S.-Z. Chen, C.-C. Wu, J. Mater. Chem. 21 (2011) 9546–9552.
[12] J.E. Adams, W.W. Mantulin, J.R. Huber, J. Am. Chem. Soc. 95 (1973) 5477–5481.
[13] R.J. Holmes, S.R. Forrest, Y.J. Tung, R.C. Kwong, J.J. Brown, S. Garon, M.E. Thompson, Appl. Phys. Lett. 82 (2003) 2422–2424.
[14] S. Tokito, T. Iijima, Y. Suzuri, H. Kita, T. Tsuzuki, F. Sato, Appl. Phys. Lett. 82 (2003) 569–571.
[15] I. Tanaka, Y. Tabata, S. Tokito, Chem. Phys. Lett. 400 (2004) 86–89.
[16] P. Schrögel, A. Tomkevičienė, P. Strohriegl, S.T. Hoffmann, A. Köhler, C. Lennartz, J. Mater. Chem. 21 (2011) 2266–2273.
[17] S.T. Hoffmann, P. Schrögel, M. Rothmann, R.Q. Albuquerque, P. Strohriegl, A. Köhler, J. Phys. Chem. B 115 (3) (2011) 414–421.
[18] V. Adamovich, J. Brooks, A. Tamayo, A.M. Alexander, P. Djurovich, B.W. D'Andrade, C. Adachi, S.R. Forrest, M.E. Thompson, New J. Chem. 26 (2002) 1171–1178.
[19] J. He, H. Lui, X. Dai, X. Ou, J. Wang, S. Tao, X. Zhang, P. Wang, D. Ma, J. Phys. Chem. C 113 (2009) 6761–6767.
[20] R. Zostautiene, J.V. Grazulevicius, Y.M. Lai, W.B. Wang, J.H. Jou, S. Grigalevicius, Synthetic Metals 161 (2011) 92–95.
[21] S.-J. Su, T. Chiba, T. Takeda, J. Kido, Adv. Mater. 20 (2008) 2125–2130.
[22] S.-J. Su, C. Cai, J. Kido, Chem. Mater. 23 (2) (2011) 274–284.
[23] C. Adachi, S.R. Forrest, US Patent 6 (2002) 458–475.
[24] J. Yin, S.-L. Zhang, R.-F. Chen, Q.-D. Ling, W. Huang, Phys. Chem. Chem. Phys. 12 (2010) 15448–15458.
[25] P. Strohriegl, J.V. Grazulevicius, Adv. Mater. 14 (2002) 1439–1452.
[26] Y. Shirota, J. Mater. Chem. 10 (2000) 1–25.
[27] R. Schmechel, H. Von Seggern, Phys. Status Solidi A 201 (2004) 1215–1235.
[28] Y. Kuwabara, H. Ogawa, H. Inada, N. Noma, Y. Shirota, Adv. Mater. 6 (2004) 677–679.
[29] M.-H. Tsai, H.-W. Lin, H.-C. Su, T.-H. Ke, C.-C. Wu, F.-C. Fang, Y.-L. Liao, K.-T. Wong, C.-I. Wu, Adv. Mater. 18 (2006) 1216–1220.
[30] M.-F. Wu, S.-J. Yeh, C.-T. Chen, H. Murayama, T. Tsuboi, W.-S. Li, I. Chao, S.-W. Liu, J.-K. Wang, Adv. Funct. Mater. 17 (2007) 1887–1895.
[31] J.P. Perdew, W. Yue, Phys. Rev. B: Condens. Matter Mater. Phys. 33 (1986) 8800–8802.
[32] A.D. Becke, Phys. Rev. A: At., Mol. Opt. Phys. 36 (1988) 3098–3100.
[33] A. Schäfer, H. Horn, R. Ahlrichs, J. Chem. Phys. 97 (1992) 2571–2577.
[34] D. Andrae, U. Häußermann, M. Dolg, H. Stoll, H. Preuss, Theor. Chim. Acta 77 (1990) 123–141.
[35] A. Schäfer, C. Huber, R. Ahlrichs, J. Chem. Phys. 100 (1994) 5829–5835.
[36] A. Klamt, J. Phys. Chem. 99 (1995) 2224–2235.
[37] R. Ahlrichs, M. Bär, M. Häser, H. Horn, C. Kölmel, Chem. Phys. Lett. 162 (1989) 165–169.
[38] M. Bold, C. Lennartz, M. Prinz, H.-W. Schmidt, M. Thelakkat, M. Bäte, C. Neuber, W. Kowalsky, C. Schildknecht, H.-H. Johannes, WO Patent (2005) 019373.
[39] N. Langer, K. Kahle, C. Lennartz, O. Molt, E. Fuchs, J. Rudolph, C. Schildknecht, S. Watanabe, G. Wagenblast, WO Patent (2009) 003898.
[40] A.S. Demir, Ö. Reis, M. Emrullahoglu, J. Org. Chem. 68 (2003) 10130–10134.
[41] H.O. Wirth, O. Königstein, W. Kern, Liebigs Ann. Chem. 634 (1960) 84–104.
[42] J.F. Ambrose, R.F. Nelson, J. Electrochem. Soc. 115 (11) (1968) 1159–1164.
[43] J.F. Ambrose, L.L. Carpenter, R.F. Nelson, J. Electrochem. Soc. 122 (7) (1975) 876–894.
[44] R.J. Holmes, B.W. D'Andrade, S.R. Forrest, X. Ren, J. Li, M.E. Thompson, Appl. Phys. Lett. 83 (2003) 3818–3820.

and charges inside the EMLs may suffer faster degradation condition due to bimolecular phenomena such as exciton-charge quenching process [5,6].

We use delayed electroluminescence (EL) measurements to gain insights about the phenomena governing the EL efficiency loss with prolonged electrical driving of PHOLEDs. In this work, PHOLEDs containing HBLs of 2,9-dimethyl-4,7-diphenyl-1,10-phenanthroline (BCP) or BAlq, two widely used hole blocking materials, are investigated The study also utilizes specially designed PHOLEDs that include a 4-[dicyanomethylene]-2-t-butyl-6-(1,1,7,7-tetramethyljulolidyl-9-enyl)-4H-pyran (DCJTB)-doped "sensor" layers. The results show a strong correlation between the extent of hole blockage capacity of the HBL and the rate of deterioration in device EL efficiency, pointing to the major role that the build-up of hole space charges in the emitting layer (EML) plays in EL degradation. In this regard, the use of a strongly blocking material significantly increases the build-up of holes in the EML, and accelerates EL degradation.

2. Experimental

Indium-tin-oxide (ITO) is used as an anode, and 100 nm thick Mg:Ag capped with Ag is employed as a cathode. The ITO substrates are cleaned with water, acetone and isopropanol in an ultrasonic bath followed by O_2 plasma treatment. All the organic materials and the cathode metals are deposited using thermal evaporation in vacuum condition at a base pressure of about 4×10^{-6} torr. In this study, PHOLEDs based on archetypical *4,4′-bis(carbazol-9-yl)biphenyl* (CBP) and *tris(2-phenylpyridine)iridium(III)* ($Ir(ppy)_3$) host–guest phosphorescent system in the emitting layer are used. *N,N′-di(naphthalene-1-yl)-N,N′-diphenyl-benzidine* (NPB) and aluminum tris(8-hydroxyquinoline) (Alq_3) are utilized as hole transport layer and electron transport layer (ETL), respectively. In devices with HBL, a 10 nm thick layer of BCP or BAlq is inserted between the emitting layer and the ETL. In devices with sensor layer, DCJTB is doped at 1 vol.% in a ~5 nm thick portion of the ETL, adjacent to the EML or HBL. Detailed device structures and measurement techniques are outlined in the following section.

3. Result and discussion

Fig. 1 shows changes in EL intensity with driving time in devices of the following structures:

- ITO/NPB (50 nm)/CBP:$Ir(ppy)_3$ (92%:8%, 40 nm)/Alq_3 (30 nm)/Mg:Ag/Ag (9:1, 100 nm) (named as No HBL).
- ITO/NPB (50 nm)/CBP:$Ir(ppy)_3$ (92%:8%, 40 nm)/BAlq (10 nm)/Alq_3 (30 nm)/Mg:Ag/Ag (9:1, 100 nm) (named as BAlq HBL).
- ITO/NPB (50 nm)/CBP:$Ir(ppy)_3$ (92%:8%, 40 nm)/BCP (10 nm)/Alq_3 (30 nm)/Mg:Ag/Ag (9:1, 100 nm) (named as BCP HBL).

All devices are driven using an AC driving scheme [14] at an average current density of 20 mA/cm^2. The initial luminance and driving voltage of these devices are as shown in Table 1. As can be seen from the figure, the device with BCP HBL shows a significantly lower EL stability compared to the other two devices. The other two devices, on the other hand, show similar EL stability trends. We also measured the EL stability, also using AC driving, at the same initial luminance of 2000 cd/m^2. The results are shown in the inset of Fig. 1. Clearly in both aging schemes, the device with the BCP HBL shows much lower EL stability, whereas the devices with BAlq HBL and no HBL demonstrate the similar EL stability trends. We note that the observed stability is similar to that reported by some groups for the same device structure [15,16] but lower in comparison to other reports [17]. The wide variation in stability can be attributed to variations in ITO and organic materials obtained from different suppliers. In our case, the materials are purchased from the Luminescence Technology and are used as received.

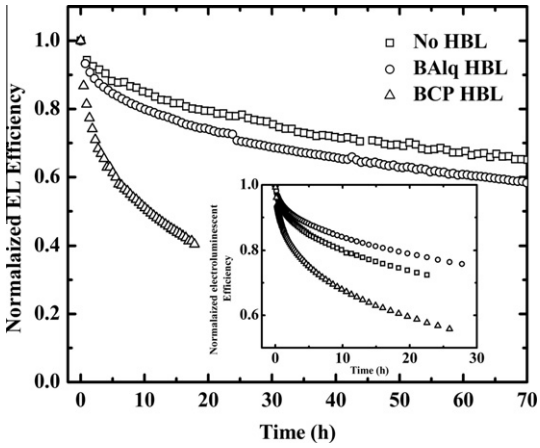

Fig. 1. Normalized EL efficiency versus time of devices without HBL and with BAlq and BCP HBLs, under AC driving at an average current density of 20 mA/cm^2. Inset: Normalized EL efficiency versus time of an identical set of devices also driven using AC driving at an initial luminance of 2000 cd/m^2.

To investigate the extent by which the HBLs reduce the leakage of holes from the EML towards the cathode, and any possible correlations with the observed changes in device stability when a HBL is used, we study a series of similar devices that contain a DCJTB-doped zone in the ETL, to act as a sensor layer. Fig. 2 shows a schematic energy band diagram of these devices, whereas Table 2 gives the driving voltage and EL intensity at 20 mA/cm^2 current density. Clearly the driving voltage of these devices is very similar to those without the sensor layer (<0.5 V) demonstrating that the presence of the sensor layer does not significantly

Table 1
Electrical and optical characteristics of the devices at 20 mA/cm^2 current density.

Device	Voltage (V)	Brightness (cd/m^2)	CIE
No HBL	10.4	1790	0.330, 0.597
BAlq HBL	10.58	2850	0.337, 0.597
BCP HBL	10.87	4130	0.331, 0.602

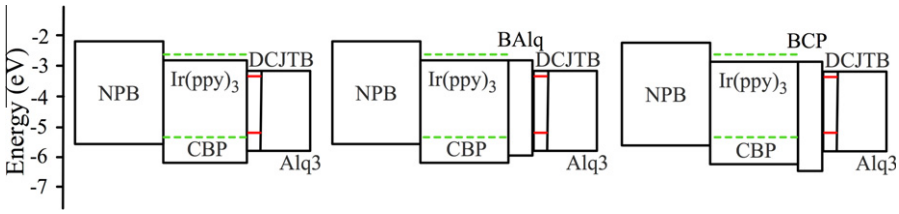

Fig. 2. Schematic structure of devices A, B and C. Layer thicknesses used for these devices are as follow: NPB = 40 nm, CBP:Ir(ppy)$_3$ = 40 nm, Alq$_3$ = 25 nm, Alq$_3$:DCJTB = 5 nm, BAlq = 10 nm, and BCP = 10 nm.

Table 2
Electrical and optical characteristics of the devices at 20 mA/cm^2 current density.

Device	Voltage (V)	Brightness (cd/m^2)	CIE
A	10.8	1640	0.371, 0.576
B	10.6	3200	0.345, 0.601
C	10.9	4660	0.336, 0.605

modify charge injection and transport in the devices. We also measured the EL stability of these devices and found to be very similar to ones without sensor layer. Fig. 3 shows EL spectra collected from the same devices. As expected, all devices show strong emission bands in the green range, with the characteristic Ir(ppy)$_3$ peak at 511 nm. The spectrum of device A is slightly broader in the red range, suggestive of some red emission from DCJTB sensor layer as would be expected due to the absence of HBL. To gain more insights about differences among these devices, we study them using delayed EL measurements. In this technique, a device is driven using a square pulse driving scheme, with a forward bias of 10 V and a pulse width of 0.5 ms (the pulse is sufficiently long for prompt EL to reach its steady-state intensity). The optical shutter opens to collect delayed EL around 0.3 ms after the forward bias is turned off, which is significantly longer than the lifetime of Ir(ppy)$_3$ triplet state lifetime (<1 μs) to ensure the absence of any contributions from prompt EL in the collected signal. As such, any collected signal will arise from the radiative decay of excitons that are formed, after the bias

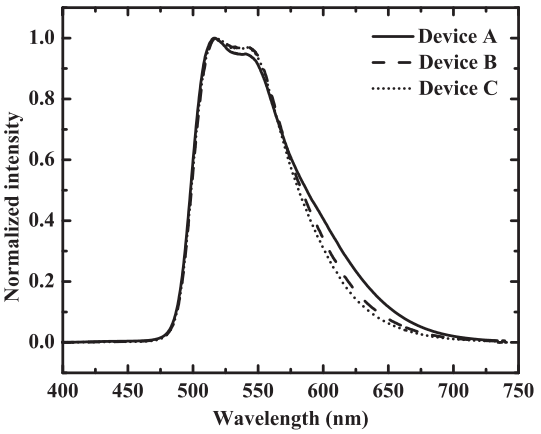

Fig. 3. Prompt EL spectra of devices A, B and C.

is removed, by means of (i) delayed recombination of detrapped charges, or (ii) various bimolecular exciton interactions. In order to distinguish between these processes, a 0.5 ms reverse bias pulse, of magnitude −10 V, is applied on the devices during the delayed EL signal collection, and subsequent changes in delayed EL characteristics are recorded. The detailed timing setup for delayed EL measurement was reported in our previous work [18], and is shown schematically in Fig. 4. As can be seen from the figure, delayed EL spectra show much more pronounced emission from DCJTB (611 nm peak band) in case of devices A (no HBL) and B (BALq HBL), but not in case of device C (BCP HBL) revealing that, unlike BCP, hole blockage by BAlq is only partial. The fact that emission from the DCJTB sensor layer is much more pronounced in delayed EL (i.e. Fig. 5) versus prompt EL (i.e. Fig. 3) can be attributed to the fact that holes are much less mobile in Alq$_3$ (due to its very low hole mobility) and therefore get essentially trapped on reaching the ETL. As residual electrons get swept back from the EML and HBL towards the cathode by the reverse bias pulse, they recombine with these trapped holes producing the observed delayed EL from the sensor layer. Regardless of the exact mechanism, the results in Fig. 5 convincingly prove that more holes reach the ETL in case of device B (BAlq HBL) than in case of device C (BCP HBL).

Finding that the use of a marginally blocking HBL (i.e. BAlq) results in a marginal decrease in device EL stability (from Fig. 1), whereas the use of a strongly blocking HBL (i.e. BCP) results in a significant decrease in EL stability, the question whether the observed changes in EL stability in Fig. 1 are due to variations in the extent of accumulation of holes in the EML naturally arises. To determine the relative concentration of trapped charges in the EML of these devices, we measure changes in their delayed EL intensity

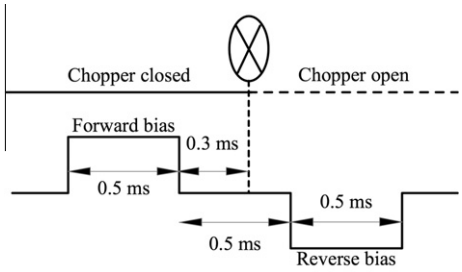

Fig. 4. Schematic diagram of the driving and signal collection timing scheme.

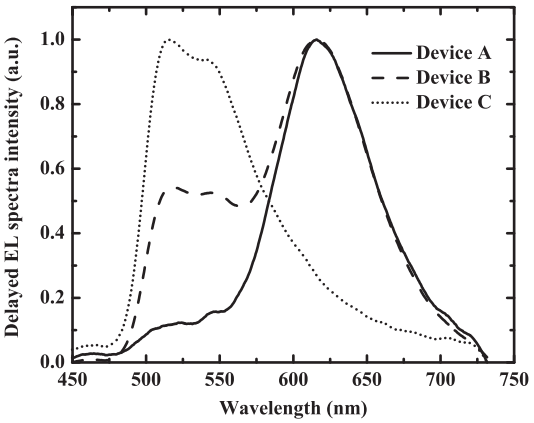

Fig. 5. Delayed EL spectra of devices A, B and C.

with time, monitoring the effect of the reverse bias pulse, following the previously established methodology [13]. For these measurements, devices without the sensor layer, (and therefore identical to the ones used in EL stability measurements of Fig. 1) are used in order to ensure that all delayed EL originates from the EML. Fig. 6a–c shows the delayed EL signal versus time elapsed from the end of the forward bias pulse obtained from the devices without HBL, with BAlq HBL and with BCP HBL, respectively; collected before and again after 20 hours of electrical aging at 20 mA/cm^2 current density in each case (denoted by "fresh" and "aged" on the figures in each case). As can be seen from the figures the application of the reverse bias causes a sudden increase in delayed EL intensity, which appears as a spike. The appearance of spike is an indication of a sudden release of trapped charges, which then recombine producing electroluminescence. A comparison of the spike heights in the fresh devices correlate with the expected variation in the extent of a hole space charge build-up in the EML among the three devices, with the device without the HBL showing the smallest spike (hence the smallest space charge), whereas the device with the strongly blocking HBL (i.e. BCP) demonstrating the highest spike (hence the largest space charge). Furthermore, a comparison of the spike heights due to aging reveals that the device without the HBL demonstrates the smallest increase, whereas the device with the strongly blocking HBL (i.e. BCP) demonstrates the largest increase, indicating the largest increase in the number of trapped charges in the EML upon prolonged electrical driving in the latter. The results therefore show a strong correlation between the accumulation of holes in the EML and the loss in EL efficiency of the PHOLEDs. In this regard, the efficiency loss may be due to increased exciton-polaron annihilation, which, as a bimolecular interaction, will increase with the concentration of holes trapped in the EML. The increase in trapped charges with electrical aging suggests that the effect may also be associated with an increase in concentration of deep charge traps, which can act as non-radiative recombination centers, and hence also contribute to the loss in device efficiency.

Although the results show a clear correlation between the extend of charge accumulation by the HBL and device stability, it is possible that variations in device stability also arise from chemical reactions between Ir(ppy)$_3$ and the HBL, as was observed in Ir(MDQ)$_2$acac based PHOLEDs before [12]. To test this possibility, we study a series of devices containing a neat CBP layer in between the EML and the HBL and compare them with control devices that do not have the neat CBP layer. The devices structure is as follows:

- ITO/NPB (50 nm)/CBP:Ir(ppy)$_3$ (92%:8%, 35 nm)/CBP (5 nm)/BAlq (10 nm)/Alq$_3$ (30 nm)/Mg:Ag/Ag (9:1, 100 nm) (named as BAlq-5 nm CBP spacer).
- ITO/NPB (50 nm)/CBP:Ir(ppy)$_3$ (92%:8%, 40 nm)/ BAlq (10 nm)/Alq$_3$ (30 nm)/Mg:Ag/Ag (9:1, 100 nm) (named as BAlq-Control).

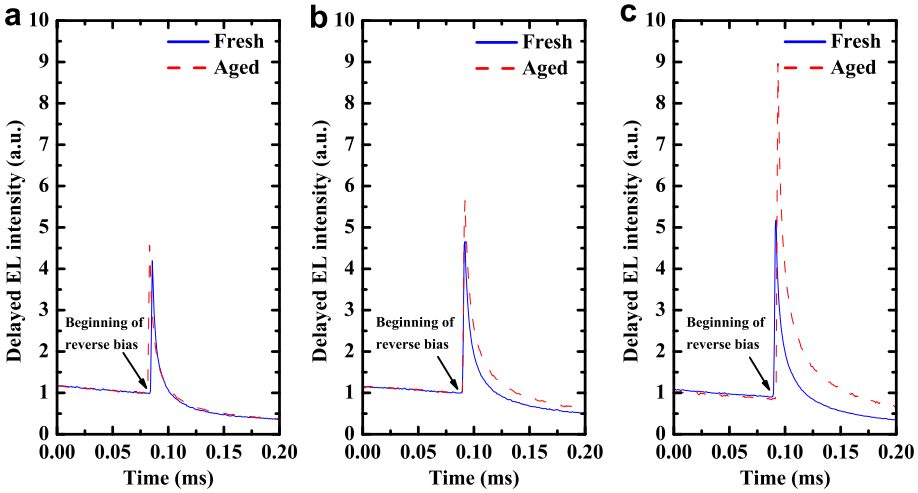

Fig. 6. Delayed EL intensity of devices (a) without HBL, (b) with BAlq HBL and (c) with BCP HBL, collected before (fresh) and after aging (aged) for 20 h at 20 mA/cm^2 current density.

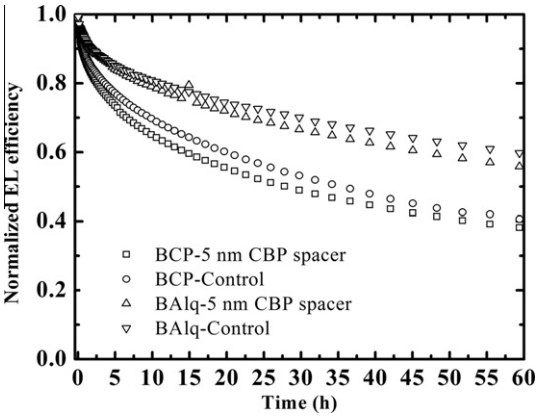

Fig. 7. Normalized EL efficiency versus time of devices with and without CBP spacer layer under AC driving at an average current density of 20 mA/cm^2.

- ITO/NPB (50 nm)/CBP:Ir(ppy)$_3$ (92%:8%, 35 nm)/CBP (5 nm)/BCP(10 nm)/Alq$_3$ (30 nm)/Mg:Ag/Ag (9:1, 100 nm) (named as BCP-5 nm CBP spacer).
- ITO/NPB (50 nm)/CBP:Ir(ppy)$_3$ (92%:8%, 40 nm)/BCP (10 nm)/Alq$_3$ (30 nm)/Mg:Ag/Ag (9:1, 100 nm) (named as BCP-Control).

Fig. 7 shows the EL stability of the devices. As can be seen from the figure devices with the neat CBP spacer layer show similar EL stability to the corresponding control devices indicating that reactions between the emitter and HBL do not play a major role in our devices, which can perhaps be attributed to the fact that we are using a different emitter.

To that end, device stability is strongly influenced by the use of a HBL, where the use of a strongly blocking material (e.g. BCP) will significantly increase the build-up of holes in the EML, and hence accelerate the EL degradation of the device.

4. Summary and conclusions

In summary, delayed EL measurements are used to investigate electroluminescence stability in PHOLEDs containing typical HBLs. The results show a strong correlation between the extent of hole blockage capacity of the HBL and the deterioration in device EL efficiency, pointing to the major role that the build-up of hole space charges in the emitting layer plays in EL degradation. In this regard, the use of a strongly blocking material (e.g. BCP) significantly increases the build-up of holes in the EML, and accelerates EL degradation.

Acknowledgements

Financial support to this work by DALSA Corporation and the Natural Science and Engineering Research Council of Canada (NSERC) is gratefully acknowledged.

References

[1] Y. Kawamura, K. Goushi, J. Brooks, J.J. Brown, H. Sasabe, C. Adachi, Appl. Phys. Lett. 86 (2005) 071104.
[2] C. Adachi, M.A. Baldo, M.E. Thompson, S.R. Forrest, J. Appl. Phys. 90 (2001) 5048.
[3] M.E. Kondakova, T.D. Pawlik, R.H. Young, D.J. Giesen, D.Y. Kondakov, C.T. Brown, J.C. Deaton, J.R. Lenhard, K.P. Klubek, J. Appl. Phys. 104 (9) (2008) 094501.
[4] M. Pfeiffer, S.R. Forrest, K. Leo, M.E. Thompson, Adv. Mater. 14 (2002) 22.
[5] N.C. Giebink, B.W. D'Andrade, M.S. Weaver, J.J. Brown, S.R. Forrest, J. Appl. Phys. 105 (2009) 124614.
[6] N.C. Giebink, B.W. D'Andrade, M.S. Weaver, P.B. Mackenzie, J.J. Brown, M.E. Thompson, S.R. Forrest, J. Appl. Phys. 103 (2008) 044509.
[7] K.S. Yook, S.E. Jang, J.Y. Lee, Electrochem. Solid-State Lett. 13 (10) (2010) J122–J124.
[8] J. Lee, J. Lee, J. Lee, H. Chu, Org. Electron. 11 (2010) 1159–1164.
[9] R. Meerheim, S. Scholz, S. Olthof, G. Schwartz, S. Reineke, K. Walzer, K. Leo, J. Appl. Phys. 104 (2008) 1.
[10] S. Lee, J. Seo, J. Seo, G. Kim, Y. Jin, Y. Kim, J. Nanosci. Nanotechnol. 9 (2009) 7044–7047.
[11] B. Chin, C. Lee, Adv. Mater. 19 (2007) 2061–2066.
[12] S. Scholz, R. Meerheim, K. Walzer, K. Leo, Proc. of SPIE 6999 (2008) 69991B.
[13] H. Zamani Siboni, Y. Luo, H. Aziz, J. Appl. Phys. 109 (2011) 044501.
[14] Y. Luo, H. Aziz, Z.D. Popovic, G. Xu, J. Appl. Phys. 99 (2006) 054508.
[15] Y. Tsai, S. Wang, S. Chen, S. Su, F. Juang, Thin Solid Films 517 (2009) 5338.
[16] J. Kang, D. Lee, H. Park, J. Kim, W. Jeong, Y. Park, S. Lee, K. Go, J. Lee, J. Kim, Org. Elec. 9 (2008) 452.
[17] R.C. Kwong, M.R. Nugent, L. Michalski, T. Ngo, K. Rajan, Y. Tung, M.S. Weaver, T.X. Zhou, M. Hack, M.E. Thompson, S.R. Forrest, J.J. Brown, Appl. Phys. Lett. 81 (2002) 162.
[18] Z.D. Popovic, H. Aziz, J. Appl. Phys. 98 (2005) 13510.

In this paper, highly efficient blue phosphorescent OLEDs have been achieved by using a new emitter, iridium(III) bis[(3,4,5-trifluorophenyl)-pyridinato-N,$C^{2'}$] picolinate (F_3Irpic). Using the typical mCP host, blue emission with a maximum power efficiency of 18.1 lm/W has been realized. The power efficiency can be further increased to 33.7 lm/W by using a host of UGH2. Performance of the device is among the best reported for blue OLEDs.

2. Experimental details

The cyclometalating ligand 1-(3,4,5-trifluorophenyl)-pyridine was prepared via a Suzuki coupling reaction between 1-bromopyridine and 3,4,5-trifluorophenyl boronic acid. Synthesis of the final Ir complex involved two key steps. In the first step, $IrCl_3$ was reacted with excess of the synthesized ligands to produce a chloro-bridged Ir dimer. This dimer can be readily converted to the monomeric complex F_3Irpic by replacing the bridging chlorides with Picolinic Acid in the presence of Na_2CO_3. The synthetic pathway towards the preparation of F_3Irpic is outlined in Scheme 1. The identity was confirmed by 1H-nuclear magnetic resonance, elemental analysis, and mass spectrometry. MS (m/z): 730; ^{1}H NMR (Acetone, 300 MHz): δ: 7.16–7.21 (t, 1H), δ: 7.36–7.40 (t, 1H), 7.65–7.66 (d, 2H), 7.75–7.88 (m, 2H), 7.92–8.00 (m, 3H), 8.13–8.20 (m, 4H), 8.67–8.69 (d, 1H). Anal. Calcd. for $IrC_{28}H_{14}N_3O_2F_6$: C, 46.03; H, 1.93%; N, 5.75%. Found: C, 45.63; H, 2.00%; N, 5.70%.

Absorption and photoluminescence spectra were recorded, respectively with a Perkin–Elmer Lambda 2S UV–Vis spectrophotometer and a Perkin–Elmer LS50B luminescence spectrophotometer. The highest occupied molecular orbital (HOMO) value of the Ir complex was measured via ultraviolet photoelectron spectroscopy (UPS). The lowest unoccupied molecular orbital (LUMO) value was determined from the difference between the HOMO energy and the band gap determined from the optical absorption edge.

OLEDs were fabricated by vacuum deposition on ITO-coated glass substrates with a sheet resistance of 30 Ω/square. Before deposition, the ITO substrate was first carefully cleaned, dried in an oven at 120 °C, and then treated with UV-ozone before loaded into a deposition chamber. Organic layers were then sequentially deposited onto the ITO substrate at a rate of 2–4 Å/s and a pressure below 5×10^{-6} mbar. Electroluminescence (EL) spectra and CIE color coordinates were measured with a Spectrascan PR650 photometer. Current–voltage–luminescence characteristics were measured with a computer-controlled Keithley 236 source meter under ambient conditions.

3. Results and discussion

Iridium(III) bis[(3,4,5-trifluorophenyl)-pyridinato-N,$C^{2'}$] picolinate (F_3Irpic) was synthesized in house. The molecular structure of F_3Irpic (Scheme 1), which has been confirmed with ^{1}H nuclear magnetic resonance, mass spectrometry and elemental analysis, is similar to that of FIrpic except for the three fluorine atoms substituted at the 3,4,5-position of the phenylpyridine ligand. Fig. 1 shows the absorption and photoluminescence (PL) spectra of F_3Irpic in dilute dichloromethane solution. The PL spectrum of F_3Irpic shows a blue emission with a main emission peak centered at 479 nm and a smaller peak at 509 nm. The shape of the PL spectrum is similar to that of FIrpic except for a red-shift of 8 nm [18]. On the other hand, the photoluminescence quantum yield of F_3Irpic in chloroform solution was measured to be 0.67 using FIrpic (Φ_f: 0.50) as a calibration standard, which is higher than that of FIrpic. The higher PL quantum yield of F_3Irpic should be attributed to more fluorine atoms substituted in the ligand than FIrpic [20].

OLEDs were made by doping F_3Irpic in mCP with a device structure of ITO/NPB (40 nm)/*x*% F_3Irpic:mCP (30 nm)/BAlq (40 nm)/LiF (0.5 nm)/Al (80 nm). In the devices, ITO (indium tin oxide) and LiF/Al are the anode and the cathode, respectively; 4,4′-bis[*N*-(1-naphthyl)-*N*-phenyl amino] biphenyl (NPB) is the hole transporting layer (HTL), and aluminum

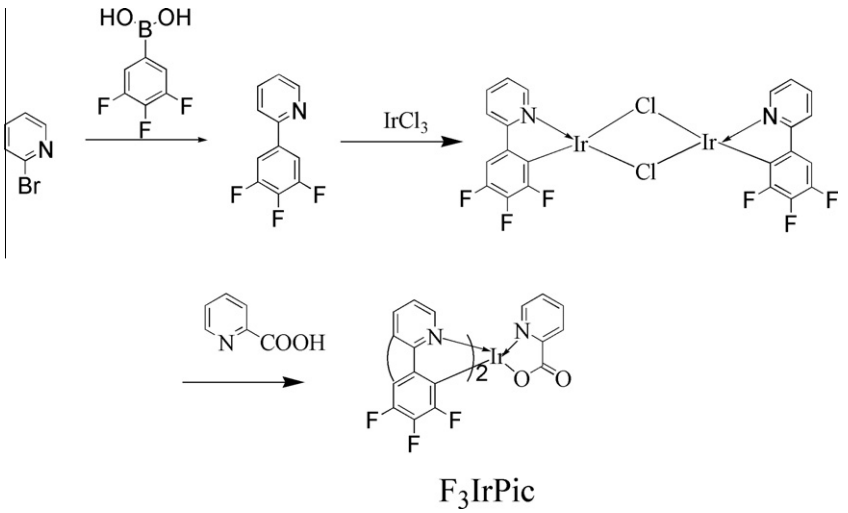

F_3IrPic

Scheme 1. Synthetic route of F_3Irpic.

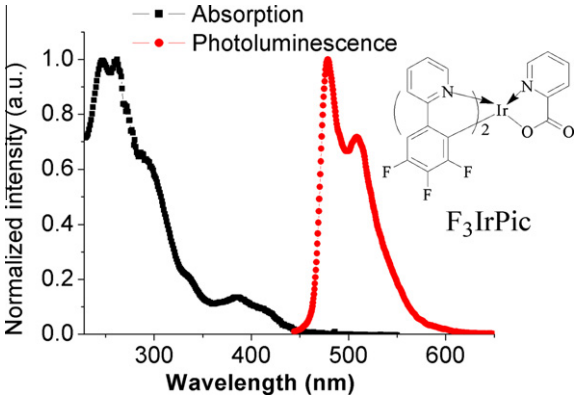

Fig. 1. Absorption and emission spectra of F_3Irpic, inset is its molecular structure.

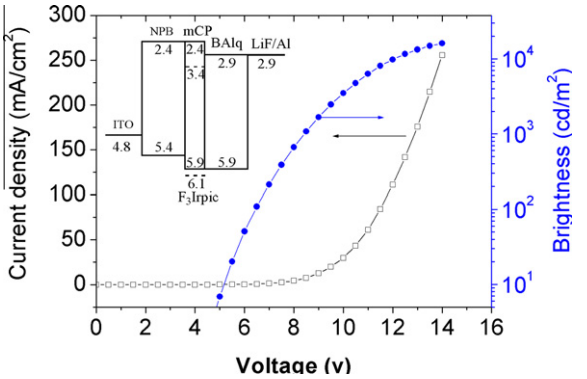

Fig. 3. *I–V–L* characteristics of the device, inset is the energy level diagram of the device.

(III) bis(2-methyl-8-quinolinato)4-phenylphenolate (BAlq) is the electron transporting layer (ETL). The F_3Irpic doped mCP layer is the emission layer (EML).

The devices with different concentration of F_3Irpic shows almost the same EL spectra (Fig. 2) as the PL spectrum (Fig. 1) of the Ir complex. Current and power efficiency of the best performing device (4% F_3Irpic in mCP) are shown in inset of Fig. 2. This device shows a maximum external quantum efficiency of 9.8%. The corresponding power (current) efficiency is 18.1 lm/W (25.9 cd/A), which is much higher than that of a similarly structured device using FIrpic dopant (7.5%, 8.9 lm/W) [19]. The good performance of the device should be attributed to the higher PL quantum yield of F_3Irpic than FIrpic. Current–brightness–voltage characteristics of this F_3Irpic (4%):mCP device are shown in Fig. 3. It has a turn-on voltage (at a brightness of 1 cd/m^2) of 4.3 V and delivers a maximum brightness of 15 000 cd/m^2 at a voltage of 13.5 V and a current density of 215 mA/cm^2. A schematic energy level diagram for the device is shown in the inset of Fig. 3. The HOMO level of F_3Irpic determined with UPS is 6.1 eV. The LUMO level as determined from the HOMO level and the optical absorption edge is 3.4 eV. As shown in the energy level diagram, the HOMO level of F_3Irpic (6.1 eV) is lower than that of mCP (5.9 eV). This suggests that the F_3Irpic might not be effective trap for the holes and thus decreases the chance of forming exciton in the phosphorescent emitter.

To address this problem, the mCP host was replaced by UGH2 which has a much larger energy gap. Chemical structure and the corresponding energy level diagram for the device are shown in Fig. 4. It can be noted that the HOMO and LUMO levels of the Ir complex are entirely bracketed by those of the UGH2 host. This suggests that the Ir molecules would be effective traps for both electrons and holes injected into the UGH2 layer. This is clear beneficial for exciton formation at the Ir molecules. It was found that the optimized device has a configuration of ITO/NPB (40 nm)/mCP (10 nm)/8% F_3Irpic:UGH2 (20 nm)/BAlq (40 nm)/LiF (0.5 nm)/Al (80 nm). The mCP layer is used as an interim layer to facilitate hole injection from the HTL into EML to overcome the large energy difference (1.8 eV) between NPB and UGH2.

Current efficiency–brightness–power efficiency characteristics of F_3Irpic:UGH2 device are shown in Fig. 5. This device shows blue emission (see inset of Fig. 5) with a peak centered at 482 nm and a sub-peak at 512 nm. The F_3Irpic:UGH2 device gives a maximum external quantum efficiency of 14.3%. The maximum power (current) efficiency of the device is 33.7 lm/W (37.6 cd/A), which is much higher than that of the F_3Irpic:mCP device. The high efficiency of the device is considered to arise from the following three aspects. Firstly, the high PL quantum yield of the F_3Irpic contributes to the high device efficiency; secondly, the good device structure can facilitate the injection and transport of electrons and holes; thirdly, the energy levels of F_3Irpic are entirely bracketed by UGH2, which induced the effective traps of the dopant for both electrons and holes injected into the host. Similar to other phosphorescent OLEDs, efficiency of the device decreases as the brightness increases. However, it is interesting to note that even at a brightness of 1000 cd/m^2, the efficiency of the device is still higher than 20 cd/A (9 lm/W). As far as we know, performance of this device is among the best values reported for blue OLEDs.

In summary, highly efficient blue phosphorescent OLEDs have been achieved by using a new emitter iridium(III)

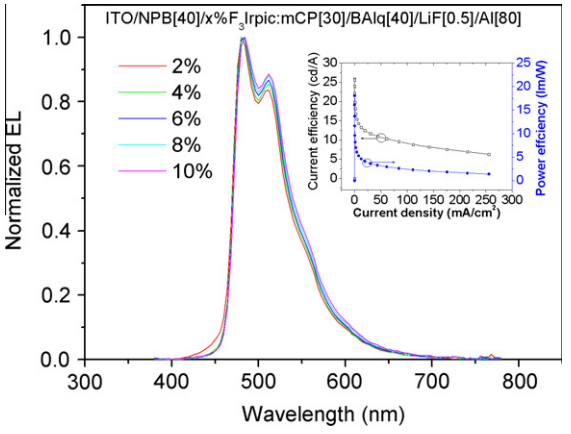

Fig. 2. EL spectra of the device at different doping concentrations, inset is the current efficiency–current density–power efficiency characteristics.

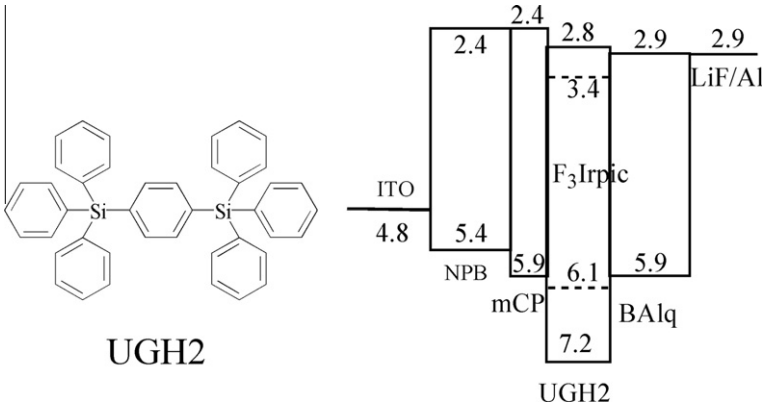

Fig. 4. The chemical structure of UGH2; the energy level diagram of device II.

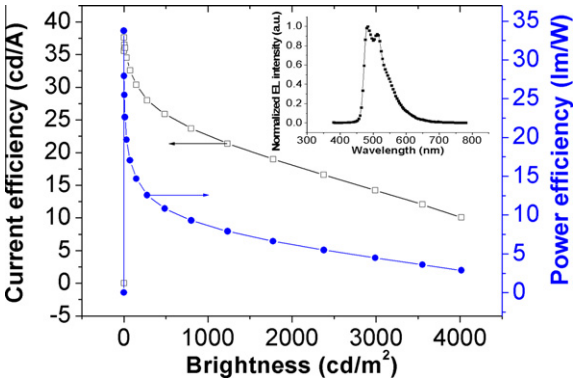

Fig. 5. The current efficiency–brightness–power efficiency characteristics of device II, the inset is the EL spectrum.

bis[(3,4,5-trifluorophenyl)-pyridinato-N,$C^{2'}$] picolinate (F_3Irpic). For a mCP:4%F_3Irpic device, blue emission with a maximum power efficiency of 18.1 lm/W has been realized, which is much higher than that of similarly structured FIrpic based device. The emission peak is located at 480 nm with a subpeak at 511 nm. By using an optimized device structure with a host of UGH2, performance of the device is substantially increased to give a maximum power efficiency up to 33.7 lm/W and an almost unchanged EL spectrum.

Acknowledgments

This work was supported by the Innovation and Technology Commission (Grant No. ITP/011/08NP) of Hong Kong SAR. S.L. Tao would like to thank financial supports from the National Natural Science Foundation of China (NSFC Grant 21002011), "the Fundamental Research Funds for the Central Universities", "the Research Fund for the Doctoral Program of Higher Education of China (20100185120015)" and Jiangsu Key Laboratory for Carbon-Based Functional Materials and Devices, Soochow University, Suzhou, P.R. China.

References

[1] J. Kido, M. Kimura, K. Nagai, Science 267 (1995) 1332.
[2] S. Reineke, F. Lindner, G. Schwartz, N. Seidler, K. Leo, Nature 459 (2009) 234.
[3] R.S. Sun, S.R. Forrest, Appl. Phys. Lett. 91 (2007) 263503.
[4] Y.R. Sun, N.C. Giebink, H. Kanno, B.W. Ma, M.E. Thompson, S.R. Forrest, Nature 440 (2006) 908.
[5] M.A. Baldo, D.F. O'Brien, Y. You, A. Shoustikov, S. Sibely, M.E. Thompson, S.R. Forrest, Nature 395 (1998) 151.
[6] C. Adachi, M.A. Baldo, M.E. Thompson, S.R. Forrest, J. Appl. Phys. 90 (2001) 5048.
[7] Y.C. Chiu, J.Y. Hung, Y. Chi, C.C. Chen, C.H. Chang, C.C. Wu, Y.M. Cheng, Y.C. Yu, G.H. Lee, P.T. Chou, Adv. Mater. 21 (2009) 2221.
[8] S.C. Lo, R.E. Harding, C.P. Shipley, S.G. Stevenson, P.L. Burn, I.D.W. Samuel, J. Am. Chem. Soc. 131 (2009) 16681.
[9] C.F. Chang, Y.M. Cheng, Y. Chi, Y.C. Chiu, C.C. Lin, G.H. Lee, P.T. Chou, C.C. Chen, C.H. Chang, C.C. Wu, Angew. Chem. Int. Ed. 47 (2008) 4542.
[10] N. Chopra, J. Lee, Y. Zheng, S.H. Eom, J. Xue, F. So, Appl. Phys. Lett. 93 (2008) 143307.
[11] H. Sasabe, J. Takamatsu, T. Motoyama, S. Watanabe, J. Kido, Adv. Mater. 22 (2010) 5003.
[12] S.O. Jeon, S.E. Jang, H.S. Son, J.Y. Lee, Adv. Mater. 23 (2011) 1436.
[13] S.O. Jeon, K.S. Yook, C.W. Joo, J.Y. Lee, Adv. Mater. 22 (2010) 1872.
[14] N. Chopra, J.S. Swensen, E. Polikarpov, L. Cosimbescu, F. So, A.B. Padmaperuma, Appl. Phys. Lett. 97 (2010) 033304.
[15] L. Xiao, S.J. Su, Y. Agata, H. Lan, J. Kido, Adv. Mater. 21 (2009) 1271.
[16] Y.Y. Lyu, J. Kwak, O. Kwon, S.H. Lee, D. Kim, C. Lee, K. Char, Adv. Mater. 20 (2008) 2720.
[17] P.I. Shih, C.H. Chien, C.Y. Chuang, C.F. Shu, C.H. Yang, J.H. Chen, Y. Chi, J. Mater. Chem. 17 (2007) 1692.
[18] S. Tokitoa, T. Iijima, Y. Suzuri, H. Kita, T. Tsuzuki, F. Sato, Appl. Phys. Lett. 83 (2003) 569.
[19] R.J. Holmes, S.R. Forresta, Y.J. Tung, R.C. Kwong, J.J. Brown, S. Garon, M.E. Thompson, Appl. Phys. Lett. 82 (2003) 2422.
[20] F. Babudri, G.M. Farinola, F. Naso, R. Ragnia, J. Mater. Chem. 12 (2007) 1003.

efficiency remain unsatisfied for high color gamut full color display or high color rendition illumination applications.

Au, one of the metals with low absorption, low reflection and high transmission, would be potentially an ideal cathode material for top-emitting WOLEDs [17]. However, few works have been reported on using Au as a low reflection and semitransparent cathode for top-emitting WOLEDs [18], mainly due to the high work function (~5.1 eV) of Au, rendering it unsuitable as a cathode material for injecting electrons. In this work, we demonstrate that with a 5 nm Yb (Ytterbium) modification layer, Au can be an excellent cathode for injecting electrons. The Au based tri-cathode-layer Yb (5 nm)/Au (15 nm)/MoO_3 (35 nm) exhibits an average reflection of 9.8% over the visible wavelength, significantly lower than 24% for the Ag based tri-cathode-layer Yb (5 nm)/Ag (15 nm)/MoO_3 (30 nm). By employing the low reflection Au based tri-cathode-layer, the microcavity effects have been weakened largely. Thus, high efficiency and high color rendition top-emitting WOLEDs with evenly separated R, G and B emission peaks have been achieved. At a high luminance of 1000 cd/m^2, the top-emitting WOLEDs exhibit an efficiency of 23 cd/A, 10.5 lm/W, a 1931 Commission International de L'Eclairage (CIE) coordinate of (0.36, 0.42) and a high color rendering index (CRI) of 85. The top-emitting WOLEDs demonstrated here would be an ideal candidate for high resolution full color active-matrix display or indoor lighting applications.

2. Experimental

Bis(3,5-difluoro-2-(2-pyridyl)phenyl)-(2-carboxypyridyl) iridium(III), FIrPic, and bis(2-benzo[*b*]thiophen-2-yl-pyridine)(acetylacetonate)iridium(III), Ir(btp)$_2$(acac) with main emission peak at 475 and 612 nm were selected as sky blue and saturated red emitter, respectively. In order to generate the white spectra with three evenly separated R, G and B emission peaks, a new yellowish-green emitter bis(5-(trifluoromethyl)-2-*p*-tolylpyridine) (acetylacetonate)iridium(III) **1** with emission peak at 544 nm was specially designed and employed in this study [1]. The top-emitting WOLEDs were fabricated in a multi-source vacuum chamber at a base pressure of around 5×10^{-7} Torr with structure glass/Al (100 nm)/MoO_3 (8 nm)/NPB (20, 30, 40 nm)/6% Ir(btp)$_2$(acac):CDBP (10 nm)/4% **1**:CDBP (3 nm)/12% FIrPic:CDBP (5 nm)/TAZ (40 nm)/Yb 5 nm/Au (or Ag) (15 nm)/MoO_3 (35, 30 nm), (NPB: *N*,*N*′-bis(naphthalen-1-yl)-*N*,*N*′-bis(phenyl)-benzidine; CDBP: 4,4′-bis(carbazol-9-yl)-2,2′-dimethylbiphenyl; TAZ: 3-(4-biphenyl)-4-phenyl-5-*tert*-butylphenyl-1,2,4-triazole), where Al, MoO_3 and NPB function as reflective anode, hole-injection and hole-transporting layer, respectively, CDBP works as host, TAZ serves as exciton-blocking and electron-transporting layer, Yb/Au (or Ag)/MoO_3 acts as semitransparent tri-cathode-layer. The energy level and molecular structure of the emitters are shown in Fig. 1. The transmission and reflection spectra of the tri-cathode-layer were characterized by UV–Vis spectrophotometer. The current density–voltage–luminance characteristics of the devices were measured by the HP4145B semiconductor parameter analyzer and a calibrated UDT PIN-25D silicon photodiode. The electroluminescent (EL) spectra were obtained with the PR650 spectrophotometer.

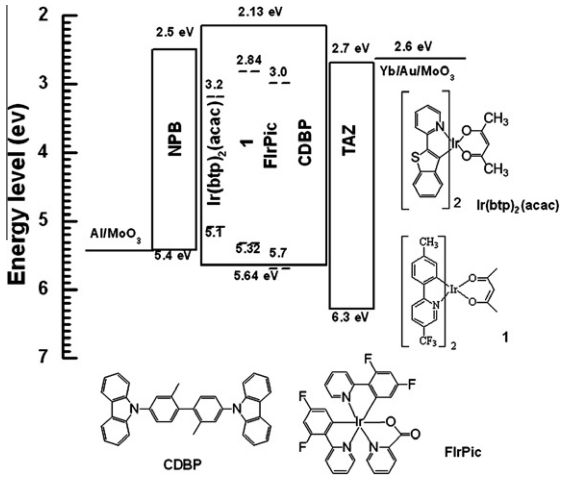

Fig. 1. Energy level and molecular structure of the materials employed in this study. The values of energy level are taken from literature.

3. Results and discussion

To alleviate the microcavity effects of the top-emitting WOLEDs, important parameters which affect the interference are analyzed first. The top-emitting OLEDs with the emission layers sandwiched between two reflective metal electrodes can be treated as a Fabry–Perot cavity optically [8,9,13,19–22]. Light emitting from the top semitransparent electrode and light reflected by the bottom reflective electrode interfere with each other. The emission intensity at λ is enhanced when the cavity effective length L_{eff} satisfies the below equation [8,20]:

$$L_{eff} = \frac{(\phi_{tm} + \phi_{bm})\lambda}{4\pi} + \sum_i n_i d_i = m\frac{\lambda}{2}\ (m:\ \text{integer}), \qquad (1)$$

where ϕ_{tm} and ϕ_{bm} are the phase shift of the light reflected by the top and bottom electrode, respectively; n_i and d_i are the refractive index and thickness of the organic layers, respectively. The cavity behaves like an optical filter which modulates the free space emission with the modulation spectra given by [8,13,19–21]:

$$I_{cav}(\lambda) \propto \frac{1 + R_1 + 2\sqrt{R_1}\cos\left(\frac{4\pi L_1}{\lambda} + \phi_{bm}\right)}{1 + R_1R_2 - 2\sqrt{R_1R_2}\cos\left(\frac{4\pi L}{\lambda} + \phi_{bm} + \phi_{tm}\right)} T_2, \qquad (2)$$

where L_1 is the optical distance between the exciton main recombination zone and the bottom reflective electrode; L is optical length of the organic layers; R_1 and R_2 are the reflectance of the bottom and top electrode, respectively; T_2 is the transmittance of the top electrode. The full width at half maximum (FWHM) of the $I_{cav}(\lambda)$ can be estimated by [8,9,13]:

$$\text{FWHM} = \frac{\lambda^2}{2L_{eff}} \times \frac{1 - \sqrt{R_1R_2}}{\pi\sqrt[4]{R_1R_2}}, \qquad (3)$$

From Eq. (3), one can see that larger reflectance of either electrode results in smaller FWHM, implying a stronger interference presented in the cavity. In order to obtain

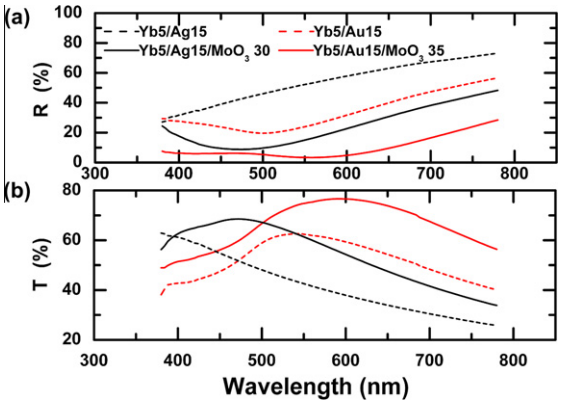

Fig. 2. Reflection (a) and transmission (b) spectra of the Ag and Au based semitransparent cathodes as measured by UV–VIS spectrometer.

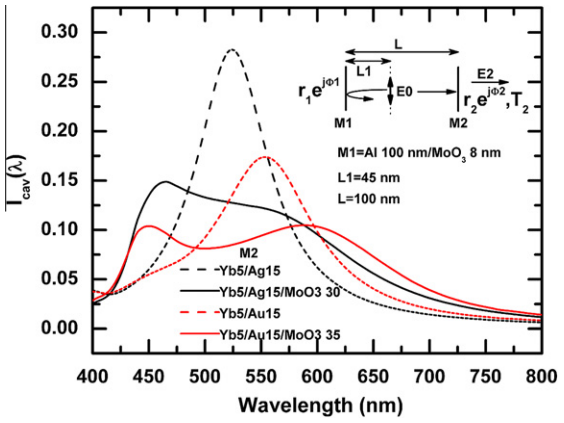

Fig. 3. Simulated cavity modulation spectra. Inset shows the physical model used in the simulation. The reflectance, phase shift and transmistance of the bottom anode $M1$ = Al 100 nm/MoO_3 8 nm and top cathode $M2$ are calculated by the transfer matrix method. The refractive indexes of the materials employed are taken from literature.

broadband emission spectra, one has to maximize the FWHM by reducing the reflection of either electrode. It is more desirable to reduce the reflection of the top electrode, since reducing the reflection of the bottom electrode, though effective, are at a cost of decreasing the light coupling efficiency.

Among the metal materials, thin film of Ag and Au are two mostly selected semitransparent top electrode materials due to their intrinsically low absorption and high transmission. Fig. 2 compares the measured reflection and transmission spectra of the Ag and Au based semitransparent top cathodes. It can be seen that the Au based top cathodes exhibit a substantially lower reflection over the visible wavelength than that of the Ag. Also, at yellow to red color, the transmittance of the Au based top cathodes is higher than that of the Ag based top cathodes. For example, the average reflectance (transmittance) of Yb (5 nm)/Au (15 nm) is 34% (52%), significantly lower (higher) than 54% (42%) for Yb (5 nm)/Ag (15 nm). By capping the semitransparent top cathodes with an index matching layer with optimized thickness, the reflectance (transmittance) of the Au and Ag based top cathodes are further reduced (enhanced). For example, the average reflectance (transmittance) has been remarkably reduced (enhanced) from 34% (52%) for the Au top cathodes without index matching layer to 9.8% (66%) for the Au top cathodes with 35 nm MoO_3 index matching layer. The low reflection of Yb (5 nm)/Au (15 nm)/MoO_3 (35 nm) suggests a good possibility of achieving a weakened interference cavity, and hence top-emitting WOLEDs with broadband emission spectra may be expected by employing this low reflection top cathode.

To evaluate the interference effects of the cavity with the low reflection top cathodes, cavity modulation spectra $I_{cav}(\lambda)$ are simulated. Although Eq. (2) provides a simple calculation formulation for $I_{cav}(\lambda)$, important parameters like dipole orientation, ***s***, ***p*** polarization, light emitting angles, exciton recombination zone and diffusing length are omitted. It is thus inaccurate to use Eq. (2) to describe the optical characteristics of the cavity. A rigorous electromagnetic modeling is adopted to accurately simulate the modulation spectra of the cavity [22]. Fig. 3 inset shows the physical model used in the simulation. Organic layers with thickness of L = 100 nm are sandwiched between the bottom reflective anode $M1$ = Al (100 nm)/MoO_3 (8 nm) and top semitransparent cathode $M2$. The distance between the exciton main recombination zone and the bottom anode is assumed to be $L1$ = 45 nm. The exciton diffusing length is assumed to be 15 nm. The reflectance, transmittance and phase shift of $M1$, $M2$ are calculated by the transfer matrix method by considering ***s***, ***p*** polarization. The modulation spectra of the cavity with different $M2$ are shown in Fig. 3. It can be clearly seen that with lower reflection $M2$, the modulation spectra exhibit wider FWHM. For example, with $M2$ = Yb (5 nm)/Ag (15 nm), the spectra exhibit a clear interference peak at 525 nm and a FWHM of only 78 nm; thus it is unlikely to obtain broadband white emission spectra in such cavity due to strong modulation of the cavity at green color. While by replacing Ag with low reflection Au, the intensity of the interference peak is suppressed and the FWHM is broadened to 110 nm. Further capping an optimized index matching layer reduces the reflection of $M2$ and broadens the FWHM accordingly. For example, the FWHM is broadened to 194 nm and 256 nm for $M2$ = Yb (5 nm)/Ag (15 nm)/MoO_3 (30 nm) and $M2$ = Yb (5 nm)/Au (15 nm)/MoO_3 (35 nm), respectively. Due to alleviation of the interference, the cavity with $M2$ = Yb (5 nm)/Au (15 nm)/MoO_3 (35 nm) exhibits a rather flat modulation intensity from 440 to 600 nm, implying a good possibility of obtaining broadband white emission spectra with equal R, G and B intensity in such cavity.

To verify this assertion, top-emitting WOLEDs with different top cathodes were fabricated. Fig. 4 shows the EL spectra of the devices with different top cathodes. For devices with Yb (5 nm)/Ag (15 nm) cathode, due to strong interference at λ = 525 nm as predicted by the simulated cavity modulation spectra, the green emission is enhanced significantly while the blue and red emission are suppressed, resulting in unbalanced white spectra as shown in Fig. 4a inset. For the devices with Ag and Au based tri-cathode-layer, the cavity length was tuned deliberately

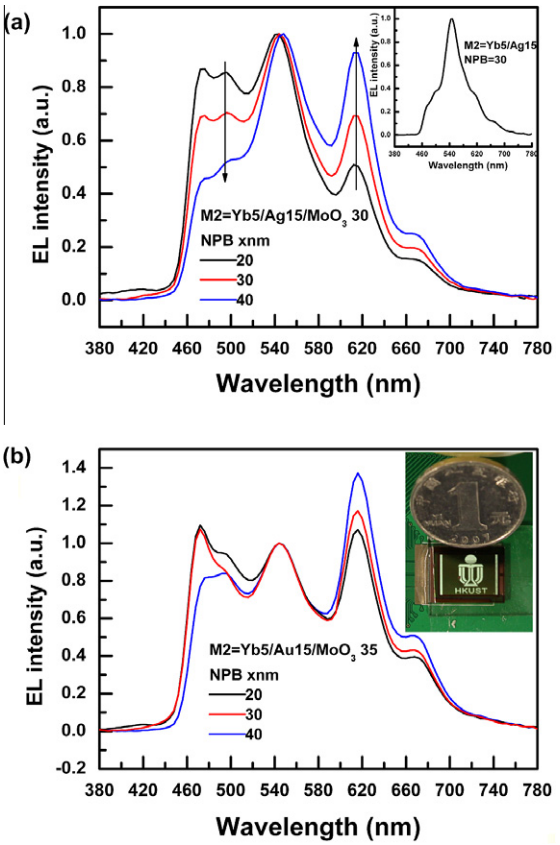

Fig. 4. (a) EL spectra of the devices with Ag based tri-cathode-layer. Inset shows the EL spectra of the devices with Yb (5 nm)/Ag (15 nm) top cathode. (b) EL spectra of the devices with Au based tri-cathode-layer. Inset shows a photo of the Si based SVGA+ microdispaly developed in this study. All devices were driven at 8 V for measuring the EL spectra.

by changing the thickness of NPB to further compare the interference effects of the cavity with different top cathodes. As shown in Fig. 4a, for devices with Ag based tri-cathode-layer, as NPB thickness increases, the blue emission decreases quickly while the red emission enhances rapidly, which may be attributable to the interference effects or shifting of the recombination zone. Also, the spectra exhibit slightly red-shift as the cavity length increases, a typical phenomenon in interference cavity. However, for the devices with Au based tri-cathode-layer, the white spectra only exhibit a slighted change as the increased of cavity length, which may be mainly caused by the shifting of the recombination zone. Noted that, both devices have the same emission and injection layers, thus the exciton recombination zone should also be identical. The severe change and red shifting white spectra as the increased of cavity length of the devices with Ag based tri-cathode layer are therefore most likely caused by interference effects; hence to obtain balanced white emission, one should carefully tune the thickness of the cavity length. While the relatively stable white spectra as the increased of cavity length of the devices with Au based tri-cathode-layer implies a much weakened interference effect; hence broadband white spectra with evenly separated R, G, B peaks and equal intensity are much easier to obtain, as shown in Fig. 4b. At NPB = 30 nm, the white spectra exhibit a CIE coordinate of (0.36, 0.42) and a high CRI of 85, rendering such top-emitting WOLEDs to be ideal candidate for display or lighting applications. We have successfully applied such top-emitting WOLEDs in the Si based microdisplay with SVGA+ resolution, as shown in Fig. 4b inset. It is noted that the emission color of the demonstrated top-emitting WOLEDs is not pure white and the CIE coordinate is far from (0.33, 0.33). To remedy this deficiency, deep fluorescent blue emitter like 4,4′-bis(9-ethyl-3-carbazovinylene)-1,1′-biphenyl (BcZVBi) may be employed to replace the sky blue emitter FIrPic [1].

The viewing characteristics of the white spectra are further examined. As shown in Fig. 5a, for the devices with Ag based tri-cathode-layer, the red emission decreases while the blue emission increases as the increased of viewing angle, mainly due to the reduction of cavity length viewed from an oblique angle. While the red emission remains unchanged regardless of the change of viewing angle for the devices with Au tri-cathode-layer as shown in Fig. 5b, again confirms a neglectable interference effect. However, the blue emission decreases as the increased of viewing angle, which is attributable to the strong absorption of the Au at the blue color region. At oblique angle, light see a thicker Au layer than that of their cousins at normal angle, thus leading to lower blue emission intensity at oblique angle. Fig. 5c and d show the EL spectra under different driving voltages. At high voltage, the exciton recombination zone shifts towards the green/red emission layer, thus one observes a decreasing blue emission and an increased red emission. The CIE coordinates changing from (0.34, 0.40) at 6 V to (0.36, 0.42) at 10 V for the devices with Au based tri-cathode layer.

Fig. 6 compares the key characteristics of the top-emitting WOLEDs with the Ag and the Au tri-cathode-layer. Both devices show similar current density–voltage–luminance and efficiency–luminance characteristics due to their identical structures; for example, both devices turn on at 3.8 V for 1 cd/m^2 and at ~7 V for 1000 cd/m^2, indicating that with the modification of Yb electron injection layer, Au works excellently as a cathode [17,23] despite its high work function. The devices with the Au based tri-cathode-layer exhibit a slightly higher efficiency than that of the devices with the Ag based tri-cathode-layer, which may be mainly due to the higher transmission of the Au based tri-cathode-layer than that of the Ag based tri-cathode layer [17]. For example, at a typical application luminance level of 1000 cd/m^2, the devices with the Au tri-cathode-layer demonstrate an efficiency of 23 cd/A and 10.5 lm/W, higher than 21 cd/A and 9.1 lm/W for the devices with the Ag based tri-cathode-layer. Further optimization, for example, electrical doping the charge transporting layer [24], employing new emitters/host with high carrier mobility and efficiency, applying out-coupling techniques [25,26], can be employed to boost the device performance.

4. Summary

In conclusion, the interference effects of the microcavity can be greatly alleviated by reducing the reflection of the

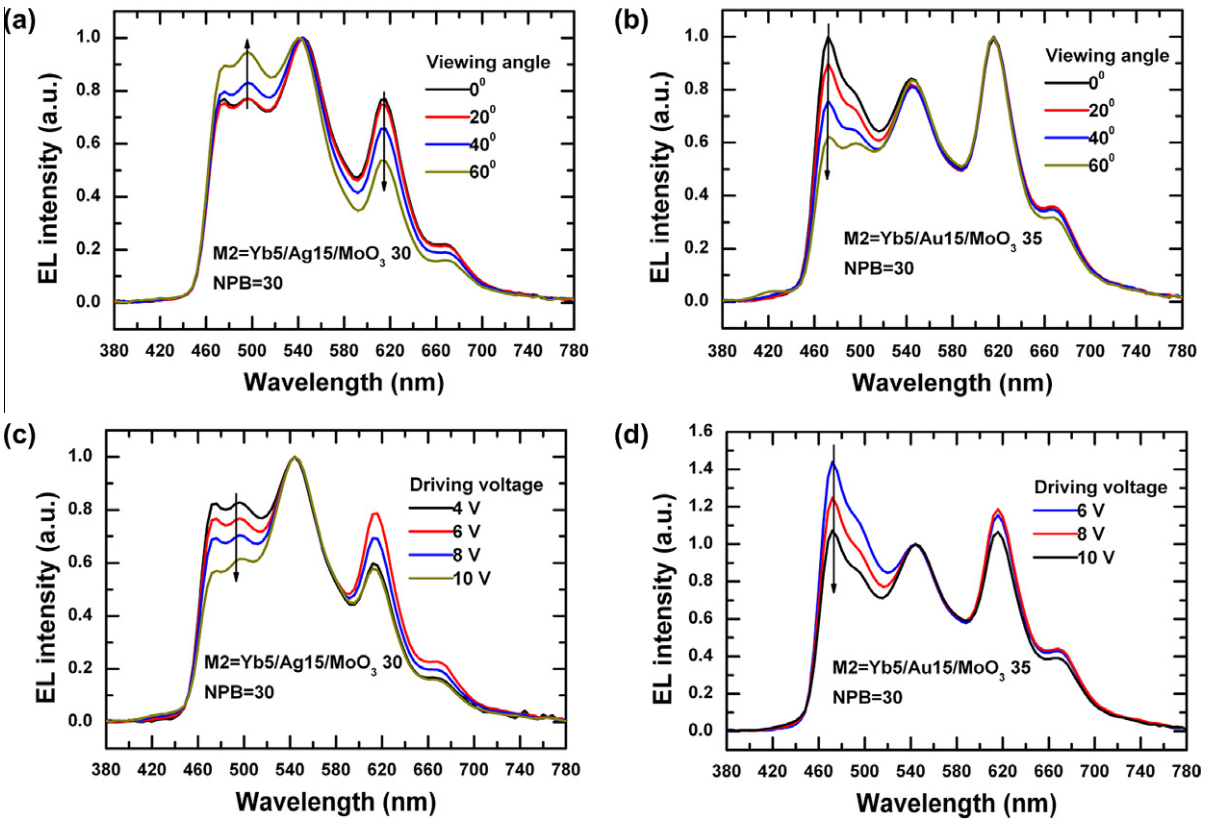

Fig. 5. (a) EL spectra of the devices with Ag based (a) and Au based (b) tri-cathode-layer at different viewing angle. EL spectra of the devices with Ag based (c) and Au based (d) tri-cathode-layer at different driving voltage.

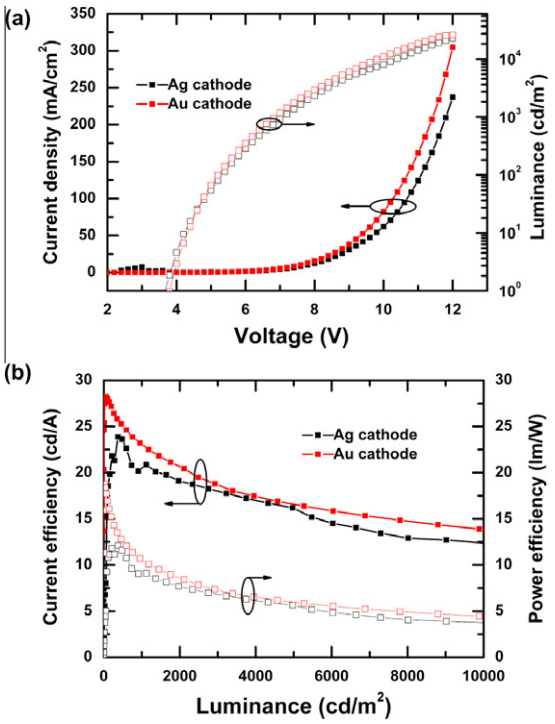

Fig. 6. Current density–voltage–luminance (a) and efficiency–luminance (b) characteristics of the devices with Ag and Au based tri-cathode-layer.

top cathode. Au, modified by a 5 nm Yb electron injection layer, can not only be an excellent cathode for injecting electrons, but also exhibits lower reflection and higher transmission than that of the mostly used Ag top cathode. By employing the low reflection Yb (5 nm)/Au (15 nm)/MoO_3 (35 nm) cathode, top-emitting WOLEDs with evenly separated R, G and B emission peaks have been demonstrated. At a luminance of 1000 cd/m^2, the top-emitting WOLEDs exhibit a CIE coordinate of (0.36, 0.42), a high CRI of 85 and an efficiency of 23 cd/A, 10.5 lm/W. As well, the spectra of the top-emitting WOLEDs demonstrate a very weak angle dependence due to the neglectable interference effects. The top-emitting WOLEDs demonstrated here, which have been successfully applied in the Si based microdisplay, would be an ideal candidate for high resolution active-matrix display or indoor lighting applications.

Acknowledgments

The authors thank Prof. Wai-Yeung Wong's group for providing the green-yellowish emitter **1**, and Mr. Pengfei Sun for driving the microdisplay panel. This work was supported by the Hong Kong Government Research Grants Council Grant Number 614410 and AOE/P0308PG2.

References

[1] S. Chen, G. Tan, W.-Y. Wong, H.-S. Kwok, White organic light-emitting diodes with evenly separated red, green and blue colors for

efficiency/color rendition trade-off optimization, Adv. Funct. Mater. doi:10.1002/adfm.201100895, 2011.
[2] S. Chen, H.-S. Kwok, Top-emitting white organic light-emitting diodes with a color conversion cap layer, Org. Electron. 12 (2011) 677–681.
[3] <http://www.emagin.com/oled-microdisplays/>.
[4] J.-J. Lih, C.-I. Chao, C.-C. Lee, Novel pixel design for high-resolution AMOLED displays with a shadow mask, J. Soc. Inf. Display 15 (2007) 3–7.
[5] C.-H. Chang, H.-C. Cheng, Y.-J. Lu, K.-C. Tien, H.-W. Lin, C.-L. Lin, C.-J. Yang, C.-C. Wu, Enhancing color gamut of white OLED displays by using microcavity green pixels, Org. Electron. 11 (2010) 247–254.
[6] T. Ishibashi, J. Yamada, T. Hirano, Y. Iwase, Y. Sato, R. Nakagawa, M. Sekiya, T. Sasaoka, T. Urabe, Active matrix organic light-emitting diode display based on "super top emission" technology, Jpn. J. Appl. Phys. 45 (2006) 4392–4395.
[7] S. Kim, S. Lee, M. Kim, J. Song, E. Hwang, S. Tamura, S. Kang, H. Kim, C. Kim, J. Lee, J. Kim, S. Cho, J. Cho, M.C. Suh, H. Kim, A 3.0-in. 308-ppi WVGA AMOLED with a top-emission white OLED and color filter, J. Soc. Inf. Display 17 (2009) 145–149.
[8] J. Cao, X. Liu, M.A. Khan, W. Zhu, X. Jiang, Z. Zhang, S. Xu, RGB tricolor produced by white-based top-emitting organic light-emitting diodes with microcavity structure, Curr. Appl. Phys. 7 (2007) 300–304.
[9] S.-F. Hsu, C.-C. Lee, S.-W. Hwang, C.-H. Chen, Highly efficient top-emitting white organic electroluminescent devices, Appl. Phys. Lett. 86 (2005) 253508.
[10] M. Mazzeo, F.D. Sala, F. Mariano, G. Melcarne, S. D'Agostino, Y. Duan, R. Cingolani, G. Gigli, Shapping white light through electroluminescent fully organic coupled microcavities, Adv. Mater. 22 (2010) 4696–4700.
[11] R.S. Cok, J.D. Shore, Microcavity white-emitting OLED devices, J. Soc. Inf. Display 17 (2009) 617–627.
[12] P. Freitag, S. Reineke, S. Olthof, M. Furno, B. Lüssem, K. Leo, White top-emitting organic light-emitting diodes with forward directed emission and high color quality, Org. Electron. 11 (2010) 1676–1682.
[13] M. Thomschke, R. Nitsche, M. Furno, K. Leo, Optimized efficiency and angular emission characteristics of white top-emitting organic electroluminescent diodes, Appl. Phys. Lett. 94 (2009) 083303.
[14] H. Kannp, Y. Sun, S.R. Forrest, High-efficiency top-emissive white-light-emitting organic electroluminescent devices, Appl. Phys. Lett. 86 (2005) 263502.
[15] M.-T. Lee, M.-R. Tseng, Efficient, long-life and lambertian source of top-emitting white OLEDs using low-reflectivity molybdenum anode and co-doping technology, Curr. Appl. Phys. 8 (2008) 616–619.
[16] G. Xie, Z. Zhang, Q. Xue, S. Zhang, L. Zhao, Y. Luo, P. Chen, B. Quan, Y. Zhao, S. Liu, Highly efficient top-emitting white organic light-emitting diodes with improved contrast and reduced angular dependence for active matrix displays, Org. Electron. 11 (2010) 2055–2059.
[17] G.Z. Ran, G.L. Ma, Y.H. Xu, L. Dai, G.G. Qin, Light extraction efficiency of a top-emission organic light-emitting diode with an Yb/Au double-layer cathode and an opaque Si anode, Appl. Optics 45 (2006) 5871–5876.
[18] X. Zhu, J. Sun, X. Yu, M. Wong, H.-S. Kwok, High-performance top-emitting white organic light-emitting devices, Jpn. J. Appl. Phys. 46 (2007) 4054–4058.
[19] T. Shiga, H. Fujikawa, Y. Taga, Design of multiwavelength resonant cavities for white organic light-emitting diodes, J. Appl. Phys. 93 (2003) 19–22.
[20] S. Han, C. Huang, Z.-H. Lu, Color tunable metal-cavity organic light-emitting diodes with fullerene layer, J. Appl. Phys. 97 (2005) 093102.
[21] C.-L. Lin, H.-W. Lin, C.-C. Wu, Examining microcavity organic light-emitting devices having two metal mirrors, Appl. Phys. Lett. 87 (2005) 021101.
[22] H. Benisty, H.D. Neve, C. Weisbuch, Impact of planar microcavity effects on light extraction – part I: basic concepts and analytical trends, IEEE J. Quantum Electron. 34 (1998) 1612–1631.
[23] S.L. Lai, M.Y. Chan, M.K. Fung, C.S. Lee, L.S. Hung, S.T. Lee, Applications of Ytterbium in organic light-emitting devices as high performance and transparent electrodes, Chem. Phys. Lett. 366 (2002) 128–133.
[24] K. Walzer, B. Maennig, M. Pfeiffer, K. Leo, Highly efficient organic devices based on electrically doped transport layers, Chem. Rev. 107 (2007) 1233–1271.
[25] C.-C. Liu, S.-H. Liu, K.-C. Tien, M.-H. Hsu, H.-W. Chang, C.-K. Chang, C.-J. Yang, C.-C. Wu, Microcavity top-emitting organic light-emitting devices integrated with diffuser for simultaneous enhancement of efficiencies and viewing characteristics, Appl. Phys. Lett. 94 (2009) 103302.
[26] Z. Wang, Z. Chen, L. Xiao, Q. Gong, Enhancement of top emission for organic light-emitting diode via scattering surface plasmons by nano-aggregated outcoupling layer, Org. Electron. 10 (2009) 341–345.

investigate the subcells directly within the tandem device and to monitor the impact of the top cell coating on the bottom cell performance.

2. Experimental

ITO-coated glass substrates were structured and plasma etched (Diener Pico) with Argon for 120 s at 30 W and a base pressure of 0.38 mbar. Afterwards, the substrates were spin-coated (Laurell CZ-650 series, 1000 rpm, 55 s) with a dichlorobenzene solution loaded with 48 mg/ml of PCBM ([6,6]-phenyl-C61-butyric acid methyl ester, Solenne) and P3HT (poly(3-hexylthiophene), Rieke) in a ratio of 0.9:1.0 and dried under ambient solvent atmosphere for 15 min leading to a 160 nm thick photo active layer. Thin layers of $LiCoO_2$ (~1 nm) and Al (4 nm) were then sputtered (von Ardenne Anlagentechnik GmbH CS 730 S) to define the work function of the bottom cell cathode and to provide additional protection from sputter damage by the following sputtered n-type ZnO:Al (doping: 2-wt.% Aluminum) layer (15–300 nm). The recombination layer was plasma etched using the same parameters like for ITO with the etching time reduced to 60 s. Next, a layer of PEDOT:PSS (Orgacon pH-neutral (pH = 7) from Agfa (abbr. PpH, 60 nm) or Baytron P AI 4083 from H.C. Starck diluted 1:1 with deionized water (abbr. P4083, 20 nm)) was spincoated with 5000 rpm for 55 s. For the top cell absorber, the same P3HT:PCBM blend was used as for the bottom cell. The 160 nm thick top cell layer was spincoated with 1000 rpm for 55 s and dried under ambient solvent atmosphere for 15 min. The cathode was evaporated (Balzers) in UHV ($<10^{-3}$ Pa) incorporating a 1.2 nm LiF interlayer and the 120 nm aluminum cathode.

Current voltage analysis was carried out with a WACOM solar simulator (class AAA, AM 1.5G) and a Keithley 238 current source measure unit.

3. Discussion

We fabricated tandem solar cells comprising different ZnO:Al recombination layer thicknesses. A P4083 p-type layer in the top cell was included in each case. The tandem cell open-circuit voltage was used as an indication of device performance. For a functional tandem device, the open-circuit voltage must be approximately twice the single-cell open-circuit voltage. Our result is presented in (Fig. 1, ♦). We can identify two regions: one stable area above 45 nm thickness which is the maximum value of the open-circuit voltage. A region with decreasing open-circuit voltage of linear tendency is found for decreasing recombination layer thickness. Since the P4083 is acidic and might damage the recombination layer, we replaced it with a PpH formulation [5] (▲). Interestingly, we observe the same behavior for the open-circuit voltage like before except that the linearily decreasing region is shifted approximately 20 nm to thinner recombination layers. This observation is consistent with SEM measurements which showed the loss of 10–20 nm ZnO:Al due to etching when P4083 was coated on top. Undiluted P4083 formulations resulted in increasing losses of ZnO:Al of up to 50 nm.

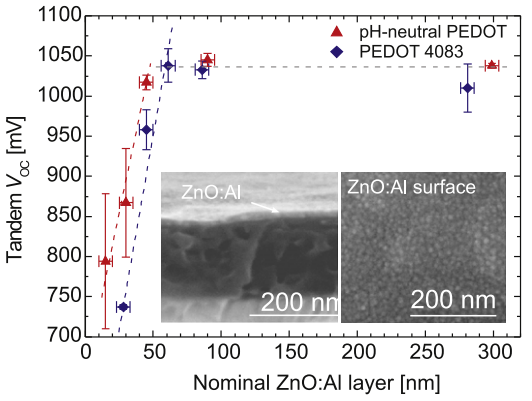

Fig. 1. Tandem cell open circuit voltages for various ZnO:Al recombination layer thicknesses which have to be at least 45 nm thick to achieve properly working devices. SEM cross section and surface image of a with 15 nm ZnO:Al coated bottom cell show a closed layer.

Hence we propose that more diluted P4083 formulations would suppress significant material losses of ZnO:Al and allow its use for even thinner recombination layers. This procedure would be advantageous since PpH is known to have an altered work function compared to P4083 [6] and may be less compatible to some materials energy levels.

The distinctive statistical spread in (Fig. 1) of the open circuit voltage for 15 nm and 30 nm tandem devices utilizing PpH can be attributed to a not absolutely homogeneous layer deposition of the sputter equipment. For deposition of ZAO we use a round sputter target and the reference layer thickness has been taken from the center position while the actual ZAO layer thickness decreases with increasing distance to the target center. For very thin layers slight changes in the ZAO layer thickness will result in a significant alteration of the open circuit voltage. Further, we also looked at the statistical spread of the fill factor as well as the short circuit current (Fig. 2). There, the relative error was in the same order of magnitude as for the open circuit voltage and diminished with increasing

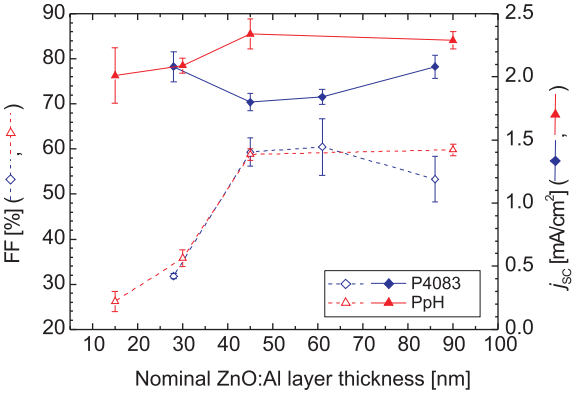

Fig. 2. Fill factor and short circuit current for different ZnO:Al layer thicknesses. For the FF we observe the same behavior as for the open circuit voltages while the short circuit current is only slightly dependent on the ZnO:Al layer thickness.

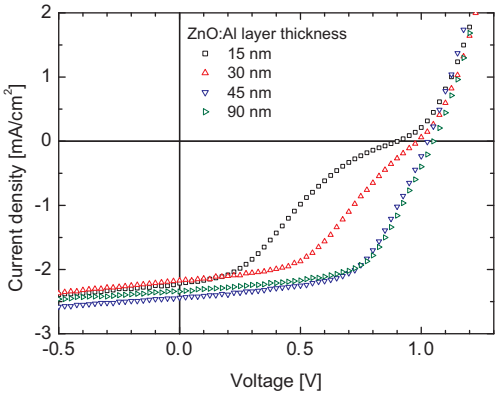

Fig. 3. Current–voltage characteristics for different ZnO:Al recombination layers coated with PpH. Functional devices are obtained for ZnO:Al layers around 45 nm.

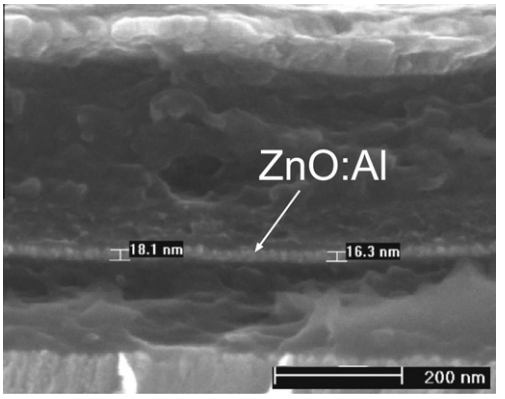

Fig. 4. SEM cross section of a tandem device comprising a nominal 15 nm ZnO:Al layer in combination with PpH.

layer thickness while the improvement of the fill factor can be mainly ascribed to the reduction of the S-shape behavior.

Tandem devices comprising a PpH layer are further investigated by evaluating the shape of the current voltage characteristics (Fig. 3). For ZnO:Al layers around 45 nm thickness we obtain functional tandem devices with a normal *IV* shape. Tandem cell *IV*s comprising thinner recombination layers result in S-shaped curves which are more pronounced for thinner layers. Here we would like to point out that even for the best obtained devices comprising 15 nm ZAO and 900 mV open circuit voltage the S-shape is still present. The S-shape only occurs in the fourth quadrant without affecting other regions. Since this effect is only observable for very thin layers, we first investigated the integrity of the ZnO:Al layer. SEM measurements (Fig. 1, bottom images) of the thinnest (15 nm) sputtered recombination layer show a closed surface layer confirmed by the top view and is also approved by Fig. 4 which shows a closed ZnO:Al layer after PpH coating in a completed tandem device. Further, SEM top view images of 45 nm and 90 nm ZnO:Al show increasing grain size for extended sputter time and layer thickness. According to Guillén and Herrero [19], smaller grain sizes will lead to reduced charge carrier densities and low mobilities which could result in charge accumulation and S-shape formation. These characteristics are consistent with our observation of increased tandem series resistance when the ZnO:Al layer thickness was decreased. Another possible mechanism is interface degradation leading to S-shape *IV* curves due to oxidation of the aluminum interlayer. Thin ZnO:Al layers might not be able to prevent sufficiently oxygen diffusion into the aluminum interlayer thus forming an insulating layer. Though the process leading to S-shape *IV* curves cannot be concluded definitively, both explanations result in low electron mobility and charge accumulation at the cathode side of the recombination layer and are modeling the S-shape.

By increasing its thickness to 300 nm, ZnO:Al is suitable as an intermediate electrode ($\sigma \approx 1100$ S/cm) for subcell characterization (Fig. 5). In this three-terminal structure it is also possible to monitor the bottom cell after each top cell coating step. For this purpose the bottom cell was annealed (135 °C for 10 s) after sputtering the middle

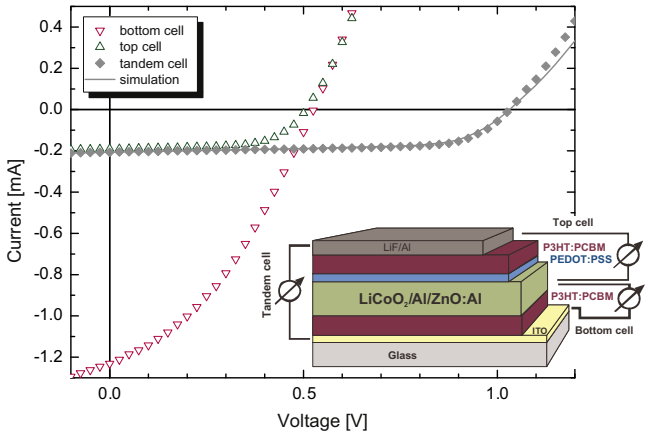

Fig. 5. *IV* characteristics of a complete tandem solar cell and its subcells. The subcells *IV*s can be used to simulated tandem *IV* by voltage summation at equal subcell currents and is in good agreement to the experimental curve. The deviation of the series resistance is due to the (double) utilization of the ZnO:Al as electrode leading to an increased resistance.

electrode to remove sputter damage [20–22]. Our result is presented in Fig. 6 and shows only slight deviations in the short-circuit current after each process step. We attribute the loss in current to degradation of the P3HT bottom cell caused by the long exposure time to ambient atmosphere during device fabrication of the top cell and subsequent device characterization. We conclude from these findings that the top cell coating process has no substantial impact on the bottom cell performance and also that the 300 nm ZnO:Al recombination layer acts as a protection layer.

In a parallel investigation, the impact of P4083 on ZnO nanoparticle layers was investigated and compared to the results from sputtered ZnO:Al layers. Measurements revealed that the ZnO is more susceptible to etching than ZnO:Al layers with an increased loss of material: approx. 50 nm even for diluted P4083. Taking the material loss into account, we were able to build working tandem devices comprising P4083 and a ZnO nano particle layer with device parameters that are comparable to devices utilizing PpH (Fig. 7). For these devices the bottom cell absorber thickness has been adjusted to 50 nm in order to improve

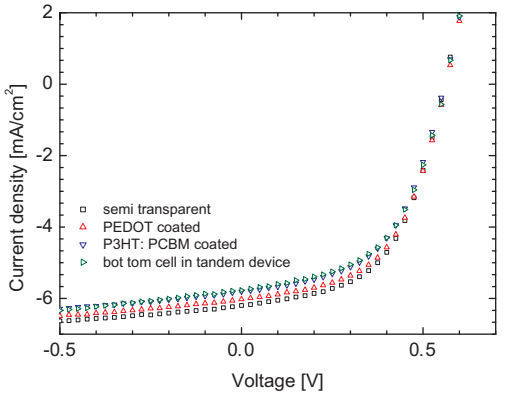

Fig. 6. Bottom cell measured with the ZnO:Al recombination layer as electrode. The measurement was carried out after each subsequent top cell coating step and shows no substantial impact. The deviation is attributed to the normal degradation of the non-encapsulated P3HT bottom cell.

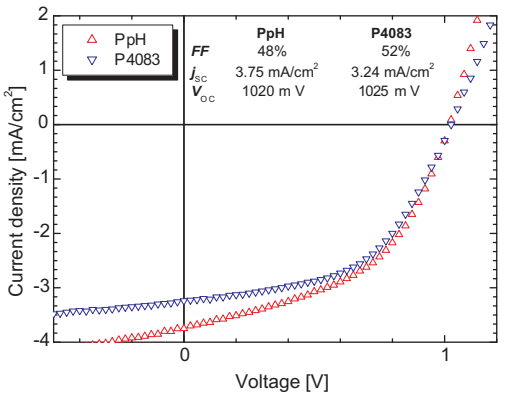

Fig. 7. *IV* characteristics of tandem cells comprising ZnO nano particles in the recombination layer in combination with PpH and P4083 which show comparable device parameters.

the overall current of the tandem device and a 1:2 vol. diluted PpH was used to get a 30 nm PEDOT:PSS layer like for ZnO:Al comprising tandem solar cells. The results show that tandem solar cells comprising ZnO nanoparticles instead of sputtered Zno:Al as recombination layer lead to similar results regarding the impact of PEDOT:PSS acidity. However, the long-term chemical stability of a ZnO/PEDOT:PSS or ZnO:Al/PEDOT:PSS junction might be affected and thus requires sufficiently effective encapsulation barrier against moisture to prevent interface degradation.

4. Conclusion

Sputtered ZnO:Al was used as a recombination layer and middle electrode in tandem solar cells with P3HT:PCBM absorber layers. Although P4083 is acidic and removes a thin layer of about 20 nm ZnO:Al, the choice of PEDOT:PSS formulations had no impact on the device performance. The removed layer can be compensated by increasing the initial ZnO:Al layer thickness accordingly. Moreover, we propose that ZnO:Al loss due to P4083 can be reduced by using more diluted formulations. The ZnO:Al was more resistant against etching than ZnO nanoparticles which were successfully used as recombination layer in combination with P4083. Properly working tandem devices required a ZnO:Al recombination layer of at least 45 nm thickness. Below this critical thickness, S-shape behavior in the *IV* curve was observed which we attribute to low electron mobility at the bottom cell recombination layer interface. In-device characterization of subcells enabled the investigation of subsequent top cell layer coating. No negative impact on the bottom cell performance was observed.

Acknowledgments

This work is funded by the DFG within the SPP 1355. We thank Dr. T. Magorian Friedlmeier for careful reading and corrections as well as Prof. U. Lemmer for inspiring discussions.

References

[1] W. Shockley, H.J. Queisser, Detailed balance limit of efficiency of p–n junction solar cells, J. Appl. Phys. 32 (1961) 510–519.
[2] G. Dennler, M.C. Scharber, T. Ameri, P. Denk, K. Forberich, C. Waldauf, C.J. Brabec, Design rules for donors in bulk-heterojunction tandem solar cells-towards 15% energy-conversion efficiency, Adv. Mater. 20 (2008) 579.
[3] J.Y. Kim, K. Lee, N.E. Coates, D. Moses, T.-Q. Nguyen, M. Dante, A.J. Heeger, Efficient tandem polymer solar cells fabricated by all-solution processing, Science 317 (2007) 222.
[4] D. Lee, W. Ki Bae, I. Park, D.Y. Yoon, S. Lee, C. Lee, Transparent electrode with ZnO nanoparticles in tandem organic solar cells, Sol. Energy Mater. Sol. Cells 95 (2011) 365–368.
[5] J. Gilot, M.M. Wienk, R.A.J. Janssen, Double and triple junction polymer solar cells processed from solution, Appl. Phys. Lett. 90 (2007) 143512.
[6] D.J.D. Moet, P. de Bruyn, P.W.M. Blom, High work function transparent middle electrode for organic tandem solar cells, Appl. Phys. Lett. 96 (2010) 153503–153504.
[7] J. Gilot, M.M. Wienk, R.A.J. Janssen, Optimizing polymer tandem solar cells, Adv. En. Mater. 22 (2010) E67–E71.
[8] A.G.F. Janssen, T. Riedl, S. Hamwi, H.-H. Johannes, W. Kowalsky, Highly efficient organic tandem solar cells using an improved connecting architecture, Appl. Phys. Lett. 91 (2007) 073519.

[9] D.W. Zhao, X.W. Sun, C.Y. Jiang, A.K.K. Kyaw, G.Q. Lo, D.L. Kwong, Efficient tandem organic solar cells with an Al/MoO_3 intermediate layer, Appl. Phys. Lett. 93 (2008) 083305.
[10] K. Kawano, N. Ito, T. Nishimori, J. Sakai, Open circuit voltage of stacked bulk heterojunction organic solar cells, Appl. Phys. Lett. 88 (2006) 073514.
[11] B. Joon Lee, H. Jung Kim, W.-i. Jeong, J.-J. Kim, A transparent conducting oxide as an efficient middle electrode for flexible organic tandem solar cells, Sol. Energy Mater. Sol. Cells 94 (2010) 542–546.
[12] J. Sakai, K. Kawano, T. Yamanari, T. Taima, Y. Yoshida, A. Fujii, M. Ozaki, Efficient organic photovoltaic tandem cells with novel transparent conductive oxide interlayer and poly(3-hexylthiophene): fullerene active layers, Sol. Energy Mater. Sol. Cells 94 (2010) 376–380.
[13] X. Guo, F. Liu, B. Meng, Z. Xie, L. Wang, Efficient tandem polymer photovoltaic cells using inorganic metal oxides as a transparent middle connection unit, Org. Electron. 11 (2010) 1230–1233.
[14] B.H. Yang, Q.L. Song, C.M. Li, Z.S. Lu, New architecture for accurate characterization of the behavior of individual sub-cells within a tandem organic solar cell, Energy Environ. Sci. 1 (2008) 389–394.
[15] X. Guo, F. Liu, W. Yue, Z. Xie, Y. Geng, L. Wang, Efficient tandem polymer photovoltaic cells with two subcells in parallel connection, Org. Electron. 10 (2009) 1174–1177.
[16] S. Sista, Z. Hong, M.-H. Park, Z. Xu, Y. Yang, High-efficiency polymer tandem solar cells with three-terminal structure, Adv. Mater. 22 (2010) E77–E80.
[17] A. Hadipour, B. de Boer, P.W.M. Blom, Solution-processed organic tandem solar cells with embedded optical spacers, J. Appl. Phys. 102 (2007) 074506.
[18] T. Minami, Transparent conducting oxide semiconductors for transparent electrodes, Semicond. Sci. Technol. 20 (2005) S35–S44.
[19] C. Guillén, J. Herrero, Optical, electrical and structural characteristics of Al:ZnO thin films with various thicknesses deposited by DC sputtering at room temperature and annealed in air or vacuum, Vacuum 84 (2010) 924–929.
[20] E. Ahlswede, J. Hanisch, M. Powalla, Influence of cathode sputter deposition on organic solar cells, Appl. Phys. Lett. 90 (2007) 063513.
[21] J. Hanisch, E. Ahlswede, M. Powalla, Contacts for semitransparent organic solar cells, Eur. Phys. J. Appl. Phys. 37 (2007) 261.
[22] J. Hanisch, E. Ahlswede, M. Powalla, All-sputtered contacts for organic solar cells, Thin Solid Films 516 (2008) 7241.

operation is <2 V [15]. There are many types of aromatic hydrocarbons other than picene, *i.e.*, one-dimensional (1D) and two-dimensional (2D) extended aromatic hydrocarbons. In 1D extended hydrocarbon molecules, there are two types of molecules, [*n*]acnene and [*n*]phenacene; [*n*]acene consists of a linear fusion of benzene rings, while [*n*]phenacene consists of a zigzag fusion of benzene rings; [11]phenacene has already been synthesized [16]. Very recently, we reported characteristics of FET with thin films of [7]phenacene, and with various solid gate dielectrics [17]. The p-channel operation at absolute threshold voltage $|V_{TH}|$ as low as 20 V was realized for [7]phenacene FET with Ta_2O_5 gate dielectric, and the stable FET operation exhibiting the μ as high as 0.75 $cm^2 V^{-1} s^{-1}$ was also recorded [17]. For the lower $|V_{TH}|$ operation, *i.e.*, higher density of carrier-injection, the ionic liquid gate dielectrics should be tried for the [7]phenacene.

In this letter, we have fabricated the [7]phenacene TFTs with two ionic liquids, [1-ethyl-3-methylimidazolium][bis(trifluoromethanesulfonyl)imide] (emim[TFSI]) and [1-butyl-3-methylimidazolium][hexafluorophosphate] (bmim[PF_6]); the molecular structure of [7] phenacene is shown in Fig. 1(a). The characteristics of [7]phenacene TFTs with ionic liquid gate dielectrics are investigated in order to establish the application of 1D extended hydrocarbons to low-voltage operated transistors and to clarify the hole-accumulation process in the transistors, *i.e.*, the device physics of organic TFTs with ionic liquids. Here, we refer expediently as [7]phenacene TFT for the transistor with ionic liquid since its operation mechanism is different from the EDL FET, as is described later. The operation mechanism in [7]phenacene TFT with ionic liquid is identified in this study. On the other hand, [7]phenacene transistor with solid gate dielectric is defined as [7]phenacene FET because of its clear field-effect transistor operation.

2. Experimental

Sample of [7]phenacene was synthesized and purified to be ~99.9% according to the previous report [18]. A commercially available SiO_2 (400 nm)/Si wafer was washed by acetone and methanol, H_2O_2/H_2SO_4 and ultrapure water. [7]phenacene thin film FETs with solid gate dielectrics of SiO_2 (400 nm) and HfO_2 (50 nm) were fabricated for a comparison with those with ionic liquids. The surface of SiO_2 was coated by hexamethyldisilazane (HMDS). The HfO_2 was not formed on SiO_2/Si but on Si substrate by use of ion beam spattering, and the surface was covered with parylene (25 nm). Thickness of [7]phenacene thin films were 30 nm except for the devices (thickness of 60 and 480 nm) used for measurement of thickness dependence of I_D–t plot (Fig. 5(b)) and the device (thickness of 60 nm) used for investigation of I_D evolution with different ionic liquids (Fig. 5(c)). Thickness of Au source/drain electrodes is 50 nm. The thin films of [7]phenacene and Au source/drain electrodes were formed by thermal evaporation at 10^{-7} Torr. The molecular structures of two ionic liquids, emim[TFSI] and bmim[PF_6], are shown in Fig. 1(a). The liquid of emim[TFSI] was used as gate dielectric in the [7]phenacene TFT device, and the gel of bmim[PF_6] was used as the gate dielectric. The bmim[PF_6] gel was prepared according to the following procedure. (1) Poly(styrene-*b*-ethylene oxide-*b*-styrene) [PS-PEO-PS] and

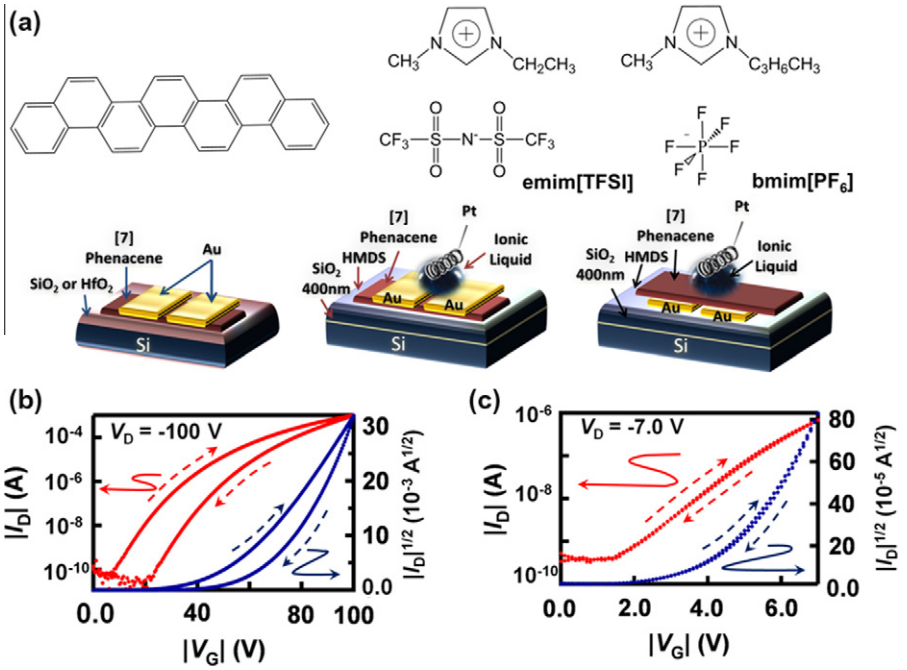

Fig. 1. (a) Molecular structures of [7]phenacene and ionic liquids (emim[TFSI] and bmim[PF_6]). Device structures of [7]phenacene thin film FETs with solid gate dielectrics (left), those of [7]phenacene FETs with ionic liquid gate dielectrics in the different device structures (middle and right). Transfer curves of [7]phenacene FET with (b) SiO_2 and (c) HfO_2 gate dielectrics. $V_D = -100$ V for (b) and $V_D = -7.0$ V for (c).

bmim[PF6] were dissolved at weight ratio of 1:9 in CH_2Cl_2, and the solution was stirred for 16 h at room temperature and CH_2Cl_2 were evaporated. (2) The remaining solid was heated at 343 K under Ar atmosphere for 7 h.

All device structures of [7]phenacene transistors with solid and ionic liquid gate dielectrics are shown in Fig. 1(a). The capacitance per area of EDL, C_{IL}, with the ionic liquids, emim[TFSI] and bmim[PF6], were estimated to be 9.3 and 9.7 μF cm^{-2}, respectively, and the capacitance per area of oxide gate insulator, C_O, for SiO_2 and HfO_2 were estimated to be 8.1 and 83 nF cm^{-2}, respectively. The C_{IL} and C_O were determined by extrapolating the $C_{IL}(v)$ and $C_O(v)$ measured at AC frequency v of 20 Hz–1000 kHz to 0 Hz; the obtained capacitance corresponds to DC capacitance. The AC bias voltage of 1.0 V was applied to determine the capacitance per area. Actually, the C_{IL} is twice as high as the capacitance per area, C_{area}, measured directly for ionic liquid because of the formation of two EDLs under AC bias application.

Platinum (Pt) wire coil was contacted to the ionic liquid as gate electrode (see Fig. 1(a)). The channel length L and channel width W were 30 μm and 2.2–4.8 mm, respectively, except for devices used for obtaining I_D–t plots shown in Fig. 5(b) and (c) where L = 30 μm and W = 200 μm. The transistor characteristics were measured in an Ar-filled glove box, and the reproducibility of characteristics was confirmed with at least three devices. The μ values were determined from the saturation drain currents for all transistors using normal MOS formula. The values of C_O were used for estimation of μ's in [7]phenacene FETs with solid gate dielectrics, while the C_{IL} values were used for estimation of μ's in [7]phenacene TFTs with ionic liquids.

3. Results and discussion

Transfer curves of [7]phenacene thin film FETs with SiO_2 and HfO_2 (left device structure in Fig. 1(a)) are shown in Fig. 1(b) and (c), respectively. Clear p-channel FET characteristics are observed in both FET devices. The maximum absolute drain current $|I_D|^{max}$ reaches 10^{-4} A at gate voltage V_G of −100 V and drain voltage V_D of −100 V for the [7]phenacene FET with SiO_2 gate dielectric. The μ for [7]phenacene FET with SiO_2 gate dielectric was estimated to be 8.4 x 10^{-1} cm^2 V^{-1} s^{-1} from the saturation drain current measured at V_D = −100 V, and the $|V_{TH}|$ was 55 V. Thus, the μ was quite high but the high absolute V_G, $|V_G|$, was necessary for FET operation. Furthermore, the on–off ratio and subthreshold swing S were 4.2×10^7 and 5.8 V decade^{-1}, respectively, for [7]phenacene FET with SiO_2 gate dielectric. The on–off ratio is quite high but the S is not so good. Thus, the serious problem for the [7]phenacene FET with thick SiO_2 gate dielectric is the high voltage operation caused by the low C_O of SiO_2 gate dielectric.

On the other hand, the μ value for the [7]phenacene FET with HfO_2 gate dielectric was 1.6×10^{-2} cm^2 V^{-1} s^{-1} from the saturation drain current measured at V_D = −7 V, and the $|V_{TH}|$ was 4.5 V. This device operates at low voltage but the μ is still lower by approximately a factor of 50 than that for [7]phenacene FET with 400 nm thick SiO_2 gate dielectric. The on–off ratio and S were 1.8×10^3 and 1.5 V decade^{-1}, respectively, for [7]phenacene FET with HfO_2 gate dielectric. In this device, the S is not so good regardless of the low $|V_{TH}|$. Nevertheless, the best record of μ (8.4×10^{-1} cm^2 V^{-1} s^{-1} for [7]phenacene FET with SiO_2) and the best record of $|V_{TH}|$ (4.5 V for [7]phenacene FET with HfO_2) are improved in comparison with the values, $\mu = 7.5 \times 10^{-1}$ cm^2 V^{-1} s^{-1} and $|V_{TH}|$ = 22 V, reported previously [17]. For a realization of [7]phenacene transitor exhibiting both high μ and low $|V_{TH}|$, we turn to ionic liquid gate dielectrics.

For [7]phenacene TFTs with ionic liquids, we adopted two types of device structures as shown in middle and right of Fig. 1(a). In this text, the transistor characteristics of the device shown in middle of Fig. 1(a) are mainly investigated. Here, in the middle device structure, the ionic liquids are directly contacted to the Au source/drain electrodes, but the conductivity was not observed between

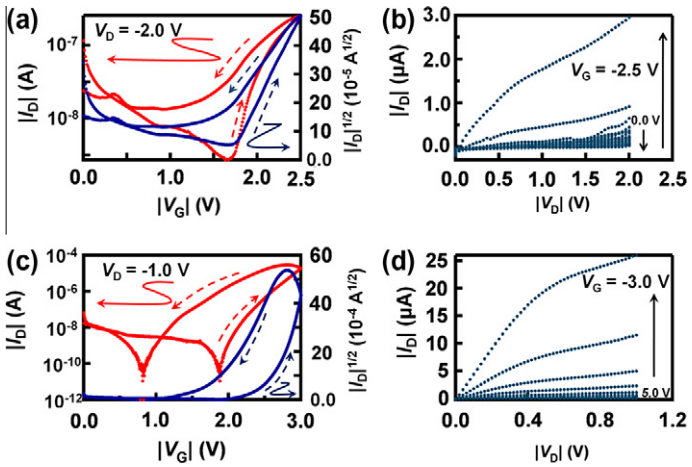

Fig. 2. (a) Transfer and (b) output curves of [7]phenacene thin film FET with emim[TFSI]. (c) Transfer and (d) output curves of [7]phenacene thin film FET with bmim[PF_6]. The device structure refers to the middle device in Fig. 1(a). V_D = −2.0 V for (a) and V_D = −1.0 V for (c). The V_G in the output curves are also shown in graphs, (b) and (d).

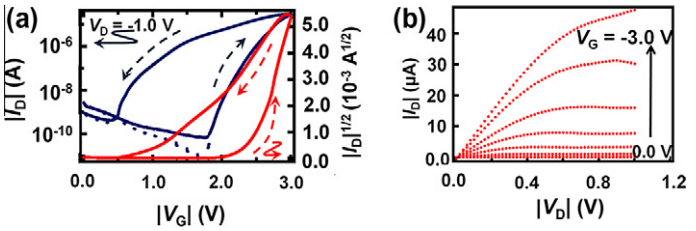

Fig. 3. (a) Transfer and (b) output curves of [7]phenacene thin film FET with bmim[PF_6]. The device structure refers to the right device in Fig. 1(a). $V_D = -1.0$ V for (a). The V_G in the output curves are also shown in graph, (b).

electrodes without [7]phenacene thin films, indicating the ion conductivity is negligible in ionic liquids.

Transfer and output curves of [7]phenacene TFT with emim[TFSI] (middle device structure in Fig. 1(a)) are shown in Fig. 2(a) and (b), respectively. The p-channel transistor characteristics are observed in this TFT device, and the μ was estimated to be 1.0×10^{-3} cm^2 V^{-1} s^{-1} from the transfer curves in saturation regime measured at $V_D = -2.0$ V and the $|V_{TH}|$ was 1.7 V. This device operated at very low $|V_{TH}|$, but the μ is lower than the μ values, 8.4×10^{-1} and 1.6×10^{-2} cm^2 V^{-1} s^{-1}, in [7]phenacene FETs, respectively, with SiO_2 and HfO_2. The [7]phenacene TFT with emim[TFSI] may not provide the prospective for practical application of [7]phenacene owing to the extremely low μ value ($\sim 10^{-3}$ cm^2 V^{-1} s^{-1}) regardless of the low $|V_{TH}|$. The on–off ratio and S were 93 and 200 mV/decade, respectively. This S is smaller by one or two orders of magnitude than those for [7]phenacene FETs with solid gate dielectrics, but the on–off ratio is quite low. The low on–off ratio originates from the off-current as high as 10^{-9} A. Such a high off-current was found in poly(3-hexylthiophene) (P3HT) FET with polymer electrolyte, and the phenomenon was attributed to the ionic charge current produced by using drop of gate electrolyte [19]. The use of ionic liquid drop may also cause the high off-current in our device, although the off-current of [7]phenacene TFT with emim[TFSI] is actually much smaller than that in the P3HT FET with electrolyte gate drop [19].

The output curves show a weak ambipolar property that the I_D decreases with an increase in $|V_G|$ from 0.0 to 1.0 V. The transfer curve also shows a slow increase with a decrease in $|V_G|$ below 1.7 V, suggesting the ambipolar property in this TFT. Here it should be pointed out that such a behavior observed in the P3HT FET with polymer electrolyte gate dielectric was not attributed to the ambipolar electronic current but additional ionic current caused by electrochemical reaction [20]. This fact implies that the interpretation of the ambipolar like behavior observed is not so simple in [7]phenacene TFT with emim[TFSI] gate dielectric. The discussion on the electrochemical reaction in [7]phenacene TFTs with ionic liquids is fully described later.

Transfer and output curves of [7]phenacene TFT with bmim[PF_6] (middle device structure in Fig. 1(a)) are shown in Fig. 2(c) and (d), respectively. The p-channel characteristics are also observed in this TFT device, and the μ was estimated to be 2.6×10^{-1} cm^2 V^{-1} s^{-1} from the transfer curve at $V_D = -1.0$ V in saturation regime, and the $|V_{TH}|$ was 2.7 V. This device operates with the high μ value comparable to that, 8.6×10^{-1} cm^2 V^{-1} s^{-1}, recorded for [7]phenacene FET with thick SiO_2 gate dielectric. Namely, the [7]phenacene TFT with bmim[PF_6] realizes both high mobility and low voltage operation. The on–off ratio and S were 1.9×10^7 and 89 mV/decade. The on–off ratio is also comparable to that for [7]phenacene FET with thick SiO_2 gate dielectric, and the S is close to the theoretical limited value, 60 mV/decade at room temperature. This S value is smaller by one–two orders of magnitude than that for [7]phenacene FETs with solid gate dielectrics. The output curves did not show the ambipolar properties, contrary to those for [7]phenacene TFT with emim[TFSI] (Fig. 2(b)). Thus [7]phenacene TFT with bmim[PF_6] is substantially superior to that with emim[TFSI].

We further made [7]phenacene TFT with bmim[PF_6] in the device structure shown in right of Fig. 1(a) and investigated its transport characteristics. The transfer and output curves are shown in Fig. 3(a) and (b), respectively. P-channel characteristics were observed and the μ, |VTH|, on–off ratio and S were evaluated to be 2.8×10^{-1} cm^2 V^{-1} s^{-1}, 2.5 V, 2.9×10^7 and 107 mV/decade, respectively, from the transfer curve in saturation regime (VD = −1.0 V). These values are almost consistent with those for [7]phenacene TFT with bmim[PF_6] (middle device in Fig. 1(a)). This result is a little surprising for us, because [7]phenacene thin film FET was expected not to operate in the device structure shown in right of Fig. 1(a), from the analogy of picene thin film FET [3]. The picene thin film FET with SiO_2 gate dielectric and Au source/drain electrodes did not operate in the bottom contact structure in which the picene thin films are deposited and formed on Au source/drain electrodes. Actually, it is found, for the picene thin film FET in the bottom contact structure, that the large hole-injection barrier-height is formed between Au source/drain electrodes and the picene thin films, *i.e.,* the formation of picene thin film on Au electrodes produces large hole-injection barrier. It is natural for us to predict large hole-injection barrier-height for [7]phenacene FET, because the crystal structure of [7]phenacene thin films on the SiO_2 and the electronic structure are similar to those of picene [17], and the [7]phenacene thin films are formed on Au electrodes in right of Fig. 1(a). The fact, that the excellent transistor characteristics for [7]phenacene TFT in the device structure shown in right of Fig. 1(a) is observed, suggests the destruction of the hole-injection barrier, which is probably owing to high density of hole accumulation at channel region of [7]phenacene thin films. This result is consistent with the

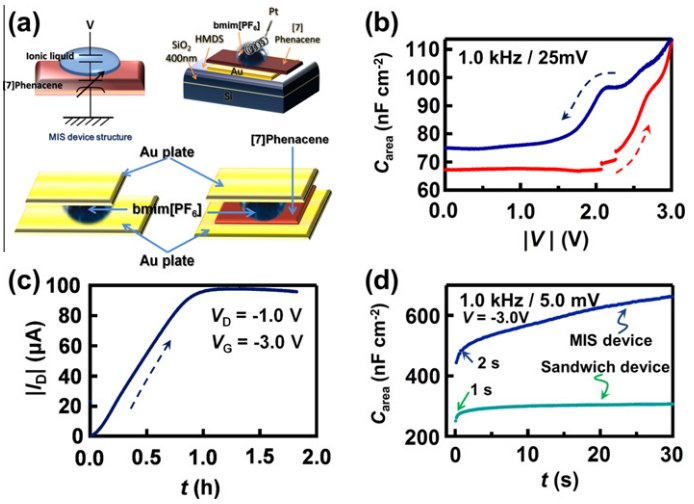

Fig. 4. (a) Schematic representation of MIS device (top left), and device structures of [Pt(wire coil)–bmim[PF_6]-[7]phenacene-Au(thin films)] MIS device (top right) , [Au(plate)–bmim[PF_6]-Au(plate)] sandwich device (bottom left) and [Au(plate)–bmim[PF_6]-[7]phenacene-Au(plate)] MIS device (bottom right). The bias voltage applying to the MIS device is represented as *V*. (b) C_{area}–*V* plot measured in the [Pt(wire coil)–bmim[PF_6]-[7]phenacene-Au(thin films)] MIS device. (c) $|I_D|$ plot as a function of *t* measured in [7]phenacene FET with bmim[PF_6] (middle device in Fig. 1(a)). (d) C_{area}–*t* in the [Au(plate)–bmim[PF_6]-Au(plate)] sandwich device and the [Au(plate)–bmim[PF_6]-[7]phenacene–Au(plate)] MIS device. The AC frequency is 1 kHz for (b) and (d), while the AC bias voltage for estimating capacitance is 25 and 5 mV for (b) and (d), respectively. The DC bias voltages are also shown in graphs of (c) and (d), *i.e.*, $V_D = -1.0$ V and $V_G = -3.0$ V in (c), and $V = -3.0$ V in (d).

fact that [7]phenacene TFT is electrochemical (EC) transistor, as described later.

Fig. 4(a) shows the schematic representation of metal–insulator-semiconductor (MIS) device (top left in (Fig. 4(a)), Pt–bmim[PF_6]-[7]phenacene-Au (top right in Fig. 4(a)), which implies two series of capacitors; metal, insulator and semiconductor refer to Pt electrode, bmim[PF6] and [7]phenacene, respectively. In this device, the Au electrode was grounded. The C_{area} measured in the MIS device is plotted as a function of absolute applied bias voltage |*V*|, as shown in Fig. 4(b). Here it is important to notice that the *V* is the same role as the V_G in the TFT device. Actual measurement condition is described in figure caption of Fig. 4(b). As seen from Fig. 4(b), the C_{area} drastically increases with an increase in |*V*| above 2.0 V. The $|V_{TH}|$ for C_{area}–*V* plot can be estimated to be 2.3 V. The transfer curves of TFTs corresponding to this MIS device are shown in Fig. 2(c) and Fig. 3(a). The $|V_{TH}|$ for the TFT device was 2.5–2.7 V as described previously, whose value is consistent with 2.3 V estimated from C_{area}–*V* plot (Fig. 4(b)). This C_{area}–*V* curve shows the hole accumulation above 2.3 V in forward application of |*V*|.

The time (*t*) dependence of the absolute maximum drain current, $|I_D|^{max}$, for [7]phenacene TFT with bmim[PF_6] measured at $V_D = -1.0$ V and $V_G = -3.0$ V is shown in Fig. 4(c); the device structure is shown in middle of Fig. 1(a). The value increases monotonously with an increase in *t* and almost saturates above 1 h, suggesting time necessary for the hole accumulation. The I_D in [7]phenacene TFT with bmim[PF_6] (Fig. 4(c)) reaches 100 μA at 1 h. Furthermore, the time scale (~1 h = 3600 s) of I_D evolution in [7]phenacene TFT with bmim[PF_6] is different from that (~1 s) in EDL FETs [19–23]. This suggests that the I_D evolution in [7]phenacene TFT with bmim[PF_6] cannot be related to that for EDL FET but to electrochemical doping of PF_6^-, *i.e.*, the [7]phenacene TFT is a electrochemical (EC) TFT. Thus, the evolution of $|I_D|$ (Fig. 4(c)) may be an indirect indication of penetration of PF_6^- to bulk region of [7]phenacene thin films; as described later, the penetration of PF_6^- ions can produce large amounts of holes into the bulk region to realize the absolute I_D as high as 100 μA.

Here it is important to say that the time required for EDL formation is probably approximately 1s because the C_{IL} for Au–bmim[PF_6]-Au sandwich device (bottom left in Fig. 4(a)) was detected at 20 Hz – 1 kHz and AC bias voltage of 1 V without DC bias voltage, as described in the experimental section. Next the C_{area} for Au–bmim[PF_6]-Au sandwich device was measured at 1 kHz and AC bias voltage of 5 mV and DC bias voltage of −3 V. The C_{area} is plotted as a function of *t* in Fig. 4(d), where the starting time corresponds to the time when the DC bias voltage is applied. This experiment was carried out to know the formation process of EDL under DC bias voltage application ($V = -3$ V); this bias voltage is consistent with the V_G of −3 V used for I_D–*t* measurement (Fig. 4(c)). The C_{area} rapidly increases within 1 s and saturates above 20 s.

Furthermore, we measured evolution of C_{area} in the Au–bmim[PF_6]-[7]phenacene–Au MIS device. The *t* dependence of C_{area} in the MIS device is shown in Fig. 4(d). The C_{area} increases rapidly up to 2 s and saturates above 90 s. This C_{area}–*t* curve reflects both EDL formation and penetration of PF_6^- into [7]phenacene thin films by application of −3 V. The time scale is shorter by one–two orders of magnitude than that of I_D–*t* plot shown in Fig. 4(c). The C_{area}–*t* plot in Au–bmim[PF_6]-Au detects only the EDL formation process, while that in the Au–bmim[PF_6]-[7]phenacene–Au MIS device detects both processes of EDL and

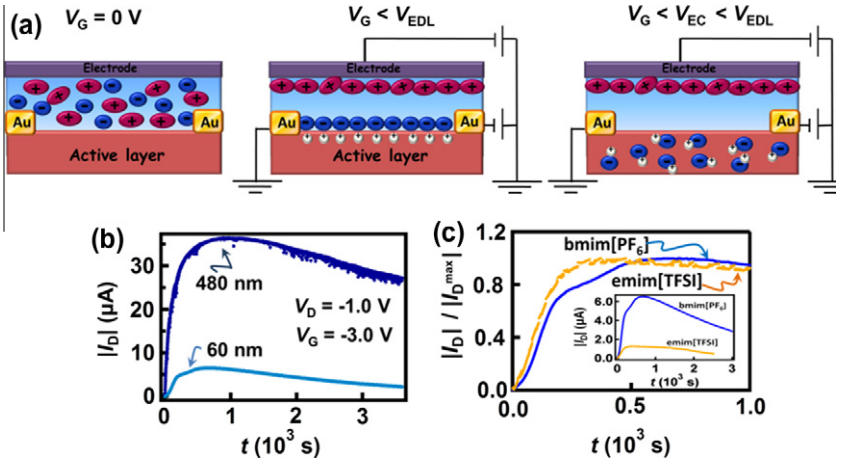

Fig. 5. (a) Schematic representation of ionic liquid capacitor at each V_G. EDL and EC capacitors are shown, respectively, in middle and right of (a). (b) $|I_D|$–t plots for 60 and 480 nm thick [7]phenacene TFTs with bmim[PF_6]. (c) Normalized $|I_D|$–t plots for [7]phenacene TFTs with emim[TFSI] and bmim[PF_6]; normalization is performed by dividing the measured $|I_D|$ by the maximum $|I_D|$. Inset of (c): $|I_D|$–t plots for [7]phenacene TFTs with emim[TFSI] and bmim[PF_6]. Thickness of [7]phenacene is 60 nm for (c). The L and W are the same in all devices in (b) and (c), as described in the experimental section.

electrochemistry (penetration of PF_6^-). The time, <2 s, required for EDL formation in the MIS device is consistent with that in Au–bmim[PF_6]-Au device, implying that the penetration process of PF_6^- to [7]phenacene thin films does not affect the EDL formation in short time region. As a consequence, the penetration process starts in longer time region than several seconds. To sum up, the time, <2 s, required for EDL formation (Fig. 4(d)) is exactly shorter than the time scale for I_D evolution by penetration of PF_6^- (Fig. 4(c)).

It is found that the polymer FETs with polymer electrolytes and ionic liquids show two types transistor operation, EDL FET (electrostatic carrier doping) and EC transistor (electrochemical doping) [19–23]. We fully discuss characteristics of [7]phenacene EC TFTs based on the model presented for polymer FETs. As seen from Fig. 5(a), when V_G is not applied to ionic liquid ($V_G = 0$), the anions and cations are dissolved in ionic liquid. When negative bias voltage is applied to ionic liquid ($V_G < V_{EDL} < 0$), the EDLs are formed on both the active layer side and gate electrode side; the V_{EDL} refers to the threshold voltage for EDL FET. The cations (anions) are close to gate electrode (active layer). Holes are accumulated in one or two monolayer(s) of active layer at the interface between active layer and ionic liquid. The anions may penetrate into the active layer together with hole carries when high negative V_G is applied ($V_G < V_{EC} < V_{EDL}$); the V_{EC} means the threshold voltage for EC TFT and the V_{TH} determined from transfer curves (Figs. 2 and 3) in [7]phenacene TFTs with ionic liquids corresponds to V_{EC}. Holes are weekly bound to anions, but at sufficiently high hole density, the screening of the Coulomb attraction occurs and metallic behavior is observed in channel region. This transition is recognized as 'Mott-transition' by Yuen et al. [22]. The channel region is the whole of active layer, *i.e.*, the region in which anion penetrate. Thus the EC TFT is a bulk transistor, and the performance is reversible. Here it should be noted that the I_D values in forward transfer curves in Fig. 2(a) and (c), and Fig. 3(a) are too low below $|V_{TH}| = |V_{EC}| \sim 2$ V despite of the formation of EDL. This suggests the localization of holes caused by the strong Coulomb attraction force between PF_6^- (or $TFSI^-$) and hole at EDL region. In other word, the [7]phenacene TFTs with emim[TFSI] and bmim[PF_6] may not provide the detectable I_D owing to the strong attractive force even if the EDL capacitor is formed.

It is interesting to know whether the electrochemical doping may occur in the transistors with single crystals (SC) of organic semiconductor since ion diffusion/penetration may be prevented because of high crystallinity and a few grain boundaries. In the case of organic thin films used in this study, the ion diffusion/penetration may effectively occur because of existence of many defects and grain boundaries, leading to EC transistor. Actually, a slow increase in I_D shown in Fig. 4(c) reflects the characteristics of electrochemical doping into three dimensional (3D) bulk region of [7]phenacene thin films. To investigate characteristics of [7]phenacene SC transistor with ionic liquids is of importance to clarify the microscopic process of electrochemical doping or ion penetration/diffusion to active layer. The investigation with SC transistor is now in progress.

Fig. 5(b) shows the $|I_D|$–t plots for two [7]phenacene TFTs with bmim[PF_6] which have different thickness of [7]phenacene thin films (60 and 480 nm); the V_D and V_G applied are −1.0 and −3.0 V, respectively. If the [7]phenacene TFT with bmim[PF_6] is an EC TFT, the maximum $|I_D|$ should be different owing to the different thickness, since the EC TFT is based on electrochemical doping of PF_6^- to the whole region of [7]phenacene thin films. Both $|I_D|$ values increase with an increase in t and gradually decrease above 1000 s. As seen from Fig. 5(b), the maximum $|I_D|$ for 480 nm thick [7]phenacene TFT is six times as high as that for 60 nm thick TFT, supporting that these TFTs operate in bulk region of [7]phenacene thin films and the TFT is an EC transistor. The reason why the decrease in $|I_D|$

above 1000 s is observed remains to be clarified, but the tendency is observed for most of $|I_D|$–t data (Fig. 4(c), Fig. 5(b) and (c)). A recent preliminary experiment with spin probe method shows a clear decreases in hole-concentration in the time region when the $|I_D|$ decreases [24]. That is, the decrease is not associated with localization of holes. Further investigation is necessary for clarifying the origin.

Furthermore, we discussed on hysteresis in transfer curves of [7]phenacene TFTs with emim[TFSI] and bmim[PF_6] (Figs. 2(a) and (c)). The hysteresis in [7]phenacene TFT with bmim[PF_6] is larger than that with emim[TFSI]. The reverse transfer curve in [7]phenacene TFT with bmim[PF_6] is much higher than the forward transfer curve. We measured the I_D as a function of t for [7]phenacene TFTs with emim[TFSI] and bmim[PF_6], and the normalized $|I_D|$–t plots are shown in Fig. 5(c); the normalization is done by dividing the $|I_D|$ by the maximum $|I_D|$ value. The $|I_D|$ evolution in TFT with bmim[PF_6] is slower than that with emim[TFSI], *i.e.*, the penetration of PF_6^- into [7]phenacene thin films is slower. The slower penetration/diffusion of PF_6^- can reasonably explain the characteristics or hysteresis observed in transfer curves (Fig. 2(a) and (c)), because the slow diffusion may provide a slow response for decrease in $|V_G|$ and it may still cause an increase in $|I_D|$ when $|V_G|$ decreases.

However, the behavior observed in Fig. 5(c) cannot be explained by the simple idea that small size of anion (PF_6^-) more rapidly penetrates into the thin films than large size of anion ($TFSI^-$). Here, we have to consider that the bmim[PF_6] is gel and emim[TFSI] is liquid (not gel). If the viscosity of ionic liquid is taken into account, larger hysteresis in [7]phenacene TFT with bmim[PF_6] may be reasonably explained because high viscosity of bmim[PF_6] gel leads to low diffusion coefficient, *i.e.*, PF_6^- ions cannot effectively penetrate into thin films. Therefore, the slow penetration of PF_6^- causes the hysteresis in transfer curve because of a slow response for applied V_G.

As seen from inset of Fig. 5(c), the $|I_D|$ is higher by an order of magnitude in [7]phenacene TFT with bmim[PF_6] than that with emim[TFSI], which is consistent with the characteristics of transfer/output curves shown in Fig. 2. The results suggest that bmim[PF_6] is a better ionic liquid for electrochemical doping than emim[TFSI]. This may be due to that anion size (PF_6^-) is so small that large amounts of PF_6^- can be doped into the [7]phenacene thin films, although long time is required to completely penetrate, producing high absolute I_D in [7]phenacene TFT with bmim[PF_6].

4. Conclusion

We fabricated [7]phenacene TFT with two different ionic liquids. The low voltage operation and high field-effect mobility are realized in [7]phenacene TFT with bmim[PF_6]. The device performance is superior to the low-voltage operated [7]phenacene FET with HfO_2, indicating availability of bmim[PF_6] gel. Furthermore, the excellent device performance of [7]phenacene TFT with bmim[PF_6] in the device structure shown in right of Fig. 1(a) suggests the destruction of hole-injection barrier by high density of hole accumulation, which may present one way for the smooth carrier injection in organic transistor, *i.e.*, high-density carrier-accumulation. If this is the case, we may expect the destruction of not only hole-barrier but also electron-barrier in this type of TFTs. The most important conclusion of this study is that [7]phenecene TFT operates electrochemically, *i.e.*, EC TFT (not EDL FET). The operation mechanism was confirmed from I_D–t and C_{area}–t measurements (Figs. 4 and 5). The time scale of transistor characteristics in [7]phenacene TFTs with emim[TFSI] and bmim[PF_6] is different from that in typical EDL FETs [19–23]. Thickness dependence of thin films in I_D–t plot in [7]phenacene TFT with bmim[PF_6] provided a conclusive evidence that this TFT operated electrochemically in bulk region of thin films. We stress the importance to clarify the operation mechanism in organic thin film transistors with ionic liquids, for new application of organic transistors with ionic liquid gate dielectrics. The technique of EC transistor, or electrochemical doping with ionic liquid may be available for high density carrier accumulation to control physical properties of organic materials.

Acknowledgements

This work was partly supported by a Grant-in-Aid (22244045) from MEXT, Japan, by the Japan Science and Technology Agency and by the Support Unit for Strategic Programs of Okayama University.

References

[1] H. Okamoto, N. Kawasaki, Y. Kaji, Y. Kubozono, A. Fujiwara, M. Yamaji, J. Am. Chem. Soc. 130 (2008) 10470.
[2] N. Kawasaki, Y. Kubozono, H. Okamoto, A. Fujiwara, M. Yamaji, Appl. Phys. Lett. 94 (2009) 043310.
[3] Y. Kaji, R. Mitsuhashi, X. Lee, H. Okamoto, T. Kambe, N. Ikeda, A. Fujiwara, M. Yamaji, K. Omote, Y. Kubozono, Org. Electron. 10 (2009) 432.
[4] Y. Kaji, N. Kawasaki, X. Lee, H. Okamoto, Y. Sugawara, S. Oikawa, A. Ito, H. Okazaki, T. Yokoya, A. Fujiwara, Y. Kubozono, Appl. Phys. Lett. 95 (2009) 183302.
[5] X. Lee, N. Kawasaki, M. Suekiyo, Y. Sugawara, A. Fujiwara, Y. Kubozono, Org. Electron. 11 (2010) 1394.
[6] R. Mitsuhashi, Y. Suzuki, Y. Yamanari, H. Mitamura, T. Kambe, N. Ikeda, H. Okamoto, A. Fujiwara, M. Yamaji, N. Kawasaki, Y. Maniwa, Y. Kubozono, Nature 464 (2010) 76.
[7] K. Ueno, S. Nakamura, H. Shimotani, A. Ohmoto, N. Kimura, T. Nojima, H. Aoki, Y. Iwasa, M. Kawasaki, Nature Mater. 7 (2008) 855.
[8] J.T. Ye, S. Inoue, K. Kobayashi, H.T. Yuan, H. Shimotani, Y. Iwasa, Nature Mater. 9 (2010) 125.
[9] H. Shimotani, G. Diguet, Y. Iwasa, Appl. Phys. Lett. 86 (2005) 022104.
[10] H. Shimotani, H. Asanuma, J. Takeya, Y. Iwasa, Appl. Phys. Lett. 89 (2006) 203501.
[11] H. Shimotani, H. Asanuma, Y. Iwasa, Jpn. J. Appl. Phys. Part.1 46 (2007) 3613.
[12] J.H. Cho, J. Lee, H. Yiyong, B.S. Kim, T.P. Lodge, C.D. Frisbie, Adv. Mater. 20 (2008) 989.
[13] T. Uemura, M. Yamagishi, S. Ono, J. Takeya, Appl. Phys. Lett. 95 (2009) 103301.
[14] J. Lee, L.G. Kaake, J.H. Cho, X.-Y. Zhu, T.P. Lodge, C.D. Frisebie, J. Phys. Chem. 113 (2009) 8972.
[15] K. Ogawa, Y. Kaji, N. Kawasaki, R. Eguchi, T. Takayanagi, H. Okamoto, A. Fujiwara, T. Kambe, Y. Kubozono, submitted.
[16] F.B. Mallory, K.E. Butler, A.C. Evans, E.J. Brondyke, C.W. Mallory, C. Yang, A. Ellenstein, J. Am. Chem. Soc. 119 (1997) 2119.

[17] Y. Sugawara, Y. Kaji, K. Ogawa, R. Eguchi, S. Oikawa, H. Gohda, A. Fujiwara, Y. Kubozono, Appl. Phys. Lett. 98 (2011) 013303.
[18] F.B. Malloy, K.E. Bultler, A.C. Evans, E.J. Brondyke, C.W. Malloy, Tetrahedron Lett. 37 (1996) 7173.
[19] L. Herlogsson, X. Crispin, N.D. Robinson, M. Sandberg, O.-J. Hagel, G. Gustafsson, M. Berggren, Adv. Mater. 19 (2007) 97.
[20] E. Said, O. Larsson, M. Berggren, X. Crispin, Adv. Funct. Mater. 18 (2008) 3529.
[21] M. Hamedi, L. Herlogsson, X. Crispin, R. Marcilla, M. Berggren, O. Inganas, Adv. Mater. 21 (2009) 573.
[22] J.D. Yuen, A.S. Dhoot, E.B. Namdas, N.E. Coates, M. Heeney, I. McCulloch, D. Moses, A.J. Heeger, J. Am. Chem. Soc. 129 (2007) 14367.
[23] J. Lee, J.G. Kaake, J.H. Cho, X.-Y. Zhu, T.P. Lodge, C.D. Frisbie, J. Phys. Chem. C113 (2009) 8972.
[24] Y. Nagasaki, Y. Kaji, Y. Kubozono, T. Kambe, unpublished data.

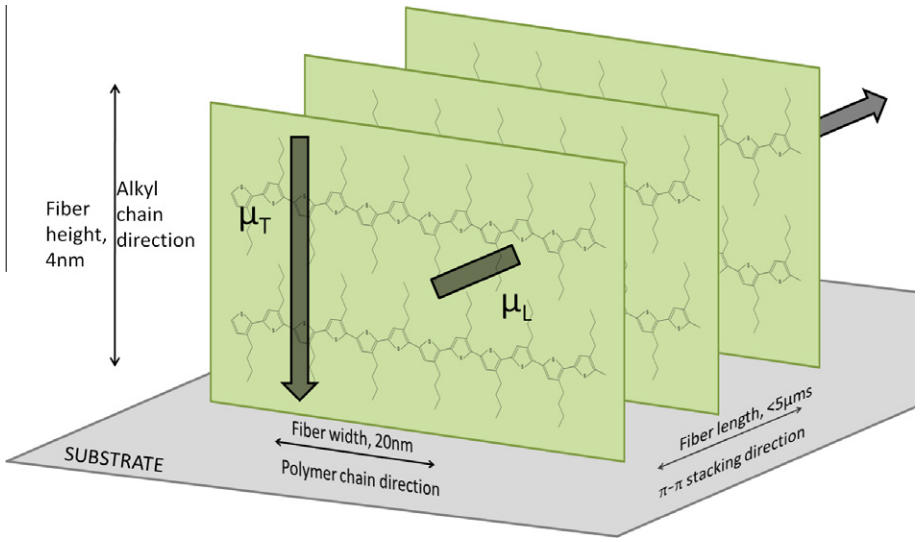

Fig. 1. Schematic of the P3BT nanofiber and the two investigated charge transport directions. μ_T is the transversal mobility and μ_L is the longitudinal mobility.

along the height of one NF, μ_T for transversal mobility. With this approach, charge transport anisotropy in P3AT NFs will be evidenced, since we find at least four orders of magnitude difference between μ_L and μ_T.

2. Experimental

P3AT NFs were synthesized as described in Ref. [8]. P3AT denotes a family of conjugated polymer of which the number of C atoms in the side chain can vary. In this study, we use poly(3-butylthiophene) (P3BT), four C atoms, poly(3-hexylthiophene) (P3HT), six C atoms, and poly(3octylthiophene) (P3OT), eight C atoms. The M_n values [in kg mol^{-1}] as obtained by GPC *versus* polystyrene standards in chlorobenzene at 60 °C Ref. [8] were (PDI between parentheses) 19.5 (2.29) for P3BT, 23.6 (1.95) for P3HT, and 28.0 (1.66) for P3OT. Regioregularities as obtained by ^{1}H-NMR Ref. [8] were 96.5, 94.0, and 97 for P3BT, P3HT and P3OT, respectively. Nanofibers were prepared in *o*-chlorotoluene (P3BT), *p*-xylene (P3HT) and pinane (P3OT) as described in Ref. 8 at 0.4, 1 and 0.5 wt.% concentrations and then diluted to the concentrations of 0.005 to 0.001 wt.% used in this work. From tapping mode AFM measurements (for which the resolution is better than in CAFM), NFs heights and widths are typically 4 nm and 20 nm respectively, independent of the alkyl chain length. It is known that when used with appropriate high work function electrodes, such as Au or Pt, they behave like p-type semiconductors [11].

The transistor structure used consists of a highly n-doped Si wafer (acting as the gate electrode) with a SiO_2 gate dielectric on top of it (gate capacitance per unit area, C_o = 16.9 nF cm^{-2}). A self-assembled monolayer of hexamethyldisilazane (HMDS) was used to passivate the SiO_2 layer. A thin drain electrode (10 nm Pt layer on top of 2 nm Ti adhesion layer) was patterned by standard photolithography. Thin electrodes were chosen to prevent NFs disruptions. The source, drain and gate electrodes were connected by a voltage source internal to the AFM and an external one (Keithley 2400), both sources being grounded to the tip potential. The NFs were deposited on the transistor by drop-casting.

The Veeco multimode AFM equipped with the Nanoscope IIIa controller, the quadrex module and the CAFM module were used. We employed two kinds of CAFM tip: $PtIr_5$ and Au coated tips from Nanosensors. Both tips give similar results and have a spring constant of 0.2 N/m. To avoid any degradation on the soft polymer NFs a low contact force (∼0.3 nN, deduced from force-curve measurements) was employed. Assuming a Young's modulus for P3BT [12] of ∼1 GPa, a tip radius of 25 nm (typical for CAFM tips) and using the Hertz mechanic model [13], we find a contact radius of ∼2 nm. To avoid sample contamination and tip oxidation, all the measurements were performed in a home-made glove box with oxygen concentration lower than 50 ppm and humidity concentration lower than 10 ppm.

3. Results and discussion

CAFM is a current sensitive AFM technique in which a metal coated AFM tip scans a sample under a user defined bias voltage. CAFM can be used in the spectroscopic mode and in the imaging mode. In the spectroscopic mode, the tip is fixed on a specific position on the sample while an *I*/*V* characteristic is performed. In the imaging mode, topography and current maps are simultaneously recorded at fixed voltage and enable to distinguish high and poor conductive regions.

3.1. Longitudinal transport, μ_L

The measurements shown in this paragraph are for P3BT. Longitudinal charge transport is studied by building

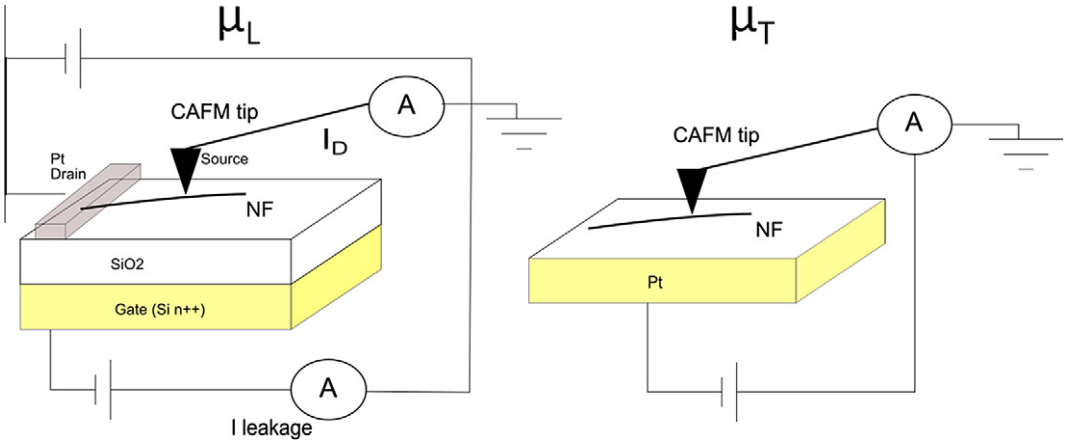

Fig. 2. Left: transistor structure for measuring longitudinal mobility, μ_L. Right: sandwich structure for measuring transversal mobility, μ_T.

a transistor with one electrode being the mobile CAFM tip, as depicted in Fig. 2. The purpose is to measure the current flowing from the drain electrode to the CAFM tip via the NFs which are deposited in between. Fig. 3A and B show the topographic image of the NFs and the corresponding current map for a fixed drain voltage V_D and a varying gate voltage V_G. We observe that the correlation between both maps is remarkable: the current is zero where no NFs are present in the topography, which is logic since there is no pathway for holes to flow from the tip to the drain electrode. On the other hand, when the tip touches a NF we see that the current becomes positive since an electrical transport channel is found. When scanning the sample from the top to the bottom of the image, V_G is progressively decreased and leads to an increase of the NFs conductivity as this is expected for a p-type semiconductor. This indicates that the gate electrode is well connected. If alternatively, we fix the CAFM tip on one NF and perform, in the spectroscopic mode, several V_D sweeps at different fixed V_G, we obtain the output characteristic of Fig. 3C showing the linear and saturation regimes. This proves that our transistor is operating properly.

We have checked that our measurements are non-destructive since two successive mappings on the same area give very similar topographic and current maps. However, when we increase the current flowing through the individuals NFs (by changing adequately V_D and V_G) up to a value of about 5 nA, we have observed that the current jumps immediately to zero. In other words, the maximum current I_{max} we have measured without NFs destruction is about 4 nA. Taking 20 nm for the width of a NF and 1 nm for the thickness of the accumulation layer, we obtain a maximum current density of about 2 kA/cm^2, near the value (700 A/cm^2) reported by Ref. [9].

Compared to a standard transistor structure with two fixed electrodes, the main benefit of this mobile electrode transistor is that we can choose the quantity of NFs under investigation. In particular, by placing the tip very close to the drain electrode and by depositing NFs from very dilute dispersions, it is possible to measure μ_L on one single NF.

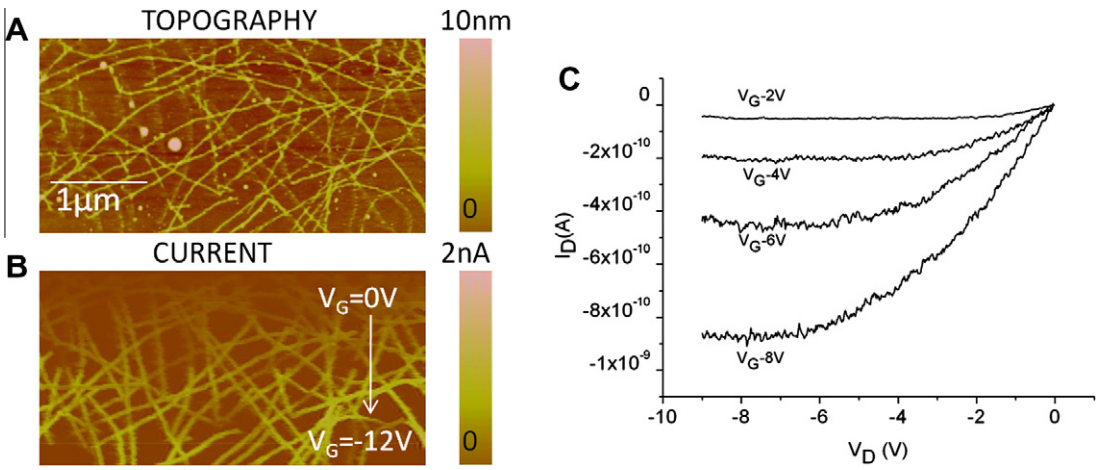

Fig. 3. (A and B) show the topography and current images obtained on P3BT NFs at fixed $V_D = -4$ V and changing V_G. The current is increased as V_G is decreased. Fig. 3C shows the output characteristic when the tip is fixed on a P3BT NF demonstrating the expected linear and saturation regimes for a p-type semiconductor.

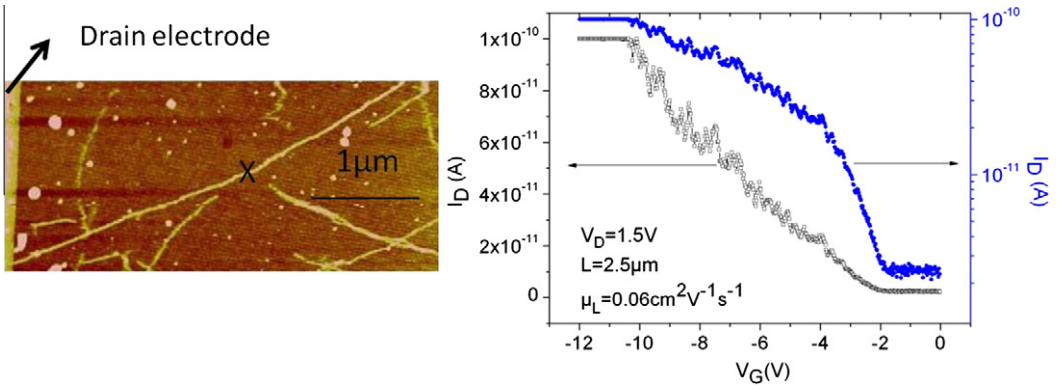

Fig. 4. Topographic image of one P3BT NF touching the drain electrode at the left extremity of the image and the transfer characteristic taken at point X from which μ_L is fitted.

The strategy is illustrated on Fig. 4. First, an isolated NF touching the drain electrode is located. This is done without drain bias which would cause instabilities in the image due to the metal–metal contact. Once the target NF is identified and the image is very stable, the tip is fixed on the desired location and a transfer characteristic is performed as shown in Fig. 4. After the I/V measurement is done, we check that the NF is not destroyed by re-imaging the NF.

Before extracting any mobility values, some interesting points can be deduced from the transfer characteristic. We observe that the onset voltage, i.e. the voltage at which conduction starts in the log plot, is close to zero. This is an indication that the transistor does not suffer from hole and electron trapping which are known to move the onset voltage towards negative and positive voltage respectively [14]. This is due to our home-made glove box which prevents oxygen and water contamination.

Because the tip radius is small (~25 nm) and the channel length (<3 µm) is smaller than for conventional transistors, we have to check that the contact resistance R_c is not limiting the current measurements. This can be done in the imaging mode where we measure the current along one NF in function of the NF length as described in detail in Fig. 5.

The total resistance R_{tot} can be written as the sum of the contact resistance and the channel resistance: $R_{tot} = R_c + R_{channel} = R_c + \frac{\rho L}{Wh}$ with L the channel length, W the channel width and ρ the NFs resistivity. The extrapolation of the measured resistance at zero length gives an estimation of the contact resistance. As depicted in Fig. 5, we find $R_c \sim 1\ G\Omega \pm 1\ G\Omega$. Although this number can seem huge, the worst case value (2 GΩ) is still small enough compared to the intrinsic NF resistance to be considered as not influencing the results. The reason is that with the CAFM-based transistor on one single NF, we usually measure current lower than 100 pA at a bias of a few volts. This provides a minimum value for the total resistance of 20 GΩ much higher than the worst case R_c value. This conclusion that R_c is not perturbing the measurements can also be deduced from the slope of the transfer characteristic at highly negative V_G. If R_c was limiting the results, we would have observed a decrease of the absolute slope of the curve at high negative V_G, which is not the case.

Finally, the longitudinal mobility μ_L is extracted from the slope of the transfer characteristic in the negative gate voltage region: $\mu_L = \frac{L}{WC_oV_D} \cdot \frac{\partial I_D}{\partial V_G}$ where $W = 20$ nm (equals here to the width of one NF), I_D is the transistor current

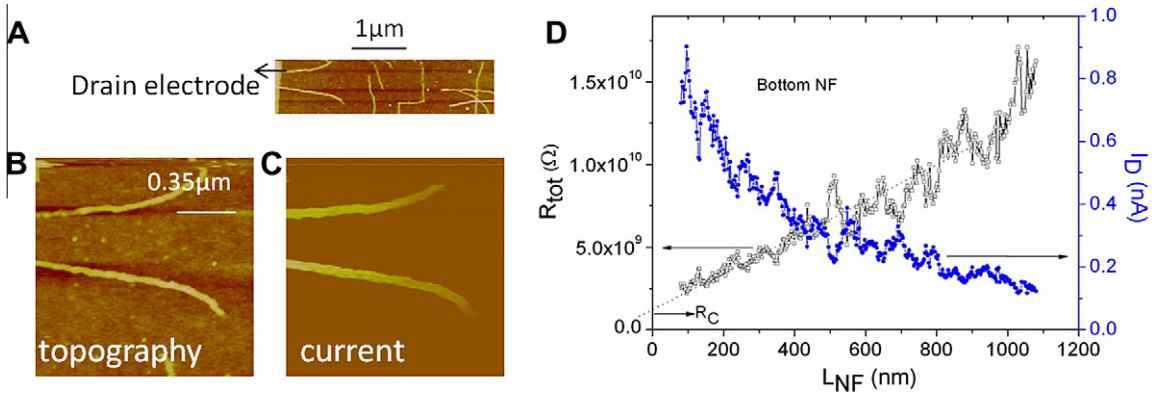

Fig. 5. Evaluation of the contact resistance. (A): topographic map showing two independent NFs touching the drain electrode. (B and C): zoomed topographic and current maps of A where the drain electrode is 80 nm on the left of the image. (D): Current profile along the bottom NF of C (LNF denotes the length of the NF starting from the drain electrode). From the extrapolation of the total resistance R_{tot} at zero length, we can extract the contact resistance R_C.

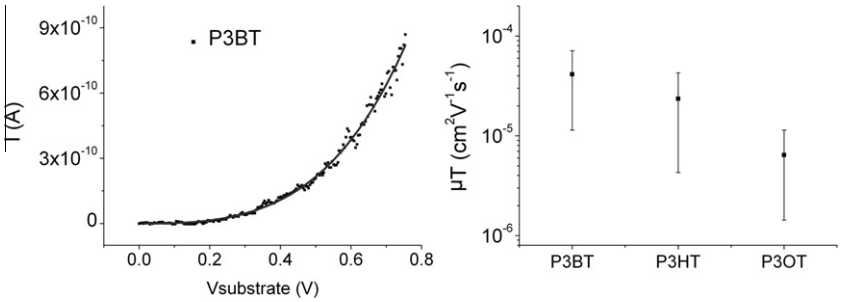

Fig. 6. Typical transversal *I*/*V* curve obtained on single P3BT NF (dots: experimental points, line: fit to Eq. (2)) and the transversal mobility for P3BT, P3HT and P3OT NFs.

and *L* the NF's length between the drain electrode and the X label as deduced from the topographic map. The measurement was done on about ten independent P3BT NFs and led to the following result: μ_L 0.07 ± 0.03 $cm^2\,V^{-1}\,s^{-1}$. It corresponds to a hopping time between two chains of about 100 ps.

There have been several papers reporting that the longitudinal mobility on films of NFs [11] and web of NFs [2] is not influenced by the alkyl side chain length. The same question arises for one single NF. To our knowledge, there are no reports on isolated P3BT NF and only two reports on P3HT NF: one from Merlo et al. [6] (0.06 $cm^2\,V^{-1}\,s^{-1}$) and one very recent by Shimomura et al. [10] (0.05 $cm^2\,V^{-1}\,s^{-1}$). We see that our mobility value for P3BT (0.07 $cm^2\,V^{-1}\,s^{-1}$) is very comparable to these P3HT values. This is a suggestion that μ_L is alkyl chain length independent for one single NF.

Using the acoustic deformation potential scattering theory [15] the mobility in one ideal single crystal has been calculated to be 31 $cm^2\,V^{-1}\,s^{-1}$ for P3HT [16] which is almost three orders of magnitude higher than μ_L. Moreover, we note also that μ_L is not larger than best mobility values ($\sim$0.1 $cm^2\,V^{-1}\,s^{-1}$) for semi-crystalline self-organized P3HT films [17,18] for which it has been proved that the molecular orientation at the dielectric interface is the crucial factor [11]. These comparisons confirm the fact that one NF cannot be seen as one single crystalline region but instead is a superposition along its length of single crystalline regions with a characteristic length around 5 nm as suggested by the authors of Ref. [10]. Density functional theory calculations on crystal structure of P3HT have suggested that a likely structural disorder is one in which one of the polymer backbone within a lamella runs in the direction opposite to the majority [19].

From a technological point of view, we consider that the knowledge of μ_L and I_{max} is interesting for applications engineers to decide whether the NFs can be used or not as interconnecting wires in molecular electronics.

3.2. Transversal transport, μ_T

To investigate charge transport along the height of one NF, we used the sandwich geometry depicted in Fig. 2. The NFs were drop-cast and gently N_2 flushed on a conducting substrate. We have chosen Pt for its low roughness (<1 nm) and the fact that its work function (5.6 eV) is close to the highest occupied molecular orbital of P3BT ($\sim$5.3 eV). Since the NFs are deposited on a metal and the NFs surface coverage is low, measurements in the imaging mode (mapping at constant voltage) would lead to metal–metal contacts and consequently to shortcut currents which are orders of magnitude out of range, making the amplifier saturated and the images unstable. Consequently, measurements are forbidden in the imaging mode and restricted to the spectroscopic mode. In order to get reproducible and non-destructive measurements, we follow an appropriate strategy. Firstly, we acquire several successive topography maps at zero bias until the images are very stable. Secondly, we zoom in successively several times until the tip can be positioned on the target NF. Thirdly, the *I*/*V* characteristic is recorded. Finally, after zooming out, the same area is imaged and compared with the image before the *I*/*V* sweep to check that the NF is not destroyed by the measurement. To check the tip cleanliness, which is critical when investigating soft materials, *I*/*V* sweeps on the Pt electrode were regularly done in a short voltage range (+/− 100 mV to limit the current). Tips with a linear *I*/*V* response (ohmic behavior) were considered as good and used for the NFs while tips with other responses were disregarded.

A typical *I*/*V* curve obtained on a single P3BT NF is shown in Fig. 6. Due to the high work function of tip and bottom electrode, we can rule out electron current and consider our device as hole only. Diode characteristics on conjugated polymer are usually associated with space-charge limited current (SCLC) transport [20] and fitted by the Mott-Gurney law [21,22]: $J_{plannar} = \frac{9}{8}\varepsilon_r\varepsilon_0\mu_{T,V}\frac{V^2}{h^3}$ where *J* is the current density, ε_r (=3) is the relative dielectric permittivity of the active layer, ε_0 is the permittivity of free space, *V* is the applied voltage, and *h* is the NF height. Usually, a Poole–Frenkel form is used to take into account the field dependence of the mobility $\mu_{T,V}(V) = \mu_T e^{0.89\gamma(V/h)^{0.5}}$ (1) where μ_T is the zero field mobility, γ is proportional to the field dependence of the mobility. These equations are valid for devices with two plane electrodes where the field lines are perpendicular to the electrodes. For CAFM measurements, the geometry is much different at the tip sample contact and it leads to a current density significantly higher close to the tip. Reid et al. [23] have shown that the use of the standard above equations on CAFM data causes a mobility overestimation by up to three orders of magnitude depending on the ratio of the tip contact diameter, *d*, to the sample thickness, *h*. They propose the following correction: $\frac{J_{CAFM}}{J_{plannar}} = \frac{8}{9}\alpha\delta\left(\frac{h}{d}\right)^{1.6\pm0.1}$ (2)

where $\alpha = 8.2$ and $\delta = 7.8 \pm 1$. In our case, $h = 4$ nm and $d = 4$ nm which gives a correction factor of about 57.

We have performed measurements on isolated NFs of P3BT, P3HT and P3OT (at least ten independent NFs of each) and fitted the I/V curves to Eq. (2). However, the classic way to prove indisputably the SCLC character of the transport is to check that the current scales as $\propto 1/L^{1.4}$ (or $\propto 1/L^3$ for the planar device). Unfortunately, we cannot tune our sample thickness since the NF's height is fixed. Irrespective of the polymer, we find a typical value for γ of $\sim 1 \times 10^{-4}$ $m^{1/2} V^{-1/2}$ which is of the same order of magnitude as for reported values on conjugated polymers studied with CAFM [23,24]. On the other hand, we have found a remarkable dependence for μ_T with the alkyl side chain length as observed on Fig. 6. As explained in the experimental part, the NFs thickness is found to be alkyl chain length independent and therefore is not responsible for the variability of μ_T. The transversal mobility μ_T is found to decrease with the number of carbon atoms on the side chain. This suggests that longer alkyl chains reduce the efficiency of charge hopping from polymer chain to polymer chain. This statement is only valid if the NFs are oriented with the alkyl chain direction perpendicular to the substrate like depicted in Fig. 1. A detailed structural characterization of the NFs concluded that all of the polymer NFs strongly orient with the alkyl chain direction perpendicular to the substrate [8]. Moreover, the passivation of SiO_2 with HMDS is known to promote the same orientation. Then, we argue that the big majority of NFs segments orient like in Fig. 1 even if we cannot rule out that locally on some spots the NFs are slightly twisted or turned.

To our opinion, a better accuracy than one order of magnitude on μ_T seems difficult to reach because important factors like the contact force and contact diameter which have shown to play a crucial role [25] are hard to control or evaluate. In particular, the contact force has tendency to increase while scanning the sample probably due to tip voltage induced contact forces.

To our knowledge, charge transport investigation along the NF height is reported here for the first time. It is interesting to see that μ_L is three to four orders of magnitude higher than μ_T even if the applied field is much bigger for the transversal configuration [26] which is known to increase the mobility. This was expected since it is known that the fiber direction is a fast charge transport direction (through the π-orbital's overlap) while the alkyl side chain direction is much slower. It is also valuable to point out that, even if small, μ_T is not zero and therefore this has to be taken into account when designing devices architectures where transversal current in NFs is undesired.

4. Conclusion

In conclusion, charge transport in one single P3AT NF has been investigated along two distinct directions. We have developed a CAFM-based transistor which allows us to measure the longitudinal mobility along the length, corresponding to the π–π stacking direction, of one NF: $\mu_L = 0.07 \pm 0.03$ $cm^2 V^{-1} s^{-1}$. Then, in a second configuration, NFs were used in a sandwich structure and we have found a transversal mobility along the height, corresponding to the alkyl chain direction, of one NF: $\mu_T \sim 10^{-5}$–10^{-6} $cm^2 V^{-1} s^{-1}$ depending on the length of the alkyl side chain. With this approach charge transport anisotropy in P3AT NFs has been evidenced, yielding at least four orders of magnitude difference between μ_L and μ_T. We consider that the knowledge of I_{max}, μ_L and μ_T is an important step towards the use of conjugated polymer nanofibers in electronic applications.

Acknowledgements

This work was supported by the FWO (Fund for Scientific Research, Flanders, Belgium) project nanofibers R-1226, the IWT-SBO project 'POLYSPEC' and the Interreg project 'Organext'.

References

[1] G.A. O'Brien, A.J. Quinn, D.A. Tanner, G. Redmond, Adv. Mater. 18 (2006) 2379–2383.
[2] S. Samitsu, T. Shimomura, S. Heike, T. Hashizume, K. Ito, Macromolecules 43 (2010) 7891–7894.
[3] B. Berson, R. De Bettignies, S. Bailly, S. Guillerez, Adv. Funct. Mater. 17 (2007) 1377–1384.
[4] S. Bertho, W.D. Oosterbaan, V. Vrindts, J. D'Haen, T.J. Cleij, L. Lutsen, J. Manca, D. Vanderzande, Org. Electron. 10 (2009) 1248–1251.
[5] K.J. Ihn, J. Moulton, P.J. Smith, Polym. Sci. Part B: Polym. Phys. 31 (1993) 735.
[6] J.A. Merlo, C.D. Frisbie, J. Polym. Sci. Part B: Polym. Phys. 41 (2003) 2674.
[7] S. Samitsu, T. Shimomura, S. Heike, T. Hashizume, K. Ito, Macromolecules 41 (21) (2008) 8000–8010.
[8] W.D. Oosterbaan, V. Vrindts, S. Berson, S. Guillerez, O. Douhéret, B. Ruttens, J. D'Haen, P. Adriaensens, J. Manca, L. Lutsen, D. Vanderzande, J. Mater. Chem. 19 (2009) 5424–5435.
[9] J.A. Merlo, C.D. Frisbie, J. Phys. Chem. B 108 (2004) 19169–19179.
[10] T. Shimomura, T. Takahashi, Y. Ichimura, S. Nakagawa, K. Noguchi, S. Heike, T. Hashizume, Phys. Rev. B 83 (2011) 115314.
[11] W.D. Oosterbaan, J-C. Bolsée, A. Gadisa, V. Vrindts, S. Bertho, J. D'Haen, T.J. Cleij, L. Lutsen, C.R. McNeill, L. Thomsen, J.V. Manca, D. Vanderzande, Adv. Funct. Mater. 20 (2010) 792.
[12] S. Miyauchi, T. Kondo, K. Oshima, T. Yamauchi, M. Shimomura, H. Mitomo, J. Appl. Polym. Sci. 85 (7) (2002) 1429–1433.
[13] According to the Hertz model, the contact radius, r, is given $r^3 = 3FR/4E$ with $1/E = (1 - \nu_1^2)/E_1 + (1 - \nu_2^2)/E_2$ where F is the load, R is the tip radius and E is the Young's modulus. With $E_1 = 195$ GPa, $\nu_1 = 0.38$ for $PtIr_5$ and $E_2 = 1$ GPa, $\nu_2 = 0.35$ for polymer, r is found to be around 2 nm.
[14] J-C. Bolsée, J.V. Manca, Synth. Met. 161 (2011) 789–793.
[15] N. Karl, in: R. Farchioni, G. Grosso (Eds.), Organic Electronic Materials, Springer, Berlin, 2001.
[16] J.E. Northrup, Phys. Rev. B 76 (2007) 245202.
[17] H. Sirringhaus, P.J. Brown, R.H. Friend, M.M. Nielsen, K. Bechgaard, B.M.W. Langeveld-Voss, A.J.H. Spiering, R.A.J. Janssen, E.W. Meijer, P. Herwig, D.M. de Leeuw, Nature 401 (1999) 685–688.
[18] J.F. Chang, B. Sun, D.W. Breiby, M.M. Nielsen, T.L. Solling, M. Gilles, I. McCulloch, H. Sirringhaus, Chem. Mater. 16 (2004) 4772–4776.
[19] W. Xie, Y.Y. Sun, S.B. Zhang, J.E. Northrup, Phys. Rev. B 83 (2011) 184117.
[20] P.W.M. Blom, M.J.M. de Jong, J.J.M. Vleggaar, Appl. Phys. Lett. 68 (1996) 23.
[21] M.A. Lampert, P. Mark, Current injection in solids, Academic, New York, 1970.
[22] N.F. Mott, R.W. Gurney, Electronic processes in ionic crystals, oxford university press, London, 1948.
[23] O.G. Reid, K. Munechika, D.S. Ginger, Nano Lett. 8 (6) (2008) 1602–1609.
[24] H-N. Lin, H-L. Lin, S-S. Wang, L-S. Yu, G-Y. Perng, S-A. Chen, S-H. Chen, Appl. Phys. Lett. 81 (14) (2002) 2572.
[25] W. Frammelsberger, G. Benstetter, J. Kiely, R. Stamp, Appl. Surf. Sci. 253 (2007) 3615–3626.
[26] For longitudinal configuration: $E \sim 10^6$ $V.m^{-1}$. For transversal configuration: $E \sim 10^8$ $V.m^{-1}$.

organic/organic interface had a direct and pronounced impact on the performance of up-conversion devices (external efficiency, turn-on voltage, etc.) MoO_3-doped CuPc as the interface layer, the device showed the highest photon-to-photon conversion efficiency of 0.81 W/W%.

2. Experiment

The inorganic detector structure was prepared using *n*-GaAs substrate in a VEECO GEN-II molecular beam epitaxy (MBE) system. In the MBE chamber the surface oxide was desorbed at 580 °C, and a GaAs layer was grown as a buffer. Then, the thirty $In_{0.2}Ga_{0.8}As$/GaAs multiple quantum wells (MQWs) were grown under an Ga/In flux ratio of 2.2, which 8-nm-thick InGaAs wells were separated by 20-nm-thick GaAs barrier layers. Finally, the *p*-GaAs layer was grown as the interface layer for the up convertor. Fig. 1 shows a sketch of the up convertor. The first step in the device fabrication was to grow a 150-nm-thick SiO_2 layer on the top surface of the *p*-GaAs layer using plasma-enhanced chemical vapor deposition. This was for the purpose of preventing short circuits between the top electric contact and the underlying semiconductor substrate since the OLED layers would be only 140 nm thick. Square windows were patterned using standard photolithography and were chemically etched onto the SiO_2 layer. A metal contact In was deposited onto the back side of the *n*-GaAs substrate of the $In_{0.2}Ga_{0.8}As$/GaAs MQWs sample, serving as the common bottom contact for the up conversion devices. The *p*-GaAs surface is boiled in a mixture of sulfuric acid and phosphoric acid (H_2SO_4:H_3PO_4 = 3:1) to remove oxides for 5 min, then, ultrasonic cleaned in ethanol for 10 min, finally, washed in deionized water.

Then, the sample was placed into an organic molecular beam deposition system (OMBD) with the vacuum about 3×10^{-7} Torr. The OLED layers were deposited on top of the exposed *p*-GaAs areas. *N*,*N*′-bis-(1-naphthl)-diphenyl-1,1′-biphenyl-4,4′-diamine (NPB), 10-(2-benzothiazolyl)-2,3,6,7-tetrahydro-1,1,7,7-tetramethyl-1H,5H,11H-(1)-benzopyropyrano (6,7,8-i, j) quinolizin-11-one (C545T):tris(8-hydroxyquinoline)aluminum (Alq_3) and Alq_3 were used as hole transport, emitting and electron transport layers, respectively. And the thickness of NPB, C545T:Alq_3 and Alq_3 in these devices are 75, 30 and 30 nm, respectively. The MoO_3, CuPc and MoO_3-doped CuPc as hole injection layer in OLED, or the interface layer between inorganic detector structure and OLED, were investigated. On the top of organic layers of these devices are LiF (1 nm)/Al (25 nm) cathodes under identical conditions, which is partially transparent to green light.

The emission area of the devices was 0.01 cm^2 as determined by the overlap area of the anode and the cathode. The current density–voltage–luminescence (*J*–*V*–*L*) characteristics of the devices were measured by a ST-86LA spot photometer and a computer controlled Keithley electrometer 2400 at room temperature in ambient atmosphere. Veeco NanoScope 3D atomic force microscope (AFM) measurements were performed to characterize the surface morphology of the MoO_3-doped CuPc films and *p*-GaAs.

3. Results and discussion

We designed and fabricated the light up-conversion devices from 980 to 520 nm by direct tandem integration of an OLED and an inorganic photo detecting structure. As shown in Fig. 1, in this hybrid device, the *p*-GaAs top layer

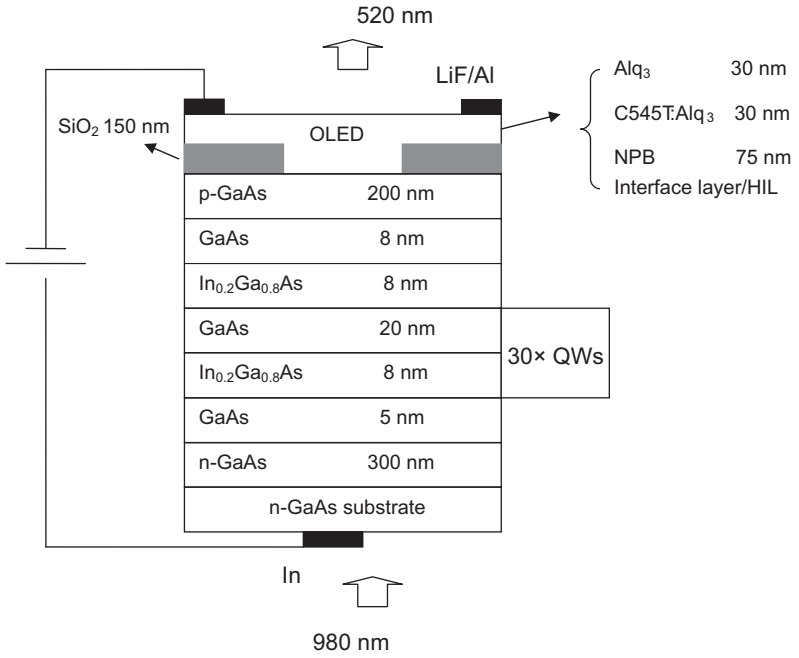

Fig. 1. Schematic diagram of up conversion device.

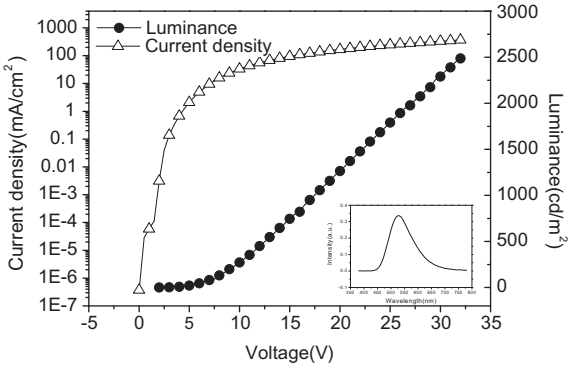

Fig. 2. Current density–voltage–luminance characteristics of device A under a 980 nm IR illumination. Inside picture is the spectrum of device A at 20 V.

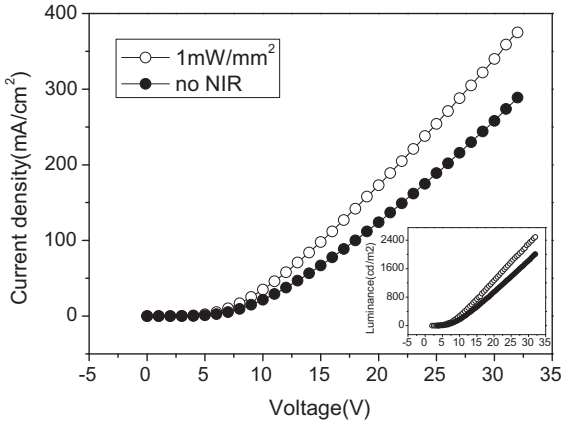

Fig. 3. Current density-voltage characteristics of device A under no IR and 1 mW/mm^2 illumination. Inside picture is the luminance–voltage characteristics of device A.

of inorganic photo detecting structure as the anode of the OLED. Under bias condition, the OLED component is under forward bias and the *p–i–n* detector component is under reverse bias. The input IR light was absorbed by the InGaAs/GaAs MQWs layer generating photocarriers, the photocarriers were then injected into the organic layers in OLED and emit green light from Al cathode surface. The injection of hole from *p*-GaAs layer is modulated by incoming 980 nm light. The interface layer between the organic and inorganic layers thus plays a vital role in such up-conversion devices.

Therefore, we fabricated three up convertor devices, which chose different interface layer (or hole injection layer in OLEDs), MoO_3-doped CuPc (device A), MoO_3 (device B) and CuPc (device C) [15]. The thickness of interface layer is 5 nm in all devices. Firstly, Fig. 2 shows the luminance–voltage–current density curves of the device A under a 980 nm IR illumination. The input NIR power density was around 1 mW/mm^2. The device with MoO_3-doped CuPc layer (50 V/V%, volume ratio) show significantly reduced operation voltages. The operation voltage of 2.8 V at 0.1 mA/cm^2 was achieved (The turn-on voltage is 2.6 V at 1 cd/m^2). As the device bias continued to increase, the current density (photocurrent density plus dark current density) increased rapidly up to ~200 mA/cm^2 at 20 V. Correspondingly, the output luminance of green emission (peaked at 520 nm) from OLED component arrived at 1264 cd/m^2 at 20 V. The luminance of this up-convertor device was even brighter than that of a LCD screen (about 200 cd/m^2). The results indicated that holes were injected from *p*-GaAs to organic layers efficiently, and the inorganic-organic interface had an excellent electrical connection in this device. Fig. 3 is plotted the voltage-current density of device A at no IR and 1 mW/mm^2 illumination, thus the turn-on voltage of the integrated device is increased from 2.8 to 3.8 V at same current density when there is no IR irradiation. Under dark condition (i.e., no input NIR illumination), the brightness of the device is also small, only 942 cd/m^2 at a bias of 20 V resulted from dark current density. OLED external power efficiency (W/A) can be calculated by assuming that the upconversion device is a Lambertian source, according to reference [11], the calculated optical power efficiency (W/A) = luminance efficiency $\times \pi/488$. The 488 lm/W is the effective power conversion constant that is normalized by the OLED emission spectrum (peaked in 520 nm). The overall external up conversion efficiency can then be calculated by multiplying the detector responsivity (A/W) and the OLED optical power efficiency (W/A), and the results are plotted in Fig. 4. It can be found that the highest external power efficiency of 0.015 W/A is achieved at the bias of

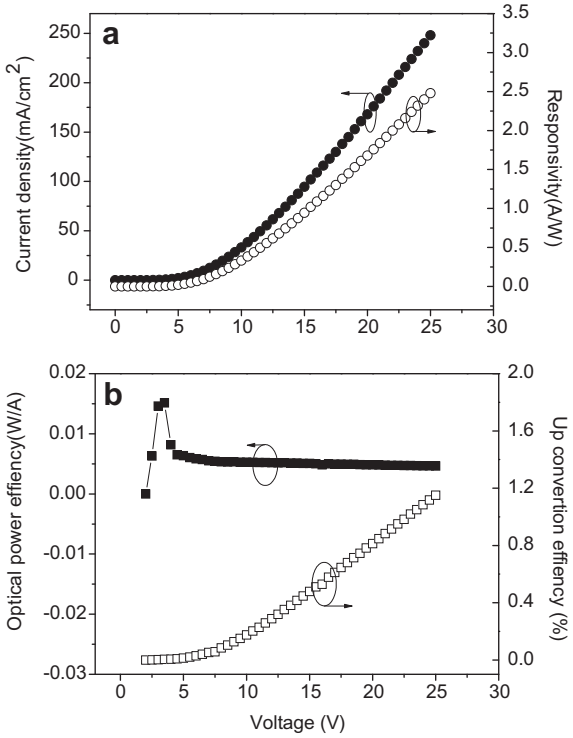

Fig. 4. (a) Current density and device responsivity versus voltage of device A and (b) optical power efficiency and up conversion efficiency versus voltage of device A.

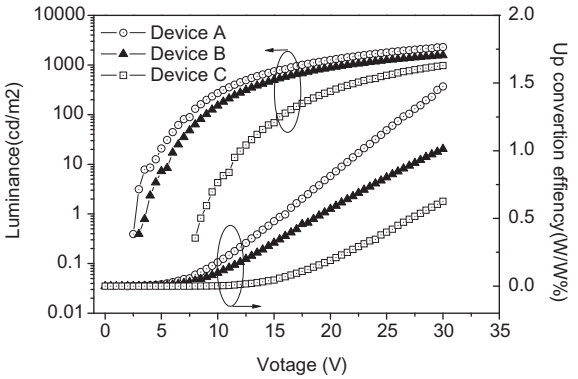

Fig. 5. Luminance and up conversion efficiency versus voltage characteristics of devices A, B, and C listed.

Table 1
The performance of devices A, B, and C in this work.

Device	Driving voltage at 1 cd/m^2 (V)	Luminance at 20 V (cd/m^2)	Upconversion efficiency at 20 V (W/W%)
A	2.6	1264	0.81
B	3.6	885	0.56
C	8.6	295	0.19

3.5 V, then it began to decrease to about 0.005 W/A at 10 V with little change in the bias. However, the overall external up conversion efficiency increased with the voltage, agreeing with the aforementioned current density-voltage characteristics. It increased up to around 0.81% W/W at a bias of 20 V. Under a bias of 20 V and an input 980 nm near infrared radiation of 1 mW/mm^2, the NIR induced green-light luminance reached up to 1264 cd/m^2, which was visible even under normal daytime light condition. Secondly, by comparing the three interface layers for device performance, we found that the appropriate interface layer is crucial for the organic and inorganic composite light up conversion device. As shown in Fig. 5 and Table 1, the turn-on voltage is 2.6, 3.6 and 8.6 V at 1 cd/m^2 for devices A, B, and C, respectively. Then, at the bias of 20 V, device brightness and upconversion efficiency is on the order of device A > device B > device C. Thus, these molybdenum oxide and organic materials composite as interface layer between the inorganic photo detecting structure and OLED is better than the single oxides or organic materials.

Fig. 6 shows AFM images of 50 V% MoO_3-doped CuPc (a), MoO_3 (b), and CuPc (c) films on glass substrates, the *p*-GaAs surface (d) of the inorganic photo detecting structure. The surface root-mean-square (RMS) roughness of 50 V% MoO_3-doped CuPc (a), MoO_3 (b), CuPc (c) and the *p*-GaAs surface (d) are 0.94, 2.06, 2.52 and 0.70 nm, respectively. The doped film owns a best smooth surface in these

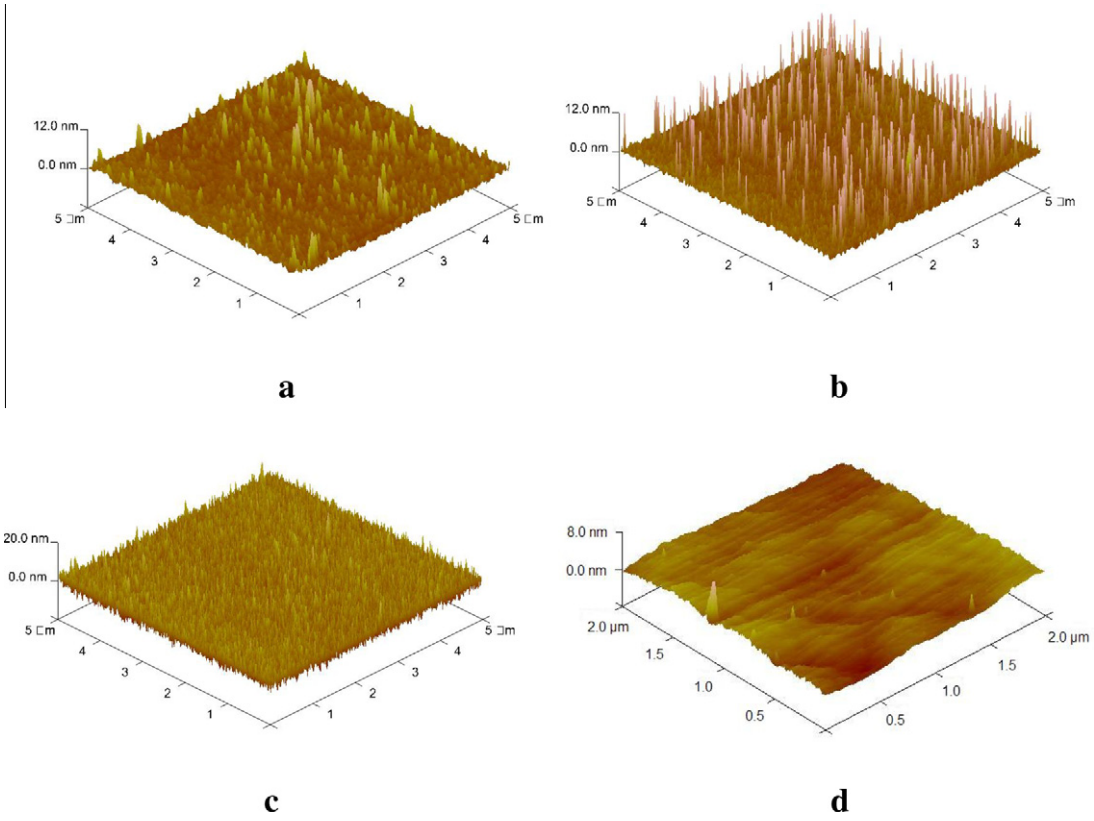

Fig. 6. The AFM images of 50 V% MoO_3-doped CuPc (a), MoO_3 (b), CuPc (c) films (about 50 nm) on glass substrates and the *p*-GaAs surface (d) of the inorganic photo detecting structure.

three organic layers. Moreover, the surface roughness of the composite films and *p*-GaAs are very small, but very close which is helpful for the ultimate device performance.

4. Conclusions

In conclusion, we have demonstrated the design, fabrication, and characterization of a hybrid optical up-convertor from 980 to 520 nm through direct tandem integration of an inorganic $In_{0.2}Ga_{0.8}As/GaAs$ MQWs photodetector and an OLED. Efficient carrier injection across the inorganic-organic interface was achieved by the insertion of a thin MoO_3-doped CuPc layer. The NIR induced green-light luminance reached up to 1264 cd/m^2 at a bias of 20 V under an input 980 nm NIR power density of 1 mW/mm^2. The appropriate interface layer of the hybrid devices lowered the turn-on voltage to 2.6 V for an output luminance of 1.0 cd/m^2. The maximum external upconversion efficiency of an optimized device at 20 V is 0.81%. It is worthy to note that large leakage current in this photo-detector affects the detector responsivity, thereby further affecting the device performance of the up-convertor. We think that surface leakage current caused by surface defect states is the key ingredient in our devices. In the following work, we are continuing to examine this issue related to surface passivation to reduce the leakage current, and thus further improve the performance of the up-convertor.

Acknowledgments

We acknowledge the supports from National Natural Science Foundation of China (NNSFC 60876043), Beijing Municipal Natural Science Foundation (Grant No. 2112040), and Beijing Nova Program (Grant No. 2010B056).

References

[1] D. Ban, H. Luo, H.C. Liu, Z.R. Wasilewski, A.J. SpringThorpe, R. Glew, M. Buchanan, J. Appl. Phys. 96 (2004) 5243–5348.
[2] Y. Yang, W.Z. Shen, H.C. Liu, S.R. Laframboise, S. Wicaksono, S.F. Yoon, K.H. Tan, Appl. Phys. Lett. 94 (2009) 093504.
[3] Lai Zhao, Pete Thompson, N.N. Faleev, D.W. Prather, Ian Appelbaum, Appl. Phys. Lett. 90 (2007) 121132.
[4] H. Luo, D. Ban, H.C. Liu, Z.R. Wasilewski, M. Buchanan, Appl. Phys. Lett. 88 (2006) 073501.
[5] Y. Sun, N.C. Giebink, H. Kanno, B. Ma, M.E. Thompson, S.R. Forrest, Nature 440 (2006) 908.
[6] Y.J. Lu, C.H. Chang, C.L. Lin, C.C. Wu, H.L. Hsu, L.J. Chen, Y.T. Lin, Nishikawa Ryuji, Appl. Phys. Lett. 92 (2008) 123303.
[7] S. Shi, D. Ma, Phys. Status Solidi A 206 (2009) 2641.
[8] L. Li, M. Guan, G. Cao, Y. Li, Y. Zeng, Solid State Commun. 150 (2010) 1683–1685.
[9] J. Ni, T. Tano, Y. Ichino, T. Hanada, T. Kamata, N. Takada, K. Yase, Jpn. J. Appl. Phys. 40 (2001) L948–L951.
[10] M. Chikamatsu, Y. Ichino, N. Takada, M. Yoshida, T. Kamata, K. Yase, Appl. Phys. Lett. 81 (2002) 769–771.
[11] D. Ban, S. Han, Z.H. Lu, T. Oogarah, A.J. SpringThorpe, H.C. Liu, Appl. Phys. Lett. 90 (2007) 093108.
[12] J. Chen, D. Ban, X. Feng, Z. Lu, S. Fathololoumi, A.J. SpringThorpe, H.C. Liu, Appl. Phys. Lett. 103 (2008) 103112.
[13] Jun Chen, Dayan Ban, Michael G. Helander, Zhenghong Lu, Marcel Graf, Philip Poole, H.C. Liu, IEEE Photonics Technol. Lett. 21 (2009) 1447.
[14] F. So, D.Y. Kim, K.R. Choudhury, J.W. Lee, D.W. Song, G. Sarasqueta, Nano Lett. 11 (5) (2011) 2109–2113.
[15] L. Li, M. Guan, G. Cao, Y. Li, Y. Zeng, Appl. Phys. A. 99 (2010) 251–254.

niques are commonly used to deposit polymer films due to their high solubility in various solvents; the long polymer chains facilitate uniform film formation across the entire substrate. In general, small molecules exhibit better electrical and optical properties than polymers; therefore, development of solution-based patterning techniques for small molecule devices is of great interest [8,9].

Recent advances in film deposition and patterning techniques have enabled the fabrication of micro-OLEDs with fine pixel sizes. Micro-pixels are commonly prepared by patterning the anode or cathode by using photolithography, and blocking the electrode contacting area with insulating materials [5]. Organic small molecules can be deposited with solution-based techniques with the proper solvent. Techniques such as an ink-jet printing [10,11], roll to roll processing [12], or screen printing [13,14] have been demonstrated, but these techniques have limited resolution due to large droplet size and spreading of the solution. Micro/nano-contact printing techniques have been developed as a substitute for traditional fabrication techniques utilizing solution-processible characteristics [15–17].

Besides precise patterning, uniform film deposition is required over large areas and the organic materials must function properly in the display. Organic materials must maintain a uniform amorphous state during the fabrication process since device performance strongly depends on the morphological properties of the film, affecting color purity, device efficiency, and device lifetime. OLEDs require balanced electron and hole current transport to generate efficient electroluminescence [18]. Electron transport materials (e.g. Alq3) are chemically and environmentally sensitive to their processing and operating conditions. Any morphological transformation such as cluster formation or crystallization may alter the overlap of the π molecular orbitals, negatively impacting OLED function via red-shift of the emisson spectrum or decrease in quantum efficiency due to increased non-radiative recombination rates. In addition, the device could experience a significant decrease in lifetime [19–21]. Therefore, proper fabrication techniques and materials properties will be necessary to minimize imperfections so as to achieve functioning devices [22,23].

Here, we demonstrate a pixel patterning method by combining spin-casting with a structured hydrophobic surface to achieve directed self-assembly of Alq3 pixels with well-defined pixel size and long-range order. OLED structures based upon Alq3/TPD have been studied widely since these materials typically produce efficient performance for green emitting displays [24,18]. The device structure in this report consists of stacks of PEDOT/TPD/Alq3/LiF/Al [25,26]. This solution-based spin-on patterning technique can resolve the problems of local pixel placement and size through the use of photolithography, which allows higher resolution patterning of OLED pixels compared to shadow masking; here, we demonstrate pixels as small as 10 μm. A potential application of the spin-on patterning technique is in microdisplays [27]. A microdisplay is a moderate to high-resolution, small-diagonal display that is typically placed closer than 10-in. (~25 cm) to the eyes. Desired resolutions are 800 × 600 and 1280 × 1024 (SVGA, XGA, and SXGA formats), with active areas between 5 and 80 mm^2 and pixel sizes between 5 and 30 μm [28].

2. Experimental

2.1. Materials

Tris(8-hydroxyquinoline) aluminum (Alq3, Aldrich) was purified by sublimation and *N*,*N*-bis(3-methylphenyl)-*N*,*N*-diphenylbenzidine (TPD, Aldrich) was used as received. Poly(3,4-ethylendioxythiophene)-poly (styrenesulfonate) (PEDOT) (2.8 wt. % dispersion in H_2O, low-conductivity grade) was diluted with 1:1 ratio in DI water and sonicated before deposition. Octadecyl-trichlorosilane (OTS, Gelest, Inc.) was used as received. Chloroform (ACS reagent) was used as received without further purification. ITO/glass was purchased from Delta technology (ITO thickness: 100 nm, substrate thickness: 0.7 mm, sheet resistance, R_s: 1525 Ω, nominal transmittance: > 78%).

2.2. Thin film characterization

P-type silicon wafers [100] (1–10 Ω cm) were used as substrates to prepare Alq3 films for morphology scanning by atomic force microscopy (AFM), X-ray diffraction (XRD), and photoluminescence (PL) intensity versus wavelength. The wafer was diced into rectangular pieces, sonicated for 10 min at room temperature, rinsed with DI water, and then cleaned with a hot 'piranha solution' (25% concentrated hydrogen peroxide, 75% concentrated sulfuric acid) for 1 h to remove organic contaminants and strip the native silicon dioxide surface layer. Finally, the treated substrates were sonicated and thoroughly rinsed with DI water and dried in dry nitrogen flow. Alq3 solution was prepared with a concentration of 0.5 wt.% in chloroform in a clean room with short-UV filtered lighting to prevent photo-oxidation in the solution state. Alq3 solution was then spin-cast at 3000 rpm for 30 s on the cleaned Si substrate, which results in uniform 50 nm Alq3 thin films.

2.3. Pixel patterning

The pixel patterning process is illustrated in Fig. 1. Micro-channel or square well arrays with widths ranging from 10 to 100 μm and depths of 0.2 μm covering a total active area 6 × 6 mm^2 were fabricated in silicon using standard micro-fabrication techniques. A 500 nm silicon dioxide layer was grown by thermal oxidation as a wet etching mask. The SiO_2/Si wafers were cleaned as follows: sequential ultrasonic rinse in acetone, methanol, isopropyl alcohol, DI water, and baked at 200 °C prior to deposition of photoresist. The microchannels or wells were patterned by photolithography using Shipley 1813 positive photoresist and then developed with Shipley 352. The photoresist-patterned wafer was baked on a hot plate at 120 °C for 5 min. The wafer was etched with buffered oxide etch (BOE) to define the KOH etching mask in SiO_2. The patterned wafer was then etched to 0.2 μm with 60 wt.% KOH at 60 °C with high speed stirring to prevent formation of vapor on the Si surface, and then the SiO_2 mask was removed with BOE. The wafer was diced into 13 × 13 mm^2 squares. The diced substrates were oxidized by oxygen plasma for 1 min, resulting in a fresh silicon oxide layer

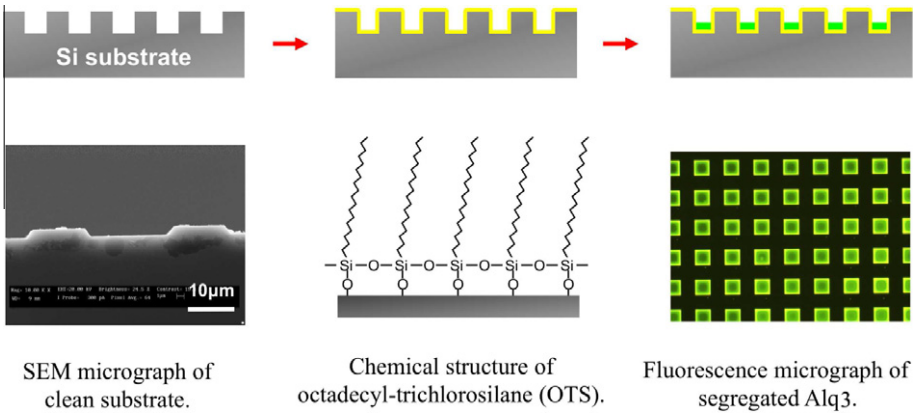

Fig. 1. Schematic of the spin-casting process onto pre-patterned substrates.

of 1.0–1.2 nm with a high density of silanol (Si–OH) groups. The substrates were treated in 1 mM OTS/toluene solution for 1 h and rinsed thoroughly with toluene and chloroform in an ultrasonic bath for 10 min each, leaving a monolayer with thickness 2–3 nm [29]. The OTS treated substrates were hydrophobic with a water contact angle of $\sim 100°$. Alq3 solution was prepared as before and drop-cast through a 0.4 μm pore size filter onto the spinning patterned substrate at 3000 rpm for 30 s. The addition of hydrophobic OTS to the surface discourages the adsorption of Alq3, thereby resulting in selective deposition in the pre-patterned micro-channels or wells [30,31]. The organic molecules on top are unstable and move toward the edges of the substrate during spinning, but the organic molecules on the bottom are trapped in the pre-patterned micro-channels or wells.

2.4. OLED fabrication

The bottom-emitting structure with a PEDOT hole injection layer consists of the following layers: ITO/PEDOT/Alq3:TPD/LiF/Al, as shown in Fig. 2. Despite the advantages of solution-based techniques, the solvent used can chemically destroy any pre-deposited layers. Therefore, here we make use of a single emissive layer consisting of a mixture of Alq3 as the electron transport and emissive material and TPD as the hole transport material. Mixed layers have been reported before, with vapor phase deposition [19] and spin-casting [32].

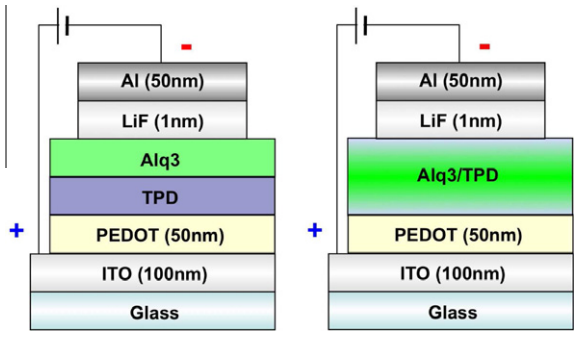

Fig. 2. Bottom emitting structure of Alq3-based OLED (left) and modified OLED structure incorporating TPD and Alq3 into the same layer (right).

The process of fabricating a bottom-emitting structure using the spin-on patterning technique is presented in Fig. 3. Insulating micro-channels and wells were fabricated in SiO_2 using microfabrication techniques. Two types of devices were made-pixel patterned devices and reference (i.e. large pixel) devices. For pixel patterned devices, insulating micro-wells were fabricated in SiO_2/ITO/glass as follows. SiO_2 was deposited onto ITO/glass substrates (bottom-emitting structure) by plasma-enhanced chemical vapor deposition (PECVD, Oxford Plasmalab 80) to a thickness of 0.2 ± 0.01 μm as determined by ellipsometry (Woollam V-VASE) and contact profiling (Tencor P-10 Profilometer). Substrates were ultrasonically-cleaned in DI water and wells of widths 10–100 μm were patterned in photoresist as described previously, across a 6×6 mm^2 area. The patterned substrates were dry-etched by RIE (Oxford Plasmalab 80) using CF_4 with etching rate 35–37 nm/min. Substrates were treated with 1 mM OTS as described previously. For reference devices, the SiO_2 layer was patterned into four 11×2 mm^2 macro-pixels, and OTS treatment was not performed.

Diluted PEDOT was filtered through a 0.4 μm pore size filter and spin-cast at 3000 rpm for 1 min, yielding ~50 nm film. The PEDOT film was cured in an oven at 120°C for 1 h to drive off water solvent and improve adhesion, then taped off to remove residue on the top of pre-patterned wells. An Alq3/TPD mixture was dissolved with 1 wt.% in chloroform in an ultrasonic bath for 10 min. This mixture was drop-cast through a 0.4 μm pore size filter on the spinning substrate, resulting in a thickness of the active organic layer of ~100 nm.

For electrical tests, the substrates were protected from light until being loaded into a thermal evaporation system. LiF and Al were sequentially deposited as the electron injection layer and cathode, respectively, with a base pressure less than 10^{-6} Torr. The devices were completed by packaging with an optical adhesive (Norland Product Inc.), covered by a thin glass slide under long wavelength UV exposure. Pertinent fabrication procedures were performed in a glove box with nitrogen ambient to prevent photo-oxidation of the organic films.

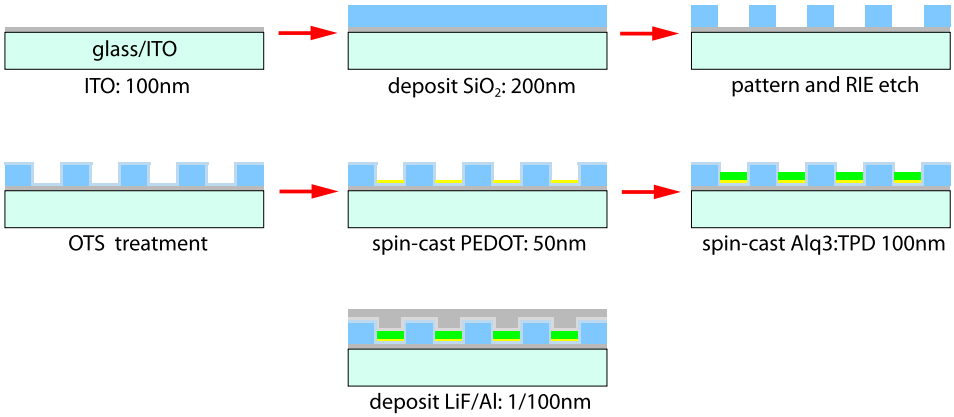

Fig. 3. Process flow for fabrication of bottom emitting OLED by using the spin-on method.

2.5. OLED characterization

All organic film thicknesses were measured by ellipsometry (Woollam V-VASE) and surface profilometry (Tencor P-10). Amorphous Alq3 film morphology was observed by atomic force microscopy (AFM) using intermittent-contact mode with low spring force constant (40 N/m) and resonance frequency 325 kHz. The quality of the film was assessed by RMS roughness measurement. XRD investigation was carried out with a Cu K-alpha standard radiation source ($\lambda = 1.54060$) with an acceleration voltage of 45 kV and a current flow of 40 mA. The PL intensity versus wavelength was measured by a SPEX fluorolog (HORIBA Jobin Yvon Inc.) at excitation wavelength 365 nm. The excitation source is a xenon lamp which is filtered through a monochromator with bandwidth approximately 15 nm (−5/+10). Collection is performed through a second monochromator connected to a photomultiplier tube for detection. EL spectra (luminescence intensity versus wavelength) were measured by a multichannel spectrometer. Luminescence–current–voltage characteristics (L–J–V) were measured by using a digital voltmeter (computer controlled Keithley 236 source). The completed OLEDs were mounted onto the surface of a silicon photodiode module (PIN-10D, OSI optoelectronics) in the forward emission direction for EL measurement. All of the measurements were performed in air.

3. Results and discussion

3.1. Characterization of spin-cast films

The morphological properties were investigated by atomic force microscopy (AFM) and X-ray diffraction (XRD). AFM scanning of spin-cast Alq3 showed smooth and uniform films with no obvious cracks or pinholes, with 2.9 Å RMS surface roughness, as indicated in Fig. 4. Interestingly, spin-casting produced a smoother surface than thermal evaporation (RMS roughness 3.7 Å). XRD scans indicated that Alq3 films prepared by both thermal evaporation and spin-casting are in the glassy amorphous state.

Fig. 4(c) shows the typical photoluminescence (PL) emission peak of Alq3 film around 520 nm. The PL spectrum can be disturbed by impurities, stress, or morphological deformations in the film during the deposition process. If the film undergoes stress during deposition, the PL emission peak blue shifts, while the formation of crystalline structures in the film causes the emission peak to red shift [23,2,3]. Thus, PL measurement provides a sensitive diagnostic of film

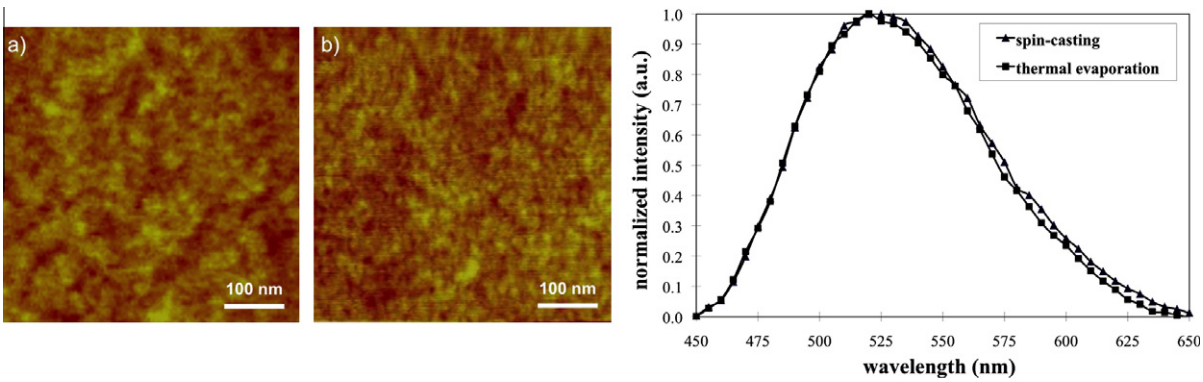

Fig. 4. AFM topographic scans across 500 × 500 nm areas: (a) thermally evaporated film (thickness 50 nm, RMS roughness 3.7 Å) and (b) spin-cast film (thickness 50 nm, RMS roughness 2.9 Å). PL spectra of Alq3 film (c) deposited by thermal evaporation (square symbol) and by spin-casting (circle symbol). The excitation wavelength is 365 nm.

properties. As shown in Fig. 4, the emission spectra of spin-cast and thermally-evaporated Alq3 films are consistent.

3.2. Pixel patterning

The organic films formed in the pre-patterned channels and wells with pixel sizes ranging from 10 to 100 μm were observed by fluorescence microscopy, as shown in Fig. 5. Without OTS treatment, a uniform film of Alq3 forms across the entire substrate.

3.3. Reference OLED characterization

We tested the effect of spin casting a hole injection layer PEDOT between the ITO interface and the Alq3:TPD organic layer prepared by spin-casting (previous reports

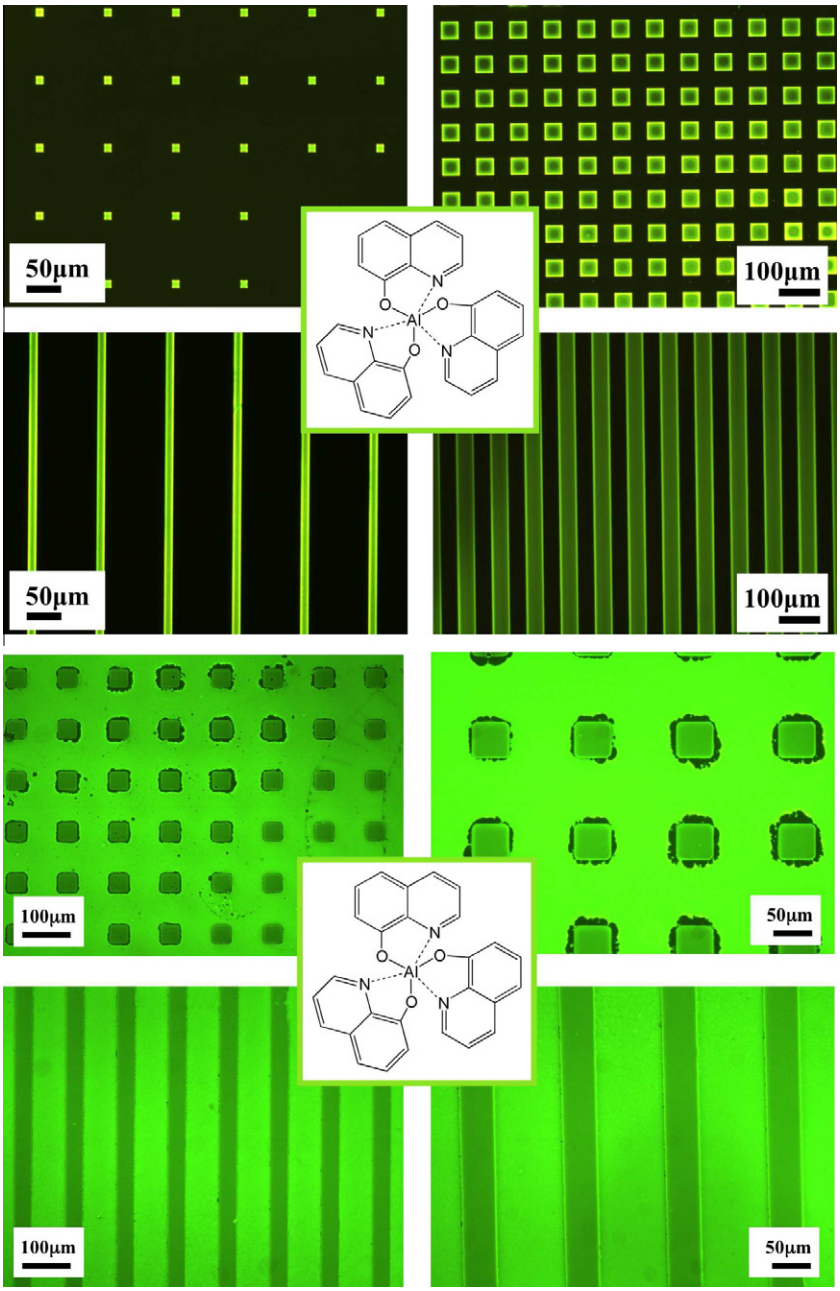

Fig. 5. Photoluminescence images of spin-cast Alq3 onto patterned substrates treated with the OTS monolayer (upper group) and without the OTS monolayer (lower group). The widths of the square pixels (wells) are 10 μm (top left) and 50 μm (top right), and the widths of the stripe pixels are 10 μm (bottom left) and 50 μm (bottom right), respectively. Excitation is at 365 nm.

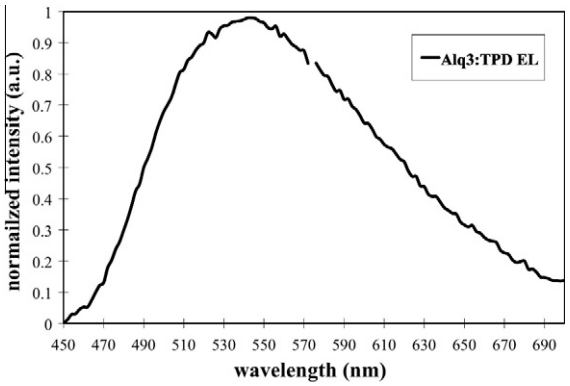

Fig. 6. Electroluminescence spectrum of the reference OLED using a mixed Alq3:TPD layer.

of using PEDOT have been with evaporated Alq3 and TPD layers). A smooth organic interface results in reduction of electrical shorts and the threshold voltage. Roughness characterization by AFM shows that the PEDOT layer is smoother (RMS roughness: 4.1 Å) than the underlying ITO layer (RMS roughness: 8.4 Å), but subsequent deposition of Alq3:TPD increases roughness (RMS roughness: 7.5 Å). The low roughness of our results may be due to the polished ITO/glass substrate, which is smoother than ITO/glass used in other published reports (RMS ~ 1–3 nm) [33]. For comparison, a report of Alq3/TPD evaporated onto ITO obtained RMS roughness of 1.7 nm [34].

Fig. 6 shows the electroluminescence spectrum of the Alq3:TPD based OLED, which shows the expected broad peak starting from 450 to 800 nm and maximum EL intensity at 542 nm. This spectrum is close to that of typical Alq3-based OLEDs but red-shifted compared to the PL spectrum of spin-cast Alq3 film. The shifting is likely due to mixing of Alq3 and TPD [19,32].

Fig. 7 shows the L–J–V characteristics of devices with and without the PEDOT layer. The effect of PEDOT is to reduce the turn-on voltage to ~6 V from ~7.5 V without PEDOT (here, we define the turn-on voltage as the applied voltage required to obtain light emission above the background level). PEDOT reduces the energy barrier by about 0.2 eV between the anode (ITO) and HTL (TPD) layers, which improves hole injection and transport [35]. Charge injection and transport are primarily responsible for operating voltage and luminous efficiency. We do not expect to obtain higher efficiency than a single heterojunction device prepared by thermal evaporation since we use a mixed HTL:ETL layer to achieve a one step patterning process. The PEDOT device shows lower current density above 11 V and lower electroluminescence intensity above 13 V as compared to the non-PEDOT device. However, electroluminescence as a function of current density exhibited by the PEDOT device shows that it operates more efficiently than the non-PEDOT device. This is because the hole current is limited by injection and PEDOT increases hole injection to TPD, which drives an increase in the electron/hole recombination rate.

3.4. Patterned OLED characterization

In the spin patterning technique, obtaining an amorphous film with uniform surface coverage in the pre-patterned regions is the main objective, because the local current density with applied voltage strongly depends on film qualities [34]. Fig. 8 shows scanning electron microscopy (SEM) and photoluminescence images of the patterned OLED pixels. The SEM images (a) and (b) were taken after dry-etching the SiO_2 layer. The photoluminescence images were taken after deposition of the OTS monolayer and spin-casting of the Alq3:TPD layer. One limitation of this spin-on patterning technique is that the solution is driven into the edges of the pre-patterned channels or wells. Sample (c) is prepared by spin-casting Alq3:TPD on an OTS treated substrate without a PEDOT layer. The image clearly shows accumulation of organic at the edges, which will eventually drop device efficiency. Uniform thickness is important since the operating voltage required for light emission is strongly dependent on the thickness of the organic materials. PEDOT can be deposited on the OTS treated pre-patterned substrate as a hole injection layer. In addition, the PEDOT layer prevents edge accumulation as shown in photoluminescence image (d) through the increased affinity of Alq3:TPD to PEDOT.

The micro-patterned device without the OTS layer operates without current leakage, and with lower threshold voltage (about 4.4 V) and higher current density as compared to the reference device, as shown in the J–V curves of Fig. 9. Furthermore, from the L–J plot, it is clear that the EL efficiency is higher. This may be due, in part, to the fact that our patterned device structure bears similarity to the low-index grid structure that has been shown to significantly increase light extraction (i.e. external quantum efficiency) [36].

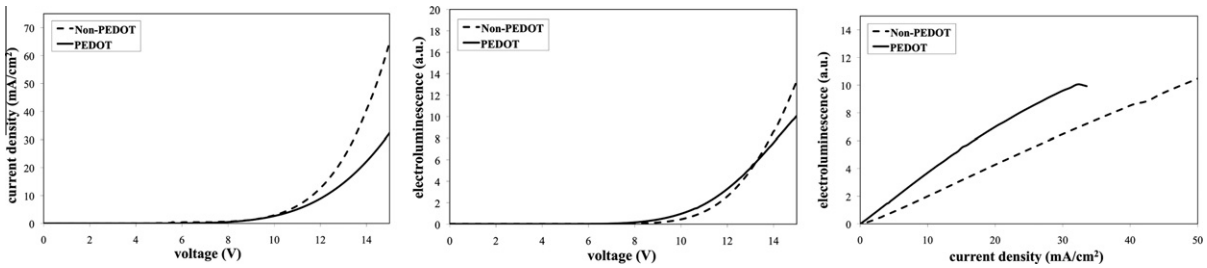

Fig. 7. J–V (left), L–V (middle) and L–J (right) characteristics of unpatterned reference OLED based upon a spin-cast Alq3:TPD layer with and without PEDOT. The active area is 0.22 cm^2.

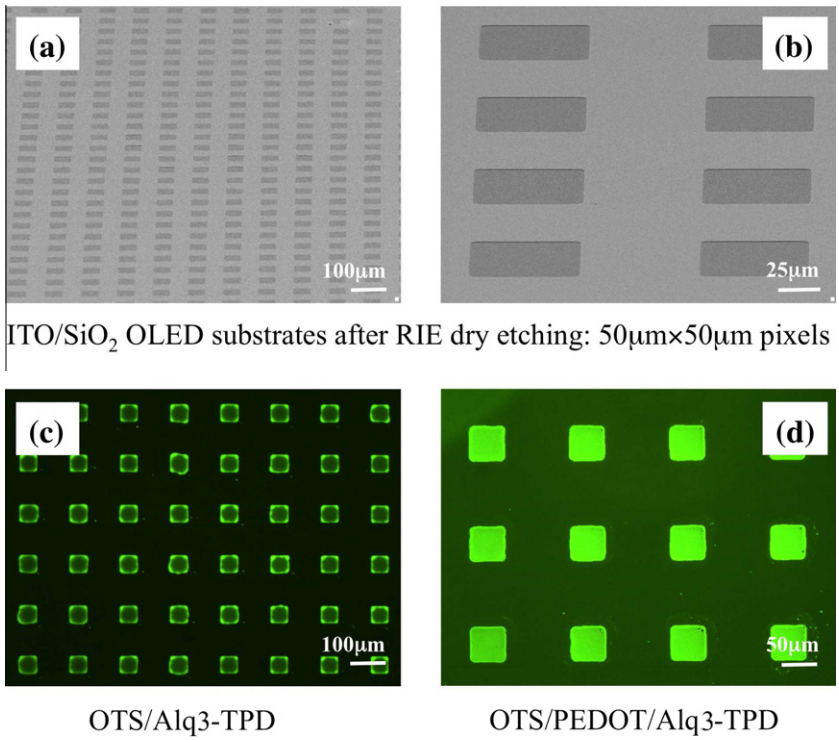

Fig. 8. Scanning electron microscopy images: (a) and (b) pixel size 50 μm; photoluminescence images of 50 μm OLED pixels: (c) without PEDOT, (d) with PEDOT. Excitation is at 365 nm.

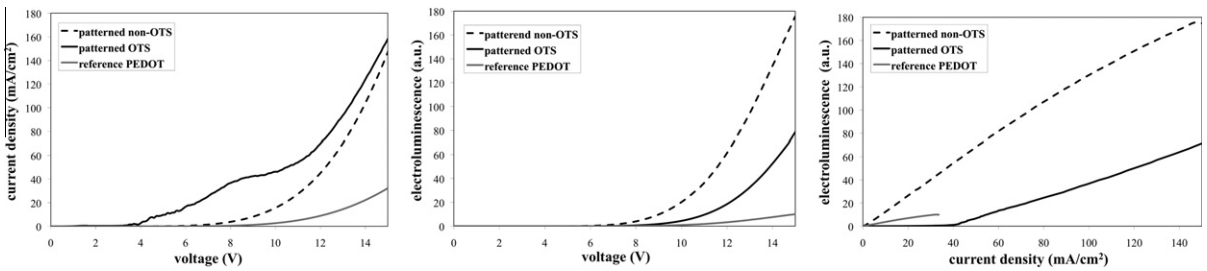

Fig. 9. J–V (left), L–V (middle) and L–J (right) characteristics of pixelated OLED based upon a spin-cast Alq3:TPD layer for non-OTS and OTS devices. Total active pixel area is 0.04 cm^2.

In the micro-patterned OTS device, there is no current leakage observed at low voltages, but an abrupt change of current occurs in the J–V characteristics beyond 4 V, with a turn-on voltage about 5.8 V. This device operates with higher current density than the non-OTS device, which could be the result of a thinner active layer, increased hole injection, and/or reduced resistance through the OTS layer at the inorganic–organic interface, perhaps via incomplete OTS coverage. The EL intensity of the OTS device at the same voltage is lower, suggesting that the increased current density leads to Joule heating rather than resulting in light emission. Indeed, the EL intensity versus current plot shows that the non-OTS device is more efficient, warranting further study on the role of the OTS layer on the electrical properties of the device, along with optimizations in the fabrication process.

4. Conclusions

In summary, we have demonstrated a solution-based patterning technique for fabricating high-resolution Alq3 OLED pixels based upon spin-casting combined with a structured surface consisting of etched channels or wells. The structured surface is modified with OTS, which serves to direct solution into the etched areas. This method achieves precise pixel placement and geometry, and long-range order dictated by photolithographic methods. However, we need to better understand the role of OTS on the electrical device properties, and further efforts to improve device performance are needed. It should be noted that OTS is a well-known gate dielectric layer for OTFT's [37]. The functional role of OTS in this fabrication method is as a hydrophobic layer [38], so organic monolayers with other

terminal ends should be investigated for possible improvements in device performance. In general, this technique should also be compatible with conjugated polymers [30,38] and may offer a promising solution to front-end patterning of molecular organic semiconductors for high resolution large-area, low-cost display applications.

References

[1] K. Liao, OLED market outlook, Tech. rep., DisplaySearch (2008).
[2] J.N. Bardsley, International OLED technology roadmap, IEEE Journal of Selected Topics in Quantum Electronics 10 (1) (2004) 3–9.
[3] C.C. Wu, C.W. Chen, C.L. Lin, C.J. Yang, Advanced organic light-emitting devices for enhancing display performances, Journal of Display Technology 1 (2) (2005) 248–266.
[4] H. Klauk (Ed.), Organic Electronics: Materials, Manufacturing, and Applications, Wiley-VCH, 2006.
[5] S.R. Forrest, The path to ubiquitous and low-cost organic electronic appliances on plastic, Nature 428 (6986) (2004) 911–918. http://dx.doi.org/10.1038/nature02498.
[6] S.R. Forrest, Ultrathin organic films grown by organic molecular beam deposition and related techniques, Chemical Reviews 97 (6) (1997) 1793–1896. http://dx.doi.org/10.1021/cr941014o.
[7] G.J. Burger, E.J.T. Smulders, J.W. Berenschot, T.S.J. Lammerink, J.H.J. Fluitman, S. Imai, High-resolution shadow-mask patterning in deep holes and its application to an electrical wafer feed-through, Sensors and Actuators A: Physical 54 (1–3) (1996) 669–673. http://www.sciencedirect.com/science/article/B6THG-3TTDFRM-3J/2/7ebeb64c2d9e2c6cb37adc427dc71272.
[8] G.P. Collins, Next stretch for plastic electronics, Scientific American 291 (2) (2004) 74–81.
[9] W. Brutting (Ed.), Physics of Organic Semiconductors, Wiley-VCH, 2006.
[10] T.R. Hebner, C.C. Wu, D. Marcy, M.H. Lu, J.C. Sturm, Ink-jet printing of doped polymers for organic light emitting devices, Applied Physics Letters 72 (5) (1998) 519–521. http://link.aip.org/link/?APL/72/519/1.
[11] T. Shimoda, K. Morii, S. Seki, H. Kiguchi, Inkjet printing of light-emitting polymer displays, MRS Bulletin 28 (11) (2003) 821.
[12] P.C. Kao, S.Y. Chu, C.Y. Zhan, L.C. Hsu, W.C. Liao, Fabrication of organic light-emitting devices on flexible substrates using a combined roller imprinting and photolithography-patterning technique, Journal of Vacuum Science & Technology B: Microelectronics and Nanometer Structures 24 (3) (2006) 1278–1282. http://link.aip.org/link/?JVB/24/1278/1.
[13] Z. Bao, Y. Feng, A. Dodabalapur, V.R. Raju, A.J. Lovinger, High-performance plastic transistors fabricated by printing techniques, Chemistry of Materials 9 (6) (1997) 1299–1301. http://dx.doi.org/10.1021/cm9701163.
[14] K. Mori, T. Ning, M. Ichikawa, T. Koyama, Y. Taniguchi, Organic light-emitting devices patterned by screen-printing, Japanese Journal of Applied Physics 39 (Part 2, No. 9A/B) (2000) L942–L944. doi:10.1143/JJAP.39.L942. http://jjap.ipap.jp/link?JJAP/39/L942.
[15] T. Granlund, T. Nyberg, L.S. Roman, O. Inganas, Patterning of polymer light-emitting diodes with soft lithography, Advanced Materials 12 (4) (2000) 269–273.
[16] X. Cheng, Y. Hong, J. Kanicki, L.J. Guo, High-resolution organic polymer light-emitting pixels fabricated by imprinting technique, Journal of Vacuum Science & Technology B: Microelectronics and Nanometer Structures 20 (6) (2002) 2877–2880. http://link.aip.org/link/?JVB/20/2877/1.
[17] C.Y. Cheng, F.C.N. Hong, Fabrication of organic light-emitting diode arrays on flexible plastic substrates by imprint lithography, Japanese Journal of Applied Physics 45 (11) (2006) 8915–8919. http://jjap.ipap.jp/link?JJAP/45/8915.
[18] W. Li, R.A. Jones, S.C. Allen, J.C. Heikenfeld, A.J. Steckl, Maximizing Alq3 OLED internal and external efficiencies: charge balanced device structure and color conversion outcoupling lenses, Journal of Display Technology 2 (2) (2006) 143–152. http://jdt.osa.org/abstract.cfm?URI=jdt-2-2-143.
[19] E.M. Han, L.M. Do, N. Yamamoto, M. Fujihira, Crystallization of organic thin films for electroluminescent devices, Thin Solid Films 273 (1–2) (1996) 202–208. http://www.sciencedirect.com/science/article/B6TW0-3VR9X1X-4N/2/a9c5727b7452e3186a3b49c402e549b6.
[20] H. Aziz, Z. Popovic, S. Xie, A.M. Hor, N.X. Hu, C. Tripp, G. Xu, Humidity-induced crystallization of tris (8-hydroxyquinoline) aluminum layers in organic light-emitting devices, Applied Physics Letters 72 (7) (1998) 756–758. http://link.aip.org/link/?APL/72/756/1.
[21] S.Y. Kim, K.Y. Kim, Y.-H. Tak, J.-L. Lee, Dark spot formation mechanism in organic light emitting diodes, Applied Physics Letters 89 (13) (2006) 132103–138108. http://link.aip.org/link/?APL/89/132108/1.
[22] J. Shinar (Ed.), Organic Light-Emitting Devices: A Survey, Springer-Verlag, 2002.
[23] L.S. Hung, C.H. Chen, Recent progress of molecular organic electroluminescent materials and devices, Materials Science and Engineering: R: Reports 39 (5–6) (2002) 143–222. http://www.sciencedirect.com/science/article/B6TXH-473MBJY-1/2/c3e2151c53ae7eefff7ef8bdeb4d059e.
[24] W.H. Kim, A.J. Makinen, N. Nikolov, R. Shashidhar, H. Kim, Z.H. Kafafi, Molecular organic light-emitting diodes using highly conducting polymers as anodes, Applied Physics Letters 80 (20) (2002) 3844–3846. http://link.aip.org/link/?APL/80/3844/1.
[25] L.S. Hung, C.W. Tang, M.G. Mason, Enhanced electron injection in organic electroluminescence devices using an Al/LiF electrode, Applied Physics Letters 70 (2) (1997) 152–154. http://link.aip.org/link/?APL/70/152/1.
[26] H. Mu, W. Li, R. Jones, A. Steckl, D. Klotzkin, A comparative study of electrode effects on the electrical and luminescent characteristics of Alq3/TPD OLED: improvements due to conductive polymer (PEDOT) anode, Journal of Luminescence 126 (1) (2007) 225–229.
[27] D. Armitage, I. Underwood, S.T. Wu, Microdisplays move outside the box, OE Magazine (2002) 28–30.
[28] W.E. Howard, O.F. Prache, Microdisplays based upon organic light-emitting diodes, IBM Journal of Research and Development 45 (1) (2001) 115–127.
[29] T. Manifar, A. Rezaee, M. Sheikhzadeh, S. Mittler, Formation of uniform self-assembly monolayers by choosing the right solvent: OTS on silicon wafer, a case study, Applied Surface Science 254 (15) (2008) 4611–4619. http://www.sciencedirect.com/science/article/B6THY-4RR1 NKC-5/2/b99f1389364860129b0bacf9e2570d4c.
[30] Z. Zhang, Z. Wang, R. Xing, Y. Han, How to form regular polymer microstructures by surface-pattern-directed dewetting, Surface Science 539 (1–3) (2003) 129–136. http://www.sciencedirect.com/science/article/pii/S0039602803007854.
[31] N. Herzer, M.M. Wienk, P. Schmit, A.B. Spoelstra, C.E. Hendriks, S.D. Oosterhout, S. Hoeppener, U.S. Schubert, Fabrication of PEDOT-OTS-patterned ITO substrates, Journal of Materials Chemistry 20 (32) (2010) 6618–6621. http://dx.doi.org/10.1039/C0JM01468K.
[32] N. Suganuma, C. Adachi, T. Koyama, Y. Taniguchi, H. Shiraishi, A 200×2 mm array of organic light-emitting diodes and their anisotropic electroluminescence, Applied Physics Letters 74 (9) (1999) 1206–1208. 10.1063/1.123500.
[33] Q. Huang, J. Li, T.J. Marks, G.A. Evmenenko, P. Dutta, Triarylamine siloxane anode functionalization/hole injection layers in high efficiency/high luminance small-molecule green- and blue-emitting organic light-emitting diodes, Journal of Applied Physics 101 (9) (2007) 093101. http://dx.doi.org/10.1063/1.2719276 doi:10.1063/1.2719276.
[34] H. Mu, H. Shen, D. Klotzkin, Dependence of film morphology on deposition rate in ITO/TPD/Alq3/Al organic luminescent diodes, Solid-State Electronics 48 (10–11) (2004) 2085–2088. http://www.sciencedirect.com/science/article/B6TY5-4CTCRMH-C/2/946adf51755d123404ca6684832f9baf.
[35] C.W. Tang, S.A. VanSlyke, Organic electroluminescent diodes, Applied Physics Letters 51 (12) (1987) 913–915. http://dx.doi.org/10.1063/1.98799 doi:10.1063/1.98799.
[36] Y. Sun, S.R. Forrest, Enhanced light out-coupling of organic light-emitting devices using embedded low-index grids, Nature Photonics 2 (8) (2008) 483–487. http://dx.doi.org/10.1038/nphoton.2008.132.
[37] Y.-Y. Lin, D. Gundlach, S. Nelson, T. Jackson, Stacked pentacene layer organic thin-film transistors with improved characteristics, Electron Device Letters, IEEE 18 (12) (1997) 606–608. http://dx.doi.org/10.1109/55.644085 doi:10.1109/55.644085.
[38] L. Xue, Y. Han, Pa ttern formation by dewetting of polymer thin film, Progress in Polymer Science 36 (2) (2011) 269–293. http://www.sciencedirect.com/science/article/pii/S0079670010000675.

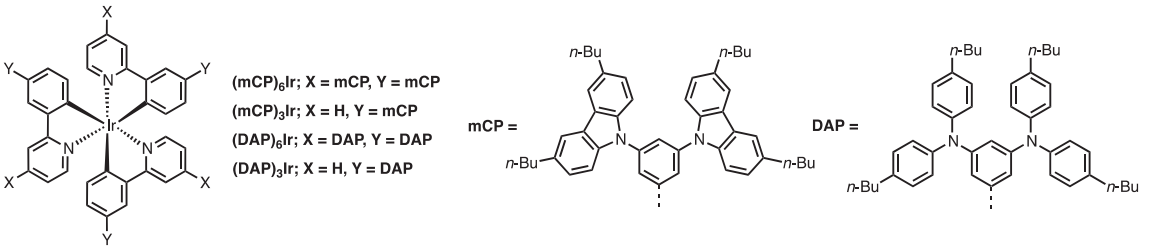

Scheme 1. Chemical structure of the iridium complexes.

bulky dendrons, **(mCP)$_6$Ir** and **(DAP)$_6$Ir** (Scheme 1). Both of the complexes showed higher PLQE in a neat film than that of half-surrounded **(mCP)$_3$Ir** and **(DAP)$_3$Ir**, well-supporting the results reported in the literature [9]. Solution-processed OLED with **(mCP)$_6$Ir** showed high efficiencies, 19 lm/W, 32 cd/A, and 12% of external quantum efficiency at 100 cd/m^2, and 11 lm/W, 25 cd/A, 9.1% at 1000 cd/m^2. The energy levels of the surrounding dendrons intensely affected the charge injection into the emitting layer and the device performance.

2. Results and discussion

Scheme 2 shows synthesis route of **(mCP)$_6$Ir**, **(DAP)$_6$Ir**, and **(DAP)$_3$Ir**. The ligands of the complexes, **2**, **5**, and **6**, were synthesized via several steps of palladium catalyzed coupling reactions. The complexes were prepared from the two steps of complexation. First, a mixture of iridium chloride trihydrate and excess of the ligands afforded dichloro bridged dimer complexes, **7**, **8**, and **9**. Second, the dimers were reacted by the ligands with silver trifluorom-

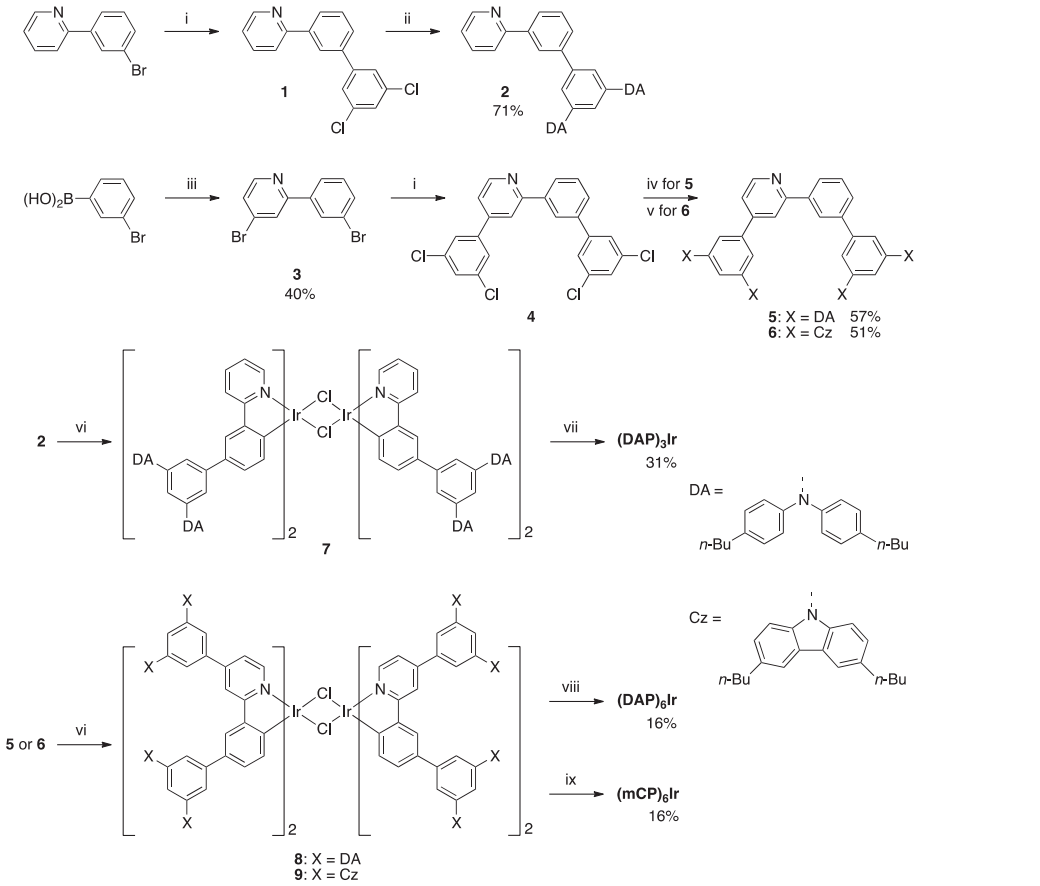

Scheme 2. Synthetic procedure of (**DAP)$_3$Ir**, (**DAP)$_6$Ir** and (**mCP)$_6$Ir**: (i) 3,5-dichlorophenylboronic acid, Pd(PPh$_3$)$_4$, K$_2$CO$_3$ aq., THF, N$_2$, reflux, (ii) di(4-(*n*-butyl)phenyl)amine, Pd$_2$(dba)$_3$, PCy$_3$, NaO*t*-Bu, toluene, N$_2$, reflux, (iii) 2,4-dibromopyridine, Pd$_2$(dba)$_3$, dppf, K$_2$CO$_3$ aq., toluene, N$_2$, reflux, (iv) di(4-(*n*-butyl)phenyl)amine, Pd$_2$(dba)$_3$, P(Cy)$_3$, NaO*t*-Bu, toluene, N$_2$, reflux, (v) 3,6-di(*n*-butyl)carbazole, Pd(OAc)$_2$, P(*t*-Bu)$_3$, NaO*t*-Bu, *o*-xylene, N$_2$, 120 °C, (vi) IrCl$_3$·3H$_2$O, H$_2$O, 2-ethoxyethanol, N$_2$, 130 °C, (vii) **2**, CF$_3$SO$_3$Ag, diglyme, N$_2$, 130 °C, (viii) **5**, CF$_3$SO$_3$Ag, diglyme, N$_2$, 130 °C, (ix) **6**, CF$_3$SO$_3$Ag, ethyldiglyme, N$_2$, 150 °C.

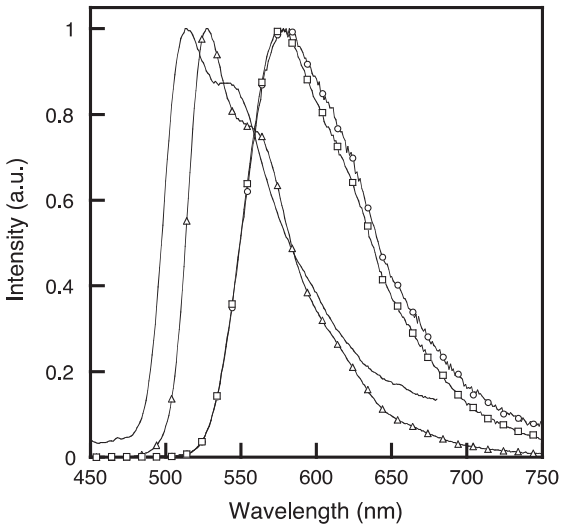

Fig. 1. Photoluminecence spectra of **(mCP)$_3$Ir** (solid line), **(mCP)$_6$Ir** (circle), **(DAP)$_3$Ir** (triangle), and **(DAP)$_6$Ir** (square) in a neat film.

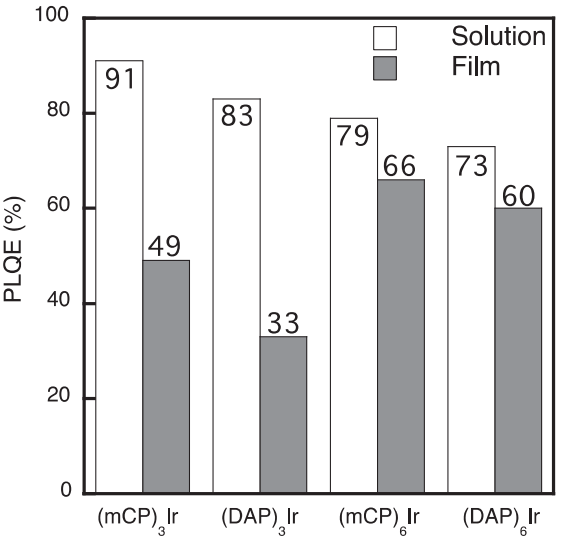

Fig. 2. Photoluminescent quantum efficiencies (PLQEs) of the compounds in a neat film or a toluene solution (2×10^{-6} mol L^{-1}).

ethane sulfonate to give homoleptic functionalized complexes. The complexes were fully characterized by ^{1}H-NMR, matrix-assisted laser desorption/ionization time-of-flight (MALDI) mass spectrometry (MS), and elemental analysis.

Photoluminescence of the neat film of the complexes fully-surrounded by the six bulky dendrons showed the peaks around 580 nm for **(mCP)$_6$Ir** and 577 nm for **(DAP)$_6$Ir**, and the spectra were red-shifted compared with the emission of the less-surrounded complexes around 514 nm for **(mCP)$_3$Ir** and 528 nm for **(DAP)$_3$Ir** (Fig. 1). These results indicated that substitution on 3-position of phenyl ring did not change emission color of Ir(ppy)$_3$, but substitution on 4-position of pyridine ring made the emission red-shifted. The emission of Ir(ppy)$_3$ is mainly ascribed to triplet metal-to-ligand charge transfer (^{3}MLCT) transition. Its highest occupied molecular orbital (HOMO) corresponds to *d* orbital of Ir and lowest unoccupied molecular orbital (LUMO) correspond to π^* orbital of ppy ligand, especially pyridine part of the ligand. That is why electron-donating group on pyridine ring decrease the energy gap of π–π^* and LUMO level, on the other hand the same electron-donating group on 3-position of phenyl ring does not affect the pyridine ring because of less π-conjugation via *meta*-linkage [27,28].

PLQEs of the complexes in the neat film are important parameter to estimate the shielding effect of the surrounding dendrons to Ir(ppy)$_3$. PLQEs of the toluene solution and the films were measured by using an integrating sphere system under 331 nm excitation (Fig. 2). In a diluted solution, all complexes showed higher PLQE than 70%, which are comparable to 85% of unsubstituted Ir(ppy)$_3$. This result demonstrated that these surrounding dendrons are optically inert and does not affect the emission efficiency of Ir(ppy)$_3$ core. The fully-surrounded complexes, **(mCP)$_6$Ir** and **(DAP)$_6$Ir**, showed high PLQE even in a neat film, which is comparable to PLQE in a dilute solution. On the other hand, the half-surrounded complexes, **(mCP)$_3$Ir** and **(DAP)$_3$Ir**, showed much lower PLQE in a neat film than that in a dilute solution. These complexes are facial isomers, therefore, in **(mCP)$_3$Ir** and **(DAP)$_3$Ir**, a some space around pyridyl groups of Ir(ppy)$_3$ core are opened and their three dimensional structure is like a hemisphere, shown in Fig. 3, resulting in only partial suppression of concentration-quenching in a neat film of an iridium complex. However, in **(mCP)$_6$Ir** and **(DAP)$_6$Ir**, the bulky host dendrons fully surrounded Ir(ppy)$_3$ and effectively prevented the intermolecular interaction between Ir(ppy)$_3$s. There are still small amount of reduction of PLQEs from a solution to a neat film, due to the concentration-quenching even in the fully-substituted complexes. The substituted host dendrons are not enough large to completely suppress the interaction between the core complexes. Adachi et al. reported that an average distance between iridium complexes in a doped film critically influenced on PLQE [29]. Förster type energy transfer between Ir(ppy)$_3$ cores through an overlap of the emission and the absorption causes a decrease of neat film PLQY. If the average distance between iridium complexes is shorter than Förster radius, a strong quenching occurs. The stronger quenching of **(mCP)$_3$Ir** in the neat film than that of **(mCP)$_6$Ir** is due to the shorter average distance between the cores derived from a less number of bulky host dendrons of **(mCP)$_3$Ir** than that of **(mCP)$_6$Ir**. Substitution of more branched and larger dendrons to the core complexes are desirable to achieve the complete suppression of concentration-quenching.

HOMO level of the complexes and the surrounding host dendrons themselves, 3,5-(3,6-di(*n*-butyl)carbazol-9-yl)benzene **DAP** and 3,5-(*N*,*N*-di(4-(*n*-butyl)phenyl)amine) benzene **mCP**, were estimated from ionization potentials measured by photoelectron yield spectroscopy (Fig. 4). LUMO levels of **DAP** and **mCP** were estimated from the difference of optically obtained energy gap and ionization potential. LUMO level of the dendrimer complexes are still unknown because the optically obtained energy gap dose

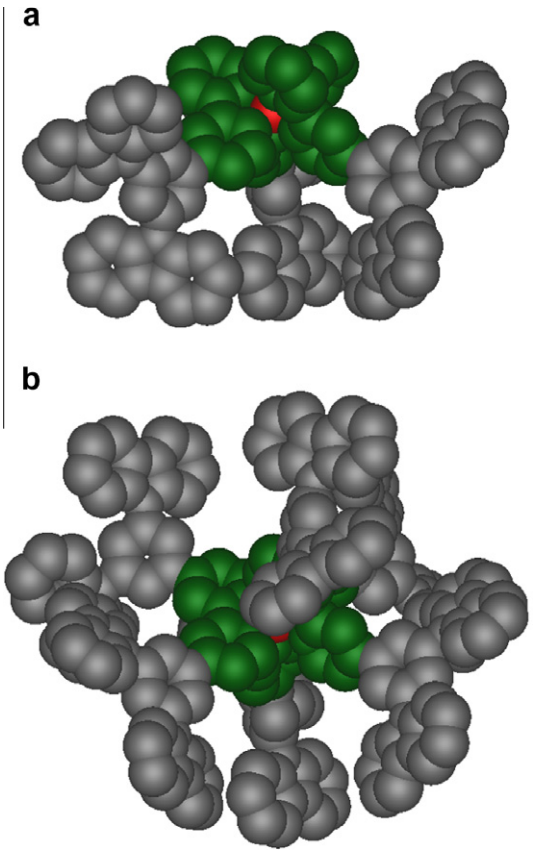

Fig. 3. The optimized structures of: (a) **(mCP)$_3$Ir** and (b) **(mCP)$_6$Ir** by PM6 calculation. The butyl groups were replaced to hydrogen in calculation.

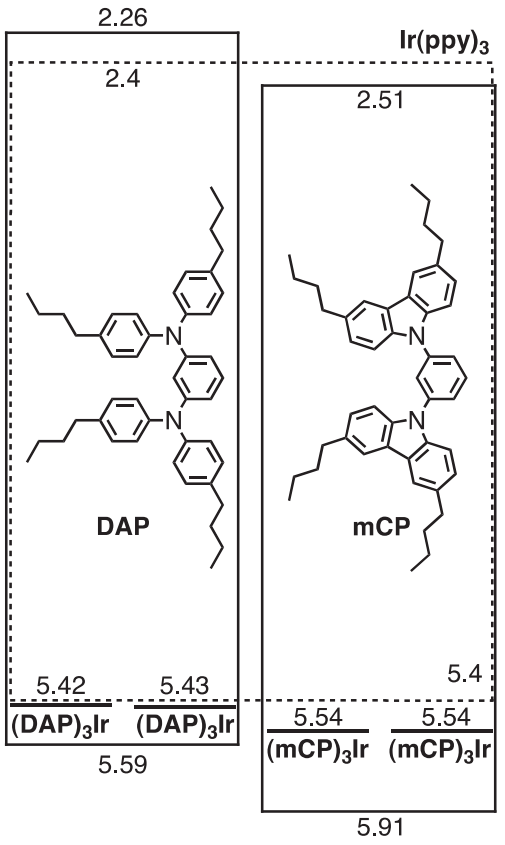

Fig. 4. HOMO and LUMO levels of the surrounding host groups, **DAP** (fine solid line) and **mCP** (fine solid line), and Ir(ppy)$_3$ (dotted line), and HOMO levels of the complexes (thick solid line). Chemical structure of **DAP** and **mCP**.

not correspond to HOMO–LUMO gap in the case of Ir(ppy)$_3$ derivatives. HOMO levels of the dendrimer complexes were close to that of Ir(ppy)$_3$, rather than that of the surrounding host dendrons. This result suggest that HOMO are mainly located on the central Ir(ppy)$_3$ group.

Single layer devices with the configuration of ITO/poly(3,4-ethylenedioxythiophene) (PEDOT): poly(styrene sulfonic acid) (PSS) (40 nm)/**(DAP)$_3$Ir**, **(DAP)$_6$Ir**, or **(mCP)$_6$Ir** (120 nm)/LiF (1 nm)/Al (100 nm) and double layer devices with the configuration of ITO/PEDOT:PSS (40 nm)/**(DAP)$_3$Ir**, **(DAP)$_6$Ir**, or **(mCP)$_6$Ir** (60 nm)/bis-4,6-(3,5-di-4-pyridylphenyl)-2-methylpyrimidine (B4PyMPm) (60 nm)/LiF (1 nm)/Al (100 nm) were fabricated. In single layer devices, **(DAP)$_3$Ir** and **(DAP)$_6$Ir** exhibited higher current density than **(mCP)$_6$Ir**, probably because HOMO level of **(DAP)$_3$Ir** and **(DAP)$_6$Ir** are shallower than **(mCP)$_6$Ir** to enhance hole injection from PEDOT:PSS (Fig. 5). Therefore, hole current should be dominant in single layer devices. However, in contrast to the result of the current density–voltage plots, **(mCP)$_6$Ir** showed higher luminance than the others. As well as the luminance, current efficiencies of the single layer device with **(mCP)$_6$Ir** were much higher than those of the other two complexes. This improvement showed that the surrounding **mCP** dendron has better electron injection and/or electron transport property than **DAP** dendron to improve charge balance. The double layer devices were fabricated using B4PyMPm as an electron transporting and hole-blocking material on the emitting layer. **DAP**-surrounding complex, **(DAP)$_3$Ir** and **(DAP)$_6$Ir**, showed higher current density, as well as single layer device. This results suggest that hole current is still excess even in the device with electron transporting layer. High luminance was obtained at much lower voltage, and the efficiency were drastically improved. In the device with **(mCP)$_6$Ir**, thickness of the emitting layer was reduced from 60 to 40 nm to improve charge balance, resulting in increasing efficiencies (Table 1). Current efficiency of the device with **(mCP)$_6$Ir** was 32 cd/A, 19 lm/W, 12% at 100 cd/m^2, and 25 cd/A, 11 lm/W, 9.1% at 1000 cd/m^2. There have been several reports on solution-processed phosphorescence OLED with dendrimer iridium complexes, and their high efficiencies, as mentioned in Section 1. However the most of papers emphasized peak efficiencies at a low current density and luminance, and did not revealed the efficiencies at practically high luminance, e.g. for lighting application. The efficiencies with our fully-surrounded Ir(ppy)$_3$ are one of high values among the solution-processed OLED ever reported.

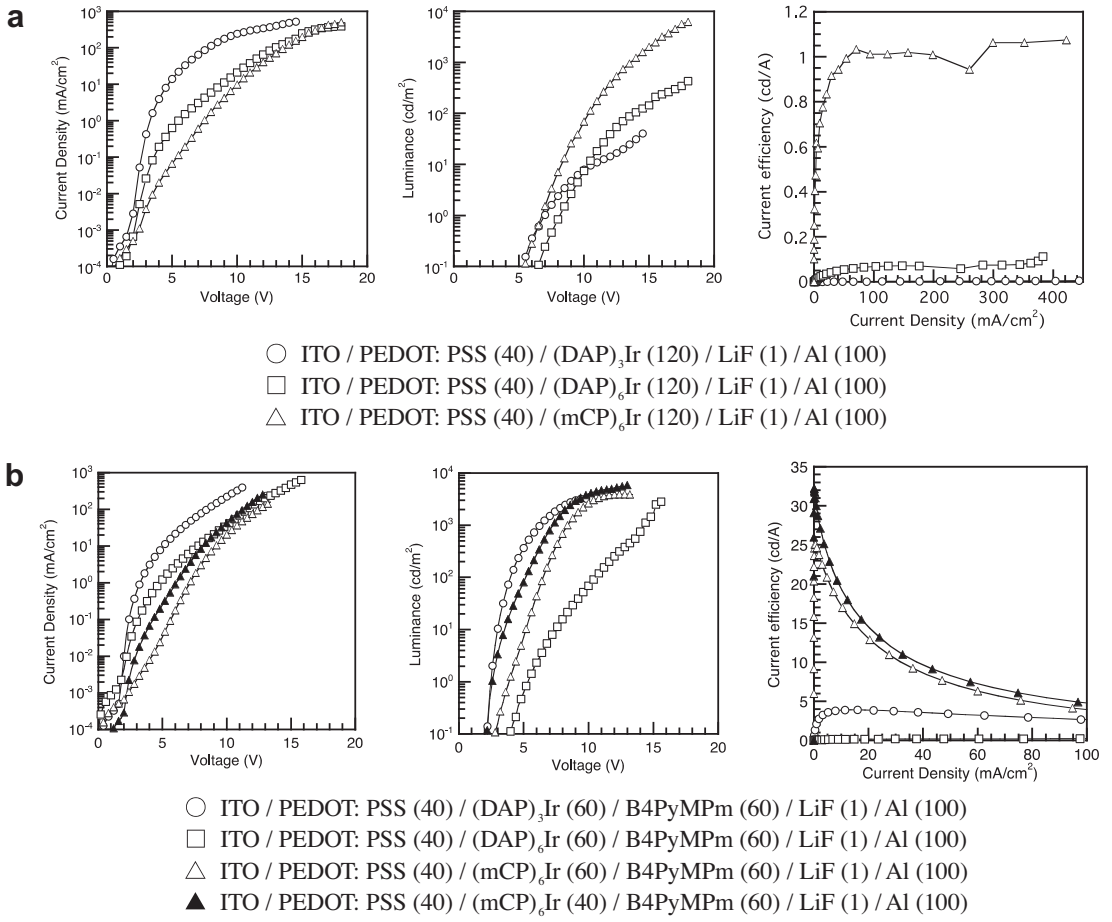

Fig. 5. Current density–voltage, luminance–voltage, and current efficiency–voltage characteristics of the single layer device (a) and the double layer device (b).

Table 1
Efficiencies of the solution-processed OLEDs.

Device structure	Compound	100 cd/m^2				1000 cd/m^2			
		Voltage (V)	η_P (lm W^{-1})	η_C (cd A^{-1})	η_{EXT} (%)	Voltage (V)	η_P (lm W^{-1})	η_C (cd A^{-1})	η_{EXT} (%)
Single layer	**(DAP)$_3$Ir**	–	–	–	–	–	–	–	–
	(DAP)$_6$Ir	13.9	0.016	0.071	0.028	–	–	–	–
	(mCP)$_6$Ir	10.3	0.23	0.75	0.29	13.6	0.23	1.0	0.39
Double layer	**(DAP)$_3$Ir**	4.0	2.6	3.2	1.0	6.3	1.9	3.8	1.1
	(DAP)$_6$Ir	10.5	0.057	0.19	0.075	14.3	0.065	0.30	0.11
	(mCP)$_6$Ir	6.5	12	25	9.4	8.4	7.8	21	7.8
	(mCP)$_6$Ir[a]	5.2	19	32	12	7.3	11	25	9.1

[a] Thickness of emitting layer is 40 nm.

3. Conclusion

We synthesized the solution processable iridium complexes for OLEDs, surrounded by diphenylamine derivatives or carbazole derivatives. The fully surrounded complexes, **(DAP)$_6$Ir** and **(mCP)$_6$Ir**, by six host dendrons showed high PLQE in a neat film, comparable to their PLQE in a dilute solution, demonstrating that the surrounding host dendrons efficiently suppressed intermolecular interaction between central Ir complexes and prevented concentration quenching. Not only PLQE of the complex but also energy levels and charge transporting property of the surrounding host dendron are important to achieve high efficiencies in a device. The complex, **(mCP)$_6$Ir**, fully surrounded by six carbazole type hosts showed much better performance, compared with the complexes surrounded by arylamine type hosts, because of well balanced charge injection and transporting in the devices.

4. Experimental

4.1. Measurements

^{1}H-NMR spectra were measured in deuterated solvents on a JEOL ECX 400 MHz spectrometer. Mass spectra were recorded on a JEOL JMS-K9 for electron impact-ionization (EI) or an Applied Biosystems Voyager DE-PRO for matrix-assisted laser desorption/ionization-time-of-flight (MALDI-TOF) from dithranol (DITH) in linear or reflection mode. Elemental analyses were carried out by the Elemental Analysis Service, Yamagata University, Japan. Thermal gravimetric analysis (TGA) was performed on Seiko SII EXSTAR 6000 and TGA/DTA 6200 analyzers. Differential Scanning Calorimetry (DSC) was performed on a Perkin–Elmer Diamond DSC calorimeter. Ionization potentials were measured with a photoelectron spectrometer surface analyzer (RIKEN KEIKI AC-3). UV–visible absorption spectra were recorded of solutions in chloroform or films on quartz with a Shimadzu UV-3150 spectrometer. PL spectra were recorded on a Jobin Yvon Fluoromax-4 fluorometer. PL quantum efficiencies were measured on a Hamamatsu C9920-01 calibrated integrating sphere system under nitrogen. Light emitting devices were fabricated on indium tin oxide (ITO) coated glass substrates, which were prepared by ultrasonication sequentially in detergent, methanol, 2-propanol and acetone, then exposed to UV–ozone under ambient conditions for 15 min. PEDOT:PSS was spin-coated as an anode buffer layer on pre-cleaned ITO substrate. On the top of PEDOT:PSS layer, dendrimers were spin-coated from 1,2-dichloroethane or toluene solution. The electron transporting material B4PyMPm was deposited by thermal evaporation at less than 1×10^{-4} Pa. The aluminum cathode was deposited through a shadow mask at less than 1×10^{-4} Pa. The active area of each device is 2 mm × 2 mm. Layer thickness calibration was performed using a Dektak 3 surface profilometer. The EL spectra were measured on a Hamamatsu PMA-11 photonic multichannel analyzer. The current–voltage (*I–V*) characteristics and luminance of the devices were measured using a Keithley 2400 Source Meter and Konica Minolta CS-200 chromameter, respectively. External quantum efficiencies were calculated assuming a Lambertian emission pattern and considering all spectral features in the visible region.

5. Materials

2-(3-(3,5-Dichlorophenyl)phenyl)pyridine **1**: a mixture of 2-(3-bromophenyl)pyridine (1.20 g, 5.13 mmol), 3,5-dichlorophenylboronic acid (1.97 g, 10.3 mmol), K_2CO_3 (1.42 g, 10.3 mmol), and THF (100 ml) was deoxygenated by bubbling N_2 for 30 min. After that, $Pd(PPh_3)_4$ (0.240 g, 0.208 mmol) and degassed deionized water (5.2 ml) were added in the mixture, and then the mixture was refluxed under N_2 for 24 h. The mixture was allowed to cool to room temperature, and then diethylether was added. The organic layer was washed by deionized water, dried over magnesium sulfate, and filtered. The solvent was removed in vacuo and the residue was purified by column chromatography over silica using a chloroform–ethyl acetate mixture (30:1) as eluent to give the compound **1** (1.26 g, 82%). δ_H(400 MHz, CD_2Cl_2) 8.67 (1H, d, J = 4.1 Hz), 8.23 (1H, s), 8.02 (1H, d, J = 7.3 Hz), 7.82–7.76 (2H, m), 7.61–7.53 (4H, m), 7.37 (1H, t, J = 1.8 Hz), 7.27 (1H, td, J = 5.7, 1.8 Hz). *m/z* [EI] 299: (M^+). Found: C, 67.74; H, 3.60; N, 4.45. $C_{17}H_{11}C_{l2}N$ requires C, 68.02; H, 3.69; N, 4.67%.

2-(3-(3,5-Bis(di-(4-*n*-butylphenyl)amino))phenyl)phenyl)pyridine **2**: the compound **1** (0.500 g, 1.67 mmol), di(4-(*n*-butyl)phenyl)amine (1.41 g, 5.00 mmol), sodium *tert*-butoxide (0.721 g, 7.50 mmol), $Pd_2(dba)_3$ (0.114 g, 0.125 mmol), and $P(Cy)_3$ (0.0701 g, 0.250 mmol) in a sealed tube was degassed in vacuo and filled with N2. After that, degassed toluene (5.0 ml) was added into the mixture, and then the mixture was refluxed for 24 h. After the mixture was allowed to cool to room temperature, diethylether was added. The organic layer was washed by deionized water, dried over magnesium sulfate, and filtered. The solvent was removed in vacuo, and the residue was purified by column chromatography over silica using chloroform and a hexane–chloroform mixture (from 1:0 to 0:1) as eluent to give the compound **2** (0.929 g, 71%). δ_H(400 MHz, CD_2Cl_2) 8.62 (1H, d, J = 5.0 Hz), 7.97 (1H, s), 7.88 (1H, d, J = 6.4 Hz), 7.74–7.67 (2H, m), 7.41–7.38 (2H, m), 7.22 (1H, td, J = 5.7, 1.4 Hz), 7.04–6.97 (16H, m), 6.81 (2H, d, J = 2.3 Hz), 6.67 (1H, t, J = 1.8 Hz), 2.52 (8H, t, J = 7.8 Hz, -$\underline{CH_2}CH_2CH_2CH_3$), 1.58–1.50 (8H, m, -$CH_2\underline{CH_2}CH_2CH_3$), 1.38–1.29 (8H, m, -$CH_2CH_2\underline{CH_2}CH_3$), 0.90 (12H, t, J = 7.4 Hz, -$CH_2CH_2CH_2\underline{CH_3}$). *m/z* [EI] 791: ($M^+$). Found: C, 86.49; H, 7.75; N, 5.24. $C_{57}H_{63}N_3$ requires C, 86.65; H, 8.04; N, 5.32%.

4-Bromo-(2-(3-bromophenyl))pyridine **3**: the mixture of 3-bromophenylboronic acid (2.81 g, 14.0 mmol), 2,4-dibromopyridine (3.31 g, 14.0 mmol), K_2CO_3 (3.87 g, 28.0 mmol), deionized water (14 ml), and toluene (60 ml) was deoxygenated by bubbling N_2 for 30 min. After that, $Pd_2(dba)_3$ (0.385 g, 0.420 mmol) was added, and then the mixture was refluxed for 36 h. After the mixture was allowed to cool to room temperature, diethylether was added. The organic layer was washed by deionized water, dried over magnesium sulfate, and filtered. The solvent was removed in vacuo, and the residue was purified by column chromatography over silica using a hexane–dichloromethane mixture (from 1:0 to 0:1) as eluent to give the compound **3** (1.76 g, 40%). δ_H(400 MHz, $CDCl_3$) 8.50 (1H, d, J = 5.0 Hz), 8.14 (1H, t, J = 1.8 Hz), 7.89–7.87 (2H, m, ArH), 7.56 (1H, d, J = 7.8 Hz), 7.43 (1H, dd, J = 5.3, 1.4 Hz), 7.34 (1H, t, J = 8.0 Hz). *m/z* [EI] 313: (M^+), Found: C, 42.41; H, 2.02; N, 4.45. $C_{11}H_7Br_2N$ requires C, 42.21; H, 2.25; N, 4.48%.

2-(3-(3,5-Dichlorophenyl)phenyl)-4-(4-(3,5-dichlorophenyl)phenyl)pyridine **4**: the compound **3** (1.75 g, 5.59 mmol), 3,5-dichlorophenylboronic acid (4.26 g, 22.3 mmol), K_2CO_3 (1.55 g, 11.2 mmol), deionized water (5.6 ml), and toluene (95 ml) was deoxygenated by bubbling N_2 for 30 min. After that, $Pd(PPh_3)_4$ (0.224 g, 0.194 mmol) was added, and then the mixture was refluxed for 24 h. After the mixture was allowed to cool to room temperature, diethylether was added. The organic layer was washed by deionized water, dried over magnesium sulfate, and filtered. The solvent was removed in vacuo, and the residue was purified by column chromatography over silica using a hex-

ane–chloroform mixture (from 1:0 to 0:1) as eluent to give the compound **4** (2.01 g) as a crude. The crude product was directly used for next step without further purification. δ_H(400 MHz, $CDCl_3$) 8.73 (1H, s), 8.18 (1H, s), 7.99 (1H, dt, *J* = 7.1, 1.8 Hz), 7.84 (1H, s), 7.58–7.50 (6H, m), 7.40 (1H, t, *J* = 1.8 Hz), 7.37 (1H, dd, *J* = 5.0, 1.8 Hz), 7.30 (1H, t, *J* = 1.8 Hz).

2-(3-(3,5-Bis(di(4-*n*-butylphenyl)amino))phenyl)phenyl)-4-(3-(3,5-bis(di(4-*n*-butylphenyl)amino))phenyl)pyridine **5**: the mixture of di(4-*n*-butylphenyl)amine (18.0 g, 64.0 mmol), crude **4** (3.56 g), sodium *tert*-butoxide (8.85 g, 96.0 mmol), and toluene (80 ml) was deoxygenated by bubbling N_2 for 30 min. After that, $Pd_2(dba)_3$ (1.47 g, 1.60 mmol), PCy_3 (1.79 g, 6.40 mmol) was added, and then the mixture was refluxed for 24 h. After the mixture was allowed to cool to room temperature, diethylether was added. The organic layer was washed by deionized water, dried over magnesium sulfate, and filtered. The solvent was removed in vacuo, and the residue was purified by column chromatography over silica using a hexane–chloroform mixture (from 1:0 to 0:1) and a hexane–chloroform mixture (from 1:0 to 1:3) as eluent, respectively, to give the compound **5** (7.30 g, 57%). δ_H(400 MHz, CD_2Cl_2) 8.52 (1H, d, *J* = 5.0 Hz), 7.99 (1H, s), 7.74 (1H, s), 7.65 (1H, s), 7.36 (2H, d, *J* = 4.6 Hz), 7.16 (1H, s), 7.04–6.96 (32H, m), 6.78 (4H, t, *J* = 2.1 Hz), 6.72 (1H, t, *J* = 1.8 Hz), 6.66 (1H, t, *J* = 1.8 Hz) 2.51 (16H, t, *J* = 7.6 Hz, -$\underline{CH_2}CH_2CH_2CH_3$), 1.57–1.50 (16H, m, -$CH_2\underline{CH_2}CH_2CH_3$), 1.37–1.28 (16H, m, -$CH_2CH_2\underline{CH_2}CH_3$), 0.90 (24H, t, *J* = 7.3 Hz, -$CH_2CH_2CH_2\underline{CH_3}$). [MALDI:DITH] (*m*/*z*) 1424.9: (MH^+). Found: C, 86.55; H, 8.48; N, 4.84. $C_{103}H_{117}N_5$ requires C, 86.81; H, 8.28; N, 4.91%.

2-(3-(3,5-Bis(3,6-di(*n*-butyl)carbazol-9-yl)phenyl)phenyl-4-(3,5-bis(3,6-di(*n*-butyl)carbazol-9-yl)phenyl))pyridine **6**: the mixture of 3,6-di-*n*-butylcarbazole (7.21 g, 25.8 mmol), crude **4** (1.91 g), palladium(II) acetate (0.231 g, 1.03 mmol), K_2CO_3 (10.7 g, 77.4 mmol), and *o*-xylene (40 ml) was deoxygenated by bubbling N_2 for 30 min. After that, P(*t*-Bu)$_3$ (0.75 ml, 3.10 mmol) was added, and then the mixture was refluxed for 24 h. After the mixture was allowed to cool to room temperature, diethylether was added. The organic layer was washed by deionized water, dried over magnesium sulfate, and filtered. The solvent was removed in vacuo, and the residue was purified by column chromatography over silica using a hexane–chloroform mixture (from 1:0 to 1:1) as eluent to give the compound **6** (3.84 g, 51%). δ_H(400 MHz, CD_2Cl_2) 8.75 (1H, d, *J* = 5.0 Hz), 8.45 (1H, s), 8.06 (1H, s), 8.04 (1H, d, *J* = 1.8 Hz), 7.98 (2H, d, *J* = 1.8 Hz), 7.95 (2H, d, *J* = 1.8 Hz), 7.91 (8H, s), 7.88 (1H, t, *J* = 1.8 Hz), 7.78–7.76 (2H, m), 7.61–7.56 (2H, m), 7.49 (8H, dd, *J* = 8.2, 5.0 Hz), 7.22 (8H, dt, *J* = 8.2, 2.0 Hz), 2.77 (16H, t, *J* = 7.8 Hz, -$\underline{CH_2}CH_2CH_2CH_3$), 1.70–1.63 (16H, m, -$CH_2\underline{CH_2}CH_2CH_3$), 1.43–1.34 (16H, m, -$CH_2CH_2\underline{CH_2}CH_3$), 0.93 (24H, t, *J* = 7.3 Hz, -$CH_2CH_2CH_2\underline{CH_3}$), [MALDI:DITH] (*m*/*z*) 1417.17: (MH^+), Found: C, 87.14; H, 8.02; N, 4.88. $C_{103}H_{109}N_5$ requires C, 87.30; H, 7.75; N, 4.94%.

7: the mixture of **2** (1.00 g, 1.27 mmol), iridium chloride trihydrate (0.186 g, 0.527 mmol), deionized water (8.5 ml), and 2-ethoxyethanol (36 ml) was heated at 130 °C for 24 h under N_2. After the solvent was removed in vacuo, the residue was washed with K_2CO_3 aq. (0.33 M, 6.0 ml) and deionized water to give crude compound **7**. The crude product was directly used for next step without further purification.

5.1. $(DPA)_3Ir$

The mixture of **7** (0.933 g), **5** (1.25 g, 1.58 mmol), silver trifluoromethanesulfonate (0.162 g, 0.632 mmol), and diglyme (31 ml) was heated at 130 °C under N_2 for 114 h. After the mixture was allowed to cool to room temperature, insoluble part was removed by column chromatography over silica using dichloromethane as eluent. The solvent was removed in vacuo, and then the residue was purified by chromatography over silica using a dichloromethane–hexane mixture (2:3) as eluent. Further purification by preparative TLC using a dichloromethane–hexane mixture (15:8) as eluent gave the complex **$(DPA)_3Ir$** (0.415 g, 31%). δ_H(400 MHz, CD_2Cl_2) 7.81–7.78 (3H), 7.60–7.55 (6H), 7.48–7.45 (3H), 7.03–6.94 (48H, m), 6.88–6.84 (3H), 6.78–6.72 (8H), 6.66–6.59 (6H), 2.54 (24H, t, *J* = 7.5 Hz, -$\underline{CH_2}CH_2CH_2CH_3$), 1.52–1.72 (24H, m, -$CH_2\underline{CH_2}CH_2CH_3$), 1.32–1.52 (24H, m, -$CH_2CH_2\underline{CH_2}CH_3$), 0.94 (36H, t, *J* = 7.3 Hz, -$CH_2CH_2CH_2\underline{CH_3}$). δ_C(100 MHz, CD_2Cl_2) 14.1, 22.7, 34.0, 35.3, 115.2, 116.1, 119.2, 122.4, 122.6, 124.4, 128.6, 129.2, 132.9, 136.5, 137.2, 137.5, 143.9, 144.4, 145.6, 147.4, 149.4, 160.8, 166.2. [MALDI:DITH] (*m*/*z*) 2559.68: (MH^+). Found: C, 80.40; H, 7.17; N, 4.88. $C_{171}H_{186}IrN_9$ requires C, 80.24; H, 7.32; N, 4.93%.

8: the mixture of **5** (2.50 g, 1.75 mmol), iridium chloride trihydrate (0.258 g, 0.731 mmol), deionized water (12 ml), and 2-ethoxyethanol (49 ml) was heated at 130 °C for 24 h under N_2. After the solvent was removed in vacuo, the residue was washed with K_2CO_3 aq. (0.33 M, 38 ml) and deionized water to give crude compound **8** (2.41 g). The crude product was directly used for next step without further purification.

5.2. $(DAP)_6Ir$

The mixture of **8** (2.41 g), **5** (4.80 g, 3.37 mmol), silver trifluoromethanesulfonate (0.225 g, 0.877 mmol), and diglyme (15 ml) was heated at 130 °C under N_2 for 192 h. The mixture was allowed to cool to room temperature, and then purified by column chromatography over silica using a dichloromethane–hexane mixture (1:2 and 1:3, respectively) as eluent. Further purification by preparative TLC using a dichloromethane–hexane mixture (1:3) as eluent gave the complex **$(DPA)_6Ir$** (0.526 g, 16%). δ_H(400 MHz, CD_2Cl_2) 7.72 (3H, s), 7.52 (3H, s), 7.31 (3H, d, *J* = 5.9 Hz), 7.00–6.94 (96H, m), 6.70–6.63 (21H, m), 6.59–6.55 (6H, m), 2.51 (48H, t, *J* = 7.7 Hz, -$\underline{CH_2}CH_2CH_2CH_3$), 1.57–1.50 (48H, m, -$CH_2\underline{CH_2}CH_2CH_3$), 1.37–1.28 (48H, m, -$CH_2CH_2\underline{CH_2}CH_3$), 0.89 (72H, t, *J* = 7.3 Hz, -$CH_2CH_2CH_2\underline{CH_3}$). δ_C(100 MHz, CD_2Cl_2) 166.1, 161.1, 149.6, 149.3, 149.2, 147.1, 145.6, 145.1, 144.2, 140.0, 138.1, 137.4, 137.1, 133.0, 129.3, 129.2, 128.8, 124.7, 124.3, 122.3, 120.9, 116.9, 116.8, 115.98, 115.95, 115.3, 114.4, 35.2, 33.97, 33.95, 22.7, 14.0. [MALDI:DITH] (*m*/*z*) 4462.45: (MH^+), Found: C, 83.30; H, 7.83; N, 4.64. $C_{309}H_{348}IrN_{15}$ requires C, 83.13; H, 7.86; N, 4.71%.

9: the mixture of **6** (1.70 g, 1.19 mmol), iridium chloride trihydrate (0.175 g, 0.496 mmol), deionized water (8.0 ml), and 2-ethoxyethanol (33 ml) was heated at 130 °C for 24 h under N_2. After the solvent was removed in vacuo, the residue was washed with K_2CO_3 aq. (0.33 M, 24 ml) and deionized water to give crude compound **9** (1.79 g). The crude product was directly used for next step without further purification.

5.3. *(mCP)$_6$Ir*

The mixture of **9** (1.46 g), **6** (2.89 g, 2.03 mmol), silver trifluoromethanesulfonate (0.498 g, 1.94 mmol), and ethyldiglyme (10 ml) was heated at 150 °C under N_2 for 133 h. The mixture was allowed to cool to room temperature, and then purified by column chromatography over silica using a dichloromethane–hexane mixture (1:3) as eluent, twice, to give the complex **(mCP)$_6$Ir** (0.316 g, 16%). δ_H(400 MHz, CD_2Cl_2) 8.28 (3H, s), 8.09 (3H, s), 7.93–7.89 (15H, m), 7.86 (24H, dd, J = 4.6, 1.4 Hz), 7.82 (3H, t, J = 1.8 Hz), 7.61 (3H, t, J = 1.8 Hz), 7.44 (12H, d, J = 8.7 Hz), 7.40 (12H, d, J = 8.2 Hz), 7.34–7.29 (6H, m), 7.15–7.11 (27H, m), 2.72 (48H, t, J = 7.6 Hz, -$\underline{CH_2}CH_2CH_2CH_3$), 1.67–1.59 (48H, m, -$CH_2\underline{CH_2}CH_2CH_3$), 1.41–1.31 (48H, m, -$CH_2CH_2\underline{CH_2}CH_3$), 0.92 (72H, t, J = 7.3 Hz, -$CH_2CH_2CH_2\underline{CH_3}$). δ_C(100 MHz, CD_2Cl_2) 166.5, 162.2, 148.0, 147.9, 145.4, 144.6, 141.3, 140.5, 139.9, 139.2, 139.0, 137.8, 135.1, 134.7, 132.0, 129.3, 126.7, 126.6, 124.8, 123.7, 123.6, 123.5, 122.9, 122.7, 121.9, 121.6, 119.6, 119.4, 117.4, 109.5, 109.3, 35.5, 34.42, 34.40, 29.7, 22.4, 13.8. [MALDI:-DITH] (m/z) 4439.73: (MH^+), Found: C, 83.58; H, 7.10; N, 4.78. $C_{309}H_{324}N_{15}$ requires C, 83.58; H, 7.35; N, 4.73%.

Acknowledgment

This work was supported by Grant-in-Aid for Young Scientists (A) No. 21685014 from MEXT, Japan.

References

[1] R.F. Service, Science 310 (2005) 1762.
[2] F. So, J. Kido, P. Burrows, MRS Bull. 33 (2008) 663.
[3] S. Reineke, F. Lindner, G. Schwartz, N. Seidler, K. Walzer, B. Lüssem, K. Leo, Nature 459 (2009) 234.
[4] C.-W. Han, S.-H. Pieh, H.-S. Pang, J.-M. Lee, H.-S. Choi, S.-K. Hong, B.-S. Kim, Y.-H. Tak, N.-Y. Lee, B.-C. Ahn, SID Int. Symp. Dig. Tech. 41 (2010) 136.
[5] M.A. Baldo, D.F. O'Brien, Y. You, A. Shoustikov, S. Sibley, M.E. Thompson, S.R. Forrest, Nature 395 (1998) 151.
[6] M.A. Baldo, S. Lamansky, P.E. Burrows, M.E. Thompson, S.R. Forrest, Appl. Phys. Lett. 75 (1999) 4.
[7] J.M. Lupton, I.D.W. Samuel, M.J. Frampton, R. Beavington, P.L. Burn, Adv. Funct. Mater. 11 (2001) 287.
[8] J.P.J. Markham, S.C. Lo, S.W. Magennis, P.L. Burn, I.D.W. Samuel, Appl. Phys. Lett. 80 (2002) 2645.
[9] S.-C. Lo, T.D. Anthopoulos, E.B. Namdas, P.L. Burn, I.D.W. Samuel, Adv. Mater. 17 (2005) 1945.
[10] T. Sato, D.-L. Jiang, T. Aida, J. Am. Chem. Soc. 121 (1999) 10658.
[11] A.W. Freeman, S.C. Koene, P.R.L. Malenfant, M.E. Thompson, J.M.J. Fréchet, J. Am. Chem. Soc. 122 (2000) 12385.
[12] S. Bettington, M. Tavasli, M.R. Bryce, A. Beeby, H. Al-Attar, A.P. Monkman, Chem. Eur. J. 13 (2007) 1423.
[13] T.-H. Kwon, M.K. Kim, J. Kwon, D.-Y. Shin, S.J. Park, C.-L. Lee, J.-J. Kim, J.-I. Hong, Chem. Mater. 19 (2007) 3673.
[14] G. Zhou, W.-Y. Wong, B. Yao, Z. Xie, L. Wang, Angew. Chem. Int. Edit. 46 (2007) 1149.
[15] B. Liang, L. Wang, Y. Xu, H. Shi, Y. Cao, Adv. Funct. Mater. 17 (2007) 3580.
[16] J. Ding, J. Lü, Y. Cheng, Z. Xie, L. Wang, X. Jing, F. Wang, Adv. Funct. Mater. 18 (2008) 2754.
[17] G.-J. Zhou, W.-Y. Wong, B. Yao, Z. Xie, L. Wang, J. Mater. Chem. 18 (2008) 1799.
[18] J. Ding, B. Wang, Z. Yue, B. Yao, Z. Xie, Y. Cheng, L. Wang, X. Jing, F. Wang, Angew. Chem. Int. Edit. 48 (2009) 6664.
[19] R. Guan, Y. Xu, L. Ying, W. Yang, H. Wu, Q. Chen, Y. Cao, J. Mater. Chem. 19 (2009) 531.
[20] S. Gambino, S.G. Stevenson, K.A. Knights, P.L. Burn, I.D.W. Samuel, Adv. Funct. Mater. 19 (2009) 317.
[21] S.-C. Lo, R.E. Harding, C.P. Shipley, S.G. Stevenson, P.L. Burn, I.D.W. Samuel, J. Am. Chem. Soc. 131 (2009) 16681.
[22] J.J. Kim, Y. You, Y.-S. Park, J.-J. Kim, S.Y. Park, J. Mater. Chem. 19 (2009) 8347.
[23] V. Adamovich, J. Brooks, A. Tamayo, A.M. Alexander, P.I. Djurovich, B.W. D'Andrade, C. Adachi, S.R. Forrest, M.E. Thompson, New J. Chem. 26 (2002) 1171.
[24] B.W. D'andrade, S.R. Forrest, J. Appl. Phys. 94 (2003) 3101.
[25] N. Iguchi, Y.-J. Pu, K. Nakayama, J. Kido, J. Photopolym. Sci. Technol. 20 (2007) 73.
[26] N. Iguchi, Y.-J. Pu, K. Nakayama, M. Yokoyama, J. Kido, Org. Electron. 10 (2009) 465.
[27] P.J. Hay, J. Phys. Chem. A 106 (2002) 1634.
[28] F.-M. Hwang, H.-Y. Chen, P.-S. Chen, C.-S. Liu, Y. Chi, C.-F. Shu, F.-I. Wu, P.-T. Chou, S.-M. Peng, G.-H. Lee, Inorg. Chem. 44 (2005) 1344.
[29] Y. Kawamura, J. Brooks, J.J. Brown, H. Sasabe, C. Adachi, Phys. Rev. Lett. 96 (2006) 17404.

chlorobenzene (CB) or 1,2-dichlorobenzene (DCB) for film casting. Solvent choice and solution concentration have been shown to be critical factors for polymer OPV device performance [23–25] due to the variation in nanocrystalline domain sizes that occurs in each case. This warrants an investigation of the interaction between these organic solvents and MPc thin films for small molecule OPV devices.

Here we use GLAD to fabricate nanostructured ZnPc films for improving OPV device performance. GLAD is a physical vapor deposition technique that employs substrate rotation (described by the angle variable ϕ) and oblique substrate angles relative to the incoming vapor flux (α) during deposition, in order to create porous columnar films [26–29]. We fabricate a variety of planar and nanostructured ZnPc films and study the effects of exposure to CB and DCB. By identifying sensitivities to these solvents, we are able to optimize the performance of ZnPc/PCBM devices through control of the initial ZnPc film morphology and the choice of solvent used to cast PCBM.

2. Experimental

2.1. ZnPc thin film deposition and characterization

ZnPc was acquired from Sigma–Aldrich and was purified at least twice via thermal gradient sublimation at 400 °C. All ZnPc thin films were deposited at high vacuum ($<2 \times 10^{-7}$ Torr) in a GLAD apparatus [27] with a throw distance of 34 cm. Unless otherwise stated, films were grown by using a source temperature of 390–400 °C resulting in a deposition rate of 0.7 Å/s at normal incidence. All GLAD films were preceded by a 10 nm planar layer grown at normal incidence immediately prior to GLAD deposition, to prevent any direct contact between the anode and the acceptor. All GLAD films described here are slanted post (SP) films made using the ϕ-sweep substrate motion technique [19,30–32]. Unless otherwise stated, we used a substrate rotation angle of $\gamma = 30°$ and one full sweep cycle per 4–5 nm of film growth when using the ϕ-sweep technique.

Solvent-treated films were achieved by either placing four drops ($\sim$200 μL) of solvent on the film surface from a glass pipet and spinning the solvent off at 1000 rpm (spin treatment), or by bathing the film sample in 5 mL of solvent in a glass petri dish for 10 min and then allowing the solvent to volatilize off the film under ambient conditions after removal from the bath (soak treatment). For device fabrication, the soak treatment was replaced with a drop treatment whereby four drops of solvent were placed on the film surface and allowed to volatilize under ambient conditions. The drop treatment provides very similar morphologies to the soak treatment.

Images were acquired using a Hitachi S-4800 field emission SEM. UV–Vis absorbance data was acquired using a Perkin Elmer Lambda 900 UV/VIS/NIR spectrophotometer. Absorbance was calculated as the negative logarithm of the transmittance spectrum.

XRD patterns were collected using a Bruker D8 diffractometer equipped with a Cu source and scintillometer using 1.0 mm antiscatter and 0.6 mm receiving slits. Diffractometer calibration and instrument resolution was determined using a silver behenate reference standard. XRD peak fits were performed with gnuplot 4.4 using pseudo-Voight peak shapes and linear backgrounds between 5.5° and 8.1° scattering angle for patterns collected using theta/two theta geometry. Detector resolution was determined to be 0.21° FWHM; uncertainty in peak position was ±0.04°.

2.2. OPV device fabrication and characterization

OPV devices were fabricated on anodes of ITO on glass (8–12 Ω/□, Delta Technologies), coated with a thin layer of PEDOT:PSS (Clevios P VP Al 4083). ITO was cleaned via sonication in IPA followed by an oxygen plasma etch. PEDOT:PSS was applied undiluted, spun at 4000 rpm for 30 s, and baked at 80 °C for 10 min in air. Following ZnPc deposition, PCBM (American Dye Source) was applied at 30 mg/mL in either CB or DCB (Sigma–Aldrich), and spun in air for 30 s at 1000 rpm. The top electrode, consisting of 15 nm bathocuproine (BCP, Sigma–Aldrich) and 80 nm Al (Lesker), was deposited through a shadow mask over five rectangular device areas of 0.20 cm^2 each, in a glovebox evaporator.

Current–voltage characteristics of OPV devices were taken in air using a Keithley 2400 source meter, under AM 1.5 G simulated irradiation (Oriel 91191 1000 W). Light intensity was calibrated against a KG-5 filtered Si reference cell (PV Measurements, Inc., model PVM624). Device performance numbers are reported as averages over several (5–10) devices.

Depth profiling was performed via secondary ion mass spectrometry (SIMS), by alternating sputtering and analysis processes using a ToF SIMS IV instrument (ION-TOF GmbH). A chopped 25 keV Bi^+ ion beam with a current of 0.7 pA was used as the primary source to analyze an area of 40×40 μm^2, while O_2^+ was used as the sputtering source, operated at 1 kV/55 nA over a crater area of 200×200 μm^2.

3. Results and discussion

3.1. ZnPc thin film structuring

3.1.1. Nanostructured ZnPc films via GLAD

Thin films of ZnPc were grown under several sets of conditions by varying the film thickness, the angle between the incoming vapor flux and the substrate normal (α) and the substrate rotation behavior during deposition (described by the angle variable γ). In Fig. 1 we show a planar ZnPc film compared to several slanted post (SP) GLAD films grown using different α values, which illustrates the effect of α on morphology. In particular, the film porosity increases with α, as expected due to increased shadowing [28]. With the exception of the film in Fig. 1b, which was grown with no substrate motion, a ϕ-sweep substrate motion program was used to grow each GLAD film, as specified in Section 2.

Ideally, the donor layer morphology would have columns with diameter close to that of its exciton diffusion

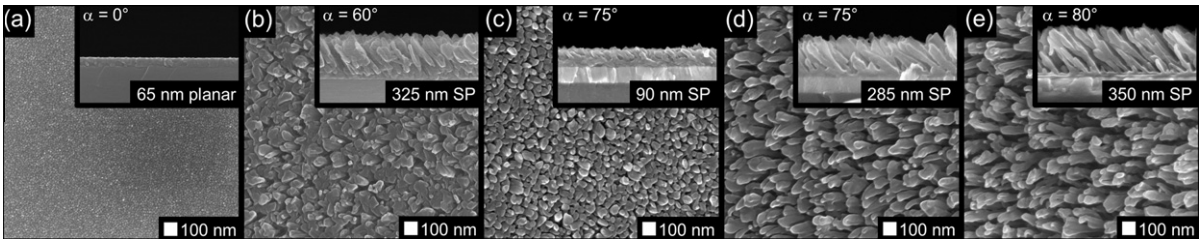

Fig. 1. Aerial and cross-sectional views of various planar and slanted post (SP) ZnPc thin films. The angle of incidence (α) is shown in each case. The substrates in each case are (a, b) Si and (c–e) PEDOT:PSS coated ITO.

length (15 nm for ZnPc [33]), with a thickness or length of around 200 nm [34]. The films shown in Fig. 1d and e begin to mimic this arrangement and are grown to even greater thicknesses while maintaining relatively uniform average column diameters.

3.1.2. Solvent effects on ZnPc films

One route to completing active layer fabrication using nanostructured ZnPc films is to fill them with PCBM in solution. In this case, it is critical to understand the sensitivity of ZnPc films to the solvents used for PCBM casting. To investigate this, we exposed planar and nanostructured ZnPc films to CB and DCB under different conditions, the results of which are shown in Fig. 2. The first condition mimics device fabrication conditions, by spinning the solvent off the film surface immediately after it is applied (the spin treatment, shown in Fig. 2a and b). The second condition involves placing the film sample in a bath of solvent for 10 min and then removing the sample and allowing the solvent to volatilize under ambient conditions (the

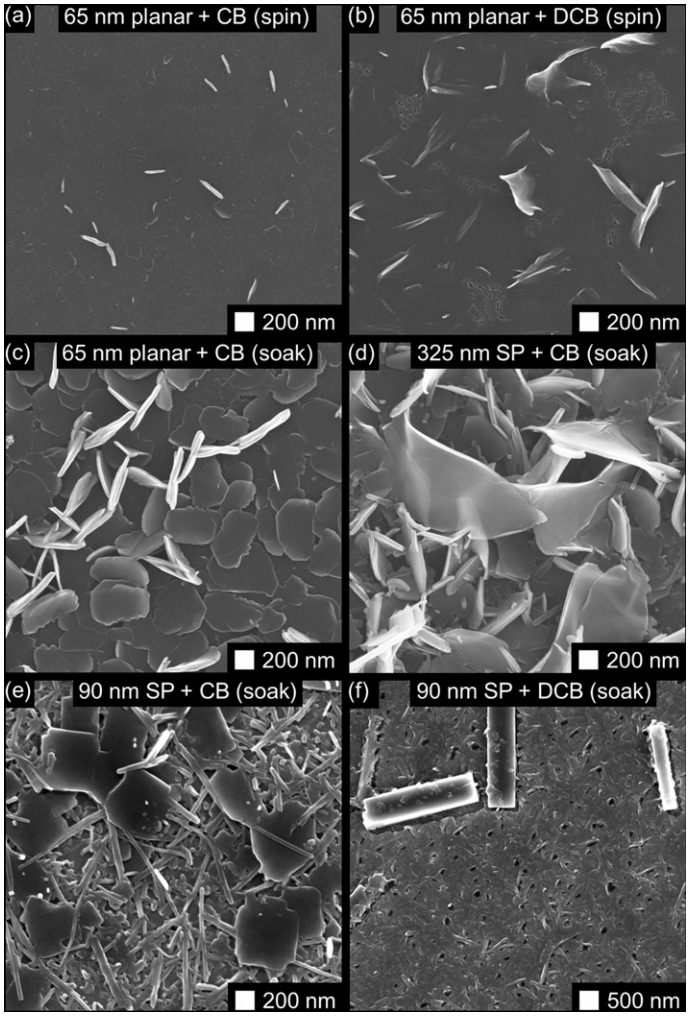

Fig. 2. Aerial views of solvent-treated ZnPc thin films. The untreated versions of these films are shown in Fig. 1.

soak treatment, shown in Fig. 2c–f). This is a similar approach to what has been used previously to improve the performance of CuPc films in OPV devices [13,14]. In addition, we measured absorbance spectra of the solvents after soaking ZnPc films to identify dissolved material (shown in Fig. S1.1 of the Supplementary data). From this we determined the solubility of a ZnPc thin film to be 0.2 μg/mL in CB and 0.5 μg/mL in DCB, based on the molar extinction coefficient determined by Whalley [35]. Modest solubility of ZnPc and other MPc complexes has been observed elsewhere as well [14,36–39].

The films exhibited a significant degree of recrystallization as a result of these solvent exposures, with each combination of solvent treatment and ZnPc film morphology yielding a unique morphology. The film surface can be roughened even with very short solvent exposure times, as seen in Fig. 2a and b. In this case, DCB appears to have a much stronger effect, suggesting that solvent choice may be a critical factor under device fabrication conditions. A greater degree of recrystallization occurs for longer exposure times, with CB generally leading to platelet formations (most evident in Fig. 2c) and DCB leading to large rectangular box structures (Fig. 2f). Similar ZnPc structures have been prepared before, albeit with radically different conditions [40]. Interestingly, the platelet thicknesses closely match the exciton diffusion length of ZnPc (15 nm [33]), which should provide strong exciton dissociation efficiency. Thus, an ordered arrangement of such structures could be expected to perform well in photovoltaic devices. However, additional changes in the film structure were evident after the solvent exposure, from both a crystallinity and absorbance perspective.

The XRD data in Fig. 3 shows the ZnPc films' crystallinity changes due to the solvent treatment. In all cases, the most prominent observed peak was α (010), centered at ca. 6.82° scattering angle, consistent with what has been observed previously for MPc films [41].The α (010) peak intensity is enhanced by the solvent treatment for the planar film, but decreases significantly for the SP film. In both cases, the DCB-treated film showed a higher α (010) peak than the CB-treated film. Interestingly, the α (001) peak, centered at ca. 7.37° scattering angle, became much stronger in the SP film upon solvent treatment with DCB.

The absorbance profiles shown in Fig. 4 also reveal significant changes in the film as a result of solvent exposure. Spin treatments did not affect absorbance significantly, except for DCB on a planar film where we observed a new peak in the 850 nm region. For the soak treatments, we observed significant changes to the Q band (500–800 nm), suggesting compositional changes in addition to the morphological changes. We investigate the photovoltaic properties of some of these solvent textured films in the following section, but for now we note that ZnPc films respond differently to these two solvents, while being sensitive to both.

3.2. ZnPc/PCBM OPV devices

3.2.1. Bilayer devices: choice of solvent and solution temperature

As a control study, bilayer OPV devices were fabricated with the following architecture: ITO (120 nm)/PEDOT:PSS

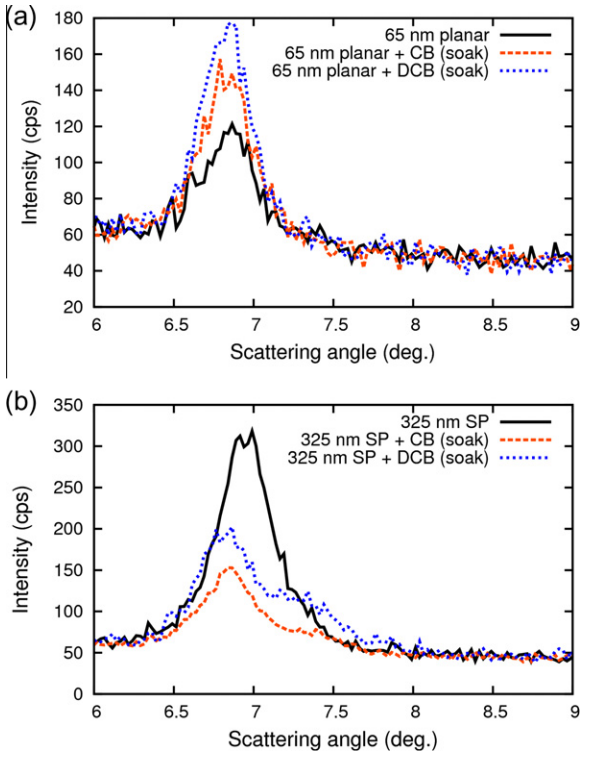

Fig. 3. Effects of solvent treatments on the XRD patterns of (a) planar and (b) nanostructured ZnPc thin films.

(40 nm)/ZnPc (50 nm)/PCBM (70 nm)/BCP (15 nm)/Al (80 nm). We varied the PCBM solution temperature to vary the interaction between the ZnPc film and the solvent. Cross-sectional views of these devices are shown in Fig. 5, which reveal subtle distinctions in the abruptness of the ZnPc/PCBM interface. Though the overall active layer thickness remains constant, the most well-defined boundary between ZnPc and PCBM occurs when the PCBM is applied cold (Fig. 5a). *I–V* curves for these devices are shown in Fig. 6, and device performance metrics are summarized in Table 1.

As seen in the *I–V* curves, the solution temperature has little impact when using CB as the solvent. However, a significant improvement is seen in the photocurrent when we switch the solvent to DCB. We postulate that the difference between using CB and DCB is due to a different degree of material mixing at the ZnPc/PCBM interface. Specifically, the interface may become more of a mixed heterojunction structure when using DCB than CB due to a greater degree of solubility. We investigate this further in the following sections.

The ZnPc layer used here is thicker than what is typically used in such devices, the purpose of which is to allow an investigation of the unique structures in the solvent-treated films (which, under 50 nm thickness, cease to form platelet structures) as well as to provide an absorption-matched comparison to thicker GLAD-structured devices. Both of these tasks are addressed in the following section.

3.2.2. Nanostructured devices

Photovoltaic devices were fabricated with the same layer structure as in the previous section, but here we

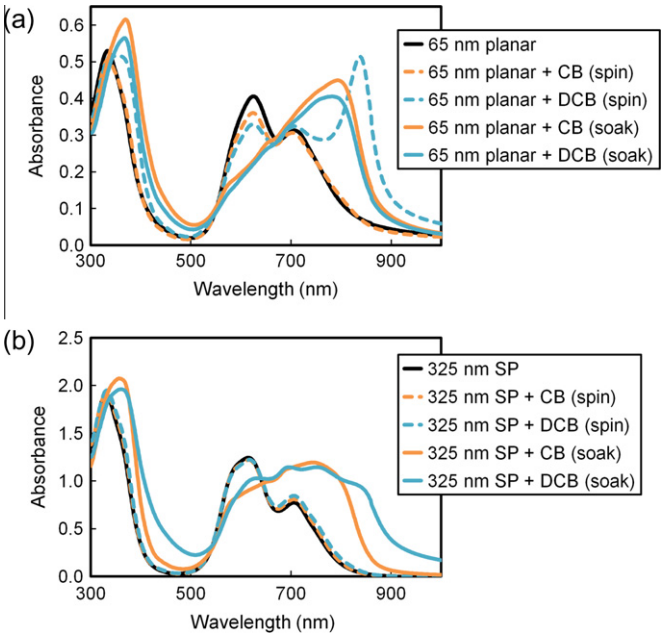

Fig. 4. Effects of solvent treatments on the absorbance of (a) planar and (b) nanostructured ZnPc thin films.

replace the planar layer with structured ZnPc films. The structuring is accomplished either by depositing with GLAD or by direct exposure of a planar film to solvents using a drop treatment, which affords very similar morphologies to the soak treatment discussed earlier. Fig. 7 shows cross-sectional views of the PCBM-coated ZnPc films for each of these two approaches. Fig. 7a is the PCBM-coated version of a 50 nm planar ZnPc film treated with CB and Fig. 7b is the PCBM-coated version of Fig. 1c. We noted that the PCBM solutions in both CB and DCB wet the ZnPc films very well, enabling effective filling of the structured films.

With the solvent-structured approach, the platelets seen in Fig. 2c largely maintain their structure during the coating process (Fig. 7a), which translates into sharp peaks and ridges across the PCBM coating. These contours are still apparent after depositing the BCP/Al electrode (see Fig. 7c), which suggests that CB is not as able to dissolve ZnPc when being used as the PCBM carrier.

When using the slanted post (SP) ZnPc structured film, the PCBM coating not only fills the film completely but also

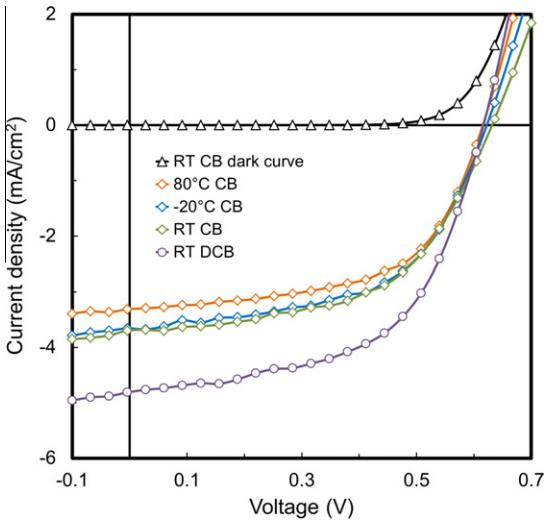

Fig. 6. Current–Voltage characteristics of bilayer ZnPc/PCBM OPV devices made using different PCBM solvents and solution temperatures.

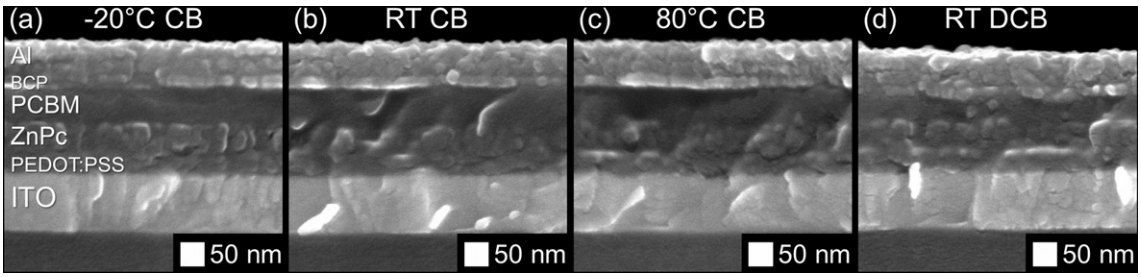

Fig. 5. Cross-sectional views of bilayer ZnPc/PCBM OPV devices. The PCBM solvent and solution temperature used in each case are denoted in the image.

Table 1
OPV device performance parameters for various bilayer and structured ZnPc/PCBM OPV devices.

ZnPc film morphology	α	Solvent treatment	PCBM solvent	J_{sc} (mA/cm^2)	V_{oc} (V)	η (%)	FF	R_s (Ω cm^2)
50 nm planar	0°	–	CB	3.67 ± 0.09	0.624 ± 0.004	1.37 ± 0.04	0.57 ± 0.01	19.3 ± 3.8
50 nm planar	0°	–	CB(−20 °C)	3.68 ± 0.04	0.617 ± 0.004	1.33 ± 0.02	0.56 ± 0.02	18.6 ± 1.3
50 nm planar	0°	–	CB(80 °C)	3.39 ± 0.11	0.614 ± 0.002	1.24 ± 0.05	0.57 ± 0.03	22.1 ± 5.9
50 nm planar	0°	–	DCB	4.88 ± 0.16	0.618 ± 0.006	1.74 ± 0.06	0.55 ± 0.04	15.6 ± 2.5
50 nm planar	0°	CB	CB	4.09 ± 0.08	0.638 ± 0.001	1.12 ± 0.02	0.41 ± 0.05	15.8 ± 1.4
50 nm planar	0°	DCB	CB	2.30 ± 0.28	0.562 ± 0.016	0.56 ± 0.07	0.41 ± 0.06	12.4 ± 1.3
20 nm planar	0°	–	CB	5.69 ± 0.13	0.637 ± 0.005	2.10 ± 0.08	0.55 ± 0.07	10.2 ± 1.0
20 nm planar	0°	–	DCB	6.82 ± 0.31	0.615 ± 0.014	2.27 ± 0.19	0.51 ± 0.08	9.9 ± 0.9
10 nm planar + 20 nm SP	75°	–	CB	5.94 ± 0.22	0.640 ± 0.002	2.29 ± 0.08	0.57 ± 0.09	10.3 ± 0.4
10 nm planar + 20 nm SP	75°	–	DCB	7.52 ± 0.23	0.629 ± 0.005	2.86 ± 0.09	0.57 ± 0.10	9.1 ± 0.5
10 nm planar + 90 nm SP	75°	–	CB	6.63 ± 0.23	0.583 ± 0.006	1.88 ± 0.06	0.46 ± 0.11	12.9 ± 1.0
10 nm planar + 90 nm SP	75°	–	DCB	8.79 ± 0.09	0.552 ± 0.005	1.99 ± 0.10	0.39 ± 0.12	10.6 ± 0.4

leaves a much smoother top surface (shown in Fig. 7b). In addition, the overburden could be controlled by varying the spin speed during PCBM application. OPV devices were made with several of these structured morphologies and thicknesses. Additional bilayer devices were also made, with a 20 nm thick ZnPc layer (as is common for these devices). We ensured that the bilayer devices had comparable absorption to the structured devices in order to isolate the effects of morphology alone on photovoltaic performance (see Fig. 8). The results of all these devices are summarized in Table 1, and current–voltage behavior of the key structured devices is shown in Fig. 9. EQE measurements were performed (see Supplementary data), which showed that the relative contributions of the different absorption bands did not vary significantly when using different ZnPc morphologies or PCBM solvents.

As shown in Fig. 9, solvent treatment prior to PCBM coating hindered device performance in both cases. Despite somewhat ideal structures being formed with CB treatment, the performance drop is likely due to the disorder present in the film morphology as well as potential

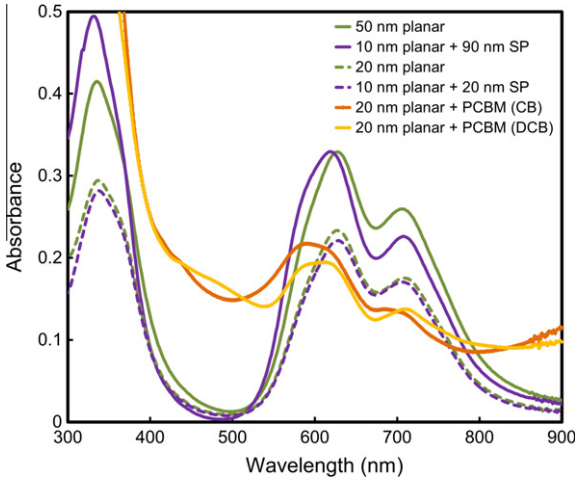

Fig. 8. Absorbance of various planar, structured, and PCBM-coated ZnPc thin films.

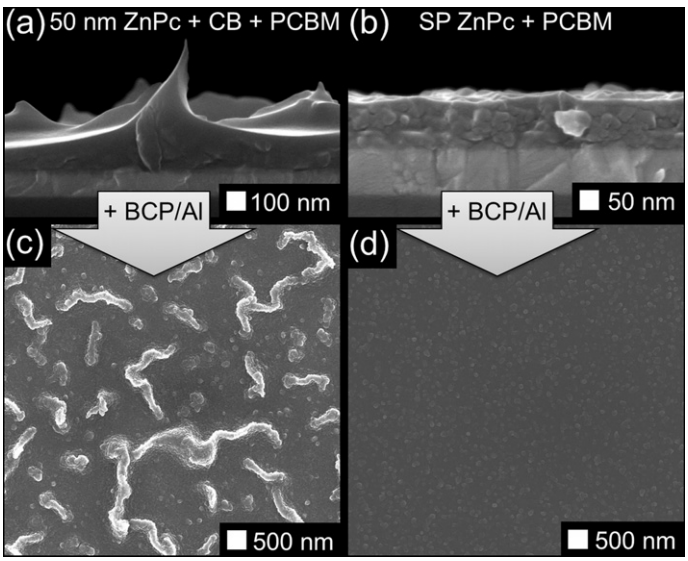

Fig. 7. Cross-sectional views of PCBM coated ZnPc films and aerial views of the corresponding Al electrode on each. The ZnPc film and solvent used in each case was (a, c) 50 nm planar + CB, CB, and (b, d) 90 nm SP via GLAD, DCB.

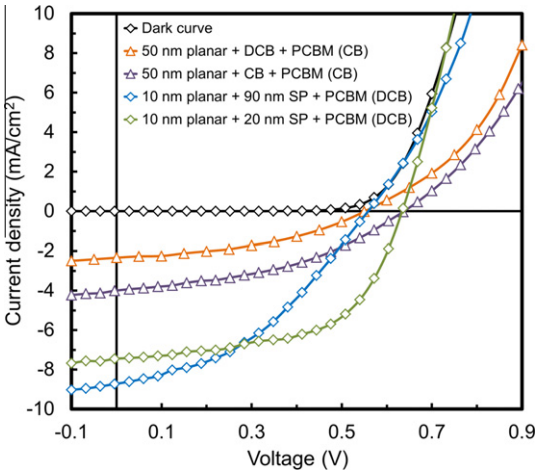

Fig. 9. Current–Voltage behavior of various structured ZnPc/PCBM OPV devices.

changes in film composition, as discussed earlier. In the case of DCB treatment, the structures created are far from ideal to begin with (large rectangular boxes with dimensions of 500 nm or greater, as shown in Fig. 2f). We confirmed by SEM that these large box structures were not dissolved during PCBM coating and were still present after complete device fabrication. Thus, the lower performance is not surprising. However, the fact that photovoltaic activity is still seen in these devices likely means that some of the ZnPc material remains as a planar layer, while the rest is organized into box structures.

Upon examining the performance of the SP films in devices, we see that the thicker film is able to generate the highest short circuit current density (J_{sc}).This is due to the increased light absorption, as shown in Fig. 8. However, the large active layer thickness allows the poor charge carrier properties of these organic materials to limit the collection of free charges, leading to a low fill factor (FF). In addition, exposure to air may be a greater concern for thick structured ZnPc films, whose larger surface area could permit more severe contamination than less textured films. As a result, the highest photoconversion efficiency is still observed when using the thin structured ZnPc film (10 nm planar + 20 nm SP). In this case, an average photoconversion efficiency of 2.86% is achieved when using DCB as the PCBM solvent. The best result among these devices was 3.0%, which is near the performance of some of the best ZnPc devices to date [9,42,43]. It is possible that these results could be further improved by using $PC_{71}BM$ in place of $PC_{61}BM$, as demonstrated elsewhere [44,45].

Overall, the ZnPc morphology improvements created with GLAD provide photoconversion performance enhancement regardless of the amount of material in the

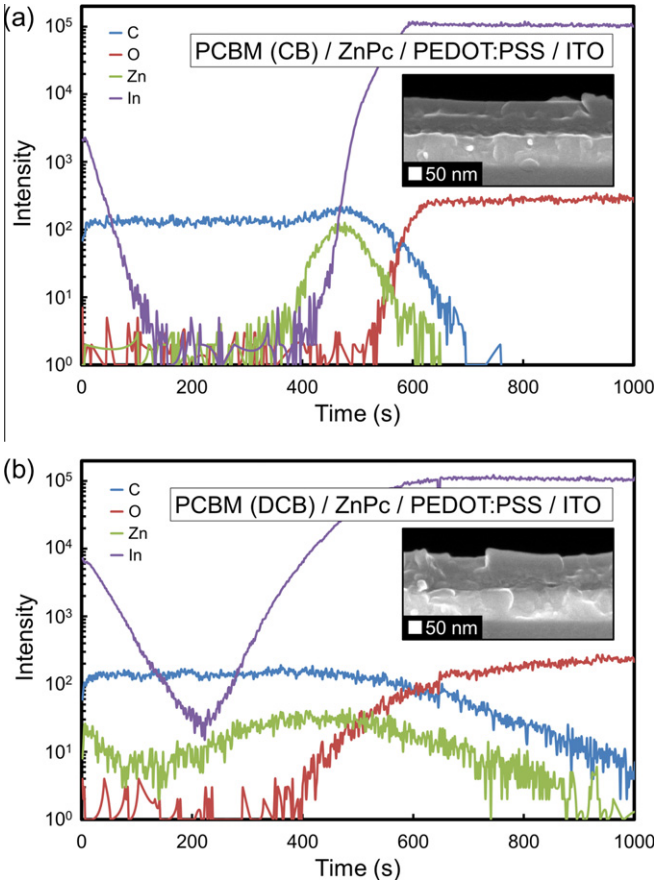

Fig. 10. SIMS depth profiles for thin bilayer ZnPc/PCBM OPV devices, without top electrodes, using (a) CB and (b) DCB as the PCBM solvent.

device. In other words, with all else being equal, a 10 nm planar + 90 nm SP film always outperforms the 50 nm planar film. Similarly, a 10 nm planar + 20 nm SP film always outperforms the 20 nm planar film. We note that the series resistances of the devices using a 50 nm planar film are nearly 50% higher than for devices using a 10 nm planar + 90 nm SP film. Remarkably, the series resistances of thick GLAD-structured devices is as low as the thinnest planar and nanostructured devices. In this case it is evident that the nanostructured architecture promotes better charge transport while containing the same amount of material as the bilayer device. The absorbance profiles of these films are used as grounds to determine that they contained a comparable amount of material (see Fig. 8). Also, in Fig. 8 we see that as the films grow thicker and their morphologies deviate more significantly (between planar and GLAD), so do their absorbance profiles. This is similar to that observed previously with SP CuPc thin films [19].

The absorbance profiles reveal an important difference between the thin bilayer devices prepared using CB vs. DCB as the PCBM solvent, and that is the amount of material stripped off by the solvent during the coating process. We note that the ZnPc absorbance peak around 600–620 nm is lower when using DCB than when using CB, suggesting that DCB is more able to dissolve the ZnPc material while holding 30 mg/mL PCBM. Along with the depth profiles in the following section, this supports the notion that the superior performance observed when using DCB over CB is due to more significant mixing at the interface.

3.3. Depth profiling of thin bilayer device architectures

To further investigate the degree of material mixing at the interface between ZnPc and PCBM, we performed depth profiling via secondary ion mass spectrometry (SIMS) on thin bilayer devices that used either CB or DCB as the PCBM solvent, without a top electrode. Thus, the architecture of the analyzed samples is: ITO (120 nm)/PEDOT:PSS (40 nm)/ZnPc (20 nm)/PCBM (40 nm). The results are shown in Fig. 10.

We see that when using CB as the PCBM solvent, the Zn is well-confined to a specific interval. However, when using DCB as the solvent, the Zn is spread throughout the entirety of the device and is even present at the surface. This further supports the notion that the difference in photovoltaic performance between using CB and DCB (as seen in Table 1) is related to the degree of ZnPc/PCBM mixing during the PCBM casting process.

Finally, it is interesting to note that in each case there was a significant amount of indium present at the surface of the PCBM layer. Migration of indium has been observed previously in OPV devices [46] and OLEDs [47,48]; its impact on these devices will be left for future study.

4. Conclusion

The effects of organic solvents on ZnPc thin films were studied and used to optimize nanostructured ZnPc/PCBM OPV devices. We observe significant recrystallization of ZnPc thin films upon exposure to CB and DCB, which tend to create platelet formations and box structures, respectively, regardless of the initial film morphology. We find that the overall ZnPc film morphology is maintained when coating with PCBM in these solvents, but a degree of material mixing occurs that is dependent on the solvent. This indicates that a planar donor layer can yield either a bilayer or mixed heterojunction, depending on the solvent used to cast the acceptor. When using a nanostructured donor layer, such as a GLAD film, the end result can then be a combination of the interdigitated donor and acceptor layers with a mixed heterojunction forming throughout the acceptor region. This provides an alternative approach to the well-established co-deposition techniques that are routinely used in fabricating mixed heterojunction OPV active layers, while additionally allowing the use of ideal donor layer morphologies.

Photovoltaic performance in our ZnPc/PCBM OPV devices appears to be strongly related to ZnPc film morphology and thickness, as well as PCBM solvent. Our best result in this work is achieved with a 10 nm planar + 20 nm slanted post ZnPc film morphology while using DCB as the PCBM solvent, which exhibits photoconversion efficiencies of up to 3.0%. This work provides motivation for continued optimization of small molecule OPV devices through a combination of direct donor material structuring and optimal solvent choice for casting the acceptor layer (or vice versa).

Acknowledgments

The authors gratefully acknowledge financial support from the Natural Sciences and Engineering Research Council of Canada (NSERC), Alberta Innovates – Technology Futures (AITF), Micralyne Inc., the University of Alberta, and the National Research Council – National Institute for Nanotechnology (NRC-NINT). JV acknowledges NSERC, AITF and SPIE for scholarship support. The authors would also like to thank Tate Hauger for OPV device testing, Brian Worfolk for assistance with the ZnPc solubility study, Michael Taschuk for useful discussions and setting up the EQE system (with Torsten Dorschel), the NINT Microscopy Group, and the Alberta Centre for Surface Engineering and Science (ACSES) for SIMS analysis.

Appendix A. Supplementary data

Supplementary data associated with this article can be found, in the online version, at doi:10.1016/j.orgel.2011.09.005.

References

[1] C.W. Tang, Two-layer organic photovoltaic cell, Appl. Phys. Lett. 48 (1986) 183–185.
[2] F. Yang, M. Shtein, S.R. Forrest, Controlled growth of a molecular bulk heterojunction photovoltaic cell, Nat. Mater. 4 (2005) 37–41.
[3] J.Y. Kim, K. Lee, N.E. Coates, D. Moses, T.Q. Nguyen, M. Dante, A.J. Heeger, Efficient tandem polymer solar cells fabricated by all-solution processing, Science 317 (2007) 222–225.
[4] H. Y Chen, J.H. Hou, S.Q. Zhang, Y.Y. Liang, G.W. Yang, Y. Yang, L. P Yu, Y. Wu, G. Li, Polymer solar cells with enhanced open-circuit voltage and efficiency, Nat. Photonics 3 (2009) 649–653.

[5] T.D. Nielsen, C. Cruickshank, S. Foged, J. Thorsen, F.C. Krebs, Business market and intellectual property analysis of polymer solar cells, Sol. Energy Mater. Sol. Cells 94 (2010) 1553–1571.
[6] P. Peumans, S. Uchida, S.R. Forrest, Efficient bulk heterojunction photovoltaic cells using small-molecular-weight organic thin films, Nature 425 (2003) 158–162.
[7] J. Xue, B.P. Rand, S. Uchida, S.R. Forrest, A hybrid planar–mixed molecular heterojunction photovoltaic cell, Adv. Mater. 17 (2005) 66–71.
[8] R. Pandey, R.J. Holmes, Graded donor-acceptor heterojunctions for efficient organic photovoltaic cells, Adv. Mater. 22 (2010) 5301–5305.
[9] S. Pfuetzner, C. Mickel, J. Jankowski, M. Hein, J. Meiss, C. Schuenemann, C. Elschner, A.A. Levin, B. Rellinghaus, K. Leo, M. Riede, The influence of substrate heating on morphology and layer growth in C(60):ZnPc bulk heterojunction solar cells, Org. Electron. 12 (2011) 435–441.
[10] C. Schunemann, C. Elschner, A.A. Levin, M. Levichkova, K. Leo, M. Riede, Zinc phthalocyanine - Influence of substrate temperature, film thickness, and kind of substrate on the morphology, Thin Solid Films 519 (2011) 3939–3945.
[11] D. Placencia, W. Wang, R.C. Shallcross, K.W. Nebesny, M. Brumbach, N.R. Armstrong, Organic photovoltaic cells based on solvent-annealed textured titanyl phthalocyanine/C_{60} heterojunctions, Adv. Funct. Mater. 19 (2009) 1913–1921.
[12] W. Wang, D. Placencia, N.R. Armstrong, Planar and textured heterojunction organic photovoltaics based on chloroindium phthalocyanine (ClInPc) versus titanyl phthalocyanine (TiOPc) donor layers, Org. Electron. 12 (2011) 383–393.
[13] S. Karak, S.K. Ray, A.J. Dhar, Improvement of efficiency in solar cells based on vertically grown copper phthalocyanine nanorods, J. Phys. D: Appl. Phys. 43 (2010) 245101.
[14] H. Xi, Z. Wei, Z. Duan, W. Xu, D. Zhu, Facile method for fabrication of nanostructured cupcthin films to enhance photocurrent generation, J. Phys. Chem. C 112 (2008) 19934–19938.
[15] M. Hirade, H. Nakanotani, M. Yahiro, C. Adachi, Formation of organic crystalline nanopillar arrays and their application to organic photovoltaic cells, ACS Appl. Mater. Interfaces 3 (2011) 80–83.
[16] J.G. Van Dijken, M.D. Fleischauer, M.J. Brett, Morphology control of CuPc thin films using glancing angle deposition, Proc. 33rd IEEE Photov. Spec. Conf (2008) 1222–1225.
[17] Y. Zheng, R. Bekele, J. Ouyang, J. Xue, Organic photovoltaic cells with vertically aligned crystalline molecular nanorods, Org. Electron. 10 (2009) 1621–1625.
[18] N. Li, S.R. Forrest, Tilted bulk heterojunction organic photovoltaic cells grown by oblique angle deposition, Appl. Phys. Lett. 95 (2009) 123309.
[19] J.G. Van Dijken, M.D. Fleischauer, M.J. Brett, Controlled nanostructuring of CuPc thin films via glancing angle deposition for idealized organic photovoltaic architectures, J. Mater. Chem. 21 (2011) 1013–1019.
[20] G. Wei, S. Wang, K. Renshaw, M.E. Thompson, S.R. Forrest, Solution-processed squaraine bulk heterojunction photovoltaic cells, ACS Nano 4 (2010) 1927–1934.
[21] A. Sanchez-Diaz, R. Pacios, U. Munecas, T. Torres, E. Palomares, Charge transfer reactions in near IR absorbing small molecule solution processed organic bulk-heterojunction solar, Org. Electron. 12 (2011) 329–335.
[22] F. Liang, F. Shi, Y. Fu, L. Wang, X. Zhang, Z. Xie, Z. Su, Donor–acceptor conjugates-functionalized zinc phthalocyanine: Towards broad absorption and application in organic solar cells, Sol. Energy Mater. Sol. Cells 94 (2010) 1803–1808.
[23] J. Liu, Y. Shi, Y. Yang, Solvation-induced morphology effects on the performance of polymer-based photovoltaic devices, Adv. Funct. Mater. 11 (2001) 420–424.
[24] H. Hoppe, M. Niggemann, C. Winder, J. Kraut, R. Hiesgen, A. Hinsch, D. Meissner, N.S. Sariciftci, Nanoscale morphology of conjugated polymer/fullerene-based bulk-heterojunction solar cells, Adv. Funct. Mater. 14 (2004) 1005–1011.
[25] Y. Liang, L. Yu, A new class of semiconducting polymers for bulk heterojunction solar cells with exceptionally high performance, Acc. Chem. Res. 43 (2010) 1227–1236.
[26] K. Robbie, M.J. Brett, A. Lakhtakia, Chiral sculptured thin films, Nature 384 (1996) 616.
[27] K. Robbie, M.J. Brett, Sculptured thin films and glancing angle deposition: Growth mechanics and applications, J. Vac. Sci. Technol. A-Vac. Surf. Films 15 (1997) 1460–1465.
[28] J.J. Steele, M.J. Brett, Nanostructure engineering in porous columnar thin films: recent advances, J. Mater. Sci. Mater. Electron. 18 (2007) 367–379.
[29] M.M. Hawkeye, M.J. Brett, Glancing angle deposition: fabrication, properties, and applications of micro- and nanostructured thin films, J. Vac. Sci. Technol. A 25 (2007) 1317–1335.
[30] M.O. Jensen, M.J. Brett, Periodically structured glancing angle deposition thin films, IEEE Trans. Nanotechnol. 4 (2005) 269–277.
[31] D.A. Gish, M.A. Summers, M.J. Brett, Morphology of periodic nanostructures for photonic crystals grown byglancing angle deposition, Photonics Nanostruct. 4 (2006) 23–29.
[32] M.A. Summers, M.J. Brett, Optimization of periodic column growth inglancing angle deposition for photoniccrystal fabrication, Nanotechnology 19(2008) 415203.
[33] Y. Terao, H. Sasabe, C. Adachi, Correlation of hole mobility, exciton diffusion length, and solar cell characteristics in phthalocyanine/fullerene organic solar cells, Appl. Phys. Lett. 90 (2007) 103515.
[34] F. Yang, S.R. Forrest, Photocurrent generation in nanostructured organic solar cells, ACS Nano 2 (2008) 1022–1032.
[35] M. Whalley, Conjugated macrocycles. Part XXXII, J. Chem. Soc. (1961) 866–869.
[36] C.C. Leznoff, A.B.P. Lever (Eds.), Phthalocyanines: Properties and Applications, VCH: New York, 1989, 1993, 1996, Vols 1–4.
[37] S. Schumann, R.A. Hatton, T.S. Jones, Organic photovoltaic devices based on water-soluble copper phthalocyanine, J. Phys. Chem. C 115 (2011) 4916–4921.
[38] A. Slodek, D. Wohrle, J.J. Doyle, W. Blau, Metal complexes of phthalocyanines in polymers as suitable materials for optical limiting, Macromol. Symp. 235 (2006) 9–18.
[39] S.M.T. Nunes, F.S. Sguilla, A.C. Tedesco, Photophysical studies of zinc phthalocyanine and chloroaluminum phthalocyanine incorporated into liposomes in the presence of additives, Braz. J. Med. Biol. Res. 37 (2004) 273–284.
[40] Z. Guo, B. Chen, M. Zhang, J. Mu, C. Shao, Y. Liu, Zinc phthalocyanine hierarchical nanostructure with hollow interior space: solvent-thermal synthesis and high visible photocatalytic property, J. Colloid Interface Sci. 348 (2010) 37–42.
[41] I. Bruder, J. Schoneboom, R. Dinnebier, A. Ojala, S. Schafer, R. Sens, P. Erk, J. Weis, What determines the performance of metal phthalocyanines (MPc, M=Zn, Cu, Ni, Fe) in organic heterojunction solar cells? A combined experimental and theoretical investigation, Org. Electron. 11 (2010) 377–387.
[42] W. Zeng, K.S. Yong, Z.M. Kam, F. Zhu, Y. Li, Effect of blend layer morphology on performance of ZnPc:C_{60} -based photovoltaic cells, Appl. Phys. Lett. 97 (2010) 133304.
[43] B. Yu, L. Huang, H. Wang, D. Yan, Efficient organic solar cells using a high-quality crystalline thin film as a donor layer, Adv. Mater. 22 (2010) 1017–1020.
[44] X. Xi, W. Li, J. Wu, J. Ji, Z. Shi, G. Li, A comparative study on the performances of small molecule organic solar cells based on CuPc/C(60) and CuPc/C(70), Sol. Energy Mater. Sol. Cells 94 (2010) 2435–2441.
[45] S.H. Park, A. Roy, S. Beaupre, S. Cho, N. Coates, J.S. Moon, D. Moses, M. Leclerc, K. Lee, A.J. Heeger, Bulk heterojunction solar cells with internal quantum efficiency approaching 100%, Nat. Photonics 3 (2009) 297–303.
[46] M. Jorgensen, K. Norrman, F.C. Krebs, Stability/degradation of polymer solar cells, Sol. Energy Mater. Sol. Cells 92 (2008) 686–714.
[47] M.P. de Jong, L.J. van IJzendoorn, M.J.A. de Voigt, Stability of the interface between indium-tin-oxide and poly(3,4-ethylenedioxythiophene)/poly(styrenesulfonate) in polymer light-emitting diodes, Appl. Phys. Lett. 77 (2000) 2255–2257.
[48] Y.H. Kim, S.H. See, J. Noh, S.H. Han, Performance and stability of electroluminescent device with self-assembled layers of poly(3,4-ethylenedioxythiophene)–poly(styrenesulfonate) and polyelectrolytes, Thin Solid Films 510 (2006) 305–310.

possible to bring organic materials into degenerate semiconductor or metallic regimes by incorporating relatively small amounts of conductive fillers [2]. Thus, developing polymer-based composites using thermoelectric and conducting fillers is a logical and promising strategy for creating a new class of thermoelectric materials with sufficient mechanical properties, including flexibility.

In 2008, Yu et al. [2] fabricated carbon nanotube (CNT)/PVAc composites and investigated their thermoelectric properties upon CNT addition. The researchers showed that the electrical conductivity can be dramatically increased by creating a network of CNTs in the composite, while the thermal conductivity and Seebeck coefficient remained relatively insensitive to the filler concentration. A thermoelectric figure of merit (*ZT*) greater than 0.006 was achieved with a CNT concentration of 20 wt.% at room temperature. The study by Yu et al. was the first investigation into the use of CNT/polymer composites as thermoelectric materials. In 2010, Kim et al. [3] reported a maximum *ZT* of ~0.02 at room temperature for a polymer composite containing 35 wt.% SWCNTs. In the study, the main polymer matrix was copolymer latex containing vinyl acetate and ethylene. The stabilizer that was used to disperse the CNTs in water was PEDOT:PSS, a widely used conducting polymer, which was doped with DMSO. Electrically insulating gum Arabic (GA) also was studied for a comparison. Composites were made with two different CNTs (XM-CNT and SWCNT) at 2–15 wt.% CNT concentrations and 1:1–1:4 ratios of CNT to PEDOT:PSS; the structures were dried at room temperature and/or 80 °C. In the preparation procedure, CNTs were added to the conducting polymer as fillers to impart more electrical conductivity and ensure a high thermoelectric figure of merit. Meng et al. [4] and Yao et al. [5] fabricated composites consisting of a CNT network as the main matrix and polyaniline (PANI), a conductive polymer, as a coating additive to the CNTs. Meng et al. reported significantly enhanced Seebeck coefficients and power factors in the multi-walled CNTs (MWCNT)/PANI composites, which were several times larger than either of their individual components. The best *ZT* value obtained was 0.003 for a 15.8 wt.% MWCNT/PANI composite. Yao et al. fabricated single-walled CNTs (SWCNT)/PANI composites with a maximum ZT of 0.004 at 41.4 wt.% SWCNT.

In the above cited studies, the effect of the CNT type on the thermoelectric performance of the CNT/polymer composite was not investigated. It has been known that different types of CNTs exhibit different electrical conductivities and Seebeck coefficients. At 300 K, the Seebeck coefficients of individual SWCNTs and MWCNTs are about 42 μV/K [6] and 82 μV/K [7], respectively. The Seebeck coefficients of SWCNT and MWCNT films [4,8] are comparable and have values of around 20–25 μV/K. With regard to electrical conductivity, metallic SWCNT rope exhibits values around 10,000–30,000 S/cm [9], while electrical conductivities of approximately 200–2000 S/cm have been obtained for individual MWCNTs [10,11]. For films or networks composed of CNTs, electrical conductivity becomes one or two orders of magnitude lower than that of individual CNTs and varies depending on the degree of aggregation. While the electrical conductivity of SWCNT films is about 2000 S/cm [12], that of MWCNT mat is approximately 10 S/cm [13].

Given the aforementioned findings, the CNT type would directly influence the thermoelectric performance of their composites. In this study, the thermoelectric properties of CNT/Nafion nanocomposite films with three different types of CNTs were investigated. The CNT/Nafion nanocomposites were prepared from aqueous solutions of CNT/Nafion and SWCNTs, few-walled CNTs (FWCNTs), and MWCNTs were employed in the structures. A water soluble polymer, Nafion, which also contains hydrophobic nature in its backbone, has exhibited good affinity with CNTs and provides enhanced solubility in an aqueous solution without additional surfactants. As a result, films on a substrate were readily fabricated by the doctor blading method. The electrical properties of the CNT/Nafion nanocomposites were primarily affected by the CNTs since the Nafion acts as an electrically non-conducting matrix, while the thermal conductivity of the composites was dominated by the Nafion matrix; electrical and thermal transport are separated. The electrical conductivity and Seebeck coefficient of the nanocomposites were measured as a function of the type and concentration of CNTs at room temperature. For all three kinds of CNTs, both the electrical conductivity and the Seebeck coefficient increased as the concentration of CNTs was increased. While the electrical conductivity was dependent on the type of CNT, the behavior of the Seebeck coefficient was relatively independent of the CNT type. This indicates that high-energy-charges can participate in transport processes irrespective of the type of CNT.

2. Experimental

2.1. Preparation of CNT/Nafion nanocomposites

SWCNT (ASA-100F), FWCNT (CMP-310F), and MWCNT (CM-95) that are purchased from Hanwha Nanotech were purified according to the "Fenton Chemistry Method" reported by Wang et al. [14] Briefly, pristine CNTs were stirred in 1 N HCl and H_2O_2 (7/3 by weight) at 60 °C for 4 h. The resulting CNTs were filtered and washed with deionized water until the filtrated solution had a pH of 7. The pristine CNTs were heated for 4 h at 292 °C before the Fenton Chemistry purification in order to remove amorphous carbon impurities. The purity of the CNTs, as determined by thermogravimetric analysis (TGA), was >95%. The purified CNTs were mixed with a Nafion solution in deionized (DI) water (5% by weight, Aldrich). The solution was then briefly sonicated (30 min) and stirred overnight. The CNT/Nafion composite solutions were cast onto glass plates that were cleaned by sequential washing with ethanol and acetone under sonication. The composite solution was then doctor-bladed to form the films. The thickness of the film is 2–5 μm.

2.2. Characterization

The four-probe method was used to measure the electrical conductivities of the CNT/Nafion nanocomposites. A

Keithley 2400 was employed as a source meter. The Seebeck coefficient was extracted by applying a temperature gradient along the sample while measuring the thermoelectric voltage. Two T-type thermocouples were used to measure temperatures and voltages simultaneously. Two thermoelectric devices, one as a heat source and another as a heat sink, were used to create a temperature gradient across the samples. The measured Seebeck coefficient was calibrated due to the Seebeck coefficient of the Cu wire of the T-type thermocouple, which is 1.7 μV/K [15]. The thermal conductivity of the samples was extracted by measuring the thermal diffusivity using the laser flash technique (Netzsch LFA 457 MicroFlash) and the specific heat as measured with a differential scanning calorimeter (Netzsch Differential Scanning Calorimeter (DSC) 200).

3. Results and discussion

For the preparation of the CNT/polymer composites, an effective dispersion of CNTs within the polymer matrix is quite a challenge since CNTs have poor solubility due to strong van der Waals interactions. Nafion, a water soluble perfluorosulfonated polymer, has been successfully used to solubilize CNTs in alcoholic solutions so as to form homogeneous composites [16,17]. The hydrophobic main chain of Nafion can wrap the surface of CNTs, while the polar side chain can provide solubility in polar solvents. A photo of a diluted SWCNT/Nafion composite (5 wt.% SWCNT in Nafion) solution in DI-water is shown in Fig. 1(a). A stable homogeneous dispersion of the composites is clearly evident. Stability was reasonably maintained at various SWCNT concentrations. Photos of aqueous SWCNT/Nafion composite solutions over a range of SWCNT/Nafion weight ratios (1/9–5/5) are shown in Fig. 1(b). The dispersion stability was intact after one month, indicating that the Nafion can efficiently solubilize a significant amount of CNTs for a long period of time. The aqueous dispersion and the solution stability of FWCNT and MWCNT-based composites were even more improved because SWCNTs have a stronger tendency toward self-aggregation [18–20]. CNT/Nafion composite-based films were prepared using the doctor blade method, which is popular for micron-thick polymer film fabrication. The fabrication of crack-free CNT/Nafion composite films via a solution process has been demonstrated by Luo et al. [17]. The resulting films exhibited enhanced mechanical properties with strong flexibility and high electrical conductivity. A doctor-bladed SWCNT/Nafion composite film (5 μm thick) on a glass plate is shown in Fig. 1(c). The surface of the films was relatively smooth without noticeable cracks.

Scanning electron microscopy (SEM) images of a 7 wt.% SWCNT/Nafion composite and a 50 wt.% SWCNT/Nafion composite are shown in Fig. 2(a) and (b), respectively. The SWCNTs were homogeneously dispersed within the Nafion matrix, which is indicative of effective wrapping of the SWCNTs by the Nafion in an aqueous solution. As the SWCNT/Nafion ratio was increased, more SWCNTs were observed in the SEM images (Fig. 2(a) and (b)), which indicates that the SWCNTs were homogeneously dispersed within the composite films.

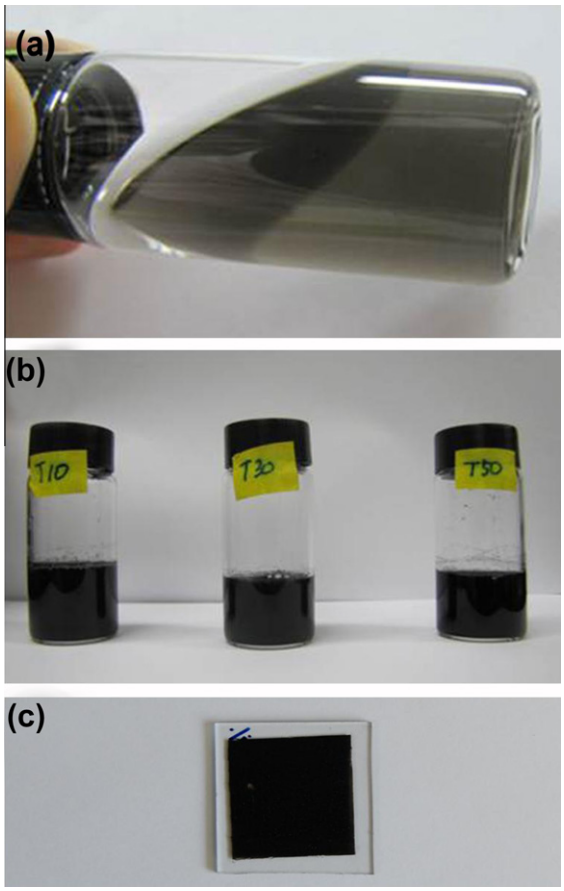

Fig. 1. Photos of (a) a diluted SWCNT/Nafion (5 wt.% SWCNT in Nafion) solution in deionized (DI) water, (b) a range of SWCNT/Nafion composite (1/9–5/5 by weight ratio) solutions in DI water one month after preparation, (c) a SWCNT/Nafion composite film prepared via the doctor blade method. The film was relatively uniform with a thickness of ~5 μm.

The electrical conductivities of the CNT/Nafion nanocomposites are shown in Fig. 3(a). The electrical conductivities of all of the composites increased as the CNT concentration was increased. These conductivities saturated at ~30 wt.% CNT loading in Nafion. Note that even the lowest CNT concentration (10 wt.%) in the composites is much higher than the conventional percolation threshold of CNT/polymer composites (~ a few %), thus the electrical conductivity at 10 wt.% CNT loading was not significantly lower than in the 30 wt.% CNT-loaded films (they were the same order of magnitude), which indicates the efficient percolation of charges. The optimized electrical conductivity of the CNT/Nafion composites (13 S/cm) was similar to the values obtained in a previous report (12.5 S/cm) [17], although the CNT loading in that study was 10 wt.% more than in our composites. Such a result indicates that our composites contained well-dispersed and efficiently interconnected CNTs within a matrix of Nafion. The SWCNT/Nafion composites exhibited relatively lower conductivities when compared to the FWCNT and MWCNT-based composites. For fully connected CNT networks, the electrical conductivity can be somewhat limited by the CNT–CNT contact resistance [21,22]. Taking

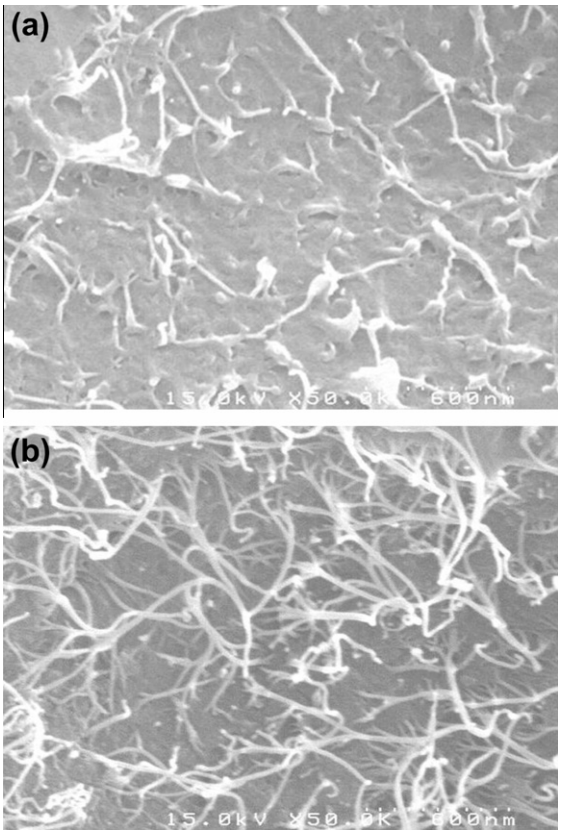

Fig. 2. Scanning electron microscopy (SEM) images of SWCNT/Nafion composites: (a) 7 wt.% and (b) 50 wt.% of SWCNTs in Nafion.

into account that the conductivity of individual CNTs is dependent on various factors such as the surface functionality, tube diameter, length, wall thickness, and bundle size, the conductivity of the composites will be governed by the electrical properties of the CNTs themselves and the contact resistance among the Nafion-wrapped CNTs. In the case of a SWCNT-based mat or composite films, the conductivity significantly varies depending on the ratio of metallic to semiconducting tubes. This is because the contact resistance between semiconducting and metallic junctions is significantly greater than that in metallic–metallic junctions [23]. Since our SWCNTs possessed a typical composition (1:2 for metallic:semiconducting) [23], the higher electrical conductivities of the FWCNT and MWCNT-based composites are not surprising and are consistent with the findings of other reports [24,25]. Based on Fig. 3(a), we deduce that a CNT concentration of 30% should be enough to obtain an optimum electrical conductivity. The highest observed electrical conductivity in this study was 13 S/cm from the 30 wt.% MWCNT/Nafion composites.

The Seebeck coefficients of the CNT/Nafion nanocomposites with respect to the CNT concentration are shown in Fig. 3(b). All of the films, irrespective of the type and concentration of CNTs, exhibited p-type conduction, which means that the majority of charge carriers are holes. When charge carriers from the thermoelectric effect are transported in

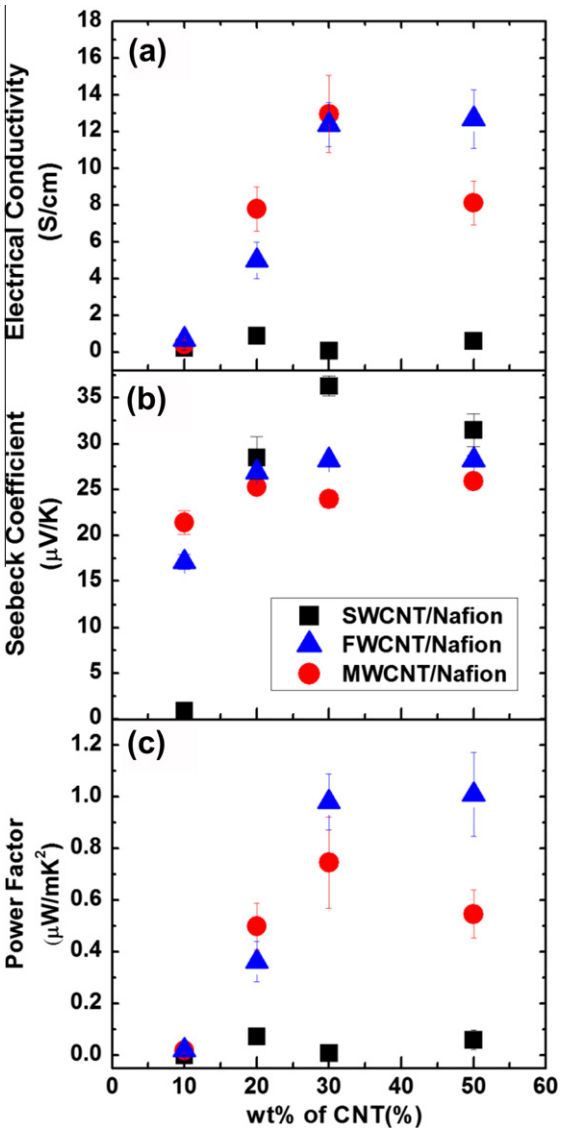

Fig. 3. (a) Electrical conductivity [S/cm], (b) Seebeck coefficient [μV/K], and (c) power factor [W/m-K^2] versus CNT weight percent.

conducting networks (CNTs in this study) within a non-conducting matrix, such as Nafion, the Seebeck coefficient of the composites should depend on the Seebeck coefficient of the networked materials. As mentioned previously, although the Seebeck coefficients of individual CNTs are dependent on the type of CNT (the Seebeck coefficients of the SWCNTs and MWCNTs are about 42 μV/K [6] and 82 μV/K [7], respectively), the Seebeck coefficients of SWCNT and MWCNT mats [4,24] are comparable to each other and are approximately 20–25 μV/K. The Seebeck coefficient is related to the transport of energetic charges, whereas the electrical conductivity is related to the transport of all mobile charges [2,3]. Charge transport in CNT mats is hindered by junctions such as metallic CNT-semiconductor CNT junctions, metallic CNT–metallic CNT junctions, etc. The fact that the Seebeck coefficients of CNT

mats are independent of the CNT type suggests that energetic charges transported regardless of the junction types in SWCNT mats. In our nanocomposites, behavior similar to that seen in CNT-based mats was observed. The Seebeck coefficients of the CNT/Nafion composites which contains >20 wt.% of CNTs ranged from 25–35 μV/K, and there was no significant difference among the types of CNTs (SWCNT, FWCNT, MWCNT) whereas the dependency on the types of CNTs was observed in the 10 wt.% CNT loaded composites. The CNT/Nafion nanocomposites have a different morphology from the CNT mats: Nafion-wrapped-CNTs are connected to each other in the composites, whereas the pure CNTs are connected in the mats. The fact that the Seebeck coefficients of CNT/Nafion composites with higher CNT concentration (20 wt.%) are independent of the type of CNT is an indicator that energetic charges have sufficient energy to transport through the Nafion-wrapped CNTs. This inter-CNT resistance should be even higher than that in CNT mats. Resistance due to metallic CNT-semiconductor CNT junctions should not be affected. Therefore, the Seebeck coefficient of CNT/Nafion nanocomposites should be independent of the CNT type. However, in the composites with 10 wt.% CNT loading, the higher inter-CNT resistance of the Nafion-wrapped CNT could influence to the transport of the energetic charges thus the Seebeck coefficients of the composites. The lower CNT loaded (10 wt.%) composites exhibited relatively reduced values of Seebeck coefficients; especially the SWCNT/Nafion (10 wt.%) displayed much lower values of Seebeck coefficient (0.9 μV/K) than other samples. This result indicates that both the connectivity of CNTs and the inter-CNT resistance determine the Seebeck coefficients of the composites.

The power factors ($S^2\sigma$) of the CNT/Nafion composites are shown in Fig. 3(c). Since the Seebeck coefficients were almost independent of the CNT type and the electrical conductivities were dependent on the type of CNT at the high CNT concentrations, the composites exhibiting higher electrical conductivities possessed higher power factors. The power factor of the FWCNT/Nafion composites was as high as 1 μW/m-K^2, whereas one-tenth of this power factor was observed in the SWCNT/Nafion composites. The thermal conductivity of the 5 wt.% FWCNT/Nafion composites was determined to be ~0.3 W/m-K at room temperature. The thermal conductivity of CNT mats is around 30 W/m-K [26], whereas that of polymer in general is around 0.2 W/m-K at room temperature. This suggests that weak van der Waals bonding in the Nafion significantly contributes to thermal transport. It has been previously reported that the thermal conductivity of CNT/polymer composites is relatively insensitive to the CNT concentration [4,5]. CNT/Nafion thermal conductivity is dominated by the polymer matrix, whereas the electrical transport is dominated by the CNTs themselves. In this scenario, electrical transport can be separated from thermal transport. While the estimated thermoelectric figure of merit of ~0.001 for the CNT/Nafion films is not comparable to that of inorganic materials at this time, the work presented here demonstrates that separating electrical and thermal transport should serve as a scheme to increase the thermoelectric figure of merit.

4. Conclusions

We investigated the thermoelectric properties of CNT/Nafion nanocomposites using various types of CNTs. It was found that the electrical conductivities of the CNT/Nafion composites were primarily affected by the type and concentration of CNTs since the Nafion act as an electrically non-conducting matrix. For all three kinds of CNTs, both the electrical conductivity and the Seebeck coefficient increased as the concentration of CNTs was increased. While the electrical conductivity was dependent on the type of CNT, the behavior of the Seebeck coefficient was relatively insensitive of the CNT type. The Seebeck coefficient is related to the transport of energetic charges, whereas the electrical conductivity is related to the transport of all mobile charges [2,3]. Therefore, energetic carriers that contribute to the Seebeck coefficient would not see barriers such as the metallic CNT-semiconductor CNT junctions in SWCNT/Nafion nanocomposites at high enough concentration. The thermal conductivity of the composites was governed by the polymer matrix. As such, electrical and thermal transport can be separated. This study could prove quite useful in the design and synthesis of polymer composites for thermoelectric applications.

Acknowledgements

WK acknowledges financial support from the Basic Science Research Program through the National Research Foundation of Korea (NRF) funded by the Ministry of Education, Science and Technology (grant numbers 2010-0000610 and 2010-0021487). SYJ thanks financial support by the research program 2011 of Kookmin University in Korea.

References

[1] M.S. Dresselhaus, G. Chen, M.Y. Tang, R.G. Yang, H. Lee, D.Z. Wang, et al., New directions for low-dimensional thermoelectric materials, Adv. Mater. 19 (8) (2007) 1043–1053.
[2] C. Yu, Y.S. Kim, D. Kim, J.C. Grunlan, Thermoelectric behavior of segregated-network polymer nanocomposites, Nano Lett. 8 (12) (2008) 4428–4432.
[3] D. Kim, Y. Kim, K. Choi, J.C. Grunlan, C. Yu, Improved thermoelectric behavior of nanotube-filled polymer composites with poly(3, 4-ethylenedioxythiophene) poly(styrenesulfonate), ACS Nano 4 (1) (2010) 513–523.
[4] C. Meng, C. Liu, S. Fan, A promising approach to enhanced thermoelectric properties using carbon nanotube networks, Adv. Mater. 22 (4) (2010) 535–539.
[5] Q. Yao, L. Chen, W. Zhang, S. Liufu, X. Chen, Enhanced thermoelectric performance of single-walled carbon nanotubes/polyaniline hybrid nanocomposites, ACS Nano 4 (4) (2010) 2445–2451.
[6] C.H. Yu, L. Shi, Z. Yao, D.Y. Li, A. Majumdar, Thermal conductance and thermopower of an individual single-wall carbon nanotube, Nano Lett. 5 (9) (2005) 1842–1846.
[7] P. Kim, L. Shi, A. Majumdar, P.L. McEuen, Thermal transport measurements of individual multiwalled nanotubes, Phys. Rev. Lett. 87 (21) (2001) 215502.
[8] T.D. Van, V.D. Dzung, T. Yamada, T.T. Bui, K. Hata, S. Sugiyama, Integration of SWNT film into MEMS for a micro-thermoelectric device, Smart Mater. Struct. 19 (7) (2010) 075003.
[9] A. Thess, R. Lee, P. Nikolaev, H.J. Dai, P. Petit, J. Robert, et al., Crystalline ropes of metallic carbon nanotubes, Science 273 (5274) (1996) 483–487.
[10] T.W. Ebbesen, H.J. Lezec, H. Hiura, J.W. Bennett, H.F. Ghaemi, T. Thio, Electrical conductivity of individual carbon nanotubes, Nature 382 (6586) (1996) 54–56.

[11] H.J. Dai, E.W. Wong, C.M. Lieber, Probing electrical transport in nanomaterials: conductivity of individual carbon nanotubes, Science 272 (5261) (1996) 523–526.
[12] W.J. Ma, L. Song, R. Yang, T.H. Zhang, Y.C. Zhao, L.F. Sun, et al., Directly synthesized strong, highly conducting, transparent single-walled carbon nanotube films, Nano Lett. 7 (8) (2007) 2307–2311.
[13] I.N. Mazov, V.L. Kuznetsov, S.I. Moseenkov, A.V. Ishchenko, A.I. Romanenko, O.B. Anikeeva, et al., Electrophysical and electromagnetic properties of pure MWNTs and MWNT/PMMA composite materials depending on their structure, Fullerenes, Nanotubes, Carbon Nanostruct. 18 (4–6) (2010) 505–515.
[14] Y. Wang, H. Shan, R.H. Hauge, M. Pasquali, R.E. Smalley, A highly selective, one-pot purification method for single-walled carbon nanotubes, J. Phys. Chem. B 111 (6) (2007) 1249–1252.
[15] A.W. Van Herwaarden, P.M. Sarro, Thermal sensors based on the Seebeck effect, Sens. Actuators 10 (3–4) (1986) 321–346.
[16] J. Wang, M. Musameh, Y.H. Lin, Solubilization of carbon nanotubes by Nafion toward the preparation of amperometric biosensors, J. Am. Chem. Soc. 125 (9) (2003) 2408–2409.
[17] C. Luo, X.L. Zuo, L. Wang, E.G. Wang, S.P. Song, J. Wang, et al., Flexible carbon nanotube-polymer composite films with high conductivity and superhydrophobicity made by solution process, Nano Lett. 8 (12) (2008) 4454–4458.
[18] A. Hirsch, Functionalization of single-walled carbon nanotubes, Angew. Chem. Int. Ed. 41 (11) (2002) 1853–1859.
[19] N. Karousis, N. Tagmatarchis, D. Tasis, Current progress on the chemical modification of carbon nanotubes, Chem. Rev. 110 (9) (2010) 5366–5397.
[20] P. Singh, S. Campidelli, S. Giordani, D. Bonifazi, A. Bianco, M. Prato, Organic functionalisation and characterisation of single-walled carbon nanotubes, Chem. Soc. Rev. 38 (8) (2009) 2214–2230.
[21] Z. Yao, C.L. Kane, C. Dekker, High-field electrical transport in single-wall carbon nanotubes, Phys. Rev. Lett. 84 (13) (2000) 2941–2944.
[22] A. Buldum, J.P. Lu, Contact resistance between carbon nanotubes, Phys. Rev. B 63 (16) (2001).
[23] Y.P. Sun, W. Wang, K.A.S. Fernando, Y. Lin, M.J. Meziani, L.M. Veca, et al., Metallic single-walled carbon nanotubes for conductive nanocomposites, J. Am. Chem. Soc. 130 (4) (2008) 1415–1419.
[24] Y.K. Gun'ko, M.T. Byrne, Recent advances in research on carbon nanotube-polymer composites, Adv. Mater. 22 (15) (2010) 1672–1688.
[25] F.H. Gojny, M.H.G. Wichmann, B. Fiedler, I.A. Kinloch, W. Bauhofer, A.H. Windle, et al., Evaluation and identification of electrical and thermal conduction mechanisms in carbon nanotube/epoxy composites, Polymer 47 (6) (2006) 2036–2045.
[26] J. Hone, M.C. Llaguno, N.M. Nemes, A.T. Johnson, J.E. Fischer, D.A. Walters, et al., Electrical and thermal transport properties of magnetically aligned single walt carbon nanotube films, Appl. Phys. Lett. 77 (5) (2000) 666–668.

intensity of such a DC device is dominated by the wavelengths corresponding to the emission of underlying blue OLED and emission from the down conversion material. Therefore, the device spectra are not very broad and limit the color rendering index (CRI). Our approach tries to overcome this disadvantage: We fabricate white top-emitting OLEDs with a heterosystem of two different organic layers. Utilizing two down conversion materials helps to obtain a DC device with a broad emission spectrum, an improved CRI, and a better control of color coordinates with thickness of down conversion materials.

2. Experimental

The blue OLED device consists of glass substrate/aluminum 40 nm/silver as bottom contact 15 nm/hole transport layer *N*,*N*,*N*′,*N*′-tetrakis (4-methoxyphenyl)-benzidine (MeO-TPD) doped with 2 wt.% Novaled dopant (NDP2) 25 nm/electron blocking layer *N*,*N*′-di(naphthalen-2-yl)-*N*,*N*′-diphenyl-benzidine (α-NPD) 10 nm/fluorescent blue emitter system 2-methyl-9,10-bis(napthalen-2-yl) anthracene (MADN) doped with 1 wt.% of 2,5,8,11 -tetra-tert-butylperylene (TBPe) 10 nm/hole blocking layer tris(8-hydroxy-quinolinato)aluminum (Alq_3) 10 nm/electron transporting layer 4,7-diphenyl-1,10-phenanthroline (BPhen) coevaporated with cesium (Cs) 10 nm/semi-transparent top contact Ag 15 nm. The dopant NDP2 has similar electrical properties to a known dopant F4-TCNQ, but F4-TCNQ is known to contaminate the evaporation chamber, therefore NDP2 is used. The thicknesses for different layers of the blue device are optimized by optical simulation [17]. The DC materials used in this study are the deep red emitter 4-dicyanomethylene-2-methyl-6-*p*-dimethylaminostyryl-4*H*-pyran (DCM) doped at 1 wt.% in an Alq_3 matrix and a yellow fluorescent dye *N*4,*N*41′-bis-(4-tert-butyl-phenyl)-*N*4,*N*4′-di-fluoranthen-3-yl-diphenylether-4,4′-diamine (OYSE). The OLED structures of the fabricated devices A, B, and C are shown in Fig. 1.

The thicknesses of DC layers are determined by previous experiments on bottom emitting devices. All devices are fabricated in an UHV chamber (Kurt Lesker) with a base pressure $<10^{-7}$ mbar. The deposition rates for all materials are in the range of 0.2–1.5 Å/s and thicknesses are measured with quartz crystals. The photoluminescence spectra of single layers are measured with the luminescence spectrometer Fluoromax from HORIBA Jobin Yvon GmbH. Transmission and reflection measurements are done at the spectral photometer UV-3101 from Shimadzu Deutschland GmbH. The current–voltage characteristics of the devices are measured by source measure unit (Keithley SMU2400) and a silicon photodiode (HAMAMATSU). The spectral emission is detected by an absolute calibrated CAS100 spectrometer. Angular resolved electroluminescence spectra are measured with a goniophotometer. The efficiencies are calculated with respect to the goniophotometer measurements [18].

3. Results and discussion

Fig. 2 shows the absorbance and photoluminescence spectra of 80 nm films of the down conversion materials on quartz substrates superposed with the photoluminescence spectrum of MADN:TBPe. The photoluminescence spectrum of MADN:TBPe exhibits peak at 460 nm followed two shoulders at 490 nm and 525 nm. It can be observed that DCM and OYSE have high absorption at the wavelength corresponding to maximum emission (460 nm) of the blue OLED. DCM and OYSE have strong emission in the deep red (670 nm) and in the yellow region (556 nm), respectively. In the system Alq_3:DCM, the Alq_3 host allows Foerster energy transfer to DCM and also acts as a spacer for DCM molecules to prevent the quenching of emission [19]. For an efficient Foerster energy transfer from the host to the dopant there should be a strong overlap between the photoluminescence spectrum of the host and absorption spectrum of the dopant, which is illustrated in Fig. 2. Further, there is a significant overlap of blue emit-

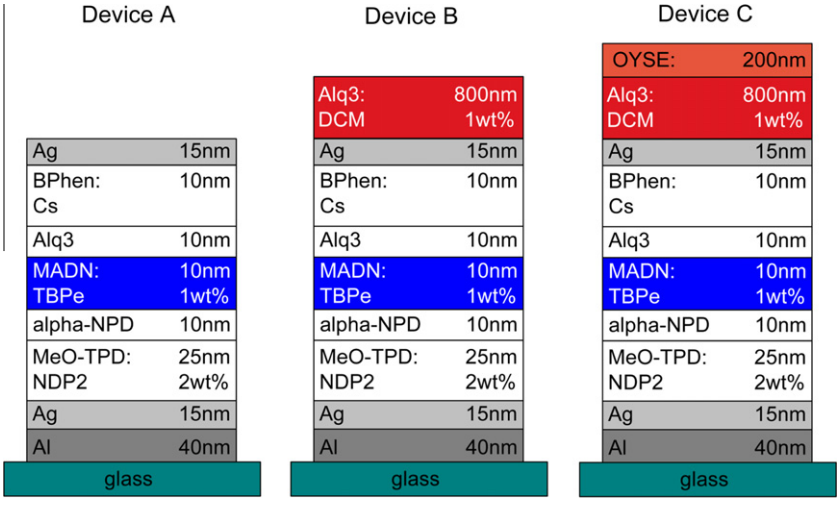

Fig. 1. Layer architectures of the fabricated devices. Additionally to the blue top-emitting OLED (device A), a single down conversion layer of Alq_3:DCM (device B) and a heterosystem of Alq_3:DCM/OYSE (device C) is applied. (For interpretation of the references to color in this figure legend, the reader is referred to the web version of this article.)

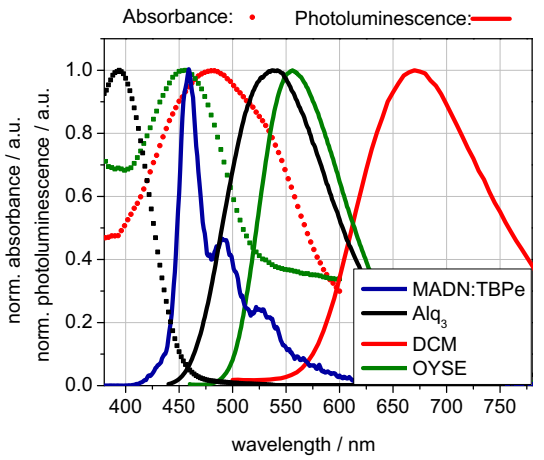

Fig. 2. Absorbance spectra of the materials Alq_3, OYSE and DCM and photoluminescence spectra for Alq_3, OYSE, DCM and MADN:TBPe for single layers. The DC materials are chosen such that there is a high overlap between the photoluminescence spectrum of blue material and the absorbance of the DC materials to enable efficient energy transfer. (For interpretation of the references to colour in this figure legend, the reader is referred to the web version of this article.)

ter photoluminescence spectrum with the absorption spectrum of DCM. Direct absorption of blue light by DCM and re-emission is also likely to contribute to DC device spectrum. The peak wavelength of photoluminescence spectrum exhibits a red shift with increased doping of DCM in Alq_3 with maximum photoluminescence intensity at around 1 wt.% [20]. The incorporation of an OYSE layer serves to fill the spectral gap between red and blue regions of the visible spectrum.

The majority of DCOLEDs reported in literature are bottom emission OLEDs [9–14]. Usually an ITO coated glass substrate separates the organic layer of the OLED stack and DC layer. The mechanism of color conversion in such devices can simply be attributed to light absorption and re-emission by the DC layers. For an Alq_3:DCM DC layer, blue light absorbed by Alq_3 can be transferred non-radiatively to DCM dopant molecules by Foerster energy transfer. However, in top-emitting OLEDs a second mechanism of color conversion may operate in parallel to absorption and re-emission. Previously it has been demonstrated that in systems, where two organics films are separated by a thin metallic layer, radiative energy transfer can occur from the decaying dipoles of the emitter to acceptor molecules in the other organic layer, mediated by the surface plasmon polaritons (SPPs), existing on both sides of the metal [21–23]. For both devices B and C the emitting dipoles are close to the 15 nm thick Ag top contact (20–30 nm). It is likely that the energy from decaying blue emitting dipoles can couple to SPP modes near surface of thin Ag film and this energy can then be further transferred to DCM dopant via the SPPs existing on the other side of the metal.

The inset in Fig. 3 shows the current–voltage (I–V) curves for the devices A, B, and C. It is noteworthy, that the I–V curves of all devices are almost identical. This shows that the DC layers have no effect on the electrical properties of the device. Fig. 3 illustrates the normalized

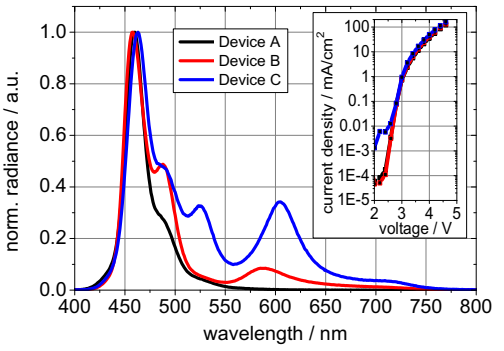

Fig. 3. Normalised EL spectrum for the devices A, B and C. The emission from Alq_3:DCM and OYSE proves the principle of down conversion in top-emitting OLEDs. Inset: I–V characteristics of devices A, B and C have very similar behavior. This demonstrates the additional DC layer(s) have no impact on the electrical behavior of the device.

EL spectrum at 1000 cd/m^2 of the devices A, B, and C. The spectra of devices B and C have peaks at 580 nm and 602 nm, respectively. These maxima arise from the light generated in the DC layers. These peaks do not exactly correspond to the photoluminescence maximum of DC materials but rather to a peak which represents the net sum of emission from individual DC materials. The shoulder observed at 525 nm in MADN:TBPe photoluminescence spectrum is suppressed in electroluminescence spectra of devices A and B due to the cavity structure. Further, the blue part of the spectra of the devices B and C are much broader compared to the reference blue device A, which is related to an additional capping layer effect [24].

The device C exhibits cold white CIE color coordinates of (0.27, 0.26) with a color rendering index of 60 and correlated color temperature (CCT) of 17,200 K (Fig. 4). A shift towards the planckian locus is observed for the devices B and C. The warm white point A can be achieved by an enhanced contribution of OYSE and Alq_3:DCM, which might be realized with thicker DC layers.

Furthermore, it is observed that the electroluminescence spectrum of device C is stable with variation of the applied current. The blue emitting device A exhibits an electroluminescence (EL) spectrum which is stable against

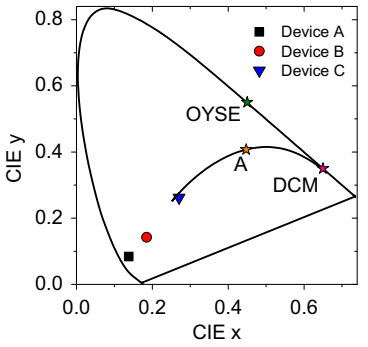

Fig. 4. CIE color coordinates for the three devices. By tuning the layer thicknesses of the down conversion layers an adjustment of the coordinates towards the planckian locus is realized.

the measurement angle θ ($0° < \theta < 90°$) as shown in Fig. 5(a), while for the device C the spectrum has a strong angular dependence as depicted in Fig. 5(b). The blue part of the spectrum for devices A and C show a similar angular dependence. For the device C, the change in angular spectra is most pronounced in the yellow and red parts of the emission spectrum which also corresponds to the maximum of photoluminescence from the DC materials OYSE and Alq_3:DCM, respectively. This is due to the fact that the down converted light undergoes strong microcavity effects when it enters the cavity through the semitransparent cathode. At the normal observation angle for device C, the emission from OYSE is not clearly visible. However, at angles of 40–50° one can clearly see the spectral contribution from both OYSE and Alq_3:DCM. To make the angular spectrum more stable, one could utilise a scattering layer or a microlens foil on top of the DC layer.

To have a more accurate estimate of the amount of down conversion, one must consider the light emitted not only in the forward direction but also for larger viewing angles. Therefore the photon flux (PF) of the devices A, B, and C is calculated by measuring and integrating the EL spectra from viewing angles of 0–90°. The photon flux is depicted in the following formula by

$$PF = \frac{2\pi}{hc} \int \int \lambda I_e[\lambda, \theta] \sin\theta d\lambda d\theta$$

where h and c represent Planck's constant and speed of light in vacuum, respectively. I_e denotes the spectral radiant intensity as a function of wavelength λ and viewing angle θ.

In Fig. 6, the relative contribution to the photon flux by the down conversion components in devices B and C is depicted. The strong absorption of the DC layers lead to a loss of blue light. In the case of Alq_3:DCM, the peak of the blue emission is reduced by a factor of 1.8; for the heterosystem Alq_3:DCM/OYSE by a factor of 6.2. Hence, the contribution of blue, yellow, and red light can be well adjusted using thickness variations of the DC-layers.

Fig. 7 shows the external quantum efficiency (EQE) and luminous efficacy of the devices in dependence of the current density. The EQE of device A is higher than of devices B and C. Interestingly, the EQE is reduced almost by a factor of 2 when applying the heterosystem. The decrease is mainly due to the limited photoluminescence quantum yield (PLQY) and absorption by the down conversion materials, PLQY for Alq_3:DCM is nearly 60% [25] and 69.4% for OYSE. The luminous efficacy is enhanced for the devices

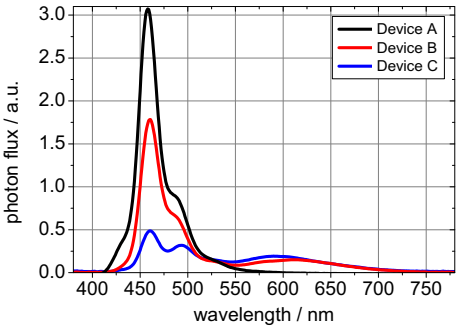

Fig. 6. Photon flux for the three devices at a current of 3 mA. The strong decrease in the blue spectrum is due to absorption by Alq_3:DCM and OYSE.

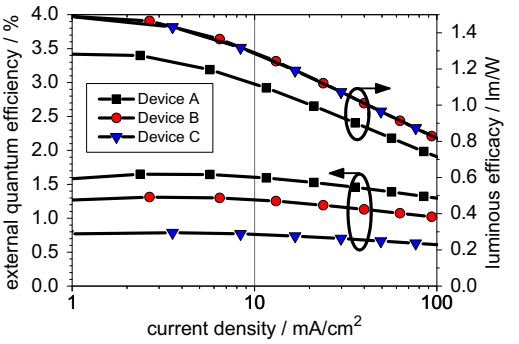

Fig. 7. External quantum efficiency (EQE) and luminous efficacy (LE) vs current density for devices A, B and C. The blue device shows nearly twice the external quantum efficiency of the heterosystem DCOLED. The down conversion devices B and C have higher luminous efficacy than the blue system as the device spectra are pronounced in the region of the eye sensitization curve. (For interpretation of the references to colour in this figure legend, the reader is referred to the web version of this article.)

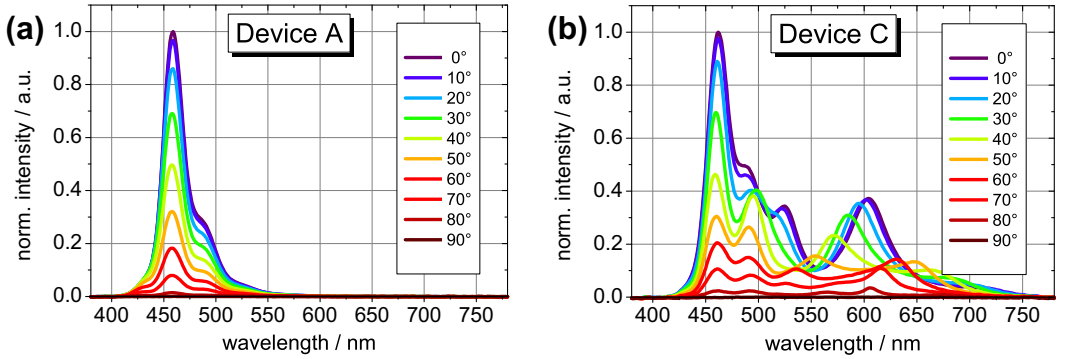

Fig. 5. Angular dependent EL spectrum for device A and C at 3 mA. The spectra are normalized to the peak of the 0° spectrum. While the blue OLED (a) shows an angular stable spectrum, the DC-OLED (b) exhibits a strong shift only in the yellow and red parts of the spectrum with increasing viewing angle. (For interpretation of the references to color in this figure legend, the reader is referred to the web version of this article.)

with DC layer, which is a result of the stronger overlap of the spectrum with the eye sensitization $V(\lambda)$ curve.

4. Conclusion

Top emitting white organic LEDs are demonstrated with a single- and a heterosystem of organic DC layers. For the heterosystem, the conversion in both layers has been demonstrated. The white OLED has a broad emission spectrum with spectral contributions from each of the two down conversion materials. At 1000 cd/m^2 the white DCOLED has color coordinates of (0.27, 0.26) with the current efficacy, luminous efficacy and external quantum efficiency values of 1.4 cd/A, 0.88 lm/W and 0.83%, respectively. The DC device efficiencies can be substantially increased by using phosphorescent blue emitters instead of fluorescent ones. Furthermore, DC layer thicknesses can be optimized in terms of the color point and light outcoupling.

References

[1] C.W. Tang, S.A. VanSlyke, Organic electroluminescent diodes, Appl. Phys. Lett. 51 (1987) 913.
[2] S. Reineke, F. Lindner, G. Schwartz, N. Seidler, K. Walzer, B. Lüssem, K. Leo, White organic light-emitting diodes with fluorescent tube efficiency, Nature 459 (2009) 234–238.
[3] A. Misra, P. Kumar, M.N. Kamalasanan, S. Chandra, White organic LEDs and their recent advancements, Semicond. Sci. Technol. 21 (2006) R35–R47.
[4] R.S. Deshpande, V. Bulovic, S.R. Forrest, White-light-emitting organic electroluminescent devices based on interlayer sequential energy transfer, Appl. Phys. Lett. 75 (1999) 888.
[5] S. Tasch, E.J.W. List, O. Ekström, W. Graupner, G. Leising, P. Schlichting, U. Rohr, Y. Geerts, U. Scherf, K. Müllen, Efficient white light-emitting diodes realized with new processable blends of conjugated polymers, Appl. Phys. Lett. 71 (1997) 2883.
[6] Yao-Shan Wua, Shiao-Wen Hwang, Hsian-Hung Chen, Meng-Ting Lee, Wen-Jian Shen, Chin H. Chen, Efficient white organic light emitting devices with dual emitting layers, Thin Solid Films 488 (2005) 265.
[7] C.-H. Kim, J. Shinar, Bright small molecular white organic light-emitting devices with two emission zones, Appl. Phys. Lett. 80 (2002) 2201.
[8] G. Leising, S. Tasch, C. Brandstätter, F. Meghdadi, G. Froyer, L. Athouel, Red-green-blue light emission from a thin film electroluminescence device based on parahexaphenyl, Adv. Mater. 9 (1997) 33.
[9] S. Chen, H.-S. Kwok, "Top-emitting white organic light-emitting diodes with a colour conversion cap layer", Org. Electronics 12 (2011) 677.
[10] A.R. Duggal, J.J. Shiang, C.M. Heller, D.F. Foust, Organic light-emitting devices for illumination quality white light, Appl. Phys. Lett. 80 (2002) 3470.
[11] A.R. Duggal, J.J. Shiang, D.F. Foust, L.G. Turner, W.F. Nealon, J.C. Bortscheller, Large Area White OLEDs, SID Digest 36 (2005) 28.
[12] A. Mikami, High efficiency white-light-emitting organic devices coupled with lateral colour conversion layer, in: 19th Annual Meeting of the IEEE, Lasers and Electro-Optics Society, LEOS, 2006.
[13] C. Li, M. Ichikawa, B. Wei, Y. Taniguchi, H. Kimura, K. Kawaguchi, K. Sakurai, A high colour stability white organic light-emitting diode by colour conversion within hole injection layer, Opt. Express 15 (2007) 608.
[14] Y.B. Yuan, S. Li, Z. Wang, H.T. Xu, X. Zhou, White organic light-emitting diodes combining vacuum deposited blue electrophosphorescent devices with red surface colour conversion layers, Opt. Express 17 (2009) 1577.
[15] B.C. Krummacher, V. Choong, M.K. Mathai, S.A. Choulis, F. So, Highly efficient white organic light-emitting diode, Appl. Phys. Lett. 88 (2006) 113506.
[16] W. Ji, L. Zhang, R. Gao, L. Zhang, W. Xie, H. Zhang, B. Li, Top-emitting white organic light-emitting devices with down-conversion phosphors: theory and experiment, Opt. Express 16 (2008) 15489.
[17] M. Furno, R. Meerheim, M. Thomschke, S. Hofmann, B. Lüssem, K. Leo, Outcoupling efficiency in small-molecule OLEDs: from theory to experiment, Proc. SPIE 7617 (2010) 761716.
[18] S. Hofmann, M. Thomschke, P. Freitag, M. Furno, B. Lüssem, K. Leo, Top-emitting organic light-emitting diodes: influence of cavity design, Appl. Phys. Lett. 97 (2010) 253308.
[19] C.W. Tang, S.A. VanSlyke, C.H. Chen, Electroluminescence of doped organic thin films, J. Appl. Phys. 65 (1989) 3610.
[20] J. Jakabovic, T.C. Wong, O. Lengyel, J. Kovac, C.S. Lee, S.T. Lee, Optical properties investigations of organic Alq3 layers doped by DCM, in: The Fourth International Conference on Advanced Semiconductor Devices and Microsystems (ASDAM), Slovakia, 2002, p. 35.
[21] P. Andrew, W.L. Barnes, Energy transfer across a metal film mediated by surface plasmon polaritons, Science 306 (2004) 1002.
[22] K.H. An, M. Shtein, K.P. Pipe, Surface plasmon mediated energy transfer of electrically-pumped excitons, Opt. Express 18 (2010) 4041.
[23] K.-C. Tien, M.-S. Lin, Y.-H. Lin, C.-H. Tsai, M.-H. Shiu, M.-C. Wei, H.-C. Cheng, C.-L. Lin, H.-W. Lin, C.-C. Wu, Utilizing surface plasmon polariton mediated energy transfer for tunable double-emitting organic light-emitting devices, Org. Electronics 11 (2010) 397.
[24] M. Thomschke, R. Nitsche, M. Furno, K. Leo, Optimized efficiency and angular emission characteristics of white top-emitting organic electroluminescent diodes, Appl. Phys. Lett. 94 (2009) 083303.
[25] G.Y. Zhong, J. He, S.T. Zhang, Z. Xu, Z.H. Xiong, H.Z. Shi, X.M. Ding, W. Huang, X.Y. Hou, In situ photoluminescence investigation of doped Alq, Appl. Phys. Lett. 80 (2002) 4846.

acid (PTCDA) has been used at the anode, whereby the improved stacking of the ClAlPc molecules led to an increase in short-circuit current density J_{sc} of 25% [10]. For organic transistors, the use of self-assembled monolayers (SAMs) is a well-established technique for the control of the growth [11]. Using this approach, the molecular orientation of ClAlPc molecules could be changed from face-on (parallel to the substrate) to edge-on (normal to the substrate) by treating a SiO_2 substrate with octadecyltrichlorosilane [12]. For OPVCs, SAMs have been used to treat the anode, though here the aim has typically been to adjust the ITO work function, rather than adjusting the growth of subsequent layers [13–16].

To obtain a BHJ that combines good transport properties with efficient exciton separation, the control of morphology and growth is even more critical. For example, the co-evaporation of a planar phthalocyanine (Pc) and C_{60} at room temperature will typically lead to an amorphous film [17,18]. Compared to the pure CuPc layer these amorphous films have poor hole mobilities, limiting cell efficiency. By applying an elevated substrate temperature (T_{sub}) during Pc:C_{60} deposition, the efficiency can be improved compared to deposition at room temperature [19]. Also here, the growth surface can have a large impact on the solar cell performance, with films grown on 3,4-polyethylenedioxythiophene:polystyrenesulfonate (PEDOT:PSS) showing a different morphology and lower efficiency compared to devices with films grown directly on ITO [20].

For ClAlPc, Li et al. showed that the surface area of the films could be increased by using oblique angle vacuum deposition [21]. This resulted in an increase in J_{sc} in their ClAlPc/C_{60} cells, thereby showing that ClAlPc cells could be improved with a bulk heterojunction approach. First promising results for co-evaporated ClAlPc:C_{70} BHJ cells have already been reported [22], where T_{sub} was shown to have a strong impact on the growth of the blend, with nanocrystal formation at an elevated temperature from 370–390 K. Consequently, J_{sc} and *FF* were enhanced significantly, resulting in a power conversion efficiency of 4.1%.

In this article, we will further investigate the growth of ClAlPc for BHJ solar cells. We will focus on the use of structural templating layers, an approach which has already proven successful in planar heterojunction cells, but has not been thoroughly investigated for their role to improve BHJ-based cells. The two different surfaces we compare as templating layers are molybdenum oxide (MoO_3) and MoO_3 treated with a SAM of 1H,1H,2H,2H-perfluorodecyltrichlorosilane (FDTS). First, pure ClAlPc films were grown on top of these surfaces, and the influence of T_{sub} on the film properties was investigated. Planar HJ solar cells were then produced from these pure films to probe how the different growth properties affect the ensuing solar cell performance.

Next, we proceed by growing co-evaporated ClAlPc:C_{60} films at elevated T_{sub} in order to grow crystalline BHJ layers. Here, we observe a significant device performance improvement depending on the presence of an initial pure ClAlPc templating layer underneath the BHJ layer. Bulk heterojunction solar cells produced with these blends all show increased current with respect to the planar HJ devices, with power conversion efficiencies (η) greater than 4%.

2. Experimental

Glass substrates coated with ITO (Kintec, 85 nm, sheet resistance <20 $\Omega\,\square^{-1}$) arevv cleaned by subsequent ultrasonic treatment in detergent, de-ionized water, acetone, and iso-propanol, for 5 min each, followed by an ultraviolet-ozone treatment for 900 s. On the samples for film characterization, a 25 nm thick layer of PEDOT:PSS (HC Starck Clevios P) was deposited. Prior to FDTS surface modification, 10 nm of MoO_3 is evaporated at a rate of $\sim$1 Å s^{-1} and pressure of $\sim10^{-7}$ Torr in a vacuum chamber. Then FDTS is applied by vapor phase deposition in a home-built oven under reduced pressure (140 °C, 30 min.).

The MoO_3 ($\sim$550 °C), ClAlPc ($\sim$350 °C), C_{60} ($\sim$380 °C) and bathocuproine (BCP) ($\sim$150 °C) materials are evaporated at a rate of $\sim$1 Å s^{-1} in a vacuum chamber at a pressure of $\sim10^{-7}$ Torr. The mixed ClAlPc:C_{60} (1:1) layer was formed by keeping both rates constant at 0.5 Å s^{-1}. Deposition rates are determined from calibration of the film thickness, measured ex-situ by spectroscopic ellipsometry (Sopra GESP-5). All organic materials are purified before loading into the chamber by thermal gradient sublimation. T_{sub} was elevated with heat lamps, calibrated by thermocouple measurements. Before subsequent layers were deposited on the heated layer, samples were cooled to $\sim$40 °C. The cathode, Ag ($\sim10^{-7}$ Torr; 1.5 Å s^{-1}), is deposited through a shadow mask, without breaking vacuum.

X-ray reflectivity (XRR) measurements were performed on a PANalytical X'Pert Pro Materials Research Diffractometer using Cu Kα radiation. An integration time of 7 s per 2θ of 0.01° was used for scanning $\theta/2\theta$. Absorptance spectra are measured with a Shimadzu UV-1601PC. The surface morphology was studied with atomic force microscopy (AFM) using a Picoscan PicoSPM LE scanning probe in tapping mode. Static contact angle measurements were performed on MoO_3 and ClAlPc films with an OCA-20 contact angle meter from DataPhysics Instruments GmbH with SCA20 software.

Electrical characterization of the solar cells is performed with a Keithley 2602 measurement unit. Cells are measured in the dark (see supplementary information) and under 100 mW cm^{-2} AM1.5G simulated solar illumination. Solar illumination is applied using an Abet solar simulator, calibrated with a Fraunhofer certified photovoltaic cell. For all studied device architectures, 6 cells with active areas of 0.134 cm^2 were measured, where the best performing (highest power conversion efficiency) is reported here.

A commercial set-up (Bentham) is used to measure the external quantum efficiency (*EQE*). Light from a Xe arc lamp (300–670 nm) and a quartz halogen lamp (670–900 nm) is chopped, coupled into a monochromator and aimed at the device. The resulting current is sent through a Bentham477 current pre-amplifier, then arriving in the Bentham485 lock-in amplifier. Calibration is done with a certificated Si cell. The integration of these EQEs over the solar spectrum [23] is listed in Tables 1 and 2 as J_{EQE}. The same optics and measurement setup is used with a DTR6 integrating sphere to determine the reflection.

Table 1
J_{sc}, V_{oc}, *FF* and efficiency η measured for 100 mW cm^{-2} AM1.5G simulated solar illumination. J_{EQE} is the current density as calculated by integration of the *EQE* over the AM1.5G solar spectrum.

Structure	J_{sc} (mA cm^{-2})	J_{EQE} (mA cm^{-2})	V_{OC} (V)	*FF* (%)	η (%)
(a) MoO_3/ClAlPc (RT)/C_{60}/BCP/Ag	4.9	4.7	0.80	62	2.4
(b) MoO_3/FDTS/ClAlPc (RT)/C_{60}/BCP/Ag	6.3	6.3	0.70	52	2.3
(c) MoO_3/ClAlPc (105 °C)/C_{60}/BCP/Ag	5.3	5.0	0.72	49	1.9
(d) MoO_3/FDTS/ClAlPc (105 °C)/C_{60} /BCP/Ag	8.9	8.7	0.53	65	3.0

Table 2
J_{sc}, V_{oc}, *FF* and efficiency η measured for 100 mW cm^{-2} AM1.5G simulated solar illumination. J_{EQE} is the current density as calculated by integration of the *EQE* over the AM1.5G solar spectrum.

Structure	J_{sc} (mA cm^{-2})	J_{EQE} (mA cm^{-2})	V_{oc} (V)	*FF* (%)	η (%)
(e) MoO_3/ClAlPc:C_{60} (105 °C)/C_{60}/BCP/Ag	9.1	7.9	0.78	32	2.2
(f) MoO_3/FDTS/ClAlPc:C_{60} (105 °C)/C_{60}/BCP/Ag	10.8	9.0	0.58	49	3.1
(g) MoO_3/ClAlPc (105 °C)/ClAlPc:C_{60} (105 °C)/C_{60}/BCP/Ag	10.7	9.3	0.74	61	4.8
(h) MoO_3/FDTS/ClAlPc (105 °C)/ClAlPc:C_{60} (105 °C)/C_{60}/BCP/Ag	10.6	9.6	0.62	54	3.5

3. Results and discussion

3.1. Effect of substrate surface and temperature on planar HJ cells

3.1.1. Characterization of pure ClAlPc films

Four samples are prepared to study the influence of temperature and substrate surface on the film growth of ClAlPc:

a) ITO/25 nm PEDOT:PSS/5 nm MoO_3/50 nm ClAlPc (T_{sub} = room temperature (RT))
b) ITO/25 nm PEDOT:PSS/5 nm MoO_3/FDTS/50 nm ClAlPc (T_{sub} = RT)
c) ITO/25 nm PEDOT:PSS/5 nm MoO_3/50 nm ClAlPc (T_{sub} = 105 °C)
d) ITO/25 nm PEDOT:PSS/5 nm MoO_3/FDTS/50 nm ClAlPc (T_{sub} = 105 °C)

To study the orientation of the ClAlPc molecules with respect to the substrate, an X-ray reflectivity (XRR) measurement is performed. The PEDOT:PSS in the structures functions as a flattening layer on top of ITO in order to get a well-defined XRR signal. For ClAlPc grown at RT, only peaks at $2\theta = 21.2°$ (not shown) and $2\theta = 30.1°$ are detected, corresponding to peaks of the ITO substrate (Fig. 1a and b). The absence of ClAlPc peaks suggests the films have very limited crystalline order and are likely amorphous. At T_{sub} = 105 °C, the ClAlPc films exhibit an increased crystallinity. For the films on MoO_3, (Fig. 1c) a peak at $2\theta = 27.1°$ (d = 3.3 Å) corresponds to diffraction from the (001) plane of phase I ClAlPc [24,12], indicating that the ClAlPc molecules are parallel to the substrate (face-on orientation). This can be expected when the substrate-molecule interactions are strong [25]. In order to quantify these interactions, contact angle measurements were performed with four different liquids (de-ionized water, ethylene glycol, diiodomethane and decane) in order to calculate the polar and dispersive component of the surface energy by applying the Owens–Wendt–Rabel–Kaelble method [26]. Due to the rather apolar nature of organic semiconductors, it is mainly the dispersive component that can be correlated to the substrate-molecule interaction. For ClAlPc a dispersive component of 30.2 mN/m was derived, compared to 25.5 mN/m for MoO_3, thereby indicating that ClAlPc-MoO_3 interactions are significant.

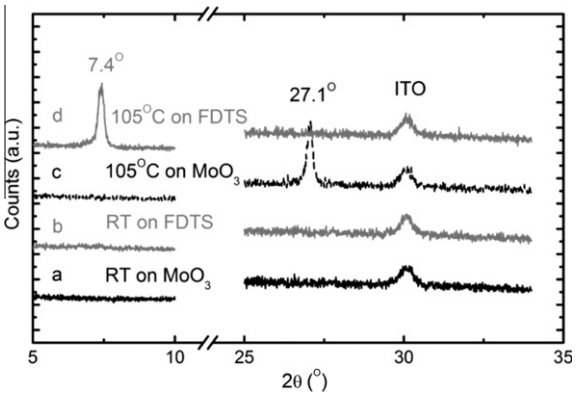

Fig. 1. X-ray reflectivity measurements of (a) ITO/PEDOT:PSS/MoO_3/ClAlPc (RT); (b) ITO/PEDOT:PSS/MoO_3/FDTS/ClAlPc (RT); (c) ITO/PEDOT:PSS/MoO_3/ClAlPc (105 °C); (d) ITO/PEDOT:PSS/MoO_3/FDTS/ClAlPc (105 °C). A constant offset is added between the graphs for visual clarity; in between $2\theta = 10°$ and $2\theta = 25°$ no ClAlPc peak was observed, hence the break.

For FDTS, a peak at $2\theta = 7.4°$ (d = 11.9 Å) implies that the ClAlPc molecules adopt an edge-on orientation (Fig. 1d). Molecule–molecule interactions are stronger than substrate-molecule interactions in this case (dispersive component of the surface energy is 11.2 mN/M for FDTS [26]), favoring a growth where the ClAlPc molecules are facing each other rather than the substrate.

Due to the fact that different phases of ClAlPc have distinct absorption features [27], the absorption of the pure thin films is also characterized. The ClAlPc films grown at RT both show a very similar quite featureless absorptance profile, with the Q-band peaking at a wavelength of λ = 760 nm, consistent with an amorphous film growth (Fig. 2a and b) [28]. When grown at 105 °C, the films show

quite different absorptance profiles, suggesting that not only orientation of the molecules is influenced by the substrate, but that the crystalline phase of the ClAlPc is also substrate-dependent. On MoO_3, the Q-band absorption maximum shifts slightly to $\lambda = 770$ nm, while a more pronounced shoulder appears at $\lambda = 716$ nm (Fig. 2c). This absorption profile is very similar to that of phase I of titanyl phthalocyanine (TiOPc) [27]. In phase I, the phthalocyanine molecules are slightly distorted, thereby lifting the doubly degenerate excited state and splitting it into two absorption bands whose transition moments are orthogonal [27]. On FDTS, the Q-band peak undergoes a very pronounced red-shift to $\lambda = 824$ nm, with a profile that was previously identified to belong to phase II (Fig. 2d), a phase with an even stronger molecular distortion. This phase is further distinguished by very close π-π atomic contacts and a highly polarized excited state [28].

Topographical AFM images reveal rather smooth films when grown at RT, with root mean square (*rms*) roughness values of 2.6 nm on MoO_3 (Fig. 3a) and 3.9 nm on FDTS (Fig. 3b). As a consequence, the ratio of the surface area and the projected area are close to one, as expressed by the folding ratios (*FR*) of $FR_{MoO3,RT} = 1.03$ and $FR_{FDTS,RT} = 1.11$, respectively. At 105 °C, rougher films with larger crystallites are observed. On MoO_3, the crystallites have a pyramidal structure, with a high roughness of *rms* = 35.6 nm and an increased surface area with $FR_{MoO3,105\ °C} = 1.38$ (Fig. 3c). In order to study the initial stages of film growth, a sample with a thinner ClAlPc thickness of 5 nm was characterized (Fig. 3c bis, *rms* = 13.4 nm). Here, ClAlPc was found to grow in an island (i.e., Volmer–Weber) mode, as described before for ClAlPc growth on SiO_2, whereby ClAlPc adatoms aggregate in discrete islands that preferentially expand in the vertical direction [12]. On FDTS, the crystal shapes look more disk-like, while the 50 nm ClAlPc film is slightly smoother than on MoO_3 with *rms* = 14.7 nm and $FR_{FDTS,105\ °C} = 1.21$ (Fig. 3d). In Fig. 3d bis, a 5 nm thick ClAlPc film grown in the same conditions covers almost the whole substrate (*rms* = 4.8 nm). This suggests that this growth mode can be described as the Stranski–Krastanov or layer-island growth mode [12]. In fact, upon close inspection of Fig. 3d bis, molecular planes can even be discerned.

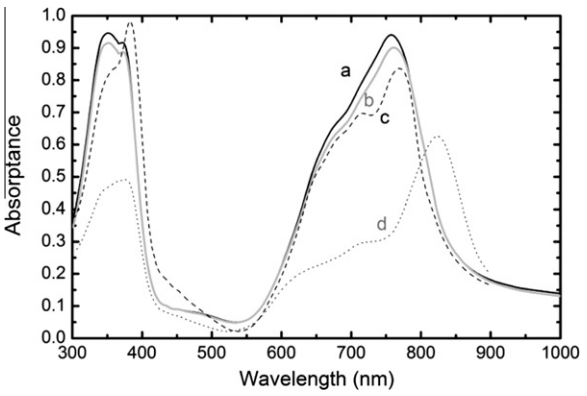

Fig. 2. UV–Vis absorptance of (a) ITO/PEDOT:PSS/MoO_3/ClAlPc (RT): black solid curves; (b) ITO/PEDOT:PSS/MoO_3/FDTS/ClAlPc (RT): grey solid curves; (c) ITO/PEDOT:PSS/MoO_3/ClAlPc (105 °C): black dashed curves; (d) ITO/PEDOT:PSS/MoO_3/FDTS/ClAlPc (105 °C): grey dotted curves.

In summary: at RT, ClAlPc grows as a conformal, amorphous film independent of the substrate surface. When the substrate is heated to 105 °C, the grown films are rougher and more crystalline in nature. On MoO_3, the ClAlPc molecules will be face-on and in phase I, whereas on FDTS, molecules adept an edge-on and phase II orientation.

3.1.2. Characterization of ClAlPc/C_{60} planar HJ solar cells

In order to study whether the investigated film properties have an influence on solar cell performance, the following devices are produced:

a) ITO/5 nm MoO_3/20 nm ClAlPc (T_{sub} = RT)/40 nm C_{60}/10 nm BCP/100 nm Ag
b) ITO/5 nm MoO_3/FDTS/20 nm ClAlPc (T_{sub} = RT)/40 nm C_{60}/10 nm BCP/100 nm Ag
c) ITO/5 nm MoO_3/20 nm ClAlPc (T_{sub} = 105 °C)/40 nm C_{60}/10 nm BCP/100 nm Ag
d) ITO/5 nm MoO_3/FDTS/20 nm ClAlPc (T_{sub} = 105 °C)/40 nm C_{60}/10 nm BCP/100 nm Ag

When comparing the solar cells grown at RT, it can be noticed that MoO_3 devices show slightly higher V_{oc} and fill factor (V_{oc} = 0.8 V and *FF* = 62%) compared to FDTS devices (V_{oc} = 0.7 V and *FF* = 52%) (c.f. Fig. 4 and Table 1). This can best be explained by the fact that MoO_3 forms a better electrical contact with ClAlPc than FDTS, due to a better alignment between the work function of the electrode and the ClAlPc highest occupied molecular orbital (HOMO) [14,29]. The samples on FDTS also show a higher J_{sc} of 6.3 mA cm^{-2} than those on MoO_3 (J_{sc} = 4.9 mA cm^{-2}). We suspect that the MoO_3 contact dissociates or quenches excitons [30,31]. The FDTS would then act as an exciton blocking layer [32], thereby hindering the loss of excitons at the contact.

The solar cells on MoO_3 exhibit a lower V_{oc} (V_{oc} = 0.72 V) and *FF* (*FF* = 49%) when the samples were heated during ClAlPc deposition (c.f. Table 1c). Here it is not clear whether this lower performance is related to the phase change from amorphous to phase I, or to the roughening of the donor layer (see Fig. 3c), which causes more shunting currents (see suppl. Info).

On FDTS, the heating results in a dramatic reduction of V_{oc} to 0.53 V. This shift we attribute to the phase change from amorphous ClAlPc to phase II. It was previously reported by Alloway et al. that ClAlPc grown edge-on on perylenetetracarboxylicdianhydride-*N*,*N*′-bis (butyl)imide (C4-PTCDI) has a lower ionization potential (E_{HOMO} = 5.1 eV) than ClAlPc with face-on orientation on PTCDA (E_{HOMO} = 5.4 eV) [33]. This shift in ionization potential was then attributed to a speculated phase-change. As it is well established that V_{oc} is strongly correlated to the difference in HOMO of the donor and the lowest unoccupied molecular orbital (LUMO) of the acceptor [34–36], such an energy shift can explain the lower V_{oc} observed here. Most striking is the current density increase to J_{sc} = 8.9 mA/cm^2. Together with a *FF* of 65%, this gives rise to a considerable planar HJ cell efficiency of $\eta = 3\%$. In order to get better insight as to the origin of this photocurrent increase,

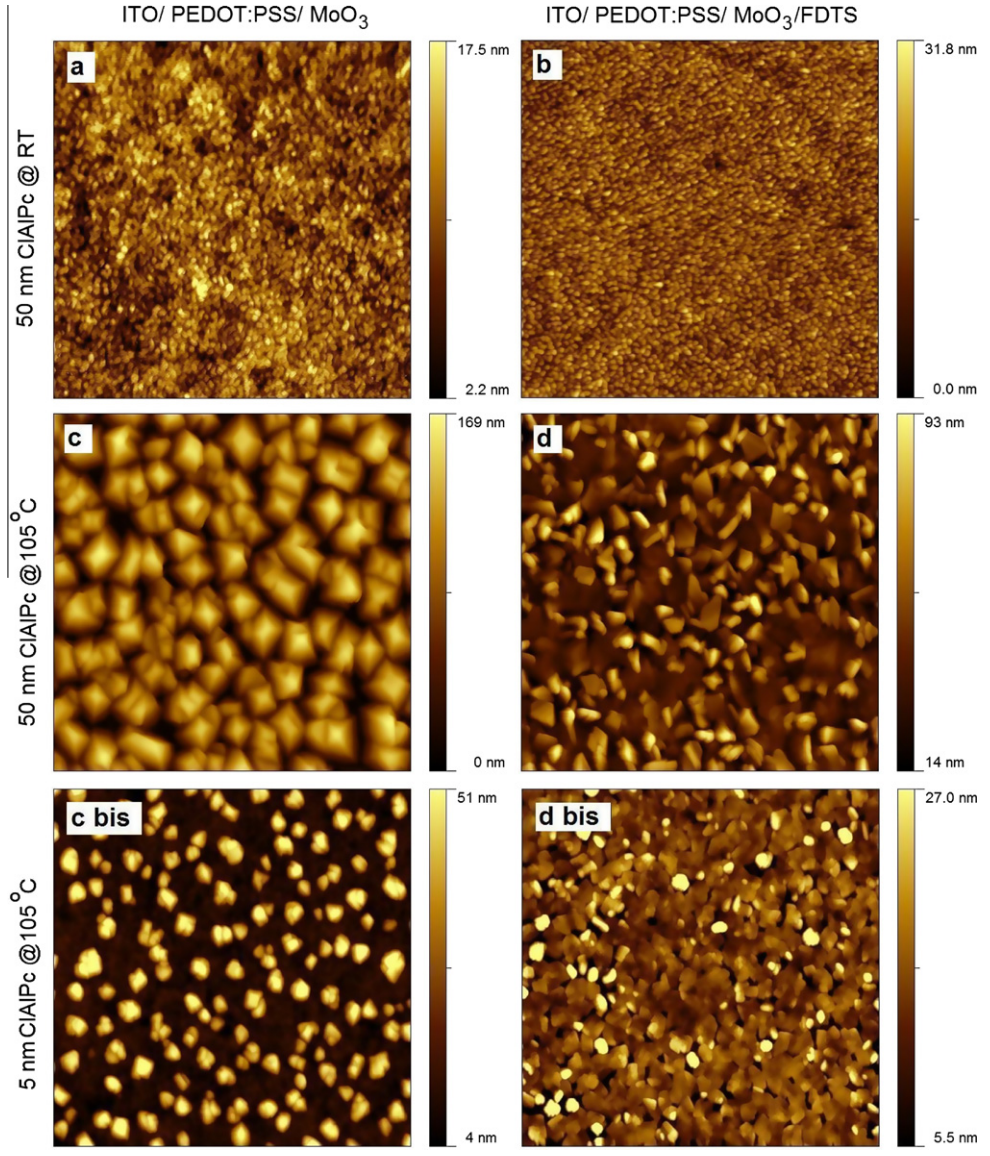

Fig. 3. Topographic AFM images (2500 × 2500 nm). (a), (b), (c) and (d) labeled as in Figs. 1 and 2. (c bis) and (d bis) are similar samples as (c) and (d), but with only 5 nm ClAlPc instead of 50 nm ClAlPc.

spectral response and reflectivity measurements are performed.

When we compare the external quantum efficiency (*EQE*) spectra of the heated ClAlPc cells on MoO_3 and FDTS (Fig. 5c and d respectively), we can see that two effects lead to a higher J_{sc} on FDTS. First: the red-shifted absorption profile on FDTS allows the cell to harvest a broader portion of the solar spectrum, and second: the *EQE* of the cells on FDTS is overall higher. A similar effect has been observed before for solvent annealed, phase II TiOPc. [37] The *EQE* can be further analyzed with the following formula [38]:

$$EQE(\lambda, V) = \eta_A(\lambda)\eta_{ED}\eta_{CT}(V)\eta_{CC}(V) \quad (1)$$

Here, η_A is the absorption efficiency. The reflectivity of the device shown in Fig. 5 (dashed and dotted curves) represents η_A: all light that is not reflected (100−*R*, in %) is absorbed in either the organic layers, the substrate, or the electrodes. Therefore, η_A alone cannot explain the increased EQE on FDTS, as the absorption on FDTS around $\lambda = 700$ nm is lower than that on MoO_3. Exciton diffusion efficiency (η_{ED}) expresses how many excitons reach the D/A interface before recombination. This can typically be improved by either increasing the D/A surface or by increasing the exciton diffusion length. According to the AFM data (Fig. 3) the D/A area should be higher on MoO_3 ($FR_{MoO3,105\ °C} = 1.38$) than on FDTS ($FR_{FDTS,105\ °C} = 1.21$), so according to this effect one would rather expect higher J_{sc}

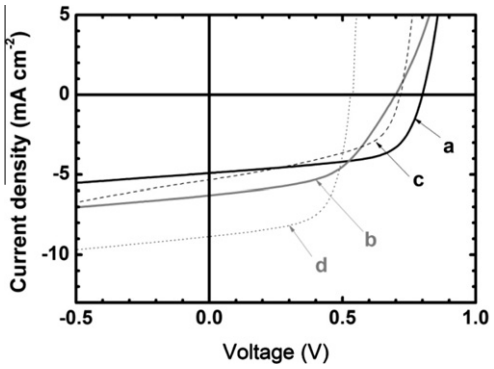

Fig. 4. Current density–voltage (*J–V*) curves for 100 mW cm^{-2} AM1.5G simulated solar illumination, of (a) ITO/MoO_3/ClAlPc (RT)/C_{60}/BCP/Ag: black solid curves; (b) ITO/MoO_3/FDTS/ClAlPc (RT) /C_{60}/BCP/Ag: grey solid curves; (c) ITO/MoO_3/ClAlPc (105 °C) /C_{60}/BCP/Ag: black dashed curves; (d) ITO/MoO_3/FDTS/ClAlPc (105 °C) /C_{60}/BCP/Ag: grey dotted curves.

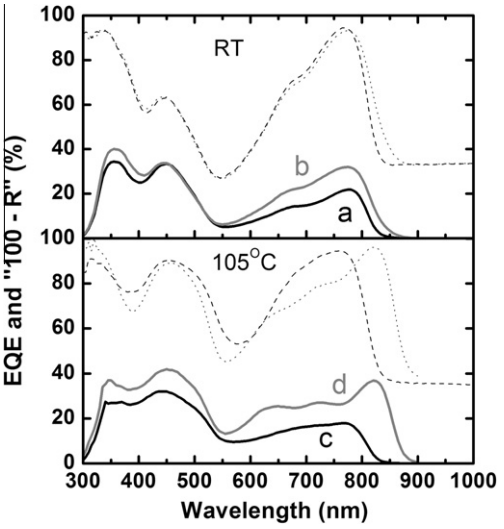

Fig. 5. Measured external quantum efficiency (*EQE*) and absorption spectra (100−R, in %) of devices on MoO_3 (EQE: black solid curves, 100−R: dashed curve) or on FDTS (EQE: grey solid curves, 100−R: dotted curve), with ClAlPc processed with the substrate at room temperature (top panel) or at 105 °C (bottom panel).

on MoO_3. Moreover, an increase of the exciton diffusion length in ClAlPc does not explain why the *EQE* signal of C_{60} (the peak around $\lambda = 460$ nm) also increases on FDTS. When charges are dissociated, they still need to reach an electrode and they will do so with a charge collection efficiency η_{CC}. For η_{CC} to be able to explain the device trends, however, one would expect this to be correlated with the *FF* of the devices, and for the devices at RT this seems not to be the case. There, the device on FDTS shows the highest EQE (Fig. 5a and b), while it has at the same time a lower *FF* than the device on MoO_3 (Table 1a and b).

Following this process of elimination, it seems that the increased *EQE* on FDTS is most likely related to a more efficient charge transfer process (η_{CT}) at the D/A interface. The difference in η_{CT} on MoO_3 and FDTS is likely related to both the different phase and the different orientation of the ClAlPc molecules in the cells.

3.2. Effect of substrate surface and temperature on bulk heterojunction cells

3.2.1. Characterization of co-evaporated ClAlPc:C_{60} films

To investigate how co-evaporated ClAlPc:C_{60} blends grow on different substrates, the following structures were fabricated:

a) ITO/25 nm PEDOT:PSS/5 nm MoO_3/100 nm ClAlPc:C_{60} (T_{sub} = 105 °C)
b) ITO/25 nm PEDOT:PSS/5 nm MoO_3/FDTS/100 nm ClAlPc:C_{60} (T_{sub} = 105 °C)
c) ITO/25 nm PEDOT:PSS/5 nm MoO_3/5 nm ClAlPc (T_{sub} = 105 °C)/100 nm ClAlPc:C_{60} (T_{sub} = 105 °C)
d) ITO/25 nm PEDOT:PSS/5 nm MoO_3/FDTS/5 nm ClAlPc (T_{sub} = 105 °C)/100 nm ClAlPc:C_{60} (T_{sub} = 105 °C)

Here, all the ClAlPc:C_{60} blends (ratio 1:1) are evaporated at 105 °C as we are aiming to grow crystalline, phase-separated BHJ layers. For structures (g) and (h), a 5 nm ClAlPc templating layer was grown before blend deposition, to see whether such a film can influence the growth of the overlying blend.

The XRR measurements show that the ClAlPc component in the blend still grows preferentially face-on on MoO_3 and edge-on on FDTS (Fig. 6e and f). However, the intensity of the peaks at, respectively, $2\theta = 27.1°$ and $2\theta = 7.4°$, is lower for the blended layers than for the pure layers of Fig. 1. When the 5 nm pure ClAlPc layer is grown before blend deposition, XRR signals become more pronounced, especially for the samples on FDTS. As the increase in signal is too strong to come from the 5 nm film itself, we ascribe this to a templating effect. The pure ClAlPc layer grows as a crystalline seed layer, which then templates the growth of the blend towards a similar preferred crystalline orientation [39].

The absorptance spectra of the blends on MoO_3 (Fig. 7e and g) more closely resemble that of the pure

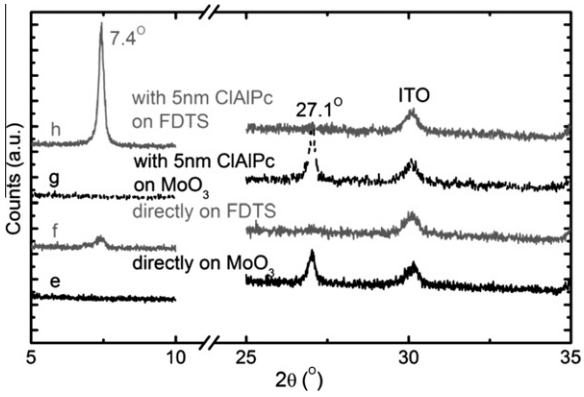

Fig. 6. X-ray reflectivity measurements of (e) ITO/PEDOT:PSS/MoO_3/ClAlPc:C_{60} (105 °C); (f) ITO/PEDOT:PSS/MoO_3/FDTS/ClAlPc:C_{60} (105 °C); (g) ITO/PEDOT:PSS/MoO_3/ClAlPc (105 °C)/ClAlPc:C_{60} (105 °C); (h) ITO/PEDOT:PSS/MoO_3/FDTS/ClAlPc (105 °C)/ClAlPc:C_{60} (105 °C).

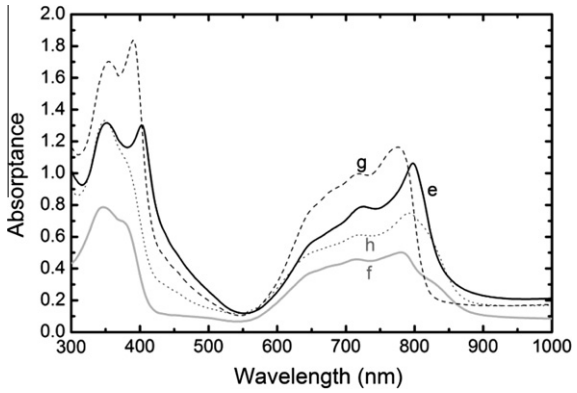

Fig. 7. UV–Vis absorptance of (e) ITO/PEDOT:PSS/MoO_3/ClAlPc:C_{60} (105 °C): black solid curves; (f) ITO/PEDOT:PSS/MoO_3/FDTS/ClAlPc:C_{60} (105 °C): grey solid curves; (g) ITO/PEDOT:PSS/MoO_3/ClAlPc (105 °C)/ClAlPc:C_{60} (105 °C): black dashed curves; (h) ITO/PEDOT:PSS/MoO_3/FDTS/ClAlPc (105 °C)/ClAlPc:C_{60} (105 °C): grey dotted curves.

film (Fig. 2c), when a templating layer is applied. So, in addition to a preferred orientation, the templating layer can also help to achieve a certain ClAlPc phase in the blend. On FDTS (Fig. 7f and h), both films show a red-shifted Q-band absorption shoulder at $\lambda > 800$ nm. These absorption signals are not as pronounced as the signal for a pure ClAlPc film on FDTS (Fig. 2d), but also here the templating layer helps to reinforce this red-shifted absorption feature.

According to AFM images, growing ClAlPc:C_{60} blends directly on MoO_3 results in very rough films with *rms* = 51.4 nm (Fig. 8e). Islands 0.5 μm in size are formed, and the space in between the islands is filled with smaller crystallites. These islands have a more irregular shape than those of the 50 nm pure ClAlPc film grown under similar conditions (Fig. 3c). As already shown in Fig. 3c bis, the templating layer consists of crystallites with a height of about 40 nm and width of 100–200 nm, spread over the surface. When the ClAlPc:C_{60} blend is grown on top of this layer, they form islands with a very similar spacing as the template crystallites (Fig. 8g). This hints that the pure ClAlPc crystallites of the templating layer form nucleation sites, around which the subsequently deposited ClAlPc:C_{60} blend grows. This results in smaller, more closely spaced ClAlPc:C_{60} islands compared to the film without a templating layer.

Images of the blends grown on FDTS, with and without a templating layer, are shown in Fig. 8f and h. Also here, it can be seen that the templating layer (Fig. 3d bis) has an impact on the growth of the blend layer, although in this case the use of a templating layer leads to larger islands.

3.2.2. Characterization of bulk heterojunction devices

The co-evaporated films studied above were then incorporated into bulk heterojunction solar cells with the following structures:

a) ITO/5 nm MoO_3/100 nm ClAlPc:C_{60} (T_{sub} = 105 °C)/40 nm C_{60}/10 nm BCP/100 nm Ag

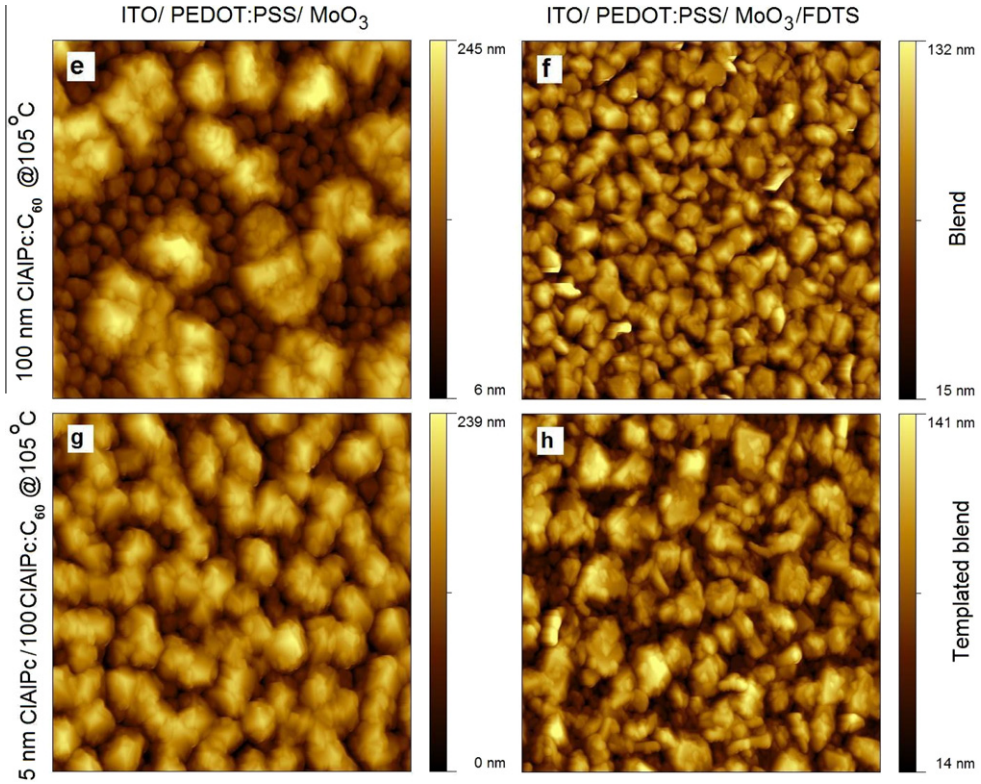

Fig. 8. Topographic AFM images (2500 × 2500 nm). (e), (f), (g) and (h) labeled as in Figs. 6 and 7.

b) ITO/5 nm MoO_3/FDTS/100 nm ClAlPc:C_{60} (T_{sub} = 105 °C)/40 nm C_{60}/10 nm BCP/100 nm Ag
c) ITO/5 nm MoO_3/5 nm ClAlPc (T_{sub} = 105 °C)/100 nm ClAlPc:C_{60} (T_{sub} = 105 °C)/40 nm C_{60}/10 nm BCP/100 nm Ag
d) ITO/5 nm MoO_3/FDTS/5 nm ClAlPc (T_{sub} = 105 °C)/100 nm ClAlPc:C_{60} (T_{sub} = 105 °C)/40 nm C_{60}/10 nm BCP/100 nm Ag

All of the produced bulk heterojunction cells show an increased J_{sc} compared to the planar HJ cells (Fig. 9 and Table 2). The planar HJ cells were partially limited by exciton diffusion, but within a bulk heterojunction the generated excitons do not have to diffuse as far to reach a D/A junction. The *EQE* spectra and reflectivity data (plotted as 100−*R* (%)) are shown in Fig. 10. These spectra make clear that the current of all these devices is generated over a wide wavelength region, ranging from λ = 300–800 nm. Reflectivity data show that near λ = 700 nm, about 90% of incident light gets absorbed, while both the *EQE* and "100−*R*" spectra are becoming relatively featureless. This indicates that absorption is nearing saturation. But while about 90% of the light gets absorbed in the devices, maximum *EQE* is only ≈40%. This indicates that even in the BHJ devices, internal quantum efficiency is still quite low, leaving room for possible future enhancement. Integration of the *EQE* over the AM1.5G solar spectrum is listed in Table 2 as J_{EQE}. Differences in between J_{sc} and J_{EQE} can be attributed to spectral mismatch between the solar simulator and the ideal AM1.5G spectrum.

Both for devices on MoO_3 and on FDTS, the use of a 5 nm ClAlPc templating layer results in an improved *FF*. (On MoO_3: $FF_{no\ template}$ = 32% versus $FF_{templated}$ = 61%; On FDTS: $FF_{no\ template}$ = 49% versus $FF_{templated}$ = 54%). This improved *FF* is ascribed to the higher crystallinity of the templated films, and hence better morphology and transport.

Unlike planar HJ cells, the templated bulk heterojunction structures can combine relatively high J_{sc} with decent *FF*s. But similar to the planar HJ cells, the BHJ cells on FDTS show a decreased V_{oc}. As a result, highest performance is on MoO_3, where the best cell reached a power conversion

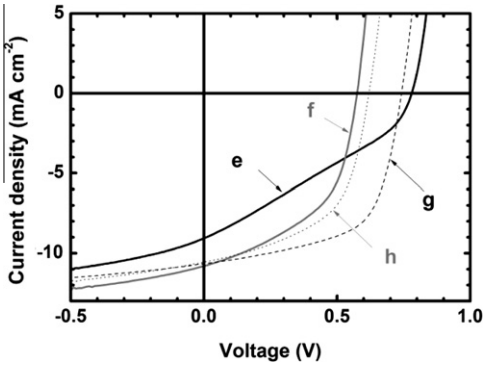

Fig. 9. Current density–voltage (*J*–*V*) curves for 100 mW cm^{-2} AM1.5G simulated solar illumination, of (e) ITO/MoO_3/ClAlPc:C_{60} (105 °C)/C_{60}/BCP/Ag: black solid curves; (f) ITO/MoO_3/FDTS/ClAlPc:C_{60} (105 °C)/C_{60}/BCP/Ag: grey solid curves; (g) ITO/MoO_3/ClAlPc (105 °C)/ClAlPc:C_{60} (105 °C)/C_{60}/BCP/Ag: black dashed curves; (h) ITO/MoO_3/FDTS/ClAlPc (105 °C)/ClAlPc:C_{60} (105 °C)/C_{60}/BCP/Ag: grey dotted curves.

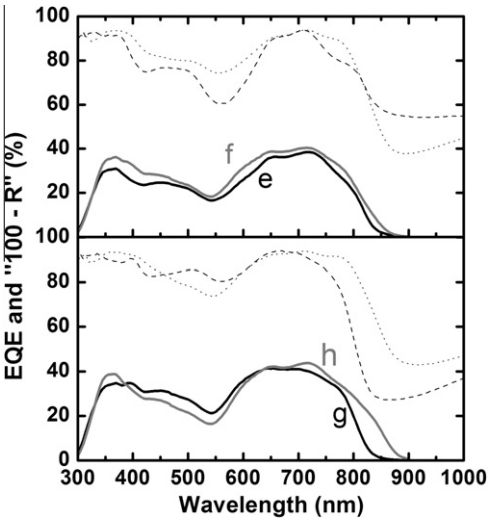

Fig. 10. Measured external quantum efficiency (EQE) and absorption spectra (100−R, in %) of bulk heterojunctions on MoO_3 (EQE: black solid curves, 100−R: dashed curve) or FDTS (EQE: grey solid curves, 100−R: dotted curve), with ClAlPc processed directly on the substrate (top panel) or on top of a ClAlPc templating layer (bottom panel).

of η = 4.8%. When this value is corrected for spectral mismatch, a value of $\eta_{corrected} = (J_{EQE} \times FF \times V_{oc})/P_{light}$ = 4.2% is obtained.

4. Conclusion

In conclusion, we have investigated ClAlPc films grown on either FDTS or MoO_3. At RT, the ClAlPc films grow amorphous, independent of the surface. When heated to 105 °C, ClAlPc grows face-on on MoO_3, with a phase I-like absorption profile. On FDTS, the film is characterized as edge-on, phase II. These films are then used to fabricate planar HJ cells. On FDTS, the induced phase is accompanied by a lower V_{oc}, but also by a higher current, leading to 3% efficient planar HJ cells. The higher current on FDTS compared to MoO_3 is believed to be caused by two effects: the FDTS surface would quench fewer excitons than the MoO_3 surface, and the exciton charge transfer would be more efficient for phase II ClAlPc.

Next, ClAlPc and C_{60} are co-evaporated on FDTS and MoO_3 substrates. In order to achieve an enhanced crystallinity, a thin pure "templating" layer of ClAlPc proved advantageous. When the films were used in bulk heterojunction cells, the more crystalline films grown on top of a templating layer showed higher *FF* than devices without templating layers. The use of the co-evaporated bulk heterojunctions ensured high photocurrents, independent of the growth surface. Here, the higher V_{oc} of devices on MoO_3 was beneficial, with devices showing efficiencies greater than 4% as a result.

Acknowledgements

The research leading to these results has received funding from the European Community's Seventh Framework

Programme (FP7/2007-2013) under grant agreement 212311 of the ONE-P project. K.V. acknowledges the Institute for the Promotion of Innovation through Science and Technology in Flanders (IWT-Vlaanderen) for financial support.

Appendix A. Supplementary data

Supplementary data associated with this article can be found, in the online version, at doi:10.1016/j.orgel.2011.08.031.

References

[1] M.A. Green, K. Emery, Y. Hishikawa, W. Wart, Prog. Photovolt: Res. Appl. 19 (2011) 84–92.
[2] C.W. Tang, Appl. Phys. Lett. 48 (1986) 183.
[3] G. Yu, J. Gao, J.C. Hummelen, F. Wudl, A.J. Heeger, Science 270 (1995) 1789–1791.
[4] P. Peumans, S. Uchida, S.R. Forrest, Nature 425 (2003) 158.
[5] D. Cheyns, B.P. Rand, P. Heremans, Appl. Phys. Lett. 97 (2010) 033301.
[6] R.F. Bailey-Salzman, B.P. Rand, S.R. Forrest, Appl. Phys. Lett. 91 (2007) 013508.
[7] S.W. Cho, L.F.J. Piper, A. DeMasi, A.R.H. Preston, K.E. Smith, K.V. Chauhan, P. Sullivan, R.A. Hatton, T.S. Jones, J. Phys. Chem. C 114 (2010) 1928–1933.
[8] C.H. Cheng, J. Wang, G.T. Du, S.H. Shi, Z.J. Du, Z.Q. Fan, J.M. Bian, M.S. Wang, Appl. Phys. Lett. 97 (2010) 083305.
[9] B. Yu, L. Huang, H. Wang, D. Yan, Adv. Mater. 22 (2010) 1017–1020.
[10] K.V. Chauhan, P. Sullivan, J.L. Yang, T.S. Jones, J. Phys. Chem. C 14 (2010) 3304–3308.
[11] S.A. DiBenedetto, A. Facchetti, M.A. Ratner, T.J. Marks, Adv. Mater. 21 (2009) 1407–1433.
[12] L. Li, W. Hu, H. Fuchs, L. Chi, Adv. Energy Mater. 1 (2011) 188–193.
[13] A. Sharma, A. Haldi, P.J. Hotchkiss, S.R. Marder, B. Kippelen, J. Appl. Phys. 105 (2009) 074511.
[14] N. Beaumont, I. Hancox, P. Sullivan, R.A. Hatton, T.S. Jones, Energy Environ. Sci. 4 (2011) 1708–1711.
[15] S. Khodabakhsh, B.M. Sanderson, J. Nelson, T.S. Jones, Adv. Funct. Mater. 16 (2006) 95–100.
[16] R.M. Cook, L.-J. Pegg, S.L. Kinnear, O.S. Hutter, R.J.H. Morris, R.A. Hatton, Adv. Eng. Mater. 1 (2011) 440–447.
[17] J. Xue, B.P. Rand, S. Uchida, S.R. Forrest, J. Appl. Phys. 98 (2005) 124902.
[18] J. Xue, B.P. Rand, S. Uchida, S.R. Forrest, J. Appl. Phys. 98 (2005) 124903.
[19] S. Pfuetzner, J. Meiss, A. Petrich, M. Riede, K. Leo, Appl. Phys. Lett. 94 (2009) 253303.
[20] W. Zeng, K.S. Yong, Z.M. Kam, F. Zhu, Y. Li, Appl. Phys. Lett. 97 (2010) 133304.
[21] N. Li, S. Forrest, Appl. Phys. Lett. 95 (2009) 123309.
[22] K. Harada, T. Edura, C. Adachi, Appl. Phys. Express 3 (2010) 121602.
[23] Global tilt ASTM G173-03 Reference Spectrum http://rredc.nrel.gov/solar/spectra/am1.5/.
[24] K.J. Wynne, Inorg. Chem. 23 (1984) 4658–4663.
[25] S. Verlaak, S. Steudel, P. Heremans, D. Janssen, M.S. Deleuze, Phys. Rev. B 68 (2003) 195409.
[26] D. Janssen, R. De Palma, S. Verlaak, P. Heremans, W. Dehaen, Thin Solid Films 515 (2006) 1433–1438.
[27] J. Mizuguchi, G. Rihs, H.R. Karfunkel, J. Phys. Chem. 99 (1995) 16217–16227.
[28] T. Saito, W. Sisk, T. Kobayashi, S. Suzuki, T. Iwayanagi, J. Phys. Chem. 97 (1993) 8026–8031.
[29] Irfan, H. Ding, Y. Gao, D.Y. Kim, J. Subbiah, F. So, Appl. Phys. Lett. 96 (2010) 073304.
[30] Y. Nakayama, K. Morii, Y. Suzuki, H. Machida, S. Kera, N. Ueno, H. Kitagawa, Y. Noguchi, H. Ishii, Adv Funct. Mater. 19 (2009) 3746–3752.
[31] X.Y. Sun, Q.L. Song, M.L. Wang, X.M. Ding, X.Y. Hou, Z.G. Zhou, F.Y. Li, J. Appl. Phys. 104 (2008) 103702.
[32] B.E. Lassiter, R.R. Lunt, C.K. Renshaw, S.R. Forrest, Optics Express A 18 (2010) A444–A450.
[33] D.M. Alloway, N.R. Armstrong, Appl. Phys. A 95 (2009) 209–218.
[34] B.P. Rand, D.P. Burk, S.R. Forrest, Phys Rev B 75 (2007) 115327.
[35] C.J. Brabec, A. Cravino, D. Meissner, N.S. Sariciftci, T. Fromherz, M.T. Rispens, L. Sanchez, J.C. Hummelen, Adv. Funct. Mater. 11 (2001) 374–380.
[36] A. Gadisa, M. Svensson, M.R. Andersson, O. Inganäs, Appl. Phys. Lett. 84 (2004) 1609–1611.
[37] D. Placencia, W. Wang, R.C. Shallcross, K.W. Nebesny, M. Brumbach, N.R. Armstrong, Adv. Funct. Mater. 19 (2009) 1913–1921.
[38] B.P. Rand, J. Genoe, P. Heremans, J. Poortmans, Prog. Photovolt: Res. Appl. 15 (2007) 659–676.
[39] T. Sakurai, R. Fukusawa, K. Saito, K. Akimoto, Org. Electron. 8 (2007) 702–708.

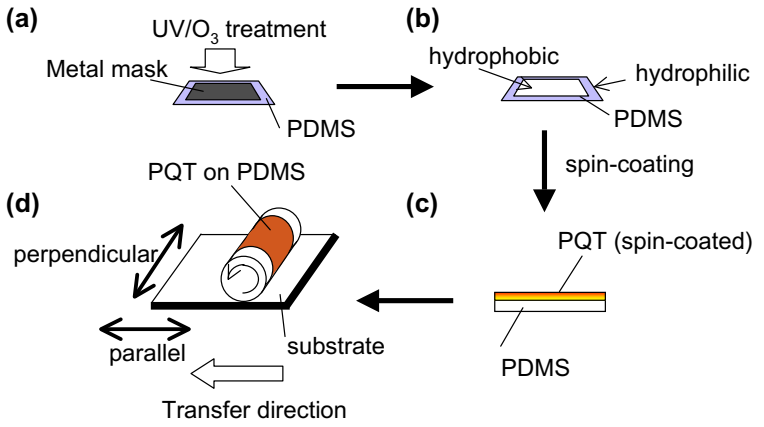

Fig. 1. Schematic diagram of roll-transfer printing. (a) and (b) Creation of a peripheral hydrophilic region on the PDMS stamp. (c) Spin coating the PQT film onto the PDMS stamp. (d) Roll-transfer printing of the PQT film onto the substrate.

toluene solution [16]. Our roll-transfer printing method is illustrated in Fig. 1. A 0.5 wt.% toluene solution of PQT (M_w = 18,000, American Dye Source Inc.) was spin-coated onto a poly(dimethylsiloxane) (PDMS) stamp (SIM-260, ShinEtsu Chem.). Before use, traces of remaining siloxane oligomers were extracted from PDMS using a Soxhlet extractor with hexane. Prior to spin coating, the peripheral area of the PDMS stamp was treated with a UV/O_3 cleaner to form a hydrophilic region, which allows the formation of a PQT film on hydrophobic region. The obtained PQT thin film (~50-nm thick) was dried in a Petri dish for 10 min, before laminating the inked stamp on a glass cylinder (ϕ = 40 mm). The inked stamp was then applied to the substrate heated on a hot plate (80–150 °C), and printing was achieved by rotating the cylinder. OFET fabrication was completed by evaporating Au source–drain electrodes on the PQT surface. The channel length and width were 50 μm and 1.5 mm, respectively.

FET measurements of the fabricated devices were performed under ambient condition. The polarized UV–vis absorption was measured using the PQT films printed on OTS-treated glass substrates (Corning 7059) and normalized at a wavelength of 540 nm. In-plane grazing-incidence X-ray diffraction (GIXD) measurements were performed using Cu-Kα X-rays (~8.0 keV) with a rotating target energy of 9 kW (45 kV–200 mA) and an incident beam angle of 0.2°.

3. Results and discussions

Fig. 2(a) shows the polarized UV–vis absorption spectra of a PQT film fabricated using the roll-transfer printing method at a substrate temperature of 130 °C. Absorption peaks at 512, 547, and 587 nm are identified as absorptions of π–π lamella stacking [17]. The transferred PQT film clearly exhibits strong optical anisotropy, and light polarized parallel to the transfer direction is more strongly absorbed than that polarized perpendicular to the transfer direction, indicating that the main chains of PQT are uniaxially aligned in the transfer direction. Fig. 2(b) shows the relationship between the transfer temperature and optical

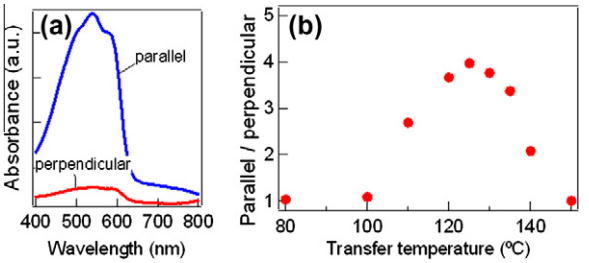

Fig. 2. (a) Polarized UV–vis absorption spectra of the PQT film prepared by roll-transfer printing at 130 °C on an OTS-treated glass substrate. (b) Effect of the transfer temperature on optical anisotropy in the transferred PQT film.

anisotropy. When the substrate temperature is kept at 80 °C (solid phase) in the transfer process, the transferred films are found to be isotropic. The optical anisotropies appear when the transfer temperature is increased to above 100 °C and disappear above 140 °C, between which corresponds to the temperature range that PQT possesses the thermotropic liquid crystal phase [15]. At a transfer temperature of 150 °C, PQT films show isotropic properties because of the transition from a liquid crystal to an isotropic phase. These results clearly show that film transfer at liquid–crystal phase temperatures is an essential factor for achieving uniaxial alignment.

Fig. 3 shows the in-plane GIXD patterns in the perpendicular and parallel directions of a PQT film transferred at 130 °C before and after annealing at 135 °C for 5 min. In Fig. 3(a) and (b), the peak at $2\theta = 21.2°$, produced by π-stacking (0 1 0), and a broad structure around $2\theta = 24.2°$, caused by high-density π-stacking (0 1 0), are observed [17]. The peak intensity in the parallel direction is greater than that in the perpendicular direction, which clearly shows that the main chains of PQT molecules are aligned in the parallel direction. Further, the in-plane GIXD patterns do not have a lamella diffraction peak, indicating that the thiophene rings of the aligned PQT molecules are oriented perpendicular to the substrate (edge-on structure), as illustrated in the inset of Fig. 3. After annealing, the peak

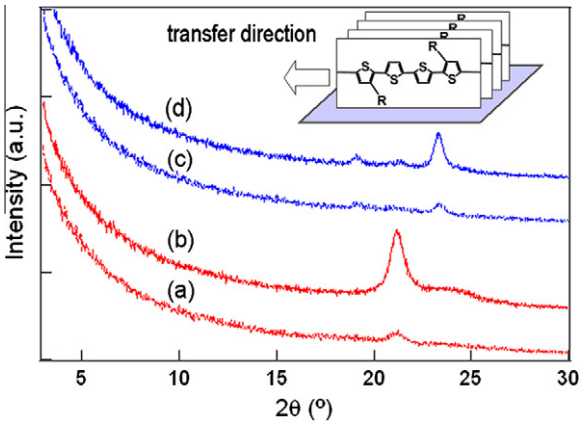

Fig. 3. In-plane GIXD patterns of the PQT film prepared by roll-transfer printing at 130 °C before and after annealing at 135 °C for 5 min in vacuum. GIXD patterns were measured (a) perpendicular and (b) parallel to the transfer direction in the as-prepared film. GIXD patterns were measured (c) perpendicular and (d) parallel to the transfer direction in the annealed film. The inset shows the molecular conformation in a PQT film prepared by roll-transfer printing.

intensity at $2\theta = 21.2°$ decreases and that at $2\theta = 24.2°$ increases (Fig. 3(c) and (d)), indicating that the crystal structure becomes denser by annealing. We note that the anisotropy of peak intensity persists, indicating that the uniaxial alignment is preserved even after annealing.

Fig. 4(a) and (b) shows the typical electrical characteristics (output and transfer curves) of PQT FETs fabricated using the roll-transfer printing method, measured in parallel and perpendicular to the transfer direction, respectively. The devices were fabricated at a transfer temperature of 140 °C and then annealed at 135 °C for 5 min (the highest mobility was achieved with this condition). The PQT film exhibits strong anisotropy of field -effect mobility. The mobilities in the parallel direction show high values of 0.17 ± 0.02 cm^2/Vs, which are 8 times

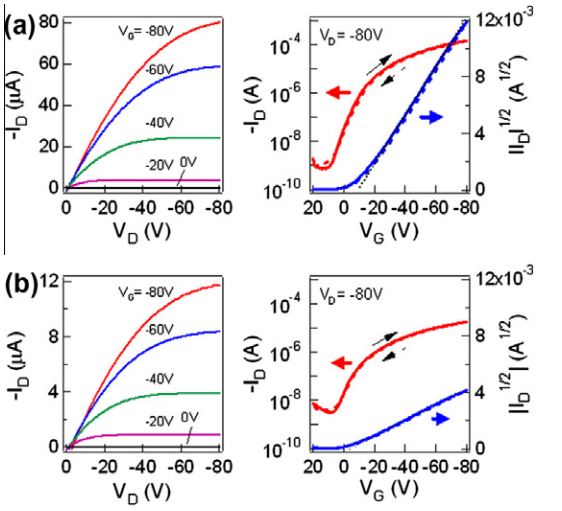

Fig. 4. Typical output (drain current I_D–drain voltage V_D) and transfer (I_D–gate voltage V_G) curves of PQT FETs fabricated by the roll-transfer printing method in (a) parallel and (b) perpendicular directions.

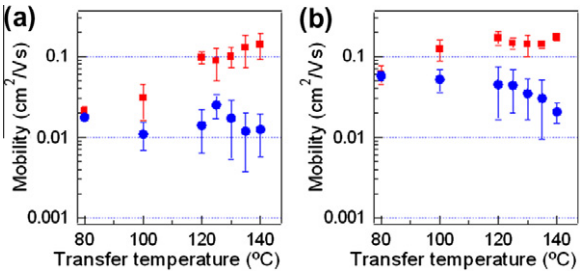

Fig. 5. Effect of the transfer temperature on the mobility anisotropy in PQT films (a) before annealing and (b) after annealing at 135 °C for 5 min in vacuum.

greater than those in the perpendicular direction (0.021 ± 0.006 cm^2/Vs).

Fig. 5(a) and (b) shows the relationships between the transfer temperature and the mobility anisotropy before and after annealing at 135 °C for 5 min, respectively. It can be seen in Fig. 5(a) that the PQT films transferred at 80 °C are electrically isotropic and those transferred in the liquid crystal phase (120–140 °C) exhibit strong electrical anisotropy, implying that the molecular alignment is attributed to the roll transfer at liquid crystal phase temperatures. For transfer temperatures above 140 °C, the transfer-printing process was impaired by the dewetting of the film, and reliable data could not be obtained. We also see that mobility anisotropy increases when the transfer temperature exceeds 130 °C, and a relatively strong mobility anisotropy appears even below the solid-to-liquid crystal transition temperature (110 °C) [15]; this result somewhat differs from the results of optical absorption measurements. An increase in the mobility anisotropy at higher temperatures can be caused by an improvement in the film crystallinity associated with increasing temperature. A PQT film transferred at 100 °C is electrically anisotropic, but optically almost isotropic. Since PQT shows a gradual transition from the solid to the liquid crystal phase [15], the film partially changes to a liquid crystal at 100 °C, which leads to uniaxial alignment at the substrate surfaces. The observed mobility anisotropy can be attributed to the molecular alignment just above the substrate surface because the charge transport in OFETs mainly reflects molecular ordering at the insulator/semiconductor interface [1]. On the contrary, heat conduction is not sufficient for causing phase change across the entire region of the film during printing, and this results in a small optical anisotropy. We believe that the driving force of molecular alignment is the shear stress associated with the roll-transfer processes and that molecular alignment easily occurs by relatively low shear stress when PQT is in the liquid crystal phase. We note that annealed films still show large mobility anisotropies, although their ratios are decreased as compared with those of the as-prepared films (Fig. 5(b)). Higher mobilities in the annealed devices would result from the crystal phase changing to the high-density π-stacking of the PQT molecules, as shown in Fig. 3.

The average mobility in the parallel direction is approximately 0.17 cm^2/Vs when the film was transferred at 140 °C, which is almost 3 times higher than that in isotropic

films such as the film transferred at 80 °C (0.06 ± 0.01 cm^2/Vs) and spin-coated films (0.06 ± 0.02 cm^2/Vs, not indicated in Fig. 5). The maximum mobility in the parallel direction is 0.28 cm^2/Vs, which is higher than that of isotropic PQT films in the previous literature (0.2 cm^2/Vs) [18]. Electrical anisotropies of polythiophene films have been reported previously; however, in many cases, the mobilities achieved are relatively low [12,14]. One of the reasons for a low mobility is responsible for polymer chain conformation. Nagamatsu et al. reported that anisotropic polyalkylthiophenes prepared by the friction transfer method are stacked parallel to the substrate (face-on structure) [11]. This face-on structure is less suitable for lateral charge transfer than the edge-on structure [19,20]. In contrast, PQT films fabricated by the roll-transfer printing method have an edge-on structure, and therefore, their charge mobility in the lateral direction is very high, which is advantageous for conventional OFETs. Moreover, the present roll-transfer printing method does not need any alignment layers for molecular ordering, which allows the fabrication of a semiconductor film even on hydrophobic substrates such as an OTS-treated SiO_2 substrate. This is another advantage for achieving high-performance OFETs because hydrophobic self-assembled monolayers are well known to enhance molecular ordering, which leads to the enhancement of charge mobility.

4. Conclusions

In summary, we have presented the roll-transfer printing method to fabricate the aligned thin film of polymer semiconductors. The method is based on the enhancement of shear-stress effects associated with roll-transfer printing in the thermotropic liquid crystal phase of polymer semiconductors. We have shown that roll-transfer printed PQT films are uniaxially aligned parallel to the transfer direction and have an edge-on structure. We also observed the anisotropic electrical properties of OFETs associated with the molecular alignment. The enhanced mobility in the parallel direction is at least 8 times higher than that in the perpendicular direction, and the highest mobility achieved was 0.28 cm^2/Vs. Our results suggest important strategies for fabricating high-performance OFETs by printing.

References

[1] H. Sirringhaus, Adv. Mater. (Weinheim, Germany) 17 (2005) 2411.
[2] M.L. Chabinyc, A. Salleo, Chem. Mater. 16 (2004) 4509.
[3] J.A. Rogers, Z. Bao, K. Baldwin, A. Dodabalapur, B. Crone, V.R. Raju, V. Kuck, H. Katz, K. Amundson, J. Ewing, P. Drzaic, PNAS 98 (2001) 4835.
[4] Y.H. Kim, S.K. Park, J.I. Han, D.G. Moon, W.K. Kim, M.G. Kwak, Proc. Int. Display Workshop (2002) 255.
[5] V. Subramanian, J.M.J. Fréchet, P.C. Chang, D.C. Huang, J.B. Lee, S.E. Molesa, A.R. Murphy, D.R. Redinger, S.K. Volkman, Proc. IEEE 93 (2005) 1330.
[6] T. Kushida, T. Nagase, H. Naito, Appl. Phys. Lett. 98 (2011) 063304.
[7] H. Sirringhaus, R.J. Wilson, R.H. Friend, M. Inbasekaran, W. Wu, E.P. Woo, M. Grell, D.D.C. Bradley, Appl. Phys. Lett. 77 (2000) 406.
[8] L. Kinder, J. Kanicki, P. Petroff, Synth. Met. 146 (2004) 181.
[9] L. Zeng, F. Yan, S.K.-H. Wei, S.W. Culligan, S.H. Chen, Adv. Funct. Mater. 19 (2009) 1978.
[10] T. Yasuda, K. Fujita, T. Tsutsui, Y. Geng, S.W. Culligan, S.H. Chen, Chem. Mater. 17 (2005) 264.
[11] S. Nagamatsu, W. Takashima, K. Kaneto, Y. Yoshida, N. Tanigaki, K. Yase, K. Omote, Macromolecule 36 (2003) 5252.
[12] S. Nagamatsu, W. Takashima, K. Kaneto, Y. Yoshida, N. Tanigaki, K. Yase, Appl. Phys. Lett. 84 (2004) 4608.
[13] H.A. Becerril, M.E. Roberts, Z. Liu, J. Locklin, Z. Bao, Adv. Mater. (Weinheim, Germany) 20 (2008) 2588.
[14] M. Karakawa, M. Chikamatsu, Y. Yoshida, M. Oishi, R. Azumi, K. Yase, Appl. Phys. Express 1 (2008) 061802.
[15] N. Zhao, G.A. Botton, S. Zhu, A. Duft, B.S. Ong, Y. Wu, P. Liu, Macromolecules 37 (2004) 8307.
[16] T. Kushida, T. Nagase, H. Naito, Org. Electron 11 (2010) 1323.
[17] B.S. Ong, Y. Wu, P. Liu, S. Gardner, J. Am. Chem. Soc. 126 (2004) 3378.
[18] P. Liu, Y. Wu, H. Pan, B.S. Ong, S. Zhu, Macromolecules 43 (2010) 6368.
[19] H. Sirringhaus, P.J. Brown, R.H. Friend, M.M. Nielsen, K. Bechgaard, B.M. Langeveld-Voss, A.J.H. Spiering, R.A.J. Janssen, E.W. Meijer, P. Herwig, D.M. de Leeuw, Nature (London) 401 (1999) 685.
[20] R.J. Kline, M.D. McGehee, M.F. Toney, Nat. Mater. 5 (2006) 222.

However, in terms of more practical device applications, solid-state device structure is more preferable to CAFM or STM testbeds [12]. Furthermore, with CAFM or STM tools, it is not trivial to perform temperature-variable electrical characterizations to investigate charge conduction mechanisms, and it is generally difficult to determine the actual contact junction area. Therefore, a more comprehensive study based on a statistical analysis of the electrical properties induced by conformational changes in azobenzene-derivative molecules using a solid-state device structure is important for understanding the conduction mechanism and for more practical device applications.

In this study, we report the electrical properties of azobenzene-derivative ([4-(phenylazo)phenoxy]hexane-1-thiol) molecular junctions in which the azobenzene moiety is linked to an alkanethiol (with six carbon atoms). Specifically, we studied the photo-induced conductance changes between the trans- and cis-isomers of this molecule through statistical analysis. The absorption spectrum was determined by UV–Vis spectroscopy to confirm the conformational changes between trans- and cis-isomers by an external light trigger. In addition, temperature-variable electrical characterization and transition voltage spectroscopy analysis were performed to understand the charge transport mechanisms in both isomers.

2. Experimental

As schematically described in Fig. 1a, the molecular junctions were fabricated on a p-type Si (100) substrate covered by a thermally grown 6000 Å-thick SiO_2 layer. Conventional optical lithography was used to pattern the bottom electrodes prepared from Au (800 Å)/Ti (50 Å) using an electron-beam evaporator. Photoresist (PR) (AZ1512) was spin-coated on top of the bottom electrodes for electrical isolation. After isolation, square holes with side length of 30–100 μm were created through PR layer by optical lithography to expose the Au bottom electrodes. The devices with PR patterns were then annealed for at least 2 h at 180 °C to make the PR layer insoluble in ethanol during the formation of self-assembled monolayers (SAMs) on the Au bottom electrode. We used an azobenzene-derivative ([4-(phenylazo)phenoxy]hexane-1-thiol) consisting of two phenyl rings linked by an N=N double bond. These azobenzene-derivative molecules have two distinct isomers: trans- (extended form) and cis-isomer (compact form) depending on the wavelength of irradiating light (Fig. 1d). We prepared trans- and cis-isomer devices in the following way. First, SAMs (~1 mM) of trans-isomer were formed on the Au bottom electrode in a nitrogen-filled glove box with an oxygen level less than ~10 ppm for 1–2 days under visible light irradiation (400–500 nm). After the formation of trans-isomer azobenzene SAMs, several devices were illuminated by UV light (365 nm) in a darkroom for one hour, a period of time sufficient to guarantee a complete conformational change from the trans- to cis-isomer. Next, poly(3,4-ethylene-dioxythiophene) stabilized with poly (4-styrenesulphonic acid) (PEDOT:PSS) was spin-coated onto the tops of all devices to prevent electrical shorts between bottom Au electrode and a deposited Au top electrode [13,14]. The Au top electrode was deposited through a shadow mask using the electron-beam evaporator, which acted as a self-aligned etching mask during the removal of exposed PEDOT:PSS. Finally, the remaining PEDOT:PSS outside the junctions was removed by reactive ion etching using O_2 gas.

The current–voltage (I–V) characterization of the fabricated molecular devices was carried out using a probe station and a semiconductor parameter analyzer (HP4155A) in ambient air at room temperature. And, the temperature variable I–V characterization was also performed in a cryostat system (ST-100 from Janis Co.) at the temperature ranging from 77 to 290 K. The absorption spectra of the azobenzene-derivative molecules in chloroform were characterized by using a UV–Vis spectroscopy measurement (PerkinElmer Lambda 750).

3. Results and discussion

3.1. photo-induced isomers

The photo-induced isomers of azobenzene derivatives are distinguished by the different physical and optical properties of the two configurations (trans- and cis-isomers), which can be observed through changes in their respective absorption spectra, dipole moments, refractive indices, and molecular conformations [15,16]. Before fabricating molecular devices, we measured the absorption spectra of the azobenzene derivative in chloroform to confirm the conformational changes upon external light irradiation. Fig. 2a shows the absorption spectra of our azobenzene derivatives in chloroform using UV–Vis spectroscopy. Generally, the absorption spectra of azobenzene derivatives are characterized by two distinct band peaks consisting of an intense band peak near 350 nm (UV region) and a weak band peak between 400 and 450 nm (visible region) [17]. The absorption transition near 350 nm is denoted as the $\pi\pi^*$ transition, which represents the rotation motion of the upper phenyl ring at the site of the N=N double bond for the trans-cis photoisomerization process. The absorption transition between 400 and 450 nm is denoted as the $n\pi^*$ transition, which represents the inversion motion of the upper phenyl ring at the same site [18]. The $n\pi^*$ transition is known to be prohibited for the trans-isomer, but it is allowed for the cis-isomer [19]. However, although the $n\pi^*$ transition of the trans-isomer is originally forbidden, a small amount of $n\pi^*$ transition peak is observed due to vibronic coupling between the $n\pi^*$ and $\pi\pi^*$ states [19].

In the trans-isomer, the two band peaks near 350 nm and between 400 and 450 nm were observed by UV–Vis spectroscopy (the blue curve in Fig. 2a). The $\pi\pi^*$ transition peak is relatively dominant compared with the $n\pi^*$ transition peak. After the trans-isomer was irradiated with UV light for 90 min in a darkroom, the intensity of the $n\pi^*$ transition peak increased because the $n\pi^*$ transition is allowed for the cis-isomer, and the $\pi\pi^*$ transition peak decreased (however, it was still intense compared with the $n\pi^*$ transition peak). From this photo-induced transition, we estimated the ratio of trans- to cis-photoisomerization from the spectra in solution. From the ratio of absorbance peak between trans- and cis-isomers at ~350 nm, the

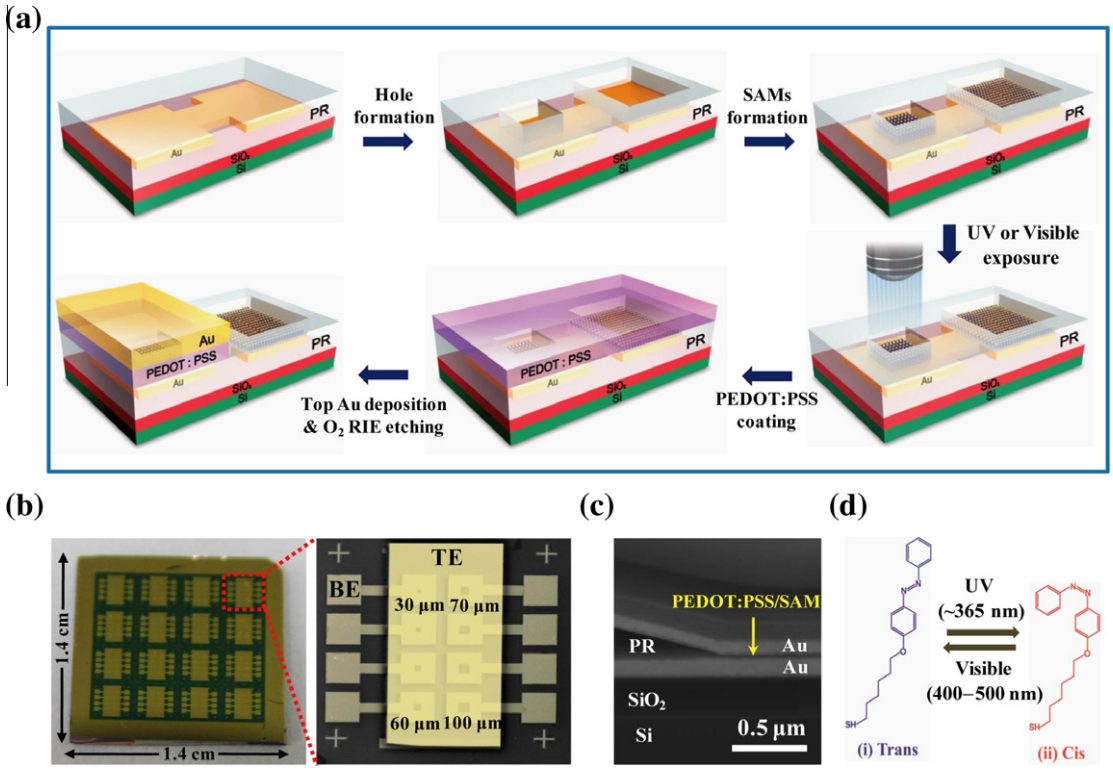

Fig. 1. (a) The process flow of device fabrication. (b) Photographic and SEM images of molecular junctions. A total of 128 junctions with square holes and side lengths of 30–100 μm are formed; BE and TE (yellow) denote the bottom and top electrodes, respectively. (c) Cross-sectional high-resolution SEM image of a molecular junction. (d) Molecular configurations of the trans- and cis-isomers. (For interpretation of the references to colour in this figure legend, the reader is referred to the web version of this article.)

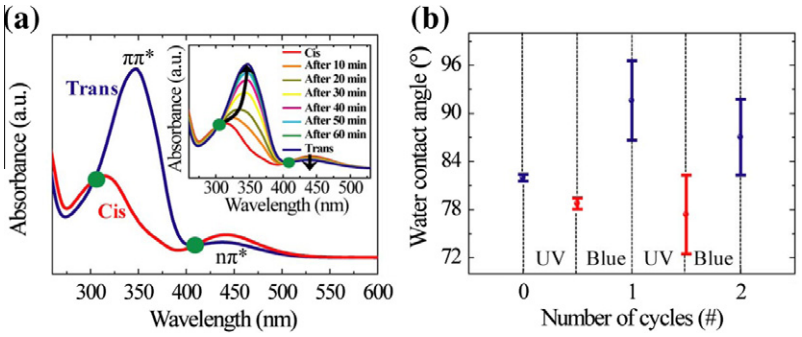

Fig. 2. (a) Absorption spectra of trans- (blue) and cis- (red) isomers in chloroform. Inset shows the evolution from cis- to trans-isomer upon visible light (~436 nm) exposure. The two green circular symbols represent the isosbestic points. (b) The evolution of water contact angle of the trans-isomer (blue symbols) and cis-isomer (red symbols) on Au substrate after UV (~365 nm) and blue light (~412 nm) irradiation, respectively. (For interpretation of the references to colour in this figure legend, the reader is referred to the web version of this article.)

trans- to cis-isomerization was found to be ~63%. This value suggests that all of the trans-isomers in solution are not completely changed to cis-isomers.

Furthermore, we investigated the conformational changes from the cis- to trans-isomer for the azobenzene derivative. Inset of Fig. 2a shows the evolution of the absorption spectrum of the cis-isomer (red curve) with visible light (~412 nm) exposure at 10-min intervals. The $\pi\pi^*$ transition peak of the cis-isomer increased and the $n\pi^*$ transition peak decreased upon visible light irradiation. After an hour of visible light irradiation, the cis-isomer was completely converted back into the trans-isomer. Note that the solvent of chloroform may evaporate during the UV–Vis measurement, but the effect of solvent evaporation would be negligible at least during the period of our measurement time, because the two isosbestic points did not change noticeably.

To elucidate the trans-cis photoisomerization behavior of azobenzene derivative on Au surface, it is necessary to confirm the conformational changes by external light. The

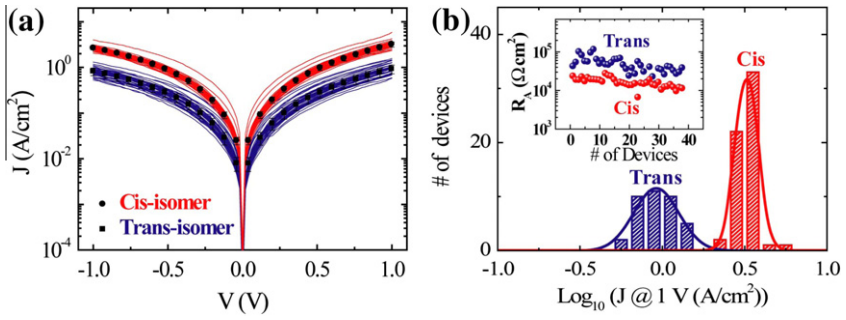

Fig. 3. (a) *J–V* curves on a logarithmic scale for trans-isomer (blue) and cis-isomer (red). The symbols and error bars represent the average and standard deviation of the current density for all the measured devices (~50 devices for each isomer case), respectively. (b) A histogram of *J* at 1 V for the trans- and cis-isomers. The solid lines are Gaussian fitting curves. The inset shows the distribution of the resistance-area products (R_A) for the trans- and cis-isomers. (For interpretation of the references to colour in this figure legend, the reader is referred to the web version of this article.)

evolution of the water contact angle on Au surface of azobenzene SAMs was monitored as a function of external irradiation wavelengths in Fig. 2b. Before UV light irradiation (~365 nm) on SAMs, the contact angle of pristine SAMs was about 81 ± 0.4°. After UV light irradiation for 90 min in a dark room, the contact angle decreased to 78 ± 0.6°, which is attributed to the trans- to cis-isomerization [21]. And, after subsequent visible light irradiation (~412 nm) for 90 min, the contact angle increased to 91 ± 4° due to cis- to trans-isomerization.

Also, we conducted the repeatable cycling measurements and confirmed the water contact angle values were reproducible for two cycles. This difference of water contact angle on trans- and cis-isomer on Au surface is mainly attributed to different top contact group and dipole moment [22]. The top contact group of trans-isomer is constituted by hydrophobic CH_3 group. In the cis-isomer, the azo (N=N bond) or phenyl group is exposed by UV light irradiation. Therefore, the surface wettability for two isomers is different.

3.2. Electrical properties and charge transport mechanism

Using the metal–molecule–metal device structure shown in Fig. 1, we statistically studied the electrical properties of the two isomers. Fig. 3a shows the current density–voltage (*J–V*) characteristics of the trans- and cis-isomer-based molecular junctions. We plotted the *J–V* curves for ~50 molecular junctions of each isomer in Fig. 3a. The important point is that the current densities of the cis-isomer junctions were higher than those of the trans-isomer junctions. To statistically compare the electrical characteristics of the trans- and cis-isomers, histograms of the logarithmic current densities (log*J*) at 1 V were plotted for both isomers, as shown in Fig. 3b. The histograms of the trans- and cis-isomer did not overlap (except for slight tails) and had distinct ranges of current density. The representative current densities were determined as the mean values of Gaussian fittings of the histograms and were found to be ~0.93 and 3.21 A/cm^2 for the trans-isomer and cis-isomer junctions, respectively. It is noted that the photoisomerization from trans- to cis-isomer might be suppressed in SAMs as compared with that in solution because the azobenzene derivatives in self-assembled monolayers are highly densely packed and subsequently there is lack of free volume in the interior of the monolayers [20]. Therefore, it is considered that the ratio of photoisomerization in SAMs may become smaller than that in solution.

Because the junction areas were different in our case (with side lengths of 30–100 μm), we considered the product of the resistance (*R*) and area (*A*), i.e., R_A (=$R \times A$), to be a junction-area-compensated quantity [23]. The obtained resistance-area products R_A of the trans- and cis-isomers were well distributed, as shown in the inset of Fig. 3b. The average R_A values were determined to be $(4.73 \pm 2.20) \times 10^4$ and $(1.40 \pm 0.40) \times 10^4\ \Omega\,cm^2$ for the trans- and cis-isomers, respectively.

To investigate the conduction mechanisms of the trans- and cis-isomers, a temperature-variable characterization was performed. Fig. 4a shows an Arrhenius plot [ln(J) versus 1/*T*] with curves at different biases ranging from 0.6 to 1.0 V in increments of 0.1 V. The temperature was varied from 77 to 290 K in increments of 40 K. For the trans-isomer (top of Fig. 4a), there were no significant changes in the slopes of the Arrhenius curves as the temperature was varied. This temperature-independent behavior indicates that the main charge transport mechanism in the trans-isomer is a tunneling in the measured bias range [24]. For the cis-isomer (bottom of Fig. 4a), the Arrhenius plot also showed a negligible temperature dependence (except for a very slight dependence at high temperature), suggesting that the overall conduction mechanism in the cis-isomer is also tunneling. If tunneling is the main conduction mechanism, the junction current density varies exponentially with the distance of tunneling pathway. The current density (*J*) for the molecular junction is described as:

$$J = J_0 \exp(-\beta\, d) \quad (1)$$

where J_0 is a constant, *d* is the tunneling distance, and β is the tunneling decay factor that represents charge transport efficiency through the molecules [25].

The molecular tunneling distances of the trans- and cis-isomers between the two electrodes were estimated using the Cambridge Scientific Chem3D software at 22.73 and

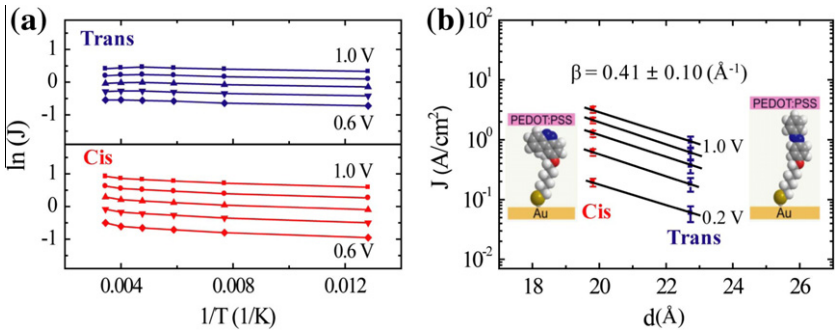

Fig. 4. (a) Arrhenius plot [ln(J) versus 1/T] for the trans- and cis-isomers at different voltages ranging from 0.6 to 1.0 V (0.1 V step). (b) A semilog plot of J as a function of molecular tunneling distance (d) for the trans- and cis-isomers at different voltages. The slopes represent the tunneling decay factor β (~0.41 Å^{-1}).

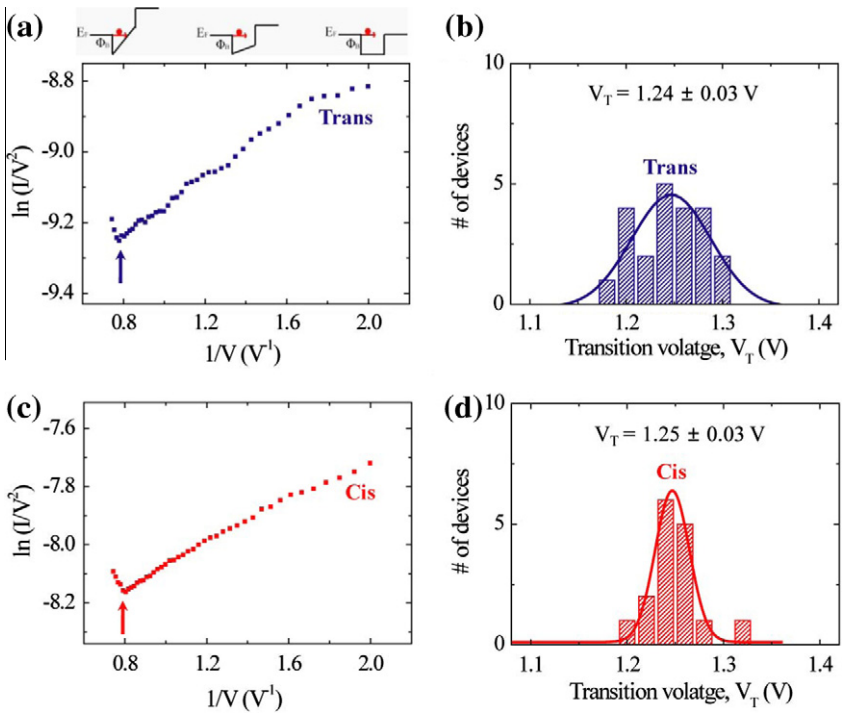

Fig. 5. (a and c) Representative plots of ln(I/V^2) versus ($1/V$) for the trans- and cis-isomers. The arrows indicate the transition point from DT to FN tunneling for the trans- and cis-isomers. (b and d) The statistical histograms of transition voltage (V_T) for the trans- and cis-isomers.

19.81 Å, respectively. Details of the determination of the molecular tunneling distances for the trans- and cis-isomers are provided in Fig. S2 in the Supplementary Data. Because the current density of the molecular tunneling junctions obeys (Eq. (1)), we plotted a semilog plot of the current density versus molecular tunneling distances for the trans- and cis-isomers, as shown in Fig. 4b. The estimated tunneling decay factor β was then obtained from the slopes [25] and found to be 0.41 ± 0.10 Å^{-1} at different biases. The observed β value in our study is similar to previously reported values in the literature [26,27]. Note that there is a variation in tunneling distance between the two electrodes because of defects in molecular layer [28] and imperfect interconversion of the molecules. Therefore, the experimental values of J are log-normally distributed as shown in Fig. 3b, and the estimated decay constant (β) represents the averaged degree of decay in our molecular junctions.

It is useful to analyze the tunneling transport with a conventional energy band model [29,30]. In the tunneling regime, when the applied bias is less than the barrier height ($V < \Phi_B/e$), charge transport exhibits direct tunneling (DT), and the barrier shape appears as a trapezoidal shape. On the other hand, when the applied bias is larger than the barrier height ($V > \Phi_B/e$), the charge transport is the field emission (or Fowler-Nordheim, FN) tunneling,

and the barrier shape appears as a triangular shape [29]. The important point is that the transition of the charge transport from DT to FN tunneling accompanies an inflection in a plot of $\ln(I/V^2)$ versus $(1/V)$ [30]. This inflection point is called the transition voltage (V_T), and this technique is termed transition voltage spectroscopy (TVS) [29,31]. The TVS method provides useful information about the location of the frontier molecular orbital (the highest occupied molecular orbital (HOMO) or lowest unoccupied molecular orbital (LUMO)) with respect to the Fermi level of the electrodes. Therefore, from the analysis of V_T by TVS characterization, one can estimate the energy offset between a metal electrode's Fermi energy and the frontier molecular orbital, which provides an estimated value of the barrier height (Φ_B); note V_T may not be identical to Φ_B. Plots of $\ln(I/V^2)$ versus $(1/V)$ for the trans-isomer (blue curve) and the cis-isomer (red curve) are shown in Fig. 5a and c, respectively (here, the applied bias was from 0 to 1.5 V). In the low-bias regime, this plot exhibits a logarithmic decay in the DT transport regime. Between the two charge transport regimes, an inflection point in the plot of $\ln(I/V^2)$ versus $(1/V)$ was observed (indicated by arrows). This inflection point is the transition voltage (V_T); it was determined to be ~1.25 V for both the trans- and cis-isomers (a small difference in V_T for the two isomers is within the error range). Fig. 5b and d shows statistical histograms for the V_T values of the trans- (22 devices) and cis-isomers (16 devices); Statistically, the V_T value was determined to be 1.24 ± 0.03 for the trans-isomer and 1.25 ± 0.03 V for the cis-isomer. This suggests that the energy offset, i.e., the barrier height (Φ_B), is also similar for both isomers regardless of the conformational change [32]. Note that the difference of conductance between the two isomers has also been reported in terms of the changes in their molecular electronic properties [33] (The details are described in the Supplementary Data).

To probe the positions of the HOMO levels of the SAMs on Au, we performed ultraviolet photoelectron spectroscopy (UPS) for each isomer. The UPS method has been used to estimate the work functions of metals and the HOMO levels of organic thin films [34,35]. We observed no significant difference between the HOMO levels of the trans- and cis-isomers on an Au substrate from the UPS measurements (for details, see Fig. S3 in the Supplementary Data). The UPS measurement result indicates that the electronic structure (HOMO level) of our molecule did not change on conversion from the trans- to the cis-isomer, meaning that the barrier height was also similar for the two isomers. Therefore, based on our study, we suggest that the main origin of the higher conductance of the cis-isomer is the difference in the molecular tunneling distance rather than the barrier height. This was confirmed by the fact that the V_T values of the trans- and cis-isomers are indeed similar: ~1.25 V (Fig. 5).

4. Conclusions

In conclusion, we performed a statistical study on the electrical characteristics of an azobenzene-derivative molecular junction in a solid-state device platform. This molecule was reversibly converted from its trans- to cis-isomer by irradiation with UV light (~365 nm) and from its cis- to trans-isomer with visible light (400–500 nm). The conductance of cis-isomer (compact form) was higher than that of trans-isomer (extended form). From the temperature-variable electrical characterization, transition voltage spectroscopy analysis, and ultraviolet photoelectron spectroscopy measurement, the current density difference between the two isomers can be explained by the reduction in the molecular tunneling distance through the molecules sandwiched between the two electrodes.

Acknowledgements

This work was supported by the National Research Laboratory program; a Korean National Core Research Centre grant; the World Class University program of the Korean Ministry of Education, Science, and Technology; the Program for Integrated Molecular Systems at GIST. We thank Ja Min Koo and Yun Hee Jang for discussions throughout this study.

Appendix A. Supplementary data

Supplementary data associated with this article can be found, in the online version, at doi:10.1016/j.orgel.2011.08.017.

References

[1] H. Song, Y. Kim, Y.H. Jang, H. Jeong, M.A. Reed, T. Lee, Nature 462 (2009) 1039.
[2] K. Mohanta, A.J. Pal, Org. Electron. 10 (2009) 960.
[3] D.W. Steuerman, H.-R. Tseng, A.J. Peters, A.H. Flood, J.O. Jeppesen, K.A. Nielsen, J.F. Stoddart, J.R. Heath, Angew. Chem. Int. Ed. 43 (2004) 6486.
[4] M. Alemani, M.V. Peters, S. Hecht, K.-H. Rieder, F. Moresco, L. Grill, J. Am. Chem. Soc. 128 (2006) 14446.
[5] A.S. Kumar, T. Ye, T. Takami, B.-C. Yu, A.K. Flatt, J.M. Tour, P.S. Weiss, Nano Lett. 8 (2008) 1644.
[6] U. Pischel, Angew. Chem. Int. Ed. 46 (2007) 4026.
[7] M. Irie, Chem. Rev. 100 (2000) 1685.
[8] M.-M. Russew, S. Hecht, Adv. Mater. 22 (2010) 3348.
[9] U. Jung, O. Filinova, S. Kuhn, D. Zargarani, C. Bornholdt, R. Herges, O. Magnussen, Langmuir 26 (2010) 13913.
[10] J.M. Mativetsky, G. Pace, M. Elbing, M.A. Rampi, M. Mayor, P. Samorì, J. Am. Chem. Soc. 130 (2008) 9192.
[11] G. Pace, V. Ferri, C. Grave, M. Elbing, C. von Hänisch, M. Zharnikov, M. Mayor, M.A. Rampi, P. Samorì, Proc. Nat. Acad. Sci. 104 (2007) 9937.
[12] A.J. Kronemeijer, H.B. Akkerman, T. Kudernac, B.J. van Wees, B.L. Feringa, P.W.M. Blom, B. de Boer, Adv. Mater. 20 (2008) 1467.
[13] H.B. Akkerman, P.W.M. Blom, D.M. de Leeuw, B. de Boer, Nature 441 (2006) 69.
[14] P.A. Van Hal, E.C.P. Smits, T.C.T. Geuns, H.B. Akkerman, B.C. De Brito, S. Perissinotto, G. Lanzani, A.J. Kronemeijer, V. Geskin, J. Cornil, P.W.M. Blom, B. De Boer, D.M. De Leeuw, Nat. Nanotechnol. 3 (2008) 749.
[15] C. Gahl, R. Schmidt, D. Brete, E.R. McNellis, W. Freyer, R. Carley, K. Reuter, M. Weinelt, J. Am. Chem. Soc. 132 (2010) 1831.
[16] B.-Y. Choi, S.-J. Kahng, S. Kim, H. Kim, H.W. Kim, Y.J. Song, J. Ihm, Y. Kuk, Phys. Rev. Lett. 96 (2006) 156106.
[17] K. Hoffmann, F. Marlow, J. Caro, Adv. Mater. 9 (1997) 567.
[18] N. Tamai, H. Miyasaka, Chem. Rev. 100 (2000) 1875.
[19] N. Biswas, S. Umapathy, Chem. Phys. Lett. 236 (1995) 24.
[20] J.-I. Anzai, S.-I. Sakasegawa, T. Takemura, T. Osa, Mater. Sci. Eng. C2 (1994) 107.
[21] N. Delorme, J.-F. Bardeau, A. Bulou, F. Poncin-Epaillard, Langmuir 21 (2005) 12278.
[22] C.L. Feng, G. Qu, Y. Song, L. Jiang, D. Zhu, Surf. Interface Anal. 38 (2006) 1343.

[23] G. Wang, T.-W. Kim, Y.H. Jang, T. Lee, J. Phys. Chem. C 112 (2008) 13010.
[24] W. Wang, T. Lee, M.A. Reed, Phys. Rev. B 68 (2003) 035416.
[25] I. Katsouras, V. Geskin, A.J. Kronemeijer, P.W.M. Blom, D.M. de Leeuw, Org. Electron. 12 (2011) 857.
[26] V. Ferri, M. Elbing, G. Pace, M.D. Dickey, M. Zharnikov, P. Samorì, M. Mayor, M.A. Rampi, Angew. Chem. 120 (2008) 3455.
[27] A. Salomon, D. Cahen, S. Lindsay, J. Tomfohr, V.B. Engelkes, C.D. Frisbie, Adv. Mater. 15 (2003) 1881.
[28] C.A. Nijhuis, W.F. Reus, G.M. Whitesides, J. Am. Chem. Soc. 132 (2010) 18386.
[29] J.M. Beebe, B. Kim, C.D. Frisbie, J.G. Kushmerick, ACS Nano 2 (2008) 827.
[30] J.M. Beebe, B. Kim, J.W. Gadzuk, C.D. Frisbie, J.G. Kushmerick, Phys. Rev. Lett. 97 (2006) 026801.
[31] E.H. Huisman, C.M Guédon, B.J. van Wees, S.J. van der Molen, Nano Lett. 9 (2009) 3909.
[32] S. Martin, W. Haiss, S.J. Higgins, R.J. Nichols, Nano Lett. 10 (2010) 2019.
[33] K. Smaali, S. Lenfant, S. Karpe, M. Ocąfrain, P. Blanchard, D. Deresmes, S. Godey, A. Rochefort, J. Roncali, D. Vuillaume, ACS Nano 4 (2010) 2411.
[34] B.R. Chalamala, Y. Wei, R.H. Reuss, S. Aggarwal, B.E. Gnade, R. Ramesh, J.M. Bernhard, E.D. Sosa, D.E. Golden, Appl. Phys. Lett. 74 (1999) 1394.
[35] B. Kim, J.M. Beebe, Y. Jun, X.-Y. Zhu, C.D. Frisbie, J. Am. Chem. Soc. 128 (2006) 4970.

titanium oxide (TiO*x*) [12–15], zinc oxide (ZnO) [16–20], LiF [21], cesium carbonate (Cs_2CO_3) [22–25], indium sulfide (In_2S_3) [26], or self-propagating molecule-based assemblies (SPMAs) [27], are usually used as an ECL in such inverted PSCs, due to their large band gaps and the well electron extraction property.

For the fabrication of thin films of inorganic n-type semiconductors as the ECL, a variety of growth methods have been employed, including sol–gel [28], thermal deposition, and atomic layer deposition (ALD) [18,29]. Among these fabrication techniques, the ALD possesses several unique capabilities, including uniform film growth, low processing temperature, low defect density, and precise control of chemical composition and film thickness at a maximum rate of one monolayer per cycle. ALD has been used to form an ECL (i.e., ZnO and TiO_2) and encapsulating films (e.g., Al_2O_3) for PSCs [18,29–31].

In this work, the feasibility of ALD-grown cadmium sulfide (CdS) film as an ECL in the inverted PSCs is explored. CdS being an n-type compound semiconductor with high electron affinity, wide direct band gap (2.4–2.5 eV), relatively high electron mobility, and environmental stability, is widely used as an n-type buffer layer for thin film photovoltaic devices [32,33], and can be fabricated by various techniques, such as ALD [34], chemical vapor deposition (CVD) [35], atomic layer epitaxy (ALE) [36], pulsed laser deposition [37], and so on. Here, the ALD-grown CdS films were obtained at relatively low temperature with high uniformity, and efficient inverted PSCs with a blended poly(3-hexylthiophene):[6,6]-phenyl C61 butyric acid methyl ester (P3HT:PCBM) photoactive layer were achieved by integrating with an ALD-grown CdS film as an ECL.

2. Experiment

2.1. Atomic layer deposition process

The CdS films with various thicknesses were grown by ALD on pre-cleaned and 15 min UV-ozone treated ITO glass substrates, which were conducted by a Savannah 100 ALD system from Cambridge Nanotech, Inc. The ALD growth process of polycrystalline CdS films on ITO substrates is schematically shown in Fig. 1, which was performed under the optimum operating conditions using the dimethyl cadmium (DMCd) and *in situ* generated H_2S precursors [34]. The temperature of ITO-coated glass substrates with a sheet resistance of 20 Ω/sq was kept at 150 °C, which is suitable to protect conductive substrates and to avoid the breakdown of DMCd precursor. The process pressure was 2×10^{-1} Torr with high-purity N_2 (flow rate = 10 sccm) as the carrier and purging gas. As depicted in Fig. 1, the optimized ALD cycle settings for CdS films were followed with 0.015 s pulse of H_2S, 10 s purge of N_2, 0.015 s pulse of DMCd, 10 s purge of N_2. The thickness of ALD-deposited CdS films per cycle was determined to be ~0.35 Å by alpha-SE™ Spectroscopic Ellipsometer. As demonstrated previously [34], the growth rate of CdS films is self-limited and will be saturated with respect to the DMCd pulse time of 0.4 s, and the N_2 purge time of 10 s is sufficient to remove the excess reactants.

2.2. Fabrication of inverted devices

The device structure of the inverted PSCs was ITO/CdS/P3HT:PCBM/MoO_3/Al. Throughout the device fabrication process, all the process parameters were fixed except for the film thickness of the CdS layer. After the deposition of CdS films by ALD, the resulting substrates were transferred into a N_2-filled glove box for the preparation of the P3HT:PCBM photoactive layer, which was spin-coated from a 1:1 weight-ratio solution in chlorobenzene with a concentration of 40 mg/mL, followed by annealing on a hot plate at 130 °C for 20 min in glove box. The thickness of the resulting P3HT:PCBM blend film was determined to be approximately 125 nm. Then, to complete the PSC devices, the samples were transferred into the high vacuum chamber with a base pressure of 1×10^{-6} Torr for the thermal evaporation of a 1.5 nm-thick MoO_3 layer as a buffer layer for hole collection and a 100 nm-thick Al anode through shadow masks. The device area, as defined by the overlap between the ITO and Al electrodes, was 0.1 cm^2. For comparison, the inverted devices employing CdS films with four different thicknesses were fabricated with the identical process parameters during the same batch processing.

2.3. Thin film and device characterization

The thickness of CdS films was calibrated by the alpha-SE™ Spectroscopic Ellipsometer. Surface morphology and roughness were characterized with atomic force microscopy (AFM) (Veeco MultiMode V) in tapping mode. The UV–vis absorption and transmission measurements of the samples were recorded at room temperature with a Perkin Elmer Lambda 750 UV/Vis/NIR spectrophotometer. High-resolution transmission electron microscopy (HRTEM) images and selected area diffraction (SAD) patterns were taken by an FEI Tecnai G2 F20 X-TWIN operated using an accelerating voltage of 200 kV with samples by separating CdS from the ITO substrate. The contact angle of water on the surfaces of CdS films was determined by SCA20 contact angle measurement system (sessil drop method). Elemental composition and the electronic structures of the films were determined by ultraviolet and X-ray photoelectron spectroscopies (UPS and XPS) in a Kratos AXIS Ultra-DLD ultra-high vacuum system (a base pressure of 3×10^{-10} Torr) with HeI excitation (21.22 eV for UPS) and monochromatic Al Kα source (1486.6 eV for XPS). Details of the experimental setup for UPS and XPS measurements have been given elsewhere [38,39].

Photovoltaic measurements were conducted at room temperature in air without any device encapsulation. The current density–voltage (*J–V*) characteristics of the inverted PSC devices were examined with a programmable Keithley 2612 source meter under simulated air mass (AM) 1.5G illumination (Newport-Oriel solar simulators with integrated intensity = 100 mW/cm^2), which was calibrated with a silicon photodiode.

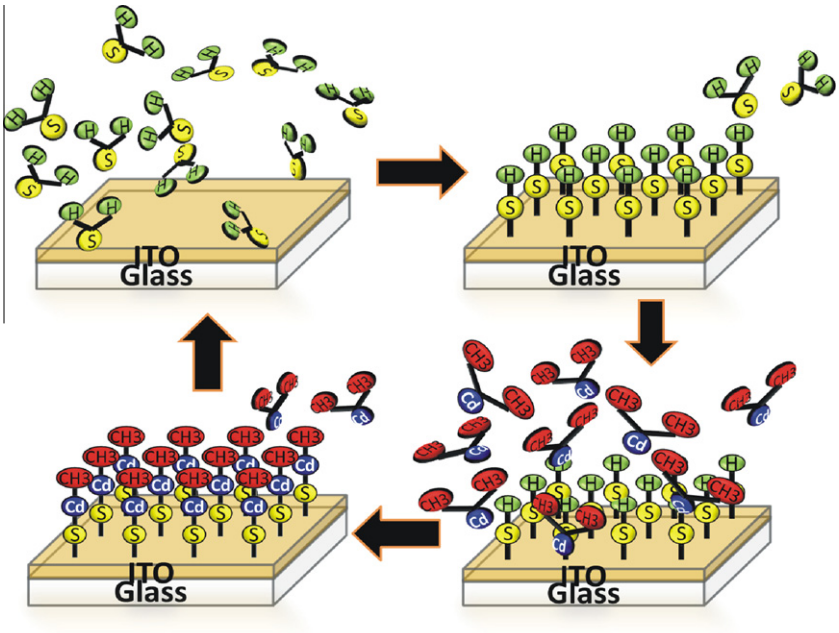

Fig. 1. Schematic of the atomic layer deposition process for CdS films based on precursors of diethyl cadmium (DMCd) and *in situ* generated H_2S.

3. Results and discussion

The surface morphology and roughness of the ALD-grown CdS films on ITO glass surfaces were investigated by AFM. Fig. 2 shows the AFM micrographs of ALD-grown CdS films with a thickness of 3.5 nm (100 cycles), 10.5 nm (300 cycles), 17.5 nm (500 cycles), and 38.5 nm (1100 cycles), respectively, where the film thickness is dependent on the cycle numbers. It is evident in Fig. 2 that there is negligible change in the surface features for CdS films with increasing thickness, in which uniform CdS films composed of similar distinct crystal grains can be observed. The root mean square (RMS) roughness values, as summarized in Table 1, are almost identical with respect to the variation in film thicknesses. The crystallinity of the ALD-grown CdS films has been estimated by HRTEM. As shown in Fig. 3, the HRTEM image and SAD pattern confirm the presence of polycrystalline CdS grains. However, due to sulfur vacancies as discussed later by XPS measurement, the non-stoichiometric structure in ALD-deposited CdS films results in the derivation of the SAM pattern in comparison with zinc blende (cubic) and wurtzite (hexagonal) crystals of CdS [34]. As reported in the literature, the polycrystalline CdS film by ALD is the mixture of zinc blende (cubic) and wurtzite (hexagonal) crystals, and the transition between these two phases strongly depends upon factors such as deposition method, temperature, time, and precursors [34].

In order to characterize the composition of ALD-deposited CdS films, the XPS measurements were carried out. Fig. 4 shows the XPS spectra for the ALD-grown CdS films with different thicknesses, where the Cd 3d and S 2p XPS core level spectra exhibit symmetric line shapes. With increasing the CdS thickness, the binding energies of Cd $3d_{5/2}$ (and S $2p_{3/2}$) peaks gradually shift from 405.5 eV (and 162.0 eV) to 405.9 eV (and 162.3 eV), respectively. According to the quantitative analysis of Cd 3d and S 2p core level spectra, the atomic Cd-to-S ratio were determined to be approximate 1.60:1, as listed in Table 1. It is found that the CdS films by ALD are not stoichiometric within the error of the XPS characterization due to the sulfur vacancies, whereas there is no noticeable change in the spectral shape.

The key factors of ALD-grown CdS films affecting the electrical properties of the CdS ECL were examined to obtain the optimal performance from the inverted PSCs. Fig. 5 plots the *J–V* characteristics of inverted PSCs employing CdS films as an ECL under AM 1.5G irradiation with the intensity of 100 mW/cm^2 and in dark. Table 1 summarizes the device parameters. Reasonable photovoltaic effect was observed with the incorporation of CdS film. It is noted that when the CdS thickness is less than 3.5 nm, the device exhibits an antidiode behavior with a poor performance, resulting in short-circuit current density (J_{SC}) of 9.88 mA/cm^2, open-circuit voltage (V_{OC}) of 0.55 V, fill factor (FF) of 39.71%, and the PCE of only 2.16%. However, with the increase of CdS thickness, the PSC devices shows a remarkable improvement with the increase of CdS thickness, and the device with 17.5 nm-thick CdS yields the best device performance, providing the PCE of 3.33%. The major improvement in device performance with the incorporation of 17.5 nm-thick CdS film arises from the higher FF and V_{OC}, while the J_{SC} remained almost unchanged. These results clearly demonstrate that CdS can act as an efficient ECL to enhance the efficiency of inverted PSCs. In addition, the further increase of CdS thickness leads to a reduction in J_{SC} and V_{OC}. For instance, the inverted device incorporating a CdS film with a thickness over 38.5 nm shows a reduced PCE (2.6%) with lower J_{SC}, V_{OC}, and FF.

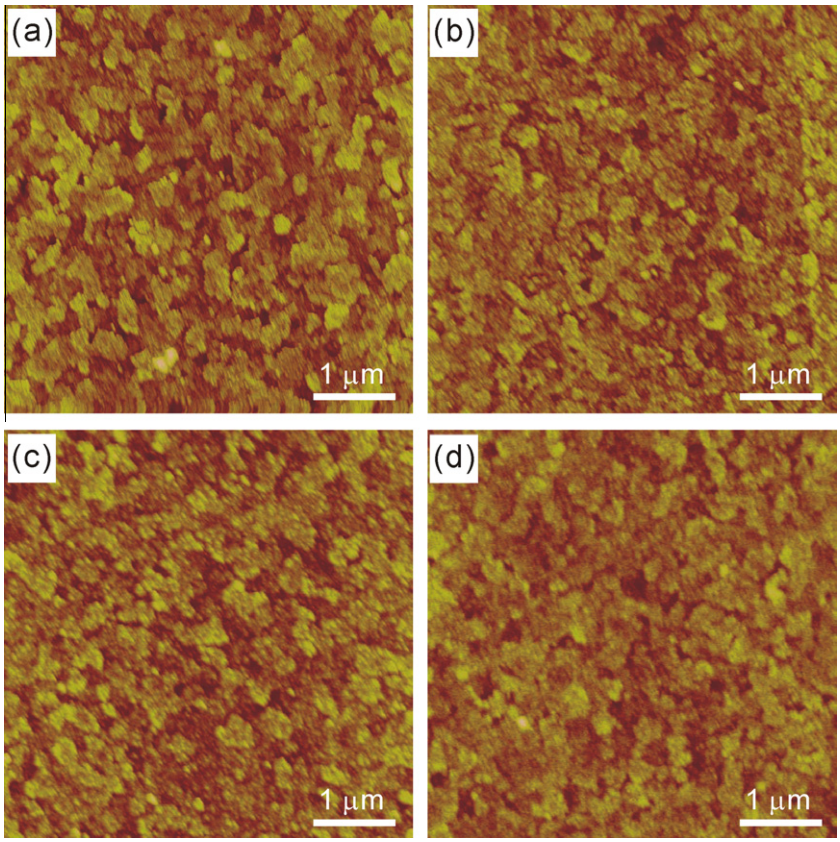

Fig. 2. AFM images of ALD-grown CdS films on ITO substrates with the thicknesses: (a) 3.5 nm, (b) 10.5 nm, (c) 17.5 nm, and (d) 38.5 nm.

Table 1
Characteristics of ALD-grown CdS films and device performance parameters of inverted polymer solar cells with CdS as the electron collection layer. The series resistance (Rs) was determined from the dark *J*–*V* characteristics shown in Fig. 5(b).

CdS (nm)	Roughness (nm)	Cd/S ratio	Contact angle (°)	V_{OC} (V)	J_{SC} (mA/cm^2)	FF (%)	PCE (%)	Rs (Ω)
3.5	2.16	1.77	49.5	0.55	9.88	39.71	2.16	1495.5
10.5	1.93	1.62	54.5	0.59	9.07	57.97	3.10	58.82
17.5	2.07	1.67	55.8	0.61	8.94	61.11	3.33	59.65
38.5	1.75	1.32	54.0	0.56	8.69	53.37	2.60	67.93

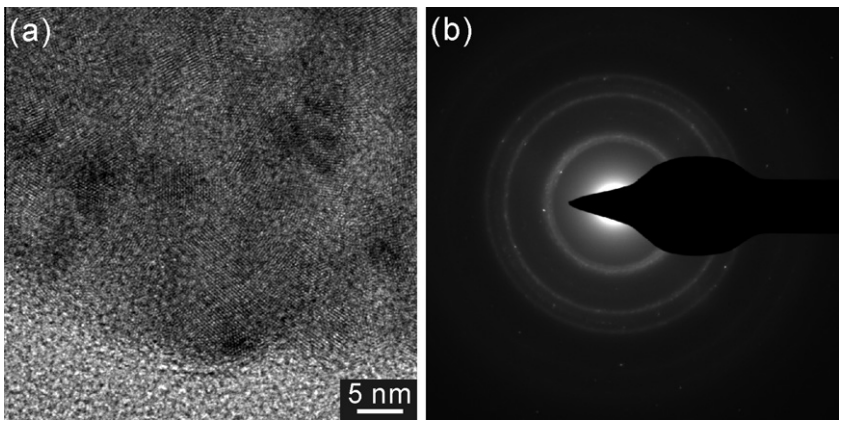

Fig. 3. (a) HRTEM image and (b) selected area diffraction (SAD) pattern of ALD-grown CdS film.

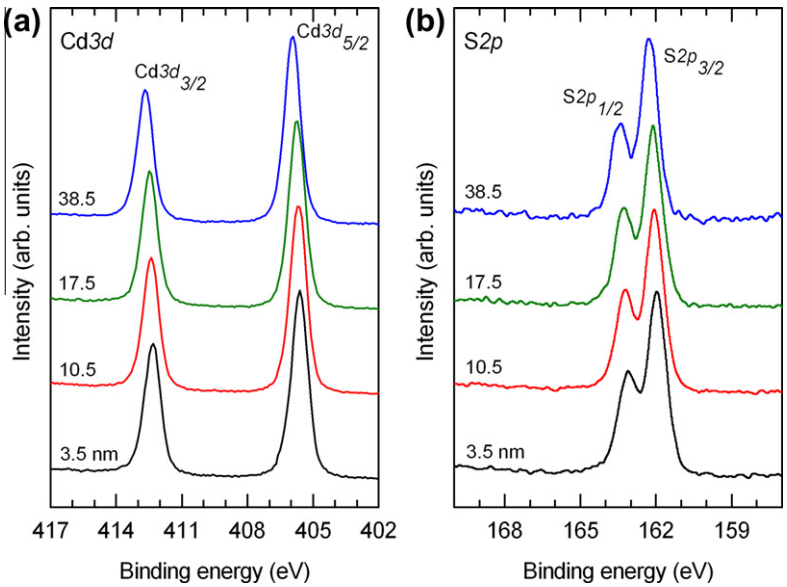

Fig. 4. (a) Cd 3d and (b) S 2p XPS core level spectra of ALD-grown CdS films with different thicknesses.

To understand the influence of ALD-grown CdS films with different thicknesses on the device performance, the optical transmittance of the CdS films on ITO glass was performed with UV–vis spectroscopy. The transmittance spectra of the CdS films shown in Fig. 6 indicate the thickness-dependent transmittance in the range below 500 nm. The inset of Fig. 6 shows the absorption spectra of the CdS film, the P3HT:PCBM layer, and CdS/P3HT:PCBM bilayer, respectively, where an increase in the absorption below 500 nm is clearly seen due to the strong absorption of CdS film near the band gap edge of CdS. In addition, it is obvious that the film thickness did not appear to have impact on the band gap except for the transmittance.

It has been demonstrated that controlling the surface energy of the buffer layer can result in an enhanced performance of the inverted PSCs due to the optimized morphology of the photoactive layer [40]. As shown in Table 1, the contact angle of water on the surface of CdS films was measured, revealing little fluctuation of the surface energy with respect to the variation of CdS film thickness. It has also been confirmed that the morphology of the P3HT:PCBM films spin-coated on CdS/ITO substrates are insensitive to the CdS surface, exhibiting the similar morphology (not shown here). As reflected by the contact angle measurement, the surface energy of the CdS films cannot be speculated to the reason behind the efficiency variation in inverted structure PSCs.

Further surface property studies were carried out by UPS measurement on the electronic structures of CdS films. Fig. 7(a) shows the secondary electron cutoff of the ALD-grown CdS films with different thicknesses on ITO substrates, which can be used to determine the work function of CdS films by the intercept between the background level and the extrapolation of the leading edge in the high binding energy region. According to the UPS measurement, the work function of UV-ozone treated ITO substrate is determined to be 4.8 eV, while the corresponding work function of CdS films deposited on the ITO surface is reduces to about 3.9 eV, which keeps almost identical with respect to the variation of the film thickness. On the other hand, the valence band maximum (VBM) of the CdS films can be determined from the UPS spectra in Fig. 7(b), which locates at 2.2 eV below Fermi level (E_F). Taking into account the band gap obtained from the UV absorption edge in the inset of Fig. 6, the conduction band minimum (CBM) of the CdS film is 0.2 eV above E_F, indicating the n-type semiconducting property of the ALD-grown CdS films.

Fig. 8 displays the secondary-electron cutoff and the zoom-in HOMO region of 10 nm-thick P3HT:PCBM blend spin-coated on ALD-grown CdS films with various thickness. It is evident that the UPS signals of the highest occupied molecular orbital (HOMO) features are dominated by the P3HT component due to the accumulation of P3HT at the blend surface, which is consistent with previous reports [41]. As shown in Fig. 8(a), the spin-coating of the blended P3HT:PCBM layer on CdS films only induces a slight vacuum level shift (~0.1–0.2 eV) within the error of the UPS measurement, leading to a work function of ~3.8 eV. The ionization potential (IP) value of P3HT extracted from the UPS spectra is around 4.55 eV by taking into account the work function of ~3.8 eV and HOMO edge of 0.75 eV below E_F. However, the energy levels of PCBM cannot be clearly distinguished from the UPS spectra of the P3HT:PCBM blend layers due to the vertical phase separation as demonstrated previously [41], and will be assumed to be vacuum-level (VL) aligned with that of P3HT [42].

The electronic structures of the MoO_3/P3HT:PCBM interface were also investigated, since a stable MoO_3 thin film was selected as the hole extraction layer in the inverted configuration. Fig. 9 shows UPS spectra of the corresponding interface with increasing MoO_3 overlayer thicknesses. It is obvious that deposition of the MoO_3

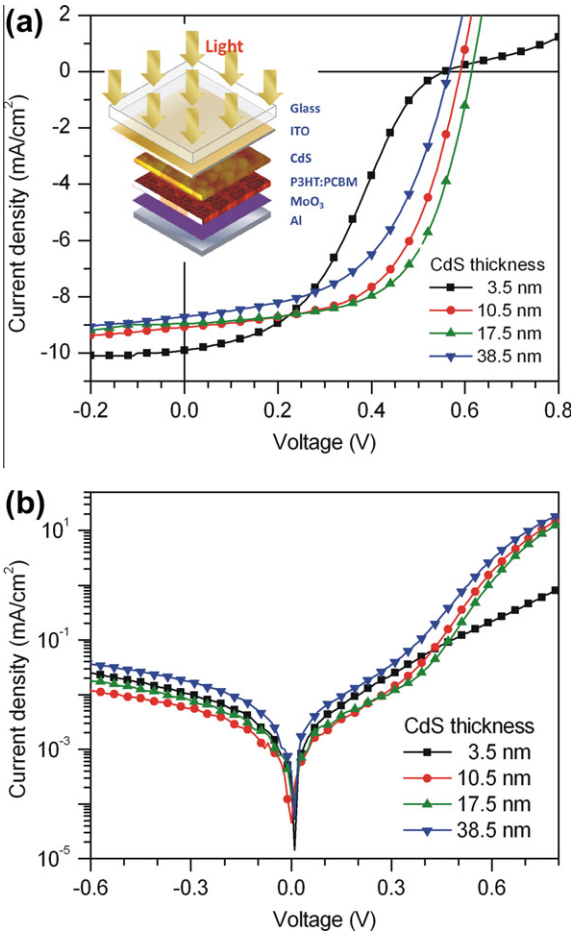

Fig. 5. *J–V* characteristics of the inverted polymer solar cells incorporating ALD-grown CdS films with various thicknesses (a) under 100 mW/cm^2 AM 1.5G simulated solar illuminations and (b) in darkness. Inset in (a) is the device structure of inverted P3HT:PCBM solar cell.

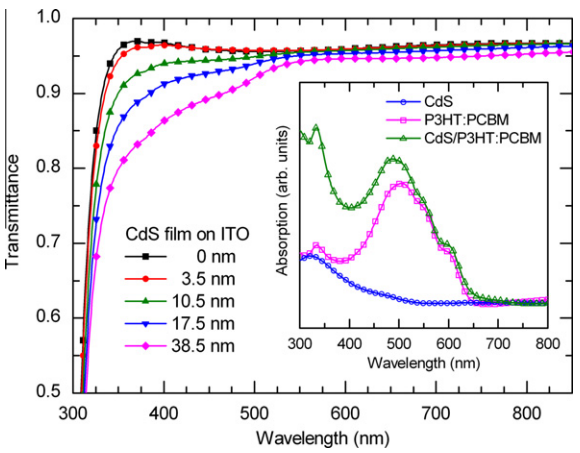

Fig. 6. Optical transmittance spectra of ALD-grown CdS films with various thicknesses on ITO substrate. The inset shows the absorption spectra of 17.5 nm-thick CdS, 125 nm-thick P3HT:PCBM, and the CdS/P3HT:PCBM layers, respectively.

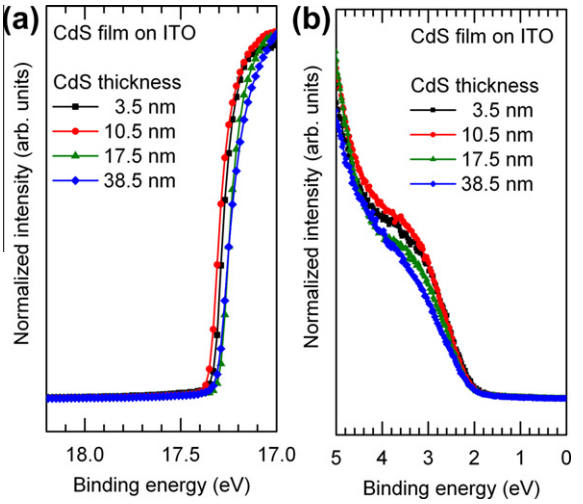

Fig. 7. (a) The secondary electron cutoff region and (b) enlarged HOMO region of the UPS spectra of CdS films deposited on ITO substrates with various thicknesses.

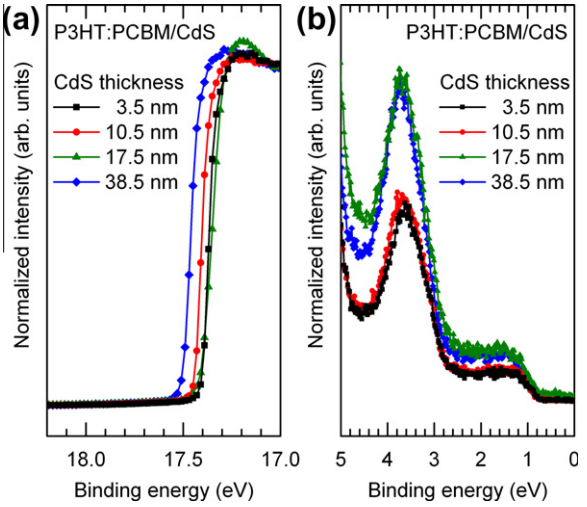

Fig. 8. (a) The secondary electron cutoff region and (b) enlarged HOMO region of the UPS spectra of a 10 nm-thick P3HT:PCBM layer spin-casted on various CdS films.

overlayer results in a progressive shift (~1.4 eV) of the secondary electron cutoff towards lower binding energy region, which corresponds to the increase of the work function and the formation of interface dipole. According to Fig. 9(b), the VBM of a 1.5 nm-thick MoO_3 layer is estimated to be at 2.8 eV below E_F. Considering the energy gap of 3.1 eV, MoO_3 exhibits an n-type semiconductor property with E_F slightly pinned below the CBM, which is in good agreement with previous reports [43].

Using the results from UPS measurements, the energy level offsets directly at the interface can be accurately determine by considering the interface dipole formation. Fig. 10 illustrates the energy level diagram for the inverted PSC with a CdS ECL. Here, HOMO (or VBM) positions are

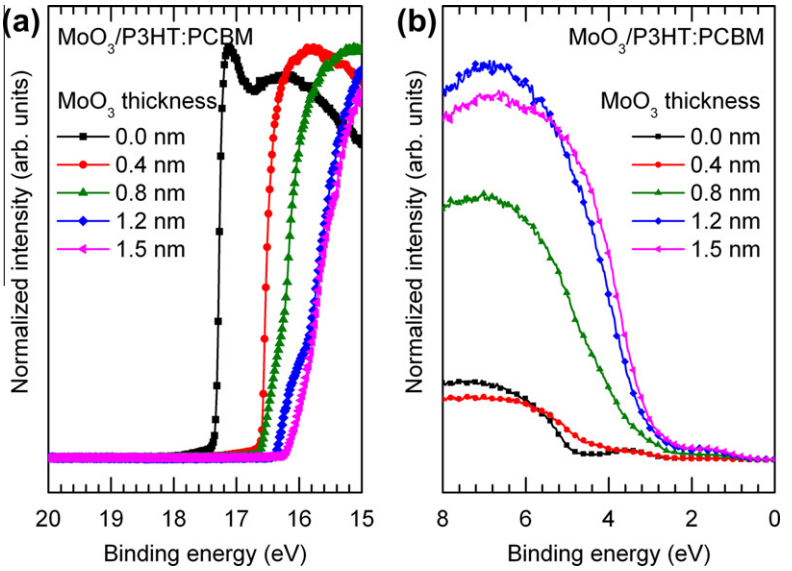

Fig. 9. (a) The secondary electron cutoff region and (b) the enlarged HOMO region of the UPS spectra of the incremental deposition of a MoO_3 layer on the P3HT:PCBM film.

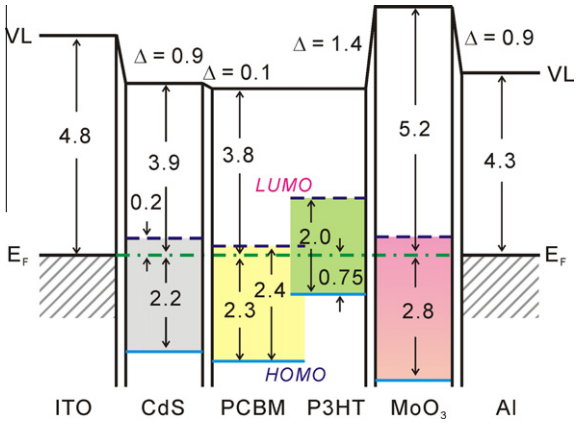

Fig. 10. Schematic energy level diagram of the component materials used in the inverted configuration, where the VL and HOMO (or VBM) positions are derived from the UPS measurements, and the LUMO (or CBM) is derived from optical gaps plus HOMO.

extracted from the UPS spectra, and the lowest unoccupied molecular orbital (LUMO) (or CBM) positions are estimated by adding the energy gaps. E_F is aligned across the interfaces in a thermodynamic equilibrium state, and the VL shift determined by the secondary electron cutoff is compensated with the interface dipole formation (Δ). In addition, the HOMO and LUMO levels of PCBM in the P3HT:PCBM blend were referred to the values of pristine PCBM layer in the literature [41], which are aligned with that of P3HT with a common VL. It is evident that the energy level lineup across the inverted PSC is not consistent with the traditional concepts of common VL alignment [42]. In addition, Fig. 10 implies that the CdS film between ITO cathode and P3HT:PCBM layer provides a better energy level matching due to the well-aligned CBM of CdS film with the LUMO of the electron acceptor PCBM. Therefore, the ALD-grown CdS film is indicative of efficient electron collection and transport from the P3HT:PCBM photoactive to the ITO cathode.

To get additional insight into the origin of the observed PCE enhancements with respect to the variation of CdS thickness, the contact resistance of the inverted devices was examined from the dark *J–V* characteristics in Fig. 5(b). As shown in Table 1, a strong correlation between the series resistance (Rs) and the resultant device performance can be obtained. The Rs variation of inverted PSC with ALD-grown CdS films follows the PCE results. For ALD-grown CdS films with a thickness lower than 17.5 nm, the Rs decreases with the CdS thickness, and then increases with a thicker CdS film. As a result, a higher Rs can lead to a reduction in FF and J_{SC}, hence a reduction in PCE [44]. The results clearly reveal that the Rs might be one of the reasons behind the improved efficiency of inverted structure PSCs with ALD-grown CdS films as an ECL.

4. Conclusions

In summary, efficient inverted polymer solar cells were achieved by using ALD-grown CdS films as the electron collection layer. The CdS films by ALD using DMCd and *in situ* generated H_2S precusors can be obtained at relatively low growth temperatures ($\leqslant$150 °C) with high uniformity, and the sulfur vacancy induces an n-type semiconducting property as determined by UPS and XPS measurements. The suitable energy level alignment at the ITO/CdS/PCBM interface is favorable to electron extraction through CdS to the ITO cathode. With the optimized CdS film thickness, the power conversion efficiency increases to 3.33% under AM1.5G 100 mW/cm^2 irradiation. The results define a promising pathway for the fabrication of efficient inverted polymer solar cells.

Acknowledgements

The authors acknowledge the financial support by the National Natural Science Foundation of China (No. 91027041, 61007020, 61036009, 60937001, 61107022), National Basic Research Program of China (973 program) (No. 2011CB808404, 2010CB934502, 2009CB623703), the Research Fund for the Doctoral Program of Higher Education of China (No. 20093201120019, 20103201120019), the Natural Science Foundation of Jiangsu Province (No. BK2010003), and a Project Funded by the Priority Academic Program Development of Jiangsu Higher Education Institutions (PAPD).

References

[1] P.W.M. Blom, V.D. Mihailetchi, L.J.A. Koster, D.E. Markov, Adv. Mater. 19 (2007) 1551.
[2] S. Günes, H. Neugebauer, N.S. Sariciftci, Chem. Rev. 107 (2007) 1324.
[3] G. Dennler, M.C. Scharber, C.J. Brabec, Adv. Mater. 21 (2009) 1323.
[4] L.M. Chen, Z.R. Hong, G. Li, Y. Yang, Adv. Mater. 21 (2009) 1434.
[5] G. Li, V. Shrotriya, J. Huang, Y. Yao, T. Moriarty, K. Emery, Y. Yang, Nat. Mater. 4 (2005) 864.
[6] L.H. Hoppe, N.S. Sariciftci, J. Mater. Chem 16 (2006) 45.
[7] J.Y. Kim, K. Lee, N.E. Coates, D. Moses, T.Q. Nguyen, M. Dante, A.J. Heeger, Science 317 (2007) 222.
[8] C.Y. Li, T.C. Wen, T.H. Lee, T.F. Guo, J.C.A. Huang, Y.C. Lin, Y.J.J. Hsu, Mater. Chem. 19 (2009) 1643.
[9] M. Jorgensen, K. Norrman, F.C. Krebs, Sol. Energy Mater. Sol. Cells 92 (2008) 686.
[10] S.K. Hau, H.L. Yip, A.K.Y. Jen, Polym. Rev. 50 (2010) 474.
[11] Z. Xu, L.M. Chen, G.W. Yang, C.H. Huang, J.H. Hou, Y. Wu, G. Li, C.S. Hsu, Y. Yang, Adv. Funct. Mater. 19 (2009) 1227.
[12] C. Waldauf, M. Morana, P. Denk, P. Schilinsky, K. Coakley, S.A. Choulis, C.J. Brabec, Appl. Phys. Lett. 89 (2006) 233517.
[13] G.K. Mor, K. Shankar, M. Paulose, O.K. Varghese, C.A. Grimes, Appl. Phys. Lett. 91 (2007) 152111.
[14] M.H. Park, J.H. Li, A. Kumar, G. Li, Y. Yang, Adv. Funct. Mater. 19 (2009) 1241.
[15] T. Kuwabara, C. Iwata, T. Yamaguchi, K. Takahashi, ACS Appl. Mater. Interfaces 2 (2010) 2254.
[16] M.S. White, D.C. Olson, S.E. Shaheen, N. Kopidakis, D.S. Ginley, Appl. Phys. Lett. 89 (2006) 143517.
[17] A.K.K. Kyaw, X.W. Sun, C.Y. Jiang, G.Q. Lo, D.W. Zhao, D.L. Kwong, Appl. Phys. Lett. 93 (2008) 221107.
[18] H. Cheun, C. Fuentes-Hernandez, Y.H. Zhou, W.J. Potscavage, S.J. Kim, J. Shim, A. Dindar, B. Kippelen, J. Phys. Chem. C 114 (2010) 20713.
[19] J. Gilot, I. Barbu, M.M. Wienk, R.A.J. Janssen, Appl. Phys. Lett. 91 (2007) 113520.
[20] F.C. Krebs, T. Tromholt, M. Jorgensen, Nanoscale 2 (2010) 873.
[21] C.J. Brabec, S.E. Shaheen, C. Winder, N.S. Sariciftci, P. Denk, Appl. Phys. Lett. 80 (2002) 1288.
[22] G. Li, C.W. Chu, V. Shrotriya, J. Huang, Y. Yang, Appl. Phys. Lett. 88 (2006) 253503.
[23] H.H. Liao, L.M. Chen, Z. Xu, G. Li, Y. Yang, Appl. Phys. Lett. 92 (2008) 173303.
[24] J.S. Huang, G. Li, Y. Yang, Adv. Mater. 20 (2008) 415.
[25] C.S. Kim, S. Lee, L.L. Tinker, S. Bernhard, Y.L. Loo, Chem. Mater. 21 (2009) 4583.
[26] M.R.R. Menon, M.V. Maheshkumar, K. Sreekumar, C.S. Kartha, K.P. Vijayakumar, Sol. Energy Mater. Sol. Cells 94 (2010) 2212.
[27] L. Motiei, Y. Yao, J. Choudhury, H. Yan, T.J. Marks, M.E. van der Boom, A. Facchetti, J. Am. Chem. Soc. 132 (2010) 12528.
[28] Y.M. Sun, J.H. Seo, C.J. Takacs, J. Seifter, A.J. Heeger, Adv. Mater. 23 (2011) 1679.
[29] C.Y. Chang, F.Y. Tsai, J. Mater. Chem. 21 (2011) 5710.
[30] C.Y. Chang, C.T. Chou, Y.J. Lee, M.J. Chen, F.Y. Tsai, Org. Electron. 10 (2009) 1300.
[31] J.C. Wang, W.T. Weng, M.Y. Tsai, M.K. Lee, S.F. Horng, T.P. Perng, C.C. Kei, C.C. Yu, H.F. Meng, J. Mater. Chem. 20 (2010) 862.
[32] I. Repins, M.A. Contreras, B. Egaas, C. DeHart, J. Scharf, C.L. Perkins, B. To, R. Noufi, Prog. Photovoltaics 16 (2008) 235.
[33] X.X. Jiang, F. Chen, H. Xu, L.G. Yang, W.M. Qiu, M.M. Shi, M. Wang, H.Z. Chen, Sol. Energy Mater. Sol. Cells 94 (2010) 338.
[34] J.R. Bakke, H.J. Jung, J.T. Tanskanen, R. Sinclair, S.F. Bent, Chem. Mater. 22 (2010) 4669.
[35] Q. Liu, G.B. Mao, Surf. Rev. Lett. 16 (2009) 469.
[36] Y. Luo, M. Han, D.A. Slater, R.M. Osgood, J. Vac. Sci. Technol. 18 (2000) 438.
[37] B. Ullrich, H. Sakai, Y. Segawa, Thin Solid Films 385 (2001) 220.
[38] H.X. Wei, J. Li, Z.Q. Xu, Y. Cai, J.X. Tang, Y.Q. Li, Appl. Phys. Lett. 97 (2010) 083302.
[39] Q.Y. Bao, J.P. Yang, J.X. Tang, Y.Q. Li, C.S. Lee, S.T. Lee, Org. Electron. 11 (2010) 1578.
[40] X. Bulliard, S.G. Ihn, S. Yun, Y. Kim, D. Choi, J.Y. Choi, M. Kim, M. Sim, J.H. Park, W. Choi, K. Cho, Adv. Funct. Mater. 20 (2010) 4381.
[41] Z. Xu, L.M. Chen, M.H. Chen, G. Li, Y. Yang, Appl. Phys. Lett. 95 (2009) 013301.
[42] J.X. Tang, C.S. Lee, S.T. Lee, J. Appl. Phys. 101 (2007) 064504.
[43] Q.Y. Bao, J.P. Yang, Y.Q. Li, J.X. Tang, Appl. Phys. Lett. 97 (2010) 063303.
[44] Z.Q. Xu, J. Li, J.P. Yang, P.P. Cheng, J. Zhao, S.T. Lee, Y.Q. Li, J.X. Tang, Appl. Phys. Lett. 98 (2011) 253303.

can effectively increase the electrical conductivity to several hundred Siemens per centimeter. However, due to the low Seebeck coefficient, the highest ZT can only reach $\sim 10^{-3}$ around room temperature, which is still insufficiently high for practical application. The ICPs with specific dopants indeed provide the excellent and stable electric conductivities needed, but it is generally difficult to obtain a high Seebeck coefficient simultaneously. A significant enhancement in ZT has been achieved by synthesizing specially designed copolymers with a high electrical conductivity, e.g., poly(2,5-dimethoxyphenylenevinylene-co-phenylenevinylene) and poly(2,5-diethoxyphenylenevinylene-co-phenylenevinylene), which exhibit a greatly improved ZT of $\sim 10^{-2}$ and $\sim 10^{-1}$, respectively [15,16].

As a popular commercial conducting polymer, the water-dispersible poly(3,4-ethylenedioxythiophene):poly (styrenesulfonate) (PEDOT:PSS) has become one of the most promising conductive polymers and has been widely applied in modern photoelectronic devices [17]. The TE investigations for PEDOT:PSS can be traced back to 2002, when Kim et al. established that the Seebeck coefficient decreases with the addition of the dielectric solvent of dimethyl sulfoxide (DMSO) [10]. The topic began to attract growing interest until in 2009 numerous results were published regarding both as-received PEDOT:PSS and blended composites [10–12,18]. Although the addition of DMSO has been widely accepted as an effective approach to greatly increase the electrical conductivity by several orders of magnitude, in the meantime, the Seebeck coefficient also drastically decreases, even with a very small addition, e.g., 0.5 wt.%, and seems to have less change with the variation of the DMSO concentration [11].

Due to the difficulty of independently controlling the Seebeck coefficient and electrical conductivity, blending of different organic/inorganic TE materials provides a simple and potential way to individually optimize these two parameters of the blended TE composites. For instance, Zhang et al. have demonstrated one design of organic–inorganic hybrid films, i.e., one Bi_2Te_3 granular layer coated with one thick PEDOT:PSS layer, and obtained a power factor of $\sim 16\ \mu W/mK^2$, which is much lower than their theoretical prediction using a simplified ideal model [12]. See et al. have also presented an in situ synthesis of the composite of the Te nanorods and PEDOT:PSS, which has a maximum Seebeck coefficient of 163 μV/K and power factor of $\sim 70\ \mu W/mK^2$ [18]. All these hybrid results indicate that no matter whether the TE heteromaterials are integrated in parallel or serial methods, the final TE performance is directly correlated with that of the individual components [12]. It is thus of great importance and meaningful to make efforts to enhance the TE performance of all components, especially the polymers, such as the PEDOT:PSS polymers in the above cases.

In this paper, the effects of the ammonium formate (AF) dopants on the Seebeck coefficient, electrical conductivity, power factor and microstructures of the commercial PEDOT:PSS films are presented. It has been reported that AF can cut off alkyl groups or side chains from benzene [19]. The results motivated us to examine if AF can be a promising dopant to effectively tune the electrical properties of conducting polymers. In addition, since AF will decompose into formamide and water with the presence of heat [20], in our experience, a two-step drying process was specially designed to form PEDOT:PSS films with nano/micro-fractures in which significant phonon scattering may occur, reducing the thermal conductivity of the films. During the first drying step at lower temperature, the only solvent, water, will be gently removed to create dried AF blended PEDOT:PSS films and a very small fraction of the AF dopants will also decompose into the gas phase. The following higher-temperature step will make the trapped solid AF dopants almost decompose to simultaneously form open or closed voids or channels randomly distributed over the films.

2. Experiment

Commercial PEDOT:PSS and AF were purchased from H.C. Starck (Clevios PH 500, 1.0–1.4 wt.%) and Showa Chemical Inc., respectively, and used without further purification. The received PEDOT:PSS solution was doped with 5, 10, 20 and 50 wt.% AF, and respectively denoted as P5, P10, P20, and P50. It must be noted that the weight percentages mentioned above are expressed only by the respective weight percentages of the solid content irrespective of the water solvent, not the whole solution mixture. The 5 wt.% DMSO doped and raw PEDOT:PSS solutions were also prepared for comparison. The chemical structures are shown in Fig. 1. The glass slides were cut into $2.5 \times 2.5\ cm^2$ pieces as the substrates and washed with ultrasonic cleaning processes in detergent, deionized water, and isopropyl alcohol, sequentially. An approximate 100 μL of each prepared PEDOT:PSS solution was dropped onto the as-cleaned glass substrate using a micropipette and spread evenly. The deposited sample was firstly dried in air at 40 °C for 1 h mainly to drive off the H_2O solvent and then kept at 80 °C for another 1 h to further remove the residual solvent as well as to evaporate the AF dopants.

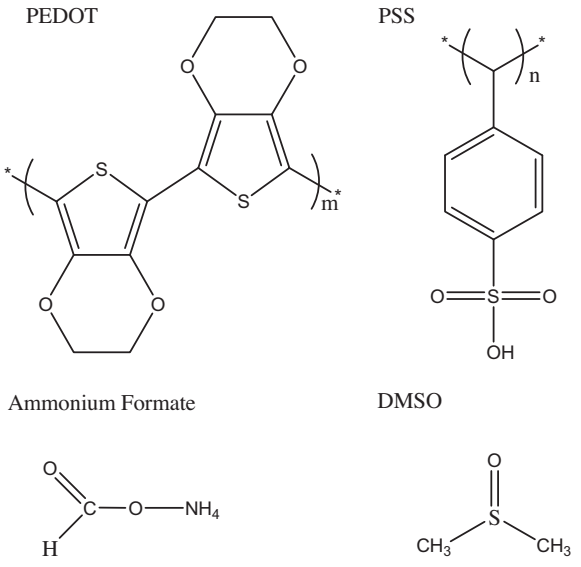

Fig. 1. Chemical structures of PEDOT, PSS, AF, and DMSO.

The final thickness of each dried PEDOT:PSS film was in the range of ~4–6 μm.

The sheet resistance and the electrical conductivity were measured with an automated four-point probe system (Resistest RT-80/Resistage RT-80, Napson Corporation). The corresponding carrier concentration and Hall mobility were characterized with a Hall system (Accent HL5500). The cross-section SEM images provided the accurate thicknesses needed. For the Seebeck coefficient measurement, a maximum temperature gradient of 10 °C was created between two electrodes with an interval of 1.0 cm. The Seebeck voltage and temperature difference were recorded in situ for obtaining the Seebeck coefficients. The samples for the scanning electron microscope (SEM; JSM-6500, JEOL) were broken in liquid nitrogen to avoid plastic deformation of the films. Thermogravimetry analysis (TGA, Q500, TA instruments) was deployed not only to understand the decomposition process of AF but also to characterize the thermostability of the produced films. All TGA samples were pre-heated at 40 °C for 10 min. The time-resolved decomposition of the as-received AF powders at 80 °C and the temperature-dependent weight loss of the prepared PEDOT:PSS films up to 800 °C were respectively recorded. The furnace chamber was constantly purged with nitrogen to minimize the effect of oxygen and to serve as a carrier gas, taking waste out of the chamber. The UV–Vis absorption spectra were recorded with a UV–Vis spectrophotometer (Evolution 300, Thermo Scientific). Thermal conductivity was analyzed by placing a free-standing polymer film between two stacking copper pillars. A heat source generates heat from the bottom of the lower pillar and heat flows upward, through the sample, and then into the upper pillar. Temperatures were measured at certain points of the two pillars to calculate the speed of the heat flow and thermal conductivity of the polymer film.

3. Results and discussion

Fig. 2 shows the cross-section and top-view SEM images of the unmodified and AF-doped PEDOT:PSS films, respectively. In contrast to the very smooth and flat surface of the unmodified PEDOT:PSS, the surface roughness as well as the morphological defect within the film, e.g., the cracks, voids and column structures, obviously increase with the increase of the AF dopant, especially when the AF exceeds 20 wt.%. It is difficult to spread the PEDOT:PSS solution with AF dopants over 50 wt.% since the strong ionic interaction among the AF salts will make the solution gel.

In order to identify the role of AF on the fracture structures, TGA analysis was performed on the as-received AF powders to understand its decomposition behavior. As can be seen in Fig. 3(a), the weight of the AF powders decreases approximately as a linear function with the heating time at 80 °C and approaches complete decomposition after 100 min. It is thus clear that the structural fractures of the PEDOT:PSS films as observed in Fig. 2 were mainly created

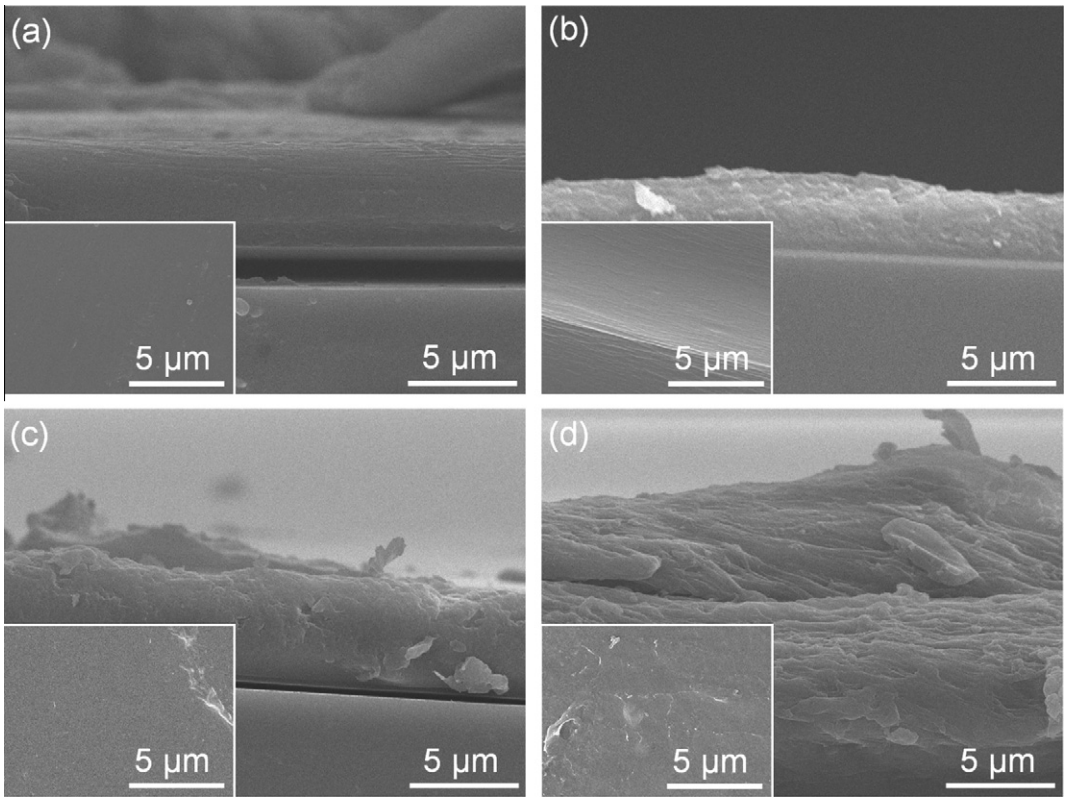

Fig. 2. The cross-section and top-view (inset) SEM images of (a) PH 500, (b) P10, (c) P20, and (d) P50. (e) Image of the close-up of the crack formed during sample preparation.

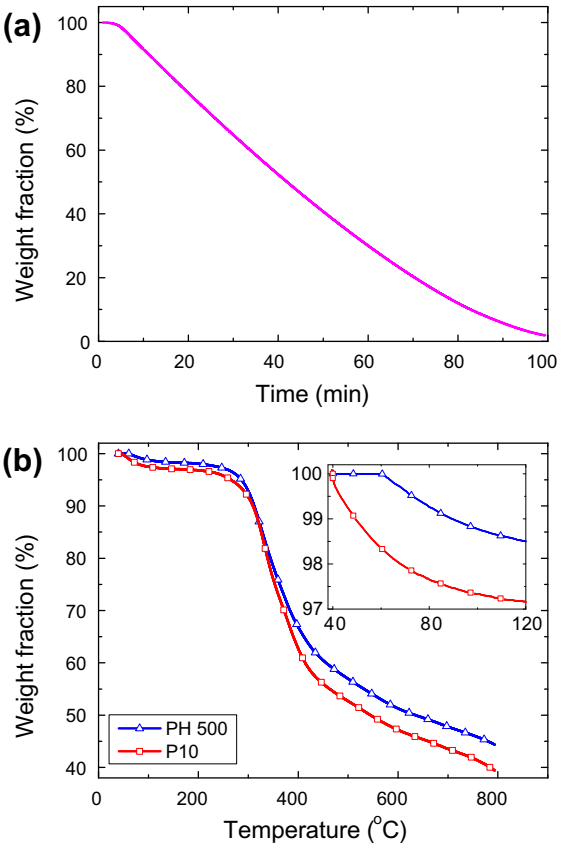

Fig. 3. TGA curves of (a) as-received AF powders and (b) PH 500 and P10.

during the second drying process, i.e., 80 °C for 60 min, due to the violent decomposition of AF at this condition. Because of the lower mechanical strength of the PEDOT:PSS film, the decomposition gas will be released toward the film surface or just trapped in the films. When the three-dimensional pores or channels are open to atmosphere, the inner gas will be exhausted by the gravity of the PEDOT:PSS films to form collapsed two-dimensional interfaces.

Fig. 3(b) is the temperature dependence of the weight loss of PH 500 and P10 from 40 to 800 °C. Basically, the TGA curves for PH 500 and P10 are quite similar to our expectation, since PH 500 is the only main component for both cases. A drastic weight loss of P10 found at the very beginning stage up to ~100 °C should originate from the further decomposing of the residual AF, as discussed above. As can be seen, at 80 °C, i.e., the temperature of the second drying step, the weight loss difference between PH 500 and P10 remains at less than 1.5%, indicating the possible residual level of AF. The adding of AF seems not to affect the thermostability of the PH 500 films. As displayed, the substantial decomposition for both PH 500 and P10 found at ~300 °C is close to that for traditional Polyimide (PI), which is commonly used for flexible substrates in electronic devices. Therefore, the thermostability of the present AF-doped PH 500 film is sufficient for future applications of the soft thermoelectric devices.

Table 1
Seebeck coefficients (S), sheet resistances (R), electrical conductivities (σ), and power factors (P) of the as-received and modified PEDOT:PSS films.

	R (Ω/□)	σ (S/cm)	S (μV/K)	P (μW/mK^2)
PH 500	825.57	1.21	12.4	0.019
DMSO-doped	2.93	524.30	11.6	7.06
P5	21,590	0.11	30.6	0.010
P10	619,100	0.019	220.0	0.092
P10′	323,640	0.036	436.3	0.69

P10′:P10 solution stored at 10 °C for 1 month.

Table 2
Carrier concentrations (n), Hall mobilities (μ_H), and calculated electrical conductivities (σ_H) of the as-received and modified PEDOT:PSS films.

	n (cm^{-3})	μ_H (cm^2/Vs)	σ_H (S/cm)
PH 500	5.5×10^{18}	2.96	2.64
DMSO-doped	1.1×10^{21}	3.81	670
P10	4.3×10^{17}	1.43	0.0984

Table 1 summarizes the measured thermoelectric properties of the as-received and modified PEDOT:PSS films. The most notable changes are that the electrical conductivity of the AF doped film decreases by one to two orders of magnitude compared to the unmodified PH 500. For further evaluation of the electrical conductivity, Hall measurements were carried out and the results confirmed that all the prepared films were hole-type carrier domination. In the p-type semiconductors, the electrical conductivity σ can be expressed by the relationship:

$$\sigma = e\, n\, \mu_H \tag{2}$$

where e, n, and μ_H is the electronic charge, carrier concentration, and Hall mobility, respectively. As can be seen in Table 2, the electrical conductivity of the pristine and modified PEDOT:PSS films obtained from the product of these two competing factor, n and μ_H, is of the same order of magnitude as that measured by 4-point probe method as shown in Table 1, indicating the reliability of the present measurements. Obviously, the largely decreased electrical conductivity of the AF doped PEDOT:PSS film (P10), was mainly caused by the one-order-of-magnitude reduction in the carrier concentration. This probably results from the interaction between the AF molecules and PSS monomers, and thus inhibits the role of the carrier supplier of PSS for PEDOT. Checking the results in Table 2, the Hall mobility shows relatively less variation (<50%) with dopants, either the DMSO or the AF.

In addition to the electrical conductivity, it is noteworthy that the Seebeck coefficient for P10 as displayed in Table 1 is ~20 times higher than that for as-received PH 500 as well as the widely-synthesized DMSO-modified PH 500. Generally, the Seebeck coefficient will be affected, either increasing or decreasing, even with only slight doping, e.g., the DMSO, but will not effectively vary with the doping concentration. It is surprising in the present case that the Seebeck coefficient significantly enhances with the AF doping concentration.

A theoretical derivation of Seebeck coefficient (S) is expressed as [21]:

$$S(T) = \frac{1}{eT}\frac{\int [E_F(T) - E]\delta\sigma(E)dE}{\int \delta\sigma(E)dE} \quad (3)$$

where E_F is the Fermi level and $\delta\sigma(E)$ the differential conductivity at energy E. This equation holds for both band and hopping transport. With the further assumption of unipolar charge carrier transport at one narrow transport level (E_T), Eq. (3) can be written as:

$$S(T) = \frac{E_F(T) - E_T}{eT} \quad (4)$$

The energy difference E_F(T)−E_T is correlated to the carrier concentration as well known [22]. The variation of about one order decrease of the carrier concentration will great increase the $E_F(T)$−E_T, and thus enhance the Seebeck coefficient according to Eq. (4). Similar tendency between the carrier concentration and thermoelectric properties, including the electrical conductivity and the Seebeck coefficient can also be observed in doped organic semiconductors [21].

In addition to the direct evidence of the carrier concentration influence on the electrical conductivity and Seebeck coefficient, here we further consider another phenomenon that might happen in the present AF doped system and affect these two parameters, σ and S. It has been reported that AF can substitute double bonds sites and cut off side groups with the presence of catalysts [19,23,24]. Thus, it is reasonable to consider that the double bonds on PEDOT will be partially damaged by AF. The conjugation length of PEDOT will thus be reduced and the lowered density of states of the conducting bands and valence bands lead to a wider band gap. Martin et al. have experimentally proven the correlation between the conjugation length and the band gap by analyzing UV–Vis spectra of samples with a precisely controlled conjugation length from one oligomer to six oligomers. They found that the UV–Vis absorption energy E_{abs} (eV) were found to be ruled by the following equation derived from Kuhn's electron gas model [25].

$$E_{abs} = V_0 + \left(\frac{h^2}{4mL_0^2} - \frac{V_0}{4}\right)\frac{1}{N + 0.5} \quad (5)$$

where V_0 is the amplitude which corrects the free electron gas model, h the Plank constant, m the mass of the electron, L_0 the unit length of the conjugation, and N the number of conjugated bonds. Since N is much larger than 0.5 in the present case, the absorption energy E_{abs} shows a linear relation with $1/N$. As a result, the blue shift of the UV–Vis peak should increase with the decreasing of conjugation length. The slight decrease of the Hall mobility of P10 as observed in Table 2 might also be correlated to the possible decrease of conjugation length. The UV–Vis spectra of the prepared films shown in Fig. 4 represent a large blue shift for the AF-doped PH 500, which provides reliable evidence of the widening of the band gaps. As previously discussed, the widened band gap should mainly originate from the great decrease of the carrier concentration of the AF doped films.

According to the definition of the power factor, either increased electrical conductivity or especially the Seebeck coefficient is of great importance to enhance the power factor. However, these two parameters generally cannot be increased simultaneously due to the inverse relation to the gap between E_T and E_F of the material, i.e., when the gap becomes wider, a higher Seebeck coefficient can be obtained, whereas a lower electrical conductivity will be presented. This trade-off has also been one of the major problems for all categories of thermoelectric materials. Although the electrical conductivity decreases by two orders of magnitude due to the doping of 10 wt.% AF (P10), the one order of magnitude increase in the Seebeck coefficient leads to an overall one order increase in the power factor, compared with the pristine PH 500. A similar tendency can also be found in the case of P5.

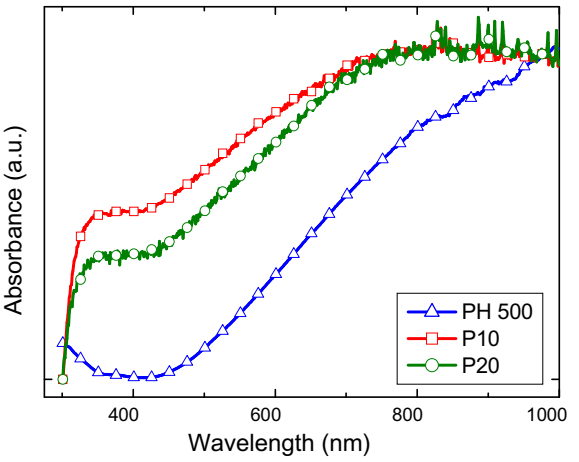

Fig. 4. The normalized UV–Vis absorption spectra of PH 500, P10, and P20.

In order to investigate the AF doping effect on the phonon scattering and to estimate the ZT value, the thermal conductivity of P10′ was measured near the room temperature. The obtained thermal conductivity of 0.18 W/mK is close to that of the PH 500 film with 5% DMSO (0.32 W/mK) [26] and PH 500 pellet with 10% DMSO (0.17 W/mK) [27] been reported. The estimated ZT value of P10′ would thus be 1.1×10^{-3} at room temperature. This result indicates that not only can electrical conductivity modification improve the ZT value, but TE behavior can also be enhanced by modifying the Seebeck coefficient to a comparative value regarding other works.

Another interesting phenomenon is observed that when the prepared AF doped film is stored at lower temperatures (~10 °C) in refrigerator for a period of time, the Seebeck coefficient increases with the storage time. For instance, the Seebeck coefficient of P10 rises from the initial 220 to 436.3 μV/K after 1 month storage. The solution was kept in a refrigerator at all times and only taken out for sample coating. The mechanism of this effect on especially the Seebeck coefficient is not clear so far.

4. Conclusion

In summary, we have successfully incorporated AF into Clevios PH 500 with various concentrations from 5 to 50 wt.% to form continuous films with distinct

thermoelectric properties and microstructures. With the increase of the AF doping, the Seebeck coefficient discernibly varied in a pretty wide range in which a maximum of 436.3 μV/K was found for 10 wt.% AF (P10′), i.e., ~40 times greater in magnitude, compared with 12.4 μV/K for pure PH 500. The greatly increased Seebeck coefficient, as well as the accompanying decreased electrical conductivity, probably originates from the reduction of the conjugation length of PEDOT by AF, as evidenced by the UV–Vis spectra. The best power factor obtained is 0.69 $\mu W/mK^2$, which is one order higher than that of pristine PH 500, but it is still lower than PH 500 blend with 5 wt.% DMSO, due to its lack of electrical conductivity. Nevertheless, this work provides a new procedure to increase the Seebeck coefficient of the polymer by simple blending, which has not previously been reported. In addition, AF also plays an important role in the formation of the closed or open pores and channels by thermal decomposing of AF, as can be seen in SEM images. These nano/micro-defects are considered to effectively scatter phonons and thus to further enhance the thermoelectric performance.

References

[1] D.M. Rowe (Ed.), CRC Handbook of Thermoelectrics, CRC Press, Boca Raton, 1995.

[2] J.P. Fleurial, A. Borshchevsky, T. Caillat, R. Ewell, New materials and devices for thermoelectric applications, Annu. Meet. – Am. Inst. Chem. Eng. 2 (1997) 1080–1085.

[3] J. Wüsten, K. Potje-Kamloth, Organic thermogenerators for energy autarkic systems on flexible substrates, J. Phys. D 41 (2008) 135113.

[4] R.B. Aïch, N. Blouin, A. Bouchard, M. Leclerc, Electrical and thermoelectric properties of poly(2,7-carbazole) derivatives, Chem. Mater. 21 (2009) 751–757.

[5] H.J. Goldsmid, R.W. Douglas, The use of semiconductors in thermoelectric refrigeration, Br. J. Appl. Phys. 5 (1954) 386–390.

[6] C.J. Vineis, A. Shakouri, A. Majumdar, M.G. Kanatzidis, Nanostructured thermoelectrics: big efficiency gains from small features, Adv. Mater. 22 (2010) 3970–3980.

[7] F. Yakuphanoglu, B.F. Şenkal, A. Saraç, Electrical conductivity, thermoelectric power, and optical properties of organo-soluble polyaniline organic semiconductors, J. Electron. Mater. 37 (2008) 930–934.

[8] F. Yakuphanoglu, B.F. Şenkal, Electronic and thermoelectric properties of polyaniline organic semiconductor and electrical characterization of Al/PANI MIS diode, J. Phys. Chem. C 111 (2007) 1840–1846.

[9] K. Bender, E. Gogu, I. Hennig, D. Schweitzer, H. Müenstedt, Electric conductivity and thermoelectric power of various polypyroles, Synth. Met. 18 (1987) 85–88.

[10] J.Y. Kim, J.H. Jung, D.E. Lee, J. Joo, Enhancement of electrical conductivity of poly(3,4-ethylenedioxythiophene)/poly(4-styrenesulfonate) by a change of solvents, Synth. Met. 126 (2002) 311–316.

[11] K.C. Chang, M.S. Jeng, C.C. Yang, Y.W. Chou, S.K. Wu, M.A. Thomas, Y.C. Peng, The thermoelectric performance of poly(3,4-ethylenedioxythiophene)/poly(4-styrenesulfonate) thin films, J. Electron. Mater. 38 (2009) 1182–1188.

[12] B. Zhang, J. Sun, H.E. Katz, F. Fang, R.L. Opila, Promising thermoelectric properties of commercial PEDOT:PSS materials and their Bi_2Te_3 powder composites, ACS Appl. Mater. Inter. 2 (2010) 3170–3178.

[13] N. Toshima, H. Yan, M. Kajita, Y. Honda, N. Ohno, Novel synthesis of polyaniline using iron(III) catalyst and ozone, Chem. Lett. 29 (2000) 1428–1429.

[14] H. Yan, N. Sada, N. Toshima, Thermal transporting properties of electrically conductive polyaniline films as organic thermoelectric materials, J. Therm. Anal. Calorim. 69 (2002) 881–887.

[15] Y. Hiroshige, M. Ookawa, N. Toshima, High thermoelectric performance of poly(2,5-dimethoxyphenylenevinylene) and its derivatives, Synth. Met. 156 (2006) 1341–1347.

[16] Y. Hiroshige, M. Ookawa, N. Toshima, Thermoelectric figure-of-merit of iodine-doped copolymer of phenylenevinylene with dialkoxyphenylenevinylene, Synth. Met. 157 (2007) 467–474.

[17] O.F. Yilmaz, S. Chaudhary, M. Ozkan, A hybrid organic–inorganic electrode for enhanced charge injection or collection in organic optoelectronic devices, Nanotechnology 17 (2006) 3662–3667.

[18] K.C. See, J.P. Feser, C.E. Chen, A. Majumdar, J.J. Urban, R.A. Segalman, Water-processable polymer–nanocrystal hybrids for thermoelectrics, Nano Lett. 10 (2010) 4664–4667.

[19] N.C. Ganguly, S. Dutta, M. Datta, Mild and efficient deprotection of allyl ethers of phenols and hydroxycoumarins using a palladium on charcoal catalyst and ammonium formate, Tetrahedron Lett. 47 (2006) 5807–5810.

[20] A. Brann, On the preparation of formamide, J. Am. Chem. Soc. 40 (1918) 793–796.

[21] A. Nollau, M. Pfeiffer, T. Fritz, K. Leo, Controlled n-type doping of a molecular organic semiconductor: naphthalenetetracarboxylic diabhydride (NTCDA) doped with bis(ethylenedithio)–tetrathiafulvalene (BEDT–TTF), J. Appl. Phys. 87 (2000) 4340–4343.

[22] S.M. Sze, Kwok K. Ng, Physics of Semiconductor Devices, third ed., John Wiley and Sons, America, 2007 (Section 1.4).

[23] S. Gowda, K. Abiraj, D.C. Gowda, Reductive cleavage of azo compounds catalyzed by commercial zinc dust using ammonium formate or formic acid, Tetrahedron Lett. 43 (2002) 1329–1331.

[24] B.C. Ranu, A. Sarkar, Regio- and stereoselective hydrogenation of conjugated carbonyl compounds via palladium assisted hydrogen transfer by ammonium formate, Tetrahedron Lett. 35 (1994) 8649–8650.

[25] R.E. Martin, U. Gubler, C. Boudon, V. Gramlich, C. Bosshard, J.P. Gisselbrecht, P. Günter, M. Gross, F. Diederich, Poly(triacetylene) oligomers: characterization, and estimation of the effective conjugation length by electrochemical, UV/Vis, and nonlinear optical methods, Chem. Eur. J. 3 (1997) 1505–1512.

[26] M. Scholdt, H. Do, J. Lang, A. Gall, A. Colsmann, U. Lemmer, J.D. Koenig, M. Winkler, H. Boettner, Organic semiconductors for thermoelectric applications, J. Electron. Mater. 39 (2010) 1589–1592.

[27] F.X. Jiang, J.K. Xu, B.Y. Lu, Y. Xie, R.J. Huang, L.F. Li, Thermoelectric performance of poly(3,4-ethylenedioxythiophene):poly(styrenesulfonate), Chin. Phys. Lett. 25 (2008) 2202–2205.

formation of a coffee ring along the initial contact line of the droplet which leads to a non-uniform morphology of the surface and a sparse active layer matrix [7]. This consequently leads to poorly performing solar cells since it prevents the escalating and elongating of P3HT crystals which are crucial for high efficiency, as proven by the improvements made by the thermal annealing process. Therefore, some research groups have tried new ways to avoid these inevitable problems. Green et al. reported spray deposited P3HT:PCBM films from various organic solvents with different boiling points [8]. Recently, Park et al. showed that the fabrication of sprayed solvent over-layer method gives highly efficient devices [9]. Furthermore, Susanna et al. presented high power conversion efficient solar cell by optimizing the parameters of the spray system, especially using a co-solvent mixture [10].

In this work, we specially investigate the film formation, surface topography and the morphology of active layer through additional solvent spray coating with various solvents, such as chlorobenzene (CB), chloroform (CF), ortho-dichlorobenzene (DCB) and ortho-dichlorobenzene/mesitylene (DCB/Mes). Furthermore, we studied the causes behind low fill factors (*FF*) and short circuit current-densities (J_{sc}) that occur in conventionally spray coated films. This additional solvent spraying immediately follows the active layer deposition by spray coating of mixed solution of P3HT:PCBM in CB that followed the spray coating of the electron-blocking layer of poly (3,4-ethylenedioxy thiophene):poly(styrene sulfonate) (PEDOT:PSS). We also investigated the combination of this additional solvent spraying process with post-annealing one so as to improve the phase separation of bulk heterojunction.

2. Experimental

We prepared thin films and solar cells based on a 1:0.8 mixture of P3HT (Rieke Metal) and (6, 6)-phenyl-PCBM (Nano C) dissolved in CB using both spray coating and spin-coating processes. Indium-tin-oxide (ITO) coated glass substrates (Geomatec, 5 Ω/cm^2) were first patterned by etching and then cleaned thoroughly with a sequence of solvents: detergent, deionized water, acetone and isopropanol, for 10 min each in an ultrasonic bath. The cleaned substrates were purified further by oxygen plasma treatment with oxygen for 10 min. The substrates were then spin coated with a 0.45 μm filtered PEDOT:PSS solution (Clevios P), purchased from HC Starck, at 4000 rpm for 60 s to produce a 40 nm thick layer. The substrates were subsequently heated on a hotplate in air at 200 °C for 10 min to remove excess water. The active layer containing a mixture of P3HT and PCBM was prepared with a concentration of 22.5 mg/ml stirred in ultrasonic cleaner at 50 °C for 2 h. Then, for the spray coating process, the airbrush was powered by N_2 gas at 70 psi, a relatively low pressure that ensures fine atomization and prevents blowing off the droplets already deposited on the substrate. The distance of the airbrush from the substrate was 10 cm. For the additional spray coating, pristine CB, CF, DCB and DCB/Mes were sprayed onto the active layers for 1 min at a rate of about 100 μl/min. The wet solvent on the active layer was evaporated for about 5 s. Additional control of the deposition conditions was achieved by varying the solution flux and the speed of the airbrush relative to the substrate.

Thermal annealing was performed at 150 °C in a glove box. Then after titanium tetraisopropoxide in ethanol (10 μl/3 ml) was spin coated at 4000 rpm as precursor of TiO_x layer, it was left at room temperature for 20 min to hydrolyze and form TiO_x. Aluminum (100 nm) top electrodes were deposited by thermal evaporation in ultra-high vacuum 5×10^{-3} Pa. The photovoltaic characteristics were measured under nitrogen atmosphere using an Agilent 4156C parameter analyzer under AM1.5G (100 mW/cm^2) simulated illumination using a solar simulator with a 1000 W Xenon arc lamp.

UV–visible absorption spectra were obtained using a Shimadzu UV-1601PC UV–visible spectrophotometer. Thin polymer films were deposited onto previously cleaned quartz slides with the same settings used for the production of solar cells.

The two-dimensional local characteristics of OSCs were obtained by laser beam induced current (LBIC), which was uniquely equipped to produce quantitative maps of local quantum efficiency with relative ease. To investigate the effect of the additional solvent sprayed on the morphology of the active layer, X-ray diffraction (XRD) and surface profiler were used. The morphology of the active layer was observed by transmission electron microscopy (TEM) (JEOL, 2000FX).

3. Results and discussion

The device performance of spray coated films was investigated based on the common device configuration: glass-ITO/PEDOT:PSS/P3HT-PCBM/additional pure solvent/TiO_x/Al. Because single droplets are deposited by the nitrogen gas pressure on the substrate, the surface of the active layer is more irregular compared to the film of spin-coated devices. The film is formed by the spreading of droplets and the combining of adjacent droplets with the vaporization of the organic solvents. The film morphology is not only affected by the characteristic of solution such as vapor pressure, boiling point, surface tension but also the flux of the droplets and ambient condition. If the droplets are not sprayed at a high solution flow rate or a solvent with very low vapor pressure is not used, the independent droplets are accumulated rather than interconnected with each other.

The images of surface profiler after additionally spray coating various solvents are presented in Fig. 1. Due to residues and pinholes, the scale bar of Fig. 1(b) and (c) range widely from 1 μm to 2 μm. The surface profile of both however indicates that there is no remarkable change in the film when compared to the film in Fig. 1(a). However, the surface topography of Fig. 1(d) and (e) indicates significant differences in the film formation. The second spray deposition redissolves the sprayed active layer and some dissolved droplets merge to form a larger one more easily. The difference in the surface film forming dynamics is attributed to low vapor pressure of DCB. In case we spray excess quantity of DCB solvent, all droplets are redissolved

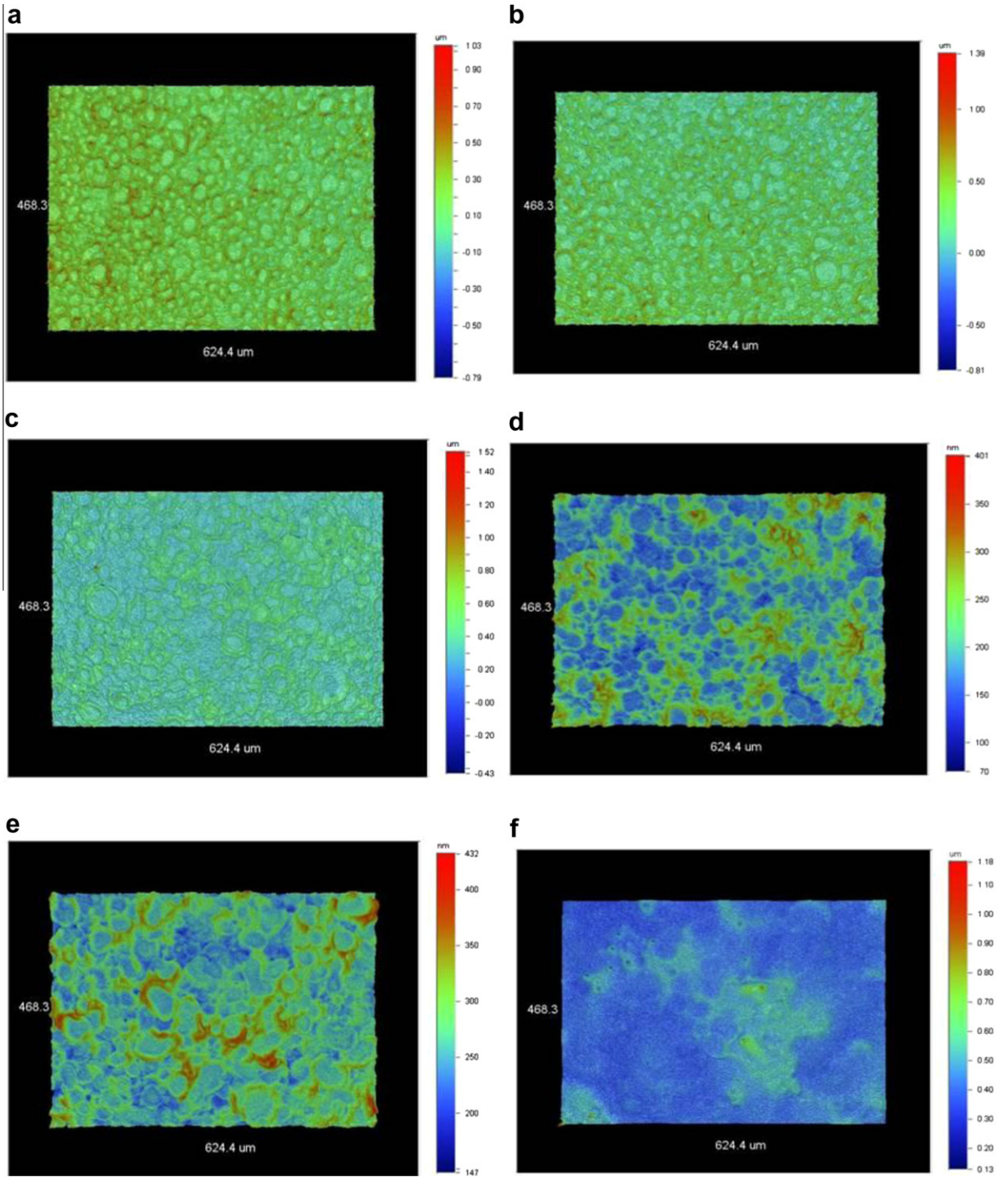

Fig. 1. Surface profiles representing the surface topographies of glass-ITO/PEDOT:PSS/P3HT-PCBM/additional solvent coating. Each device was fabricated by (a) without any solvent (b) CB (c) CF (d) DCB/Mes (e) DCB (F) excess DCB. Note that the scale bars of the color indexes for each deivce were different one another.

and form three distinct regions; partly undissolved region, entirely dissolved region and residue region. If we can select the photoactive area to examine the efficiency, we would expect that the performance is higher than the spin coated one occasionally (see Table 1), taking into account the solvent annealing effect and good roughness. However, excess solvent coated device is not reproducible and compatible for large area cell.

Nanomorphological change achieved by additional solvent spray was reflected in the performance enhancement

Table 1
The device performance and characteristic of glass-ITO/PEDOT:PSS/P3HT-PCBM/various solvent spray coating/TiO_x/Al.

Description	E_{ff} (%)	J_{sc} (mA/cm^2)	V_{oc} (V)	FF	R_s (Ω cm^2)	R_{sh} (KΩ cm^2)	Rms (nm)	Active layer thickness (nm)
Ref.(w/o)	0.97	4.34	0.51	0.23	22.28	0.294	59.1	171
CB	1.51	5.13	0.57	0.51	16.30	0.493	128.0	298
CF	1.36	5.19	0.55	0.48	20.32	0.381	60.9	274
DCB + mesitylene	1.81	6.83	0.59	0.45	14.44	0.226	39.1	231
DCB	1.95	6.70	0.58	0.50	12.12	0.315	31.1	215
DCB (excess)	2.44	6.75	0.60	0.61	7.01	0.771	51.3	173
Spin coated (air)	2.03	5.87	0.62	0.56	10.19	0.610	9.8	109

in characteristic properties of OSCs as summarized in Table 1. The device fabricated from additionally sprayed with CB has V_{oc} = 0.57, J_{sc} = 5.13 mA/cm^2, FF = 0.51 and E_{ff} = 1.51%. Notably, the J–V characteristic of the device sprayed with DCB (V_{oc} = 0.58, J_{sc} = 6.67 mA/cm^2, FF = 0.50 and E_{ff} = 1.95%) are similar to the performance of spin coated devices in air. The value of RMS and thickness of active layer represent that CB and CF solvent just add up, whereas DCB and DCB/Mes solvent dissolve and reconstruct the previous layer.

Based on this result, we selected DCB solvent for additional solvent spray and continue to investigate the change of morphology in four cases, (a) CB solution of P3HT-PCBM spray coating (ref.) (b) ref./annealed (c) ref./DCB solvent spraying (d) ref./DCB solvent spraying/annealed, as shown in Fig. 2. Comparing Fig. 2(a) and (c), it is evident that the numerous pinholes and the thick edge of the droplet partially disappear after the additional solvent spraying. This can be due to the dissolution and interconnection of isolated active layer droplets in the presence of DCB droplets. This is confirmed by the significant reduction of the surface roughness in rms of the devices in Fig. 2(a) and (c), which have values of 68.22 nm and 34.84 nm, respectively. However, it can be said that the morphology of surface in micrometer scale does not seem to be affected by thermal annealing at 150 °C as there are no remarkable change between Fig. 2(a)–(d). The computed surface roughness in rms only differs slightly between pre- and post-annealing for conventionally sprayed (68.2 nm and 63.4 nm, respectively) and additionally solvent sprayed (34.8 nm and 28.8 nm, respectively) devices. Therefore, we suggest that the ridge-like features remain in surface unless physical change such as melting occurs in the

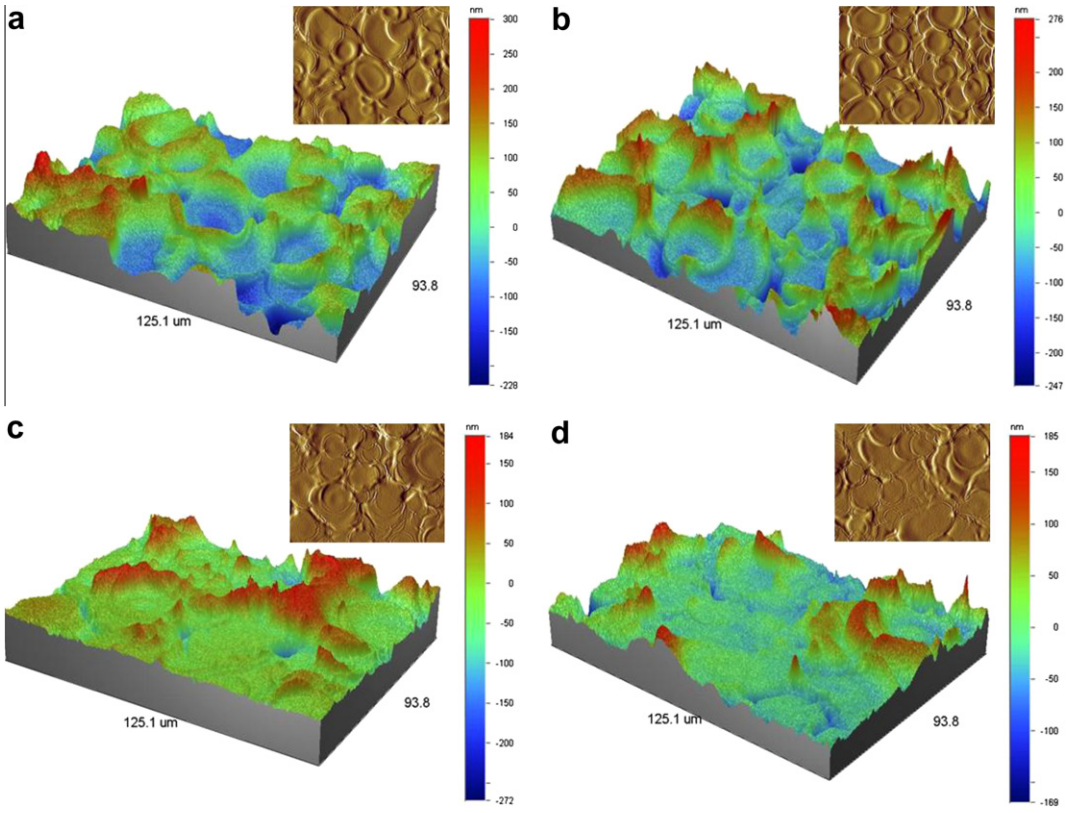

Fig. 2. Surface profiles representing the surface topographies of glass-ITO/PEDOT:PSS/P3HT-PCBM/solvent coating with or without annealing. Each device was fabricated by (a) CB solution of P3HT-PCBM spray coating (ref.) (b) ref./annealed (c) ref./DCB solvent spraying (d) ref./DCB solvent spraying/annealed.

boundary. Nevertheless, it was reported that a high surface roughness does not really connote poor device performance for spray coating [11]. However when the surface roughness also reflects the distribution and physical change of the droplets inside the layer as above, the measured rms of the surface is a good criterion for estimating the final device performance.

The images of LBIC also show distinctively spatial and non-uniform distribution of droplets in conventional spray coated device. The image of Fig. 3(a) proves that pinholes are largely present on the surface of the conventionally sprayed device and was distributed over a large area, as indicated by the irregular and yellowish color. As for the device with additional solvent spraying in Fig. 3(b), a more homogenous red coloring is observed, which indicates higher current density generated in the light. The dark red color in Fig. 3(b) is consistent with better result of the *J–V* characteristic curves, as mentioned below.

When the nanoscale morphology of the active layer is examined by TEM, in Fig. 4(a) the film of the conventionally sprayed device shows aggregation made of sparse dots. This is largely due to atomized droplets from the nozzle during the spray coating process that have relatively lower opportunities to form donor–acceptor domains compared to droplets in a successive coating method such as spin coating. The insufficient donor–acceptor interpenetrating networks formed in spray coating cannot efficiently induce charge separation and transport. Moreover, though phase separation has occurred in thermal annealing, the effect of heat treatment would be restricted because the droplet is physically isolated each other, as shown in Fig. 4(b). However, the film with the additionally sprayed DCB exhibits a different morphology, as shown in Fig. 4(c). White, hair-like nanofibers increase conspicuously so that the total image becomes blurred. This morphological characteristic is more pronounced, that is, light and darkness is more contrasted as phase separation is accelerated, after thermal annealing (see Fig. 4(d)).

To find out how the additional sprayed solvent works for enhancing the crystallization of P3HT, we examined the XRD pattern of each device in Fig. 5(a). The effect of the rate of spray coating to P3HT crystallization was also studied in Fig. 5(b). Usually, the rate of spray coating is controlled by the carrier gas pressure. For the slow spraying process used for the construction of the devices in Fig. 5(b), the rate is that of the conventional spray method, wherein the carrier gas pressure is 70 psi. This carrier gas pressure is the minimum that can be used such that spray coating could still be done in this experiment. Meanwhile, the use of the fast spray coating rate (300 psi) kept the P3HT:PCBM layer wet and slowed down the drying time brought a similar effect of solvent annealing [4]. This may be the cause why the crystallite size of P3HT for fast sprayed device is larger as compared to the slow sprayed device, as shown in Fig. 5(b). Interestingly, the additional solvent sprayed device in Fig. 5(a) has a comparable high peak to the fast sprayed one. This indicates that the additional solvent spray process could also induce the solvent annealing effect. The difference however between the fast spraying and the additional solvent spraying is that with the additional spray coating process, elimination of most of the pinholes and thick edges of the active layer is also possible due to the dissolution (viz. dissolving) of the previously sprayed droplets. Moreover, the thickness and roughness of the active layer is more reproducible and easier to control through the additional spray coating process. The normalized XRD pattern shows the effect of the additional solvent coating at the peak of P3HT crystalline with diffraction angle at $2\theta = 5.6°$, which corresponds to (100) packing. As shown in Fig. 5(a) devices with additional solvent sprayed shows sharp and intensive peak at $2\theta = 5.6°$, while the conventional device exhibits a relatively broader and lower peak. Although we can expect that the fast sprayed device has higher efficiency, the practical application to the fabrication of commercial devices would be difficult because of low reproducibility and tough handling. Therefore, additional solvent coating in conjunction with slow-speed spray coating fabrication can be a good alternative. Since this method promotes the reduction of unavoidable disadvantages in the spray coating process by prolonging the drying time and promoting the reorganization of the matrix in the P3HT:PCBM layer. This is con-

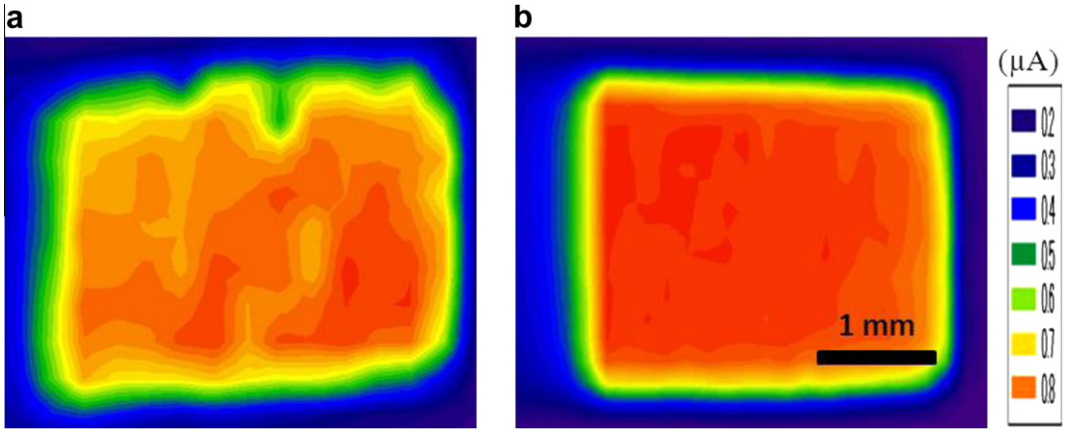

Fig. 3. LBIC (5 mW He-Ne laser 632 nm irradiation with 0.3 mm beam width and 0.2 mm scan step) images of glass-ITO/PEDOT:PSS/P3HT-PCBM fabricated through CB solution of P3HT-PCBM spray coating followed by (a) annealing, (b) DCB solvent spraying/annealing.

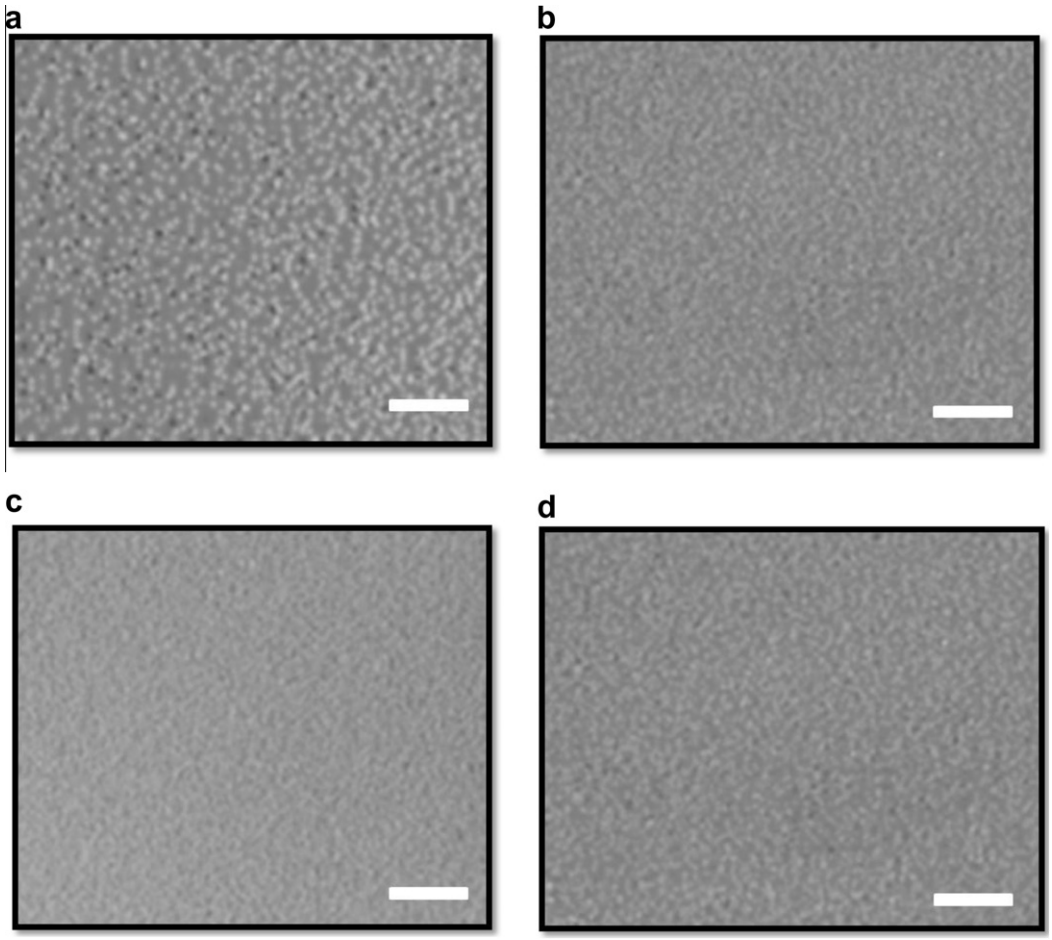

Fig. 4. TEM images of glass-ITO/PEDOT:PSS/P3HT-PCBM/solvent spray coating with or without annealing/TiO_x/Al as follows: (a) CB solution of P3HT-PCBM spray coating (ref.), (b) ref./annealed, (c) ref./DCB solvent spraying, (d) ref./DCB solvent spraying/annealed. The conditions of thermal annealing were performed at 150 °C for 30 min. The scale bar is 10 nm.

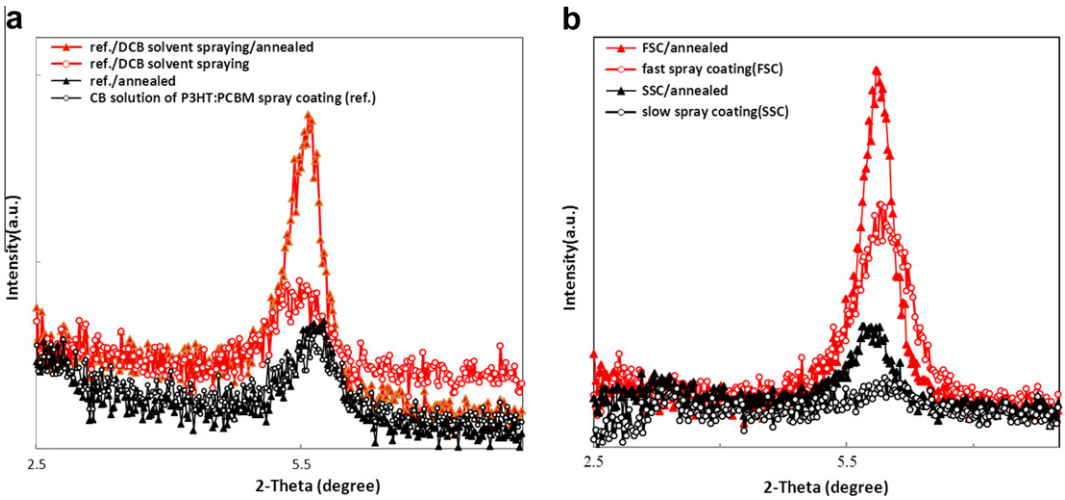

Fig. 5. Normalized XRD patterns of glass-ITO/PEDOT:PSS/P3HT-PCBM/solvent spray coating with or without annealing/TiO_x/Al fabricated by (a) CB spray coating (ref.), ref./annealed, ref./DCB solvent spraying, ref./DCB solvent spraying/annealed, (b) fast spray coating(FSC), FSC/annealed, slow spray coating(SSC), SSC/annealed.

Table 2
The comparison of P3HT crystallite size in each device of glass-ITO/PEDOT:PSS/P3HT-PCBM/solvent spray coating with or without annealing.

	CB solution of P3HT:PCBM spray coating(Ref.)	Ref./ annealed	Ref./DCB solvent spraying	Ref./DCB solvent spraying/annealed	SSC[a]	SSC/ annealed	FSC[b]	FSC/ annealed
Crystallite size (nm)	7.92	11.37	10.80	14.67	7.21	10.73	10.69	18.33

[a] SSC: slow spray coating.
[b] FSC: fast spray coating.

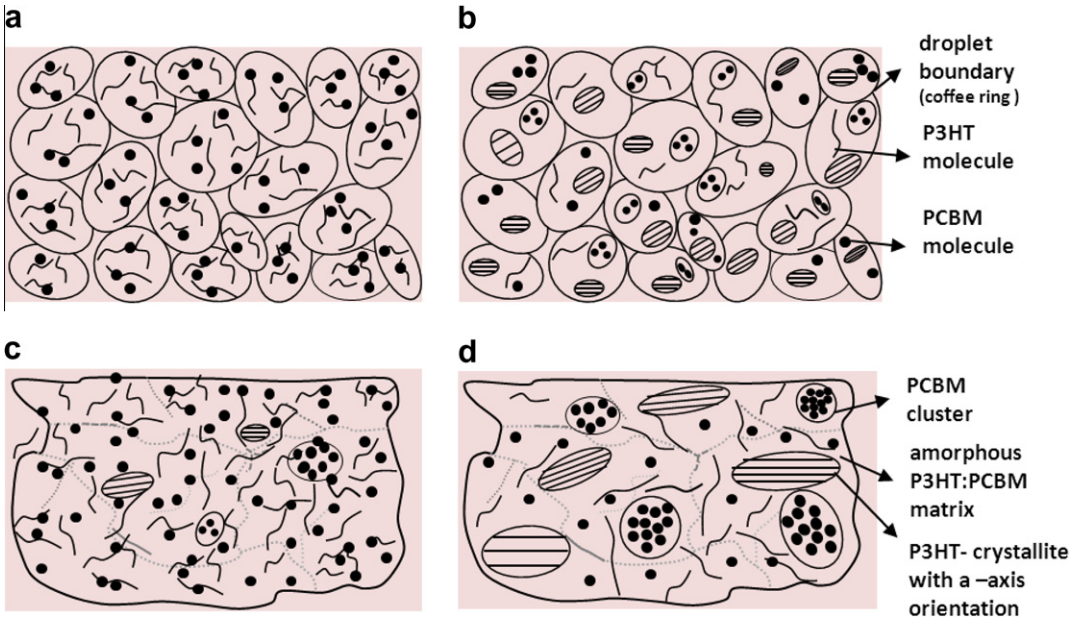

Fig. 6. Schematic picture showing the microscopic change of active layer in the process of additional solvent spraying and thermal annealing. Each device stands for (a) CB solution of P3HT-PCBM spray coating (ref.) (b) ref./annealed (c) ref./DCB solvent spraying (d) ref./DCB solvent spraying/annealed.

firmed by the measured crystallite size as summarized in Table 2. The mean size of the polymer crystallite, L, was estimated from Bragg's law and Scherrer's relation [12]. The crystallite size of P3HT in a conventionally spray coated device changed from 7.92 nm to 11.37 nm after thermal annealing. On the other hand, the crystallite size has almost doubled, L = 14.67 nm, after the additional solvent spray process. The enhancement probably result from the reorganizing P3HT:PCBM matrix with the long drying process.

On the basis of the result above, we can predict a structural change upon additional solvent spraying and thermal annealing in this experiment. Upon thermal annealing, the V_{oc} was found to decrease, while both the J_{sc} and the FF increased significantly. This phenomenon is attributed mainly to an enhancement of the charge-carrier transport, by a larger hole mobility, a reduced dispersivity, and a reduced recombination kinetics [13–16]. X-ray investigations allowed the development of a microscopic picture of the annealing process, as depicted in Fig. 6. This macroscopic representation of the active layer before and after the spray coating and annealing process was developed from the spin-coating model presented in Ref. [12]. Several detailed morphological studies revealed that the organization of the P3HT:PCBM is modified upon annealing [13,17,18], with fibrillar-like P3HT crystals embedded in a matrix believed to comprise mostly of PCBM nanocrystals and amorphous P3HT[12]. Fig. 6(a) and (b) illustrates the process of a typical enhancement of the external quantum efficiency (EQE) upon thermal annealing in a conventional device. However, we can forecast that the morphological limitation in a spray coated active layer like isolated droplets holds back reorganization of the P3HT:PCBM and eventually blocks the enhancement upon thermal annealing in Fig. 6(b). This is because of the coffee ring effect [7] wherein a thick boundary effectively binds every droplet tightly. When additional solvent droplets with low vapor pressure such as DCB are sprayed on an active layer, the solvent enter into the space of previously deposited droplets, as shown in Fig. 6(c). Upon contact, the solvent droplets immediately dissolve the dried droplets and the thick boundary, filling up the gap between them. Then, two droplets start to connect to form a larger droplet. The repetitive recombination of droplets allows for the formation of semi-crystalline lamellar morphologies with higher order architectures. That is, by taking the additional solvent spray coating process, solvent annealing effect can be obtained by controlling the total time of spraying and flow rate of sprayed droplets. In addition, this

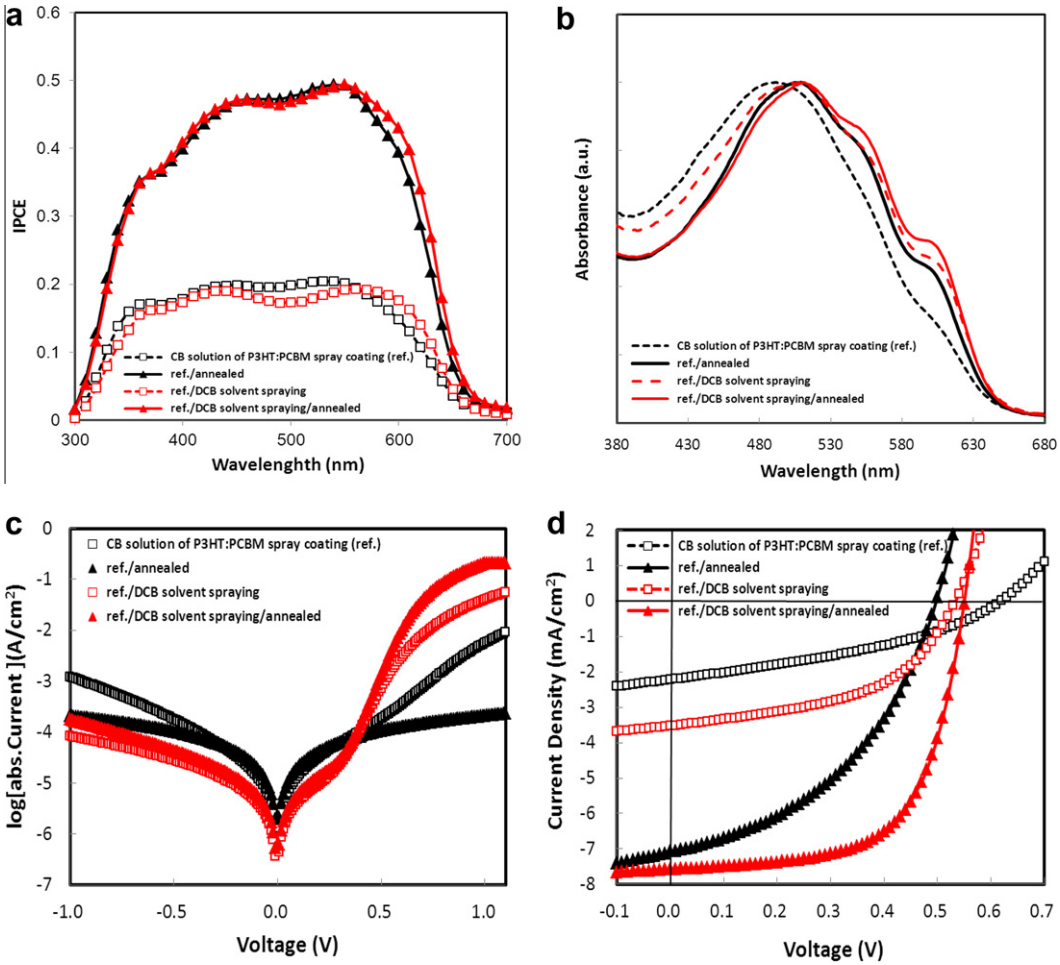

Fig. 7. (a) the corresponding *IPCE* spectra (b) UV–vis spectra (c) dark current (d) *J–V* curve of OSCs of glass-ITO/PEDOT:PSS/P3HT-PCBM/solvent spray coating with or without annealing/TiO_x/Al (100 mW/cm^2, AM 1.5G) fabricated by the spray coating.

solvent annealing effect provides well-developed morphology to maximize the effect of thermal annealing, such that PCBM nanocrystals and amorphous P3HT have a higher chance to connect and reorganize in a matrix. In the cases that the amount of additional solvent and spray time is not sufficient, the boundary between droplets is not perfectly dissolved, as depicted in Fig. 6(c) and (d).

Fig. 7(a) shows characteristics of the incident photon-to-current efficiency (IPCE) curves, for devices with additional solvent spraying. It is found that devices with additional solvent spraying has the maximum IPCE at 560 nm, broader peak above 600 nm wavelength compared to an untreated one. It is interesting that the current density calculated by the integration of the IPCE graph is not much different between the device with and without the additional solvent spraying, despite the considerable difference in efficiency, as shown in Fig. 7(d). The IPCE result indicates that the majority of enhancement of efficiency results from charge-carrier transport and the balance between hole and electron mobility. The effect of additional solvent spraying on P3HT:PCBM layer is also observed in the obtained UV–vis spectra, as shown in Fig. 7(b). For P3HT:PCBM films, the solvent annealed films have the most prominent vibronic features, indicating strong interchain–interlayer interactions among the P3HT chains as well as good polymer ordering in the blend films [19–22]. The quick removal of the solvent like in spray coating favors a uniform P3HT:PCBM distribution and prevents the formation of highly ordered lamella by disrupting the interchain interactions between P3HT chains. Since the thickness of each active layer was controlled to be the same at 230 nm, the characteristically vibronic absorption shoulder at 600 nm originates from the enhancement of crystallinity of P3HT. The vibronic shoulder of the additionally solvent sprayed active layer, without thermal annealing, shows a peak similar to that of a conventional device with thermal annealing. It means that the additional solvent spraying contribute to enhancement of crystallinity. It is also assumed that the additional solvent coating induces improvement of photovoltaic characteristic somewhat, although it is not as remarkable as thermal annealing.

The notable result of additional solvent spraying process is revealed in the *J–V* characteristic curves as shown in Fig. 7(d). It shows the optimal device performance is obtained upon annealing at 150 °C for 30 min, with 3.06% power conversion efficiency (PCE), which is twice the PCE

of a conventionally sprayed device (1.49%). The main reason for the higher PCE of the additional solvent spray coated OSC is slightly increased V_{oc} and higher *FF*. Although the factors affecting *FF* have not been completely identified yet, it has generally been accepted that *FF* is derived from the morphology of the active layer, charge-carrier transport, the balance between hole and electron mobility, and the interface of layers in OSC [23]. The particular distinguishable feature is that the shunt resistance (R_{sh}) increases after the additional solvent spraying, as shown in Fig. 7(c). Considering that the R_{sh} depends on the internal condition of layer, we can expect that the additional solvent spraying induce improvement of the morphology of active layer by delaying drying time while solvent droplets penetrate into previous droplets of active layer and allow for redissolution and diffusion.

4. Conclusions

We have investigated the film formation, surface topography and the morphology of active layer of OSCs through spray coating with various additional solvent. Since the additional solvent spraying process, especially with DCB, is accompanied by a slow drying process and the reorganization of the P3HT:PCBM matrix, it effectively induces a larger crystallite of P3HT and helps overcome the non-uniform morphology of the matrix. All of the morphological changes in a P3HT:PCBM system after this process and subsequent thermal annealing resulted in improvement of photon absorption, better exciton dissociation, and more efficient and balanced transportation of free charges to the electrodes, reflected in higher values of *FF* and J_{sc}. All of this therefore corresponds to better overall efficiencies for corresponding solar cell devices. The additional spray coating of DCB solvent resulted in the doubling of the performance, compared to conventionally sprayed devices. In conclusion, this additional solvent spraying is promising as an auxiliary method to overcome some inevitable hindrances of spray coating. In addition, this simple method can be applied to other coating method such as an inkjet printing, which has relatively similar surface and morphology.

Acknowledgements

The authors are indebted to Prof. Yoshinobu Tsujii of the Institute of Chemistry, Kyoto University for using the surface profiler. They are also obliged to Dr. Tetsuya Ogawa of Kyoto University and Dr. Hiroyuki Nomoto of Kumamoto University for their kind guidance on the TEM observation. This work is partially supported by the New Energy and Industrial Technology Development Organization (NEDO) of the Ministry of Economy, Trade, and Industry (METI), Core Research of Evolutional Science & Technology Agency (CREST) from Japan Science Technology Agency (JST), and the Global Center of Excellence (GCOE) Program of Kyoto University from the Ministry of Education, Culture, Sports, Science and Technology in Japan (MEXT).

References

[1] S.E. Shaheen, R. Radspinner, N. Peyghambaria, G.E. Jabbour, Appl. Phys. Lett. 79 (2001) 2996.
[2] P. Schilinsky, C. Waldauf, C.J. Brabec, Adv. Funct. Mater. 16 (2006) 1669.
[3] C.N. Hoth, S.A. Choulis, P. Schilinsky, C.J. Brabec, Adv. Mater. 19 (2007) 3973.
[4] B.-K. Yu, D. Vak, J. Jo, S.-I. Na, S.-S. Kim, M.-K. Kim, D.-Y. Kim, IEEE J. Select. Topics Quantum Electron. 16 (2010) 1838.
[5] D. Vak, S.-S. Kim, J. Jo, S.-H. Oh, S.-I. Na, J. Kim, D.-Y. Kim, Appl. Phys. Lett. 91 (2007) 081102.
[6] T. Matsutani, K. Yamamoto, J. Phys.: Conf. Ser. 272 (2011) 012015.
[7] R.D. Deegan, O. Bakajin, T.F. Dupont, G. Huber, S.R. Nagel, T.A. Witten, Nature 389 (1997) 827.
[8] R. Green, A. Morfa, A.J. Ferguson, N. Kopidakis, G. Rumbles, S.E. Shaheen, Appl. Phys. Lett. 92 (2008) 033301.
[9] H.-Y. Park, K. Kim, D.Y. Kim, S.-K. Choi, S.M. Jo, S.-Y. Jang, J. Mater. Chem. 21 (2011) 4457.
[10] G. Susanna, L. Salamandra, T.M. Brown, A. Reale, Sol. Energy Mater. Sol. 95 (2011) 1775.
[11] L.-M. Chen, Z. Hong, W.L. Kwan, C.-H. Lu, Y.-F. Lai, B. Lei, C.-P. Liu, Y. Yang, ACS Nano 4 (2010) 4744.
[12] T. Erb, U. Zhokhavets, G. Gobsch, S. Raleva, B. Stühn, P. Schilinsky, C. Waldauf, C.J. Brabec, Adv. Funct. Mater. 15 (2005) 1193.
[13] T.J. Savenije, J.E. Kroeze, X. Yang, J. Loos, Adv. Funct. Mater. 15 (2005) 1260.
[14] V.D. Mihailetchi, H.X. Xie, B. de Boer, L.J.A. Koster, P.W.M. Blom, Adv. Funct. Mater. 16 (2006) 699.
[15] J. Huang, G. Li, Y. Yang, Appl. Phys. Lett. 87 (2005) 112105.
[16] A. Pivrikas, G. Juška, A. Mozer, M. Scharber, K. Arlauskas, N. Sariciftci, H. Stubb, R. Österbacka, Phys. Rev. Lett. 94 (2005) 176806.
[17] X. Yang, J. Loos, S.C. Veenstra, W.J.H. Verhees, M.M. Wienk, J.M. Kroon, M.A.J. Michels, R.A.J. Janssen, Nano Lett. 5 (2005) 579.
[18] W. Ma, C. Yang, X. Gong, K. Lee, A.J. Heeger, Adv. Funct. Mater. 15 (2005) 1617.
[19] R.D. McCullough, S. Tristram-Nagle, S.P. Williams, R.D. Lowe, M. Jayaraman, J. Am. Chem. Soc. 15 (1993) 4910.
[20] T.-A. Chen, X. Wu, R.D. Rieke, J. Am. Chem. Soc. 117 (1995) 233.
[21] H. Sirringhaus, Science 280 (1998) 1741.
[22] H. Sirringhaus, P.J. Brown, R.H. Friend, M.M. Nielsen, K. Bechgaard, B.M.W. Langeveld-Voss, A.J.H. Spiering, R.A.J. Janssen, E.W. Meijer, P. Herwig, D.M. de Leeuw, Nature 401 (1999) 685.
[23] M.-S. Kim, B.-G. Kim, J. Kim, ACS Appl. Mater. Interfaces 1 (2009) 1264.

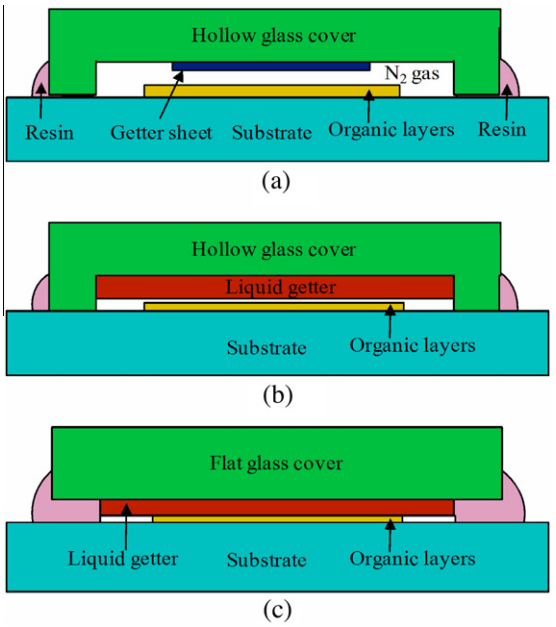

Fig. 1. Schematic view of OLED structures based on (a) conventional glass encapsulation, (b) getter-filled hollow glass (GFHG) encapsulation, and (c) getter-coated flat glass (GCFG) encapsulation.

is in contact with the OLED device. Moreover, such a material should be capable of absorbing gas emitting from the OLED device or moisture diffusing into the device from the outside. In our previous study [14], we filled a thermally conductive epoxy resin in a glass cover. However, it can not absorb oxygen or moisture because no moisture getter material is involved. The typical getter materials include zeolite tablet or powder, an oxide (BaO, CaO), or a reactive metal (such as Ba and its alloys with other metals such as Al) [15]. CaCO3 particles were calcinated into highly crystalline calcium oxide (CaO) nanoparticles, which are used as active materials for water absorption [15]. Fine zirconium powders were used as the active materials in a porous zirconium–graphite getter (named as SAES Getters), which is not for oxygen but for hydrogen sorption [16]. Those getters are not readily filled into the glass cap. Recently, SAES Getters Co., Ltd., developed a liquid getter (AqvaDry), which is UV- or thermally curable. Such a liquid getter can be easily filled into the glass cap. Moreover, it is highly transparent once it is UV-cured. In this paper, we investigate the thermal and barrier properties of the moisture getter-filled encapsulations for OLEDs. It is demonstrated that the heat dissipation capability of the moisture getter-filled encapsulation is degraded due to a bad contact between the OLED device and the heat transferring getter. However, it is enhanced by coating the liquid getter on a flat glass cover and sealing the OLED device with it. Though the thermal property is enhanced with this scheme, yet its barrier property is degraded. We demonstrate that both thermal and barrier properties can be enhanced by simply increasing the thickness of an Al cathode in the presence of buffer layers.

2. Experiments

For experiments, we purchased UV-curable liquid getter (AqvaDry ODF-U) from SAES Getters Co., Ltd. The UV-cured 50-μm-thick moisture-getter film shows the optical transmittance more than 95% within the visible wavelength range and the refractive index of 1.493. The moisture capacity of 350-μm-thick getter film with the area of 1.5 cm × 1.5 cm is 2.42 mg, which is almost equivalent to that of a commercial DYNIC getter [17]. It discharges moisture over 200 °C, indicating that it does not discharge again under normal operating conditions of OLEDs. The liquid getter was coated on cover glasses using a bar-coater (YBA baker applicator, YOSIMITSU, JAPAN). The coated liquid-getter films were UV-cured for 30–60 s under 60 mW/cm^2 UV power. To eliminate remaining gas, we carried out a thermal annealing on a hot plate at 90 °C for 1 h. We fabricated phosphorescent green OLED devices that consist of a 150-nm-thick indium–tin-oxide (ITO) for anode, 10-nm-thick LG-101 for a hole injection layer (HIL), 25-nm-thick 4,40-bis[*N*-(1-nathyl)-*N*-phenylamino] biphenyl (NPB) for a hole transport layer (HTL), 25-nm-thick 4,4′-*N*,*N*′-dicarbazolylbiphenyl (CBP) doped with tris(2-phenylpyridinate) iridium(III) (Ir(ppy)$_3$, 8 wt.%) for an emitting layer (EML), 10-nm-thick *m*-bis-(triphenylsilyl) benzene (UGH3) for a hole/exciton blocking layer (HBL), 30-nm-thick LG-201 doped with lithium quinolate (LiQ, 50 wt.%) for an electron transport layer (ETL), and 150-nm-thick aluminum (Al) for cathode. The emission area of OLED is 4 mm^2. To seal OLEDs, an epoxy resin (XNR 5570-B1, Nagase ChemteX Corp.) is dispensed on the edge sides of the glass cover and cured using a UV lamp (Ultra violet cure M/C, SEI MYUNG VACTRON). The epoxy resin exhibits the moisture permeability of 18 g/m^2·day at 60 °C and 90% relative humidity and the glass transition temperature of 144 °C. We attached a Polynetwork flexible heat sink (PN-FHB050 N) [18] in the form of bonding sheet to the outer surface of the glass cover. It consists of a 50-μm-thick copper sheet and 35-μm-thick thermal radiation layer. The bonding sheet has the thermal conductivity of 0.86 W/m-K. All encapsulation process was carried out in a glove box below 10 ppm H_2O.

As a glass cover, we have used two different types of glasses. One is a hollow glass cover and the other one is a flat glass cover. The liquid getter is filled in the hollow glass cover (Fig. 1(b)), whereas it is coated on the flat glass cover (Fig. 1(c)). For comparison, we have used those hollow glass covers that are different in depth (100 and 350 μm). Namely, the 0.7-mm-thick glass cover is hollowed out so that its thickness becomes 100 or 350 μm and thus the moisture getter can be filled therein. In this paper, an OLED device based on this method is referred to as a getter-filled hollow glass-encapsulated OLED (GFHG-OLED). The liquid getter filled in the hollow glass cover is shrunk during the UV-curing process, possibly leaving a nitrogen gas-filled gap and thus blocking off the heat transfer. It is avoidable by coating and UV-curing the liquid getter on the flat glass cover. We have also employed those flat glass covers that are different in thickness (0.2 and 0.7 mm). An OLED device based on this scheme is

referred to as a getter-coated flat glass-encapsulated OLED (GCFG-OLED). Just in case that the moisture getter may cause damage to the organic layers, we have inserted a buffer layer that consists of a 40-nm-thick NPB and 50-nm-thick lithium fluoride (LiF) in both devices.

3. Results and discussions

We have first investigated the optical transmittance of moisture getter-filled glass encapsulations for different time slots. To this end, the glass substrate without OLED device involved was encapsulated with the 100-μm-thick hollow glass cover where the moisture getter is filled. We carried out a stress testing of the samples at 85 °C and 85% relative humidity. During the stress testing, we took out the samples from a thermo-hygrostat and measured their transmittance using UV/Vis spectrometer (PG Instrument Ltd.) with glass as the reference. The initial transmittance of the 100-μm-thick moisture getter-filled encapsulation was measured to be 95% at 520 nm. It is observed from Fig. 2 that the initial transmittance decreased gradually with time. As the moisture getter absorbs oxygen or moisture, its color is changed to white and thus its transmittance is decreased. Because there is no out-gassing involved in this case, such a reduction in transmittance arises mainly from oxygen or moisture diffusing through the epoxy seal over time.

As a reference device, we fabricated an OLED device based on the conventional glass encapsulation where a moisture getter sheet (DYNIC Corp.) was inserted. We measured the surface temperature distribution of the device with and without the heat sink and presented the results in Fig. 3(a and b). Shown in Fig. 3(c) is the transient variation of the maximum surface temperature measured at 8 V. It is observed that heat is dissipated only by 7.7 °C (60.2 → 52.5 °C) with the heat sink. Such a small reduction in the surface temperature even in the presence of the heat sink is attributed to the fact that remaining nitrogen gas

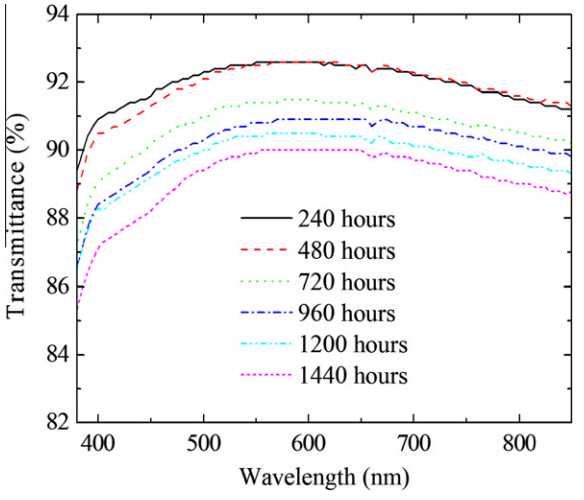

Fig. 2. Measured transmittance of 100-μm-thick moisture getter-filled glass encapsulation for different time slots at 85 °C and 85% relative humidity.

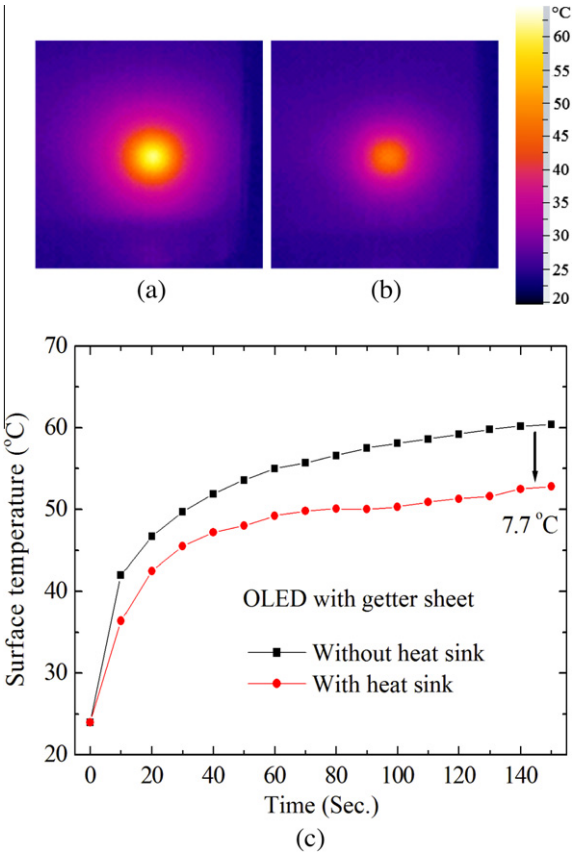

Fig. 3. Surface temperature distribution over the conventional glass-encapsulated OLED (a) without and (b) with heat sink, and (c) transient variation of the maximum surface temperature measured at 8 V.

blocks off the heat transfer from the OLED device to the heat sink because nitrogen gas has the thermal conductivity of 0.024 W/m K [19], which is much lower than that (≈1.0 W/m K) of glass.

With attempt to dissipate heat more effectively, we fabricated GFHG-OLEDs and measured their thermal property as presented in Fig. 4. Using the 350-μm-thick hollow glass cover, however, the maximum surface temperature is reduced only by 10 °C (from 60 to 50 °C) with the heat sink. Although the maximum surface temperature is reduced further (62.3 → 46.8 °C) using a thinner (100-μm-thick) hollow glass cover, such a small reduction in heat is unexpected because the thermal conductivity of UV-cured getter is close to 0.1–0.3 W/m·K, which is much higher than that of nitrogen gas. It is most likely that there still exists a nitrogen gas-filled gap between the OLED device and the moisture getter, which is induced by the shrinkage of the liquid getter during the UV-curing process. Therefore, such a gas-filled gap is unavoidable using a hollow glass cover.

To eliminate the gas-filled gap completely, we employed a flat glass cover where the liquid getter is bar-coated. With this scheme, we fabricated GCFG-OLEDs and measured their thermal property as presented in Fig. 5. It is clearly seen even with the naked eye (Fig. 5(a and b))

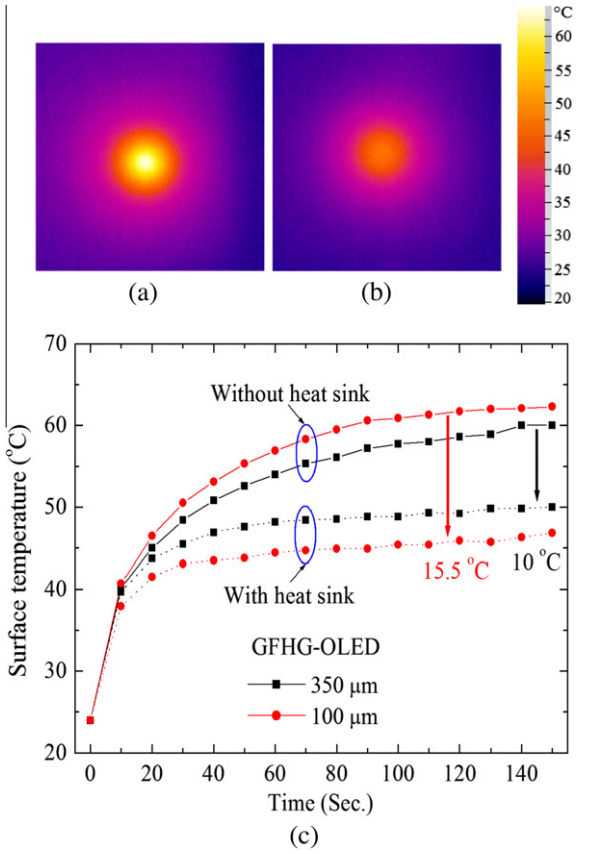

Fig. 4. Surface temperature distribution over the 100-μm-thick GFHG-OLED (a) without and (b) with heat sink, and (c) transient variation of the maximum surface temperature measured at 8 V for different thicknesses of hollow glass.

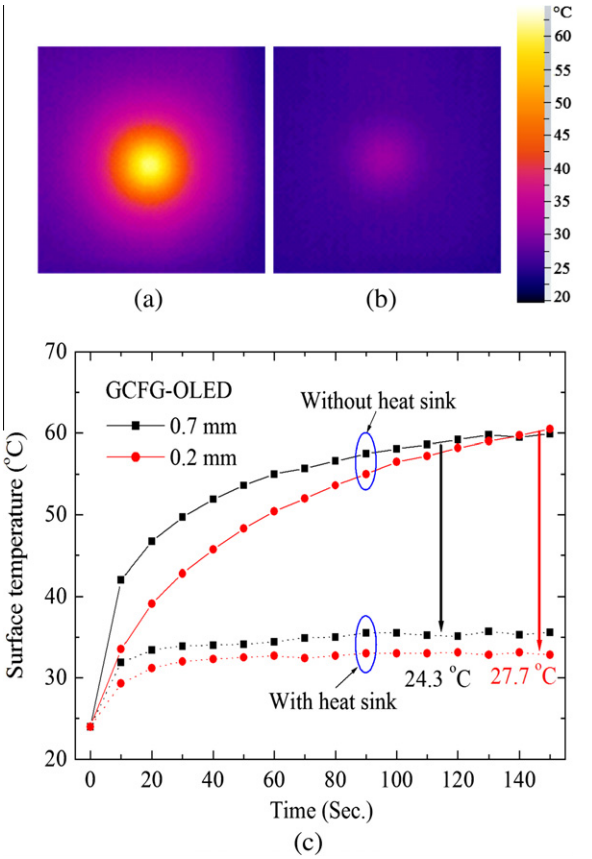

Fig. 5. Surface temperature distribution over the 0.2-mm-thick GCFG-OLED (a) without and (b) with heat sink, and (c) transient variation of the maximum surface temperature measured at 8 V for different thicknesses of flat glass.

that heat is dissipated to a great extent. The maximum surface temperature is reduced by 24.3 °C (from 59.9 to 35.6 °C) with the 0.7-mm-thick flat glass cover, while reduced further by 27.7 °C (from 60.5 to 32.8 °C) with the 0.2-mm-thick flat glass cover. Comparing with the results in Fig. 4, the surface temperature is reduced more than 10 °C. This result indicates that a contact at the interface between the organic device and the moisture getter is excellent and consequently heat is dissipated effectively through the thermally conductive moisture getter.

To investigate the gas diffusion barrier property of those getter-filled glass encapsulations, we measured the luminance variation of those devices over time at 85 °C and 85% relative humidity and presented the results in Fig. 6. The initial luminance of the devices was 1500 cd/m^2. It is evident that GCFG-OLEDs show poorer gas diffusion barrier, compared with GFHG-OLEDs. Although a removal of gas-filled gap enhances the heat dissipation in GCFG-OLEDs, it seems that a direct contact of the moisture getter with the OLED device causes damage to the organic layers even in the presence of the buffer layer. This was confirmed by the emission images measured by microscope (ECLIPSE L300, NIKON) in Table 1. Once oxygen or moisture diffuses into the OLED device, there appear dark spots that are non-emissive area. Those dark spots are extended over

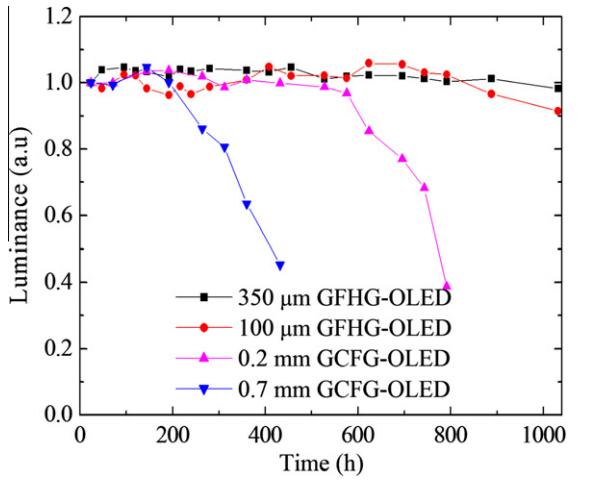

Fig. 6. Luminance of those OLED devices as a function of time under conditions of 85 °C and 85% relative humidity.

time and thus shorten the device lifetime. As evident in Table 1, the dark spots are extended much earlier in GCFG-OLEDs than in GFHG-OLEDs. In GCFG-OLEDs, the moisture

Table 1
Images of dark spots in those OLED devices for different time slots at 85 °C and 85% relative humidity.

	Glass Encapsulation	350 μm GFHG-OLED	100 μm GFHG-OLED	0.2 mm GCFG-OLED	0.7 mm GCFG-OLED
24 hours					
120 hours					
240 hours					
360 hours					
480 hours					
600 hours					
720 hours					
840 hours					

getter absorbs out-gases from the OLED device or moisture diffused from the outside. However, the organic device is damaged once the moisture getter absorbs them because the moisture-absorbed getter is in directly contact with the organic layer. Otherwise, the dark spots would be expanded as slowly as in GFHG-OLEDs. Moreover, the boundary between the dispensed epoxy resin and the coated moisture getter on the flat glass cover is not clear. If the moisture getter is located close to the epoxy resin as depicted in Fig. 1(c), there arises some damage to the getter during the epoxy dispensing and UV-curing process. Namely, the UV-cured getter reacts with the moist epoxy to produce oxidative degradation, which obviously speeds up an expansion of dark spots, especially near the edge sides of the glass cap in GCFG-OLEDs [see Table 1]. Meanwhile, the conventional glass encapsulation shows the best gas barrier performance because a DYNIC getter sheet inserted into the hollow glass cover stays away from the epoxy resin and no direct contact with the organic layers is involved.

To reduce damage to the moisture getter by the epoxy resin, we left a little space (3 mm) between them. In this case, care is taken to ensure that the moisture getter area is larger than the organic light-emitting area. We also increased the thickness of the Al cathode to enhance the passivation effect or rather reduce damage induced by the direct contact between the moisture getter and the organic device. It is known that the Al cathode also works as a passivation layer since it covers the organic light-emitting layers. As such, the passivation effect is expected to be

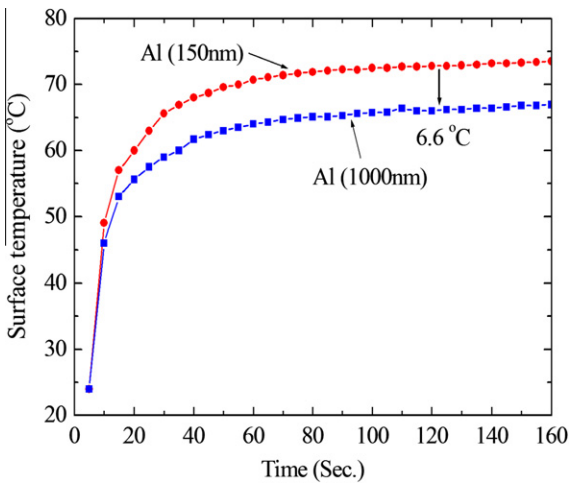

Fig. 7. Transient variation of the maximum surface temperature of conventional glass-encapsulated OLEDs with heat sink for different Al thicknesses.

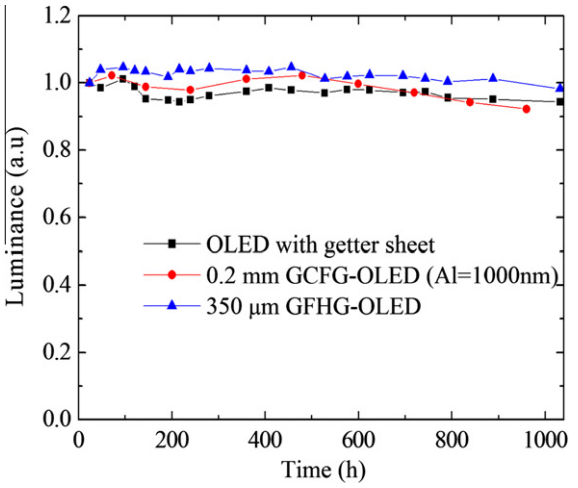

Fig. 8. Luminance of OLED devices as a function of time under conditions of 85 °C and 85% relative humidity.

enhanced by simply increasing the thickness of the Al cathode. This scheme also reduces the surface temperature because heat is dissipated horizontally through the thick Al metal. To verify it, we increased the thickness of the Al cathode from 150 to 1000 nm for the conventional glass-encapsulated OLEDs and measured their surface temperature. As evident in Fig. 7, the maximum surface temperature is reduced by 6.6 °C (from 73.5 to 66.9 °C), which is induced obviously by the thick Al cathode. Considering these, we fabricated GCFG-OLEDs and measured the luminance variation with time at 85 °C and 85% relative humidity. The initial luminance of each device was the same as that (1500 cd/m^2) in Fig. 6. As evident in Fig. 8, the operating lifetime of the GCFG-OLED is much enhanced, which is even comparable with the conventional glass-encapsulated OLED. The increased operational lifetime of GCFG-OLED results from the enhanced gas diffusion barrier property, which is obtained by the thick Al cathode and a reduction of damage to the moisture getter by the epoxy resin. Furthermore, heat was dissipated more (by 30.5 °C from 62.4 to 31.9 °C) with the flexible heat sink, compared with the result (by 27.7 °C) in Fig. 5(c). This result demonstrates that the thermal conductivity of OLED can be enhanced further by the use of the high thermal conductivity GCFG encapsulation. If the gas diffusion barrier property of encapsulation is as good as the conventional glass encapsulation, a higher thermal conductivity encapsulation is preferred because it can effectively dissipate the Joule heat and thus boost the thermal stability [20]. Due to Joule heating induced by high current injection during operation, there arise thermal degradations such as a reduction of luminance, short lifetime, and large spectral shift of OLEDs, which are mainly related to the low glass transition temperature (T_g) of organic molecules. Therefore, the use of the high thermal conductivity GCFG encapsulation along with a heat sink is demanded to ensure the stable operation at high luminances.

4. Conclusion

We investigated the thermal and barrier properties of moisture getter-filled glass encapsulations for OLEDs. It was found that, in the presence of a slim and flexible heat sink, the getter-coated flat glass encapsulation showed the best thermal performance, followed by the getter-filled hollow glass encapsulation and then the conventional glass encapsulation. However, the getter-coated flat glass encapsulation exhibited the poorest gas diffusion barrier property because the moist surface of the getter damages the organic layers. We demonstrated that the barrier property of the getter-coated flat glass-encapsulated OLEDs was much enhanced by increasing the thickness of the Al cathode in the presence of the buffer layer, which also brought in a further reduction of the surface temperature.

Acknowledgement

This work was supported by the IT R&D program of MKE/IITA. [2009-F-016-01, Development of Eco-Emotional OLED Flat-Panel Lighting.]

References

[1] C.W. Tang, S.A. Vanslyke, Appl. Phys. Lett. 51 (1987) 913.
[2] J.H. Burroughes, D.D.C. Bradley, A.R. Brown, R.N. Marks, K. Mackay, R.H. Friend, P.L. Burns, A.B. Holmes, Nature 347 (1990) 539.
[3] K. Leo, Science 310 (2005) 1762.
[4] Y. Sun, N. Giebink, H. Kanno, B. Wa, M.E. Thompson, S.R. Forrest, Nature (London) 440 (2006) 908.
[5] J. Shinar, Organic Light-Emitting Devices: A Survey, AIP Press, 2004.
[6] J. Kalinowski, Organic Light-Emitting Diodes: Principles, Characteristics, and Processes, Marcel Dekker, New York, 2005.
[7] P.E. Burrows, V. Bulovic, S.R. Forrest, L.S. Sapochack, D.M. McCarty, M.E. Thompson, Appl. Phys. Lett. 65 (1994) 2922.
[8] J.D. Affinito, M.E. Gross, C.A. Coronado, G.L. Graff, E.N. Greenwell, P.M. Martin, Thin Solid Films 63 (1996) 290–291.
[9] A.P. Ghosh, L.J. Gerenser, C.M. Jarman, J.E. Fornalik, Appl. Phys. Lett. 86 (2005) 223503-1.
[10] G. Nisato, M. Kuilder, P. Bouten, L. Moro, O. Philips, N. Rutherford, SID 00 Digest XXXIV (2003) 88.
[11] J. Meyer, D. Schneidenbach, T. Winkler, S. Hamwi, T. Weimann, P. Hinze, S. Ammermann, H.H. Johannes, T. Riedl, W. Kowalsky, Appl. Phys. Lett. 94 (2009) 233305-1.
[12] A.B. Chwang, M.A. Rothman, S.Y. Mao, R.H. Hewitt, M.S. Weaver, J.A. Silvernail, K. Rajan, M. Hack, J.J. Brown, X. Chu, L. Moro, T. Krajewski, N. Rutherford, Appl. Phys. Lett. 83 (2003) 413.
[13] F.L. Wong, M.K. Fung, S.L. Tao, S.L. Lai, W.M. Tsang, K.H. Kong, W.M. choy, C.S. Lee, S.T. Lee, J. Appl. Phys. 104 (2008) 14509-1.
[14] J.W. Park, H.K. Ham, C.Y. Park, Org. Electron. 12 (2011) 227.
[15] J.H. Park, S.G. Oh, Mater. Res. Bull. 44 (2009) 110.
[16] Y.H. Xiong, X.Y. Wei, G.R. Qin, P. Yuan, C.H. Mao, J. Du, Vacuum 82 (2008) 737.
[17] http://www.dynic.com.hk/eng/OLED_EN.html.
[18] http://polynetwork.asia/eindex.html.
[19] http://www.engineeringtoolbox.com/thermal-conductivity-d_429.html.
[20] Y.S. Tsai, S.H. Wang, C.H. Chen, C.L. Cheng, T.C. Liao, Appl. Phys. Lett. 95 (2009) 233306.

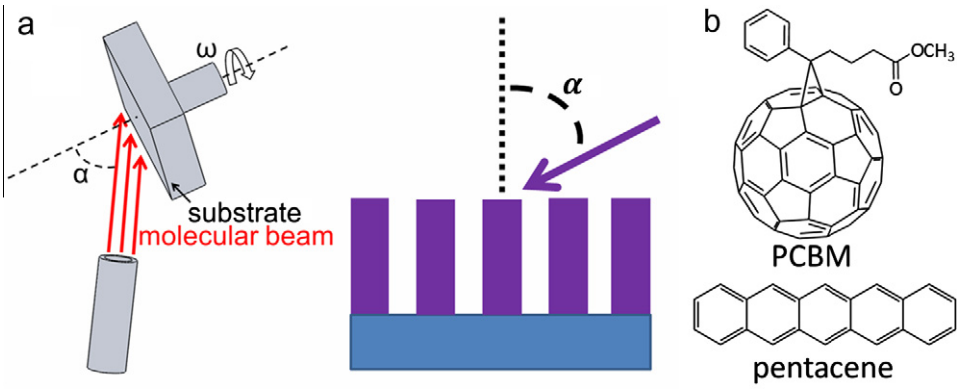

Fig. 1. (a) Schematic of glancing angle deposition, (b) chemical structure of pentacene and PCBM.

holes due to shadowing of the molecular beam. Further device performance improvement was achieved by inserting a thin pentacene electron-blocking layer before NCA growth to prevent electron current leakage to the anode.

2. Experimental

Pentacene (purchased from Sigma–Aldrich) was deposited by GLAD on glass substrates coated with 20 Ω/square indium tin oxide (ITO) in a high vacuum chamber (base pressure $\sim 3 \times 10^{-7}$ mbar). A computer-controlled stepper motor was used to facilitate sample rotation about the substrate surface normal. The molecular flux incidence angle α and the substrate rotation rate ω were set to 85° and 6 rounds per minute, respectively during nanocolumn (NC) growth. The distance between the center of the substrate and the evaporation source was 15 cm, and the deposition rate at the substrate was ca. 1 Å/s, as monitored by a quartz-crystal microbalance which vertically faced the evaporation source.

OPVCs were fabricated by spin-coating PCBM dissolved in chlorobenzene (28 mg/ml) onto the NCA at 25 rounds per second in a nitrogen glove box. The pentacene/PCBM interdigitated structures were subsequently annealed at 85 °C for 20 min to remove residual solvent and to facilitate improved PCBM infiltration into the voids between the pentacene NCs. An 8 nm thick exciton-blocking layer of bathocuproine (BCP) [12,13] was deposited onto the structure before a 100 nm thick Sm cathode was evaporated in high vacuum (base pressure $\sim 8 \times 10^{-8}$ mbar). The current density–voltage characteristics in dark and under illumination (2.5 mW/cm^2, Solux C6 halogen lamp, close to daylight spectrum in the visible region) were measured in vacuum (2×10^{-8} mbar) with a Keithley 2400 sourcemeter, and the sample morphology was investigated with a HITACHI S-4100 field-emission scanning electron microscope (SEM), after sputter-coating the samples with a thin conductive Au layer.

3. Results and discussion

The formation of nanocolumns is due to a shadowing effect of molecular islands with respect to the incoming material flux, aggravated by the large oblique incident deposition angle. During deposition a large fraction of the flux is captured by taller grains that continue growing at the expense of their dying neighbors. Fig. 2(b)–(d) shows representative topography and cross-section micrographs of pentacene columnar structures grown by GLAD on ITO. Compared with the typical flat and homogeneous morphology of vertically deposited pentacene thin films on ITO, displayed in Fig. 2(a), almost square shaped crystalline pentacene nanocolumns (NCs) and large gaps between them persist for the deposition using GLAD. The polycrystalline structure of pentacene NCs, which is important to obtain high charge carrier mobility for a low solar cell series resistance, has been demonstrated earlier by Zhang et al. [7]. The diameter of the columns in our samples is predominantly in the range of 120–180 nm and the column area-density is about 3×10^7 mm^{-2}. The cross-section view (Fig. 2(c) and (d)) reveals that the height of the individual columns is rather uniformly about 210 nm, except few higher protrusions. There are always small gaps between columns, even for locally high area-densities.

The interpenetrating donor–acceptor structure was obtained by PCBM solution spin coating onto the pentancene NCAs. As shown in Fig. 3(a), spin coating with low concentration PCBM solution (18 mg/ml in chlorobenzene) left the underlying pentacene NCs still clearly visible. Although such a highly corrugated surface easily leads to electrical shorts [14,15], our observation implies that pentacene NCs still stand vertically on the ITO substrate, not impeded by PCBM spin coating, and that PCBM infiltration into gaps between NCs occurred, as can be seen in Fig. 3(b). With a higher concentration PCBM solution (28 mg/ml), a rather smooth surface was obtained and the gaps were filled adequately by PCBM (see Fig. 3(c) and (d)).

The structure of all investigated OPVC variants is shown in Fig. 4. For comparison with OPVCs that have pentacene NCs, an optimized bi-layer planar heterojunction OPVC employing ITO/PEDOT:PSS/50 nm pentacene/30 nm PCBM/8 nm BCP/100 nm Sm (structure A) were fabricated at room temperature, as suggested in [16]. Interdigitated OPVC fabrication was done by BCP and cathode (Sm) deposition in high vacuum (structure B). The BCP thin film was used as

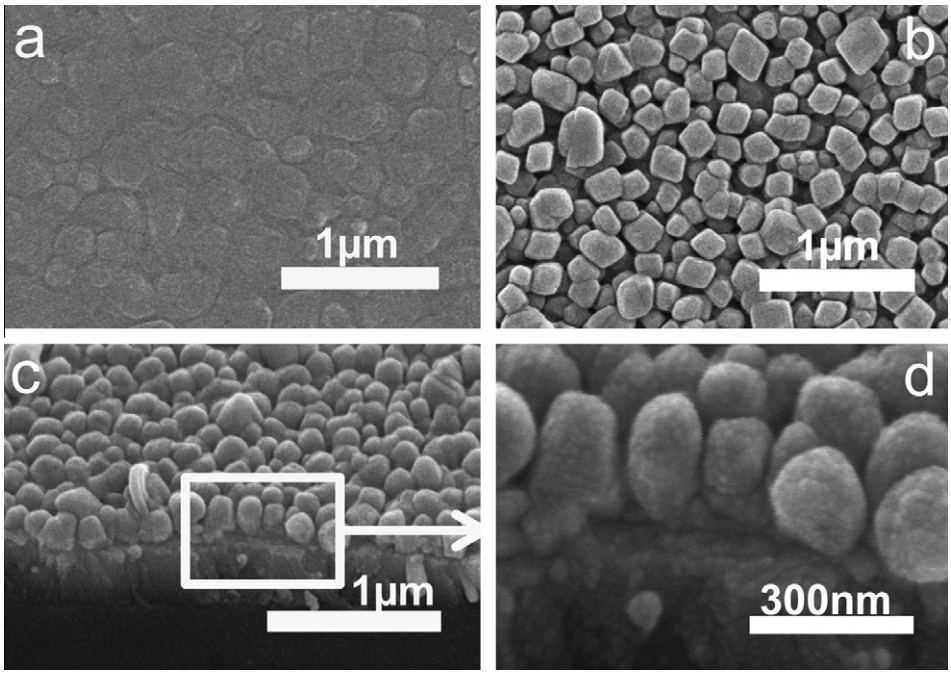

Fig. 2. SEM micrographs of pentacene films on ITO. (a) Top view of vertically deposited pentacene, (b) top view of a GLAD pentacene nanocolumn array (NCA), (c) and (d) cross-section views of a GLAD pentacene NCA.

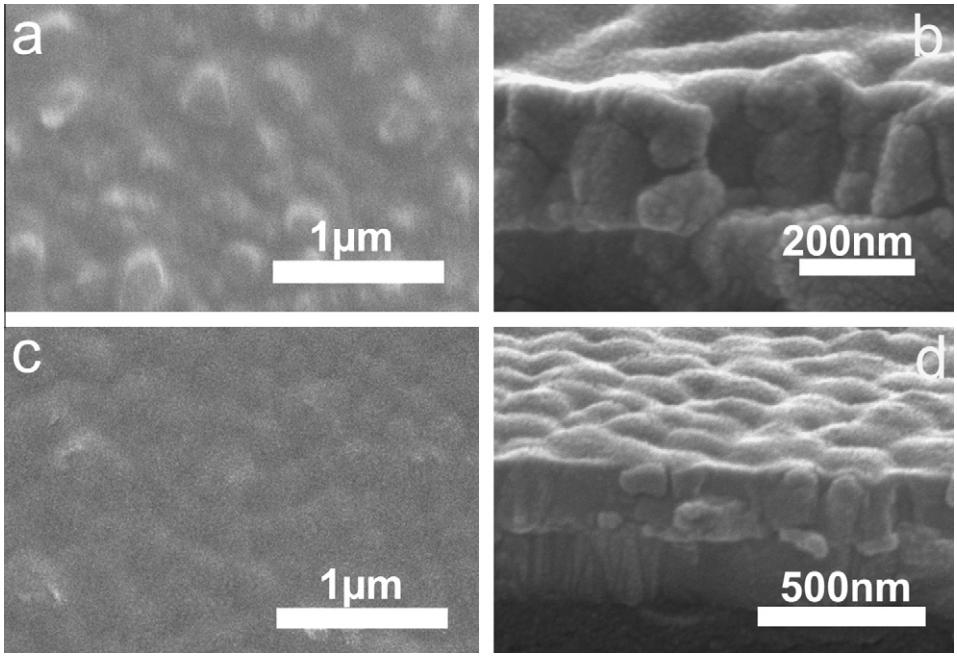

Fig. 3. SEM micrographs of PCBM solution deposited onto pentacene NCAs. (a) and (b) Top and cross-section views of low concentration (18 mg/ml) PCBM solution, (c) and (d) top and cross-section views of high concentration (28 mg/ml) PCBM solution.

an exciton-blocking layer and as protection-layer for the active donor/acceptor layer during metal deposition. The current density–voltage characteristics of interdigitated OPVCs and reference bi-layer cells (measured at 2.5 mW/cm^2 illumination from a halogen lamp) are shown in Fig. 5, the characteristic parameters summarized in Table 1. The open-circuit voltage (V_{oc}) of the cell with structure B is slightly increased from 0.47 V to 0.50 V. However, the short circuit current density (J_{sc}) of interdigitated cells with structure B is more than doubled compared to that of the reference bi-layer cell under the same illumination condition. The improved performance of interdigitated cells is

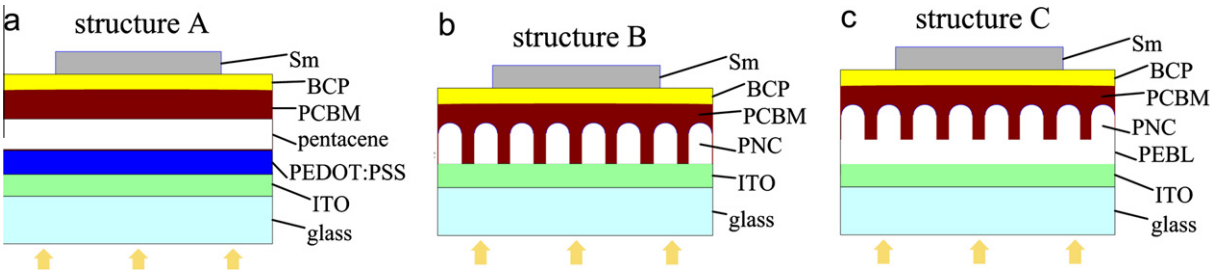

Fig. 4. Structures of the investigated OPVCs. (a) Planar bi-layer structure, (b) PNC (pentacene nanocolumn) structure, (c) PEBL (pentacene electron-blocking layer) combined with PNC.

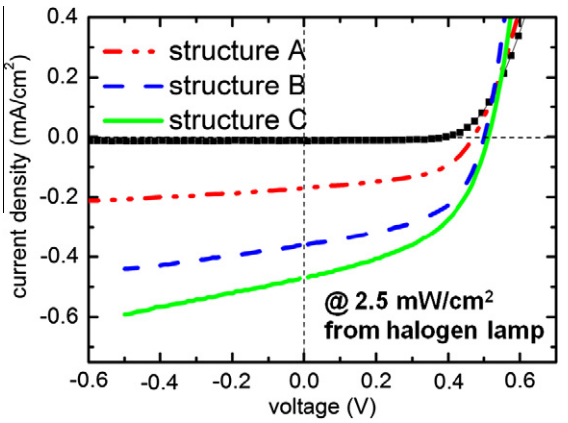

Fig. 5. Current density–voltage characteristics of NC heterojunction and improved devices compared with bi-layer heterojunction devices at the same illumination density (2.5 mW/cm^2 illumination from a halogen lamp). Squares with the black line show the characteristics of all three devices in dark.

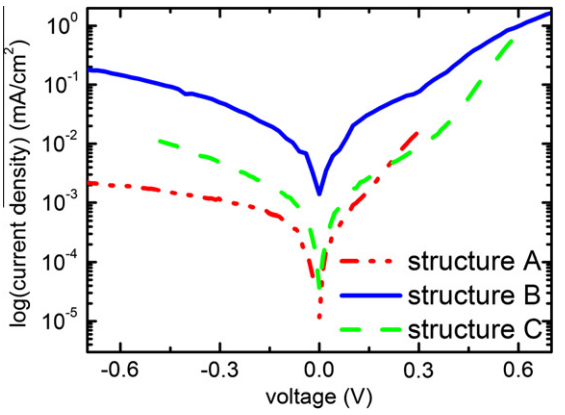

Fig. 6. Current density–voltage characteristics in dark for the three device structures.

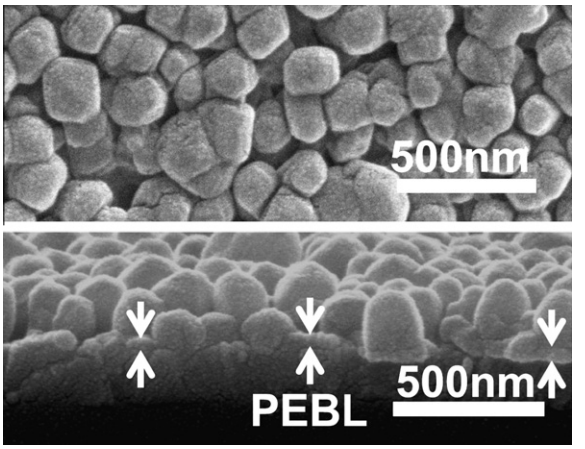

Fig. 7. Top and cross-section view of pentacene nanocolumn array grown on a 10 nm thick PEBL.

attributed to the increased active interface area due to the pentacene NCs. From the SEM images we estimate an increased interface area with NCs by a factor of three, which in principle could increase J_{sc} threefold as well, if there are no other factors impacting device performance. Since J_{sc} in structure B OPVCs was only doubled compared to structure A, we expect additional effects to play a role. Considering the characteristics of devices in the dark, shown on a logarithmic scale in Fig. 6, a much lower area specific shunt resistance of structure B devices was obtained (approx. 0.02 MΩ cm^2) compared to that of structure A devices (approx. 2.86 MΩ cm^2) [17]. The reason of the low shunt resistance could be due to current leakage paths produced by infiltration of the PCBM acceptor phase to the bottom electrode, which do not occur in the planar bi-layer reference device.

To eliminate the problem of leakage paths, a 10 nm thick pentacene film was deposited on ITO before growing pentacene NCs as an electron-blocking layer, shown as structure C in Fig. 4(c). As seen from Fig. 7, there is no marked difference of pentacene NCs compared to those in Fig. 3 except for the thin pentacene electron-blocking layer, except for a slightly decreased FF. A remarkably increased J_{sc} resulted (see Fig. 5 and Table 1), owing to the increased shunt resistivity (approx. 1 MΩ cm^2), see Fig. 6. Hence, the influence of current leakage paths is reduced but not eliminated totally. We suggest that employing a heavily p-doped thin film as electron-blocking layer might be helpful to further improve device performance. Nevertheless, the characteristics of interdigitated OPVCs employing pentacene NCs were improved significantly improved by utilizing the thin electron-blocking layer. The J_{sc} improvement now reached more than 90% of the expected threefold increase due to increased active

Table 1
Characteristic performance parameters of OPVCs. Open circuit voltage (V_{oc}), short circuit current (J_{sc}), fill factor (FF).

	Structure A	Structure B	Structure C
V_{oc} (V)	0.47	0.50	0.51
J_{sc} (mA cm^{-2})	0.17	0.36	0.47
FF	0.51	0.51	0.48
$V_{oc}J_{sc}$FF	0.04	0.09	0.12

interface area. While we cannot provide power conversion efficiency values under standard illumination conditions (due to our experimental setup in vacuum, see experimental section), we estimate that devices with structure C (interdigitated) have an efficiency of ca. 4%, as opposed to only ca. 1.5% for those with structure A (planar), at 2.5 mW/cm^2 illumination from a halogen lamp with an emission spectrum close to daylight in the visible region.

4. Conclusion

In conclusion, vertically aligned crystalline pentacene NCs with a diameter of ~160 nm were grown by GLAD. Interdigitated OPVCs structures were achieved by spin-coating PCBM onto the pentacene NCs, which lead to a threefold increase of active donor/acceptor interface area compared to planar bi-layer structures. By employing an additional planar thin pentacene electron-blocking layer, J_{sc} was increased from 0.17 mA cm^{-2} to 0.47 mA cm^{-2}, corresponding to over 90% of the expected increase due to larger interface area. The remarkable conversion efficiency of OPVCs based on NC structures proves that it is an effective architecture to eliminate charge transport and exciton diffusion bottlenecks while maximizing the interface area. Other materials as donors and/or acceptors employed in similar structures will most likely lead to significant further improvements in OPVCs performance in the future.

Acknowledgement

SY acknowledges the China Scholarship Council for an individual research fellowship.

Reference

[1] C.W. Tang, Two-layer organic photovoltaic cell, Appl. Phys. Lett. 48 (1986) 183–185.
[2] G. Yu, J. Gao, J.C. Hummelen, F. Wudl, A.J. Heeger, Polymer photovoltaic cells: enhanced efficiencies via a network of internal donor–acceptor heterojunctions, Science 270 (1995) 1789–1791.
[3] J.J.M. Halls, C.A. Walsh, N.C. Greenham, E.A. Marseglia, R.H. Friend, S.C. Moratti, A.B. Holmes, Efficient photodiodes from interpenetrating polymer networks, Nature 376 (1995) 498–500.
[4] P. Peumans, S. Uchida, S.R. Forrest, Efficient bulk heterojunction photovoltaic cells using small molecular-weight organic thin films, Nature 425 (2003) 158–162.
[5] F. Yang, M. Shtein, S.R. Forrest, Controlled growth of a molecular bulk heterojunction photovoltaic cell, Nat. Mater. 4 (2005) 37–41.
[6] Y. Zheng, R. Bekele, J.M. Ouyang, J.G. Xue, Organic photovoltaic cells with vertically aligned crystalline molecular nanorods, Org. Electron. 10 (2009) 1621–1625.
[7] J. Zhang, I. Salzmann, S. Rogaschewski, J.P. Rabe, N. Koch, F.J. Zhang, Z. Xu, Arrays of crystalline C60 and pentacene nanocolumns, Appl. Phys. Lett. 90 (2007) 193117.
[8] P.C.P. Hrudey, K.L. Westra, M.J. Brett, Highly ordered organic Alq_3 chiral luminescent thin films fabricated by glancing-angle deposition, Adv. Mater. 18 (2006) 224–228.
[9] K. Robbie, M.J. Brett, Sculptured thin films and glancing angle deposition: growth mechanics and applications, J. Vac. Sci. Technol. A 15 (1997) 1460.
[10] Y.P. Zhao, D.X. Ye, G.C. Wang, T.M. Lu, Novel nano-column and nano-flower arrays by glancing angle deposition, Nano Lett. 2 (2002) 351.
[11] L. Abelmann, C. Lodder, Oblique evaporation and surface diffusion, Thin Solid Films 305 (1997) 1–21.
[12] M. Vogel, S. Doka, Ch. Breyer, M.Ch. Lux-Steiner, K. Fostiropoulos, On the function of a bathocuproine buffer layer in organic photovoltaic cells, Appl. Phys. Lett. 89 (2006) 163501.
[13] H. Gommans, B. Verreet, B.P. Rand, R. Muller, J. Poortmans, P. Heremans, J. Genoe, On the role of bathocuproine in organic photovoltaic cells, Adv. Funct. Mater. 18 (2008) 3686–3691.
[14] Ch. Seungkeun, J.P. William Jr., K. Bernard, Area-scaling of organic solar cells, J. Appl. Phys. 106 (2009) 054507.
[15] M. Vogel, S. Doka, C. Breyer, M.C. Lux-Steiner, K. Fostiropoulos, Relation between the barrier interface and the built-in potential in pentacene/C60 solar cell, Appl. Phys. Lett. 89 (2006) 163501.
[16] V.S. Reddy, S. Karak, S.K. Ray, A. Dhar, Photovoltaic properties of pentacene/[6,6]-phenyl C61 butyric acid methyl ester based bilayer hetero-junction solar cells, J. Phys. D Appl. Phys. 42 (2009) 145103.
[17] S.M. Sze, Physics of Semiconductor Devices, 2nd ed., Wiley, New York, 1981.

To employ R2R gravure for properly simulating and integrating all printed fTFTs (PTFTs) on plastic foils, at first, each components of PTFTs should be able to R2R gravure print on poly(ethylene terephthalate) (PET) foils with reliable physical dimensions. In other words, gate electrodes, dielectric layers, active layers and drain–source electrodes should be R2R printed on PET foils with sophisticated and reliable structures. However, printing reliable fTFTs using R2R gravure is strongly depending on the rheology of inks for printing electrodes, dielectrics and active layers. Furthermore, those inks should be cured with minimum influences on the substrates under 150 °C for less than 5 s to provide practical printing speed with plastic or paper webs. Since inks to meet above requirement in R2R gravure are only commercially available for electrodes and dielectric layers, but not for active layers, we are using an inkjet with dispersed individual single walled carbon nanotubes (SWNTs) solution as an active ink to print SWNT network structures as active layers. Furthermore, since the network structures of SWNTs as active layers on SiO_2 dielectric layer with Si wafer show reasonably low operation voltages (<20 V) [18,19] employing inkjet printed SWNT network structures as active layers on all gravure printed gate electrodes, dielectric layers and drain–source electrodes on PET foils will be very valuable approach to introduce a practical way of producing fTFTs. Therefore, although whole fTFTs could not be printed by R2R gravure at this moment, it is very valuable to verify that R2R gravure printed gate electrodes, dielectric layers and drain–source electrodes on plastic film are eligible with inkjet-printed active layers using SWNT ink and expandable to integrate PTFTs on the plastic foils with well matched to their simulation results.

In this paper, we would like to show that all printing process based on R2R gravure and inkjet on plastic foils is reliable and integrable fTFTs for the production of flexible and costless macro-electronic devices such as RFID tags, sensors and signage. For this purpose, basic building blocks in integrated circuits such as fTFTs, inverter and ring oscillator, were printed. Furthermore, we analyzed frequency performance and electrical properties related to the SWNT network of the printed circuits by referring a previously reported organic semiconductor based PTFT model [20] and spice simulation model which may enable to describe the static and dynamic behaviors of the printed SWNT based PTFTs with sufficient accuracy.

In printing fTFTs on plastic foils, R2R gravure (AVACO, Korea) (Fig. 1a) and inkjet (DMP-2800, Dimatix, USA) (Fig. 1b) were used with PET foils (SKC, Korea) with the thickness of 70 μm. For R2R gravure-printing precursors, containing gate electrodes, dielectric layers, drain–source electrodes and wires, silver nanoparticle based gravure inks (PG-007, Paru Co., Korea) and a high dielectric ink based on $BaTiO_3$ nanoparticles (PD-100 Paru Co., Korea) were respectively used by adding appropriate amounts of ethylene glycol and hexanol to control viscosity and surface tension. The optimized viscosities and surface tensions of silver nanoparticles and $BaTiO_3$ nanoparticles with R2R gravure printing speed of 12 m/min were respectively the viscosity of 200 cP and the surface tension of 30–36 mN/m. To directly employ SWNTs in printing fTFTs as an active material with a reasonable on current level and on–off ratio for the production of PTFTs, well dispersed individual SWNTs (HiPco, Carbon Nanotechnology Laboratory, Rice University) in aqueous solution with sodium dodecylsulfate (SDS) was inkjet printed on the R2R gravure printed gate electrodes, dielectric layers and drain–source electrodes on PET, called precursor at here (Fig. 2a). In this work, inkjet printed all SWNT network layers were dried under vacuum oven at 35 °C for 1 h and then, gently washed by DI water to remove SDS residues. The resulting devices were further dried under vacuum at 35 °C for 1 h.

Using mentioned R2R gravure printer and inks, we obtained the parabolic gate electrodes (Fig. 3a) with a peak thickness of 680 nm, a line width of 297 μm and a surface roughness of about 30 nm, and dielectric layer with a peak thickness of 2.48 μm and a surface roughness of 200 nm (Fig. 3b). The drain–source electrodes were continuously R2R gravure printed at 3rd printing unit in Fig. 1a using the same gravure inks to print gate electrodes. The height of drain–source electrodes were about 680 nm as shown in the cross-sectional SEM image (Fig. 3b). The details of R2R gravure printed electrodes could be referred from our previous report [9]. For the active layer, we considered SWNTs, having high intrinsic mobility and stability, as a network structure of active layer because the network structure of SWNTs will overcome the surface roughness of the printed dielectric layers and long channel length (150 μm) [13,21–23]. We used a long channel length to compensate the limit of overlay printing registration accuracy of 20 μm. To print active layers on the R2R gravure printed precursors, we print well dispersed individual SWNTs as an active layer by using inkjet printer (Dimatix Materials Printer, 16 nozzles at 254 μm spacing) as shown in Fig. 1b. In this work, since drive (low current) and load (high current) PTFTs were needed to design printed circuits, inverter and multi-stage ring oscillator, using only p-channel PTFTs, we changed the network density of SWNTs in the active layer by managing inkjet printing times (drive: printing one time and load: printing three times) to adjust I_{DS} (drain/source current) instead of having different physical dimensions such as channel length and width. This will be a big advantage of using printing method in integrating SWNT based TFTs over the photolithography.

Fig. 2 shows the R2R gravure printed precursor (Fig. 2a) (include gate, dielectric layer, drain and source electrodes) and all printed fTFT (Fig. 2b) with a channel length of L = 150 μm and width of W = 3000 μm. All electrical characterization of PTFTs was carried out under ambient conditions using a semiconductor parameter analyzer (Agilent 4155C), and typical IV characteristics were shown in Fig. 4. The variation in the output characteristics as shown in Table 1 is mainly originated from the misalignment of printed drain–source electrodes on the printed active layer which causes uneven parasitic capacitances. Because of this effect, the effective channel mobility is changed. Another reason for the uneven electrical characteristics of the PTFTs may due to the variation in the surface roughness, waviness and thickness of the electrodes and dielectric layer through R2R gravure printing process. To find out a key factor among major factors influencing on PTFTs, we measured and calculated mobility based on the attained

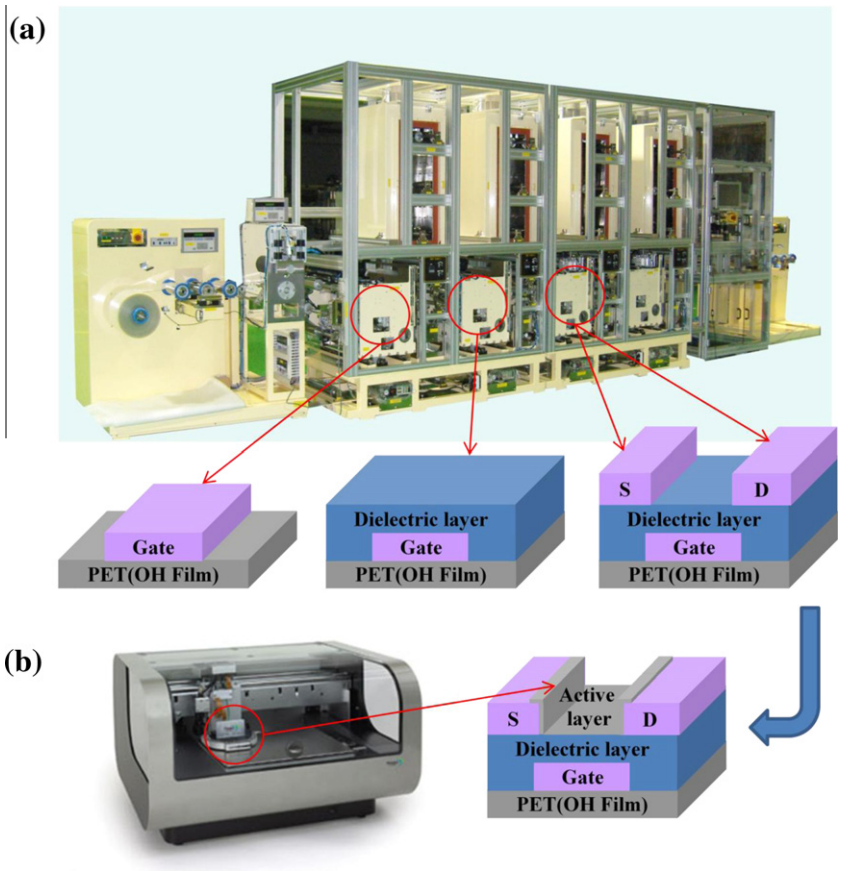

Fig. 1. Actual image of R2R gravure with four color units (a) and inkjet printer (b).

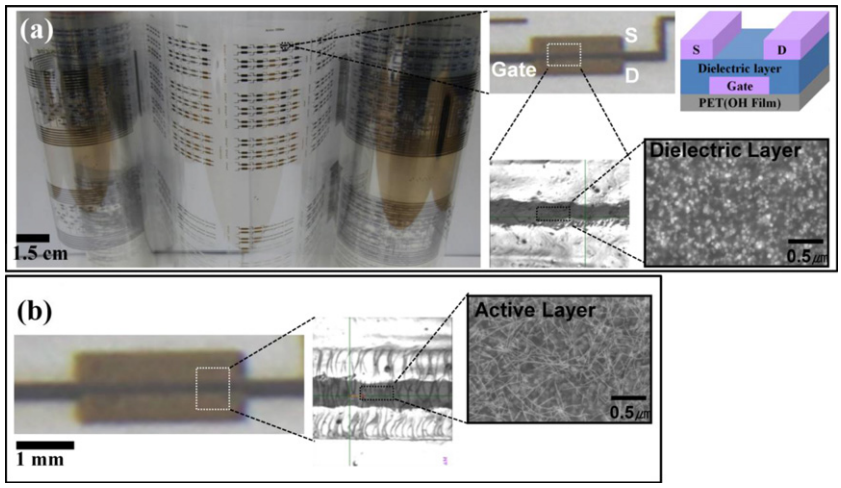

Fig. 2. Optical image of R2R gravure printed precusor and SEM image of R2R gravure printed dielectric layer between drain and source electrodes (a). All printed TFT and SEM image of SWNT (b) as an active layer using the inkjet printing method.

parasitic capacitances generated by misalignment between printed gate and drain–source electrodes. As shown in Table 1, the influence of parasitic capacitance on the major parameters such as transconductance, mobility and threshold voltage is dominant. Therefore, the minor things such as the variation in the surface roughness, waviness and thickness of the gravure printed electrodes and dielectric layer would not consider in this paper. Although the at-

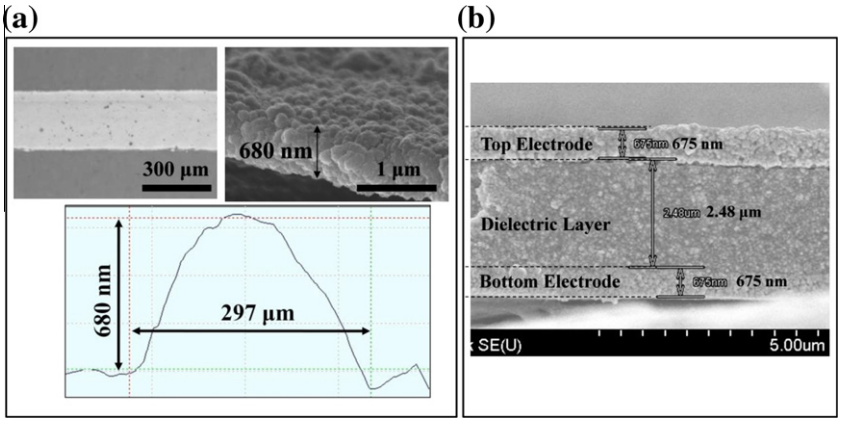

Fig. 3. Optical image, cross-sectional SEM image and cross-sectional profile (a) of the optimized surface roughness, line widening and thickness of printed electrode. Cross-sectional SEM image (b) of the R2R gravure printed precursor.

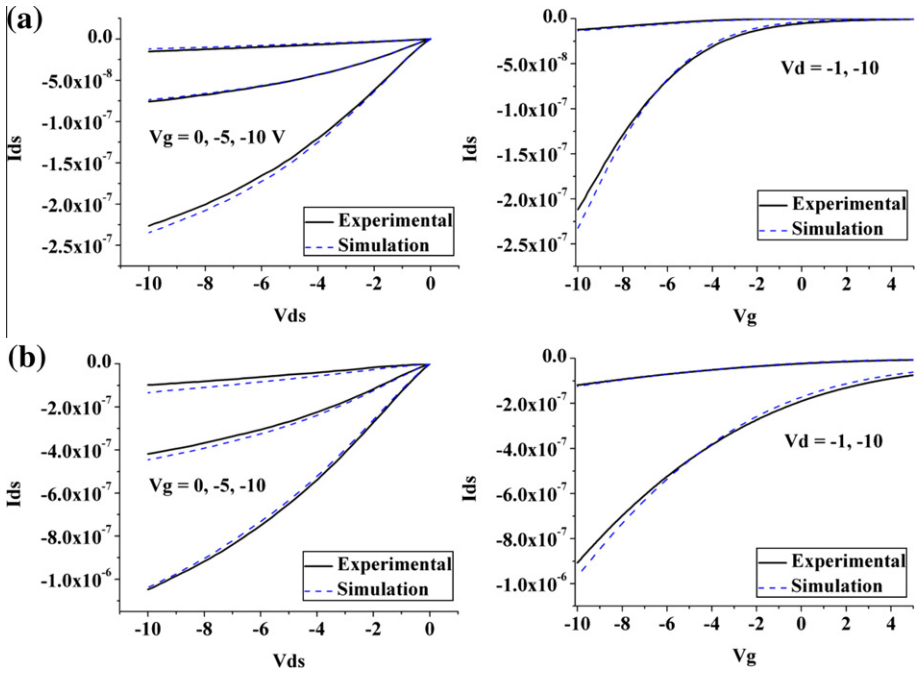

Fig. 4. Simulated and measured *IV* characteristic curve of the SWNT based PTFT for the driver (a) and load (b), respectively.

tained mobilities of SWNT based PTFTs (Table 1) are modest, the mobility can be simply improved by reducing the channel length and defect sites of network structure of SWNTs. Table 1 shows the measured and the calculated output at V_g of −10 V for each 10 different PTFTs (five driver fTFTs, five load fTFTs) with the consideration of parasitic capacitances between gate–drain and gate–source electrodes. Since those parasitic capacitances are strongly relied on the overlay printing registration accuracy and waviness of printing process between gate and drain–source electrodes, the electrical properties of PTFTs are strongly depending on the overlay printing registration accuracy of the R2R gravure printing process. Based on the observed electrical characteristics and standard equation for Si based TFT, we have extracted the parameters of electronic property of the PTFTs to design simulation model which describes the static and the dynamic behaviors of all printed SWNTn–fTFTs with sufficient accuracy.

The modeling of the PTFTs was performed using AIM-extract and AIM-spice software. The software includes various TFT models. Among of them, we employed the level 15 model (amorphous-silicon TFT model) [24] which shows the behavior of organic semiconductors in similar [20,25,26]. The parameters for the PTFT were determined in two steps. In the first step, the mobility was calculated from the measured output and transfer characteristics following standard equations [20] (refer the Supplementary Information). In the second step, the parameter extractor

Table 1
The measured and calculated properties of printed SWNT–TFTs (ε_r: relative dielectric constant, g_m: transconductance, S.S: sub-threshold swing, V_{TH}: threshold voltage, u: mobility).

Sample number	Dielectric thickness		Parasitic cap		Channel L/W (μm)	On current	Off current	On/off ratio from V_g-I_{DS} (Vds-I_{DS})	g_m (nS)	S.S (V/dec)	V_{TH} (V)	u (cm^2/V s)
	Cap.	ε_r	*G–D*	*G–S*								
			Length									
Driver 1	2.9 μm		7 pF	9.3 pF	150/3000	455 nA	8.1 nA	1000 (56)	1.35	2.1	−1.9	0.014
	4.8 nF	15	100 μm									
Driver 2	2.9 μm		10 pF	9.9 pF	150/3000	348 nA	8.9 nA	1000 (39)	0.84	3.6	−3	0.009
	4.8nF	15	100 μm									
Driver 3	2.9 μm		9.6 pF	10 pF	150/3000	332 nA	3.7 nA	1000 (90)	0.56	2.1	−2.2	0.006
	4.8 nF	15	100 μm									
Driver 4	2.9 μm		7 pF	5.8pF	150/3000	239 nA	2.3 nA	1000 (104)	0.41	1.6	−3.1	0.007
	4.8 nF	15	100 μm									
Driver 5	2.9 μm		6.4 pF	7.8pF	150/3000	413 nA	2.0 nA	1000 (207)	0.84	2.3	−2.1	0.009
	4.8 nF	15	100 μm									
Load 1	2.9 μm		7.3 pF	11 pF	150/3000	3.2 μA	220 nA	1000 (15)	11.9	6.1	−1	0.12
	4.8 nF	15	100 μm									
Load 2	2.9 μm		11 pF	10 pF	150/3000	2.88 μA	192 nA	200 (15)	10.3	9	−0.3	0.11
	4.8 nF	15	100 μm									
Load 3	2.9 μm		11.5 pF	8.4pF	150/3000	2.22 μA	103 nA	1000 (21)	6.1	5.9	−1.1	0.063
	4.8 nF	15	100 μm									
Load 4	2.9 μm		9.5 pF	7.3pF	150/3000	3.48 μA	228 nA	1000 (15)	20	6.3	−1.8	0.21
	4.8 nF	15	100 μm									
Load 5	2.9 μm		7.3 pF	7 pF	150/3000	2.98 μA	170 nA	800 (18)	8.95	6.4	−0.6	0.093
	4.8 nF	15	100 μm									

of AIM-spice was used to fit the whole parameter set for the level 15 model. Using the extracted value from the PTFTs, a good agreement between simulation and experimental results could be achieved. Fig. 4a and b shows the *IV* characteristic curves of the PTFT simulation model (blue[1] dash line) and the measured values (black solid line) of the drive and load transistor.

The inverter is the most basic building block for the construction of electronic circuits. Fig. 5a shows p-channel based inverter which consists of drive p-channel PTFT and load p-channel PTFT with same physical dimension. In this work, the network density of SWNTs at the channel was tuned by jetting times of inkjet to control the current levels instead of having different physical dimension. Fig. 5b shows the measured inverter transfer characteristic curve (black solid line) and the simulation model (blue dash line) for p-channel based all printed inverter with gain of 3.4.

Using the described SWNTn–PTFT and inverter model, a five-stage ring oscillator circuit was simulated and then printed. Fig. 6a shows the optical image of the printed five-stage ring oscillator. This circuit is composed of five inverters, each inverter consisted of two p-channel PTFTs. To measure the ring oscillator frequency performance, the output stage of the five-stage ring oscillator was connected in series with a voltage follow circuit and a common voltage of −10 V was applied. The ring oscillator starts oscillating if the supply voltage reaches an onset value, which depends on circuit design, overlap capacitance, threshold voltage, and on/off ratio. With the five-stage ring oscillator mentioned above, the onset voltage was about

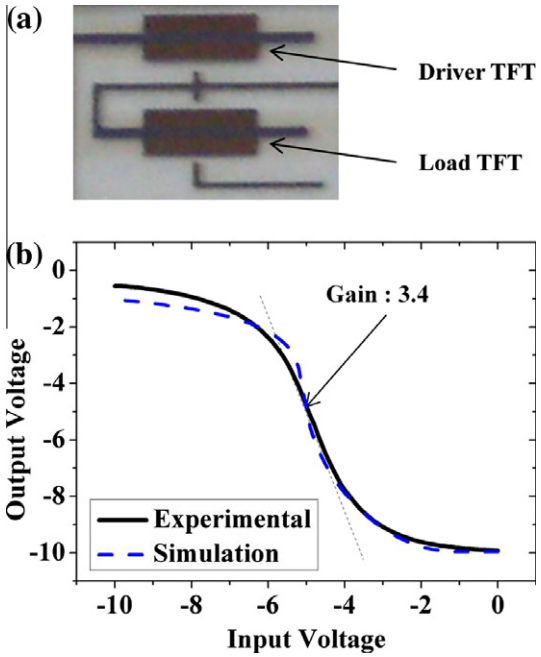

Fig. 5. Optical image of printed inverter (a), and simulated and measured dc characteristic curve of the printed inverter.

−8 V, and with a supply voltage of −10 V, a frequency of 114.6 Hz was reached (Fig. 6b, black solid line). This is equivalent to a stage delay of 1.75 ms.

The ring oscillator frequency is limited by the charging and discharging time of the capacitive load of a stage output, which is the sum of the input capacitance of the following stage and a parasitic capacitance. Therefore, the

[1] For interpretation of color in Figs. 4–6 the reader is referred to the web version of this article.

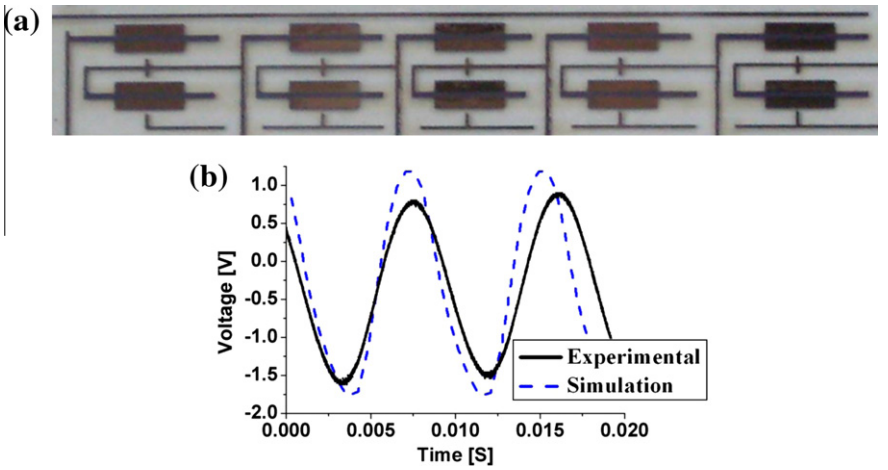

Fig. 6. Optical image of all printed p-channel inverter based five-stage ring oscillator (a) and simulated and measured output signal of the printed five-stage ring oscillator.

delay per stage of a ring oscillator could be estimated by using the RC (resistor–capacitor) charging/discharging circuit which can be written as Eq. (1) [27]

$$t = M \times R \times C = M \times C \times \frac{V_{OSC}}{I_{DS}} \quad (1)$$

where, M is the constant value which has 5–10 in RC circuit, C is the total overlap capacitance in the five stage ring oscillator, V_{osc} is the oscillation amplitude, and I_{DS} is the current that is switched. In our five-stage ring oscillator, C = 28 pF, V_{osc} is 2.58 V, and the I_{DS} is measured with semiconductor parameter analyzer (Agilent 4155C) to be 0.76 μA. The total delay of all the stages is calculated to be $(10 \times (10 \times C + C_{probe}) \times V_{osc}/I)$ = 9.95 ms (equivalent to a stage delay of 2 ms). C_{probe} is the probe capacitance which is 13 pF for the probe used in our measurement. In this research, all electrical measurements of the PTFT, inverter, and five-stage ring oscillator were carried out under ambient conditions using a semiconductor parameter analyzer (Agilent 4155C) and set up with DC power supply (HP 1245), a function generator (Tektronix AFG 3022), LCR meter (Agilent E4980A), and a digital oscilloscope (Tektronix DPO 4032).

The simulation result (Fig. 6b, blue dot line) shows the amplitude of 2.91 V and oscillation frequency of 123.1 Hz in a good agreement with the measured output signal (Fig. 6b, black solid line). However the amplitude of the simulated output is higher than measured output. The reason for this discrepancy could be caused by the input impedance of the measurement equipment. This load on the output of the oscillator can be responsible for the lower oscillation amplitude and frequency.

In summary, R2R gravure and inkjet printing process were employed for the fabricating the SWNTn–TFTs on plastic foils to show the possibility of all R2R gravure printed circuits. Based on the fully printed SWNTn–PTFTs on PET foils, we have made a simulation model for an inverter and a five-stage ring oscillator. The inverter had gain of 3.4 with a good agreement between simulation and experimental results. Based on the known our knowledge, the attained gain of 3.4 under the operation voltage of 10 V is highest one among fully printed fTFTs on plastic foils. The printed ring oscillator exhibited 114.6 Hz of oscillation frequency and 1.75 ms per stage of propagation stage delay at Vds = −10 V. The calculated oscillation frequency based on each inverters and simulation model of five-stage ring oscillator respectively had a stage delay time of 1.99 and 1.62 ms at Vds = −10 V with high output voltage accuracy. The mismatch between simulated and experimental values is pretty acceptable with a circuit design using reasonable number of transistors, but may be noticeable as increasing number of transistors because electrical performance of TFTs is going to more strongly influenced on the roughness of gate dielectric layers and even small misalignment of drain–source electrodes [28–30]. Therefore, controlling roughness of R2R gravure printed dielectric layers and overlay printing registration accuracy need to be first addressed for the integration of SWNTn–PTFTs on plastic foils. This result indicates that more complex circuits can be easily simulated with the viewpoint of static and dynamic behavior, and the circuits made of all printed fTFTs can be applicable to flexible electronics with a modest supply voltage (<20 V) in mass production.

Acknowledgments

We are grateful to the World Class University Program at Sunchon National University and MKE for their support in the research consortium for developing roll-to-roll printed RFID tags.

Appendix A. Supplementary data

Supplementary data associated with this article can be found, in the online version, at doi:10.1016/j.orgel.2011.09.006.

References

[1] W. Fix, A. Ullmann, J. Ficker, W. Clemens, Appl. Phys. Lett. (81) (2002) 1735.

[2] S.H. Han, S.M. Cho, J.H. Kim, J.H. Kim, J.W. Choi, J. Jang, Appl. Phys. Lett. (89) (2006) 093504.
[3] P.F. Baude, D.A. Ender, M.A. Haase, T.W. Kelley, D.V. Muyres, S.D. Theiss, Appl. Phys. Lett. 82 (2003) 3964.
[4] B. Crone, A. Dodabalapur, R. Sarpeshkar, A. Gelperin, H.E. Katz, Z. Bao, J. Appl. Phys. 91 (2002) 10140.
[5] P. Mach, S.J. Rodriguez, R. Nortrup, P. Wiltzius, J.A. Rogers, Appl. Phys. Lett. 78 (2001) 3592.
[6] H.E.A. Huitema, G.H. Gelinck, J.B.P.H. van der Putten, K.E. Kuijk, K.M. Hart, E. Cantatore, D.M. de Leeuw, Adv. Mater. 14 (2002) 1201.
[7] V. Subramianian, J.M.J. Frechet, P.C. Chang, D.C. Huang, J.B. Lee, S.E. Molesa, A.R. Murphy, D.R. Redinger, S.K. Volkman, Proc. IEEE 93 (2005) 1330.
[8] N. Lim, J. Kim, S. Lee, N. Kim, G. Cho, IEEE Trans. Adv. Pack. 32 (2009) 72.
[9] M. Jung, J. Kim, J. Noh, N. Lim, C. Lim, G. Lee, H. Kang, K. Jung, A.D. Leonard, J.M. Tour, G. Cho, IEEE Trans. Elec. Dev. 57 (2010) 571.
[10] J. Noh, D. Yeom, C. Lim, H. Cha, J. Han, J. Kim, Y. Park, V. Subramanian, G. Cho, IEEE Trans. Elec. Pack. Man. 33 (2010) 275.
[11] M. Voigt, A. Guite, D. Chung, R. Khan, A. Campbell, D. Bradley, F. Meng, J. Steinke, S. Tierney, I. McCulloch, H. Penxten, L. Lutsen, O. Douheret, J. Manca, U. Brokmann, K. Sonnichsen, D. Hulsenberg, W. Bock, C. Barron, N. Blanckaert, S. Springer, J. Crupp, A. Mosley, Adv. Func. Mat. 20 (2010) 239.
[12] B. Crone, A. Dodabalapur, Y.-Y. Lin, R.W. Filas, Z. Bao, A. Laduca, R. Sarpeshkar, H.E. Katz, W. Li, Nature 403 (2004) 521.
[13] Q. Cao, H.S. Kim, N. Pimparkar, J.P. Kulkarni, C. Wang, M. Shim, K. Roy, M.A. Alam, J.A. Rogers, Nature 454 (2008) 495.
[14] W. Clemens, W. Fix, J. Ficker, A. Knobloch, A. Ullmann, J. Mater. Res. 19 (2004) 1963.
[15] T.W. Kelley, P.F. Baude, C. Gerlach, D.E. Ender, D. Muyres, M.A. Haase, D.E. Vogel, S.D. Theiss, Chem. Mater. 16 (2004) 4413.
[16] A.C. Huebler, F. Doetz, H. Kempa, H.E. Katz, M. Bartzsch, N. Brandt, I. Hennig, U. Fuegmann, S. Vaiyanathan, J. Granstrom, S. Liu, A. sydorenko, T. Zilliger, G. Schmidt, K. Preissler, E. Reichmanis, P. Eckerle, F. Richter, T. Fischer, U. Hahn, Org. Elect. 8 (2007) 480.
[17] M. Hambsch, K. Reuter, M. Stanel, G. Schmidt, H. Kempa, U. Fugmann, U. Hahn, A.C. Hubler, Mat. Sci. Eng. B 170 (2010) 93.
[18] S. Hur, A. Gaur, O. Park, M. Shim, J. Rogers, J. Appl. Phys. 98 (2005) 114302.
[19] P. Beecher, P. Servati, A. Rozhin, A. Colli, V. Scardaci, S. Pisana, T. Hasan, A. Flewitt, J. Rogers, G. Hsieh, Appl. Phys. 102 (2007) 043710.
[20] M. Bartzsch, H. Kempa, M. Otto, A. Hubler, D. Zielke, Org. Elec. 8 (2007) 431.
[21] A. Javey, J. Guo, Q. Wang, M. Jundstrom, H. Dai, Nature 424 (2003) 654.
[22] Z. Chen, J. Appenzeller, Y. Lin, J. Oakley, A. Rinzler, J. Tang, S. Wind, P. Solomon, P. Avouris, Science 311 (2006) 1735.
[23] M. Ha, Y. Xia, A. Green, W. Zhang, M. Renn, C. Kim, M. Hersam, C. Frisbie, ACS Nano. 8 (2010) 4388.
[24] Aim-Software, AIM-Spice Reference Manual, Version 4.0a, 2004.
[25] F. Schauer, J. Appl. Phys. 86 (1999) 524.
[26] P.V. Necliudov, M.S. Shur, D.J. Gundlach, T.N. Jackson, J. Appl. Phys. 88 (2000) 6594.
[27] Y.Y. Lin, A. Dodabalapur, R. Sarpeshkar, Z. Bao, W. Li, K. Baldwin, V.R. Raju, H.E. Katz, Appl. Phys. Lett. 74 (1999) 2714.
[28] S.E. Fritz, T.W. Kelley, C.D. Frisbie, J. Phys. Chem. B 109 (2005) 10574.
[29] S. Steudel, S. Vusser, S. Jonge, D. Janssen, S. Verlaak, J. Genoe, P. Heremans, Appl. Phys. Lett. 85 (2004) 4400.
[30] D. Knipp, R.A. Street, A.R. Volkel, Appl. Phys. Lett. 82 (2003) 3907.

process of ITO thin film and sputtering process also increases the complexity of device fabrication.

Although many efforts have been made on the T/SOLEDs, fabricating white T/SOLEDs with microcavity effects still leaves a door open. The difference in luminance, efficiency and chromaticity coordinates for the emission from both sides was hardly avoided in T/SOLEDs owing to an asymmetric structure of light propagation. In this article, we designed and fabricated a new type of SWOLED with the same electrode composition of a semitransparent multilayer of $(Ag/Alq_3)_2$ and $(Alq_3/Ag)_2$ as the cathode and anode, respectively. The device showed few differences in luminance, efficiency and spectra from both sides. Furthermore, this kind of electrode can be potentially fabricated on the soft substrate for flexible OLEDs, like the similar structure electrodes (for example, ITO/Ag/ITO, Al/Alq_3/Al, ZnS/Ag/WO_3) utilized in flexible OLEDs [27–29].

We designed SWOLED (device A) consisting of glass substrate/$(Alq_3/Ag)_n$/MoO_3 (1.5 nm)/4,4′,4″-tris(3-methylphenyl-phenylamino)-triphenylamine (*m*-MTDATA, 30 nm)/*N*,*N*′-bis-(1-naphthyl)-*N*,*N*′-diphenyl-1, 1-biphenyl-4,4′-diamine (NPB, 10 nm)/4,4′-bis(2,2′-diphenylvinyl)-1,1′-biphenyl (DPVBi, 15 nm)/4,4-*N*,*N*-dicarbazole-biphenyl (CBP, 3 nm)/CBP:bis(2-(2-fluorphenyl)-1,3-benzothiozolato-*N*, C2′)iridium(acetylacetonate) [$(F–BT)_2Ir(acac)$] (7 nm)/4,7-diphenyl-1,10-phenanthroline (Bphen, 35 nm)/LiF (1 nm)/Al (1 nm)/$(Ag/Alq_3)_n$. In this device, *m*-MTDATA, NPB, DPVBi, CBP:(F–BT)2Ir(acac), Bphen, and LiF/Al/Ag/M/A/M were used as the hole injection layer (HIL), hole transporting layer (HTL), blue emitting layer, orange emitting layer, electron transporting layer (ETL), respectively. The neat CBP was introduced to separated blue and orange emitting layers to avoid the Dexter energy transfer between the two emitters. For comparison, the bottom-emitting device (ITO glass substrate) with the same organic layers (device B) and 100 nm Al as a cathode was fabricated. The thickness of each layer was optimized according to the analysis below. The deposition of layers and the measure of devices characteristics were described before [16]. The transmission spectrum was measured by means of ultraviolet/visible spectrometer (UV 1700, Shimadzu).

Fig. 1a shows the transmittance and reflectance spectra of the electrodes with different thickness of Alq_3. Considering the transmittance and electrical characteristics of the electrodes, a thin Ag layer can have high transmittance and a thick Ag layer can have high conduction, 22 nm Ag layer is chosen. As can be seen, the peak of transmittance/reflectance shift to longer wavelength as the thickness of Alq_3 increased. As depicted in Ref. [30], two resonant cavity modes are necessary in our devices. In order to obtain high effective microcavity devices, a moderate transmittance and reflectance is need near the resonant wavelengths (RWs) 448 and 590 nm, so 80 or 85 nm Alq_3 is chose. Fig. 1b shows the absorption spectra of the electrodes. We can see that a larger absorption is obtained at long wavelength region. Considering the absorption of the electrodes, 85 nm Alq_3 layer is better due to lower absorption of electrode than that of 80 nm Alq_3.

In addition, we calculated the cavity emission by considering wavelength-independent intrinsic luminescence spectra of the emitters [31] in order to clarify the microcavity effect in the device and optimize the parameters of device A. The peak wavelength of the resonant cavity mode is dependent on the optical thickness of the cavity region and the Bragg peak wavelength of the electrodes [32]. Thus, in order to adjust the position of the resonant peak, we only change the thickness of the hole injection layer and electron transporting layer and hold other layers constant when altering the optical thickness of the cavity region. Fig. 2a and b shows the cavity emission from Ag side (cathode side) and glass side (anode side), respectively. Different thickness active layers, 90, 100, 110, 130, and 150 nm are adopted and the thickness of the electrodes is constant, 22 and 85 nm for Ag and Alq_3, respectively. We can see that two resonant peaks are obtained and the RWs shift towards longer wavelength region with the active layers thickness increasing. In order to obtain high effective device we choose the thickness of 100 nm for active layers considering the emission peaks of blue (DPVBi, emission peak at 448 nm) and yellow [$(F–BT)_2Ir(acac)$, emission peak at 548 and a shoulder peak at 590 nm] emitters. Meanwhile, we can see that almost the same emission can be obtained from both sides of the device.

In addition, we can also confirm the position of the resonant peak by utilizing the Fabry–Perot peak condition

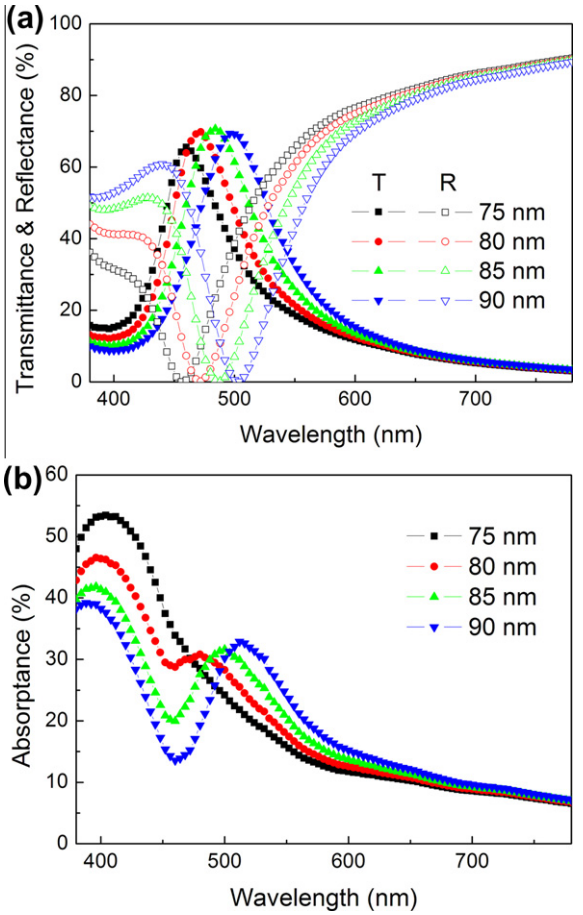

Fig. 1. (a) The transmittance, reflectance and (b) absorption spectra of the electrodes with different Alq_3 thickness.

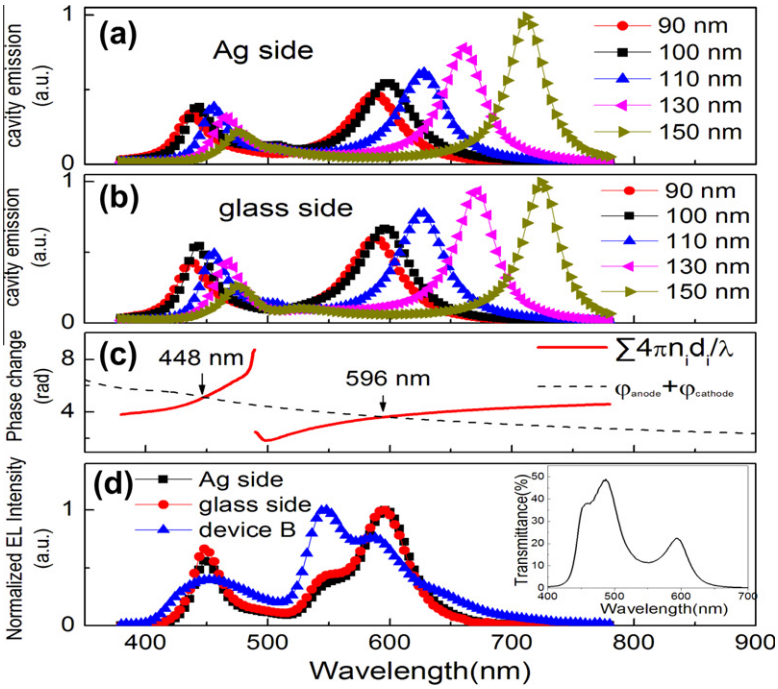

Fig. 2. The cavity emission from (a) Ag side (cathode) and (b) glass side (anode) with different thickness active layers; (c) the calculated round-trip phase changes for 100 nm organic layers between two electrodes and the phase changes for two electrodes; (d) the normalized measured EL spectra for devices A and B. Inset is the measured transmission for device A.

[33]. The resonant wavelength (RW) condition of the microcavity for normal incidence is determined by the below equation:

$$\sum_i \frac{4\pi d_i n_i(\lambda)}{\lambda} - \varphi_{\text{cathode}}(0,\lambda) - \varphi_{\text{anode}}(0,\lambda) = 2m\pi$$

where λ is the emission wavelength, $\varphi_{\text{cathode}}(0, \lambda)$ and $\varphi_{\text{anode}}(0, \lambda)$ are the angle- and the wavelength-dependent phase changes on reflection from top cathode and bottom anode, respectively, and m is an integer that defines the mode number (in our work, we choose $m = 0$), $n_i(\lambda)$ and d_i are the refractive index and thickness of organic layers.

Fig. 2c shows the calculated round-trip phase changes for 100 nm organic layers sandwiched between two reflection electrodes [i.e., $\varphi_1(\lambda) = \Sigma 4\pi n_i(\lambda) d_i/\lambda$], and the phase shift at two reflective electrodes [i.e., $\varphi_2(\lambda) = \varphi_{\text{cathode}}(\lambda) + \varphi_{\text{anode}}(\lambda)$] in forward direction. The points of the intersection of $\varphi_1(\lambda)$ and $\varphi_2(\lambda)$ are the RWs of the device. Two RWs at 448 and 596 nm will occur in the designed device. The detail calculations were described before [14,15]. Fig. 2d shows the normalized measured EL spectra at voltage of 8 V for devices A and B in forward direction. The spectrum of the device B shows two main peaks at 448 and 548 nm originating from DPVBi and $(F–BT)_2Ir(acac)$, respectively. The shoulder peak is at 590 nm. Device A shows two resonant emission peaks at 448 and 596 nm for both sides, which are in excellent agreement with the calculated results. It can be seen that the spectra for Ag- and glass-side have only little difference. In other words, we can obtain almost the same emission from both sides with this structure. Comparing these two devices, the narrower full width at half maximum (FWHM) of the DPVBi and $(F–BT)_2Ir(acac)$ emission in device A is observed (for example, the FWHM of the $(F–BT)_2Ir(acac)$ is 90 nm for device B and 28 nm for device A). This result also indicates that strong microcavity effect is occurred in this SWOLED. Inset shows the measured transmittance of the device in forward direction. As can be seen, the device has two transmission peaks at 487 and 592 nm and a shoulder peak at 456 nm, which is the characteristic of periodic structure electrodes.

Fig. 3a and b shows the normalized EL spectra at viewing angle of 0°, 30°, and 60° and a voltage of 8 V for Ag side and glass side, respectively. As can be seen, the experiment results (solid symbols) are in excellent agreement with the simulated results (open symbols) and the details of calculation is described before [16]. With the viewing angle increasing, the RWs shift to a shorter wavelength due to the microcavity effect for either Ag side (upper) or glass side (down). A white emission was obtained with CIE coordinates (0.424 and 0.347) [(0.402 and 0.344)] at a viewing angle of 0° and changing to (0.419 and 0.379) [(0.399 and 0.376)] at 30° and (0.368 and 0.456) [(0.351 and 0.458)] at 60° for Ag side (glass side). Fig. 4a and b shows the normalized measured EL spectra at voltage of 6, 8, and 10 V for device A in forward direction, for Ag side and glass side, respectively. We can see that the spectra are fairly stable over a range of operation voltages for both sides. In other words, the CIE coordinates are stable within the operation voltage, which are very important in displays and lighting. Fig. 3c indicates the measured angular distribution of the

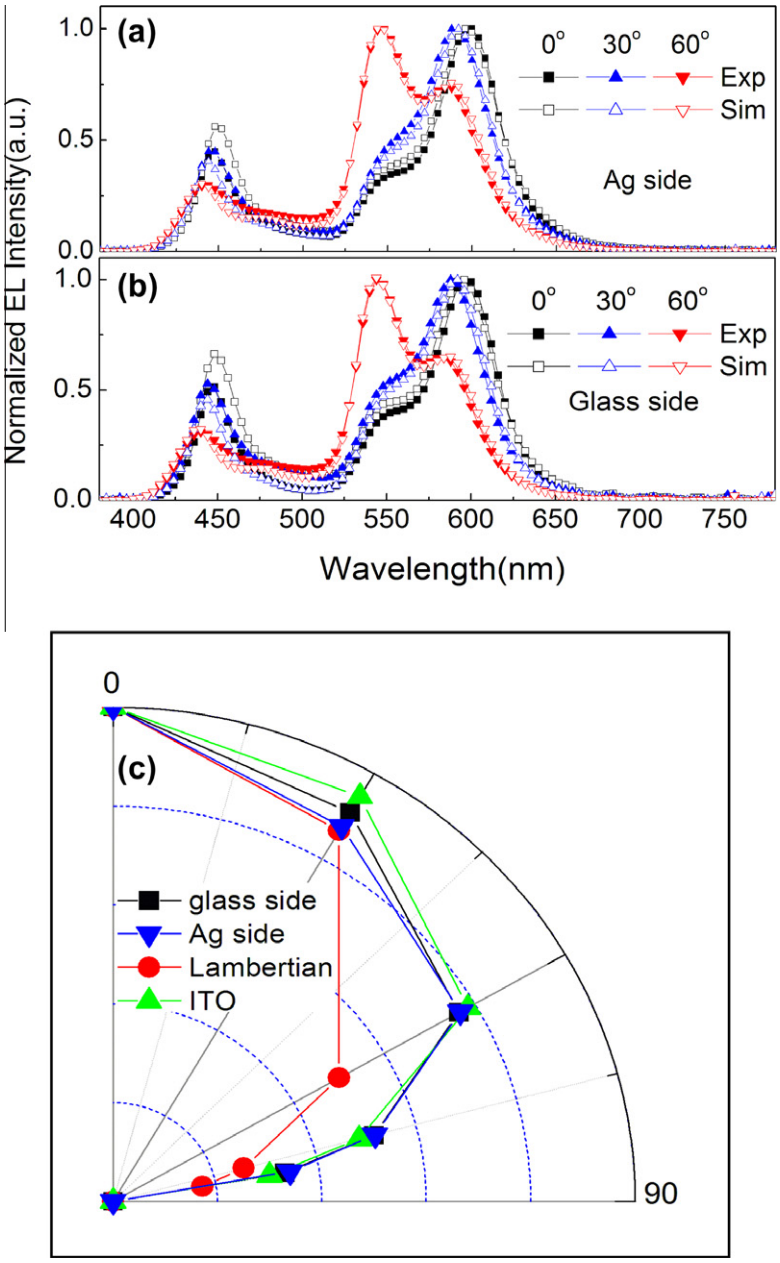

Fig. 3. (a) The normalized experimental (Exp) and simulated (Sim) EL spectra at different viewing angles and voltage of 8 V for (a) Ag side and (b) glass side; (c) the measured angular distribution of the devices and the red solid circle represents a Lambertian-type distribution. (For interpretation of the references to color in this figure legend, the reader is referred to the web version of this article.)

devices and the red solid circle represents a Lambertian-type distribution. We can see that the emission of SWOLED has the similar angular distribution as that of ITO-based OLED, which is a super-Lambertian distribution [16].

Fig. 5a shows the current density–luminance–voltage characteristics of the SWOLED. There is only little difference in luminance from both sides. For example, at the driving voltage of 10 V, the luminance for the Ag side and glass side is 2550 and 2423 cd/m^2, respectively. Fig. 4b shows the forward direction efficiency of the device A and B. The maximum efficiencies from Ag side and glass side of the SWOLED are 4.14 and 4.32 cd/A, respectively. The maximum total EL efficiency of the device is 8.46 cd/A, which is comparable to the corresponding bottom-emitting WOLED (9.20 cd/A).

Fig. 6 shows the transmittance, reflectance, and absorption spectra of the cathode (electrode 1) and anode (electrode 2). As can be seen, the two electrodes almost have the same spectral response, which ensures the uniform optical characteristics of the two sides for the SWOLED.

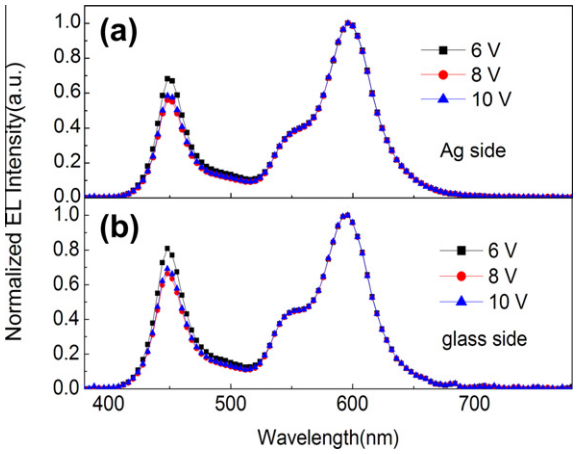

Fig. 4. The normalized measured EL spectra of device A at voltage of 6, 8, and 10 V, (a) Ag side and (b) glass side.

The loss due to the absorption by multilayer electrode is about 30%. The absorption at the RW is 20% (RW = 448 nm) and 15% (RW = 596 nm). Fig. 7 shows the ratio of air mode, glass mode, and nonemissive mode (waveguide mode and surface plasmon polaritons) to the total emission as a function of wavelength simulated by numerical method of the finite-difference time-domain (FDTD) [34]. The inset is the normalized PL spectra of the DPVBi and

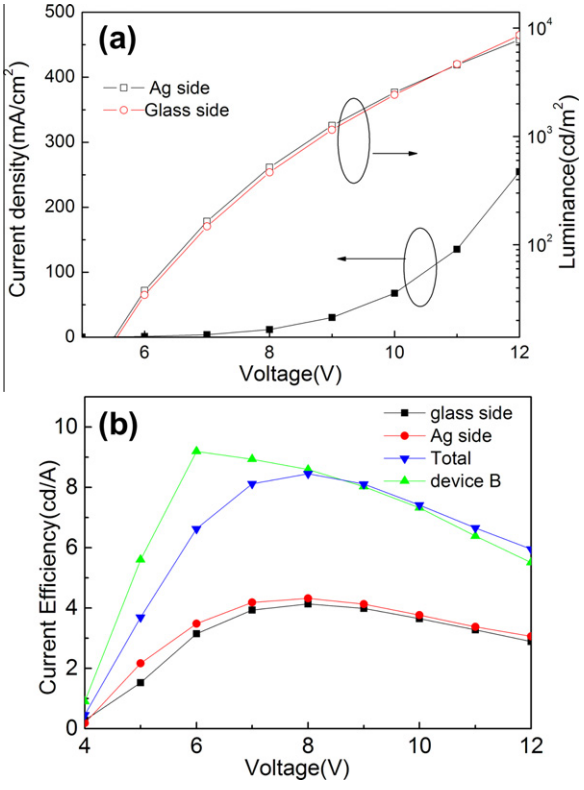

Fig. 5. (a) The voltage–current density–luminance characteristics of the devices; (b) the efficiency–voltage characteristics.

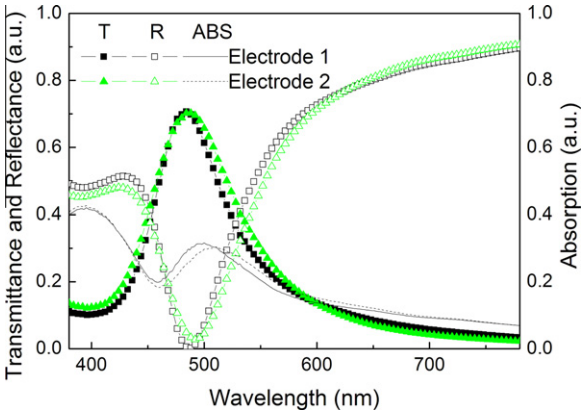

Fig. 6. The transmittance, reflectance and absorption spectra of the electrodes.

CBP:$(F–BT)_2Ir(acac)$. Thus, the light extraction efficiency of the SWOLED could be defined as $\eta_{ext} = \int_{380}^{780}[k_1 S_b(\lambda) + (1-k_1)S_y(\lambda)]\eta_{air}(\lambda)d\lambda$, where k_1 is the weight of the blue emission to the white emission. $S_b(\lambda)$ and $S_y(\lambda)$ are the photoluminescence (PL) spectrum normalized with its area of the blue and yellow emitting material. $\eta_{air}(\lambda)$ is the air mode of the SWOLED as function of wavelength. According to the EL spectra of the SWOLED, the weight of the blue emission to the white emission is about 40%. Thus, the calculated light extraction efficiency of the SWOLED is 11.3% which is less than that of the bottom device (~20%). However, the radiative quantum efficiency of the emissive materials will increase in the microcavity device due to the presence of the Purcell effect [35]. The calculated Purcell factor for the blue and yellow emitting material is 2.3 and 3.2 in the SWOLED, respectively. The PL quantum efficiency of DPVBi and CBP: $(F–BT)_2Ir(acac)$ are 0.4 and 0.62. Then, the improvement of the radiative quantum efficiency of DPVBi and $(F–BT)_2Ir(acac)$ is about 50% and 35%, respectively. As a result, the efficiency of the SWOLED is comparable to that of the corresponding bottom-emitting OLED.

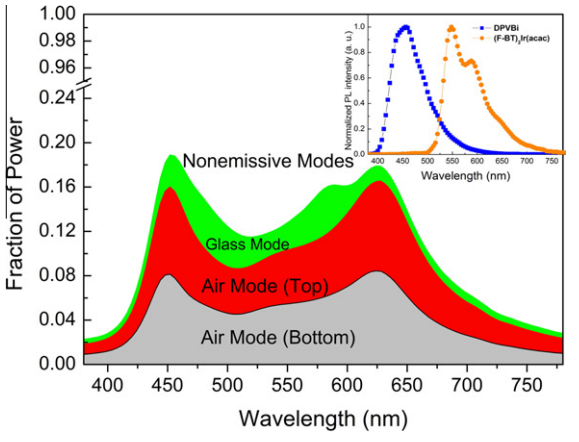

Fig. 7. The ratio of air mode, glass mode, and nonemissive mode to the total emission as a function of wavelength.

In summary, the SWOLED with $(Ag/Alq_3)_2$ electrodes was demonstrated, which showed few differences in luminance, spectra and efficiency. The total efficiency of the SWOLED is comparable to the corresponding bottom-emitting OLED. By changing optical thickness of the cavity region, we can adjust the RWs of the device. In fact, we can also adjust the optical characteristics (including the RWs and transmittance) of the device by adjusting the parameters of the electrodes. The results will provide guidance in fabrication of OLEDs with optimum performance, such as high efficiency, pure color emission, required transmittance, and flexible devices. At present, the SWOLEDs have the cavity effect which leads to an angular dependent EL emission. However, the devices can be used as the screens of mobile phones and smartphones that do not need high quality at a large viewing angle.

Acknowledgments

This work was supported by the National Natural Science Foundation of China (Grant Nos. 60937001, 11074096, 61077045, 61177026, 60723002, 10774060, and 10974071) and New Century Excellent Talents in University (No. 100446).

References

[1] R.H. Jordan, A. Dodabalapur, M. Strukeji, Appl. Phys. Lett. 68 (1996) 1192.
[2] H. Mattoussi, H. Murata, C.D. Merritt, Y. Lizumi, J. Kido, Z.H. Kafafi, J. Appl. Phys. 86 (1999) 2642.
[3] G. Gustafsson, Y. Cao, G.M. Treacy, F. Klavetter, N. Colaneri, A.J. Heeger, Nature 357 (1992) 477.
[4] G. Gu, P.E. Burrows, S. Venkatesh, S.R. Forrest, M.E. Thompson, Opt. Lett. 22 (1997) 172.
[5] A.B. Chwang, M.A. Rothman, S.Y. Mao, R.H. Hewitt, M.S. Weaver, J.A. Silvernail, K. Rajan, M. Hack, J.J. Brown, X. Chu, L. Moro, T. Krajewski, N. Rutherford, Appl. Phys. Lett. 83 (2003) 413.
[6] J.S. Lewis, M.S. Weaver, IEEE J. Sel. Top. Quant. 10 (2004) 45.
[7] B.J. Chen, X.W. Sun, S.C. Tan, Opt. Express 13 (2005) 937.
[8] G. Gu, V. Bulović, P.E. Burrows, S.R. Forrest, M.E. Thompson, Appl. Phys. Lett. 68 (1996) 2606.
[9] A. Yamamori, S. Hayashi, T. Koyama, Y. Taniguchi, Appl. Phys. Lett. 78 (2001) 3343.
[10] G. Parthasarathy, C. Adachi, P.E. Burrows, S.R. Forrest, Appl. Phys. Lett. 76 (2000) 2128.
[11] G. Parthasarathy, P.E. Burrows, V. Khalfin, V.G. Kozlov, S.R. Forrest, Appl. Phys. Lett. 72 (1998) 2138.
[12] S.F. Hsu, C.C. Lee, S.W. Hwang, C.H. Chen, Appl. Phys. Lett. 86 (2005) 253508.
[13] H. Kanno, Y. Sun, S.R. Forrest, Appl. Phys. Lett. 86 (2005) 263502.
[14] W.Y. Ji, L.T. Zhang, T.Y. Zhang, G.Q. Liu, W.F. Xie, S.Y. Liu, H.Z. Zhang, L.Y. Zhang, B. Li, Opt. Lett. 34 (2009) 2703.
[15] W.Y. Ji, L.T. Zhang, T.Y. Zhang, W.F. Xie, H.Z. Zhang, Org. Electron. 11 (2009) 202.
[16] W.Y. Ji, L.T. Zhang, R.X. Gao, L.M. Zhang, W.F. Xie, H.Z. Zhang, B. Li, Opt. Express. 16 (2008) 15489.
[17] C.J. Lee, R.B. Pode, J.I. Han, D.G. Moon, Appl. Surf. Sci. 253 (2007) 4249.
[18] P.E. Burrows, V. Khalfin, G. Gu, S.R. Forrest, Appl. Phys. Lett. 73 (1998) 435.
[19] G. Gu, V. Khalfin, S.R. Forrest, Appl. Phys. Lett. 73 (1998) 2399.
[20] G. Gu, G. Parthasarathy, P.E. Burrows, P. Tian, I.G. Hill, A. Kahn, S.R. Forrest, J. Appl. Phys. 86 (1999) 4067.
[21] P.E. Burrows, G. Gu, S.R. Forrest, E.P. Vicenzi, T.X. Zhou, J. Appl. Phys. 87 (2000) 3080.
[22] H. Peng, X. Zhu, J. Sun, Z. Xie, S. Xie, M. Wong, H. Kwok, Appl. Phys. Lett. 87 (2005) 173505.
[23] Q. Huang, K. Walzer, M. Pfeiffer, V. Lyssenko, G. He, K. Leo, Appl. Phys. Lett. 88 (2006) 113515.
[24] J. Meyer, T. Winkler, S. Hamwi, S. Schmale, H.H. Johannes, T. Weimann, P. Hinze, W. Kowlasky, T. Riedl, Adv. Mater. 20 (2008) 3839.
[25] T.Y. Zhang, L.T. Zhang, W.Y. Ji, W.F. Xie, Opt. Lett. 34 (2009) 1174.
[26] M.H. Lu, M.S. Weaver, T.X. Zhou, M. Rothman, R.C. Kwong, M. Hack, J.J. Brown, Appl. Phys. Lett. 81 (2002) 3921.
[27] J. Lewis, S. Grego, B. Chalamala, E. Vick, D. Temple, Appl. Phys. Lett. 85 (2004) 3450.
[28] L. Duan, S. Liu, D. Zhang, J. Qiao, G. Dong, L. Wang, Y. Qiu, J. Phys. D: Appl. Phys. 42 (2009) 075103.
[29] H. Cho, C. Yun, J.W. Park, S. Yoo, Org. Electron. 10 (2009) 1163.
[30] In our work, we achieve white light emission by complementary color, blue (emission peak at 448 nm) and yellow (emission peak at 548 nm). So a cavity with two resonant cavity modes is enough. The device with electrode $(Ag/Alq_3)_2$ can has two peak wavelengths according to our report [Ji et al., Curr. Appl. Phys. 11 (2011) 1410], so we choose $n = 2$ in this work. The peak wavelength of the resonant cavity mode is dependent on the optical thickness of the cavity region and the Bragg peak wavelength of the electrodes as depicted in Ref. [32]. We choose 85 nm Alq_3 layer to make the electrode have two Bragg peak wavelengths near 448 and 590 nm.
[31] P. Freitag, S. Reineke, S. Olthof, M. Furno, B. Lüssem, K. Leo, Org. Electron. 11 (2010) 1676.
[32] D.P. Puzzo, M.G. Helander, P.G. O'Brien, Z.B. Wang, N. Solheilnia, N. Kherani, Z.H. Lu, G.A. Ozin, Nano Lett. 11 (2011) 1457.
[33] A.B. Djurišić, A.D. Rakić, Appl. Opt. 41 (2002) 7650.
[34] A. Chutinan, K. Ishihara, T. Asano, M. Fujita, S. Noda, Org. Electron. 6 (2005) 3.
[35] S. Nowy, B.C. Krummacher, J. Frischeisen, N.A. Reinke, W. Brütting, J. Appl. Phys. 104 (2008) 123109.

semiclassical Marcus charge transfer (CT) rate theory [8] has long been used to describe the charge transport in organic semiconductors [9–11]. By comparison, it has been known for more than 10 years that charge mobility of highly pure and defect-free molecular single crystals decreases with temperature following a negative power law [12,13], which has been taken as strong evidence for band-like transport in organic semiconductors. Later, a temperature-independent mobility has been observed in pentacene OTFTs which further complicates the charge transport mechanism [2]. In fact, there are structural defects in organic semiconductors [6,14] which can create localized electronic states to influence the charge transport [15,16]. To include the effect of traps for charge transport, a multiple trapping and release model has been developed where charge transport occurs in delocalized bands, but is restrained by a distribution of shallow traps near band edges [17–19]. Most of the charge carriers are assumed to be trapped in localized states. The amount of released charge carriers to an extended-state transport level depends on the energy level of the localized states, the temperature, and the gate voltage. However, unlike inorganic semiconductors where atoms are strongly bound by covalent interactions, molecules in organic semiconductors are held together by weak interactions between adjacent molecules [20,21], which results in a narrow bandwidth. Furthermore, the strong thermal fluctuation of transfer integrals can destroy the translational symmetry of the electronic Hamiltonian [22], so the mean free path of charge carriers becomes shorter than the lattice constant at high temperature [23]. Thus, the extended-state transport is unlikely in organic semiconductors. To avoid the band-like picture, a variable-range hopping model has then been proposed [24]. In this model, the charge transport is governed by thermally activated tunneling of carriers between localized states, but a carrier may either hop over a small distance with a high activation energy or hop over a long distance with a low activation energy. While this theory seems to be able to explain the gate voltage and the temperature dependence of the mobility in the literature, it still suffers from a lack of physical justification [25]. Instead, the picture of carrier hopping between neighboring localized states has successfully described the charge transport in organic semiconductors [26–28] although the band-like transport cannot be explained from the hopping model with the semiclassical Marcus CT rate theory. To reconcile the discrepancy, a quantum CT rate theory with first-order perturbative nature has been used to study the charge transport in organic semiconductors [29,30]. It is found that the nuclear tunneling effect can largely reduces the activated energy between two adjacent localized states, which then leads to the band-like transport in organic semiconductors. The importance of quantum treatment for the nuclear degrees of freedom has also been pointed out during the simulation for organic photovoltaic material [31]. Thus, it is helpful to understand the charge transport in organic semiconductors by using a CT rate theory beyond the semiclassical Marcus CT rate theory. Along this way, it is found that the molecular packing in organic semiconductors often makes the first-order perturbative approximation in the semiclassical Marcus CT theory invalid [32], so a quantum CT rate theory without weak electronic coupling approximation has been applied to study the charge transport in perfect organic semiconductors [33]. To simulate the mobility in polycrystalline organic semiconductors, the effect of traps should be further included. It has been widely accepted that traps are mainly located at boundaries between grains in polycrystalline organic semiconductors [34–36], which are believed to be bottlenecks to the charge transport in OTFTs [16,37]. Among the models of grain boundaries (GBs) focusing specifically on the role the GBs play in the charge transport through organic semiconductor devices, most share an element that electrostatic barriers are present at the grain–grain interfaces which arise from traps localized at the GBs, whereas grains are basically free of traps [15,34,35,38]. These simulations have shown that it is necessary to consider the conduction processes through both the grains and the boundaries separating them for a deeper understanding of the device and satisfying the needs of the circuit designer.

In the present paper, we propose a model for charge transport in the polycrystalline organic semiconductors, where the charge transport is governed by hopping, i.e., the thermally activated tunneling of carriers between adjacent localized states, but energy barriers are present at boundaries between grains which can scatter the charge carriers when the charge carriers try to hop across the GBs. The present authors have ever used sexithiophene crystal structures in high-temperature (HT) and low-temperature (LT) phases which have been shown in Fig. 1 to show the influence of molecular packing for the mobility versus temperature [33]. In the present paper, we continue to use these two crystal structures to investigate the effect of traps for charge transport in polycrystalline organic semiconductors so that the effect of molecular packing can be seen at the same time. Since the charge transport in OTFTs is mainly confined within the first few layers of the organic semiconductor/insulator interface [39], the present work only deals with two-dimensional (2D) charge transport properties [33]. The paper is organized as follows: In Section 2, we describe the theoretical model and method to calculate the CT rates and to simulate the charge mobility in polycrystalline organic semiconductors. In Section 3, we display the numerical results and discussions. The conclusion is drawn in Section 4.

2. Theoretical methodology

2.1. Model for polycrystalline organic semiconductors

Atomic force microscope images of organic semiconductors have shown that a polycrystalline organic material is composed of small crystallitic grains joined together by GBs between them [6]. These grains have a distribution of sizes and irregular shapes, and the angle between the orientations of the adjoining grains is often large. The boundary between grains consists of a few molecular layers of disordered molecules resulting from different orientations of neighboring grains. Thus, the polycrystalline organic semiconductor has a complex microstructure. To

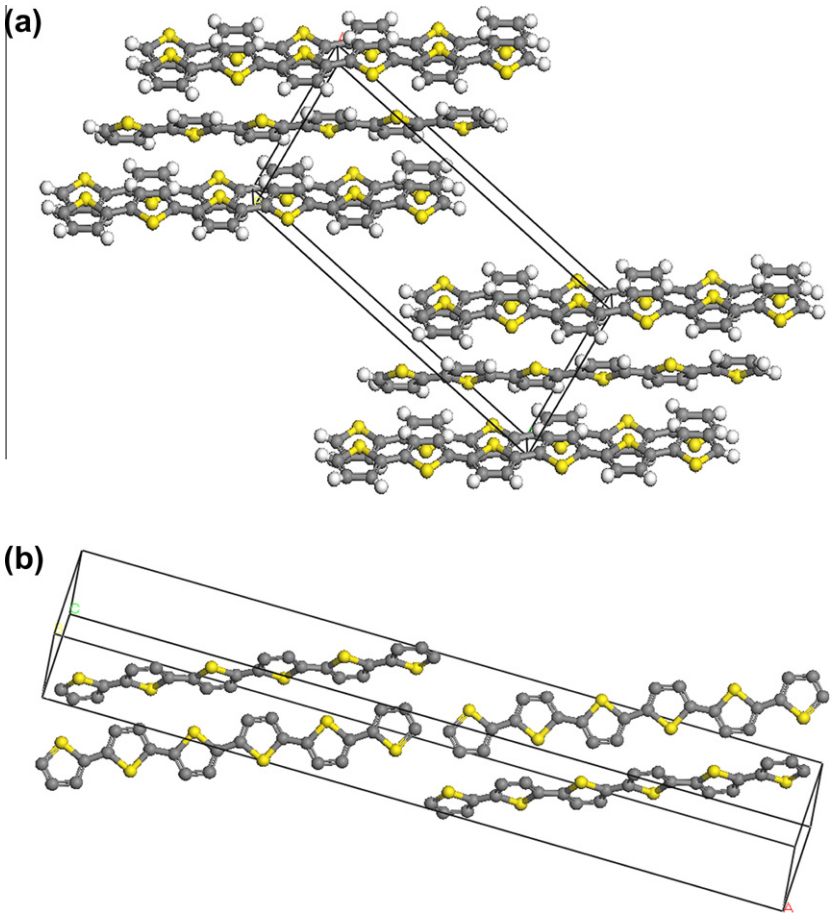

Fig. 1. Crystal structures of sexithiophene: (a) the unit cell of the HT phase; (b) the unit cell of the LT phase.

simplify the model, we notice that Gaussian distributions of grain sizes lead to little variation of the mobility with respect to the model with uniform grain sizes [38]. Meanwhile, the mobility has a strong dependence on the grain size [40,41] showing that charge transport is mainly limited by GBs [42]. In addition, theoretical calculations have shown that in most cases the width of GBs is negligibly small as compared to the grain size [34]. Therefore, we assume that the crystals in OTFTs are composed of identical square crystallites having a grain size of L nm. We also assume that the molecules are arranged in a periodic manner within each crystallite so no scattering takes place in the grains. We further assume that the boundary between grains is of negligible thickness compared to L so scattering only takes place when charge carriers try to hop across the GBs. In fact, these assumptions have been widely used to simulate the charge transport in polycrystalline inorganic semiconductors [43,44].

2.2. Method for charge transfer rates and mobilities

Recently, we have proposed a quantum CT rate theory without weak electronic coupling approximation to simulate the charge transport in perfect organic semiconductors [33]. Based on the above assumptions we have made, the CT rates in the grains of polycrystalline organic semiconductors can be computed with the quantum CT rate theory without weak electronic coupling approximation. Since the details of the quantum CT rate theory without electronic coupling approximation has been shown in our recent work [33], a brief description for this theory is given below.

The carrier hopping between neighboring molecules in organic semiconductors is a self-exchange two-state CT reaction, so the system can be described by a spin-boson Hamiltonian [45]:

$$H = V\sigma_x + \sum_{j=1}^{N}\left[\frac{p_j^2}{2m_j} + \frac{1}{2}m_j\omega_j^2\left(x_j - \frac{c_j}{m_j\omega_j^2}\sigma_z\right)^2\right]. \quad (1)$$

Here, N is the number of intramolecular vibrational modes, V is the electronic coupling between the donor and acceptor states, x_j and p_j are the position and momentum of the jth normal mode with mass m_j and frequency ω_j, respectively, c_j is the coupling strength between the charge carrier and nuclear vibration for the jth normal mode, and $\sigma_x = |1\rangle\langle 2| + |2\rangle\langle 1|$ and $\sigma_z = |1\rangle\langle 1| - |2\rangle\langle 2|$ are the Pauli matrices. It has been shown that the frequency ω_j and the reorganization energy λ_j can be easily computed

[29,33,46] from the normal mode analysis with DUSHIN program [47], so the coupling strength c_j can be obtained with the relationship $c_j^2 = \frac{1}{2} m_j \omega_j^2 \lambda_j$. Meanwhile, the electronic coupling between the donor and acceptor states can be obtained from a direct method [48,49], which has been shown to be reliable in the literature [32].

Having obtain the Hamiltonian for the CT reaction, we start from the real-time flux–flux correlation function (FFCF) [50], then the rigorous quantum mechanical rate constant can be written as

$$K = \int_{-\infty}^{\infty} dt C_{ff}(t), \tag{2}$$

where the real-time FFCF $C_{ff}(t)$ has the form

$$C_{ff}(t) = \frac{V^2}{\hbar^2 Z} \mathrm{Tr}\left[e^{-\beta H} e^{iHt/\hbar} \sigma_y e^{-iHt/\hbar} \sigma_y\right]. \tag{3}$$

Here, $Z = \mathrm{Tr}[e^{-\beta H}]$ is the sum of partition functions for the donor and acceptor states, $\sigma_y = i(|2\rangle\langle 1| - |1\rangle\langle 2|)$ is the Pauli matrix, and $\beta = 1/k_B T$ where T is the temperature and k_B is the Boltzmann constant. It has been shown that the CT rates are often dominated by stationary phase point trajectories in imaginary time [51]. For the self-exchange CT reaction, one of the stationary phase points occurs at a pure imaginary time $\tau_{st} = i\beta\hbar/2$ [52]. The integral in Eq. (2) can then be translated to an integral over the line $t' = \tau_{st} - t$ through the standard contour integral methodology:

$$k = \int_{\tau_{st}-\infty}^{\tau_{st}+\infty} dt C_{ff}(\tau_{st} - t). \tag{4}$$

When the Wick's rotation $t \to -i\tau$ is introduced, Eq. (4) in terms of the time integral of the real-time FFCF becomes the imaginary part of the integral of imaginary-time FFCF

$$k = \mathrm{Im} \int C_{ff}(\tau_{st} + i\tau) d\tau \tag{5}$$

with the imaginary-time FFCF

$$C_{ff}(\tau) = \frac{V^2}{\hbar^2 Z} \mathrm{Tr}\left[e^{-(\beta\hbar - \tau)H/\hbar} \sigma_y e^{-\tau H/\hbar} \sigma_y\right]. \tag{6}$$

To calculate the imaginary part of a diverging integral in Eq. (5), the saddle point approximation is made for the imaginary-time FFCF, that is, we write the imaginary-time FFCF as $C_{ff}(\tau_{st} + i\tau) = e^{-\phi(\tau_{st} + i\tau)}$ and expand $\phi(\tau_{st} + i\tau)$ at τ_{st} to get $\phi(\tau_{st} + i\tau) \approx \phi(\tau_{st}) - \frac{1}{2}\phi''(\tau_{st})\tau^2$, then the quantum CT rate constant is expressed as

$$K = C_{ff}(\tau_{st}) \sqrt{\frac{2\pi}{C''_{ff}(\tau_{st})/C_{ff}(\tau_{st})}}. \tag{7}$$

It is obvious that the imaginary-time FFCF at τ_{st} is required to obtain the CT rates in the grains. A path integral Monte Carlo route has been given to compute the imaginary-time FFCF [33], which is a simplified version of the calculation of real-time correlation functions by Cao et al. [53].

For the charge transport at GBs, it has been accepted that there exists an energy barrier at each boundary between grains [15,34,35,38]. When the grain size is small, the traps can be seemed to be uniformly distributed, so Horowitz et al. have shown a relationship between the mobility and the energy barrier E_{gb} at GBs as $\mu = \mu_0 e^{-E_{gb}/k_B T}$ where μ_0 is the trap-free mobility in grains [40]. It has been shown that the extended-state transport model is invalid above 150 K for oligoacenes [23] which have larger transfer integrals than the sexithiophene and the CT rates are present in sexithiophene crystals [32,33]. Therefore, a different assumption is made in the present paper that the energy barrier has a direct relationship with the CT rate (k_{gb}) at GBs:

$$K_{gb} = k e^{-E_{gb}/k_B T}. \tag{8}$$

The reason for such assumption is that the molecules near GBs are usually distributed irregularly [6,40], so the electronic couplings between molecules in different grains change rapidly and can vary several orders of magnitude [30,54] which can prevent charge carriers to transport from one grain to the other grain and may be a possible origin of the energy barriers at GBs. Thus, the energy barrier E_{gb} can represent the extent of molecular disorder near the boundaries between grains. While the relationship between k_{gb} and E_{gb} cannot be accurately expressed with Eq. (8), we do not expect the results to be qualitatively different as long as k_{gb} increases strongly with decreasing the barrier height at GBs, which has been verified by different group [24,38]. When the CT rates in the grains and across the GBs have been obtained, a random walk method is then used to simulate the charge mobility with Einstein relation $\mu = eD/k_B T$ [29,46,55] where the diffusion coefficient $D = \lim_{t\to\infty}(l(t)^2/4t)$ for the 2D charge transport. The averaged squared displacement $l(t)^2 = \frac{1}{K}\sum_{i=1}^{K} l_i(t)^2$ can reach an approximately linear function of simulation time t when the number K of trajectories for random walk is 5000 (Fig. 2). Then the effect of the GBs in polycrystalline organic semiconductors is naturally included into the charge mobility. If the grain size is small enough such that the charge carrier is scattered by the GBs for each hopping, the hopping time is $e^{E_{gb}/k_B T}$ times larger than that in perfect organic semiconductors, so Horowitz et al's relation $\mu = \mu_0 e^{-E_{gb}/k_B T}$ is easily obtained.

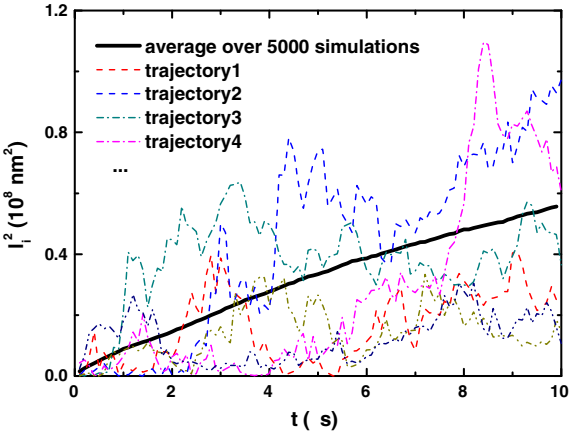

Fig. 2. Squared displacement $l_i(t)^2$ versus simulation time for a 2D sexithiophene layer with L = 60 nm and E_{gb} = 100 meV at room temperature. Each thin line represents an individual simulation of the random walk. The thick solid line means the average over 5000 simulations.

3. Results and discussion

The present model is only used to investigate the charge transport in sexithiophene polycrystals above 200 K because the energy band model is inapplicable above this temperature [23] where the thermal fluctuation can destroy the translational symmetry of the electronic Hamiltonian. The CT rates in perfect organic semiconductors based on the sexithiophene crystal structures in HT and LT phases have been obtained with Eq. (7) in our previous work [33], which can be used as the CT rates in the grains for the present model. Then the CT rates at GBs can be easily obtained from Eq. (8) if the energy barrier at GBs is given. The structural defects in polycrystalline organic semiconductors usually form shallow traps at GBs [16,41,56] and the barrier height from the traps can be changed by tuning the gate voltage [37,40]. It has been shown that the barrier height varies from 0 to 150 meV in sexithiophene for different gate voltages [34], so the energy barrier in this region is used into Eq. (8) to calculate the CT rates at boundaries between grains.

Fig. 3 shows the charge mobility of the polycrystalline organic semiconductor based on the sexithiophene crystal structure in HT phase for different energy barriers at GBs. The grain size varies from 60 to 300 nm in Fig. 3, which has been obtained as a function of substrate temperature in oligothiophene field-effect transistors [40]. The charge mobility in perfect organic semiconductor [33] is also shown there. It can be seen in Fig. 3(a) that the mobility increases with decreasing temperature showing that the charge transport is band-like for perfect organic semiconductor, but the mobility becomes slightly thermally activated in Fig. 3(b) when the barrier height is 25 meV, so the increase of mobility with increasing temperature can be easily obtained when the barrier height at GBs is small. When the barrier height increases to 50 meV, it is shown in Fig. 3(c) that the mobility increases consistently with temperature in the investigated temperature region for all the grain sizes, so the charge transport becomes increasingly thermally activated as the barrier height increases. However, the situation is much different when the sexithiophene crystal structure in LT phase is used to simulate the charge transport in the polycrystalline organic semiconductor. We can see in Fig. 4(b) that the mobility decreases with increasing the temperature when the barrier height is 25 meV. The thermally activated mobility cannot be observed for all the grain sizes. When the barrier height is 50 meV, Fig. 4(c) shows that the mobility increases obviously with temperature for the grain size of 60 nm and increases slightly with temperature when the grain size is 180 nm, but the mobility is almost unchanged below 350 K and then decreases slightly with increasing temperature when the grain size increases to 300 nm. When the barrier height increases to 75 meV, the thermally activated

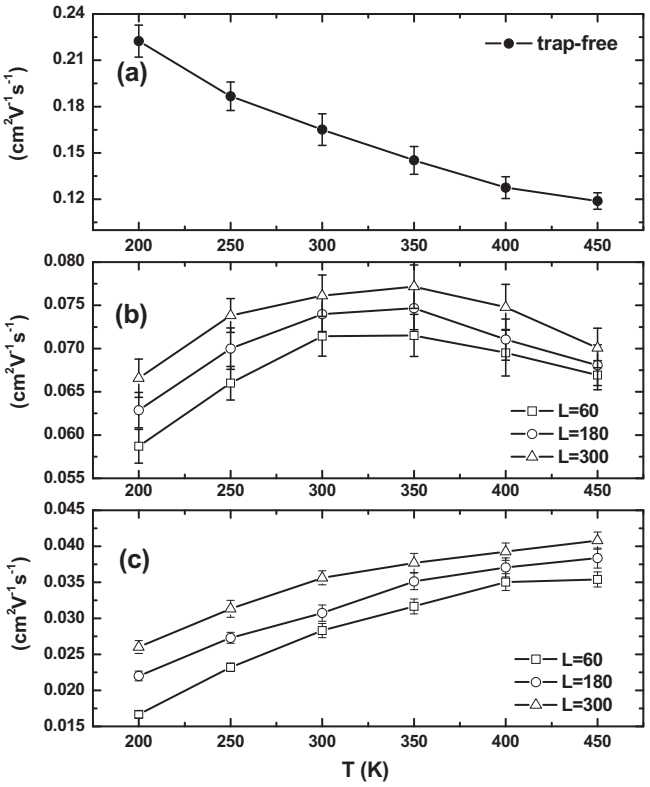

Fig. 3. The hole mobility as a function of temperature for the polycrystalline organic semiconductor based on the sexithiophene crystal structure in HT phase: (a) for E_{gb} = 0 meV or trap-free; (b) for E_{gb} = 25 meV; (c) for E_{gb} = 50 meV. The solid circles represent the trap-free mobilities; the hollow squares represent the mobilities for the grain size of 60 nm; the hollow circles represent the mobilities for the grain size of 180 nm; the hollow triangles represent the mobilities for the grain size of 300 nm.

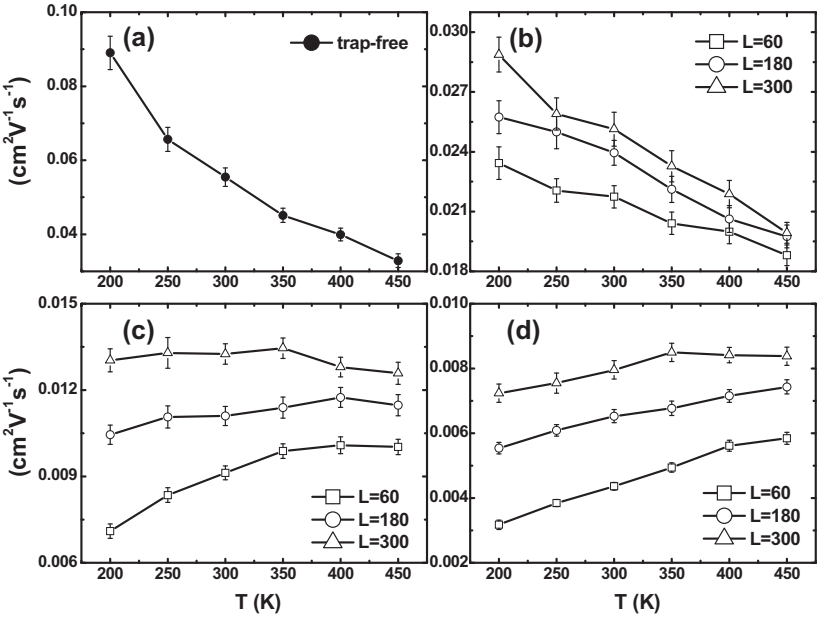

Fig. 4. The hole mobility as a function of temperature for the polycrystalline organic semiconductor based on the sexithiophene crystal structure in LT phase: (a) for E_{gb} = 0 meV or trap-free; (b) for E_{gb} = 25 meV; (c) for E_{gb} = 50 meV; (d) for E_{gb} = 75 meV. The symbols are the same as those in Fig. 3.

mobilities are observed in Fig. 4(d) for all the grain sizes. The comparison between Figs. 3 and 4 shows that the barrier height at GBs for mobility to become thermally activated is larger in HT phase than that in LT phase. This difference can be easily understood from the molecular packing in grains which actually correspond to the sexithiophene crystal structures of the HT and LT phases in Fig. 1, respectively [33]. For the HT phase, there is a displacement of about one thiophene along the long molecular axis in Fig. 1(a) for the adjacent molecules in one molecular layer. This packing manner makes the high occupied molecular orbitals of adjacent molecules in a monolayer being bonding or antibonding which can lead to large electronic couplings. However, in the LT phase, the displacement along the long molecular axis for the neighboring molecules in a monolayer is about half a thiophene ring width in Fig. 1(b), so there is some mixing between bonding and antibonding overlaps in the LT phase and the electronic couplings are then smaller than those in the HT phase [46]. It has been shown that the non-perturbative effect of these electronic couplings in the HT phase reduces the CT rates much more than those in the LT phase especially in low temperatures [33]. The CT rates, thus the mobilities, become less dependent on temperature in the HT phase than those in the LT phase, which have been shown in Figs. 3 and 4(a). When the traps at GBs are considered, the mobilities in the polycrystalline organic semiconductor based on the sexithiophene crystal structure in HT phase are easier to be thermally activated. This may be the reason that the thermally activated mobility is often obtained from experiments for sexithiophene field-effect transistors [37,40]. Recently, Yamagishi et al. have indicated that the intrinsic charge transport is band-like inside the trap-free grains, but the mobility decrease monotonically with decreasing temperatures for the whole polycrystalline organic semiconductors where the boundaries between grains are present [15], which is in excellent agreement with the present model. That is, Figs. 3 and 4 show that the mobility in grains decreases with increasing temperature while the mobility for the whole polycrystalline organic semiconductors can increase monotonically with increasing temperature when the barrier height at GBs is large. Thus, the quantum treatment for the nuclear degrees of freedom is required for understanding the band-like transport in grains [29,31] while the traps at GBs are responsible for the mobility to be thermally activated [40]. The mobilities from experiments for polycrystalline OTFTs have combined the effects of nuclear tunneling and traps at GBs. When the barrier height at GBs is much small, the contribution of band-like transport in grains will be predominant for the mobility of the whole polycrystalline organic semiconductors, so the mobility from experiments for polycrystalline OTFTs can decrease with increasing temperature. This may provide a possible explanation for the recent experiment by Sakanoue and Sirringhaus where the band-like transport has been observed for the whole polycrystalline organic semiconductors with the barrier height of several micro-electron volts at boundaries between grains [56].

The mobility has been shown to vary greatly in experiments when the sexithiophene thin films were deposited on different substrates in OTFTs. For example, the measured mobility is 0.025 $cm^2 V^{-1} s^{-1}$ when the sexithiophene thin film was deposited directly on a thermally oxidized silicon wafer [57] while the mobility can reach 0.08 $cm^2 V^{-1} s^{-1}$ when the surface of the silicon dioxide was treated with a self-assembled monolayer prior to the deposition of the sexithiophene on the substrate [58].

Thus, the properties of semiconductor/insulator interfaces are critically important to the operation of OTFTs [59]. Later, a robust connection between organic semiconductor/insulator interfaces and energy barriers at GBs has been demonstrated [60,61]. Since the majority of charge carriers in OTFTs are confined within the first few layers of the organic semiconductor/insulator interface [39], any variation of energy barriers within these layers will affect the charge carrier motion. To see this more clearly, we show the relationship between charge mobility and barrier height at GBs in Fig. 5 for the polycrystalline organic semiconductor based on the sexithiophene crystal structure in HT phase. The mobility for perfect organic semiconductors ($E_{gb} = 0$) [33] is also shown there. It is obvious in Fig. 5 that the mobility decreases rapidly as the barrier height increases even if the energy barrier at GBs is very small. For example, the mobility is about 0.16 $cm^{-2} V^{-1} s^{-1}$ when there is no energy barrier at GBs while the mobility decreases to about 0.07 $cm^{-2} V^{-1} s^{-1}$ when the barrier height at GBs is 25 meV. While the rapid variation for mobility with energy barrier at GBs is observed, we notice that the present results are still coincident with experiments [25,57,58]. The mobility (0.08 $cm^2 V^{-1} s^{-1}$) for sexithiophene in Ref. [58] corresponds to the result in Fig. 5 where a small barrier height is present at boundaries between grains while the mobility (0.025 $cm^2 V^{-1} s^{-1}$) for sexithiophene in Ref. [57] corresponds to the mobility where a large barrier height is present at grain boundaries. Comparing the preparing process for OTFTs in Refs. [57,58], it seems to show that the interface treatment with a self-assembled monolayer in organic semiconductor/insulator interface can largely reduce the energy barrier at GBs although the detailed relation between interface and energy barrier at GBs is still open for further studies. Recently, Marumoto et al. have shown that the trapping time of charge carriers at the interface greatly decreases in rubrene field-effect transistors by interface treatment with a self-assembled monolayer [62], which can be explained with the present model. When the energy barrier at GBs is largely reduced by interface treatment with a self-assembled monolayer, the CT rates at GBs are much larger than those without interface treatment with a self-assembled monolayer, so the charge carrier has a larger probability to hop across the boundaries between grains and then the trapping time in one grain is largely reduced. In addition, we can see in Fig. 5 that the influence of grain sizes is much small as compared to that of boundaries between grains. As the grain size increases from 60 to 300 nm, the mobility varies slightly in the investigated region of energy barrier. Therefore, the GB is the main bottleneck to field-effect mobility measured for the whole polycrystalline materials which is consistent with the previous conclusion [15,16,38].

The relation between mobility and grain size has also been shown in experiments for OTFTs, but incompatible conclusions have been made in the literature [38,40,63]. For example, Horowitz and Hajlaoui have shown that the mobility increases roughly linearly with increasing the grain size [40,63] while Carlo et al. have shown that the mobility decreases dramatically with decreasing the grain size when the grain size is small [38]. However, it is surprisingly found that the above discrepancy can be easily reconciled from the present model. When the grain size is small, we can see in Fig. 6(a) that the mobility increases rapidly as the grain size increases from 0 to 60 nm especially when the energy barrier at GBs is large, which

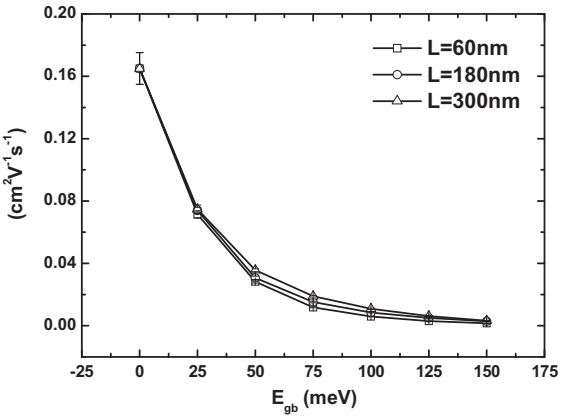

Fig. 5. The hole mobility as a function of energy barrier at grain boundaries for the polycrystalline organic semiconductor based on the sexithiophene crystal structure in HT phase at 300 K. The hollow squares represent the mobilities for the grain size of 60 nm; the hollow circles represent the mobilities for the grain size of 180 nm; the hollow triangles represent the mobilities for the grain size of 300 nm.

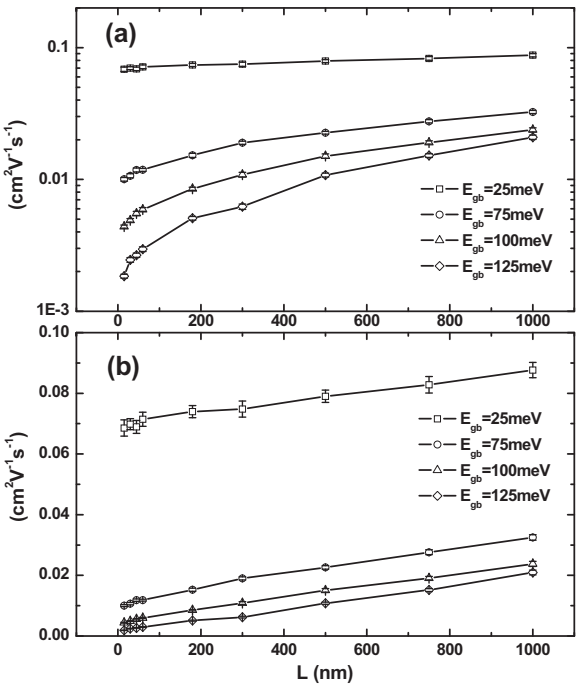

Fig. 6. The hole mobility as a function of grain size for the polycrystalline organic semiconductor based on the sexithiophene crystal structure in HT phase at 300 K: (a) linear plot; (b) log-linear plot. The hollow squares represent the mobilities for E_{gb} = 25 meV; the hollow circles represent the mobilities for E_{gb} = 75 meV; the hollow triangles represent the mobilities for E_{gb} = 100 meV; the hollow diamonds represent the mobilities for E_{gb} = 125 meV.

shows that a high energy barrier at GBs is responsible for the rapid increase of mobility with grain size. When the grain size is larger than 60 nm, we can see in Fig. 6(b) that mobility shows a roughly linear increase with grain size no matter when the barrier height at GBs is large or small, which is in good agreement with Horowitz et al. model [40]. Thus, a roughly linear dependence of mobility on grain size can be predicted from the present model for large grain size although the linear relationship between mobility and grain size has not been presumed in the present model.

4. Conclusion

In summary, we propose a model to simulate charge transport in polycrystalline organic semiconductors where the trap-free grains are separated by boundaries between them and the carrier hopping between adjacent molecules is believed as the basic transport process. The CT rates in grains are calculated from a quantum CT rate theory without weak electronic coupling approximation while the charge transport at GBs is controlled by an energy barrier between grains. The polycrystalline organic semiconductors based on the sexithiophene crystal structures in HT and LT phases are used to show the effect of GBs for charge transport. It is found that the nuclear tunneling effect is required for understanding the band-like transport in grains while the traps at GBs are responsible for mobility to be thermally activated. Meanwhile, the mobility in HT phase is easier to be thermally activated that in LT phase, which is due to that the electronic couplings in the HT-phase crystal structure are larger than those in the LT-phase crystal structure. Thus, we conclude that the charge transport in polycrystalline organic semiconductors is not only influenced by the traps at GBs but also by molecular packing in grains. It is also found that the mobility shows a roughly linear relationship with the grain size when the grains size is large while the rapid change of mobility with grain size is observed for small grain size, which reconciles the discrepancy for mobility versus grain size in experiments. Finally, we point out that the energy barrier at boundaries between grains is mainly responsible for mobility degradation observed in devices even if the barrier height is much small, so the efforts for improving the mobility should be put on reducing the barrier height during the preparing process of OTFTs. The energy barriers at GBs are still undetermined in the present study. This is due to that the present authors have fully realized that the energy barriers at GBs have close relationship with many factors, such as the organic semiconductor/insulator interface [64] which has beyond the scope in this paper and is left to a future work.

Acknowledgements

This work is supported by Open Project of State Key Laboratory of Urban Water Resource and Environment, Harbin Institute of Technology (Grant No. HC201117); the National Natural Science Foundation of China (Grant Nos. 21003030 and 20973049); and the China Postdoctoral Science Foundation (Grant No. 20110490102).

References

[1] J. Zaumseil, H. Sirringhaus, Chem. Rev. 107 (2007) 1296.
[2] S.F. Nelson, Y.-Y. Lin, D.J. Gundlach, T.N. Jackson, Appl. Phys. Lett. 72 (1998) 1854.
[3] H. Sirringhaus, N. Tessler, R.H. Friend, Science 280 (1998) 1741.
[4] V. Coropceanu, J. Cornil, D.A. da Silva Filho, Y. Olivier, R. Silbey, J.L. Brédes, Chem. Rev. 107 (2007) 926.
[5] A.R. Brown, C.P. Jarrett, D.M. de Leeuw, M. Matters, Synth. Met. 88 (1997) 37.
[6] D. Knipp, R.A. Street, A.R. Völkel, Appl. Phys. Lett. 82 (2003) 3907.
[7] J.A. Letizia, J. Rivnay, A. Facchetti, M.A. Ratner, T.J. Marks, Adv. Funct. Mater. 20 (2010) 50.
[8] R.A. Marcus, Rev. Mod. Phys. 65 (1993) 599.
[9] W.Q. Deng, W.A. Goddard III, J. Phys. Chem. B 108 (2004) 8614.
[10] Y.B. Song, C.A. Di, X.D. Yang, S.P. Li, W. Xu, Y.Q. Liu, L.M. Yang, Z.G. Shuai, D.Q. Zhang, D.B. Zhu, J. Am. Chem. Soc. 128 (2006) 15940.
[11] J.C. Sancho-García, A.J. Pérez-Jiménez, Y. Olivier, J. Cornil, Phys. Chem. Chem. Phys. 12 (2010) 9381.
[12] N. Karl, J. Marktanner, R. Stehle, W. Warta, Synth. Met. 42 (1991) 2473.
[13] V. Podzorov, E. Menard, A. Borissov, V. Kiryukhin, J.A. Rogers, M.E. Gershenson, Phys. Rev. Lett. 93 (2004) 086602.
[14] J. Lee, J.H. Kim, S. Im, J. Appl. Phys. 95 (2004) 3733.
[15] M. Yamagishi, J. Soeda, T. Uemura, Y. Okada, Y. Takatsuki, T. Nishikawa, Y. Nakazawa, I. Doi, K. Takimiya, J. Takeya, Phys. Rev. B 81 (2010) 163106(R).
[16] J.H. Chen, C.K. Tee, M. Shtein, J. Anthony, D.C. Martin, J. Appl. Phys. 103 (2008) 114513.
[17] G. Horowitz, R. Hajlaoui, P. Delannoy, J. Phys. III 5 (1995) 355.
[18] R.J. Chesterfield, J.C. McKeen, C.R. Newman, P.C. Ewbank, D.A. da Silva Filho, J.L. Brédas, L.L. Miller, K.R. Mann, C.D. Frisbie, J. Phys. Chem. B 108 (2004) 19281.
[19] R.J. Chesterfield, C.R. Newman, T.M. Pappenfus, P.C. Ewbank, M.H. Haukaas, K.R. Mann, L.L. Miller, C.D. Frisbie, Adv. Mater. 15 (2003) 1278.
[20] F.J.M. Hoeben, P. Jonkheijm, E.W. Meijer, A.P.H.J. Schenning, Chem. Rev. 105 (2005) 1491.
[21] J.D. Dunitz, A. Gavezzotti, Acc. Chem. Res. 32 (1999) 677.
[22] A. Troisi, G. Orlandi, Phys. Rev. Lett. 96 (2006) 086601.
[23] Y.C. Cheng, R.J. Silbey, D.A. da Silva Filho, J.P. Calbert, J. Cornil, J.L. Brédas, J. Chem. Phys. 118 (2003) 3764.
[24] M.C.J.M. Vissenberg, M. Matters, Phys. Rev. B 57 (1998) 12964.
[25] G. Horowitz, R. Hajlaoui, D. Fichou, A.E. Kassmi, J. Appl. Phys. 85 (1999) 3202.
[26] O. Kwon, V. Coropceanu, N.E. Gruhn, J.C. Durivage, J.G. Laquindanum, H.E. Katz, J. Cornil, J.L. Brédas, J. Chem. Phys. 120 (2004) 8186.
[27] J.L. Brédas, J.P. Calbert, D.A. da Silva Filho, J. Cornil, Proc. Natl. Acad. Sci. USA 99 (2002) 5804.
[28] Z.M. Wei, W. Hong, H. Geng, C.L. Wang, Y.L. Liu, R.J. Li, W. Xu, Z.G. Shuai, W.P. Hu, Q.R. Wang, D.B. Zhu, Adv. Mater. 22 (2010) 2458.
[29] G.J. Nan, X.D. Yang, L.J. Wang, Z.G. Shuai, Y. Zhao, Phys. Rev. B 79 (2009) 115203.
[30] L.J. Wang, Q.K. Li, Z.G. Shuai, L.P. Chen, Q. Shi, Phys. Chem. Chem. Phys. 12 (2010) 3309.
[31] D.L. Cheung, A. Troisi, J. Phys. Chem. C 114 (2010) 20479.
[32] G.J. Nan, L.J. Wang, X.D. Yang, Z.G. Shuai, Y. Zhao, J. Chem. Phys. 130 (2009) 024704.
[33] G.J. Nan, Q. Shi, Z.G. Shuai, Z.S. Li, Phys. Chem. Chem. Phys. 13 (2011) 9736.
[34] G. Horowitz, Adv. Funct. Mater. 13 (2003) 53.
[35] S. Verlaak, V. Arkhipov, P. Heremans, Appl. Phys. Lett. 82 (2003) 745.
[36] K. Puntambekar, J.P. Dong, G. Haugstad, C.D. Frisbie, Adv. Funct. Mater. 16 (2006) 879.
[37] G. Horowitz, M.E. Hajlaoui, R. Hajlaoui, J. Appl. Phys. 87 (2000) 4456.
[38] A.D. Carlo, F. Piacenza, A. Bolognesi, B. Stadlober, H. Maresch, Appl. Phys. Lett. 86 (2005) 263501.
[39] F. Dinelli, M. Murgia, P. Levy, M. Cavallini, F. Biscarini, Phys. Rev. Lett. 92 (2004) 116802.
[40] G. Horowitz, M.E. Hajlaoui, Adv. Mater. 12 (2000) 1046.
[41] R. Matsubara, N. Ohashi, M. Sakai, K. Kudo, M. Nakamura, Appl. Phys. Lett. 92 (2008) 242108.
[42] A.B. Chwang, C.D. Frisbie, J. Appl. Phys. 90 (2001) 1342.
[43] J.Y.W. Seto, J. Appl. Phys. 46 (1975) 5247.
[44] J. Levinson, F.R. Shepherd, P.J. Scanlon, W.D. Westwood, G. Este, M. Rider, J. Appl. Phys. 53 (1982) 1193.
[45] A.J. Leggett, S. Chakravarty, A.T. Dorsey, M.P.A. Fisher, A. Garg, W. Zwerger, Rev. Mod. Phys. 59 (1987) 1.
[46] X.D. Yang, L.J. Wang, C.L. Wang, W. Long, Z.G. Shuai, Chem. Mater. 20 (2008) 3205.

[47] J.R. Reimers, J. Chem. Phys. 115 (2001) 9103.
[48] T. Fujita, H. Nakai, H. Nakatsuji, J. Chem. Phys. 104 (1996) 2410.
[49] A. Troisi, G. Orlandi, Chem. Phys. Lett. 344 (2001) 509.
[50] W.H. Miller, S.D. Schwartz, J.W. Tromp, J. Chem. Phys. 79 (1983) 4889.
[51] W.H. Miller, J. Chem. Phys. 62 (1975) 1899.
[52] P.G. Wolynes, J. Chem. Phys. 87 (1987) 6559.
[53] J.S. Cao, L.W. Ungar, G.A. Voth, J. Chem. Phys. 104 (1996) 4189.
[54] A. Troisi, G. Orlandi, J. Phys. Chem. A 110 (2006) 4065.
[55] E.D. Donato, R.P. Fornari, S.D. Motta, Y. Li, Z.H. Wang, F. Negri, J. Phys. Chem. B 114 (2010) 5327.
[56] T. Sakanoue, H. Sirringhaus, Nat. Mater. 9 (2010) 736.
[57] B. Servet, G. Horowitz, S. Ries, O. Lagorsse, P. Alnot, A. Yassar, F. Deloffre, P. Srivastava, R. Hajlaoui, P. Lang, F. Garnier, Chem. Mater. 6 (1994) 1809.
[58] S. Nagamatsu, K. Kaneto, R. Azumi, M. Matsumoto, Y. Yoshida, K. Yase, J. Phys. Chem. B 109 (2005) 9374.
[59] J. Veres, S. Ogier, G. Lloyd, D. de Leeuw, Chem. Mater. 16 (2004) 4543.
[60] V. Kalihari, D.J. Ellison, G. Haugstad, C.D. Frisbie, Adv. Mater. 21 (2009) 3092.
[61] W.G. Xie, J.B. Xu, J. An, K. Xue, J. Phys. Chem. C 114 (2010) 19044.
[62] K. Marumoto, N. Arai, H. Goto, M. Kijima, K. Murakami, Y. Tominari, J. Takeya, Y. Shimoi, H. Tanaka, S. Kuroda, T. Kaji, T. Nishikawa, T. Takenobu, Y. Iwasa, Phys. Rev. B 83 (2011) 075302.
[63] G. Horowitz, M.E. Hajlaoui, Synth. Met. 122 (2001) 185.
[64] I.N. Hulea, S. Fratini, H. Xie, C.L. Mulder, N.N. Iossad, G. Rastelli, S. Ciuchi, A.F. Morpurgo, Nat. Mater. 5 (2006) 982.

making it (also) an ideal tool for patterning on foil in, for example, a R2R line.

Flexibility is introduced in an organic electronic device by the substrate material, typically being a polyester, polyimide or polycarbonate [13,14]. Paper has been reported for the fabrication of flexible electronic devices [15], although the rough surface is limiting the usage of it. Of the polyesters, poly(ethylene terephthalate) (PET) and poly(ethylene naphthalate) (PEN) are often used [16–18] and are well-studied [19,20], combining good mechanical properties and a reasonably high resistance to oxygen and water vapor penetration, making them good candidates for R2R integration. The gas permeability can be further decreased by the deposition of barrier layers such as Ormocer [21].

The fabrication of flexible electronic devices requires a process with good registration of the involved layers, in particular the registration of the source–drain contacts to the gate layer for TFTs. Flexible organic transistors have been fabricated by photolithographic patterning [22–26], stamping methods [27] and inkjet printing [28,29], all showing different advantages and disadvantages regarding registration, process temperature, feature size and device performance [1,28,30]. With conventional printing techniques, typical channel lengths in the range of 10 μm are obtained, limiting the bandwidth to 10 kHz for printable semiconductors with typical mobilities of 0.01 $cm^2/V\,s$ [31]. Fast, sub-micron transistors are, other than with conventional patterning techniques such as photolithography, readily available by NIL, being an intrinsically sub-micron and truly nanometer patterning technique. Organic thin film transistors have been demonstrated with source–drain contacts defined by thermal NIL on foil [32] and by UV NIL on glass [33], both having a photolithographically patterned bottom gate. On PET foil, gate structures have been patterned by UV NIL, followed by a backside exposure step defining the source–drain contacts in a self-aligned fashion using the previously defined gate as photomask [31].

In this study we report common gate TFTs on flexible PEN foil, in which interdigitated source–drain contacts are defined by SFIL. As such, this report aims to improve upon earlier reports [31–33] by the combination of electrode design (interdigitated), imprint process (SFIL) and choice of foil substrate (PEN). Future developments will require patterning of the gate as well and implementation into R2R for large-area device fabrication. The devices targeted here do not require any alignment step due to the chosen architecture, and can therefore be seen as the first step towards fully patterned, flexible TFTs with all functional layers defined and registered by UV NIL. The foil has been reversibly glued to a carrier for improved handling and dimensional stability during the process. SFIL has been chosen as the patterning process not only for its potential for high resolution patterning, but also and foremost for its potential for implementation in R2R. The semiconductor has been inkjet-printed, and the electronic performance of the fabricated flexible TFTs has been characterized.

2. Results and discussion

2.1. Design and process scheme

Scheme 1 shows a schematic top and side view of the here fabricated flexible thin film transistors (TFTs) in a bottom contact, bottom and common gate architecture. Source and drain, patterned by SFIL, are made of five interdigitated, 5 μm wide and spaced fingers.

Scheme 2 shows the process flow for the fabrication of common gate flexible TFTs with an SFIL-defined source–drain layer. Substrates are made of PEN foil, reversibly glued to a carrier (foil-on-carrier; FOC), coated with a metal–insulator–metal (MIM) stack. A UV-curable resist is dispensed on the substrate and brought into contact with a UV-transparent template (Scheme 2A). The template is demolded after exposure and curing of the resist with UV light, leaving an inverse replica of the template features on the substrate (Scheme 2B). The remaining residual layer is removed by reactive ion etching (Scheme 2C). Unprotected Au and Cr are subsequently removed by wet etching and ion beam etching. The remaining resist is stripped off by O_2 plasma (Scheme 2D). In the final step, two types of self-assembled monolayers (SAMs), pentafluorobenzenethiol (PFBT) and trichlorophenylsilane (TCPS) (Fig. 1), are applied before the semiconductor is deposited by inkjet-printing of a blend of 6,13-bis(triisopropylsilylethynyl) pentacene (TIPS pentacene) and polystyrene (PS) (Scheme 2E).

2.2. Fabrication

The dimensional stability and flatness of the 125 μm thick PEN foils was improved by reversibly gluing them to a carrier (foil-on-carrier; FOC), allowing conformal contact during imprinting and a reduced residual layer thickness. The MIM layer on the FOC was deposited by electron-beam evaporation of subsequently 5 nm Cr, 40 nm Au and 5 nm Cr (common gate), 100 nm Al_2O_3 (dielectric), and 5 nm Cr and 40 nm Au as the source–drain layer. Cr was used as an adhesion promoter. The quality of the imprint and the residual layer thickness remaining after imprinting are dominated by the waviness of the fabricated FOC. Significant effort has therefore been devoted to reduce the waviness and bending of the FOCs.

In first attempts, PEN foil was laminated manually, and later on with a lamination tool, onto a glue, followed by thermal curing. The difference in expansion coefficients between the PEN foil, glue and Si wafer led to such a drastic bowing of the FOC (>30 μm) that it could not be taken up by the vacuum chuck in the imprint tool. Contacting of the template on the FOC, homogeneous filling and residual layer formation were not possible due to the waviness of the foil. In the here developed FOC fabrication technique, the glue was replaced by the thermoplast poly(methyl methacrylate) (PMMA) and spincoated on a Si wafer. The PEN foil was activated by a short plasma treatment and pressed against the PMMA at an elevated temperature of

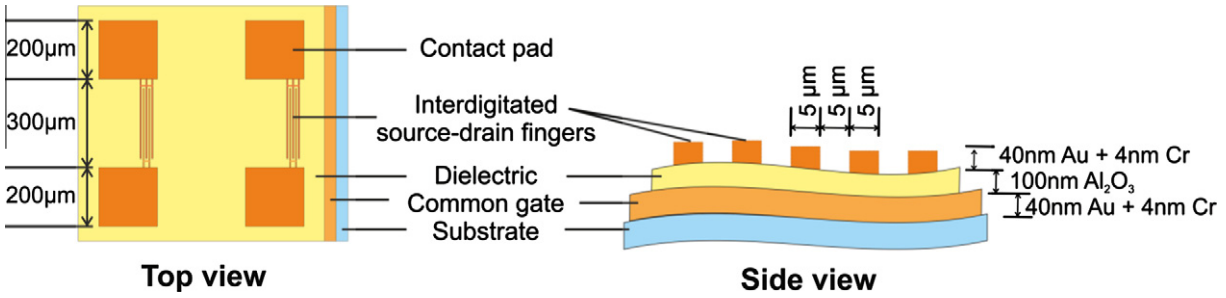

Scheme 1. Schematic top and side view of the TFT architecture. The source–drain layer defined by SFIL is patterned on top of the stack of dielectric and common gate. For each TFT, five interdigitated 5 μm wide and spaced fingers are connected to either the source (three fingers) or drain (two fingers) contact pads, having a width of 200 μm.

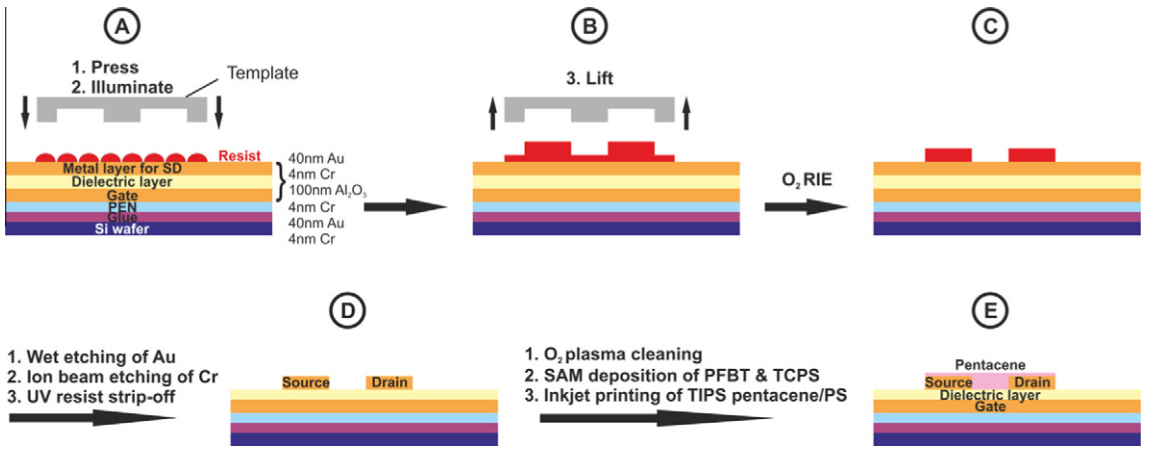

Scheme 2. Process flow for the fabrication of common gate TFTs with imprinted source–drain fingers. In the first step pL amounts of resist are drop-dispensed on the MIM stack-covered foil-on-carrier. (A) The template is pressed into the liquid UV-resist and cured for 10 s. (B) After demolding of the template (C) the thin residual layer is removed by O_2 RIE. (D) Pattern transfer into the top metal layer is followed by wet etching of the Au in KI:I_2:H_2O 4:1:40 and ion beam etching of the 5 nm Cr layer. (E) After the resist is stripped off with O_2 plasma, PFBT and TCPS self-assembled monolayers (SAMs) are deposited onto the surface and a blend of TIPS pentacene/PS is inkjet-printed on top of the interdigitated source–drain fingers.

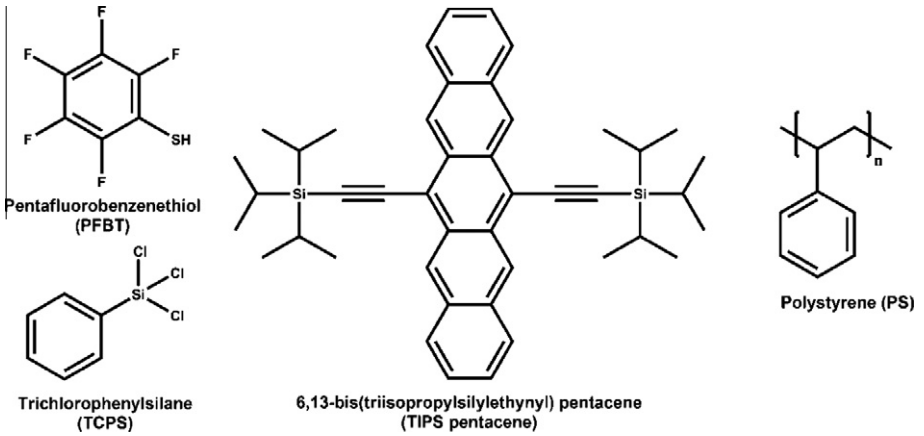

Fig. 1. Molecular structures of PFBT and TCPS, deposited as self-assembled monolayers on the Au structures and on the dielectric Al_2O_3, respectively, and of the semiconductor blend components TIPS pentacene and PS.

190 °C under 40 bar pressure with a non-patterned Si wafer in an embosser tool (Eitre 6 from Obducat). The here developed FOC fabrication technique allowed imprinting on FOCs with a bowing of less than 10 μm and surface

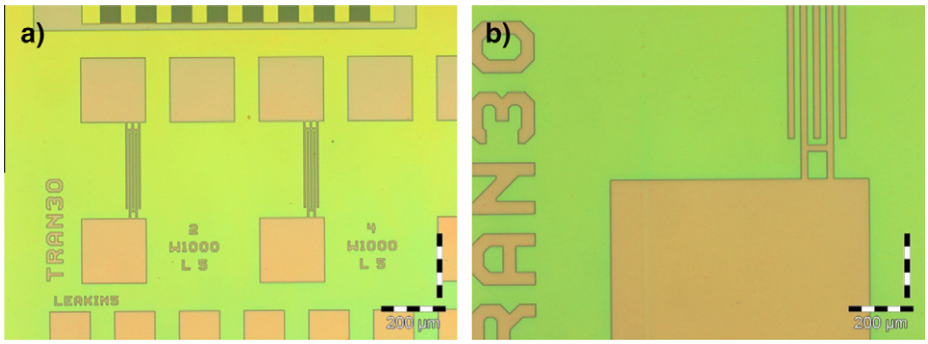

Fig. 2. Optical microscopy images of 5 µm wide and spaced interdigitated line structures connected to 200 µm wide contact pads after imprinting (Scheme 2B). The substrate is a MIM-coated PEN foil reversibly glued to a carrier.

waviness of ~1 µm (see Supporting information for surface contour plots).

The UV-transparent quartz template used as the template for imprinting, contained test features in the dimensional range of 750 nm up to 1.4 mm and the TFT features as shown in Scheme 1 on an active area of 15×15 mm^2 with a depth of 200 nm.

In the first step towards flexible, common gate TFTs with an SFIL-patterned source–drain layer, a low viscosity, organic, and UV-curable resist (MonoMat™) was field-by-field drop-dispensed in pL amounts onto the substrate (Scheme 2A). The template was brought into contact with the resist droplets under low pressure (2–3 N) and at room temperature. Capillary force action pulled the template further down spreading the resist over the active area and filling thereby the structures in the template within 60 s. Broadband UV light was guided through the template curing the resist within 3 s, leaving an inverse replica of the template features on the substrate after demolding (Scheme 2B). An anti-sticking layer (RelMat™) applied to the template before imprinting allowed easy demolding and complete pattern transfer with no residues left on the template. With the field-by-field imprinting technique SFIL, it was possible to imprint the entire FOC (diameter 100 mm) with a throughput of approximately 2 min per field.

The optical microscopy images in Fig. 2 display 5 µm wide and spaced lines connected to 200 µm square pads directly after imprinting on MIM-coated FOC. The overall residual layer thickness and the filling height of the structures were relatively homogeneous, as can be deduced from the absence of color deviations within the layers. The contrast in color suggests sharply defined edges of the imprinted structures. Pinholes and other filling errors were not observed.

After imprinting, the residual layer was removed by oxygen-based reactive ion etching (O_2 RIE) (Scheme 2C). A residual layer thickness of 80 nm was determined by profilometry before etching. Especially in the residual layer removal step, the waviness of the FOC plays an important role. Features imprinted on top of a hill of the wave have a thinner residual layer compared to features imprinted in the valley. Removal of the residual layer of features in the wave valleys partially coincides with complete removal of the features on the hills if the feature height is less than the wave height.

The source–drain areas remained covered with resist, allowing selective wet etching of the unprotected Au. The underlying Cr adhesion layer had to be removed by ion beam etching (IBE), as wet etching also lifted the Al_2O_3 dielectric layer underneath, due to weak adhesion of the oxide to the underlying gold layer. Improvement of adhesion was attempted by inserting an additional thin layer of Cr on top of the unpatterned gate metal just before oxide deposition. However, the adhesion was not sufficient to withstand the wet etching step. After IBE, the remaining resist was stripped off by O_2 plasma (Scheme 2D).

Fig. 3 shows optical microscopy images of the features after residual layer removal, wet etching of the Au, dry etching of the Cr layer, and resist strip-off. Additional examples of successful sub-micron features patterned by SFIL on FOC are given in the Supporting information. The bright yellow color indicates the Au features on the (orange colored[1]) Al_2O_3 dielectric layer. The features appear sharply defined and no pinholes were observed, deduced from the absence of bright spots in the closed orange layer.

As the TFT was made in a bottom-contact, bottom-gate architecture, the final layer added to the device was the organic semiconductor. A PFBT SAM was deposited from ethanol solution on all gold contacts to modify the charge injection [34]. TCPS was deposited by vapor deposition on all oxide surfaces to reduce electron trapping. SAMs are known to improve the molecular order of the deposited semiconductor [35]. A blend of TIPS pentacene:PS in a 2:1 w/w ratio, was inkjet-printed at a substrate temperature of 70 °C from tetraline solution onto the interdigitated source–drain fingers, leading to TIPS pentacene crystals grown from the edge to the center of the inkjet-printed droplets [36].

Fig. 4a shows an optical microscopy image of inkjet-printed TIPS pentacene/PS on the interdigitated source–drain fingers patterned by SFIL. Accurate control of the dispensing unit allowed the deposition of one drop of semiconductor on each of the four TFTs. A microscope

[1] For interpretation of color in Fig. 3, the reader is referred to the web version of this article.

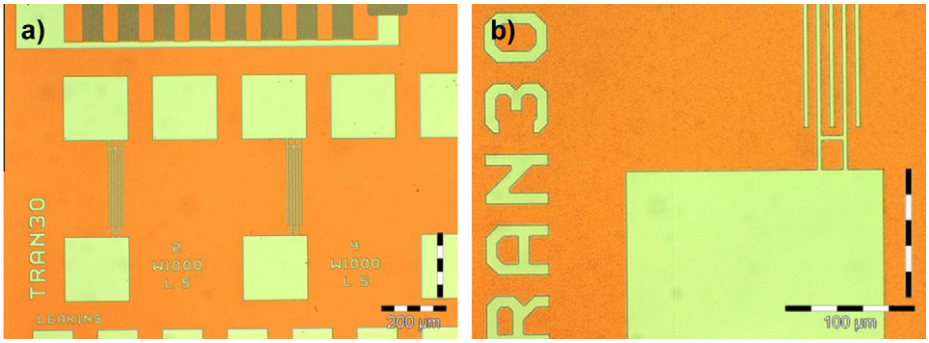

Fig. 3. Optical microscopy images of 5 μm wide and spaced interdigitated source–drain fingers connected to 200 μm wide contact pads after imprinting, residual layer removal, wet etching of the unprotected Au and dry etching of Cr and resist strip-off (Scheme 2D). The substrate is a MIM-coated PEN foil reversibly glued to a carrier.

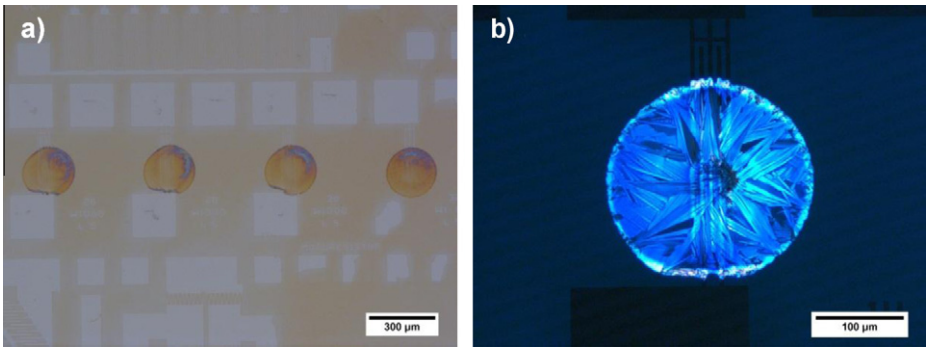

Fig. 4. Optical microscopy images of bottom contact, bottom gate TFTs with SFIL-patterned source–drain fingers on a MIM-covered FOC with inkjet-printed TIPS pentacene/PS crystals after SAM deposition of PFBT and TCPS (Scheme 2E). (a) One drop of TIPS pentacene/PS inkjet-printed on each of the four interdigitated 5 μm wide and spaced source–drain fingers. (b) Crossed polarizer optical microscopy image of one drop of TIPS pentacene/PS inkjet printed on the source–drain fingers showing a crystal growth from the edge to the center.

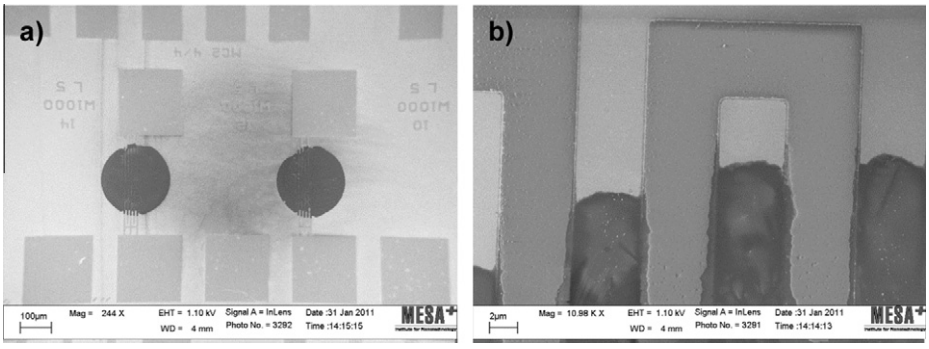

Fig. 5. High resolution SEM images after semiconductor deposition of (a) two TFTs, and (b) part of the source drain fingers displaying a line edge roughness of ~70 nm caused by wet etching.

image taken with cross polarizers shows the crystal orientation of the birefringent TIPS pentacene crystals, pointing to the center of the drop (Fig. 4b).

The high resolution SEM images in Fig. 5 show the final TFTs after semiconductor deposition, displaying a line edge roughness (LER) of about 70 nm caused by the short (10 s) wet etching of the gold. Any LER introduced by imprinting, representing an exact replica of the LER of the template, is negligibly small in comparison to the LER caused by wet etching of the gold.

2.3. Electrical characterization

Electrical characterization of the SFIL-patterned flexible TFTs was performed in a non-illuminated glove box under N_2 atmosphere. The contact to the common gate was

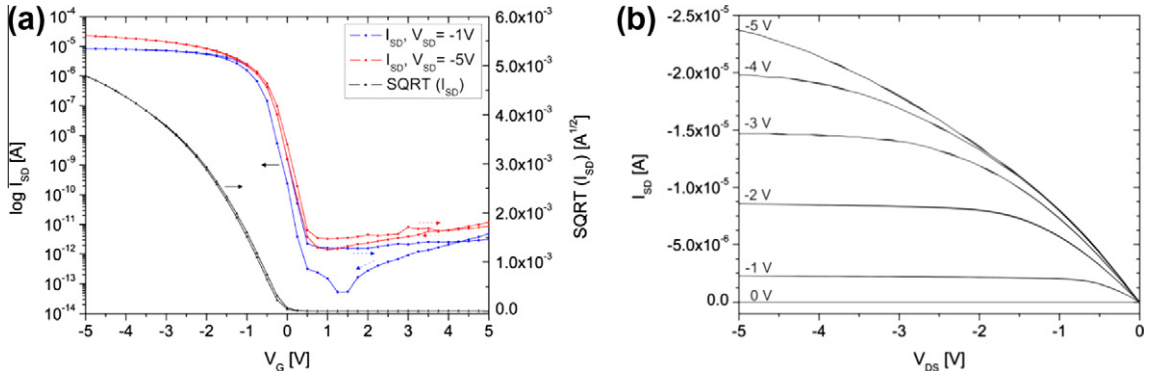

Fig. 6. (a) Transfer characteristics of an SFIL-patterned TFT in a bottom contact, bottom gate architecture. Channel length and width are 5 and 766 μm, respectively. A 100 nm thick Al_2O_3 layer served as the gate dielectric, and a blend of TIPS pentacene/PS as the semiconductor. The dashed arrows indicate the sweep direction (gate swept from +5 V → −5 V → +5 V). (b) Output characteristics of the same transistor. V_G was varied between 0 and −5 V at a step of −1 V.

established by penetrating the dielectric layer with one of the probe station needles. The source and drain contact pads were each gently contacted with another probe needle. The gate voltage was varied from 5 to −5 V in a double scan and the bias over source and drain (V_{DS}) held at −1 and −5 V. The transfer and output characteristics of the best out of six transistors with a channel length L = 5 μm and a channel width W = 766 μm arranged in a comb structure are given in Fig. 6 (see Supporting information for the transfer characteristics of the five other transistors).

From the semi-logarithmic plot (log I_{SD} vs. V_G), a subthreshold swing (SS) of 190 mV/dec, an on/off ratio of 2×10^7, and a switch-on voltage of V_{SO} = 0.4 V were obtained. The switch-on voltage was taken as the gate voltage at which the drain current is one order of magnitude higher than the off-current I_{off} [33]. From the plot of the square root of I_{SD} vs. V_G, a gate-dependent mobility of μ_{SAT} = 0.56 $cm^2\ V^{-1}\ s^{-1}$ at V_G = −0.75 V (average over all six transistors: $\mu_{SAT} = 0.37 \pm 0.08\ cm^2\ V^{-1}\ s^{-1}$) and a near-zero threshold voltage of V_{th} = −0.1 V were determined. To place the here obtained TFT data in a context, they were compared with data reported in literature for TFTs with either the same blend of inkjet-printed TIPS pentacene/PS or similar device structure and channel dimensions with the source–drain electrodes in a comb structure. The averaged mobility obtained for photolithographically defined bottom-contact, bottom-gate TFTs on poly(ethylene terephthalate) foil with a (sputtered) Al_2O_3 gate dielectric and inkjet printed TIPS pentacene on SAM-treated contacts and a channel width over length of 1000 μm/5 μm is $\mu = 0.22 \pm 0.03\ cm^2\ V^{-1}\ s^{-1}$ [37]. The mobility obtained here using imprinting is slightly higher, possibly caused by an improved LER or cleaner interfaces. Previously reported TFTs with TIPS pentacene/PS (67 wt%) blend inkjet printed on photolithographically patterned Au source–drain electrodes on highly doped n^{++} Si wafers with 140 nm thermally grown SiO_2, showed an improved mobility of $\mu_{sat} \approx 0.73\ cm^2/V\ s \pm 23\%$ for a channel length of 5 μm [36]. The on/off current and the threshold voltage of these non-flexible TFTs are very similar to the here obtained values. Only a steeper SS of 67 mV/dec was obtained. A steep SS and low V_{th}, are usually taken as evidence for a high-quality gate dielectric – semiconductor interface with few charge trapping centers [36]. The higher mobility reported for the non-flexible TFTs is believed to be due to the higher quality thermally grown gate dielectric, compared to the e-gun evaporated SiO_2 deposited on the here presented SFIL-patterned flexible transistors. The results shown here confirm that high-quality TFT devices can be made using NIL which holds promise for facile R2R production and further extension to sub-micron and nanoscale feature sizes.

3. Conclusions

In this paper we show the feasibility of SFIL as a patterning technique on flexible PEN foil for the fabrication of bottom-gate (common) and bottom-contact flexible TFTs. The here developed lamination process to create FOCs is a significant improvement to achieve better imprinting uniformity, but obviously does not impose any limitation on the flexibility of the device on foil in real-life applications as the foil can be easily delaminated afterwards. Using this R2R-compatible and downscalable technique in combination with inkjet printing excellent flexible TFTs with a performance comparable with state-of-the-art devices fabricated by optical photolithographic patterning [36–38] were obtained.

Future plans concern the fabrication of flexible, patterned-gate TFTs with all functional layers patterned by the room temperature, low pressure and high precision technique SFIL. The channel length of the flexible, all-patterned TFTs will also be reduced to the sub-micrometer regime. Downscaling into the sub-micrometer regime will result in an increased impact of the LER on the performance and dimensions of the device. Wet etching of the gold is at this stage the main factor introducing LER. Therefore, an etch process with an improved LER control, such as ion beam etching, should be introduced. The final flexible TFT fabrication process is envisioned to be R2R imprinting. R2R processing requires a patterning process independent of any alignment step, as the critical source–drain to gate overlay cannot be registered precise enough. Therefore, efforts are undertaken toward the development of a self-aligned imprinting process, implementing the fabrication

lessons learned here. As soon as device layout, process parameters and R2R implementation have been achieved, other performance issue such as mechanical stability and environmental stability will be addressed as well.

4. Experimental

4.1. Materials and methods

Imprint resist MonoMat and anti-sticking layer RELMAT were purchased from Molecular Imprints Inc. Teonex® Q65a poly(ethylene naphthalate) foil (PEN, 125 μm thick) was purchased from Dupont Teijin. 6,13-Bis(triisopropyl-silylethynyl) pentacene (TIPS pentacene) was synthesized according to literature [39]. Polystyrene (PS) $M_w \approx 9.58$ kDa ($M_n = 9.32$ kDa, PDI = 1.03) was purchased from Fluka. 1,2,3,4-Tetrahydro-naphthalene (tetraline) was purchased from Merck.

4.2. Foil-on-carriers (FOC)

FOCs were made by laminating the PEN foil to a glue, previously deposited on a double-side polished wafer. As glue, a 6 wt% solution of poly(methyl methacrylate) ($M_w = \sim 38$ kDa) dissolved in toluene, both purchased from Aldrich, was spincoated on a double-side polished wafer. The stack of glue-coated wafer, activated foil and a double-side polished (unpatterned) wafer with an 1H,1H,2H,2H-perfluorodecyltrichlorosilane anti-sticking layer applied by chemical vapor deposition, were loaded in an embossing tool (Eitre® 6 from Obducat, Malmö, Sweden). The foil was glued to the wafer by heating up the stack to 190 °C under 40 bar pressure for 500 s. The top wafer (with anti-sticking layer) was demolded at a temperature of 95 °C from the finished FOC. The PEN foil could be delaminated again from the carrier by heating to a temperature of 150 °C or by dissolving the PMMA in acetone.

The MIM layer was deposited on the FOC by e-gun evaporation of subsequently 5 nm Cr, 30 nm Au and 5 nm Cr forming the common gate, 100 nm Al_2O_3 as gate dielectric, and 5 nm Cr and 30 nm Au as source–drain metal.

4.3. Step-and-flash imprint lithography (SFIL)

The UV-transparent quartz template used for the experiments was fabricated by standard e-beam lithography and RIE techniques. The template contained, on an active area of 15×15 mm^2, test features in the dimensional range of 750 nm up to 1.4 mm and the TFT features as shown in Scheme 1 with a depth of 200 nm.

SFIL was performed with an Imprio 55 tool from Molecular Imprints Inc. The imprints were carried out at room temperature and under a force of 3 N. For improved adhesion of the imprint resist (MonoMat™), the Au surface of the FOC was activated just before use by a short O_2 plasma treatment of 5 min at 300 W and 18 sccm O_2 (Apparatus Tepla 300E). MonoMat™, after field by field drop dispensing on the substrate, filled the template within 60 s and was cured through the backside of the template for 3 s with broad band UV light (exposure dose of 80 mJ/cm^2 and $\lambda = 230$–360 nm).

4.4. Residual layer removal

The thin residual layer left after imprinting was removed by anisotropic O_2 plasma based reactive ion etching in a home build tool (Etske). At a chamber pressure of 10 m Torr and 20 sccm O_2 the residual layer was removed within 1 min at 20 W.

4.5. Direct etching

RIE opened windows in the resist layer which uncovered the Au/Cr metal layer. The 30 nm Au layer was removed by 10 s wet etching in a solution of $KI:I_2:H_2O$ 4:1:400. The 5 nm Cr adhesion layer was removed by Ar Ion beam etching with an Oxford Ionfab 300, removing the Cr layer within 3 min, controlled by an endpoint detection system.

4.6. Resist strip-off

Remaining resist was stripped off in a Tepla 300E, by generation of an 300 W O_2 plasma (18 sccm) for 10 min.

4.7. Self-assembled monolayers

PFBT was deposited by 15 min exposure to a 10 mM PFBT solution in ethanol, followed by rinsing with ethanol and N_2 blow drying. N_2 was utilized as carrier gas bubbling through TCPS in a closed chamber at atmospheric pressure for 15 min to deposit TCPS on all oxide areas. The substrates were baked 2 min at 100 °C on a hotplate after flushing the chamber with N_2 to remove the side product (hydrochloric acid) of the condensation reaction.

4.8. Semiconductor deposition

An ink-jet printing setup with a high-precision vertical translation stage and a Microfab glass nozzle (type MJ-ATP-01-50-DLC, 50 μm orifice diameter) was used to print the blend of TIPS pentacene (20 mg/ml):PS (10 mg/ml) in a blending ratio of 2:1. Droplets with a volume of 50 pL were jetted on demand, onto transistor substrates kept at a temperature of 70 °C. All printing experiments were performed in ambient clean room conditions [36].

Acknowledgments

The author would like to thank Hans Mertens and Shuo Kang for their support in dry etching of the Cr adhesion layer and Bas van der Putten for SAM depositions. The program Lithography on flexible substrates of the Holst Centre is acknowledged for financial support.

Appendix A. Supplementary data

Supplementary data associated with this article can be found, in the online version, at doi:10.1016/j.orgel.2011.09.020.

References

[1] D. Braga, G. Horowitz, High-performance organic field-effect transistors, Adv. Mater. 21 (2009) 1–14.
[2] P.F. Baude, D.A. Ender, M.A. Haase, T.W. Kelley, D.V. Muyres, S.D. Theiss, Pentacene-based radio-frequency identification circuitry, Appl. Phys. Lett. 82 (2003) 3964–3966.
[3] V. Subramanian, P.C. Chang, J.B. Lee, S.E. Molesa, S.K. Volkman, Printed organic transistors for ultra-low-cost RFID applications, IEEE Trans. Compon. Packag. Technol. 28 (2005) 742–747.
[4] T. Kietzke, Recent advances in organic solar cells, Adv. Opt. Electron. (2007) 40285.
[5] B. Geffroy, P. le Roy, C. Prat, Organic light-emitting diode (OLED) technology: materials, devices and display technologies, Polym. Int. 55 (2006) 572–582.
[6] S.H. Ahn, L.J. Guo, Large-area roll-to-roll and roll-to-plate nanoimprint lithography: a step toward high-throughput application of continuous nanoimprinting, ACS Nano 3 (2009) 2304–2310.
[7] H. Schift, Nanoimprint lithography: an old story in modern times? A review, J. Vac. Sci. Technol. B 26 (2008) 458–480.
[8] M.D. Austin, H.X. Ge, W. Wu, M.T. Li, Z.N. Yu, D. Wasserman, S.A. Lyon, S.Y. Chou, Fabrication of 5 nm linewidth and 14 nm pitch features by nanoimprint lithography, Appl. Phys. Lett. 84 (2004) 5299–5301.
[9] S.Y. Chou, P.R. Krauss, P.J. Renstrom, Imprint of sub-25nm vias and trenches in polymers, Appl. Phys. Lett. 67 (1995) 3114–3116.
[10] S.Y. Chou, P.R. Krauss, P.J. Renstrom, Imprint lithography with 25-nanometer resolution, Science 272 (1996) 85–87.
[11] J. Haisma, M. Verheijen, K.V.D. Heuvel, J.V.D. Berg, Mold-assisted nanolithography: a process for reliable pattern replication, J. Vac. Sci. Technol. B 14 (1996) 4124–4128.
[12] P. Ruchhoeft, M. Colburn, B. Choi, H. Nounu, S. Johnson, T. Bailey, S. Damle, M. Stewart, J. Ekerdt, S.V. Sreenivasan, J.C. Wolfe, C.G. Willson, Patterning curved surfaces: template generation by ion beam proximity lithography and relief transfer by step and flash imprint lithography, J. Vac. Sci. Technol. B 17 (1999) 2965–2969.
[13] R. Parashkov, E. Becker, G. Ginev, T. Riedl, H.-H. Johannes, W. Kowalsky, All-organic thin-film transistors made of poly(3-butylthiophene) semiconducting and various polymeric insulating layers, J. Appl. Phys. 95 (2004) 1594–1596.
[14] D.R. Hines, A. Southard, M.S. Fuhrer, Poly(3-hexylthiophene) thin-film transistors with variable polymer dielectrics for transfer-printed flexible electronics, J. Appl. Phys. 104 (2008) 024510.
[15] A.C. Siegel, S.T. Phillips, M.D. Dickey, N. Lu, Z. Suo, G.M. Whitesides, Foldable printed circuit boards on paper substrates, Adv. Funct. Mat. 20 (2010) 28–35.
[16] S. Logothetidis, A. Laskarakis, Organic against inorganic electrodes grown onto polymer substrates for flexible organic electronics applications, Thin Solid Films 518 (2009) 1245–1249.
[17] J. Zhang, C.M. Li, M.B. Chan-Park, Q. Zhou, Y. Gan, F. Qin, B. Ong, T. Chen, Fabrication of thin-film organic transistor on flexible substrate via ultraviolet transfer embossing, Appl. Phys. Lett. 90 (2007) 243502.
[18] G.F. Wang, X.M. Tao, H.M. Huang, Influence of the deposition temperature on the structure and performance of tris(8-hydroxyquinoline) aluminum based flexible organic light-emitting devices, Appl. Surf. Sci. 253 (2007) 4463–4466.
[19] D. van den Berg, M. Barink, P. Giesen, E. Meinders, I. Yakimets, Hygroscopic and thermal micro deformations of plastic substrates for flexible electronics using digital image correlation, Polymer Testing 30 (2011) 188–194.
[20] I. Yakimets, D. MacKerron, P. Giesen, K.J. Kilmartin, M. Goorhuis, E.R. Meinders, W.A. MacDonald, Polymer substrates for flexible electronics: achievements and challenges, Adv. Mat. Res. 93–94 (2010) 5–8.
[21] S. Logothetidis, Flexible organic electronic devices: materials, process and applications, Mater. Sci. Eng. B 152 (2008) 96–104.
[22] D.K. Hwang, C. Fuentes-Hernandez, J. Kim, W.J. Potscavage, S.-J. Kim, B. Kippelen, Top-gate organic field-effect transistors with high environmental and operational stability, Adv. Mat. 23 (2011) 1293–1298.
[23] H.E.A. Huitema, G.H. Gelinck, J.B.P.H. van der Putten, K.E. Kuijk, C.M. Hart, E. Cantatore, P.T. Herwig, A.J.J.M. van Breemen, D.M. de Leeuw, Plastic transistors in active-matrix displays, Nature 414 (2001) 599.
[24] M. Péter, F. Furthner, J. Deen, W.J.M. de Laat, E.R. Meinders, Lithographic patterning of metals on flexible plastic foils, Thin Solid Films 517 (2009) 3081–3086.
[25] W.J.M. de Laat, M. Péter, F. Furthner, P.T.M. Giesen, C.-Q. Gui, E.R. Meinders, Submicron patterning on Flexible Substrates by Reduction Optical Lithography, Emerging Lithographic Technologies XII, Proc. SPIE 6921 (2008) 69212F, doi: 10.1117/12.771947.
[26] I. Barbu, M.G. Ivan, P. Giesen, M. vd Moosdijk, E.R. Meinders, Advances in mask-less and mask-based optical lithography on plastic flexible substrates, Proc. SPIE 7520 (2009) 75200A, doi: 10.1117/12.837171.
[27] D.W. Li, L.J. Guo, Micron-scale organic thin film transistors with conducting polymer electrodes patterned by polymer inking and stamping, Appl. Phys. Lett. 88 (2006) 063513.
[28] A.C. Arias, S.E. Ready, R. Lujan, W.S. Wong, K.E. Paul, A. Salleo, M.L. Chabinyc, R. Apte, R.A. Street, Y. Wu, P. Liu, B. Ong, All jet-printed polymer thin-film transistor active-matrix backplanes, Appl. Phys. Lett. 85 (2004) 3304–3306.
[29] H.-Y. Tseng, V. Subramanian, All inkjet-printed, fully self-aligned transistors for low-cost circuit applications, Org. Electron. 12 (2011) 249–256.
[30] G. Gelinck, P. Heremans, K. Nomoto, T.D. Anthopoulos, Organic transistors in optical displays and microelectronic applications, Adv. Mat. 22 (2010) 3778–3798.
[31] U. Palfinger, C. Auner, H. Gold, A. Haase, J. Kraxner, T. Haber, M. Sezen, W. Grogger, G. Domann, G. Jakopic, J.R. Krenn, B. Stadlober, Fabrication of n- and p-type organic thin film transistors with minimized gate overlaps by self-aligned nanoimprinting, Adv. Mat. 22 (2010) 5115–5119.
[32] U. Haas, H. Gold, A. Haase, G. Jakopic, B. Stadlober, Submicron pentacene-based organic thin film transistors on flexible substrates, Appl. Phys. Lett. 91 (2007) 043511.
[33] C. Auner, U. Palfinger, H. Gold, J. Kraxner, A. Haase, T. Haber, M. Sezen, W. Grogger, G. Jakopic, J.R. Krenn, G. Leising, B. Stadlober, Residue-free room temperature UV-nanoimprinting of submicron organic thin film transistors, Org. Electron. 10 (2009) 1466–1472.
[34] S.R. Saudari, Y.J. Lin, Y. Lai, C.R. Kagan, Device configurations for ambipolar transport in flexible, pentacene transistors, Adv. Mat. 22 (2010) 5063–5068.
[35] M. Mas-Torrent, C. Rovira, Role of molecular order and solid-state structure in organic field-effect transistors, Chem. Rev. (2011), doi: 10.1021/cr100142w.
[36] X. Li, W.T.T. Smaal, C. Kjellander, B. van der Putten, K. Gualandris, E.C.P. Smits, J. Anthony, D.J. Broer, P.W.M. Blom, J. Genoe, G. Gelinck, Charge transport in high-performance ink-jet printed single-droplet organic transistors based on a silylethynyl substituted pentacene/insulating polymer blend, Org. Electron. 12 (2011) 1319–1327.
[37] B.K.C. Kjellander, W.T.T. Smaal, J.E. Anthony, G.H. Gelinck, Inkjet printing of tips-pen on soluble polymer insulating films: a route to high-performance thin-film transistors, Adv. Mat. 22 (2010) 4612–4616.
[38] S.H. Lee, M.H. Choi, S.H. Han, D.J. Choo, J. Jang, S.K. Kwon, High-performance thin-film transistor with 6,13-bis(triisopropylsilylethynyl) pentacene by inkjet printing, Org. Electron. 9 (2008) 721–726.
[39] J.E. Anthony, J.S. Brooks, D.L. Eaton, S.R. Parkin, Functionalized pentacene: improved electronic properties from control of solid-state order, J. Am. Chem. Soc. 123 (2001) 9482–9483.

Since a successful hybridization of RG-O/conducting polymer requires RG-O platelets to be fully exfoliated in a suspension and provide a modified and active sites for the hybridization, we used PIL to modify the surface of RG-O platelets. The specific PIL of poly(1-vinyl-3-ethyimidazolium) salts was explored to stabilize RG-O platelets to be suspended in organic solvent, and provide an effective linkage during the polymerization of PEDOT molecules on the RG-O surface. The resulting hybrid material of RG-O and PEDOT are found to be readily dispersed as a colloidal system without any agglomeration and its film showed synergistic effects in terms of electrical conductivity and thermal stability.

2. Experimental

2.1. Synthesis of graphene oxide and poly(ionic liquid)

Graphite oxide (GO) powder was prepared from graphite flakes using modified Hummers method [17,18]. Briefly, 5 g of graphite (Bay carbon SP-1) and 3.75 g of $NaNO_3$ were placed in a flask. Then, 375 mL of H_2SO_4 was added while stirring in an ice-water bath, and 25 g of $KMnO_4$ were slowly added for 1 h. Stirring was continued for 2 h in the ice-water bath. The reaction mixture was washed with deionized water, and reacted with a 30 wt.% aqueous solution of H_2O_2 to complete oxidation. The ions of oxidant and other inorganic impurity were removed by repeating cycle of centrifugation, removal of the supernatant liquid, and redispersing the solid using 3 wt.% HCl aqueous solution. Finally, the solid was dispersed again in water using ultrasonication for 2 h and centrifuged at 6000 rpm for 30 min to remove the multilayered species.

PIL of poly(1-vinyl-3-ethylimidazolium) salts bearing the bis(trifluoromethylsulfonyl)amide anion (NTf_2^- or $CF_3SO_2–N–SO_2CF_3$) was synthesized according to a previously reported procedure [19,20].

2.2. Poly(ionic liquid)-mediated thermal reduction of graphene oxide in propylene carbonate

Graphene oxide (G-O) suspension with a concentration of 1 mg/mL was obtained by dispersing GO powder in propylene carbonate (PC) with the aid of mild sonication

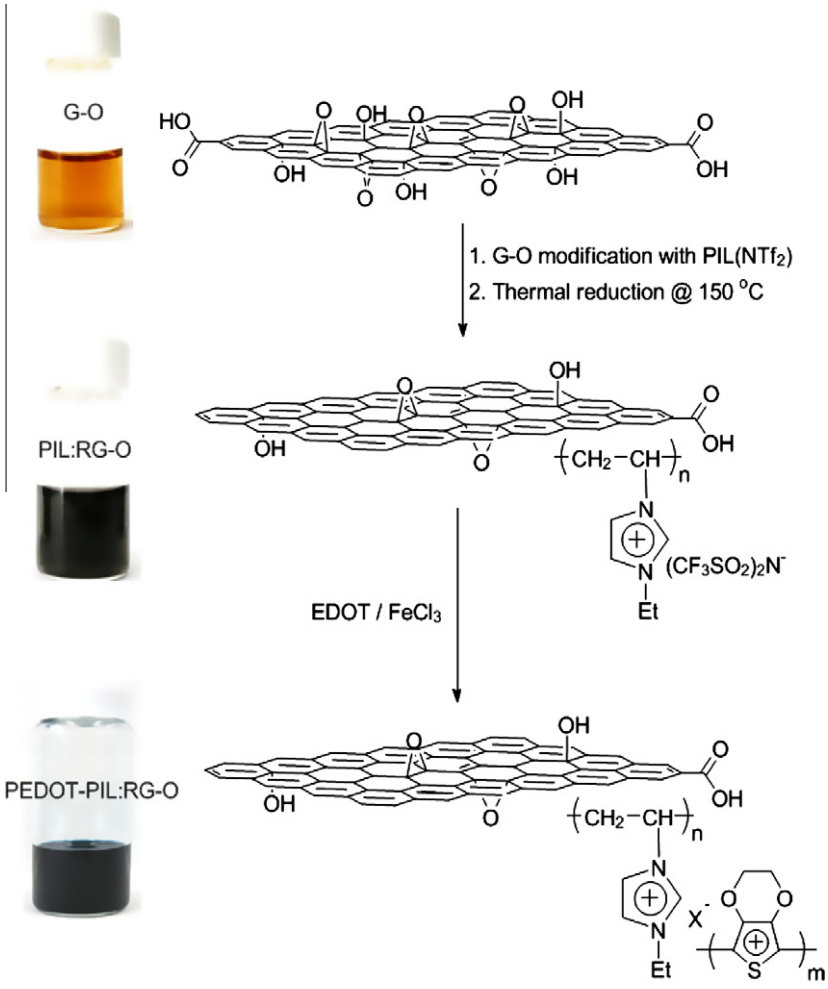

Fig. 1. The process for preparation of PIL:RG-O hybrids with conducting polymer PEDOT using poly(ionic liquids).

for 30 min. Then, PIL was added to the G-O suspension in PC and stirred for 30 min to produce PIL-modified G-O. PIL-modified G-O was prepared with different ratios of PIL/G-O (1/1, 3/1, 5/1, 10/1) by weight. In a typical process, 300 mg of PIL(NTf_2^-) were dissolved in 30 mL of anhydrous PC and added to 60 mL of G-O suspension. Under continues stirring, heating these mixture at 150 °C for 3 h yielded a thermally reduced RG-O modified with PIL (PIL:RG-O), as previously reported [21]. After cooling, a part (*e.g.*, 10 mL) of heated suspension was filtered through a Omnipore membrane (JGWP, 0.2 μm pore size, Millipore, Ireland) to obtain the resultant PIL:RG-O, followed by drying at 80 °C in vacuum for 2 days.

2.3. Hybridization of PIL-modified reduced graphene oxide and conducting polymer

The as-prepared PIL:RG-O suspension was subjected to hybridization with PEDOT. In situ polymerization of EDOT was carried out by chemical oxidative method in PIL:RG-O suspension. Typical preparation procedure for the PIL-mediated hybridization of RG-O and PEDOT (PEDOT-PIL:RG-O) composites is as follows: a mixture of EDOT (0.268 g), 1.25 mL of PIL:RG-O suspension and 60 mL of PC were introduced into a 250 mL one-necked round bottom flask and stirred for 1 h. The chemical polymerization was effected by the addition of a solution of Iron(III) chloride ($FeCl_3$, 0.30 g in 20 mL PC) into the mixture and the reaction was continued under vigorous stirring for 48 h at room temperature, yielding organic solvent dispersible PEDOT-PIL:RG-O composites. For comparison, the PIL-modified PEDOT (without any RG-O) (PEDOT:PIL) sample was also prepared separately under same conditions.

2.4. Characterization

Fourier transform infrared (FT-IR) spectra were recorded on a Nicolet Avatar 320 using KBr pellets. X-ray photoelectron spectroscopy (XPS) measurements were performed with ESCA2000 (VG Microtech) system using a monochromatized aluminum Kα anode. Raman spectra were recorded over 500–4000 cm^{-1} with an excitation wavelength of 642.8 nm using RFS-100/S Raman spectrometer equipment. Thermogravimetric analysis (TGA) measurement was performed at a heating rate of 10 °C min^{-1} under nitrogen flow using a NETZSCH STA 409 PC/PG

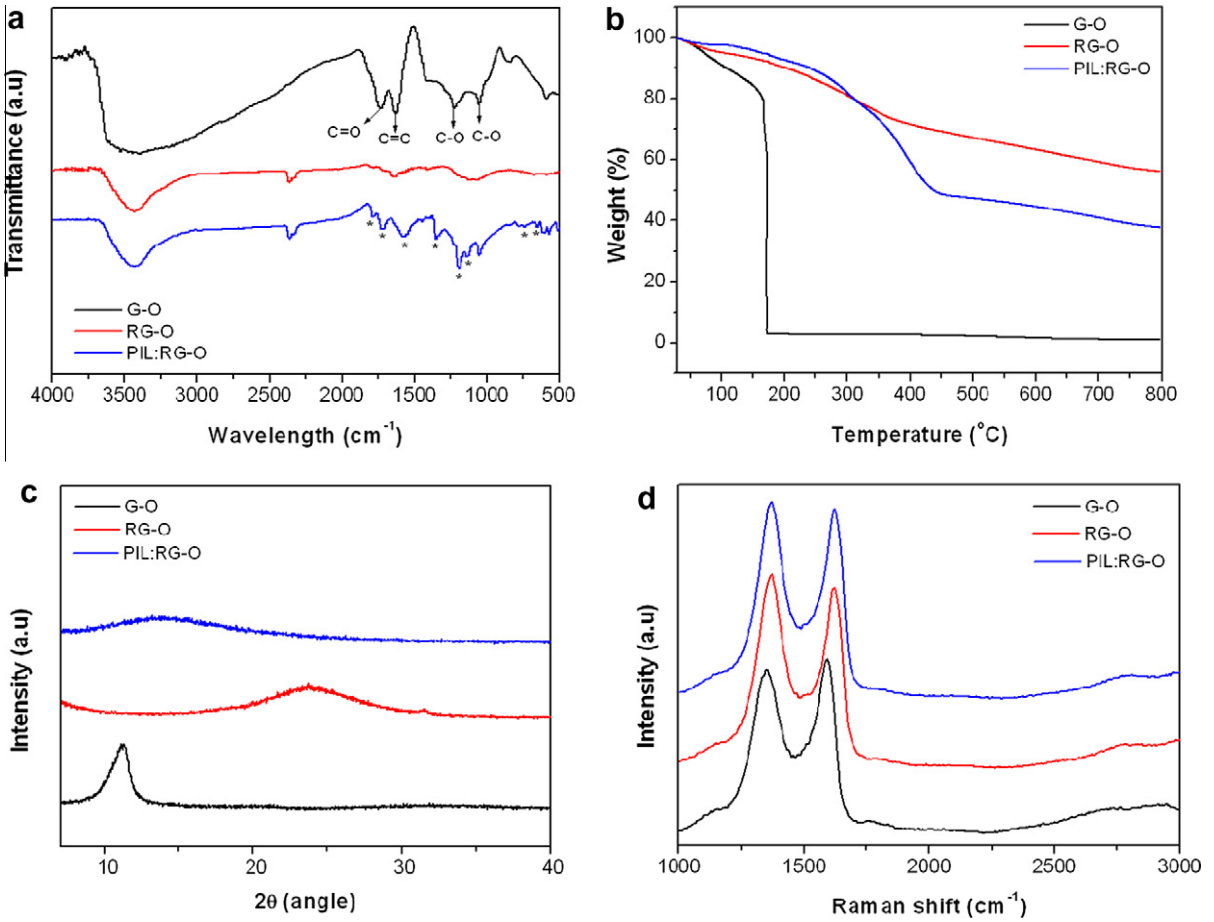

Fig. 2. (a) FTIR, (b) TGA, (c) XRD, and (d) Raman spectra of G-O (black curve), RG-O (red curve) and PIL:RG-O (blue curve). (For interpretation of the references to color in this figure legend, the reader is referred to the web version of this article.)

instrument. X-ray diffraction (XRD) data were collected on a Rigaku D/Max Ultima II Powder X-ray diffractometer. Scanning electron microscopy (SEM) images were recorded using a JEOL JSM-700F microscope operated at 15.0 kV. High resolution transmission electron microscopy (HR-TEM) images were obtained using a TECNAI 20 operating at 200 kV and equipped with energy dispersive X-ray fluorescence spectrometer for EDX analysis. Atomic force microscopy (AFM) measurements were performed in tapping mode with an AFM XE-100 (Park System). The surface resistance was obtained using a four-point probe method (CMT-SR2000N) at room temperature.

3. Results and discussion

A hybrid of RG-O and PEDOT was obtained through a two-step procedure illustrated in Fig. 1. The first step involved thermal reduction of G-O in the presence of PIL and this process typically resulted in the RG-O modified with PIL. In the second step, we carried out in situ chemical polymerization of EDOT in PIL:RG-O suspension using $FeCl_3$ as an oxidizing agent. This process leads to the formation of a hybridized material PEDOT-PIL:RG-O that are homogeneously dispersed as a colloidal system in PC.

3.1. Thermal reduction of the PIL-functionalized graphene oxide in propylene carbonate

The addition of PIL into G-O suspension in propylene carbonate (PC) typically yielded the PIL-modified G-O by the electrostatic interaction between the cation in PIL and negatively charged G-O platelets. Then, heating this suspension at 150 °C led to the reduced graphene oxide modified with PIL. Fig. 2a shows the FT-IR spectra of G-O, RG-O and PIL:RG-O. The spectra of G-O sheets (black curve) showed C=O (1725 cm^{-1}), aromatic C=C (1621 cm^{-1}), carboxy C–O (1382 cm^{-1}), epoxide/ether C–O (1231 cm^{-1}), and alkoxy/alkoxide C–O stretches (1027 cm^{-1}). The RG-O (red curve) showed a decrease in C=O and C–O stretch peak intensities, indicating de-oxygenation of the RG-O sheets after thermal reduction. In the FT-IR spectra of PIL:RG-O (blue curve), the peaks at 1792, 1569, 1352, 1189, 744, and 647 cm^{-1} correspond to the PIL(NTf_2^-), indicating an adsorption of PIL(NTf_2^-) onto the RG-O surface.

Fig. 2b shows the TGA data of RG-O (red curve) and PIL:RG-O (blue curve) in comparison with pristine G-O (black curve). G-O shows a continuing weight loss of

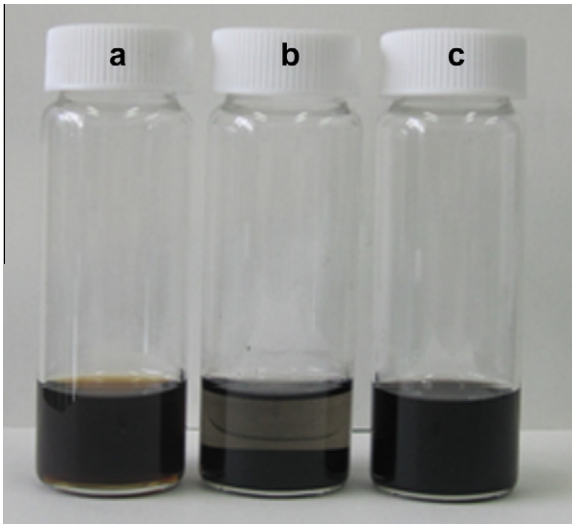

Fig. 3. Photograph of (a) G-O, (b) RG-O, and (c) PIL:RG-O dispersed in propylene carbonate after 3 days of free-standing.

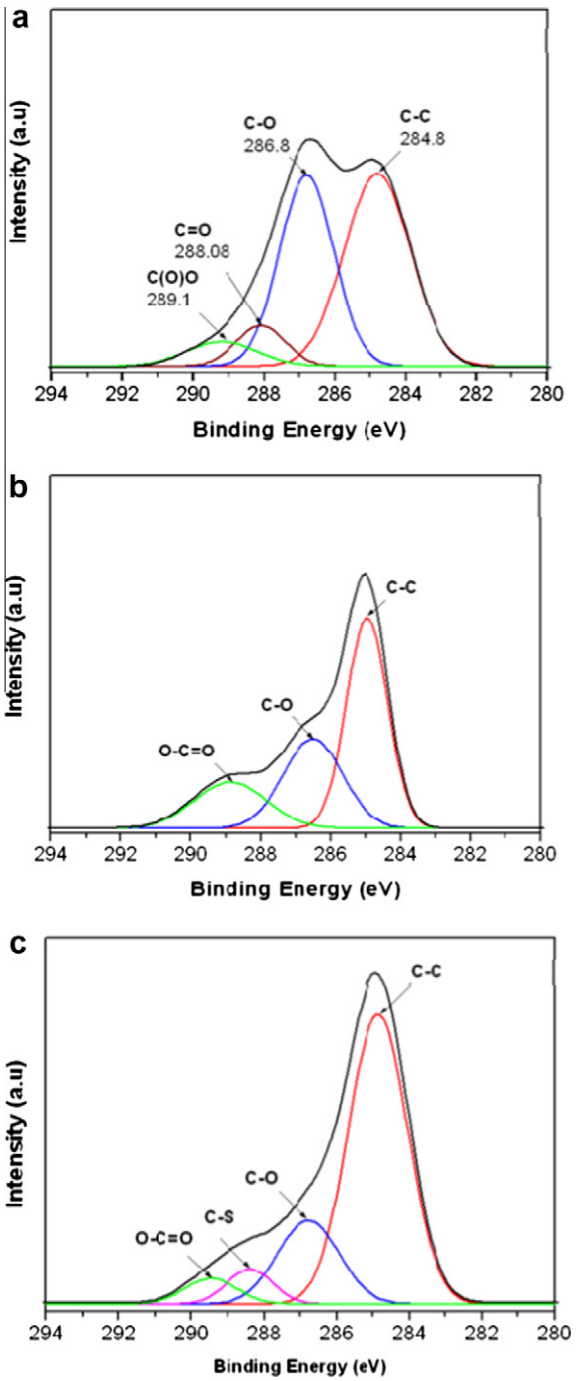

Fig. 4. C 1s XPS spectra of (a) G-O, (b) RG-O, and (c) PIL:RG-O.

7–8% in the temperature range up to 80 °C, and this is related to the removal of physisorbed water. A weight loss around 168 °C can be ascribed to the decomposition of different oxygen containing groups in the G-O layer [22]. The weight loss of RG-O (red curve) is much smaller due to a decreased amount of oxygen functional groups in the RG-O. For the case of PIL:RG-O (blue curve), the weight loss of 25% occurs from 316 to 428 °C, possibly due to the decomposition of the surface-bound PIL molecules.

The XRD patterns of G-O, RG-O and PIL:RG-O are shown in Fig. 2c. Similar to the previous report, G-O and RG-O showed a XRD peak at $2\theta = 11.2°$ and 23.8°, indicating an interlayer spacing of ~0.78 nm and ~0.36 nm. The decreased interlayer spacing for RG-O is due to the removal of oxygen-based functional groups on the basal plane by thermal reduction. Compared with RG-O, the PIL:RG-O showed a broad peak at $2\theta = 13.9°$, indicating an increased interlayer spacing of ~0.62 nm. This suggests that PIL are coated on the surface of RG-O surface and act as a spacer for RG-O platelets with an increased interlayer spacing.

Raman spectroscopy was employed to investigate a change in the graphitic structure during the reduction process of RG-O and PIL:RG-O as shown in Fig. 2d. The Raman spectrum shows a typical D band (1332 cm^{-1}) and G band (1560 cm^{-1}) for G-O, which corresponds to the presence of sp^3 defects and tangential vibration of sp^2 carbon atoms in hexagonal plane, respectively. While the intensity ratio of D and G band (I_D/I_G) of G-O is about 0.82, the I_D/I_G of RG-O increased to 1.12 due to a decrease in the average size of the sp^2 carbon network upon thermal reduction of the exfoliated G-O [22,23]. In case of PIL:RG-O, the I_D/I_G was measured as 1.03 which is lower than that of RG-O. This suggests that PIL:RG-O has decreased density of defects compared with RG-O without PIL.

The thermal reduction of G-O in the presence of PIL produces a suspension of PIL:RG-O in PC. While the reduction of G-O without PIL resulted in an agglomerated RG-O sheets which can be viewed as black particles in the vial (Fig. 3b), the PIL:RG-O was found to be dispersed as a homogeneous colloidal system with no visible agglomerates (Fig. 3c). This dispersion can be filtered to obtain PIL:RG-O platelets that can be re-dispersed in a wide range of organic solvents such as PC, acetone, acetonitrile (AN), dimethylformamide (DMF), *N*-methyl-pyrollidone (NMP) and nitromethane (NM). It should be noted that an increase in the amount of PIL added to G-O suspension enhances the stability of suspension (Fig. S-1, supporting information). When the PIL/G-O weight ratio is equal to or lower than 3/1, PIL:RG-O in PC precipitated out after several days, suggesting that PIL concentration was not sufficient to fully stabilize RG-O platelets in PC. On the other hand, when the ratio is higher than 5/1, the dispersion remained stable for more than 6 months.

The chemical composition of G-O, RG-O, and PIL:RG-O was investigated by XPS. The C 1s XPS spectrum of G-O (Fig. 4a) can be deconvoluted into four main components

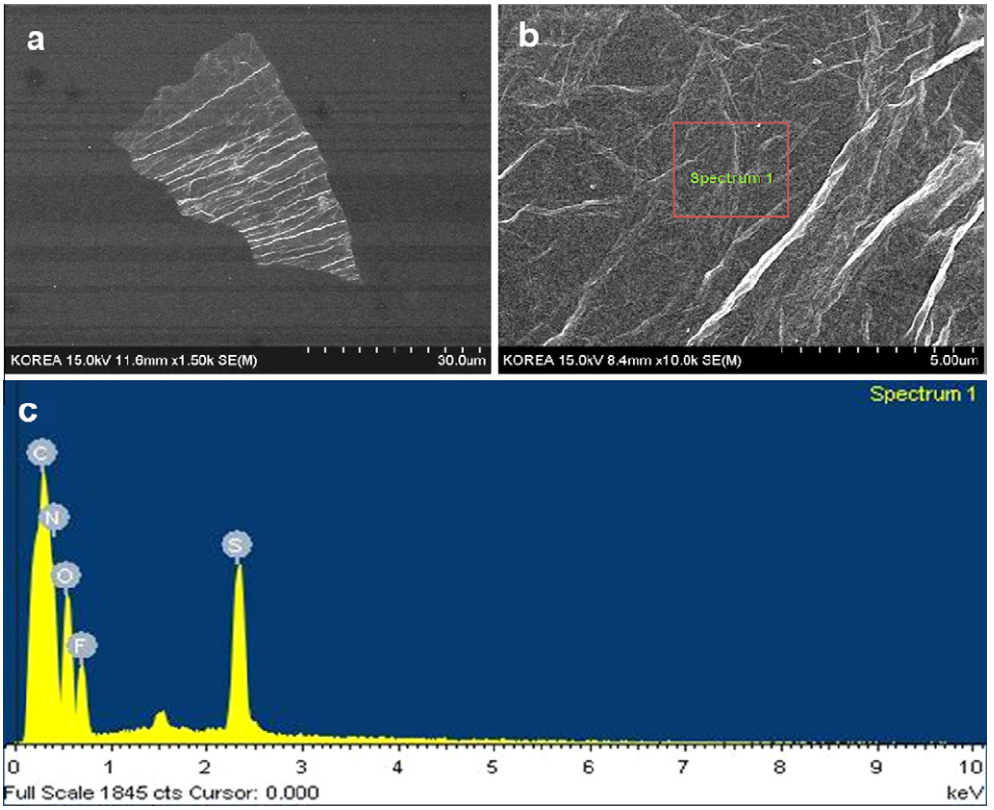

Fig. 5. (a and b) SEM image with different magnification of PIL:RG-O and (c) the EDX spectra corresponding to panel b.

corresponding to carbon atoms in different functional groups: the non-oxygenated ring C (284.8 eV), the C in C–O bonds (286.8 eV), the carbonyl C (C=O, 288.0 eV), and the carboxylate carbon (O–C=O, 289.1 eV). As shown in Fig. 4b, RG-O sample showed a decreased intensity of these oxygen groups confirming the effective removal of oxygen groups by thermal reduction [21]. The C 1s XPS spectrum of PIL:RG-O (Fig. 4c) also shows the removal of oxygen groups on the G-O basal plane and the subsequent restoration of sp^2-hybridized carbon network. Moreover, the C/O atomic ratio calculated from the XPS spectra is 2.0, 6.2 and 8.6 for G-O, RG-O and PIL:RG-O, respectively. The higher C/O atomic ratio observed for PIL:RG-O is attributed to the fact that the thermal reduction of G-O platelets occurred more rapidly in the presence of PIL, than in a control experiment with no PIL present [21]. The rapid reduction of suspended G-O described here may come from the reducing capability of imidazolium-based PIL, which has been previously reported for ionic liquid reduction of Au precursors [24]. Additionally, there is a new component at 288.4 eV corresponding to the C in the C–S bonds of NTf_2^- (CF_3SO_2–N–SO_2CF_3) anion, suggesting the existence of PIL on the RG-O surfaces.

A top-view SEM image of PIL:RG-O deposited on Si/SiO_2 substrates (Fig 5a) reveals that the RG-O platelets are individually isolated. In Fig. 5b, it can be seen that the surface of RG-O was covered with a thin layer of PIL molecules, which is also evidenced by energy dispersive X-ray (EDX) analysis in Fig. 5c.

TEM was used to investigate the level of exfoliation and the dispersion. As can be seen in Fig. 6a, PIL:RG-O material was observed as thin platelets with some folded area and small fragments. In the selected area electron diffraction (SAED) patterns (inset of Fig. 6a), a ring-like pattern consisting of many diffraction spots was observed indicating a random overlay of individual RG-O platelets coated with PIL, or from folds that cause overlays [21]. Fig. 6b shows an AFM image and height profile from the sample, confirming that PIL:RG-O are comprised of large-scale (several μm) and isolated graphitic sheets with some winkles. From the AFM height profile, the thickness of PIL:RG-O was measured as 1.64 nm that is higher than that of theoretical thickness of a single layer graphene (0.34 nm) [25], G-O platelets exfoliated in water (~1 nm) [26,27], and RG-O in PC (~0.6 nm) [21]. The higher thickness value for PIL:RG-O is likely due to the PIL coating of RG-O platelet [28].

Fig. 7 shows the surface resistivity vs. weigh ratio of PIL/G-O. The surface resistivity was measured for PIL:RG-O

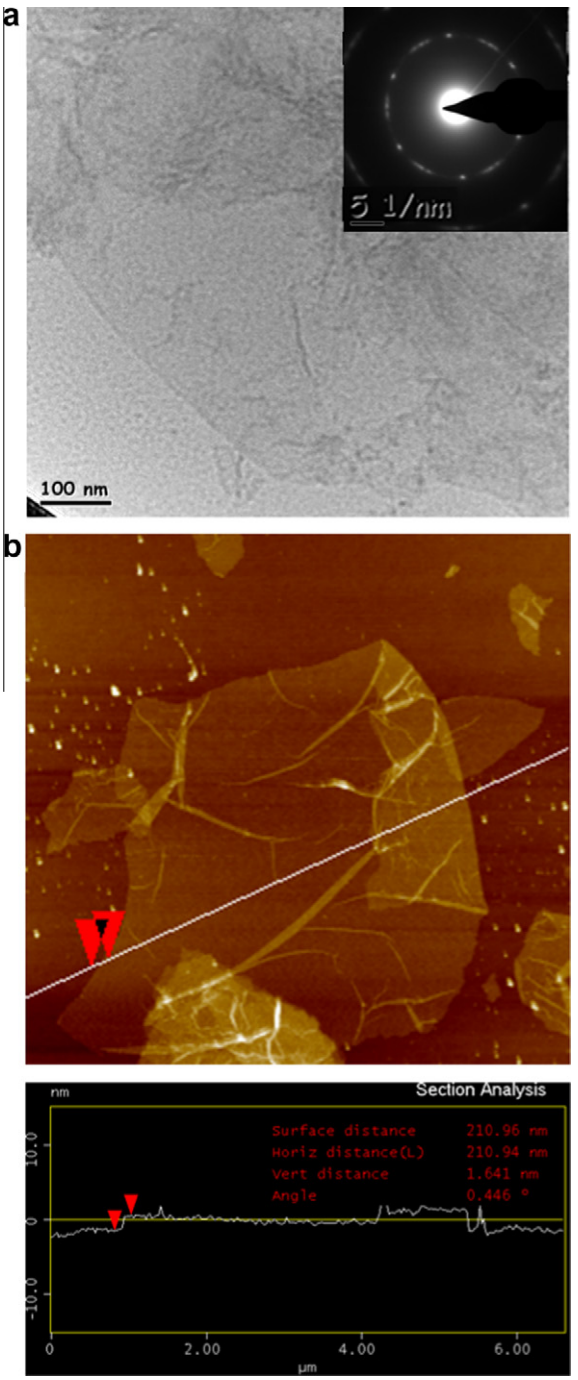

Fig. 6. (a) TEM and (b) AFM histogram shows the statistic analysis of PIL:RG-O sample. The inset in (a) is the SAED patterns from PIL:RG-O sheet.

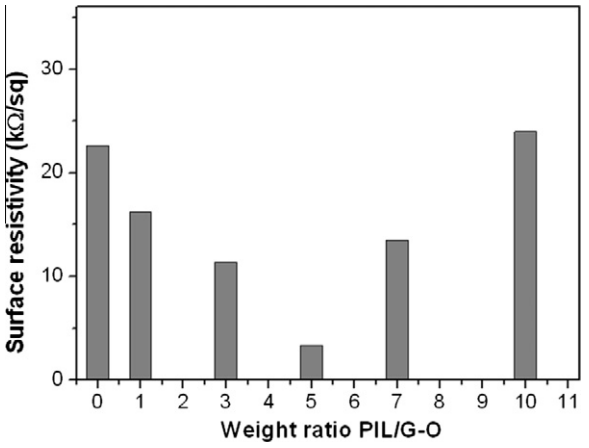

Fig. 7. The surface resistivity of PIL:RG-O films with different weight ratios of PIL vs. G-O.

using a standard four-probe method. For the measurement, the PIL:RG-O paper-like films with the film thickness of ~534 nm (Fig. S-2, SI) were prepared by casting PIL:RG-O suspension on the Si/SiO2 wafer. The randomly stacked PIL:RG-O film was peeled off the substrate and subject to the resistivity measurement. The surface resistivity of PIL:RG-O decreases from 22.6 to 3.3 kΩ/sq with increasing PIL/G-O ratio of up to 5. This result suggest that the sp^2-carbon network is more effectively restored in the PIL:RG-O than RG-O. However, when PIL/G-O ratio is above 5, the surface resistivity increases to 23 kΩ/sq, indicating that an excess of PIL negatively affects the electrical connectivity of PIL:RG-O platelets. Therefore, the optimized PIL/G-O ratio was set as 5 and further experiments were carried out.

3.2. Hybridization of PIL-modified reduced graphene oxide and conductive polymer

In this section, we describe the preparation and characterization of PEDOT-PIL:RG-O composites by in situ polymerization of EDOT (Fig. 1, step 2), in which EDOT is polymerized in the presence of PIL:RG-O. The driving force for the formation of hybridized PEDOT and PIL:RG-O is likely due to electrostatic attraction between opposite charges. Since the growing PEDOT chains have positive charge and PIL carries a negative charge by NTf_2^- anions, it is conceivable that PIL on the RG-O surface function as a charge balancing stabilizer to the positively doped PEDOT chains during the polymerization process.

Fig. 8a shows the FT-IR spectra of the PEDOT-PIL:RG-O composite and pristine PEDOT-PIL. The characteristic bands for the PEDOT-PIL:RG-O composites appear in the range of 500–4000 cm^{-1}, showing almost the same numbers and positions of the main peaks as in the pristine PEDOT:PIL; C–C stretching in the thiophene ring (1350 cm^{-1}), vibration modes of the ethylenedioxy group (1207 and 1093 cm^{-1}), S–O stretched vibration (988 cm^{-1}) and vibration modes of the PIL(NTf_2^-) (1790, 1400 and 780 cm^{-1}). However, there were two additional peaks at 1725 and 1634 cm^{-1}, corresponding to the stretching modes of the aromatic C=C in RG-O sheets.

The chemical composition of the PEDOT-PIL:RG-O composites were also investigated by XPS spectra. The C 1s XPS spectrum (Fig. 8b) of the composite film can be deconvoluted into four main components corresponding to carbon atoms in different functional groups: the non-oxygenated ring C (284.9 eV), the C–O (286.4 eV), C–S (287.7 eV) and the C=O (289.5 eV). Moreover, the S 2p core-line spectra (Fig. 8c) showed the peak at 168.2 eV (NTf_2^- anion in the PIL dopant), and the lower binding energy peaks at 165.3 and 164.1 eV (spin-split doublets of sulfur atoms in PEDOT backbone), which confirms the existence of PEDOT.

SEM was used to observe the fine morphological structure of the composites. Fig. 9 shows representative SEM images of PEDOT-PIL:RG-O. In the top-view image (Fig. 9a), the conducting polymer formed a continuous phase with the RG-O submerged in the polymer phase, while cross-section image (Fig. 9b) shows stacked RG-O sheets of which their surfaces are likely to be covered with PEDOT. A TEM image of the composite sample (Fig. 9c)

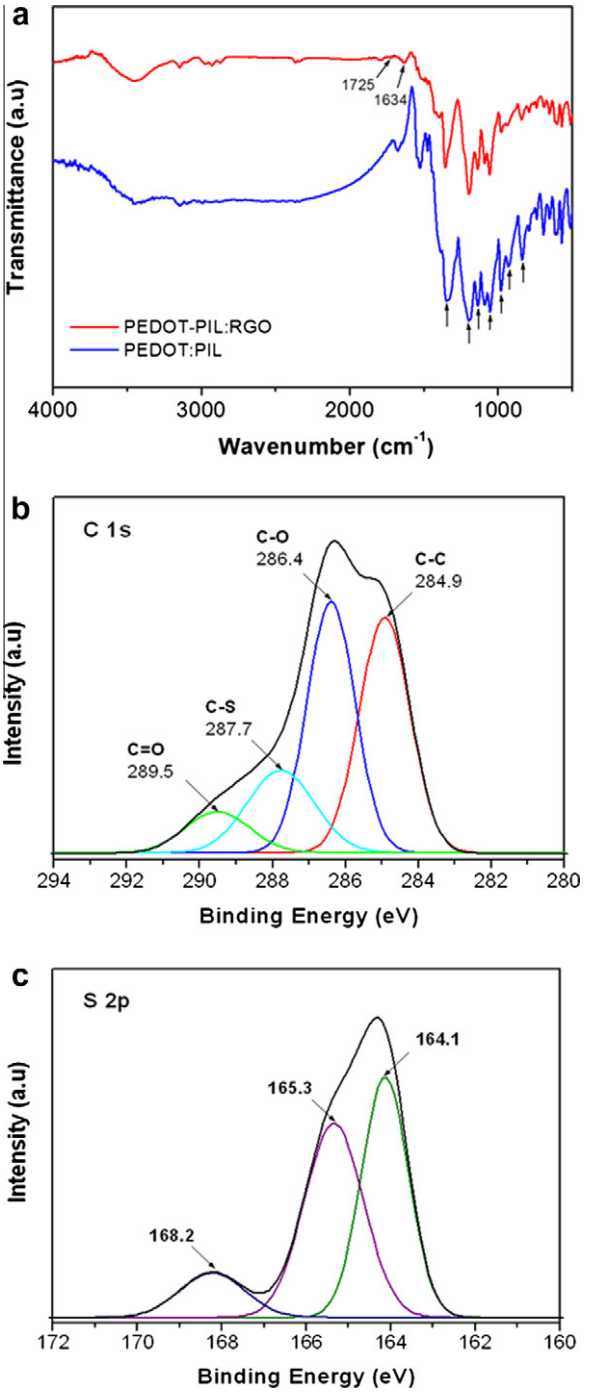

Fig. 8. (a) FTIR curves of PEDOT-PIL:GR-O (blue line) and pristine PEDOT-PIL (red line). (b) C 1s and (c) S 2p spectra of PEDOT-PIL:RG-O composites. (For interpretation of the references to color in this figure legend, the reader is referred to the web version of this article.)

displays that each RG-O sheet is encapsulated by PEDOT. The PEDOT attachment on the RG-O sheet was also confirmed by the EDX analysis (Fig. S-3), in which the sulfur from the PEDOT was found. AFM image (Fig. 9d) also reveals that PEDOT-PIL:RG-O is composed of thin platelets

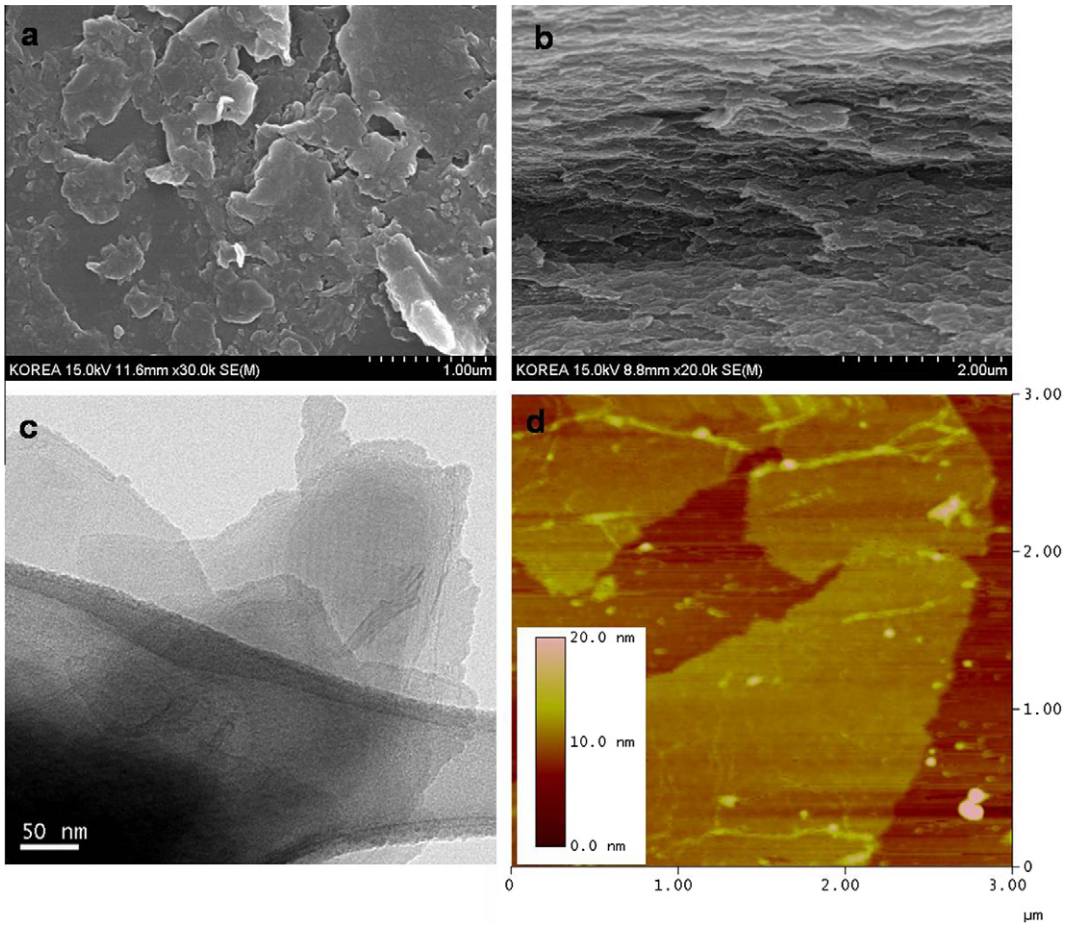

Fig. 9. (a) Top-view, (b) cross-section SEM image, (c) TEM image of PEDOT-PIL:RG-O composites, and (d) AFM image of PEDOT-PIL:RG-O composites.

with some wrinkles. The large surface area of RG-O was covered by a thin layer of PEDOT with the total thickness 10–15 nm.

In order to investigate the role of PIL:RG-O on the electrical properties of conducting polymer composites, slab samples were prepared by solvent casting PEDOT–PIL:RG-O suspension onto the filter, followed by drying at 80 °C for 2 h and further annealing at 200 °C for 3 h under argon atmosphere. The conductivity of sample was calculated from the value of sheets resistivity and thickness (measured by SEM). As shown in Fig. 10a, while the PIL-modified PEDOT sample (PEDOT:PIL without RG-O) showed a conductivity of 0.92 S/cm, PEDOT-PIL:RG-O hybrid composite showed enhanced conductivity values of up to 20 S/cm with increasing PIL:RG-O contents in the composites. The conductivity value of the composite film increases sharply with increasing PIL:RG-O loading level up to 0.3 wt.%, and then saturates over PIL:RG-O concentration, which gives an estimation that a percolation threshold is in the proximity of 0.1 wt.%. This percolation threshold value is comparable to the values previously reported in graphene/polystyrene composites [29,30]. Moreover, the enhancement of conductivity observed for this composite is consistent with other graphene/conducting polymer composites including PEDOT/G-O composites (5 S/cm) [31], polypyrrole/GO composites (7 S/cm) [32], graphene/polyaniline composites mediated by PIL (7.5 S/cm) [33], and graphene/polyaniline nanofiber composite samples (16.8 S/cm) [34]. Such enhancement could be explained by the better electrical connectivity between the RG-O platelets afforded by interconnecting PEDOT chains.

To evaluate the possible application of hybrid composite as a transparent electrode, 1.3 wt.% of PEDOT-PIL:RG-O composites (with 0.3 wt.% of RG-O in the composite) was dispersed in AN and coated on PET film to form 500-nm-thick conductive layer. This film showed a surface resistivity of 1.5×10^4 Ω/sq with light transmittance of 86.0% at 550 nm. Considering the optical transmittance of PET film itself 87.6%, PEDOT-PIL:RG-O caused a transmittance loss less than 2%. Moreover, upon treatment of $SOCl_2$ solution for 1 h the PEDDOT-PIL:RG-O composite film shows further decrease in the surface resistivity to 5.3×10^3 Ω/sq. On the other hand, the hybrid composites can be spin-coated onto glass substrate to form a homogeneous conductive composite film with a thickness of 50 nm layer as shown in Fig. 10b. The PEDOT-PIL:RG-O film was showed a surface resistivity of 9.6×10^4 Ω/sq with a transparence of 91.18%. Subsequently, the sample was annealed at 200 °C for 3 h to remove the residual solvent and oxygen-containing functional groups from RG-O. After

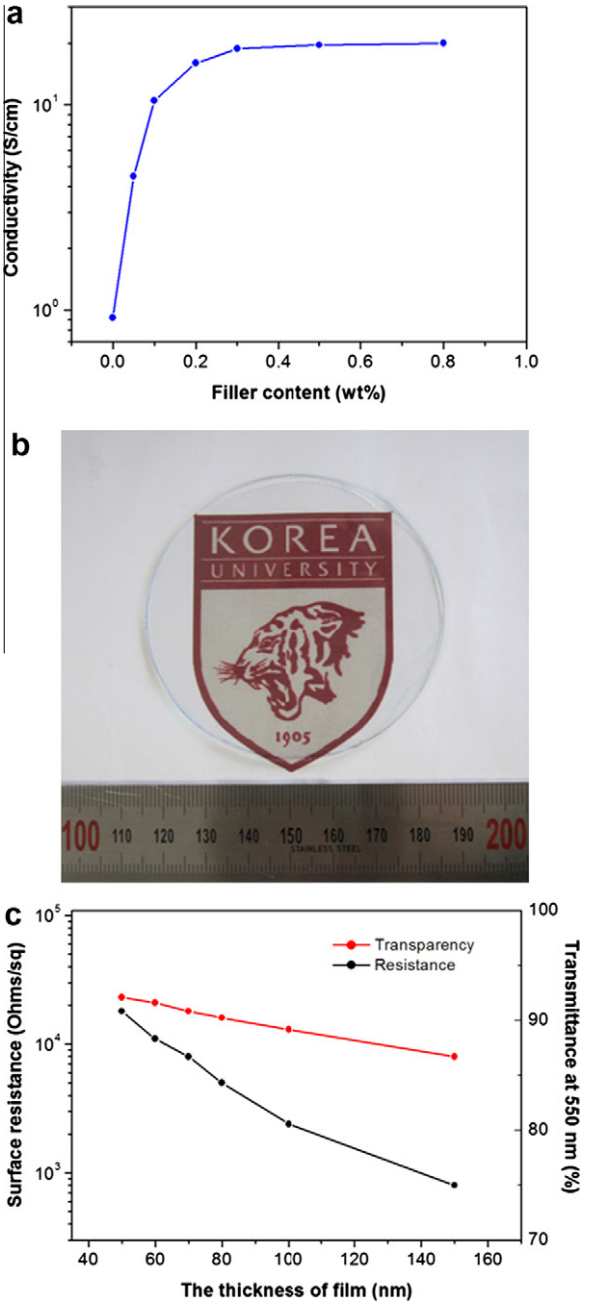

Fig. 10. (a) The electrical conductivity of PEDOT-PIL:RG-O composite films as a function of PIL:RG-O content in the composites. (b) A photograph of PEDOT-PIL:RG-O on glass substrate using a spin-coating method with KU logo underneath. And (c) sheet surface resistance and transmittance varies with different thicknesses of films.

annealing we found that the surface resistivity of film decreased from 9.6×10^4 to 1.8×10^4 Ω/sq without any significant change in light transmittance. In Fig. 10c, the surface resistivity and transmittance varies with thicknesses of films. As the film thickness increases, the surface resistivity decreases at the expense of light transmittance. For example, a surface resistivity of 800 Ω/sq can be obtained with 150 nm film thickness, but transmittance was decreased to 86.8%. The transparent and conductive properties of the present film are consistent with other reports involving graphene/poly(3,4-ethylenedioxy thiophene) composite films [35,37], RG-O thin films [38–42], and lower than that of the aqueous dispersible graphene/PEDOT:PSS composite electrode in term of conductivity [43,44]. However, at the same time, the hybrid materials described here have additional advantages in that it is dispersible in a range of organic solvents and free of water with no acidic moieties like PSS, which may be valuable for its long-term utilization in many practical applications such as organic light emitting diodes and organic photovoltaic cells [45,46].

The thermal stability of the PEDOT-PIL:RG-O composites was also investigated and compared with that of pristine PEDOT:PIL as shown in Fig S-4. The PEDOT:PIL showed an onset degradation temperature at 298 °C and a weight loss was ~78%. On the other hand, the PEDOT-PIL:RG-O hybrid composite showed the decomposition temperature of 312 °C, with the weight loss of ~54%. These results suggest that the coupling of PIL:RG-O and PEDOT could delay the thermal degradation of PEDOT chains due to a strong interaction between PEDOT matrix and PIL:RG-O. Therefore, the advantage of this method for fabricating RG-O/conducting polymer is that PIL-modified RG-O not only enhances the solubility of reduced graphene oxide, but also functions as ionic stabilizers and/or counterions of conducting polymer to facilitate the formation of homogeneous composites on the molecular scale.

4. Conclusions

In this work, we have demonstrated hybridization of graphene/PEDOT composite with an aid of PIL. Here, PIL coating on the surface of the RG-O platelets plays dual roles by increasing the solubility of RG-O in organic solvents and providing effective anchoring sites to bond with PEDOT chains. It was found that this results in good electrical conductivity due to inter-sheets enhanced carrier hopping. This non-acidic, organic solvent dispersible PEDOT-PIL:RG-O hybrid composites holds a great potential for application in optoelectronic devices especially where transparency, electrical conductivity, and stability properties are required.

Acknowledgements

This work was supported by InsCon Tech. Co. Ltd., Korea, and Korea Ministry of Environment as the Eco-Innovation Project (Global-Top Project).

Appendix A. Supplementary data

Supplementary data associated with this article can be found, in the online version, at doi:10.1016/j.orgel.2011.09.012.

References

[1] A.K. Geim, K.S. Novoselov, The rise of graphene, Nat. Mater. 6 (2007) 183.

[2] K.S. Novoselov, A.K. Geim, S.V. Morozov, D. Jiang, M.I. Katsnelson, I.V. Grigorieva, S.V. Dubonos, A.A. Firsov, Two-dimensional gas of massless Dirac fermions in graphene, Nature (438) (2005) 197.
[3] K.S. Novoselov, A.K. Geim, S.V. Morozov, D. Jang, Y. Zhang, S.V. Dubonos, Electric field effect in atomically thin carbon films, Science 306 (2004) 666.
[4] K.S. Kim, Y. Zhao, H. Jang, S.Y. Lee, J.M. Kim, K.S. Kim, J.H. Ahn, P. Kim, J.Y. Choi, B.H. Hong, Large-scale pattern growth of graphene films for stretchable transparent electrodes, Nature 457 (2009) 706.
[5] C. Berger, Z.M. Song, X.B. Li, X.S. Wu, N. Brown, C. Naud, D. Mayou, T. Li, J. Hass, A.N. Marchekov, E.H. Conrad, P.N. First, W.A. de Heer, Electronic confinement and coherence in patterned epitaxial graphene, Science 312 (2006) 1191.
[6] S. Park, R.S. Ruoff, Chemical methods for the production of graphenes, Nat. Nanotechnol. 4 (2009) 217.
[7] S. Gilje, S. Han, M.S. Wang, M.S. Wang, K.L. Wang, R.B. Kaner, A chemical route to graphene for device applications, Nano Lett. 7 (2007) 3394.
[8] W. Gao, L.B. Alemary, L. Gi, P.M. Ajayan, New insights into the structure and reduction of graphite oxide, Nat. Chem. 1 (2009) 403.
[9] F. Schedin, A.K. Geim, S.V. Morozov, E.W. Hill, P. Blake, M.I. Katsnelson, K.S. Novoselov, Detection of individual gas molecules adsorbed on graphene, Nat. Mater. 6 (2007) 652.
[10] J.S. Bunch, A.M. van der Zande, S.S. Verbridge, I.W. Frank, D.M. Tanenbaum, J.M. Parpia, Electromechanical resonators from graphene sheets, Science 315 (2007) 490.
[11] M.D. Stoller, S. Park, Y. Zhu, J. An, R.S. Ruoff, Graphene-based ultracapacitors, Nano Lett. 8 (2008) 3498.
[12] S. Gilje, S. Han, M.S. Wang, K.L. Wang, R.B. Kaner, A chemical route to graphene for device applications, Nano Lett. 7 (2007) 3394.
[13] H. Wang, Q. Hao, X. Yang, L. Lu, X. Wang, A nanostructured graphene/polyaniline hybrid material for supercapacitors, Nanoscale 2 (2010) 2164.
[14] S. Biswas, L.T. Drzal, Multilayered nanoarchitecture of graphene nanosheets and polypyrrole nanowires for high performance supercapacitor electrodes, Chem. Mater. 22 (2010) 5667.
[15] W. Hong, Y. Xu, G. Lu, C. Li, G. Shi, Transparent graphene/PEDOT–PSS composite films as counter electrodes of dye-sensitized solar cells, Electrochem. Commun. 10 (2008) 1555.
[16] L.G. de Arco, Y. Zhang, C.W. Schlenker, K. Ryu, M.E. Thompson, C. Zhou, Continuous, highly flexible, and transparent graphene films by chemical vapor deposition for organic photovoltaics, ACS Nano 4 (2010) 2865.
[17] W.S. Hummers, R.E. Offeman, Preparation of graphitic oxide, J. Am. Chem. Soc. 80 (1958) 1339.
[18] Y. Liang, D. Wu, X. Feng, K. Mullen, Dispersion of graphene sheets in organic solvent supported by ionic interactions, Adv. Mater. (21) (2009) 1679.
[19] R. Marcilla, J.A. Blazquez, J. Rodríguez, J.A. Pomposo, D. Mecerreyes, Tuning the solubility of polymerized ionic liquids by simple anion-exchange reactions, J. Polym. Sci. Part A: Polym. Chem. 42 (2004) 208.
[20] T.Y. Kim, T.H. Lee, J.E. Kim, R.M. Kasi, C.S.P. Sung, K.S. Suh, Organic solvent dispersion of poly(3, 4-ethylenedioxythiophene) with the use of polymeric ionic liquid, J. Polym. Sci. Part A: Polym. Chem. 46 (2008) 6872.
[21] Y. Zhu, M.D. Stoller, W. Cai, A. Velamakanni, R.D. Piner, D. Chen, Exfoliation of graphite oxide in propylene carbonate and thermal reduction of the resulting graphene oxide platelets, ACS Nano 4 (2010) 1227.
[22] S. Stankovich, D.A. Dikin, R.D. Piner, K.A. Kohlhaas, A. Kleinhammes, Y. Jia, Synthesis of graphene-based nanosheets via chemical reduction of exfoliated graphite oxide, Carbon 45 (2007) 1558.
[23] F. Tuinstra, J.L. Koenig, Raman spectrum of graphite, J. Chem. Phys. 53 (1970) 1126.
[24] J. Dupond, J.D. Scholten, On the structural and surface properties of transition-metal nanoparticles in ionic liquids, Chem. Soc. Rev. 39 (2010) 780.
[25] A.J. Patil, J.L. Vickery, T.B. Scott, S. Mann, Aqueous stabilization and self-assembly of graphene sheets into layered bio-nanocomposites using DNA, Adv. Mater. 21 (2009) 3159.
[26] C. Chen, Q.H. Yang, Y. Yang, W. Lv, Y. Wen, P.X. Hou, M. Wang, H.M. Cheng, Self-assembled free-standing graphite oxide membrane, Adv. Mater. 21 (2009) 3007.
[27] M.J. McAllister, J.L. Li, D.H. Adamson, H.C. Schniepp, A.A. Abdala, J. Liu, Single sheet functionalized graphene by oxidation and thermal expansion of graphite, Chem. Mater. 19 (2007) 4396.
[28] T.Y. Kim, H.W. Lee, J.E. Kim, K.S. Suh, Synthesis of phase transferable graphene sheets using ionic liquid polymers, ACS Nano 4 (2010) 1612.
[29] S. Stankovich, D.A. Dikin, G.H.B. Dommett, K.M. Kohlhaas, E.J. Zimney, E.A. Stach, R.D. Piner, S.T. Nguyen, R.S. Ruoff, Graphene-based composite materials, Nature 442 (2006) 282.
[30] N. Liu, F. Luo, H. Wu, Y. Liu, C. Zhang, J. Chen, One-step ionic-liquid-assisted electrochemical synthesis of ionic-liquid-functionalized graphene sheets directly from graphite, Adv. Funct. Mater. 18 (2008) 1518.
[31] Y. Han, Y. Lu, Characterization and electrical properties of conductive polymer/colloidal graphite oxide nanocomposites, Compos. Sci. Technol. 69 (2009) 1231.
[32] Y. Han, Y. Lu, Preparation and characterization of graphite oxide/polypyrrole composites, Carbon 45 (2007) 2394.
[33] X. Zhou, T. Wu, B. Hu, G. Yang, B. Han, Synthesis of graphene/polyaniline composite nanosheets mediated by polymerized ionic liquid, Chem. Commun. 46 (2010) 3663.
[34] K. Zhang, L.L. Zhang, X.S. Zhao, J. Wu, Graphene/polyaniline nanofiber composites as supercapacitor electrodes, Chem. Mater. 22 (2010) 1392.
[35] Y. Xu, Y. Wang, J. Liang, Y. Huang, Y. Ma, X. Wan, Y. Chen, A hybrid material of graphene and poly (3, 4-ethyldioxythiophene) with high conductivity, flexibility, and transparency, Nano Res. 2 (2009) 343.
[36] K.S. Choi, F. Liu, J.S. Choi, T.S. Seo, Fabrication of free-standing multilayered graphene and poly(3, 4-ethylenedioxythiophene) composite films with enhanced conductive and mechanical properties, Langmuir 26 (2010) 12902.
[37] K.Y. Jo, T.M. Lee, H.Y. Choi, J.H. Park, D.J. Lee, D.W. Lee, B.S. Kim, Stable aqueous dispersion of reduced graphene nanosheets via non-covalent functionalization with conducting polymers and application in transparent electrodes, Langmuir 27 (2011) 2014.
[38] X. Li, G. Zhang, X. Bai, X. Sun, X. Wang, E. Wang, H. Dai, Highly conducting graphene sheets and Langmuir-Blodgett films, Nat. Nanotechnol. 3 (2008) 538.
[39] G. Eda, G. Fanchini, M. Chhowalla, Large-area ultrathin films of reduced graphene oxide as a transparent and flexible electronic material, Nat. Nanotechnol. 3 (2008) 270.
[40] C. Mattevi, G. Eda, S. Agnoli, S. Miller, K.A. Mkhoyan, O. Celik, D. Mastrogiovanni, G. Granozzi, E. Garfunkel, M. Chhowalla, Evolution of electrical, chemical, and structural properties of transparent and conducting chemically derived graphene thin films, Adv. Funct. Mater. 19 (2009) 2577.
[41] Y. Zhu, W. Cai, R.D. Piner, A. Velamakanni, R.S. Ruoff, Transparent self-assembled films of reduced graphene oxide platelets, Appl. Phys. Lett. (95) (2009) p. 103104–1–3.
[42] G. Eda, Y.Y. Lin, S. Miller, C.W. Chen, W.F. Su, M. Chhowalla, Transparent and conducting electrodes for organic electronics from reduced graphene oxide, Appl. Phys. Lett. (92) (2008) p. 233305–1–3.
[43] H. Chang, G. Wang, A. Yang, X. Tao, X. Liu, Y. Chen, Z. Zheng, A transparent, flexible, low-temperature, and solution-processible graphene composite electrode, Adv. Funct. Mater. 20 (2010) 2893.
[44] S.B. Bon, L. Valentili, J.M. Kenny, Preparation of extended alkylated graphene oxide conducting layers and effect study on the electrical properties of PEDOT:PSS polymer composites, Chem. Phys. Lett. 494 (2010) 264.
[45] M.P. de Jong, L.J. van Ijzendoorn, M.J.A. de Voigt, Stability of the interface between indium-tin-oxide and poly(3, 4-ethylenedioxythiophene)/poly(styrenesulfonate) in polymer light-emitting diodes, Appl. Phys. Lett. 77 (2000) 2255.
[46] T.Y. Kim, M.W. Suh, S.J. Kwon, T.H. Lee, J.E. Kim, Y.J. Kim, M.P. Hong, K.S. Suh, Poly(3, 4-ethylenedioxythiophene) derived from poly(ionic liquid) for the ues as hole-injecting materials in organic light-emitting diodes, Macromol. Rapid Commun. 30 (2009) 1477.

propanol followed by DI water. The bottom PEDOT:PSS electrode was spin coated onto the plastic substrate at 1500 rpm for 30 s followed by 5000 rpm for 30 s to get a smooth film. The film was dried at 110 °C for 30 min in air. P(VDF-TrFE) copolymer powder was dissolved in methyl ethyl ketone (MEK) to get a 2 wt.% solution. The filtered solution was then spun on the PEDOT:PSS film at 6000 rpm for 60 s followed by a soft bake for 30 min at 80 °C. The films were then annealed in vacuum at 140 °C for 4 h to improve the crystallinity [2,13,16]. The PEDOT:PSS electrodes were approximately 110 ± 10 nm thick and P(VDF-TrFE) film was ~100 ± 10 nm thick, measured using a Dektak profilometer. Finally, the top PEDOT:PSS electrode was spun and etched using RF oxygen plasma with patterned gold (Au) layer as a hard mask. For comparison, a sample with Au and Pt as top and bottom electrodes, respectively was also made with the same P(VDF-TrFE) thickness.

Surface morphology was studied using Atomic Force Microscopy (Agilent 5400) and Scanning Electron Microscopy (Nova NanoSEM 630 FESEM). The crystallinity and inter-planar distance of polymer chains was evaluated using Grazing Incidence X-ray Diffraction (Bruker D8 Discover) while the bonding and dipole orientation was analyzed using Fourier-transform infrared spectroscopy (FT-IR, ThermoScientific Nicolet iS10). The electrical characterization was performed using the Keithley 4200 semiconductor analyzer while polarization-voltage and fatigue tests were done using the Premier Precision II ferroelectric tester (Radiant Technologies Inc.).

3. Results and discussion

Fig. 1(a) and (b) shows the surface morphology of platinum and PEDOT:PSS surfaces, respectively. The root mean square (R_{rms}) roughness values for Pt and PEDOT:PSS over 1 μm^2 area are comparable and are 0.44 nm and 0.55 nm, respectively. Fig. 1(c) and (d) shows P(VDF-TrFE) films grown on Pt and PEDOT:PSS surfaces, respectively. The data show that the P(VDF-TrFE) film grown on the polymer surface is smoother than on the Pt surface with a roughness value of 1.28 versus 2.3 nm. Fig. 1(e) and (f) shows Scanning Electron Microscopy (SEM) images of P(VDF-TrFE) films grown on Pt and PEDOT:PSS. The figure indicates a difference in the nucleation and grain growth rates of the films on the two respective electrodes. The average grain size of P(VDF-TrFE) is much smaller (~75–80 nm) when grown on a polymer, compared to a metal surface (~160–170 nm). This result should not be surprising since the surface roughness of the bottom electrode has an effect on nucleation rate of the P(VDF-TrFE) film, with rougher surface leading to higher nucleation rate [17]. The higher nucleation rate limits the grain growth leading to smaller grains, as observed in our films. Additionally the higher nucleation rate and smaller grain size leads to a smoother P(VDF-TrFE) film on PEDOT:PSS as suggested by the AFM data.

Grazing Incidence X-ray Diffraction (GIXRD) was used to compare the phase and orientation of the P(VDF-TrFE) films on the respective electrodes. Fig. 2 shows that P(VDF-TrFE) films on Pt substrate exhibit a peak centered at $2\theta \sim 19.95°$, characteristic of the ferroelectric β phase and reflection from the (110) and (200) planes. The inter-planar distance was calculated to be approximately 4.44 Å and is consistent with earlier studies [16]. In comparison, the P(VDF-TrFE) films grown on PEDOT:PSS exhibit a peak at $2\theta \sim 19.53°$, indicating a larger inter-planar distance. The XRD peaks indicate that the P(VDF-TrFE) films on Pt electrodes have larger crystallite size than films on PEDOT:PSS electrodes, with a full-width-half-maxima (FWHM) of 1.67° and 2.2°, respectively, as confirmed by the SEM images.

In P(VDF-TrFE) films, it is important that the chain direction (*c* axis) is oriented parallel to the film surface because polarization is induced in the *b*-axis direction, perpendicular to the chain axis [18–20]. There have been some studies on techniques to control the preferential orientation of P(VDF-TrFE) chains by nano-imprint lithography and using nanostructured electrodes [20,21]. We have analyzed the orientation of the P(VDF-TrFE) films as a function of growth on polymer and metal electrodes under identical annealing temperatures (140 °C) and thickness (100 nm). The dipoles in P(VDF-TrFE) strongly interact with the applied field, when it is perpendicular to the dipole direction. We used *p*-polarized FT-IR analysis of the ferroelectric polymer films, which has an electric field component parallel to the plane of the substrate. It has been reported that the FT-IR bands at 1288 and 850 cm^{-1} are associated with CF_2 symmetric stretching vibration and are characteristic bands of the trans-zigzag formation (β phase)-indicating dipole moments parallel to the *b* axis [16,18,19]. It can be easily seen from Fig. 3 that 1288 cm^{-1} peak is relatively stronger on the film grown on Pt, therefore *b* axis (and dipoles) of the polymer is perpendicular to the film. The 1400 cm^{-1} band which is characteristic of the CH_2 wagging vibration has dipoles parallel to the polymer chain *c* axis. For a baseline region of 1417.48–1378.43 cm^{-1}, the area under the 1400 cm^{-1} band shows that this peak is relatively stronger on PEDOT:PSS (Area of 0.2074) compared to Pt (Area of 0.1431). This indicates that for P(VDF-TrFE) films grown on PEDOT:PSS electrodes, a significant portion of the copolymer chain tilts vertically, which is undesirable for vertical polarization as most dipoles are parallel to substrate. All other peaks in the FT-IR spectrum of P(VDF-TrFE) film grown on PEDOT:PSS can be attributed to the PEDOT:PSS layer itself as can be seen from the IR spectra of the PEDOT:PSS in Fig. 3.

Ferroelectric behavior of our capacitors was tested using polarization–electric field hysteresis measurements. In Fig. 4, the hysteresis loops for the all-polymer device show a remnant polarization (P_r) of 7.5 $\mu C/cm^2$ and coercive field (E_c) of 60 ± 5 MV/m. These values show a remarkable improvement compared to earlier studies using polymer electrodes on plastic substrates. Xu et al. [22] had earlier reported a P_r of 7.6 $\mu C/cm^2$ and an E_c of 130 MV/m with an all polymer capacitor with Polyaniline and PEDOT:PSS as top and bottom electrodes, respectively on a plastic substrate. Our all polymer, flexible and transparent device also compares well with the device with metal electrodes which show a P_r of 7.5 $\mu C/cm^2$ and E_c of

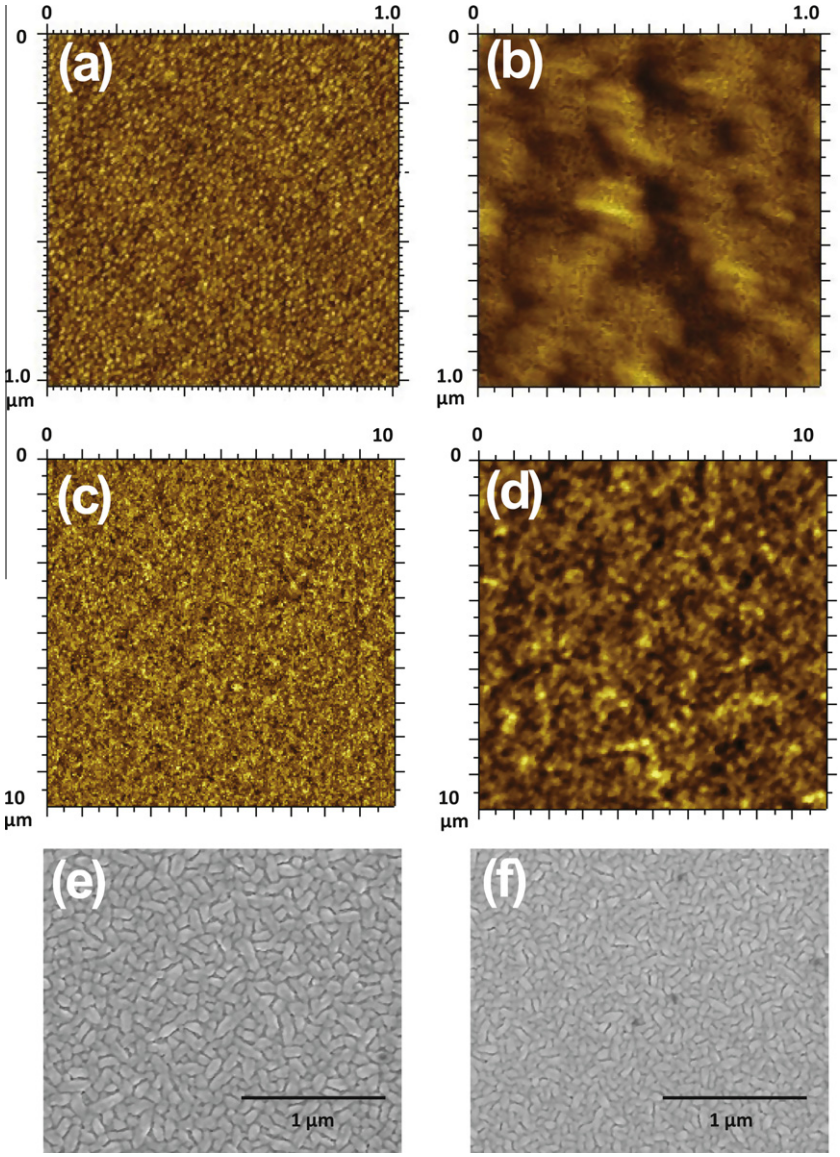

Fig. 1. AFM topography images of (a) Pt surface (b) PEDOT:PSS surface (c) P(VDF-TrFE) grown on Pt surface (d) P(VDF-TrFE) grown on PEDOT:PSS surface. SEM images of (e) P(VDF-TrFE) grown on Pt surface (f) P(VDF-TrFE) grown on PEDOT:PSS surface.

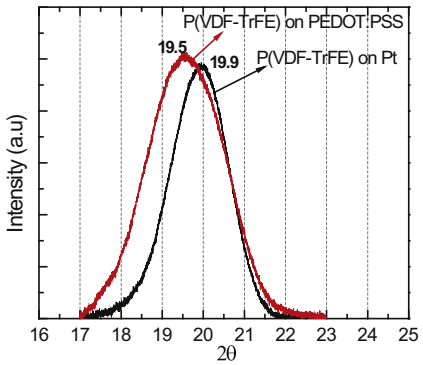

Fig. 2. Grazing Incidence XRD spectra of P(VDF-TrFE) films on Pt and PEDOT:PSS electrodes.

54 ± 5 MV/m. The slightly higher coercive field could be attributed to the smaller grain size as well as the unfavorable orientation of P(VDF-TrFE) chains on the polymer electrode as seen from the FT-IR data. Fig. 5 shows that the switching current response of the all polymer devices is almost identical to the device with metal electrodes with a peak switching current density ~20 μA/cm^2.

Leakage current mechanisms in dielectric films are usually controlled by space charge limited current (SCLC), interface limited Schottky emission (SE) or bulk limited Frenkel-Poole (FP) emission. Schottky emissions involve carrier injection from the electrodes into the conduction band of the dielectric over a barrier height while FP emissions involves field-assisted thermionic emission of carriers trapped in the dielectric film [23,24].

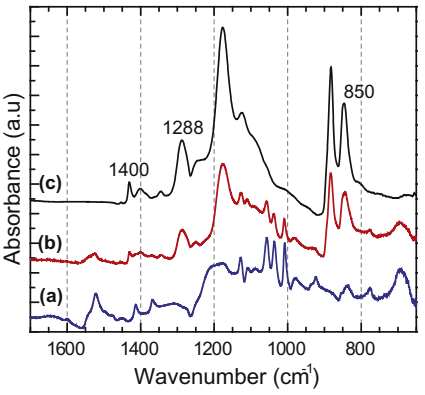

Fig. 3. *p* Polarized FT-IR spectra of (a) spin coated PEDOT:PSS (b) P(VDF-TrFE) film (~110 ± 10 nm) on PEDOT:PSS and (c) P(VDF-TrFE) film on a Pt substrate.

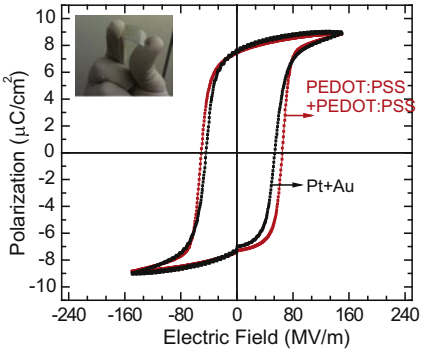

Fig. 4. Hysteresis loops at a frequency of 1 Hz and electric field of 150 MV/m from devices with platinum/gold electrodes and with PEDOT:PSS top and bottom electrodes.

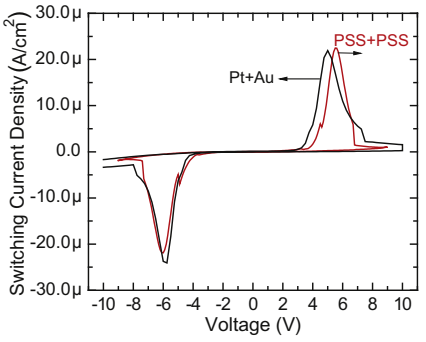

Fig. 5. Switching current response from devices with platinum/gold electrodes and with PEDOT:PSS top and bottom electrodes.

The best fit of *J–V* response for the all-polymer device is plotted for ln(*J*) versus $V^{1/2}$ as seen in the inset in Fig. 6. Linear behavior of this plot suggests that leakage current is controlled either by Schottky or Frenkel Poole emission. FP emissions are independent of the work functions of the electrodes and display symmetric *I–V* characteristics [23,25]. A look at Fig. 6, shows the asymmetry of the leakage current response which confirms that FP emission is unlikely in our devices.

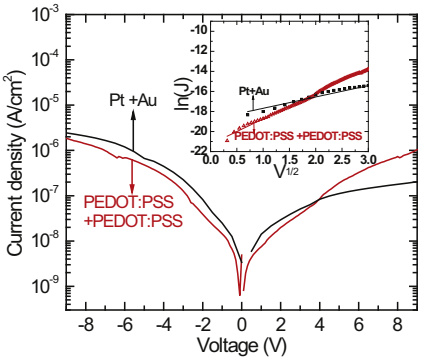

Fig. 6. *I–V* characteristics of devices with platinum/gold electrodes and PEDOT:PSS electrodes. The inset shows a plot of current density versus voltage$^{0.5}$ measured at room temperature.

The Schottky controlled leakage current is given by:

$$J = AT^2 exp\left(\frac{aE^{0.5} - \emptyset_B}{kT}\right) \quad (1)$$

where *A* is the effective Richardson's constant, *T* is temperature, *E* is applied electric field, $\emptyset_B$ is barrier height and *a* is a constant [23].

According to Fig. 6, the current response in our devices shows dependence on the work functions of the electrodes, confirming an interface limited Schottky emission process. The device with metal electrodes shows lower leakage current in the forward bias regime because of the higher work function of bottom Pt electrode (5.65 eV) compared to the top Au electrode (5.1 eV). The devices with PEDOT:PSS top and bottom electrodes show symmetric *I–V* curves. The Highest Occupied Molecular Orbital (HOMO) for PEDOT:PSS is 5.3 eV which explains the slightly lower leakage current compared to the Au top electrode devices in the reverse bias regime.

There have been various studies published on the effect of applied voltage profile, frequency, crystallinity and operating temperature on polarization fatigue, but most of these studies were done using metal electrodes [26–30]. Xu et al. [14,15] reported much improved fatigue properties at different temperatures when using conducting polymers as interface layers but this was done on Si substrates. Another study using Polyaniline and PEDOT:PSS polymer electrodes on flexible substrates showed poor fatigue performance (58% retention after 10^5 cycles) and concluded the need to study different polymers for improvement of fatigue properties [22].

The fatigue performance of our devices was studied as a function of electric field. Fig. 7 shows fatigue test results performed at applied electric fields of 55, 80 and 100 MV/m at a frequency of 1 kHz. These fields correspond to the coercive, intermediate and saturation fields, respectively. It can be seen from Fig. 7(b) that the device with PEDOT:PSS polymer electrodes performs considerably better compared to metal electrodes [Fig. 7(a)]. At a field of 100 MV/m, the all polymer device retains about 80% of its initial polarization after 10^6 cycles, while the device with metal electrodes retains only about 55%. It has been

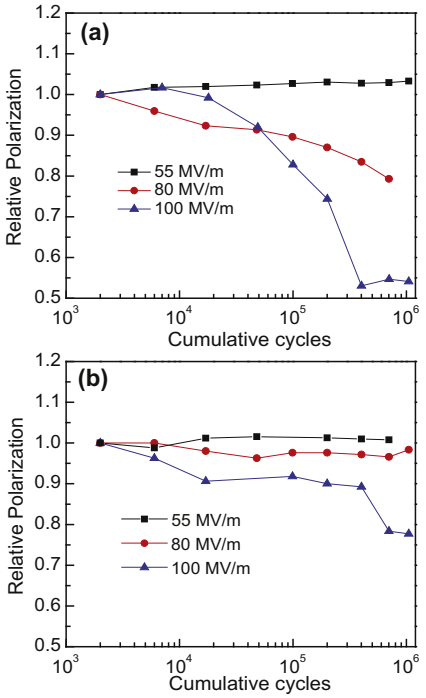

Fig. 7. Electrical fatigue properties of P(VDF-TrFE) films showing relative polarization for P_r (a) with platinum and gold electrodes (b) with PEDOT:PSS electrodes.

proposed that fatigue in P(VDF-TrFE) film is related to the injection of charges from electrodes which are subsequently trapped at crystallite boundaries and defects, inhibiting ferroelectric switching and leading to faster fatigue rates [26,29,30]. It is likely that the use of polymer electrodes reduces charge injection into the PVDF-TrFE (due to lower carrier concentration in the polymer compared to metal electrodes), resulting in less trapped charges, therefore lower fatigue rates, as shown in Fig. 7.

4. Conclusion

In summary, we have fabricated all-polymer, flexible and transparent ferroelectric capacitors on PEN substrate. Electrical characterization showed that the all-polymer capacitors showed comparable ferroelectric properties ($P_r \sim 7.5$ μC/cm^2, $E_c \sim 60 \pm 5$ MV/m) and I–V characteristics to capacitors with metal electrodes. At the same time our polymer devices have much improved fatigue performance compared to ferroelectric capacitors with metal electrodes and previously published polymer electrodes.

Acknowledgments

The authors would like to thank Mr. Ahad Syed from the Advanced Nanofabrication Core Facility and Dr. Dongkyu Cha from the Imaging and Characterization Core facility at KAUST for their support. H.N.A. acknowledges the financial support from the KAUST baseline fund.

References

[1] Q.-D. Ling, D.-J. Liaw, C. Zhu, D.S.-H. Chan, E.-T. Kang, K.-G. Neoh, Prog. Polym. Sci. 33 (2008) 917.
[2] R.C.G. Naber, K. Asadi, P.W.M. Blom, D.M. de Leeuw, B. de Boer, Adv. Mater. 22 (2010) 933.
[3] A.J.J.M. van Breemen, J.B.P.H. van der Putten, R. Cai, K. Reimann, A.W. Marsman, N. Willard, D.M. de Leeuw, G.H. Gelinck, Appl. Phys. Lett. 98 (2011) 183302.
[4] Y.J. Park, I.-s. Bae, S.J. Kang, J. Chang, C. Park, IEEE Trans. Electr. Insul. 17 (2010) 1135.
[5] T. Furukawa, M. Date, M. Ohuchi, A. Chiba, J. Appl. Phys. 56 (1984) 1481.
[6] T. Furukawa, H. Matsuzaki, M. Shina, Y. Tajitsu, Jpn. J. Appl. Phys. 24 (1985) 661.
[7] C.A. Nguyen, P.S. Lee, N. Ng, H. Su, S.G. Mhaisalkar, J. Ma, F.Y.C. Boey, Appl. Phys. Lett. 91 (2007) 042909.
[8] K. Noda, K. Ishida, A. Kubono, T. Horiuchi, H. Yamada, K. Matsushige, J. Appl. Phys. 93 (2003) 2866.
[9] F. Xia, B. Razavi, H. Xu, Z.Y. Cheng, Q.M. Zhang, J. Appl. Phys. 92 (2002) 3111.
[10] K. Kimura, H. Ohigashi, Jpn. J. Appl. Phys. 25 (1986) 383.
[11] Y. Tajitsu, Jpn. J. Appl. Phys. 34 (1995) 5418.
[12] G. Vizdrik, S. Ducharme, V. Fridkin, S. Yudin, Phys. Rev. B 68 (2003) 094113.
[13] R.C.G. Naber, P.W.M. Blom, A.W. Marsman, D.M. de Leeuw, Appl. Phys. Lett. 85 (2004) 2032.
[14] H. Xu, X. Liu, X. Fang, H. Xie, G. Li, X. Meng, J. Sun, J. Chu, J. Appl. Phys. 105 (2009) 034107.
[15] H. Xu, J. Zhong, X. Liu, J. Chen, D. Shen, Appl. Phys. Lett. 90 (2007) 092903.
[16] D. Mao, M.A. Quevedo-Lopez, H. Stiegler, B.E. Gnade, H.N. Alshareef, Org. Electron. 11 (2010) 925.
[17] I. Chung, J.K. Lee, I.K. Yoo, Integr. Ferroelectr. 10 (1995) 99.
[18] A.A. Prabu, K.J. Kim, C. Park, Vib. Spectrosc. 49 (2009) 101.
[19] N.M. Reynolds, K.J. Kim, C. Chang, S.L. Hsu, Macromolecules 22 (1989) 1092.
[20] Y.J. Park, S.J. Kang, C. Park, E. Woo, K. Shin, K.J. Kim, Appl. Phys. Lett. 90 (2007) 222903.
[21] Z. Hu, M. Tian, B. Nysten, A.M. Jonas, Nat. Mater. 8 (2009).
[22] H. Xu, X. Fang, X. Liu, S. Wu, Y. Gu, X. Meng, J. Sun, J. Chu, J. Appl. Polym. Sci. 120 (2011) 1510.
[23] H.N. Al-Shareef, D. Dimos, J. Am. Ceram. Soc. 80 (1997) 3127.
[24] B. Nagaraj, S. Aggarwal, T.K. Song, T. Sawhney, R. Ramesh, Phys. Rev. B 59 (1999) 16022.
[25] L. Pintilie, I. Vrejoiu, D. Hesse, G. LeRhun, M. Alexe, Phys. Rev. B 75 (2007).
[26] G.-D. Zhu, X.-Y. Luo, J.-H. Zhang, Y. Gu, IEEE Trans. Electr. Insul. 17 (2010) 1172.
[27] S. Horie, K. Ishida, S. Kuwajima, K. Kobayashi, H. Yamada, K. Matsushige, Jpn. J. Appl. Phys. 47 (2008) 1259.
[28] S. Nozaki, K. Ishida, A. Matsumoto, S. Horie, S. Kuwajima, H. Yamada, K. Matsushige, Thin Solid Films 516 (2008) 2450.
[29] G. Zhu, Z. Zeng, L. Zhang, X. Yan, Appl. Phys. Lett. 89 (2006) 102905.
[30] G. Zhu, Z. Zeng, Q. Zhang, X. Yan, R. Liu, J. Appl. Phys. 103 (2008) 084125.

was synthesized according to the method described before [11]. All the materials were purified twice by thermal gradient sublimation before experiments. The device structure is shown in Fig. 2b inset. Six nanometer *p*-6P film was sublimed onto SiO_2/Si(n++) substrate at the substrate temperature of 180 °C. 1.8 nm TiOPc film was sublimed subsequently onto the *p*-6P film to form a weak epitaxy growth (WEG) ultrathin film as reported [12]. The deposition was performed under a pressure of 10^{-4}–10^{-5} Pa at a rate of about 1 nm/min. The finger electrodes were sublimed with a shadow mask on top of the organic film in another vacuum chamber to obtain TiOPc ultrathin film device. Each device contains seven pairs of fingers with each finger of 3 mm length and 100 μm distance between each other. About 1 nm F_{16}CuPc was directly depositated onto the 1.8 nm TiOPc device at room temperature substrate to obtain bilayer device. One nanometer WEG F_{16}CuPc film was also prepared to obtain F_{16}CuPc ultrathin film device for contrast.

2.2. Films characterization and sensor test

The morphology and surface potential of the organic thin films were characterized by SPI 3800N instrument (Seiko Instruments Inc.) by tapping mode and lift mode, respectively. A freshly cleaved highly oriented pyrolytic graphite (HOPG) is used as standard to determine the tip work function of KPFM measurements [13]. The wide angle X-ray diffraction (XRD) pattern was taken from a D8 discovery thin-film diffractometer with Cu Kα radiation (=1.54056 Å). The selected voltage and current were 40 kV and 35 mA, respectively.

All the devices have been stored in air for 48 h before sensor test. The electrical measurement was taken by Keithley 2636A double channel source measurement at the voltage of 1 V. Two mass flow controllers (MFC) (BROOKS 5850S) were used to control the flow rate of air stream used as carrier gas and NO_2 stream to generate diluted NO_2 sample of 2, 3 and 4 ppm. The flow rate in

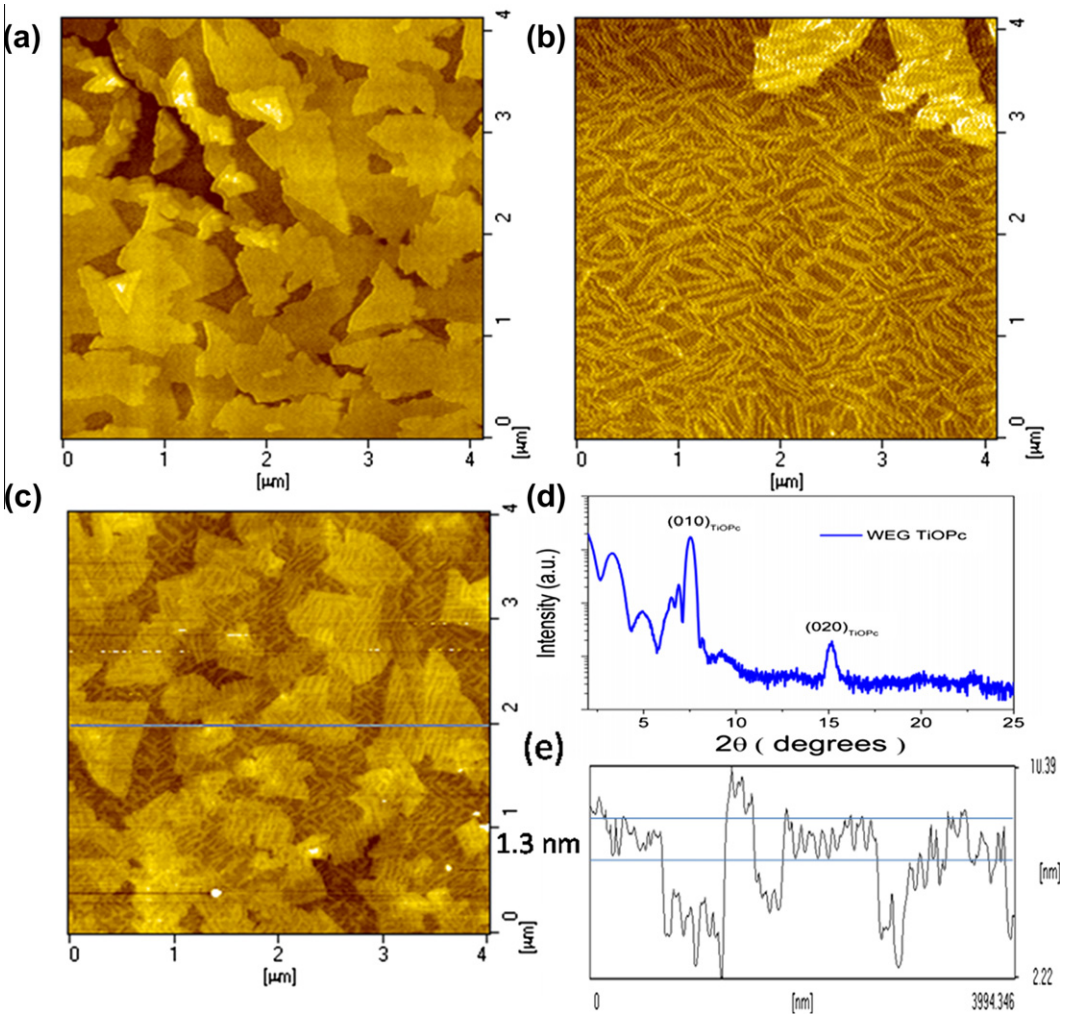

Fig. 1. Surface morphology of (a) TiOPc monolayer, (b) 1 nm WEG F_{16}CuPc film and (c) F_{16}CuPc–TiOPc bilayer film. The X-ray diffraction of 20 nm WEG TiOPc is shown in (d) and the section profile of bilayer is shown in (e).

the test was fixed at 120 sccm (standard cm^3 per min) and the gas inlet tubes were made of PTFE to avoid analyte adsorption. The sensor test was realized by exposing the devices to a constant flow of NO_2 gas doses in a homemade PTFE test chamber which was of 50 ml internal volume at the temperature of 295 K and relative humidity of 18%. Each dose in Fig. 2a lasted 10 min and the carrier gas air was used during the interval. Measurement with longer NO_2 exposure time of 30 min with 150 min carrier gas interval was also performed for bilayer device to study the response and baseline character, shown in Fig. 2b. Two devices were placed in the chamber for simultaneous mounting at a time.

3. Results and discussion

The morphology of the WEG TiOPc and F_{16}CuPc film is shown in Fig. 1a and b. The film is made up of packed lamellar-like crystals with a lamella size of about 1 μm. The XRD of 20 nm WEG TiOPc film is shown in Fig. 1c. Results prove that TiOPc molecules are standing up on the *p*-6P film in Phase II (triclinic, space group *P*1, $a = 12.166$ Å, $b = 12.584$ Å, $c = 8.641$ Å, $\alpha = 96.28°$, $\beta = 95.03°$, and $\gamma = 67.86°$), and (0 1 0) is the contact plane [14,15]. The sharp diffraction peaks also demonstrate that the WEG TiOPc film is highly oriented, the π–π conjugation direction is parallel to substrate which is consistent with the carrier transport direction. Subsequently, 1 nm F_{16}CuPc was deposited on the TiOPc ultrathin film to form a bilayer film. The top layer F_{16}CuPc presents a discontinuous stripe-like morphology on TiOPc surface shown in Fig. 1b. The section profile is shown in Fig. 1d. F_{16}CuPc grown on TiOPc layer has an average height of 1.3 nm, which means the F_{16}CuPc is standing up on the TiOPc lamella and its π–π conjugation direction favors the heterojunction formation. The root mean square (RMS) roughness of the TiOPc film is 1.6 nm and of bilayer film is 2.1 nm. The nanostructure has led to more grain boundaries although it does not significantly enrich the surface area of the bilayer device.

As we focused on the heterojunction effect in gas sensing, only one kind of analyte was used in sensor measurement. The NO_2 gas sensing property is performed under 1 V voltage for all the devices. The sensing character of 6 nm *p*-6P film has been proved before to have no detectable signal toward NO_2 and gas response of the WEG film mainly comes from the phthalocyanine layer [16]. The relative response is shown in Fig. 2a and the bilayer device shows a significant increase compared with TiOPc and F_{16}CuPc ultrathin layer device. The relative response to 2 ppm NO_2 is 3.48 for ultrathin TiOPc layer and is 0.16 for 1 nm F_{16}CuPc film, both are much smaller than that of 9.56 for bilayer device. The 1 nm WEG F_{16}CuPc film shows very weak positive response to NO_2 due to its poor continuity. Positive response is rarely reported for n-type semiconductor and the reason is not clear, the weak signal suggests that the film thickness has strong influence on device performance. The obvious positive response of TiOPc film and bilayer film indicates that the devices work in the hole transport mode and the carriers are mainly transported in TiOPc layer in bilayer device due to TiOPc layer continuity.

The response of ultrathin TiOPc film shows obvious two steps of adsorption, an initial fast step and a followed slow step. However, the response of 1 nm F_{16}CuPc film is extremely poor and it shows no clear sign of slow adsorption step. It also reflects in bilayer device that the transition from initial fast to slow adsorption is not that obvious, which may be a combined effect of the top layer F_{16}CuPc and bottom layer TiOPc. These devices did not reach their saturation region during the test so measurement with longer NO_2 exposure time of 30 min and a followed 150 min carrier gas interval was performed for TiOPc–F_{16}CuPc bilayer device, shown in Fig. 2b. It can be seen that the bilayer device still shows no clear sign of reaching saturation region but its response shows NO_2 concentration dependence is similar to that measured in Fig. 2a. This is quite normal for organic semiconductor gas sensor due to the slow adsorption and desorption effect especially at room temperature.

The baseline of TiOPc–F_{16}CuPc bilayer device has lifted 2.8 nA at the end of the test in Fig. 2a, however, it has lifted 1.8 nA at the end of the test with long exposure and recover time shown in Fig. 2b. This means that the bilayer device is hard to fully recover to baseline value even in 150 min, so this portion of the response is irreversible. In our earlier report, KPFM results of film doping revealed that grain boundaries took longer time to release the adsorbed analytes than crystal grains. The bilayer film has F_{16}CuPc nanocrystalline on its surface and this means that there are much more grain boundaries on bilayer surface than on bare TiOPc layer surface. The slow desorption effect is enhanced by adding F_{16}CuPc layer so the bilayer is

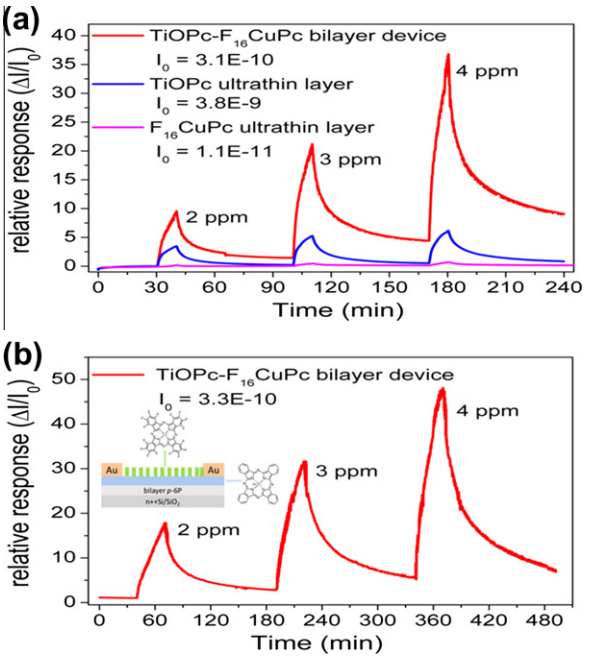

Fig. 2. (a) Relative response of the three devices to NO_2 pulse as a function of time. The relative response is defined as normalized increase of device current. (b) The section view of bilayer device structure and the molecular structure of F_{16}CuPc and TiOPc.

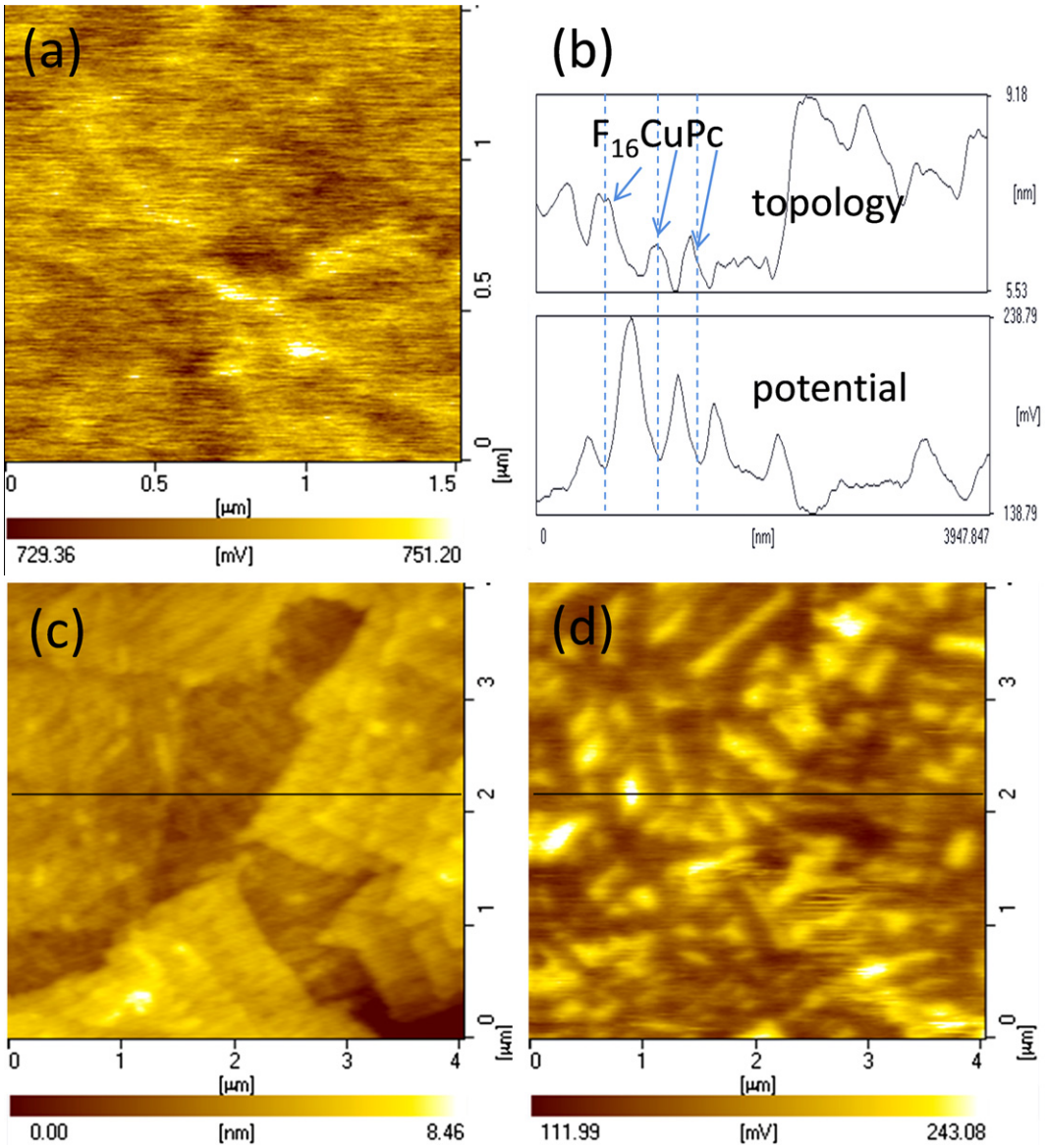

Fig. 3. KPFM results of (a) WEG TiOPc monolayer. (c) Topology of bilayer and (d) the relevant KPFM results of bilayer. The section profile of bilayer is compared in (b).

slow in desorption. The *p*-6P layer could also be slightly doped by NO_2 due to slow diffusion effect as it is exposed through gaps of TiOPc islands [16]. These are the reasons for the baseline shift in these devices.

Previous reports demonstrated that surface grain boundaries are the main adsorption sites in the film [17], and there are energy barriers at the grain boundaries [18]. In polycrystalline film the crystal size is hard to precisely control and the nano-sized crystalline does not favor the carrier transport. In WEG TiOPc film, the exposed surface area is mainly crystal grains which is homogeneous and favors the carrier transport. By depositing 1 nm F_{16}CuPc, the TiOPc crystal grain is covered with F_{16}CuPc nanocrystalline which forms heterostructure and changes the redox character of the film. The analytes adsorbed at bilayer surface generate hole carriers, and adjust the barrier height and affect the device conductivity.

In order to interpret the heterostrcture at the interface of the bilayer device, we measured and compared the surface potential of TiOPc ultrathin film (Fig. 3a) and TiOPc–F_{16}CuPc bilayer film (Fig. 3d) by KPFM method [19]. The surface potential value is obtained by measuring the difference of Fermi energy level between the sample and the scanning tip in our KPFM setup. According to Anderson rule, the Fermi level aligned at the interface thus the change of surface potential at the film interface represents the change of local vacuum level, which indicates the energy band bending at the interface. The surface potential

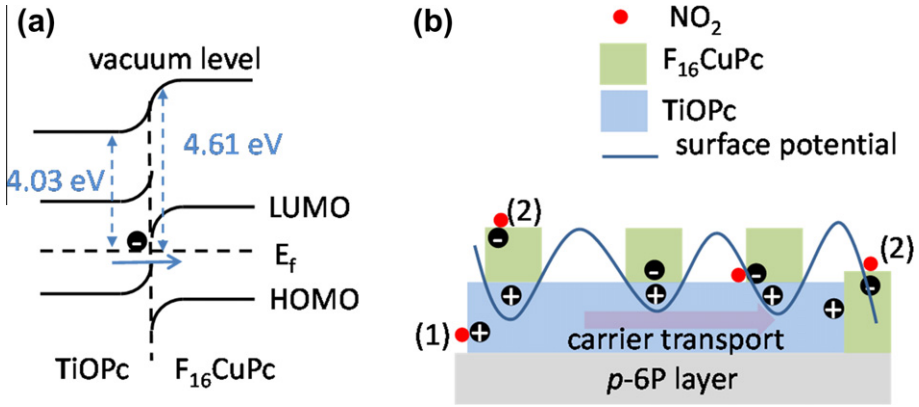

Fig. 4. (a) Interface electronic structure of TiOPc and F_{16}CuPc based on KPFM results. (b) Sensing model of bilayer sensor. Process (1) is related to TiOPc native grain boundary NO_2 adsorption and process (2) is related to local electron accumulating area (heterojunction area) NO_2 adsorption.

of TiOPc ultrathin film is 4.03 eV and that of TiOPc–F_{16}CuPc bilayer is 4.61 eV. This means the local vacuum level of TiOPc–F_{16}CuPc bilayer is higher than that of TiOPc layer, which indicates an upward bending of the local vacuum level of F_{16}CuPc layer referencing to the TiOPc layer. The schematic interfacial electronic structure is obtained (Fig. 4a) according to the band gap and electron affinity of TiOPc and F_{16}CuPc material, which is the intrinsic properties of semiconductor. The energy band of TiOPc is bending upwards and that of F_{16}CuPc is bending downwards. This means the F_{16}CuPc layer is electron accumulating and the TiOPc layer is hole accumulating at the interface. But as the F_{16}CuPc layer is only 1 nm and the film is poorly continuous, its band bending is far from saturation region.

Fig. 3b gives the section profile of bilayer film in topography (Fig. 3c) and potential (Fig. 3d). The dashed line points at the peak in topography of F_{16}CuPc crystalline and it corresponds to the valley in potential image. It proves directly that the F_{16}CuPc nanocrystalline has formed obvious electron rich area on bilayer surface. There is a surface potential fluctuation varying from 30 to 80 mV between the top F_{16}CuPc layer and the bottom TiOPc layer. As the heterojunction effect can be controlled by varying the top layer thickness or by choosing different top layer materials, the surface potential of bilayer can be tailored to fit different analytes. There is report on using functional material as top layer to realize sensor selectivity, here we use a physical way to control device response [20]. The conductivity is slightly decreased for the bilayer device although hole carriers are accumulated in the TiOPc lamellas. The reason is complex because the initial conductivity of TiOPc ultrathin film is in 10^{-9} level and the decrease is not obvious.

According to the above analysis, Fig. 4b gives the model of bilayer sensor. The transport channel is mainly in TiOPc layer as is suggested by film morphology. As is reported before, crystal grains and grain boundaries are all involved in analyte adsorption in WEG film [16]. The grain boundaries take the leading role in gas sensing in 1.8 nm TiOPc film shown as process (1). After the heterojunction is formed in the bilayer, the electron rich F_{16}CuPc area on the bilayer surface lowers down the activation energy for analyte reduction and these F_{16}CuPc crystallines help to adsorb analytes. The generated carriers adjust the F_{16}CuPc–TiOPc heterojunction so to influence the TiOPc layer conductivity, shown as process (2). It is necessary to point out that a small portion of F_{16}CuPc has reached down to *p*-6P layer as there are gaps between TiOPc islands. The joint area between F_{16}CuPc and TiOPc also forms heterojunction. The heterojunction area acts as extra active sites on the surface, and it plays a role much alike the grain boundaries without hindering the film conductive path in TiOPc layer. The NO_2 molecules adsorbed by F_{16}CuPc accept electrons and thus adjust the band bending of heterojunction and TiOPc conductivity. As the film surface owns more active sites, the bilayer shows obvious enhanced relative response and its detection limit reaches ppb level.

4. Conclusions

In conclusion, we have successfully fabricated a TiOPc–F_{16}CuPc bilayer gas sensor with heterojunction formed at their interface. The bilayer device shows obvious increase in relative response than ultrathin TiOPc film and F_{16}CuPc film at room temperature to NO_2 below 5 ppm. The detection limit of bilayer device is down to 250 ppb. The enhanced response is attributed to the p–n heterojunction formed at bilayer interface. The heterojunction effect has led to electron accumulating area at bilayer film surface and it makes the film more reductive to NO_2. The F_{16}CuPc nanostructure on TiOPc surface act as extra active sites besides grain boundaries and they adsorb analyte more effectively. We suggest that it provides a new manner to obtain highly sensitive room temperature gas sensor.

Acknowledgments

This work was financially supported by The National Natural Science Foundation of China (51133007) and The National Basic Research Program (2009CB939702).

References

[1] K.K. Khun, A. Mahajan, R.K. Bedi, SnO_2 thick films for room temperature gas sensing applications, Journal of Applied Physics 106 (2009) 124509.

[2] S.-W. Fan, A.K. Srivastava, V.P. Dravid, Nanopatterned polycrystalline ZnO for room temperature gas sensing, Sensors and Actuators B: Chemical 144 (2010) 159–163.

[3] Y.-L. Lee, C.-Y. Hsiao, C.-H. Chang, Y.-M. Yang, Effects of sensing temperature on the gas sensing properties of copper phthalocyanine and copper tetra-tert-butyl phthalocyanine films, Sensors and Actuators B: Chemical 94 (2003) 169–175.

[4] B. Bott, T.A. Jones, A highly sensitive NO_2 sensor based on electrical-conductivity changes in phthalocyanine films, Sensors and Actuators 5 (1984) 43–53.

[5] F.I. Bohrer, C.N. Colesniuc, J. Park, M.E. Ruidiaz, I.K. Schuller, A.C. Kummel, W.C. Trogler, Comparative gas sensing in cobalt, nickel, copper, zinc and metal-free phthalocyanine chemresistors, Journal of the American Chemical Society 131 (2009) 478–485.

[6] M. Passard, A. Pauly, J.P. Blanc, S. Dogo, J.P. Germain, C. Maleysson, Doping mechanisms of phthalocyanines by oxidizing gases – Application to gas sensors, Thin Solid Films 237 (1994) 272–276.

[7] A. Das, R. Dost, T. Richardson, M. Grell, J.J. Morrison, M.L. Turner, A nitrogen dioxide sensor based on an organic transistor constructed from amorphous semiconducting polymers, Advanced Materials 19 (2007) 4018.

[8] J. Li, Y. Lu, Q. Ye, M. Cinke, J. Han, M. Meyyappan, Carbon nanotube sensors for gas and organic vapor detection, Nano Letters 3 (2003) 929–933.

[9] R.D. Yang, T. Gredig, C.N. Colesniuc, J. Park, I.K. Schuller, W.C. Trogler, A.C. Kummel, Ultrathin organic transistors for chemical sensing, Applied Physics Letters 90 (2007) 263506.

[10] S.-W. Fan, A.K. Srivastava, V.P. Dravid, UV-activated room-temperature gas sensing mechanism of polycrystalline ZnO, Applied Physics Letters 95 (2009) 142106.

[11] F. Garnier, G. Horowitz, X.Z. Peng, D. Fichou, Structural basis for high carrier mobility in conjugated oligomers, Synthetic Metals 45 (1991) 163–171.

[12] H. Wang, D. Song, J. Yang, B. Yu, Y. Geng, D. Yan, High mobility vanadyl-phthalocyanine polycrystalline films for organic field-effect transistors, Applied Physics Letters 90 (2007) 253510.

[13] W.N. Hansen, G.J. Hansen, Standard reference surfaces for work function measurements in air, Surface Science 481 (2001) 172–184.

[14] M. Brinkmann, J.-C. Wittmann, M. Barthel, M. Hanack, C. Chaumont, Highly ordered titanyl phthalocyanine films grown by directional crystallization on oriented poly(tetrafluoroethylene) substrate, Chemistry of Materials 14 (2002) 904–914.

[15] J. Mizuguchi, G. Rihs, H.R. Karfunkel, Solid-state spectra of titanylphthalocyanine as viewed from molecular distortion, The Journal of Physical Chemistry 99 (1995) 16217–16227.

[16] W. Xiujin, J. Shiliang, W. Haibo, Y. Donghang, Room temperature nitrogen dioxide chemresistor using ultrathin Vanadyl-Phthalocyanine as active layer, doi:10.1016/j.snb.2011.07.021.

[17] T. Someya, H.E. Katz, A. Gelperin, A.J. Lovinger, A. Dodabalapur, Vapor sensing with alpha, omega-dihexylquarterthiophene field-effect transistors: the role of grain boundaries, Applied Physics Letters 81 (2002) 3079–3081.

[18] H. Huang, H. Wang, J. Zhang, D. Yan, Surface potential images of polycrystalline organic semiconductors obtained by Kelvin probe force microscopy, Applied Physics A: Materials Science and Amp; Processing 95 (2009) 125–130.

[19] H.B. Wang, X.J. Wang, H.C. Huang, D.H. Yan, Isotype heterojunction between organic crystalline semiconductors, Applied Physics Letters 93 (2008).

[20] J. Huang, J. Sun, H.E. Katz, Monolayer-dimensional 5,5′-Bis(4-hexylphenyl)-2,2′-bithiophene transistors and chemically responsive heterostructures, Advanced Materials 20 (2008) 2567–2572.

efficient solid-state emitters based on pyrene, such as 1,3,6,8-tetrakis[4-(1,2,2-triphenylvinyl)phenyl]pyrene (TTPEPy) [10] and 1,2-diphenyl-1,2-dipyrenylethene (DPDPyE) [11]. Non-doped OLEDs fabricated by using TTPEPy, and DPDPyE as emitters exhibit sky-blue, and green lights with high efficiencies up to 12.3, and 10.2 cd/A, respectively. However, pyrene has seldom been considered for the construction of yellow or red luminescent materials [12]. In this work, we present our study on a novel yellow emitter 1,3,6,8-tetrakis[(triisopropylsilyl)ethynyl]pyrene (TTIPSEPy), which consists of a 1,3,6,8-tetraethynylpyrene core and four triisopropylsilyl peripheral substituents. The single crystal structure, thermal stability, electrochemical and photophysical properties of TTIPSEPy are investigated. Multiplayer OLEDs using TTIPSEPy as non-doped emitter are fabricated and studied.

2. Experimental

2.1. General

Tetrahydrofuran (THF) was distilled from sodium benzophenone ketyl under nitrogen immediately prior to use. 1,3,6,8-Tetrabromopyrene [13] was prepared according to the literature method. All the other chemicals and regents were purchased from Aldrich and used as received without further purification. ^{1}H and ^{13}C NMR spectra were measured on a Bruker AV 300 spectrometer in deuterated chloroform using tetramethylsilane (TMS; $\delta = 0$) as internal reference. UV spectra were measured on a UV-2450 spectrophotometer. Photoluminescence was recorded on a RF-5301pc spectrofluorometer. The MALDI-TOF mass spectrum was recorded on a GCT premier CAB048 mass spectrometer. Elemental analysis was performed on an Elementary Vario EL analyzer. Cyclic voltammetric measurement on sample film was carried out in a conventional three-electrode cell containing 0.1 M Bu_4NPF_6 in acetonitrile solution at room temperature. A platinum working electrode, a platinum wire counter electrode, and an Ag/AgCl reference electrode were used for the measurement. The experiment was calibrated with the ferrocene/ferrocenium (Fc/Fc^+) redox system.

2.2. Synthesis

1,3,6,8-Tetraiodopyrene: *n*-Butyllithium (1.6 M in hexane, 6 mL, 9.6 mmol) was added dropwise into a THF suspension solution (100 mL) of 1,3,6,8-tetrabromopyrene (1 g, 2 mmol) at −78 °C. After the solution was stirred for 3 h, iodine (4.2 g, 9.6 mmol) was added into the solution in three portions. After being warmed to room temperature and stirred for 2 h, the mixture was poured into water. The precipitate was filtrated, washed by saturated sodium thiosulfate solution and water and dried under vacuum to a constant weight. The obtained pale green solid (1.2 g), 1,3,6,8-tetraiodopyrene, was used for the following reaction directly without further purification and characterization due to its poor solubility in common organic solvents.

1,3,6,8-Tetrakis[(triisopropylsilyl)ethynyl]pyrene (TTIPSEPy): 1,3,6,8-Tetraiodopyrene (0.7 g, 1 mmol) was added into a mixture of (triisopropylsilyl)acetylene (1 g, 6 mmol), copper(I) iodide (20 mg, 0.1 mmol), $Pd(PPh_3)_4$ (0.11 g, 0.1 mmol), and triphenylphosphine (10.5 mg, 0.04 mmol) in dry 100 mL diisopropylamine. After the solution was purged with nitrogen for half an hour, the reaction was refluxed under nitrogen for 24 h. After filtration and solvent evaporation, the residue was purified by silica gel column chromatography, using *n*-hexane/dichloromethane as eluent. TTIPSEPy was obtained as a greenish yellow solid in 92% yield (0.85 g). ^{1}H NMR (300 MHz, $CDCl_3$), δ (TMS, ppm): 8.67 (s, 4H), 8.28 (s, 2H), 1.26–1.23 (m, 84H). ^{13}C NMR (75 MHz, $CDCl_3$), δ (TMS, ppm): 135.2, 132.8, 127.7, 124.4, 119.7, 105.4, 98.9, 19.5, 12.1. HRMS: m/z 922.8466 (M^+, calcd 922.6120). Anal. Calcd for $C_{60}H_{90}Si_4$: C, 78.02; H, 9.82. Found: C, 77.95; H, 9.78.

2.3. X-ray crystallography

Crystal data for TTIPSEPy: $C_{60}H_{90}Si_4$, $M_w = 923.68$, triclinic, P-1, $a = 11.1306(3)$, $b = 11.7481(3)$, $c = 12.8102(3)$ Å, $\alpha = 77.772(2)$, $\beta = 75.612(2)$, $\gamma = 65.072(2)^\circ$, $V = 1460.43(6)$ Å^3, $Z = 1$, $D_c = 1.050$ g cm^{-3}, $\mu = 0.136$ mm^{-1} (MoKα, $\lambda = 0.7107$ Å), $F(000) = 506$, $T = 173.0$ K, $2\theta_{max} = 50.00$ (99.0%)°, 16,974 measured reflections, 5688 independent reflections ($R_{int} = 0.0349$), GOF on $F^2 = 1.019$, $R_1 = 0.0783$, w$R_2 = 0.1769$ (all data), Δe 0.505 and −0.225 eÅ^3.

Deposited crystal data number: CCDC 817287 for TTIPSEPy.

2.4. Device fabrication and measurements

In a general procedure, indium-tin oxide (ITO)–coated glass substrates were etched, patterned, and washed with detergent, deionized water, acetone, and ethanol in turn. PEDOT:PSS (Baytron P® Al 4083) was spin coated onto the ITO substrates under ambient atmosphere yielding a layer of 10 nm, and then it was baked at 120 °C for 30 min to remove residual water. All the organic layers were subsequently thermally deposited in a vacuum chamber at a base pressure of 8×10^{-5} Pa. After that a 100-nm-thick Ag capping layer was deposited through a 2-mm-wide opening array to fulfill the device fabrication. In all devices, a thin layer of Ca about 8 nm was deposited to enhance the electron injection ability on the Ag cathode. A quartz crystal oscillator placed near the substrate was used to monitor the thickness of each layer, which was calibrated ex situ using Ambios Technology XP-2 surface profilometer. The active area of device was 6 mm^2. EL spectra and chromaticity coordinates were measured with a SpectraScan PR650 photometer. Current density–voltage–luminance measurements were recorded simultaneously using a Keithley 4200 semiconductor parameter analyzer combined with a Newport multifunction 2835-C optical meter, with luminance was measured in the forward direction. All device characterizations were carried out under ambient laboratory air at room temperature.

3. Results and discussion

The synthetic route to TTIPSEPy is illustrated in Scheme 1. TTIPSEPy was facilely synthesised by Sonogash-

ira coupling of 1,3,6,8-tetraiodopyrene with (triisopropylsilyl)acetylene in a high yield of 92%. Thermogravimetric analysis gave a decomposition temperature of 377 °C for TTIPSEPy, indicating that the compound was thermally stable for application in OLEDs. The single crystals of TTIPSEPy were grown from hexane/dichloromethane mixture and analyzed by X-ray diffraction crystallography. The crystal structure and B3LYP/6-31G(d) calculated molecular orbital amplitude plots of HOMO and LUMO of TTIPSEPy are shown in Fig. 1. The pyrene ring is well conjugated with four exterior acetylene units. The electron clouds in both HOMO and LUMO are distributed on this conjugated backbone, suggesting that the central conjugation system predominantly controls the photophysical properties of this compound in the disperse phase.

TTIPSEPy exhibits fine-structured absorption spectrum with absorption maximum at 440 nm in dilute THF solution (Fig. 2A), associated with the π–π^* transition of the conjugated backbone. The film of TTIPEPy shows absorption maximum at 442 nm, which is slightly red-shifted comprared with that in solution. The absorption edge of TTIPSEPy in solution is very sharp and is located at 458 nm, whereas that in film is broad and extends up to 540 nm (Fig. 2B). A new absorption shoulder is observed in the wavelength range of 450–540 nm that can be assigned to the charge-transfer transitions induced by *J*-aggregation. TTIPSEPy shows blue emission with a peak at 446 nm and a shoulder at 472 nm in dilute THF solution, which resembles to that of 1,3,6,8-tetrakis[(trimethysilyl)ethynyl]pyrene [14], indicating that the different–sized trialkylsilyl substituents at periphery have little influence on the emission property of the 1,3,6,8-tetraethynylpyrene core in solution. The fluorescence quantum yield (Φ_F) of TTIPSEPy in THF solution is 8.7%, measured by a relative method using 9,10-diphenylanthracene (Φ_F = 90% in cyclohexane) as standard. This Φ_F value is lower than those of pyrene and most pyrene derivatives [9], probably due to the self-absorption effect as implied by the partial overlapping of absorption and emission spectra (Fig. 2A) in solution. Howerve, the PL of TTIPSEPy becomes redder and broader in the single crystal state. The emission spectrum red-shifts to green region with two emission peaks at 490 and 510 nm. Moreover, the PL further moves to yellow region in the solid amorphous film with emission maxiumum at 553 nm, which is bathochromatically shifted by 107 nm compared with that in solution (Fig. 2B). Concerning the PL of 1,3,6,8-tetrakis[(trimethysilyl)ethynyl]pyrene, its emission maximum in film state is located at ~650 nm, and is strongly red-shifted by about 200 nm than that in solution [14]. The hypsochromic shift in PL of TTIPSEPy film relative to 1,3,6,8-tetrakis[(trimethysilyl)ethynyl]pyrene film can be interpreted as that the more bulky triisoporpylsilyl substitutents have reduced π–π interactions to some extent in film state. Nevertheless, the broader absorption and the bathochromically shifted PL of TTIPSEPy in film compared with those in solution clearly suggest that there are strong intermolecular interactions between TTIPSEPy molecules in the condensed phase. TTIPSEPy exhibits a high Φ_F value of 100% in film, measured by a calibrated integrating sphere, being more than 10-fold higher than that in solution. The unity emission efficiency of TTIPSEPy in film reveals that it is an outstanding solid-state emitter.

To further understand the optical property of TTIPSEPy in the solid-state, we investigate the crystal structure of TTIPSEPy. As displayed in Fig. 3A–C, the pyrene rings of two adjacent TTIPSEPy molecules are stacked in a parallel pattern. However, the overlapping between adjacent pyrene rings is inadequate, which undermines the strong π–π interactions between TTIPSEPy molecules in crystalline. CH$\cdots\pi$ hydrogen bonds with a distance of 2.856 Å are formed between the hydrogen atoms of the triisopropylsilyl groups in one TTIPSEPy molecule and the π cloud of the pyrene ring in another molecule. A distance of 5.614 Å is found between the parallelly located acetylene units of the adjacent TTIPSEPy molecules. These findings suggest that weak intermolecular interactions may exist in the crystals, which accounts for the redder PL of TTIPSEPy in crystalline state, as compared to that in solution. However, the remarkable bathochromatic shift in PL of TTIPSEPy film should stem from strong π–π interactions between pyrene rings. The proposed *J*-type packing model of TTIPSEPy molecules in film state is illustrated in Fig. 3D, where the TTIPSEPy molecules are stacked parallely and closely, and strong π–π interactions are formed between pyrene rings. The formation of such kind of *J*-aggregation should be responsible for the drastic bathochromatic shift and notable emission efficiency enhancement in film state [11,15,16].

Cyclic voltammetry measurement was carried out to determine the energy levels of TTIPSEPy in film state. Fig. 4 shows the cyclic voltammogram of TTIPSEPy film, in which oxidation and reduction peaks are found at 1.45 and −1.68 V, respectively. The onset oxidation potential of TTIPSEPy film is at 1.01 eV, corresponding to the estimated HOMO energy level of −5.41 eV [HOMO = $-(E^{ox}_{onset} + 4.4)$ eV]. This value is quite close to that of a widely used hole transport material *N*,*N*′-di(1-naphthyl)-*N*,*N*′-diphenyl-benzidine (NPB, −5.4 eV) [5], indicating that the holes can be facilely injected to TTIPSEPy film. The

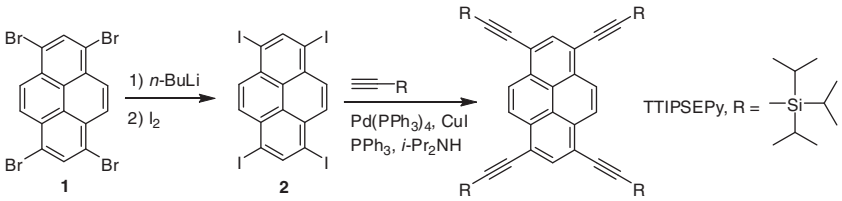

Scheme 1. Synthetic route to TTIPSEPy.

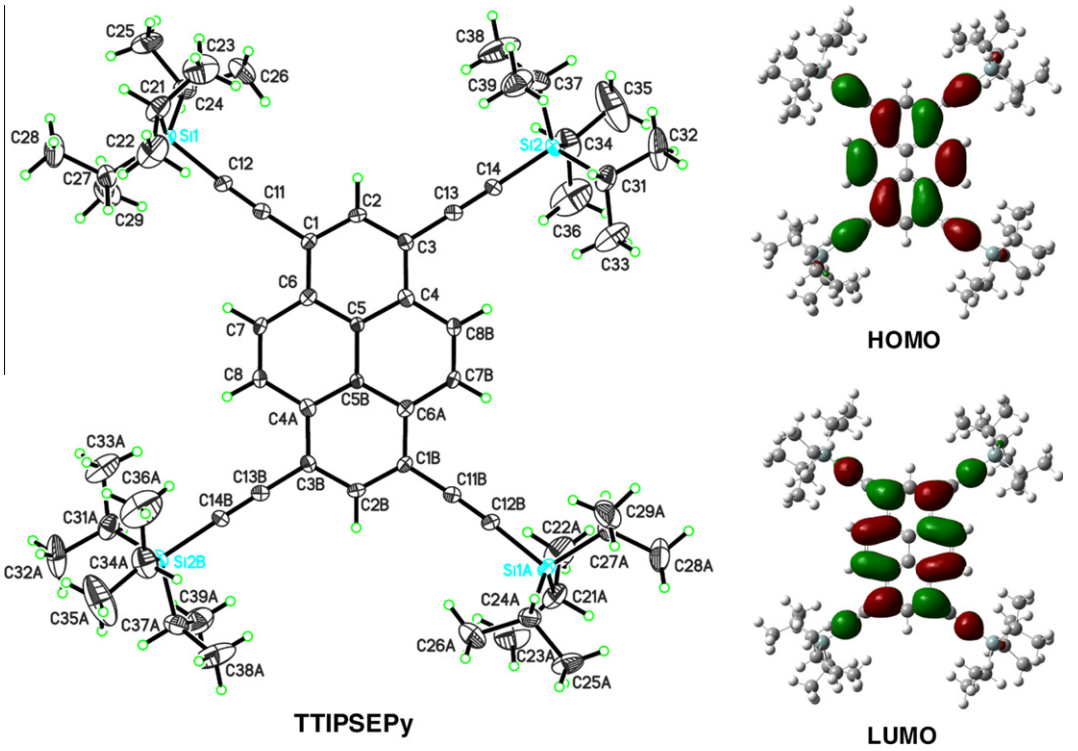

Fig. 1. ORTEP drawing and B3LYP/6-31G(d) calculated molecular orbital amplitude plots of HOMO and LUMO of TTIPSEPy.

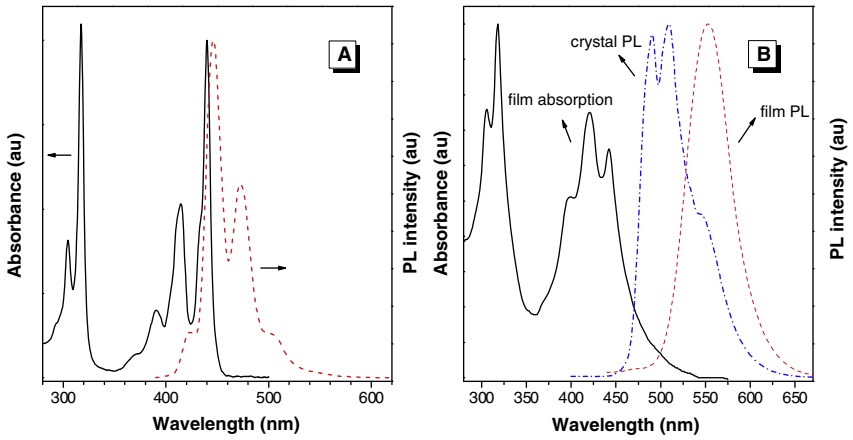

Fig. 2. Absorption and PL spectra of TTIPSEPy (A) in dilute THF solution (10 μM) and (B) in the solid state.

onset reduction potential (E^{re}_{onset}) of TTIPSEPy film is found at −1.21 V, from which the LUMO energy level of −3.19 eV is derived [LUMO = $-(E^{re}_{onset} + 4.4)$ eV]. The value is lower than those of electron transport materials aluminum(III)bis(2-methyl-8-quinolinato)4-phenylphenolate (BAlq, −2.7 eV) [17] and 1,3,5-tris(2-*N*-phenylbenzimidazolyl)benzene (TPBI, −2.7 eV) [18], and equal to that of 2,9-dimethyl-4,7-diphenyl-1,10-phenanthroline (BCP, −3.2 eV) [19], indicating that TTIPSEPy film is in favor of electron injection and transport. The rather low LUMO energy level is presumably due to the electron-withdrawing effect of triisoporpylsilylacetylene [20]. The energy band gap (E_{exp}) calculated from the electrochemically determined HOMO and LUMO energy levels is 2.22 eV, which is in good accordance with that obtained from the threshold of absorption spectrum of TTIPSEPy film (2.30 eV).

The highly efficient solid-state PL of TTIPSEPy encouraged us to investigate its application in non-doped OLEDs. We fabricated multilayer devices by vapor deposition process with the configurations listed in Table 1. A control device was also fabricated adopting rubrene as emitter. The EL spectra and performance curves of the devices are displayed in Figs. 5 and 6, respectively. Devices A and B with a configuration of ITO/PEDOT:PSS (10 nm)/NPB (35 nm)/

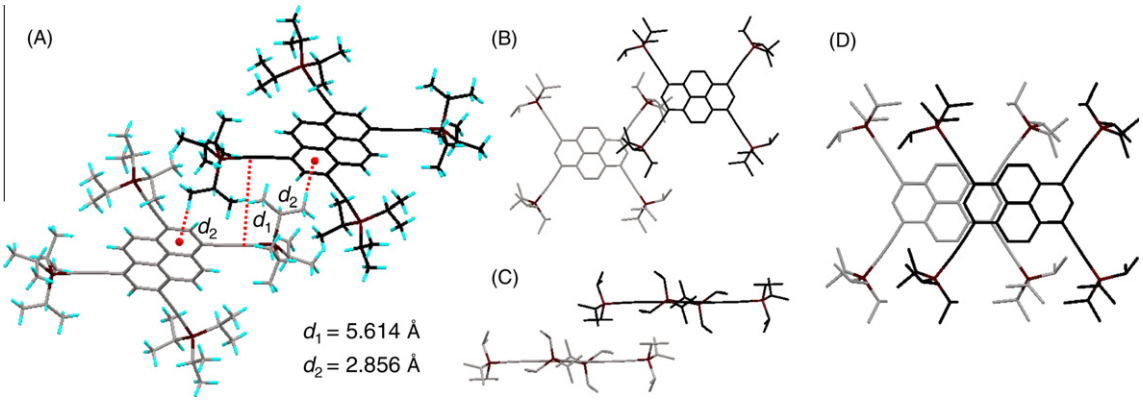

Fig. 3. (A) C–H···π hydrogen bonds between adjacent molecules of TTIPSEPy in crystals. (B) Top and (C) side views of adjacent molecules of TTIPSEPy in crystals along the plane of pyrene ring. (D) Proposed stacking pattern of TTIPSEPy molecules in the film state.

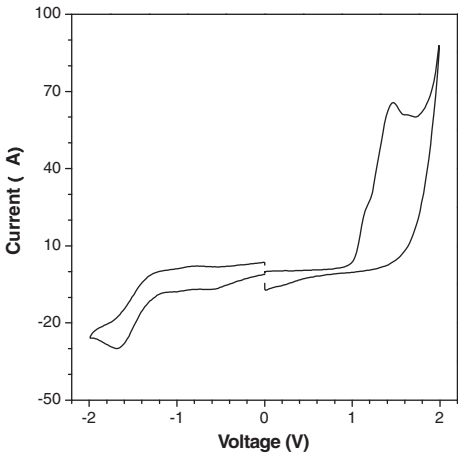

Fig. 4. Cyclic voltammogram of TTIPSEPy film measured in acetonitrile containing 0.1 M Bu_4NPF_6, scant rate 100 mV/s.

TTIPSPEy (*x* nm)/BCP (36 nm)/Ca (8 nm)/Ag (100 nm), where *x* = 13 nm for device A and *x* = 25 nm for device B, are turned on at a quite low voltage of 2.2 V. They emit yellow light peaked at 560 nm, corresponding to the Commission International de l'Eclairage (CIE) chromaticity coordinates of (0.44, 0.53). Both devices show stable EL, whose spectra profiles change little against applied voltage increases (Fig. 5A). These EL spectra are close to the PL spectrum of the TTIPSEPy film, revealing that both EL and PL originate from the same radiative-decay process of singlet excitons. The EL efficiency is enhanced obviously when the thinkness of TTIPSEPy layer increases as indicated in Fig. 6C. Device B shows a maximum current efficiency ($\eta_{c,max}$) of 7.1 cd/A, and a maximum power efficiency ($\eta_{p,max}$) of 8.3 lm/W, which are much higher than those of device A (4.2 cd/A, and 3.6 lm/W). In general, thickening the emitting layer will enhance the recombination efficiency of holes and electrons in it, and consequently improves the device efficiency. We also investigated the effect of electron-transporting layers on the performances of the devices. When keep TTIPSEPy thickness unchanged and use different electron-transporting layers in devices C and D, the EL spectra vary slightly (Fig. 5B) but the turn-on voltages, L_{max} and $\eta_{c,max}$ change remarkably (Table 1). The turn-on voltages of devices C and D are 4.4 and 5.0 V, respectively, which are more than 2-fold higher than that of device B. Device D with a configuration of ITO/PEDOT:PSS (10 nm)/NPB (35 nm)/TTIPSEPy (25 nm)/TPBI (36 nm)/Ca (8 nm)/Ag (100 nm), where TPBI is used as electron-transporting as well as hole-blocking layer, exhibits the highest L_{max} and $\eta_{c,max}$ (Table 1). It radiates brilliantly yellow light peaked at 552 nm (CIE = 0.41, 0.56) with a L_{max} of 26,400 cd/m^2 and a $\eta_{c,max}$ of 9.2 cd/A. On the other hand, the data attained from TTIPSEPy-based devices A–D are much better than those from rubrene-based control device E (Table 1, Fig. S2 and S3). They are also

Table 1
EL properties of TTIPSEPy and rubrene in non-doped OLEDs.[a]

EML	ETL	λ_{EL} (CIE) (nm)	V_{on} (V)	L_{max} (cd/m^2)	$\eta_{c,max}$ (cd/A)	$\eta_{p,max}$ (lm/W)
A: TTIPSEPy (13 nm)	BCP	560 (0.44, 0.53)	2.2	19 220	4.2	3.6
B: TTIPSEPy (25 nm)	BCP	560 (0.44, 0.53)	2.2	21 230	7.1	8.3
C: TTIPSEPy (25 nm)	BAlq	557 (0.44, 0.54)	4.4	24 140	8.6	4.1
D: TTIPSEPy (25 nm)	TPBI	552 (0.41, 0.56)	5.0	26 400	9.2	2.9
E: rubrene (25 nm)	TPBI	553 (0.42, 0.55)	3.1	13 750	2.2	1.2

[a] Device configuration: ITO/PEDOT:PSS (10 nm)/NPB (35 nm)/EML/ETL (36 nm)/Ca (8 nm)/Ag (100 nm). EML = emitting layer, ETL = electron-transporting layer, λ_{EL} = EL maximum, V_{on} = turn-on voltage at 1 cd/m^2, L_{max} = maximum luminance, $\eta_{c,max}$ = maximum current efficiency. NPB = *N*,*N*′-di(1-naphthyl)-*N*,*N*′-diphenyl-benzidine, BCP = 2,9-dimethyl-4,7-diphenyl-1,10-phenanthroline, BAlq = aluminum(III)bis(2-methyl-8-quinolinato)4-phenylphenolate, TPBI = 1,3,5-tris(2-*N*-phenylbenzimidazolyl)benzene.

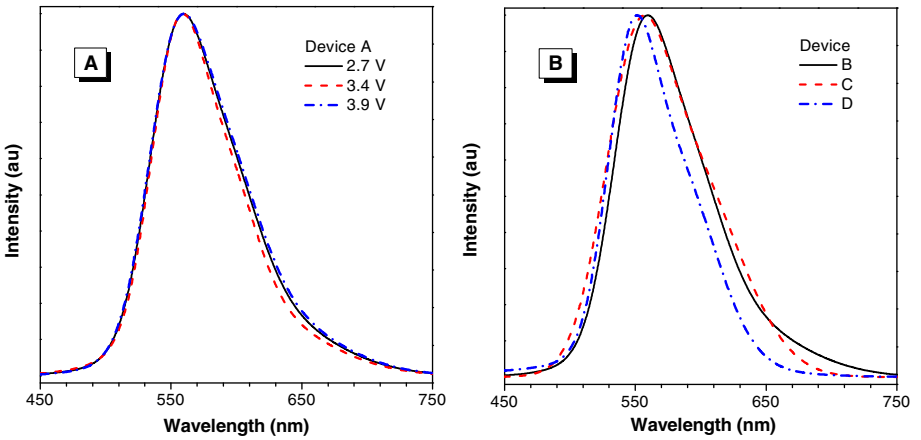

Fig. 5. (A) EL spectra of TTIPSEPy in device A at bias voltages. (B) EL spectra of TTIPSEPy in devices B–D.

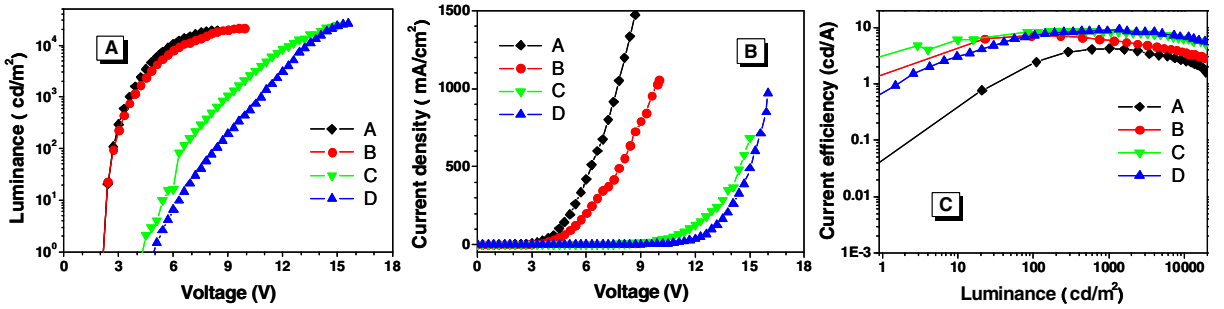

Fig. 6. Plots of (A) luminance versus voltage, (B) current density versus voltage and (C) current efficiency versus luminance in devices A–D.

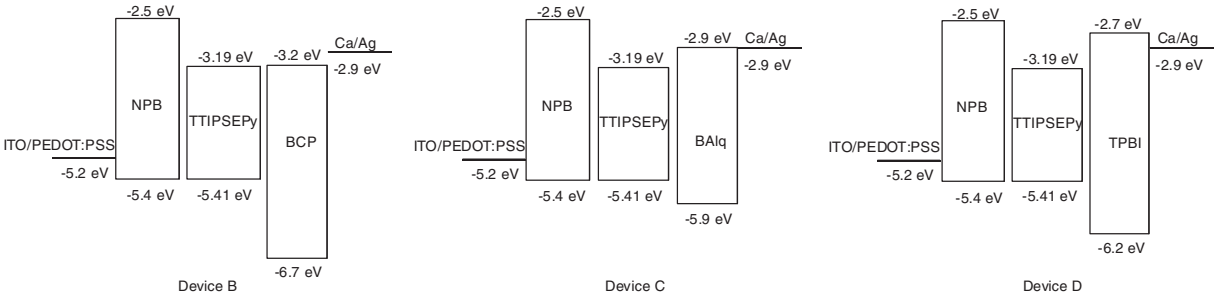

Fig. 7. The energy band structures of devices B–D.

close to the best results of rubrene-doped devices in literatures [3]. Such good EL performances are attributable to the high Φ_F in the solid-state and matched energy levels of TTIPSEPy.

To get a better understanding of the mechanism behind the changes in performances of devices B–D, the energy levels of TTIPSEPy and various electron-transporting layers are taken into consideration. Fig. 7 illustrates the energy level diagrams of devices B–D. The LUMO energy level of BCP (−3.2 eV) is lower than those of BAlq (−2.9 eV) and TPBI (−2.7 eV), which facilitates the electron injection. Moreover, the electron mobility of BCP (1.0×10^{-3} $cm^2 V^{-1} s^{-1}$) [21] is 100-fold higher than that of TPBI (1.0×10^{-5} $cm^2 V^{-1} s^{-1}$) [22]. Both factors account for the lowest turn-on voltage of device B. On the other hand, the HOMO energy level of TPBI (−6.2 eV) is lower than that of BAlq (−5.9 eV), which confines holes and excitions in the emitting layer more effectively. Meanwhile, the higher LUMO energy level of TPBI faciliates more efficient electron injection to emitting layer from TPBI layer. The combination of these two effects in device D leads to the highest L_{max} and $\eta_{c,max}$ values among these devices.

4. Conclusion

In summary, a novel simple-structured chromophore composed by a 1,3,6,8-tetraethynylpyrene core and four

triisopropylsilyl peripheral substituents (TTIPSEPy) is synthesised and characterized. TTIPSEPy is thermally stable and shows yellow PL with unity emission efficiency in film state. High performance non-doped OLEDs have been fabricated using TTIPSEPy as emitter, exhibiting yellow EL (CIE = 0.41, 0.56) with luminance and efficiency up to 26,400 cd/m^2 and 9.2 cd/A, respectively. To the best of our knowledge, these values are better than those of non-doped yellow fluorescent OLEDs ever reported [6]. The facile synthesis and outstanding PL and EL properties of TTIPSEPy suggest that it is a promising candidate for the fabrication of non-doped yellow and white OLEDs. Systematic investigations on structure–property relationship of similar chromophores constructed by 1,3,6,8-tetraethynylpyrene cores and different-sized peripheral substituents are in progress.

Acknowledgments

The work reported in this paper was partially supported by the National Natural Science Foundation of China (21074028). Z.J.Z. acknowledges Natural Science Foundation of Zhejiang Province (Y4110331) and the Initial Funding of Hangzhou Normal University (HSQK0085).

Appendix A. Supplementary data

Supplementary data associated with this article can be found, in the online version, at doi:10.1016/j.orgel.2011.09.019.

References

[1] (a) C. Vijayakumar, V.K. Praveen, A. Ajayaghosh, Adv. Mater. 21 (2009) 2059;
(b) R. Wang, J. Peng, F. Qiu, Y. Yang, Z. Xie, Chem. Commun. (2009) 6723;
(c) C. Gu, T. Fei, Y. Lv, T. Feng, S. Xue, D. Lu, Y. Ma, Adv. Mater. 22 (2010) 2702.

[2] (a) B.W. D'Andrade, M.E. Thompson, S.R. Forrest, Adv. Mater. 14 (2002) 147;
(b) D.S. Qin, Y. Tao, Appl. Phys. Lett. 86 (2005) 113507;
(c) C.H. Kim, J. Shinar, Appl. Phys. Lett. 80 (2002) 2201.

[3] (a) K.-Y. Peng, C.-W. Huang, C.-Y. Liu, S.-A. Chen, Appl. Phys. Lett. 91 (2007) 093502;
(b) T.-H. Liu, Y.-S. Wu, M.-T. Lee, H.-H. Chen, C.-H. Liao, C.H. Chen, Appl. Phys. Lett. 85 (2004) 4304;
(c) S.H. Kim, S. Park, J.E. Kwon, S.Y. Park, Adv. Funct. Mater. 21 (2011) 644.

[4] (a) S.L. Lai, S.L. Tao, M.Y. Chan, T.W. Ng, M.F. Lo, C.S. Lee, X.H. Zhang, S.T. Lee, Org. Electron. 11 (2010) 1511;
(b) L. Li, J. Yu, X. Tang, T. Wang, W. Li, Y. Jiang, J. Lumin. 128 (2008) 1783;
(c) Q. Xue, S. Zhang, G. Xie, Z. Zhang, L. Zhao, Y. Luo, P. Chen, Y. Zhao, S. Liu, Solid-State Electron. 57 (2011) 35.

[5] (a) S. Chen, Z. Zhao, B.Z. Tang, H.S. Kwok, J. Phys. D: Appl. Phys. 43 (2010) 095101;
(b) S. Chen, Z. Zhao, Z. Wang, P. Lu, Z. Gao, Y. Ma, B.Z. Tang, H.S. Kwok, J. Phys. D: Appl. Phys. 44 (2011) 145101.

[6] (a) Y. Zhou, J.W. Kim, R. Nandhakumar, M.J. Kim, E. Cho, Y.S. Kim, Y.H. Jang, C. Lee, S. Han, K.M. Kim, J.-J. Kim, J. Yoon, Chem. Commun. 46 (2010) 6512;
(b) Z. Zhao, S. Chen, J.W.Y. Lam, C.K.W. Jim, C.Y.K. Chan, Z. Wang, P. Lu, C. Deng, H.S. Kwok, Y. Ma, B.Z. Tang, J. Phys. Chem. C 114 (2010) 7963;
(c) H. Cao, Z. Chen, Y. Liu, B. Qu, S. Xu, S. Cao, Z. Lan, Z. Wang, Q. Gong, Synth. Met. 157 (2007) 427;
(d) C. Fave, T.-Y. Cho, M. Hissler, C.-W. Chen, T.-Y. Luh, C.-C. Wu, R. Réau, J. Am. Chem. Soc. 125 (2003) 9254.

[7] (a) Z.I. Zhang, X.Y. Jiang, S.H. Xu, T. Nagatomo, O. Omoto, J. Phys. D: Appl. Phys. 31 (1998) 32;
(b) Y.-S. Wu, T.-H. Liu, H.-H. Chen, C.H. Chen, Thin Solid Films 496 (2006) 626.

[8] (a) C.T. Chen, Chem. Mater. 16 (2004) 4389;
(b) H. Bi, K. Ye, Y. Zhao, Y. Yang, Y. Liu, Y. Wang, Org. Electron. 11 (2010) 1180;
(c) X. Gong, S. Wang, D. Moses, G.C. Bazan, A.J. Heeger, Adv. Mater. 17 (2005) 2053.

[9] (a) K.-C. Wu, P.-J. Ku, C.-S. Lin, H.-T. Shih, F.-I. Wu, M.-J. Huang, J.-J. Lin, I.-C. Chen, C.-H. Cheng, Adv. Funct. Mater. 18 (2008) 67;
(b) S.T. Tao, Z.K. Peng, X.H. Zhang, P.F. Wang, C.-S. Lee, S.-T. Lee, Adv. Funct. Mater. 15 (2005) 1716;
(c) C. Tang, F. Liu, Y.-J. Xia, L.-H. Xie, A. Wei, S.-B. Li, Q.-L. Fan, W. Huang, J. Mater. Chem. 16 (2006) 4074;
(d) Z. Zhao, X. Xu, F. Wang, G. Yu, P. Lu, Y. Liu, D. Zhu, Synth. Met. 156 (2006) 209;
(e) J.N. Moorthy, P. Natarajan, P. Venkatakrishnan, D.-F. Huang, T.J. Chow, Org. Lett. 9 (2007) 5215;
(f) Z. Zhao, S. Chen, C. Deng, J.W.Y. Lam, C.Y.K. Chan, P. Lu, Z. Wang, B. Hu, X. Chen, P. Lu, H.S. Kwok, Y. Ma, H. Qiu, B.Z. Tang, J. Mater. Chem. 21 (2011) 10949;
(g) T. Kumchoo, V. Promarak, T. Sudyoadsuk, M. Sukwattanasinitt, P. Rashatasakhon, Chem.–Asian J. 5 (2010) 2162.

[10] Z. Zhao, S. Chen, J.W.Y. Lam, P. Lu, Y. Zhong, K.S. Wong, H.S. Kwok, B.Z. Tang, Chem. Commun. 46 (2010) 2221.

[11] Z. Zhao, S. Chen, J.W.Y. Lam, Z. Wang, P. Lu, F. Mahtab, H.H.Y. Sung, I.D. Williams, Y. Ma, H.S. Kwok, B.Z. Tang, J. Mater. Chem. 21 (2011) 7210.

[12] (a) Z. Zhao, J.-H. Li, X. Chen, X. Wang, P. Lu, Y. Yang, J. Org. Chem. 73 (2009) 383;
(b) Z. Zhao, J.-H. Li, X. Chen, P. Lu, Y. Yang, Org. Lett. 10 (2008) 3041;
(c) Y. Zhou, J.W. Kim, M.J. Kim, W.-J. Son, S.J. Han, H.N. Kim, S. Han, Y. Kim, C. Lee, S.-J. Kim, D.H. Kim, J.-J. Kim, J. Yoon, Org. Lett. 12 (2010) 1272.

[13] G. Venkataramana, S. Sankararaman, Eur. J. Org. Chem. (2005) 4162.

[14] S. Shanmugaraju, S.A. Joshi, P.S. Mukherjee, J. Mater. Chem. 21 (2011) 9130.

[15] (a) S. Varghese, S. Das, J. Phys. Chem. Lett. 2 (2011) 863;
(b) B.-K. An, S.-K. Kwon, S.-D. Jung, S.Y. Park, J. Am. Chem. Soc. 124 (2002) 14410;
(c) Z. Wang, H. Shao, J. Ye, L. Tang, P. Lu, J. Phys. Chem. B 109 (2005) 19627.

[16] (a) R. Nandy, M. Subramoni, B. Varghese, S. Sankararaman, J. Org. Chem. 72 (2007) 938;
(b) S. Sankararaman, G. Venkataramana, B. Varghese, J. Org. Chem. 73 (2008) 2404;
(c) G. Venkataramana, S. Sankararaman, Org. Lett. 8 (2006) 2739.

[17] B.D. Chin, M.C. Suh, M.H. Kim, S.T. Lee, H.D. Kim, H.K. Chung, Appl. Phys. Lett. 86 (2005) 133505.

[18] Z. Zhao, X. Xu, H. Wang, P. Lu, G. Yu, Y. Liu, J. Org. Chem. 73 (2008) 594.

[19] M.A. Baldo, S. Lamansky, P.E. Burrows, M.E. Thompson, S.R. Forrest, Appl. Phys. Lett. 75 (1999) 4.

[20] Z. Zhao, D. Liu, F. Mahtab, L. Xin, Z. Shen, Y. Yu, C.Y.K. Chan, P. Lu, J.W.Y. Lam, H.H.Y. Sung, I.D. Williams, B. Yang, Y. Ma, B.Z. Tang, Chem.–Eur J. 17 (2011) 5998;
(b) Z. Zhao, P. Lu, J.W.Y. Lam, B. Yang, Y. Ma, B.Z. Tang, Sci. China Ser. B 53 (2010) 2311.

[21] H. Fukagawa, N. Yokoyama, S. Irisa, S. Tokito, Adv. Mater. 22 (2010) 4775.

[22] S.-J. Su, T. Chiba, T. Takeda, J. Kido, Adv. Mater. 20 (2008) 2125.

of these derivatives [9]. Increasing the number of thiophene units, on the other hand, leads to reduction of the ionization potential (IP) as well as the optical band gap [12]. Thus, use of dicyanovinyl endgroups and variation of oligomer backbone result in oligothiophene structures for which an efficient exciton dissociation in heterojunctions to the acceptor C60 takes place [12]. For planar heterojunction (PHJ) solar cells based on DCVnTs, power conversion efficiencies (PCE) of up to 3.4% with an open circuit voltage of up to 1 V were reported [13]. Most recently, optimization of the mixed layer morphology by use of substrate heating resulted in PCEs of 4.9% in DCV6T-Bu(1,2,5,6):C60 and 5.2% in DCV5T:C60 mixed heterojunction solar cells [14,15].

In this work, in contrast to Ref. [14], we study neat vacuum deposited films of the α-ω-bis-(dicyanovinylen)-sexithiophene DCV6T-Bu(1,2,5,6) (DCV6T-Bu), comprising six thiophene rings and four butyl side-chains at the first, second, fifth and sixth thiophenes (see inset of Fig. 1). Compared to the formerly introduced in Ref. [16] DCV6T-Et(2,2,5,5) (DCV6T-Et), which comprised two ethyl side chains at the second and fifth thiophene, DCV6T-Bu has the same thiophene backbone and differs only in the side chain length and pattern. The molecular structure of the reported material was intentionally modified utilizing longer side chains with asymmetrical substitution aiming at enhanced solubility, thus improved purity upon synthesis, and promotion of self-organization. We report on the morphology and optical properties of the neat DCV6T-Bu films, discussing the effect of the molecular structure on the molecular arrangement and packing in the solid state. We show that more ordered film morphology is obtained as a result of the modified substitution in DCV6T-Bu as compared to DCV6T-Et. Deposition on substrates at elevated temperature leads to enhanced crystalline growth as confirmed by the presented structural and spectroscopic data. On the basis of these results, using the charge extraction by linearly increasing voltage (CELIV) method, we study the hole mobility of heated and nonheated DCV6T-Bu films. Finally, contrary to Ref. [14] dealing with the optimization of mixed heterojunction solar cells, here, we discuss the performance of DCV6T-Bu/C60 PHJ solar cells comparing devices with and without deposition at elevated substrate temperature.

2. Experimental

The samples for the ultraviolet–visible (UV–Vis) absorption spectroscopy, X-ray diffraction (XRD), atomic force microscopy (AFM) measurements as well as the solar cell devices were prepared by thermal evaporation in high vacuum at a base pressure of $\leqslant 6 \times 10^{-6}$ mbar and deposition rate of 0.1–0.2 Å/s. Nominal layer thicknesses were determined using quartz crystal monitor calibrated beforehand using a second crystal placed at the sample position.

UV–Vis absorption spectroscopy and AFM measurements were carried out on DCV6T-Bu films deposited on quartz glass substrates. Neat or precovered with 15 nm C60 (Bucky, USA) Si wafers were used as substrates for the XRD studies. Two CELIV devices and two solar cells comprising DCV6T-Bu/C60 PHJs were prepared on indium tin oxide (ITO)-precovered glass substrates (Thin Film devices Inc., sheet resistance of 30 Ω/sq). All substrates were cleaned subsequently in acetone, ethanol and isopropanol, and after that blow-dried in nitrogen. The nominal thickness of the DCV6T-Bu layers was 20 nm for all samples grown on quartz glass, independent of the substrate temperature (assumed density $\rho = 1.3$ g/cm^3). For the XRD measurements, 50 nm DCV6T-Bu films were deposited on 30 °C- and 6 nm, 10 nm, and 50 nm on 90 °C-substrates, respectively.

The absorption of the layers in the UV–Vis spectral range was measured in transmission mode using a two-beam spectrometer UV 3100 (Shimadzu Corporation). The

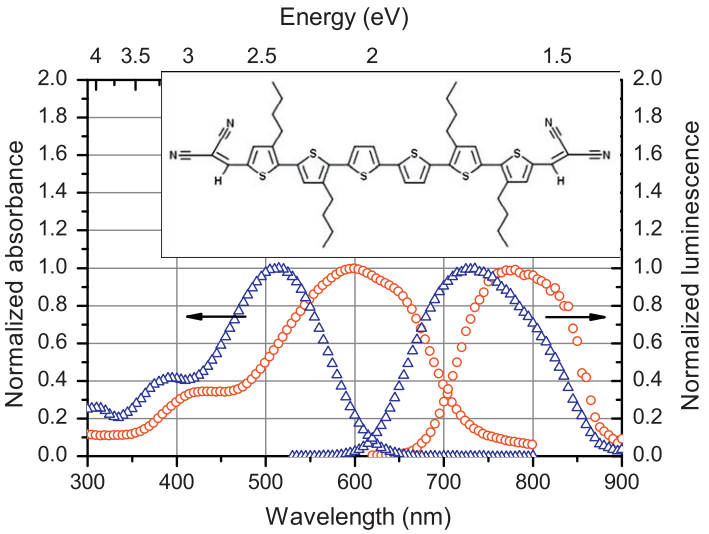

Fig. 1. Normalized absorbance and PL spectra of DCV6T-Bu in dichloromethane solution (open triangles) and in thin film (open circles). The thickness of the film is 30 nm. PL is measured by excitation at the corresponding wavelength of maximum absorption. Inset: chemical structure of the DCV6T-Bu(1,2,5,6) molecule.

surface topography of the samples was studied by AFM using a Digital Instrument NanoScope IIIa microscope in tapping mode. XRD investigations were carried out by means of X-ray diffractometer URD-6 (Seifert FPM, Germany) designed in Bragg–Brentano geometry using monochromatized Cu-K_α radiation with wavelength of 1.5418 Å. The XRD patterns of the samples were recorded in symmetrically coupled ω-2θ specular scan mode, where 2θ is the diffraction angle and $\omega = \theta$ is the X-ray incidence angle. Other details of the XRD experiment could be found in [17].

The mobility of DCV6T-Bu was measured using the charge extraction by linearly increasing voltage method (CELIV) as described in Refs. [18,19]. The CELIV devices were built of DCV6T-Bu/C60 planar heterojunctions in the layer structure (thickness given in brackets in nm): ITO / C60 (20) / DCV6T-Bu (x) / Au (10) / Al (90) with x = 57 nm and x = 60 nm for device I and II, respectively. For comparison of the effect of different DCV6T-Bu film morphologies on the hole mobility, device I was prepared at room temperature (RT) substrate (T_{sub} = RT), while for device II a substrate temperature of (90 ± 10)°C (T_{sub} = 90 °C) was used during the deposition of DCV6T-Bu. Both electrons and holes are extracted from the devices. However, the presented experiments determine the hole mobility of DCV6T-Bu, since the signal is dominated by the slower carrier and electrons in C60 have the by far higher mobility, reported to be as high as 6 cm^2/Vs [23]. A blue light emitting diode is used to illuminate the CELIV devices prior to applying the voltage pulse in order to increase the amount of extractable charges.

The layer structures of solar cells A and B are (thickness given in brackets in nm): ITO / n-C60 (10) / C60 (15) / DCV6T-Bu (10) / BPAPF (5)/ p-BPAPF (50)/ NDP9 (1) / Au (40).

Device A was produced without substrate heating, meaning the substrate temperature (T_{sub}) during all deposition steps was around 24 °C, whereas in device B a substrate temperature T_{sub} = (90 ± 5)°C was applied during the deposition of the DCV6T-Bu layer in order to facilitate enhanced crystalline growth. We produced three solar cells of device type A and four solar cells of device type B on one substrate, respectively. The deviations between the characteristic parameters of the nominally equal solar cells were <1% in the open circuit voltage V_{oc}, <2.5% in the fill factor FF, and <2% in the short circuit current j_{sc}. For the hole transport layer (HTL) 9,9-bis[4-(N,N-bis-biphenyl-4-yl-amino)phenyl]-9H-fluorene (BPAPF, Lumtec) was used because this material provides a high IP of 5.6 eV, determined by ultraviolet photoelectron spectroscopy (UPS), and is therefore well matched to the IP of DCV6T. This is important to avoid transport barriers between the HTL and the donor [20–22]. For doping of C60, the n-dopant NDN1 from Novaled AG (Dresden, Germany) was used with a ratio of 3 wt% (weight percent). BPAPF was doped with the p-dopant NDP9 from the same company and a ratio of 10 wt%. DCV6T-Bu (Heliatek GmbH, Dresden, Germany) and the dopants were used as received without further purification. C60 and BPAPF were purified by thermal gradient sublimation at least twice before deposition.

The current-voltage (J-V) characteristics were recorded with a source measure unit 2400 Sourcemeter (Keithley) under a sun simulator 16S-003-300 (Solar Light Company Inc.), using an aperture mask of 3.0 mm^2. The nominal area given by the overlap of ITO ground contact and metal top contact is 6.2 mm^2. The intensity is monitored by the calibrated reference diode S1337-33BQ (Hamamatsu) and subsequently corrected for mismatch, in order to provide intensity values corresponding to standard sun spectrum AM1.5G. For the external quantum efficiency (EQE) measurement, a homemade setup based on a xenon arc lamp, a monochromator (Cornerstone 260), and a lock-in amplifier (Signal Recovery SR 7265) was used. The setup was calibrated with the same reference diode S1337-33BQ (Hamamatsu).

All measurements discussed above were performed at RT.

3. Results and discussion

3.1. Morphology and optical properties

In solution, the absorption behavior of DCV6T-Bu is similar to that of the previously studied DCV6T-Et [16]. As can be seen in Fig. 1, the absorption band is broad and featureless. It thus relates to rotational disorder of the thiophene rings in the dissolved state. The photoluminescence (PL) spectrum is slightly structured, suggesting planarization of the molecule upon excitation [24]. Simultaneously, the peak to peak shift between absorption and emission is rather large, 0.72 eV, thus indicating significant change in conformation upon excitation. In the thin film, the absorption and PL peak positions are shifted to lower energies. The displacement of absorption and emission bands relative to solution and the observed broadening of absorption indicate solid state aggregation resulting from increased molecular interactions.

The molecular structure of DCV6T-Bu obviously influences the spectral response of the material in the solid state. Compared to DCV6T-Et [16], the absorption band of the DCV6T-Bu film is shifted further to longer wavelengths by about 23 nm and displays pronounced vibronic substructure evident by the shoulder at 650 nm. The presence of absorption fine structure is generally attributed to planarization of the thiophene backbone in the solid state [25] and indicates the better self-organization of the DCV6T-Bu molecules in the thin film deposited on RT-substrate. The high absorption coefficient with a maximum value of $(3.2 \pm 0.3) \times 10^5$ cm^{-1} [14] and the broad spectrum in the visible range of DCV6T-Bu are prerequisites for a promising performance when utilized as absorber material in organic solar cells.

An XRD pattern of a 50 nm DCV6T-Bu film deposited on Si substrate kept at RT is depicted in Fig. 2. As can be seen, in contrast to the DCV6T-Et derivative which is characterized by a rather amorphous structure when deposited on RT-substrate [16], the DCV6T-Bu film shows an XRD reflection at 2θ = 7.83°. In the ω-2θ scan mode, only Bragg reflections from lattice planes oriented parallel to the sample surface can be detected. The derived interplane distance d equals 11.29 Å. Using the Scherrer equation with constant K set to 0.94 [26] and an appropriate instrumental correction, a

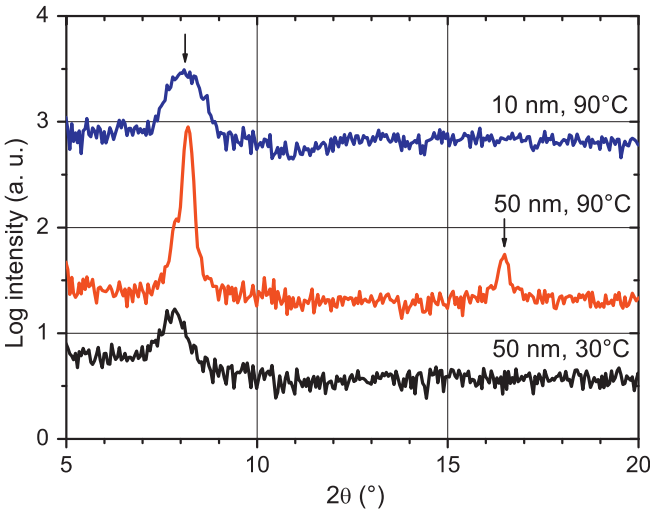

Fig. 2. XRD patterns of DCV6T-Bu deposited on Si-wafer kept at RT and 90 °C temperature. The substrate contribution is subtracted from the XRD patterns. The XRD patterns of the different samples are shifted vertically for easier comparison. The observed XRD reflections are indicated by arrows. The corresponding film thicknesses and substrate temperatures are displayed in the graph. Determined values of interplane distances and crystallite sizes are summarized in Table 1.

Table 1
Central-angle 2θ position, corresponding interplane distance d and full width at half maximum (FWHM) of the observed XRD reflections, and calculated crystallite size D for DCV6T-Bu films of various thickness grown on neat Si wafer and on 15 nm-thick C60 underlayer at different substrate temperatures.

DCV6T-Bu on Si	2θ (°)	d (Å)	FWHM (°)	D (nm)
50 nm / 30 °C	7.83	11.29	0.64	13.4 ± 0.2
50 nm / 90 °C	8.19	10.78	0.22	49 ± 4
10 nm / 90 °C	8.09	10.92	1.03	8.1 ± 0.1
DCV6T-Bu on C60				
10 nm / 90 °C	8.20	10.78	1.28	7.0 ± 0.1
6 nm / 90 °C	8.15	10.84	1.59	5.5 ± 0.1

crystallite size D along the substrate normal of 13.4 nm is determined (see XRD data in Table 1). Accordingly, the XRD result affirms that the modification of the alkyl side chains from ethyl to butyl and the alteration in substitution pattern promote better molecular arrangement at RT-deposition of DCV6T-Bu compared to the previously introduced DCV6T-Et [16].

XRD patterns of DCV6T-Bu films with thickness of 10 nm and 50 nm deposited at 90 °C substrate temperature on Si are depicted in Fig. 2. According to the increasing number of XRD reflections and their intensity, the XRD patterns of the films grown on elevated substrate temperature evidence better crystallinity compared to the film grown on RT-substrate. The interplane distance d, corresponding to scattering planes parallel to the substrate surface, is reduced to 10.78 Å for the 50 nm sample (vs. 11.29 Å for the 50 nm at RT-substrate), pointing at film relaxation induced by the substrate heating. Similar film relaxation is established upon increasing film thickness (cp. data in Table 1). The crystallite size D along the substrate normal equals 8.1 nm and 49 nm for the 10 nm and 50 nm film, respectively. Thus, the films grown on heated substrate are crystalline through the whole film thickness. The larger interplane distance observed for DCV6T-Bu as compared to that of DCV6T-Et (cp. to d = 8.5 Å for DCV6T-Et film grown at 90 °C-substrate, Ref. [16]) might be related to the longer alkyl side-chains, resulting in a less dense packing of the DCV6T-Bu molecules. Correspondingly, although having the same thiophene backbone and end groups, both derivatives might crystallize in different structures due to the different side chain length and substitution pattern. Knowledge of the crystal structure is essential to rationalize the molecular orientation in the films as well as the solid state absorption spectra and transport properties. However, crystal structure determination needs an extensive analysis of suitable single crystals which we were not able to grow up to now. In Ref. [17] an attempt is performed to index the reflections observed in the XRD pattern of DCV6T-Bu powder and to make assumptions about the possible unit cell. Accordingly, the reflections in the XRD patterns of the DCV6T-Bu films (Fig. 2) correlate to nearly parallel orientation of the DCV6T-Bu molecules inclined at about 19° with respect to the substrate as described in Ref. [17].

In addition to the films deposited directly on Si, layer arrangement relevant to a real OPV stack was also investigated by means of XRD. Fig. 3 depicts the XRD patterns of 6 nm and 10 nm DCV6T-Bu films grown on 15 nm-thick C60 underlayer. The reference C60 film is at least X-ray amorphous. Its XRD pattern exhibits an enhanced intensity in vicinity of 2θ-angle position of the 111 C60 reflection [27]. The DCV6T-Bu films on top of C60 are crystalline with interplane distances decreasing with film thickness and crystalline domains extending vertically over the whole film thickness (see data in Table 1). Thus the films on C60 underlayer follow the tendencies observed for the neat films grown directly on Si at 90 °C substrate temperature. Accordingly, they show enhanced crystallinity when deposited on substrate at elevated temperature which is a

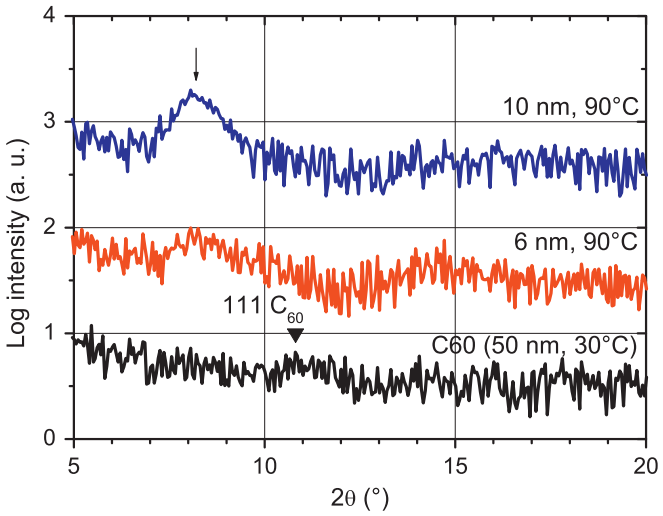

Fig. 3. XRD patterns of DCV6T-Bu films deposited at 90 °C substrate temperature on top of 15 nm C60 underlayer. The XRD pattern of neat C60 underlayer is presented for comparison. The studied film thicknesses and substrate temperatures are indicated in the graph. The substrate contribution is subtracted from the XRD patterns. For the purpose of comparison, the XRD patterns of the different samples are shifted vertically. The observed XRD reflection of DCV6T-Bu is marked by an arrow. The theoretical 2θ-angle position of the 111 C60 reflection according to [27] is indicated by triangle. Determined values of interplane distances and crystallite sizes are summarized in Table 1.

beneficial quality for OSC application since better transport properties are expected.

Extensive analysis and details on calculations of the XRD, and additionally X-ray reflectivity data concerning the DCV6T-Bu films deposited on the neat and precovered by C60, or other organic layers used in OPV stacks, Si-wafers will be published elsewhere [17].

Fig. 4 displays the alteration in the absorption response of the neat DCV6T-Bu films in dependence on substrate temperature. Upon increasing substrate temperature the absorption band gradually shifts to longer wavelengths and a distinct structure evolves. At temperatures above 100 °C the low energy peak shifts by about 16 nm compared to the initial shoulder at RT-substrate. Additionally, at the high energy side a shoulder shifting from 550 nm to 560 nm can be distinguished. Accordingly, the film grown at 90 °C substrate temperature is characterized by the highest overall absorption (integrated from 300 nm to 850 nm) while the films grown at yet higher temperatures show enhanced absorption at longer wavelengths. The changes in DCV6T-Bu absorption are similar to the alterations reported for regioregular poly(3-alkylthiophenes) [28,29], attributed to increased interchain interactions and hence are explained by a better molecular arrangement induced by the

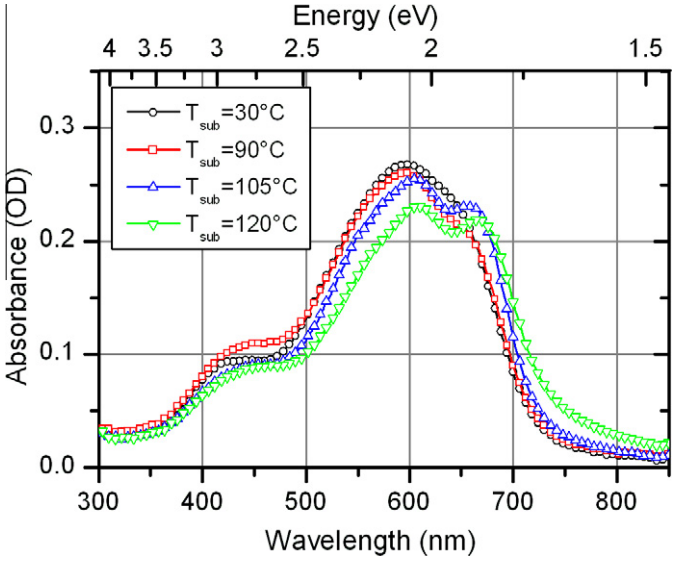

Fig. 4. Absorbance of DCV6T-Bu films deposited at different substrate temperatures on quartz glass. All films are 20 nm thick.

substrate heating. The results of absorption spectroscopy are in agreement with the presented XRD data, which reveal evolution of the film morphology toward enhanced crystallization upon growth at elevated substrate temperature. Heating of the substrate facilitates molecular surface diffusion, thus allowing ordered films with larger crystallites. Consequently, configurational disorder is reduced resulting in the well-resolved vibronic fine structure apparent in the absorption band. On the other hand, the closer packing of the molecules induced by the crystal structure leads to increased molecular interactions giving rise to the observed red shift. In solar cell application the red shift of absorption adapts better to the sun spectrum and hence more photons can be harvested.

The morphology of the DCV6T-Bu films probed by AFM is presented in Fig. 5. On RT-substrate, the film is characterized by a smooth surface with root mean square roughness (rms) of only 1.4 nm. Due to the rapid nucleation process at this temperature, condensation results in a large number of fine and homogeneous grains. With increasing substrate temperature up to 90 °C, the grains agglomerate to build chain-like aggregates. Correspondingly, the surface roughness increases, reaching values of about 2 nm. This morphology relates to stronger tendency to crystallization and is thus consistent with the results from UV–Vis absorption and XRD analysis. Higher substrate temperature leads to increased molecular surface diffusion which favors the lateral growth. For the 105 °C-substrate, the surface becomes rougher with clusters reaching lateral sizes up to 200 nm. Thus, higher substrate temperature promotes the film organization and consequently results in enhanced crystalline growth. Further increase of the substrate temperature to 120 °C causes a change in the film morphology to even larger clusters with lateral size of 500 nm to 800 nm and height of 12 nm to 20 nm, being more or less separated from each other. The surface roughness is enhanced to a considerable value of 6.7 nm and the clusters comprise distinct steps and terraces. The step height is estimated to lie between 1.0 nm and 1.5 nm and thus corresponds to the interplane distance d of about 11 Å for heated DCV6T-Bu films determined by XRD. Compared to the maximum length of a DCV6T-Bu molecule, estimated to be about 3.2 nm, the step height suggests a parallel or at least strongly tilted orientation of the molecule long axis toward the substrate plane for the sample deposited at 120 °C substrate temperature. This conclusion is in line with the strong absorption of the films that indicates a significant component of the molecular transition dipoles oriented parallel to the substrate as well as with the derived from XRD molecular inclination of 19° [17]. However, according to the presented AFM results, the very coarse morphology with large clusters and voids in-between might be the cause for the decrease in absorption, observed for the DCV6T-Bu films grown at high substrate temperatures.

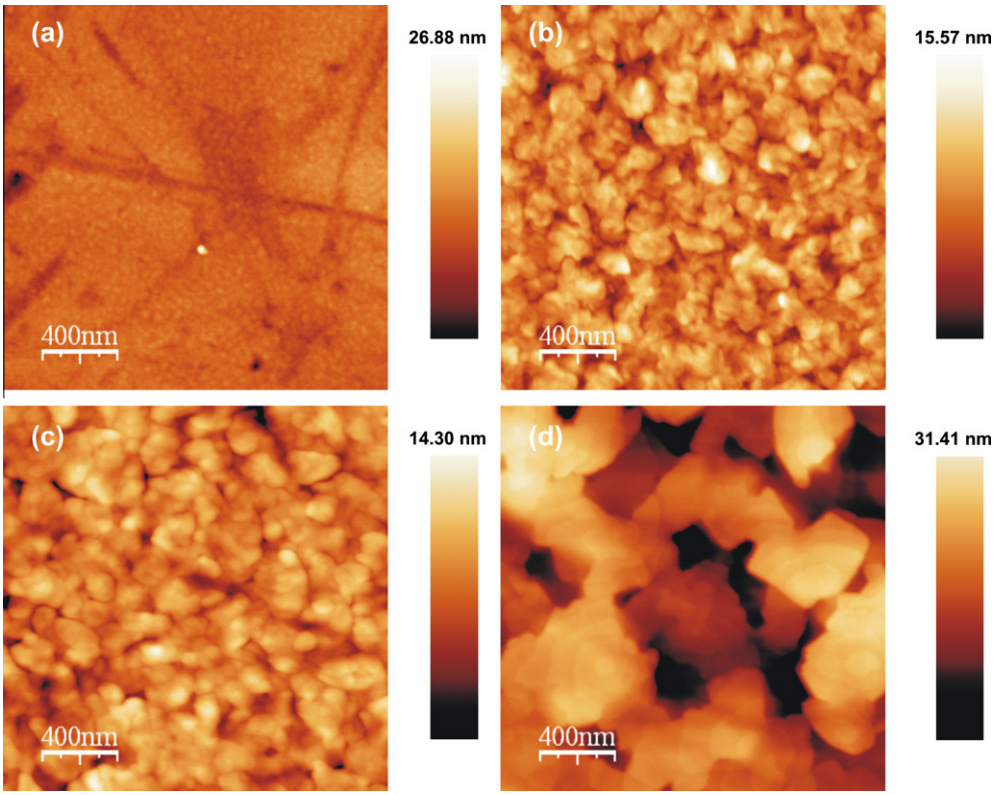

Fig. 5. AFM micrographs of DCV6T-Bu grown on quartz glass substrates kept at different substrate temperatures during deposition: (a) 30 °C, (b) 90 °C, (c) 105 °C, and (d) 120 °C. The films are 20 nm thick.

3.2. Electrical properties

As the morphology of the neat DCV6T-Bu films changes toward increased crystallinity when grown on a heated substrate, mobility variation of the charge carriers is expected. In order to prove the effect of modified morphology on the charge transport properties, CELIV measurements on devices comprising DCV6T-Bu films deposited at RT (device I) and ~90 °C (device II) substrate temperature were carried out. Fig. 6 shows the evaluated hole mobility values for the CELIV-devices I and II as Arrhenius plot. In both devices a clear thermal activation of mobility is observed, as can be seen from the linear development in both graphs. The corresponding activation energy for device I (T_{sub} = RT) and II (T_{sub} = 90 °C) are 186 meV and 87 meV, respectively. The lower activation energy value for the heated device II is consistent with its higher crystallinity, which is expected to lower the energetical disorder of the molecular states, thereby reducing the average barrier height between hopping steps during the charge transport. However, comparing the mobilities measured at a temperature of 300 K and an electric field of 90,000 V/cm (i.e. 0.9 V applied at 100 nm), mobility values of $\mu = 1.0 \times 10^{-6}$ cm^2/Vs for device I and $\mu = 3.1 \times 10^{-7}$ cm^2/Vs for device II, respectively, are obtained. Another sample, nominally equal to device I, exhibited mobility of 2.4×10^{-7} cm^2/Vs. Thus, contrary to the general expectation that charge carrier mobility could be increasing in the more crystalline phase, there is no significant increase of μ in the heated device II compared to the nonheated device I. Since the accurate crystal structure of DCV6T-Bu is not yet determined, it is difficult to clarify the reasons for this behavior. It could be speculated that, despite the expected preferred orientation of planar molecules lying nearly parallel to the substrate, self organization at elevated substrate temperature does not facilitate a better π-stacking in upright direction. We thus suggest a rather parallel to the substrate plane growth direction of the π-stacks and nearly perpendicular to the substrate plane butyl side-chains. Hence, in spite of the relative high molecular order, the low mobility values are interpreted to be a result of impeded charge transport by the alkyl side-chains.

3.3. Solar cells

Fig. 7 shows the J-V characteristics of solar cell devices A and B comprising DCV6T-Bu/C60 PHJs. In these cells we utilize a DCV6T-Bu layer thickness of only 10 nm, mainly out of two reasons. Firstly, the obtained hole mobility is very low and thus it is to be expected that larger layer thicknesses would impede efficient extraction of holes, thereby decreasing the fill factor (FF). This effect was already presented in Ref. [21] for the derivative DCV6T-Et. Secondly, the thickness of 10 nm lies in the range of the exciton diffusion length, and thus a higher layer thickness would lead to inefficient exciton collection [21]. For better comprehension, in Fig. 7 the J-V characteristics of only one out of several measured solar cells is exemplarily displayed for device type A and B, respectively. However, the deviations between nominally equal solar cells are such small that the displayed characteristic parameters are valid for all measured solar cells, besides in solar cells of type A fill factors in the range of 67–68% were measured while in solar cells of type B the FF differs in the range of 66–68%. Comparing devices A and B, it can be seen that both provide a nearly equal open circuit voltage around V_{oc} = 0.80 V and FF. However, device B, prepared at T_{sub} = 90 °C during deposition of the DCV6T-Bu layer, exhibits higher short circuit current of density 4.0 mA/cm^2 while device A, prepared without substrate heating, reaches only 3.4 mA/cm^2. From Fig. 8, showing the EQE of the corresponding solar cells of type A and B, it can be seen that the improvement of photocurrent in the heated device B originates from higher EQE in the wavelength range of DCV6T absorption. Especially in the red absorption region, i.e. from 550 nm to 700 nm, the EQE is increased and we also observe a more distinct formation of the lowest energy absorption feature (at 650 nm), similar to the findings of the UV–Vis spectra of DCV6T-Bu single layers. Although for the presented set of samples grown on quartz glass

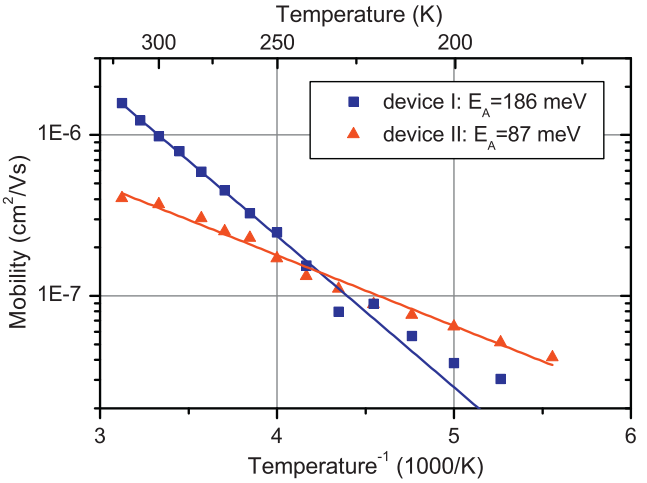

Fig. 6. Thermal activation of mobility measured by CELIV at devices I (T_{sub} = RT) and II (T_{sub} = 90 °C) at a voltage of 2.5 V.

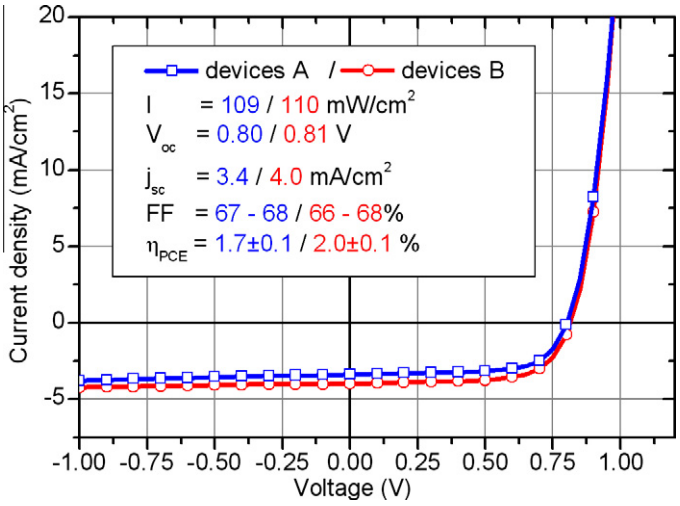

Fig. 7. Current-voltage (J-V) characteristics of one solar cell of type A and B, respectively. The characteristic parameters of the solar cells A and B are given in the inset. All devices comprise a DCV6T-Bu/C60 PHJ. The substrate temperature during deposition of the DCV6T-Bu layer is T_{sub} = 24 °C and T_{sub} = 90 °C, respectively. For measurements, an aperture mask of 3.0 mm^2 was used while the nominal area is 6.2 mm^2. The intensity and subsequently the efficiency are corrected for spectral mismatch.

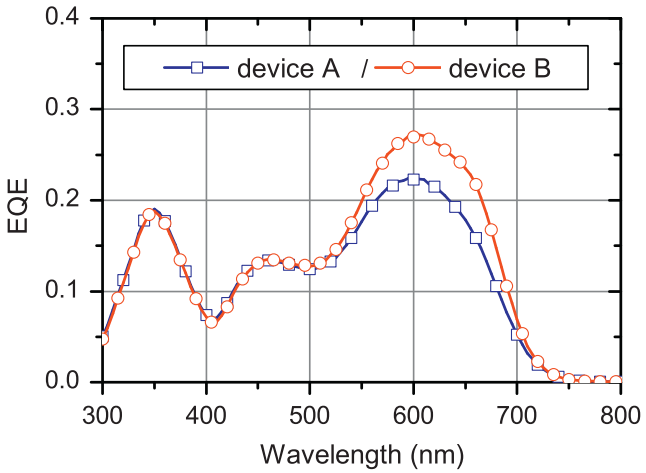

Fig. 8. External quantum efficiency (EQE) spectra of one solar cell of type A and B, respectively. These devices comprise DCV6T-Bu/C60 PHJs. The substrate temperature during deposition of the DCV6T-Bu layer is T_{sub} = 24 °C and T_{sub} = 90 °C, respectively.

(Fig. 4) the absorbance of the RT-film in the region 550–650 nm is slightly higher than that of the 90 °C-film, our studies show that in general for neat DCV6T-Bu and DCV6T-Et layers the increase of substrate temperature from RT to 90 °C during deposition results in enhanced absorption at longer wavelengths. This behavior is observed for films on glass or quartz glass substrates, and also for films having a hole transport material as an underlayer (e.g. compare to data in Ref. [14]). Furthermore, in the case of DCV6T-Bu we do not expect considerable alteration of the DCV6T-Bu growth morphology on C60 compared to that on quartz glass. Parameters, such as surface roughness and crystalline state of the substrate (or underlayer) could affect the molecular surface diffusion and thus for example the molecular orientation or the degree of crystallinity of the DCV6T-Bu film. Quartz glass and C60 have similar surface roughness of about 1–1.8 nm and are amorphous or in the case of C60 at least X-ray amorphous. Thus, we assume that the higher EQE at substrate temperature of 90 °C is due to the increase of absorption of the DCV6T-Bu layer grown on C60 in the heated solar cell device B. Finally, device B reaches a higher power conversion efficiency of PCE = 2.0 ± 0.1% than device A with PCE = 1.7 ± 0.1%. The solar cell improvement upon substrate heating during DCV6T-Bu deposition only arises from the higher photocurrent, which we attribute to the improvement of DCV6T-Bu absorption, especially in the red wavelength region. However, we do not observe indications for better charge transport capabilities, since the FF is unaffected. This is consistent with the CELIV results, showing no substantial increase of charge carrier mobility in the DCV6T-Bu layers grown on heated substrates.

4. Conclusions

Compared to the formerly introduced DCV6T-Et(2,2,5,5) [16], which comprises four ethyl side chains, the modified molecular structure of DCV6T-Bu results in optimized morphology with better molecular arrangement in the solid state. For DCV6T-Bu neat films, growth on RT-substrate already results in ordered aggregation. Self-organization is further improved when substrate heating during film deposition is used. The enhanced crystalline growth is verified by XRD studies, showing that the films deposited at elevated substrate temperature are crystalline across the whole film thickness. Red shifted absorption with distinct vibronic substructure and rough three-dimensional film morphology are attributed to the better structural order and thus are consistent with the results of XRD analysis. However, although the modified morphology should result in favorable transport properties, CELIV measurements indicate that the DCV6T-Bu hole mobility does not improve upon substrate heating. On the other hand, lower activation energy is derived for the 90 °C-device, which is consistent with the improved molecular organization in the heated DCV6T-Bu film. In DCV6T-Bu/C60 PHJ solar cells an increased photocurrent is observed when DCV6T-Bu is grown at elevated substrate temperature. This is attributed to the changes in DCV6T-Bu absorption. The charge transport capabilities seem unaffected by the heating, as can be seen from the FF, which does not change at elevated substrate temperature and thus supports the results of CELIV measurements.

Acknowledgements

The authors thank Dr. Selina Olthof for the UPS measurements, and Toni Meyer and Dr. André Merten (both IAPP) for the solar cell characterization measurements. Financial support by the Europäische Fonds für regionale Entwicklung (EFRE) and the Freistaat Sachsen (project No. 12717/2112) as well as the Bundesministerium für Bildung und Forschung (BMBF project No. 13N9872) is gratefully acknowledged.

References

[1] F. Garnier, A. Yassar, R. Hajlaoui, G. Horowitz, F. Deloffre, Control of the mesoscopic organization of conjugated thiophene oligomers, induced by self-assembly properties, Electrochim. Acta 39 (1994) 1339–1344.
[2] G. Horowitz, F. Garnier, A. Yassar, R. Hajlaoui, F. Kouki, Field-effect transistor made with a sexithiophene single crystal, Adv. Mater. 8 (1996) 52–54.
[3] D. Fichou, Structural order in conjugated oligothiophenes and its implications on opto-electronic devices, J. Mater. Chem. 10 (2000) 571–588.
[4] A.B. Tamayo, B. Walker, T.-Q. Nguyen, A low band gap, solution processable oligothiophene with a diketopyrrollopyrrole core for use in organic solar cells, J. Phys. Chem. C 112 (2008) 11545–11551.
[5] M. Mazzeo, D. Pisignano, L. Favaretto, G. Barbarella, R. Cingolani, G. Gigli, Bright oligothiophene-based light emitting diodes, Synth. Met. 139 (2003) 671–673.
[6] A. Mishra, C.-Q. Ma, P. Bäuerle, Functional oligothiophenes: molecular design for multidimensional nanoarchitectures and their applications, Chem. Rev. 109 (2009) 1141–1276.
[7] S. Hotta, K. Waragay, Alkyl-substituted oligothiophenes: crystallographic and spectroscopic studies of neutral and doped forms, J. Mater. Chem. 1 (1991) 835–842.
[8] F. Garnier, A. Yassar, R. Hajlaoui, G. Horowitz, F. Deloffre, B. Servet, S. Ries, P. Alnot, Molecular engineering of organic semiconductors: design of self-assembly properties in conjugated thiophene oligomers, J. Am. Chem. Soc. 115 (1993) 8716–8721.
[9] T.M. Pappenfus, M.W. Burand, D.E. Janzen, K.R. Mann, Synthesis and characterization of tricyanovinyl-capped oligothiophenes as low-band-gap organic materials, Org. Lett. 5 (2003) 1535–1538.
[10] G. Barbarella, M. Zambianchi, L. Antolini, P. Ostoja, P. Maccagnani, A. Bongini, E.A. Marseglia, E. Tedesco, G. Gigli, R. Cingolani, Solid-state conformation, molecular packing, and electrical and optical properties of processable β-methylated sexithiophenes, J. Am. Chem. Soc. 121 (1999) 8920–8926.
[11] S. Steinberger, A. Mishra, E. Reinold, J. Levichkov, C. Uhrich, M. Pfeiffer, P. Bäuerle, Vacuum-processed small molecule solar cells based on terminal acceptor-substituted low-band gap oligothiophenes, Chem. Commun. 47 (2011) 1982–1984.
[12] R. Schueppel, K. Schmidt, C. Uhrich, K. Schulze, D. Wynands, J.L. Brédas, E. Brier, E. Reinold, H.-B. Bu, P. Baeuerle, B. Maennig, M. Pfeiffer, K. Leo, Optimizing organic photovoltaics using tailored heterojunctions: a photoinduced absorption study of oligothiophenes with low band gaps, Phys. Rev. B 77 (2008) 085311.
[13] K. Schulze, C. Uhrich, R. Schueppel, K. Leo, M. Pfeiffer, E. Brier, E. Reinold, P. Baeuerle, Efficient vacuum-deposited organic solar cells based on a new low-bandgap oligothiophene and fullerene C_{60}, Adv. Mater. 18 (2006) 2872–2875.
[14] D. Wynands, M. Levichkova, K. Leo, C. Uhrich, G. Schwartz, D. Hildebrandt, M. Pfeiffer, M. Riede, Increase in internal quantum efficiency in small molecular oligothiophene: C_{60} mixed heterojunction solar cells by substrate heating, Appl. Phys. Lett. 97 (2010) 073503.
[15] R. Fitzner, E. Reinold, A. Mishra, E. Mena-Osteritz, H. Ziehlke, C. Körner, K. Leo, M. Riede, M. Weil, O. Tsaryova, A. Weiß, C. Uhrich, M. Pfeiffer, P. Bäuerle, Dicyanovinyl-substituted oligothiophenes: structure–property relationships and application in vacuum-processed small-molecule organic solar cells, Adv. Funct. Mater. 21 (2011) 897–910.
[16] D. Wynands, M. Levichkova, M. Riede, M. Pfeiffer, P. Baeuerle, R. Rentenberger, P. Denner, K. Leo, Correlation between morphology and performance of low bandgap oligothiophene: C60 mixed heterojunctions in organic solar cells, J. Appl. Phys. 107 (2010) 014517.
[17] A.A. Levin, M. Levichkova, D. Hildebrandt, M. Klisch, A. Weiss, D. Wynands, C. Elschner, M. Pfeiffer, K. Leo, M. Riede, Effect of film thickness, type of buffer layer, and substrate temperature on the morphology of dicyanovinyl-substituted sexithiophene films, Thin Solid Films, 2011, accepted for publication.
[18] G. Juska, K. Arlauskas, M. Viliunas, J. Kocka, Extraction current transients: new method of study of charge transport in microcrystalline silicon, Phys. Rev. Lett. 84 (2000) 4946–4949.
[19] G. Juska, K. Arlauskas, R. Osterbacka, H. Stubb, Time-of-flight measurements in thin films of regioregular poly(3-hexyl thiophene), Synth. Met. 109 (2000) 173–176.
[20] C. Uhrich, D. Wynands, S. Olthof, M.K. Riede, S. Sonntag, K. Leo, B. Maennig, M. Pfeiffer, Origin of open circuit voltage in planar and bulk heterojunction organic thin-film photovoltaics depending on doped transport layers, J. Appl. Phys. 104 (2008) 043107.
[21] D. Wynands, B. Maennig, M. Riede, K. Leo, E. Brier, E. Reinold, P. Bäuerle, Organic thin film photovoltaic cells based on planar and mixed heterojunctions between fullerene and a low bandgap oligothiophene, J. Appl. Phys. 106 (2009) 054509.
[22] W. Tress, K. Leo, M. Riede, Influence of hole-transport layers and donor materials on open-circuit voltage and shape of I–V curves of organic solar cells, Adv. Funct. Mater. 21 (2011) 2140–2149.
[23] T.D. Anthopoulos, B. Singh, N. Marjanovic, N.S. Sariciftci, A.M. Ramil, H. Sitter, M. Colle, D.M. de Leeuw, High performance n-channel organic field-effect transistors and ring oscillators based on C-60 fullerene films, Appl. Phys. Lett. 89 (2006) 213504.
[24] I.B. Berlman, On an empirical correlation between nuclear conformation and certain fluorescence and absorption characteristics of aromatic compounds, J. Phys. Chem. 74 (1970) 3085–3093.
[25] M. Turbiez, P. Frère, M. Allain, C. Videlot, J. Ackermann, J. Roncali, Design of organic semiconductors: tuning the electronic properties of π-conjugated oligothiophenes with the 3,4-ethylenedioxythiophene (EDOT) building block, Chem. Eur. J. 11 (2005) 3742–3752.

[26] J.I. Langford, A rapid method for analysing the breadths of diffraction and spectral lines using the Voigt function, J. Appl. Crystallogr. 11 (1978) 10–14.
[27] H.-B. Bürgi, R. Restori, D. Schwarzenbach, Structure of C_{60}: partial orientational order in the room-temperature modification of C_{60}, Acta Crystallogr. B 49 (1993) 832–838. Inorganic Crystal Structure Database (ICSD) code 73661.
[28] T.A. Chen, X.M. Wu, R.D. Rieke, Regiocontrolled synthesis of poly(3-alkylthiophenes) mediated by rieke zinc - their characterization and solid-state properties, J. Am. Chem. Soc. 117 (1995) 233–244.
[29] P.J. Brown, D.S. Thomas, A. Köhler, J.S. Wilson, J.-S. Kim, C.M. Ramsdale, H. Sirringhaus, R.H. Friend, Effect of interchain interactions on the absorption and emission of poly(3-hexylthiophene), Phys. Rev. B 67 (2003) 064203.

in a nitrogen atmosphere at a heating rate of 10 °C/min. The cyclic voltammetry measurements were performed by a procedure described earlier [10].

UV light source was high-pressure mercury lamp with standard wavelength distributions (280–400 nm) and output power of ~1800 mW/cm^2. Radiation dosage was controlled by irradiation time.

Thin films of polycarbazole **PKOx** were prepared by spin-coating from its toluene solution (2–10 mg/ml), which additionally contained 7 wt.% of {4-[(2-hydroxytetradecyl)-oxyl]-phenyl}-phenyliodonium hexafluorantimonate (**PhIA**) as initiator for the cationic polymerization of oxetane units. The films were irradiated by the UV light source for about 2 min at room temperature. Afterwards, to further advance the crosslinking process in the growing network, the films were annealed at 120 °C for 5 min. Then the cross-linked films were rinsed with toluene and finally heated to 180 °C for 5 min to remove the radical cations formed upon polymerization. The resulting polymer networks were found to be insoluble in any common solvent. The cross-linking experiments were done with films of thickness of 15–100 nm. We have also tested thermal cross-linking of the polymers, however the obtained layers were partially soluble and were not suitable for preparation of OLEDs.

PKOx-based multilayer electroluminescent devices were fabricated on glass substrates and had the typical structure of the organic layers sandwiched between a bottom ITO anode and a top metal cathode. Before use in device fabrication, the substrates were prepared as described earlier [11]. The insoluble hole transporting networks were made by spin-coating a 15–100 nm layer of the polycarbazole **PKOx** containing the initiator onto the substrates and by following cross-linking as described earlier. 100 nm layer of green light emitting polymer (**GEP**) – poly(9,9-dioctylfluorene)-*co*-(2,5-dioctyloxyphenylene-*co*-benzothiadiazole) [12] was spin-coated from toluene solution onto the cross-linked network. Ca/Al electrode was done at a pressure of 310^{-6} mbar in vacuum evaporation equipment. Device without hole injecting/transporting layer (configuration: ITO/**GEP**/[Ca/Al]) and PEDOT-based device (ITO/PEDOT/**GEP**/[Ca/Al]) were also prepared for comparison.

The current–voltage and luminance–voltage characteristics of the devices were recorded using a computer controlled Keithley 2400 source meter and a PR650 Spectrometer. All measurements were performed at ambient conditions in air.

2.2. Materials

1,5-Cyclooctadiene (COD), 2,2′-bipyridyl (ByPy) and bis(1,5-cyclooctadiene)nickel (Ni[COD]$_2$) were purchased from Aldrich. All the chemicals were used without further purification.

3,6-Diiodo-9-(2-ethylhexyl)carbazole (**1**) was prepared by alkylation of 3,6-diiodo-9H-carbazole in a two phase system [11]. 3,6-Diodo-9-[6-(3-ethyloxetan-3-ylmethoxy)hexyl]carbazole (**2**) was prepared by the reaction of 3,6-diodo-9-(6-bromohexyl)carbazole with 3-hydroxymethyl-3-ethyl-oxetane [13].

Poly{(9-(2-ethylhexyl)-3,6-carbazole)-stat-9-[6-(3-ethyloxetan-3-ylmethoxy)hexyl]-3,6-carbazole} (**PKOx**). The co-polymer was prepared according to general procedure of Yamamoto polycondensation for dihaloaromatic compounds using Ni[COD]$_2$ as a coupling agent [14]. 3,6-Diiodo-9-(2-ethylhexyl)carbazole (**1**) (0.41 g, 0.78 mmol), 3,6-diodo-9-[6-(3-ethyloxetan-3-ylmethoxy)hexyl]-carbazole (**2**) (0.48 g, 0.78 mmol), ByPy (0.56 g, 3.6 mmol) and Ni[COD]$_2$ (1.05 g, 3.82 mmol) were placed into a Schlenk tube under argon. Dry THF (10 ml) and COD (0.31 ml) were added, and the reaction mixture was stirred at 80 °C for 2 days. The polymer was extracted into chloroform, and the organic phase was washed with water and dried over $MgSO_4$, and the solvent was removed by rotary evaporation. The residue was dissolved in chloroform and precipitated into methanol/2 M HCl. After extracting the crude solid with acetone and re-precipitation, the polymer was obtained in 51% with number-average molecular weight of 17,000 and polydispersity of 1.7. ^{1}H NMR ($CDCl_3$): δ = 0.72–0.98 (m, 9H, $3 \times C\underline{H}_3$), 1.12–1.71 (m, 16H, $2 \times C\underline{H}_2CH_3$, $OCH_2C\underline{H}_2C\underline{H}_2C\underline{H}_2$, $-C\underline{H}_2C\underline{H}_2C\underline{H}_2CH_3$), 1.78–1.93 (m, 2H, $NCH_2C\underline{H}_2CH_2$), 2.01–2.19 (m, 1H, $C\underline{H}[CH_2-]_3$), 3.23–3.44 (m, 4H, $CC\underline{H}_2O$ and $OC\underline{H}_2CH_2$), 3.82–4.44 (m, 8H, $2 \times C\underline{H}_2$ of oxetane ring, $NC\underline{H}_2CH_2-$, $NC\underline{H}_2CH-$), 7.19–7.46 (m, 4H, ArH), 7.62–7.83 (m, 4H, ArH), 8.32–8.74 (m, 4H, ArH). IR (KBr): 3058 (CH_{ar}), 2953, 2925, 2853 ($CH_{aliphatic}$), 1496, 1462 (C=C_{ar}), 1310 (C–N), 1112 (C–O–C), 879, 824, 802 (CH=CH).

3. Results and discussion

The synthetic route towards the carbazole-based copolymer (**PKOx**) is shown in Scheme 1. The random copolymerization of the monomers 3,6-diiodo-9-(2-ethylhexyl)carbazole (**1**) and 3,6-diodo-9-[6-(3-ethyloxetan-3-ylmethoxy)hexyl]carbazole (**2**) was accomplished under standard Yamamoto conditions [14] using bis(1,5-cyclooctadiene)nickel(0), 2,2′-bipyridyl, and cyclooctadiene as the coupling agent. The actual percentage of incorporated *N*-alkylcarbazol-3,6-diyl moieties from comonomer **1** was calculated by comparing the relative intensities of the $(-CH_2)_3C\underline{H}$ proton signal of the 2-ethylhexyl group at about 2.1 ppm to the intensity of the $-NCH_2C\underline{H}_2-$ signals ($\delta \sim 1.85$ ppm) of the monomer **2**. The estimated composition of the copolymer was very close to that which was predicted from the monomer feed ratio (1:1).

The newly synthesized copolymer was first characterized by IR and ^{1}H NMR spectroscopy. The characterization data are in good agreement with the proposed structures. The material was well soluble in common organic solvents, such as chloroform and THF at room temperature. Transparent thin films of these materials could be prepared by spin coating from solutions.

The thermal behavior of the copolymer **PKOx** was studied by DSC and TGA under nitrogen atmosphere. The material demonstrates high thermal stability. An initial mass loss is observed at a temperature of >390 °C (TGA with a heating rate of 10 °C/min). The copolymer was obtained as amorphous material. When a sample of **PKOx** was

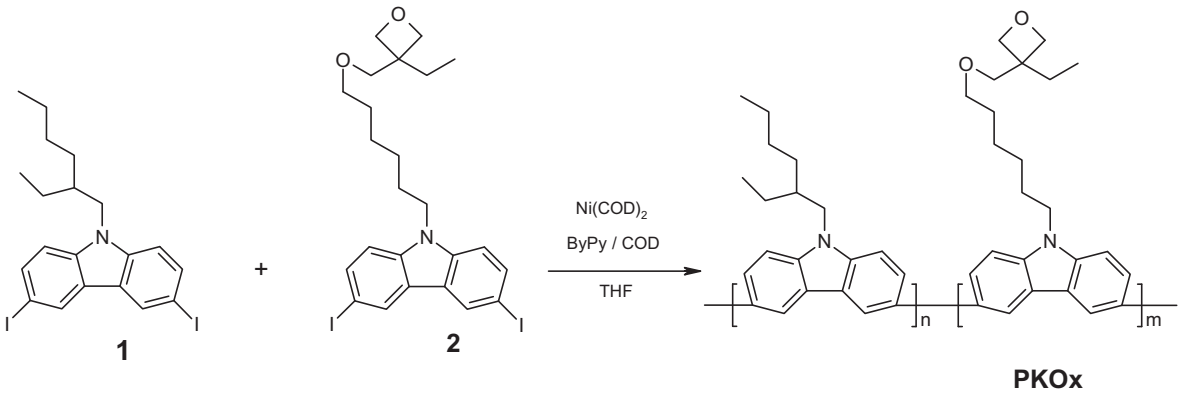

Scheme 1.

heated a glass transition temperature T_g was observed at 119 °C. Cooling down and repeated heating again revealed only the glass transition.

The electrochemical properties (redox behavior) of the new copolymer was studied by cyclic voltammetry for an determination of the HOMO energy level that controls the hole injection (and transport) properties. Our cyclic voltammetry measurements were calibrated with a ferrocene standard [15]. In the anodic scan, the onset of oxidation for **PKOx** occurred at 0.82 V corresponding to a HOMO value of *ca.* −5.2 eV, according to an empirical relationship proposed by De Leeuw [16]. The LUMO energy of the copolymer was estimated by subtracting the optical band gap to be *ca.* −1.85 eV.

The copolymer **PKOx** as cross-linkable material was used for the preparation of insoluble hole transporting layers. Photoinitiated cross-linking of thin **PKOx** layers containing 2–7 wt.% of cationic photoinitiator **PhIA** was carried out as described in Section 2. The solubility of the cross-linked layers was studied by recording UV–vis spectra of the layers before and after rinsing with toluene which is suitable solvent both for the non-cross-linked **PKOx** layer as well as for the green polymeric emitter (**GEP**, poly(9,9-dioctylfluorene)-*co*-(2,5-dioctyloxyphenylene-*co*-benzothiadiazole) as the emitter layer. If the cross-linking was carried out with 2–5 wt.% of the photoinitiator, the films were still partially soluble. In contrast, cross-linking with 7 wt.% of the photo-initiator yielded fully insoluble films as documented by practically unchanged absorption spectra of the films (Fig. 1 shows the UV–vis results for **PKOx** films crosslinked by using 7 wt.% of the photoinitiator **PhIA**).

The crosslinked **PKOx** networks were then tested as hole transporting layers of double-layer OLEDs with the configuration ITO/crosslinked **PKOx**/**GEP**/(Ca/Al). The hole transporting layers were made by spin-coating solutions of copolymer and initiator onto ITO substrates as *ca.* 50 nm thick layers followed by photo-crosslinking as described in Section 2. Poly(9,9-dioctylfluorene)-*co*-(2,5-dioctyloxyphenylene-*co*-benzothiadiazole) **GEP** was used as green polymeric emitter.

When a positive voltage was applied to the OLED devices a bright green electroluminescence of the GEP

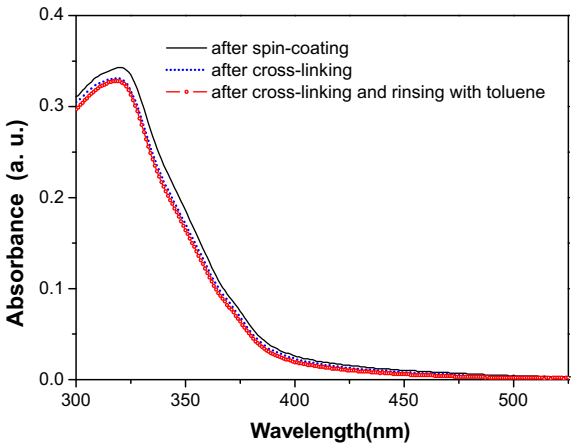

Fig. 1. Absorption spectra of **PKOx** films after spin-coating, cross-linking and rinsing with toluene.

emitter was observed with an emission maximum peaking at *ca.* 528 nm (see Fig. 2). This implies that the hole transporting **PKOx** network allows for an efficient hole injection

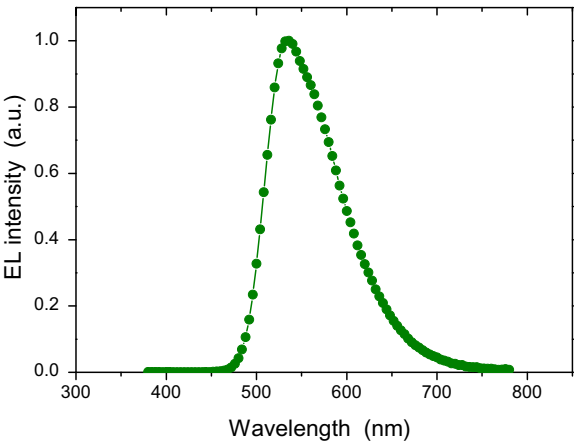

Fig. 2. Normalized electroluminescence spectrum of the device: ITO/crosslinked **PKOx**/**GEP**/(Ca/Al).

at the anode followed by charge carrier recombination with electrons (injected at the cathode) within the emissive GEP layer. No spectroscopic sign for exciplex formation at the interface between hole transporting and emitter layer was observed.

Fig. 3 shows OLED characteristic of the described device. The plots for a device (configuration: ITO/PEDOT (50 nm)/GEP/[Ca/Al]) containing a PEDOT hole transporting layer is also presented in the Fig. 3 for comparison. The rather low turn-on voltage of 3.5 V, defined as the voltage where electroluminescence (EL) becomes detectable, the maximum brightness of *ca.* 15000 cd/m^2, and the relatively low operational voltage (~6 V@100 cd/m^2) of the device suggest that the cross-linked **PKOx** material acts as an efficient hole transporting layer. The comparison with PEDOT-based OLED shows that both the devices show similar efficiencies; however only the device with the cross-linked **PKOx** layer demonstrates a stable operation at voltages up to 16 V. It should be mentioned that a device without hole injecting/transporting layer (configuration: ITO/GEP/[Ca/Al]) demonstrated an efficiency only of 0.2 cd/A.

The cross-linked copolymer layers were also tested in multilayer devices with the configuration ITO/PEDOT/crosslinked **PKOx**/GEP/(Ca/Al) containing both a PEDOT layer for hole injection and **PKOx** layers of different thickness for hole transport. The OLED devices in general exhibit low turn-on voltages of 4–4.5 V, a maximum brightness of 8300–13,700 cd/m^2 (@16–20 V), and a maximum photometric efficiency of 8.2–8.5 cd/A (see Fig. 4). Among these OLEDs, devices containing a hole transporting **PKOx** layer of *ca.* 30 nm displayed the best overall performance (turn-on voltage of *ca.* 4 V and a maximum photometric efficiency of *ca.* 8.5 cd/A). Hereby, the hole transporting **PKOx** network improves both device efficiency and operational stability at high voltages if compared to devices without the **PKOx** layer. The device characteristics observed for our devices are also superior to those of related multilayer systems containing structurally different carbazole-based networks as hole injection layer and the GEP emitter as reported earlier [7,8]. The device characteristics compare to those of many related cross-linkable systems recently reviewed in literature [3,4,6].

In conclusion, carbazole-based copolymers containing side-chain oxetanyl groups as photo-crosslinkable moieties have been successfully synthesized and characterized. Insoluble, photo-crosslinked layers of these copolymers have been obtained as thin films. The crosslinked networks have been tested as hole injection/hole transporting layers of OLED devices in combination with a green polymeric emitter (GEP). Our best devices exhibited a low turn-on voltage of *ca.* 4 V, combined with a maximum brightness of 13,700 cd/m^2 and a maximum photometric efficiency of *ca.* 8.5 cd/A.

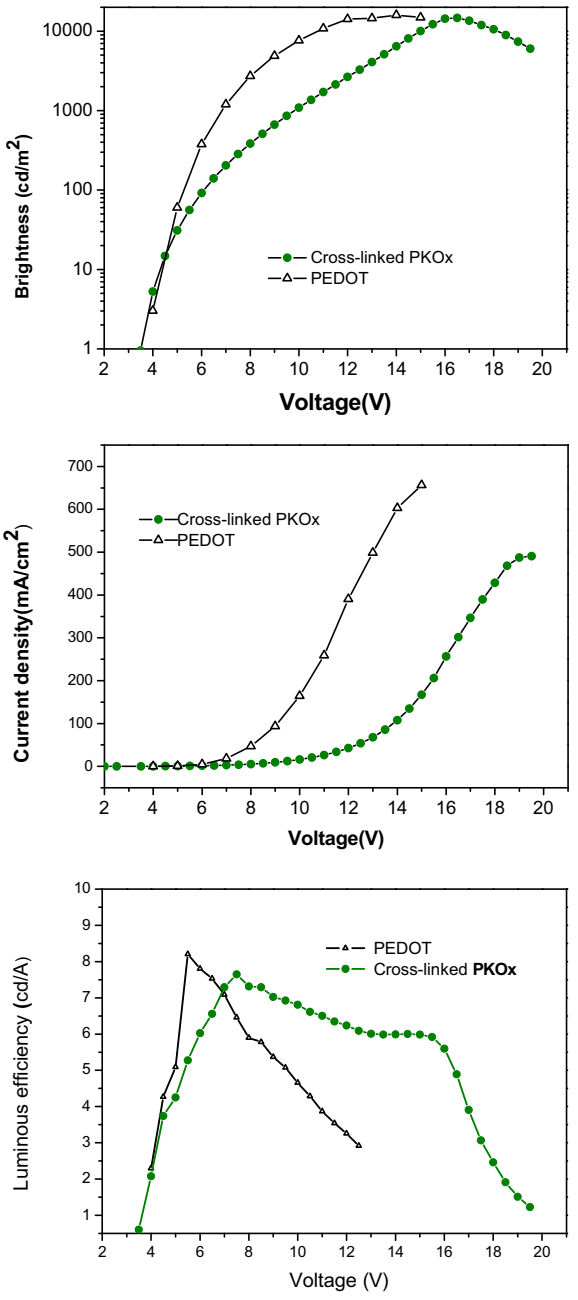

Fig. 3. OLED characteristics of the devices: ITO/PEDOT or crosslinked **PKOx**/**GEP**/(Ca/Al).

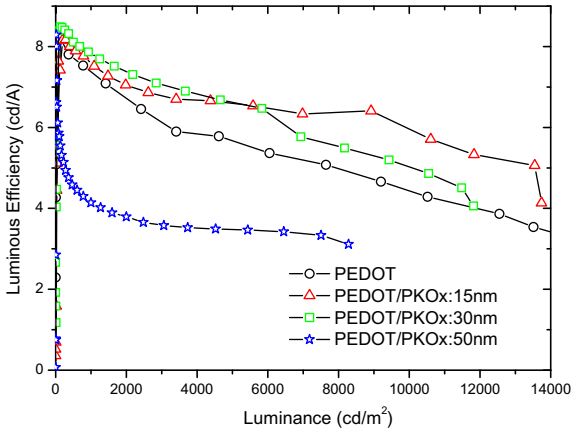

Fig. 4. Luminous efficiency of the devices: ITO/PEDOT/crosslinked **PKOx** (0–50 nm)/**GEP**/(Ca/Al).

Acknowledgements

The OLED materials were prepared in the frame of Project funded by a Grant No. MIP-063/2011 from the Research Council of Lithuania. Financial support from the Alexander von Humboldt Foundation (Germany) for S.G. is also gratefully acknowledged.

References

[1] W.-F. Su, Y. Chen, Polymer 52 (2011) 77.
[2] C.D. Muller, A. Falcou, N. Reckefuss, M. Rojahn, V. Wiederhirn, P. Rudati, H. Frohne, O. Nuyken, H. Becker, K. Meerholz, Nature 421 (2003) 829 (and references therein).
[3] O. Nuyken, S. Jungermann, V. Wiederhirn, E. Bacher, K. Meerholz, Monat Fur Chemie 137 (2006) 811 (and references therein).
[4] F. Huang, Y.-J. Cheng, Y. Zhang, M.S. Liu, A.K.-Y. Jen, J. Mater. Chem. 18 (2008) 4495.
[5] (a) B.H. Wallikewitz, D. Hertel, K. Meerholz, Chem. Mater. 21 (2009) 2912;
(b) J. Schelter, G.F. Mielke, A. Kohnen, J. Wies, S. Kober, O. Nuyken, K. Meerholz, Macromol. Rapid Commun. 31 (2010) 1560.
[6] K. Mullen, U. Scherf (Eds.), Organic Light Emitting Devices – Synthesis, Properties and Applications, Wiley-VCH, Weinheim, 2005.
[7] S. Lengvinaite, J.V. Grazulevicius, S. Grigalevicius, B. Zhang, J. Yang, Z. Xie, L. Wang, Synth. Met. 158 (2008) 213.
[8] S. Lengvinaite, J.V. Grazulevicius, S. Grigalevicius, R. Gu, W. Dehaen, V. Jankauskas, B. Zhang, Z. Xie, Dyes Pigm. 85 (2010) 183.
[9] S. Lengvinaite, J.V. Grazulevicius, B. Zhang, Z. Xie, S. Grigalevicius, React. Funct. Polym. 71 (2011) 574.
[10] G. Jiang, B. Yao, Y. Geng, Y. Cheng, Z. Xie, L. Wang, X. Jin, F. Wang, Macromolecules 36 (2006) 1403.
[11] (a) J. Simokaitiene, S. Grigalevicius, J.V. Grazulevicius, R. Rutkaite, K. Kazlauskas, S. Jursenas, V. Jankauskas, J. Sidaravicius, J. Optoelectron. Adv. Mater. 8 (2006) 876–882;
(b) V. Vaitkeviciene, S. Grigalevicius, J.V. Grazulevicius, V. Jankauskas, V.G. Syromyatnikov, Eur. Polymer J. 42 (2006) 2254.
[12] P. Herguth, X. Jiang, M.S. Liu, A.K.Y. Jen, Macromolecules 35 (2002) 6094.
[13] S. Lengvinaite, J.V. Grazulevicius, V. Jankauskas, S. Grigalevicius, Synth. Met. 157 (2007) 529.
[14] P.L. Burn, A. Kraft, D.R. Baigent, D.D.C. Bradley, A.R. Brown, R.H. Friend, R.W. Gymer, A.B. Holmes, R.W. Jackson, J. Am. Chem. Soc. 115 (1993) 10117.
[15] R. Borner, W. Paulus, R. Schollhorn, B. Kabius, J. Schubert, Adv. Mater. 7 (1995) 55.
[16] D.M. De Leeuw, M.M.J. Simenon, A.R. Brown, R.E.F. Einerhand, Synth. Met. 87 (1997) 53.

interface area and loss of excitons by enhanced charge carrier collection due to improved mobilities and closed percolation paths.

The series of oligothiophenes end capped with the acceptor group dicyanovinyl DCV_2-nT ($n = 3,4,5,6$) has been studied intensely [11–13,15,18]. The increase of the thiophene chain shifts the highest occupied molecular orbital (HOMO) upwards while the lowest unoccupied molecular orbital (LUMO) is less affected. Photoinduced absorption spectroscopy (PIA) showed that this directly influences the energy and charge transfer processes between the oligothiophene and the commonly used acceptor C_{60} [15].

In the paper, the influence of morphological change induced by the deposition on substrates of different temperature (T_{sub}) on charge separation and transport is investigated for dicyanovinyl–quinquethiophenes. The molecular structure of DCV_2-5T (Bu_4) is shown in Fig. 1. In blend layers with the acceptor fullerene C_{60} efficient charge separation occurs. Neat and blend layers with C_{60} (1:1 by volume) deposited at room temperature ($T_{sub} = 30$ °C) as well as blend layers with C_{60} (1:1 by volume) deposited at $T_{sub} = 80$ °C are investigated by their optical properties (absorbance) and by photoinduced absorption spectroscopy (PIA). The visible signatures of triplet excitons and donor cations in PIA are investigated with respect to existing recombination models. Hence, their lifetime and effective generation rate are determined. This procedure is carried out for four different measurement temperatures: 10, 100, 200, and 295 K. Likewise, lifetimes and generation rates for the heated and unheated samples are compared. The PIA results are complemented by mip (metal-intrinsic-p-doped) solar cell devices. In order to shed more light on the nature of the detected cation signatures, we carry out impedance spectroscopy on the solar cell devices and determine time constants for trapped and free charge carriers.

2. Material and methods

DCV_2-5T (Bu_4) is synthesized according to a route published elsewhere [14]. The materials are purified prior to sample preparation: DCV_2-5T (Bu_4) is purified by recrystallization and degassing, C_{60} (Bucky, USA) is purified twice by vacuum gradient sublimation. The thin films are prepared via thermal vapor deposition in ultra high vacuum on glass substrates, solar cells on tin-doped indium oxide (ITO) coated glass (Thin Film Devices, USA, sheet resistance of 30 Ω/sq.) with a base pressure of 10^{-8} mbar and evaporation rates of 0.2 Å s^{-1}. The film thickness is controlled by quartz crystal monitors which are calibrated in advance for every material evaporated.

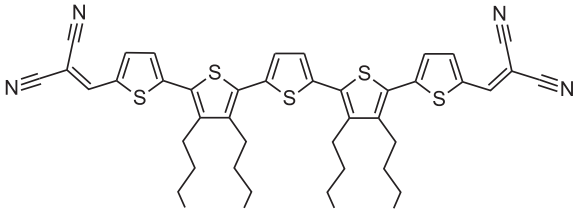

Fig. 1. Molecular structure of DCV_2-5T (Bu_4) with the butyl side chains attached to the second and fourth thiophene ring.

Linear absorption measurements are conducted with a UV–vis spectrometer (Shimadzu UV-2101/3101).

Flat and bulk heterojunction solar cells are prepared layer by layer without breaking the vacuum and are encapsulated after processing using a glass cover under nitrogen atmosphere. The layer structure of the bulk heterojunction solar cells is as follows: ITO/15 nm C_{60}/20 nm DCV_2-5T (Bu_4):C_{60} (1:1 by volume)/5 nm 9,9-bis[4-(*N*,*N*-bis-biphenyl-4-yl-amino) phenyl]-9H-fluorene (BPAPF, Lumtec, Taiwan; ionization potential measured by UPS 5.6 eV)/50 nm BPAPF doped with p-dopant NDP9 (Novaled AG, Germany) with a doping concentration of 10 wt.%/1 nm NDP9/50 nm Au. BPAPF is purified at least twice by vacuum gradient sublimation prior to sample preparation; NDP9 is used as received. We use this proprietary material due to a better processability, but doping of materials with low lying HOMO can be achieved in a comparable way using WO_3 [19]. The flat heterojunction layer structure is similar to the bulk layer stack: ITO/15 nm C_{60}/6 nm DCV_2-5T (Bu_4)/5 nm BPAPF/50 nm BPAPF:NDP9 (10 wt.%)/1 nm NDP9/50 nm Au. The cell area for bulk and flat heterojunction cells is 6.4 mm^2.

External quantum efficiency (EQE) measurements for solar cell devices are conducted at a custom-made setup utilizing a xenon arc lamp, a monochromator (Newport Cornerstone), and a lock-in amplifier (Signal Recovery 7265 DSP). A silicon reference diode (Hamamatsu S1337) is used to calibrate the setup.

$J - V$ characteristics are measured using an automated setup consisting of a source-measure unit (Keithley SMU 2400) and an AM 1.5G sun simulator (KHS Technical Lighting SC1200). The intensity is monitored with a silicon photodiode (Hamamatsu S1337). The mismatch between the spectrum of the sun simulator and the AM 1.5G spectrum is determined by taking these spectra as well as the spectral responses of the reference diode and the sample (from EQE measurements) into account.

Photoinduced absorption (PIA) is measured with a custom-made setup using the 532 nm mode of an frequency doubled CW Nd:YVO_4 laser (spectra physics Millenia) as pump beam which is chopped by an acousto optical modulator (AOM). The pump intensity is around 20 mW on a spot of 3 mm diameter and can be reduced by several orders of magnitude employing the AOM and neutral density filters. The probe beam is provided by a tungsten halogen lamp. The PIA signal is recorded in a transmission geometry, passes a monochromator and is detected either by a silicon photodiode or, for the near infrared region, an indium-galium-arsenide photodiode by utilizing lock-in techniques. The samples are cooled down to 10, 100, and 200 K, by keeping them in helium vapor in a continuous flow cryostat (Janis Research STVP-100). Room temperature measurements 295 K are performed as well. The PIA spectra are recorded from 2.07 eV (600 nm) down to 0.78 eV (1590 nm) and are corrected for luminescence of the sample. To determine lifetimes the modulation frequency of the pump beam can be varied from 1 to 10^6 Hz. PIA-samples contain neat and blend layer of one

compound on the same substrate and are encapsulated with a cover glass in a glovebox under nitrogen atmosphere attached to the vacuum chamber system used for evaporation.

Impedance spectroscopy measurements are performed in dark and under illumination at room temperature with an Autolab PGSTAT302N. The probe signal has an amplitude of 15 mV (rms) and the frequency is varied from 100 Hz to 1 MHz for the measurements under illumination and from 100 mHz to 1 MHz in dark. Illumination is provided by a halogen lamp. The results are presented in terms of Modulus and Phase of the complex impedance. Additionally the real part of the dielectric constant is used, assuming unitary vacuum capacitance: $\varepsilon(\omega) = Y(\omega)/(j\omega C_v)$ such that the real part of the dielectric permittivity coincides with the device capacitance function.

3. Results and discussion

3.1. OSC devices

Three solar cell devices are presented to illustrate the improved device performance caused by substrate heating during the active layer deposition. A flat heterojunction device with a 6 nm layer of DCV_2-5T (Bu_4) (device **A**), a bulk heterojunction device with a 1:1 by volume blend layer DCV_2-5T (Bu_4):C_{60} with a thickness of 20 nm (device **B**), and a bulk heterojunction with the same device structure but the substrate heated to 80 °C while the active layer is deposited (device **C**). Fig. 2a shows the $J - V$ characteristics of the three devices, Fig. 2b shows the corresponding EQE curves. The device parameter are summarized in Table 1. Device **A** exhibits a high fill factor (FF) of 61% and the open circuit voltage (V_{oc}) of 1.02 V corresponds to former values obtained with DCV_2-5T (Bu_4)[13,15]. The device shows good performance with only little recombination losses as can be seen from the good saturation factor $Sat. = J(0\,V)/J(-1\,V)$.

The main part of the photocurrent is due to DCV_2-5T (Bu_4) as can be seen in the corresponding EQE spectrum (compare also the neat and blend layer absorption spectra in Fig. 3). For the bulk layer device **B** J_{sc} increases due to the increased content of D and A. However, *FF* and V_{oc} decrease compared to the flat junction caused by increased recombination. The saturation factor increases which hints to a strong voltage dependence of charge carrier collection. The bulk layer device deposited at elevated substrate temperatures (T_{sub} = 80 °C) **C** clearly shows improved performance compared to the unheated device: *FF* increases again and V_{oc} reaches the value of the flat junction (device **A**), J_{sc} increases and accordingly the device efficiency increases. However, recombination losses still lead to a lower *FF* than in the flat junction and consequently to a slightly larger saturation factor. The EQE spectra show that the contribution of the donor material to the photocurrent is increased by substrate heating while the contribution of C_{60} remains constant.

3.2. Absorption

In Fig. 3 the absorbance of blend layers of DCV_2-5T (Bu_4):C_{60} (1:1 by volume) for different substrate temperatures 30 °C (i.e. room temperature), 80 °C, and 110 °C is shown. For comparison, the absorbance of a neat layer DCV_2-5T (Bu_4) at room temperature is depicted. The blend layer spectra consist of a broad absorption band between 1.5 and 3.0 eV which is due to the absorption of the donor molecule (compare to the neat layer spectrum), the contribution at energies above 3.0 eV is attributed to C_{60}. The strong background and increase for energies above 4.0 eV is caused by the substrate and the encapsulation of the sample (both glass) which could not be corrected by reference measurements here. For the 80 °C sample slight changes compared to the room temperature absorbance can be observed: the red shoulder gets slightly more pronounced and the absorption maximum is slightly decreased.

For even higher substrate temperatures of 110 °C the spectrum is shifted to the blue compared to the blend layers at lower substrate temperatures and even to the neat layer spectrum. A blue shifted absorption spectrum has been attributed to a lower degree of molecular ordering

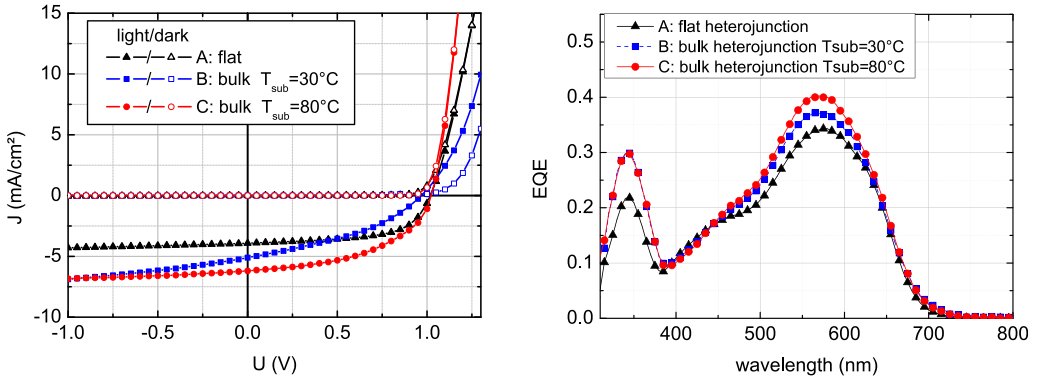

(a) J-V characteristics (b) EQE spectra

Fig. 2. Solar cell characteristics and EQE spectra of a flat heterojunction comprising 6 nm of DCV_2-5T (Bu_4) (device **A**), a bulk heterojunction with a 20 nm blend layer DCV_2-5T (Bu_4):C_{60} (1:1, by volume) (device **B**), and a bulk heteorjunction with the same device architecture like device **B** but with the active layer deposited at a substrate temperature of 80 °C (device **C**). The stack design is described in Section 2.

Table 1
Solar cell parameters corresponding to the characteristics shown in Fig. 2a. The intensity is mismatch corrected with respect to the reference diode.

	V_{oc} (V)	J_{sc} (mA/cm^2)	*FF* (%)	*Sat.*	*I* (mW/cm^2)	η (%)
A: flat	1.02	3.7	61	1.0	99	2.3
B: bulk T_{sub} = 30 °C	0.97	4.7	38	1.4	100	1.7
C: bulk T_{sub} = 80 °C	1.02	5.8	49	1.1	100	2.9

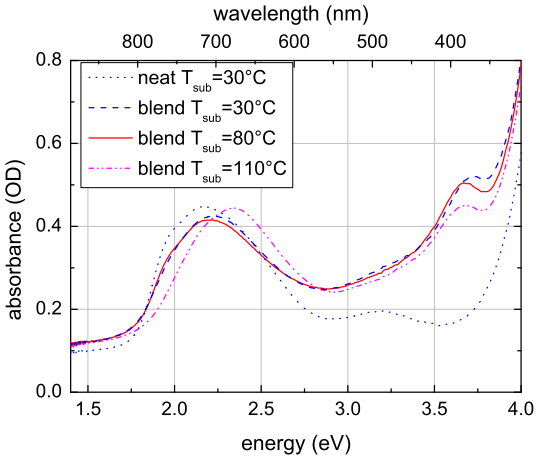

Fig. 3. Absorbance of a neat layer DCV_2-5T (Bu_4) (30 nm, dotted blue line) and a 1:1 (by volume) blend layer DCV_2-5T (Bu_4):C_{60} (60 nm, dashed blue line), both layers are deposited at room temperature. The absorbance of a 1:1 (by volume) blend layer DCV_2-5T (Bu_4):C_{60} (60 nm) is shown for different substrate temperatures: 80 °C (red line) and 110 °C (pink dashed dotted line). (For interpretation of the references to colour in this figure legend, the reader is referred to the web version of this article.)

[20]. The neat layer at room temperature shows the preferred conformation in which DCV_2-5T (Bu_4) molecules arrange due to self assembly, here also the attached alkyl side chains have major impact on the neat layer nanomorphology [21]. A vibronic substructure is slightly visible with a shoulder at 1.7 eV and the absorbance is larger than in the blend layer. The neat layer morphology seems to be suppressed when blending the material with C_{60}. However, an increased crystallinity of the donor material can be achieved by substrate heating [11].

3.3. PIA spectroscopy

Long-living photoexcited species and their recombination dynamics are investigated with photoinduced absorption spectroscopy performed with standard CW photomodulation techniques. The signal dependence on the modulation frequency and the pump intensity provides information on the lifetimes and the recombination mechanisms of the metastable states. The PIA signal $-\Delta T/T$ depends on the absorption cross σ of the observed transition, the film thickness d, and the density of photoexcited states n. When assuming small signals $|-\Delta T/T| \ll 1$ and thin films, the signal is given by [23]

$$-\frac{\Delta T}{T}(E,t) = \sigma(E) dn(t),$$

where n can be described by the monomolecular rate equation

$$\frac{dn(t)}{dt} = g(t) - \frac{1}{\tau} n(t),$$

with the monomolecular lifetime τ, and the generation of the excited state $g(t)$ which is proportional to the excitation intensity I. The sample is excited with a modulated pump laser (modulation frequency ω). A sinusoidal generation $g(t) = \alpha\gamma\ I(1 + \cos(\omega t))$ is chosen, where α is the absorption of the ground state and γ denotes the quantum efficiency of the generated photoexcitation. The analytical stationary solution is complex and the *in phase* (*IPh*) and *out of phase* (*OPh*) components are [24–26]:

$$\left(-\frac{\Delta T}{T}\right)_{IPh} = d\sigma\alpha\gamma I \frac{\tau}{1+(\omega\tau)^2} \qquad (1)$$

$$\left(-\frac{\Delta T}{T}\right)_{OPh} = d\sigma\alpha\gamma I \frac{\omega\tau^2}{1+(\omega\tau)^2}$$

Hence, under quasi steady state conditions ($\omega\tau \ll 1$) the PIA signal depends on the lifetime of the excited state and its effective generation rate ($g' = d\sigma\alpha\gamma I$). Note that g' has the units s^{-1} only if the intensity is counted as photon-flux I_p ($[I_p] = \#cm^{-2}\,s^{-1}$, number of photons per area and second) rather than as power per area ($[I] = mW\,cm^{-2}$). Both intensity notations can be correlated by $I = E_p I_p$, using the photon energy $E_p = h\,c\lambda^{-1}$, with the Planck constant h, the velocity of light c and the excitation laser wave length λ = 532 nm. The effective generation rate g' is not an absolute measure of the quantum yield of the respective species, since the absorption cross-section σ of the excited

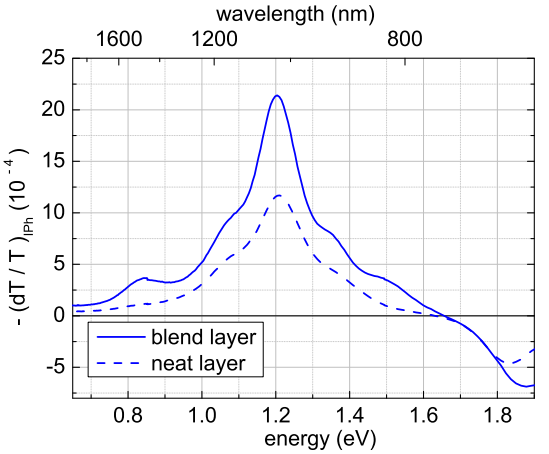

Fig. 4. Neat (dashed blue line) and blend layer (blue solid line) PIA spectra of DCV_2-5T (Bu_4) measured at 10 K. (For interpretation of the references to colour in this figure legend, the reader is referred to the web version of this article.)

species is generally not known. Generation rates displayed in the following are effective generation rates.

In Fig. 4 PIA spectra at 10 K for a neat layer DCV_2-5T (Bu_4) and a blend layer DCV_2-5T (Bu_4):C_{60} (1:1 by volume) deposited at room temperature are shown. In the neat layer a dominant contribution (1.2 eV) accompanied by two shoulders is observed. In the blend layer two additional features can be observed at 0.8 eV and 1.5 eV. From time dependent density functional theory calculations (see Ref. [15]) the feature at 1.2 eV is assigned to a transition of the DCV_2-5T (Bu_4) triplet exciton while the contributions at 0.8 eV and 1.5 eV are attributed to transitions of the DCV_2-5T (Bu_4) cation. The shoulders of the triplet peak might be due to vibronic transitions of the triplet exciton.

By varying the modulation frequency at a fixed spectral position, e.g. the maxima of the spectra shown in Fig. 4, the lifetime and the effective generation rate of the corresponding state can be determined. For the triplet exciton in neat and blend layers we find that a model comprising two monomolecularly decaying species yields the best fitting results. We here determine a long living species (τ = 200–300 μs) with very low effective generation rates and a short living species ($\tau \approx$ 50–80 μs) with an effective generation rate one order of magnitude higher than the long living species. Lifetime analysis at the spectral position of the shoulders yields similar results as the main maximum which is a hint for the shoulders being part of vibronic modes of the triplet exciton. The origin of the two species is discussed elsewhere [21].

The cation transitions (0.8 and 1.5 eV in the blend layer) exhibit different dynamics than the triplet excitons. For higher frequencies the slopes of *IPh* and *OPh* show deviations from the −2 and −1 behavior (typical for mono- and bimolecular dynamics). This deviation indicates dispersive recombination, i.e. a mono- or bimolecular process superimposed by a distribution of lifetimes [28,29]. In the simplest case dispersive recombination can be modelled with the empirical Cole–Cole model [31]. The expressions for the *IPh* and *OPh* component transfer to:

$$\left(-\frac{\Delta T}{T}\right)_{IPh} = d\sigma\alpha\gamma I\tau \frac{1+\cos(\frac{\pi a}{2})(\omega\tau)^a}{1+2\cos(\frac{\pi a}{2})(\omega\tau)^a+(\omega\tau)^{2a}}, \qquad (2)$$

$$\left(-\frac{\Delta T}{T}\right)_{OPh} = d\sigma\alpha\gamma I\tau \frac{\sin(\frac{\pi a}{2})(\omega\tau)^a}{1+2\cos(\frac{\pi a}{2})(\omega\tau)^a+(\omega\tau)^{2a}}$$

where $0 < a \leqslant 1$ denotes the degree of dispersion (a = 1 equals pure monomolecular/bimolecular decay).

The two cation transitions exhibit lower effective generation rates compared to the triplet exciton and lifetimes around 400–500 μs, the degree of dispersion is reflected in the fit parameter a which shows values around 0.8.

Fitting curves can be found in the Supplementary informations in Fig. 12. The fit parameters g' and τ are summarized in Table 2 for the central triplet transition as well as the cation transitions for the neat and blend layer at 10 K for an intensity of 35 mW/cm^2. Fit parameter for the whole intensity range can be found in the Supplementary information Fig. 13. The generation rate of the triplet exciton in the neat layer is only slightly lower than in the blend layer but the lifetimes in neat and blend layer differ by 30 μs. The differences in the amplitude of the triplet transition are thus caused to major extent by the different lifetimes of triplet excitons in neat and blend layer. Schueppel et al. [15] explained the enhanced triplet amplitude in DCV_2-5T (Bu_4):C_{60} by an indirect population of the triplet level via a bound charge transfer state (CT). The DCV_2-5T triplet level is claimed to be energetically lower than the CT state and a fraction of the CT excitons recombine to the triplet exciton, hence a part of the initially created excitons is lost in the triplet state [15,30]. We do not find a significant difference in the effective generation rates of triplets in neat and blend layers. However, the triplet excitons in the blend layer can either be generated intrinsically (as in the neat layer) via intersystem crossing (ISC) or by a back transfer via a CT state.

3.3.1. Temperature dependence

To understand the PIA spectra taken at more realistic temperatures for OSC device operation than 10 K, i.e. room temperature (295 K), it is crucial to be aware of the signal evolution with the measurement temperature. In Fig. 5a the PIA spectrum of DCV_2-5T (Bu_4):C_{60} is shown for 10, 100, 200 and 295 K. The signal decreases with increasing measurement temperature. This can mainly be assigned to the decrease of the excited state lifetime: at low temperatures the molecular vibrations are mostly frozen while for higher temperatures molecular vibrations become more prominent and increase the non-radiative decay of excited states. Hence, the additional decay channel present at higher temperatures leads to smaller excited state lifetimes.

Fig. 5b shows the temperature dependent spectra of DCV_2-5T (Bu_4):C_{60} normalized to the triplet transition at 1.2 eV. Here, the cation transitions grow with temperature compared to the triplet exciton. A third transition of the DCV_2-5T (Bu_4) cation at 1.7 eV becomes visible, as predicted from DFT calculations [15]. A detailed analysis of the excited state dynamics with temperature exhibits a decrease of the triplet (1.2 eV) lifetime as well as the

Table 2
Fit parameters for DCV_2-5T (Bu_4) (neat) and DCV_2-5T (Bu_4):C_{60} (blend) layers at 10 K derived from the fitting procedure described above. For the triplet peak only the values of the short living species are shown since it is dominating the spectrum and most likely is due to triplet excitons. The excitation intensity is 35 mW/cm^2.

		Triplet 1.2 eV		Cation 1.5 eV		Cation 0.8 eV	
	I (mW/cm^2)	g' (s^{-1})	τ (μs)	g' (s^{-1})	τ (μs)	g' (s^{-1})	τ (μs)
Neat	35	2.3	51	–	–	–	–
Blend	35	2.9	84	0.28	580	0.35	450

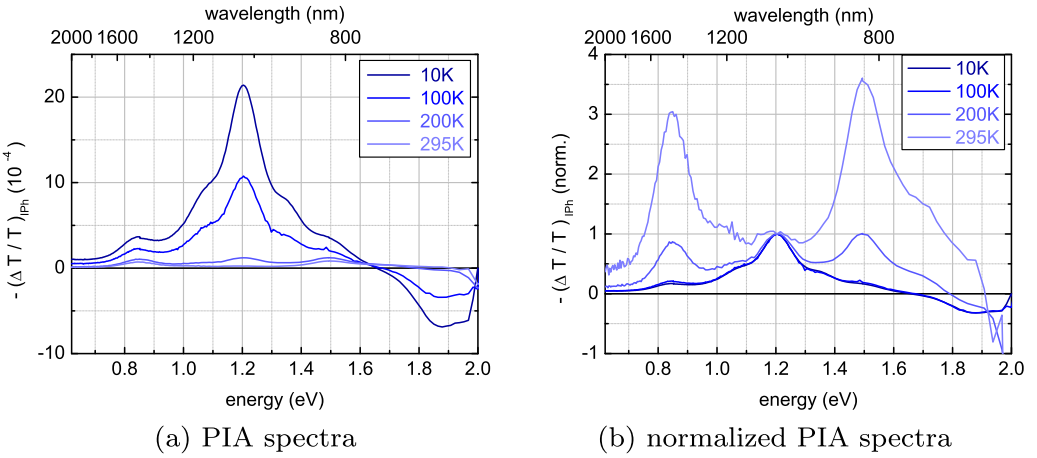

Fig. 5. PIA spectra of DCV_2-5T (Bu_4):C_{60} deposited at room temperature in dependence of the measurement temperature. The left side depicts the actual spectra whereas the right side shows the same spectra normalized to the triplet transition at 1.2 eV.

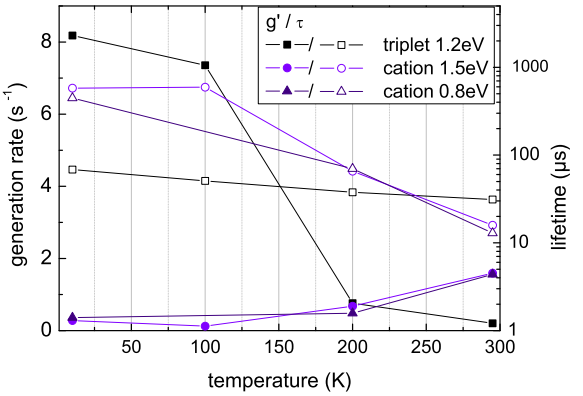

Fig. 6. Lifetimes and effective generation rates for triplets (black open and filled squares), the cation at 1.5 eV (light violet open and filled circles) and the cation at 0.8 eV (dark violet open and filled triangles) in DCV_2-5T (Bu_4):C_{60} in dependence of measurement temperature. The values are taken at an excitation intensity of 35 mW/cm^2. (For interpretation of the references to colour in this figure legend, the reader is referred to the web version of this article.)

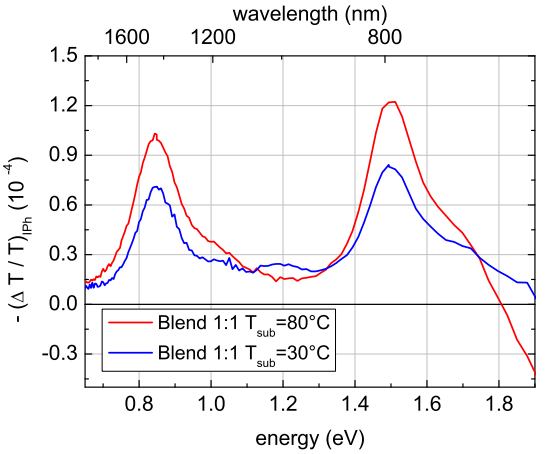

Fig. 7. PIA Spectra of a DCV_2-5T (Bu_4):C_{60} blend layer deposited at room temperature (blue line) and a DCV_2-5T (Bu_4):C_{60} layer deposited at 80 °C (red line). The spectra are taken at a temperature of 295 K. (For interpretation of the references to colour in this figure legend, the reader is referred to the web version of this article.)

effective generation rate with increasing temperature. Likewise, the effective cation generation increases while the temperature rises. The cation lifetime decreases with increasing temperature but with a much steeper slope than the triplet lifetime. The simultaneous increase in effective cation generation and decrease in effective triplet exciton generation as well as the above assumption that triplet excitons in the blend are created via a CT state hint for an improved charge generation involving temperature activated processes. The lifetimes and effective generation rates for triplets and cations derived for the four different temperatures are depicted in Fig. 6.

3.3.2. Comparison of heated and unheated blend layers at room temperature

The PIA spectra of blend layers deposited on heated and nonheated substrates at a measurement temperature of 10 K do not show significant differences. The data is shown in the Supplementary informations. Fig. 7 shows the PIA spectra of a blend layer DCV_2-5T (Bu_4):C_{60} deposited at room temperature (blue curve) and of a blend layer DCV_2-5T (Bu_4):C_{60} deposited at a substrate temperature of 80 °C (red curve) measured at 295 K. The peaks are due to optical transitions of the donor cation (1.5 and 0.8 eV). The transition of the DCV_2-5T (Bu_4) triplet exciton (1.2 eV) is no longer visible since its lifetime is strongly decreased at 295 K. In the blend layer deposited at room temperature, there is still a slight hint of the triplet transition, while in the heated blend layer there is no trace of the triplet transition left. The amplitude of the cation signatures in the heated layer is stronger than in the blend layer deposited at room temperature. The excitation conditions are comparable for both spectra (the excitation intensity is even slightly lower for the heated sample, comp. Table 5). An analysis of the recombination dynamics reveals the

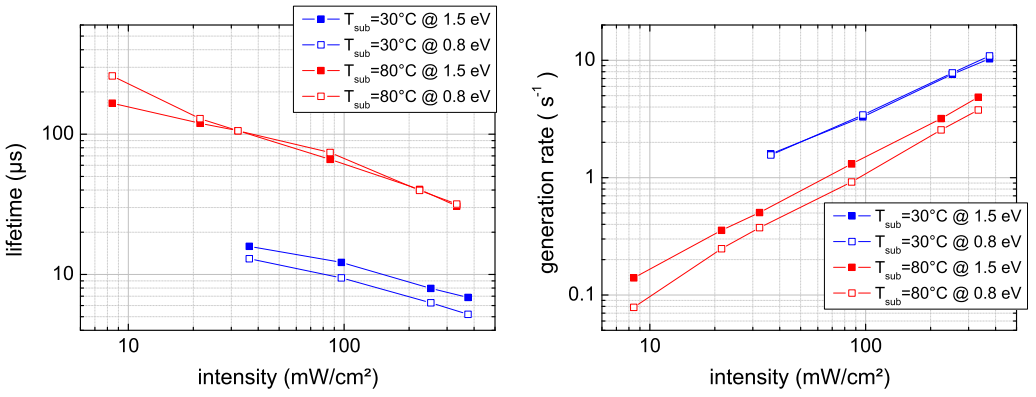

Fig. 8. Lifetimes and effective generation rates evaluated for the cation transitions (1.5 and 0.8 eV) in DCV_2-5T (Bu_4):C_{60} deposited at room temperature (blue symbols) and deposited at 80 °C (red symbols) in dependence of excitation intensity. The data is fitted with a dispersive recombination model (Eq. 2). (For interpretation of the references to colour in this figure legend, the reader is referred to the web version of this article.)

Table 3
Fit parameter for DCV_2-5T (Bu_4) and DCV_2-5T (Bu_4):C_{60} layers at 295 K derived from the fitting procedure described above. The excitation intensity is 100 mW/cm^2.

		Cation (1.5 eV)		Cation (0.8 eV)	
T_{sub} (°C)	I (mW/cm^2)	g' (s^{-1})	τ (µs)	g' (s^{-1})	τ (µs)
30 °C	100	3.4	12	3.5	9
80 °C	100	1.5	61	1.1	67

origin of the increased amplitude in the heated layer to be a strongly increased cation lifetime. For data evaluation again the dispersive model is chosen (Eq. 2). Fig. 8a shows the lifetime evaluated for the two cation transitions in the heated and the unheated layer in dependence of the excitation intensity. The values determined for lifetime and effective generation for the two different cation transitions match each other well. It is evident that the cation lifetime in the heated blend layer exceeds that of the unheated layer by almost one order of magnitude. The intensity dependence of the lifetime suggests a bimolecular mechanism being responsible for the recombination of cations. The effective generation rate on the other hand is larger in the unheated layer by almost a factor of three. Table 3 summarizes the effective generation and lifetime of cations for an excitation intensity of 100 mW/cm^2. The fit parameter a is constant with intensity and for both the heated and the unheated layer shows a value of ≈0.7.

Clarke et al. recently showed by transient absorption techniques that for polymer-fullerene blends a post process annealing of the film resulted in an acceleration of recombination dynamics assigned to a reduction in the trap depth of the system [32]. They further stated that the origin of trap states must be structural/conformational, i.e. upon annealing the molecule planarizes which leads to smoother energetical distribution of states. They also observed an increase in charge carrier generation upon annealing, which was attributed to a change in the ionization potential of P3HT [33] affecting the driving force that leads to charge separation. Contrary to this we observe a decrease in cation generation upon substrate heating. However, studies on PFB:F8BT showed a systematic decrease in charge carrier generation with annealing temperature [34].

The area under the cation peaks in the PIA spectrum in Fig. 7, should correlate with the short circuit current of the solar cell devices presented in Section 3.1. The area under the peaks is determined by using a gaussian fit. Comparing the heated and unheated layer yields a ratio of

$$\overline{g'\tau} = \frac{[A_{1.5\ \mathrm{eV}} + A_{0.8\ \mathrm{eV}}]_{\mathrm{heated}}}{[A_{1.5\ \mathrm{eV}} + A_{0.8\ \mathrm{eV}}]_{\mathrm{room\ temperature}}} = 1.7$$

while the ratio of the short circuit currents only yields a value of 1.2, thus, is not clearly correlated. The question is whether the observed cation transitions belong to free carriers that contribute to the photocurrent or if the signature is mainly caused by trapped holes that do not contribute to the current.

For P3HT:PCBM systems lifetimes of trapped carriers were determined to be in the range from 3 µs to ms, while free carriers were determined in the range below 3 µs [32].

3.4. Impedance spectroscopy

To investigate the characteristic time constants of free and trapped carriers in blends of DCV_2-5T (Bu_4):C_{60}, we analyze the impedance spectra of the solar cell devices **B** and **C** (comp. Section 3.1). Since PIA is an optical measurement carried out on layers without external voltage applied or current flowing, a direct comparison with the impedance spectroscopy (IS) results is not possible. However, IS can provide important information on the dynamics of charge carriers, giving us the possibility to distinguish trap states and free charges from their characteristic lifetimes [35,36].

In order to perform the electrical characterization under the same conditions as analyzed by PIA, we focus first on the open-circuit case at different light intensities, since no charges are extracted as for the PIA measurements. The resulting impedance spectra are presented in a Bode

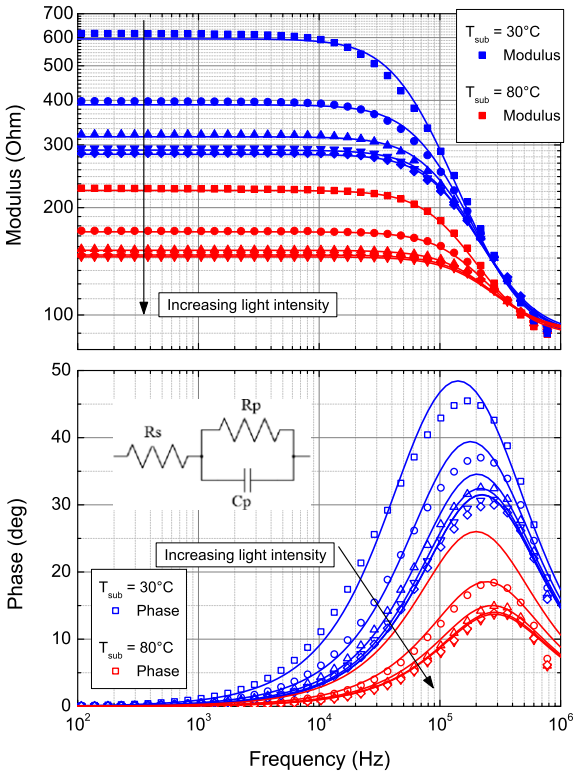

Fig. 9. Bode plot for solar cell devices **B** (blue symbols) and **C** (red symbols). The fitting curves are presented as continuous lines and the equivalent circuit used is shown as inset. (For interpretation of the references to colour in this figure legend, the reader is referred to the web version of this article.)

plot (Fig. 9). From the Bode plot we observe that the solar cell impedance spectra can be divided in two regions. For high frequencies the absolute value of the impedance presents a plateau and the phase approaches low values, it means that a resistor in line with a capacitor is dominating the response. For lower frequencies the phase reaches a maximum value and then decreases, while the modulus increases until a second plateau at small frequencies. This behavior is typical of an RC parallel connection. The equivalent circuit used to fit the data is therefore composed by a series resistance and one RC parallel element. The series resistance takes into account the ohmic contribution of the contacts and the transport layers. The value of the capacitor is composed by two different contributions: the polarization of the intrinsic layers, that is the geometrical capacitance, and the accumulation of photo-generated charges, also called chemical capacitance or diffusion capacitance [37].

The fitting circuit is shown in Fig. 9 and the resulting curves are shown as continuous lines. The fitting results are presented in Table 4, together with the estimated density and lifetime of the free charges. The chemical capacitance is calculated from the parallel capacitance C_p subtracting the geometrical value of the intrinsic layer. The latter is estimated from capacitance measurements in dark under different reverse bias voltages (not shown). The calculation of accumulated free charge density is performed by multiplying the chemical capacitance by the applied open-circuit voltage. The effective lifetime is the characteristic time of the parallel RC circuit, still considering as capacitance the chemical capacitance and is shown in Fig. 10 varying the illumination intensity. The results are affected by errors coming from the geometrical capacitance estimation, the voltage drop across the series resistance and uncertainties in the fitting results. We estimate the overall error to be in the range of 10–20%, still acceptable for an estimation of the order of magnitude for both charge density and lifetime. The charge carrier lifetime in the heated device **C** is by a factor of 1.4 larger than in the unheated device **B**.

From the IS measurements it is apparent that the free charges have an effective lifetime in the range of 1–5 μs for a measured charge density in the range of 1–3×10^{17} cm^{-3}, in agreement with previous results for polymer solar cells [38,39].

The cation lifetimes observed from PIA are almost one order of magnitude higher. There is therefore the possibility that they belong to trap states and not to free charges. By analyzing the capacitance spectra it is in principle possible also to observe the effect of trap states in the device electrical response, visible as an additional capacitance for frequencies lower than the characteristic trapping–

Table 4
Equivalent circuit values obtained by fitting the measured spectra shown in Fig. 9 at different illumination intensities. The charge density and lifetime are calculated from the C_p after subtracting the geometrical capacitance of the intrinsic layer.

I (mW/cm^2)	R_s (Ω)	R_p (Ω)	C_p (F)	Charge density (10^{17} cm^3)	Charge lifetime (μs)
*Device **B***					
250	85.59	509.3	5.8266E−9	1.40	2.65
410	86.76	301.9	6.2256E−9	1.51	2.32
510	87.24	228.9	6.4857E−9	1.57	2.14
570	87.49	202.6	6.5917E−9	1.62	2.03
610	88.51	193.8	6.5817E−9	1.63	1.93
*Device **C***					
240	87.23	136.3	9.3506E−9	2.35	3.73
380	88.5	82.61	1.0956E−8	2.76	3.09
480	89.37	62.47	1.2282E−8	3.11	2.86
520	89.92	57.4	1.2482E−8	3.16	2.70
600	89.74	55.81	1.2798E−8	3.24	2.73

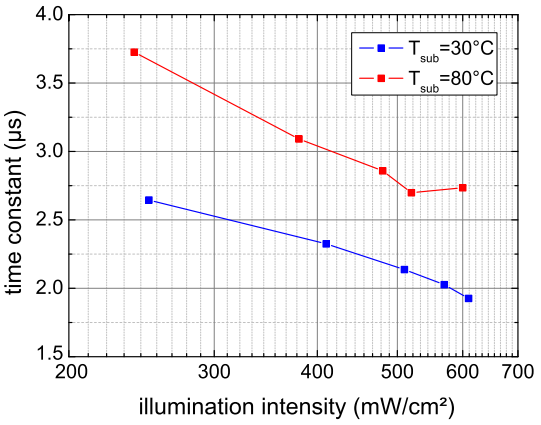

Fig. 10. Effective charge carrier lifetime for the unheated device **B** (blue squares) and the heated device **C** (red squares). (For interpretation of the references to colour in this figure legend, the reader is referred to the web version of this article.)

detrapping time-constant [40,41]. This is unfortunately not possible under illumination, since the high density of photo-generated charges induces a capacitance drop at low frequencies as consequence of the strong recombination process [42]. The capacitance function of device **B** and **C** under different illumination is depicted in Fig. 15 in the Supplementary informations. We therefore measure the solar cells in dark at 0 V bias, again without current flowing. The measured spectra are shown in Fig. 11. In this case, the parallel resistance reaches very high values since no free charges are produced inside the intrinsic layers and the conductivity is drastically reduced. Under these conditions, the impedance phase reaches much higher values and it is possible to measure the capacitance function down to very low frequencies. From the capacitance spectra there is no significant trap contribution visible above 1 Hz. For lower values an increase is visible, at least for the device evaporated on heated substrate, which presents an imaginary part of the impedance large enough (higher phase) to be measured without too much noise.

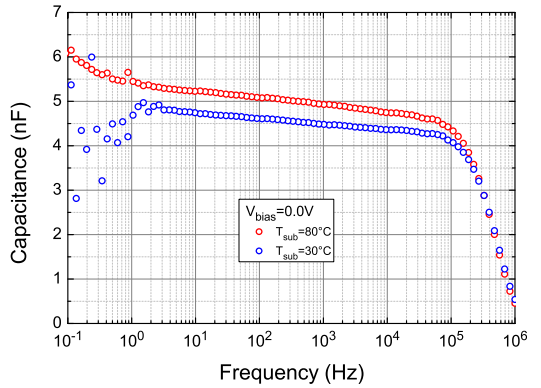

Fig. 11. Capacitance function of the solar cell devices **B** (blue symbols) and **C** (red symbols) measured in the dark at 0 V bias. (For interpretation of the references to colour in this figure legend, the reader is referred to the web version of this article.)

We can conclude from the IS investigation, that free charges have a lifetime in the range of 1–5 µs, while trap states are not giving a significant contribution for these devices and they start to respond with a characteristic time in the range of 1 s. From the comparison with PIA results, we also conclude that the observed cation states are most probably carriers that are not entirely free, but can rather be classified as shallow traps that still contribute to the photocurrent. The higher charge density observed in device **C**, together with the increased lifetime and improved fill factor and saturation of the IV curves (Fig. 2), are indications of reduced recombination for the active layer being deposited on a heated substrate. The observed increase in lifetime upon heating is visible both in optical and electrical measurements and can be attributed to a better spatial arrangement of the donor and acceptor phase, which improves the spatial separation of charges and percolation paths, and thus preventing bimolecular recombination.

4. Conclusion

The device performance of solar cells using an active bulk heterojunction layer of DCV_2-5T (Bu_4):C_{60} (1:1, by volume) deposited on heated substrates increases compared to devices deposited at room temperature. We have shown that the improved device performance can be correlated to an increase of the lifetime of charge carriers, that we attribute to a better phase separation in the heated bulk layer.

Acknowledgements

The authors thank the Deutsche Forschungsgemeinschaft (DFG) for funding this work within the scope of the priority progam SPP 1355 “Elementarprozesse der organischen Photovoltaik”. This work has partly been funded by the Bundesministerium für Bildung und Forschung (BMBF) within the project 13N9720. Additionally we would like to thank David Wynands (IAPP) for fruitful discussions.

Appendix A. Supplementary data

Fitting curves and parameters at 10 K for neat and blend layers; Comparison of heated and unheated blend layers at 10 K; Capacitance function of solar cell devices under illumination. Supplementary data associated with this article can be found, in the online version, at doi:10.1016/j.orgel.2011.09.015.

References

[1] 8.3% Efficient small molecule organic solar cells on 1.1 cm^2 area, made by Heliatek/IAPP, certified at Fraunhofer ISE (Freiburg), see the news section of <http://www.heliatek.com/>, 2010 (accessed 20.5.2011).
[2] 8.3% Efficient polymer device on an area >1 cm^2, made by Konarka, certified at NREL, see the newsroom of <http://www.konarka.com/>, 2010 (accessed 20.5.2011).
[3] M. Hiramoto, H. Fujiwara, M. Yokoyama, J. Appl. Phys. 72 (1992) 3781–3787.
[4] J.J.M. Halls, C.A. Walsh, N.C. Greenham, E.A. Marseglia, R.H. Friend, S.C. Moratti, A.B. Holmes, Nature 376 (1995) 498–500.

[5] G. Yu, J. Gao, J.C. Hummelen, F. Wudl, A.J. Heeger, Science 270 (1995) 1789–1791.
[6] D. Meissner, J. Rostalski, Syn. Met. 121 (2001) 1551–1552.
[7] C. Pannemann, V. Dyakonov, J. Parisi, O. Hild, D. Wöhrle, Syn. Met. 121 (2001) 1585–1586.
[8] F. Padinger, R.S. Rittberger, N.S. Sariciftci, Adv. Funct. Mater. 13 (2003) 85–88.
[9] C.R. McNeill, J.J.M. Halls, R. Wilson, G.L. Whiting, S. Berkebile, M.G. Ramsey, R.H. Friend, N.C. Greenham, Adv. Funct. Mater. 18 (2008) 2309–2321.
[10] M. Vogel, J. Strotmann, B. Johnev, M. Ch. Lux-Steiner, K. Fostiropoulos, Thin Solid Films 511 (2006) 367–370.
[11] D. Wynands, M. Levichkova, M. Riede, M. Pfeiffer, P. Baeuerle, R. Rentenberger, P. Denner, K. Leo, J. Appl. Phys. 107 (2010) 014517.
[12] D. Wynands, B. Männig, M. Riede, K. Leo, E. Brier, E. Reinold, P. Baeuerle, J. Appl. Phys. 106 (2009) 054509.
[13] K. Schulze, M. Riede, E. Brier, E. Reinold, P. Baeuerle, K. Leo, J. Appl. Phys. 104 (2008) 074511.
[14] K. Schulze, C. Uhrich, R. Schüppel, K. Leo, M. Pfeiffer, E. Brier, E. Reinold, P. Bäuerle, Adv. Mater. 18 (2006) 2872–2875.
[15] R. Schueppel, K. Schmidt, C. Uhrich, D. Wynands, J.L. Brédas, E. Brier, E. Reinold, H.-B. Bu, P. Baeuerle, B. Maennig, M. Pfeiffer, K. Leo, Phys. Rev. B 77 (2008) 085311.
[18] R. Fitzner, E. Reinold, A. Mishra, E. Mena-Osteritz, H. Ziehlke, C. Körner, K. Leo, M. Riede, M. Weil, O. Tsaryova, A. Weiß, C. Uhrich, M. Pfeiffer, P. Bäuerle, Adv. Funct. Mater. 21 (2011) 897–910.
[19] J. Meyer, S. Hamwi, S. Schmale, T. Winkler, H.-H. Johannes, T. Riedl, W. Kowalsky, J. Mater. Chem. 19 (2009) 702–705.
[20] P.J. Brown, D.S. Thomas, A. Köhler, J.S. Wilson, J.-S. Kim, C.M. Ramsdale, H. Sirringhaus, R.H. Friend, Phys. Rev. B 67 (2003) 064203.
[21] H. Ziehlke, R. Fitzner, C. Koerner, R. Gresser, E. Reinold, P. Bäuerle, K. Leo, M. Riede, J. Phys. Chem. A 115 (2011) 8437.
[23] G. Lanzani (Ed.), Photophysics of Molecular Materials, Wiley-Interscience, Weinheim, 2006, pp. 183–259 (Chapter 5).
[24] C. Botta, S. Luzatti, R. Tubino, D.D.C. Bradley, R.H. Friend, Phys. Rev. B 48 (1993) 14809–14817.
[25] G. Dellepiane, C. Cuniberti, D. Comoretto, G. Figar, A. Piaggi, A. Borghesi, Phys. Rev. B 48 (1993) 7850–7856.
[26] M. Westerling, C. Vijila, R. Österbacka, H. Stubb, Chem. Phys. Lett. 286 (2003) 315–320.
[28] M. Westerling, C. Vijila, R. Österbacka, H. Stubb, Phys. Rev. B 69 (2004) 245201.
[29] O. Epshtein, G. Nakhmanovich, Y. Eichen, E. Ehrenfreund, Phys. Rev. B. 63 (2001) 125206.
[30] D. Veldman, S.C.J. Meskers, R.A.J. Janssen, Adv. Funct. Mater. 19 (2009) 1939–1948.
[31] K.S. Cole, R.H. Cole, J. Chem. Phys. 9 (1941) 341–351.
[32] T.M. Clarke, F.C. Jamieson, J.R. Durrant, J. Phys. Chem. C 113 (2009) 20934–20940.
[33] T.M. Clarke, A.M. Ballantyne, J. Nelson, D.D.C. Bradley, J.R. Durrant, Adv. Funct. Mater. 18 (2008) 4029–4035.
[34] C.R. McNeill, S. Westenhoff, C. Groves, R.H. Friend, N.C. Greenham, J. Phys. Chem. C 111 (2007) 19153–19160.
[35] J. Bisquert, Phys. Rev. B 77 (2008) 235203.
[36] G. Garcia-Belmonte, A. Munar, E. Barea, J. Bisquert, I. Ugarte, R. Pacios, Org. Electron. 9 (2008) 847–851.
[37] S.M. Sze, K.K. Ng, Physics of Semiconductor Devices, third ed., Wiley Interscience, Hoboken, NJ, 2006.
[38] C.G. Shuttle, B. O'Regan, A.M. Ballantyne, J. Nelson, D.D.C. Bradley, J. de Mello, J.R. Durrant, Appl. Phys. Lett. 92 (2008) 93311.
[39] C. Shuttle, B. O'Regan, A. Ballantyne, J. Nelson, D. Bradley, J. Durrant, Phys. Rev. B 78 (2008) 113201.
[40] J.D. Cohen, D. Lang, Phys. Rev. B 25 (1982) 5321–5350.
[41] D. Ray, L. Burtone, K. Leo, M. Riede, Phys. Rev. B 82 (2010) 125204.
[42] N. Nguyen, M. Schmeits, H. Loebl, Phys. Rev. B 75 (2007) 75307.

ORGANIC ELECTRONICS
materials • physics • chemistry • applications

Editors:

Prof. Chihaya Adachi — Center for Future Chemistry, Kyushu University, 744 Motooka, Nishi, Fukuoka 819-0395, Japan, Fax: +81-92-802-3294, e-mail: adachi@cstf.kyushu-u.ac.jp

Prof. Paul Heremans — imec, Kapeldreef 75, B-3001 Leuven, Belgium, Tel: +32 16 281521, e-mail: heremans@imec.be

Prof. René Janssen — Molecular Materials and Nanosystems, Eindhoven University of Technology, P.O. Box 513, 5600 MB Eindhoven, The Netherlands, Fax: +31 40 2451036, e-mail: r.a.j.janssen@tue.nl

Prof. Antoine Kahn — Department of Electrical Engineering, Princeton University, Princeton, NJ 08544, USA, Fax: +1-609-258-6279, e-mail: kahn@princeton.edu

Associate Editorial Board:

V.M. AGRANOVICH (Moscow)
Y. CAO (Guangzhou)
A. DODABALAPUR (Austin)
M. FUJIHIRA (Yokohama)
N. PEYGHAMBARIAN (Tucson)
Z. POPOVIC (Mississauga)
W. RIESS (Rüschlikon)
Y. SHIROTA (Osaka)
C. TALIANI (Bologna)
T. TSUTSUI (Fukuoka)
E. UMBACH (Würzburg)

Founding Editors:

Prof. Donal Bradley, Prof. Stephen Forrest, Prof. Norbert Karl and Prof. Kazuhiko Seki

Aims and scope

Organic Electronics is a primary journal whose interdisciplinary focus is organic materials, devices and phenomena, with application to devices such as organic light emitting diodes, thin film transistors, photovoltaic cells, etc.

Papers suitable for publication in this journal cover such topics as photoconductive and electronic properties of organic materials, thin film growth and characterization, charge and exciton transport, organic electronic and optoelectronic devices, etc.

Organic Electronics provides the only forum for both applied and fundamental contributions spanning the many different disciplines addressing the wide range of electronic properties and applications of organic materials. A Letters section is included for rapid publication of short articles announcing significant and highly original results.

Advertising information

If you are interested in advertising or other commercial opportunities please e-mail Commercialsales@elsevier.com and your enquiry will be passed to the correct person who will respond to you within 48 hours.

Abstracted/indexed in:

Current Contents: Engineering, Technology and Applied Sciences; El Compendex Plus; Engineering Index; INSPEC; Physics Briefs; Science Citation Index, expanded; Chemistry Citation Index; Current Contents: Physics, Chemistry and Engineering Science. Also covered in the abstract and citation database SciVerse Scopus®. Full text available on SciVerse ScienceDirect®.

Publication information: *Organic Electronics* (ISSN 1566-1199). For 2011, Volume 12 (12 issues) is scheduled for publication. Subscription prices are available upon request from the Publisher or from the Elsevier Customer Service Department nearest you or from this journal's website (http://www.elsevier.com/locate/orgel). Further information is available on this journal and other Elsevier products through Elsevier's website (http://www.elsevier.com). Subscriptions are accepted on a prepaid basis only and are entered on a calendar year basis. Issues are sent by standard mail (surface within Europe, air delivery outside Europe). Priority rates are available upon request. Claims for missing issues should be made within six months of the date of dispatch.

Orders, claims, and journal enquiries: please contact the Elsevier Customer Service Department nearest you:

St. Louis: Elsevier Customer Service Department, 3251 Riverport Lane, Maryland Heights, MO 63043, USA; phone: (877) 8397126 [toll free within the USA]; (+1) (314) 4478878 [outside the USA]; fax: (+1) (314) 4478077; e-mail: JournalCustomerService-usa@elsevier.com

Oxford: Elsevier Customer Service Department, The Boulevard, Langford Lane, Kidlington, Oxford OX5 1GB, UK; phone: (+44) (1865) 843434; fax: (+44) (1865) 843970; e-mail: JournalsCustomerService-EMEA@elsevier.com

Tokyo: Elsevier Customer Service Department, 4F Higashi-Azabu, 1-Chome Bldg, 1-9-15 Higashi-Azabu, Minato-ku, Tokyo 106-0044, Japan; phone: (+81) (3) 5561 5037; fax: (+81) (3) 5561 5047; e-mail: JournalsCustomerServiceJapan@elsevier.com

Singapore: Elsevier Customer Service Department, 3 Killiney Road, #08-01 Winsland House I, Singapore 239519; phone: (+65) 63490222; fax: (+65) 67331510; e-mail: JournalsCustomerService-APAC@elsevier.com

USA mailing notice: *Organic Electronics* (ISSN 1566-1199) is published monthly by Elsevier B.V., Radarweg 29, 1043 NX Amsterdam, the Netherlands. Periodical postage paid at Rahway NJ and additional mailing offices.

USA POSTMASTER: Send change of address to *Organic Electronics*, Elsevier Customer Service Department, 3251 Riverport Lane, Maryland Heights, MO 63043, USA.

AIRFREIGHT AND MAILING in USA by Mercury International Limited, 365 Blair Road, Avenel, NJ 07001.

Printed in the Netherlands

For a full and complete Guide for Authors, please go to: http://www.elsevier.com/locate/orgel